Organic Electronics 11 (2010) 1–9

Contents lists available at ScienceDirect

Organic Electronics

journal homepage: www.elsevier.com/locate/orgel

Synthesis of liquid crystalline benzothiazole based derivatives: A study of their optical and electrical properties

Gitish K. Dutta [a], S. Guha [b,*], Satish Patil [a,*]

[a] Solid State and Structural Chemistry Unit, Indian Institute of Science, Bangalore 560 012, India
[b] Department of Physics and Astronomy, University of Missouri, Columbia, Missouri 65211, USA

ARTICLE INFO

Article history:
Received 7 July 2009
Received in revised form 19 August 2009
Accepted 12 September 2009
Available online 18 September 2009

Keywords:
Benzothiazole
Donor–acceptor
Liquid crystal
Mobility
OFET

ABSTRACT

Two new donor–acceptor type liquid crystalline semiconductors based on benzothiazole have been synthesized. Their structural, photophysical and electronic properties were investigated using X-ray diffraction, atomic force microscopy, cyclic voltammetry, UV–Vis, photoluminescence, and Raman spectroscopy. The liquid crystalline behaviour of the molecules was thoroughly examined by differential scanning calorimetry (DSC) and optical polarizing microscope. The DSC and thermogravimetric analysis (TGA) show that these materials posses excellent thermal stability and have decomposition temperatures in excess of 300 °C. Beyond 160 °C both molecules show a smectic A liquid crystalline phase that exists till about 240 °C. Field-effect transistors were fabricated by vacuum evaporating the semiconductor layer using standard bottom gate/top contact geometry. The devices exhibit p-channel behaviour with hole mobilities of 10^{-2} cm^2/Vs.

© 2009 Elsevier B.V. All rights reserved.

1. Introduction

π-Conjugated organic materials have been the subject of recent research work due to their optical, electronic properties as well as their applications in many fields such as organic light-emitting diodes (OLED) [1–3], photovoltaic cells [4–7], thin film organic field-effect transistors (OFETs) [8–13]. The organic molecules used in electronic and opto-electronic devices are generally divided into two groups: small molecules and polymers. For field-effect transistors, small organic molecules and oligomers are extensively used rather than polymeric materials. The most notable examples include pentacene [14–16], rubrene [17–20] and oligothiophene derivatives [21–24]. In the best cases, the room temperature mobility of crystalline organic semiconductors can reach the value of around 0.1–20 $cm^2 V^{-1} S^{-1}$ [25]. A majority of these organic molecules are hole conductors although ambipolar and *n*-type materials are also known [26–32]. The major challenge in device fabrication is to achieve favourable alignment of molecules between source and drain contacts enabling efficient charge transport through the semiconducting medium [33,34]. In this context, liquid crystalline materials are promising candidates as active semiconductor layers in organic electronics [35–43]. Supramolecular organization of the organic semiconductor in a thin film can be enhanced through the utilization of the liquid crystalline material [44–50]. Liquid crystalline phase can induce highly ordered, closely packed structures, leading to high mobilities within the domain boundaries [51,52]. Introduction of π-conjugated moieties into a liquid crystalline material gives many advantages in charge transport properties arising from their self-assembling nature [53–58]. They must contain a rigid, conjugated core, which is responsible for the semiconducting behaviour of the molecule. In the past few years, considerable efforts have been made to design, synthesize, and characterize such type of π-conjugated liquid crystalline materials [59–62]. In particular; smectic liquid crystalline materials because of their spontaneous alignment are good candidates for such applications. Their

* Corresponding authors. Tel.: +91 80 22932651; fax: +91 80 23601310.
E-mail addresses: guhas@missouri.edu (S. Guha), satish@sscu.iisc.ernet.in (S. Patil).

1566-1199/$ - see front matter © 2009 Elsevier B.V. All rights reserved.
doi:10.1016/j.orgel.2009.09.012

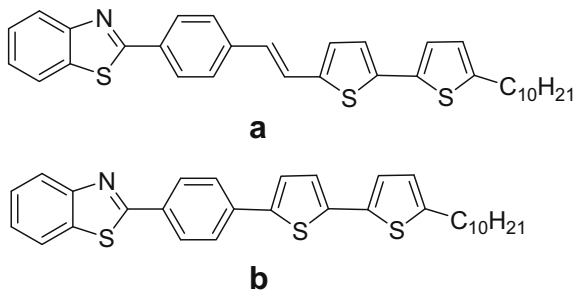

Fig. 1. Chemical structures of compounds a and b.

self-assembling property produces multidomain films with no physical grain boundaries between the domains thus facilitating hopping of charge carriers more easily.

In our search for organic semiconductors for OFET application we focused on benzothiazole based organic molecules (Fig. 1) because of their liquid crystalline properties. We have designed and synthesized two donor–acceptor (D–A) type benzothiazole based molecules showing interesting liquid crystalline and semiconducting properties. In both molecules, the core benzothiazole ring acts as an electron acceptor unit because of the presence of sulphur and nitrogen atoms and alkyl substituted thiophene ring as a donor because of its high electron donating ability and charge carrier mobilities. These molecules show a smectic A liquid crystalline phase above the melting temperature, which results in a good alignment and packing of the molecule in the solid state. Also, the materials exhibit p-type FET behaviour with hole mobility of 10^{-2} cm^2/Vs and on/off current ratio of 1×10^3. With additional surface modification of the gate dielectric layer, it is conceivable that the transport properties of OFETs may further improve. The AFM studies of the annealed samples show a dewetting of the surface with smooth morphology.

2. Results and discussion

2.1. Synthesis and characterization

The synthetic route to compounds (a) and (b) are summarized in the Scheme 1. Benzothiazole core were synthesized according to method described in literature [63] and bithiophene derivatives were synthesized by reported procedure [64,65]. The final derivatives were synthesized by Wittig reaction and Stille cross coupling and purified by column chromatography [66,67].

2.2. Optical and electrochemical properties of the compounds

The optical and electrochemical properties of the compounds are summarized in the Table 1. The photophysical properties of these two derivatives were investigated using UV–Vis and photoluminescence spectroscopy. The absorption and emission spectra of these two compounds in solution ($CHCl_3$) and solid state are depicted in Fig. 2. Compound (a) shows two strong absorption peaks at 318 nm and 395 nm in solution and photoluminescence peak at around 504 nm (in solution) and 587 nm (in solid state). The absorption peak at 318 nm belongs to the π–π^* transition and the absorption peak at 395 nm corresponds to a charge transfer band of the donor–acceptor system [68]. Compound (b), on the other hand predominantly shows only one strong absorption peak at 390 nm in solution which belongs to the charge transfer band; the photoluminescence is observed at ~462 nm in solution and 550 nm in solid state. In case of compound (a) the donor and acceptor units are linked through a vinyl bond which inhibits a charge transfer process from the donor thiophene ring to acceptor benzothiazole ring. As a consequence both π–π^* transition and charge transfer bands are observed in the absorption spectrum. In compound

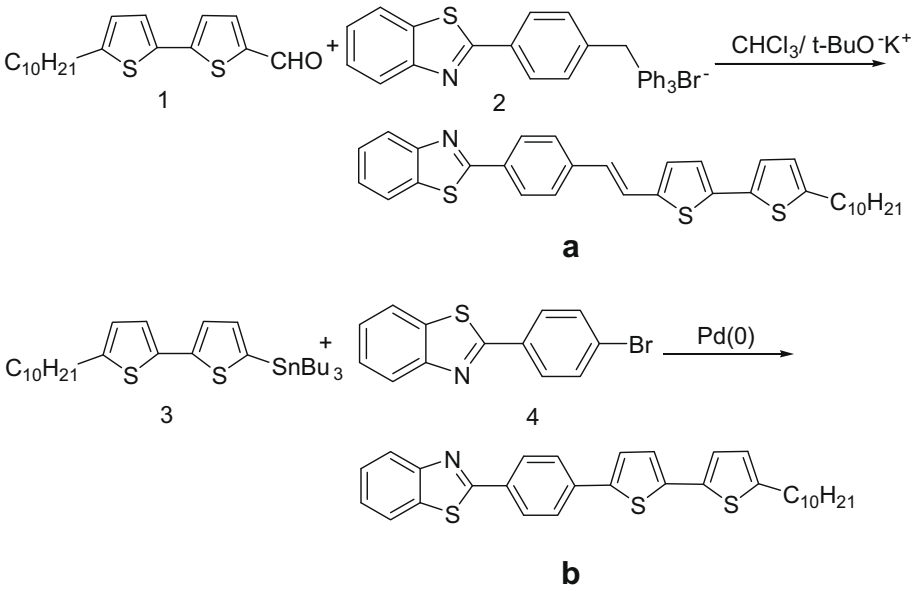

Scheme 1. Synthesis routes to a and b.

Table 1
Optical and electrochemical properties of the compounds.

Compounds	Film		Solution			CV		
	λ_{abs} (nm)	λ_{em} (nm)	λ_{abs} (nm)	λ_{em} (nm)	E_g (eV)	E_{ox}^{onset} (V)	E_{HOMO} (eV)	LUMO (eV)
a	318	587	395	504	2.6	0.35	−5.17	−2.57
b	325	550	390	462	2.8	0.37	−5.19	−2.39

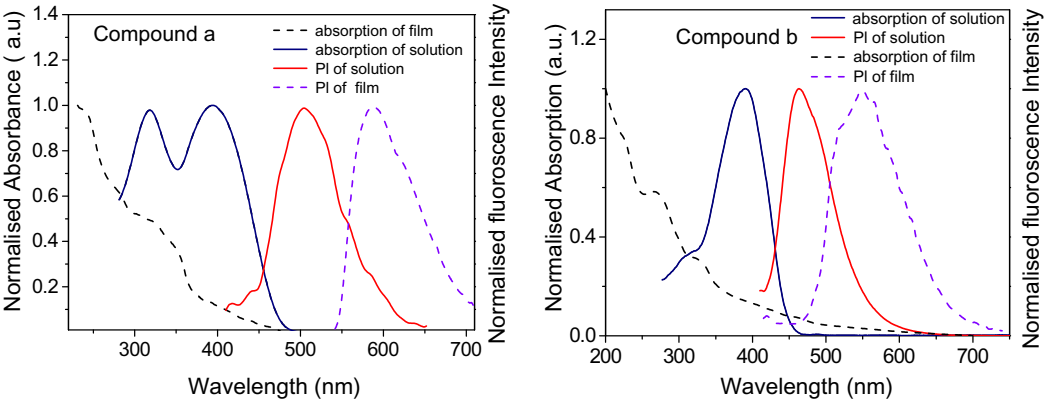

Fig. 2. UV–Vis absorption and photoluminescence spectra of compounds a and b.

(b) the donor and acceptor units are directly linked allowing a strong charge transfer process, and as a result only one peak is observed in the absorption spectrum. For both the molecules there is no sharp absorption peak in the solid state due to aggregation. The emission maxima in the solid state were observed at longer wavelengths than those in solution (80–90 nm red shift) indicating the presence of a strong interaction between the molecules (packing effect) [69] in the solid state, which is essential for good device performance. The optical band gaps, E_g, were approximated from the onset of the low energy side of the absorption spectra (λ_{onset}, solution) to the baseline. Further, the HOMO–LUMO energy levels were calculated by cyclic voltammetry measurements. The oxidation onset for the compound (a) and (b) were 0.35 and 0.37 eV, respectively, and their corresponding HOMO energy levels are −5.17 and −5.19 eV (Table 1). HOMO energy levels have been calculated by using equation HOMO = $-(E_{ox}^{onset} + 4.8)$ (eV). The LUMO levels were estimated from HOMO values and values of optical band gaps according to the equation: LUMO = HOMO + E_g^{opt} (eV). These results show that the introduction of vinyl linkage between benzothiazole and bithiophene unit inhibits donor–acceptor charge transfer and increases the effective conjugation length, thus lowering the band gap by about 0.2 eV.

2.3. Structure and morphology

To study the crystallinity of the materials, X-ray diffraction studies were performed from drop cast films that were annealed at 120 °C (Fig. 3). From the diffraction pattern it seems that both the materials are crystalline. Compound (a) exhibits distinct diffraction peaks at $2\theta = 5.7°$ and 8.3° with d-spacings of 15.2 Å and 10.5 Å corresponds to intermolecular distances. Similarly, compound (b) shows two sharp diffraction peaks at $2\theta = 6.0°$ and 8.7° with d-spacings of 14.6 Å and 10.0 Å corresponds to intermolecular distances. For both the compounds, several reflections in the wide-angle regions (between 7.6 Å and 3.6 Å), occur because of the organization within the 3D lattice and the reflections at around 3.6 Å may be due to π–π stacking of mesogens [40].

Raman scattering is particularly informative on chemical composition, segmental orientation, conformational distribution and phase identification in organic semiconductors. Fig. 4 shows the Raman spectra of as-is powder samples for both compounds. They were measured in a perfect backscattering geometry with less than 2 mW incident laser power on a 50 μm^2 area of the sample. The 1620 cm^{-1} Raman peak in compound (a) originates from the C=C stretch motion of the vinyl group [70], which is absent in compound (b). The Raman peaks in the 1600 cm^{-1} region in both compounds are from the intra-ring C–C stretch motion (ring breathing) of the phenyl group [71]. The 1564/1560 cm^{-1} peak arises from a C=C stretch motion of the phenyl ring. The Raman peaks in the 1470–1490 cm^{-1} region in both compounds are attributed to the benzothiazole unit [72]. These peaks arise from C–H bending and C–N stretch motions. The C–N stretch mode is usually an infrared active mode that may become Raman active due a lowering of the symmetry of the molecule. In compound (a) the 1487 cm^{-1} peak is seen only as a shoulder. The 1447 cm^{-1} Raman frequency in both compounds are from the C=C ring stretch motion of the thiophene unit. In thiophene-based polymers the 1447 cm^{-1} appears as an intense peak in the Raman spectrum [73]. Future Raman scattering studies from biased OFET struc-

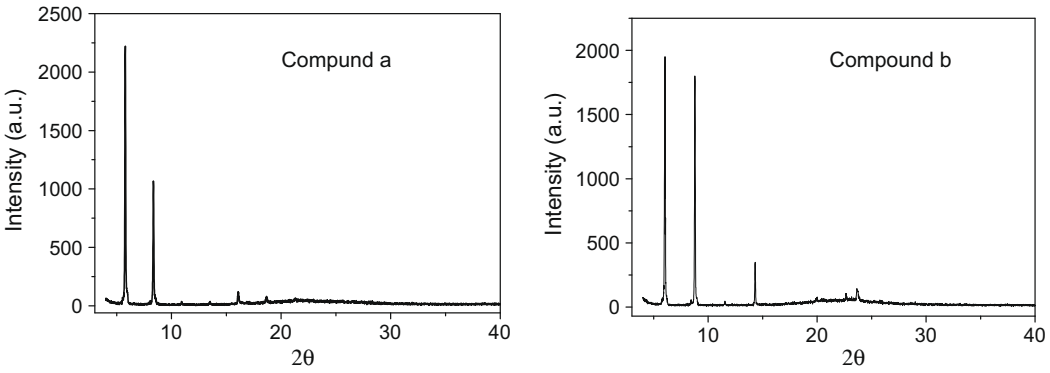

Fig. 3. Room temperature powder XRD of thin films of compounds a and b.

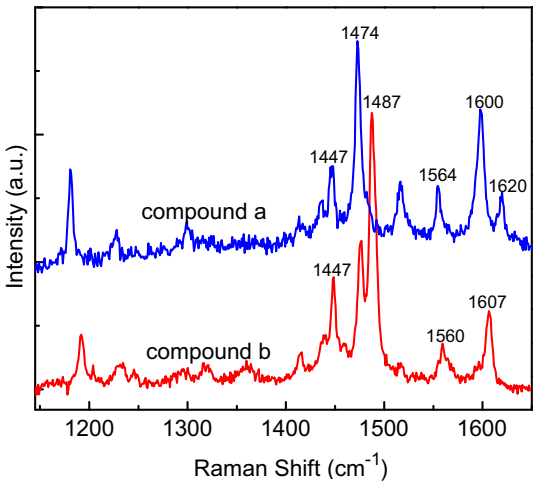

Fig. 4. Raman spectra of compounds a and b.

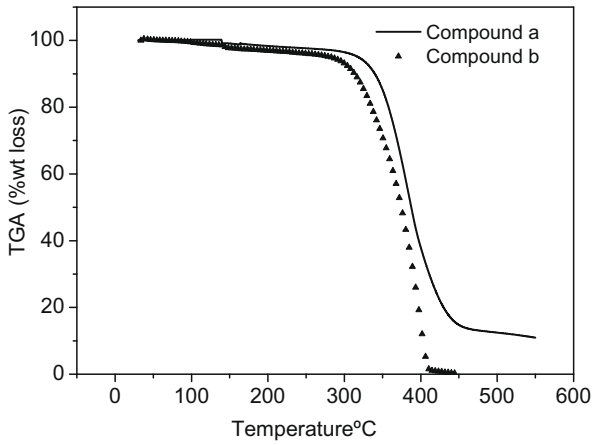

Fig. 5. TGA of compounds a and b.

tures of both compounds will yield information on the nature of electron–phonon coupling associated with charge transport mechanism in such devices.

2.4. Thermal and liquid crystalline properties

The thermal stability of the compounds (a) and (b) were investigated using thermal gravimetric analysis (TGA) and differential scanning calorimetry (DSC). Both the compounds have an excellent thermal stability, with decomposition temperatures of 320 °C (compound a) and 300 °C (compound b) as shown in Fig. 5. At temperature around 158 °C compound (a) starts melting and a liquid crystalline phase appears. This liquid crystalline phase exist up to 240 °C and a new nematic phase appears between 240 °C and 253 °C before it turns into a completely isotropic phase at around 260 °C. The existence of the nematic phase for compound (a) has been confirmed from a clear transition at 240 °C in DSC (Fig. 6). The optical polarizing images of the nematic and smectic A phase are shown in Fig. 7. Compound (b), on the other hand, starts to melt at around 177 °C and forms a smectic A phase existing up to 239 °C, beyond which it becomes a completely isotropic phase at 250 °C as shown in DSC (Fig. 6). The optical polarizing images of smectic A phase and crystalline phase were given in Fig. 7. All the phase transition temperatures including their change of enthalpy are given in the Table 2.

2.5. AFM analysis

A thin film of compound (a) was evaporated on cleaned Si wafers under vacuum evaporation (10^{-6} mbar). The thickness of the films ranged from 60 to 80 nm. Two films were utilized for the AFM studies: one as-is and the other thermally annealed. The latter was placed in an oven (under nitrogen atmosphere) and slowly heated to 120 °C and kept at this temperature for a few hours. It was then heated to 160 °C, left at this temperature for a few hours and then slowly brought back to room temperature. These temperatures were chosen to match the changes in the crystalline phase with temperature. We simultaneously recorded AFM topography and phase images. Fig. 8 shows the topography and phase images of the as-grown [(a) and (b)] and annealed sample [(c) and (d)]. The annealed samples clearly show a dewetting of the surface but with a very smooth morphology. The rms roughness of the two samples for 1 μm × 1 μm area decreased from

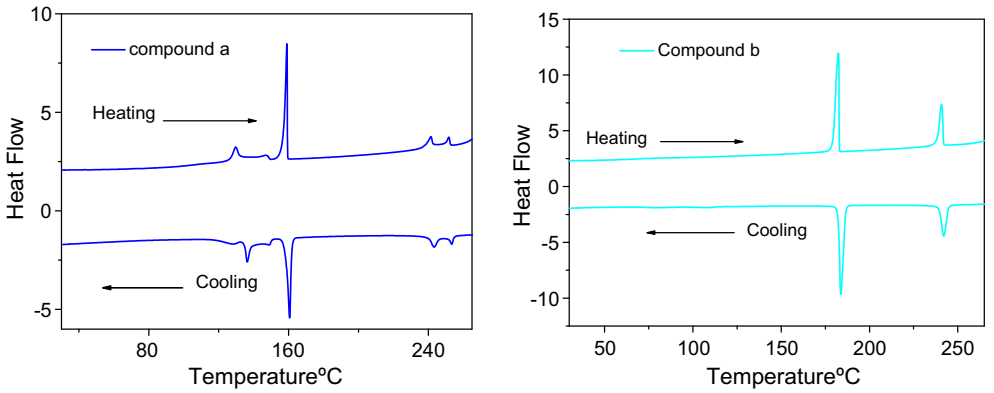

Fig. 6. DSC of compounds a and b (scan rate is 10 °C/min under N_2).

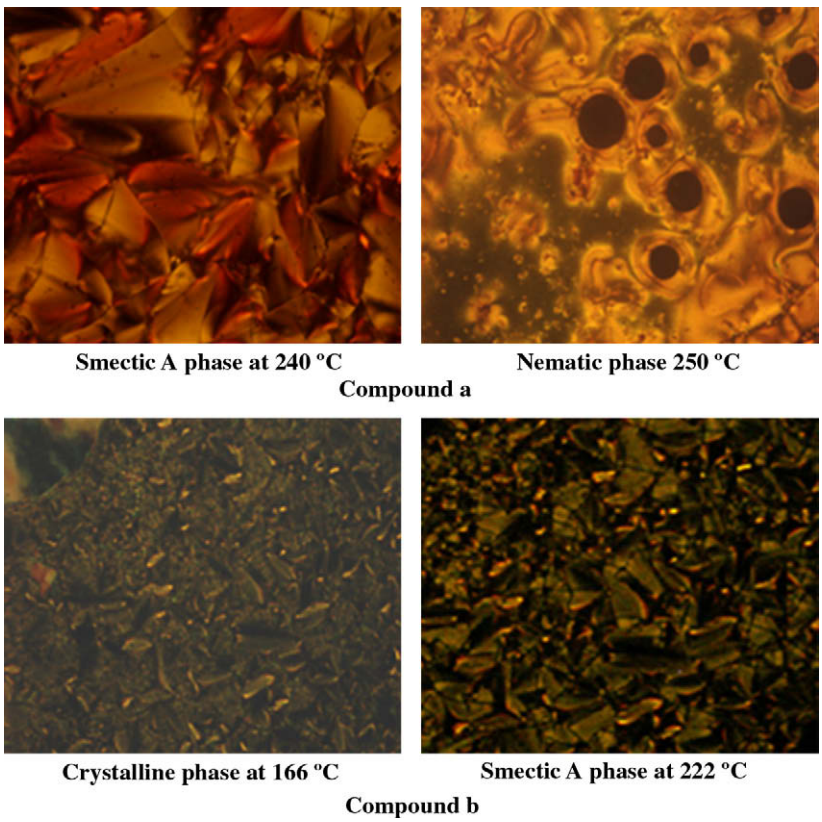

Fig. 7. Optical polarizing microscopic images of compounds a and b.

Table 2
Phase transition temperatures and their corresponding Enthalpy changes.

Compounds	T_t (Cr–S_A)	ΔH(Cr–S_A) (J/gm)	T_t (S_A–N)	ΔH(S_A–N) (J/gm)	T_t (N–I)	ΔH(N–I) (J/gm)
a	158 °C	18.40	239	1.85	250	1.08
b	177 °C	30.35	–	–	234	15.91

Transition temperatures and enthalpies determined by DSC at scan rate = 10 °C/min. (Cr = crystalline phase, S_A = smectic A phase, N = nematic phase and I = isotropic phase, T_t is transition temperature and ΔH = enthalpy change.)

~3.2 nm in the as-grown sample to ~0.7 nm in the annealed sample. At this point it is not clear if the dewetting of the annealed sample may be avoided by treating the Si surface differently. We are currently exploring different

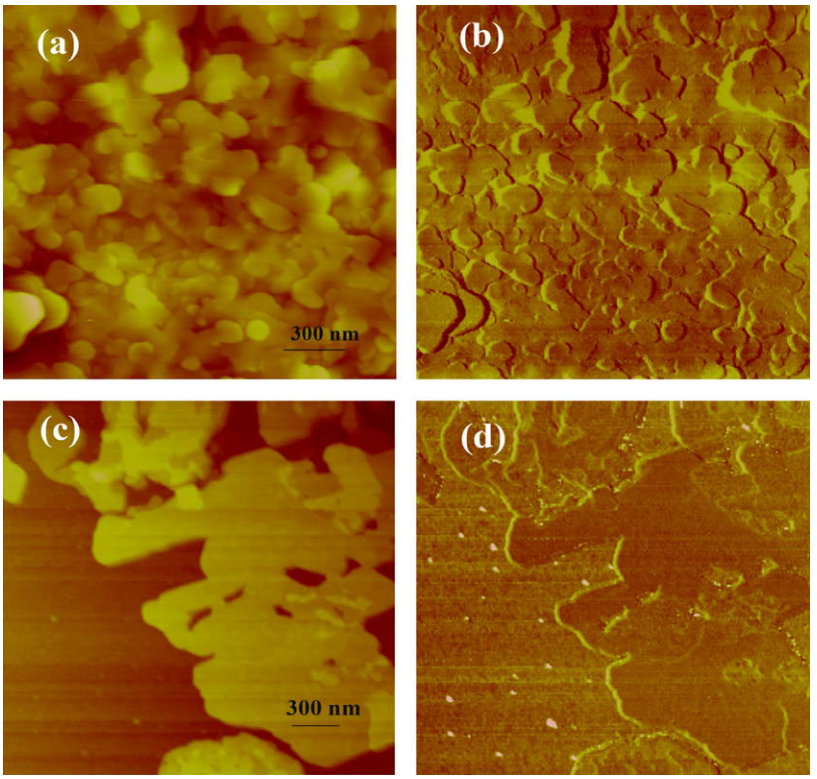

Fig. 8. AFM images of as-grown and annealed samples of compound a.

chemical treatments of Si and Si/SiO_2 interfaces for thin film growth of such liquid crystalline molecules since the small rms roughness of annealed films is extremely beneficial from the device aspect if the film coverage were better. Due to the issues with the annealed films all devices were fabricated with as-is evaporated films of compounds (a).

2.6. Field-effect transistor performance

Thin film transistors were fabricated by vacuum deposition of compound (a). The devices were fabricated using a top-contact bottom gate structure. In this work no surface modification of the Si/SiO_2 layers were done and all organic films were grown at room temperature. The devices exhibit p-channel performance. Although the output transistor characteristics from FETs fabricated with compound (b) were similar to compound (a), the former exhibited large leakage currents. It is not clear whether the leakage current in compound (b) mainly originates from the morphology of the film owing to grain boundaries and whether this can be circumvented using different gate dielectric layers. Systematic studies for improving FET characteristics using different surface modification and gate dielectrics from both compounds are in progress.

Fig. 9 shows the transfer characteristics for a forward and reverse sweep from an OFET using compound (a); the inset shows the output characteristics where the drain-source voltages were swept from 0 to −20 V. The highest hole mobility, calculated from the saturation regime (V_{DS} = −60 V), was estimated as 0.01 cm^2/Vs. The on/off ratio was obtained as 10^3 from I_{DS} at V_{GS} = 0 V and V_{GS} = −60 V; the threshold voltages were relatively low at

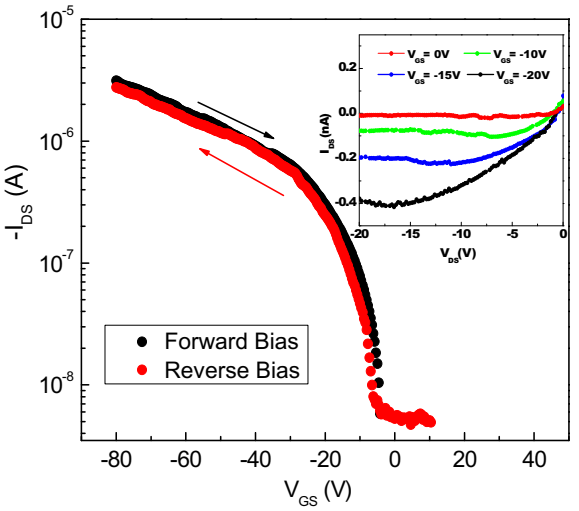

Fig. 9. The transfer characteristics for a forward and reverse sweep and output characteristics (inset) from an OFET fabricated using compound a.

~7 V. We point out that there is a lot of room for improvement for device performance. It is well established that surface modification by octyltrichlorosilane (OTS) or hexamethyldisilazane (HMDS) self-assembled monolayers can improve charge carrier mobilities and on/off ratios by more than an order of magnitude [67]. The results presented here are a proof of concept that the liquid crystalline benzothiazole compounds are excellent candidates for application in organic electronics.

3. Conclusions

Two new liquid crystalline donor–acceptor type benzothiazole derivatives have been synthesized by simple synthetic methods and characterized by optical absorption and photoluminescence spectroscopies, Raman scattering, differential scanning calorimetry, and thermogravimetric analysis. The field-effect transistor performance of one of the benzothiazole compounds shows that these materials have a great potential for future application in organic devices.

4. Experimental details

4.1. Synthesis

All chemicals were purchased from S.D. Fine Chemicals Ltd.; Mumbai, India and Spectrochem Pvt. Ltd.; Mumbai, India, except tributyltinchloride, $Pd(PPh_3)_4$ and potassium tert-butoxide which were bought from Sigma Aldrich.

^1H NMR and ^{13}C NMR spectra were recorded using Bruker 400 MHz. Chemical shifts were given in parts per million and coupling constants (J) in Hertz.

4.1.1. Synthesis of 2-(4-((E)-2-(5-(5-decylthiophen-2-yl)thiophen-2-yl)vinyl)phenyl)benzo[d] thiazole (a)

To a solution of 5-(5-decylthiophen-2-yl)thiophene-2-carbaldehyde (1) (0.617 g, 1.08 mmol) and Wittig salt (2) (0.347 g, 1.03 mmol) in dry $CHCl_3$ was added t-BuO^-K^+ (0.139 g, 1.2 mmol) in ethanol at room temperature. After allowing the mixture refluxing for 4 h, water was added and extracted with $CHCl_3$. The organic phase was dried over sodium sulphate. After removal of the solvent, the residue was purified by silica gel column chromatography with 30% chloroform and hexane as the eluent. Yield 67%.

^1H NMR (400 MHz, $CDCl_3$): δ 8.02–8.00 (m, 3H), 7.85–7.83 (d, J = 8 Hz, 1H), 7.51–7.49 (d, J = 8 Hz, 2H), 7.45–7.41 (dt, 1H), 7.34–7.30 (dt, 1H), 7.23–7.19 (d, J = 16 Hz, 1H), 6.95–6.39 (m, 3H), 6.84–6.80 (d, J = 16 Hz, 1H), 6.62–6.60 (d, J = 8 Hz, 1H), 2.75–2.71 (t, J = 8 Hz, 2H), 1.63–1.53 (m, 4H), 1.30–1.18 (m, 12H), 0.83–0.80 (t, J = 8 Hz, 3H).

^{13}C NMR (400 MHz, $CDCl_3$): δ 146.00, 140.71, 137.63, 129.53, 128.10, 127.95, 127.72, 126.40, 125.20, 124.90, 123.47, 123.44, 123.41, 121.61, 31.88, 31.58, 30.19, 29.55, 29.32, 29.06, 22.67, 14.10.

ESIMS [Found: m/z 542.1 $[M+H]^+$, Calcd. for $C_{33}H_{35}NS_3$ $[M+H]^+$: 541.19.

Anal. Calcd. for $C_{33}H_{35}NS_3$: C, 73.15; H, 6.51; N, 2.59; S, 17.75. Found C, 71.84; H, 6.19; N, 3.64; S, 16.10.

4.1.2. Synthesis of 2-(4-(5-(5-decylthiophen-2-yl)thiophen-2-yl)phenyl)benzo[d]thiazole (b)

Tributyl(5-(5-decylthiophen-2-yl)thiophen-2-yl)stannane (3) (0.515 gm, 0.86 mmol) and 2-(4-bromophenyl)benzo[d]thiazole (4) (0.250 g, 0.86 mmol) were dissolved in 25 ml of dry DMF. $Pd(PPh_3)_4$ (50 mg, 0.04 mmol) was added and the mixture was stirred for 16 h at 95 °C. After cooling to room temperature the solvent was removed in rotavapor and the yellow color solid compound was purified by column chromatography (SiO_2/chloroform:Hexane (v:v 1:1)) to give b as a yellow solid. Yield 65%.

^1H NMR (400 MHz, $CDCl_3$): δ 8.11–8.045 (m, 3H), 7.93–7.91 (d, J = 8 Hz, 1H), 7.72–7.70 (d, J = 8.3 Hz, 2H), 7.52–7.49 (dt, 1H), 7.41–7.38 (dt, 1H), 7.33–7.32 (d, J = 3.7, 1H), 7.11–7.10 (d, J = 3.7 Hz, 1H), 7.05–7.04 (d, J = 3.5 Hz, 1H), 6.71–6.70 (d, J = 3.4 Hz, 1H), 2.82–2.79 (t, J = 8 Hz., 2H), 1.71–1.66 (m, 4H), 1.36–1.19 (m, 12H), 0.89–0.86 (t, J = 6.9 Hz, 3H).

^{13}C NMR (400 MHz, $CDCl_3$): δ 146.32, 140.94, 138.79, 136.37, 134.22, 128.15, 126.45, 125.75, 125.26, 124.76, 124.00, 123.68, 123.12, 121.61, 31.90, 31.59, 30.21, 29.55, 29.34, 29.08, 22.67, 14.09.

ESIMS [Found: m/z 516.2 $[M+H]^+$, Calcd for $C_{31}H_{33}NS_3[M+H]^+$: 515.17.

Anal, Calcd. for $C_{31}H_{33}NS_3$:C, 72.19; H, 6.45; N, 2.72; S, 18.65. Found C, 72.26; H, 6.29; N, 3.33; S, 18.21.

4.2. Instrumental analysis

Thermal properties were studied under nitrogen atmosphere on Mettler DSC-1 instrument. Thermal gravimetric analysis (TGA) was conducted on Mettler Toledo TGA/SDTA 851e (temperature rate 10° C/min under N_2). The electrochemical properties of both the molecules were examined by using cyclic voltammetry (CH instrument). The electrolyte solution employed were 0.1 M Bu_4NPF_6/THF solution using platinum as working electrode and Ag/Ag+ as the reference electrode at a scan rate of 100 mVs^{-1} under Argon atmosphere.

Absorption spectra were recorded on Perkin Elmer (Lambda 35) UV–Vis Spectrometer and fluorescence emission spectra were recorded by using Perkin Elmer Spectrofluorophotometer (LS 50B) for both solution as well as solid state. Films of the two molecules were fabricated on quartz substrate from orthodichlorobenzene solution by spin casting. The absorption and fluorescence spectra of solution state were taken in chloroform (conc. 1×10^{-5} mol/L). Optical polarizing microscopic images of liquid crystalline phase were taken by Olympus- BX-51 polarizing microscope.

The AFM measurement was performed with a Nanoscope IIIa (Veeco Instruments, Inc.) operating in the tapping mode. Commercial ultra-sharp, rectangular silicon cantilevers made by Micromasch ($250 \times 35 \times 1.7$ μm^3) were used having a nominal spring constant of ~0.35 N/m and a resonance frequency of ~33 kHz.

The Raman spectra were collected using an Invia Renishaw spectrometer attached to a confocal microscope with $a \times 50$ long working distance objective and a 785 nm line

of a diode laser as the excitation wavelength. Typical laser power was a few mW on the sample.

OFET Fabrication: The devices were fabricated using a top-contact bottom gate structure with gold source and drain electrodes. A heavily p-doped silicon (1 0 0) wafer was used as the gate electrode with 200 nm bare SiO_2 layer as the gate dielectric insulator. Thin films (100 nm) of compound (a) were deposited on SiO_2 by vacuum sublimation at a rate of 0.2 Å/s under a pressure of 10^{-6} mbar. The substrate was kept at room temperature. Patterned Au layers of thickness 60 nm were deposited for the source (S)–drain (D) contacts. Typical S–D channel length (L) and width (W) for OFETs were 500 μm and 5 mm, respectively. The device characteristics were measured at room temperature with two source meters, Keithley 2400 and Keithley 236, configured together using a program written in LabView. The source–drain current and the source-gate leakage currents were measured with Keithley 236, which has a resolution of 10 fA.

Acknowledgement

We thank department of science and technology (DST) for financial support and G.K. Dutta thanks UGC for Junior Research Fellowship. SG acknowledges the IREE award from the National Science Foundation (NSF) ECCS-0523656 and NSF ECCS-0823563 for partial support of this work.

References

[1] J. Kido, M. Kimura, K. Nagai, Science 267 (1995) 1332.
[2] B.W.D. Andrade, S.R. Forrest, Adv. Mater. 16 (2004) 1585.
[3] A.R. Duggal, J.J. Shiang, C.M. Heller, D.F. Foust, Appl. Phys. Lett. 80 (2002) 3470.
[4] N.S. Sariciftci, D. Braun, C. Zhang, V.I. Srdanov, A.J. Heeger, G. Stucky, F. Wudl, Appl. Phys. Lett. 62 (1993) 585.
[5] J.E. Anthony, Chem. Rev. 106 (2006) 5028.
[6] L.S. Mende, U. Bach, R.H. Baker, T. Horiuchi, H. Miura, S. Ito, S. Uchida, M. Gratzel, Adv. Mater. 17 (2005) 813.
[7] M. Svensson, F. Zhang, S.C. Veenstra, W.J.H. Verhees, J.C. Hummelen, J.M. Kroon, O. Inganas, M.R. Andersson, Adv. Mater. 15 (2003) 988.
[8] C.D. Dimitrakopoulos, P.R.L. Malenfant, Adv. Mater. 14 (2002) 99.
[9] M. Torrent, C. Rovira, Chem. Soc. Rev. 37 (2008) 827.
[10] D.H. Kim, J.T. Han, Y.D. Park, Y. Jang, J.H. Cho, M. Hwang, K. Cho, Adv. Mater. 18 (2006) 719.
[11] A.R. Murphy, J. Liu, C. Luscombe, D. Kavulak, J.M.J. Frechet, R.J. Kline, M.D. McGehee, Chem. Mater. 17 (2005) 4892.
[12] Y. Sakamoto, T. Suzuki, M. Kobayashi, Y. Gao, Y. Fukai, Y. Inoue, F. Sato, S. Tokito, J. Am. Chem. Soc. 126 (2004) 8138.
[13] Y. Kunugi, K. Takimiya, Y. Toyoshima, K. Yamashita, Y. Aso, T. Otsubo, J. Mater. Chem. 14 (2004) 1367.
[14] V.Y. Butko, X. Chi, D.V. Lang, A.P. Ramirez, Appl. Phys. Lett. 83 (2003) 4773.
[15] T. Sekitani, T. Someya, Jpn. J. Appl. Phys. 46 (2007) 4300.
[16] K. Shibata, H. Wada, K. Ishikawa, H. Takezoe, T. Moria, Appl. Phys. Lett. 90 (2007) 193509.
[17] T. Takahashi, T. Takenobu, Appl. Phys. Lett. 88 (2006) 033505.
[18] E. Menard, V. Podzorov, S.H. Hur, A. Gaur, M.E. Gershenson, J.A. Rogers, Adv. Mater. (Weinheim) 16 (2004) 2097.
[19] R. Zeis, C. Besnard, T. Siegrist, C. Schlockermann, X. Chi, C. Kloc, Chem. Mater. 18 (2006) 244.
[20] A. Saeki, S. Seki, T. Takenobu, Y. Iwasa, S. Tagawa, Adv. Mater. 20 (2008) 920.
[21] L. Torsi, A. Dodabalapur, L.J. Rothberg, A.W.P. Fung, H.E. Katz, Science 272 (1996) 1462.
[22] S.A. Ponomarenko, S. Kirchmeyer, A. Elschner, B.H. Huisman, A. Karbach, D. Drechsler, Adv. Funct. Mater. 13 (2003) 591.
[23] G. Horowitz, M.E. Hajlaoui, Adv. Mater. 12 (2000) 1046.
[24] Y. Sun, Y. Liu, D. Zhu, J. Mater. Chem. 15 (2005) 53.
[25] N. Karl, Synth. Met. 133 (2003) 649.
[26] L.L. Chua, J. Zaumseil, J.F. Chang, E.C.W. Ou, P.K.H. Ho, H. Sirringhaus, R.H. Friend, Nature 434 (2005) 194.
[27] S. Ando, R. Murakami, J.I. Nishida, H. Tada, Y. Inoue, S. Tokito, Y. Yamashita, J. Am. Chem. Soc. 127 (2005) 14996.
[28] E.J. Meijer, D.M. Leeuw, S. Setayesh, E. Veenendaal, B.H. Huisman, P.W.M. Blom, J.C. Hummelen, U. Scherf, T.M. Klapwijk, Nat. Mater. 2 (2003) 678.
[29] J. Jang, J.W. Kim, N. Park, J.J. Kim, Organ. Electron. 9 (2008) 481.
[30] J. Huang, M. Yi, I.A. Hümmelgen, D. Ma, Organ. Electron. 10 (2009) 210.
[31] H.N. Tsao, W.P.Z. Liu, W. Osikowicz, W.R. Salaneck, K. Mullen, Adv. Mater. 20 (2008) 2715.
[32] S.I. Noro, T. Takenobu, Y. Iwasa, H.C. Chang, S. Kitagawa, T. Akutagawa, T. Nakamura, Adv. Mater. 20 (2008) 3399.
[33] L. Burgi, T. Richards, M. Chiesa, R.H. Friend, H. Sirringhaus, Synth. Met. 146 (2004) 297.
[34] A.L. Briseno, S.C.B. Mannsfeld, M.M. Ling, S. Liu, R.J. Tseng, C. Reese, M.E. Roberts, Y. Yang, F. Wudl, Z. Bao, Nature 444 (2006) 913.
[35] F. Zhang, M. Funahashi, N. Tamaoki, Organ. Electron. 10 (2009) 73.
[36] M. O'Neill, S.M. Kelly, Adv. Mater. 15 (2003) 1135.
[37] S. Sergeyev, W. Pisula, Y.H. Geerts, Chem. Soc. Rev. 36 (2007) 1902.
[38] Y. Shimizu, K. Oikawa, K. Nakayama, D. Guillon, J. Mater. Chem. 17 (2007) 4223.
[39] M. Funahashi, J. Hanna, Phys. Rev. Lett. 78 (1997) 2184.
[40] K. Oikawa, H. Monobe, K. Nakayama, T. Kimoto, K. Tsuchiya, B. Heinrich, D. Guillon, Y. Shimizu, M. Yokoyama, Adv. Mater. 19 (2007) 1864.
[41] A.J.J.M. van Breemen, P.T. Herwig, C.H.T. Chlon, J. Sweelssen, H.F.M. Schoo, S. Setayesh, W.M. Hardeman, C.A. Martin, D.M. de Leeuw, J.J.P. Valeton, C.W.M. Bastiaansen, D.J. Broer, A.R. Popa-Merticaru, S.C.J. Meskers, J. Am. Chem. Soc. 128 (2006) 2336.
[42] M. Funahashi, F. Zhang, N. Tamaoki, Adv. Mater. 19 (2007) 353.
[43] F. Zhang, M. Funahashi, N. Tamaoki, Appl. Phys. Lett. 91 (2007) 063515.
[44] S. Laschat, A. Baro, N. Steinke, F. Giesselmann, C. Hgele, G. Scalia, R. Judele, E. Kapatsina, S. Sauer, A. Schreivogel, M. Tosoni, Angew. Chem. Int. Ed. 46 (2007) 4832.
[45] S. Chandrasekhar, N.V. Madhusudana, Annu. Rev. Mater. Sci. 10 (1980) 33.
[46] M. Suarez, J.M. Lehn, S.C. Zimmerman, A. Skoulios, B. Heinrich, J. Am. Chem. Soc. 120 (1998) 9526.
[47] T. Chuard, R. Deschenaux, J. Mater. Chem. 12 (2002) 1944.
[48] M.A. Loi, E.D. Como, F. Dinelli, M. Murgia, R. Zamboni, F. Biscarini, M. Muccin, Nat. Mater. 4 (2004) 81.
[49] J. Piris, M.G. Debije, N. Stutzmann, B.W. Laursen, W. Pisula, M.D. Watson, T. Bjornholm, K. Müllen, J.M. Warman, Adv. Funct. Mater. 14 (2004) 1053.
[50] M. Heeney, C. Bailey, M. Giles, M. Shkunov, D. Sparrowe, S. Tierney, W. Zhang, I. McCulloch, Macromolecules 37 (2004) 5250.
[51] S.D. Feyter, F.C. De Schryver, Chem. Soc. Rev. 32 (2003) 139.
[52] L.S. Mende, A. Fechtenkötter, K. Müllen, E. Moons, R.H. Friend, J.D. MacKenzie, Science 293 (2001) 1119.
[53] F. Garnier, R. Hajlaoui, A.E. Kassmi, G. Horowitz, L. Laigre, W. Porzio, M. Armanini, F. Provasoli, Chem. Mater. 10 (1998) 3334.
[54] T. Yasuda, H. Ooi, J. Morita, Y. Akama, K. Minoura, M. Funahashi, T. Shimomura, T. Kato, Adv. Funct. Mater. 19 (2009) 411.
[55] S. Yazaki, M. Funahashi, T. Kato, J. Am. Chem. Soc. 130 (2008) 13206.
[56] T. Kato, T. Yasuda, Y. Kamikawa, M. Yoshio, Chem. Commun. (2009) 729.
[57] J. Cornil, D. Beljonne, J.P. Calbert, J.L. Bredas, Adv. Mater. 13 (2001) 1053.
[58] C.H. Lee, T. Yamamoto, Tetrahedron Lett. 42 (2001) 3993.
[59] J.C. Maunoury, J.R. Howse, M.L. Turner, Adv. Mater. 19 (2007) 805.
[60] Y.S. Park, D. Kim, H. Lee, B. Moon, Org. Lett. 8 (2006) 4699.
[61] S.R. Amrutha, M. Jayakannan, J. Phys. Chem. B 113 (2009) 5083.
[62] K. Yoshino, T. Kohno, T. Uno, T. Morita, G. Tsukamoto, J. Med. Chem. 29 (1986) 820.
[63] P. Frre, J.M. Raimundo, P. Blanchard, J. Delaunay, P. Richomme, J.L. Sauvajol, J. Orduna, J. Garin, J. Roncali, J. Org. Chem. 68 (2003) 7254.
[64] C. Zhao, Y. Zhang, M. Ng, J. Org. Chem. 72 (2007) 6364.
[65] G. Barbarella, L. Favaretto, G. Sotgiu, M. Zambianchi, L. Antolini, O. Pudova, A. Bongini, J. Org. Chem. 63 (1998) 5497.
[66] R. Tang, Z. Tan, Y. Li, F. Xi, Chem. Mater. 18 (2006) 1053.
[67] S. Tirapattur, M. Belletete, N. Drolet, M. Leclerc, G. Durocher, Chem. Phys. Lett. 370 (2003) 799.

[68] J.H. Tsai, C.C. Chueh, M.H. Lai, C.F. Wang, W.C. Chen, B.T. Ko, Ch. Ting, Macromolecules 42 (2009) 1897.
[69] E. Mulazzi, A. Ripamonti, J. Wery, B. Dulieu, S. Lefrant, Phys. Rev. B 60 (1999) 1659.
[70] C. Volz, M. Arif, S. Guha, J. Chem. Phys. 126 (2007) 064905.
[71] R. Sun, J. Yao, S. Li, R. Gu, Vib. Spectrosc. 47 (2008) 38.
[72] M. Baibarac, M. Lapkowski, A. Pron, S. Lefrant, I.J. Baltog, J. Raman Spectrosc. 29 (1998) 825.
[73] J. Zaumseil, H. Sirringhaus, Chem. Rev. 107 (2007) 1296.

Organic Electronics 11 (2010) 10–15

Contents lists available at ScienceDirect

Organic Electronics

journal homepage: www.elsevier.com/locate/orgel

Three-dimensional anisotropic density of states distribution and intrinsic-like mobility in organic single crystals

B. Fraboni [a,*], A. Fraleoni-Morgera [b], A. Cavallini [a]

[a] Dipartimento di Fisica, Università di Bologna, viale Berti Pichat 6/2, 40127 Bologna, Italy
[b] Sincrotrone Trieste, Strada Statale Km 163.5, 34102 Basovizza (Trieste), Italy

ARTICLE INFO

Article history:
Received 27 May 2009
Received in revised form 10 September 2009
Accepted 15 September 2009
Available online 19 September 2009

Keywords:
Molecular electronics
Anisotropic mobility
Density of states distribution
Organic single crystal
Solution-grown crystals

ABSTRACT

Organic semiconducting molecules are receiving a large attention because of their potential applications, spanning from OLEDs to plastic photovoltaics to bio-chemical sensors. However, the electronic transport properties of these materials are still not fully understood, and organic single crystals (OSCs) may represent model materials for assessing the charge transport mechanisms, thanks to their high purity and molecular order. Here we show for the first time that solution-grown, millimiter-sized organic single crystals of 4-hydroxycyanobenzene (4HCB) possess a clear and reproducible three-dimensional anisotropy in their main transport parameters: (i) charge carrier mobility, (ii) distribution of the electronic density of states and (iii) deep traps energy and concentration, and we report intrinsic-like three-dimensional mobility values for these crystals. These findings demonstrate that the electronic spatial anisotropy of OSCs extends well beyond the carrier mobility, and open the way to the development of novel electronic device architectures based on the simultaneous exploitation of different electronic responses along the three spatial directions of the crystal.

© 2009 Elsevier B.V. All rights reserved.

1. Introduction

Organic semiconductors are considered promising materials for implementing low-cost and large-scale produced electronics [1–8]. Among the most attractive prospects in this field are the possibility of tailoring functionalities by molecular design [9] and the realization of flexible devices [10–12], distinctive and unique features that open the way to the attainment of versatile and multifunctional electronic systems. However, in order to achieve this goal, a number of issues relative to the charge transport in organic materials are yet to be clarified. In particular, a clear and well defined comprehension of the electronic behaviour of these materials (including a complete description of the fundamental electronic states of the charge carriers) has still to be gained and related to their structural properties.

In this view, organic single crystals (OSCs) offer the possibility to effectively probe the electronic behaviour of organic materials. In fact, thanks to their long-range molecular order, they limit charge carrier trapping and hopping phenomena due to grain boundaries, interfaces and structural imperfections, and provide an almost ideal work bench for the study of intrinsic electronic transport. Nonetheless, the low symmetry of organic molecules leads to anisotropically packed crystal structures, that affect their transport properties (for example, the direction of the strongest π-orbitals overlap usually coincides with the direction of the highest carrier mobility [13–19]). This asymmetry, on one hand introduces difficulties in a clear understanding of the transport behaviour of organic semiconductors, but on the other hand it offers the tool to investigate the correlation between the three-dimensional molecular stacking order of OSCs and their recently found

* Corresponding author. Address: Department of Physics, University of Bologna, viale Berti Pichat 6/2, Bologna 40127 Italy. Tel.: +39 0512095806; fax: +39 0512095113.
E-mail address: beatrice.fraboni@unibo.it (B. Fraboni).

1566-1199/$ - see front matter © 2009 Elsevier B.V. All rights reserved.
doi:10.1016/j.orgel.2009.09.014

anisotropic electronic transport properties. In particular, in the last years different mobilities have been measured along the two dimensions (2D) in the main crystal plane for micro- or nanometer sized organic single crystals, either vapour deposited [13–19] or solution-grown [20–22].

These findings, associated to the intrinsic three-dimensional (3D) molecular asymmetry and packing anisotropy of OSCs, suggest that the anisotropic behaviour of the electronic transport could actually extend into the 3D realm. Indeed, we have recently showed that 4-hydroxycyanobenzene (4HCB) single crystals exhibit a three-dimensional anisotropic mobility, although this has been assessed using two different measurement techniques along the three crystallographic directions [23].

Another point to be considered when dealing with OSCs transport properties is that hardly avoidable differences in the crystal growth conditions and in the experimental method used to determine the mobility (usually based on a field effect transistor, FET) lead to significant discrepancies in the carrier mobility values reported for the same type of OSC (e.g. for rubrene single crystals: [7,13–17,19,24–27]). In fact, the device fabrication processes and the defects at the crystal/gate dielectric interface unpredictably affect the absolute measured mobility, as well as its reproducibility [7,15,17,26,28]. The already mentioned inherent structural anisotropy of OSCs introduces additional complexity to this issue.

Finally, besides carrier mobility other transport parameters are of fundamental importance in determining the electronic behaviour of a semiconductor: the density of states (DOS) distribution, the concentration of the electrically active electronic states and their energy level have to be known in order to develop a consistent charge transport model. This knowledge becomes even more fundamental if the mentioned parameters vary along the three different dimensions in space, especially if novel electronic device architectures have to be developed. For example, monocrystal-based, single gated devices capable of delivering source-drain responses where the gain depends on the spatial direction along which the electrodes are aligned, may be envisaged as useful tools for lowering the amount of components of a single chip. However, up to date, a full assessment of the 3D anisotropy of the carrier transport properties of OSCs is still lacking.

In this work we show that, by means of Space Charge-Limited Current (SCLC) and photocurrent spectroscopy analyses, it is possible to carry out on solution-grown, macroscopic 4-hydroxycyanobenzene (4HCB) single crystals (Fig. 1) a complete characterization of several key electronic transport parameters. In particular, we determine (i) the majority carrier mobility, (ii) the density of states (DOS) distribution of the intrinsic electronic states, (iii) their concentration and (iv) their energy levels in the band gap. We bring to evidence that all of these properties are clearly anisotropic in the crystal three dimensions, with very good reproducibility over more than 30 different crystals. Moreover, we compare the carrier mobilities found along the two main crystal axes *a* and *b* using the SCLC method with the corresponding ones determined on 4HCB crystals by means of the air–gap FET technique [22,23]. From this comparison, the remarkable agreement between the two sets of values obtained with two different and independent experimental techniques points to the likely intrinsicity of the found mobility values.

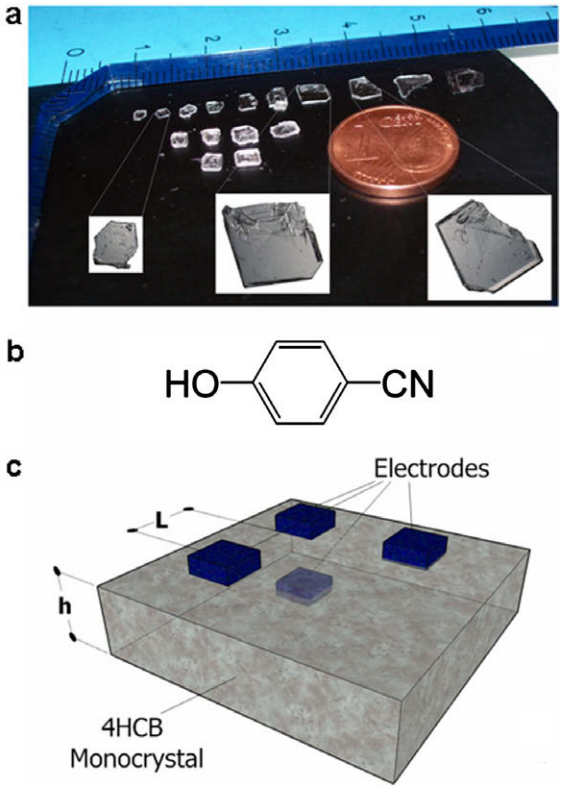

Fig. 1. (a) Examples of solution-grown 4HCB single crystals investigated in this work, (b) chemical structure of 4-hydroxycyanobenzene (4HCB) and (c) layout of the electrical contacts used for the electronic transport characterization.

2. Experimental

4HCB was purchased from FLUKA (99+%). The raw material was dissolved in pure ethylic ether (technical grade), and the solvent was allowed to slowly evaporate under a hood in standard laboratory conditions. The resulting 4HCB crystals have been washed thoroughly with warm petroleum ether. About 150 mg of so-purified 4HCB crystals were dissolved in 10 ml of ethylic ether, filtered through a 0.45 μm Teflon filter and left in a 500 ml beaker covered by a petri dish, at controlled temperature (approximately 6 °C) for about 48 h. A complete and slow evaporation of the solvent delivered beautiful and transparent crystals, left on the bottom of the beaker. Following this procedure, crystals with thickness varying from 150 μm to 600 μm may be grown. The higher the concentration of 4HCB in ether, the bigger (in size and thickness) the obtained crystals. The crystals have been gently removed from the beaker using a spatule, and used for the preparation of the devices with no further treatment. The molecular packing and orientation of the 4HCB crystals with respect to the crystal axes have been investigated by X-ray diffraction measurements, that assessed a clear

3D packing anisotropy [22]. The thickness of the crystals has been measured by optical microscopy methods.

All the electrical measurements reported in this paper have been done at room temperature in darkness using a Keithley Source-Meters 2400 and Electrometers 617 and 6512. Data were acquired at a slow gate voltage sweep, with different sweep rates. No significant hysteresis or time relaxation were observed. The ohmic contacts on 4HCB were fabricated using silver epoxy (Epo-Tek E415G) at a fixed distance, in order to form pairs of contact pads perpendicular to each other (Fig. 1c).

As already reported in the literature [22] the performance of the air–gap FETs fabricated with these contacts assessed the p-type conductivity of the material and the good hole injecting properties of the electrical contacts. Spectral photocurrent (PC) measurements were carried out in the planar configuration with an optical flux of 1×10^{13} photons/cm^2 at $\lambda = 450$ nm. PC spectra were recorded in air at 295 K. The low-level injection conditions ensured that no alteration in the crystal electrical response was induced by the PC measurements, as assessed by comparing many consecutively acquired PC spectra. A good reproducibility of the electrical measurements has been assessed over many tested crystals. No sign of permanent ageing or degradation of the crystals was observed, neither from the *I–V* curves nor from PC analyses.

3. Results and discussion

We have carried out current–voltage analyses using the Space Charge-Limited Current (SCLC) method [29,30] along all of the three spatial direction of 4HCB crystals. SCLC is a relatively easy-to-handle room temperature method that, if properly applied, allows to determine several relevant bulk transport parameters of OSCs, such as the carrier mobility and the concentration, the energy and density of states distribution of the dominant deep traps [31,32]. SCLC curves have a symmetric character for positive and negative biases and are characterized by a linear region (ohmic) followed by a Space Charge Limited (SCL) one and finally by the Trap-Filled-Limited (TFL) region, when a steep increase of the current occurs (Fig. 2). Such a behaviour is related to the balance between thermally generated and injected carriers, and to the occupation of the dominant deep traps in the material. At $V \geqslant V_{TFL}$ (the voltage at which the SCL/TFL transition occurs) the charge injected by the contacts fills all the traps and the transport enters the trap-free regime, with a sharp current increase. For a given distribution of states, the equations describing the SCL *J–V* characteristics can be obtained by solving simultaneously the current equation and the Poisson's equation. In order to do so, however, the following assumptions are usually introduced: (i) to consider unipolar majority carrier transport (holes in our case [22]); (ii) to neglect the density of thermal carriers with respect to injected carriers; and (iii) to assume the diffusion term in the current equation to be small with respect to the drift term.

Two different sample geometries can be used for SCLC measurements, i.e. the sandwich-like one (with electrical contacts on opposite sides of the crystal) and the planar gap-like one (with the two contacts on the same surface) [31–34]. In the sandwich geometry the transport is assumed to be one-dimensional and follows the Mott and Gurney model [35], that describes transport in bulk material:

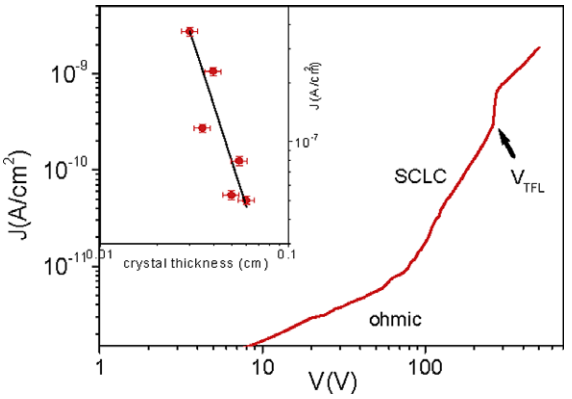

Fig. 2. Typical SCLC characteristic of a 4HCB single crystal. The ohmic, SCLC and Trap-Fill-Limited Voltage (V_{TFL}) are highlighted. The inset shows the L^{-3} dependence of the measured current as a function of the crystal thickness, assessing the occurrence of proper bulk conduction during the SCLC analyses.

$$J = \frac{9}{8}\varepsilon\mu\frac{V^2}{L^3}$$

where *J* is the current density for the applied voltage *V*, *L* is the thickness of the organic layer (electrode separation), ε is the dielectric constant of the material and μ is the carrier mobility. In the planar geometry, the transport is two-dimensional (2D) and has been modelled by Geurst [36] as:

$$J = \frac{2}{\pi}\varepsilon\mu\frac{V^2}{L^2} \quad (1)$$

where *L* is the electrodes separation (see Fig. 1c). In this case the thickness of the organic layer, *h*, becomes a key parameter for the determination of the type of transport: for $L/h > 200$ the 2D law (Eq. (2)), will dominate the carrier transport, while bulk, 1D transport (Eq. (1)) occurs if $L/h < 10$ [33]. We applied these models to our data and, since the thickness of the examined 4HCB crystals varied between 150 and 600 μm, L/h was always small enough to grant 1D transport also in the planar electrode configuration.

A typical curve measured in the sandwich geometry along axis *c* of a 350 μm thick 4HCB crystal is shown in Fig. 2, where the ohmic, SCLC and TFL regimes are highlighted. The inset of Fig. 2 reports the L^{-3} dependence of the measured current as a function of the crystal thickness, at a constant electric field of 9×10^3 V/cm, and assesses the occurrence of proper bulk conduction transport during SCLC analyses [30,32]. SCLC measurements on axes *a* and *b* were carried out in the planar electrode configuration.

The intrinsic-like carrier mobility μ_{SCLC} can be obtained from Eq. (1) calculated at $V = V_{TFL}$. We have measured SCLC curves along axes *a*, *b* and *c* over 30 different (in size and thickness) crystals, finding maximum mobility values of

1×10^{-1}, 4×10^{-2} and 2×10^{-5} cm^2/Vs, respectively (Table 1, column μ_{SCLC}–Max). The average mobility values for each axis are also reported in Table I (column μ_{SCLC}–Ave), and both the maxima and average values show clear anisotropic behaviour along the three different crystal directions.

We recently reported anisotropic mobilities in similar 4HCB crystals measured with air–gap FETs (columns μ_{FET}-Max and -Ave in Table 1) [23]. Air–gap FETs offer the advantage of reducing the influence of the interface with the gate dielectric, that usually lowers the effective mobility value [7,15,17,26,28].

A comparison between the μ_{SCLC} and the FET-measured one (μ_{FET}) brings to evidence that: (i) for each axis the SCLC-measured mobility is always higher or, in the worst case, equal to the FET-determined one. These observations point to the intrinsic nature of the mobility values determined by SCLC, to the reliability of the SCLC technique as a mobility measurement tool and to the overall good electronic quality of solution-grown 4HCB crystals; (ii) both FET and SCLC measurements deliver maximum and average values that do not differ much. The limited difference between the μ_{SCLC} and the μ_{FET} values confirms that air–gap OFETs may provide a mobility measurement tool able to minimize interface effects induced by the gate dielectric [7,26,28], one of the major cause for mobility reduction in OFETs.

Fig. 3 shows the mobility measured along each one of the three axes of the very same crystal for three different crystals, highlighting a marked and reproducible 3D anisotropic transport in each of the three. It is also noteworthy that each crystal has been repetitively measured along the three axes, providing reproducible results. The consistency of the measured values over several different crystals, which even had different dimensions, confirms that the measured mobilities may be actually considered as intrinsic to the crystal, and that the measurements did not affect their electronic properties, although all the tests were carried out in normal laboratory atmosphere and at room temperature.

Another very important transport parameter that can be obtained from the SCLC method is an estimate of the density of electrically active traps in the material, N_T, using the relation $N_T = \varepsilon V_{TFL}/(eL^2)$, where e is the electron charge, with the underlying assumption that the traps are uniformly distributed in the material. We thus calculated N_T for each crystallographic axis and the average trap density found along each crystallographic axis is reported in Table 1 (column N_T). While along axis a and axis b the concentration of traps is substantially comparable, the same parameter is one order of magnitude higher for axis c. These findings are in line with the higher mobilities found along axes a and b with respect to axis c, and confirm the inherently anisotropic nature of the electronic parameters of OSCs.

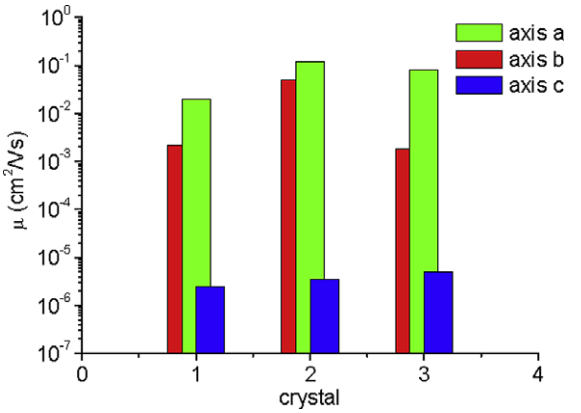

Fig. 3. Charge carrier mobility measured by SCLC along the three different spatial directions on the same crystal for three different crystals, clearly showing the anisotropy and reproducibility of the measurements.

The shape of the SCLC curve reflects the increment of the space charge with respect to the shift of the Fermi level as a function of the applied bias, and thus mirrors the energy dependence of the density of states (DOS) distribution. By analyzing the SCLC curves with a differential analysis method developed by Nespurek and Sworakowky [37,38], it is possible to extract an energy distribution of states $h(E_F)$ directly from a single current–voltage curve:

$$h(E_F) = \frac{x_1 x_2 \varepsilon V}{2eL^2 kT(m-1)} \tag{2}$$

The position of the Fermi level, E_F, can be obtained using the following equation:

$$E_F = kT \ln \frac{L}{x_1 N_v e \mu} + kT \ln \frac{J}{V} \tag{3}$$

where is $m = d(\ln J)/d(\ln V)$, $x_1 = (2m-1)/m$, $x_2 = (m-1)/m$ and N_V is the effective density of states in the highest occupied molecular orbital (here $N_V = 5 \times 10^{21}$ cm^{-3}).

We have hence analyzed the SCLC curves obtained along the 3 crystal axes according to this model, and we have obtained the three DOS distributions shown in Fig. 4. One has to keep in mind that by assuming a unipolar

Table 1
Charge carrier mobility μ_{SCLC} and trap density N_T, obtained from the SCLC analysis of J–V curves with the Mott–Gurney theory for the three crystal axes a, b and c. N_T^* is the trap density evaluated from the differential analysis of SCLC curves. μ_{FET} is the charge carrier mobility obtained from OSC FET measurements. Average values, measured over 30 crystals.

Crystal axis	μ_{FET} (cm^2/Vs)[23]		μ_{SCLC} (cm^2/Vs)		N_T (cm^{-3})	N_T^* (cm^{-3})
	Max.	Ave.	Max.	Ave.		
a	8×10^{-2}	3×10^{-2}	1×10^{-1}	5×10^{-2}	3×10^{11}	9×10^{12}
b	9×10^{-3}	5×10^{-3}	2×10^{-2}	6×10^{-3}	1×10^{11}	4×10^{12}
c	–	–	2×10^{-5}	5×10^{-6}	5×10^{12}	2×10^{13}

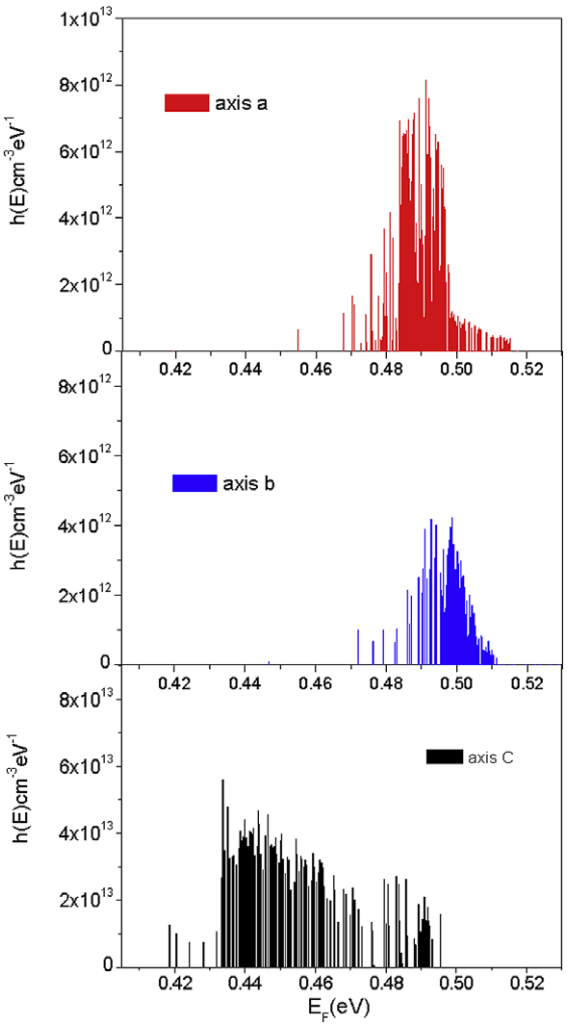

Fig. 4. The DOS distribution of the electrically active states obtained from SCLC measurements along the three spatial directions of 4HCB crystals, showing an anisotropic energy distribution and concentration of states.

majority carrier type conduction (holes in our case), the method of Nespurek and Sworakowski allows to reveal only the deep states that interact with the majority carrier band (the valence band in our case) This means that the peak energies in the $h(E_F)$ functions shown in Fig. 4 correspond to the dominant hole deep states.

In the planar axis *a* the DOS is centered at an energy of (0.49 ± 0.01) eV, along axis *b* at an energy of (0.50 ± 0.01) eV, while along axis *c* the DOS is shifted at (0.45 ± 0.02) eV (the associated error is estimated from the scattering of the data within the various investigated crystals). Trap states at comparable energies have been recently reported along one of the axes of rubrene single crystals [32,39] and in pentacene [40]. Further evidence on the presence of deep electrically active states in 4HCB crystals is provided by spectral PC analyses, that we carried out along axes *a* and *b* on the same crystal. The photoconductivity yield spectrum is reported in Fig. 5, showing the HOMO–LUMO transport edge located at 4.5 eV, followed by exciton related features at energies >4.0 eV. A large band of deeper states is clearly visible at lower energies in the spectrum, starting at 4.0 eV and peaking at approx. 0.50 eV from the HOMO–LUMO gap, a value in line with the results obtained from the above reported SCLC analyses on the DOS energy distribution. In addition, from Fig. 5 it is also evident that the number of electrons excited per incident photon is larger along axis *a* than along axis *b*, again in good agreement with the DOS distributions reported in Fig. 4, where the density of states is higher along *a* than along *b*.

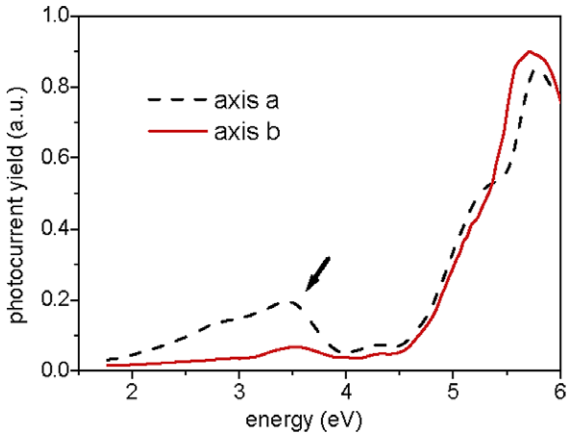

Fig. 5. Photocurrent yield as a function of the incident photon beam energy for 4HCB single crystals, along the two planar direction of the crystals, axis *a* (dotted line) and axis *b* (solid line). The arrow highlights the peak associated to the band of states located in the band-gap corresponding to the DOS distribution found by SCLC analyses.

The $h(E_F)$ distribution represents the actual density of trapped carriers $N_T(E)$ [30,32] and it is hence possible to exploit it to obtain trap density values along the three axes *a*, *b* and *c*, $N^*_{Ta,b,c}$ more accurate than the previously calculated ones. In fact, the density of traps $N_{Ta,b,c}$ extracted from the V_{TFL} method and reported in Table 1 is often underestimated, due to inhomogeneities in the trap distribution and to the occurrence of Poole–Frenkel effects at voltages close to V_{TFL}, that hinder a complete filling of all the traps [41]. The more accurate determination of the trap densities $N^*_{Ta,b,c}$, also reported in Table 1 for the three crystal axes, delivers again anisotropic values along the three crystal axes, and in line (although, as expected, higher in absolute values) with the corresponding $N_{Ta,b,c}$.

4. Conclusions

In conclusion, we have grown from solution high quality, millimiter-sized organic single crystals of 4HCB that allowed us to carry out a complete 3D characterization of their electrical transport properties. By means of SCLC measurements we evidenced a clear 3D anisotropy for several main electronic transport parameters of the crystals, namely (i) the charge carrier mobility, (ii) the DOS distribution of the electrically active deep states, (iii) the concentration and (iv) the energy of dominant carrier traps. We reproducibly determined these parameters along the three different crystal axes over a large number of samples,

using a differential analysis of SCLC curves and photocurrent spectroscopy to investigate the energy states in the *a*–*b* plane, and we showed examples of anisotropic mobilities measured in all the three dimensions of the same single 4HCB monocrystal. Moreover, the comparison between the mobility values obtained by SCLC analyses and by air–gap OFET measurements demonstrate a remarkable agreement, confirming that air–gap OFET measurements consistently reduce the effects of interface states on the mobility. Finally, the permanence of anisotropic 3D mobility even after repeated *I*–*V* measurements demonstrates the fair robustness of the 4HCB solution-grown crystals under room temperature and atmosphere conditions.

These results indicate that solution-grown, macroscopic and easily obtainable 4HCB organic single crystals may be considered as model compounds for a deeper understanding of the anisotropic transport behaviour of organic semiconductors. As an outlook, the here demonstrated 3D electronic anisotropy of OSCs opens the way towards the realization of novel electronic devices, based on the exploitation and control of transport parameters that differ in the three spatial directions, for fully functional 3D device architectures.

Acknowledgements

The authors acknowledge financial support by the Italian Research Ministry, under the project PRIN 2006.

References

[1] S. Forrest, Nature 428 (2004) 911.
[2] A. Dodabalapour, Mater. Today 9 (2006) 24.
[3] C. Brabec, Sol. Energy Mater. Sol. Cells 83 (2004) 273.
[4] B. Geffro, P. le Roy, C. Prat, Polymer Int. 55 (2006) 572.
[5] A. Misra, P. Kumar, M. Kamalasanan, C. Chandra, Semicond. Sci. Technol. 21 (2006) R35.
[6] A. Briseno et al., Nature 444 (2006) 913.
[7] T. Kawanishi et al., Appl. Phys. Lett. 93 (2008) 23303.
[8] H. Alves, E. Molinari, H. Xie, A. Morpurgo, Nat. Mater. 7 (2008) 574.
[9] A. Facchetti et al., J. Am. Chem. Soc. 126 (2004) 13859.
[10] G. Gelinck et al., Nat. Mater. 3 (2004) 106.
[11] A. Loi, I. Manunza, A. Bonfiglio, Appl. Phys. Lett. 86 (2005) 103512.
[12] M. Zirkl et al., Adv. Mater. 19 (2007) 2241.
[13] V. Sundar et al., Science 303 (2004) 1644.
[14] R. Zeis et al., Chem. Mater. 18 (2006) 244.
[15] E. Menard, V. Podzorov, S. Gaur, M. Gershenson, J. Rogers, Adv. Mater. 16 (2004) 2097.
[16] R. de Boer, M. Gershenson, A. Morpurgo, V. Podzorov, Phys. Status Solidi A (2004) 1302.
[17] V. Podzorov et al., Phys. Rev. Lett. 93 (2004) 86602.
[18] J. Lee, S. Roth, Y. Park, Appl. Phys. Lett. 88 (2006) 25216.
[19] C. Reese, Z. Bhao, Mater. Today 10 (2007) 27.
[20] Q. Tang et al., Adv. Mater. 20 (2008) 2947.
[21] S. Mannsfeld et al., Adv. Funct. Mater. 17 (2007) 1617.
[22] B. Fraboni et al., Org. Electron. 9 (2008) 974.
[23] B. Fraboni et al., Adv. Mater. 21 (2009) 5.
[24] V. Podzorov, V. Pudalov, M. Gershenson, Appl. Phys. Lett. 83 (2003) 4345.
[25] R. de Boer, N. Iosad, A. Stassen, T. Klapwijk, A. Morpurgo, Appl. Phys. Lett. 86 (2005) 32103.
[26] J. Takeya et al., Phys. Rev. Lett. 98 (2007) 196804.
[27] K. Nakayama et al., Appl. Phys. Lett. 93 (2008) 153302.
[28] C. Cheung, K. Kwok, S. Tse, S. So, J. Appl. Phys. 103 (2008) 093705.
[29] M. Lampert, P. Mark, In Current Injection in Solids, Academic Press, New York, 1970.
[30] M. Pope, C. Swenberg, in: Electronic Processes in Organic Crystals and Polymers, Oxford Scient. Publ., Oxford, UK, 1999.
[31] (a) T. Cesca, A. Gasparotto, B. Fraboni, Appl. Phys. Lett. 93 (2008) 102114;
(b) T. Cesca, A. Gasparotto, E. Piana, B. Fraboni, J. Appl. Phys. 102 (2007) 93711.
[32] D. Braga, N. Battaglini, A. Yassar, G. Horowitz, M. Campione, A. Sassella, A. Borghesi, Phys. Rev. B 77 (2008) 115205.
[33] O. Jurchescu, T. Palstra, Appl. Phys. Lett. 88 (2006) 122101.
[34] D. Lang et al., Phys. Rev. Lett. 93 (2004) 86802.
[35] N. Mott, R. Gurney, Electronic Processes in Ionic Crystals, Clarendon Press, Oxford, 1940.
[36] J. Geurst, Phys. Status Solidi 15 (1966) 107.
[37] S. Nespurek, J. Sworakowski, Phys. Status Solidi A 41 (1977) 619.
[38] J. Sworakowski, S. Nespurek, Vacuum 38 (1989) 7.
[39] C. Krellner et al., Phys. Rev. B 75 (2007) 245115.
[40] D. Lang et al., Phys. Rev. Lett. 93 (2004) 76601.
[41] M. Campos, Mol. Cryst. Liq. Cryst. 18 (1972) 105.

Organic Electronics 11 (2010) 16–22

Contents lists available at ScienceDirect

Organic Electronics

journal homepage: www.elsevier.com/locate/orgel

High electron mobility layers of triazines for improving driving voltages, power conversion efficiencies, and operational stability of organic light-emitting diodes

Toshinori Matsushima [a], Mayumi Takamori [b], Yuichi Miyashita [b], Yoko Honma [b], Tsuyoshi Tanaka [b], Hidenori Aihara [c], Hideyuki Murata [a,*]

[a] School of Materials Science, Japan Advanced Institute of Science and Technology, 1-1 Asahidai, Nomi, Ishikawa 923-1292, Japan
[b] Tokyo Research Laboratory, TOSOH Corporation, 2743-1 Hayakawa, Ayase, Kanagawa 252-1123, Japan
[c] Frontier Materials Chemistry Group, Sagami Chemical Research Center, 2743-1 Hayakawa, Ayase, Kanagawa 252-1193, Japan

ARTICLE INFO

Article history:
Received 19 May 2009
Received in revised form 18 September 2009
Accepted 20 September 2009
Available online 25 September 2009

Keywords:
Organic light-emitting diodes
Electron-transport materials
Triazines
Stability
Operation voltage

ABSTRACT

We have shown that triazine compounds of 2-biphenyl-4-yl-4,6-bis-(4′-pyridin-2-yl-biphenyl-4-yl)-[1,3,5]triazine (DPT) and 2,4-bis-biphenyl-4-yl-6-(4′-pyridin-2-yl-biphenyl-4-yl)-[1,3,5]triazine (MPT) work as excellent electron-transport layers (ETLs) of organic light-emitting diodes (OLEDs). By replacing a typical ELT of tris(8-hydroxyquinoline) aluminum (Alq_3) with the DPT ETL and the MPT ETL, driving voltages and power conversion efficiencies of OLEDs operated at a current density of 50 mA cm^{-2} are improved from 7.7 ± 0.2 V and 1.41 ± 0.10 lm W^{-1} (Alq_3) to 6.0 ± 0.1 V and 1.62 ± 0.09 lm W^{-1} (DPT) and 5.2 ± 0.1 V and 1.88 ± 0.18 lm W^{-1} (MPT), respectively. Half lifetimes of the OLEDs operated at the same current are also enhanced from 3200 h (Alq_3) to 4200 h (MPT) by using the MPT ETL. The reduction in driving voltage is found to arise from more efficient electron injection at interfaces of DPT/cathode (a barrier height of ≈0.61 eV) and MPT/cathode (a barrier height of ≈0.51 eV) than at an interface of Alq_3/cathode (a barrier height of ≈0.73 eV) as well as better electron mobilities of DPT (8.7×10^{-5} cm^2 V^{-1} s^{-1} at an electric field of 5.0×10^5 V cm^{-1}) and MPT (1.4×10^{-4} cm^2 V^{-1} s^{-1} at the same field) than that of Alq_3 (4.1×10^{-6} cm^2 V^{-1} s^{-1} at the same field [Naka et al., Synth. Met. 111–112 (2000) 331.]). A high-mobility electron-transport material of 4,7-diphenyl-1,10-phenanthroline (BPhen) is also used as an ETL for comparison of OLED characteristics.

© 2009 Elsevier B.V. All rights reserved.

1. Introduction

Although organic light-emitting diodes (OLEDs) have been significantly developed over the last decade [1,2], driving voltages, power conversion efficiencies, and operational stability of OLEDs must be further improved for practical applications, such as flat panel displays. In general, organic materials used for OLEDs are basically insulators having carrier mobilities lower than 10^{-3} cm^2 V^{-1} s^{-1} [3–6]. Also, carrier injection barrier heights of several hundred meV are present at heterojunction interfaces of electrode/organic and organic/organic in OLEDs [7,8]. Therefore, high electric fields are required to overcome the low mobilities and the barrier heights, degrading the OLED performances. In particular, electron mobilities are known to be much lower than hole mobilities in most organic materials [3–6]. If a high-mobility electron-transport material (ETM) can be developed, it will be possible to further improve the OLED performances.

Various ETMs have been reported and used to date, such as oxadiazoles [9], triazoles [10], phenanthrolines [11], and triazines [12]. Klenkler et al. recently demonstrated that replacing tris(8-hydroxyquinoline) aluminum

* Corresponding author. Tel.: +81 761 51 1531; fax: +81 761 51 1149.
E-mail address: murata-h@jaist.ac.jp (H. Murata).

1566-1199/$ - see front matter © 2009 Elsevier B.V. All rights reserved.
doi:10.1016/j.orgel.2009.09.016

(Alq_3) with a triazine compound of 4,4′-bis-[2-(4,6-diphenyl-1,3,5-triazinyl)]-1,1′-biphenyl (BTB) as an electron-transport layer (ETL) can reduce driving voltages of OLEDs from 6.86 V to 4.51 V at a current density of 25 mA cm^{-2} [13]. Thus, we focus our attention on triazines among the ETMs due to their characteristics of wide energy gaps and high electron-transport [13,14]. From results of synthesizing and testing a wide variety of triazine derivatives, 2-biphenyl-4-yl-4,6-bis-(4′-pyridin-2-yl-biphenyl-4-yl)-[1,3,5]triazine (DPT) and 2,4-bis-biphenyl-4-yl-6-(4′-pyridin-2-yl-biphenyl-4-yl)-[1,3,5]triazine (MPT) are found to work as excellent ETLs of OLEDs. The chemical structures of DPT and MPT are shown in Fig. 1. Results of time-of-flight (TOF) measurements reveal that vacuum-deposited films of these triazines have very good electron mobilities of 8.7×10^{-5} cm^2 V^{-1} s^{-1} (DPT) and 1.4×10^{-4} cm^2 V^{-1} s^{-1} (MPT) at an electric field of 5.0×10^5 V cm^{-1}, which are one-to-two orders of magnitude higher than that of Alq_3 (4.1×10^{-6} cm^2 V^{-1} s^{-1} at the same field [4,6]), but are slightly lower than that of an ETL material, 4,7-diphenyl-1,10-phenanthroline (BPhen) (5.8×10^{-4} cm^2 V^{-1} s^{-1} at the same field [6]). Moreover, higher LUMO (lowest unoccupied molecular orbital) energy levels of DPT (-2.97 ± 0.02 eV) and MPT (-3.07 ± 0.02 eV) lead to efficient electron injection from a cathode when compared with Alq_3 (-2.85 ± 0.02 eV) and BPhen (-2.83 ± 0.02 eV). In other words, the electron mobilities and the electron injection barrier heights can be modified by changing the number of pyridine substitutes in a triazine framework.

In this study, we have shown that driving voltages of OLEDs operated at a current density of 50 mA cm^{-2} are reduced from 7.7 ± 0.2 V (Alq_3) to 7.0 ± 0.2 V (BPhen), 6.0 ± 0.1 V (DPT), and 5.2 ± 0.1 V (MPT) by replacing the typical Alq_3 ETL with the ETLs of BPhen, DPT, and MPT due to the enhanced electron injection and/or transport. Power conversion efficiencies at 50 mA cm^{-2} are also improved from 1.41 ± 0.10 lm W^{-1} (Alq_3) to 1.55 ± 0.07 lm W^{-1} (BPhen), 1.62 ± 0.09 lm W^{-1} (DPT), and 1.88 ± 0.18 lm W^{-1} (MPT) due to the voltage reduction mentioned above. Among OLEDs investigated in this study, an OLED with the MPT ETL has the longest half lifetime of 4200 h under operation at 50 mA cm^{-2}. For better understanding of the improved OLED performances, details of optical, electrical, and thermal characteristics of DPT and MPT are investigated.

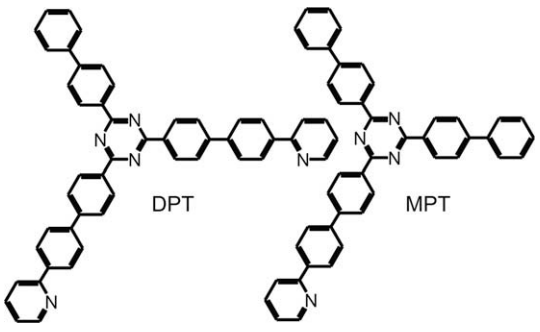

Fig. 1. Chemical structures of molecules of DPT and MPT.

2. Experimental

The devices (A)–(F), whose structures are shown in Fig. 2a, were fabricated using a vacuum deposition condition as previously reported in Ref. [15]. The ITO, the α-NPD, and the LiF stand for indium tin oxide as a hole-injecting anode layer, *N*,*N*′-diphenyl-*N*,*N*′-bis(1-naphthyl)-1,1′-biphenyl-4,4′-diamine as a hole-transport layer (HTL) [16], and lithium fluoride as an electron injection layer (EIL) [17], respectively. Since use of a very thin hole-injection layer (HIL) of molybdenum oxide (MoO_3) can improve both driving voltages, power conversion efficiencies, and operational stability of OLEDs [15,18,19], a 0.75 nm MoO_3 HIL was introduced between the ITO and the α-NPD for all devices. The completed devices were encapsulated together with an oxygen and moisture absorbing desiccant sheet using a glass cap and an ultraviolet curing epoxy resin inside a nitrogen-filled glove box. The driving voltages, the current densities, the external quantum efficiencies, the luminance, and the power conversion efficiencies of the devices were measured using conditions as previously reported in Ref. [15]. The changes in voltage and luminance with operational time were measured under dc driving of (A)–(F) at 50 mA cm^{-2} at room temperature to estimate the voltage increase rates and the half lifetimes, at which the luminance drops to one-half of the initial luminance.

To investigate the electron injection and transport characteristics of Alq_3, BPhen, DPT, and MPT, the electron-only devices (I)–(VIII), whose structures are shown in Fig. 2b, were fabricated using a similar condition as previously reported in Ref. [15]. To prevent hole-injection from the ITO anode, 2,9-dimethyl-4,7-diphenyl-1,10-phenanthroline (BCP) having a high ionization potential energy level of −6.25 eV was inserted as a hole-blocking layer (HBL) between the ITO and the ETL in (I)–(VIII). In fact, all electron-only devices exhibited no electroluminescence (EL) during their current density–voltage measurements.

3. Results and discussion

3.1. Optical, electrical, and thermal characteristics of DPT and MPT

The UV–vis absorption spectra and the fluorescence (FL) spectra of 50 nm films of DPT and MPT on quartz substrates are shown in Fig. 3. The films of DPT and MPT have the almost similar optical characteristics. The absorption peak wavelengths of DPT and MPT are 332 nm and 325 nm, respectively. The FL spectra of the films are nearly mirror images of the absorption spectra. The FL peak wavelengths of DPT and MPT are 431 nm and 424 nm, respectively [20]. Moreover, the ionization potential energy levels of DPT and MPT are measured to be -6.06 ± 0.02 eV and -6.25 ± 0.02 eV, respectively, using an AC-2 photoelectron yield spectrometer (Riken Keiki). The electron affinity energy levels of DPT and MPT are roughly estimated to be -2.97 ± 0.02 eV and -3.07 ± 0.02 eV, respectively, by subtracting the absorption onset energies [≈3.09 eV (400 nm) for the DPT film and

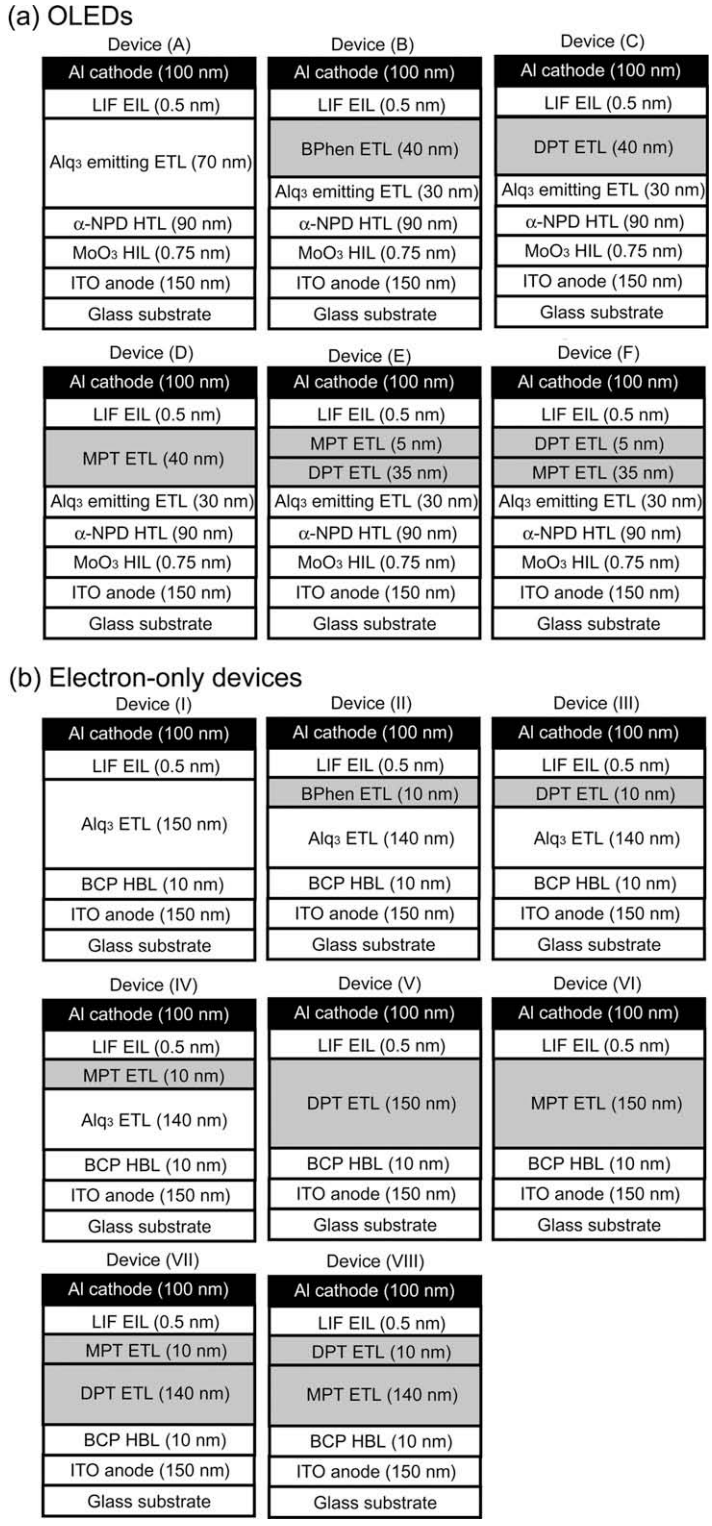

Fig. 2. Schematic structures of (a) OLEDs (A)–(F) and (b) electron-only devices (I)–(VIII).

≈3.18 eV (389 nm) for the MPT film] from the ionization potential energy levels.

The energy-level diagrams of the OLEDs and the electron-only devices estimated using the above-mentioned technique are depicted in Fig. 4a and b, respectively. The smaller-energy-gap layer of Alq_3 (≈2.86 eV) is sandwiched between the wider-energy-gap layers of α-NPD (≈3.05 eV), BPhen (≈3.38 eV), DPT (≈3.09 eV), and MPT (≈3.18 eV),

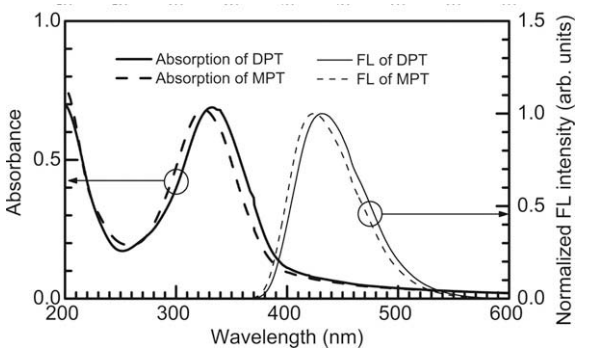

Fig. 3. UV–vis absorption spectra and FL spectra of vacuum-deposited films of DPT and MPT on quartz substrates. FL spectra were measured using excitation light wavelengths at absorption maxima.

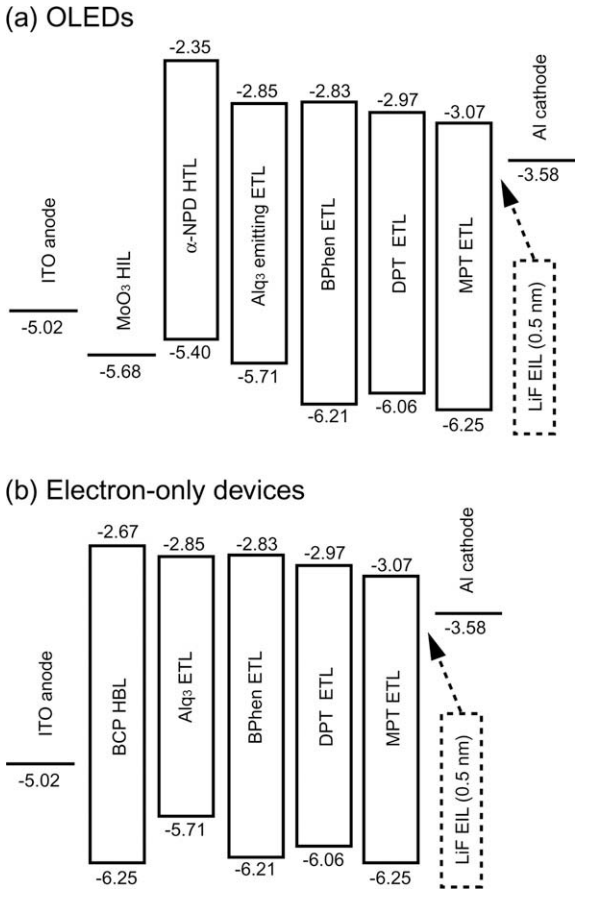

Fig. 4. Energy-level diagrams of (a) OLEDs (A)–(F) and (b) electron-only devices (I)–(VIII).

indicating that Alq_3 excitons are well confined in the Alq_3 layer. Moreover, the electron injection barrier heights at the interfaces of Alq_3/Al, BPhen/Al, DPT/Al, and MPT/Al are calculated to be ≈0.73 eV, ≈0.75 eV, ≈0.61 eV, and ≈0.51 eV, respectively, from the differences between the electron affinity energy levels of the ETLs and the work function energy level of the Al cathode (Fig. 4a). Comparing these barrier heights, more efficient electron-injection is expected to occur at the interfaces of DPT/Al and MPT/Al than at the interfaces of BPhen/Al and Alq_3/Al. It is noted that these barrier heights may be overestimated since a LiF EIL has been used between an ETL and an Al cathode layer to enhance electron injection from Al [17]. However, we suppose that the qualitative comparison of the electron-injection characteristics is possible using the above-mentioned barrier heights.

In addition to the smaller electron injection barrier heights, the films of DPT and MPT have very good electron transport abilities. The electron mobilities of the films are analyzed using structures of glass substrate/ITO (110 nm)/DPT (870 nm) or MPT (1550 nm)/Al (100 nm) with a TOF measurement condition as previously reported in Ref. [5]. The electron transients of DPT and MPT have less clear plateaus (Fig. 5a). The electron transit time (t_{TR}) of DPT and MPT is estimated from a change in slope in the double logarithmic plots as shown in Fig. 5b. The electron mobilities (μ) of the films under a wide range of electric fields are determined from the relationship [4–6] $\mu = L^2/(t_{TR}V)$ (1), where L is the cathode–anode spacing and V is the voltage. The μ of these films is found to be field dependent (Fig. 5c). Here, the field-dependent mobility [4–6] can be expressed as $\mu = \mu_0 \exp(\beta E^{0.5})$ (2), where μ_0 is the zero field mobility, β is the field dependence parameter, and E is the electric field. Fitting the μ-$E^{0.5}$ plots with Eq. (2) yields $\mu_0 = 3.6 \times 10^{-6}$ cm^2 V^{-1} s^{-1} and $\beta = 4.5 \times 10^{-3}$ cm$^{0.5}$ V$^{-0.5}$ (DPT) and $\mu_0 = 5.8 \times 10^{-6}$ cm^2 V^{-1} s^{-1}

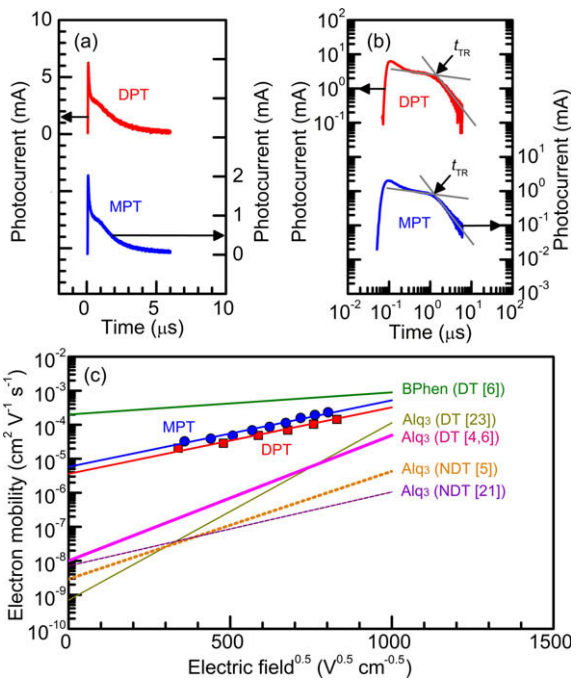

Fig. 5. (a) Double linear plots and (b) double logarithmic plots of TOF electron transients from DPT and MPT at electric field of 5.8×10^5 V cm^{-1} and (c) electric field dependence of TOF electron mobilities of DPT and MPT, which is compared with that of previously reported TOF electron mobilities estimated from dispersive transport (DT) and non-dispersive transport (NDT) of Alq_3 [4–6,21,23] and DT of BPhen [6].

and $\beta = 4.5 \times 10^{-3}$ cm$^{0.5}$ V$^{-0.5}$ (MPT) (Fig. 5c). It has been shown that electron transients of Alq_3 films are changed from a non-dispersive shape to a dispersive shape by exposing the films to oxygen and water atmosphere [5,21,22]. The μ obtained from non-dispersive transport (NDT) and dispersive transport (DT) of Alq_3 [4–6,21,23] and BPhen [6] is plotted together with that of DPT and MPT in Fig. 5c. The reported μ of Alq_3 is slightly dependent upon research groups. As can be seen in Fig. 5c, the measured μ of DPT and MPT is found to be the intermediate values between those of Alq_3 (for example, $\mu_0 = 1.0 \times 10^{-8}$ cm^2 V^{-1} s^{-1} and $\beta = 8.5 \times 10^{-3}$ cm$^{0.5}$ V$^{-0.5}$ [4,6]) and BPhen ($\mu_0 = 2.0 \times 10^{-4}$ cm^2 V^{-1} s^{-1} and $\beta = 1.5 \times 10^{-3}$ cm$^{0.5}$ V$^{-0.5}$ [6]) and is, however, comparable to those of triazine compounds previously reported [13,24,25].

The thermal characteristics of DPT and MPT are investigated using differential scanning calorimetry (DSC 200, SEIKO). The measured glass transition temperatures of DPT and MPT are 136 °C and 108 °C, respectively, and the measured melting temperatures of DPT and MPT are 340 °C and 279 °C, respectively. The observed high glass transition temperatures are expected to provide high thermal stability for the OLEDs operated at elevated temperature.

3.2. Injection and transport of electrons in OLEDs and electron-only devices

We investigate that how the use of the ETLs of Alq_3, BPhen, DPT, and MPT affects the driving voltages of the OLEDs. The current density–voltage characteristics of (A)–(D) are shown in Fig. 6a. The driving voltages of (A)–(D) operated at a current density of 50 mA cm^{-2} are summarized in Table 1. Replacing the Alq_3 ETL with the BPhen ETL reduces the driving voltages from 7.7 ± 0.2 V (A) to 7.0 ± 0.2 V (B) at 50 mA cm^{-2}. Since the electron injection barrier heights at the interfaces of Alq_3/Al (≈0.73 eV) and BPhen/Al (≈0.75 eV) are almost similar, the voltage reduction is attributable to the highest electron mobility observed in the BPhen ETL (Fig. 5c). On the other hand, the driving voltages at 50 mA cm^{-2} are reduced from 7.7 ± 0.2 V (A) to 6.0 ± 0.1 V (C) and 5.2 ± 0.1 V (D) by replacing the Alq_3 ETL with the DPT ETL and the MPT ETL due to the decrease in electron injection barrier height from ≈0.73 eV (Alq_3/Al) to ≈0.61 eV (DPT/Al) and ≈0.51 eV (MPT/Al) as well as the increase in electron mobility by one-to-two orders of magnitude (see Fig. 5c). Although the electron mobility of the BPhen ETL is higher than those of the DPT ETL and the MPT ETL, the driving voltage of (B) with the BPhen ETL (7.0 ± 0.2 V) becomes higher than those of (C) with the DPT ETL (6.0 ± 0.1 V) and (D) with the MPT ETL (5.2 ± 0.1 V), indicating that the decrease in electron injection barrier height is more advantageous than the increase in electron mobility to reducing the voltages. To double-check the change in the driving voltages of (A)–(D), the electron-only devices (I)–(IV), the structures of which are shown in Fig. 2b, were fabricated and tested. The current density–voltage characteristics of the electron-only devices (I)–(IV) (Fig. 6b) are found to be changed in the manner similar to those of the OLEDs (A)–(D) (Fig. 6a).

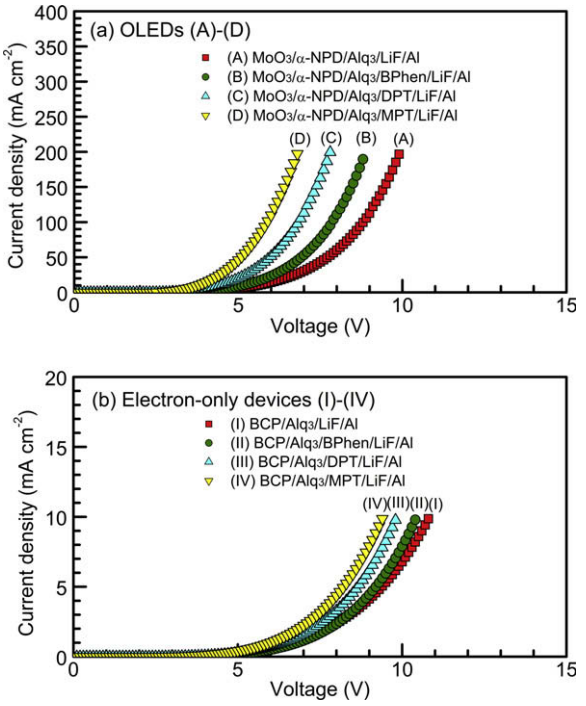

Fig. 6. (a) Current density–voltage characteristics of (a) OLEDs (A)–(D) and (b) electron-only devices (I)–(IV).

As discussed in the previous Section 3.1., the difference in the electron injection barrier height between the interfaces of DPT/cathode and MPT/cathode is only ≈0.1 eV. Also, the ratio of the mobility of the MPT ETL to the mobility of the DPT ETL is as small as ≈1.6. Therefore, we investigate that either electron injection or electron transport plays an important role in improving the driving voltage of (D) relative to (C). To do this, the current density–voltage characteristics of the OLEDs (C)–(F) and the electron-only devices (V)–(VIII) are compared (Fig. 7a and b). The structures of (C)–(F) and (V)–(VIII) are also shown in Fig. 2a and b, respectively. Using a 5 nm MPT ETL between the DPT ETL and the LiF EIL leads to a reduction in the driving voltage from 6.0 ± 0.1 V (C) to 5.4 ± 0.1 V (E). On the other hand, the driving voltages increase from 5.2 ± 0.1 V (D) to 5.8 ± 0.1 V (F) by inserting a 5 nm DPT ETL between the MPT ETL and the LiF EIL. The similar change in voltage is observed in the electron-only devices (V)–(VIII). In general, while transport-limited currents (such as space-charge-limited currents) are changed proportional to carrier mobilities [26], injection-limited currents (such as tunneling injection currents and thermionic emission currents) exponentially increase with decreasing barrier heights [7,27,28]. From these, we infer that the decrease in electron injection barrier height by ≈0.1 eV predominantly reduces the driving voltages of the OLEDs than the increase in electron mobility by ≈1.6 times, which is in good agreement with the results discussed previously using the BPhen ETL.

In all devices, we observed green EL from electrically excited Alq_3 molecules. The shapes and the peak tops

Table 1
Driving voltages, luminance, external quantum efficiencies, power conversion efficiencies, half lifetimes, and voltage increase rates of (A)–(F) operated at 50 mA cm^{-2}.

Device	Driving voltage (V)	Luminance (cd m^{-2})	External quantum efficiency (%)	Power conversion efficiency lm W^{-1}	Half lifetime (h)	Voltage increase rate (V h^{-1})
(A) Alq_3	7.7 ± 0.2	1622 ± 129	0.98 ± 0.02	1.41 ± 0.10	3200	4.1×10^{-4}
(B) BPhen	7.0 ± 0.2	1599 ± 94	0.99 ± 0.03	1.55 ± 0.07	400	8.0×10^{-3}
(C) DPT	6.0 ± 0.1	1540 ± 98	0.99 ± 0.01	1.62 ± 0.09	2800	1.4×10^{-4}
(D) MPT	5.2 ± 0.1	1557 ± 133	0.97 ± 0.02	1.88 ± 0.18	4200	1.0×10^{-4}
(E) DPT/MPT	5.4 ± 0.1	1547 ± 102	0.97 ± 0.01	1.83 ± 0.11	3700	1.2×10^{-4}
(F) MPT/DPT	5.8 ± 0.1	1512 ± 130	0.99 ± 0.01	1.68 ± 0.15	2900	1.7×10^{-4}

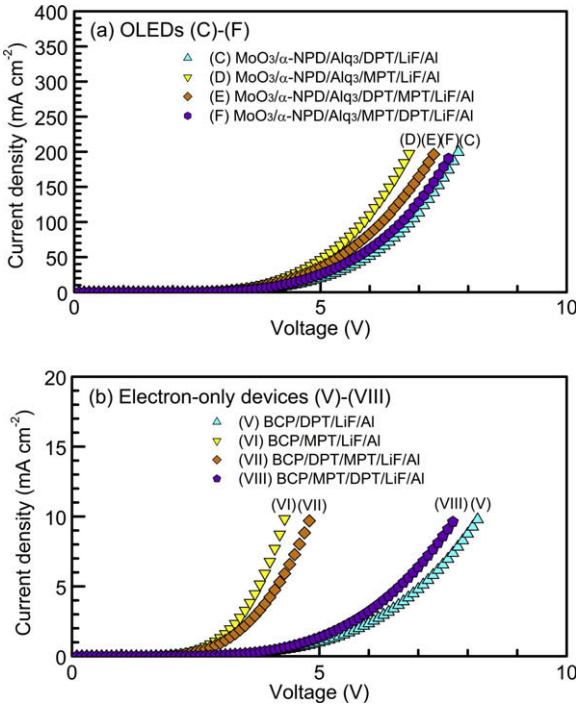

Fig. 7. (a) Current density–voltage characteristics of (a) OLEDs (C)–(F) and (b) electron-only devices (V)–(VIII).

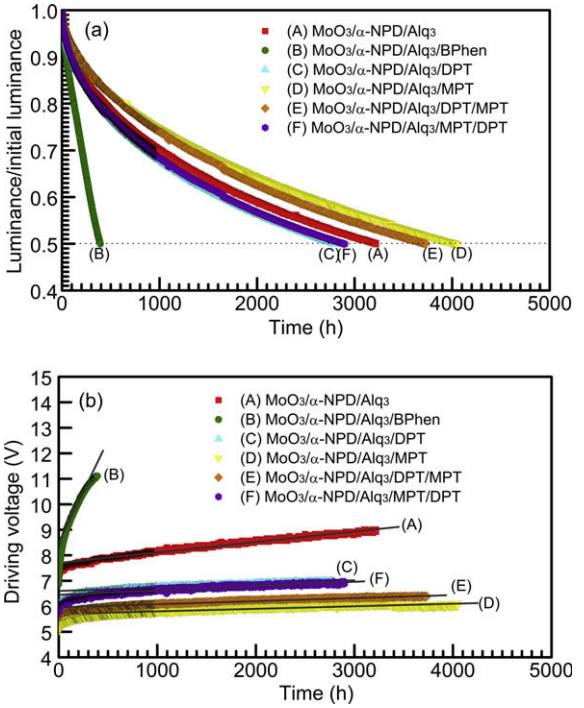

Fig. 8. (a) Luminance/initial luminance-time characteristics and (b) driving voltage–time characteristics of OLEDs (A)–(F) operated at 50 mA cm^{-2}.

(528–530 nm) of the EL spectra are consistent with those previously reported [16,29,30] and they are independent of current densities. A carrier recombination efficiency of electrons and holes in a carrier recombination zone is known to affect current density–voltage characteristics [26]. However, the external quantum efficiencies of (A)–(F) at 50 mA cm^{-2} are almost similar (≈1%) (Table 1), indicating that a change in carrier recombination efficiency causes a negligible effect on the driving voltages of the OLEDs. On the other hand, the power conversion efficiencies at 50 mA cm^{-2} are improved from 1.41 ± 0.10 lm W^{-1} (A) to 1.88 ± 0.18 lm W^{-1} (D) due to the voltage reduction discussed above (Table 1).

3.3. Operational stability of OLEDs

The luminance/initial luminance-time (L/L_0–t) characteristics and the driving voltage–time (V–t) characteristics of (A)–(F) are shown in Figs. 8a and b, respectively. The half lifetimes of the OLEDs are determined to be 3200 h (A), 400 h (B), 2800 h (C), 4200 h (D), 3700 h (E), and 2900 h (F) (Table 1) from Fig. 8a [31]. Moreover, the straight-line approximation of the V–t curves (the solid lines in Fig. 8b) gives the voltage increase rates: 4.1×10^{-4} V h^{-1} (A), 8.0×10^{-3} V h^{-1} (B), 1.4×10^{-4} V h^{-1} (C), 1.0×10^{-4} V h^{-1} (D), 1.2×10^{-4} V h^{-1} (E), and 1.7×10^{-4} V h^{-1} (F) (Table 1). The longest half lifetime of 4200 h and the lowest voltage increase rate of 1.0×10^{-4} V h^{-1} obtained in (D) are excellent values when compared with previously reported OLEDs based on α-NPD and Alq_3 [15,16].

Replacing the Alq_3 ETL with the MPT ETL increases the half lifetimes from 3200 h (A) to 4200 h (D). Although the half lifetime of (C) with the DPT ETL (2800 h) is shorter than that of (A) with the Alq_3 ETL (3200 h), inserting the 5 nm MPT ETL between the DPT ETL and the LiF EIL (the DPT/MPT/LiF unit) enhances the lifetimes from 2800 h (C)

to 3700 h (E). On the other hand, the lifetimes are degraded from 4200 h (D) to 2900 h (F) by using the MPT/DPT/LiF unit. In the case of the BPhen ETL, the device (B) has the shortest lifetime of 400 h among the devices. From these results, inserting the MPT layer between the ETL and the LiF EIL is found to be more important for the operational stability of the OLEDs than using the layers of Alq_3, BPhen, and DPT. Since various degradation models of Alq_3-based OLEDs have been proposed [32], the proposed degradation models cannot fully explain the lifetime results obtained in this work. Detailed degradation mechanisms of the OLEDs are now under investigation.

4. Conclusions

We have shown that triazine films of DPT and MPT have very good electron mobilities of 8.7×10^{-5} cm^2 V^{-1} s^{-1} (DPT) and 1.4×10^{-4} cm^2 V^{-1} s^{-1} (MPT) at an electric field of 5.0×10^5 V cm^{-1}, which are much higher than that of Alq_3 (4.1×10^{-6} cm^2 V^{-1} s^{-1} at the same field [4,6]), but are slightly lower than that of BPhen (5.8×10^{-4} cm^2 V^{-1} s^{-1} at the same field [6]). Moreover, the triazine films have higher LUMO energy levels of -2.97 ± 0.02 eV (DPT) and -3.07 ± 0.02 eV (MPT) than the films of Alq_3 (-2.85 ± 0.02 eV) and BPhen (-2.83 ± 0.02) have, resulting in that electron injection at interfaces of DPT/cathode and MPT/cathode is more facile than that at interfaces of Alq_3/cathode and BPhen/cathode. By comparing performances of OLEDs having the ETLs of Alq_3, BPhen, DPT, and MPT, a decrease in electron injection barrier height at the ETL/cathode interfaces is found to predominantly reduce driving voltages of the OLEDs than an increase in electron mobility of the ETLs. Thus, the OLED having the MPT ETL has the lowest driving voltage of 5.2 ± 0.1 V, the highest power conversion efficiency of 1.88 ± 0.18 lm W^{-1}, and the longest half lifetime of 4200 h at a current density of 50 mA cm^{-2} among the OLEDs investigated in this study. These results indicate that MPT with the high electron mobility and the high LUMO energy level is a promising candidate for use as an ETL for fabricating high-performance OLEDs.

References

[1] S.R. Forrest, Nature (London) 428 (2004) 911.
[2] N. Koch, Chem. Phys. Chem. 8 (2007) 1438.
[3] M. Kitamura, T. Imada, S. Kato, Y. Arakawa, Jpn. J. Appl. Phys. 43 (2004) 2326.
[4] S. Naka, H. Okada, H. Onnagawa, Y. Yamaguchi, T. Tsutsui, Synth. Met. 111–112 (2000) 331.
[5] G.G. Malliaras, Y. Shen, D.H. Dunlap, H. Murata, Z.H. Kafafi, Appl. Phys. Lett. 79 (2001) 2582.
[6] S. Naka, H. Okada, H. Onnagawa, T. Tsutsui, Appl. Phys. Lett. 76 (2000) 197.
[7] I.D. Parker, J. Appl. Phys. 75 (1994) 1656.
[8] T. Matsushima, K. Goushi, C. Adachi, Chem. Phys. Lett. 435 (2007) 327.
[9] C. Adachi, T. Tsutsui, S. Saito, Appl. Phys. Lett. 55 (1989) 1489.
[10] J. Kido, C. Ohtaki, K. Hongawa, K. Okuyama, K. Nagai, Jpn. J. Appl. Phys. 32 (1993) L917.
[11] H. Nakada, S. Kawami, K. Nagayama, Y. Yonemoto, R. Murayama, J. Funaki, T. Wakimoto, K. Imai, Polym. Prepr. Jpn. 35 (1994) 2450.
[12] R. Fink, C. Frenz, M. Thelakkat, H.-W. Schmidt, Macromolecules 30 (1997) 8177.
[13] R.A. Klenkler, H. Aziz, A. Tran, Z.D. Popovic, G. Xua, Org. Electron. 9 (2008) 285.
[14] H. Inomata, K. Goushi, T. Masuko, T. Konno, T. Imai, H. Sasabe, J.J. Brown, C. Adachi, Chem. Mater. 16 (2004) 1285.
[15] T. Matsushima, G.-H. Jin, H. Murata, J. Appl. Phys. 104 (2008) 051501.
[16] S.A. Van Slyke, C.H. Chen, C.W. Tang, Appl. Phys. Lett. 69 (1996) 2160.
[17] L.S. Hung, C.W. Tang, M.G. Mason, Appl. Phys. Lett. 70 (1997) 152.
[18] T. Matsushima, Y. Kinoshita, H. Murata, Appl. Phys. Lett. 91 (2007) 253504.
[19] T. Matsushima, H. Murata, J. Appl. Phys. 104 (2008) 034507.
[20] FL quantum efficiencies of films of DPT and MPT are measured to be 55 ± 1% and 54 ± 1% using an integrating sphere system (C9920, Hamamatsu Photonics).
[21] S.C. Tse, H.H. Fong, S.K. So, J. Appl. Phys. 94 (2003) 2033.
[22] H.H. Fong, S.K. So, J. Appl. Phys. 98 (2005) 023711.
[23] R.G. Kepler, P.M. Beeson, S.J. Jacobs, R.A. Anderson, M.B. Sinclair, V.S. Valencia, P.A. Cahill, Appl. Phys. Lett. 66 (1995) 3618.
[24] Y.-D. Zhang, K.G. Jesperson, M. Kempe, J.A. Kornfield, S. Barlow, B. Kippelen, S.R. Marder, Langmuir 19 (2003) 6534.
[25] T. Yamamoto, S. Watanabe, H. Fukumoto, M. Sato, T. Tanaka, Macromol. Rapid Commun. 27 (2006) 317.
[26] M.A. Lampert, P. Mark, Current Injection in Solids, Academic Press, New York, 1970.
[27] R.H. Fowler, L. Nordheim, Proc. R. Soc. London Ser. A 119 (1928) 173.
[28] T. Matsushima, C. Adachi, Thin Solid Films 516 (2008) 5069.
[29] T. Dobbertin, M. Kroeger, D. Heithecker, D. Schneider, D. Metzdorf, H. Neuner, E. Becker, H.-H. Johannes, W. Kowalsky, Appl. Phys. Lett. 82 (2003) 284.
[30] P.-C. Kao, S.-Y. Chu, Z.-X. You, S.J. Liou, C.-A. Chuang, Thin Solid Films 498 (2006) 249.
[31] Luminance decay curves shown in Fig. 8a are well fitted using stretched exponential decay equation, which is given by $L/L_0 = \exp[-(t/\tau)^{\alpha}]$, where τ and α is fitting parameters [C. Féry, B. Racine, D. Vaufrey, H. Doyeux, S. Cinà, Appl. Phys. Lett. 87 (2005) 213502].
[32] H. Aziz, Z.D. Popovic, Chem. Mater. 16 (2004) 4522.

Organic Electronics 11 (2010) 23–28

Contents lists available at ScienceDirect

Organic Electronics

journal homepage: www.elsevier.com/locate/orgel

Efficient solution-processed hybrid polymer–nanocrystal near infrared light-emitting devices

Kaushik Roy Choudhury, Dong Woo Song, Franky So *

Department of Materials Science and Engineering, University of Florida, Gainesville, Florida 32611, USA

ARTICLE INFO

Article history:
Received 24 July 2009
Received in revised form 31 August 2009
Accepted 20 September 2009
Available online 26 September 2009

Keywords:
Hybrid organic/inorganic
Nanocrystal
Polymer
Light-emitting device
Infrared

ABSTRACT

We report solution-processed hybrid LEDs, emitting infrared light with enhanced efficiency, based on PbSe nanocrystal (NC) lumophores embedded a conjugated polymer forming the nanocomposite active layer. The effect of device geometry and the NC-polymer blend composition on device performance is studied in detail. Increasing the PbSe NC concentration leads to a substantial decrease in device current, and an increase in efficiency and turn-on voltage. Analysis of the device data indicates that the PbSe NCs act as carrier traps and radiative recombination centers. With optimized concentration of NC emitters and active layer thickness, the devices exhibit an external electroluminescence quantum efficiency of 0.83% at a peak emission wavelength of 1280 nm.

© 2009 Elsevier B.V. All rights reserved.

1. Introduction

Colloidal semiconductor nanocrystals (NCs), by virtue of the large tunability in their bandgap, high luminance efficiency, narrow spectral emission and high photo-stability, are an attractive choice as lumophores as well as sensitizers in next-generation optoelectronic devices such as light-emitting diodes (LEDs) [1–3], photodetectors [4,5] and solar cells [6–8]. Their compatibility with facile low-temperature solution-processing opens up the possibility of fabricating organic/inorganic hybrid devices at low-cost with device performance similar to their inorganic counter-parts. For electroluminescent device applications, combining the advantages of the rapidly developing organic LED (OLED) technology with the attractive properties of semiconductor NCs has led to advances in these hybrid LEDs: the external quantum efficiency (EQE) has improved by over two orders of magnitude, and highly saturated color emission across the visible spectrum has been achieved. Several hybrid light emitters employing visible-range NCs and organic semiconductors have been demonstrated with maximum EQEs up to 2% [9,10]. On the other hand, little work has been done to explore such devices emitting at infrared (IR) wavelengths, although large area near-IR emitters and absorbers can lend themselves to a number of applications including chemical spectroscopy, night vision and biomedical sensing. Additionally, electroluminescent sources with activity in the 1.3–1.55 μm window can specifically find applications in optical communications. Owing to the paucity of molecular and polymeric organic semiconductors with efficient tunable emission beyond 1 μm wavelength, the use of semiconductor NCs emitting in the near-IR offers a particularly attractive alternative. However, only a few infrared electroluminescent hybrid devices been reported to date and they have shown low external quantum efficiencies [2,11,12].

Early work on hybrid LEDs primarily focused on wide-gap semiconductor NCs emitting at visible wavelengths. The first published work on hybrid LEDs incorporating colloidally grown semiconductor NCs by Colvin and co-workers [1] demonstrated low device efficiency, limited by inefficient charge injection and poor charge transport. A fundamentally different device architecture of hybrid LEDs by Coe et al. [3], seeking to isolate the functionalities of charge transport and exciton recombination, utilized a

* Corresponding author.
E-mail address: fso@mse.ufl.edu (F. So).

1566-1199/$ - see front matter © 2009 Elsevier B.V. All rights reserved.
doi:10.1016/j.orgel.2009.09.017

monolayer of NCs as the emitter in a multilayer structure similar to heterostructure OLEDs. This approach resulted in significant improvement in device efficiency. Subsequent enhancement in luminous power efficiency was achieved by Jen and co-workers by optimizing charge injection through the use of thermally polymerized hole transport layer (HTL) [13] and by thermal annealing of the emission layer [10]. In IR emitting hybrid devices, the highest external electroluminescence quantum efficiency (ELQE) achieved was ca. 0.5% using core–shell InAs/ZnSe NCs as lumophores [2]. However, in solution processable LEDs with PbSe or PbS NCs as the IR emitters, external EQEs have been limited to only ~0.001% and 0.27%, respectively [11,12]. Given the high photoluminescence quantum yield of these IV–VI semiconductor NCs [14] in solution, a proper choice of active layer composition and design of device architectures should lead to higher IR emission efficiency.

In this study, we demonstrate solution-processed hybrid infrared LEDs with enhanced efficiency using PbSe NCs as lumophores dispersed in a conjugated polymer to form a nanocomposite electro-active layer. Among the IV–VI semiconductors, PbSe NCs constitute an interesting system because of the ease of realizing quantum modulated optical properties in the infrared range. Due to the large Bohr exciton radius in PbSe, about 46 nm, quantum confinement effects begin to appear at relatively large particle dimensions and wavelength tunability can easily be achieved. Additionally, highly reproducible colloidal synthesis yields PbSe NCs with narrow size distribution and well-defined band-edge excitonic transitions tunable between 0.9 and 2.0 eV. To fabricate infrared emitting hybrid LEDs, PbSe NCs were homogeneously dispersed in a conjugated polymer matrix to form the nano-composite used for the electro-active layer. The effect of device geometry and polymer blend composition on device performance was studied in detail. We found that both the operating voltage and the NIR emission quantum efficiency increase with increasing concentration of NCs in the polymer matrix. The increase in operating voltage and EQE suggests that the NCs act as traps for both electrons and holes resulting in an increase in radiative recombination at the NC sites. The concentration of NC emitters and the thickness of the active layer were optimized, yielding devices with an external ELQE of 0.83% which is significantly higher than the efficiencies reported previously [11,12].

2. Experimental

2.1. Nanocrystal synthesis and processing

We tailored the synthesis of NCs by making appropriate variations to existing literature methods [15] to obtain highly monodispersed, discretely luminescent and easily solution processable NCs over a wide range of synthetically accessible sizes. In a typical reaction, PbO (4 mmol) and oleic acid (11 mmol) were added to 1-octadecene (35 ml). The reaction mixture was stirred under heat and argon flow for 45 min. When the temperature reaches 155 °C, 12 mmol of 1 M TOP-Se (selenium dissolved in trioctylphosphine) and 0.11 ml of DPP (diphenyl phosphine) were rapidly injected. The resulting NCs are withdrawn in two aliquots (typically after 30 s and 60 s) and quenched with cold toluene (~15 ml). Subsequently the NCs are precipitated and extracted by adding acetone and ethanol followed by centrifugation.

Following previously established procedures, those that lead to narrow NC size distribution and remove excess unreacted organics and reaction byproducts, a rigorous three-step post synthesis washing of NCs was adopted without compromising the colloidal stability. After an initial precipitation with acetone and ethanol, the precipitate is dissolved in toluene and kept in a freezer for 10 min to initiate the precipitation of salts. The sample is then centrifuged and the NC containing supernatant is removed. Ethanol is added to the supernatant and a second precipitation is carried out. The resulting precipitate is again dissolved in toluene and a final precipitation with a mixture of acetone and ethanol is carried out. Finally, the NCs are dried under argon, and dissolved in chlorobenzene for device fabrication or tetrachloroethylene for optical characterization.

2.2. Device fabrication

To fabricate the light-emitting devices studied herein, a 40 nm layer of poly(3,4-ethylenedioxythiophene) doped with poly(styrenesulfonic acid) (PEDOT:PSS) was spin coated on pre-cleaned indium tin oxide (ITO) coated substrates and baked in air at 180 °C for 20 min. PEDOT:PSS serves as a hole injection layer and also planarizes the ITO surface to prevent any unwarranted shorts. Monodispersed NCs and poly[2-methoxy-5-(2′-ethyl-hexyloxy)-1,4-phenylene vinylene] (MEH-PPV) were blended in chlorobenzene in various proportions to yield different active-layer compositions. This solution was then spin casted as the active-layer on the PEDOT:PSS coated substrates and baked under N_2 at 60 °C for 15 min. Subsequently, an 8 nm layer of the electron transporting and hole-blocking material bathocuproine (BCP) was deposited by thermal evaporation in a chamber pressure below 2×10^{-6} Torr. Finally, a composite metal cathode of LiF/Al was evaporated through a shadow mask.

2.3. Nanocrystal and device characterization

The absorption spectra of colloidal NCs in tetrachloroethylene were collected using a Varian Cary 500 UV–vis-near-IR spectrophotometer. A SPEX 270M spectrometer was used for acquisition of the emission spectra. Transmission electron microscopy (TEM) images were obtained using a JEOL model JEM-200CX microscope at an acceleration voltage of 200 kV.

The current–voltage-emission measurements were performed on the devices in the ambient on a test fixture using a Keithley 2400 source meter interfaced in conjunction with a Thorlabs InGaAs photodiode (model # FGA21-CAL) with NIST traceable calibration. A longpass filter with short-wavelength cutoff at 830 nm was used to eliminate any visible emission from the polymer matrix. Electroluminescence quantum efficiency in the infrared was determined by measuring emission intensity in the forward

direction and converting it to total external emission. EL spectra were recorded using an Ocean Optics near-IR spectrometer (model NIR256-2.1) with an InGaAs detector array.

3. Results and discussion

3.1. Nanocrystal characterization

Fig. 1a shows typical near-IR absorption and photoluminescence (PL) spectra for ~4 nm diameter PbSe NCs and Fig. 1b shows the size-tunable IR absorption for the NCs with diameters ranging from 3 nm to 7 nm. The TEM micrograph image shown in the inset of Fig. 1a showing the uniformity of the d-spacing of the planes of the highly regular 2-dimensional hcp lattice confirms the characteristic narrow size distribution [evident also from the full width at half maximum (FWHM) of the PL spectrum ~130 nm] of the PbSe NCs obtained without any post-synthetic size selective processing. Based on the tunable absorption spectra (shown in Fig. 1b) spanning a wide range of infrared wavelengths (1000–1900 nm), we expect this device platform to yield solution-processed IR emitters.

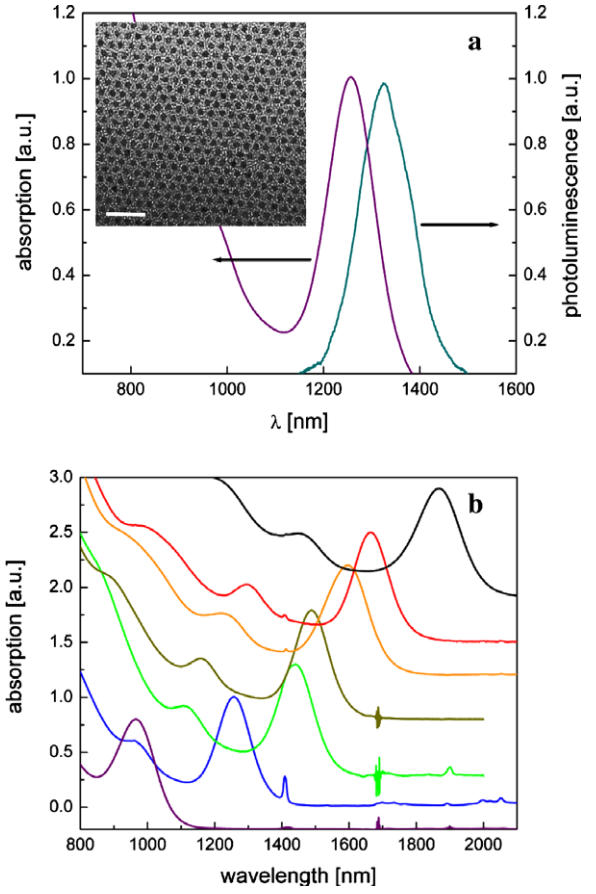

Fig. 1. (a) Typical absorption (peak at 1260 nm) and photoluminescence (peak at 1320 nm) spectra of 4 nm sized PbSe NCs. The inset shows a transmission electron micrograph image of the same particles; scale bar 20 nm. (b) Size-tunable absorption spectra of PbSe NCs (diameter ~2.5–6.5 nm) in the infrared.

3.2. Hybrid polymer/nanocrystal LEDs

Hybrid LEDs with semiconductor NCs dispersed in a conjugated polymer have previously been reported. However, the reported efficiencies were usually quite low due to the unfavorable alignment of the conduction/valence band edges of the wide-gap NCs with the highest occupied molecular orbital (HOMO) and lowest unoccupied molecular orbital (LUMO) energies of the conjugated polymer and inefficient energy/charge transfer from the polymers to the NCs. For narrow gap semiconductors such as PbSe, both the conduction and valence band edges of the NCs are in close proximity of the LUMO–HOMO gap of many conjugated polymers, and it is expected that energy/charge transfer from the host polymer to the PbSe NCs should be more efficient. In this work, MEH-PPV was used as the polymer matrix. Fig. 2 shows the device architecture employed and the energy levels of the PbSe NC based LEDs. The HOMO–LUMO energies of the polymer [16] and BCP [17] are obtained from the literature. The valence and conduction band levels of the NCs employed here (~4 nm diameter) are estimated using optical absorption data and reported bulk energy levels [18] and considering quantum size effects [19]. MEH-PPV has been widely used for polymer LEDs and its HOMO energy matches the valence band edge of these NCs. At the same time, the conduction band edge of the NCs is well within the bandgap of MEH-PPV and efficient electron transfer from the polymer to the PbSe NCs is expected. It should be noted that organometallically synthesized PbSe NCs are capped with a layer of oleate ligands to prevent aggregation and to passivate their surfaces. Due to the insulating nature of the organic ligands, the presence of a large amount of capping groups can result in inefficient charge transfer [20]. Thus, to achieve efficient EL from these lumophores, high purity NCs free of excess organics are important. To realize this end, the NCs were subject to a rigorous three-step post-synthesis washing (see experimental section) to eliminate excess organics and reaction byproducts without compromising the colloidal stability.

The electro-optical characteristics of an LED with a polymer/NC blend containing 1% NCs by weight are shown in Fig. 3a. The device turns on at around 3 V which is significantly lower than the previous devices with PbSe NCs in a multilayered device architecture [11]. The peak external quantum efficiency (EQE) of this hybrid LED device is ~0.1%. Fig. 3b displays the EL spectra of different devices incorporating NCs of varying sizes. The EL spectrum for each device resembles the PL spectrum of the corresponding NC solution and demonstrates the tunability of the hybrid LEDs emitting at 1290 nm, 1350 nm, and 1440 nm. The spectral FWHM of the devices shown in Fig. 3b is less than 0.14 eV, demonstrating the narrow IR emission spectra from the NCs.

3.3. Effect of nanocrystal concentration

To better understand the device characteristics, the EL properties of the hybrid LEDs were studied as a function of NC concentration. Four different concentrations of PbSe NCs in MEH-PPV films were explored for device fabrica-

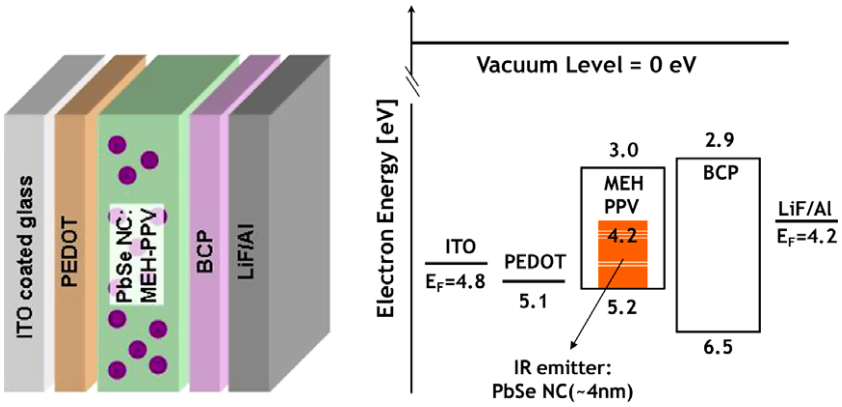

Fig. 2. Device structure and energy levels of constituent materials of the hybrid LED consisting of NC-polymer composite active layer.

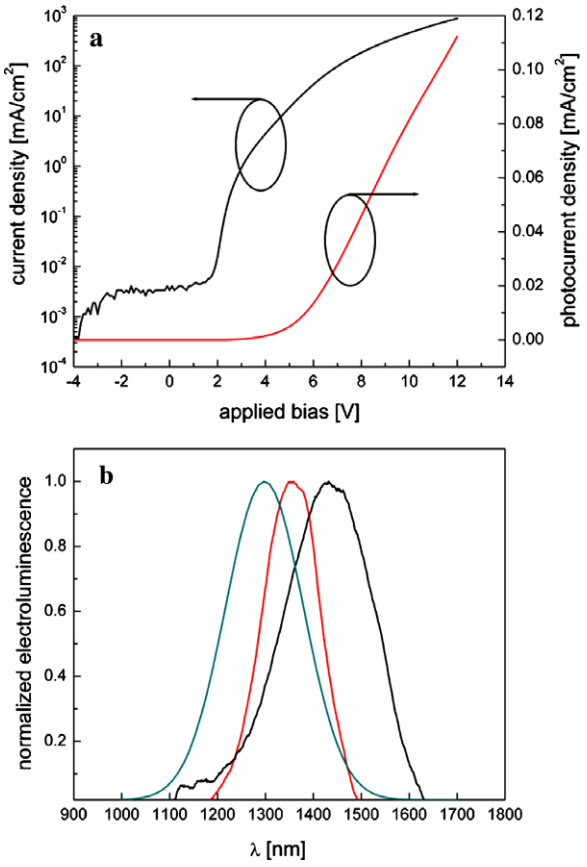

Fig. 3. (a) Hybrid infrared LED performance characteristics (current–voltage-photocurrent) of a device containing 1 wt.% PbSe NCs. (b) Normalized infrared electroluminescence spectra of different NC based hybrid LEDs tuned through choice of NC size (diameter ~3–4.5 nm).

tion: 1%, 3%, 6%, and 9% of NCs by weight. Fig. 4a shows the current density–voltage (J–V) curves for the hybrid LEDs with different compositions. The current–density decreases monotonically with increasing amount of NCs in the polymer layer at all operating voltages. To compare device performances, data from a device with a neat MEH-PPV emitting layer of the same thickness as the NC-dispersed devices are also included in the same figure. The dependence of IR light emission intensity on applied bias is illustrated in Fig. 4b. It is observed that the IR light emission intensity increases as the amount of NCs is increased from 1 wt.% to 3 wt.%, but reduces with further increase in NC content. The device with a neat MEH-PPV layer exhibits orange emission with an EQE of ~1%. Addition of the NCs increases the luminescence from the NCs at the expense of MEH-PPV emission. In fact, for the devices containing 9 wt.% NCs, the EQE from MEH-PPV emission is reduced by 90% of its value, to about ~0.1%. Additionally the turn-on voltage for the devices also increases as the amount of NCs in the film is increased.

The NIR EQE of the hybrid LEDs with varying amount of NCs as a function of device current density is displayed in Fig. 4c. At low current densities, the EQE increases from the device containing 1 wt.% NCs to the one having 3 wt.% NCs, but reduces for devices with higher amount of NCs. However, at current densities larger than 10 mA/cm^2, the device containing 6 wt.% NCs exhibits the highest external IR EQE with a peak value of 0.65%. Interestingly, the efficiencies of all hybrid LEDs remain reasonably flat over a wide range of device current densities and across the entire voltage range, without showing any significant roll-off, which indicates there is good charge balance in the devices.

The EL EQE of the hybrid LEDs depends strongly on the efficiency of excitation transfer to the NC emitters. It has been suggested that both neutral-excitation energy transfer (Förster mechanism) due to dipole–dipole interactions and direct injection of carriers are possible routes of NC excitation in hybrid LEDs [2,12]. Both these mechanisms depend strongly on the distance separating the donor and acceptor involved. As shown in the J–V plots in Fig. 4a, increasing the amount of NCs in our hybrid LEDs reduces the device currents significantly, especially at low operating voltages. For example, at 5 V the current density in the device containing 9 wt.% NCs is two orders lower than that in the neat MEH-PPV device. The decrease in current indicates that the PbSe NC sites in the polymer matrix act as charge trapping centers. The conduction band edge of PbSe NCs (~4.27 eV) is well within the en-

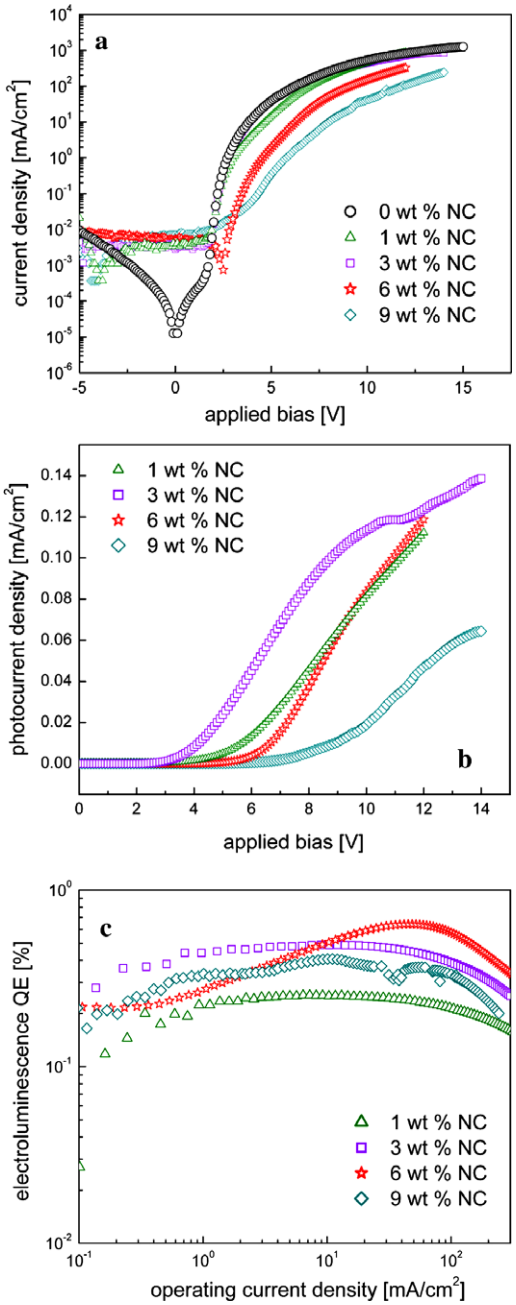

Fig. 4. Electro-optical characteristics of hybrid LEDs incorporating different amounts of NCs. (a) Current density–voltage curves. For comparison, data from an identical control device without the NCs is also plotted. (b) Infrared light emission intensity as a function of applied bias. (c) External quantum efficiencies as a function of operating current density.

ergy gap of MEH-PPV (with a LUMO level 3.0 eV) [16,21] and it favors the transfer of electrons from the polymer to the NCs, resulting in strong electron trapping in the NCs. At the same time, given that the small difference in HOMO energies of MEH-PPV (5.2 eV) [16,21] and the PbSe NCs (~5.27 eV) [22] and the fact that MEH-PPV is a hole transporting polymer, the presence of NC traps should not have a strong effect in hole transport. Therefore the addition of NCs would further increase the hole dominance. The BCP layer acts as a hole blocker and its presence enhances the recombination of blocked holes with trapped electrons in the NCs, resulting in increase in EL efficiency. It should be noted that the carrier trapping proposed here is different from carrier trapping due to chemical or structural defects. Carrier trapping due to defects leads to increase in voltage and decrease in EL efficiency. On the other hand, carrier trapping due to lumophores leads to enhancement in EL. In fact, carrier trapping leading to EL has also been observed in dye-dispersed polymer OLEDs where the drive voltage also increases with the dye doping concentration [23,24]. The increase in the turn-on voltage with higher NC content is also consistent with the presence of NC charge traps [25]. Thus, direct carrier injection into the NC emitters due to charge trapping plays an important role in determining the recombination efficiency in these hybrid LEDs. Increased carrier trapping leads to more efficient exciton formation on the NC emitting sites, resulting in higher luminescence efficiency. This is also evidenced by the significant suppression of MEH-PPV emission from the polymer host with increasing NC content in the composite. The presence of a long chain organic capping ligand can raise concern regarding the efficiency of charge transfer. However, the conformation of single chain ligands on a high curvature NC surface leaves significant portions of the surface accessible for electronic contact by the surrounding matrix [26]. It has already been demonstrated, that even the relatively long capping ligands do not impede excitation transfer to a great extent [27,28]. It should also be noted that aggregation of NCs should not be an issue here because the difference in photoluminescence and electroluminescence spectra is insignificant.

3.4. Effect of electro-active layer thickness

If the NCs act as carrier traps, increase in layer thickness increases the electron and hole trapping probability. While NC-doped MEH-PPV is hole dominant, increasing the layer thickness probably improves the charge balance due to enhanced spreading of carriers over a larger distance. As a result, we expect that the EL efficiency increases with increasing thickness of the electro-active layer. To investigate further the mechanism of trapping and EL emission, the effect of the electro-active layer thickness on the performance of the hybrid LEDs containing 6 wt.% NCs was studied. Fig. 5 shows the peak EQE of these devices as a function of nanocomposite emission layer thickness. The EQE increases with device thickness, and peaks at a value of 0.83% in a hybrid LED having a 210 nm thick active layer. Devices with active layers thicker than 210 nm showed a marked reduction in current density and EL emission efficiency. It should be noted that the peak efficiency shifts to higher current density as the device thickness increases, indicating that charge balance is improved at higher current density with thicker layer. It is also evident from the *J–V* data that an increase in active layer thickness leads to reduced current density. As the charge carriers travel through greater distances across the devices with in-

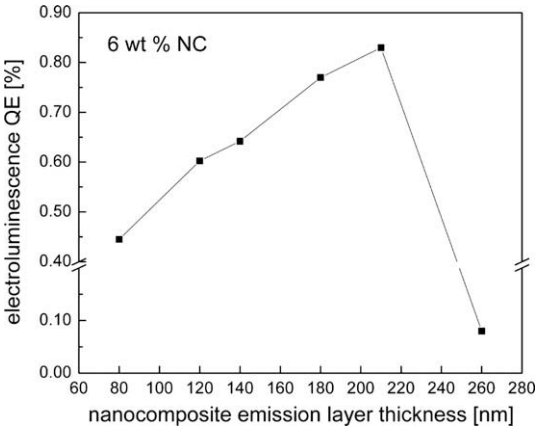

Fig. 5. External infrared electroluminescence QE as a function of active nanocomposite layer thickness for the hybrid LEDs containing 6 wt.% NCs.

creased thickness, their probability of being trapped by the PbSe NCs increases. This increased trapping efficiency results in reduced device current and enhanced EL efficiency. It should be noted that ITO has strong absorption in the NIR wavelength range being studied here. For example, the optical transmission of the ITO substrates used for device fabrication is 55% to 65% in the wavelength range between 1000 nm and 1500 nm. Taking into account the ITO absorption, the maximum EQE of our hybrid LEDs should be ~1.2% if the ITO electrode is replaced with a non-infrared-absorbing electrode. Assuming that this device has a light extraction efficiency similar to OLEDs (20%), the overall internal quantum efficiency should be ~6%, which is significantly higher than the results reported previously [11,12].

4. Conclusions

In conclusion, we demonstrated hybrid solution-processed, IR LEDs based on PbSe NC emitters. We investigated and optimized devices based on a nanocomposite blend architecture and achieved a maximum external quantum efficiency of 0.83% at a peak emission wavelength of 1280 nm. This constitutes a significant improvement over previous reports of NC based IR LEDs, but there are several approaches in device engineering and materials optimization that can lead to further enhancement in performance. For example, optimized core–shell NC structures can prevent delocalization of carriers injected into the NC while allowing for efficient energy exchange with the surrounding matrix, leading to higher internal radiative efficiency.

Acknowledgements

The authors acknowledge the support of the Defense Advanced Research Projects Agency and the US Army Aviation and Missile Research, Development, and Engineering Center (AMRDEC) XLS program (contract number W31P4Q-08-1-0003). The authors thank the Major Analytical Instrumentation Center at the University of Florida for instrumentation support for TEM, and Dr. Aubrey Dyer and Dr. Richard Farley for help in colloidal NC optical characterization.

References

[1] V.L. Colvin, M.C. Schlamp, A.P. Alivisatos, Nature 370 (1994) 354.
[2] N. Tessler, V. Medvedev, M. Kazes, S. Kan, U. Banin, Science 295 (2002) 1506.
[3] S. Coe, W.K. Woo, M. Bawendi, V. Bulovic, Nature 420 (2002) 800.
[4] G. Konstantatos, I. Howard, A. Fischer, S. Hoogland, J. Clifford, E. Klem, L. Levina, E.H. Sargent, Nature 442 (2006) 180.
[5] N. Cho, K. Roy Choudhury, R.B. Thapa, Y. Sahoo, T. Ohulchanskyy, A.N. Cartwright, K.S. Lee, P.N. Prasad, Adv. Mater. 19 (2007) 232.
[6] W.U. Huynh, J.J. Dittmer, A.P. Alivisatos, Science 295 (2002) 2425.
[7] I. Gur, N.A. Fromer, M.L. Geier, A.P. Alivisatos, Science 310 (2005) 462.
[8] B. Sun, N.C. Greenham, Phys. Chem. Chem. Phys. 8 (2006) 3557.
[9] S. Coe-Sullivan, J.S. Steckel, W.K. Woo, M.G. Bawendi, V. Bulovic, Adv. Funct. Mater. 15 (2005) 1117.
[10] Y.H. Niu, A.M. Munro, Y.J. Cheng, Y. Tian, M.S. Liu, J. Zhao, J.A. Bardecker, I.J. Plante, D.S. Ginger, A.K.Y. Jen, Adv. Mater. 19 (2007) 3371.
[11] J.S. Steckel, S. Coe-Sullivan, V. Bulovic, M. Bawendi, Adv. Mater. 15 (2003) 1862.
[12] G. Konstantatos, C. Huang, L. Levina, Z. Lu, E.H. Sargent, Adv. Funct. Mater. 15 (2005) 1865.
[13] J. Zhao, J.A. Bardecker, A.M. Munro, M.S. Liu, Y.H. Niu, I.K. Ding, J. Luo, B. Chen, A.K.Y. Jen, D.S. Ginger, Nano Lett. 6 (2006) 463.
[14] B.L. Wehrenberg, C. Wang, P. Guyot-Sionnest, J. Phys. Chem. B 106 (2002) 10634.
[15] J.S. Steckel, B.K.H. Yen, D.C. Oertel, M.G. Bawendi, J. Am. Chem. Soc. 128 (2006) 13032.
[16] I.D. Parker, Proc. SPIE 51 (1994) 2144.
[17] W. Gao, A. Kahn, Appl. Phys. Lett. 82 (2003) 4815.
[18] V. Sholin, A.J. Breeze, I.E. Anderson, Y. Sahoo, D. Reddy, S.A. Carter, Sol. Energy Mater. Sol. Cells 92 (2008) 1706.
[19] Al.L. Efros, A.L. Efros, Sov. Phys. Semicond. 16 (1982) 772.
[20] C.A. Leatherdale, C.R. Kagan, N.Y. Morgan, S.A. Empedocles, M.A. Kastner, M. Bawendi, Phys. Rev. B 62 (2000) 2699.
[21] D.H. Choi, M.J. Cho, K.I. Han, I.H. Chang, J.S. Song, J.H. Kim, S.H. Paek, S.H. Choi, Synth. Met. 156 (2006) 685.
[22] X. Jiang, R.D. Schaller, S.B. Lee, J.M. Pietryga, V.I. Klimov, A.A. Zakhidov, J. Mater. Res. 22 (2007) 2204.
[23] K. Tada, M. Onoda, Jpn. J. Appl. Phys. 44 (2005) 4165.
[24] Y. Xu, X. Zhang, J. Peng, Q. Niu, Y. Cao, Semicond. Sci. Technol. 21 (2006) 1373.
[25] K.C. Kao, W. Hwang, Electrical Transport in Solids, International Series in the Science of the Solid State, vol. 14, Pergamon, New York, 1981.
[26] A. Badia, L. Cuccia, L. Demers, F. Morin, R.B. Lennox, J. Am. Chem. Soc. 119 (1997) 2682.
[27] K. Roy Choudhury, Y. Sahoo, T. Ohulchanskyy, P.N. Prasad, Appl. Phys. Lett. 87 (2005) 073110.
[28] T.F. Chang, S. Musikhin, L. Bakueva, L. Levina, M.A. Hines, P.A. Cyr, E.H. Sargent, Appl. Phys. Lett. 84 (2004) 4295.

Organic Electronics 11 (2010) 29–35

Contents lists available at ScienceDirect

Organic Electronics

journal homepage: www.elsevier.com/locate/orgel

Length-scale effects on electrical and thermal transport in polyaniline thin films

Jiezhu Jin [a], Qing Wang [a], M.A. Haque [b,*]

[a] Department of Materials Science and Engineering, The Pennsylvania State University, University Park, PA 16802, USA
[b] Department of Mechanical and Nuclear Engineering, The Pennsylvania State University, University Park, PA 16802, USA

ARTICLE INFO

Article history:
Received 27 July 2009
Received in revised form 16 September 2009
Accepted 19 September 2009
Available online 25 September 2009

Keywords:
Conducting polymer
Polyaniline
Electrical conductivity
Thermal conductivity
Length-scale effect

ABSTRACT

Conducting polymers are prevalently used in organic and flexible electronics and energy conversion devices. While their thermo-physical properties are well characterized for different processing and doping conditions, very little is known about the effect of length-scale, especially their thermal conductivity and thermal contact resistance of their interfaces with substrates. In this paper we develop an analytical model to capture the heat transfer in ultra-thin polyaniline thin films and their interfaces with other substrate materials. The model is demonstrated on 20–1000 nm thick 50% camphor-sulphonic acid doped polyaniline films patterned on silicon substrate using photolithography and reactive ion etching. The four-probe based technique allows simultaneous electrical and thermal characterization. Experimental results show a 500% and 200% increase in the in-plane thermal conductivity and electrical conductivity, respectively as the film thickness is increased from 20 nm to 1000 nm. These findings suggest up to 300% improvement in thermoelectric performance for 20 nm thick films when compared to the bulk. Such strong length-scale effects are observed to decay rapidly after 100 nm film thickness and can be attributed to the enhanced phonon scattering at the surface and interface boundaries at length-scales comparable to phonon mean free paths.

© 2009 Elsevier B.V. All rights reserved.

1. Introduction

Conducting polymer thin films are prevalently used in state of the art organic/flexible micro-electronic [1,2] and optoelectronic [3,4] systems, solid state energy conversion devices [5–7] and novel composites [8,9]. In particular, polyaniline (PANI, also known as the organic metal) stands out among conducting polymers because of its facile synthesis and tailorable conductivity arising from its unique doping/de-doping chemistry based on acid/base reactions and more importantly, metallic transport property [10,11]. It is a popular organic electronics material with applications including electrodes for rechargeable batteries, sensors, super-capacitors, electro-chromic displays [12]. Accordingly, the issues of electrical conductivity and compatibility with micro-electronic processing have received the most attention. The literature shows that the electrical conductivity is strongly dependent on the preparation conditions, doping chemistry and temperature [8,11–19]. Thermal transport properties, on the other hand, are comparatively less studied with only few reports on the thermal conductivity of microscale PANI films [5,20]. In fact, thermal conductivity of polyaniline is found to remain unchanged at the micro and meso scales [21], which leads researchers to focus on enhancing the electrical conductivity for better electrode or thermoelectric conversion performances.

While synthesis and doping chemistry are the two most investigated routes towards advanced conducting polymeric materials, the motivation for this paper comes from the relatively unexplored opportunities due to the

* Corresponding author.
E-mail address: mah37@psu.edu (M.A. Haque).

1566-1199/$ - see front matter © 2009 Elsevier B.V. All rights reserved.
doi:10.1016/j.orgel.2009.09.018

'length-scale effects' on electrical and thermal transport. The first rationale behind our approach is that as materials dimensions approach the mean free path of electrons and phonons, strong length-scale effects are expected to manifest in novel thermo-physical properties [22–24]. The second rationale is that the ever-continuing trend in miniaturization results in unfamiliar problems that can be only dealt with fundamental understanding in the length-scale effects. For example, only ten years ago, thermal management of electronics was an emerging issue, which now is regarded to be a major problem. As switching speed and circuit density increase, thermal transport will become increasingly critical in determining the operating temperature for organic electronics [22]. This is because the heat dissipation density increases non-linearly (L^{-1}) with the characteristic length-scale (L) [25]. Unfortunately, there are only a few studies in the literature that investigate length-scale effects on electrical properties at the 10–100 nm range [26,27]. On the other hand, existing thermal conductivity studies on conducting polymers only involve relatively thicker films [20,28], where the effects of geometric (film thickness) and microstructural (disordered or partially disordered structures inside films) confinement are virtually non-existent. It is important to note that there is not a single study in the literature on the thermal contact resistance of the conducting polymer based interfaces, even though such interfaces are ubiquitous in organic electronics.

While the four-probe electrical characterization technique has been universally applicable across length-scales, thermal characterization of nanoscale materials is particularly challenging. To enable simultaneous electrical and thermal characterization, we adopt the 3ω technique, which also uses four electrodes to heat up the specimen and extract the thermal conductivity by sensing the temperature changes. Here, an alternating current $I(\omega)$ is passed through the specimen, generating thermal waves that diffuse along the specimen thickness direction and modulating the resistance at 2ω frequency. The resulting voltage drop across the specimen, $V = I(\omega)R$, contains the third harmonics, 3ω, which is proportional to the temperature rise of the heater and can be used to calculate the thermal properties of the specimen [29,30]. For conducting materials, the specimen is required to be freestanding [28,31], which not only makes it impossible to measure the thermal contact resistance at the substrate interfaces but also makes specimen fabrication challenging especially for soft polymeric materials with nanometer scale thickness.

In the next section, we develop an analytical model that modifies the conventional 3ω technique to relax the freestanding specimen restriction and thus allows simultaneous characterization of electrical and thermal conductivity as well as thermal contact resistance at the interface with the substrate. The four-probe electrical conductivity measurements are very straightforward and will not be discussed in detail. We then present the experimental details and analyze the results to draw conclusions on the length-scale effects on the electrical and thermal transport in nanoscale polyaniline thin films.

2. Analytical model for thermal transport in thin films

The essence of the model developed in this study is to relax the restriction that the specimen must be released from the substrate by explicitly accounting for the heat loss to the substrate in one-dimensional heat conduction equation. Fig. 1a shows cross-sectional view of the specimen with four electrodes. The two outer probes (1 and 4) are used to supply AC electric current, and the two inner probes (2 and 3) are used to measure the voltage across the specimen. The applied sinusoidal current source ($I = I_0 \sin \omega t$) leads to Joule heating which is equal to $I^2(R_0 + \delta R)$, where δR is the resistance fluctuation of the specimen and is proportional to the temperature oscillation. A scanning electron micrograph of the top view of the setup is shown in Fig. 1b.

The heat generation and one-dimensional heat conduction through the specimen are given by [31],

$$\rho C_p \frac{\partial \theta(x,t)}{\partial t} = \kappa \frac{\partial^2 \theta(x,t)}{\partial x^2} + \frac{I_0^2 \sin^2 \omega t}{LS}(R_0 + R'\theta(x,t)) \tag{1}$$

where L and S are the length between the voltage contacts and the cross-section area of the specimen, respectively. ρ, C_p and κ are the density, specific heat and thermal conductivity. R_0 is the initial electrical resistance of the specimen at initial temperature T_0. R' is the resistance derivative of temperature $R' = \left(\frac{dR}{dT}\right)_{T_0}$ at T_0. $\theta(x,t) = T(x,t) - T_0$ is the temperature change, t is the time, x is the coordinate along the length and also the heat flow direction. In order to relax the constraint of suspended specimen, we consider balancing the heat loss across the contact to the underlying substrate $\theta(x,t)A/\sum R_t$ in the one-dimensional heat conduction equation by the introduction of underlying thermal resistance $\sum R_t$ (in the unit of m^2K/W), where A is the contact area between the specimen and substrate. The total underlying thermal resistance $\sum R_t$ is the sum of the interfacial contact resistance and the substrate conduction resistance, i.e. $\sum R_t = R_{t,\mathrm{cont}} + R_{t,\mathrm{cond}}$. Thermal resistance from the substrate can be approximated from $R_{t,\mathrm{cond}} = \frac{\lambda_s}{\kappa_s}$, where $\lambda_s = \sqrt{\alpha_s/2\omega}$ is the thermal penetration depth in the substrate, α_s is the thermal diffusivity and κ_s is the thermal conductivity of the substrate. By subtracting the thermal resistance of the substrate from the total resistance $\sum R_t$, the value of the interfacial thermal resistance can be found.

The introduction of underlying thermal resistance $\sum R_t$ turns one-dimensional heat conduction equation to be,

$$\rho C_p \frac{\partial \theta(x,t)}{\partial t} = \kappa \frac{\partial^2 \theta(x,t)}{\partial x^2} + \frac{I_0^2 \sin^2 \omega t}{LS}(R_0 + R'\theta(x,t)) - \frac{\theta(x,t)A}{LS\sum R_t} \tag{2}$$

By setting $\alpha = \kappa/\rho C_p$, $b = I_0^2 R_0/LS\rho C_p$, $c = I_0^2 R'/LS\rho C_p$, $d = A/LS\sum R_t \rho C_p$, the equation can be rewritten as

$$\frac{\partial \theta(x,t)}{\partial t} - \alpha \frac{\partial^2 \theta(x,t)}{\partial x^2} - (c \sin^2 \omega t - d)\theta(x,t) = b \sin^2 \omega t \tag{3}$$

with the following initial and boundary conditions

$$\theta(0,t) = 0, \quad \theta(L,t) = 0, \quad \theta(x,-\infty) = 0 \tag{4}$$

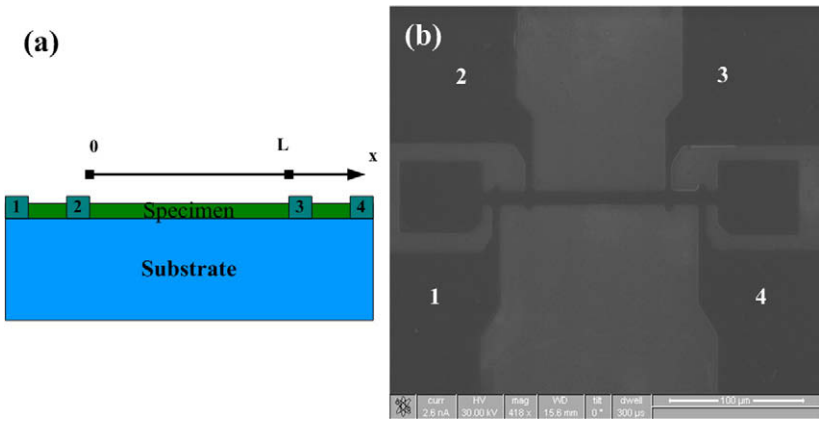

Fig. 1. (a) Cross-sectional view of the four-probe configuration (b) scanning electron microscope image of the geometry of the specimen (viewed from the top). The darker region is PANI thin film and lighter region is thermally grown silicon oxide. Scale bar is 100 μm.

The impulse theorem is employed to solve the Eq. (3)

$$\theta(x,t)=\int_{-\infty}^{t} z(x,t;\tau)\,d\tau \tag{5}$$

where $z(x,t;\tau)$ satisfies

$$\frac{\partial z}{\partial t}-\alpha\frac{\partial^2 z}{\partial x^2}-(c\sin^2\omega t-d)z=0 \tag{6}$$

with the initial and boundary conditions,

$$z(0,t)=0,\quad z(L,t)=0,\quad z(x,\tau^+)=b\sin^2\omega\tau \tag{7}$$

Fourier series can be used to expand $z(x,t;\tau)$,

$$z(x,t;\tau)=\sum_{n=1}^{\infty}U_n(t;\tau)\sin\frac{n\pi x}{L} \tag{8}$$

Substitute Eq. (8) into Eq. (6),

$$\sum_n\left[\frac{dU_n}{dt}+\left(\alpha\frac{n^2\pi^2}{L^2}-c\sin^2\omega t+d\right)U_n\right]\sin\frac{n\pi x}{L}=0 \tag{9}$$

We now set $\lambda=\alpha\frac{n^2\pi^2}{L^2}+d$.

When $c\ll\lambda$, $c\sin^2\omega t$ can be neglected, that is

$$\frac{I_0^2R'L\sum R_t}{n^2\pi^2\kappa\sum R_tS+LA}\ll 1 \tag{10}$$

Non-trivial solution of Eq. (9) is

$$\frac{dU_n}{dt}+\left(\alpha\frac{n^2\pi^2}{L^2}-c\sin^2\omega t+d\right)U_n=0 \tag{11}$$

If condition (10) can be satisfied, the solution of Eq. (11) is

$$U_n(t;\tau)=C_ne^{-\left(\alpha\frac{n^2\pi^2}{L^2}+d\right)(t-\tau)} \tag{12}$$

From initial condition in (7) and Fourier expansion in (8), we know

$$z(x,t;\tau)=\sum_n\frac{2b}{n\pi}[1-(-1)^n]\sin^2\omega\tau e^{-(\alpha\frac{n^2\pi^2}{L^2}+d)(t-\tau)}\times\sin\frac{n\pi x}{L} \tag{13}$$

We now apply the impulse theorem again to find $\theta(x,t)$,

$$\theta(x,t)=\int_{-\infty}^{t}z(x,t;\tau)\,d\tau=\sum_{n=1}^{\infty}\left\{\frac{b}{n\pi}[1-(-1)^n]\sin\frac{n\pi x}{L}\frac{1}{\lambda}\left[1-\frac{\sin(2\omega t+\phi_n)}{\sqrt{1+\cot^2\phi_n}}\right]\right\} \tag{14}$$

where $\tan\phi_n=\frac{\lambda}{2\omega}$.

For $n=1$, the temperature difference becomes,

$$\theta(x,t)=\frac{2b}{\pi}\sin\frac{\pi x}{L}\frac{1}{\lambda}\left[1-\frac{\sin(2\omega t+\phi)}{\sqrt{1+\cot^2\phi}}\right] \tag{15}$$

and the resistance variation can be obtained as

$$\delta R=\frac{R'}{L}\int_0^L\theta(x,t)\,dx=\frac{4bR'}{\pi^2\lambda}\left[1-\frac{\sin(2\omega t+\phi)}{\sqrt{1+\cot^2\phi}}\right] \tag{16}$$

The voltage of the specimen as the product of the total resistance $R+\delta R$ and the current $I_0\sin\omega t$ contains a 3ω component $V_{3\omega}(t)$. The root-mean-square value of 3ω voltage is

$$V_{3\omega}=\frac{\sqrt{2}I_0R'b}{\pi^2\lambda}\frac{1}{\sqrt{1+(2\omega/\lambda)^2}} \tag{17}$$

If $2\omega\ll\lambda$, the root-mean-square value of 3ω voltage becomes

$$V_{3\omega}\approx\frac{\sqrt{2}I_0^3R_0R'L}{\pi^4\kappa S+\frac{\pi^2LA}{\sum R_t}} \tag{18}$$

The average temperature change of the specimen can be calculated from Eq. (14)

$$\bar{\theta}\approx\frac{4I_0^2R_0L}{\pi^4\kappa S+\frac{\pi^2LA}{\sum R_t}} \tag{19}$$

By extracting the linear relationship between $V_{3\omega}$ and I_0^3 from the measurement, and combining Eqs. (18) and (19) and the heat balance Eq. (20),

$$\frac{I_0^2}{2LS}(R_0 + R'\overline{\theta}) = \frac{\overline{\theta}A}{LS\sum R_t} + \rho C_p \overline{\theta}\lambda \quad (20)$$

κ and $\sum R_t$ can be simultaneously determined, where λ^{-1} is the thermalization time,

$$\lambda = \frac{\kappa\pi^2}{L^2\rho C_p} + \frac{A}{LS\sum R_t \rho C_p}$$

3. Experimental details

The PANI specimens for this study were prepared using chemical oxidation based polymerization. CSA and PANI in the emeraldine base form are mixed in a 0.5 M ratio of CSA to phenyl-N repeat unit using a mortar and pestle and then added to the m-cresol while stirring. The solution is magnetically stirred for 48 h with an initial heating at 60 °C for 90 min to make the solution homogenous before ultrasonication for 6 h. The solution is filtered using syringe filters of 450 nm and 200 nm before casting the film. The film is obtained by spin coating the homogeneous solution onto thermally grown silicon oxide substrate and subsequently drying for 24 h and annealing for 4 h. In the experimental setup shown in Fig. 1, the PANI thin film serves as both the specimen heater and temperature sensor. To minimize the contact resistance between the electrical pads and the contact probes, a thin layer of aluminum is deposited on top of PANI thin film. A two-step lithographic process is employed to pattern the specimen and then overlay aluminum in the form of four pads by photolithography. In the second-step, PANI thin film is patterned using front-side alignment photolithography to achieve the 110-μm long, 10-μm wide filament-like specimens. Details of the fabrication processes and calibration are given in [32]. The thickness of the PANI specimens was varied from 20 to 1000 nm and measured using an atomic force microscope. Conductive epoxy is applied to connect the four pads to small diameter alloy wires that are used for electrical connections to minimize the conduction loss.

The specimen is mounted in a vacuum chamber and the temperature is maintained at 300 K. Radiation losses are minimized by shielding and convection losses are reduced by operating in a vacuum of 0.3 torr. A Keithley 6221 is used to supply constant amplitude current source to the two outer pads. The third harmonic voltages across the two inner pads are picked up by a lock-in amplifier (Stanford Research Systems SR 830). The third harmonic voltages are measured from 1 to 30 Hz. The time constant which determines the bandwidth of low pass filter is set to be 30–300 s. To satisfy Eq. (10), the input current I_0 is limited to 0.05 μA or below to increase the measurement accuracy and keep the specimen undamaged by the heat generated due to the high resistance of the specimen. The phase of the lock-in at each frequency is zeroed to improve the phase accuracy for small amplitude current and all line filters are turned off to keep them from interfering with the 3ω signals. Finally, the thermal conductivity of the specimen is evaluated by measuring the third harmonic dependence of the current.

4. Experimental results and discussion

The frequency range of AC current from 1 to 30 Hz is used to fulfill the frequency limit: $2\omega \ll \lambda$, i.e., $2\omega \ll \frac{\kappa\pi^2}{\rho C_p L^2} + \frac{A}{\rho C_p LS\sum R_t}$. In order to measure the thermal conductivity using the above method, the low frequency limit should be established by obtaining the frequency dependence of the root-mean-square (rms) value of the third harmonic voltage $V_{3\omega}$. Fig. 2a shows the frequency dependence of $V_{3\omega}$ in measuring the thermal conductivity of 20-nm thick PANI films. As shown in Fig. 2a, the voltage measured at the third harmonic decreases as the frequency is increased. By fitting the curve shown in Fig. 2a to Eq. (17), the value of λ was found to be on the order of 100 s^{-1}. Meanwhile, C_P was also extracted. For frequencies below 5 Hz, we can consider $2\omega \ll \lambda$. The low frequency limit is established by setting the frequency at 3 or 4 Hz for all the thicknesses. Hence the thermal conductivity can be derived from Eq. (18) by the current dependence of voltage $V_{3\omega}$. Fig. 2b shows the applied current dependence of voltage $V_{3\omega}$ of 20-nm thick PANI films at 4 Hz. The amplitude of the current varies from 0.005 to 0.05 μA. The signal follows well the predicted third power law as shown in Eq. (18). Relationship between $\sum R_t$ and k is extracted according to Eq. (18) and Fig. 2b. By the combination of Eqs. (18), (19) and (20), the in-plane thermal conductivity of the 20-nm thick PANI thin film is calculated to be 0.0406 W/m K, and the underlying total thermal resistance is 0.806 K m^2/W by subtracting the thermal resistance of the substrate from the total resistance $\sum R_t$. The high interfacial thermal resistance could be attributed to many factors, including surface characteristics of the interfacial region and adhesion of PANI with the substrate.

Fig. 2c and d presents the measured rms value of 3ω voltages in the frequency range 1–30 Hz and the linear relationship between $V_{3\omega}$ and I_0^3 of 110-nm thick PANI films, respectively. For other thicknesses, it has also been found that the applied current dependence of voltage $V_{3\omega}$ of PANI films follows the predicted third power law as shown in Eq. (18). By substituting the interfacial thermal resistance of 0.806 K m^2/W and the linear relationship between $V_{3\omega}$ and I_0^3 into Eq. (18), the thermal conductivities of PANI films at different thicknesses are determined.

Fig. 3a shows the experimental results on electrical conductivity of polyaniline films as a function of film thickness. Very strong thickness effect is observed at the 1–100 nm length-scale, which can be attributed to the increasing packing density of the polymer as the thickness increases, leading to higher volumes of metallic transporting regions composed of polaronic conducting segments randomly oriented in the disordered matrix. There is a significant difference in the scattering mechanism in the PANI compared to metals, as shown by the difference between the dashed line (the Mayadas–Shatzkes [33] model for electron scattering in metals) and the solid line for the experimental results obtained in this study. This observation indirectly supports the polaron (electron in phonon cloud) model of conduction in polyaniline [34], where the electron–phonon scattering is more dominant compared to the electron surface/interface scattering as in metals.

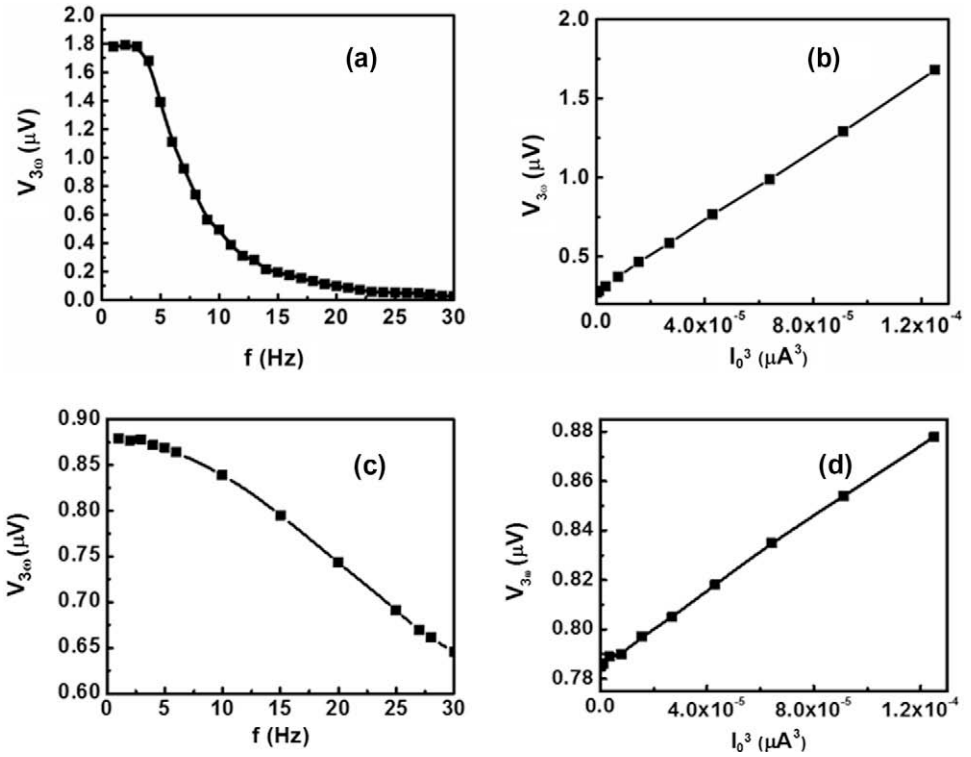

Fig. 2. Frequency dependence of the third harmonic in the range of 1–30 Hz of (a) 20 nm and (c) 110 nm thick PANI films. The amplitude I_0 of the supplied current is 0.05 μA. Dependence of the third harmonic on the applied current of (b) 20 nm and (d) 110 nm thick PANI films at 4 and 3 Hz, respectively.

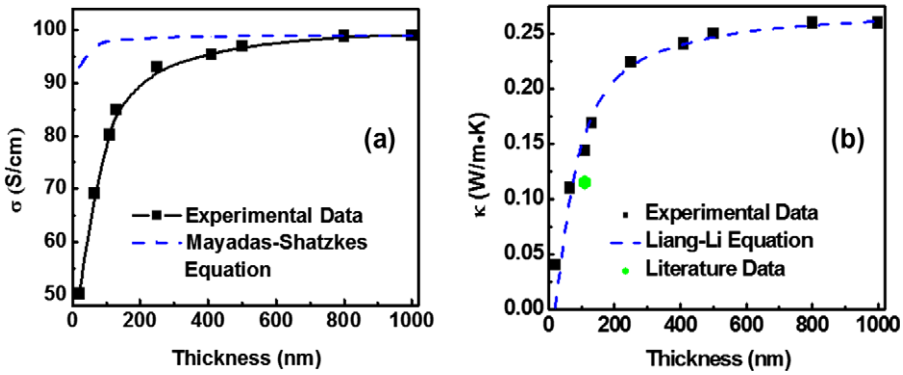

Fig. 3. (a) Electrical conductivity of PANI thin films as a function of film thickness. The dashed curve represents the analytical expression for metals. (b) Thermal conductivity of PANI thin films as a function of film thickness. The symbol ⬢ is the data of the thinnest film from literature [28]. The dashed curve represents the analytical expression [24].

Fig. 3b shows the thickness dependence of the thermal conductivity of polyaniline. Also shown is the data obtained for the thinnest specimen in the existing literature. The thinnest specimens (20 nm) exhibit the smallest value of thermal conductivity 0.0406 W/m K, and the thickest specimens (1 μm) presents the largest value of 0.26 W/m K. As the thickness increases from 20 to about 130 nm, the thermal conductivity increases rapidly from 0.0406 to 0.166 W/m K. Such strong thickness dependence diminishes rather dramatically after 130 nm thickness, and the values converge to the bulk value after 800 nm thickness.

Fig. 3b also shows a curve fitted to the experimental data according to Liang and Li [24] as shown below,

$$\kappa = \kappa_b p \exp\left(-\frac{l_0}{t}\right)\left[\exp\left(\frac{-(\alpha-1)}{t/L_0-1}\right)\right]^{\frac{3}{2}} \quad (\mathrm{W/m\,K}) \qquad (21)$$

where t is the thickness, k_b is the bulk value of thermal conductivity, p is the surface roughness parameter in the range of 0–1, and α is a material constant related to the atomic structure. For the phonon mean free path l_0, we use the estimated value 10 nm [28]. L_0 is a critical size of

material and is assumed as 10 nm in the fitted curve. The fitted results are the product of k_b and p is 0.2772 W/m K, and $\alpha = 4.135$. The analytical model [24] is derived based on the phonon surface scattering and the size confinement of phonon transport in the nanoscale semiconducting systems. Although the mechanism is not developed for polyaniline, its underlying phonon dominance agrees with our experimental data very well.

To explain the observed thickness dependence of thermal conductivity, we note that heat energy is transmitted via electrons and phonons in PANI [35]. The total thermal conductivity k comes from the contributions of those two heat carriers. The literature suggests that the phonon contribution to thermal conductivity may be predominantly high for thin films due to the polaron lattice imperfections in nano-scale films [20]. Therefore, the thermal conductivity can be expressed as

$$k = k_p + k_e \approx k_p = \frac{1}{3} c v l \tag{22}$$

where c is the phonon heat capacity, v is the phonon velocity and l is the phonon mean free path. Because heat conduction mainly depends on the phonon transport in nanometer film, the thermal conductivity is governed by the phonon heat capacity and mean free path. In ordered materials, it is reasonable to assume a constant heat capacity provided that the films are not as thin as atomic layers. However, for the case of disordered organic materials, the influence of structure and defect on volumetric heat capacity cannot be neglected. This is because the thermal properties of organic films are highly sensitive to their microstructural features [36]. With the reduction of film thickness, the volumetric heat capacity is decreased due to the interplay among atomic-scale disorder, porosity, partial crystallinity, and molecular orientation [28].

Another important reason leading to the size dependence of thermal conductivity is the phonon mean free path. On one hand, the collision probability of phonons increases with thickness reduction due to the confinement, which leads to the decrease of the efficiency in heat conduction. On the other hand, the heat conduction is greatly influenced by the nanometer film surface/interface. As the size decreases and the surface–volume ratio increases, the large surface and interface boundary scattering of phonons impose additional resistance to thermal transport and reduces the thermal conductivity of thin films. In addition, there is widespread acceptance that PANI forms a heterogeneous structure in its emeraldine salt (ES) form, in which small domains of highly ordered polymer are surrounded by less ordered material [10]. As PANI film becomes thinner, the amorphous regions are increased, hence the chains are more twisted or the polymer chain discontinues so that the mean free path of phonon is remarkably decreased. According to the classic kinetic theory, the mean free path of phonons in PANI thin films has been estimated to be on the order of 10 nm [28]. The thinnest specimen (20 nm) in our study approaches the mean free path. Therefore, phonon boundary scattering plays the most vital role in the significant reduction of the thermal conductivity of 20 nm thick films compared with thicker films. When the film thickness is between 20 nm and 130 nm, the thermal conductivity is greatly affected by the phonon–phonon scattering due to the confinement and phonon boundary scattering at the interface or surface. When the films are thicker than 130 nm, the nature of structural disorder, imperfection, molecular conformation leads to the increase of the thermal conductivity with the film thickness. When the films are 800 nm thick, the size effect of thermal conductivity is no longer observed, due to the constant phonon heat capacity and mean free path in the bulk films.

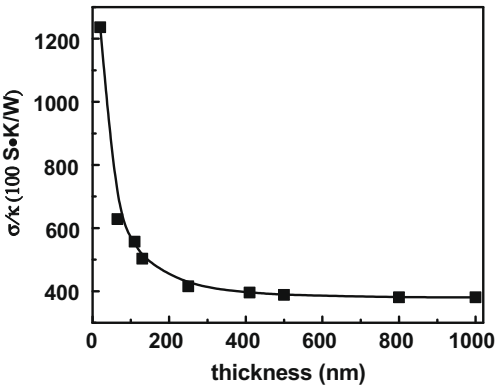

Fig. 4. Ratio of electrical to thermal conductivity (σ/κ) as a function of polyaniline film thickness.

The findings on length-scale effects on electrical and thermal transport in nanoscale polyaniline films predict unfavorable consequences of miniaturization, mainly because of the very low thermal conductivity. However, it also indicates promising performance enhancing aspects for thermoelectric applications. The efficiency of a thermoelectric material is reflected by the value of the dimensionless thermoelectric figure-of-merit (ZT) calculated according to the following equation,

$$ZT = S^2 T\left(\frac{\sigma}{k}\right) \tag{23}$$

where S is the Seebeck coefficient, σ is the electrical conductivity, T is the absolute temperature, and κ is the thermal conductivity. A good thermoelectric material has a high ZT value at the operating temperature, which is determined by the ratio of electrical conductivity and thermal conductivity, assuming S is constant. This ratio is shown as a function of film thickness in Fig. 4. Here, the length scale effect on the phonon dominated thermal transport outweighs the electronic conduction, hence the magnitude of the ratio is very large for the ultra-thin films. However, as the film thickness increases, thermal conductivity increases, thereby lowering the value of the conductivity ratio, which rapidly converges to the bulk value at 130 nm.

5. Conclusion

We present an experimental technique that allows simultaneous characterization of electrical and thermal conductivity and thermal contact resistance of ultra-thin film specimens on insulating substrates. The technique is based on a analytical model we developed to extend the conventional four-probe based (3ω) technique for thermal

characterization to specifically account for the heat loss to the substrate, which enables us to relax the freestanding specimen constraint. The model also allows the extraction of the thermal contact resistance of the specimen-substrate interface. Measurements on PANI thin films in the range of 20 nm −1 micron reveal a strong thickness dependence of thermal conductivity below 130 nm. The size effect rapidly diminishes for films thicker than 800 nm. The size effect on thermal conductivity is attributed to restrictions of the phonon mean free path length and heat capacity. The phonon boundary scattering is the major factor reducing the thermal conductivity of micro- and nanoscale films, and the trend for size effect is expected to be more significant for further reduced thicknesses. In addition, phonon–phonon scattering due to the confinement, structural factors including crystallinity, polymer chain orientation, molecular conformation and imperfection gradually increases, resulting in the decrease of thermal conductivity with the reduction in thin film thickness. The findings of this study suggest that the length-scale effects on electrical and thermal transport can be exploited for better performance thermoelectric applications.

Acknowledgement

M.A. Haque gratefully acknowledges the support from the Korea Institute of Machinery & Materials and the National Science Foundation (CMMI 0555420).

References

[1] A. Moliton, R.C. Hiorns, Review of electronic and optical properties of semiconducting pi-conjugated polymers: applications in optoelectronics, Polymer International 53 (2004) 1397–1412.
[2] K. Ziemelis, Putting it on plastic, Nature 393 (1998) 619–620.
[3] C. Tengstedt, A. Crispin, C.H. Hsu, C. Zhang, I.D. Parker, W.R. Salaneck, M. Fahlman, Study and comparison of conducting polymer hole injection layers in light emitting devices, Organic Electronics 6 (2005) 21–33.
[4] Y.A. Udum, A. Durmus, G.E. Gunbas, L. Toppare, Both p- and n-type dopable polymer toward electrochromic applications, Organic Electronics 9 (2008) 501–506.
[5] N. Toshima, Conductive polymers as a new type of thermoelectric material, Macromolecular Symposia 186 (2002) 81–86.
[6] S.K. Hau, H.-L. Yip, J. Zou, A.K.Y. Jen, Indium tin oxide-free semi-transparent inverted polymer solar cells using conducting polymer as both bottom and top electrodes, Organic Electronics 10 (2009) 1401–1407.
[7] M.-Y. Chang, C.-S. Wu, Y.-F. Chen, B.-Z. Hsieh, W.-Y. Huang, K.-S. Ho, T.-H. Hsieh, Y.-K. Han, Polymer solar cells incorporating one-dimensional polyaniline nanotubes, Organic Electronics 9 (2008) 1136–1139.
[8] J. Anand, S. Palaniappan, D.N. Sathyanarayana, Conducting polyaniline blends and composites, Progress in Polymer Science 23 (1998) 993–1018.
[9] H. Zengin, W.S. Zhou, J.Y. Jin, R. Czerw, D.W. Smith, L. Echegoyen, D.L. Carroll, S.H. Foulger, J. Ballato, Carbon nanotube doped polyaniline, Advanced Materials 14 (2002) 1480–1483.
[10] E.R. Holland, S.J. Pomfret, P.N. Adams, A.P. Monkman, Conductivity studies of polyaniline doped with CSA, Journal of Physics-Condensed Matter 8 (1996) 2991–3002.
[11] A. Varela-Alvarez, J.A. Sordo, G.E. Scuseria, Doping of polyaniline by acid-base chemistry: density functional calculations with periodic boundary conditions, Journal of the American Chemical Society 127 (2005) 11318–11327.
[12] A.J. Heeger, Semiconducting and metallic polymers: The fourth generation of polymeric materials (Nobel lecture), Angewandte Chemie-International Edition 40 (2001) 2591–2611.
[13] J.K. Avlyanov, Y.G. Min, A.G. Macdiarmid, A.J. Epstein, Polyaniline – conformational-changes induced in solution by variation of solvent and doping level, Synthetic Metals 72 (1995) 65–71.
[14] C.O. Yoon, M. Reghu, D. Moses, Y. Cao, A.J. Heeger, Transports in blends of conducting polymers, Synthetic Metals 69 (1995) 255–258.
[15] E.R. Holland, S.J. Pomfret, P.N. Adams, L. Abell, A.P. Monkman, Doping dependent transport properties of polyaniline-CSA films, Synthetic Metals 84 (1997) 777–778.
[16] E. Banka, W. Luzny, Structural properties of polyaniline protonated with camphorsulfonic acid, Synthetic Metals 101 (1999) 715–716.
[17] J.Y. Shimano, A.G. MacDiarmid, Polyaniline, a dynamic block copolymer: key to attaining its intrinsic conductivity?, Synthetic Metals 123 (2001) 251–262
[18] K. Lee, S. Cho, S.H. Park, A.J. Heeger, C.W. Lee, S.H. Lee, Metallic transport in polyaniline, Nature 441 (2006) 65–68.
[19] V.N. Prigodin, F.C. Hsu, J.H. Park, O. Waldmann, A.J. Epstein, Electron–ion interaction in doped conducting polymers, Physical Review B 78 (2008) 035203.
[20] J.E. de Albuquerque, W.L.B. Melo, R.M. Faria, Determination of physical parameters of conducting polymers by photothermal spectroscopies, Review of Scientific Instruments 74 (2003) 306–308.
[21] H. Yan, T. Ohta, N. Toshima, Stretched polyaniline films doped by (+/−)10-camphorsulfonic acid: anisotropy and improvement of thermoelectric properties, Macromolecular Materials and Engineering 286 (2001) 139–142.
[22] J. Feng, T.W. Ellis, Thermal management for semiconductor devices with conductive polymers, Synthetic Metals 135 (2003) 155–156.
[23] J.P. Reifenberg, M.A. Panzer, S. Kim, A.M. Gibby, Y. Zhang, S. Wong, H.S.P. Wong, E. Pop, K.E. Goodson, Thickness and stoichiometry dependence of the thermal conductivity of GeSbTe films, Applied Physics Letters 91 (2007) 111904.
[24] L.H. Liang, B.W. Li, Size-dependent thermal conductivity of nanoscale semiconducting systems, Physical Review B 73 (2006) 153303.
[25] D. Duvivier, O. Van Overschelde, M. Wautelet, Nanogeometry, European Journal of Physics 29 (2008) 467–474.
[26] R.V. Plank, N.J. DiNardo, J.M. Vohs, Growth and characterization of vapor-deposited polyaniline on Cu(1 1 0), Physical Review B 55 (1997) R10241.
[27] H. Li, H. Qiu, K. Fang, J. Li, C. Fang, Characteristics of the polyaniline films vacuum deposited at a high background pressure, Synthetic Metals 156 (2006) 1097–1101.
[28] P.B. Kaul, K.A. Day, A.R. Abramson, Application of the three omega method for the thermal conductivity measurement of polyaniline, Journal of Applied Physics 101 (2007) 083507.
[29] D.G. Cahill, Thermal-conductivity measurement from 30-K to 750-K: the 3-omega method, Review of Scientific Instruments 61 (1990) 802–808.
[30] C. Dames, G. Chen, 1 omega, 2 omega, and 3 omega methods for measurements of thermal properties, Review of Scientific Instruments 76 (2005) 124902.
[31] L. Lu, W. Yi, D.L. Zhang, 3 Omega method for specific heat and thermal conductivity measurements, Review of Scientific Instruments 72 (2001) 2996–3003.
[32] J.Z. Jin, M.P. Manoharan, Q. Wang, M.A. Haque, In-plane thermal conductivity of nanoscale polyaniline thin films, Applied Physics Letters 95 (2009) 033113.
[33] A.F. Mayadas, M. Shatzkes, Electrical-resistivity model for polycrystalline films: the case of arbitrary reflection at external surfaces, Physical Review B 1 (1970) 1382–1389.
[34] S. Stafstrom, J.L. Bredas, A.J. Epstein, H.S. Woo, D.B. Tanner, W.S. Huang, A.G. Macdiarmid, Polaron lattice in highly conducting polyaniline – theoretical and optical studies, Physical Review Letters 59 (1987) 1464–1467.
[35] S.D. George, S. Saravanan, M.R. Anantharaman, S. Venkatachalam, P. Radhakrishnan, V.P.N. Nampoori, C.P.G. Vallabhan, Thermal characterization of doped polyaniline and its composites with CoPc, Physical Review B 69 (2004) 235201.
[36] K.E. Goodson, Y.S. Ju, Heat conduction in novel electronic films, Annual Review of Materials Science 29 (1999) 261–293.

Organic Electronics 11 (2010) 36–40

Contents lists available at ScienceDirect

Organic Electronics

journal homepage: www.elsevier.com/locate/orgel

Red phosphorescent organic light-emitting diodes with indium tin oxide/single organic layer/Al simple device structure

Chul Woong Joo, Soon Ok Jeon, Kyoung Soo Yook, Jun Yeob Lee *

Department of Polymer Science and Engineering, Dankook University, Jukjeon-dong, Suji-gu, Yongin-si, Kyeonggi-do 448-701, Republic of Korea

ARTICLE INFO

Article history:
Received 29 July 2009
Received in revised form 17 September 2009
Accepted 19 September 2009
Available online 12 October 2009

Keywords:
Simple device structure
Phosphine oxide
High efficiency
Organic light-emitting diodes

ABSTRACT

A simple red phosphorescent organic light-emitting diode with a device structure of indium tin oxide (ITO)/single organic layer/Al was developed using a mixed host emitting layer of 2,7-bis(diphenylphosphoryl)spiro[fluorene-7,11′-benzofluorene] (SPPO21) and *N*,*N*′-di(1-naphthyl)-*N*,*N*′-diphenylbenzidine (NPB). Holes were directly injected from the ITO to the emitting layer through the NPB, while electrons were injected from the Al to the emitting layer through the SPPO21. The quantum efficiency of the simple device was comparable to that of the common red device.

© 2009 Elsevier B.V. All rights reserved.

1. Introduction

Phosphorescent organic light-emitting diodes (PHOLEDs) use triplet excitons for light emission and they have been known to be better than fluorescent organic light-emitting diodes (OLEDs) in terms of quantum efficiency. They showed four times higher quantum efficiency than the fluorescent OLEDs and a theoretical maximum internal quantum efficiency of 100% has already been reported [1–3]. Therefore, the PHOLEDs can replace the fluorescent OLEDs in practical applications.

Although the PHOLEDs are better than fluorescent OLEDs in terms of the quantum efficiency, the PHOLEDs have a complicated device structure to maximize the recombination efficiency of holes and electrons. Hole/exciton blocking layers have generally been used in the PHOLEDs to block the hole leakage and prevent the triplet exciton quenching by the electron transport layer [4,5]. Electron/exciton blocking layers were also critical to the quantum efficiency of the PHOLEDs and the quantum efficiency was greatly improved using the high triplet energy electron/exciton blocking layers [6–11]. Holes, electrons and excitons were confined inside the emitting layer in the device with the hole/exciton and electron/exciton blocking layers. The blocking layers were typically used in the PHOLEDs, but the high quantum efficiency could also be obtained in the PHOLEDs without the blocking layers by controlling the charge transport properties of the host materials [12,13]. It was reported that the hole/exciton blocking layer could be omitted by using the electron transport type host material with the recombination zone near the hole transport layer. The use of the high triplet energy hole transport material was effective to achieve high quantum efficiency without the hole/exciton blocking layers [9].

The device structure of the PHOLEDs could be further simplified by developing strong electron transport type host material which can transport electrons from the electron injection layer/cathode to the emitting layer [12,13]. The number of organic layers between the anode and the emitting layer could also be reduced by proper combination of the hole transport material and the triplet host material. A high triplet energy hole transport material with the highest occupied molecular orbital (HOMO) for efficient hole injection could play a role of the hole transport layer and the electron/exciton blocking layer [9]. It was

* Corresponding author. Tel./fax: +82 31 8005 3585.
E-mail address: leej17@dankook.ac.kr (J.Y. Lee).

1566-1199/$ - see front matter © 2009 Elsevier B.V. All rights reserved.
doi:10.1016/j.orgel.2009.09.019

reported that a single layer hole transport structure was enough to balance holes and electrons in the light-emitting layer. In this way, a simple PHOLED with three layers made up of the hole transport layer, the emitting layer and the electron injection layer between the anode and the cathode were developed [13]. However, it was difficult to further simplify the device structure due to high driving voltage and low quantum efficiency.

In this work, a single layer device with only the emitting layer between the anode and the cathode was developed using a novel phosphine oxide type host material. It was demonstrated that the combination of the hole transport type host material and the phosphine oxide type host material which can play a role of a host material and an electron injection material was effective to fabricate the single layer PHOLEDs. The device performances of the single layer red PHOLEDs were comparable to those of common red PHOLEDs with separate charge transport layers.

2. Experimental

The 2,7-bis(diphenylphosphoryl)spiro[fluorene-7,11′-benzofluorene] (SPPO21) was synthesized by the phosphonation reaction of the dibrominated spiro[fluorene-7,11′-benzofluorene]. The SPPO21 single layer device had a device configuration of indium tin oxide (ITO, 150 nm)/*N*,*N*′-di(1-naphthyl)-*N*,*N*′-diphenylbenzidine (NPB):SPPO21:iridium(III) bis(2-phenylquinoline)acetylacetonate (Ir(pq)$_2$acac, 100 nm, 2%)/Al (200 nm). A standard device with a device configuration of ITO (150 nm)/*N*,*N*′-diphenyl-*N*,*N*′-bis-[4-(phenyl-m-tolyl-amino)-phenyl]-biphenyl-4,4′-diamine (60 nm)/NPB(30 nm)/(4,4′-*N*,*N*′-dicarbazole)biphenyl (CBP):Ir(pq)$_2$acac (30 nm, 10% doping)/2,9-dimethyl-4,7-diphenyl-1,10-phenanthroline (BCP, 5 nm)/tris(8-hydroxyquinoline)aluminum(Alq$_3$, 20 nm)/LiF (1 nm)/Al (200 nm) was also fabricated to compare device performances of the single layer devices. The relative ratio of the NPB to SPPO21 was 10:90, 25:75, 40:60 and 50:50 in weight ratio. Three devices were abbreviated as device I, device II, device III and device IV, respectively. Device structures and chemical structures of the emitting materials are shown in Fig. 1. Organic materials were deposited at a deposition rate of 0.1 nm/s and the relative composition of the host material was controlled by managing the deposition rate of each host material. The devices were encapsulated with a getter and a glass lid after cathode deposition. Voltage sweep of the single layer devices were carried out to obtain current density–voltage–luminance relationship. Energy levels of the materials were determined by cyclic voltametry and ultraviolet–visible absorption spectroscopy. Photovoltaic measurements of the devices were carried out with a solar simulator (Abet Co.) at AM 1.5 condition (100 mW/cm^2). The device performances of the blue PHOLEDs was measured with Keithley 2400 source measurement unit and CS1000 spectroradiometer.

3. Results and discussion

The phosphine oxide type host material, SPPO21, has the HOMO level of 6.12 eV, the lowest unoccupied molecular orbital (LUMO) level of 2.57 eV and the triplet energy level of 2.32 eV. The LUMO level of the SPPO21 is suitable for electron injection and the triplet energy of the SPPO21 is wide enough for efficient energy transfer from the SPPO21 to the red emitting triplet dopant materials. Therefore, it can be used as the electron transport type host material for red PHOLEDs. However, the HOMO level of the SPPO21 is not appropriate for hole injection from the anode to the SPPO21 layer. The hole injection can be improved by the hole transport type host material and

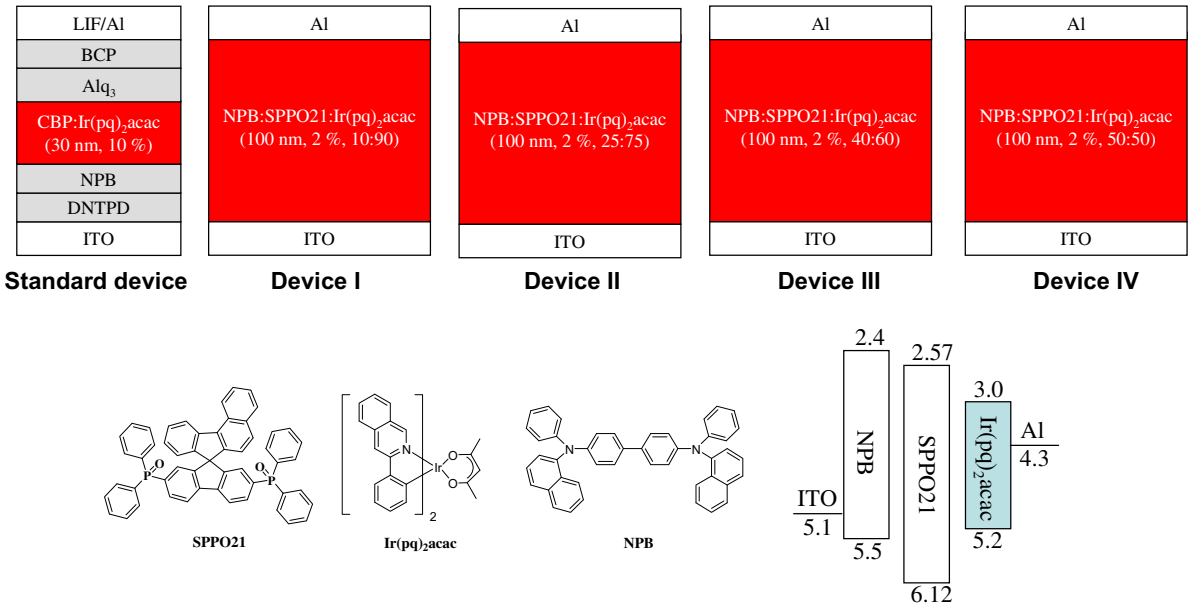

Fig. 1. Chemical structures of the organic materials and device structures of the single layer devices.

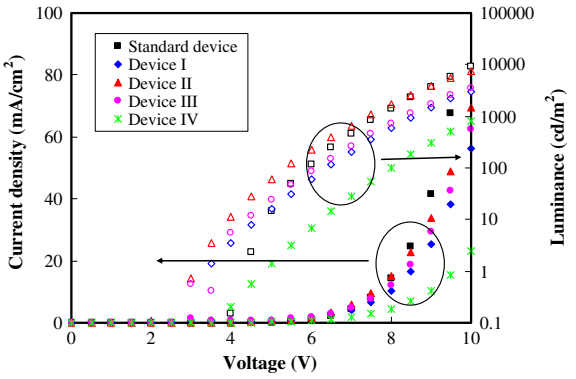

Fig. 2. Current density–voltage and luminance–voltage curves of the single layer red phosphorescent organic light-emitting diodes.

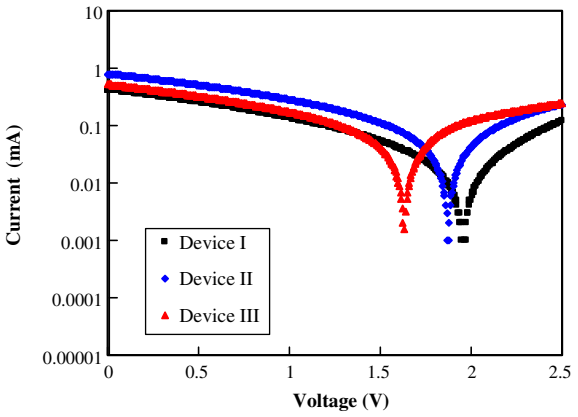

Fig. 3. Current–voltage curves of the single layer red phosphorescent organic light-emitting diodes under exposure to AM 1.5 solar simulator.

the mixing of the hole transport type host with the SPPO21 may enhance the hole injection from the anode to the emitting layer. NPB was chosen as the hole transport type host material due to its triplet energy of 2.3 eV for an energy transfer to the red triplet dopant and the HOMO level of 5.5 eV for direct hole injection from the indium tin oxide anode.

Fig. 2 shows the current density–voltage–luminance curves of the single layer PHOLEDs with different host compositions in the light-emitting layer. The highest current density was observed in the device II with the NPB:SPPO21(25:75) host in the light-emitting layer. There was little difference of the current density in the device I and device III. The high current density of the device II can be explained by the efficient hole injection from the ITO and electron injection from the Al electrode to the emitting layer. The hole injection is effective through the NPB material with strong hole transporting properties, while the electron injection is efficient through the electron transport type SPPO21 material. Therefore, both holes and electrons are effectively injected from the ITO and Al electrode to the emitting layer. In the case of the device I, poor hole injection from the ITO to the emitting layer reduces the current density of the device in spite of the high electron density. Similarly, poor electron injection from the Al cathode to the emitting layer may be responsible for the low current density of the device III. The current density of the device IV was even lower than that of the device III due to poor electron injection. This result implies that the probability for the formation of percolation path for the charge transport is high in the device II, while the percolation path is not formed in the device I, device III and device IV. The luminance of the single layer devices followed the similar relationship as the current density.

To investigate the origin for the direct electron injection from the Al to the emitting layer, the built-in potential of the device was measured using the photovoltaic experiments. The single layer device was exposed to the solar simulator at air mass (AM) 1.5 (100 mW/cm^2) condition and the open circuit voltage (Voc) of the device was measured. Fig. 3 shows the current density–voltage curves of the simple devices under exposure to AM 1.5 solar simulator. The Voc of the simple device I was 1.97 V and it was reduced in the device II (1.88 V) and device III (1.63 V). The Voc corresponds to the built-in potential of the device and it reflects the energy level difference between the anode and the cathode [14]. The ITO electrode has the work function of 5.1 eV from our photoelectron spectroscopic measurements and the Al has the work function of 4.3 eV. Therefore, the built-in potential of the device with the ITO anode and the Al cathode should be around 0.8 eV. However, the built-in potential was greatly increased in the simple device, indicating that the there is a band bending at the interface between the mixed host structure and the electrodes. The NPB does not form any complex with the ITO, while the SPPO21 can induce the band bending through the charge transfer complex formation between the phosphine oxide unit and the Al electrode [15]. Therefore, the work function of the Al is modified by the SPPO21 and the built-in potential is increased. The interface band bending is significant in the device with the high SPPO21 content due to the extensive interfacial contact between the SPPO21 and the Al. The built-in potential was greatly reduced in the device III due to low SPPO21 content, which explains the low current density of the device III. The high energy barrier for electron injection is one of the important reasons for the low current density. As a reference, the built-in potential of the NPB:Alq_3 single layer device was 0.9 eV.

Quantum efficiency of the single layer devices are shown in Fig. 4. High quantum efficiency was obtained in the device II, while the device I, device III and device IV showed much lower quantum efficiency than the device II. In general, the quantum efficiency of the PHOLEDs is determined by the charge balance and triplet exciton quenching by the charge transport layers or cathodes. In terms of the charge balance, the device II is better than the device I or device III because the hole and electron current density was similar in the device II. The electron carriers was much more than the hole carriers in the device I, while hole carriers are much more than the electron carriers in the device III and device IV. The holes and electrons unbalance in the light-emitting layer decreases the quantum efficiency of the device I, device III and device IV. This can be confirmed in the current density–voltage

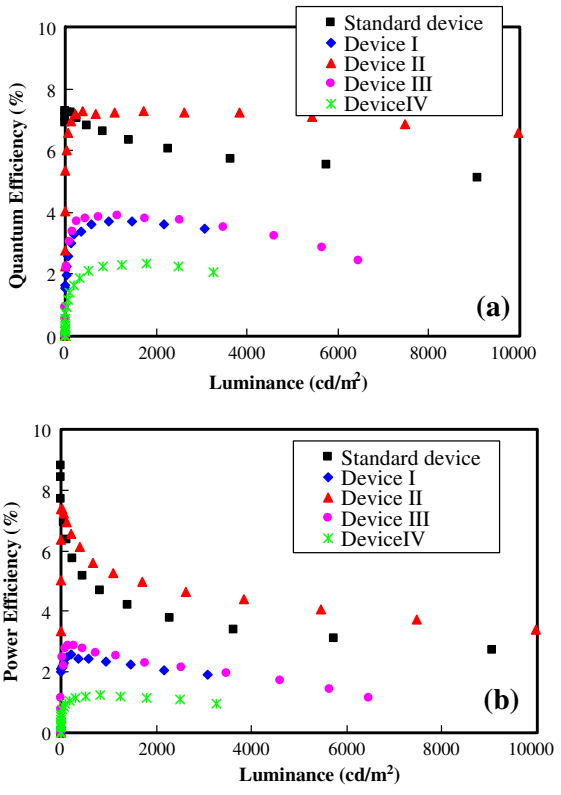

Fig. 4. Quantum efficiency–luminance (a) and power efficiency–luminance (b) curves of the single layer devices.

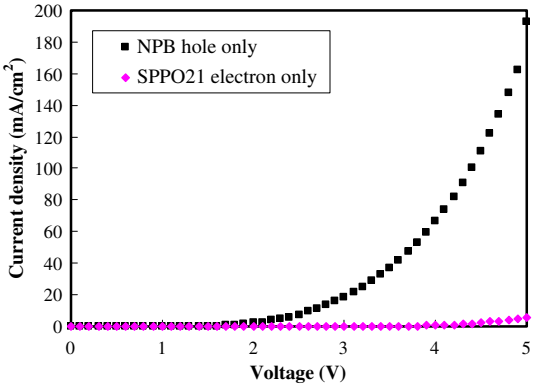

Fig. 5. Current density–voltage curves of the hole only device of the NPB and the electron only device of the SPPO21.

curves of the hole only device of the NPB and the electron only device of the SPPO21 (Fig. 5). The hole current density was much higher than the electron current density and the charge balance could be optimized in the device with high SPPO21 content. The other factor for the low quantum efficiency in the device I, device III and device IV is triplet exciton quenching by the anode and the cathode. It has been known that the recombination zone of the emitting layer in the PHOLEDs should be away from the cathode. As reported in the early work, the triple exciton quenching is significant in the device with the recombination zone near

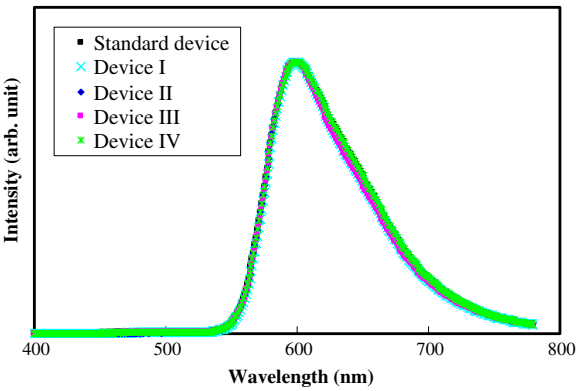

Fig. 6. Electroluminescence spectra of the single layer red PHOLEDs.

the electrode. The recombination zone of the device is close to the anode side when the electron transport type host material is rich in the mixed host structure, while the exciton formation zone is close to the electron transport layer side in the device when the hole transport type host material is rich in the mixed host structure. Therefore, there is a high probability for the exciton quenching by the electrode in the device I, device III and device IV. In the case of the device II, the exciton quenching by the electrode can be reduced due to broad recombination zone. The quantum efficiency of the device II was 7.3% at 1000 cd/m^2 and the current efficiency was 11.4 cd/A. The quantum efficiency of the device II was better than that of the standard device with CBP host in the light-emitting layer and common charge transport layers. The improved charge balance in the emitting layer and low probability for the triplet exciton quenching may be responsible for the high quantum efficiency of the device II compared with the standard device. The efficiency roll-off was also better in the device II, which may be due to broad recombination zone in the device II. Therefore, it was possible to develop the single organic layer PHOLEDs which show better performances than the common red PHOLEDs. The direct hole injection from the ITO to the NPB and direct electron injection from the Al to the SPPO21 were responsible for the high quantum efficiency and low driving voltage in the single layer device. The power efficiency of the devices followed the same trend as the quantum efficiency.

Electroluminescence (EL) spectra of the single layer red PHOLEDs are shown in Fig. 6. There was little difference of the EL spectra in the single layer devices with different host compositions in the emitting layer. This indicates that the same EL spectra as the standard device can be obtained in the single layer devices.

4. Conclusions

In conclusion, high efficiency single layer red PHOLEDs could be developed using the hole transport type NPB and the electron transport type SPPO21 as the host materials in the light-emitting layer. Holes were directly injected from the anode through the NPB and electrons could be directly injected from the cathode through the SPPO21 layer. Band bending at the interface between the

mixed emitting layer and the Al cathode by the SPPO21 layer was critical to fabricate the single layer devices without any electron injection layer and any charge transport layer. Therefore, the device structure of the PHOLEDs could be simplified without sacrificing the device performances by using the phosphine oxide type SPPO21 host material.

Acknowledgement

This work was supported by the IT R&D program of MKE/KEIT. [2009-F-017-01, Development of Fundamental Technologies for Flexible Combined-Function Organic Electronic Device].

References

[1] C. Adachi, M.A. Baldo, M.E. Thompson, S.R. Forrest, J. Appl. Phys. 90 (2001) 5048.
[2] S.-J. Su, D. Tanaka, Y.-J. Li, H. Sasabe, T. Takeda, J. Kido, Org. Lett. 10 (2008) 941.
[3] L. Xiao, S.-J. Su, Y. Agata, H. Lan, J. Kido, Adv. Mater. (2009), doi:10.1002/adma.200802034.
[4] M.A. Baldo, M.E. Thompson, S.R. Forrest, Pure Appl. Chem. 71 (1999) 2095.
[5] M. Ikai, Y. Sakamoto, T. Suzuki, Y. Taga, Appl. Phys. Lett. 79 (2001) 156.
[6] V. Adamovich, S. Ramansky, P.I. Djurovich, A. Tamayo, M.E. Thompson, B. Andrade, S.R. Forrest, Org. Electron. 4 (2003) 77.
[7] Y. Wang, Appl. Phys. Lett. 85 (2004) 4848.
[8] S.H. Kim, J. Jang, J.Y. Lee, Appl. Phys. Lett. 90 (2007) 223505.
[9] S.O. Jeon, K.S. Yook, C.W. Joo, J.Y. Lee, K. Ko, J. Park, Y.G. Baek, Appl. Phys. Lett. 93 (2008) 063306.
[10] S. Tokito, M. Suzuki, F. Sato, M. Kamachi, K. Shirane, Org. Electron. 4 (2003) 105.
[11] M. Suzuki, S. Tokito, F. Sato, T. Igarashi, K. Kondo, T. Koyama, T. Yamaguchi, Appl. Phys. Lett. 86 (2005) 103507.
[12] S.O. Jeon, K.S. Yook, C.W. Joo, J.Y. Lee, Appl. Phys. Lett. 94 (2009) 013301.
[13] W.S. Jeon, T.J. Park, J.J. Park, S.Y. Kim, J. Jang, J.H. Kwon, R. Pode, Appl. Phys. Lett. 92 (2008) 113311.
[14] G.G. Malliaras, J.R. Salem, P.J. Brock, J.C. Scott, J. Appl. Phys. 84 (1998) 1583.
[15] K.U. Jeong, I.Y. Park, I.C. Kim, T.H. Yoon, J. Appl. Polym. Sci. 80 (1999) 1198.

Organic Electronics 11 (2010) 41–49

Contents lists available at ScienceDirect

Organic Electronics

journal homepage: www.elsevier.com/locate/orgel

Synthesis, crystal structure and photo- and electro-luminescence of the coumarin derivatives with benzotriazole moiety

Tianzhi Yu [a,*], Peng Zhang [a,b], Yuling Zhao [b], Hui Zhang [a], Jing Meng [a], Duowang Fan [a], Lili Chen [c], Yongqing Qiu [c]

[a] Key Laboratory of Opto-Electronic Technology and Intelligent Control (Lanzhou Jiaotong University), Ministry of Education, Lanzhou 730070, China
[b] School of Chemical and Biological Engineering, Lanzhou Jiaotong University, Lanzhou 730070, China
[c] Institute of Functional Material Chemistry, Faculty of Chemistry, Northeast Normal University, Changchun 130024, China

ARTICLE INFO

Article history:
Received 15 July 2009
Received in revised form 22 September 2009
Accepted 23 September 2009
Available online 9 October 2009

Keywords:
Synthesis
Coumarin derivative
Benzotriazole
Photo- and electroluminescence

ABSTRACT

Two new coumarin derivatives containing an electron-transporting moiety (benzotriazole), 7-*N*,*N*-diethylamino-3-(benzotriazol-1-yl)coumarin (DABTC-1) and 7-*N*,*N*-diethylamino-3-(benzotriazol-2-yl)coumarin (DABTC-2), were synthesized and characterized by element analysis, ^{1}H NMR, FT-IR and UV–vis absorption spectra. Their structures were determined by X-ray crystallography single crystal analysis. The photoluminescent behaviors of the compounds in both solution and solid states were observed, they exhibit strong blue and blue–green emissions under ultraviolet light excitation, respectively. The energy levels of the HOMO and LUMO of the compounds have been calculated with density functional theory (DFT) and time-dependent density functional theory (TD-DFT) at B3LYP/6-31G(d) level. The electroluminescent devices with the compounds as the emitters were fabricated.

© 2009 Elsevier B.V. All rights reserved.

1. Introduction

Organic light-emitting diodes (OLEDs) based on organic materials are known to be highly efficient and are capable of producing a wide range of colors, which have attracted considerable interest and constitute a rapidly developing field due to their potential use in the development of energy-efficient, low-cost, full-color, flat-panel displays and other emissive products [1–4].

Coumarin derivatives exhibit not only excellent biological and medical activities [5], but also have super thermal stability and outstanding optical properties including an extended spectral response, high quantum yields, superior photostability. Optical applications of these compounds, such as laser dyes, nonlinear optical chromophores, fluorescent whiteners, fluorescent probes, polymer science, optical recording and solar energy collectors, have been widely investigated [6–12]. More important, coumarin dyes were used as blue, green and red dopants in organic light-emitting diodes (OLEDs) [13–15]. However, coumarin dyes are easily self-quenched in high concentration due to the intermolecular interactions and aggregations, so as the light-emitting materials they are always doped in the host materials at appropriate concentration to fabricate OLEDs with reasonable, luminant efficiency [16–19]. 7-*N*,*N*-diethylaminocoumarin dyes substituted at 3-position with an electron-withdrawing group are a typical class of D-A structure molecules and exhibit strong fluorescence [20–22]. So some of these coumarin derivatives have been used in the fabrication of OLEDs through doping in polymer matrix or Alq_3 thin layer as guest-emitting materials [23].

Recently, we synthesized two new coumarin derivatives, 7-*N*,*N*-diethylamino-3-(benzotriazol-1-yl)coumarin (DABTC-1) and 7-*N*,*N*-diethylamino-3-(benzotriazol-2-yl)-coumarin (DABTC-2), using the Knoevenagel type of condensation reaction (Scheme 1). The compounds exhibit strong blue and blue-green emissions under ultraviolet light excitation, respectively. Here, the photophysical properties of the compounds in diluted chloroform

* Corresponding author. Tel.: +86 931 4956935; fax: +86 931 4938756.
E-mail address: Ytz823@hotmail.com (T. Yu).

1566-1199/$ - see front matter © 2009 Elsevier B.V. All rights reserved.
doi:10.1016/j.orgel.2009.09.023

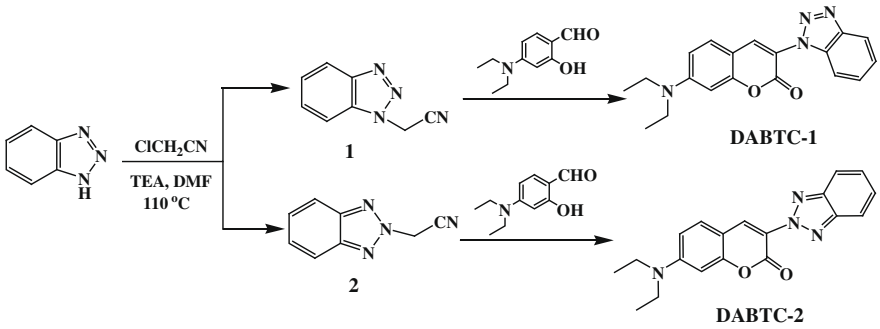

Scheme 1. Synthetic routes of 7-*N*,*N*-diethylamino-3-(benzotriazol-1-yl)coumarin and 7-*N*,*N*-diethylamino-3-(benzotriazol-2-yl)coumarin.

solutions and thin films were investigated in detail. We fabricated the electroluminescence devices by vacuum vapor-deposited film with doped with the compounds as emission materials and investigated the electroluminescent properties.

2. Experimental details

2.1. Materials and methods

4-(*N*,*N*′-diethylamino) salicylaldehyde from Zhejiang Huadee Dyestuff Chemical Co. Ltd. (China) was recrystallized from ethanol. 1H-benzotriazole (BTA) from Aldrich was used without further purification. Triethylamine, piperidine and chloroacetonitrile were analytical grade reagents from Tanjin Fuchen Chemical Reagent Factory. 4,4′-bis(9-carbazolyl) biphenyl (CBP), 2-(4-biphenylyl)-5-(4-tert-butylphenyl)-1,3,4-oxadiazole (Bu-PBD), 4,4′,4″-tris-N-naphthyl-*N*-phenylamino-triphenylamine (2-TNATA) and *N*,*N*′-bis-(naphthyl)-*N*,*N*′-diphenyl-1,1′-biphenyl-4,4′-diamine (NPB) were purchased from Electro-Light Technology Corp., Beijing. The other solvents were analytical grade reagents.

IR spectra (400–4000 cm^{-1}) were measured on a Shimadzu IRPrestige-21 FT-IR spectrophotometer. ^1H NMR spectra were obtained on Unity Varian-500 MHz. C, H, and N analyses were obtained using an Elemental Vario-EL automatic elemental analysis instrument. Melting points were measured by using an X-4 microscopic melting point apparatus made in Beijing Taike Instrument Limited Company, and the thermometer was uncorrected. UV–vis absorption and photoluminescent spectra were recorded on a Shimadzu UV-2550 spectrometer and on a Perkin–Elmer LS-55 spectrometer, respectively. The electroluminescent spectra were measured on a Hitachi MPF-4 spectrometer.

2.2. Synthesis and characterization of 7-N,N-diethylamino-3-(benzotriazol-1-yl)coumarin (DABTC-1) and 7-N,N-diethylamino-3-(benzotriazol-2-yl)coumarin (DABTC-2)

The synthetic routes were shown in scheme 1.

2.2.1. 2-(1H-benzotriazol-1-yl)acetonitrile (**1**) and 2-(1H-benzotriazol-2-yl)acetonitrile (**2**)

The intermediates **1** and **2** were synthesized by condensation of 1*H*-benzotriazole with chloroacetonitrile in DMF at reflux in the presence of triethylamine according to the method reported by Sanna et al. [24].

2.2.2. 7-N,N-diethylamino-3-(benzotriazol-1-yl)coumarin (DABTC-1)

1.93 g (10 mmol) of 4-(*N*,*N*′-diethylamino) salicylaldehyde, 1.67 g (10.6 mmol) 2-(1*H*-benzotriazol-1-yl)acetonitrile (**1**) were dissolved in 16 mL of anhydrous alcohol and treated with piperidine (0.6 mL). The reaction mixture was refluxed with stirring for 49 h, treated with HCl (3.5%), and boiled for 5 h. After the reaction was finished, the resulting mixture was poured into 50 mL of water and extracted with dichloromethane (3 × 50 mL). The organic phase was washed with water (2 × 50 mL) and dried over anhydrous $MgSO_4$. After filtering, the filtrate was evaporated to dryness under reduced pressure. The crude was purified by chromatography on silica gel using ethyl acetate/petroleum ether (1:6, v/v) as the eluent to give 7-*N*,*N*-diethylamino-3-(benzotriazol-1-yl)coumarin (DABTC-1) (1.12 g, 33.5%). m.p. 164–165 °C. 1H NMR: (500 MHz, $CDCl_3$, δ, ppm): 8.116 (d, J = 4.8 Hz, 1H, Aryl-H), 8.049 (s, 1H, 4-H), 7.619–7.594 (m, 1H, Aryl-H), 7.565–7.554 (m, 1H, Aryl-H), 7.540–7.516 (m, 1H, Aryl-H), 7.434–7.388 (m, 1H, Aryl-H), 6.678 (d, J = 7.9 Hz, 1H, Aryl-H), 6.608 (s, 1H, Aryl-H), 3.503–3.451 (m, 4H, $-CH_2-$), 1.261 (t, J = 6.4 Hz, 6H, $-CH_3$). IR (KBr pellet cm^{-1}): 3060 (Aryl-CH), 2971, 2929, 2891 (Alkyl-CH), 1728 (C=O, lactone), 1628 (C=C), 1590, 1524, 1421, 1250, 1121, 752. Anal. Calc. for $C_{19}H_{18}O_2N_4$ (%): C, 68.25; H, 5.43; N, 16.76. Found: C, 68.53; H, 5.57; N, 16.84.

2.2.3. 7-N,N-diethylamino-3-(benzotriazol-2-yl)coumarin (DABTC-2)

0.49 g (2.53 mmol) of 4-(*N*,*N*′-diethylamino) salicylaldehyde, 0.40 g (2.53 mmol) 2-(1*H*-benzotriazol-2-yl)acetonitrile (**2**) were dissolved in 12 mL of absolute alcohol, and then piperidine (0.2 mL) was dropped under ice bath. The mixture was stirred for 12 h at room temperature, treated with HCl (3.5%) and boiled for 5 h. After the reaction was finished, the resulting mixture was poured into 20 mL of water and extracted with dichloromethane (3 × 20 mL). The organic phase was washed with water and dried over anhydrous $MgSO_4$. After filtering, the filtrate was evaporated to dryness under reduced pressure. The crude was purified by chromatography on silica gel using ethyl acetate/petroleum ether (1:6, v/v) as the eluent to give 7-

N,*N*-diethylamino-3-(benzotriazol-2-yl)coumarin (DABTC-2) (0.63 g, 74.8%). m.p. 156–158 °C. ^{1}H NMR: (500 MHz, $CDCl_3$, δ, ppm): 8.280 (s, 1H, 4-H), 7.954 (d, J = 4.8 Hz, 2H, Aryl-H), 7.441–7.264 (m, 3H, Aryl-H), 6.682 (d, J = 8 Hz, 1H, Aryl-H), 6.608 (s, 1H, Aryl-H), 3.484–3.440 (m, 4H, $-CH_2-$), 1.255 (t, J = 5.2 Hz, 6H, $-CH_3$). IR (KBr pellet cm^{-1}): 3067 (Aryl-CH), 2975, 2925, 2871 (Alkyl-CH), 1731 (C=O, lactone), 1624 (C=C), 1573, 1517, 1421, 1233, 1125, 745. Anal. Calc. for $C_{19}H_{18}O_2N_4$ (%): C, 68.25; H, 5.43; N, 16.76. Found: C, 68.51; H, 5.72; N, 16.37.

2.3. Crystallography

Suitable crystals of DABTC-1 and DABTC-2 were obtained by evaporation of ethyl acetate solutions, respectively. The diffraction data were collected with a Bruker Smart Apex CCD area detector using a graphite-monochromated Mo Kα radiation (λ = 0.71073 Å) at 20 °C. The structures of DABTC-1 and DABTC-2 were solved by using the program SHELXL and Fourier difference techniques, and refined by full-matrix least-squares method on F^2. All hydrogen atoms were added theoretically. The crystals and experimental data of DABTC-1 and DABTC-2 are shown in Table S1. The selected bond lengths and bond angles of DABTC-1 and DABTC-2 are listed in Tables S2 and S3, respectively.

2.4. Quantum chemical calculations

The structure of DABTC-1 and DABTC-2 were optimized by semiempirical density functional theory (DFT) using a B3LYP/6-31G (d) basis set. The structural energies of DABTC-1 and DABTC-2 were calculated at B3LYP/6-31G(d) levels. The structure optimization and energy calculations were performed with the GAUSSIAN 98 program.

2.5. OLEDs fabrication

The multilayer OLEDs were fabricated by vacuum-deposition method. ITO-coated glass with a sheet resistance $R_\square \sim 20\ \Omega/\square$ was cut into 3 cm × 3 cm plates and etched in dilute hydrochloric acid for 20 min. Then the ITO substrates were routinely cleaned by ultrasonic treatment in solvents and then cleaned by exposure to an UV–ozone ambient. All organic layers were sequentially deposited without breaking vacuum (2×10^{-4} Pa). Thermal deposition rates for organic materials, LiF and Al were ~2 Å/s, ~1 Å/s and 10 Å/s, respectively. The active area of the devices was 12 mm^2. The EL spectra were measured on a Hitachi MPF-4 fluorescence spectrometer. The characterization of brightness–current–voltage (B–I–V) were measured with a 3645 DC power supply combined with a 1980A spot photometer and were recorded simultaneously. All measurements were done in the air at room temperature without any encapsulation.

3. Results and discussion

3.1. X-ray crystal structures of DABTC-1 and DABTC-2

The crystal structures and packing diagrams of DABTC-1 and DABTC-2 are given in Figs. 1–4, respectively. The crystal data and experimental details are shown in Table S1. The selected bond lengths and bond angles of DABTC-1 and DABTC-2 are listed in Tables S2 and S3, respectively.

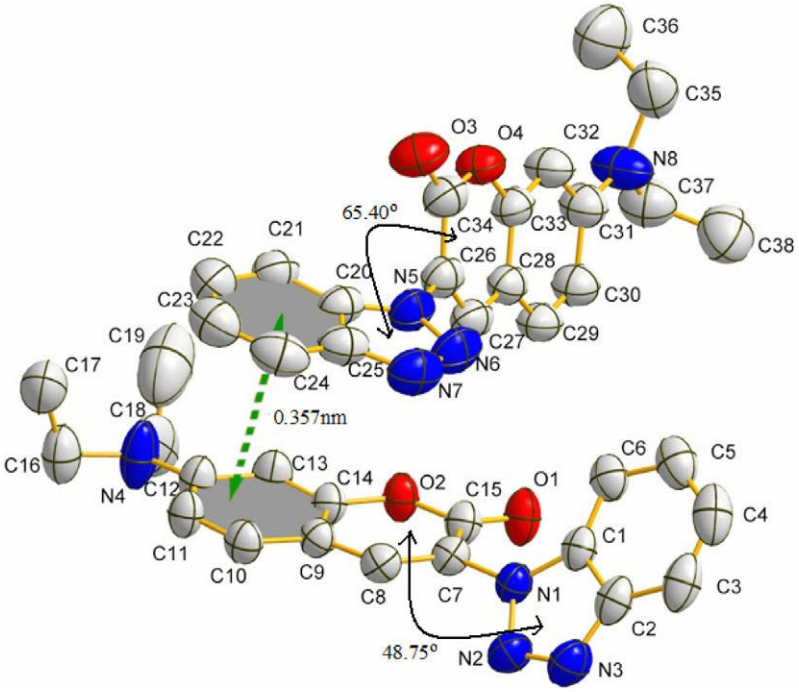

Fig. 1. Crystal structure of DABTC-1.

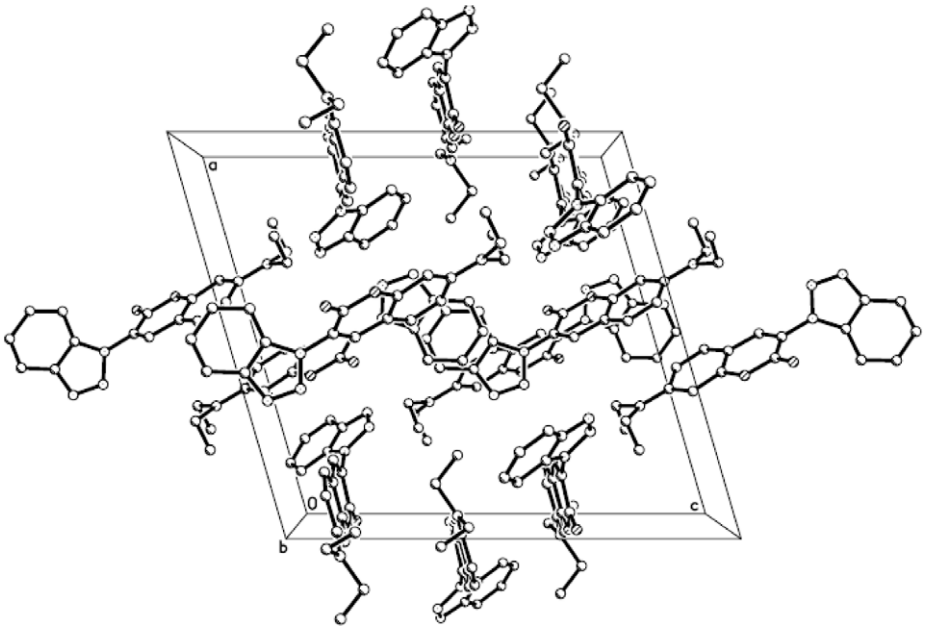

Fig. 2. Packing diagram of molecules of DABTC-1 along *a*-axis. H atoms are omitted for clarity.

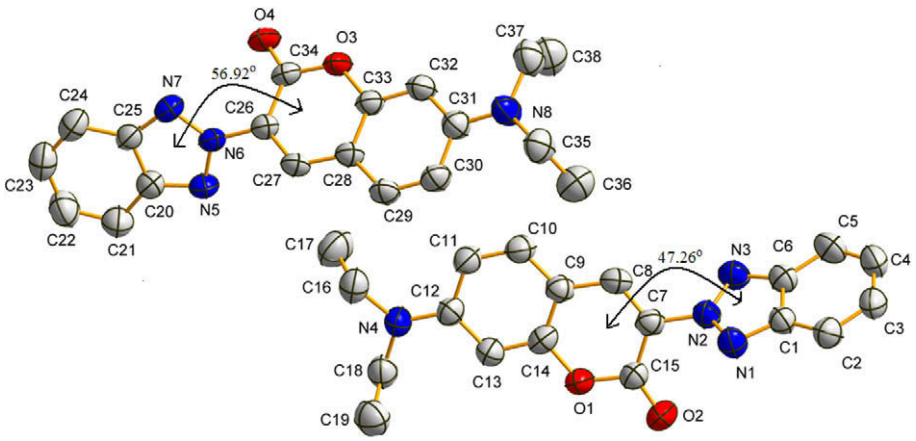

Fig. 3. Crystal structure of DABTC-2.

Acceptable crystals of DABTC-1 for X-ray analysis were obtained by slow evaporation of ethyl acetate solution, and the structure was measured by X-ray crystallography. The crystal of DABTC-1 belongs to the monoclinic space group $P2_1/c$, $a = 15.920(2)$ Å, $b = 12.8933(18)$ Å, $c = 17.083(3)$ Å, $\beta = 106.299(3)°$, $U = 3365.7(9)$ Å^3, $Z = 8$, $D_c = 1.320$ g cm^{-3}, $\mu = 0.089$ mm^{-1}. As shown in Fig. 1, there is an asymmetric unit consisted of two molecules in crystal structure of DABTC-1 due to the different space configuration of two ethylic groups of diethylamine in 7-position of coumarin ring. These two molecules are space conformers, the benzotriazole skeleton of one DABTC-1 molecule cross-paralleled and superposed with the coumarin ring of other DABTC-1 molecule, and the distance of the planes is about 3.6 Å. In addition, the benzotriazole skeletons are not coplanar with the coumarin rings in these two molecules, the dihedral angles are 65.40° and 48.75°, respectively.

The packing diagram for unit cell of DABTC-1 was shown in Fig. 2. There is cross ABAB-type stacking between the benzotriazole group of one DABTC-1 molecule and the coumarin ring of other DABTC-1 molecule, the interplanar (A···B) distance is approximately 3.6 Å, which means weak intermolecular π–π stacking interaction between DABTC-1 molecules in crystal lattice.

Acceptable crystals of DABTC-2 for X-ray analysis were also obtained by slow evaporation of ethyl acetate solution. The crystal of DABTC-2 belongs to the monoclinic space group $P2_1/c$, $a = 17.416(5)$ Å, $b = 12.743(4)$ Å, $c = 15.707(5)$ Å, $\beta = 102.527(5)°$, $U = 3403.1(18)$ Å^3, $Z = 8$, $D_c = 1.305$ g cm^{-3}, $\mu = 0.088$ mm^{-1}. Similarly, there is also an asymmetric unit consisted of two molecules in crystal structure of DABTC-2 due to the different space configuration of two ethylic groups of diethylamine in 7-position of coumarin ring (Fig. 3). Compared with DABTC-1, these

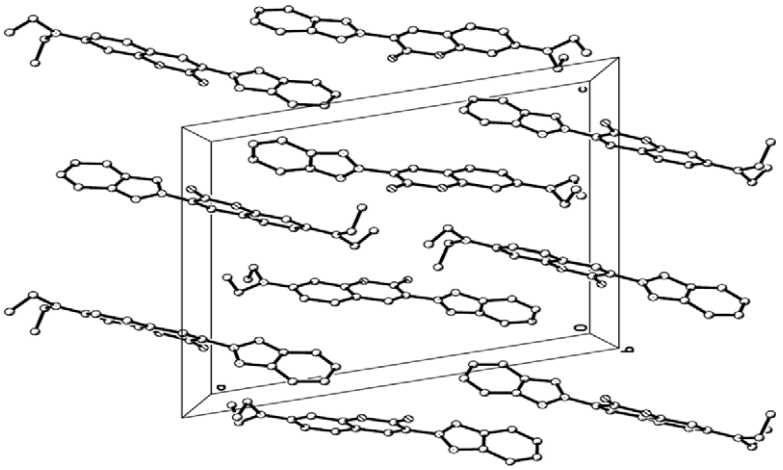

Fig. 4. Packing diagram of molecules of DABTC-2 along *c*-axis. H atoms are omitted for clarity.

space conformers did not neither parallel nor superpose each other. As shown in Fig. 4, there is no intermolecular π–π stacking interaction between DABTC-2 molecules in crystal lattice. From the crystal structure of DABTC-2, we can see that the benzotriazole skeletons are not also coplanar with the coumarin rings in these two molecules, the dihedral angles are 56.92° and 47.26°, respectively.

3.2. Absorption and fluorescence of DABTC-1 and DABTC-2

UV–vis absorption spectra of DABTC-1 and DABTC-2 in diluted chloroform solutions are given in Fig. 5. It is shown that the absorption spectrum of DABTC-1 exhibits absorptions at 253 nm and 414 nm, respectively. The absorption spectrum of DABTC-2 is similar to that of DABTC-1, there are two absorption at 253 nm and 424 nm. An important feature of the absorption spectrum of DABTC-2 is shown that the second absorption band at 424 nm was bathochromically shifted by about 10 nm with respect to that of DABTC-1 in which the second absorption band is at 414 nm, it can be generally deduced that the conjugative effect of the 2-substituted benzotriazole derivative (i.e. DABTC-2) is larger than that of the 1-benzotriazolyl isomer (i.e. DABTC-1).

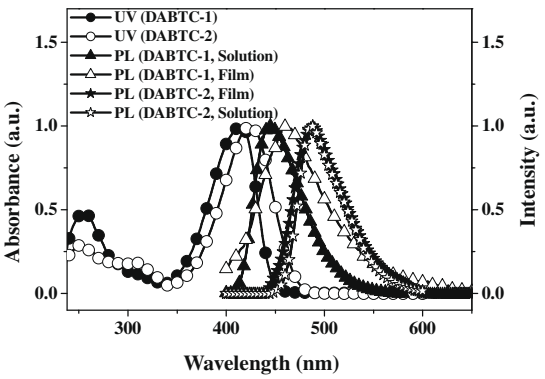

Fig. 5. UV–Vis absorption and photoluminescent spectra of the compounds in dilute chloroform solutions and the solid films.

Fig. 5 also shows the photoluminescent spectra of DABTC-1 and DABTC-2 in dilute chloroform solutions and the solid films. It is shown that DABTC-1 compound exhibits bright blue emission with peak at 447 nm and DABTC-2 compound exhibits bright blue–green emission at 485 nm in dilute solution, and the emission peak of DABTC-2 was red-shifted by about 38 nm compared with that of DABTC-1 due to the larger conjugation of molecule in DABTC-2. Compared with the emission spectra in the solutions, the emission peaks of the solid films of DABTC-1 and DABTC-2 are observed at 462 and 485 nm, respectively. The emission peak of DABTC-1 in the solid film was bathochromically shifted by 15 nm with respect to that in the solution, and much broader emission band of the solid film brought about the compact piling of the solids was occurred, suggesting that the compound in the solid film has more intermolecular interaction than that in solution situation, and thus may lead to change of the emission band. The emission spectrum of the film of DABTC-2 was similar to that of the solution, the emission peaks were at 485 nm, but the former was little broader than the latter. The differences between the films and the solutions were explained by the crystal structures of DABTC-1 and DABTC-2. There was weak intermolecular π–π stacking interaction between DABTC-1 molecules in crystal lattice, whereas no intermolecular π-π stacking interaction between DABTC-2 molecules existed in crystal lattice.

UV–vis absorption and photoluminescent spectra of coumarin 6 (C6) and 7 (C7) in diluted chloroform solutions show the maximum peaks at 456 nm (C6), 437 nm (C7), 490 nm (C6) and 491 nm (C7), respectively [25]. Compared with commercial coumarin 6 and 7, although the structure of DABTC-2 is similar to that of coumarin 6 and 7, UV–vis absorption and photoluminescent spectra of DABTC-2 shift to blue due to the electron-withdrawing benzotriazole substituents at 3-position.

The photoluminescence behaviors of DABTC-1 and DABTC-2 vs. the concentrations in chloroform solutions were shown in Fig. 6. It was found that the emission spectral features of DABTC-1 and DABTC-2 changed with the solution concentrations. The concentration required for

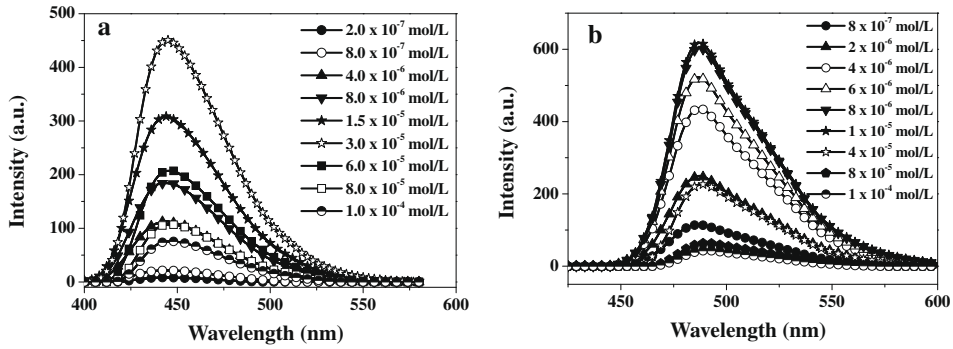

Fig. 6. The emission spectra of DABTC-1 (a) and DABTC-2 (b) in dilute chloroform solutions at room temperature.

the maximum emission intensity was different in DABTC-1 and DABTC-2, which implies that concentration plays an important role in the different dye molecules. There is the strongest blue emission at about concentration of 3.0×10^{-5} mol/L for DABTC-1 and 8.0×10^{-6} mol/L for DABTC-2, respectively. When the concentrations were lower than these concentrations, the relative emission intensities increased gradually with increasing the concentrations. When the concentrations were higher than these concentrations, the emission intensities were decreasing.

3.3. Fluorescence quantum yield of the compound **3** ($\Phi_{F,3}$)

Fluorescence quantum yields of DABTC-1 and DABTC-2 in chloroform solution were checked with anthracene, respectively. The quantum yield (Φ_F) were calculated according to the relationship [26,27]:

$$\Phi_F = \Phi_F^S \frac{\int_0^\infty I_F(\tilde{\nu})d\tilde{\nu}}{\int_0^\infty I_F^S(\tilde{\nu})d\tilde{\nu}} \left(\frac{1-10^{-A^S}}{1-10^{-A}}\right)\left(\frac{n}{n^S}\right)^2$$

where Φ_F^S is the quantum yield of anthracene as standard, which was assumed to be 0.25 for all environments [27]. The integral $\int_0^\infty I_F(\tilde{\nu})d\tilde{\nu}$ and $\int_0^\infty I_F^S(\tilde{\nu})d\tilde{\nu}$ are the areas under the emission curves of the investigated and standard compound, respectively. A and A^S are the absorbances at the wavelength of excitation, n and n^S are the refractive indices for the investigated and standard, respectively. In the research, the $\Phi_{F,\ DABTC\text{-}1}$ and $\Phi_{F,\ DABTC\text{-}2}$ are 0.53 and 0.69, respectively. Fluorescence quantum yields of Coumarin 6 ($\Phi_{F,\ Coumarin\ 6}$) in acetonitrile is 0.63 [28]. Fluorescence quantum yields of DABTC-1 and DABTC-2 are comparative to that of coumarin 6.

3.4. Quantum chemical calculations

From the crystal structures of DABTC-1 and DABTC-2 (Figs. 1 and 3), it was found that there were two molecules in the crystal structures. For the sake of quantum chemical calculations, we chose one molecule of them to optimize DABTC-1 and DABTC-2 geometrical structures, respectively. B3LYP/6-31G(d) optimized structures of DABTC-1 and DABTC-2 are close to their X-ray crystallographic data. The HOMO and LUMO levels of DABTC-1 and DABTC-2 were deduced using the DFT method as shown in Figs. S1 and S2, respectively. It can be seen that the levels of HOMO and LUMO of DABTC-1 were −5.510 eV and −1.589 eV, and the energy gap between HOMO and LUMO is about 3.921 eV. For DABTC-2, the data were −5.487 eV, −1.594 eV and 3.893 eV, respectively. It can be also found that the electron density distributions of the HOMO orbitals were different from that of the HOMO orbitals for DABTC-1 and DABTC-2.

The UV–vis absorption spectra of DABTC-1 and DABTC-2 were also calculated by the time-dependent density functional theory (TD-DFT) at the same level. The experimental and calculated data for the lower-lying singlet states of DABTC-1 and DABTC-2 were listed in Table 1. As shown in Table 1, there are some discrepancies between theoretical and experimental data due to several influencing factors, such as solvent effect and intermolecular interaction. It has been found that the lowest energy absorption at 414 nm for DABTC-1 or 424 nm for DABTC-2 was an excitation from the HOMO to the LUMO. The transition occurring at 253 nm was attributed to the electronic $\pi \rightarrow \pi^*$ transition from the HOMO to the LUMO+2 for DABTC-1 or from the HOMO−2 to the LUMO+1 for DABTC-2, respectively.

Table 1
Absorption spectra data of DABTC-1 and DABTC-2.

Compound	Transition character	OSC[a]	$\lambda_{max,\ cal.}$ (nm)	$\lambda_{max,\ exp.}$ (nm)[b]	Transition feature
DABTC-1	HOMO → LUMO	0.7397	369.32	414	$\pi \rightarrow \pi^*$
	HOMO → LUMO+2	0.1583	243.25	253	$\pi \rightarrow \pi^*$
DABTC-2	HOMO → LUMO	0.9473	378.24	424	$\pi \rightarrow \pi^*$
	HOMO−2 → LUMO+1	0.1778	233.37	253	$\pi \rightarrow \pi$

[a] Oscillator strength coefficients (f).
[b] λ_{max} in dichloromethane solvent.

3.5. OLED performance

The molecular structures of the materials and the devices with the configuration of ITO/2-TNATA (5 nm)/NPB (40 nm)/CBP: DABTC-1 or CBP: DABTC-2 (× wt%, 30 nm)/PBD (30 nm)/LiF (1 nm)/Al (100 nm) were depicted in Fig. 7. DABTC-1: CBP or DABTC-2: CBP was employed as the emitter, 2-TNATA, NPB, and PBD were used as hole injection, hole transport and electron transport materials, respectively. LiF was used as the electron–injection layer.

Fig. 8 shows the EL spectra of the devices with DABTC-1 and DABTC-2 doped at concentrations of 1.0 wt% at different driving voltages. The intensities of EL emissions increase gradually with increasing the driving voltages, but the emission spectral features do not change. The devices of DABTC-1 exhibit blue emissions with the maximum peaks at ca. 462 nm, the devices of DABTC-2 exhibit blue–green emissions with the maximum peaks at ca. 485 nm. The EL spectra of DABTC-1 and DABTC-2 are identical to the PL spectra of them in the solid films, respectively. Such results indicate that these emissions take place from DABTC-1 and DABTC-2 molecules.

Fig. 9 shows the representative luminance-current density–voltage characteristics of the devices doped DABTC-1 with different concentrations. At the doped concentration of 1.0 wt%, the device shows a turn-on voltage about 12 V, and the luminance reaches as high as 40 cd/m^2 at 21 V. At the doped concentration of 2.0 wt%, a turn-on voltage of the device is about 8.5 V, and the maximal luminance reaches 48 cd/m^2 at 15 V.

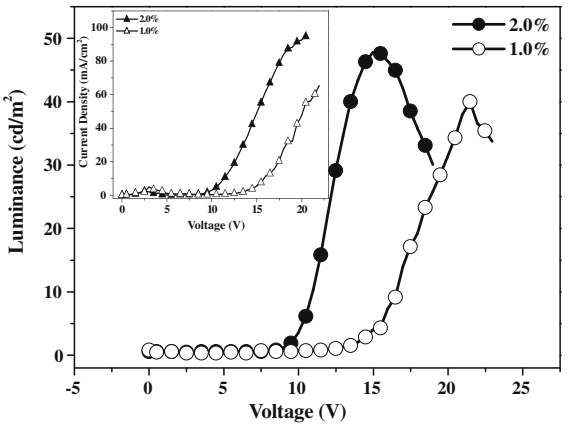

Fig. 9. The luminance vs. voltage and current density vs. voltage (inset) curves of the devices with different DABTC-1 concentrations.

Fig. 10 shows the representative luminance-current density–voltage characteristics of the devices doped DABTC-2 with different concentrations. The turn-on voltages of the devices at the doped concentrations of 1.0 wt% and 2.0 wt% were 10 V and 6 V, respectively. The maximal luminances were 371 cd/m^2 at 23 V for the device doped

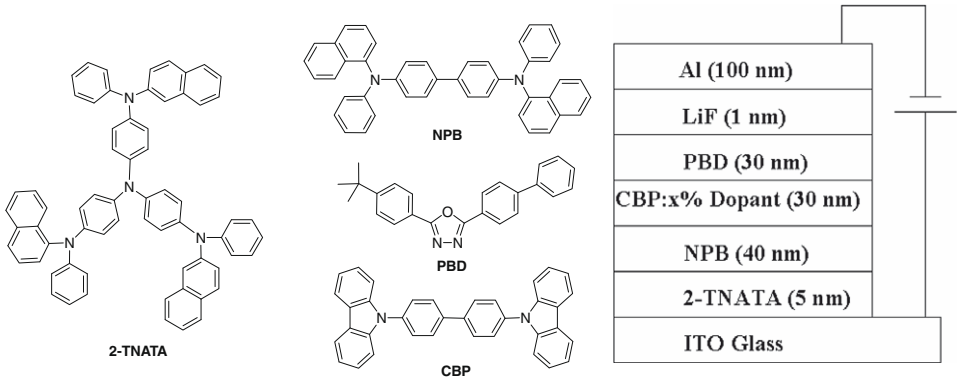

Fig. 7. The molecular structures of materials and the structure of EL devices.

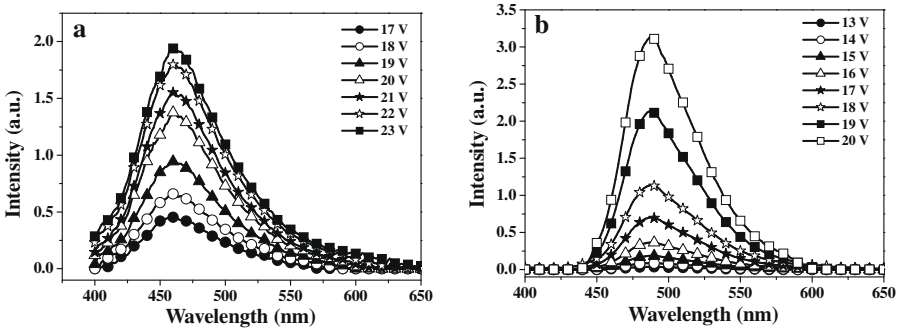

Fig. 8. EL spectra of the devices used DABTC-1 (a) and DABTC-2 (b) as dopants at different applied voltages. The devices with the configuration of ITO/2-TNATA (5 nm)/NPB (40 nm)/CBP: dopant (1.0 wt%, 30 nm)/PBD (30 nm) / LiF (1 nm)/Al (100 nm).

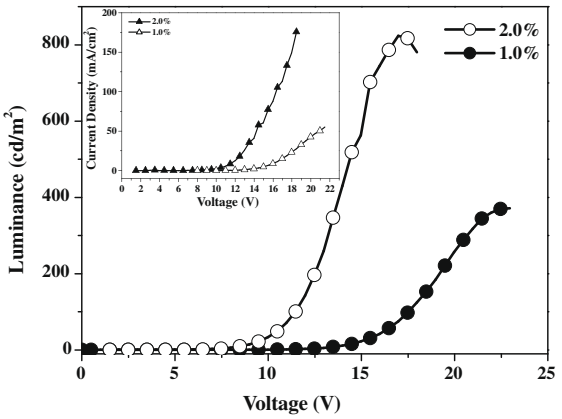

Fig. 10. The luminance vs. voltage and current density vs. voltage (inset) curves of the devices with different DABTC-2 concentrations.

concentration of 1.0 wt% and 823 cd/m^2 at 17 V for the device doped concentration of 2.0 wt%, respectively.

Fig. 11 shows the relationships between current efficiency and the current density in the devices with various DABTC-1 and DABTC-2 doping concentrations. It is shown that all doped devices have higher efficiencies at low current densities, and then the efficiencies fall off at higher current densities. The above finding indicates that the electron hole recombination may not be effective under high current density, revealing that the present host, CBP, might not be an optimal host material. The present device performance could be further improved by substituting other host candidates. Table 2 summarized the performances of the devices with various DABTC-1 and DABTC-2 doping concentrations in CBP host. It was shown that the 2 wt% DABTC-1 and DABTC-2 doped devices had better efficiencies.

It was interesting to note that the turn-on voltages of the devices decreased with the increasing of compounds (DABTC-1 or DABTC-2) doping concentration in the CBP host from Figs. 9 and 10. In view of the structures of the two compounds, they were substituted by the electron-withdrawing benzotriazoles regarded as accptors [29] and used as electron-transporting materials [30]. Furthermore, the host material CBP can provide good hole-transporting properties [31]. With DABTC concentration

Table 2
EL performances of DABTC-1 and DABTC-2 doped devices.

Compound		Maximum efficiency (cd/A)	Efficiency at 20 mA/cm^2 (cd/A)
DABTC-1	1.0 wt%	0.33 @ 0.22 mA/cm^2	0.09
	2.0 wt%	0.60 @ 0.10 mA/cm^2	0.15
DABTC-2	1.0 wt%	1.81 @ 0.16 mA/cm^2	0.97
	2.0 wt%	1.63 @ 0.40 mA/cm^2	1.05

increasing, the conductive characteristics of the devices was considerably improved, and the turn-on voltages of the devices were reduced. It was shown that benzotriazole group had excellent electron-transporting ability in these EL devices. From Figs. 9 and 10, it was found that the luminance of DABTC-2 devices was very stronger than that of DABTC-1 devices due to the larger conjugation of molecule in DABTC-2. Similarly, it was found that the current efficiency of DABTC-2 devices was higher than that of DABTC-1 devices (Fig. 11).

From above results, it was indicated that the performance of the DABTC-2 doped devices is be superior to that of the DABTC-1 doped devices.

3.6. Conclusions

We designed and prepared two new coumarin derivatives containing an electron-transporting moiety (benzotriazole), 7-*N*,*N*-diethylamino-3-(benzotriazol-1-yl)coumarin (DABTC-1) and 7-*N*,*N*-diethylamino-3-(benzotriazol-2-yl)coumarin (DABTC-2). The photoluminescent behaviors of the compounds in both solution and solid states were investigated and discussed. The doped devices fabricated from DABTC-1 or DABTC-2 doped in CBP show the EL spectra of DABTC-1 or DABTC-2 is identical to the PL spectra of them in the solid films, respectively. The ITO/2-TNATA (5 nm)/NPB (40 nm)/CBP: DABTC-1 (2.0 wt%, 30 nm)/PBD (30 nm)/LiF (1 nm)/Al (100 nm) device displayed the pure blue emission, a maximum luminous efficiency of 0.15 cd/A at the current density of 20 mA/cm^2, and maximum luminance of 48 cd/m^2 at 15 V. At the same condition, the DABTC-2 doped devices exhibited the brighter blue–green emission, a maximum luminous efficiency of 1.05 cd/A at the current density of 20 mA/cm^2, and maximum luminance of 823 cd/m^2 at 17 V.

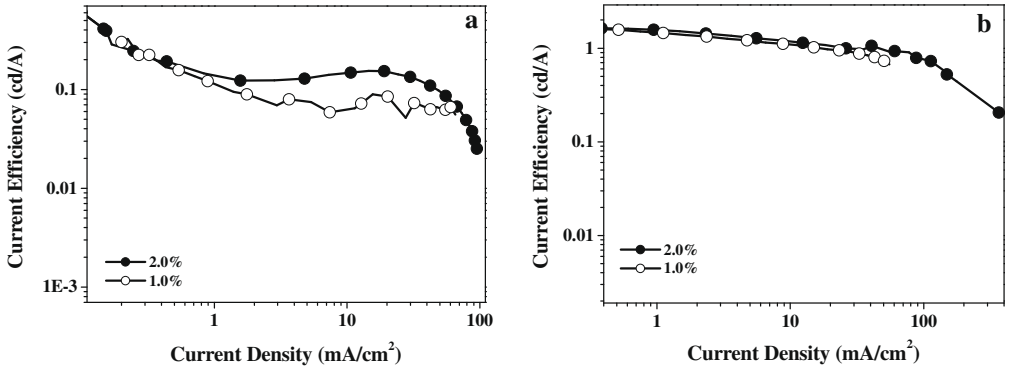

Fig. 11. Current efficiency-current density characteristics of the doped devices with various DABTC-1 (a) and DABTC-2 (b) concentrations.

Acknowledgements

This work was supported by the National Natural Science Foundation of China (Grant 60776006), the Program for Changjiang Scholars and Innovative Research Team in University (IRT0629) and also supported by 'Qing Lan' talent engineering funds (QL-05-23A) by Lanzhou Jiaotong University.

Appendix A. Supplementary material

The crystallographic data (excluding structure factors) of DABTC-1 and DABTC-2 had been deposited with the Cambridge Crystallographic Center as supplementary publication No. CCDC 733174 and No. CCDC 733173, respectively. Tables S1–S3 and Figs. S1 and S2 are given as supplementary information. Supplementary data associated with this article can be found, in the online version, at doi:10.1016/j.orgel.2009.09.023.

References

[1] C.W. Tang, S.A. VanSlyke, Appl. Phys. Lett. 51 (1987) 913–915.
[2] J.R. Sheats, H. Antoniadis, M. Hueschen, W. Leonard, J. Miller, R. Moon, D. Roitman, A. Stocking, Science 273 (1996) 884–888.
[3] R.H. Friend, R.W. Gymer, A.B. Holmes, J.H. Burroughes, R.N. Marks, C. Taliani, D.D.C. Bradley, D.A. Dos Santos, J.L. Bredas, M. LÖglund, M. LÖglund, W.R. Salaneck, Nature 397 (1999) 121–128.
[4] J. Shinar, R. Shinar, J. Phys. D: Appl. Phys. 41 (2008) 133001.
[5] K.C. Fylaktakidou, D.J. Hadjipavlou-Litina, K.E. Litinas, D.N. Nicolaides, Curr. Pharm. Des. 10 (2004) 3813.
[6] G. Jones, W.R. Jackson, C. Choi, W.R. Bergmark, J. Phys. Chem. 89 (1985) 294.
[7] T. Hiroshi, O. Yosho, I. Juzo, I. Masato, T. Atsushi, Jpn. Kokai Tokkyo Koho 1990 (1990) (CODEN: JKXXAF JP 02126241 A2 19900515 Heisei).
[8] H.E. Patel, K.R. Desai, J. Inst. Chem. 68 (1996) 78.
[9] D. Ray, P.K. Bharadwaj, Inorg. Chem. 7 (2008) 2252.
[10] S.R. Trenor, A.R. Shultz, B.J. Love, T.E. Long, Chem. Rev. 104 (2004) 3059.
[11] T.T. Hung, Y.J. Lu, W.Y. Liao, C.L. Huang, IEEE T. Magn. 2 (2007) 867.
[12] K. Hara, K. Sayama, Y. Ohga, A. Shinpo, S. Suga, H. Arakawa, Chem. Commun. (2001) 569.
[13] M. Fujiwara, N. Ishida, M. Satsuki, S. Suga, J. Photopolym. Sci. Technol. 2 (2002) 237.
[14] C.W. Tang, S.A. VanSlyke, C.H. Chen, J. Appl. Phys. 65 (1989) 3610.
[15] M. Mitsuya, T. Suzuki, T. Koyama, H. Shirai, Y. Taniguchi, Appl. Phys. Lett. 77 (2000) 3272.
[16] C.H. Chen, C.W. Tang, J.M. Shi, K.P. Klubek, US Patent 6020078, 2000.
[17] M.T. Lee, C.K. Yen, W.P. Yang, H.H. Chen, C.H. Liao, C.H. Tsai, C.H. Chen, Org. Lett. 8 (2004) 1241.
[18] J.L. Lai, J.S. Shiu, C.W. Kuo, US Patent 6727362 B1, 2004.
[19] T.Z. Yu, P. Zhang, Y.L. Zhao, H. Zhang, J. Meng, D.W. Fan, Org. Electron. 10 (2009) 653–660.
[20] B.B. Raju, T.S. Varadarajan, Laser Chem. 16 (1995) 109–120.
[21] J. Griffiths, V. Millar, G.S. Bahra, Dyes Pigments 28 (1995) 327–339.
[22] N. Kitamura, T. Fukagawa, S. Kohtani, S. Kitoh, K.-K. Kunimoto, R. Nakagaki, J. Photochem. Photobiol. A: Chem. 188 (2007) 378–386.
[23] T. Mori, K. Obata, K. Imaizumi, T. Mizutani, Appl. Phys. Lett. 69 (1996) 3309–3311.
[24] P. Sanna, A. Carta, M.E.R. Nikookar, Eur. J. Med. Chem. 35 (2000) 535–543.
[25] U.S. Raikar, C.G. Renuka, Y.F. Nadaf, B.G. Mulimani, A.M. Karguppikar, M.K. Soudagar, Spectrochim. Acta Part A 65 (2006) 673–677.
[26] K.A. Kozyra, J.R. Heldt, H.A. Diehl, J. Heldt, J. Photochem. Photobiol. A: Chem. 152 (2002) 199–205.
[27] M. Kaholek, P. Hrdlovič, J. Photochem. Photobiol. A: Chem. 127 (1999) 45–55.
[28] G. Jones II, W.R. Jackson, C. Choi, J. Phys. Chem. 89 (1985) 294–300.
[29] R. Lygaitisa, A. Matoliukstytea, N. Kreiveniene, J.V. Grazulevicius, J. Photochem. Photobiol. A: Chem. 167 (2004) 163–168.
[30] S.H. Ahn, M. Czae, E.R. Kim, H. Lee, S.H. Han, J. Noh, M. Hara, Macromolecules 34 (2001) 2522–2527.
[31] H. Kanai, S. Ichinosawa, Y. Sato, Synth. Met. 91 (1997) 195–196.

Organic Electronics 11 (2010) 50–56

Contents lists available at ScienceDirect

Organic Electronics

journal homepage: www.elsevier.com/locate/orgel

Surface photovoltage method for evaluation of exciton diffusion length in fluorene–thiophene based copolymers

Jiří Toušek [a,*], Jana Toušková [a], Ivo Křivka [a], Petra Pavlačková [b], Drahomír Výprachtický [b], Věra Cimrová [b,*]

[a] Charles University in Prague, Faculty of Mathematics and Physics, Department of Macromolecular Physics, V Holešovičkách 2, 180 00 Prague 8, Czech Republic
[b] Institute of Macromolecular Chemistry, Academy of Sciences of the Czech Republic, Heyrovsky sq. 2, 162 06 Prague 6, Czech Republic

ARTICLE INFO

Article history:
Received 26 June 2009
Received in revised form 18 September 2009
Accepted 28 September 2009
Available online 3 October 2009

Keywords:
Conjugated polymers
Thin films
Fluorene–thiophene
Surface photovoltage
Diffusion length

ABSTRACT

The surface photovoltage method was used for the study of polymer layers made of copolymers based on fluorene and thiophene derivatives, particularly for the determination of exciton diffusion lengths. The surface photovoltage (SPV) in a polymer layer is the result of dissociation of photogenerated free excitons in electric field of the space charge region (SCR), which forms spontaneously at the surface. Our conception of the SPV calculates both currents from the bulk and currents from the SCR where recombination is considered. Fitting theory to the experimental data allows estimation of the diffusion length and the thickness of the SCR regardless of the thickness of the layers. Photovoltage spectra were measured under illumination from both the free surface (SPV_{fs}) and the substrate (SPV_{sub}) side of the layers. For the copolymers under study the diffusion length was determined to be 20–23 nm.

© 2009 Elsevier B.V. All rights reserved.

1. Introduction

Conjugated polymers such as polyfluorenes, polythiophenes and their derivatives are of interest as promising active materials for optoeletronic devices such as polymer light-emitting diodes (PLEDs), organic solar cells, and organic thin film transistors [1–4]. The use of semiconducting organic materials as an active layer in optoelectronic devices offers some advantages in processing and new possibilities of device fabrication. One very important parameter essentially influencing the operation of optoelectronic devices is the diffusion length of the excitons, which is connected with their lifetime and mobility. The exciton diffusion length in various conjugated polymers was reported to be in the range from 4 to 20 nm [5–17]. Quenching of luminescence is often used for diffusion length determination [5,6] but it requires the preparation of variously thick layers with exactly the same structure and also a quencher for which titania or C_{60} are mostly used. Another method, namely fitting of theoretical quantum efficiency to measured data needs complete cells [5,7]. On the other hand, the non-destructive surface photovoltage (SPV) method has been widely used for determination of diffusion length of minority charge carriers in thick samples of inorganic semiconductors [18]. It employs internal electric field of a space charge region spontaneously formed at the surface of the materials and is indicated also in organic semiconductors e.g. [19,20]. This region is consequence of surface states which arise e.g. due to oxygen adsorption or diffusion.

In this paper, we used this technique modified for determination of exciton diffusion length in thin polymer films made of two copolymers based on fluorene and thiophene derivatives in the main backbone (see Fig. 1), which differ each other in the substitution of thiophene ring in the position 3 by the alkyl chain (**FIPT**) or the pyrene derivative **FPyT**. Our model is performed assuming a layer with a neutral bulk and one space charge region (SCR) at the free surface. After illumination excitons are created both in the

* Corresponding authors.
E-mail addresses: jiri.tousek@mff.cuni.cz (J. Toušek), cimrova@imc.cas.cz (V. Cimrová).

1566-1199/$ - see front matter © 2009 Elsevier B.V. All rights reserved.
doi:10.1016/j.orgel.2009.09.025

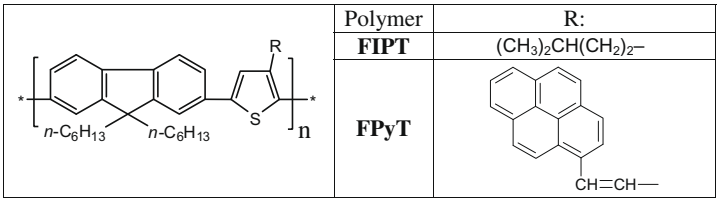

Fig. 1. Structure of alternating fluorene-thiophene copolymers under study.

bulk and in the SCR. The model considers that the bulk/SCR interface is the place where the charge separation occurs. The opposite surface is supposed to be a sink for excitons, which represents their losses by surface recombination.

To obtain the SPV signal from the bulk the continuity equation is solved. The second contribution to the signal comes from the SCR taking possible recombination in account. Total SPV signal is a sum of the both contributions. The SPV measurement at various wavelengths gives information on the diffusion length of excitons in the bulk and on the SCR thickness. The usual way of diffusion length evaluation by the SPV technique assumes a thin SCR with negligible losses of photogenerated carriers [21]. Consequently, it fails in samples with a thick SCR.

The advantage of our SPV model used here is its applicability to arbitrary thickness of the layers and its possibility to apply it to samples with arbitrary thickness of the SCR and of the bulk. From the photoelectric point of view the polymer layer acts as a thick or as a thin in different parts of the spectrum. For example if the polymer bulk thickness d is 100 nm, the exciton diffusion length L is 20–30 nm, and with the measured absorption coefficient α, there is a large wavelength region where the polymer layer cannot be considered as a thin layer according to the definition given by the following inequalities: $d \leqslant L$, $\alpha d \leqslant 1$ which hold for thin layers.

We have used our model to the evaluation of diffusion length in inorganic materials [22,23]. Recently, we have also applied the SPV method for characterization of organic layers made of fluorene–thiophene copolymer **FIPT**. We briefly reported the first result that the photovoltage consists from the contributions of thick SCR and thin neutral bulk and evaluated the diffusion length [24]. In this paper, we solved also the second case with thin SCR layer and a thick bulk region that is shown on the second fluorene–thiophene copolymer **FPyT**, which possesses similar absorption as **FIPT**, but differs in both SPV and photoluminescence spectra. Sensitivity of the SPV spectra to the diffusion length is demonstrated by a set of theoretical curves for the both cases i.e. for thick and thin SCR, and also for both cases of illumination (from the free surface and the substrate side).

2. Experimental

2.1. Samples and characterization

Alternating fluorene–thiophene copolymers, **FIPT** and **FPyT**, are displayed in Fig. 1. The copolymers were synthesized by Suzuki coupling reaction of 9,9-dihexylfluorene and 3-substituted (with 3-methylbutyl and 2-(pyren-1-yl)-vinyl, respectively) thiophene units. Detailed syntheses of monomers and polymers are described in our previous papers [25,26]. Average molecular weights of **FIPT** were $M_w = 26{,}250$, $M_n = 7800$, and **FPyT** $M_w = 26{,}460$, $M_n = 11{,}110$. Polymer films were prepared by spin coating from tetrahydrofuran solutions onto fused silica substrates for optical studies and onto indium-tin oxide (ITO) substrate for SPV study. All solutions were filtered with 0.45 μm Millex-FH13 Millipore syringe filters prior to spin coating. The films were dried in vacuum (10^{-3} Pa) at 353 K for 1 h. Thin polymer layers were prepared from good solvents under optimized conditions for spin coating and their homogeneity was checked by optical microscopy. Layer thicknesses were in the range 100–1000 nm as measured by KLA-Tencor P-10 profilometer. UV–vis spectra were measured on a Perkin–Elmer Lambda 35 spectrometer and PL spectra using a Perkin–Elmer LS55 spectrofluorometer.

2.2. Surface photovoltage measurement

The photovoltage generated in the polymer films was measured in a sandwich structure between two ITO electrodes with a Mylar sheet at the film surface serving as a dielectric layer. A capacitive couple is formed in this way. The sample was irradiated by low-intensity monochromatic light chopped with a low frequency of 11 Hz generating an alternating voltage which was measured between a transparent conductive electrode capacitively coupled to the sample and an appropriate back electrode by lock-in amplifiers Stanford SR 810 and SR 830. The SPV spectra were measured using a Jobin–Yvon H 25 spectrometer at constant impinging photon flux density ($\sim 10^{14}$ photons cm^{-2} s^{-1}) and subsequently corrected for the transparency of the electrodes. The light intensity was checked during the measurement by spectral independent Thermopile TS-100 (IPHT Jena). The SPV spectra were taken at room temperature and in air. Maximum values of the photovoltage were 30–50 μV.

3. Results and discussion

Typical SPV spectra of **FIPT** and **FPyT** samples under irradiation from the free surface (SPV_{fs}) and from the substrate (SPV_{sub}) are shown in Fig. 2. It can be seen that the SPV spectra of these two copolymers are significantly different, whereas the absorption spectra for the copolymers (see Fig. 3) are similar. The lowest-energy absorption maxima, corresponding to the absorption of the conjugated backbone, are located at 401 and 391 nm for **FIPT** and

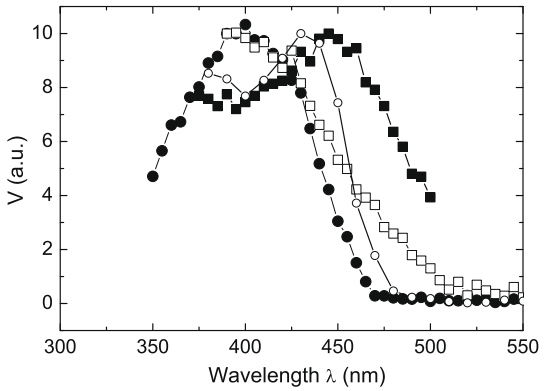

Fig. 2. Normalized SPV spectra measured for polymer layers under illumination from the free surface side: **FIPT** (open circles) and **FPyT** (open squares), and under illumination from the substrate side: **FIPT** (solid circles) and **FPyT** (solid squares).

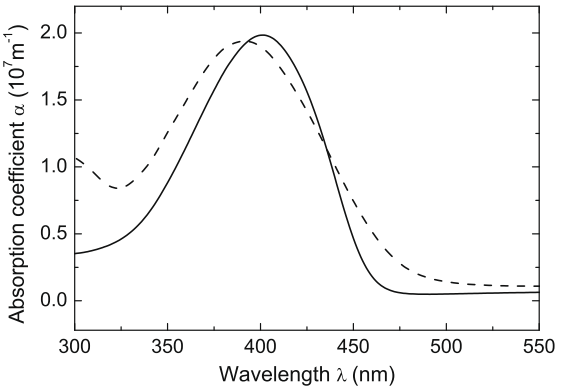

Fig. 3. UV-Vis absorption spectra of the copolymers **FIPT** (solid) and **FPyT** (dashed) measured in thin films prepared on fused silica substrate.

FPyT, respectively. The onset of the absorption is at about 470 nm for **FIPT** thin film, whereas for **FPyT** it is at a longer wavelength ca. 500 nm, which indicates a lower band gap value for **FPyT** than for **FIPT**. The optical energy band gap (E_g) was evaluated from the thin film absorption edge as 2.76 and 2.65 eV for **FIPT** and **FPyT**, respectively. The maximum of SPV_{sub} spectrum for **FIPT** is located at 400 nm similarly as the absorption one and also the shape is similar to that of the absorption spectrum, whereas the SPV_{fs} spectrum maximum is at 445 nm, i.e. shifted to longer wavelengths. In the case of **FPyT**, SPV_{sub} spectrum significantly differs from the absorption spectrum, with its maximum being shifted to longer wavelengths; on the other hand, SPV_{fs} spectrum follows roughly the absorption one.

Electronic structure of the copolymers was determined from electrochemical study. The onset of oxidation potential was nearly the same for both polymers. Using this value, HOMO levels E_{IP} at about 5.3 eV were estimated. From the onset of the reduction, electron affinity (LUMO level) of 2.8 eV was obtained for **FIPT** and a higher electron affinity of 3 eV was determined for **FPyT**. These results show that the condition on the interface substrate ITO-copolymer is similar for both materials under study.

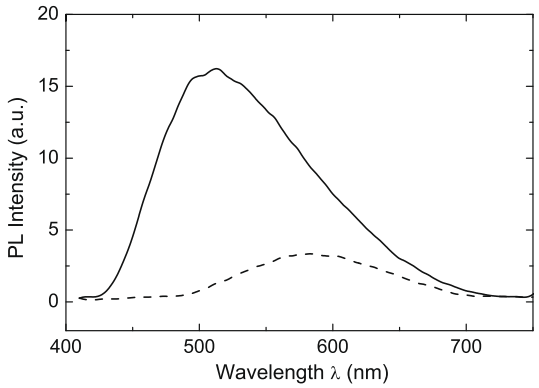

Fig. 4. Photoluminescence spectra of the copolymers **FIPT** (solid) and **FPyT** (dashed) measured in thin films prepared on fused silica substrate.

Photoluminescence (PL) of the two polymers in thin films significantly differs. As can be seen from Fig. 4, broad-band PL spectra were observed for both polymers, but the intensity and the position of their maxima significantly differ. The PL intensity is much lower in **FPyT** than in **FIPT**. The PL maximum for **FIPT** is located at 499 nm, whereas for **FPyT** it is at 580 nm, significantly red-shifted. This red-shift and a very large Stokes shift demonstrate more pronounced aggregation of **FPyT** molecules than **FIPT** ones.

To explain the SPV experimental data we use our earlier calculations [23,27]. The polymer layers under study were considered as homogenous medium for SPV study similarly as in other macroscopic optical or electrical studies. Results of SPV measurements performed on the different places of the samples did not show any non-homogeneity.

Measurements of photovoltage spectra show only one SCR and the polarity of the voltage indicates its position at the free surface (Appendix A). Hence, a structure with a bulk region and one SCR at its free surface is considered in the theoretical fitting (Fig. 5). Our measurements were performed in the ambient atmosphere; therefore the separation of charge carriers generated in the SCR is influenced by oxygen. The role of oxygen is not yet fully understood. Oxygen acts as an electron acceptor and may negatively charge the layer surface. The influence of oxygen on the charge separation and on the modulated SPV signal is discussed and shown by Zidon et al. [28]. In our case, oxygen molecules can catch electrons from the dissociated photogenerated excitons and shorten the drift length of these minority carriers. This causes a decrease in the probability of charge separation in the SCR and consequently the signal lowering. The excitons generated in the bulk, which

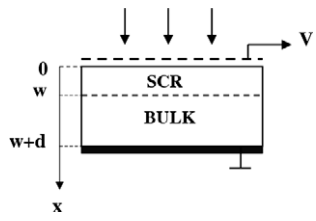

Fig. 5. Schematic view of the sample for SPV measurement.

diffuse to the SCR/bulk interface, are separated into free electrons and holes at the interface and contribute to the SPV signal that is added to the SPV from the SCR.

Let us note that the SPV measurement configuration does not allow for obtaining values of the quantum efficiency. It operates only with relative values that are proportional to the internal quantum efficiency.

Usually, there are several relaxation processes in the layers, influencing the form of the SPV pulses [29]. In our experiment the chopper frequency of 11 Hz was sufficiently low to obtain saturated pulses not influenced by relaxations. This fact together with experimentally verified linear relation between the photovoltage and the light intensity leads to proportionality between the photovoltage V and the photogenerated current J

$$V \sim J \tag{1}$$

Unit area of the samples is considered. The photogenerated current is formed both in the neutral bulk (thickness d) and in the space charge region (thickness w) at the free surface (Fig. 5). In the case of the free surface illumination the component from the neutral bulk is calculated by solving the usual diffusion equation

$$d^2\Delta p/dx^2 - \Delta p/L^2 = -\alpha I/D \exp(-\alpha[w+x]) \tag{2}$$

where Δp is the concentration of photogenerated free excitons, L is their diffusion length, and I is the density of the photon flux entering into the sample with the absorption coefficient α. The boundary condition characterizing sweep of excitons at the bulk-SCR boundary is

$$\Delta p(w) = 0 \tag{3a}$$

Another condition is represented by recombination at the bottom contact:

$$Dd\Delta p/dx|_{x=w+d} = -s\Delta p(w+d) \tag{3b}$$

where D is the exciton diffusion coefficient and s is the surface recombination velocity. Instead of s a dimensionless parameter $S \equiv sL/D$ is further used. Diffusion current J_b from the bulk can be simply obtained as

$$J_b = eDd\Delta p/dx|_{x=w}. \tag{4}$$

The component of the current from the SCR J_s is usually calculated as:

$$J_s = e\int_0^w g(x)dx = eI(1-\exp[-\alpha w]) \tag{5}$$

where $g(x) = \alpha I \exp(-\alpha x)$ is the generation rate. In the case of recombination in the SCR

$$J_s = e\int_0^w G(x)g(x)dx. \tag{6}$$

$G(x)$ is the gain factor characterizing losses by recombination in the SCR ($G \leqslant 1$) and according to Shockley–Ramo theorem [30] $G(x) = (l_n(x) + l_p(x))/w = (\mu_n\tau_n E(x) + \mu_p\tau_p E(x))/w$. $G(x)$ shows the contribution of each photogenerated carrier to the current J_s. $E(x)$ is the electric field in the SCR while $l_{n,p}$, $\mu_{n,p}$, $\tau_{n,p}$ are drift length, mobility and carrier lifetime of electrons and holes, respectively. A constant concentration of bound charges in the SCR is considered leading to linear electric field and a linear dependence of l_n, l_p versus x. The drift lengths at the surface are characterized by l_{n0}, l_{p0} values [23] and together with the thickness w of the SCR determine the drift lengths at arbitrary point in the SCR. Final equations for the currents J_b and J_s are shown in the Appendix B. As it was demonstrated in [22] the currents are mutually independent and can be added, giving the total photocurrent. Similar calculation can be made if illumination comes from the substrate side (Appendix B).

Let us assume and analyze two cases, which well applicable to our copolymers under study:

1. a thick SCR (w) and a thin bulk layer (d), i.e. $w > d$,
2. a thin SCR (w) and a thick bulk layer (d), i.e. $w < d$.

Theoretical SPV curves for the case 1 were calculated using absorption coefficients of **FIPT** (from Fig. 3) for $w = 100$ nm, $d = 25$ nm, $S = 1$, $l_{n0} = l_{p0} = 1$ nm and different L for illumination from the free surface side (Fig. 6) and substrate side (Fig. 7).

It can be clearly recognized from Fig. 6 that the shape of SPV_{fs} spectrum for illumination from the free surface side significantly depends on the value of exciton diffusion

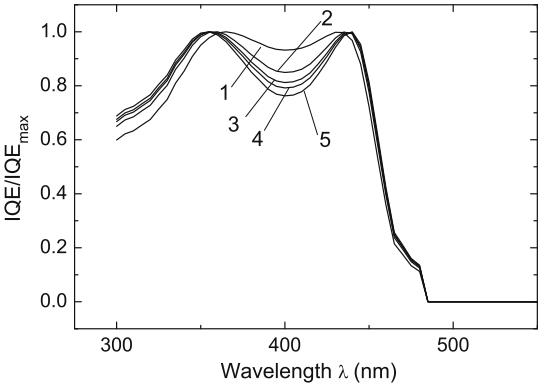

Fig. 6. Normalized theoretical SPV spectra for illumination from the free surface side calculated using $w = 100$ nm, $d = 25$ nm, $S = 1$, $l_{n0} = l_{p0} = 1$ nm and absorption coefficient values of **FIPT** for various diffusion length 1: $L = 5$ nm, 2: $L = 10$ nm, 3: $L = 15$ nm, 4: $L = 20$ nm, 5: L = 30nm.

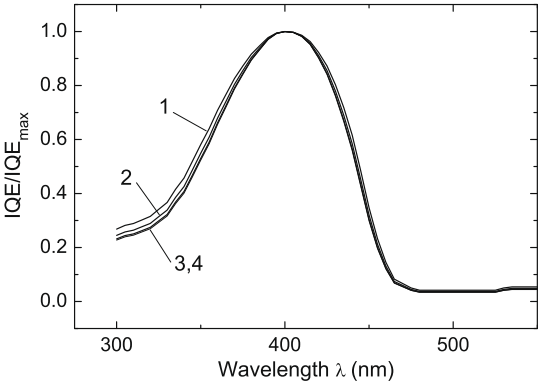

Fig. 7. Normalized theoretical SPV spectra for illumination from the substrate side calculated using $w = 100$ nm, $d = 25$ nm, $S = 1$, $l_{n0} = l_{p0} = 1$ nm and absorption coefficient values of **FIPT** for various diffusion length 1: $L = 5$ nm, 2: $L = 10$ nm, 3: $L = 20$ nm, 4: $L = 30$ nm

length L. As the diffusion length L increases the minimum of the signal becomes deeper in the region of maximum absorption. On the other hand, for illumination from the substrate side the SPV theoretical curves for various L values differ only slightly (Fig. 7) so that the diffusion length determination is not reliable.

Absorption coefficients for **FPyT** were used in the case of a thin SCR and a thick bulk layer. SPV theoretical curves for various L values differ only slightly for illumination from the free surface side and significantly for illumination from the substrate side (Figs. 8 and 9). In this case, the diffusion length can be determined from the SPV_{sub} spectra measured for the illumination from the substrate side. It should be stressed that using the absorption coefficient evaluated from the measurement in transmission the fitting is reasonable only in the spectral region of absorption because the absorption coefficient in the tail of the absorption differs from the intrinsic one. The reason for this is the fact that some fraction of the absorption in the tail of the absorption originates from reflection losses [31].

On the basis of theoretical analysis outlined above, SPV spectra measured for **FIPT** samples under irradiation from both sides are typical ones for the case 1 of a thick SCR (w) and a thin bulk layer (d), whereas SPV spectra measured for **FPyT** represent the case 2 of a thin SCR (w) and a thick bulk layer (d). The best theoretical fits to experimental data are shown in Figs. 10 and 11 for **FIPT** and **FPyT**, respectively.

For **FIPT** the diffusion length $L = 20$ nm was evaluated from the SPV_{fs} spectrum, whereas for **FPyT** from the SPV_{sub} one as $L = 23$ nm. For **FIPT**, the theoretical fit (solid lines) reveals that the SCR spreads across a greater part (100 nm) of the layer whereas the bulk region is very thin (25 nm). The SPV_{sub} signal is proportional to the absorption coefficient, which means that in this case the diffusion length modifies the spectrum only weakly. For **FIPT**, a low ratio of the drift lengths and thickness of the SCR that were evaluated by the fitting means that the SCR layer is not efficient. Absolute values of the SPV_{fs} were much lower than those of SPV_{sub}. This corresponds to a high recombi-

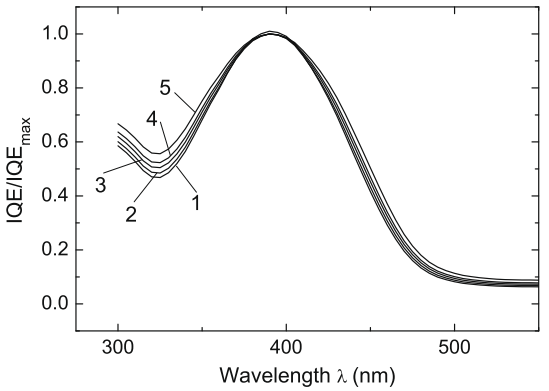

Fig. 8. Normalized theoretical SPV spectra for illumination from the free surface side calculated using $w = 2$ nm, $d = 137$ nm, $S = 1$, $l_{n0} = l_{p0} = 1$ nm and absorption coefficient values of **FPyT** for various diffusion length 1: $L = 5$ nm, 2: $L = 10$ nm, 3: $L = 15$ nm, 4: $L = 20$ nm, 5: $L = 30$ nm.

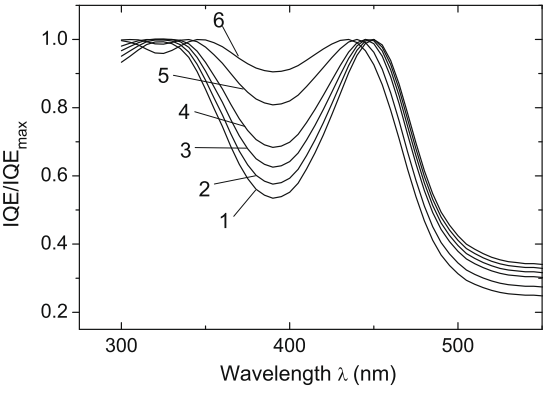

Fig. 9. Normalized theoretical SPV spectra for illumination from the substrate side calculated using $w = 2$ nm, $d = 137$ nm, $S = 1$, $l_{n0} = l_{p0} = 1$nm and absorption coefficient values of **FPyT** for various diffusion length 1: $L = 5$ nm, 2: $L = 10$ nm, 3: $L = 15$ nm, 4: $L = 20$ nm, 5: $L = 30$ nm, 6: $L = 40$ nm.

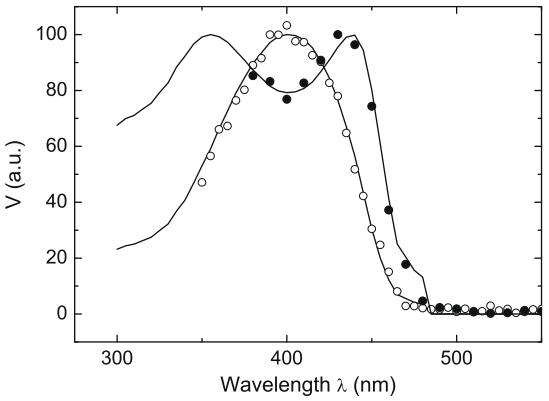

Fig. 10. Normalized SPV spectra measured on **FIPT** layers under illumination from the free surface side (solid circles) and from the substrate (open circles). Full lines are theoretical curves obtained as the best fit with $d = 25$ nm, $w = 100$ nm and $L = 20$ nm, $l_{n0} = l_{p0} = 1$nm.

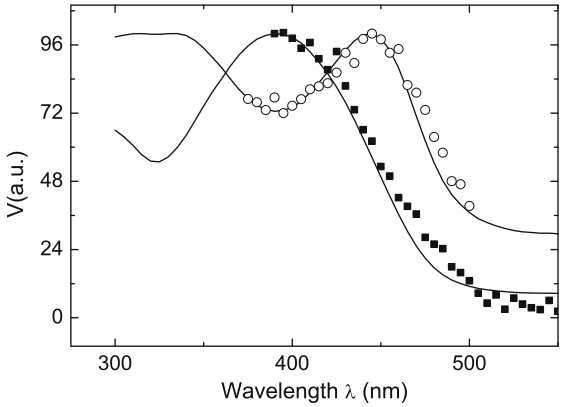

Fig. 11. Normalized SPV spectrum measured on **FPyT** layers under illumination from the substrate side (open circles) and from the free surface side (solid squares). Full lines are theoretical curves obtained as the best fit with $d = 137$ nm, $w = 2$ nm, $L = 23$ nm, $l_{n0} = l_{p0} = 1$nm.

nation rate in the SCR and a negligible contribution of this region to the SPV signal.

If the free surface is illuminated, weakly absorbed low energy photons penetrate deep into the material and generate a higher signal than the more absorbed photons in the SCR. This causes a local minimum in the region of the highest absorption.

In contrast to the **FIPT** samples, in **FPyT** the SCR is very thin (2 nm) in comparison with the thickness of the bulk (137 nm) as evaluated by fitting the theory to SPV_{sub}. Under illumination from the substrate side, and in the region of high absorption the excitons are generated far from the bulk/SCR interface and an SPV minimum appears. Higher signals correspond to weakly absorbed photons penetrating deeper into the material. All these spectra are in accordance with the theoretical results shown in Figs. 6, 7 and 9. The SPV_{fs} signals of **FPyT** were also measured (Fig. 11) but the spectrum did not correspond so well to the theory because most of the generated signal comes from the very thin SCR at the surface where a linear electric field cannot be assumed in general. The sum of thickness of the bulk and of the SCR agrees well with the thickness of the samples as measured with the profilometer, namely 125 nm for **FIPT** and 140 nm for **FPyT**.

For the **FIPT** samples with thin bulk region, the diffusion length value of 20 nm was estimated with 10% accuracy by fitting the theory to the SPV_{fs} spectrum measured under illumination from the free surface side of the samples. The accuracy of the thickness of the SCR was 6%. The diffusion length in the **FPyT** samples with relatively thick bulk region was 23 nm with 15% accuracy as estimated by fitting the theory to experiments carried out under illumination from the substrate side. The accuracy of the thickness of the bulk was 4%. In general, we have found that a satisfactory fit with the experiment cannot be attained with parameter combinations falling outside the frame of accuracy.

As already mentioned in Section 1 the exciton diffusion length in conjugated polymers according to the literature varies from 4 to 20 nm [5–17] depending not only on the material but also on the method applied for its measurement. The diffusion lengths in the range 17–23 nm as evaluated from SPV method for our copolymers belong to the higher ones determined for conjugated polymers. Such higher values were also obtained for MEH-PPV (20 nm) from the analysis of luminescence as a function of the film thickness [16] and was also reported in phenylene vinylene oligomers, where an estimate of the exciton diffusion range of 20 nm was obtained from the photoluminescence quenching at the Ca interface [17]. It should be noted that our SPV measurements were performed with much lower light intensity as compared with the measurements where lower diffusion lengths were determined. Our results show that SPV measurements are an alternative way of studying exciton diffusion and suitable method for the determination of the diffusion length.

The theoretical analysis of SPV experimental spectra measured for **FIPT** and **FPyT** within the frames of the model described in this paper is in very good agreement with the photoluminescence study on thin films. Thick SCR with short drift lengths found in **FIPT** samples show a high recombination rate in this region, which leads to higher PL intensity. On the other hand, thin SCR in **FPyT** material can yield only low PL intensity. Indeed, the PL intensity in **FPyT** is lower than in **FIPT**.

4. Conclusions

The surface photovoltage method was used for the photophysical study of copolymer layers. Measurement of photovoltage of **FIPT** and **FPyT** copolymer layers revealed that only one space charge region is present in the samples. This region, that is much thicker in **FIPT** than in **FPyT**, is localized at their free surface. Photovoltage spectra were taken under illumination of the free surface and substrate side. Their evaluation indicates a high recombination rate in quite thick SCR of the **FIPT** layers, which agrees with high PL intensity in these films. It was shown that the main contribution to the photovoltage comes from the bulk region because of a small signal from the SCR. The theory presented here was fitted to the spectra allowing evaluation of the exciton diffusion length and thickness of the space charge region. The diffusion length in the **FIPT** and **FPyT** layers was 20 ± 2 nm and 23 ± 3 nm, respectively.

Acknowledgements

We acknowledge the support of the Ministry of Education, Youth and Sports of the Czech Republic (Grant Nos. 1M06031 and MSM 0021620834), the Grant Agency of the Academy of Sciences of the Czech Republic (Grant No. IAA4050409) and the Grant Agency of the Czech Republic (Grant No. 202/09/1206).

Appendix A

Presence of two space charge regions, one at the free surface and another at the semiconductor/ITO interface would lead to two voltage signals of opposite sign generated after illumination. Change in the sign in the SPV spectrum would appear after illumination of the top or the bottom surface indicating two different SCRs in this way [27]. Such effect was not found in the measurement so that only one SCR was considered in our samples. The space charge regions at the ITO/molecular layers and at the free surface of the layers were demonstrated in [19] where only the latter significantly contributed to the photovoltage.

In our samples position of the SCR was determined from the direction of the photogenerated current influencing the phase of the signal measured by lock-in amplifier. Using Si solar cell for calibration, it was found that the SCR was at the free surface.

Appendix B

Electrons and holes from dissociated excitons create the current in the SCR, while minority carriers control the bulk current.

The illumination from the free surface side generates the current $J_1 = J_{s1} + J_{b1}$ [32,27] where

$$
\begin{aligned}
J_{s1} &= J_{ps1} + J_{ns1} \\
&= \frac{e\alpha I}{w}\int_0^w l_{p0}\left(1-\frac{x}{w}\right)\exp(-\alpha x)dx \\
&\quad + \frac{e\alpha I}{w}\int_0^{l_{n1}} x\exp(-\alpha x)dx \\
&\quad + \frac{e\alpha I}{w}\int_{l_{n1}}^w l_{n0}\left(1-\frac{x}{w}\right)\exp(-\alpha x)dx \\
&= \frac{eIl_{po}}{w}\left\{1+\frac{1}{\alpha w}(\exp(-\alpha w)-1)\right\} \\
&\quad + \frac{eIl_{no}}{w}\left\{\exp(-\alpha l_{n1})\left(1-\frac{l_{n1}}{w}-\frac{1}{\alpha w}\right)+\frac{1}{\alpha w}\exp(-\alpha w)\right\} \\
&\quad + \frac{eI}{\alpha w}(1-\exp(-\alpha l_{n1}))-\frac{eIl_{n1}}{w}\exp(-\alpha l_{n1})
\end{aligned}
$$

and

$$
\begin{aligned}
J_{b1} &= \frac{eI\alpha L}{1-\alpha^2L^2}\,\frac{\exp(-\alpha w)}{\{(1-S)\exp(-d/L)+(1+S)\exp(d/L)\}} \\
&\quad \times[(1+S)\exp(d/L)-(1-S)\exp(-d/L) \\
&\quad + 2\exp(-\alpha d)(\alpha L-S)]-eI\exp(-\alpha w)\frac{\alpha^2L^2}{1-\alpha^2L^2}
\end{aligned}
$$

I is the photon flux entering into the sample, l_{p0}, l_{n0} are the drift lengths corresponding to the maximum electric field in the SCR. The minority carriers drift length maximum is $l_{n1} = l_{n0}/(1 + l_{n0}/w)$, which follows from limitation by the SCR boundary [32].

The dimensionless surface recombination velocity is $S \equiv sL/D$ where D is the exciton diffusion coefficient and s is the surface recombination velocity at the substrate.

The illumination from the substrate side generates the current $J_2 = J_{s2} + J_{b2}$ where

$$
\begin{aligned}
J_{s2} &= J_{ps2} + J_{ns2} \\
&= \frac{e\alpha I}{w}\exp(-\alpha d)\int_0^w l_{p0}\frac{x}{w}\exp(-\alpha x)dx \\
&\quad + \frac{e\alpha I}{w}\frac{l_{n0}}{w}\exp(-\alpha d)\int_0^{l_{n1}} x\exp(-\alpha x)dx \\
&\quad + \frac{e\alpha I}{w}\exp(-\alpha d)\int_{l_{n1}}^w (w-x)\exp(-\alpha x)dx \\
&= \frac{eIl_{po}}{w}\exp(-\alpha d)\left\{\frac{1}{\alpha w}(1-\exp(-\alpha w))-\exp(-\alpha w)\right\} \\
&\quad + \frac{eIl_{no}}{w}\exp(-\alpha d)\left\{(1-\exp(-\alpha l_{n1}))\frac{1}{\alpha w}\right. \\
&\quad \left.-\frac{l_{n1}}{w}\exp(-\alpha l_{n1})\right\}+eI\exp(-\alpha d) \\
&\quad \times\left\{\exp(-\alpha l_{n1})(1-\frac{l_{n1}}{w}-\frac{1}{\alpha w})+\frac{1}{\alpha w}\exp(-\alpha w)\right\}
\end{aligned}
$$

and

$$
\begin{aligned}
J_{b2} &= \frac{eI\alpha L}{1-\alpha^2L^2}\,\frac{1}{\{(1-S)\exp(-d/L)+(1+S)\exp(d/L)\}} \\
&\quad \times\{2(\alpha L+S)+\exp(-\alpha d)[(1-S)\exp(-d/L) \\
&\quad -(1+S)\exp(d/L)]\}-eI\exp(-\alpha d)\frac{\alpha^2L^2}{1-\alpha^2L^2}
\end{aligned}
$$

Meaning of the symbols is the same as above.

References

[1] A. Skotheim, J.R. Reynolds (Eds.), Conjugated Polymers, CRC Press, Taylor and Francis Group, Boca Raton, 2007.
[2] S.S. Sun, N.S. Sariciftci (Eds.), Organic Photovoltaics, Taylor and Francis, 2005.
[3] Z. Li, H. Meng (Eds.), Organic Light-Emitting Materials and Devices, Taylor and Francis, 2007.
[4] K. Mullen, U. Scherf, Organic Light Emitting Devices: Synthesis, Properties and Applications, Wiley-VCH, 2006.
[5] P. Peumans, A. Yakimov, S.R. Forrest, J. Appl. Phys. 93 (2003) 3693.
[6] M. Theander, A. Yartsev, D. Zigmantas, V. Sundström, W. Mammo, M. Andersson, O. Inganäs, Phys. Rev. B61 (2000) 12957.
[7] T. Stübinger, W. Brütting, J. Appl. Phys. 90 (2001) 3632.
[8] A. Haugeneder, M. Neges, C. Kallinger, W. Spirkl, U. Lemmer, J. Feldmann, U. Scherf, E. Harth, A. Gügel, K. Müllen, Phys. Rev. B 59 (1999) 15346.
[9] Y. Wu, Y.C. Zhou, H.R. Wu, Y.Q. Zhan, J. Zhou, S.T. Zhang, J.M. Zhao, Z.J. Wang, X.M. Ding, X.Y. Hou, Appl. Phys. Lett. 87 (2005) 044104.
[10] D.E. Markov, J.C. Hummelen, P.W.M. Blom, A.B. Sieval, Phys. Rev. B 72 (2005) 45216.
[11] D.E. Markov, P.W.M. Blom, Phys. Rev. B 72 (2005) 161401.
[12] D.E. Markov, E. Amsterdam, P.W.M. Blom, A.B. Sieval, J.C. Hummelen, Phys. Chem. A 109 (2005) 5266.
[13] S.R. Scully, M.D. McGehee, J. Appl. Phys. 100 (2006) 034907.
[14] Ch. Goh, S.R. Scully, M.D. McGehee, J. Appl. Phys. 101 (2007) 114503.
[15] A.J. Lewis, A. Ruseckas, O.P.M. Gaudin, G.R. Webster, P.L. Burn, D.W. Samuel, Org. Electr. 7 (2006) 452.
[16] T.J. Savenije, J.M. Warman, A. Goossens, Chem. Phys. Lett. 287 (1998) 148.
[17] V. Choong, Y. Park, Y. Gao, T. Wehrmeister, K. Müllen, B.R. Hsieh, Appl. Phys. Lett. 69 (1996) 1492.
[18] L. Kronik, Y. Shapira, Surf. Sci. Rep. 37 (1999) 1.
[19] E. Moons, A. Goossens, J. Phys. Chem. B 101 (1997) 8492.
[20] J.N. Barisci, R. Stella, G.M. Spinks, G.G. Wallace, Synth. Met. 124 (2001) 407.
[21] A.M. Goodman, J. Appl. Phys. 32 (1961) 2550.
[22] J. Toušek, J. Toušková, Sol. Energy Mater. Solar Cells 92 (2008) 1020.
[23] J. Toušek, J. Toušková, E. Belas, L. Votoček, Phys. Status Sol. (A) 204 (2007) 2381.
[24] J. Toušek, P. Pavlačková, V. Cimrová, J. Toušková, Macromol. Symp. 268 (2008) 96.
[25] D. Výprachtický, V. Cimrová, P. Pavlačková, I. Kmínek, Macromol. Symp. 268 (2008) 120.
[26] P. Pavlačková, V. Cimrová, D. Výprachtický, I. Kmínek, Macromol. Symp. 268 (2008) 105.
[27] J. Toušek, D. Kindl, J. Toušková, Sol. Energy Mater. Solar Cells 29 (2000) 64.
[28] Y. Zidon, Y. Shapira, T. Ditrich, L. Otero, Phys. Rev. B 75 (2007) 195327.
[29] Y. Zidon, Y. Shapira, T. Ditrich, Appl. Phys. Lett. 90 (2007) 142103.
[30] Z. He, Nucl. Instrum. Meth. A463 (2001) 250.
[31] V. Cimrová, D. Neher, S. Kostromine, Th. Bieringer, Macromolecules 32 (1999) 8496.
[32] J. Toušek, Phys. Status Sol. (A) 128 (1991) 531.

Organic Electronics 11 (2010) 57–61

Contents lists available at ScienceDirect

Organic Electronics

journal homepage: www.elsevier.com/locate/orgel

Towards organic light-emitting diode microdisplays with sub-pixel patterning

Fabian Ventsch, Malte C. Gather, Klaus Meerholz *

Department of Chemistry, University of Cologne, Luxemburgerstr. 116, D-50939 Cologne, Germany

ARTICLE INFO

Article history:
Received 21 July 2009
Received in revised form 25 September 2009
Accepted 26 September 2009
Available online 12 October 2009

Keywords:
OLED
Top-emitter
Microdisplay

ABSTRACT

We report on solution processed top-emitting organic light-emitting diodes (TEOLEDs) that are compatible with TFT- and CMOS-substrates, thus being applicable in full-color microdisplays. In this device geometry TEOLEDs offer highly tunable and controllable color-coordinates. Compared to the standard sRGB-colorspace the color gamut is increased by 18%. The CIE (*Commission internationale de l'éclairage)* color coordinates are more saturated in the red and green spectral region and comparable in the blue region. Brightness levels of 1000 cd/m^2 are reached at voltages below 7 V for all colors which is within the operating voltage range of CMOS-backplanes. The polymeric emitters are crosslinkable and can be patterned in a UV-lithography process. The achieved minimum feature size is suitable for high resolution microdisplays.

© 2009 Elsevier B.V. All rights reserved.

1. Introduction

For several years the interest in organic light-emitting diodes (OLEDs) has shifted from rather simple devices such as monochrome displays to complex full-color active-matrix displays. In this context, increasing amounts of money are invested in the commercialization of displays based on OLED-technology. As a preliminary highlight, this trend resulted in the implementation of an 11 in. OLED-TV (XEL-1) by Sony in 2007. The main effort in this field is to increase display sizes. However, there is also an ever increasing demand for mobile TV and video equipment. Here it is necessary to decrease pixel size in order to build very small displays (typically below 1.5 in. diagonal) with high resolution. These so-called microdisplays are the key components in video goggles. By use of magnifying optics an enlarged image of the display is projected directly into the human eye.

Today an overwhelming share of the display market is held by liquid crystal (LC)-technology and hence any new technology has to compete against it. In LC-displays white light from a backlight is converted into red, green and blue (RGB) by color filters laminated on top of the LC-cell. The gap between filter and LC-cells leads to partial illumination of adjacent sub-pixels and, therefore, to a loss in color gamut. This effect becomes worse with decreasing pixel size and hence puts a fundamental limit to the resolution of microdisplays. Underwood et al. [1] established a microdisplay in which the LC-cell was replaced by a white-emitting OLED (see Fig. 1a). This reduces the power consumption and simplifies the fabrication process of the microdisplays but does not solve the problem of the limited color gamut.

Here, we propose a process for the fabrication of a high resolution microdisplay in which red-, green- and blue-emitting OLEDs form the sub-pixels of the display. To achieve this, thin films of RGB-emitting materials will be deposited from solution and be structured via direct UV-lithography in order to define the color of corresponding sub-pixels (see Fig. 1b). The used electroluminescent materials are oxetane-functionalized and can be crosslinked through cationic ring opening polymerisation. In the presence of a photo acid generator (PAG) this reaction can be initiated by UV-light giving the material photoresist-like properties [2,3]. As light and color are generated in the same layer, crosstalk between sub-pixels is eliminated and a large color gamut is expected. The pixel size in a microdisplay

* Corresponding author.
E-mail address: Klaus.Meerholz@uni-koeln.de (K. Meerholz).

1566-1199/$ - see front matter © 2009 Elsevier B.V. All rights reserved.
doi:10.1016/j.orgel.2009.09.026

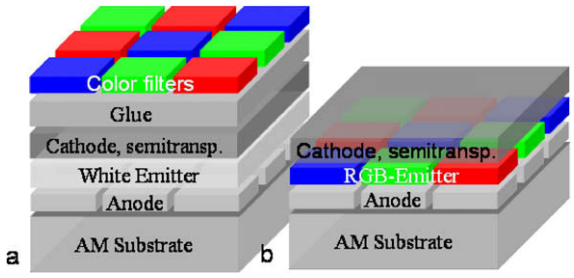

Fig. 1. (a) Schematic of a commercial OLED-based microdisplay using a polymeric white emitter and color filters. (b) RGB sub-pixel approach proposed here.

with VGA resolution (640 × 480 pixels) amounts to a few micrometers. We have already demonstrated that direct lithographic patterning of electroluminescent polymers yields minimum feature sizes down to 2 μm [3].

In contrast to direct lithography of solution processed OLED materials, vacuum deposition of small molecules through shadow masks is not a suitable option for the fabrication of microdisplays: The quality of the shadow masks suffers from material being deposited onto it over time. This leads to a gradual reduction of the actual pixel size and to an enhanced formation of disruptive particles on the OLED. For the small pixels of microdisplays, the required OLED quality is only ensured for very few evaporation procedures per shadow mask [4].

It is obvious that top-emitting OLEDs (TEOLEDs) are favorable over bottom-emitting ones (BEOLEDs) when working with opaque complementary metal oxide semiconductor (CMOS) backplanes. These active transistor backplanes are necessary to display complex content. There are two possible geometries for TEOLEDs: Inverted OLEDs with a transparent top-electrode [5–7] as well as cavity TEOLEDs [8–10]. The latter allow for better control of the emission characteristics due to the layer-thickness-dependent microcavity effect. Especially since many polymeric emitters show a broad emission spectrum (see Fig. 3c), the control of both, spectral width and peak wavelength, is beneficial to achieve primary color coordinates suitable for display applications.

In general, a cavity TEOLED consists of a metallic mirror which is usually the anode of the OLED, a stack of organic layers, and a semi-transparent metallic cathode. In this Fabry–Perot-cavity-like geometry, light is reflected between the two metallic layers. Light with wavelengths matching the criterion for constructive interference after reflection at each metal layer is amplified and emitted through the semi-transparent mirror. Light with other wavelengths is weakened or even suppressed from being coupled out [11–13]. As a consequence, the cavity thickness determines the emitted peak wavelength, and the cavity quality defines the spectral width.

2. Experimental

On CMOS surfaces, titanium nitride (TiN) is usually used as hole-injection layer (HIL). Due to its rather high work function of about −5 eV vs. vacuum [14], TiN is not capable of efficiently injecting holes to the electroluminescent copolymers used in this work (E_{HOMO} = −5.4 eV [15]). This problem can be circumvented by the addition of a molybdenum oxide (MoO_3)-layer (−5.3 eV [16]). When used in a cavity structure, MoO_3 is preferable to the commonly used 3,4-poly(ethylendioxythiophen)-poly(styrolsulfonat) (PEDOT) for transparency reasons.

We investigated TEOLEDs on glass substrates with a highly reflecting silver (Ag) anode due to our standard OLED processing. However, silver is not suitable in standard CMOS fabrication process. Thus, to demonstrate that the results are of relevance for a true CMOS process, we investigated in addition TEOLEDs containing an aluminum (Al)/(TiN)/(MoO_3) anode on a CMOS dummy substrate.

The silver anode, the HIL (MoO_3) and the cathode layers (barium and silver) were vacuum deposited in a Leybold Univex 450 chamber. The emitting polymers were spin-coated from solution in nitrogen atmosphere. Crosslinking was initiated by exposure to UV-light. A softcuring step at 90 °C on a hotplate is essential to allow chain propagation and promote further crosslinking. In crosslinked areas the polymer film becomes insoluble. Finally, the film is rinsed with toluene to remove non-exposed material. The subpixels in the future microdisplays will be developed in the same manner. Here, the entire layer is crosslinked to emulate the future conditions in microdisplays. At last, a postbaking step at 200 °C is applied.

For comparison of current–voltage–luminescence (*J–V–L*) curves and for color point characterization, OLEDs have been investigated in the top-emitting as well as in the bottom-emitting geometry. The cavity TEOLEDs consisted of the following layer stack:

Glass/Ag (150 nm)/MoO_3 (30 nm)//XR (90 nm) or
XG (70 nm) or XB (35 nm)//Ba (4 nm)/Ag (20 nm).

Using an Al mirror instead of an Ag mirror will change the optical characteristics of the cavity for a given layer thickness due to the difference in reflectivity. However, this can be compensated by re-adjusting the thickness of the emitting layer, thus, leading to identical spectral output. To study the influence on the OLED performance we fabricated a red-emitting device with Al mirror (CMOS dummy). The entire layer stack of the CMOS dummy was:

Si/Al (100 nm)/TiN (10 nm)/MoO_3 (30 nm)//
XR (100 nm)//Ba (4 nm)/Ag (20 nm).

The sequence of the BEOLED stack was:

Glass/ITO (160 nm)/MoO_3 (30 nm)//XR (80 nm) or
XG (80 nm) or XB (70 nm)//Ba (4 nm)/Ag (150 nm).

Each diode has an active area of 7.9 mm^2.

3. Results and discussion

3.1. Device performance

In Fig. 2 current density, luminance and current efficiencies are presented for TEOLEDs. Brightness levels of 1000 cd/m^2 for red and blue and 10,000 cd/m^2 for green

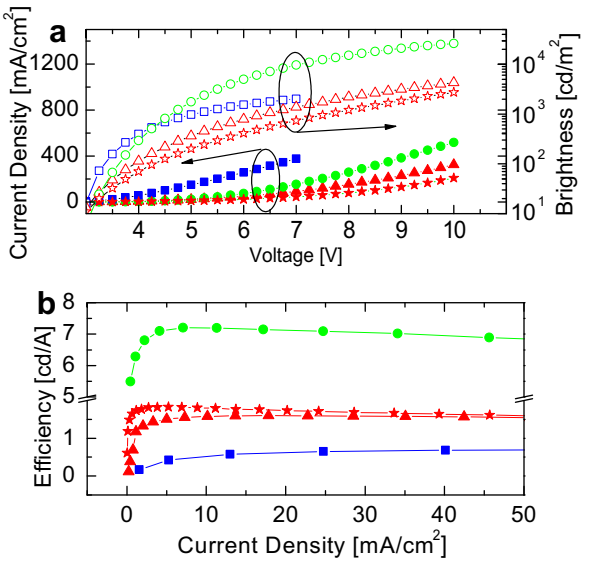

Fig. 2. (a) Current density (closed symbols) and brightness (open symbols) versus voltage, for red (triangles = Ag/MoO_3-anode, stars = Al/TiN/MoO_3-anode), green (circles) and blue (squares) TEOLEDs (b) Current efficiency versus voltage (symbols see (a)). (For interpretation of the references to colour in this figure legend, the reader is referred to the web version of this article.)

were achieved at voltages of <7 V and a current density of <40 mA/cm^2. Comparing the efficiencies of the TEOLEDs and BEOLEDs, similar values are achieved for the red and the green emitter (see Table 1). In this case the losses due to absorption at the semi-transparent cathode are compensated by the light amplification in forward direction due to microcavity effects.

The decrease in efficiency of the blue emitter in the TEOLED case can be attributed to differences in optical and electrical device performance of TEOLEDs and BEOLEDs: the emission width of the polymeric blue emitter is broad with a significant amount of emission in the green region of the spectrum (see Fig. 3). In the BEOLED geometry this fraction of green leads to sky-blue emission. The layer thickness (70 nm) in this case is chosen to achieve optimum electrical performance (balancing efficiency and operating voltage). Deep blue emission with corresponding color coordinates is obtained in the TEOLED geometry at layer thicknesses of 35 nm (first maximum of emission) and 140 nm (second maximum). This is contrary to the optimum layer thickness in terms of efficiency and operating voltage. High leakage currents for the thin layers (35 nm) and high driving voltages for the thick layers (140 nm) are observed. Besides reducing the electrical performance, the spectral blue-shift leads to a decrease in current-efficiency as the brightness is corrected by the

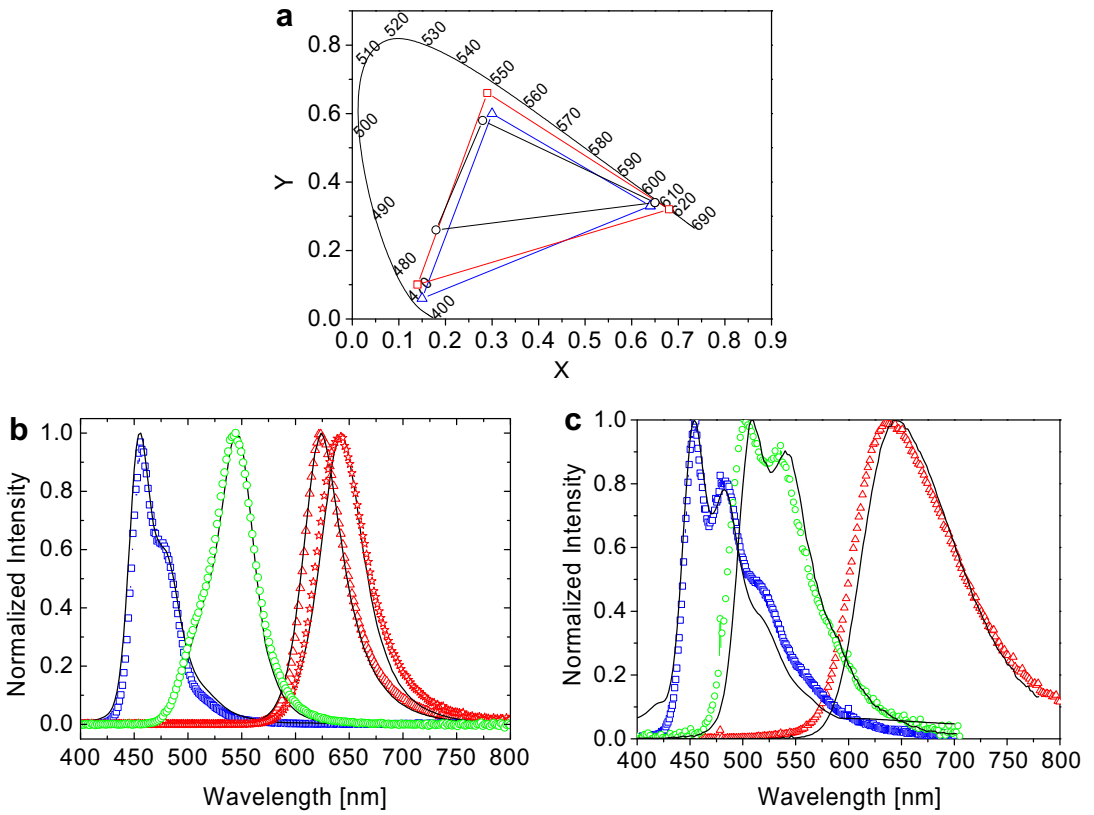

Fig. 3. (a) Color coordinates of TEOLEDs (squares) BEOLED (circles) and sRGB color space for CRTs (triangles). EL spectra of blue (squares), green (circles), red (triangles = Ag/MoO_3-anode, stars = Al/TiN/MoO_3-anode) TEOLEDs (b) and BEOLEDs (c) and Etfos simulations (solid lines).

Table 1
Efficiency and color coordinates for RGB emitters in TEOLED and BEOLED geometry.

	$XR_{Al\ Mirror}$	$XR_{Ag\ Mirror}$	$XG_{Ag\ Mirror}$	$XB_{Ag\ Mirror}$
TEOLED				
Layer thickness [nm]	100	90	70	35
η_{max} [cd/A] (CIE-values)	1.8 (0.69; 0.31)	1.6 (0.68; 0.32)	7.2 (0.29; 0.66)	0.7 (0.14; 0.10)
BEOLED				
Layer thickness [nm]	/	80	80	70
η_{max} [cd/A] (CIE-values)	/	1.2 (0.65; 0.34)	9.4 (0.28; 0.58)	2.0 (0.18; 0.26)

sensitivity of the human eye. In order to distinguish the fractions of eye-sensitivity correction and electrical device performance, we normalized the device efficiency by the overlap integral of the EL-spectrum and the eye-sensitivity curve and then compared these "quasi quantum efficiencies". It turns out that 32% of the efficiency decrease can be attributed to the color shift to deeper blue. The remaining percentage (68%) of efficiency decrease has thus to be due to electrical device performance.

Comparing the red-emitting TEOLED device featuring an Ag/MoO_3 anode with the CMOS dummy (Al/TiN/MoO_3-anode), reduced current- and light output at a given voltage are observed in the latter case. This is mainly due to a decrease in electric field resulting from the enlarged layer thickness. The current efficiency is slightly increased while λ_{max} is red-shifted. The increase in efficiency is probably due to an enlarged internal quantum efficiency due to a better charge carrier balance in the CMOS dummy device. Optical simulations show that the expected output is even reduced by a factor of 0.45 (see Supplementary data). With respect to the electrical characteristics of green- and blue-emitting materials on a CMOS dummy device, we expect similar results.

3.2. Color characteristics

In Figs. 3b and 3c the electroluminance spectra of bottom- and top-emitting OLEDs are shown. The experimental spectra were confirmed by optical simulations using Fluxim Etfos 1.3 [17]. Assuming an exciton density that is maximum at the HIL/EML interface and decays exponentially towards the cathode with a 1/e width of 20 nm [18], simulation and experimental results are in excellent agreement. Due to microcavity effects, narrowband emission is achieved in case of the TEOLED devices. In comparison to the BEOLEDs, this results in a higher color purity and, therefore, better primary CIE-values (see also Fig. 3a). Especially for the blue emitter much better color coordinates are achieved. Overall, our TEOLEDs achieve better values than required by the sRGB color space which defines the limits for computer monitors and HDTVs. In particular, the red and green emission is more saturated than required. In this case the slightly red-shifted emission of the CMOS dummy device compared with our standard TEOLED has no significant effect on the color coordinate.

The blue nearly meets the sRGB specifications. By a comparison of the areas of the color triangles [19], we conclude that the color gamut is increased by 18% (see Fig. 3a).

Calculated from the primary color coordinates, the fraction of emission required from each of the RGB TEOLEDs to obtain white emission, i.e. CIE(x, y) = (0.33; 0.33) is (RGB) = (0.26; 0.61; 0.13). The corresponding maximum current efficiency for white light emission is 4.9 cd/A at a brightness level of 1000 cd/m^2. This corresponds to a value of 5 cd/A achieved in BEOLED geometry [3], i.e. the properties are fully conserved.

4. Summary

In conclusion, we investigated solution processed crosslinkable electroluminescent materials in top- and bottom-emitting OLEDs. We showed the advantages of TEOLEDs over BEOLEDs in terms of color tuning. We also demonstrated that our TEOLEDs are suitable for high color gamut and high brightness displays. Due to their photoresist like properties, they can be directly patterned via UV-lithography and hence will allow for high resolution microdisplays. The next step will be to process and investigate the TEOLED stack and arrays of RGB sub-pixels on CMOS-backplanes for microdisplays. We already demonstrated, that on a CMOS dummy substrate the electrical and optical characteristics are essentially preserved.

Acknowledgement

We thank Herbert Metzner (University of Cologne) and the technical workshop for technical support, EU/Hypoled for funding and U. Vogel and D. Kreye (both Fraunhofer IPMS, Dresden) for fruitful discussions and for the supply with CMOS dummy wafers.

Appendix A. Supplementary data

Supplementary data associated with this article can be found, in the online version, at doi:10.1016/j.orgel.2009.09.026.

References

[1] I. Underwood, G. Kelly, R. Woodburn, P-OLED microdisplays, in: IEEE LEOS Annual Meeting Conference Proceedings, vol. 1–2, 2006, p. 438.
[2] C.D. Muller, A. Falcou, N. Reckefuss, M. Rojahn, V. Wiederhirn, P. Rudati, H. Frohne, O. Nuyken, H. Becker, K. Meerholz, Multi-colour organic light-emitting displays by solution processing Nature 421 (2003) 829.
[3] M.C. Gather, A. Koehnen, A. Falcou, H. Becker, K. Meerholz, Solution-processed full-color polymer organic light-emitting diode displays fabricated by direct photolithography, Adv. Funct. Mater. 17 (2007) 191.
[4] J.W. Hamer, A. Yamamoto, G. Rajeswaran, S.A. Van Slyke, Mass production of full-color AMOLED displays, SID Dig. 39 (2005) 1902.
[5] G. Parthasarathy, G. Gu, S.R. Forrest, A full-color transparent metal-free stacked organic light emitting device with simplified pixel biasing, Adv. Mater. 11 (1999) 907.
[6] H.K. Kim, D.G. Kim, K.S. Lee, M.S. Huh, S.H. Jeong, K.I. Kim, T.Y. Seong, Plasma damage-free sputtering of indium tin oxide cathode layers

for top-emitting organic light-emitting diodes, Appl. Phys. Lett. 86 (2005) 183503.
[7] Y.Q. Li, L.W. Tan, X.T. Hao, K.S. Ong, F.R. Zhu, L.S. Hung, Flexible top-emitting electroluminescent devices on polyethylene terephthalate substrates, Appl. Phys. Lett. 86 (2005) 153508.
[8] Q. Huang, K. Walzer, M. Pfeiffer, K. Leo, M. Hofmann, T. Stubinger, Performance improvement of top-emitting organic light-emitting diodes by an organic capping layer: an experimental study, J. Appl. Phys. 100 (2006) 064507.
[9] C.J. Lee, R.B. Pode, D.G. Moon, J.L. Han, N.H. Park, S.H. Baik, S.S. Ju, On the problem of microcavity effects on the top emitting OLED with semitransparent metal cathode, Phys. Status Solidi A Appl. Res. 201 (2004) 1022.
[10] H.J. Peng, J.X. Sun, X.L. Zhu, X.M. Yu, M. Wong, H.S. Kwok, High-efficiency microcavity top-emitting organic light-emitting diodes using silver anode, Appl. Phys. Lett. 88 (2006) 073517.
[11] A. Dodabalapur, L.J. Rothberg, T.M. Miller, Color variation with electroluminescent organic semiconductors in multimode resonant cavities, Appl. Phys. Lett. 65 (1994) 2308.
[12] A. Dodabalapur, L.J. Rothberg, R.H. Jordan, T.M. Miller, R.E. Slusher, J.M. Phillips, Physics and applications of organic microcavity light emitting diodes, J. Appl. Phys. 80 (1996) 6954.
[13] J.H. Hou, J. Wu, Z.Y. Xie, L.X. Wang, Tuning the emissive colour of top-emitting organic light-emitting diodes by using exterior multilayer films, J. Phys. D: Appl. Phys. 42 (2009) 035107.
[14] J. Westlinder, G. Sjoblom, J. Olsson, Variable work function in MOS capacitors utilizing nitrogen-controlled TiNx gate electrodes, Microelectr. Eng. 75 (2004) 389.
[15] M.C. Gather, F. Ventsch, K. Meerholz, Embedding organic light-emitting diodes into channel waveguide structures, Adv. Mater. 20 (2008) 1966.
[16] H.J. Bolink, E. Coronado, J. Orozco, M. Sessolo, Efficient polymer light-emitting diode using air-stable metal oxides as electrodes, Adv. Mater. 21 (2009) 79.
[17] A.G. Fluxim, Dr. Beat Ruhstaller, Dorfstrasse 7, CH-8835 Feusisberg, Switzerland.
[18] A. Koehnen, M.C. Gather, N. Riegel, P. Zacharias, K. Meerholz, Enhanced efficiency of multilayer organic light-emitting diodes with a low-refractive index hole-transport layer: an effect of improved outcoupling?, Appl Phys. Lett. 91 (2007) 113501.
[19] R.J. Xie, N. Hirosaki, T. Takeda, Wide color gamut backlight for liquid crystal displays using three-band phosphor-converted white light-emitting diodes, Appl. Phys. Exp. 2 (2009) 022401.

Organic Electronics 11 (2010) 62–66

Contents lists available at ScienceDirect

Organic Electronics

journal homepage: www.elsevier.com/locate/orgel

Effects of solution processing and thermal annealing on the phosphorescence of iridium(III) complex-cored dendrimer films

J.C. Ribierre [a], C.J. Yates [a], A. Ruseckas [a], S.V. Staton [b], P.L. Burn [c,*], I.D.W. Samuel [a,**]

[a] Organic Semiconductor Centre, SUPA, School of Physics and Astronomy, University of St. Andrews, North Haugh, St. Andrews, Fife KY16 9SS, United Kingdom
[b] Department of Chemistry, University of Oxford, Chemistry Research Laboratory, Mansfield Road, Oxford OX1 3TA, United Kingdom
[c] Centre for Organic Photonics & Electronics, University of Queensland, Chemistry Building, Queensland 4072, Australia

ARTICLE INFO

Article history:
Received 20 May 2009
Received in revised form 24 September 2009
Accepted 26 September 2009
Available online 3 October 2009

Keywords:
OLED
Blend
Phase separation
Morphology
Processing
Phosphorescence

ABSTRACT

We present evidence that the photoluminescence (PL) spectrum, PL kinetics and PL efficiency of solution-cast films of a phosphorescent *fac*-tris(2-phenylpyridyl)iridium(III)-cored dendrimer are not affected by the choice of solvent and thermal annealing. In contrast, when the dendrimer is dispersed into a 4,4′-bis(*N*-carbazolyl)biphenyl (CBP) host, thermal annealing induces phase separation at a micrometer scale, which results in incomplete energy transfer from CBP to the dendrimer. The insensitivity of the dendrimer film morphology and PL properties to the casting conditions and thermal treatment shows the advantage of host-free electrophosphorescent dendrimers for the further development of light-emitting displays, whilst blended systems are potentially more suitable for photovoltaic applications.

© 2009 Published by Elsevier B.V.

1. Introduction

There has been considerable interest in the optical and electrical properties of conjugated dendrimers in the recent past owing to their prospective applications in organic light-emitting diodes (LEDs) [1–3], optical amplifiers and lasers [4]. In particular, phosphorescent dendrimers containing a *fac*-tris(2-phenylpyridyl)iridium(III) [Ir(ppy)$_3$] core have been used to make efficient solution-processable LEDs with external quantum efficiencies as high as 16% [1]. Iridium(III) complexes are capable of harvesting light from both singlet and triplet excitons [5] and internal electroluminescence quantum efficiencies of nearly 100% has been achieved [6]. In addition, these materials present good colour tunability and are attractive for display and lighting applications.

Solution processable materials such as conjugated dendrimers or polymers have the advantage over light-emitting small molecules of being suitable for simple solution processing techniques such as spin-coating and inkjet printing. It is now well established that the morphology and photophysical properties of conjugated polymer films are strongly affected by the solvent used for the spin-coating and also by thermal annealing [7–15]. They have to be carefully manipulated to achieve the best performance in devices. For instance, the interplay between film morphology and photophysical properties of polyfluorene has been investigated in detail [13] and strong variations of lasing performance with phase morphology were reported by Shkunov et al. [14]. In addition, the conformation of the molecules and the local morphology at the film/substrate interface can vary greatly with the solvent, depending on its polarity and its aromaticity [11]. Different experimental techniques including neutron reflectivity [16] and Fourier-transform infrared spectroscopy measurements [17] have also been performed to study the polymer film morphology and probe the interfacial interactions in order to relate

* Corresponding author. Tel.: +617 33467614; fax: +617 33469273.
** Corresponding author. Tel.: +44 1334463114; fax: +44 1334463104.
E-mail addresses: p.burn2@uq.edu.au (P.L. Burn), idws@st-and.ac.uk (I.D.W. Samuel).

1566-1199/$ - see front matter © 2009 Published by Elsevier B.V.
doi:10.1016/j.orgel.2009.09.027

PL properties and film structure. In contrast, the influence of solution processing and thermal annealing on the molecular organization of phosphorescent [Ir(ppy)$_3$]-cored dendrimer thin films and their photophysical properties has not been investigated yet. In order to make further progress and guide future innovation in the field of phosphorescent dendrimer LEDs, it is now essential to identify the existence or not of such morphological effects and to improve our understanding of the structure–property relationships in these materials.

In this manuscript, we investigate how the photophysical properties of an [Ir(ppy)$_3$]-cored phosphorescent dendrimer with first generation phenylene-based dendrons and 2-ethylhexyloxy surface groups (IrG1) in neat films and blended into a 4,4′-bis(*N*-carbazolyl)biphenyl (CBP) host are affected by the film preparation conditions. In particular, we examine the influence of the solvent used for film deposition by spin-coating, the concentration of the dendrimer solution, the spin-speed and thermal annealing on the PL spectra, PL quantum yield (PLQY) and PL kinetics. Importantly, no significant changes in the PL properties of the neat film are observed with change in processing solvent or thermal annealing, indicating that the dendrimers form robust morphologically stable thin films. In contrast, annealing the blended film gives rise to a strong phase separation, which substantially modifies the PL properties. Using three different microscopy techniques, one measuring the photoluminescence [confocal laser scanning microscopy (CLSM)], one giving topographical information [atomic force microscopy (AFM)] and one observing the optical transmission of the sample [scanning near-field optical microscopy (SNOM)], we demonstrate the formation of large domains (up to 15 μm) rich in IrG1 dendrimer after the thermal annealing. The results are of strong interest for the development of efficient electrophosphorescent devices and support the desirability of developing solution-processed host-free phosphorescent dendrimer LEDs.

2. Experimental

The chemical structures of the materials used in this study are shown in Fig. 1. For the neat film preparation, IrG1 was dissolved into a range of organic solvents: chloroform, dichloromethane, tetrahydrofuran, chlorobenzene and toluene. Only chloroform was used to form the IrG1:CBP (20:80 wt.%) blended film due to the poor solubility of CBP in other solvents. The films were deposited by spin-coating onto precleaned quartz substrates with spin-speeds ranging from 1000 to 5000 rpm. Thermal annealing was carried out at 180 °C for 2 h in vacuum at 2×10^{-4} mbar. The thickness of the films was determined by spectroscopic ellipsometry and checked from the value of their absorbance. The absorption spectra were recorded by a Cary Varian model 300 absorption spectrophotometer and the PL spectra were measured by a Jobin Yvon Fluoromax 2 fluorimeter. Film PLQYs were determined using an integrating sphere under a flowing nitrogen atmosphere according to the method reported by Greenham et al. [18]. The samples were excited from a HeCd laser emitting at 325 nm with an excitation power of about 0.15 mW.

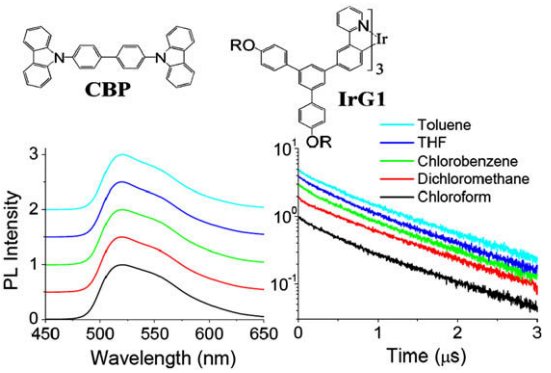

Fig. 1. PL spectra and PL kinetics detected at 520 nm of spin-coated IrG1 neat films prepared using a range of solvents. The spectra and kinetics are offset vertically for clarity. From top to bottom, the curves are obtained with films made from toluene, tetrahydrofuran (THF), chlorobenzene, dichloromethane and chloroform. The film thicknesses were in the range of 170–200 nm. The excitation wavelength was 355 nm. The chemical structure of the molecules used in this work is given in the inset. R = 2-ethylhexyl.

Time-resolved PL measurements were performed by a time-correlated single-photon counting system. Samples were excited at 393 nm by a pulsed laser diode (Picoquant) or at 355 nm by the third harmonic of a pulsed Nd:YAG laser. For the triplet–triplet exciton annihilation experiments, the 355 nm excitation light at a repetition rate of 10 kHz was focused onto the samples with a spot size of 0.3 mm diameter. All time-resolved PL measurements were carried out at room temperature and in a vacuum of $<8 \times 10^{-4}$ mbar. Spatially-resolved topographical, optical transmission and photoluminescence measurements were performed using a commercial microscope (alpha-SNOM, WITec GmbH) which allows scanning near field transmission measurements to be obtained simultaneously with AFM (contact or tapping mode) measurements. Simultaneous measurements of photoluminescence and topography are also possible using the light emanating from the tip as a near field excitation source. In addition the microscope can be used as a scanning laser confocal microscope. Sample topography was recorded simultaneously to the transmission mode data obtained at 393 nm with the Picoquant laser diode. CLSM and PL spectroscopy measurements were performed using the HeCd laser at 325 nm as excitation source. The PL signal was dispersed by a monochromator to allow wavelength discrimination. Both the transmission and the PL emission of the sample were detected by an avalanche photodiode.

3. Results and discussion

We have investigated the influence of the processing solvent on the PL properties of IrG1 neat films, using both non-aromatic and aromatic solvents. The films had thicknesses ranging from 170 to 200 nm. The green phosphorescent emission is due to the radiative decay of the metal-to-ligand charge transfer triplet state (^{3}MLCT) to the ground state [5,6,19,20]. As shown in Fig. 1, the PL spectra and the PL kinetics of IrG1 dendrimer neat films are independent of the solvent used for the spin-coating. The PLQYs

and the $1/e$ PL lifetimes measured for the films cast from a range of solvents were $65 \pm 5\%$ and 0.8 μs, respectively, with no significant difference between samples. This result clearly demonstrates that the photophysical properties of IrG1 neat films are insensitive to the processing solvents.

We have also studied the influence of the solvent on the triplet exciton diffusion in IrG1 neat films. Fig. 2a shows the PL decays measured in the neat film spin-coated from a THF solution for various excitation densities. As shown in previous work, triplet–triplet exciton annihilation processes [21–24] are responsible for the faster PL decays at high excitation densities. The density of triplet excitons $N(t)$ is proportional to the phosphorescence intensity and can be expressed by a rate equation: $dN/dt = -N/\tau - \gamma N^2$ where τ is the PL lifetime without annihilation and γ is the annihilation rate constant. If γ is time independent, a solution of this equation is:

$$\frac{1}{N(t)} = \left[\frac{1}{N_0} + \gamma\tau\right] \exp(t/\tau) - \gamma\tau \quad (1)$$

where the initial exciton density N_0 can be obtained from the energy density of the absorbed excitation laser pulse. In Fig. 2b, the inverse of the exciton density measured in the IrG1 neat film spin-coated from a THF solution is plotted as a function of $\exp(t/\tau)$. The γ value can be directly determined from the slope of the fitting curves calculated from Eq. (1). In the IrG1 neat films, the best fits were obtained with $\gamma = (6.3 \pm 1) \times 10^{-12}$ cm^3 s^{-1}, and did not depend on the solvent used for the film deposition. For diffusion limited annihilation in a three dimensional case, the exciton diffusion constant D can then be calculated from the annihilation rate constant using $\gamma = 4\pi D R_a$ where R_a is the reaction radius for which hopping is slower than annihilation and can be approximated as the core-core distance R_{eff} between neighboring phosphorescent emitters. This intermolecular distance can be estimated using a film density of 1.1 g/cm^3 [21] and assuming the molecules to be spherical. Our result leads to an exciton diffusion constant D equal to $(2.65 \pm 0.5) \times 10^{-6}$ cm^2 s^{-1} [21] and shows that the average intermolecular spacing between nearest neighbor chromophores and thus the molecular arrangement remain the same and independent of the processing solvent used to form the film.

Thermal annealing is another way to modify the morphology of polymer thin films. By heating the film near or above the glass transition temperature (T_g), macromolecules can in principle relax to more thermodynamically stable conformations and cause substantial changes in their electrical and optical properties [9,12]. We have examined the effects of thermal annealing on the photophysical properties of both the neat film of IrG1 and the 20 wt.% blend. Previous study has shown that the PLQY of 80% measured in films of this pristine (as deposited) blend is close to that of IrG1 in degassed solution [19], indicating that concentration quenching has been essentially suppressed. As shown in Fig. 3, heating the dendrimer neat film at 180 °C (which is around 50 °C higher than the T_g reported for the bulk [25]) for 2 h in vacuum does not induce any changes in the PL spectrum and the PL kinetics. It is worth noting that a similar thermal annealing in the presence of oxygen leads to a much faster PL decay and a strong

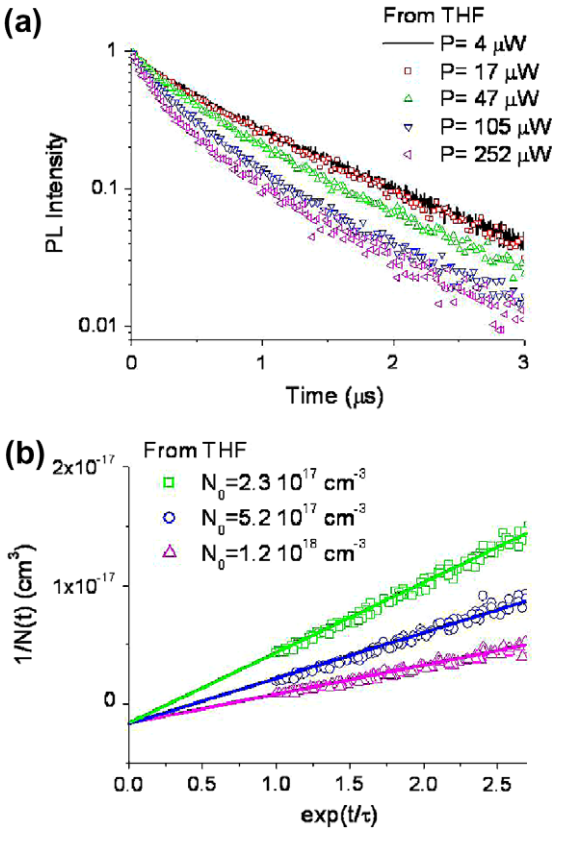

Fig. 2. (a) PL decays measured at 520 nm under different laser excitation densities in IrG1 neat film spin-coated from a THF solution. The initial intensities were normalized. (b) Plot of the reciprocal of the exciton density *versus* $\exp(t/\tau)$ in IrG1 neat film spin-coated from THF at various excitation densities.

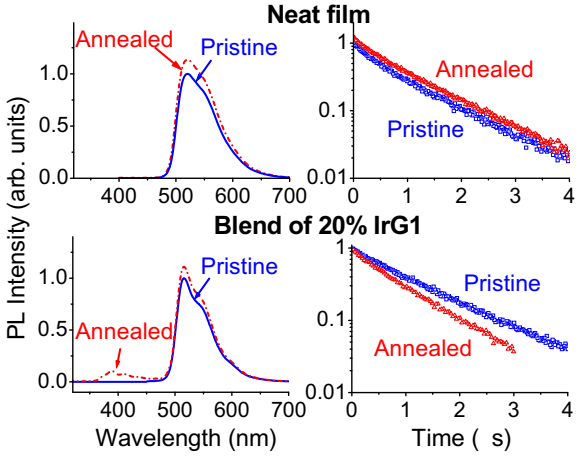

Fig. 3. PL spectra and kinetics of IrG1 neat films and IrG1:CBP (20:80 wt.%) blended films before and after a thermal annealing at 180 °C for 2 h in vacuum. The excitation wavelengths for the PL spectra were 390 and 310 nm for the neat film and the blend, respectively. The PL kinetics were measured at 520 nm with excitation at 393 nm. Spectra and kinetics are scaled vertically for clarity.

decrease in the phosphorescence efficiency due to photo-oxidation of the film. The PL spectrum of the pristine blend (before annealing) recorded with excitation at 310 nm, where CBP molecules have strong absorption, shows emission from IrG1 only, which indicates that excitation energy is transferred quickly from CBP to IrG1 (Fig. 3). In contrast, the annealed blend shows some blue fluorescence at around 400 nm from the CBP host, which suggests that energy transfer from CBP to IrG1 is much slower than in pristine blends (Fig. 3). The $1/e$ PL lifetime of IrG1 in the pristine blend of 1.1 μs is longer than that in the neat IrG1 film and can be explained by slower diffusion of triplets to any quenchers in the film [19,21]. The phosphorescence lifetime in the blend decreases to 0.8 μs with annealing and is the same as in the neat IrG1 film.

As a first step to investigate the change in blend morphology caused by thermal annealing, AFM and optical transmission measurements on a confocal microscope were performed to study the topography of the annealed blend. The blend before annealing is known to have a very smooth surface and to be homogeneous with no evident phase separation [19,21]. In contrast, the annealed blend (Fig. 4a) shows large domains (up to 15 μm) with a height variation profile of about a micrometer (Fig. 4c). The transmission signal shown in Fig. 4b was measured at 393 nm where only IrG1 absorbs significantly (see the absorption spectra of CBP and IrG1 in Fig. 4d) and correlates very well with the topography of the annealed blend. The transmission image shows exactly the same island distribution of the AFM image but with inverted contrast: low transmission of raised domains and higher transmission in inter-island regions. These results suggest that the islands are regions rich in IrG1.

Spatially-resolved PL spectroscopy using the CLSM technique was also performed to gain further insights into the molecular organization of the phase-separated annealed blend. An excitation wavelength of 325 nm was chosen in this experiment to observe the photoluminescence from both IrG1 and CBP. Note that the needs for different lasers (laser diode for the optical transmission image at 393 nm and HeCd laser for the fluorescence image) means that we were not able to probe exactly the same regions of the annealed sample using these two techniques. Fig. 5a show the CSLM fluorescence images at various emission wavelengths each of them with 10 nm bandwidth (FWHM). The images taken at emission wavelengths in the range from 480 to 600 nm show strong luminescence from the islands up to ~20 μm in size, whereas at 390 and 420 nm the islands are dark and some luminescence is observed in the regions between them. The PL spectrum of the islands (Fig. 5b) agrees well with the IrG1 emission in the bulk films (see Fig. 1), and shows no sign of CBP emission at wavelengths <430 nm, and hence the islands predominantly contain IrG1. The PL spectrum of the inter-island region shows only the blue fluorescence (<430 nm), indicating that the inter-island regions only

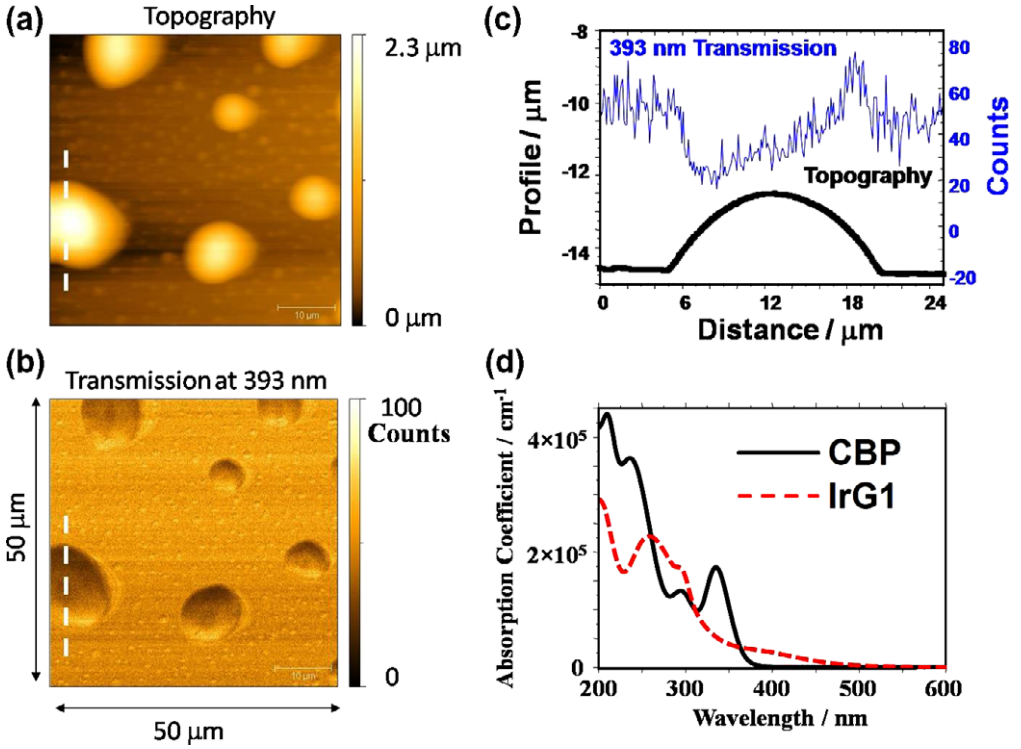

Fig. 4. SNOM micrographs demonstrating the phase separation between IrG1 and CBP after thermal annealing of the 20 wt.% blend. Panels (a) and (b) show the topography and the transmission mode measurement at 393 nm, respectively. Panel (c) gives the profiles of both the topography and the transmission mode measurement at 393 nm along the dashed white lines shown in (a) and (b). Panel (d) shows the wavelength-dependence of the absorption coefficients measured for IrG1 and CBP neat films determined by ellipsometry.

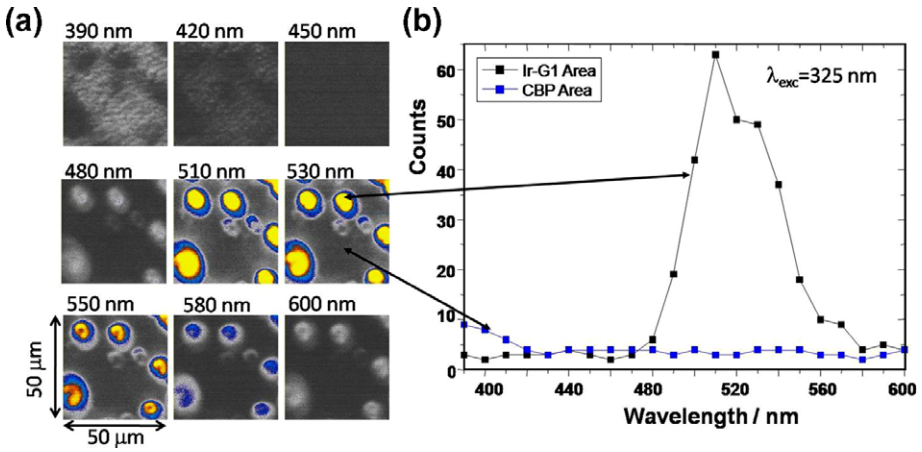

Fig. 5. (a) Photoluminescence images obtained with a confocal scanning laser microscope for the annealed 20 wt.% blend at different emission wavelengths varying from 390 to 600 nm. The excitation wavelength was 325 nm. (b) PL spectra recorded in IrG1-rich and CBP areas indicated by the arrows in (a).

contain CBP. However, it is possible that the island regions contain some CBP. If it is the case, no CBP fluorescence can be observed because the energy transfer from CBP to IrG1 is very fast in well-mixed blends. The images shown in Figs. 4 and 5 provide clear evidence of the phase separation into IrG1-rich and CBP domains when the phosphorescent blends are annealed. This work also demonstrates that spatially-resolved PL spectroscopy is a powerful tool to explore the morphology and the molecular organization of phosphorescent organic LED materials.

4. Conclusion

In summary, the effects of the solvent used for the film preparation by spin-coating and thermal annealing on the PL properties of neat and blended films of a phosphorescent [Ir(ppy)$_3$]-cored dendrimer have been investigated in detail. The results indicate excellent consistency of the properties of the film for a wide range of processing conditions for the neat films. We find that PL spectra, PL kinetics, PL efficiency and exciton diffusion of the neat films remain the same. This is potentially very attractive for applications as the need for complex process control is reduced. We also show that heating a phosphorescent dendrimer neat film at a temperature as high as 180 °C for several hours in vacuum does not alter its photophysical properties. Such thermal stability is another important factor for the choice of [Ir(ppy)$_3$]-cored dendrimers as light-emitting materials for the next generation of displays and lighting. In contrast, a strong phase separation was observed in the blend of the dendrimer with CBP and is likely to occur in other phosphorescent composite materials. Whilst phase separation may be useful for bulk heterojunction solar cells, our results strongly support the interest in developing host-free dendrimers for LEDs.

References

[1] S.-C. Lo, N.A.H. Male, J.P.J. Markham, S.W. Magennis, P.L. Burn, O.V. Salata, I.D.W. Samuel, Adv. Mater. 14 (2002) 975.
[2] T.D. Anthopoulos, M.J. Frampton, E.B. Namdas, P.L. Burn, I.D.W. Samuel, Adv. Mater. 16 (2004) 557.
[3] S.-C. Lo, T.D. Anthopoulos, E.B. Namdas, P.L. Burn, I.D.W. Samuel, Adv. Mater. 17 (2005) 1945.
[4] J.R. Lawrence, G.A. Turnbull, I.D.W. Samuel, G.J. Richards, P.L. Burn, Opt. Lett. 29 (2004) 869.
[5] M.A. Baldo, D.F. O'Brien, Y. You, A. Shoustikov, S. Sibley, M.E. Thompson, S.R. Forrest, Nature 395 (1998) 151.
[6] C. Adachi, M.A. Baldo, M.E. Thompson, S.R. Forrest, J. Appl. Phys. 90 (2001) 5048.
[7] T.-Q. Nguyen, R.C. Kwong, M.E. Thompson, B.J. Schwartz, Appl. Phys. Lett. 76 (2000) 2454.
[8] T.-Q. Nguyen, V. Doan, B.J. Schwartz, J. Chem. Phys. 110 (1999) 4068.
[9] T.-Q. Nguyen, I.B. Martini, J. Liu, B.J. Schwartz, J. Phys. Chem. B 104 (2000) 237.
[10] J. Liu, Y. Shi, L. Ma, Y. Yang, J. Appl. Phys. 88 (2000) 605.
[11] Y. Shi, J. Liu, Y. Yang, J. Appl. Phys. 87 (2000) 4254.
[12] J. Liu, T.F. Guo, Y. Yang, J. Appl. Phys. 91 (2002) 1595.
[13] A.J. Cadby, P.A. Lane, H. Mellor, S.J. Martin, M. Grell, C. Giebeler, D.D.C. Bradley, M. Wohlgennant, C. An, Z.V. Vardeny, Phys. Rev. B 62 (2000) 15604.
[14] M.N. Shkunov, R. Osterbacka, A. Fujii, K. Yoshino, Z.V. Vardeny, Appl. Phys. Lett. 74 (1999) 1648.
[15] I.D.W. Samuel, G. Rumbles, C.J. Collison, S.C. Moratti, A.B. Holmes, Chem. Phys. 227 (1998) 75.
[16] W.J. Mitchell, P.L. Burn, R.K. Thomas, G. Fragnetto, J.P.J. Markham, I.D.W. Samuel, J. Appl. Phys. 95 (2004) 2391.
[17] J. Liu, T.F. Guo, Y. Shi, Y. Yang, J. Appl. Phys. 89 (2001) 3668.
[18] N.C. Greenham, I.D.W. Samuel, G.R. Hayes, R.T. Phillips, R.R. Kessener, S.C. Moratti, A.B. Holmes, R.H. Friend, Chem. Phys. Lett. 241 (1995) 89.
[19] E.B. Namdas, A. Ruseckas, I.D.W. Samuel, S.-C. Lo, P.L. Burn, J. Phys. Chem. B 108 (2004) 1570.
[20] W.J. Finkenzeller, H. Yersin, Chem. Phys. Lett. 377 (2003) 299.
[21] J.C. Ribierre, A. Ruseckas, I.D.W. Samuel, K. Knights, S.V. Staton, N. Cumpstey, P.L. Burn, Phys. Rev. Lett. 100 (2008) 017402.
[22] E.B. Namdas, A. Ruseckas, I.D.W. Samuel, S.-C. Lo, P.L. Burn, Appl. Phys. Lett. 86 (2005) 091104.
[23] M.A. Baldo, C. Adachi, S.R. Forrest, Phys. Rev. B 62 (2000) 10967.
[24] A. Suna, Phys. Rev. B 1 (1970) 1716.
[25] S.-C. Lo, E.B. Namdas, P.L. Burn, I.D.W. Samuel, Macromolecules 36 (2003) 9721.

Organic Electronics 11 (2010) 67–73

Contents lists available at ScienceDirect

Organic Electronics

journal homepage: www.elsevier.com/locate/orgel

Existence of optimum intermolecular spacing for maximum exciton diffusion length in tris(2-phenylpyridine) iridium(III)

Y. Divayana, X.W. Sun *

School of Electrical and Electronic Engineering, Nanyang Technological University, Nanyang Avenue, Singapore 639798, Singapore

ARTICLE INFO

Article history:
Received 21 July 2009
Received in revised form 22 September 2009
Accepted 26 September 2009
Available online 6 October 2009

Keywords:
Organic materials
Exciton diffusion
Forster energy transfer
Quenching
Organic light-emitting diode
Organic solar cell

ABSTRACT

A study of one-dimensional exciton diffusion in tris(2-phenylpyridine) iridium(III) molecules as a function of intermolecular spacing is reported. We show for the first time the existence of an optimum intermolecular spacing that gives the longest diffusion length in [Ir(ppy)$_3$] molecules. When the intermolecular spacing is too short, the long-range excitonic quenching becomes dominant; on the other hand, when it is too long, the exciton energy transfer is miniscule. A specially-designed organic light-emitting diode with separate exciton formation and emission was constructed to measure the one-dimensional exciton diffusion length. The maximum one-dimensional exciton diffusion length for this material is around 8.5 nm for an inter-molecular separation of around 4.5 nm.

© 2009 Elsevier B.V. All rights reserved.

1. Introduction

Performance of organic light-emitting diodes (OLEDs) and photovoltaic (OPV) depends much on the dynamics of the exciton migration (diffusion). The relatively long exciton diffusion length (L_D) of triplet excitons enables a highly efficient white OLED with small electroluminescence efficiency roll-off by separating singlet and triplets into two independent channels [1]. In OPV devices, a longer L_D allows the utilization of a thick absorption layer that maximizes the light absorption. Although bulk-heterojunction OPV devices create donor–acceptor interface that is highly folded such that photogenerated excitons find an interface within a distance L_D of their generation sites [2,3], carrier transport is much obstructed by the multi-domains associated with the structure [4]. Therefore a longer L_D is still preferred. Understanding of exciton diffusion in organic semiconductor is therefore imperative.

Exciton diffusion in organic semiconductor has been subjected to theoretical and experimental studies for many years. Movaghar et al. [5,6] modeled the exciton diffusion and energy relaxation by both Monte Carlo simulation and a numerical analytic theory utilizing a Förster energy transfer between adjacent molecules. An improved model by Madigan and Bulovic is capable to fit very well with the experimental results [7] which shows that exciton diffusion in organics is truly governed by the long-range dipole–dipole interaction. These studies suggest that a more compact molecular material should posses a larger L_D due to a higher energy transfer rate.

Tris(2-phenylpyridine) iridium(III) [Ir(ppy)$_3$] has been used in organic light-emitting diode (OLED) to harvest the triplet excitons, which increases the efficiency by almost four times [8]. The emission layer of the OLED is normally formed by a host–guest system obtained by co-evaporating a small amount of guest molecule [Ir(ppy)$_3$] in the matrix of host material. Most excitons are formed in the matrix host which then transfers its energy to the guest molecules where final emission takes place. Recently, it was observed that Ir(ppy)$_3$ also suffers from a long-range excitonic quenching which is responsible for

* Corresponding author.
E-mail address: exwsun@ntu.edu.sg (X.W. Sun).

1566-1199/$ - see front matter © 2009 Elsevier B.V. All rights reserved.
doi:10.1016/j.orgel.2009.09.029

the concentration quenching [9–11]. Concentration quenching is represented by a persistent drop in quantum efficiency as the concentration of guest molecule increases. The quenching mechanism is reported to follow a similar Förster-type process with R^{-6} dependence, where R is the intermolecular spacing [9–11]. Correspondingly, our current understanding on exciton diffusion will be modified with the presence of this long-range quenching mechanism.

In this work we investigate the impact of the long-range quenching process to the exciton diffusion in $Ir(ppy)_3$. Exciton diffusion involves energy transfer to the adjacent molecules by Förster process [12]. In the presence of the long-range quenching there is an optimum value of intermolecular distance that gives the longest L_D. Besides demonstrating the first evidence of the existence of this optimum intermolecular spacing, we also present for the first time a direct method of measuring L_D in organic semiconductor.

2. Theory

To illustrate the effect of inter-molecular distance to the exciton diffusion, we utilized two models of exciton diffusion by adding in the long-range quenching process, as is shown in the following. The first one is based on the detailed-balance approach developed by Movaghar et al. [6]. The second one is based on the stochastic random flight model developed by Markov [13]. For the first approach, let's consider a one-dimensional molecular arrangement with a lattice spacing of R and exciton concentrations of (..., P_{i-1}, P_i, P_{i+1}, ...). We assume that the exciton transfer, which is governed by the Förster process, only occurs between adjacent molecules. This assumption is valid due to the R^n, ($n > 3$) dependence of the transfer rate. Based on this assumption, we can write the exciton (P) dynamics as,

$$\frac{dP_i}{dt} = -\frac{P_i}{\tau_r} + \{\chi_F P_{i-1} - 2\chi_F P_i + \chi_F P_{i+1}\} - 2\chi_{nr} P_i \quad (1)$$

where τ_r is the exciton lifetime, and χ_F is the Förster energy transfer rate, which can be written as [6]

$$\chi_F(R) = (1/\tau_r)(R_F/R)^6 \quad (1a)$$

For the case of a plane-to-plane interaction, Eq. (1a) should be integrated across the planar surface, thus we have $\chi_F(R) = \frac{2\pi\sigma R_F^6}{\tau_r}\int_0^\infty \frac{rdr}{(r^2+R^2)^3}$, which can be reduced to

$$\chi_F(R) = (1/\tau_r)\frac{\pi}{2}\sigma R_F^6 (1/R)^4 = (1/\tau_r)(R_{F2D}/R)^4 \quad (1b)$$

where σ is the plane surface density, R_F and R_{F2D} is the Förster radius and 2D modified Förster radius, respectively, and the long-range quenching rate is [9–11]

$$\chi_{nr}(R) = \begin{cases} (1/\tau_r)(R_{nr}/R)^6 \quad \text{for point-to-point} & (1.c) \\ (1/\tau_r)\frac{\pi}{2}\sigma R_{nr}^6 (1/R)^4 = (1/\tau_r)(R_{nr2D}/R)^4 & \\ \quad \text{for plane-to-plane} & (1.d) \end{cases}$$

where R_{nr} and R_{nr2D} is the lossy radius and 2D modified lossy radius, respectively. The steady state solution of Eq. (1) for the exciton distribution is $P_{i+1}/P_i = P_i/P_{i-1} = c = 1 + \Pi - \sqrt{\Pi}\sqrt{\Pi+2} \approx 1 - \sqrt{2\Pi}$, where $\Pi = \chi_{nr}/\chi_F + 1/2[\tau_r\chi_F]^{-1}$. At a distance x from the initial molecule, the exciton density becomes $P(x) = P(0)c^{\left(\frac{x}{R}\right)} = P(0)\exp^{\left(\frac{x}{R/\ln c}\right)}$. Hence the diffusion length can simply be written as $L_D = -R/\ln c \approx R/\sqrt{2\Pi}$.The second approach is based on Markov model where random flight of excitons in a lattice is considered [13]. In this case, the exciton diffusion occurs by incoherent hopping between the nearest-neighbor with a hopping rate (χ_F), which is related to the diffusion constant (D) by: $D = R^2(2\chi_F)/2$ [14]. The diffusion length can simply be written as $L_D = \sqrt{D\tau_t}$, where τ_t is the total exciton lifetime. Adding in the long-range quenching into the Markov isotropic model, the exciton lifetime can be written as $\tau_t^{-1} = \tau_r^{-1} + 2\chi_{nr}$. The exciton diffusion length can be written as:

$$L_D = \sqrt{\frac{R^2\chi_F}{(\tau_r^{-1} + 2\chi_{nr})}} = R/\sqrt{2\Pi} \quad (2)$$

For a plane-to-plane energy transfer, $L_D = R/\sqrt{2\left(\frac{R_{nr2D}}{R_{F2D}}\right)^4 + \left(\frac{R}{R_{F2D}}\right)^4}$. Both the Moghavar and Markov models yield the same result. Eq. (2) shows that there exists an optimum intermolecular spacing (R) that gives the longest L_D. When R is large, the energy transfer process between the molecules is miniscule. On the other hand, when R is small, the long-range quenching process takes place therefore reducing the L_D. It should be noted that Eqs. (1) and (2) only apply for one-dimensional exciton diffusion. However similar behavior is also expected in three-dimensional case.

It is worth mentioning that in the above analysis, we excluded the lateral long-range quenching interaction within the planar sheet of $Ir(ppy)_3$ and the non-radiative losses. This is meaningful as the lateral interaction only adds a constant value (independent of R) in the transfer rate, which can be absorbed in the equation as a non-radiative loss. Assuming the guest molecules in the planar layer are homogeneously distributed in a 2D square lattice with inter-molecular separation of a, the summation of the long-range quenching interaction within the planar guest layer (2D) can be written as:

$$\chi_{nr2D} = \int_a^\infty \frac{1}{\tau_r}\left(\frac{R_{nr}}{r}\right)^6 \sigma 2\pi r dr = \frac{2\pi\sigma R_{nr}^6}{\tau_r}\int_a^\infty \frac{rdr}{r^6} \quad (3)$$

where σ is the surface density of the guest layer (for the case of square lattice, $\sigma = a^{-2}$). The long-range quenching interaction within the guest layer is:

$$\chi_{nr2D} = \frac{\pi}{2\tau}\left(\frac{R_{nr}}{a}\right)^6 \quad (4)$$

The overall long-range quenching interaction is therefore,

$$\chi_{nr} = \frac{\pi}{2\tau}\left(\frac{R_{nr}}{a}\right)^6 + \frac{\pi}{2\tau}\sigma R_{nr}^2\left(\frac{R_{nr}}{R}\right)^4 \quad (5)$$

Addition of the lateral long-range quenching interaction will not affect the result shown in Eq. (2).

3. Experimental

To verify experimentally the variation of L_D as a function of intermolecular spacing, we investigated the exciton diffusion and quenching utilizing a blue OLED with a single exciton source [15]. The blue OLED has a structure of ITO/NPB/BCP/Alq_3/Mg:Ag, where ITO is indium–tin–oxide as the anode, NPB is N,N′-di(naphth-2-yl)-N,N′-diphenyl-benzidine as the hole transporting layer, BCP is 2,9-dimethyl-4,7-diphenylphenanthroline as the hole blocking layer, Alq_3 is tris-(8-hydroxyquinoline) aluminum as the electron transporting layer, and Mg:Ag is a mixture of magnesium and silver (ratio 10:1) as the cathode. Detail of the fabrication and measurement can be found elsewhere [15]. For this structure, the barriers for both hole and electron exist at the NPB/BCP interface. Since holes experience a larger barrier at BCP (1.1 eV) [16] than electrons at NPB (0.6 eV) [16], the recombination and exciton formation take place in the NPB layer.

Using the basic blue OLED structure, we shall study the exciton diffusion in Ir(ppy)$_3$ molecules in the following. As the exciton is absent at the BCP side, Ir(ppy)$_3$ was deposited as the guest molecule in the BCP-host by sequential doping [Ir(ppy)$_3$/BCP multiple-layer] [9]. In this system, the exciton from NPB transfers its energy to Ir(ppy)$_3$ nearest to the NPB/BCP interface (Fig. 1). The excitons then diffuse within the Ir(ppy)$_3$ molecules. To detect the exciton distribution, a thin sensing layer (red emission) of bis(2-phenylquinoline) (acetylacetonate) iridium(III) [Ir(2-phq)$_2$(acac)] is deposited after the Ir(ppy)$_3$. By varying the thickness of the BCP-host layer, the exciton diffusion as a function of intermolecular spacing in Ir(ppy)$_3$ can be studied.

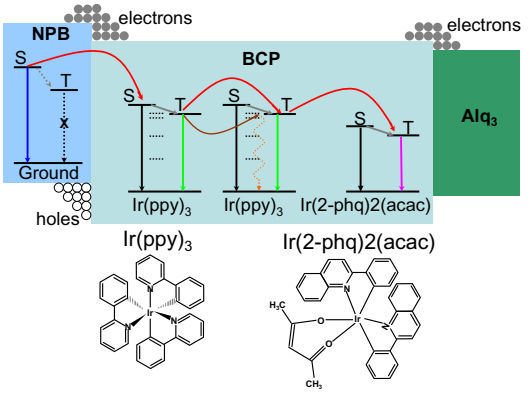

Fig. 1. Illustration of the OLED structure utilized to study exciton diffusion in Ir(ppy)$_3$. The excitons are formed at the NPB layer with a peak concentration at the NPB/BCP interface. The exciton in NPB transfers its energy to the nearest Ir(ppy)$_3$ molecules via Förster process (red arrow) [singlet–singlet (S–S)]. Due to a large inter-system crossing rate (grey arrow) because of the large spin–orbit coupling, the singlet exciton in Ir(ppy)$_3$ decays into a triplet state. The triplet (T) exciton then diffuses to an adjacent Ir(ppy)$_3$ molecule by Förster process (red arrow). However there is also a chance that the triplet exciton transfers via long-range quenching process (brown arrow) to the vibrational mode (dotted lines) of the adjacent Ir(ppy)$_3$, resulting in non-radiative decay (dotted orange arrow). To detect the exciton distribution, a Ir(2-phq)$_2$(acac) layer emitting red color (pink arrow) is deposited at the end. Also shown are the molecular structure of Ir(ppy)$_3$ and Ir(2-phq)$_2$(acac). (For interpretation of the references to colour in this figure legend, the reader is referred to the web version of this article.)

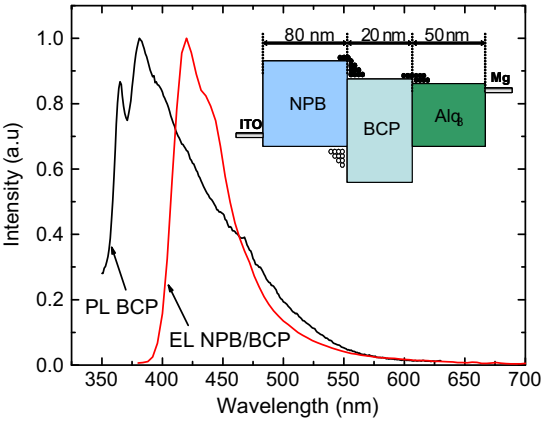

Fig. 2. Photoluminescence of BCP and electroluminescence of blue OLED. The inset shows the energy diagram of the blue OLED. (For interpretation of the references to colour in this figure legend, the reader is referred to the web version of this article.)

4. Result and discussion

4.1. Exciton distribution in blue OLED

Before we study the L_D, we shall first investigate the exciton distribution in the blue OLED. The inset of Fig. 2 shows the band energy of the blue OLED. The electroluminescence (EL) spectrum of the blue OLED is shown in Fig. 2. Also shown in Fig. 2 is the photoluminescence (PL) spectrum of the BCP. It can be seen that there is no BCP emission, thus the exciton is only formed at NPB layer.

To study the exciton distribution at NPB layer, we fabricated device with a structure of ITO/NPB (80-d nm)/DCJTB (0.1 nm)/NPB(d nm)/BCP (20 nm)/Alq_3 (50 nm), where DCJTB is 4-(dicyanomethylene)-2-tert-butyl-6-(1,1,7, 7-tetramethyljulolidin-4-yl-vinyl)-4H-pyran, and d varies from 10, 20, 30 to 50 nm as shown by the inset of Fig. 3a. DCJTB emits red light peaking at 590 nm. Fig. 3a shows the emission spectra for devices with various d's. It can be seen that the NPB (or DCJTB) peak increases (or decreases) with the increase of d. In Fig. 3b, we plotted the intensity of the NPB and DCJTB as a function of d. Also shown in the figure is the fitting curves that follows $(1 - \exp[-d/L_D])$ [red line] and $(\exp[-d/L_D])$ [blue line]. It can be seen that the fit and the data match well with $L_D = 22 \pm 3$ nm. This relatively long L_D may also indicate that the formation of exciton occurs throughout the NPB layer with the peak rate at the NPB/BCP interface.

4.2. Energy transfer rate between NPB, Ir(ppy)$_3$ and Ir(2-phq)$_2$(acac)

We then investigated the exciton energy transfer rate between NPB and Ir(ppy)$_3$. To do this, we deposited a thin layer of 0.5 nm Ir(ppy)$_3$ in the BCP layer with varying distance from NPB/BCP interface. The structure is NPB

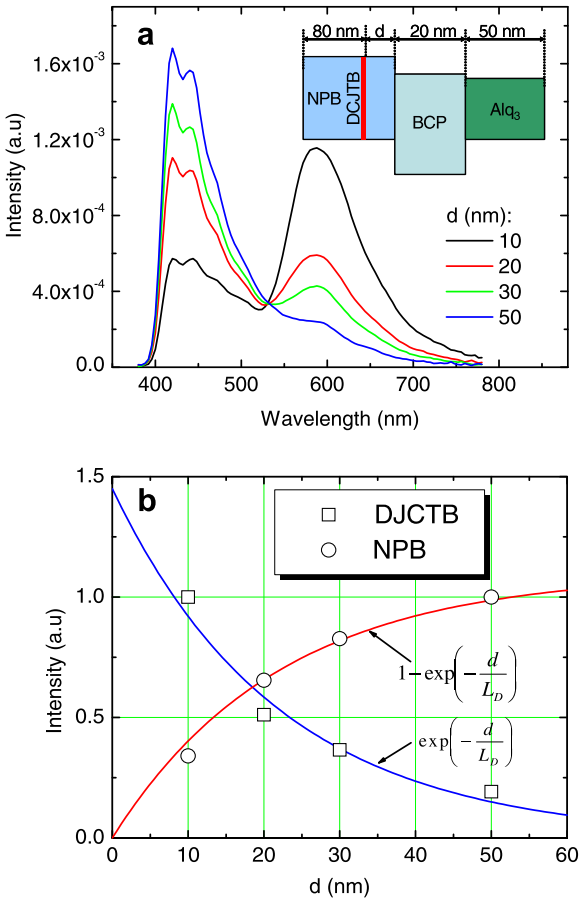

Fig. 3. (a) Emission spectra for devices with various *x*'s. The inset shows the energy diagram of the ITO/NPB/DCJTB/NPB/BCP/Alq_3/Mg structure. (b) Normalized peak intensity of DCJTB and NPB as a function of *x*. Also shown are the fitting curves which obey $(1-\exp[-d/L_D])$ and $\exp[-d/L_D]$.

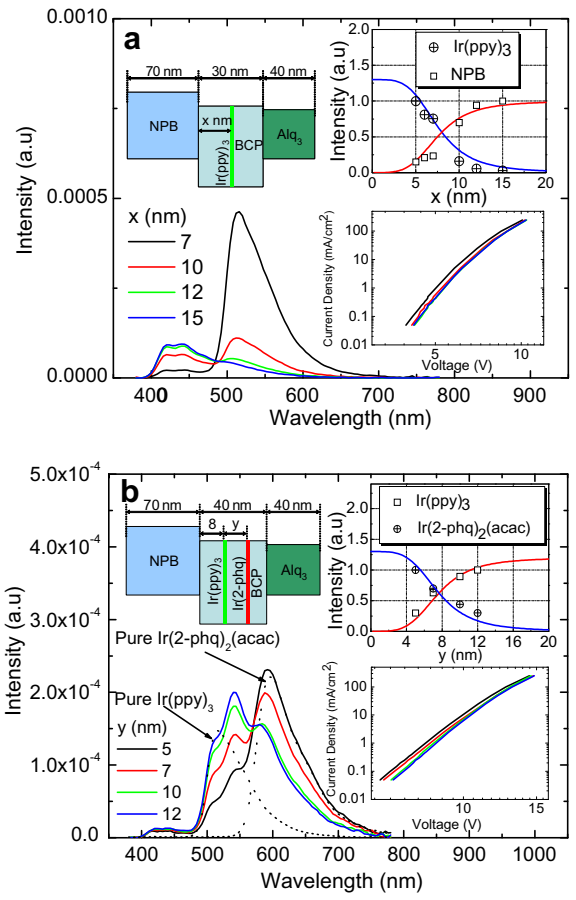

Fig. 4. (a) The emission spectra for devices with different values of *x*. The inset shows the normalized peak intensity of the NPB and $Ir(ppy)_3$ as a function of *x*. The lower inset shows the current density versus voltage curves for devices with different values of *x*. Also shown by the inset is the energy diagram of the corresponding device. (b) The emission spectra for devices with different values of *y*. Emission spectra of pure $Ir(ppy)_3$ and $Ir(2\text{-phq})_2(acac)$ are also shown. The inset shows the normalized peak intensity of the $Ir(ppy)_3$ and $Ir(2\text{-phq})_2(acac)$ as a function of y. The lower inset shows the current density versus voltage curves for devices with different values of y. Also shown by the inset is the energy diagram of the corresponding device.

(70 nm)/BCP (*x* nm)/$Ir(ppy)_3$ [0.5 nm]/BCP (30 − *x* nm)/Alq_3 (40 nm), where *x* varies from 5, 6, 7, 10, 12, to 15 nm as shown by the inset of Fig. 4a. Fig. 4a shows the emission spectra for device with different *x*'s. It can be seen that the $Ir(ppy)_3$ [or NPB] peak decreases [or increases] sharply with the increase of *x*. This is because the transfer rate from NPB to $Ir(ppy)_3$ exciton is distance dependent. The inset shows the peak intensity of NPB and $Ir(ppy)_3$ peaks as a function of *x*. The intensity of the $Ir(ppy)_3$ peak can be written as $\chi_F/(\chi_F+\tau_r^{-1}) = (1+(x/R_{F2D})^4)^{-1}$ [17]. It is clear that the $Ir(ppy)_3$ peaks can be fitted well using a plane-to-plane type Förster transfer rate [blue line]. The intensity of the NPB peak on the other hand can be written as $\tau_r^{-1}/(\chi_F+\tau_r^{-1}) = (1+(R_{F2D}/x)^4)^{-1}$ [17]. And similarly, the data are fitted well using a plane-to-plane type Förster transfer rate [red line], with R_{F2D} = 7.5 ± 0.6 nm. The lower inset in Fig. 4a shows the current density versus voltage relationship for devices with different values of *x*. It can be seen that there is no significant change in the current–voltage profile, which indicates that the variation of the emission spectrum is unrelated with charge trapping in $Ir(ppy)_3$ layer.

We then studied the exciton energy transfer rate between the $Ir(ppy)_3$ and the sensing layer $Ir(2\text{-phq})_2(acac)$. Devices with a structure of NPB (70 nm)/BCP (8 nm)/$Ir(ppy)_3$ [0.5 nm]/BCP(*y* nm)/$Ir(2\text{-phq})_2(acac)$ [0.1 nm]/BCP (32 − *y* nm)/Alq_3 (40 nm) was fabricated, where *y* varies from 5, 7, 10 to 12 nm as shown by the inset of Fig. 4b. Fig. 4b shows the emission spectra for different *y*'s. Similar to the results in Fig. 4a, there is a clear variation of emission spectrum due to energy transfer. The inset shows the peak intensities of $Ir(ppy)_3$ and $Ir(2\text{-phq})_2(acac)$ as a function of *y*. The simulation fits the experimental data well based on the Förster type of energy transfer with R_{F2D} = 7.5 ± 0.6 nm (as shown by the solid line). The lower inset in Fig. 4b shows the current density versus voltage curves for devices with different values of *y*. It can be seen that only slight shift in voltage is observed for different *y*'s. This indicates that the changes in the emission spectrum is not caused by direct exciton formation at $Ir(2\text{-phq})_2(acac)$. Exciton formation at $Ir(2\text{-phq})_2(acac)$ requires the presence

of both hole and electron carriers. Any variation of emission spectrum signifies changes in carrier flow within the device, hence should be reflected by the current density versus voltage curves.

4.3. Exciton diffusion length as a function of intermolecular spacing

Finally, to study the L_D in Ir(ppy)$_3$ molecules, we fabricated two different structures where Ir(ppy)$_3$ was deposited as the guest molecule in the BCP-host by sequential doping [Ir(ppy)$_3$/BCP multiple-layer] [9]. The thickness of the Ir(ppy)$_3$/BCP multiple-layer is fixed (Fig. 5a). The Ir(ppy)$_3$/BCP multiple-layer consists of [Ir(ppy)$_3${0.5 nm}/BCP(R nm)] N times/Ir(ppy)$_3$ [0.5 nm]. The BCP layer thickness determines the intermolecular spacing between the Ir(ppy)$_3$ molecules.

Structure A consists of NPB (70 nm)/BCP (7 nm)/{Ir(ppy)$_3$/BCP multiple-layer} [24 nm]/BCP (5 nm)/Ir(2-phq)$_2$(acac) (0.1 nm)/BCP (5 nm)/Alq$_3$ (40 nm). The (R, N) varies from (6 nm, 4), (8 nm, 3), to (12 nm, 2). For structure B, the thickness of the Ir(ppy)$_3$/BCP multiple-layer was fixed at 12 nm. Structure B consists of NPB (70 nm)/BCP (7 nm)/{Ir(ppy)$_3$/BCP multiple-layer} [12 nm]/BCP (7 nm)/Ir(2-phq)$_2$(acac) (0.1 nm)/BCP (5 nm)/Alq$_3$ (40 nm). The (R, N) varies from (2 nm, 6), (3 nm, 4), (4 nm, 3), to (6 nm, 2). For all devices in each structure, the sensing Ir(2-phq)$_2$(acac) layers are at the same distance from the NPB/BCP interface [18].

Fig. 5a shows the emission spectrum for structure A and B with different (R, N)'s. For structure A, it can be seen that the Ir(ppy)$_3$ peak increases with the increase of R. The Ir(2-phq)$_2$(acac) peak on the other hand is maximum for R = 6 nm. This shows L_D is the longest for device with (R, N) = (6 nm, 4) since the position of the Ir(2-phq)$_2$(acac) layer is approximately the same for all devices. The smaller Ir(2-phq)$_2$(acac) peak intensity for R > 6 nm can be understood due to a weak Förster energy transfer between the Ir(ppy)$_3$.

For structure B, it can be seen that the Ir(2-phq)$_2$(acac) peak decreases as R decreases. This shows the exciton diffusion to the Ir(2-phq)$_2$(acac) decreases with the decrease of R. The Ir(ppy)$_3$ peak decreases even more with the decrease of R. For device with R < 6 nm, the long-range quenching process increases, reducing the L_D as suggested in the beginning. The emission of the Ir(ppy)$_3$ molecule also reduces as a result of the increasing long-range quenching process. This agrees with our theory well for reduced L_D. Maximum exciton diffusion is obtained for R = 6 nm. The exciton distribution in the Ir(ppy)$_3$ layers can be written as $p(x) = L_D^{-1}\exp(-xL_D^{-1})$, where L_D is a function of intermolecular spacing R. In the case where there is an absorbing layer [Ir(2-phq)$_2$(acac)] with different emission spectrum positioned at a distance d from the boundary (x = 0), the emission will consist of that the original molecules [Ir(ppy$_3$)] and the absorbing molecules [Ir(2-phq)$_2$(acac)]. Unlike diffusion, where the energy transfers between different layers are unidirectional, the energy transfer from Ir(ppy)$_3$ to the Ir(2-phq)$_2$(acac) is one-way only, therefore the overall energy

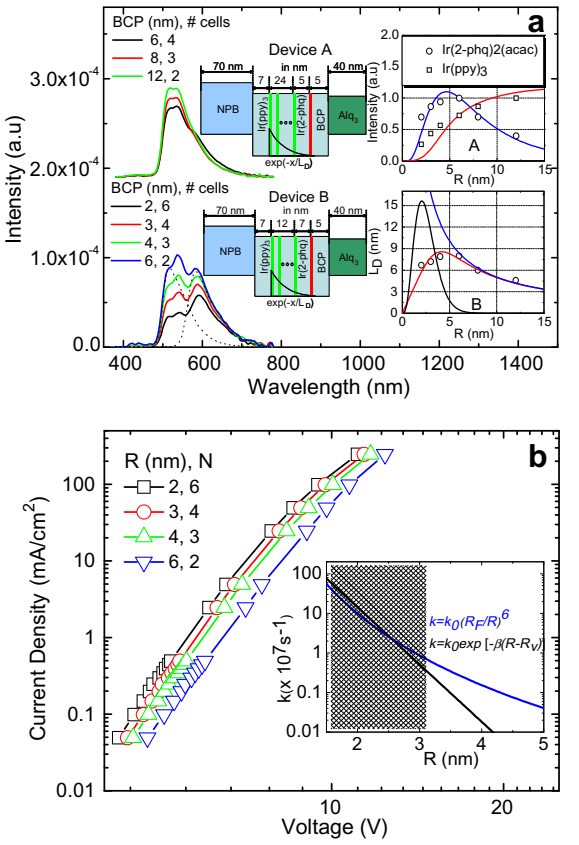

Fig. 5. (a) The emission spectra of devices with structure A (upper) and structure B (lower). The inset shows the respective energy diagram of structure A and B. Also shown in the energy diagram is the illustration of exponentially distributed excitons. The inset A shows the intensity of the Ir(ppy)$_3$ and Ir(2-phq)$_2$(acac) peaks as a function of thickness of BCP layer separating two adjacent Ir(ppy)$_3$ layers (R). Peak intensities of devices with structure A and B are normalized with respect to device with R = 6 nm. Inset B shows the corresponding L_D value for devices with different value of R. (b) Current density versus voltage curves for device B. Inset in (b) shows the exciton hopping rate as function of intermolecular spacing (R). Black and blue lines are the hopping rate based on Dexter and Förster processes, respectively. It can be seen that at the range of the data presented at Ref. [15] shown here inside the grid-box, both model show a similar characteristic. (For interpretation of the references to colour in this figure legend, the reader is referred to the web version of this article.)

transfer to the [Ir(2-phq)$_2$(acac)] is much larger than the diffusion rate, hence the intensity can be written as:

$$I_{Ir(ppy)3} = \frac{\tau_r^{-1}}{\tau_r^{-1} + 2\chi_{Fnr}} \int_0^d p(x)dx = \frac{1}{(1 + 2\tau_r\chi_{Fnr})}\left(1 - \exp\left(-\frac{d}{L_D(R)}\right)\right) \quad (6)$$

$$I_{Ir(2\text{-}phq)2(acac)} = \int_d^\infty p(x)dx = \exp\left(-\frac{d}{L_D(R)}\right) \quad (7)$$

The inset A of Fig. 5a shows the intensity of the Ir(ppy)$_3$ and Ir(2-phq)$_2$(acac) as a function of BCP layer separating the Ir(ppy)$_3$ layers (R). It can be seen that the Ir(2-phq)$_2$(acac) peak intensity is maximum for R = 6 nm, which indi-

cates the longest L_D. The blue line shows the fit using Eq. (6) while the red line using Eq. (7). It can be seen that a reasonable agreement between the theory and experimental data were achieved. In the inset B of Fig. 5a, we plotted the corresponding L_D obtained from experimental data (open circle) and calculated from Eq. (2) with (red line) and without (blue line) the inclusion of the long-range quenching process. It should be noted that the large variation in the emission spectrum is only reflected by the small changes in the L_D value because of the logarithmic relation. Inclusion of the long-range quenching process is clearly necessary to fit the experimental data. For the fit, we used L_D = 8 nm for R = 6 nm (see below). From the fit in inset B, the Förster (R_{F2D}) and lossy (R_{nr2D}) radius are about 7.1 ± 0.3 nm and 3.5 ± 0.2 nm, respectively, with maximum L_D = 8.5 nm at R = 4.5 nm. The R_{F2D} value is close with that obtained for NPB–Ir(ppy)$_3$. On the other hand, the R_{nr2D} value is similar with that reported previously [9]. R_F and R_{nr} can be calculated assuming that the surface density of the planar 0.5 nm Ir(ppy)$_3$ layer is around (1^{-2}–2^{-2} nm^{-2}). Using the relation between R_F and R_{F2D} [Eq. (1)], R_F = 3.4–4.3 nm and R_{nr} = 2.1–2.7 nm were obtained. The R_{nr} value is very close with that reported previously [10].

Another point needs to be addressed is the possibility of Ir(ppy)$_3$ triplet exciton back-transferring the energy to the BCP triplet which then diffuses via BCP. Previous report has shown that the triplet energy of BCP (2.5 eV) is only slightly larger than that of Ir(ppy)$_3$ (2.4 eV) [19]. This small difference in the energy level suggests that the triplet is not well confined in the Ir(ppy)$_3$. The significance of the back-energy transfer from Ir(ppy)$_3$ to BCP can be seen by analyzing the experimental results. Let's examine Fig. 4b for example, where we showed the interaction between Ir(ppy)$_3$ and Ir(2-phq)$_2$(acac). A large back-energy transfer to BCP will lead to exciton diffusion directly via the BCP instead of Ir(ppy)$_3$. In this case, only the emission spectrum of the Ir(2-phq)$_2$(acac) is expected to vary, not the Ir(ppy)$_3$, since only the Ir(2-phq)$_2$(acac) layer is positioned differently. However, it is clear from Fig. 4b that both Ir(ppy)$_3$ and Ir(2-phq)$_2$(acac) peaks vary accordingly, which indicates that the energy transfer is mainly due to Förster process. Secondly, it can be seen for device B in Fig. 5 that the addition of the Ir(ppy)$_3$ layers is able to extend the exciton distribution up to 19 nm, which indicates that exciton diffusion is occurred between the Ir(ppy)$_3$ layers. Furthermore it has been well reported in the literature that BCP acts as a good exciton blocker [1,8]. In an OLED system that utilizes 4,4′-bis(N-carbazolyl)biphenyl (CBP) (with higher triplet energy of 2.6 eV [19]) as the host and with BCP as the exciton blocker, the triplet exciton is found to be efficiently confined within the CBP, which indicates effective exciton blocking by BCP [1]. Hence it is safe to say that the excitons are well confined within the Ir(ppy)$_3$ layer.

Fig. 5b shows the current–voltage characteristics for devices with various (R, N). It can be seen that despite of the large variation of R and N, the current–voltage profile is barely changed (maximum shift of 1 V). This signifies that the charge trapping at the Ir(ppy)$_3$ layers is minimum. The influence of charge trapping to the light emission can be further considered insignificant for the following reason. Charge trapping in Ir(ppy)$_3$ layer will cause devices with larger N to emit more green and red light. However, from the experimental result it can be seen that, N does not correlate linearly with the emission peak intensity. For device A, the highest N gives smaller green but larger red emissions. On the other hand for device B, the highest N gives smaller green and red emissions. Hence the consequence of charge trapping to the interpretation of our result can be neglected. Recently, Ribierre et al. studied the triplet–triplet exciton annihilation dynamics in Iridium(III)-centered dendrimers [11]. They discovered a similar Förster type of excitonic quenching, but discussed the exciton diffusion in term of a hopping (Dexter) process [20]. However, the limited range of intermolecular spacing (1.8–3.2 nm) available for the analysis could mislead to the conclusion that exciton diffusion is governed by Dexter process. In fact, at such intermolecular spacing (1.8–3.2 nm), the data can be fitted well with either Dexter or Förster (with R_F = 4.5 nm) processes. In inset of Fig. 5b we plotted the Dexter and Förster energy transfers as function of intermolecular spacing. It can be seen that at a small intermolecular spacing as reported by Ribierre et al. (1.8–3.2 nm), the data can be fitted with both Dexter and Förster processes. The data start to deviate at R > 3 nm. For the Förster transfer rate R_F = 4.5 nm. The fitted R_F is close to the value obtained experimentally (R_F = 3.4–4.3 nm). Moreover, exciton diffusion by Dexter process will lead to a non-monotonous L_D characteristic as a function of intermolecular spacing, which fails to fit the experimental data for a larger intermolecular spacing. Also shown in inset B of Fig. 5a is the L_D calculated by assuming that the exciton diffusion is governed by Dexter process (black line) with a hopping rate of $k = k_0 \exp[-\beta(R - R_v)]$ with $k_0 = 4\times 10^9\ s^{-1}$, $\beta = 0.33\ \text{A}^{-1}$ and $R_v = 1$ nm [11]. These parameters were directly taken from Ref. [12]. For the calculation, we modified the Dexter process for the case of plane-to-plane interaction. In plane-to-plane interaction, the Förster process decays as R^{-4} while the Dexter process decays as $R \cdot \exp[-\beta(R - R_v)]$. It can be seen that, due to the nature of the Dexter process, the L_D drops very fast as R increases, which cannot be fitted with the experimental data.

To confirm the value of L_D for the optimum intermolecular spacing, we then perform another experiment, by fabricating a structure with fixed intermolecular spacing with different values of N. The structure is NPB (70 nm)/BCP (7 nm)/[Ir(ppy)$_3$ {0.5 nm}/BCP (6 nm)]N times/Ir(ppy)$_3$ [0.5 nm]/BCP (5 nm)/Ir(2-phq)$_2$(acac) [0.1 nm]/BCP (28–6N nm)/Alq$_3$ (40 nm), where N is varied from 1 to 4. Fig. 6 shows the emission spectra for devices with various N's. The intensity of Ir(2-phq)$_2$(acac) and Ir(ppy)$_3$ as a function of N or thickness of Ir(ppy)$_3$/BCP multiple-layer is shown in the inset. The Ir(2-phq)$_2$(acac) and Ir(ppy)$_3$ peaks can be fitted with $(1 - \exp(-d/L_D))$ [red line] and $\exp(-d/L_D)$ [blue line], respectively. Based on the plot, the L_D is determined to be 8 ± 2 nm for R = 6 nm.

It is worth mentioning that the total thickness of our device is more than 120 nm, and a Ir(2-phq)$_2$(acac) was used as an absorber, so that surface quenching can be neglected [11]. In fact, there was no Alq$_3$ emission observed, indicating the absence of exciton diffusion toward the interface.

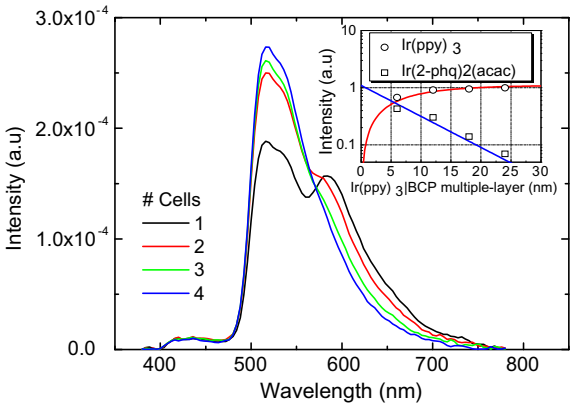

Fig. 6. The emission spectra for devices with different numbers of cells (N). The inset shows the normalized peak intensity of $Ir(ppy)_3$ and $Ir(2\text{-phq})_2(acac)$ as a function of the thickness of $Ir(ppy)_3$/BCP multiple-layer.

5. Conclusion

In conclusion, we have shown that there is an optimum intermolecular spacing that gives the largest L_D. This is because the exciton in organic semiconductor experiences two competing processes (Förster and long-range quenching processes). We found a good fit between theoretical and experimental data. This result will have tremendous impact to the development of OLED and OPV devices which rely heavily on exciton diffusion. Similar mechanisms are expected for other organic semiconductor and for singlets, though experimental verification is needed.

Acknowledgement

Y.D. would like to thank the Singapore Millennium Foundation (SMF) for the financial support.

References

[1] Y. Sun et al., Nature 440 (2006) 908.
[2] P. Peumans, S. Uchida, S.R. Forrest, Nature 425 (2003) 158.
[3] J.J.M. Halls et al., Nature 376 (1995) 6540.
[4] J.-I. Nakamura, K. Murata, K. Takahashi, Appl. Phys. Lett. 87 (2005) 132105.
[5] B. Movaghar, J. Phys. C 13 (1980) 4915.
[6] B. Movaghar et al., Phys. Rev. B 33 (1986) 5545.
[7] C. Madigan, V. Bulovic, Phys. Rev. Lett. 96 (2006) 046404.
[8] M.A. Baldo et al., Appl. Phys. Lett. 75 (1999) 4.
[9] Y. Divayana, X.W. Sun, Phys. Rev. Lett. 99 (2007) 143003.
[10] Y. Kawamura et al., Phys. Rev. Lett. 96 (2006) 017404.
[11] J.C. Ribierre et al., Phys. Rev. Lett. 100 (2008) 017402.
[12] T. Förster, Discuss. Faraday Soc. 27 (1959) 7.
[13] S. Chandrasekhar, Rev. Mod. Phys. 15 (1943) 1.
[14] E.B. Namdas et al., Appl. Phys. Lett. 86 (2005) 091104.
[15] Y. Divayana et al., Appl. Phys. Lett. 89 (2006) 173511.
[16] C. Shen, A. Kahn, I.G. Hill, in: W.R. Salaneck et al. (Eds.), Conjugated Polymer and Molecular Interfaces, Marcel Dekker Inc., New York, 2002.
[17] S.R. Scully et al., Adv. Mater. (Weinheim, Ger.) 19 (2007) 2961.
[18] To minimize the direct exciton energy transfer from NPB to Ir(ppy)3 to Ir(2-phq)2(acac) through Förster transfer (without diffusion), the first Ir(ppy)3 layer was deposited 7 nm away from NPB/BCP interface. Furthermore, the Ir(2-phq)2(acac) is deposited 7 nm from the final Ir(ppy)3 layer (structure B). This guarantees the contribution of direct exciton energy transfer from NPB to the first Ir(ppy)3 layer to Ir(2-phq)2(acac) to be close to zero, $\left[1+(7\text{ nm}/R_{F2D(\text{NPB}-\text{Ir(ppy)}_3)})^4\right]^{-1}\times[1+(19\text{ nm}/R_{F2D(\text{Ir(ppy)}-\text{Ir}(2-\text{phq}))})^4]^{-1}\sim 0.008$. A direct energy transfers from NPB to the Ir(2-phq)2(acac) sensing layer is also unlikely since they are separated by 26 nm.
[19] M.A. Baldo, S.R. Forrest, Phys. Rev. B 62 (2000) 10958.
[20] D.L. Dexter, J. Chem. Phys. 21 (1953) 836.

Organic Electronics 11 (2010) 74–80

Contents lists available at ScienceDirect

Organic Electronics

journal homepage: www.elsevier.com/locate/orgel

An X-shaped solution-processible oligomer having an anthracene unit as a core: A new organic light-emitting material with high thermostability and efficiency

Jing Sun [a], Hongliang Zhong [a], Erjian Xu [a], Danli Zeng [a], Jianhua Zhang [b], Hongguang Xu [c], Wenqing Zhu [b], Qiang Fang [a,*]

[a] Key Laboratory of Organofluorine Chemistry and Laboratory for Polymer Materials Shanghai Institute of Organic Chemistry, Chinese Academy of Sciences, 345 Lingling Road, Shanghai 200032, PR China
[b] Key Laboratory of Advanced Display and System Applications, Shanghai University, Ministry of Education, 149 Yanchang Road, Shanghai 200072, PR China
[c] R&D Center for Flat Panel Display Technology, SVA Company, Shanghai 200081, PR China

ARTICLE INFO

Article history:
Received 13 July 2009
Received in revised form 17 September 2009
Accepted 30 September 2009
Available online 20 October 2009

Keywords:
Organic light-emitting diodes
π-Conjugated oligomers
Anthracene derivatives
Optical properties
Electrochemical properties

ABSTRACT

A new X-shaped solution-processible oligomer with a glass transition temperature of higher than 200 °C based on an anthracene derivative was prepared, and it showed good hole-transporting ability in organic light-emitting diodes (OLED). Such oligomer was also employed as the emitting layer to give the devices showing blue emission.

© 2009 Elsevier B.V. All rights reserved.

1. Introduction

In the recent years, there has been an increasing interest in the synthesis and characterization of the π-conjugated molecules with topologically special structure such as cruciform or X-shaped [1–12]. Those molecules show highly electrochemical and photoluminescent activities, and easily form amorphous glass in the solid state. Moreover, some of them display sensitivity to proton and metals [2,3]. Such interesting properties of the molecules are desired for the application in optoelectronic field as the materials in non-linear optical device [4,5], light-emitting diodes [7,11], organic field-effect transistors [12] and chemical sensors [2,3].

Compared with the linear conjugated molecules, the conjugated cruciform compounds show spatially separated energy levels of HOMO and LUMO, and each branch of the molecules possess independent properties, which are suitable for the applications of chemical sensors [2]. It is more important the π-aggregation is depressed in the conjugated cruciform molecules due to the special 3D structure of the molecules [13], and such properties probably are useful for fabrication of the optoelectronic devices with excellent properties. Undoubtedly, investigation on the relationship between the chemical structure of the cruciform compounds and properties of the molecules is very necessary.

* Corresponding author. Tel./fax: +86 21 5492 5337.
E-mail address: qiangfang@mail.sioc.ac.cn (Q. Fang).

1566-1199/$ - see front matter © 2009 Elsevier B.V. All rights reserved.
doi:10.1016/j.orgel.2009.09.030

It is noted that there are few building models for the cruciform compounds. E.g., the reported cruciform molecules are mainly formed by the models that each branch of the molecules is extended from a benzene (or a thiophene) ring [14,15]. Thus, exploring and developing new building models of the π-conjugated molecules with cruciform structure are desired.

To build a new structure of the cruciform compounds, a better choice is employing anthracene as a starting unit because an anthracene unit possesses four active positions, e.g., 2,6- and 9,10-positions, in which the covalent bonds are easily formed. When an anthracene unit contains π-conjugated substituted groups both at 2,6- and 9,10-positions, those molecules are topologically cross-shaped (or X-shaped). On the other hand, anthracene-based derivatives have been widely used as organic optoelectronic materials owing to their high fluorescence quantum yields [16], implying that studying the derivatives with new structure is helpful to find new kind of the anthracene-based materials. Hence, we designed and synthesized a new anthracene-based oligomer **8**, whose structure is shown in Scheme 1. Such oligomer shows good hole-transporting ability in organic light-emitting diodes. Moreover, employing the oligomer as the emitting layer gives the devices showing blue emission. Herein, we report the details.

2. Experimental

2.1. Materials

2,7-Dibromo-9,9-diethyl-fluorene (**1**) [17a], 2,6-dibromoanthraquinone (**4**) [17b], pinacol(4-(*N*,*N*-diphenylamino)l-phenyl)boronate (**6**) [17c] were prepared as previously reported. $[Bu_4N]ClO_4$ (Bu = butyl) was an industrial product and purified by recrystallized three times from a mixture of ethyl acetate and cyclohexane and dried over P_2O_5 under vacuum at room temperature for three days. All solvents were dehydrated and distilled under an inert atmosphere before use.

2.2. Instrumentation

Elemental analysis was taken with a Carlo Erba 1106 elemental analyzer. ^{1}H NMR spectra were carried out on a Bruker DRX 300 spectrometer and ^{13}C NMR spectra were carried out on a Bruker DRX 400 spectrometer. UV–Vis absorption and photoluminescence spectra were measured with a Hitachi U-2910 spectrophotometer and a Hitachi F-4500 fluorescence spectrophotometer, respectively. Cyclic voltammetry (CV) for the cast films were measured in an acetonitrile solution of $[Bu_4N]ClO_4$ (0.10 M, Bu = butyl) at a scan rate of 100 mV/s under argon using (0.10 M $AgNO_3$)/Ag and platinum wire as reference and counter electrodes, respectively. A CHI 600B analyzer was used for the measurements. DSC was determined with TA Instrument DSC Q200 at a heating and cooling rate of 10 °C min^{-1} under nitrogen flow.

2.3. LED device fabrication

On a cleaning ITO glass, a layer PEDOT-PSS (50 nm, Bayer AG) was applied. A layer of **11** (10 mg/mL in $CHCl_3$ for the application of hole-transporting layer, 20 mg/mL in $CHCl_3$ for the application of light-emitting layer) was then spin-coated on the substrate. After dried 2 h in a glove box at 60 °C, Alq_3 (30 nm), LiF, Ca (120 nm) and Al (100 nm) were deposited on the compound film by thermal evaporation, respectively, under a vacuum of 10^{-4} Pa. The measurements of the properties of the devices were operated at room temperature in air. The EL spectra were recorded on a photometer PR 705.

2.4. Synthesis of the compounds

2.4.1. Synthesis of (2-bromo-9,9-diethyl-9H-fluoren-7-yl)trimethylsilane (**2**)

Under an argon atmosphere, a solution of *n*-BuLi in hexane (1.6 M, 11.8 mL, 18.8 mmol) was added slowly at −78 °C to a solution of **1** in anhydrous THF. The mixture was stirred for 1 h at −78 °C before adding chlorotrimethylsilane (6.0 g, 55.3 mmol). The reactants were warmed to room temperature and stirred for 3 h, poured into water of 200 mL, and extracted with hexane. The organic layer was washed with water and dried over Na_2SO_4. **2** was obtained as a colorless oil by column chromatography on silica gel with hexane as the eluent. 6.80 g, yield of 99%. ^{1}H NMR (300 MHz, $CDCl_3$, δ in ppm): 7.68 (d, 1H), 7.69 (d, 1H), 7.52 (d, 1H), 7.46–7.49 (m, 3H), 2.04 (m, 4H), 0.33–0.38 (m, 15H).

2.4.2. Synthesis of (7-(1,3,2-dioxaborinan-2-yl)-9,9-diethyl-9H-fluoren-2-yl)trimethylsilane (**3**)

A solution of *n*-BuLi in hexane (1.6 M, 12.5 mL, 20.0 mmol) was added slowly to a solution of **2** (6.79 g, 18.2 mmol) in anhydrous THF (80 mL) at −78 °C. The mixture was stirred for 1 h at −78 °C before triisopropyl boronate (10.3 g, 54.6 mmol) was added. The reactants were warmed to room temperature, stirred for 24 h, poured into a large mount of water (200 mL), and extracted with ethyl acetate. The organic layer was washed with brine and dried over Na_2SO_4. After removal of the solvent under reduced pressure, the residue was obtained as the boric acid (6.05 g, yield of 98.4%) as white solid. To a solution of the boric acid (6.05 g, 17.9 mmol) in toluene (150 mL), 1,3-propanediol (4.15 g, 54.6 mmol) was added, and the mixture was stirred at 110 °C for 10 h. After being cooled to room temperature, the solution was washed with water, dried over Na_2SO_4, and evaporated to remove the solvent. The obtained crude product was purified by column chromatography using a mixture solvent of hexane and ethyl acetate (8:1, v/v) as the eluent to afford a white solid **3** (6.30 g, yield of 93.1%). ^{1}H NMR (300 MHz, $CDCl_3$, δ in ppm): 7.69–7.78 (m, 4H), 7.47 (m, 2H), 4.21 (t, 4H), 2.06 (m, 6H), 0.27–0.32 (m, 15H). ^{13}C NMR (100 MHz, $CDCl_3$, δ in ppm): 149.56, 149.13, 143.90, 142.11, 139.38, 132.46, 131.76, 127.91, 127.54, 119.22, 118.96, 62.02, 55.89, 32.60, 27.46, 8.59. FT-IR (KBr pellets, cm^{-1}): 2960, 2852, 1608, 1482,

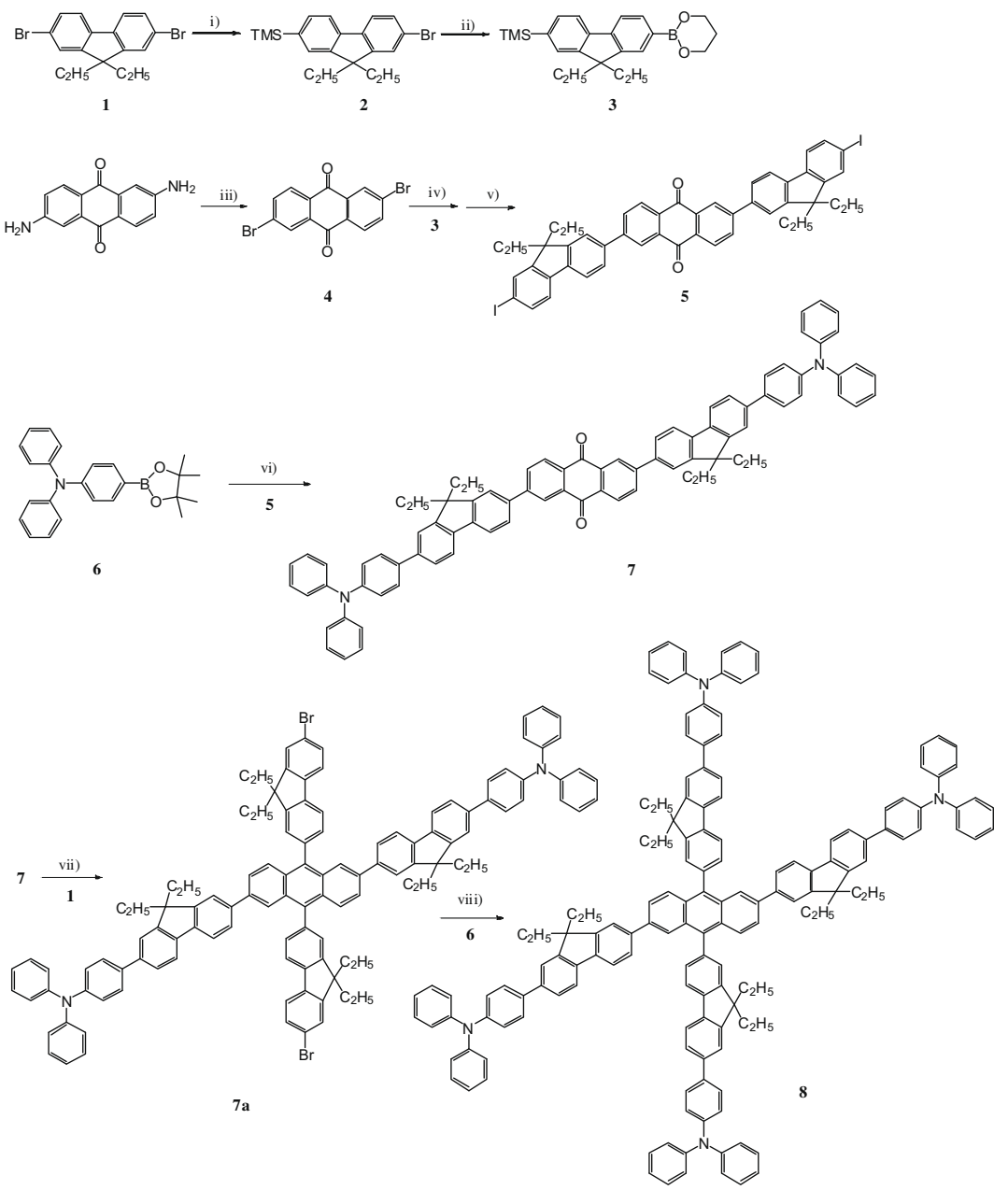

Scheme 1. Synthetic procedure of the oligomer **8**. Reagents and conditions: (i) (1) *n*-BuLi, THF, −78 °C, (2) TMSCl, −78 °C to room temperature; (ii) (1) *n*-BuLi, THF, −78 °C, (2) (*i*-PrO)$_3$B, −78 °C to room temperature; (3) 1,3-propanediol, toluene, 110 °C; (iii) *t*-BuONO, $CuBr_2$, CH_3CN, 65 °C; (iv) $Pd(PPh_3)_4$, aq. K_2CO_3, toluene, 80 °C; (v) ICl, $CHCl_3$, 0 °C to room temperature; (vi) $Pd(PPh_3)_4$, aq. K_2CO_3, toluene, 80 °C; (vii) 1) *n*-BuLi, THF, (2) KI, $NaH_2PO_2{\cdot}H_2O$, AcOH, 120 °C; (viii) $Pd(PPh_3)_4$, K_2CO_3, THF, 80 °C.

1426, 1313, 1277, 1250, 1230, 1156, 1266, 857, 841, 820, 754, 684. MS (EI): 378 (M^+).

2.4.3. Synthesis of 2,6-dibromoanthraquinone (*4*)

2,6-Diaminoanthraquinone (2.9 g, 12 mmol) was added to a solution of t-BuONO (3.62 mL, 2.8 g, 27 mmol) and $CuBr_2$ (6.0 g, 27 mmol) in CH_3CN (50 mL) at 65 °C. The mixture was stirred for 3 h and then slowly poured into 20% aqueous HCl solution (200 mL). The precipice was filtered, washed with water, CH_3CN, and benzene. Finally, the more pure product was obtained by washing with benzene. (3.75 g, yield of 84%).

2.4.4. Synthesis of 2,6-bis(9,9-diethyl-7-iodo-9H-fluoren-2-yl) anthraquinone (*5*)

Under an argon atmosphere, a mixture of **4** (1.85 g, 5.07 mmol), **3** (4.31 g, 11.4 mmol), $Pd(PPh_3)_4$ (0.29 g, 0.25 mmol) and K_2CO_3 (3.22 g, 23.3 mmol) in THF

(80 mL) and distilled water (40 mL) was stirred for 48 h at 80 °C. After being cooled to room temperature, the mixture was extracted with $CHCl_3$. The organic layer was washed with water and dried over with anhydrous Na_2SO_4. After removal of the solvents, the residue was recrystallized with a mixture solvent of toluene and ethanol to yield a yellow solid, which was dissolved in anhydrous $CHCl_3$ (3.02 g in 60 mL), and to the obtained solution was added a mixture of ICl in methylene chloride solution (1.0 M, 8.4 mL, 8.4 mmol) under an argon atmosphere at 0 °C. After warmed to room temperature, the reactants were stirred for 4 h, then poured into aqueous $NaHSO_3$ (5% w/w, 200 mL). The mixture was extracted with $CHCl_3$ and the organic layer was washed with water before being dried over with Na_2SO_4. After evaporated to remove the solvent, the residue was purified by recrystallization with toluene to give **5** as a crude product with a yield of 69%. ^{1}H NMR (300 MHz, $CDCl_3$, δ in ppm): 8.64 (s, 2H), 8.45 (d, 2H), 8.12 (d, 2H), 7.83 (d, 2H), 7.69–7.77 (m, 8H), 7.53 (d, 2H), 2.11 (m, 8H), 0.37 (t, 12H). ^{13}C NMR (100 MHz, $CDCl_3$, δ in ppm): 183.11, 152.75, 150.46, 147.25, 141.95, 140.36, 138.14, 134.12, 132.36, 132.28, 132.16, 128.18, 126.61, 125.51, 121.73, 121.62, 120.45, 93.26, 56.70, 32.73, 8.56. FT-IR (KBr pellets, cm^{-1}): 2958, 1672, 1592, 1453, 1399, 1313, 969, 816, 746, 479. MS (MALDF-TOF): 900.3 (M^+).

2.4.5. Synthesis of 2,6-bis(7-(4-(diphenylamino)phenyl)-9,9-diethyl-9H-fluoren-2-yl)-anthraquinone (7)

Under an argon atmosphere, a mixture of **5** (1.88 g, 2.08 mmol), **6** (1.70 g, 4.58 mmol), $Pd(PPh_3)_4$ (0.12 g, 0.10 mmol) and K_2CO_3 (1.32 g, 9.57 mmol) in THF (50 mL) and distilled water (25 mL) was stirred for 48 h at 80 °C. After being cooled to room temperature, the mixture was extracted with $CHCl_3$. The organic layer was washed with water and dried over anhydrous Na_2SO_4. After removal of the solvents, the residue was purified by column chromatography on silica gel using a mixture solvent of petroleum ether and CH_2Cl_2 (1:1, v/v) as the eluent to obtain **7** as an orange powder (1.98 g, yield of 83.8%). ^{1}H NMR (300 MHz, $CDCl_3$, δ in ppm): 8.67 (d, 2H), 7.46 (d, 2H), 8.14 (d, 2H), 7.23–7.88 (m, 8H), 7.27–7.32 (m, 8H), 7.17 (m, 12H), 7.05 (m, 4H), 2.16 (m, 8H), 0.42 (t, 12H). ^{13}C NMR (100 MHz, $CDCl_3$, δ in ppm): 138.41, 151.50, 151.31, 147.91, 147.68, 147.45, 142.55, 140.41, 139.79, 137.82, 135.62, 134.37, 132.51, 132.29, 129.53, 128.39, 128.06, 126.74, 125.89, 125.67, 124.62, 124.27, 123.19, 121.68, 121.31, 120.60, 120.50, 56.74, 33.14, 8.91. FT-IR (KBr pellets, cm^{-1}): 3032, 2962, 2874, 1673, 1591, 1514, 1492, 1464, 1377, 1310, 1281, 817, 747, 695, 497. MS (MALDF-TOF): 1136.0 (M^+). Elemental analysis: Calcd for $C_{84}H_{68}N_2O_2$: C, 88.86; H, 5.86; N, 2.47. Found: C, 88.77; H, 6.00; N, 2.13.

2.4.6. Synthesis of 2,6,9,10-tetra(7-(4-(diphenylamino)phenyl)-9,9-diethyl-9H-fluoren-2-yl)-anthracene (8)

A solution of *n*-BuLi (1.6 M, 1.38 mL, 2.21 mmol) in hexane was added slowly to a solution of **1** (839 mg, 2.21 mmol) in anhydrous THF (30 mL) at −78 °C, and the mixture was stirred for 1 h at the same temperature. Then a solution of **7** (627 mg, 0.55 mmol) in anhydrous THF was added to the mixture. The reactants were allowed to slowly warm to room temperature, stirred for 24 h and poured to water of 200 mL. The mixture was extracted with ethyl acetate, and the obtained organic layer was washed with brine and dried over Na_2SO_4. Column chromatography on silica gel with hexane:$CHCl_3$:ethyl acetate (30:10:4) as the eluent afford an intermediate (901 mg, yield of 93.8%) as an orange glass. ^{1}H NMR (300 MHz, $CDCl_3$, δ in ppm):7.86 (s, 2H), 7.41–7.72 (m, 32H), 7.25–7.30 (m, 8H), 7.16 (m, 12H), 7.04 (m, 4H), 3.36 (s, 2H), 1.96–2.11 (m, 16H), 0.27–0.41 (m, 24H). ^{13}C NMR (100 MHz, $CDCl_3$, δ in ppm): 152.76, 151.03, 149.60, 147.92, 147.32, 145.96, 142.06, 141.77, 141.10, 140.44, 140.05, 139.88, 139.81, 139.19, 135.75, 130.33, 129.51, 129.33, 128.03, 127.30, 126.50, 126.21, 125.83, 124.57, 124.31, 123.13, 121.75, 121.42, 121.35, 121.28, 121.21, 120.35, 120.08, 119.55, 76.94, 56.85, 56.44, 32.97, 8.88, 8.65. FT-IR (KBr pellets, cm^{-1}): 3543, 3033, 2963, 2920, 2875, 2852, 1592, 1514, 1493, 1464, 1377, 1313, 1279, 1006, 908, 815, 753, 734, 697. MS (MALDF-TOF): 1738.3 (M^+).

Under an argon atmosphere, the above mentioned intermediate (901 mg, 0.52 mmol), was added to a mixture of potassium iodide (861 mg, 5.2 mmol) and sodium hypophosphite hydrate (1.10 g, 10.4 mmol) in acetic acid (50 mL), and the mixture was stirred for 19 h at 120 °C. After being cooling to room temperature, the mixture was filtered and washed with water. The residue was purified by column chromatography on silica gel using a mixture of petroleum ether and $CHCl_3$ (2:1, v/v) as the eluent to give **7a** as a green–yellow powder, 658 mg, yield of 74.5%. ^{1}H NMR (300 MHz, $CDCl_3$, δ in ppm): 8.06 (s, 2H), 7.98 (d, 2H), 7.90 (d, 2H), 7.64–7.79 (m, 8H), 7.50–7.59 (m, 20H), 7.25–7.31 (m, 8H), 7.13–7.17 (m, 12H), 7.04 (m, 4H), 1.97–2.14 (m, 16H), 0.53 (m, 12H), 0.28–0.38 (m, 12H). ^{13}C NMR (100 MHz, $CDCl_3$, δ in ppm): 152.42, 150.87, 150.81, 149.78, 147.67, 147.05, 139.83, 139.54, 138.53, 137.57, 135.51, 130.40, 130.22, 129.60, 129.24, 127.74, 127.57, 126.33, 125.57, 125.45, 124.31, 124.05, 122.86, 121.48, 121.37, 121.17, 120.96, 119.96, 119.89, 56.72, 56.14, 32.82, 32.69, 8.70, 8.58. FT-IR (KBr pellets, cm^{-1}): 2962, 2918, 2974, 2851, 1592, 1541, 1493, 1455, 1377, 1313, 1278, 883, 812,752, 754, 696. MS (MALDF-TOF): 1702.8 ($(M-1)^+$). Elemental analysis: Calcd for $C_{118}H_{98}Br_2N_2$: C, 83.18; H, 5.80; N, 1.64; Br, 9.38. Found: C, 82.93; H, 6.10; N, 1.61; Br, 9.32.

The obtained green–yellow powder (200 mg, 0.12 mmol), mentioned above was added to a mixture of **6** (96 mg, 0.26 mmol), $Pd(PPh_3)_4$ (14 mg, 0.012 mmol) and K_2CO_3 (250 mg, 1.81 mmol) in THF (40 mL) containing distilled water (15 mL). The reactants were stirred for 48 h at 80 °C. After being cooled to room temperature, the mixture was extracted with $CHCl_3$. The organic layer was washed with water and dried over with anhydrous Na_2SO_4. After removal of the solvent, the residue was purified by column chromatography on silica gel using a mixture solvent of petroleum ether and CH_2Cl_2 (3:2, v/v) as the eluent to give **8** as a yellow–green powder, 190 mg, yield of 79.5%. ^{1}H NMR (300 MHz, $CDCl_3$, δ in ppm): 8.12 (s, 2H), 8.02 (d, 2H), 7.94 (m, 4H), 7.78 (d, 2H), 7.61–7.71(m, 14H), 7.49–7.58 (m, 14H), 7.23–7.33 (m, 18H), 7.12–7.22 (m, 22H), 7.05 (m, 8H), 2.17 (m, 8H), 1.99

(m, 8H), 0.54–0.60 (m, 12H), 0.28–0.38 (m, 12H). ^{13}C NMR (100 MHz, $CDCl_3$, δ in ppm): 150.91, 150.82, 150.33, 147.72, 147.68, 147.13, 147.03, 140.87, 140.62, 140.36, 139.92, 139.75, 139.65, 139.53, 137.81, 137.68, 135.62, 135.84, 130.51, 130.25, 129.71, 129.29, 127.84, 127.75, 126.18, 126.05, 125.74, 125.56, 125.36, 124.53, 124.34, 124.17, 124.08, 122.90, 122.86, 121.51, 121.05, 120.97, 120.10, 119.52, 119.91, 119.77, 56.48, 56.16, 33.12, 33.01, 8.84, 8.58. FT-IR (KBr pellets, cm^{-1}): 3036, 2961, 2917, 2873, 2851, 1592, 1513, 1492, 1467, 1376, 1313, 1279, 1177, 883, 813, 752, 695. MS (MALDF-TOF): 2033.0 (M^+). Elemental analysis: Calcd for $C_{154}H_{126}N_4$: C, 91.00; H, 6.25; N, 2.76. Found: C, 90.52; H, 6.56; N, 2.30.

3. Results and discussion

3.1. Synthesis

Oligomer **8** was built from 2,6-dibromoanthraquinone, fluorene boric ester and triphenylamine boric ester, and the synthesis procedure is shown in Scheme 1, and the detailed preparation and characterization of the oligomer are listed in experimental section. **8** was an amorphous powder and can easily form a film on a glass plate by using a spin-coating method, suggesting that the oligomer possesses good solution-processability, which is desire for the fabrication of the optoelectronic devices.

3.2. Thermal stability and optical properties

Thermal properties of **8** were characterized by differential scanning calorimetry (DSC), and the result is shown in Fig. 1. As can be seen from Fig. 1, **8** shows a glass transition temperature, T_g, of 223 °C, which is higher than those of most of the well-known small molecule materials used in optoelectronic fields [18], and even higher than those of some polymeric materials [19], indicating that the oligomer possesses high thin film morphological stability. Moreover, no obvious crystallization peak was observed during a scanning from 50 to 300 °C, demonstrating that **8** has a limited tendency to crystallize.

The basic photophysical properties of **8** were characterized by UV–Vis and photoluminescent (PL) spectra. The

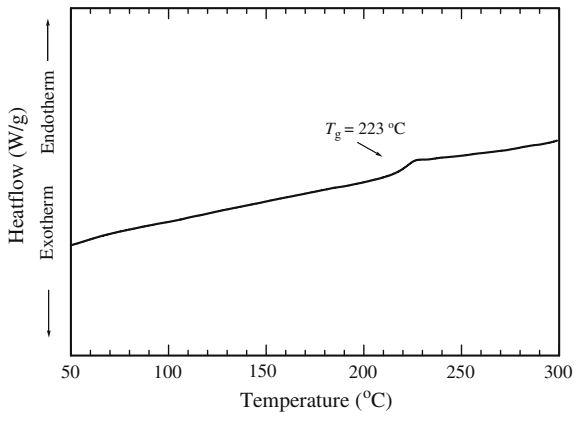

Fig. 1. DSC trace of **8**.

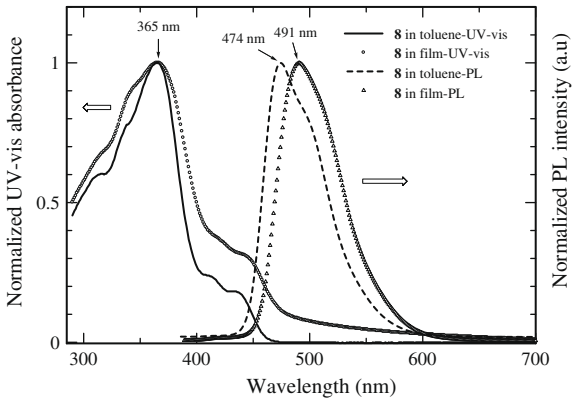

Fig. 2. UV–Vis and PL spectra of **8** in toluene and in the solid state.

spectra are displayed in Fig. 2. The oligomer exhibits a maximum absorption peak at 365 nm in both toluene and in the solid state, whereas the onset position of its absorption band in the solid state has a red-shift, suggesting the existence of part π-stacking structure in the oligomer. It is noted that a compound composed of a fluorene unit and two triphenylamine units showed an absorption peak at about 370 nm [20], thus, the maximum absorption peak at 365 nm in Fig. 2 is attributed to the electronic transition (π–π*) along the backbone of a fluorene unit linked with a triphenylamine group. The weak absorption peaks at 400–450 nm are also observed in Fig. 2, which are probably derived from the anthracene unit in **8**, the similar absorption peaks were found in our previous work concerning a polymer containing anthracene unit as side chain [21].

The photoluminescent (PL) spectrum of **8** in toluene shows a main peak at 474 nm with a quantum yield of 62% (estimated with a 0.5 M H_2SO_4 solution of quinine as a reference), similar to the PL spectra of poly(9,9-alkylfluorene-alt-triphenylamine) [22]. In the solid state, **8** gives a maximum emission peak at 491 nm with an absolute PL quantum yield of 24%, measured by using a calibrated integrating sphere. Here, the main emission peak of **8** has a red-shift of 17 nm relative to that in the solution, indicating the existence of the interaction between the molecules in the solid state, similar phenomena were also observed in poly(9,9-alkylfluorene-alt-triphenylamine) [23] and the fluorene–anthracene compounds [24].

3.3. Electrochemical properties

The electrochemical behavior of **8** was measured by cyclic voltammetry (CV) of its cast film on a Pt plate, and the result is shown in Fig. 3. The electrochemical oxidation (or p-doping) of **8** starts at about 0.60 V versus Ag^+/Ag, and gives a p-doping peak at 1.02 V. The corresponding reduction peak appears at 0.18 V. According to the relationship between the oxidation onset potential (E_{ox}^{onset}) and HOMO level value as $-(E_{ox}^{onset} + 4.4)$ [24], the HOMO energy level of **8** is estimated as $-(0.60 + 4.4) = -5.00$ eV. Relative to the triphenylamine derivatives with HOMO value of about 5.7 eV, that of **8** is close to the work function of ITO glass (4.5–4.8 eV) [25]. This result implies that **8** is very suitable for OLEDs as a hole-transport layer (HTL). Consequently,

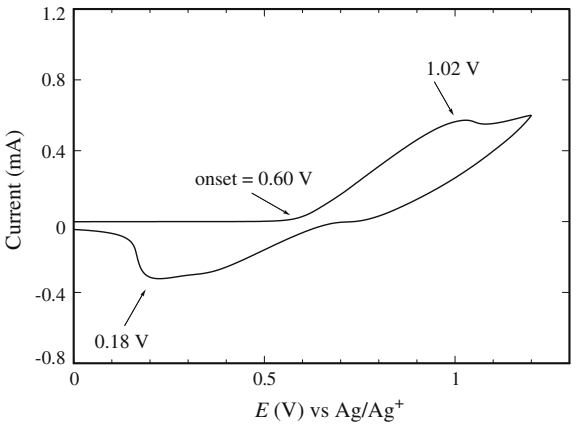

Fig. 3. CV curve of a cast film of **8** on a Pt electrode (wire) with a sweep rate of 100 mV s^{-1} in an acetonitrile solution of 0.10 M $[Bu_4N]ClO_4$. The applied potential is 0.0–1.5 V.

the LUMO value of **8** is calculated by subtraction of the optical bandgap E^{opt} (eV) from the HOMO value, given as −2.41 eV.

3.4. Electroluminescence properties

To evaluate the performance of **8** as a HTL in OLEDs, three non-optimized OLED devices were fabricated with

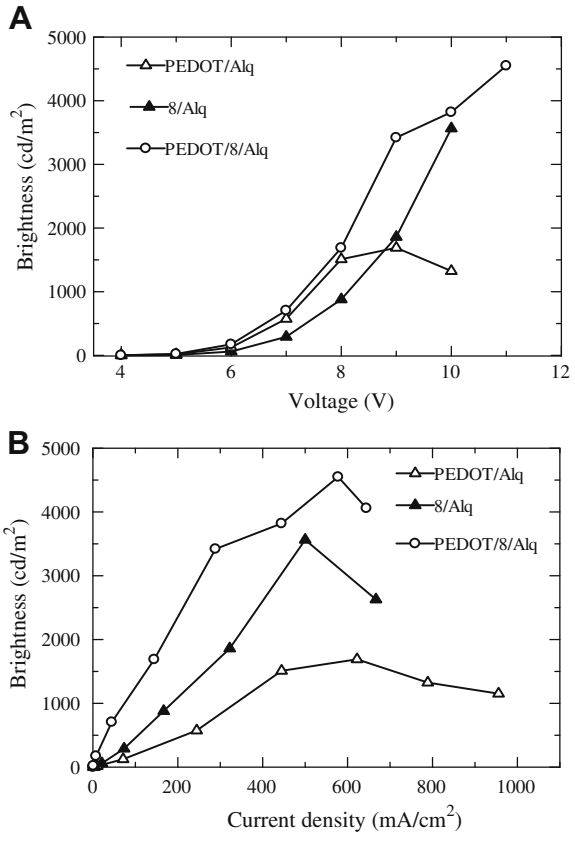

Fig. 4. *B–V* (A) and *B–I* curves (B) of the three devices.

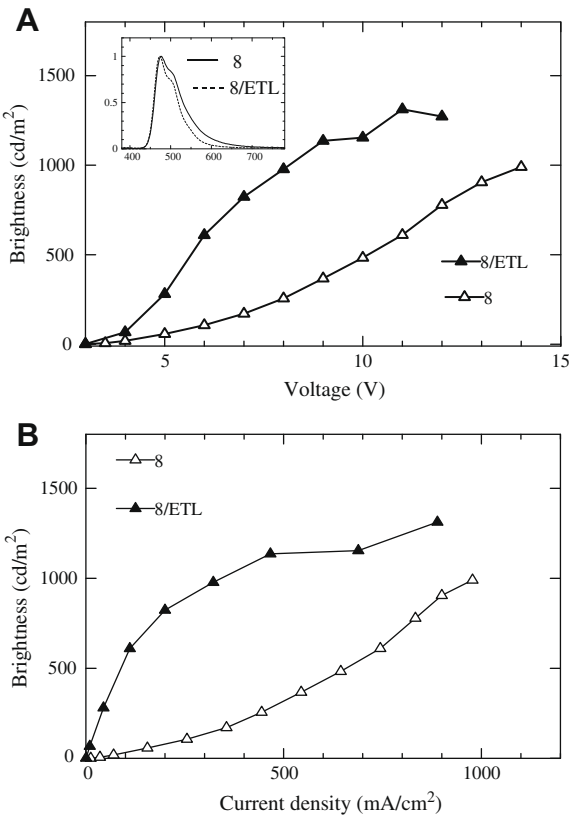

Fig. 5. *B–V* (A) and *B–I* curves (B) of a device based on **8.**

the following configuration: (1) ITO/PEDOT:PSS/Alq/LiF/Ca/Al (device PEDOT/Alq); (2) ITO/**8**/Alq/LiF/Ca/Al (device 8/Alq) and (3) ITO/PEDOT:PSS/**8**/Alq/LiF/Ca/Al (device PEDOT/8/Alq). Here, PEDOT-PSS was employed as a hole-injection material that had been widely used in OLEDs. Moreover, a commercially available electron transport material, Alq, was used as both electron transport layer and emitting layer. All devices showed green emission derived from Alq, illuminating that the holes from the anode (ITO) and the electrons from the cathode (Ca/Al) combine in the Alq layer. The *B–V* (brightness versus operation voltage) and *B–I* (brightness versus current density) characteristics of the devices shows in Fig. 4. As can be seen form Fig. 4, device 8/Alq shows a maximum brightness of about 3600 cd/m^2 at 10 V, which is much higher than that of the device PEDOT/Alq only with PEDOT as a hole-injection layer, suggesting that oligomer **8** shows good hole-transport ability. Interestingly, when **8** was used together with PEDOT-PSS, the device (PEDOT/8/Alq) shows higher brightness and luminous efficiency. Its maximum brightness was 4549 cd/m^2 at 11 V and the maximum current efficiency reached 2.32 cd/A. Moreover, the maximum external quantum efficiencies (Max EQE) of the devices showed an order of PEDOT/Alq (0.11%) < 8/Alq (0.26%) < PEDOT/8/Alq (0.57%). Those results indicate that a combination of **8** and a commercial PEDOT-PSS may obtain a better performance in OLEDs, and that oligomer **8** could be used as a new component in OLEDs.

The high absolute PL quantum yield of **8** inspired us to investigate its application in OLED as a light-emitting layer. A device was fabricated with the configuration of ITO/PEDOT:PSS/**8**/LiF/Ca/Al (device 8). The *B–V* curve and efficiency of the device are shown in Fig. 5. As shown in Fig. 5, device 8 shows light-blue emission with a maximum emission peak of 478 nm, which has a slight blue-shift relative to that of its PL emission in the solid state. Device 8 exhibits a low turn-on voltage of 3.5 V, whereas its efficiency is very low (maximum current efficiency = 0.1 cd/A, and Max EQE = 0.043%). This may be due to the unbalance between the hole-transport and the electron transport in the device, derived from the strong hole-transporting ability of **8**. Considering the good electron transport of a bitriazine derivative developed by our group [26], we designed a new configuration of the device using the bitriazine derivative as electron transport layer (ETL) to adjust the balance between the electron transport and the hole-transport in the device. The new device has a configuration of ITO/PEDOT:PSS/**8**/ETL/LiF/Ca/Al (device 8/ETL), and shows the same emission color as that of device 8 with a maximum emission peak of 474 nm (Fig. 5, the insert), but its efficiency is much higher than that of device 8 (for device 8/ETL, maximum current efficiency = 0.6 cd/A and Max EQE = 0.29%), implying that **8** also shows good emitting properties.

4. Conclusion

A new anthracene derivative containing four triphenylamine groups was prepared. Such oligomer is solution-processible with a glass transition temperature of higher than 200 °C, and it showed good hole-transporting ability in organic light-emitting diodes. Such compound was also employed as the emitting layer to give the devices showing blue emission.

Acknowledgements

Financial support from National Natural Science Foundation of China (NSFC, No. 20872171) is gratefully acknowledged. Q. Fang thanks the financial support from Key Laboratory of Advanced Display and System Applications (Shanghai University), Ministry of Education of China (No. A.05-0408-07-003).

References

[1] (a) W.J. Oldham, R.J. Lachicotte, G.C. Bazan, J. Am. Chem. Soc. 120 (1998) 2987;
(b) S. Wang, W.J. Oldham, R.A. Hudack, G.C. Bazan, J. Am. Chem. Soc. 122 (2000) 5695.
[2] (a) P.L. McGrier, K.M. Solntsev, J. Schonhaber, S.M. Brombosz, L.M. Tolbert, U.H.F. Bunz, Chem. Commun. (2007) 2127;
(b) A.J. Zucchero, J.N. Wilson, U.H.F. Bunz, J. Am. Chem. Soc. 128 (2006) 11872;
(c) W.W. Gerhardt, A.J. Zucchero, J.N. Wilson, C.R. South, U.H.F. Bunz, M. Weck, Chem. Commun. (2006) 2141.
[3] J.A. Marsden, J.J. Miller, L.D. Shirtcliff, M.M. Haley, J. Am. Chem. Soc. 127 (2005) 2464.
[4] (a) H. Kang, P. Zhu, Y. Yang, A. Facchetti, T.J. Marks, J. Am. Chem. Soc. 126 (2004) 15974;
(b) H. Kang, G. Evmenenko, P. Dutta, K. Clays, K. Song, T.J. Marks, J. Am. Chem. Soc. 128 (2006) 6194.
[5] C. Lambert, W. Gaschler, G. Noll, M. Weber, E. Schmalzlin, C. Brauchle, K. Meerholz, J. Chem. Soc. Perkin Trans. 2 (2001) 964.
[6] S. Sengupta, P. Purkayastha, Org. Biomol. Chem. 1 (2003) 436.
[7] H.C. Yeh, R.H. Lee, L.H. Chan, T.Y.J. Lin, C.T. Chen, E. Balasubramaniam, T.-Y. Tao, Chem. Mater. 13 (2001) 2788.
[8] S. Fratiloiu, K. Senthilkumar, F.C. Grozema, H. Christian-Pandya, Z.I. Niazimbetova, Y.J. Bhandari, M.E. Galvin, L.D.A. Siebbeles, Chem. Mater. 18 (2006) 2118.
[9] S. Sengupta, S. Muhuri, Tetrahedron Lett. 45 (2004) 2895.
[10] D. Lalibert, T. Maris, J.D. Wuest, Can. J. Chem. 82 (2004) 386.
[11] (a) Z. Xie, B. Yang, F. Li, G. Cheng, L. Liu, G. Yang, H. Xu, L. Ye, M. Hanif, S. Liu, D. Ma, Y. Ma, J. Am. Chem. Soc. 127 (2005) 14152–14153;
(b) Z. Xie, B. Yang, G. Cheng, L. Liu, F. He, F. Shen, Y. Ma, S. Liu, Chem. Mater. 17 (2005) 1287.
[12] (a) A. Zen, A. Bilge, F. Galbrecht, R. Alle, K. Meerholz, J. Grenzer, D. Neher, U. Scherf, T. Farrell, J. Am. Chem. Soc. 128 (2006) 3914;
(b) A. Bilge, A. Zen, M. Forster, H. Li, F. Galbrecht, B.S. Nehls, T. Farrell, D. Neher, U. Scherf, J. Mater. Chem. 16 (2006) 3177.
[13] (a) C.W. Wu, H.H. Sung, J. Polym. Sci. Polym. Chem. 44 (2006) 6765;
(b) J.X. Yang, X.T. Tao, C.X. Yuan, Y.X. Yan, L. Wang, Z. Liu, Y. Ren, M.H. Jiang, J. Am. Chem. Soc. 127 (2005) 3278.
[14] (a) X.B. Sun, Y.Q. Liu, S.Y. Chen, W.F. Qiu, G. Yu, Y.Q. Ma, T. Qi, H.J. Zhang, X.J. Xu, D.B. Zhu, Adv. Funct. Mater. 16 (2006) 917;
(b) H.Y. Wang, J.C. Feng, G.A. Wen, H.J. Jiang, J.H. Wan, R. Zhu, C.M. Wang, W. Wei, W. Huang, New J. Chem. 30 (2006) 667.
[15] X.M. Liu, J. Xu, X. Lu, C. He, Macromolecules 39 (2006) 1397.
[16] (a) M.T. Bernius, M. Inbasekaran, J. O'brien, W.S. Wu, Adv. Mater. 12 (2000) 1737;
(b) U. Scherf, E.J.W. List, Adv. Mater. 14 (2002) 477;
(c) K. Danel, T.H. Huang, J.T. Lin, Y.T. Tao, C.H. Chuen, Chem. Mater. 14 (2002) 3860;
[d] A.K. Tripathi, M. Heinrich, T. Chen, J.P. Siegrist, Adv. Mater. 19 (2007) 2097;
(e) A.C. A Culligan, J.U. Wallace, K.P. Klubek, C.W. Tang, S.H. Chen, Adv. Funct. Mater. 16 (2006) 148.
[17] (a) D.W. Price, J.M. Tour, Tetrahedron 59 (2003) 3131;
(b) S.K. Lee, W.J. Yang, J.J. Choi, C.H. Kim, S.J. Jeon, B.R. Cho, Org. Lett. 7 (2005) 323;
(c) Y.J. Pu, T. Kurata, M. Soma, J. Kido, H. Nishide, Synth. Met. 143 (2004) 207.
[18] S.A. Van Slyke, C.H. Chen, C.W. Tang, Appl. Phys. Lett. 69 (1996) 2160.
[19] (a) E. Bellmann, G.E. Jabbour, R.H. Grubbs, N. Peyghambarian, Chem. Mater. 12 (2000) 1349;
(b) C. Schmitz, P. Pösch, M. Thelakkat, H.W. Schmidt, A. Montali, K. Feldman, P. Smith, C. Weder, Adv. Funct. Mater. 11 (2001) 41;
(c) X.C. Li, Y.Q. Liu, M.S. Liu, A.K.Y. Jen, Chem. Mater. 11 (1999) 1568;
(d) J.P. Liu, A.R. Hlil, A.S. Hay, T. Maindron, J.P. Dodelet, J. Lam, M. D'iorio, J. Polym. Sci. Polym. Chem. 38 (2000) 2740.
[20] Q. Fang, B. Xu, B. Jiang, H. Fu, W. Zhu, X. Jiang, Z. Zhang, Synth. Met. 155 (2005) 206.
[21] J. Du, Q. Fang, D. Bu, S. Ren, A. Cao, X. Chen, Macromol. Rapid Commun. 26 (2005) 1651.
[22] M. Redecker, D. Bradley, M. Inbasekaran, W. Wu, E. Woo, Adv. Mater. 11 (1999) 241.
[23] W. Cui, Y. Wu, H. Tian, Y. Geng, F. Wang, Chem. Commun. (2008) 1017.
[24] S. Janietz, D.D.C. Bradley, M. Grell, C. Giebeler, M. Inbasekaran, E.P. Woo, Appl. Phys. Lett. 73 (1998) 2453.
[25] T. Ishida, H. Kobayashi, Y. Nakato, J. Appl. Phys. 73 (1993) 4344.
[26] H. Zhong, E. Xu, D. Zeng, J. Du, J. Sun, S. Ren, B. Jiang, Q. Fang, Org. Lett. 10 (2008) 709.

Organic Electronics 11 (2010) 81–88

Contents lists available at ScienceDirect

Organic Electronics

journal homepage: www.elsevier.com/locate/orgel

High-performance poly(3-hexylthiophene) top-gate transistors incorporating TiO_2 nanocomposite dielectrics

Feng-Yu Yang [a,*], Meei-Yu Hsu [a], Gue-Wuu Hwang [a], Kuo-Jui Chang [b]

[a] Materials and Chemical Laboratories, Industrial Technology Research Institute, 195, Sec. 4, Chung Hsing Road, Chutung, Hsinchu 310, Taiwan
[b] Department of Electronics Engineering and Institute of Electronics, National Chiao Tung University, Hsinchu 300, Taiwan

ARTICLE INFO

Article history:
Received 2 July 2009
Received in revised form 30 September 2009
Accepted 6 October 2009
Available online 13 October 2009

Keywords:
Nanocomposites
TiO_2
Top-gate
Organic filed-effect transistor

ABSTRACT

This paper describes the fabrication of top-gate P3HT organic field effect transistors (OFETs) incorporating polymer/TiO_2 nanocomposite bilayer dielectrics. The TiO_2 nanocomposite comprised PVP, the cross-linking agent PMF, and TiO_2 nanoparticles (NPs), which possessed rod-like anatase structures and were solution-processable using polar solvents; thus, the composite dielectric solutions were easy to be prepared for the use in top-gate OFET devices without damaging and dissolution of the underlying P3HT film. SEM and AFM images revealed the high uniformity of the nanocomposite films. To determine the effects of the composite dielectrics with/without TiO_2 on the performance of the OFET devices, we inserted a buffer layer of PMMA between the semiconductor layer and the gate dielectric to maintain a constant semiconductor–dielectric interface. The device incorporating the PMMA/TiO_2 nanocomposite bilayer gate dielectric operated effectively at supply voltages within 20 V, with a good mobility (μ) of 1.5×10^{-2} $cm^2 V^{-1} s^{-1}$, which was three times greater than that of the devices featuring the PMMA/PVP/PMF dielectric; the on/off ratio of nanocomposite device (8.6×10^6) was significantly better than that of the PVP/PMF device (1.5×10^5). The PMMA/TiO_2 nanocomposite was also performed acceptably at supply voltages of less than 10 V. The performance of the OFET incorporating a single dielectric layer of the TiO_2 nanocomposite ($\mu = 0.001$ $cm^2 V^{-1} s^{-1}$; on/off ratio = 5.7×10^2) was inferior to those of the bilayer gate dielectric devices.

© 2009 Elsevier B.V. All rights reserved.

1. Introduction

During the past decade, organic field effect transistors (OFETs) have attracted a great deal of interest because of their potential use in such applications as radio frequency identification tags, flexible displays, and smart cards [1–4]. Although traditional OFETs must be operated at high voltage (usually exceeding 40 V) to output a high current, typical low-end applications would require very low available operating voltages. Recently, low-voltage OFETs have been reported that incorporate ultrathin high-capacitance gate dielectrics, such as self-assembled monolayers (SAMs) [5–8] and thin polymers [9–12], high-dielectric-constant (high-k) inorganic metal-oxide gate dielectrics [13–17], or polymer electrolyte dielectrics [18–20]. For example, Halik et al. [5] reported pentacene-based FETs employing SAMs as ultrathin gate dielectrics that operated at 2 V with a field effect mobility of 1 $cm^2 V^{-1} s^{-1}$. Although this approach shows great promise, the ability to integrate it into a large-volume coating process remains questionable. Ultrathin polymer dielectrics have the advantage that they could be applied through solution processing, but this technique remains problematic because of the generation of pinholes during the deposition process [10]. The films of high-k metal oxides, such as Al_2O_3, Ta_2O_5, and TiO_2,

* Corresponding author. Tel.: +886 3 5912643; fax: +886 3 5827694.
E-mail address: FengYuYang@itri.org.tw (F.-Y. Yang).

1566-1199/$ - see front matter © 2009 Elsevier B.V. All rights reserved.
doi:10.1016/j.orgel.2009.10.002

are usually deposited using sputtering or high-temperature sintering processing, which are not compatible with low-cost, large-area plastic electronics. The combination of polymers and metal oxides is a relatively new development for the preparation of solution-processed high-*k* nanocomposite gate dielectrics for low-voltage OFETs [21–24]. The reported OFETs incorporating metal-oxide nanocomposite gate dielectrics have mostly been based, however, on thermally evaporated pentacene as the semiconductor layer and mostly based on bottom-gate OFET geometries. Little has been known about top-gate devices which were fabricated using solution-processed semiconductors and featuring metal-oxide nanocomposite gate dielectrics [24].

Top-gate OFET structures have many advantages over bottom-gate devices. For example, the gate dielectric and top-gate metal could also be used as the passivation layers to protect the devices from degradation by outdoor moisture, oxygen, and UV or visible light. In addition, the gate lines can be prepared conveniently and the channel length can be defined as small as is allowable photolithographically. Although top-gate architectures have great potential for use in the fabrication of low-cost, large-area OFETs on flexible substrates, their assembly remains very challenging because it requires successive multilayer depositions (semiconductor, gate dielectric, gate electrode) in which great care must be taken when selecting the materials and their processing solvents.

For the fabrication of top-gate OFETs, the first requirement is that the semiconductor layer remains intact during deposition of the overlying dielectric layers. Among the top-gate P3HT OFETs reported to date, the solvents that have been used to process the polymer gate dielectrics have been 2-butanone [25], ethyl acetate [26,27], *n*-butanol [27], and *N*-methylpyrrolidinone (NMP) [27], which are all polar solvents. Therefore, if we are to develop solution-processable polymer/metal-oxide nanocomposites from these solvents, the metal-oxides must be not only dispersible in polar solvents but also compatible with the selected polymers to prevent phase separation during the film formation process.

In previous studies, we demonstrated the blending of poly(vinyl phenol) (PVP) and poly(melamine-*co*-formaldehyde) (PMF) as the gate dielectrics for bottom-gate devices [28]. The transistors showed good performances, however, operated at high voltage (−40 V). We also demonstrated solution-processed oleic acid-capped TiO_2 (OA-TiO_2) dielectrics for low-voltage-driven bottom-gate devices [29]. We found, however, that the OA-TiO_2 was dispersible only in nonpolar solvents, such as toluene and xylene, which are good solvents for dissolving semiconductors; thus, the OA-TiO_2 can not be applied directly onto the semiconductor as the top-gate dielectrics nor homogeneously blended with the polar PVP polymer. In this present study, we modified the OA-TiO_2 nanoparticles (NPs) from hydrophobic to hydrophilic to improve both their solubility in polar solvents and their compatibility with the PVP polymer matrix. We then investigated the blending of the modified OA-TiO_2 NPs with polymers and studied their applicability as dielectrics in top-gate OFETs.

2. Experiments

2.1. Materials

Poly(vinyl phenol) (PVP) (M_w = 20,000), the cross-linking agent poly(melamine-*co*-formaldehyde) (PMF) (M_w = 511), poly(methyl methacrylate) (PMMA) (M_w = 540,000) and diethyl (2-cyanoethyl) phosphonate ($NC(CH_2)_2PO_2(OEt)_2$, DCP) were obtained from Sigma–Aldrich. Chlorobenzene, *n*-butanol, ethyl acetate, and acetone were also purchased from Sigma–Aldrich and used without further purification. The hydrophobic OA-TiO_2 NPs were obtained through the hydrolysis of titanium tetraisopropoxide using the literature procedure [30]. The hydrophilic TiO_2 NPs (DCP-TiO_2) were synthesized by heating a mixture of OA-TiO_2 (0.2 g) and DCP (0.1 g) in chlorobenzene (2 mL) at 100 °C for 24 h and then evaporating the solvent under vacuum. Regioregular P3HT was purchased from Aldrich and purified through Soxhlet extractions with hexane and CH_2Cl_2 to remove low-molecular-weight chains.

2.2. Film fabrication and characterization

For the PVP dielectric, the weight percentage ratio of PVP and the cross-linking agent PMF in formulations (blends) was 8:4 in hexanol; for the TiO_2 nanocomposite, the weight percentage ratio of PVP, PMF, and DCP-TiO_2 was 8:4:12. Both formulations were spin-coated and the resulting films were then hardened through baking at 180 °C for 30 min. The thicknesses of the corresponding PVP films were determined using cross-sectional SEM. The morphologies of the TiO_2 nanocomposite films were evaluated using AFM (Nanoscope IIIa, Digital Instruments). The rms surface roughnesses were determined over an area of 9 μm^2. Absorption spectra of the corresponding films were measured using a Perkin–Elmer Lambda 950 UV–vis spectrometer. The phase of the crystalline TiO_2 NPs was analysed by powder X-ray diffraction (XRD: Philips Xpert XRD system), with Cu Kα radiation at a scanning speed of 10 min^{-1}. The dispersion characteristics of the TiO_2 NPs in organic media were evaluated by dynamic light scattering analyzer (DLS: Malvem Zetasizer Nano).TGA was performed using a Perkin–Elmer TGA 7.

2.3. Device fabrication and electrical measurements

A silicon wafer presenting thermally grown SiO_2 (d = 120 nm) was used as the substrate. The source and drain electrodes (Pt) having channel widths and lengths of 500 and 10 μm, respectively, were prepared using a photolithography/Pt (20 nm) deposition/lift-off (acetone) process. After spin-coating of P3HT as the semiconductor, the PMMA (1 wt.% in ethyl acetate) and the PVP or TiO_2 nanocomposite was then spin-coated onto the P3HT layer as a gate dielectric layer. Gold gate electrodes were deposited and patterned using the same methods used to prepare the source and drain electrodes. To characterize the leakage currents and capacitances of the PVP and TiO_2 nanocomposite films, metal–insulator–metal (MIM) capacitor structures were prepared by sandwiching the insulator

materials between the ITO and the Au electrode (dot area = 0.000415 cm^2). The capacitances were measured using a Keithley 590 CV capacitance analyzer operated at 100 kHz. All *I–V* measurements for our OFET and MIM devices were taken at room temperature under ambient conditions using an Agilent 4156C semiconductor parameter analyzer.

3. Results and discussion

This study began with the synthesis of TiO_2 NPs. The resulting OA-TiO_2 NPs have been reported to possess the anatase phase; our NPs were cylindrical in shape (20 nm long and 4 nm wide, as measured using transmission electron microscopy (TEM), Fig. 1a). The OA-TiO_2 film was solution-processable from toluene or chlorobenzene. We used scanning electron microscopy (SEM) imaging of the fracture edge to examine the uniformity of the OA-TiO_2 film. Fig. 1b reveals that the OA-TiO_2 layer exhibited good uniformity with a homogeneous NP dispersion. To synthesize hydrophilic TiO_2 NPs, we performed a surface modification of the OA-TiO_2 NPs by heating them in the presence of DCP in chlorobenzene at 100 °C for 24 h. The product DCP-TiO_2 NPs, which could be redispersed in polar solvents, such as isopropyl alcohol (IPA) and *n*-butanol, formed films that also exhibited good uniformity (Fig. 1c). Thus, we suspected that the DCP-TiO_2 NPs would be a good candidate material for use as a metal-oxide for mixing with a polymer matrix to form homogeneous nanocomposites that could be processed using polar solvents.

Because it is difficult to observe the modification layer on the surface of the TiO_2 NPs directly from TEM micrographs, we monitored the formation of the modification layer (DCP and OA) on the surface of the TiO_2 NPs using thermo gravimetric analysis (TGA). Fig. 2 presents typical TGA heating curves of the OA-TiO_2 and DCP-TiO_2 NPs. The mass profile reveals a major weight loss between 150 and 600 °C that is due to evaporation of the modification layer of the TiO_2. For OA-TiO_2 NPs, the TGA curve displays a ca. 43% weight loss (oleic acid), indicating a residue of ca. 57 wt.% inorganic TiO_2. For the DCP-TiO_2 NPs, the coverage of the NPs was ca. 54 wt.% (oleic acid and DCP), i.e., the inorganic TiO_2 residue was ca. 46 wt.%.

Fig. 3 displays the X-ray diffraction (XRD) patterns of the synthesized OA-TiO_2 and DCP- TiO_2 NPs. Both sets of

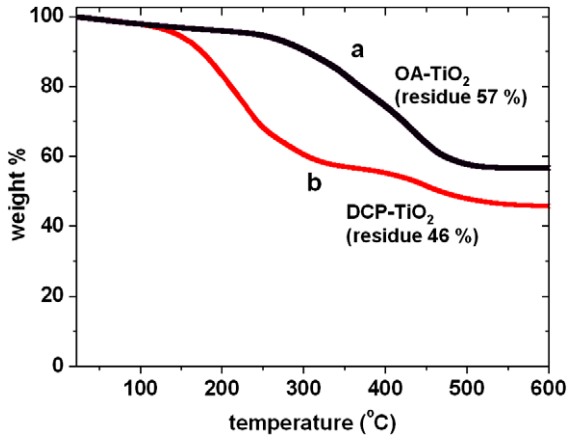

Fig. 2. Heating curves of OA-TiO_2 (curve a) and DCP-TiO_2 (curve b) nanoparticles.

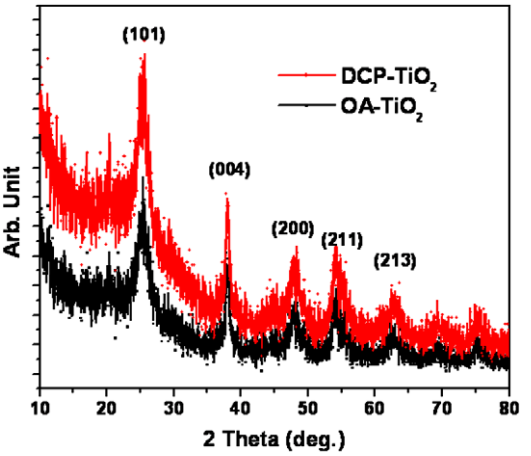

Fig. 3. XRD powder pattern of the OA-TiO_2 and DCP-TiO_2 nanorods.

reflections can be indexed to anatase; the (1 0 1), (0 0 4), (2 0 0), (2 1 1), and (2 1 3) planes provided the strongest reflections, indicating that the crystallinity of the TiO_2 was not changed after performing the surface ligand modification. The characteristic line broadening of diffraction peaks was consistent with the nanosized crystalline do-

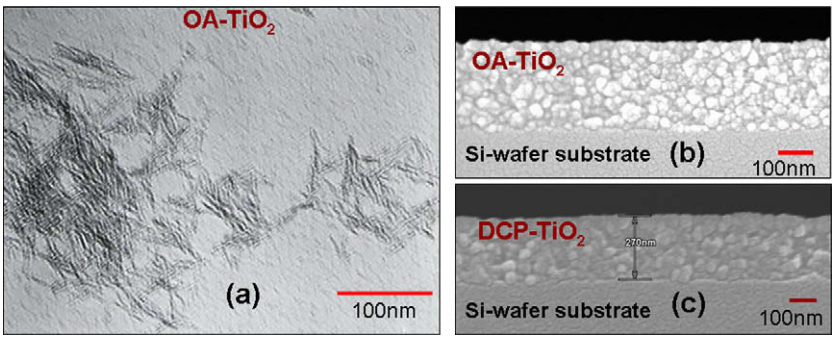

Fig. 1. (a) TEM image of the OA-TiO_2 nanorods, (b) cross-sectional SEM image of the OA-TiO_2 layer, (c) cross-sectional SEM image of DCP-TiO_2 layer. All scale bars are 100 nm.

mains and the sharp peak and narrow width of the signal for the (0 0 4) plane implied the formation of nanorods that grew anisotropically. These results are consistent with the TEM analysis.

Fig. 4 presents the particle size distributions of the DCP-TiO_2 NPs and OA-TiO_2 NPs that we measured using a dynamic light scattering (DLS) analyzer. The average particle size of the OA-TiO_2 NPs was ca. 35 nm in chlorobenzene, indicating that they were well dispersed in the organic medium (curve c). The DCP-TiO_2 NPs that we dispersed in *n*-butanol, a polar solvent, exhibited good dispersion stabilities with an average particle size of 22 nm (curve a), such that they have great potential for blending with polar polymer matrices. Interestingly, the DCP-TiO_2 NPs also displayed good dispersibility (102 nm) in chlorobenzene (curve d), although they had agglomerated to some extent relative to their dispersion in *n*-butanol. It thus implied that the DCP-TiO_2 NPs, resulting from the DCP ligands treated OA-TiO_2 NPs, still possessed small fraction of hydrophobic OA groups on their surfaces.

Among the polymer gate dielectrics reported in the literatures [7,31], the cross-linked PVP exhibits particularly good dielectric properties and high carrier mobilities of 3–5 $cm^2 V^{-1} s^{-1}$ when using pentacene as the semiconductor [32,33]. Hence, in this paper, we selected PVP as the polymer matrix for mixing with the DCP-TiO_2 NPs. For comparison, we prepared two types of gate dielectrics: a typical PVP/PMF blend gate dielectric (denoted "PVP/PMF"), which we obtained by mixing PVP (8 wt.%) with PMF (4 wt.%) in *n*-butanol, and a PVP/PMF/DCP-TiO_2 blend gate dielectric (denoted "TiO_2 nanocomposite") prepared at weight percentage ratio of 8:4:12 in *n*-butanol. We spin-coated these two dielectric films from solution and cured them at the temperature of 180 °C for 30 min. The DLS analysis in Fig. 4b reveals that the dispersibility of the TiO_2 nanocomposite was 35.2 nm in *n*-butanol, indicating that the NPs and polymers formed a uniform and homogeneous dispersion. In addition, the SEM cross-sectional image of the nanocomposite also displays a uniform NP/polymer blend (Fig. 5a); the tapping mode AFM image (Fig. 5b) exhibits the root-mean-square (rms) surface roughness of 2.29 nm, revealing the high uniformity of the PVP/PMF/DCP-TiO_2 blends, although the rms surface roughness of the neat PVP/PMF film was smaller at 0.58 nm (rms data from 3×3 μm scale). Thus, the TiO_2 nanocomposite in this study was not only soluble in polar solvents but also formed uniform films with homogeneous TiO_2 NP dispersion, all of which are desirable properties for solution-processable gate dielectrics for fabricating top-gate OFETs.

We measured the leakage currents and capacitances of the PVP/PMF and TiO_2 nanocomposite dielectrics using Au/

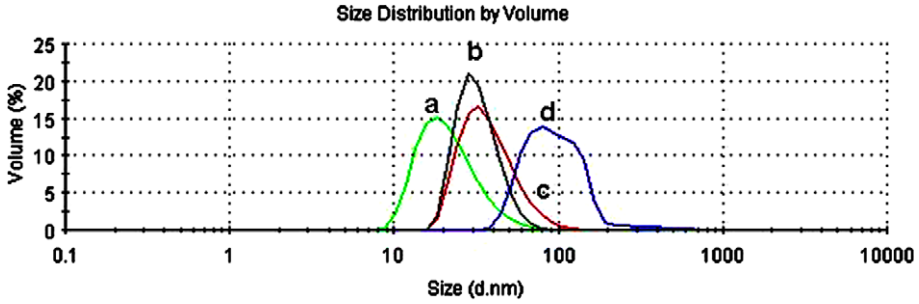

Fig. 4. Dynamic light scattering (DLS) analysis of the TiO_2 nanoparticles. (curve a) DCP-TiO2 in *n*-butanol; (curve b) PVP/PMF/DCP-TiO_2 nanoparticles blends; (curve c) OA-TiO_2 in Cl-benzene; (curve d) DCP-TiO_2 in Cl-benzene.

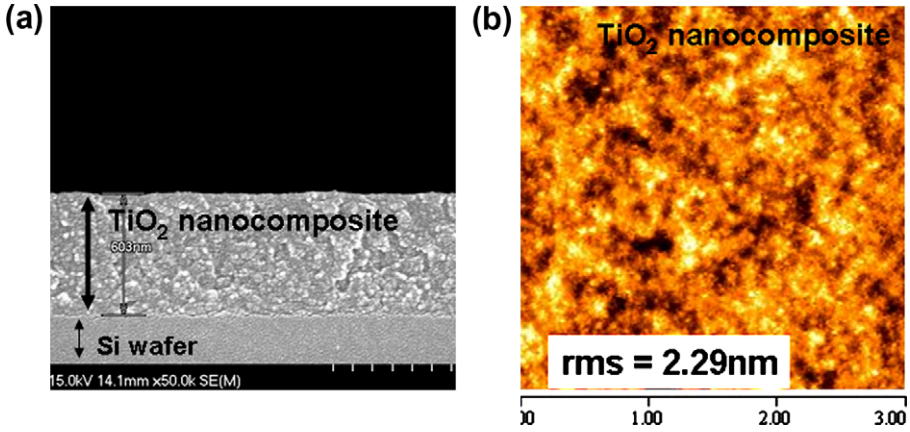

Fig. 5. (a) SEM cross-sectional image of TiO_2 nanocomposite film. (b) AFM image of the surface of the high-*k* nanocomposite film.

dielectric/ITO glass structures through capacitance–voltage (C–V) and current density–electric field (J–E) tests. Fig. 6 reveals that the PVP/PMF film exhibited a current density of 5×10^{-8} A cm^{-2} at 40 V, which is close to the value reported previously [32]. The current density of the TiO_2 nanocomposite (6×10^{-7} A cm^{-2} at 40 V) was only one order of magnitude higher than that of the low-k PVP film. The inset to Fig. 6 displays the C–V characteristics of the TiO_2 nanocomposite. From the capacitance (9.5 nF cm^{-2}) and the thickness (678 nm) of the film, we estimated the dielectric constant k to be 7.3. In contrast, the value of k of the PVP/PMF film was 4.9. Obviously, the increased value of k of the nanocomposite was due to the addition of the TiO_2 NPs in the polymer matrix of the PVP/PMF blends. Next, we deposited the TiO_2 nanocomposite and the PVP/PMF onto P3HT OFETs to study the effects of the high-k (k = 7.3) and low-k (k = 4.9) materials. We note that both the TiO_2 nanocomposite and PVP/PMF films exhibited excellent chemical resistance to the bases typically found in positive photoresist developers. Thus, we defined the region of the gate electrodes by using a photolithography/Au-deposition (50 nm)/lift-off process, rather than a traditional process of vacuum-deposition through a shadow mask.

All of the OFETs were fabricated with the top-gate geometry depicted in Fig. 7. A crystal silicon was used as a substrate. The semiconductor, P3HT, was spin-coated from a toluene solution and the resulting film was self-isolated between the source and drain electrodes (Fig. 7b) [34]. Because the performance of OFETs is influenced dramatically by the nature of the semiconductor–insulator interface [31,35], and because we expected the P3HT–high-k and P3HT–low-k dielectric interfaces to exhibited different morphologies and crystallinities, we capped the P3HT layer by spin-coating a buffer layer (d = 50–60 nm) of PMMA (k = 3.5) from ethyl acetate solution to maintain a constant semiconductor–dielectric interface and then spin-coated the two dielectrics from n-butanol solution

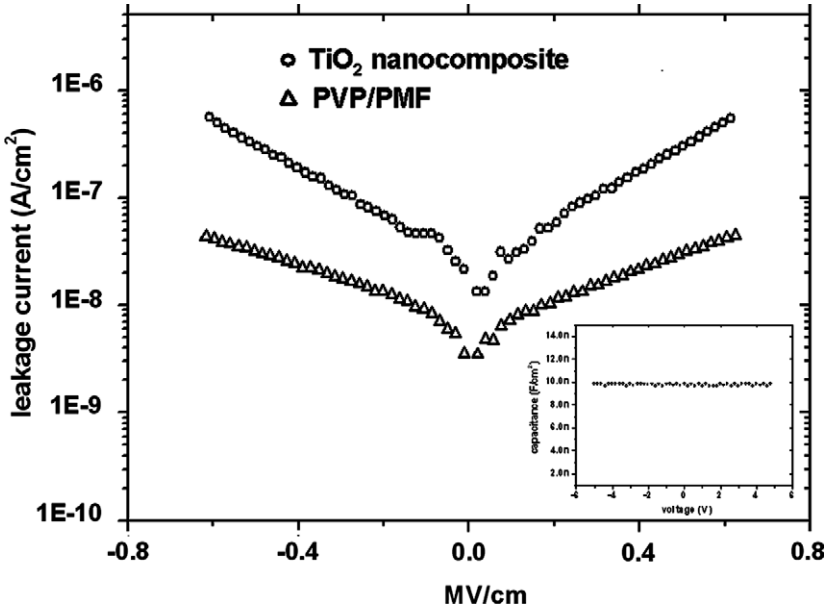

Fig. 6. Plots of current density and capacitance (inset) as a function of the applied voltage for the PVP/PMF and TiO_2 nanocomposite films.

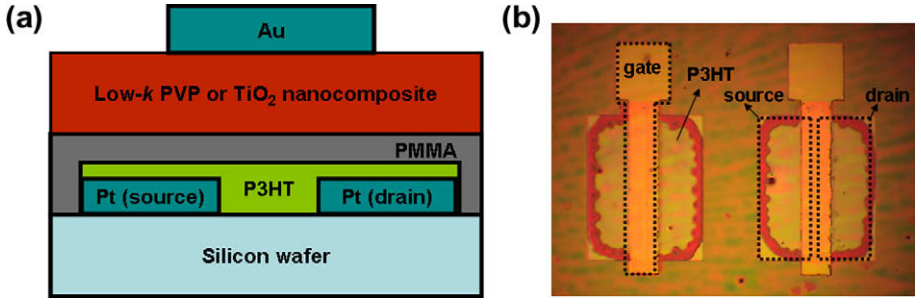

Fig. 7. (a) Device structure of the top-gate, bottom-contact configuration employed in this study. (b) Optical micrograph of stripe electrodes having a channel length of 500 μm and a width of 10 μm.

onto the resulting substrates. After deposition of the gate electrodes, we obtained two OFETs with stacked (bilayer) structures of the PMMA/TiO_2 nanocomposite and PMMA/PVP/PMF dielectrics, respectively, which allowed us to study the different effects of the high-k and low-k dielectrics. For convenience, we name the P3HT OFET incorporating the bilayer of PMMA/PVP/PMF (d = 420 nm) as "transistor 1"; the P3HT OFET featuring the PMMA/TiO_2 nanocomposite (d = 450 nm) is "transistor 2"; the P3HT OFET containing a single layer of the TiO_2 nanocomposite is "transistor 3." Using the following equation

$$1/C_{\text{total}} = 1/C_{\text{PMMA}} + 1/C_{\text{PVP}} \quad (1)$$

and the above dielectric constants k of the PVP/PMF and TiO_2 nanocomposite, we calculated the capacitances of the two bilayer dielectrics to be 8.12 and 11.1 nF cm^{-2}, respectively.

Fig. 8 displays the drain current–drain voltage curves (I_d–V_d) obtained from our P3HT OFETs incorporating the bilayer gate dielectrics. Both types of devices demonstrated desirable TFT characteristics at operating voltages of less than 20 V. To the best of our knowledge, this device is the first reported example of a top-gate P3HT OFET featuring solution-processed TiO_2 nanocomposites as gate dielectrics. From the output characteristics, the maximum saturation current of transistor 2 (PMMA/TiO_2 nanocomposite; 1.4 μA) under a gate bias (V_g) of −20 V was significantly greater that that of transistor 1 (PMMA/PVP/PMF; ca. 0.3 μA). These results clearly demonstrate the benefits that high-k TiO_2 NPs contribute to the performance of OFETs.

We used the following equation to determine the carrier mobility (μ) and the threshold voltage (V_{th}):

$$\sqrt{I_{D,SAT}} = \sqrt{\frac{W\mu C_{ox}}{2L}}(V_G - V_{th}) \quad (2)$$

where $I_{D,SAT}$ is the saturated drain current, C_{ox} is the gate capacitance per unit area, W and L are the conducting channel width and length, respectively, V_{th} is the threshold voltage, and V_G is the gate applied voltage. We extracted the mobilities from the slopes of the linear plots of the square root of the drain current versus the gate voltage (Fig. 9).

Table 1 lists all of the electrical parameters of these OFETs. When we operated transistor 1 (C = 8.12 nF cm^{-2}) within 20 V (V_{ds} = –20 V; V_{gs} = + 20 to −20 V), the mobility in the saturation region and the threshold voltage were 0.003 cm^2 V^{-1} s^{-1} and 1.43 V, respectively. The on/off ratio was ca. 1.5 × 10^5. For transistor 2 (C = 11.1 nF cm^{-2}), the mobility and threshold voltage were 0.015 cm^2 V^{-1} s^{-1} and −1.33 V, respectively, with an on/off ratio of 8.4 × 10^6; thus, the mobility of transistor 2 was ca. five times higher than that of transistor 1. This implies that the mobility of P3HT devices in this case is dependent of the capacitances of the gate dielectrics. The enhanced mobility obtained for devices with higher capacitance (i.e. higher field-induced carrier concentration in the conducting channel) indicated that the presence of a larger number of electronic defect states in the channel effectively trapping the carriers at small carrier concentration. Similar observations have been made in previous studies [36–38]. To achieve low-operating-voltage OFETs, we tested the performance of transistors 1 and 2 within 10 V (V_{ds} = −10 V; V_{gs} = +10 to −10 V). Fig. 9b reveals that transistor 1 exhibited a mobility of 0.002 cm^2 V^{-1} s^{-1} and a threshold voltage of 2.48 V, with an on/off ratio of 1.5 × 10^4; the mobility of transistor 2 (0.006 cm^2 V^{-1} s^{-1}) was three times better than that of transistor 1, and its on/off ratio (6.5 × 10^5) was 40 times better. These results clearly demonstrate the advantages that TiO_2 NPs materials provide toward improving the performances of OFETs in terms of their mobilities and on/off ratios.

For comparison, we investigated the performance of transistor 3, the P3HT OFET incorporating a single layer of the TiO_2 nanocomposite (C = 10.8 nF cm^{-2}) as the gate dielectric. When operated within 20 V, transistor 3 exhibited an acceptable mobility of 0.0011 cm^2 V^{-1} s^{-1} and a threshold voltage of 0.41 V, but its on/off ratio (5.7 × 10^2)

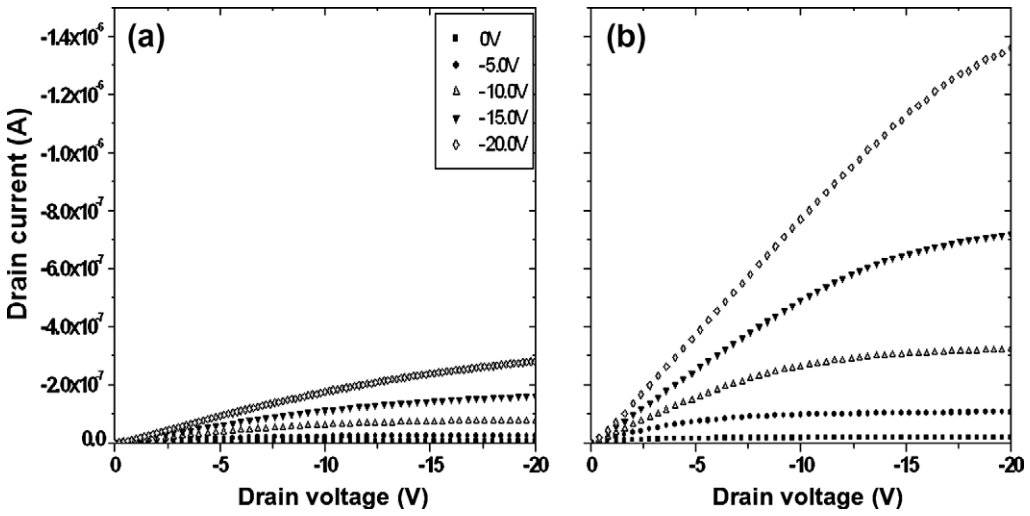

Fig. 8. Output characteristics of (a) transistor 1 and (b) transistor 2.

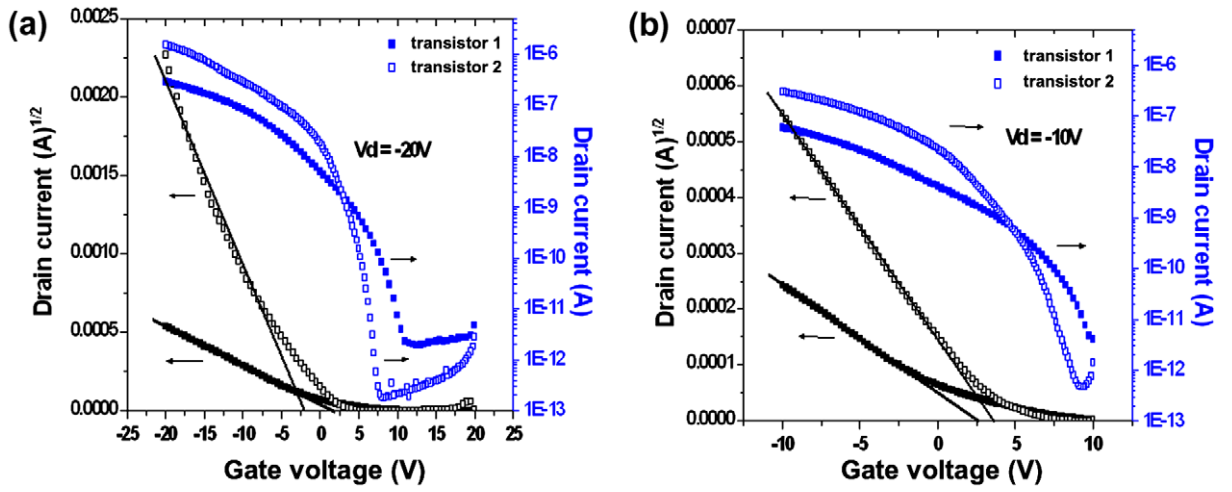

Fig. 9. Transfer characteristics of transistor 1 and transistor 2: (a) $V_{ds} = -20$ V (b) $V_{ds} = -10$ V.

Table 1
Electrical characteristics of P3HT OFETs with bilayer (PMMA/PVP/PMF and PMMA/TiO_2 nanocomposite) and single layer (high-k nanocomposite) gate dielectrics.

Sample	Gate dielectric (bilayer or single layer)	C (nF cm^{-2})	Operating conditions	μ (cm^2 V^{-1} s^{-1})	On/off ratio	V_{th} (V)
Transistor 1	PMMA/PVP/PMF	8.12	$V_{ds} = -20$ V, $V_{gs} = +20$ to -20 V	3.1×10^{-3}	1.5×10^5	1.43
Transistor 2	PMMA/TiO_2 nanocomposite	11.1		1.5×10^{-2}	8.4×10^6	−1.33
Transistor 1	PMMA/PVP/PMF	8.12	$V_{ds} = -10$ V, $V_{gs} = +10$ to -10 V	1.9×10^{-3}	1.5×10^4	2.48
Transistor 2	PMMA/TiO_2 nanocomposite	11.1		6.1×10^{-3}	6.5×10^5	3.40
Transistor 3	TiO_2 nanocomposite (d = 600 nm)	10.8	$V_{ds} = -20$ V, $V_{gs} = +20$ to -20 V	1.1×10^{-3}	5.7×10^2	0.41

was dramatically inferior to those of the devices featuring bilayer gate dielectrics because its off-current (ca. 10^{-9} A) was ca. 2–3 orders of magnitude larger than those of transistor 1 (ca. 10^{-11} A) and transistor 2 (ca. 10^{-12} A). We suspect that the high off-current of transistor 3 might be due to the poor interface morphology induced by the relatively high-k material, the introduction of impurities at the interface during the preparation of the nanocomposite sample, or the high-temperature curing process having damaged the interface [26]. Therefore, the presence of PMMA as a buffer layer between the composite dielectric and the semiconductor was of vital importance to the high performance of these low-voltage top-gate transistors. Wang et al. [14] reported bottom-gate P3HT OFETs incorporating sputtered TiO_2 and bilayer SiO_2/TiO_2 gate insulators that operated within 10 V and exhibited mobilities of 0.005 and 0.032 cm^2 V^{-1} s^{-1}, respectively. Although our transistors operated with lower mobilities, they are the first examples of top-gate P3HT OFETs to have been prepared using simple, solution-processed TiO_2 nanocomposite gate dielectrics that had been fabricated at moderate temperatures.

4. Conclusions

We have synthesized novel DCP-TiO_2 NPs that are dispersible in polar solvents. Furthermore, the surfaces of these NPs are compatible with PVP, providing homogeneous polymer/NP blends, as evidenced from SEM and AFM images. The leakage current of the TiO_2 nanocomposite was only one order of magnitude larger than that of the PVP/PMF, suggesting again the uniformity of the organic/inorganic blends. We fabricated P3HT OFETs incorporating the PMMA/PVP/PMF and the PMMA/TiO_2 nanocomposite as bilayer gate dielectrics. When operated within 20 V, the OFET featuring the TiO_2 nanocomposite exhibited a higher mobility (0.015 cm^2 V^{-1} s^{-1}) and on/off ratio (8.5×10^6) than those of the PVP/PMF device. Furthermore, when operated within 10 V, this device retained a good mobility (0.006 cm^2 V^{-1} s^{-1}) and on/off ratio (6.5×10^5). Thus, our TiO_2 nanocomposite is a promising solution-processed gate dielectric for low-voltage top-gate OFETs.

Acknowledgment

We thank the Ministry of Economic Affairs, Taiwan, for financially supporting this research.

References

[1] H. Sirringhaus, T. Kawase, R.H. Friend, T. Shimoda, M. Inbasekaran, W. Wu, E.P. Woo, Science 290 (2000) 2123.
[2] L.-L. Chua, J. Zaumseil, J.-F. Chang, E.C.W. Ou, P.K.H. Ho, H. Sirringhaus, R.H. Friend, Nature 434 (2005) 194.
[3] B. Crone, A. Dodabalapur, Y.Y. Lin, R.W. Filas, Z. Bao, A. LaDuca, R. Sarpeshkar, H.E. Katz, W. Li, Nature 403 (2000) 521.
[4] J.H. Burroughes, D.D.C. Bradley, A.R. Brown, R.N. Marks, K. Mackay, R.H. Friend, P.L. Burns, A.B. Holmes, Nature 347 (1990) 539.

[5] M. Halik, H. Klauk, U. Zschieschang, G. Schmid, C. Dehm, M. Schutz, S. Maisch, F. Effenberger, M. Brunnbauer, F. Stellacci, Nature 431 (2004) 963.
[6] H. Klauk, U. Zschieschang, J. Pflaum, M. Halik, Nature 445 (2007) 745.
[7] A. Facchetti, M.H. Yoon, T.J. Marks, Adv. Mater. 17 (2005) 1705.
[8] Y.D. Park, D.H. Kim, Y. Jang, M. Hwang, J.A. Lim, K. Cho, Appl. Phys. Lett. 87 (2005) 243509.
[9] M.H. Yoon, H. Yan, A. Facchetti, T.J. Marks, J. Am. Chem. Soc. 127 (2005) 10388.
[10] L.L. Chua, P.K.H. Ho, H. Sirringhaus, R.H. Friend, Appl. Phys. Lett. 84 (2004) 3400.
[11] S.Y. Yang, S.H. Kim, K. Shin, H. Jeon, C.E. Park, Appl. Phys. Lett. 88 (2006) 173507.
[12] Y.Y. Noh, H. Sirringhaus, Org. Electron. 10 (2009) 174.
[13] C.D. Dimitrakopoulos, S. Purushothaman, J. Kymissis, A. Callegari, J.M. Shaw, Science 283 (1999) 822.
[14] L.A. Majewski, R. Schroeder, M. Grell, Adv. Funct. Mater. 15 (2005) 1017.
[15] G. Wang, D. Moses, A.J. Heeger, H.-M. Zhang, M. Narasimhan, R.E. Demaray, J. Appl. Phys. 95 (2004) 316.
[16] J. Lee, J.H. Kim, S. Im, Appl. Phys. Lett. 29 (2003) 2689.
[17] C.S. Kim, S.J. Jo, S.W. Lee, W.J. Kim, H.K. Baik, Appl. Phys. Lett. 88 (2006) 243515.
[18] M.J. Panzer, C.D. Frisbie, J. Am. Chem. Soc. 127 (2005) 6960.
[19] J. Lee, M.J. Panzer, Y. He, T.P. Lodge, C.D. Frisbie, J. Am. Chem. Soc. 129 (2007) 4532.
[20] J.H. Cho, J. Lee, Y. He, B.S. Kim, T.P. Lodge, C.D. Frisbie, Adv. Mater. 20 (2008) 686.
[21] F.C. Chen, C.W. Chu, J. He, Y. Yang, Appl. Phys. Lett. 85 (2004) 3295.
[22] F.C. Chen, C.S. Chuang, Y.S. Lin, L.J. Kung, T.H. Chen, H.P.D. Shieh, Org. Electron. 7 (2006) 435.
[23] A. Maliakal, H. Katz, P.M. Cotts, S. Subramoney, P. Mirau, J. Am. Chem. Soc. 127 (2005) 14655.
[24] Q.J. Cai, Y. Gan, M.B. Chan-Park, H.B. Yang, Z.S. Lu, Q.L. Song, C.M. Li, Z.L. Dong, Appl. Phys. Lett. 93 (2008) 113304.
[25] K. Muller, I. Paloumpa, K. Henkel, D. Schmeiber, Mat. Sci. Eng. C 26 (2006) 1028.
[26] H.G.O. Sandberg, T.G. Backlund, R. Osterbacka, H. Stubb, Adv. Mater. 16 (2004) 1112.
[27] H.G.O. Sandberg, T.G. Backlund, R. Osterbacka, M. Shkunov, D. Sparrowe, I. McCulloch, H. Stubb, Org. Electron. 6 (2005) 142.
[28] F.Y. Yang, K.J. Chang, M.Y. Hsu, C.C. Liu, J. Mater. Chem. 18 (2008) 5927.
[29] F.Y. Yang, K.J. Chang, M.Y. Hsu, C.C. Liu, Org. Electron. 9 (2008) 925.
[30] P.D. Cozzoli, A. Kornowski, H. Weller, J. Am. Chem. Soc. 125 (2003) 14539.
[31] J. Veres, S. Ogier, G. Lloyd, D.D. Leeuw, Chem. Mater. 16 (2004) 4543.
[32] H. Klauk, M. Halik, U. Zschieschang, G. Schmid, W. Radlik, W. Weber, J. Appl. Phys. 92 (2002) 5259.
[33] M. Halik, H. Klauk, U. Zschieschang, T. Kriem, G. Schmid, W. Radlik, K. Wussow, Appl. Phys. Lett. 81 (2002) 289.
[34] K.J. Chang, F.Y. Yang, C.C. Liu, M.Y. Hsu, T.C. Liao, H.C. Cheng, Org. Electron. 10 (2009) 815.
[35] J. Veres, S.D. Ogier, S.W. Leeming, D.C. Cupertino, S.M. Khaffaf, Adv. Funct. Mater. 13 (2003) 199.
[36] C. Jung, A. Maliakal, A. Sidorenko, T. Siegrist, Appl. Phys. Lett. 90 (2007) 062111.
[37] Y. Jang, D.H. Kim, Y.D. Park, J.H. Cho, M. Hwang, K. Cho, Appl. Phys. Lett. 87 (2005) 152105.
[38] D.K. Hwang, C.S. Kim, J.M. Choi, K. Lee, J.H. Park, E. Kim, H.K. Baik, J.H. Kim, S. Im, Adv. Mater. 18 (2006) 2299.

Organic Electronics 11 (2010) 89–94

Contents lists available at ScienceDirect

Organic Electronics

journal homepage: www.elsevier.com/locate/orgel

Role of air exposure in the improvement of injection efficiency of transition metal oxide/organic contact

C.H. Cheung [a], W.J. Song [b], S.K. So [a,*]

[a] Department of Physics and Centre for Advanced Luminescence Materials, Hong Kong Baptist University, Kowloon Tong, Hong Kong, China
[b] Devision of Functional Materials and Nano Devices, Ningbo Institute of Material Technology and Engineering, Chinese Academy of Science, Ningbo, People's Republic of China

ARTICLE INFO

Article history:
Received 16 June 2009
Received in revised form 10 September 2009
Accepted 6 October 2009
Available online 13 October 2009

Keywords:
Transition metal oxides, Charge injection
Organic semiconductor
Injection efficiency

ABSTRACT

Oxygen or air exposure to transition metal oxides (TMOs) was demonstrated to be essential in improving the hole injection (HI) efficiency at the contact formed by TMOs and small organic hole transporter. Current–voltage (*J–V*) and dark-injection space-charge-limited current (DI-SCLC) techniques were used to cross-examine the TMO/organic contacts. The hole transporter under investigation was *N,N′*-diphenyl-*N,N′*-bis(1-naphthyl)(1,1′biphenyl)-4,4′diamine (NPB). The improvement was attributed to the reduction in the energy barrier at TMO/NPB interface, which was a consequence of the work function enhancement of TMO by the oxidation of oxygen in air.

© 2009 Elsevier B.V. All rights reserved.

1. Introduction

Organic semiconductors have received tremendous attention for optoelectronic applications in recent decades with various advantages such as low cost processing and structural flexibility [1,2]. Owing to the low intrinsic carrier concentration in organic semiconductors, external charge injection from a contact electrode is necessary for making the semiconductors electrically conducting. As a matter of fact, efficient carrier injection at electrode/organic contact is critically important in 'turning on' organic optoelectronic devices and thus realizing devices with high efficiency [3]. For hole injection, ideally, if interface dipole is negligible, the hole injection efficiency is mainly determined by the energy barrier between the work function of anode and the highest occupied molecular orbital (HOMO) level of organic hole transporting layer (HTL) [4]. A smaller barrier should result in a better efficiency. The most efficient injection contact, i.e. an Ohmic contact, appears in the absence of an injection barrier.

Indium tin oxide (ITO) is the preferred anode for organic optoelectronic devices due to its optical transparency in visible spectrum. However, with a work function of ~4.8 eV, a finite energy barrier always exists at ITO/HTL interface as most HT materials possess high-lying HOMO levels (>5.4 eV). To date, the most commonly used method to minimize the ITO/organic barrier is to insert a hole injection layer (HIL) between ITO and HTL [3,5]. Different HI materials were realized, such as copper phthalocyanine (CuPc) [3] and polyethylene dioxythiophene polystyrene sulfonate (PEDOT:PSS) [5], but an Ohmic contact has not been achieved yet. Recently, transition metal oxides (TMOs) with high work functions have been shown to be promising candidates to facilitate hole injection and improve the performance of organic optoelectronic devices [6–10]. Popular oxides include molybdenum trioxide (MoO_3), vanadium pentoxide (V_2O_5) and tungsten trioxide (WO_3). While most reports aim at showing the improved performance of devices by TMOs, a critical factor, the

* Corresponding author.
E-mail address: skso@hkbu.edu.hk (S.K. So).

1566-1199/$ - see front matter © 2009 Elsevier B.V. All rights reserved.
doi:10.1016/j.orgel.2009.10.003

preparation condition (substrate temperature and oxygen partial pressure, etc.) of TMOs, which strongly affects the stoichiometry of TMOs and their work functions, was neglected.

In this study, we address the injection problems encountered in using TMOs as HIL. We will show that the post-treatment of TMO films (MoO_3, V_2O_5, and WO_3) at different oxygen partial pressures before HTL deposition can affect the HI efficiency into an organic HTL, *N,N′*-diphenyl-*N,N′*-bis(1-naphthyl)(1,1′biphenyl)-4,4′diamine (NPB). NPB is a widely used amorphous HT material in OLEDs [11]. It has excellent film forming ability and air stability; it also exhibits trap-free HT property. Besides, similar to many common small-molecule HT materials, NPB has a high-lying HOMO level of 5.4 eV. Therefore, NPB is an ideal candidate for examining charge transport and injection mechanism in amorphous organic semiconductors [12,13]. Two electrical techniques, current–voltage (*J–V*) and dark-injection space-charge-limited-current (DI-SCLC) techniques, are employed to perform the examination. These techniques have been demonstrated to be valuable tools for injection contact examination [12,14,15]. Besides, carrier mobility of NPB can also be evaluated by DI-SCLC techniques [16]. The carrier mobility deduced from DI-SCLC technique will be compared to those obtained from independent time-of-flight (TOF) technique. In addition, X-ray photoemission spectroscopy (XPS) was employed to study the surface composition and the stoichiometry of TMO films.

2. Experimental

TMOs and NPB were purchased from Strem Chemicals and E-ray, respectively. Details of TOF experiments have been reported elsewhere [17]. For *J–V* and DI-SCLC experiments, samples have the general structures of ITO/TMO(20 nm)/NPB(~4 μm)/Ag. Prior to film deposition, ITO-coated glass slides were cleaned by using sequential baths of deconex, de-ionized water, and acetone. Subsequently, the ITO substrates were exposed to UV–ozone [18]. TMOs and NPB were thermally evaporated onto the substrates at rates of 0.05 and 1 nm/s, respectively. Since only hole injection was considered, 100 nm of Ag was used to be the hole collecting and electron blocking cathode. All films were deposited inside a high vacuum evaporator with a base pressure of about 10^{-6} Torr. In the following, instead of MoO_3, V_2O_5 and WO_3, we will use the notation of MoO_x, V_2O_x, and WO_x, to represent the stoichiometry of thermally evaporated TMOs film. Non-stoichiometric TMO films are usually obtained from thermal evaporation [19]. There are three kinds of devices used in this work. Their differentiation is based on how the TMO layer was modified prior to the deposition of the NPB layer. They are distinguished as follows: Method A – the TMO film was not modified, i.e., TMO and NPB were deposited sequentially under the same vacuum; Methods B and C – the TMO films were exposed to air and oxygen for 10 min, respectively, prior to the deposition of NPB. All film thicknesses were measured *in situ* by a quartz crystal sensor and *ex situ* by a step profilometer (Tencor Alpha-Step 500). After fabrication, the samples were immediately loaded inside a vacuum cryostat with a pressure of less than 10^{-3} Torr for measurements. All measurements were performed at room temperature. The *J–V* experiments were carried out with a computer-controlled Keithley Source-Measure Unit (model 236). For DI-SCLC experiments, the samples were subjected to a rectangular voltage pulse by using a pulse generator (HP model 241B) for injecting holes into the samples. A digital oscilloscope was used to capture the voltage across a current sensing resistor, which was connected in series to the samples. The current can be computed afterwards. For XPS, MoO_x was taken for surface composition study. Two samples were fabricated: Sample 1 – 20 nm MoO_x covered with 100 nm NPB, by which the two films were deposited sequentially on top of ITO in the same vacuum; Sample 2 – bare MoO_x film on top of ITO. The buried MoO_x film in sample 1 represents the MoO_x film without gas exposure, while the film in sample 2 corresponds to air-exposed oxide. The XPS experiment was performed inside Kratos AXIS ULTRA^{DLD} system using monochromic Al Kα radiation as the X-ray source and the surface composition can be determined. The surface composition of MoO_x in sample 1 can be characterized only after the removal of the NPB layer by Ar^+ ion sputtering.

3. Results and discussion

Fig. 1a shows the *J–V* characteristics for devices having the structure of ITO/HIL/NPB/Ag, where the HIL = PEDOT:PSS, TMOs with and without air exposure. Ideally, if an organic material is trap-free and under the condition of Ohmic injection contact, the steady-state current should follow the space-charge-limited current (SCLC) (J_{SCL}) [20]:

$$J_{SCL} = \frac{9}{8}\mu_0\varepsilon_0\varepsilon_r \exp(0.89\beta\sqrt{F})\frac{F^2}{d} \quad (1)$$

where ε_0 is the permittivity in free space, ε_r is the dielectric constant (~3 for organic materials), F is the applied electric field strength and d is the thickness of organic layer respectively. The factor β is the Poole–Frenkel slope, which indicates the sensitivity of carrier mobility of material with respect to applied electric field. Carrier mobility of materials with smaller β shows less field-dependence. On the other hand, μ_0 is zero-field mobility, i.e., the mobility when $F = 0$. Both β and μ_0 can be obtained from independent time-of-flight experiments, and were found to be $1.3 \times 10^{-3}(\mathrm{cm/V})^{-1/2}$ and $2.7 \times 10^{-4}\mathrm{cm}^2/\mathrm{Vs}$, respectively [21]. In addition, the HI efficiency (η_{INJ}), can be obtained from the *J–V* characteristics and is given by [22]:

$$\eta_{INJ} = J_{INJ}/J_{SCL} \quad (2)$$

where J_{INJ} and J_{SCL} are, respectively, the measured and computed hole current from Eq. (1).

The solid line in Fig. 1a is the computed theoretical J_{SCL} which serves as the upper bound for the experimental current density. PEDOT:PSS has been demonstrated to be an promising HIL for OLEDs. The *J–V* characteristic of device with PEDOT:PSS here is used as a reference showing how

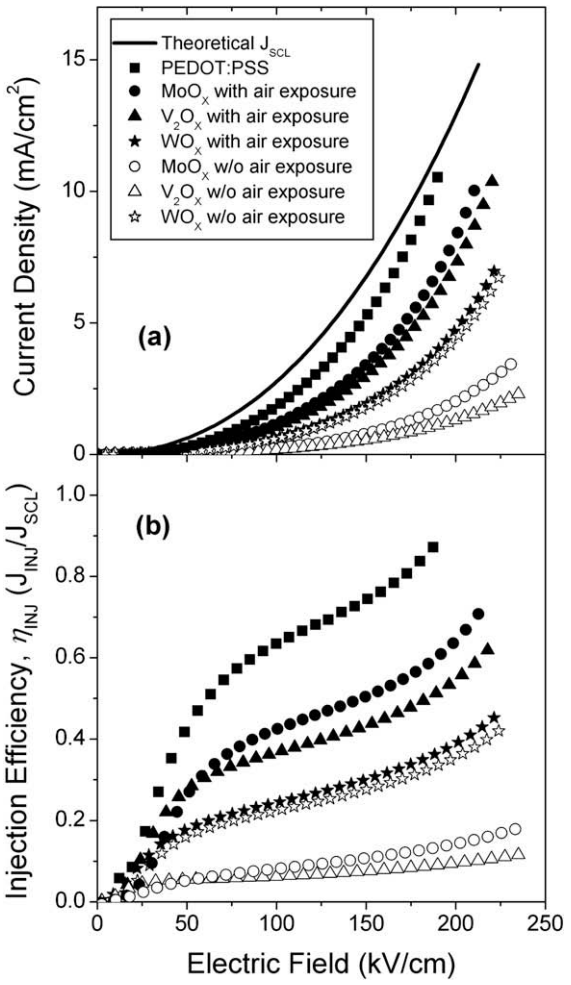

Fig. 1. (a) Current–voltage (J–V) characteristics and (b) injection efficiency plot of ITO/HIL/NPB/Ag devices using different HIL materials. The HILs are PEDOT:PSS, MoO_x, V_2O_x, and WO_x. For the TMOs, closed and open symbols correspond to the TMOs with and without air exposure, respectively.

an efficient HIL behaves. Clearly, at high field, the experimental J–V curves nearly overlap with the theoretical one for the PEDOT:PSS device, which indicates the HIL can form nearly Ohmic contact with NPB. On the other hand, those devices with HIL = air-exposed TMOs show larger deviations between experimental and theoretical J–V curves when compared to PEDOT:PSS device, indicating poorer injection condition. Furthermore, for those devices with HIL = TMOs without air exposure (except for WO_x), the measured J–V curves deviate substantially from the theoretical curve. This indicates the currents flowing through the devices are completely injection limited.

Substantial improvement in current density was observed from the devices with HIL = TMOs after air exposure. Fig. 1(b) shows the HI efficiency (η_{INJ}) plot of all the anodes. Same as J–V characteristics, when the TMOs are exposed to air, the HI efficiency has a marked improvement when compared to those without air exposure. About fivefold increase in η_{INJ} can be found when $F > 50$ kV/cm. The improvements clearly reveal that the hole injection at the TMO/NPB interface is enhanced upon exposing the oxides to air before the deposition of NPB, which is solely originated from the reduced injection barrier at TMO/NPB interface. The observations are, perhaps, not surprising. TMOs have been demonstrated to be the materials for gas sensors [23,24]. Their work functions change upon exposing to different gases. Exposing the oxides to oxidizing/reducing gases will result in an increase/decrease of their work functions. In air, the oxidizing constituent is oxygen. In order to verify if the improvement is solely originated from the oxygen exposure, samples with oxygen-exposed TMOs were fabricated.

Fig. 2a shows the J–V characteristics for NPB, with ITO/MoO_x as hole injecting anodes. The solid lines are the computed theoretical J_{SCL} using Eq. (1). In Fig. 2a, solid triangles (▲), open square (□) and open circle (○) represent the samples with no gas-exposed MoO_x (device A), air-exposed

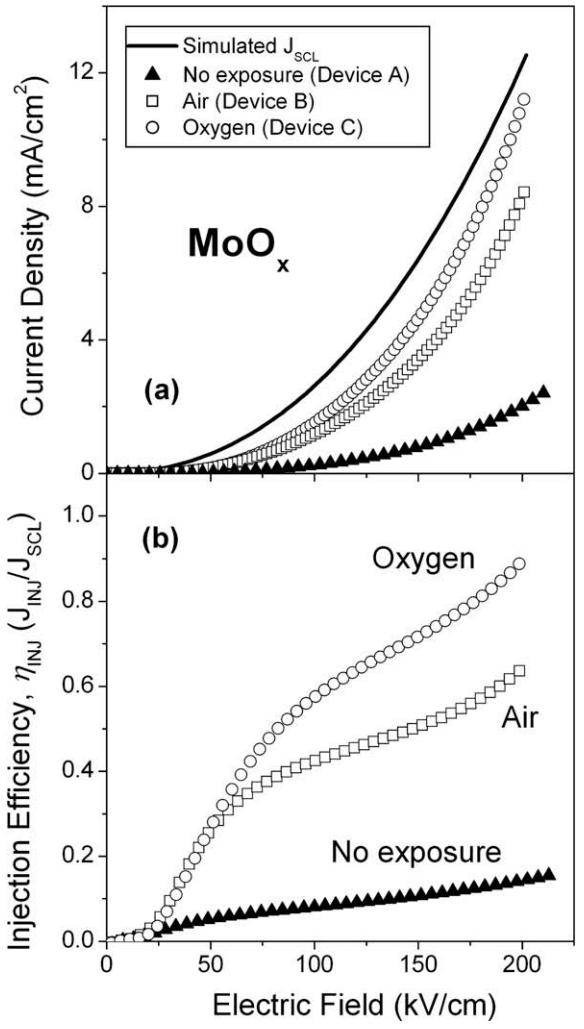

Fig. 2. (a) J–V characteristics and (b) injection efficiency plot of ITO/MoO_x/NPB/Ag devices. The MoO_x were treated differently in these devices: device A (▲) – no gaseous exposure; device B (□) – exposed to air for 10 min; device C (○) – exposed to oxygen for 10 min. In (a), the solid line is the simulated J–V curve using SCLC theory.

MoO_x (device B) and oxygen-exposed MoO_x (device C), respectively. Same as device B, substantial improvement in current density was observed from device C, when compared to that of device A. In addition, deviation between the theoretical fit and the experimental J–V curves from device C is smaller when compared to device B, in the entire range of electric field. Fig. 2b shows the HI efficiency plots for the corresponding TMOs containing devices. The results are consistent with the observations from the J–V plots, showing improved η_{INJ} from gas-exposed TMOs. The contacts of device C have the best η_{INJ} among all the devices, especially when $F > 50$ kV/cm. Analogous experiments were performed on V_2O_x, and the results are summarized in Table 1. The table shows η_{INJ} at two different applied electric field strengths, $F = 100$ kV/cm and 150 kV/cm. Same observation of η_{INJ} improvement can be found from V_2O_x containing devices. Since WO_x showed no effect upon air exposure, only MoO_x and V_2O_x were taken to be further investigated here. The discrepancy between η_{INJ} of oxygen-exposed and air-exposed TMOs is likely due to the presence of moisture in air, which acts as a reducing agent for TMOs [23]. Moisture counteracts the effect of oxygen and will reduce the effect of work function enhancement of oxides. In addition, the η_{INJ} of PEDOT:PSS/NPB contact were found to be 0.64 and 0.74 at $F = 100$ kV/cm and 150 kV/cm from Fig. 1b, respectively. Oxygen-exposed TMOs show comparable injection performance to PEDOT:PSS, which suggests that TMOs can be an alternative choice for HIL in OLEDs to replace PEDOT:PSS, with an additional advantage of being the top electrodes of organic thin film transistors (OTFTs).

Besides J–V characteristics, the injection behavior of TMO/NPB contacts was further examined by DI-SCLC experiment. Fig. 3a shows the DI signals at 100 V ($F = 250$ kV/cm) from all the devices (A, B and C). The signals from device B and C clearly exhibit the characteristics which resemble the ideal DI transient as shown in Fig. 3b, while the signal from device A is featureless. The ideal current transient reaches a maximum at a well-defined flight time τ_{DI} and decays to a saturated value after a long time. This transient can only be observed if the following conditions are satisfied: (i) anode/organic contact is Ohmic and (ii) organic/cathode contact is electron blocking. The transient current density $J(t)$ can be derived from Poisson's equation for a trap-free material under the condition of unipolar Ohmic injection. The carrier mobility μ_{DI} can be calculated as follows [25]:

$$\mu_{DI} = \frac{0.787 d^2}{\tau_{DI} \cdot V} \quad (3)$$

where τ_{DI} is the arrival time of the fastest carriers at the non-injecting electrode, and is related to the space-charge free carrier transit time τ by $\tau_{DI} = 0.787\tau$; d and V are the organic layer thickness and voltage applied across the sample. In Fig 3a, we can clearly extract the τ_{DI} from devices B and C while no distinct τ_{DI} appeared from device A.

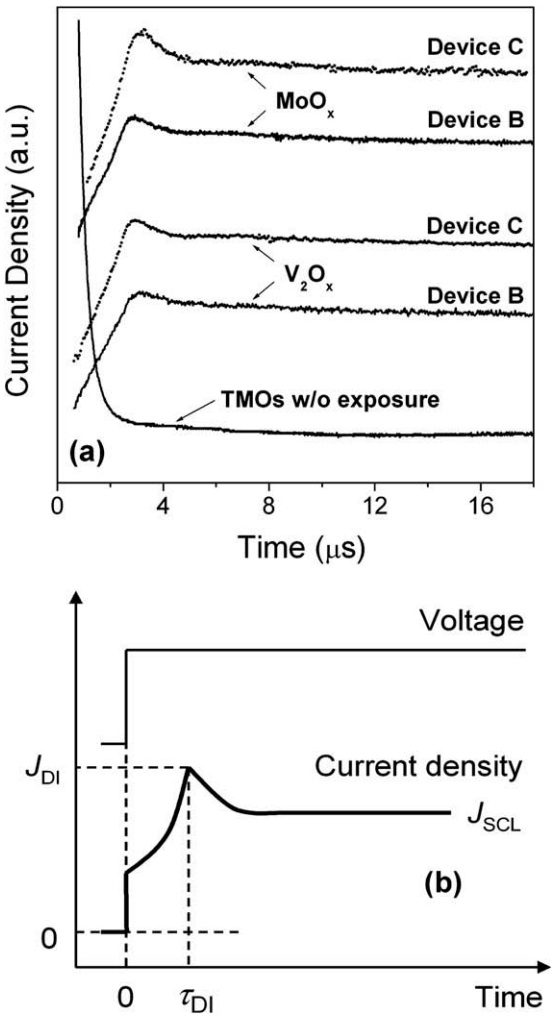

Fig. 3. (a) DI-SCLC transients from device A, B and C at 100 V ($F = 250$ kV/cm). (b) An ideal DI-SCLC transient.

Moreover, the DI transients under different applied voltages were measured. From Eq. (3), we can extract the hole transit time and hence the hole mobilities of NPB from the DI transients. The results from MoO_x containing devices are summarized in Fig. 4. The values of hole mobilities of NPB extracted from all the devices are consistent to the reported values [12,21]. In Fig. 4, device C (○) shows slightly higher hole mobilities than device B (■). Fig. 4 also

Table 1
Summary of HI efficiency (η_{INJ}) of different oxide contacts.

	MoO_x		V_2O_x	
	$F = 100$ kV/cm	$F = 150$ kV/cm	$F = 100$ kV/cm	$F = 150$ kV/cm
w/o gas exposure	0.08	0.11	0.06	0.08
Air exposure	0.43	0.51	0.37	0.43
O_2 exposure	0.58	0.72	0.6	0.75

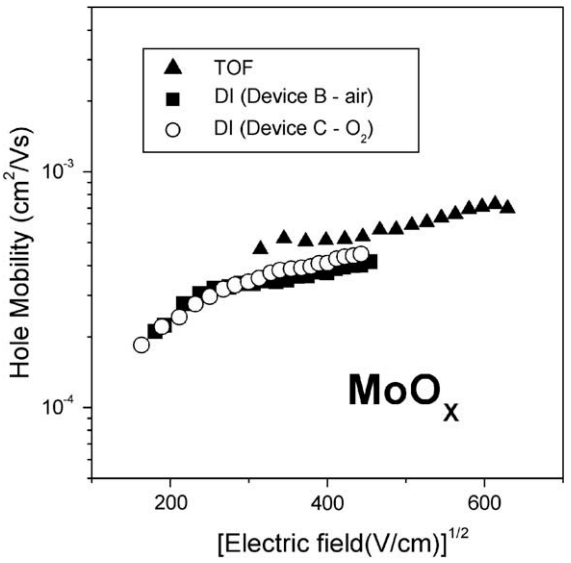

Fig. 4. The hole mobilities of NPB against the square root of the electric field at 290 K derived from DI-SCLC and TOF techniques for ITO/MoO_x/NPB/Ag devices.

shows the hole mobilities of NPB obtained from independent TOF experiment. In TOF, as the charge carriers inside NPB are optically generated by pulse laser, problems related to the injection contact can be neglected. Therefore, carrier mobility from TOF reveals the actual mobility of materials. The mobilities obtained from DI experiments are in good agreement to those from TOF. Same observation can also be found from V_2O_x containing devices. The small discrepancy can be originated from the imperfectly Ohmic injection from the oxides contact. Larger discrepancy can be found in the range of small electric field, as the injection barrier height is lowered upon increasing the applied voltages. The observation is consistent to that of *J–V* experiment showing incomplete overlap between the measured *J–V* curves and the theoretical fits, especially when *F* is small. Although significant difference cannot be found from the DI mobilities evaluated from the devices B and C, the observation of DI transients from those devices with gas-exposed TMOs indicate the contacts are nearly Ohmic. On the other hand, absence of DI transients and the large deviation between measured and theoretical *J–V* curve indicate the contacts formed by TMOs with no gas exposure and NPB (device A) are significantly injection limited. The contact transition from non-Ohmic to nearly Ohmic further verifies the air/oxygen exposure is essential for reducing the energy barrier at TMO/NPB interface.

Energy barrier reduction at the TMO/NPB interface after air/oxygen exposure is solely originated from the gas sensing properties of TMOs. As mentioned above, exposing the oxides to oxidizing gases will result in an increase of their work functions. The mechanism of work function enhancement in our case can be understood as follows. Under an oxygen deficient environment, i.e. low oxygen partial pressure (pO_2), TMOs undergo reduction by losing oxygen, which creates an oxygen vacancy and generates electrons contributing to *n*-type conductivity. This situation is similar to the case of doping donor atoms into an intrinsic inorganic semiconductor, which will shift the Fermi level of semiconductor towards the conduction band. Under this circumstance, non-stoichiometric TMOs are produced. While at high pO_2, oxygen is incorporated at an oxygen vacancy and takes two electrons from the valence band of TMOs, leaving two holes to contribute to *p*-type conductivity. This will shift the Fermi level to the valence band [26,27]. As the work function equals to the difference between the vacuum level and Fermi level, the shift of Fermi level results in the variation of work function. In order to

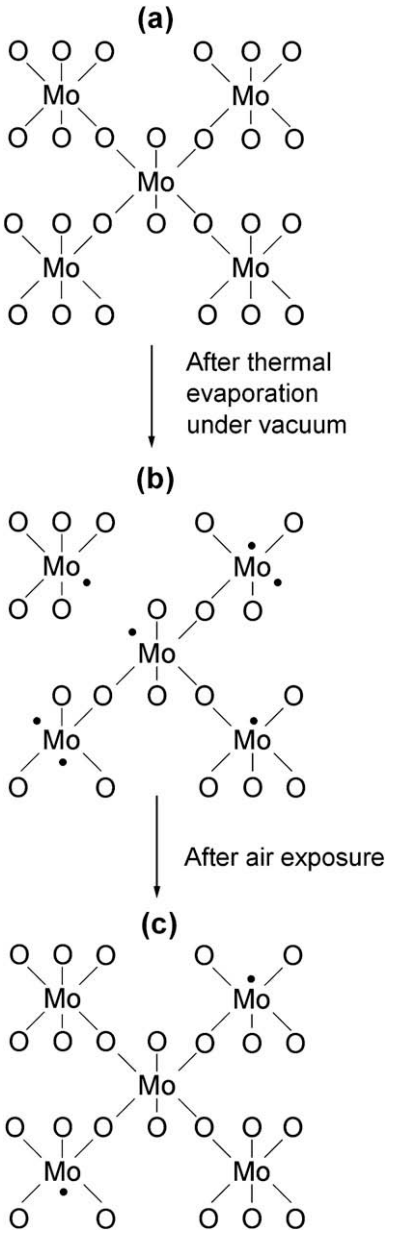

Fig. 5. Bond representation of (a) stoichiometric MoO_3 prior to evaporation; (b) thermally evaporated MoO_x film under vacuum; (c) MoO_x after exposing to air. The dots (●) denote the electrons left behind after the loss of O-atoms in the lattice.

verify if the air-exposed TMO film has different oxygen content to that without gas exposure, complementary X-ray photoemission spectroscopy (XPS) experiment was performed on MoO_x films. By monitoring the ratio of the peak areas of Mo 3d and O 1s, the values of x in the MoO_x films with and without air exposure were found to be 2.6 and 1.4 respectively, which suggests the oxygen content increases upon air exposure. The value of $x \sim 2.6$ from air-exposed MoO_x film is also consistent to the value from Kanno et. al. ($x \sim 2.7$) [19].

Fig. 5 shows a schematic diagram of the redox reactions of MoO_3 during our fabrication. In our case, the deposition of TMO film was carried out inside a vacuum evaporator, which provides an oxygen deficient environment. The outcome is the creation of oxygen vacancies inside the film, which shifts the Fermi level towards the conduction band and thus reduces the work function of the oxide as outlined above (Fig. 5b). However, upon air/oxygen exposure, oxygen will be incorporated back to the oxide films at the oxygen vacancies. For every oxygen vacancies, the process removes up to two electrons. The overall result is a net increase in the work function due to the lowering of the Fermi level of the oxide (Fig. 5c). As a result, the work function of oxide is enhanced, which reduces the energy barrier at TMO/NPB, and improves the HI efficiency.

In contrast to MoO_x and V_2O_x, WO_x behaves differently for the work function enhancement in this study. In this case, the *J–V* characteristics in Fig. 1 showed that only a small improvement can be found when WO_x is exposed to air. This is an indication that thermally evaporated WO_x film remains highly stoichiometric, with relatively few oxygen vacancies. According to the work of Molenda et al., a slightly non-stoichiometric species, $WO_{2.7}$, can only be created from WO_3 in ultra-high vacuum environment [28]. However, in our case, the film deposition was carried out under high vacuum ($\sim 10^{-6}$ Torr). So, it is unlikely that the non-stoichiometric oxide can be formed, and thus, the reduction of the oxide by oxygen does not occur. As a result, variation of the work function of WO_x cannot be observed and thus, the HI efficiency improvement cannot be found in WO_x. On the other hand, even in low vacuum environment, non-stoichiometric MoO_3 and V_2O_5 can be easily obtained [29], which are consistent to our observation as discussed above.

4. Conclusion

In conclusion, we demonstrate that exposing a TMO film to air can effectively reduce the energy barrier at TMO/NPB interface, and improve the HI efficiency. *J–V* and DI-SCLC techniques were used to cross-examine the injection behavior of the contacts. The origin of improvement is attributed to the oxidation of TMOs by oxygen upon air exposure. Finally, we emphasize that this improvement is not only valuable for enhancing the performance of organic optoelectronic devices, but also providing an insight for the fabrication of transition metal oxide films.

Acknowledgements

Support of this research by the Research Grant Council of Hong Kong and the Research Committee of Hong Kong Baptist University under Grant #HKBU211107E, #HKBU211209E and FRG/07-08/II-66 is gratefully acknowledged.

References

[1] Y. Shirota, H. Kageyama, Chem. Rev. 107 (2007) 953.
[2] S.C. Tse, K.K. Tsung, S.K. So, Appl. Phys. Lett. 90 (2007) 213502.
[3] S.A. VanSlyke, C.H. Chen, C.W. Tang, Appl. Phys. Lett. 69 (1996) 2160.
[4] H. Ishii, K. Sugiyama, E. Ito, K. Seki, Adv. Mater. 11 (1999) 605.
[5] A. Kahn, N. Koch, W. Gao, J. Polym. Sci. B: Polym. Phys. 41 (2003) 2529.
[6] S. Tokito, K. Noda, Y. Taga, J. Phys. D: Appl. Phys. 29 (1996) 2750.
[7] C.W. Chu, S.H. Li, C.W. Chen, V. Shrotriya, Y. Yang, Appl. Phys. Lett. 87 (2005) 193508.
[8] H. Kanno, R.J. Holmes, Y. Sun, S. Kena-Cohen, S.R. Forrest, Adv. Mater. 18 (2006) 339.
[9] T. Matsushima, Y. Kinoshita, H. Murata, Appl. Phys. Lett. 91 (2007) 253504.
[10] H. You, Y. Dai, Z. Zhang, D. Ma, J. Appl. Phys. 101 (2007) 026105.
[11] C. Adachi, K. Nagai, N. Tamoto, Appl. Phys. Lett. 66 (1995) 2679.
[12] S.C. Tse, S.W. Tsang, S.K. So, J. Appl. Phys. 100 (2006) 063708.
[13] C.H. Cheung, K.K. Tsung, K.C. Kwok, S.K. So, Appl. Phys. Lett. 93 (2008) 083307.
[14] P.S. Davids, I.H. Campbell, D.L. Smith, J. Appl. Phys. 82 (1997) 6319.
[15] C. Giebeler, H. Antoniadis, D.D.C. Bradley, Y. Shirota, Appl. Phys. Lett. 72 (1998) 2448.
[16] D. Poplavskyy, W. Su, F. So, J. Appl. Phys. 98 (2005) 014501.
[17] C.H. Cheung, K.C. Kwok, S.C. Tse, S.K. So, J. Appl. Phys. 103 (2008) 093705.
[18] S.K. So, W.K. Choi, C.H. Cheng, L.M. Leung, C.F. Kwong, Appl. Phys. A: Mater. Sci. Process. 68 (1999) 447.
[19] H. Kanno, N.C. Giebink, Y. Sun, S.R. Forrest, Appl. Phys. Lett. 89 (2006) 023503.
[20] P.N. Murgatroyd, J. Phys. D 3 (1970) 151.
[21] S.K. So, S.C. Tse, K.L. Tong, J. Disp. Tech. 3 (2007) 225.
[22] M. Abkowitz, J.S. Facci, J. Rehm, J. Appl. Phys. 83 (1998) 2670.
[23] J.L.G. Fierro, Metal Oxides: Chemistry and Applications, CRC Taylor and Francis, 2006 (Chapter 22).
[24] S.S. Sunu, E. Prabhu, V. Jayaraman, K.I. Gnanasekar, T.K. Seshagiri, T. Gnanasekaran, Sensor. Actuat. B 101 (2004) 161.
[25] M.A. Lampert, P. Mark, Current Injection in Solids, Academic, New York, 1970;
K.C. Kao, W. Hwang, Electrical Transport in Solids, Pergamon, Oxford, 1981.
[26] J.L.G. Fierro, Metal Oxides: Chemistry and Applications, CRC Taylor and Francis, 2006 (Chapter 3).
[27] P.A. Cox, Transition Metal Oxides: An Introduction to their Electronic Structure and Properties, Oxford Science Publications, 1992 (Chapter 1).
[28] J. Molenda, A. Kubik, Phys. Stat. Sol. (b) 191 (1995) 471.
[29] O.M. Hussain, K.S. Rao, Mater. Chem. Phys. 80 (2003) 638.

Organic Electronics 11 (2010) 95–99

Contents lists available at ScienceDirect

Organic Electronics

journal homepage: www.elsevier.com/locate/orgel

Full-swing organic inverters using a charged perfluorinated electret fabricated by means of mass-printing technologies

K. Reuter [a,*], H. Kempa [a], K.D. Deshmukh [b], H.E. Katz [b], A.C. Hübler [a]

[a] Institute for Print and Media Technology, Chemnitz University of Technology, Reichenhainer Straße 70, D-09126 Chemnitz, Germany
[b] Department of Materials Science and Engineering, Johns Hopkins University, 3400 North Charles Street, 103 Maryland Hall, Baltimore, MD 21218, USA

ARTICLE INFO

Article history:
Received 6 July 2009
Received in revised form 5 October 2009
Accepted 7 October 2009
Available online 13 October 2009

Keywords:
Flexible electronics
Organic field-effect transistors
Dielectrics
Electret

ABSTRACT

We report on the successful fabrication of full-swing charged organic inverter circuits by means of continuous mass-printing technologies. Using an electrostatic charged perfluorinated gate dielectric (Cytop™), we demonstrate depletion-mode and enhancement-mode transistors with the same organic semiconductor in top-gate device structure.

The threshold voltage of the printed p-type transistors can be shifted by injecting stable positive charges by means of a corona discharge or contact charging.

© 2009 Elsevier B.V. All rights reserved.

1. Introduction

The development of new cost-efficient applications like large area electronic circuits on flexible substrates requires solution-processing techniques. Several printing methods such as inkjet [1–3], screen printing [4] and pad printing [5] have been proposed. However, all of these techniques have limited throughput due to the slow process speed. In 2007, we demonstrated a fully integrated circuit completely manufactured by continuous mass-printing technologies [6]. The oscillator consisting of p-type enhancement-mode transistors only, was made by a single unipolar organic semiconductor (OSC), resulting in high circuit complexity and limited swing. While complementary circuits are desirable because of the high signal integrity and low power consumption, printable air-stable n-type semiconductors are rarely published yet [7,8].

One way to overcome these problems is the use of a so-called electret material as the dielectric in the organic field effect transistor (OFET). An electret is a type of dielectric that exhibits a quasi-permanent electric field due to dipolar polarization or trapped homopolar charge layers [9]. Corona charging, a common tool in xerographic printing processes, can be used to create electret properties in organic field-effect transistors and control their threshold voltage [10–12]. The high stability of the electret state, which is known to be higher than 10 years for some materials [13], makes electrostatic charging a promising technology for the realization of certain mass-printed circuits. Additionally, non-volatile transistor memories with long retention times could be realized. In this paper, we report on mass-printed full-swing inverter circuits based on positively charged top-gate-transistors with the perfluorinated material Cytop™ as the dielectric.

2. Experimental

For the preparation of the top-gate OFET's we used solution processable materials only, which allow the realization of mass-printed electronic devices.

The device architecture, the printable materials and the deposition method are summarized in Fig. 1. For material testing we prepared OFET's by a combination of gravure

* Corresponding author. Tel.: +49 037153135600; fax: +49 037153123619.
E-mail address: kay.reuter@mb.tu-chemnitz.de (K. Reuter).

1566-1199/$ - see front matter © 2009 Elsevier B.V. All rights reserved.
doi:10.1016/j.orgel.2009.10.004

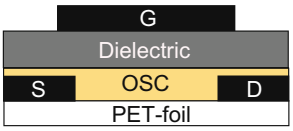

layer	material	deposition method
Gate	PEDOT:PSS	dispensed
Dielectric	Cytop	Spin On
OSC	TIPS-Pentacene	Spin On
S-D	PEDOT:PSS	gravure printing

Fig. 1. Device architecture, materials and method of application used for the charging tests.

printing, spin-coating and dispensing. As substrate we used a smooth commercially available (DuPont Tejin) polyester foil (PET) with a surface roughness of 8 nm.

Source–drain-electrodes are gravure-printed with an in-house reformulated water-based dispersion of poly (3,4-ethylenedioxythiophene) doped with poly (styrenesulfonate) (PEDOT:PSS), which is commercially available as Clevios P® from H.C Starck. The process speed was of the order of 1 m/s. The channel length was $L = 60$ μm and the channel width W was 30 mm. The layer thickness was measured to be 200 nm with a surface roughness $R_a = 20$ nm, determined using the profilometer Dektak 8 from Veeco. As active semiconductor (OSC) we used triisopropylsilyl (TIPS) pentacene, which was synthesized via standard methods published by the Anthony's group [14]. The OSC was spin-coated from a 0.5% toluene-solution with a spinning speed of 3000 rpm for 20 s and annealed for 5 min with a temperature of 120 °C. The resulting layer thickness was measured to be 80 nm. As organic dielectric we used the amorphous poly-perfluoro-alkenyl vinyl ether (Cytop CTL-809M, $\varepsilon_r = 2.1$), which is known for its excellent charge stability [15]. Cytop layers were prepared by spin-coating the 9% solution with a spinning speed of 1500 rpm for 20 s and a subsequent annealing step at 120 °C for 15 min. The thickness of the electret layer was measured to be 1.4 μm.

For electrostatic charging we tested the corona charging technique [16,17], as well as contact charging [18,19], to implant charges into the electret material.

Corona charging (wire-to-grid method) is done before dispensing the conductive gate on top of charged dielectric. Therefore we applied a corona voltage of +10 kV to a tungsten wire for a charging time of $t = 5$ min. The surface potential was controlled by the voltage of a metal grid, which is located above the test sample. After charging, the surface potential was measured with an electrostatic voltmeter (Trek model 368A). Due to the very low surface energy of the Cytop layer ($\sigma = 12$–14 mN/m), we used a mixture of a highly conductive PEDOT:PSS solution (Clevios FE) and the fluorinated surfactant DuPont Zonyl FSO for the gate electrode, which reduces the surface tension of the polymer solution and therefore improves the wetting properties on the insulating surface. The gate material was annealed for 5 min at 100 °C to remove the solvent. Contact charging was done by applying a high depletion voltage to the OFET for variable times, while the source and drain electrodes were grounded.

Fully mass-printed OFET's were realized by a combination of gravure printing and flexography in the same layer configuration under the same drying conditions as the spin-coated ones. Source–drain structures were gravure-printed on a flexible PET foil as described above. The OSC, organic dielectric and the gate electrode were applied by flexo-printing with a fixed process speed of 0.1 m/s. As printing form we used an anilox roll with a cell volume 24.9 ml. Optimized transistor performance was achieved by printing TIPS-pentacene from a 1% tetralin solution. To achieve insulating dielectric layers, we flexo-printed the 9% Cytop solution three times over the desired regions. The resulting layer thickness was measured to be 1.9 μm. For the gate layer we again used an in-house reformulated PEDOT:PSS solution mixed with the surfactant Zonyl FSO (0.5 mass %).

All devices were electrically characterized by sweeping the gate voltage V_{GS} from +60 to −60 V with a constant source–drain-voltage of $V_{SD} = -10$ V under ambient conditions. The threshold voltage is defined as the gate voltage at which the square root of the source–drain current begins to increase substantially and was extracted as the x-intercept of the transfer curve ($I_{DS}^{0.5}$ vs. V_G). The mobility was determined by a standard procedure from the slope of the transfer curve [20].

3. Results and discussion

Fig. 2 shows the transfer curves of corona charged top-gate OFET's with different surface potentials. We applied a positive corona voltage (V_C) of +10 kV to the tungsten wire, while the surface potential was controlled by the voltage of a metallic grid (V_{Grid}), which is located above the sample. Consequently, the free gate electrode side of the dielectric is charged positively. The charge density Uncharged transistors show typical p-type accumulation behaviour with a threshold voltage of $V_{th} = -5$ V. Under zero gate-voltage condition no charge accumulation can

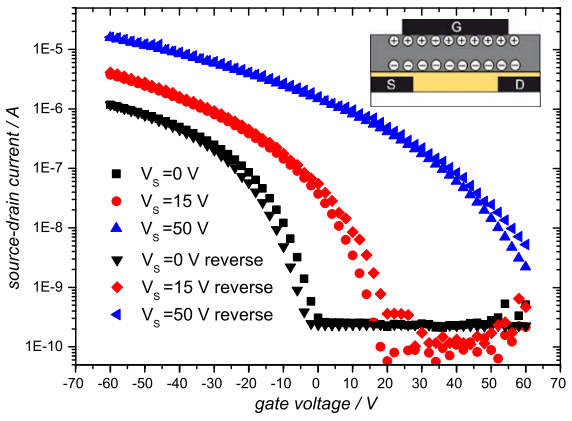

Fig. 2. Semilogarithmic I_{DS}–V_G curves of corona charged OFET's with different surface potentials measured at $V_{DS} = -10$ V. The inset shows the proposed mechanism of the threshold voltage shift. The transistors were prepared by spin-coating as shown in Fig. 1. W/L-ratio is 500 and the capacitance was measured to be 2 nF/cm^2.

be observed. With increasing surface potential V_S of the charged dielectric, the threshold voltage shifts towards higher positive gate voltages. Charged transistors show depletion mode characteristic with threshold voltages of V_{th} = +7 V (V_C = +10 kV, V_{Grid} = +20 V, V_S = +15 V) and of V_{th} = +37 V (V_C = +10 kV, V_{Grid} = +60 V, V_S = +50 V), respectively. The hysteresis observed in the transfer characteristic was <1 V. The mobility changes insignificantly from $1.3 * 10^{-2}$ cm^2/V s (uncharged sample) to $1.1 * 10^{-2}$ cm^2/V s (sample charged to V_S = 50 V). The charge density stored in the dielectric can be estimated to be $1.4 * 10^{-8}$ C/cm^2 for a surface potential of V_S = 15 V and $4.8 * 10^{-8}$ C/cm^2 for V_S = 50 V.

The gate leakage current did not exceed 10 nA for the uncharged as well as the charged transistors. The shift of the threshold voltage can be attributed to the presence of stored charge carriers in the dielectric. The result is an electrostatic induction effect at the interface of the dielectric and the semiconductor, increasing the number of hole carriers in the channel. Consequently the transistors reach on-state under zero gate-voltage condition.

Huang et al. reported positive threshold voltage shifts in bottom-gate devices with nonpolar dielectrics (SiO_2 and glass resin) by means of negative corona charging [10,11]. Scharnberg et al. [21] reported negative threshold voltage shifts for negative corona charging of the encapsulation layer (Teflon AF) in bottom-gate transistors. The mechanism behind the threshold voltage shift is explained by the electrostatic attraction or repellency of charge carriers on the semiconductor–dielectric interface caused by homopolar corona charges in the electret layer.

We observe positive threshold voltage shifts for positive corona charging in the top-gate architecture, indicating that in our case, the accumulation of majority charge carriers in the transistor channel cannot be explained by homopolar space charges residing completely in the dielectric. The result is consistent with previous observations, that positive threshold voltage shifts can be observed for negative corona charging of semiconductor side of the dielectric in bottom-gate architecture [10,11]. Consequently we can exclude, that the mechanism behind the threshold voltage shift is caused by a change of the surface chemistry at the semiconductor–dielectric interface.

However, we conclude that the corona discharge injects static charges somewhere between (or at) the surface of the dielectric and the dielectric–semiconductor interface. The charge may be in form of homopolar space charges that fill traps directly in the semiconductor, or oriented dipoles that have negative ends pointed toward the semiconductor, also causing the prefilling of traps in the semiconductor, and hence a threshold voltage shift in the transistor.

Due to the high complexity of corona discharges, we tested contact charging as another possibility to influence the threshold voltage of OFET's, which was first reported by Katz et al. [22]. Similar results, but with much smaller programming times, were reported by Baeg et al. [23,24]. By applying a high depletion voltage charge can be transferred from the gate electrode and/or the semiconductor to the electrets and stored at sites inside the dielectric.

In Fig. 3a the transfer curve of a transistor before and after applying a depletion voltage of V_{Write} = +200 V for t = 1 s is shown. The threshold voltage changes significantly from V_{th} = −2 V (pristine) to V_{th} = +40 V. Applying high accumulation voltages of V_{Write} = −200 V for up to 10 s results in threshold voltage shifts of <5 V towards lower positive gate voltages.

This applies for pristine as well as charged transistors.

The excellent charge stability is proved by repeated measurement of the transistor. After 1 month the threshold voltage reduces only by 5 V. Fig. 3b shows that the amount of transferred charge, and hence the threshold voltage shift, strongly depends on the applied electric field ($E = V_{Write}/d$) as well as on the writing time. By increasing the electric field, the necessary writing time to create a sufficient threshold voltage shift of about 10 V (transition from accumulation-mode to depletion mode) can be reduced to t = 10 ms, which makes this technology attractive for a possible roll-to-roll process. However, it is not clear

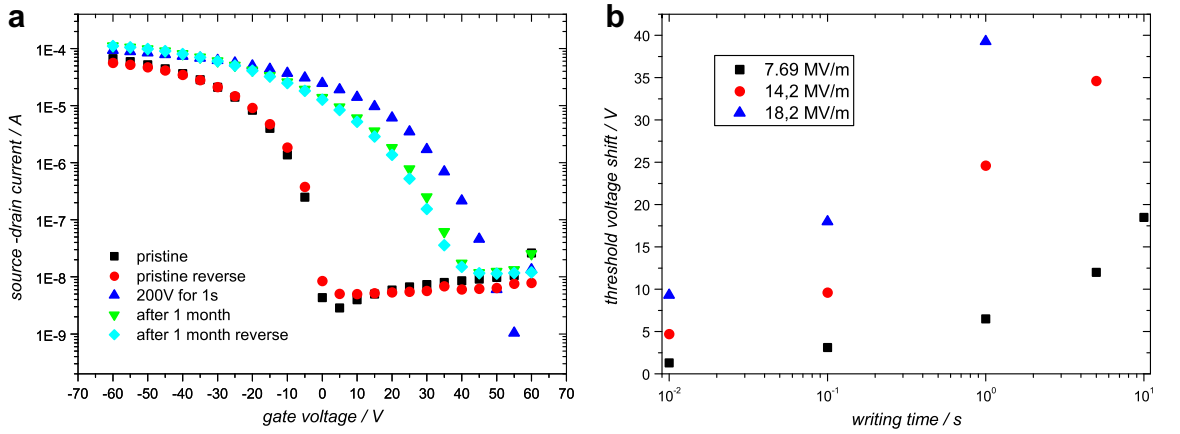

Fig. 3. (a) Semilogarithmic I_{DS}–V_G curve of a transistor before (pristine) and after contact charging with a writing voltage of V_w = 200 V for 1 s measured at V_{DS} = −10 V and (b) shows the threshold voltage shift of the contact charged OFET's depending on the applied electric field. The transistors were prepared by spin-coating as shown in Fig. 1.

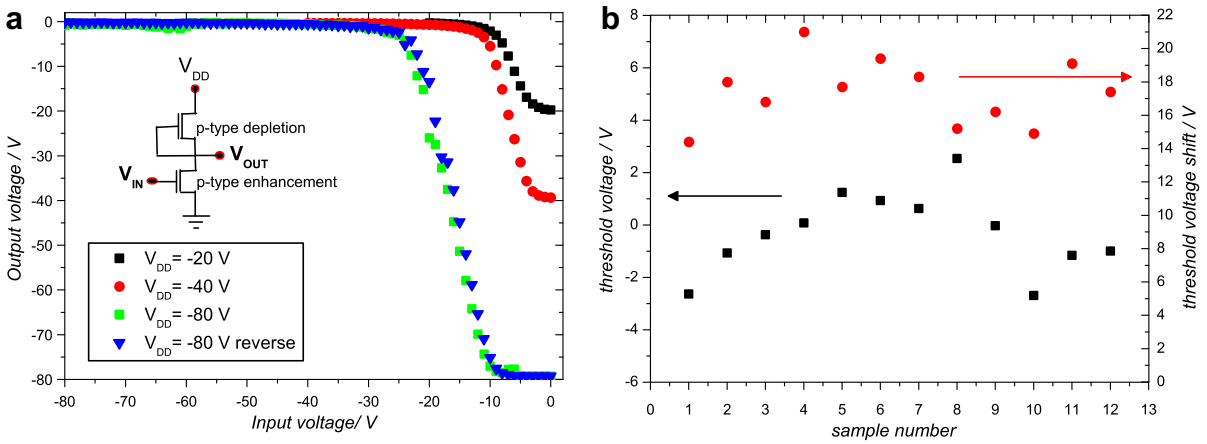

Fig. 4. (a) Static voltage transfer characteristic of a printed inverter device measured for supply voltages V_{DD} of −20 V, −40 V and −80 V. The inset shows the circuit diagram of the inverter comprising of a p-type depletion-mode load and a p-type enhancement drive transistor. (b) Statistical data of the printed transistors with the distribution of the threshold voltage (black squares) and their corresponding threshold voltage shifts (red dots) for a depletion voltage of 200 V for 1 s. (For interpretation of the references to colour in this figure legend, the reader is referred to the web version of this article.)

whether the threshold voltage shift is caused by the injection of electrons from the semiconductor into the dielectric or due to charge transfer from the gate electrode to the dielectric.

Additionally, we demonstrate fully mass-printed organic inverters based on a contact charged Cytop layers. The printed transistors exhibit good electrical performance with a saturated mobility of $1–3 * 10^{-2}$ cm^2/V s, a threshold voltage between −3 and 2 V and On/Off-ratios of about 10^3. The capacitance was measured to be 2 nF/cm^2. Consequently, we built up inverters, which consists of a p-type accumulation-mode drive and a p-type depletion-mode load transistor (see inset Fig. 4a), each with the same geometrical dimensions (W/L-ratio = 500). The uncharged printed transistors were brought from accumulation-mode to depletion mode by applying a writing voltage of V_{Write} = +200 V for t = 1 s. The threshold voltage uniformity of the printed transistors, as well as their threshold voltage shift is illustrated in Fig. 4b. We observed threshold voltage shifts of 17.4 V with a standard deviation of 1.9 V for the tested transistors. The smaller threshold voltage shift in comparison to the spin-coated samples (Fig. 3b), can be explained by the higher dielectric layer thickness, resulting in a lower writing field for the same applied voltage.

The static voltage characteristic of a unipolar inverter device is shown in Fig. 4a. For negative values of drive voltages (V_{DD}) and input voltages (V_{IN}) the inverter works in the third quadrant of the output voltage (V_{OUT}) vs. (V_{IN}) plot. Our devices show nearly full-swing characteristic with a small hysteresis, similar to complementary inverters reported recently [25,26]. The voltage gain, which was measured to be 3.6 (V_{DD} = −20 V), 5.7 (V_{DD} = −40 V) and 7.2 (V_{DD} = −80 V), is comparable to results obtained in [10].

The gain can be increased by adapting the transistor dimensions [27], while using a symmetrical distribution of the threshold voltage (e.g. V_{th} = −5 V for the drive and V_{th} = +5 V for the load transistor). This can be done for instance by increasing the channel width of the drive transistor with respect to the load transistor. So the output current under zero gate-voltage condition of the load transistor can be tuned, to match the output characteristic of the drive transistor.

4. Conclusions

We successfully demonstrated fully mass-printed unipolar logic gates with improved device performance by using the electret Cytop as the gate dielectric for the OFET's. The threshold voltage of transistors can be shifted with the injection of electric charges into the dielectric by means of corona charging or contact charging. The injected charges exhibit excellent stability in comparison with other competing materials [21]. Full-swing inverters can be realized without using complementary semiconductors [8,25] or the use of competing technologies to influence the threshold voltage of the transistors [28–30]. In particular, the ability to charge the printed transistors within a few milliseconds makes this technology attractive for roll-to-roll processes, an application which is under investigation.

Acknowledgements

We thank J.E. West for helpful discussions and M. Stanel, G. Schmidt, K. Weigelt, M. Hambsch, S. Voigt, N. Wetzold, B. Meier for technical support. We thank the German Research Foundation (DFG), the NSF (ECS-0601356) and DOE (DE-FG02-07ER46465) for funding.

References

[1] K.E. Paul, W.S. Wong, S.E. Ready, R.A. Street, Appl. Phys. Lett. 83 (2003) 2070.
[2] Y. Noh, X. Cheng, H. Sirringhaus, J.I. Sohn, M.E. Welland, D.J. Kang, Appl. Phys. Lett. 91 (2007) 043109.
[3] C.W. Sele, T. Werne, R.H. Friend, H. Sirringhaus, Adv. Mater. 17 (2005) 8.
[4] J.A. Rogers, Z. Bao, V.R. Raju, Appl. Phys. Lett. 72 (1998) 2716.

[5] A. Knobloch, A. Manuelli, A. Bernds, W. Clemens, J. Appl. Phys. 96 (2004) 4.
[6] A.C. Huebler, F. Doetz, H. Kempa, H.E. Katz, M. Bartzsch, N. Brandt, I. Hennig, U. Fuegmann, S. Vaidyanathan, J. Granstrom, S. Lui, A. Sydorenko, T. Zillger, G. Schmidt, K. Preissler, E. Reichmanis, P. Eckerle, F. Richter, T. Fischer, U. Hahn, Org. Electr. 8 (2007) 480.
[7] B.K. Crone, A. Dodabalapur, R. Sarpeshkar, R.W. Filas, Y.Y. Lin, Z. Bao, J.H. O'Neill, W. Li, H.E. Katz, J. Appl. Phys. 89 (2001) 9.
[8] H. Yan, Z. Chen, Y. Zheng, C. Newman, J.R. Quinn, F. Dötz, M. Kastler, A. Facchetti, Nature (2009) 07727.
[9] G.M. Sessler, Electrets, third ed., vol. 1, Laplacian Press, Morgan Hill, California, 1998.
[10] C. Huang, J.E. West, H.E. Katz, Adv. Funct. Mater. 17 (2007) 142–153.
[11] C. Huang, H.E. Katz, J. Appl. Phys. 100 (2006) 114512.
[12] R. Swödiauer, G.S. Neugeschwandtner, S. Bauer-Gogonea, S. Bauer, Appl. Phys. Lett. 75 (1999) 3998.
[13] Z. Xia, R. Gerhard-Multhaupt, W. Künstler, A. Wedel, R. Danz, J. Phys. D: Appl. Phys. 32 (1999) L83–L85.
[14] J.E. Anthony, J.S. Brooks, D.L. Eaton, S.R. Parkin, J. Am. Chem. Soc. 123 (2001) 9482–9483.
[15] Y. Sakane, Y. Suzuki, N. Kasagi, in: Proc. IEEE, ISE.13 Conf., Tokyo, 2008, p. 13.
[16] J. Chang, P. Lawless, T. Yamamoto, IEEE Trans. Plasma Sci. 19 (1991) 6.
[17] J.A. Giacometti, O.N. Oliveira, IEEE Trans. Electr. Insul. 27 (1992) 5.
[18] J. Lowell, A.C. Rose-Innes, Adv. Phys. 29 (1980) 947–1023.
[19] A.R. Akande, J. Lowell, J. Phys. D: Appl. Phys. 20 (1987) 565–578.
[20] A.R. Brown, C.P. Jarret, D.M. Leeuw, M. Matters, Syn. Met. 88 (1997) 37–55.
[21] M. Scharnberg, V. Zaporojtchenko, R. Adelung, F. Faupel, C. Pannemann, T. Diekmann, U. Hilleringmann, Appl. Phys. Lett. 90 (2007) 013501.
[22] H.E. Katz, X.M. Hong, A. Dodabalapur, R. Sarpeshkar, J. Appl. Phys. 91 (2002) 3.
[23] K. Baeg, Y. Noh, J. Ghim, S. Kang, H. Lee, D. Kim, Adv. Mater. 18 (2006) 3179–3183.
[24] K. Baeg, Y. Noh, J. Ghim, B. Lim, D. Kim, Adv. Funct. Mater. 18 (2008) 1–8.
[25] M.P. Walser, W.L. Kalb, T. Mathis, T.J. Brenner, B. Batlogg, Appl. Phys. Lett. 94 (2009) 053303.
[26] M.S. Oh, W. Choi, K. Lee, D.K. Hwang, S. Im, Appl. Phys. Lett. 93 (2008) 033510.
[27] H. Klauk, D.J. Gundlach, T.N. Jackson, IEEE Electr. Dev. Lett. 20 (1999) 289.
[28] N. Benson, M. Schidleja, C. Melzer, R. Schmechel, H. von Seggern, Appl. Phys. Lett. 89 (2006) 182105.
[29] K. Hizu, T. Sekitani, T. Someyaa, J. Otsuki, Appl. Phys. Lett. 90 (2007) 093504.
[30] A. Wang, I. Kymissis, V. Bulović, A.I. Akinwande, Appl. Phys. Lett. 89 (2006) 112109.

Organic Electronics 11 (2010) 100–108

Contents lists available at ScienceDirect

Organic Electronics

journal homepage: www.elsevier.com/locate/orgel

Growth of pentacene thin films by in-line organic vapor phase deposition

Cedric Rolin *, Karolien Vasseur, Jan Genoe, Paul Heremans

IMEC, Polymer and Molecular Electronics, Kapeldreef 75, 3001 Leuven, Belgium

ARTICLE INFO

Article history:
Received 6 July 2009
Received in revised form 28 September 2009
Accepted 7 October 2009
Available online 13 October 2009

Keywords:
OVPD
Pentacene
Thin film transistor
Roll-to-roll
Sheet-to-sheet
In-line
Reel-to-reel

ABSTRACT

We present the extension of the organic vapor phase deposition technique to an in-line geometry, in which the sample travels underneath an elongated showerhead that sprays molecules transported by a stream of carrier gas. Highly uniform pentacene films are grown at web speeds of up to 2.1 m/min, equivalent to an average deposition rate of 105 Å/s in a static system. With transistor mobilities of up to 1.5 cm^2/V s, these pentacene films are of high electrical quality. Importantly, this quality is conserved up to the highest deposition speeds. We discuss the relationships between in-line deposition rate, morphology and crystallinity of the deposited pentacene films and their electrical characteristics.

© 2009 Elsevier B.V. All rights reserved.

1. Introduction

In the recent years, circuits based on organic field effect transistors (OFETs) have been investigated for potential applications such as back panels for flexible displays and transponder circuits for RFID tags. Two approaches have been explored for the processing of organic circuits at the lab-scale: (i) the first one, stimulated by the printing industry, based on printing technologies to apply and pattern films from soluble materials. (ii) the second one, inspired by the microelectronic industry, makes use of photolithography to pattern thin films often deposited by vacuum thermal evaporation (VTE). The former approach has the potential advantage of low-cost high-throughput production [1,2], while the latter approach has delivered the best performing organic circuits so far [3,4]. A future industrial scale roll-to-roll or sheet-to-sheet production of organic circuits would have to combine the advantages of both approaches: it should associate cost-effective processing steps to a sufficient performance of the final organic circuits.

The deposition of the organic semiconductor is a critical step in the fabrication sequence. The selected technique should deposit thin films at a high speed over large substrates with a well-controlled morphology, high uniformity and good reproducibility of the electrical characteristics. Due to its good electrical performance, pentacene is the small organic molecule that has attracted most of the attention. It is generally processed at the lab-scale by VTE. The maximum deposition rate that VTE can reach is set by the poor heat conductivity of the organic powder and is limited around ~2 Å/s. Above that value, the evaporated molecular flux fluctuates too much to guarantee reproducibility [5]. Such a deposition rate remains far away from the high speed constraint set by, for example, roll-to-roll processing, since the growth of a functional 30 nm thick pentacene film over a substrate of a limited area takes at least 150 s. In addition, using flash evaporation, Gundlach et al. demonstrated that pentacene thin film electrical characteristics greatly suffer from growth at too high rates [6]. This apparently sets a hard limit on

* Corresponding author. Tel.: +32 16 28 81 42; fax: +32 16 28 15 01.
E-mail address: cedric.rolin@imec.be (C. Rolin).

1566-1199/$ - see front matter © 2009 Elsevier B.V. All rights reserved.
doi:10.1016/j.orgel.2009.10.005

the maximum deposition rate at which pentacene can be processed at the industrial scale.

An alternative to VTE for the growth of pentacene thin films is organic vapor phase deposition (OVPD) [7,8]. In OVPD, the source material is sublimed into a stream of hot carrier gas. The molecules undergo a convective transport through a hot-wall chamber to a cooled substrate on which they condense to form a film. OVPD has already been shown for the deposition of high quality pentacene thin films with rates of up to 10 Å/s [9,10]. This technique proves to be quite flexible in terms of tool design. The first instruments, inspired from purification systems, were based on a single differentially heated quartz glass tube containing both the source cell and the substrate [7]. Later on, OVPD instruments inspired from Chemical Vapor Deposition techniques were designed, where the evaporation and condensation steps are physically separated and the spreading of the process gas over the substrate is finely controlled by means of a showerhead [11]. As a result, OVPD presents a number of industrially important advantages [5,12]: (i) high material utilization efficiency and thickness uniformity; (ii) low vacuum operation; (iii) high deposition rates; (iv) fewer particles due to hot-wall chamber and gas flush; (v) flexibility in the design of the tool.

In this work, we demonstrate high performance pentacene thin films grown at unprecedented high speeds using a roll-to-roll compatible in-line OVPD tool. The relation between growth parameters, deposition speed and OFET mobility is discussed.

2. Experimental

2.1. In-line OVPD instrument

The in-line OVPD system used in this work was built in house and is schematically depicted in Fig. 1. The top part of the furnace encloses two gas lines: the source line and the dilution line. The amount of nitrogen carrier gas injected in each line is controlled by means of mass flow controllers. The source line comprises a source cell loaded with the organic powder. The bottom of the furnace envelops the deposition chamber. Injection of the process gas from the gas lines into the chamber is performed by an elongated showerhead whose appropriate design ensures a uniform distribution of the gas onto the susceptor passing several centimeters underneath. The susceptor consist of a trolley that is moving at a controlled speed along rails in a direction perpendicular to the long edge of the showerhead. Its temperature is controlled by means of a water chiller. The trolley top surface dimensions allow for the mounting of 4″ diameter substrates. This mobile trolley simulates well an infinitely-long continuously moving substrate, even though its finite size gives rise to edge effects that are absent in a roll-to-roll process. Finally, the deposition chamber is equipped on one side with a loadlock, allowing for fast loading and unloading of samples, and on the other side with a blind flange that would easily accommodate a second processing chamber.

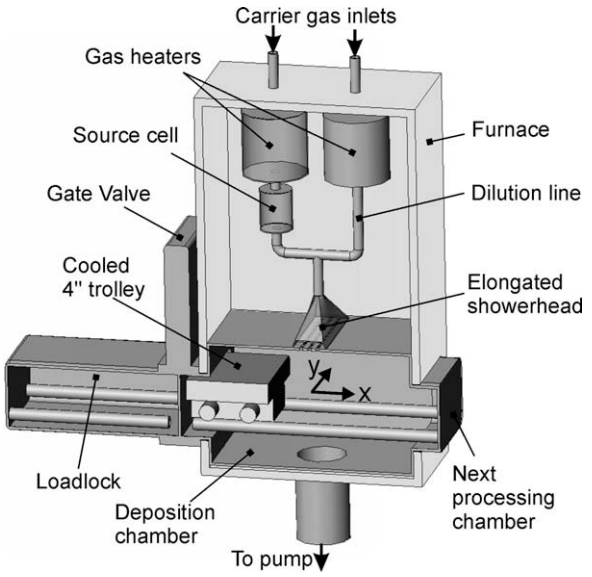

Fig. 1. Schematics of the OVPD tool used in this work. The *x* and *y* axis show the convention used in this work.

2.2. Pentacene deposition parameters

Pentacene is purchased from Aldrich and used as received without further purification. Approximately 500 mg of material powder is loaded into the source cell. For pentacene deposition, the furnace temperature is set between 260 and 320 °C and the carrier gas flow through the source cell is varied between 10 and 200 sccm. Using the dilution line, the total carrier gas flow injected in the chamber through the showerhead is set between 150 and 5000 sccm. The chamber pressure is regulated between 0.1 and 10 mbar independently of the total carrier gas flow by means of a flow control valve. The trolley is kept at a temperature between 50 and 80 °C. In order to meet the constraints of roll-to-roll processing, the trolley velocity is kept constant (between 0.1 and 10 mm/s) during a run and the travel distance is set to the maximum allowed by the dimensions of the chamber. Depending on the deposition speed, several passes under the showerhead can be needed to achieve the desired film thickness.

2.3. Thin film characterization

The film thickness is systematically measured post-growth using ellipsometry (SOPRA GES5). The morphology of the organic polycrystalline film is characterized by atomic force microscopy (AFM) operated in tapping mode (Agilent 5100). Finally, film crystallinity is characterized by XRD (PANalytical X'Pert Pro Materials Research Diffractometer).

The electrical characterization of the pentacene thin films is carried out through the fabrication of top contact OFETs. Fig. 2 shows schematically the structure of these devices. A highly doped n++ silicon wafer is used as gate. A 145-nm thick thermal SiO_2 layer serves as gate dielectric. Prior to pentacene deposition, the wafer is successively

rinsed in deionized water, acetone and isopropanol. It is further cleaned by a 2-min exposure to a 100-W O_2 plasma. Next, the clean gate dielectric is treated with a 10-nm thick poly-(α-methyl-styrene) (PαMS) film which is spin-coated at 4000 rpm for 30 s from a 0.1% solution in toluene, and let dried at 120 °C for 2 min. Then a 30-nm thick pentacene film is grown by in-line OVPD. Finally, gold source and drain contacts are deposited by evaporation through a shadow mask, delivering top contact OFETs with a channel width of 2000 μm and a channel length varying between 50 and 200 μm. Between pentacene deposition and device characterization, samples were often exposed to ambient for up to 12 h without noticeable damage.

These devices are characterized in a nitrogen atmosphere. The OFET transfer curves were typically measured in saturation mode, by sweeping back and forth the gate voltage between −20 and +5 V, while keeping a permanent voltage of −20 V between the source and drain electrodes. Thin film mobilities are extracted from these measurements as described in Ref. [13], using relative dielectric constant values of 3.9 for SiO_2 and 2.2 for PαMS.

3. Modeling of the growth

In in-line OVPD, the process gas injected by the elongated showerhead into the chamber undergoes a rapid relaxation, leading to a broadening of the flow of convectively transported organic species. As a consequence, the organic flux condensing on the substrate is a function of the position x relative to the showerhead long axis. By extension, we define the deposition rate profile $r(x)$ of an in-line instrument as the deposition rate experienced by a point on the susceptor as a function of its position x. Fig. 3 shows a profile $r(x)$ typically observed in our instrument. During a deposition run, a sample lying on the trolley sweeps the deposition rate profile, experiencing a varying deposition rate.

3.1. In-line deposition rate

In an in-line process, the average deposition rate r_{avg} can be evaluated by integrating the deposition rate profile $r(x)$:

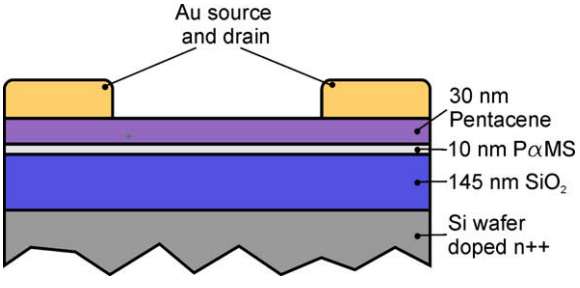

Fig. 2. Schematics of the top contact OFET devices fabricated for electrical characterization of pentacene thin film.

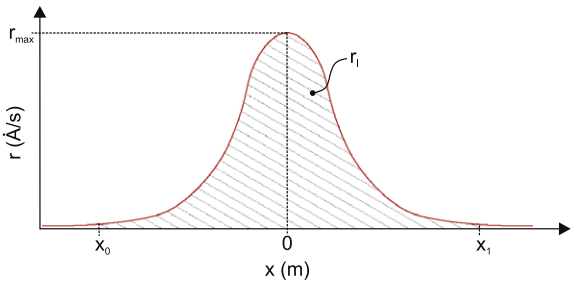

Fig. 3. Schematics of a deposition rate profile $r(x)$ typically observed in our in-line OVPD instrument. The central long axis of the showerhead is located in position $x = 0$, where the deposition rate is maximum (r_{max}). The area below the curve $r(x)$ and in this space interval defines the in-line deposition rate r_l.

$$r_{avg} = \frac{1}{x_1 - x_0} \int_{x_0}^{x_1} r(x)dx, \tag{1}$$

where x_0 and x_1 are, respectively, the starting point and the end point of the movement described by a considered substrate point under the showerhead. A practical way to evaluate r_{avg}, is to divide the final sample thickness d by its exposure time $t_1 - t_0$ to the incident organic flux, where t_0 is the starting time and t_1 the final time. Since the trolley is moving at a constant velocity v_t, there is a direct relationship between travel length and time. r_{avg} can be written:

$$r_{avg} = \frac{d}{t_1 - t_0} = \frac{d \cdot v_t}{x_1 - x_0}. \tag{2}$$

However, if the travel length $x_1 - x_0$ is longer than the width of the profile $r(x)$, the considered point is not permanently exposed to the incident flux. This leads to an underevaluation of r_{avg}. A correct evaluation requires the knowledge of $r(x)$ which depends on the system architecture and on processing parameters. A better parameter is the in-line deposition rate r_l defined by combining Eqs. (1) and (2):

$$r_l = \int_{x_0}^{x_1} r(x)dx = d \cdot v_t. \tag{3}$$

Indeed d and v_t are two easily accessible parameters, which renders r_l easily accessible for the experimentalist and comparable from system to system. As illustrated in Fig. 3, r_l also corresponds to the area under the deposition rate profile $r(x)$. A convenient unit for r_l is $\mu m^2/s$.

Industrially, the roll-to-roll processing speed is often expressed in terms of web speed (in m/min). This is the foil velocity needed to get a full functional coating. The roll-to-roll deposition of a 30-nm pentacene film at a web speed of 1 m/min requires a deposition rate $r_l = 500\ \mu m^2/s$.

However, as the community is using Å/s in order to qualify the deposition speed of a system, it is convenient to express r_l in this unit in order to convey a feeling for the growth speed. In the definition of r_{avg} in Eq. (2), $t_1 - t_0$, the time during which the sample is effectively exposed to the incident flux, is not an easily accessible parameter. However, another way to look at the problem is to simply take the time spent by the sample under the showerhead. This time is equal to the sample length l di-

vided by the trolley velocity. An average deposition rate in Å/s can then be expressed as:

$$r_{avg} \cong \frac{d \cdot v_t}{l}. \quad (4)$$

Calculated in this way, the deposition rate is inversely proportional to the substrate length. It is therefore important to specify the length on which this value is calculated. Since our trolley handles 4″ substrates, it is decided to use a l of 100 mm. This delivers a deposition rate comparable to the deposition rate reached in 4″ lab-scale VTE systems.

3.2. Finite element analysis of the deposition rate profile

The shape of the deposition rate profile is an important deposition characteristic that is unfortunately not easily accessible. A way to grasp it is a finite element analysis of the process gas flow within the chamber. Since the molecular mean free path remains small in comparison to the deposition chamber dimensions, the fluid behavior within this chamber can be accurately described using continuum models. The thermal nitrogen flow and the convective and diffusive transport of diluted organic species are solved on a geometry close to the actual in-line OVPD tool using a commercially available software.

The bulk properties and boundary conditions used to solve the nitrogen flow are similar to experimental operation conditions. The bulk properties and boundary conditions of the convective and diffusive transport model are the following: the diffusion coefficient of pentacene in nitrogen is calculated to be approximately 5e−3 m^2/s [14]; complete condensation is simulated by setting a concentration of 0 mol/m^3 as boundary condition on the susceptor surface; the flux of organic molecules at the inlet of the system is evaluated to be about 1e−4 mol/s at 300 °C [15]. In order to fit the experimental data, the numerically calculated deposition rate profile is multiplied by a single fitting parameter that covers the effects of out-of-equilibrium evaporation and non-complete condensation.

4. Results and discussion

4.1. Deposition rate profile and thickness uniformity

A way to measure the deposition rate profile of the in-line system is to grow a pentacene film over an immobile 4″ wafer lying right under the showerhead. The thickness is mapped by ellipsometry along a line crossing the center of the wafer along the x direction. The circles in Fig. 4 represent the deposition rate profile as measured on a film deposited in static conditions using typical growth parameters. Note that on the edges of the measured profile, the deposition rate profile has still a significant value. The reason for that is that for our system geometry and for the used parameters, the deposition rate profile is wider than the trolley length. Therefore, the static experiment can only capture the central part of the $r(x)$ peak represented in Fig. 3.

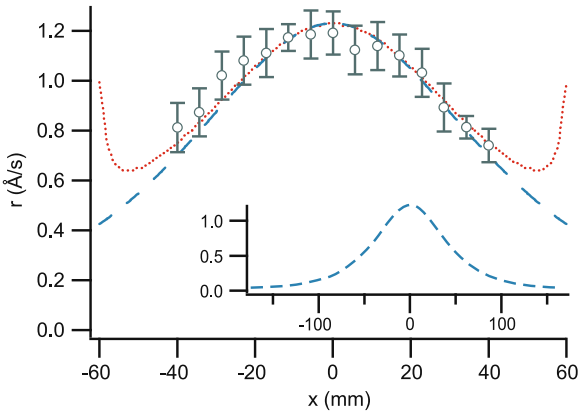

Fig. 4. Deposition rate profiles $r(x)$. Circles: as measured by ellipsometry along the central line of a typical pentacene film grown on an immobile 4″ wafer. Lines: numerically calculated profiles in conditions equivalent to the experimental ones. Dotted line: short susceptor geometry close to the trolley geometry. Dashed line: susceptor as long as the chamber dimensions. The inset shows the full width of the simulated profile on a long susceptor. Following Eq. (3), integration of this profile delivers a $r_l = 12.9\ \mu m^2/s$.

Fig. 4 also shows two deposition rate profiles obtained by numerical simulation and fitted to the experimental data. They were obtained by simulating the process gas flow around a "short" susceptor, similar to the real trolley, and around a "long" susceptor, as long as the chamber length. The strong increase in deposition rate on the edges of the short susceptor originates from the finite length of the susceptor: the thinning of the carrier gas boundary layer on the edges leads to an enhanced deposition. In the case of the long susceptor, the edge effects disappear and the deposition rate profile appears in its full extent. The in-line deposition rate r_l corresponding to this profile can be calculated from Eq. (3) by profile integration. Choosing experimental values as travel boundaries x_0 and x_1, we extract a $r_l = 12.9\ \mu m^2/s$.

Using the growth parameters of Fig. 4, we deposit pentacene on a susceptor travelling at constant speed underneath the showerhead. Fig. 5 shows a mapping of the thickness of a pentacene film grown in these conditions over a 4″ wafer. The standard deviation of the thickness over the whole wafer surface is low: 1.1%. The showerhead long axis is parallel to the vertical y direction of the image. Uniformity along this direction is optimized by carefully engineering the design of the showerhead. The smooth movement of the trolley ensures the uniformity along the horizontal x direction. However, in Fig. 5, the thickness on the left and right sides appears to be higher than in the center. This is a consequence of the edge effects revealed by the simulation on short susceptor in Fig. 4. In a roll-to-roll system with an infinite substrate, the uniformity along the horizontal direction should further improve. Following Eq. (3), the in-line deposition rate of the layer represented in Fig. 5 is calculated by multiplying the final thickness with the trolley velocity. A value of 13.2 $\mu m^2/s$ is extracted at the center of the wafer, which is close to the 12.9 $\mu m^2/s$ predicted by the long profile integration.

4.2. Growth speed optimization

A systematic study of the influence of in-line OVPD pentacene growth parameters on in-line deposition rate r_l has been carried out, the output of which is shown in Fig. 6. In OVPD, the organic flux condensing on the substrate is determined by the succession of evaporation and transport phenomena taking place within the system [15]. An analytical model of the evaporation exists [16] that can successfully explain the behavior of r_l as a function of the source flow n_s and the furnace temperature T_{fur} visible in Fig. 6a. This model also predicts that r_l drops with an increase in source cell pressure. Regarding the transport of organic species within the OVPD chamber, it can be shown by numerical simulation that conditions that favor an increase in carrier gas velocity also enhance convective transport of organic species towards the pump ports and therefore lower the chamber material utilization efficiency η_{ut}.

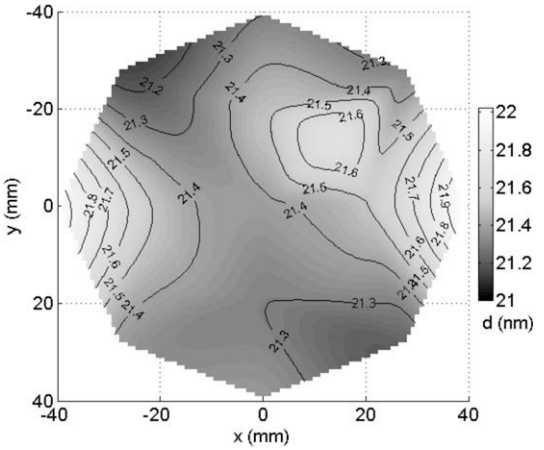

Fig. 5. Mapping of the thickness d of a typical pentacene film grown by in-line OVPD over a 4″ wafer. The thickness standard deviation over the wafer is ±1.1%. Following Eq. (3), multiplication of the layer thickness with trolley velocity delivers a $r_l = 13.2\ \mu m^2/s$.

An increase in total flow n_{tot} increases the source cell pressure and lowers chamber efficiency, explaining the important drop of r_l with n_{tot} in Fig. 6b. On the other hand, an increase of chamber pressure P slightly increases source cell pressure but improves chamber efficiency. These two effects counteract each other, explaining the limited effect of P on r_l seen in Fig. 6c.

Another studied parameter is the trolley velocity v_t depicted in Fig. 6d. A priori, an acceleration of the trolley should trigger an inversely proportional decrease of the fi-

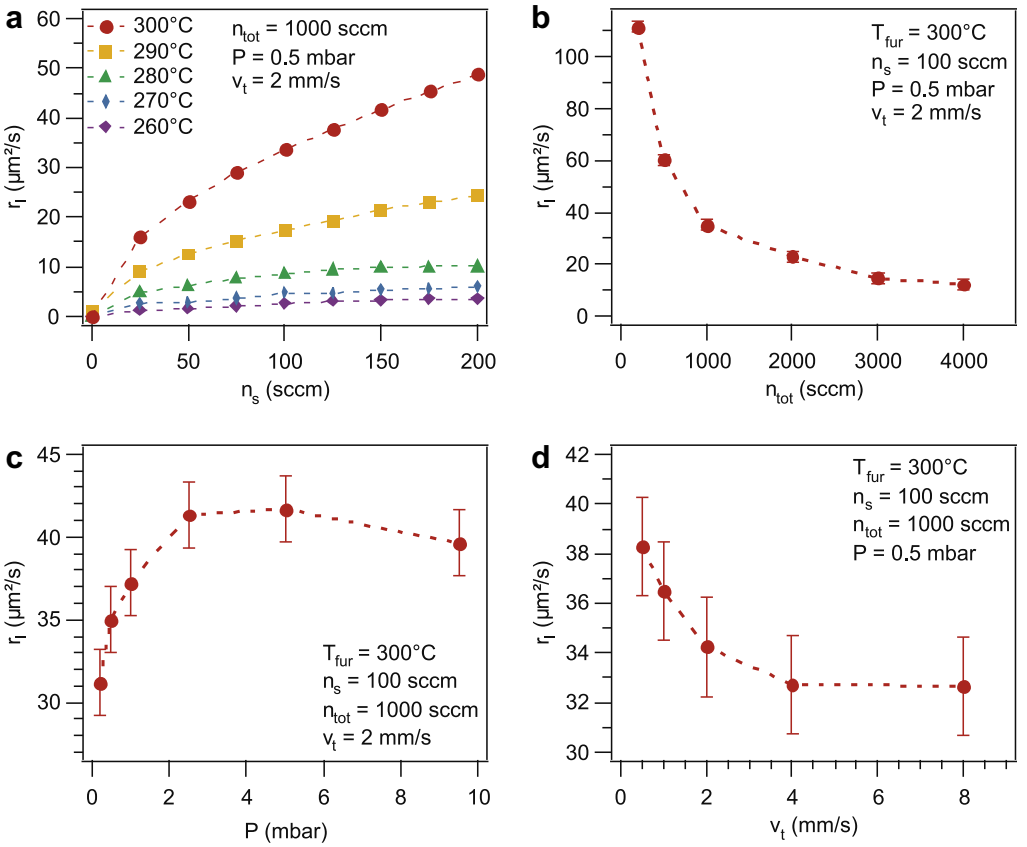

Fig. 6. Dependence of in-line deposition rate r_l on growth parameters. (a) r_l vs. source cell flow and furnace temperature; (b) r_l vs. total flow; (c) r_l vs. chamber pressure; (d) r_l vs. trolley velocity. The insets in each graph show the values of the growth parameters kept constant for all experimental points of the considered graph.

nal thickness d, leaving the in-line deposition rate r_l unchanged. However, r_l appears to be greater at low v_t. It is only at higher velocities that r_l becomes independent of v_t. The reason for the (small) decrease is unclear. It could be related to effects due to the finite size of the trolley.

As the main motivation of in-line processing is to enhance the production throughput, the OVPD growth parameters have been optimized to reach high in-line deposition rates. The graphs of Fig. 6 reveal that the two parameters that influence the most r_l are the furnace temperature and the total carrier gas flow. To reach the highest deposition speeds, T_{fur} is set at 320 °C and n_{tot} is decreased to 150 sccm. With these conditions, we reach an in-line deposition rate of 1055 μm²/s. This corresponds to a web speed of 2.1 m/min and to a 4″ static average deposition rate of 105 Å/s. Such a high speed is two orders of magnitude over what VTE usually reaches. Only Shtein et al., using organic vapor jet deposition could reach higher deposition rates for pentacene, but on dots with a diameter smaller than 100 μm [17].

4.3. Functional pentacene films grown at high speeds

In addition to deposition speed optimization, we studied the evolution of the electrical quality of pentacene thin films processed in-line and at high deposition speed. In order to establish a benchmark to assess our electrical results, control samples were fabricated, based on VTE-deposited pentacene layers. These samples have an OFET top-contact structure similar to the one displayed in Fig. 2. Two structural variations were simultaneously tested in this control experiment: (i) variation on the dielectric pretreatment: OFETs were fabricated with and without the PαMS layer on top of SiO_2; (ii) variation on pentacene deposition rate: both a low and a high rate were tested.

Measurement output for this set of VTE control samples is shown in Fig. 7. As expected, the pentacene layer deposited at a low rate (0.2 Å/s) on PαMS delivers the best transistor, with a saturation hole mobility μ_{sat} of 0.8 cm²/V s and a threshold voltage V_T of −0.6 V. In the absence of surface pretreatment, μ_{sat} is almost halved while other transistor characteristics remain good. This beneficial effect of PαMS on charge transport has also been observed by others [18] and justifies the systematic use of this pretreatment. Depositing pentacene at high rates (5.2 Å/s) results in an important worsening of transistor characteristics: μ_{sat} drops while V_T and the subthreshold slope greatly increase. These effects are attributed to a global increase of the trap density within the transistor channel [13]. This

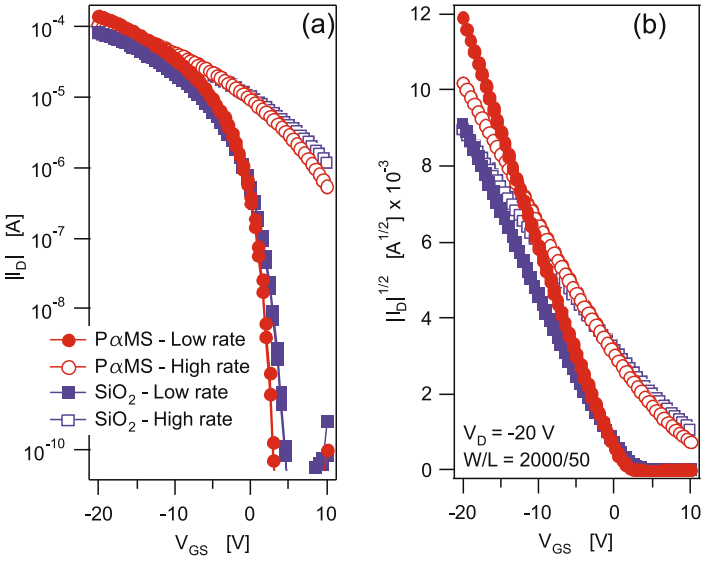

(c)

	0.2 Å/s		5.2 Å/s	
PαMS	0.77	-0.6	0.29	7.1
SiO_2	0.43	-0.2	0.19	9.7
	μ_{sat} (cm^2/Vs)	V_T (V)	μ_{sat} (cm^2/Vs)	V_T (V)

Fig. 7. Measurement of top contact OFETs based on VTE-deposited pentacene thin films. In these control experiments, dielectric pretreatment and pentacene deposition rate are varied. Logarithmic (a) and square-root (b) plots of transfer curves measured in saturation on four samples with different preparations. (c) Table summarizing transistor performances of the four samples.

points towards a very defective microstructure of the pentacene polycrystalline layer grown at high speed by VTE [19].

Fig. 8 shows typical transfer and output curves measured on a top contact OFET based on a pentacene thin film deposited by in-line OVPD. The transistor characteristics are apparently well-behaved: V_{ON} close to 0 V, the steep subthreshold slope (<0.4 V/dec) and the negligible hysteresis indicate high purity and low trap density. The saturation hole mobility μ_{sat} of this device is 1.01 cm^2/V s. These transistor characteristics advantageously compare to those of the best VTE control sample of Fig. 7. However, a major difference lies in pentacene growth speeds: $r = 0.2$ Å/s for the VTE control sample and $r_l = 431$ $\mu m^2/s$, equivalent to a $r_{avg} = 43$ Å/s, for the device shown in Fig. 8, which is based on an in-line OVPD-deposited pentacene film.

In fact, similar OFET characteristics were observed on most of the pentacene films prepared with the in-line OVPD, up to the highest speeds [20]. The observation that thin film electrical properties do not suffer from increased growth speeds contradicts previous reports [6]. It also opposes what we observed during the VTE control experiment of Fig. 7 according to which pentacene deposition at too high rates leads to inferior transistor characteristics. On the contrary, using certain conditions of in-line OVPD deposition, the opposite trend was even observed. Fig. 9a shows the evolution of the saturation mobility measured on thin films deposited at low total flow, with an increasing furnace temperature. This graph reveals that, in those conditions, the saturation mobility linearly increases with the logarithm of the in-line deposition rate. In order to study this effect in more details, three samples present in Fig. 9a are selected. They all have a pentacene thickness of 100 nm and are deposited with in-line deposition speeds of, respectively, I = 21, II = 343 and III = 961 $\mu m^2/s$. They are characterized by XRD in Fig. 9b and by AFM in Fig. 9c.

Pentacene growth on an inert substrate such as PαMS follows the description by Stranski–Krastanov [21]: after a two-dimensional layered growth, there is a transition towards a three-dimensional island growth, which, in the case of pentacene, appears to be mostly terraced. Such dendritic terraced islands are visible on all three AFM micrographs in Fig. 9c. Terrace step height is about 15 Å, indicating that the pentacene molecules are oriented with their long axis close to the normal direction of the substrate. In sample I, islands are larger than in other samples, but their center is often split into small high grains. Terraced islands are smaller in sample II and III but remain reasonably large considering the high growth speeds. At such speeds, a second mode of three-dimensional growth appears under the form of dispersed networks of fine needles, with a height of up to 200 nm. In VTE-grown pentacene films, bulkier needles become apparent with deposition rates above ~1.5 Å/s [22].

The XRD spectra of all three samples in Fig. 9b reveal the presence of a family of peaks attributed to reflection on the (0 0 1) planes. This confirms that *ab* planes of the crystal are parallel to the substrate. This is characteristic of layered and terraced growth. The interplanar distance d_{001} extracted from the spectra is 15.4 Å, typical of the "thin film" phase T of pentacene [23]. Moreover, a second family of peaks is also apparent on the three spectra, but with less intensity. It is also attributed to reflection on the (0 0 1) planes but with an interplanar distance of $d_{001} = 14.4$ Å, typical of the "bulk phase" B of pentacene [23]. The occurrence of such polymorphism within one pentacene thin film is usually thickness dependent, but can also be triggered by growth conditions [24]. Finally, two supplementary peaks at $2\theta = 19.3°$ and 24.0° are visible in the spectra of sample II and III. These correspond to interplanar distances of, respectively, 4.6 and 3.7 Å. These distances could be attributed to reflection on, respectively, (1 1 0) and (½ 0 0) planes in pentacene, revealing crystals with a different orientation relative to the substrate. These peaks could be characteristic of needles visible in the AFM micrographs of these two samples.

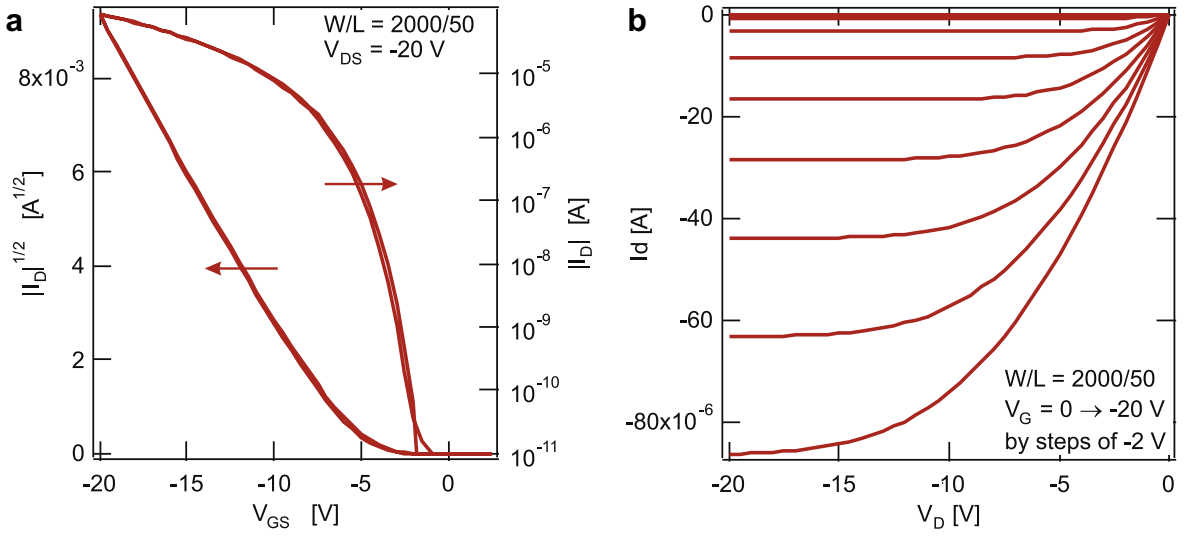

Fig. 8. Measurement of a typical top contact OFET based on a pentacene thin film deposited by in-line OVPD with a $r_l = 431$ $\mu m^2/s$, equivalent to a $r_{avg} = 43$ Å/s on a 4″ substrate. (a) Transfer curve measured in saturation; (b) output curve.

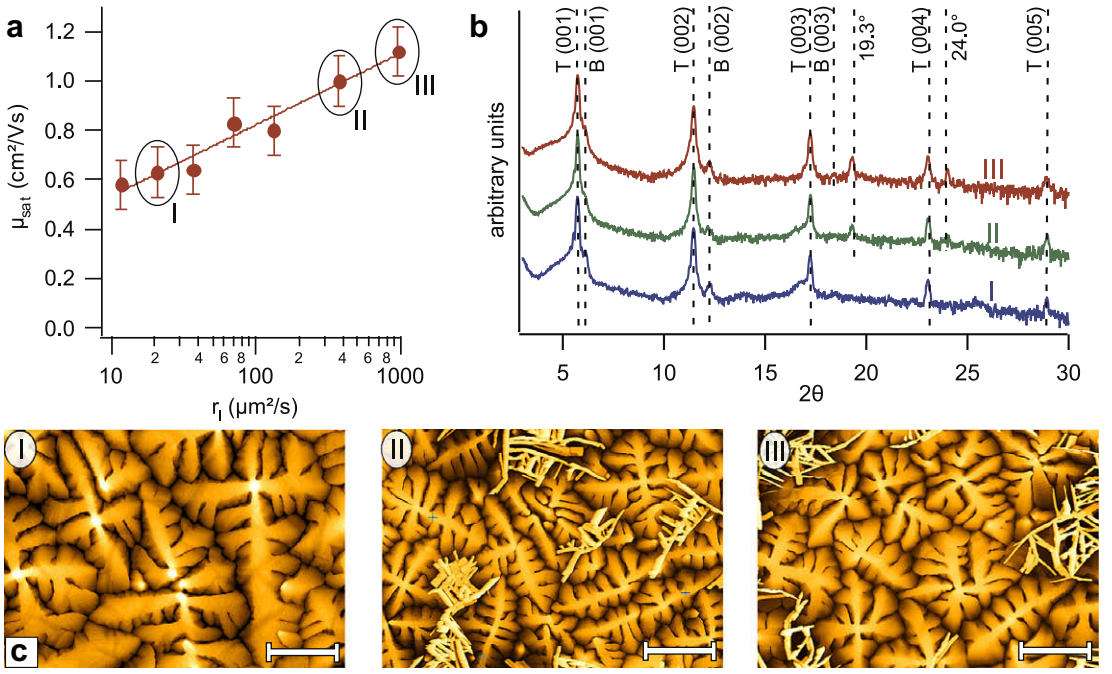

Fig. 9. (a) Top contact saturation mobility vs. logarithm of the in-line deposition rate. The linear fit is drawn as a guide for the eye. r_l of the selected samples are: I = 21, II = 343 and III = 961 μm^2/s. The selected samples have a pentacene thickness of 100 nm. (b) XRD spectra of the selected samples. T denotes thin film phase and B, bulk phase. (c) AFM images of the selected samples. Bars are 2 μm long.

The AFM and XRD data are not sufficient to clarify the improvement of the saturation mobility with the in-line deposition rate visible in Fig. 8a. The AFM data shows that, contrarily to what is usually observed in static systems [16], terraced island size does not drastically reduce upon an increase in deposition speed. The XRD data reveals that all three samples are of good crystalline quality, with T(0 0 l) peaks that are intense and repeated up to high orders [25]. Both characterization techniques show evidences that thin films conserve their good electrical performances up to the highest deposition rates. It is generally accepted that the electrical quality of a pentacene thin film is strongly dependent on the morphology of the first layered pentacene monolayers formed on the dielectric [26]. In in-line OVPD, considering the progressive deposition rate profile $r(x)$ measured in Fig. 4, these first monolayers are formed at low deposition rate. We tentatively attribute the good electrical performance of our pentacene films grown at high average speeds to this slow formation of the first monolayers.

Finally, other OVPD process parameters are equally important for the electrical properties of in-line deposited pentacene films. Electrical characteristics generally improve when the film is deposited at a lower pressure and at substrate temperatures above 60 °C. Furthermore, when growing at low in-line deposition rates, a too low total flow is harmful for the electrical characteristics. Using these basic rules, a sample grown at 41 μm^2/s, using a pressure of 0.5 mbar, a total flow of 1000 sccm and a substrate temperature of 65 °C reached a mobility of 1.4 cm^2/V s. At higher speeds, a mobility of 1.5 cm^2/V s is obtained on a sample grown at 751 μm^2/s, using a pressure of 0.1 mbar, a total flow of 350 sccm and a substrate temperature of 65 °C.

5. Conclusion

The OVPD technique has been successfully extended to an in-line geometry, with the susceptor undergoing a linear movement under an elongated showerhead. Experimental measurements reveal the spatial evolution of the deposition rate whose full profile is obtained by means of numerical simulations. As a consequence of the reduced dimensionality of the in-line system, the in-line deposition rate is defined that characterizes in-line growth speeds. A systematic parameter study using pentacene as a test material permits to draw calibration curves of the system and to define high deposition speed conditions. Pentacene is grown with thickness standard deviation as low as 1.1% over a 4″ substrate and an in-line deposition rate of up to 1055 μm^2/s. This corresponds to a web speed of 2.1 m/min and to a 4″ static deposition rate of 105 Å/s. Electrical properties of pentacene are probed via top-contact thin film transistors measurements. These transistors show high saturation mobilities (up to 1.5 cm^2/V s) and excellent characteristics that are conserved up to the highest deposition rates. This result opposes the usual observation that high pentacene deposition rates are very harmful to transistor characteristics. In contrast to pentacene layers deposited in static systems, the morphology of our pentacene films does not suffer from high growth speeds: grain sizes stay reasonable and crystalline order remains high. We attribute the conservation of excellent electrical prop-

erties up to the highest growth speeds to the progressive deposition profile that ensures a slow formation of the first pentacene monolayers. This work shows that in-line OVPD is a very promising candidate for the sheet-to-sheet and roll-to-roll processing of small molecular weight organic semiconductors.

Acknowledgments

This work was performed in a collaboration between IMEC and TNO in the frame of the HOLST Centre. C.R. acknowledges the F.R.I.A. and K.V. acknowledges the Institute for the Promotion of Innovation through Science and Technology in Flanders (IWT-Vlaanderen) for PhD grants. The authors acknowledge the financial support of EC-funded project ONE-P (FP7 Grant No. 212311).

References

[1] A.C. Huebler, F. Doetz, H. Kempa, H.E. Katz, M. Bartzsch, N. Brandt, I. Hennig, U. Fuegmann, S. Vaidyanathan, J. Granstrom, S. Liu, A. Sydorenko, T. Zillger, G. Schmidt, K. Preissler, E. Reichmanis, P. Eckerle, F. Richter, T. Fischer, U. Hahn, Org. Electron. 8 (2007) 480.
[2] A. Knobloch, A. Manuelli, A. Bernds, W. Clemens, J. Appl. Phys. 96 (2004) 2286.
[3] G.H. Gelinck, E. Huitema, E. van Veenendaal, E. Cantatore, L. Schrijnemakers, J. van der Putten, T. Geuns, M. Beenhakkers, J. Giesbers, B.-H. Huisman, E. Meijer, E.M. Benito, F. Touwslager, A. Marsman, B. van Rens, D. de Leeuw, Nat. Mater. 3 (2004) 106.
[4] K. Myny, M. Beenhakkers, N. van Aerle, G.H. Gelinck, J. Genoe, W. Dehaene, P. Heremans, Int. Solid-State Circ. Conf. Dig. Tech. Papers 206 (2009).
[5] S.R. Forrest, Nature 428 (2004) 911.
[6] D.J. Gundlach, Y.Y. Lin, T.N. Jackson, S.F. Nelson, D.G. Schlom, IEEE Electron. Dev. Lett. 18 (1997) 87.
[7] M.A. Baldo, M. Deutsch, P.E. Burrows, H.F. Gossenberger, M. Gerstenberg, V.S. Ban, S.R. Forrest, Adv. Mater. 10 (1998) 1505.
[8] OVPD is a technology by UDC exclusively licensed to AIXTRON for equipment manufacturing. The term OVPD is a trademark of AIXTRON.
[9] M. Shtein, J. Mapel, J.B. Benziger, S.R. Forrest, Appl. Phys. Lett. 81 (2002) 268.
[10] C. Rolin, S. Steudel, K. Myny, D. Cheyns, S. Verlaak, J. Genoe, P. Heremans, Appl. Phys. Lett. 89 (2006) 203502.
[11] T.X. Zhou, T. Ngo, J.J. Brown, M. Shtein, S.R. Forrest, Appl. Phys. Lett. 86 (2005) 021107.
[12] J.K. Mahon, T.X. Zhou, S.R. Forrest, M. Schwambera, N. Meyer, Solid State Technol. 45 (2002) 131.
[13] C. Horowitz, Adv. Mater. 10 (1998) 365.
[14] R.B. Bird, W.E. Stewart, E.N. Lightfoot, Transport Phenomena, second ed., Wiley, New York, 2002.
[15] M. Shtein, H.F. Gossenberger, J.B. Benziger, S.R. Forrest, J. Appl. Phys. 89 (2001) 1470.
[16] C. Rolin, K. Vasseur, S. Schols, M. Jouk, G. Duhoux, R. Müller, J. Genoe, P. Heremans, Appl. Phys. Lett. 93 (2008) 033305.
[17] M. Shtein, P. Peumans, J.B. Benziger, S.R. Forrest, J. Appl. Phys. 96 (2004) 4500.
[18] T.W. Kelley, P.F. Baude, C. Gerlach, D.E. Ender, D. Muyres, M.A. Haase, D.E. Vogel, S.D. Theiss, Chem. Mater. 16 (2004) 4413.
[19] S. Verlaak, C. Rolin, P. Heremans, J. Phys. Chem. B 111 (2007) 139.
[20] C. Rolin, S. Steudel, P. Vicca, J. Genoe, P. Heremans, Appl. Phys. Express 2 (2009) 086503.
[21] J.A. Venables, G.D.T. Spiller, M. Hanbücken, Rep. Prog. Phys. 47 (1984) 399.
[22] M. Kitamura, Y. Arakawa, J. Phys. Condens. Matter 20 (2008) 184011.
[23] C.D. Dimitrakopoulos, A.R. Brown, A. Pomp, J. Appl. Phys. 80 (1996) 2501.
[24] T. Kakudate, N. Yoshimoto, Appl. Phys. Lett. 90 (2007) 081903.
[25] A.C. Durr, F. Schreiber, M. Munch, N. Karl, B. Krause, V. Kruppa, H. Dosch, Appl. Phys. Lett. 81 (2002) 2276.
[26] F. Dinelli, M. Murgia, P. Levy, M. Cavallini, F. Biscarini, D.M.D. Leeuw, Phys. Rev. Lett. 92 (2004) 116802.

Organic Electronics 11 (2010) 109–114

Contents lists available at ScienceDirect

Organic Electronics

journal homepage: www.elsevier.com/locate/orgel

Effect of metal ions on the switching performance of polyfluorene-based organic non-volatile memory devices

Tae-Wook Kim [1], Seung-Hwan Oh, Joonmyoung Lee, Hyejung Choi, Gunuk Wang, Jubong Park, Dong-Yu Kim, Hyunsang Hwang, Takhee Lee *

Department of Materials Science and Engineering, Gwangju Institute of Science and Technology, Gwangju 500-712, Republic of Korea

ARTICLE INFO

Article history:
Received 29 July 2009
Received in revised form 29 September 2009
Accepted 6 October 2009
Available online 13 October 2009

Keywords:
Organic memory device
Polyfluorene
Metal ion

ABSTRACT

We investigated the switching behavior of the polyfluorene-derivatives (WPF-oxy-F) with and without metal ions (Ca^{2+} and Na^{+}). Basic memory behavior (e.g., current–voltage sweep, cumulative probability and retention) was not significantly affected by the metal ions, and the materials displayed an on/off ratio of more than three orders of magnitude, as well as good device-to-device uniformity and $>10^4$ s of retention time. However, the threshold voltage of Na-WPF-oxy-F containing Na^{+} was found to be lower than that of Ca-WPF-oxy-F containing Ca^{2+}, due to the looser binding between the sodium ion and the ethylene oxide unit in Na-WPF-oxy-F. Both Ca-WPF-oxy-F and Na-WPF-oxy-F showed area dependence in the low resistance state, implying that localized current flow is assisted by metal ions. In addition, the response time of Ca- and Na-WPF-oxy-F was faster than that of WPF-oxy-F, suggesting possible modulation of memory performance by the addition of metal ions in the polymer layer.

© 2009 Elsevier B.V. All rights reserved.

1. Introduction

Recently, organic based electronic devices have been intensively studied due to their flexibility, low cost, ease of fabrication and printing capabilities [1–5]. With the rapid development of information technology, the demand for inexpensive and high density data storage media has increased. Organic non-volatile memory devices have been some of the most promising candidates for next generation storage media [6–17].

There have been many efforts to develop optimal structures and fabrication methods for organic non-volatile memory devices [6–17]. Many research groups have tried to develop novel organic materials or mixtures of host polymer material and metallic nanoparticles that exhibit good memory performance [13,15–17]. Recently, we demonstrated sub-micron scale polymer non-volatile memory devices fabricated using a scalable via-hole structure that showed potential for high density polymer non-volatile memory applications [18]. In addition, combined transistor and organic memory device (one transistor and one resistor, 1T-1R) and combined organic diode and organic memory device (one diode and one resistor, 1D-1R) structures were shown to prevent random accessibility in organic non-volatile memory applications [19,20]. Although they showed satisfactory switching behavior, the devices lacked the performance necessary for realistic memory applications without sophisticated control of the switching parameters or an understanding of the switching mechanism. Joo et al. determined operation voltage threshold behavior in organic based memory devices by controlling ionization of a copper electrode [21], and showed the memory behavior dependence on field strength and temperature. Ma et al. reported organic non-volatile memory devices with controlled copper–ion concentrations within the organic layer [22]. However, the specific effects of metal ions on the switching behavior of organic memory

* Corresponding author. Tel.: +82 62 9702313; fax: +82 62 9702304.
E-mail address: tlee@gist.ac.kr (T. Lee).
[1] Current Address: Department of Materials Science and Engineering, University of Washington, Seattle, Washington 98195, USA.

1566-1199/$ - see front matter © 2009 Elsevier B.V. All rights reserved.
doi:10.1016/j.orgel.2009.10.006

devices have not been thoroughly investigated, and it is possible that addition of metal ions in organic memory devices could be used to control switching parameters.

In this study, the effects of metal ions on memory performance and specific switching parameters were investigated. Our results show that while the basic current–voltage characteristics of the polyfluorene-derivative were not significantly affected by the addition of metal ions, studies on the change in threshold voltage, area dependence of each resistance state and transient responses indicated that metal ions assisted localized conduction and induced faster responses.

2. Experimental

Single component polyfluorene-derivative memory devices were fabricated in metal–insulator–metal (MIM) structures on heavily doped p-type (1 0 0) silicon (p^+ Si) substrates (0.001–0.015 Ω cm). After the typical ultrasonic cleaning processes with acetone, methanol, and DI water, silicon wafers were treated with diluted HF to remove the native oxide layer and eliminate the possible role of interfacial SiO_2 layer on the switching behavior. Poly[(9,9-bis((6′-(*N*,*N*,*N*-trimethylammonium)hexyl)-2,7-fluorene)-alt-(9,9-bis(2-(2-methoxyethoxy)ethyl)-fluorene)] dibromide (denoted WPF-oxy-F) and its derivatives (Ca-WPF-oxy-F and Na-WPF-oxy-F) was used as an active layer, schematically shown in Fig. 1 [23]. The three kinds of polyfluorene-derivatives were first dissolved in methanol at a concentration of 10 mg/ml, and then were spin coated on the highly doped p-type silicon substrate. Typically, spin-coating was performed at 2000 rpm for 30 s, and the resulting thickness of the films was ~60 nm. To improve the film uniformity and eliminate the solvent from the films, the films were baked at 150 °C for 20 min on a hotplate in a nitrogen-filled glove box. The top electrodes of the MIM devices were patterned with a shadow mask with square patterns of four different sizes: $50 \times 50\ \mu m^2$, $100 \times 100\ \mu m^2$, $200 \times 200\ \mu m^2$ and $400 \times 400\ \mu m^2$. A 100 nm thick Ag layer was deposited as the top electrode using a thermal evaporator under a pressure of $\sim 10^{-6}$ torr. The memory device structure is schematically shown in Fig. 1d.

X-ray photoelectron spectroscopy (XPS) measurements were carried out using a MultiLab2000 (THERMO VG SCIENTIFIC) system equipped with monochromatised Mg Kα radiation at $h\nu = 1253.6$ eV at a pressure of 1×10^{-9} Pa ($\sim 7.5 \times 10^{-12}$ torr). The binding energies were calibrated to the C1s peak at 285 eV. Both room temperature current–voltage (*I*–*V*) measurements and pulsed *I*–*V* measurements were conducted using a semiconductor parameter analyzer (HP4155C). Additionally, transient voltage response tests were performed with a two-channel pulse generator (Agilent Technology 81104A) and a two-channel oscilloscope (Tektronix TDS 3054B), which were connected to a PC with a general purpose interface bus (GPIB) using a Labview program. The Ag top electrode was connected to a signal line, and the bottom electrode was used as a grounding electrode. All electrical characterization was performed under ambient conditions.

3. Results and discussion

To investigate the effect of metal ions on memory performance, we used WPF-oxy-F and its derivatives bound with mobile metal ions (sodium and calcium) [23]. Chemical structures are shown in Fig. 1. These materials were denoted Na-WPF-oxy-F when containing sodium ions and

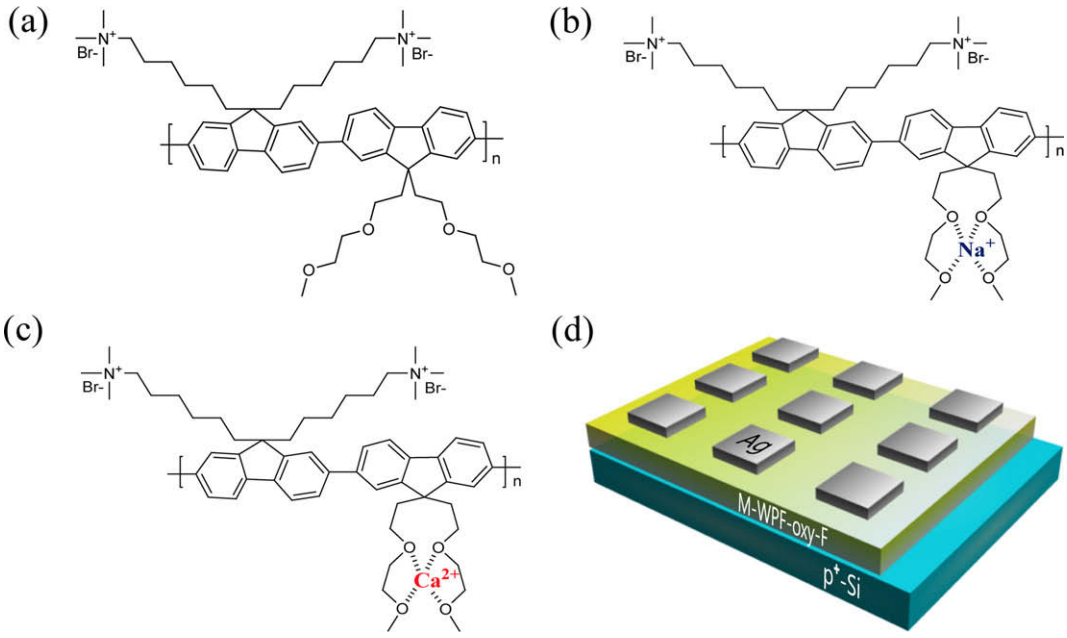

Fig. 1. Chemical structures of polyfluorene-derivatives (a) WPF-oxy-F, (b) Na-WPF-oxy-F and (c) Ca-WPF-oxy-F. (d) Schematic of MIM-type organic nonvolatile memory device.

Ca-WPF-oxy-F when containing calcium ions. The polyfluorene-derivatives with and without metal ions were used as active layers in metal–insulator–metal (MIM) type polymer non-volatile memory devices. To verify the existence of metal ions in M-WPF-oxy-F (where M indicates a metal ion), we performed X-ray photoelectron spectroscopy (XPS) analysis. Fig. 2 shows the XPS spectra of the oxygen 1s (O 1s) peak for each polyfluorene-derivative. For WPF-oxy-F, the O 1s peak equaled ~533 eV, indicating no binding between metal ions and the ethylene oxide unit. On the other hand, the M-WPF-oxy-F series with Na and Ca ions showed Na^+–O and Ca^{2+}–O binding in the O1s spectra as shown in Fig. 2, indicating binding between Na^+ or Ca^{2+} ions and the ethylene oxide unit [24,26]. Because Ca^{2+}–O has a higher binding energy than Na^+–O, binding between Ca^{2+} and the ethylene oxide unit is stronger than that of Na^+ [27].

The MIM polymer memory device structure is shown in Fig. 1d. In our previous work, we reported current–voltage (I–V) characteristics of WPF-oxy-F in an MIM structure [17]. Reversible switching behavior was observed within the range of 5 to −3 V. The initial state of the polymer memory devices was a high resistance state (HRS). When a positive bias was applied to the top electrode, the current began to increase gradually, and then abruptly jumped to around 3–4 V as the material changed from a HRS to a low resistance state (LRS), as shown in Fig. 3. Conversely, when a reverse voltage sweep was performed on the devices from 5 to −3 V, the current was maintained at a LRS and then decreased somewhat abruptly, indicating a change from a LRS to a HRS. Despite structural differences among these polyfluorene-derivatives, switching behavior was relatively uniform (Fig. 3).

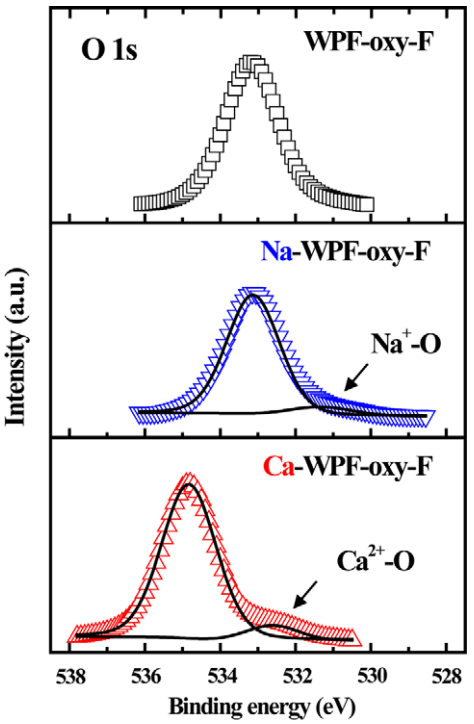

Fig. 2. XPS spectra of oxygen 1s peaks for WPF-oxy-F, Na-WPF-oxy-F and Ca-WPF-oxy-F.

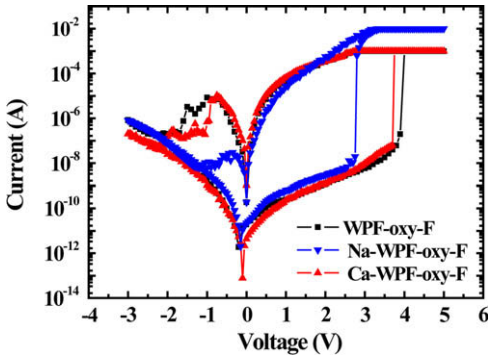

Fig. 3. Semi-log scale I–V characteristics of WPF-oxy-F, Na-WPF-oxy-F and Ca-WPF-oxy-F with a cell size of 50 × 50 μm^2.

To investigate the effects of metal ions on polyfluorene-derivatives, we characterized their basic memory performance. Fig. 4a shows the cumulative probability of resistance values (cell size of 50 × 50 μm^2). We measured a total of 81 memory devices (20 WPF-oxy-F devices, 37 Na-WPF-oxy-F devices and 24 Ca-WPF-oxy-F devices). The HRS of the three polymer memory devices showed very narrow resistance distributions. The distributions of the LRS were within two orders of magnitude, a slightly wider distribution than that of HRS. However, on/off ratios

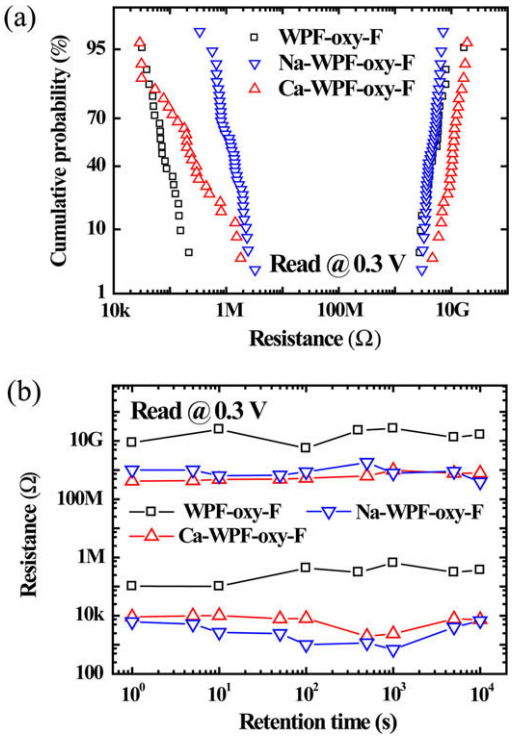

Fig. 4. (a) A Cumulative probability data sets of WPF-oxy-F, Na-WPF-oxy-F and Ca-WPF-oxy-F. (b) Retention characteristics of WPF-oxy-F, Na-WPF-oxy-F and Ca-WPF-oxy-F measured at room temperature.

of mean resistance values for each type of polymer memory devices were still more than three orders of magnitude, indicating excellent device-to-device uniformity in these polyfluorene-derivatives. Fig. 4b shows the retention characteristics of each polymer memory device. Written and erased data were held more than 10^4 s while maintaining on/off ratios of more than three orders of magnitude during the retention characterization. The metal ions did not show any distinct effects on basic memory performance (i.e., *I–V* sweeps, device-to-device uniformity and retention characteristics).

We also investigated the effect of metal ions on the threshold voltages and on/off ratios. Fig. 5a shows the distributions of threshold voltage (i.e., the voltage when changing from a HRS to LRS) for each polymer memory device. Although the three kinds of polyfluorene-derivatives had different average threshold voltages, most devices were within the voltage range of 2.5–4.0 V. For example, when we plot the histogram on the threshold voltage for Na-WPF-oxy-F (inset of Fig. 5a), we see a distribution of threshold voltages within 1 V around 2.8 V, indicating reliable switching performance. The other memory devices also showed similar distributions (data not shown). A previous study on the effect of metal ions on switching behavior reported that switching behavior is controlled by two processes: metal ionization and ion drift [21]. Electric field strongly influences the switching behavior, and the switching probability increases sharply around the threshold electric field [21]. In M-WPF-oxy-F containing metal ions, the metal ions are incorporated into the ethylene oxide side groups (see Fig. 1). It is well known that the ethylene oxide unit can be used as a channel for transport of mobile ions even in solid state [24,25]. Hence, when the devices are in the writing process, it is expected that the mobile ions in the ethylene oxide units are rearranged with an applied bias and form conducting current path [27]. This would affect the threshold voltage of the polymer memory devices. The looser bond between the ethylene oxide unit and Na^+ ion (as compared to Ca^{2+} ions, as explained in Fig. 2) results in Na^+ ions moving more easily than Ca^{2+} ions under the same bias conditions. Therefore, Na-WPF-oxy-F displayed a lower threshold voltage than Ca-WPF-oxy-F.

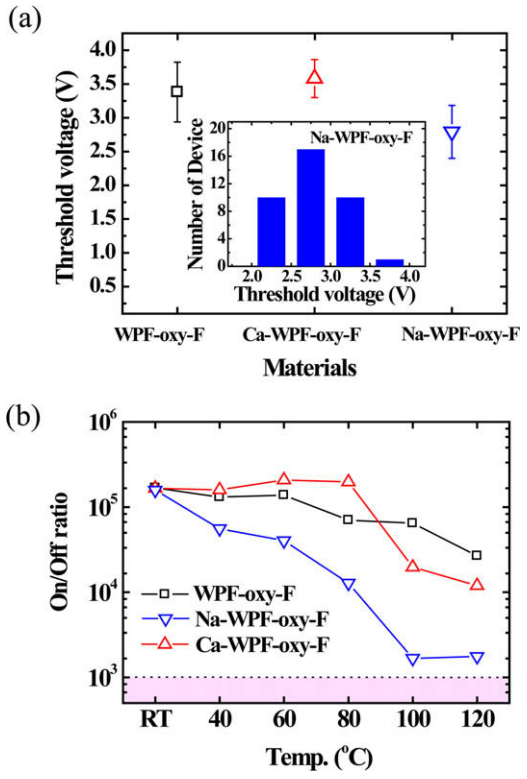

Fig. 5. (a) Distributions of threshold voltage of organic non-volatile memory devices with WPF-oxy-F, Na-WPF-oxy-F and Ca-WPF-oxy-F. Inset shows the histogram of threshold voltage for Na-WPF-oxy-F. (b) Comparisons of on/off ratios of three kinds of polyfluorene-derivatives measured at various temperatures.

Fig. 5b shows the on/off ratios of polymer memory devices at different temperatures. The on/off ratios were measured by the voltage sweep method and read at 0.3 V. In the initial state (at room temperature), all the memory devices showed on/off ratios of more than five orders of magnitude. Although the on/off ratios started to decrease after 60 °C, they retained on/off ratios of more than three orders of magnitude, indicating reliable switching behavior. Only WPF-oxy-F showed a gradual decrease in its on/off ratio. This decrease was due to the increase of leakage current in the HRS, which is enhanced by the hopping current as temperature increases [28]. The on/off ratios of Ca- and Na-WPF-oxy-F reduced considerably near 80 °C due to both hopping current increases and high-temperature activated metal ion movement through the ethylene oxide side groups. Na-WPF-oxy-F showed more rapid on/off ratio reduction with increasing temperature than Ca-WPF-oxy-F. This phenomenon is also related to the different binding energies between the ethylene oxide unit and the Na^+ and Ca^{2+} ions.

To help understand the switching mechanism, we characterized the size dependence of the resistance values of both the HRS and the LRS, as shown in Fig. 6a. The resistance of the polyfluorene-derivative with metal ions (Ca- and Na-WPF-oxy-F) clearly scaled with the reciprocal of the cell size, indicating that the current flowed through the whole cell area in the HRS [28]. This suggests that the metal ions, which exist in polymer layer randomly, allow the current to flow through the whole area in the HRS. On the other hand, dispersed metal ions in each polymer layer are arranged by applied bias and arranged metal ions act as a main current path in the LRS. Most of current flows happen through this current path. Hence the low resistance values of the two polymer materials with metal ions did not change significantly with cell size [29]. One should consider that ionic conduction also partially contributes to the current flow in metal ion based polymer materials. However, unlike Ca- and Na-WPF-oxy-F, the resistance of the WPF-oxy-F did not show any clear size dependence in both LRS and HRS, as can be seen in Fig. 6a. Especially, the slope of log (R)–log (area) at high resistance states observed below 1. This behavior implies that current flows in WPF-oxy-F are affected by not only localized current flows but also space charge limited conduction [17].

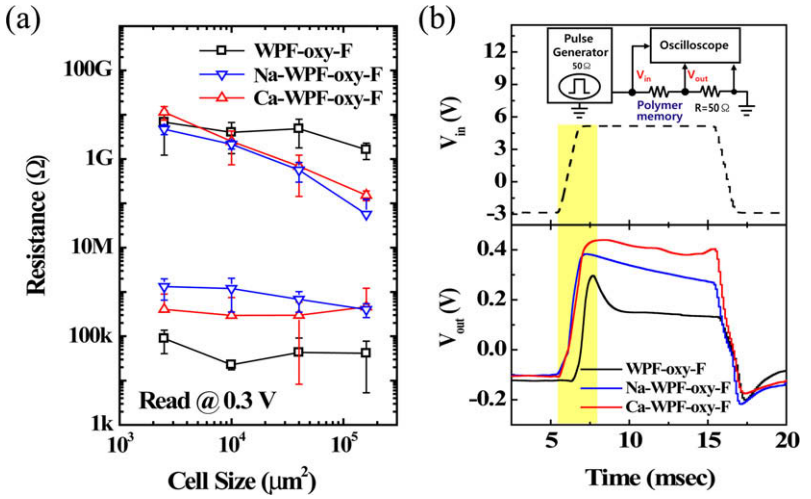

Fig. 6. (a) Resistance values of the on and off states of the three kinds of polyfluorene-derivative memory devices as a function of junction area. (b) Transient response characteristics of the three kinds of polyfluorene-derivative memory devices. The inset shows the circuit of measurement method.

Table 1
Summary of basic switching properties of organic non-volatile memory devices with WPF-oxy-F, Ca-WPF-oxy-F and Na-WPF-oxy-F.

	Band gap [24] [eV]	On/off ratio	*V*th [V]	Response time [μs]	Retention time [s]	Area dependence of HRS
WPF-oxy-F	~2.8	~10^4	3.4 ± 0.5	~2000	~10^4	No
Ca-WPF-oxy-F	~2.8	~10^4	3.6 ± 0.3	~10	~10^4	Yes
Na-WPF-oxy-F	~2.8	~10^4	3.0 ± 0.4	~10	~10^4	Yes

To further study the effects of metal ions on memory performance, we measured pulse delay times for the three kinds of polymer memory devices. The inset in Fig. 6b shows a schematic of the transient response measurements. We monitored input and output voltage pulses using an oscilloscope, and the data are shown in Fig. 6b. By monitoring output voltage (V_{out}) through a 50 Ω external resistor, we estimated the response times for each polymer memory device with cell size of 50 × 50 μm^2. In this analysis, the response time was the delay time between when an input voltage pulse was applied to the device in the HRS and when it switched to the LRS, as shown in the yellow region of Fig. 6b. The transient responses of Ca- and Na-WPF-oxy-F were very similar (~10 μs writing process). On the other hand, the transient response of WPF-oxy-F was ~2 ms, a much slower writing process response. This difference in response time is mainly due to the metal ions that make current paths in the polymer layer.

The properties of the three polymer memory devices are summarized in Table 1. While they show similar memory characteristics (e.g., similar *I*–*V* hysteresis, room-temperature on/off ratio and retention time), considerable differences can be seen in the threshold voltages, on/off ratios as temperature increases, area dependences and response times. Thus, metal ions in the polymer layer can play an important role in the design of polymer memory devices with low voltage operation and fast response. One can expect more sophisticated control of polymer memory device performance with use of various metal ions.

4. Conclusions

We synthesized polyfluorene-derivatives (WPF-oxy-F) with and without metal ions (Ca^{2+} and Na^+) and compared the switching behaviors of each polyfluorene-derivative. Although basic memory behavior (current–voltage characteristics, cumulative probability and retention) was not significantly affected by the metal ions, Ca-WPF-oxy-F and Na-WPF-oxy-F showed area dependence in the high resistance state, implying that metal ions assist localized current flow. The threshold voltage of Na-WPF-oxy-F was lower than that of Ca-WPF-oxy-F because of more efficient Na^+ movement in Na-WPF-oxy-F. In addition, the Ca- and Na-WPF-oxy-F response time was faster than that of WPF-oxy-F, indicating that memory performances could be controlled with the addition of metal ions in the polymer layer.

Acknowledgements

This work was supported by the National Research Laboratory (NRL) Programs of the Korea Science and Engineering Foundation (KOSEF), the Program for Integrated Molecular System at GIST and the SystemIC2010 project of the Korea Ministry of Knowledge Economy.

References

[1] C.D. Müller, A. Falcou, N. Reckefuss, M. Rojahn, V. Wiederhirn, P. Rudati, H. Frohne, O. Nuyken, H. Becker, K. Meerholz, Nature 421 (2003) 829.

[2] G. Darlinski, U. Böttger, R. Waser, H. Klauk, M. Halik, U. Zschieschang, G. Schmid, C. Dehm, J. Appl. Phys. 97 (2005) 093708.
[3] T.W. Lee, Y. Byun, B.W. Koo, I.N. Kang, Y.Y. Lyu, C.H. Lee, L. Pu, S.Y. Lee, Adv. Mater. 17 (2005) 2180.
[4] J.Y. Kim, K. Lee, N.E. Coates, D. Moses, T.Q. Nguyen, M. Dante, A.J. Heeger, Science 317 (2007) 222.
[5] S.-I. Na, S.-S. Kim, J. Jo, D.-Y. Kim, Adv. Mater. 20 (2008) 4061.
[6] D. Wei, J.K. Baral, R. Österbacka, A. Ivaska, J. Mater. Chem. 16 (2008) 1853.
[7] L.D. Bozano, B.W. Kean, M. Beinhoff, K.R. Carter, P.M. Rice, J.C. Scott, Adv. Funct. Mater. 15 (2005) 1933.
[8] M. Karakawa, M. Chikamatsu, Y. Yoshida, R. Azumi, K. Yase, C. Nakamoto, Macromol. Rapid Commun. 28 (2007) 1479.
[9] C.H. Tu, Y.S. Lai, D.L. Kwong, IEEE Electron Device Lett. 27 (2006) 354.
[10] A. Bandhopadhyay, A.J. Pal, J. Phys. Chem. B 107 (2003) 2531.
[11] B. Mukherjee, A.J. Pal, Appl. Phys. Lett. 85 (2004) 2116.
[12] J. Ouyang, C.W. Chu, C.R. Szmanda, L. Ma, Y. Yang, Nat. Mater. 3 (2004) 918.
[13] R.J. Tseng, C. Tsai, L. Ma, J. Ouyang, C.S. Ozkan, Y. Yang, Nat. Nanotechnol. 1 (2006) 72.
[14] Y. Chen, G.Y. Jung, D.A.A. Ohlberg, X. Li, D.R. Stewart, J.O. Jeppesen, K.A. Nielsen, J.F. Stoddart, R.S. Williams, Nanotechnology 14 (2003) 462.
[15] C. Pearson, J.H. Ahn, M.F. Mabrook, D.A. Zeze, M.C. Petty, K.T. Kamtekar, C. Wang, M.R. Bryce, P. Dimitrakis, D. Tsoukalas, Appl. Phys. Lett. 91 (2007) 123506.
[16] Q.-D. Ling, E.-T. Kang, K.-G. Neoh, Y. Chen, X.-D. Zhuang, C. Zhu, D.S.H. Chan, Appl. Phys. Lett. 92 (2008) 143302.
[17] T.-W. Kim, S.-H. Oh, H. Choi, G. Wang, D.-Y. Kim, H. Hwang, T. Lee, Appl. Phys. Lett. 92 (2008) 253308.
[18] T.-W. Kim, H. Choi, S.-H. Oh, M. Jo, G. Wang, B. Cho, D.-Y. Kim, H. Hwang, T. Lee, Nanotechnology 20 (2009) 025201.
[19] T.-W. Kim, H. Choi, S.-H. Oh, G. Wang, D.-Y. Kim, H. Hwang, T. Lee, Adv. Mater. 21 (2009) 2497.
[20] H.-T. Lin, Z. Pei, J.-R. Chen, Y.-J. Chan, IEEE Electron Device Lett. 30 (2008) 18.
[21] W.-J. Joo, T.-L. Choi, K.-H. Lee, Y. Chung, J. Phys. Chem. B 111 (2007) 7756.
[22] L. Ma, Q. Xu, Y. Yang, Appl. Phys. Lett. 84 (2004) 4908.
[23] S.-H. Oh, S.-I. Na, Y.-C. Nah, D. Vak, S.-S. Kim, D.-Y. Kim, Org. Electron. 8 (2007) 773.
[24] F.M. Gray, Polymer Electrolytes, Royal Society of Chemistry, Cambridge, 1997.
[25] Q. Pei, Y. Yang, J. Am. Chem. Soc. 118 (1996) 7416.
[26] P.R. Ettireddy, G.S. Panagiotis, J. Phys. Chem. B 108 (2004) 7794.
[27] N.R. Dhumal, S.P. Gejji, Chem. Phys. 323 (2006) 595.
[28] G. Pfister, C.H. Griffiths, Phys. Rev. Lett. 40 (1978) 659.
[29] P.G. Lecomber, A.E. Owen, W.E. Spear, J. Hajto, A.J. Snell, W.K. Choi, M.J. Rose, S. Reynolds, J. Non-Cryst. Solids 77/78 (1985) 1373.

Organic Electronics 11 (2010) 115–122

Contents lists available at ScienceDirect

Organic Electronics

journal homepage: www.elsevier.com/locate/orgel

On the dendritic growth and field emission of amorphous AlQ_3 nanowires

Chun-Pei Cho [a], Tsong-Pyng Perng [b,c,*]

[a] Department of Applied Materials and Optoelectronic Engineering, National Chi Nan University, Nantou 54561, Taiwan
[b] Department of Materials Science and Engineering, National Tsing Hua University, Hsinchu 30013, Taiwan
[c] Department of Chemical Engineering and Materials Science, Yuan Ze University, Chung-Li 32003, Taiwan

ARTICLE INFO

Article history:
Received 16 August 2009
Received in revised form 10 October 2009
Accepted 11 October 2009
Available online 20 October 2009

Keywords:
AlQ_3 nanowires
Dendritic growth
Photoluminescence
Field emission

ABSTRACT

Amorphous AlQ_3 nanowires were fabricated by vapor condensation under a cold trap. Their diameter distributed in a small range of 35–60 nm, but their length was dramatically changed by working pressure. Longer and thinner nanowires could be obtained at a lower working pressure. The most appropriate condition to fabricate long and fine nanowires was to set boat temperature at 410 °C and to control the working pressure of Ar at 1.33×10^3–3.99×10^3 Pa. A higher density of nanowires was observed at a lower working pressure. The dendritic growth mechanism caused by a temperature gradient was proposed to explain the formation of branched nanowires. Due to the absence of quantum confinement effect, the nanowires did not exhibit a PL blue shift as their sizes shrank. When higher density of nanowires were formed at a lower working pressure, stronger PL intensity could be revealed on the emission spectra. The amorphous nanowires also exhibited field-emission behavior. Their $E_{turn\text{-}on}$ ranged from 3 to 20 V/μm and frequently approximated to 10 V/μm, comparable to those of most inorganic 1D nanostructures but somewhat larger than that of CNTs. Larger thickness caused by a higher deposition rate at a higher boat temperature could lead to a smaller $E_{turn\text{-}on}$.

Crown Copyright © 2009 Published by Elsevier B.V. All rights reserved.

1. Introduction

Nanostructures have received continuously growing interests owing to the peculiar and fascinating properties superior to their bulk counterparts. With a size between the molecules and bulk solid-state structures, nanostructured materials exhibit hybrid properties which are still not completely understood today. The small size of nanostructured materials may result in different electronic, optical, magnetic, chemical, and mechanical properties, and thereby they may be more suitable for noble applications. It is important to develop new advanced nanomaterials for electronics, biotechnology, environment or energy applications. Lots of effort has been devoted to the design and synthesis of new nanomaterials. However, most of the researches were concentrated on inorganic materials. By contrast, the studies related to organic or organometallic nanomaterials were comparatively fewer [1–19]. The development of "soft" nanomaterials is absolutely an inevitable tendency in future nanotechnology. Consequently, organic and organometallic nanomaterials merit more investigation due to their excellent flexibility, high photoconductivity, nonlinear optical effect and low cost [20–22].

It is generally accepted that one-dimensional (1D) nanomaterials such as wires, rods, belts and tubes, provide a good system for investigation of the dependence of electrical and thermal transports or mechanical properties on dimensionality. They are also expected to play important roles as interconnects and functional units in electronic and optoelectronic nanoscaled devices. Nevertheless, in comparison with quantum dots and wells, the advancement of 1D nanomaterials has been slow due to the difficulties associated with the synthesis and fabrication of 1D nanomaterials with well-controlled dimensions, morphology, phase purity, and chemical composition. In this study, we have demonstrated that an organometallic

* Corresponding author. Address: Department of Materials Science and Engineering, National Tsing Hua University, Hsinchu 30013, Taiwan.
E-mail address: tpperng@mx.nthu.edu.tw (T.-P. Perng).

1566-1199/$ - see front matter Crown Copyright © 2009 Published by Elsevier B.V. All rights reserved.
doi:10.1016/j.orgel.2009.10.007

semiconductor named tris (8-hydroxyquinolinato) aluminium (AlQ_3), could be employed to fabricate long and fine amorphous nanowires under a cold trap by an accessible vapor condensation approach. Since the efficient electroluminescence (EL) from a bilayer organic light emitting device (OLED) was reported, AlQ_3 has become one of the most successful electron transport and emitting materials [23]. It offers the possibilities of flexible displays, more facile deposition of wide-area film, cheaper purification cost, and more versatile color specificity which most inorganic semiconductors do not have [24]. To generate AlQ_3 nanostructures with various geometries has become possible by adjusting the working parameters during the vapor condensation process [2–5]. Some interesting phenomena and optoelectronic properties have been discovered in this work. The growth mechanism of branched AlQ_3 nanowires could be explained by a temperature gradient and the presence of an interface allowed to move forward into sufficiently supercooled gaseous phase. Previously, the field emission of conjugated polymers and organic compound has been reported [25–27]. The amorphous AlQ_3 nanowires also exhibited field mission characteristics comparable to those of some inorganic nanostructures such as SiC or SiCN nanorods [28,29]. In addition, the low working temperatures for vapor condensation is compatible with most electronic processes. Thus this is a brand-new territory and of great potential for optoelectronic applications.

2. Experimental

AlQ_3 nanowires were fabricated by a vapor condensation system which mainly consisted of a process chamber, a pumping system, a heating system and a gauge system. The setup has been presented elsewhere previously [30]. The nanowires were grown on two kinds of substrates: *n*-type (1 0 0) silicon wafer and ITO-coated glass. The Si substrate was used mainly for SEM examination, whereas the conductive ITO-coated glass was employed for field-emission measurement. The morphology and size of the AlQ_3 nanostructures fabricated by vapor condensation were independent of substrate category. The pretreatment of substrates included two steps: rinse and drying. The silicon and ITO substrates were ultrasonically rinsed in acetone and then in isopropyl alcohol, respectively, for 15 min. Subsequently, they were taken out of the solvents and dried by purging with N_2 gas. Commercial AlQ_3 powder (TCI Ltd., T1527, purity >95.0%) was placed on the graphite boat. The silicon or ITO-coated glass substrates were stuck at the underside of the concave stainless steel plate which was 10 cm above the graphite boat. The DC current applied to the graphite boat was supplied by an AC transformer and modulated by the sensitive feedback through a thermocouple contact with the graphite boat. At first, the process chamber was evacuated to a vacuum of 2.7×10^{-4} Pa in 1 h, and then various pressures inside the chamber could be achieved by injecting Ar gas. The pressure was controlled in the range of 1.33×10^3–6.67×10^3 Pa. Subsequently, liquid nitrogen was poured into the concave stainless steel plate for rapid cold trap of the substrates. When the temperature of graphite boat reached 400–420 °C, the commercial AlQ_3 powder started to sublime to form amorphous nanowires on the cold substrates. Most impurities in the commercial powder could be eliminated in the evacuation and sublimation processes, so the nanowires obtained were much purer than the powder.

A field emission scanning electron microscope (FESEM, JEOL JSM-6330F) was used to examine the morphologies of the nanowires on silicon substrates. Due to the poor conductance of AlQ_3, an ultra-thin gold film was sputtered onto the specimen to get clearer image. A low angle X-ray diffraction spectrometer (MAC SIENCE MXP-18, Cu-Kα1) was employed to examine the crystallinity of the nanowires on silicon substrates. A photoluminescence (PL) system composed of a He–Cd excitation laser, a spectrometer and a photomultiplier was utilized to measure the PL spectra of the nanowires. The detection range of wavelength was from 350 to 1000 nm. The field-emission characteristics of the AlQ_3 nanowires were detected by a field emission measuring system mainly comprising a vacuum chamber, a power supply (Keithley 237) and a set of anode–cathode configuration. The anode was a small Pt sphere with a diameter of 650 μm. The specimen was placed on the cathode plate in the stainless steel holder. The movement and position of the anode sphere could be precisely controlled by a triple axis XYZ stage so that local measurement of emission current and a zero-point calibration were achievable. ITO-coated glasses were used as the substrates for field-emission measurement.

3. Results and discussion

3.1. Amorphous AlQ_3 nanowires

When the temperature of the graphite boat reaches 400 °C, AlQ_3 nanowires with an average diameter of 34, 42 and 45 nm are fabricated in Ar of 1.33×10^2, 1.33×10^3 and 3.99×10^3 Pa, respectively, as shown in Fig. 1. It is not easy to estimate the real lengths of the nanowires obtained in Ar of 1.33×10^2 and 1.33×10^3 Pa because they tangle and entwine together. Fig. 1a shows that the length is approximately several μm, whereas Fig. 1b reveals a smaller length than that in Fig. 1a. Nanowires with a length smaller than 1 μm are obtained in Ar of 3.99×10^3 Pa, as shown in Fig. 1c. Similar results are also observed as the temperature of the graphite boat is higher (410 and 420 °C). As displayed in Fig. 2, when the boat temperature is 410 °C, AlQ_3 nanowires with an average diameter of 35, 41, 46 and 60 nm are fabricated in Ar of 1.33×10^2, 1.33×10^3, 3.99×10^3 and 6.67×10^3 Pa, respectively. Fig. 2a–c reveal that the lengths of the nanowires is up to several μm, whereas that in Fig. 2d is smaller than 1 μm. If the boat temperature is further raised to 420 °C, AlQ_3 nanowires with an average diameter of 35 and 44 nm are obtained in Ar of 1.33×10^3 and 3.99×10^3 Pa, respectively, as shown in Fig. 2e and f. The length shown in Fig. 2e is estimated to be several μm, but that in Fig. 2f is smaller than 1 μm.

The above results illustrate that the boat temperature does not have a conspicuous influence on the dimension

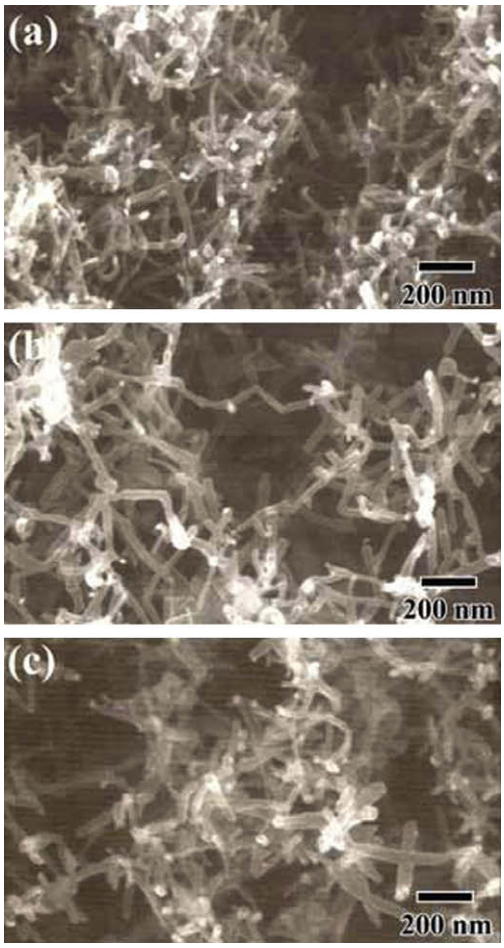

Fig. 1. AlQ_3 nanowires fabricated under a cold trap as the temperature of graphite boat is 400 °C in Ar of (a) 1.33×10^2 Pa, (b) 1.33×10^3 Pa, and (c) 3.99×10^3 Pa.

of nanowires. Unlike a wide distribution of the AlQ_3 nanoparticles [3], the diameter of the nanowires slightly increases with working pressure and its distribution is in a small range of 35–60 nm. On the other hand, the length of nanowires is dramatically changed by altering working pressure. Longer and thinner nanowires can be achieved at a lower working pressure. After the systematic studies, it is concluded that the most appropriate condition for fabrication of long and fine nanowires is to set the boat temperature at 410 °C and to control the Ar pressure at between 1.33×10^3 and 3.99×10^3 Pa. Moreover, a higher density of nanowires is observed at a lower working pressure, indicating that more nanowires congregate in the same area. Similar to AlQ_3 nanoparticles [3], the nanowires formed by vapor condensation are also amorphous, as demonstrated by the XRD pattern in Fig. 3, which shows the crystallinity of the commercial powder as well.

3.2. Growth mechanism

Unlike the fabrication of AlQ_3 nanoparticles in He [3], AlQ_3 nanowires were fabricated in Ar of various working pressures. Ar as well as He is inert gas, and they belong to the same group in the periodic table. Compared to the smaller He atom, an Ar atom has larger volume and weight. Probably due to the different size and gravity from the inert gaseous atoms, AlQ_3 nanostructures with dissimilar geometries could be fabricated in different working gases. How the atomic size and gravity influence the formation of various nanostructures should be further explored by theoretical calculation, which is not included in this work.

The growth of AlQ_3 nanowires is greatly related to the low temperature of the cold substrate and the working pressure in the process chamber. The Ar pressure should be controlled in the range of 1.33×10^2–6.67×10^3 Pa, otherwise abnormal nanostructures, rather than wire-like nanostructures, would be formed. It was found that the most appropriate Ar pressure for achieving fine and long nanowires was between 1.33×10^3 and 3.99×10^3 Pa. A dendritic growth mechanism caused by the temperature gradient is proposed to explain the formation of AlQ_3 nanowires during the vapor condensation process. When the graphite boat reaches the sublimation temperature, AlQ_3 molecules acquire enough energy to sublime and move upward to the cold substrate. As soon as they arrive at the substrate, the molecules freeze quickly and release the latent heat of fusion. Consequently, the temperature of the region where the molecules freeze on the substrate rises. However, the temperature ahead of this region drops because of a heat flow from the frozen solid into the gaseous phase, as schematically presented in Fig. 4. Subsequently, the condition becomes unstable. In the presence of any small perturbation, primary branches of nanowires may grow out from these positions into the gaseous phase. The resulting structures may also become quite complicated, with secondary branches forming on the primary ones, and possibly with tertiary branches forming on the secondary ones, ... and so on, as depicted in Fig. 4b and c.

The reason for the branched growth of AlQ_3 nanowires is not difficult to understand. As shown in Fig. 4b, section *aa* stands for the interface between the solid and gaseous phases where the primary branches start to form. On the other hand, the average temperature at section *bb* is lower than that at section *aa*, so a falling temperature gradient generates. The temperature gradient is responsible for the formation of primary branches. Once the primary branches have formed, the growth at section *aa* becomes slow because supercooling gets small here and the latent heat of fusion tends to further decrease its magnitude. Then secondary branches form because there is also a falling temperature gradient starting at point A on the primary arm and moving toward point B in front ($T_A > T_B$), as displayed in Fig. 4c. Tertiary branches also form for the same reason. Consequently, the branched growth of AlQ_3 nanowires can be attributed to the presence of an interface allowed to move forward into the sufficiently supercooled gaseous phase.

3.3. Photoluminescence

The same as AlQ_3 nanoparticles [3], the nanowires do not exhibit blue shift on their PL emission spectra when their sizes shrink because the molecules are bonded

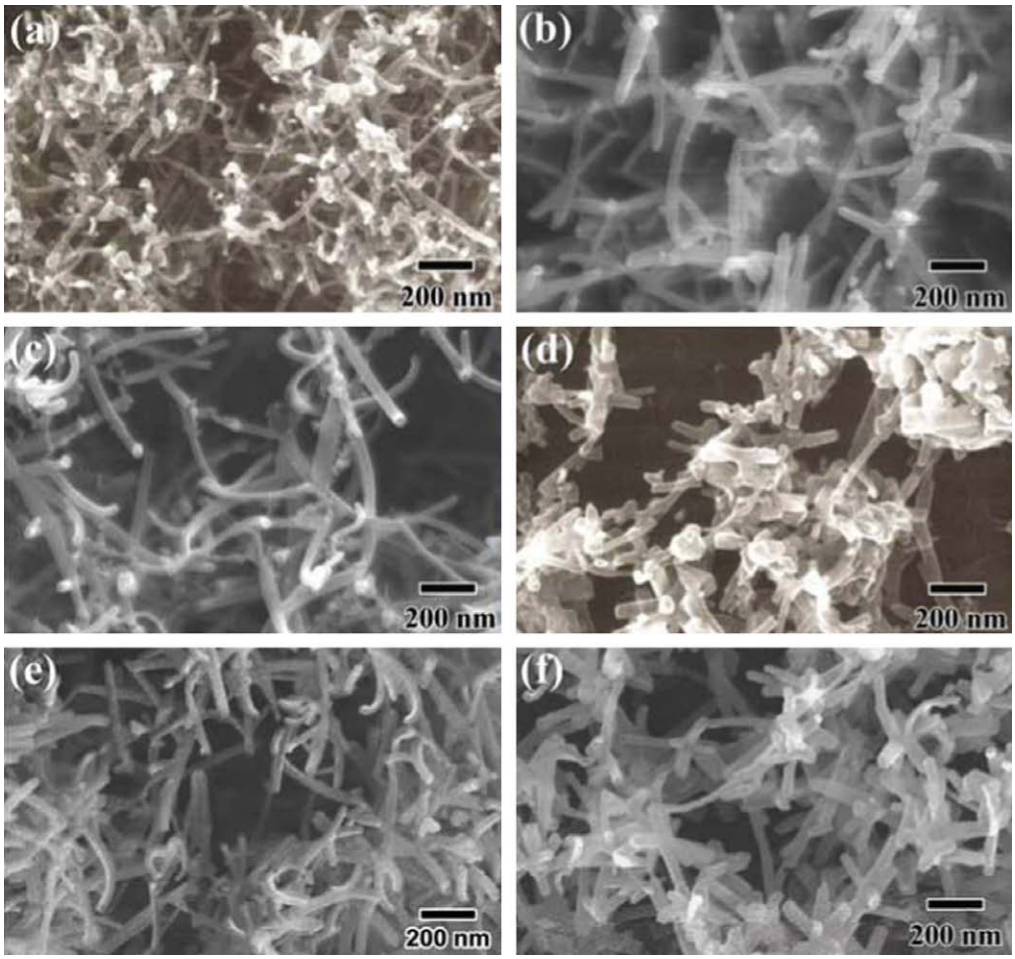

Fig. 2. AlQ_3 nanowires fabricated under a cold trap when the temperature of graphite boat is 410 °C in Ar of (a) 1.33×10^2 Pa, (b) 1.33×10^3 Pa, (c) 3.99×10^3 Pa, (d) 6.67×10^3 Pa, and when the temperature of graphite boat is 420 °C in Ar of (e) 1.33×10^3 Pa and (f) 3.99×10^3 Pa.

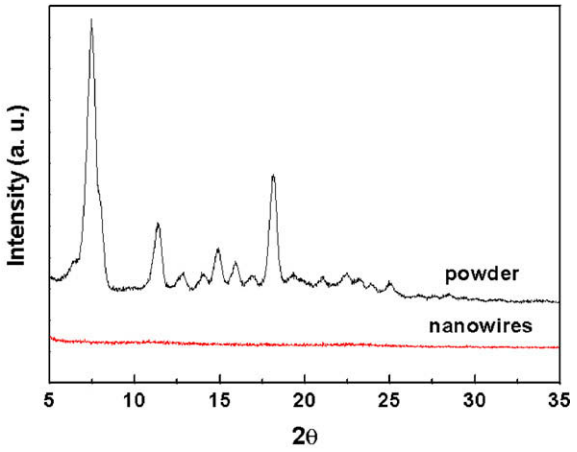

Fig. 3. XRD patterns of AlQ_3 nanowires and commercial powder.

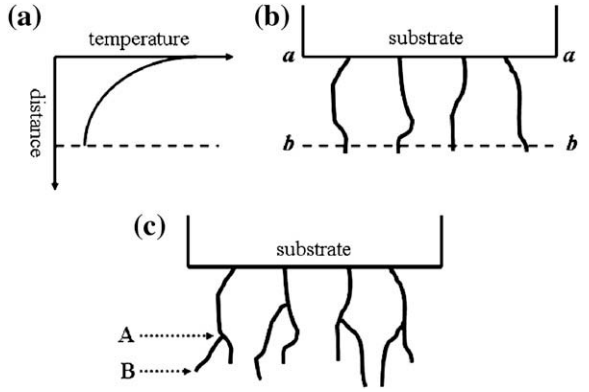

Fig. 4. Schematic growth mechanism of AlQ_3 nanowires. (a) The temperature in advance of section *aa* drops and a falling temperature gradient generates. (b) The primary branches of nanowires grow out. (c) T_A is higher than T_B so the secondary branches form.

together merely by weak van der Waals force. Quantum confinement effect is not expected to exist in this kind of organometallic material [31]. Previous literature has demonstrated that both AlQ_3 nanoparticles and nanowires ex-

hibit a stronger PL emission than that of AlQ_3 thin film [30]. Similar results are also demonstrated in this work. The specific surface area of nanowires is much larger than that of the film, so enhanced absorption of excitation light and a stronger PL emission are observed. The emission ranges of various nanowires are from 4400 to 7200 Å, and the maximum intensities are all located at around 5270 Å, as shown in Fig. 5. The PL spectra of the nanowires fabricated in Ar of 1.33×10^2, 1.33×10^3 and 3.99×10^3 Pa when the boat temperature is 400 and 410 °C are displayed in Fig. 5a and b, respectively. Stronger PL intensity is revealed from the nanowires fabricated at a lower working pressure. Unlike AlQ_3 nanoparticles [3], the nanowires have a narrow distribution of diameter, and a decreased diameter is not supposed to influence their PL property. The enhanced PL intensity can be attributed to the higher density of nanowires formed at a lower working pressure. Higher density indicates that more nanowires congregate in the same area and increases the absorption of excitation light, leading to a stronger PL emission accordingly.

3.4. Field emission

Thanks to the large aspect ratio and field enhancement factor (β) of 1D nanostructures, they have become promising candidates as the field-emission electron source for applications such as field-emission electron microscope, electron source of X-ray and field-emission displays, etc. Lots of effort has been devoted to 1D inorganic nanomaterials such as carbon nanotubes (CNTs), SiC nanowires and nanorods, SiCN nanorods, ZnO nanotips and nanowires, GaN nanorods and CuO nanofibers for a long time [32–42]. Among them, CNTs are one of the most widely investigated materials. It is demonstrated in this work that amorphous AlQ_3 nanowires fabricated by vapor condensation also exhibit field-emission behavior. Their low turn-on field ($E_{\text{turn-on}}$) and high current density are comparable to those of most inorganic 1D nanostructures.

The famous Fowler–Nordheim (F–N) equation [43] is also applicable to AlQ_3 nanowires. The straight line obtained by plotting $\ln(J/E^2)$ versus $1/E$ is regarded as a typical signature of field-emission phenomenon. According to the F–N equation, the slope (m) of the straight line is related to work function (ϕ) and β. As long as m is achieved, β can be calculated if ϕ is already known, or ϕ can be calculated if β is already known. The schematic energy diagram of bulk AlQ_3 material is depicted in Fig. 6a. The dissociation energy from the LUMO to vacuum is around 3.0 eV [44]. Because an exponential distribution of trap states with a characteristic energy 0.15 eV exists below the LUMO and the quasi-Fermi level lies in where the traps distribute, the ϕ of AlQ_3 bulk material is between 3.0 and 3.15 eV.

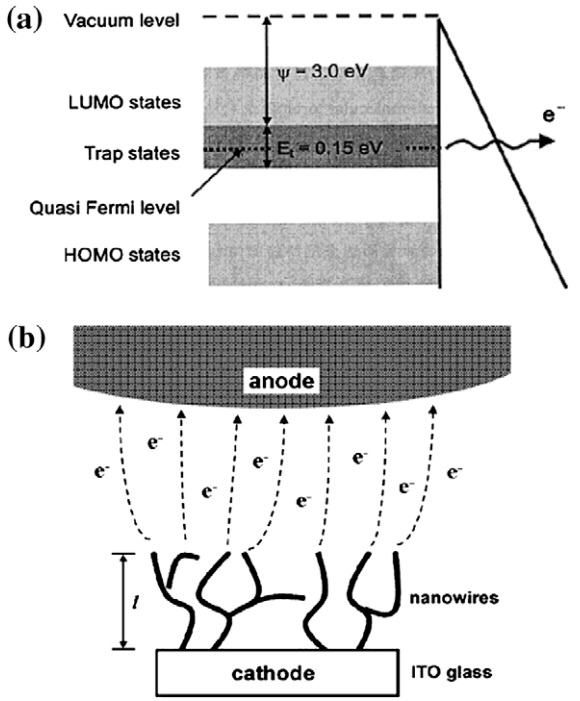

Fig. 6. (a) Schematic energy diagram of AlQ_3 bulk material. (b) Schematic electron emission process from the branched AlQ_3 nanowires.

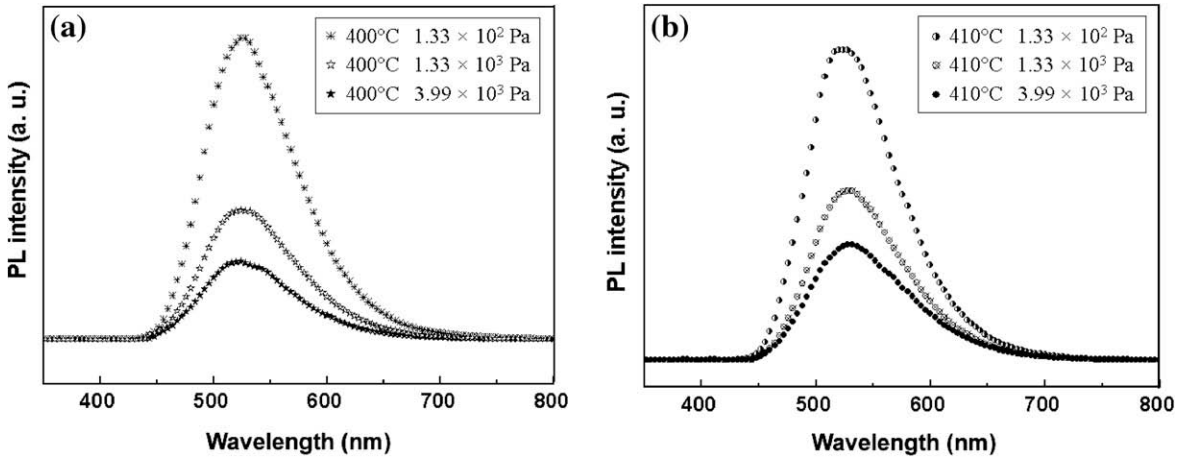

Fig. 5. PL spectra of the AlQ_3 nanowires fabricated in Ar of various working pressures when the boat temperature is (a) 400 °C and (b) 410 °C.

Thus $\phi = 3.15$ eV is used to calculate the β of AlQ_3 nanostructures. According to the report by Tarntair et al. [29], β is related to the geometry of nanostructures and can be expressed by the ratio of the length (l) and radius (r) of an individual nanostructure ($\beta = l/r$). A larger β can be obtained when a nanostructure has a larger l and a smaller r. That is, longer and thinner nanostructures should be more advantageous to field emission.

Fig. 7a shows the J–E curves of various AlQ_3 nanowires. As the applied field is 20 V/μm, the nanowires fabricated at a boat temperature of 400 °C in Ar of 1.33×10^2, 1.33×10^3 and 3.99×10^3 Pa can bear a current density of 31.90, 0.15 and 2.81 mA/cm^2, respectively (curves a–c). The nanowires fabricated at a boat temperature of 410 °C in Ar of 1.33×10^2, 3.99×10^3 and 6.67×10^3 Pa can bear a current density of 13.81, 12.42 and 44.27 mA/cm^2, respectively (curves d–f). With a boat temperature of 420 °C, the nanowires fabricated in Ar of 1.33×10^3 and 3.99×10^3 Pa can bear a current density of 6.25 and 32.49 mA/cm^2, respectively (curves g and h). Table 1 reveals that the current density of AlQ_3 nanowires can not be correlated to their geometries. The maximum current density can be as large as almost 50 mA/cm^2, implying the possibility of employing amorphous AlQ_3 nanowires as emitters with high bearing capacity.

Generally, the magnitude of $E_{\text{turn-on}}$ is regarded as an index of determining whether a nanostructure exhibits a good field-emission characteristic. The $E_{\text{turn-on}}$ is defined as the electric field required to reach a current density of 10 μA/cm^2, and it usually varies with different materials, structures, geometries or measuring instruments. In Fig. 7a, the $E_{\text{turn-on}}$ of curves a, b and c are 10.23, 19.91

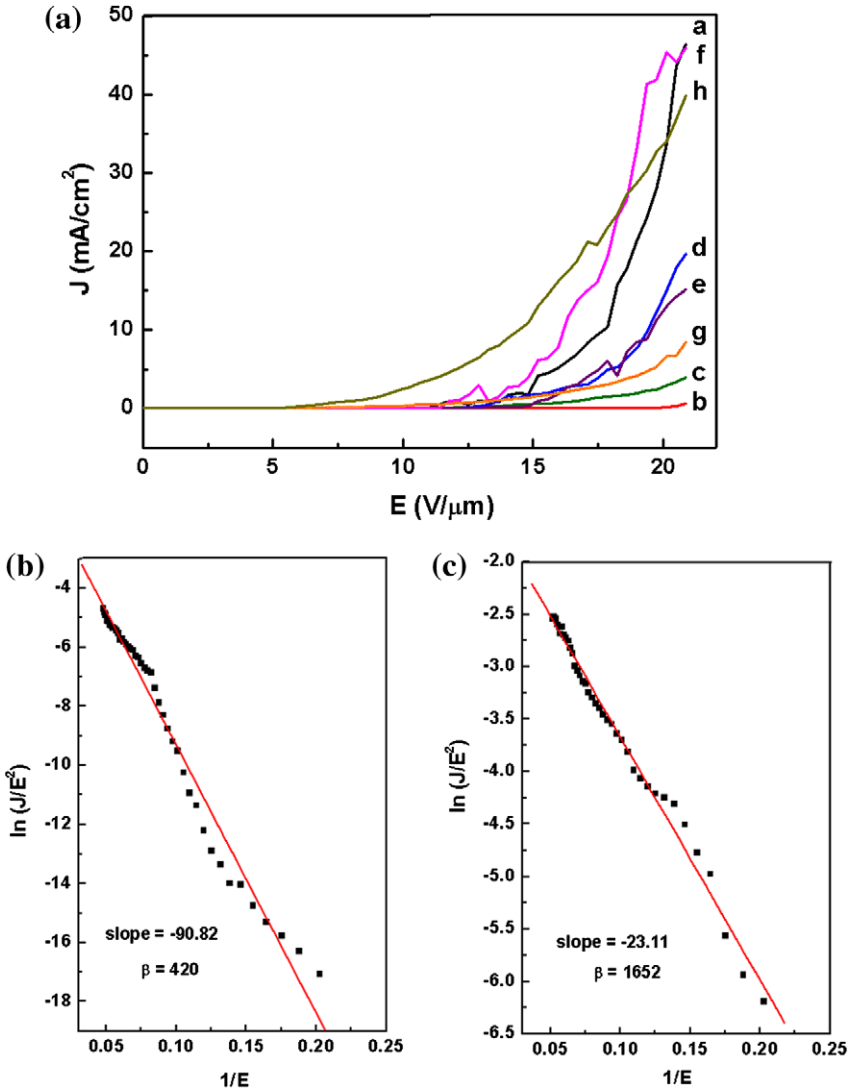

Fig. 7. (a) J–E curves of the AlQ_3 nanowires fabricated at a boat temperature of 400 °C in Ar of 1.33×10^2 (curve a), 1.33×10^3 (curve b), 3.99×10^3 Pa (curve c), at a boat temperature of 410 °C in Ar of 1.33×10^2 (curve d), 3.99×10^3 (curve e), 6.67×10^3 Pa (curve f), and at a boat temperature of 420 °C in Ar of 1.33×10^3 (curve g) and 3.99×10^3 Pa (curve h), respectively. (b) F–N plots transformed from the J–E curves c and h. The straight lines yielded from the high field region demonstrate the field-emission behavior of amorphous AlQ_3 nanowires.

Table 1
$E_{turn\text{-}on}$, $J_{E=20}$ (the current density when the applied field is 20 V/μm) and β estimated from curves a–h of Fig. 7a.

Sample	T (°C)	Ar pressure (Pa)	d (nm)	$E_{turn\text{-}on}$ (V/μm)	$J_{E=20}$ (mA/cm^2)	β
a	400	1.33×10^2	34	10.23	31.91	271
b	400	1.33×10^3	42	19.91	0.15	39
c	400	3.99×10^3	45	10.18	2.81	420
d	410	1.33×10^2	35	9.93	13.81	207
e	410	3.99×10^3	46	11.04	12.42	256
f	410	6.67×10^3	60	10.37	44.27	264
g	420	1.33×10^3	35	3.07	6.25	1445
h	420	3.99×10^3	44	3.21	32.49	1652

and 10.18 V/μm, respectively. For curves d, e and f, the $E_{turn\text{-}on}$ are 9.93, 11.04 and 10.37 V/μm, respectively, whereas for curves g and h, the $E_{turn\text{-}on}$ are 3.07 and 3.21 V/μm, respectively. Table 1 reveals that the $E_{turn\text{-}on}$ of the amorphous AlQ_3 nanowires ranges from 3 to 20 V/μm and frequently approximates to 10 V/μm. This is comparable to those of most inorganic nanostructures but somewhat larger than that of CNTs [32–42,45,46]. Table 1 also discloses that the magnitude of $E_{turn\text{-}on}$ does not correlate to the geometries (diameters) of the nanowires neither. It can be seen that the nanowires fabricated at a boat temperature of 420 °C exhibit a smaller $E_{turn\text{-}on}$. This may be ascribed to the larger film thickness caused by a higher deposition rate.

By plotting $ln(J/E^2)$ versus $1/E$, the *F–N* plots of various AlQ_3 nanowires are obtained. The *F–N* plots transformed from the *J–E* curves c and h in Fig. 7a are given in Fig. 7b and c, respectively, as examples to demonstrate the field-emission behavior of amorphous AlQ_3 nanowires. After obtaining the *F–N* plots, the slopes of the straight lines yielded from the high field region can be estimated, and the corresponding β can then be calculated by substituting the slopes into the *F–N* equation, as displayed in Table 1. According to the definition by Tarntair et al. [29], the l of nanowires can be obtained if the r and β are known, or the β can be calculated if the r and l of nanowires are known. However, the β obtained by estimating the l and r from the SEM micrographs (Figs. 1 and 2) does not match with those calculated from the slopes of the *F–N* plots. Therefore, the definition by Tarntair et al. has to be corrected herein in order to apply to AlQ_3 nanowires. As illustrated in Fig. 4, AlQ_3 nanowires have branched rather than well aligned structures. The process of electrons emitting from the nanowires can be proposed as follows. When an external voltage is applied, the electrons from the cathode are transported through the branches, and then emit from the tips of the branches to the anode, as depicted in Fig. 6b. Consequently, the "l" calculated by multiplying the β with r should be defined as the cross-section thickness of AlQ_3 nanowires, rather than the length of a branch or an individual nanowire. The total thickness of the nanowires deposited on the ITO substrate is calculated and ranges from 3.5 to 9.5 μm. However, the thickness of those fabricated at a boat temperature of 420 °C is over 25 μm, much longer than others. This can be attributed to a higher deposition rate as the boat temperature is higher. Thus larger total thickness of AlQ_3 nanowires results in not only a smaller $E_{turn\text{-}on}$ but also a larger β, which are beneficial for superior field emission.

The comparison in the field-emission properties of amorphous AlQ_3 nanowires with some inorganic and metallic nanomaterials were accomplished [29,32–36,41,45,46]. In terms of the above data and discussion, the $E_{turn\text{-}on}$ of the amorphous nanowires ranges from 3 to 20 V/μm and is usually close to 10 V/μm. Their filed emission characteristic is worse than CNTs, but is comparable to inorganic nanostructures such as SiC or SiCN nanorods [28,29]. The small $E_{turn\text{-}on}$ of some inorganic and metallic nanomaterials may be ascribed to their aligned structures [33–35,41,45,46]. If aligned AlQ_3 nanowires could be obtained, they may become more promising emitters for field emission. Moreover, AlQ_3 nanowires are prepared by a low temperature process, which is more compatible with most electronic processes, so they may find potential applications in electronic or optoelectronic devices.

4. Conclusions

AlQ_3 nanowires could be fabricated under a cold trap by vapor condensation. The diameter of the nanowires was slightly influenced by working pressure and its distribution was in a small range of 35–60 nm. Their length was dramatically changed by working pressure. Longer and thinner nanowires were obtained at a lower working pressure. The most appropriate condition for fabricating long and fine nanowires was to set boat temperature at 410 °C and to control Ar pressure at between 1.33×10^3 and 3.99×10^3 Pa. A higher density of nanowires was observed at a lower working pressure. By XRD analysis, it could be demonstrated that all the AlQ_3 nanowires were amorphous. Their growth was greatly related to the low temperature of substrate and the working pressure in the process chamber. A dendritic growth mechanism caused by a temperature gradient was proposed to explain the formation of AlQ_3 nanowires. The branched growth could be attributed to the presence of an interface allowed to move forward into sufficiently supercooled gaseous phase.

Quantum confinement effect was not expected to appear in AlQ_3 because the molecules were bonded together merely by weak van der Waals force. Thus the nanowires should not exhibit a PL blue shift as their sizes shrank. Stronger PL intensity was revealed when higher density of nanowires were formed at a lower working pressure. This work also demonstrated that AlQ_3 nanowires exhibited field-emission behavior. The $E_{turn\text{-}on}$ of the nanowires ranged from 3 to 20 V/μm and frequently approximated to 10 V/μm. Their low $E_{turn\text{-}on}$ were comparable to those

of most inorganic 1D nanostructures but somewhat larger than that of CNTs, implying the possibility of using them as emitters with high bearing capacity. The magnitude of $E_{\text{turn-on}}$ did not correlate to the geometries (diameters) of the nanowires. Larger film thickness caused by a higher deposition rate at a higher boat temperature led to a smaller $E_{\text{turn-on}}$. If aligned AlQ_3 nanowires could be obtained, they may become more promising emitters for field-emission applications.

References

[1] J.J. Chiu, C.C. Kei, T.P. Perng, W.S. Wang, Adv. Mater. 15 (2003) 1361.
[2] C.P. Cho, C.A. Wu, T.P. Perng, Adv. Funct. Mater. 16 (2006) 819.
[3] C.P. Cho, T.P. Perng, Nanotechnology 17 (2006) 3756.
[4] C.P. Cho, C.Y. Yu, T.P. Perng, Nanotechnology 17 (2006) 5506.
[5] C.P. Cho, T.P. Perng, Nanotechnology 18 (2007) 125202.
[6] J.X. Huang, R.B. Kaner, J. Am. Chem. Soc. 126 (2004) 851.
[7] H. Hasegawa, I. Kubota, S. Mashiko, Thin Solid Films 438 (2003) 352.
[8] C.P. Cho, T.P. Perng, J. Nanosci. Nanotechnol. 8 (2008) 69.
[9] W. Chen, Q. Peng, Y.D. Li, Adv. Mater. 20 (2008) 2747.
[10] Y.S. Zhao, C.A. Di, W.S. Yang, G. Yu, Y.Q. Liu, J.N. Yao, Adv. Funct. Mater. 16 (2006) 1985.
[11] H.B. Liu, J.B. Li, C.S. Lao, C.S. Huang, Y.L. Li, Z.L. Wang, D.B. Zhu, Nanotechnology 18 (2007) 495704.
[12] H.B. Liu, Q. Zhao, Y.L. Li, Y. Liu, F.S. Lu, J.P. Zhuang, S. Wang, L. Jiang, D.B. Zhu, D.P. Yu, L.F. Chi, J. Am. Chem. Soc. 127 (2005) 1120.
[13] A.M. Collins, S.N. Olof, J.M. Mitchels, S. Mann, J. Mater. Chem. 19 (2009) 3950.
[14] R.O. Al-Kaysi, C.J. Bardeen, Chem. Commun. (2006) 1224.
[15] Y.S. Zhao, H.B. Fu, F.Q. Hu, A.D. Peng, J.N. Yao, Adv. Mater. 19 (2007) 3554.
[16] Y.S. Zhao, H.B. Fu, F.Q. Hu, A.D. Peng, W.S. Yang, J.N. Yao, Adv. Mater. 20 (2008) 79.
[17] Y.S. Zhao, H.B. Fu, A.D. Peng, Y. Ma, D.B. Xiao, J.N. Yao, Adv. Mater. 20 (2008) 2859.
[18] J.H. Kim, Y.N. Jung, J.W. Chung, B.K. An, S.Y. Park, Small 5 (2009) 804.
[19] J.W. Chung, H. Yang, B. Singh, H. Moon, B.K. An, S.Y. Leed, S.Y. Park, J. Mater. Chem. 19 (2009) 5920.
[20] Y. Cao, I.D. Parker, G. Yu, C. Zhang, A.J. Heeger, Science 397 (1999) 414.
[21] A. Noy, A.E. Miller, J.E. Klare, B.L. Weeks, B.W. Woods, J.J. DeYoreo, Nano Lett. 2 (2002) 109.
[22] J.H. Lim, C.A. Mirkin, Adv. Mater. 14 (2002) 1474.
[23] C.W. Tang, S.A. VanSlyke, Appl. Phys. Lett. 51 (1987) 913.
[24] J.R. Sheats, H. Antoniadis, M. Hueschen, W. Leonard, J. Miller, R. Moon, D. Roitman, A. Stocking, Science 273 (1996) 884.
[25] I. Musa, D.A.I. Munindrasdasa, G.A.J. Amaratunga, W. Eccleston, Nature 395 (1998) 362.
[26] J.C. She, J. Chen, S.Z. Deng, X.G. Zheng, N.S. Xu, Ultramicroscopy 79 (1999) 149.
[27] J.C. She, Y.Y. Yang, X.M. Chen, J. Chen, S.Z. Deng, X.G. Zheng, N.S. Xu, Thin Solid Films 349 (1999) 225.
[28] X.T. Zhou, N. Wang, C.K. Au, H.L. Lai, H.Y. Peng, I. Bello, C.S. Lee, S.T. Lee, Mater. Sci. Eng. 119 (2000) A286.
[29] F.G. Tarntair, C.Y. Wen, L.C. Chen, J.J. Wu, K.H. Chen, P.F. Kuo, S.W. Chang, Y.F. Chen, W.K. Hong, H.C. Cheng, Appl. Phys. Lett. 76 (2000) 2630.
[30] J.J. Chiu, W.S. Wang, C.C. Kei, T.P. Perng, Appl. Phys. Lett. 83 (2003) 347.
[31] A.P. Alivisatos, Science 271 (1996) 933.
[32] H. Murakami, M. Hirakawa, C. Tanaka, H. Yamakawa, Appl. Phys. Lett. 76 (2000) 1776.
[33] S.Z. Deng, Z.S. Wu, J. Zhou, N.S. Xu, J. Chen, J. Chen, Chem. Phys. Lett. 356 (2002) 511.
[34] Z.W. Pan, H.L. Lai, F.C.K. Au, X.F. Duan, W.Y. Zhou, W.S. Shi, N. Wang, C.S. Lee, N.B. Wong, S.T. Lee, Adv. Mater. 12 (2000) 1186.
[35] H.C. Lo, D. Das, J.S. Hwang, K.H. Chen, C.H. Hsu, C.F. Chen, L.C. Chen, Appl. Phys. Lett. 83 (2003) 1420.
[36] C.J. Lee, T.J. Lee, S.C. Lyu, Y. Zhang, H. Ruh, H.J. Lee, Appl. Phys. Lett. 81 (2002) 3648.
[37] Y.W. Zhu, H.Z. Zhang, X.C. Sun, S.Q. Feng, J. Xu, Z. Zhao, B. Xiang, R.M. Wang, D.P. Yu, Appl. Phys. Lett. 83 (2003) 144.
[38] C.X. Xu, X.W. Sun, Appl. Phys. Lett. 83 (2003) 3806.
[39] H.M. Kim, T.W. Kang, K.S. Chung, J.P. Hong, W.B. Choi, Chem. Phys. Lett. 377 (2002) 491.
[40] J. Chen, S.Z. Deng, N.S. Xu, W.X. Zhang, X.G. Wen, S.H. Yang, Appl. Phys. Lett. 83 (2003) 746.
[41] C.T. Hsieh, J.M. Chen, H.H. Lin, H.C. Shih, Appl. Phys. Lett. 83 (2003) 3383.
[42] Y.B. Li, Y. Bando, D. Golberg, Appl. Phys. Lett. 82 (2003) 1962.
[43] R. Fowler, L.W. Nordheim, Proc. R. Soc. London 119 (1928) 173.
[44] H. Murata, C.D. Merritt, Z.H. Kafafi, IEEE J. Select. Top. Quantum Electron. 4 (1998) 119.
[45] J. Zhou, N.S. Xu, S.Z. Deng, J. Chen, J.C. She, Z.L. Wang, Adv. Mater. 15 (2003) 1835.
[46] Y.B. Li, Y. Bando, D. Golberg, K. Kurashima, Appl. Phys. Lett. 81 (2002) 5048.

Organic Electronics 11 (2010) 123–126

Contents lists available at ScienceDirect

Organic Electronics

journal homepage: www.elsevier.com/locate/orgel

Low-voltage organic thin-film transistors with hydrophobic hafnium oxynitride film as gate insulator

Li-Shiuan Tsai, Chung-Hwa Wang, Wei-Yu Chen, Wen-Chieh Wang, Jennchang Hwang *

Department of Materials Science and Engineering, National Tsing Hua University, Taiwan

ARTICLE INFO

Article history:
Received 11 August 2009
Received in revised form 11 October 2009
Accepted 11 October 2009
Available online 29 October 2009

Keywords:
OTFT
HfON
Pentacene
Gate dielectric

ABSTRACT

An excellent gate dielectric of amorphous HfON (a-HfON) can be fabricated by flashing a Hf metal layer prior to a-HfON deposition. Nitrogen incorporation in the HfON film can reduce leakage current density from 8×10^{-7} to 10^{-7} A/cm^2. And surface roughness of a-HfON is reduced by the flash Hf metal layer from 1.9 to 1.2 nm. With the flash Hf metal layer, field effect mobility (0.17 cm^2/V s), threshold voltage (−0.3 V), subthreshold swing (−0.209 V/decade), and on/off current ratio (3.2×10^3) can be achieved for organic thin-film transistors with a-HfON gate dielectric.

© 2009 Elsevier B.V. All rights reserved.

1. Introduction

Organic thin-film transistors (OTFTs) have received attention in the applications of flat panel displays and flexible electronics [1–3]. Pentacene, a fused-ring polycyclic aromatic hydrocarbon, is one of the promising materials for the active layers in OTFTs since it exhibits high field effect mobility among organic materials [4,5]. For pentacene-based OTFTs, SiO_2 is frequently used as the gate dielectric and the threshold voltage is about 10 V for a SiO_2 layer of 100 nm thick. In order to lower the threshold voltage, two approaches have been often used. One is to reduce the thickness of the gate dielectric [6]. However, a very thin gate dielectric may have the leakage current problem [7]. The other is to use a high-*k* material as the gate dielectric [8,9]. Hafnium dioxide (HfO_2) is a high-*k* material with very good chemical stability, which has been used to fabricate pentacene-based OTFTs with a low threshold voltage [5,8,10]. The HfO_2 is in a form of amorphous since the deposition is operated at low temperature (150 °C). Nitrogen incorporated amorphous HfO_2 (a-HfO_2) is also an attractive material since it exhibits higher dielectric permittivity than intrinsic a-HfO_2 [11]. The a-HfON film can reduce further the threshold voltage. However, the amorphous HfON (a-HfON) film has been used as the gate dielectric in silicon-based thin-film transistors, rather than OTFTs.

In this article, we present an excellent gate dielectric film of a-HfON fabricated by flashing a Hf metal layer prior to a-HfON deposition. The requirements for a good gate dielectric are low leakage current density, low surface roughness and high-*k*. Low leakage current density can be achieved by the nitrogen incorporation in the HfON film. And surface roughness can be reduced by the flash Hf metal layer. The pentacene-based OTFTs with the a-HfON gate dielectric on a flash Hf metal layer exhibits very good device performance. Various OTFTs with different HfO_2-related gate dielectrics, such as a-HfO_2, a-HfON and a-HfON with a flash Hf metal layer, are fabricated for comparison.

* Corresponding author.
E-mail address: jch@mx.nthu.edu.tw (J. Hwang).

1566-1199/$ - see front matter © 2009 Elsevier B.V. All rights reserved.
doi:10.1016/j.orgel.2009.10.008

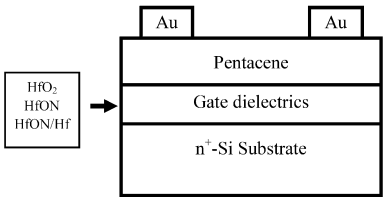

Fig. 1. Schematic showing the structure of an organic thin film transistor with bottom gate and top contact. An ultra-thin Hf metal layer is flashed onto Si(1 0 0) prior to the deposition of gate dielectric.

2. Experimental section

The HfON films with and without a Hf-flash metal layer were chosen as the gate dielectrics for pentacene-based OTFTs. Fig. 1 shows the schematic of a pentacene based OTFT structure. The n^+-Si(1 0 0) wafers were cleaned in the deionized water, and then ultrasonically cleaned in acetone. The n^+-Si(1 0 0) wafers were dipped in a dilute HF solution ($HF:H_2O = 1:100$) in order to remove the native oxide. HfON films of about 50 nm thick were then deposited on the as-dipped n^+-Si(1 0 0) wafers at low-temperature (150 °C) in a radio-frequency (RF) sputtering chamber. The as-dipped n^+-Si(1 0 0) wafers were first transferred to the RF sputtering chamber that was pumped down to a base pressure to 2×10^{-6} torr. The chamber was admitted with a mixing gas of Ar, O_2, and N_2. Mass flow controllers (MFCs) were used to monitor the flow ratio of the mixed gas. The working pressure was 0.25 mtorr. Before the HfON film deposition, a Hf metal layer was flashed onto n^+-Si(1 0 0) by RF sputtering. The Ar flow rate was set to 10 sccm and the RF gun power was operated at 100 W. The bonding characteristics of the HfON films were characterized using X-ray photoelectron spectroscopy (XPS; ESCA1600). With a shadow mask pattern, pentacene films were deposited onto the HfON gate dielectrics with or without a Hf-flash metal layer. The thickness of the pentacene film was about 80 nm and the deposition rate was 0.5 Å/s, which was monitored by a quartz crystal oscillator. The substrate temperature was heated to 50 °C, and work pressure was pumped to 1×10^{-6} torr. Finally, Au was deposited as the source/drain electrodes. Au film thickness was 100 nm, and the shadow mask was used to define the pad. The device channel width and length were defined as 1000 and 100 μm. A metal–insulator–metal (MIM) structure (Al/HfON/Al) with same film thickness of HfON (30 nm) was fabricated to measure the gate leakage current density and the dielectric constant. The area of the Al pad was 1650×1000 μm^2. All electrical characteristics were measured using Agilent 4155c and Agilent 4284 analyzers.

Table 1
AFM measurements and the corresponding surface roughness, leakage current density of HfON dielectrics with different Hf-flash metal layers.

	a-HfO_2	a-HfON	a-HfON/Hf
Ra (nm)	2.3	1.9	1.2
J_{leak} (A/cm^2)	8×10^{-7}	10^{-7}	10^{-7}

3. Results and discussion

Surface roughness and leakage current density (J_{leak}) are critical in the fabrication of an excellent gate dielectric for OTFTs [6,12]. Polycrystalline HfO_2 is not appropriate for gate dielectric since it exhibits high surface roughness and J_{leak} due to the existence of grain boundaries. Amorphous HfO_2 (a-HfO_2) film is a better choice for gate dielectrics since it may exhibit low surface roughness and J_{leak} by removing grain boundaries. In our work, three a-HfO_2 related materials (a-HfO_2, a-HfON, and a-HfON with a flash Hf metal layer) are compared and evaluated to be gate dielectrics in terms of surface roughness and J_{leak}. The evaluation results are listed in Table 1. The a-HfO_2 film was deposited onto Si(1 0 0) by magnetron sputtering Hf metal target in a chamber flowing with a mixed gas of Ar/O_2 (flow rate ratio = 2:4) at 150 °C and 30 W RF gun power. The surface roughness (*Ra*) is ~2.3 nm and J_{leak} is around 8×10^{-7} A/cm^2. By incorporating nitrogen into a-HfO_2 using the gas flow ratio $Ar:O_2:N_2 = 2:4:14$, the *Ra* value of the a-HfON film is reduced to 1.9 nm and the J_{leak} is lowered down to 10^{-7} A/cm^2 at an electric field of 1 MV/

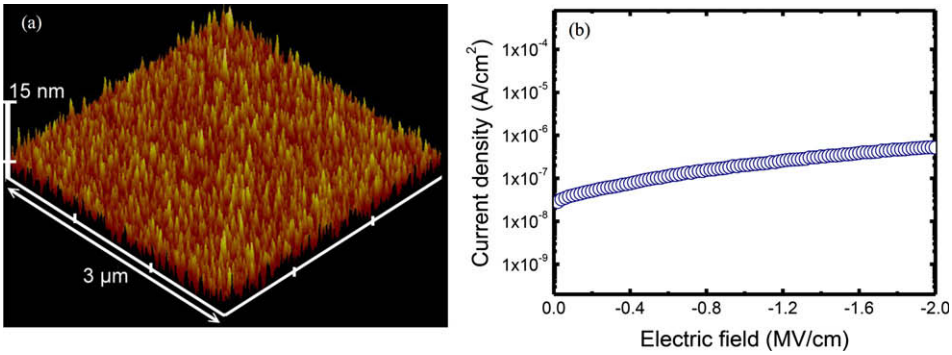

Fig. 2. (a) AFM image showing the 150 °C HfON film with a Hf-flash metal layer. The scanning size is 3×3 μm^2. (b) Leakage current density of the Al–HfON–Al structure as a function of electric field. The maximum bias voltage in OTFT operations corresponds to the electric field of 1 MV/cm.

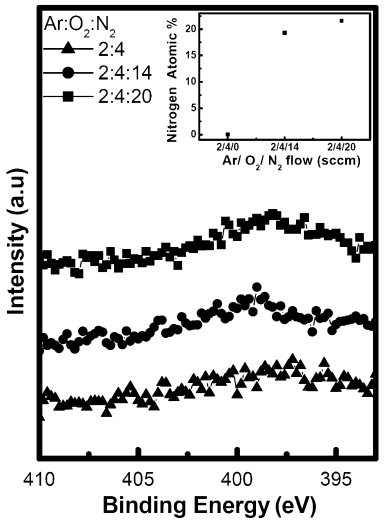

Fig. 3. XPS N 1s core levels excited from the HfON films deposited with different gas flow ratios. The gas flow ratios of $Ar/O_2/N_2$ are 2/4/0, 2/4/14 and 2/4/20. Inset shows the nitrogen atomic percentage at different gas flow ratio.

cm, in agreement with the previous observation reported by Kang et al. [11]. However, the surface roughness of the HfON film is not good enough for gate dielectric. When an ultra-thin Hf metal is flashed on Si(1 0 0) prior to the deposition of the a-HfON film, surface roughness can be reduced down to 1.2 nm shown in Fig. 2a. The corresponding J_{leak} remains at about the same magnitude as that of HfON, shown in Fig. 2b. This suggests that flashing Hf metal does not create more leakage paths.

The incorporation of nitrogen into a-HfO_2 is further characterized using XPS.

Fig. 3 shows the N 1s core electrons emitted different HfON films deposited at different gas flow ratio of $Ar/O_2/N_2$. The N 1s core level increases in intensity with the N_2 ratio, supporting that N incorporation occurs simply by adding N_2 in the mixed gas of Ar/O_2. The nitrogen concentration at different gas flow ratio of $Ar/O_2/N_2$ is estimated by the relative peak area of Hf 4f, O 1s, and N 1s and plotted in the inset in Fig. 3. Note that N 1s slightly shifts toward lower binding energy when gas flow ratio $Ar/O_2/N_2$ changes from 2:4:14 to 2:4:20. The slight energy shift is probably due to the change of the amorphous environment of nitrogen atom in a-HfON. Moreover, N_2 ratio should be higher than O_2 one for nitrogen incorporation to occur. This implies that the efficiency of nitrogen incorporation into a-HfO_2 is not high due to the stronger bond energy of Hf-O. The incorporation of nitrogen into a-HfO_2 is also confirmed by the increase of dielectric constant. The dielectric constants of different HfON films were measured using a test structure of Al/HfON/Al. The dielectric constants of HfON are determined to be 18, 21.1 and 21.3 for the gas flow ratio $Ar:O_2:N_2 = 2:4:0$, 2:4:14 and 2:4:20, respectively.

A 50 nm HfON film ($Ar:O_2:N_2 = 2:4:14$) with the Hf-flash metal layer was chosen as the gate dielectric to illustrate the electrical characteristics of pentacene-based OTFTs. Fig. 4a shows the transfer characteristics of the HfON–OTFT with a Hf-flash metal layer. The HfON–OTFT is saturated at a relatively low gate voltage (~3 V). The field effect mobility (μ_{FE}), threshold voltage (V_{TH}), on/off current ratio (I_{on}/I_{off}) and subthreshold swing (S.S.) are determined to be 0.17 $cm^2/V\,s$, −0.3 V, $\sim 10^3$ and 209 mV/decade, respectively. The subthreshold swing is close to the theoretical minimum value, $(kT/q \cdot \ln(10) = \sim 60$ mV/decade) [13]. The HfON–OTFT can be operated in the saturation region at low drain bias (~1.5 V), as shown in the output characteristics of the HfON–OTFT in Fig. 4b.

The electrical characteristics of pentacene-based OTFTs with different gate dielectrics (a-HfO_2, a-HfON, and a-HfON with a flash Hf metal layer) are determined for comparison and tabulated in Table 2. Among these three gate dielectrics, a-HfO_2–OTFT exhibits the lowest μ_{FE} value of 0.038 $cm^2/V\,s$. When nitrogen is incorporated into a-HfO_2, μ_{FE} increases to 0.086 $cm^2/V\,s$. For a-HfON with a flash Hf metal layer, μ_{FE} reaches to 0.17 $cm^2/V\,s$ much higher than that of a-HfO_2–OTFT. The enhancement of the μ_{FE} value is attributed to low surface roughness (1.2 nm) and low

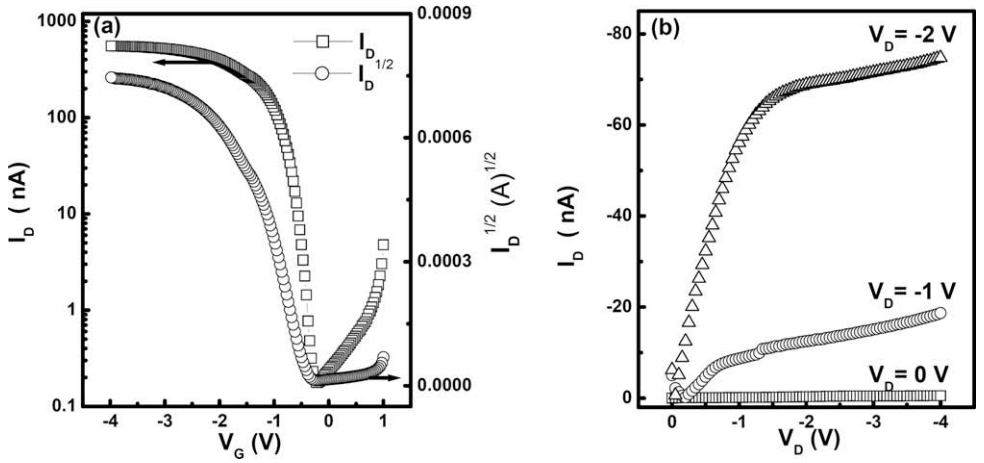

Fig. 4. (a) Transfer characteristics of the OTFT with HfON gate dielectric on a flash Hf metal layer. (b) The corresponding output characteristics.

Table 2
Electric properties of OTFTs with different gas flow ratio and Hf-flash metal layer.

	μ_{FE} (cm^2/V s)	V_{th} (V)	I_{on}/I_{off}	S.S. (V/decade)	Interface trap density (cm^{-2} eV^{-1})
a-HfO_2	0.038	−0.9	3×10^3	−0.319	3.14×10^{13}
a-HfON	0.086	−0.7	0.9×10^3	−0.368	3.8×10^{13}
a-HfON/Hf	0.17	−0.3	3.2×10^3	−0.209	1.9×10^{13}

leakage current density (10^{-7} A/cm^2). By lowering surface roughness, the scattering probably is reduced in the transport channel at the pentacene/a-HfON interface so that μ_{FE} is enhanced. Moreover, the reduction of leakage current density makes the drain current higher such that a higher value of μ_{FE} can be obtained. Similarly, the V_{TH} value of OTFTs reduces from −0.9 to −0.7 V when nitrogen is incorporated into a-HfO_2. The slight reduction of V_{TH} is attributed to the generation of negative fixed charges due to the replacement of oxygen by nitrogen. For a-HfON with a flash Hf metal layer, V_{TH} reduces further down from −0.7 to −0.3 V. The flash Hf metal layer is very thin, which is transformed into a-HfON at the interface during the deposition process of a-HfON. The extra formation of a-HfON due to the flash Hf metal layer is not expected to reduce V_{TH}. In 2008, Suemori et al. reported that the V_{TH} value of a pentacene based OTFT was reduced by smoothing the surface roughness of SiO_2 gate dielectric [14]. The V_{TH} shift was attributed to lattice distortion in pentacene layers deposited on rough SiO_2 surfaces. The V_{TH} shift is 0.4 V in our work that is thus attributed to the reduction of surface roughness. For OTFTs with either one of the three gate dielectrics (a-HfO_2, a-HfON, and a-HfON with a flash Hf metal layer), the I_{on}/I_{off} values are about the same. The I_{on}/I_{off} value of the a-HfON–OTFT with a flash Hf metal layer is slightly higher, which is attributed to its lowest leakage current density.

Since the subthreshold swing represents the interface quality and the trap behavior [15], the maximum interface trap density is approximated to be [16],

$$N_{SS} = \left[\frac{S \cdot \log(e)}{kT/q} - 1\right] \cdot \frac{C_i}{q}$$

where S is the subthreshold swing; C_i is the capacitance per unit area; k is Boltzmann's constant, and T is the absolute temperature. Substituting $C_i = 787$ nf/cm^2 and $S =$ 209 mV/decade, the approximate interface trap density is determined to be 1.9×10^{13} cm^{-2} eV^{-1} for the a-HfON–OTFT with the flash Hf metal layer. The trap density is lower than that of a-HfO_2–OTFT and a-HfON–OTFT. This indicates that the defects at the pentacene/a-HfON interface can be lowered by flashing a very thin Hf metal layer before depositing HfON film. Very probably, the defects at the pentacene/a-HfON are strongly affected by the surface roughness of a-HfON. With a smoother surface, a better quality of pentacence can be deposited on the surface of a-HfON at the beginning of the deposition. And the reduction of the interface trap density would speed up the carrier transport, which is in agreement with the increase of μ_{FE}.

4. Conclusion

In conclusion, a-HfON–OTFTs exhibits better device performance than a-HfO_2–OTFTs since nitrogen incorporation into a-HfO_2 can reduce leakage current density. The device performance of a-HfON–OTFTs can be further improved by flashing a very thin Hf metal layer on the bottom gate electrode before depositing the a-HfON gate dielectric. The flash Hf metal layer helps to reduce surface roughness of the a-HfON gate dielectric. The fabrication of the Hf flashed a-HfON gate dielectric is a low temperature process (150 °C), which may be applicable to either metal or polymer substrates and is potentially useful for soft organic electronics.

Acknowledgement

The work is sponsored by National Science Council, R.O.C., through the project NSC 97-2221-E-007-018-MY3.

References

[1] Q. Cao, Z.T. Zhu, M.G. Lemaitre, M.G. Xia, M. Shim, J.A. Rogers, Appl. Phys. Lett. 88 (2006) 3.
[2] T.W. Kelley, P.F. Baude, C. Gerlach, D.E. Ender, D. Muyres, M.A. Haase, D.E. Vogel, S.D. Theiss, Chem. Mater. 16 (2004) 4413–4422.
[3] C.D. Dimitrakopoulos, P.R.L. Malenfant, Adv. Mater. 14 (2002) 99.
[4] C. Mattheus, G. Wijs, R. Groot, T. Palstra, J. Am. Chem. Soc. 125 (2003) 6323.
[5] T.W. Kelley, L.D. Boardman, T.D. Dunbar, D.V. Muyres, M.J. Pellerite, T.P. Smith, J. Phys. Chem. B 107 (2003) 5877–5881.
[6] A. Facchetti, M.H. Yoon, T.J. Marks, Adv. Mater. 17 (2005) 1705.
[7] G.M. Wang, D. Moses, A.J. Heeger, H.M. Zhang, M. Narasimhan, R.E. Demaray, J. Appl. Phys. 95 (2004) 316–322.
[8] G.D. Wilk, R.M. Wallace, J.M. Anthony, J. Appl. Phys. 89 (2001) 5243–5275.
[9] M. Houssa, L. Pantisano, L.A. Ragnarsson, R. Degraeve, T. Schram, G. Pourtois, S. De Gendt, G. Groeseneken, M.M. Heyns, Mater. Sci. Eng. R Rep. 51 (2006) 37–85.
[10] C.S. Kim, S.J. Jo, S.W. Lee, W.J. Kim, H.K. Baik, S.J. Lee, D.K. Hwang, S. Im, Semi. Sci. Technol. 21 (2006) 1022–1025.
[11] C.S. Kang, H.J. Cho, R. Choi, Y.H. Kim, C.Y. Kang, S.J. Rhee, C.W. Choi, M.S. Akbar, J.C. Lee, IEEE Trans. Electr. Dev. 51 (2004) 220–227.
[12] J. Veres, S. Ogier, G. Lloyd, D. de Leeuw, Chem. Mater. 16 (2004) 4543–4555.
[13] M. McDowell, I.G. Hill, J.E. McDermott, S.L. Bernasek, J. Schwartz, Appl. Phys. Lett. 88 (2006) 3.
[14] K. Suemori, S. Uemura, M. Yoshida, S. Hoshino, N. Takada, T. Kodzasa, T. Kamata, Appl. Phys. Lett. 93 (2008) 3.
[15] C.R. Newman, C.D. Frisbie, D.A. Da Silva, J.L. Bredas, P.C. Ewbank, K.R. Mann, Chem. Mater. 16 (2004) 4436–4451.
[16] K.N.N. Unni, S. Dabos-Seignon, J.M. Nunzi, J. Phys. D-Appl. Phys. 38 (2005) 1148–1151.

Organic Electronics 11 (2010) 127–136

Contents lists available at ScienceDirect

Organic Electronics

journal homepage: www.elsevier.com/locate/orgel

Understanding the effect of semiconductor thickness on device characteristics in organic thin film transistors by way of two-dimensional simulations

Dipti Gupta [a,b,*], Yongtaek Hong [b]

[a] Department of Materials and Metallurgical Engineering, Indian Institute of Technology, Kanpur 208016, India
[b] School of Electrical Engineering and Computer Science, Seoul National University, San 56-1 Shillim-Dong, Kwanakgu, Seoul 151-744, South Korea

ARTICLE INFO

Article history:
Received 20 July 2009
Received in revised form 20 September 2009
Accepted 17 October 2009
Available online 22 October 2009

Keywords:
Organic thin film transistor
Device simulation
Pentacene
Semiconductor thickness
Semiconductor–insulator interface
Low-mobility-layer
Energy band offset
Morphology

ABSTRACT

This paper investigates the dependence of organic thin film transistor (OTFT) characteristics with semiconductor (pentacene) thickness by way of two-dimensional drift–diffusion simulations. The extracted field-effect mobility of the as-measured top contact devices exhibits a variation as the pentacene thickness changes from 10 to 100 nm. Device simulation of an ideal OTFT does not exhibit any dependence on semiconductor thickness, as expected. Therefore, in simulations, the physical behavior related to charge transport at the pentacene–insulator interface and in the bulk is systematically introduced in order to model the experimentally observed device characteristics. These effects are simulated by incorporating a low-mobility-layer adjacent to the dielectric, and energy level shift in the same layer as compared to the bulk pentacene to induce confinement towards the insulator, and bulk donor traps in the pentacene film above a certain thickness (~35 nm). Finally, verification between the simulated and experimental device characteristics is obtained as a function of pentacene thickness.

© 2009 Elsevier B.V. All rights reserved.

1. Introduction

Thin film transistors using organic semiconductors as the active materials are considered to be an important component in low-cost, large-area applications such as active-matrix displays, identification tags, sensors and other low-end applications. Organic thin film transistors (OTFT) are also in competition with amorphous silicon TFTs because they demonstrate comparable performance level and better compatibility with the processing on flexible/plastic substrates [1,2]. OTFTs have shown impressive progress in the recent years, however, a lot of research is still needed to make these devices commercial grade and competitive to traditional inorganic-based transistors. It is now well realized that most of the room for improvement lies in understanding the interfaces and the physical properties (i.e., morphology) of organic semiconductors. Any inhomogeneity/defects at the interface or in the semiconducting film not only have adverse effect on the device performance but also hinder in determining the intrinsic properties of the organic semiconductor correctly.

One of the issues related to the above-mentioned effects is the dependence of device performance on the semiconductor thickness. In principle, the device mobility should be unaffected by the semiconductor thickness, because it is well known that most of the charge is accumulated in few nanometers of the semiconductor near the insulator, eliminating the effect of rest of the film [3,4]. However, several studies [4–15] have reported effects of

* Corresponding author. Address: Department of Materials and Metallurgical Engineering, Indian Institute of Technology, Kanpur 208016, India.
E-mail address: dipti.kanpur@gmail.com (D. Gupta).

1566-1199/$ - see front matter © 2009 Elsevier B.V. All rights reserved.
doi:10.1016/j.orgel.2009.10.009

active layer thickness on OTFT performance with a variety of organic semiconductors and in a range of semiconductor thickness (from ~2 nm to ~500 nm). The explanation of such behavior is often attributed to organic semiconductor morphology, semiconductor–insulator interfaces, and access resistances. Although efforts have been taken to describe it properly, comprehensive understanding is still lacking due to the experimental limitations in providing evidences. In this regard, physical modeling and simulation methods becomes utmost important to fully understand the device mechanisms and maximize their performances.

This paper builds on the previous efforts by combining the numerical simulation techniques with the experiments to fully understand the dependence of device characteristics with semiconductor thickness. The simulated results in the normal conditions did not show the experimentally observed thickness dependence, which was also expected as per the standard field-effect models. The physical behavior associated with the semiconductor–insulator interface and the morphology of the semiconductor in the simulation is then step-wise incorporated in order to model the device characteristics accurately. The pentacene film close to the insulator is simulated with different properties as compared to the bulk film in order to account for the known structural discontinuities and interaction of charge carrier with the surface polarons at the polar dielectric surfaces. The morphological dependence of pentacene film with thickness is simulated by including the bulk traps above a certain thickness of pentacene films. The simulated parameters are then adjusted to have a reasonable match with the experimental results.

2. Experiment and device simulation procedure

2.1. Experiment

Fig. 1a illustrates the schematic diagram of the top contact devices with the axes and dimensions as marked. A highly doped silicon wafer (n++) provides a common gate electrode and a uniform 200 nm thick layer of thermally grown SiO_2 on this wafer serves as a gate dielectric. The source and drain electrodes made of 50 nm thick gold are deposited through a shadow mask, which yield a channel length (L) of 30 μm and channel width (W) of 1.0 mm, respectively. Pentacene as the organic semiconductor film is deposited by thermal evaporation at the rate of 0.03–0.04 nm/s at substrate temperature of 65 °C.

2.2. Method of extraction of mobility

The prevalent method, for a grounded source, to extract the field-effect mobility is by using the expressions that describe the drain current (I_D) for crystalline MOSFETs [16]. From simple FET theory, the device characteristics is described by the following equation:

$$I_D = \frac{W\mu C_i}{L}\left[(V_G - V_T)V_D - V_D^2/2\right] \quad (1)$$

where V_D is (drain-source voltage, V_G is (gate-source voltage, μ is the field-effect mobility, V_T is the threshold voltage, and C_i is the capacitance per unit area of the gate insulator. In the linear regime, where $V_D \ll V_G - V_T|$) Eq. (1)) can be simplified to

$$I_D = \frac{W\mu C_i}{L}(V_G - V_T)V_D \quad (2)$$

The field-effect mobility in the linear regime is extracted from the transconductance, which is defined as

$$g_m = \frac{\partial I_D}{\partial V_G} \quad (3)$$

For small and constant V_D device, the mobility is calculated from the relationship

$$\mu = \frac{L \cdot g_m}{W \cdot C_i \cdot V_D} \quad (4)$$

It is to be noted that the mobility as a function of gate voltage can be obtained from Eq. (4) [16]. The threshold voltage is determined from the intercept of the fitting line used to extract the mobility in the linear regime (I_D–V_G) characteristics.

2.3. Device simulation procedure

The two-dimensional device simulator ATLAS (Silvaco) is used for numerical simulations. ATLAS incorporates the physics that govern charge carrier transport and applies it to the dimensions of the device being studied. Further details can be found in Ref. [17]. Although, its applicability to organic materials is limited, it can still predict the qualitative device characteristics correctly [17–20]. The bandgap of pentacene is taken as 2.2 eV, electron affinity (E_A) as 2.8 eV, density of states as 2×10^{21} cm^{-3}, doping concentration as 3×10^{16} cm^{-3}, and dielectric constant as 4. The work function of the source, drain and gate electrode is assumed to be 5.0 eV [17].

3. Results and discussion

3.1. Effect of pentacene thickness

Fig. 1b illustrates the experimental output curves for top contact devices at gate voltage, $V_G = -20$ V, for pentacene thicknesses of 10, 20, 35, 50, 80 and 100 nm, respectively. In order to make a comparison, the simulated curves for the same pentacene thicknesses are also superimposed on the experimental curves. The value of the mobility for the simulations is taken as 0.14 cm^2/Vs, which is equal to the value obtained experimentally for a device with pentacene thickness of 50 nm at $V_D = -5$ V and $V_G = -15$ V. Clearly, there is a mismatch in the trend of the drain current variation with pentacene thickness between experimental and simulated curves. According to the experiments, the drain current increases at any drain voltage (V_D) until a pentacene thickness of 35 nm, and then the

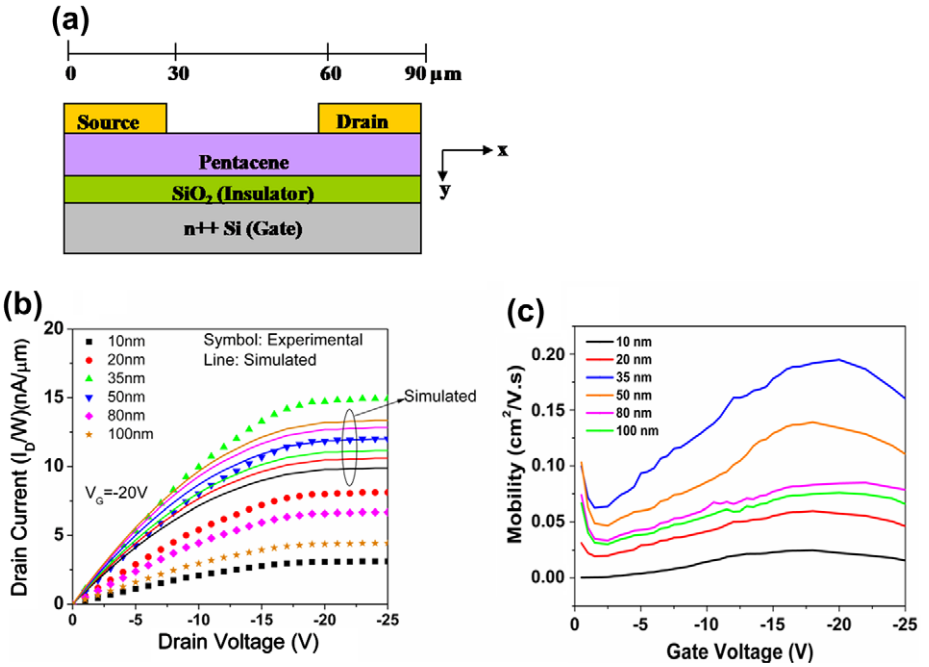

Fig. 1. (a) Schematic diagram of the top contact devices. The scale represents dimensions in microns. (b) A comparison of the output curves for the experimental (symbol) and the simulated (line) devices as a function of pentacene thickness (10–100 nm) at $V_G = -20$ V. (c) Extracted mobility of the devices as a function of gate voltage for pentacene thickness of 10, 20, 35, 50, 80 and 100 nm, respectively (at $V_D = -5$ V).

current decreases. However, the corresponding simulated drain current demonstrates a slight monotonic increase with the pentacene thickness.

The field-effect mobilities, according to the method described in Section 2.2, are also extracted as a function of gate voltage, and are plotted for various pentacene thicknesses at $V_D = -5$ V in Fig. 1c. It is evident from Fig. 1c that the mobility shows a variation with gate voltage, which is generally the case with organic transistors [3,21,22]. The reason for such a gate voltage dependence of mobility is often attributed to the organic material characteristics and also to the insulator–semiconductor interfaces [21,22]. As demonstrated in Fig. 1c, the trend of mobility variation with pentacene thickness is similar to the drain current for all gate voltages, where the values of mobility is highest for pentacene thickness of 35 nm. In order to make a comparison between the mobility obtained from the experimental data and from the simulated device characteristics, the mobility values at $V_D = -5$ V and $V_G = -15$ V are plotted as a function of pentacene thickness in Fig. 2a. Similar to the behavior of the drain current, the experimentally obtained mobility value peaks at 35 nm, whereas simulated data does not demonstrate a major effect of pentacene thickness.

It is clear that simulated device characteristics are only very slightly affected by pentacene thickness, and not to the extent of experimental observations. This small thickness dependence in the simulated results can be explained by the current density profile (Fig. 2b), which is taken across the pentacene at the center of the channel region (shown by a dashed vertical line in the inset of Fig. 2b). Fig. 2b shows that in all the devices with varying pentacene thickness, most of the current flows through a very thin region (called as accumulation region), approximately 5 nm, near the dielectric surface. The slight increase in the drain current with pentacene thickness is thus due to the increase in bulk current. However, its contribution to the total drain current is very little and hence no significant effect on the device characteristics could be observed by varying the pentacene thickness.

Since the experimentally obtained device mobility exhibits a significant pentacene thickness dependence, which is not adequately simulated, it is advisable to incorporate additional features in the simulation in order to model the device characteristics accurately. In the simulation, the physical behavior related to charge transport in the first few layers adjacent to the dielectric is not modeled. The first few layers, where most of the charge transport occurs, may have low mobility as compared to the bulk film. This low mobility may be caused by structural defects, discontinuities, low surface coverage or due to the charge-surface phonon interaction caused by the polar oxide dielectric [23–29]. Kirova and Bussac [26] and Hulea et al. [30] demonstrated through calculations that the charge carrier in the organic film interacts with the surface phonons of the polar dielectrics, which leads to its self-trapping and formation of the long range surface polaron. This result in increased effective mass and mid gap states, which tends to reduce the mobility of the material near the dielectric surface. The similar conclusion is also drawn by Houilli et al. [27], where they performed calculations on the bandwidth and effective mass of the organic semiconductor

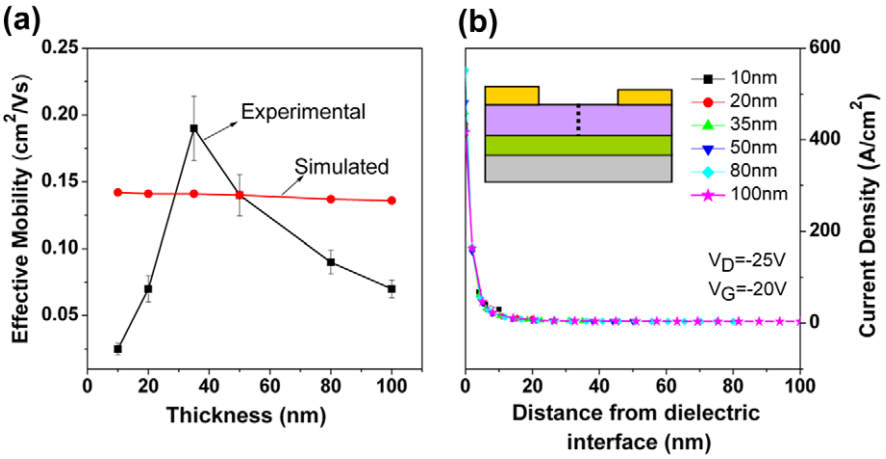

Fig. 2. (a) A comparison of the mobility values for the experimental and the simulated devices as a function of pentacene thickness at $V_D = -5$ V and $V_G = -15$ V. (b) Current density profile taken across the pentacene thickness in the center of the region between the source and drain contacts, as shown by a dashed vertical line in the inset.

layers near the polar dielectric by accounting for the dielectric polarizability and the charge-phonon interaction. They observed that the band-width of the organic semiconducting material near the gate dielectric decreases, while the effective mass increases, as compared to the bulk values. Through potentiometry studies on the pentacene monolayer on an oxide surface, Puntambekar et al. [25] also revealed potential drops in and between the pentacene grains, which also points that the region near the dielectric interface may have low mobility.

Apart from affecting the properties of the organic semiconductor film near the dielectric, the charge transport in this region may also get affected due to the inter layer surface potential differences in the pentacene film and charge distribution in the gate dielectric. Puntambekar et al. [25] demonstrated through surface potential studies that there exists a difference in potential between the first and the second monolayer of pentacene, forcing the mobile carriers more towards the vicinity of the dielectric. Huilli et al. [27] also showed this effect, where they study the polarizability of the channel and concluded that polarization interaction energy of the charge in the dielectric attract the mobile carriers towards it. Since the interface may be defective, this causes mobile charge carriers to probe all the non-idealities associated with the dielectric interface, which further affects the charge transport properties near the dielectric interface [25,27].

Based on this discussion, following two points emerge:

(a) A monolayer of pentacene may have low mobility in comparison to the bulk pentacene. Hereafter this layer is referred as low-mobility-layer.
(b) Mobile charge, for reasons not precisely understood, is preferentially forced to this low-mobility region.

Thus for the realistic simulations, these two effects should also be incorporated, which are systematically introduced in order to match with the experimental data.

3.2. Introduction of a low-mobility-layer at the pentacene–SiO_2 interface and its effect on the device behavior with pentacene thickness

To evaluate the effect of the low-mobility-layer at the insulator surface, we incorporated a 1.5 nm thick layer at the dielectric interface, as depicted in Fig. 3a. The thickness of this layer according to the pentacene crystal structure on SiO_2 is about one monolayer [31,32]. To observe the effect of the lower values of mobility of this layer as compared to the bulk mobility value on the device characteristics, we first reduced its mobility by 10 times as compared to the bulk mobility of 0.14 cm^2/Vs. It is found that the saturation current decreases approximately by 2.5 times with the introduction of a low-mobility-layer, which is due to the 10 times reduction in the drain current in the accumulation region. As already mentioned, the accumulation region is roughly 5 nm thick, therefore reducing the mobility of first 1.5 nm in this region by 10 times leads to a total reduction in the drain current approximately by 2.5 times.

The effective mobility extracted from the simulated curves for this device having a low-mobility-layer (mobility = 0.014 cm^2/Vs) is 0.08 cm^2/Vs at $V_D = -5$ V and $V_G = -15$ V, as compared to the bulk mobility value of 0.14 cm^2/Vs. However, the measured effective mobility of a similar device is 0.14 cm^2/Vs. Therefore, in order to achieve this effective mobility in simulations, we then need to increase the bulk mobility value to 0.28 cm^2/Vs. A good matching with the experiments and simulations could be established, by using the above mobility values. Lowering the mobility of this low-mobility-layer by a decade further causes the drain current to reduce by 1.3 times, while the effective device mobility reduces to 0.115 cm^2/Vs at $V_D = -5$ V and $V_G = -15$ V. Further reduction by a decade in the mobility of low-mobility-layer does not cause significant difference in the over-all device performance.

Next, a study on pentacene thickness dependence incorporating a 1.5 nm thick low-mobility-layer (mobil-

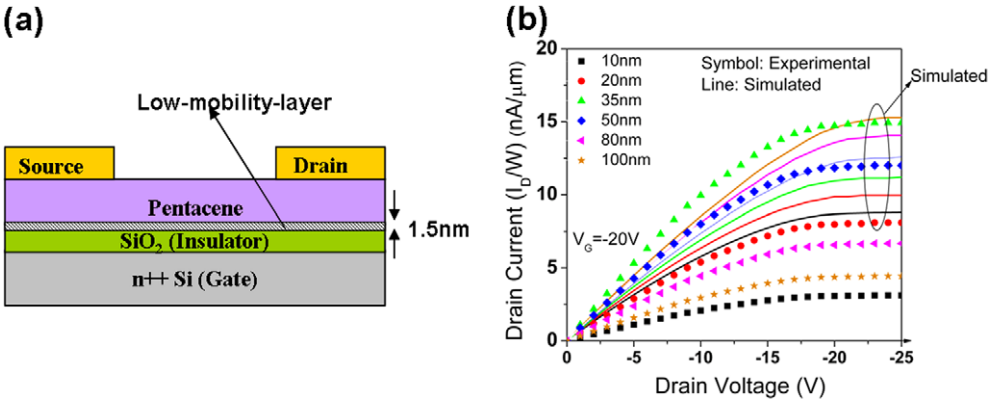

Fig. 3. (a) Schematic diagram of the device depicting 1.5 nm thick low-mobility-layer adjacent to the pentacene–dielectric interface. (b) A comparison of the output characteristics of the simulated devices with the low-mobility-layer at the dielectric surface and the experimental curves, as a function of pentacene thickness at $V_G = -20$ V. The mobility of the low-mobility-layer is 0.014 cm^2/Vs and bulk mobility is 0.28 cm^2/Vs, respectively.

ity = 0.014 cm^2/Vs) is carried out in order to accurately simulate the experimentally observed thickness dependence. Fig. 3b illustrates the superimposed experimental and simulated output characteristics at $V_G = -20$ V with pentacene thicknesses with the bulk mobility as 0.28 cm^2/Vs. It is clear from Fig. 3b that no similarity in the device characteristics between the simulated and experimental curves could be established as a function of pentacene thickness. When comparing with Fig. 1b, now the drain current depends more strongly on the pentacene thickness. However, the simulated device characteristics are still different in two ways from the measured results. First, the simulated drain current increases monotonically as thickness increases, whereas, as-measured drain current is maximum at pentacene thickness of 35 nm. Second, the drain current difference measured for various pentacene thicknesses is much greater than that simulated. Also, the extracted device mobility from the simulated curves shows different characteristics than the experiments. As shown in Fig. 4a the extracted mobility after a pentacene thickness of 35 nm becomes almost constant for simulated devices, whereas it starts decreasing in the as-measured ones.

The nature of the simulated device characteristics could be understood by considering the downwards vertical electric field (in y-direction), which decreases on increasing the pentacene thickness (illustrated in Fig. 4b, at the pentacene–insulator interface in the center of channel). The presence of low-mobility-layer at the dielectric interface and higher electric field for the thinner pentacene films forces more charge carriers to pass through this low-mobility-layer, causing greater reduction in the drain current for thinner devices. The initial increase in mobility with pentacene thickness is thus due to the reduced vertical electric field. However, after a certain value, the channel current is primarily conducted above the low-mobility-layer and the subsequent increase in the drain current is due to the increased bulk current. The above results clearly mark the fact that the incorporation of a low-mobility-layer at the dielectric interface has the greatest effect on thinner films, and after a certain thickness, it does not have any significant effect on the device mobility on increasing the pentacene thickness. Nonetheless, it is clear that the incorporation of low-mobility channel region alone does not allow us to simulate the measured results.

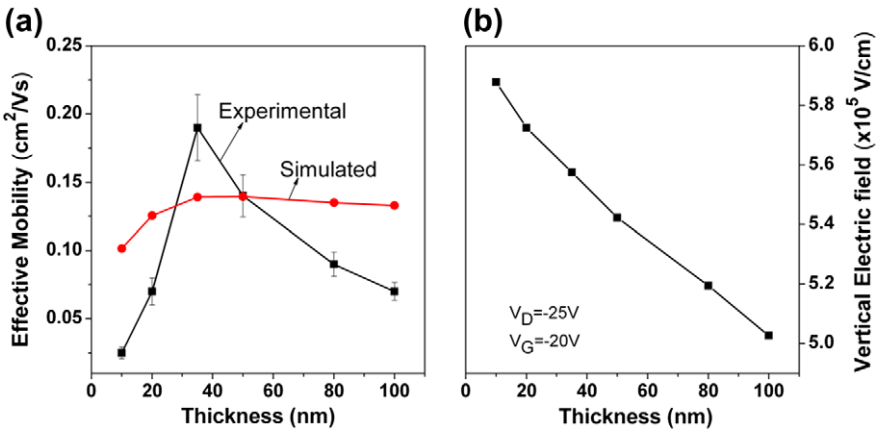

Fig. 4. (a) Extracted device mobility as a function of pentacene thickness for top contact devices on incorporating the low-mobility-layer at $V_D = -5$ V and $V_G = -15$ V, and (b) electric field at the pentacene–dielectric interface, in the middle of the channel. The mobility of the low-mobility-layer is 0.014 cm^2/Vs and bulk mobility is 0.28 cm^2/Vs.

Hence, it is important to include also the preferential forcing (confinement) of charge near the dielectric interface, as discussed in the next section.

3.3. Introducing charge confinement towards near semiconductor–dielectric interface

Since the insertion of the low-mobility-layer at the dielectric interface alone is not able to explain the observed pentacene thickness dependence on mobility values, the additional option of confinement of the mobile channel towards the low-mobility-layer is invoked. This could be accomplished in two ways. First, by the application of a negative charge at the semiconductor–insulator interface or secondly, by the introduction of an energy band offset in the low-mobility-layer with respect to the bulk film.

3.3.1. Negative interface charge

In order to induce confinement of the channel a negative interface charge of the magnitude $q \times 1 \times 10^{12}$ C cm^{-2} (q is the charge on an electron) is applied. On applying the interface charges, the drain current increases and shifts the threshold voltage towards negative gate voltages for all pentacene thicknesses, but does not impact the device mobility. Therefore, including a negative interface charge does not accomplish the objective of effective confinement of charge near the dielectric interface, and yet the threshold voltage shifts significantly. Therefore, confinement of charge near dielectric interface is simulated by another way, as discussed next.

3.3.2. Energy band offset between the low-mobility-layer and bulk pentacene

Based on observations discussed at the end of Section 3.1, electrostatic potential measurements indicated that carriers are preferentially forced in region near the dielectric interface. The reason for this behavior is not well established. Furthermore, the commercial simulator in use here does not contain any models to physically simulate the carrier confinement. Hence, to confine carrier near the dielectric interface, an energy band offset between the low-mobility-layer and bulk pentacene is introduced in such a way that it facilitates the charge migration towards the low-mobility-layer. Fig. 5a shows the energy band diagram of pentacene film depicting the energy band offset between the low-mobility-layer and the bulk pentacene. To force the mobile charge towards the low-mobility-layer, the electron affinity (E_A) value of the low-mobility-layer (E_{A1}) is reduced in comparison to its value in the bulk pentacene (E_{A2}), while keeping the band gap (E_g) value same for both the regions.

With this method of charge accumulation near the interface, the experimental and the simulated transfer curve with an energy band offset value of 0.1 eV between the low-mobility-layer and bulk pentacene is compared. The device characteristics are simulated with the mobility of the low-mobility-layer as 0.014 cm^2/Vs, bulk mobility as 0.28 cm^2/Vs, and pentacene thickness of 50 nm. As expected, the drain current is reduced on introducing this offset, which is due to the charge transfer from the bulk pentacene towards the low-mobility-layer. The effective device mobility reduces to 0.09 cm^2/Vs as compared to the mobility value of 0.14 cm^2/Vs. The threshold voltage shifts to −1.7 V (experimentally −1.9 V). Since the energy band offset produced the expected result of reducing the device mobility, without producing a significant change in the threshold voltage, this method of introducing energy band offset in the low-mobility-layer to confine the charge towards the dielectric interface is preferable.

The magnitude of band offset also affects the device characteristics, which is shown in Fig. 5b by the extracted mobility value with the offset values of 0.0, 0.1 and 0.2 eV, respectively. On increasing the energy band offset value, effective device mobility decreases, indicating more confinement of the mobile charges towards the dielectric interface. Additionally, on including the energy band offset, the mobility of the low-mobility region has much greater effect on the effective mobility of the device. This is illustrated by Fig. 5c which shows the change in over-all device mobility value as a function of the mobility of the low-mobility-layer with an energy band offset value of 0.1 eV.

Apart from the effective mobility value, the charge transport behavior also changes on reducing the mobility value of this low-mobility-layer. For the sake of illustration, the mobility value of this low-mobility-layer are taken as 1×10^{-2}, 1×10^{-3}, and 1×10^{-5} cm^2/Vs. Fig. 5d depicts the current density profile taken across the pentacene thickness in the center of the region between the source and drain contacts, as shown by a dashed vertical line in the inset of Fig. 5d. It is observed that on decreasing the mobility value of the low-mobility-layer by 10 times as compared to the bulk mobility value, the channel becomes very thin and confined to the low-mobility-layer, and the contribution of bulk current to the total current is insignificant. On decreasing the mobility value of the low-mobility-layer to 1×10^{-3} cm^2/Vs, the value of the current passing through the low-mobility-layer reduces. However, now the fraction of the current through bulk is significant. On further decreasing the value of the low-mobility-layer to 1×10^{-5} cm^2/Vs, we observe that current does not at all flow through the low-mobility-layer. Instead, the maximum drain current flows through the layer just above the low-mobility-layer. The bulk conduction also increases and it is almost half of the value of the maximum current density. Further decrease in the mobility value of the low-mobility-layer does not cause any significant difference in the current density profile.

3.3.3. Combined effect of energy band offset and mobility of low-mobility-layer: comparison with experiments

In this section, the simulation parameters that yield results similar to the measurements as a function of pentacene thickness are determined. To match the extracted mobility from the simulated curves with the experimental mobility values, the effect of the various mobility values of the low-mobility-layer and the values of the energy band offset are studied.

Fig. 6a illustrates the extracted effective mobility values as a function of pentacene thickness with a mobility value of 0.014 cm^2/Vs for the low-mobility-layer and the energy

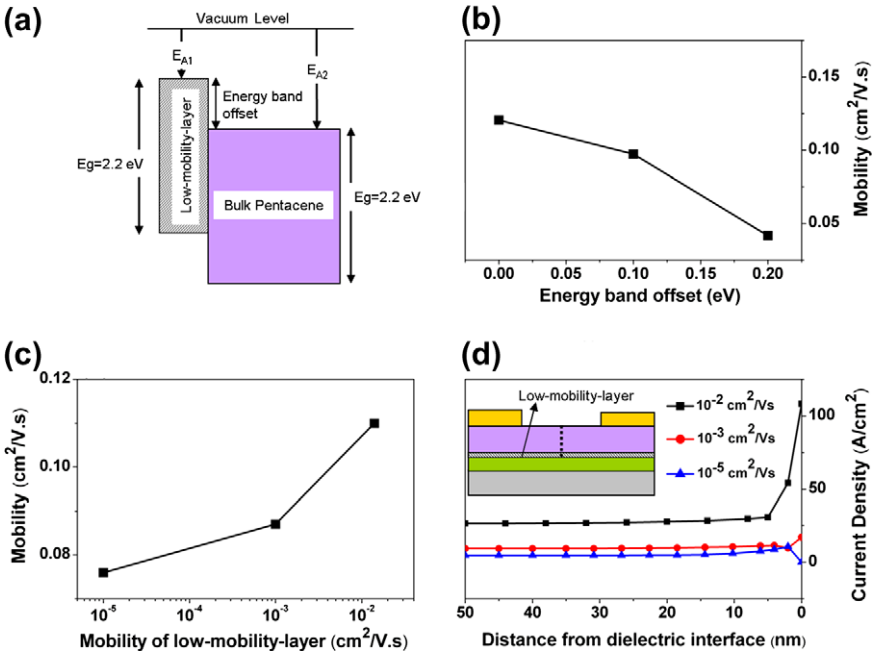

Fig. 5. (a) Schematic diagram of the energy levels in the low-mobility-layer and bulk of the pentacene film, (b) extracted mobility values as a function of the magnitude of energy band offset at $V_D = -5$ V and $V_G = -15$ V, (c) extracted mobility values as a function of the mobility of the low-mobility-layer at an energy band offset of 0.1 eV at $V_D = -5$ V and $V_G = -15$ V, and (d) current density profile in the cross-section of the device as a function of the mobility of the low-mobility-layer ($V_D = -40$ V and $V_G = -20$ V). The mobility of the low-mobility-layer is 0.014 cm^2/Vs and bulk mobility is 0.28 cm^2/Vs. Pentacene thickness is 50 nm.

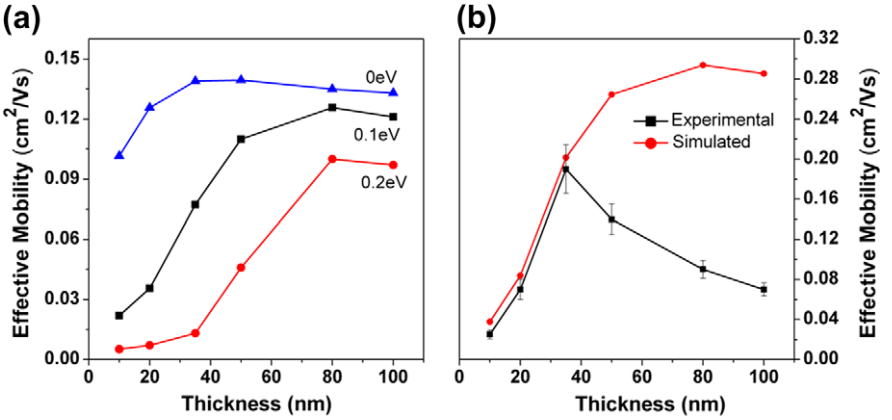

Fig. 6. (a) Effective mobility as a function of pentacene thickness for different values of the energy band offset between the low-mobility-layer and bulk pentacene at $V_D = -5$ V and $V_G = -15$ V. The mobility of the low-mobility-layer is 0.014 cm^2/Vs and bulk mobility is 0.28 cm^2/Vs. (b) Comparison of experimental and simulated mobility value as a function of pentacene thickness. The mobility of the low-mobility-layer is 1×10^{-4} cm^2/Vs and bulk mobility is 1.3 cm^2/Vs. The energy band offset value is 0.11 eV.

band offset value of 0.0, 0.1 and 0.2 eV. It can be seen that the variation in the magnitude of extracted device mobility with pentacene thickness increases when energy band offset between the low-mobility-layer and bulk pentacene is included. For energy band offset value of 0.1 eV, the mobility value increases gradually until 80 nm of thickness and then decreases slightly. While for an energy band offset value of 0.2 eV, device mobility value first increases slightly till 35 nm, then increases rapidly till 80 nm and then becomes almost constant. This variation with thickness as a function of energy band offset magnitude is a result of variations in electric fields, which vary with energy band offset magnitude as well as with the thickness. Whereas higher thickness reduces confinement, the higher energy offset promotes it.

The experimentally determined mobility, as in Fig. 2a increases up to a thickness of 35 nm and then decreases. In case of mobility determined from simulated curves

(see Fig. 6b), the quantitative behavior of mobility up to 35 nm is better matched for an energy band offset value of 0.11 eV, the mobility of low-mobility-layer as $\sim 1 \times 10^{-4}$ cm^2/Vs and bulk mobility as 1.3 cm^2/Vs. However, after 35 nm, no match could be obtained, which is discussed in the next section.

3.4. Introducing bulk traps for thicker pentacene films

After matching the mobility up to pentacene thickness of 35 nm, it is still found that mobility extracted from the simulated curves continued to increase till 100 nm. This would have been the case if the film growth was uniform along the thickness. It has been pointed out that the molecular crystal packing and grain size varies as the pentacene film thickness is increased [33–37]. Furthermore, pentacene films exhibit several crystal structures depending on the thickness [33–37]. Due to the variation in morphology with thickness, more grain boundaries begin to appear, which acts as trapping centers for the mobile charge [38,39]. Table 1 lists the grain size [recorded through atomic force micrographs (AFM)] variation with the pentacene thickness. It is found that until pentacene thickness of 35 nm, the average grain size remains ~0.85 μm. After further increasing the film thickness, the grain size reduces and reaches to 0.15 μm for the 100 nm thick pentacene films.

To explain the experimental results as a function of thickness, we then introduced bulk traps in the region above 35 nm of pentacene thickness, as illustrated in Fig. 7a. Fig. 7b shows a combination of bulk donor type trap concentration and its trap level from the valence band edge, which yields the drain current at $V_D = -25$ V and $V_G = -20$ V within 10% of the measured value in the same condition. Based on this figure, a trap level of 0.4 eV is selected, which produces a reasonable match between the experimental and simulated curves, if bulk donor trap concentration of 4×10^{16} cm^{-3} for 50 nm thick film and 6×10^{16} cm^{-3} for 80 and 100 nm thick films, are chosen.

Table 1
Average grain size as a function of pentacene thickness.

Thickness (nm)	Average grain size (nm)
10	0.8
20	0.85
35	0.85
50	0.55
80	0.3
100	0.25

The superimposed simulated and experimental output curves are depicted in Fig. 8a. The extracted mobility values from the experiments and simulations are also illustrated in Fig. 8b. The extracted mobility values from simulations after substituting these trap levels matches well with the experimentally determined mobility. This indicates that the devices face several non-regularities, which are expressed in the form of low-mobility of the pentacene layers that are associated with the dielectric, existence of energy band offset between the interface layers and the bulk, and the bulk traps due to the structural defects like grain boundaries. The combined effect of these features causes the extracted mobility to depend on the film thickness, which in an ideal case should have been absent. It also signifies the importance of optimizing the thickness of organic semiconductor in order to have enhanced as well as reliable device performance.

The effect of the bulk traps could be illustrated by the current density profile taken across a vertical section in the pentacene film in the center of channel. Fig. 9 illustrates the comparison of the current density profile in device with and without the bulk traps in pentacene film, taken across the pentacene in the middle of channel. It is found that on introducing the bulk traps, the bulk conduction reduces drastically. Since the bulk traps produce resistance, the current is less likely to flow through the bulk. This reduction in bulk current is proportional to the area in which these bulk traps reside. Since bulk traps reside in larger area in 100 nm thick film as compared to 50 and 80 nm thick films, the reduction in the drain current is highest for the 100 nm film. Therefore the bulk current which initially was a significant part of the drain current in thicker films has almost no contribution now. Due to this reduction in bulk current, the over-all drain current decreases.

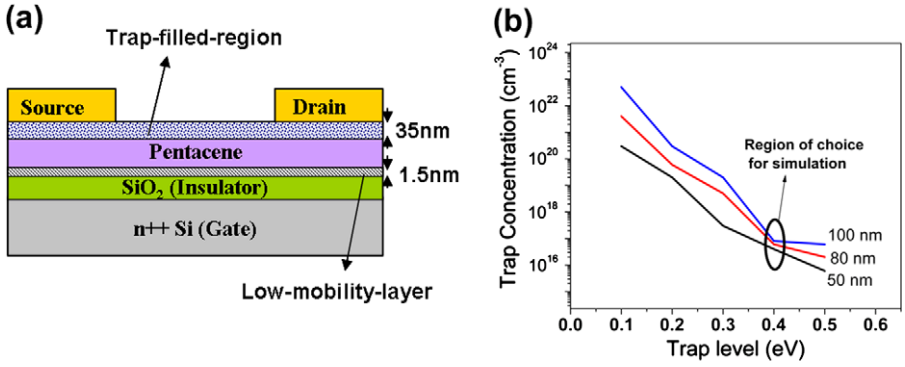

Fig. 7. (a) Schematic diagram of the device depicting low-mobility-layer, and trap filled region above the pentacene thickness of 35 nm. (b) Comparison of trap energy level and trap concentration for 50–100 nm thick pentacene films.

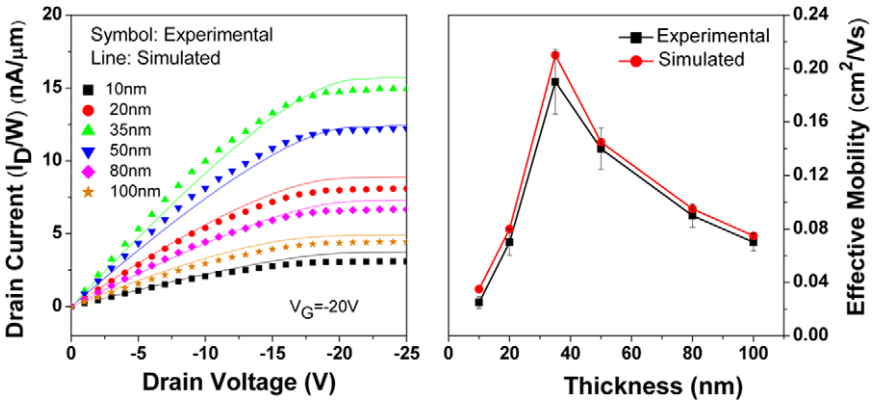

Fig. 8. A comparison of simulated and experimental (a) output curves and (b) mobility value (at $V_D = -5$ V and $V_G = -15$ V) as a function of pentacene thickness. The mobility of the low-mobility-layer and bulk pentacene is taken as 1×10^{-4} cm^2/Vs and 1.3 cm^2/Vs, respectively. The energy band offset value is 0.11 eV. The trap concentration is taken as 4×10^{16} cm^{-3} for 50 nm thick film and 6×10^{16} cm^{-3} for 80 and 100 nm thick films, respectively.

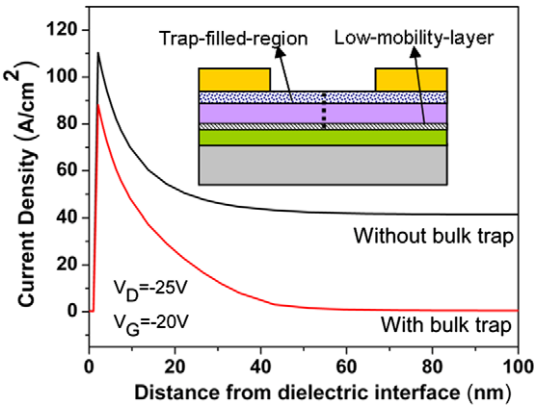

Fig. 9. Current density profile for 100 nm thick pentacene film showing the effect of traps above 35 nm thick pentacene.

4. Conclusions

The observed pentacene thickness dependence on the device characteristics is attributed to the structural inhomogeneities of the region near pentacene/dielectric interface and in the bulk film. The interfacial region is modeled by assigning a 1.5 nm thick layer adjacent to the dielectric a lower mobility value as compared to the bulk pentacene and introducing an energy band offset between this layer and the bulk pentacene. The defects in the bulk film are modeled by introducing donor type traps above a certain thickness (~35 nm) of the pentacene film. The mobility of the low-mobility-layer is estimated to be $\sim 1 \times 10^{-4}$ cm^2/Vs with an energy level shift of the magnitude 0.11 eV. Based on these values, an optimum bulk mobility value of 1.3 cm^2/Vs for pentacene films is estimated, which is significantly higher than obtained from transistor measurements. It is also inferred that in the presence of the above-mentioned defects at the semiconductor–insulator interface and in the bulk of the film, the intrinsic mobility of the material is disguised and one is not able to measure the true mobility of the material through the field-effect measurements.

References

[1] S.F. Nelson, Y.-Y. Lin, D.J. Gundlach, T.N. Jackson, Appl. Phys. Lett. 72 (1998) 1854.
[2] J.S. Campbell, L.D. Bozano, Adv. Mater. 19 (2007) 1452.
[3] G. Horowitz, R. Hajlaoui, H. Bouchriha, R. Bourguiga, M. Hajlaoui, Adv. Funct. Mater. 13 (2003) 53.
[4] F. Dinelli, M. Murgia, P. Levy, M. Cavallini, F. Biscarini, D. de Leeuw, Phys. Rev. Lett. 92 (2004) 116802.
[5] A. Dodabalapur, L. Torsi, H.E. Katz, Science 268 (1995) 270.
[6] J. Lee, K. Kim, J.H. Kim, S. Im, D.Y. Jung, Appl. Phys. Lett. 82 (2003) 4169.
[7] E.L. Granstrom, C.D. Frisbie, J. Phys. Chem. B 103 (1999) 8842.
[8] M. Kiguchi, M. Nakayama, T. Shimada, K. Saiki, Phys. Rev. B 71 (2005) 353321.
[9] R. Ruiz, A. Papadimitratos, A.C. Mayer, G.G. Malliaras, Adv. Mater. 17 (2005) 1795.
[10] S. Jung, Z. Yao, Appl. Phys. Lett. 86 (2005) 083505.
[11] J.B. Chang, V. Subramaniam, Appl. Phys. Lett. 88 (2006) 233513.
[12] P.V. Pesavento, K. Puntambekar, C.D. Frisbie, J.C. McKeen, P.P. Ruden, J. Appl. Phys. 99 (2006).
[13] S. Hoshino, T. Kamata, K. Yase, J. Appl. Phys. 92 (2002).
[14] R. Schroeder, L. Majewski, M. Grell, Appl. Phys. Lett. 83 (2003) 3201.
[15] A. Takshi, A. Dimopoulos, J.D. Madden, Solid-State Electron. 52 (2008) 107.
[16] S.M. Sze, Physics of Semiconductor Devices, second ed., John Wiley and Sons.
[17] D. Gupta, M. Katiyar, D. Gupta, Org. Electron. 10 (2009) 775.
[18] A. Bolognesi, M. Berliocchi, M. Manenti, A.D. Carlo, P. Lugli, K. Lmimouni, C. Dufour, IEEE Trans. Electron Dev. 51 (2004) 1997.
[19] S. Scheinert, G. Paasch, M. Schrodner, J. Appl. Phys. 92 (2002) 330.
[20] S. Cherian, C. Donley, D. Mathine, L. LaRussa, W. Xia, N. Armstrong, J. Appl. Phys. 96 (2004) 5638.
[21] G. Horowitz, R. Hajlaoui, D. Fichou, A. El. Kassmi, J. Appl. Phys. 85 (1999).
[22] M. Mottagghi, G. Horowitz, Org. Electron. 7 (2006) 528.
[23] A.F. Stassen, R.W. de Boer, N.N. Iosad, A.F. Morpurgo, Appl. Phys. Lett. 85 (2004) 3899.
[24] S. Steudel, S. De Vusser, S. De Jonge, D. Janssen, S. Verlaak, J. Genoe, P. Heremans, Appl. Phys. Lett. 85 (2004) 4400.
[25] K. Puntambekar, J. Dong, G. Haugstad, C.D. Frisbie, Adv. Funct. Mater. 16 (2006) 879.
[26] N. Kirova, M.-N. Bussac, Phys. Rev. B 68 (2003) 235312.
[27] H. Houilli, J.D. Picon, L. Zuppiroli, M. Bussac, J. Appl. Phys. 100 (2006) 23702.
[28] H.G.O. Sandberg, G.L. Frey, M.N. Shkunov, H. Sirringhaus, R.H. Friend, Langmuir 18 (2002) 101706.
[29] J. Veres, S.D. Ogier, S.W. Leeming, D.C. Cupertino, S. Mohialdin Khaffaf, Adv. Funct. Mater. 13 (2003) 199.

[30] N. Hulea, S. Fratini, H. Xie, C.L. Mulder, N.N. Iossad, G. Rastelli, S. Ciuchi, A.F. Morpurgo, Nat. Mater. 5 (2006) 982.
[31] S.E. Fritz, S.M. Martin, C.D. Frisbie, M.D. Ward, M.F. Toney, J. Am. Chem. Soc. 126 (2004) 4084.
[32] R. Ruiz, D. Choudhary, B. Nickel, T. Toccoli, K.C. Chang, A.C. Mayer, P. Clancy, J.M. Blakely, R.L. Headrick, S. Iannotta, G.G. Malliaras, Chem. Mater. 16 (2004) 4497.
[33] C.C. Mattheus, G.A. de Wijs, R. de Groot, T.T.M. Palstra, J. Am. Chem. Soc. 125 (2002) 6323.
[34] T. Kakudate, N. Yoshiimoto, Y. Saito, Appl. Phys. Lett. 90 (2007).
[35] L.F. Drummy, D.C. Martin, Adv. Mater. 17 (2005) 903.
[36] T. Jentzch, H.J. Juepner, K.W. Brzezinka, A. Lau, Thin Solid Films 315 (1998) 273.
[37] I.P.M. Bouchoms, W.A. Schoonveld, J. Vrijmoeth, T.M. Klapwijk, Synth. Met. 104 (1999) 175.
[38] S. Verlaak, C. Rolin, P. Heremans, J. Phys. Chem. B 111 (2007) 139.
[39] G. Horowitz, M.E. Hajlaoui, Synth. Met. 122 (2001) 185.

Organic Electronics 11 (2010) 137–145

Contents lists available at ScienceDirect

Organic Electronics

journal homepage: www.elsevier.com/locate/orgel

Deep blue, efficient, moderate microcavity organic light-emitting diodes

Hyoung Kun Kim [a,1], Sang-Hwan Cho [b,1], Jeong Rok Oh [a], Yong-Hee Lee [b], Jun-Ho Lee [c], Jae-Gab Lee [c], Soo-Kang Kim [d], Young-Il Park [d], Jong-Wook Park [d], Young Rag Do [a,*]

[a] Department of Chemistry, Kookmin University, Seoul 136-702, Republic of Korea
[b] Department of Physics, Korea Advanced Institute of Science and Technology, Daejeon 350-710, Republic of Korea
[c] School of Advanced Materials Engineering, Kookmin University, Seoul 136-702, Republic of Korea
[d] Department of Chemistry/Display Research Center, The Catholic University of Korea, Bucheon 420-743, Republic of Korea

ARTICLE INFO

Article history:
Received 14 August 2009
Received in revised form 1 October 2009
Accepted 17 October 2009
Available online 23 October 2009

Keywords:
Organic light-emitting diodes
Microcavity
Bragg mirror
Blue

ABSTRACT

Two types of microcavity blue organic light-emitting diodes (OLEDs) with a dielectric Bragg mirror (two different center wavelengths, type-A ≈ 465, type-B ≈ 470 nm) were designed to achieve the color coordinates of NTSC blue standard and enhance the quantum efficiency in the normal direction. A moderate microcavity OLED was defined as a microcavity OLED with a single pair of TiO_2/SiO_2 high/low dielectric layers inserted between an indium tin oxide (ITO) layer and a glass substrate. The moderate microcavity blue OLED doped with 9,10-bis(3′,5′-diphenylphenyl)-10-(3″,5″-diphenylbiphenyl-4″-yl)anthracene (TAT) exhibited excellent color coordinates (type-A; $x = 0.143$, $y = 0.068$, type-B; $x = 0.139$, $y = 0.081$), which were better than the color coordinates of the NTSC standard (0.140, 0.080) and the TAT-doped conventional noncavity OLED (0.156, 0.094). There were approximately 60% and 54% improvement in the relative quantum efficiency of the type-B TAT-doped moderate microcavity OLED, respectively, compared to those of the conventional noncavity reference OLED (ITO = 150 nm) and other reference type-II with an identical ITO layer thickness (ITO = 85 nm). These improvements in color coordinates and the relative quantum efficiency were attributed to the optimization of narrowed spectrum bandwidth and enhanced integrated spectrum intensity in the TAT-doped blue OLED, resulting from the effective microcavity effect.

© 2009 Elsevier B.V. All rights reserved.

1. Introduction

Organic light-emitting diodes (OLEDs) are used widely as ideal emissive devices in lighting and flat panel displays on account of their low driving voltage, low power consumption, high color gamut, high contrast and rapid response [1–4]. For full color display applications, it is essential to develop high performance red-, green-, and blue-emitting OLEDs with high EL efficiency, good thermal properties, and long device lifetime as well as pure color coordinates (1931 Commission Internationale de l'Eclairage (CIE) x, y coordinates). To develop stable, efficient and saturated red to green and blue OLEDs, the general approach is to design and synthesize new organic small molecules as emitters in OLEDs. Many organic small molecules for red [5–7], green [8,9] and blue emitters [10–19] have been synthesized. Recently, high efficient and pure red fluorescent and green OLEDs have been developed with CIE x, y coordinates and electrical efficiencies of (0.67, 0.23) and 11 cd/A and (0.29, 0.64) and 21 cd/A, respectively. However, the color purity and efficiency of the blue-light emitters are still lower than the requirements for balancing with red and green emitters for full color displays. Therefore, improvements in the blue emitting performance are necessary, particularly for large display

* Corresponding author.
E-mail address: yrdo@kookmin.ac.kr (Y.R. Do).
[1] These authors contributed equally to this work.

1566-1199/$ - see front matter © 2009 Elsevier B.V. All rights reserved.
doi:10.1016/j.orgel.2009.10.011

applications, such as digital video displays (DVD) and laptop computer screens, which require a larger color gamut. In particular, blue emitters require the CIE x, y coordinates of the National Television System Committee (NTSC) blue color standard (0.14, 0.08). With this respect, synthesizing new blue emitters with a narrow band and saturated color might help in obtaining a deep blue color. Many types of blue emitters have been studied extensively, and considerable effort has been made to improve their blue EL performance [10–19]. Thus far, the best results of a deep blue-light emitter are anthracene-cored derivatives with excellent color coordinates (0.156, 0.088) and good electrical efficiency [19]. The color coordinates of anthracene-cored derivatives are still inferior to the NTSC blue color standard. Therefore, further improvements in blue color and luminescence efficiency are essential for applications to large display devices, such as televisions and computer screens. However, the broad emission spectra due to both vibronic transitions and strong inhomogeneous broadening of the transitions in various organic molecules make it difficult to develop deep blue color OLEDs using a new type of blue emitter only.

Another way of overcoming the problem of limited color purity of blue OLEDs is the optical modification of the OLED structure and filtering out the unwanted long wavelength emission. With this respect, a simple modification of the OLED structure, i.e. the insertion of organic layers into a microcavity structure has been investigated extensively in recent years owing to the enhanced luminescence, narrowing bandwidth, and tunable emission color [20–32]. Microcavity OLEDs can be divided into two categories: one is OLEDs embedded in a weak cavity structure [20], and the other is insertion into a strong cavity structure [21–32]. The former is a conventional OLED structure, in which the central organic layers are sandwiched between an aluminum (Al) metal cathode and an indium tin oxide (ITO) anode. On the other hand, the latter uses a conventional Al electrode and semitransparent metal mirror [21–24] or an ITO anode coated onto a dielectric Bragg mirror [25–32]. As previously reported, the weak microcavity has relatively minor effects on the electroluminescence (EL) performance [20]. However, the strong microcavity modifies the photonic mode density within the OLED significantly, improving the EL performance and tuning the color purity from a homogeneously broadened emitter at the microcavity resonance [21–32].

The use of metal mirrors enhances the EL efficiency and luminance in the top- or bottom-emitting OLEDs significantly but their narrowing capability of the emission spectrum from the metal mirror still does not satisfy the NTSC pure blue. Recently, Mudler et al. [21] obtained a high efficient and deep blue color (0.116, 0.136) OLED from a sky blue phosphorescent OLED using a strong microcavity structure with a semitransparent Ag anode. Although the color purity of the phosphorescent OLED was improved significantly using a strong metal mirror-based microcavity, it is necessary to control the detailed peak position and bandwidth of the emission spectrum in order to approach the NTSC blue color standard.

On the other hand, dielectric mirrors reduce the bandwidth of the EL spectrum considerably but the improvement in OELD efficiency is not as high as the metal-based strong microcavity. In the early stages of dielectric-based microcavity OLEDs, Tokito et al. [28,29] reported that the purity of red, green and blue obtained in microcavity OLEDs was superior to the NTSC standard. However, the total enhancement of their device by integration over all angles and wavelengths was not reported. Recently, Zhang et al. [30] and Jung et al. [31] reported the tuning of the emission color and improvement in EL efficiency simultaneously by simply adjusting the cavity length and carefully designing the device structures. They narrowed the emission spectrum of blue, green and red OLEDs significantly, but improved the green and red efficiency only. Quite recently, Cho et al. [32] reported that moderate microcavity formed by an Al cathode and one pair of high- and low-index (SiN_x/SiO_2) dielectric layers enhanced the efficiency of sky blue OLEDs (0.110, 0.216) by more than 26%. Although there are many papers on the enhanced output of the emission peaks from microcavity OLEDs, there are few reports on the high efficient and saturated blue OLEDs, which are more efficient than noncavity conventional OLEDs and have a deeper color than the NTSC blue color standard (0.14, 0.08). This paper reports microcavity OLEDs containing dielectric Bragg mirrors with a finely tunable peak position and a bandwidth of EL emission that achieves enhanced external quantum efficiency and a deep blue color ($y \leqslant 0.08$). The significant change in bandwidth, external quantum efficiency and color of the microcavity OLEDs with three different pairs and two lattice constants of high- and low-index dielectric layers was examined in order to gain a better understanding of the effect of the degree of microcavity TiO_2/SiO_2 layers on the efficiency and color purity of 9,10-bis(3′,5′-diphenylphenyl)-10-(3‴,5‴-diphenylbiphenyl-4″-yl)anthracene (TAT)-doped OLEDs. Among the various microcavity OLEDs, a moderate microcavity OLED was defined as a microcavity OLED with only a single pair of TiO_2/SiO_2 layers inserted between the indium tin oxide (ITO) layer and a glass substrate to achieve the NTSC blue standard and enhance the normally directed quantum efficiency.

2. Experimental

Fig. 1 shows a schematic diagram of the microcavity OLED with one, two and four pairs of high- and low-index pair of dielectric Bragg mirrors. Two types of reference blue OLEDs were fabricated with a commercialized emitter in the following configurations: ITO (150 nm or 85 nm)/4,4′,4″-tris(*N*-(2-naphthyl)-*N*-phenylamino)triphenylamine [2-TNATA] (49 nm)/*N*,*N*′-bis(naphthalen-1-yl)-*N*,*N*′-bis(phenyl)benzidine [NPB] (12 nm)/9,10-bis(3′,5′-diphenylphenyl)-10-(3‴,5‴-diphenylbiphenyl-4″-yl)anthracene [TAT] (30 nm)/8-hydroxyquinolinealuminium [Alq_3] (24 nm)/LiF (1 nm)/Al (150 nm). The optical lengths of the type-A and type-B TAT-doped microcavity blue OLEDs were attributed to the different optimized structures summarized in Table 1. In the type-A microcavity blue OLEDs, one, two and four pairs of high-(TiO_2) and low-index (SiO_2) layers were placed between the ITO layer and glass substrate to control the top reflectivity of the reflection band.

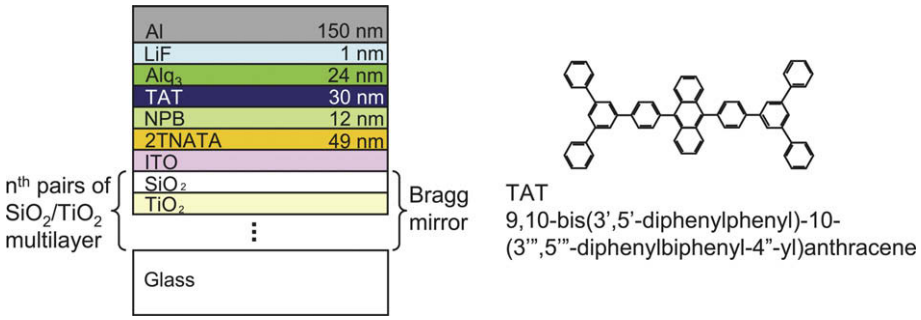

Fig. 1. Schematic diagram of a microcavity OLED device and chemical structure of TAT.

Fig. 1 also shows the chemical structures of the blue emitting material (TAT) in this experiment. As reported previously [19], TAT was purified employing a silica column and recrystallization, was characterized with nuclear magnetic resonance (NMR), Fourier transform infrared (FT-IR), and fast atom bombardment mass (FAB-MS) analysis. Boration and Suzuki aryl–aryl coupling reactions were used in all syntheses. The detailed synthesis route and characterization results of TAT are reported elsewhere [19].

To examine the effect of the dielectric Bragg mirrors experimentally, OLEDs were fabricated on two reference substrates (conventional reference (ITO = 150 nm) and reference type-II (ITO = 85 nm) and two types (type-A one pair and type-B one pair) of dielectric Bragg mirrors covering the substrates. Table 1 summarizes the thicknesses and sheet resistances of each sample. Mono-color OLED samples were fabricated with an active area of $2.0 \times 2.0\ mm^2$. High-index TiO_2 ($n = 2.3$) and low-index SiO_2 ($n = 1.46$) thin films were deposited alternatively on glass substrates in a single chamber using an e-beam evaporation technique [33]. The ITO layer was then deposited by magnetron sputtering with no intentional heating, and organic layers corresponding to 2-TNATA, NPB, TAT, and Alq_3 as well as a LiF film (as EIL) and aluminum metal cathode were evaporated sequentially to fabricate both the reference and microcavity devices. Finally the OLEDs were encapsulated with 0.7 mm Corning cover glass.

The current–voltage (I–V) characteristics of the electroluminescence (EL) devices fabricated were obtained using a Keithley 2611 electrometer. The EL spectra, EL brightness and color coordinates were obtained with a spectrophotometer (PSI Co., Ltd.) and a Minolta CS-1000A. The enhancement ratio of the quantum efficiency was obtained by comparing the normally directed light output of microcavity OLEDs at 10 mA/cm^2 to that of a conventional reference OLED (ITO = 150 nm).

3. Results and discussion

As reported previously [29–32], the electrical efficiency, relative quantum efficiency and color purity of the microcavity OLEDs depend on the thickness of the ITO, organic, low-index, and the high-index layers, respectively. The finite-difference time-domain (FDTD) simulations were used to determine the resonance wavelength of the cavity by varying the thickness of the ITO, low-index (SiO_2), and high-index layers (TiO_2). Dielectric Bragg mirrors with two different lattice constants were also inserted into the blue OLEDs in an attempt to tune the position of the blue emission peaks. Here, two types of quarter-wave stacks were designed to have center wavelengths of ≈465 (type-A) and 470 nm (type-B). The thicknesses of the ITO, low-index, and high-index layers are defined as the values when a deep blue color was realized. The reflectance (R) and transmittance (T) of the two types of quarter-wave stacks consisting of alternating low-index SiO_2 and high-index TiO_2 were measured as a function of the number of periods. As shown in Fig. 2, the reflectance of the type-A Bragg mirrors at the blue region increased with increasing periodic number of stacks. The central wavelength of the reflectance band shifted toward a bluish color with increasing number of high/low stacks, which is consistent with those in the calculation. The inset in Fig. 2 shows a side-view scanning electron microscopy (SEM) image of a real fabricated type-A dielectric multilayer comprised of alternate TiO_2 and SiO_2 quarter-wave films of the fourth periods. As shown in Table 1 and Fig. 2, the thicknesses

Table 1
The designed and fabricated thicknesses of the ITO, TiO_2, and SiO_2 films for the two types of reference OLEDs and two types of microcavity OLEDs along with the sheet resistances of ITO for each sample.

		Noncavity OLEDs		Microcavity OLEDs			
				Type-A			Type-B
		Conventional reference	Reference type-II	One pair	Two pairs	Four pairs	One pair
Thickness (nm)	ITO	150	85	80			85
	SiO_2	–	–	80			82
	TiO_2	–	–	50			51
Sheet resistance (±2 Ω/□)		13	47	34	44	41	36

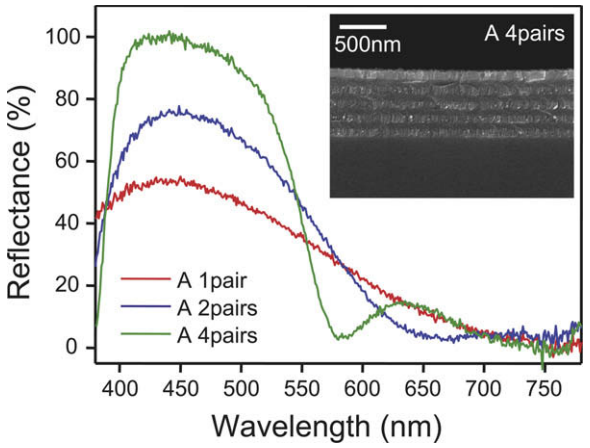

Fig. 2. The measured diffusive reflectance spectra of two and four pairs of TiO_2/SiO_2 high/low stacks coated on glass substrate. The inset shows a side-view scanning electron microscopy (SEM) image of the fourth periods of $[TiO_2/SiO_2]$ films coated with the ITO film.

of the TiO_2/SiO_2 films match those of the dielectric films in the designed Bragg mirrors satisfactorily.

In order to compare the performance of the conventional noncavity OLED and the type-A microcavity OLEDs, the color coordinates, brightness, electrical efficiency and power efficiency should be considered. The normalized EL spectra of both type-A devices and the conventional reference (ITO = 150 nm) device (Fig. 3a) indicates that an increase in the periodic number of stacks decreases the full width at half maximum (FWHM) of the emission spectrum up to ~9 nm (four pairs) [29,30]. Single-mode blue emissions with peak wavelength of 460–466 nm with reduced FWHMs were realized by simply increasing the periodic number of SiO_2/TiO_2 stacks. Compared to the conventional noncavity devices with a broader EL spectrum (≈55 nm FWHM), controlling both the narrowness and position of the emissive spectrum will be of great benefit in optimizing the color purity of blue OLED for applications to display devices [32]. Fig. 3b shows the relative EL spectra of the conventional OLED and type-A OLEDs with the periodic number of stacks at a viewing angle of 0°. The intensity of the EL spectra increased with increasing periodic number of stacks up to two pairs and then decreased with further increases. This decrease in EL intensity in the four pairs of TiO_2/SiO_2 stacks was attributed to the increased reflectance and reduced transmittance of blue light, as shown in Fig. 2. The figure compares the normally directed emission spectra recorded at a constant current density (10 mA/cm^2) for the conventional noncavity OLED and type-A microcavity OLEDs with a periodic number of stacks. The results show that at the main peak wavelength, the emission intensity of the type-A microcavity OLEDs with one, two, and four pair stacks was 2.3, 3.3, and 2.2 higher than that of the conventional reference OLED, respectively. Moreover, the EL spectra of the microcavity OLEDs were narrowed and shifted, indicating the microcavity effect. Therefore, the thicknesses of the ITO, low- and high-index layer affect the spectral characteristics [30]. Our FDTD calculations were also used to determine

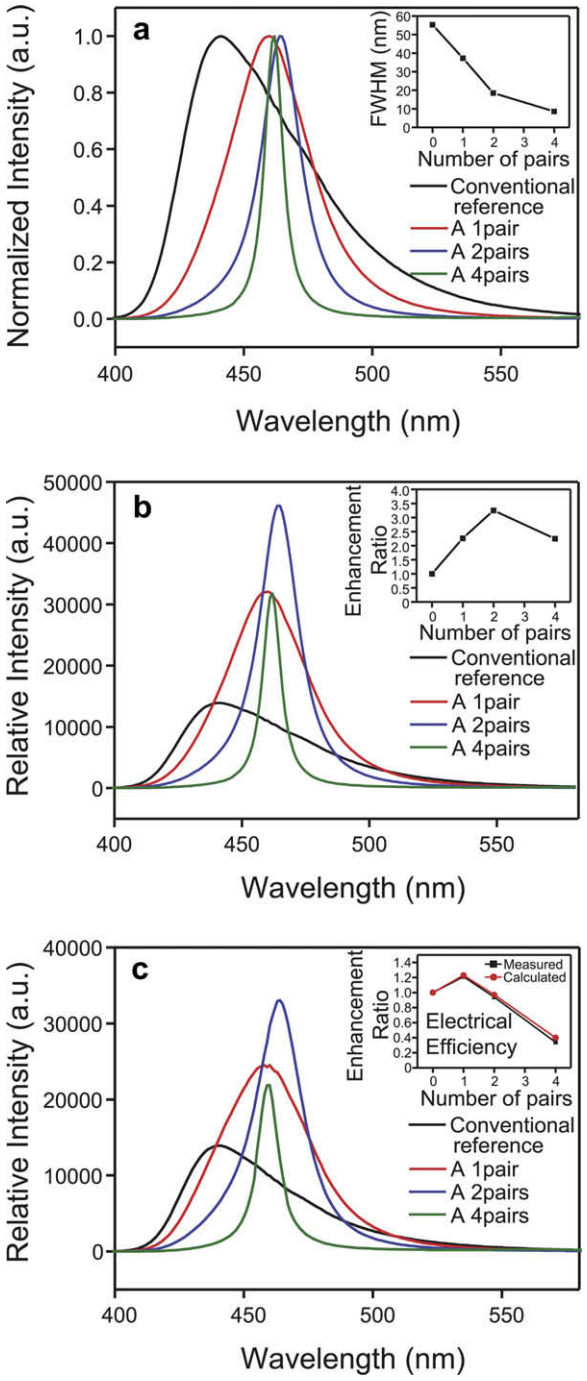

Fig. 3. (a) Normalized EL spectra and (b) relative EL spectra of the conventional reference OLED (ITO = 150 nm) and type-A microcavity OLEDs with the periodic number of high/low stacks at viewing angle of 0°. The inset in (a) shows the relationship between the full width at half maximum (FWHM) of the EL spectrum and the periodic number of high/low stacks, and the inset in (b) shows the relationship between the EL spectrum intensity and the periodic number of high/low stacks. (c) Calculated EL spectra of the conventional reference OLED (ITO = 150 nm) and type-A microcavity OLEDs with the periodic number of high/low stacks at viewing angle of 0°. The inset in (c) shows the relationship between the calculated and measured electrical efficiency along normal direction and the periodic number of high/low stacks.

the normally directed emission spectrum and electrical efficiency of type-A microcavity OLEDs with one, two and four pair stacks, indicating an improvement in the relative electrical efficiency of this device of ≈23%. Fig. 3c shows the calculated emission spectra and relative electrical efficiency of the type-A microcavity OLEDs. Fig. 3b and c confirm that the calculated shape of the emission spectra and the enhancement of the electrical efficiency are very similar to those of the measured spectra and electrical efficiency in the normal direction.

Fig. 4a and b shows the current density (J)–normal direction luminance (L)–voltage (V) characteristics of the conventional noncavity reference OLEDs and type-A microcavity OLEDs with the periodic number of stacks. The J of the conventional reference OLED increased faster with increasing voltage than those of all microcavity OLEDs. The superior J–V characteristics was attributed to the enhanced hole injection from the thicker ITO anode of the conventional OLED with a lower resistance, as summarized in Table 1. On the other hand, the dependence of J for all type-A microcavity OLEDs showed similar trends due to the similar sheet resistance of the ITO anodes, irrespective of the periodic number of stacks. Fig. 4b shows that the difference between the L–V curves of the conventional OLED

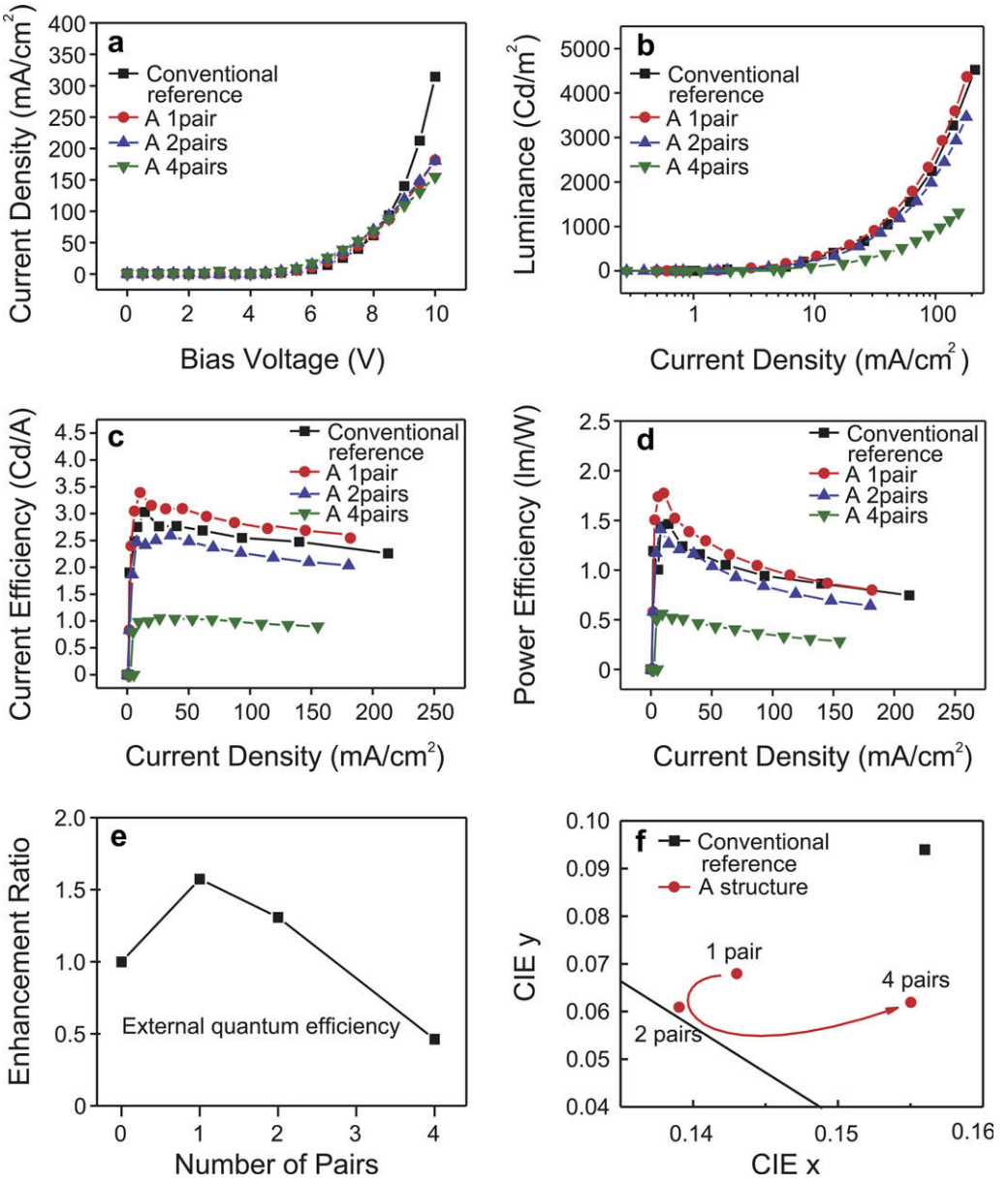

Fig. 4. (a) Current density–bias voltage characteristics, (b) current density–normal direction luminance characteristics, (c) current density–electrical efficiency characteristics, (d) current density–power efficiency characteristics (e) enhancement ratio of the quantum efficiency in the normal direction and (f) CIE color coordinates of the conventional reference OLED (ITO = 150 nm) and type-A microcavity OLEDs with a periodic number of high/low stacks at a viewing angle of 0°. (For interpretation of the references to colour in this figure legend, the reader is referred to the web version of this article.)

and the microcavity OLEDs with the periodic number of stacks is larger than that between the *J–V* curves. This figure also shows the different trends of the *L–V* curves of the microcavity OLEDs as a function of the periodic number of stacks. The microcavity OLEDs with increasing number of quarter-wave stacks showed decreased brightness due to the different dependences of the microcavity effect on the periodic number of stacks. Although higher color purity was achieved by increasing the microcavity effect, the luminous efficiency was reduced despite the enhanced peak intensity due to the loss of light around the shoulder of the peak at 480 nm, which has high eye sensitivity. It appears that when dielectric mirrors are used, there is some trade-off between the color purity and luminance for blue-emitting materials.

Fig. 4c and d shows the relationship between the current efficiency–current density and power efficiency–current density of the conventional reference OLED and type-A microcavity OLEDs. The current efficiency at 10 mA/cm^2 in the normal direction for the conventional noncavity reference OLED was 2.8 cd/A, whereas the efficiencies for the type-A microcavity OLEDs with one, two and four pairs of quarter-wave stacks were 3.2, 2.4, and 1.0 cd/A, indicating that the current efficiency of conventional reference OLED in the normal direction is slightly lower than that in the type-A microcavity OLED containing a single pair of quarter-wave stacks. Fig. 4d also shows a similar relationship of power efficiency–current density with the number of quarter-wave stacks. Although the current and power efficiencies of the moderate microcavity blue OLED with one pair of high-low stacks is slightly higher than that of the noncavity blue OLED, the photons emitted from the microcavity blue OLEDs was significantly enhanced by the microcavity effect, as illustrated by the emission spectra in Fig. 3b.

For a systematic comparison of these OLEDs, the enhancement ratio of the quantum efficiency was defined as the ratio of the normally directed light output of microcavity OLEDs or other reference OLEDs to that of a conventional reference OLED (ITO = 150 nm). This enhancement ratio only shows how much the EL quantum efficiency at 10 mA/cm^2 of microcavity OLEDs was improved relative to that of a conventional noncavity reference OLED. Fig. 4e shows the enhancement ratio of the quantum efficiencies of each OLED. In contrast to the trends in current efficiency, the quantum efficiency of type-A microcavity OLEDs with a single pair of quarter-wave stacks was superior to that of the conventional reference OLED. However, the microcavity OLEDs with a higher number of pairs of quarter-wave stacks showed lower quantum efficiency. The normally directed quantum efficiency of the type-A microcavity OLEDs with a single pair of high and low-index layers was 1.57 higher than that of the conventional reference OLED. As expected, with the resonant wavelength set to 465 nm (19 nm longer than the PL peak of TAT), the type-A moderate microcavity device with a single pair of quarter-wave stacks showed the significantly enhanced quantum efficiency compared to the conventional reference OLED device. Even with brightness slightly higher than the conventional OLEDs, the quantum efficiency of the microcavity OLEDs with a single pair of quarter-wave stacks was significantly higher than that of the conventional OLED device. This was attributed to the lower eye sensitivity of more pure blue moderate microcavity OLEDs. In addition, Fig. 4f shows that the CIE color coordinates of the type-A microcavity OLEDs with a different number of quarter-wave stacks were purer than those of the conventional noncavity OLED. The increased color purity with the increasing number of high/low stacks was attributed to the blue shift and narrowing of the emission spectrum due to the enhanced microcavity effect. In particular, the moderate microcavity OLED with a single pair of high/low stacks showed a deeper blue and higher quantum efficiency than the conventional noncavity OLED.

The angular dependence of the emission spectrum was also examined because changes in color with changing viewing angle are undesirable for display applications [28,29]. Fig. 5a and b shows the angle dependence of the emission spectra of a conventional reference OLED (ITO = 150 nm) and a type-A microcavity OLED with a single pair of high/low stacks at room temperature, respectively. The figures show negligible angular dependence in the peak shape of the conventional reference OLED but a blue shift in the emission spectrum of the microcavity OLED with a single pair of high/low stacks. The CIE coordinates were used to assess the color changes in the OLEDs. Fig. 6 shows the angular dependence of the CIE color coordinates for the conventional reference OLED and type-A microcavity OLED with a single pair of high/low stack on a chromaticity diagram. When viewed from the normal direction, the CIE color coordinates for the conventional reference OLED and moderate microcavity OLED were $(0.156, 0.094)$ and $(0.143, 0.068)$, respectively. This suggests that the light emitted by the moderate microcavity OLED has deeper color purity than the conventional reference standard. The results also show that the color change ratio of the moderate microcavity OLED ($\Delta x = 13\%$, $\Delta y = 15\%$) became slightly worse than that of the conventional reference OLED ($\Delta x = 1\%$, $\Delta y = 31\%$) as the viewing angle was changed up to 60° of the normal. In contrast to the color change in the conventional reference OLED ($0.156, 0.094 \rightarrow 0.157, 0.123$) and the angular dependence of color purity of the moderate microcavity OLED ($0.143, 0.068 \rightarrow 0.161, 0.058$) showed improved color purity with increased viewing angle. The improved color purity and comparable angular dependence of the color purity are another advantage that the moderate microcavity OLEDs have over conventional reference OLEDs.

The far-field pattern of the integrated spectrum intensity was measured to determine the physical characteristics underlying the angular dependence of a single EL emission intensity. The far-field photon radiation from the OLED devices was measured directly with a photodiode, 1 mm^2 in area, which was located 10 cm from the radiation source. Fig. 7 compares the far-field profiles of the conventional reference and moderate microcavity OLEDs cut along the horizontal line. It shows that the noncavity OLED radiates into air in a manner consistent with a Lambertian source. It also suggests that the moderate microcavity OLEDs show only small variations in their angular radiation patterns over a large angular span. Therefore, the far-field profiles of the moderate microcav-

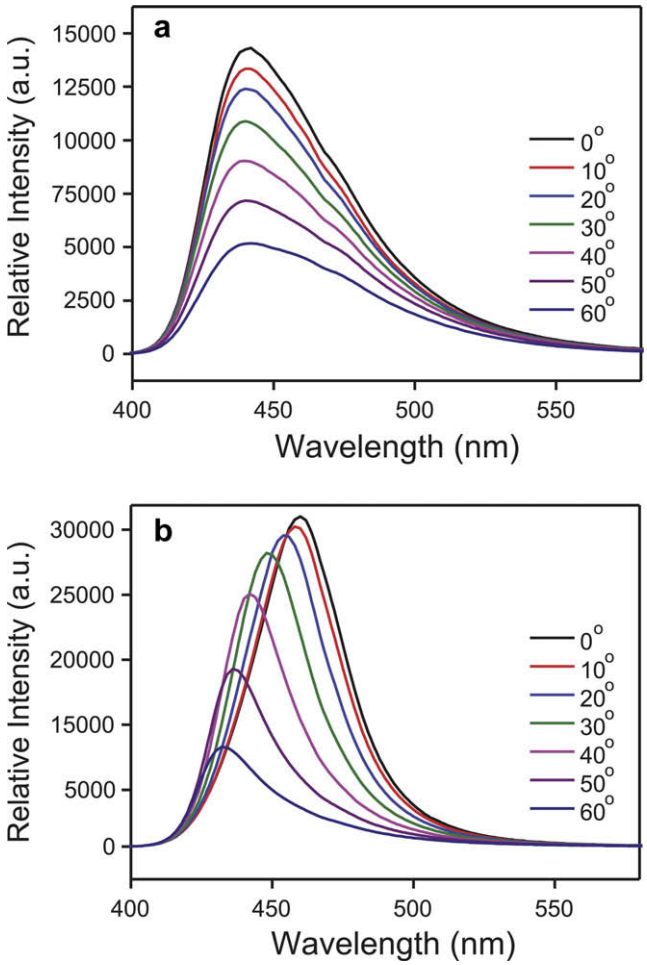

Fig. 5. Viewing angle dependence of the EL spectra of (a) conventional reference OLED (ITO = 150 nm) and (b) type-A moderate microcavity OLED with a single pair of high/low stacks.

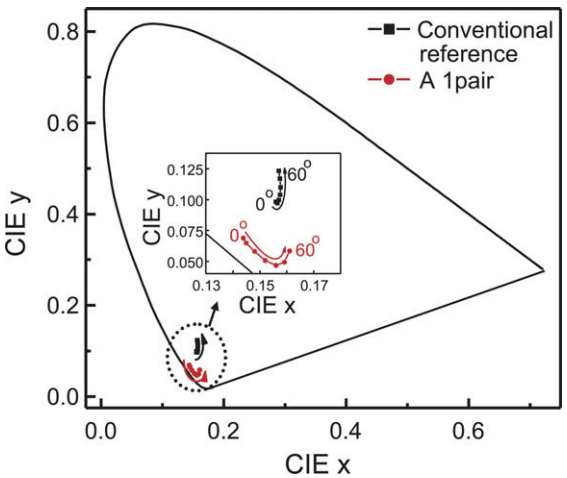

Fig. 6. Viewing angle dependence of the Commission Internationale de l'Eclairage (CIE) color coordinates of the conventional reference OLED (ITO = 150 nm) and type-A moderate microcavity OLED with a single pair of high/low stacks under 10 mA/cm^2 of current density.

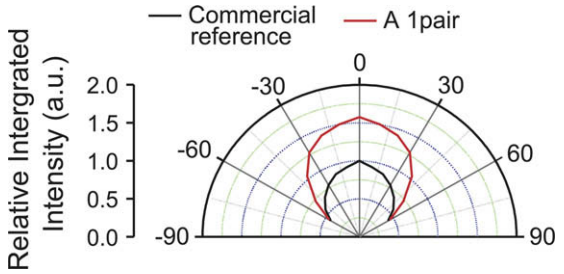

Fig. 7. The viewing angle dependence of integrated EL intensity profiles of conventional reference OLED (ITO = 150 nm) and type-A moderate microcavity OLED with a single pair of high/low stacks under 10 mA/cm^2 of current density.

ity OLEDs with a single pair of high/low stacks were similar to that of the conventional reference OLEDs.

To achieve the NTSC blue color from TAT-doped blue OLED, the tunable effects of the microcavity (type-A one pair and type-B one pair) on OLEDs were examined by controlling the central wavelength of the dielectric Bragg

mirror. OLEDs were fabricated on two reference substrates (conventional reference (ITO = 150 nm) and reference type-II (ITO = 85 nm)) and two moderate microcavity substrates (type-A: λ_{cen} = 465 nm, type-B: λ_{cen} = 470 nm) deposited with a single pair of high/low stacks, side by side for comparison. Consistent with the simulated results, Fig. 8 suggests that the emission spectrum of the type-B microcavity OLED was shifted slightly to a longer wavelength compared to that of the type-A microcavity OLEDs. This indicates that the emission spectra of two types of moderate microcavity OLEDs were narrower than those of the two reference OLEDs. Fig. 8 also shows the CIE color coordinates in the normal direction for the reference OLEDs and moderate microcavity OLEDs. The color coordinates of a thin ITO (85 nm) coated reference type-II OLED was slightly higher than that of the conventional reference OLED (ITO = 150 nm). This means that the reduced ITO thickness of the noncavity OLED have a minor effect in controlling the color purity and EL performance. As mentioned above, the light emitted from the moderate microcavity OLEDs had deeper color purity than that emitted by both types of reference OLEDs. The color coordinates (x = 0.139, y = 0.081) of the type-B moderate microcavity OLED with a single pair of high/low stacks was very close to the color coordinates of NTSC blue (x = 0.140, y = 0.080). Therefore, a pure blue color was obtained from TAT-doped blue OLEDs simply by introducing a single pair of TiO_2/SiO_2 high/low dielectric stacks on the substrate.

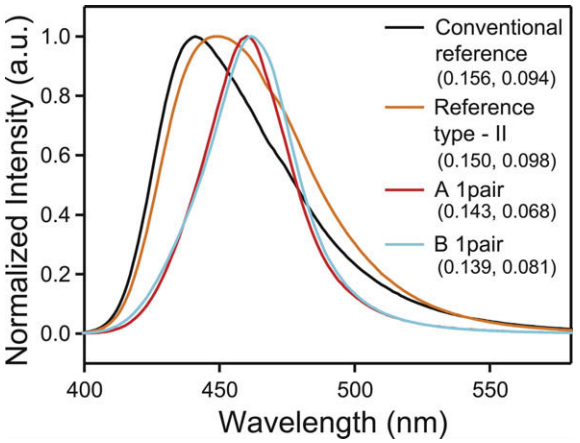

Fig. 8. The normalized EL spectra and CIE color coordinates of the conventional reference OLED (ITO = 150 nm), reference type-II OLED, type-A moderate microcavity, and type-B moderate microcavity OLED under a current density of 10 mA/cm^2.

The electroluminescence measurements showed the current density–luminance characteristics of the four types of OLEDs with and without the microcavity high/low stack. The luminance values of the two types of moderate microcavity OLEDs and reference OLEDs measured in the normal direction ($\theta = 0^\circ$) under dc excitation at 10 mA/cm^2 were 320 (type-A one pair, ITO thickness of 80 nm), 340 (type-B one pair, ITO thickness of 85 nm), 280 (conventional, ITO thickness of 150 nm), and 290 cd/m^2 (conventional, ITO thickness of 85 nm). Fig. 9 shows the current efficiency and enhancement ratio of the normally directed quantum efficiency for two conventional OLEDs and two types of moderate microcavity OLEDs. For the conventional OLEDs, the current efficiencies and relative quantum efficiencies at 10 mA/cm^2 in the normal direction were 2.8 cd/A and 1.00 (conventional reference) and 2.9 cd/A and 1.04 (reference type-II). By comparison, the current efficiencies and quantum efficiencies of the type-A and type-B moderate microcavity OLEDs were 3.2 cd/A, 1.57 and 3.4 cd/A, 1.60, respectively. This indicates that the current efficiencies of the moderate microcavity OLEDs in the normal direction are higher than those of the corresponding conventional OLEDs. Moreover, the relative quantum efficiencies of the type-A and type-B moderate microcavity OLEDs in the normal direction were 57% and 60% higher than those of the corresponding conventional reference OLEDs. This also suggests that the type-B moderate microcavity OLED with color purity close to the NTSC blue standard had higher efficiency than both conventional reference OLEDs and reference type-II with an ITO layer of identical thickness.

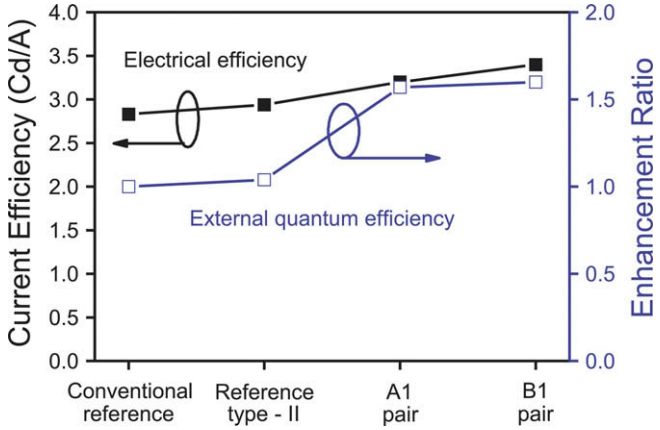

Fig. 9. Electrical efficiency and the enhancement ratio of the normally directed quantum efficiency of the conventional reference OLED (ITO = 150 nm), reference type-II OLED, type-A moderate microcavity, and type-B moderate microcavity OLED under current density of 10 mA/cm^2.

4. Conclusion

This study examined the effects of inserting dielectric Bragg mirrors in an OLED with the aim of achieving NTSC pure blue and enhancing its relative quantum efficiency. First the FDTD method was used to calculate the resonance wavelength of the cavity while varying the thickness of the organic and high/low dielectric layers. The introduction of a single pair of TiO_2/SiO_2 high/low stacks into the OLED structure (denoted as a moderate microcavity OLED) is an effective way of enhancing the quantum efficiency and achieving a NTSC pure blue color from a TAT-based blue OLED. It was demonstrated experimentally that the incorporation of two types of moderate microcavity OLEDs with a single pair of high/low stacks achieved pure blue CIE color coordinates (type-A; $x = 0.143, y = 0.068$, type-B; $x = 0.139$, $y = 0.081$). The type-A and type-B moderate microcavity OLED showed more than 57% and 60% improvement in relative quantum efficiency in the normal direction, respectively, compared to the conventional reference OLED (ITO = 150 nm) in the normal direction. They also improved the relative quantum efficiency by more than 51% and 54%, respectively, compared to the reference type-II (ITO = 85 nm). In addition, the moderate microcavity OLED is more favorable for the angular dependence of the color purity and EL intensity. This simple technique of introducing a dielectric Bragg mirror with a single pair of high/low dielectric stacks into a TAT-doped blue OLED can be generalized for the development of efficient and saturated blue OLEDs from the standpoint of realizing a deep blue color in computer and television screens, and for full color display applications.

Acknowledgments

This study was supported by grant number 2008-03573 of the Nano R&D Program and grant number R11-2005-048-00000-0 of the ERC program through the Korea Science and Engineering Foundation, funded by the Ministry of Education, Science and Technology. This study was partly supported by the IT R&D program of Ministry of Knowledge Economy/Institute for Information Technology Advancement (2009-F-020-01). This work was also supported by the faculty research program 2009 of Kookmin University of Korea. H.K. Kim and S.-H. Cho contributed equally to this work.

References

[1] C.W. Tang, S.A. Van Slyke, C.H. Chen, J. Appl. Phys. 65 (1989) 3610.
[2] C. Adachi, T. Tsutsui, S. Saito, Appl. Phys. Lett. 55 (1989) 1489.
[3] M.A. Baldo, M.E. Thompson, S.R. Forrest, Nature 403 (2000) 750.
[4] C.C. Wu, Y.T. Lin, K.T. Wong, R.T. Chen, Y.Y. Chien, Adv. Mater. 16 (2004) 61.
[5] Y.S. Yao, Q.X. Zhou, X.S. Wang, Y. Wang, B.W. Zhang, J. Mater. Chem. 16 (2006) 3512.
[6] B.J. Jung, J.I. Lee, H.Y. Chu, L.M. Do, J.M. Lee, H.K. Shim, J. Mater. Chem. 15 (2005) 2470.
[7] T. Tsuzuki, S. Tokito, Adv. Mater. 19 (2007) 276.
[8] M. Cocchi, D. Virgili, V. Fattori, D.L. Rochester, J.A.G. Williams, Adv. Funct. Mater. 17 (2007) 285.
[9] K.T. Kamtekar, C. Wang, S. Bettington, A.S. Batsanov, I.F. Perepichka, M.R. Bryce, J.H. Ahn, M. Rabinal, M.C. Petty, J. Mater. Chem. 16 (2006) 3823.
[10] J. Luo, Y. Zhou, Z.-Q. Niu, Q.-F. Zhou, Y. Ma, J. Pei, J. Am. Chem. Soc. 129 (2007) 11314.
[11] P.-I. Shih, C.-Y. Chuang, C.-H. Chien, E.W.-G. Diau, C.-F. Shu, Adv. Funct. Mater. 17 (2007) 3141.
[12] C.J. Tonzola, A.P. Kulkarni, A.P. Gifford, W. Kaminsky, S.A. Jenekhe, Adv. Funct. Mater. 17 (2007) 863.
[13] R. Gómez, D. Veldman, B.M.W. Langeveld, J.L. Segura, R.A.J. Janssen, J. Mater. Chem. 17 (2007) 4274.
[14] S.J. Lee, J.S. Park, K.-J. Yoon, Y.-I. Kim, S.-H. Jin, S.K. Kang, Y.-S. Gal, S.W. Kang, J.Y. Lee, J.-W. Kang, S.-H. Lee, H.-D. Park, J.-J. Kim, Adv. Funct. Mater. 18 (2008) 3922.
[15] C. Hosokawa, H. Higashi, H. Nakamura, T. Kusumoto, Appl. Phys. Lett. 67 (1995) 3853.
[16] M.-T. Lee, C.-H. Liao, C.-H. Tsai, C.H. Chen, Adv. Mater. 17 (2005) 2493.
[17] S. Liu, F. He, H. Wang, H. Xu, C. Wang, F. Li, Y. Ma, J. Mater. Chem. 18 (2008) 4802.
[18] K. Kreger, M. Bäte, C. Neuber, H.-W. Schmidt, P. Strohriegl, Adv. Funct. Mater. 17 (2007) 3456.
[19] S.-K. Kim, B. Yang, Y. Ma, J.-H. Lee, J.-W. Park, J. Mater. Chem. 18 (2008) 3376.
[20] V. Bulovic, V.B. Khalfin, G. Gu, P.E. Burrows, D.Z. Garbuzov, S.R. Forrest, Phys. Rev. B 58 (1998) 3730.
[21] C.L. Mulder, K. Celebi, K.M. Milaninia, M.A. Baldo, Appl. Phys. Lett. 90 (2007) 211109.
[22] H. Peng, J. Sun, X. Zhu, X. Yu, M. Wong, H.-S. Kwok, Appl. Phys. Lett. 88 (2006) 073517.
[23] C.-L. Lin, H.-W. Lin, C.-C. Wu, Appl. Phys. Lett. 87 (2005) 021101.
[24] C.-L. Lin, T.-Y. Cho, C.-H. Chang, C.-C. Wu, Appl. Phys. Lett. 88 (2006) 081114.
[25] A. Dodabalapur, L.J. Rothberg, T.M. Miller, E.W. Kwock, Appl. Phys. Lett. 64 (1994) 2486.
[26] T. Tsutsui, N. Takada, S. Saito, E. Ogino, Appl. Phys. Lett. 65 (1994) 1868.
[27] R.H. Jordan, L.J. Rothberg, A. Dodabalapur, R.E. Slusher, Appl. Phys. Lett. 69 (1996) 1997.
[28] S. Tokito, K. Noda, Y. Taga, Appl. Phys. Lett. 68 (1996) 2633.
[29] S. Tokito, T. Tsutsui, Y. Taga, J. Appl. Phys. 86 (1999) 2407.
[30] H. Zhang, H. You, W. Wang, J. Shi, S. Guo, M. Liu, D. Ma, Semicond. Sci. Technol. 21 (2006) 1094.
[31] B.-Y. Jung, C.K. Hwangbo, J. Korean Phys. Soc. 49 (2006) 2112.
[32] S.-H. Cho, Y.-W. Song, J.-G. Lee, Y.-C. Kim, J.H. Lee, J. Ha, J.-S. Oh, S.Y. Lee, S.Y. Lee, K.H. Hwang, D.-S. Zang, Y.-H. Lee, Opt. Exp. 16 (2008) 12632.
[33] J.R. Oh, S.-H. Cho, Y.-H. Lee, Y.R. Do, Opt. Exp. 17 (2009) 7450.

Organic Electronics 11 (2010) 146–149

Contents lists available at ScienceDirect

Organic Electronics

journal homepage: www.elsevier.com/locate/orgel

Letter

Stability of large-area molecular junctions

Hylke B. Akkerman [a], Auke J. Kronemeijer [a], Jan Harkema [a], Paul A. van Hal [b], Edsger C.P. Smits [a,b], Dago M. de Leeuw [a,b,*], Paul W.M. Blom [a]

[a] Molecular Electronics, Zernike Institute for Advanced Materials, University of Groningen, Nijenborgh 4, NL-9747AG Groningen, The Netherlands
[b] Philips Research Laboratories, High Tech Campus 4, NL-5656AE Eindhoven, The Netherlands

ARTICLE INFO

Article history:
Received 22 July 2009
Received in revised form 14 September 2009
Accepted 14 September 2009
Available online 18 September 2009

Dedicated to the memory of Professor Bert de Boer, who passed away January 2009.

Keywords:
Molecular electronics
Molecular devices
Self-assembled monolayers
Stability
Alkanedithiols

ABSTRACT

The stability of molecular junctions is crucial for any application of molecular electronics. Degradation of molecular junctions when exposed to ambient conditions is regularly observed. In this report the stability of large-area molecular junctions under ambient conditions for more than two years is presented. Furthermore, the thermal stability of molecular junctions at elevated temperatures is investigated. A transition temperature at 50 °C was observed for molecular junctions based on self-assembled monolayers of alkanedithiols, above which the resistance decreases exponentially with temperature. This transition temperature limits the process window during fabrication and the temperature window during operation.

© 2009 Elsevier B.V. All rights reserved.

The field of molecular electronics has grown exponentially after the seminal theoretical paper of Aviram and Ratner [1], predicting that a single molecule can operate as a rectifying diode. Electronic transport through molecules has since then been investigated experimentally in many different device geometries [2,3]. The most studied systems are self-assembled monolayers (SAMs) of alkane(di)thiols on gold [4–6]. The resistance of Au/SAM Au junctions exponentially increases with increasing molecular length and is independent of temperature, indicating that charge transport is due to non-resonant tunneling [7–9]. Progress in the study of discrete devices is severely hampered by limited reliability, stability, and especially, yield. Electrical shorts in the SAM are readily formed upon vapor deposition of the top electrode [10]. An illustration is the statistical analysis which has been reported for manually measured molecular junctions with a diameter of 2 μm and evaporated metal top electrodes [11]. The yield of the functional junctions was 156 out of 13,440 junctions fabricated, or 1.2%. Formation of shorts can be prevented by applying a conducting barrier layer between the SAM and the top electrode. A yield of unity has been reported for discrete large-area junctions by using the conducting polymer poly(3,4-ethylene-dioxythiophene) stabilized with polystyrene sulphonic acid, henceforth abbreviated as PEDOT:PSS, as a barrier [12]. Even for devices as large as 100 μm in diameter, the PEDOT:PSS layer prevents shorts. The technology is suitable for upscaling, integration and incorporation of functionality. More than 20,000 molecular junctions, discrete and connected in series, were fabricated simultaneously on a single 150 mm wafer in a semi-automated process [13]. Functionality was demonstrated by switchable conductance realized with diarylethene molecular photoswitches

* Corresponding author. Address: Molecular Electronics, Zernike Institute for Advanced Materials, University of Groningen, Nijenborgh 4, NL-9747AG Groningen, The Netherlands.
E-mail address: dago.de.leeuw@philips.com (D.M. de Leeuw).

1566-1199/$ - see front matter © 2009 Elsevier B.V. All rights reserved.
doi:10.1016/j.orgel.2009.09.013

[14]. A prerequisite for any application is a shelf life extending years. Furthermore, the temperature window for operation needs to be determined. Here we investigate the electrical transport in molecular junctions as a function of storage time and at elevated temperatures.

Discrete large-area molecular junctions were fabricated according to previously published procedure [2,13–16]. By photolithography, vertical interconnects (vias) are created on top of the gold bottom electrodes. A monolayer of alkanedithiols is self-assembled on the exposed gold bottom electrodes within the vertical interconnects. The conducting polymer interlayer of PEDOT:PSS is spincoated on top after the self-assembly process. In the final step Au top electrodes are evaporated and the redundant PEDOT:PSS is etched away with reactive ion etching to prevent parasitic currents. The resulting molecular junctions have the SAM completely encapsulated by photoresist on the sides of the vertical interconnect and protected by the conducting polymer PEDOT:PSS on top. A schematic presentation of the device geometry and a micrograph of an actual junction are presented in Fig. 1.

The current density of C12-dithiol junctions as a function of bias is presented in Fig. 2a. The density is an average over 10 devices, half of them with a diameter of 40 μm and half of them of 80 μm in diameter. The *I–V* curves of the molecular junctions exhibit a super linear increase due to tunneling, as confirmed by low temperature measurements [7,12]. To investigate the stability of the molecular junctions, the samples were stored in air for subsequent measurements. Molecular junctions have been stored and remeasured after 2.5 years. There is only a minor change of a factor less than two after storage for 888 days, or 2.5 years. In Fig. 2b the resistances of the 10 discrete junctions are presented separately.

To determine the maximum operation temperature, the transport in the junctions was investigated as a function of temperature. The junctions are loaded in the probe station and set under vacuum. The temperature of the system was systematically increased up to 110 °C. The temperature was raised in steps of 10 °C and kept for 5 min at each temperature before performing *I–V* scans on 2 or 3 junctions at these temperatures. Subsequently, the temperature was raised and kept constant for 5 min again, before performing the next measurements.

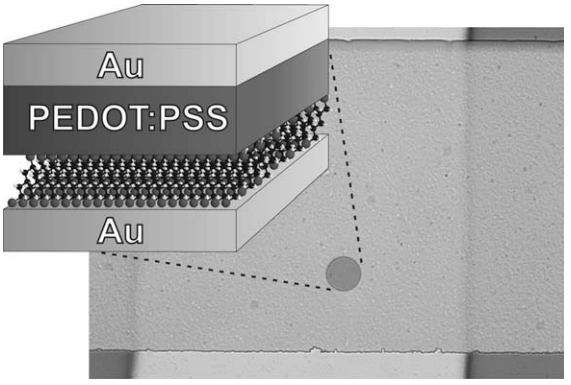

Fig. 1. A micrograph of a molecular junction of 100 μm in diameter. In this image the top Au electrode is 20 nm thick and therefore partially transparent. A schematic representation of the junction with the stacked layers of Au/SAM/PEDOT:PSS/Au is shown in the inset.

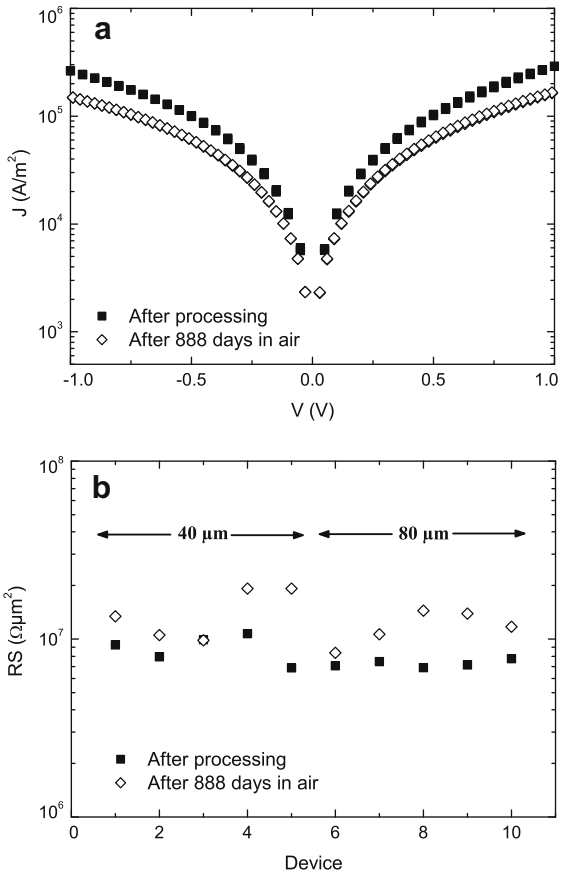

Fig. 2. Stability of large-area molecular junctions in ambient environment. (a) *J–V* traces of devices with a C12-dithiol self-assembled monolayer. The average current density is plotted of 10 junctions, where the *J–V* characteristics from the junctions after processing (■) are compared to the same junctions stored in air for 888 days (◇). The normalized resistance at 0.1 V for the 10 measured individual junctions of 40 and 80 μm in diameter is presented in (b). No dependence on device area is observed for the small increase in resistance after almost 2.5 years storage in air.

Fig. 3a shows the normalized resistance as a function of anneal temperature. Data are presented for different lengths of the alkanedithiols, *i.e.* C8, C10, C12, and C14. For comparison a junction without a SAM present (PEDOT:PSS-only device) is included. The resistances of all junctions decrease with increasing anneal temperature. We note that the change in resistance is irreversible. Since the maximum temperature inside the probe station is 110 °C, the samples were annealed at 150 °C and 200 °C for 15 min on a hotplate in air to investigate the decrease in resistance at higher temperatures. Towards high temperatures, all junctions approach the resistance value of a PEDOT:PSS-only device. The transition temperature is defined as shown in Fig. 3b, by the intercept between low and high temperature fits. Surprisingly, the transition temperature does not depend on the length of the molecules and is at 50 °C for all junctions. Below this temperature

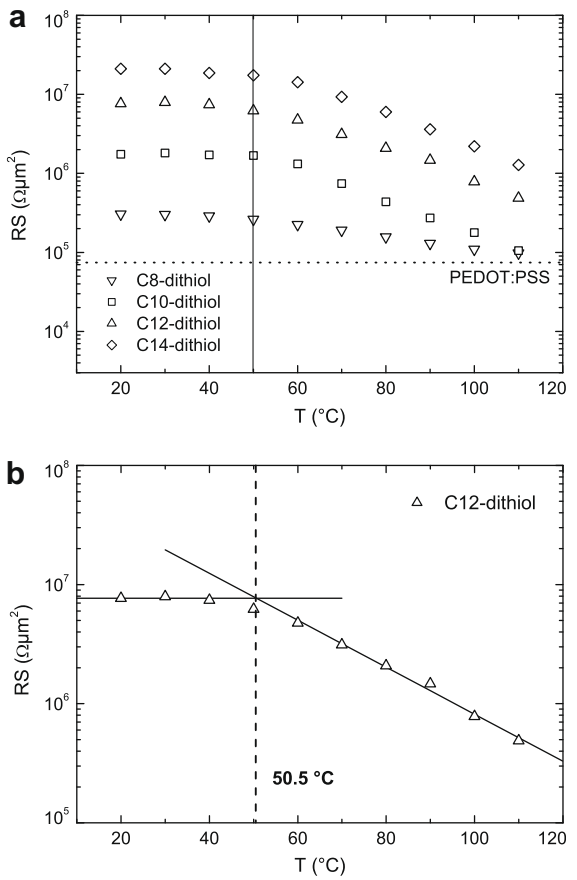

Fig. 3. (a) Normalized resistance at 0.1 V, *RS*, as a function of increasing temperature. For alkane(di)thiols with lengths C10, C12, and C14 a similar trend is observed with increasing temperature, independent of molecule length. C8 shows a different trend since the normalized resistance approaches that of PEDOT:PSS only junctions (represented by the dotted line) at higher temperatures. All SAMs show a transition temperature around 50 °C, after which the resistance is decreasing exponentially with increasing temperature. (b) The transition temperature is determined by calculating the intersection between the average *RS* value of 20–40 °C and the linear fit to the data for 70–110 °C.

no changes in resistance are observed. Above the transition temperature the resistance decreases exponentially with increasing temperature.

The formation of shorts due to PEDOT:PSS filaments can be excluded. When conducting filaments of PEDOT:PSS would form at a specific temperature, irrespective of the length of the SAM, the decrease in resistance would be more pronounced for higher resistances, hence longer molecules.

Thermal stability of SAMs on Au surfaces has been studied extensively [17–23]. Phase transitions and desorption of alkanethiol monolayers on Au(1 1 1) have been observed at elevated temperatures with STM [20,21,24–27]. The two dimensional melting temperature of alkanethiol SAMs increases with increasing chain length of the alkane backbone [22,23,27]. The transition temperature in the junctions being independent of chain length can therefore not yet be explained. The formation of an incommensurate phase as observed by Fenter and coworkers is similar to our observations [28]. While absolute transition temperatures are strongly dependent on coverage of the monolayer, the temperature for the commensurate–incommensurate phase transition is shown to be independent of molecular length, however, only for *n*-alkanethiols with $n \geqslant 14$.

To summarize, we investigated the stability of large-area molecular junctions at temperatures up to 110 °C. Long term stability at room temperature was demonstrated, when stored in ambient conditions. After 888 days in air without UV shielding or any other precautions, no significant change was observed in the current–voltage characteristics of molecular junctions. At elevated temperatures, a transition point was found at 50 °C, which is independent of the molecule length. Up to 50 °C no changes in resistance are observed, whilst above the transition temperature a decrease of the normalized resistance was observed. The observed exponential decrease in resistance for temperatures exceeding 50 °C is similar for all SAMs irrespective of the molecular length of the alkanedithiols. The upper limit of 50 °C is a strong limitation for the applicability of molecular electronics.

Acknowledgements

The research was financially supported by the Zernike Institute for Advanced Materials, The Netherlands Organization for Scientific Research (NWO, Vidi grant) and NanoNed, a national nanotechnology program coordinated by the Dutch Ministry of Economic Affairs.

References

[1] A. Aviram, M.A. Ratner, Chem. Phys. Lett. 29 (1974) 277.
[2] H.B. Akkerman, B. de Boer, J. Phys. Condens. Matter 20 (2008) 013001.
[3] H. Haick, D. Cahen, Prog. Surf. Sci. 83 (2009) 217.
[4] M.D. Porter, T.B. Bright, D.L. Allara, C.E.D. Chidsey, J. Am. Chem. Soc. 109 (1987) 3559.
[5] J.C. Love, L.A. Estroff, J.K. Kriebel, R.G. Nuzzo, G.M. Whitesides, Chem. Rev. 105 (2005) 1103.
[6] C. Vericat, M.E. Vela, G.A. Benitez, J.A.M. Gago, X. Torrelles, R.C. Salvarezza, J. Phys. Condens. Matter 18 (2006) R867.
[7] W. Wang, T. Lee, M.A. Reed, Rep. Prog. Phys. 68 (2005) 523.
[8] K. Slowinski, R.V. Chamberlain, C.J. Miller, M. Majda, J. Am. Chem. Soc. 119 (1997) 11910.
[9] Y.H. Kim, J. Tahir-Kheli, P.A. Schultz, W.A. Goddard III, Phys. Rev. B 73 (2006) 235419.
[10] B. de Boer, M.M. Frank, Y.J. Chabal, W. Jiang, E. Garfunkel, Z. Bao, Langmuir 20 (2004) 1539.
[11] T.W. Kim, G. Wang, H. Lee, T. Lee, Nanotechnology 18 (2007) 315204.
[12] H.B. Akkerman, P.W.M. Blom, D.M. de Leeuw, B. de Boer, Nature 441 (2006) 69.
[13] P.A. Hal, E.C.P. Smits, T.C.T. Geuns, H.B. Akkerman, B.C. de Brito, S. Perissinotto, G. Lanzani, A.J. Kronemeijer, V. Geskin, J. Cornil, P.W.M. Blom, B. de Boer, D.M. de Leeuw, Nat. Nanotechnol. 3 (2008) 794.
[14] A.J. Kronemeijer, H.B. Akkerman, T. Kudernac, B.J. van Wees, B.L. Feringa, P.W.M. Blom, B. de Boer, Adv. Mater. 20 (2008) 1467.
[15] H.B. Akkerman, R.C.G. Naber, B. Jongbloed, P.A. van Hal, P.W.M. Blom, D.M. de Leeuw, B. de Boer, Proc. Natl. Acad. Sci. USA 104 (2007) 11161.
[16] H.B. Akkerman, A.J. Kronemeijer, P.A. van Hal, D.M. de Leeuw, P.W.M. Blom, B. de Boer, Small 4 (2007) 100.
[17] R.G. Nuzzo, E.M. Korenic, L.H. Dubois, J. Chem. Phys. 93 (1990) 767.
[18] T. Ishida, H. Fukushima, W. Mizutani, S. Miyashita, H. Ogiso, K. Ozaki, H. Tokumoto, Langmuir 18 (2002) 83.
[19] B. Rai, P. Sathish, C.P. Malhotra, Pradip, K. Ayappa, Langmuir 20 (2004) 3138.

[20] Y. Qian, G. Yang, J. Yu, T.A. Jung, G.Y. Liu, Langmuir 19 (2003) 6065.
[21] Q. Guo, X. Sun, R.E. Palmer, Phys. Rev. B 71 (2005) 035406.
[22] N. Prathima, M. Harini, N. Rai, R.H. Chandrashekara, K.G. Ayappa, S. Sampath, S.K. Biswas, Langmuir 21 (2005) 2364.
[23] P. Fenter, P. Eisenberger, K.S. Liang, Phys. Rev. Lett. 70 (1993) 2447.
[24] R.L. McCarley, D.J. Dunaway, R.L. Willicut, Langmuir 9 (1993) 2775.
[25] N. Nishida, M. Hara, H. Sasabe, W. Knoll, Jpn. J. Appl. Phys. 36 (1997) 2379.
[26] L.B. Picraux, C.D. Zangmeister, J.D. Batteas, Langmuir 22 (2006) 174.
[27] G. Yang, G.Y. Liu, J. Phys. Chem. B 107 (2005) 8746.
[28] P. Fenter, Self-assembled monolayers of thiols, in: A. Ulman (Ed.), Thin Films, vol. 24, Academic Press, San Diego, p. 111.

Organic Electronics 11 (2010) 150–153

Contents lists available at ScienceDirect

Organic Electronics

journal homepage: www.elsevier.com/locate/orgel

Letter

A light-emitting memristor

Alexander A. Zakhidov [a], Byungki Jung [a], Jason D. Slinker [b], Héctor D. Abruña [c], George G. Malliaras [a,*]

[a] Department of Materials Science and Engineering, Cornell University, Ithaca, NY 14853-1501, USA
[b] Department of Chemistry, California Institute of Technology, Pasadena, CA 91125, USA
[c] Department of Chemistry and Chemical Biology, Cornell University, Ithaca, NY 14853-1301, USA

ARTICLE INFO

Article history:
Received 11 May 2009
Received in revised form 14 September 2009
Accepted 16 September 2009
Available online 19 September 2009

Keywords:
Memristor
Ionic transition metal complex

ABSTRACT

A light-emitting memristor (LEM) is reported based on a metal/mixed conductor/metal structure, where the mixed conductor is the ionic transition metal complex ruthenium(II) tris(bipyridine) with hexafluorophosphate counter ions. The device shows memory effects upon the application of an ac bias, in both current and electroluminescence intensity. The observation of memory in light emission offers the potential for optical read-out of the state of memristive devices.

© 2009 Elsevier B.V. All rights reserved.

1. Introduction

In 1971, Leon Chua introduced the concept of a missing fundamental passive element in electronics called the memristor (short for memory resistor) [1]. The prediction of the existence of the memristor was based on conceptual symmetry arguments which followed from the description of basic passive circuit elements as defined by the relation between two of the four fundamental circuit variables, namely voltage V, current I, charge q, and magnetic flux Φ. Chua demonstrated that memristors could not be obtained by any combination of the other three fundamental elements: resistors, capacitors and inductors. A memristor is characterized by its memristance $M(q)$, which is the time-dependent rate of change of the magnetic flux in respect to the electric charge:

$$M(q(t)) = \frac{\partial \Phi(t)}{\partial q(t)} \tag{1}$$

Since magnetic flux is the time integral of voltage and charge is the time integral of current I, one may write that:

$$M(q(t)) = \frac{V(t)}{I(t)} \tag{2}$$

which is more convenient since voltage and current can be easily measured in an experiment.

The essential property of a memristor is its memory – the dependence of resistance on the operational history of the device. At the time that the theoretical properties of a memristor were described, there was no experimental demonstration of a memristor as a two-terminal passive element. Chua proposed the modeling of a memristor with electric circuits, with at least 15 transistors and other passive elements [1]. Potential applications in programmable logic, signal processing, neural networks, and control systems have been proposed [2]. The ideal memristor response in terms of $M(q(t))$ is a step function at $q = 0$ between an "on" and an "off" state.

Interest in memristors was recently renewed when Williams et al. demonstrated the first memristor as a passive, two-terminal element made from a thin (5 nm) film of TiO_2 sandwiched between two Pt metal electrodes [3]. The

* Corresponding author. Tel.: +1 607 255 1956; fax: +1 607 255 2365.
E-mail address: ggm1@cornell.edu (G.G. Malliaras).

1566-1199/$ - see front matter © 2009 Elsevier B.V. All rights reserved.
doi:10.1016/j.orgel.2009.09.015

memristance of the device was attributed to ion drift in the film and a subsequent modulation of the bulk conductivity [1]. It was further postulated that memristive behavior should be common in nanoscale electronics devices, in which high electric fields can induce ionic motion. In terms of response, this was not an ideal memristor, and there was a transition region between the "on" and "off" states, as one would expect for a realistic material.

In this vein, it is of interest to explore memristors from other materials, particularly materials that might offer enhanced functionality. Molecular electronic materials are currently being used in large-area flat panel displays and are also being developed for solar cells and memory devices. These materials offer unique properties such as solution processing, compatibility with mechanically flexible and large-area substrates, and wide tunability of properties through chemical synthesis [4]. As a result, they can bring new forms and functions to the memristor. In this letter, we report on a two-terminal memristor that is capable of electroluminescence (EL); hence the name light-emitting memristor (LEM). We use the well-studied ionic transition metal complex (iTMC) ruthenium(II) tris(bipyridine) with hexafluorophosphate counter ions, $[Ru(bpy)_3]^{2+}(PF_6^-)_2$, and demonstrate devices in which not only the current, but also the electroluminescence exhibits a memory effect. Light emission gives memristors new functionality, and might enable new features such as optical read-out.

$[Ru(bpy)_3]^{2+}(PF_6^-)_2$ is a mixed conductor, possessing the ability to conduct both ionic (the PF_6^- ions) and electronic (injected from metal electrodes) carriers under an applied bias [5–11]. In metal/{$[Ru(bpy)_3]^{2+}(PF_6^-)_2$}/metal devices, the redistribution of the PF_6^- ions upon the application of a bias creates an ionic space charge near each electrode (excess PF_6^- near the anode and uncompensated $[Ru(bpy)_3]^{2+}$ near the cathode). This assists in the injection of electrons and holes [7,10,11], which recombine in the bulk of the $[Ru(bpy)_3]^{2+}$ layer to form excitons, a fraction of which recombine radiatively to give rise to light emission.

2. Experimental

The LEM device was fabricated as follows: Stock solutions of 40 mg/ml of $[Ru(bpy)_3]^{2+}(PF_6^-)_2$ in acetonitrile and 25 mg/ml of poly(methyl methacrylate) (Aldrich; average $M_w \sim 300{,}000$) in acetonitrile were prepared separately and combined in a 1:1 volume ratio. A film was fabricated by spin coating onto a clean ITO glass slide at 1000 rpm for 60 s, to give a final film thickness of 120 nm. The film was baked for 2 h at 120 °C and a 300 Å-thick Au electrode was thermally evaporated on top of the films at a pressure of 3.0×10^{-6} Torr and at a rate of 1 Å/s. The devices were tested using a Keithley 236 source measure unit and a Labsphere modular integrating sphere with a calibrated Si photodetector. Fabrication and testing took place in a nitrogen glove box.

3. Results and discussion

The typical dependence of the current $I(t)$ under an applied harmonic bias $V(t)$ is shown in Fig. 1A. The observed time delay between the maxima in voltage and current is a result of memristive behavior. Fig. 1B shows the corresponding I–V plot, which follows Chua's prediction and corresponds to a Lissajous curve. Fig. 2A shows the time dependence of the intensity of electroluminescence ($L(t)$), which exhibits the same time delay with respect to voltage as did the current. Fig. 2B shows the corresponding plot of light intensity vs. voltage.

The highest occupied molecular orbital (HOMO) of $[Ru(bpy)_3]^{2+}$ is at 5.8 eV and its lowest unoccupied molecular orbital (LUMO) is at 3.2 eV. The large barriers from the ITO (work function ~4.3 eV) and Au (work function of ~5.1 eV) electrodes imply that there is little electronic charge injection immediately after the application of a bias. This is the OFF state where the electronic current is negligible and no light emission is observed. However, as the ions redistribute near the ITO/organic and organic/Au interfaces, charge injection commences and the ON state is reached [11]. The asymmetry in current and light intensity between positive and negative bias can be attributed to the difference in the work functions of ITO and Au, causing different injection barriers.

The memristive effect in these devices depends on the frequency of the applied signal. In order to illustrate this, Fig. 3 shows the frequency dependence of the phase shift – calculated by dividing the time delay between the maxima of $I(t)$ (or $L(t)$) and $V(t)$ peaks by the period of the ap-

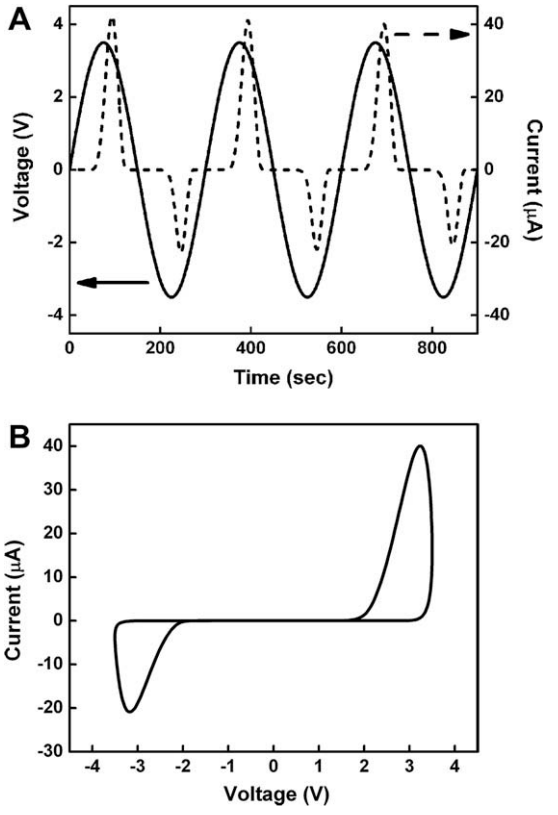

Fig. 1. (A) The applied bias at 3.33 mHz (solid line) and resulting current (dashed line) as function of time, and (B) the corresponding current vs. voltage plot. Bias applied with respect to ITO electrode.

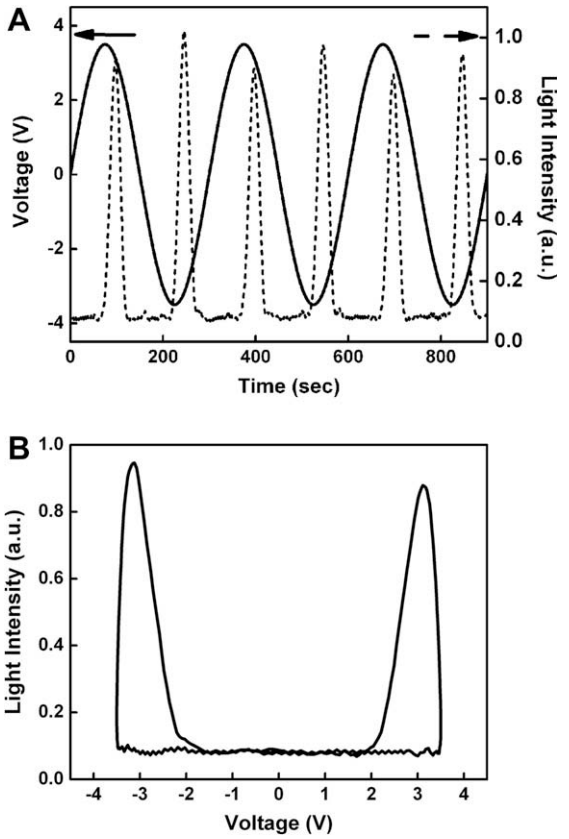

Fig. 2. (A) The applied bias at 3.33 mHz (solid line) and resulting electroluminescence intensity (dashed line) as function of time, and (B) the corresponding intensity vs. voltage plot.

plied signal. Interestingly, there is a phase shift maximum near 3.3 mHz, with decreasing phase shifts for lower and higher frequencies. We can account for this behavior by considering ionic space charge effects: at low frequencies, the ion movement is fast enough to follow the applied bias, so little memory effect is observed. The current (or light intensity) vs. voltage curves in this regime look qualitatively similar to the curves in Figs. 1B and 2B, but the magnitudes of both current and light intensity are higher and there is less hysteresis. In contrast, at high frequencies, the ions cannot respond fast enough to enable significant electronic carrier injection. Therefore, the current in this regime is mostly due to ionic displacement (hence there is no light emission) and follows the voltage signal without a time lag. The maximum phase shift corresponds to a time period around 300 s, consistent with the slow turn-on times of iTMC devices [11].

Due to the low ionic conductivity of PF_6^- ions, the time response of the memristor presented here is too slow for practical applications. However, there are several ways to improve the time response of devices made from iTMCs. For instance, decreasing the thickness of the iTMC layer makes the device turn-on faster. Unfortunately, this also lowers its efficiency, owing to exciton quenching at the electrodes [12]. Increasing the applied bias reduces the turn-on time but also leads to shorter device lifetime [5].

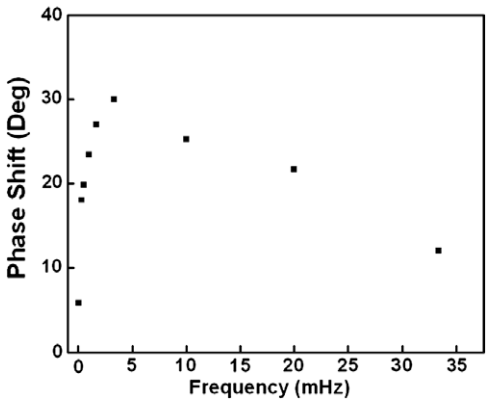

Fig. 3. Phase shift dependence on the frequency of the applied bias.

Changing the counter ion from PF_6^- to ClO_4^- or BF_4^- reduces the turn-on times but is also accompanied by a faster degradation of the device, as observed by the decreasing light output over time [6,13,14]. One of the most effective ways to improve the time response of iTMC light-emitting device is to increase the ionic conductivity [15–21]. For instance, incorporation of the ionic liquid 1-butyl-3-methylimidazolium hexafluorophosphate enabled ac operation of $[Ru(bpy)_3]^{2+}(PF_6^-)_2$ devices at 60 Hz [19].

Even though the device presented here does not show non-volatility, it is still a memristor due to its strong dependence of resistance on charge. Upon application of a bias in a "rested" device, it takes several minutes to observe electroluminescence. The resulting ion distribution is retained for several minutes after the bias is removed. Therefore, if a bias is immediately reapplied, the time to observe electroluminescence would be much shorter. A memory switch could be fabricated using this device that would operate with a retention time/switching time ratio acceptable for some applications (e.g. for bio-inspired circuits). As was recently pointed out [22], thin metal oxide memristors are not completely non-volatile either, with their retention time depending on temperature, applied voltage and materials parameters.

The memristive behavior in electroluminescence observed here is not limited to $[Ru(bpy)_3]^{2+}(PF_6^-)_2$ light-emitting devices. Solid-state light-emitting devices possessing mixed ionic and electronic conductivity belong to a general class of devices termed light-emitting electrochemical cells, which have been studied for over a decade [23–28]. Virtually all of these devices should, likewise, exhibit memory effects. With recent advances in the understanding of their mechanism of device operation [10,23,24] and with better control of their turn-on time [15–21,29,30], these devices might contribute to data storage and computing.

Acknowledgements

This work was supported by the National Science Foundation and the ELI program at Cornell University. The work was performed in part at the Cornell NanoScale Facility, a member of the National Nanotechnology Infrastructure

Network, which is supported by the National Science Foundation (Grant ECS-0335765).

References

[1] L.O. Chua, Memristor – the missing circuit element, IEEE Trans. Circuits Theory 18 (1971) 507–519.

[2] G.S. Snider, US Patent No. 7,203,789 (10 May 2004); B.L. Mouttet, US Patent No. 7,302,513 (3 April 2006); G. Snider, US Patent No. 7,359,888 (31 Jan 2003); B.L. Mouttet, US Patent Application No. 11/976,927 (30 October 2007).

[3] D.B. Strukov, G.S. Snider, D.R. Stewart, R.S. Williams, The missing memristor found, Nature 453 (2008) 80–83.

[4] G.G. Malliaras, R.H. Friend, An organic electronics primer, Phys. Today 58 (2005) 53–58.

[5] E.S. Handy, A.J. Pal, M.F. Rubner, Solid-state light-emitting devices based on the tris-chelated ruthenium(II) complex. 2. tris(bipyridyl) ruthenium(II) as a high-brightness emitter, J. Am. Chem. Soc. 121 (1999) 3525–3528.

[6] F.G. Gao, A.J. Bard, Solid-state organic light-emitting diodes based on tris(2,2′-bipyridine) ruthenium(II) complexes, J. Am. Chem. Soc. 122 (2000) 7426–7427.

[7] J.D. Slinker, D. Bernards, P.L. Houston, H.D. Abruña, S. Bernhard, G.G. Malliaras, Solid state electroluminescent devices based on transition metal complexes, Chem. Commun. (2003) 2392–2399.

[8] H.J. Bolink, L. Cappelli, E. Coronado, M. Gratzel, E. Orti, R.D. Costa, P.M. Viruela, M.K. Nazeeruddin, Stable single-layer light-emitting electrochemical cell using 4,7-diphenyl-1,10-phenanthroline-bis(2-phenylpyridine)iridium(III) hexafluorophosphate, J. Am. Chem. Soc. 128 (2006) 14786–14787.

[9] J. Moran-Mirabal, J.D. Slinker, J.A. DeFranco, S.S. Verbridge, R. Ilic, S. Flores-Torres, H.D. Abruña, G.G. Malliaras, H.G. Craighead, Electrospun light-emitting nanofibers, Nano Lett. 7 (2007) 458–463.

[10] J.D. Slinker, J.A. DeFranco, M.J. Jaquith, W.R. Silveira, Y.W. Zhong, J.M. Moran-Mirabal, H.C. Craighead, H.D. Abruña, J.A. Marohn, G.G. Malliaras, Direct measurement of the electric-field distribution in a light-emitting electrochemical cell, Nat. Mater. 6 (2007) 894–899.

[11] J.D. Slinker, J. Rivnay, J.S. Moskowitz, J.B. Parker, S. Bernhard, H.D. Abruña, G.G. Malliaras, Electroluminescent devices from ionic transition metal complexes, J. Mater. Chem. 17 (2007) 2976–2988.

[12] K.W. Lee, J.D. Slinker, A.A. Gorodetsky, S. Flores-Torres, H.D. Abruña, P.L. Houston, G.G. Malliaras, Photophysical properties of tris(bipyridyl)ruthenium(II) thin films and devices, Phys. Chem. Chem. Phys. 5 (2003) 2706–2709.

[13] M. Buda, G. Kalyuzhny, A.J. Bard, Thin-film solid-state electroluminescent devices based on tris(2,2′-bipyridine)ruthenium(II) complexes, J. Am. Chem. Soc. 124 (2002) 6090–6098.

[14] H. Rudmann, S. Shimida, M.F. Rubner, Solid-state light-emitting devices based on the tris-chelated ruthenium(II) complex. 4. High-efficiency light-emitting devices based on derivatives of the tris(2,2′-bipyridyl)ruthenium(II) complex, J. Am. Chem. Soc. 124 (2002) 4918–4921.

[15] C.H. Lyons, E.D. Abbas, J.K. Lee, M.F. Rubner, Solid-state light-emitting devices based on the trischelated ruthenium(II) complex. 1. Thin film blends with poly(ethylene oxide), J. Am. Chem. Soc. (1998) 12100–12107.

[16] J.C. Leprêtre, A. Deronzier, O. Stéphan, Light-emitting electrochemical cells based on ruthenium(II) using crown ether as solid electrolyte, Synthetic Met. 131 (2002) 175–183.

[17] S.T. Parker, J.D. Slinker, M.S. Lowry, M.P. Cox, S. Bernhard, G.G. Malliaras, Improved turn-on times of iridium electroluminescent devices by use of ionic liquids, Chem. Mater. 17 (2005) 3187–3190.

[18] H.J. Bolink, L. Cappelli, E. Coronado, A. Parham, P. Stossel, Green light-emitting solid-state electrochemical cell obtained from a homoleptic iridium(III) complex containing ionically charged ligands, Chem. Mater. 18 (2006) 2778–2780.

[19] J.D. Slinker, J. Rivnay, J.A. DeFranco, D.A. Bernards, A.A. Gorodetsky, S.T. Parker, M.P. Cox, R. Rohl, S. Flores-Torres, H.D. Abruña, G.G. Malliaras, Direct 120 V, 60 Hz operation of an organic light emitting device, J. Appl. Phys. 99 (2006) 074502-1–074502-5.

[20] H.-C. Su, F.-C. Fang, T.-Y. Hwu, H.-H. Hsieh, H.-F. Chen, G.-H. Lee, S.-M. Peng, K.-T. Wong, C.-C. Wu, Highly efficient orange and green solid-state light-emitting electrochemical cells based on cationic Ir^{III} complexes with enhanced steric hindrance, Adv. Funct. Mater. 17 (2007) 1019–1027.

[21] S. Graber, K. Doyle, M. Neuburger, C.E. Housecroft, E.C. Constable, R.D. Costa, E. Ortí, H.J. Bolink, A supramolecularly-caged ionic iridium(III) complex yielding bright and very stable solid-state light-emitting electrochemical cells, J. Am. Chem. Soc. 130 (2008) 14944–14945.

[22] D.B. Strukov, R.S. Williams, Exponential ionic drift: fast switching and low volatility of thin-film memristors, Appl. Phys. A 94 (2009) 515–519.

[23] Q.B. Pei, G. Yu, C. Zhang, Y. Yang, A.J. Heeger, Polymer light-emitting electrochemical cells, Science 269 (1995) 1086–1091.

[24] J.C. deMello, Interfacial feedback dynamics in polymer light-emitting electrochemical cells, Phys. Rev. B 66 (2002) 235210-1–235210-5.

[25] D.J. Dick, A.J. Heeger, Y. Yang, Q.B. Pei, Imaging the structure of the p–n junction in polymer light-emitting electrochemical cells, Adv. Mater. 8 (1996) 985–987.

[26] N.D. Robinson, J.-H. Shin, M. Berggren, L. Edman, Doping front propagation in light-emitting electrochemical cells, Phys. Rev. B 74 (2006) 155210-1–155210-5.

[27] Q. Sun, Y. Li, Q. Pei, Polymer light-emitting electrochemical cells for high-efficiency low-voltage electroluminescent devices, J. Display Technol. 3 (2007) 211–224.

[28] G. Yu, Y. Cao, M. Andersson, J. Gao, A.J. Heeger, Polymer light-emitting electrochemical cells with frozen p–i–n junction at room temperature, Adv. Mater. 10 (1998) 385–388.

[29] E. Zysman-Colman, J.D. Slinker, J.B. Parker, G.G. Malliaras, S. Bernhard, Improved turn-on times of light-emitting electrochemical cells, Chem. Mater. 20 (2008) 388–396.

[30] L.S.C. Pingree, D.B. Rodovsky, D.C. Coffey, G.P. Bartholomew, D.S. Ginger, Scanning Kelvin probe imaging of the potential profiles in fixed and dynamic planar LECs, J. Am. Chem. Soc. 129 (2007) 15903–15910.

Organic Electronics 11 (2010) 154–158

Contents lists available at ScienceDirect

Organic Electronics

journal homepage: www.elsevier.com/locate/orgel

Letter

Hybrid TiO_x/fluoropolymer bi-layer dielectrics for low-voltage complementary inverters

Chao-Feng Sung [a], Dhananjay Kekuda [d], Li Fen Chu [c], Fang-Chung Chen [a], Shiau-Shin Cheng [c], Yuh-Zheng Lee [b], Meng-Chyi Wu [c], Chih-Wei Chu [a,d,*]

[a] Department of Photonics and Display Institute, National Chiao Tung University, Hsinchu 30013, Taiwan
[b] Industrial Technology Research Institute, Hsinchu 31040, Taiwan
[c] Department of Electrical Engineering, National Tsing Hua University, Hsinchu 30013, Taiwan
[d] Research Center for Applied Sciences, Academia Sinica, Taipei 11529, Taiwan

ARTICLE INFO

Article history:
Received 27 August 2009
Received in revised form 10 September 2009
Accepted 21 September 2009
Available online 25 September 2009

Keywords:
Organic
Titanium oxide
Dielectrics
Thin-film transistors

ABSTRACT

In this article, low temperature processed, reactively evaporated titanium oxide layers were utilized as gate dielectrics for achieving low voltage driven transistors and complementary inverters. The surface of the gate dielectric was modified by an ultra thin (~30 nm) fluoropolymer Cytop® layer which partially helped to reduce the leakage in the dielectric films and also enhanced the organic transistor performance. The current investigation demonstrates the ability of these high capacitance bi-layer dielectrics ($k \sim 20$). The combined p-type and n-type field-effect transistors show similar saturation mobility ~0.3 cm^2/Vs to achieve low voltage driven complementary circuits with output gain of 22. Low temperature processing of these dielectric layers make them easily integrated.

© 2009 Elsevier B.V. All rights reserved.

1. Introduction

Recently, interest in organic electronics is rapidly emerging due to its easy processing routes and cheaper production costs. Organic solar cells, organic thin-film transistors (OTFTs), complementary inverters and light emitting diodes have been the focus of invention by majority of researchers in this area [1–3]. Various materials have been investigated as candidates for the active layers for organic/inorganic TFTs [4,5]. Among organic TFTs, Pentacene has derived much attention due to its planar structure and high mobility. Moreover, Pentacene can be easily evaporated so that the growth mechanisms are easily controlled through deposition rate, thickness and the substrate temperatures. When employed as active layers in a planar geometry, Pentacene based OTFTs have resulted in field-effect mobilities ~1 $cm^2/V\,s^{-1}$, ensuring that they can be the possible replacements for the amorphous Si transistors in near future [6,7]. However, one of the challenging issues in OTFTs is to reduce the operative voltages of the devices. Utilization of high dielectric constant oxides is the plausible route to achieve low voltage driven transistors and complementary inverters [8–10]. Some of the oxides which derived much attention as gate dielectrics are Ta_2O_3 [11,12], YO_x [13], TiO_2 [8,14,15], MgO [16] etc. Roughness, density of surface traps and dielectric constants of the dielectric layer are the key issues to be addressed while designing the OTFTs [11,17]. It is anticipated that surface of these oxides can be modified by a thin polymer layer coating which eventually smoothens the dielectric surface and helps in increasing the breakdown field [18]. Utilization of such bi-layer dielectrics is the main topic of current investigation [11,15]. Because of their highly hydrophilic surfaces, these oxide films are not suitable for direct growth of the organic semiconductor due to the probable undesirable interface modifications [19]. The polymer

* Corresponding author. Address: Research Center for Applied Sciences, Academia Sinica, Taipei 11529, Taiwan. Tel.: +886 2 2789 8000.
E-mail address: gchu@gate.sinica.edu.tw (C.-W. Chu).

1566-1199/$ - see front matter © 2009 Elsevier B.V. All rights reserved.
doi:10.1016/j.orgel.2009.09.020

layers atop gate oxide ensures organic–organic interface between the active layers and gate dielectrics which is of non-interacting nature and provide better interface [20]. Considering all these factors, in this study, we have grown low temperature processed titanium oxide (TiO_x) dielectric layers by a simple reactive evaporation process. The surface modification was achieved by a solution processed fluoropolymer Cytop® layers. We also have demonstrated the low-voltage operation of the complementary inverter consisting of Pentacene and PTCDI-C8 as p- and n-type semiconductors, respectively.

2. Experimental

The devices were fabricated on the indium tin oxide (ITO)-coated glass substrates (10–20 Ω/□, sheet resistance), acting as gate electrode. Prior to the device fabrication, the ITO substrates were cleaned by TFD4 detergent (Franklab, France) and deionized water in an ultrasonic bath and were treated with UV-ozone for 15 min. In order to implement low-voltage operation of the organic thin-film transistors, we used the high-k metal oxides TiO_x as gate insulators. The chamber was pumped down to $\sim 10^{-6}$ Torr before the TiO_x deposition. The films were deposited by reactive evaporation of Ti in an oxygen environment. The flow rate of the oxygen gas was maintained by means of a mass flow controller. During the TiO_x deposition process, the partial pressure was optimized at 2×10^{-4} Torr. The as-deposited films were subjected to post-deposition annealing process at a temperature of 150 °C, and the evaporation rate of 1.0 Å was fixed during the deposition. However, the resultant TiO_x dielectrics caused a high grain boundary leakage current. To reduce such leakage currents, a dilute 1 wt% Cytop® CTL-809 M (Asahi Glass, Tokyo, Japan) was spin-coated over the TiO_x-covered ITO glass substrates at a rotation speed of 2000 rpm for 60 s, followed by baking at 100 °C to remove the residual solvent. The spin coating process was carried out under nitrogen environment in glove box. In order to achieve the low-voltage complementary circuits, p-type Pentacene and n-type N-N′-dioctyl-3,4,9,10-perylene tetracarboxylic diimide (PTCDI-C8) were, respectively, patterned on the TiO_x layer using shadow masks by thermal evaporation.

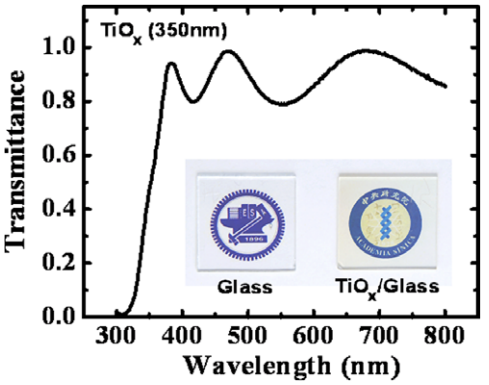

Fig. 1. UV–vis transmission spectra for TiO_x thin film. Inset: photographic images of the TiO_x films grown on glass and a bare glass.

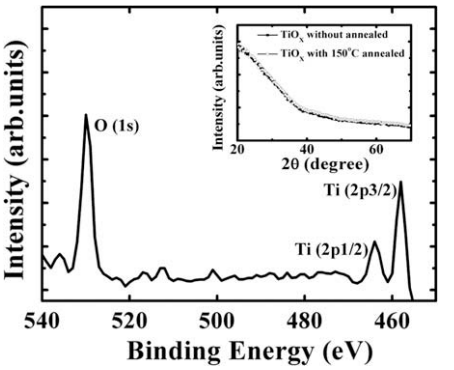

Fig. 2. X-ray photoelectron spectroscopic (XPS) spectra of TiO_x thin film. Inset: X-ray diffraction (XRD) spectra of TiO_x thin film with/without annealing.

The deposition rate was fixed to 0.5 Å/s for the evaporation of both Pentacene and PTCDI-C8 which were deposited onto the gate dielectric under a high vacuum 10^{-6} Torr. Both the thicknesses of Pentacene and PTCDI-C8 films were 50 nm. Finally, the metal (Au) was deposited on semiconductors through a shadow mask as the contact electrodes. The current–voltage (I–V) characteristics of OTFTs were measured in N_2 by Keithley semiconductor analyzer (4200-SCS). The C–V measurement was performed by a HP 4980A precision LCR meter. The films were subjected to X-ray diffraction (XRD) to ascertain nature of crystallinity

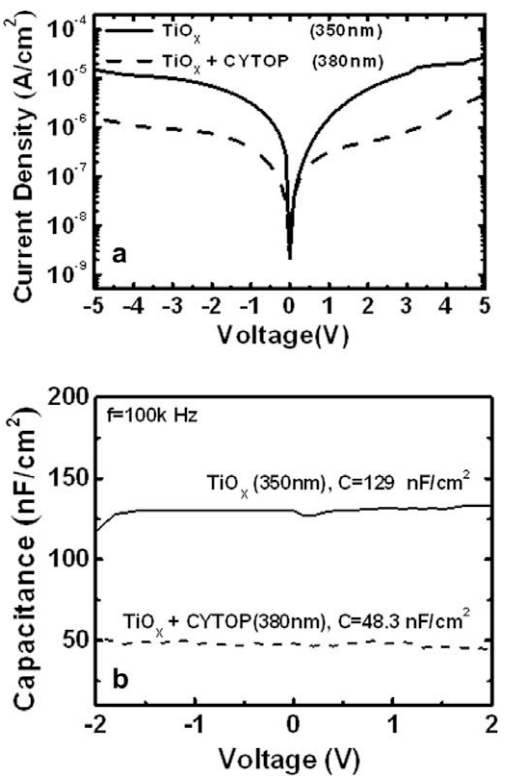

Fig. 3. (a) Current density vs. electric field characteristics of the TiO_x and TiO_x/polymer gate dielectrics. (b) Capacitance vs. voltage curves measured at 100 kHz for TiO_x and TiO_x/polymer.

in the films. The XRD measurements were performed using a Philips X' Pert-Pro diffractometer with Cu Kα radiation of wavelength $\lambda = 1.54$ Å.

3. Results and discussion

Optical band gap of TiO_x without intentional doping is ~3.4 eV [21]. Its wide band gap makes it transparent in the visible region of the electromagnetic spectrum and hence are suitable for the transparent electronics applications. Fig. 1 displays the transmission spectrum of the reactively evaporated TiO_x films grown on glass. Inset provides the photographic images of the TiO_x films grown on glass and that of a bare glass. The highly transparent nature of the films is clearly visible from the figure. Thickness of the layer was ~350 nm as measured from the thickness profilometer. The optical transmission spectra of the reactively evaporated TiO_x films are highly transparent (transmittance >78%) in the visible region. The high transmittances indicate fairly smooth surfaces and relatively good film homogeneity.

In order to further characterize the oxide films, X-ray photoelectron spectroscopy was carried out. Fig. 2 shows the high resolution XPS spectra of the TiO_x films deposited on glass substrate. As shown in the figure, titanium peaks were located 458 eV (Ti $2p_{3/2}$) and 464 eV (Ti $2p_{1/2}$), the oxygen peak (O 1S) was positioned at 530 eV. The elemental analysis of the films resulted in corresponding atomic composition of 66.3 and 33.7 for titanium and oxygen, respectively. Hence, it was found that the composition is

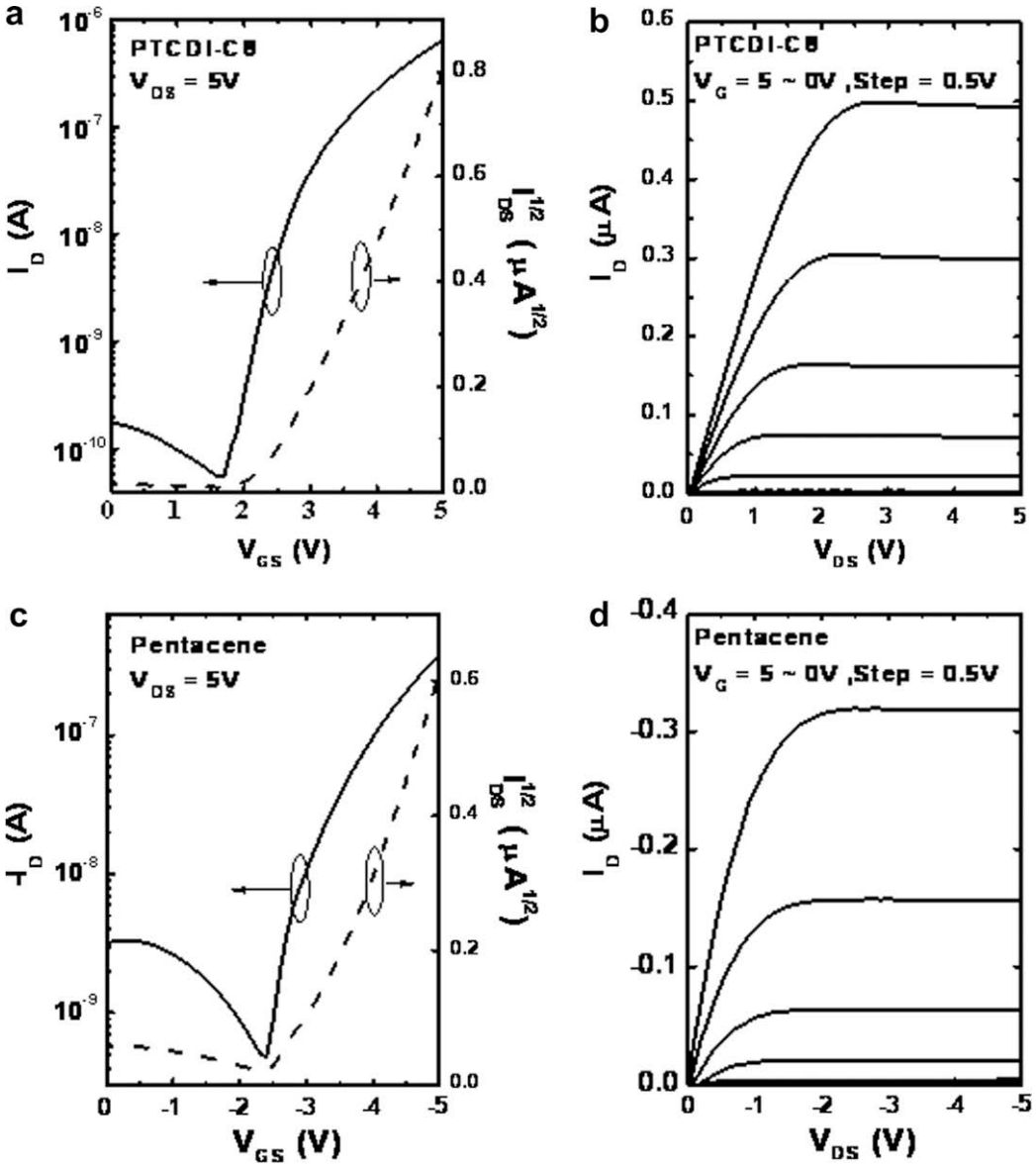

Fig. 4. (a) Transfer and (b) output characteristics of the n-type (PTCDI-C8) OTFTs. (c) Transfer and (d) output characteristics of the p-type (Pentacene) OTFTs.

close to the ideal value of 2, indicating that the films are stoichiometric in nature and the current reactive evaporation is desired for the effective conversion of Ti into TiO_x films at room temperature. Fig. 2 inset shows the X-ray diffraction pattern of TiO_x thin films grown on glass substrates by reactive evaporation. The absence of any well defined diffraction peaks indicates that the films are amorphous in nature. For comparison both unannealed and annealed films are shown in the figure. As can be seen from the figure, annealing at 150 °C did not help in inducing any crystallinity in the films. In the case of oxides, the grain size tends to increase with increasing annealing temperatures as a result of which the surface roughness also increases. Since the higher surface roughness is not desired for the gate dielectric applications, high-temperature annealing process was not carried out for the films. Amorphous nature of the oxide films ensures that the grain boundary effects will be minimal. Hence, it is expected to lead to reduced charge trapping at the interface. Amorphous nature of the gate dielectric films is also found in the literature.

In order to achieve low-voltage operation in OTFTs, the high-k materials are always used as the gate insulators, which can afford greater surface charge density and also reduce the operating voltages of OTFTs. The TiO_x has lately been used as a high-k gate dielectric material and many groups have researched about this metal oxide [14,15,20]. In general, the TiO_x films have usually fabricated through rf/dc sputtering, sol–gel, solution processing, and were used as dielectrics for OTFTs. However, almost such methods need to high-temperature annealing. Their dielectric constant values of the TiO_x films are in the range of 11–41. In the present study, the TiO_x films are deposited by reactive evaporation of Ti without any high-temperature treatment. The electrical properties of the films are investigated by current–density–voltage J–V and capacitance–voltage C–V characteristics of the Au/Cytop®/TiO_x/ITO sandwich structures. As shown in Fig. 3b, the TiO_x film has relatively high capacitance (Ci = 129 nF/cm^2) and the dielectric constant of the TiO_x extracted from capacitance–voltage (C–V) measurement is as high as 51. In order to avoid leakage current and surface modification, the fluoropolymer Cytop® thin film is used to stack on the TiO_x film through solution processing. The leakage current density of the bi-layer dielectric has successfully compressed than that of the single TiO_x layer as seen in Fig. 3a. For the bi-layer insulator, the bottom layer of the thick TiO_x enhances the dielectric constant of the insulator, and the top layer of the ultrathin Cytop® acts as a roughness-smoothing layer and hydrophobic surface treatment. As the metal–insulator–metal capacitors, we have measured the capacitance of 48.3 nF/cm^2 for an Au/Cytop®/TiO_x/ITO sandwich, and the total dielectric constant of the dual-layered gate dielectric was 20. Hence, in order to reconcile the advantages of high dielectric constant for operating at low operating voltages and polymer dielectric for better interface, it is desirable to employ bilayer gate dielectrics as demonstrated by the electrical properties.

OTFTs were fabricated using the above mentioned bilayer dielectrics using a top contact geometry with a channel length (L) of 120 μm and width (W) of 2 mm. While the

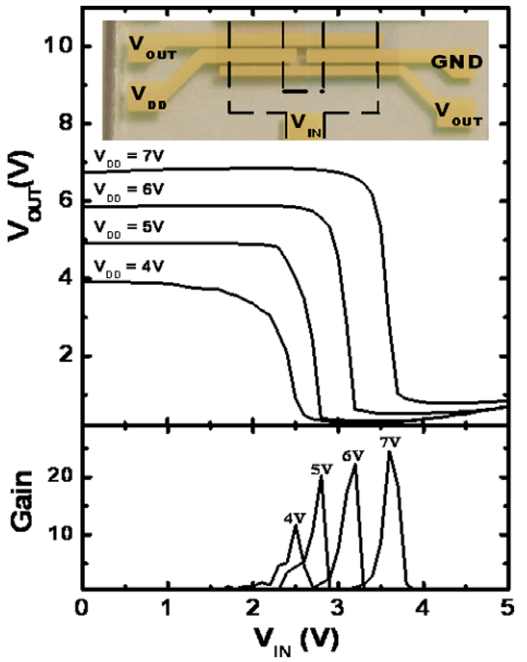

Fig. 5. Output voltage (top) and small-signal gain (bottom) plotted with respect to the input voltage for supply voltages between 4 and 7 V. Inset: photograph of a complementary Pentacene/PTCDI-C8 circuit.

Pentacene OTFTs exhibited a typical p-channel conduction, PTCDI-C8 OTFTs resulted in a n-type OTFT characteristics. It is worth noting that the operative voltages for both the devices is only 5 V depicting that these devices can be operated at low voltages. Output curves are the plots of drain current as a function of source to drain voltages are shown in Fig. 4b and d. Maximum saturation drain current of 0.5 μA for PTCDI-C8 transistor and 0.3 μA for Pentacene transistor are achieved under a gate bias of ±5 V. The field-effect mobility (μ) and threshold voltage (V_T) were extracted from the measured transfer curve (Fig. 4a and c) by comparing it with the standard current–voltage equation for a transistor in the saturation regime [22]. The PTCDI-C8 and Pentacene OTFTs had high field-effect mobilities of 0.33 and 0.31 cm^2/Vs, and exhibited low threshold voltage of 2.7 and −3.1 V, respectively. It reveals that the high-performance and low-voltage organic thin-film transistors can be accomplished though the high-k metal oxide. The PTCDI-C8 OTFTs exhibited a slightly higher on/off ratio ($\sim 10^4$) compared to the Pentacene OTFTs ($\sim 10^3$). Overall, the values of the filed-effect mobilities are relatively high both in n-channel transistors and p-channel transistors operating at low voltages, and the low threshold voltage will enable us to achieve the low-voltage operation of the inverter.

Finally, we have also demonstrated the organic complementary inverters with PTCDI-C8 and Pentacene OTFTs, fabricated on TiO_x/Cytop® double dielectric layers. The static inverter characteristic of a complementary Pentacene/PTCDI-C8 is shown in Fig. 5, and the inverter operated at low voltages (V_{DD}) in the range of 4–7 V. When the organic complementary inverters operated at a low voltage of 5 V, it shows a maximum voltage gain of 22. Thus, we conclude that our TiO_x/Cytop® double layer is a promising

new gate dielectric for realizing a low-operating-voltage PTCDI-C8 and Pentacene OTFTs and subsequent complementary inverters. Therefore, the logic circuits operating at low voltage can be realized by these low-voltage devices.

4. Conclusion

In summary, we have successfully implemented low-voltage operation organic thin-film transistors by using the high-k metal oxides TiO_x/thin polymer as gate insulators. The titanium oxide films are deposited by reactive evaporation of Ti in an oxygen environment without high-temperature annealing. The total dielectric constant of the dual-layered gate dielectric is 20 enabled us to achieve a high capacitance dielectric for low-voltage operation. By using TiO_x/Cytop® as insulator, we were able to manufacture high quality PTCDI and Pentacene organic OTFTs with exceptionally low leakage and relatively low operating voltage. The PTCDI-C8 and Pentacene OTFTs possess field-effect mobilities of 0.33 and 0.31 cm^2/Vs, and threshold voltage of 2.7 and −3.1 V, respectively. In addition, the organic complementary inverters operated at a low voltage of 5 V with a voltage gain of 22. Thus, we conclude that our TiO_x/Cytop® double layer is a promising new gate dielectric for realizing a low voltage driving OTFTs.

Acknowledgment

We thank the National Science Council (NSC 96-2221-E-001-017-MY2 and NSC 96-2628-E-007-030-MY2) and Academia Sinica for financial support.

References

[1] D. Braga, G. Horowitz, Adv. Mater. 21 (2009) 1473.
[2] C.W. Chu, H. Yang, W.J. Hou, J. Huang, G. Li, Y. Yang, Appl. Phys. Lett. 92 (2008) 103306.
[3] W. Ma, C. Yang, X. Gong, K. Lee, A.J. Heeger, Adv. Funct. Mater. 15 (2005) 1617.
[4] A. Facchetti, Mater. Today 10 (2007) 28.
[5] Dhananjay, Chih-Wei Chu, Appl. Phys. Lett. 91 (2007) 132111.
[6] H. Klauk, D.J. Gundlach, J.A. Nichols, T.N. Jackson, IEEE Trans. Electron Dev. 46 (1999) 1258.
[7] M. Shtein, J. Mapel, J.B. Benziger, S.R. Forrest, Appl. Phys. Lett. 81 (2002) 268.
[8] F.C. Chen, C.S. Chuang, Y.S. Lin, L.J. Kung, T.H. Chen, H.P.D. Shieh, Org. Electron. 7 (2006) 435.
[9] H. Klauk, U. Zschieschang, J. Pflaum, M. Halik, Nature 445 (2007) 745.
[10] J.B. Koo, C.H. Ku, J.W. Lim, S.H. Kim, Org. Electron. 8 (2007) 552.
[11] A.L. Deman, J. Tardy, Org. Electron. 6 (2005) 78.
[12] C. Bartic, H. Jansen, A. Campitelli, S. Borghs, Org. Electron. 3 (2002) 65.
[13] D.K. Hwang, C.S. Kim, J.M. Choi, K. Lee, J.H. Park, E. Kim, H.K. Baik, J.H. Kim, S. Im, Adv. Mater. 18 (2006) 2299.
[14] C.S. Chuang, F.C. Chen, H.P.D. Shieh, Org. Electron. 8 (2007) 767.
[15] L.A. Majewski, R. Schroeder, M. Grell, Adv. Mater. 17 (2005) 192.
[16] Y. Irokawa, Y. Nakano, M. Ishiko, T. Kachi, J. Kim, F. Ren, B.P. Gila, A.H. Onstine, C.R. Abernathy, S.J. Pearton, C.C. Pan, G.T. Chen, J.I. Chyi, Appl. Phys. Lett. 84 (2004) 2919.
[17] L. Fumagalli, D. Natali, M. Sampietro, E. Peron, F. Perissinotti, G. Tallarida, S. Ferrari, Org. Electron. 9 (2008) 198.
[18] T. Umeda, D. Kumaki, S. Tokito, Org. Electron. 9 (2008) 545.
[19] S.J. Mun, J.M. Choi, K.H. Lee, K. Lee, S. Im, Appl. Phys. Lett. 93 (2008) 233301.
[20] Y. Lu, W.H. Lee, H.S. Lee, Y. Jang, K. Cho, Appl. Phys. Lett. 94 (2009) 113303.
[21] T.G. Lei, H.H. Bo, S.J. Da, Chinese Phys. Lett. 22 (2005) 1787.
[22] F. Garnier, Organic-based thin-film transistors, in: C.R. Kagan, P. Andry (Eds.), Thin-Film Transistors, Marcel Dekker Inc., New York, 2003, p. 307.

Organic Electronics 11 (2010) 159–163

Contents lists available at ScienceDirect

Organic Electronics

journal homepage: www.elsevier.com/locate/orgel

Letter

Pentacene thin-film on organic/inorganic nanohybrid dielectrics for ZnO charge injection memory transistor

Sung Hoon Cha [a], Aaron Park [a], Kwang H. Lee [a], Seongil Im [a,*], Byoung H. Lee [b], Myung M. Sung [b]

[a] Institute of Physics and Applied Physics, Yonsei University, Seoul 120-749, Republic of Korea
[b] Department of Chemistry, Hanyang University, Seoul 133-791, Republic of Korea

ARTICLE INFO

Article history:
Received 10 August 2009
Received in revised form 14 September 2009
Accepted 22 September 2009
Available online 26 September 2009

Keywords:
Thin-film transistor
Flash memory
Pentacene
Organic–inorganic nanohybrid
ZnO

ABSTRACT

We report on the fabrication of ZnO-channel charge injection memory thin-film transistors (TFTs). Our non-volatile memory TFT has a thin pentacene on top of a dielectric sandwich which has 3 nm-thin inserted potential well as a hole trap layer. The thin pentacene in contact with Au top electrode supports effective hole injection from pentacene into the inserted well under +8 V programming gate pulse while those injected holes are effectively ejected out under −8 V pulse, so that ZnO channel below the dielectric may have two different current states: write and erase. Our device operates at less than 2 V and shows a retention time of about 1000 s after programmed at +8 V, along with an effective program/erase ratio of 5–20.

© 2009 Elsevier B.V. All rights reserved.

1. Introduction

Glass- or plastic-based electronics have steadily been developed with organic and oxide semiconductors as active channels for their thin-film transistor (TFT) component [1–3]. Since memory circuits with TFTs are regarded highly important for the future electronics on glass or plastics, non-volatile memory TFTs have been developed with ferroelectric polymers [4–7] or with charge injection gate [8–10] dielectrics. In the case of ferroelectric field effect transistors, however, the operating voltage was quite high ranging from minimum 15 to maximum 80 V, due to the thickness of the ferroelectric polymer. While the charge injection type memory TFTs operate at a little lower voltage of ~12 V than that of ferroelectric memory TFT, they expose a critical drawback: poor erase performance [8]. Low voltage-driven memory TFTs with good program/erase properties using charge-injection mechanism has thus hardly been reported. Here, we have fabricated ZnO-channel non-volatile memory TFT with unique top gate structure, as an effort to resolve such issues: good erase performance and low voltage switching. Our charge injection memory TFT has thin pentacene layer on top of oxide-organic nanohybrid dielectric sandwich which has 3 nm-thin inserted oxide-organic nanohybrid potential well. The thin pentacene in contact with Au top electrode supports effective hole injection from pentacene into the inserted dielectric well under +8 V programming gate pulse, while those injected holes are effectively ejected out under −8 V pulse for erase, so that ZnO channel below the dielectric may have two different current states.

2. Experimental section

On a clean glass substrate (Corning Eagle 2000), Al source/drain electrodes were patterned by thermal evaporation. Then, a 70-nm-thick ZnO film was deposited at room temperature (RT) by rf sputtering, to be active patterned channel. After that, nanohybrid dielectric multi-layers were deposited on ZnO channel by repeating a cyclic molecular layer deposition (MLD), which is a deposition

* Corresponding author. Tel.: +82 2 2123 2842; fax: +82 2 392 1592.
E-mail address: semicon@yonsei.ac.kr (S. Im).

1566-1199/$ - see front matter © 2009 Elsevier B.V. All rights reserved.
doi:10.1016/j.orgel.2009.09.021

process to achieve multi-units of inorganic (AlO_x or TiO_x) monolayer-organic self-assembled monolayer (SAM), e.g., $1AlO_x$–SAM = 1 molecular unit with 1.1 nm thickness; the details of the oxide–SAMu formation and MLD were very recently reported [11], while the molecular units of AlO_x-SAM and TiO_x –SAM were described in Fig. 1a. Our organic–inorganic hybrid (e.g., oxide–SAMu) dielectric has a specifically designed sandwich structure that includes a trap layer of TiO_x–SAMu (3.3 nm) between a 2.2 nm AlO_x–SAMu for gate charge tunneling and an 11 nm-thick AlO_x–SAMu for blocking the ZnO-channel charges. After the definition of sandwich dielectrics, 15–50 nm-thick pentacene (Aldrich Chem. Co., ~99% purity) as hole injection layer was deposited on the dielectric. Finally, the Au top-gate electrode was patterned on pentacene by thermal evaporation. The nominal channel length (L) and width (W) were 90 and 500 μm, respectively. Top-gate flash memory transistor has three layers in its general dielectric structure: tunneling layer in contact with channel, trapping layer, and blocking layer beneath the gate electrode [12–15]. However, in contrast to general flash memory transistor scheme, our memory device has an opposite dielectric layer stacking, as shown in the device cross-section of Fig. 1a. Plan view of the device is also shown in the right-side photograph (Fig. 1b). All of our device characterizations, except memory dynamics, were carried out in the dark at RT by using a semiconductor parameter analyzer (HP 4155C, Agilent Technologies). Memory dynamics were measured by a setup using a function generator (AFG310, Sony/Tektronix) and an oscilloscope (TDS210, Tektronix).

3. Results and discussion

Fig. 1c is absorption spectra as the plots of the squared angular frequency absorption coefficient ($\alpha^2\omega^2$) with respect to photon energy, that were obtained from 20 nm-thick TiO_x–SAMu and identically-thick AlO_x–SAMu layers deposited on sapphire substrates. According to the spectra, the optical bandgap of TiO_x –SAMu is estimated to be ~3.9 eV while that of AlO_x –SAMu appeared greater than 7 eV. We thus expect that the accumulated holes would tunnel from pentacene into the TiO_x–SAMu quantum well through the thin AlO_x–SAMu under a strong (+) gate pulse, to be confined there as illustrated in the band diagram of Fig. 1d. As a result, non-volatile memory effects are induced. The holes injected by the (+) pulse would induce the increase of channel electron density and drain current at the bottom ZnO channel while those holes may tunnel back to pentacene by (−) pulse resulting in the decrease of channel electron density.

The charge injection memory effects are clearly displayed in the transfer curves of Fig. 2. Considerable memory window appears through the gate voltage (V_G) sweep that ranges from −4 to 7 V and this window was again proved by pulsing our pristine TFT device with ±8 V. We applied +8 V write-pulse (pulse condition: V_G = +8 V 1 s with ground source/drain, $V_D = V_S = 0$ V) onto the gate to achieve blue color transfer curves in a low voltage range (−1 to +2 V) and then applied −8 V erase-pulse to get green curves in the same low voltage range. It is interesting to note that the write- and erase-levels are quite well

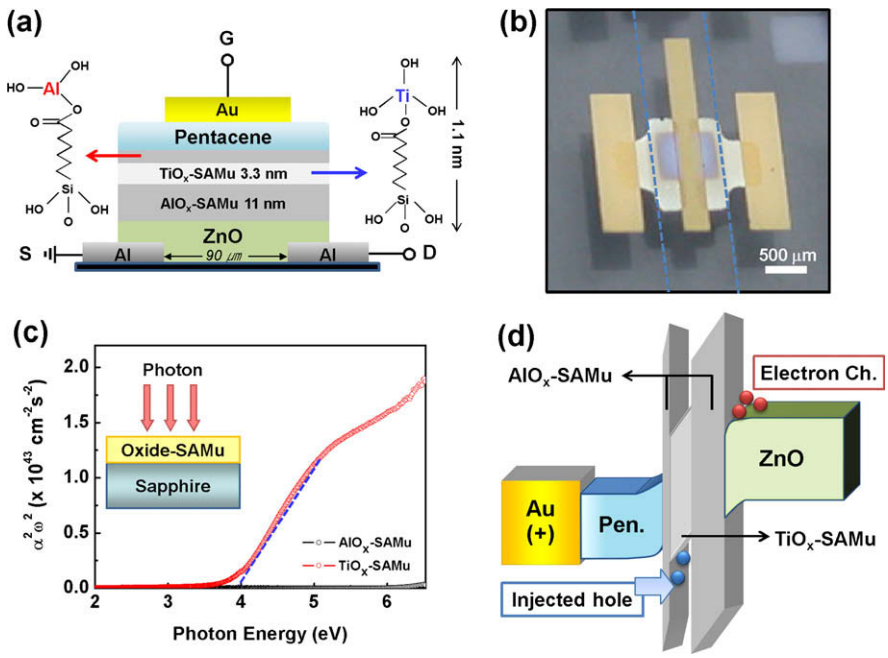

Fig. 1. (a) Schematic cross-section of our hole injection memory TFT using ZnO channel and pentacene top layer. The sandwich dielectric is composed of organic–inorganic hybrid multi-layers: 2.2 nm-thin AlO_x–SAMu, 3.3 nm-thin TiO_x–SAMu, and 11 nm-thin AlO_x–SAMu. (b) Photographic image of the top-view ZnO–TFT. (c) Absorption spectra of our dielectric materials of 20 nm-thin AlO_x–SAMu (black line) and the same thin TiO_x–SAMu (red line) layers. (d) Band diagram of our memory TFT.

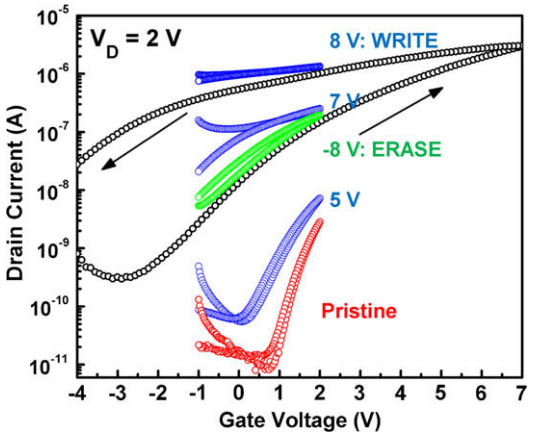

Fig. 2. Main transfer characteristics of the memory TFT were achieved from a gate voltage (V_G) sweep between −4 and +7 V, while low voltage transfer curves between −1 and 2 V gate bias were also obtained after write (+8 V) and erase (−8 V) pulses. Program (write) characteristics depend on the gate voltage; optimum was 8 V.

matched to those (black curves) from large gate-bias sweep. The red transfer curves are for the pristine device, whose initial device performance is not good (with a saturation mobility ~0.05 $cm^2/V\,s$) because we intentionally use Au (high work function ~5.1 eV) as top-gate electrode, which is largely mismatched with the Fermi level of ZnO (~4.3 eV) [16]. However, when +8 V gate pulse is applied, the drain current increases drastically to 10^{-6} A level (saturation mobility ~0.3 $cm^2/V\,s$) and it decreases to about 10^{-8} A with −8 V pulse. This write–erase switching was repetitively observed. These memory behaviors with the pulse are again confirmed in the transistor output curves of Fig. 3a and b. The drain current (I_D) obtained by +8 V 1 s gate pulse for program (write) appears ~10 times higher than that of erase state (by −8 V pulse).

The reason why the current at the erase state does not turn back to the original pristine state in Fig. 2 is because −8 V does not make the same electric field for the dielectric as +8 V does. Instead, the −8 V makes lower electric field for the dielectric itself, since the depleted ZnO and pentacene layers take part in the voltage dividing under

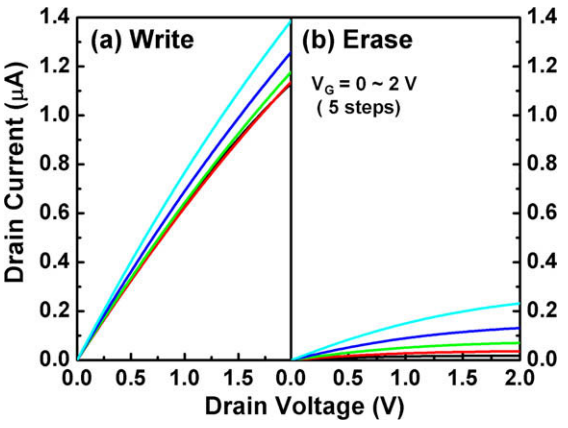

Fig. 3. Drain current–drain voltage (I_D–V_D) output curves of ZnO–TFT after ±8 V 1 s pulses for (a) write and (b) erase.

the negative gate bias. Nevertheless, our results for erase are relatively much effective compared to those of the previously reported ZnO-based memory TFTs with normal floating gate structures, where the carrier ejection performance (erase) was very poor [8,17]. In our present device, 8 V turned out to be an effective value for hole tunneling. As shown in the figure, 5 and 7 V were not large enough to fully turn on the memory device. We thus regard 8 V as a critical value. The maximum gate leakage current was ~2 nA for our memory TFT devices (not shown here). In addition, all the transfer curves have displayed quite stable operations in a low voltage range (−1 to +2 V), hardly showing any hysteresis. It is because the interface between our AlO_x–SAMu dielectric and channel semiconductors (either ZnO or pentacene) is very stable as we previously reported [18,19].

Fig. 4a shows the capacitance–voltage (C–V) measurement results from pentacene-semiconductor/dielectric insulator/metal (MIS) structure, confirming that some of the accumulated holes are really injected from the thin pentacene into the inserted TiO_x–SAMu dielectric well. Some of the accumulated interface holes tunnel into the inserted dielectric layer at a high (+) voltage in the end of the up-arrow process. Once the inserted thin dielectric becomes electrically positive by the hole injection, the hole depletion process of pentacene (down-arrow sweeping) becomes easier with the well-confined holes than without. But then, all of the confined holes are ejected into the pentacene through the down-arrow sweeping at a high (−) voltage. These hole injection and ejection, causing a memory window, were almost exactly repeated without much deviation as shown in the figure. The right and left insets illustrate the hole injection (at +4 V) and ejection (at −4 V), respectively. The memory window approximately deduces the (+) hole charge density difference $\Delta Q_{h(+)}$ between write and erase states by the following equation [13]:

$$\Delta V_{FB} = -\frac{\Delta Q_h}{C_{ox}} \times \frac{x_{(+)}}{x_{tot}},$$

where ΔV_{FB} is the flat band voltage shift obtained from the memory window (~2 V), C_{ox} is total capacitance of the dielectric (~127 nF/cm^2), $x_{(+)}$ is the thickness of injected (+) charge location (=5.5 nm, sum of inserted and tunneling layer thickness) and x_{tot} is 16.5 nm as the total dielectric thickness. Now ΔQ_h is deduced as $\sim 5 \times 10^{12}\ e/cm^2$, where e is electron charge and the ΔQ_h value is regarded reasonable in light of usual charge injection carrier density [20].

Based on these non-volatile memory properties of Figs. 2 and 4a, we set up a non-volatile memory inverter with 22 MΩ load-resistance as shown in the inset of Fig. 4b. According to the input gate voltage sweep (from −4 to +8 V), the memory inverter displays permanent hysteresis window and transition voltage shift (~5 V) with the voltage gain of ~5. For instance, two different output voltages (V_{out}) exist at an input voltage (V_{in}) of 1 V; the two V_{out} states (=1.5 and 7.5 V) after the respective write (+8 V) and erase (−8 V) pulses were substantially displayed along with the memory inverter curves. (See the results from V_{in} sweep in the range from 0 to 1.5 V, as blue and green curves.) This means that our memory device approaches

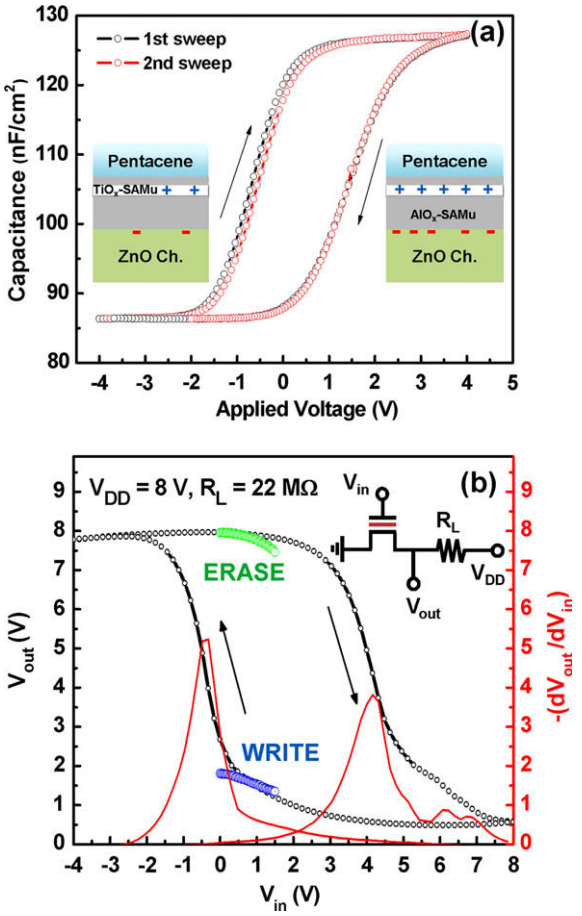

Fig. 4. (a) *C–V* curves of our sandwich structured dielectrics with 15 nm-thick pentacene layer. The holes injected from the accumulated pentacene induce a hysteresis. The inset briefly shows the injection and ejection mechanism. (b) Static voltage transfer characteristics (VTC) of our ZnO–TFT connected to load resistor (R_L) of 22 MΩ. Due to the large window, we clearly obtain two V_{out} states at 1 V (=V_{in}) (blue:+8 V pulsed; green: −8 V pulsed).

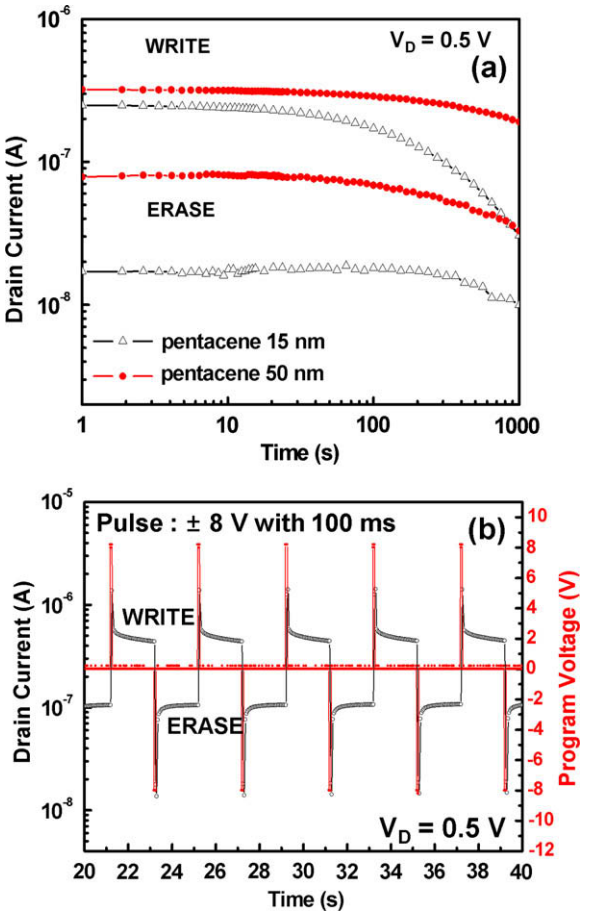

Fig. 5. (a) Retention of the write and erase state for our memory TFT with 15 nm- and 50 nm-thick pentacene. (b) Dynamic retention behavior observed under periodic pulses.

to practical applications readily demonstrating the write and erase states.

Retention properties at static and dynamic switching were measured under a condition of $V_G = 0$ V and $V_D = 0.5$ V as shown in Fig. 5a and b, respectively. For the static retention properties of the ZnO-channel flash memory TFT, ±8 V 1 s pulses were applied onto the gate of the devices with 15 nm- and 50 nm-thin top pentacene. Large on/off (=write/erase) ratio of ∼20 was observed from the TFT with 15 nm-thin pentacene although its effective retention time was only as long as approximately few hundred seconds (Fig. 5a). This short retention was lengthened to higher than ∼1000 s adopting a little thick pentacene top layer (∼50 nm) but then on/off ratio was reduced to ∼4. Fig. 5b shows the dynamic retention properties with the ZnO device with 15 nm-thin pentacene top layer when the write/erase current ratio was measured by alternating ±8 V 100 ms pulses in 4 s period. Write/erase states were clearly distinguished and the ratio was persistent to be ∼5, which is still effective to resolve the two states.

Fig. 6a and b displays the results from subsidiary experiments on ZnO memory TFT without pentacene top layer. As shown in the transfer curves of Fig. 6a, memory hysteresis window was relatively narrow and in particular, +8 V pulse could not make high on-state current unlike the case with pentacene top layer. It seems that without top pentacene the embedded TiO_x–SAMu in the ZnO–TFT has only minor density of injected holes. In other words, the Au gate electrode could not effectively supply high density holes into the embedded well without the assistance of pentacene interlayer and it is understandable. The retention curves of Fig. 6b again reflect the low write-state current, which is an order of magnitude lower than that of ZnO–TFT with pentacene top layer as observed in Fig. 5a. Retention time also appeared much inferior to the case with pentacene top layer (Fig. 5b), that may now play as a buffer to keep the trapped hole charges from occasional recombining with the electrons in gate electrode. We regard that this is a reasonable explanation, since according to Fig. 5b the ZnO device with 50 nm-thick pentacene buffer shows improved retention time property compared to that with 15 nm-thin buffer which may allow some regional contact between Au electrode and dielectric surface [21].

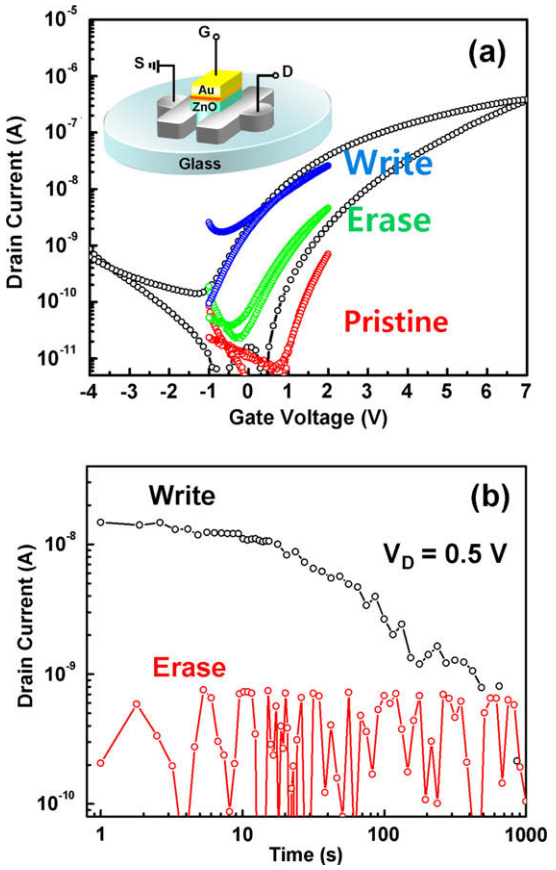

Fig. 6. (a) Transfer (V_G–I_D) and (b) retention characteristics of ZnO–TFT without pentacene top layer. Reduced memory window size and write-state current were observed.

4. Conclusion

In summary, we have fabricated non-volatile flash memory TFTs with ZnO layer for electron channel and with pentacene top layer for gate hole injection. With the assistance of 15–50 nm-thin pentacene, the accumulated holes were effectively injected into inserted TiO_x–SAMu potential well. The repetitive injection and ejection processes were very stable at ±8 V showing good memory window in light of memory transfer curves, memory inverter curves, and dynamic retention curves. Although the retention time after 8 V 1 s pulse appears not that long, our flash memory TFT demonstrates a promising non-volatile memory effects operating at low voltages.

Acknowledgements

This work was supported by the KOSEF (NRL Program: Grant No. 2009-8-0403), by the MKE [IT R&D Program (2008-8-0613), fundamental R&D Program for Core Technology of Materials (2008-8-1410)], by Seoul R&BD Program (ST090839), and by the Brain Korea 21 Program. S.H. Cha acknowledges the Seoul Science Fellowship.

References

[1] T. Sekitani, M. Takamiya, Y. Noguchi, S. Nakano, Y. Kato, T. Sakurai, T. Someya, Nat. Mater. 6 (2007) 413.
[2] M. Ofuji, K. Abe, H. Shimizu, N. Kaji, R. Hayashi, M. Sano, H. Kumomi, K. Nomura, T. Kamiya, H. Hosono, IEEE Electron Device Lett. 28 (2007) 273.
[3] M.S. Oh, K. Lee, K.H. Lee, S.H. Cha, J.M. Choi, B.H. Lee, M.M. Sung, S. Im, Adv. Funct. Mater. 19 (2009) 726.
[4] R.C.G. Naber, C. Tanase, P.W.M. Blom, G.H. Gelinck, A.W. Marsman, F.J. Touwslager, S. Setayesh, D.M. De Leeuw, Nat. Mater. 4 (2005) 243.
[5] S.H. Noh, W. Choi, M.S. Oh, D.K. Hwang, K. Lee, S. Im, S. Jang, E. Kim, Appl. Phys. Lett. 90 (2007) 253504.
[6] S. Ducharme, T.J. Reece, C.M. Othon, R.K. Rannow, IEEE Trans. Device Mater. Rel. 5 (2005) 720.
[7] R. Schroeder, L.A. Majewski, M. Grell, Adv. Mater. 16 (2004) 633.
[8] H. Yin, S. Kim, C.J. Kim, I. Song, J. Park, S. Kim, Y. Park, Appl. Phys. Lett. 93 (2008) 172109.
[9] Y. Guo, C. Di, S. Ye, X. Sun, J. Zheng, Y. Wen, W. Wu, G. Yu, Y. Liu, Adv. Mater. 21 (2009) 1954.
[10] X. Cai, C.P. Gerlach, C.D. Frisbie, J. Phys. Chem. C 111 (2007) 452.
[11] B.H. Lee, M.K. Ryu, S. Choi, K.H. Lee, S. Im, M.M. Sung, J. Am. Chem. Soc. 129 (2007) 16034.
[12] B.J. Hinds, T. Yamanaka, S. Oda, J. Appl. Phys. 90 (2001) 6402.
[13] R.S. Muller, T.I. Kamins, M. Chan, Device Eelectronics for Integrated Circuits, third ed., John Wiley & Sons, New York, 2003 (Chapter 8).
[14] S. Kolliopoulou, P. Dimitrakis, P. Normand, H. Zhang, N. Cant, S.D. Evans, S. Paul, C. Pearson, A. Molloy, M.C. Petty, D. Tsoukalas, J. Appl. Phys. 94 (2003) 5234.
[15] T. Chen, K. Wu, H. Chung, C. Kao, IEEE Electron Device Lett. 25 (2004) 205.
[16] K. Lee, J.H. Kim, S. Im, Appl. Phys. Lett. 88 (2006) 023504.
[17] S.H. Cha, M.S. Oh, K.H. Lee, J.M. Choi, B.H. Lee, M.M. Sung, S. Im, IEEE Electron Device Lett. 29 (2008) 1145.
[18] S.H. Cha, M.S. Oh, K.H. Lee, S. Im, B.H. Lee, M.M. Sung, Appl. Phys. Lett. 92 (2008) 023506.
[19] K.H. Lee, J.-M. Choi, S. Im, B.H. Lee, K.K. Im, M.M. Sung, S. Lee, Appl. Phys. Lett. 91 (2007) 123502.
[20] S. Choi, Y.-K. Cha, B.-S. Seo, S. Park, J.-H. Park, S. Shin, K.S. Seol, J.-B. Park, Y.-S. Jung, Y. Park, Y. Park, I.-K. Yoo, S.-H. Choi, J. Phys. D: Appl. Phys. 40 (2007) 1426.
[21] S. Mun, J.-M. Choi, K.H. Lee, K. Lee, S. Im, Appl. Phys. Lett. 93 (2008) 233301.

Organic Electronics 11 (2010) 164–168

Contents lists available at ScienceDirect

Organic Electronics

journal homepage: www.elsevier.com/locate/orgel

Letter

The initial interface formation between Al and tris-(8-hydroquinoline) aluminum (Alq_3) with LiF interlayer

Jung Han Lee [a], Dae Won Moon [a,b], Yeonjin Yi [a,b,*]

[a] Department of Nano Surface Science, Korea University of Science and Technology, 52 Eoeun-Dong, Yuseong-Gu, Daejeon 305-333, Republic of Korea
[b] Division of Industrial Metrology, Korea Research Institute of Standards and Science, 1 Doryong-Dong, Yuseong-Gu, Daejeon 305-340, Republic of Korea

ARTICLE INFO

Article history:
Received 22 April 2009
Received in revised form 3 July 2009
Accepted 22 September 2009
Available online 26 September 2009

Keywords:
OLED
Metal–organic interface
Metal diffusion
LiF
Alq_3
Al
Ion scattering
MEIS

ABSTRACT

The interface between Al and tris-(8-hydroquinoline) aluminum (Alq_3) was studied using *in situ* medium energy ion scattering spectroscopy. We compared two interfaces of Al/LiF/Alq_3 and Al/Alq_3 with the elemental depth profile of each interface. The thin LiF changes the interfacial structures significantly; the excess Li in the LiF layer diffuses into Alq_3 while F does not. In addition, the Al diffusion into the Alq_3 layer during the initial stages of Al deposition is reduced significantly compared to the interface without the LiF interlayer. The LiF interlayer makes a more abrupt metal–organic interface, which would contribute to the efficiency and stability of the organic light-emitting device.

© 2009 Elsevier B.V. All rights reserved.

Organic electronic devices are promising candidates which can substitute for the Si-based electronic devices because of their simple fabrication process, flexibility and cheap manufacturing cost. For instance, the development of organic light-emitting diodes (OLED) has already reached the level for mass production. However, fundamental understanding of organic devices has not kept pace with the development of the manufacturing process. One of these issues is the physical structures of the interface between the metal electrode and the organic material layer. Various groups have studied the metal–organic interface, which has revealed that the interface has a crucial role in the performance and lifetime of such devices. In 1997, Hung et al. [1] reported the LiF electron injection layer (EIL) in the OLED which initiated research on the insulator EILs in the organic devices. The LiF EIL at the interface between the metal electrode and the organic layer has shown good device performance. The introduction of LiF EIL is regarded as a key architecture for the advanced OLED. Thus, many reports about this EIL have been published.

There have been many efforts to find the mechanism of how a thin LiF layer – or other EIL materials such as NaCl, CsCl and NaF – enhances the performance of OLED. The photoemission measurements have been mainly performed to reveal the interfacial electronic structure which is responsible for the enhancement [2,3]. EILs reduce the work function of the metal electrode, and so lower the electron injection barrier at the interface. Thus it improves the electron injection efficiency dramatically. Though the LiF shows device performance enhancement clearly, its distribution inside the device and the chemical interaction with other materials in the device are still in discussion. In previous studies, the chemical interaction in Al/LiF/tris-(8-hydroxyquinolate) aluminum (Alq_3) has been explained by the reaction of $Al + 3LiF + Alq_3 \rightarrow AlF_3 + 3Li^{+} + Alq_3^{-}$ [4].

* Corresponding author. Address: Division of Industrial Metrology, Korea Research Institute of Standards and Science, 1 Doryong-Dong, Yuseong-Gu, Daejeon 305-340, Republic of Korea. Tel.: +82 42 868 5299; fax: +82 42 868 5032.
E-mail address: yeonjin@kriss.re.kr (Y. Yi).

1566-1199/$ - see front matter © 2009 Elsevier B.V. All rights reserved.
doi:10.1016/j.orgel.2009.09.022

However, there is no clear report for the Li liberation and the behavior of free Li in the device. In another viewpoint, it has been suggested that the presence of the LiF interlayer prevents Al diffusion into Alq_3 [5]. However, these results are not very clear because of the destructive analysis such as secondary ion mass spectroscopy (SIMS) or X-ray photoemission spectroscopy (XPS) depth profiles. Recently, we showed the suitability of the medium energy ion scattering spectroscopy (MEIS) technique for studying the organic thin films and obtained good results for Al diffusion into the Alq_3 layer [6].

In this letter, we studied the physical structures of LiF film deposited on the Alq_3 layer and its behaviors during the initial stage of the Al layer formation on it. We chose the Al/LiF/Alq_3 system since they are the most widely used materials in organic devices, and their characteristics are well known. We measured the MEIS spectra before and after depositing Al on bare Alq_3 and after each stepwise deposition of Al on LiF-covered Alq_3. To analyze the MEIS data, an ion scattering simulation code was used [7]. All film preparation and MEIS measurements were carried out *in situ*. We obtained information about the behavior of Li in the Al/LiF/Alq_3 structure and the effect of LiF layer on Al diffusion into Alq_3 layer.

Alq_3 (Sigma–Aldrich) and LiF (99.99%, Sigma–Aldrich) were thermally deposited (~1.0 nm/min) from an alumina crucible heated with Ta wire. Al metal was thermally evaporated from an Al wire (99.9999%, Nilaco) inserted into the alumina tube wound with Ta wire. Al metal was deposited on Alq_3 or LiF/Alq_3 film at the rate of 0.05 nm/min. All samples were prepared on Si (1 0 0) substrates having a natural oxide layer (SiO_2). The Si substrates were cleaned by ultrasonication in acetone and rinsed with deionized water. The thickness of the film was monitored with a quartz microbalance and confirmed with an α-step and the simulation of the MEIS spectra. All film depositions were conducted in the preparation chamber with a pressure of 1×10^{-7} torr at room temperature.

The quantitative elemental analysis and depth profile of the films were investigated by MEIS. A detailed measurement setup is described in a previous report [6]. In this study, we used two scattering geometries. Generally, we used a H^+ ion beam with an incident angle of 54.7° ([1 1 1] direction of the Si substrate) and an exit angle of 0° ([1 0 0] direction of the Si substrate) from the surface normal ([1 0 0] exit geometry). A different geometry was set with an identical incident angle but an exit angle of 54.7° ([1 1 1] exit geometry). In this geometry, the energy splitting between different elements decreases, while the scattering cross section increases. Consequently, it is possible to get the spectrum of light elements with much better statistics. All measurements were carried out in the scattering chamber with a pressure of 1×10^{-9} torr.

First, we analyzed the single LiF layer deposited on the Si substrate quantitatively. In Fig. 1, the MEIS spectrum is obtained from the sample LiF (1 nm)/SiO_2. The gray symbol is the measured spectrum and the red line is the simulated result. Five peaks are lined up in the order of elemental number. Si and O peaks originated from the native oxide (SiO_2) on the Si substrate and the C peak from the carbon contamination on the SiO_2 surface. To confirm the composition of the LiF film, we simulated the spectra with a composition ratio of Li:F = 1:1 (green line). However, the simulated spectrum, especially on the F height, does not fit with the experimental spectrum. The F concentration is rather small (red line for the best fit) compared to the stoichiometric LiF. We obtained a concentration ratio of Li:F = 1:0.8 from the fitting parameters. This excess Li might have originated from the partial dissociation of LiF during the deposition process.

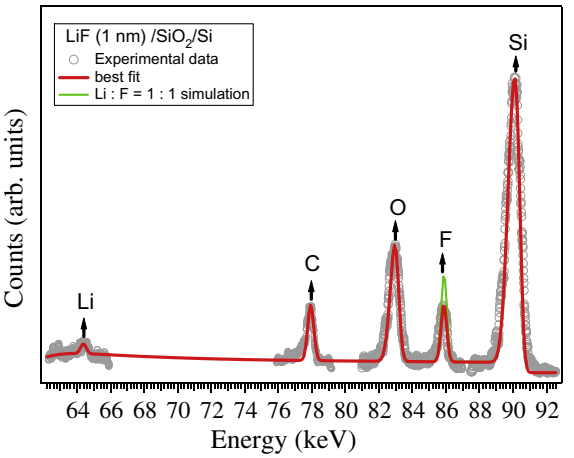

Fig. 1. Measured MEIS spectrum from the sample of LiF/SiO_2/Si versus simulated result. Traces of open symbol are measured spectrum, and the red line is the simulated result. The green line indicates the shape of the F peak when Li:F = 1:1. (For interpretation of the references to colour in this figure legend, the reader is referred to the web version of this article.)

Fig. 2 shows the Li and F spectra of LiF (1.5 nm)/Alq_3 (6 nm)/SiO_2 and Al (1 nm)/LiF (1.5 nm)/Alq_3 (6 nm)/SiO_2 measured with [1 1 1] exit geometry. We chose thin LiF thickness known for the optimum device performance [1]. The Li and F peaks show different shapes. While the Li peak shows tails at the lower energy side, F shows only a single peak without following tails. (The F tail region is seen in the Fig. 3. The F peak in Fig. 2 seems to be overlapped with another peak at lower energy side, but the lower energy overlap is nothing more than the SiO_2 substrate signal in [1 1 1] exit geometry.) These indicate that Li diffuses into Alq_3 significantly but F does not. The diffused Li could be the excess Li shown in Fig. 1 or liberated Li by the chemical interaction with Al and Alq_3 [4].

With the Al deposition (red line), the amount of the F peak shift to lower energy is smaller than that of the Li peak. (The energy resolution of MEIS is about 100 eV.) This means that some part of Li diffuses into the Alq_3 layer, but F remains at the surface region relatively. This is consistent with the previous SIMS study showing that Li and F have maximum density at different positions [8]. One possible driving force for the F immobilization could be the Al–F interaction forming the AlF_3 species [4].

In Fig. 3, the MEIS spectra measured in [1 0 0] exit geometry are presented as a function of Al thickness. Each spectrum corresponds to the sample of Al (1, 2, and 4 nm)/LiF (1.5 nm)/Alq_3 (10 nm) deposited on the SiO_2 substrate. While the surface Al and O peaks increase as Al is deposited, the C, F and Si peaks are shifted to low energy because

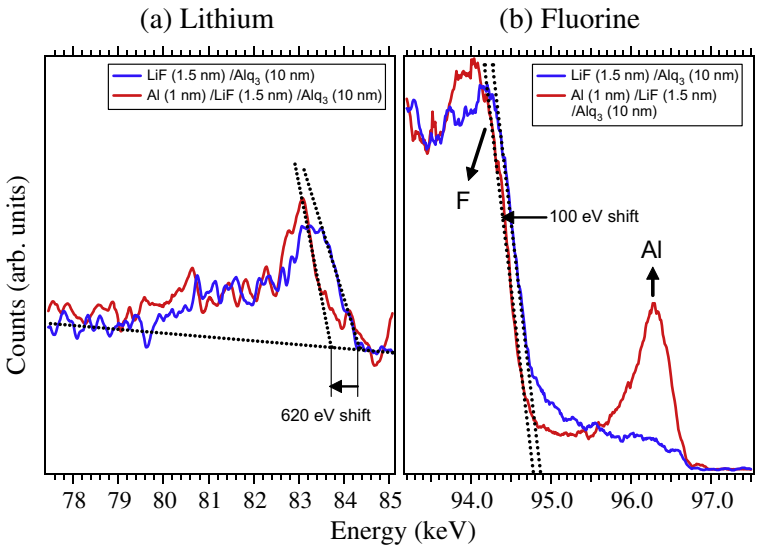

Fig. 2. Li and F spectra measured from the sample of LiF (1.5 nm)/Alq_3 (6 nm) (blue) and Al (1 nm)/LiF (1.5 nm)/Alq_3 (6 nm) (red) with [1 1 1] exit. (a) Li spectrum spreads from surface to the region of Alq_3, indicating the Li diffusion into Alq_3 layer. (b) The low energy shift of the F peak is smaller than the Li peak, implying negligible F diffusion. (For interpretation of the references to colour in this figure legend, the reader is referred to the web version of this article.)

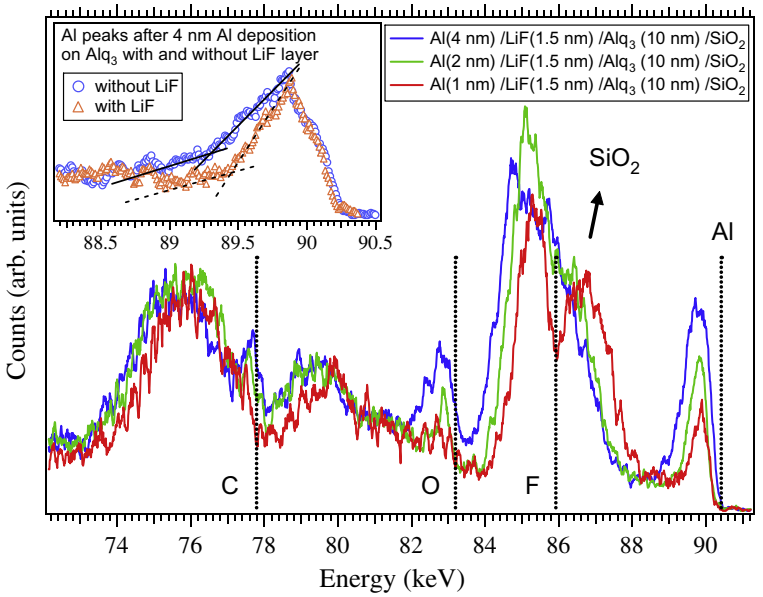

Fig. 3. Measured MEIS spectra from the sample of Al (1, 2, and 4 nm)/LiF (1.5 nm)/Alq_3 (10 nm)/SiO_2 with the step-by-step deposition. The inset shows the different Al peak width according to the existence of LiF interlayer.

they are buried under the surface Al layer. As mentioned in Fig. 2, F shows a sharp peak without significant tails on the low energy side, meaning negligible diffusion. The inset shows the Al peak after 4 nm Al deposition on Alq_3 (10 nm)/SiO_2 (orange) and on LiF (1.5 nm)/Alq_3 (10 nm)/SiO_2 (blue). It clearly shows the different Al peak width between the two interfaces. With the LiF layer, the peak width is reduced significantly, implying that the interfacial diffusion of Al decreases significantly. That is, Al makes a more abrupt interface with the LiF interlayer.

In Fig. 4A, the depth profile of each element is presented in order to see the changes of the Al/LiF/Alq_3 interface with successive Al deposition. Thus, they show the evolution of elemental depth profile during the initial Al layer formation. We also presented control experiment of Al/Alq_3 interface in Fig. 4B from our previous results [6]. We fitted all spectra in Fig. 3 and used the Alq_3 density of 1.3 g/cm^3 [6] to convert the area density to the depth dimension. Each diagram represents the interface of (a) 1 nm, (b) 2 nm and (c) 4 nm Al deposited on LiF (1.5 nm)/Alq_3

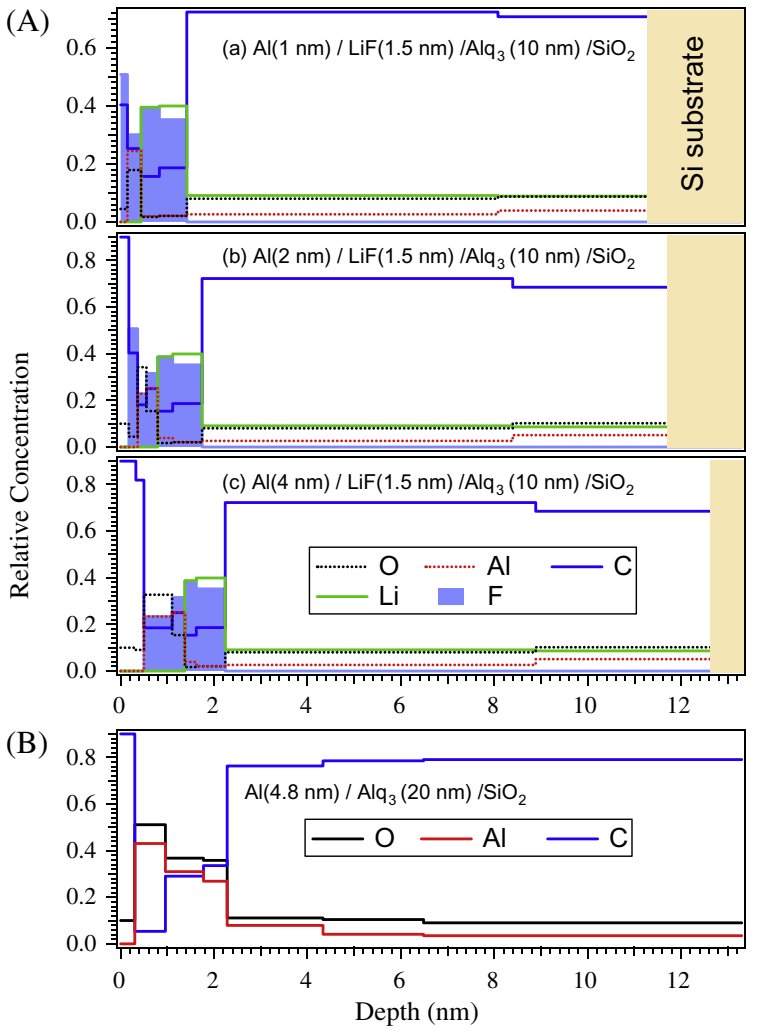

Fig. 4. (A) Depth profiles of key elements (C, O, Al, F and Li) during the Al deposition. (a–c) Indicates successive deposition of Al on LiF/Alq_3/SiO_2 corresponding to the Fig. 2. (B) The depth profile of Al on Alq_3 without LiF layer [6].

(10 nm)/SiO_2 which correspond to the spectra in Fig. 3. At the initial deposition stage (a), small amounts of Al diffuse into the Alq_3 layer and reach the SiO_2 interface. However, the Al diffusion into Alq_3 layer is highly diminished compared to the interface without the LiF interlayer (B). The diffused Li into the Alq_3 layer is clearly seen as explained in Fig. 2. After this stage, Al is only stacked on the LiF layer without significant penetration into Alq_3 (b). Then, the Al forms a thick layer and is oxidized with residual water or oxygen from the vacuum chamber (c). The oxidation of Al is also decreased compared to the interface of (B) Al/Alq_3. The F species in the vicinity of Al could prevent Al oxidation, which could be caused by the interaction between Al and F [4]. That is, the metallic Al is consumed to be reacted into AlF_3 and there are little metallic Al atoms to be reacted with residual oxygen/water. However, further studies for the detailed interaction mechanism and the effect of oxidation on the diffusion are needed. These reduced diffusion and oxidation would contribute to the improvement of device performance in terms of luminescence quenching site elimination [9] and interfacial resistance reduction [10].

In summary, we studied the interface structure of LiF/Alq_3 and Al/LiF/Alq_3 with *in situ* medium energy ion scattering spectroscopy. Excess Li was found in the single LiF layer deposited on the SiO_2 substrate and some Li diffused into the Alq_3 film when LiF was deposited on the Alq_3 layer. The Al diffusion into the Alq_3 layer was significantly diminished with the LiF interlayer compared to the case without LiF. That is, a more abrupt interface is formed at the Al/LiF/Alq_3 than at the Al/Alq_3 surface. The reduction of Al diffusion and abrupt interface formation attributes to the enhancement of device performance.

Acknowledgement

This work was supported by Korea Research Council of Fundamental Science and Technology (KRCF) through the KRISS project of "Development of Advanced Industrial

Metrology" and a research project of the Korea Research Foundation (Grant No. 2009-0070876).

References

[1] L.S. Hung, C.W. Tang, M.G. Mason, Appl. Phys. Lett. 70 (1997) 152.
[2] H. Ishii, K. Sugiyama, E. Ito, K. Seki, Adv. Mater. 11 (1999) 605.
[3] A. Kahn, N. Koch, W. Gao, J. Polym. Sci. Polym. Phys. 41 (2003) 2529.
[4] M.G. Mason, C.W. Tang, L.S. Hung, P. Raychaudhuri, J. Madathil, D.J. Giesen, L. Yan, Q.T. Le, Y. Gao, S.T. Lee, L.S. Liao, L.F. Cheng, W.R. Salaneck, D.A. dos Santos, J.L. Bredas, J. Appl. Phys. 89 (2001) 2756.
[5] Q.T. Le, L. Yan, Y. Gao, M.G. Mason, D.J. Giesen, C.W. Tang, J. Appl. Phys. 87 (2000) 375.
[6] J.H. Lee, Y. Yi, D.W. Moon, Appl. Phys. Lett. 93 (2008) 153307.
[7] J. Kido, T. Matsumoto, Appl. Phys. Lett. 73 (1998) 2866.
[8] H. Heil, J. Steiger, S. Karg, M. Gastel, H. Ortner, H. von Seggern, M. Stossel, J. Appl. Phys. 89 (2001) 420.
[9] J. Birgerson, M. Fahlman, P. Broms, W.R. Salaneck, Synth. Met. 80 (1996) 125.
[10] J. Zaumseil, K.W. Baldwin, J.A. Rogers, J. Appl. Phys. 93 (2003) 6117.

Organic Electronics 11 (2010) 169–174

Contents lists available at ScienceDirect

Organic Electronics

journal homepage: www.elsevier.com/locate/orgel

Letter

Organic inverter using two transistors with different channel thicknesses

Sung-jin Mun [a], Kimoon Lee [a], Kwang H. Lee [a], Min Suk Oh [b], Seongil Im [a,*]

[a] Institute of Physics and Applied Physics, Yonsei University, Seoul 120-749, Republic of Korea
[b] Korea Electronics Technology Institute (KETI), Seongnam 463-816, Republic of Korea

ARTICLE INFO

Article history:
Received 12 August 2009
Received in revised form 23 September 2009
Accepted 26 September 2009
Available online 3 October 2009

Keywords:
Thin-film transistor
Pentacene
Inverter
Dielectric

ABSTRACT

We report on p-channel depletion mode organic inverter composed of two pentacene thin-film transistors (TFTs), which have different channel thickness each other. Adopting thin hydrophilic AlO_x as dielectric, the 25 nm-thin channel pentacene TFT showed lower threshold voltage (V_{TH}) than that of 50 nm-thick channel-TFT, while on hydrophobic poly-4-vinyphenol (PVP) dielectric the results became opposite. We utilized the different V_{TH} caused by different channel thickness to operate the inverter that consists of driver- and load-TFTs. The 50 nm-thick pentacene operated as the channel layer of driver-TFT on AlO_x, but on PVP dielectric the 25 nm-thin pentacene layer played as the driver channel. Maximum voltage gain of ~22 under −8 V supply voltage was achieved when the dielectric layer was optimized.

© 2009 Elsevier B.V. All rights reserved.

1. Introduction

Pentacene-based thin-film transistors (TFTs) have attracted much attention due to their potentials use in transparent, flexible and low cost electronics circuits: sensors, display backplane and rectifiers for radio frequency identification (RFID) [1–6]. Pentacene inverter has thus been studied and fabricated with several methodologies as a fundamental element of conventional integrated circuit on glass or plastic. Among the methodologies, using different W/L ratios for the load- and driver-TFTs [7], changing the dielectric surface of load- or driver-TFTs [8], adopting different polymer dielectrics for load and driver [9,10], and even using dual-gate for the driver-TFTs [11] have been reported for pentacene inverter, all of which were based on the effort to change threshold voltage (V_{TH}) of load- or driver-TFTs; the main concept of organic inverter implemented by previous researchers was to make the V_{TH} of load-TFT smaller than that of driver-TFT, so that the effective channel resistance of load-TFT might be smaller for desirable inverter operation. In the present study, we adopt another but more simple way to change the V_{TH} of load-TFTs and achieve an organic inverter: changing the channel thickness, since we observed the change of V_{TH} and drain current (I_D) (or effective channel resistance) with varying thickness of pentacene channel on both hydrophilic oxide and hydrophobic polymer dielectrics [12]. We have thus fabricated the depletion-mode inverters, where pentacene channel of load-TFT has different thickness from that of driver on hydrophilic or hydrophobic dielectric surfaces.

2. Experimental

For OTFT substrates, we used indium-tin-oxide (ITO)/glass that was cleaned with acetone, methanol, and de-ionized water, in that order. ITO gate electrodes were patterned by wet etching. Then we deposited three kinds of dielectrics: sputter-deposited AlO_x [13], optimally-cured poly-4-vinyphenol (PVP) [14,15], and AlO_x–PVP bilayer [8]. Pentacene (Aldrich Chem. Co., 99% purity, no other distillation) active channel layers were patterned on the dielectric layers through a shadow mask by thermal evaporation at room temperature (RT). We fixed the pentacene deposition rate to 1 Å/s. For source/drain (S/D) of the pentacene TFTs

* Corresponding author. Tel.: +82 2 2123 2842; fax: +82 2 392 1592.
E-mail address: semicon@yonsei.ac.kr (S. Im).

1566-1199/$ - see front matter © 2009 Elsevier B.V. All rights reserved.
doi:10.1016/j.orgel.2009.09.024

and also for inverter connection, Au was evaporated onto the pentacene channels at RT. Nominal channel length (L) and width (W) of our pentacene TFTs were 90 and 500 μm, respectively. We used two different pentacene-thicknesses for load- and driver-TFTs: 25 and 50 nm for OTFT inverter with dielectric AlO_x, but vice versa for other

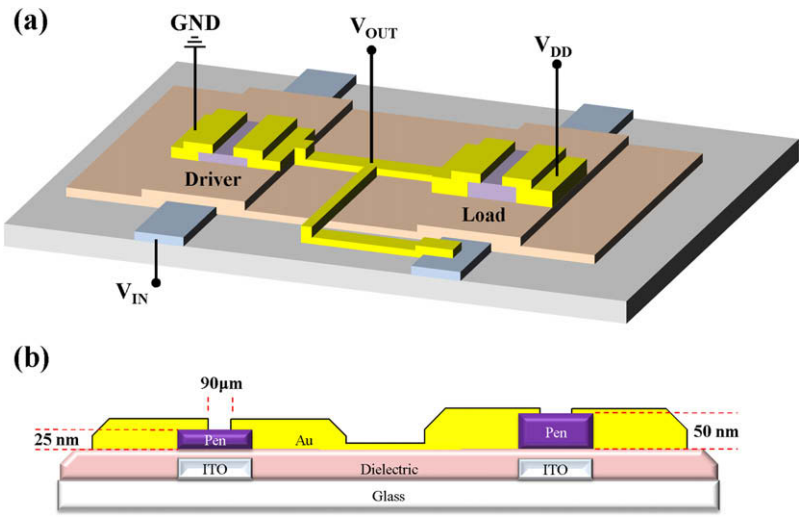

Fig. 1. (a) Schematic 3D structure of our inverter with two p-channel OTFTs. Each OTFT has different pentacene-thickness, so that different V_{TH} is obtained. The W/L ratio of both transistors is 500/90 μm. (b) Schematic 2D cross-section of the inverter.

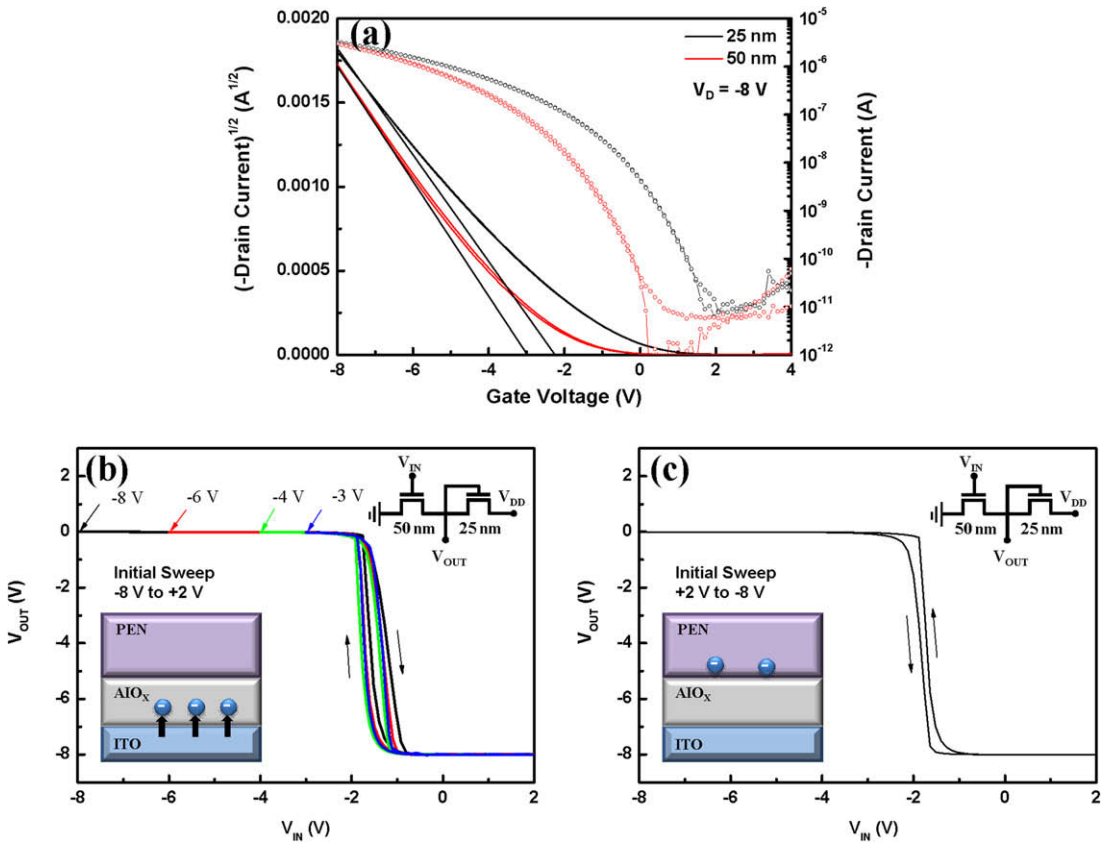

Fig. 2. (a) $\sqrt{-I_D}$–V_G and $\log_{10}(-I_D)$–V_G plots obtained from our pentacene TFTs with AlO_x dielectric at $V_D = -8$ V. (b) VTC of the inverter on AlO_x as obtained in different V_{IN} sweep range. Driver-OTFT has 50 nm-thick pentacene channel while load-OTFT does 25 nm-thin pentacene. Arrows indicate the starting V_{IN} for sweep (−3, −4, −6, and −8 V). (c) VTC of the inverter on AlO_x as obtained from opposite V_{IN} sweep direction (from +2 to −8 V). Hysteresis direction changed opposite.

devices with PVP dielectric. Fig. 1a shows the three-dimensional schematic of our inverter while Fig. 1b does its cross-section.

3. Results and discussion

3.1. Organic inverter with hydrophilic AlO_x dielectric

Fig. 2a shows the I_D versus gate voltage (V_G) transfer curves of two pentacene TFTs with 100 nm-thick AlO_x dielectric that was deposited by 50 W rf sputtering of Al_2O_3 target (~99.999%) at RT. Both OTFTs with 25 and 50 nm-thick channel appear very stable with little hysteresis, but one with 25 nm-thin channel displays smaller V_{TH} and higher on-state current [13]. Since we previously observed the similar results from pentacene TFTs on hydrophilic SiO_2 dielectric where I_D and mobility gradually decreased with pentacene thickness due to thickness-induced resistance [12] (the parasitic resistance through thickness between the metal/pentacene interface and the channel), we set-up a TFT inverter utilizing the thickness effects on hydrophilic AlO_x in the present study [13]; 25 nm-thin pentacene channel was used for load-TFT due to its lower effective channel resistance, (which can be defined by channel resistance + thickness-induced resistance) while 50 nm-thick channel for driver-TFT. Driver-TFT shows a good saturation mobility (~0.5 $cm^2/V\,s$) and high on/off current ratio (~5×10^5), also displaying $V_{TH} = -3$ V in a low operating V_G range below −8 V. Load-TFT displays similar saturation mobility of ~0.46 $cm^2/V\,s$ and the same decent on/off ratio (~5×10^5) but with smaller $V_{TH} = -2.2$ V. As a result from the two OTFTs, we obtained a high gain inverter, whose voltage transfer curves (VTCs) are displayed under a constant supply voltage (V_{DD}) of −8 V but in the different sweep ranges of driver input (V_{IN}, from −3 to 2 V, −4 to 2 V, −6 to 2 V, and −8 to 2 V) in Fig. 2b. Starting V_{IN} is indicated by arrows and a maximum output voltage gain ($-dV_{OUT}/dV_{IN}$) was ~18. VTCs show some hysteresis at output voltage (V_{OUT}) switching, and all the hysteresis appears almost the same regardless of V_{IN} range when the sweep started from negative voltages to reach the positive values. During V_{IN} sweep, electron injection from ITO gate electrode into AlO_x or time-dependent charge trapping at the pentacene/

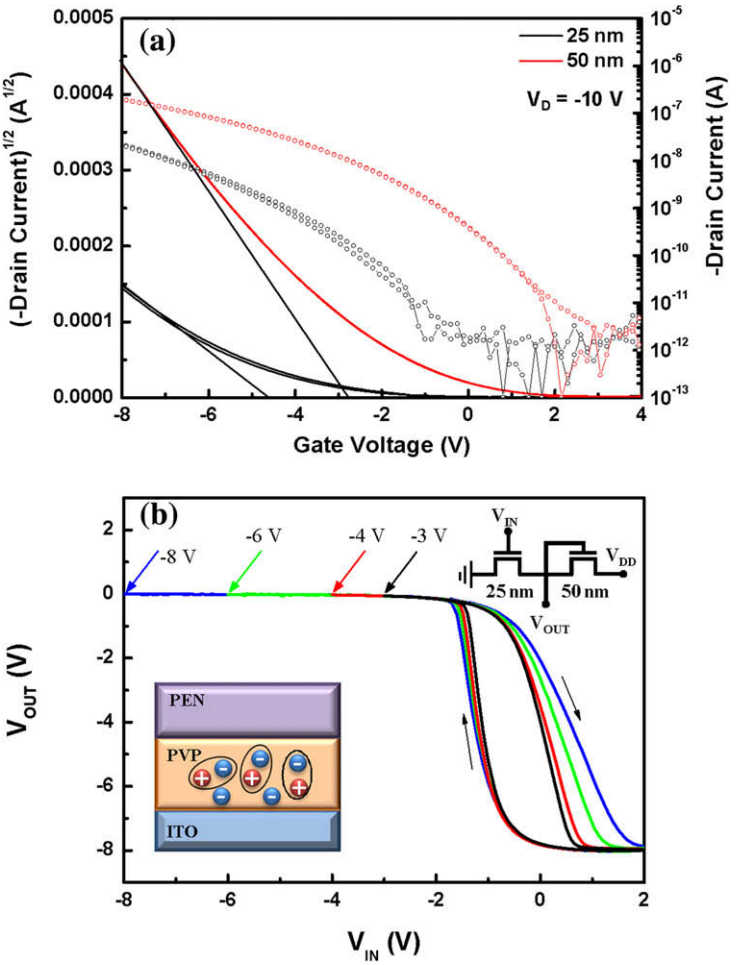

Fig. 3. (a) $\sqrt{-I_D}$–V_G and $\log_{10}(-I_D)$–V_G plots obtained from our pentacene TFTs with 230 nm-thick PVP dielectric at $V_D = -10$ V. (b) VTC of the inverter on PVP as obtained under various V_{IN} ranges. Arrows indicate the starting V_{IN} for sweep (−3, −4, −6, and −8 V). Driver-OTFT has 25 nm-thin pentacene channel while load-OTFT does 50 nm-thick pentacene.

dielectric interfaces are expected and such mobile charge behavior causes the visible hysteresis in the driver-TFT side [14–18]. If our pentacene TFT driver of this inverter was influenced by time-dependent charge trapping at the pentacene/dielectric interfaces, the hysteresis direction would appear opposite to the present direction [7]. (See the hysteresis arrows.) Therefore, the observed VTC hysteresis is attributed to the electron injection from the ITO gate as illustrated in the inset in Fig. 2b [19]. (It is also to be kept in mind that unlike the V_G sweep of transfer curve, the V_{IN} sweep exerts serious gate bias-stress onto the driver-TFT because V_{OUT} maintains 0 V during some time of V_{IN} sweep.) However, when we swept the V_{IN} from +2 V to reach −8 V, the VTC hysteresis direction changed opposite to that of Fig. 2b as shown in another VTC of Fig. 2c. This means that other hysteresis mechanism due to electron trapping also exists for this inverter with thin AlO_x dielectric whose surface is strongly polar and hydrophilic to trap some density of electrons [7,17,18]. We regard that both electron trapping and gate electron injection exist for this inverter probably competing each other.

3.2. Organic inverter with hydrophobic PVP dielectric

We also tested the case of PVP polymer for an inverter dielectric, on which OTFT with 25 nm-thin pentacene channel has lower on-state I_D and larger V_{TH} than that with 50 nm-thick channel. The transfer curves of Fig. 3a show the very results, supporting previous reports that a hydrophobic dielectric surface has an optimum pentacene channel thickness around 50 nm [12]. Unlike the case on hydrophilic oxide of large surface energy, the pentacene channel on hydrophobic dielectric does not have perfect coverage if it is too thin [12], so that the effective channel resistance of 25 nm-thin pentacene must be larger than that of 50 nm-thick channel which may perfectly cover the PVP dielectric making good channel/dielectric interface. In this case, we set-up an inverter taking 50 nm-thick pentacene as the channel of load-TFT because this TFT with 50 nm-thick channel has lower V_{TH} (−3.6 V) than that (−6 V) with 25 nm-thin pentacene channel, which is now contrary to the case on hydrophilic AlO_x. Although OTFTs with this polymer dielectric did not show any gate-bias

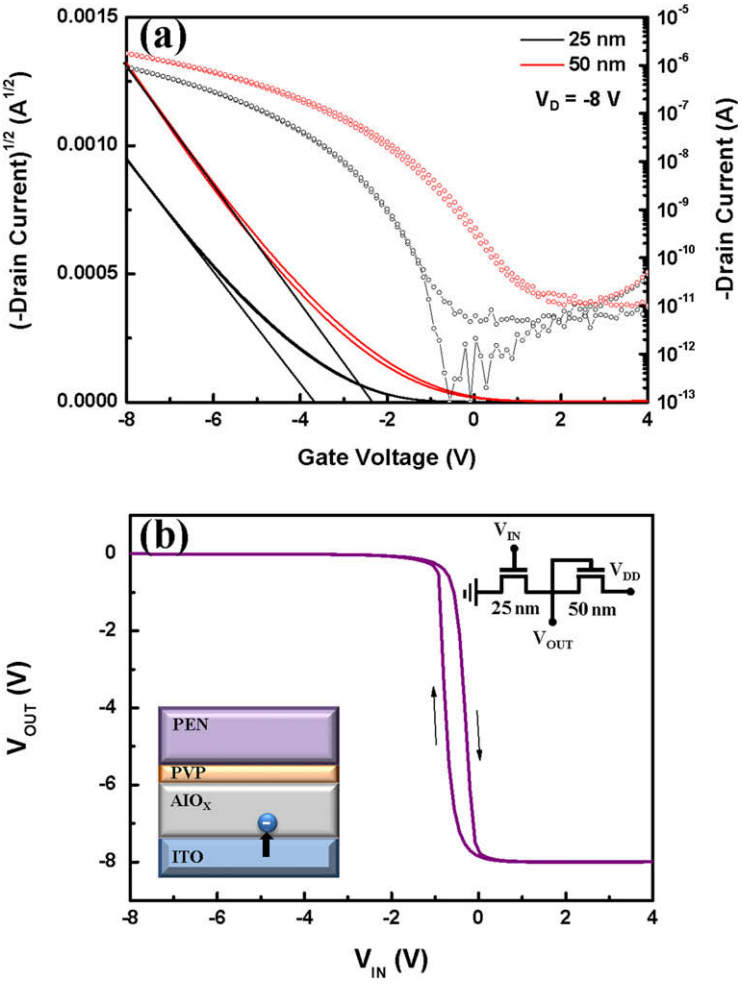

Fig. 4. (a) $\sqrt{-I_D}$–V_G and $\log_{10}(-I_D)$–V_G plots obtained from our pentacene TFTs with AlO_x–PVP bilayer dielectric at $V_D = -8$ V. (b) VTC of the inverter on AlO_x–PVP bilayer. VTC behavior was improved in respects of voltage gain and hysteresis. (V_{IN} starts at −8 V.)

hysteresis in their transfer curves, our inverter VTCs behavior displayed very large hysteresis depending on V_{IN} sweep range. (Fig. 3b) Thickness of the PVP film was approximately 230 nm as measured by optical method (model ST2000DLXn, K-MAC) and we attribute the large hysteresis to the gate-bias stress on driver-TFT. The stress would easily cause gate electron injection into the thick PVP as well as cause electric dipoles in PVP. The dipoles in PVP are slowly depolarized even at a positive (+) V_{IN} during the sweep. We explained this slow polarization effects in previous reports [14,15]. Due to this effect added to the gate electron injection, the size of hysteresis appears large and evidently increases with the V_{IN} range increase. The inset of Fig. 3b illustrates the remnant dipoles and remnant electrons.

In order to minimize such V_{IN}-induced hysteresis that we observe from electron injection, slow polarization, and electron trapping, we prepared another inverter with 45 nm-thin PVP/100 nm-thick AlO_x double layer dielectric. Fig. 4a shows the I_D versus V_G transfer curves obtained from the OTFTs with 45 nm-thin PVP/100 nm-thick AlO_x double layer dielectric. Since pentacene channel was in contact with hydrophobic PVP surface, the device of 50 nm-thick pentacene channel showed higher on-state I_D and lower V_{TH} than those of 25 nm-thin channel. According to $\sqrt{-I_D}$–V_G curve, the pentacene TFT with 25 nm-thin channel has a saturation mobility of ~0.5 cm^2/V s and a high on/off current ratio of $\sim 10^6$ with $V_{TH} = -4$ V while the other one with 50 nm-thick pentacene shows a little higher saturation mobility (~0.6 cm^2/V s) and lower $V_{TH} = -2.5$ V. We thus took the TFT with 25 nm-thin channel as driver-TFT and the other one as load-TFT. The VTCs of this inverter with PVP/AlO_x double dielectric are displayed in Fig. 4b and show improved features in respects of voltage gain ($-dV_{OUT}/dV_{IN} = \sim 22$) and the size of hysteresis, compared to those of other inverters with AlO_x or with PVP single layer (Figs. 2b and 3b). Through the organic/inorganic double layer approach, we may reduce the hysteresis induced by gate electrons injected into AlO_x because electric field stress is divided into PVP and AlO_x, simultaneously minimizing the slow polarization effects in PVP which is now thin enough to neglect the effect [8,15].

3.3. Device statistics on the V_{TH} values of driver- and load-TFTs

Fig. 5a shows the V_{TH} values of our TFTs as the functions of thickness and substrate. We randomly selected at least 12 pentacene TFTs consisting 6 pairs of inverter for this statistic plot. As shown in the plot, the V_{TH} of 25 nm-thin channel-TFT appeared always lower than that of 50 nm-thick channel-TFT on hydrophilic AlO_x dielectric, to be −2.5 V as an average value while that of 50 nm-thick channel-TFT was −3.4. (Deviation bar is also noted.) In contrast, the situation becomes opposite when we use PVP dielectric surface for pentacene channel. In this case, the V_{TH} of 25 nm-thin channel-TFT appeared always larger than that of 50 nm-thick channel-TFT as we expected from previous results. It is also noted that our V_{TH} values obtained from our optimized devices on PVP/AlO_x dielectric has much reduced deviations. Our pentacene inverters with the PVP/AlO_x dielectric have also been tested for their aging properties. Fig. 5b displays two VTC curves of a random selected organic inverter with the PVP/AlO_x dielectric; one of the curves was obtained after 3 months passed since initially measured. As shown in the figure, our device displayed almost the same VTC characteristics except a little shift of transition voltage even after 3 months, implying that this organic inverter is relatively stable in aging (as long as we have kept the device in 1 Torr desiccator for the time).

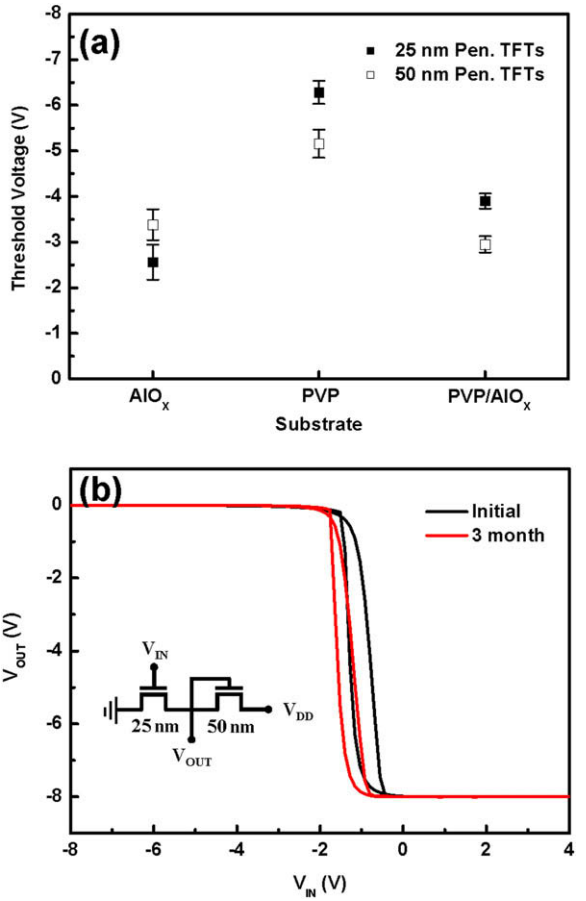

Fig. 5. (a) V_{TH} values of our TFTs as the functions of thickness and substrate. (b) VTC curves of a random selected organic inverter with the PVP/AlO_x dielectric; one of the curves was obtained after 3 months passed since initially measured. Our organic inverter appears relatively stable in aging (as long as we have kept the device in 1 Torr desiccator for the time).

4. Conclusion

We have fabricated p-channel depletion mode inverter using two pentacene TFTs with different channel thicknesses. Since on hydrophilic AlO_x dielectric the V_{TH} of 25 nm-thin channel-TFT is lower than that of 50 nm-thick channel-TFT, the thinner channel-TFT was used as load while the thicker channel-TFT became driver in the inverter. The driver and load set-up for inverter became opposite on hydrophobic PVP dielectric surface, where the V_{TH} of thinner channel-TFT is larger. Our optimized inverters

with 45 nm-thin PVP/100 nm-thick AlO_x double layer dielectric demonstrate a high voltage gain of ~22 under −8 V supply voltage, since the double dielectric layer effectively prevents the slow polarization and gate electron injection. We conclude that this channel thickness approach is quite a promising way to achieve organic inverter without complexity.

Acknowledgments

Authors acknowledge the financial support from KOSEF (NRL program: Grant No. 2009-8-0403), from MKE (the fundamental R&D Program for Core Technology of Materials: No. 2008-8-1410, the IT R&D Program for Smart window with transparent electronic devices: No. 2008-8-0613), Information Display R&D center, one of the 21st Century Frontier R&D Program: No. F0004022-2009], and Brain Korea 21 program.

References

[1] H. Klauk, U. Zschieschang, J. Pflaum, M. Halik, Nature (London, UK) 445 (2007) 745.
[2] B.N. Pal, J. Sun, B.J. Jung, E. Choi, A.G. Andreou, H.E. Katz, Adv. Mater. (Weinheim, Germany) 20 (2008) 1023.
[3] M.S. Oh, K. Lee, K.H. Lee, S.H. Cha, J.-M. Choi, B.H. Lee, M.M. Sung, S. Im, Adv. Funct. Mater. 19 (2009) 726.
[4] U. Zschieschang, H. Klauk, M. Halik, G. Schmid, C. Dehm, Adv. Mater. (Weinheim, Germany) 15 (2003) 1147.
[5] T.B. Singh, P. Senkarabacak, A. Tanda, C. Lackner, R. Hagelauer, G. Horowitz, N.S. Sariciftci, Appl. Phys. Lett. 89 (2006) 033512.
[6] S.D. Wang, K. Kanai, Y. Ouchi, K. Seki, Org. Electron. 7 (2006) 457.
[7] J.B. Koo, S.J. Yun, J.W. Lim, S.H. Kim, C.H. Ku, S.C. Lim, J.H. Lee, T. Zyung, Appl. Phys. Lett. 89 (2006) 033511.
[8] J.-M. Choi, J.H. Kim, S. Im, Appl. Phys. Lett. 91 (2007) 083504.
[9] C.A. Lee, S.H. Jin, K.D. Jung, J.D. Lee, B.-G. Park, Solid-State Electron. 50 (2006) 1216.
[10] C. Baek, S. Seo, Appl. Phys. Lett. 94 (2009) 153305.
[11] J.B. Koo, C.H. Ku, J.W. Lim, S.H. Kim, Org. Electron. 8 (2007) 552.
[12] S. Mun, J.-M. Choi, K.H. Lee, K. Lee, S. Im, Appl. Phys. Lett. 93 (2008) 233301.
[13] J. Lee, K. Kim, J.H. Kim, D.-Y. Jung, S. Im, Appl. Phys. Lett. 82 (2003) 4169.
[14] D.K. Hwang, K. Lee, J.H. Kim, J.H. Park, E. Kim, S. Im, Appl. Phys. Lett. 89 (2006) 093507.
[15] D.K. Hwang, M.S. Oh, J.M. Hwang, J.H. Kim, S. Im, Appl. Phys. Lett. 92 (2008) 013304.
[16] D.K. Hwang, J.H. Park, J. Lee, J.-M. Choi, J.H. Kim, E. Kim, S. Im, J. Electrochem. Soc. 153 (2006) G23.
[17] L.-L. Chua, J. Zaumseil, J.-F. Chang, E.C.-W. Ou, P.K.-H. Ho, H. Sirringhaus, R.H. Friend, Nature (London, UK) 434 (2005) 194.
[18] G. Gu, M.G. Kane, J.E. Doty, A.H. Firester, Appl. Phys. Lett. 87 (2005) 243512.
[19] C.A. Lee, D.-W. Park, K.-D. Jung, B. Kim, Y.C. Kim, J.D. Lee, B.-G. Park, Appl. Phys. Lett. 89 (2006) 262120.

Organic Electronics 11 (2010) 175–178

Contents lists available at ScienceDirect

Organic Electronics

journal homepage: www.elsevier.com/locate/orgel

Letter

A monolithically integrated organic photodetector and thin film transistor

C. Kyle Renshaw [a], Xin Xu [a,b], Stephen R. Forrest [a,c,d,*]

[a] Department of Physics, University of Michigan, Ann Arbor, MI 48109, USA
[b] Department of Electrical Engineering, Princeton University, Princeton, NJ 08544, USA
[c] Department of Electrical Engineering and Computer Science, University of Michigan, Ann Arbor, MI 48109, USA
[d] Department of Materials Science and Engineering, University of Michigan, Ann Arbor, MI 48109, USA

ARTICLE INFO

Article history:
Received 7 August 2009
Received in revised form 27 September 2009
Accepted 30 September 2009
Available online 8 October 2009

Keywords:
Small molecule
Photodetector
Thin film transistor
Integration

ABSTRACT

We demonstrate a vacuum deposited molecular organic photodetector (OPD) integrated with a top gate, bottom-contact, pentacene-based organic thin film transistor (OTFT) for use as a switchable organic passive pixel sensor in focal plane imaging arrays. The heterojunction OPD consists of a 110 Å thick film of the donor, boron subphthalocyanine chloride, and a 325 Å thick film of the acceptor, C_{60}. The OTFT switch allows the photodetector to be switched between an active (ON) state with a light intensity dependent photocurrent peaking at 20 nA, and an inactive (OFF) state with current <50 pA, corresponding to an 8-bit dynamic range. The integrated device has a spectral coverage from wavelengths of 400–600 nm, and a pixel switching frequency >400 kHz. The integrated structure is fabricated at room temperature, making this circuit compatible with low cost, flexible plastic substrates.

© 2009 Elsevier B.V. All rights reserved.

Recent interest in organic semiconductors has led to the development of many devices and applications opportunities previously unattainable with inorganic semiconductors. Inexpensive organic materials can be readily deposited onto transparent and flexible substrates, and in non-planar geometries with potential uses in, for example, displays, imaging, and solar energy harvesting [1]. In particular, organic photodetectors (OPD) have been demonstrated with broad spectral coverage and high specific detectivity [2], while simple passive-matrix OPD focal plane arrays have been fabricated on such non-planar surfaces as hemispheres [3,4]. A second component required for many electronic applications is the organic thin film transistor (OTFT), demonstrated using an organic semiconductor channel [5]. Examples of integrated circuits that combine electrical and optical functions include drive transistors combined with organic light emitting devices (OLEDs) [6]. Hybrid [7] and monolithic [8] photodetectors [7] or photoconductors [8] integrated with transistors have also been demonstrated for scanning and imaging applications using complex laser drilling [7] or lithographic processes and inkjet printing [8] techniques.

Here, we demonstrate a boron subphthalocyanine chloride (SubPc)/C_{60} photodetector monolithically integrated in series with a top gate, pentacene OTFT switch for use as a passive pixel sensor [9] in imaging focal plane array applications that require a low OFF current [3,4]. The integrated structure is fabricated by sequential layer growth using vacuum thermal evaporation of the small molecular weight organic materials. The pixel is activated using the OTFT by applying a negative gate voltage which turns the transistor to the ON (i.e. conducting) state, permitting photocurrent from the OPD to be collected at the source. The device has an 8-bit dynamic range and allows for >400 kHz switching.

A cross-section of the integrated circuit is shown in Fig. 1a. The OPD was fabricated by vacuum thermal evaporation onto a commercially patterned 200 μm wide stripe of 100 nm thick, 20 Ω/sq. indium tin oxide (ITO) precoated on a glass substrate. Prior to organic thin film deposition, the substrate was solvent cleaned and UV ozone treated as described elsewhere [10]. All organic materials were

* Corresponding author. Address: Department of Physics, University of Michigan, Ann Arbor, MI 48109, USA.
E-mail address: stevefor@umich.edu (S.R. Forrest).

1566-1199/$ - see front matter © 2009 Elsevier B.V. All rights reserved.
doi:10.1016/j.orgel.2009.09.028

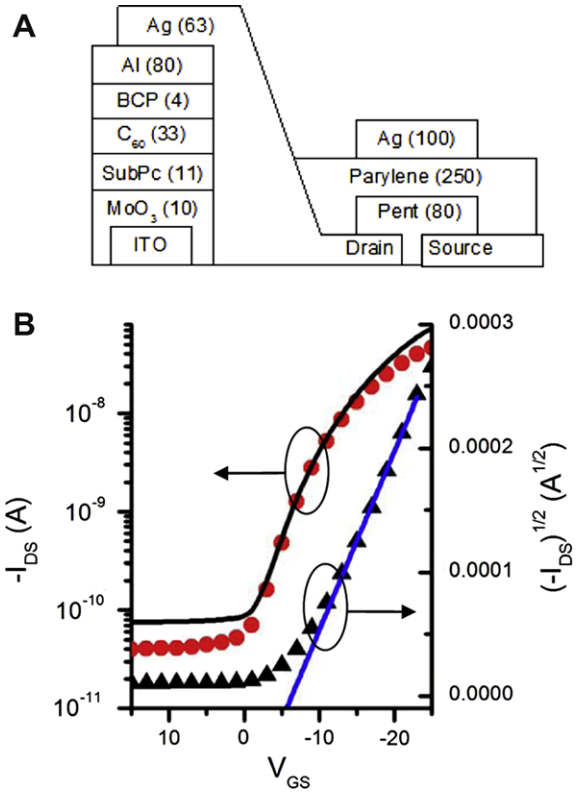

Fig. 1. (a) Schematic cross-section of the integrated pixel structure. Layer thicknesses in parentheses are in nanometers. (b) Top gate pentacene OTFT transfer characteristic at a drain-source voltage of $V_{DS} = -17.5$ V (solid line) and -7.5 V (circles) for a 500 μm wide by 25 μm long channel. Also shown is the square root of drain-source current, $(I_{DS})^{1/2}$, (triangles) with fit to pinch-off region (straight solid line).

purified by vacuum thermal gradient sublimation and were deposited at 1 Å/s in a vacuum chamber with a base pressure of 1×10^{-6} torr unless otherwise stated. Prior to deposition of the photoactive layers, a 10 nm thick MoO_3 film was deposited onto the ITO at 0.2 Å/s as a hole transport and electron blocking layer that reduces photodetector dark current [11]. The active layers consisted of a 110 Å thick film of SubPc followed by a 325 Å thick film of C_{60}. Subsequently, a 40 Å thick layer of exciton blocking and electron transporting bathocuproine was deposited [12]. The cathode, an 800 Å thick Al stripe that was either 100 or 500 μm wide, was deposited through a shadow mask aligned with the ITO anode across the anode stripe defining the detector area. The top gate OTFT was subsequently grown adjacent to the detector with the drain connected to the detector cathode, forming the passive pixel sensor circuit [9]. The OTFT layers were also grown by vacuum thermal evaporation except for the gate insulator. Here, parylene-C gate dielectric was deposited at room temperature after vaporization and pyrolysis [13] to prevent any damage to the pentacene channel. The OTFT structure consists of (from substrate to top gate): a 625 Å thick Ag layer for the drain and source contacts deposited through a second, aligned mask, an 800 Å thick pentacene channel layer (deposited at 0.2 Å/s for the first 300 Å, and 0.5 Å/s for the remainder), and a 250 nm thick parylene-C insulator followed by a 1000 Å thick Ag top gate electrode. Channel widths of 100 μm and 500 μm were employed, each with gate lengths of 25 and 50 microns. During deposition the device was kept in vacuum or in an ultrahigh purity (<1 ppm O_2 or H_2O) N_2 glovebox except when exposed to air after the cathode, pentacene, and parylene-C deposition steps.

Independent steady state electrical characterizations of both the OTFT and OPD were obtained using a semiconductor parameter analyzer. The OPD was tested in the dark and under illumination at powers as high as 0.33 mW/cm^2, at a wavelength of $\lambda = 578$ nm using a Hg lamp with a notch filter. A quartz-tungsten lamp chopped at 190 Hz synchronized with a lock-in amplifier, and filtered by a monochromator was used to determine the detector spectral response. Optical power intensity was measured using a calibrated Si photodetector. The optical pulse response was measured using a N_2 pumped dye laser at $\lambda = 581$ nm with a pulse energy of 5 μJ and duration of 1.5 ns. The switching response of the OTFT was measured using an oscilloscope and a pulse generator connected to the OTFT gate.

The OTFT with a gate width to length ratio of $W/L = 20$ for a gate width of $W = 500$ μm had a drain-source current, I_{DS}, ON/OFF ratio of 700 when the gate-source voltage, V_{GS}, was varied from -25 V to +15 V (voltages are relative to the source at ground) and at a drain-source voltage of $V_{DS} = -17.5$ V. The OFF current was approximately $I_{OFF} = 80$ pA as shown in the transfer characteristics of Fig. 1b. At low V_{DS}, I_{OFF} is reduced but more slowly than the reduction in the ON current resulting in a reduced ON/OFF ratio. Analysis of the transfer characteristics in the pinch-off regime yields a pentacene mobility of $\mu = 0.0025$ cm^2/V s and threshold voltage of $V_{th} = 7$ V according to: $I_{DS} = \frac{1}{2}\frac{W}{L}\mu C_i(V_{GS} - V_{th})^2$, where $C_i = 8$ nF/cm^2 is the capacitance of the parylene-C gate dielectric. The resistance of the OTFT, extracted from I_{DS} vs. V_{DS}, is 220 MΩ at $V_{DS} = -5$ V with $V_{GS} = -20$ V. The relatively high resistance and low mobility of the OTFT is due to the top gate, bottom-contact configuration, and air exposure between the pentacene and parylene depositions. Growth of the pentacene channel at elevated temperatures also is known to increase the hole mobility [14].

The current–voltage (I–V) characteristic of a 200 μm × 500 μm OPD at a wavelength of $\lambda = 578$ nm is shown in Fig. 2, with the wavelength-dependent external quantum efficiency (EQE) shown in the inset. The SubPc response peak at $\lambda = 580$ nm and the broader C_{60} peak at $\lambda = 450$ nm are apparent [15]. Under reverse bias, the C_{60} peak increases significantly relative to that of SubPc due to increased field-induced exciton dissociation in the thin film bulk [16].

The anode-source current, I_{AS}, of the integrated device is shown in the inset of Fig. 3 for $V_{AS} = -5.0$ V. In the ON state at $V_{GS} = -20$ V, the pixel provides an intensity dependent photocurrent that is suppressed in the OFF state. The ON state photocurrent is plotted in Fig. 3 as a function of power intensity and shows an 8-bit dynamic range of $DR = \Delta I_{max}/\Delta I_{min} = (I_{max} - I_{dark})/(I_{min} - I_{dark}) = 300$, where I_{max} is the current that is reduced by 1 dB from the linear

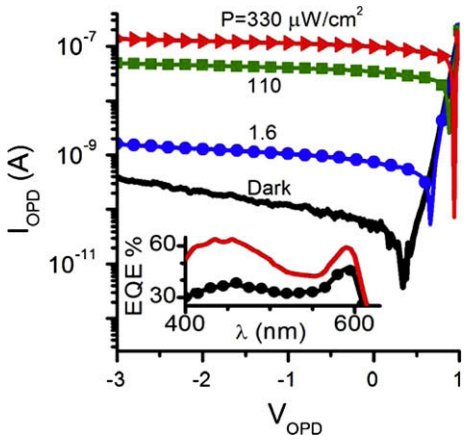

Fig. 2. Steady state current–voltage (I_{OPD}–V_{OPD}) characteristics for a 200 μm × 500 μm SubPc/C_{60} based OPD in the dark (solid line) and illuminated at a wavelength of $\lambda = 578$ nm at 1.6 μW/cm^2 (circles), 110 μW/cm^2 (squares), and 330 μW/cm^2 (triangles). Inset: Spectral dependence of external quantum efficiency (EQE) of the OPD, at 0 V (solid line) and at −2.5 V (circles).

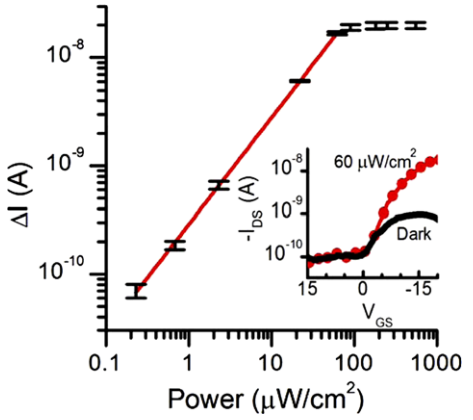

Fig. 3. Power intensity dependent photocurrent of an integrated pixel with a 200 μm × 500 μm OPD, and a 500 μm wide × 25 μm long OTFT channel, illuminated at a wavelength of $\lambda = 578$ nm. The photocurrent, ΔI, is the illuminated current minus the dark current. The pixel is in the ON state, with gate-source voltage of −20 V, and the anode-source voltage is $V_{AS} = -5$ V. The line is a linear fit of log(ΔI) to log(P) with a slope of 1.01 ± 0.02 and an intercept corresponding to a responsivity of 0.29 A/W. Inset: The anode-source current, I_{AS}, in the dark (solid line) and illuminated at 60 μW/cm^2 (circles) for $V_{AS} = -5$ V with V_{GS} varied from +15 V to −20 V.

response of current vs. incident optical power, I_{dark} is the OPD dark current, and I_{min} is the minimum current distinguishable from I_{dark}. This *DR* is lower than expected from the transfer characteristic since $V_{AS} = -5.0$ V is restricted to low voltage to avoid damaging the OPD. The line is a fit of log(ΔI) to log(P) and yields a slope of 1.01 ± 0.02 and intercept of −6.54 ± 0.06, corresponding to a responsivity of 0.29 A/W at $\lambda = 581$ nm.

The response of the pixel to a 1.5 ns optical pulse at $\lambda = 581$ nm is shown in Fig. 4 with $V_{GS} = -20$ V and OPD-anode to OTFT-source voltage, V_{AS}, of −5 V. The signal is

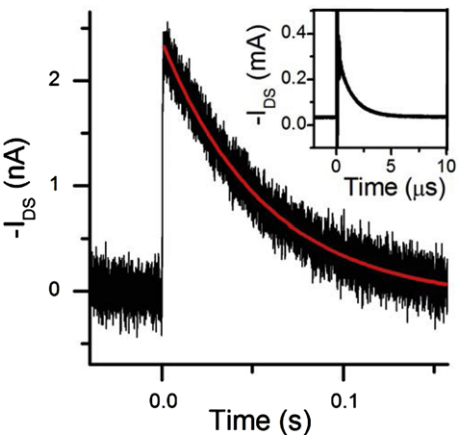

Fig. 4. Optical pulse response through a 1 MΩ load of an integrated pixel, with a 200 μm × 100 μm OPD and a 500 μm wide × 25 μm long OTFT channel. The optical pulse is 1.5 ns long with a pulse energy of 5 μJ centered at a wavelength of $\lambda = 581$ nm. The anode-source current, I_{AS}, decays exponentially with a 60 ms time constant, shown by the fit (red line). Inset: OTFT switching response of the pixel with 5 kΩ load due to a 800 ms long, gate-source voltage pulse of −20 V. The response time of 1.3 μs corresponds to a frequency response of >400 kHz. (For interpretation of the references to colour in this figure legend, the reader is referred to the web version of this article.)

measured on an oscilloscope with a 1 MΩ load that is much less than the channel resistance, and an exponential fit has a decay time of 60 ms. The response time of the OPD alone is approximately 10 ns [2], and the long response time corresponds to discharge through the OTFT. Improving the mobility of the OTFT by improving molecular ordering of the pentacene film and preventing air exposure between the channel and gate insulator deposition steps can reduce the time required to extract photogenerated charge from the pixel. The electrical pulse response of the integrated device under illumination is shown in the inset of Fig. 4, with $V_{AS} = -10$ V and with a 50 ms long pulse of $V_{GS} = -20$ V applied to the transistor gate. A resistance–capacitance (RC) time of 1.3 μs is required to charge the OTFT using a 5 kΩ load, resulting in a switching frequency of 400 kHz.

The OPD has a linear response over more than 5 decades in power intensity, so the *DR* is limited by the performance of the OTFT which limits the photocurrent of the OPD at high light intensity. For small photocurrents, the OTFT operates in a linear, resistive regime where $V_{DS} \propto I_{DS}$, and all the photocurrent can be extracted through the transistor. For large currents, the OTFT saturates and the forward bias on the OPD is diminished since the total voltage across the circuit, $V_{AS} = V_{OPD} + V_{DS}$, is fixed. This restricts the photocurrent to the ON current of the OTFT. The OTFT ON current could realistically be improved toward reported values of 10^{-6} A by improving fabrication techniques [17]. This would result in a dynamic range of 13 bits for the same dark current.

This device has applications in systems that require low dark current, for example, sensors with multiple detectors sharing a common output as is typical of most imaging focal plane arrays. The integrated OTFT in the OFF state re-

duces the OPD dark current by a factor of 10, enabling the fabrication of a sensor comprised of 10×10 array blocks with integrated OFF currents comparable to that of a single detector. Optimization of the OTFT performance to reported OFF currents <4 pA characteristic of discrete, top gate pentacene OTFTs can extend array sizes to $>100 \times 100$ [18]. Since the vertical integration achieved using layer-by-layer growth requires no complex patterning processes, it preserves the potential low cost of organic electronics. In addition, the room temperature processing including gate insulator deposition makes this process compatible with flexible plastic substrates.

In conclusion, we have demonstrated a monolithically integrated, small molecular weight OPD plus OTFT passive pixel sensor circuit with an 8-bit dynamic range, a switching time of >400 kHz, and an OFF current of <50 pA. This circuit has applications in focal plane detector arrays for high sensitivity imaging applications.

Acknowledgement

The authors thank Universal Display Corporation for financial support.

References

[1] G.H. Gelinck, H.E.A. Huitema, E.V. Veenendaal, E. Cantatore, et al., Nat. Mater. 3 (2004) 106.
[2] M.S. Arnold, J.D. Zimmerman, C.K. Renshaw, X. Xu, R.R. Lunt, C.M. Austin, S.R. Forrest, Nano Lett. 9 (2009) 3354.
[3] X. Xu, M. Mihnev, A. Taylor, S.R. Forrest, Appl. Phys. Lett. 94 (2009) 043313.
[4] X. Xu, M. Davanco, X.F. Qi, S.R. Forrest, Org. Electron. 9 (2008) 1122.
[5] C.D. Dimitrakopoulos, D.J. Mascaro, IBM J. Res. Dev. 45 (2001) 11.
[6] L. Zhou, A. Wanga, S. Wu, J. Sun, S. Park, T.N. Jackson, Appl. Phys. Lett. 88 (2006) 083502.
[7] T. Someya, Y. Kato, S. Iba, Y. Noguchi, T. Sekitani, H. Kawaguchi, T. Sakurai, IEEE Trans. Electron Dev. 52 (2005) 11.
[8] I. Nausieda, K. Ryu, I. Kymissis, A.I. Akinwande, V. Bulovic, C.G. Sodini, IEEE Trans. Electron Dev. 55 (2008) 527.
[9] D. Renshaw, P.B. Denyer, G. Wang, M. Lu, ASIC image sensors, IEEE Int. Symp. Circ. Sys. (1990).
[10] R.F. Salzman, J. Xue, B.P. Rand, A. Alexander, M.E. Thompson, S.R. Forrest, Org. Electron. 6 (2005) 242.
[11] N. Li, B.E. Lassiter, R.R. Lunt, G. Wei, S.R. Forrest, Appl. Phys. Lett. 94 (2009) 023307.
[12] M. Vogel, S. Doka, Ch. Breyer, M.C. Lux-Steiner, K. Fostiropoulos, Appl. Phys. Lett. 89 (2006) 163501.
[13] P. Kramer, A.K. Sharma, E.E. Hennecke, H. Yasuda, J. Polym. Sci. Polym. Chem. 22 (2003) 475.
[14] D.J. Dundlach, Y.Y. Lin, T.N. Jackson, S.F. Nelson, D.G. Schlom, IEEE Electron Dev. Lett. 18 (1997) 87.
[15] H. Gommans, B. Verreet, B.P. Rand, R. Muller, J. Poortmans, P. Heremans, J. Genoe, Adv. Funct. Mater. 18 (2008) 3686.
[16] P. Peumans, A. Yakimov, S.R. Forrest, J. Appl. Phys. 93 (2003) 3693.
[17] W.L. Kalb, K. Mattenberger, B. Batlogg, Phys. Rev. B 78 (2008) 035334.
[18] C.R. Newman, R.J. Chesterfield, M.J. Panzer, C.D. Frisbie, J. Appl. Phys. 98 (2005) 084506.

Organic Electronics 11 (2010) 179–183

Contents lists available at ScienceDirect

Organic Electronics

journal homepage: www.elsevier.com/locate/orgel

High efficiency red phosphorescent organic light-emitting diodes with single layer structure

Woo Sik Jeon [a], Tae Jin Park [a], Kyeong Heon Kim [b], Ramchandra Pode [c,*], Jin Jang [a], Jang Hyuk Kwon [a,*]

[a] Department of Information Display, Kyung Hee University, Dongdaemoon-gu, Seoul 130-701, Republic of Korea
[b] Department of Chemistry, Kyung Hee University, Dongdaemoon-gu, Seoul 130-701, Republic of Korea
[c] Department of Physics, Kyung Hee University, Dongdaemoon-gu, Seoul 130-701, Republic of Korea

ARTICLE INFO

Article history:
Received 22 August 2009
Received in revised form 12 September 2009
Accepted 17 October 2009
Available online 22 October 2009

Keywords:
Red
Single layer
Phosphorescent
OLED

ABSTRACT

We report simple red phosphorescent devices comprising single layer configuration using a tris[1-phenylisoqunolinato-C2,N]iridium (III) ($Ir(piq)_3$) dopant concentration as low as 1 wt.% in mixed host systems. The driving voltage of 5.4 V to reach the brightness of 1000 cd/m^2 in the mixed emitting layer of *N*,*N*′-diphenyl-*N*,*N*′-bis(1,1′-biphenyl)-4,4′-diamine (NPB) and bis(10-hydroxybenzo[h]quinolinato)beryllium ($Bebq_2$) is reported. Maximum current and power efficiency values of 9.44 cd/A and 10.62 lm/W are obtained in this single layer structure PHOLEDs, respectively. It is believed that the direct injection of charge carriers to the organic layer and high carrier mobility therein are the keys to the simplification of the device structure.

Crown Copyright © 2009 Published by Elsevier B.V. All rights reserved.

1. Introduction

Organic light-emitting devices (OLEDs) have made significant stride in recent days [1] and the technology has already been commercialized to mobile flat panel display applications. In phosphorescent OLEDs (PHOLEDs), required for high brightness and display applications, almost maximum theoretical limit of external quantum efficiency (EQE) has been achieved in several color devices [2–4]. Thermal evaporation technique and complicated fabrication process consisting of multiple layers for charge carriers balancing and exciton confinement [5–7] are employed in highly efficient phosphorescent OLEDs. In order to overcome such complex device architecture, many good approaches are enduring until now. High efficiency devices with pure organic bi-layered OLEDs have been reported by several researchers [8–10]. Furthermore, bi-layered devices consisting of an organic single layer with a buffer layer on the electrode have also been reported without any significant improvement of the device performances [11–14]. However, truly organic single layered approach is almost rare. To date, only an exclusive article on the red emitting PHOLED single layer device with a tris[1-phenylisoqunolinato-C2,N]iridium (III) ($Ir(piq)_3$) (21 wt.%) doped in TPBi (100 nm) with low values of current and power efficiencies under 3.7 cd/A and 3.2 lm/W at 1 cd/m^2 have been reported, respectively [15].

In this paper, we have demonstrated efficient and simple red PHOLEDs with only single organic layer using thermal evaporation technique. The key to the simplification is the direct injection of holes and electrons into the mixed host materials through electrodes. In conventional OLEDs, usually the Fermi energy gap between cathode (~2.9 eV) and surface treated anode (~5.1 eV) is about 2.0–2.2 eV which is close to the red light emission energy (1.9–2.0 eV). As a consequence, red devices do not at all require any charge injection and transporter layer if the host material has proper HOMO (highest occupied molecular orbital) and

* Corresponding authors. Tel.: +82 2 961 0948; fax: +82 2 961 9154.
E-mail addresses: rbpode@khu.ac.kr (R. Pode), jhkwon@khu.ac.kr (J.H. Kwon).

1566-1199/$ - see front matter Crown Copyright © 2009 Published by Elsevier B.V. All rights reserved.
doi:10.1016/j.orgel.2009.10.010

LUMO (lowest unoccupied molecular orbital) energy levels. However, such host materials are very rare. The most suitable option to address such issues is to employ the mixed host system to adequately match the energy levels between emitting host and electrodes. Mixed host system of electron transporting and hole transporting materials to inject electrons and holes from electrodes into the organic layer without any barrier has been studied, respectively and employed for the charge balance. Thus, hole type host materials are required to have HOMO energy levels at 5.1–5.4 eV to match with the Fermi energy of surface treated ITO (5.1 eV). While 2.8–3.0 eV LUMO energy levels of electron transporting host materials are necessary to match the Fermi level of cathode. 4,4′,4″-Tris(*N*-3-methylphenyl-*N*-phenyl-amino)triphenylamine(m-MTDATA) and *N*,*N*′-diphenyl-*N*, *N*′-bis(1,1′-biphenyl)-4,4′-diamine (α-NPB) were used as the hole transporting host materials. Bis(10-hydroxybenzo[h]quinolinato)beryllium ($Bebq_2$) with 2.8 eV LUMO energy was used as the electron transport host material and $Ir(piq)_3$ was employed as a red phosphorescent guest.

2. Experimental

m-MTDATA and α-NPB as hole transporting host materials, $Bebq_2$ as an electron transporting host material, and $Ir(piq)_3$ as a red dopant were purchased from Gracel Corporation. To fabricate OLED devices, clean glass substrates precoated with a 150-nm-thick indium tin oxide (ITO) layer with a sheet resistance of ~20 Ω/sq were used. Line patterns of ITO were formed on glass by photolithography process. The ITO glass was cleaned by sonification in an isopropylalcohol and acetone, rinsed in deionized water, and finally irradiation in a UV-ozone chamber. All organic materials were deposited by the vacuum evaporation technique under a pressure of $\sim 2.0 \times 10^{-7}$ Torr. The deposition rate of organic layers was about 1 A/s. Subsequently, LiF and Al were deposited in another vacuum deposition system without breaking vacuum. Deposition rates of LiF and Al were 0.1 and 5–10 A/s, respectively. The current density–voltage (*J*–*V*) and luminance–voltage (*L*–*V*) data of red PHOLEDs were measured by Keithley 2635 A and Minolta CS-1000A, respectively. The red PHOLED emitting area was 2 mm^2 for all the samples studied in the present work.

3. Results and discussion

Fig. 1 shows the energy band-diagram of the single layer red PHOLEDs used in the present work. For the evaluation of single layer with different mixed host systems, the following devices were fabricated:

Device A: ITO/m-MTDATA:$Bebq_2$:$Ir(piq)_3$ [1–4 wt.%, 100 nm]/LiF (0.5 nm)/Al (100 nm).
Device B: ITO/α-NPB:$Bebq_2$:$Ir(piq)_3$ [1–4 wt.%, 100 nm]/LiF (0.5 nm)/Al (100 nm).

The ratio of the hole and electron transporting hosts was fixed to 1:1. The doping concentrations were varied

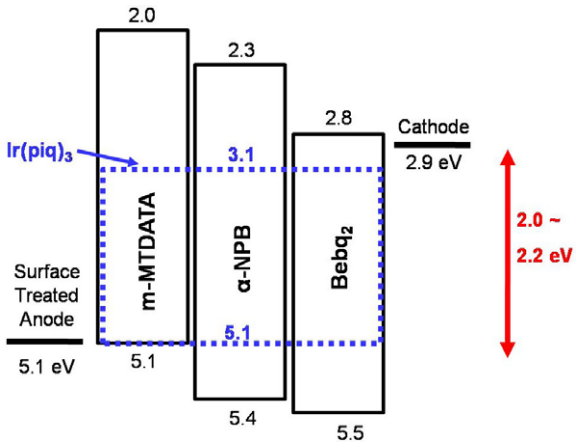

Fig. 1. Energy band-diagram of the single layer red PHOLEDs.

from 1% to 4% to optimize the device performance. Table 1 shows the performance of red PHOLEDs devices comprising a single emitting layer. The current and power efficiencies values of 7.44 cd/A, and 3.43 lm/W at 1000 cd/m^2 brightness value are reported in 4 wt.% doped device A, respectively. The driving voltage (to reach 1000 cd/m^2) is 6.9 V. Very similar device performances are obtained in 2 wt.% doped device A. The optimum doping condition for device A seems to be 4 wt.% as the highest efficiency is observed at an acceptable brightness value (1000 cd/m^2). Whereas, the driving voltage, current and power efficiencies values of 5.4 V, 9.02 cd/A, and 5.25 lm/W at brightness value of 1000 cd/m^2 are reported in device B with 1 wt.% of optimum doping condition, respectively. Maximum current efficiency for devices A and B were appeared for the 4 and 1 wt.% of $Ir(piq)_3$ doped mixed hosts, respectively. The color coordinates are (0.66, 0.33) or (0.67, 0.32) for all devices. Even in 1% doped device, a good red emission color is observed. The results of device B (1 wt.%) is significantly superior to $Ir(piq)_3$ doped multilayer red PHOLEDs [16]. In our previous study, the doping concentration in PHOLEDs can be reduced until 1–2% range with higher efficiency when HOMO–HOMO and LUMO–LUMO differences between host and dopant molecules are provided within ~0.3 eV [17]. Device B displays exactly similar behavior although HOMO–HOMO gap is relatively higher than device A. However, unlike device B, similar device properties in device A regardless of doping condition from 1% to 4% are obtained. The self quenching by dopants seems to be not so serious in this device A. This indicates that the emission zone of device A is very broad and the charge balance is also relatively poor. As a result, the efficiency of device A is low compared to device B and 4% doped condition in device A seems to have a little better charge balance.

The *J*–*V*–*L* curve and efficiency characteristics of devices A and B are shown in Fig. 2. The best efficiency yields of 9.44 cd/A (EQE 14.6%) and 10.62 lm/W are noticed in the device B as shown in Fig. 2b. As seen from the results of Fig. 2a, the driving voltage in device A with m-MTDATA:$Bebq_2$:$Ir(piq)_3$ [4 wt.%] is 6.9 V at the bright-

Table 1
Device performances of various single red devices with different doping concentration.

	Device A			Device B		
	1% Doping	2% Doping	4% Doping	1% Doping	2% Doping	4% Doping
Turn on voltage (at 1 cd/m^2)	2.5 V	2.4 V	2.3 V	2.4 V	2.4 V	2.4 V
Operating voltage (at 1000 cd/m^2)	7.2 V	7.1 V	6.9 V	5.4 V	5.4 V	5.3 V
Maximum current and power efficiency	8.12 cd/A	8.19 cd/A	8.04 cd/A	9.44 cd/A	8.36 cd/A	7.04 cd/A
	7.84 lm/W	9.86 lm/W	10.96 lm/W	10.62 lm/W	9.82 lm/W	8.11 lm/W
Current and power efficiency (at 1000 cd/m^2)	7.28 cd/A	7.34 cd/A	7.44 cd/A	9.02 cd/A	8.26 cd/A	7.04 cd/A
	3.18 lm/W	3.29 lm/W	3.43 lm/W	5.25 lm/W	4.80 lm/W	4.10 lm/W
CIE (x, y) (at 1000 cd/m^2)	(0.66, 0.33)	(0.67, 0.32)	(0.67, 0.32)	(0.66, 0.33)	(0.67, 0.32)	(0.67, 0.32)

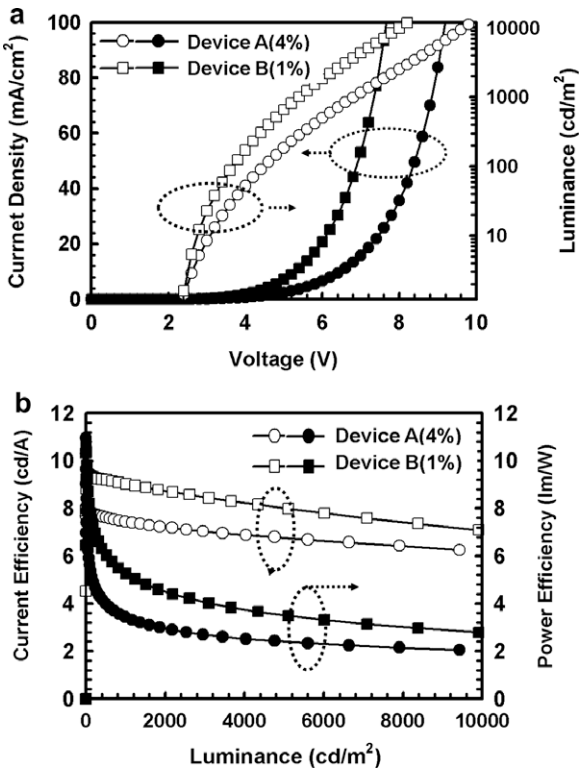

Fig. 2. J–V–L and efficiency characteristics of single layer red PHOLEDs. J–V–L characteristics, (b) L vs. current and power efficiencies characteristics.

ness of 1000 cd/m^2. The device B with α-NPB:Bebq$_2$:Ir(piq)$_3$ [1 wt.%] shows a driving voltage of 5.4 V at 1000 cd/m^2. In m-MTDATA, no barrier for hole injection from the surface treated ITO (5.1 eV) to the HOMO (5.1 eV) of the m-MTDATA exists. Further, this energy level matches with the HOMO (5.1 eV) of the Ir(piq)$_3$. While, electrons injected from the cathode move freely on the LUMO energy of Bebq$_2$. In case of the device B, the HOMO energy in the α-NPB material at 5.4 eV as against 5.1 eV in the surface treated ITO (HOMO difference ~0.3 eV) offers some barrier to the hole injection into the emitting layer. While electrons injected from cathode move freely over the LUMO energy of Bebq$_2$. In order to understand the injection barrier situation in m-MTDATA and α-NPB, J–V of hole only devices were investigated. An ideal Ohmic contact [18] at ITO and m-MTDATA interface was reported. Whereas, the NPB hole only device had reported to have injection limited current behavior. When a buffer layer like PEDOT:PSS (poly(3,4-ethylenedioxythiophene)-poly(4-stylenesulfonate) or C60 was introduced at ITO interface, the Ohmic characteristic was observed in this device [19,20]. Form these previously reported results, a high value of driving voltage in the α-NPB mixed device B due to the high barrier to hole injection into the emitting layer was expected. However in reality, the device B with α-NPB hole transporting host shows a lower driving voltage implying a low resistance to the current flow. Here, devices A and B were realized using two different hole transporting host materials having different charge carriers transport abilities, particularly the hole mobility. α-NPB has an ambipolar transporting ability with the hole mobility faster than that of m-MTDATA [21]. Thus, mobilities of hole carriers in these mixed host single layer systems rather than hole injection barrier at the ITO/mixed host interface seems to be crucial in deciding the driving voltage. In order to elucidate the conduction and emission processes in single layer devices, we have fabricated following several devices and investigated.

We have made devices C and D without Ir(piq)$_3$ dopant and results were compared with those of devices A and B, respectively. Fig. 3 shows J–V characteristics of devices A, B, C, and D. Results on bi-layered ITO/α-NPB (40 nm)/Bebq$_2$:Ir(piq)$_3$ (10 wt.%, 50 nm)/LiF (0.5 nm)/Al (100 nm) red emitting PHOLEDs [16], reproduced here for better

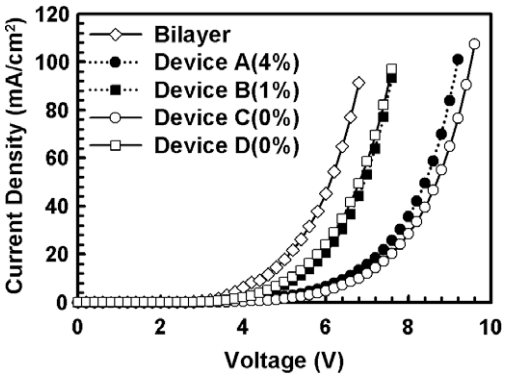

Fig. 3. J–V characteristics of bi-layered ITO/α-NPB (40 nm)/Bebq$_2$:Ir(piq)$_3$ (10 wt.%, 50 nm)/LiF (0.5 nm)/Al (100 nm) red emitting PHOLED and devices A–D.

comparison, show a low driving voltage value of 4.5 V to reach a luminance of 1000 cd/m^2. As displayed in Fig. 3, both devices C and D (undoped) show *J–V* characteristics similar to Ir(piq)$_3$ doped devices A and B, respectively. Furthermore in our devices A and B, hole and electron injection barriers by dopant molecules are negligible due to no barrier at ITO and cathode interfaces, respectively. Doping in the device may affect carrier mobility due to carrier trapping by dopant molecules. Usually, *J–V* characteristics of PHOLEDs are changed significantly by adding dopant molecules when HOMO–HOMO and LUMO–LUMO differences between host and dopant molecules are high over 0.3 eV. In device A and B, these energy differences are within 0.3 eV. In this case, the change of *J–V* characteristic is very small because trapped charges in dopant molecules easily overcome to host energy level by thermal energy. Such behavior is already reported in our previous study [17]. Described results demonstrate that the conduction of current in a hole and electron transporting mixed host layer is almost independent of (i) the charge trapping at dopant molecules and (ii) hole injection barrier at the ITO/mixed host interface. Further, all mixed single layer devices offer a high resistance to current flow than bi-layered red device with hetero junction (see Fig. 3). The interesting and intriguing results on *J–V* in mixed host single layer devices may be explained on the basis of existing knowledge on carrier mobilities in organic materials. α-NPB exhibits an ambipolar transporting ability with electron and hole mobility values of 9×10^{-4} and 6×10^{-4} cm^2/Vs, respectively [22], while the hole mobility value in m-MTDATA is 3×10^{-5} cm^2/Vs. Earlier, it was shown that the charge transport behaviors in mixed thin films of α-NPB and Alq$_3$ are sensitive to (i) compositional fraction, and (ii) charge carriers mobilities of neat compounds [22]. The 1:1 mixed layer of α-NPB and Alq$_3$ appeared to give lower charge carrier mobility of 10^{-2}–10^{-3} order than neat films [22]. As a consequence, the fast current flow in the device B despite the large hole injection barrier is attributed to the high hole mobility value and ambipolar nature of α-NPB. Higher driving voltage of single layer devices compared to the bilayer device is also well understood by the decrease in carrier mobility in the mixed host system.

Since the charge transport behaviors in mixed hosts are sensitive to the composition and intrinsic mobilities in neat films, the location of the recombination region may be important to understand the device efficiency. To investigate the recombination zone position, we have evaluated three devices with doped emissive layer located at different positions as:

(1) Device A-(L): ITO/m-MTDATA:Bebq$_2$:Ir(piq)$_3$ [4 wt.%, 30 nm]/m-MTDATA:Bebq$_2$ [70 nm]/LiF (0.5 nm)/Al (100 nm).
(2) Device A-(C): ITO/m-MTDATA:Bebq$_2$ [35 nm]/m-MTDATA:Bebq$_2$:Ir(piq)$_3$ [4 wt.%, 30 nm]/m-MTDATA:Bebq$_2$ [35 nm]/LiF (0.5 nm)/Al (100 nm).
(3) Device A-(R): ITO/m-MTDATA:Bebq$_2$ [30 nm]/m-MTDATA:Bebq$_2$:Ir(piq)$_3$ [4 wt.%, 70 nm]/LiF (0.5 nm)/Al (100 nm).

Similarly, devices B-(L), (C) and (R) were fabricated using α-NPB instead of m-MTDATA and 1 wt.% of Ir(piq)$_3$. The doping region was fixed to 30 nm in all devices. The anode side doped devices show the best current efficiency performance as displayed in Fig. 4 (devices A-(L) and B-(L)), indicating that the recombination zone is around the ITO/mixed host interface. Further, the emission efficiency performance deteriorates as the doped region is moved toward the cathode side. High current efficiency in α-NPB/Bebq$_2$ mixed host system is the consequences of the better charge balance in the recombination zone. Fig. 5 shows electroluminescence (EL) spectra dependence on the emission zone location in doped and undoped devices. Broad and clean EL peak at 620 nm in undoped mixed m-MTDATA/Bebq$_2$ host organic device C is due to exciplex emissions. While the strong and asymmetric EL emission peak at 620 in devices A-(L) to A-(R) due to emissions of exciplex and Ir(piq)$_3$ red phosphorescent dopant are noticed. In these devices, exciplexes are formed as the energy difference between HOMO of m-MTDATA and LUMO of Bebq$_2$ is about 2.3 eV. Whereas in case of fully doped (device B) and undoped (device D) α-NPB/Bebq$_2$ mixed devices, clean peaks at 510 and 620 nm due to strong emission of Bebq$_2$ and Ir(piq)$_3$ dopant are appeared, respectively. Upon moving the doped region toward the anode side, EL spectra show both emission peaks at 510 and 620 nm due to Bebq$_2$ host and Ir(piq)$_3$ dopant, respectively, but with the reduced intensity of 510 nm emission peak of Bebq$_2$. The electron charge carriers are transported over the LUMO of Bebq$_2$ through the doped region and reach the anode side, resulting in the emission due to Bebq$_2$ host. Although holes are easily injected into the m-MTDATA/Bebq$_2$ organic layer (device A), they are slowly transported due to low hole mobility in m-MTDATA which is further reduced in the mixed host system. While transport behavior in α-NPB/Bebq$_2$ mixed host system is relatively better due to the high hole mobility in α-NPB. Whereas, electrons in both doped devices A and B are transported freely over the LUMO of the Bebq$_2$. These results corroborate that the recombination zone in devices A and B are located between the anode and the center of the emitting layer.

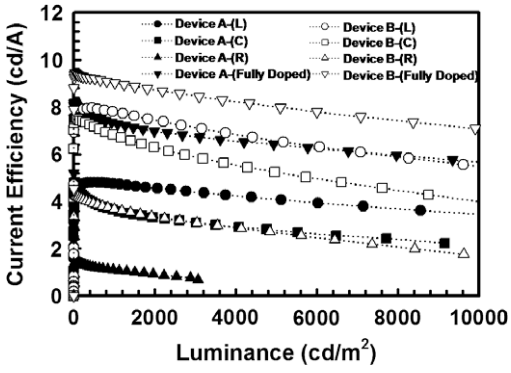

Fig. 4. *L*-Efficiency characteristics of various single layer devices fabricated with different locations of doped regions.

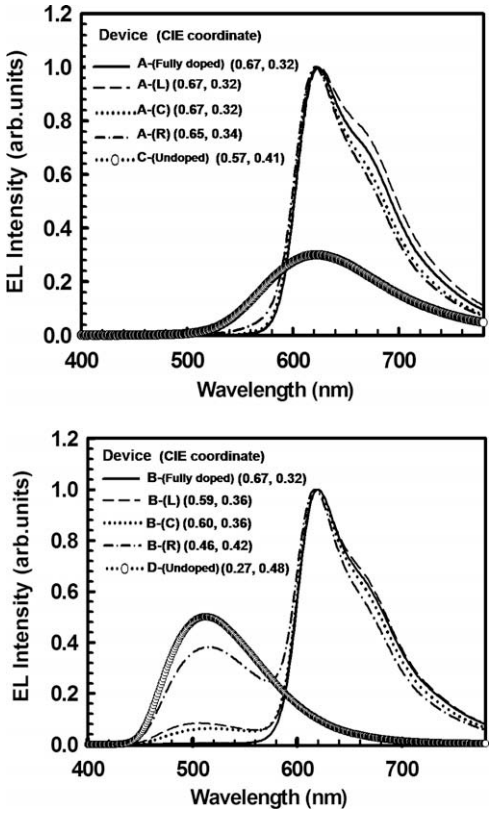

Fig. 5. Electroluminescence (EL) spectra of various single layer devices fabricated with different locations of doped regions at the brightness of 1000 cd/m^2.

4. Conclusions

In conclusion, we have demonstrated high efficiency red PHOLEDs comprising only single emitting layer. The key to the simplification is the direct injection of holes and electrons into the mixed host materials through electrodes. The driving voltage of 5.4 V to reach the 1000 cd/m^2 and maximum current and power efficiency values of 9.44 cd/A and 10.62 lm/W, respectively, in the α-NPB/$Bebq_2$ mixed single layer structure PHOLEDs with the $Ir(piq)_3$ dopant as low as 1 wt.% are obtained. We found that carrier mobility is significantly important parameter to simplify the device architecture. The obtained characteristics of red PHOLEDs pave the way to simplify the device structure with reasonable reduction in the manufacturing cost of passive and active matrix OLEDs.

Acknowledgement

This research was accomplished with support from the Ministry of Commerce, Industry, and Energy of the Korean government.

References

[1] M. Pfeiffer, S.R. Forrest, K. Leo, M.E. Thomson, Adv. Mater. 14 (2002) 1633.
[2] D. Tanakai, H. Sasabe, Y.J. Li1, S.J. Su, T. Takea, J. Kido, J. Appl. Phys. 47 (2007) L10.
[3] N. Chopra, J.W. Lee, Y. Zheng, S.H. Eom, J.G. Xue, F. So, Appl. Phys. Lett. 93 (2008) 143307.
[4] B.W. D'Andrade, J. Esler, C. Lin, V. Adamovich, S. Xia, M.S. Weaver, R. Kwon, J.J. Brown, IMID08 8 (2008) 1109.
[5] M.A. Baldo, S.R. Forrest, Phys. Rev. B 62 (2000) 10958.
[6] K. Coushi, R. Kwon, J.J. Brown, H. Sasabe, C. Adachi, J. Appl. Phys. 95 (2004) 7798.
[7] D. Tanaka, H. Sasabe, Y.J. Li, S.-J. Su, T. Takeda, J. Kido, Jpn. J. Appl. Phys. 2, Lett. (Jpn.) 46 (2007) L10.
[8] W.S. Jeon, T.J. Park, S.Y. Kim, R. Pode, J. Jang, J.H. Kwon, Appl. Phys. Lett. 93 (2008) 063303.
[9] J. Meyer, S. Hamwi, T. Bülow, H.-H. Johannes, T. Riedl, W. Kowalsky, Appl. Phys. Lett. 91 (2007) 113506.
[10] Z.W. Liu, M.G. Helander, Z.B. Wang, Z.H. Lu, Appl. Phys. Lett. 94 (2009) 113305.
[11] Q. Huang, J. Cui, H. Yan, J.G.C. Veinot, T.J. Marks, Appl. Phys. Lett. 81 (2002) 3528.
[12] Y. Gao, L. Wang, D. Zhang, L. Duan, G. Dong, Y. Qiu, Appl. Phys. Lett. 82 (2003) 155.
[13] H.F. Wang, L.D. Wang, Z.X. Wu, D.Q. Zhang, J. Qiao, Y. Qui, X.G. Wang, Appl. Phys. Lett. 88 (2006) 131113.
[14] S.C. Tse, K.K. Tsung, S.K. So, Appl. Phys. Lett. 90 (2007) 213502.
[15] Z. Liu, M.G. Helander, Z. Wang, Z. Lu, Org. Electron. 10 (2009) 1146.
[16] T.J. Park, W.S. Jeon, J.J. Park, S.Y. Kim, Y.K. Lee, J. Jang, R. Pode, J.H. Kwon, Appl. Phys. Lett. 92 (2008) 113308.
[17] W.S. Jeon, T.J. Park, S.Y. Kim, R. Pode, J. Jang, J.H. Kwon, Org. Electron. 10 (2009) 240.
[18] C. Giebeler, H. Antoniadis, D.D.C. Bradley, Yasuhiko Shirota, Appl. Phys. Lett. 72 (1998) 2448.
[19] S.C. Tse, S.W. Tsang, S.K. So, J. Appl. Phys. 100 (2006) 063708.
[20] Y.-M. Koo, S.-J. Choi, T.-Y. Chu, O.-K. Song, W.-J. Shin, J.-Y. Lee, J.C. Kim, T.-H. Yoon, J. Appl. Phys. 104 (2008) 123707.
[21] S.C. Tse, K.C. Kwok, S.K. So, Appl. Phys. Lett. 89 (2006) 262102.
[22] S.W. Liu, J.H. Lee, C.C. Lee, C.T. Chen, J.K. Wang, Appl. Phys. Lett. 91 (2007) 142106.

Organic Electronics 11 (2010) 184–187

Contents lists available at ScienceDirect

Organic Electronics

journal homepage: www.elsevier.com/locate/orgel

Small molecule based mixed interlayer for color control of solution processed multilayer white polymer light-emitting diodes

Kyoung Soo Yook, Chul Woong Joo, Soon Ok Jeon, Jun Yeob Lee *

Department of Polymer Science and Engineering, Dankook University, Jukjeon-dong, Suji-gu, Yongin, Gyeonggi 448 701, Republic of Korea

ARTICLE INFO

Article history:
Received 8 August 2009
Received in revised form 21 September 2009
Accepted 17 October 2009
Available online 22 October 2009

Keywords:
Multilayer stacked white polymer light-emitting diodes
Color control
Transfer printing

ABSTRACT

Solution processed multilayer stacked white polymer light-emitting diodes (WPLEDs) with small molecule based interlayer for color and charge balance management were developed. The multilayer stacked WPLEDs were fabricated by a stamp transfer printing method and a mixed interlayer of 4,4′,4″-tris(N-carbazolyl)triphenylamine (TCTA) and 3-(biphenyl-4-yl)-4-phenyl-5-(4-tert-butylphenyl)-1,2,4-triazole (TAZ) was inserted at the interface between a yellow and a blue emitting layer. Electroluminescence spectra and efficiency of the multilayer stacked WPLEDs could be effectively managed by changing the composition of the TCTA:TAZ mixed interlayer.

© 2009 Elsevier B.V. All rights reserved.

1. Introduction

White polymer light-emitting diodes (WPLEDs) are promising as devices for applications in displays, light sources and general lighting because of their advantages such as simple processing and simple device structure. However, the device performances of the WPLEDs are inferior to those of small molecule based white organic light-emitting diodes fabricated by a vacuum thermal evaporation [1,2]. Many factors such as purity of the polymer material, corrosion of the indium tin oxide (ITO) by an acidic hole injection layer, electron leakage to the hole transport layer and limitation of multilayer stacking of polymer materials have been proposed as the main reasons for the poor device performances of the polymer based devices [3,4]. In particular, the limitation of the multilayer stacking of polymer materials is one of important factors for the poor device performances in WPLEDs.

There have been several studies to fabricate multilayer stacking structures in the PLEDs. An alcohol soluble or water soluble emitting material was developed to prepare multilayer structures and the WPLEDs with the alcohol soluble emitting material were reported [5]. Crosslinkable polymer emitting materials were also synthesized to fabricate multilayer stacked PLEDs and they were effective to prepare the WPLEDs with multiple emitting layers [6]. However, these approaches require the synthesis of functionalized or crosslinkable materials and common polymer or soluble materials cannot be used.

A method to fabricate multilayer structures with common polymer materials is to apply dry patterning method to form a thin film. A laser induced thermal imaging was effective to deposit polymer films on the substrate and a stamp transfer printing method could be used to make polymer thin film without any damage to the polymer film underneath [7]. Polydimethylsiloxane (PDMS) stamp has been typically used for the stamp transfer printing and polymer films could be transferred from the PDMS to the substrate by heat and pressure during contact [8–10]. Our group already demonstrated that the stamp transfer printing method could be utilized for the preparation of multilayer device structure [11,12].

In this work, color tunable multilayer stacked WPLEDs were fabricated by the stamp transfer printing and the device performances of the multilayer stacked WPLEDs

* Corresponding author. Tel./fax: +82 31 8005 3585.
E-mail address: leej17@dankook.ac.kr (J.Y. Lee).

1566-1199/$ - see front matter © 2009 Elsevier B.V. All rights reserved.
doi:10.1016/j.orgel.2009.10.012

were investigated according to the interlayer structures. An efficient color control of the WPLEDs by the small molecule interlayer was demonstrated.

2. Experimental

A device structure of indium tin oxide (ITO, 150 nm)/polyethylene-3,4-dioxythiophene:polystyrenesulfonate (PEDOT:PSS, 60 nm)/yellow emitting layer(15 nm)/4,4′,4″-tris(N-carbazolyl)triphenylamine (TCTA):3-(biphenyl-4-yl)-4-phenyl-5-(4-tert-butylphenyl)-1,2,4-triazole (TAZ) (10 nm)/blue emitting layer (60 nm)/LiF/Al was used. The interlayer was a mixed layer of the TCTA and TAZ. The relative compositions of the TCTA:TAZ interlayer were 100:0 (device I), 90:10 (device II) and 75:25 (device III). A polyfluorene based Blue C polymer from Dow chemical was a blue emitting material, while polyphenylenevinylene based supper yellow polymer from Merck was a yellow emitting material. The yellow emitting material was spin-coated from a 0.2 wt% toluene solution, while the blue material was spin-coated from a 0.5 wt% toluene solution. The blue material was spin-coated on a Si substrate and then it was transferred to the substrate coated with the yellow polymer and the TCTA:TAZ interlayer using a PDMS stamp. Detailed procedure for the preparation of the PDMS stamp was reported in previous work [12]. Device structures and energy levels of the materials are shown in Fig. 1. Current density–voltage–luminance and electroluminescence (EL) characteristics of the devices were obtained by Keithley 2400 source measurement unit and a Minolta CS 1000 spectroradiometer.

3. Results and discussion

The interlayer in the white organic light-emitting diodes (WOLEDs) is important for the color management and charge balance control and it was generally used in small molecule based WOLEDs [1]. However, the interlayer could not be used in the WPLEDs as it was difficult to fabricate multilayer stacked structures in the WPLEDs. Film orthogonality could not be guaranteed due to the intermixing of the polymer materials during spin coating of one polymer on the other polymer. The problem can be solved by utilizing the stamp transfer printing method and the WPLEDs with controlled light emission were fabricated using the small molecule interlayer structure.

Fig. 2 shows the current density–voltage–luminance curves of the multilayer stacked WPLEDs with the small molecule interlayer. The current density of the device was dependent on the interlayer structure and the WPLED with the TCTA:TAZ (75:25) interlayer showed the highest current density. The current density of the WPLED with the pure TCTA interlayer was much lower than those of other devices with the mixed interlayer structure. The current density of the white device with multiple emitting layers is generally determined by the energy levels of the emitting layers and the interlayer. Efficient hole and electron transport in the emitting layer lead to high current density, while energy barrier within the emitting layer reduces the current density of the device. In the case of the interlayer, a bipolar type interlayer is usually effective to improve the current density because holes and electrons can be transported through the interlayer. In the device I

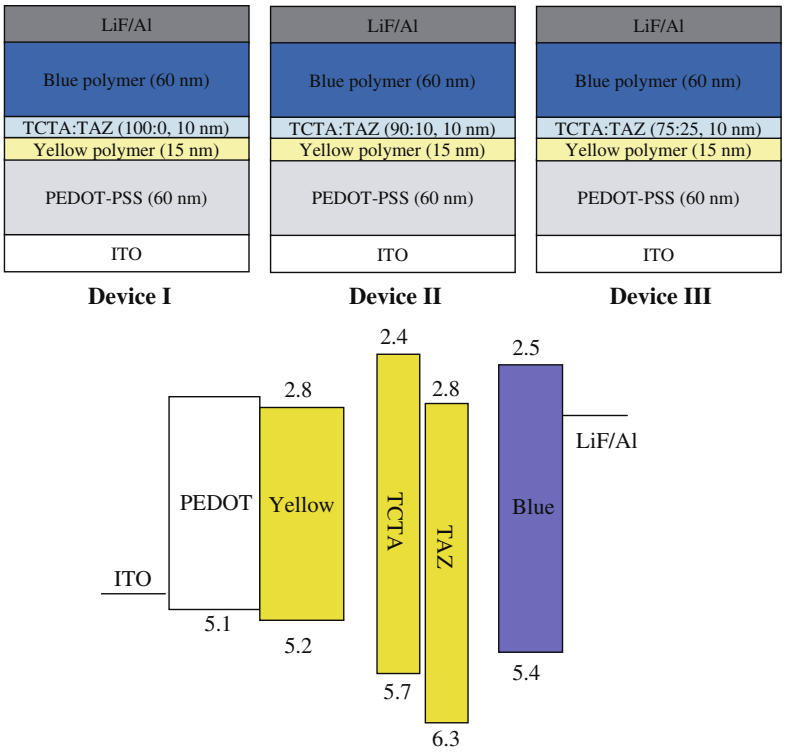

Fig. 1. Device structures and energy levels of the white polymer light-emitting diodes fabricated in this work.

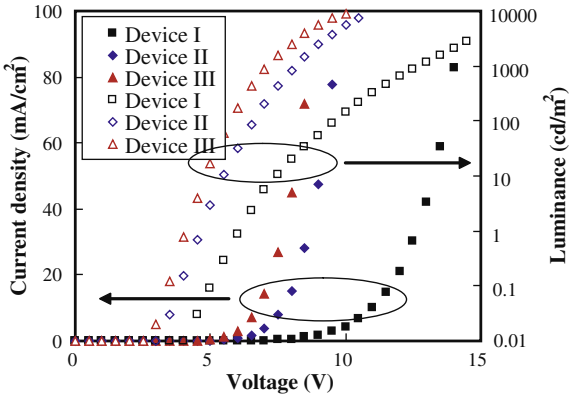

Fig. 2. Current density–voltage–luminance curves of the white polymer light-emitting diodes with the TCTA:TAZ interlayer.

with the TCTA interlayer, the holes can be transported from the yellow emitting layer to the blue emitting layer, while electrons are blocked by the TCTA interlayer due to the lowest unoccupied molecular orbital (LUMO) of 2.4 eV. The poor electron transport through the TCTA interlayer reduces the current density of the WPLED in spite of the efficient hole transport. The current density was greatly improved in the device II and device III because both the hole transport type TCTA and electron transport type TAZ were used in the interlayer. The holes can be transported through the TCTA, while electrons can be transported through the TAZ, resulting effective holes and electrons transport through the interlayer. The rather high current density of the device III compared with the device II is due to better electron transport through the TAZ. High TAZ content in the interlayer facilitates the electron transport though the interlayer. The luminance of the WPLEDs followed the similar trend as the current density.

The quantum efficiency and current efficiency of the WPLEDs are shown in Fig. 3. The quantum efficiency of the WPLED with the mixed interlayer was much higher than that of the WPLED with the TCTA interlayer. The mixed interlayer balances the transport of the holes and electrons through the interlayer, resulting in charge balance in the yellow and blue emitting layer. However, the TCTA blocks electron injection from the blue emitting layer to the yellow emitting layer, leading to poor charge balance in the emitting layer. Compared with the quantum efficiency of the yellow and blue single layer devices [13], the quantum efficiency of the WPLED was rather high due to efficient charge transport control through the interlayer. The quantum efficiency of the WPLED with the TCTA:TAZ interlayer was even higher than that of the stacked WPLEDs reported earlier [11,13]. This indicates that the light emission of the multilayer stacked WPLEDs can be effectively managed by the TCTA:TAZ interlayer. The current efficiency of the WPLEDs was also improved by the TCTA:TAZ interlayer and a current efficiency of 6.1 cd/A was obtained in the device III with the TCTA:TAZ (75:25) interlayer. The efficiency roll-off was also improved in the mixed interlayer devices due to the balance charge injection through the interlayer.

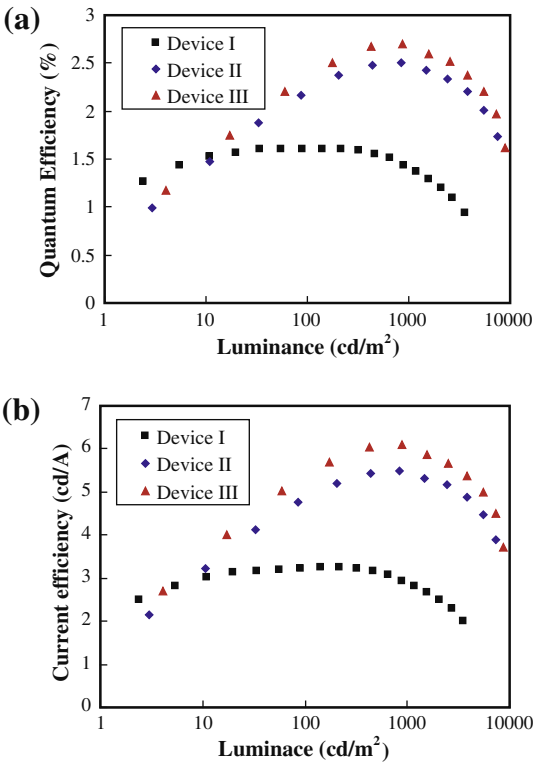

Fig. 3. Quantum efficiency–luminance (a) and current efficiency–luminance (b) curves of the white polymer light-emitting diodes with the TCTA:TAZ interlayer.

The EL spectra of the WPLEDs with the TCTA:TAZ mixed interlayer are presented in Fig. 4 according to the composition of the interlayer. The increase of the TAZ content in the interlayer strengthens the yellow emission due to strong electron transport properties of the TAZ. The emission zone is shifted from the blue emitting layer to the yellow emitting layer due to more electron injection through the interlayer. The use of the TCTA interlayer increases the

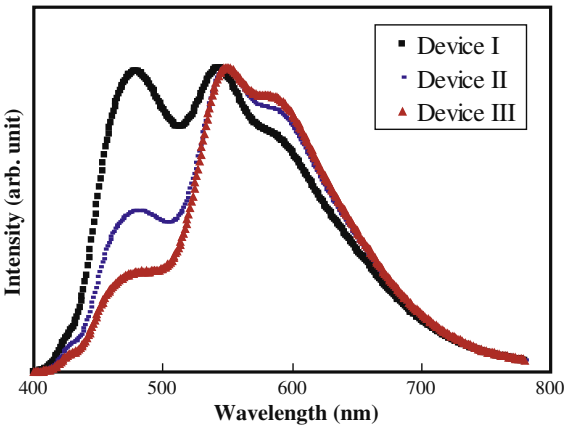

Fig. 4. Electroluminescence spectra of the white polymer light-emitting diodes with the TCTA:TAZ interlayer. The spectra were obtained at 1000 cd/m².

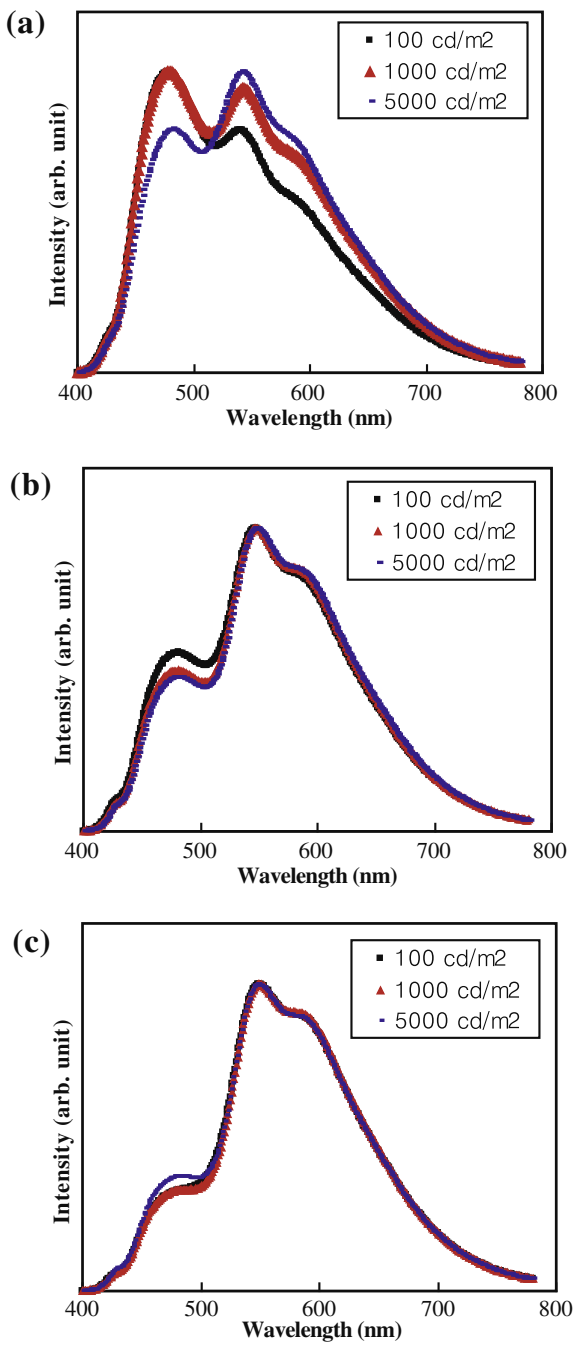

Fig. 5. Electroluminescence spectra of the white polymer light-emitting diodes with the TCTA:TAZ interlayer according to the luminance of the devices. (a) Device I, (b) Device II and (c) Device III.

blue intensity because of more hole injection from the yellow emitting layer to the blue emitting layer. The yellow and blue emission was balanced in the device II with the TCTA:TAZ (9:1) and a color coordinate of (0.38, 0.43) was obtained. The color coordinates of the device I and device III were (0.32, 0.39) and (0.41, 0.46).

The color change of the WPLEDs was measured according to the luminance of the devices (Fig. 5). The color change of the WPLEDs was minimized in the device III with TCTA:TAZ (75:25). The color change depends on the recombination zone shift according to the driving voltage of the devices. The use of the mixed interlayer in the WPLEDs balanced the hole and electron injection at low and high luminances, leading to the stable EL spectra in the device III. Similar result was reported in the small molecule based white devices in our previous work [14]. The color change was significant in the device I with only TCTA interlayer.

4. Conclusion

In summary, the device performances of the multilayer stacked WPLEDs could be effectively managed by the small molecule based TCTA:TAZ interlayer. The emission zone of the WPLEDs could be controlled by managing the composition of the interlayer and the efficiency of the device was also improved by the mixed interlayer. The interlayer approach can be useful in the fabrication of the multilayer stacked WPLEDs in the future because of balanced charge transport and effective color control.

Acknowledgements

This study was supported by a grant (M2009010025) from the Fundamental R&D Program for Core Technology of Materials funded by the Ministry of Knowledge Economy (MKE), Republic of Korea.

References

[1] Y. Sun, N.C. Giebink, H. Kanno, B.W. Ma, M.E. Thompson, S.R. Forrest, Nature 440 (2006) 908.
[2] K.S. Yook, S.O. Jeon, C.W. Joo, J.Y. Lee, M.S. Kim, H.S. Choi, S.J. Lee, C.W. Han, Y.H. Tak, Org. Electron. 10 (2009) 681.
[3] J. Kim, R.H. Friend, I. Grizzi, J.H. Burroughes, Appl. Phys. Lett. 87 (2005) 023506.
[4] P.K.H. Ho, J. Kim, J.H. Burroughes, H. Becker, S.F.Y. Li, T.M. Brown, F. Cacialli, R.H. Friend, Nature 404 (2000) 481.
[5] X. Niu, C. Qin, B. Zhang, J. Yang, Z. Xie, Y. Cheng, L. Wang, Appl. Phys. Lett. 90 (2007) 203513.
[6] J. Li, T. Sano, Y. Hirayama, K. Shibata, Syn. Metal 159 (2009) 36.
[7] J.Y. Lee, S.T. Lee, Adv. Mater. (Weinheim, Germany) 16 (2004) 51.
[8] L. Chen, P. Degenaar, D.D.C. Bradley, Adv. Mater. (Weinheim, Germany) 20 (2008) 1679.
[9] Y.N. Xia, G.M. Whitesides, Annu. Rev. Mater. Sci. 28 (1998) 153.
[10] B.D. Gates, Q.B. Xu, M. Stewart, D. Ryan, C.G. Willson, G.M. Whitesides, Chem. Rev. (Washington, DC) 105 (2005) 1171.
[11] S.O. Jeon, C.W. Joo, K.S. Yook, J.Y. Lee, Appl. Phys. Lett. 94 (2009) 093303.
[12] C.W. Joo, K.S. Yook, S.O. Jeon, J.Y. Lee, Org. Electron. 10 (2009) 372.
[13] C.W. Joo, S.O. Jeon, K.S. Yook, J. Phys. D: Appl. Phys. 42 (2009) 105115.
[14] K.S. Yook, S.O. Jeon, C.W. Joo, J.Y. Lee, J. Ind. Eng. Chem. 15 (2009) 420.

Organic Electronics 11 (2010) 188–194

Contents lists available at ScienceDirect

Organic Electronics

journal homepage: www.elsevier.com/locate/orgel

Electronic structure of anode interface with molybdenum oxide buffer layer

Kaname Kanai [a,*], Kenji Koizumi [b], Satoru Ouchi [c], Yoshiaki Tsukamoto [c], Kei Sakanoue [c], Yukio Ouchi [b], Kazuhiko Seki [b]

[a] Research Core for Interdisciplinary Sciences, Okayama University, 3-1-1 Tsushima-naka, Okayama 700-8530, Japan
[b] Graduate School of Science, Nagoya University, Furo-cho, Chikusa-ku, Nagoya 464-8602, Japan
[c] Panasonic Corporation, 3-1-1 Yagumo-naka-machi, Moriguchi City, Osaka 570-8501, Japan

ARTICLE INFO

Article history:
Received 21 August 2009
Received in revised form 21 September 2009
Accepted 17 October 2009
Available online 4 November 2009

Keywords:
MoO_3
Oxygen vacancy
Ultraviolet photoemission spectroscopy
Inverse photoemission spectroscopy

ABSTRACT

The electronic structure at the α-NPD/MoO_3/Au interfaces has been investigated with ultraviolet photoemission spectroscopy (UPS), X-ray photoemission spectroscopy (XPS) and inverse photoemission spectroscopy (IPES). It was found that the MoO_3 layer contains some number of oxygen vacancies prior to any treatment and gap states are induced by the partial filling of the unoccupied 4d orbitals of molybdenum atoms neighboring oxygen vacancies. The α-NPD thickness dependence of XPS spectra for the α-NPD/MoO_3 system clearly showed that molybdenum atoms at the surface of the MoO_3 film were reduced by α-NPD deposition through the charge-transfer interaction between the adsorbed α-NPD and the molybdenum atoms. This reduction at the α-NPD/MoO_3 interface formed a large interface dipole layer up to −1.79 eV. The deduced energy-level diagram for the α-NPD/MoO_3/Au interfaces describes the energy-level matching that explains well the significant reduction in the hole-injection barrier due to the MoO_3 buffer layer.

© 2009 Elsevier B.V. All rights reserved.

1. Introduction

MoO_X was first introduced as a buffer layer in an organic electroluminescent device (OLED) by Tokito et al. in 1996 [1]. By placing the MoO_X layer between the hole-transporting layer (HTL) and anode, the operational voltage of the device was reduced and its efficiency was enhanced. These improvements were attributed to the lowering of the hole-injection barrier at the HTL/MoO_X interface. Since the first report by Tokito et al., similar improvements in device efficiency have been reported for OLEDs with both small molecule and conducting polymer layers [2–9]. Moreover, the MoO_3 buffer layer also offers advantages over the lifetime of the device, such as less contamination of anode surface which significantly improves stability of anode interface. The improvement of device performance has been attributed to the enhancement of the hole-injection and recombination efficiencies at the HTL/MoO_X interface. Recently, Wang et al. reported the electronic structure at the *N*,*N*′-di(naphthalene-1-yl)-*N*,*N*′-diphenyl-benzidine (α-NPD)/MoO_3/indium tin oxide (ITO) interface, as observed by ultraviolet photoemission spectroscopy (UPS) [10]. They concluded that the reduction in the hole-injection barrier is due to the formation of an interfacial dipole layer at the MoO_3/ITO interface, which shifts the vacuum level upward. Consequently, the highest occupied molecular orbital (HOMO) of the α-NPD layer becomes relatively close to the Fermi level (E_F) of ITO. However, it has been observed that device efficiency improves over a wide range of MoO_3 thickness [9]. Even for devices with a thick MoO_3 buffer layer up to 20 nm, the device efficiency and lifetime are significantly improved. To interpret these results, it is necessary to better understand the hole-transport mechanism through the MoO_3 layer. In previous reports, information is lacking on the hole-transporting levels of

* Corresponding author. Tel.: +81 86 251 8715; fax: +81 86 251 8705.
E-mail address: kaname@cc.okayama-u.ac.jp (K. Kanai).

1566-1199/$ - see front matter © 2009 Elsevier B.V. All rights reserved.
doi:10.1016/j.orgel.2009.10.013

the MoO_3 layer. The topmost valence band of the MoO_3 layer remains far below E_F of the anode and HOMO of the α-NPD layer since MoO_3 is an insulator with a wide band gap of about 3.1 eV; such a wide band gap would be expected to result in a large hole-injection barrier at the MoO_3/ITO interface.

In this study, we used UPS, X-ray photoemission spectroscopy (XPS) and inverse photoemission spectroscopy (IPES) to systematically investigate the details of the electronic structure of the α-NPD/MoO_X/Au interfaces. It was found that gap states, which are generated by partial filling of unoccupied 4d orbitals of molybdenum atoms neighboring oxygen vacancies, are formed within the energy gap of the MoO_3 layer. The gap states align with the topmost hole-transporting states of the α-NPD layer and play an important role in energy-level matching at the α-NPD/MoO_3/Au interfaces.

2. Experimental

α-NPD and MoO_3 samples were purchased from Aldrich Chemical Co. and Mitsuwa Chemicals Co. Ltd., respectively. The purity of the α-NPD and MoO_3 samples were 99% and 99.9999%, respectively. Silicon substrates with an atomically flat surface were used for the measurements of thickness dependence. The MoO_3 film was evaporated onto a clean Au-coated Si substrate. Then, α-NPD film was evaporated onto the MoO_3 film in a stepwise fashion. The evaporation rates for MoO_3 and α-NPD were about 0.3 nm/min and 0.1 nm/min, respectively. The rates were constant over the course of the evaporation. Annealing of MoO_3 film was performed at 300 °C for 10 min under an ultrahigh vacuum (UHV). The evaporation of the materials was performed under UHV (base pressure $<1 \times 10^{-7}$ Pa). The specimens were transported to the analysis chamber without being exposed to air. The UPS and XPS measurements were performed in an analysis chamber (base pressure $<5 \times 10^{-8}$ Pa), using an electron spectrometer (Omicron spectrometer, EA125). The He I resonance line at 21.22 eV was used as the excitation source for UPS measurements. IPES measurements were performed in the analysis chamber (base pressure $<1 \times 10^{-7}$ Pa), using a home-made electron-gun and a band-pass-type photon-detector with a combination of a SrF_2 window and KCl-coated channeltron [11].

3. Results and discussion

Fig. 1 displays the XPS spectra of MoO_3 films for Mo 3d core levels. The thickness dependence of the spectra for as-grown MoO_3 films is shown in Fig. 1a. The numbers on the right axis denote the MoO_3 film thickness t. The spectrum of the MoO_3 film with thickness of 20 nm shows a single Mo $3d_{3/2}$ and $3d_{5/2}$ doublet, which indicates the presence of only one type of molybdenum(VI) oxo-species. The binding energies of the Mo $3d_{3/2}$ and $3d_{5/2}$ doublet are 235.6 eV and 232.5 eV, respectively, which are lower than those of the MoO_3 crystal [12]. The observed values of the binding energy are close to the reported values for the MoO_3/Al_2O_3 system [13]. The discrepancy in the binding energy between the MoO_3 film and crystal reflects the presence of two-dimensional or monomeric molybdenum(VI) oxo-species in the film. From a fitting analysis with a Gaussian/Lorentzian mixing function, it was found that a single doublet could not resolve the observed XPS spectra of the films with thickness less than 15 nm. On the other hand, the fitting results are of sufficient quality when a second doublet is introduced. The binding energies of the two individual doublets are almost constant for all the spectra of the MoO_3 films, regardless of film thickness. The doublet at the lower binding energy (234.4 eV and 231.3 eV for Mo $3d_{3/2}$ and $3d_{5/2}$, respectively) corresponds to molybdenum(V) oxo-species [14], which indicates that reduced molybdenum is present in the evaporated MoO_3 film. The area of the doublet at lower binding energy decreases with increasing MoO_3 thickness. This reflects the decrease in reduced molybdenum with increasing the MoO_3 thickness. The reduced molybdenum could not be detected in film with thickness of 20 nm. In order to confirm the assignment of the doublet at the lower binding energy, XPS spectra of annealed MoO_3 films were acquired for comparison. The top spectrum in Fig. 1a was obtained for the MoO_3 film (t = 20 nm) annealed at 300 °C for 10 min. It is known that annealing induces the reduction of the molybdenum of MoO_3 by the introduction of the oxygen vacancies [12]. In fact, the spectra of the molybdenum(V) species were significantly enhanced after annealing. The fitting analysis shows that the binding energy of the doublet at the lower binding energy agrees with that of the as-grown films. From the XPS results, it can be concluded that oxygen vacancies are present in the evaporated MoO_3 film. Fig. 1b shows the α-NPD thickness dependence of the XPS spectra. α-NPD was deposited onto the annealed MoO_3 film in a stepwise fashion. By increasing the α-NPD thickness, the contribution to the spectra from the molybdenum(V) species increases, indicating that the surface molybdenum atoms are reduced by the adsorption of α-NPD. As discussed later, this electron donation from the adsorbed α-NPD to the MoO_3 surface induces a large dipole layer at the α-NPD/MoO_3 interface.

The UPS-IPES spectra of the as-grown and annealed MoO_3 films are shown in Fig. 2a. The density of states (DOS) calculated by the "density functional theory (DFT) + U" method is also shown for comparison [15]. The UPS-IPES spectra of the as-grown and annealed films are well explained by the calculated DOS, showing that the films mostly consist of stoichiometric MoO_3. The occupied band labeled "A" just below the energy gap is mainly composed of oxygen 2sp orbitals, and the unoccupied band labeled "B" just above the energy gap is mainly composed of molybdenum 4d orbitals. The energy gap is defined as the energy difference between the top of the O 2sp valence band and the bottom of the Mo 4d conduction band, which are indicated by vertical lines in the figure. The deduced energy gap of the as-grown film is about 3.2 eV. It was found that the energy gap decreased slightly to 3.1 eV upon annealing. In the spectra of both the as-grown and annealed films, there are small peaks just below E_F, which are denoted by asterisks. The calculated DOS does not explain these peaks. Fig. 2b shows the MoO_3 thickness dependence of the UPS spectra for the as-grown MoO_3 film in the vicinity of E_F. The peak around 1 eV decreases with increasing film thickness and is

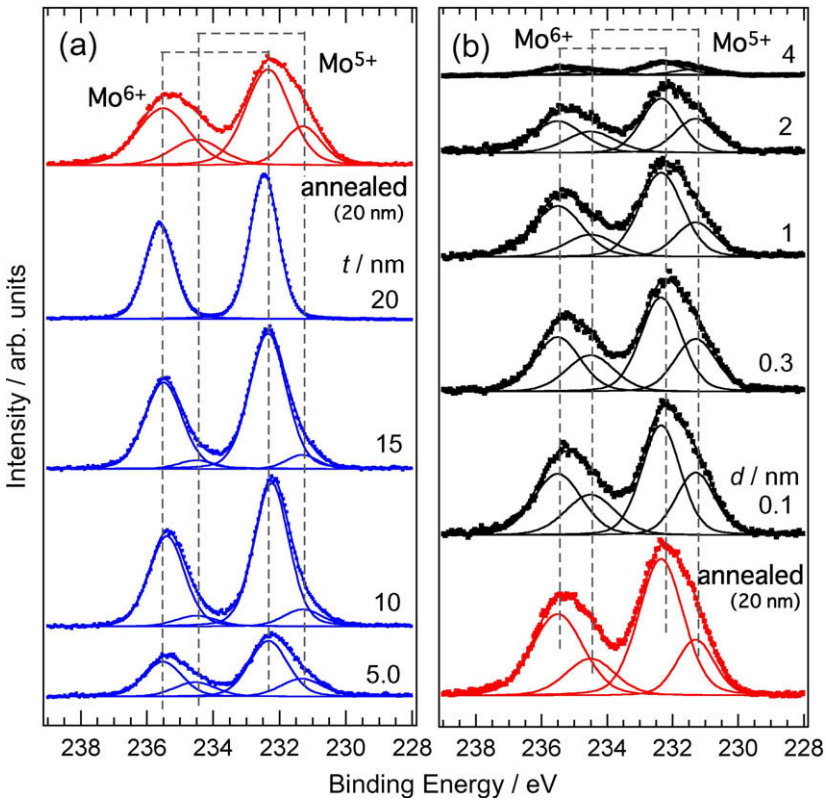

Fig. 1. XPS spectra of MoO_3 films for Mo 3d core levels. Bottom axes represent binding energy with respect to E_F of the substrate. (a) MoO_3 thickness (t) dependence of the XPS spectra for MoO_3 film deposited on Au substrate in a stepwise fashion. (b) α-NPD thickness (d) dependence of the XPS spectra for α-NPD film deposited on annealed MoO_3 film (t = 20 nm) in a stepwise fashion. Solid lines represent Gaussian/Lorentzian mixing functions for fitting analysis and resultant curves of the fitting on the experimental data. Full width at half maximum for fitting functions is 1.2 eV. Binding energies for fitting functions for the two doublets are constant.

almost completely obscured in the spectrum of the film with thickness of 2.0 nm. On the other hand, a new shoulder structure appears at around the 1.9 eV in the spectra of films with thickness of 1.5 nm and 2.0 nm, as indicated by vertical lines. In order to investigate the nature of the peak observed at 1 eV, we re-examined the effect of annealing on the spectrum. The top spectrum in Fig. 2b was obtained for the annealed MoO_3 film (t = 20 nm). A prominent peak appears at around 1 eV. This peak appears to be associated with the oxygen vacancies introduced by annealing. A similar peak was observed in the UPS spectra of the intermediate molybdenum oxide crystals, Mo_4O_{11} and $Mo_{18}O_{52}$ [12]. From DFT cluster studies, this peak was found to correspond to the gap state caused by partial filling of unoccupied 4d orbitals of molybdenum atoms neighboring oxygen vacancies [12]. When oxygen is removed to yield a neutral final product, it leaves a negative charge behind, which is distributed over the atoms close to the vacancy and compensates for some of the positive charge of the molybdenum atoms. Thus, the oxygen vacancy increases the occupancy of local molybdenum 4d orbitals. In fact, as can be seen in Fig. 2a, the unoccupied Mo 4d orbitals contribute less to the IPES spectra after annealing. As discussed in regards to Fig. 1a, the XPS spectra indicate the presence of the oxygen vacancies in the MoO_3 films up to the thickness of about 15 nm. On the other hand, the UPS results in Fig. 2b show that the gap states disappear in the thinner film with thickness of 2.0 nm. One possible reason for this inconsistency between the XPS and UPS results is the difference in their probing depth. UPS measurement possesses higher sensitivity to the surface states of the sample than XPS. However, roughly speaking, the probing depths of UPS and XPS are not much different in this experiment. The typical probing depths of XPS and UPS in this experiment are 2 nm and 1 nm, respectively, and thus both measurements are sufficiently surface sensitive. It has been reported that MoO_3 crystals with oxygen vacancies introduced by mild ion bombardment have a gap state at the 2.1 eV [12]. It should be noted that the binding energy of the shoulder structures in the UPS spectra of as-grown films with thickness of 1.5 nm and 2.0 nm is very close to the gap states of the above mentioned MoO_3 crystal containing oxygen vacancies. Therefore, the shoulder structures can possibly be assigned to the gap states that result from the oxygen vacancies that differ from those in the thinner films. The studies of the intermediate molybdenum oxide crystals showed that the nature of the gap states strongly depends on the chemical state of the oxygen vacancy [12]. The gap states at around 1.9 eV are present even in MoO_3 films with thickness up to 20 nm, although they are very small.

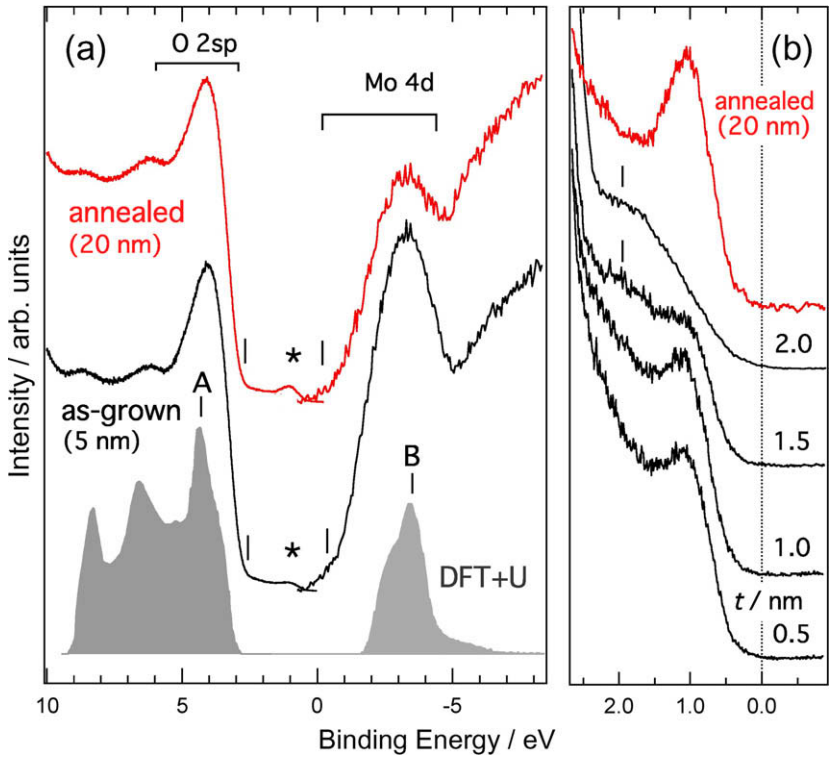

Fig. 2. (a) Combined UPS-IPES spectra for as-grown MoO_3 film (t = 5 nm) and annealed MoO_3 film (t = 20 nm). Bottom axis: binding energy with respect to E_F. Calculated DOS (filled spectra at bottom) calculated by DFT + U method is displayed for comparison. DOS data are cited from Ref. [15]. Energies for occupied and unoccupied parts of DOS were individually shifted to reproduce the observed spectra. (b) MoO_3 thickness (t) dependence of UPS spectra of as-grown MoO_3 film near E_F. Top spectrum shows UPS spectrum of annealed MoO_3 film. The top of the O 2sp valence band and the bottom of the Mo 4d conduction band are indicated by vertical lines. Asterisks denote the gap states which are caused by oxygen vacancies.

Fig. 3 shows the α-NPD thickness dependence of the UPS spectra. The results for the α-NPD films deposited on the as-grown (t = 20 nm) and annealed MoO_3 films (t = 20 nm) are shown in Fig. 3a and b, respectively. The numbers on the right axes denote the α-NPD thickness d. As discussed above, the gap states exits within the energy gap of the MoO_3 films even in the case of the as-grown film. The gap states can be seen at around 1.9 eV in the spectrum of the as-grown MoO_3 film in Fig. 3a. Both in the cases of the as-grown film (a) and the annealed MoO_3 films (b), the spectral features of α-NPD appear in the spectra of films with thickness greater than 4.0 nm. The spectra of films with thickness of 4.0 nm and 10 nm are in reasonably good agreement with the reported α-NPD spectrum [16]. On the other hand, differing spectra were obtained for films with thickness less than 1 nm. For example, the spectrum of the film for which d = 1.0 nm on the as-grown MoO_3 has a single broad peak at around 0.9 eV, while the spectra of the films for which d = 4.0 and 10 nm show two peaks around the 1.2 eV. These results indicate that there is a characteristic electronic structure right at the α-NPD/MoO_3 interface through the interaction between adsorbed α-NPD and the MoO_3 surface. Neither DFT calculations for anion nor cation of α-NPD reproduce the spectra. Although we have lacked detailed information regarding the chemical species produced at the interface until now, based on the XPS results shown in Fig. 1b, it was found that the molybdenum atoms at the MoO_3 surface are reduced by the deposition of α-NPD. Therefore, the cationic species of α-NPD must be generated by a charge-transfer interaction between the adsorbed α-NPD and molybdenum atoms at the MoO_3 surface. The vertical lines in the figures indicate the onset positions of the spectral peaks, which correspond to the topmost hole-transporting states of the films. It should be noted that the onset positions of the α-NPD films are very close to those corresponding to the gap states of MoO_3 films.

Fig. 4 summarizes the α-NPD thickness (d) dependence of the vacuum level (VL), HOMO and C 1s core level energies for α-NPD films on the as-grown and annealed MoO_3 films. As d increases, the VL sharply decreases at the α-NPD/MoO_3 interface, which represents the formation of an interfacial dipole layer. Here, the magnitude of interfacial dipole layer is defined as the energy difference between the VL of the MoO_3 film (d = 0 nm) and that of the α-NPD film with thickness of 4 nm. The magnitudes of interfacial dipole layers of the as-grown and annealed MoO_3 films are denoted as Δ and Δ', respectively. The deduced values of Δ and Δ' are −1.79 eV and −1.54 eV, respectively. Assuming that there is a weak interaction between the adsorbed organic molecule and the substrate surface such as van der Waals interactions, the typical magnitude of the interfacial dipole layer has been found to be less than −1 eV [17]. The large negative values of Δ and Δ' at the α-NPD/MoO_3 interface indicates that a charge-transfer interaction between the adsorbed α-NPD

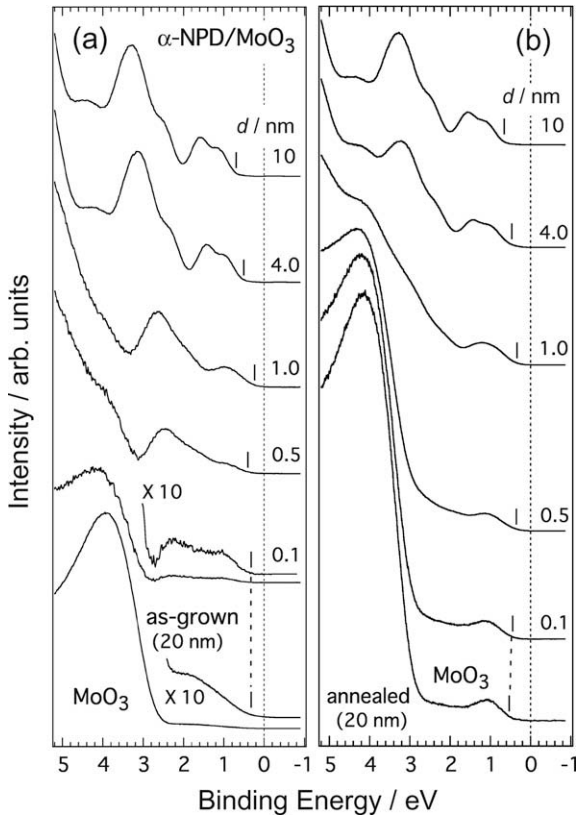

Fig. 3. α-NPD thickness (d) dependence of UPS spectra for α-NPD film deposited on as-grown MoO_3 film (t = 20 nm) (a) and annealed MoO_3 film (t = 20 nm) (b). Vertical lines denote onset position of the spectra.

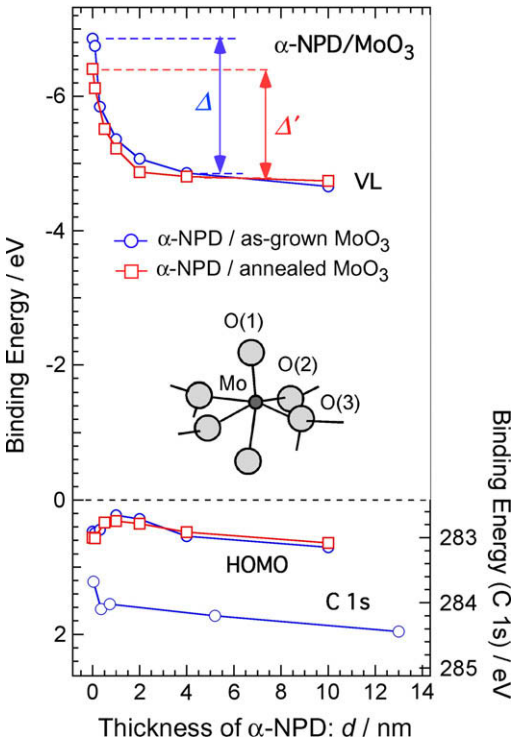

Fig. 4. α-NPD thickness (d) dependence of VL, HOMO and C 1s core level energies for α-NPD film deposited on as-grown MoO_3 film (open circle) and annealed MoO_3 film (box). Bottom axis: α-NPD thickness d. Left axis: binding energies of VL and HOMO. Right axis: binding energy of C 1s core level. Inset: octahedral MoO_6 cluster which is a building unit for MoO_3 crystal.

and MoO_3 film surface forms a cationic α-NPD layer at the interface. This is consistent with the α-NPD thickness dependence of the XPS spectra shown in Fig. 1b, which shows the reduction of the molybdenum atoms at the MoO_3 surface as a result of α-NPD deposition. The difference between Δ and Δ' is primarily due to the difference of the VL between the as-grown and annealed MoO_3 films (d = 0 nm). The inset in Fig. 4 depicts an octahedral MoO_6 cluster, which is the building unit of the MoO_3 crystal. The different oxygen sites are labeled as O(1), O(2) and O(3), respectively. If the O(1) site is removed by annealing, an electric dipole would form pointing outward. This scenario explains well the observed decrease in the VL of the MoO_3 film due to annealing. However, the vacancy formation energy for the removal of an oxygen is about 7 eV for each of the oxygen sites [12]. This means that it is quite difficult to remove oxygen from the fully stoichiometric MoO_3 surface by annealing at 300 °C. These oxygen vacancies can be produced only on a reduced MoO_3 surface already containing oxygen vacancies. As discussed with regard to Fig. 2, some vacancies are already present in the evaporated MoO_3 film, and thus it is possible to produce additional oxygen vacancies by annealing. However, it is difficult to specify the site of the oxygen vacancy. The difference in VL between the as-grown and annealed film indicates only that annealing induces the formation of the interfacial dipole by the introduction of oxygen vacancies, where the outside of the MoO_3 film is positively charged. In films with thickness greater than 4 nm, the energies of VL, HOMO and C 1s core level monotonically decrease as thickness increases.

The deduced schematic energy diagrams for α-NPD/MoO_3/Au interfaces are shown in Fig. 5. Fig. 5a depicts the energy diagram of α-NPD/Au as previously reported [16]. The hole-injection barrier of the α-NPD/Au interface was reported to be 1.4 eV. The large Δ formed at the interface results in a very large hole-injection barrier. The energy diagrams of the as-grown and annealed MoO_3 buffer layers are depicted in Fig. 5b and c, respectively. The following points should be emphasized here: (1) the positive interfacial dipole Δ at the MoO_3/Au interface is canceled out by the negative dipole Δ' at the α-NPD/MoO_3 interface, (2) the gap states nearly align with the topmost hole-transporting states of the α-NPD layer at the α-NPD/MoO_3 interface. As a result of (1) the HOMO position in the α-NPD/MoO_3/Au system is much closer to E_F of the substrate compared with that of the α-NPD/Au system, in which α-NPD is in direct contact with the substrate surface. The gap states provide hole-transporting levels from the substrate to the α-NPD layer through the MoO_3 layer. There is a small injection barrier of 0.28 eV (0.32 eV) at the as-grown (annealed) MoO_3/Au interface, and there is a negligibly small barrier at the α-NPD/MoO_3 interface as a result of (2). These results reasonably explain the improved hole-injection efficiency due to the MoO_3 buffer layer as well

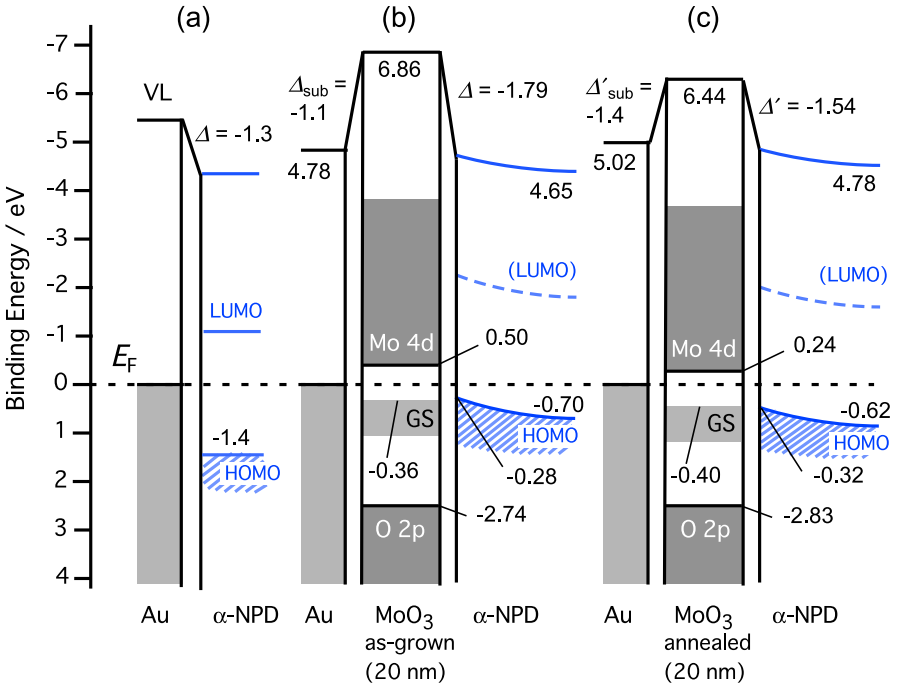

Fig. 5. Schematic energy diagrams for α-NPD/Au (a), α-NPD/as-grown MoO_3/Au (b) and α-NPD/annealed MoO_3/Au (c) interfaces. Left axis: binding energy with respect to E_F. Δ_{sub}, Δ, Δ'_{sub} and Δ' represent values of interfacial dipole layers estimated by UPS experiments. Numbers written in the figures are binding energy based on UPS and IPES results. Data for α-NPD/Au (a) were cited from Ref. [15]. "GS" in (a) and (b) refers to gap states.

as the hole-transport mechanism through the thick MoO_3 layer. Although the difference between the as-grown and annealed MoO_3 films is small, the density of gap states in the annealed film is larger than that in the as-grown film. Thus, the gap states are located at higher binding energy and the hole-injection barrier is slightly larger.

Finally, it should be noted that the interfacial dipoles (Δ_{sub}, Δ, Δ'_{sub} and Δ') observed in this work are much larger that those reported by Wang et al. [10]. For example, their reported value of Δ_{sub} for the MoO_3/ITO interface was −0.5 eV, which is much smaller than the value of Δ_{sub} obtained for the MoO_3/Au interface (Δ_{sub} = −1.1 eV) in this work. It can be reasonably assumed that this difference is due to differences in substrate material. On the other hand, their reported value of Δ for the α-NPD/MoO_3 interface (Δ = −0.05 eV) is also much smaller than that observed for the same interface in this work (Δ = −1.79 eV). However, the hole-injection barriers at the α-NPD/MoO_3 interface are nearly identical in both works. The hole-injection barrier observed by Wang et al. was 0.25 eV, while in this work it was found to be 0.28 eV. This strongly suggests the alignment of E_F between the substrate and α-NPD through the MoO_3 buffer layer. The gap states located just below E_F of the MoO_3 film are possibly impurity states that donate electrons to the conduction band since the molybdenum atoms neighboring oxygen vacancies are accepting some amount of electrons. Thus, such an "*n*-doped MoO_3 film" has some electron carriers that are thermally activated and can achieve the alignment of E_F with the substrate. Charge-transfer between the α-NPD and MoO_3 surfaces might occur, allowing the α-NPD/MoO_3 interface to reach thermal equilibrium.

4. Conclusion

The electronic structure at the α-NPD/MoO_3/Au interfaces was investigated with UPS, XPS and IPES. It was found that the MoO_3 layer contains some number of oxygen vacancies prior to any treatment and gap states are induced by the partial filling of the unoccupied 4d orbitals of molybdenum atoms neighboring oxygen vacancies. The α-NPD thickness dependence of XPS spectra for the α-NPD/MoO_3 system clearly showed that molybdenum atoms at the surface of the MoO_3 film were reduced by α-NPD deposition through the charge-transfer interaction between the adsorbed α-NPD and the molybdenum atoms. This reduction at the α-NPD/MoO_3 interface formed a large interface dipole layer up to −1.79 eV. The deduced energy-level diagram for the α-NPD/MoO_3/Au interfaces described the energy-level matching that explained well the significant reduction in the hole-injection barrier due to the MoO_3 buffer layer. In particular, it was found that the gap states align with the topmost hole-transporting states of the α-NPD layer and there is almost ohmic contact between them. The MoO_3 layer is possibly "*n*-doped" by the electron-rich molybdenum atoms neighboring the oxygen vacancies, and this might be the origin of the energy-level alignment at the α-NPD/MoO_3/Au interfaces.

Acknowledgments

This work was supported in part by a Grant-in-Aid for Scientific Research (S) (Grant No. 19105005) from the Ministry of Education Culture, Sports, Science and Technology

of Japan (MEXT), and Special Coordination Funds for Promoting Science and Technology from MEXT.

References

[1] S. Tokito, K. Noda, Y. Taga, J. Phys. D 29 (1996) 2750.
[2] K.J. Reynolds, J.A. Barker, N.C. Greenham, R.H. Friend, G.L. Frey, J. Appl. Phys. 92 (2002) 7556.
[3] J.H. Li, J. Haung, Y. Yang, Appl. Phys. Lett. 90 (2007) 173505.
[4] X. Zhu, J. Sun, X. Yu, M. Wong, H.S. Kwok, Jpn. J. Appl. Phys. 46 (2007) 1033.
[5] H.J. Bolink, E. Coronado, D. Repetto, M. Sessolo, E.M. Barea, J. Bisquert, G.G. Belmonte, J. Prochazka, L. Kavan, Adv. Funct. Mater. 18 (2008) 145.
[6] T. Matsushita, Y. Kinoshita, H. Murata, Appl. Phys. Lett. 91 (2007) 253504.
[7] C.W. Chu, S.H. Li, C.W. Chen, V. Shrotriya, Y. Yang, Appl. Phys. Lett. 87 (1999) 193508.
[8] C.W. Chen, Y.J. Lu, C.C. Wu, E.H. Wu, C.W. Chu, Y. Yang, Appl. Phys. Lett. 87 (1999) 193508.
[9] H. You, Y. Dai, Z. Zhang, D. Ma, J. Appl. Phys. 101 (2007) 026105.
[10] F. Wang, X. Qiao, T. Xiong, D. Ma, Org. Electron. 9 (2008) 985.
[11] K. Kanai, K. Akaike, K. Koyasu, K. Sakai, T. Nishi, Y. Kamizuru, T. Nishi, Y. Ouchi, K. Seki, Appl. Phys. A 95 (2009) 309.
[12] R. Tokarz-Sobieraj, K. Hermann, M. Witko, A. Blume, G. Mestl, R. Schlögl, Surf. Sci. 489 (2001) 107.
[13] Yu.V. Plyuto, I.V. Babich, I.V. Plyuto, A.D. Van Langeveld, J.A. Moulijn, Appl. Surf. Sci. 119 (1997) 11.
[14] Á. Koós, A. Oszkó, F. Solymosi, Appl. Surf. Sci. 253 (2007) 3022.
[15] R. Coquet, D.J. Willock, Phys. Chem. Chem. Phys. 7 (2005) 3819.
[16] A. Wan, J. Hwang, F. Amy, A. Kahn, Org. Electron. 6 (2005) 47.
[17] H. Ishii, K. Sugiyama, E. Ito, K. Seki, Adv. Mat. 11 (1999) 605.

Organic Electronics 11 (2010) 195–201

Contents lists available at ScienceDirect

Organic Electronics

journal homepage: www.elsevier.com/locate/orgel

Heteroepitaxy growth high performance films of perylene diimide derivatives

Lizhen Huang [a,b], Feng Zhu [a], Chengfang Liu [a,b], Haibo Wang [a], Yanhong Geng [a], Donghang Yan [a,*]

[a] State Key Laboratory of Polymer Chemistry and Physics, Changchun Institute of Applied Chemistry, Chinese Academy of Sciences, Changchun 130022, China
[b] Graduate School of Chinese Academy of Sciences, Beijing 100039, China

ARTICLE INFO

Article history:
Received 21 September 2009
Received in revised form 19 October 2009
Accepted 19 October 2009
Available online 25 October 2009

Keywords:
Organic semiconductor films
Perylene diimide derivatives
Heteroepitaxy
Organic thin film transistors
Weak epitaxy growth

ABSTRACT

High performance films of phenyl substituted perylene diimide are obtained by heteroepitaxy growth through Weak Epitaxy Growth technique. As epitaxially grown on the *para*-sexiphenyl (*p*-6P) ordered layers, the *N*,*N*′-di-phenyl perylene tetracarboxylic diimide (PTCDI-Ph) grows to form continuous and highly oriented films with large grain size, which possess low density of grain boundary and smooth surface. This quality films bring about improvement of two orders of magnitude in mobility compare to the traditional films, and present relative good air stability. Ambipolar transport behavior was also observed as tuning the thickness of *p*-6P.

© 2009 Elsevier B.V. All rights reserved.

1. Introduction

Organic semiconductors have attracted considerable interest for several decades, owing to their various applications in organic thin film transistors, organic light-emitting diodes, and organic solar cells [1–4]. Some of the applications such as complementary integrated circuits, organic p/n junction devices, both hole-transporting (p-type) and electron transporting (n-type) materials are needed. However, performance of n-type materials is being challenge because most of organic semiconductors usually present hole-transporting property. During the past decades, much progress has been made in exploiting high performance n-type materials, typical material families are C_{60} and its derivatives [5–7], Perylene and naphthalene diimide derivatives [8–13], substituted oligothiophene derivatives [14,15], substituted pentacene derivatives [16], and some metal phthalocyanine compounds [17–19]. Among them, perylene diimide derivatives (PTCDIs) bear most attention for their good performance, high electron affinities and good chemical stability. In addition they are commercial pigments which can be readily synthesized [20]. According to recent works, strategy from materials design has been widely studied and significantly promotes the performance of PTCDIs [21–27]. However, the film growth of PTCDIs has received less attention [12,28,29] and work had scarcely paid close attention on film growth strategy, which affects the device performance to a great extent. Most of the PTCDIs growing on amorphous substrate (SiO_2) present small grain size with random orientation. Even large grain size has obtained at high temperature, concomitant cracks result in poor film continuity. Besides, it is known that the performance of flexible alkyl substituted PTCDIs (0.6–2.1 cm^2/Vs) is quite better than the PTCDIs bearing phenyl or methyl substituent (10^{-5}–10^{-2} cm^2/Vs) [10,22,30]. The reason of this is unclear so far but it might greatly relative to the film quality, since the PTCDIs with flexible alkyl end groups usually are liquid crystals which possess the ability to self-organize into highly ordered structure [31]. Recent work proposed that the film quality also influenced the air stability which is a grave problem of n-type materials [32]. Hence, study on achieving high quality film is

* Corresponding author. Tel.: +86 0431 85262165; fax: +86 0431 85262266.
E-mail address: yandh@ciac.jl.cn (D. Yan).

1566-1199/$ - see front matter © 2009 Elsevier B.V. All rights reserved.
doi:10.1016/j.orgel.2009.10.014

important for the further development of perylene diimides derivatives.

Organic-organic heteroepitaxy is an effective approach to grow highly ordered films with controlled orientation and morphology [33,34]. However, most studies of heteroepitaxy growth are based on the single-crystal substrate. It greatly limited their applications on the devices. Recently, a method named "Weak Epitaxy Growth" made the heteroepitaxy can be realized on the ordinary amorphous substrate e.g. SiO_2, polymer, on which an ordered layer of rod-like molecule was introduced between the substrate and organic semiconductor films, and high substrate temperature was applied [35,36]. The rod-like molecules possess the layer-by-layer growth manner and easily to form large-area crystalline domains, which benefit the overlayer growth. Previous work has also pointed out that inserting an ordered buffer layer (such as pentacene) can increase the molecular wettability of the substrate, and thus improve the crystalline of the overlayer, leading to high performance [7,37]. Here, we explore the heteroepitaxy growth of one of perylene diimides derivatives, *N*,*N*′-diphenyl perylene tetracarboxylic diimide (PTCDI-Ph), on the crystalline layer of rod-like molecules *para*-sexiphenyl (*p*-6P). The results displayed that the PTCDI-Ph was successfully heteroepitaxially grown on the *p*-6P layers, forming highly oriented single-crystal-like films. Organic transistors with the epitaxial films as the active layer exhibit electron mobility up to 0.2 cm^2/Vs in the ambient condition, which is two orders of magnitude higher than common films, simultaneously show relative good air stability.

2. Experimental

2.1. Materials and samples preparation

The *p*-6P was synthesized according to Ref. [38], and *N*,*N*′-di-phenyl perylene tetracarboxylic diimide (PTCDI-Ph) was synthesized according to Ref. [39]. All the materials were purified twice by thermal sublimation prior to experiments. A heavily doped n-type silicon wafer with a 300 nm thermal oxidation SiO_2 layer (dielectric capacitance $C = 10$ nF cm^{-2}) was used as the substrates. The *p*-6P of various thicknesses was deposited on the previously cleaned SiO_2 substrate, and PTCDI-Ph with different thicknesses were then deposited on the *p*-6P thin films. The deposition was performed under a pressure of 10^{-4}–10^{-5} Pa at a rate of about 1 nm/min with a substrate temperature at 180 °C. For the transistor fabrication, Au was deposited on the organic films by thermal evaporation as the source and drain contacts with a shadow mask in vacuum at 10^{-4} Pa. The channel length and width are 200 μm and 6000 μm, respectively.

2.2. Characterization of organic films and transistors

2.2.1. Atomic force microscopy

Film morphology was imaged by a SPI 3800/SPA 300HV (Seiko Instruments Inc., Japan) with tapping mode. A 150 μm scanner and a commercially available SiN4-cantilevel with a spring constant of 2 N/m were used. *X-ray diffraction measurements*: The wide angle XRD pattern were taken from a D8 discovery thin film diffractometer with Cu Kα radiation (=1.54056 Å). The selected voltage and current were 40 kV and 35 mA, respectively.

2.2.2. Transmission electron microscope measurements

Organic films of PTCDI-Ph/*p*-6P were deposited on the SiO_2 substrate, subsequently a carbon thin film which was used as support layer was deposited on the films. The films were separated from SiO_2 surface by floating from 10% HF solution, and then transferred to a copper grid for measurements. The selected area electron diffraction was performed by JEOL JEM-1011 transmission electron microscope operated at 100 kV. In order to provide weaker-intensity beam and high contrast, dark field was used for experiments.

2.2.3. Transistor measurements

Current–voltage tests were performed with the two keithley 236 source-measurement unit under ambient conditions at room temperature.

3. Results and discussion

3.1. Film morphologies and structural properties

Molecular structures of PTCDI-Ph and *p*-6P are given in Fig. 1. Fig. 1a and b show morphologies of 2 nm PTCDI-Ph grown on *p*-6P with thickness of 2 nm. Domains of *p*-6P monolayer were clearly observed (details of the growth of *p*-6P have been published else where [40,41]), and differences of film morphology of PTCDI-Ph grown on *p*-6P domain and on bare SiO_2 are obviously displayed. On the *p*-6P monolayer islands, large size ribbon-like crystals of PTCDI-Ph with several preferred orientations were formed (Fig. 1b), which is much better than that on the bare SiO_2 (Fig. 1g and h). As the thickness of *p*-6P increased to 5 nm, bilayer domains of *p*-6P were formed (Fig. 1d). On the *p*-6P bilayer islands, as Fig. 1e shows, all ribbon-like crystals nearly show one orientation, implying well-defined epitaxy relation exists between the *p*-6P and PTCDI-Ph. All the crystals on the *p*-6P layers show layer-by-layer growth fashion at the early stage, whereas additional readily coalescence between adjacent grains, leading to smooth and continuous films with low density of grain boundaries. As the thickness of PTCDI-Ph increases to 20 nm, morphology is the same as the film at the early stage except appearance of some needle-like crystals originated from the island growth manner (Fig. 1c and f). This is greatly different from the morphology of PTCDI-Ph directly grown on the SiO_2 substrate, which shows small size and randomly oriented (Fig. 1l). The epitaxial films with large size and continuous grains greatly decrease the grains boundaries which is the primary limit to high performance.

The out of plane X-ray diffraction of the films present strong intensity diffraction peaks, revealing highly order (Fig. 2). PTCDI-Ph films grown on SiO_2 and *p*-6P monolayer present a primary peak with a d spacing of 17.17 Å, slightly different from the (1 0 0) peak of bulk phase (with

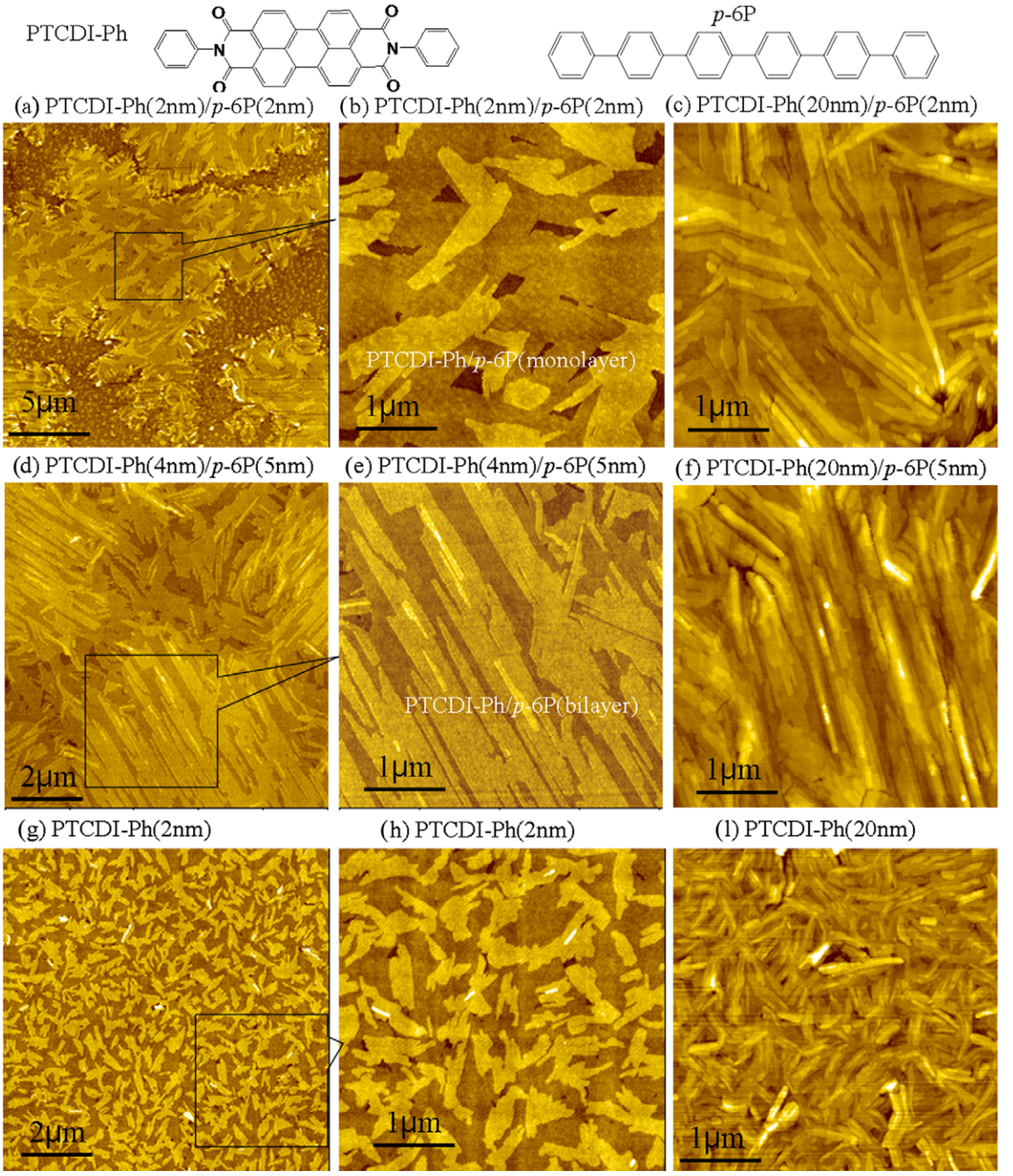

Fig. 1. Molecular structures of PTCDI-Ph and *p*-6P, AFM morphologies of (a) 2 nm thickness PTCDI-Ph on 2 nm *p*-6P, (b) zoom image of (a), (c) 20 nm thickness PTCDI-Ph on 2 nm *p*-6P, (d) 4 nm thickness PTCDI-Ph on 5 nm *p*-6P, (e) zoom image of (d), (f) 20 nm thickness PTCDI-Ph on 5 nm *p*-6P, (g) 2 nm thickness PTCDI-Ph on bare SiO_2, (h) zoom image of (g), (l) 20 nm thickness PTCDI-Ph on bare SiO_2.

a lattice spacing of 16.60 Å). On the *p*-6P bilayer, besides the diffraction peak with the d spacing of 17.17 Å, the PTCDI-Ph films mainly present another strong diffraction peak with a d spacing of 16.10 Å. This result implies that different polymorphs exist in the epitaxial films. Here different d spacing imply tilt angle between the molecular long axis and the substrate is variant. Detailed information about this was being investigated. Nevertheless, the (1 0 0) orientation corresponds that PTCDI-Ph molecule upright on the substrate, meaning the π–π stack direction parallel

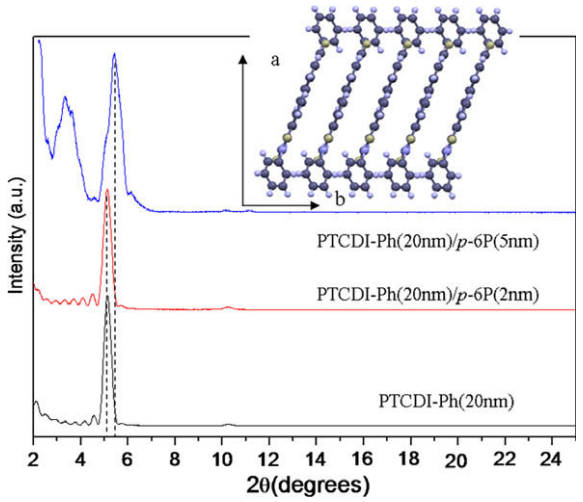

Fig. 2. Out of plane X-ray diffraction patterns of films of 20 nm thickness PTCDI-Ph grown on *p*-6P (2 nm and 5 nm) and on bare SiO_2, the inset gives the out of plane orientation of the PTCDI-Ph.

to the film plane, which is ideal for the in-plane charge transport.

Selected area electron diffraction was performed to investigate the epitaxy relationship between PTCDI-Ph and *p*-6P. On the *p*-6P monolayer, in the selected area with a diameter of 3.5 μm, diffraction pattern consists of one (0 0 1) zone of *p*-6P, demonstrating that each domain of *p*-6P presents single-crystal structure. (Fig. 3a) However, several sets diffraction of PTCDI-Ph appearance indicated that several orientations coexist on the *p*-6P monodomain, agreed well with the AFM results and the corresponding electron micrograph. The reciprocal vectors of PTCDI-Ph shows featureless relation with the *p*-6P, implied incommensurate growth of PTCDI-Ph on the *p*-6P monolayer. On the *p*-6P bilayer domain, besides the diffraction pattern of *p*-6P, only one set of in-plane orientation of PTCDI-Ph presents, indicating the PTCDI-Ph grown on each *p*-6P island shows only one orientation, consistent with the AFM results (Fig. 3b). Clear and strong intensity of the diffraction spots of PTCDI-Ph reveal that the epitaxial films present single-crystal-like structure. In-plane parameters of PTCDI-Ph calculated from diffraction pattern are: $d_{(010)} = 4.98$ Å, $d_{(002)} = 7.96$ Å, $\alpha = 90^{o}$. The lattice parameters are greatly different from the bulk phase, it can ascribe to "thin film phase". What's more, the lattice vectors of two materials are perfectly coincidence. The c* axis of PTCDI-Ph is parallel to the a* axis of *p*-6P, and the b* axis of PTCDI-Ph parallel to the b* axis of *p*-6P. In addition, along the a* direction, there exists a perfect lattice match relationship: $d_{(002)\text{PTCDI-Ph}} = d_{(100)p\text{-6P}}$, along the b* axis of *p*-6P, the lattice mismatch between $d_{(010)p\text{-6P}}$ and $d_{(010)\text{PTCDI-Ph}}$ is about 10%. All the results suggest information of commensurate epitaxy between the PTCDI-Ph and *p*-6P. Fig. 3c gives the model of the commensurate epitaxy, the epitaxy relationship is: $(1\,0\,0)_{\text{PTCDI-Ph}}//(0\,0\,1)_{p\text{-6P}}$, $[0\,0\,1]_{\text{PTCDI-Ph}}//[1\,0\,0]_{p\text{-6P}}$, $[0\,1\,0]_{\text{PTCDI-Ph}}//[0\,1\,0]_{p\text{-6P}}$. Additionally, large discrepancy of PTCDI-Ph on *p*-6P monolayer and bilayer was found in the morphology and structure, which might attribute to the difference of the phase and structure between *p*-6P monolayer and bilayer [42]. Combined the electron diffraction pattern and corresponding morphology, the PTCDI-Ph crystal anisotropic grown along the b axis direc-

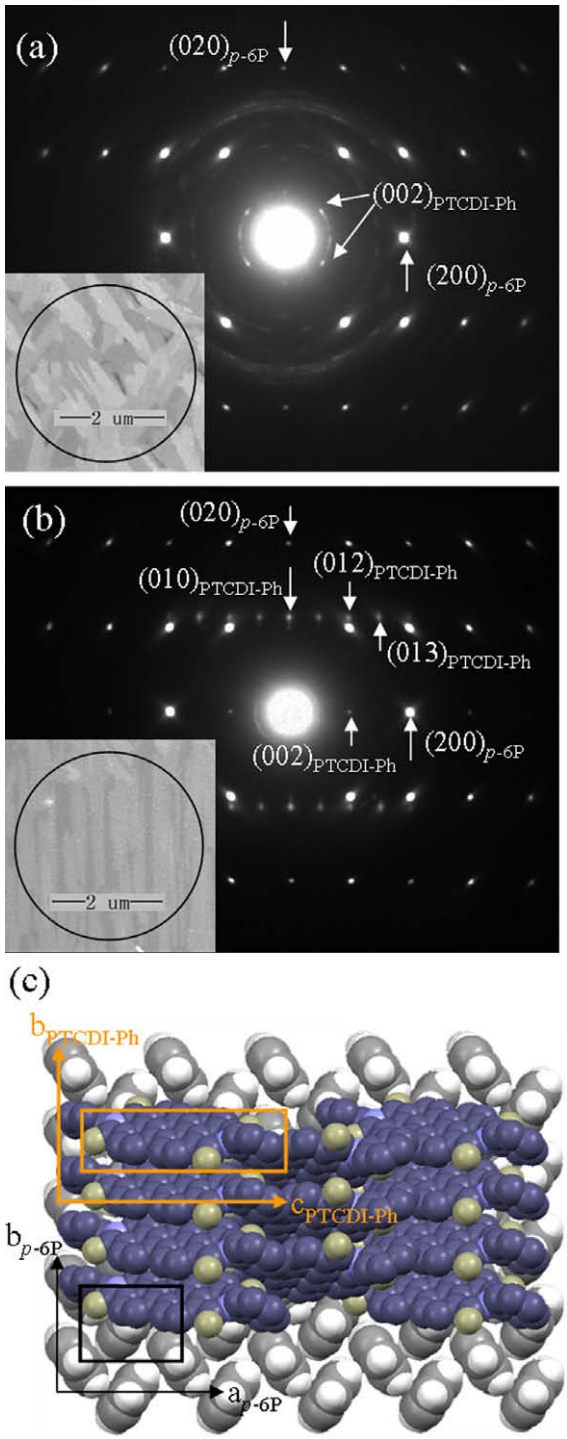

Fig. 3. (a), (b) Selected area electron diffraction patterns of 4 nm thickness PTCDI-Ph grown on *p*-6P monolayer and *p*-6P bilayer, and its corresponding electron micrograph, (c) schematic diagram of epitaxy relationship between PTCDI-Ph and *p*-6P (top view).

tion, owing to the strong π–π interaction. Such growth behavior is desired for the organic thin film transistors.

3.2. Transistor performance based on the epitaxial films

Top-contact bottom gate transistors with the epitaxial films as the active layer were fabricated to investigate the performance of the PTCDI-Ph films, the device configuration was shown in Fig. 4a. For comparison, devices with different thicknesses of *p*-6P and no *p*-6P were fabricated. The field-effect mobility was summarized in Table 1, the thickness of PTCDI-Ph is 20 nm of all the devices. The devices basing the epitaxial films show extraordinary performance improvement compare to the device with traditional film (no *p*-6P). For PTCDI-Ph directly grown on SiO_2/Si substrate, a field-effect electron mobility of about 0.001 cm^2/Vs was obtained, while as the 1 nm *p*-6P inserted, the electron mobility increases to 0.01 cm^2/Vs. As the thickness of *p*-6P increase to 2 nm, the electron mobility is up to 0.1 cm^2/Vs, which can be compared with most fashion n-type materials. Fig. 4b shows the typical transfer curve of devices with and without *p*-6P, besides the enhancement in mobility, the threshold voltage and current on/off ratio are also greatly improved. As the *p*-6P thickness up to 3 nm, the *p*-6P domains impinge with each other, forming a continuous film, which results in the formation of a hole transport channel (the *p*-6P is a p-type materials). Hence, the transistors present ambipolar transport behavior. Fig. 4c and d gives the output characteristics of ambipolar transistors with PTCDI-Ph (20 nm)/*p*-6P (3 nm), its hole mobility and electron mobility extract from the transfer characteristics is 0.09 cm^2/Vs and 0.17 cm^2/Vs, respectively. Its notable that the enhanced hole mobility is nearly 3 times higher than the *p*-6P single component (0.02 cm^2/Vs), which is similar to the phenomenon observed in 2,5-bis (4-biphenylyl) bithiophene (BP2T)/copper-hexadecafluoro phthalocyanine ($F_{16}CuPc$) system [43,44]. It implies that effect like charge transfer may be occurs in the interface of *p*-6P/PTCDI-Ph, which favored the charge transport in the interface. Details of the effect need further study. Continuing to increase thickness of *p*-6P, ambipolar charge transport dominate, but the hole mobility reduced. The thicken of *p*-6P causing the influence from the effect of organic-organic interface on the hole transport decreases, led to a mobility nearly equal to *p*-6P single component (0.02 cm^2/Vs). The electron mobility of ambipolar transistors slightly increases as the *p*-6P thickness increase. The maximum mobility of PTCDI-Ph

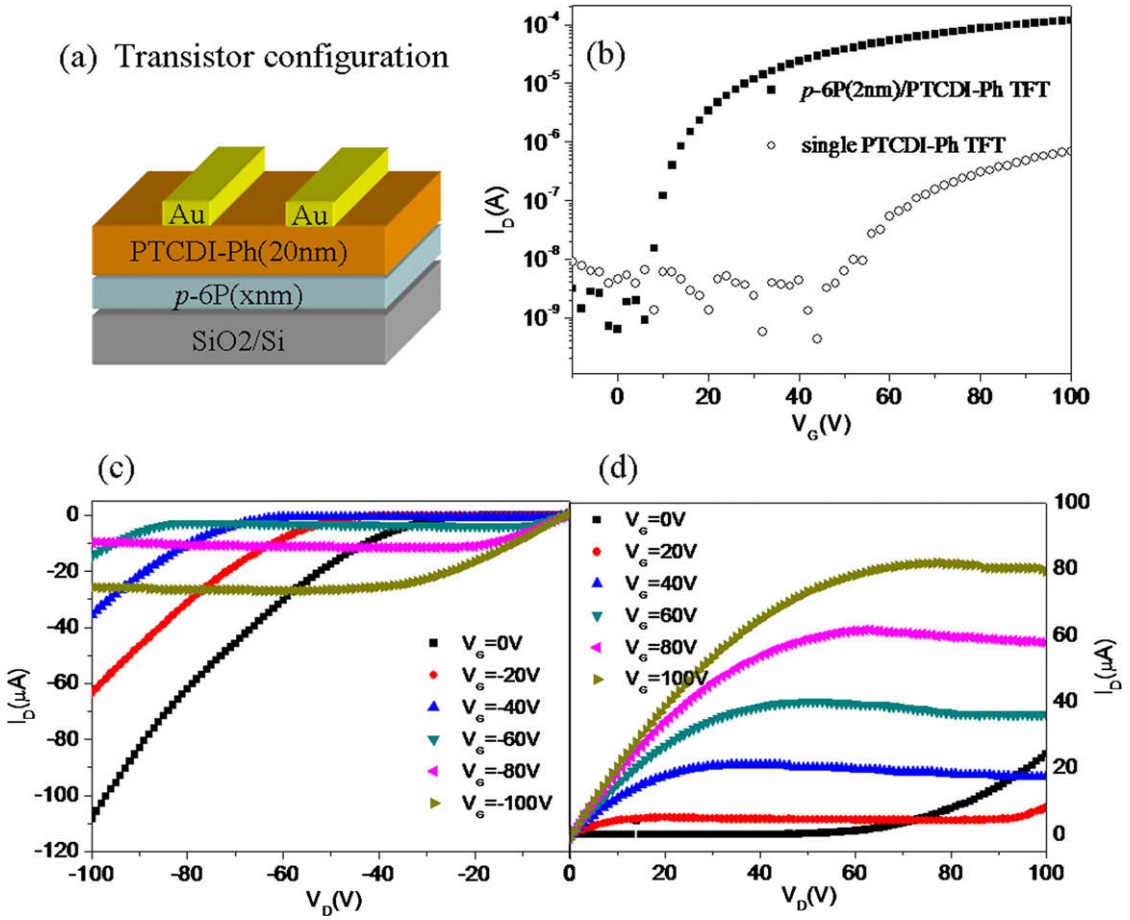

Fig. 4. (a) The transistors configuration, (b) the transfer characteristics of transistors of based on PTCDI-Ph films grown on 2 nm *p*-6P and bare SiO_2, V_{DS} = 100 V, (c), (d) output characteristics of ambipolar transistor basing on PTCDI-Ph (20 nm)/*p*-6P (3 nm) for positive and negative gate biases.

Table 1
The mobility of transistors based on PTCDI-Ph grown on *p*-6P with various thicknesses.

Devices	Hole mobility (cm^2/Vs)	Electron mobility (cm^2/Vs)
PTCDI-Ph	–	0.001–0.002
p-6P (1 nm)/PTCDI-Ph	–	0.01
p-6P (2 nm)/PTCDI-Ph	–	0.1–0.15
p-6P (3 nm)/PTCDI-Ph	0.06–0.09	0.1–0.17
p-6P (5 nm)/PTCDI-Ph	0.02	0.15–0.2

can be up to 0.2 cm^2/Vs, which is the best performance of this material in ambient condition until now.

The great improvement in electron mobility of the epitaxial films is consistent with the morphology results. Comparing to the non epitaxial films, the epitaxial films with lager grain size are highly oriented and continuous, which is benefit to the carrier transport. In addition, the low density of grain boundary of the epitaxial films is responsible for the increased electron mobility. The thickness of *p*-6P increasing means the coverage of *p*-6P on substrate increase, via, the coverage of epitaxial films increase. Owing to the oriented, large size and continuous crystals of epitaxial films, the grain boundary decreased dramatically, led to high electron mobility and low threshold voltage. On the other hand, recent studies reveal that the Si–OH groups on the bare SiO_2 substrate are the efficient traps for electrons but not for holes [45]. These interface traps greatly affect the n-channel field-effect, thus the inserted *p*-6P layer maybe reduced the traps on the SiO_2 surface worked as a buffer layer [46–49]. However, compare to the performance of PTCDI-Ph grown on the substrate modified with OTS which shows a mobility of 0.017 cm^2/Vs in glove box (The OTS treatment was an efficient method to reduce the traps and improve the mobility) [22], the electron mobility of epitaxial films is also one order of magnitude higher. Hence, the improvement mainly attribute to the good film morphology, although the *p*-6P may be play a role in reducing the electron traps originating from the Si–OH groups on the bare SiO_2 substrate.

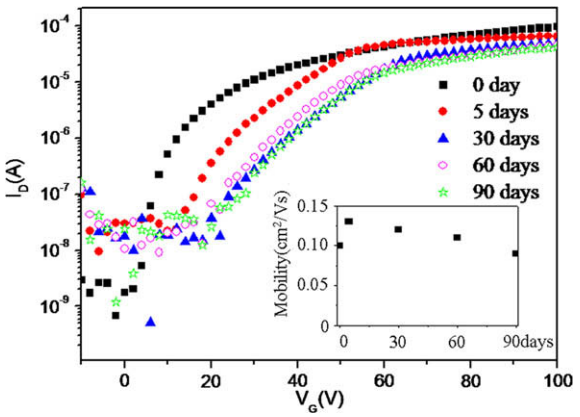

Fig. 5. Air-stability measurements of transistors based on PTCDI-Ph (20 nm)/*p*-6P (2 nm), V_{DS} = 100 V, the inset gives the mobility evolution as the function of time.

Performance evolution of the epitaxial film TFTs as the function of time exposing in ambient condition was carried out by tracking the transfer characteristics. In the first 5 days, the mobility slight increased from 0.1 cm^2/Vs to 0.13 cm^2/Vs, and then gradually decreased (Fig. 5). After exposing in ambient for 90 days, the mobility still retain as high as 0.09 cm^2/Vs, which is rarely for the n-type materials. The good stability of the mobility might attribute to the few grain boundaries and smooth interface in the epitaxial films, which effectively decrease the physical absorption of the environment gases. On the other hand, the inserted *p*-6P layer which might reduce the electron traps on the SiO_2 substrate is also responsible for the good stability. The threshold voltage shifts from 5 V to 18 V after exposure for 5 days, but remains at 20–30 V as exposing more time, and the current on/off ratio slightly decreases from 10^5 to 10^4.

4. Conclusions

In summary, we have obtained high mobility films of PTCDIs by heteroepitaxy growth using the Weak Epitaxy Growth technique. Through epitaxial grown on the *p*-6P ordered layer, the PTCDI-Ph films present highly crystalline, oriented and continuous morphology, and commensurate epitaxy relationship was found between PTCDI-Ph and *p*-6P. The high quality films, which possess low density of grain boundary and smooth surface, bring about improvement of two orders of magnitude in the mobility, simultaneously exhibit relative good stability in ambient condition. Hence, the organic–organic heteroepitaxy provide a new path to achieve high performance films of perylene diimides derivatives.

Acknowledgements

This work was supported by the National Natural Science Foundation of China (50773079 and 50803063) and The National Basic Research Program (2009CB939702).

References

[1] C.D. Dimitrakopoulos, P.R.L. Malenfant, Organic thin film transistors for large area electronics, Adv. Mater. 14 (2002) 99–117.
[2] C.W. Tang, Two-layer organic photovoltaic cell, Appl. Phys. Lett. 48 (1986) 183–185.
[3] C.W. Tang, S.A. VanSlyke, Organic electroluminescent diodes, Appl. Phys. Lett. 51 (1987) 913–915.
[4] W. Brütting, Physics of Organic Semiconductors, Wiley-VCH-Verlag GmbH & Co. KGaA, 2006.
[5] E. Frankevich, Y. Maruyama, H. Ogata, Mobility of charge-carriers in vapor-phase grown C-60 single-crystal, Chem. Phys. Lett. 214 (1993) 39–44.
[6] K. Hoshimono, S. Fujimori, S. Fujita, S. Fujita, Semiconductor-like carrier conduction and its field-effect mobility in metal-doped C-60 thin-films, Jpn. J. Appl. Phys. 32 (1993) L1070–L1073.
[7] K. Itaka, M. Yamashiro, J. Yamaguchi, M. Haemori, S. Yaginuma, Y. Matsumoto, M. Kondo, H. Koinuma, High-mobility C60 field-effect transistors fabricated on molecular-wetting controlled substrates, Adv. Mater. 18 (2006) 1713–1716.
[8] P.R.L. Malenfant, C.D. Dimitrakopoulos, J.D. Gelorme, L.L. Kosbar, T.O. Graham, A. Curioni, W. Andreoni, N-type organic thin-film transistor with high field-effect mobility based on a N,N′-dialkyl-34910-perylene tetracarboxylic diimide derivative, Appl. Phys. Lett. 80 (2002) 2517–2519.

[9] H.E. Katz, A.J. Lovinger, J. Johnson, C. Kloc, T. Siegrist, W. Li, Y.Y. Lin, A. Dodabalapur, A soluble and air-stable organic semiconductor with high electron mobility, Nature 404 (2000) 478–481.
[10] S. Tatemichi, M. Ichikawa, T. Koyama, Y. Taniguchi, High mobility n-type thin-film transistors based on *N*,*N*′-ditridecyl perylene diimide with thermal treatments, Appl. Phys. Lett. 89 (2006) 112108.
[11] Y. Hosoi, Y. Furukawa, High performance n-channel organic field-effect transistors based on *N*,*N*′-dioctyl-34910-perylene tetracarboxylic diimide, Mol. Cryst. Liq. Cryst. 462 (2007) 37–43.
[12] R.J. Chesterfield, J.C. McKeen, C.R. Newman, P.C. Ewbank, D.A. da Silva, J.L. Bredas, L.L. Miller, K.R. Mann, C.D. Frisbie, Organic thin film transistors based on N-alkyl perylene diimides: charge transport kinetics as a function of gate voltage and temperature, J. Phys. Chem. B 108 (2004) 19281–19292.
[13] M.M. Ling, P. Erk, M. Gomez, M. Koenemann, J. Locklin, Z.N. Bao, Air-stable n-channel organic semiconductors based on perylene diimide derivatives without strong electron withdrawing groups, Adv. Mater. 19 (2007) 1123–1127.
[14] A. Facchetti, M.H. Yoon, C.L. Stern, H.E. Katz, T.J. Marks, Building blocks for n-type organic electronics: regiochemically modulated inversion of majority carrier sign in perfluoroarene-modified polythiophene semiconductors, Angew. Chem. Int. Ed. 42 (2003) 3900–3903.
[15] A. Facchetti, M. Mushrush, H.E. Katz, T.J. Marks, n-Type building blocks for organic electronics: a homologous family of fluorocarbon-substituted thiophene oligomers with high carrier mobility, Adv. Mater. 15 (2003) 33–38.
[16] Y. Sakamoto, T. Suzuki, M. Kobayashi, Y. Gao, Y. Fukai, Y. Inoue, F. Sato, S. Tokito, Perfluoropentacene: high-performance pb n junctions and complementary circuits with pentacene, J. Am. Chem. Soc. 126 (2004) 8138–8140.
[17] Z.A. Bao, A.J. Lovinger, J. Brown, New air-stable n-channel organic thin film transistors, J. Am. Chem. Soc. 120 (1998) 207–208.
[18] D. Song, H.B. Wang, F. Zhu, J.L. Yang, H.K. Tian, Y.H. Geng, D.H. Yan, Phthalocyanato tin(IV) dichloride: an air-stable high-performance n-type organic semiconductor with a high field-effect electron mobility, Adv. Mater. 20 (2008) 2142–2144.
[19] D. Song, F. Zhu, B. Yu, L. Huang, Y. Geng, D. Yan, Tin (IV) phthalocyanine oxide: an air-stable semiconductor with high electron mobility, Appl. Phys. Lett. 92 (2008) 143303.
[20] K.Y. Law, Organic photoconductive materials: recent trends and developments, Chem. Rev. 93 (1993) 449–486.
[21] B.A. Jones, M.J. Ahrens, M.H. Yoon, A. Facchetti, T.J. Marks, M.R. Wasielewski, High-mobility air-stable n-type semiconductors with processing versatility: dicyanoperylene-34:910-bis-(dicarboximides), Angew. Chem. Int. Ed. 43 (2004) 6363–6366.
[22] H.Z. Chen, M.M. Ling, X. Mo, M.M. Shi, M. Wang, Z. Bao, Air stable n-channel organic semiconductors for thin film transistors based on fluorinated derivatives of perylene diimides, Chem. Mater. 19 (2007) 816–824.
[23] Y. Hosoi, D. Tsunami, I. Hisao, Y. Furukawa, Air-stable n-channel organic field-effect transistors based on *N*,*N*′-bis(4-trifluoromethylbenzyl)perylene-3,4,9,10-tetracarboxylic diimide, Chem. Phys. Lett. 436 (2007) 139–143.
[24] J.C. Huang, L.G. Yang, X. Mo, M.M. Shi, M. Wang, H.Z. Chen, Influence of fluorination position on aggregate structure and electron transport of perylene diimide derivatives, Acta Chim. Sinica 65 (2007) 1051–1056.
[25] B.A. Jones, A. Facchetti, M.R. Wasielewski, T.J. Marks, Tuning orbital energetics in arylene diimide semiconductors. Materials design for ambient stability of n-type charge transport, J. Am. Chem. Soc. 129 (2007) 15259–15278.
[26] R.T. Weitz, K. Amsharov, U. Zschieschang, E.B. Villas, D.K. Goswami, M. Burghard, H. Dosch, M. Jansen, K. Kern, H. Klauk, Organic n-channel transistors based on core-cyanated perylene carboxylic diimide derivatives, J. Am. Chem. Soc. 130 (2008) 4637–4645.
[27] R. Schmidt, J.H. Oh, Y.S. Sun, M. Deppisch, A.M. Krause, K. Radacki, H. Braunschweig, M. Konemann, P. Erk, Z.A. Bao, F. Wurthner, High-performance air-stable n-channel organic thin film transistors based on halogenated perylene bisimide semiconductors, J. Am. Chem. Soc. 131 (2009) 6215–6228.
[28] M. Petit, R. Hayakawa, Y. Wakayama, T. Chikyow, Early stage of growth of a perylene diimide derivative thin film growth on various Si(0 0 1) substrates, J. Phys. Chem. C 111 (2007) 12747–12751.
[29] B.A. Jones, A. Facchetti, M.R. Wasielewski, T.J. Marks, Effects of arylene diimide thin film growth conditions on n-channel OFET performance, Adv. Funct. Mater. 18 (2008) 1329–1339.
[30] G. Horowitz, F. Kouki, P. Spearman, D. Fichou, C. Nogues, X. Pan, F. Garnier, Evidence for n-type conduction in a perylene tetracarboxylic diimide derivative, Adv. Mater. 8 (1996) 242–244.
[31] C.W. Struijk, A.B. Sieval, J.E.J. Dakhorst, M. van Dijk, P. Kimkes, R.B.M. Koehorst, H. Donker, T.J. Schaafsma, S.J. Picken, A.M. van de Craats, J.M. Warman, H. Zuilhof, E.J.R. Sudholter, Liquid crystalline perylene diimides: architecture and charge carrier mobilities, J. Am. Chem. Soc. 122 (2000) 11057–11066.
[32] Y.G. Wen, Y.Q. Liu, C.A. Di, Y. Wang, X.N. Sun, Y.L. Guo, J. Zheng, W.P. Wu, S.H. Ye, G. Yu, Improvements in stability performance of *N*,*N*′-dialkyl perylene diimide-based n-type thin-film transistors, Adv. Mater. 21 (2009) 1631–1635.
[33] G. Koller, S. Berkebile, J.R. Krenn, F.P. Netzer, M. Oehzelt, T. Haber, R. Resel, M.G. Ramsey, Heteroepitaxy of organic b organic nanostructures, Nano Lett. 6 (2006) 1207–1212.
[34] M. Campione, L. Raimondo, A. Sassella, Heteroepitaxy of alpha-quaterthiophene on tetracene single crystals, J. Phys. Chem. C 111 (2007) 19009–19014.
[35] H.B. Wang, F. Zhu, J.L. Yang, Y.H. Geng, D.H. Yan, Weak epitaxy growth affording high-mobility thin films of disk-like organic semiconductors, Adv. Mater. 19 (2007) 2168–2171.
[36] J. Yang, D. Yan, Weak epitaxy growth of organic semiconductor thin films, Chem. Soc. Rev. 38 (2009) 2634–2645.
[37] M. Haemori, J. Yamaguchi, S. Yaginuma, K. Itaka, H. Koinuma, Fabrication of highly oriented rubrene thin films by the use of atomically finished substrate pentacene buffer layer, Jpn. J. Appl. Phys., Part: I 44 (2005) 3740–3742.
[38] F. Garnier, G. Horowitz, X.Z. Peng, D. Fichou, Structural basis for high carrier mobility in conjugated oligomers, Synthetic Met. 45 (1991) 163–171.
[39] Z.D. Popovic, R.O. Loutfy, A.-M. Hor, Photoconductivity studies of perylene tetracarboxyl-diimides, Can. J. Chem. 63 (1985) 134–139.
[40] J.L. Yang, T. Wang, H.B. Wang, F. Zhu, G. Li, D.H. Yan, Ultrathin-film growth of para-sexiphenyl (I): submonolayer thin-film growth as a function of the substrate temperature, J. Phys. Chem. B 112 (2008) 7816–7820.
[41] J.L. Yang, T. Wang, H.B. Wang, F. Zhu, G. Li, D.H. Yan, Ultrathin-film growth of para-sexiphenyl (II): formation of large-size domain and continuous thin film, J. Phys. Chem. B 112 (2008) 7821–7825.
[42] J.L. Yang, T. Wang, H.B. Wang, F. Zhu, G. Li, D.H. Yan, Weak epitaxy growth of metal-free phthalocyanine on p-sexiphenyl monolayer and double-layer films, J. Phys. Chem. B 112 (2008) 3132–3137.
[43] J.W. Shi, H.B. Wang, D. Song, H. Tian, Y.H. Geng, D.H. Yan, n-Channel ambipolar and p-channel organic heterojunction transistors fabricated with various film morphologies, Adv. Funct. Mater. 17 (2007) 397–400.
[44] Y. Gao, H. Ding, H. Wang, D. Yan, Electronic structure of interfaces between copper-hexadecafluoro-phthalocyanine 2,,5-bis(4-biphenylyl) bithiophene, Appl. Phys. Lett. 91 (2007). 142112-3.
[45] L.-L. Chua, J. Zaumseil, J.-F. Chang, E.C.-W. Ou, P.K.-H. Ho, H. Sirringhaus, R.H. Friend, General observation of n-type field-effect behaviors in organic semiconductors, Nature (London) 434 (2005) 194–199.
[46] T. Takahashi, T. Takenobu, J. Takeya, Y. Iwasa, Ambipolar organic field-effect transistors based on rubrene single crystals, Appl. Phys. Lett. 88 (2006). 033505-3.
[47] F.-C. Chen, C.-H. Liao, Improved air stability of n-channel organic thin-film transistors with surface modification on gate dielectrics, Appl. Phys. Lett. 93 (2008). 103310-3.
[48] S. Tanida, K. Noda, H. Kawabata, K. Matsushige, Ultrathin polymer gate buffer layer for air-stable, low-voltage, n-channel organic thin-film transistors, Polym. Adv. Technol. online, doi:10.1002/pat.1474.
[49] K.N.N. Unni, A.K. Pandey, J.M. Nunzi, N-channel organic field-effect transistors using *N*,*N*′-ditridecylperylene-3410-tetracarboxylic diimide and a polymeric dielectric, Chem. Phys. Lett. 407 (2005) 95–99.

Organic Electronics 11 (2010) 202–206

Contents lists available at ScienceDirect

Organic Electronics

journal homepage: www.elsevier.com/locate/orgel

High-contrast and high-efficiency microcavity top-emitting white organic light-emitting devices

Wenyu Ji [a,b], Letian Zhang [a], Zhang Tianyu [a], Wenfa Xie [a,*], Hanzhuang Zhang [b,*]

[a] State Key Laboratory on Integrated Optoelectronics, College of Electronic Science and Engineering, Jilin University, Changchun 130012, People's Republic of China
[b] Department of Physics, Jilin University, Changchun 130023, People's Republic of China

ARTICLE INFO

Article history:
Received 5 September 2009
Received in revised form 28 September 2009
Accepted 25 October 2009
Available online 29 October 2009

Keywords:
White OLED
Top-emitting
Microcavity
High-contrast

ABSTRACT

Microcavity top-emitting white organic light-emitting devices (TEWOLEDs) with M/(Alq_3/Ag)$_2$ anode (M = Ag, Au or Al, Alq_3 is tris (8-hydroxyquinoline) aluminum) were investigated. All devices show white emission and the optical properties of the anode play an important effect on the efficiency and contrast of the devices. The maximum efficiencies of the top-emitting devices are comparable to the corresponding bottom one and the contrasts of top-emitting devices are much higher than that of the bottom one. The results indicated that such TEWOLEDs are compatible with complementary metal oxide semiconductor or organic thin film transistor techniques which using Au or Al as electrode.

© 2009 Elsevier B.V. All rights reserved.

1. Introduction

Top-emitting organic light-emitting devices have attracted intense attention because of its enormous potential in flat-panel displays, especially for microdisplays on opaque silicon substrate. Top-emitting white organic light-emitting device (TEWOLED) combined with color filter and driving circuit [such as organic thin film transistor (OTFT) or complementary metal oxide semiconductor (CMOS)] is the most effective method to obtain high-resolution displays. In addition, TEWOLEDs will be superior to bottom one because they can fabricate on opaque and flexible substrates such as metal foils, which is cheaper than ITO. However, it remains a challenge to generate white light in TEOLEDs because of the strong microcavity effects in the devices and there are a few reports on TEWOLEDs [1–6]. In our previous work [7], the TEWOLED with one-dimensional metallic-dielectric photonic crystal (MDPC) comprised of Ag/Alq_3 (Alq_3 = tris (8-hydroxyquinoline) aluminum) as anode are investigated. A two-peak or three-peak TEWOLED could be achieved by adjusting the thickness of the Alq_3 layers in the MDPC.

Ag is used as the anode in TEOLEDs due to its lower absorption loss in the visible range and highest conductivity among electrode materials, while Au or Al was used as electrode in OTFT [8–10] or CMOS [11–13], usually. Thus, TEWOLED with appropriate electrode will simplify the fabrication process of the integrated device. In this letter, we report the TEWOLEDs based on microcavity effect with M/(Alq_3/Ag)$_2$ anode (M = Ag, Al, or Au). The effect of the different M on the performance of the device is discussed. The result indicated such TEWOLED is compatible with CMOS or OTFT techniques.

2. Experimental

The top-emitting devices with a structure of silica coated silicon substrate/M (150 nm)/Alq_3 (75 nm)/Ag (20 nm)/Alq_3 (45 nm)/Ag (20 nm)/MoO_x (1.5 nm)/4,4′,4″-*tris*(3-methylphenyl-phenylamino)-tripheny-lamine (m-MTDATA, 28 nm)/*N*,*N*′-bis-(1-naphthyl)-*N*,*N*′-diphenyl-

* Corresponding authors.
E-mail addresses: xiewf@jlu.edu.cn (W. Xie), zhanghz@mail.jlu.edu.cn (H. Zhang).

1566-1199/$ - see front matter © 2009 Elsevier B.V. All rights reserved.
doi:10.1016/j.orgel.2009.10.016

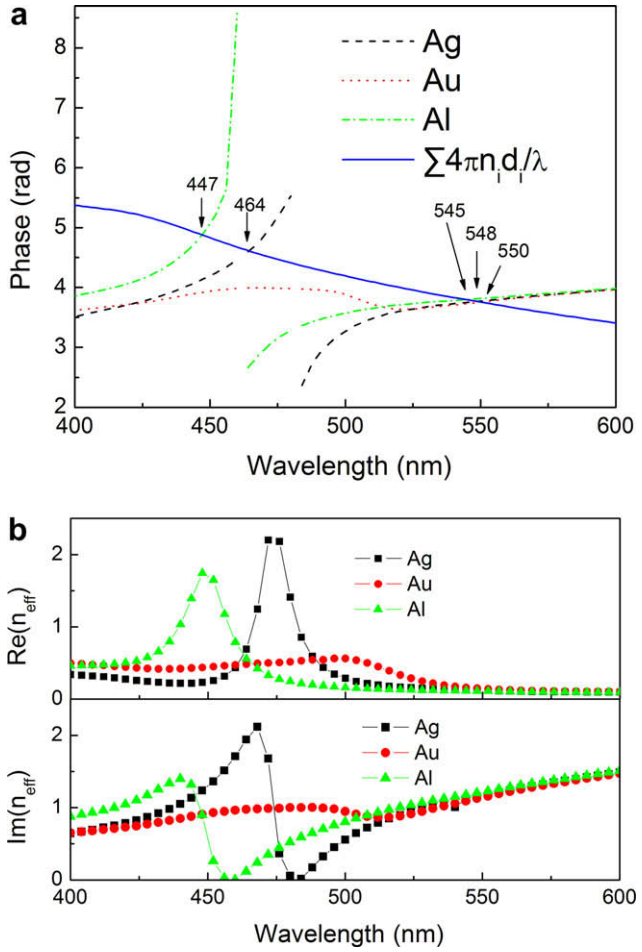

Fig.1. (a) The calculated round-trip phase changes for 95 nm organic layers between two electrodes and the phase changes on two electrodes for normal incidence; and (b) the calculated effective refractive index of three anodes.

1,1-biphenyl-4,4'-diamine (NPB, 10 nm)/4,4′-bis(2,2′-diphenylvinyl)-1,1′-biphenyl (DPVBi, 15 nm)/4,4-*N*,*N*-dicarbazole-biphenyl (CBP, 3 nm)/CBP:bis(2-(2-fluorphenyl)-1,3-benzothiozolato-N,C2′) iridium(acetylacetonate) [(F–BT)$_2$Ir(acac)] (7 nm)/4,7-diphenyl-1,10-phenanthroline (Bphen,30 nm)/LiF (1 nm)/Al (1 nm)/Ag (20 nm)/MoO_x (35 nm) were fabricated. 1.5 nm MoO_x, m-MTDATA, NPB, DPVBi, CBP:(F-BT)$_2$Ir(acac), Bphen, LiF/Al/Ag and 35 nm MoO_x were used as buffer layer, hole injection layer, hole transporting layer, blue emitting layer, orange emitting layer, electron transporting layer, cathode and light out-coupling layer, respectively. M = Ag, Au, or Al for devices A, B, or C, respectively. For comparison, the bottom-emitting device (ITO glass substrate) with the same organic layers (device D) was fabricated. All films were deposited at pressure below 4×10^{-6} Torr. Detailed processes of fabrication and measurement for OLEDs have been described in previous paper [5].

3. Results and discussion

The resonant wavelength (RW) conditions of the microcavity for normal incidence is determined by the Fabry–Perot peak condition [14]. Fig. 1a shows the calculated round-trip phase changes for 95 nm organic layers sandwiched between two reflection electrodes (i.e., $\varphi_1(0,\lambda) = \sum_i \frac{4\pi d_i n_i(\lambda)}{\lambda}$, where λ is the emission wavelength, $n_i(\lambda)$ and d_i are the refractive index and thickness of organic layers), and the phase changes at two reflective electrodes (i.e., $\varphi_2(0,\lambda) = \varphi_{\text{cathode}}(0,\lambda) + \varphi_{\text{anode}}(0,\lambda)$, $\varphi_{\text{cathode}}(0,\lambda)$ and $\varphi_{\text{anode}}(0,\lambda)$ are the angle- and the wavelength-dependent phase changes on reflection from top cathode and bottom anode, respectively; incidence medium is Bphen and m-MTDATA for cathode and anode, respectively). The points of the intersection of $\varphi_1(0,\lambda)$ and $\varphi_2(0,\lambda)$ are the RWs of the devices. As can be seen, the RWs were different for M = Ag (464 and 548 nm), Al (447 and 545 nm), and Au (550 nm). Two resonant emission peaks were achieved in the devices with M = Ag and Al. But only one intersection was observed for M = Au anode. To explain this phenomenon, we calculated the effective refractive index of the anodes with the transfer matrix theory [15]. The results are shown in Fig. 1b. The phase change on reflection is relative to the refractive index of the incidence and reflectance medium. For the anode with M = Au, the real part and imaginary part of n_{eff} is flat rela-

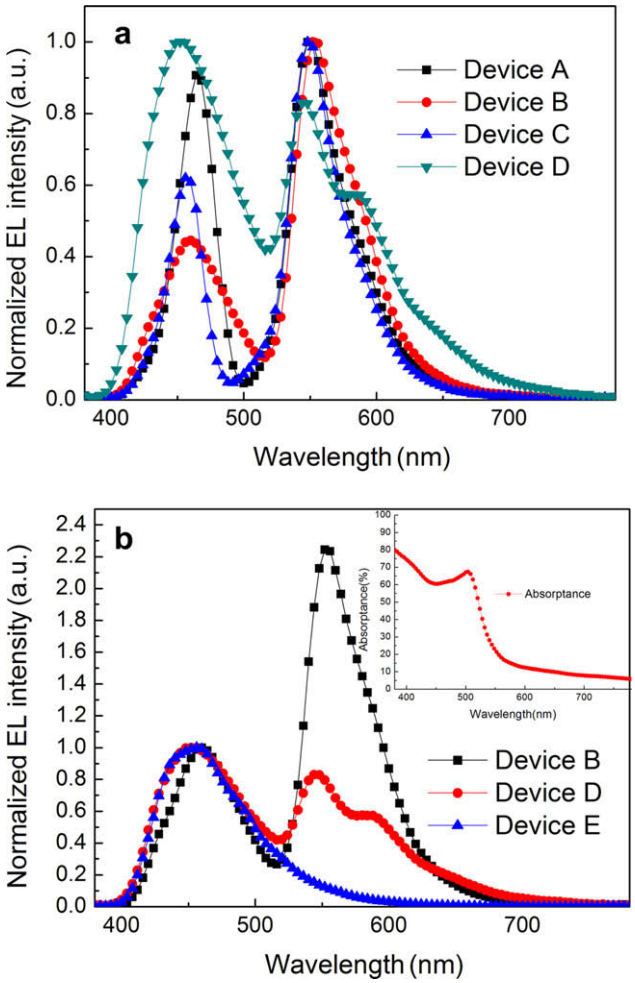

Fig. 2. (a) The normalized measured EL spectra of devices A, B, C and D at voltage of 8 V, and (b) the normalized measured EL spectra of devices B, D, and E at voltage of 8 V. Insert is the absorption for anode with M = Au.

tive to that of other two anodes. As a result, the reflection phase changes were also flat for anode with M = Au. So one intersection was obtained for device with M = Au, and two intersections for the other two.

Fig. 2a shows the normalized measured EL spectra at voltage of 8 V and viewing angle of 0° for devices A, B, C, and D. The spectrum of the device D shows two main peaks at 452 and 544 nm originating from DPVBi and $(F\text{-}BT)_2Ir(acac)$. As can be seen, the spectrum of the devices show two emission peaks, 464 and 548 nm, 460 and 552 nm, 456 and 548 nm for devices A, B, and C, respectively. The emission peaks of all the devices are in excellent agreement with calculated results. The narrowness of the full width at half maximum (FWHM) of the DPVBi and $(F\text{-}BT)_2Ir(acac)$ emission in devices A and C is observed. These results indicated that microcavity effect, which will produce a narrowing of the emission spectra of the device [16], was occurred in device A and C.

The distinct narrowness of the FWHM is only observed for $(F\text{-}BT)_2Ir(acac)$ emission in device B. We presumed that the microcavity effect was almost eliminated for blue emission in this device. To further prove this, we built the bottom-emitting device (ITO glass substrate, device E) with the same organic layers except using 10 nm DPVBi replacing CBP (3 nm) and CBP: $(F\text{–}BT)_2Ir(acac)$ (7 nm) layers. Fig. 2b shows the normalized measured EL spectra at voltage of 8 V for devices B, D, and E. We can see that the blue emission for device D is the same as that for device E. This implied that the blue emission of device D originating from DPVBi. Similarly, device B showed almost the same blue emission as device E except slight red shifts at short wavelength. Insert is the absorption for anode with M = Au. As can be seen, for the wavelength less than 450 nm the absorption is higher. We attribute the red shifts to the absorption of the anode. And the low reflection of this anode at short wavelength zone as shown in Fig. 3 almost eliminates the microcavity effects for the blue emission.

Fig. 4a–c shows the normalized measured EL spectra at voltage of 6 V and viewing angle of 0°, 30°, and 60° for devices A, B, and C, respectively. Obvious change of the blue emission is observed in devices A and C. However, it is inconspicuous for device B. This is also a proof that the microcavity effect is almost eliminated for the blue emis-

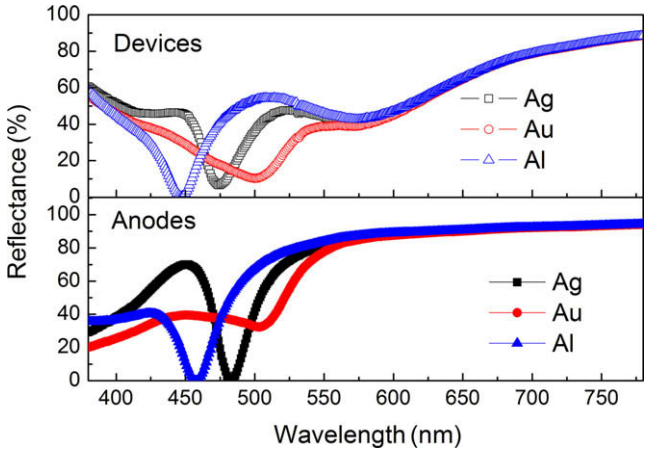

Fig. 3. The reflectance of the devices (top) and anodes (bottom).

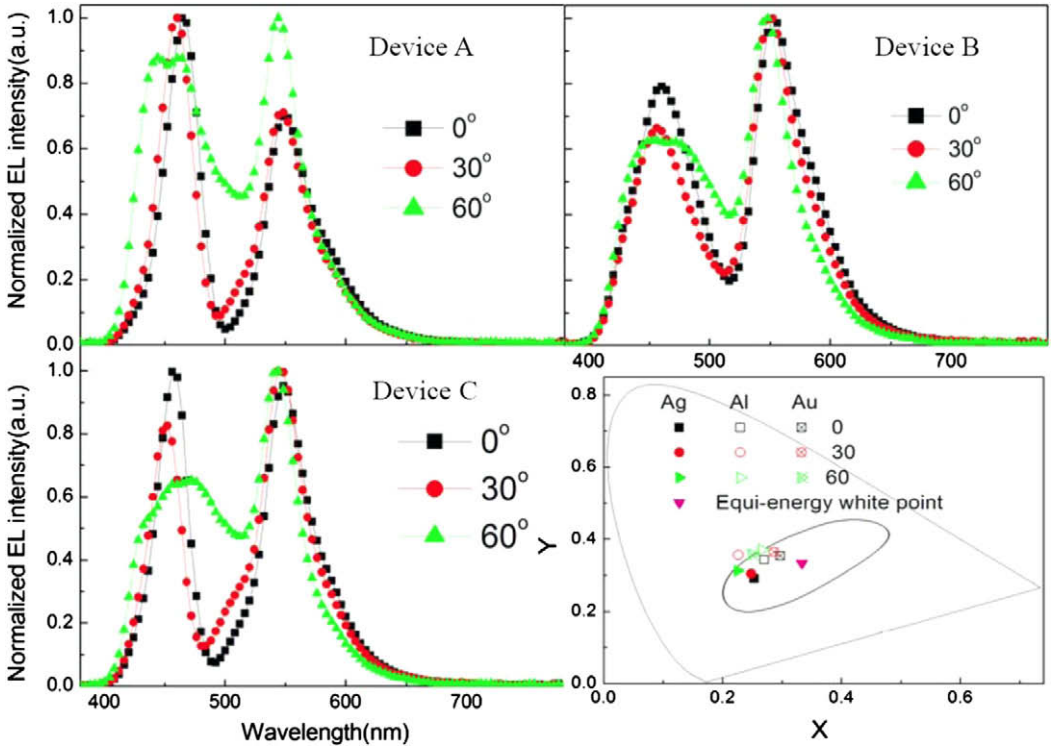

Fig. 4. The normalized EL spectra of the white TEOLED at viewing angle of 0°, 30°, and 60° for devices A, B, and C and the CIE coordinate of devices at different viewing angles.

sion in device B. Fig. 4d is the CIE coordinates of devices at viewing angle of 0°, 30°, and 60° (at a driving voltage of 6 V). We can see that a warm white emission at viewing angle of 0°, 30°, and 60° was obtained.

Fig. 5 shows the voltage–current density–luminance characteristics of the devices A, B, and C. The luminance of the devices A, B and C is 7565, 8335, and 8936 cd/m^2 at 11 V, respectively. Insert is the efficiencies versus voltage characteristics of the devices. The maximum current efficiency of the devices are 8.2, 7.7, 8.4, and 7.3 cd/A for devices A, B, C, and D, respectively. The high efficiency of top-emitting device can attributed to the microcavity effect in the devices.

The pixel contrast ratio (PCR) of devices is investigated as depicted in Refs. [17,18]. The light source D65 is utilized for calculation. In the calculation, the brightness of the devices at on- and off-state is set to be 1000 and 0 cd/m^2. The PCR of devices A, B, and C is 52:1, 63:1, and 48:1 under an ambient illumination of 140 lx, corresponding to an enhancement of 86%, 104% and 79% over that of device D.

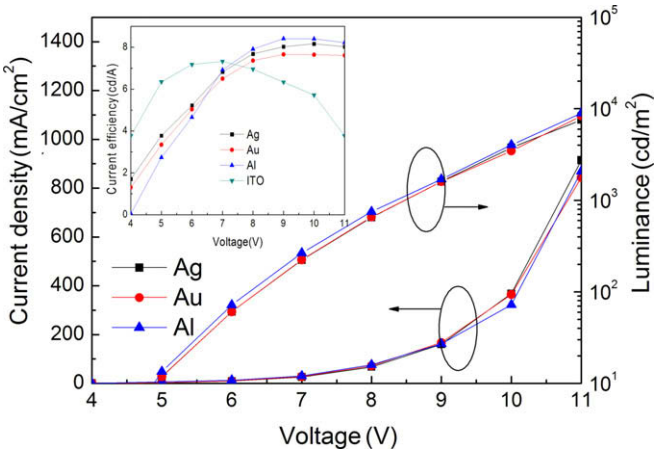

Fig. 5. The voltage–current density–luminance characteristics of the devices. Insert the efficiency–voltage characteristics of the white devices.

The obvious improvement of PCR in devices A, B, and C originates from the reduction of reflectance in the whole visible region and the anode plays an important role in the absorption of ambient light, especially for the device with M = Au (Fig. 3).

4. Conclusion

In summary, the top-emitting white organic light-emitting devices with a M/(Alq_3/Ag)$_2$ (M = Ag, Au, or Al) anode are demonstrated. The device with M = Al shows the highest efficiency and device with M = Au gives the highest contrast. The results indicated M/(Alq_3/Ag)$_2$ is an effective anode for top-emitting white OLED and is compatible with CMOS or OTFT techniques.

Acknowledgments

This work was supported by the National Natural Science Foundation of China (Grant Nos. 60937001, 60606017, 60707016, 60723002, 10774060), the Ministry of Science and Technology of China (Grant No. 2010CB327701), and Graduate Innovation Fund of Jilin University (Grant No. 20091007).

References

[1] H. Kanno, Y.R. Sun, S.R. Forrest, Appl. Phys. Lett. 86 (2005) 263502.
[2] S.F. Hsu, C.C. Lee, S.W. Hwang, C.H. Chen, Appl. Phys. Lett. 86 (2005) 253508.
[3] M.T. Lee, M.R. Tseng, Curr. Appl. Phys. 8 (2008) 616.
[4] M.S. Kim, C.H. Jeong, J.T. Lim, G.Y. Yeom, Thin Solid Films 11 (2008) 3590.
[5] W.Y. Ji, L.T. Zhang, R.X. Gao, L.M. Zhang, W.F. Xie, H.Z. Zhang, B. Li, Opt. Express 16 (2008) 15489.
[6] M. Thomschke, R. Nitsche, M. Furno, K. Leo, Appl. Phys. Lett. 94 (2009) 083303.
[7] W.Y. Ji, L.T. Zhang, T.Y. Zhang, G.Q. Liu, W.F. Xie, S.Y. Liu, H.Z. Zhang, L.Y. Zhang, B. Li, Opt. Lett. 34 (2009) 2703.
[8] N.T. Salim, K.C. Aw, W. Gao, Z.W. Li, B. Wright, Microelectron. Eng. 86 (2009) 2127.
[9] C.H. Li, F. Pan, F. Zhu, D. Song, H. Wang, D.H. Yan, Semicond. Sci. Technol. 24 (2009) 085009.
[10] D.J. Yun, S.H. Lim, T.W. Lee, S.W. Rhee, Org. Electron. 10 (2009) 970.
[11] M. Fischer, M. Nägele, D. Eichner, C. Schöllhorn, R. Strobel, Sens. Actuators, A: Phys. 52 (1996) 140.
[12] K.A. Honer, G.T.A. Kovacs, Sens Actuators, A: Phys. 91 (2001) 386.
[13] L.S. Pakula, H. Yang, H.T.M. Pham, P.J. French, P.M. Sarro, J. Micromech. Microeng. 14 (2004) 1478.
[14] A.B. Djurišić, A.D. Rakic, Appl. Opt. 41 (2002) 7650.
[15] C.L. Mitsas, D.I. Siapkas, Appl. Opt. 34 (1995) 1678.
[16] A. Dodabalapur, L.J. Rothberg, R.H. Jordan, T.M. Miller, R.E. Slusher, J.M. Phillips, J. Appl. Phys. 80 (1996) 6954.
[17] J.A. Dobrowolski, B.T. Sullivan, R.C. Bajcar, Appl. Opt. 31 (1992) 5988.
[18] Z.Y. Xie, L.S. Hung, Appl. Phys. Lett. 84 (2004) 1207.

Organic Electronics 11 (2010) 207–211

Contents lists available at ScienceDirect

Organic Electronics

journal homepage: www.elsevier.com/locate/orgel

The role of the dielectric interface in organic transistors: A combined device and photoemission study

Philipp Stadler [a,*], Anna M. Track [b], Mujeeb Ullah [c], Helmut Sitter [c], Gebhard J. Matt [c], Georg Koller [b], Thokchom B. Singh [a], Helmut Neugebauer [a], N. Serdar Sariciftci [a], Michael G. Ramsey [b]

[a] Linz Institute for Organic Solar Cells (LIOS) and Institute for Physical Chemistry, Johannes Kepler University Linz, Altenbergerstr. 69, 4040 Linz, Austria
[b] Institute for Physics, University of Graz, Universitätsplatz 3, 8010 Graz, Austria
[c] Institute of Semiconductor and Solid State Physics, Johannes Kepler University Linz, Altenbergerstr. 69, 4040 Linz, Austria

ARTICLE INFO

Article history:
Received 17 August 2009
Received in revised form 19 October 2009
Accepted 23 October 2009
Available online 29 October 2009

Keywords:
Organic field effect transistor
Ultra-violet photoemission spectroscopy
Interface dipole
Energy level alignment
Threshold voltage shift

ABSTRACT

Here the device performance is shown to be directly related to the measured electronic level alignment at the dielectric interface in C_{60} organic field effect transistors (OFETs). We compare C_{60} on two dielectrics: Al_2O_3 and a divinyltetramethyldisiloxane-bis(benzocyclobutene) (BCB)–Al_2O_3 bilayer. The improved transistor performance and the lowering of the threshold voltage by 0.8 V due to the BCB interlayer are reflected in the ultra-violet photoemission data. These show a 0.8 eV difference in the work function and a concomitant shift in the C_{60} valence band. By following the work function the improvement is shown to be due to the dipole at the organic BCB–C_{60} interface.

© 2009 Elsevier B.V. All rights reserved.

1. Introduction

Interface engineering in organic field effect transistors (OFETs) has become the key issue in designing devices with acceptable electrical transport properties. The crucial part is to design the interface between the dielectric and the organic semiconductor [1]. It has been demonstrated that by introducing a polymeric layer on an oxidic dielectric surface the overall device performance can be enhanced. Recent publications demonstrate well performing transistors with passivation layers of various thin polymeric insulators as well as transistors with self assembled molecules (SAMs) grown on silicon dioxide and Al_2O_3 [2–6]. Factors ranging from film morphology through to issues of electronic level alignment could all be playing a role. While device activity has concentrated on modifying the inorganic dielectric surface with SAMs or polymer dielectrics, little work has considered the possibility of charge rearrangements at the interface of such modifiers with the organic semiconductor. Recently theoretical modelling has suggested that improvements in transfer characteristics and rigid shifts of the threshold voltage can result from the introduction of permanent space charge or dipole layers at the organic semiconductor/dielectric interface [7]. In particular the introduction of a BCB divinyltetramethyldisiloxane-bis(benzocyclobutene) interlayer between the inorganic dielectric (Al_2O_3, SiO_2) and the organic semiconductor has been reported to yield low operating voltages and high mobilities [2–4]. Apart from suggestions of it acting as a passivation layer removing hydroxyl groups from the semiconductor dielectric interface little is known of the function of BCB interlayers. Till now very few combined studies of device characteristic and photoemission investigations of the energy level alignment of device structures can be found in literature [8]. Moreover, to our knowledge there have been no such studies where a

* Corresponding author. Tel.: +43 732 2468 8854; fax: +43 732 2468 8770.
E-mail address: Philipp.Stadler@jku.at (P. Stadler).

1566-1199/$ - see front matter © 2009 Elsevier B.V. All rights reserved.
doi:10.1016/j.orgel.2009.10.017

comparison of device structures with and without interlayer has been made.

In this work transistors using C_{60} and a bilayer of BCB–Al_2O_3, which has been reported to have low operation voltage (~1 V) and high mobilities (<3 $cm^2 V^{-1} s^{-1}$) [2,3], were used to explore the role in the improved performance due to the BCB interlayer. Here a systematic study of two insulator-C_{60} structures, with and without BCB, is made. We compare the performance of the field effect transistors and show that the improvement of the OFET with BCB can be directly related to the differences in energy level alignment as measured by ultra-violet photoemission spectroscopy (UPS). Moreover, from studies of each interface the improvement in device performance arising from the polymeric interlayer is shown to be generated by an in-built potential at the BCB-interlayer/organic semiconductor interface.

2. Experimental section

Here we use the same OFET system as Zhang et al. [3] and we systematically compare the interface of C_{60} and BCB–Al_2O_3 to the interface of C_{60} and Al_2O_3 alone to understand its role in the improved performance. To allow meaningful comparison we fabricated two bottom-gate/top contact transistors, such that both the Al_2O_3 alone and the bilayer Al_2O_3–BCB exhibit the same geometric capacitance, as depicted in Fig. 1. Additionally using 55 nF cm^{-2} dielectric layers provide transistors operating at gate voltages in the range of 1 V and a mobility of 1 $cm^2 V^{-1} s^{-1}$. To combine the transistor with the photoemission spectroscopy the same MIS structures are studied by UPS with the samples prepared in a controlled way using the same batch at once and a blind sample as a reference for the surface characterization.

2.1. OFET fabrication and characterization

BCB precursor solution and C_{60} was purchased from Aldrich and Merck respectively. The C_{60} was purified in a further re-sublimation process before evaporation. 200 nm of Al are deposited on a glass substrate at a rate of 10 Å s^{-1}. For the Al_2O_3 gate insulator a 145 nm and an 85 nm film respectively is electrochemically grown on the Al following the instructions from Majevski et al. [9] and Schröder et al. [10]. The generated oxide was then rinsed and treated with distilled water at 80 °C in the ultra sonic bath and finally dried at 200 °C. For the polymer layer a 1 wt% BCB precursor solution in mesitylene was spun onto the 85 nm thick aluminium oxide film at 1500 rpm and afterwards annealed at 150 °C for cross linking. By controlling the Al_2O_3 thickness we obtained two systems (Al_2O_3 layer and Al_2O_3–BCB bilayer) with similar surface roughness of 1.5 nm RMS and with the same measured geometric capacitance C_p of 55 nF cm^{-2}. The thicknesses were measured by capacitance measurements (Al–Al_2O_3–Al) and checked by cross section scanning electron microscopy. For the semiconductor a 300 nm C_{60} film was deposited in high vacuum using hot wall epitaxy technique at a substrate temperature of 140 °C and a growth rate of 0.5 Å s^{-1} [11]. The morphologies, as determined by AFM of the C_{60} films on the two substrates are found to be similar. For the source-drain contacts LiF/aluminium (0.6 and 50 nm) [12] was evaporated using a 70 μm shadow mask for the channel and a channel width W of 2 mm. The OFETs were characterized using Agilent E5273A 2-channel-source unit.

2.2. UPS measurements at dielectric-semiconductor interface

For the UV photoemission spectroscopy metal–insulator–semiconductor structures were prepared in the following way: A 5 nm thin layer of aluminium oxide was electrochemically grown on aluminium and treated afterwards as mentioned in Section 2.1. For the BCB surface, the 1% precursor solution was directly spun onto oxidized aluminium and cured at 200 °C as for the transistor. In a further step the C_{60} was deposited by thermal evaporation at a rate of 1 A s^{-1} at a substrate temperature of 78 K in order to guarantee homogenous covering. The thickness of the C_{60} is 2 nm (3–4 molecule layers) as determined by a quartz microbalance calibrated for C_{60}. The samples were then characterized by HeI (21.2 eV) UPS in ultra high vac-

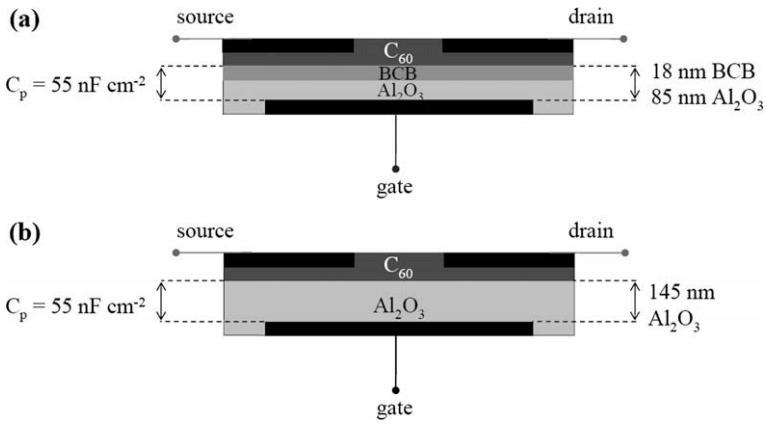

Fig. 1. Schematic of the OFET structures studied with (a) and without (b) a BCB layer on Al_2O_3. Both structures exhibit the same geometric capacitance of 55 nF cm^{-2}.

uum using a Specs PHIOBOS hemispherical energy analyser. The valence band spectra were recorded in both normal and 45° off normal emission angles and the work functions were determined from the secondary electron cut off in normal emission with a bias of 10 V. For all films XPS spectra were taken and no significant contamination was observed.

3. Results and discussion

3.1. OFET characterization

The device characteristic with and without BCB are compared in Fig. 2a and b which show the output characteristics and the transfer characteristics taken in the linear regime ($U_{gate} > U_{drain}$), respectively. Data presented here are recorded when the gate voltage U_{gate} as well as the drain voltage U_{drain} are applied in ascending and descending mode with 1 s integration time per step. Both figures reflect the same trend, however, the transistor with the BCB interlayer performs significantly better in all respects. It has a higher source-drain current I_{ds}, a higher depletion and accumulation amplitude, a sharper onset, a higher on/off ratio and a lower hysteresis. The observed hysteresis in the transfer curve is reduced for the BCB–C_{60} and the charge charier mobility μ in the range of 1 $cm^2 V^{-1} s^{-1}$ is in good agreement to earlier results of C_{60} on BCB [2,13,14].

The most striking difference of the two systems is the tremendous change in the threshold voltage U_{th}: To extract the exact threshold value in the linear regime, the transconductance change or second derivative (SD) method is selected [15]. The method estimates U_{th} as the gate voltage at which the derivative of the transconductance (dI/dU_{gate}) is maximum [16]. It works around the problem of series resistances and is shown to give reliable values for organic (*n*-channel) systems [17]. In Fig. 3a, the second derivative of the transfer characteristics d^2I/dU^2_{gate} is presented showing two maxima. The device with BCB shows a distinct and sharp peak, whereas for the device without BCB the peak is rather broad and ill-defined.

The peak maximum corresponds to the threshold voltage U_{th} of the transistor system which shifted from +725 mV in the Al_2O_3–C_{60} interface system to −75 mV in the BCB–C_{60} interface system. The device with the BCB interlayer has a 0.8 V lower U_{th}.

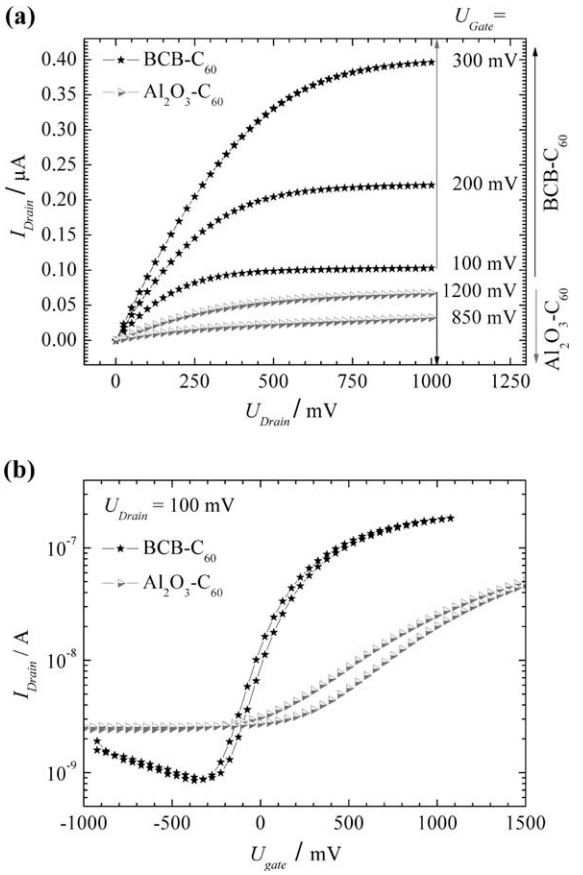

Fig. 2. Output characteristics (a) and transfer characteristics (b) in the linear regime ($U_{drain} < U_{gate} - U_{th}$) of both OFETs with (dark) and without (light) BCB layer on Al_2O_3.

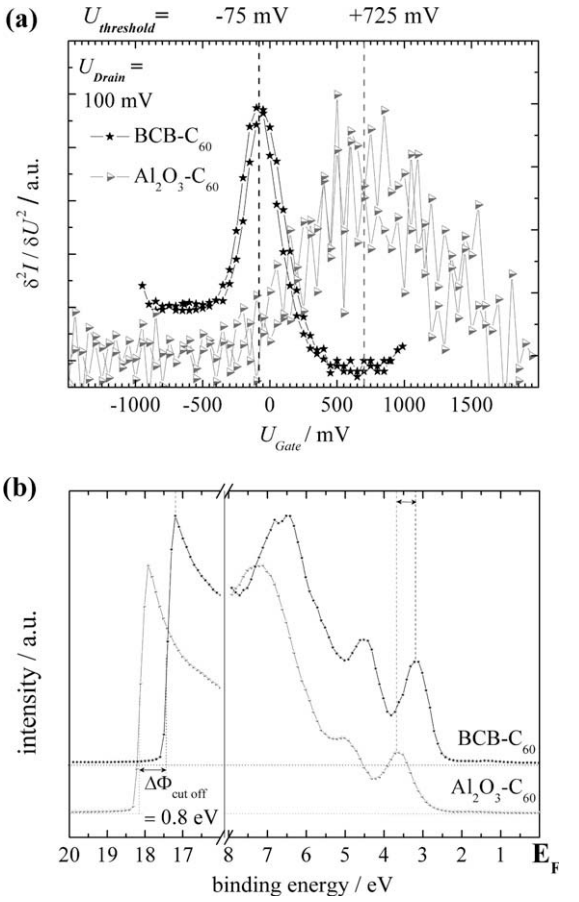

Fig. 3. (a) Shift of threshold voltage ΔU_{th} as seen in the second derivative of the transfer characteristics in OFETs with (dark) and without (light) BCB layer. (b) The UV photoemission spectrum of C_{60} on Al_2O_3 (light) and on BCB (dark) referenced to the Fermi energy. The shift in the HOMO and in the secondary electron cut-off $\Delta\Phi$ is indicated.

3.2. Photoemission studies

Photoemission measurements of ex situ prepared films on dielectric substrates are particularly challenging as contamination and charging effects can be misleading and care has to be taken. In Fig. 3b the UPS spectra of $Al/Al_2O_3/BCB/C_{60}$ and $Al/Al_2O_3/C_{60}$ thin film structures are shown referenced to the Fermi energy obtained from a metal substrate. In both cases the valence band fingerprint of the uppermost C_{60} layer is well defined with a quality approaching that of in situ UHV prepared C_{60} films [18]. This, combined with the fact that the ionisation potential of C_{60} in both cases are in agreement with literature values [18], shows that contamination and charging effects are minor.

The comparison of Fig. 3a and b illustrates the link between the device thresholds U_{th} and the electronic level alignment observed in the UPS spectra with BCB and without BCB. Clearly, introducing the BCB interlayer leads to a rigid shift of the entire photo emission spectrum to lower binding energy relative to the Fermi level. The shift of the HOMO-peak is measured to be 0.6 eV whereas the shift in the secondary cut-off, the change in the work function, is 0.8 eV. Thus the change in the measured C_{60} electronic level alignment induced by the BCB layer is the same as the lowered threshold voltage measured in the device with BCB.

To determine where and why the BCB has lowered the threshold voltage UPS spectra were measured at each layer in the device. This is summarized in Fig. 4 where the energy relations of the studied metal–insulator–semiconductor (MIS) systems for all interfaces with the work function measured for each layer are indicated. For the pure inorganic dielectric device without BCB (Fig. 4a) we measured a large work function drop to 2.7 eV on oxidation of the aluminium surface followed by a very small increase of the work function to 2.9 eV when the C_{60} film is grown on the oxide. Similar changes have been observed in in situ model studies [19,20]. In contrast, what is seen in Fig. 4b, is that on applying BCB to the Al_2O_3 surface the work function drops further to 2 eV. Then when C_{60} is grown on the BCB surface there is a large increase of the work function to 3.7 eV. At both BCB interfaces (Al_2O_3 and C_{60}) significant dipoles are formed and clearly BCB cannot be considered simply a passive spacer layer. The large work function increase at the BCB–C_{60} interface is the prime determinant of the improved device performance.

The result suggests that a significant interface dipole is formed at the BCB–C_{60} interface. This is surprising as generally organic–organic interfaces display vacuum level alignment with no significant interface dipoles. However in recent model studies [21] significant interface dipoles at organic–organic interfaces have been observed and were attributed to integer charge transfer (ICT) that is the formation of polaronic charge transfer states. Indeed the observed work function increase for C_{60} on P3HT has been attributed to this effect [21].

The C_{60} level alignments on the two gate dielectrics measured in the UPS are consistent with the two threshold voltages measured for the OFETs. Gate voltages of −0.075 V (BCB–C_{60}) and +0.725 V (Al_2O_3–C_{60}), would shift the HOMO level in both cases to around 2.8 eV below the Fermi level of the source. As C_{60} is a *n*-type semiconductor it is the LUMO relative to the Fermi energy of the source that is critical. Given a C_{60} affinity level of ~2.5 eV above the HOMO [21,22] one sees that the device threshold is obtained when the electron affinity is positioned slightly below the Fermi level of the source.

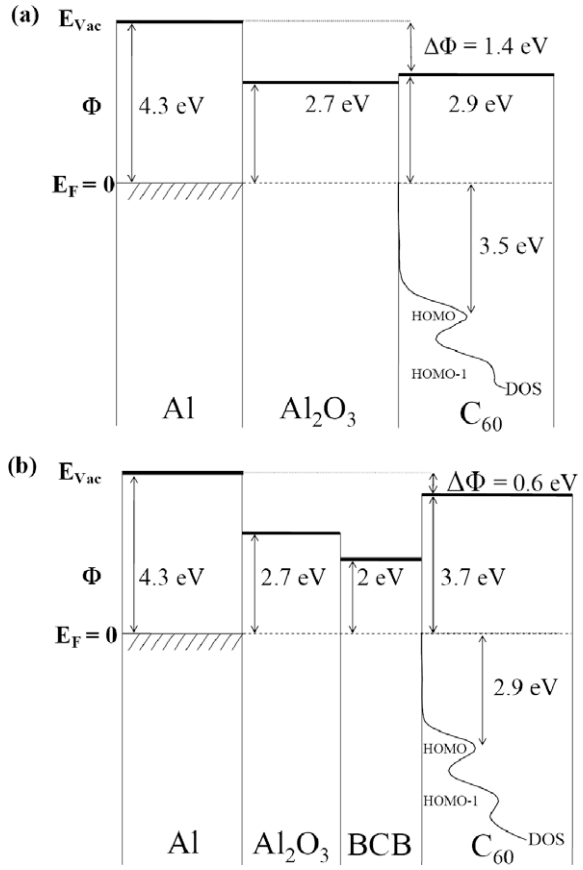

Fig. 4. Measured energy level diagrams of the two metal–insulator–semiconductor (MIS) structures studied without (a) and with (b) BCB between C_{60} and Al_2O_3. The Fermi level is the reference level and the work function at each layer are indicated. Note the large work function change at the BCB–C_{60} interface (b) and that the difference in the final work function between the two structures is 0.8 eV.

4. Conclusion

To conclude we studied two different interfaces between an organic semiconductor (C_{60}) and oxide (Al_2O_3) and an organic polymer (BCB) respectively. At the BCB interlayer dipoles are formed, which lower the threshold voltage and improve the transistor performance. The 0.8 V difference in the threshold voltage of the two device structures has been shown to be directly related to the 0.8 eV work function differences and is consistent with the band offset of C_{60} in each device. Photoemission investigations at all interfaces clearly indicate that the dipole formed at the BCB–C_{60} interface is the prime determinant for the improved device threshold. The magnitude and mechanism of this shift suggests detailed studies into tailoring

organic–organic interfaces on the gate dielectric could be very promising for optimizing device performance.

Acknowledgments

Work at Johannes Kepler University Linz and University of Graz was performed within the Nationales Forschungs Netzwerk (NFN) "Interface controlled and functionalised organic thin films" from the Austrian Foundation for Advancement of Scientific Research (FWF P15629).

References

[1] M. Mottaghia, G. Horowitz, Org. Electron. 7 (2006) 528–536.
[2] X.-H. Zhang, B. Kippelen, Appl. Phys. Lett. 93 (2008) 133305.
[3] X.-H. Zhang, B. Domercq, B. Kippelen, Appl. Phys. Lett. 91 (2007) 092114.
[4] L.-L. Chua, J. Zaumseil, J.-F. Chang, E.C.-W. Ou, P.K.-H. Ho, H. Sirringhaus, R.H. Friend, Nature 434 (2005) 195.
[5] C. Celle, C. Suspène, J.-P. Simonato, S. Lenfant, M. Ternisien, D. Vuillaume, Org. Electron. 10 (2009) 119–126.
[6] H. Klauk, U. Zschieschang, M. Halik, J. Appl. Phys. 102 (2007) 074514.
[7] S. Possanner, K. Zojer, P. Pacher, E. Zojer, F. Schürrer, Adv. Funct. Mater. 19 (2009) 958–967.
[8] Yunseok Jang, Jeong Ho Cho, Do H. Kim, Y.D. Park, M. Hwang, K. Cho, Appl. Phys. Lett. 90 (2007) 132104.
[9] L.A. Majewski, R. Schroeder, M. Grell, P.A. Glarvey, M.L. Turner, J. Phys. D: Appl. Phys. 37 (2004).
[10] R. Schroeder, L.A. Majewski, M. Grell, Adv. Mater. 16 (2004) 633.
[11] A. Andreev, C. Teichert, G. Hlawacek, H. Hoppe, R. Resel, D.-M. Smilgies, H. Sitter, N.S. Sariciftci, Org. Electron. 5 (2004) 23–27.
[12] C. Brabec, S. Shaheen, C. Winder, P. Denk, N.S. Sariciftci, Appl. Phys. Let. 80 (2002) 1288–1290.
[13] T. Anthopoulos, T.B. Singh, N. Marjanovic, N.S. Sariciftci, A. Ramil, H. Sitter, M. Cölle, D. de Leeuw, Appl. Phys. Lett. 89 (2006) 213504-1.
[14] T.B. Singh, N.S. Sariciftci, Annual Review of Material Research 36 (2006) 199–230.
[15] G. Horowitz, Adv. Mater. 10 (1998) 365–377.
[16] H.-S. Wong, M.H. White, T.J. Krutsick, R.V. Booth, Solid-State Electron. 30 (1987) 953.
[17] D. Boudinet, G.L. Blevennec, C. Serbutoviez, J.M. Verilhac, H. Yan, G. Horowitz, J. Appl. Phys. 105 (2009) 084510.
[18] S.J. Kang, Y. Yi, C.Y. Kim, S.W. Cho, M. Noh, K. Jeong, C.N. Whang, Syn. Met. 156 (2006) 32–37.
[19] J. Ivanco, B. Winter, L. Gregoratti, M. Kiskinova, F.P. Netzer, M.G. Ramsey, Appl. Phys. Lett. 85 (2004) 585–587.
[20] R.I.R. Blyth, S.A. Sardar, F.P. Netzer, M.G. Ramsey, Appl. Phys. Lett. 77 (2000) 1212–1214.
[21] W. Osikowicz, M.P. de Jong, W.R. Salaneck, Adv. Mater. 19 (2007) 4213–4217.
[22] I.F. Torrente, K.J. Franke, J.I. Pascual, J. Phys.: Condens. Matter 20 (2008) 184001.

Organic Electronics 11 (2010) 212–217

Contents lists available at ScienceDirect

Organic Electronics

journal homepage: www.elsevier.com/locate/orgel

Fermi level equilibrium at donor–acceptor interfaces in multi-layered thin film stack of TTF and TCNQ

S. Braun *, X. Liu, W.R. Salaneck, M. Fahlman

Department of Physics, Chemistry and Biology – IFM, Linköping University, S-581 83 Linköping, Sweden

ARTICLE INFO

Article history:
Received 20 August 2009
Received in revised form 29 September 2009
Accepted 25 October 2009
Available online 4 November 2009

Keywords:
Integer charge transfer model
ICT-model
Organic–organic interfaces
Organic donor
Organic acceptor
TTF
TCNQ
Fermi level pinning
Organic solar cells
Hetero-junctions
Interfaces
Organic electronics
Photoelectron spectroscopy
UPS

ABSTRACT

Organic hetero-junctions in multi-layered thin film stacks comprising alternate layers of the molecular donor – tetrathiafulvalene (TTF) and the acceptor – tetracyanoquinodimethane (TCNQ), have been studied by ultraviolet photoelectron spectroscopy (UPS). We show that the energy level alignment at the organic–organic interfaces in the stacks depends only upon the relative energy structure of the donor and acceptor molecules, in particular, the molecular integer charge transfer (ICT) states. The observed interfacial dipoles, across the multi-layered organic stacks, correspond to the difference in energy between the positive and the negative charge transfer states of the molecules constituting the interface. Consequently, Fermi level across the multi-layer system is pinned to those states, since the energetic conditions for the charge transfer across the interface are fulfilled. Hence the energy level alignment at donor–acceptor interfaces studied can be rationalized on the basis of integer charge transfer model (ICT-model). Moreover, we present the photoelectron spectra where 0.85 eV shift of the highest occupied molecular orbital (HOMO) of TTF during formation of TCNQ over-layer is directly observed. These studies contribute to the understanding of the nature of the offset between the frontier electronic levels of the donor and acceptor components which is of high importance in the engineering of efficient organic solar cells.

© 2009 Elsevier B.V. All rights reserved.

1. Introduction

The understanding of electronic structure of organic materials and energy level alignment at all-organic and hybrid interfaces is the subject of many recent extensive research efforts. In particular, photoelectron spectroscopy has been a very fruitful tool for elucidation of the electronic properties of thin organic films [1]. A detailed knowledge of the electronic structure of condensed molecular solid films and even conjugated polymers has contributed significantly to emerging industrial applications in the area of organic electronics.

Organic electronic devices are usually composed of several thin film layers that facilitate various functionalities, *e.g.,* charge injection and transport, recombination/extraction of charges, as discussed elsewhere [2–4]. Within such multilayer thin film architectures are contained interfaces, the properties of which influence and control device operational characteristics. Consequently, a detailed understanding of the interfaces involved in organic electronic devices is critical for improvement of device performance. Particularly important for device operation is electronic level alignment. The significance of this topic is related to the fact that interfacial energetics determines the conditions for the injection of charges from electrodes and charge transport across the device. According to a simple model, energy level alignment at given interface can be estimated by simply lining up the separately observed

* Corresponding author. Tel.: +46 0 13 288916; fax: +46 0 13 288968.
E-mail address: slawomir.braun@liu.se (S. Braun).

1566-1199/$ - see front matter © 2009 Elsevier B.V. All rights reserved.
doi:10.1016/j.orgel.2009.10.018

electronic structures of organic layers. However, as found by Seki and co-workers, this assumption is not valid in many cases [5]. It has been shown that various phenomena, *e.g.* formation of chemical bonds, charge transfer, "push-back effect" or adsorption of molecules, result in the formation of interfacial dipoles, which result in a vacuum level offset [6]. Such vacuum level discontinuity imposes a relative shift between the energy levels of materials constituting interface. Hence the magnitude of the interfacial dipole is an essential parameter to fully characterize interface energetics. The interfacial dipole can be used as a tool to enhance charge injection properties of an electrode. The magnitude of the dipole can be engineered through various surface modifications [7–9]. However, a complete and systematic understanding of energy level alignment has not yet been achieved. Interfacial interactions have been addressed by a large number of theoretical and experimental studies [10–14]. The concept of induced density of interface states (IDIS), based on the interaction between metals and organics has been developed to predict trends in the magnitude of interfacial dipole [15]. For a class of weakly interacting interfaces, the integer charge transfer (ICT) model was recently proposed [16,17]. This semi-empirical model originates from the photoelectron spectroscopy, which reveals characteristic trends in energy level alignment of various organic semiconductors [18–20]. The model predicts that for a large-enough range of work functions, a "Z" shaped ("Mark of Zorro") type of dependence between substrate work function and the work function of the organic layer adjacent to the substrate should be obtained. Hence, for a range of substrates with different work functions, and a given organic material, a transition between vacuum level alignment and Fermi level pinning should occur if the substrate work function enables charge transfer between the substrate and the organic over-layer. The interface will then be in equilibrium when the Fermi level of the conductive substrate is pinned at interfacial states in the organic layer, near the HOMO or LUMO levels of the molecular material. The pinning levels are determined by properties of the organic layer, defined by the nature of the charge transfer states. According to the experimental data, when the Fermi level of the metallic substrate falls within the gap (vacuum level alignment regime) any barriers for charge injection (or lack thereof) are dependent of the work function of the electrode and follow Schottky–Mott limit behavior, *i.e.,* they scale linearly with the work function of the electrode. Within the pinning regimes, when the electrode work function enables interfacial charge transfer, the barriers, if any, has a constant value determined by energy of integer charge transfer states [16–22]. In the context of device engineering, the model predicts that the charge injection barriers can be modified by changing the work function of an electrode only within certain limits [20,23–26]. Considerable interest has been also directed toward more complex systems, containing more than one organic over-layer [27–31]. Such multi-layered structures can help understanding the electronic processes in organic electronic devices.

Recently we have shown that the energetics across a multi-layered structure depends on the interplay between

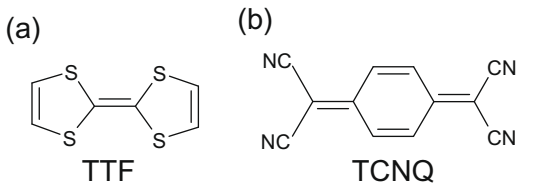

Fig. 1. The molecular structures of the organic molecules studied: (a) tetrathiafulvalene (TTF), (b) tetracyanoquinodimethane (TCNQ).

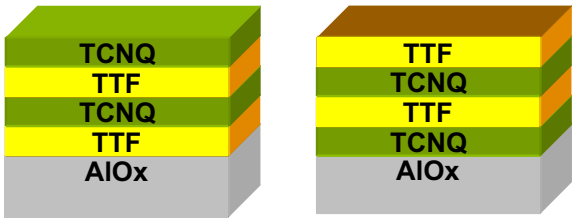

Fig. 2. Schematic drawing illustrating the molecular stacks studied.

electrode work function and the charge transfer states in organic over-layers [32]. Consequently, the magnitude of the dipole may be dependent on the sequence in which adjacent layers are present in the stack of thin film layers. Those points out the complexity of the interfacial energetics that must be addressed in the consideration of real organic-based devices.

In this report, we focus on the energy level alignment at interfaces in a multi-layer donor–acceptor organic stack. Organic donors and acceptors are commonly used in various applications where their unique properties associated with high electron affinity alternatively low ionization potential are exploited. They are often utilized to form charge-transfer complexes that are used to enhance electronic properties or they serve as the active entity to facilitate charge separation in photovoltaic cells [33,34]. In the present case, the molecular donor–acceptor pair of tetrathiafulvalene (TTF) and tetracyanoquinodimethane (TCNQ) (see Figs. 1 and 2), has been studied [35,36]. The stacks of up to four layers have been prepared in different deposition sequences. In addition, particular attention has been paid to whether TTF or TCNQ is adjacent to the substrate, as shown in Fig. 3. The results obtained on such stacks revealed that the influence of the substrate on the organic–organic interfaces is confined to the first two organic layers, and that subsequent layers exhibit exactly the same interfacial off-sets, independent of the substrate. Moreover by a careful choice of the substrate work function the position of HOMO level of the molecular donor (TTF) at the interface with the acceptor (TCNQ) could be directly observed by photoelectron spectroscopy.

2. Experimental

The multilayer stacks comprising thin films of TTF and TCNQ were prepared in situ under ultra high vacuum (UHV) conditions by physical vapor deposition (PVD). The

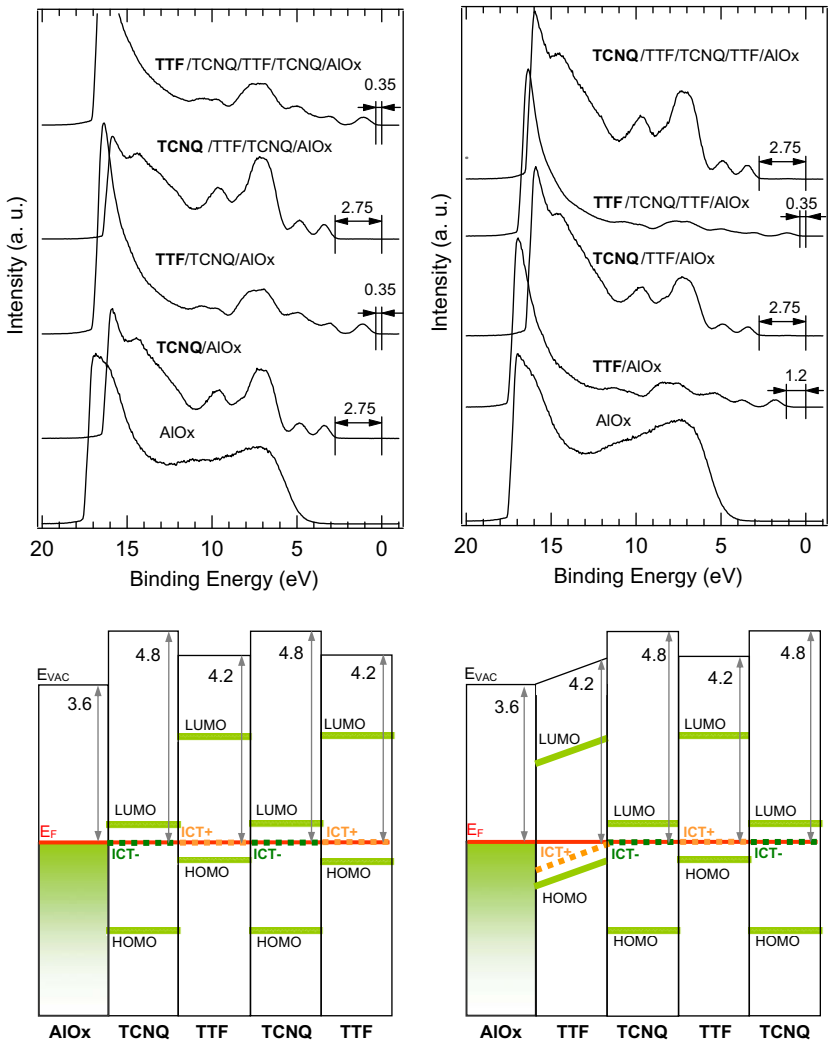

Fig. 3. UPS spectra and the corresponding diagrams of energy level alignment of interfaces at multilayer stacks of TTF and TCNQ.

molecules: TTF and TCNQ were purchased from Sigma–Aldrich. The deposition rate was set to approximately: 5 Å/min, as calibrated from the attenuation of the Au(4f) core level line of a gold substrate, measured by X-ray photoelectron spectroscopy (XPS). The aluminium substrate with a native oxide has been used. During the film growth and measurement, the substrates were cooled to −100 °C.

Ultraviolet photoelectron spectroscopy (UPS) was used to examine the correlation between the substrate work function and the energy level alignment at the organic–organic interfaces formed upon deposition of the donor and acceptor molecules. This technique is especially suited for such studies, since it enables direct probing of the occupied valence electronic levels as well as the vacuum levels, and therefore also of vacuum level shifts, upon forming the interface. The value of the vertical ionization potential (IP) is measured as the onset of the HOMO edge versus the vacuum level. UPS measurements were performed using monochromatized HeI radiation ($h\nu$ = 21.2 eV) in a spectrometer of our own design and construction [37]. The measurement sequence involved characterization of the bare substrates followed by stepwise deposition and characterization of molecular add-layers.

3. Results and discussion

Thin films of the molecular donor – TTF and the acceptor – TCNQ, have been subsequently deposited onto AlO*x* substrate. As shown in Fig. 2, the deposition sequence has been varied so either TTF or TCNQ has been put in direct contact with AlO*x*. In both cases there are four molecular layers deposited on the substrate in order to study the energy level alignment across the multi-layered organic stack.

As shown in Fig. 3, upon deposition of TCNQ onto AlO*x*, the dipole of 1.2 eV is present at the interface. Consequently, this dipole shifts the vacuum level (E_{VAC}) from 3.6 eV, as observed for AlO*x*, to the value of 4.8 eV. This shift sets the substrate Fermi level (E_F) in the vicinity of

LUMO of TCNQ that is located at 4.5 eV [R. Murdey, private commun.]. The obtained result is in line with the previously reported energy level alignment of TCNQ on the various substrates [38]. In those cases, the interfacial dipole scales with substrate work function in such a manner that the substrate Fermi level stayed pinned at about 4.8 eV. In the case reported here, the low work function of the AlO*x* (3.6 eV) also enables charge transfer between the substrate and the TCNQ molecules. In this process, it is expected that charges are transferred to the LUMO-derived states and the substrate Fermi level is pinned in the vicinity to LUMO [39].

The Fermi level, which is pinned at 4.8 eV upon deposition of TCNQ, is the reference level for TTF over-layer. As TTF is deposited onto TCNQ to form TTF/TCNQ/AlO*x* stack, the interfacial dipole appears but in the reverse direction with respect to the TCNQ/AlO*x* interface. This can be rationalized on the basis of integer charge transfer model. Since the charge transfer state of TTF is at 4.2 eV it is then 0.6 eV lower than the position of Fermi level (4.8 eV). In order to reach equilibrium, the Fermi level aligns with the TTF pinning level and the interfacial dipole is formed. The magnitude of the dipole corresponds directly to the difference between the Fermi level and the positive pinning level of TTF. As revealed by UPS and shown in Fig. 3, the same mechanism is observed when the next molecular layers are deposited. The Fermi level stays aligned to the positive integer charge transfer state (ICT+) of TTF and the negative charge transfer state (ICT−) of TCNQ. Consequently the vacuum level shift is equal to the energy difference of those charge transfer states. There are alternating positive and negative dipoles of the same magnitude equal 0.6 eV at each consecutive interface.

The stack of TTF and TCNQ layers has been also studied in the configuration where TTF layer has been deposited first onto AlO*x*. As shown in Fig. 3 the deposition of the first layer does not change vacuum level and there is no dipole at the interface. This situation is apparently different from the cases studied by Murdey et al. when TTF was deposited on the substrates with work function ranging from 4.3 to 5.1 eV. As depicted in Fig. 4, within this range of work functions, the magnitude of the dipole scales with the substrate work function in such a way that the substrate Fermi level is pinned at the constant distance from HOMO level of TTF. The lack of interfacial dipole in the case of TTF/AlO*x* indicates that there is no charge transfer between TTF and AlO*x*. This can be rationalized on the basis of the ICT-model. Since the work function of AlO*x* substrate (3.6 eV) is lower than the positive pinning level of TTF (4.2 eV), there is no favorable condition for charge transfer between organic layer and the substrate. Consequently, the lack of interaction does not alter the electronic conditions at the interface and leads to the observed vacuum level alignment. In the next step, a thin layer of TCNQ has been deposited onto TTF/AlO*x*. As shown in Fig. 3, this leads to a large work function shift of 1.2 eV (the vacuum level is lifted upward to the value of 4.8 eV). The observed energy level alignment at this organic–organic interface is attributed to the favorable energetic conditions for charge transfer between those two organic materials. Even though TTF does not alter the vacuum level position set by AlO*x*, the

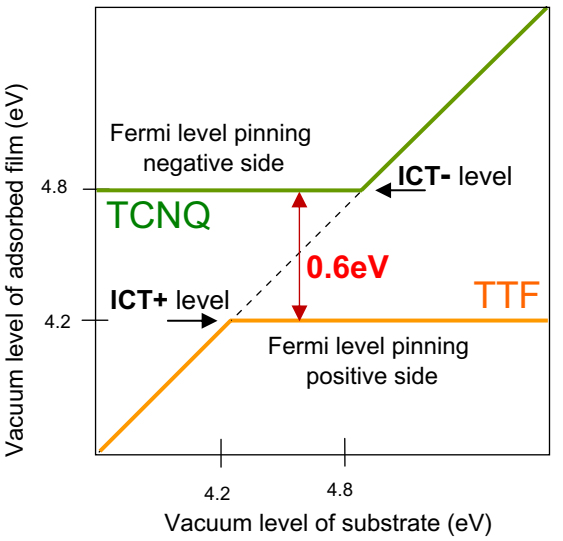

Fig. 4. Schematic drawing presenting energy level alignment regimes for TTF and TCNQ as a function of substrate work function.

Fermi level, which is set at 3.6 eV versus vacuum level, enables charge transfer between TTF and TCNQ. Consequently, upon deposition of TCNQ, the vacuum level observed for TTF is shifted to the value of the pinning level of TCNQ (4.8 eV). Note that the work function shift (1.2 eV) is larger than the interface dipole of 0.6 eV obtained at the TTF/TCNQ and TCNQ/TTF interfaces (0.6 eV being the difference between the ICT+(TTF) and ICT−(TCNQ) energies). Hence additional charge must be transferred across the interface to bring the system into equilibrium. This may be facilitated by transferring charge from the AlO*x* substrate through the TTF layer to the TCNQ at the TCNQ/TTF interface, which would lead to a linear potential gradient over the TTF layer, as schematically pictured in Fig. 3. More charges could be transferred from the TTF layer extending further away from the interface, creating a "band-bending-like" potential gradient over that region. Alternatively, some contribution to the observed work function shift may originate from the polarization effect, as suggested in the recent work of Avilov et al. [40].

On such TCNQ/TTF/AlO*x* structure the third and fourth organic layer was deposited to finally form the stack in the following configuration: TCNQ/TTF/TCNQ/TTF/AlO*x*. As revealed by the photoelectron spectra the two top most interfaces follow the path of alternating vacuum level shifts that correspond to the 0.6 eV difference between the pinning levels of TTF and TCNQ. Hence the energy level alignment of those top interfaces is invariant versus the deposition sequence. This, in turn, leads to the conclusion that the influence of the substrate work function on the energy level alignment at organic ad-layers is confined to the first two layers in a multi-layered stack *e.g.* where the first layer is adjacent to the substrate.

The direct observation of HOMO level of a molecular layer, while building the interface with another organic material, is often obscured by the similarity in the binding energies of those levels. The overlapping contributions in photoelectron signal introduce apparent ambiguity in

interpretation of the spectra. This problem is circumvented in the present studies: when TCNQ layer is deposited on TTF/AlO*x* the onset of HOMO level of TCNQ is present at 2.75 eV. In the case of the TTF layer, when deposited on AlO*x*, the HOMO onset is at 1.2 eV. Hence, the large difference in the binding energy of HOMO peaks gives a unique opportunity for a direct observation of the position of HOMO level of the molecular donor – TTF versus Fermi level, upon building the interface with TCNQ.

As shown in Fig. 5, the HOMO level of TTF deposited on AlO*x* moves towards Fermi level as the coverage of TCNQ increases. At the same time, the gradual shift of vacuum level at this interface, from 3.6 to 4.2 eV, has been observed. The total shift of HOMO level of TTF, measured between the neat TTF film and the TTF film with 8 nm thick overlayer of TCNQ is 0.85 eV. With the increasing thickness of TCNQ the HOMO peak of TTF becomes less intense, as shown in Fig. 5. This is the effect of the gradually prevailing contribution to the photoelectron signal from TCNQ. The leading edge of the highest molecular orbital of TTF is finally observed at 0.35 eV from Fermi level. As shown in Fig. 6, this value is already reached for the less than 8 nm thick TCNQ. This new position of HOMO edge (0.35 eV) is similar to the position observed when the TCNQ layer obeys the Fermi level pinning regime. Note that the HOMO leading edge of TTF does not reach the Fermi level which could be an expected result in the scenario of charge transfer. However, for a very small molecule strong localization of transferred charges could lead to Coulomb gap that would prevent appearance of the density of states at the Fermi level.

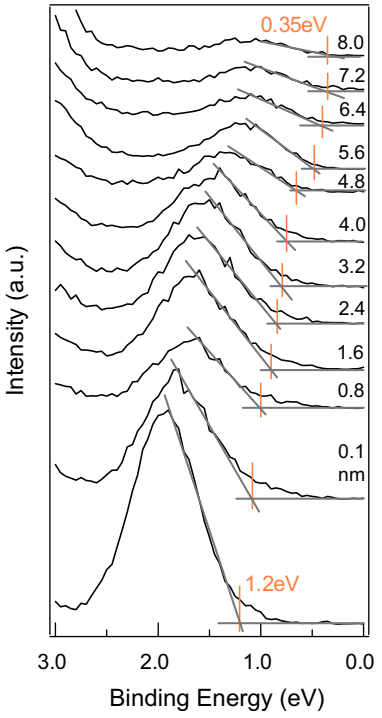

Fig. 5. UPS spectra of HOMO of TTF for different thickness of TCNQ overlayer.

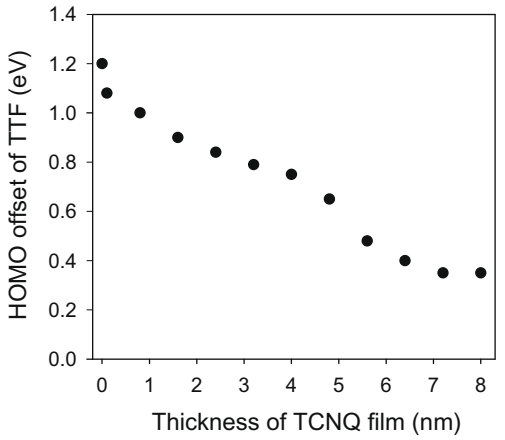

Fig. 6. Binding energy shift of HOMO edge versus thickness of TCNQ overlayer.

Recently, Duhm et al. reported that for the ordered film of α,ω-dihexyl-sexithiophene (DH6T), energy level alignment can be dependent on the orientation of the molecules due to the collective electrostatic effect of the highly anisotropic intramolecular charge distribution [41]. This dependence is manifested by the changes in ionization potential of the molecular film that for DH6T riches value of 0.6 eV. In the case of TTF/TCNQ interface, we do observe a difference between vacuum level shift (0.6 eV) and HOMO shift of TTF (0.85 eV), which points out that the ionization potential of TTF molecules in vicinity of TCNQ over-layer is changed by 0.25 eV. This, in turn, would suggest reorientation of some TTF molecules as the effect of changes in electrostatic field caused by charge transfer at the interface. To clarify this issue, however, the further research including assessment of the molecular orientation of the TTF and TCNQ films is needed.

In theory, the evolution of the TTF HOMO edge upon TCNQ deposition could be used to differentiate between the linear potential drop or "band-bending-like" potential gradient over the TTF layer (discussed in connection with Fig. 3) as the UPS signal is attenuated by the TCNQ overlayer and we are hence probing more and more shallow into the TTF layer as the TCNQ thickness increases. However, as we do not believe that the TCNQ over-layer grows uniformly, we refrain from attempting such an analysis, leaving the question open until more reliable techniques such as energy dependent depth probing at a synchrotron radiation light facility has been performed.

4. Summary

The interfaces between thin films of donor – TTF and acceptor – TCNQ have been studied by means of ultraviolet photoelectron spectroscopy. We demonstrated that the energy level alignment across the multilayer stack of thin films of molecular donor and acceptor is interdependent on the molecular integer charge transfer states and the sequence in which the layers are deposited on the substrate. These results are reminiscent to the previously studied interfaces of CBP and m-MTDATA deposited on the high

work function polymer: PEDOT-PFESA [32]. Since the studied structures include four organic layers, we have verified that across the stack of those layers, the observed interfacial dipoles (0.6 eV) are such that the Fermi level stays pinned to either positive or negative charge transfer state of TTF and TCNQ, respectively. There is however an exception to this scenario. When TTF layer is adjacent to the aluminum substrate, the work function increase upon TCNQ deposition has the magnitude of 1.2 eV. This result is rationalized on the basis of integer charge transfer model with an additional potential gradient over the TTF layer, supported by the experimental results on the TTF HOMO evolution. These studies contribute to the understanding of the nature of the offset between the frontier electronic levels of the donor and acceptor components which is of high importance in the engineering of efficient organic solar cells.

Acknowledgments

The authors acknowledge financial support from the Swedish Research Council (project grant, and Linneus center) and the Knut and Alice Wallenberg Foundation.

References

[1] W.R. Salaneck, S. Stafström, J.L. Brédas, Conjugated Polymer Surfaces and Interfaces: Electronic and Chemical Structure of Interfaces for Polymer Light Emitting Devices, Cambridge University Press, Cambridge, 1996.
[2] R.H. Friend, R.W. Gymer, A.B. Holmes, J.H. Burroughes, R.N. Marks, C. Taliani, D.D.C. Bradley, D.A.D. Santos, J.L. Brédas, M. Lögdlund, W.R. Salaneck, Nature 397 (1999) 121.
[3] C.W. Tang, S.A. VanSlyke, C.H. Chen, J. Appl. Phys. 65 (1989) 3610.
[4] H. Sirringhaus, N. Tessler, R.H. Friend, Science 280 (1998) 1741.
[5] H. Ishii, K. Sugiyama, E. Ito, K. Seki, Adv. Mater. 11 (1999) 605.
[6] X. Crispin, V. Geskin, A. Crispin, J. Cornil, R. Lazzaroni, W.R. Salaneck, J.-L. Brédas, J. Am. Chem. Soc. 124 (2002) 8131–8141.
[7] N. Koch, S. Duhm, J.P. Rabe, A. Vollmer, R.L. Johnson, Phys. Rev. Lett. 95 (2005) 237601.
[8] L. Lindell, A. Burquel, F.L.E. Jakobsson, V. Lemaur, M. Berggren, R. Lazzaroni, J. Cornil, W.R. Salaneck, X. Crispin, Chem. Mater. 18 (2006) 4246.
[9] C. Tengstedt, A. Kanciurzewska, M.P.D. Jong, S. Braun, W.R. Salaneck, M. Fahlman, Thin Solid Films 515 (2006) 2085.
[10] G. Heimel, L. Romaner, E. Zojer, J.L. Brédas, Acc. Chem. Res. 41 (2008) 721.
[11] G. Heimel, L. Romaner, E. Zojer, J.L. Brédas, Nano Lett. 7 (2007) 932.
[12] G. Heimel, L. Romaner, J.-L. Brédas, E. Zojer, Phys. Rev. Lett. 96 (2006) 196806.
[13] S. Kera, Y. Yabuuchi, H. Yamane, H. Setoyama, K.K. Okudaira, A. Kahn, N. Ueno, Phys. Rev. B 70 (2004) 085304.
[14] K. Seki, N. Hayashi, H. Oji, E. Ito, Y. Ouchi, H. Ishii, Thin Solid Films 393 (2001) 298.
[15] H. Vázquez, R. Oszwaldowski, P. Pou, J. Ortega, R. Pérez, F. Flores, A. Kahn, Europhys. Lett. 65 (2004) 802.
[16] M. Fahlman, A. Crispin, X. Crispin, S.K.M. Henze, M.P.D. Jong, W. Osikowicz, C. Tengstedt, W.R. Salaneck, J. Phys.: Condens. Matter 19 (2007) 183202.
[17] S. Braun, W.R. Salaneck, M. Fahlman, Adv. Mater. 21 (2009) 1.
[18] C. Tengstedt, W. Osikowicz, W.R. Salaneck, I.D. Parker, C.-H. Hsu, M. Fahlman, Appl. Phys. Lett. 88 (2006) 053502.
[19] A. Crispin, X. Crispin, M. Fahlman, M. Berggren, W.R. Salaneck, Appl. Phys. Lett. 89 (2006) 213503.
[20] S. Braun, W. Osikowicz, Y. Wang, W.R. Salaneck, Org. Electron. 8 (2007) 14.
[21] L. Lindell, M. Unge, W. Osikowicz, S. Stafström, W.R. Salaneck, X. Crispin, M.P.D. Jong, Appl. Phys. Lett. 92 (2008) 163302.
[22] Z. Xu, L.-M. Chen, M.-H. Chen, G. Li, Y. Yang, Appl. Phys. Lett. 95 (2009) 013301.
[23] S.W. Tsang, S.C. Tse, K.L. Tong, S.K. So, Org. Electron. 7 (2006) 474.
[24] S.W. Tsang, M.W. Denhoff, Y. Tao, Z.H. Lu, Phys. Rev. B 78 (2008) 081301.
[25] A. Sharma, A. Haldi, P.J. Hotchkiss, S.R. Marder, B. Kippelen, J. Appl. Phys. 105 (2009) 074511.
[26] X. Cheng, Y.-Y. Noh, J. Wang, M. Tello, J. Frisch, R.P. Blum, A. Vollmer, J.P. Rabe, N. Koch, H. Sirringhaus, Adv. Funct. Mater. 19 (2009) 2407.
[27] N.R. Armstrong, W. Wang, D.M. Alloway, D. Placencia, E. Ratcliff, M. Brumbach, Macromolecules 30 (2009) 717.
[28] S. Olthof, R. Meerheim, M. Schober, K. Leo, Phys. Rev. B 79 (2009) 245308.
[29] Y. Wang, W. Gao, S. Braun, W.R. Salaneck, F. Amy, C. Chan, A. Kahn, Appl. Phys. Lett. 87 (2005) 193501.
[30] A. Rajagopal, C.I. Wu, A. Kahn, J. Appl. Phys. 83 (1998) 2649.
[31] J.X. Tang, C.S. Lee, S.T. Lee, J. Appl. Phys. 101 (2007) 064504.
[32] S. Braun, M.P.D. Jong, W. Osikowicz, W.R. Salaneck, Appl. Phys. Lett. 91 (2007) 202108.
[33] W. Gao, A. Kahn, Org. Electron. 3 (2002) 53.
[34] G. Yu, J. Gao, J.C. Hummelen, F. Wudl, A.J. Heeger, Science 270 (1995) 1789.
[35] L.B. Coleman, M.J. Cohen, D.J. Sandman, F.G. Yamagishi, A.F. Garito, A.J. Heeger, Solid State Commun. 12 (1973) 1125.
[36] J.R. Kirtley, J. Mannhart, Nature 7 (2008) 520.
[37] W.R. Salaneck, R. Bergman, J.-E. Sundgren, A. Rockett, T. Motooka, J.E. Greene, Surf. Sci. 198 (1988) 461.
[38] R.J. Murdey, W.R. Salaneck, Jpn. J. Appl. Phys. 44 (2005) 3751.
[39] S. Braun, W.R. Salaneck, Chem. Phys. Lett. 438 (2007) 259.
[40] I. Avilov, V. Geskin, J. Cornil, Adv. Funct. Mater. 19 (2009) 624.
[41] S. Duhm, G. Heimel, I. Salzmann, H. Glowatzki, R.L. Johnson, A. Vollmer, J.P. Rabe, N. Koch, Nat. Mater. 7 (2008) 326.

Organic Electronics 11 (2010) 218–226

Contents lists available at ScienceDirect

Organic Electronics

journal homepage: www.elsevier.com/locate/orgel

Modeling and simulation of electronic and excitonic emission properties in organic host–guest systems

Il-Soo Park, Soon-Ryong Park, Dae-Yup Shin, Jun-Sik Oh, Won-Jun Song, Ji-Hwan Yoon *

OLED R&D Center, Samsung Mobile Display Co. Limited, San #24 Nongseo-Dong, Giheung-gu, Yongin-si, Gyunggi-do 446-711, Republic of Korea

ARTICLE INFO

Article history:
Received 30 July 2009
Received in revised form 19 October 2009
Accepted 26 October 2009
Available online 1 November 2009

Keywords:
Host
Guest
Hopping
Trapping
Excitonic emission

ABSTRACT

We propose electronic and excitonic emission models for the quantitative simulation of organic light emitting diodes comprising host–guest system in emission layer. The electronic model contains the thermionic injection at the electrodes, the charge transport with the field- or doping-dependent mobility, and Langevin's recombination. The excitonic emission model includes radiative (or nonradiative) decay, exciton diffusion, singlet–triplet intersystem-crossing, exciton annihilation, and polaron quenching. Förster and Dexter energy transfers as well as exciton blocking are also added to the excitonic emission model for the simulation of phosphorescent host–guest system. When these models are applied to a series of tris(2-phenylpyridine) iridium ($Ir(ppy)_3$)-doped 4,4′-bis(*N*-carbazolyl)-1,1′-biphenyl (CBP) devices with various doping concentration, the simulated electronic and excitonic emission properties are in good agreement with experimental results. The real devices show gentle efficiency roll-off at high $Ir(ppy)_3$ concentration and current efficiency reversion between 10% and 15% doping concentrations at over 20 mA cm^{-2}, which are successfully realized by the proposed models in which triplet–triplet annihilation in host sites is considered. It is also numerically demonstrated that exciton confinement in emitting layer by controlling the energy, lifetime, and diffusion of exciton results in improvement of luminance efficiency of the devices.

© 2009 Elsevier B.V. All rights reserved.

1. Introduction

Since the first appearances of a bi-layer organic light emitting diode (OLED) [1], electrochemical doping (host–guest system) has been widely used to improve the efficiency of multi-layer OLEDs. Understanding carrier injection, transport, and exciton formation in the doped system is the important issue for optimizing the devices and requires in-depth study of electronic and excitonic emission mechanisms. There have been proposed several theoretical models for OLEDs, but most of them are focused on the simple devices without doping [2–6] and only few reported on host–guest system [7–9], in which guests were simply treated as trap sites and carrier transport through guest sites were not considered. The carrier transport through both host and guest sites have been reported [10–13], however, there is no study in which the mechanism is applied to the simulation of the electronic properties of OLEDs. Meanwhile, simple excitonic emission models have been applied for the simulation of OLEDs, considering radiative (or nonradiative) decay, and exciton diffusion [3,5]. The concept of intersystem-crossing (ISC), exciton annihilation, and polaron quenching were often added to those models [14–17]. In some cases, Förster and Dexter energy transfers [18,19] were also included for the excitonic mechanisms, but unclearly implemented in a diffusion term [20] or limitedly applied to studies of transient photo-luminescence [15–17]. There was a case in which the Förster energy transfer is used in an excitonic emission model of steady state device simulation [9], however, exciton blocking phenomena [21,22] were not

* Corresponding author. Tel.: +82 31 2097744; fax: +82 31 2094867.
E-mail address: jihwan.yoon@samsung.com (J.-H. Yoon).

1566-1199/$ - see front matter © 2009 Elsevier B.V. All rights reserved.
doi:10.1016/j.orgel.2009.10.020

considered in the studies because the model dealt with only fluorescent dopant.

In this paper, we propose electronic and excitonic emission models for the simulation of electrochemically-doped OLEDs. The electronic model basically contains the thermionic injection at the electrodes, the charge transport with field-dependent mobility, and Langevin's recombination. For the calculation of the electronic properties in electrochemically-doped layer, hopping and trapping with field- and doping-dependent mobility in host and guest sites are also considered. For the simulation of excitonic emission, Dexter energy transfer as well as Förster energy transfer between host and guest excitons is added into the model proposed by Baldo et al. [14] and exciton blocking is treated as diffusion-like transfer containing Boltzmann factor at organic/organic interfaces. In order to verify our electronic and excitonic emission models, a series of green-emitting phosphorescent OLEDs are prepared by varying doping concentration from 1% to 15%. The experimentally-obtained current density(J)–voltage(V)–luminance(L) characteristics of the devices are compared with the theoretically-calculated ones.

2. Theory

2.1. Electronic model

Fig. 1 schematically shows the proposed hole/electron transport mechanism in undoped and doped layers. The carriers injected from electrode move along the hopping distance (d_o) in the undoped layer with a field-dependent mobility, experiencing trapping and detrapping between transport and trap sites. At the interface between undoped layers, the carriers penetrate the barriers between the layers with the probability related with energy difference and energetic disorder [3]. At the interface between undoped and doped layers, the carriers penetrating into host sites move along the host hopping distance (d_h), whilst the carriers penetrating into guest sites move along the guest hopping distance (d_g). These carriers also experience trapping and detrapping between transport and trap sites of host (or guest), and at the same time, trapping and detrapping between transport sites of host and guest.

The field-dependent mobility at room temperature in undoped layer is expressed as below from Bässler's Gaussian disorder model [3,23]

$$\mu(F)_{RT} = \mu_{o,RT} \cdot \exp(C_{RT} \cdot \sqrt{F}), \tag{1}$$

where F is electric field, $\mu_{o,RT}$ and C_{RT} are zero-field mobility and electric-field-activation parameter at room temperature, respectively. In doped layer, the effective mobilities in host and guest can be modified by considering the decrease of wavefunction overlap factor [23], and the change of field dependency [24] with increasing hopping distance

$$\mu_h * (F)_{RT} = \mu_{ho,RT} \cdot \exp\left[2\left(1 - \frac{d_h}{d_{ho}}\right)\right] \cdot \exp\left[\left(\frac{d_h}{d_{ho}}\right)^{\alpha} C_{hRT} \cdot \sqrt{F}\right], \tag{2.1}$$

$$\mu_g * (F)_{RT} = \mu_{go,RT} \cdot \exp\left[2\left(1 - \frac{d_g}{d_{go}}\right)\right] \cdot \exp\left[\left(\frac{d_g}{d_{go}}\right)^{\alpha} C_{gRT} \cdot \sqrt{F}\right], \tag{2.2}$$

where subscript o means the condition of zero concentration of guest and d is doping-dependent hopping distance. We use the host hopping distance, $d_h = d_o/(1-c)^{1/3}$ and the guest hopping distance, $d_g = d_o/c^{1/3}$, $d_o = d_{ho} = d_{go} = 1$ nm and $\alpha = 0.5$, where c is doping concentration (c = 0–1).

The numerical framework for steady state simulation is based on conventional drift-diffusion models [5,7,9]. In this study, we consider the transport and recombination in guest site in addition to those in host site. The electronic properties are then described with the following Poisson's, current continuity, and current equations:

$$\nabla^2 V = -\frac{q}{\varepsilon_r \varepsilon_o}\left(p_h + p_{ht} - n_h - n_{ht} + p_g + p_{gt} - n_g - n_{gt}\right), \tag{3}$$

$$\nabla \cdot J_{p_h} + U^t_{p_h p_{ht}} + U^f_{p_h p_g} + U^r_{p_h n_h} + U^r_{p_h n_{ht}} = 0, \tag{4.1}$$

$$\nabla \cdot J_{n_h} - U^t_{n_h n_{ht}} - U^f_{n_h n_g} - U^r_{p_h n_h} - U^r_{n_h p_{ht}} = 0, \tag{4.2}$$

$$\nabla \cdot J_{p_g} + U^t_{p_g p_{gt}} - U^f_{p_h p_g} + U^r_{p_g n_g} + U^r_{p_g n_{gt}} = 0, \tag{4.3}$$

$$\nabla \cdot J_{n_g} - U^t_{n_g n_{gt}} + U^f_{n_h n_g} - U^r_{p_g n_g} - U^r_{n_g p_{gt}} = 0, \tag{4.4}$$

$$J_{p_h} = -q\left(D_{p_h}\nabla p_h + \mu^*_{p_h} p_h \nabla V\right), \tag{5.1}$$

$$J_{n_h} = q\left(D_{n_h}\nabla n_h - \mu^*_{n_h} n_h \nabla V\right), \tag{5.2}$$

$$J_{p_g} = -q\left(D_{p_g}\nabla p_g + \mu^*_{p_g} p_g \nabla V\right), \tag{5.3}$$

$$J_{n_g} = q\left(D_{n_g}\nabla n_g - \mu^*_{n_g} n_g \nabla V\right), \tag{5.4}$$

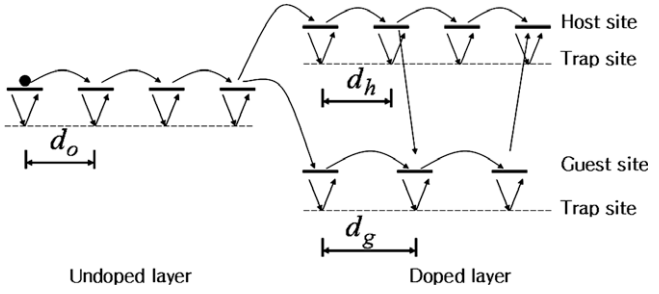

Fig. 1. Proposed electron transport mechanism in undoped and doped layers.

where V is externally-applied voltage, q is electronic charge, ε_r is relative permittivity, ε_o is permittivity of free space, p is hole density, n is electron density, t is trap, J is current density, U^t is trapping rate between transport and trap sites, U^f is trapping rate between host and guest transport sites, U^r is Langevin's recombination rate, and D is carrier diffusion constant obtained from Einstein relationship ($D = \mu \cdot k_BT/q$, where k_BT is the thermal energy).

In Eq. (4.1), the hole trapping rate between host transport and trap sites is given by [3]

$$U^t_{p_h p_{ht}} = \mu^*_{p_h} F \sigma_t \left[p_h (N_{tp_h} - p_{ht}) - p_{ht} (N_{\mathrm{hHOMO}} - p_h) \exp\left(-\frac{E_{tp_h}}{k_B T} \right) \right], \tag{6}$$

where σ_t is cross section for carrier trapping, N_t is density-of-states (DOS) of trap, E_t is trap energy level, and N_{HOMO} is DOS of the highest occupied molecular orbital (HOMO). In this study, we use $\sigma_t = 5d_o^2$ and $N_{\mathrm{hHOMO}} = d_h^{-3}$ [3]. The electron trapping rate in host or the hole and electron trapping rates in guest can be derived as an equivalent form to Eq. (6).

The hole trapping rate between host and guest transport sites is driven by

$$U^f_{p_h p_g} = \mu^*_{ph} F \sigma_t \left[p_h (N_{\mathrm{gHOMO}} - p_g) - p_g (N_{\mathrm{hHOMO}} - p_h) \exp\left(-\frac{\Delta E^H_{hg}}{k_B T} \right) \right], \tag{7.1}$$

or

$$U^f_{p_h p_g} = -\mu^*_{pg} F \sigma_t \left[p_g (N_{\mathrm{hHOMO}} - p_h) - p_h (N_{\mathrm{gHOMO}} - p_g) \exp\left(-\frac{\Delta E^H_{hg}}{k_B T} \right) \right], \tag{7.2}$$

where ΔE^H_{hg} is energy difference between host and guest HOMO levels. We set $N_{\mathrm{gHOMO}} = d_g^{-3}$. Eq. (7.1) is used when the guest HOMO level is energetically above the host HOMO level and vice versa for Eq. (7.2). The electron trapping rate between host and guest transport sites is equivalent to Eqs. (7.1) and (7.2).

The host recombination rates considering free-free and free-trap cases are given by [3]

$$U^r_{p_h n_h} = \frac{q}{\varepsilon_r \varepsilon_o} \left(\mu^*_{p_h} + \mu^*_{n_h} \right) p_h n_h, \tag{8.1}$$

$$U^r_{p_h n_{ht}} = \frac{q}{\varepsilon_r \varepsilon_o} \mu^*_{p_h} p_h n_{ht}, \tag{8.2}$$

$$U^r_{n_h p_{ht}} = \frac{q}{\varepsilon_r \varepsilon_o} \mu^*_{n_h} p_{ht} n_h. \tag{8.3}$$

The guest recombination rates are equivalent to Eqs. (8.1)–(8.3). The source terms for exciton rate equations are then considered to be only the free-free recombination rates ($U^r_{p_h n_h}$ and $U^r_{p_g n_g}$: see Eq. (11)) because it was reported that the exciton by a free-trap recombination has the other bound state of electron [25]. In this study, we exclude the recombination rates between charges in host and guest because exciton is supposed to be Frenkel exciton rather than charge-transfer exciton or Mott–Wannier exciton.

For device simulation, additional information is necessary: (1) boundary condition, (2) injection model. Here, Schottky contact boundary condition [26] is adopted. The potential at anode and cathode (V_{anode} and $V_{cathode}$) can be written as

$$V_{anode} = \frac{1}{q} \left(\phi_p - \frac{E_g}{2} + qV \right), \tag{9.1}$$

$$V_{cathode} = \frac{1}{q} \left(\frac{E_g}{2} - \phi_n \right), \tag{9.2}$$

where E_g is energy gap of the material adjacent to the electrode and ϕ is barrier height at the electrode. For injection model, we use Scott's injection model [27],

$$J_{INJ} = 4\psi^2 N_o q \mu F \exp\left(\frac{-\phi}{k_B T} \right) \exp(f^{1/2}), \tag{10.1}$$

$$\psi(f) = \frac{1}{f} + \frac{1}{\sqrt{f}} - \frac{1}{f} \left(1 + 2\frac{1}{\sqrt{f}} \right)^{1/2}, \tag{10.2}$$

$$f = \frac{q^3 F}{4\pi \varepsilon_r \varepsilon_o (k_B T)^2}, \tag{10.3}$$

where N_o is density of charge hopping sites, ψ is slowly varying function of electric field, and f is the usual Schottky barrier lowering effect. Here, we set $N_o = d_o^{-3} = 10^{21}$ cm^{-3}.

Finally, by self-consistent calculation using Eqs. (3)–(5), the local recombination rate for excitonic emission properties as well as the spatial distribution of charge carriers and current density in the device comprising host–guest system is obtained.

2.2. Excitonic emission model

The rate equations for singlet density (S) and triplet density (T) use Langevin's recombination rate (U^r) as a source, and include radiative (r) and nonradiative (nr) decay, exciton diffusion, singlet–triplet ISC, exciton annihilation (T–T,S–S,S–T), and polaron (P) quenching (S–P and T–P) mechanism [14–17]. Additionally, the exothermic energy transfers are implemented in host–guest system as shown in Fig. 2: (1) Förster energy transfer between host singlet and guest singlet, (2) Dexter energy transfer between host singlet and guest singlet, and (3) Dexter energy transfer between host triplet and guest triplet. The final form of exciton rate equations in steady state are

$$\frac{3}{4} U^r_{p_h n_h} - K^{h\to g}_{DET:T} T_h + K^{g\to h}_{DET:T} T_g + k^h_{\mathrm{ISC}} S_h - \frac{T_h}{\tau^h_{rT}} - \frac{T_h}{\tau^h_{nrT}} - \kappa^h_{TP}(n_h + p_h) T_h - \kappa^h_{TT} T_h^2 - \nabla\left(\tilde{D}^h_T \nabla T_h \right) = 0, \tag{11.1}$$

$$\frac{1}{4} U^r_{p_h n_h} - K^{h\to g}_{FET} S_h + K^{g\to h}_{FET} S_g - K^{h\to g}_{DET:S} S_h + K^{g\to h}_{DET:S} S_g - k^h_{\mathrm{ISC}} S_h + \frac{1}{5} \kappa^h_{TT} T_h^2 - \frac{S_h}{\tau^h_{rS}} - \frac{S_h}{\tau^h_{nrS}} - \kappa^h_{ST} T_h S_h - \kappa^h_{SP}(n_h + p_h) S_h - \frac{\kappa^h_{SS}}{2} S_h^2 - \nabla\left(\tilde{D}^h_S \nabla S_h \right) = 0, \tag{11.2}$$

$$\frac{3}{4} U^r_{p_g n_g} + K^{h\to g}_{DET:T} T_h - K^{g\to h}_{DET:T} T_g + k^g_{\mathrm{ISC}} S_g - \frac{T_g}{\tau^g_{rT}} - \frac{T_g}{\tau^g_{nrT}} - \kappa^g_{TP}(n_g + p_g) T_g - \kappa^g_{TT} T_g^2 - \nabla\left(\tilde{D}^g_T \nabla T_g \right) = 0, \tag{11.3}$$

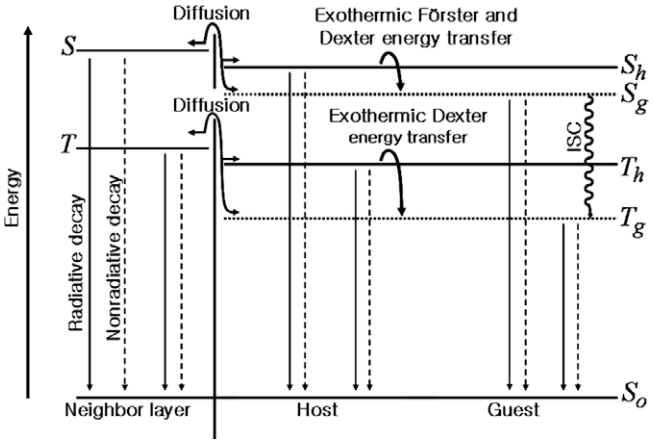

Fig. 2. Proposed excitonic emission mechanism in undoped and doped layers.

$$\frac{1}{4}U^r_{p_g n_g} + K^{h\to g}_{FET}S_h - K^{g\to h}_{FET}S_g + K^{h\to g}_{DET:S}S_h - K^{g\to h}_{DET:S}S_g - k^g_{ISC}S_g + \frac{1}{5}\kappa^g_{TT}T^2_g - \frac{S_g}{\tau^g_{rS}} - \frac{S_g}{\tau^g_{nrS}} - \kappa^g_{ST}T_gS_g - \kappa^g_{SP}(n_g + p_g)S_g - \frac{\kappa^g_{SS}}{2}S^2_g - \nabla\left(\tilde{D}^g_S\nabla S_g\right) = 0, \quad (11.4)$$

where K is energy transfer rate, k is decay rate, κ is annihilation or quenching rate, τ is exciton lifetime, $\tilde{D}$ is exciton diffusion constant. *FET*, *DET*:*S*, and*DET*:*T* denote Förster energy transfer, Dexter energy transfer for singlet and triplet, respectively.

In doped layer, the exciton diffusion constant is assumed to be changed by doping ratio-dependent hopping distance [14], and therefore, modified by multiplying exp[2(1 − d/d_o)]. As the exciton energy can be transferred to adjacent layers by an energy transfer mechanism, we assume that the exciton diffuses to the adjacent layers with the probability expressed as Boltzmann factor, exp(−$\Delta E/k_BT$), where ΔE is the difference of exciton energy between two layers. The average exciton diffusion constant at the interface is obtained by multiplying the probability.

In Eqs. (11.1)–(11.4), Förster energy transfer rate from host singlet to guest singlet is given by [18]

$$K^{h\to g}_{FET} = \frac{1}{\tau^h_{rS}}\left(\frac{R_F}{R}\right)^6, \quad (12)$$

where τ^h_{rS} is radiative lifetime of host singlet, R is average separation distance between host and guest sites, and R_F is Förster radius.

Dexter energy transfer is regarded as a purely quantum-mechanical effect, therefore, does not have a classical analogy [18,19]. We relate Dexter energy transfer rates from host singlet (or triplet) to guest singlet (or triplet) to the lifetime of exciton, the average separation distance of host and guest sites (R), effective Bohr radius (R_B), and Dexter radius (R_D) as the following rate model:

$$K^{h\to g}_{DET:S} = \frac{10^3}{\tau^h_{tS}}\exp\left[\frac{2(R_D - R)}{R_B}\right], \quad (13.1)$$

$$K^{h\to g}_{DET:T} = \frac{10^3}{\tau^h_{tT}}\exp\left[\frac{2(R_D - R)}{R_B}\right], \quad (13.2)$$

where τ_t is total lifetime ($\tau_t^{-1} = \tau_r^{-1} + \tau_{nr}^{-1}$). R_B is $0.053(\varepsilon^h_r + \varepsilon^g_r)/2$ nm, and R_D is a critical distance at which energy transfer rate reaches maximum (3 orders of magnitude higher than the other decay rates) when Dexter radius is same as the separation distance of host and guest sites.

Finally, the singlet and the triplet densities of host (or guest) are calculated by using Eq. (11), and then the luminance from guest singlet and triplet can be obtained as follows [3]:

$$L^S_g = \frac{1}{\varepsilon_r}k_m h\nu\frac{1}{\pi}\sum\frac{S_g}{\tau_{rS}}d_o, \quad (14.1)$$

$$L^T_g = \frac{1}{\varepsilon_r}k_m h\nu\frac{1}{\pi}\sum\frac{T_g}{\tau_{rT}}d_o, \quad (14.2)$$

where k_m is constant for daylight-adopted human eye (k_m = 683 lm/W), $h\nu$ is the energy of the emitted photons.

3. Experiments

In order to verify the proposed electronic and excitonic emission models, a series of green-emitting phosphorescent OLEDs were prepared by varying doping concentration of tris(2-phenylpyridine) iridium ($Ir(ppy)_3$) from 1% to 15%. The green phosphorescent devices (4 mm^2 active area) were fabricated with the configurations of ITO (150 nm)/DNTPD (60 nm)/NPB (30 nm)/CBP:$Ir(ppy)_3$ (30 nm)/BCP (5 nm)/Alq_3 (20 nm)/LiF (1 nm)/Al (200 nm), where ITO, DNTPD, NPB, CBP, BCP and Alq_3 are indium tin oxide, *N*,*N*′-diphenyl-*N*,*N*′-bis-[4-(phenyl-*m*-tolyl-amino)-phenyl]-biphenyl-s′4-diamine, *N*,*N*′-di(1-naphtyl)-*N*,*N*′-diphenylbenzidine, 4,4′-bis(*N*-carbazolyl)-1,1′-biphenyl, 2,9-dimethyl-4,7-diphenyl-phenanthroline and tris(8-hyroxyquinloine) aluminum, respectively. $Ir(ppy)_3$ was doped in CBP with the ratio of 1%, 5%, 10% and 15% and the thickness of CBP:$Ir(ppy)_3$ was maintained constant (30 nm). ITO glass substrates with a sheet resistance of 10 Ω/sq were cleaned successively with acetone and isopropyl alcohol in an ultrasonic bath for 10 min and dried at 120 °C for 2 h before set in a vacuum evaporator (~10^{-4} Pa). DNTPD, NPB, EML, and Alq_3 were thermally deposited at a rate of 1.0 Å/s. The deposition rate of $Ir(ppy)_3$ was adjusted according to the doping ratio (1%, 5%, 10% and 15%). After

Table 1
Parameters for the materials used in the simulation (underline: experimentally-obtained, double underline: theoretically-calculated).

	DNTPD	NPB	BCP	Alq_3	CBP	$Ir(ppy)_3$
HOMO (eV)	−5.20	−5.47	−6.52	−5.70	−6.09	−5.38
LUMO (eV)	−2.13	−2.40	−2.54	−2.90	−2.48	−2.34
μ_{po} (cm^2/V s)	9.76×10^{-5}	4.88×10^{-4}	5.47×10^{-8}	5.47×10^{-10}	5.10×10^{-4}	1.00×10^{-7}
$C^P_{RT}(cm/V)^{1/2}$	5.77×10^{-4}	5.77×10^{-4}	5.59×10^{-3}	5.59×10^{-3}	1.98×10^{-3}	1.00×10^{-3}
μ_{no} (cm^2/V s)	9.76×10^{-7}	9.76×10^{-7}	7.90×10^{-7}	7.90×10^{-9}	3.31×10^{-5}	1.00×10^{-7}
$C^n_{RT}(cm/V)^{1/2}$	5.77×10^{-4}	5.77×10^{-4}	8.68×10^{-3}	8.68×10^{-3}	3.49×10^{-3}	1.00×10^{-3}
λ_S (nm)	427	431	376	484	372	455
λ_T (nm)	511	535	483	622	437	498

deposition of organic materials, LiF and Al were successively deposited at a deposition rate of 0.1 Å/s and 2.0 Å/s, respectively. The *J–V–L* characteristics of the devices were measured with Keithley 236 source measurement unit and PR650 Spectrascan® colorimeter (Photoresearch, Inc.) at room temperature.

4. Input parameters

For the calculation of electronic and excitonic emission properties, many kinds of input parameters are required. The material properties used in the simulation are listed in Table 1, where the experimentally-obtained and theoretically-calculated data are highlighted by underline and double underline, respectively. As many different values of HOMO and LUMO for a material are shown in several articles [28–30] and there is little information of *S*, *T* energy in published articles, we theoretically-calculated those parameters using quantum-mechanical methods. The calculation processes are: firstly, all reported molecular structure was optimized at a DND/GGA(P91) level of theory using Dmol3 module (Material Studio, Accelrys software) and secondly, time-dependent density functional theory calculation was performed at a B3LYP/6-31G* level of theory using the Gaussian03 code to obtain the data of HOMO, LUMO, *S* and *T* energy. Most of carrier mobility are extracted from the published experimental results [31–33]. It is assumed that $100\mu_{n_NPB} = \mu_{p_NPB}$, $\mu_{DNTPD} = \mu_{NPB}$, $\mu_{BCP} = 100\mu_{Alq_3}$ (the electron mobility of BCP is reported to be at least an order of magnitude higher than that of Alq_3 [34]). Considering low mobility of Ir complex, we use $\mu_n = \mu_p = 10^{-7}\exp(10^{-3}\sqrt{F})$ for the mobility of $Ir(ppy)_3$ [35].

As there is also little information for exciton lifetime and diffusivity except those for $Ir(ppy)_3$ and CBP [17,29], we set the properties of materials as follows: (1) $\tau^S_r = 10^{-9}$ s, $\tau^S_{nr} = 10^{-7}$ s for CBP and $Ir(ppy)_3$ and $\tau^S_r = 10^{-7}$ s, $\tau^S_{nr} = 10^{-9}$ s for the other materials, (2) $\tau^T_r = 10^{-4}$ s, $\tau^T_{nr} = 10^{-6}$ s for non-phosphorescent materials and $\tau^T_r = 10^{-6}$ s, $\tau^T_{nr} = 10^{-4}$ s for $Ir(ppy)_3$, (3) $\widetilde{D}_S = 10^{-4}(cm^2/s)$ and $\widetilde{D}_T = 5 \times 10^{-6}(cm^2/s)$ for all materials, which implies that the diffusion lengths are 3 nm and 22 nm for singlet and triplet, respectively. (4) $k_{ISC} = 10^{-11}\ s^{-1}$ for metal complex material ($Ir(ppy)_3$) in order to apply strong spin–orbit coupling. The rates of polaron quenching and exciton annihilation are extracted by fitting the simulations to experimental results. For the other parameters such as trap information, injection barrier heights, etc., we use the common values as shown in Table 2. As LiF can be regarded as a barrier for electron injection from cathode, its contribution is included in ϕ_n (for the calculation of luminance (Eq. (14)), ITO and Al are assumed to be completely transparent and reflective, respectively).

Table 2
Common material parameters.

Parameter	Value
$N_{tp} = N_{tn}$	$1.0 \times 10^{18}\ cm^{-3}$
$E_{tp} = E_{tn}$	0.2 eV
ϵ_r	3
n_i	$1.0 \times 10^{11}\ cm^{-3}$
$\phi_p = \phi_n$	0.3 eV
V_{bi}	4.7 V
R_F	3.2 nm
R_D	1.12 nm

5. Results and discussion

Understanding distributions of charge carrier densities and recombination rates (or exciton densities) makes physical interpretation of the different behaviors of devices possible. Fig. 3 shows the simulated spatial distributions of electron and hole densities and recombination rates in the devices doped with 1% and 15% $Ir(ppy)_3$ at an applied voltage (9 V) (the zero position is anode). The carriers injected from the electrodes move along with different mobility in each layer and pile up at the interface between layers or penetrate into the adjacent layers. The simulation results show that (1) electrons and holes are abundant at both edges of EML, where the recombination rate is highest, (2) inside EML, the density of electrons and holes in host are higher than that in guest due to the high DOS of host, and consequently, recombination occurs mainly in host, and (3) as the concentration of $Ir(ppy)_3$ in EML is increased, the density of electrons and holes in guest is increased and therefore, the recombination in guest is increased.

The calculated *J–V* curves for the devices doped with 1%, 5%, 10%, and 15% of $Ir(ppy)_3$ are compared with experimentally-obtained ones in Fig. 4, which shows that the theoretical *J–V* curves are reasonably in good agreement with experimental ones. There is little difference in *J–V* characteristics of the devices with various

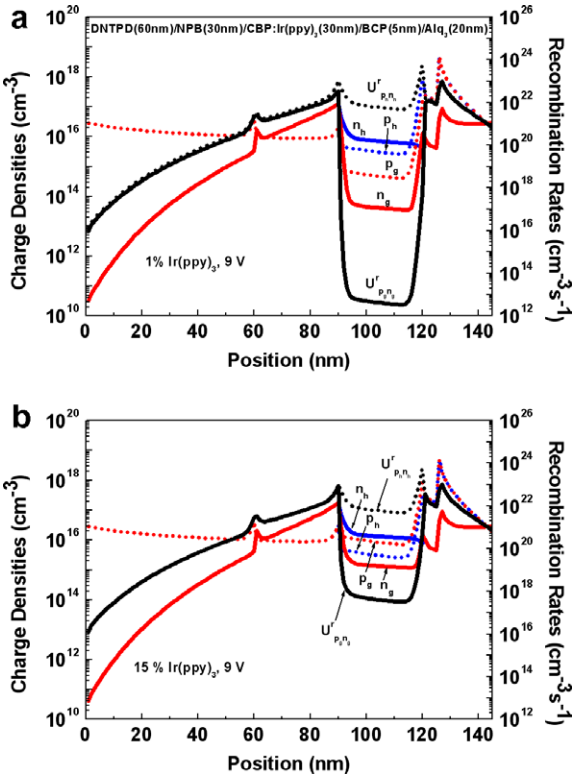

Fig. 3. Spatial distributions of the carrier densities and recombination rates of the device doped with $Ir(ppy)_3$: (a) 1% and (b) 15%.

doping concentrations, even though the real devices show relatively large variations compared with the simulated results. The similar *J–V* characteristics irrespective of doping concentration is assumed to be because most of voltage is dropped in Alq_3 layer due to the very low mobility of Alq_3 (see Table 1) and the thickness of EML is too thin (30 nm) to affect the total current of the device. Consequently, overall current density is not significantly affected by the mobility change of host and/or guest material as shown in Eq. (2) (the variations in the *J–V* curves of the real devices could be ascribed to the experimental deviations resulted from the parameters such as trap density, built-in potential, effective barrier height at EML interface, trap activation energy, etc. [36]).

As described in Eq. (14), luminance is related to exciton densities per radiative lifetime (i.e. emission rate). The simulated spatial distributions of the recombination and emission rates of the device doped with 1% and 15% $Ir(ppy)_3$ are shown in Fig. 5. The emission rates are very low in all layers except EML, which can be ascribed to fast nonradiative decay, low charge confinement, and charge unbalance in the layers. In EML, the recombination rate in host is much higher than that in guest, however, the emission from guest triplet is dominant. This is because: (1) the singlet and triple emission in host are reduced by Förster and Dexter energy transfers and nonradiative decay, and (2) the guest singlet emission is suppressed by the decay through ISC. Increase of $Ir(ppy)_3$ concentration in EML results in increase of guest emission rate, which could be simply ascribed to increase of recombination in guest. However, considering that the singlet and triplet emission rates of host are largely decreased at 15% of $Ir(ppy)_3$, the high guest emission rate at high $Ir(ppy)_3$ concentration is assumed to be due to the increase of energy transfer from host. The triplet emission is more broadly distributed in EML due to long diffusion length of triplet, and is sharply decreased at both end of EML due to exciton diffusion (triplet energy of $Ir(ppy)_3$ is 0.172 eV higher than NPB and only 0.077 eV lower than BCP as shown in Table 1).

From the fitting process of energy transfer radius (Fig. 6a), we obtain R_D = 1.12 nm for 5% $Ir(ppy)_3$:CBP device

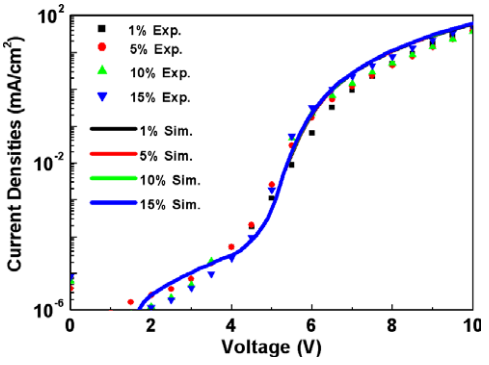

Fig. 4. Experimental and calculated current densities with voltage for the devices doped with 1%, 5%, 10%, and 15% of $Ir(ppy)_3$.

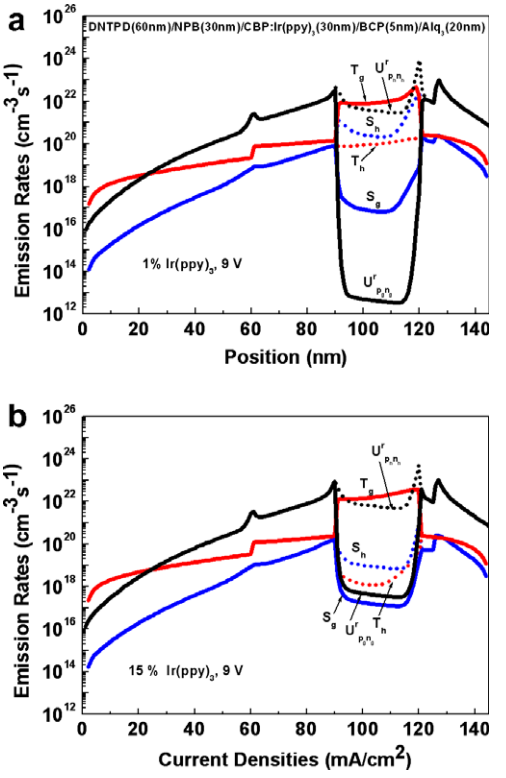

Fig. 5. Spatial distributions of the recombination and emission rates of the device doped with $Ir(ppy)_3$: (a) 1% and (b) 15%.

at a fixed value of R_F (3.2 nm [37]) (the current efficiency–current density curve at R_D = 1.12 nm is not fitted well in high current density region because exciton quenching or annihilation is not considered yet. The curve fitting in high current density region will be discussed later). Fig. 6b shows the doping concentration dependencies of energy transfer rate ratio ($K \cdot \tau$) for various Förster and Dexter radius, which is obtained by using the energy transfer rate equations (Eq. (12) and (13)). In Fig. 6b, $K \cdot \tau = 10$ implies that the energy transfer rate is 10 times higher than radiative or nonradiative decay rates. For example, Förster (at R_F = 3.2 nm) and Dexter (at R_D = 1.12 nm) energy transfers occur fast enough at over 2.5% and 9% doping concentration, respectively. The average separation distance of host and guest sites (R) can be obtained from the analytic form $R = 2.6603(100c)^{-0.25}$ nm for Förster energy transfer (which is extracted from the exact distances for the several doping concentration under the condition of crystal structure with the hopping distance of d_o = 1 nm) and $R = 1.7136\exp(-1.53c)$ nm for Dexter energy transfer (which is modified in order to avoid overestimation (underestimation) for smaller (larger) R than R_D in the simple Perrin model [38]).

In Fig. 7a, the current efficiency data simulated at R_F = 3.2 nm and R_D = 1.12 nm are compared with experimental results for all doping concentrations (1%, 5%, 10%, and 15%). The simulated results are in good agreement with experimental ones in low current density region. Overall, the current efficiency is increased with doping concentration, which is due to increase of energy transfer. The reason for higher current efficiency at 10% $Ir(ppy)_3$ than at 15% $Ir(ppy)_3$ is assumed to be because: (1) Förster and Dexter energy transfers sufficiently occur at over 9% $Ir(ppy)_3$ as shown in Fig. 6b, (2) host recombination rate decreases as guest concentration increases due to the reduction of host DOS, and (3) exciton blocking decreases as guest concentration increases due to the increase of guest exciton diffusivity as described in Eq. (11). In high current density region, there is typical efficiency roll-off

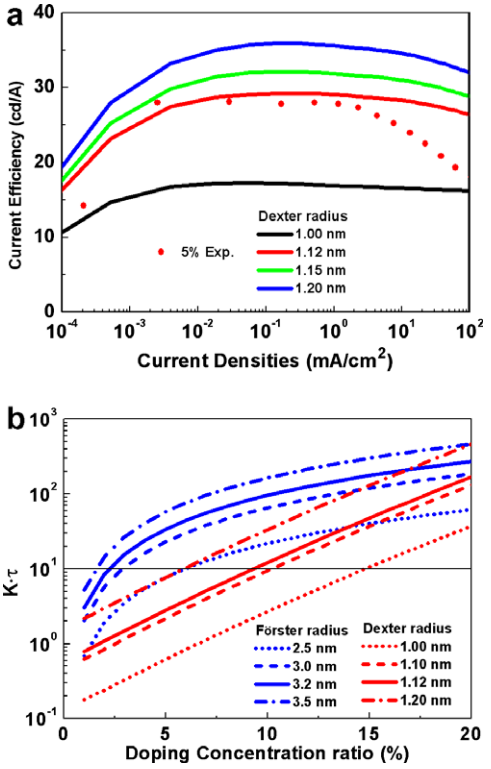

Fig. 6. (a) Dexter radius dependency of current efficiency for the device with 5% $Ir(ppy)_3$. (b) Doping concentration dependency of the energy transfer rate ratio ($K \cdot \tau$) for various Förster and Dexter radius. The horizontal solid line is $K \cdot \tau = 10$.

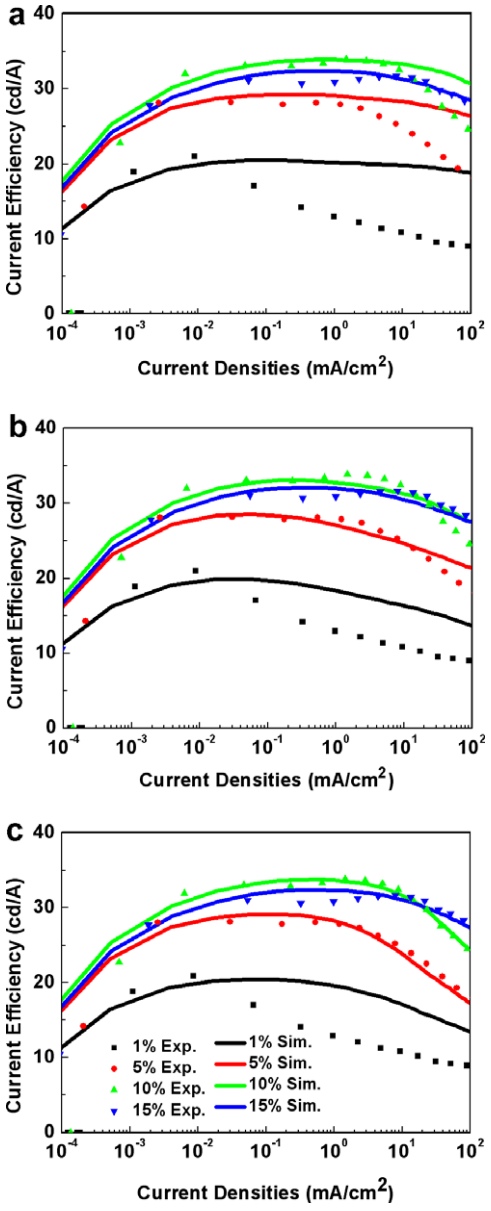

Fig. 7. Comparison of experimental and calculated current efficiency as a function of current density under the condition of (a) no quenching or annihilation, (b) host triplet–polaron quenching ($\kappa_{TP}^h = 3\times 10^{-11}$ cm^3 s^{-1}), and (c) host triple–triplet annihilation ($\kappa_{TT}^h = 2\times 10^{-9}$ cm^3 s^{-1}) for the devices doped with 1%, 5%, 10%, and 15% $Ir(ppy)_3$.

irrespective of doping concentration. Interestingly, the roll-off starting points of experimental curves are shifted to higher current density with increasing doping concentration and the roll-off slope becomes gentle at 15% Ir(ppy)$_3$, which consequently brings about the reversion of current efficiency between 10% and 15% at over 20 mA cm^{-2}. Such tendency of current efficiency roll-off can be fitted by considering polaron quenching or exciton annihilation, which is supposed to mainly occur in host sites because host recombination decreases as the doping concentration increase. The gentle roll-off at 15% Ir(ppy)$_3$ is assumed to be due to higher energy transfer rate compared with other decay rates (radiative, nonradiative, and annihilation decays). When the host *T*–*P* quenching ($\kappa^h_{TP} = 3 \times 10^{-11}$ cm^3 s^{-1}) is included to calculation, the current efficiency roll-off becomes too gentle to fit experimental results and the current efficiency reversion between 10% and 15% Ir(ppy)$_3$ is not expected as shown in Fig. 7b. This implies that polaron quenching is not the main reason for the current efficiency roll-off. When host *T*–*T* annihilation ($\kappa^h_{TT} = 2 \times 10^{-9}$ cm^3 s^{-1}) is considered, the steep roll-off and the current efficiency reversion are successfully realized except 1% Ir(ppy)$_3$ as shown in Fig. 7c. For 1% Ir(ppy)$_3$, it seems that the current efficiency roll-off cannot be obtained using common annihilation parameters, which is assumed to be because host emission (which generally shows low quantum efficiency) occurs significantly in high current density region due to very low DOS of 1% guest. Fig. 8 shows that emission at 460 nm is increased as the current density is increased, supporting that the steep efficiency roll-off at 1% Ir(ppy)$_3$ is ascribed to host emission.

In Fig. 9, several approaches to obtain high current efficiency are presented. Firstly, when the radiative lifetime of guest triplet is set to be reduced by 1 order (from 10^{-6} to 10^{-7} s), the shorten diffusion length (7.1 nm) leads to the increase of maximum current efficiency by more than 1.3 times compared with experimental result (case I). This implies that the use of the material with short triplet lifetime could be an efficient way to improve device efficiency. Meanwhile, there is no change in the roll-off tendency irrespective of the lifetime of guest, which is because *T*–*T* annihilation occurs mainly in host site (if the origin of *T*–*T* annihilation were guest site, the current efficiency roll-off

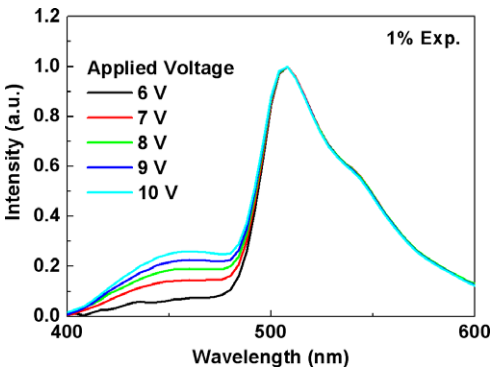

Fig. 8. Electroluminescence spectra for the device doped with 1% Ir(ppy)$_3$ according to voltage.

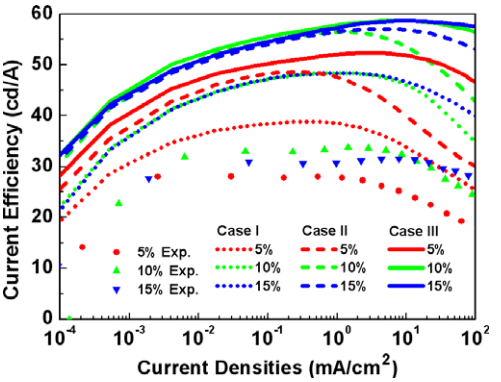

Fig. 9. Current efficiency as a function of current density, simulated under the condition of case I (1 order reduction of radiative lifetime of guest triplet), case II (reduction of *S* and *T* wavelength in HTL and ETL (λ_S = 350 nm, λ_T = 400 nm)), and case III (1 order reduction of radiative and nonradiative lifetime of host triplet) for the devices doped with 5%, 10%, and 15% Ir(ppy)$_3$.

should be gentle). Secondly, when the singlet and triplet wavelength in HTL and ETL are reduced (λ_S = 350 nm and λ_T = 400 nm), the maximum current efficiency is calculated to be about 1.8 times higher compared with experimental result (case II), which implies that hole transporting and/or electron transporting materials with high singlet and/or triplet energy could block exciton diffusion at the end of EML, consequently, increasing current efficiency. Finally, the current efficiency roll-off in high current region is improved by one order-reducing radiative and nonradiative lifetime of host triplet ($\tau^T_r = 10^{-5}$ s $\cdot$ $\tau^T_{nr} = 10^{-7}$ s), i.e. increase of energy transfer results in reduction of *T*–*T* annihilation in host [see Eq. (13)] (case III).

6. Summary

We propose electronic and excitonic emission models for organic light emitting devices comprising a host–guest system in emission layer. The basic electronic model contains thermionic injection at the electrodes, charge transport, and Langevin's recombination. Especially, charge transport mechanisms in organic host–guest systems are described as (1) hopping through the transport sites of host and guest with field- and doping-dependent mobility, (2) trapping between host (or guest) transport and trap sites, and (3) trapping between host and guest transport sites. Then, the spatial distribution of carriers, current density, and local recombination rates in host and guest sites is obtained from self-consistent calculation using Poisson's, current continuity, and current equations. The excitonic emission model includes (1) radiative and nonradiative decay, (2) exciton diffusion by exciton energy difference between materials, (3) singlet–triplet intersystem crossing, (4) Förster energy transfer between host singlet and guest singlet, (5) Dexter energy transfers between host singlet and guest singlet, or host triplet and guest triplet, (6) singlet–singlet, singlet–triplet, and triplet–triplet annihilation, (7) singlet–polaron and triplet–polaron quenching. Then, the spatial distributions of exciton and luminance

are obtained from the calculation of exciton rate equations and the summation of emission rate in EML, respectively.

In order to verify the proposed electronic and excitonic emission models, the simulated results are compared with experimental data of a series of phosphorescent (Ir(p-py)$_3$:CBP) organic electroluminescent devices with various doping concentration. When Förster and Dexter radius is set to be 3.2 nm and 1.12 nm, respectively, the simulated current density–current efficiency curves are in good agreement with experimental data for various doping concentration (5%, 10%, 15%), proving the validity of our model. It is also numerically demonstrated that (1) efficiency roll-off in high current density region is resulted from triplet–triplet annihilation (dominant) and triplet–polaron quenching, (2) exciton confinement in emission layer by controlling lifetime, diffusion constant and energy of exciton is important to improve device efficiency, (3) it is necessary to maximize energy transfer and intersystem-crossing in order to increase current efficiency. Finally, it is concluded from these results that the proposed models can be powerful simulation tools to analyze experimental data and design optimized device structures.

References

[1] C.W. Tang, S.A. VanSlyke, Appl. Phys. Lett. 51 (1987) 913.
[2] Y. Kawabe, M.M. Morrell, G.E. Jabbour, S.E. Shaeen, B. Kippelen, N. Peyghambarian, J. Appl. Phys. 84 (1998) 5306.
[3] J. Staudigel, M. Stößel, F. Steuber, J. Simmerer, J. Appl. Phys. 86 (1999) 3895.
[4] E. Tutiš, M.N. Bussac, B. Masenelli, M. Carrard, L. Zuppiroli, J. Appl. Phys. 89 (2001) 430.
[5] B. Ruhstaller, T. Beierlein, H. Riel, S. Karg, J.C. Scott, W. Riess, IEEE J. Sel. Top. Quantum Electron. 9 (2003) 723.
[6] S.J. Konezny, D.L. Smith, M.E. Galvin, L.J. Rothberg, J. Appl. Phys. 99 (2006) 064509.
[7] J. Yang, J. Shen, J. Appl. Phys. 84 (1998) 2105.
[8] F. Nüesch, D. Berner, E. Tutiš, M. Schaer, C. Ma, X. Wang, B. Zhang, L. Zuppiroli, Adv. Funct. Mater. 15 (2005) 323.
[9] C.-C. Lee, M.-Y. Chang, P.-T. Huang, Y.C. Chen, Y. Chang, S.-W. Liu, J. Appl. Phys. 101 (2007) 114501.
[10] D.M. Pai, J.F. Yanus, M. Stolka, J. Phys. Chem. 88 (1984) 4714.
[11] H. Murata, C.D. Merritt, Z.H. Kafafi, IEEE J. Sel. Top. Quantum Electron. 4 (1998) 119.
[12] Y.T. Tao, C.W. Ko, E. Balasubramaniam, Thin Solid Films 417 (2002) 61.
[13] I.I. Fishchuk, A.K. Kadashchuk, A. Vakhnin, Yu. Korosko, H. Bässler, B. Souharce, U. Scherf, Phys. Rev. B 73 (2006) 115210.
[14] M.A. Baldo, R.J. Holmes, S.R. Forrest, Phys. Rev. B 66 (2002) 035321.
[15] J. Kalinowski, W. Stampor, M. Cocchi, D. Virgili, V. Fattori, P. Di Marco, Chem. Phys. 297 (2004) 39.
[16] T. Tsuboi, N. Aljaroudi, Opt. Mater. 27 (2005) 1859.
[17] N.C. Giebink, Y. Sun, S.R. Forrest, Org. Electron. 7 (2006) 375.
[18] N.J. Turro, Modern Molecular Photochemistry, University Science Books, Sausalito, CA, 1991.
[19] D.L. Dexter, J. Chem. Phys. 21 (1953) 836.
[20] S. Verlaak, D. Cheyns, M. Debucquoy, V. Arkhipov, P. Heremans, Appl. Phys. Lett. 85 (2004) 2405.
[21] Y. Wang, Appl. Phys. Lett. 85 (2004) 4848.
[22] S.H. Kim, J. Jang, J.Y. Lee, Appl. Phys. 90 (2007) 223505.
[23] H. Bässler, Phys. Status Solidi (b) 175 (1993) 15.
[24] H.H. Fong, K.C. Lun, S.K. So, Chem. Phys. Lett. 353 (2002) 407.
[25] W. Shockley, W.T. Read Jr., Phys. Rev. 87 (1952) 835.
[26] S. Selberherr, Analysis and Simulation of Semiconductor Devices, Springer-Verlag, Wien, NY, 1984.
[27] J.C. Scott, G.G. Malliaras, Chem. Phys. Lett. 299 (1999) 115.
[28] J.H. Kim, E.J. Nam, S.Y. Hong, B.O. Kim, S.M. Kim, S.S. Yoon, J.H. Suh, Y. Ha, Y.K. Kim, Mater. Sci. Eng. C 24 (2004) 167.
[29] M.A. Baldo, S.R. Forrest, Phys. Rev. B 62 (2000) 10958.
[30] H. Kajii, T. Tsukagawa, H. Okuno, T. Taneda, K. Yoshino, Y. Ohmori, Thin Solid Films 393 (2001) 388.
[31] H. Matsushima, S. Naka, H. Okada, H. Onnagawa, Curr. Appl. Phys. 5 (2005) 305.
[32] W.-Y. Hung, T.-H. Ke, Y.-T. Lin, C.-C. Wu, T.-H. Hung, T.-C. Chao, K.-T. Wong, C.-I. Wu, Appl. Phys. Lett. 88 (2006) 064102.
[33] S. Naka, H. Okada, H. Onnagawa, Y. Yamaguchi, T. Tsutsui, Synthetic Met. 111–112 (2000) 331.
[34] N. Matsusue, Y. Suzuki, H. Naito, Jpn. J. Appl. Phys. 44 (2005) 3691.
[35] T. Yasuda, Y. Yamaguchi, D.-C. Zou, T. Tsutsui, Jpn. J. Appl. Phys. 41 (2002) 5626.
[36] H.A. Al Attar, A.P. Monkman, Adv. Funct. Mater. 16 (2006) 2231.
[37] B.W. D'Andrade, M.A. Baldo, C. Adachi, J. Brooks, M.E. Thompson, S.R. Forrest, Appl. Phys. Lett. 79 (2001) 1045.
[38] A. Monguzzi, R. Tubino, F. Meinardi, Phys. Rev. B 77 (2008) 155122.

Organic Electronics 11 (2010) 227–237

Contents lists available at ScienceDirect

Organic Electronics

journal homepage: www.elsevier.com/locate/orgel

Modification of gold source and drain electrodes by self-assembled monolayer in staggered n- and p-channel organic thin film transistors

Damien Boudinet [a,*], Mohamed Benwadih [a], Yabing Qi [b], Stéphane Altazin [a], Jean-Marie Verilhac [a], Michael Kroger [b], Christophe Serbutoviez [a], Romain Gwoziecki [a], Romain Coppard [a], Gilles Le Blevennec [a], Antoine Kahn [b], Gilles Horowitz [c]

[a] CEA/LITEN/LCI, 38054 Grenoble, France
[b] Department of Electrical Engineering, Princeton University, Princeton, NJ 08544, United States
[c] ITODYS, CNRS UMR 7086 Université Paris Diderot, 75205 Paris Cedex 13, France

ARTICLE INFO

Article history:
Received 6 August 2009
Received in revised form 19 October 2009
Accepted 27 October 2009
Available online 30 October 2009

Keywords:
Organic thin film transistors
Contact resistance
Self-assembled monolayer
Transfer line method

ABSTRACT

We report on the effect of the deposition of self-assembled monolayers (SAMs) on the source and drain electrodes on the contact resistance and mobility in organic thin film transistors (OTFTs). Ultraviolet photoelectron spectroscopy (UPS) shows a variation of the work function of the electrodes depending on the SAM. OTFTs were fabricated with solution processible Polyera ActivInk™ N1400, TIPS-pentacene and TFB, giving access to both polarities of transistors and to both crystalline and amorphous materials. The transfer line method (TLM) was used to separately estimate the contact resistance and mobility. A clear correlation is found between the work function of the modified electrodes and the corresponding contact resistance. The effect on mobility is more puzzling, and tentatively attributed to morphological effects.

© 2009 Elsevier B.V. All rights reserved.

1. Introduction

During the last decade, the development of new organic materials with enhanced electrical properties and ease of processing have led to organic field-effect transistors (OTFTs) with higher electrical performance [1–5]. More and more works report on mobility higher than 1 $cm^2/V\,s$ for both n- and p-channel OTFTs.

With the emergence of more robust materials, processible from solution, and with higher electrical properties, reduction of the transistor channel length is becoming one of the major challenges for the future years. Smaller transistors would help in designing circuits with higher working frequencies [6].

As performance is improving and channel length is decreasing, charge injection at source and drain electrodes is becoming the major impediment to further improvements [7–10]. For practical reasons, the vast majority of OTFT have contact electrodes made of gold. The high work function of atomically clean gold (5.2 ± 0.2 eV) matches most of the p-channel organic semiconductors Highest Occupied Molecular Orbital (HOMO) energy level [11–13]. For n-channel OTFTs however, a lower work function electrode is required to optimize electron injection in the Lowest Unoccupied Molecular Orbital (LUMO).

Some works have been reported on transistors fabricated using low WF metals such as calcium [14,15]. However, low WF metals tends to oxidize very quickly in ambient atmosphere. Process under high vacuum is needed for the fabrication and the characterization of such devices. For the fabrication of organic circuits, the use of the same metal is preferred to reduce the number of fabrication step.

An elegant way for tuning the work function of gold is the use of self-assembled monolayers (SAM) [16–22]. Since the first report by Campbell and coworkers [16], several works have been reported, mostly on p-channel OTFTs.

* Corresponding author.
E-mail address: damien.boudinet@cea.fr (D. Boudinet).

1566-1199/$ - see front matter © 2009 Elsevier B.V. All rights reserved.
doi:10.1016/j.orgel.2009.10.021

Yet, the effect of modifying gold with SAM on electrical performance of OTFTs is still controversial. Several works have attributed the improvement resulting from a modification of the source and drain electrodes by SAMs to a morphological effect [22,23]. However, more recent results tend to indicate that the mechanism of barrier height reduction described by Campbell may also lead to a modulation of the contact resistance in transistors.

In this paper, we investigate the effect of various SAMs on both n- and p-channel OTFTs, including polycrystalline and amorphous semiconductors. Ultraviolet photoelectron spectroscopy (UPS) is used to validate the concept in terms of work function of the modified gold electrodes. Transistors are then fabricated and characterized with various SAMs. The transfer line method (TLM) [19–21] is used to investigate and separate the effect of the SAMs on both the contact resistance and mobility. Results show that the contact resistance varies with the electrode work function (WF) and in agreement with the UPS data. Variations in the charge carrier mobility in the case of polycrystalline semiconductor are attributed to morphological effects, which are investigated by atomic force microscopy (AFM).

2. Experimental

2.1. Samples for SAMs characterization

Substrates were prepared by evaporating 200 nm of Au on Si, rinsing in acetone under nitrogen atmosphere and heating at 120 °C for 2 min. 4-Methyl(sulfanyl)thiophenol (MeSTP), 4-methoxythiophenol (MeOTP), 4-methylthiophenol (MeTP), 4-aminothiophenol (ATP), 4-nitrothiophenol (NOTP), cysteamine (CT), 1-decanethiol (DT), 1H,1H,2H,2H-perfluorooctanethiol (PFOT), and 1H,1H,2H,2H-perfluorodecanethiol (PFDT) were bought from Sigma–Aldrich. One millimolar solutions in ethanol were prepared, in which samples were immersed at room temperature for a period of 5 h. They were then rinsed thoroughly with pure ethanol and dried in a N_2 gas stream before being transferred into the vacuum system.

2.2. UPS

Measurements were performed in ultra-high vacuum (base pressure 10^{-10} Torr) using both He I and He II lines (21.22 and 40.81 eV, respectively) from a He discharge lamp. The photon flux was kept low to prevent photon-induced sample damage. The energy resolution was 0.15 eV.

2.3. Transistor fabrication and characterization

Polyethylene naphthalate (PEN) films were used as flexible substrates (Fig. 1). Thirty nanometer thick Au source and drain electrodes were deposited by plasma vapour deposition and patterned by photolithography. Transistors with a width of 1 cm and channel length of 5, 10, 20, 40, and 100 μm were fabricated.

Self-assembled monolayers were deposited the same way as for UPS and contact angle samples. For n-channel transistors, a *N,N*-dialkylsubstituted-(1,7&1,6)-dicyanoperylene-3,4:9,10-bis(dicarboximide) derivative (Polyera ActivInk™ N1400) bought from Polyera Corporation was diluted in 1,2-dichloro-benzene at a concentration of 8 mg mL^{-1} and spin-coated at 1200 revolutions per minute (rpm). For p-channel transistors, poly[9,9-dioctyl-fluorene-

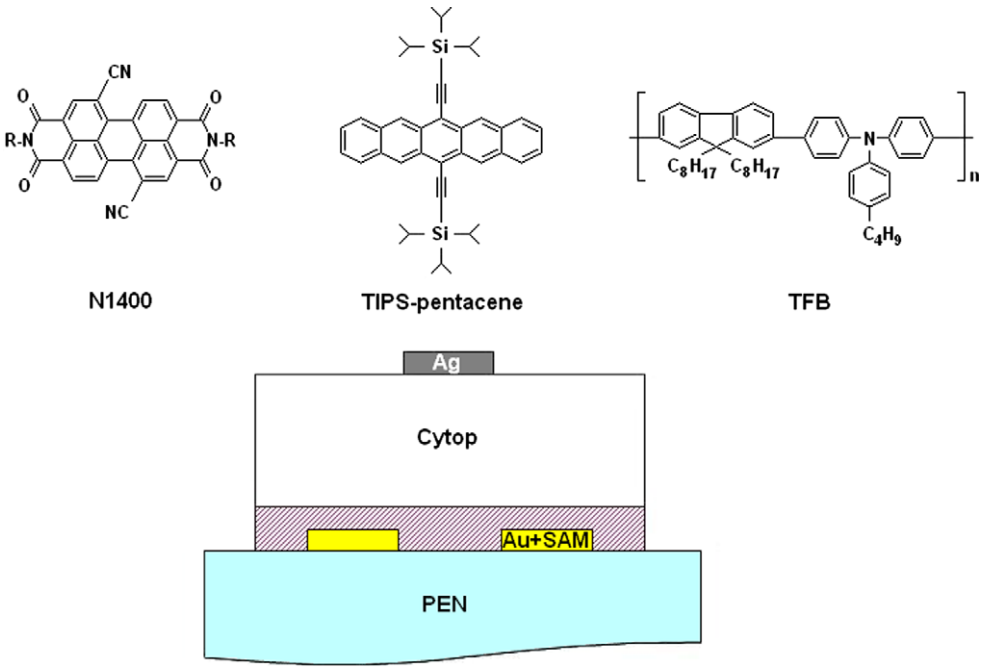

Fig. 1. Formula of the different semiconductor used in the study, and schematic of the fabricated devices.

co-*N*-(4-butylphenyl)-diphenylamine] (TFB) and 6,13-bis(triisopropylsilylethynyl) pentacene (TIPS-pentacene) were used as the active layer at a concentration of 16 and 12 mg mL^{-1} in mesythylene and toluene, respectively. Solutions were spin-coated at 1000 rpm. In all cases, the semiconductor films were cured for the three materials at a temperature of 115 °C for 5 min to eliminate the solvent. For all the spin-coating steps of the process, the plastic substrates were mounted on a silicon wafer using a drop of ethanol.

Cytop™ dielectric was then spin-coated on top of the semiconductor and cured at 100 °C for 20 min. The thickness of the layer was measured with a profilometer around 1.2 μm. To promote adhesion of the gate electrode on the highly hydrophobic insulating layer, solution of Nafion diluted at 30 mg mL^{-1} in isopropanol was spin-coated at 1000 rpm. Finally an Ag ink gate electrode was printed by ink-jet using a Dimatix set up.

Electrical measurements were performed at room temperature in air by using a parameter analyser (HP4145, Hewlett-Packard). Morphological characterization was carried out with an Innova AFM operating in the intermittent contact mode on samples specifically prepared for that purpose. The substrates consisted of PEN and patterned gold electrodes with the different SAMs that were prepared exactly the same way as for the transistors and on top of which the semiconductor was spin-coated.

2.4. Electrical parameters extraction

The transfer characteristic in the linear regime (V_D = 1 V for Polyera ActivInk™ N1400, V_D = 5 V for TIPS-pentacene, and V_D = 10 V for TFB) was measured on devices with various channel length (L = 5, 10, 20, 40, and 100 μm) prepared in the same run. From these characteristics, the threshold voltage was first extracted from the peak of the second derivative of the gate voltage dependent drain current, as described previously [21]. The next step consisted of calculating the width corrected total resistance as a function of $V_G - V_T$. According to the TLM, this resistance can be decomposed into the contact resistance R_C in series with the channel resistance. A representative example of the channel length dependent resistance for various values of $V_G - V_T$ is shown in Fig. 2. The contact resistance corresponds to the extrapolation of the straight line to zero channel length.

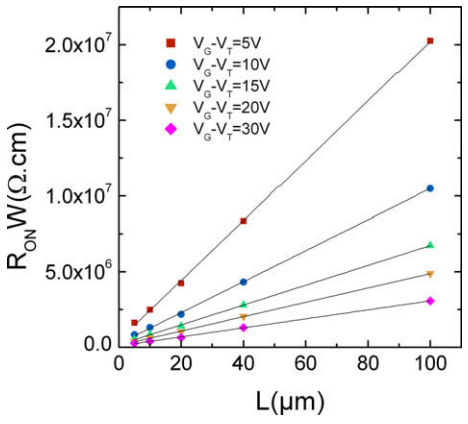

Fig. 2. Representative example of width normalized resistance versus channel length curves. The resistance is computed from the transfer characteristic at a drain voltage of 1 V.

3. Results

3.1. SAMs characterization

Fig. 3 gives the chemical structure of the different molecules used for the SAMs. To understand the effects of the different SAMs on transistors performance, we characterized them by UPS and contact angle measurements.

The UPS spectra of three representative samples are shown in Fig. 4. The work function, defined as the energy difference between the vacuum level (E_{vac}) of the film and the Fermi level (E_F), was determined from the secondary electron cut-off energy. The WF of the bare Au reference was 4.75 eV, which is a standard value for an Au surface exposed to the ambient. The WF of the SAM-modified Au was found to range from 4.18 to 5.44 eV. For example, the WF of the Au modified by PFDT SAM was measured at 5.44 eV, in good agreement with previous results [20], and 0.69 eV higher than that of bare Au. On the other hand, the work function of gold modified with MeTP was 4.28 eV, 0.47 eV lower than that of Au.

The contact angle with water (Table 1) is an indication of surface energy, and in turn depends on the nature of the terminal group of the SAM. We first note that the contact angle is smaller for the thiophenol molecules than for the corresponding alkanethiolate, which has been attributed to the polar nature of the phenol adsorbate [24]. The effect of the terminal group on the contact angle allows us to classify their impact on surface energy as follows (listed in order of decreasing surface energy): $NH_2 = NO_2 > OCH_3 > SCH_3 > CH_3 > CF_3$. We finally note that the very low contact angle found with cysteamine can be attributed to a poorly organized layer, due to the very short alkyl chain and the resulting low interchain coupling.

3.2. N-channel polycrystalline OTFTs

For each semiconductor, transistors were fabricated with various electrodes and channel lengths. We first report the results on n-channel transistors. Fig. 5 gives the transfer characteristic of some of the devices.

For long channel transistors, the devices with PFDT exhibit the largest ON current and the highest mobility, as shown in Fig. 5b. Interestingly, the transistors fabricated with hydrophobic DT and PFOT also exhibit a larger mobility than others. When the channel length decreases down to 5 μm, the transistors with PFDT deliver the lowest current, which can be attributed to a high contact resistance. Similarly, the low WF of the gold + MeOTP system can be associated with the corresponding high current at short channel length. We also note that electrodes made of bare gold and gold + CT, which show almost the same WF, yield very similar transfer characteristics.

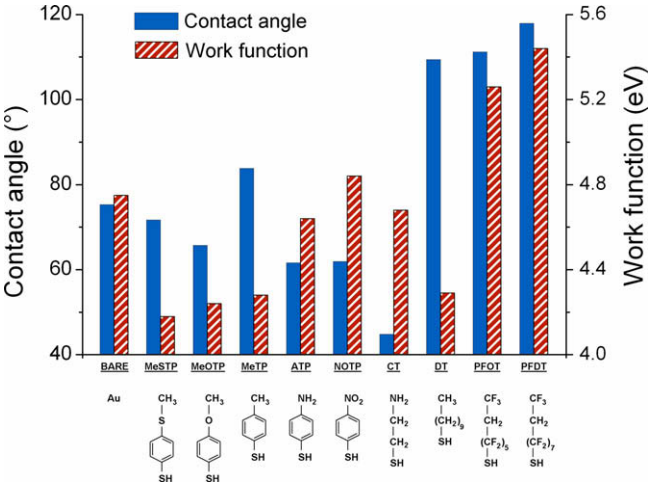

Fig. 3. Molecules used in the SAMs and corresponding Au/SAM work function measured by UPS and contact angle measured with water. Name of the molecule from left to right: 4-(methylsulfanyl)-thiophenol (MeSTP), 4-methoxythiophenol (MeOTP), 4-methylthiophenol (MeTP), 4-aminothiophenol (ATP), 4-nitrothiophenol (NOTP), cysteamine (CT), 1-decanethiol (DT), 1H,1H,2H,2H-perfluorodecanethiol (PFDT), 1H,1H,2H,2H-perfluorooctanethiol (PFOT).

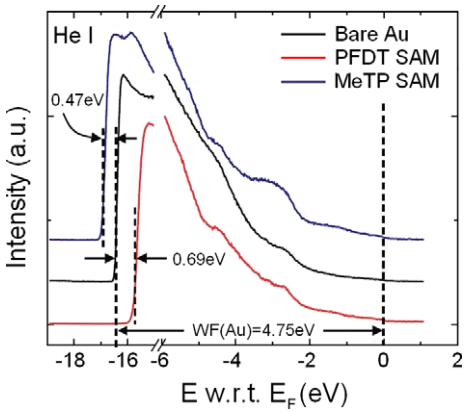

Fig. 4. He I UPS spectra of the bare Au substrate and of the PFDT and MeTP SAMs on Au samples.

The main electrical parameters of each device are listed in Table 1. For short channel, the high work function electrodes PFDT, PFOT and NOTP produce transistors with low effective mobility.

We also shown in Fig. 6 the output characteristics for source/drain electrodes modified with MeTP and PFOT. It has been reported [25,26] that transistors suffering from very high contact resistance present some non-linearity at the origin of the I_D–V_D curves. Interestingly, Polyera ActivInk N1400™ does not seem to give rise to such non-linearity.

We estimated the contact resistance R_C with the transfer line method (TLM) as described in the Section 2. Because none of the devices was affected by non-linearity at the origin, we were able to work with drain voltages as low as 1 V. For each SAM, eight transistors of each length were fabricated and characterized. The contact resistance and mobility are reported in Fig. 5. We note that R_C varies linearly with $1/(V_G - V_T)$, which is a

Table 1
Main electrical parameters for n-channel transistors with various source and drain electrodes for an applied drain voltage of 1 V.

Electrode	Contact angle (°)	WF (eV)	μ_E (cm^2/V s)[a]	μ_C (cm^2/V s)[b]	V_T (V)[c]	I_{ON}/I_{OFF}[d]	R_C (MΩ cm)[e]
MeSTP	71.7 ± 1.4	4.19	0.022	0.055	5	3.1×10^6	0.163
MeOTP	65.7 ± 1.3	4.24	0.034	0.057	3.5	6.4×10^6	0.094
MeTP	83.8 ± 1.7	4.28	0.029	0.070	1.5	1.3×10^6	0.093
DT	109.5 ± 1.7	4.29	0.055	0.139	1	1.1×10^4	0.207
ATP	61.6 ± 1.5	4.64	0.017	0.073	1.5	4.2×10^6	0.284
CT	44.8 ± 0.8	4.68	0.015	0.051	6	2.2×10^4	0.257
Bare	75.3 ± 1.7	4.75	0.016	0.057	3	3.4×10^6	0.327
NOTP	61.9 ± 1.4	4.84	0.012	0.058	6.5	2.1×10^6	0.441
PFOT	111.2 ± 0.8	5.26	0.009	0.169	8	3.1×10^5	0.540
PFDT	117.9 ± 1.7	5.44	0.005	0.184	1	7.3×10^3	0.676

[a] Effective mobility computed from classical equation at $V_G - V_T = 30$ V for 5 μm long transistors.
[b] Corrected mobility from TLM measurements at $V_G - V_T = 30$ V.
[c] Threshold voltage extracted by the second derivative method.
[d] ON/OFF ratio for 5 μm long transistors with OFF current taken at minimum of the transfer characteristic and ON current taken at 40 V.
[e] Contact resistance from the TLM measurements taken at $V_G - V_T = 30$ V.

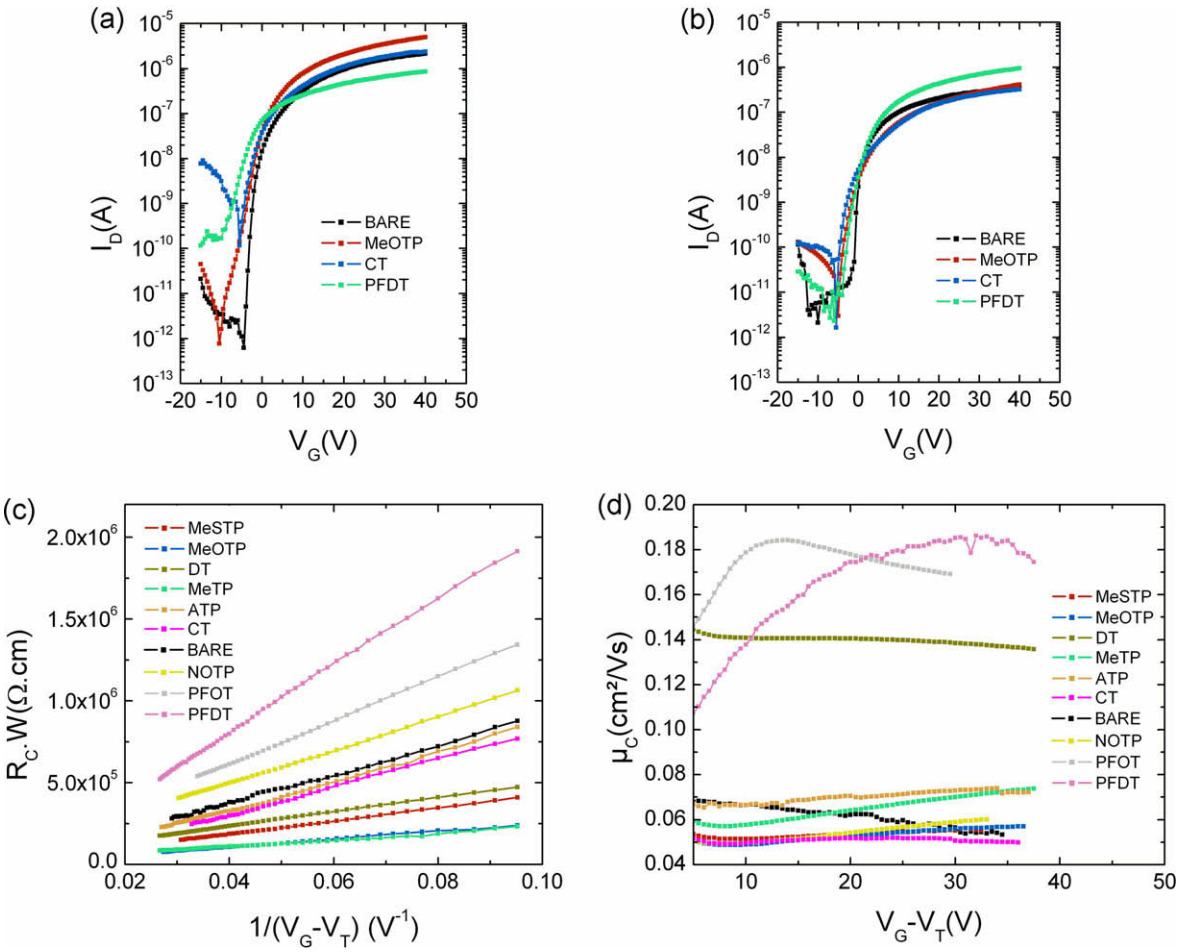

Fig. 5. Transfer characteristics in the linear regime (V_D = 1 V) with different modified electrodes for (a) 5 μm long and (b) 100 μm long transistors made with Polyera ActivInk™ N1400. (c) contact resistance, and (d) mobility corrected for the contact resistance, extracted from TLM.

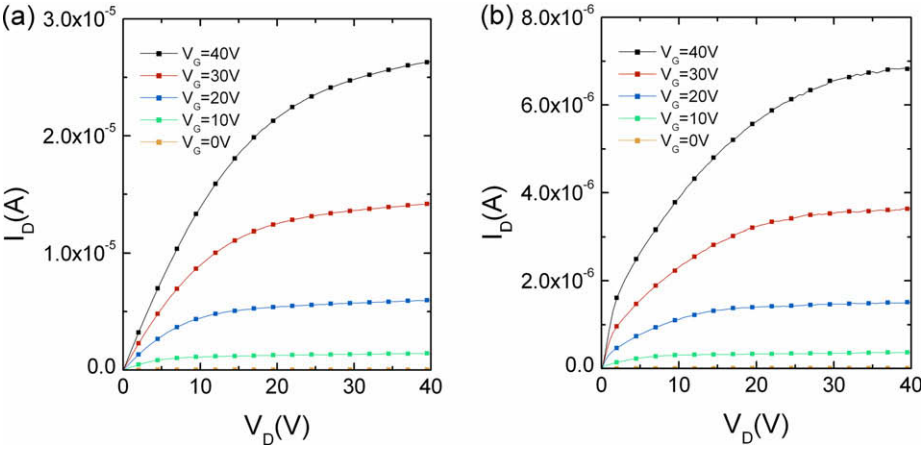

Fig. 6. Output characteristics for n-channel transistor fabricated with (a) MeOTP and (b) PFDT.

common feature in transistors with staggered configuration [27].

The extracted contact resistance nicely matches the WF of the corresponding electrodes. The LUMO of Polyera ActivInk™ N1400 is given by the supplier at around 4.3 eV. Electrodes with DT, MeTP, MeOTP and MeSTP have respective WF equal to 4.29, 4.28, 4.24, and 4.19 eV, respectively, which adequately match the LUMO

level. It is therefore not surprising that they offer the lowest contact resistance. Electrodes made of bare gold, gold + CT and gold + ATP have similar WF and exhibit almost the same contact resistance. Finally, the higher WF of gold + NOTP, gold + PFOT and gold + PFDT leads to devices with the highest contact resistance.

Interestingly, transistors fabricated with highly hydrophobic SAMs exhibit higher mobility when corrected for the contact resistance. This was already reported [28] and was attributed to morphological effects. We carried out AFM and optical polarized microscope imaging on the semiconductor films deposited on various SAMs. Representative pictures are given in Fig. 7.

Optical microscope images of films grown on gold + CT show a very small grain size. This can also be seen on the corresponding AFM picture. When the contact angle increase (from 45° for gold + CT to 84° for gold + MeTP), grains become larger, leading to an increase in mobility. The effect on the grain size is even more pronounced for very hydrophobic SAMs as shown in Fig. 7c for gold + PFOT (111°). The mobility corrected for the contact resistance for transistors made with DT, PFOT, and PFDT was found the highest among all the SAMs tested.

3.3. P-channel polycrystalline OTFTs

The effect of the SAMs on transistors made with the polycrystalline small molecule TIPS-pentacene are presented next. We limit ourselves to the most relevant SAMs. Table 2 reports the main electrical parameters for the different device fabricated.

Fig. 8 shows the output characteristics of transistors with the high WF PFOT (Fig. 8a), and low WF MeOTP (Fig. 8b). We note some non-linearity at the origin of the curves in the case of MeOTP. For this reason, TLM measurements were conducted at a drain voltage of 5 V.

The parameters extracted from TLM on TIPS-pentacene transistors are displayed in Table 2 and Fig. 9 Like for Polyera ActivInk™ N1400, the contact resistance and WF are closely correlated.

The mobility corrected for the contact resistance increases with the contact angle, the most hydrophilic surfaces corresponding to the highest mobility. A similar effect of surface energy on semiconductor morphology was already reported [29]. Optical microscope images of the semiconductor films are presented in Fig. 10. With hydrophilic surfaces, TIPS-pentacene forms very large grains offering the highest mobility when corrected for the contact resistance. When deposited on hydrophobic SAMs, the semiconductor adopts a very different morphology, which can account for the lower mobility. We finally note that, like for Polyera ActivInk™ N1400, the threshold voltage seems to be independent of the SAM.

3.4. P-channel amorphous OTFTs

Lastly, we investigated the influence of the SAMs on transistors made with amorphous TFB. As in the case of TIPS-pentacene, we limited the study to the most relevant SAMs. In Fig. 11, the output characteristics of transistors with two different SAMs are presented. The HOMO level of TFB was reported in the literature to be between 5.3 and 5.5 eV [30]. With high WF source and drain elec-

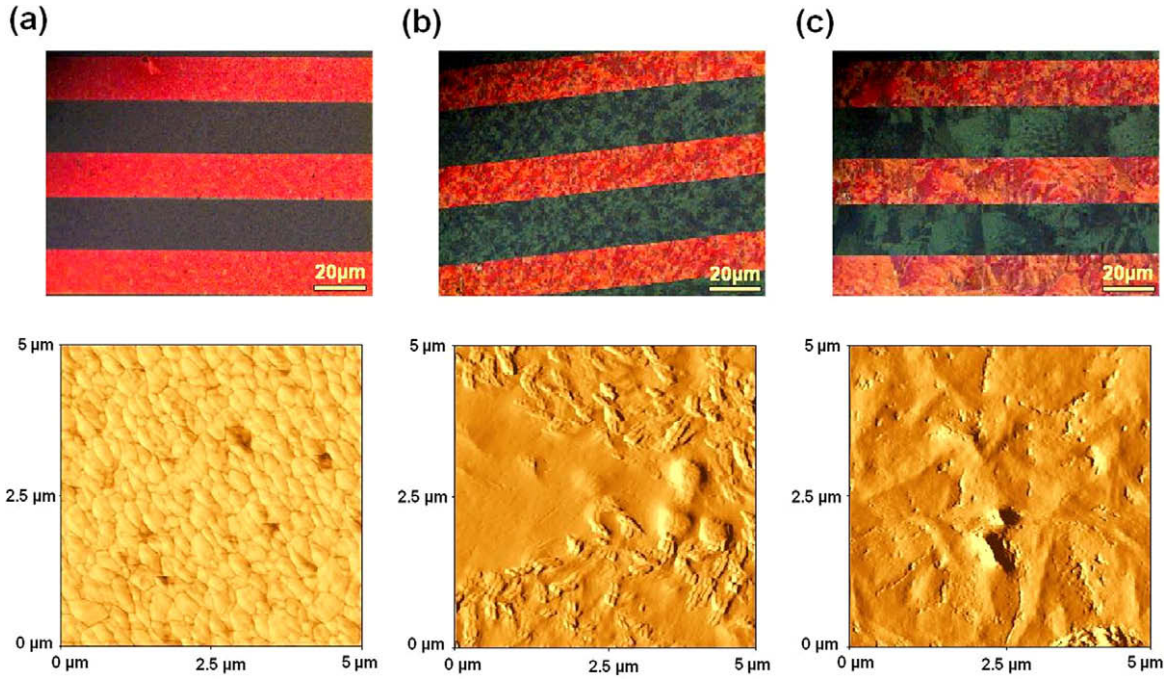

Fig. 7. Optical microscope and AFM images of Polyera ActivInk™ N1400 on various substrates: (a) CT, (b) MeTP, and (c) PFOT.

Table 2
Main electrical parameters for polycrystalline p-channel transistors with different source and drain electrodes for an applied drain voltage of 5 V.

Electrode	Contact angle (°)	WF (eV)	μ_E (cm^2/V s)[a]	μ_C (cm^2/V s)[b]	V_T (V)[c]	I_{ON}/I_{OFF}[d]	R_C (MΩ cm)[e]
MeTP	83.8 ± 1.7	4.28	0.022	0.067	−5.5	3.6×10^5	2.332
DT	109.5 ± 1.7	4.29	0.011	0.063	−5	1.3×10^5	2.361
Bare	75.3 ± 1.7	4.75	0.047	0.155	−9	3.6×10^5	0.998
NOTP	61.9 ± 1.4	4.84	0.103	0.189	−6	8.4×10^5	0.291
PFOT	111.2 ± 0.8	5.26	0.026	0.065	−6	1.8×10^5	0.105
PFDT	117.9 ± 1.7	5.44	0.036	0.059	−4.5	2.7×10^5	0.021

[a] Effective mobility computed from classical equation at $V_G - V_T = 30$ V for 5 μm long transistors.
[b] Corrected mobility from TLM measurements at $V_G - V_T = 30$ V.
[c] Threshold voltage extracted by the second derivative method.
[d] ON/OFF ratio for 5 μm long transistors with OFF current taken at minimum of the transfer characteristic and ON current taken at 40 V.
[e] Contact resistance from the TLM measurements taken at $V_G - V_T = 30$ V.

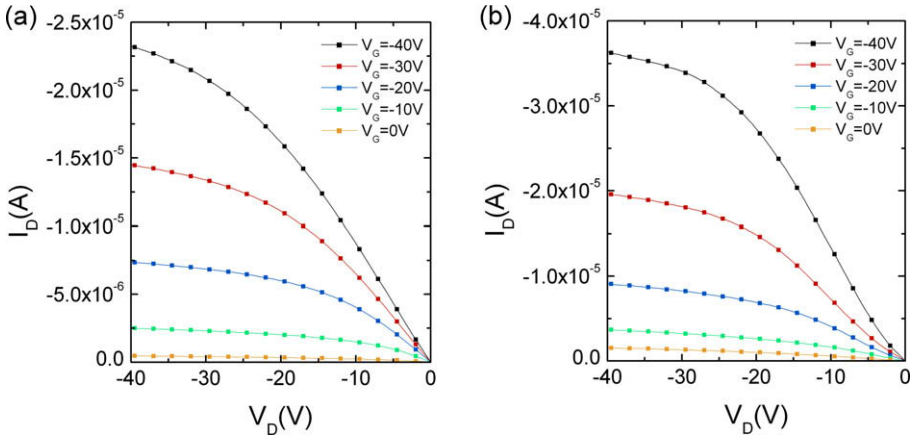

Fig. 8. Output characteristics for polycrystalline p-channel transistor fabricated with (a) PFOT and (b) MeOTP.

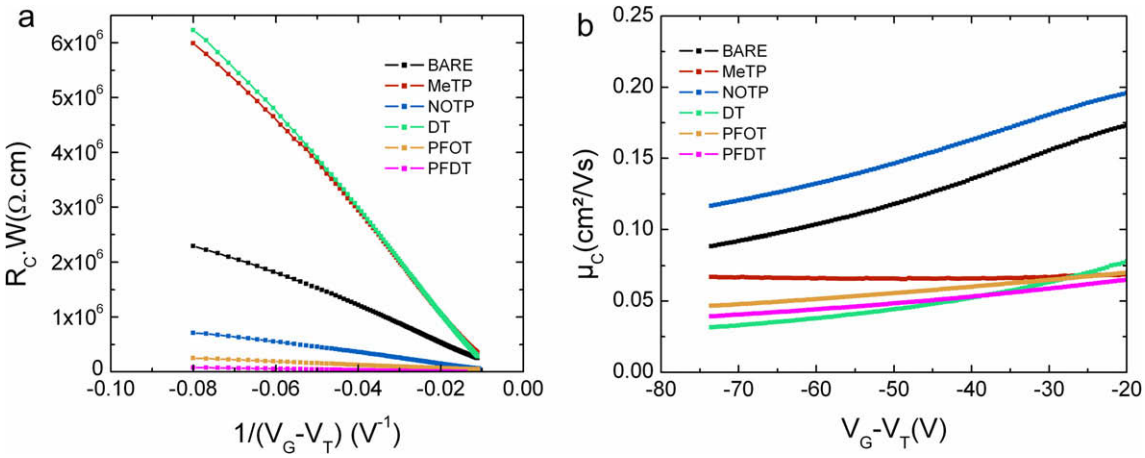

Fig. 9. (a) Contact resistance and (b) mobility extracted for TLM on polycrystalline p-channel OTFTs.

trodes, the onset of the characteristics is highly linear. However, with low work-function electrodes, the characteristics are affected by a significant non-linearity at the origin.

The transfer characteristics in the saturation regime ($V_D = 100$ V) and the corresponding square root of the drain current as a function of the gate voltage are given in Fig. 12.

The saturation mobility is computed from the slope of the curves in Fig. 12b as:

$$\mu_{SAT} = \frac{2 * \text{slope} * L}{W * \text{Cox}} \quad (1)$$

Interestingly, when the applied gate voltage is large enough, all the devices have similar mobility (curves on

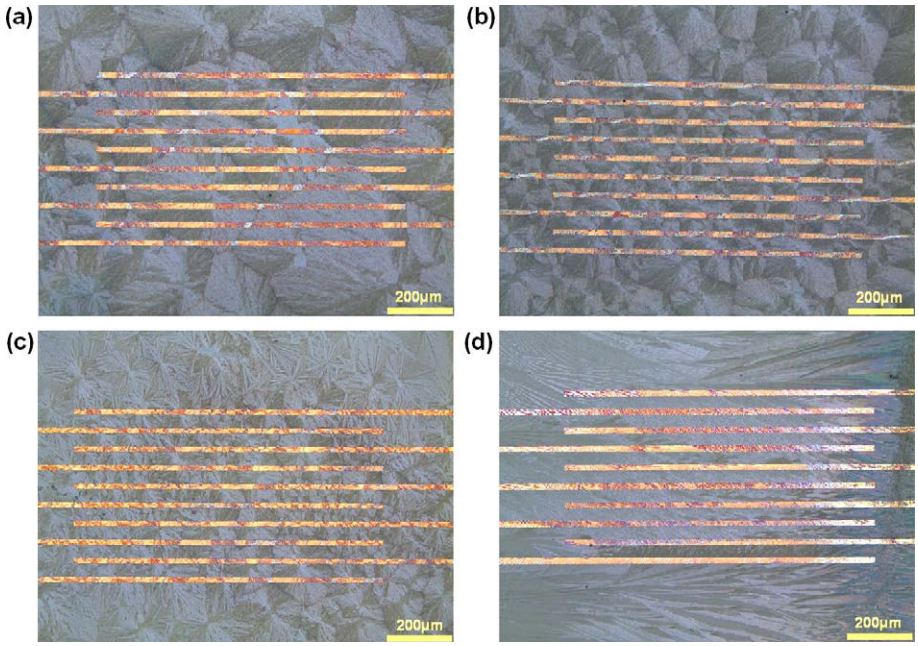

Fig. 10. Optical microscope picture of TIPS-pentacene with different source/drain electrode: (a) NOTP, (b) bare gold, (c) MeTP, and (d) DT.

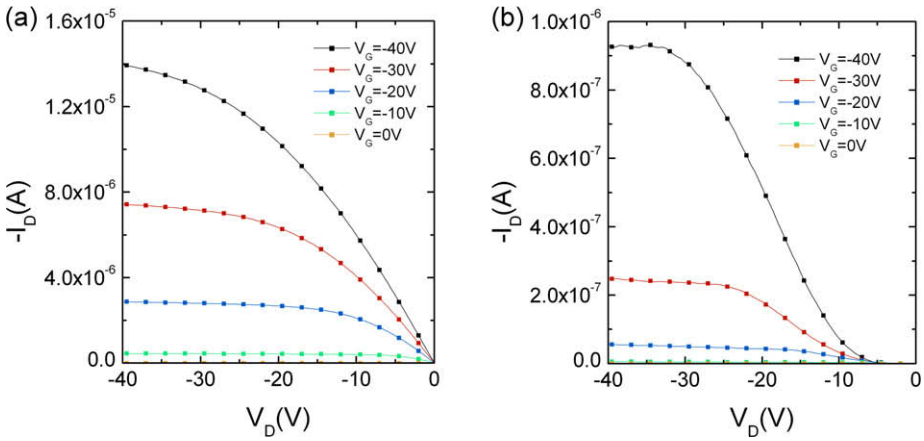

Fig. 11. Output characteristics of amorphous p-channel transistors made with source and drain electrodes treated with (a) PFDT and (b) MeOTP.

Fig. 12b have similar slope). In the case of amorphous TFB, morphological effects are non-existent. The threshold voltage extracted in the saturation regime (using the linear extrapolation of the curves in Fig. 12b) is strongly affected by the WF of the source and drain electrodes. Table 3 sums up the main electrical parameters of the different devices.

Because of the large non-linearity observed in Fig. 11b, we conducted the TLM investigation at an applied drain voltage of 10 V to ensure that transistors were operating in the linear regime. Compare to polycrystalline materials, amorphous TFB presents a huge dependence of the contact resistance with the drain voltage. This is reflected by an increased of the threshold voltage with the contact resistance, and a more and more pronounced non-linearity at the origin of the output characteristics. At a drain voltage of 10 V, we found a linear dependence of the drain current with the gate voltage for each SAM ensuring the validity of the transfer line method. The contact resistance and mobility are drawn in Fig. 12c and d.

The evolution of the contact resistance is in agreement with the WF of the respective source and drain electrodes. The lower mobility found for low WF electrodes cannot be explained by morphological effects like in the case of the polycrystalline materials. Because of the very high threshold voltages and higher applied drain voltages (10 V), TLM results for low WF electrodes are given for a smaller range of $V_G - V_T$. Mobility in TFB semiconductor was previously reported to be highly gate voltage dependent [31,32]. Due to variation of the threshold voltage, the extracted mobility is lower.

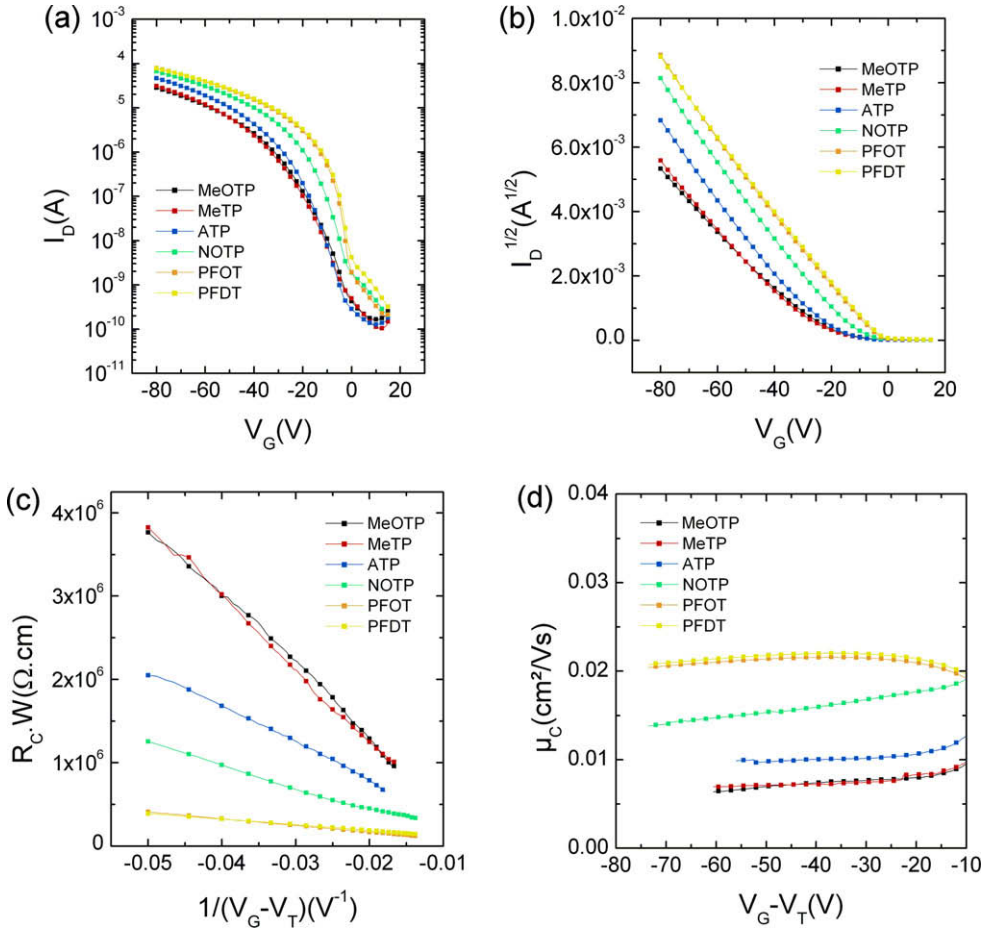

Fig. 12. (a) Transfer characteristics and (b) square root of the drain current as a function of the gate voltage for 20 μm long amorphous p-channel transistors in the saturation regime (V_D = 100 V). (c) Contact resistance extracted from TLM. (d) Mobility corrected for the contact resistance extracted from TLM.

Table 3
Main electrical parameters in the saturation regime (V_D = 100 V) and the linear regime (V_D = 10 V) for amorphous TFB p-channel transistors with different source/drain electrodes.

Electrode	WF (eV)	μ_{SAT} (cm^2/V s)[a]	μ_E (cm^2/V s)[b]	μ_C (cm^2/V s)[c]	V_T (V)[d]	I_{ON}/I_{OFF}[e]	R_C (MΩ cm)[f]
MeOTP	4.24	0.021	0.0024	0.0072	−31.5	1.72×10^5	1.78
MeTP	4.28	0.026	0.0026	0.0073	−29.5	2.99×10^5	1.64
ATP	4.64	0.033	0.0059	0.0101	−20	3.67×10^5	1.04
NOTP	4.84	0.036	0.0078	0.0159	−12	3.18×10^5	0.55
PFOT	5.26	0.037	0.0154	0.0215	−5.5	4.08×10^5	0.20
PFDT	5.44	0.037	0.0125	0.0219	−5	2.39×10^5	0.22

[a] Saturation effective mobility computed from Eq. (1) at V_G = 80 V.
[b] Linear effective mobility computed from classical equation at $V_G - V_T$ = 40 V for 5 μm long transistors.
[c] Corrected mobility from TLM measurements at $V_G - V_T$ = 40 V.
[d] Threshold voltage extracted by the second derivative method.
[e] ON/OFF ratio for 5 μm long transistors with OFF current taken at minimum of the transfer characteristic and ON current taken at 40 V.
[f] Contact resistance from the TLM measurements taken at $V_G - V_T$ = 40 V.

4. Discussion

Charge injection at metal-organic semiconductor interfaces is mainly controlled by the alignment of energy level at both sides of the interface [12]. Using SAMs, it is possible to tune the barrier at the interface and thus tune the contact resistance. However, several studies have also attributed the improvement resulting from a modification of the source and drain electrodes by SAMs to a morphological effect [9,10,33].

Using the TLM method, we were able to separate the effect of the SAMs on mobility and contact resistance in both n-channel and p-channel polycrystalline OTFTs. Fig. 13 shows the variation of the contact resistance as a function

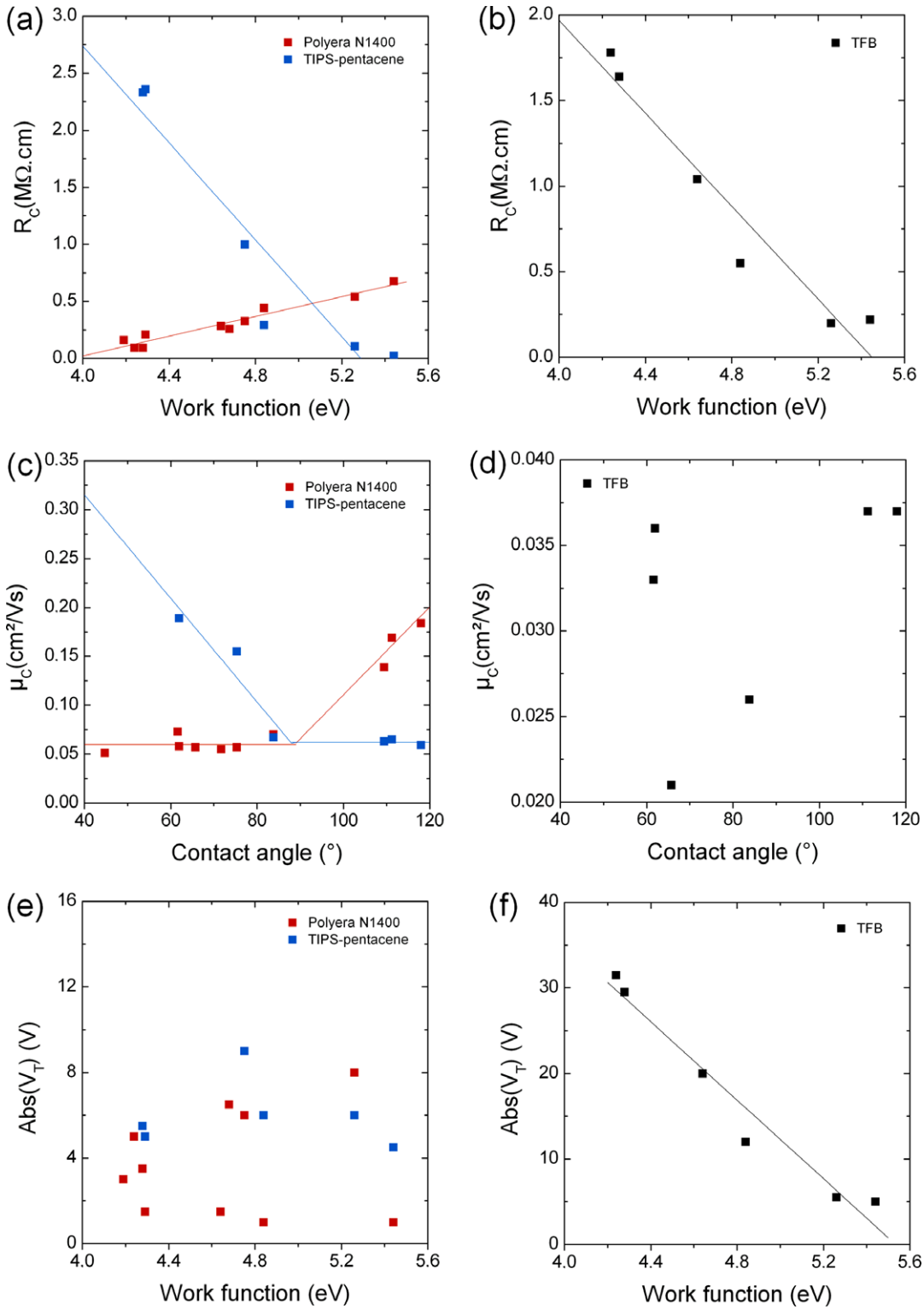

Fig. 13. (a and b): Contact resistance as a function of the work function of the modified electrodes for the different studied semiconductor. (c and d): Mobility corrected for the contact resistance as a function of the contact angle of the modified electrodes for the different studied semiconductor. (e and f): Threshold voltage as a function of the work function of the modified electrode for the different studied semiconductor. Experimental data are linearly fitted when relevant.

of the work function of source/drain electrodes. For both Polyera ActivInk N1400™ and TIPS-pentacene, the clear correlation between the two parameters presents strong evidence for the effect of the SAMs on the injection barrier height at the interface. A similar behaviour was found for amorphous TFB as already reported in the literature [34]. Of importance is the fact that the trend reverses when passing from the n-channel to the p-channel devices. That is, the contact resistance increases with the WF in the first case, while it decreases in the second one. These trends are in perfect agreement with an increase of the electron barrier in n-channel devices, and a reduction of the hole barrier in p-channel transistors.

The effect of the SAMs on the mobility is less clear and seems to largely depend on the nature of the semiconductor. Fig. 13 also reports on the variation of the mobility as a function of the contact angle. For TIPS-pentacene, the mobility is constant for contact angles lower than 90°, and linearly increases above this value. A similar behaviour has been reported for evaporated pentacene [29]. Surprisingly, a reverse trend is observed with Activink N1400, indicating that in this case, a more hydrophilic substrate yields a better morphological organisation in the semiconductor film. This unexplained discrepancy deserves further investigation. We finally note that the contact angle has practically no effect on the mobility of TFB, which can be attributed to the amorphous (isotropic) character of this compound. We also found a clear interdependence between the threshold voltage and the work function of the electrodes for the amorphous material (Fig. 13). In the case of the polycrystalline materials, we did not find any obvious dependence for the threshold voltage.

5. Conclusion

We have characterized a set of 10 SAM-modified source/drain electrodes and investigated the effect of the different SAMs on electrical performance of OTFTs. For the first time, the work was conducted on both n- and p-channel semiconductors. The use of TLM measurements allowed us to separate the effect of SAMs on contact resistance and channel mobility. We found a clear relationship between the contact resistance and the work function of source/drain electrodes for each semiconductor.

In the case of polycrystalline semiconductor, the mobility corrected for contact resistance is linked to the surface energy of the electrodes, as measured by the contact angle with water. For n-channel (p-channel) transistors, mobility was found constant for contact angles smaller (larger) than 90° and linearly increasing when the surface became more hydrophobic (hydrophilic). Optical microscope and AFM images were used to link this variation of mobility to the morphology of the semiconductor. In the case of amorphous TFB, the most affected parameter is the threshold voltage. We find a linear dependence between the threshold voltage and the work function of the electrodes.

References

[1] J. Zaumseil, H. Sirringhaus, Chem. Rev. 107 (2007) 1296–1323.
[2] A. Facchetti, Mater. Today 10 (2007) 28–37.
[3] G. Horowitz, J. Mater. Res. 19 (2004) 1946–1962.
[4] Z. Bao, Adv. Mater. 12 (2000) 227–230.
[5] C.R. Newman, C.D. Frisbie, D.A. Da Silva Filho, J.-L. Brédas, P.C. Ewbank, K.R. Mann, Chem. Mater. 16 (2004) 4436–4451.
[6] Y.-Y. Noh, N. Zhao, M. Caironi, H. Sirringhaus, Nat. Nanotechnol. 2 (2007) 784–789.
[7] D.J. Gundlach, L. Zhou, J.A. Nichols, T.N. Jackson, P.V. Necliudov, M.S.J. Shur, J. Appl. Phys. 100 (2006) 024509.
[8] T.D. Anthopoulos, D.M. de Leeuw, E. Cantatore, P. Van't Hof, J. Alma, J.C. Hummelen, J. Appl. Phys. 98 (2005) 054503.
[9] B.H. Hamadani, D. Natelson, J. Appl. Phys. 97 (2005) 064508.
[10] L. Burgi, T.J. Richards, R.H. Friend, H. Sirringhaus, J. Appl. Phys. 94 (2003) 6129–6137.
[11] I.G. Hill, D. Milliron, J. Schwartz, A. Kahn, Appl. Surf. Sci. 166 (2000) 354–362.
[12] H. Ishii, K. Sugiyama, E. Ito, K. Seki, Adv. Mater. 11 (1999) 605–625.
[13] A. Kahn, N. Koch, W. Gao, J. Polym. Sci. B: Polym. Phys. 41 (2003) 2529–2548.
[14] T. Yasuda, T. Tsutsui, Jap. Soc. Appl. Phys. 45 (2006) L595–L597.
[15] T. Yasuda, T. Tsutsui, Chem. Phys. Lett. 402 (2005) 395–398.
[16] I.H. Campbell, S. Rubin, T.A. Zawodzinski, J.D. Kress, R.L. Martin, D.L. Smith, Phys. Rev. B 54 (1996) 14321–14324.
[17] B. de Boer, A. Hadipour, M.M. Mandoc, T. van Woudenbergh, P.W.M. Blom, Adv. Mater. 17 (2005) 621–625.
[18] B.H. Hamadani, D.A. Corley, J.W. Ciszek, J.M. Tour, D. Natelson, Nano Lett. 6 (2006) 1303–1306.
[19] M. Mottaghi, G. Horowitz, Org. Electron. 7 (2006) 528–536.
[20] P. Marmont, N. Battaglini, P. Lang, G. Horowitz, J. Hwang, A. Kahn, C. Amato, P. Calas, Org. Electron. 9 (2008) 419–424.
[21] D. Boudinet, G. Le Blevennec, C. Serbutoviez, J.-M. Verilhac, H. Yan, G. Horowitz, J. Appl. Phys. 105 (2009) 084510.
[22] C. Bock, D.V. Pham, U. Kunze, D. Kafer, G. Witte, A. Terfort, Appl. Phys. Lett. 91 (2007) 052110.
[23] D.J. Gundlach, J.E. Royer, S.K. Park, S. Surbramanian, O.D. Jurchescu, B.H. Hamadani, A.J. Moad, R.J. Kline, L.C. Teague, O. Kirillov, C.A. Richter, J.G. Kushmerick, L.J. Richter, S.R. Parkin, T.N. Jackson, J.E. Anthony, Nat. Mater. 7 (2008) 216–221.
[24] J.F. Kang, A. Ulman, S. Liao, R. Jordan, G. Yang, G.-Y. Liu, Langmuir 17 (2001) 95–106.
[25] P.V. Necliudoc, M.S. Shur, D.J. Gundlach, T.N. Jackson, Solid-State Electron. 47 (2003) 259–262.
[26] D.J. Gundlach, K.P. Pernstich, G. Wilckens, M. Grüter, S. Haas, B. Batlogg, J. Appl. Phys. 98 (2005) 064502.
[27] T.J. Richards, H. Sirringhaus, J. Appl. Phys. 102 (2007) 094510.
[28] B. Yoo, T. Jung, D. Basu, A. Dodabalapur, B.A. Jones, A. Facchetti, M.R. Wasielewski, T.J. Marks, Appl. Phys. Lett. 88 (2006) 082104.
[29] S.Y. Yang, K. Shin, C.E. Park, Adv. Funct. Mater. 15 (2005) 1806–1814.
[30] J. Hwang, E.-G. Kim, J. Liu, J.-L. Bredas, A. Duggal, A. Kahn, J. Phys. Chem. C 111 (2007) 1378–1384.
[31] C. Tanase, E.J. Meijer, P.W.M. Blom, D.M. de Leeuw, Phys. Rev. Lett. 191 (2003) 216601.
[32] M. Redecker, D.D.C. Bradley, M. Inbasekaran, W.W. Wu, E.P. Woo, Adv. Mater. 11 (1999) 241–246.
[33] C. Block, D.V. Pham, U. Kunze, D. Kafer, G. Witte, A. Terfort, Appl. Phys. Lett. 91 (2007) 052110.
[34] K. Asadi, F. Gholamrezaie, A.C.P. Smits, P.W.M. Blom, B. De Boer, J. Mater. Chem. 17 (2007) 1947–1953.

Organic Electronics 11 (2010) 238–246

Contents lists available at ScienceDirect

Organic Electronics

journal homepage: www.elsevier.com/locate/orgel

Reduced efficiency roll-off in highly efficient and color-stable hybrid WOLEDs: The influence of triplet transfer and charge-transport behavior on enhancing device performance

Qi Wang [a], Cheuk-Lam Ho [b], Yongbiao Zhao [a], Dongge Ma [a,*], Wai-Yeung Wong [b,*], Lixiang Wang [a]

[a] State Key Laboratory of Polymer Physics and Chemistry, Changchun Institute of Applied Chemistry, Chinese Academy of Sciences, Graduate School of the Chinese Academy of Sciences, Changchun 130022, PR China

[b] Department of Chemistry and Centre for Advanced Luminescence Materials, Hong Kong Baptist University, Waterloo Road, Kowloon Tong, Hong Kong, PR China

ARTICLE INFO

Article history:
Received 17 June 2009
Received in revised form 28 October 2009
Accepted 1 November 2009
Available online 10 November 2009

Keywords:
Triplet emission
Iridium complexes
White light
Carbazole
Organic light-emitting diodes

ABSTRACT

By wisely utilizing combinations of exciton-managed orange-phosphorescence/sky blue-fluorescence, we report on high-efficiency white organic light-emitting diodes (WOLEDs) with high color-stability together with reduced efficiency roll-off. Two WOLEDs with the peak current efficiencies of 34.5 and 42.5 cd A^{-1} which slightly shift to 34.2 and 40.0 cd A^{-1} at 1000 cd m^{-2} are demonstrated. Systematic investigations focused on the effects of hole-injection buffer layer, thickness of emitting-layer (EML) and the stepwise-doping profile of orange phosphorescent EML on the device performance have been performed. It is evidently shown that careful management of the triplet/singlet excitons and charge-carriers is key to realizing such high performance of the devices. The results will beyond doubt be helpful to the design of both material and device structure for high-performance WOLEDs and next-generation solid-state lighting sources.

© 2009 Elsevier B.V. All rights reserved.

1. Introduction

White organic light-emitting diode (WOLED) technology is one of the most stormy developing classes of organic photonic devices nowadays due to its merits of high resolution and possible flexibility for large-scale production of solid-state lighting sources and full-color OLEDs [1]. Among the various methods that have been proposed to realize WOLEDs [2–9], electrophosphorescence is outstanding due to its demonstrated potential for achieving unity internal quantum efficiency through the simultaneous harvesting of both singlet and triplet excitons [8–10]. Accordingly, all-phosphorescence-based WOLEDs often have the highest reported efficiencies because of their possibility to achieve up to 100% internal quantum efficiency (IQE). However, problems in this architecture remain in terms of the undesired color-stability over the entire process associated with the short operational lifetime of blue phosphor, and the significant efficiency roll-off at high brightness observed due to the strong triplet–triplet or triplet-charge annihilation [11]. Furthermore, the approximate 0.8 eV exchange energy losses in power efficiency resulted from the energetic relaxation following intersystem crossing from the conductive host into the blue emissive triplet state represent another drawback. Although all-fluorescence-based WOLEDs can give less pronounced efficiency roll-off and eliminate the unfavorable exchange energy losses, the obtained maximum IQE based on this only-singlet-harvesting system is limited to 25% by quantum statistics [6,7].

An effective method to solve this conflict is by introducing both fluorescent (F) and phosphorescent (P) emitters into one WOLED, in particular the combination of high-efficiency red and green (or orange) P emitters with blue

* Corresponding authors. Tel.: +86 431 85262357; fax: +86 431 85262873.
E-mail addresses: mdg1014@ciac.jl.cn (D. Ma), rwywong@hkbu.edu.hk (W.-Y. Wong).

1566-1199/$ - see front matter © 2009 Elsevier B.V. All rights reserved.
doi:10.1016/j.orgel.2009.11.001

F dye. Recent conceptual advancement leads to several types of P/F architectures [12–15]. One exciting example is via the combination of stacked F–P–F emitters in an ambipolar host proposed by Sun et al. [12a]. It is unique in that the singlets and triplets are harvested along independent channels, and hence nearly resonant energy transfer (either from the singlet or triplet) from the host to dopants for both species can be realized, and meanwhile eliminating the 0.5–1.0 eV exchange energy losses. Accordingly, their demonstrated WOLEDs exhibited very high efficiency together with reduced efficiency roll-off [12b].

As the efficiency of WOLEDs has experienced step-by-step increase over the past years, the research focus is now shifting towards the issues such as reducing the efficiency roll-off at high luminance and enhancing the device color-stability in order to satisfy the future lighting requirements [16,17]. A lot of endeavors in improving these issues have been made, e.g., manipulating singlet and triplet excitons within an ambipolar host [12], the design of exciton-confining structure [16], broadening the exciton formation zone [9], the utilization of single host system [9e,f] or p–i–n junction [13] architectures. However, we note that these elegant and high-performance WOLEDs need somewhat complicated fabrication processes, limiting their further practical applications. In general, highly efficient WOLEDs with high color-stability and reduced efficiency roll-off based on a simpler structure seem more promising but examples that can greatly resolve this issue are still very limited.

To loosen this bottleneck, we have recently reported on a novel organometallic phosphor **Ir(Cz–CF$_3$)** (see Fig. 1 for its structure) with its intrinsic multifunctional features that can yield very high-efficiency orange emission [15]. Furthermore, a simple two-wavelength P/F WOLED by combining this orange phosphor and a sky blue fluorophore was successfully fabricated. However, as compared to the previously reported all-phosphor WOLEDs, the efficiency of this P/F WOLED is yet unsatisfactory (~26 cd A^{-1}). Besides, in order to give a further performance improvement for the WOLEDs before real commercialization, a deep understanding of the device operational mechanism is still needed. Aiming at both issues, we extend here our previous work by largely enhancing the efficiency (up to ~42 cd A^{-1}) of this simple P/F white emission device, cooperating both the improvement in color-stability and efficiency roll-off. Comprehensive studies correlating the influence of the P emitting-layer (EML) thickness, hole-injection buffer layer and stepwise-doping profile in orange EML to the device performance are subsequently carried out, from which a complete scenario of the working principle of this unique P/F WOLED is clearly depicted. It is noted that carefully managing the triplet transfer and charge-transport via the introduction of such multifunctional material and smart device engineering are essential to the realization of such high electroluminescence (EL) performance. Such knowledge would undoubtedly provide a new avenue for the rational design of heavy metal electrophosphors together with the device structure for ultra-high performance WOLEDs in the future.

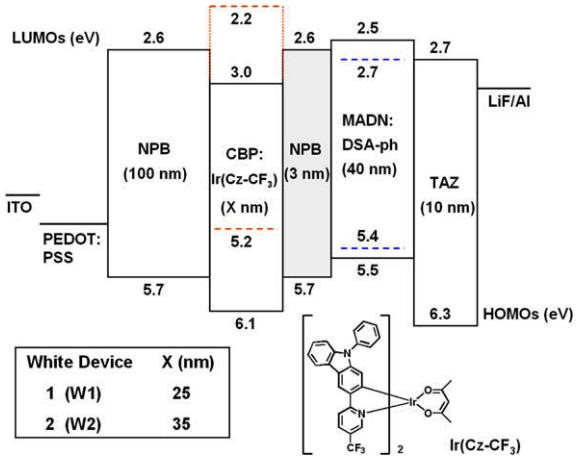

Fig. 1. Configuration (and the energy-level diagram) of the WOLED and molecular structure of **Ir(Cz–CF$_3$)**. The energy levels (in eV) are taken from Refs. [9g,h,18,19].

2. Experimental

The synthesis of **Ir(Cz–CF$_3$)** followed the procedures as described previously [15]. The fabricated devices were grown on clean glass substrates pre-coated with a 180 nm thick layer of indium tin oxide (ITO) with a sheet resistance of 10 Ω per square. The ITO surface was treated by oxygen plasma for 2 min, following degreased in ultrasonic solvent bath and then dried at 120 °C before it was loaded into an evaporator. All layers were grown by thermal evaporation in a high vacuum system with pressure of less than 5×10^{-4} Pa without breaking the vacuum. The various device structures were described in the text. In the deposition of the doping layers, deposition rates of both host and guest were controlled with their correspondingly independent quartz crystal oscillators. The evaporation rates were monitored by frequency counter, and calibrated by Dektak 6 M Profiler (Veeco). The overlap between ITO and Al electrodes was 4×4 mm^2 as the active emissive area of the devices. Current density–voltage–brightness characteristics were measured by using a Keithley source measurement unit (Keithley 2400 and Keithley 2000) with a calibrated silicon photodiode. The EL spectra were measured by JY SPEX CCD3000 spectrometer. All the measurements were carried out in ambient conditions.

3. Results and discussion

3.1. Design and fabrication of P/F hybrid WOLEDs

Several strategies are employed to enhance the EL performance of our WOLEDs. First, in common OLEDs the free electrons will combine with holes to form excitons with a singlet-to-triplet formation ratio of χ_S/χ_T in the vicinity of the main exciton-recombination zone. To effectively harvest the singlet excitons with relatively short diffusion length, the blue F layer is placed adjacent to this region, allowing for a resonant singlet energy transfer via Förster

process onto the fluorophore. On the other hand, the generated non-radiative triplets, however, which have lifetimes that are several orders of magnitude larger than singlets, typically have long diffusion lengths, and hence can migrate into the P region which is separated from the main exciton formation zone by a thin interlayer to ensure orange emission. According to this assignment, singlets and triplets can be channeled to their respective emitting species (F and P) through parallel pathways, thus greatly avoiding the exchange energy losses suffered in all-phosphor white emission devices, although some unavoidable energy losses associated with the long triplet diffusion cannot be totally eliminated.

Secondly, in conventional electrophosphorescent OLEDs one main drawback is the large efficiency roll-off at high brightness values due to the strong triplet–triplet or exciton-charge annihilations associated with the intense exciton pile-up or the intrinsically narrow exciton-recombination zone at the EML side(s) [9c]. One powerful method to solve this problem is to lower the triplet density by expanding the exciton formation region. Here, we introduce an ambipolar host for P dopant that allows a distributed exciton formation region across the full EML width to realize this goal. Furthermore, as discussed above, the process of the triplet diffusion between layers is also greatly beneficial to the formation of an extended emission zone, hence decreasing the efficiency roll-off by reducing exciton quenching [9a–f].

Next, it is noted that both careful control of triplet diffusion and wise management of electron- or hole-charges distribution provide good means of achieving a balanced white emission [3,4,9]. Therefore, in this hybrid WOLED a thin (~3 nm) hole-transporting interlayer is introduced between P and F layers to facilitate the hole injection into F layer and block electrons on this side to guarantee blue emission, maintaining the balanced white light, on the one hand. It can also prevent backward triplet energy transfer to F dopant which would otherwise decay non-radiatively, on the other hand (see Section 3.5). Finally, to achieve high color-stability in our WOLEDs, we utilize the energy-level difference between the P dopant and the host, which can lower both electron and hole mobility in the device to maintain the recombination ratio constant, thus stabilizing the EL spectrum with changing operational voltage (see Section 3.5).

Given these considerations, we put forward the structure of the hybrid WOLEDs in Fig. 1. The blue layer is composed of 0.75 wt.% *p*-bis(*p*-*N*,*N*-diphenyl-aminostyryl)benzene (DSA-Ph) doped 2-methyl-9,10-di(2-naphthyl)anthracene (MADN) [18], while 4 wt.% **Ir(Cz–CF$_3$)** doped 4,4′-*N*,*N*′-dicarbazole-biphenyl (CBP) constitutes the orange layer. Here, we choose *N*,*N*′-diphenyl-*N*,*N*′-bis(1-naphthylphenyl)-1,1′-biphenyl-4,4′-diamine (NPB) as the thin interlayer between F and P regions. 3-(4-Biphenyl)-4-phenyl-5-(4-*tert*-butylphenyl)-1,2,4-triazole (TAZ) is selected as the electron-transporting layer. To further improve the hole injection from the indium tin oxide (ITO) anode into the hole-transporting layer (HTL) of NPB, poly(3,4-ethylenedioxythiophene):poly(styrenesulfonate) (PEDOT:PSS) is introduced, which is important to the realization of high EL performance (see Section 3.3).

3.2. Orange EML-thickness dependent EL performance

We first examine the influence of phosphor-layer thickness on the EL efficiency and spectrum of the device by fabricating two WOLEDs, that is, W1 with 25 nm-thick orange EML while 35-nm thick orange EML for W2, as shown in Fig. 1. The dopant concentrations were optimized in their respective monochromatic devices before WOLED fabrication. From Fig. 2a, as compared to W1, W2 gives more intense orange emission relative to its blue counterpart, which suggests that more excitons will be trapped or harvested by **Ir(Cz–CF$_3$)** with increasing its thickness (to be discussed in detail below). Since this orange phosphor is much more efficient than the blue fluorophore, W2 exhibits the maximum forward viewing current efficiency (CE) and power efficiency (PE) of 42.5 cd A^{-1}and 24.9 lm W^{-1}, while W1 gives the maximum CE and PE of 34.5 cd A^{-1}and 17.0 lm W^{-1}, respectively (Fig. 2b). We note that these results outperform in efficiency some of the best reported all-phosphor WOLEDs in the literature [8,9a–d].

Besides the realization of high efficiency, we note here that issues on the simultaneous chromatic stability and efficiency roll-off are well resolved in this P/F hybrid WOLED. As seen from Fig. 2a, when the voltage increases from 8 to 12 V, the variations of the Commission Interna-

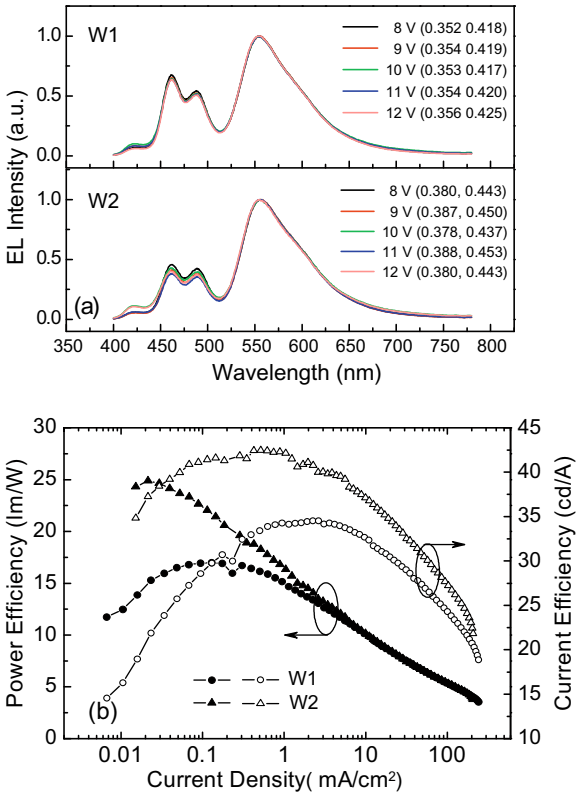

Fig. 2. (a) Electroluminescent (EL) spectra of W1 and W2 at different voltages. (b) Power and current efficiencies as a function of current density for W1 and W2.

tionale de L'Eclairage (CIE) coordinates of W1 and W2 are (0.004, 0.007) and (0.008, 0.010), respectively, which are comparable to or even much smaller than some of the high-performance single- or multi-EML WOLEDs demonstrated before [5–9]. Furthermore, as shown in Fig. 2b, this P/F WOLED exhibited less pronounced efficiency roll-off, yet at an illumination-relevant brightness of 1000 cd m^{-2}, the CE of W1 and W2 can still reach 34.2 cd A^{-1} and 40.0 cd A^{-1}, respectively, while the PE are 12.6 lm W^{-1} for W1 and 13.5 lm W^{-1} for W2. Overall, this P/F-based WOLED can reveal a better trade-off among efficiency/reduced efficiency roll-off/color-stability, demonstrating its great potential for lighting applications. Table 1 summarizes the EL efficiencies of W1 and W2 at different brightness values.

3.3. The influence of hole buffer layer

In OLEDs, an effective way to enhance the EL performance is by modifying the electrodes via the addition of buffer layer(s) to improve the charge injection and the stability of the electrode interfaces [19]. For our WOLED a proper selection of hole buffer layer is of vital importance. To give a clear illustration, a control device with CuPc modified ITO anode was fabricated. Fig. 3 depicts the device structure and its EL performance.

The maximum CE and PE of the control device dramatically decrease to 15.1 cd A^{-1} and 5.3 lm W^{-1} (Fig. 3a), with the CIE coordinates ranging from (0.382, 0.447) at 7 V to (0.374, 0.457) at 14 V (Fig. 3b). In this case, one would assume an efficiency enhancement via increasing the thickness (e.g., expanded to 25 or 35 nm as in W1 or W2) of the P layer in the control device. However, this straightforward method proved to be ineffective since any thicker phosphorescent layer (>20 nm) will render the orange emission overwhelm its blue counterpart, and hence we cannot even get yellowish-white emission as was found in the control device. Besides, we note that the thickness of HTL (NPB) also strongly influences the EL spectrum of the device. The thicker the NPB layer, the more the orange emission. Hence, we optimized the thickness of NPB as 50 nm in CuPc modified device (Fig. 3a) considering the issues of both device efficiency and EL spectrum performance.

Apparently, the introduced PEDOT:PSS buffer layer is essential in realizing the high EL performance (consider W2 with its highest CE of 42.5 cd A^{-1}, and its nearly the same EL spectral shape as the control device). Fig. 4 compares the current density–voltage characteristics of the device with CuPc or PEDOT:PSS modified anode. It is clear that the current density is enhanced dramatically in PEDOT:PSS modified device as compared to its CuPc counterpart, which indicates that the hole-injection barrier between ITO and NPB can be lowered by introducing the PEDOT:PSS buffer layer in order to facilitate the hole injection and transportation in the device. We note that this greatly benefits to the enhancement of device PE by reducing the driving voltage. Moreover, according to the previous reports, this hole buffer can smooth the anode surface and efficiently block the electrons within the device to reduce the current leakage, which contribute to the enhancement of device performance as well [20].

Table 1
EL efficiencies of W1 and W2 at different brightness values.

Brightness (cd m^{-2})	EQE (%)[a]	CE (cd A^{-1})	PE (lm W^{-1})
100	11.4, 14.0[b]	32.4, 41.9	16.1, 20.0
500	12.1, 13.9	34.2, 41.5	14.3, 15.8
1000	12.0, 13.4	34.2, 40.0	12.6, 13.5

[a] EQE: external quantum efficiency; CE: current efficiency; PE: power efficiency.
[b] The former value is from W1 whereas the latter belongs to W2.

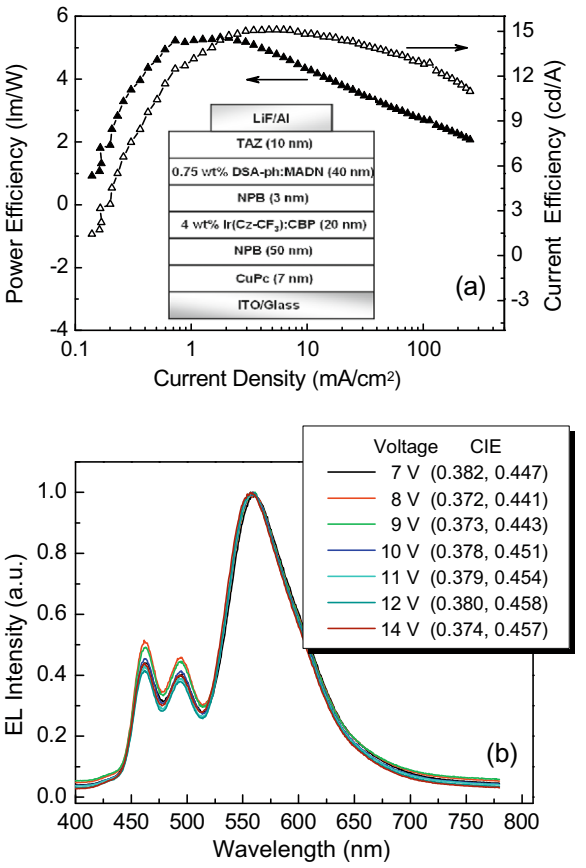

Fig. 3. (a) Power and current efficiencies as a function of current density and (b) EL spectra of the control WOLED with CuPc modified anode. The inset in (a) depicts the device structure.

3.4. Stepwise-doping profile in orange emissive region

In OLEDs the charge or exciton transport inside the EML is one of the most important issues for determining the EL performance, especially in the host–guest doped system [9a–f,12]. Therefore, a deep understanding of the underlying carrier transport or exciton diffusion characteristics is essential in revealing the device operational mechanism [21]. In order to understand how the introduced **Ir(Cz–**

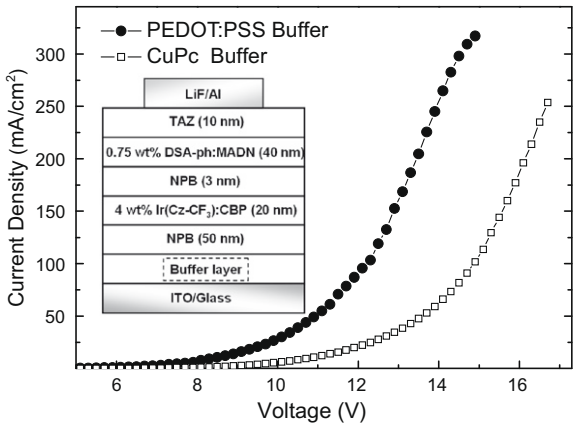

Fig. 4. Current density–voltage characteristics of the devices with CuPc or PEDOT:PSS modified anode.

CF_3) dopant functions on hole charges in this P/F WOLED, a stepwise-doping profile in the orange EML is proposed [22].

To give a clear illustration, two types of devices (Devices A and B) with an opposite stepwise-doping sequence in the orange EML were fabricated, as depicted in the upside of Fig. 5. Also shown are their corresponding EL spectra at different voltages (Fig. 5a and 5b). Apparently, in Device A the orange emission is increased dramatically relative to the blue with increasing voltage, while in Device B a completely opposite result is observed upon increasing the voltage. Fig. 5c depicts the variations of the CIE coordinates of the two devices. Evidently, a visible red-shift is observed in Device A while a large blue-shift appears in Device B with increasing voltage. Furthermore, it is found that the color-shifts in both devices are much larger than that of W2 in which the 4 wt.% doped **Ir(Cz–CF_3)** is uniformly distributed within the whole orange region (see the enlarged image in inset of Fig. 5c).

Several key issues should be clarified before our further analyses. Firstly, in a doped system the dopant may influence the charge-transportation behavior in different ways depending on its energy-level relative to the host. If the dopant has a higher-lying highest occupied molecular orbital (HOMO) with respect to the host HOMO, the dopant molecules can then act like hole-traps [23,24]. Secondly, it has been demonstrated that CBP exhibited bipolar transport property and relatively higher hole mobility [25]. Therefore, in this P/F WOLED, the main exciton formation region should be located close to the NPB/MADN interface, considering the dominant hole and electron transport characteristics of NPB and MADN, respectively. Finally, for organic semiconductors, we assume that the charge transportation is governed by hopping model between dopant sites [23].

According to the device energy-level diagram (Fig. 1), the HOMO level of **Ir(Cz–CF_3)** is much higher than that of CBP, indicating that the phosphor may act as good hole trappers, thanks to the presence of the electron-rich carbazolyl ring. In this case, some mobile holes transported in the orange EML would be trapped by the dopant molecules. Given the deep hole-trapping depth (~0.9 eV) which is defined as the HOMO energy-level difference between **Ir(Cz–CF_3)** and CBP, the detrapping probability is low, and hence the hole mobility will be lowered. Besides, since the hole mobility of CBP is nearly one order of magnitude higher than its electron counterpart, the hole charges should be distributed rather uniformly throughout the orange EML, except for the sudden rise and fall at the junctions [25]. Combining both results, the hole-trapping effect of **Ir(Cz–CF_3)** in CBP host is quite anticipated and shown to be efficient [9e,f,21–24].

Therefore, in the case of Device A, when the stepwise-doping profile in orange EML is arranged by a 4 wt.%–3 wt.%–2 wt.%–1 wt.% sequence towards the blue-layer side, an internal electric field guided to the blue-layer direction (see Device A in Fig. 5) is subsequently formed across the orange EML, considering that a higher concentration of **Ir(Cz–CF_3)** will capture more holes than its lower counterpart and the potential drop is most related to the total amount of charges inside the layer [26]. Accordingly, this internal electric field formed will significantly facilitate the electron injection across the thin NPB layer into the orange EML to combine with the trapped holes, forming excitons which then are available for **Ir(Cz–CF_3)** molecules as the voltage increases. The overall results are the continuous shift of the recombination distribution away from the main exciton formation zone (i.e., NPB/MADN interface) towards the orange-layer side [21c], resulting in a large increase in orange emission relative to blue emission with increasing voltage, consistent with the experimental results (Fig. 5a). However, when the stepwise-doping profile is arranged by a 1 wt.%–2 wt.%–3 wt.%–4 wt.% sequence, as shown in Device B, an internal electric field with the opposite direction as compared to Device A is subsequently formed across the orange EML. In this case, the formed internal electric field will tremendously retard the electron injection into the orange layer, leading to a reduction of orange emission with respect to its blue counterpart with increasing voltage (Fig. 5b). The overall results evidently reveal the hole-trapping character of **Ir(Cz–CF_3)** in CBP host.

On the other hand, as shown in Fig. 1, **Ir(Cz–CF_3)** has a higher-lying lowest unoccupied molecular orbital (LUMO) with respect to CBP. This large LUMO level difference (~0.8 eV) can effectively block the direct injection of electrons into **Ir(Cz–CF_3)** sites, preventing the shift of recombination zone as the operational voltage increases. Furthermore, the electrons tunneled into the CBP layer can be scattered at the dopant sites. Then the average free path of electrons is shortened and the electron drift velocity becomes lowered, leading to a reduction of electron mobility [24]. Direct experimental evidence for this hypothesis is provided by examining the current density–voltage characteristics of electron-only devices with or without **Ir(Cz–CF_3)** dopant in the CBP layer. As shown in Fig. 6, the significant decrease of current density in **Ir(Cz–CF_3)** doped device strongly proves that the orange dopant can indeed induce a reduced electron mobility in the CBP host.

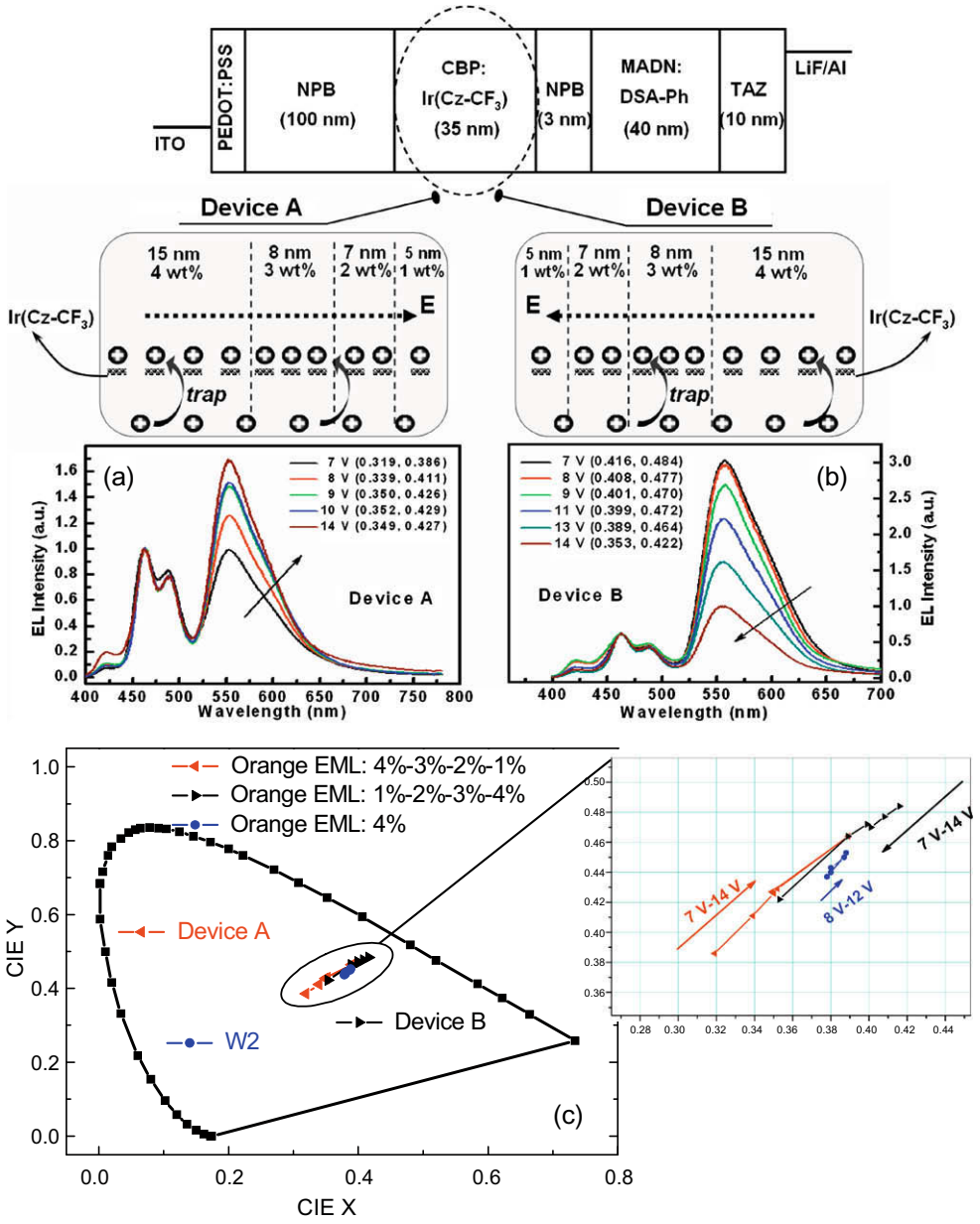

Fig. 5. Configuration of WOLEDs with stepwise-doping profile in orange EML. Device A follows 15 nm–4 wt.%, 8 nm–3 wt.%, 7 nm–2 wt.%, and 5 nm–1 wt.% doped **Ir(Cz–CF$_3$)** sequence towards the CBP/internal-NPB interface, while Device B follows a reverse sequence of doping concentration, that is, 5 nm–1 wt.%, 7 nm–2 wt.%, 8 nm–3 wt.%, and 15 nm–4 wt.% originated from the NPB-HTL/CBP interface. The formed internal electric field (E) across the orange region is also shown (dotted lines). EL spectra of Devices A and B with different voltages are depicted in (a) and (b), respectively. (c) Summarizes the variations of the CIE coordinates of Devices A, B, and W2.

3.5. Origin of the high EL performance

As illustrated above, the energy-level difference between **Ir(Cz–CF$_3$)** and CBP enables the dopant to play different roles on holes and electrons in the device. Acting as deep hole-traps, they may capture hole-carriers and then lower the hole-transport across the orange EML. Alternatively, due to the large LUMO level difference between **Ir(Cz–CF$_3$)** and CBP, the electrons injected may collide with the positive barriers and be scattered by these barriers, leading to a reduction of the drift velocity due to an increase of the total transit path [23]. Therefore, the mobilities of both holes and electrons are reduced in the white light-emitting device.

It has been evidently demonstrated that the reduction of charge mobility associated with this host–guest energy-level difference will lead to the recombination ratio to be constant in each EML, thus greatly stabilizing the EL spectrum with a change of voltage [24]. As mentioned earlier, the large host–guest LUMO difference can prevent

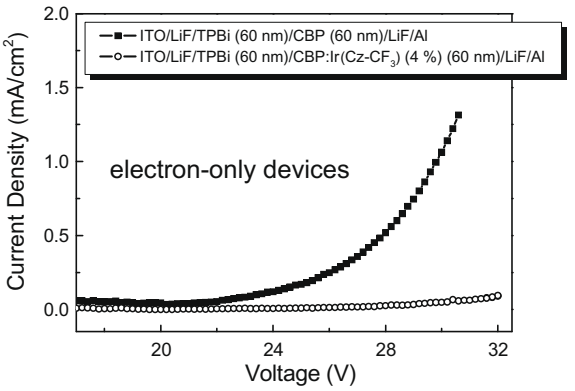

Fig. 6. Current density–voltage characteristics of electron-only devices with or without **Ir(Cz–CF$_3$)** dopant in CBP layer. Here, the addition of an electron-transporting layer 2,2′,2″-(1,3,5-phenylene)tris-(1-phenyl-1*H*-benzimidazole) (TPBi) with high electron mobility serves to block the hole diffusion into the CBP (or doped CBP) layer and prevent the breakdown of the tested film with increasing operational voltage.

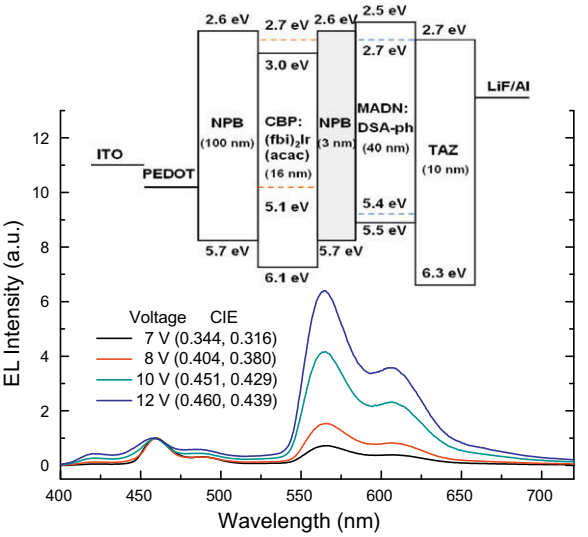

Fig. 7. EL spectrum of the device with (fbi)$_2$Ir(acac) dopant in CBP (see inset for its structure) instead of **Ir(Cz–CF$_3$)** at different voltages.

the direct electron injection into **Ir(Cz–CF$_3$)** sites, which maintains the stability of exciton-recombination zone in the device. From Fig. 5c, the rather small color-shift even in a wide range of operational voltages observed in W2 provides a strong evidence for the above analysis. Furthermore, we note that the carrier trapping process is also beneficial to the device performance since the trapped exciton fraction is not subject to diffusive transport loss, and the reduced triplet accumulation at the orange EML edges can decrease the triplet quenching, thus representing a trade-off between high color-stability and reduced efficiency roll-off. Herein, the tiny spectral variation in W2 is attributed to the asymmetric electron and hole mobility values. The relatively low electron mobility increases rapidly with the electric field. Therefore, more electrons can move throughout the CBP/internal-NPB heterojunction continuously, inject into the orange EML, and combine with the trapped holes to form excitons which are then available for **Ir(Cz–CF$_3$)** molecules, leading to more intense orange emission relative to the blue one. Clearly, the notorious voltage-dependent-color-shift problem can be solved by using this smart method which can bear the critical demands of commercial lighting applications.

Recall that a thicker orange EML in WOLEDs leads to more orange emission with respect to its thinner counterpart (compare W2 with W1). Given the unique property of **Ir(Cz–CF$_3$)**, there should be more electrons and holes captured and then they recombine to form excitons on the multifunctional dopant sites with increasing its thickness, thus making more orange light contribution, as illustrated in Fig. 2a.

To further demonstrate the importance of **Ir(Cz–CF$_3$)** in this hybrid WOLED, another device was fabricated by replacing this orange dopant with another iridium phosphor bis(2-(9,9-diethyl-9*H*-fluoren-2-yl)-1-phenyl-1*H*-benzoimidazole-*N*,C^3)iridium(acetylacetonate) (fbi)$_2$Ir(acac) [27]. Fig. 7 shows the device structure and its corresponding EL spectrum at different voltages. The LUMO offset between (fbi)$_2$Ir(acac) and NPB is rather small (~0.1 eV), indicating that the electrons tunneled from the internal-NPB layer could inject resonantly into the (fbi)$_2$Ir(acac) LUMO and transport by hopping on dopant sites [9e,f,18,28]. In this case, the fraction of excitons (singlets or triplets) directly formed on (fbi)$_2$Ir(acac) molecules via the combination of the trapped holes and the channeled electrons will be markedly increased, leading to overwhelmed orange emission with respect to the blue with increasing voltage, as shown in Fig. 7. In particular, the variations of the CIE coordinates of (fbi)$_2$Ir(acac) based device are $\Delta X = 0.116$ and $\Delta Y = 0.123$, which are nearly one order of magnitude larger than that of W1 or W2. This fact evidently demonstrates that the introduced **Ir(Cz–CF$_3$)** is important to achieve the rather high color-stability in the resulting WOLED.

Furthermore, it is noted that the smart device engineering is essential to the realization of a high EL efficiency together with a reduced efficiency roll-off. As discussed above, the added hole-type NPB interlayer between P and F regions plays an important role in maintaining the balanced white emission. Besides, this interlayer, with high triplet energy ($T_1 \sim 2.29$ eV), can suppress triplet quenching between phosphorescent and fluorescent regions. Experimental evidence to support this point is provided here, in which it is found that the PL intensity of a 30 nm layer of 4 wt.% **Ir(Cz–CF$_3$)** doped CBP is nearly unchanged, if a 4 nm layer of NPB is evaporated directly on top [13c]. Since NPB does not absorb the photon energy in the spectral range of **Ir(Cz–CF$_3$)** emission together with the fact that the triplet energy of NPB (~2.29 eV) is higher than that of **Ir(Cz–CF3)** (~2.24 eV), this result clearly demonstrates that the generated triplet excitons can flexibly transport across this thin spacer bridge into the orange EML and then decay radiatively, without being absorbed by the triplet state of the internal-NPB or backward-energy-transferred to the blue F dopant which would otherwise decay non-radiatively. In such device the blue fluorescent dopants harvest a majority of singlet energy, with the remainder of triplets diffusing into the **Ir(Cz–CF$_3$)** doped CBP layer to

excite the orange phosphor. Herein one assumption for the above analysis is that the triplet energy of MADN is larger than that of **Ir(Cz–CF3)**, rendering the triplet diffusion into the phosphorescent region can possibly happen. On the other hand, because of the rather low doping concentration of DSA-ph (0.75 wt.%), the generated triplets near the NPB/MADN interface cannot efficiently energy transfer to the fluorophore by either Förster or Dexter mechanism. Besides, direct singlet transfer from the blue species to the lower-energy orange phosphor is forbidden because of their inherently short diffusion lengths [12]. This architecture is unique in that the singlet and triplet excitons can be harvested along completely independent channels which avoids the exchange energy losses, allowing for increased power efficiency. Additionally, as expected, the process of the extended triplet diffusion and the introduction of ambipolar CBP host both allow a distribution of excitons to form in the multiple regions, thus achieving a rather small efficiency roll-off at high current density (Fig. 2b) by decreasing the exciton-charge or exciton–exciton quenching which is yet the main bottleneck to be addressed in the development of today's phosphorescent WOLEDs [11]. Overall, by virtue of the multifunctional iridium phosphor combined with the smart device engineering, we can carefully control the charge-carrier transport and diffusion of singlet or triplet excitons between or within layer(s) to reveal a better trade-off for the EL efficiency/reduced efficiency roll-off/color-stability which is necessary for constructing high-performance WOLEDs.

4. Conclusions

We report on simple and color-stable two-wavelength WOLEDs with high efficiency together with reduced efficiency roll-off at high luminance. The devices exploit a blue fluorescent dopant in exchange for a phosphorescent species to avoid the exchange energy losses and create parallel pathways to channel nearly all of the triplet energy to orange phosphor while retaining the singlet energy exclusively on the blue-fluorescence. Systematic studies on the device working mechanism have been subsequently performed from which the origin of the high EL performance of the WOLED is clearly revealed. We note that the wise management of charge-carrier transport coupled with triplet diffusion in the device is key to enhancing the device performance. Given the good compromise among the efficiency, color-stability and reduced efficiency roll-off, the present study can act as a good benchmark to resolve the trade-off hurdle of these issues. Besides, this study can also make a positive impact on the advance of both the development of new host–guest system and of efficient white emission device structures, which will excel in the realization of next-generation solid-state indoor lighting sources [29].

Acknowledgements

The authors thank the Foundation of Jilin Research Council (20080337), Foundation of Changchun Research Council (2007GH06), Science Fund for Creative Research Groups of NSFC (20621401) and Ministry of Science and Technology of China (863 Program No. 2006AA03A161, 973 Program Nos. 2009CB930603, 2009CB623604) for the support of this research. L.W. thanks NSFC (50633040) for financial support. W.-Y.W. thanks the Hong Kong Research Grants Council (HKBU 202106) and the Hong Kong Baptist University (FRG2/08-09/111) for financial support. C.-L. Ho is thankful for a postdoctoral fellowship from the Hong Kong Baptist University.

References

[1] (a) S.R. Forrest, Org. Electron. 4 (2003) 45;
(b) F. So, J. Kido, P. Burrows, MRS Bull. 33 (2008) 663;
(c) B.W. D'Andrade, Nat. Photonics 1 (2007) 33;
(d) B.W. D'Andrade, S.R. Forrest, Adv. Mater. 16 (2004) 1585.
[2] (a) H.B. Wu, J.H. Zou, F. Liu, L. Wang, A. Mikhailovsky, G.C. Bazan, W. Yang, Y. Cao, Adv. Mater. 20 (2008) 696;
(b) J.S. Huang, G. Li, E. Wu, Q.F. Xu, Y. Yang, Adv. Mater. 18 (2006) 114;
(c) Y. Zhang, F. Huang, Y. Chi, A.K.-Y. Jen, Adv. Mater. 20 (2008) 1;
(d) X. Gong, S. Wang, D. Moses, G.C. Bazan, A.J. Heeger, Adv. Mater. 17 (2005) 2053.
[3] (a) B.W. D'Andrade, S.R. Forrest, J. Appl. Phys. 94 (2003) 3101;
(b) E.L. Williams, K. Haavisto, J. Li, G.E. Jabbour, Adv. Mater. 19 (2007) 197.
[4] (a) J. Kalinowski, M. Cocchi, D. Virgili, V. Fattori, J.A.G. Williams, Adv. Mater. 19 (2007) 4000;
(b) M. Cocchi, J. Kalinowski, D. Virgili, V. Fattori, S. Develay, J.A.G. Williams, Appl. Phys. Lett. 90 (2007) 163508.
[5] (a) J. Kido, H. Shionoya, K. Nagai, Appl. Phys. Lett. 67 (1995) 2281;
(b) D. Qin, Y. Tao, J. Appl. Phys. 97 (2005) 044505;
(c) K.O. Cheon, J. Shinar, Appl. Phys. Lett. 81 (2002) 1738;
(d) S.L. Lai, M.Y. Chan, M.K. Mung, C.S. Lee, S.T. Lee, Appl. Phys. Lett. 90 (2007) 203510.
[6] (a) H. Baek, C. Lee, J. Appl. Phys. 103 (2008) 124504;
(b) S.-H. Yang, M.-H. Liu, Y.-K. Su, J. Appl. Phys. 100 (2006) 083111;
(c) C.-H. Hsiao, C.-F. Lin, J.-H. Lee, J. Appl. Phys. 102 (2007) 094508;
(d) C.-H. Kim, J. Shinar, Appl. Phys. Lett. 80 (2002) 2201;
(e) B.C. Krummacher, V.-E. Choong, M.K. Mathai, S.A. Choulis, F. So, F. Jermann, T. Fiedler, M. Zachau, Appl. Phys. Lett. 88 (2006) 113506;
(f) M.-H. Ho, S.-F. Hsu, J.-W. Ma, S.-W. Hwang, P.-C. Yeh, C.H. Chen, Appl. Phys. Lett. 91 (2007) 113518;
(g) J.H. Jou, Y.S. Chiu, R.Y. Wang, H.C. Hu, C.P. Wang, H.W. Lin, Org. Electron. 7 (2006) 8;
(h) J.H. Jou, M.H. Wu, C.P. Wang, Y.S. Chiu, P.H. Chiang, H.C. Hu, R.Y. Wang, Org. Electron. 8 (2007) 735.
[7] (a) C.-C. Chang, J.-F. Chen, S.-W. Hwang, C.H. Chen, Appl. Phys. Lett. 87 (2005) 253501;
(b) F.W. Guo, D.G. Ma, Appl. Phys. Lett. 87 (2005) 173510;
(c) S.L. Lai, M.Y. Chan, M.K. Fung, C.S. Lee, S.T. Lee, J. Appl. Phys. 101 (2007) 014509;
(d) M.-H. Ho, T.-M. Chen, P.-C. Yeh, S.-W. Hwang, C.H. Chen, Appl. Phys. Lett. 91 (2007) 233507;
(e) T.-W. Lee, T. Noh, B.-K. Choi, M.-S. Kim, D.W. Shin, J. Kido, Appl. Phys. Lett. 92 (2008) 043301;
(f) S.J. Yeh, H.Y. Chen, M.F. Wu, L.H. Chan, C.L. Chiang, H.C. Yeh, C.T. Chen, J.H. Lee, Org. Electron. 7 (2006) 137.
[8] (a) P.-I. Shih, C.-F. Shu, Y.-L. Tung, Y. Chi, Appl. Phys. Lett. 88 (2006) 251110;
(b) S. Tokito, T. Iijima, T. Tsuzuki, F. Sato, Appl. Phys. Lett. 83 (2003) 2459;
(c) H. Kanno, R.J. Holmes, Y. Sun, S. Kena-Cohen, S.R. Forrest, Adv. Mater. 18 (2006) 339;
(d) B.P. Yan, C.C.C. Cheung, S.C.F. Kui, H.F. Xiang, V.A.L. Roy, S.J. Xu, C.M. Che, Adv. Mater. 19 (2007) 3599;
(e) X.F. Qi, M. Slootsky, S.R. Forrest, Appl. Phys. Lett. 93 (2008) 193306;
(f) T.-H. Kim, H.K. Lee, O.O. Park, B.D. Chin, S.-H. Lee, J.K. Kim, Adv. Funct. Mater. 6 (2006) 611;
(g) G.-J. Zhou, C.-L. Ho, W.-Y. Wong, Q. Wang, D.-G. Ma, L.-X. Wang, Z.-Y. Lin, T.B. Marder, A. Beeby, Adv. Funct. Mater. 18 (2008) 499;
(h) W.-Y. Wong, C.-L. Ho, Z.Q. Gao, B.X. Mi, C.H. Chen, K.W. Cheah, Z.Y. Lin, Angew. Chem. Int. Ed. 45 (2006) 7800;
(i) Q. Wang, J.Q. Ding, Z.Q. Zhang, D.G. Ma, Y.X. Cheng, L.X. Wang, J.

Appl. Phys. 105 (2009) 076101;
(j) G.-J. Zhou, Q. Wang, C.-L. Ho, W.-Y. Wong, D.-G. Ma, L.-X. Wang, Z.-Y. Lin, Chem. Asian J. 3 (2008) 1830.
[9] (a) B.W. D'Andrade, R.J. Holmes, S.R. Forrest, Adv. Mater. 16 (2004) 624;
(b) B.W. D'Andrade, M.E. Tompson, S.R. Forrest, Adv. Mater. 14 (2002) 147;
(c) Y. Sun, S.R. Forrest, Appl. Phys. Lett. 91 (2007) 263503;
(d) B. Ma, P.I. Djurovich, S. Garon, B. Alleyne, M.E. Thompson, Adv. Funct. Mater. 16 (2006) 2438;
(e) Q. Wang, J.Q. Ding, D.G. Ma, Y.X. Cheng, L.X. Wang, X.B. Jing, F.S. Wang, Adv. Funct. Mater. 19 (2009) 84;
(f) Q. Wang, J.Q. Ding, D.G. Ma, Y.X. Cheng, L.X. Wang, F.S. Wang, Adv. Mater. 21 (2009) 2397;
(g) N. Iguchi, Y.-J. Pu, K. Nakayama, M. Yokoyama, J. Kido, Org. Electron. 10 (2009) 465.
[10] (a) C.-H. Yang, Y.-M. Cheng, Y. Chi, C.-J. Hsu, F.-C. Fang, K.-T. Wong, P.-T. Chou, C.-H. Chang, M.-H. Tsai, C.-C. Wu, Angew. Chem. Int. Ed. 46 (2009) 2418;
(b) S. Krishnamurthy, T.K. Hatwar, J. Spindler, J.R. Vargas, C.T. Brown, M.J. Helber, M. Ricks, W. Begley, L. Cosimbescu, Proc. SPIE 5937 (2009) 106.
[11] (a) J. Kalinowski, W. Stampor, J. Mężyk, M. Cocchi, D. Virgili, V. Fattori, P. Di Marco, Phys. Rev. B 66 (2002) 235321;
(b) N.C. Giebink, S.R. Forrest, Phys. Rev. B 77 (2009) 235215;
(c) J. Kalinowski, W. Stampor, J. Szmytkowski, D. Virgili, M. Cocchi, V. Fattori, C. Sabatini, Phys. Rev. B 74 (2009) 085316;
(d) Q. Wang, J.Q. Ding, Y.X. Cheng, L.X. Wang, D.G. Ma, J. Phys. D: Appl. Phys. 42 (2009) 065106.
[12] (a) Y. Sun, N.C. Giebink, H. Kanno, B. Ma, M.E. Thompson, S.R. Forrest, Nature 440 (2006) 908;
(b) Y. Sun, N.C. Giebink, S.R. Forrest, Org. Electron. 7 (2006) 375.
[13] (a) G. Schwartz, M. Pfeiffer, S. Reineke, K. Walzer, K. Leo, Adv. Mater. 19 (2007) 3672;
(b) G. Schwartz, S. Reineke, K. Walzer, K. Leo, Appl. Phys. Lett. 92 (2008) 053311;
(c) G. Schwartz, K. Fehse, M. Pfeiffer, K. Walzer, K. Leo, Appl. Phys. Lett. 89 (2006) 083509.
[14] J.H. Seo, J.H. Park, Y.K. Kim, J.H. Kim, G.W. Hyung, K.H. Lee, S.S. Yoon, Appl. Phys. Lett. 90 (2007) 203507.
[15] C.-L. Ho, W.-Y. Wong, Q. Wang, D.G. Ma, L.X. Wang, Z.Y. Lin, Adv. Funct. Mater. 18 (2008) 928.
[16] S.-J. Su, E. Gonmori, H. Sasabe, J. Kido, Adv. Mater. 20 (2008) 4189.
[17] M.C. Gather, R. Alle, H. Becker, K. Meerholz, Adv. Mater. 19 (2007) 4460.
[18] M.-T. Lee, H.-H. Chen, C.-H. Liao, C.-H. Tsai, C.H. Chen, Appl. Phys. Lett. 85 (2004) 3301.
[19] (a) C.-W. Chen, Y.-J. Lu, C.-C. Wu, E.H.-E. Wu, C.-W. Chu, Y. Yang, Appl. Phys. Lett. 87 (2005) 241121;
(b) H. You, Y.F. Dai, Z.Q. Zhang, D.G. Ma, J. Appl. Phys. 101 (2007) 026105.
[20] (a) J. Ouyang, C.-W. Chu, F.-C. Chen, Q.F. Xu, Y. Yang, Adv. Funct. Mater. 15 (2005) 203;
(b) S. Bange, A. Kuksov, D. Neher, A. Vollmer, N. Koch, A. Ludemann, S. Heun, J. Appl. Phys. 104 (2008) 104506;
(c) K.R. Choudhury, J. Lee, N. Chopra, A. Gupta, X. Jiang, F. Amy, F. So, Adv. Funct. Mater. 19 (2009) 491.
[21] (a) N. Matsusue, S. Ikame, Y. Suzuki, H. Naito, Appl. Phys. Lett. 85 (2004) 4046;
(b) S.M. King, H.A. Al-Attar, R.J. Evans, A. Congreve, A. Beeby, A.P. Monkman, Adv. Funct. Mater. 16 (2006) 1043;
(c) C.-H. Chen, H.-F. Meng, Appl. Phys. Lett. 86 (2005) 201102.
[22] B.D. Chin, M.C. Suh, M.-H. Kim, S.T. Lee, H.D. Kim, H.K. Chung, Appl. Phys. Lett. 86 (2005) 133505.
[23] K.K. Tsung, S.K. So, Appl. Phys. Lett. 92 (2008) 103315.
[24] Y.-S. Park, J.-W. Kang, D.M. Kang, J.-W. Park, Y.-H. Kim, S.-K. Kwon, S.C. Shin, J.-J. Kim, Adv. Mater. 20 (2008) 1957.
[25] N. Matsusue, Y. Suzuki, H. Naito, Jpn. J. Appl. Phys. 44 (2005) 3691.
[26] T. Van Woudenbergh, J. Wildeman, P.W.M. Blom, Phys. Rev. B 71 (2005) 205216.
[27] W.-S. Huang, J.T. Lin, C.-H. Chien, Y.-T. Tao, S.-S. Sun, Y.-S. Wen, Chem. Mater. 16 (2004) 2480.
[28] C. Adachi, M.A. Baldo, M.E. Thompson, S.R. Forrest, J. Appl. Phys. 90 (2001) 5048.
[29] (a) S.J. Yeh, M.F. Wu, C.T. Chen, Y.H. Song, Y. Chi, M.H. Ho, S.F. Hsu, C.H. Chen, Adv. Mater. 17 (2005) 285;
(b) M.F. Wu, S.J. Yeh, C.T. Chen, H. Murayama, T. Tsuboi, W.S. Li, I. Chao, S.W. Liu, J.K. Wang, Adv. Funct. Mater. 17 (2007) 1887;
(c) T. Tsuzuki, S. Tokito, Adv. Mater. 19 (2007) 276;
(d) J.-J. Lin, W.-S. Liao, H.-J. Huang, F.-I. Wu, C.-H. Cheng, Adv. Funct. Mater. 18 (2008) 485;
(e) X.-M. Yu, H.-S. Kwok, W.-Y. Wong, G.-J. Zhou, Chem. Mater. 18 (2006) 5097;
(f) C.-L. Ho, M.-F. Lin, W.-Y. Wong, W.-K. Wong, C.H. Chen, Appl. Phys. Lett. 92 (2008) 083301.

Organic Electronics 11 (2010) 247–254

Contents lists available at ScienceDirect

Organic Electronics

journal homepage: www.elsevier.com/locate/orgel

Enhancing color gamut of white OLED displays by using microcavity green pixels

Chih-Hao Chang, Hsing-Chieh Cheng, Yin-Jui Lu, Kun-Cheng Tien, Hao-Wu Lin, Chun-Liang Lin, Chih-Jen Yang, Chung-Chih Wu *

Department of Electrical Engineering, Graduate Institute of Photonics and Optoelectronics, and Graduate Institute of Electronics Engineering, National Taiwan University, Taipei 10617, Taiwan, ROC

ARTICLE INFO

Article history:
Received 31 August 2009
Received in revised form 25 October 2009
Accepted 1 November 2009
Available online 6 November 2009

Keywords:
White OLEDs
Microcavity
Color gamut

ABSTRACT

The combination of white organic light-emitting devices (OLED) and color filters is one of the most promising technologies for full-color OLED displays. Yet, the transmission spectra of most available color filters are broad and poorly match the electroluminescence spectra of white OLEDs, yielding less saturated filtered colors and small color gamut for displays. In this work, we report that by employing the microcavity structure only in green pixels for such OLED display technology, one can simultaneously achieve simplification the manufacturing process, enhancement of color performances, and enhancement in efficiencies for OLED displays.

© 2009 Elsevier B.V. All rights reserved.

1. Introduction

White organic light-emitting devices (WOLEDs) have attracted wide attention due to their potential applications in displays and solid-state lighting (SSL) [1,2]. For full-color display applications, the combination of WOLEDs and color filters is one of the most promising technologies, since it avoids the precise shadow-masking often used in the separate red–green–blue (RGB) pixilation, and thus is beneficial to realizations of higher display resolutions and large-area scale-up. However, for this technique challenges exist in generation of white electroluminescence (EL) with wide visible spectra and their perfect match with the transmittance of color filters (CFs) [3–5]. Typically, broad EL spectra of white emission can be achieved either by mixing two complementary colors or three primary colors. Yet, the transmission spectra of most available CFs are broad and poorly match the EL spectra of WOLEDs. Hence, the filtered EL usually exhibit poorly saturated colors and yield small color gamut than the NTSC standard.

In 2004, Sony reported that the white emitter with pixilated microcavity structures combined with CFs can achieve high brightness and good color saturation in full-color active-matrix OLED displays [6]. In general, microcavity OLEDs consist of a highly reflective back mirror electrode and a semi-transparent output mirror electrode. When appropriately tailored, microcavity OLEDs can produce narrowed/more saturated EL and brightness enhancement [7–9], useful for constructing energy-efficient displays with color saturation comparable to the NTSC standard. In Sony's configuration, WOLEDs were embedded in the microcavity structure and individual RGB emissions from RGB sub-pixels were created by adjusting the microcavity resonant wavelength of each sub-pixel. It was accomplished through depositing and patterning the indium–tin-oxide (ITO) layers of different thicknesses for the respective RGB sub-pixels. The schematic configuration is shown in Fig. 1a. Depositing and patterning ITO into different thicknesses, however, complicates the fabrication and thus is not convenient for mass production [10].

In the WOLED + CF display technology, the most significant issue resulting from residual emission with the imperfect filtration is unsaturated green emission. With

* Corresponding author. Tel.: +886 2 33663636; fax: +886 2 23689178.
E-mail address: chungwu@cc.ee.ntu.edu.tw (C.-C. Wu).

1566-1199/$ - see front matter © 2009 Elsevier B.V. All rights reserved.
doi:10.1016/j.orgel.2009.11.002

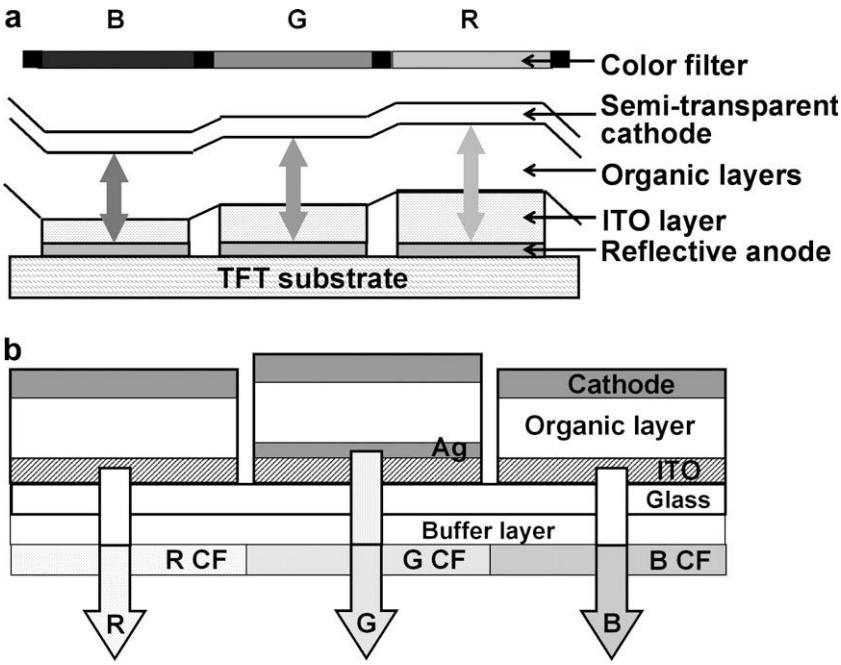

Fig. 1. (a) The schematic diagram of the WOLED + CF display with pixilated microcavity developed by Sony in 2004 and (b) the schematic diagram of the WOLED + CF display by using microcavity green pixels. The buffer layer in (b) could be an index-matching adhesive.

the band-pass nature of green color filters, modifying optical properties of CF or OLED materials would give only limited improvement and shall not solve the problem completely. Nevertheless, by employing the microcavity structure only in green pixels may compensate this weakness and also substantially simplify the manufacturing process (versus Sony's configuration). For instance, one possible WOLED + CF configuration with microcavity green pixels is schematically shown in Fig. 1b. In such an approach, a thin metal layer of one thickness is deposited and patterned only on the ITO anode of green pixels, and then the fabrication of WOLEDs of a same structure for all RGB pixels can be carried out simultaneously.

2. Experimental

2.1. OLED fabrication

All compounds used were subject to temperature-gradient sublimation under high vacuum before use. OLEDs were fabricated on the ITO-coated glass substrates with multiple organic/metal layers sandwiched between the transparent bottom indium–tin-oxide (ITO) anode and the top metal cathode. The organic and metal layers were deposited by vacuum evaporation in a vacuum chamber with a base pressure of $<10^{-6}$ Torr. The deposition system permits the fabrication of the complete device structure in a single vacuum pump-down without breaking vacuum. The deposition rate of organic layers was kept at ~0.2 nm/s. The active area of the device is $2 \times 2\ mm^2$, as defined by the shadow mask for cathode deposition.

2.2. Device characterizations

Current–voltage–luminance (I–V–L) characterization of the devices was measured using an Agilent 4155B semiconductor parameter analyzer and a Si photodiode calibrated with Photo Research PR650. EL spectra of devices were collected by a calibrated CCD spectrograph. To measure the EL spectra of WOLED + CF, color filters were attached to the devices by employing index-matching oil. Transmission spectra of CFs were measured using a spectrophotometer.

3. Results and discussion

Two types of WOLEDs were fabricated and tested. In Type-I devices (Devices A and B, Fig. 2a), the emissive dopants of two complementary colors (red and blue) were used to form a two-component white EL. In Type-II devices (Devices C and D, Fig. 2b), the emissive dopants of three primary colors (red, green, and blue) were used to form a three-component white EL. Both Type-I and II devices used two different anodes, i.e. ITO for non-cavity Devices A/C and ITO/thin Ag (30 nm) for microcavity Devices B/D, respectively. In Devices B and D, the thin silver was chosen as semi-transparent reflective anode for the microcavity structure because of its low absorption/high reflection in the visible range and the lowest resistance among electrode materials [11,12]. By controlling the thickness of anode and organic layers, the resonant wavelength was adjusted to match the transmittance of the green color filters. The transmission spectra of RGB color filters used in this study (micrometer-thick color filters coated on the glass substrate) are shown in Fig. 3.

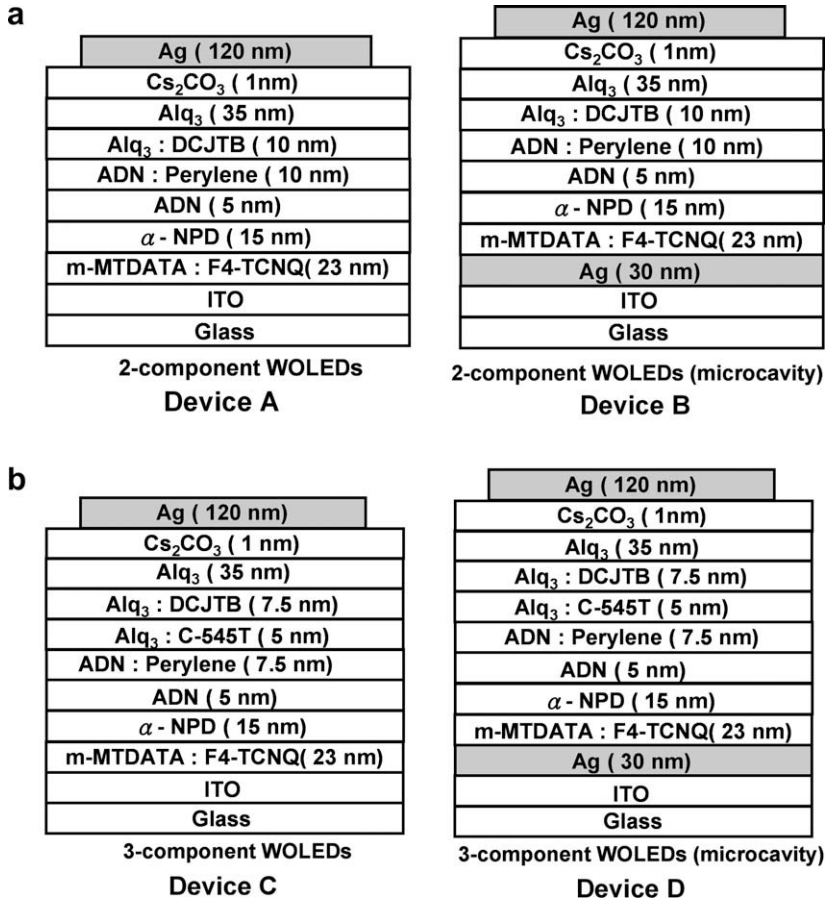

Fig. 2. (a) The structures of two-component WOLEDs (Type-I devices): non-cavity Device A and microcavity Device B and (b) the structures of three-component WOLEDs (Type-II devices): non-cavity Device C and microcavity Device D.

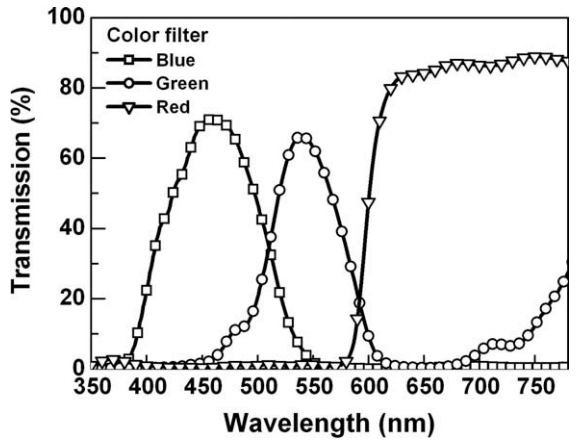

Fig. 3. Transmission spectra of color filters used in this study (micrometer-thick RGB color filters coated on the glass substrate).

3.1. Color performances of two-component white OLEDs + CFs

In Type-I devices, the organic layers and the cathode were: m-MTDATA: F4-TCNQ 2.0 wt% (23 nm)/α-NPD (15 nm)/ADN (5 nm)/ADN: Perylene 1.0 wt% (10 nm)/Alq_3: DCJTB 0.3 wt% (10 nm)/Alq_3 (35 nm)/Cs_2CO_3 (1 nm)/Ag (120 nm). In these devices, 4,4′,4″-Tris(N-3-methylphenyl-N-phenyl-amino) triphenylamine (m-MTDATA) doped with 2 wt% of 2,3,5,6-tetrafluoro-7,7,8,8-tetracyanoquinodimethane (F4-TCNQ) was used as the *p*-doped hole-injection layer (HIL) [13–15]. The p-type doping (F4-TCNQ) facilitates carrier (hole) injection between anode (ITO or silver) and organic materials. N,N′-bis(naphthalen-1-yl)-N,N′-bis(phenyl)-benzidine (α-NPD) and Tris(8-hydroxyquinolinato) aluminium (Alq_3) were used as the hole-transport layer (HTL) and electron-transport layer (ETL), respectively. A 5 nm-thickness 9,10-Di(naphth-2-yl)-anthracene (ADN) layer was used as a buffer layer between HTL and emitting layers [16,17]. The blue emitting layer was composed of 9,10-Di(naphth-2-yl)anthracene (ADN) doped with 1.0 wt% Perylene; the red emitting layer was composed of Alq_3 doped with 0.3 wt% 4-(Dicyanomethylene)-2-tert-butyl-6-(1,1,7,7-tetramethyljulolidin-4-yl-vinyl)-4H-pyran (DCJTB) [18–20]. Cs_2CO_3 and Ag were used as the electron-injection layer (EIL) and cathode, respectively [21,22]. Two types of anodes, ITO for non-cavity Device A and ITO/thin Ag (30 nm) for microcavity Device B, were used, respectively. The layer thickness and the doping concentration were adjusted to achieve white EL for non-

cavity WOLEDs and the wavelength-selected green emission for the microcavity structure (i.e. match the resonant wavelength with the green CF) simultaneously. All the materials used in devices are shown in Fig. 4.

The EL spectra of Type-I devices at 1000 cd/m^2 are shown in Fig. 5a. With carefully adjusting the relative ratio of the two complementary colors in Type-I devices, the EL spectrum of Device A exhibited a white emission with CIE coordinates of (0.34, 0.30), which is close to the equal-energy white at $CIE_{x,y}$ = (0.33, 0.33). One notices that there is absence of the green part in EL of Type-I Devices A. In microcavity Device B, to ensure sufficient light emission through the thin Ag anode, the thickness of silver was set at 30 nm to avoid serious power loss. As such, the microcavity effect is not strong enough to remove completely residual emission in the blue and red ranges, but they are already largely suppressed. The resonant wavelength of Device B was set at 531 nm and the device showed green emission with $CIE_{x,y}$ = (0.23, 0.65).

To measure the EL spectra of WOLED + CF, color filter plates were attached to the devices by employing index-matching oil. Fig. 5b and c show the filtered normalized EL spectra and the color gamut of Type-I Devices (A and B) when combined with CF. In Device A, the filtered EL spectra exhibited rather saturated blue and red colors at $CIE_{x,y}$ = (0.13, 0.11) and $CIE_{x,y}$ = (0.67, 0.32), respectively. On the contrary, the weak intensity in the green region broadened the filtered green emission and produced an unsaturated green color at $CIE_{x,y}$ = (0.28, 0.61). In Device B, the residual blue and red emission was further suppressed by the green CF and the filtered green EL was further narrowed. As shown in Fig. 5c, with the microcavity structure, the filtered green emission (along the normal direction) shifted from $CIE_{x,y}$ = (0.28, 0.61) (Device A) to $CIE_{x,y}$ = (0.25, 0.70) (Device B). By adopting the microcavity green pixel, the color gamut of the WOLED + CF display could be enlarged from 74.6% NTSC (Device A) to 91.2% NTSC (using the microcavity Device B for the green pixel)

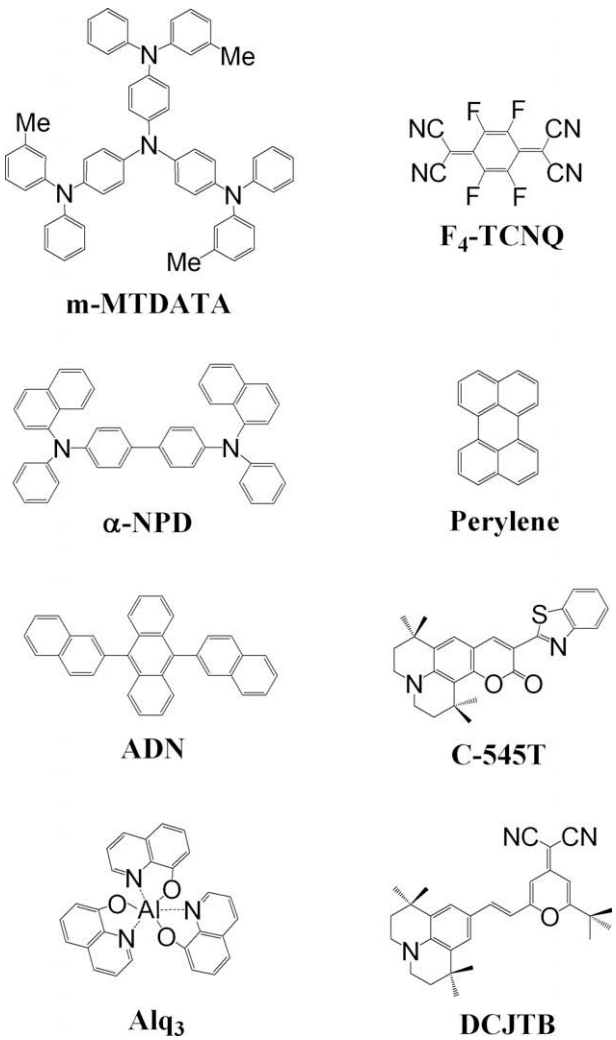

Fig. 4. Chemical structures of materials used in devices.

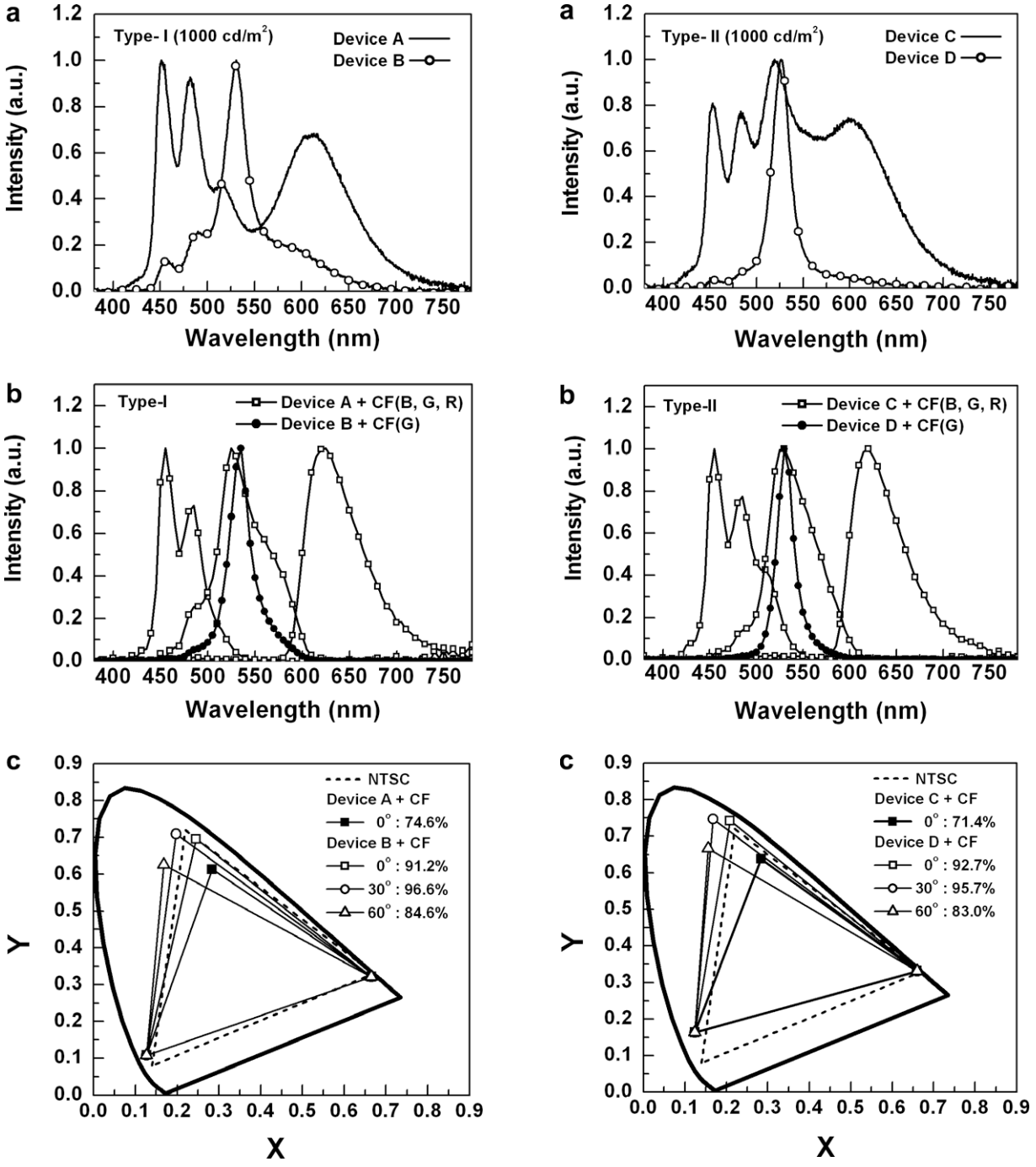

Fig. 5. (a) The normalized EL spectra of Type-I devices in the normal direction, (b) the normalized EL spectra of Type-I devices coupled with CF, and (c) color gamut of Type-I devices coupled with CF at different viewing angles.

Fig. 6. (a) The normalized EL spectra of Type-II devices in the normal direction, (b) the normalized EL spectra of Type-II devices coupled with CF, and (c) color gamut of Type-II devices coupled with CF at different viewing angles.

in the normal direction. Fig. 5c also shows the CIE coordinates of EL of microcavity Device B at different viewing angles, which shows slight blue shift with viewing angles. As such, the color gamut of the WOLED + CF display employing the microcavity green pixel would vary from 91.2% NTSC at 0°, to 96.6% NTSC at 30°, and to 84.6% NTSC at 60°. Therefore, enlarged color gamuts could be obtained over wide viewing angles. In general, the microcavity effect induces slight blue shift of the EL spectrum/peak (color) of the microcavity green pixel with viewing angles [9]. Near the viewing angle of 30°, the EL happens to reaches the

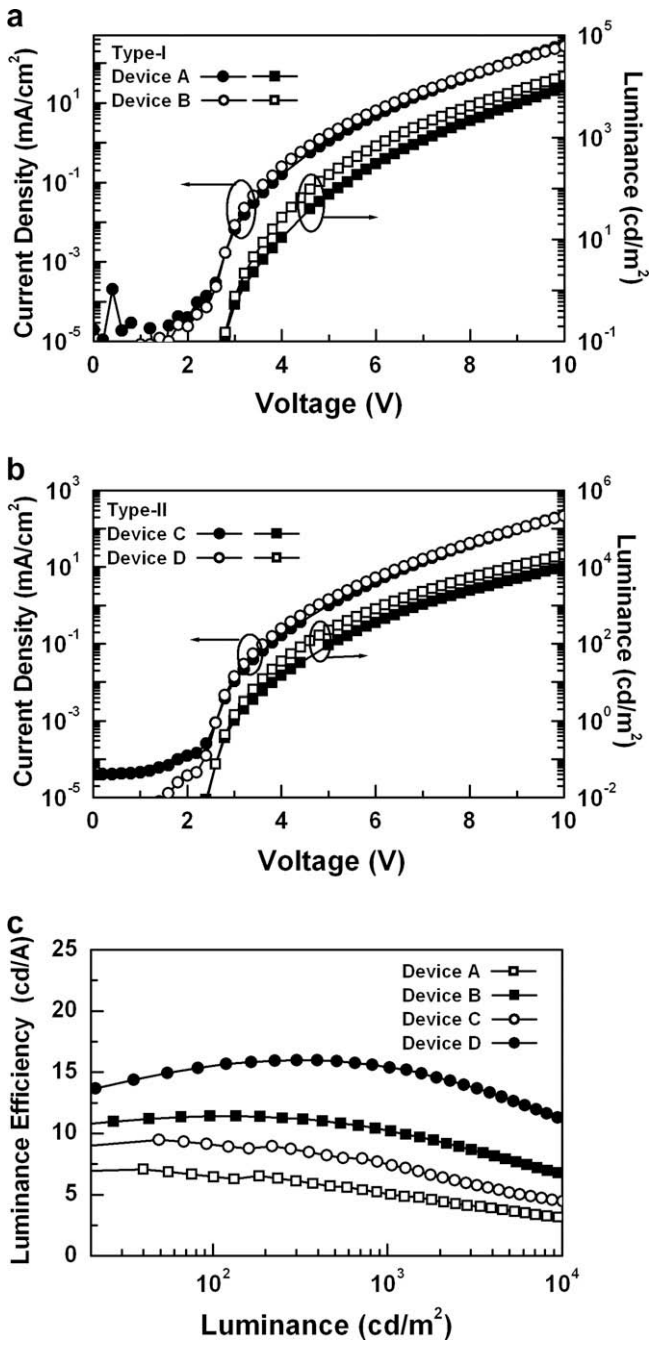

Fig. 7. (a) Current–voltage–luminescence (*I–V–L*) characteristics of Type-I devices, (b) current–voltage–luminescence (*I–V–L*) characteristics of Type-II devices, and (c) luminance efficiency vs. luminance of Type-I and II devices.

most saturated green, thus giving the largest color gamut. We also checked the viewing-angle characteristics of microcavity Device B without CF. Without green CF, the color gamut of the WOLED + CF display would have a significant variation from 89.54% NTSC at 0° to 29.14% NTSC at 60°. Therefore, the results indicate that the CF not only purifies emission colors but also reduces the color shift with viewing angles in the current technology.

3.2. Color performances of three-component white OLEDs + CFs

Triple emission layers were used in Type-II devices. The organic layers and cathode in Type-II devices were: m-MTDATA: F4-TCNQ (23 nm)/α-NPD (15 nm)/ADN (5 nm)/ADN: Perylene 1.0 wt% (7.5 nm)/Alq_3: C545T 1.0 wt% (5 nm)/Alq_3: DCJTB 0.3 wt% (7.5 nm)/Alq_3 (35 nm)/Cs_2CO_3

(1 nm)/Ag (120 nm). In Type-II devices, Alq_3 doped with 2,3,6,7-Tetrahydro-1,1,7,7,-tetramethyl-1H,5H,11H-10- (2-benzothiazolyl) quinolizino-[9,9a,1gh] coumarin (C545T) was used as the green emitting layer (Fig. 4) [23,24]. ITO was used as the anode for the non-cavity device C and ITO/thin Ag (30 nm) was used as the composite anode for the microcavity Device D.

Fig. 6a shows the EL spectra of Type-II devices at 1000 cd/m^2. With the addition of the green emitting layer and the emphasis of green emission, the EL spectrum of Type-II Device C exhibited a greenish white color with $CIE_{x,y}$ = (0.34, 0.40). The larger EL intensity in green wavelengths of Type-II devices enhances the microcavity effect in the microcavity Type-II Device D, giving a much sharper green EL. Comparing the EL spectra of microcavity devices of both types (Devices B and D), one notices that the residual blue and red emissions were much more suppressed in Device D. The resonant wavelength in Device D was set at 526 nm and the device showed more saturated green EL at $CIE_{x,y}$ = (0.22, 0.67).

Fig. 6b and c shows the normalized filtered EL spectra and the color gamut of Type-II Devices (C and D) when combined with CF. Compared to the two-components WOLED Device A, the additional green emitter in Device C does not improve color gamut of the WOLED + CF (71.4% NTSC for Device C vs. 74.6% NTSC for Device A; partially due to the degradation of the filtered blue color in addition to the broad filtered green color). In microcavity Device D + CF, the filtered green emission produced even more saturated green color at $CIE_{x,y}$ = (0.21, 0.74), and the color gamut of the WOLED + CF display could be enlarged from 71.4% NTSC to 92.7% NTSC (using microcavity Device D for the green pixel) in the normal direction. As in the previous case, the microcavity structure combined with CF could mitigate the color shift with viewing angles. The color gamut of the WOLED + CF display employing the microcavity green pixel vary from 92.7% NTSC at 0°, to 95.7% NTSC at 30°, and to 83.0% NTSC at 60°, still showing enlarged color gamuts over wide viewing angles. In general, the microcavity effect induces slight blue shift of the EL spectrum/peak (color) of the microcavity green pixel with viewing angles [9]. Near the viewing angle of 30°, the EL happens to reaches the most saturated green, thus giving the largest color gamut.

3.3. Current–voltage–luminescence (I–V–L) characteristics of all devices

Current–voltage–luminescence (*I–V–L*) characteristics of Type-I and Type-II devices are shown in Fig. 7a and b, respectively. For both types of devices, both the non-cavity and microcavity devices show similar *I–V* characteristics, indicating the effectiveness of the p-type conductive doping (in the hole-injection layer) for facilitating hole injection from the Ag anode. The luminance efficiency vs. luminescence for all Type-I and Type-II devices are shown in Fig. 7c. The non-cavity Type-II device (Device C) shows higher luminance efficiency than the non-cavity Type-I device (Device A), partly because the green dopant was used in Type-II devices. For the same type of devices, the microcavity device also shows higher luminance efficiency than the non-cavity device (Device B vs. Device A and Device D vs. Device C), partly due to eyes being more sensitive to the green color and partly due to microcavity effects on brightness enhancement.

Table 1
Luminance efficiency of WOLED + CF.

Device	Luminance efficiency (cd/A) (at 10^3 cd/m^2)			
	Original	+CF_Blue	+CF_Green	+CF_Red
Type-I				
A	5.49	0.56	1.57	1.33
B	10.23	—	5.10	—
Type-II				
C	7.72	0.70	2.89	1.28
D	14.96	—	8.08	—

The luminance efficiencies of all the devices with/without color filters are listed in Table 1. For Type-I devices, the efficiencies of filtered green EL (at 1000 cd/m^2) for Devices A and B are 1.57 and 5.1 cd/A, respectively. For Type-II devices, the efficiencies of filtered green EL (at 1000 cd/m^2) for Devices C and D are 2.89 and 8.08 cd/A, respectively. It is interesting to note that owing to the better match between the EL spectra of the microcavity OLEDs (B and D) and the transmission of the green color filter, the efficiency loss caused by the color filter (for green pixels) is substantially lower, compared to the case of the conventional WOLED. Hence, by employing the microcavity structure merely in green pixels of the WOLED + CF technology, one can simultaneously achieve simplification the manufacturing process, enhancement of color performances, and enhancement in efficiencies for OLED displays.

4. Conclusions

The combination of WOLEDs and color filters is one of the most promising technologies for full-color OLED displays. Yet, the transmission spectra of most available CFs are broad and poorly match the EL spectra of WOLEDs, yielding less saturated filtered colors and small color gamut. In this work, we report that by employing the microcavity structure only in green pixels for the WOLED + CF display technology, one can simultaneously achieve simplification the manufacturing process, enhancement of color performances, and enhancement in efficiencies for OLED displays.

Acknowledgements

The authors gratefully acknowledge the financial support from National Science Council.

References

[1] J. Kido, M. Kimura, K. Nagai, Science 267 (1995) 1332–1334.
[2] B.W. D'Andrade, S.R. Forrest, Adv. Mater. 16 (2004) 1585–1595.
[3] J.P. Spindler, T.K. Hatwar, M.E. Miller, A.D. Arnold, M.J. Murdoch, P.J. Kane, J.E. Ludwicki, S.A. Van Slyke, SID 05 Digest (2005) 36–39.
[4] H. Kanno, Y. Hamada, K. Nishimura, K. Okumoto, N. Saito, K. Mameno, K. Shibata, Jpn. J. Appl. Phys. 45 (2006) L947–L950.
[5] Y.-J. Lu, C.-H. Chang, C.-L. Lin, C.-C. Wu, H.-L. Hsu, L.-J. Chen, Y.-T. Lin, R. Nishikawa, Appl. Phys. Lett. 92 (2008) 123303.

[6] M. Kashiwabara, K. Hanawa, R. Asaki, I. Kobori, R. Matsuura, H. Yamada, T. Yamamoto, A. Ozawa, Y. Sato, S. Terada, J. Yamada, T. Sasaoka, S. Tamura, T. Urabe, SID 04 Digest (2004) 1017–1019.
[7] C.-L. Lin, H.-W. Lin, C.-C. Wu, Appl. Phys. Lett. 87 (2005) 021101.
[8] C.-C. Wu, C.-W. Chen, C.-L. Lin, C.-J. Yang, J. Disp. Technol. 1 (2005) 248–266.
[9] C.-L. Lin, H.-C. Chang, K.-C. Tien, C.-C. Wu, Appl. Phys. Lett. 90 (2007) 071111.
[10] S.-F. Hsu, C.-C. Lee, S.-W. Hwang, C.H. Chen, Appl. Phys. Lett. 86 (2005) 253508.
[11] C.-C. Wu, C.-L. Lin, P.-Y. Hsieh, H.-H. Chiang, Appl. Phys. Lett. 84 (2004) 3966–3968.
[12] H. Peng, X. Zhu, J. Sun, Z. Xie, S. Xie, M. Wong, H.-S. Kwok, Appl. Phys. Lett. 87 (2005) 173505.
[13] M. Pfeiffer, A. Beyer, T. Fritz, K. Leo, Appl. Phys. Lett. 73 (1998) 3202–3204.
[14] X. Zhou, J. Blochwitz, M. Pfeiffer, A. Nollau, T. Fritz, K. Leo, Adv. Funct. Mater. 11 (2001) 310–314.
[15] X. Zhou, M. Pfeiffer, J. Blochwitz, A. Werner, A. Nollau, T. Fritz, K. Leo, Appl. Phys. Lett. 78 (2001) 410–412.
[16] Y. Li, M.K. Fung, Z. Xie, S.-T. Lee, L.-S. Hung, J. Shi, Adv. Mater. 14 (2002) 1317–1321.
[17] J. Shi, C.W. Tang, Appl. Phys. Lett. 80 (2002) 3201–3203.
[18] C.H. Chen, J. Shi, C.W. Tang, Macromol. Symp. 125 (1997) 1–48.
[19] C.H. Chen, C.W. Tang, J. Shi, K.P. Klubek, Thin Solid Films 363 (2000) 327–331.
[20] Z.Y. Xie, L.S. Hung, S.T. Lee, Appl. Phys. Lett. 79 (2001) 1048–1050.
[21] C.-W. Chen, Y.-J. Lu, C.-C. Wu, E.H.-E. Wu, C.-W. Chu, Y. Yang, Appl. Phys. Lett. 87 (2005) 241121.
[22] C.-I. Wu, C.-T. Lin, Y.-H. Chen, M.-H. Chen, Y.-J. Lu, C.-C. Wu, Appl. Phys. Lett. 88 (2006) 152104.
[23] C.H. Chen, C.W. Tang, Appl. Phys. Lett. 79 (2001) 3711–3713.
[24] M.-T. Lee, C.-K. Yen, W.-P. Yang, H.-H. Chen, C.-H. Liao, C.-H. Tsai, C.H. Chen, Org. Lett. 6 (2004) 1241–1244.

Organic Electronics 11 (2010) 255–265

Contents lists available at ScienceDirect

Organic Electronics

journal homepage: www.elsevier.com/locate/orgel

Percolation paths for charge transports in *N,N′*-diphenyl-*N,N′*-di(*m*-tolyl)benzidine (TPD)

Tomonori Yamada [a], Tohru Sato [b,c], Kazuyoshi Tanaka [b], Hironori Kaji [a,*]

[a] Institute for Chemical Research, Kyoto University, Uji, Kyoto 611-0011, Japan
[b] Department of Molecular Engineering, Graduate School of Engineering, Kyoto University, Kyoto 615-8510, Japan
[c] Fukui Institute for Fundamental Chemistry, Kyoto University, Takano-Nishihiraki-cho 34-4, Sakyo-ku, Kyoto 606-8103, Japan

ARTICLE INFO

Article history:
Received 14 September 2009
Accepted 1 November 2009
Available online 6 November 2009

Keywords:
Organic LED, Marcus theory
Charge transfer integral
Reorganization energy
Quantum chemical calculation

ABSTRACT

We investigated charge transports in *N,N′*-diphenyl-*N,N′*-di(*m*-tolyl)benzidine (TPD), a well-known hole-transport material for organic light-emitting diodes (OLEDs), in the orthorhombic and monoclinic polymorphs. Based on Marcus theory, charge-transfer rate constants in both the polymorphs were investigated by calculating the reorganization energies and charge transfer integrals. The rate constants for hole transfers, k_{CT}^{+}, were calculated to be two to three orders of magnitude larger than those for electron transfers, k_{CT}^{-}, for both the polymorphs. The small k_{CT}^{-} values result not only from the large reorganization energies for electron transfers but also from the small electron transfer integrals. To investigate the charge transfer integrals in more detail, the contributions of respective moieties of TPD molecules, nitrogen, central biphenylene, outer phenyl, and outer tolyl moieties, to charge transfer integrals were analyzed separately. From the analysis, the small electron transfer integrals compared to hole transfer integrals were found to originate from little contribution of LUMO to the outer phenyl and outer tolyl moieties, which has close intermolecular contacts. In contrast, HOMO spreads over these moieties, which results in relatively large hole transfer integrals. Holes can transport through these moieties with close contacts. Percolated hole-transport paths, consisting of consecutive molecular pairs with large hole transfer integrals, and therefore, large k_{CT}^{+}, exist in both the polymorphs, showing the good hole-transport property.

© 2009 Elsevier B.V. All rights reserved.

1. Introduction

Charge transports in organic materials are of immense interest for device applications such as organic light-emitting diodes (OLEDs) [1,2], organic field effect transistors [3,4], and organic solar cells [5,6], and intensive studies have been carried out to understand the charge transport properties [7–47]. Charge transports in several organic crystals with particularly strong intermolecular interactions were reported to be described by the band theory at low temperatures [7,8]. In contrast, organic materials with weak intermolecular interactions, including materials for OLEDs, are known to transport charges by the hopping mechanism [9–13]. The hole- and electron-transfer processes are described by the following Eqs. (1) and (2), respectively

$$M_A + M_B^+ \rightarrow M_A^+ + M_B \quad (1)$$

$$M_A + M_B^- \rightarrow M_A^- + M_B \quad (2)$$

The charge-transfer rate constant, k_{CT}, for each process can be given by Marcus theory [9,10] as

$$k_{CT} = \frac{4\pi^2}{h} H_{AB}^2 \frac{1}{\sqrt{4\pi\lambda k_B T}} \exp\left(-\frac{\lambda}{4k_B T}\right) \quad (3)$$

* Corresponding author. Tel.: +81 774 38 3149; fax: +81 774 38 3148.
E-mail address: kaji@scl.kyoto-u.ac.jp (H. Kaji).

1566-1199/$ - see front matter © 2009 Elsevier B.V. All rights reserved.
doi:10.1016/j.orgel.2009.11.003

where λ is the reorganization energy, H_{AB} is the charge transfer integral (or the electronic coupling matrix element) between the relevant two molecules, and T is the temperature. The h and k_B are the Planck and Boltzmann constants, respectively. The parameters of key importance for charge-transfer processes are λ and H_{AB}. The value of λ is the sum of internal and external reorganization energies. The former has been quantified by quantum chemical calculations for an isolated molecule [14–17], as the summation of λ_1 and λ_2, both of which are represented by the energy differences as follows

$$\lambda_1 = E(\text{charged state in neutral geometry}) - E(\text{charged state in charged geometry}) \quad (4)$$

$$\lambda_2 = E(\text{neutral state in charged geometry}) - E(\text{neutral state in neutral geometry}) \quad (5)$$

The external reorganization energy is related to intermolecular interaction and the contribution to the total reorganization energy has been considered to be small [18,19].

To quantify H_{AB} values, geometrically symmetric neutral dimers have been often considered [20–25]. Halves of the splittings of HOMO and LUMO caused by intermolecular interactions in the dimer system correspond to H_{AB} values for the hole transfer, H_{AB}^{+}, and electron transfer, H_{AB}^{-}, respectively. However, this method is ineffective when the geometry of the dimer is asymmetric and the HOMO or LUMO is unequally distributed between the two molecules. In contrast, the following equations provide the H_{AB}^{+} value, irrespective of the symmetry

$$\begin{vmatrix} \alpha_A - E & \beta - ES \\ \beta - ES & \alpha_B - E \end{vmatrix} = 0 \quad (6)$$

Here, $\alpha_A = \langle \Phi^A_{HOMO} | \mathbf{H} | \Phi^A_{HOMO} \rangle$, $\alpha_B = \langle \Phi^B_{HOMO} | \mathbf{H} | \Phi^B_{HOMO} \rangle$, $\beta = \langle \Phi^A_{HOMO} | \mathbf{H} | \Phi^B_{HOMO} \rangle$, $S = \langle \Phi^A_{HOMO} | \Phi^B_{HOMO} \rangle$, and E is the energy. $\mathbf{H}$ is the electronic Hamiltonian. Φ^A_{HOMO} and Φ^B_{HOMO} are HOMOs of isolated molecules, A and B, respectively. Noting that Φ^A and Φ^B are a non-orthogonal basis set, an effective electronic coupling value, H_{AB}^{+}, is given by Eq. (7) through Löwdin's transformation [26,48].

$$H_{AB}^{+} = \frac{\beta - \frac{\alpha_A + \alpha_B}{2} S}{1 - S^2} \quad (7)$$

For the calculations of H_{AB}^{-} values, LUMOs of isolated molecules, Φ^A_{LUMO} and Φ^B_{LUMO}, are used instead of Φ^A_{HOMO} and Φ^B_{HOMO}.

Until now, the evaluations of H_{AB} values have been performed for several asymmetric organic molecular pairs [27–30]. However, the evaluations of H_{AB} values for OLEDs materials have not been carried out, except for tris(8-hydroxyquinoline) aluminum(III) (Alq_3) [30]. To estimate H_{AB} values for materials in OLEDs, investigations of the amorphous structures are desired; however, they have been difficult to access so far. Therefore, in Ref. [30], the β-Alq_3 crystalline structure was used for the calculations of H_{AB}, assuming that the relative geometries of molecular pairs in the amorphous state are similar to those in the β-crystalline state.

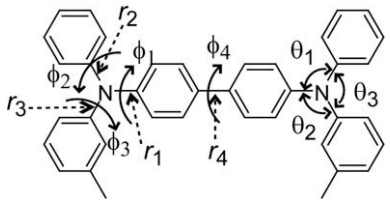

Fig. 1. The chemical structure of TPD. The θ, ϕ, and r represent respective bond angles, torsion angles, and bond lengths, respectively.

In this paper, we focus on charge transports in *N*,*N*′-diphenyl-*N*,*N*′-di(*m*-tolyl)benzidine (TPD) (Fig. 1), considering "*percolation paths*" for charge transports. TPD is a well-known hole-transport material for OLEDs [2,31–45]. Its reorganization energies for hole transfer, λ^+, and electron transfer, λ^-, have been evaluated by density functional theory (DFT) calculations, revealing that the value of λ^+ (0.28 or 0.29 eV) is much smaller than that of λ^- (0.56 eV) [15,16]. The calculations result in the ratio of the hole-transfer rate constant and electron-transfer rate constant, k_{CT}^{+}/k_{CT}^{-}, of 21 when we assume $H_{AB}^{+} = H_{AB}^{-}$ in Eq. (3) [16]. The value has been used to qualitatively explain the results of time-of-flight experiments [37,45] that TPD is superior for hole transports. However, the experimental results, that the electron mobility of TPD is a few or several orders of magnitude smaller than the hole mobility [37,45], cannot be explained by the ratio, $k_{CT}^{+}/k_{CT}^{-} = 21$. To quantify the k_{CT} values and to understand its charge transport property in more detail, the estimation of H_{AB} values is inevitable. In this paper, we evaluate the H_{AB} values using relative intermolecular geometries in TPD crystals as in the above case of Alq_3, because there have been also no data concerning the amorphous structure of TPD, except for the intramolecular structural parameters [44]. For TPD crystals, two different polymorphs, orthorhombic [41] and monoclinic [42], have been reported. We calculate H_{AB} values for both the polymorphs. To understand the charge transports in devices, percolated charge transport paths between the electrodes should be considered. We also investigate the percolation paths for charge transports, which consist of consecutive molecular pairs with large k_{CT} values. Only when percolation paths do exist, charges can be transported from one electrode to the counter electrode by the hopping mechanism [9–13].

2. Computational details

The molecular structures of TPD in its neutral, cationic and anionic states were optimized by DFT method using the B3LYP functional, which employs the gradient correction of the exchange functional with three parameters by Becke [49,50] and the correlation functional by Lee et al. [51]. The 6-31G(d) basis set was used. The values of λ^+ and λ^- were calculated for the DFT-optimized structures by both B3LYP/6-31G(d) and extended Hückel levels. As described above, the contribution of the external reorganization energy to the total reorganization energy has been considered to be small [18,19], and has been neglected [14–16,19]. Similarly, we only considered the internal

reorganization energy in the calculations of the reorganization energy, according to these preceding studies.

For the calculations of H_{AB} values, we used packing structures in the orthorhombic and monoclinic polymorphs of TPD described in Refs. [41,42], respectively. All the pairs of neighboring two molecules were taken from respective polymorphs, and the values of H_{AB} were calculated for the pairs from Eq. (7), using the values of α_A, α_B, β, and S. The calculations of H_{AB}^{+} and H_{AB}^{-} values by *ab intio* and DFT methods have sometimes failed [25] and semi-empirical calculations have been often performed [21–26]. Following these preceding studies, we used extended Hückel method to calculate H_{AB} values. All the calculations were carried out with Gaussian 03 program [52].

3. Results and discussion

3.1. Reorganization energies

For the reorganization energy calculations, TPD in the neutral, cationic, and anionic states were optimized by DFT method. Important optimized parameters, the bond angles, θ_1, θ_2, and θ_3, the torsion angles, ϕ_1, ϕ_2, ϕ_3, and ϕ_4, and the bond lengths, r_1, r_2, r_3, and r_4 (see Fig. 1), are listed in Table 1. The magnitude of geometrical change by anionization is larger than that by cationization, especially concerning the torsion angles. Table 2 shows the calculated λ values. Reflecting the torsion angle differences between the neutral and charged states, the λ^{-} value was calculated to be larger than λ^{+} value for both the DFT and extended Hückel calculations. The DFT-calculated λ values in this study are almost consistent with a previous report [16] as shown in Table 2. Although the extended Hückel calculations provide smaller λ values for both the hole and electron transports, the values of k_{CT}^{+}/k_{CT}^{-} at 300 K under the assumption of $H_{AB}^{+} = H_{AB}^{-}$, are almost consistent between the DFT and the extended Hückel results; hole-transfer rate constants are 20–30 times larger than the electron-transfer rate constants.

3.2. Frontier orbitals

Fig. 2 illustrates the HOMO and LUMO of TPD in the neutral state calculated at DFT B3LYP/6-31G(d) and extended Hückel levels for the above DFT-optimized geometry. Table 3 shows the square of the MO coefficients of respective segments in percentage. In Table 3, the respective segments, the nitrogen, biphenylene, phenyl, and tolyl moieties, are represented as "N," "BP," "Ph," and "To," respectively. The subscript of "L" or "R" means left or right part of the molecule in Fig. 2. For example, "N_L" indicates the left nitrogen of the molecule. For the HOMO, the DFT and extended Hückel results are almost equivalent. The contributions from one nitrogen, N_X, (X = L or R) and one benzene-ring in biphenylene parts, BP_X, are 15 and 16–18%, respectively. The contributions from one benzene-ring in phenyl, Ph_X, and tolyl, To_X, are 9% for both the moieties. On the other hand, the LUMO is more

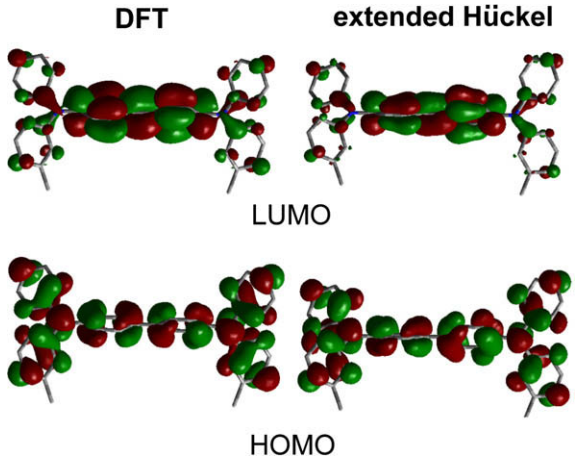

Fig. 2. The HOMO and LUMO of TPD calculated by DFT B3LYP/6-31G(d) and extended Hückel methods for the DFT-optimized geometry. The value for the surfaces is 0.02 a.u.

Table 1
Optimized parameters of TPD in its neutral, cationic, and anionic states. The parameters are defined in Fig. 1.

	θ_1 (°)	θ_2 (°)	θ_3 (°)	ϕ_1 (°)	ϕ_2 (°)	ϕ_3 (°)	ϕ_4 (°)	r_1 (Å)	r_2 (Å)	r_3 (Å)	r_4 (Å)
Neutral	120	120	120	41.0	41.3	42.5	35.8	1.42	1.42	1.42	1.48
Cation	121	121	118	26.1	48.8	49.2	20.6	1.39	1.43	1.43	1.46
Anion	119	119	122	61.4	31.3	31.7	8.7	1.44	1.41	1.41	1.44

Table 2
Reorganization energies of TPD for hole transfer and electron transfer calculated by DFT B3LYP/6-31G(d) and extended Hückel levels.

		λ_1 (eV)	λ_2 (eV)	λ (=λ_1+λ_2) (eV)	k_{CT}^{+}/k_{CT}^{-} [a]
DFT	Hole	0.131	0.141	0.272	27
	Electron	0.305	0.269	0.574	
	Hole[b]	0.13	0.15	0.28	21
	Electron[b]	0.27	0.29	0.56	
Extended Hückel	Hole	0.031	0.117	0.148	20
	Electron	0.280	0.124	0.404	

[a] Based on Eq. (3) at T = 300 K, neglecting the difference of the values of H_{AB}^{+} and H_{AB}^{-}.
[b] The values are taken from Ref. [16].

Table 3
Contributions of the nitrogen (N), biphenylene (BP), phenyl (Ph), and tolyl (To) moieties of TPD to the HOMO and LUMO calculated by DFT B3LYP/6-31G(d) and extended Hückel calculations. The subscript of "L" or "R" indicates the left or right side of the molecule in Fig. 2.

		N_L	N_R	BP_L	BP_R	Ph_L	Ph_R	To_L	To_R
DFT	HOMO	15.0	15.0	17.4	16.1	9.0	8.9	9.3	9.3
	LUMO	0.6	0.5	36.8	35.9	6.6	6.2	6.7	6.7
Extended Hückel	HOMO	14.7	14.7	17.8	17.8	8.7	8.7	8.7	8.7
	LUMO	0.5	0.5	42.6	42.6	3.7	3.7	3.1	3.1

localized on the biphenylene part and contributions from the other parts are notably small, although some difference is found between the DFT and extended Hückel results for the LUMO. For the extended Hückel calculations, the contribution from BP_X is 42.6%, whereas those from N_X, Ph_X, and To_X, are 0.5, 3.7, and 3.1%, respectively.

3.3. Molecular pairs in TPD crystals

Fig. 3a and b shows the unit cell of TPD in the orthorhombic and monoclinic polymorphs reported by Kennedy et al. [41] and Zhang et al. [42], respectively. We designate four molecules in respective unit cells as I, II, III, and IV. We define the cell in Fig. 3 as cell (0 0 0), and neighboring cells at the $+a$, $-a$, $+b$, $-b$, $+c$, and $-c$ directions are represented as (1 0 0), (−1 0 0), (0 1 0), (0 −1 0), (0 0 1), and (0 0 −1), respectively. We refer to a molecule X (X = I, II, III, or IV) in the cell (abc) (a, b, c = −1, 0, or 1) as X(abc). For example, I(0 0 0) denotes molecule I in the cell (0 0 0). In the orthorhombic polymorph, as shown in Table 4, I(0 0 0) is surrounded by two molecules of I, four molecules of II, two molecules of III, and eight molecules of IV. Except for the above pairs between I and II, II(0 0 0) is surrounded by two molecules of II, eight molecules of III, and two

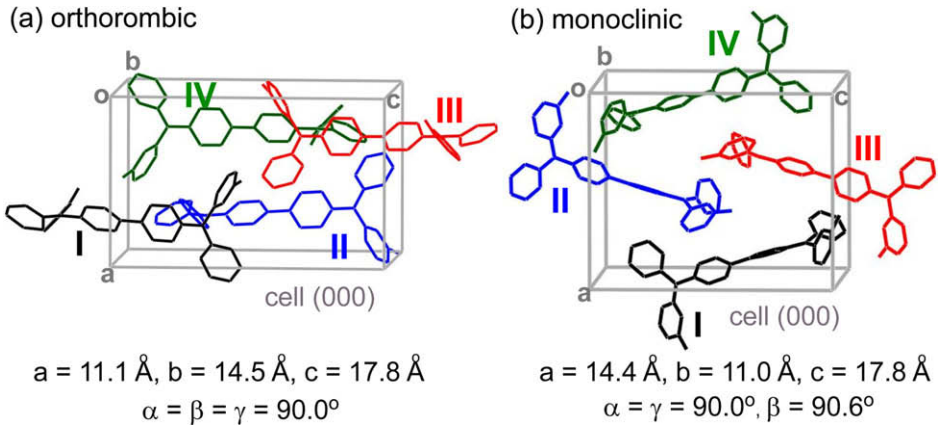

Fig. 3. Four molecules classified into the unit cell (0 0 0) in (a) orthorhombic and (b) monoclinic polymorphs of TPD. For each polymorph, the molecules are designated as I, II, III, and IV.

Table 4
Molecular pairs in the *orthorhombic* polymorph of TPD.

I	II	III		IV	
Pairs with I(0 0 0)					
1. I(0 0 1)	3. II(0 0 0)	7. III(0 0 −1)		9. IV(0 0 0)	13. IV(1 −1 0)
2. I(0 0 −1)	4. II(0 −1 0)	8. III(1 0 −1)		10. IV(1 0 0)	14. IV(1 0 −1)
	5. II(0 0 −1)			11. IV(0 −1 0)	15. IV(0 −1 −1)
	6. II(0 −1 −1)			12. IV(0 0 −1)	16. IV(1 −1 −1)
Pairs with II(0 0 0)					
–	17. II(0 0 1)	19. III(0 0 0)	23. III(1 1 0)	27. IV(0 0 0)	
	18. II(0 0 −1)	20. III(1 0 0)	24. III(1 0 −1)	28. IV(1 0 0)	
		21. III(0 1 0)	25. III(0 1 −1)		
		22. III(0 0 −1)	26. III(1 1 −1)		
Pairs with III(0 0 0)					
–	–	29. III(0 0 1)		31. IV(0 0 0)	33. IV(0 0 1)
		30. III(0 0 −1)		32. IV(0 −1 0)	34. IV(0 −1 1)
Pairs with IV(0 0 0)					
–	–	–		35. IV(0 0 1)	
				36. IV(0 0 −1)	

molecules of IV. Also except for above pairs between I and III, and II and III, III(0 0 0) is surrounded by two molecules of III and four molecules of IV. As the rest, IV(0 0 0) is sandwiched by two molecules of IV. In total, thirty-six pairs, numbered from 1 to 36 in Table 4, were considered for the calculations of H_{AB} values. Likewise, H_{AB} values were calculated for thirty-six pairs in the monoclinic polymorph, which are numbered from 37 to 72 in Table 5.

3.4. "Hole" transports in orthorhombic TPD

The H_{AB}^{+} values for the orthorhombic polymorph are represented in Fig. 4a as filled squares. The H_{AB}^{+} values are notably large for the pairs of 7 (I(0 0 0)–III(0 0 −1)), 8 (I(0 0 0)–III(1 0 −1)), 27 (II(0 0 0)–IV(0 0 0)), and 28 (II(0 0 0)–IV(1 0 0)). Since all these pairs are geometrically equivalent, their H_{AB}^{+} values are the same, 6.4 meV. The pairs are illustrated in Figs. 5a and 6a. The second largest H_{AB}^{+} values are for the pairs of 4 (I(0 0 0)–II(0 −1 0)), 6 (I(0 0 0)–II(0 −1 −1)), 31 (III(0 0 0)–IV(0 0 0)), and 33 (III(0 0 0)–IV(0 0 1)). They are also geometrically equivalent with each other, and all the H_{AB}^{+} value are 4.5 meV. Figs. 5b and 6b show the pairs. For the remaining pairs, the values are 6.4×10^{-2}–1.8 meV.

By using the H_{AB}^{+} values, the k_{CT}^{+} values were calculated at $T = 300$ K, according to Eq. (3). Here, we used the above-mentioned λ^{+} value of 0.148 eV. The results are shown in Fig. 4b as filled squares. The k_{CT}^{+} values are 4.2×10^{7}–4.3×10^{11} s^{-1}. The maximum value is for the pairs of 7, 8, 27, and 28, reflecting their large H_{AB}^{+} values. It can be expected that holes are favorably transported along the *a*-axis through the periodic pairs of 7 and 8, or 27 and 28, as shown in Fig. 5a. The k_{CT}^{+} values in the pairs of 4, 6, 31, and 33 are also in the same order, 10^{11} s^{-1}. Using the periodic pairs of 4 and 6, or 31 and 33, holes can be transported macroscopically along the *c*-axis (see Fig. 5b). Combinations of the pairs in Fig. 5a and b can be also used for effective hole-transport paths in the *a*–*c* plane. For hole transports in the *b*-direction, the pairs of 3, 4, 5, and 6, or 31, 32, 33, and 34 can be used as shown in Fig. 7. The k_{CT}^{+} values for the pairs of 3, 5, 32, and 34 are smaller than those for the pairs of 7 and 4 by about one order of magnitude. Therefore, the hole transports along the *b*-axis are expected to be ineffective compared with those along the *a*- and *c*-axes.

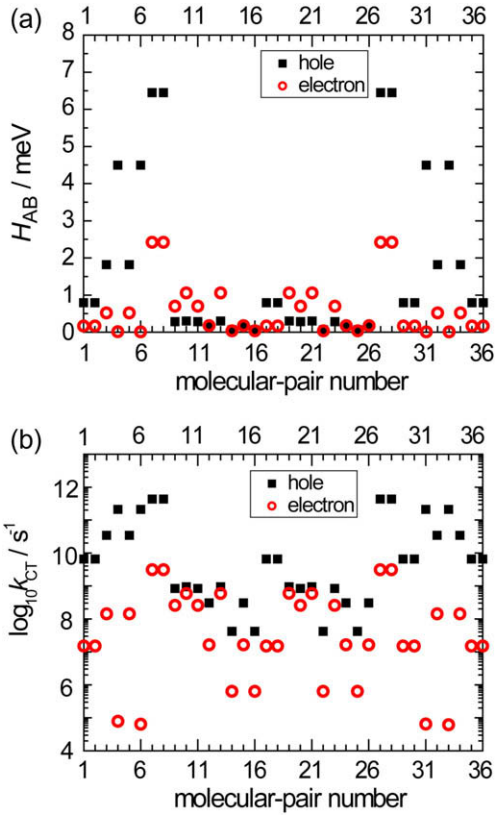

Fig. 4. (a) The values of hole transfer integrals, H_{AB}^{+}, and electron transfer integrals, H_{AB}^{-}, calculated by extended Hückel method for the thirty-six molecular pairs in the orthorhombic polymorph of TPD. (b) The values of hole-transfer rate constants, k_{CT}^{+}, and electron-transfer rate constants, k_{CT}^{-}, at 300 K calculated using the H_{AB} values in (a). For the calculations, the reorganization energies of $\lambda^{+} = 0.148$ and $\lambda^{-} = 0.404$ eV were used, which were calculated by extended Hückel method.

Table 5
Molecular pairs in the *monoclinic* polymorph of TPD.

I	II	III		IV	
Pairs with I(0 0 0)					
37. I(0 0 1)	39. II(0 0 0)	43. III(0 0 0)	47. III(1 1 0)	51. IV(1 0 0)	
38. I(0 0 −1)	40. II(1 0 0)	44. III(1 0 0)	48. III(1 0 −1)	52. IV(1 1 0)	
	41. II(0 0 1)	45. III(0 1 0)	49. III(0 1 −1)		
	42. II(1 0 1)	46. III(0 0 −1)	50. III(1 1 −1)		
Pairs with II(0 0 0)					
–	53. II(0 0 1)	55. III(0 0 −1)		57. IV(0 0 0)	61. IV(1 1 0)
	54. II(0 0 −1)	56. III(0 1 −1)		58. IV(1 0 0)	62. IV(1 0 −1)
				59. IV(0 1 0)	63. IV(0 1 −1)
				60. IV(0 0 −1)	64. IV(1 1 −1)
Pairs with III(0 0 0)					
–	–	65. III(0 0 1)		67. IV(0 0 0)	69. IV(0 0 1)
		66. III(0 0 −1)		68. IV(1 0 0)	70. IV(1 0 1)
Pairs with IV(0 0 0)					
–	–	–		71. IV(0 0 1)	
				72. IV(0 0 −1)	

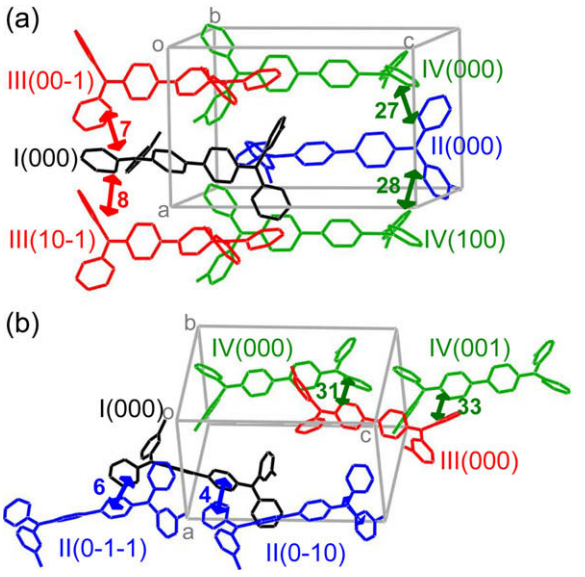

Fig. 5. (a) Representations of the molecular pairs with the largest hole-transfer rate constant in the orthorhombic polymorph, 7 (I(0 0 0)–III(0 0 −1)), 8 (I(0 0 0)–III(1 0 −1)), 27 (II(0 0 0)–IV(0 0 0)), and 28 (II(0 0 0)–IV(1 0 0)). Percolation paths for hole transports along the *a*-axis can be formed by the periodic pairs of 7 and 8, or 27 and 28. (b) The pairs with relatively large hole-transfer rate constants, 4 (I(0 0 0)–II(0 −1 0)), 6 (I(0 0 0)–II(0 −1 −1)), 31 (III(0 0 0)–IV(0 0 0)), and 33 (III(0 0 0)–IV(0 0 1)). The periodic pairs of 4 and 6, or 31 and 33 can be percolation paths for hole transports along the *c*-axis.

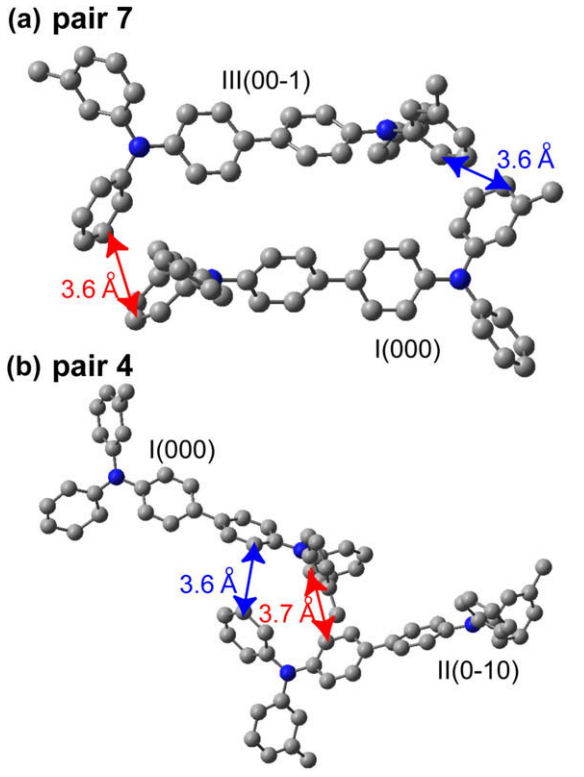

Fig. 6. Representations of short inter-segment C–C distances for the molecular pairs of (a) 7 (I(0 0 0)–III(0 0 −1)) and (b) 4 (I(0 0 0)–II(0 −1 0)).

From the calculations, the values of S in Eq. (7) were found to be small, which results in $1 \gg S^2$. Therefore, Eq. (7) can be reduced to $H_{AB}^{+} = |\beta - \{(\alpha_A + \alpha_B)/2\}S|$. Moreover, H_{AB}^{+} is found to be almost proportional to β, due to the well-known relation, $\beta \cong K\{(\alpha_A + \alpha_B)/2\}S$, where $K = 1.75$ is a Wolfsberg–Helmholz constant [53,54]. Therefore, the contribution of respective segments, the nitrogen, biphenylene, phenyl, and tolyl, for the H_{AB}^{+} values can be investigated by "*segmental β values*", calculated as $\langle \Phi_{HOMO}^{segA} | \mathbf{H} | \Phi_{HOMO}^{segB} \rangle$. Here, Φ_{HOMO}^{segA} and Φ_{HOMO}^{segB} are linear combinations of atomic orbitals in the respective segments of the molecules A and B. Tables 6 and 7 summarize the segmental β values for hole transfer, β^{+}, for respective segmental pairs in the pair of 7 and 4, respectively. Both the positive and negative values appear in the Tables, but the signs are not important and the absolute values are compared in the following discussion.

It is found from Table 6 that the following segment pairs provide large segmental $|\beta^{+}|$ values for the pair 7; (i) the pair of Ph_L of I(0 0 0) and Ph_L of III(0 0 −1), (ii) that of To_L of I(0 0 0) and Ph_L of III(0 0 −1), and (iii) that of To_R of I(0 0 0) and To_R of III(0 0 −1). For the pair 4, as shown in Table 7, followings are notable; the pair of BP_R of I(0 0 0) and Ph_L of II(0 −1 0), (ii) that of Ph_R of I(0 0 0) and BP_L of II(0 −1 0), (iii) that of To_R of I(0 0 0) and BP_L of II(0 −1 0), and (iv) that of To_R of I(0 0 0) and BP_R of II(0 −1 0). Tables 6 and 7 also show the inter-segment distances. It is found that segment pairs with short inter-segment distances generally provide large segmental $|\beta^{+}|$ values. Note that the inter-segment distances in Tables 6 and 7 are the shortest internuclei distances (here, we neglect the hydrogen nuclei). When we use the centers of gravity of each segment as the

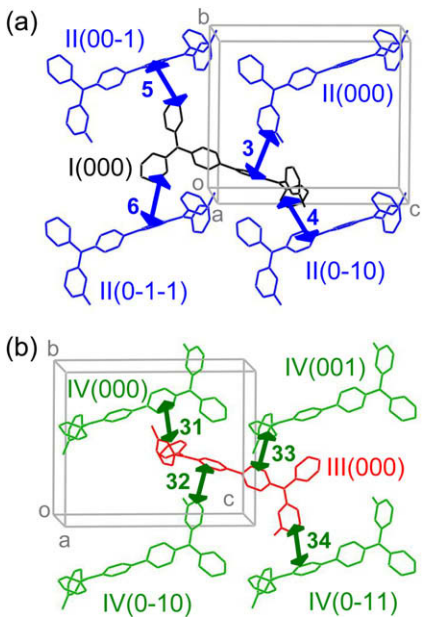

Fig. 7. Molecular pairs of (a) 3 (I(0 0 0)–II(0 0 0)), 4 (I(0 0 0)–II(0 −1 0)), 5 (I(0 0 0)–II(0 0 −1)), and 6 (I(0 0 0)–II(0 −1 −1)) and (b) 31 (III(0 0 0)–IV(0 0 0)), 32 (III(0 0 0)–IV(0 −1 0)), 33 (III(0 0 0)–IV(0 0 1)), and 34 (III(0 0 0)–IV(0 −1 1)) in the orthorhombic polymorph of TPD. They can convey holes in the direction of the *b*-axis.

Table 6
The segmental β values for charge transfer and shortest inter-segment C–C, C–N, or N–N distances in the molecular pair **7**, I(0 0 0)–III(0 0 −1). The respective contributions from the nitrogen (N), biphenylene (BP), phenyl (Ph), and tolyl (To) moieties in the left (L) and right (R) sides of TPD molecules in Fig. 6a are shown.

		III(0 0 −1)							
		N_L	N_R	BP_L	BP_R	**Ph_L**	To_L	Ph_R	**To_R**
Segmental β^+ (meV)									
I(0 0 0)	N_L	0.0	0.0	−1.2	0.0	0.3	0.0	0.0	0.0
	N_R	0.0	0.0	0.0	0.0	0.0	0.0	0.0	0.0
	BP_L	0.0	0.0	−0.8	−0.4	0.0	0.0	0.0	0.0
	BP_R	0.0	−0.2	0.0	−0.9	0.0	0.0	0.2	0.6
	Ph_L	0.0	0.0	0.3	0.0	**−3.8**	0.0	0.0	0.0
	To_L	0.0	0.0	1.6	0.0	**−5.7**	0.0	0.0	0.0
	Ph_R	0.0	0.0	0.0	0.0	0.0	0.0	0.0	0.0
	To_R	0.0	0.1	0.0	0.0	0.0	0.0	0.3	**−3.6**
Segmental β^- (meV)									
I(0 0 0)	N_L	0.0	0.0	−0.2	0.0	−0.1	0.0	0.0	0.0
	N_R	0.0	0.0	0.0	0.0	0.0	0.0	0.0	0.0
	BP_L	0.0	0.0	1.3	−5.0	0.0	0.0	0.0	0.0
	BP_R	0.0	−0.1	0.0	−0.5	0.0	0.0	0.1	0.4
	Ph_L	0.0	0.0	0.0	0.0	**0.2**	0.0	0.0	0.0
	To_L	0.0	0.0	−0.4	0.0	**0.0**	0.0	0.0	0.0
	Ph_R	0.0	0.0	0.0	0.0	0.0	0.0	0.0	0.0
	To_R	0.0	0.0	0.0	0.0	0.0	0.0	0.3	**0.4**
Inter-segment C–C, C–N, or N–N distances (Å)									
I(0 0 0)	N_L	5.8	9.3	4.1	6.1	4.6	7.2	9.4	9.8
	N_R	13.7	6.4	10.0	6.8	13.5	14.8	6.1	5.0
	BP_L	6.6	6.4	3.8	4.0	5.7	7.9	6.6	6.6
	BP_R	9.9	4.7	6.4	3.9	9.5	11.2	4.9	3.8
	Ph_L	4.8	10.0	4.0	6.6	**3.7**	6.1	10.5	10.4
	To_L	5.5	9.4	4.1	6.2	**3.6**	6.9	9.0	10.2
	Ph_R	14.8	7.8	11.2	8.2	14.5	16.0	7.5	6.2
	To_R	13.5	4.7	9.5	5.9	13.5	14.5	3.8	**3.6**

Table 7
The segmental β values for charge transfer and shortest inter-segment C–C, C–N, or N–N distances in the molecular pair **4**, I(0 0 0)–II(0 −1 0). The respective contributions from the nitrogen (N), biphenylene (BP), phenyl (Ph), and tolyl (To) moieties in the left (L) and right (R) sides of TPD molecules in Fig. 6b are shown.

		II(0 −1 0)							
		N_L	N_R	**BP_L**	**BP_R**	**Ph_L**	To_L	Ph_R	To_R
Segmental β^+ (meV)									
I(0 0 0)	N_L	0.0	0.0	0.0	0.0	0.0	0.0	0.0	0.0
	N_R	0.0	0.0	0.1	0.0	−0.1	0.0	0.0	0.0
	BP_L	0.0	0.0	0.0	0.0	0.0	0.0	0.0	0.0
	BP_R	0.0	0.0	0.0	0.0	**−6.1**	0.0	0.0	0.0
	Ph_L	0.0	0.0	0.0	0.0	0.0	0.0	0.0	0.0
	To_L	0.0	0.0	0.0	0.0	0.0	0.0	0.0	0.0
	Ph_R	0.0	0.0	**−2.9**	0.0	0.8	0.0	0.0	0.0
	To_R	0.0	0.0	**−4.3**	**2.7**	0.3	0.0	0.0	0.0
Segmental β^- (meV)									
I(0 0 0)	N_L	0.0	0.0	0.0	0.0	0.0	0.0	0.0	0.0
	N_R	0.0	0.0	0.1	0.0	0.0	0.0	0.0	0.0
	BP_L	0.0	0.0	0.0	0.0	0.0	0.0	0.0	0.0
	BP_R	0.0	0.0	0.0	0.0	**0.9**	0.0	0.0	0.0
	Ph_L	0.0	0.0	0.0	0.0	0.0	0.0	0.0	0.0
	To_L	0.0	0.0	0.0	0.0	0.0	0.0	0.0	0.0
	Ph_R	0.0	0.0	**−1.0**	−0.1	−0.2	0.0	0.0	0.0
	To_R	0.0	0.0	**0.8**	**−0.2**	−0.2	0.0	0.0	0.0
Inter-segment C–C, C–N, or N–N distances (Å)									
I(0 0 0)	N_L	12.9	19.4	13.2	16.1	8.7	13.6	19.1	20.1
	N_R	6.2	9.4	4.8	6.45	4.2	7.6	9.3	10.2
	BP_L	9.3	15.2	9.2	11.9	5.4	10.3	14.9	15.9
	BP_R	6.6	10.9	5.7	7.8	**3.6**	8.0	10.7	11.6
	Ph_L	12.3	19.8	12.9	16.2	8.0	12.7	19.7	20.5
	To_L	14.1	19.8	14.2	16.9	9.9	14.9	19.3	20.6
	Ph_R	5.2	7.5	**3.7**	4.8	4.1	6.6	8.2	7.8
	To_R	5.6	6.8	**3.8**	**3.8**	4.2	6.8	6.3	8.1

inter-segment distance instead, distinct relationship between the segmental $|\beta^+|$ value and the inter-segment distance was not found. Although the inter-segment distance is one of the most crucial factors to provide large segmental $|\beta^+|$ values, they are also affected by other factors. For example, relatively large segmental $|\beta^+|$ value of 1.6 meV is found for To_L of I(0 0 0) and BP_L of III(0 0 −1) in the pair 7 (the inter-segment distance is 4.1 Å). In contrast, the pair of To_R of I(0 0 0) and Ph_R of III(0 0 −1) provides only 0.3 meV, although the inter-segment distance is as short as 3.8 Å. One of the other factors, which affect segmental $|\beta^+|$ values, will be relative orientations between the segments. Another factor is the localization of frontier orbitals. The above results suggest that the phenyl and tolyl rings have great significances to the H_{AB}^+ in both the pairs of 7 and 4, originating from the relatively large contributions to the HOMO and the short inter-segment distances. The situation is substantially different for electron transport in spite of the same intermolecular geometry. This is due to the localization of LUMO as shown later.

3.5. "Electron" transports in orthorhombic TPD

Fig. 4a also shows the H_{AB}^- values for the orthorhombic polymorph as open circles. It is found that the values are smaller than those for HOMOs; all the values are smaller than 2.4 meV. From the H_{AB}^- values, the k_{CT}^- values in Eq. (3) were calculated at $T = 300$ K, using the λ^- value of 0.404 eV. The results are shown in Fig. 4b as open circles. It is clearly shown that the maximum k_{CT}^- value, 3.1×10^9 s^{-1} is two orders of magnitude less than the maximum k_{CT}^+ value. The minimum k_{CT}^- value, 6.2×10^4 s^{-1} is two to three orders smaller compared to the minimum k_{CT}^+ value. The smaller k_{CT}^- values explain the poor electron-transport property of TPD, which is found in this study to originate from the small H_{AB}^- values as well as the large λ value.

The segmental β values for the electron transfer, β^-, in the pairs of 7 and 4 are also shown in Tables 6 and 7, respectively. For the segment pairs with large segmental $|\beta^+|$ values, such as the pair of Ph_L of I(0 0 0) and Ph_L of III(0 0 −1), the segmental $|\beta^-|$ values are found to be small, although the relative geometry of the molecular pairs are the same. The difference originates from the difference of HOMO and LUMO; LUMO is localized on the biphenylene part and the contributions of the other segments are small as shown above (see Fig. 2 and Table 3). Instead, the pair of BP_L of I(0 0 0) and BP_R of III(0 0 −1) provides the segmental $|\beta^-|$ value of 5.0 meV, which is larger than that of the corresponding segmental $|\beta^+|$ value, 0.4 meV. This is also due to the localization of LUMO on the biphenylene part.

3.6. "Hole" transports in monoclinic TPD

Filled squares in Fig. 8a represent the H_{AB}^+ values for the monoclinic polymorph of TPD. It is found that the values in the pairs of 51 (I(0 0 0)–IV(1 0 0)), 52 (I(0 0 0)–IV(1 1 0)), 55 (II(0 0 0)–III(0 0 −1)), and 56 (II(0 0 0)–III(0 1 −1)) are remarkable. These pairs are shown in Figs. 9a, 10a, and 10b. The geometries of the former two pairs, 51 and 52, are equivalent with each other. Also, those of the later two pairs, 55 and 56, are equivalent. The difference between the former two pairs and latter two pairs is slight, which originates from the lower symmetry of the monoclinic polymorph compared with the orthorhombic polymorph. It is also found from Fig. 8a that the H_{AB}^+ values for the pairs of 39 (I(0 0 0)–II(0 0 0)), 41 (I(0 0 0)–II(0 0 1)), 67 (III(0 0 0)–IV(0 0 0)), and 69 (III(0 0 0)–IV(0 0 1)) are relatively large. These pairs are illustrated in Figs. 9b, 10c, and 10d. The geometries of the pairs, 39 and 67, are equivalent and those of the pairs, 41 and 69, are also equivalent.

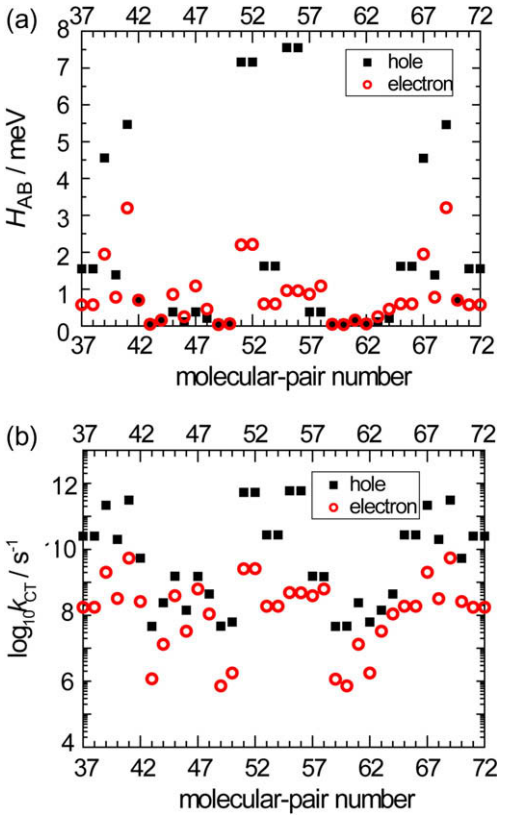

Fig. 8. (a) The values of hole transfer integrals, H_{AB}^+, and electron transfer integrals, H_{AB}^-, calculated by extended Hückel method for the thirty-six molecular pairs in the monoclinic polymorph of TPD. (b) The values of hole-transfer rate constants, k_{CT}^+, and electron-transfer rate constants, k_{CT}^-, at 300 K calculated using the H_{AB} values in (a). For the calculations, the reorganization energies of $\lambda^+ = 0.148$ and $\lambda^- = 0.404$ eV were used.

It should be noted that the pairs of 51, 52, 55, and 56 are similar to the pair 7 (and 8, 27, 28) in the orthorhombic polymorph, as shown in Figs. 6 and 10. Therefore, large segmental $|\beta^+|$ values are obtained for the same segmental pairs between spatially close Ph_X and/or To_X rings in the pairs of 51, 52, 55, and 56, as in the case of the pair 7 (see Tables S1 and S2 in the supporting information). The pairs of 39, 41, 67, and 69 are similar to the pair 4 (and 6, 31, 33) in the orthorhombic polymorph, also as shown in Figs. 6 and 10. Therefore, as in the case of the pair 4, the dominant contribution for the intermolecular HOMO coupling is provided for the segmental pairs between spatially close BP_X and Ph_X, or BP_X and To_X (see segmental $|\beta^+|$ values in Tables S3 and S4 in the supporting information).

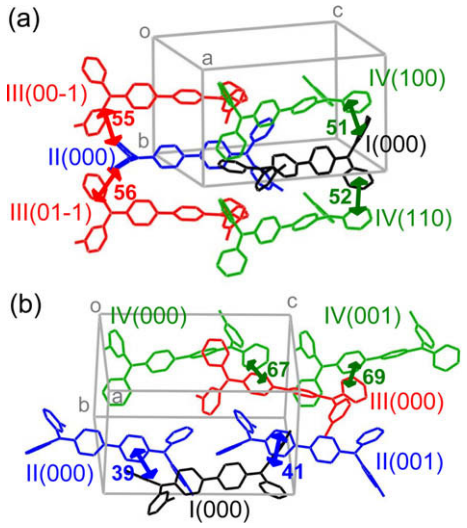

Fig. 9. (a) Representations of the molecular pairs with large hole-transfer rate constants in the monoclinic polymorph, 51 (I(0 0 0)–IV(1 0 0)), 52 (I(0 0 0)–IV(1 1 0)), 55 (II(0 0 0)–III(0 0 −1)), and 56 (II(0 0 0)–III(0 1 −1)). Percolation paths for hole transports along the *b*-axis can be formed by the periodic pairs of 51 and 52, or 55 and 56. (b) The pairs with relatively large hole-transfer rate constants, 39 (I(0 0 0)–II(0 0 0)), 41 (I(0 0 0)–II(0 0 1)), 67 (III(0 0 0)–IV(0 0 0)), and 69 (III(0 0 0)–IV(0 0 1)). The periodic pairs of 39 and 41, or 67 and 69 can be percolation paths for hole transports along the *c*-axis.

The k_{CT}^{+} values at $T = 300$ K are shown in Fig. 8b as filled squares. Large k_{CT}^{+} values in the order of $10^{12}\,s^{-1}$ are obtained for the pairs of 51, 52, 55, and 56, reflecting the H_{AB}^{+} values. Therefore, holes can be conveyed along the *b*-axis through the periodic pairs of 51 and 52, or 55 and 56, as illustrated in Fig. 9a. Also, the periodic pairs of 39 and 41, or 67 and 69, which provide the k_{CT}^{+} values larger than $10^{11}\,s^{-1}$, can transport holes macroscopically along the *c*-axis, as illustrated in Fig. 9b. Combinations of these pairs can also convey holes effectively in the *b* and *c* plane. For hole transports in the *a*-direction, the pairs of 39, 40, 41, and 42, or 67, 68, 69, and 70 can be used as illustrated in Fig. 11. However, the transports are expected to be inferior to those along the *b*- and *c*-axes due to the smaller k_{CT}^{+} values for these pairs.

3.7. "Electron" transports in monoclinic TPD

The H_{AB}^{-} values for the monoclinic polymorph of TPD are also shown in Fig. 8a as open circles. All the H_{AB}^{-} values are less than 3.2 meV, meaning the small intermolecular electronic couplings of LUMOs. The segmental β values for the pairs of 51, 55, 39, and 41 are shown in Tables S1–S4 in the supporting information. As in the case of the orthorhombic polymorph, the intermolecular LUMO couplings between the Ph_X and/or To_X rings are small due to the localization of LUMO on the biphenylene moiety, which results in the small H_{AB}^{-} values.

The k_{CT}^{-} values at $T = 300$ K are represented in Fig. 8b as open circles. The values, which results in 10^{5}–$10^{10}\,s^{-1}$, are found to two to three orders smaller than the k_{CT}^{+} values, as

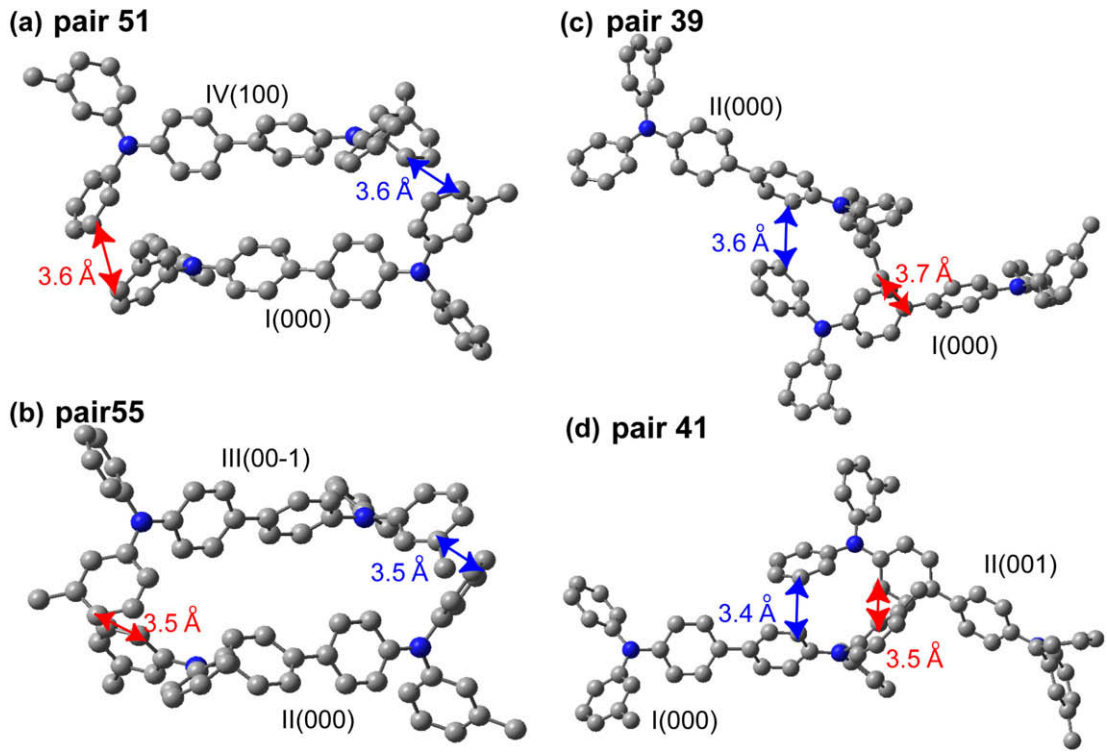

Fig. 10. Representations of some short inter-segment C–C distance for the molecular pairs of (a) 51 (I(0 0 0)–IV(1 0 0)), (b) 55 (II(0 0 0)–III(0 0 −1)), (c) 39 (I(0 0 0)–II(0 0 0)), and (d) 41 (I(0 0 0)–II(0 0 1)).

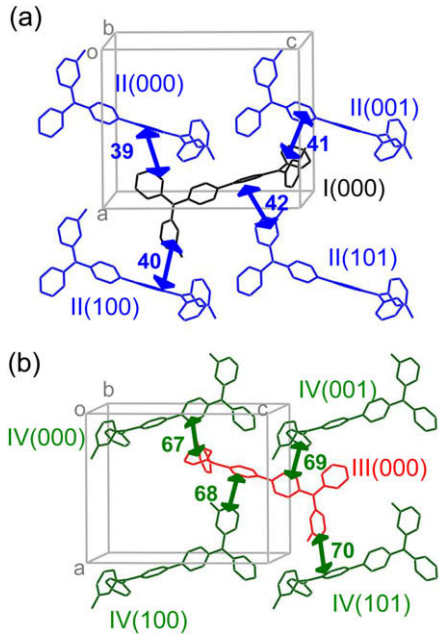

Fig. 11. Molecular pairs of (a) 39 (I(0 0 0)–II(0 0 0)), 40 (I(0 0 0)–II(1 0 0)), 41 (I(0 0 0)–II(0 0 1)), and 42 (I(0 0 0)–II(101)) and (b) 67 (III(0 0 0)–IV(0 0 0)), 68 (III(0 0 0)–IV(1 0 0)), 69 (III(0 0 0)–IV(0 0 1)), and 70 (III(0 0 0)–IV(1 0 1)) in the monoclinic polymorph of TPD. They can convey holes in the direction of the *a*-axis.

in the case of orthorhombic polymorph. Therefore, the electron-transport property of TPD is poor due to the small H_{AB}^{-} values as well as the large λ^{-} value also for the monoclinic polymorph, which is the same conclusion for the orthorhombic polymorph.

4. Conclusion

We have calculated the rate constants for Marcus-type charge transfers and have investigated percolation paths for charge transports in both the orthorhombic and monoclinic polymorphs of TPD. For hole transports, it was found that effective percolation paths exist along specific directions in both the polymorphs. HOMO of TPD delocalizes over the whole molecule, and the outer phenyl and tolyl rings of TPD were found to play an important role for the intermolecular hole transfer integrals due to the inter-segmental close contact between molecular pairs. In contrast to hole transfers, the electron-transfer rate constants are much smaller in both the polymorphs. The smaller electron-transfer rate constants originate not only from the larger reorganization energy but also from smaller electron transfer integrals. LUMO of TPD localizes on the central biphenylene segments, which results in small inter-segmental charge transfers between outer phenyl and tolyl rings in molecular pairs, in spite of the close segmental contacts.

We showed that the shape of HOMO and LUMO and intermolecular packings are crucial for charge transfer integrals. In OLEDs, TPD is used in the amorphous state. This study on the segmental contribution to charge transfer integrals shows that the intermolecular packing is crucial for charge transports. Electron transport properties would be better, if paths consisting of consecutive molecular pairs with close contact at the biphenylene segments are percolated. To be exact, information on intermolecular packing in the amorphous state is necessary to quantify the charge transfer integrals. In order to clarify the amorphous structure and to discuss the charge transports in the amorphous state, two-dimensional double-quantum solid-state NMR experiments [55–58] are now in progress in our laboratory.

Acknowledgement

This research was supported by a Grant-in-Aid for Scientific Research on Priority Areas (19029025), the Ministry of Education, Culture, Sports, Science and Technology (MEXT), and Grants-in-Aids for Scientific Research (A) (21245044) and Exploratory Research (21655068), Japan Society for the Promotion of Science (JSPS), Japan. This research work was also supported partly by Collaborative Research Program for Young Scientists of the Academic Center for Computing and Media Studies (ACCMS) and Institute for Information Management and Communication (IIMC), Kyoto University. The computation time was provided by ACCMS, Kyoto University.

Appendix A. Supplementary data

Supplementary data associated with this article can be found, in the online version, at doi:10.1016/j.orgel.2009.11.003.

References

[1] C.W. Tang, S.A. VanSlyke, Appl. Phys. Lett. 51 (1987) 913.
[2] C. Adachi, S. Tokito, T. Tsutsui, S. Saito, Jpn. J. Appl. Phys. 27 (1988) L269.
[3] F. Garnier, R. Hajlaoui, A. Yassar, P. Srivastava, Science 265 (1994) 1684.
[4] Z. Bao, A. Dodabalapur, A. Lovinger, J. Appl. Phys. Lett. 69 (1996) 4108.
[5] N. Sariciftci, L. Smilowitz, A.J. Heeger, F. Wudl, Science 258 (1992) 1474.
[6] P. Peumans, A. Yakimov, S.R. Forrest, J. Appl. Phys. 93 (2003) 3693.
[7] L.B. Schein, C.B. Duke, A.R. McGhie, Phys. Rev. Lett. 40 (1978) 197.
[8] Y.C. Cheng, R.J. Silbey, D.A. da Silva Filho, J.P. Calbert, J. Cornil, J.L. Brédas, J. Chem. Phys. 118 (2003) 3764.
[9] R.A. Marcus, J. Chem. Phys. 24 (1956) 966.
[10] R.A. Marcus, N. Sutin, Biochim. Biophys. Acta 811 (1985) 265.
[11] H. Bässler, Phys. Stat. Sol. B 175 (1993) 15.
[12] P.F. Barbara, T.J. Meyer, M.A. Ratner, J. Phys. Chem. 100 (1996) 13148.
[13] H. Sirringhaus, P.J. Brown, R.H. Friend, M.M. Nielsen, K. Bechgaard, B.M. Langeveld-Voss, A.J.H. Spiering, R.A.J. Janssen, E.W. Meijer, P. Herwig, D.M. de Leeuw, Nature 410 (1999) 685.
[14] K. Sakanoue, M. Motoda, M. Sugimoto, S. Sakaki, J. Phys. Chem. A 103 (1999) 5551.
[15] M. Malagoli, J.L. Brédas, Chem. Phys. Lett. 327 (2000) 13.
[16] B.C. Lin, C.P. Cheng, Z.P.M. Lao, J. Phys. Chem. A 107 (2003) 5241.
[17] T. Sato, K. Shizu, T. Kuga, K. Tanaka, H. Kaji, Chem. Phys. Lett. 458 (2008) 152.
[18] I. Vilfan, Phys. Stat. Sol. B 59 (1973) 351.
[19] J.J. Kwiatkowski, J. Nelson, H. Li, J.L. Brédas, W. Wenzel, C. Lennartz, Phys. Chem. Chem. Phys. 10 (2008) 1852.
[20] L. Rodriguez-Monge, S. Larsson, J. Phys. Chem. 100 (1996) 6298.
[21] J. Cornil, D. Beljonne, J.P. Calbert, J.L. Brédas, Adv. Mater. 13 (2001) 1053.

[22] J.L. Brédas, J.P. Calbert, J. Cornil, Proc. Natl. Acad. Sci. USA 99 (2002) 5804.
[23] G.R. Hutchison, M.A. Ratner, T.J. Marks, J. Am. Chem. Soc. 127 (2005) 16866.
[24] J. Kirkpatrick, J. Nelson, J. Chem. Phys. 123 (2005) 084703.
[25] A. Datta, S. Mohakud, S.K. Pati, J. Chem. Phys. 126 (2007) 144710.
[26] V. Coropceanu, J. Cornil, D.A. da Silva Filo, Y. Olivier, R. Silbey, J.L. Brédas, Chem. Rev. 107 (2007) 926.
[27] K. Tanaka, Y. Asai, T. Sato, T. Kuga, T. Yamabe, M. Tokumoto, Chem. Phys. Lett. 259 (1996) 574.
[28] A. Farazdel, M. Dupuis, E. Clementi, A. Aviram, J. Am. Chem. Soc. 112 (1990) 4206.
[29] L. Rodriguez-Monge, S. Larsson, Int. J. Quantum Chem. 61 (1997) 847.
[30] B.C. Lin, C.P. Cheng, Z.Q. You, C.P. Hsu, J. Am. Chem. Soc. 127 (2005) 66.
[31] M. Stolka, J.F. Yanus, D.M. Pai, J. Phys. Chem. 88 (1984) 4707.
[32] J. Kido, M. Kimura, K. Nagai, Science 267 (1995) 1332.
[33] V. Bulović, G. Gu, P.E. Burrows, S.R. Forrest, M.E. Thompson, Nature 380 (1996) 29.
[34] H. Ishii, K. Seki, IEEE Trans. Electron. Dev. 44 (1997) 1295.
[35] D.F. O'Brien, P.E. Burrows, S.R. Forrest, B.E. Koene, D.E. Loy, M.E. Thompson, Adv. Mater. 10 (1998) 1108.
[36] H. Murata, C.D. Merritt, Z.H. Kafafi, IEEE J. Sel. Top. Quantum Electron. 4 (1998) 119.
[37] H. Mattoussi, H. Murata, C.D. Merritt, Y. Iizumi, J. Kido, Z.H. Kafafi, J. Appl. Phys. 86 (1999) 2642.
[38] K. Seki, N. Hayashi, H. Oji, E. Ito, Y. Ouchi, H. Ishii, Thin Solid Films 393 (2001) 298.
[39] J. Cornil, N.E. Gruhn, D.A. dos Santos, M. Malagoli, P.A. Lee, S. Barlow, S. Thayumanavan, S.R. Marder, N.R. Armstrong, J.L. Brédas, J. Phys. Chem. A 105 (2001) 5206.
[40] M. Malagoli, M. Manoharan, B. Kippelen, J.L. Brédas, Chem. Phys. Lett. 354 (2002) 283.
[41] A.R. Kennedy, W.E. Smith, D.R. Tackley, W.I.F. David, K. Shankland, B. Brown, S.J. Teat, J. Mater. Chem. 12 (2002) 168.
[42] Z. Zhang, E. Burkholder, J. Zubieta, Acta Cryst. C 60 (2004) o452.
[43] K. Shankland, A.R. Kennedy, W.I.F. David, J. Mater. Chem. 15 (2005) 4838.
[44] H. Kaji, T. Yamada, N. Tsukamoto, F. Horii, Chem. Phys. Lett. 401 (2005) 246.
[45] P. Cusumano, S. Gambino, J. Electron. Mater. 37 (2008) 231.
[46] P. Poolmee, M. Ehara, S. Hannongbua, H. Nakatsuji, Polymer 46 (2005) 6474.
[47] B. Saha, M. Ehara, H. Nakatsuji, J. Phys. Chem. A 111 (2007) 5473.
[48] P.O. Löwdin, J. Chem. Phys. 18 (1950) 365.
[49] A.D. Becke, Phys. Rev. A 38 (1988) 3098.
[50] A.D. Becke, J. Chem. Phys. 98 (1993) 5648.
[51] C.T. Lee, W.T. Yang, R.G. Parr, Phys. Rev. B 37 (1988) 785.
[52] M.J. Frisch, et al., Gaussian 03, Revision E.01, Gaussian, Inc., Wallingford CT, 2004.
[53] M. Wolfsberg, L. Helmholz, J. Chem. Phys. 20 (1952) 837.
[54] R. Hoffmann, J. Chem. Phys. 39 (1963) 1397.
[55] K. Schmidt-Rohr, Macromolecules 29 (1996) 3975.
[56] K. Schmidt-Rohr, W. Hu, N. Zumbulyadis, Science 280 (1998) 714.
[57] H. Kaji, K. Schmidt-Rohr, Macromolecules 33 (2000) 5169.
[58] H. Kaji, K. Schmidt-Rohr, Macromolecules 34 (2001) 7368.

Organic Electronics 11 (2010) 266–272

Contents lists available at ScienceDirect

Organic Electronics

journal homepage: www.elsevier.com/locate/orgel

High-color-rendering pure-white phosphorescent organic light-emitting devices employing only two complementary colors

Chih-Hao Chang [a], Chung-Chia Chen [a], Chung-Chih Wu [a,*], Sheng-Yuan Chang [b], Jui-Yi Hung [b], Yun Chi [b,*]

[a] Department of Electrical Engineering, Graduate Institute of Photonics and Optoelectronics, Graduate Institute of Electronics Engineering, National Taiwan University, Taipei, Taiwan 10617, ROC
[b] Department of Chemistry, National Tsing Hua University, Hsinchu, Taiwan 300, ROC

ARTICLE INFO

Article history:
Received 8 September 2009
Received in revised form 26 October 2009
Accepted 1 November 2009
Available online 6 November 2009

Keywords:
Osmium complex
Iridium complex
White OLEDs
Color rendering index

ABSTRACT

We report successful fabrication of high-color-rendering pure-white phosphorescent organic light-emitting devices (OLEDs) by employing a true-blue iridium complex Ir(dfbp-py)(fbppz)$_2$ and a wide-bandwidth yellow emitting osmium complex Os(bptz)$_2$(dppee). The two-component phosphorescent white OLED exhibited a high color rendering index (CRI) of 81 and CIE$_{x,y}$ coordinates close to the ideal white emission (0.33, 0.33). By doping the yellow phosphors into the hole-transport layer and the electron-transport layer adjacent to the blue-emitting layer and thereby forming a triple-emitting-layer device structure, we obtained WOLED which exhibited rather stable colors at different biases/brightnesses. Such high-CRI pure-white two-component WOLEDs yielded EL efficiencies of up to 9.5%, 22.9 cd/A, and 20 lm/W for the forward directions.

© 2009 Elsevier B.V. All rights reserved.

1. Introduction

With intrinsically high quantum efficiency, white-emitting organic light-emitting devices (WOLEDs) incorporating phosphorescent emitters have become the most promising candidates for meeting the stringent efficiency requirements in lighting applications [1,2]. For high-quality white-light illumination, WOLEDs with CIE$_{x,y}$ coordinates similar to those of the blackbody radiation (with a correlated color temperature (CCT) between 2500 and 6500 K), and a color rendering index (CRI) above 80 are required [3]. Intuitively, the CRI can be enhanced by increasing the number of dopants to extend the spectral range of the electroluminescence (EL). For instance, in 2002, D'Andrade et al. demonstrated that the CRI of phosphorescent WOLEDs could be greatly improved from 50 to 83 by using three (red, green and bluish-green) phosphorescent dopants instead of two complementary (red and bluish-green) dopants [4]. As another example, in 2006 the same group combined blue fluorophors and red/green phosphors to generate white EL, in which deeper blue emission was obtained from the singlet emission of the fluorophors (to relax the requirement for the more challenging true-blue phosphors with high emission efficiencies) while red/green emission was obtained from the triplet emission of the phosphors [5]. In such hybrid WOLEDs, the CRI was improved to 85. In 2007, Schwartz et al. also successfully demonstrated high-CRI WOLEDs (CRI = 86) using a similar hybrid fluorophor/phosphor approach [6]. However, the adoption of a larger number of emissive dopants not only complicates device fabrication, but also renders the color control in WOLEDs fraught with difficulties. In addition, most reported phosphorescent WOLEDs yielded warm white, which would limit their applications in lighting.

As such, generating white electrophosphorescence using less dopants (e.g. two complementary colors) while retaining a useful CRI is highly desired, since it would

* Corresponding authors. Tel.: +886 2 33663636; fax: +886 2 23689178 (C.-C. Wu).
E-mail addresses: chungwu@cc.ee.ntu.edu.tw (C.-C. Wu), ychi@mx.nthu.edu.tw (Y. Chi).

1566-1199/$ - see front matter © 2009 Elsevier B.V. All rights reserved.
doi:10.1016/j.orgel.2009.11.004

vastly simplify the device structures of WOLEDs. To achieve such a goal, it is necessary to develop complementary-color phosphors with extended bandwidths as well as good color rendering capabilities. Until recently, one of the major bottlenecks in implementing high-CRI two-component phosphorescent WOLEDs was the lack of efficient blue phosphors generating enough light output in the shorter wavelength region. For instance, the adoption of the common bluish-green phosphor FIrpic in the two-component WOLEDs generally yielded a poor CRI of <70 due to deficient color rendering in the blue region [7–9]. However, this can be compensated by adopting novel true-blue organic phosphors developed recently [10–13]. On the other hand, from the perspective of color mixing, wide-bandwidth complementary yellow phosphors are also needed to generate white emission with high CRI. In this paper, through the employment of a recently developed true-blue iridium complex Ir(dfbppy)(fbppz)$_2$ and a newly developed wide-bandwidth yellow osmium complex Os(bptz)$_2$(dppee) in appropriate device architectures, we report two-component pure-white phosphorescent WOLEDs with CRI of >80 and CIE coordinates close to the ideal equal-energy white emission (0.33, 0.33).

2. Experimental

2.1. Materials

The blue phosphorescent iridium complex Ir(dfbppy)(fbppz)$_2$, where dfbppy and fbppz stand for 4-*tert*-butyl-2-(2,4-difluorophenyl)pyridinato and 3-(trifluoromethyl)-5-(4-*tert*-butylpyridyl) pyrazolate, and the yellow phosphorescent osmium complex Os(bptz)$_2$(dppee), where bptz and dppee stands for 3-*tert*-butyl-5-(2-pyridyl)-1,2,4-triazolate and cis-1,2-bis(diphenylphosphino) ethene, whose chemical structures are shown in Fig. 1a, were employed in the preparation of two-component WOLEDs. As shown in literature, the heteroleptic Ir^{III} complex Ir(dfbppy)(fbppz)$_2$ revealed true-blue phosphorescence with CIE$_y$ of ~0.2 [10,13]. In particular, placing bulky tertiary butyl substituents around the chelates had improved dispersion of dopant in the host matrix and reduced back energy transfer from dopant to host due to their increased spatial separation [13,14]. On the other hand, the yellow emitting Os(II) complex Os(bptz)$_2$(dppee), showing a featureless emission peak centered at λ = 611 nm, phosphorescence lifetime τ_{obs} = 1 μs and emission quantum yield ϕ = 0.3 in degassed CH_2Cl_2 solution, was synthesized from treatment of $Os_3(CO)_{12}$ with bptzH and dppee in sequence, employing the synthetic methodology that described in literature [15].

Selected spectral data of Os(bptz)$_2$(dppee): MS (FAB, ^{192}Os): *m*/*z* 990 (M^+). ^{1}H NMR (500 MHz, d_6-acetone, 298 K): δ8.04 (t, J_{HH} = 9.0 Hz, 4H), 7.83–7.71 (m, 2H), 7.59–7.55 (m, 4H), 7.36 (dd, J_{HH} = 7.5, 7.0 Hz, 2H), 7.29 (dd, J_{HH} = 8.0, 7.0 Hz, 4H), 7.05–7.03 (m, 4H), 6.85 (dd, J_{HH} = 7.5, 7.3 Hz, 4H), 6.79–6.75 (m, 6H), 1.46 (s, 18H). ^{31}P NMR (202 MHz, d_6-acetone, 298 K): δ31.04 (s). Anal. Calcd. for $C_{48}H_{48}N_8OsP_2$: C, 58.29; N, 11.33; H, 4.89. Found: C, 58.26; N, 11.24; H, 4.85.

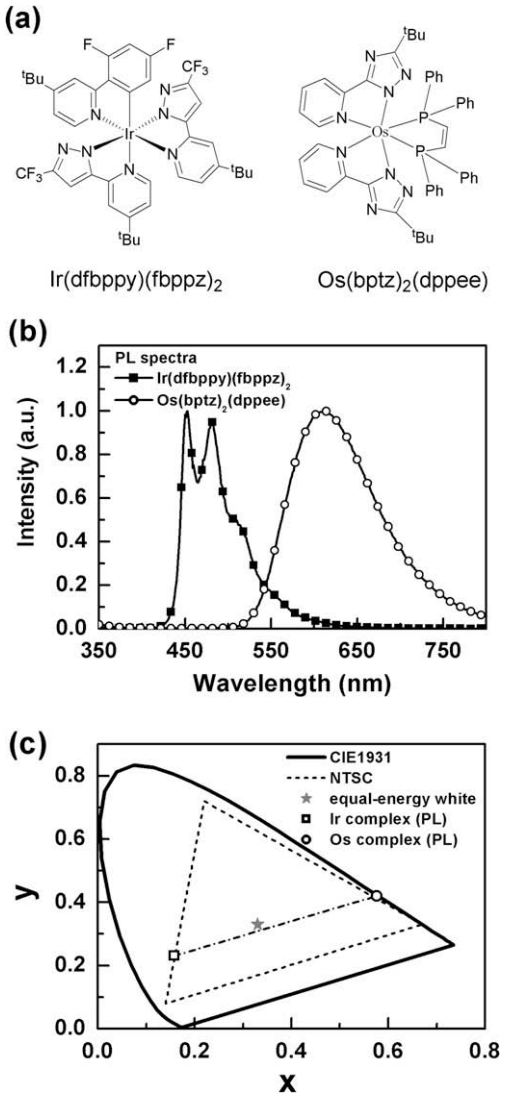

Fig. 1. (a) Chemical structures, (b) PL spectra (measured in CH_2Cl_2), and (c) CIE coordinates (PL) of Ir(dfbppy)(fbppz)$_2$ and Os(bptz)$_2$(dppee).

2.2. OLED fabrication

All synthesized compounds were subject to temperature-gradient sublimation under high vacuum before use. OLEDs were fabricated on the ITO-coated glass substrates with multiple organic layers sandwiched between the transparent bottom indium–tin–oxide (ITO) anode and the top metal cathode. The organic and metal layers were deposited by thermal evaporation in a vacuum chamber with a base pressure of <10^{-6} torr. The deposition rate of organic layers was kept at ~0.2 nm/s. The deposition system permitted the fabrication of the complete device structure in a single pump-down without breaking vacuum. The active area of the device was 2 × 2 mm^2, as defined by the shadow mask for cathode deposition.

2.3. Device characterizations

Current–voltage–luminance (*I–V–L*) characterization of the devices was measured using an Agilent 4155B semiconductor parameter analyzer and a Si photodiode calibrated with Photo Research PR650. EL spectra of devices were collected by a calibrated CCD spectrograph. Total photon output from the device (either from the viewing direction or from all directions of the device) was measured in an integrating sphere containing a calibrated photodetector.

3. Results and discussions

3.1. Emission properties of the Ir and Os complexes

Photoluminescence (PL) of Ir and Os complexes were measured using a Charge-Coupled Device (CCD) spectrograph and the 325 nm line of the He-Cd laser as the excitation source. For determining PL quantum yields, the samples were mounted in a calibrated integrating sphere coupled with the CCD spectrograph. By comparing the spectral intensities of the excitation laser and the PL emission, quantum yields (PLQY) were determined [16].

The structural drawings, PL spectrum of Ir(dfbppy)(fbppz)$_2$ and Os(bptz)$_2$(dppee) in CH_2Cl_2 and their corresponding CIE coordinates are shown in Fig. 1a–c, respectively. The PL quantum yield of Ir(dfbppy)(fbppz)$_2$ in degassed CH_2Cl_2 is calculated to be 0.68, for which true-blue emission showed a CIE$_y$ close to 0.2, while the PL spectrum of Os(bptz)$_2$(dppee) in CH_2Cl_2 revealed a yellow–orange emission with a quantum yield of 0.3.

With the CIE coordinates shown in Fig. 1c, these two phosphors are indeed quite complementary in colors and appropriate combinations of these two colors could possibly generate nearly ideal white emission with CIE coordinates close to (0.33, 0.33) (Fig. 1c). The main PL peak of Ir(dfbppy)(fbppz)$_2$ locates at 449 nm and is accompanied by the vibronic bands peaking at 479 and 507 nm and extending into the blue–green region, which together would provide color rendering in the shorter wavelength region. The yellow emitter Os(bptz)$_2$(dppee) exhibits a

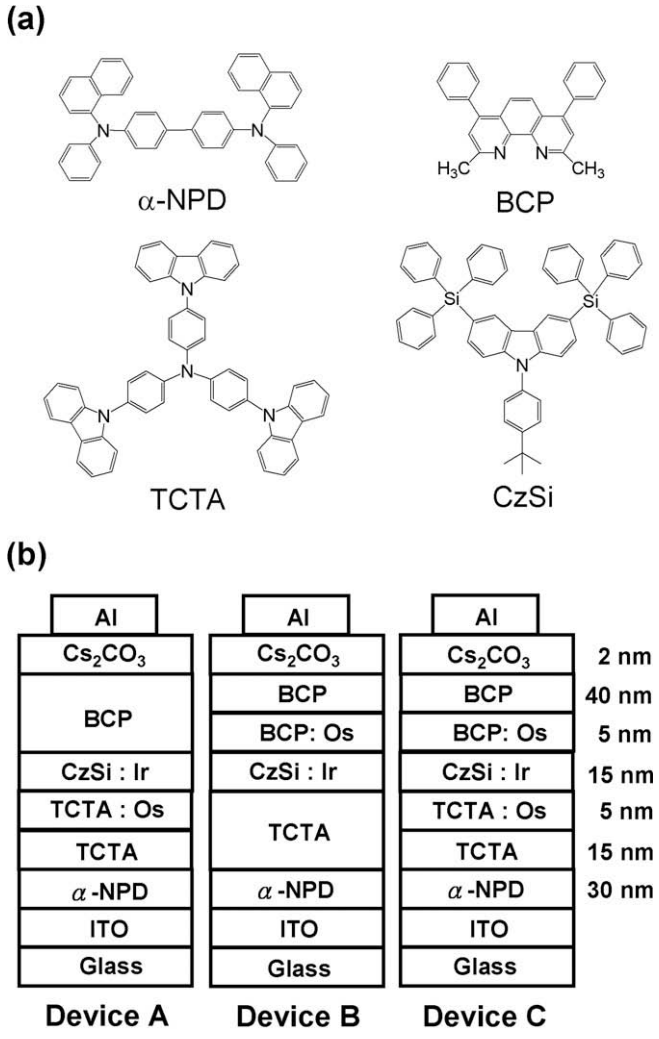

Fig. 2. (a) Structural drawings of materials used in the fabrication of OLEDs; (b) Schematic structures of the various OLED devices.

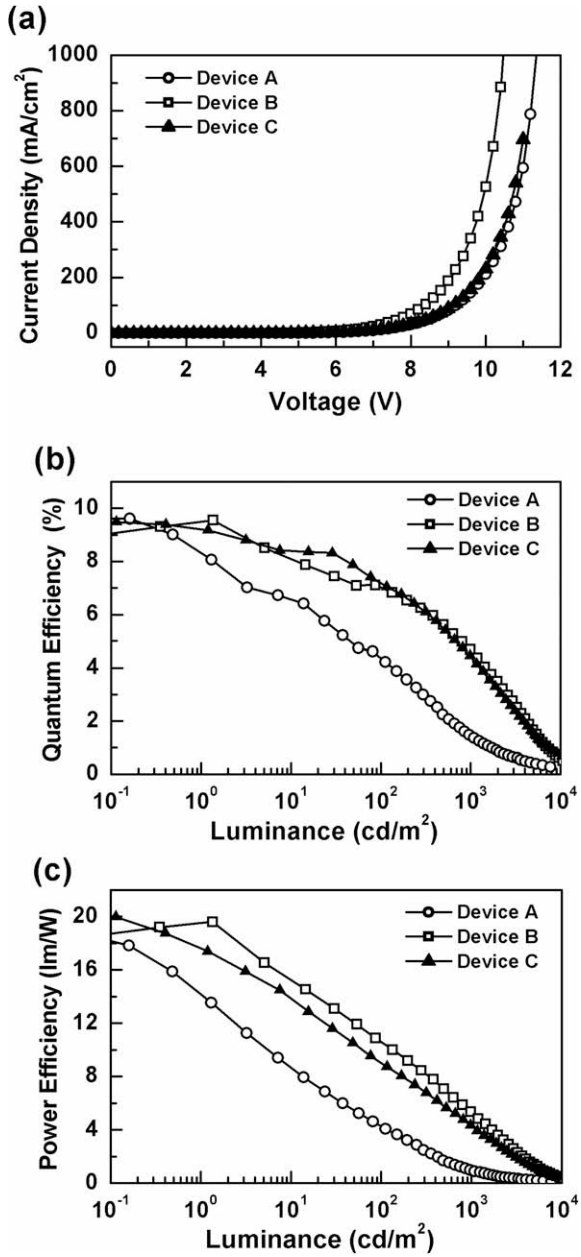

Fig. 3. (a) Current–voltage (*I–V*) characteristics, (b) external quantum efficiency versus luminance, and (c) power efficiency versus luminance for devices A, B and C.

broad PL peak at 611 nm and full-width at half-maximum (FWHM) of 120 nm, covering the spectral range all the way to saturated red. The exceeding large FWHMs of both the blue and yellow emission render possible fabrication of two-component phosphorescent WOLEDs with high CRI, if appropriate color mixing could be implemented by certain device architectures.

3.2. WOLEDs with double emitting layers

In general, the WOLED device structures can be roughly classified into single- and multiple-emitting-layer (EML)

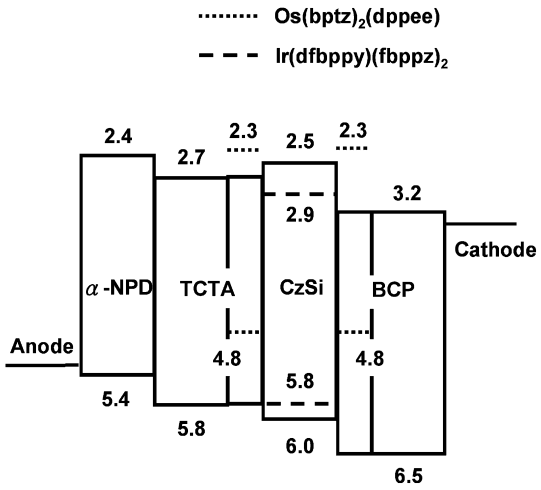

Fig. 4. The energy levels of different materials used in devices.

architectures. The fabrication of WOLEDs with the single EML is usually difficult because the multiple dopants and the host have to be evaporated simultaneously with precise ratio control. Furthermore, the relative intensities of the different emissions might vary upon variation of the operational biases. On the other hand, the device structure with multiple EMLs sometimes suffers from shifting of the recombination zone (RZ) upon increasing the biases. As such, the buffer layer is often inserted between the EMLs to prevent the RZ shift and to stabilize the emission color [17,18]. However, the hindered carrier transport at the buffer layer might degrade the power efficiency. In this work, without adopting the buffer layer, we studied various architectures for multiple-EML WOLEDs, with the aim of achieving stabilized colors. Three multiple-EML WOLED structures without the buffer layer were fabricated in this study (Fig. 2).

To prevent the back transfer of the triplet excitons from the blue phosphors to the host material, a wide-gap host 9-(4-*tert*-butylphenyl)-3,6-bis(triphenylsilyl)-9*H*-carbazole (CzSi), with a large triplet energy of 3.02 eV, was adopted for the blue-emitting layer [19]. In considering the carrier-transport properties and the energy-gap matching, both the hole-transport material 4,4′,4″-tris(carbazole-9-yl)-triphenylamine (TCTA) and the electron-transport material 2,9-dimethyl-4,7-diphenyl-1,10-phenanhroline (BCP) were tested as the host for the yellow emitting layer. Both are commonly used in green to red phosphorescent OLEDs [20]. From the phosphorescence measurements at 77 K, triplet energies of TCTA and BCP were determined to be 2.79 and 2.54 eV, respectively, both larger than that of $Os(bptz)_2(dppee)$. Hence, the yellow emitter was doped in the carrier transport layer (BCP or TCTA or both) next to the blue EML.

We first tested two architectures with double EMLs. The first device configuration (device A, in which the blue phosphor was doped into the CzSi, while the yellow phosphor was doped into TCTA) was: ITO/α-NPD (30 nm)/TCTA (10 nm)/TCTA doped with 1 wt.% of $Os(bptz)_2(dppee)$ (5 nm)/CzSi doped with 6 wt.% of $Ir(dfbppy)(fbppz)_2$

(15 nm)/BCP (50 nm)/Cs_2CO_3 (2 nm)/Al (150 nm). 4,4′-bis[N-(1-naphthyl)-N-phenyl-amino]biphenyl (α-NPD) and TCTA were used as the hole-transport layer (HTLs), BCP as the electron-transport layer (ETL), and Cs_2CO_3 as the electron-injection layer (EIL). ITO and Al were used as the anode and cathode respectively. In device B, the yellow emitter was doped into the electron-transport layer BCP. The configuration of device B was: ITO/α-NPD (30 nm)/TCTA (15 nm)/CzSi doped with 6 wt.% of Ir(dfbppy)(fbppz)$_2$ (15 nm)/BCP doped with 2 wt.% of Os(bptz)$_2$(dppee) (5 nm)/BCP (45 nm)/Cs_2CO_3 (2 nm)/Al (150 nm). The chemical structures of the materials used and the device structures are shown in Fig. 2.

The current–voltage (*I–V*) characteristics of devices A and B are shown in Fig. 3a. From the *I–V* curves, the lower voltage of device B compared to that of device A suggested hole trapping associated with the yellow emitter in TCTA. Fig. 4 depicts the energy levels of materials used in the devices. The energy levels of hosts and carrier-transport materials were collected from the literatures while energy levels of the phosphorescent dopants [Os(bptz)$_2$(dppee), Ir(dfbppy)(fbppz)$_2$] were determined by cyclic voltammetry (CV) [10,19,21,22]. The ionization potential of Os(bptz)$_2$(dppee) (4.8 eV) is substantially lower than those of TCTA, CzSi and Ir(dfbppy)(fbppz)$_2$ (all of which range between 5.8 and 6.0 eV). In view of such an energy-level relationship, it is expected that the Os complexes will function as effective hole traps in TCTA in device A [23–28], but less likely as electron traps in BCP in device B.

The EL spectra of devices A and B at different brightness levels are shown in Fig. 5a and b, respectively. With more contribution from the blue Ir complex and significantly less emission from the yellow Os complex, device A exhibited a bluish-white EL. Such EL characteristics indicated that the exciton formation occurred predominantly inside the CzSi layer, perhaps closer to the CzSi/BCP interface (even though the Os complex in TCTA demonstrated certain hole-trapping characteristics), since the CzSi was dominated by hole-transporting [19,29]. The significant efficiency roll-off in device A might also be associated with such a scenario, since the electron-transporting BCP (with lower triplet energy of 2.54 eV) can quench the high-energy triplet excitons of Ir(dfbppy)(fbppz)$_2$) (2.8 eV) near the interface. On the other hand, doping the yellow Os complex into the electron-transporting BCP near the CzSi/BCP interface (device B) greatly enhanced the yellow emission from the Os complex, resulting in a white EL with CIE coordinates close to (0.33, 0.33) (Table 1). This was due to the fact that the exciton formation zone was almost entirely located at the CzSi/BCP interface. Thus, the increased yellow emission was likely the result of both the direct exciton formation on the Os complex and the energy transfer from the Ir complex (or host) to the Os complex. Furthermore, although both devices A and B exhibited similar EL efficiencies at low current densities (peak external EL quantum efficiencies of 9% and 9.6% for devices A and B, respectively; Fig. 3b and Table 1), the efficiency roll-off in device B was nevertheless much less pronounced.

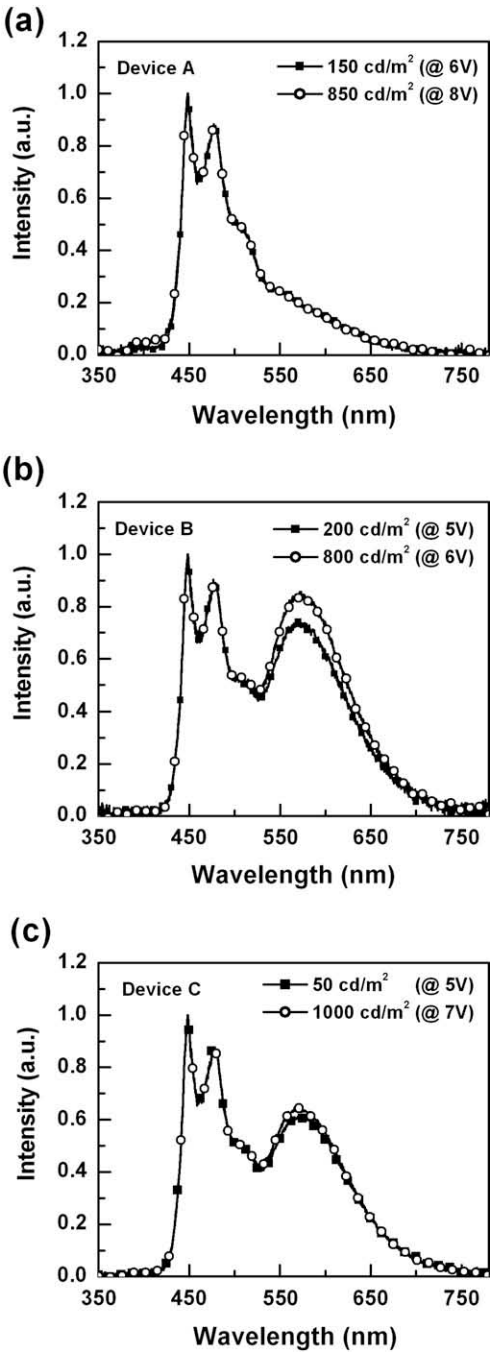

Fig. 5. Normalized EL spectra of OLED devices A, B and C at different brightness levels. EL spectra of all devices were collected at some fixed driving voltages (e.g. 4, 5, 6, 7, 8, 9 V, etc.), and the EL spectra shown in a–c represent those observed at the voltages giving brightness levels closest to 100 and 1000 cd/m^2 for each device.

3.3. WOLEDs with triple emitting layers

Although device B yielded nearly pure white EL, its CRI value was still below 80 and the color variation with brightness levels was noticeable. For device B, the intensity

Table 1
EL characteristics of devices A, B and C.

		Device A (2 EML)	Device B (2 EML)	Device C (3 EML)
External quantum efficiency (%)	Peak	9.6	9.6	9.5
	10^2 cd/m^2	4.2	6.8	7.0
Luminance efficiency (cd/A)	Peak	21.5	22.5	22.9
	10^2 cd/m^2	7.5	15.3	15.0
Power efficiency (lm/W)	Peak	18.8	19.6	20.0
	10^2 cd/m^2	4.1	10.0	8.7
Max. brightness (cd/m^2) (V)		7731 (11.6 V)	13368 (10.8 V)	10271 (11.0 V)
CIE coordinates	$\sim10^2$ cd/m^2	(0.211, 0.249)	(0.324, 0.343)	(0.311, 0.327)
	$\sim10^3$ cd/m^2	(0.208, 0.245)	(0.339, 0.354)	(0.314, 0.332)
CRI/CCT (K)	$\sim10^2$ cd/m^2	–	79 / 5861	81 / 6592
	$\sim10^3$ cd/m^2	–	78 / 5229	81 / 6400

of yellow emission grew relative to the intensity of the blue emission and the CRI dropped with the bias/brightness. It might imply that the exciton recombination zone migrated towards the BCP EML when the bias was increased, leading to larger contribution from the yellow emission of the Os complex. Such effects may be suppressed or reduced by utilizing the hole trapping phenomenon in the device structure A; the hole-trapping mechanism might be used to retard the shift of the recombination zone toward the BCP interface and thus to stabilize EL colors with biases.

Based on these considerations, we further tested a device C with the yellow Os complex doped into portions of both the hole-transport layer TCTA and electron-transport layer BCP adjacent to the blue-emitting layer. The configuration of device C with triple EMLs was: ITO/α-NPD (30 nm)/TCTA (10 nm)/TCTA doped with 1 wt.% of $Os(bptz)_2(dppee)$ (5 nm)/CzSi doped with 6 wt.% of $Ir(dfbppy)(fbppz)_2$ (15 nm)/BCP doped with 2 wt.% of $Os(bptz)_2(dppee)$ (5 nm)/BCP (45 nm)/Cs_2CO_3 (2 nm)/Al (150 nm) (shown in Fig. 2). In Fig. 3a, one observed that device C exhibited *I–V* characteristics very similar to those of device A (and higher voltage than device B), indicating similar hole-trapping effects from the $Os(bptz)_2(dppee)$ doped TCTA. Fig. 5c shows the EL spectra of device C at different brightness levels. The corresponding CIE coordinates of the EL spectra are tabulated in Table 1. For the brightness from <10^2–10^3 cd/m^2, the device exhibited nearly pure white EL with CIE coordinates of (0.311, 0.327)–(0.314, 0.332), which are close to the ideal equal-energy white (0.33, 0.33). With a color variation of only about (0.003, 0.005), the color was rather stable, indicating the effectiveness of the aforementioned device strategy and architecture. Furthermore, the CRI of device C at different brightness levels (Table 1) were higher than 80 (81 indeed). To the best of our knowledge, reports of two-component pure-white phosphorescent OLEDs with a CRI of >80 are very rare.

The EL efficiency characteristics of device C were similar to those of device B (Fig. 3(b), 3c and Table 1). The device C exhibited peak EL efficiencies of 9.5% photon/electron, 22.9 cd/A, and 20 lm/W for the forward directions. At the practical brightness of 100 cd/m^2, the forward efficiency remained high at around 7.0%, 15.0 cd/A, and 8.7 lm/W. For lighting applications, the light emitted from all surfaces of the substrate can in principle be redirected to the forward direction via certain lighting fixtures; hence the total efficiency of the device was also characterized by using an integrating sphere setup [30]. The total quantum and power efficiencies measured in our sphere setup were about 1.7× larger than the forward viewing efficiencies, which were consistent with previous reports [3,31–33]. In this regard, device C indeed had a total peak external quantum efficiency and a total power efficiency of 16.2% and 34 lm/W, respectively.

4. Conclusions

In conclusion, by utilizing a true-blue iridium complex $Ir(dfbppy)(fbppz)_2$ and a wide-bandwidth yellow osmium complex $Os(bptz)_2(dppee)$, we obtained a highly efficient phosphorescent WOLEDs. The two-component phosphorescent WOLED exhibited a high CRI of 81 and CIE coordinates close to the ideal white emission (0.33, 0.33). By doping the yellow phosphors into the hole-transport layer and the electron-transport layer adjacent to the blue-emitting layer and thereby forming a triple-emitting-layer device structure, we obtained WOLED which exhibited rather stable colors at different biases/brightnesses. Such high-CRI pure-white two-component WOLEDs yielded EL efficiencies of up to 9.5%, 22.9 cd/A, and 20 lm/W for the forward directions.

Acknowledgements

The authors gratefully acknowledge the financial support from National Science Council and Ministry of Economic Affairs of Taiwan.

References

[1] Y. Sun, S.R. Forrest, Appl. Phys. Lett. 91 (2007) 263503.
[2] S. Reineke, F. Lindner, G. Schwartz, N. Seidler, K. Walzer, B. Lüssem, K. Leo, Nature 459 (2009) 234–238.
[3] B.W. D'Andrade, S.R. Forrest, Adv. Mater. 16 (2004) 1585–1595.
[4] B.W. D'Andrade, M.E. Thompson, S.R. Forrest, Adv. Mater. 14 (2002) 147–151.
[5] Y. Sun, N.C. Giebink, H. Kanno, B. Ma, M.E. Thompson, S.R. Forrest, Nature 440 (2006) 908–912.
[6] G. Schwartz, M. Pfeiffer, S. Reineke, K. Walzer, K. Leo, Adv. Mater. 19 (2007) 3672–3676.
[7] C.-H. Chang, Y.-J. Lu, C.-C. Liu, Y.-H. Yeh, C.-C. Wu, J. Disp. Technol. 3 (2007) 193–199.
[8] S.H. Kim, J. Jang, J.Y. Lee, Appl. Phys. Lett. 91 (2007) 123509.

[9] X.-M. Yu, H.-S. Kwok, W.-Y. Wong, G.-J. Zhou, Chem. Mater. 18 (2006) 5097–5103.
[10] C.-H. Yang, Y.-M. Cheng, Y. Chi, C.-J. Hsu, F.-C. Fang, K.-T. Wong, P.-T. Chou, C.-H. Chang, M.-H. Tsai, C.-C. Wu, Angew. Chem. Int. Ed. 46 (2007) 2418–2421.
[11] C.-F. Chang, Y.-M. Cheng, Y. Chi, Y.-C. Chiu, C.-C. Lin, G.-H. Lee, P.-T. Chou, C.-C. Chen, C.-H. Chang, C.-C. Wu, Angew. Chem. Int. Ed. 47 (2008) 4542–4545.
[12] Y.-C. Chiu, J.-Y. Hung, Y. Chi, C.-C. Chen, C.-H. Chang, C.-C. Wu, Y.-M. Cheng, Y.-C. Yu, G.-H. Lee, P.-T. Chou, Adv. Mater. 21 (2009) 2221–2225.
[13] C.-H. Chang, C.-C. Chen, C.-C. Wu, C.-H. Yang, Y. Chi, Org. Electron. 10 (2009) 1364–1371.
[14] S.M. King, H.A. Al-Attar, R.J. Evans, A. Congreve, A. Beeby, A.P. Monkman, Adv. Funct. Mater. 16 (2006) 1043–1050.
[15] Y.-M. Cheng, G.-H. Lee, P.-T. Chou, L.-S. Chen, Y. Chi, C.-H. Yang, Y.-H. Song, S.-Y. Chang, P.-I. Shih, C.-F. Shu, Adv. Funct. Mater. 18 (2008) 183–194.
[16] J.C. de Mello, H.F. Wittmann, R.H. Friend, Adv. Mater. 9 (1997) 230–232.
[17] S. Tokito, T. Iijima, T. Tsuzuki, F. Sato, Appl. Phys. Lett. 83 (2003) 2459–2461.
[18] C.-L. Ho, W.-Y. Wong, Q. Wang, D. Ma, L. Wang, Z. Lin, Adv. Funct. Mater. 18 (2008) 928–937.
[19] M.-H. Tsai, H.-W. Lin, H.-C. Su, T.-H. Ke, C.-C. Wu, F.-C. Fang, Y.-L. Liao, K.-T. Wong, C.-I. Wu, Adv. Mater. 18 (2006) 1216–1220.
[20] G. He, M. Pfeiffer, K. Leo, M. Hofmann, J. Birnstock, R. Pudzich, J. Salbeck, Appl. Phys. Lett. 85 (2004) 3911–3913.
[21] V.I. Adamovich, S.R. Cordero, P.I. Djurovich, A. Tamayo, M.E. Thompson, B.W. D'Andrade, S.R. Forrest, Org. Electron. 4 (2003) 77–87.
[22] B.W. D'Andrade, S. Datta, S.R. Forrest, P. Djurovich, E. Polikarpov, M.E. Thompson, Org. Electron. 6 (2005) 11–20.
[23] P.-I. Shih, C.-F. Shu, Y.-L. Tung, Y. Chi, Appl. Phys. Lett. 88 (2006) 251110.
[24] F. Huang, P.-I. Shih, C.-F. Shu, Y. Chi, A.K.-Y. Jen, Adv. Mater. 21 (2009) 361–365.
[25] C.-H. Chang, Y.-H. Lin, C.-C. Chen, C.-K. Chang, C.-C. Wu, L.-S. Chen, W.-W. Wu, Y. Chi, Org. Electron. 10 (2009) 1235–1240.
[26] N. von Malm, J. Steiger, R. Schmechel, H. von Seggern, J. Appl. Phys. 89 (2001) 5559–5563.
[27] H. Aziz, Z.D. Popovic, Appl. Phys. Lett. 80 (2002) 2180–2182.
[28] V.V. Jarikov, Appl. Phys. Lett. 92 (2008) 244103.
[29] M.-H. Tsai, T.-H. Ke, H.-W. Lin, C.-C. Wu, S.-F. Chiu, F.-C. Fang, Y.-L. Liao, K.-T. Wong, Y.-H. Chen, C.-I. Wu, A.C.S. Appl, Mater. Interf. 1 (2009) 567–574.
[30] S.R. Forrest, D.D.C. Bradley, M.E. Thompson, Adv. Mater. 15 (2003) 1043–1048.
[31] S. Möller, S.R. Forrest, J. Appl. Phys. 91 (2002) 3324–3327.
[32] B.W. D'Andrade, J.J. Brown, Appl. Phys. Lett. 88 (2006) 192908.
[33] Y. Sun, S.R. Forrest, Nature Photon. 2 (2008) 483–487.

Organic Electronics 11 (2010) 273–278

Contents lists available at ScienceDirect

Organic Electronics

journal homepage: www.elsevier.com/locate/orgel

Correlating photocurrent spectra and electrical transport parameters in organic field effect transistors

B. Fraboni [a,*], R. DiPietro [a], A. Cavallini [a], P. Cosseddu [b,c], A. Bonfiglio [b,c], J.-O. Vogel [d], J.P. Rabe [d], N. Koch [d]

[a] Dipartimento di Fisica, Università di Bologna, viale Berti Pichat 6/2, 40127 Bologna, Italy
[b] Dipartimento di Ingegneria Elettrica ed Elettronica, Università di Cagliari, piazza d'Armi, 09123 Cagliari, Italy
[c] CNR-INFM S3 via Campi 213/a 41100 Modena, Italy
[d] Humboldt-Universität zu Berlin, Institut für Physik, Newtonstr. 15, 12489 Berlin, Germany

ARTICLE INFO

Article history:
Received 15 June 2009
Received in revised form 13 October 2009
Accepted 1 November 2009
Available online 6 November 2009

Keywords:
Charge transport
Field effect transistor
Density of electronic states
Photocurrent spectroscopy

ABSTRACT

We used photocurrent spectroscopy to study the electronic density of states distribution in thin films of sexithiophene and an alkylated analog, both at the band edge and inside the band-gap. The presented photocurrent spectroscopy analyses provide direct experimental evidence for a modification of the distribution of the electronic density of states in an organic field effect transistor (OFET) channel induced by the modulation of the effective carrier density by the gate voltage. We observe a correlation between a gate voltage induced increase of the carrier density in the channel and a broadening of the distribution of the electronic states around the band edge. We also detected the formation of deep electrically active states within the band-gap of sexithiophene OFETs, induced by the exposure to air and light. These results are in good agreement with the evolution of the macroscopic transport parameters of the devices, i.e., carrier mobility and threshold voltage, as a function of the exposure time to light and atmosphere.

© 2009 Elsevier B.V. All rights reserved.

1. Introduction

Organic semiconducting materials offer the possibility of implementing innovative applications, such as flexible light emitting diodes, photovoltaic cells, and organic field effect transistors (OFETs). The determination and the understanding of organic semiconductor charge transport properties and the electronic states energy distribution are important for further improving device performance. However, these issues are still not unequivocally resolved [1–4]. Since most organic electronic devices rely heavily on the electrical conduction properties of the material, it is necessary to achieve a thorough understanding of the physical mechanism of charge carrier (photo-) generation, transport, trapping and recombination. Charge transport in organic semiconductors can be impacted by different, often interdependent parameters. For instance, the carrier mobility (the transport parameter that can be directly derived from electrical characterization of an OFET) is affected by temperature, electrical field, and, in particular, by the charge carrier density, because charge transport at room temperature in most organic semiconductors occurs *via* carrier hopping through an energetically disordered manifold of localized states [1,2,5,6]. The energy distribution of the states that dominate the transport processes has been shown to have a Gaussian shape with its width σ [5,7,8]. It has been show from theoretical models [9] and quantum chemical calculations [10] that the presence of charged species on a molecule causes a major modification of the electronic energetic structure due to the formation of polarons. Also, the presence of a high charge carrier

* Corresponding author.
E-mail address: beatrice.fraboni@unibo.it (B. Fraboni).

1566-1199/$ - see front matter © 2009 Elsevier B.V. All rights reserved.
doi:10.1016/j.orgel.2009.11.005

density has the effect of increasing the disorder of the energy landscape within the organic semiconductor, thus broadening the Gaussian density of states (DOS) distribution [7,11–13].

The exposure of OFETs to atmosphere and a prolonged operation are two factors known to affect the macroscopic transport parameters of the devices (i.e., mobility and threshold voltage) by introducing deep electrically active trapping states [14–17]. Photocurrent (PC) spectroscopy [18] provides information on the density of states distribution inside the forbidden gap (deep states) and near the band edge, where the photocurrent follows the classical power function of the photon energy, as does the absorption coefficient α, $I_{PC}(\hbar\omega) \sim \alpha \sim (\hbar\omega - E_G)^2$, where E_G is the energy gap, I_{PC} is the collected photocurrent and $\hbar\omega$ is the photon energy, even if for energies above the band-gap the condition $I_{PC}(\hbar\omega) \sim \alpha$ becomes invalid due to the strong increase in optical absorption [19,20].

The goal of the present work is twofold: (i) to investigate how the effective distribution of the electrically available states near the band edge is affected by the modification of the DOS due to variation of the charge carrier density and (ii) to characterize the formation of deep electrically active states within the band-gap.

For that purpose, we fabricated various p-type OFETs with sexithiophene (6T) or α,ω-dihexylsexithiophene (DH6T) as the active semiconductor, and measured the key macroscopic transport parameters, i.e., the hole mobility μ and the threshold voltage V_T. Moreover, we investigated the distribution of the electrically active states by spectral photocurrent (PC) analyses as a function of the carrier concentration in the channel, which was modified by varying the applied gate voltage. We observed a modification of the photoresponse induced by the electrically active states distribution (their energy and width) as a function of the charge carrier concentration in the OFET channel. In addition, we studied the effects induced by prolonged exposure to air and light at room temperature on the transport properties (μ and V_T) and the PC spectra of 6T OFETs.

2. Experimental

OFET devices were fabricated by evaporating gold contacts on a heavily doped *n*-Si/SiO_2 substrate (the *n*-Si is the gate of the transistor) with a 0.5 μm thick SiO_2 dielectric layer. The Au source and drain contacts defined the OFET channel width (50 μm) and length (5 mm). Typically 30 nm thick layers of 6T (Sigma Aldrich) or DH6T (H.C. Stark GmbH) were then thermally evaporated (pressure below 2×10^{-7}mbar, deposition rate ca. 4 Å/min; for final device structure see Fig. 1). An Agilent HP 4155 Semiconductor Parameter Analyzer, provided with gold tips for contacting the electrodes, was used to carry out drain-source current (I_{ds}) measurements as a function of gate voltage (V_G).

Photocurrent spectroscopy measurements were carried out on these OFET structures in air and at room temperature. A low bias was applied to the drain electrode (<2 V) and the current was measured through a load resistance. The light source was a 150 W Quartz Tungsten Halogen lamp coupled to a Jarrel monochromator and mechanically chopped at low frequency (<20 Hz). The photocurrent was measured as a function of light wavelength (varied in the range λ = 300–750 nm) using a current amplifier connected to a digital lock-in amplifier (Stanford Research 850). The energy resolution was 0.01 eV at 2.40 eV. The photon flux was measured with a calibrated Si photodiode. PC measurements were done at low-level injection conditions (1×10^{13} photons/cm^2 at λ = 450 nm). No indications for sample degradation were observed in the PC spectra during experiments, as assessed by comparing consecutively acquired spectra.

3. Results and discussion

The average values of the key transport parameters of OFETs with 6T and DH6T are summarized in Table 1. Despite the very similar molecular structure of the conjugated part of the two employed molecules, two striking differences can be noted: (i) DH6T devices exhibit a higher hole mobility than 6T devices; (ii) 6T devices show a negative threshold voltage, whereas DH6T devices have a positive threshold voltage. Therefore, DH6T features an accumulation layer of charge carriers (holes) at the semiconductor/dielectric interface even at zero gate bias, and a high positive bias is needed to completely deplete the channel (OFET "off-state"). These observations were highly reproducible, and were measured for both bottom contact and top contact control-device configurations, and for OFETs fabricated on a flexible substrate (Mylar®) [22].

The observed difference in hole mobility between 6T and DH6T OFETs is likely due to a better structural and morphological quality of DH6T layers [21,22]. The terminal hexyl groups of DH6T enable an improved long range molecular ordering on the substrates [21–24], resulting in a lower density of grain boundaries in thin films [12]. The substantial number of holes present in DH6T OFET channels at zero gate voltage has been explained by a high susceptibility of this material to p-type doping by oxygen

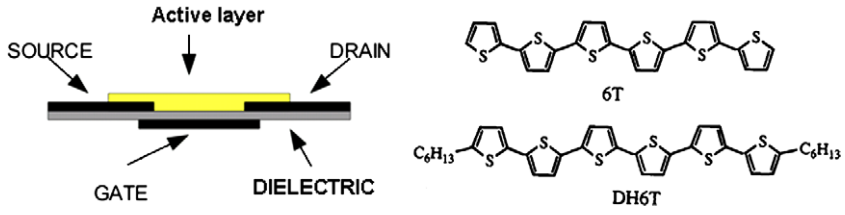

Fig. 1. Schematic layout of the OFET devices, and chemical structure of 6T and DH6T.

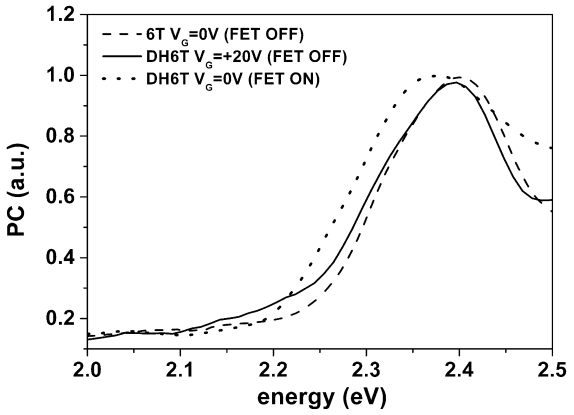

Fig. 2. Photocurrent yield (electron/photon) spectra of 6T and DH6T OFETs for different gate voltages, normalized to each curve maximum.

(*e.g.*, due to air exposure) due to its 0.2 eV lower ionization energy than 6T [21].

Fig. 2 shows the PC spectra near the fundamental optical transition (at 2.4 eV [25]) of 6T and DH6T OFETs. The almost coinciding position of the strong absorption band indicates that the effective conjugation length of the substituted DH6T molecules essentially equals that of 6T [26]. V_T values of these devices were −4 V (6T) and +12 V (DH6T). Therefore, PC measurements were done by applying V_G = 0 V (6T) and V_G = +20 V (DH6T) in order to have both OFETs in the "off-state". In this state, both organic materials exhibit a similar onset of electrical transport at *ca.* 2.25 eV. The energy distribution of the electrically available states has an almost Gaussian-like shape for both devices in the "off-state". For comparison, Fig. 2 also shows the PC spectrum of DH6T in an "on-state", i.e., for V_G = 0 V, thus with a much higher density of holes in the channel. PC spectra of DH6T OFETs in the "on-state" show a modification in the distribution of the density of the electronic transport states with the onset of the electrical transport shifting to lower energies (*ca.* 2.18 eV).

More insight into the effects of varying the charge carrier density in the OFET channel on the occupation of the electronic states distribution is provided by the PC spectra reported in Fig. 3, which zooms in on the band edge DOS distribution of a 6T OFET under different gate bias voltages (V_G = +20 V, V_G = 0 V and V_G = −20 V; i.e., going from "off-state" to "on-state"). It is evident that the energy distribution of the electrically active states varies, shifting towards lower energy when the device is turned on (V_G = −20 V). Fitting the PC spectra at the band edge of 6T OFETs with a Gaussian-like curve yields that its width increases by 0.12 eV when it passes from the "off–state" to the "on-state".

A similar behavior was reported for chemically doped organic semiconductors where the width of the Gaussian shaped density of states was assumed to increase as the charge carrier density increases [7,11] due to the local electric field induced by the presence of charges. This local electric field is responsible for the alteration of the potential landscape in the active material. The increase in energetic disorder due to the presence of charges may broaden

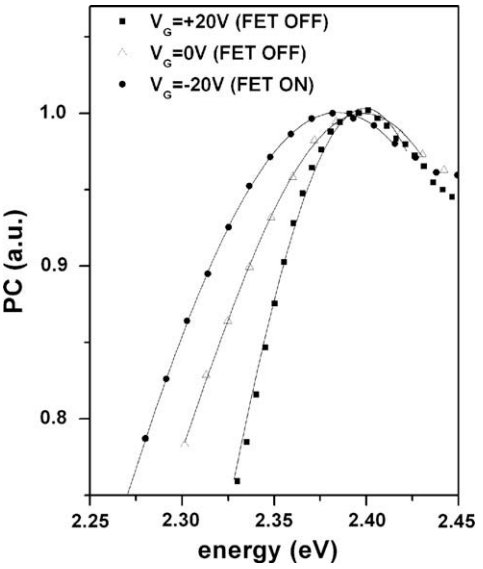

Fig. 3. Band edge details of the photocurrent yield (electron/photon) spectra of a 6T OFET for different gate voltages, normalized to each curve maximum (solid curves). The Gaussian fits to the experimental data are the dashed curves.

the effective DOS distribution by increasing the available and effective transport states in the band tails [7,12,13].

The polaronic nature of mobile charges has also the effect of modifying the energy levels of the molecules on which they are located: the presence of the polaron induces the formation of levels between the HOMO and LUMO gap and modifies the band edge shape. These effects, quantitatively predicted using quantum chemical calculations [10], have been investigated on thiophenes by Charge Modulation Spectroscopy (CMS) measurements [27], showing an induced absorption below the HOMO–LUMO transition, and a bleaching of the neutral π–π^* transition. The rearrangement of the molecular energy levels can create additional disorder in the energy landscape of the 6T layer.

Another noteworthy factor that has to be taken into account when interpreting photoconductivity spectra in organic materials is the efficiency of charge generation, which is usually low due to strong exciton effects. The presence of a larger concentration of charge carriers in the channel and of a stronger electric field when the OTFT is in the on-state, might affect the processes of light absorption and photogeneration of carriers, enhancing the photoconductivity response below the band edge region. Our results, reported in Fig. 3, suggest that this effect is not highly correlated to the presence of intense electric fields in the active material, since we observe a decrease in the DOS broadening (i.e. a decrease in the PC signal) when the OTFT is strongly depleted of charges in the off-state (V_G = +20 V).

We now turn towards the effects induced by prolonged exposures to air and light, at room temperature, on the transport properties and on the PC spectra of 6T OFETs. Two sets of 6T samples, labeled A and B, respectively, were

exposed to different ambient conditions: set B was exposed to atmosphere and light while set A was exposed to light while kept under vacuum. The change of the transport parameters and of the PC spectra was monitored after one month and after three months and the results are shown in Fig. 4. Samples A, exposed to light in vacuum, exhibit a moderate variation of the PC spectrum, the relative amplitude of the two major peaks (at 2.4 eV and at 2.8 eV) decreases from 1.5 to 1.1, mainly due to the marked decrease of the peak at 2.8 eV More pronounced modifications occur in samples B, where the relative amplitude of the two major peaks markedly decreases, due to the almost complete disappearance of the peak at 2.8 eV. At the same time, an interesting feature appears below the band-gap, where the behavior of the PC signal at ca.1.55 eV indicates the onset of photoemission of carriers from deep levels [18], that were not present in fresh as-deposited devices, but become electrically active after one month and more of exposure to air and light.

The macroscopic effects of such modifications can be monitored following the evolution of the main transport parameter of the OFETs, namely, the mobility and the threshold voltage, which are reported in Table 2 for samples A and B. Since the mobility remains almost constant for A samples, while it clearly decreases in the B ones, we assume a correlation between this behavior and the modifications observed in the corresponding PC spectra and discuss the origin of these effects.

The features that appear below the band-gap can be explained by the interaction of oxygen with organic semiconductors: it is known that oxygen diffuses into organic semiconductors, where it has recently been proposed to act as a dopant through the formation of electrically active deep states, induced by an electrochemical process during the interaction with the host organic molecule. These deep states have been theoretically modeled for pentacene where they should be located at about 0.29 eV from the valence band [31]. The slope variation that we observe in the PC spectra of the aged 6T devices and that indicates the onset of emission of carriers from trapped states is associated to an optical absorption at about 1.6 eV, i.e. much deeper in the gap.

Indeed, a strong increase in the doping level of organic materials induces an increase in the below band-gap transitions associated to polaron states, as observed by IR analyses on Ion Gel-gated polymer thin-film transistors [32]. It has been reported that polarons in photoexcited 6T are characterized by two electronic transitions (detected by photoinduced absorption) below the band-gap, i.e., at 0.8 eV and 1.54 eV [25]. The PC spectra of aged devices indicate the onset of emission of carriers from trapped states that could be attribute tosingly charged polaron

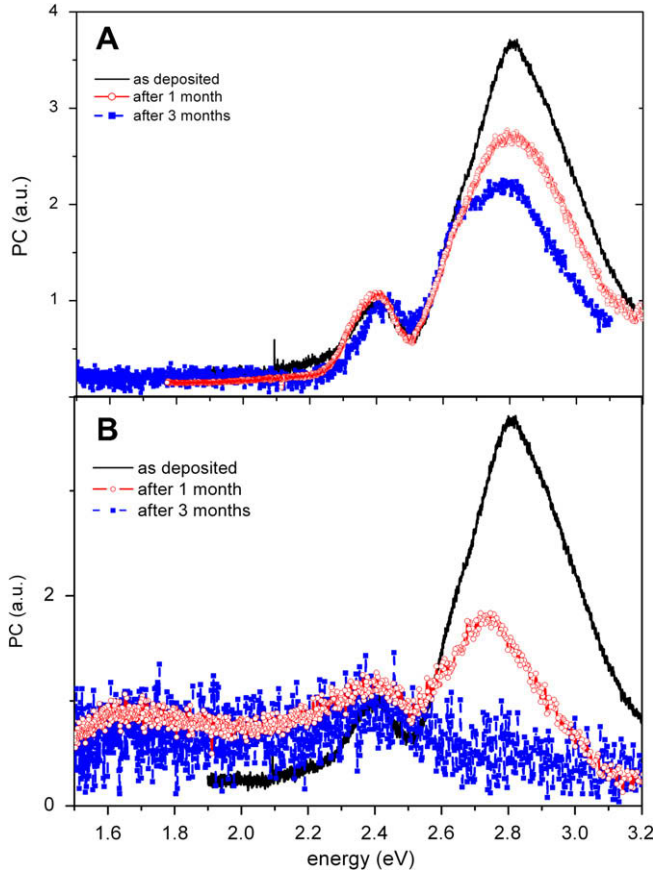

Fig. 4. Photocurrent spectra of the band edge and below-band-edge region for samples A and B monitoring their evolution with exposure time to vacuum and light (samples A) and air and light (samples B).

Table 1
Extracted parameter values (mobility and threshold voltage) for 6T and DH6T OFETs.

	Si/SiO_2 substrate	
	V_T (V)	μ (cm^2/Vs)
6T	−4	8.7×10^{-3}
DH6T	+12	6.8×10^{-2}

Table 2
Extracted parameter values (mobility and threshold voltage) for 6T OFETs following exposure to light in vacuum (set of samples A) and in air (set of samples B).

	6T			
	A		B	
	V_T (V)	μ (cm^2/Vs)	V_T (V)	μ (cm^2/Vs)
As deposited	+28	2×10^{-3}	+20	2×10^{-3}
1 Month	−18	3×10^{-3}	+7	8×10^{-4}
3 Months	−20	4×10^{-3}	0	7×10^{-4}

states [18], also in good agreement with the polaron induced absorption observed with Charge Modulation Spectroscopy [27]. Indeed, not all doping-induced polarons in the ground state contribute to mobile charge carriers at room temperature, because of notable Coulomb interactions. However, after optical excitation of a polaron to a higher lying state the charge carrier can more easily overcome the Coulomb attraction of the dopant and thus becomes a mobile charge; i.e., photoconductivity is enhanced.

Our PC results thus indicate that one month and longer exposure to air and light enhances the formation of bound polaron states (i.e., charged states) in 6T films, likely due to oxygen adsorbed from atmosphere (note that we cannot formally rule out similar effects due to water), interacting with the 6T chain and changing its charge state.

The increase in polaron concentration affects the charge carrier transport and induces a marked reduction of the carrier mobility by trapping and enhanced scattering effects [11], as reported in Table 2.

The threshold voltage shifts to more negative values in both sets of samples, and this effect normally attributed to bias stress [14] when a negative gate voltage is applied. In our case we can assume the same mechanism acting in both sets of devices [28] as, during PC analyses the gate voltage is kept at 0 V while V_{DS} = +10 V, thus inducing an effective negative potential difference between the gate and the channel. It is noteworthy that the decrease is less marked in samples B, intentionally exposed to oxygen, with respect to samples A, possibly due to oxygen doping effects that may shift the threshold voltage towards more positive voltages, thus balancing the negative V_T drift. However, the behavior of V_T under bias stress and atmosphere exposure may be affected by a number of different factors that are still being debated [15–17].

In addition, the exact nature of the broad band at 2.8 eV is still under discussion [29,30], but its modification, clearly observed in both samples A and B, is not related to a reduction of the carrier mobility, since the peak markedly decreases with aging in samples A while the mobility remains almost constant (Table 2).

4. Conclusions

In conclusion, we carried out photocurrent spectroscopy analyses on 6T and DH6T OFETs and we directly assessed a correlation between the distribution of the electronic density of states and the charge carrier population in the channel. We induced a modulation of the occupation of the density of states at the electrical band edge by varying the charge carrier concentration in the OFET channel, through applying an external voltage to the gate. As the carrier density in the OFET channel increases, the distribution of the electronic density of states is modified and the Gaussian-like shape of the transport states increases in width by 0.12 eV. We studied the effects induced by a prolonged exposure to air and light on 6T OFETs. The observed changes of the macroscopic transport parameters (reduction of the mobility and shift of the threshold voltage) were correlated to the modifications of the distribution of the electronic density of states at the band edge and in the activation of deep trapping states attributed to the formation of polaron states. PC analyses provide thus a useful tool for the in the investigation of transport phenomena in organic thin-film transistors. Table 1.

Acknowledgements

The authors thank H.C. Starck GmbH for providing DH6T, and acknowledge financial support by the Italian Research Ministry under the project PRIN 2006 "Plastic BioFET", the European Commission under the Integrated Project PROETEX, as well as the Deutsche Forschungsgemeinschaft (Sfb448). NK acknowledges support by the Emmy Noether-Program (DFG).

References

[1] G. Horowitz, M. Hajlaoui, R. Hajlaoui, J. Appl. Phys. 87 (2000) 4456.
[2] C. Tanase, E.J. Meijer, P.W.M. Blom, D.M. de Leeuw, Phys. Rev. Lett. 91 (2003) 216601.
[3] M. Vissenberg, M. Matters, Phys. Rev. B 57 (1998) 12964.
[4] H. Houili, E. Tutis, I. Batistic, L. Zuppiroli, J. Appl. Phys. 100 (2006) 33702.
[5] W. Pasveer, J. Cottaar, C. Tanase, R. Coehoorn, P. Bobbert, P. Blom, D. de Leeuw, M. Michels, Phys. Rev. Lett. 94 (2005) 206601.
[6] I.I. Fishchuk, V.I. Arkhipov, A. Kadashchuk, P. Heremans, H. Bässler, Phys. Rev. B 76 (2007) 045210.
[7] V. Arkhipov, P. Heremans, E. Emelianova, G. Adriaenssens, H. Bassler, Appl. Phys. Lett. 82 (2003) 3245.
[8] I. Hulea, H. Brom, A. Houtepen, D. Vanmaekelberg, J. Kelly, E. Meulenkamp, Phys. Rev. Lett. 93 (2004) 166601.
[9] A.J. Heeger, S. Kivelson, J.R. Schrieffer, W.-P. Su, Rev. Mod. Phys. 60 (3) (1988) 781.
[10] D. Beljonne, J. Cornil, H. Sirringhaus, P.J. Brown, M. Shkunov, R.H. Friend, J.L. Brédas, Adv. Funct. Mater. 11 (3) (2001) 229.
[11] V. Arkhipov, E. Emelianova, P. Heremans, H. Bassler, Phys. Rev. B 72 (2005) 235202.
[12] J. Zhou, Y. Zhou, J. Zhao, C. Wu, X. Ding, X. Hou, Phys. Rev. B 75 (2007) 153201.
[13] V. Arkhipov, P. Heremans, E. Emelianova, H. Bassler, Phys. Rev. B 71 (2005) 45214.
[14] D. Knipp, R. Street, A. Voelkel, J. Ho, J. Appl. Phys. 93 (2003) 347.
[15] D. Knipp, J. Northrup, Adv. Mater. 21 (2009) 5.
[16] H. Gomes et al., Appl. Phys. Lett. 84 (2004) 3184.

[17] A. Salleo, F. Endicott, R. Street, Appl. Phys. Lett. 86 (2005) 263505.
[18] R. Bube, Photconductivity of Solids, Wiley & Sons, New York, 1960.
[19] R. Zhang, X. Chen, J. Lu, W. Shem, J. Appl. Phys. 102 (2007) 123708.
[20] S. Shamuilia et al., J. Appl. Phys. 104 (2008) 114103.
[21] J.O. Vogel, I. Salzmann, R. Opitz, S. Duhm, B. Nickel, J.P. Rabe, N. Koch, J. Phys. Chem. B 51 (2007) 14097.
[22] P. Cosseddu, J.-O. Vogel, B. Fraboni, J.P. Rabe, N. Koch, A. Bonfiglio, Adv. Mater. 21 (2009) 344.
[23] F. Garnier, A. Yassar, R. Hajlaoui, G. Horowitz, F. Deloffre, B. Servet, S. Ries, P. Alnot, J. Am. Chem. Soc. 115 (1993) 8716.
[24] A. Facchetti, M. Mushrush, M. Yoon, G. Hutchinson, M. Ratner, T. Marks, J. Am. Chem. Soc. 126 (2004) 13859.
[25] P.A. Lane, X. Wei, Z. Vardeny, J. Poplawski, E. Ehrenfreund, M. Ibrahim, A. Frank, Chem. Phys. 210 (1996) 229.
[26] A. Yassar, J. Phys. Chem. 99 (1999) 9155.
[27] M.G. Harrison, R.H. Friend, F. Garnier, A. Yassar, Synth. Met. 67 (1994) 215.
[28] S.G.J. Mathijssen, M. Colle, H. Gomes, E.C.P. Smits, B. de Boer, I. McCulloch, P.A. Bobbert, D.M. de Leeuw, Adv. Mater. 19 (2007) 2785.
[29] D. Fichou, J. Mater. Chem. 10 (2000) 571.
[30] A. Stradomska, P. Petelenz, Org. Electron. 7 (2006) 551.
[31] D. Knipp, J. Northrup, Adv. Mater. 21 (2009) 1.
[32] J. Lee, L.G. Kaake, J. Ho Cho, X.-Y. Zhu, T.P. Lodge, C.D. Frisbie, J. Phys. Chem. C 113 (2009) 8972–8981.

Organic Electronics 11 (2010) 279–284

Contents lists available at ScienceDirect

Organic Electronics

journal homepage: www.elsevier.com/locate/orgel

Dynamical study of polaron–bipolaron scattering in conjugated polymers

Z. Sun [a], Y. Li [a], K. Gao [a], D.S. Liu [a,b,*], Z. An [c,*], S.J. Xie [a]

[a] School of Physics, State Key Laboratory of Crystal Materials, Shandong University, Jinan 250100, China
[b] Department of Physics, Jining University, Qufu 273155, China
[c] College of Physics, Hebei Normal University, Shijiazhuang 050016, China

ARTICLE INFO

Article history:
Received 12 July 2009
Received in revised form 1 October 2009
Accepted 3 November 2009
Available online 10 November 2009

Keywords:
Polymers
Polarons
Bipolarons

ABSTRACT

We simulate the scattering processes between a negative polaron and a positive bipolaron in a conjugated polymer chain using mixed quantum classical molecular dynamics. The simulations are performed based on the Su–Schrieffer–Heeger (SSH) model modified to include electron–electron interactions, a Brazovskii–Kirova symmetry-breaking term, and an external electric field. It is found that there exist a critical electric field, below which the polaron and bipolaron can scatter into an excited polaron. If the external electric field is higher than the critical electric field, the polaron and bipolaron will pass through each other and continue moving as isolated ones. Because the excited polaron can decay to the polaron state through emitting a photon, our results indicate that the interactions between polarons and bipolarons can open a channel for electroluminescence.

© 2009 Elsevier B.V. All rights reserved.

1. Introduction

Since the discovery that a conjugated organic polymer, poly(paraphenylene vinylene) (PPV), can be used as the active component in light-emitting diodes (LEDs) [1], much effort has been devoted to the study of the properties of organic conjugated materials. Conjugated polymers, as quasi-one-dimensional materials, have property that their structure can be easily distorted due to the strong electron-lattice interaction [2]. As a result, charges added to the polymer chain by doping, charge injection, or photoexcitation will induce self-localized electron states called polarons or bipolarons. A polaron has a spin $\pm 1/2$ and a charge ±e, whereas a bipolaron is spinless with charges ±2e [3]. It has been generally accepted that the polarons can recombine to form singlet and triplet excitons, in which the singlet exciton is radiative. However, to our knowledge, less attention has been paid to the recombination and products of polarons and bipolarons.

Bipolarons were hypothesized to exist in conjugated polymers almost 30 years ago [2] and studied extensively over the years. It was well accepted that bipolarons can be formed in doped polymers [4–7], while their formation in pristine photoexcited polymers was still an open question [8]. In addition, in studies on bipolarons it appeared that the stability of a bipolaron is questionable in the absence of oppositely charged ions [9]. In this paper, we are interested in the recombination processes between a polaron and a bipolaron with opposite charges. Total energy estimates indicate that two extra electrons may go either into two independent polarons or into a bipolaron [10]. There is a subtle balance between the two situations. The optical data of some polymers showed clearly signals involving polarons and bipolarons [3,11], which testifies the coexistence of polarons and bipolarons in conjugated polymers. Therefore, there is a possibility that polarons collide with bipolarons, and investigating the interactions between polarons and bipolarons seems to be necessary and significant.

* Corresponding authors. Address: School of Physics, Shandong University, Jinan 250100, China. Tel.: +86 531 8837035x8369 (D.S. Liu), tel.: +86 311 86268257 (Z. An).
E-mail addresses: liuds@sdu.edu.cn (D.S. Liu), zan@hebtu.edu.cn (Z. An).

1566-1199/$ - see front matter © 2009 Elsevier B.V. All rights reserved.
doi:10.1016/j.orgel.2009.11.006

Recently, Kadashchuk and coworkers reported an experimental study of trions in a PPV derivative [12]. They pointed out that the capture of a positive bipolaron by a deeply trapped negative polaron is one of the mechanism of trion formation. Onodera [13] investigated the interactions among polaron and bipolaron excitations within the framwork of the Brazovskii and Kirova continuum model of *cis*-polyacetylene. The results showed that polarons and bipolarons can freely pass through each other without attractive or repulsive interactions. Swanson et al. [14] pointed out that a positive (negative) polaron and a negative (positive) bipolaron produce a polaron and phonons. However, the results are simply based on a conjecture, not be convinced yet. Very recently, Ge et al. [15] theoretically investigated the scattering process between a negative polaron and a positive bipolaron in a single polymer chain. They employed an adiabatic molecular dynamics method (in which the electrons are in their eigenstates at any instant), and thought the reaction between a polaron and a bipolaron produces a positive polaron and emits a photon. From these works, we can see that all the results for the polaron–bipolaron interaction are not consistent, so that further investigations are needed.

In this paper, we present results from a numerical study of the dynamics of scattering between a negative polaron and a positive bipolaron in a polymer chain under the influence of an external electric field. The dynamics is performed by using a nonadiabatic evolution method where electron transitions between instantaneous eigenstates are allowed in contrast to the so-called adiabatic dynamics with fixed level occupation. We mainly give our attention to the products and their yields for the polaron–bipolaron reaction.

The paper is organized as follows. Section 2 describes the model and parameters used. The results are presented in Section 3. The summary and conclusions are given in Section 4.

2. Model and method

We use the following model Hamiltonian:

$$H = H_{\mathrm{SSH}} + H_{ee} + H_E. \tag{1}$$

The first term of Eq. (1) expresses the Su–Schrieffer–Heeger (SSH) Hamiltonian [16]:

$$H_{\mathrm{SSH}} = -\sum_{i,s} t_{i,i+1}\left(c^{\dagger}_{i,s}c_{i+1,s} + c^{\dagger}_{i+1,s}c_{i,s}\right) + \frac{1}{2}K\sum_i (u_{i+1}-u_i)^2 + \frac{1}{2}M\sum_i \dot{u}_i^2, \tag{2}$$

where $t_{i,i+1} = t_0 - \alpha(u_{i+1}-u_i) + (-1)^i t_e$, t_0 is the transfer integral of π electrons in a regular lattice, α is the electron-lattice coupling constant, and u_i is the lattice displacement of the i-th site from its equidistant position. t_e is introduced to lift the ground-state degeneracy for non-degenerate polymers. The operator $c^{\dagger}_{i,s}(c_{i,s})$ creates (annihilates) a π electron with spin s at the i-th site. The last two terms on the right hand side of Eq. (2) represent the lattice harmonic potential energy and the lattice kinetic energy, where K is the elastic constant of a σ bond and M the mass of a CH group.

The second term of Eq. (1) expresses the electron–electron interactions:

$$H_{ee} = U\sum_{i,s}\left(c^{\dagger}_{i,s}c_{i,s} - \frac{1}{2}\right)\left(c^{\dagger}_{i,-s}c_{i,-s} - \frac{1}{2}\right) + V\sum_{i,s,s'}\left(c^{\dagger}_{i,s}c_{i,s} - \frac{1}{2}\right)\left(c^{\dagger}_{i+1,s'}c_{i+1,s'} - \frac{1}{2}\right), \tag{3}$$

where U and V are the on-site and nearest-neighbor Coulomb repulsion strengths, respectively. In this paper, these extended-Hubbard-type interactions are treated within the unrestricted Hartree–Fock approximation.

The electric field is included in the Hamiltonian as a scalar potential, which gives the following contribution to the Hamiltonian:

$$H_E = |e|E\sum_{i,s}(ia + u_i)\left(c^{\dagger}_{i,s}c_{i,s} - \frac{1}{2}\right). \tag{4}$$

The model parameters we use in this work are those generally chosen for polyacetylene, [2] $t_0 = 2.5$ eV,$\alpha = 4.1$ eV/Å, $t_e = 0.05$ eV, $K = 99.0$ eV/Å^2, $M = 1349.14$ eVfs^2/Å^2 and $a = 1.22$ Å. As for the electron–electron interaction, $U = 0.5t_0$, $V = U/3$.

Within the unrestricted Hartree–Fock approximation, the time-dependent Schrödinger equations for one-particle wave functions are expressed in the following form:

$$i\hbar\frac{\partial}{\partial t}\psi_{k,s}(i,t) = H^s_{i,i+1}(t)\psi_{k,s}(i+1,t) + H^s_{i,i-1}(t)\psi_{k,s}(i-1,t) + H^s_{i,i}(t)\psi_{k,s}(i,t), \tag{5}$$

with

$$H^s_{i,i+1}(t) = -t_{i,i+1} - V\tau_s(i,t), \tag{6}$$

$$H^s_{i,i-1}(t) = -t_{i-1,i} - V\tau^*_s(i-1,t), \tag{7}$$

$$H^s_{i,i}(t) = U\left[\rho_{-s}(i,t) - \frac{1}{2}\right] + V\sum_{s'}[\rho_{s'}(i+1,t) + \rho_{s'}(i-1,t) - 1], \tag{8}$$

where the density $\rho_s(i,t)$ and bond density $\tau_s(i,t)$ are expressed as

$$\rho_s(i,t) = \sum_k{}'\psi_{k,s}(i,t)\psi^*_{k,s}(i,t), \tag{9}$$

$$\tau_s(i,t) = \sum_k{}'\psi_{k,s}(i,t)\psi^*_{k,s}(i+1,t). \tag{10}$$

Here the sum over the index k is over those occupied single-particle states. The equation of motion for the lattice is

$$M\ddot{u}_i = -K[u_{i+1}(t) - u_{i-1}(t) - 2u_i(t)] + \alpha\sum_s\{[\tau_s(i,t) - \tau_s(i-1,t)] + H.c.\} + |e|E\sum_s\left[\rho_s(i,t) - \frac{1}{2}\right]. \tag{11}$$

The above set of equations are numerically solved by discretizing the time with an interval Δt which is chosen

to be sufficiently small so that the change in the electronic Hamiltonian during that interval may be negligible small. For all the results presented below, we choose a time step of $\Delta t = 0.005$ fs.

By introducing electron eigenstates at each moment, the solutions of the time-dependent Schrödinger equations can be put in the form:

$$\psi_{k,s}(n,t_{j+1}) = \sum_l \left[\sum_m \phi^*_{l,s}(m)\psi_{k,s}(m,t_j)\right] \times e^{-i(\epsilon_l \Delta t/\hbar)}\phi_{l,s}(n), \quad (12)$$

where $\{\phi_{l,s}\}$ and $\{\epsilon_{l,s}\}$ are the eigenfunctions and the eigenvalues of the electronic part in the Hamiltonian H at a given time t_j. The lattice equations are written as

$$u_i(t_{j+1}) = u_i(t_j) + \dot{u}_i(t_j)\Delta t + \frac{F_i(t_j)}{2M}(\Delta t)^2, \quad (13)$$

$$\dot{u}_i(t_{j+1}) = \dot{u}_i(t_j) + \frac{F_i(t_{j+1}) + F_i(t_j)}{2M}\Delta t. \quad (14)$$

Hence, the electronic wave functions and the lattice displacement at the $(j+1)$th time step are obtained from the jth time step.

At time t_j, the wave functions $\{\psi_{k,s}(i,t_j)\}$ can be expressed as a series expansion of the eigenfunctions $\{\phi_{l,s}\}$ at that moment:

$$\psi_{k,s}(i,t_j) = \sum_{l=1}^{N} C^s_{l,k}(t_j)\phi_{l,s}(i), \quad (15)$$

where $C^s_{l,k}$ are the expansion coefficients. The occupied number for eigenstate $\phi_{l,s}$ is

$$n_{l,s}(t_j) = \sum_k{}' |C^s_{l,k}(t_j)|^2. \quad (16)$$

$n_{l,s}(t_j)$ contains information concerning the redistribution of electrons among the energy levels.

It is well known that removing or adding electrons to conjugated polymers creates lattice distortion in the form of polarons or bipolarons [17,2]. The formation of a polaron or bipolaron state not only induces lattice distortion but also lets the highest occupied molecular orbit (HOMO) and the lowest unoccupied molecular orbit (LUMO) enter the original energy gap and become localized deep levels [2]. In Fig. 1, we show the schematic diagram of energy levels for a polymer chain containing a negative polaron and a positive bipolaron. We can see that there are four levels in the gap. The left two levels ε^u_p and ε^d_p come from the polaron, in which the upper one is occupied by one electron and the lower one occupied by two. The right two levels ε^u_{bp} and ε^d_{bp} come from the bipolaron, and they are empty.

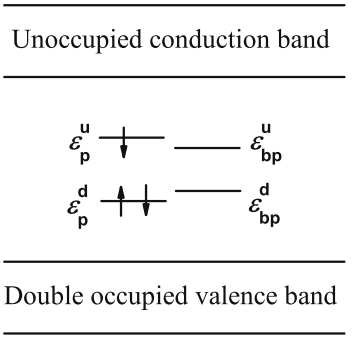

Fig. 1. The schematic diagram of energy levels for a polymer chain containing a negative polaron and a positive bipolaron.

In our simulations, a 200-site chain is considered, which is long enough to contain two independent excitations at the beginning. Before the external electric field turns on, a negative polaron is located at the 60th site while a positive bipolaron at the 140th site. They are well enough separated to ensure that they are non-interacting at the beginning. Starting from the initial conditions, the scattering processes between them driven by the external electric field are investigated.

In the following, we will focus on the evolution of the staggered lattice configuration $r_n(t)$ as

$$r_n(t) = (-1)^n \frac{u_{n-1}(t) + u_{n+1}(t) - 2u_n(t)}{4}. \quad (17)$$

3. Results and discussion

Simulations are carried out for a number of different field strengths. In these simulations, a critical electric field strength, $E_C = 0.8 \times 10^5$ V/cm , is found corresponding to markedly different behavior of the polaron and bipolaron dynamics. If the external electric field is lower than the critical electric field, the polaron and bipolaron scatter into a new state. If the external electric field is higher than the critical electric field, the polaron and bipolaron pass through each other, and continue moving in more or less the same way as before.

Fig. 2 shows the lattice evolution for the polaron–bipolaron scattering process in the external electric fields of 0.7×10^5 V/cm and 0.8×10^5 V/cm. As shown in Fig. 2a, driven by the external electric field, the polaron and bipolaron are accelerated and quickly approach their saturation velocity. At about 160 fs, they begin to contact. Due to the high kinetic energies of them, the polaron first passes through the bipolaron. However, after that, the polaron turns around and moves back following with the bipolaron. This explicitly shows that there is a strong attraction between the polaron and bipolaron. A short time later at about 300 fs, the polaron and bipolaron recombine into a new state. We can see that such a state corresponds to only one lattice deformation. What are the characteristics of this new state? We will analyze it later.

In a slightly higher electric field, as shown in Fig. 2b, the polaron and bipolaron simply pass through each other when they come into collide. After that, they recollect and continue moving as a polaron and a bipolaron along the chain.

We also find that the critical electric field is sensitive to the electron–electron interaction parameters U and V. The critical electric field strength increases as the electron–electron interaction parameters increase. This is easy to be understood. As U and V increase, the attraction between electron and hole gets strong, i.e., the attraction between the polaron and bipolaron becomes strong. Thus, passing through each other becomes difficult for the polaron and bipolaron.

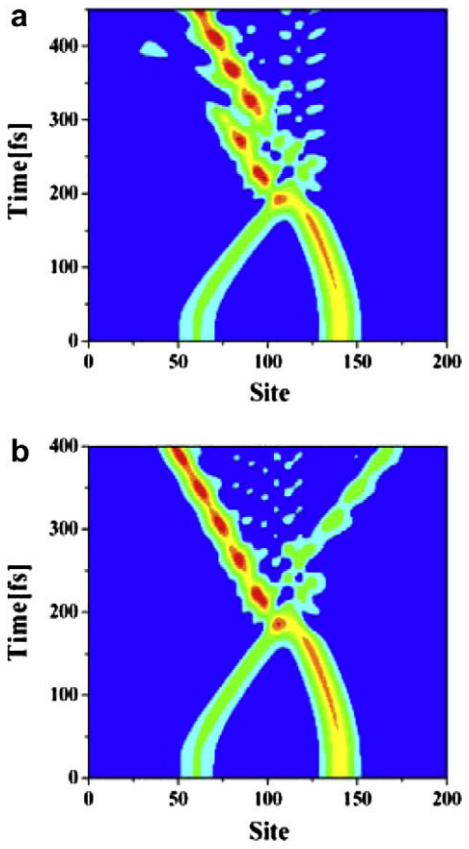

Fig. 2. Time dependence of r_n for the polaron–bipolaron scattering in different external electric fields, (a) $E = 0.7 \times 10^5$ V/cm and (b) $E = 0.8 \times 10^5$ V/cm.

In addition, if the electron–electron interaction is neglected ($U = V = 0$), we find that the polaron and bipolaron can easily pass through each other even in very weak electric fields. These results are quite consistent with the results obtained by Onodera [13].

To recognize the new state formed after the polaron–bipolaron collision, we first display the time evolution of occupied number of the intragap levels ε_p^u, ε_p^d, ε_{bp}^u and ε_{bp}^d in Fig. 3. Before 300 fs, the occupied numbers of the four levels are almost invariable, which means that the polaron and bipolaron all keep their isolation. After 300 fs, however, the occupied number of level ε_p^u rapidly drops to about zero, while the occupied number of level ε_{bp}^u quickly increases to about 0.3. At the same time, the occupied number of the other two levels ε_p^d and ε_{bp}^d still remain invariable. These results indicate that the reduced electrons in level ε_p^u may transfer to level ε_{bp}^u or level in conduction band with some probability after collision. Explicitly, electron transfer from polaron level ε_p^u to bipolaron level ε_{bp}^u and levels in conduction band will induce forming excited polarons and free carriers.

As shown above, the polaron–bipolaron interaction induces electron redistribution among levels. It also can be said that there are other electronic states mixed into the initial electronic state after the polaron–bipolaron collision. As indicated by the results displayed in Fig. 3, we found that there are mainly three electronic states mixed together after collision, which are shown in Fig. 4. State (a) denotes the initial electron distribution. So this state still contains a polaron and a bipolaron. State (b) denotes the electron in level ε_p^u transferred to level ε_{bp}^u. This state actually contains an excited polaron. As for state (c), it denotes the electron in level ε_p^u being excited to the conduction band. So this state contains a free carrier and a bipolaron. We do not draw the other possible states as we have found that the yields of other states are very small compared with these three states.

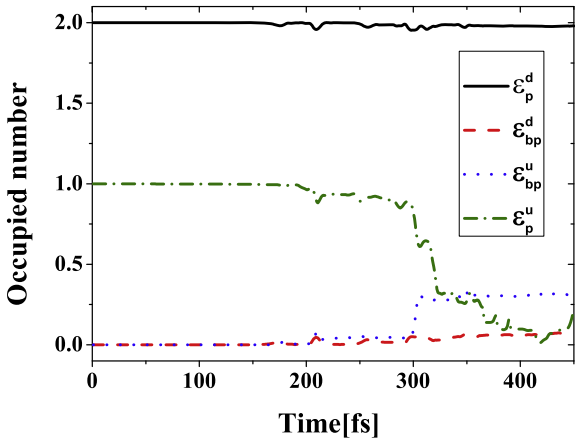

Fig. 3. Time evolution of the occupied number of the intragap energy levels, $E = 0.7 \times 10^5$ V/cm.

In the following, we will calculate the yields for these three states using a projection method [18]. The evolved wavefunction of the whole system $|\Psi(t)\rangle$ can be constructed by the single electron evolutional wavefunction $\{\psi_k(n,t)\}$ as a Slater determinant. After each evolution step, the evolved state $|\Psi(t)\rangle$ is projected onto the space of eigenstates of the system. The relative yield $I_K(t)$ for a given eigenstate $|\Phi_K\rangle$ is then obtained from:

$$I_K(t) = |\langle \Phi_K | \Psi(t) \rangle|^2. \tag{18}$$

The eigenstate $|\Phi_K\rangle$ is constructed by $\{\phi_{l,s}(n)\}$ which are the eigenfunctions of the electronic part of the Hamiltonian H. $|\Phi_K\rangle$ can be any state of interest, e.g., the states (a), (b) and (c).

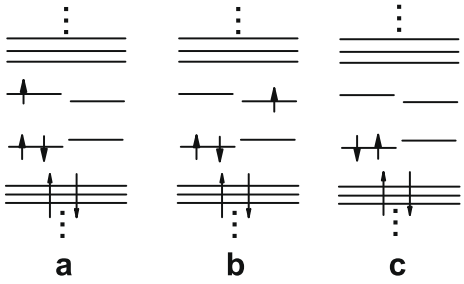

Fig. 4. The initial states and other mixed states after the polaron–bipolaron collision.

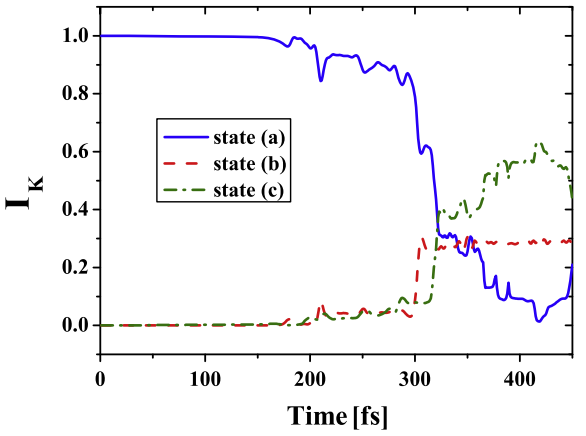

Fig. 5. Time dependence of the yields for states (a)–(c) which are shown in Fig. 4, $E = 0.7 \times 10^5$ V/cm.

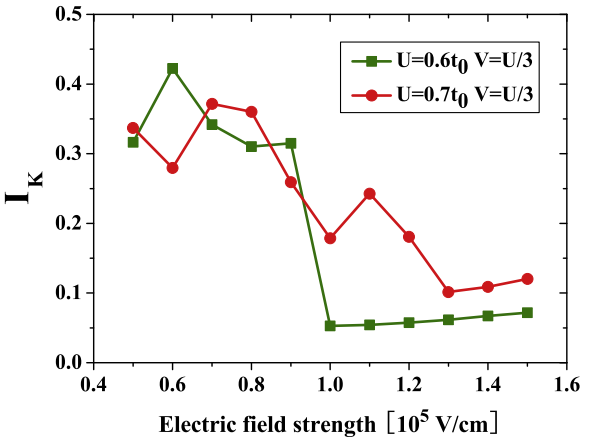

Fig. 7. Average yields of state (b) as a function of electric field strength for different electron–electron interactions.

Fig. 5 shows the time dependence of the yields for states (a), (b) and (c) during the polaron–bipolaron interaction. It can be seen that the yield of state (a) keeps 100% before 200 fs. This is because the polaron does not interact with the bipolaron before this time. From 200 to 300 fs, the yield of state (a) drops about 10%, which means that some other states, e.g., states (b) and (c), must mix into state (a). After 300 fs, the yield of state (a) sharply drops. At the same time, the yields of states (b) and (c) increase to about 30% and 40%, respectively. This explicitly shows that states (b) and (c) appear after the collision. As we have known, state (b) contains an excited polaron, and state (c) contains a free carrier. Thus, the results indicate that excited polaron and free carrier can be produced by the polaron–bipolaron interaction.

We also calculate the yields of states (a), (b) and (c) for different electric fields. We average the yields for these three states over the last 200 fs since their yields distinctly increased. The results are displayed in Fig. 6. Below the critical electric field strength, the yields of states (a), (b) and (c) oscillate in a large scope. It shows that the attraction between the polaron and bipolaron dominates their motions.

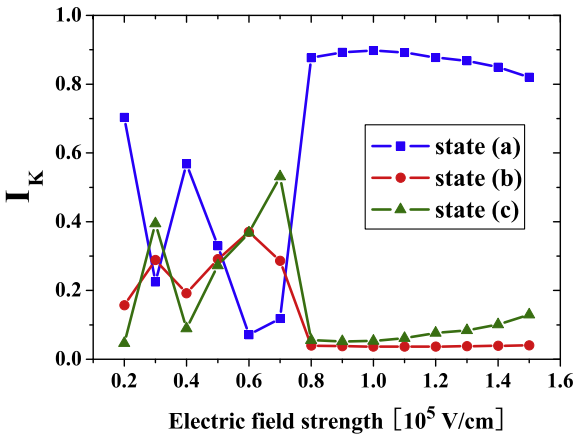

Fig. 6. Average yields for states (a)–(c) as a function of electric field strength.

However, just above the critical electric field strength, the yield of state (a) sharply increases to about 90% , while the yields of states (b) and (c) decrease quickly all to about 4%. As we have known from Fig. 4(a), state (a) contains a polaron and a bipolaron. It shows that the external field dominates the motion of the polaron and bipolaron in this case.

In Fig. 7, we display electric field dependence of the average yields of state (b) for different electron–electron interactions. It can be seen that the variation of the electron–electron interaction parameters U and V does not lead to significant change in the qualitative behavior of the yield of state (b). In addition, the results also show that the critical electric field increases as the electron–electron interaction parameters increase: $E_C = 1.0 \times 10^5$ V/cm for $U = 0.6t_0$ and $V = U/3$, $E_C = 1.3 \times 10^5$ V/cm for $U = 0.7t_0$ and $V = U/3$.

From the results above, an important channel for the polaron–bipolaron reaction can be written as

$$P^- + BP^{2+} \rightarrow P^{*+}, \tag{19}$$

where P^- denotes a negative polaron, BP^{2+} a positive bipolaron, and P^{*+} an excited positive polaron. It is worth noting that the excited polaron can decay to the polaron state through emitting a photon. Therefore, it is expected that the polaron–bipolaron reaction can contribute to electroluminescence in conjugated polymers.

From the above results, it can be seen that the electronic state of the system also have large probability to keep the initial state especially under weak electric fields, as shown in Fig. 6. In this condition, the polaron and bipolaron coalesce into a bound state due to the electron–phonon interaction and the Coulomb interaction between them. The bound state formed by a polaron and a bipolaron with opposite charges is called a trion [12] or a charged exciton [19]. Obviously, the polaron–bipolaron bound state has lower energy than separate ones so that it is more stable.

4. Conclusion

We have investigated the scattering processes between a negative polaron and a positive bipolaron in a conjugated

polymer chain. This study was carried out through numerical calculations using an improved version of the SSH model modified to include electron–electron interactions via an extended Hubbard Hamiltonian, a symmetry-breaking term and an external electric field. The time-dependent unrestricted Hartree–Fock equation and the equation of motion for the time-dependent lattice displacements form a coupled set that was numerically integrated over the time in a self-consistent way.

Initially, the negative polaron and the positive bipolaron are accelerated by an external electric field. They quickly approach saturation velocity before collision. A critical electric field is found corresponding to markedly different behavior of polaron and bipolaron dynamics. Below the critical electric field, the polaron and bipolaron can scatter into an excited polaron with high yield. The excited polaron can decay to the polaron state through emitting a photon, so that the polaron–bipolaron reaction shows a contribution to the electroluminescence in conjugated polymers beside the polaron recombination. Above the critical electric field, the polaron and bipolaron will pass through each other and continue moving as isolated ones.

Acknowledgments

This work was supported by the National Basic Research Program of China (Grant No. 2009CB929204), the National Natural Science Foundation of China (No. 10874100) and the Hebei Province Outstanding Youth Science Fund (Grant No. A2009001512).

References

[1] J.H. Burroughes, D.D.C. Bradley, A.R. Brown, R.N. Marks, K. Mackay, R.H. Friend, P.L. Burn, A.B. Holmes, Nature 347 (1990) 539.
[2] A.J. Heeger, S. Kivelson, J.R. Schrieffer, W.P. Su, Rev. Mod. Phys. 60 (1988) 781.
[3] P.A. Lane, X. Wei, Z.V. Vardeny, in: N.S. Sariciftci (Ed.), Spin-dependent Recombination Processes in π-Conjugated Polymers, World Scientific, Singapore, 1997, p. 292.
[4] F. Genoud, M. Guglielmi, M. Nechtschein, E. Genies, M. Salmon, Phys. Rev. Lett. 55 (1985) 118.
[5] Yukio Furukawa, J. Phys. Chem. 100 (1996) 15644.
[6] Yukihiro Shimoi, Shuji Abe, Phys. Rev. B 50 (1994) 14781.
[7] C.H. Lee, G. Yu, A.J. Heeger, Phys. Rev. B 47 (1993) 15543.
[8] E.M. Conwell, H.A. Mizes, ***Synth. Meter. 78 (1996) 201.
[9] E.M. Conwell, in: N.S. Sariciftci (Ed.), Are Bipolarons Photogenerated in PPV?, World Scientific, Singapore, 1997, p 489.
[10] J. Cornil, D. Beljonne, J.L. Brédas, J. Chem. Phys. 103 (1995) 842.
[11] P.A. Lane, X. Wei, Z.V. Vardeny, Phys. Rev. Lett. 77 (1996) 1544.
[12] Andrey Kadashchuk, Vladimir I. Arkhipov, Chang-Hwan Kim, Joseph Shinar, D.-W. Lee, Y.-R. Hong, Jung-Il Jin, Paul Heremans, Heinz Bässler, Phys. Rev. B 76 (2007) 235205.
[13] Y. Onodera, Phys. Rev. B 30 (1984) 775.
[14] L.S. Swanson, J. Shinar, A.R. Brown, D.D.C. Bradley, R.H. Friend, P.L. Burn, A. Kraft, A.B. Holmes, Phys. Rev. B 46 (1992) 15072.
[15] Li Ge, Sheng Li, Thomas F. George, Xin Sun, Phys. Lett. A 372 (2008) 3375.
[16] W.P. Su, J.R. Schrieffer, A.J. Heeger, Phys. Rev. Lett. 42 (1979) 1698; W.P. Su, J.R. Schrieffer, A.J. Heeger, Phys. Rev. B 22 (1980) 2099.
[17] S.A. Brazovskii, N. Kirova, Sov. Phys. JETP 33 (1981) 4; D.K. Campbell, A.R. Bishop, K. Fesser, Phys. Rev. B 26 (1982) 6862.
[18] Z. Sun, Y. Li, S.J. Xie, Z. An, D.S. Liu, Phys. Rev. B 79 (2009) 201310(R).
[19] Li Ge, Thomas F. George, Xin Sun, Phys. Status Solidi B 246 (2009) 1642.

Organic Electronics 11 (2010) 285–290

Contents lists available at ScienceDirect

Organic Electronics

journal homepage: www.elsevier.com/locate/orgel

Effect of the ordered 2D-dot nano-patterned anode for polymer solar cells

Dong Hwan Wang [a], Dae-Geun Choi [b], Ki-Joong Lee [b], Jun-Ho Jeong [b], So Hee Jeon [c], O Ok Park [a,*], Jong Hyeok Park [d,*]

[a] Department of Chemical and Biomolecular Engineering (BK21 Graduate Program), Interdisciplinary Program for Polymers, Korea Advanced Institute of Science and Technology, 335 Gwahangno, Yuseong-gu, Daejeon 305-701, Republic of Korea
[b] Research Park, KIMM (Korea Institute of Machinery and Materials), 104, Jang-dong, Yuseong-gu, Daejeon 305-343, Republic of Korea
[c] Department of Nano Manufacturing Technology, Korea Institute of Machinery and Materials, 171, Jang-dong, Yuseong-gu, Daejeon 305-343, Republic of Korea
[d] Department of Chemical Engineering, Sungkyunkwan University, Suwon 440-746, Republic of Korea

ARTICLE INFO

Article history:
Received 6 August 2009
Received in revised form 28 October 2009
Accepted 3 November 2009
Available online 10 November 2009

Keywords:
Organic solar cells
Nanoimprinting
Nano-pattern

ABSTRACT

A patterned conducting IZO film with well-ordered periodic dot-structures with 50 or 200 nm deep features has been constructed by nanoimprinting technique as the anode of an organic solar cell. The use of the patterned anode leads to an increase in the short circuit current (J_{sc}) from 7.03 to 8.94 mA/cm^2 and the power conversion efficiency (PCE) from 1.05 to 1.71% compared to the flat anode. The open circuit voltage (V_{oc}) is also affected by nano-patterned structure. The PCE is also influenced by the aspect ratio of the pattern structure.

© 2009 Elsevier B.V. All rights reserved.

1. Introduction

Research into the development of thin film photovoltaic devices based on a polymer-fullerene heterojunction as an active layer has progressed in recent years [1–6]. From [6,6]-phenyl C61-butyric acid methyl ester (PCBM) and conjugated polymers in bulk-heterojunction (BHJ) polymer solar cells, worldwide interest related to enhancing device performance has increased. The positive impact of polymer-based solar cells make them suitable for low-cost processes involving solution-based spin casting, realizing large area processability, and a flexible device with a polymer property [7]. Device performance is closely connected to the external photocurrent density, which is affected by photo-generated free electrons and holes from exciton in active layer systems. Another factor is the method of transferring the charges through the donor and acceptor phases smoothly toward each electrode [8]. Therefore, the introduction of nanostructured architecture in organic solar cells, which assists exciton generation as well as the transport of electrons-holes, is critical for an increase of the photocurrent density, resulting in an enhancement in device performance.

Generally, the most extensively used anode in optoelectronic devices has been indium tin oxide (ITO) because of its high conductivity, high transparency, and ability to match the work function of polymer films [9]. ITO, however, is weak in continuous bending tests and requires high-temperature processing conditions during sputtering operations. On the other hand, indium zinc oxide (IZO) can be prepared easily in room-temperature processing. This implies that IZO can be applied onto polymer films with various nano-patterns owing to its low-temperature processability.

Recently, a photovoltaic device containing patterned PEDOT:PSS as a hole transporting layer using polydimethylsiloxane (PDMS) stamps was reported, showing improved charge extraction and optical absorption due to the light trapping and scattering of reflected light by the imprinted patterns [10]. Another approach has been reported related to the vertical structure of the active layer, which facilitates charge transport as well as charge separa-

* Corresponding authors.
E-mail addresses: ookpark@kaist.ac.kr (O Ok Park), lutts@skku.edu (J.H. Park).

1566-1199/$ - see front matter © 2009 Elsevier B.V. All rights reserved.
doi:10.1016/j.orgel.2009.11.007

tion with patterned TDPTD (thermally deprotectable polythiophene derivative) using Si molds in a nanoimprinting operation [11].

This study presents the effect of a highly ordered 2D-dot nano-patterned anode fabricated in a simple process with UV-curable PUA [poly(urethane acrylate)] resin. PUA resin is characterized by its large-area replication capabilities, good detachment properties with low surface energy from a releasing agent, and clearly formed 2D patterns [12]. Particularly, a patterned anode also allows well-ordered periodic structures in the upper spin-coated layer. This continuous patterned anode in a polymer solar cell can induce an increase in the interfacial area between the active layer and the anode, contributing to more effective charge harvesting.

2. Experimental details

First, patterned IZO glass was cleaned by acetone and isopropanol to remove residual organic matter. Before use, it was treated with oxygen plasma. Poly(3,4-ethylene dioxythiophene:Poly(styrene sulfonate) (PEDOT:PSS, Baytron P), well known as hole a transporting material, was spin-coated to a thickness of ~35 nm. The devices were uniformly heated using a digital controlled-hotplate at 100 °C for 5 min. An active layer consisting of P3HT and PCBM at a ratio of 1:0.6 was then spin-coated at 900 rpm for 5 s in a glove-box using chlorobenzene solvent. The average thickness of the bilayer with active layer and PEDOT:PSS confirmed by Focused Ion Beam (FIB) images was approximately 240 nm (See Supplementary material). Subsequently, a metal electrode (Al) with a thickness of 150 nm was thermally deposited under a high vacuum pressure of 6.0×10^{-7} torr. The active device area with the deposited Al electrode was confirmed in the range of 4–6 mm^2. A solar simulator with a 2500 W Xenon lamp and air mass 1.5 global (AM 1.5G) filter was used to evaluate the performance of the solar cells. The light intensity was calibrated using a silicon reference cell (Fraunhofer ISE, Certificate No. C-ISE269). *J–V* curves were measured by a Keithley 2400 source measure unit under 1 sun (100 mW/cm^2) light intensity condition. The surface morphology and the roughness of the patterned IZO glass were observed by Atomic Force Microscope (AFM) made by Veeco (USA) (non-contact tapping mode, D3100). The incident photon to current conversion efficiency (IPCE) as a function of excitation wavelength (nm) was measured with a 300 W xenon lamp (Newport) and a monochromator (Model, Newport 260). Diffuse reflectance spectra were plotted by using a UV–Visible Spectrophotometer (CARY, 100 Conc) with an integrating sphere.

3. Results and discussion

Fig. 1 shows a schematic of the fabrication sequence of the highly ordered 2D-dot nano-patterned anode for poly-

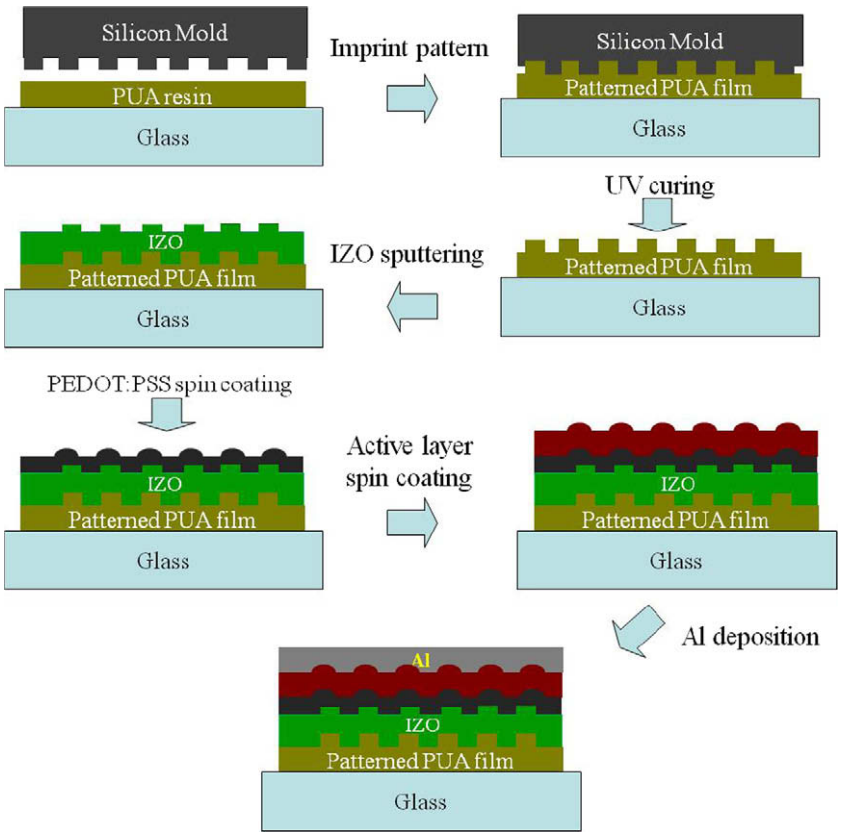

Fig. 1. Schematic of the fabrication sequence of highly ordered 2D-dot nano-patterned anode for polymer solar cells.

mer solar cells. This patterned anode was fabricated via simple imprint techniques using two different silicon master molds with heights of 50 or 200 nm and a dot space of 265 nm on a glass substrate with UV-curable PUA resin. The PUA resin was composed of tri(propylene glycol) diacrylate, trimethylolpropane triacrylate as a monomer, and 2,2-dimethoxy-2-phenylacetophenone as a photoinitiator (Aldrich). Acrylate polysiloxane (TEGO Rad 2200 N) was added as a releasing agent (1–4%). The patterned PUA film had a regular pitch size and a periodic height of the dot patterns form the UV-curing process. IZO was deposited on the patterned PUA film up to a thickness of 300 nm by RF-sputtering using a shadow mask at 400 W. The resistivity was defined to 25 Ω/□ as measured by four-point probe microscope.

To confirm of patterned PUA film and the anode for polymer solar cells, SEM images of the patterned PUA film and the IZO-coated PUA film were obtained. These are presented in Fig. 2. Fig. 2a is an top view image of an original flat PUA film on a glass substrate, and Fig. 2b and c shows top view images of a patterned PUA film with heights of either 50 or 200 nm, respectively, on glass substrates. Fig. 2d shows the side view image of a patterned IZO-coated PUA anode with a height of 200 nm. These SEM images confirm that the fabrication of the 2D-dot nano-patterned PUA films was highly ordered with a simple imprint technique. Moreover, the patterns are retained after the IZO sputter process, as shown in Fig. 2d. Fig. 2e and f are top view images of an active layer with highly ordered 2D-dot patterned PUA, 50 or 200 nm in height, respectively, with IZO after the spin coating of PEDOT:PSS (~35 nm). The surface morphology in Fig. 2e and f shows the retained well-ordered embossing structures after the spin-coating process of the P3HT/PCBM layer.

Fig. 3a–d shows AFM images of PEDOT:PSS layer with two different height patterns of the surface morphologies. From the AFM images in Fig. 3a–d, the surface morphologies of the patterned shapes retained entirely throughout the PEDOT:PSS spin-coating process. Also to confirm the patterned sequential structure of the PEDOT:PSS layer, IZO, and PUA film, we used a FIB (Focused Ion Beam) instrument. It was found that the surface morphologies retained the embossing structures after the spin-coating of PEDOT:PSS layer on the patterned IZO (See the Supplementary material, Fig. S1). Fig. 3e and f shows 52° tilted images of the entire inner structure of film prepared using a patterned anode at a height of either 50 nm or 200 nm from the FIB, respectively. These figures also show clearly sustained periodic structures from the patterned PUA up to the interfaces between the PEDOT:PSS and the active layer. The interfacial area between the PUA substrate and the anode, the anode and the PEDOT:PSS, and the PEDOT:PSS and the active layer increase in the order of precedence as they follow the first patterned structure. Therefore, the highly ordered 2D-dot nano-patterned anode from the PUA films influences the enhancement of the interfacial area between the active layer and the anode.

Fig. 4 shows the *J–V* curves of devices fabricated with IZO-coated PUA film without patterns as well as 50 or 200 nm PUA film patterned with IZO. After spin coating

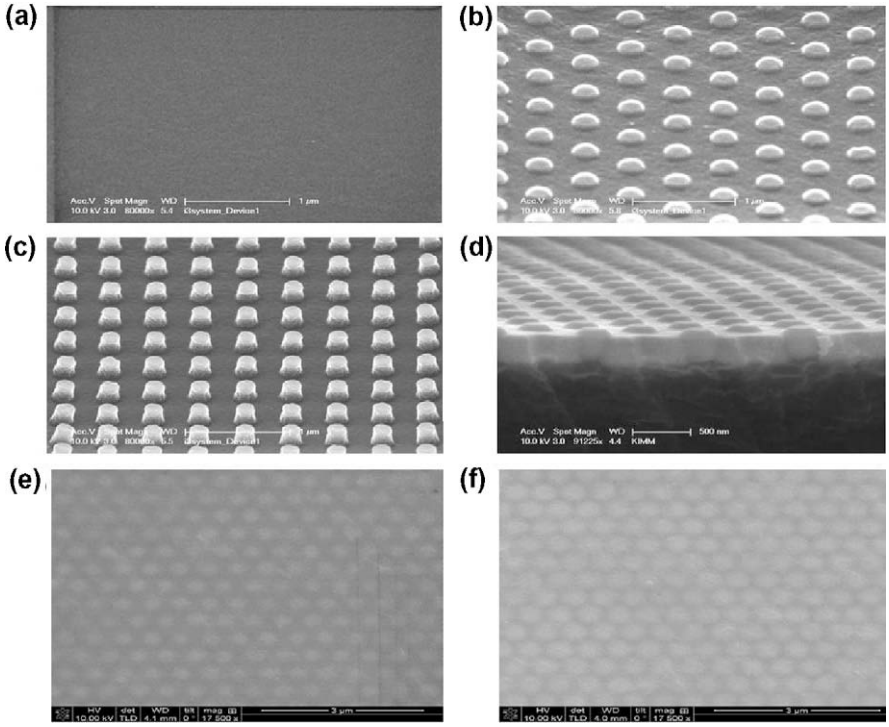

Fig. 2. SEM top view images of (a) PUA [poly(urethane acrylate)] film, (b) highly ordered patterned PUA of 50 nm height, (c) highly ordered patterned PUA of 200 nm height, and SEM side view images of (d) IZO sputted on highly ordered patterned PUA of 200 nm height, SEM top view images of (e) spin-coated active layer (~220 nm) and PEDOT:PSS (~35 nm) on highly ordered 50 nm height 2D-dot patterned PUA with IZO (f) spin coated active layer (~220 nm) and PEDOT:PSS (~35 nm) on highly ordered 200 nm height 2D-dot patterned PUA with IZO.

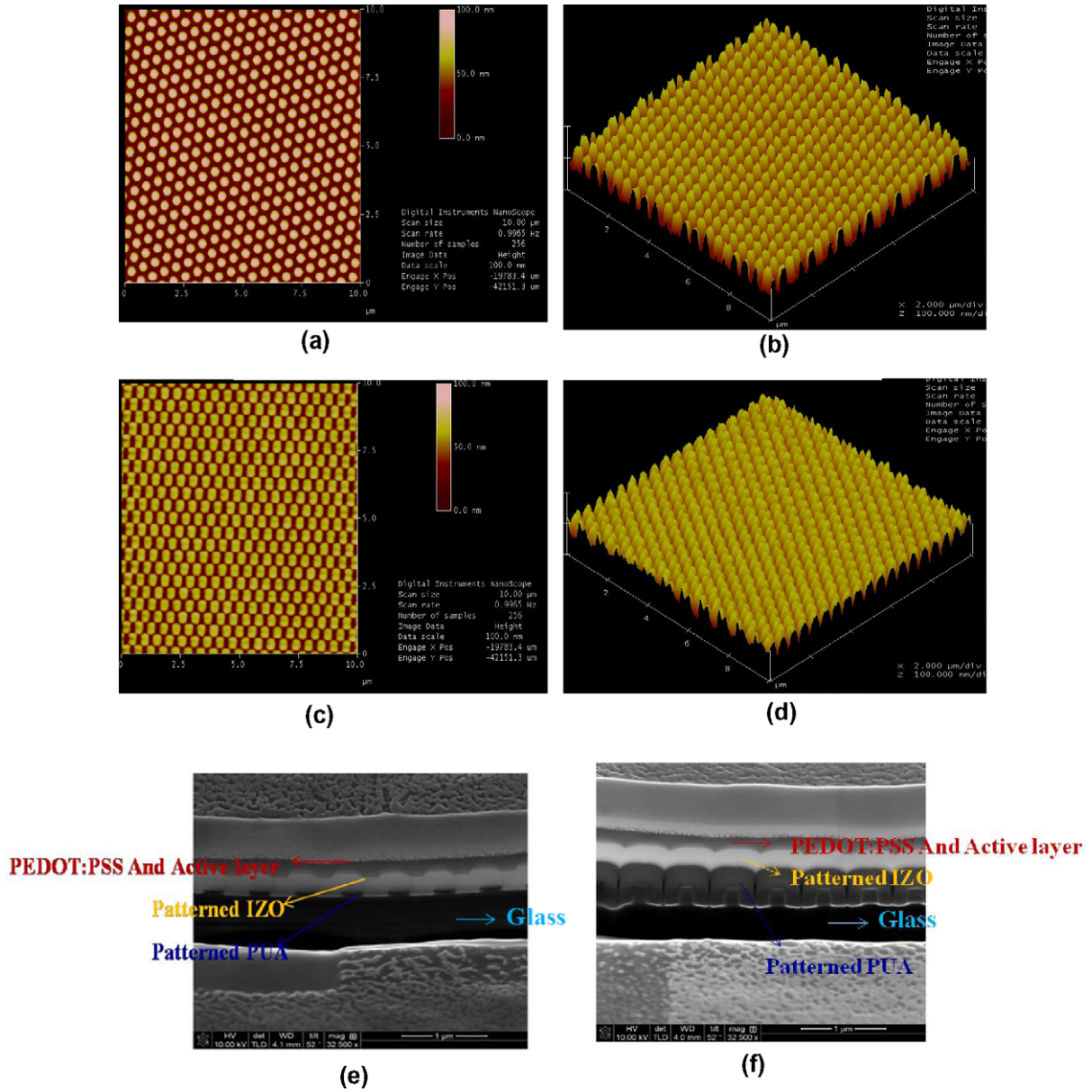

Fig. 3. AFM images of (a,b) PEDOT:PSS layer with highly ordered patterned PUA (height 50 nm) with IZO, (c,d) PEDOT:PSS layer with highly ordered patterned PUA (height 200 nm) with IZO, FIB (Focused Ion Beam) 52° tilted images (e) whole device sequential inner structure of PUA (height 50 nm) patterned with IZO, spin coated with PEDOT:PSS and an active layer (P3HT:PCBM) (f) whole device sequential inner structure of PUA (height 200 nm) patterned with IZO, spin coated with PEDOT:PSS and an active layer (P3HT:PCBM).

the active layer and Al deposition, thermal treatments such as pre-annealing or post-annealing were not performed to maintain the stable property of the PUA films. In the case of the device composed of flat PUA film with IZO in the reference device, the performance level was approximately 1.05%. However, as the patterned height of the PUA film increases, the performance of the device also increases. The factor that critically increased the efficiency of the devices with the PUA film patterned with IZO was J_{sc}. As Fig. 4 shows, the photocurrent values of the nanostructured devices were 8.67 and 8.94 mA/cm^2 at heights of 50 or 200 nm, respectively, which are larger than the 7.03 mA/cm^2 value of a cell without nano-patterns, suggesting increased the number of created charges that are collected at the electrodes. The number of charges depends on the fraction of photons absorbed (η_{abs}), the fraction of electrons-hole pairs that are dissociated (η_{diss}), and finally the fraction of charges that reach the electrodes (η_{out}) determining the overall photocurrent efficiency (η_j):

$$\eta_j = \eta_{abs} \times \eta_{diss} \times \eta_{out}$$

First possible effect for the increased photocurrent is increased optical absorption due to the dot-patterned anode. Recently, Curry's group suggested the possibility of in-

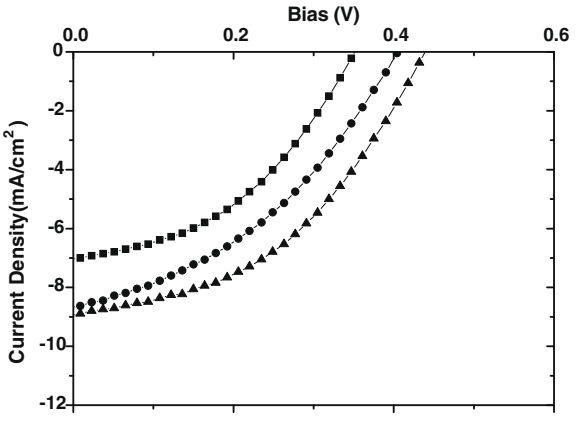

Fig. 4. *J–V* curves of devices made with flat PUA film with highly ordered patterned PUA with IZO (-■- Solar cells with IZO without patterns, -●- Solar cells with 50 nm PUA patterned film with IZO, -▲- Solar cells with 200 nm PUA patterned film with IZO).

creased optical absorption due to light trapping or scattering of reflected light by the imprint pattern when they prepared organic photovoltaic devices with patterned PEDOT:PSS layers [10]. When periodic patterns are provided on the anode of the organic solar cell, reflected light from Al electrode might be scattered or trapped in the active layer by the imprint patterns in the same manner as Curry's system. To confirm this hypothesis, optical absorption spectra were examined. The optical absorption cannot be determined directly because Al is not transparent. Instead of optical absorption, diffuse reflectance spectra were examined to measure the fraction of incident photons absorbed by the device. Fig. 5a shows diffuse reflectance spectra of the devices fabricated with IZO-coated PUA film without patterns as well as 50 nm PUA film patterned with IZO. The lower reflectivity for the device with nano-patterned anode indicates stronger absorption influencing η_{abs}. Fig. 5b shows IPCE spectra. The difference of J_{sc} between the reference device without nano-pattern and the device with 50 nm nano-pattern can be explained by this IPCE spectrum. However, the ~30% increased photocurrent cannot be fully explained by the light scattering effect. Another possible reason for the enhanced external quantum

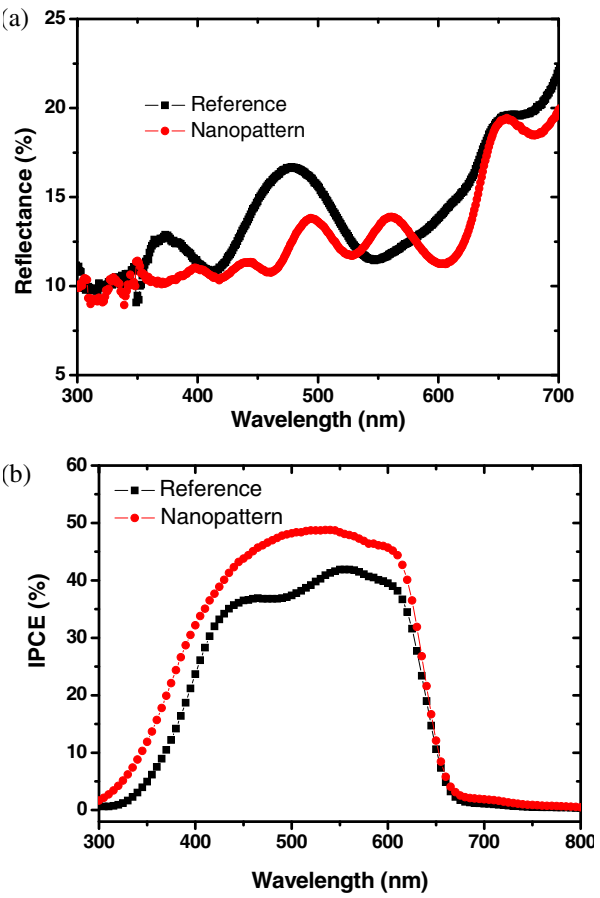

Fig. 5. (a) Diffuse reflectance spectra of the devices fabricated with IZO-coated PUA film without patterns as well as 50 nm PUA film patterned with IZO. (b) Incident-photon-to-current-efficiency (IPCE) spectra of the devices fabricated with IZO-coated PUA film without patterns as well as 50 nm PUA film patterned with IZO.

efficiency is a reduced dead ends and/or a decrease of contact resistance. In the case of BHJ cells, absorption throughout the whole P3HT/PCBM layer can generate the photocurrent, due to the efficient exciton dissociation everywhere in the BHJ layer [13]. However, it is found that

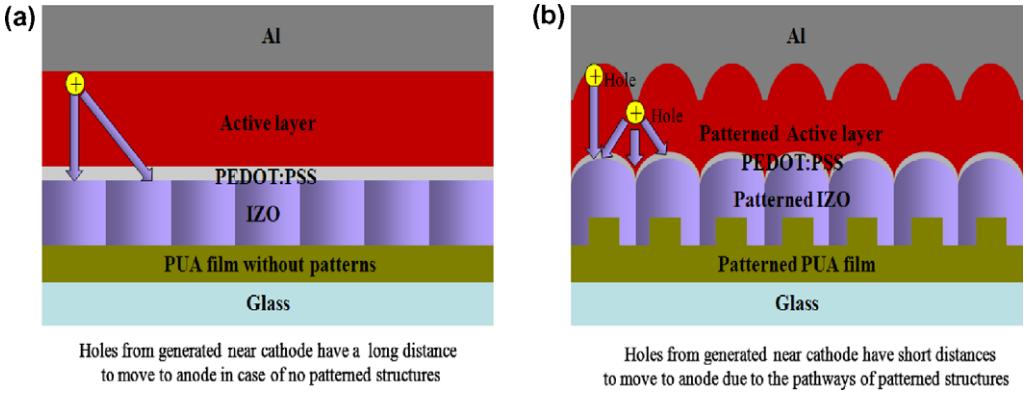

Fig. 6. Schematic diagram of the proposed devices fabricated with IZO-coated PUA film without patterns as well as IZO-coated PUA film with 2D-dot nanopatterns.

the J_{sc} increases upon increasing the temperature in the polymer/fullerene BHJ devices [14,15]. This means that a thermally activated hopping transport mechanism is obvious in the disordered morphology [16]. Therefore, the J_{sc} strongly depends on the charge-carriers mobility. Unfortunately, organic semiconductors generally have low mobilities, ranging between 10^{-5} and 10^{0} cm^2/V s [17]. Well-ordered embossing anode structures can assist with extraction of electrons and holes as it will in some regions reduce the distance they have to travel to the electrode, as shown in Fig. 6. In addition, the enlarged contact area between the active layer and the embossed pattern also might assist an efficient carrier collection. By implementation of the mechanisms discussed above, it is possible to explain the increase of PCE of a BHJ photovoltaic cell with 2D-dot nano-patterned anode.

4. Conclusion

In conclusion, P3HT/PCBM-based organic solar cells were fabricated on highly ordered 2D-dot nano-patterned anodes prepared by a nano-imprinting method. It was found that a highly ordered 2D-dot nano-patterned anode can enhance the device performance due to the large interfacial area between both of the electrodes and the active layer. This is possible because the nano-patterned structures can efficiently harvest electrons and holes from the active layer to each electrode in the IZO anode and Al cathode. Moreover, increased optical absorption due to light trapping or scattering of reflected light by the imprint pattern was also expected. A polymer solar cell based on an IZO anode makes its feasible to produce in a low-cost, room-temperature process. This technology is confidently expected to play an important role in the creation of efficient flexible polymer solar cells via nano-imprinting for practical applications in future.

Acknowledgement

This work was supported by the grant from the ERC program of the Korea Science and Engineering Foundation (KOSEF) funded by the Korea Ministry of Education, Science and Technology (MEST) (No. R11-2007-045-01002-0(2009)). Author of SKKU (J.H. Park) acknowledge the support from the Hydrogen Energy R&D Center, one of the 21st Century Frontier R&D Program, funded by the Ministry of Education, Science and Technology of Korea. Authors of KIMM (Choi and Jeong) acknowledge the support from a grant (M102KN010001-08K1401-00210) from CNMM.

Appendix A. Supplementary data

Supplementary data associated with this article can be found, in the online version, at doi:10.1016/j.orgel.2009.11.007.

References

[1] K. Kim, J. Liu, M.A.G. Namboothiry, D.L. Carroll, Appl. Phys. Lett. 90 (2007) 163511.
[2] A.J. Heeger, Angew. Chem., Int. Ed. 40 (2001) 2591.
[3] K.M. Coakley, M.D. McGehee, Chem. Mater. 16 (2004) 4533.
[4] G. Dennler, M.C. Scharber, C.J. Brabec, Adv. Mater. 21 (2009) 1.
[5] S. Gunes, H. Neugebauer, N.S. Sariciftci, Chem. Rev. 107 (2007) 1324.
[6] B.C. Thompson, J.M. Frechet, J. Angew. Chem. Rev. 47 (2008) 58.
[7] X. Yang, J. Loos, S.C. Veenstra, W.J.H. Vergees, M.M. Wienk, J.M. Kroon, M.A.J. Michels, R.J. Janssen, Nano Lett. 5 (2005) 579.
[8] V.D. Mihailetchi, H. Xie, B. de Boer, L.J.A. Koster, P.W.M. Blom, Adv. Funct. Mater. 16 (2006) 699.
[9] Y.R. Park, D.G. Jung, Y.S. Kim, Jpn. J. Appl. Phys. 47 (2008) 516.
[10] J.B. Emah, R.J. Curry, S.R.P. Silva, Appl. Phys. Lett. 93 (2008) 103301.
[11] M.S. Kim, J.S. Kim, J.C. Cho, M. Shtein, L.J. Guo, J. Kim, Appl. Phys. Lett. 90 (2007) 123113.
[12] S.J. Choi, P.J. Yoo, S.J. Baek, T.W. Kim, H.H. Lee, J. Am. Chem. Soc. 126 (2004) 7744.
[13] B. Maennig, J. Drechsel, D. Gebeyehu, P. Simon, F. Kozlowski, A. Werner, F. Li, S. Grundmann, S. Sonntag, M. Koch, K. Leo, M. Pfeiffer, H. Hoppe, D. Meissner, S. Sariciftci, I. Riedel, V. Dyakonov, J. Parisi, Appl. Phys. A 79 (2004) 1.
[14] E.A. Katz, D. Faiman, S.M. Tuladhar, J.M. Kroon, M.M. Wienk, T. Fromherz, F. Padinger, C.J. Brabec, N.S. Sariciftci, J. Appl. Phys. 90 (2001) 5343.
[15] V. Dyakonov, Physica E 14 (2002) 53.
[16] M. Pope, C.E. Swenberg, Electronic Processes in Organic Crystals and Polymers, second ed., Oxford University Press, New York, 1999.
[17] H. Hope, N.S. Sariciftci, J. Mater. Res. 19 (2004) 1924.

Organic Electronics 11 (2010) 291–298

Contents lists available at ScienceDirect

Organic Electronics

journal homepage: www.elsevier.com/locate/orgel

Influence of the semi-conductor layer thickness on electrical performance of staggered n- and p-channel organic thin-film transistors

D. Boudinet [a,*], M. Benwadih [a], S. Altazin [a], R. Gwoziecki [a], J.M. Verilhac [a], R. Coppard [a], G. Le Blevennec [a], I. Chartier [a], G. Horowitz [b]

[a] CEA/LITEN/LCI, 38054 Grenoble, France
[b] ITODYS, CNRS UMR 7086 Université Paris Diderot, 75205 Paris Cedex 13, France

ARTICLE INFO

Article history:
Received 16 September 2009
Received in revised form 30 October 2009
Accepted 3 November 2009
Available online 18 November 2009

Keywords:
Organic thin-film transistor
Contact resistance
Semi-conductor thickness

ABSTRACT

In this study, we report on the influence of the semi-conductor thickness on organic thin-film transistors (OTFTs). Devices are fabricated with a top gate/bottom contact geometry on plastic substrates. Both n-channel and p-channel OTFTs made, respectively, from a *N,N*-dialkylsubstituted-(1,7&1,6)-dicyanoperylene-3,4:9,10-bis(dicarboximide) derivative (Polyera ActivInk™ N1400) and from 6,13-bis(triisopropylsilylethynyl) pentacene (TIPS-pentacene) are studied and compared. Impact of the active semiconducting layer thickness on both contact resistance and mobility are uncorrelated by the use of the transfer line method (TLM). When increasing the thickness of the semi-conductor, we find an increasing contact resistance and a decreasing channel mobility for both n- and p-channel OTFTs. The loss of mobility with increased thickness is attributed to a degradation of the interface between the semi-conductors and the dielectric, and is studied by atomic force microscope (AFM).

© 2009 Elsevier B.V. All rights reserved.

1. Introduction

The emergence of new solution processible materials with higher electrical performance has led to significant progress in the field of OTFTs during the last decade [1–5]. Among the different transistor geometries, the staggered top gate configuration presents several technical and physical interests for solution processible organic transistors [6–9]. In this configuration, the active semiconducting–dielectric interface, where charge carriers are transported, is separated from the source and drain electrodes by the semi-conductor layer. The thickness and quality of this layer is thus of crucial importance for device performance.

Most of the works reported in the literature focused on evaporated materials [10–17] and on p-channel OTFTs. In the field of solution processed materials, Richards et al. gave a detailed study of contact resistance in top gate staggered transistors made with amorphous semiconducting polymer. Their work shows that the main cause of contact resistivity comes from the transport through the bulk film rather than injection process from gold electrode into the semi-conductor. Impact on the channel mobility and the threshold voltage was however not discussed. Recently, Verilhac et al. reported [8] an optimum thickness around 200 nm when working with staggered top gated amorphous p-channel transistors. The threshold voltage and subthreshold slope were the most affected parameters whereas the mobility was found almost constant by varying the thickness among two orders of magnitude. Huge non-linearity at the origin of the output characteristics were reported when increasing the thickness. This effect was attributed to the access resistance through the semiconducting layer which is inherent to the staggered geometry. Pesavento et al. compared [11] the impact of the

* Corresponding author.
E-mail address: damien.boudinet@cea.fr (D. Boudinet).

1566-1199/$ - see front matter © 2009 Elsevier B.V. All rights reserved.
doi:10.1016/j.orgel.2009.11.008

evaporated crystalline pentacene layer on bottom gated top contact and bottom contact transistors. In the staggered top contact configuration, for thickness higher than 100 nm, they found an increasing contact resistance and a decreasing mobility. They did not report however on the threshold voltage evolution.

From these previous works, it seems that the thickness influence may change depending on the amorphous or crystalline nature of the semi-conductor. Moreover, to our knowledge no detailed report has been published where the effect of the thickness on both contact resistance and mobility were separated in the staggered top gate configuration in the case of poly-crystalline small soluble molecules.

In this study, we fabricated both n-channel and p-channel transistors made from spin-coated small molecules (see Fig. 1). For the realization of complex organic circuits, the understanding of transistors of both polarities is necessary. To simplify the design of such circuits, similar electrical performance for n- and p-channel OTFT would be beneficial. It is also important to verify that the injection and transport mechanisms are not affected by the nature of the charge carriers.

When the semi-conductor is deposited from solution, the mechanisms of the film formation are very different from evaporated thin films. In that case, the surface morphology and roughness of the active layer are affected by parameters such as the solvent boiling point [18], the annealing temperature [19], and the surface energy of the substrate [20]. When working with very thick semi-conductor layer, a fast evaporation of the solvent can dramatically impact the roughness and the morphology of the layer, which will in turn affect the electrical performance of the devices.

In this paper, we chose the transfer line method (TLM) [21,22] to study the effect of increasing the active layer thickness on the contact resistance and the mobility. We also discussed the variation of the threshold voltage. Interestingly we found very different electrical behaviour on poly-crystalline small molecules from what was reported on amorphous polymer TFB and PTAA with the same device architecture [8].

The first part of the paper describes the fabrication process. In a second part, we report the electrical impact of increasing the semi-conductor thickness on small molecule n-channel and p-channel OTFTs. The last section is dedicated to discuss the experimental results. To account for the mobility degradation, AFM and optical microscope inspections were also conducted to get an insight at the interface between the semi-conductor and the organic insulator.

2. Materials and samples preparation

2.1. Transistor fabrication and characterization

Polyethylene naphthalate (PEN) films were used as flexible substrates. 30 nm thick Au source and drain electrodes were deposited by sputtering and patterned by photolithography. Transistors with a width of 1 cm and channel length of 5, 10, 20, 40, and 100 μm were fabricated.

In the case of n-channel transistors, 1 mM solutions of 4-methylthiophenol in ethanol were prepared, in which samples were immersed at room temperature for a period of 5 h. They were then rinsed thoroughly with pure ethanol and dried in a N_2 gas stream before semi-conductor deposition. For p-channel transistors, we followed the same procedure with 1H,1H,2H,2H-perfluorodecanethiol [23].

For n-channel transistors, a *N*,*N*-dialkylsubstituted-(1,7&1,6)-dicyanoperylene-3,4:9, 10-bis(dicarboximide) derivative (Polyera ActivInk™ N1400) [24] bought from Polyera Corporation was diluted in 1,2-dichloro-benzene at a concentration of 8 mg mL^{-1}. For p-channel transistors, 6,13-bis(triisopropylsilylethynyl) pentacene (TIPS-pentacene) [25] was used as the active layer at a concentration of 20 mg mL^{-1} in 1,2,3,4-tetrahydronaphthalene. Solutions were spin-coated at different speed to obtain different film thicknesses. The semi-conductor films were cured for both materials at a temperature of 115 °C for 5 min. Thicknesses of the active layer were measured with an alpha step profilometer.

Cytop™ dielectric [26] was then spin-coated on top of the semi-conductor and cured at 100 °C for 20 min to reach a thickness of 1.2 μm. To promote adhesion of the gate electrode on the highly hydrophobic insulating layer, solution of Nafion [27] diluted at 30 mg mL^{-1} in isopropanol was spin-coated at 1000 rpm. Finally an Ag ink gate electrode was printed by ink-jet using a Dimatix tool.

Electrical measurements were performed at room temperature in air by using a parameter analyser (HP4145, Hewlett–Packard). Morphological characterization was

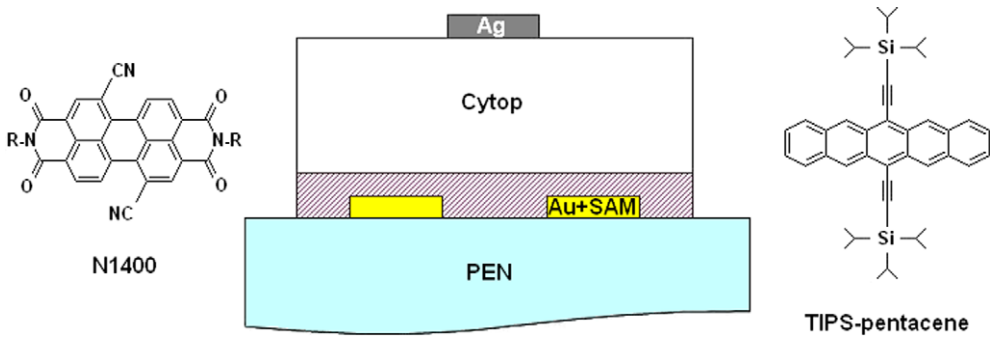

Fig. 1. Schematic of the fabricated transistors and formula of the semi-conductors used in the study.

carried out with an Innova AFM operating in the intermittent contact mode on samples specifically prepared for that purpose. The substrates consisted of Silicon on top of which the semi-conductor was spin-coated in the same condition as in the transistor fabrication.

2.2. AFM measurement

For TIPS-pentacene, 50 μm wide pictures were taken at a speed of 0.5 Hz with 256 lines. For Polyera ActivInk™ N1400, 10 μm wide pictures were taken in the same scan conditions. Roughnesses Ra and RMS were computed after a levelling of the pictures. Ra is defined as the arithmetic average of the average value roughness and is computed as Eq. (1):

$$R_a = \frac{1}{n}\sum_{i=1}^{n}|y_i| \quad (1)$$

RMS is defined as the root mean square roughness and is described by Eq. (2):

$$R_{RMS} = \sqrt{\frac{1}{n}\sum_{i=1}^{n}y_i^2} \quad (2)$$

Five pictures on five different regions of the samples were taken for each semi-conductor thickness. The reported roughness was taken as the mean value of the different scans.

2.3. Electrical parameters extraction

The transfer characteristic in the linear regime (V_D = 1 V for Polyera ActivInk™ N1400, V_D = −1 V for TIPS-pentacene) was measured on devices with various channel lengths (L = 5, 10, 20, 40, and 100 μm) prepared in the same run. From these characteristics, the threshold voltage was first extracted from the peak of the second derivative of the gate voltage dependent drain current, as described previously [7]. The next step consisted of calculating the width corrected total resistance as a function of V_G–V_T. According to the TLM, this resistance can be decomposed into the contact resistance R_C in series with the channel resistance from which the corrected mobility can be extracted. A representative example of the resistance for various values of V_G–V_T is shown in Fig. 2. The contact resistance corresponds to the extrapolation of the straight line to zero channel length.

3. Results

Fig. 3 shows the transfer characteristics in the linear regime of 20 μm long transistors for n- and p-channel OTFTs at different active layer thicknesses. Main Electrical parameters are also reported in Table 1.

Fig. 4 shows the extraction of the threshold voltage (V_T) by means of two different methods. The extrapolation in the linear region (ELR) finds the gate-voltage axis intercept of the linear extrapolation of the I_D–V_G curve at its minimum first derivative (slope) point. The value of V_T is calculated by adding $V_D/2$ to the resulting gate-voltage

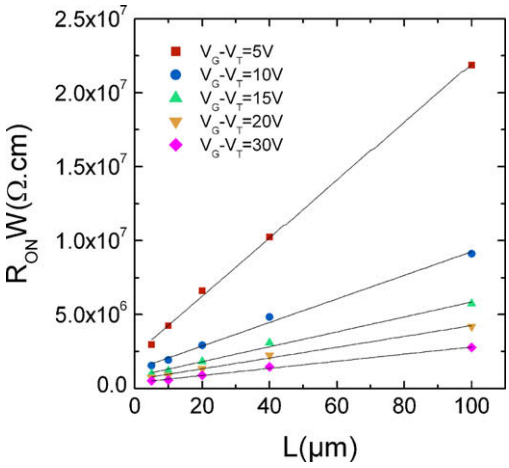

Fig. 2. Representative example of width normalized resistance versus channel length curves for n-channel OTFT. The resistance is estimated from the transfer characteristic at a drain voltage of 1 V.

intercept. We found a value of 0.5 V. The second derivative method which estimates V_T as the gate voltage at which the derivative of the transconductance (i.e., dg_m/dV_G) is maximum also gave a value of 0.5 V. In a previous study [7], we reported that for short channel OTFT, the ELR method tends to give overestimated values of V_T. As a consequence we chose to use the SD method.

V_T is not much affected by the semi-conductor thickness. Other groups also reported similar trend [13,15]. We also notice a small variation of the onset voltage (V_{ON}) defined as the lowest absolute current in the transfer characteristic from devices to devices. Variation of doping levels between the different fabricated transistors was previously reported as the origin of such variations [13,28].

We obtained very low leakage current through the gate dielectric in our transistors, leading to low OFF current and high ON/OFF ratio. Interestingly, output characteristics were not affected by the semi-conductor thickness (not shown here): we did not observe any major non-linearity at the origin of the curves for all the fabricated devices.

Fig. 5a gives the contact resistance extracted from the TLM (as described in the experimental section) with the applied gate voltage for different layer thickness. We note that R_C varies in a linear way with $1/(V_G–V_T)$ and increase for thicker film, in agreement with previous reports [9]. In a staggered geometry were charge carriers have to travel through the active layer before reaching the channel, this effect can be attributed to a smaller mobility in the normal direction of the semi-conductor [29–31].

Mobilities computed with the classical equations and extracted from the TLM method (corrected for the contact resistance) as a function of semi-conductor thickness are compared in Fig. 5b. We observe in both n-channel and p-channel OTFTs a huge drop when the semi-conductor layer becomes thicker.

4. Discussion

The almost constant threshold voltage we found in our devices tends to indicate that this parameter is not affected

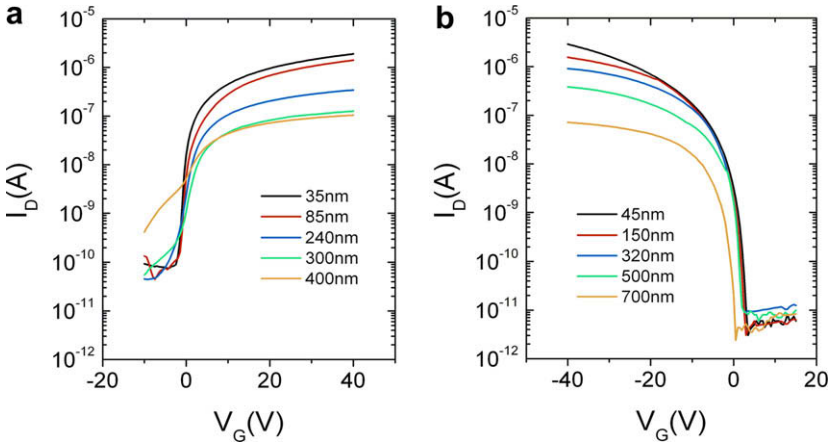

Fig. 3. Transfer characteristics in the linear regime (V_D = 1 V) of 20 μm long transistors for different semi-conductor thicknesses with (a) Polyera ActivInk™ N1400 and (b) TIPS-pentacene.

Table 1
Main electrical parameters for n- and p-channel transistors with different semi-conductor layer thicknesses for a drain voltage of 1 V.

Semi-conductor	Thickness (nm)	μ (cm^2/Vs)[a]	V_T (V)[b]	I_{ON}/I_{OFF}[c]	R_C (MΩcm)[d]
N1400	35	5.55×10^{-2}	0.5	6.98×10^4	0.14
N1400	85	6.45×10^{-2}	1.5	5.42×10^4	0.31
N1400	240	1.14×10^{-2}	1	1.02×10^4	1.35
N1400	300	7.08×10^{-3}	1	3.64×10^3	1.88
N1400	400	3.48×10^{-3}	0.5	2.65×10^3	3.72
TIPS	45	6.42×10^{-1}	−5	4.55×10^6	0.65
TIPS	150	3.84×10^{-1}	−5	9.83×10^5	0.92
TIPS	320	7.42×10^{-2}	−4	1.33×10^5	2.70
TIPS	500	3.41×10^{-2}	−4.5	8.52×10^4	4.01
TIPS	700	4.6×10^{-3}	−4.5	4.29×10^4	8.75

[a] Mobility from TLM measurements at $V_G - V_T = \pm 40$ V.
[b] Threshold voltage extracted by the second derivative method.
[c] ON/OFF ration with OFF current taken at minimum of the transfer characteristic and ON current taken at 40 V.
[d] Contact resistance from the TLM measurements taken at $V_G - V_T = \pm 40$ V.

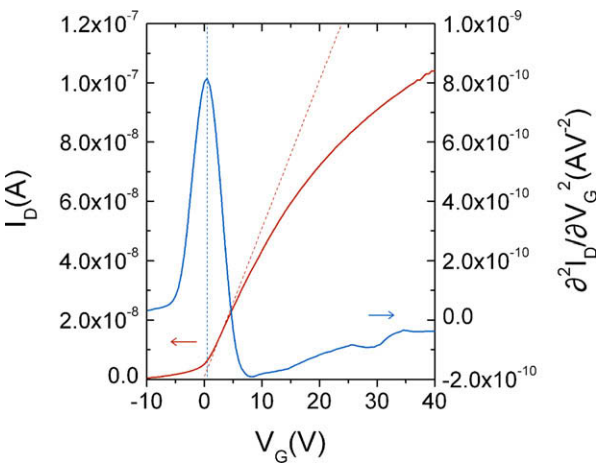

Fig. 4. Extraction of the threshold voltage for a 20 μm long n-channel OTFT. The extrapolation in the linear regime and the second derivative methods are compared.

by the semi-conductor thickness in the case of both n- and p-channel solution processed small molecule transistors. In poly-crystalline OTFTs a huge variation on V_T is generally achieved by modifying the chemical properties at the interface between the semi-conductor and the dielectric as widely reported in the literature [32,33]. Kuo et al. previously reported [15] a constant threshold voltage when changing the semi-conductor thickness in amorphous silicon devices with staggered geometry, in good agreement with our results.

Verilhac et al. on the other hand, recently reported [8] a very different trend for amorphous polymer with the same exact transistor configuration. Two distinct regimes in semi-conductor thickness were identified with an optimum for V_T around 200 nm. The authors attributed these variations to source and drain induced topologic effect and to access resistance, respectively, for low and high thickness regimes. Dependence of V_T on the semi-conductor thickness was also reported [12] on poly-crystalline pentacene by Schröeder et al.

The fact that we found an almost constant threshold voltage with the active layer thickness seems to indicate

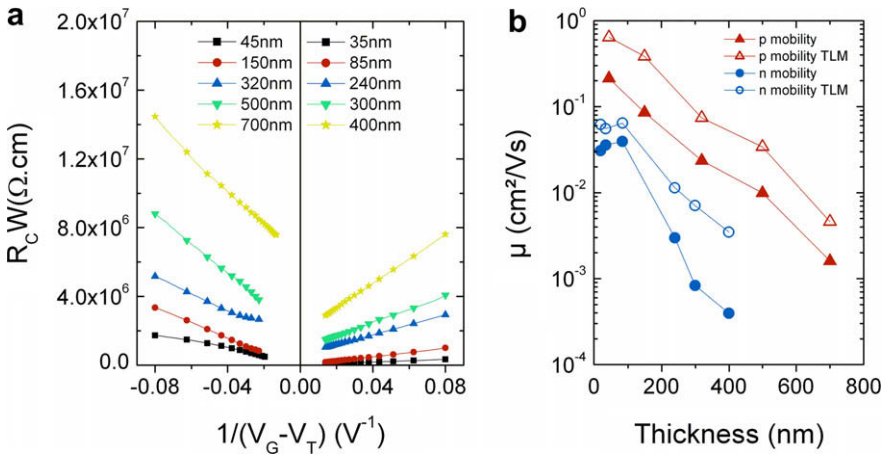

Fig. 5. (a) Contact resistance extracted from TLM measurements (left panel for p-channel OTFTs, right panel for n-channel OTFTs), and (b) comparison of the mobility corrected from contact resistance and computed from the classical equation.

that this parameter is dependent to both the geometry of the device and the nature of the semi-conductor.

In an other study where we modified the gold source and drain electrodes with self-assembled monolayers, we also found very different behaviour between amorphous poly[9,9-dioctyl-fluorene-co-*N*-(4-butylphenyl)-diphenyl-amine] (TFB) and poly-crystalline N1400 and TIPS-pentacene [23]. Variation of V_T was found dependant on the barrier height between the electrode work function and the highest occupied molecular orbital (HOMO) for amorphous TFB. In the case of poly-crystalline materials we did not find any link between these two parameters. These combined results highlight very different transport and injection mechanisms in amorphous and poly-crystalline materials.

Fig. 6a, shows the evolution of the contact resistance (R_C) as a function of the semi-conductor thickness. For both n- and p-channel OTFTs, we observe an increase in R_C with the active layer thickness. Mariucci et al. previously reported [14] that the variation of R_C was closely dependant of the device geometry. In coplanar configuration, they found an almost constant R_C, whereas this parameter was increasing with the semi-conductor thickness in the case of a staggered configuration. For thicker semiconducting films, the path that charge carriers have to cross before reaching the channel is increased which lead to a higher contact resistance. This increase in the contact resistance in staggered devices is also generally attributed to diffusion limited charges transport in thicker layer between the electrodes and the active interface [8].

From our results, and contrary to what has been previously observed for amorphous polymer, we found a huge variation in mobility with the active layer thickness. As the mobility calculated has been corrected from contact resistance, such dependence could be mainly attributed to morphological or topological effects at the semi-conductor surface.

Fig. 7 shows optical polarized microscope of both semiconductor for different thickness. In the case of TIPS-pentacene, clear change in the morphology is observed. When the layer thickness is increased, the morphology is changing from clear spherulite structure to a rod like crystallization.

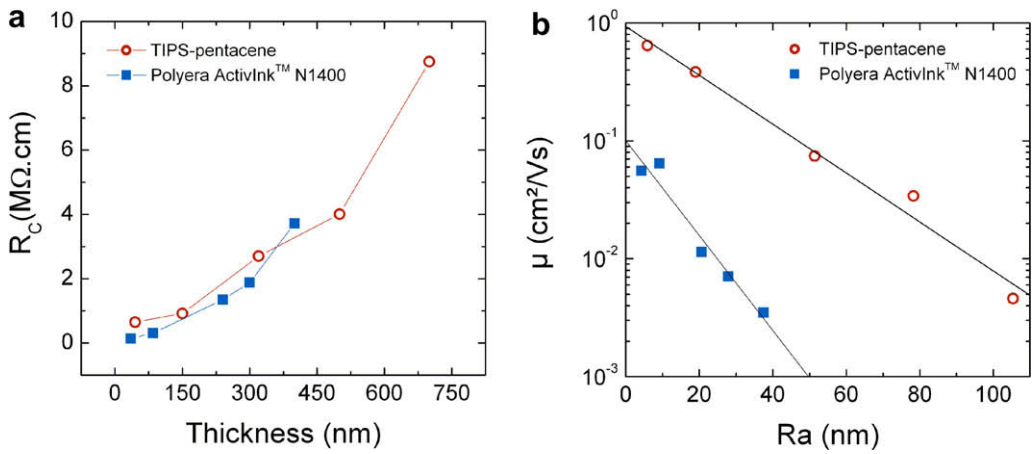

Fig. 6. (a) Variation of the contact resistance as a function of the semi-conductor thickness for both n- and p-channel devices. (b) Variation of the mobility corrected from the contact resistance as a function of the semi-conductor layer roughness (Ra) for both transistors polarity.

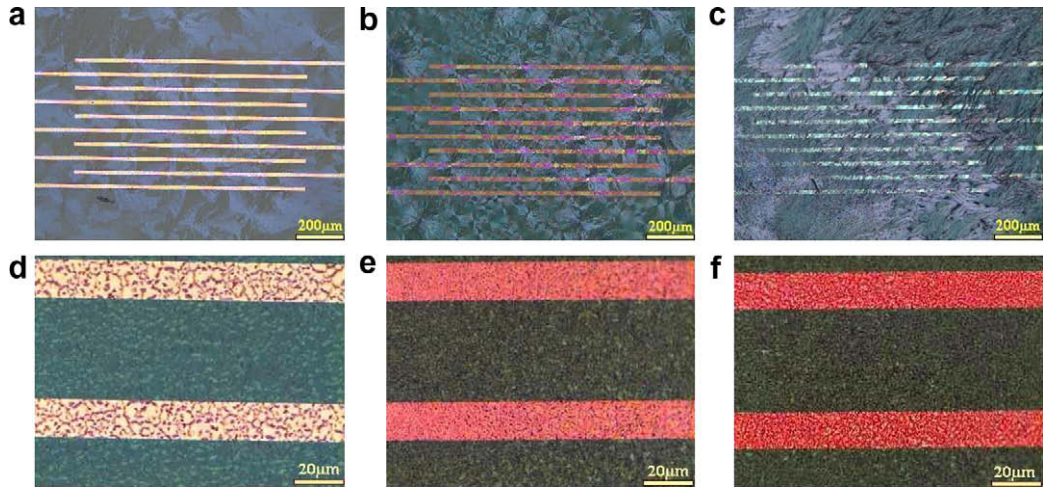

Fig. 7. Optical polarized microscope pictures on TIPS-pentacene for thicknesses of (a) 45 nm, (b) 320 nm, and (c) 700 nm and on Polyera ActivInk™ N1400 for thicknesses of (d) 35 nm, (e) 240 nm, and (f) 400 nm.

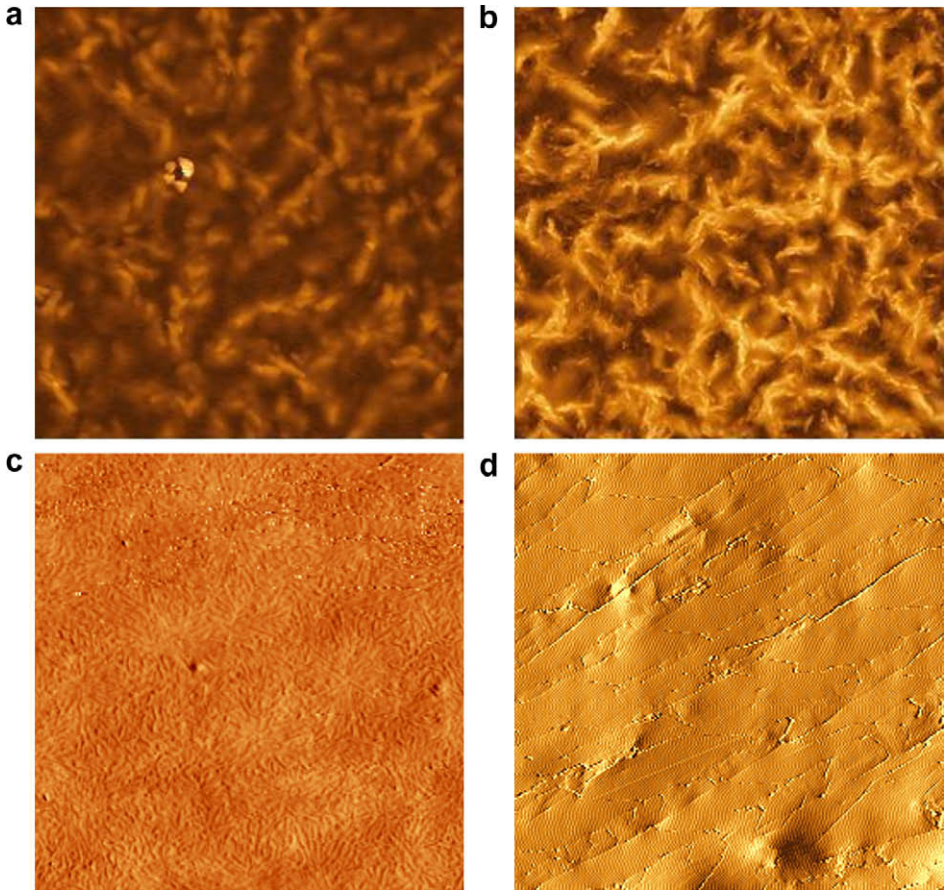

Fig. 8. AFM pictures on (a) 35 nm thick, and (b) 400 nm thick Polyera ActivInk™ N1400, and (c) 45 nm thick, and (d) 500 nm thick TIPS-pentacene. For N1400, pictures are 10 µm wide, for TIPS-pentacene, pictures are 50 µm wide.

AFM pictures on thick TIPS-pentacene also evidence cracks on top of the layer, which may be caused by solid state phase transition in the TIPS-pentacene crystals [34] and can account for the lower channel mobility. Note that in the case of n-channel OTFTs, change of optical visible variation of the morphology with the semi-conductor thickness is less clear. Complementary X-ray diffraction measurements could be processed in order to give a clearer vision

Table 2
Influence of the active layer thickness on roughness and mobility.

Semi-conductor	Thickness (nm)	Ra[a] (nm)	RMS[b] (nm)	μ (cm^2/Vs)[c]
N1400	35	4.3 ± 0.2	6.3 ± 0.6	5.55×10^{-2}
N1400	85	9.2 ± 0.3	12.3 ± 0.3	6.45×10^{-2}
N1400	240	20.6 ± 0.9	25.3 ± 1.1	1.14×10^{-2}
N1400	300	27.9 ± 4.1	34.3 ± 5.0	7.08×10^{-3}
N1400	400	37.5 ± 4.3	46.2 ± 5.3	3.48×10^{-3}
TIPS	45	5.9 ± 1.3	8.6 ± 1.8	6.42×10^{-1}
TIPS	150	18.9 ± 3.1	22.5 ± 3.5	3.84×10^{-1}
TIPS	320	51.4 ± 6.4	67.6 ± 7.4	7.42×10^{-2}
TIPS	500	78.3 ± 9.1	106.5 ± 13.1	3.41×10^{-2}
TIPS	700	105.4 ± 21.7	135.3 ± 29.6	4.6×10^{-3}

[a] Ra from 50 μm wide AFM pictures.
[b] RMS from 50 μm wide AFM pictures.
[c] Mobility from TLM measurements at $V_G - V_T = 40$ V.

of morphological aspects. However such experiments tend to be difficult on PEN due to the huge features of the substrate on X-ray spectrum.

The morphological variations come with a degradation of the semi-conductor surface smoothness which is confirmed by roughness analysis made by AFM measurement. In the bottom contact staggered geometry, the roughness of the semiconducting surface is of major importance and may impact significantly the performance of the transistor. Fig. 8 reports AFM pictures for both materials at different thicknesses. Corresponding roughnesses are reported in Table 2. For both materials, as the semi-conductor layer thickness is increased, the roughness was found higher. As an example, the 700 nm thick TIPS-pentacene film has a very high average roughness of Ra = 105 nm, while the 45 nm thick film showed much lower values around Ra = 6 nm. The very high roughness obtained can be attributed to a too fast evaporation of the solvent, which in turn leads to a poorly organized layer. In Fig. 6b we plotted the variation of the mobility as a function of the roughness Ra of the semi-conductor surface. An exponential dependence was found between the two parameters. The corresponding drop in mobility was more than two orders of magnitudes, from 0.6400 to 0.0046 cm^2/Vs. Such a trend has already been reported [35] for amorphous polymer but for another scale of roughness variation which were in the order of 1–2 nm. Such a degradation of roughness could explain the drop in contact corrected mobility as the accumulated charge carriers which are localized in a thin (~5 nm) layer at the semi-conductor–dielectric interface may be disturbed by these nano-topological effects.

5. Conclusion

We investigated the influence of the semi-conductor layer thickness on electrical performance on both n- and p-channel OTFTs. Results on both polarities followed the same trends. The threshold voltage was found constant with the active layer, opposite to other reports on amorphous semi-conductors. We believe that this parameter is dependant on both the geometry of the device and the nature of the semi-conductor.

For both types of device, contact resistance was found higher with thicker film. This result confirms the hypothesis of a diffusion limited charge transport mechanism across the semi-conductor layer.

Finally, even when corrected for the contact resistance, we found a huge decrease in the mobility when the active layer was thicker. We attributed this loss to a degradation of both the film morphology and the roughness at the interface with the dielectric, evidenced by AFM.

References

[1] J. Zaumseil, H. Sirringhaus, Chem. Rev. 107 (2007) 1296–1323.
[2] A. Facchetti, Mater. Today 10 (2007) 28–37.
[3] G. Horowitz, J. Mater. Res. 19 (2004) 1946–1962.
[4] Z. Bao, Adv. Mater. 12 (2000) 227–230.
[5] C.R. Newman, C.D. Frisbie, D.A. Da Silva Filho, J.-L. Brédas, P.C. Ewbank, K.R. Mann, Chem. Mater. 16 (2004) 4436–4451.
[6] H. Yan, Y. Zheng, R. Blache, C. Newman, S.F. Lu, J. Woerle, A. Facchetti, Adv. Mater. 20 (2008) 3393–3398.
[7] D. Boudinet, G. Le Blevennec, C. Serbutoviez, J.-M. Verilhac, H. Yan, G. Horowitz, J. Appl. Phys. 105 (2009) 084510.
[8] J.M. Verilhac, M. Benwadih, S. Altazin, S. Jacob, R. Gwoziecki, R. Coppard, C. Serbutoviez, Appl. Phys. Lett. 94 (2009) 143301.
[9] T.J. Richards, H. Sirringhaus, J. Appl. Phys. 102 (2007) 094510.
[10] M.-W. Lee, C.-K. Song, J. Korean Phys. Soc. 47 (2005) 111–115.
[11] P.V. Pesavento, K.P. Puntambekar, C.D. Frisbie, J.C. McKeen, P.P. Ruden, J. Appl. Phys. 99 (2006) 094504.
[12] R. Schroeder, L.A. Majewski, M. Grell, Appl. Phys. Lett. 83 (2003) 3201–3203.
[13] R. Schroeder, L.A. Majewski, M. Grell, Appl. Phys. Lett. 84 (2004) 1004–1006.
[14] L. Mariucci, D. Simeone, S. Cipolloni, L. Maiolo, A. Pecora, G. Fortunato, S. Brotherton, Solid-State Electron. 52 (2008) 412–416.
[15] A. Kuo, T.K. Won, J. Kanicki, Jpn. J. Appl. Phys. 47 (2008) 3362–3367.
[16] S. Gowrisanker, Y. Ai, M.A. Quevedo-Lopez, H. Jia, H.N. Alshareef, E. Vogel, B. Gnade, Appl. Phys. Lett. 92 (2008) 153305.
[17] P.V. Necliudov, M.S. Shur, D.J. Gundlach, T.N. Jackson, Solid-State Electron. 47 (2003) 259–262.
[18] Y.-H. Kim, Y.U. Lee, J.-I. Han, S.-M. Han, M.-K. Han, J. Electrochem. Soc. 154 (2007) H995–H998.
[19] D. Guo, S. Ikeda, K. Saiki, H. Miyazoe, K. Terashima, J. Appl. Phys. 99 (2006).
[20] S.-Y. Kwak, C.G. Choi, B.-S. Bae, Electrochem. Solid-State Lett. 12 (2009) G37–G39.
[21] M. Mottaghi, G. Horowitz, Org. Electron. 7 (2006) 528–536.
[22] P. Marmont, N. Battaglini, P. Lang, G. Horowitz, J. Hwang, A. Kahn, C. Amato, P. Calas, Org. Electron. 9 (2008) 419–424.
[23] D. Boudinet, M. Benwadih, Y. Qi, S. Altazin, J.-M. Verilhac, M. Kroger, C. Serbutoviez, R. Gwoziecki, R. Coppard, G. Le Blevennec, A. Kahn, G. Horowitz, Org. Electron. (2009), doi:10.1016/j.orgel.2009.10.021.
[24] T.N. Ng, S. Sambandan, R. Lujan, A.C. Arias, C.R. Newman, H. Yan, A. Facchetti, Appl. Phys. Lett. 94 (2009) 233307.
[25] J.E. Anthony, J.S. Brooks, D.L. Eaton, S.R. Parkin, J. Am. Chem. Soc. 123 (2001) 9482–9483.
[26] J. Veres, S. Ogier, G. Lloyd, D. de Leeuw, Chem. Mater. 16 (2004) 4543–4555.

[27] C. Serbutoviez, M. Benwadih, J.-M. Verilhac, US Patent 20090035565, 2009.
[28] E.J. Meijer, C. Tanase, P.W.M. Blom, E. van Veenendaal, B.-H. Huisman, D.M. de Leeuw, T.M. Klapwijk, Appl. Phys. Lett. 80 (2002) 3838–3840.
[29] J. Chen, C.K. Tee, M. Shtein, D.C. Martin, J. Anthony, Org. Electron. 10 (2009) 696–703.
[30] R.L. Headrick, S. Wo, F. Sansoz, J.E. Anthony, Appl. Phys. Lett. 92 (2008).
[31] X.L. Chen, A.J. Lovinger, Z. Bao, J. Sapjeta, Chem. Mater. 13 (2001) 1341–1348.
[32] K.P. Pernstich, S. Haas, D. Oberhoff, C. Goldmann, D.J. Gundlach, B. Batlogg, A.N. Rashida, G. Schitter, J. Appl. Phys. 96 (2004) 6431–6438.
[33] S. Kobayashi, T. Nishikawa, T. Takenobu, S. Mori, T. Shimoda, T. Mitani, H. Shimotani, N. Yoshimoto, S. Ogawa, Y. Iwasa, Nat. Mater. 3 (2004) 317–322.
[34] J. Chen, J. Anthony, D.C. Martin, J. Phys. Chem. B 110 (2006) 16397–16403.
[35] L.L. Chua, P.K.H. Ho, H. Sirringhaux, R.H. Friends, Adv. Mater. 16 (2004) 1609–1615.

Organic Electronics 11 (2010) 299–310

Contents lists available at ScienceDirect

Organic Electronics

journal homepage: www.elsevier.com/locate/orgel

Novel blue and red electrochromic poly(azomethine ether)s based on electroactive triphenylamine moieties

Hung-Ju Yen, Guey-Sheng Liou *

Functional Polymeric Materials Laboratory, Institute of Polymer Science and Engineering, National Taiwan University, 1 Roosevelt Road, 4th Sec., Taipei 10617, Taiwan

ARTICLE INFO

Article history:
Received 18 September 2009
Received in revised form 22 October 2009
Accepted 3 November 2009
Available online 10 November 2009

Keywords:
Electrochemistry
Electrochromism
Polyethers
Azomethine
Triphenylamine

ABSTRACT

Two series of red and blue electrochromic aromatic poly(azomethine ether)s (PAMEs) containing electroactive triphenylamine (TPA) moieties in the backbone were prepared from the high-temperature polycondensation reactions of newly azomethine–triphenylamine (AM–TPA)-based biphenol monomers, 4,4′-di(4-hydroxybenzylideneamino)triphenylamine (**3**) and 4,4′-di(4-hydroxybenzylideneamino)-4″-methoxytriphenylamine (**4**), with difluoro compounds, respectively. The obtained polymers were readily soluble in many organic solvents and showed useful levels of thermal stability associated with high softening temperatures (215–240 °C) and high char yields (higher than 64% at 800 °C in nitrogen). In addition, the polymer films showed reversible electrochemical oxidation with high contrast ratio and unique anodic blue/red electrochromic behaviors.

© 2009 Elsevier B.V. All rights reserved.

1. Introduction

Electrochromic materials exhibited a reversible optical change in absorption or transmittance upon electrochemically oxidized or reduced, such as transition-metal oxides, inorganic coordination complexes, organic molecules, and conjugated polymers [1]. In general, the investigation of electrochromic materials had been directed towards optical changes in the visible region proved especially useful for variable reflectance mirrors, tunable windows, and electrochromic displays.

Poly(azomethine)s (PAMs) or poly(Schiff-base)s with aromatic backbones were considered as high performance polymers [2] due to their high thermal stability [3], excellent mechanical strength [4], and good optoelectronic properties [5]. In recent years, PAMs had also been explored for applications in organic electronics, such as light-emitting materials [6], pH sensors [7], and metal-collecting polymers [8]. However, their insolubility in common organic solvents limited their processability and application [9]. One of the common approaches for increasing the solubility and processibility of PAMs without sacrificing high thermal stability was the introduction of various substituted aromatic ring into the polymer backbone [10], by using monomers with thiophene [11], phenylquinoxaline ring [12], cardo-structure [13], tetraphenylethene [14], and others [15]. Though PAMs made by vapor deposition of the monomers in a vacuum chamber have also been used as electron transporting layers in polymer light-emitting diodes [16], the preparation by solution-processable PAMs is beneficial for their fabrication of large-area, thin-film photonic devices.

The anodic oxidation pathway of electroactive TPA always associated noticeable color changed was well reported, and the electrogenerated TPA cation radical could be dimerized to form tetraphenylbenzidine (TPB), which

* Corresponding author.
E-mail address: gsliou@ntu.edu.tw (G.-S. Liou).

1566-1199/$ - see front matter © 2009 Elsevier B.V. All rights reserved.
doi:10.1016/j.orgel.2009.11.009

was more easily oxidized than the original TPA moieties [17]. Recently, we have reported some organo-soluble and high T_g aromatic polymers bearing TPA units in the main chain [18]. Because of the incorporation of bulky and three-dimensional TPA units along the polymer backbone, all the polymers were amorphous with good solubility in many aprotic solvents and exhibited excellent thin-film-forming capability.

In this contribution, we therefore synthesized the azomethine–triphenylamine (AM–TPA)-based aromatic poly(azomethine ether)s (PAMEs) from the new (AM–TPA)-based diol monomers, 4,4′-di(4-hydroxybenzylideneamino)-4″-triphenylamine (**3**) and 4,4′-di(4-hydroxybenzylideneamino)-4″-methoxytriphenylamine (**4**), with difluoro compounds, respectively. Incorporation of preformed TPA units into PAMEs allowed the retention of some of the favorable properties of polymers such as high thermal stability and glass transition temperature, whereas the ether linkages increase the solubility and enhance the film-forming ability. In addition to the general properties (such as inherent viscosities, solubility, and thermal properties), the electrochemical and electrochromic behaviors of these polymers were also investigated.

2. Experimental section

2.1. Materials

4,4′-Diaminotriphenylamine [19] (**1**) (mp: 186–187 °C), 4,4′-diamino-4″-methoxytriphenylamine [20] (**2**) (mp: 150–152 °C) and 2,5-bis(4-fluorophenyl)-1,3,4-oxadiazole [21] (**5b**) (mp: 205–206 °C) were synthesized according to a previously reported procedure. 4,4′-Difluoro-benzophenone (**5a**) (ACROS) was purified by recrystallization. Tetrabutylammonium perchlorate (TBAP) (ACROS) was recrystallized twice from ethyl acetate under a nitrogen atmosphere and then dried in vacuo prior to use. All other reagents were used as received from commercial sources.

2.2. Monomer synthesis

The general procedure is as follows: To a solution of 30.10 mmol of diamino compound was stirred in 85 mL of ethanol and heated to 70 °C under nitrogen atmosphere. After the diamino compound was dissolved, 90.40 mmol of 4-hydroxybenzaldehyde was added and the mixture was then heated to reflux. After a further 15 h of reflux, the solution was cooled and poured slowly into 300 ml of stirred methanol, and the product was collected by filtration and dried *in vacuo* at 80 °C to give yellow powders.

2.2.1. 4,4′-Di(4-hydroxybenzylideneamino)triphenylamine (**3**)

96.9 % in yield; mp of 259–260 °C (by DSC). ^{1}H NMR (300 MHz, DMSO-d_6, δ, ppm): 6.87 (d, J = 8.4 Hz, 4H, H_f), 7.00–7.03 (m, 7H, $H_a + H_c + H_d$), 7.20 (d, J = 8.4 Hz, 4H, H_e), 7.29 (t, J = 8.4 Hz, 2H, H_b), 7.75 (d, J = 8.4 Hz, 4H, H_g), 8.48 (s, 2H, –CH═N–), 10.09 (s, 2H, –OH). ^{13}C NMR (DMSO-d_6, δ, ppm): 115.6 (C^{10}), 122.2 (C^7), 122.7 (C^1), 123.3 (C^3), 124.4 (C^6), 127.7 (C^5), 129.5 (C^2), 130.5 (C^{11}), 144.9 (C^8), 146.7 (C^9), 147.3 (C^4), 158.6 (–CH═N–), 160.4 (C^{12}). Anal. Calcd (%) for $C_{32}H_{25}N_3O_2$ (483.56): C, 79.48; H, 5.21; N, 8.69. Found: C, 79.34; H, 5.36; N, 8.55. ESI-MS: calcd for $(C_{32}H_{25}N_3O_2)^+$: m/z 483.6; found: m/z 482.6.

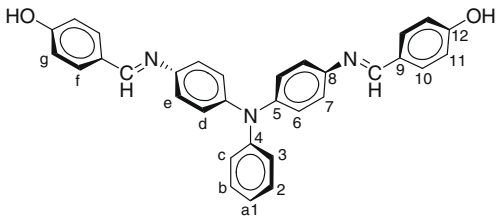

2.2.2. 4,4′-Di(4-hydroxybenzylideneamino)-4″-methoxytriphenylamine (**4**)

99.7 % in yield; mp of 293–295 °C (by DSC). ^{1}H NMR (300 MHz, DMSO-d_6, δ, ppm): 3.73 (s, 3H, $-OCH_3$), 6.86 (d, J = 8.4 Hz, 4H, H_e), 6.91–6.96 (m, 6H, $H_a + H_c$), 7.04 (d, J = 8.4 Hz, 4H, H_d), 7.73 (d, J = 8.4 Hz, 4H, H_f), 8.46 (s, 2H, –CH═N–), 10.08 (s, 2H, –OH). ^{13}C NMR (DMSO-d_6, δ, ppm): 55.3 ($-OCH_3$), 115.1 (C^2), 115.6 (C^{10}), 122.1 (C^7), 122.9 (C^6), 127.0 (C^3), 127.8 (C^5), 130.4 (C^{11}), 140.0 (C^4), 145.4 (C^8), 145.8 (C^9), 156.0 (C^1), 158.1 (–CH═N–), 160.4 (C^{12}). Anal. Calcd (%) for $C_{33}H_{27}N_3O_3$ (513.59): C, 77.17; H, 5.30; N, 8.18. Found: C, 77.15; H, 5.46; N, 8.15. ESI-MS: calcd for $(C_{33}H_{27}N_3O_3)^+$: m/z 513.6; found: m/z 512.6.

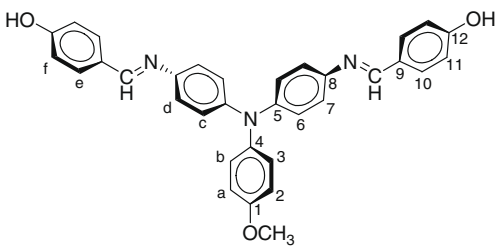

2.3. Polymer synthesis

The synthesis of PAME **Ia** was used as an example to illustrate the general synthetic procedure. To a two necked 50 ml glass reactor was charged with diol monomer **3** (0.97 g, 2 mmol), **5a** (0.44 g, 2 mmol), and 4 ml *N*-methyl-2-pyrrolidinone (NMP), 2 ml of toluene, and an excess of potassium carbonate (0.41 g, 3 mmol). The reaction mixture was heated at 150 °C for 3 h to remove water during the formation of phenoxide anions, then heated at 170 °C for 1 h, 180 °C for 3 h, and finally heated at 190 °C for 1 h. After the reaction, the obtained polymer solution was poured slowly into 400 ml of acidified methanol/water (v/v = 1/1). The precipitate was collected by filtration, washed thoroughly with hot water and methanol, and dried under vacuum at 100 °C. Reprecipitations of the polymer by NMP/methanol were carried out twice for fur-

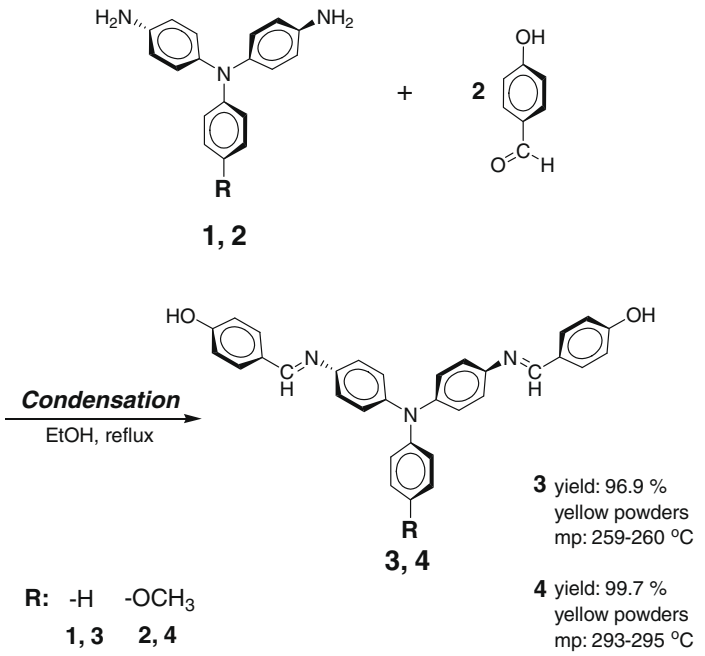

Scheme 1. Synthesis of AM–TPA-based diol monomers.

ther purification. The inherent viscosity of the obtained PAME **Ia** was 0.20 dl/g (measured at a concentration of 0.5 g/dl in NMP at 30 °C). Anal. Calcd (%) of **Ia** for $(C_{47}H_{37}N_3O_3)_n$ $(691.81)_n$: C, 81.60; H, 5.39; N, 6.07. Found: C, 79.70; H, 5.61; N, 5.90. Anal. Calcd (%) of **IIa** for $(C_{48}H_{39}N_3O_4)_n$ $(721.84)_n$: C, 79.87; H, 5.45; N, 5.82. Found: C, 77.97; H, 5.33; N, 5.89. The other PAMEs were prepared by an analogous procedure.

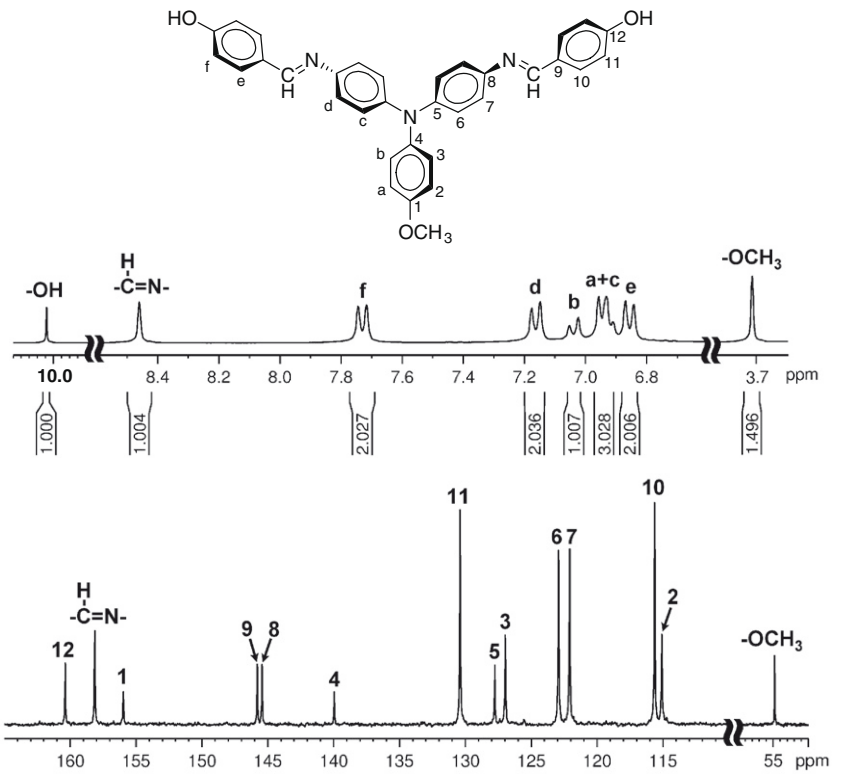

Fig. 1. ^{1}H NMR and ^{13}C NMR spectra of diol monomer **4** in DMSO-d_6.

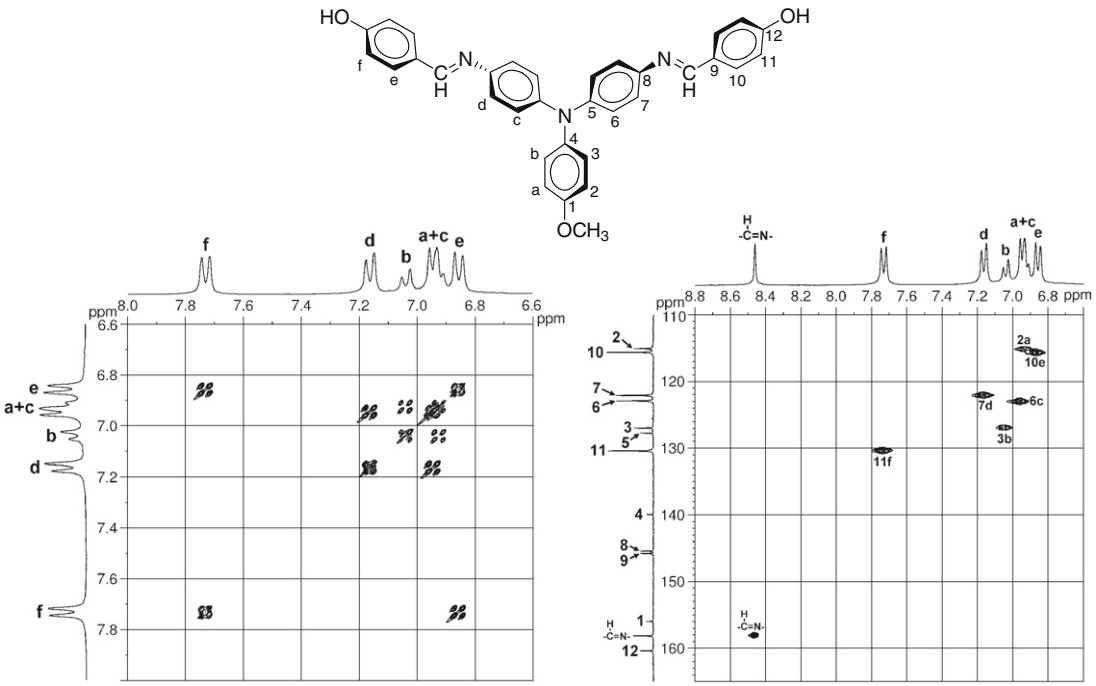

Fig. 2. H–H COSY and C–H HMQC spectra of diol monomer **4** in DMSO-d_6.

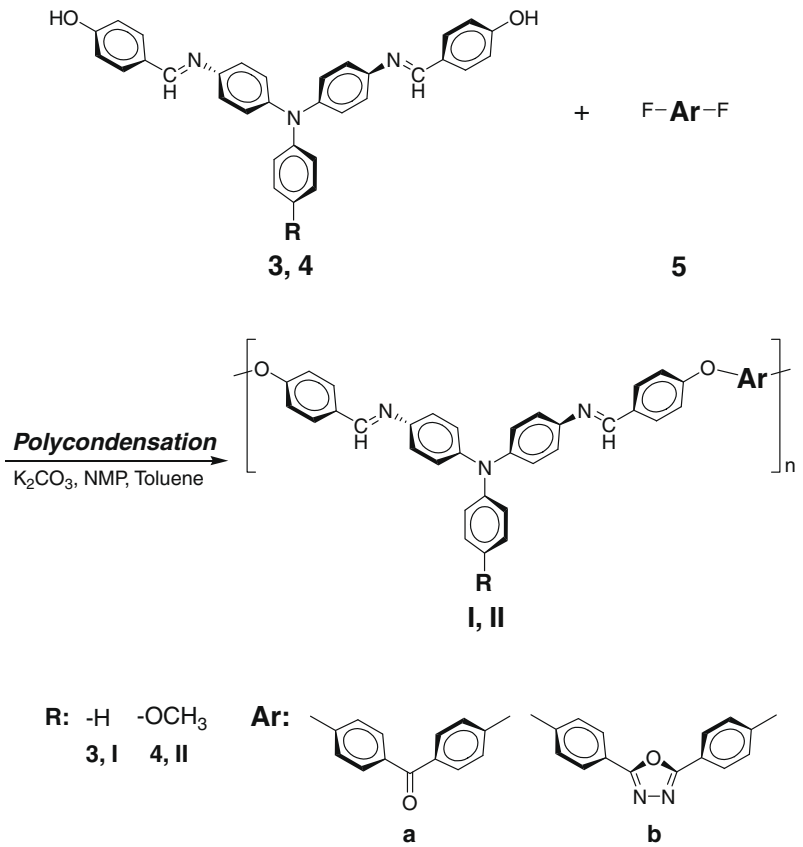

Scheme 2. Synthesis of aromatic PAMEs.

2.4. Preparation of the poly(azomethine-ether) films

A solution of polymer was made by dissolving the poly-ether sample in NMP. The homogeneous solution was poured into a glass Petri dish, which was placed in a 90 °C oven for 5 h to remove most of the solvent; then the semidried film was further dried *in vacuo* at 160 °C for 8 h. The obtained films were used for solubility tests and thermal analyses.

Table 1
Inherent viscosity[a] and solubility behavior of PAMEs.

Polymer	η_{inh} (dl/g)	Solubility in various solvent[b]						
		NMP	DMAc	DMF	DMSO	*m*-cresol	THF	$CHCl_3$
Ia	0.20	++	++	+–	+–	++	+–	+–
Ib	0.24	++	++	+–	+–	++	+–	+–
IIa	0.32	++	++	+–	+–	++	+–	+–
IIb	0.27	++	++	+–	+–	++	+–	+–

[a] Measured at a polymer concentration of 0.5 g/dl in NMP at 30 °C.
[b] The solubility was determined with a 2 mg sample in 2 ml of a solvent. ++, Soluble at room temperature; +, soluble on heating; +–, partially soluble or swelling; –, insoluble even on heating.

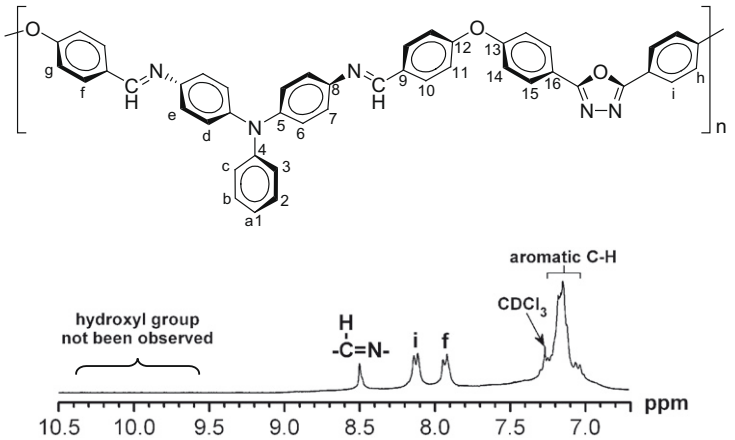

Fig. 3. ^1H NMR spectrum of PAME **Ib** in $CDCl_3$.

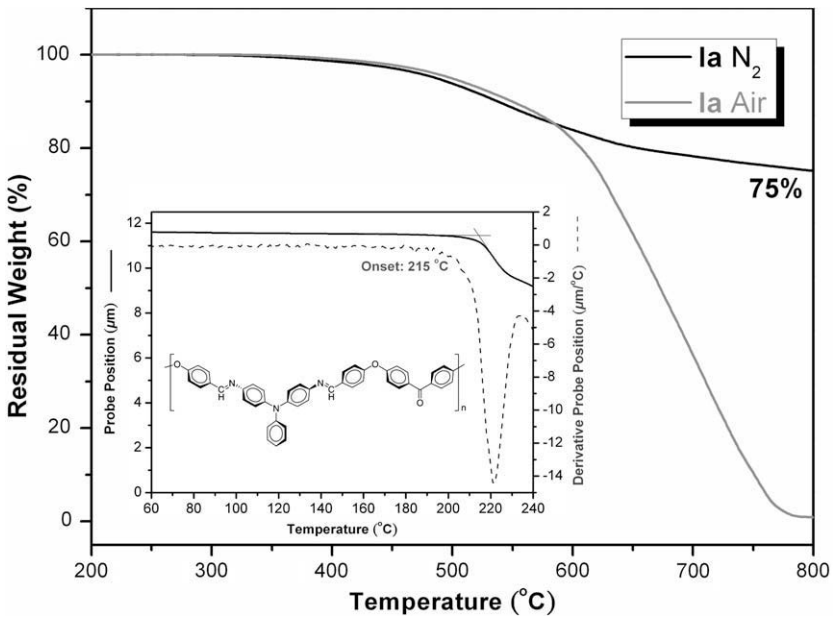

Fig. 4. TGA and TMA curves of PAME **Ia**.

Table 2
Thermal properties of PAMEs.

Polymer[a]	T_s (°C)[b]	T_d^5 (°C)[c]		T_d^{10} (°C)[c]		R_{w800} (%)[d]
		N_2	Air	N_2	Air	
Ia	215	490	500	540	550	75
Ib	219	480	480	510	515	68
IIa	227	460	475	505	525	64
IIb	240	450	460	485	495	65

[a] The polymer film samples were heated at 300 °C for 1 h prior to all the thermal analyses.
[b] Softening temperature measured by TMA with a constant applied load of 10 mN at a heating rate of 10 °C/min.
[c] Temperature at which 5% and 10% weight loss occurred, respectively, recorded by TGA at a heating rate of 20 °C/min and a gas flow rate of 30 cm^3/min.
[d] Residual weight percentages at 800 °C under nitrogen flow.

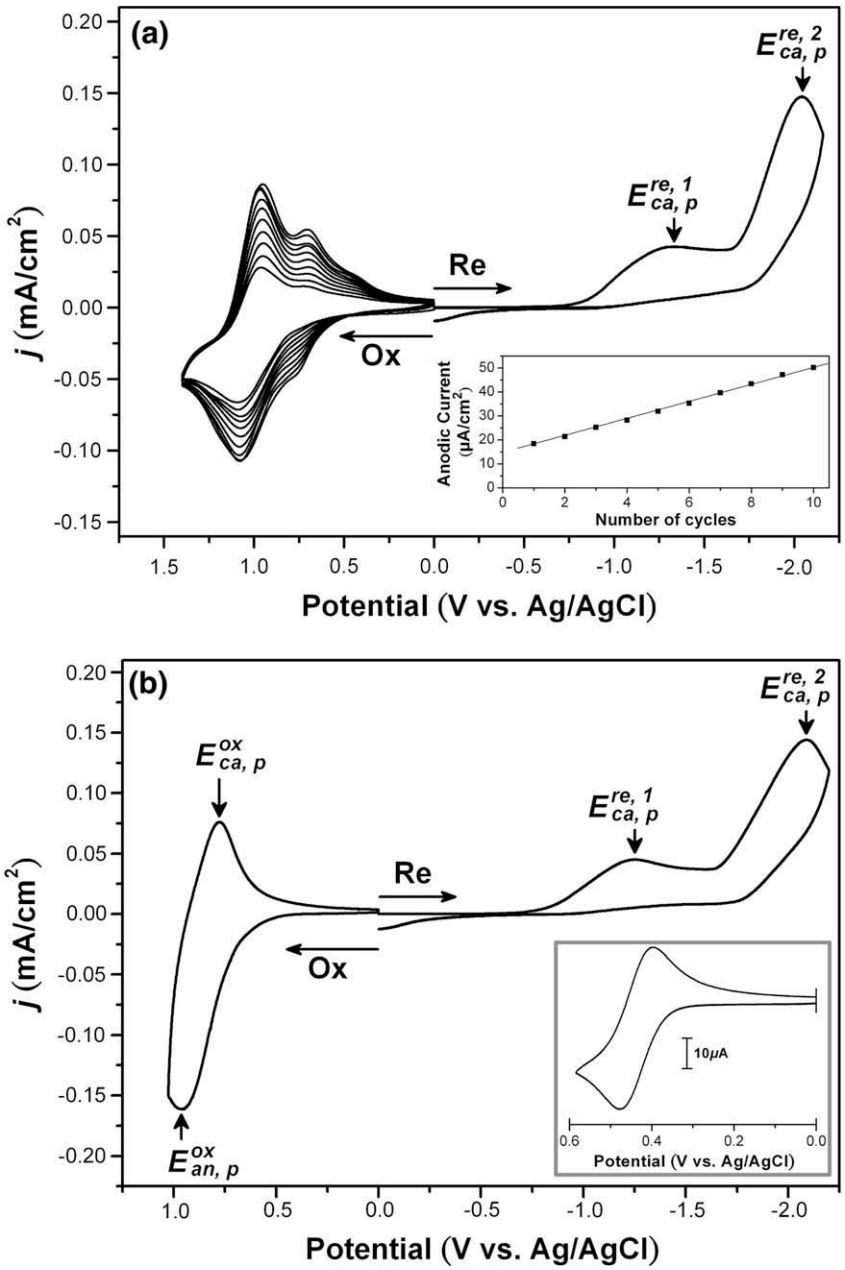

Fig. 5. Cyclic voltammogram of: (a) **Ia** and (b) **IIa** films on ITO-coated glass substrate in CH_3CN (oxidation) and DMF (reduction) solutions containing 0.1 M TBAP at scan rate of 50 and 100 mV/s, respectively. The inset showed a linear plot of the anodic current grown at 0.80 V vs. the number of scans and ferrocene, respectively.

2.5. Measurements

Elemental analyses were run in a Heraeus VarioEL-III CHNS elemental analyzer. Electrospray ionization (ESI) mass spectra were measured on LCQ Advantage mass spectrometer. NMR spectra were measured on a Bruker AC-300 MHz spectrometer in $CDCl_3$ and DMSO-d_6, and peak multiplicity was reported as follows: s, singlet; d, doublet; m, multiplet. The inherent viscosities were determined at 0.5 g/dl concentration using Tamson TV-2000 viscometer at 30 °C. Thermogravimetric analysis (TGA) was conducted with a PerkinElmer Pyris 1 TGA. Experiments were carried out on approximately 6–8 mg film samples heated in flowing nitrogen or air (flow rate = 20 cm^3/min) at a heating rate of 20 °C/min. Softening temperatures (T_s) were taken as the onset temperatures of probe displacement on the TMA traces. Electrochemistry was performed with a CH Instruments 611B electrochemical analyzer. Voltammo-

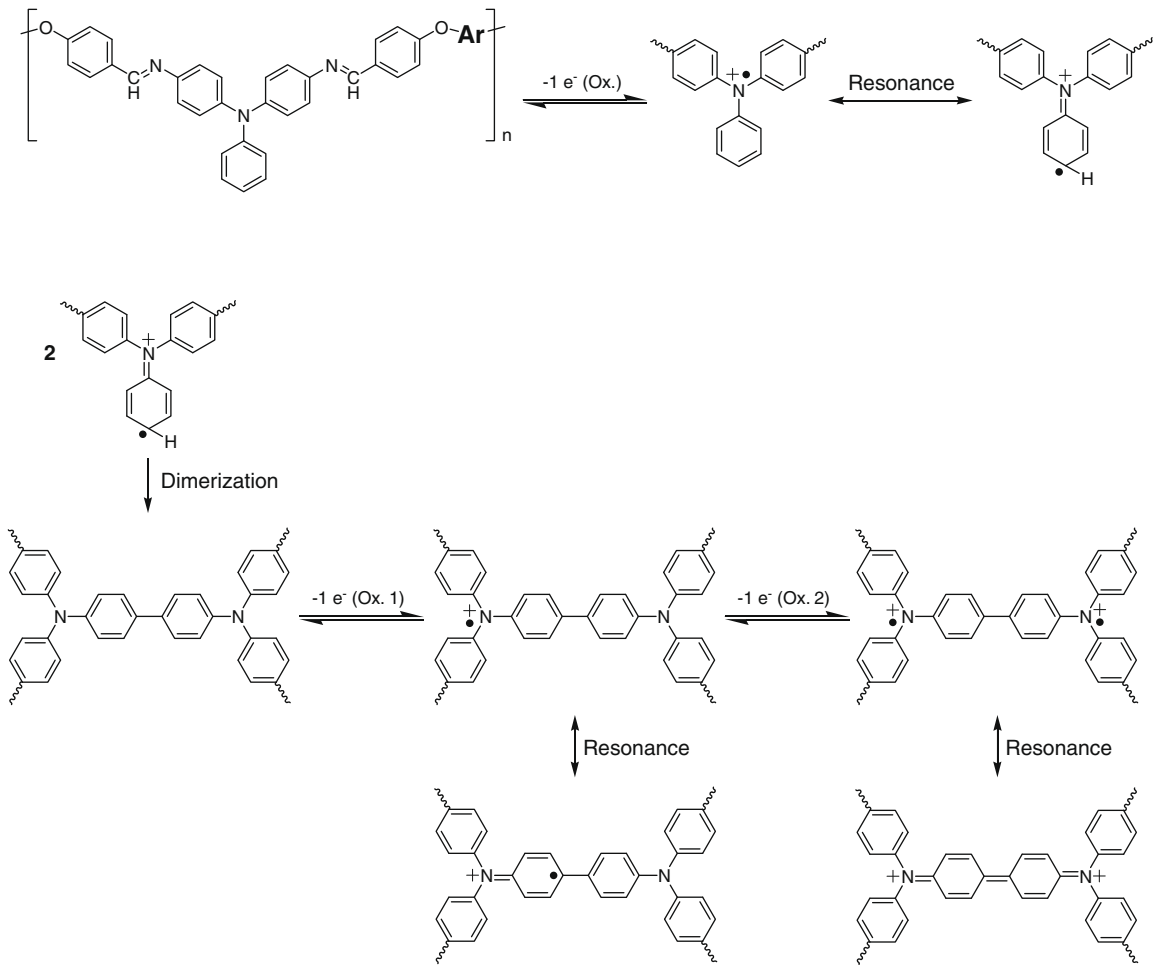

Scheme 3. Proposed reaction for electropolymerization of PAME **I**.

Table 3
Redox potentials and energy levels of PAMEs.

Index	Oxidation/V[a]		Reduction/V[b]			E_{HOMO} (eV)[c]	E_{LUMO} (eV)[c]	E_g (eV)[d]
	$E_{1/2}$	E_{onset}	E_{peak}		E_{onset}			
			1st	2nd				
Ia	1.03	0.82	−1.33	−2.04	−0.83	5.26	3.61	1.65
Ib	1.03	0.83	−1.31	−2.07	−0.79	5.27	3.65	1.62
IIa	0.87	0.70	−1.28	−2.06	−0.81	5.14	3.63	1.51
IIb	0.86	0.69	−1.27	−2.05	−0.77	5.13	3.67	1.46

[a] From cyclic voltammograms vs. Ag/AgCl in CH_3CN. $E_{1/2}$: average potential of the redox couple peaks.
[b] From cyclic voltammograms vs. Ag/AgCl in DMF.
[c] The energy levels were calculated from cyclic voltammetry and were referenced to ferrocene (4.8 eV; onset = 0.36 V).
[d] Difference between E_{HOMO} and E_{LUMO}.

grams were presented with the positive potential pointing to the left and with increasing anodic currents pointing downwards. Cyclic voltammetry (CV) was conducted with the use of a three-electrode cell in which ITO (polymer films area about 0.5 cm × 1.6 cm) was used as a working electrode. A platinum wire was used as an auxiliary electrode. All cell potentials were taken by using a homemade Ag/AgCl, KCl (sat.) reference electrode. Spectroelectrochemical experiments were carried out in a cell built from a 1 cm commercial UV–visible cuvette using Hewlett–Packard 8453 UV–Visible diode array and Hitachi U-4100 UV–vis-NIR spectrophotometer. The ITO-coated glass slide was used as the working electrode, a platinum wire as the counter electrode, and Ag/AgCl cell as the reference elec-

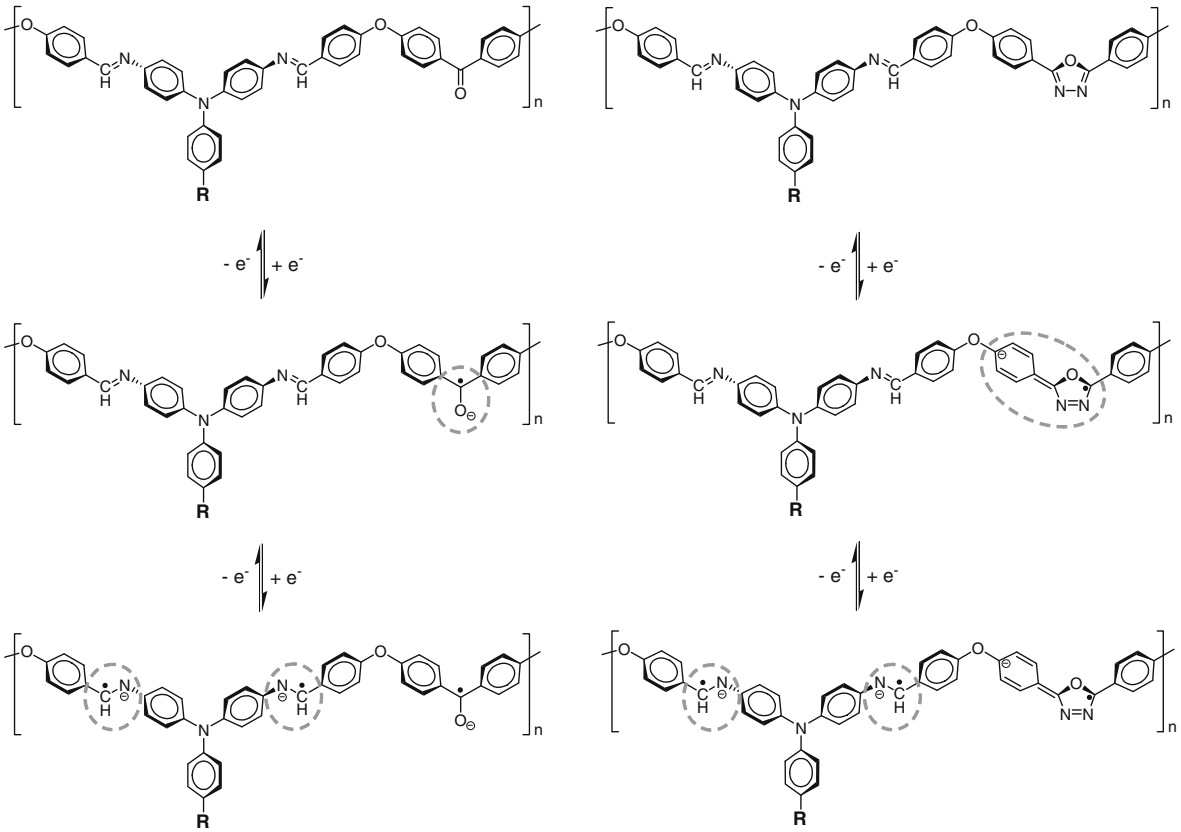

Scheme 4. Mechanism of the electrochemical reduction for PAMEs in an aprotic medium.

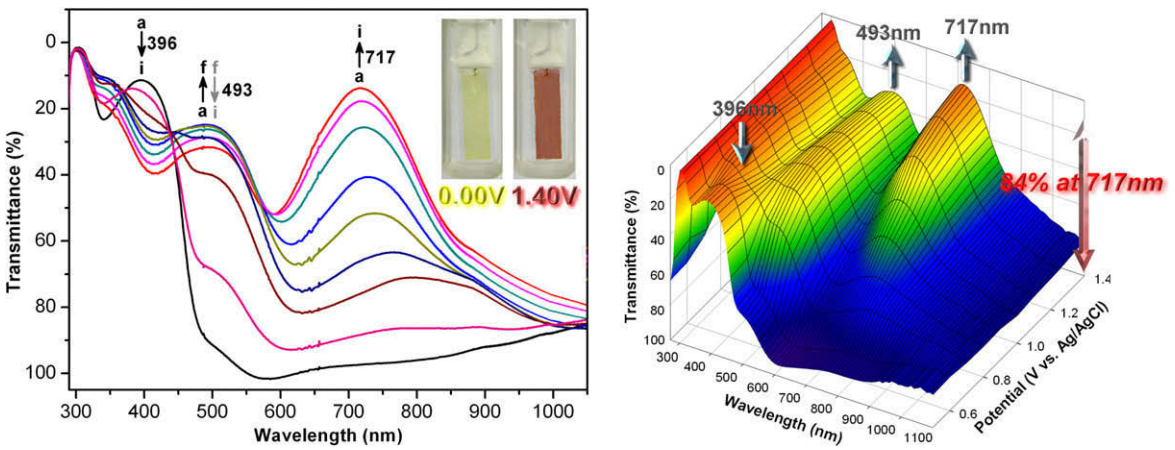

Fig. 6. Electrochromic behavior (left) at applied potentials of: (a) 0, (b) 0.60, (c) 0.70, (d) 0.80, (e) 0.90, (f) 1.00, (g) 1.10, (h) 1.25, (i) 1.40 (V vs. Ag/AgCl), and 3-D spectroelectrochemical behavior (right) from 0.50 to 1.40 (V vs. Ag/AgCl) of electropolymerized PAME **Ia** thin film (~160 nm in thickness) on the ITO-coated glass substrate in 0.1 M TBAP/CH_3CN.

trode. The thickness of the PAME thin films was measured by alpha-step profilometer (Kosaka Lab., Surfcorder ET3000, Japan). Colorimetry measurements were obtained using a Minolta CS-100A Chroma Meter. The color coordinates were expressed in the CIE 1931 *Yxy* color spaces.

3. Results and discussion

3.1. Monomer Synthesis

The new AM–TPA-based diol monomers **3** and **4** were synthesized by condensation reaction of the diamino compounds **1** and **2** with 4-hydroxybenzaldehyde, respectively (Scheme 1). Elemental analysis, MS, and NMR spectroscopic techniques were used to identify structures of the target diol monomers. Fig. 1 illustrates the ^{1}H NMR and ^{13}C NMR spectra of the diol monomer **4**. The ^{1}H and ^{13}C NMR chemical shift of CH=N at 8.46 and 158.1 ppm, respectively, were consistent with the previous reports (Fig. 1) [6b,18d]. The ^{1}H NMR chemical shift of Ar–OH shifts to low field at 10.08 ppm due to its acidity increased by the introduction of azomethine moiety. Assignments of each carbon and proton were assisted by the two-dimensional NMR spectra shown in Fig. 2, and these spectra agreed well with the proposed molecular structure.

3.2. Polymer synthesis

A series of newly TPA-based PAMEs were synthesized from the biphenol monomers **3** and **4** with corresponding difluoro compounds **5** (Scheme 2). The polymerization was carried out via potassium carbonate-mediated nucleophilic substitution reaction. All polymerization reactions proceeded homogenously and the obtained PAMEs had inherent viscosities in the range of 0.20–0.32 dl/g (Table 1). All the polymers could afford transparent and tough films via solution casting implying the formation of polymers with high molecular weight. Typical ^{1}H NMR spectrum of PAME **Ib** is illustrated in Fig. 3, and the hydroxyl group of diol monomer around 10 ppm disappeared for PAMEs confirming the completion of polymerization.

3.3. Polymer properties

3.3.1. Basic characterization

The solubility behavior of the PAMEs was investigated qualitatively, and the results were also summarized in Table 1. The TPA-based PAMEs showed good solubility in polar organic solvents such as NMP, *N,N*-dimethylacetamide (DMAc), and *m*-cresol. The enhanced solubility made these polymers as potential candidates for practical applications by spin-coating or inkjet-printing processes to afford high performance thin films for optoelectronic devices.

The thermal properties of PAMEs were examined by TGA and TMA and the typical TGA and TMA curves of representative PAME **Ia** were shown in Fig. 4, and the data were also listed in Table 2. All the prepared PAMEs exhibited good thermal stability with insignificant weight loss up to 400 °C under nitrogen or air atmosphere. The 10% weight loss temperatures of these polymers in nitrogen and air were recorded in the range of 485–540 and 495–550 °C, respectively. The concentration of carbonized residue (char yield) of these polymers in a nitrogen atmosphere was more than 64% at 800 °C. The high char yields of these polymers can be ascribed to their high aromatic content. The softening temperatures (T_s) of the polymer film samples were determined by the TMA method with a loaded penetration probe. They were obtained from the onset temperature of the probe displacement on the TMA traces and recorded in the range of 215–240 °C, depending upon the stiffness of the polymer chain.

3.3.2. Electrochemical properties

The electrochemical properties of the PAMEs were investigated by cyclic voltammetry (CV) conducted for the cast film on an indium–tin oxide (ITO)-coated glass substrate as working electrode in anhydrous CH_3CN and

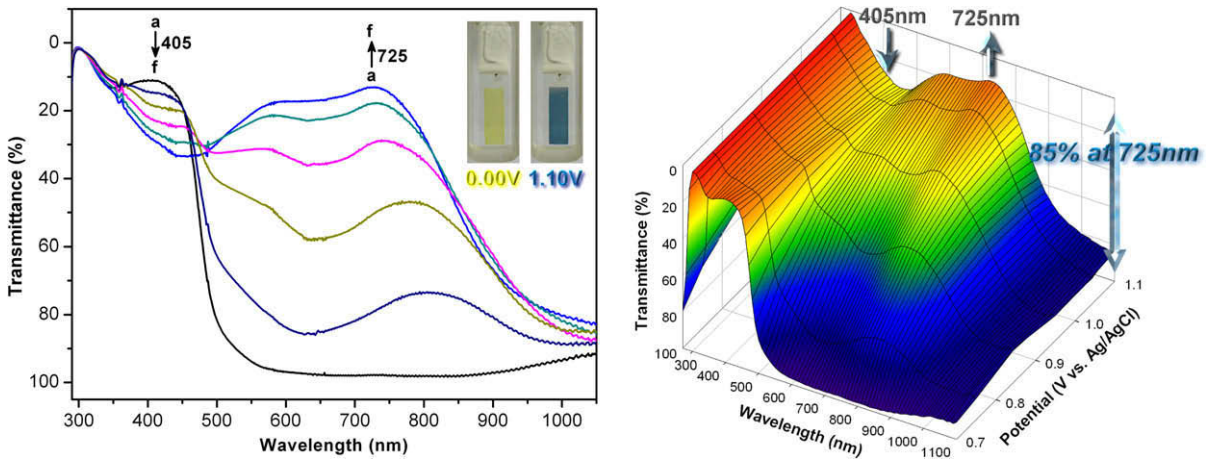

Fig. 7. Electrochromic behavior (left) at applied potentials of: (a) 0, (b) 0.75, (c) 0.85, (d) 0.95, (e) 1.05, (f) 1.10 (V vs. Ag/AgCl), and 3-D spectroelectrochemical behavior (right) from 0.70 to 1.10 (V vs. Ag/AgCl) of PAME **IIa** thin film (~160 nm in thickness) on the ITO-coated glass substrate in 0.1 M TBAP/CH_3CN.

DMF containing 0.1 M of TBAP as an electrolyte under nitrogen atmosphere for oxidation and reduction measurements, respectively. The typical CV for PAMEs **Ia** (without 4-methoxy-substituted) and **IIa** (with 4-methoxy-substituted) are shown in Fig. 5 for comparison, the results revealed one oxidation and two reduction processes for all the PAMEs. The PAME **IIa** (with 4-methoxy-substituted) exhibited lower oxidation potential than the corresponding **Ia** (without 4-methoxy-substituted) [20]. The cyclic voltammogram of PAME **Ia** indicated that TPA without 4-methoxy-substituted unit was irreversibly oxidized at applied potential range from 0 to 1.4 V upon repetitive scanning. A new pair of redox peaks corresponding to TPB was observed around 0.80 V from the second scan in Fig. 5a indicating the TPB formation during oxidation of the TPA moieties of PAME **Ia** (Scheme 3). As shown in the inset of Fig. 5a, the plot of the anodic current at 0.80 V was linearly proportional to the number of scans confirming the occurrence of the oxidative coupling at the *para*-position of TPA in PAME **I** main chains. As summarized in Table 3, the reduction behavior of PAMEs **Ia**, **IIa** and **Ib**, **IIb** were attributed the methanone and oxadiazole groups in the polymer main chain, respectively. In addition, the second reduction stage around −2.05 V could be assigned to the imine (CH═N) groups in the polymer main chains [22], and the mechanism for the electrochemical reduction of PAMEs could be depicted as in Scheme 4. During the electrochemical oxidation scanning of the PAME thin films, the color of

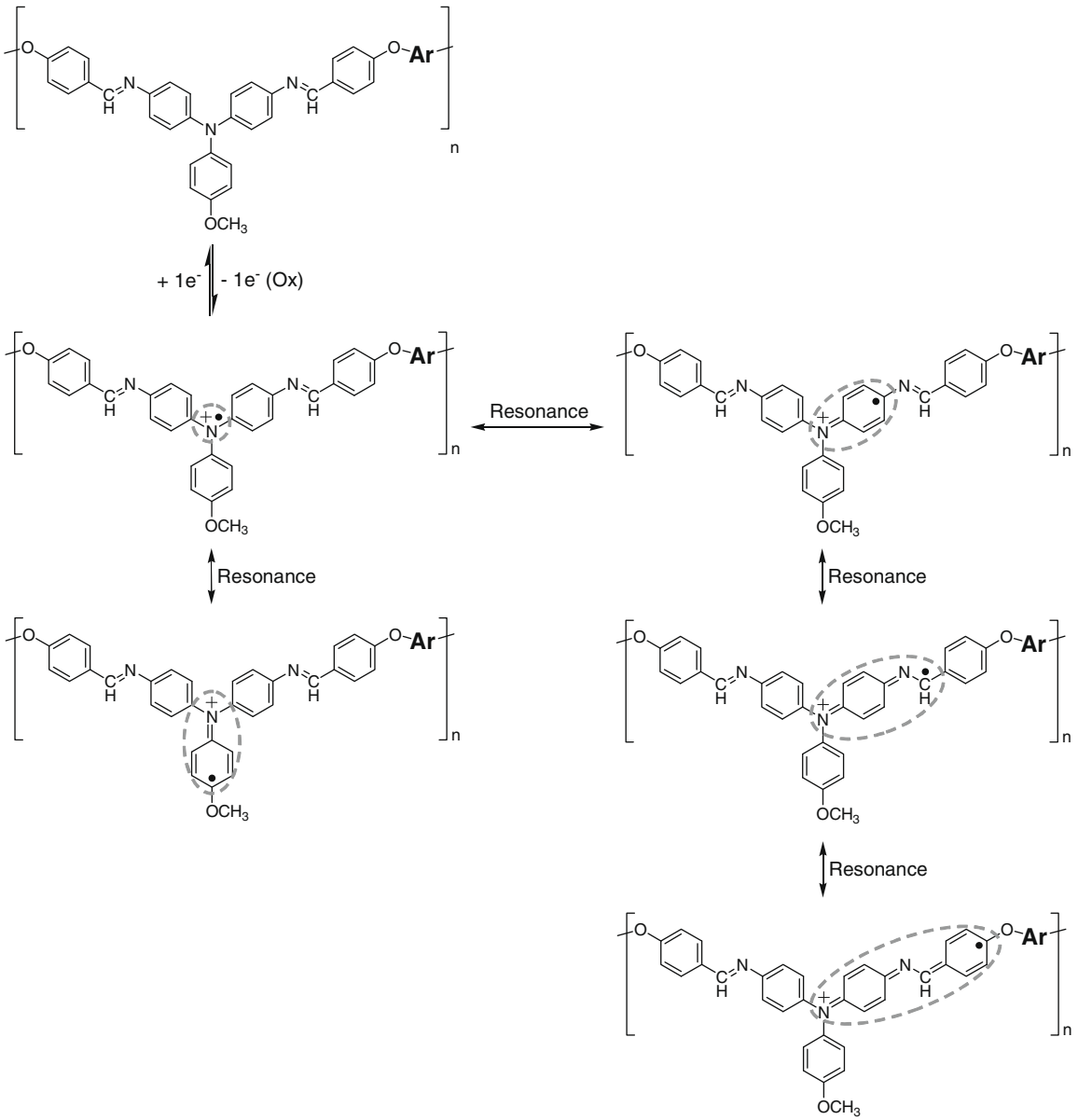

Scheme 5. Mechanism of the electrochemical oxidation for PAMEs **II**.

the film changed from yellow to red and blue for PAMEs **I** and **II**, respectively. The redox potentials of the PAMEs as well as their respective highest occupied molecular orbital (HOMO) and lowest unoccupied molecular orbital (LUMO) (on the basis of ferrocene/ferrocenium is 4.8 eV below the vacuum level with E_{onset} = 0.36 V) estimated from the onset of their oxidation or reduction in CV experiments were summarized in Table 3.

3.3.3. Spectroelectrochemical and electrochromic properties

Spectroelectrochemical experiments were used to evaluate the optical properties of the electrochromic films. The PAME film was cast on an ITO-coated glass slide, and was placed in the optical path of the light beam from a UV–vis-NIR spectrophotometer, which allowed us to acquire electronic absorption spectra under potential control in a 0.1 M TBAP/MeCN solution. The UV–vis-NIR absorbance curves correlated to applied potentials and three-dimensional transmittance-wavelength-applied potential correlation of after-oxidized **Ia** film were depicted in Fig. 6. The strong absorption at around 396 nm, characteristic for the charge-transfer complex (CTC) formation between the electron-donating TPB group and the strongly electron-accepting AM group in the neutral form (0 V), decreased and new peaks at 493 and 717 nm grew up steadily upon electrochemical oxidation (increasing applied voltage from 0 to 1.00 V). The one-electron oxidation product, a stable monocation radical TPB, exhibited absorption at 493 nm. As the anodic potential higher than 1.00 V, the absorption peak at 717 nm corresponding to the formation of a dication of TPB unit grew up. From the inset shown in Fig. 6, the PAME **Ia** film switched from a transmissive neutral state (light-yellow; *Y*: 74; *x*, 0.372; *y*, 0.444) to a highly absorbing oxidized state (red; *Y*: 13; *x*, 0.601; *y*, 0.351) with an high optical transmittance change ($\Delta\%T$) of 84%.

On the other hand, the spectroelectrochemical behavior of PAME **IIa** film shown in Fig. 7 also exhibited strong absorption at around 405 nm in the neutral form (0 V). Upon oxidation (increasing applied voltage from 0 to 1.10 V), the intensity of the absorption peak at 405 nm decreased while a new peak at 725 nm gradually increased in intensity due to the formation of a stable monocation radical of the AM–TPA unit. Furthermore, the broadened absorbance band was because of the monocation radical of AM–TPA unit having more extended conjugation length than TPA (Scheme 5), which resulted different and unique coloration from other TPA-based electrochromic materials [20,23]. From the inset shown in Fig. 7, the PAME **IIa** film switches from a transmissive neutral state (light-yellow; *Y*: 70; *x*, 0.374; *y*, 0.453) to a highly absorbing oxidized state (blue; *Y*: 10; *x*, 0.246; *y*, 0.305) with an high optical transmittance change ($\Delta\%T$) of 85% at 725 nm. Besides, the distribution of coloration across these polymer films was very homogeneous with high electrochemical stability.

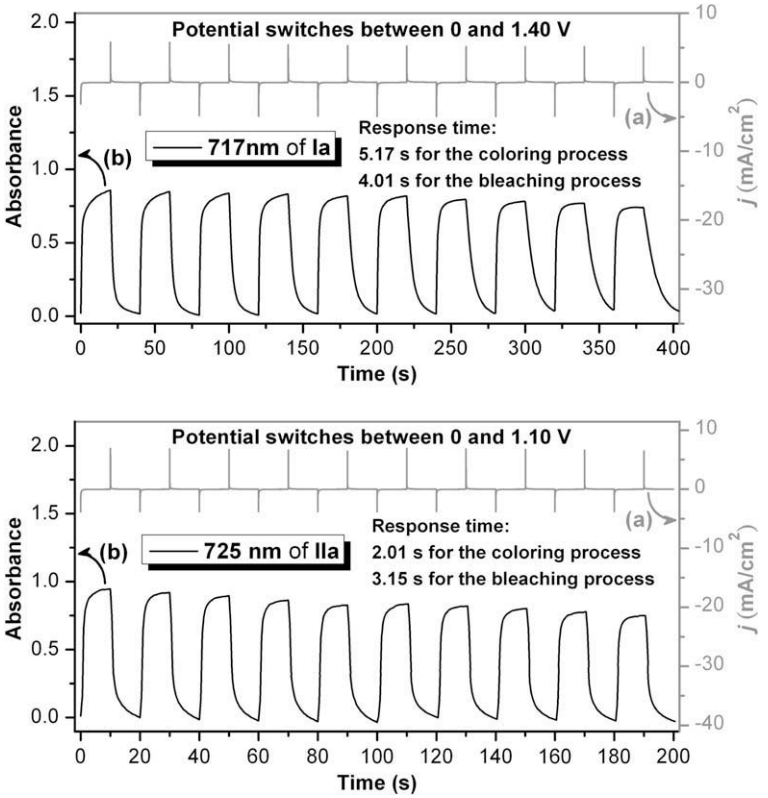

Fig. 8. (a) Current consumption and (b) electrochromic switching and absorbance change monitored for PAME thin films (~160 nm in thickness) on the ITO-coated glass substrate (coated area: 1.6 cm × 0.5 cm) in 0.1 M TBAP/CH_3CN.

For electrochromic switching studies, polymer films were cast on ITO-coated glass slides in the same manner as described above, and chronoamperometric and absorbance measurements were performed. While the films were switched, the absorbance at the given wavelength was monitored as a function of time with UV–vis-NIR spectroscopy (Fig. 8). The switching time was calculated at 90% of the full switch because it is difficult to perceive any further color change with naked eye beyond this point. The electrochromic coloration efficiency ($\eta = \delta OD/Q$) of PAMEs **Ia** and **IIa** are calculated as 162 and 195 cm^2/C, respectively [18j]. After several coloring/bleaching cyclic scans, the polymer films still exhibited good stability of electrochromic characteristics.

4. Conclusion

Two series of blue and red electrochromic aromatic PAMEs containing electroactive TPA moieties in the backbone were prepared from the potassium carbonate-mediated nucleophilic substitution reaction of newly azomethine–triphenylamine (AM–TPA)-based biphenol monomers with difluoro compounds. Introduction of electron-donating TPA groups to the polymer main chain not only afford high T_g and good thermal stability but also leads to good solubility of the PAMEs. All the obtained polymers revealed valuable electrochromic characteristics such as high contrast in visible region and unique blue/red electrochromic behavior, indicating the incorporation of azomethine groups into TPA-based polymers is a new approach for tuning the coloration changed.

Acknowledgement

The authors are grateful to the National Science Council of the Republic of China for its financial support of this work.

References

[1] (a) P.M.S. Monk, R.J. Mortimer, D.R. Rosseinsky, Electrochromism: Fundamentals and Applications, VCH, Weinheim, Germany, 1995;
(b) R.J. Mortimer, Chem. Soc. Rev. 26 (1997) 147–156;
(c) D.R. Rosseinsky, R.J. Mortimer, Adv. Mater. 13 (2001) 783–793;
(d) S. Liu, D.G. Kurth, H. Mohwald, D. Volkmer, Adv. Mater. 14 (2002) 225–228;
(e) T. Zhang, S. Liu, D.G. Kurth, C.F.J. Faul, Adv. Funct. Mater. 19 (2009) 642–652;
(f) A. Maier, A.R. Rabindranath, B. Tieke, Adv. Mater. 21 (2009) 959–963.
[2] C.J. Yang, S.A. Jenekhe, Chem. Mater. 3 (1991) 878–887.
[3] I.K. Spiliopoulos, J.A. Mikroyannidis, Macromolecules 29 (1996) 5313–5319.
[4] P. Cerrada, L. Oriol, M. Pinol, J.L. Serrano, I. Iribarren, S. Munoz Guerra, Macromolecules 29 (1996) 2515–2523.
[5] (a) N. Kiriy, V. Bocharova, A. Kiriy, M. Stamm, F.C. Krebs, H.J. Adler, Chem. Mater. 16 (2004) 4765–4771;
(b) G. Zotti, A. Randi, S. Destri, W. Porzio, G. Schiavon, Chem. Mater. 14 (2002) 4550–4557.
[6] (a) A. Kimoto, K. Masachika, J.S. Cho, M. Higuchi, K. Yamamoto, Chem. Mater. 16 (2004) 5706–5712;
(b) D. Sek, A. Iwan, B. Jarzabek, B. Kaczmarczyk, J. Kasperczyk, Z. Mazurak, M. Domanski, K. Karon, M. Lapkowski, Macromolecules 41 (2008) 6653–6663.
[7] M.K. Choi, H.L. Kim, D.H. Suh, J. Appl. Polym. Sci. 101 (2006) 1228–1233.
[8] (a) M. Cazacu, M. Marcu, A. Vlad, A. Tóth, C. Racles, J. Polym. Sci. Part A: Polym. Chem. 41 (2003) 3169–3179;
(b) J.M. Adell, M.P. Alonso, J. Barberá, L. Oriol, M. Piñol, J.L. Serrano, Polymer 44 (2003) 7829–7841.
[9] (a) H.H. Yang, Aromatic High Strength Fibers, Wiley, New York, 1989;
(b) H.R. Kricheldorf, G. Schwarz, Handbook of Polymer Synthesis, Part B, in: H.R. Kricheldorf (Ed.), Dekker, New York, 1992, pp. 1673–1684.
[10] T. Yamamoto, Z.H. Zhou, T. Kanbara, M. Shimura, K. Kizu, T. Maruyama, Y. Nakamura, T. Fukuda, B.L. Lee, N. Ooba, S. Tomaru, T. Kurihara, T. Kaino, K. Kubota, S. Sasaki, J. Am. Chem. Soc. 118 (1996) 10389–10399.
[11] (a) C. Wang, S. Shieh, E. LeGoff, M.G. Kanatzidis, Macromolecules 29 (1996) 3147–3156;
(b) O. Thomas, O. Inganas, M.R. Anderson, Macromolecules 31 (1998) 2676–2678.
[12] D.J. Klein, D.A. Modarelli, F.W. Harris, Macromolecules 34 (2001) 2427–2437.
[13] C.L. Chiang, C.F. Shu, Chem. Mater. 14 (2002) 682–687.
[14] T. Matsumoto, F. Yamada, T. Kurosaki, Macromolecules 30 (1997) 3547–3552.
[15] N. Giuseppone, G. Fuks, J.M. Lehn, Chem. Eur. J. 12 (2006) 1723–1735.
[16] (a) W. Fischer, F. Stelzer, F. Meghdadi, G. Leising, Synth. Met. 76 (1996) 201–204;
(b) M.S. Weaver, D.D.C. Bradley, Synth. Met. 83 (1996) 61–66.
[17] (a) T. Zhang, B. Toth, Anal. Chem. 72 (2000) 2533–2540;
(b) M. Oyama, K. Nozaki, S. Okazaki, Anal. Chem. 63 (1991) 1387–1392;
(c) S.C. Creason, J. Wheeler, R.F. Nelson, J. Org. Chem. 37 (1972) 4440–4446;
(d) E.T. Seo, R.F. Nelson, J.M. Fritsch, L.S. Marcoux, D.W. Leedy, R.N. Adams, J. Am. Chem. Soc. 88 (1966) 3498–3503.
[18] (a) S.H. Cheng, S.H. Hsiao, T.H. Su, G.S. Liou, Macromolecules 38 (2005) 307–316;
(b) G.S. Liou, S.H. Hsiao, N.K. Huang, Y.L. Yang, Macromolecules 39 (2006) 5337–5346;
(c) G.S. Liou, S.H. Hsiao, W.C. Chen, H.J. Yen, Macromolecules 39 (2006) 6036–6045;
(d) G.S. Liou, H.Y. Lin, Y.L. Hsieh, Y.L. Yang, J. Polym. Sci. Part A: Polym. Chem. 45 (2007) 4921–4932;
(e) G.S. Liou, C.W. Chang, Macromolecules 41 (2008) 1667–1674;
(f) S.H. Hsiao, G.S. Liou, Y.C. Kung, H.J. Yen, Macromolecules 41 (2008) 2800–2808;
(g) C.W. Chang, C.H. Chung, G.S. Liou, Macromolecules 41 (2008) 8441–8451;
(h) C.W. Chang, H.J. Yen, K.Y. Huang, J.M. Yeh, G.S. Liou, J. Polym. Sci. Part A: Polym. Chem. 46 (2008) 7937–7949;
(i) G.S. Liou, H.J. Yen, M.C. Chiang, J. Polym. Sci. Part A: Polym. Chem. 47 (2009) 5378–5385;
(j) H.J. Yen, G.S. Liou, Chem. Mater. 21 (2009) 4062–4070.
[19] Y. Oishi, H. Takado, M. Yoneyama, M. Kakimoto, Y. Imai, J. Polym. Sci. Part A: Polym. Chem. 28 (1990) 1763–1769.
[20] C.W. Chang, G.S. Liou, S.H. Hsiao, J. Mater. Chem. 17 (2007) 1007–1015.
[21] J.L. Hedrick, R. Twieg, Macromolecules 25 (1992) 2021–2025.
[22] İ. Kaya, S. Koyuncu, S. Çulhaoğlu, Polymer 49 (2008) 703–714.
[23] T.X. Su, S.H. Hsiao, G.S. Liou, J. Polym. Sci. Part A: Polym. Chem. 43 (2005) 2085–2098.

Organic Electronics 11 (2010) 311–321

Contents lists available at ScienceDirect

Organic Electronics

journal homepage: www.elsevier.com/locate/orgel

Synthesis of benzoselenadiazole-based small molecule and phenylenevinylene copolymer and their application for efficient bulk heterojunction solar cells

John A. Mikroyannidis [a,*], P. Suresh [b], G.D. Sharma [b,c,*]

[a] Chemical Technology Laboratory, Department of Chemistry, University of Patras, GR-26500 Patras, Greece
[b] Physics Department, Molecular Electronic and Optoelectronic Device Laboratory, JNV University, Jodhpur (Raj.) 342005, India
[c] Jaipur Engineering College, Kukas, Jaipur (Raj.), India

ARTICLE INFO

Article history:
Received 5 August 2009
Received in revised form 22 September 2009
Accepted 4 November 2009
Available online 10 November 2009

Keywords:
Low-band gap small molecule
Phenylenevinylene copolymer
Benzothiadiazole
Benzoselenadiazole
Organic photovoltaic solar cell
Bulk heterojunction

ABSTRACT

A new low-band gap small molecule (Se-SM), which contains dithyenyl-benzoselenadiazole as central unit and terminal cyanovinylene 4-nitrophenyls, was synthesized. In addition, a new phenylenevinylene copolymer (P) containing dithyenyl-dinitrobenzothiadiazole moieties was synthesized by Heck coupling. Se-SM showed broad absorption band with long-wavelength absorption maximum ($\lambda_{a,max}$) at ~640 nm and optical band gap (E_g^{opt}) of 1.67 eV. Copolymer P had $\lambda_{a,max}$ around 420 nm and E_g^{opt} of 2.31 eV. The dark current–voltage characteristics and incident photon to current efficiency spectra of the devices based on copolymer P and Se-SM indicates that both materials behave as p-type organic semiconductors. The power conversion efficiency (PCE) of the photovoltaic devices based on these materials is low. However, the PCE of the devices fabricated with the blends of copolymer P or Se-SM with PCBM, was improved significantly. The increase is attributed to the formation of bulk heterojunction with increased interfacial area. The effect of the incorporation of Se-SM molecule on the photovoltaic properties of copolymer P:PCBM blend has been also investigated. The overall PCE of the copolymer P:PCBM:Se-SM device is approximately 2.24%, which is further enhanced up to 3.16%, when the thermally annealed blend is used. Therefore, we conclude that the Se-SM molecule increases the light harvesting property of the blend and also provides efficient path for holes and electron in copolymer and PCBM phases, respectively.

© 2009 Elsevier B.V. All rights reserved.

1. Introduction

Conjugated polymer/fullerene bulk heterojunction (BHJ) solar cells have received increased attention because of their promising energy conversion efficiencies, solution processability, and their low cost of fabrication [1–14]. Power conversion efficiencies (PCEs), more than 5% have been reported for BHJ cells, incorporating a blend of conjugated polymer poly(3-hexylthiophene) (P3HT) as donor and fullerene derivatives as electron acceptor [5–14]. However, to achieve PCE values higher than 10%, nanoscale morphology of blend, transport properties in the device, band gap, band alignment, and device architecture must be optimized [4,15,16].

Since P3HT (with a band gap of about 1.9 eV) only absorbs up to 22% of the incident photons of solar spectrum [17], low-band-gap materials were expected to harvest more incident photons to further improve the efficiency of organic solar cells. However, BHJ devices made from

* Corresponding authors. Address: Physics Department, Molecular Electronic and Optoelectronic Device Laboratory, JNV University, Jodhpur (Raj.) 342005, India. Tel.: +91 0291 2720857; fax: +91 0291 2720856 (G.D. Sharma), tel.: +30 2610 997115; fax: +30 2610 997118 (J.A. Mikroyannidis).
E-mail addresses: mikroyan@chemistry.upatras.gr (J.A. Mikroyannidis), sharmagd_in@yahoo.com (G.D. Sharma).

1566-1199/$ - see front matter © 2009 Elsevier B.V. All rights reserved.
doi:10.1016/j.orgel.2009.11.010

these materials with PCBM are usually show low power conversion efficiency (<1%), with only a few of them demonstrated efficiencies in the range of 3–6% [18–27,9,28–35]. Most of them suffer from either (a) unmatched energy levels with respect to PCBM and thereby a low open circuit voltage (V_{oc}) or (b) low hole mobility and un-optimized morphology, leading to a low short circuit current (J_{sc}) and a small fill factor (FF).

Recently, several low-band gap conjugated polymers ($E_g < 1.8$ eV) have been employed as electron donor materials in BHJ solar cells [36,32]. Among these, benzothiadiazole-based copolymers were the most successful, showing a PCE in the range of ~1.0–5.5% [22,24,25,32]. The reasons for such high performance might be ascribed to the material properties, such as high hole mobility, structural stability in the charged state, as well as a broad absorption spectrum (E_g ~1.38 eV) [22]. Moreover, a possible route to overcome the low photovoltaic performance observed in a polymer solar cell may be the incorporation of a low-band gap small molecule [37,38]. Small molecules generally have high charge carrier mobility, monodispersity and relatively simple synthesis [39].

Color tuning to the deep-red and near-infrared (NIR) region in conjugated polymers can be also achieved by incorporating low-band gap Se-containing comonomer into the polymer backbone. Cao et al. first reported a polyfluorene copolymer with Se-containing heterocycle, benzoselenadiazole (BSeD), a selenium analogue of benzothiadiazole in different compositions [40]. He found out that incorporating Se-containing heterocycle (BSeD) into the polyfluorene main chain resulted in a significant red shift in comparison with its sulfur analogue. He also reported the synthesis and properties of the polyfluorene copolymer with another Se-containing heterocycle, 2,1,3-naphthoselenadiazole as a narrow band gap component [41]. Finally, Cao et al. reported the synthesis of two conjugated Se-containing heterocyclic monomers and their copolymerization with 9,9-dioctylfluorene. The copolymers derived, which had optical band gap of ~1.80 eV, were used for BHJ solar cells with PCBM and gave energy conversion efficiency up to 1% [42]. These results indicate that synthesizing Se-containing heterocycles with a narrower band gap moves the absorption band edge to a further deep-red or even NIR region without using the metallic complex ions.

Very recently, we have shown that the addition of a low-band gap benzothiadiazole-based small molecule in a conjugated phenylenevinylene copolymer:PCBM bulk heterojunction solar cell improves the photocurrent and power conversion efficiency [43]. In extension of this research line, we have synthesized a new low-band gap benzoselenadiazole-based small molecule (Se-SM) and incorporated it with a novel phenylenevinylene copolymer (P) for BHJ solar cells. The phenylenevinylene copolymer is a dithyenyl-dinitobenzothiadiazole derivative which was successfully synthesized by Heck coupling. The structures of Se-SM and P were designed so that the energy levels of the Se-SM lie between those of P and PCBM, in order to avoid a charge trapping in the small molecule. Both samples contain nitro groups in the terminal or the central units to broadening their absorption band [43,44]. Moreover, Se-SM contains two cyano-substituted vinylene bonds. The very strong electron withdrawing effect of the cyano group significantly affects the charge separation and charge transfer processes as well as the band gap energy of the molecule [45]. Copolymer P carries solubilizing hexyloxy side chains. The current–voltage characteristics and the incident photon to current efficiency (IPCE) spectra of the devices based on either copolymer P or Se-SM reveal that both materials behave as p-type organic semiconductors. The PCE of the devices based on blends with PCBM is about 0.52% and 1.30 for copolymer P and Se-SM, respectively. We have shown that the addition of the Se-SM small molecule in the copolymer P:PCBM bulk heterojunction solar cell increases the efficiency of the device, which is further improved up 3.16%, when thermally annealed P:PCBM:Se-SM blend is used as active layer in the device.

2. Experimental

2.1. Characterization methods

IR spectra were recorded on a Perkin–Elmer 16PC FT-IR spectrometer with KBr pellets. ^{1}H NMR (400 MHz) spectra were obtained using a Brucker spectrometer. Chemical shifts (δ values) are given in parts per million with tetramethylsilane as an internal standard. UV–vis spectra were recorded on a Beckman DU-640 spectrometer with spectrograde THF. TGA was performed on a DuPont 990 thermal analyzer system. Ground samples of about 10 mg each were examined by TGA and the weight loss comparisons were made between comparable specimens. Dynamic TGA measurements were made at a heating rate of 20 °C/min in atmospheres of N_2 at a flow rate of 60 cm^3/min. Thermomechanical analysis (TMA) was recorded on a DuPont 943 TMA using a loaded penetration probe at a scan rate of 20 °C/min in N_2 with a flow rate of 60 cm^3/min. The TMA experiments were conducted at least in duplicate to ensure the accuracy of the results. The TMA specimens were pellets of 10 mm diameter and ~1 mm thickness prepared by pressing powder of sample for 3 min under 8 kp/cm^2 at ambient temperature. The T_g is assigned by the first inflection point in the TMA curve and it was obtained from the onset temperature of this transition during the second heating. Elemental analyses were carried out with a Carlo Erba model EA1108 analyzer.

2.2. Reagents and solvents

1,4-Divinyl-2,5-bis(hexyloxy)-benzene was prepared by Stille coupling reaction of 1,4-dibromo-2,5-bis(hexyloxy)-benzene with tributylvinyltin [46]. *N,N*-Dimethylformamide (DMF) and tetrahydrofuran (THF) were dried by distillation over CaH_2. Triethylamine was purified by distillation over KOH. All other reagents and solvents were commercially purchased and were used as supplied.

2.3. Synthesis of compounds and copolymer

2.3.1. Compound 4

A flask was charged with a solution of **3** (0.38 g, 1.09 mmol) in 1,2-dichloroethane (30 mL). DMF (0.26 g,

3.61 mmol) and $POCl_3$ (0.55 g, 3.61 mmol) are added dropwise and the mixture was refluxed for 17 h under N_2. After cooling to room temperature and addition of dichloromethane (20 mL) and a saturated aqueous solution of sodium acetate (30 mL), the mixture was stirred for 2 h at room temperature. The organic phase was then washed with water and dried over $MgSO_4$. Solvent removal and column chromatography (silica gel/dichloromethane) gave 4 (0.27 g, 61%).

FT-IR (KBr, cm^{-1}): 1630, 1588, 1412, 1338, 1266, 1160, 1074, 1016, 908, 780, 670, and 614.

^1H NMR ($CDCl_3$) ppm: 9.90 (s, 2H, CHO); 7.80 (m, 2H, benzoselenadiazole); 7.23 (m, 4H, thiophene).

Anal. Calcd. for $C_{16}H_8N_2O_2S_2Se$: C, 47.65; H, 2.00, N, 6.95. Found: C, 46.20; H, 1.74, N, 6.37.

2.3.2. Compound Se-SM

A flask was charged with a solution of 4 (0.75 g, 1.09 mmol) and 4-nitrobenzyl cyanide (0.35 g, 2.18 mmol) in anhydrous ethanol (20 mL). Sodium hydroxide (0.20 g, 5.00 mmol) which was dissolved in anhydrous ethanol (20 mL) was added portionwise to the stirred solution. The mixture was stirred for 1 h at room temperature under N_2 and then was concentrated under reduced pressure. Compound Se-SM precipitated as a dark-green solid by concentration and subsequent cooling into a refrigerator. It was filtered off, washed thoroughly with water and dried. The crude product was purified by dissolution in THF and precipitation in methanol (0.43 g, 57%).

FT-IR (KBr, cm^{-1}): 2154, 1654, 1586, 1522, 1440, 1344, 1288, 1184, 1106, 1016, 854, 702.

^1H NMR ($CDCl_3$) ppm: 8.15 (m, 4H, phenylene ortho to nitro); 7.81 (m, 2H, benzosenadiazole); 7.70 (s, 2H, olefinic); 7.46 (m, 4H, phenylene meta to nitro); 7.22 (m, 4H, thiophene).

Anal. Calcd. for $C_{32}H_{16}N_6O_4S_2Se$: C, 55.57; H, 2.33, N, 12.15. Found: C, 54.73; H, 2.12, N, 11.85.

2.3.3. Copolymer P

A flask was charged with a mixture of 9 (0.4887, 0.891 mmol) 1,4-divinyl-2,5-bis(hexyloxy)benzene (0.2944 g, 0.891 mmol), $Pd(OAc)_2$ (0.0083 g, 0.037 mmol), P(*o*-tolyl)$_3$ (0.0624 g, 0.205 mmol), DMF (5 mL) and triethylamine (3 mL). The flask was degassed and purged with N_2. The mixture was heated at 90 °C for 24 h under N_2. Then, it was filtered and the filtrate was poured into methanol. The precipitate was filtered and washed with methanol. The crude product was purified by dissolution in THF and precipitation in methanol (0.46 g, 72%).

FT-IR (KBr, cm^{-1}): 2956, 2926, 2868, 1592, 1538, 1464, 1378, 1270, 1210, 1156, 1064, 962, 874, and 702.

^1H NMR ($CDCl_3$) ppm: 7.33 (m, 4H, olefinic); 7.08 (m, 4H, thiophene); 7.04 (m, 2H, phenylene); 3.94 (m, 4H, $OCH_2(CH_2)_4CH_3$); 1.80 (m, 4H, $OCH_2CH_2(CH_2)_3CH_3$); 1.33 (m, 12H, $O(CH_2)_2(CH_2)_3CH_3$); 0.92 (t, J = 7.7 Hz, 6H, $O(CH_2)_5CH_3$).

Anal. Calcd. for $C_{34}H_{36}N_4O_6S_3$: C, 58.94; H, 5.24, N, 8.08. Found: C, 57.49; H, 5.10, N, 7.85.

2.4. Electrochemical characterization

The position of the HOMO and LUMO energy levels were estimated by cyclic voltammetry measurements. This was performed on an Autolab Potentiostat PGSTAT-10, equipped with a three electrode system, in an acetonitrile solution (0.1 M) of 4-tert-butylpyridine at a potential scan of 0.05 V/s at room temperature. Three electrode systems were composed of a glassy carbon electrode coated with a thin film of copolymer P, Se-SM and PCBM, Pt and Ag electrode. The electrochemical potential was calibrated against ferrocene/ferrocenium (Fc/Fc^+).

2.5. Device fabrication and characterization

For the photovoltaic device fabrication, indium tin oxides (ITO) coated glass substrates were cleaned with detergent, de-ionized water and acetone and then dried at room temperature. The PEDOT:PSS was spin coated upon the ITO coated substrates and then dried at a temperature of 60 °C. Then the active layers copolymer P, Se-SM, P:PCBM (1:1), Se-SM:PCBM (1:1) and P:Se-SM:PCBM (1:0.5:1) were spin coated on PEDOT:PSS coated ITO substrates from a THF at 1500 rpm. The thickness of the photoactive layers is about 100 nm. Finally, the Al electrode was thermally evaporated on the top of the photoactive layer under vacuum ($\sim 10^{-5}$ Torr) to make the sandwiched structure ITO/PEDOT:PSS/organic photoactive layer/Al. The effective area of the devices is about 25 mm^2. For the thermal annealing of photoactive layer, photoactive layer deposited on the PEDOT:PSS coated ITO substrate was placed on a hot plate at 100 °C for 10 min and then cooled up to room temperature, before the final Al electrode was deposited. Current–voltage characteristics of the devices were recorded with a Keithley electrometer with a built-in power supply in the dark and under a white light illumination intensity of 100 mW/cm^2. The 100 W halogen lamp calibrated for 1.5 AM sunlight spectrum was used as light source. The intensity of the lamp was calibrated and adjusted using a energy meter equipped with silicon detector. The incident photon to current efficiency (IPCE) of the devices was measured by illuminating the device with a halogen lamp using a monochromator and measuring the resulting photocurrent with a Keithley electrometer under short circuit conditions. All the fabrications and characterization were performed in an ambient environment.

3. Results and discussion

3.1. Synthesis and characterization of small molecule Se-SM

The Se-containing small molecule (Se-SM) was synthesized by a five-step reaction sequence which is outlined in Scheme 1. Specifically, compounds **1** [47], **2** [48] and **3** [48] were synthesized according to reported methods. Dialdehyde **4** was prepared by formylation of **3** using DMF and $POCl_3$. Finally, the condensation of **4** with 4-nitrobenzyl cyanide in ethanol in the presence of NaOH afforded Se-SM. It precipitated from the reaction mixture as a dark-green solid and was purified by dissolution in THF and

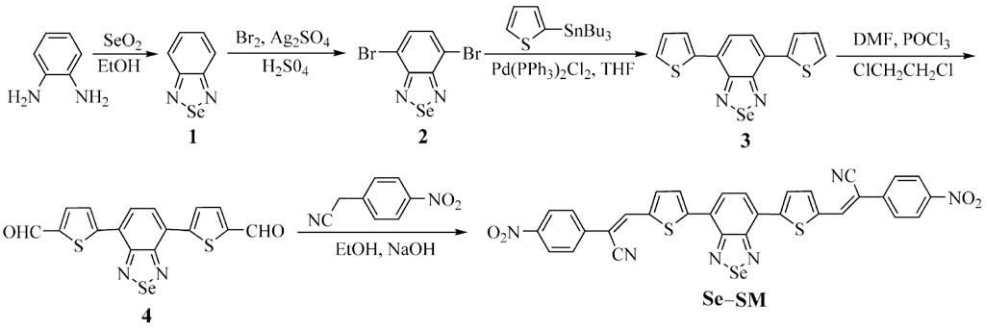

Scheme 1. Synthesis of small molecule Se-SM.

precipitation into methanol. Se-SM was soluble in THF, dichloromethane, chloroform and other common organic solvents. Thin films of Se-SM could be obtained from its solution by spin-coating even though it was a small molecule.

Table 1
Thermal, optical and electrochemical properties of Se-SM and P.

Sample	Se-SM	P
T_d[a] (°C)	517	413
Y_c[b] (%)	76	57
T_g[c] (°C)	68	56
$\lambda_{a,max}$[d] in solution (nm)	650	422
$\lambda_{a,max}$[d] in thin film (nm)	640	426
E_g^{opt}[e] (eV)	1.67	2.31
E_{onset} (red) (V)	−1.15	−1.95
HOMO (eV)	−5.25	−5.1
E_{onset} (ox) (V)	0.55	0.40
LUMO (eV)	−3.55	−2.75
E_g^{el}[f] (eV)	1.70	2.35

The HOMO and LUMO energy levels were calculated according to the equation: $-E_{LUMO} = E_{onset}$ (red) + 4.7 eV and $-E_{HOMO} = E_{onset}$ (ox) + 4.7 eV, where E_{onset} (ox) and E_{onset} (red) are the onset potentials for the oxidation and reduction processes of sample thin films vs. Ag/Ag^+ electrode.

[a] Decomposition temperature corresponding to 5% weight loss in N_2 determined by TGA.

[b] Char yield at 800 °C in N_2 determined by TGA.

[c] Glass transition temperature determined by TMA.

[d] $\lambda_{a,max}$: the absorption maxima from the UV–vis spectra in THF solution or in thin film.

[e] E_g^{opt}: optical band gap determined from the absorption onset in thin film.

[f] E_g^{el}: electrochemical band gap determined from cyclic voltammetry. $E_g^{el} = E_{LUMO} - E_{HOMO}$.

The FT-IR and ^1H NMR spectra confirmed the chemical structure of Se-SM (see Section 2). In particular, it showed characteristic absorption bands at 2154 (cyano group); 1586, 1440 (aromatic); 1522, 1344 (nitro group); 1654 (C=C olefinic stretching vibration); 1288, 854, 702 (thiophene) and 1016 cm^{-1} (cyano-substituted trans olefinic bond). The ^1H NMR spectrum of Se-SM displayed upfield signals at 8.15 (phenylene ortho to nitro) and 7.81 (benzoselenadiazole). Finally, the olefinic, the aromatic meta to nitro and the thiophene protons resonated at 7.70, 7.46 and 7.22 ppm, respectively.

Se-SM exhibited high thermal stability, which was comparable with that of heat-resistant materials, due to the absence of aliphatic moieties. In particular, it had decomposition temperature (T_d) of 517 °C, char yield (Y_c) at 800 °C of 76% in N_2, by TGA, and glass transition temperature (T_g) of 68 °C, by TMA (Table 1).

3.2. Synthesis and characterization of copolymer P

Copolymer P was synthesized by a six-step reaction sequence which is presented in Scheme 2. Particularly, compounds **5** [49], **6** [49], **7** [50], **8** [50] and **9** [51] were synthesized according to the literature. The Heck coupling of dibromide **9** with an equivalent amount of 1,4-divinyl-2,5-bis(hexyloxy)benzene gave P. This reaction took place in DMF utilizing palladium catalyst and triethylamine as acid scavenger. The hexyloxy side chains enhanced the solubility of P making it very soluble in common organic solvents. The number average molecular weight (M_n) was 12,300, by GPC, with polydispersity of 2.6.

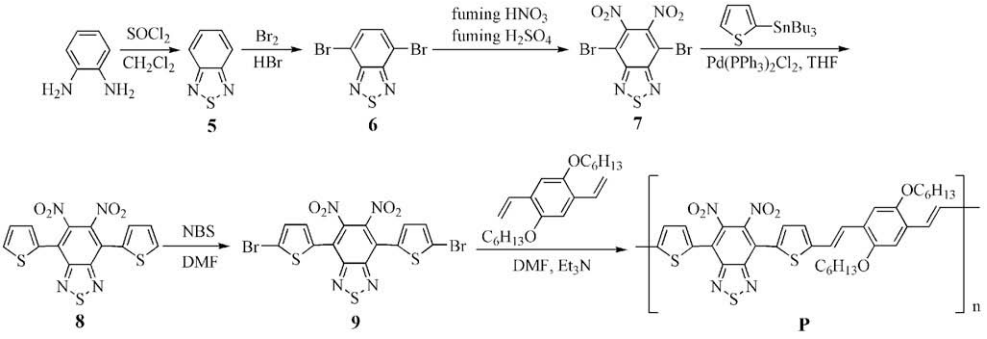

Scheme 2. Synthesis of copolymer P.

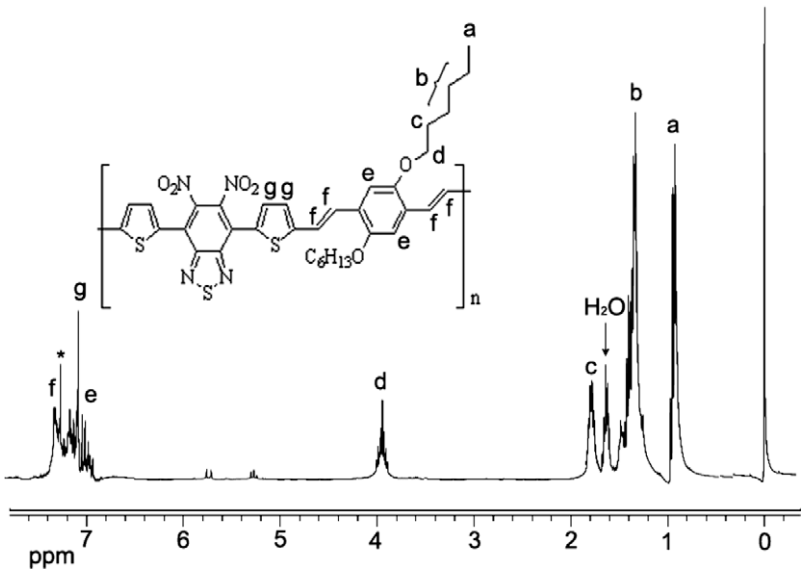

Fig. 1. ^{1}H NMR spectrum of copolymer P in $CDCl_3$ solution. The solvent peak is denoted by an asterisk.

The FT-IR spectrum of P showed characteristic absorptions at 2956, 2926 (C–H stretching of aliphatic segments); 1592, 1492, 1464 (aromatic); 1538, 1378 (NO_2); 1210, 1156 (ether bond); 1270, 874, 702 (thiophene) and 962 cm^{-1} (trans olefinic bond). The ^{1}H NMR spectrum (Fig. 1) displayed multiplets at 7.33, 7.08 and 7.04 ppm assigned to the olefinic, thiophene and phenylene protons, respectively. Finally, the aliphatic protons labelled "d", "c", "b" and "a" resonated at 3.94, 1.80, 1.33 and 0.92 ppm, respectively. The small peaks between 5 and 6 ppm are assigned to the terminal CH_2 = CH– groups.

Fig. 2 presents the TGA and TMA traces of P. No weight loss was observed up to ~300 °C. The T_d and Y_c were 413 °C and 57%, respectively (Table 1). Finally, the T_g, which was determined by TMA, was 56 °C. P exhibited lower thermal stability and T_g than Se-SM owing to the presence of the hexyloxy side chains in the former.

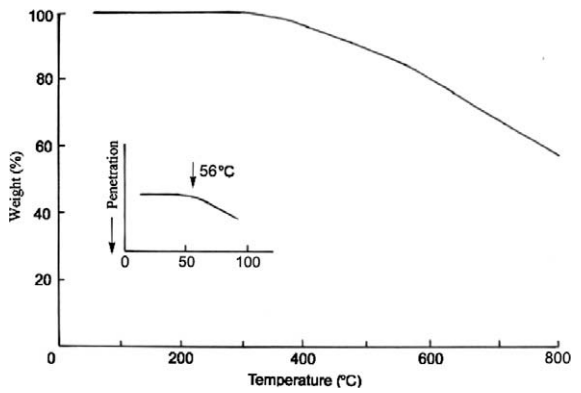

Fig. 2. TGA thermogram of copolymer P in N_2. The inset shows the TMA trace of this copolymer. Conditions: N_2 flow, 60 cm^3/min; heating rate, 20 °C/min.

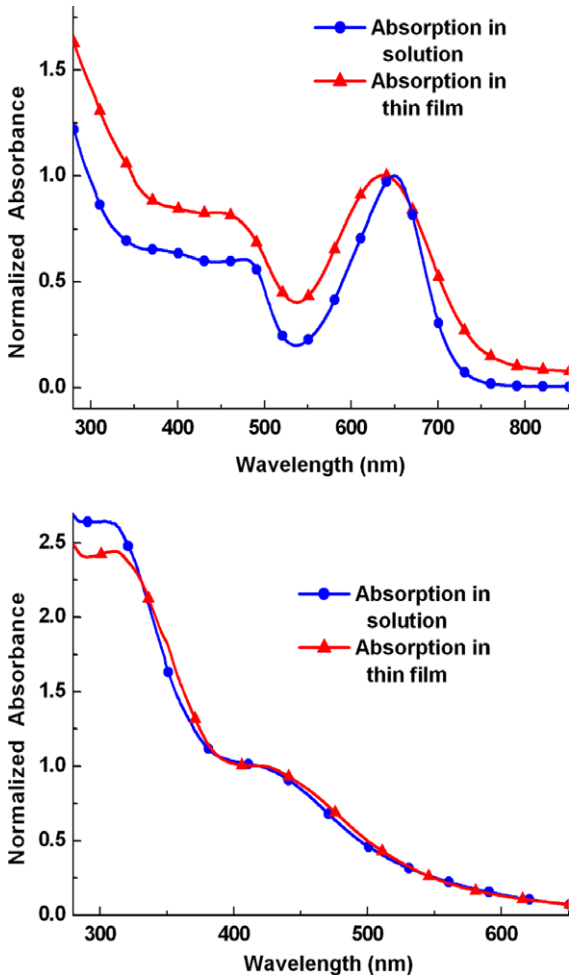

Fig. 3. Normalized UV–vis absorption spectra in solution and thin film of small molecule Se-SM (top) and copolymer P (bottom).

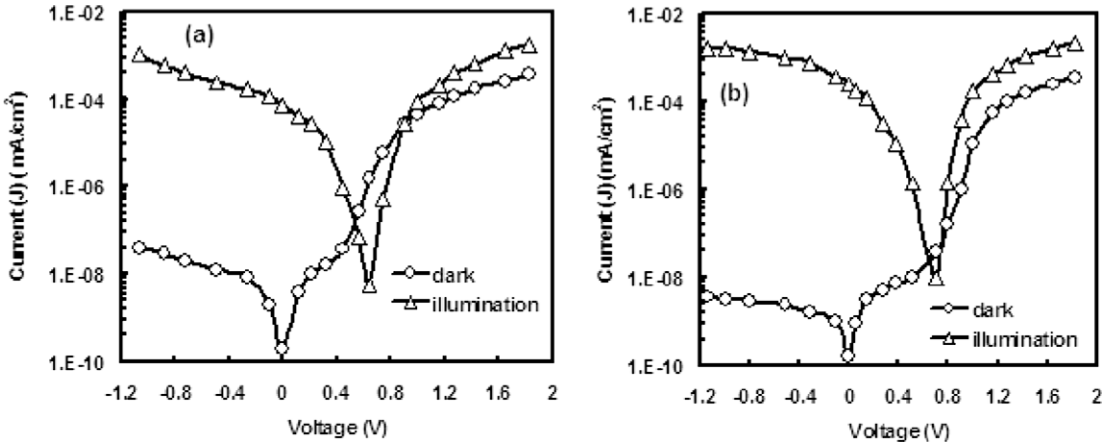

Fig. 4. Current–voltage characteristics in dark and under illumination for (a) ITO/PEDOT:PSS/copolymer P/Al and (b) ITO/PEDOT:PSS/Se-SM/Al devices.

3.3. Photophysical properties

Fig. 3 presents the UV–vis absorption spectra of Se-SM and P in both dilute (10^{-5} M) THF solution and thin film. They were normalized with respect the long-wavelength absorption peak. Table 1 summarizes all photophysical characteristics of these samples.

Se-SM showed a broad absorption bands (Fig. 3a) which were extended up to ~750 nm with long-wavelength absorption maximum ($\lambda_{a,max}$) at 650 for solution and 640 nm for thin film. This $\lambda_{a,max}$ was attributed to an intramolecular charge transfer between the central 4,7-di-2-thienyl-2,1,3-benzoselenadiazole and the terminal cyanovinylene 4-nitrophenyls. Similar absorption curves were obtained from other related compounds which have been synthesized in our laboratory [43,44]. The thin film absorption onset of Se-SM was located at 741 nm which corresponds to an optical band gap (E_g^{opt}) of 1.67 eV. The relatively low E_g^{opt} value of Se-SM suggests that this small molecule is attractive for photovoltaic applications.

Copolymer P displayed similar absorption curves (Fig. 3b) in solution and thin film which were extended about up to 500 nm with $\lambda_{a,max}$ at ~420 nm. The thin film absorption onset was at 536 nm corresponding to E_g^{opt} of 2.31 eV.

3.4. Electrical and photovoltaic properties of copolymer P and Se-SM

The current–voltage (J–V) characteristics of the ITO/PEDOT:PSS/copolymer P/Al and ITO/PEDOT:PSS/Se-SM/Al devices in dark and under illumination intensity of 100 mW/cm^2 are presented in Fig. 4. In these curves, the forward bias corresponds to the positive and negative voltage applied to ITO and Al electrode, respectively. It can be seen from this figure that the J–V characteristics show rectification effect. This can be explained by the high work function of ITO coated PEDOT:PSS and p-type semi-conductivity of both copolymer P and Se-SM. This indicates that the ITO/PEDOT:PSS/ and Al form Ohmic and Schottky barrier with both copolymer P and Se-SM, respectively. Since the HOMO level of both the copolymer P (−5.1 eV) and Se-SM (−5.25 eV) are very close to the Fermi level of PEDOT:PSS (−5.0 eV), forms a potential barrier of about 0.10 and 0.25 eV for hole injection from PEDOT:PSS into the HOMO of copolymer P and Se-SM, respectively, in their devices. This results in the formation of nearly Ohmic contact at ITO/PEDOT:PSS-organic layer. However, the Fermi level of Al (−4.3 eV) is very far from the LUMO of copolymer P (−2.8 eV) and Se-SM (−3.60 eV) thus forming a potential barrier of 1.5 and 0.9 eV for electron injection from Al to LUMO of the copolymer P and Se-SM, respectively, resulting a Schottky barrier contact. Therefore, the copolymer P behaves as p-type organic semiconductor.

We have estimated the hole mobility of copolymer P and Se-SM using the space charge limited current (SCLC) method [52]. The J–V characteristics of ITO/PEDOT:PSS/copolymer P/Au and ITO/PEDOT:PSS/Se-SM/Au devices in dark on log–log scale are shown in Fig. 5. It can be seen from this figure that in low voltage region, the log J is linearly dependent on the log V with a slope of unity. In the relatively high voltage region, the log J is also linearly

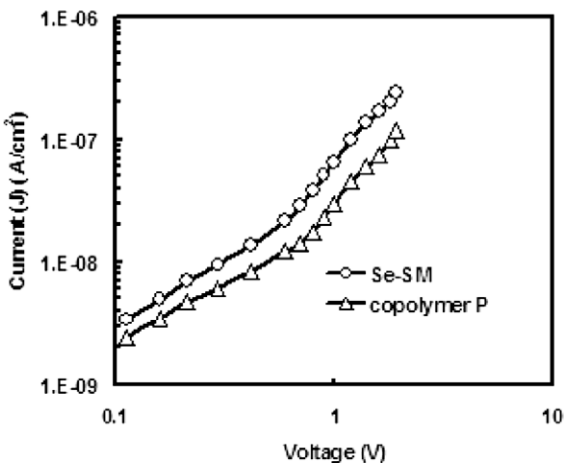

Fig. 5. Current–voltage curves in for devices based on copolymer P and Se-SM sandwiched between PEDOT:PSS coated ITO and Au electrodes in log–log scale.

dependent on the log V with a slope of two. The J–V curves in this region correspond to the trap free SCLC behavior. We estimated the hole mobility of the corresponding copolymer P and Se-SM, according to equation

$$J = \frac{9}{8}\varepsilon_r\varepsilon_o\mu_h\frac{(V - V_{bi})^2}{d^3} \quad (1)$$

where V is the applied voltage, J is the current density, ε_r and ε_o are the relative dielectric constant and permittivity of free space (8.85×10^{-12} F/m), respectively, μ_h is the hole mobility and d is the thickness of the organic layer and V_{bi} is the built-in potential which is determined by the difference between the work function of the electrodes. Using $\varepsilon_r = 3.5$, $d = 100$ nm and $V_{bi} = 0.8$ eV and fitting the curve in high voltage region with Eq. (1), the values of hole mobility are 2.3×10^{-5} cm^2/Vs and 3.4×10^{-4} for copolymer P and Se-SM, respectively.

The photovoltaic parameters, i.e., short circuit current (J_{sc}), open circuit voltage (V_{oc}), fill factor (FF) and power conversion efficiency (η) for the devices are listed in Table 2. It can be seen from this table that the open circuit voltage for both devices is almost the same and the J_{sc} for the ITO/PEDOT:PSS/Se-SM/Al device is higher than that for ITO/PEDOT:PSS/copolymer P/Al device. The V_{oc} for a Schottky barrier device is approximately equal to the work function difference between the electrodes used. In these devices we have used same electrodes and therefore the V_{oc} is quite similar. The higher value of the J_{sc} for the device based on Se-SM is attributed to the broad band absorption spectra and the low-band gap as compared to the copolymer P. The higher value of the hole mobility for the Se-SM also contributes to the higher photocurrent, resulting better charge transport in the device.

Table 2
Photovoltaic parameters of the devices using different photoactive layers sandwiched between ITO/PEDOT:PSS and Al electrodes.

Photoactive layer	Short circuit current (J_{sc}) (mA/cm^2)	Open circuit voltage (V_{oc})	Fill factor (FF)	Power conversion efficiency (η) (%)
P	0.07	0.64	0.31	0.014
Se-SM	0.25	0.74	0.38	0.07
P:PCBM	1.30	0.93	0.43	0.52
Se-SM:PCBM	2.7	0.98	0.49	1.30

In order to get more information about the formation of Schottky barrier, we measured the incident photon to current efficiency (IPCE) of both devices. The values of IPCE have been estimated using the following expression

$$\mathrm{IPCE}\,(\%) = 1240 J_{sc}/\lambda P_{in} \quad (2)$$

where J_{sc} (mA/cm^2) is the short circuit photocurrent, P_{in} (W/m^2) and λ (nm) is the illumination intensity and wavelength of the monochromatic light, respectively. The IPCE spectra of the ITO/PEDOT:PSS/copolymer P/Al and ITO/PEDOT:PSS/Se-SM/Al devices, illuminating through the Al and ITO side are shown in Fig. 6a and b. It can be seen from these figures that the shape of IPCE spectra of the devices, illuminating through the Al side closely follow the absorption spectra of the organic materials used in the device as photoactive layer. In organic photovoltaic devices, the photocurrent is due to the exciton generation upon the photoexcitation and their subsequent dissociation into free carrier at the Schottky barrier or p–n junction. Since the exciton diffusion length in most of organic semiconductors is in the range of 10–15 nm, the excitons that reaches the interface, only contributes to the photocurrent. When the device is illuminated through the Al electrode, photons corresponding to the absorption peaks of copolymer P and Se-SM are absorbed near the Al/copolymer P and Al/Se-SM in their respective devices due to the high absorption of photoactive material, generate the excitons in this region and subsequently dissociate into free carries due to the built-in field at the interface, resulting IPCE. However, photons corresponding to the low absorption coefficient of the organic materials, penetrate more into the bulk of the material. As a result, they are absorbed far from the Schottky barrier and generate excitons there. Therefore, only excitons that are generated within the distance 10–15 nm from the Schottky barrier (Al–organic layer interface), are able to reach the Schottky interface, contributes to the photocurrent. In this case only few excitons reach to the Schottky barrier and results low photocurrent in comparison to earlier case. On the other case, when the devices are illumi-

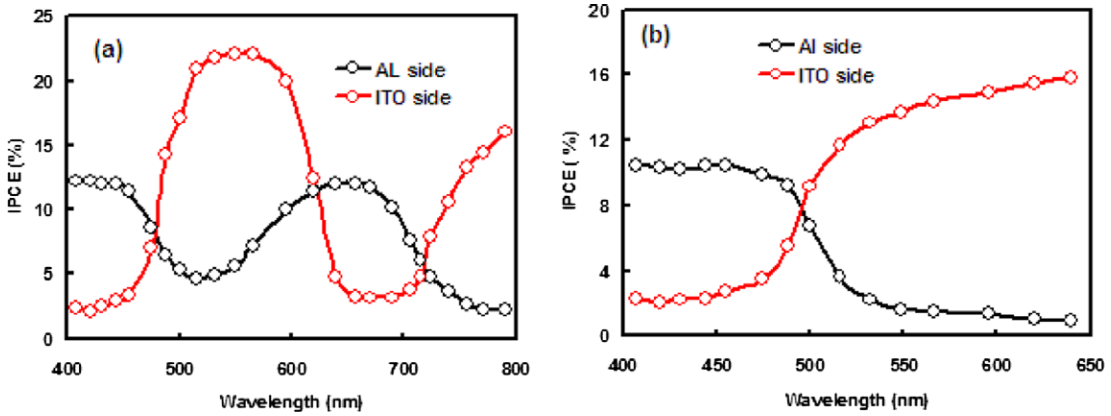

Fig. 6. IPCE spectra of (a) ITO/PEDOT:PSS/Se-SM/Al and (b) ITO/PEDOT:PSS/copolymer P/Al devices, illuminating through ITO and Al electrodes.

nated through the ITO side, only a few of the photons are able to reach the Schottky barrier, and therefore, cause limited generation of excitons leading to low photocurrent at the wavelength where the absorption coefficient is low. The excitons generated near to the Ohmic contact, i.e., ITO/PEDOT:PSS disappear due to recombination or trapping during their transportation through the organic layer towards the Schottky barrier. At the wavelengths where the absorption of the active layer is minimum, the light can penetrate deeper, allowing more excitons to be generated near the Schottky barrier, leading to higher photocurrent.

3.5. Photovoltaic properties of copolymer P or Se-SM blended with PCBM

The energy levels for the highest occupied molecular orbital (HOMO) and the lowest unoccupied molecular orbital (LUMO) of copolymer P and Se-SM were obtained by cyclic voltammetry with the method described by Bredas et al. [53] and are summarized in Table 1. The crucial factor for the effective photoinduced charge transfer in bulk heterojunction is the difference between the LUMO level of the donor and acceptor components used in the bulk heterojunction photoactive layer. This difference should be larger than that of the exciton binding energy, i.e., 0.3 eV. The difference in the LUMO levels of PCBM (acceptor) and copolymer P or Se-SM is higher. Therefore, the combination of PCBM and copolymer P or Se-SM is suitable for the photoactive layer to be used in a BHJ PV device.

Fig. 7 shows the *J–V* characteristics of the devices fabricated with copolymer P:PCBM and Se-SM:PCBM blends under the illumination intensity 100 mW/cm^2. The photovoltaic parameters of both devices are given in Table 2. The values of the power conversion efficiency of both devices are higher than those obtained for the devices fabricated with pristine copolymer P and Se-SM. This indicates that a BHJ is formed in the blend that increases the interfacial interface between the donor and acceptor. It can be seen from Table 2 that both short circuit current and open circuit voltage for the device using Se-SM:PCBM are higher than that for fabricated with copolymer P:PCBM. The higher short circuit current is attributed to the low-band gap and broad band absorption extending up to 800 nm of Se-SM and higher hole mobility in comparison to that for copolymer P, resulting to greater exciton generation in the Se-SM phase and better hole transport in the device.

In BHJ devices, if both electrodes form the Ohmic contact with the photoactive layer, the open circuit is mainly governed by the difference between the LUMO level of acceptor and HOMO level of the donor used in the device [54,55]. The work function of PEDOT:PSS almost matches the HOMO level of copolymer P or Se-SM, resulting in nearly ohmic contact for holes in the their respective BHJ devices, under the forward bias condition. On the other hand, the Al makes nearly Ohmic contact electron injection in the LUMO of PCBM. For this case the open circuit voltage is given by [54]

$$q(V_{oc} - \Delta V_b) = (\mathrm{HOMO})_{donor} - (\mathrm{LUMO})_{acceptor} \quad (3)$$

where ΔV_b is the sum of the voltage losses at each contact due to the band bending. The observed experimental values of V_{oc} for both devices are in agreement with Eq. (3). Since the position of the HOMO level for Se-SM (−5.25 eV) is more negative than that for copolymer P (−5.1 eV), results higher value of V_{oc} for device employing Se-SM:PCBM blend as compared to the device with copolymer P:PCBM blend.

3.6. Effect of incorporation of Se-SM in the copolymer P:PCBM blend

The photovoltaic performance of the photovoltaic devices using copolymer:PCBM and Se-SM:PCBM blends is low. A possible route to overcome this low performance

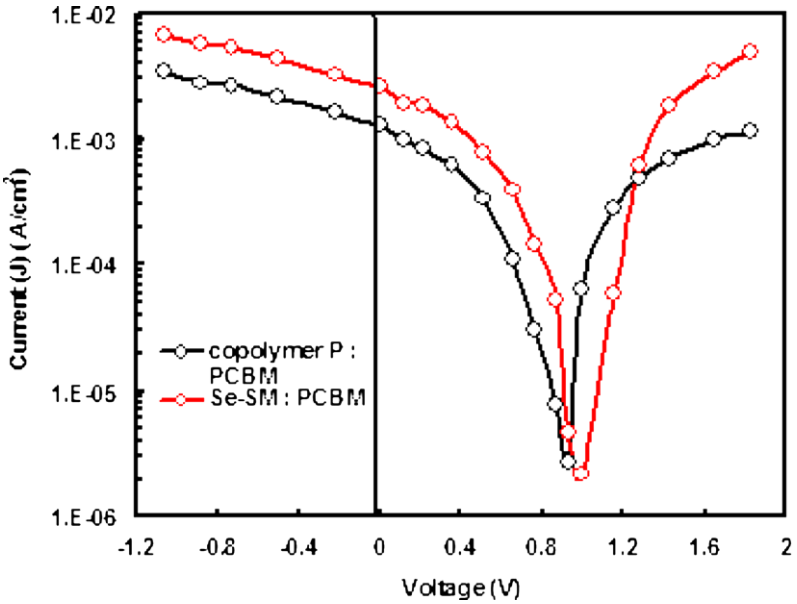

Fig. 7. Current–voltage characteristics of devices fabricated with copolymer:PCBM and Se-SM:PCBM blends under illumination.

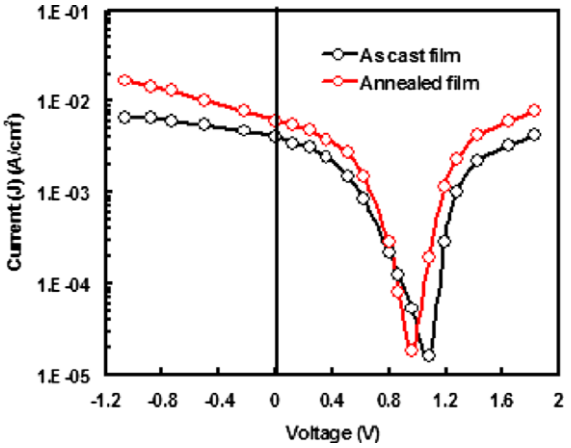

Fig. 8. Current–voltage characteristics of ITO/PEDOT:PSS/copolymer P:PCBM:Se-SM/Al devices.

might be to incorporate a low-band gap small molecule donor in the blend of polymer P:PCBM [56,57] blend with energy levels intermediate to those polymer and PCBM, in order to avoid the charge trapping in the small molecule. Since the energy levels of the Se-SM are located between the energy levels of copolymer P and PCBM, we have incorporated Se-SM in the copolymer P:PCBM blend to increase the power conversion efficiency.

Fig. 8 shows the *J–V* characteristics of the devices based on as cast and annealed copolymer P:PCBM:Se-SM blends under illumination intensity of 100 mW/cm^2. The photovoltaic parameters of the devices are summarized in Table 3. The incorporation of Se-SM in the blend improves both the short circuit current (J_{sc}) and the open circuit voltage (V_{oc}). However, the V_{oc} decreases when the annealed photoactive blend is used. This may be due to the increase in the crystalline nature of the copolymer that results in a decrease of V_{oc} because of the rise of HOMO level of the copolymer P. The rise in the HOMO level occurs as a result of increased inter-chain orbital delocalization [58]. The increase in J_{sc} with the addition of Se-SM is a result of increased absorption at the longer wavelength region, which is absent in the case of the copolymer P:PCBM blend. The absorption at the wavelength region leads increased exciton generation in the blend, and their subsequent dissociation into free charge carriers at the donor–acceptor (D–A) interfaces formed in the blend. Since Se-SM also acts as a donor, its incorporation also increases number of D–A interfaces in the blend that also increases the photoinduced charge separation.

In order to get more information about the origin of the increase in J_{sc} upon the addition of Se-SM in the copolymer P:PCBM blend, we have measured the IPCE spectra of the devices which are shown in Fig. 9. In the case of photovoltaic device based on blend without Se-SM, the IPCE peak is only in the region of 380–500 nm corresponding to the absorption spectrum of copolymer P. The increase in the IPCE of device with copolymer P:PCBM (Fig. 9b) upon thermal annealing is attributed to the increase in crystallization of the copolymer. On the other side, the device with copolymer P:PCBM:Se-SM exhibits two IPCE peaks appearing in the wavelength region of copolymer P absorption and also in the longer wavelength region of Se-SM absorption.

When the Se-SM is incorporated in copolymer P:PCBM blend, Se-SM may be located between (i) copolymer P and PCBM phases, (ii) PCBM phases and (iii) copolymer phases. The energy level diagram of the copolymer P, Se-SM, and PCBM is shown in Fig. 10. As shown in this figure, the excitons generated in Se-SM, when Se-SM is located between copolymer P and PCBM, inject electrons into PCBM and holes into copolymer P because the HOMO level of Se-SM is more negative than the HOMO level of copolymer P. However, when Se-SM is located at PCBM domain, Se-SM can only inject electrons into the PCBM domain but cannot inject holes into surrounding PCBM domain because of more negative HOMO level of PCBM. Similarly, when Se-SM is located between the copolymer P domains only holes are injected into the surrounding copolymer P. Therefore, only the Se-SM molecule, which is located between the copolymer P and PCBM, can contribute to the photocurrent.

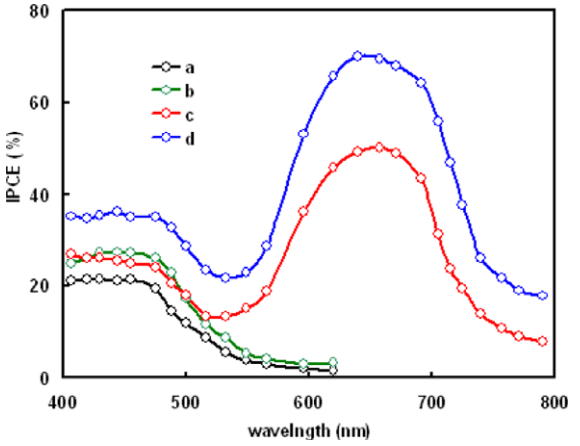

Fig. 9. IPCE spectra of the photovoltaic devices based on different blends (a) copolymer P:PCBM (as cast), (b) copolymer P:PCBM (annealed), (c) copolymer P:PCBM:Se-SM (as cast) and (d) copolymer P:PCBM:Se-SM (annealed).

Table 3
Effect of Se-SM incorporation in the copolymer P:PCBM blend on photovoltaic parameters.

Photoactive layer	Short circuit current (J_{sc}) (mA/cm^2)	Open circuit voltage (V_{oc}) (V)	Fill factor (FF)	Power conversion efficiency (η) (%)
P:PCBM:Se-SM (as cast)	4.1	1.05	0.52	2.24
P:PCBM:Se-SM (annealed)	6.1	0.92	0.54	3.16

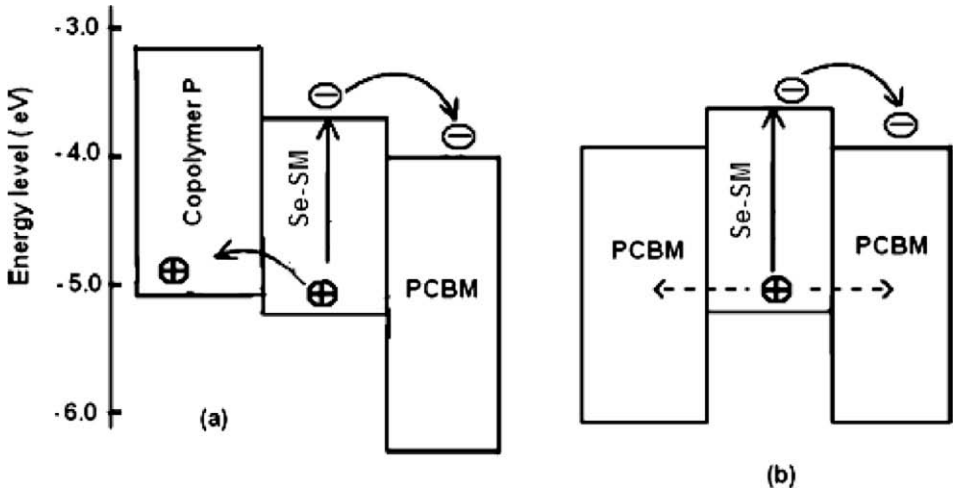

Fig. 10. Energy level diagram of Se-SM and surrounding materials: (a) Se-SM molecule is located between copolymer P and PCBM and (b) Se-SM molecule located in between two PCBM domains.

As can be seen from the IPCE spectra of the devices, the IPCE value at 640 nm increases from 48% to 70%, when the thermally annealed copolymer P:PCBM:Se-SM blend is used. However, it was observed that the optical absorption spectra do not change upon the thermal annealing. The increase in the IPCE may be attributed to the enhanced charge collection efficiency, which is improved by the formation of more crystalline nature interpenetrating network, upon thermal annealing. In addition to that, the number of the Se-SM molecules in between copolymer P and PCBM may increase upon thermal annealing because of the increased crystalline nature of the conjugated polymer and aggregation of the nano-crystalline PCBM domain. The Se-SM molecules located in the copolymer P or PCBM domain may be expelled from these domains into the interface between copolymer P and PCBM, upon thermal annealing. The combined effect of additional absorption at longer wavelength region by Se-SM molecules and Se-SM molecules located in between conjugated copolymer P and PCBM results the improvement in the J_{sc}, thereby increases the power conversion efficiency.

4. Conclusions

A new low-band gap Se-containing small molecule (Se-SM) and a phenylenevinylene copolymer (P) based on dithyenyl-dinitrobenzothiadiazole were synthesised and used for BHJ solar cells. The current–voltage characteristics in dark and IPCE spectra of devices using these materials show that both copolymer P and Se-SM behave as p-type organic semiconductor forming Ohmic and Schottky barrier with ITO coated PEDOT:PSS and Al electrodes, respectively. The power conversion efficiency of the devices based on Se-SM and copolymer P is low. However, both materials can be used as donors for bulk heterojunction with PCBM due the suitable position of their LUMO level. However, when P or Se-SM blended with PCBM, the power conversion efficiency was significantly improved resulted from the formation of bulk heterojunction between copolymer P or Se-SM and PCBM in their respective devices. The effect of the incorporation of the Se-SM on the photovoltaic properties of vinylene copolymer P:PCBM solar cell was investigated. The broader absorption of Se-SM molecules at the longer wavelength region effectively harvests the photon in this region. Moreover, the Se-SM molecules located between the copolymer P and PCBM contribute to the enhancement in the power conversion efficiency due to the effective dissociation of the generated excitons in the copolymer P phase at shorter wavelength region. A further improvement in the power conversion efficiency (3.16%) of the device based on thermally annealed copolymer P:PCBM:Se-SM is attributed to the increase in the number of Se-SM molecules in between copolymer P and PCBM domain due to increased crystallization of the copolymer P.

Acknowledgement

P. Suresh is grateful of council for Scientific and Industrial research (CSIR), Govt. of India for awarding Senior Research fellowship. We are thankful to Dr. M.S. Roy, Scientist and other members in his group, Defence Laboratory, Jodhpur for providing the cyclic voltammetry (CV) measurement facility and fruitful discussions.

References

[1] J.J.M. Halls, C.A. Walsh, N.C. Greenham, E.A. Marseglia, R.H. Friend, S.C. Moratti, A.B. Holmes, Nature 376 (1995) 498.
[2] G. Yu, J. Gao, J.C. Hummelen, F. Wudl, A.J. Heeger, Science 270 (1995) 1789.
[3] B.A. Gregg, J. Phys. Chem. B 107 (2003) 4688.
[4] K.M. Coakley, M.D. McGehee, Chem. Mater. 16 (2004) 4533.
[5] G. Li, V. Shrotriya, J. Huang, Y. Yao, T. Moriarty, K. Emery, Y. Yang, Nat. Mater. 4 (2005) 864.
[6] W. Ma, C. Yang, Y. Gong, K. Lee, A.J. Heeger, Adv. Funct. Mater. 15 (2005) 1617.
[7] M. Reyes-Reyes, K. Kim, D.L. Carroll, Appl. Phys. Lett. 87 (2005) 083506.

[8] Y. Kim, S. Cook, S.M. Tuladhar, S.A. Choulis, J. Nelson, J.R. Durrant, D.D.C. Bradley, M. Giles, I. Mcculloch, C.-S. Ha, M. Ree, Nat. Mater. 5 (2006) 197.
[9] W.-Y. Wong, X.-Z. Wang, Z. He, A.B. Djurisic, C.-T. Yip, K.-Y. Cheung, H. Wang, C.S.K. Mak, W.-K. Chan, Nat. Mater. 6 (2007) 521.
[10] S. Gunes, H. Neugebauer, N.S. Sariciftci, Chem. Rev. 107 (2007) 1324.
[11] P.W.M. Blom, V.D. Mihailetchi, L.J.A. Koster, D.E. Markov, Adv. Mater. 19 (2007) 1551.
[12] X. Yang, J. Loos, Macromolecules 40 (2007) 1353.
[13] A.C. Mayer, S.R. Scully, B.E. Hardin, M.W. Rowell, M.D. McGehee, Mater. Today 10 (2007) 28.
[14] B.C. Thompson, M.J. Fréchet, Angew. Chem., Int. Ed. 47 (2008) 58.
[15] L.J.A. Koster, V.D. Mihailetchi, P.W.M. Blom, Appl. Phys. Lett. 88 (2006) 093511.
[16] M.C. Scharber, D. Muehlbacher, M. Koppe, P. Denk, C. Waldauf, A.J. Heeger, C.J. Brabec, Adv. Mater. 18 (2006) 789.
[17] E. Bundgaard, F.C. Krebs, Sol. Energy Mater. Sol. Cells 91 (2007) 954.
[18] F. Zhang, K.G. Jespersen, C. Björström, M. Svensson, M.R. Andersson, V. Sundström, K. Magnusson, E. Moons, A. Yartsev, O. Inganäs, Adv. Funct. Mater. 16 (2006) 667.
[19] L.M. Andersson, F. Zhang, O. Inganas, Appl. Phys. Lett. 91 (2007) 071108.
[20] L.H. Slooff, S.C. Veenstra, J.M. Kroon, D.J.D. Moet, J. Sweelssen, M.M. Koetse, Appl. Phys. Lett. 90 (2007) 143506.
[21] A. Gadisa, W. Mammo, L.M. Andersson, S. Admassie, F. Zhang, M.R. Andersson, O. Inganas, Adv. Funct. Mater. 17 (2007) 3836.
[22] D. Mühlbacher, M. Scharber, M. Morana, Z. Zhu, D. Waller, R. Gaudiana, C. Brabec, Adv. Mater. 18 (2006) 2884.
[23] Z. Zhu, D. Waller, R. Gaudiana, M. Morana, D. Muhlbacher, M. Scharber, C. Brabec, Macromolecules 40 (2007) 1981.
[24] J. Peet, J.Y. Kim, N.E. Coates, W.L. Ma, D. Moses, A.J. Heeger, G.C. Bazan, Nat. Mater. 6 (2007) 497.
[25] N. Blouin, A. Michaud, M. Leclerc, Adv. Mater. 19 (2007) 2295.
[26] N. Blouin, A. Michaud, D. Gendron, S. Wakim, E. Blair, R. Neagu-Plesu, M. Belletete, G. Durocher, Y. Tao, M. Leclerc, J. Am. Chem. Soc. 130 (2008) 732.
[27] S.H. Park, A. Roy, S. Beaupre, S. Cho, N. Coates, J.S. Moon, D. Moses, M. Leclerc, K. Lee, A.J. Heeger, Nat. Photon. 3 (2009) 297.
[28] L. Liu, C.-L. Ho, W.-Y. Wong, K.-Y. Cheung, M.-K. Fung, W.-T. Lam, A.B. Djurisic, W.-K. Chan, Adv. Funct. Mater. 18 (2008) 2824.
[29] P.-T. Wu, T. Bull, F.S. Kim, C.K. Luscombe, S.A. Jenekhe, Macromolecules 42 (2009) 671.
[30] M.M. Wienk, M. Turbiez, J. Gilot, R.A.J. Janssen, Adv. Mater. 20 (2008) 2556.
[31] C.-P. Chen, S.-H. Chan, T.-C. Chao, C. Ting, B.-T. Ko, J. Am. Chem. Soc. 130 (2008) 12828.
[32] E. Wang, L. Wang, L. Lan, C. Luo, W. Zhuang, J. Peng, Y. Cao, Appl. Phys. Lett. 92 (2008) 033307.
[33] J. Hou, H.-Y. Chen, S. Zhang, G. Li, Y. Yang, J. Am. Chem. Soc. 130 (2008) 16144.
[34] Y. Liang, Y. Wu, D. Feng, S.-T. Tsai, H.-J. Son, G. Li, L. Yu, J. Am. Chem. Soc. 131 (2009) 56.
[35] J. Mei, K. Ogawa, Y.-G. Kim, N.C. Heston, D.J. Arenas, Z. Nasrollahi, T.D. McCarley, D.B. Tanner, J.R. Reynolds, K.S. Schanze, ACS Appl. Mater. Interfaces 1 (2009) 150.
[36] Y. Li, Y. Zou, Adv. Mater. 20 (2008) 2952.
[37] W.J. Belcher, K.I. Wagner, P.C. Dastoor, Sol. Energy Mater. Sol. Cells 91 (2007) 447.
[38] A. Ltaief, R.B. Chaabane, A. Bouazizi, J. Davenas, Mater. Sci. Eng. C 26 (2006) 344.
[39] M.T. Lloyd, J.E. Anthony, G.G. Malliaras, Mater. Today 10 (2007) 34.
[40] R. Yang, R. Tian, W. Yang, Q. Hou, Y. Cao, Macromolecules 36 (2003) 7453.
[41] J. Yang, C. Jiang, Y. Zhang, R. Yang, W. Yang, Q. Hou, Y. Cao, Macromolecules 37 (2004) 1211.
[42] R. Yang, R. Tian, J. Yan, Y. Zhang, J. Yang, Q. Hou, W. Yang, C. Zhang, Y. Cao, Macromolecules 38 (2005) 244.
[43] P. Suresh, P. Balraju, G.D. Sharma, J.A. Mikroyannidis, M.M. Stylianakis, ACS Appl. Mater. Interfaces 1 (2009) 1370.
[44] J.A. Mikroyannidis, M.M. Stylianakis, P. Balraju, P. Suresh, G.D. Sharma, ACS Appl. Mater. Interfaces 1 (2009) 1711.
[45] B.C. Thompson, Y.-G. Kim, T.D. McCarley, J.R. Reynolds, J. Am. Chem. Soc. 128 (2006) 12714.
[46] Q. Peng, M. Li, X. Tang, S. Lu, J. Peng, Y. Cao, J. Polym. Sci. Part A: Polym. Chem. 45 (2007) 1632.
[47] K. Klaus, J. Chem. Soc., Perkin Trans. 1: Org. Bio-Org. Chem. (7) (1972–1999) 1939–1943 (1988).
[48] X. Li, W. Zeng, Y. Zhang, Q. Hou, W. Yang, Y. Cao, Eur. Polym. J. 41 (2005) 2923.
[49] F.S. Mancilha, B.A. DaSilveira Neto, A.S. Lopes, P.F. Moreira Jr., F.H. Quina, R.S. Gonçalves, J. Dupont, Eur. J. Org. Chem. 21 (2006) 4924.
[50] E. Perzon, X. Wang, S. Admassie, O. Inganas, M.R. Andersson, Polymer 47 (2006) 4261.
[51] E. Perzon, F. Zhang, M. Andersson, W. Mammo, O. Inganas, M.R. Andersson, Adv. Mater. 19 (2007) 3308.
[52] P.W.M. Blom, M.J.M. de Jong, M.G. van Munster, Phys. Rev. B 55 (1997) R656.
[53] J.L. Bredas, R. Silbey, D.S. Boudreux, R.R. Chance, J. Am. Chem. Soc. 105 (1983) 6555.
[54] V.D. Mihailetchi, P.W.M. Blow, J.C. Hummelen, M.T. Rispend, J. Appl. Phys. 94 (2003) 6849.
[55] K. Kawano, N. Ito, T. Nishimori, J. Sakai, Appl. Phys. Lett. 88 (2006) 07354.
[56] A. Ltaief, R.B. Chaabane, A. Bouazizi, J. Davenas, Mater. Sci. Eng. C 129 (2006) 344.
[57] A.B. Tamayo, B. Walker, T.Q. Nguyen, J. Phys. Chem. C 112 (2008) 11545.
[58] K. Vandewal, A. Gadisa, W.D. Oosterbaan, J.V. Mance, Adv. Funct. Mater. 18 (2008) 2064.

Organic Electronics 11 (2010) 322–331

Contents lists available at ScienceDirect

Organic Electronics

journal homepage: www.elsevier.com/locate/orgel

Origin of damages in OLED from Al top electrode deposition by DC magnetron sputtering

Tae Hyun Gil [a,*], Christian May [a], Sebastian Scholz [b], Sebastian Franke [a], Michael Toerker [a], Hubert Lakner [a], Karl Leo [a], Stefan Keller [c]

[a] Fraunhofer Institut für Photonische Mikrosysteme, Maria-Reiche Strasse 2, 01109 Dresden, Germany
[b] Institut für Angewandte Photophysik, Technische Universität Dresden, 01062 Dresden, Germany
[c] Applied Materials GmbH, Siemens Strasse 100, 63755 Alzenau, Germany

ARTICLE INFO

Article history:
Received 14 September 2009
Received in revised form 4 November 2009
Accepted 5 November 2009
Available online 14 November 2009

Keywords:
Organic light emitting diode
Sputter damage
DC magnetron sputtering
Ellipsometry
LDI-TOF-MS
SEM/EDX

ABSTRACT

In this study, we examine organic light emitting diodes (OLEDs) having Al top electrodes deposited on organic layers by direct-current magnetron sputtering. The OLEDs consisted of electronically doped transport layers and phosphorescent emission layer were characterized by typical current–voltage–luminance measurement. They showed higher leakage currents, decreased forward currents, and corresponding increases of driving voltage after the sputter deposition on the organic layers. The OLEDs exhibited randomly distributed bright spots on the active area, and the bright spots were investigated by scanning electron microscopy/energy-dispersive X-ray spectroscopy. In order to prove the origins of sputter damage, simple organic/Al layer samples were made and investigated by ellipsometry and laser-induced desorption/ionization time-of-flight mass spectrometry. The results are compared with previous works addressing the fundamental phenomena of magnetron sputtering. We conclude that the high leakage current originated from a penetration of sputtered metal atoms into the underlying organic layers, and the decrease of forward current resulted from an interface degradation caused by the radiation of plasma, which reduces charge carrier injection preferentially at the Al/organic layer interface.

© 2009 Elsevier B.V. All rights reserved.

1. Introduction

Organic light emitting diodes (OLED) are excellent optoelectronic devices for various applications like display and general lighting due to their self-emissive characteristics, natural color expression, and comparably simple device structure. Since a multilayered organic electroluminescence device was reported [1] , its efficiency has been tremendously improved by introducing highly efficient and functional organic materials and stack optimization [2–5]. Fabrication technologies as well as organic materials also achieved great progress on large area substrates, although high deposition rate and stability of top electrode deposition are still a challenge. The top electrodes, e.g. Al or Ag, are evaporated at two or threefold higher temperature than organic materials. For this purpose, metal boats made of Ta or W are generally used to heat the electrode materials. However, such metal boats are supplied with a high power in order to exceed the vaporizing temperature of the electrode metals, which causes a gradual degradation of the boat materials. In particular, molten Al can easily wet the boat surface, resulting in a serious damage due to an extremely high current. In OLED mass production, this problem is still a critical issue in the metal electrode deposition, because it leads to a shorter equipment uptime. Due to those problems, the development of an alternative deposition method has been strongly urged by the OLED industry, especially for large area OLEDs. Magnetron sputtering method is still the best candidate for the metal

* Corresponding author. Tel.: +49 351 8823 235; fax: +49 351 8823 266.
E-mail address: tae-hyun.gil@ipms.fraunhofer.de (T.H. Gil).

1566-1199/$ - see front matter © 2009 Elsevier B.V. All rights reserved.
doi:10.1016/j.orgel.2009.11.011

deposition. Much works were done in order to apply magnetron sputtering for the top electrode deposition on organic layers [6–8], but serious damages in device were reported unfortunately. However, a positive result was also reported by Guenther et al. that only a slight voltage increase of less than 1 V was observed in case of sputtered Indium–Tin–Oxide (ITO) top electrode with a device optimization, keeping the efficiencies and the lifetime similar as for a device having a evaporated metal top electrode [9].

The first part of this study is therefore devoted to examine the OLEDs fabricated with Al cathodes by direct-current (DC) magnetron sputtering and to identify the origins of damage, especially leakage currents. In the Al sputter depositions, only the Ar flow rate was varied to alter the process pressure, which affects sputter deposition significantly. Since the process pressure plays a decisive role in changing kinetic energy of atomic particles by collisions with background Ar gases, a corresponding variation in damages of OLEDs can be expected. The fabricated OLEDs were characterized by current–voltage–luminance (I–V–L) measurements. The results are discussed on the basis of the fundamental phenomena of magnetron sputtering, and a possible damage source responsible for the high leakage current is inferred from it. Simple structures were made in order to prove a change of the electronic level structure in an organic layer after Al cathode deposition by sputtering. Each sample consisted of a single organic and Al layer deposited with the same process parameters as for the OLED fabrications. The samples were examined by ellipsometry which allows an easy access to optical constants of the materials. We employed laser desorption/ionization time-of-flight mass spectrometry (LDI–TOF–MS), which is a useful tool to detect chemical mixtures via their mass-to-charge ratio, in order to identify materials responsible for the high leakage current [10].

In the second part, radiation effects from plasma on the metal/organic interface are examined. If a substrate is immersed into the plasma, the surface of the substrate experiences impingement of radiative particles including electrons, ions and photons. The former two particles have energy corresponding to plasma potential, but the latter photons range from ultra-violet (UV) to infrared. In particular, the high-energy photons ($h\nu > 10$ eV) generated from the energy transition of excited or ionized atoms have been examined in various plasma-associated processes because the photon radiation is quite intensive in glow discharge plasma and affects a device performance significantly. While radiation-induced material damages have been studied widely in semiconductor devices, e.g. metal–oxide-semiconductor devices and bipolar transistors, or a surface modification engineering of polymers using plasma [11–13] , such effects have been rarely discussed in OLED field. During magnetron sputtering, those particles are also generated from the bulk plasma and the surface of sputter cathode considerably. Therefore, we will examine resulting influences from the plasma radiation on OLED characteristic by considering an radiation energy, which the underlying organic layer suffers differently according to the variation of sputter process parameters.

2. Experimental preparation

The samples listed in Table 1, except for the reference OLED, were fabricated in VES400 vertical In-line OLED deposition system (Applied Materials, GmbH & Co. KG) [14,15] . The VES400 consists of several vacuum chambers as shown in Fig. 1, and all the organic materials are thermally evaporated in linear type sources.

The stacks of the samples are listed in Table 1. Substrates used for OLED fabrications were cleaned with isopropanol, acetone and deionised water ultrasonically. Afterwards they were heated at 120 °C for outgassing. The substrate loading to a transport carrier was carried out in the nitrogen ambient glove box 1, and the carrier moved from glove box 1 into the loadlock chamber. The deposition processes were performed at high vacuum of 10^{-7} mbar range by passing all the process chambers. In the substrates, indium tin oxide (ITO) was predeposited on glass as a transparent anode material. For all the OLEDs including the reference OLED and the OLEDs from A to C, doped transport layers (Novaled AG.) were employed to achieve low driving voltage and high carrier transport. These organic layers, NHT5:NDP2 and NET5:NDN1, have electrical conductivity above 10^{-5} S/cm which are electrically approximately equivalent to MeO—TPD : F_4–TCNQ and BPhen:Li, respectively [4] . The emission layer consisted of 4,4-bis [N-(1-naphtyl)-N-phenyl-amino] biphenyl (α-NPD) and Iridium(III)bis(2-methyldibenzo-[f,h] quinoxaline)(acetylacetonate) ($Ir(MDQ)_2(acac)$) as a host and orange–red phosphorescent dye dopant, respectively. This emitting system allows an effective energy transfer from the host to the guest dopant because the HOMO/LUMO positions of α-NPD and the triplet energy state of $Ir(MDQ)_2(acac)$ are quite well matched. Hence an effective energy transfer of the singlet and triplet excitons from the

Table 1
Sample descriptions for experiments.

Sample	Stack	Sputter process parameter
Reference	Glass/ITO/NHT5:NDP2(190 nm)/α-NPD(10 nm)/α-NPD:$Ir(MDQ)_2(acac)$(20 nm)/NET5(10 nm)/NET5:NDN1(40 nm)/evaporated Al(100 nm)	×
A/B/C	Glass/ITO/NHT5:NDP2(190 nm)/α-NPD(10 nm)/α-NPD:$Ir(MDQ)_2(acac)$(20 nm)/NET5(10 nm)/NET5:NDN1(40 nm)/Al(100 nm)	1 (A), 2 (B), 3 (C)
D	Glass/NET5(100 nm)/evaporated Al(100 nm)	×
E/F/G	Glass/NET5(100 nm)/Al(100 nm)	1 (E), 2 (F), 3 (G)
H/I	Stainless plate/BPhen(20 nm)/Al(10 nm)	1 (H), 3 (I)

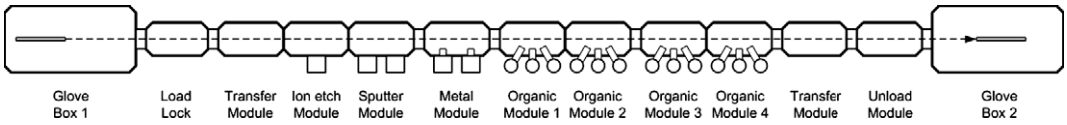

Fig. 1. Schematic illustration of In-line machine implemented for the experiments.

host to the phosphorescent dye dopant is accomplished [16].

The reference OLED was fabricated in a cluster equipment with same organic stack in order to deposit Al cathode by thermal evaporation. The Al cathodes of the sample A/B/C are deposited in the sputter chamber after depositions of organic layers. The sputter chamber equipped with two conventional magnetron sputtering cathodes is also located in the middle of the In-line machine so that Al cathodes were subsequently deposited on organic layers without vacuum break. The process parameters for Al sputtering are listed in Table 2. As indicated, three different Ar flow rates (100, 300 and 500 sccm) were selected with an equal DC power 500 W. After all the film depositions, the substrates were encapsulated in a nitrogen-filled glove box with glass including getter inside to protect the OLEDs from oxygen and water vapors. *I–V–L* characteristic of the fabricated OLEDs was measured by DMS 101 (Autronic Melchers, GmbH). The samples from D to H were made on different substrates prepared with the same preparation sequence for ITO substrates. The samples for ellipsometry and LDI–TOF–MS measurements were put into a nitrogen-filled carrier with O-ring seal directly after film deposition in order to prevent them from ambient before the measurements.

The basic setup of ellipsometry is depicted in Fig. 2. The measurements were performed twice on both sample sides. In the first measurement, linearly polarized light emitted from light source fell onto the Al film at an incoming angle $\theta = 65°$, and the optical constant of the Al film was obtained first after eliminating the constant of a thin surface aluminum oxide. Afterwards, the film-coated side of the sample was set above like Fig. 2, and the measurement was performed once more with the setup. In this case, the polarized light is reflected at the Al/organic layer interface and escapes from the sample. The light undergoes phase delays by passing through the glass and the organic layer because the refractive indices of glass and most organic materials are higher than air. The light escaping the sample is then falls onto the detector. Since the optical constants of Al films processed at different parameters were almost identical, we assumed that the optical properties of the Al film at the interface agreed with those at the air side. Since the refractive index of the glass is already known ($n \cong 1.5$), that of the organic layer is able to be extracted. By means of iterative fits, the thickness as well as the index of the organic layer was successfully obtained. The thickness of the organic layer exhibited approximately 5% deviation from the value measured by a profilometer, proving that the sample preparations were very reproducible. As an organic interlayer, NET5 (Novaled AG, Dresden) was deposited on the glass because this material undergoes sputter damage firstly in OLED.

Table 2
Process parameters for Al sputter depositions and corresponding deposition rates.

Process parameter	DC power (W)	Ar flow rate (sccm)	Pressure (mbar)	Deposition rate (nm/speed.oscillation)
1	500	100	0.001	24.86
2	500	300	0.003	18.70
3	500	500	0.005	14.75

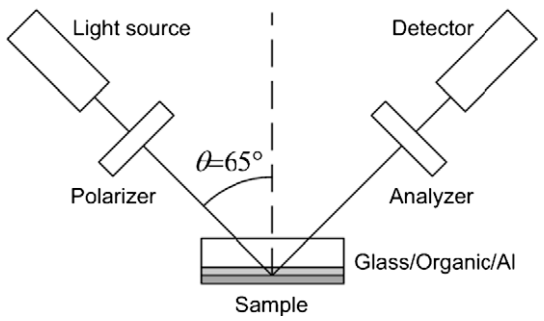

Fig. 2. Ellipsometry scheme on the sample for measurement. The optical constants of organic layer after sputter deposition are obtained from this setup.

The samples for LDI–TOF–MS were prepared on well-cleaned stainless plates. The instrument was described well by Scholz et al. [10]. The samples were placed in the analysis chamber under a vacuum of 10^{-7} mbar during measurement. The wavelength of the laser was 337 nm and the total laser intensity was 129.2 μJ/pulse. The spectra were taken at positive detection mode at a laser intensity of 75%. Three different positions at one sample were measured, and 60 spectra were gathered from each position to obtain one spectrum.

3. Results and discussion

3.1. Origin of leakage current in OLED

In Fig. 3, the *I–V–L* characteristics of the reference OLED and the OLED samples A to C are shown. Notable are high current densities at low forward voltage under 2 V and negative voltage regions in the OLEDs having sputtered Al cathode while the reference OLED shows very low current. According to the transport theory in a dielectric layer, the current at those regions exhibits $I \propto V$ characteristic in a well-fabricated device. This current obeys Ohm's law, and this ohmic current is controlled by thermally generated charges [17] . The current level is usually much lower than the trap-filled space charge limited current at higher

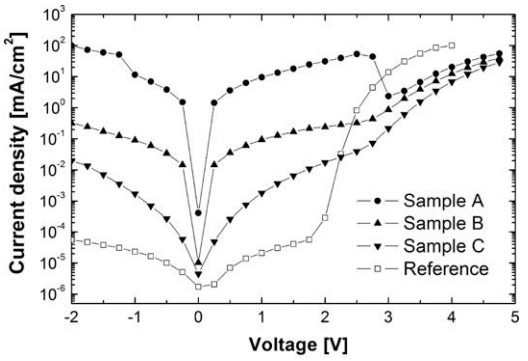

Fig. 3. *I–V* Characteristics of fabricated OLEDs. The OLEDs show high leakage currents after the Al top contact deposition using magnetron sputtering. Remarkable point in the graph is that the leakage current decreases as the process pressure increases.

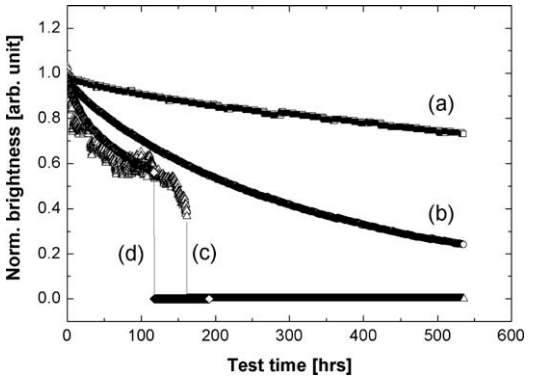

Fig. 4. Lifetime results of the fabricated OLEDs. (a) and (b) are the normalized brightness of reference OLED measured at 10 and 30 mA/cm^2, respectively. (c) From the sample B measured at 10 mA/cm^2, and (d) from the sample C measured at 30 mA/cm^2.

voltage region. When the low current density of around 10^{-4} mA/cm^2 at between ±2 V in the reference OLED is considered, the higher currents in the OLED samples A to C seem to be defects caused by sputtering deposition on the organic layers. There can be other possible reasons like shortcuts due to ITO roughness or particle contamination. However, it is certainly sputter-induced damage because an identical procedure for substrate preparation was carried out for all the samples including the reference OLED. Similar phenomena have been examined by Kim et al. for Al top electrode deposition using facing target sputter (FTS) apparatus [8] . In that study, the reason for high leakage current was explained with a formation of a metallic surface due to bombardment of energetic particles and with a current path at the interface between metal and organic layers due to local damage, quoting the study of Liao et al. and Gu et al., respectively [18,19] . In the Liao's study, the effect of energetic Ar^+ ion bombardment on tris-(8-hydroxyquinoline) aluminum (Alq_3) molecules has been examined in order to simulate sputtering deposition. They explained that the bombardment of high energetic particles destroyed molecular band structure, resulting in a formation of a metal-like conducting surface consequently. However, their experiment was not carried out by a substantial sputtering deposition, and employed an intentional 100 eV Ar^+ which is scarcely generated in Al target sputtering with Ar^+ ion at a discharge voltage around 300 V [20] . Furthermore, only a metallic surface is not thought to induce such high leakage current because the bombarded surface of organic layer makes contact with a deposited Al layer, which is incomparably more conductive.

Since these high leakage currents often result in an unstable device operation or sudden death, lifetime measurement must be performed to evaluate the stability of OLED. The measurement is also necessary to turn out a correlation between the leakage current and the lifetime. Fig. 4 contains four graphs of normalized brightness obtained from lifetime measurements. OLEDs, the reference and sample A/B/C, are supplied with the current density of 10 and 30 mA/cm^2. It should be noted in advance that the sample A, which has shown the highest leakage current, exhibited extremely short lifetime, only a few minutes, so the result is not included. As expected, the results of the reference OLED in Fig. 4a and b shows curves stably decaying in brightness at the both current densities. In contrast with the reference OLED, the sample B from Fig. 4c measures at 10 mA/cm^2 showed a faster decay, fluctuating until the sample resulted in sudden death eventually. Whereas, the sample C in Fig. 4d shows relatively more stable decay than the sample B. This result is attributed to the lower leakage current of the sample C. It is therefore manifested that the leakage current and the lifetime have an intimate correlation.

In order to compare the previous explanations of Liao et al. with our results, simple structures (samples D–G) were made for an investigation on optical properties of the organic material by ellipsometry. In Fig. 5, the curves of the optical constants obtained for NET5 layers are shown. Interestingly, there were no significant differences in the optical properties of the organic layers in spite of the high leakage currents in the OLEDs. In particular, the optical bandgaps of NET5 layers from the extinction coefficients

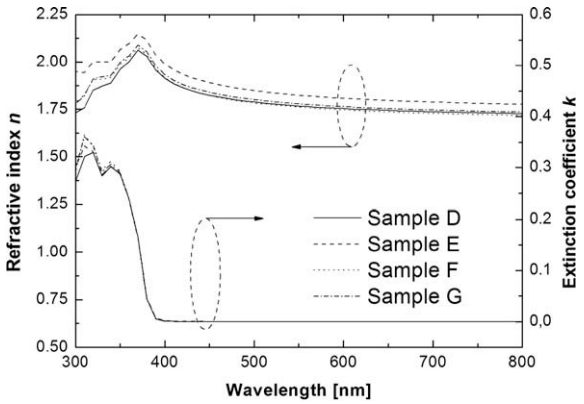

Fig. 5. Comparison of refractive indices and extinction coefficients of the samples from D to G. The NET5 layers show an identical optical gap of 3.26 eV despite of different leakage currents in the sample A–C.

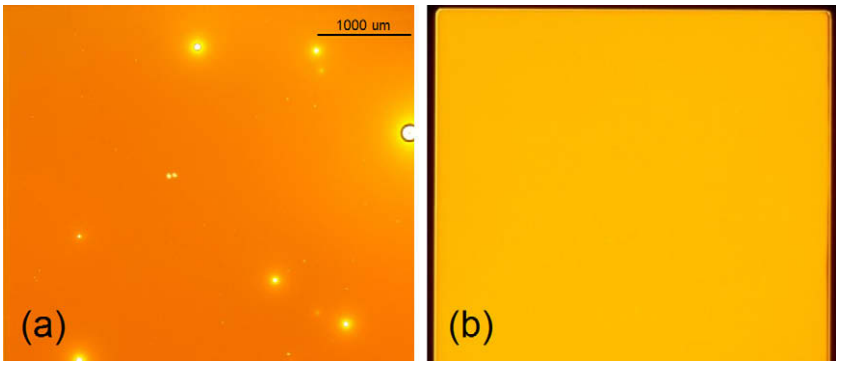

Fig. 6. Observation of the lighting surface of OLEDs at identical magnification, (a) having sputtered Al cathode and (b) evaporated Al cathode. The operation voltage was 3 V, and the resulting luminance was 160 (a) and 2700 cd/m^2 (b). Many bright spots are observed in the OLED having the sputtered Al top electrode while the reference OLED shows a homogenous lighting area.

are explicitly identical and clearly observable at 3.26 eV (λ = 380 nm); the results were also equal in other measure points as well. This means that the electronic band structure of the entire organic layer was not significantly changed after the Al sputtering and the previous explanations are not satisfactory to explain the leakage currents in our OLEDs.

The active surfaces of operating OLEDs were also observed by optical microscopy in order to find clues in detail. The surface images are shown in Fig. 6. In contrast to the results of Kim et al. [8] , the OLEDs having sputtered Al cathodes showed many localized bright spots while the reference OLED had no such spots. These bright spots indicate that more charge carriers flow through such small areas due to the higher electric field or parasitic current paths and that the charge carriers are transported not by conventional hopping conduction between organic molecules over highest occupied molecular orbital (HOMO)/lowest unoccupied molecular orbital (LUMO) level. Such current paths are therefore thought to be responsible for the high leakage currents, and it may be caused by other highly conductive species like metal filaments.

We also examined the core of the bright spots by means of scanning electron microscopy/energy-dispersive X-ray spectroscopy (SEM/EDX) after removing encapsulation glass. Fig. 7 contains two SEM images of the bright spots and EDX element map obtained from the core and the outer area of the damages. It is seen in Fig. 7a and b that the center of the bright spots was seriously destroyed and that the total OLED structure was completely molten and agglomerated again. The destroyed core was analyzed by EDX at the X-ray energy of 5 kV. The solid line spectrum is from the outer area of the center, and the filled spectrum is from the center. It is quite interesting that the element map showed similar intensities of the elements consisting of OLED. This result gives important information that such damages were not induced by external particle contamination but by existing elements in OLED. Also, these damages were not observable in an as-made device, and they were all generated during the *I–V–L* measurement. This means again that materials inside OLED like conductive metallic particles must have generated such damages, and it supports the presence of metallic current paths.

Interestingly, the leakage currents in Fig. 3 shows a decreasing trend as the process pressure increases. To understand this result, energy transfer onto the substrate from all the energetic particles generated in magnetron sputtering should be taken into account. In sputtering processes, various kinds of energetic particles are generated simultaneously from the sputtering cathode and bulk plasma, for example, ions, secondary electrons, sputtered target atoms, neutrals and also radiation particles [21–22]. The energy and the production of each particle depend on the kind of discharge gas, target material, process parameters, and power source. Such complications made the identification of dominant damage sources quite difficult and prevented the understanding of the exact damage mechanisms up to now. So we attempt to investigate the generation mechanisms referring to other researches. The highly energetic atomic particles include recoiled Ar neutrals, ions and sputtered particles. Among them, the recoiled neutrals can be either generated or not depending on the masses of incident ion and target material. Sputtering mechanism is based on atomic momentum transfer between incident and target atoms. In case of Al sputtering with Ar gas, the mass of Ar (39.95) is heavier than that of Al (26.98) so that a perfect energy transfer is accomplished. The fraction of energy lost by the incident particle is obtained as [23]

$$\zeta_L = \frac{E_t}{E_i} = \frac{\frac{1}{2} m_t v_t^2}{\frac{1}{2} m_i v_i^2} = \frac{4 m_i m_t}{(m_i + m_t)^2} \cos^2 \theta \qquad (1)$$

where E_t and E_i are respectively the kinetic energy of target and incident particles, m_t and m_i are the mass of target and incident particles, v_t and v_i are the velocity of target and incident particles. θ is the incident angle, and is assumed to be 90° in plasma sheath. If the mass relation of Ar and Al is applied in Eq. (1), ζ_L is derived as 0.962 which states an almost perfect energy transfer from the incident Ar to the Al target atoms. It means that no Ar neutrals are generated theoretically and that the energy term of Ar neutrals is neglected. Accordingly, energy variations of other components and their energy transfer are taken into account.The total energy generated from magnetron sputtering was estimated by Ekpe as

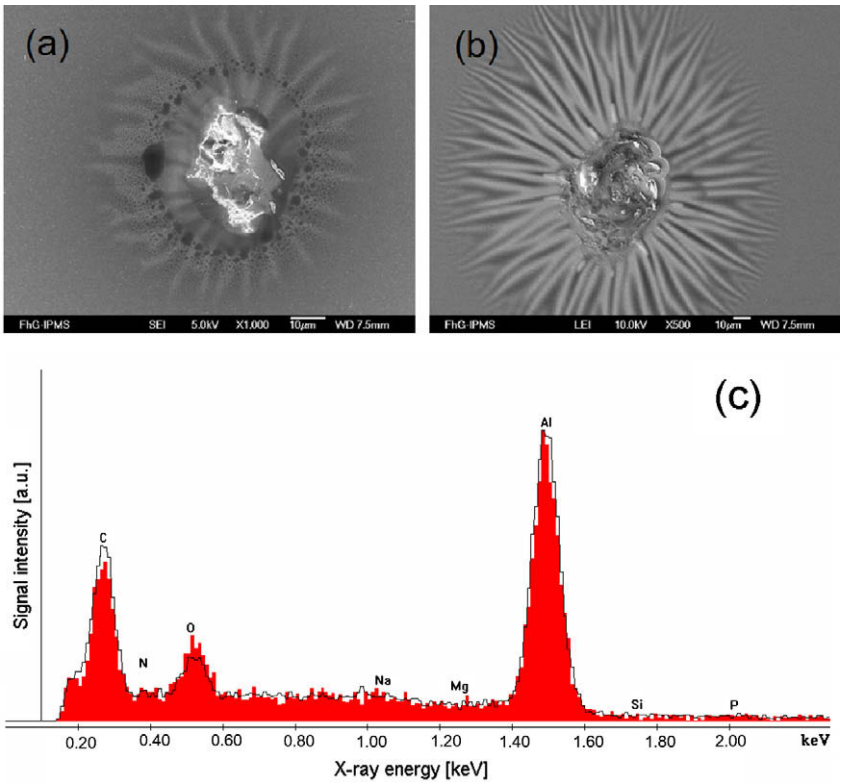

Fig. 7. SEM images of bright spots after *I–V–L* measurement and EDX element map from the core and the vicinity: (a) and (b) destroyed OLED structures through melting and agglomeration. EDX element map in Fig. 6c shows two spectra obtained from the degradation core (filled) and outer the degradation (solid line), non-destroyed region. Two spectra exhibit almost identical signal intensities throughout the elements consisting of OLED.

$$E_{\text{total}} = U + E_k + E_0\frac{R_E}{Y} + E_p + E_e + E_t \tag{2}$$

where U and E_k represent the heat of condensation and the average kinetic energy of the deposited atoms, respectively [24]. The third term represents the contribution of the reflected gas neutrals determined per sputtered atoms in terms of the yield Y. As discussed already, this term is eliminated. E_p represents the contribution of photonic radiation generated from excited atoms within plasma. E_e and E_t are the contributions of electron and thermal radiation, respectively. In this equation, however, the contribution of ions from plasma bulk onto the substrate is absent, and it should be added. Therefore, Eq. (2) is modified into

$$E_{\text{total}} = U + E_k + E_p + E_e + E_t + E_i \tag{3}$$

It is then essential to know which energy terms or elements in Eq. (3) vary with respect to process pressure. Firstly, the kinetic energy of the sputtered atoms and its changes on the process pressure is discussed. The energy and direction of the sputtered target atoms arriving at the substrate is related to the transport process from the target to the substrate. Each energy term in Eq. (3) is significantly affected by process parameters like power and operating pressure. Pressure-dependent deposition rate or film uniformity changes have been described by many researchers [25–27], and the average energy of the sputtered Al atoms was also reported to reach 19.2 eV at process conditions similar to our study. In magnetron sputtering, the transport from the sputter target to the substrate plays a significant role in film deposition and properties. Collisions and mutual energy transfer between sputtered atoms and discharge gases, depending on their energies, masses and densities, are the key factors in determining the transport process. A mean free path is introduced primarily to explain the effect of collision between particles. Since the energetic particles generated collide with the background gas atoms, the energy of the background gases should be taken into account. The mean free path λ_m is then expressed as

$$\lambda_m = \frac{k_B T}{p\sigma} \tag{4}$$

where k_B is the Boltzmann constant, T is the temperature of the sputtering gas. p is the pressure of the sputtering gas, and σ is the collision cross section for momentum transfer [28]. Referred to Eq. (4), the λ_m is decreased reciprocally with an increase of pressure. This effect is due to increase of collision frequency which can lead to a deviation of the direction by scattering and a loss of kinetic energy of the sputtered atoms, so-called thermalization. Therefore, the deposition rate decreases at higher process pressure as indicated in Table 2, and a decrease of the kinetic energy

of the sputtered atoms is thus expected.Secondly, the energy transfers by other energy terms (E_p, E_e and E_t) are discussed. In contrast to the energy of sputtered atoms, their energy transfer is increased at higher process pressure because the process time to deposit film of a same thickness becomes longer and accordingly the surface of organic layer is exposed to the plasma longer. Those plasma components are particles which change internal energy of organic molecules or deposited Al film by ionization and excitation. By continuous irradiation on the surface of organic layers or on the initial thin metal layer previous to a high reflection or screening against such irradiation, other degradation at the interface of metal and organic layer can occur. However, it is believed that they are not the major source to give rise to a high leakage current because their masses are extremely small to deliver a sufficient kinetic energy for a formation of metallic current paths.

When comparing these explanations with the OLED *I–V–L* results in Fig. 3, one can recognize that only the energy variation of the sputtered Al atoms in good agreement with the change of leakage current in OLEDs. Considering their masses and energies, the sputtered Al atoms are supposed to penetrate into the underlying organic layers much deeper than the evaporated Al atoms. Moreover, if energy is transferred further by collision cascades due to continuous atomic bombardments, highly conductive current paths can be formed locally through the organic layers. As a similar phenomenon, it was reported that even evaporated metal atoms deposited at an elevating substrate temperature up to 70 °C were also able to diffuse into a single crystalline organic diindenoperylene (DIP) film [29]. A high electric field can be then induced through the localized paths caused by metal diffusion, and it leads to highly localized currents through the OLED even at a low operation voltage, as shown in Fig. 3. The substrate temperature during deposition was measured on glass substrate by Super mole™ (ECD, Inc.). Highest temperature during Al depositions in the In-line machine was however only 26 °C as shown in Fig. 8, so the thermal energy seems not to play a significant role in producing such highly conductive paths resulted from penetration or diffusion.

By LDI–TOF–MS, we were able to identify the presence of metal particles deep in the organic layer. There are several methods to detect atomic elements in thin films like depth profiling X-ray photoemission spectroscopy (XPS) and depth profiling secondary ion mass spectrometry (SIMS). However, these instruments require an additional ion gun in order to sputter the surface of specimen. This is a quite destructive method, and the bombarded surface element can also penetrate deeper into the underlying film. In case of organic films, the intermolecular bonding is in general held by a weak van der Walls force so that such energetic metal atoms can easier penetrate through organic molecules than inorganic molecules. Therefore, it is difficult to distinguish whether such metal atoms originate from sputtering damage or depth profiling in those instruments. On the other hand, the LDI–TOF–MS can also provide in-depth information by laser-induced desorption. One

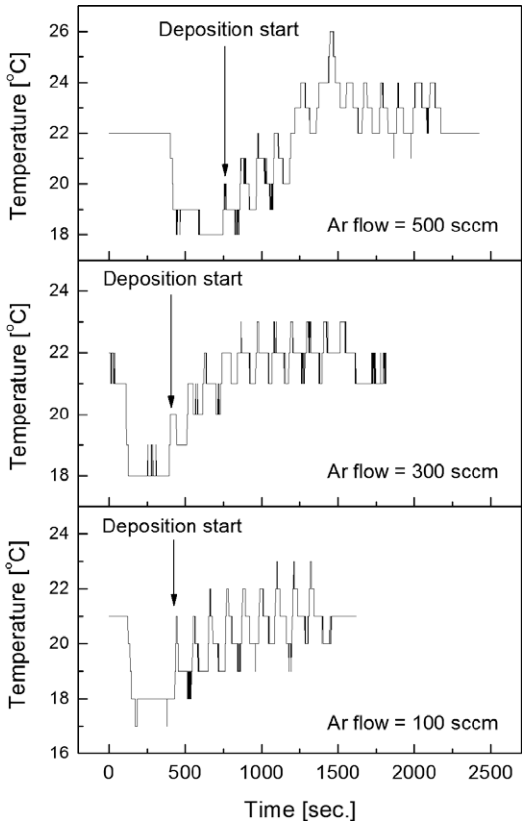

Fig. 8. Temperature variations during Al depositions at different Ar flow rates. The highest temperature is found as 26 °C at the Ar flow rate of 500 sccm which showed the longest deposition time.

important thing is that the laser intensity must be controlled at a threshold level to avoid an excess of ionizations and corresponding chemical reactions.

A shallow doping of metal atoms was reported to be beneficial to improve charge injection into the organic layers by a self-doping effect at the metal/organic layer interface [30]. However, if metal atoms exist in a deep area of organic layer, they will provide current paths interconnecting the two electrodes of OLED. The organic material BPhen used for the measurements is reported to produce a complex with Al or Ag metal atom by donor–acceptor interaction. Hence one can recognize the presence of those metal atoms from the detection of metal–organic complexes. Additionally, the quantity of the metal atoms can be compared by the intensity of spectra. Its depth resolution is unknown, but the deposited 10 nm think Al layer of the sample H and I is certainly transparent for the wavelength of the laser. Hence the given condition for the laser irradiation was same, and it enables a relative comparison of the both samples. Nevertheless, the technique is suitable to give quantitative statement about incorporated compounds and reacted molecules, even for metal on organic hetero structures [30].

In Fig. 9, two spectra of the sample H and I are shown. It is clearly seen that the sample H contains much more Al adduct ions, $[BPhen + Al]^+$ at $m/z = 359$ amu and [2BPhe-

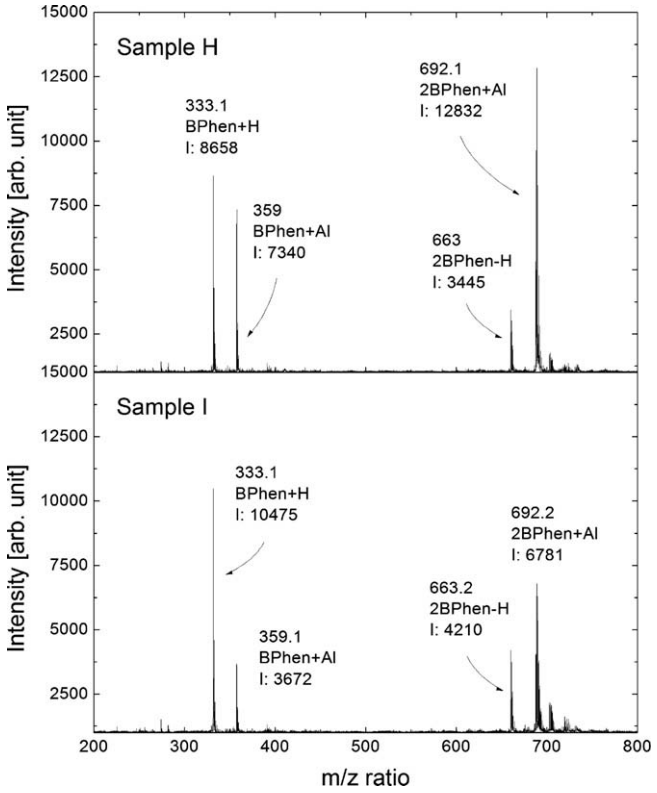

Fig. 9. LDI–TOF–MS results of sample H and I. The sample H shows much higher intensities of BPhen + Al and 2BPhen + Al complexes than the sample I, representing the existence of Al atoms inside of the BPhen layer.

n + Al]$^+$ at m/z = 692.1 amu, than the sample I. The ratios of the spectrum intensities from the existing molecules are tabulated in Table 3. This result gives a decisive evidence to clarify that more metal atoms existed inside the BPhen layer of the sample H than the sample I, supporting the penetration effect of Al atoms due to continuous bombardment effect with high-energy. Therefore, we can conclude that the penetrated Al atoms resulted in high leakage current flowing through the organic layers.

3.2. Radiation effects in OLED

The forward *I–V* in the linear scale and *L–V* characteristics of the OLEDs are plotted again and shown in Fig. 10a and b. The reference OLED exhibits a high forward current density of 100 mA/cm^2 at 4 V. On the other hand, the forward current density of the OLED from the sample A–C decreases with increasing process pressure. The forward current in OLED is the summation of hole and electron currents. The decrease of the forward current reflects a poor charge carrier injection, especially electrons from the Al cathode. It is probably due to generation of different electronics states or charge traps at the top metal/organic layer interface generated by the irradiation from plasma. Several mechanisms can be introduced to explain the degradation of interface property due to plasma radiation. Electrons fall onto a substrate faster than ions when the substrate is immersed in the plasma. The electrons can be accumulated on the surface making the interface of metal/organic layer negatively charged. Such localization of electrons can possibly modify electronic structure of organic molecules [31]. The photons with energies higher than the band gap of organic material can excite bound electrons to LUMO or higher states, generating electron–hole pairs (EHPs) [32]. When the organic molecules are excited, they may dissipate the excess energy by emitting photons as it returns to a lower energy level and eventually to the ground state. The energy can also be emitted irradiatively forming fragmented and reactive species by the opening of a bond structure and the detachment of hydrogen or an organic ligand. It is because the photon energy in plasma ranges much exceeding the binding energy of carbon–carbon covalent bonds or carbon–hydrogen bonds of organic molecules, and such unbound sites are then able to act as charge trapping sites which hinder the injection of charge carriers from the electrode.

Table 3
Calculated ratios from the spectrum intensities of the sample H and I.

Molecules for comparison	Sample H (Ar = 100 sccm)	Sample I (Ar = 500 sccm)
BPhen/BPhen-Dimer	2.51	2.488
BPhen + Al/2BPhen + Al	0.57	0.54
BPhen/Al + BPhen	1.18	2.85
BPhen-Dimer/2Bphen + Al	0.268	0.62

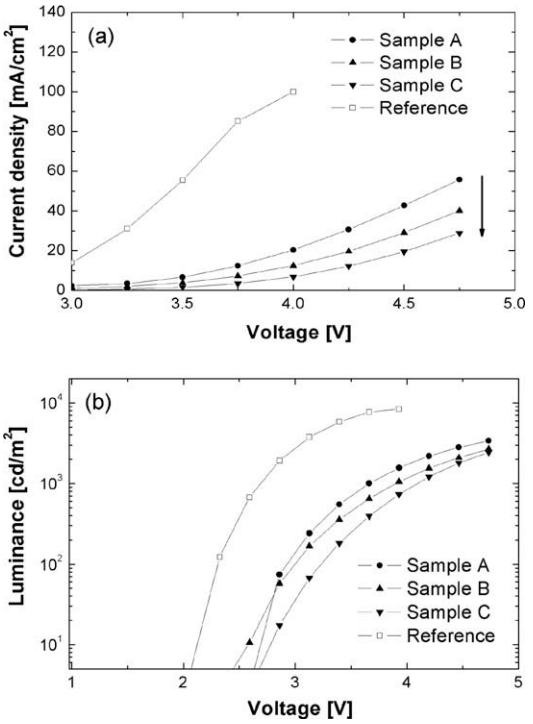

Fig. 10. Rescaled *I–V* and *L–V* characteristics of the OLEDs. The forward current and corresponding luminance decrease as the irradiative energy increases, resulted from the decrease of the deposition rate.

The generation of such degradations can be related with a total radiation energy, which is estimated as a product of radiation flux from plasma and exposure time of the organic layers. As discussed briefly in former section, the total radiation energy comprising E_p, E_e, E_t and E_i in Eq. (3) becomes larger at higher process pressure because the process time to deposit 100 nm thick Al layer in the sample C was roughly two times longer than A. Corresponding effect is clearly seen in Fig. 10a that the forward current of the sample C decreased from 57 mA/cm^2 at 4.75 V to 30 mA/cm^2 of the sample A, which is well matched with the increase of the process time. Therefore, the decrease of the forward current can be ascribed surely to the radiation out of plasma. It should be mentioned one more that this radiation effect should be separated from that of the leakage current, because the tendency of the both effects with respect to the variation of the process pressure was obviously opposite. The luminance of the OLED is undoubtedly decreased, and this yielded also a shift of driving voltage from 2.7 V of the reference OLED to almost 4 V of the other OLEDs for 1000 cd/m^2.

4. Conclusions

We demonstrated OLEDs having Al top electrode deposited by a conventional magnetron sputtering system. The Al sputtering deposition on organic layers resulted in high leakage current and lower forward current in the OLEDs fabricated. The OLEDs possessing high leakage current showed many bright spots on active area, which are thought as the result from the leakage current. The optical constants of the organic layers obtained from ellipsometry showed no changes in the optical gap of the organic layers. This means that the organic layer was not damaged seriously after Al sputter deposition and that other sources might have caused the high leakage currents. Based on the operating principle of magnetron sputtering, we concluded that the high kinetic energy of sputtered Al atoms was the dominant source responsible for the leakage current, resulting in a metal penetration into the underlying organic layers. In order to prove the metal penetration, we employed LDI–TOF–MS. At the same process parameter that OLED showed highest leakage current, the obvious existence of Al atoms deeper inside the organic layer was identified as a form of metal–organic complex. It assured that the high leakage current was caused by conductive metallic paths provided by penetrated Al metal particles into organic layer.

The effect of plasma radiation on the metal/organic layer interface was also examined. The forward current density showed a decreasing trend, as the process time became longer. This result was explained well with the increase of the radiation energy that influences the generation of the interface degradation.

We note that if the process pressure is increased further in order to reduce the leakage current in OLED, the interface will be degraded more, which leads to a higher operating voltage. Therefore, the two damages caused by magnetron sputtering are in a trade-off relation, and a thick buffer layer or modified organic layers based on *p–i–n* OLED would be helpful to obtain comparable leakage current, efficiency and lifetime with OLED having evaporated metal electrode.

Acknowledgement

This work was performed with financial support by Applied Materials GmbH & Co. KG within the OPAL project (Support Code 13N8944) funded by the Federal Ministry for Education and Research of Germany.

References

[1] C.W. Tang, S.A. VanSlyke, Appl. Phys. Lett. 51 (1987) 913.
[2] M.A. Baldo, D.F. O'Brien, Y. You, A. Shoustikov, S. Sibley, M.E. Thompson, S.R. Forrest, Nature 395 (1998) 151.
[3] M.A. Baldo, M.E. Thompson, S.R. Forrest, Nature 403 (2000) 750.
[4] K. Walzer, B. Maennig, M. Pfeiffer, K. Leo, Chem. Rev. 107 (2007) 1233.
[5] S. Reineke, F. Lindner, G. Schwartz, N. Seidler, K. Walzer, B. Lüssem, K. Leo, Nature 459 (2009) 234.
[6] L.S. Hung, C.W. Tang, Appl. Phys. Lett. 74 (1999) 3209.
[7] L.S. Hung, L.S. Liao, C.S. Lee, S.T. Lee, J. Appl. Phys. 86 (1999) 4607.
[8] H.K. Kim, S.W. Kim, K.S. Lee, K.H. Kim, Appl. Phys. Lett. 88 (2006) 083513.
[9] G. Guenther, in: Proceedings of IDMC, Invited Talk, 2009.
[10] S. Scholz, C. Corten, K. Walzer, D. Kuckling, K. Leo, Organ. Electron. 8 (2007) 709.
[11] J. Kassabov, E. Atanassova, D. Dimitrov, J. Vasileva, Thin Solid Films 169 (1989) 43.
[12] A.M. Wróbel, G. Czeremuszkin, Thin Solid Films 216 (1992) 203.
[13] A.C. Fozza, J. Roch, J.E. Klemberg-Sapieha, A. Kruse, A. Holländer, M.R. Wertheimer, Nucl. Instrum. Methods. Phys. Res. B I31 (1997) 205.

[14] U. Hoffmann, P. Netuschill, M. Bender, P. Sauer, M. Schreil, J. Amelung, K. Leo, SID Symp. Dig. Tech. Papers 34 (2003) 1410.
[15] C. May, Y. Tomita, M. Toerker, M. Eritt, F. Loeffler, J. Amelung, K. Leo, Thin Solid Films 516 (2007) 4609.
[16] R. Meerheim, S. Scholz, G. Schwartz, S. Reineke, S. Olthof, K. Walzer, K. Leo, Proc. SPIE 6999 (2008) 699917.
[17] C.R. Dutta, K. Barua, J. Phys. D: Appl. Phys. 14 (1981) L179.
[18] L.S. Liao, L.S. Hung, W.C. Chan, X.M. Ding, T.K. Sham, I. Bello, C.S. Lee, S.T. Lee, Appl. Phys. Lett. 75 (1999) 1619.
[19] G. Gu, V. Bulović, P.E. Burrows, S.R. Forrest, M.E. Thompson, Appl. Phys. Lett. 68 (1996) 2606.
[20] Tilo P. Drüsedau, Mirko Löhmann, Bernd Garke, J. Vac. Sci. Technol. A 16 (4) (1998) 2728.
[21] S.M. Rossnagel, J. Vac, Sci. Technol. A 7 (1989) 1025.
[22] S.M. Rossnagel, K.L. Saenger, J. Vac, Sci. Technol. A 7 (1989) 968.
[23] M.A. Lieberman, Principles of Plasma Discharges and Materials Processing, John Wiley & Sons, 1994.
[24] S.D. Ekpe, S.K. Dew, J. Vac. Sci. Technol. A 20 (2002) 1877.
[25] J.C. Helmer, C.E. Wickersham, J. Vac. Sci. Technol. A 4 (1986) 408.
[26] T.P. Drüsedau, M. Löhmann, B. Garke, J. Vac. Sci. Technol. A 16 (1998) 2728.
[27] A. Settaouti, L. Settaouti, Appl. Surf. Sci. 254 (2008) 5750.
[28] S.D. Ekpe, L.W. Bezuidenhout, S.K. Dew, Thin Solid Films 474 (2005) 330.
[29] A.C. Dürr, F. Schreiber, M. Kelsch, H.D. Carstanjen, H. Dosch, Adv. Mater. 14 (2002) 961.
[30] S. Scholz, Q. Huang, M. Thomschke, S. Olthof, P. Sebastian, K. Walzer, K. Leo, S. Oswald, C. Corten, D. Kuckling, J. Appl. Phys. 104 (2008) 104502.
[31] R.Q. Zhang, C.S. Lee, S.T. Lee, Chem. Phys. Lett. 326 (2000) 413.
[32] H. Yasuda, J. Macromol. Sci.-Chem. A10 (3) (1976) 383.

Organic Electronics 11 (2010) 332–337

Contents lists available at ScienceDirect

Organic Electronics

journal homepage: www.elsevier.com/locate/orgel

Charging energy, self-interaction correction and transport energy gap for a nanogap organic molecular junction

E. Abad [a,*], C. González [b], J. Ortega [a], F. Flores [a]

[a] Departmento de Física Teórica de la Materia Condensada, Universidad Autónoma de Madrid, 28049 Madrid, Spain
[b] Departamento de Superficies y Recubrimientos, Instituto de Ciencia de Materiales de Madrid (CSIC), 28049 Madrid, Spain

ARTICLE INFO

Article history:
Received 3 August 2009
Received in revised form 29 October 2009
Accepted 5 November 2009
Available online 11 November 2009

Keywords:
C_{60}
Charge neutrality level
Self-interaction correction

ABSTRACT

A C_{60} molecule sandwiched between two Au(1 1 1) based tips is used as a model system to analyze the formation of nanogap molecular junctions including charging effects and self-interaction corrections. In our approach, we combine a DFT-LDA calculation of the structural and electronic properties of the system with an analysis of the interface barrier formation based on the charge transfer and the organic Charge Neutrality Level, as described by the Induced Density of Interface States model. This allows us to determine, as a function of the tip/C_{60} distance, the self-interaction correction to the frontier molecular orbitals levels, the transport energy gap and the metal/organic barrier height. Our approach offers a fully consistent technique for analyzing a metal/organic interface at the molecular level.

© 2009 Elsevier B.V. All rights reserved.

1. Introduction

One of the most ambitious objectives in Nanoscience is to build electronic devices using individual molecules. In order to achieve this goal, a lot of work has been addressed to investigate the nanocontact between metal electrodes and a single molecule [1–14]. For example, mechanically controllable break junctions or scanning tunneling microscope tips have been used to deposit inorganic and organic molecules [15–17] between two metals, forming in this way a typical quantum dot (QD) as a possible component of a molecular electronic device.

From a fundamental point of view, the energy levels of the frontier orbitals of the molecule relative to the interface Fermi energy determine the electronic, transport and optical properties of the system [18]. Those levels depend on the detailed atomic geometry of the nanocontact, but also depend sensitively on self-interaction corrections, polarization effects and the charging energy of the molecule [19–21] and therefore cannot be determined accurately using standard density functional theory (DFT) calculations [22]. Thus, there is a critical need for the development of practical procedures to properly include those effects in a simulation of a realistic molecule/metal nanocontact.

In the last few years, a lot of experimental and theoretical work has been done to explain the mechanism responsible of the barrier height formation (and interface electrostatic dipole) between a metal and an organic monolayer. Chemical reactions [23–27], induced "pillow" (or Pauli exclusion) dipole [26,28,29], or intrinsic molecular dipoles [26,28–30] have been proposed as the main mechanisms operating at the metal organic (MO) interface. The Unified Induced Density of Interface States (IDIS)-model [30,31] combines the "pillow" and the intrinsic molecular dipoles with the charge transfer between the materials forming the interface to explain the barrier formation. Although in these studies typically a full monolayer of the organic material is assumed to be deposited on the metal, one can expect that a similar mechanism should be operative at the molecular level.

* Corresponding author. Tel.: +34 914978648; fax: +34 914974950.
E-mail addresses: enrique.abad@uam.es (E. Abad), cesar.gonzalez@icmm.csic.es (C. González), jose.ortega@uam.es (J. Ortega), fernando.flores@uam.es (F. Flores).

1566-1199/$ - see front matter © 2009 Elsevier B.V. All rights reserved.
doi:10.1016/j.orgel.2009.11.012

The C_{60} molecule has been widely studied deposited on metals [21] or forming interfaces [33,34] and it has been encapsulated as a film between two metal electrodes as part of a solar cell [35]. Some work has also been addressed to understanding the QD formed by an isolated C_{60}–molecule located between two metallic tips [12–14], but in these references those many-body corrections have been neglected.

In this paper we analyze theoretically a C_{60} sandwiched between two Au(1 1 1) based tips, as a model system for understanding the nanocontact between a metal and an organic molecule, including the many-body corrections mentioned above. We study the fully relaxed nanocontact with variable tip/tip distance, combining a DFT calculation in the local density approximation (LDA) of its geometrical and electronic properties with the induced interface potential associated with the charge transfer as described by the IDIS-model. In particular, we show how the barrier formation at the molecular level can be related to the effective intrasite charging energy of the molecule, this quantity allowing us to obtain the transport energy gap of the molecule, and the frontier molecular orbital levels, as a function of the tip–molecule distance [19,32]. In a further step, we combine the calculation of the effective on-site coulomb repulsion with a "scissor" hamiltonian [19,36] to determine selfconsistently the transport energy gap for each tip/C_{60}/tip geometry. Finally, we make contact with other theoretical and experimental approaches by analyzing the case of a single C_{60} molecule on a Au-surface.

2. Model and mechanical study

In our DFT simulations, the Au-tips consist of pyramidal-shape clusters of 46 Au atoms in a (1 1 1) geometry, with 3, 6, 10 and 27 atoms in the first, second, third and last layer respectively [38] (see Fig. 1). The Au/C_{60} interface is analyzed using the FIREBALL code [37], with a LDA-exchange correlation functional and a basis set of short-range numerical atomic-like orbitals (NAOs); the carbon atoms are described in terms of an optimized sp^3 NAOs basis [40] with cut-off radii (in a.u.): 4.5 (s), 4.5 (p), while for the Au atoms we use a sp^3d^5 basis defined with the following cut-off radii (in a.u.): 4.6 (s), 5.2 (p) and 4.1 (d) [36]. This DFT-LDA technique has been slightly modified by shifting the metal energy levels in order to have an appropriate MO level alignment before the contact is established [30,36]: in this paper we have taken initially the Au work-function 0.3 eV above the gas-phase C_{60}-midgap [34]. In addition to this shift, we have also introduced in the molecule a "scissor" operator to calculate the molecule energy gap selfconsistently (see below). The contact formation is analyzed by approaching each Au-tip in steps of 0.1 Å; after each step the atoms are relaxed to their corresponding minimum energy positions, excepting the atoms in the last Au-layer of both tips, which are fixed. The electrical conductance of the system is calculated at each step of the deformation using a Keldish–Green's function approach [41,42], together with the first-principles hamiltonian obtained after the relaxation.

Fig. 1 shows the calculated geometry of the tip/C_{60}/tip contact as a function of the distance, d, measured between the fixed Au-layers of both tips. Initially (Fig. 1A), C_{60} is attracted by the tips, its diameter increasing along the tip–tip direction (see Fig. 2b). The buckyball suffers, however, a slight rotation (Fig. 1B) in the attractive region between distances d = 23.7 and 26.4 Å, where the molecule jumps between different minima in such a way that the force cannot be calculated as the derivative of the energy (in Fig. 2a this is represented by a dashed line for the force which is only a guide to the eye, calculated smoothing the energy curve). When the force is $\sim$0, the C_{60} returns to its original orientation, and after that, the molecule starts to be compressed (Fig. 1C), shortening its diameter along the tip–tip direction. Eventually, the tips starts to break (Fig. 1D). Notice also that the maximum attractive energy for one interface is 2.2 eV, and that the maximum attractive force is (probably) in the order of 3.8 nN; as expected, this force is around twice the one calculated for a tip/nanotube contact of the same diameter [38]. Van der Waals forces are found to be small (less than 0.5 nN) and are not discussed here (see [38]).

The conductance at the Fermi level of the tip/C_{60}/tip contact (Fig. 2b) shows a maximum of $1.8G_0$ ($G_0 = 2e^2/h$) in the compressive region, while it is $\sim 0.8G_0$ for the equilibrium position. For long distances, $d > 25.7$ Å, 3 channels contribute equally to the conductance, as corresponds to the three orbitals of the lowest unoccupied molecular orbital (LUMO) level while, due to the symmetry breaking of LUMO level, only two channels contribute at short distances. At intermediate distances only one channel dominates the conductance due to the rotation of the molecule.

3. Electronic analysis: unified IDIS-model and self-interaction correction

Fig. 3 shows the density of states projected on the C_{60} orbitals for the cases A, B and C of Fig. 1. For each case, the LUMO and highest occupied molecular orbital (HOMO) levels, the molecule Charge Neutrality Level (CNL), the Fermi energy E_F (zero energy) and the metal (effective) work-function, Φ_M ($\widetilde{\Phi}_M$, see below), are shown. The CNL is calculated integrating the C_{60}-DOS up to charge neutrality conditions; as in a typical MO interface [30], the tip/C_{60}/tip contact reacts creating a mean potential, V^t, between the tips and the molecule that tries to align the organic CNL and the metal work-function: notice that Φ_M and E_F define respectively the initial and final metal Fermi energy with respect to the molecular levels.

In case A for which the "pillow" potential (associated with the compression of the metal electron tails at the MO interfaces due to the Pauli repulsion [30]) is negligible, that potential is created by the charge transfer between the two materials and, following the IDIS-description of MO interfaces [43], it can be identified with V^{IDIS} ($V^t = V^{IDIS}$, case A) such that:

$$eV^{IDIS} = (1 - S)(CNL - \Phi_M); \tag{1}$$

S being the interface screening parameter [30]. Notice also that:

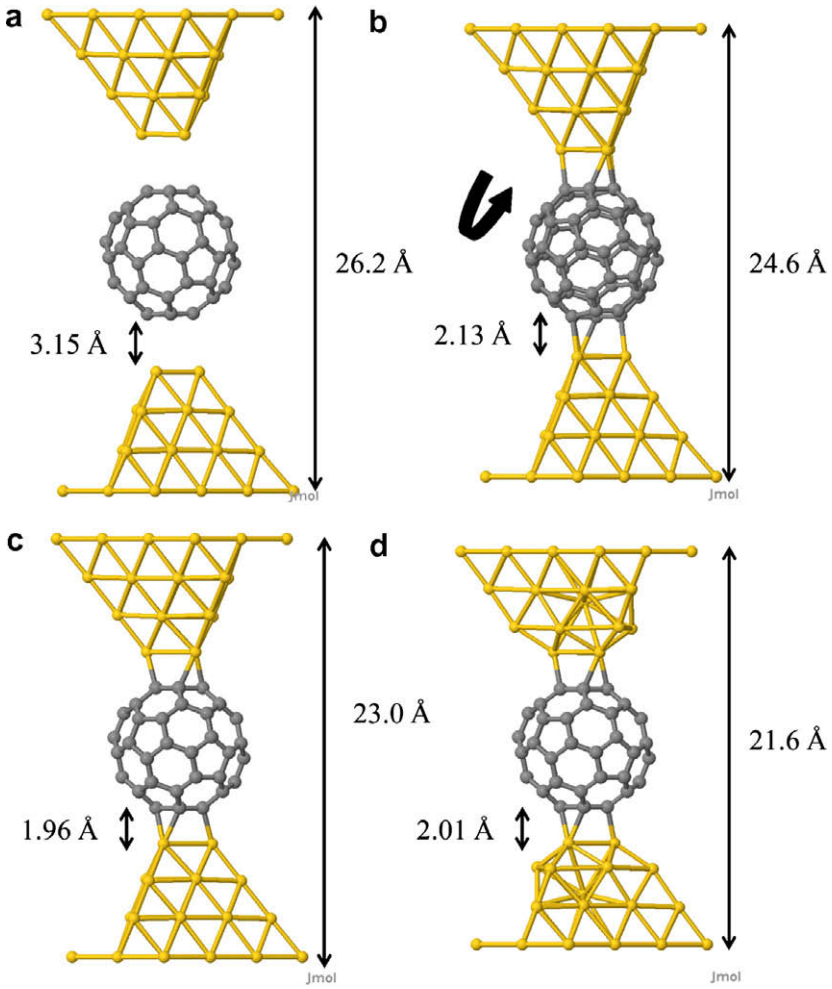

Fig. 1. (color online). Geometry of the tip/C_{60}/tip system for different values of the distance d between the fixed Au-layers. The arrow in case B suggests how the molecule rotates. (images created with Jmol [39]).

$$(CNL - E_F) = S(CNL - \Phi_M); \tag{2}$$

this equation describing how that parameter "screens" $(CNL - \Phi_M)$ to $(CNL - E_F)$.

In Fig. 3a, $CNL - \Phi_M$ = 1.1 eV and eV^{IDIS} = 0.34 eV, so that S = 0.7. We have checked, by changing in our code Φ_M fictitiously, that S is practically independent from moderate changes of the work-function value. In these calculations, the transport energy gap (the HOMO–LUMO energy difference) has been fitted to 3.6 eV (see below) moving in an opposite way the filled and empty states using a "scissor" operator, described in Ref. [36]: we stress that in $H^{scissor} = \sum_{\mu=occ.} - \Delta|\mu\rangle\langle\mu| + \sum_{\nu=empty}\Delta|\nu\rangle\langle\nu|$, $|\mu\rangle$ and $|\nu\rangle$ are the molecular orbitals of the non-interacting molecule with the deformed geometry of Fig. 1. As shown in Fig. 3a, the effect of the metal/C_{60} interaction is to broaden the HOMO and LUMO levels, in addition to the creation of V^{IDIS}: the effect of this induced potential is to shift rigidly the HOMO and LUMO levels, as well as the CNL, with respect to the metal Fermi energy. This suggests to calculate the charging energy of the molecule (the effective on-site coulomb interaction, U^{eff}) by dividing eV^{IDIS}, by the number of electrons transferred to the molecule (δn):

$$U^{eff} = \frac{eV^{IDIS}}{\delta n} = \frac{(1-S)(CNL - \Phi_M)}{\delta n} \tag{3}$$

a similar equation for the LUMO and HOMO levels has also been reported by Sau et al. [22]. Considering that $\delta n = (CNL - E_F)\widetilde{D}$, $\widetilde{D}$ being the mean density of states between the Fermi level and the CNL in the organic molecule, one can easily find that:

$$S = \frac{1}{1 + U^{eff}\widetilde{D}}; \tag{4}$$

in this equation $U^{eff}\widetilde{D}$ plays the same role that the term $4\pi e^2 D(E_F)\delta/A$ does in the elementary theory of Schottky-barriers [30,44].In our calculations, δn has been calculated using Löwdin population analysis [37] of C_{60} and Au orbitals and the CNL has been obtained by integrating the molecule DOS up to charge neutrality condition.

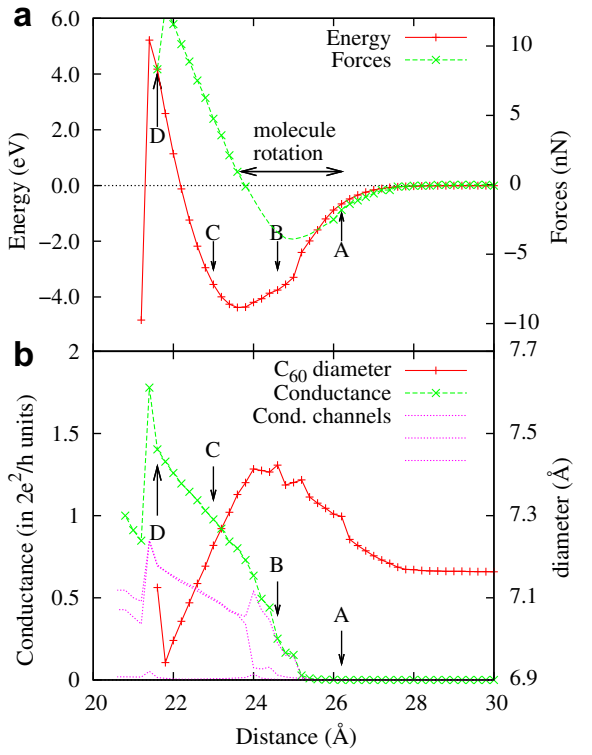

Fig. 2. (color online) (a) Energy, forces and (b) conductance at the Fermi level and the diameter of C_{60} along the contact direction, for the system shown in Fig. 1 as a function of the distance *d*.

Let us now discuss how to calculate selfconsistently the C_{60}–molecule transport energy gap. The first point to realize is that for an isolated molecule, the appropriate transport energy gap is given by the (underestimated) Kohn–Sham gap plus the self-interaction correction [19]:

$$E^t_{mol} = E^{KS}_{mol} + E^{SI}_{mol} \text{ (isolated molecule)}; \quad (5)$$

where E^{SI}_{mol} can be viewed as due to the self-interaction energy associated with the orbital charge distribution for either the HOMO or the LUMO levels [19], which we have found, for C_{60}, to be very similar. This suggests that, for a very weak MO interaction (where image potential effects are negligible), the self-interaction correction for the metal charge tunneling into the organic gap should also be the same E^{SI}_{mol}

On the other hand, image potential effects at the MO-interface induce on the metal side an opposite charge to the one appearing in the molecule, and reduce E^t_{mol} compensating partially for the self-interaction correction. Both effects taken together can be added to yield an effective charging energy that we identify with U^{eff}, as given by Eq. (3), since in this equation we include in V^{IDIS} both the self-interaction energy of the extra charge and its interaction with the opposite charge induced in the electrodes. This allows us to write for the MO-interface:

$$E^t_{mol} = E^{KS}_{mol} + U^{eff} \quad (6)$$

with U^{eff} given by Eq. (3) [22].

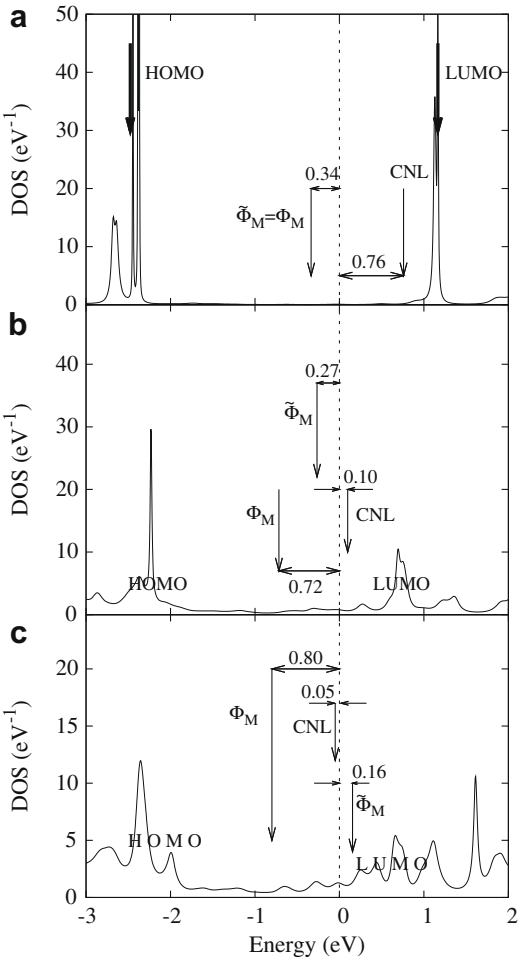

Fig. 3. (a–c) DOS (per spin) as a function of energy for geometries (A–C) in Fig. 1. Each case shows: HOMO, LUMO levels and Fermi energy (E_F, origin of energies), as well as the CNL and the (effective) work-function, ($\tilde{\Phi}_M$) Φ_M.

Then, in our calculations we determine U^{eff} and E^t_{mol} selfconsistently, using the "scissor" operator mentioned above.

1. In a first step, we define an "input" E^t_{mol} using $H^{scissor}$. This transport gap is then used in the DFT calculation.
2. From this calculation and Eq. (3) we obtain U^{eff}.
3. Then, using Eq. (6) we calculate an "output" E^t_{mol}; this new transport gap is then used to define a new "input" E^t_{mol} (step 1), defining a selfconsistent cycle.

Regarding the cases shown in Fig. 3b and c, the main difference with case A is due to the "pillow" effect that creates a potential V^{pillow} between the tips and the molecule. Then, the total potential between the two materials, V^t, can be decomposed into the IDIS, V^{IDIS}, and the "pillow", V^{pillow} potentials:

$$V^t = V^{IDIS} + V^{pillow} \quad (7)$$

V^{IDIS} being, as in case A, associated with the misalignment between the CNL and Φ_M (see Eq. (1)).

The "pillow" potential, V^{pillow}, is also the result of screening the bare one V_0^{pillow}, $V^{pillow} = SV_0^{pillow}$ [30], in the same way as $(CNL - \Phi_M)$ is screened to $S(CNL - \Phi_M) = (CNL - E_F)$. Then Eq. (7) can be rewritten as follows:

$$\begin{aligned} eV^t &= (1-S)(CNL - \Phi_M) + SeV_0^{pillow} \\ &= (1-S)(CNL - \tilde{\Phi}_M) + eV_0^{pillow} \end{aligned} \quad (8)$$

this equation shows that eV^t has a bare component, eV_0^{pillow}, independent from the interface screening, and another one, $(1-S)(CNL - \tilde{\Phi}_M)$, associated with the charge transfer between the tips and the molecule. In this component, there appears an effective metal work-function: $\tilde{\Phi}_M = \Phi_M + eV_0^{pillow}$, such that $(CNL - \tilde{\Phi}_M)$ is related to the total charge transfer between the tips and the molecule. In this way of thinking, the "Pauli exclusion" potential, V_0^{pillow}, is fully incorporated in the effective work-function $\tilde{\Phi}_M$; notice, in this regards, that the bare potential, eV_0^{pillow} in Eq. (8) also shifts the metal work-function from Φ_M to $\tilde{\Phi}_M = \Phi_M + eV_0^{pillow}$.

Fig. 3b and c shows both Φ_M and $\tilde{\Phi}_M$: the corresponding values of eV_0^{pillow} are 0.45 eV and 0.96 eV respectively. In addition to this new effect appearing in cases b and c, we also find an important broadening of the HOMO and LUMO levels that cannot be so sharply defined as in case A. This is the reason why it is necessary, in our procedure, to consider the relative shift of the metal Fermi level with respect to the CNL, instead of the metal Fermi level and either the LUMO or the HOMO levels, to define the charge transfer induced potential and calculate U^{eff}.

In our calculations for cases B and C, the initial values of $(CNL - \tilde{\Phi}_M)$ [0.37 eV (B); −0.21 eV (C)] are reduced to $(CNL - E_F) = S(CNL - \tilde{\Phi}_M)$ [0.10 eV (B); −0.05 eV (C)], yielding the following values of S: 0.26 (B) and 0.24 (C), indicating that in these two cases, for small tip–C_{60} distances the interface screening is much more effective than in case A, saturating around the energy minimum. Moreover our selfconsistent calculations yield the following values of U^{eff}: 1.6 eV (B) and 1.3 eV (C), and the following transport energy gaps: 3.2 eV (B) and 2.9 eV (C), as can be approximately appreciated from the strongly broadened HOMO and LUMO levels of those figures.

We have also calculated the case of C_{60} on a Au(1 1 1)-surface as shown in the inset of Fig. 4 in order to compare our model with other theoretical and experimental results. The DOS projected on the C_{60}–molecule for this case yields the following results: $CNL - E_F = 0.10$ eV; $E_F - \Phi_M = 0.72$ eV; and $S = 0.35$, not far from the values found for cases B and C above; we also find $U^{eff} = 1.6$ eV. Notice that in our calculations, the HOMO–LUMO gap as estimated from the calculated DOS is around 3.2 eV, slightly larger than the one measured by Lu et al. [21] using STS: 2.7 eV with an error bar of 0.3 eV, this might be due to the screening effects associated with the STS tip. It is interesting to mention that calculations of Sau et al. [22] using a GW-like approach yield $E_{gap}^{trans} = 2.5$ eV, a little too small. On the balance, we believe that the comparison with the experimental data offers a reasonable confirmation of the validity of the calculations presented here.

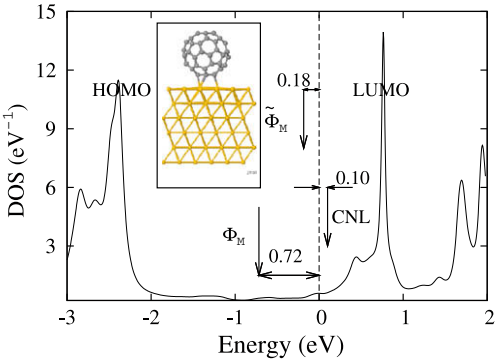

Fig. 4. (color online). DOS (per spin) as a function of energy for a single C_{60} molecule adsorbed on Au(1 1 1)-surface. Shows HOMO and LUMO levels, Fermi energy (energy origin) and (effective) metal work-function. Inset: geometry of the interface.

4. Conclusion

In conclusion, a new method is introduced to analyze the formation of a nanogap organic molecular junction, including charging effects and self-interaction corrections. In our approach, we combine a DFT-LDA calculation of the structural and electronic properties of the nanocontact with an analysis of the interface charge transfer and metal/organic molecule barrier height formation, as described by the IDIS-model. In this way, we obtain the on-site coulomb interaction, U^{eff}, associated with the injection of an electron in the molecule and calculate selfconsistently its frontier molecular orbital levels and the transport energy gap. We have illustrated this new approach, by analyzing a C_{60} molecule between two Au(1 1 1) based tips as a function of the tip–molecule distance. Our approach offers a practical fully selfconsistent technique for studying realistic single molecule nanocontacts.

Acknowledgements

This work is supported by Spanish MICIIN under contracts NAN-2004-09183-C-10-07 and MAT2007-60966, the CAM under contract 0505/MAT/0303 and the European Project MINOTOR (FP7-NMP-228424). E. Abad gratefully acknowledges financial support by the Consejería de Educación de la CAM and the FSE. C.González acknowledges the CSIC JAE-DOC contract under the program "Junta para la Ampliación de Estudios" co-funded by FSE, and the MICIIN (projects MAT-2008-01497/NAN and CSD2007-00041).

References

[1] M.A. Reed, C. Zhou, C.J. Muller, T.P. Burgin, J.M. Tour, Science 278 (1997) 252.
[2] X.D. Cui, A. Primak, X. Zarate, J. Tomfohr, O.F. Sankey, A.L. Moore, T.A. Moore, D. Gust, G. Harris, S.M. Lindsay, Science 294 (2001) 571.
[3] B. Xu, N.J. Tao, Science 301 (2003) 1221.
[4] J. Zhang, Q. Chi, A.M. Kuznetsov, A.G. Hansen, H. Wackerbarth, H.E.M. Christensen, J.E.T. Andersen, J.J. Ulstrup, Phys. Chem. B 106 (2002) 1131.
[5] N.J. Tao, Nat. Nanotechnol. 1 (2006) 173.
[6] F. Chen, J. Hihath, Z.F. Huang, X.L. Li, N.J. Tao, Annu. Rev. Phys. Chem. 58 (2007) 535.
[7] X.Y. Xiao, B.Q. Xu, N.J. Tao, Nano Lett. 4 (2004) 267.

[8] R. Stadler, K.W. Jacobsen, Phys. Rev. B 74 (2006) 161405.
[9] S. Kubatkin, A. Danilov, M. Hjort, J. Cornil, J.-L. Brédas, N. Stuhr-Hansen, P. Hedegård, T. Bjørnholm, Nature (London) 425 (2003) 698.
[10] H. Park, J. Park, A.K.L. Lim, E.H. Anderson, A.P. Alivisatos, P.L. McEuen, Nature (London) 407 (2000) 57.
[11] M.P. Shores, M. Bockrath, J.R. Long, H. Park, Nature (London) 417 (2002) 725.
[12] J.J. Palacios, Phys. Rev. B 72 (2005) 125424.
[13] J.J. Palacios, A.J. Pérez-Jiménez, E. Louis, J.A. Vergés, Phys. Rev. B 64 (2001) 115411.
[14] N. Sergueev, A.A. Demkov, H. Guo, Phys. Rev. B 75 (2007) 233418.
[15] M. Ruben, A. Landa, E. Lörtscher, H. Riel, M. Mayor, H. Görls, H.B. Weber, A. Arnold, F. Evers, Small 4 (12) (2008) 2229.
[16] A.K. Mahapatro, J. Ying, T. Ren, D.B. Janes, Nano Lett. 8 (8) (2008) 2131.
[17] M. Kiguchi, O. Tal, S. Wohlthat, F. Pauly, M. Krieger, D. Djukic, J.C. Cuevas, J.M. van Ruitenbeek, Phys. Rev. Lett. 101 (2008) 046801.
[18] G. Heimel, E. Zojer, L. Romaner, J.-L. Brédas, F. Stellacci, Nano Lett. 9 (7) (2009) 2559.
[19] F. Flores, J. Ortega, H. Vazquez, Phys. Chem. Chem. Phys. 11 (2009) 8658.
[20] E.V. Tsiper, Z.G. Soos, W. Gao, A. Kahn, Chem. Phys. Lett. 360 (2002) 47.
[21] X. Lu, M. Grobis, K.H. Khoo, S.G. Louie, M.F. Crommie, Phys. Rev. B 70 (2004) 115418.
[22] J.D. Sau, J.B. Neaton, H.J. Choi, S.G. Louie, M.L. Cohen, Phys. Rev. Lett. 101 (2008) 026804.
[23] H. Ishii, K. Sugiyama, E. Ito, K. Seku, Adv. Mater. (Weinheim, Ger.) 11 (1999) 605.
[24] I.G. Hill, J. Schwartz, A. Kahn, Org. Electron. 1 (2000) 5.
[25] C. Shen, A. Kahn, Org. Electron. 2 (2001) 89.
[26] X. Crispin, V. Geskin, A. Crispin, J. Cornil, R. Lazzaroni, W.R. Salaneck, J.L. Brédas, J. Am. Chem. Soc. 124 (2002) 8131.
[27] M. Eremtchenko, D. Bauer, J.A. Shaefer, F.S. Tautz, New J. Phys. 6 (2004) 4.
[28] P.S. Bagus, V. Staemmler, C. Wöll, Phys. Rev. Lett. 89 (2002) 096104.
[29] G. Witte, S. Lukas, P.S. Bagus, C. Wöll, Appl. Phys. Lett. 87 (2005) 263502.
[30] H. Vázquez, Y.J. Dappe, J. Ortega, F. Flores, J. Chem. Phys. 126 (2007) 144703.
[31] M.G. Betti, A. Kanjilal, C. Mariani, H. Vázquez, Y.J. Dappe, J. Ortega, F. Flores, Phys. Rev. Lett. 100 (2008) 027601.
[32] J.B. Neaton, M.S. Hybertsen, S.G. Louie, Phys. Rev. Lett. 97 (2006) 216405.
[33] C.-T. Tzeng, W.-S. Lo, J.-Y. Yuh, R.-Y. Chu, K.-D. Tsuei, Phys. Rev. B 61 (2000) 2263.
[34] L.L. Wang, H.-P. Chen, Phys. Rev. B 69 (2004) 165417;
L.L. Wang, H.-P. Chen, Phys. Rev. B 69 (2004) 045404.
[35] S.K.M. Jönsson, E. Carlegrim, F. Zhang, W.R. Salaneck, M. Fahlman, Jpn. J. Appl. Phys. 44 (2005) 3695.
[36] E. Abad, J. Ortega, Y.J. Dappe, F. Flores, Appl. Phys. A 95 (1) (2009) 119.
[37] P. Jelínek, H. Wang, J.P. Lewis, O.F. Sankey, J. Ortega, Phys. Rev. B 71 (2005) 235101;
J.P. Lewis, K.R. Glaesemann, G.A. Voth, J. Fritsch, A.A. Demkov, J. Ortega, O.F. Sankey, Phys. Rev. B 64 (2001) 195103.
[38] C. González, J. Ortega, F. Flores, D. Martínez-Martín, J. Gómez-Herrero, Phys. Rev. Lett. 102 (2009) 106801.
[39] Jmol: an open-source Java viewer for chemical structures in 3D. http://www.jmol.org/.
[40] M.A. Basanta, Y.J. Dappe, P. Jelínek, J. Ortega, Comp. Mat. Sci. 39 (2007) 759.
[41] F.J. García-Vidal, F. Flores, S.G. Davison, Prog. Surf. Sci. 74 (2003) 177.
[42] P. Jelínek, R. Pérez, J. Ortega, F. Flores, Surf. Sci. 566–568 (2004) 13.
[43] H. Vázquez, R. Oszwaldowski, P. Pou, J. Ortega, R. Pérez, F. Flores, A. Kahn, Europhys. Lett. 65 (2004) 802.
[44] E.H. Rhoderick, R.H. Williams, Metal-semiconductor Contacts, Clarendon Press, 1988.

Organic Electronics 11 (2010) 338–343

Contents lists available at ScienceDirect

Organic Electronics

journal homepage: www.elsevier.com/locate/orgel

Letter

Aminosilane monolayer-assisted patterning of conductive poly(3,4-ethylenedioxythiophene) source/drain electrodes for bottom contact pentacene thin film transistors

Ilsun Pang [a], Hyunho Kim [a], Sungsoo Kim [b], Kyunghoon Jeong [a], Hyun Suk Jung [a], Chung-Jong Yu [c], Hoesup Soh [a], Jaegab Lee [a,*]

[a] Center for Materials and Processes of Self-Assembly, School of Advanced Materials Engineering, Kookmin University, Seoul 136-702, Republic of Korea
[b] Department of Nanopolymer Materials Engineering, Pai Chai University, Daejeon 302-735, Republic of Korea
[c] Pohang Accelerator Laboratory, Pohang University of Science and Technology, Pohang 790-784, Republic of Korea

ARTICLE INFO

Article history:
Received 27 July 2009
Received in revised form 29 September 2009
Accepted 1 October 2009
Available online 8 October 2009

Keywords:
Bottom contact OTFTs
Conducting polymer
Self-assembled monolayers
Low contact resistance

ABSTRACT

This paper reports the fabrication of organic thin film transistors (OTFTs) with conducting poly(3,4-ethylenedioxythiophene) (PEDOT) electrodes using a bottom-up process consisting of the selective growth of PEDOT on a pre-patterned (3-aminopropyl)trimethoxysilane (APS) monolayer. The newly developed bottom-up process produced strongly adherent, selectively and uniformly patterned PEDOT films on oxidized substrates. In addition, the PEDOT/APS double structure showed an approximately one order of magnitude lower leakage current and contact resistance than the Au/Ti electrodes. The lower leakage current was due to the additional blocking effects by APS monolayer in the PEDOT/APS structure; the lower contact resistance was attributed to the better quality of pentacene films formed on PEDOT electrodes than that of the gold electrodes.

© 2009 Elsevier B.V. All rights reserved.

1. Introduction

Organic thin film transistors (OTFTs) have attracted considerable attention for their potential applications to low cost and low temperature fabrication of flexible devices [1–5]. Significant improvement in the performance of organic semiconductor materials, especially pentacene, has been reported [6–11]. In addition, the recent development of highly conducting π-conjugated polymers provided the possible replacement of gold electrodes, which has further reduced the material and processing cost. Conducting polymer electrodes provide a low contact resistance to semiconducting polymers due partly to the lower barrier height for hole injection, and the negligible interface morphological discontinuity at the organic–organic interface [12–14]. Among these polymers, poly(3,4-ethylenedioxythiophene) (PEDOT) has attracted particular attention as a potential electrode of OTFT and organic light emitting diodes (OLED) on account of its low band gap (1.5–1.7 eV), as well as its excellent electrochemical stability and transmittance in the visible range [15–19]. To date, a variety of methods, such as polymer dispersion with a water soluble polyelectrolyte [20], electropolymerization [21] and direct oxidative polymerization [22], have been used to produce PEDOT thin films. However, there are no reports of the production of pure thin films. Recently, Winther-Jensen and West and Kim et al. [23,24], reported that 3,4-ethylenedioxythiopene (EDOT), a monomer of PEDOT, can be vaporized simply by increasing the temperature, and these molecules can be polymerized rapidly on an oxidizing agent (for example, $FeCl_3$) – coated substrate, thereby producing pure films. However,

* Corresponding author. Tel.: + 82 2 941 0536.
E-mail address: lgab@kookmin.ac.kr (J. Lee).

1566-1199/$ - see front matter © 2009 Elsevier B.V. All rights reserved.
doi:10.1016/j.orgel.2009.10.001

in order to implement a vapor phase-polymerized PEDOT film in conventional TFTs, several issues, such as the poor adhesion of PEDOT films to the oxide substrate [25] and the lack of a scalable, simple, and inexpensive patterning method, needs to be addressed.

We previously reported [25,26] a method to pattern PEDOT thin films by the selective growth of PEDOT on a pre-patterned APS monolayer, which had been self-assembled on OTS monolayers microcontact-printed on an oxidized silicon wafer. This bottom-up process can produce a strongly adhered, selectively patterned PEDOT thin film on an oxidized Si wafer surface through the chemical bonds between the polymer and APS monolayer [26]. The strong tendency of the lone pair electrons on the N–H groups of APS monolayer to bind Fe (III) leads to a uniform distribution of ferric chloride on the APS monolayer, and can provide excellent selectivity in the presence of an OTS monolayer [25,26]. Therefore, this simple, scalable and inexpensive PEDOT patterning method was used to fabricate PEDOT bottom contact (BC) pentacene TFTs. The electrical performance of the OTFTs was also investigated. In addition, the Au BC OTFTs were fabricated and compared. Furthermore, the degree of crystallinity of pentacene thin films deposited on PEDOT electrodes as well as on gold electrodes was examined by using XRR to find out the dependence of crystallinity of pentacene on substrate materials and its effects on contact resistances.

2. Experimental

The thermally grown SiO_2 (100 nm) coated n^+-Si substrates (resistivity < 0.005 Ω cm) were cleaned using the Piranha cleaning method (H_2SO_4:H_2O_2 = 4:1), and then exposed to UV illumination to create hydroxyl (–OH) groups that can form a siloxane bond with the OTS monolayer [27]. A polydimethylsiloxane (PDMS) stamp was then used for microcontact printing to transfer the OTS SAM patterns to the SiO_2 surface, leaving a hydrophobic stamped area. The OTS coated area showed a typical water contact angle of approximately 109°. After OTS patterning, a negative pattern was formed with APS monolayers by dipping it into a silane solution (0.1 mM APS + 1 μM acetic acid in 50 ml ethyl alcohol) for 30 min. After rinsing with ethyl alcohol followed by drying with blowing N_2, a 3 wt.% $FeCl_3$ solution was spread over the monolayer surface and spun at 2500 rpm using a spin coater for 90 s. The $FeCl_3$-coated sample was placed on the top sample holder with the surface facing down in a hot wall oven. EDOT was then placed in a container. The EDOT was vaporized for 3 min at 80 °C to selectively form PEDOT films on the pre-patterned APS monolayer. The sample was rinsed with methanol, and dried in a desiccator before depositing the pentacene semiconductor layer. A 70 nm-thick pentacene layer was thermally evaporated in a vacuum of 7×10^{-6} Torr at a substrate temperature of 60 °C. The deposition rate was approximately 1 Å/s. Fig. 1 shows the fabrication sequence for the bottom contact pentacene TFTs formed on the n^+-Si substrate.

The transmission line model (TLM) patterns were used to characterize the bottom contact resistance of the PEDOT BC pentacene TFTs. The width of the TLM patterns measured from the optical images was 51 μm and the length was varied; 8, 14, 25, 46, and 84 μm. The polymer thickness and sheet resistance was measured using an ellipsometer (Sentech SE-800) and a four point probe (Chang Min Co., Ltd, Korea). The static water contact angles were measured with a goniometer (Phoenix 300, Surface Electro Optics Co. Ltd, Korea) and recorded with a CCD camera. Atomic force microscopy, AFM (SPA 400 Seiko, Japan; trapping mode, scan speed: 0.5–0.6 Hz, scan size: 10×10 μm^2) was used to measure the surface morphology. X-ray reflectivity (XRR) measurement was done at 5A HFXS beamline of Pohang Light Source with the X-ray energy of 11.6 keV in order to get information about the structures of pentacene thin films deposited on PEDOT or gold electrodes. These structures were compared with that of pentacene on OTS monolayer. Finally, a semiconductor parameter analyzer (HP4155C) was used to determine the electrical properties.

3. Results and discussion

Fig. 2a shows an optical image of a selectively formed PEDOT source and drain electrodes on a SiO_2-coated n^+-Si substrate (gate electrode). The patterned PEDOT electrodes had a defined channel width and length between 70 and 15 μm, respectively. The AFM image in Fig. 2b shows the edge of the PEDOT pattern with a tapered, smooth surface. The thickness and sheet resistance of the PEDOT thin film were 133 nm and 18 Ω/□, respectively.

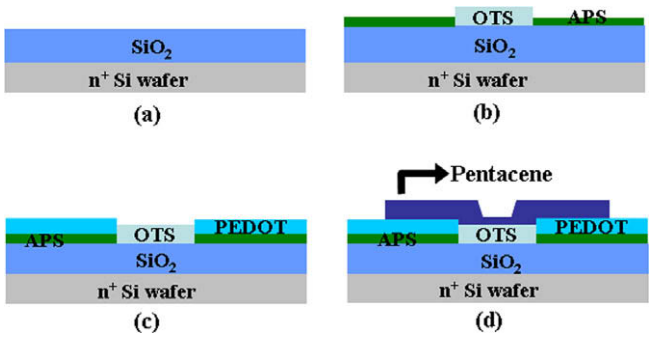

Fig. 1. Schematic diagram showing the fabrication of pentacene OTFTs of (a) dry oxidation of n^+-Si, (b) micro contact printing of OTS and then formation of APS monolayers by dipping it into silane solution, (c) selective vapor deposition of PEDOT and (d) deposition of pentacene.

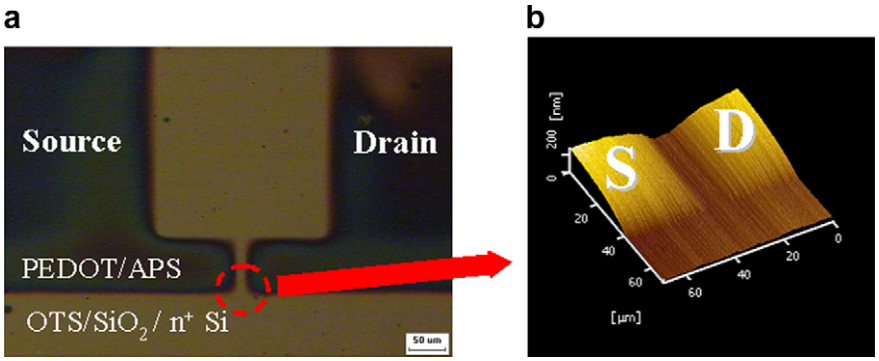

Fig. 2. (a) Optical image of selectively deposited PEDOT on APS patterns, and (b) AFM images of the gap between the source and drain electrodes of PEDOT.

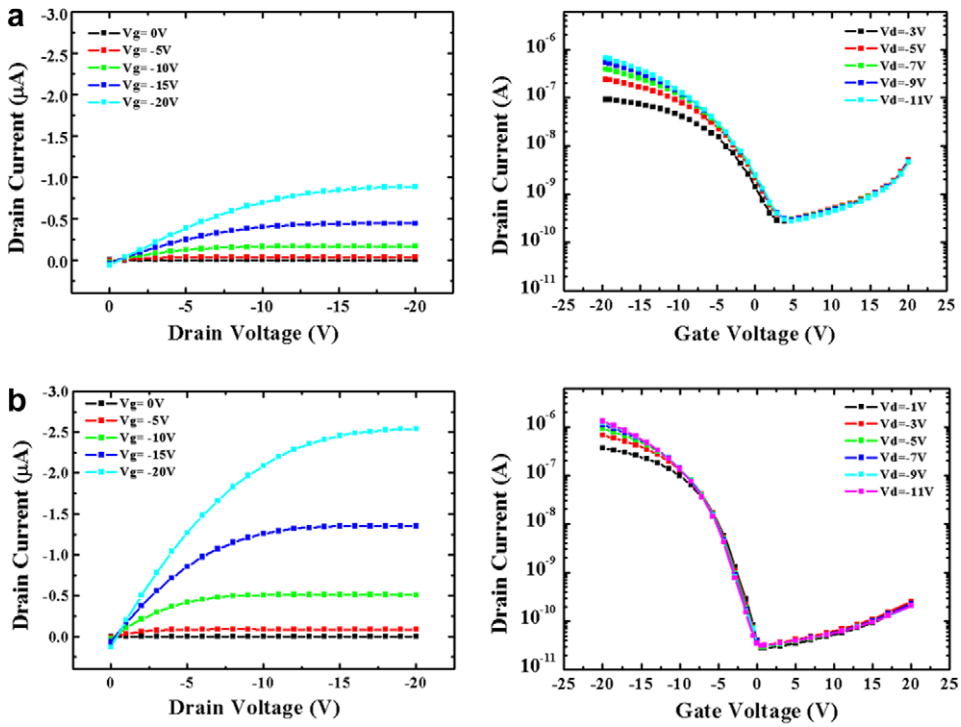

Fig. 3. Electrical characteristics of pentacene-based OTFT with (a) Au/Ti electrodes and (b) with PEDOT electrodes, respectively.

Fig. 3 shows the typical electrical output and transfer characteristics of the BC pentacene TFTs with (a) Au/Ti electrodes and (b) PEDOT electrodes, respectively. The field-effect mobility, on/off current ratio, subthreshold slope and threshold voltage of the gold BC pentacene TFTs with a channel length of 70 μm were 0.1 $cm^2/V\,s$ in the saturation regime ($V_{DS} = -11$ V), 2.4×10^3, 3.6 V/decade and −1.4 V, respectively. On the other hand, the PEDOT BC OTFTs with a channel length of 25 μm showed an improved field-effect mobility, on/off current ratio, subthreshold slope and the threshold voltage of 0.13 $cm^2/V\,s$, 1.2×10^5, 2.04 V/decade, and 0.527 V, respectively, as shown in Fig. 3b. In some OTFTs, for small V_{DS} a large fraction of V_{DS} may be dropped across the contact resistance rather than the intrinsic field-effect transistor, while at larger V_{DS} the fraction of V_{DS} dropped across the contacts may decrease and the contact resistance is less significant. Since small values of V_{DS} are used to extract linear mobility, the measured mobility may be significantly smaller than the measured saturation mobility in the case of high contact resistance. The linear mobility of the PEDOT-electrode and gold-electrode TFTs was calculated to be 0.128 $cm^2/V\,s$ and 0.058 $cm^2/V\,s$, respectively. Significantly smaller linear mobility than the saturation mobility in the gold-electrode OTFT was compared with the similar value of the linear and saturation mobility in the PEDOT-electrode device. Much higher contact resistance of gold-electrode transistor than that of PEDOT-electrode one was responsible for the decreased linear mobility. It was also noted that the significantly increased on/off current ratio for the PED-

OT contact OTFT was attributed to both the decrease in leakage current and increase in on-current. The PEDOT/APS BC OTFTs showed an approximately one order lower leakage current than the Au/Ti BC OTFTs. This was attributed to the presence of an APS monolayer between the PEDOT layer and SiO_2, which acts as an additional blocking layer to effectively reduce the leakage current [28]. The total resistance is the sum of the channel resistance and contact resistance, and the channel resistance for the two types of OTFTs is similar. Therefore, the increased on-current for the PEDOT OTFTs can be understood by comparing the contact resistance between pentacene and the electrodes (both gold and PEDOT).

The contact resistance was evaluated by fabricating TLM patterns using a selectively deposited PEDOT on a microcontact-printed APS monolayer followed by the deposition of a pentacene layer. Gold TLM patterns were fabricated using a lift-off technique for the patterning of gold pads followed by the deposition of a pentacene layer. Fig. 4 shows a plot of the corresponding resistance as a function of the distance between the pads and the voltages applied to the n^+-Si substrate. For the PEDOT TLM patterns, stable electrical *I–V* curves were measured at gate voltage of −20 V, providing contact resistances, R_C, of $1.8 \times 10^6\ \Omega$. The normalized contact resistances, R_C' (=$R_C \times W$, *W*: channel width), was 9.2 k Ω cm, which are similar to those of gold TC pentacene TFTs [29].

For the gold TLM patterns, the electrical *I–V* curve was measured at a gate voltage of −20 V, providing a slope (R_S/*W*) of $4.5 \times 10^5\ \Omega/\mu m$, which is similar to that of the PEDOT TLM structures. This suggests that the channel resistance is similar irrespective of the contact resistance. However, the corresponding contact resistance of the gold TLM was increased to $1.3 \times 10^7\ \Omega$, which is approximately one order of magnitude higher than that of the PEDOT contacts to pentacene. The increased contact resistance can be a main contributor to the decreased on-current and reduced linear mobility. In an OTFT device, the barrier height between semiconductor and electrode, and the crystalline quality of semiconductor on the electrodes are major factors determining the contact resistance. As a result, we have used XRR to determine the quality of pentacene deposited on the electrodes (PEDOT and gold) and then compared with the pentacene on OTS monolayer. We have measured X-ray specular scans of the three samples: pentacene/OTS/Si (POS), pentacene/PEDOT/Si (PPS), and pentacene/Au/Ti/Si (PATS), all of which were deposited at 60 °C. The experiment was performed at 5C2 of the Pohang Light Source (Korea). The X-ray energy was 10 keV. Fig. 5a shows true specular scans in which the background signals from the substrate are removed. True specular scans probe density variation in the normal direction to substrate surface. POS shows the typical pentacene peaks at $q = 0.41\ Å^{-1}$ from the film phase, $0.44\ Å^{-1}$ from the bulk phase and their second order peaks [30], where $q = 4\pi/\lambda \times \sin\theta$, λ is the X-ray wavelength, and θ is the incident angle to the sample surface. PPS shows a very weak and broad diffraction peak near $q = 0.41\ Å^{-1}$, but PATS does not. This difference can be more easily noted in the Patterson function which is simply the Fourier transformation of the true specular scans in normalized form [31]. It can be shown that the peak positions in the Patterson functions indicate the distances between regions where the density is changing rapidly. Fig. 5c shows the resulting Patterson functions and POS shows the typical layer spacing of pentacene 15.3 Å, in good agreement with previous reports. The Patterson function of PPS is different to that of POS, but shows four peaks (marked by the arrows) separated by 11, 14, and 13 Å which would indicate pentacene molecules tilted to the surface normal direction. The Patterson function of PATS, however, only shows the peaks corresponding to the interfaces between pentacene/Au, Au/Ti and Ti/Si; it does not indicate any layered pentacene molecules at all.

Another structural aspect of the films can be found from the off-specular scans by +0.07° and −0.07° from the specular direction as shown in Fig. 5b. These scans probe the average crystallinities of the films. The two peaks for POS are from the film phase and the bulk phase of pentacene as in the true specular scans of Fig. 5a, while PPS shows a weak peak but broad enough to include both of the pentacene phases. PATS also show a peak but the bulk phase peak is significantly suppressed. This suppression would be due to the fact that the pentacene thickness of PATS is much thinner than those of POS and PPS. Usually the film thicknesses would be estimated from the Kiessig fringes in XRR data, but the three XRR data do not show the Kiessig fringes corresponding to the thicknesses of pentacene films. The reason would be the large surface roughness of the pentacence films. The obvious Kiessig fringes in the PATS data are just from the metallic layers, Au/Ti. We, therefore, measured the thicknesses of pentacene films using AFM. The POS and the PATS were scrubbed several times with Q-tips soaked in methanol; the PPS was scrubbed just once not to remove PEDOT. The thicknesses were found to be 82.1, 83.6 and 71.1 nm for POS, PPS and PATS, respectively. Although PATS is ∼10% thinner than two others, it is still thick enough to show the bulk phase peak. A similar trend was obtained for the three films deposited at room temperature. The Patterson functions and the off-specular scans for the three films indicate that the structures of POS and PPS are the more similar than that of PATS.

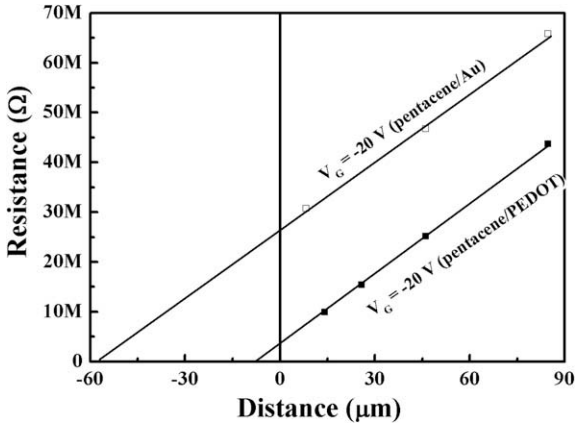

Fig. 4. The resistance as a function of the distance between the pads for gate voltage of −20 V applied in both pentacene/PEDOT structure and pentacene/Au structure.

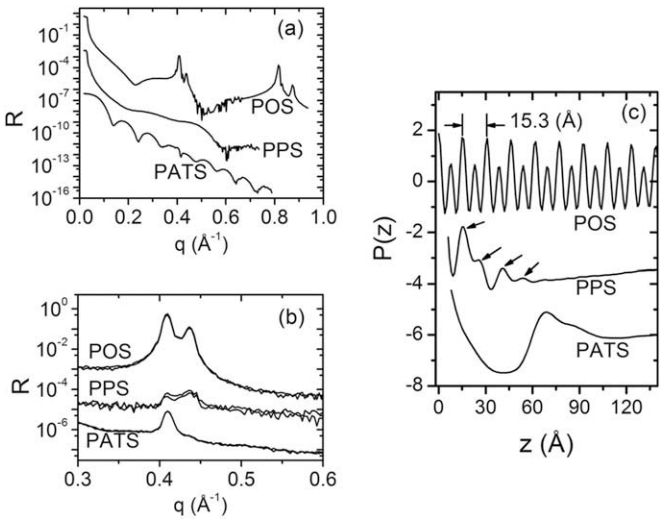

Fig. 5. (a) The true specular scans, (b) the off-specular scans and (c) the Patterson functions corresponding to (a) for three types of films: POS, PPS and PATS. Error bars are not shown in (a) and (b) for clarity. The two lines in each case of (b) represent the off-specular scans by +0.07° and −0.07° from the specular direction. POS, PPS and PATS curves in each of (a–c) are shifted vertically for clarity.

It can be concluded that the pentacene thin film evaporated on PEDOT shows better crystallinity in a region of 0–60 Å, compared with that on gold electrodes. The current flowing from the electrode-semiconductor lines to the active channel regions must be transported from the electrode–pentacene interface to the edge of the channel through the source or drain regions. Current enters the contact perpendicular to the pentacene surface and then travels through the pentacene on the electrode to reach the channel. The contact resistance from the contact to the edge of the channel can be the sum of the contact resistance between the electrode and the source/drain region of pentacene, and the sheet resistance of the pentacene of the source or drain. As a result, the better crystalline structure of pentacene on the PEDOT reduces the sheet resistance, thus leading to the lower contact resistance in PPS.

4. Conclusions

In summary, a bottom-up process was developed using a negative SAM patterning method combined with the selective growth of conducting polymer PEDOT electrodes for BC OTFTS. The negatively patterned APS monolayer provides chemically robust templates for the selective and uniform coating of $FeCl_3$ on the APS–SAM surface. This allows for the formation of highly selective patterns of PEDOT films with a smooth surface and strong adhesion to the oxide substrates. In addition, XRR analysis revealed the better crystalline structures of pentacene thin films grown on PEDOT electrodes than that on gold ones. This may be a main contributor to the lower contact resistance obtained in PPS. Furthermore, the PEDOT/APS structure effectively reduces the leakage current and provides a low contact resistance, resulting in excellent electrical characteristics. Overall, this chemically active SAM patterning and the selective growth of a conducting polymer is quite suitable for the fabrication of bottom contact TFTs.

Acknowledgement

This work was supported by the ERC (CMPS, Center for Materials and Processes of Self-Assembly) program of MOST/KOSEF (R11-2005-048-00000-0).

References

[1] K. Shibata, K. ishikawa, H. Takezoe, H. Wada, T. Mori, Appl. Phys. Lett. 92 (2008) 023305.
[2] C. Reese, M. Roberts, M. Ling, Z. Bao, Mater. Today September (2004) 20.
[3] H.E. Katz, Z. Bao, S.L. Gilat, Acc. Chem. Res. 34 (2001) 359.
[4] C.D. Dimitrakopoulos, P.R.L. Malenfant, Adv. Mater. 14 (2002) 99.
[5] Z. Bao, Adv. Mater. 12 (2000) 227.
[6] K.H. Choi, D.K. Hwang, K.M. Lee, J.H. Kim, S.I. Im, Electrochem. Solid-State Lett. 10 (2007) H114.
[7] U. Zschieschang, H. Klauk, M. Halik, G. Schmid, C. Dehm, Adv. Mater. 15 (2003) 1147.
[8] H. Klauk, M. Halik, U. Zschieschang, F. Eder, G. Schmid, C. Dehm, Appl. Phys. Lett. 82 (2003) 4175.
[9] C.S. Kim, S.J. Jo, S.W. Lee, W.J. Kim, H.K. Baik, S.J. Lee, J. Electrochem. Soc. 154 (2007) H102.
[10] T. Minari, T. Nemoto, S. Isoda, J. Appl. Phys. 99 (2006) 034506.
[11] S.Y. Yang, K. Shin, C.E. Park, Adv. Mater. 15 (2005) 1806.
[12] K. Shibata, H. Wada, K. Ishikawa, H. Takezoe, T. Mori, Appl. Phys. Lett. 90 (2007) 193509.
[13] D. Li, L.J. Guo, Appl. Phys. Lett. 88 (2006) 063513.
[14] D.J. Grundlach, Y.Y. Lin, T.N. Jackson, S.F. Nelson, D.G. Schlom, IEEE Electron Dev. Lett. 18 (1997) 87.
[15] G. Gustafsson, Y. Gao, G.M. Tracy, F. Klavetter, N. Colaneri, A.J. Heeger, Nature 357 (1993) 477.
[16] J. Gao, A.J. Heeger, J.Y. Lee, C.Y. Kim, Synth. Met. 82 (1996) 221.
[17] Y. Cao, G. Yu, C. Zhang, R. Menon, A.J. Heeger, Synth. Met. 87 (1997) 171.
[18] J.C. Scott, S.A. Carter, S. Karg, M. Angelopoulos, Synth. Met. 85 (1997) 1197.
[19] S. Cho, S.H. Park, K. Lee, J. Korean Phys. Soc. 47 (2005) 474.
[20] D. Hohnholz, H. Okuzaki, A.G. MacDiarmid, Adv. Funct. Mater. 15 (2005) 51.
[21] A. Baba, J. Lubben, K. Tamada, W. Knoll, Langmuir 19 (2003) 9058.
[22] D.M. DeLeeuw, P.A. Kraakman, P.E.G. Bongaerts, C.M.J. Mutsaers, B.B.M. Klaassen, Synth. Met. 66 (1994) 263.
[23] B. Winther-Jensen, K. West, Macromolecules 37 (2004) 4538.
[24] J. Kim, E. Kim, Y. Won, H. Lee, K. Suh, Synth. Met. 139 (2003) 485.
[25] S.S. Kim, I.S. Pang, J.G. Lee, Macromol. Rapid Commun. 28 (2007) 1574.
[26] I.S. Pang, S.S. Kim, J.G. Lee, Surf. Coat. Technol. 201 (2007) 9426.

[27] D.L. Allara, A.N. Parikh, F. Rondelez, Langmuir 11 (1995) 2357.
[28] J. Wang, X. Yan, Y. Xu, J. Zhang, D. Yan, Appl. Phys. Lett. 85 (2004) 5424.
[29] J. Zaumseil, K.W. Baldwin, J.A. Rogers, J. Appl. Phys. 93 (2003) 6117.
[30] T. Kakudate, N. Yoshimoto, Y. Saito, Appl. Phys. Lett. 90 (2007) 081903.
[31] C.-J. Yu, A.G. Richter, J. Kmetko, S.W. Dugan, A. Datta, P. Dutta, Phys. Rev. E 63 (2001) 021205.

Organic Electronics 11 (2010) 344–350

Contents lists available at ScienceDirect

Organic Electronics

journal homepage: www.elsevier.com/locate/orgel

Letter

Enhancement of the field-effect mobility of solution processed organic thin film transistors by surface modification of the dielectric

Lin Jiang [a], Jie Zhang [b], Daniel Gamota [b], Christos G. Takoudis [a,c,*]

[a] Department of Chemical Engineering, University of Illinois, 810 S. Clinton St., Chicago, IL 60607, United States
[b] Printovate Inc., Palatine, IL 60196, United States
[c] Department of Bioengineering, University of Illinois, 851 S. Morgan St., Room 218 Science and Engineering Offices(SEO), Chicago, IL 60607, United States

ARTICLE INFO

Article history:
Received 28 August 2009
Accepted 20 October 2009
Available online 23 October 2009

Keywords:
OTFT
Solution-processing
Surface modification
Organosilanes

ABSTRACT

The electrical performance of organic thin film transistors (OTFTs) is profoundly affected by organic semiconductor crystal formation and molecular ordering. The molecular ordering induced by self-assembly mechanisms can improve carrier mobility by a few orders of magnitude. In this work, the dielectric surface was modified to obtain preferred chemical functional groups that promote semiconductor ordering on the dielectric surface. OTFTs were fabricated using heavily p-doped silicon wafers as the gate electrode and thermally grown SiO_2 as the dielectric. Organosilanes, (3-mercaptopropyl)triethoxysilane and p-tolyltrimethoxysilane were used to modify the dielectric surface. Organic semiconductor, bis(triisopropylsilylethynyl) pentacene, was solution-cast as the semiconductor layer. X-ray photoelectron spectroscopy was used to characterize the modified dielectric surface. The analysis from atomic force microscopy indicated improved ordering in the semiconductor layer on silane treated dielectric surfaces. Electrical characterizations showed that the field-effect carrier mobility was enhanced by two orders of magnitude with dielectric surface modifications.

© 2009 Elsevier B.V. All rights reserved.

1. Introduction

During the past decade, organic thin film transistors (OTFTs) have been studied extensively for printed integrated circuits (p-ICs) as an alternative to traditional inorganic based (e.g., silicon) ICs. Compared to traditional inorganic TFTs, OTFTs have lower mobilities and slower switching speeds; therefore, OTFTs are more likely to suit applications requiring large area circuit distribution, structural flexibility, and low product cost. Commonly used organic semiconductors are conjugated polymers, oligomers, and small molecules [1,2]. The highest reported field-effect mobility for an OTFT was 6 cm^2/V s for a pentacene and C_{60} based OTFT fabricated using vacuum deposition [3]. High vacuum deposition processes are costly and the size of the substrate is limited by the dimensions of the vacuum chamber. Thus, these inherent limitations make this method unsuitable to meet the attributes of many OTFTs applications, such as large area and low cost. Pentacene cannot be solution processed; however, bis(triisopropylsilylethynyl) pentacene (TIPS) is a solution processable pentacene that shows great promise [4–8]. In this study, we investigate the performance of OTFTs fabricated using TIPS semiconductor material.

Previously conducted studies have demonstrated that OTFT electronic properties, such as the threshold voltage, device mobility and on/off current ratio, are strongly dependent on the preparation of the surface on which the organic film material is deposited [9–19]. Thus, surface modification is important in enhancing the electronic

* Corresponding author. Address: Departments of Chemical Engineering and Bioengineering, University of Illinois at Chicago, 851 S. Morgan St. (M/C 063), Chicago, IL 60607-7052, United States. Tel.: +1 312 355 0859/413 7677.
E-mail address: takoudis@uic.edu (C.G. Takoudis).

1566-1199/$ - see front matter © 2009 Elsevier B.V. All rights reserved.
doi:10.1016/j.orgel.2009.10.015

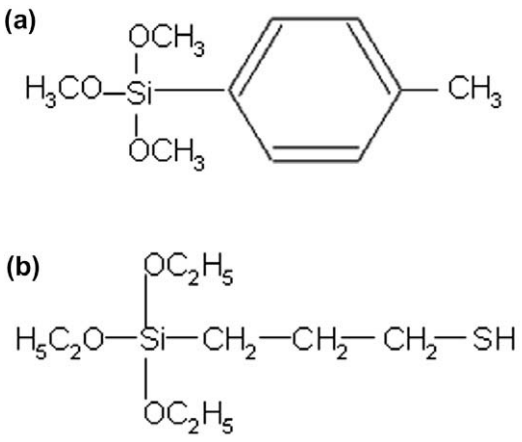

Fig. 1. Molecular structures of TTMS (a) and MPTES (b).

properties of OTFTs. During the surface modification process, a chemical moiety is selected as a self-assembling monolayer (SAM) that is applied to enhance π–π conjugation during organic semiconductor film formation [10] and to induce the local electrical field for carrier accumulation [14]. Organosilanes, such as hexamethyldisilazane (HMDS) and octyltriethoxylsilane (OTS), are commonly used SAM materials for pentacene [9–11]. These organosilanes are terminated with hydrophobic functional groups to decrease the surface energy and to enhance the ordering of pentacene molecules deposited by vacuum deposition [14,18].

In this study, for our solution-processed semiconductor material, organosilanes having hydrophilic terminal groups, such as (3-mercaptopropyl)triethoxysilane (MPTES), and organosilanes similar in chemical structure to TIPS, such as p-tolyltrimethoxysilane (TTMS), were selected as SAM candidates. The molecular structures for TTMS and MPTES are shown in Fig. 1. After surface modification with MPTES, the dielectric surface was hydrophilic which was suitable for deposition of the semiconductor film via solution processing. The existing SAM layer assisted molecular ordering of the semiconductor which in turn enhanced the field-effect mobility. The dielectric surface modified by TTMS was less hydrophilic but still enhanced semiconductor molecular ordering. It is believed that the enhanced ordering is partially due to the presence of a benzene ring in both TTMS and the semiconductor film; the benzene ring facilitates the compact alignment of the different molecules at the interface [20]. This, in turn, results in the enhancement of the field-effect mobility.

2. Experiment – device fabrication

Heavily doped p-type silicon samples (resistivity, 0.005 V cm/A) were cleaned using piranha solution, followed by rinsing in deionized (DI) water and nitrogen blow-drying. Next, the wafers were oxidized in dry oxygen at 1000 °C for 150 min resulting in the growth of a SiO_2 layer. The thermally grown SiO_2 was 150 nm-thick, measured using ellipsometry (J.A. Woollam Co., Inc., Model M-44). These samples were subjected to a second piranha treatment to obtain –OH groups on the surface of the grown SiO_2 layer. The –OH groups were required to aid the bonding of organosilanes to the surface during the subsequent processing steps [21,22]. The samples were then dipped in the organosilane solutions (10% in toluene) at room temperature for 60 min. After this step, the samples were rinsed sequentially with toluene, isopropyl alcohol (IPA) and DI water to remove excess organosilane solution followed by blow-drying with nitrogen. A gold (Au) source (S) and drain (D) of 50 nm thickness were deposited by e-beam evaporation using a shadow mask. A titanium (Ti) layer of 5 nm thickness was used as the adhesion layer. The channel length and width were 70 and 600 μm, respectively. Finally, the semiconductor precursor solution (1% TIPS in toluene) was rod-coated on the S/D to complete the fabrication of the bottom-gate field-effect transistors.

Contact angle measurements using Drop Shape Analysis Software (Version 1.00.17.0) were carried out to assess the hyrdrophobicity of the surfaces. X-ray photoelectron spectroscopy (XPS) was used to investigate the chemical composition and elemental bonding states of the dielectric surface – Kratos AXIS-165 spectrometer with a monochromatic Al Kα (1486.6 eV) X-ray source. Atomic force microscopy (AFM; Veeco MultiMode III) in the contact mode was used to probe the morphology of the semiconductor film. The OTFT electrical characterization was conducted using a Keithley 4200 Semiconductor Characterization System. The test was conducted in dark and in a nitrogen purged environment.

3. Results and discussion

The hydrophilicity of the treated surfaces was characterized by surface contact angle measurements of a water droplet on the SiO_2 surface before and after surface treatment. Initial studies were performed using HMDS and OTS; however, since surfaces treated with these organosilanes are strongly hydrophobic, they are incompatible with the selected solution-processed semiconductor films (e.g., TIPS). The incompatibility was observed during the inhomogeneous crystal formation of TIPS when rod-coated on surfaces treated by HMDS and OTS; contact angle measurements showed that the surfaces were higher than 80°. The resulting high contact angles did not enable fabrication of top contact mode transistors. TIPS material did not spread evenly over the device layer surfaces and it preferentially formed as a drop prior to solvent evaporation and therefore did not result in the formation of a continuous film. Therefore, MPTES and TTMS were selected as surface modification agent in this study.

As it is shown in Fig. 2a, MPTES and TTMS surface treatments resulted in higher surface contact angles for a water droplet than that on an untreated SiO_2 surface. This increased hydrophobicity was expected for the MTPES and TTMS-treated surfaces, because after surface modification alkyl groups are added onto the surface [16,18]. Further, the terminal group $–CH_3$ in TTMS is more hydrophobic than –SH in MPTES, which further suggests why the contact angle is larger on TTMS-treated surfaces than that on MPTES-treated ones. The capacitance values for the dielectric film modified with the different organosilanes are

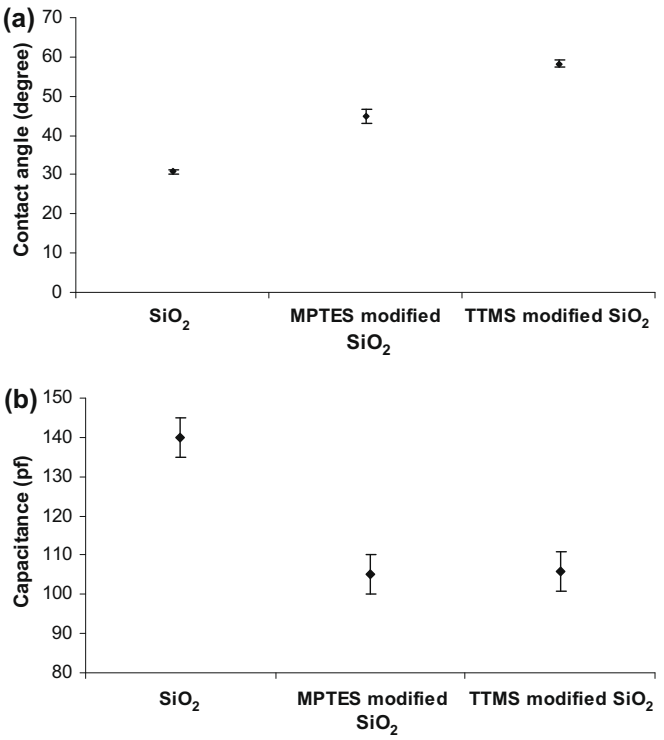

Fig. 2. DI water contact angles (a) and capacitances (b) of dry oxygen-grown SiO_2 surface, and SiO_2 surfaces modified with MPTES and TTMS.

shown in Fig. 2b; they are lower than that of the untreated SiO_2 devices. This decrease in the capacitance may be attributed to the increased overall dielectric layer thickness and the formation of the low dielectric constant (<3) [23] organosilane layer on the SiO_2 dielectric layer.

Fig. 3 shows the transfer characteristics for the OTFTs fabricated with untreated SiO_2 dielectric, and the SiO_2 dielectric modified with MPTES and TTMS. It is observed that MPTES and TTMS treatments on the SiO_2 surface improve the electrical performance of the resulting

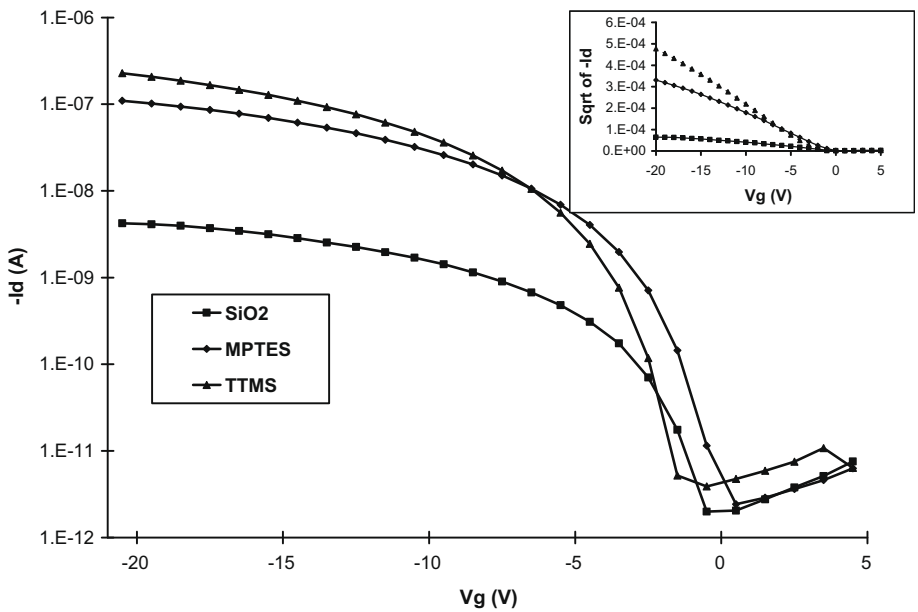

Fig. 3. Transfer curves of OTFTs with SiO_2, and SiO_2 surfaces modified with MPTES and TTMS.

transistors, as indicated by the higher measured 'on currents' and 'on/off ratios'. The field-effect mobility (μ) calculated from the transfer curves using the method published by Horowitz [24] are 4.2×10^{-5} cm^2/V s for devices with untreated SiO_2, and 0.002 and 0.005 cm^2/V s for devices with MPTES- and TTMS-treated dielectric, respectively. Devices with treated dielectric have on/off ratios that increased by at least one order of magnitude when compared to devices with untreated SiO_2. MPTES dielectric surface modification tended to shift the OTFT threshold voltage to the positive regime, while there was no apparent shift for the TTMS dielectric surface modified OTFTs. This observed shift is due to the electron accumulation properties of the terminal group on the organosilane molecule. For MPTES which has a –SH terminal group, electrons from the TIPS film are attracted by the SAM and leave behind mobile holes in the channel. Therefore, a higher positive gate bias is needed to switch off the device [16]. This electron accumulation effect is less pronounced when using TTMS which has a $–CH_3$ terminal group. Table 1 summarizes the results of the electrical parameters for these devices.

The enhanced performance of devices fabricated with TTMS and MPTES-treated dielectrics is attributed to the improvement in TIPS crystal formation when compared to TIPS crystal formation on untreated dielectrics, as seen in the AFM images presented in Fig. 4. TIPS crystals show greater ordering and alignment between the source and drain on the devices with modified dielectric surfaces (Fig. 4c and d) as compared to the randomly oriented crystals that formed on the devices fabricated with untreated SiO_2 surfaces (Fig. 4b). In the case of MPTES-treated dielectric based devices, the self-assembling layer with the hydrophilic terminal group (–SH) seemed to improve the ordering of TIPS molecules while not negatively affecting the surface wetting properties. Grazing Incidence X-ray Diffraction data seems to corroborate this conclusion. Similar to TIPS, TTMS has a benzene ring in its molecular structure, and as shown in previously published articles

Table 1
Electrical characteristics of the OTFTs with treated and untreated SiO_2 dielectric surfaces.

	Mobility (cm^2/V s)	On–off ratio	Threshold voltage (V)	Capacitance (pf)
SiO_2	0.42×10^{-4}	0.21×10^4	−0.7	140
MPTES-treated SiO_2	20×10^{-4}	4.5×10^4	0.1	105
TTMS-treated SiO_2	50×10^{-4}	5.8×10^4	−0.9	106

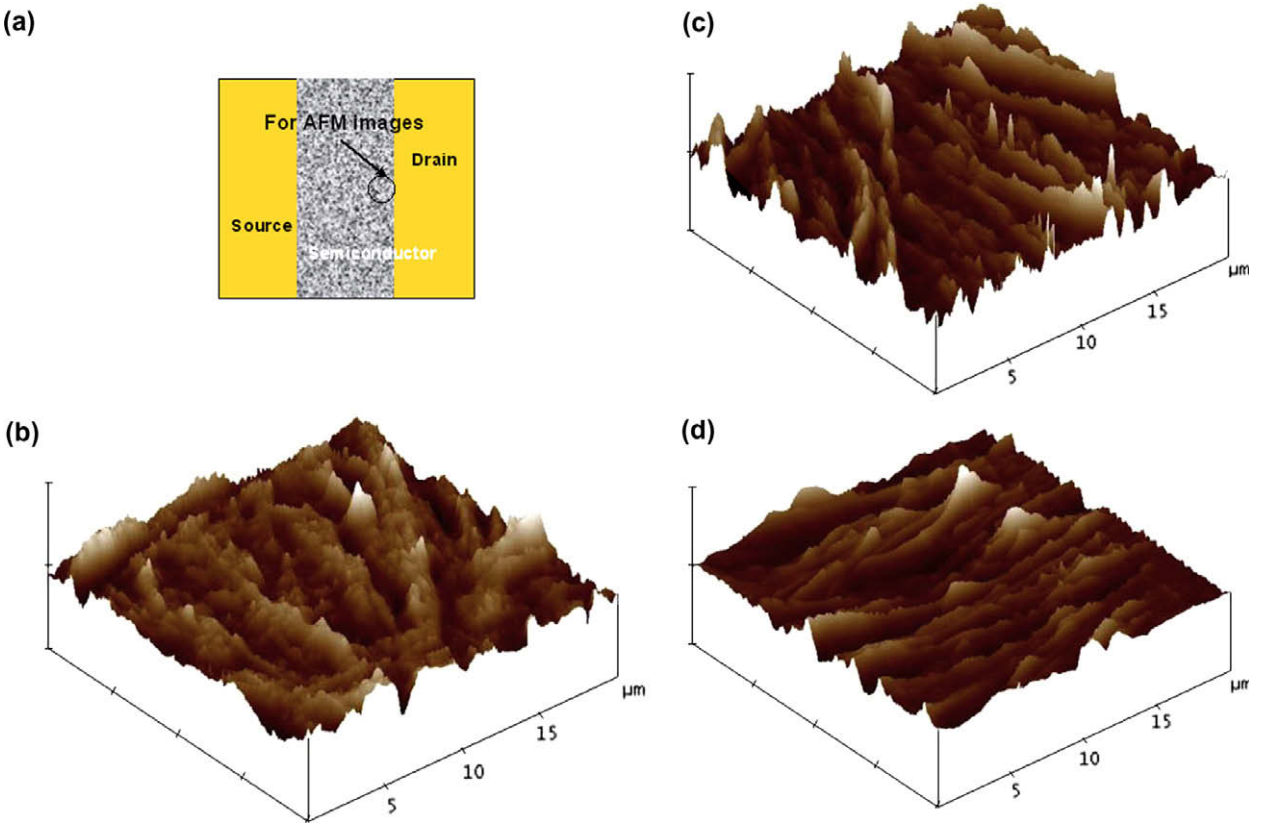

Fig. 4. AFM images of TIPS on different surfaces: top view of the OTFT and location at which the AFM images were taken from (a); atomic force micrographs of the semiconductor in the channel with SiO_2 dielectric surface untreated (b), and treated with MPTES (c) and TTMS (d). The full vertical range is 600 nm.

molecules having similar chemical structures typically, when processed, result in films with greater alignment. Therefore, improved ordering of TIPS molecules on TTMS-treated surfaces is achieved. For organic semiconductors, π–π conjugation can be enhanced by the improvement of molecular ordering which thereby increases the carrier mobility [10]. This might explain the higher field-effect mobility observed for OTFTs with the treated dielectric surfaces studied.

While contact angle measurements showed the physical property modification results after the SAM successfully bonded onto the SiO_2 surface, XPS characterization was necessary to reveal information about the chemical bonding changes at the surface before and after SAM treatments. XPS is a surface sensitive technique and chemical changes upon successful surface modification would manifest as additional peaks in the core level element scans. Based on the molecular structure shown in

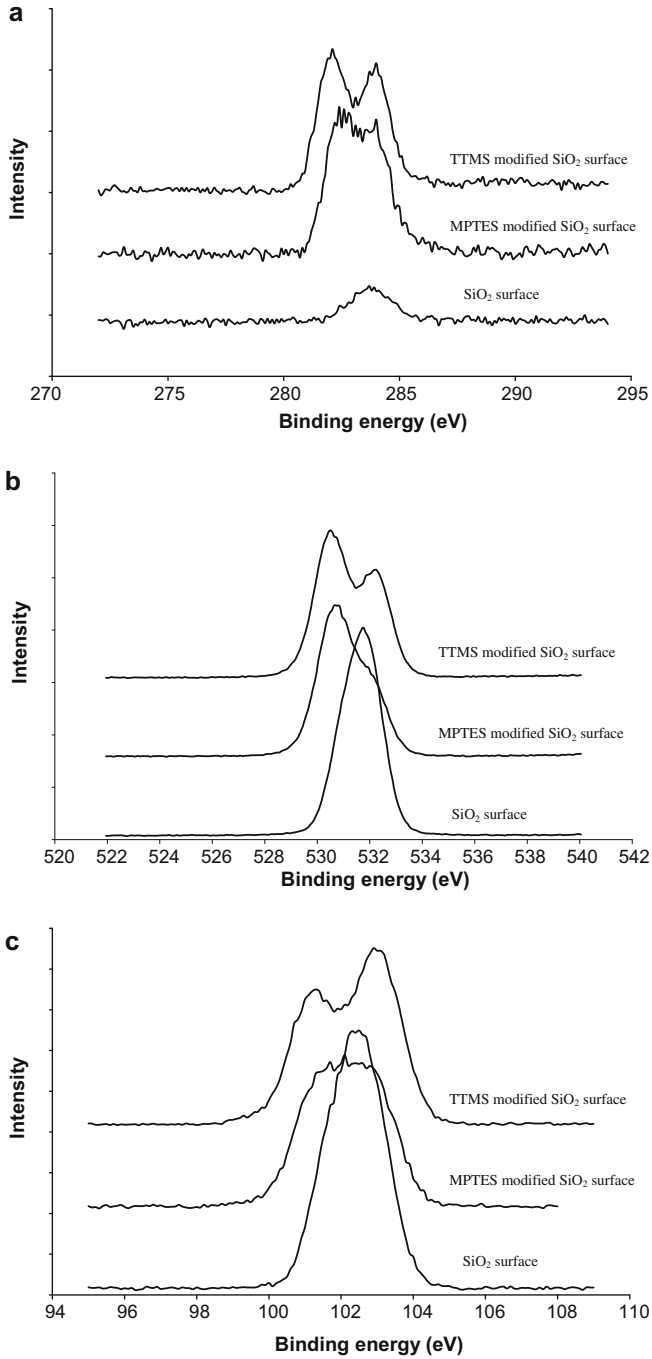

Fig. 5. XPS spectra (a) C 1s, (b) O 1s, and (c) Si 2p for SiO_2 surface, and SiO_2 surfaces treated with TTMS and MPTES.

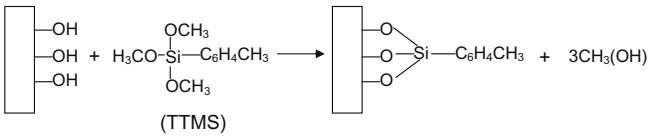

Fig. 6. Schematic chemical reaction for the surface modification of the OH-terminated SiO_2 surface using TTMS.

Fig. 1, after successful surface modification the organosilane was bonded onto the silicon oxide surface, therefore introducing, additional chemical bonds on the surface such as Si–C–C and C–Si(–O)$_3$. Fig. 5a shows the C 1s core level for the different SiO_2 surfaces. The peak at 284 eV in the case of untreated SiO_2 is attributed to carbon contamination from the ambient since there is no carbon in the silicon oxide film. Following MPTES and TTMS treatment, additional peaks appear at lower binding energy. The bonds with more electronegative atoms result in greater positive XPS chemical shift [25]. The newly formed carbon bonds, C–C, having weaker electronegativity compared to C=O appear at lower binding energy. Similarly, silicon bonds Si(–O)$_3$ from organosilanes molecules which are weaker than the bonds in SiO_2 (Si(–O)$_4$) shift towards lower binding energies, by more than 1 eV, in the Si 2p core regions [22,26] (Fig. 5c). The reaction corresponding to surface modification could be represented as indicated in Fig. 6. Based on such a reaction, if there is a monolayer formation, the chemical environment of oxygen atoms would essentially be the same as that before the reaction. But in the spectra for O 1s shown in Fig. 5b, an additional peak at a lower binding energy is observed indicating the presence of weaker bonds such as C–O besides Si–O. This could indicate that some alkoxy groups remain in the film. They are either present in the form of excess organosilanes remaining on top of the surface or in the form of incompletely removed leaving groups, probably due to steric hindrance effects from the bulky tolyl and mercaptopropyl groups.

4. Summary – conclusion

Arrays of OTFTs were fabricated using solution processable TIPS semiconductor and electrically characterized. The OTFT performance was significantly influenced by dielectric surface modifications. The SAM layers formed on the dielectric surfaces using organosilanes with polarized or aromatic functional groups improved the maximum on-current and the on/off current ratio of the fabricated OTFTs. Also, the field-effect mobility increased by two orders of magnitude resulting in a average mobility of 0.005 cm^2/V s. In addition, a shift in the threshold voltage was observed for OTFTs fabricated with dielectric surfaces modified using MPTES.

Acknowledgment

The authors would like to thank the Motorola Research Center for supporting this project.

Reference

[1] C.D. Dimitrakopoulos, D.J. Mascaro, Organic thin-film transistors: a review of recent advances, IBM J. Res. Dev. 45 (2001) 11–27.
[2] J.M. Shaw, P.F. Seidler, Organic electronics. Introduction, IBM J. Res. Dev. 45 (2001) 3–9.
[3] T.B. Singh, N.S. Sariciftci, Progress in plastic electronics devices, Annu. Rev. Mater. Res. 36 (2006) 199–230.
[4] R.L. Headrick, S. Wo, F. Sansoz, J.E. Anthony, Anisotropic mobility in large grain size solution processed organic semiconductor thin films, Appl. Phys. Lett. 92 (2008) 063302/1–063302/3.
[5] D.H. Kim, D.Y. Lee, H.S. Lee, W.H. Lee, Y.H. Kim, J.I. Han, K. Cho, High-mobility organic transistors based on single-crystalline microribbons of triisopropylsilylethynyl pentacene via solution-phase self-assembly, Adv. Mater. (Weinheim, Ger.) 19 (2007) 678–682.
[6] S.K. Park, J.E. Anthony, T.N. Jackson, Solution-processed TIPS-pentacene organic thin-film-transistor circuits, IEEE Electron Device Lett. 28 (2007) 877–879.
[7] S.K. Park, T.N. Jackson, J.E. Anthony, D.A. Mourey, High mobility solution processed 6,13-bis(triisopropyl-silylethynyl) pentacene organic thin film transistors, Appl. Phys. Lett. 91 (2007) 063514/1–063514/3.
[8] S.K. Park, C.-C. Kuo, J.E. Anthony, T.N. Jackson, High Mobility Solution-Processed OTFTs, Technical Digest – International Electron Devices Meeting, 2005, pp. 113–116.
[9] P.S. Abthagir, Y.-G. Ha, E.-A. You, S.-H. Jeong, H.-S. Seo, J.-H. Choi, Studies of tetracene- and pentacene-based organic thin-film transistors fabricated by the neutral cluster beam deposition method, J. Phys. Chem. B 109 (2005) 23918–23924.
[10] W.S. Hu, Y.T. Tao, Y.J. Hsu, D.H. Wei, Y.S. Wu, Molecular orientation of evaporated pentacene films on gold: alignment effect of self-assembled monolayer, Langmuir 21 (2005) 2260–2266.
[11] D.H. Kim, H.S. Lee, H. Yang, L. Yang, K. Cho, Tunable crystal nanostructures of pentacene thin films on gate dielectrics possessing surface-order control, Adv. Funct. Mater. 18 (2008) 1363–1370.
[12] J.-M. Kim, J.-W. Lee, J.-K. Kim, B.-K. Ju, J.-S. Kim, Y.-H. Lee, M.-H. Oh, An organic thin-film transistor of high mobility by dielectric surface modification with organic molecule, Appl. Phys. Lett. 85 (2004) 6368–6370.
[13] W.J. Kim, C.S. Kim, S.J. Jo, S.W. Lee, S.J. Lee, H.K. Baik, Observation of the hysteresis behavior of pentacene thin-film transistors in *I–V* and *C–V* measurements, Electrochem. Solid-State Lett. 10 (2006) H1–H4.
[14] S. Kobayashi, T. Nishikawa, T. Takenobu, S. Mori, T. Shimoda, T. Mitani, H. Shimotani, N. Yoshimoto, S. Ogawa, Y. Iwasa, Control of carrier density by self-assembled monolayers in organic field-effect transistors, Nat. Mater. 3 (2004) 317–322.
[15] M.C. Kwan, K.H. Cheng, P.T. Lai, C.M. Che, Improved carrier mobility for pentacene TFT by NH_3 annealing of gate dielectric, Solid-State Electron. 51 (2007) 77–80.
[16] K.P. Pernstich, S. Haas, D. Oberhoff, C. Goldmann, D.J. Gundlach, B. Batlogg, A.N. Rashid, G. Schitter, Threshold voltage shift in organic field effect transistors by dipole monolayers on the gate insulator, J. Appl. Phys. 96 (2004) 6431–6438.
[17] A. Salleo, M.L. Chabinyc, M.S. Yang, R.A. Street, Polymer thin-film transistors with chemically modified dielectric interfaces, Appl. Phys. Lett. 81 (2002) 4383–4385.
[18] S.Y. Yang, K. Shin, C.E. Park, The effect of gate-dielectric surface energy on pentacene morphology and organic field-effect transistor characteristics, Adv. Funct. Mater. 15 (2005) 1806–1814.
[19] J.E. McDermott, M. McDowell, I.G. Hill, J. Hwang, A. Kahn, S.L. Bernasek, J. Schwartz, Organophosphonate self-assembled monolayers for gate dielectric surface modification of pentacene-based organic thin-film transistors: a comparative Study, J. Phys. Chem. A 111 (2007) 12333–12338.

[20] Y. Li, X.J. He, X.L. Cao, Y.H. Shao, Z.Q. Li, F.L. Dong, Mesoscopic simulation study on the efficiency of surfactants adsorbed at the liquid/liquid interface, Mol. Simul. 31 (2005) 1027–1033.
[21] D.H. Davis, C.S. Giannoulis, R.W. Johnson, T.A. Desai, Immobilization of RGD to {1 1 1} silicon surfaces for enhanced cell adhesion and proliferation, Biomaterials 23 (2002) 4019–4027.
[22] M.C. Porte-Durrieu, C. Labrugere, F. Villars, F. Lefebvre, S. Dutoya, A. Guette, L. Bordenave, C. Baquey, Development of RGD peptides grafted onto silica surfaces: XPS characterization and human endothelial cell interactions, J. Biomed. Mater. Res. 46 (1999) 368–375.
[23] P.K. Jal, S. Patel, B.K. Mishra, Chemical modification of silica surface by immobilization of functional groups for extractive concentration of metal ions, Talanta 62 (2004) 1005–1028.
[24] G. Horowitz, Organic field-effect transistors, Adv. Mater. (Weinheim, Ger.) 10 (1998) 365–377.
[25] J.F. Watts, J. Wolstenholme, An Introduction to Surface Analysis by XPS and AES, first ed., Wiley, New York, 2003.
[26] M.R. Alexander, R.D. Short, F.R. Jones, W. Michaeli, C.J. Blomfield, A study of HMDSO/O_2 plasma deposits using a high-sensitivity and high-energy resolution XPS instrument: curve fitting of the Si 2p core level, Appl. Surf. Sci. 137 (1999) 179–183.

Organic Electronics 11 (2010) 351–355

Contents lists available at ScienceDirect

Organic Electronics

journal homepage: www.elsevier.com/locate/orgel

Letter

Polythiophene-based field-effect transistors with enhanced air stability

Yanmin Sun [a], Xiaofeng Lu [a], Shiwei Lin [a], Jeff Kettle [a], Stephen G. Yeates [b], Aimin Song [a,*]

[a] School of Electrical and Electronic Engineering, University of Manchester, Manchester M60 1QD, United Kingdom
[b] School of Chemistry, University of Manchester, Manchester M13 9PL, United Kingdom

ARTICLE INFO

Article history:
Received 18 June 2009
Received in revised form 20 October 2009
Accepted 27 October 2009
Available online 30 October 2009

Keywords:
Organic field-effect transistors
Polythiophene
Polymethylmethacrylate
Air stability

ABSTRACT

Organic field-effect transistors (OFETs) based on regioregular poly(3-hexyl-thiophene) (P3HT) have been demonstrated with improved ambient-air stability. Substrates of untreated SiO_2, octadecyltrichlorosilane (OTS)-treated SiO_2, and SiO_2 coated with a thin layer of polymethylmethacrylate (PMMA) were compared in terms of OFET electric performance and air stability. We are able to show virtually no change in transistor on/off ratio over a 3-day period in ambient air in OFETs fabricated on SiO_2-PMMA substrates. We also studied devices based on OTS-treated PMMA interface. By analyzing the surface morphology, possible mechanisms of the enhanced air stability are discussed.

© 2009 Elsevier B.V. All rights reserved.

Organic semiconductors offer the potential as a low-cost alternative to silicon in applications such as active-matrix backplanes for displays, photovoltaics, sensors and radio-frequency identification (RFID) tags [1,2]. Among the many soluble polymers, regioregular poly(3-hexyl-thiophene) (rr-P3HT) has been extensively studied in organic field-effect transistors (OFETs) due to its comparatively high hole carrier mobility, simple solution processability, and commercial availability [3–6]. However, P3HT-based OFETs typically show relatively poor ambient stability, which has limited its use in industrial applications. Experimentally, it has been shown that increased humidity, oxygen, ozone, UV light exposure as well as other species present in ambient air, could result in degradation of P3HT device performance [7–9].

In order to overcome the air stability limitations of polythiophenes, a number of approaches have been pursued. Several groups have attempted to optimize the chemical structures so as to lower the highest occupied molecular orbital (HOMO) level [10–13]. This enabled improved stability against oxidative doping, but often somewhat lowered the solubility and hence printability. Furthermore, efforts have devoted to understanding the physical mechanisms of the susceptibility of P3HT to air [7–9,14]. Holdcroft et al. reported that oxygen could form a weak charge-transfer complex with P3HT, which increases the carrier concentration and hence conductivity [7]. In contrast, Hoshino et al. reported that atmospheric water content had a greater effect on the susceptibility of the device operation to air than oxygen [8]. Interestingly, Chabinyc et al. reported that oxygen is not a strong dopant for polythiophenes in the absence of light, but ozone may have a much greater influence [9]. It is noted that less effort has so far been undertaken to enhance the air stability of actual polythiophene devices, when compared with the work to improve the carrier mobility. Recently, we reported that the stability of rr-P3HT devices were improved by utilizing a combination of a high-boiling point solvent 1,2,4-trichlorobenzene (TCB), highly hydrophobic interface treatment with a self-assembled monolayer (SAM) octadecyltrichlorosilane (OTS), and a thermal annealing process [15]. Devices fabricated using this method showed stable operation in air for a few hours. Interestingly, the same fabrication procedures also enabled P3HT devices to survive in de-ionized water for periods as long as 20 h, showing a much better stability than in ambient air [16]. The

* Corresponding author. Tel.: +44 161 306 4762.
E-mail addresses: sunym@physics.ucsb.edu (Y. Sun), A.Song@manchester.ac.uk (A. Song).

1566-1199/$ - see front matter © 2009 Elsevier B.V. All rights reserved.
doi:10.1016/j.orgel.2009.10.019

experiments demonstrated that the stability of OFETs may not only be improved by optimization of the chemical structures of the organic semiconductor but also by refining the detailed device fabrication processes.

In this paper, we report that the interface between the gate dielectric and P3HT film plays a significant role in the device performance and stability. Four different interfaces were studied: bare SiO_2, SiO_2 modified with OTS (referred to as SiO_2-OTS), SiO_2 coated a thin polymethylmethacrylate (PMMA) layer (SiO_2-PMMA), and SiO_2 substrate coated with PMMA and subsequently treated with OTS (SiO_2-PMMA-OTS). Very different air stability was observed by modification of the interface. Whereas the devices on bare SiO_2 degraded rapidly within 30 min, the OFETs based on SiO_2-PMMA substrates showed virtually no change in characteristics even after exposure in ambient air for 3 days.

Fig. 1 shows the chemical structure of rr-P3HT and a schematic of the top-contact OFETs in this study. In all cases, highly n-doped silicon wafers with a thermally grown SiO_2 (300 nm) were used. Some of the substrates were modified by OTS and/or PMMA before spin coating the organic semiconductor material. PMMA (*Mw*: 950,000, purchased from Microchem Corp, 3% in anisole) was spin coated at 4000 rpm for 2 min and a thickness of approximately 150 nm obtained. Subsequently, the sample was hard baked at a high temperature of 220 °C for 30 min in nitrogen gas environment. The hard baking process enabled PMMA films to be resistant to swelling and dissolution by TCB over the time scale of the experiment. Without such hard baking, we observed significant color change of the PMMA films once we spin coated TCB. To be more certain, we have also carried out atomic-force micrograph studies, which showed that hard baked PMMA films remained very smooth after spin coating of TCB solvent. For PMMA films only baked 180 °C, a spin-coating of TCB solvent significantly increased the film roughness. OTS was evaporated onto the sample in a nitrogen gas chamber at 140 °C for 1 h. Ellipsometry shows that the OTS layer was composed of a single monolayer with thickness approximately 2.65 nm [17]. For the substrates prior to P3HT deposition, we have imaged bare SiO_2 (RMS: 0.6 nm) and SiO_2/PMMA (RMS: 0.79 nm). In fact, the RMS values are similar to reported in literature [18]. Regioregular P3HT (purchased from Rieke Metals, and used as received) was dissolved in TCB at a concentration of 10 mg/ml and spin coated on top of the substrate at 3000 rpm for 3 min in air. The samples were then annealed at 100 °C for 2 h in nitrogen gas environment. Finally, gold source and drain electrodes, which define a channel length $L = 60$ μm and a channel width $W = 2$ mm, were deposited through a shadow mask. All P3HT devices were stored and measured in air in a 3-day period in room light.

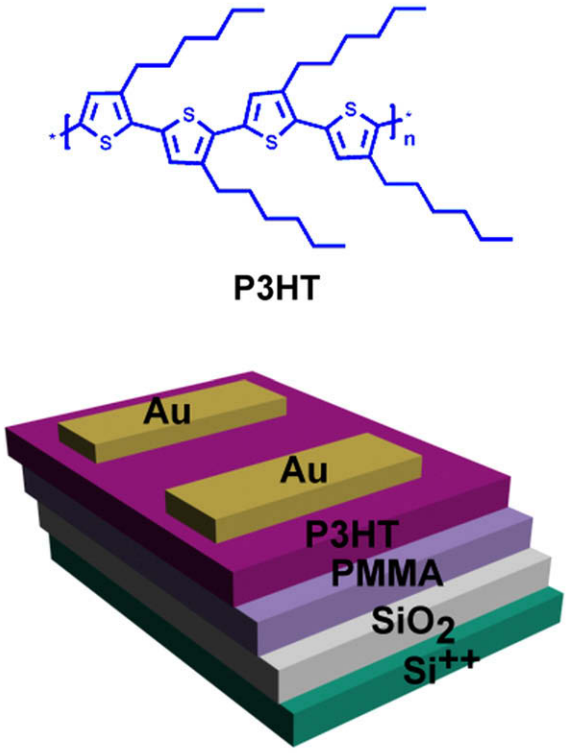

Fig. 1. The chemical structure of rr-P3HT and a schematic of the bottom gate, top-contact OFETs used in this study.

The transfer characteristics of four typical P3HT devices in the saturated regime at a drain–source voltage $V_D = -80$ V are shown in Fig. 2. A summary of the performance of the P3HT FET over time is given in Table 1. For each gate interface structure, we measured the total gate dielectric capacitance using an Agilent E4980 LCR meter and the values (10^6 Hz) are shown in Table 1. Fig. 2a shows the transfer characteristics of a P3HT FET based on a bare SiO_2 substrate after different exposure times in air. Before the first measurement, the sample was subjected to air exposure for about 15 min due to the sample transfer from the cleanroom and setting up the electrical measurement. The transfer curve indicates that the device was already severely doped as seen by a large positive threshold voltage ($V_T = 20$ V). Further doping clearly occurred after 30 min and the on/off ratio was reduced from 7×10^3 to 1×10^2 (the on/off ratio values are taken at the gate voltages of -100 V and 40 V). After the first 30 min, the rate of deterioration seemed to have significantly reduced. The on/off ratio only changed moderately in the next 3 days largely due to the increase of both the on current and off current. It is also noted that the hole mobility increased slightly after 3 days, from 0.013 to 0.019 cm^2/V s. The relatively high mobility on a bare SiO_2 substrate without any SAM treatment is most likely a result of the air doping. Recently, mobility values up to 1.8 cm^2/V s have been demonstrated in electrolyte-gated P3HT FETs with very high carrier concentrations [19–21].

Fig. 2b shows the transfer characteristic of a P3HT device based on a OTS-treated SiO_2 substrate. Here, OTS was used to promote the edge-on orientation of P3HT, which could enhance carrier mobility. For the initial measurement, the mobility was calculated to be 0.02 cm^2/V s and remained almost constant for 9 h in air. However, the on/off ratio decreased from 3×10^6 to 1.9×10^6 and the threshold voltage changed from 11 V to 18 V, indicat-

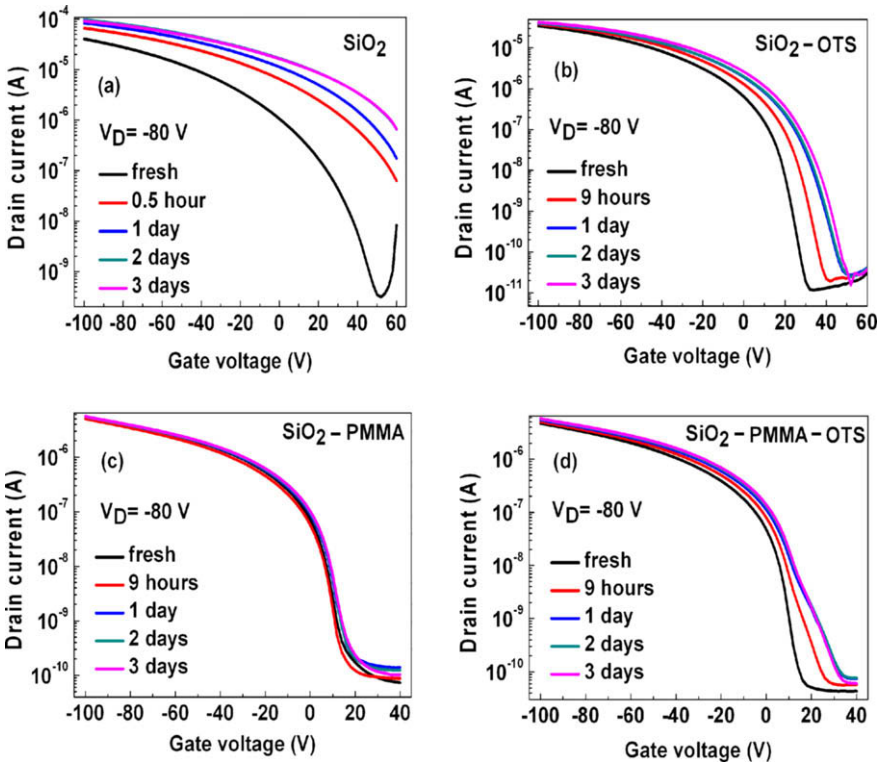

Fig. 2. The characteristics of P3HT FETs with different dielectric-semiconductor interfaces over a 3-day period.

Table 1
Summary of performance parameters of P3HT FETs with different dielectric-semiconductor interfaces over a 3-day period.

Surface	Capacitance (nF cm^{-2})	Time (days)	Mobility (cm^2/V s)	On/off ratio[a]	Threshold voltage (V)
SiO_2	11.5	0	0.013	7×10^3	20
		1	0.019	55	56
		2	0.019	28	71
		3	0.018	26	72
SiO_2-OTS	10.8	0	0.02	3×10^6	11
		1	0.019	5×10^4	23
		2	0.019	4×10^4	24
		3	0.02	1.5×10^4	27
SiO_2-PMMA	6.51	0	0.005	8×10^4	12
		1	0.005	4×10^4	13
		2	0.005	4.4×10^4	13
		3	0.005	5.5×10^4	13
SiO_2-PMMA-OTS	5.40	0	0.005	1×10^5	11
		1	0.005	6×10^4	16
		2	0.005	6×10^4	16
		3	0.005	8×10^4	16

[a] The on/off ratios for all devices were calculated at the gate voltages of −100 V and 40 V.

ing the occurrence of air doping. After the first day, the device characteristics became relatively stable, with the on/off ratio reducing from 5×10^4 to 1.5×10^4 and the threshold voltage increasing from 23 V to 27 V over the following 2 days. The air stability is clearly much better than the P3HT FET based on bare SiO_2 substrates shown in Fig. 2a. This is most likely due to the highly hydrophobic interface resulted by the OTS treatment, which inhibits water molecules being adsorbed at the interface and therefore severely affecting the device performance.

PMMA is often used in OFETs as a dielectric material, especially for oligomers [22]. By inserting a thin layer of PMMA on top of the SiO_2 prior to coating of P3HT, we found that the devices showed dramatically improved stability, with the on/off ratio virtually unchanged even after exposure in air for 3 days, as shown in Fig. 2c. The thresh-

old voltage was calculated to be 12 V, similar to the value of as-fabricated OTS-treated device. When compared to the bare SiO_2 substrate, a very different stability was obtained. We believe the improved stability arising from PMMA treatment is a consequence of H-bonding interactions arising from acid–base interactions between the acidic OH groups on the silica surface and the basic carbonyl groups on PMMA [23–25]. It has previously been reported that poly(styrene-methyl methacrylate) statistical copolymers when spin coated onto silica and heated above the glass transition temperature (T_g) of the copolymer give polymer chains that are permanently attached to the silica surface [26]. Whereas it has been previously reported that PMMA and P3HT solutions are both soluble in DCB [27]. We believe the hard bake conditions employed here give rise to high molecular weight PMMA which is strongly bound to the silica surface and which is not removed under the short contact times arising from the spin coating of the P3HT/TCB solution.

Interface plays an important role to determine the properties of OFETs. Some groups have suggested that the interface hydrophobicity could affect the device stability. A recent paper by Chen and Liao reported that the air stability of n-channel OFETs based on N,N′-dioctyl-3,4,9,10-perylene tetracarboxylic diimide was significantly improved after they modified the dielectric surfaces with hydroxyl-free polymers [28]. It was suggested that the enhanced hydrophobicity of the interface limited the absorption of humidity, and thereby retarded the degradation of the OFETs under ambient condition. In our work, the PMMA surface is also far more hydrophobic than bare SiO_2 surface, because of the lack of hydroxy groups. This may make it difficult for water molecules to attack and attach to the PMMA interface.

Since both OTS treatment and PMMA coating seemed to improve the P3HT OFET stability, we have also tried OTS treatment on PMMA-coated SiO_2 substrates. The device measurement results are shown in Fig. 2d. The resulted mobility of 0.005 $cm^2/V\,s$, on/off ratio of 1×10^5, and threshold voltage of 11 V of the as-fabricated device were almost the same as that based on the SiO_2-PMMA substrate. By considering the performance alone, the data suggest that the extra OTS treatment on PMMA layer did not improve the mobility. Meanwhile, the device stability actually reduced, although it was still much better when compared to the bare-SiO_2 device in Fig. 2a and slightly better than the device on OTS-treated SiO_2.

In order to gain an insight into the differences in ambient stability, the morphology of the P3HT films on the four different substrates were studied by using an atomic-force microscope (AFM). Comparing the AFM micrographs in Fig. 3a and b, no significant differences were observed. The values of the maximum peak-to-valley fluctuation (Z_{max}) and root-mean-square (RMS) are similar. However,

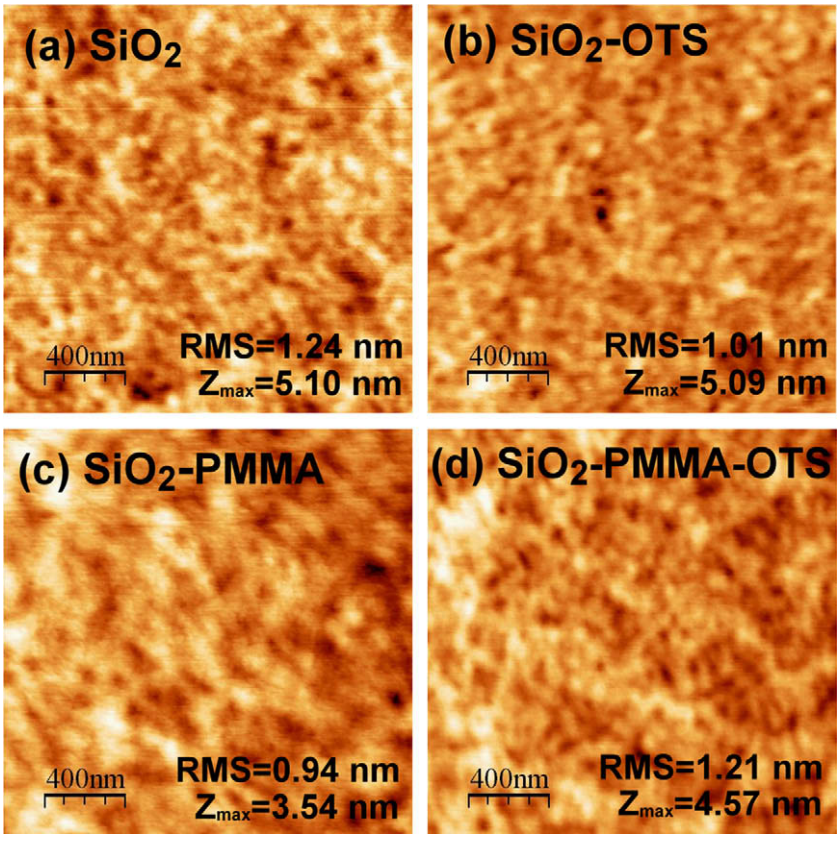

Fig. 3. AFM images of P3HT thin films on the four different dielectric-semiconductor interfaces.

both the surface roughness (RMS = 0.94 nm) and the fluctuation (Z_{max} = 3.54 nm) of P3HT on PMMA-coated SiO_2 in Fig. 3c were reduced. This suggests that the P3HT molecules are slightly more densely packed, and hence slow down the diffusion of oxygen and moisture to the gate dielectric interface where the hole transport takes place. This may also contribute to the improved stability for the P3HT devices based on PMMA-coated substrates. In Fig. 2d, it was shown that OTS treatment on PMMA surface did not improve the device stability. The corresponding AFM image in Fig. 3d indicates that the domain sizes of P3HT were similar when compared with case in Fig. 3b, which may be the reason for the reduced stability.

In summary, regioregular-P3HT devices with four different interfaces were studied. We were able to demonstrate virtually no change in the OFET electrical characteristics over a 3-day period in air, by inserting a thin PMMA buffer layer between the P3HT film and gate insulator. Such stability may have important implications in practical applications by enabling a long process window before, e.g., the encapsulation or packaging steps are applied.

References

[1] C.D. Dimitrakopoulos, P.R.L. Malenfant, Adv. Mater. 14 (2002) 99.
[2] Y.M. Sun, Y.Q. Liu, D.B. Zhu, J. Mater. Chem. 15 (2005) 53.
[3] G. Wang, J. Swensen, D. Moses, A.J. Heeger, J. Appl. Phys. 93 (2003) 6137.
[4] H. Sirringhaus, P.J. Brown, R.H. Friend, M.M. Nielsen, K. Bechgaard, B.M.W. Langeveld-Voss, A.J.H. Spiering, R.A.J. Janssen, E.W. Meijer, P. Herwig, D.M. de Leeuw, Nature (London) 401 (1999) 685.
[5] Z. Bao, A. Dodabalapur, A.J. Lovinger, Appl. Phys. Lett. 69 (1996) 4108.
[6] H. Sirringhaus, N. Tessler, R.H. Friend, Science 280 (1998) 1741.
[7] M.S.A. Abdou, F.P. Orfino, Y. Son, S. Holdcroft, J. Am. Chem. Soc. 119 (1997) 4518.
[8] S. Hoshino, M. Yoshida, S. Uemura, T. Kodzasa, N. Takada, T. Kamata, K. Yase, J. Appl. Phys. 95 (2004) 5088.
[9] M.L. Chabinyc, R.A. Street, J.E. Northrup, Appl. Phys. Lett. 90 (2007) 123508.
[10] B.S. Ong, Y. Wu, P. Liu, S. Gardner, J. Am. Chem. Soc. 126 (2004) 3378.
[11] B.S. Ong, Y. Wu, L. Jiang, P. Liu, K. Murti, Synth. Met. 142 (2004) 49.
[12] A.R. Murphy, J. Liu, C. Luscombe, D. Kavulak, J.M.J. Frechet, R.J. Kline, M.D. McGehee, Chem. Mater. 17 (2005) 4892.
[13] I. McCulloch, M. Heeney, C. Bailey, K. Genevicius, I. MacDonald, M. Shkunov, D. Sparrowe, S. Tierney, R. Wagner, W.M. Zhang, M.L. Chabinyc, R.J. Kline, M.D. McGehee, M.F. Toney, Nat. Mater. 5 (2006) 328.
[14] E.J. Meijer, C. Detcheverry, P.J. Baesjou, E. van Veenendaal, D.M. de Leeuw, T.M. Klapwijk, J. Appl. Phys. 93 (2003) 4831.
[15] L.A. Majewski, J.W. Kingsley, C. Balocco, A.M. Song, Appl. Phys. Lett. 88 (2006) 222108.
[16] L.A. Majewski, A.M. Song, J. Appl. Phys. 102 (2007) 074515.
[17] C. Boulas, J.V. Davidovits, F. Rondelez, D. Vuillaume, Phys. Rev. Lett. 76 (1996) 4797.
[18] P. Dhagat, H.M. Haverinen, R.J. Kline, Y. Jung, D.A. Fischer, D.M. DeLongchamp, G.E. Jabbour, Adv. Funct. Mater. 19 (2009) 2365.
[19] J.H. Cho, J. Lee, Y. Xia, B.S. Kim, Y. He, M.J. Renn, T.P. Lodge, C.D. Frisbie, Nat. Mater. 7 (2008) 900.
[20] R.C.G. Naber, M. Mulder, B. de Boer, P.W.M. Blom, D.M. de Leeuw, Organ. Electron. 7 (2006) 132.
[21] A.S. Dhoot, J.D. Yuen, M. Heeney, I. McCulloch, D. Moses, A.J. Heeger, Proc. Natl. Acad. Sci. 103 (2006) 11834.
[22] A. Facchetti, M.H. Yoon, T. Marks, Adv. Mater. 17 (2005) 1705.
[23] M. Kawaguchi, S. Yamagiwa, A. Takahashi, T. Kato, J. Chem. Soc., Faraday Trans. 86 (1990) 1383.
[24] M.M. Chehimi, J.F. Watts, J. Electron Spectrosc. Relat. Phenom. 63 (1993) 393.
[25] D.L. Allara, Z. Wang, C.G. Pantano, J. Non-Cryst. Solids 120 (1990) 93.
[26] T.P. Russel, P. Mansky, E. Huang, C. Hawaker, Proceedings of the Annual Meeting of the Adhesion Society, vol. 21, 1998, p. 224.
[27] A.C. Arias, F. Endicott, R.A. Street, Adv. Mater. 18 (2006) 2900.
[28] F.-C. Chen, C.-H. Liao, Appl. Phys. Lett. 93 (2008) 103310.

Organic Electronics 11 (2010) 357–362

Contents lists available at ScienceDirect

Organic Electronics

journal homepage: www.elsevier.com/locate/orgel

Spectrally selected photodiodes for colorimetric application

Maria Rosa Antognazza [a,*], Davide Musitelli [b], Stefano Perissinotto [a], Guglielmo Lanzani [a,b]

[a] Istituto Italiano di Tecnologia, via Morego 30, 16163 Genova, Italy
[b] Politecnico di Milano, Dipartimento di Fisica, P.zza L. da Vinci 32, 20133 Milano, Italy

ARTICLE INFO

Article history:
Received 12 June 2009
Received in revised form 6 November 2009
Accepted 8 November 2009
Available online 13 November 2009

Keywords:
Organic photodetectors
Colorimetry
Internal filter effect
Color sensor

ABSTRACT

We demonstrate that it is possible to fine-tune the photocurrent action spectrum of an organic photodiode, based onto a prototype semiconducting polymer, simply varying the active layer thickness and properly exploiting the filter effect of the optical absorption. The theory adopted to model the experimental data represents a useful tool to predict with accuracy the position and the spectral shape of the photovoltaic current. Based on this result, we apply our method in the colorimetric field, where a simple way to tune the spectral response of the detector unit is highly desired: we realize an organic color sensor device without any optical filtering.

© 2009 Elsevier B.V. All rights reserved.

1. Introduction

Over the last three decades, there has been a continuously increasing interest in organic photovoltaics (oPVs) research, especially focused onto the realization and the development of efficient solar cells [1–6]. Only more recently, the same attention has been deserved to organic photodetectors (oPDs) as well [7,8]. In particular, photosensors working in photovoltaics conditions may find useful application not only in technology, but also, for instance, in diagnostics, in biometry, in humanoid sciences [9,10].

Although oPV cells and oPDs share many similar features and definitely are, under many respects, similar devices, they nevertheless have to fulfill a different set of requirements. In photovoltaics, tremendous efforts have been done by many groups in order to pursue two main objectives, the improvement of the overall power conversion efficiency and the extension of the absorption range towards the near infrared. Important results have been obtained by blending conjugated polymers with high-electron affinity molecules, such as C_{60} and its soluble derivative, PCBM [3]. So, as far as photovoltaics is concerned, the main issue is to convey as much as possible the solar spectrum.

On the other side, the key parameters for photodetection are the photocurrent and the dark current intensities; state-of-the-art P3HT:PCBM bulk heterojunction diodes have been recently reported, with external quantum efficiency between 60% and 70% and dark current densities below 10 nA/cm^2 at −1 V [11]. In addition to the most conventional architectures, hybrid devices, based onto the contemporary employ of organic conjugated polymers and inorganic semiconductors as active materials, have been recently extensively explored, due to the exciting opportunity to combine the valuable properties of both materials groups, in particular in terms of charge generation and transport (see [12] for a recent review). Another fundamental factor to be considered in photodetection is represented by the spectral selectivity. The opportunity to tune and properly, finely adjust the spectral response of photodetectors within the visible range is one of their most attractive properties, which does not have a counterpart in the silicon-based technology.

Organic materials can be chemically tailored, by changing the molecular structure in order to adjust the band gap, and therefore the optoelectronic properties; anyway, this

* Corresponding author. Tel.: +39 0223993783; fax: +39 0223996126.
E-mail address: mariarosa.antognazza@polimi.it (M.R. Antognazza).

1566-1199/$ - see front matter © 2009 Elsevier B.V. All rights reserved.
doi:10.1016/j.orgel.2009.11.013

approach is often too expensive and time-consuming. A second, well-known method [13,14] to tune the spectral response consists in applying various difference potentials (which is anyway strictly required for sensitive and fast photodetection, [11]). Nevertheless, for many applications in the colorimetric and bioengineering fields (for instance in spectral biological imaging) photodiodes working at zero bias are preferable.

In this work, we use the well-known internal filter effect in order to fine-tune the spectral response of a prototype conducting polymer, simply varying the active layer thickness. We analyze the data within the framework of the Ghosh–Feng model [15]; the good agreement between the experimental action spectra and the theory provides us with a simple way to predict and/or to tune with accuracy the position and the spectral shape of the photovoltaic current, just relying onto the optical absorption and the active layer thickness. Finally, we describe an interesting application of the organic photodiodes in the colorimetric field, where the spectral tuning plays a fundamental role: it has a significant technological value, since it avoids the use of optical filters in front of the detector, and, even more importantly, it can account for a more bio-mimetic color perception, offering a simpler and direct response to the problem of metamerism (i.e., different combinations of the reflected light from two (different) objects produce the same color perception; sets of metameric colors vary in a considerable way among different sets of color-matching functions).

2. Materials and methods

The photodetectors were realized in the usual sandwich structure, adopting for simplicity a single layer approach and using as active polymer a prototype material, regioregular poly(3-hexylthiophene-2,5-diyl) (rr-P3HT). P3HT was supplied by Sigma–Aldrich with a regio-regularity of 99.5%, a molecular weight of 17,500 g/mol, and it was used without any further purification. We used glass substrates precoated with ITO as the anode; special care was taken of careful cleaning, rinsing the substrates in ultrasonic bath with (i) specific detergent in 3% water solution, (ii) deionised water, (iii) pure acetone and (iv) isopropyl alcohol. The substrates were then dried by a nitrogen flux and finally cleaned by oxygen plasma. 1,2-Dichlorobenzene solutions (concentration range between 5 and 40 g/l) of P3HT were heated at 50°, stirred and finally deposited by spin coating on pre-heated substrates, properly adjusting the parameters, in order to obtain a film of good optical quality. After deposition films were not thermally annealed. The aluminium cathodes were deposited by thermal evaporation, through shadow masks. The metal thickness was determined by a quartz microbalance; suitable values are about 120 nm. Finally, electrical contacts were realized through Au wires. Pixel area is 2×3 mm^2. The devices were realized and immediately tested in air, at room temperature. Degradation of the optoelectronic properties was observed after a week, as a $\sim$50% reduction in the measured photocurrent values.

Active film thickness for different concentrations was carefully measured by a step profiler (ALPHA STEP IQ, KLA TENCOR): obtained values are, respectively, 30, 75, 250, 340, and 440 nm; for each device we measured the photocurrent action spectrum, in photovoltaic conditions.

In action spectra measurements, the light from a tungsten lamp passes through a monochromator and is focused onto the photodiode, at 0° incidence, through the ITO electrode. The light is chopped by a mechanical chopper (operating frequency 130 Hz) and the reference signal is fed to a lock-in amplifier. System calibration was performed by replacing the organic photodiode with a silicon photodiode of known efficiency, taking into account the dark current and the spectral response of the light source and the monochromator gratings.

For the measurements of colorimetric coordinates of standard objects, the source light (whose spectral emission is close to the standard illuminant A) is focused onto calibrated color samples (LABSPHERE, SPECTRALON® color standards), and the diffused radiation is detected by the organic photodiodes at an angle of 45°, following the CIE (Commission International d'Eclairage) prescriptions. All measurements were performed in air and at room temperature.

3. Results and discussion

Measured photocurrent action spectra on different thickness photodiodes are shown in Fig. 1a, as dotted black lines. The optical absorption spectrum is also shown for comparison (dashed green line). The latter shows a weak structure probably due to the vibronic lineshape convoluted by the disorder distribution in the polymer film. In the considered range, the spectral responsivity (Fig. 1b) of the organic photodiodes changes as the active layer thickness is increased, and it presents two main features:

- A narrowing of the lineshape.
- A pronounced shift of the peak, from 560 nm (matching the absorption spectrum) to 625 nm.

The highest responsivities are obtained for 30 and 250 nm-thicknesses; the photodiode with 75 nm active layer thickness is characterized by an intermediate value, while for active layers thicker than 250 nm the measured responsivities are considerably reduced.

Maxima external quantum efficiencies (EQE) are low, as expected in pristine rr-P3HT photodiodes, with a not-optimized structure. Moreover, they critically depend on the layer thickness. Calculated values are reported in Table 1. In this work, we mainly focused onto the spectral shape, aiming at finding a simple method to predict, at a discrete level of accuracy, the photocurrent action spectrum, with the final goal of reproducing the standard observer color-matching functions (see Section 4). For practical colorimetric application it will be possible to increase the EQE of the devices, if required, by using an external signal amplifier, without affecting the optimized spectral matching and properly selecting the amplifying factor.

Traditionally, the relationship between the photocurrent and the absorption spectra has been classified as either symbatic or antibatic [14]. If the maximum photo-

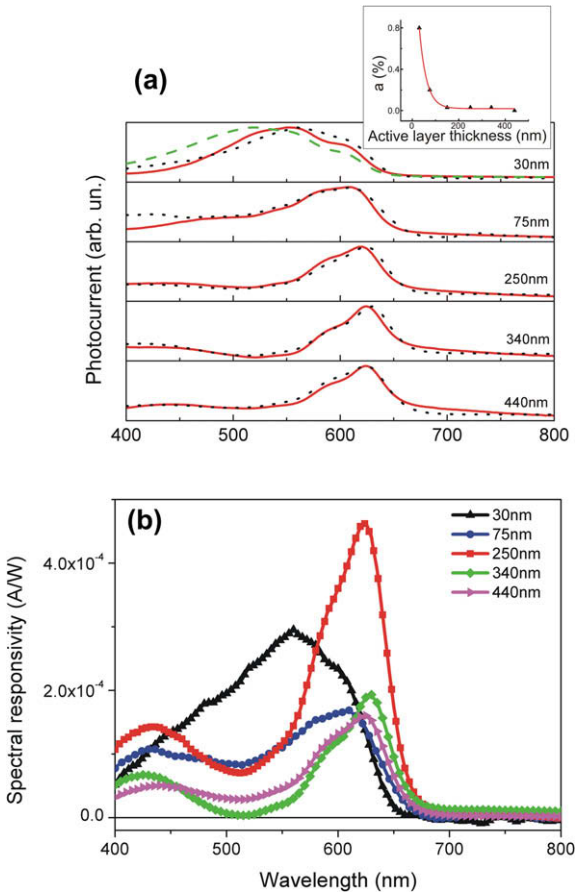

Fig. 1. (a) Normalized photocurrent action spectra of sandwich photodetectors ITO/rr-P3HT/Al, for different active layer thicknesses (dotted black lines), and theoretical spectra, as predicted from the Ghosh–Feng diffusion model (solid red lines). For comparison, the optical absorption spectrum of the polymer is also shown (dashed green line). The model reproduces with good accuracy the transition from a symbatic to an antibatic behaviour, in photovoltaic conditions. The inset reports the percentage weight of the symbatic component *a*, as obtained from the simulation procedure, as a function of the polymer thickness. (b) Measured spectral responsivities for different active layer thicknesses. (For interpretation of the references to color in this figure legend, the reader is referred to the web version of this article.)

Table 1
External quantum efficiencies of photodiodes with different active layers thicknesses.

Active layer thickness (nm)	EQE (%)
30	0.07
75	0.03
250	0.09
340	0.04
440	0.03

current coincides with the strongest photon absorption, the photocurrent response is said to be symbatic with the absorption spectrum. If the maximum of the photocurrent spectrum occurs at photon energy where the optical absorption is weakest, i.e., if the photocurrent and the absorption are almost complementary, the photocurrent response is said to be antibatic. Fig. 1 clearly shows the transition from the symbatic response to the antibatic one, for increasing active film thickness.

The antibatic behaviour has been previously reported for various polymer-based sandwich cells and attributed to the internal filter effect [13,14,16–20]: carriers are predominantly generated close to the electrode, which is opposite to the contact through which light enters the active layer. In other words, the material below the aluminium does not contribute to current generation within the device and acts solely as an optical filter, filtering out the useful light from reaching the only active charge generation region in the device. In this case the photocurrent is expected to decrease in the wavelength range of high absorbance.

Several models have been developed in the past in order to relate the photocurrent action spectrum to the optical absorption spectrum, based onto the self-absorption within the film [21–24]: all of them assume an exponential decay of the incident radiation with the distance (i.e., the Lambert–Beer law), but differ from each other in the assumed mechanisms of charge separation and transport. In this work, we use the model originally due to Simpson [25], and then applied for the first time to organic, merocyanine solar cells materials by Ghosh and Feng [15].

Two main hypotheses are assumed:

i. The absorption of the light creates excitons, that *diffuse* towards the organic material–electrode interfaces;
ii. Dissociation of the excitons into free carriers takes place *only* in proximity of the interfaces, within few exciton diffusion lengths, and not in the bulk (as in doped organic photodiodes).

Under the first assumption, the transport of excitons from the generation to the dissociation site is treated by the standard diffusion equation:

$$\frac{dn(x,t)}{dt} = \Phi N \alpha e^{-\alpha x} - \frac{dJ}{dx} - \frac{n(x,t)}{\tau} \quad (1)$$

where n is the number of excitons, Φ is the quantum efficiency of exciton generation, N is the number of incident photons per unit area per second, α is the absorption coefficient, as a function of the radiation wavelength, J is the exciton current and τ is the mean exciton lifetime.

First term on the right hand side of Eq. (1) describes exciton photogeneration, the second one is due to the exciton diffusion, while the last one is a recombination term. J is proportional to the diffusion coefficient D, and can be expressed as:

$$J = -D\frac{dn(x,t)}{dx} \quad (2)$$

Since we are interested in steady-state photocurrent, we only consider equation at equilibrium ($dn(x,t)/dt = 0$):

$$0 = D\frac{d^2n}{dx^2} - \frac{n}{\tau} + \alpha\Phi N \exp(-\alpha x) \quad (3)$$

Adopted boundary conditions are $n(x) = 0$ at $x = 0$ and $x = L$, where L is the thickness of the active layer. In this way the two electrode–organic interfaces can be both

recombination and dissociation sites for the excitons. In other words, we assume that free carriers are generated only if the excitons reach one of the two electrodes (no bulk photogeneration), so that interfaces with aluminium and ITO can be seen as 'infinite sink' either for exciton dissociation or for exciton recombination. With these boundary conditions, general solution of Eq. (3) is given by (4):

$$n = \frac{\gamma}{\beta^2 - \alpha^2}\left(\frac{e^{\beta L} - e^{-\alpha L}}{e^{-\beta L} - e^{\beta L}}\right)e^{-\beta x} - \frac{\gamma}{\beta^2 - \alpha^2}\left(\frac{e^{-\beta L} - e^{-\alpha L}}{e^{-\beta L} - e^{\beta L}}\right)e^{\beta x} + \frac{\gamma}{\beta^2 - \alpha^2}e^{-\alpha x} \tag{4}$$

where Λ is the diffusion length of excitons and:

$$\beta \equiv (\Lambda)^{-1} \equiv (D\tau)^{-1/2} \quad \text{and} \quad \gamma \equiv \frac{\alpha N \Phi}{D} \tag{5}$$

The exciton current at interfaces with ITO and aluminium, J_{ITO} and J_{Al}, is thus simply obtained by relation (2) in correspondence, respectively, to the extremes $x = 0$ and $x = L$ (for illumination from the ITO side):

$$J_{ITO} = -D\frac{dn}{dx}\bigg|_{x=0} \quad \text{and} \quad J_{Al} = -D\frac{dn}{dx}\bigg|_{x=L} \tag{6}$$

For a p-conducting material and for illumination from the ITO side, the dependence of J_{ITO} and J_{Al} on the incident photon energy gives rise, respectively, to the symbatic and antibatic response in the photocurrent action spectrum. In our case, at zero bias, the photocurrent spectra cannot be described simply by a symbatic or an antibatic response alone, but it is necessary to consider the combination of both contributions [14–20]. The two limiting cases are for thicknesses comparable to the exciton diffusion length Λ, when the spectral response is mainly symbatic, and for thicknesses much greater than Λ, when it is almost completely antibatic. For intermediate thicknesses, one should consider both the symbatic and the antibatic response. We assume that the total photocurrent J can be simply written as a linear combination of J_{ITO} and J_{Al}:

$$J = (1 - a)J_{Al} + aJ_{ITO} \tag{7}$$

where a ($0 < a < 1$) is the contribution due to the symbatic response.

Using this model, we were able to reproduce with good accuracy the experimental photoaction spectra, for different values of the active layer thickness. In the simulation procedure we first optimized the exciton diffusion length Λ, and we fixed it to $\Lambda = 10$ nm. This value has anyway to be considered as a rough estimate, since it probably slightly overestimates the recently reported values, in the range (8.5 ± 0.7)nm, obtained by specific and more precise technique [26,27]. Considering that the exciton lifetime τ is in the order of ~400 ps [27], we can give an estimation for the diffusion coefficient, D ~25E–4 cm^2/s, five times larger than the value estimated by Luer et al. [28], which anyway was to be considered as a lower limit, since they estimated D from kinetics measurement of fluorescence quenching upon exposure to oxygen. Within the framework of the Smoluchowski model [29], they assumed that the fluorophores are instantaneously deactivated upon contact with the quencher (oxygen), and that each encounter leads to quenching, with a reaction radius R = 500 pm. If these conditions are not met, or R is smaller, one obtains higher values for D.

For fixed Λ, the only free parameter is a, which has been varied between 0 and 1. Results of the simulation are shown in Fig. 1, as solid, red lines. The slight deviations of the experimental spectra from the model, more evident at the lowest and the highest wavelengths, may find an explanation taking into account that:

1. We assume the exciton dissociation efficiency as independent from the excitation wavelength;
2. We do not consider any length distribution in the polymeric chains, which would determine different exciton lifetimes.

The inset in Fig. 1 shows the best values obtained for the percentage weight of the symbatic component a, as a function of the active layer thickness. It is possible to note that the weight of the symbatic component decreases in an exponential way with the thickness, and indeed it plays a real role just in the first one hundred nanometers. For thickness ~440 nm it is almost zero, and the photocurrent is dominated by the antibatic behaviour. This is due to the unbalance in mobility (holes mobility is bigger than electrons mobility) and only a small fraction of the electrons generated near the ITO reaches the aluminium electrode and can contribute to the current. We see that the spectral response of the photodiodes stems for both charge generation and transport phenomena.

The well accordance between the experimental data and the model allows us to conclude that the interfaces at the electrodes play a fundamental role, without any relevant contribution from the bulk photogeneration: the exciton dissociation is a fully extrinsical phenomenon.

The model gives us a useful tool to predict with accuracy the photocurrent action spectrum of an organic photodetector, just on the base of its optical absorption, the exciton diffusion wavelength (which is known for many, commercial materials) and the active layer thickness. In addition, it suggests that fine tuning of the spectral response can as well be obtained using a single material and different thickness. This can be done simply changing the processing conditions (polymer concentration and/or spinning parameters). In the following, we describe an application, where the spectral tuning of the photoresponsivity is of fundamental importance, thus exploiting the thickness dependence.

4. Color measurement

Organic photodetectors may find useful applications in the colorimetric field, as color sensor devices [30]; the great advantage of the organic semiconductors technology is the possibility to reproduce the three standard observer color-matching functions (CMFs), traditionally named as Z, Y and X [31], without using any optical filtering, but simply exploiting the tunability characteristics of the active materials. To this respect a simple way to properly tune the spectral response is of crucial importance.

In this work, we exploit the symbatic/antibatic behaviour of the photocurrent in rr-P3HT sandwich devices in order to reproduce the standard colorimetric curves *Y* and *X*. More in detail we choose two different solution concentrations, corresponding to active layers of, respectively, 50 nm (mainly symbatic-type photocurrent action spectrum) and 200 nm (mainly antibatic-type). The CMF *Z* is reproduced by selecting a second material, namely methyl-substituted ladder-type *para*-polyphenylene (m-LPPP), doped with PCBM (1:1 concentration, in weight). Measured EQE at 470 nm is 1.1%. Fig. 2 shows the comparison between the experimental photocurrent action spectra and the standard CMFs (respectively, dashed and solid lines). Even if the spectral agreement is not yet fully satisfactory, nonetheless these results represent a proof of concept of the reliability of our approach. In order to directly test the possibility to use organic photodiodes as color sensor devices, we measured the colorimetric coordinates of some calibrated color standard. Obtained values are displayed in Fig. 3 (white triangles) in comparison with the calibration values in the standard system (black dots). Even if the organic color sensor devices at the present still do not meet the requirements for a commercial application, due to the spectral mismatch between the experimental and the standard CMFs, these results demonstrate the capability of organic photodiodes to measure the color of a diffusing object, representing a valuable alternative to the existing technology.

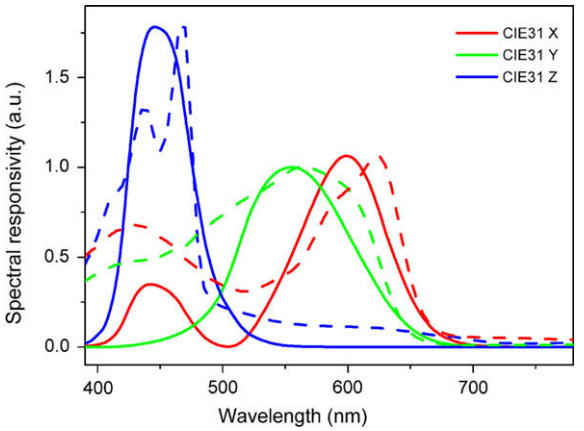

Fig. 2. Comparison between the two sets of colorimetric functions, the standard observer CIE31 (solid lines) and the experimental photocurrent spectra, properly normalized (dashed lines).

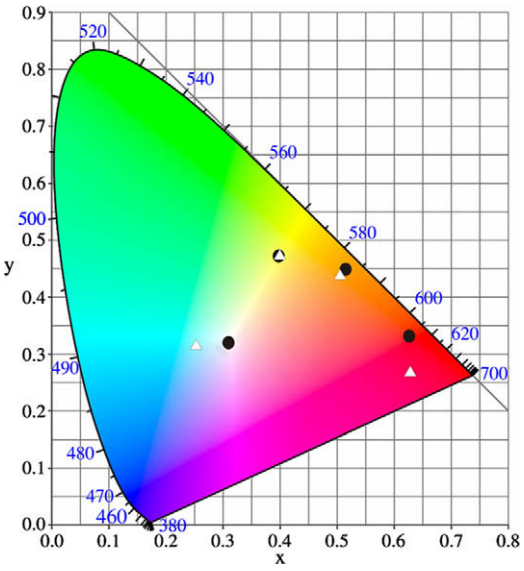

Fig. 3. Chromaticity coordinates of four calibrated color samples, as measured by organic color sensors (white triangles), in comparison with the calibration values (black dots) in the standard system CIE31. The observed deviations are due to the mismatch between the standard observer colorimetric functions and the experimental ones; nevertheless, these results can be considered as a direct proof of the capability of organic photovoltaic devices to detect and measure color stimuli. (For interpretation of the references to color in this figure legend, the reader is referred to the web version of this article.)

5. Concluding remarks

In this work, we demonstrated that, exploiting the internal filter effect, it is possible to fine-tune the photocurrent action spectrum of an organic photodiode simply varying the active layer thickness. The theory adopted to model the experimental data represents a useful tool to accurately predict the action spectrum shape, just relying onto observation of the material optical absorption and properly selecting the active layer thickness. We applied our method to a specific purpose, i.e. the realization of a color sensor device without any optical filtering, whose spectral response closely resembles the standard observer CMFs.

References

[1] C.J. Brabec, V. Djakonov, J. Parisi, N.S. Sariciftci (Eds.), Organic Photovoltaics: Concepts and Realization, 60, Springer, Berlin, Germany, 2003.
[2] H. Hoppe, N.S. Sariciftci, J. Mater. Res. 19 (2004) 1924.
[3] S. Günes, H. Neugebauer, N.S. Sariciftci, Chem. Rev. 107 (2007) 1324.
[4] C.J. Brabec, Sol. Energy Mater. Sol. Cells 83 (2004) 273.
[5] Special Issue on 'Organic Photovoltaics', MRS Bull. 30 (2005) 1.
[6] M.C. Scharber, D. Mühlbacher, M. Koppe, P. Denke, C. Waldauf, A.J. Heeger, C.J. Brabec, Adv. Mater. 18 (2006) 789.
[7] P. Peumans, A. Yakimov, S.R. Forrest, J. Appl. Phys. 93 (2003) 3693.
[8] P. Schilinsky, C. Waldauf, J. Hauch, C.J. Brabec, Thin Solid Films 451–452 (2004) 105.
[9] O. Hofmann, P. Miller, P. Sullivan, T.S. Jones, J.C. de Mello, D.C. Bradley, A.J. de Mello, Sens. Actuators B 106 (2005) 878.
[10] A. Pais, A. Banejee, D. Klotzkin, I. Papautsky, Lab Chip 8 (2008) 794.
[11] M. Ramuz, L. Bürgi, C. Winnewisser, P. Seitz, Org. Electron. 9 (2008) 369.
[12] W.J.E. Beek, R.A.J. Janssen, Hybrid polymer–inorganic photovoltaic cells, in: L. Merhari (Ed.), Hybrid Nanocomposites for Nanotechnology, Springer, New York, USA, 2009.
[13] R.N. Marks, J.J. Halls, D.D.C. Bradley, R.H. Friend, A.B. Holmes, J. Phys.: Condens. Matter 6 (1994) 1379.
[14] M.G. Harrison, J. Grüner, G.C.W. Spencer, Phys. Rev. B 55 (1997) 7831.
[15] A.K. Ghosh, T. Feng, J. Appl. Phys. 49 (1978) 5982.
[16] C.J. Harris, W.J. Belcher, P.C. Dastoor, Sol. Energy Mater. Sol. Cells 91 (2007) 1127.
[17] F. Feller, A.P. Monkman, Synth. Met. 116 (2001) 149.
[18] J.E. Kroeze, T.J. Savenije, M.J.W. Vermeulen, J.M. Warman, J. Phys. Chem. B 107 (2003) 7696.
[19] T.K. Däubler, D. Neher, H. Rost, H.H. Hörhold, Phys. Rev. B 59 (1999) 1964.
[20] C.L. Yang, Z.K. Tang, W.K. Ge, J.N. Wang, Z.L. Zhang, X.Y. Jian, Appl. Phys. Lett. 83 (2003) 1737.

[21] A.K. Ghosh, D.L. Morel, T. Feng, R.F. Shaw, C.A. Rowe Jr., J. Appl. Phys. 45 (1974) 230.
[22] W. Tang, A.C. Albrecht, J. Chem. Phys. 62 (1975) 2139.
[23] H.B. De Vore, Phys. Rev. 102 (1956) 86.
[24] A. Desormeaux, J.J. Max, R.M. Leblanc, J. Phys. Chem. 97 (1993) 6670.
[25] O. Simpson, Proc. R. Soc. London, Ser. A 238 (1957) 402.
[26] S.R. Goh, C. Scully, M.D. Mc Gehee, J. Appl. Phys. 101 (2007) 114503.
[27] P.E. Shaw, A. Ruseckas, I.W. Samuel, Adv. Mater. 20 (2008) 3516.
[28] L. Luer, H.-J. Egelhaaf, D. Oelkrug, G. Cerullo, G. Lanzani, B.-H. Huisman, D. de Leeuw, Org. Electron. 5 (2004) 83.
[29] J.R. Lakowicz, Principles of Fluorescence Spectroscopy, third ed., Springer, New York, 2006.
[30] M.R. Antognazza, P. Monti, G. Lanzani, Appl. Phys. Lett. 90 (2007) 163509.
[31] G. Wyszecki, W.S. Stiles, Color Science, second ed., Wiley, New York, 2000.

Organic Electronics 11 (2010) 363–368

Contents lists available at ScienceDirect

Organic Electronics

journal homepage: www.elsevier.com/locate/orgel

Flexible field-effect transistors from a liquid crystalline semiconductor by solution processes

Fapei Zhang [a], Masahiro Funahashi [a,*], Nobuyuki Tamaoki [b,1]

[a] Department of Chemistry and Biotechnology, School of Engineering, The University of Tokyo, 7-3-1 Hongo, Bunkyo-ku, Tokyo 113-8656, Japan
[b] Research Institute for Electronic Science, Hokkaido University, Kita 20, Nishi 10, Kita-ku, Sapporo 001-0020, Hokkaido, Japan

ARTICLE INFO

Article history:
Received 16 October 2009
Received in revised form 6 November 2009
Accepted 6 November 2009
Available online 13 November 2009

Keywords:
Liquid crystal
Liquid crystalline semiconductor
Field-effect transistor
Flexible device

ABSTRACT

We have fabricated the flexible field-effect transistors based on the liquid crystalline phenylterthiophene derivative via a solution process. A dielectric layer of polyvinyl alcohol (PVA) are deposited on a polyimide sheet substrate by a spin-coating method and then the thin film of 5-propyl-5″-(4-pentylphenyl)-2,2′:5′,2″-terthiophene is fabricated from its chlorobenzene solution on the dielectric layer by spin-coating or solution sheared deposition method. The fabricated devices exhibit good electrical performance with a hole mobility of up to 0.05 $cm^2 V^{-1} s^{-1}$ as well as excellent mechanical flexibility. The performance does not degrade at the external strain reached 3%. Our results demonstrate that liquid crystalline semiconductors are promising materials for low-cost flexible electronic devices.

© 2009 Elsevier B.V. All rights reserved.

1. Introduction

Organic field-effect transistors (FETs) exhibit high carrier mobility which can be comparable to that of amorphous silicon field-effect transistors. In general, organic FETs utilize the vacuum-deposited polycrystalline thin films of molecular crystals such as pentacene [1–3]. In contrast to expensive vacuum process, a few solution-processable organic semiconductors forming high quality polycrystalline thin films have been designed and applied to FETs [4,5]. The soluble precursors which can be converted to insoluble organic semiconductor materials, as well as the pentacenes bearing bulky substituents are the typical examples [6,7]. However the control of crystal growth in the solution processes is generally difficult and the device performances are inferior to those of the devices fabricated by vacuum process. A few conjugated polymers have been applied to the FETs with high performance [8]. However the performance significantly depends upon the crystallinity and morphology of the thin films [9].

In addition to the solution-processability, one of the recent research topics is the development of the flexible FETs. Such devices are the key components, e.g. in the electronic papers [10,11] and in the large-area active-matrix pressure sensors for artificial skin [12,13]. Someya et al. prepared the flexible FETs based on the vacuum-deposited pentacene films and fabricated the transistor arrays on flexible polymer substrates which were applied to pressure sensors [12,13]. Bao et al. fabricated the transistor arrays consisting of rubrene single crystals on the plastic substrates [14,15]. However, molecular crystals have a relatively rigid structure and the device performance degrades when a large strain is applied e.g. by bending. Moreover the fabrication of polycrystalline thin films generally needs vacuum process. It should be noted that the flexible organic FETs fabricated by solution process have been very limited.

In this paper, we report the fabrication and characterization of the flexible FETs using liquid crystalline (LC)

* Corresponding author. Tel.: +81 3 5841 7441; fax: +81 3 5841 8661.
E-mail addresses: funahashi@chembio.t.u-tokyo.ac.jp (M. Funahashi), tamaoki@es.hokudai.ac.jp (N. Tamaoki).
[1] Tel.: +81 11 706 9356; fax: +81 11 706 9357.

1566-1199/$ - see front matter © 2009 Elsevier B.V. All rights reserved.
doi:10.1016/j.orgel.2009.11.014

semiconductors by solution process. The LC semiconductors exhibit good carrier transport characteristics in their mesophases because of their crystal-like molecular packing structures and the low defect density [16–22]. In the columnar and smectic phases, the LC molecules self-organize into large domains with crystal-like molecular ordering. The close molecular packing structure and small energetic disorder in the LC phases leads to efficient intermolecular charge carrier transport. In addition, the defect density at the domain boundaries is sufficiently suppressed because of a self-healing effect by molecular thermal motion.

Fast electronic charge carrier transport has been confirmed in the discotic columnar [23–30], smectic [31–37], nematic and cholesteric phases [38–40]. The time-of-flight (TOF) measurement revealed high drift carrier mobilities exceeding 0.1 $cm^2 V^{-1} s^{-1}$ in highly ordered smectic phases of alkynylquaterthiophene [35] and bisthienylbenzene derivatives [36] as well as in the discotic columnar phases of hexaalkylthiotriphenylene derivatives [26], respectively. Time-resolved pulse-radiolysis microwave conductivity indicates high microscopic carrier mobilities comparable to molecular crystals in columnar phases of hexabenzocoronene derivatives [27–29].

Recently a few solution-processable LC semiconductors have been developed and applied to the electroluminescence devices [41–44], solar cells [45], and FETs [46–52]. The disk-like hexabenzocoronene derivatives exhibiting columnar phases were applied to the FETs in which the columns are aligned parallel to the substrates by the friction transfer [46] and zone-cast methods [47]. In contrast, it is relatively easy to control the molecular alignment of the rod-like LC molecules in the smectic phases. Oligothiophene derivatives which exhibit the highly ordered smectic phases have been applied to the FETs [48–52].

Moreover, the LC semiconductors possess not only efficient carrier transport characteristics but also softness even in the highly ordered smectic phases owing to molecular thermal motion [53]. The thermal movement of the LC molecules enables self-healing of dynamic positional disorders (which act as carrier trapping sites) within the LC material, resulting in a low defect density [54]. These LC semiconductors are expected to be conformable to the deformation made by the external strain, and therefore the formation of the defects and disorders will be suppressed. These characteristics are highly desirable in flexible electronics. However the fabrication of the flexible FETs based on the liquid crystalline semiconductors by the solution process has not been reported yet.

Recently, we have developed a LC semiconductor, 5-propyl-5″-(4-pentylphenyl)-2,2′:5′,2″-terthiophene (3-TTPPh-5); its molecular structure is shown in Fig. 1a. 3-TTPPh-5 exhibits a nematic phase between 216 °C and 202 °C and a highly ordered smectic phase below 202 °C. This compound does not crystallize when it is cooled to −50 °C. A time-of-flight measurement revealed a fast ambipolar transport in the bulk state at room temperature [49]. Hole mobility of more than 0.04 $cm^2 V^{-1} s^{-1}$ in ambient air was achieved in its FETs [50]. It should be noted that the active layers of such FETs are in the highly ordered smectic phase and not in the crystalline state when the devices are functioning. This highly ordered smectic phase should be more flexible and softer than the crystalline films. Most of the FETs based on liquid crystalline semiconductors are operated in the crystalline states [46–48,52]. The highly ordered smectic phase has a layer structure with long-range molecular ordering within the smectic layers, while there is degree of freedom for molecular thermal movement around the long axis of the LC molecules. The LC films are expected to be softer and more flexible than those based on molecular crystals.

2. Experimental

2.1. Material synthesis

3-TTPPh-5 was synthesized by a previously reported method [49]. Before the fabrication of the devices, the material was purified by silica gel column chromatography and recrystallized from cyclohexane.

2.2. Fabrication of the OFETs on the polyimide (PI) films

A 60 nm-thick Au film with a 5 nm MoO_x adhesive layer was vacuum-deposited on the surface of a 0.3 mm-thick PI sheet, and this Au film acted as the gate electrode. The dielectric layer was spin-coated (at 1500 rpm) on the Au-deposited PI sheet from a 10% aqueous solution of polyvinyl alcohol (PVA) (Tokyo Kasei, Japan) and baked overnight in a vacuum oven at 80 °C. The average thickness of the resulting PVA layer determined using a surface profiler was ca. 2.0 μm. The PVA-coated PI sheet was then immersed into a 10 mM toluene solution of octyltrichlorosilane (OTS-8) at 65–70 °C for 25 min and rinsed four times with toluene. Then a 50 nm thin film of the LC 3-TTPPh-5 was prepared by spin-coating the 0.7% solution in chlorobenzene on the PVA surface and annealed at 100 °C for 10 min in vacuum. Finally, a 60 nm-thick Au source/drain electrode was deposited under high vacuum using a shadow mask to define a top-contact FET structure with a channel length of 20–30 μm (width: 5 mm).

2.3. Fabrication of the liquid crystalline thin film of 3-TTPPh-5 by the solution sheared deposition

A few droplets of chlorobenzene solution of 3-TTPPh-5 (0.6 wt.%) were placed on a PVA-coated PI sheet which was kept at 80 °C in air, so that the solution should cover the whole surface of the substrate. Then a hydrophobic Si wafer whose surface was pretreated by the OTS-8 self-assembled monolayer was put on the surface of the solution. Drawing the upper wafer in one direction (shearing the solution) slowly, leaving the film on the PVA surface by solvent evaporation on the heated substrate.

2.4. Electrical measurement of the flexible field-effect transistors

The transistor characteristics were measured by a two-channel source meter (Kethley source meter 2612). The transistors were placed in a light-shielded box under ambi-

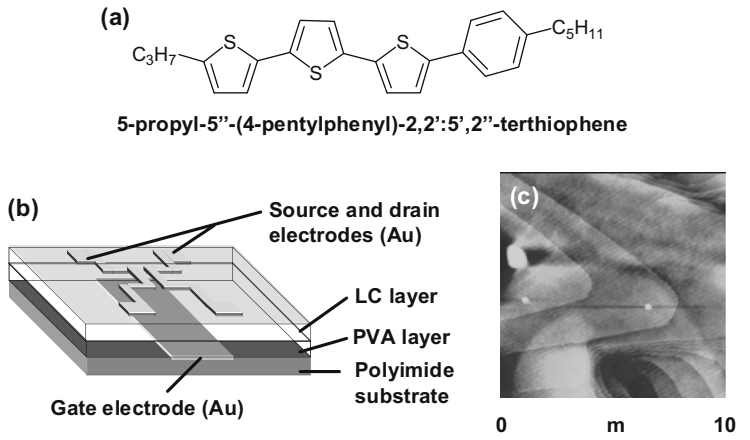

Fig. 1. (a) Molecular structure of 3-TTPPh-5. (b) A schematic image of the structure of the flexible FET fabricated on polyimide films. (c) Tapping-mode AFM topographic image of an individual grain in the annealed film of 3-TTPPh-5 prepared on the PVA surface.

ent condition with low humidity. The strain was applied to the flexible transistors by attaching them around glass cylinders. All the electrical measurements were performed at room temperature.

3. Results and discussion

The flexible thin film transistors were fabricated on the polyimide sheets with a device structure as shown in Fig. 1b. The capacitance of the PVA dielectric was estimated to be 3.5 nF cm^{-2} from its thickness by assuming the relative permittivity of the PVA as 8. Such a capacitance value was confirmed by the capacitance–frequency measurements and this value was used to calculate the hole mobility below.

The morphology and structure of the LC 3-TTPPh-5 thin films grown on the PVA surface were investigated by atomic force microscopy (AFM) and X-ray diffraction (XRD). The AFM observation revealed that the film consists of large-size plate-like grains (10–50 μm) with a lamellar structure, similar to the films formed on the SiO_2 surface [50]. Fig. 1c shows a tapping-mode AFM image within a grain exhibiting the atomically flat terraces on the surface. The films formed on the PVA surface also showed the same XRD pattern as those on the SiO_2 surface, exhibiting a highly ordered layer structure [50].

Fig. 2a and b show the output and transfer characteristics of the flexible FET using 3-TTPPh-5, measured in ambient air, respectively. The device exhibits a clear *p*-type operation. The hole mobility and current on/off ratio were found to be ca. 0.01 $cm^2 V^{-1} s^{-1}$ and 10^4, respectively. This mobility value is lower than that of the FETs of 3-TTPPh-5 formed on the rigid SiO_2/Si substrate (0.04 $cm^2 V^{-1} s^{-1}$) [50]; however, this value is comparable to that of the normal solution-processed organic FETs [55]. The unsaturation of the drain current was found to occur at the higher drain voltage in the output curves, and the threshold voltage V_T was found to shift slightly toward the positive direction with time. We propose that these phenomena are due to the presence of trace amounts of mobile sodium ions in the commercially available PVA, as recently demonstrated by Egginger et al. [56]. The movement of such ionic impurities in the PVA dielectric induces an additional electric field in the dielectric layer by gate bias; this leads to the shift of V_T and a large off-current (thereby, a low on/off ratio). However, we observed that such impurities do not significantly

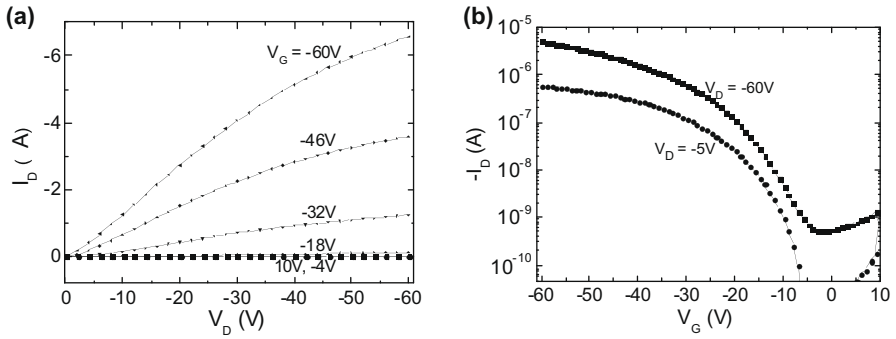

Fig. 2. (a) Output characteristics and (b) transfer curves of the flexible FET of 3-TTPPh-5 film on the bare PVA dielectric surface at room temperature. The channel length of the FET is 30 μm.

affect the value of carrier mobility in our devices. Residual water contained in the PVA layers may also influence on the unsaturation in the drain current and the shift of V_T.

In order to further improve the device performance, we carried out surface modification of the PVA dielectric using silane agents. This was owing to the presence of hydroxyl groups (–OH) on the PVA surface, similar to the SiO_2 surface. First hexamethyldisilazane (HMDS) was spin-coated on the PVA-coated PI sheets. However, there was no notable enhancement in the hole mobility in the devices. This was probably due to a weak interaction between the PVA surface and the HMDS molecules and thus the insufficient surface coverage by the alkyl chains. In the next approach, we grew a self-assembled monolayer (SAM) of octyltrichlorosilane (OTS) on PVA. The PVA-coated PI sheet was immersed into a 10 mM toluene solution of OTS at 65–70 °C for 25 min and rinsed four times with toluene. After this treatment, the contact angle of water droplets on the PVA surface increased from 30–40° (for the bare PVA) to 90°, indicating the sufficient coverage of the OTS on the PVA surface.

The OTS-treatment enhances the hole mobility, as shown in the transfer curves of the flexible 3-TTPPh-5 FETs (Fig. 3). Hole mobility of up to 0.036 $cm^2 V^{-1} s^{-1}$ has been achieved, which is close to that observed for the 3-TTPPh-5 devices on the OTS-treated SiO_2/Si substrates. The on/off ratio keeps nearly constant (10^4). We did not observe any change in the surface morphology and structure of the LC films after the OTS-modification of the PVA surface. Therefore, the mobility enhancement should be attributed to the favorable interaction between the long alkyl chains of the OTS molecules and those of the 3-TTPPh-5 molecules near the initial 2–3 layers of the LC film [57]; however, further investigation must be carried out in this regard. The off-current is slightly higher possibly due to the residual impurities introduced by the OTS-treatment of the PVA surface.

The hole mobility increases further when the liquid crystalline thin films are formed by a solution sheared deposition (SSD) method. High performance FETs based on some of solution-processable oligothiophene derivatives were produced by this method [58]. In our study, the thin film of 3-TTPPh-5 was deposited on the PVA-coated PI sheets which were kept at 80 °C in air. From optical microscopic observation, the resulting films exhibit a better film coverage on the substrate as well as the more homogenous film morphology, compared to the films deposited by spin-coating (not shown here). Moreover the films also show some degree of macroscopic orientation, similar to the observation by Bao et al. on oligothiophene films produced by the SSD method [58]. However, crystal structure of the films formed by the SSD shows no obvious change compared to those by spin-coating from the XRD results.

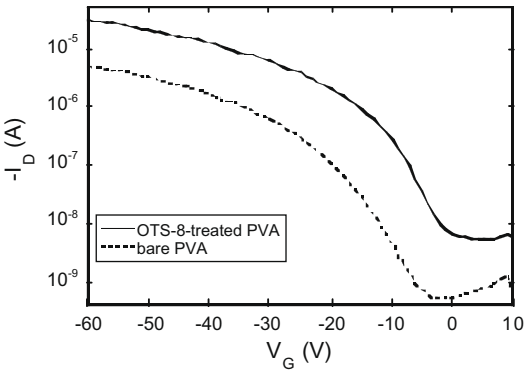

Fig. 3. Transfer curves of flexible 3-TTPPh-5 FET on the bare surface (dotted line) and on OTS-treated surface (solid line) at room temperature. The channel length of the FET is 30 μm.

Fig. 4a and b show the output and transfer characteristics of the FET prepared by the solution sheared deposition. The hole mobility and on/off ratio reach up to 0.05 $cm^2 V^{-1} s^{-1}$ and 10^5, respectively. The threshold voltage value is reduced from −18 V (for the FET prepared by spin-coating) to ca. −8 V. It should be noted that the mobility approaches the value in the bulk state (0.07 $cm^2 V^{-1} s^{-1}$) from the TOF measurement [49], which represents the upper limit of carrier transport.

We tested the mechanical flexibility of the FETs by bending the PI substrate to various radii. The flexible FETs fabricated by the solution sheared deposition on the PVA layer (on a PI substrate) exhibits the hole mobility of 0.05 $cm^2 V^{-1} s^{-1}$ and the on/off ratio of 10^5 before the application of the strain. The extent of bending was measured by attaching the flexible transistor around the cylindrical bars with different radii R, as shown in the inset of Table 1. The derived mobility and threshold voltage are shown as a function of the strain in Fig. 5. The relation between the strain ε and the bending radius R is given as $\varepsilon = d_s/2R$ for our devices. Here, d_s is the substrate thickness (PI sheet) [14,15,59]. Table 1 lists the bending radii used in our experiment and the corresponding strain values. Our flexible devices can be bent to a radius of less than 5 mm. The carrier mobility shows a slight increase with the strain and then remains constant at a high strain of 2.7%. The slight decrease in V_T with strain may be attributed to the effect of mobile ionic impurities in the dielectric layer, as mentioned above. Bending measurements could not be carried out at the smaller bending radii because of the large-size of the device and the relative rigidity of the thick PI sheet (thickness: 0.3 mm) which makes the bending difficult. However, we believe that our LC transistors are capable of functioning even under the higher strain. In addition, the AFM observation did not reveal any marked difference between the film morphologies of the bent FETs and those prior to bending.

Our results are very encouraging when compared to the data on the flexible FETs presented by the other groups [11,12,14,15]. Someya's group has fabricated the flexible pentacene TFT arrays, whose mechanical flexibility represents the best values till date [12]. However, though these devices can be operated under a strain of 2.7%, their hole mobility is decreased by 40%. Therefore, the flexible properties of our devices are comparable to and even better than the OFETs with the best flexibility available at present. It should be mentioned that these authors used the thin polymeric substrates (thickness: 0.1–0.14 mm). The substrates with a thickness of less than 0.3 mm can effectively absorb the mechanical stress and prevent mechani-

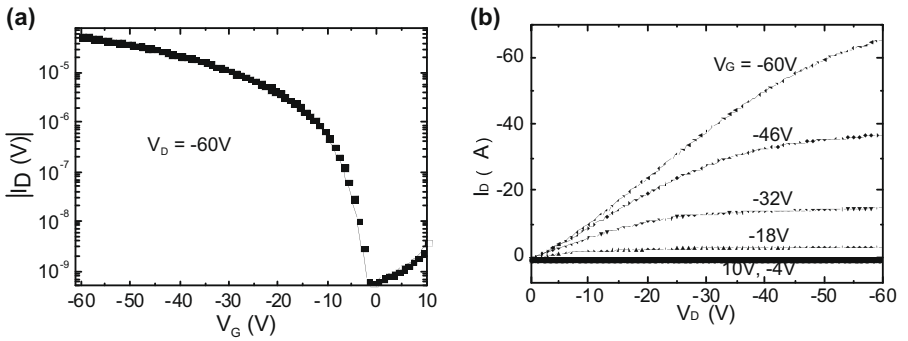

Fig. 4. (a) Output characteristics and (b) transfer curves of the flexible FET of 3-TTPPh-5 film on the PVA dielectric surface by the solution sheared deposition. The measurement was performed at room temperature. The channel length of the FET is 30 μm.

Table 1
Bending radii used in the bending experiment and the corresponding strain values.

Bending radius (mm)	12	10	7.5	5.5
Strain (%)	1.25	1.5	2.0	2.73

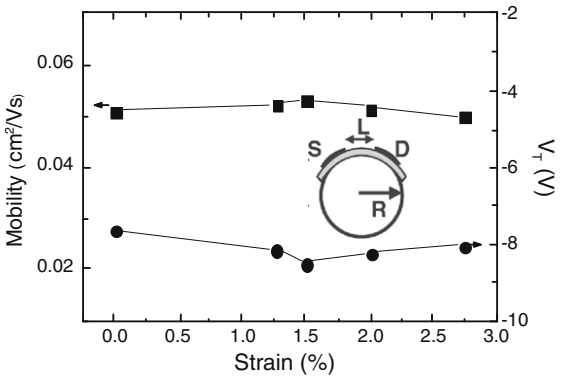

Fig. 5. The field-effect mobility and threshold voltage (V_T) of a flexible LC FET as a function of the strain at room temperature.

cal degradation of the active layer. Our PI substrates are relatively thick (0.3 mm), which may be detrimental to the flexibility of the FETs. However, our flexible LC FETs also exhibit the excellent mechanical flexibility. Better results can be expected from bending measurements if the thinner substrates are used. The excellent mechanical flexibility of LC FETs can be attributed to the inherent softness of liquid crystals. The thermal movement and self-assembling capability of the LC molecules enables self-healing of the dynamic positional disorders (carrier trapping sites) caused by mechanical deformation, and thus, carrier transport in LC semiconductors is not significantly affected by the external strain.

Besides, the large-area homogenous LC 3-TTPPh-5 thin films can be fabricated by a simple spin-coating process. The film morphology and structure are unaffected by the nature of the substrate materials and surface chemistry; these properties facilitate the fabrication of these device by practical methods such as roll-to-roll printing or ink-jet processing. Moreover, all the device fabrication steps were carried out at a low temperature (below 100 °C). These characteristics make the 3-TTPPh-5 a good candidate for large-area, low-cost flexible electronics.

4. Conclusions

In conclusion, we have fabricated the flexible FETs based on the LC 3-TTPPh-5 via solution process. The fabricated devices exhibit good electrical performance with a hole mobility of up to 0.05 $cm^2 V^{-1} s^{-1}$ and mechanical flexibility superior to the normal polycrystalline OFETs. Our results demonstrate that the LC semiconductors are promising materials for the low-cost flexible electronic devices.

Acknowledgements

This study was financially supported by the NEDO Industrial Technology Research Grant, Association of New Chemistry, and Sumitomo foundation. We thank Dr. H. Minamikawa and the Nano-Processing Facility in AIST for providing the XRD apparatus. We also thank Dr. M. Chikamatsu and Dr. R. Azumi from the Photonics Research Institute of AIST for their fruitful advice on fabrication and characterization of FET devices and Prof. T. Kato for the valuable discussion on the material design. We also thank Mitsui Chemicals for providing the polyimide sheets.

References

[1] M. Kitamura, Y. Arakawa, J. Phys.: Condens. Matter 20 (2008) 184011.
[2] T.W. Kelley, L.D. Boardman, T.D. Dunbar, D.V. Muyres, M.J. Pellerite, T.P. Smith, J. Phys. Chem. B 107 (2003) 5877.
[3] S. Lee, B. Koo, J. Shin, E. Lee, H. Park, H. Kim, Appl. Phys. Lett. 88 (2006) 162109.
[4] A.R. Murphy, J.M.J. Fréchet, Chem. Rev. 107 (2007) 1066.
[5] A.R. Murphy, P.C. Chang, P. VanDyke, J. Liu, J.M. Fréchet, V. Subramanian, D.M. DeLongchamp, S. Sambasivan, D.A. Fischer, E.K. Lin, Chem. Mater. 17 (2005) 6033.
[6] J.E. Anthony, Chem. Rev. 106 (2006) 5028.
[7] M.M. Payne, S.R. Parkin, J.E. Anthony, C.-C. Kuo, T.N. Jackson, J Am. Chem. Soc. 127 (2005) 4986.
[8] I. McCulloch, M. Heeney, C. Bailey, K. Genevicius, I. MacDonald, M. Shkunov, D. Sparrowe, S. Tierney, R. Wagner, W. Zhang, M.L. Chabinyc, R.J. Kline, M.D. McGgehee, M.F. Toney, Nat. Mater. 5 (2006) 328.

[9] R.J. Kline, M.D. McGehee, E.N. Kadnikova, J. Liu, J.M.J. Fréchet, M.F. Toney, Macromolecules 38 (2005) 3312.
[10] J.A. Rogers, Z. Bao, K. Baldwin, A. Dodabalapur, B. Crone, V.R. Raju, V. Kuck, H. Katz, K. Amundson, J. Ewing, P. Drzaic, Proc. Nat. Acad. Sci. 98 (2001) 4835.
[11] G.H. Gelinck, H.E.A. Huitema, E.V. Veenedaal, E. Cantatore, L. Schrijnemakers, J.B.P.H. van der Putten, T.C.T. Geuns, M. Beenhakkers, J.B. Giesbers, B.H. Huisman, E.J. Meijer, E.M. Benito, F.J. Touwslager, A.W. Marsman, B.J.E. van Rens, D.M. De Leeuw, Nat. Mater. 3 (2004) 106.
[12] T. Someya, T. Sekitani, S. Iba, Y. Kato, H. Kawaguchi, T. Sakurai, Proc. Nat. Acad. Sci. 101 (2004) 9966.
[13] T. Someya, Y. Kato, T. Sekitani, S. Iba, Y. Noguchi, Y. Murase, H. Kawaguchi, T. Sakurai, Proc. Nat. Acad. Sci. 102 (2005) 12321.
[14] A.L. Briseno, R.J. Tseng, M.-M. Ling, E.H.L. Falcao, Y. Yang, F. Wudl, Z. Bao, Adv. Mater. 18 (2006) 2320.
[15] A.L. Briseno, S.C.B. Mannsfeld, M.M. Ling, S. Liu, R.J. Tseng, C. Reese, M.E. Roberts, Y. Yang, F. Wudl, Z. Bao, Nature 444 (2006) 913.
[16] M. O'Neill, S.M. Kelly, Adv. Mater. 15 (2003) 1135.
[17] Y. Shimizu, K. Oikawa, K. Nakayama, D. Guillon, J. Mater. Chem. 17 (2007) 4223.
[18] S. Sergeyev, W. Pisula, Y.H. Geerts, Chem. Soc. Rev. 36 (2007) 1902.
[19] M. Funahashi, H. Shimura, M. Yoshio, T. Kato, Struct. Bonding 128 (2008) 151.
[20] M. Funahashi, Polymer J 41 (2008) 459.
[21] S. Laschat, A. Baro, N. Steinke, F. Giesselmann, C. Hägele, G. Scalia, R. Judele, E. Kapatsina, S. Sauer, A. Schreivogel, M. Tosoni, Angew. Chem. Int. Ed. 46 (2007) 4832.
[22] M. Funahashi, Transworld Res. Network, Recent Dev. Appl. Phys. 6 (2003) 839.
[23] N. Boden, R.J. Bushby, J. Clements, M.V. Jesudason, P.F. Knowles, G. Williams, Chem. Phys. Lett. 152 (1988) 94.
[24] D. Adam, F. Closs, T. Frey, D. Funhoff, D. Haarer, H. Ringsdorf, P. Schuhmacher, K. Siemensmeyer, Phys. Rev. Lett. 70 (1993) 457.
[25] N. Boden, R.J. Bushby, J. Clements, B. Movaghar, K.J. Donovan, T. Kreouzis, Phys. Rev. B 52 (1995) 13274.
[26] D. Adam, P. Schuhmacher, J. Simmerer, L. Häußling, K. Siemensmeyer, K. Etzbach, H. Ringsdorf, D. Haarer, Nature 371 (1994) 141.
[27] A.M. van de Craats, J.M. Warman, K. Müllen, Y. Geerts, J.D. Brand, Adv. Mater. 10 (1998) 36.
[28] A.M. van de Craats, J.M. Warman, A. Fechtenkötter, J.D. Brand, M.A. Harbison, K. Müllen, Adv. Mater. 11 (1999) 1469.
[29] A.M. van de Craats, J.M. Warman, Adv. Mater. 13 (2001) 130.
[30] M. Kastler, F. Laquai, K. Müllen, G. Wegner, Appl. Phys. Lett. 89 (2006) 252103.
[31] M. Funahashi, J. Hanna, Phys. Rev. Lett. 78 (1997) 2184.
[32] M. Funahashi, J. Hanna, Appl. Phys. Lett. 71 (1997) 602.
[33] M. Funahashi, J. Hanna, Appl. Phys. Lett. 76 (2000) 2574.
[34] M. Funahashi, J. Hanna, Mol. Cryst. Liq. Cryst. 410 (2004) 529.
[35] M. Funahashi, J. Hanna, Adv. Mater. 17 (2005) 5945.
[36] K. Oikawa, H. Monobe, J. Takahashi, K. Tsuchiya, B. Heinrich, D. Guillon, Y. Shimizu, Chem. Commun. (2005) 5337.
[37] T. Yasuda, H. Ooi, J. Morita, Y. Akama, K. Minoura, M. Funahashi, T. Shimomura, T. Kato, Adv. Funct. Mater. 19 (2009) 411.
[38] K.L. Woon, M.P. Aldred, P. Vlachos, G.H. Mehl, T. Stirner, S.M. Kelly, M. O'Neill, Chem. Mater. 18 (2006) 2311.
[39] M. Funahashi, N. Tamaoki, Chem. Phys. Chem. 7 (2006) 1193.
[40] M. Funahashi, N. Tamaoki, Chem. Mater. 19 (2007) 608.
[41] K. Kogo, T. Goda, M. Funahashi, J. Hanna, Appl. Phys. Lett. 73 (1998) 1595.
[42] A.E.A. Contoret, S.R. Farrar, P.O. Jackson, S.M. Khan, L. May, M. O'Neill, J.E. Nicholls, S.M. Kelly, G.J. Richards, Adv. Mater. 12 (2000) 971.
[43] T. Hassheider, S.A. Benning, H.-S. Kitzerow, M.-F. Achard, H. Bock, Angew. Chem. Int. Ed. 40 (2001) 2060.
[44] M.P. Aldred, A.E.A. Contoret, S.R. Farrar, S.M. Kelly, D. Mathieson, M. O'Neill, W.C. Tsoi, P. Vlachos, Adv. Mater. 17 (2005) 1368.
[45] L. Schmidt-Mende, A. Fechtenkötter, K. Müllen, E. Moons, R.H. Friend, J.D. MacKenzie, Science 293 (2001) 1119.
[46] A.M. van de Craats, N. Stutzmann, O. Bunk, M.M. Nielsen, M. Watson, K. Müllen, H.D. Chanzy, H. Sirringhaus, R.H. Friend, Adv. Mater. 15 (2003) 495.
[47] W. Pisula, A. Menon, M. Stepputat, I. Lieberwirth, U. Kolb, A. Tracz, H. Sirringhaus, T. Pakula, K. Müllen, Adv. Mater. 17 (2005) 684.
[48] A.J.J.M. van Breemen, P.T. Herwig, C.H.T. Chlon, J. Sweelssen, H.F.M. Schoo, S. Setayesh, W.M. Hardeman, C.A. Martin, D.M. de Leeuw, J.J.P. Valeton, C.W.M. Bastiaansen, D.J. Broer, A.R. Popa-Merticaru, S.C.J. Meskers, J. Am. Chem. Soc. 128 (2006) 2336.
[49] M. Funahashi, F. Zhang, N. Tamaoki, Adv. Mater. 19 (2007) 353.
[50] F. Zhang, M. Funahashi, N. Tamaoki, Appl. Phys. Lett. 91 (2007) 063515.
[51] F. Zhang, M. Funahashi, N. Tamaoki, Org. Electron. 10 (2009) 73.
[52] K. Oikawa, H. Monobe, K. Nakayama, T. Kimoto, K. Tsuchiya, B. Heinrich, D. Guillon, Y. Shimizu, M. Yokoyama, Adv. Mater. 19 (2007) 1864.
[53] G.W. Gray, J.W.G. Goodby, Smetic Liquid Crystals – Texture and Structures, Leonard Hill, Glasgow, Scotland, 1984.
[54] H. Maeda, M. Funahashi, J. Hanna, Mol. Cryst. Liq. Cryst. 246 (2000) 183.
[55] S. Allard, M. Forster, B. Souharce, H. Thiem, U. Scherf, Angew. Chem. Int. Ed. 47 (2008) 4070.
[56] M. Egginger, M. Irihai-Vladu, R. Schwödiauer, A. Tanda, I. Frischauf, S. Bauer, N.S. Sariciftci, Adv. Mater. 20 (2008) 1018.
[57] A. Salleo, M.L. Chabinyc, M.S. Yang, R.A. Street, Appl. Phys. Lett. 81 (2001) 4383.
[58] H.A. Becerril, M.E. Roberts, Z. Liu, J. Locklin, Z. Bao, Adv. Mater. 20 (2008) 2588.
[59] Z. Suo, E.Y. Ma, H. Gleskova, S. Wagner, Appl. Phys. Lett. 74 (1999) 1177.

Organic Electronics 11 (2010) 369–376

Contents lists available at ScienceDirect

Organic Electronics

journal homepage: www.elsevier.com/locate/orgel

Efficient near-infrared organic light-emitting diodes based on multimetallic assemblies of lanthanides and iridium complexes

Zhu-Qi Chen, Fei Ding, Zu-Qiang Bian *, Chun-Hui Huang

Beijing National Laboratory for Molecular Sciences, State Key Laboratory of Rare Earth Materials Chemistry and Applications, College of Chemistry and Molecular Engineering, Peking University, Beijing 100871, China

ARTICLE INFO

Article history:
Received 16 October 2009
Received in revised form 9 November 2009
Accepted 9 November 2009
Available online 14 November 2009

Keywords:
Near-infrared emission
Electroluminesence
Lanthanide
Multimetallic assembly

ABSTRACT

Two structurally simple Iridium(III) complexes with pyrimidin-imidazole derivatives as the ancillary ligands (Ir**1** and Ir**2**) were synthesized. Photophysical studies showed that the iridium complexes have suitable triplet energy levels for sensitizing Nd^{III}. The efficient energy transfer from Ir^{III} moiety to Nd^{III} is observed in both solutions and films. Utilizing co-deposition film of Ir–Nd assemblies as the emitting layer, nondoped OLEDs were fabricated. EL devices with a structure of NPB (1,4-bis((1-naphthylphenyl)amino)biphenyl, 30 nm)/Ir**1**-Nd(PMIP)$_3$ (1-phenyl-3-methyl-4-isobutyryl-5-pyrazolone, 1:1, 40 nm)/BCP (2,9-dimethyl-4,7-diphenyl-1,10-phenanthroline, 10 nm)/Alq_3 (tris(8-hydroxyquinoline), 30 nm) exhibited a NIR emission from Nd^{III} ions. The highest EQE achieved is 0.3%, with a maximum radiance of 6.1 μW cm^{-2} at the main emission wavelength of 1060 nm. This result provides a useful guidance for the future work of lanthanide complexes based NIR OLEDs.

© 2009 Elsevier B.V. All rights reserved.

1. Introduction

Organic light-emitting diodes (OLEDs) have been the subject of a significant research effort from both the academic and industrial communities because of their advantages in emission in a wide visible region and great potential to serve in flat-panel displays [1,2]. Near infrared (NIR) OLEDs have many potential applications such as optical communication [3,4], night-vision readable displays [5], and sensors [6]. To date, attempts to achieve NIR electroluminescence (EL) have primarily focused on low band-gap organic chromophores [7–12], polymers [13–19], transition metal complexes [6,20–24], and lanthanide complexes [25–41]. Among many low band-gap organic compounds, π-conjugated donor–acceptor (D–A) type of chromophores and polymers have been investigated for NIR materials. Yang et al. reported D–A–D oligomers that displayed the EL spectra at 815 nm [12]. OLEDs based on polymers were also developed with peaks ranged from 670 nm to 790 nm and an external an quantum efficiency (EQE) of 1.1% and 0.3%, respectively [19]. Recently Qian et al. reported the well designed D–π–A–π–D type chromophores in the OLEDs that displayed emission exclusively at 1080 nm with an EQE of 0.28% [10,11]. On the other hand, the efficiency of OLEDs is markedly improved when fluorescent emissive chromophores are replaced by phosphorescent complexes which can harvest both the singlet and triplet excitons [42–45]. The highest quantum efficiency in NIR OLEDs published so far is about 8% by Borek et al. using a Pt-based porphyrin complex. However, this OLED emits at a peak of 765 nm, which is still far away from the telecommunication window (1310 nm or 1550 nm) [22,23]. Lanthanide complexes based NIR OLEDs have shown NIR EL at a number of important wavelengths (e.g., 890, 977, 1064, 1346, and 1560 nm), being the potential candidates in optical fiber applications. It has got a great development since Curry et al. reported electroluminescence of ErQ complex [25]. Schanze et al. fabricated devices utilizing lanthanide cations in conjunction with a porphyrin/polystyrene matrix by spin-coating. The EQE ranged from 8.0×10^{-4} to 2.0×10^{-4}% [33].

* Corresponding author.
E-mail address: bianzq@pku.edu.cn (Z.-Q. Bian).

1566-1199/$ - see front matter © 2009 Elsevier B.V. All rights reserved.
doi:10.1016/j.orgel.2009.11.015

$Ln(diketonate)_3$ units with neutral N,N-bidentate chelates or phosphine oxide ligands were also developed as NIR emitting material [26–29,35–37,41]. Zhang et al. observed an EL intensity enhancement by introducing an iridium complex in emitting layer but the efficiency was not given [38]. To date, most EL performances obtained with Ln^{III} complexes had an irradiances of less than 1 $\mu W\,cm^{-2}$ and an EQE of less than 0.1%. Therefore, it is still a challenge to develop Ln^{III} based NIR OLEDs with a high efficiency for both science and technological applications.

Lanthanide emissions need to be sensitized *via* antenna chromophores because their intra-configurational 4f–4f transitions are forbidden and absorptions are very weak. The use of strongly absorbing d-block chromophores as sensitizers for the NIR emissions from f-block lanthanides has attracted more and more attentions since van Veggel and co-workers reported the first example of Nd^{III} and Yb^{III} luminescence sensitized by the transition metal complexes $Ru(bpy)_3^{2+}$ and ferrocene [46]. Subsequently, many d-block chromophores, based on related transition metals were extensively studied [47–54]. Recently our group reported the characterization of dinuclear Ir–Ln complexes that display NIR emission [55]. As most of the energy levels of these d-block chromophores are around 13,000–18,000 cm^{-1}, energy transfer from the transition metal to the lanthanide ion is most efficient and the characteristic emission from these NIR lanthanides are successfully obtained. But the application of multimetallic assembles on OLEDs has not been reported. In this contribution, we report the design and synthesis of a structurally simple Ir^{III} complex with a suitable triplet energy level for sensitizing Nd^{III}. Efficient energy transfer was observed when Ir^{III} complex served as the neutral ligand for Nd^{III} ions in both solutions and films. As the high molecular weight of the complex precludes direct thermal evaporation, we utilized co-deposition film of Ir^{III} complex and Nd^{III} complex as the emitting layer to fabricate NIR OLEDs. The highest EQE achieved was 0.3%, with a maximum radiance of 6.1 $\mu W\,cm^{-2}$ at the main emission wavelength of 1060 nm. These values are a significant improvement over previously reports.

2. Experimental

2.1. General Information

Alq_3 was synthesized according to literature procedures and sublimed twice prior to use [56]. NPB and BCP were purchased from Aldrich and used after a single sublimation. $Tb(PMIP)_3(H_2O)_2$, $Tb(PMIP)_3(TPPO)_2$ and $Tb(PMIP)_3$ Bath (PMIP = 1-phenyl-3-methyl-4-isobutyryl-5-pyrazolone; Bath = bathophenanthroline; TPPO = triphenylphosphine oxide) were synthesized according to our previous report [56]. Chromatographic separation was carried out on silica gel (200–300 mesh). The ^1H NMR spectra were recorded on a Varian 400 MHz instrument using Me_4Si as an internal reference. Mass spectra were recorded on a ZAB-HS and BIFLEX III. Elemental analyses were performed on a VARIO EL analyzer. Photoluminescence spectra and phosphorescence decay lifetimes were recorded with an Edinburgh Analytical Instruments FLS920 spectrometer after removing oxygen in the solution by a vacuum technique (3 or 4 freeze–pump–thaw cycles) [57]. EL spectra were measured by using liquid-nitrogen-cooled germanium detector on FLS 920. Absorption spectra were measured on a Shimadzu UV-3100 UV–vis spectrometer. Cyclic voltammetry was performed with a computer controlled CHI600C electrochemical workstation. The measurement was carried out at room temperature with a conventional three electrode configuration consisting of a one compartment electrolysis cell with a platinum button, a platinum wire, an Ag/AgCl working electrode, counter electrode and reference electrode. Cyclic voltammograms were obtained at a scan rate of 50 mV s^{-1} in dichloromethane after removing oxygen. The concentration of the complexes was 1.0 mM and each solution contained 0.1 M tetrabutylammonium hexafluorophosphate (TBAP) as an electrolyte.

2.2. OLED fabrication and measurement

OLED devices were fabricated by sequentially depositing organic layers using thermal evaporation in one run under high vacuum ($<8 \times 10^{-5}$ Pa) onto a pre-cleaned indium tin oxide (ITO) glass substrate with a sheet resistance of 7 Ω/sq. A shadow mask with rectangular (3×3 mm) openings was used to define the cathode of a 200 nm thick layer of $Mg_{0.9}Ag_{0.1}$ alloy with an 80 nm thick Ag cap. The thickness of the deposited layer and the evaporation speed of the individual materials were monitored in a vacuum with quartz crystal monitors. Deposition rates were maintained at 0.05–0.2 nm s^{-1} for organic materials and 0.2–0.3 nm s^{-1} for the $Mg_{0.9}Ag_{0.1}$ alloy. The visible EL spectra were measured with a Spectra Scan PR650. The current–voltage (I–V) characteristics were measured with a computer controlled Keithley 2400 Sourcemeter unit. The NIR EL irradiance was measured by using a UDT Model 261 Germanium Detector (calibrated by National Institute of Metrology PR China). A 720 nm filter SCF-50S-72R, purchased from Sigma, was used to preclude the effect of visible light. All the measurements were carried out under ambient atmosphere at room temperature. The EQE of the NIR emission was obtained by measuring the irradiance in the forward direction and assuming the external emission profile to be Lambertian.

l is the distance between the OLED and the detector (1.7 cm), e is the charge of an electron, λ is the emission wavelength (1060 nm), P_{det} is the power that the detector measures, S_1 is the area of the detector (0.25 cm^{-2}), S_2 is the area of the device (0.09 cm^{-2}), h is Planck's constant, c is the speed of light in a vacuum and I is the current injected. According to the literature, [11,58] the flux leaving the device directly, F_{ext}, can be calculated as follows:

$$F_{ext} = \int_0^{\pi/2} 2\pi L_0 \cos\theta \sin\theta d\theta = \pi L_0,$$

where L_0 is the flux per solid angle of light leaving the device directly in the forward direction.

The solid angle from the detector to the light source is as follows:

$$\omega = \frac{S_1}{l^2}$$

$$L_0 = \frac{P_{det}}{\omega}$$

So the irradiance of the device, R ($\mu W\ cm^{-2}$), can be calculated as follows:

$$R = \frac{F_{ext}}{S_2} = \frac{\pi P_{det} l^2}{S_1 S_2}$$

The number of photons can be calculated as follows:

$$N_p = \frac{F_{ext}}{h\nu} = \frac{\pi P_{det} l^2 \lambda}{S_1 hc}$$

The number of electrons can be calculated from the current injected as follows:

$$N_e = \frac{I}{e}$$

So the EQE was calculated as follows:

$$\eta_{ext} = \frac{N_p}{N_e} = \frac{\pi P_{det} l^2 \lambda e}{S_1 hcI}$$

2.3. Materials

Scheme 1 shows the synthetic route to the Ir^{III} complexes and chemical structures of Nd^{III} complexes. The bridging ligand was obtained by a one-step reaction of pyrimidine-2-carbonitrile and 4-fluorobenzene-1,2-diamine at 160 °C for 2 h [59]. Complex Ir**1** or Ir**2** was prepared from a reaction of the bridging ligand with the corresponding chloride-bridged Ir^{III} dimer: $(dfppy)_2Ir(\mu\text{-}Cl)_2Ir(dfppy)_2$ or $(ppy)_2\ Ir(\mu\text{-}Cl)_2Ir(ppy)_2$, respectively, (dfppy = 2-(4′,6′-difluorophenyl)-pyridinato-N,$C^{2'}$, ppy = 2-phenylpyridinato-N,$C^{2'}$). The iridium ion was coordinated to one N^N site of the bridging ligand, leaving the other N^N site free for chelating with Ln^{III}. PMIP was chosen as the anion ligand because it has shown good thermal-evaporation ability and sensitization ability to Ln^{III} ions in previous reports [37,60,61]. Reaction of $Nd(PMIP)_3(H_2O)_2$ with Ir**1** or Ir**2** in ethanol and recrystallization afforded the dinuclear adducts by displacement of two water ligands from the lanthanide. This synthesis is based on the well-known formation of eight-coordinate adducts between $Ln(diketone)_3$ units and N,N-bidentate chelates. Similar d–f dinuclear complexes have been described by others [49,50,53]. $Nd(PMIP)_3Bath$ and $Nd(PMIP)_3(TPPO)_2$ were also synthesized as reference materials because most reports on lanthanide based NIR OLEDs have used Bath or TPPO as the neutral ligands [27–29,34,35,37,38,41].

Synthesis of Iridium(III) bis(2-(4′,6′-difluorophenyl)-pyridinato-N,$C^{2'}$) (5-fluoro-2-(pyrimidin-2-yl)-benzo[d] imidazole) (Ir**1**): Ir**1** was synthesized in two steps. A mixture of pyrimidine-2-carbonitrile (2 mmol) and 4-fluorobenzene-1,2-diamine (2 mmol) was heated under a N_2 atmosphere at 160 °C for 2 h. The product was purified by recrystallization from ethanol with a yield of 80%. Then the mixture of this compound (1.1 mmol), anhydrous sodium carbonate (5 mmol) and $(dfppy)_2Ir(\mu\text{-}Cl)_2Ir(dfppy)_2$ (0.5 mmol) was refluxed in 2-ethoxyethanol under a N_2 atmosphere for 12 h. After cooling to room temperature, the mixture was poured into water. The crude product was obtained by filtration and then dissolved in $CHCl_3$. The solution was dried in anhydrous sodium sulfate overnight. After evaporation of the solvent, the residue was

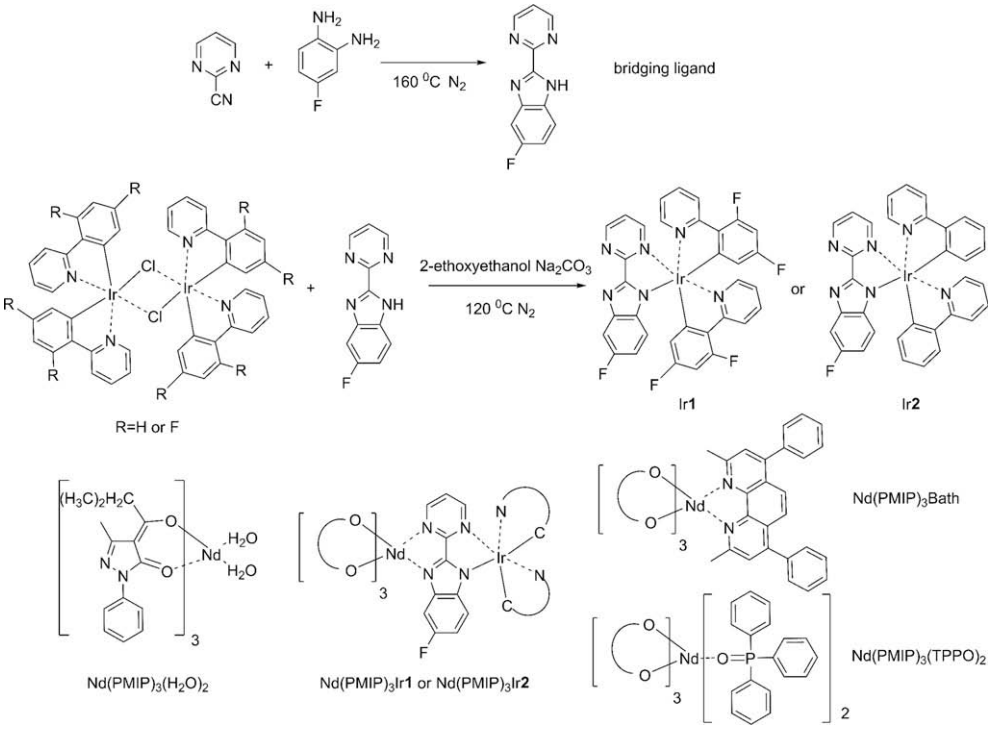

Scheme 1. Synthetic route to Ir^{III} complexes and chemical structures of the Nd^{III} complexes.

purified *via* chromatography, using a methanol–CH_2Cl_2 mixture as the eluent. The pure product was obtained as a yellow powder. Yield: 40%. HRESI (*m*/*z*, Ir**1**H$^+$, 100%): calcd. 787.11423, found 787.11771. ^{1}H NMR (400 MHz, $CDCl_3$, δ): 8.96 (s, 2H), 8.28–8.26 (d, J = 8 Hz, 4H), 7.95–7.94 (d, J = 4 Hz, 2H), 7.76–7.52 (m, 10H), 7.18 (s, 2H), 6.99–6.92 (m, 5H), 6.67–6.51 (m, 5H), 6.19–6.16 (q, 1H), 5.87–5.80 (m, 5H).

Synthesis of Iridium(III) bis(2-phenyl)-pyridinato-N,C$^{2\prime}$) (5-fluoro-2-(pyrimidin-2-yl)-benzo[d]imidazole) (Ir**2**): Ir**2** was synthesized using a procedure similar to that used for Ir**1**. Yield: 35%. HRESI (*m*/*z*, Ir**1**H$^+$, 100%): calcd. 715.15975, found 715.16000. ^{1}H NMR (400 MHz, $CDCl_3$, δ): 8.87 (s, 2H), 7.93–7.91 (m, 2H), 7.85–7.81 (t, 4H), 7.70–7.58 (m, 12H), 7.08–7.05 (m, 4H), 7.00–6.98 (m, 2H), 6.92–6.90 (m, 4H), 6.87–6.84 (m, 6H), 6.59–6.53 (t, 1H), 6.47–6.42 (m, 4H), 6.05–6.02 (q, 1H), 5.71–5.69 (q, 1H).

Synthesis of Nd(PMIP)$_3$Ir**1**: to a 1.0 mmol solution of Nd(PMIP)$_3$(H_2O)$_2$ in 20 mL ethanol 1.0 mmol Ir**1** in 50 mL ethanol was added (drop wise) while stirring and the mixture was heated to reflux for 2 h. The yellow solid was collected by filtration and purified by recrystallization from ethanol with a yield of 50%. HRESI (*m*/*z*, Nd(PMIP)$_2$Ir**1**$^+$, 100%): calcd. 1418.26432, found 1418.27013. Anal. Calcd. for $C_{77}H_{72}F_5IrN_{12}NdO_7$ (Nd(PMIP)$_3$Ir**1** + C_2H_5OH) C 54.12, H 4.25, N 9.84, found C 54.03, H 4.19, N 9.91.

Synthesis of Nd(PMIP)$_3$Ir**2**: Nd(PMIP)$_3$Ir**2** was synthesized using a procedure similar to that used for Nd(PMIP)$_3$Ir 1 with a yield of 52%. HRESI (*m*/*z*, Nd(PMIP)$_2$Ir**2**$^+$, 100%): calcd. 1344.30200, found 1344.30398. Anal. Calcd. for $C_{77}H_{76}FIrN_{12}NdO_7$ (Nd(PMIP)$_3$Ir**2** + C_2H_5OH) C 56.50, H 4.68, N 10.27, found C 56.41, H 4.59, N 10.34.

3. Results and discussion

3.1. Absorption, fluorescence and phosphorescence

The absorption spectra of Ir**1** and Ir**2** in CH_2Cl_2 (Fig. 1) show high energy bands from 220 to 380 nm, which are attributed to the π–π^* transitions of the ligand centered states. The weaker absorption bands at longer wavelengths are due to the singlet and triplet metal-to-ligand charge transfer (^{1}MLCT and ^{3}MLCT) transitions. The photoluminescence (PL) spectra of Ir**1** and Ir**2** in CH_2Cl_2 are observed as broad peaks centered at 535 nm and 565 nm, respectively. The lifetimes of the excited state (τ) for Ir**1** and Ir**2** are 1.8 μs and 1.1 μs, respectively, consistent with the emission from the triplet excited state. According to our previous study on Ir–Ln assembles [55], triplet excited energy levels of Ir**1** and Ir**2** are both suitable for Ln^{III} ions with NIR emissions.

The spectroscopic titration of addition of ND(PMIP)$_3$ (H_2O_2) into a solution of Ir**1** in ethanol (Fig. 1b) and PL spectra of films containing a 1:1 ratio of co-deposited ND(PMIP)$_3$(H_2O)$_2$ and Ir**1** or Ir**2** (Fig. 2) both show the efficient energy transfer from the d-block to the f-block. When increasing amount of Nd(PMIP)$_3$(H_2O)$_2$ is added to a solution of Ir**1** in ethanol, the intensity of iridium moiety centered emission decrease. The luminescence intensity at 535 nm of the Nd-Ir**1** (1:1) complex is 10 times lower than that of Ir**1**, indicating efficient energy transfer from Ir**1** to Nd^{III} ions. The PL spectrum of vacuum co-deposited film of Ir**1** and Nd(PMIP)$_3$ (molar ratio = 1:1) also shows strong emission from the $^4F_{3/2} \rightarrow {}^4F_{j/2}$ (j = 9, 11, 13) transitions of Nd^{III} ions (Fig. 2) while the emission from Ir**1** is quenched.

PL quantum efficiency of the emitting material is a key factor for its EL performance. Due to the relatively low efficiency and lack of a sensitive power meter working with an integral sphere at NIR wavelength, we compared the PL intensity of the following films: Nd(PMIP)$_3$, Nd(PMIP)$_3$Ir**1**, Nd(PMIP)$_3$Ir**2**, Nd(PMIP)$_3$Bath and Nd(PMIP)$_3$(TPPO)$_2$ (Fig. 2). Nd^{III} complexes with an Ir complex as the have higher PL intensity, which can be attributed to the more suitable triplet energy levels of iridium complexes for sensitizing Nd^{III} ions. All the complexes with the neutral ligand have higher PL intensity compared to that of Nd(PMIP)$_3$ because the neutral ligand offers the coordination number to the Nd^{III} ions to prevents the quenchers enter the coordination sphere and also help to harvest the light to improve the fluorescence [32].

3.2. Cyclic voltammetric studies

Cyclic voltammetry (CV) was conducted to investigate electrochemical properties of the compounds. The highest occupied molecular orbital (HOMO) and lowest unoccupied molecular orbital (LUMO) energy levels of the materials were estimated by CV and absorption spectra. The

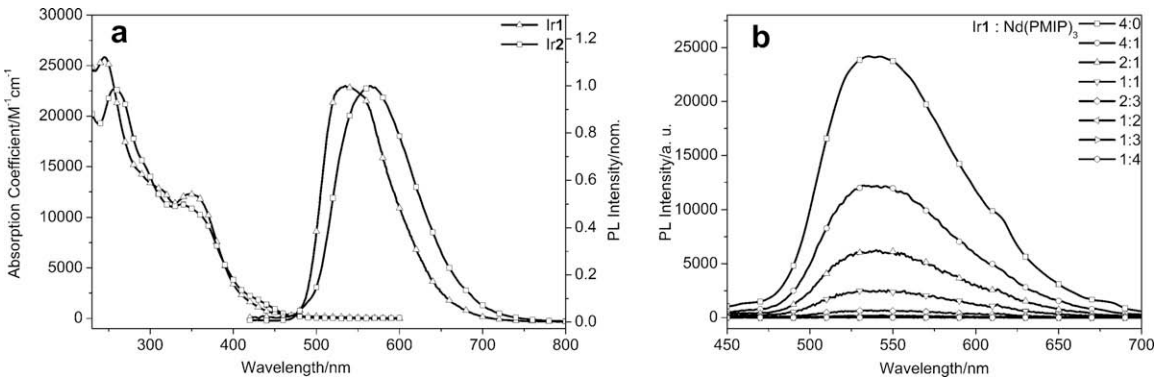

Fig. 1. (a) Absorption and PL spectra of Ir**1** and Ir**2** in dichloromethane (10^{-5} M). (b) Spectroscopic titration by dropping Nd(PMIP)$_3$(H_2O)$_2$ solutions into Ir**1** solution in ethanol (10^{-5} M).

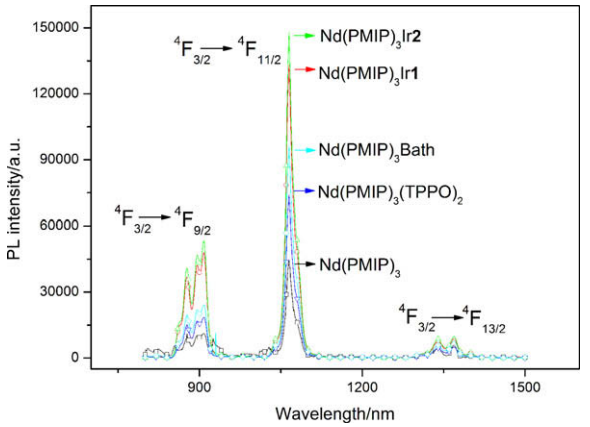

Fig. 2. PL spectra of Nd^{III} complexes at maximum exciting wavelength, measured from their 50 nm vacuum deposited films on quartz slides.

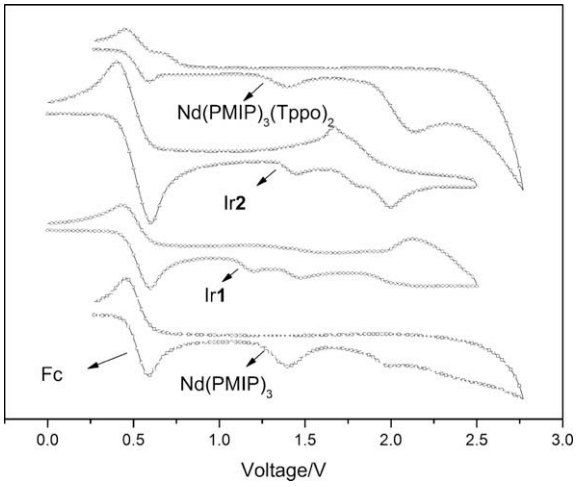

Fig. 3. Cyclic voltammograms of Ir^{III} and Nd^{III} complexes.

highest occupied molecular orbital (HOMO) energy level was calculated from the oxidation potentials by reference to the ferrocene/ferrocenium energy level of −4.8 eV. The energy gap (Eg) between HOMO and LUMO was estimated from the UV–vis absorption spectra. The LUMO energy level was deduced from the HOMO energy level and Eg. The cyclic voltammograms were shown in Fig. 3. $Nd(PMIP)_3$ and $Nd(PMIP)_3(TPPO)_2$ exhibit similar HOMO (−5.4 eV) and LUMO (−2.1 eV) energy level. The HOMO energy level of Ir**1** and Ir**2** was calculated to be −5.4 eV and −5.8 eV. The LUMO energy level was −2.5 eV and −3.1 eV, respectively.

3.3. Electroluminescence properties

All of the Nd^{III} complexes were further evaluated as emitters in NIR OLEDs. 4,4′-bis[N-(1-naphthyl)-N-phenylamino]biphenyl, (NPB), tris(8-hydroxyquinolinato) aluminum^{III} (Alq_3) and 2,9-dimethyl-4,7-diphenyl-1,10-phenanthroline (BCP) was chosen as the hole transporting, electron transporting and hole blocking materials, respectively. A Mg/Ag cathode is used to aid the electron injection and ITO anode for the hole injection. The device configuration is: ITO/NPB (30 nm)/emitting layer (40 nm)/BCP (10 nm)/Alq_3 (30 nm)/$Mg_{0.9}Ag_{0.1}$ (200 nm)/Ag (80 nm). The EL spectra are shown in Fig. 5 and the devices' performance are summarized in Table 1 and Fig. 4. Firstly, we made device A with $Nd(PMIP)_3$ as the emitter. An irradiance of 0.28 μW cm^{-2} at 14.0 mA cm^{-2} and an external quantum efficiency of 0.02% are obtained. This result is of the same order of magnitude with that of previous reports [36,41]. Then the co-deposited film, $Nd(PMIP)_3$:Ir**1** (1:1), is applied as the emitting layer of device B. Compared with device A, device B has a maximum irradiance of 6.1 μW cm^{-2}, 20 times enhancement on intensity, and an EQE of 0.3%, 15 times increase on efficiency. With $Nd(PMIP)_3$:Ir**2** (1:1) as the emitter, Device C shows an irradiance of 5.6 μW cm^{-2} and an EQE of 0.1% at low voltage. The result is lower than that of device B in some extent. Such a phenomenon is likely originated from the different highest occupied molecular orbital (HOMO) and lowest unoccupied molecular orbital (LUMO) energy levels that the complexes exhibit (Fig. 4). In device B the LUMO energy level of Ir**1** moiety is −2.5 eV, which is lower than that of $Nd(PMIP)_3$ (−2.1 eV) and the HOMO energy level of Ir**1** moiety is −5.4 eV, higher than that of $Nd(PMIP)_3$ (−5.6 eV). When electrons and holes are injected into the emitting layer, they are both trapped on the d-block moiety providing excitons. The energy is then transferred to Nd^{III} ions leading to an efficient NIR emission. However, in device C, the HOMO energy level of Ir**2** is −5.8 eV, which is 0.2 eV lower than that of $Nd(PMIP)_3$. So the holes are more likely to be injected onto the $Nd(PMIP)_3$ while electrons are trapped on the d-block moiety. Thus the exciton recombination in device C is not so efficient as that in device B. Meanwhile, device C has a larger current density at each voltage than that of device B. It can be explained by the fact that Ir**2** has a much lower LUMO energy level than that of Ir**1**, which makes electrons easier to be injected

Table 1
Electroluminescent data of NIR OLEDs based on Nd^{3+} complexes.

Device	Emitting Complex	Irradiance (μW cm^{-2})	EQE (%)		
			Highest value	J = 0.1 mA cm^{-2}	J = 10 mA cm^{-2}
A	$Nd(PMIP)_3$	0.28	0.02	0.005	0.002
B	$Nd(PMIP)_3$:Ir**1** (1:1)	6.1	0.3	0.1	0.05
C	$Nd(PMIP)_3$:Ir**2** (1:1)	5.6	0.1	0.07	0.03
D	$Nd(PMIP)_3(TPPO)_2$	2.4	0.01	NA	0.003

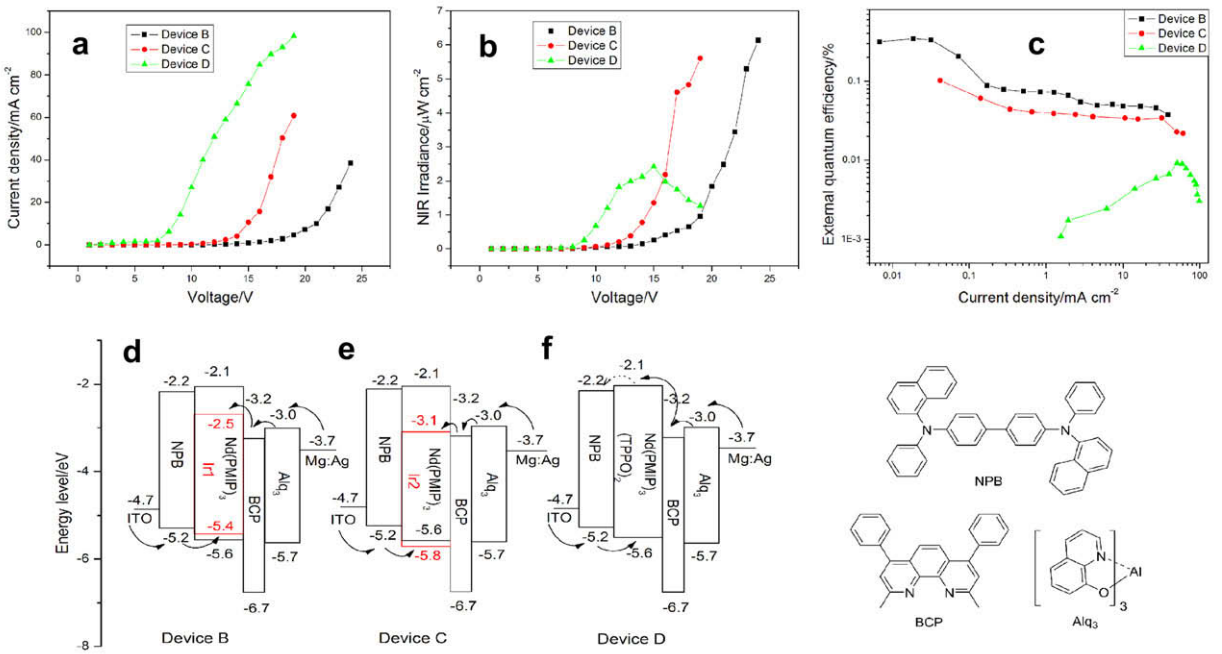

Fig. 4. (a) Current density versus voltage. (b) NIR irradiance versus voltage. (c) EQE versus current density of device B, C and D. (d), (e) and (f) Energy diagrams of device B, C and D.

from BCP layer. Strong roll-off characteristics of efficiencies at high current density are observed in all devices. The phenomenon is thought to be a result of some processes quenching the excited states [57,62,63].

To determine the difference between Ir^{III}-based antenna and traditional small molecular in serving as the neutral ligand, device D with $Nd(PMIP)_3(TPPO)_2$ as the emitter was fabricated. Surprisingly this device does not show much improvement compared to device A. Introducing TPPO moiety into the complex improves the charge-transfer ability of the emitting layer as TPPO is widely used as an electron transporting group. Thus the turn-on voltage, maximum current density and maximum irradiance of device D is improved to 6 V, 98.34 mA cm^{-2} and 2.4 μW cm^{-2}, respectively. However the highest EQE is only 0.01%. It is possible due to excitons not confined well in the emitting layer. Because of the large energy gap between the LUMO energy level of BCP and that of $Nd(PMIP)_3(TPPO)_2$ (Fig. 4f), electrons are difficult to be injected into the emitting layer at low voltages. Meanwhile holes may tunnel through the thin layer of BCP into Alq_3 layer. Thus electrons and holes are mainly combined in Alq_3 layer at low voltages. On the other hand, electrons are easy to be transferred into NPB layer at high voltages because $Nd(PMIP)_3(TPPO)_2$ have a 0.1 eV higher LUMO energy level than that of NPB. Thus as the voltage increases in device D, the combining zone for excitons moves from Alq_3 layer to Nd^{III} complex layer, and then to NPB layer. We measured the visible EL spectra of device D at different voltages. The changing of emitting zone, from Alq_3 layer to NPB layer, was observed (Fig. 6). This phenomenon is accordant with the fact that the NIR irradiance increases and then decreases as the voltage increases (Fig. 4b). The brightness of this visible emission in device D was 269 cd m^{-2} (measured without the filter), five times higher than that of device B. However the NIR EQE measured (with the filter) of device B was 10 times higher than that of device D, indicating that the 720 nm filter precluded the effect of visible light. When Bath is used instead of TPPO as the neutral ligand, device only shows blue emission from NPB. The NIR efficiency is still low (0.02%). These results

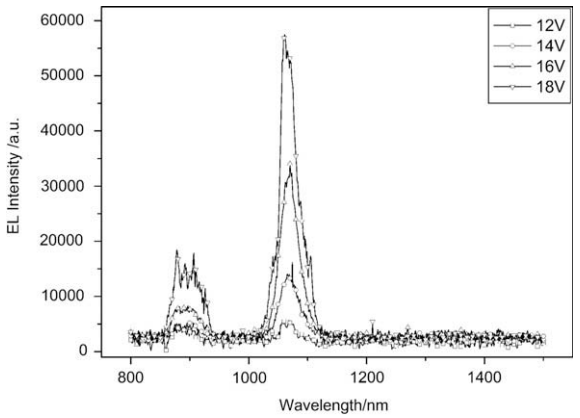

Fig. 5. EL spectra at different voltages of device B (inset: EL spectra at visible region with 720 nm filter).

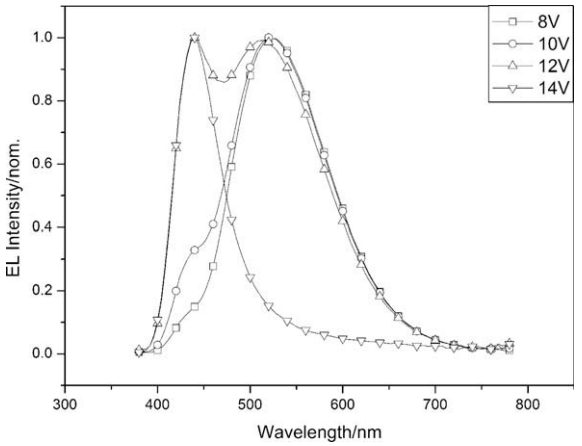

Fig. 6. EL spectra of device D at different voltages (without the 720 nm filter).

indicate that the improvements achieved in device B and C are contributed to both higher PL intensity and more suitable energy levels leading to well confined excitons.

In summary, two structurally simple iridium complexes with suitable triplet energy levels for sensitizing Nd^{III} ions have been synthesized. Efficient energy transfer from Ir^{III} moiety to Nd^{III} is observed in both solutions and films. Utilizing co-deposition film of Ir–Nd assemblies as the emitting layer, nondoped OLEDs were fabricated. The highest EQE achieved is 0.3%, with a maximum radiance of 6.1 $\mu W\,cm^{-2}$ at the main emission wavelength of 1060 nm. Further modifying on transition metal-based antenna and device optimization to further improve the performance of Ln^{III} based NIR OLEDs are in progress.

Acknowledgements

The authors are grateful to the National Basic Research Program (2006CB601103) and the NNSFC (20671006, 50772003, 90922004, 20971006, 20821091) for financial support.

References

[1] C.W. Tang, S.A. Vanslyke, Appl. Phys. Lett. 51 (1987) 913.
[2] Z.H. kafafi, Organic Electroluminescence, CRC Press, Boca Raton, FL, 2005.
[3] N. Tessler, V. Medvedev, M. Kazes, S.H. Kan, U. Banin, Science 295 (2002) 1506.
[4] L.H. Slooff, A. van Blaaderen, A. Polman, G.A. Hebbink, S.I. Klink, F. Van Veggel, D.N. Reinhoudt, J.W. Hofstraat, J. Appl. Phys. 91 (2002) 3955.
[5] K.S. Schanze, J.R. Reynolds, J.M. Boncella, B.S. Harrison, T.J. Foley, M. Bouguettaya, T.S. Kang, Near-infrared organic light emitting diodes, in: Presented at International Conference on Science and Technology of Synthetic Metals (ICSM 2002), Shanghai, PR China, Jun 29–Jul 05, 2002.
[6] E.L. Williams, J. Li, G.E. Jabbour, Appl. Phys. Lett. 89 (2006) 083506.
[7] M. Casalboni, F. De Matteis, P. Prosposito, R. Pizzoferrato, Appl. Phys. Lett. 75 (1999) 2172.
[8] H. Suzuki, Appl. Phys. Lett. 80 (2002) 3256.
[9] H. Suzuki, K. Ogura, N. Matsumoto, P. Prosposito, S. Schutzmann, Polymethine dyes as novel efficient infrared electroluminescence materials, in: Presented at 15th Korea–Japan Joint Forum on Organic Materials for Electronics and Photonics, Okinawa, Japan, 2004, 2006.
[10] G. Qian, B. Dai, M. Luo, D.B. Yu, J. Zhan, Z.Q. Zhang, D.G. Ma, Z.Y. Wang, Chem. Mat. 20 (2008) 6208.
[11] G. Qian, Z. Zhong, M. Luo, D.B. Yu, Z.Q. Zhang, Z.Y. Wang, D.G. Ma, Adv. Mater. 21 (2009) 111.
[12] Y.X. Yang, R.T. Farley, T.T. Steckler, S.H. Eom, J.R. Reynolds, K.S. Schanze, J.G. Xue, Appl. Phys. Lett. 93 (2008) 163305.
[13] D.R. Baigent, P.J. Hamer, R.H. Friend, S.C. Moratti, A.B. Holmes, Polymer electroluminescence in the near-infrared, in: Presented at International Conference on Science and Technology of Synthetic Metals (ICSM 94), Seoul, South Korea, Jul 24–29, 1994.
[14] M. Berggren, G. Gustafsson, O. Inganas, M.R. Andersson, O. Wennerstrom, T. Hjertberg, Appl. Phys. Lett. 65 (1994) 1489.
[15] S.C. Moratti, R. Cervini, A.B. Holmes, D.R. Baigent, R.H. Friend, N.C. Greenham, J. Gruner, P.J. Hamer, High electron-affinity polymers for leds, in: presented at International Conference on Science and Technology of Synthetic Metals (ICSM 94), Seoul, South Korea, Jul 24–29, 1994.
[16] M.R. Andersson, M. Berggren, O. Inganas, G. Gustafsson, J.C. Gustafssoncarlberg, D. Selse, T. Hjertberg, O. Wennerstrom, Macromolecules 28 (1995) 7525.
[17] M.X. Chen, E. Perzon, M.R. Andersson, S. Marcinkevicius, S.K.M. Jonsson, M. Fahlman, M. Berggren, Appl. Phys. Lett. 84 (2004) 3570.
[18] X.Z. Li, W.J. Zeng, Y. Zhang, Q. Hou, W. Yang, Y. Cao, Eur. Polym. J. 41 (2005) 2923.
[19] R.Q. Yang, R.Y. Tian, J.G. Yan, Y. Zhang, J. Yang, Q. Hou, W. Yang, C. Zhang, Y. Cao, Macromolecules 38 (2005) 244.
[20] C.H. Cheng, Z.Q. Fan, S.K. Yu, W.H. Jiang, X. Wang, G.T. Du, Y.C. Chang, C.Y. Ma, Appl. Phys. Lett. 88 (2006) 213505.
[21] C.J. Yang, C. Yi, M. Xu, J.H. Wang, Y.Z. Liu, X.C. Gao, J.W. Fu, Appl. Phys. Lett. 89 (2006) 233506.
[22] C. Borek, K. Hanson, P.I. Djurovich, M.E. Thompson, K. Aznavour, R. Bau, Y.R. Sun, S.R. Forrest, J. Brooks, L. Michalski, J. Brown, Angew. Chem. Int. Ed. 46 (2007) 1109.
[23] Y. Sun, C. Borek, K. Hanson, P.I. Djurovich, M.E. Thompson, J. Brooks, J.J. Brown, S.R. Forrest, Appl. Phys. Lett. 90 (2007) 213503.
[24] T.C. Rosenow, K. Walzer, K. Leo, J. Appl. Phys. 103 (2008) 043105.
[25] R.J. Curry, W.P. Gillin, Appl. Phys. Lett. 75 (1999) 1380.
[26] Y. Kawamura, Y. Wada, Y. Hasegawa, M. Iwamuro, T. Kitamura, S. Yanagida, Appl. Phys. Lett. 74 (1999) 3245.
[27] R.G. Sun, Y.Z. Wang, Q.B. Zheng, H.J. Zhang, A.J. Epstein, J. Appl. Phys. 87 (2000) 7589.
[28] Z.R. Hong, C.J. Liang, R.G. Li, F.X. Zang, D. Fan, W.L. Li, L.S. Hung, S.T. Lee, Appl. Phys. Lett. 79 (2001) 1942.
[29] Z.R. Hong, C.J. Liang, R.G. Li, D. Zhao, D. Fan, W.L. Li, Thin Solid Films 391 (2001) 122.
[30] B.S. Harrison, T.J. Foley, M. Bouguettaya, J.M. Boncella, J.R. Reynolds, K.S. Schanze, J. Shim, P.H. Holloway, G. Padmanaban, S. Ramakrishnan, Appl. Phys. Lett. 79 (2001) 3770.
[31] L.H. Slooff, A. Polman, F. Cacialli, R.H. Friend, G.A. Hebbink, F. van Veggel, D.N. Reinhoudt, Appl. Phys. Lett. 78 (2001) 2122.
[32] J. Kido, Y. Okamoto, Chem. Rev. 102 (2002) 2357.
[33] T.S. Kang, B.S. Harrison, T.J. Foley, A.S. Knefely, J.M. Boncella, J.R. Reynolds, K.S. Schanze, Adv. Mater. 15 (2003) 1093.
[34] T.S. Kang, B.S. Harrison, M. Bouguettaya, T.J. Foley, J.M. Boncella, K.S. Schanze, J.R. Reynolds, Adv. Funct. Mater. 13 (2003) 205.
[35] F.X. Zang, Z.R. Hong, W.L. Li, M.T. Li, X.Y. Sun, Appl. Phys. Lett. 84 (2004) 2679.
[36] A. O'Riordan, E. O'Connor, S. Moynihan, P. Nockemann, P. Fias, R. Van Deun, D. Cupertino, P. Mackie, G. Redmond, Thin Solid Films 497 (2006) 299.
[37] Z.F. Li, J.B. Yu, L. Zhou, H.J. Zhang, R.P. Deng, Z.Y. Guo, Org. Electron. 9 (2008) 487.
[38] D.Y. Zhang, W.L. Li, B. Chu, X. Li, L.L. Han, J.Z. Zhu, T.L. Li, D.F. Bi, D.F. Yang, F. Yan, H.H. Liu, D. Wang, Appl. Phys. Lett. 92 (2008) 093501.
[39] M.C. Silva, A.S.S. de Camargo, L.A.O. Nunes, R.A. Silva, A. Marletta, J. Non-Cryst. Solids 354 (2008) 5496.
[40] M.A. Katkova, M.E. Burin, A.A. Logunov, V.A. Ilichev, A.N. Konev, G.K. Fukin, M.N. Bochkarev, Synth. Met. 159 (2009) 1398.
[41] Z.F. Li, J.B. Yu, L. Zhou, R.P. Deng, H.J. Zhang, Inorg. Chem. Commun. 12 (2009) 151.
[42] M.A. Baldo, D.F. O'Brien, Y. You, A. Shoustikov, S. Sibley, M.E. Thompson, S.R. Forrest, Nature 395 (1998) 151.
[43] S. Lamansky, P. Djurovich, D. Murphy, F. Abdel-Razzaq, H.E. Lee, C. Adachi, P.E. Burrows, S.R. Forrest, M.E. Thompson, J. Am. Chem. Soc. 123 (2001) 4304.
[44] E. Holder, B.M.W. Langeveld, U.S. Schubert, Adv. Mater. 17 (2005) 1109.

[45] R.J. Holmes, S.R. Forrest, T. Sajoto, A. Tamayo, P.I. Djurovich, M.E. Thompson, J. Brooks, Y.J. Tung, B.W. D'Andrade, M.S. Weaver, R.C. Kwong, J.J. Brown, Appl. Phys. Lett. (2005) 87.
[46] S.I. Klink, H. Keizer, F. van Veggel, Angew. Chem. Int. Ed. 39 (2000) 4319.
[47] J.C.G. Bunzli, C. Piguet, Chem. Soc. Rev. 34 (2005) 1048.
[48] P.B. Glover, P.R. Ashton, L.J. Childs, A. Rodger, M. Kercher, R.M. Williams, L. De Cola, Z. Pikramenou, J. Am. Chem. Soc. 125 (2003) 9918.
[49] N.M. Shavaleev, L.P. Moorcraft, S.J.A. Pope, Z.R. Bell, S. Faulkner, M.D. Ward, Chem. Commun. 1134 (2003).
[50] N.M. Shavaleev, L.P. Moorcraft, S.J.A. Pope, Z.R. Bell, S. Faulkner, M.D. Ward, Chem. Eur. J. 9 (2003) 5283.
[51] S.J.A. Pope, B.J. Coe, S. Faulkner, Chem. Commun. 2004 (1550).
[52] H.B. Xu, L.X. Shi, E. Ma, L.Y. Zhang, Q.H. Wei, Z.N. Chen, Chem. Commun. 2006 (1601).
[53] J.M. Herrera, S.J.A. Pope, H. Adams, S. Faulkner, M.D. Ward, Inorg. Chem. 45 (2006) 3895.
[54] F. Kennedy, N.M. Shavaleev, T. Koullourou, Z.R. Bell, J.C. Jeffery, S. Faulkner, M.D. Ward, Dalton Trans. 2007 (1492).
[55] F.F. Chen, Z.Q. Bian, B. Lou, E. Ma, Z.W. Liu, D.B. Nie, Z.Q. Chen, J. Bian, Z.N. Chen, C.H. Huang, Dalton Trans. 5577 (2008).
[56] H. Xin, M. Shi, X.C. Gao, Y.Y. Huang, Z.L. Gong, D.B. Nie, H. Cao, Z.Q. Bian, F.Y. Li, C.H. Huang, J. Phys. Chem. B 108 (2004) 10796.
[57] C. Adachi, M.A. Baldo, S.R. Forrest, J. Appl. Phys. 87 (2000) 8049.
[58] N.C. Greenham, R.H. Friend, D.D.C. Bradley, Adv. Mater. 6 (1994) 491.
[59] M.A. Haga, M. Ishizuya, T. Kanesugi, T. Yutaka, D. Sakiyama, J. Fees, W. Kaim, Indian J. Chem. Sect. A – Inorg. Bio-Inorg. Phys. Theor. Anal. Chem. 42 (2003) 2290.
[60] S. Capecchi, O. Renault, D.G. Moon, M. Halim, M. Etchells, P.J. Dobson, O.V. Salata, V. Chrisou, Adv. Mater. 12 (2000) 1591.
[61] H. Xin, F.Y. Li, M. Shi, Z.Q.A. Bian, C.H. Huang, J. Am. Chem. Soc. 125 (2003) 7166.
[62] J. Kalinowski, W. Stampor, M. Cocchi, D. Virgili, V. Fattori, Appl. Phys. Lett. (2005) 86.
[63] J. Kalinowski, Opt. Mater. 30 (2008) 792.

Organic Electronics 11 (2010) 377–387

Contents lists available at ScienceDirect

Organic Electronics

journal homepage: www.elsevier.com/locate/orgel

What determines the performance of metal phthalocyanines (MPc, M = Zn, Cu, Ni, Fe) in organic heterojunction solar cells? A combined experimental and theoretical investigation

Ingmar Bruder [a], Jan Schöneboom [a,*], Robert Dinnebier [c], Antti Ojala [a], Stefan Schäfer [b], Rüdiger Sens [a], Peter Erk [a], Jürgen Weis [c,*]

[a] BASF SE, Carl-Bosch-Str. 38, 67056 Ludwigshafen, Germany
[b] Robert Bosch GmbH, Postfach 10 60 50, 70049 Stuttgart, Germany
[c] Max-Planck-Institut für Festkörperforschung, Heisenbergstraße 1, 70569 Stuttgart, Germany

ARTICLE INFO

Article history:
Received 4 August 2009
Received in revised form 6 October 2009
Accepted 11 November 2009
Available online 14 November 2009

Keywords:
Metal phthalocyanines
Organic heterojunction solar cells
Crystal structure
Solid state fluorescence and absorption
Ligand–metal exchange coupled states

ABSTRACT

An investigation on the MPc series (M = Zn, Cu, Ni, Fe) targeted at a fundamental understanding of the physical origin of their different performance in organic solar cells is presented. MPc/C_{60} based bilayer hetero-junction (HJC) devices were built and analyzed. The crystal structure in thin films of MPc's was explored by high resolution XRPD and AFM measurements and compared to powder data. The absorption spectra of the evaporated MPc films was observed to differ only slightly, while there was a strong fluorescence quenching for M = Cu, Ni, Fe as opposed to ZnPc. The differences in the solid state fluorescence were further explored by high-level quantum mechanical calculations. Thus, the calculations of the lowest excited states show, that there are intermediate states below the Q-band (π–π^*) excitation for all of the MPc series but ZnPc. It will be discussed, that these states are ligand–metal exchange coupled states, which are treated at the multi-reference configuration interaction (MR-CI) level, in order to account for multi-configurational mixing and double excitations. The implications of these electronic effects on exciton diffusion are discussed and related to device performance.

© 2009 Elsevier B.V. All rights reserved.

1. Introduction

Organic photovoltaic could be one solution for future energy supply because of low production costs, light weight of devices and the processibility on flexible substrates. Since Tang [1] presented a 1% efficient bilayer solar cell based on copper phthalocyanine (CuPc) and a perylene tetracarboxylic derivative (PTCBI) in 1986, enormous progress was made in research. The introduction of bulk heterojunction [2,3] and tandem device architectures [4–7] led to devices with power conversion efficiencies close or even higher than η = 6%. For a successful commerzialisation of organic photovoltaic devices it is necessary to increase the power conversion efficiency further. One possibility could be the development of new photoactive materials based on metal phthalocyanine derivatives. Therefore, it is crucial to understand the influence of the central metal atoms on the optical and electrical behavior in solar cell devices on a microscopic level.

Although metal phthalocyanines (MPc) were one of the first compounds used in organic photovoltaics, 20 years later they are still first choice due to their special physical and chemical properties, investigated by numerous experimental and theoretical [8–17,60,61] studies. Depending on the nature of the central metal atom, MPc based solar cells exhibit markedly different device performance. In this

* Corresponding authors.
E-mail addresses: Jan.Schoeneboom@BASF.com (J. Schöneboom), J.Weis@fkf.mpg.de (J. Weis).

1566-1199/$ - see front matter © 2009 Elsevier B.V. All rights reserved.
doi:10.1016/j.orgel.2009.11.016

publication, an experimental and theoretical study on zinc (Zn), copper (Cu), nickel (Ni) and iron (Fe) phthalocyanines is presented in which the fundamental physical origin of their characteristic performance in organic solar cells (Fig. 1b) was investigated. We restrict the study to metal phthalocyanines, having the same molecular structure and symmetry (D_{4h}). Thus, a straightforward comparison of their electronic structure was possible.

Since charge transport properties were supposed to depend sensitively on the thin film structure, atomic force microscope (AFM) and high resolution X-ray powder diffraction (XRPD) measurements were carried out. In the course of these investigations the relation between the known crystal structure of α-CuPc [18] and the molecular packing in vacuum deposited thin films was clarified. This relation was described incorrectly in previous publications [19–21]. The optical properties of the respective metal phthalocyanines were experimentally investigated by solid state fluorescence and absorption measurements. Significant differences in the solid-state fluorescence intensity prompted us to undertake an in-depth quantum mechanical study on the excited states of the present MPc series. Details are presented in Section 3. It will be shown, that there are states below the Q-band (π–π^*) excitation for all of the MPc series but ZnPc. These states arise from d–d excitations and ligand–metal exchange coupling. We present for the first time a treatment of these states at the ab initio multi-reference configuration interaction (MR-CI) level. Finally, the implications of these excitation effects on the exciton diffusion capabilities of the respective metal phthalocyanines will be discussed and related to device performance.

2. Experimental and results

2.1. Device setup and characterization

Hetero-junction solar cells were produced using FePc, NiPc, CuPc and ZnPc, respectively, as p-conducting and C_{60} as *n*-conducting organic layers (see Section A for sample preparation). The layer sequence ITO/MPc (10 nm −60 nm)/C_{60} (10 nm −60 nm)/Bphen (6 nm)/Ag (100 nm) was used in the present device setup. The structure of the molecules used as well as the device setup are depicted in Fig. 1. The open circuit voltage V_{oc}, the short circuit current I_{sc}, the fill factor FF and the power conversion efficiency η were obtained under simulated 100 mW/cm^2 AM 1.5 white light illumination. The illumination intensity was adjusted with a calibrated Si detector. Fig. 2 shows the *I–V* characteristics for HJC's with optimized layer setups. The respective layer parameters and key characteristics are depicted in Table 1. With an open circuit voltage V_{oc} of 550 mV, a short circuit current I_{sc} of −5.15 mA/cm^2 and an efficiency η of 1.77%, ZnPc was identified to be the best performing metal phthalocyanine in our bilayer HJC's. All other MPc's showed reduced device performance in the ordering ZnPc → CuPc → NiPc → FePc.

While the thickness of C_{60} has its optimum at 40 nm for all devices, the optimal layer thickness of the metal phthalocyanines varied from 40 nm for ZnPc to 10 nm for FePc. A complete thickness dependence of I_{sc} is depicted in Fig. 2b.

2.2. High resolution X-ray powder diffraction (XRPD)

High resolution X-ray powder diagramms were recored in order to look for a correlation between device performance and the crystal structure of vacuum deposited ZnPc, CuPc, NiPc and FePc films with thicknesses of 1 μm and 30 nm (for details see Section B). As a result, the XRPD diagramm of all investigated materials turned out to be almost identical. For the 1 μm films seven reflection peaks (Fig. 3, Table 2) were observed. At layer thicknesses of 30 nm only the strongest peak at $2\Theta = 6.8°$ could be measured. The peaks at $2\Theta = 21.27°$ and 30.17° are attributed to [2 1 1] and [2 2 2] reflections of the ITO substrate [25]. Comparing the observed reflections with previously published results of MPc films, the crystalline polymorph could be identified as α-phase [26–28] (Table 2). In agreement with present fundamental crystallographic studies [29,30], our observations show, that the crystal structure of the investigated MPc films exhibit the α-form [18], e.g. have a triclinic unit cell. Therefore, it became obvious, that

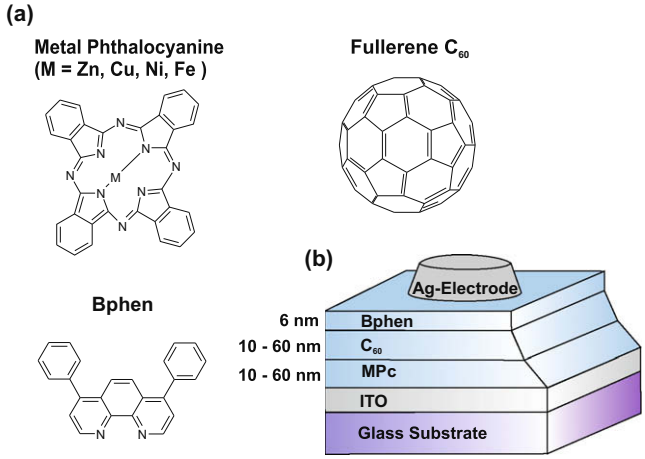

Fig. 1. (a) Chemical structure of the materials used in our bilayer hetero-junction solar cell (HJC). (b) Schematic device structure of the HJC.

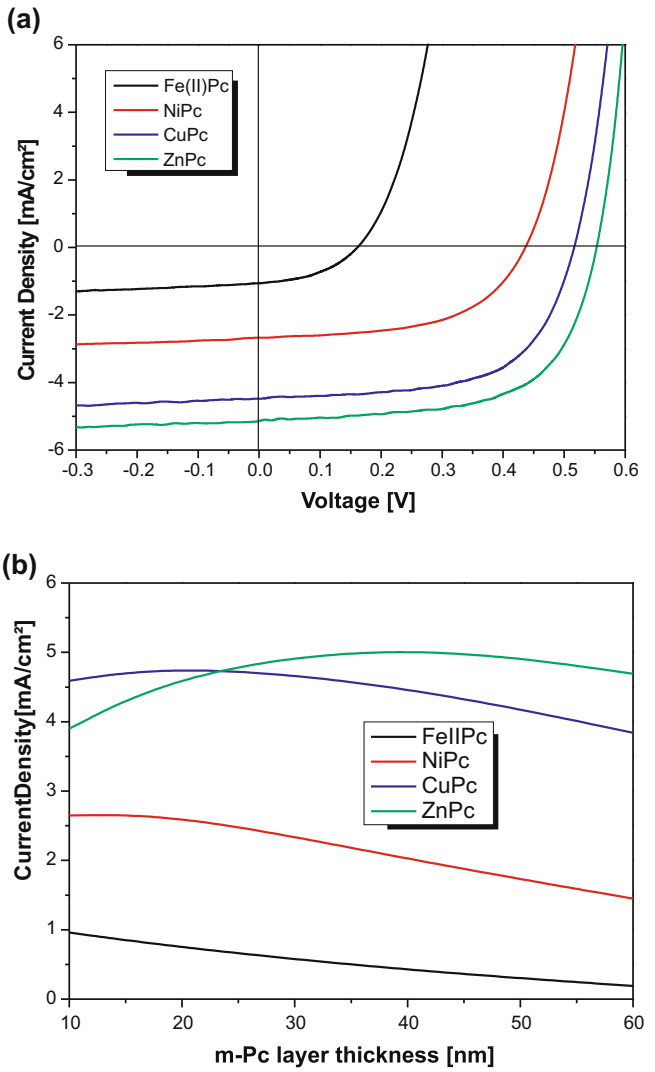

Fig. 2. (a) *I–V* curves of the investigated bilayer hetereojunction solar cells: ZnPc/C_{60}, CuPc/C_{60}, NiPc/C_{60} and FePc/C_{60}. The corresponding device data are given in Table 1. (b) Thickness dependence of the short circuit current I_{sc} (absolute value) of the MPc/C_{60} hetero-junction devices: The layer thickness of the phthalocyanines was varied from 10 nm to 60 nm, while the C_{60} layer was kept constant at 40 nm.

Table 1
Key device characteristics measured for the optimal thickness combination of the MPc and C_{60} layer. The corresponding *I–V* curves are shown in Fig. 2.

MPc	MPc/C_{60} (nm)	V_{oc} (mV)	I_{sc} (mA/cm^2)	FF (%)	η (%)
ZnPc	40/40	550	−5.15	63	1.77
CuPc	40/40	520	−4.48	61	1.42
NiPc	20/40	440	−2.67	55	0.64
FePc	10/40	160	−1.06	42	0.07

the monoclinic β modification [23], having a completely different arrangement shown in Fig. 3c, has been erroneously used to describe the crystal packing in previous publications [19–21].

For the 30 nm vacuum deposited MPc films the calculated crystallite sizes, based on the [0 1 0] reflection peak, were found to be identical to the film thickness. For the 1 μm films no domain sizes >50 nm were observed in agreement with complementary AFM studies (Fig. 4, details in Section C): With a diameter of (27.6 ± 8.7) nm NiPc shows the largest grains followed by ZnPc with (23.6 ± 8.91) nm, FePc with (22.2 ± 6.5) nm and CuPc with (21.1 ± 8.5) nm.

As no significant differences regarding packing and grain size in the different metal phthalocyanines were found, the performance variation (Table 1) of the fabricated devices is assigned tentatively to electronic properties.

2.3. Absorption and fluorescence of vaccum deposited metal phthalocyanine films

The optical absorption of all investigated MPc films was measured on quartz glass. As depicted in Fig. 5a, the 30 nm thick phthalocyanines films showed similar spectra with slight characteristic differences. With respect to the

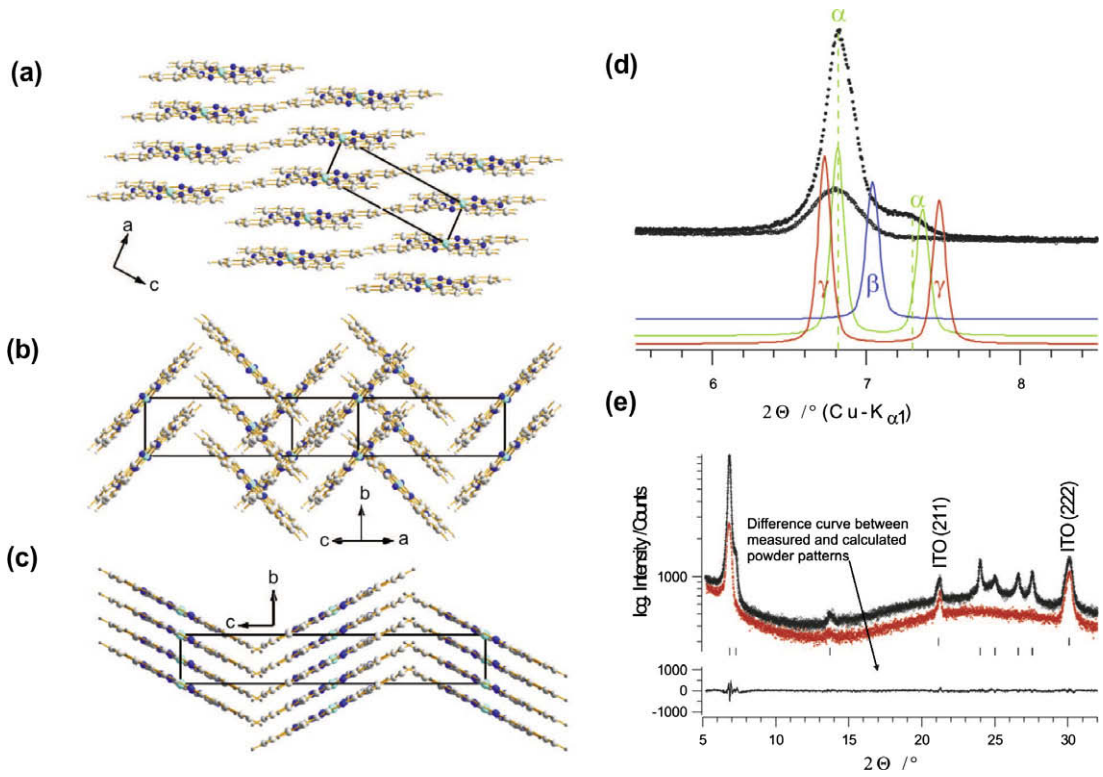

Fig. 3. (a–c) Crystal packings of three polymorphic forms of CuPc showing different arrangements of the CuPc molecules: (a) triclinic α-phase [18] showing parallel stacks in a single orientation. (b) Monoclinic β-phase [22] exhibiting a herringbone arrangement and (c) the also monoclinic γ-phase [23] with parallel stacks in a zigzag fashion with a dihedral angle of 54.8° between neighboring stacks. (d) Low angle region of powder patterns of 1 μm and 30 nm thick, vacuum deposited CuPc films on ITO, compared to calculated powder patterns of α-, β-, and γ-CuPc. (e) Full powder patterns of the 1 μm and 30 nm thick films shown partly in (d) in logarithmic intensity scale. For the 1 μm film, a calculated profile is given, consisting of a LeBail fit [24] of the ITO substrate and seven individually fitted peaks of α-CuPc. The peaks markers of the two phases and the difference curve between measured and calculated powder patterns are given below.

Table 2
Observed reflections of the 1 μm CuPc films in values of 2Θ compared with the calculated powder pattern of α, β, and γ-forms obtained from the CCDC data base. For the 30 nm films only the first reflection at $2\Theta = 6.85°$ could be detected.

Observed peaks	α-Form [18]		γ-Form [23]		β-Form [22]	
	$P\bar{1}$	*hkl*	C_2/n	*hkl*	$P2_1/a$	*hkl*
6.84	6.82	010	6.73	200	7.04	001
7.27[a]	7.37	001	7.47	002	–	–
13.72	13.66	020	13.48	400	14.12	002
24.00	23.95	10-1	23.90	111	23.85	31-2
25.01	25.00	11-1	24.82	112	–	–
26.60	26.63	10-2	26.79	312	26.66	11-3
27.56	27.55	12-1	27.53	31-3	27.65	60-2

[a] The large deviation from the theoretical peak position could be explained by the strong overlap with the first reflection.

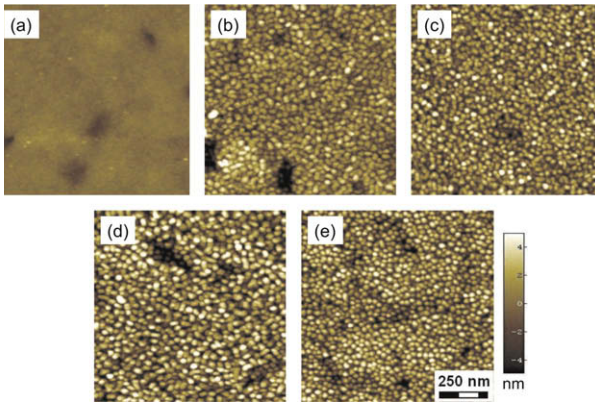

Fig. 4. AFM images of 30 nm thin films of (b) ZnPc, (c) CuPc, (d) NiP and (e) FePc grown on ITO coated glass. The used ITO (a) is in average very smooth (RMS = 0.48 nm), however slight hight differences of up to 3 nm could be detected (dark parts in the SEM picture).

current-thickness dependence shown in Fig. 2b it is concluded, that the absorption strength, which varied at most by a factor of two, could not explain the five times higher current of ZnPc compared to FePc in the present solar cells. Thus, the differences in absorption cannot account for the huge differences in the device performance of the MPc's.

The fluorescence spectra of evaporated ZnPc, CuPc, NiPc and FePc films were also measured on quartz glass. The applied technique is explained in Section D. As depicted in Fig. 5b, the fluorescence intensity of ZnPc was measured to be ninety times stronger than that of CuPc. The fluorescence of NiPc and FePc was below the detection limit. Interestingly, in contrast to the very similar structure and

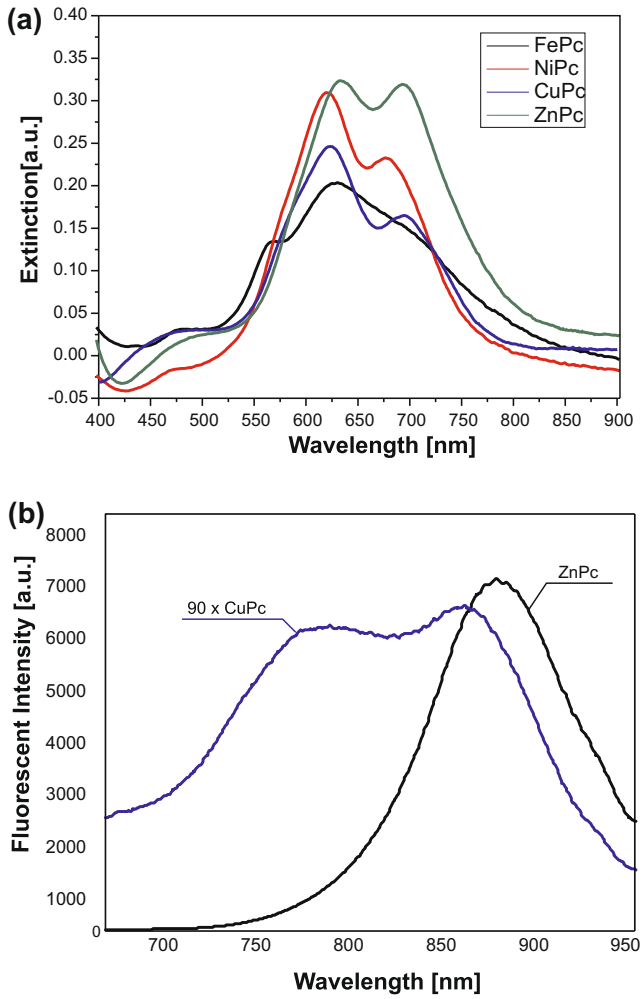

Fig. 5. (a) Absorption spectra of 30 nm thick evaporated films of ZnPc, CuPc, NiPc and Fe(II)Pc. (b) Fluorescence spectra of vacuum deposited films of CuPc and ZnPc with a thickness of 800 nm. The films were excited at a wavelength of 532 nm. The fluorescent quantum yield of CuPc is measured to be ninety times weaker than for ZnPc. The broad shape of the CuPc spectra has its origin in impurities of the vacuum deposited film.

absorption characteristics, the fluorescence quantum yield of the investigated MPc films differed tremendously from each other. These variations of the solid state fluorescence were further explored by high-level quantum mechanical calculations.

3. Computational results of ligand–metal exchange coupled states

Electronic ligand–metal exchange coupling is a general phenomenon observed in many transition metal complexes. An excellent introduction to this subject is given in Ref. [31].

It was demonstrated already in early theoretical work, e.g. on CuPc [33], that exchange coupling of the metal center with ligand triplet states gives rise to spin-allowed transitions at low energy [31], i.e. a doublet (tripdoublet) [34] state in CuPc. Results from ultrafast spectroscopy indicate that this state is responsible for efficient fluorescence quenching and intersystem crossing to the quartet [35]. While there are a number of more recent theoretical studies on the excited states of MPc's [8–17,60,61], a rigorous theoretical treatment of the ligand–metal exchange coupled states (LMEC states) is lacking to this date. Herein, we calculated the low-energy LMEC states by an *ab initio* multi-reference configuration interaction technique (MR-CI) [36], specifically the Spectroscopy-Oriented CI (SORCI) approach by Neese [32]. Our calculations explicitly take into account double-excitations and multi-configurational mixing. In the case of FePc, NiPc, and CuPc, LMEC states are located energetically well below the Q-band excitation on the phthalocyanine ligand at around 1.7 eV. Because the oscillator strength of a transition from ground state to the LMEC state is zero, the corresponding absorption features are not obvious. However, it is important to note that the LMEC states considered here are of the same spin as the respective ground states. Therefore, they may be populated on the femto- to picoseconds timescale by internal conversion from the initial ligand excited state. This process is expected to lead to a fast de-population of the initial excited

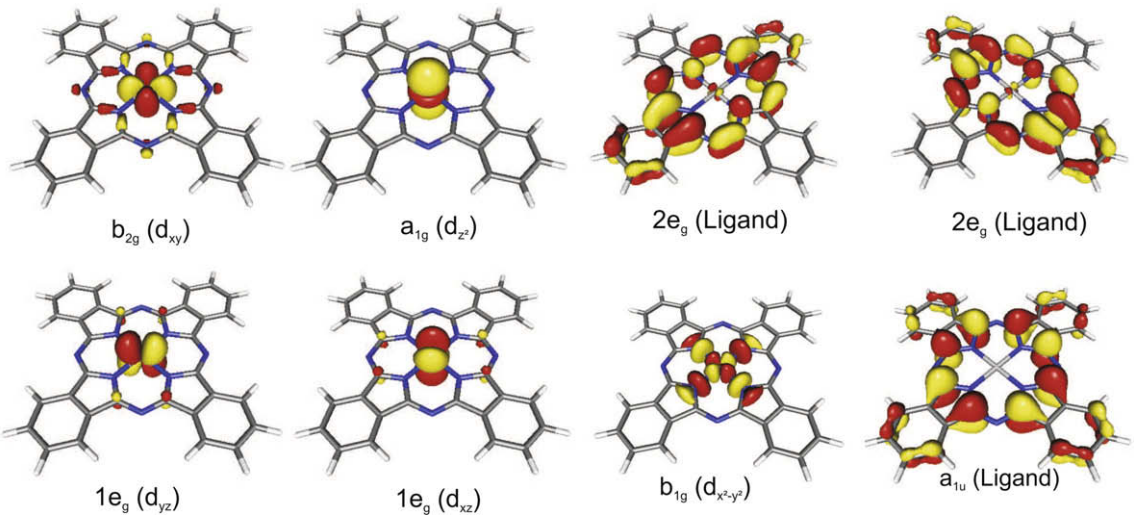

Fig. 6. Relevant frontier orbitals of the MPc's considered in the present study. Shown orbitals are state-averaged natural orbitals from a DDCI2 calculation [32] on FePc. The corresponding orbitals of ZnPc, NiPc and CuPc are qualitatively the same, with a somewhat larger admixture of ligand π and metal d_{xz}/d_{yz} orbitals.

state, and could therefore influence effectively the solid state fluorescence of the corresponding MPc's.

3.1. Relative energy of ligand–metal exchange coupled excited states

The electronic structure of the MPc series (M = Fe, Ni, Cu, Zn) in their ground and excited states is defined by differential occupations of the representative molecular orbitals (MOs) depicted in Fig. 6. Three points have to be emphasised:

1. The metal *d* orbitals give rise to the following MOs, classified according to their irreducible representation in D_{4h} symmetry: $b_{2g}(d_{xy}), a_{1g}(d_z^2), 1e_g(d_{xz,yz}), b_{1g}(d_{x^2-y^2})$.
2. The relevant ligand-based orbitals for the low-energy excitations are the a_{1u} orbital and the set of degenerate $2e_g$ orbitals.
3. The mixing of ligand and metal MOs is quite small, hence the picture of weakly exchange coupled electronic systems is justified.

Because we did not aim for the calculation of the higher-energy B-band region, the a_{2u} MO has not been included into the reference space of our calculation.

Ligand–metal exchange coupled (LMEC) states which have the same spin as ground state, and which are lower in energy than the optical excited state (the Q-band, i.e. the ligand based $a_{1u} \rightarrow 2e_g$ excitation) were found to be present for all molecules under study but ZnPc. An increasing number of electronically excited states was obtained energetically below the initially excited ligand-based π–π^* state (Q-band) going from ZnPc (zero) → CuPc with one → NiPc with two → FePc with over six excited states. In Table 3 the MR-CI ground state configurations are summarized, while the excited states are listed in Table 4. In the following, we have adopted the nomenclature for LMEC states from Ref. [31], where $^{2S+1}L(M_s)^{2S'+1}M(M'_s)$ denotes a LMEC state with a ligand L of multiplicity $(2S + 1)$ and magnetic spin quantum number M_s and a metal *M* of multiplicity $(2S' + 1)$ and magnetic spin quantum number $M_{s'}$. The nature of the LMEC states are assigned in Table 4 accordingly, where we give appropriate linear combinations to account for the correct symmetry of the wavefunctions, but have dropped orthonormality coefficients for the sake of brevity. A pictorial representation of the leading configurations is given in Fig. 7. Detailed information of the respective calculated excited states of each of the MPc's are presented in the supporting information.

4. Discussion

The similar molecular structure, packing and grain size of the MPc's as well as their absorption offers no explanation for the huge performance variation in organic solar cells. However, the solid state fluorescence spectra of the

Table 3
Ground state configurations of the MPc's.

MPc	State	Electronic configuration	CI weight
Fe(II)Pc	$^3A_{2g}$	$(b_{2g})^2, (1e_g)^2, (a_{1g})^2, (a_{1u})^2, (b_{1g})^0, (2e_g)^0$	0.83
Ni(II)Pc	$^1A_{1g}$	$(b_{2g})^2, (1e_g)^4, (a_{1g})^2, (a_{1u})^2, (b_{1g})^0, (2e_g)^0$	0.80
Cu(II)Pc	$^2B_{1g}$	$(b_{2g})^2, (1e_g)^4, (a_{1g})^2, (a_{1u})^2, (b_{1g})^1, (2e_g)^0$	0.79
Zn(II)Pc	$^1A_{1g}$	$(b_{2g})^2, (1e_g)^4, (a_{1g})^2, (a_{1u})^2, (b_{1g})^2, (2e_g)^0$	0.81

Table 4
Calculated lowest excitations of the ground state manifold (SORCI). For explanation of the nomenclature in column "nature" see text.

MPc	State	Excitation	Energy (eV)	Nature	CI weight
Fe(II)Pc	$1\,^3E_g$	$(a_{1g}) \rightarrow (1e_g)$	0.13	Metal d–d	0.81
	$1\,^3B_{2g}$	$(a_{1g},b_{2g}) \rightarrow (1e_g)$	0.69	Metal d–d	0.83
	$1\,^3A_{2u}$	$(a_{1u},a_{1g}) \rightarrow (1e_g,2e_g)$	0.89	$^3L(0)^3M(1)$–$^3L(1)^3M(0)$	0.63
	$1\,^3E_u$	$(a_{1u}) \rightarrow (2e_g)$	1.17	$^3L(0)^3M(1)$–$^3L(1)^3M(0)$	0.77
	$2\,^3A_{2u}$	$(a_{1u},a_{1g}) \rightarrow (1e_g,2e_g)$	1.49	$^3L(1)^1M(0)$(tripsinglet)	0.82
	$3\,^3A_{2u}$	$(a_{1u},a_{1g}) \rightarrow (1e_g,2e_g)$	1.62	$^1L(0)^3M(1)$(singtriplet)	0.79
Ni(II)Pc	$1\,^1E_u$	$(a_{1g},a_{1u}) \rightarrow (b_{1g},2e_g)$	2.17	$^3L(-1)^3M(1) + {}^3L(1)^3M(-1) - {}^3L(0)^3M(0)$	0.83
	$1\,^1B_{1g}$	$(a_{1g}) \rightarrow (b_{1g})$	2.50	metal d–d	0.83
	$2\,^1E_u$	$(a_{1u}) \rightarrow (2e_g)$	2.60	Ligand π–π^* (Q)	0.82
Cu(II)Pc	$1\,^2E_u$	$(a_{1u}) \rightarrow (2e_g)$	1.43	$^3L(0)^2M(1/2)$–$^3L(1)^2M(-1/2)$(tripdoublet)	0.68
	$2\,^2E_u$	$(a_{1u}) \rightarrow (2e_g)$	2.70	Ligand π–π^* (Q)	0.79
Zn(II)Pc	$1\,^1E_u$	$(a_{1u}) \rightarrow (2e_g)$	2.50	Ligand π–π^* (Q)	0.80

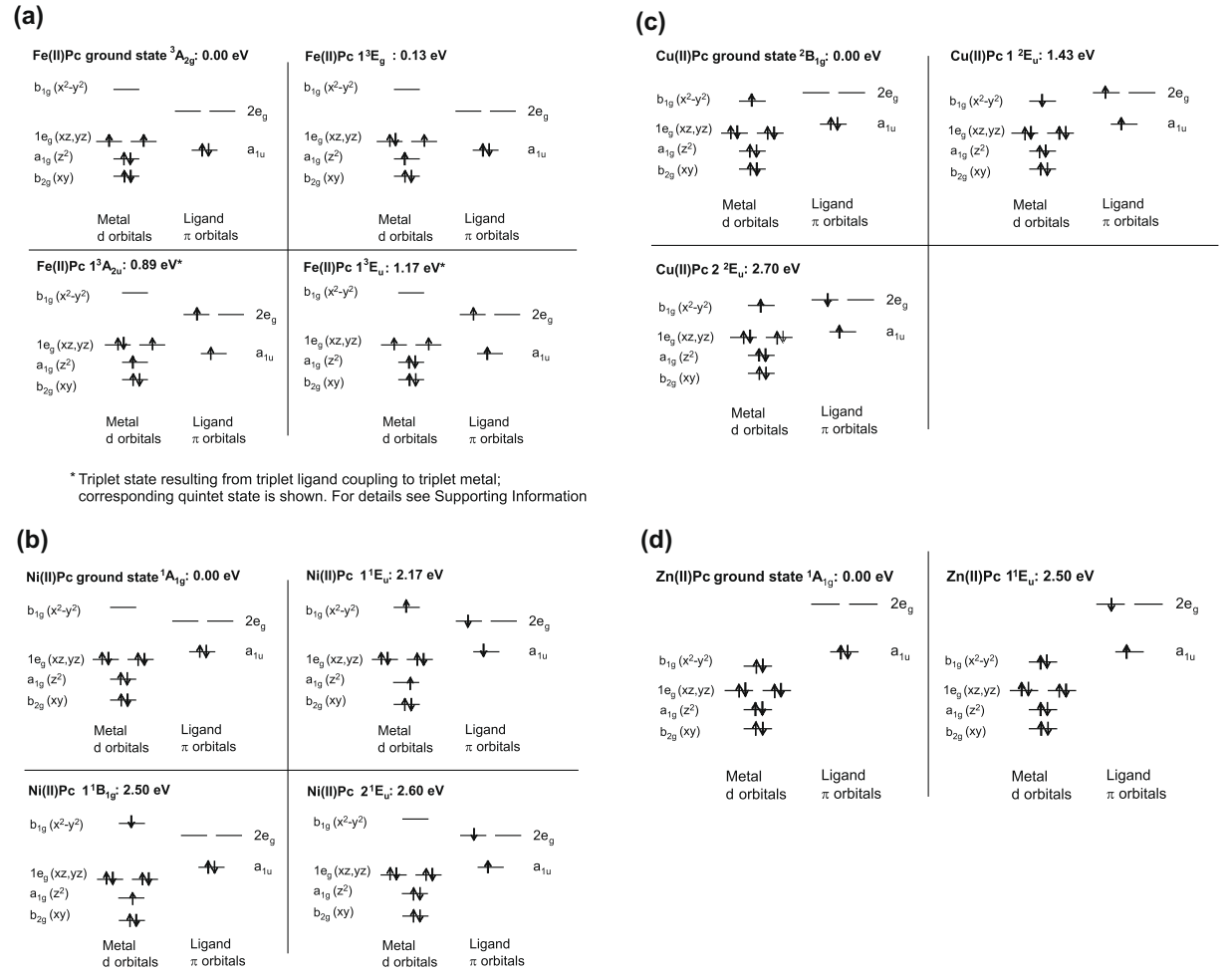

Fig. 7. Leading electronic configurations of the ground states and lowest excited states of the same spin manifold obtained from SORCI calculations for (a) FePc, (b) NiPc, (c) CuPc and (d) ZnPc. For FePc, the configuration $1\,^3B_{2g}$ (d–d excitation) state has been omitted.

investigated MPc films were shown to differ significantly from each other. Based on the quantum mechanical calculations of the excited states in the MPc's, there is a strong evidence, that the different fluorescence behaviors are based on characteristic ligand–metal exchange coupled states (LMEC states).

To correlate the influence of the LMEC states with the device performance of the respective phthalocyanines,

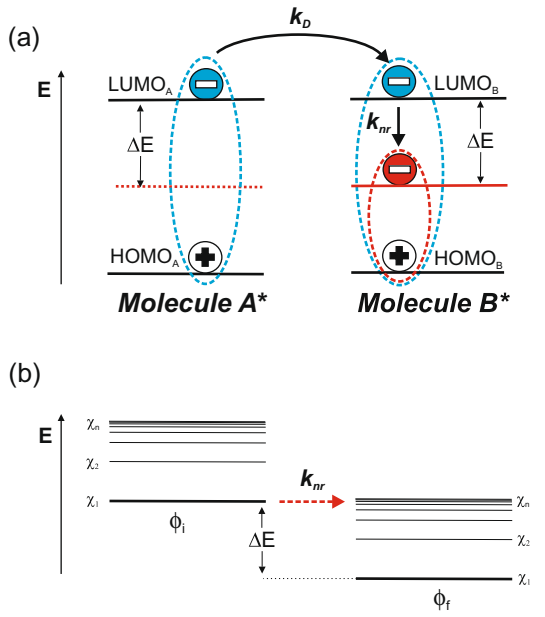

Fig. 8. (a) Schematic picture describing the influence of the calculated LMEC-state of CuPc (Table 4) on the exciton transport: CuPc has one additional calculated excitation which is lowered by a ΔE of 1.27 eV compared to the π–π^* Q-band excitation. This intermediate state has the same spin as the respective initial state and therefore may be populated on the femto- to picoseconds timescale by internal conversion. Thus, excitons moving with a rate k_D from molecule A to B (the * at A and B in the picture should indicate that the molecules are not charged but excited) towards the donor–acceptor (DA) interface could concurrently relax non-radiative with a rate k_{nr}. These relaxed excitons are now either trapped or they cannot split at the DA interface due to their strong binding. Hence, they cannot contribute to the current in an organic solar cell. (b) None radiative energy conversion in a polyatomic molecule. The rate of the none radiative deactivation processes k_{nr} depends on the density of the states ρ_v as well as on the overlap of the vibronic wavefunctions in the final and initial state.

one has to consider, that excitons diffuse after their generation towards the donor–acceptor interface[1] with a certain rate k_D. Concurrently, these excitons could relax nonradiatively with a rate k_{nr} by increasing their binding energy (Fig. 8). In case of the presence of LMEC-states below the Q-band excitation ($a_{1u} \rightarrow 2e_g$) this relaxation process is supposed to become very likely.

Therefore, it has to be discussed whether the exciton diffusion rate k_D or the none radiative relaxation k_{nr} is dominant and therefore formative for the device performance of the investigated metal phthalocyanines.

4.1. Implications of the excitation effects on the excitation energy transfer

Incoherent exciton hopping is described in the weak coupling limit, which means that interchromophore electronic coupling is weaker than the donor excited state vibrational reorganisation energy. In this case, the bimolecular rate k_D for excitation energy transfer takes the form [37]

$$k_D = \frac{2\pi}{\hbar} V_{DA}^2 F_{DA}, \tag{1}$$

where V_{DA} is the electronic coupling integral for excitation energy transfer and F_{DA} the overlap between donor emission and acceptor absorption spectra, normalized on an energy scale (derived from the Franck–Condon weighted density of states, the product of the density of vibrational states in the initial and final states and their overlap). Under the assumption of separate chromophores, V_{DA} is dominated by the Coulomb integral

$$J = \frac{1}{4\pi\varepsilon_0} \int dr_1 dr_2 \phi_A^{HO}(r_1)\phi_A^{*,LU}(r_1)\frac{1}{r_{12}}\phi_B^{HO}(r_2)\phi_B^{*,LU}(r_2). \tag{2}$$

$\phi_A^{HO}(\phi_A^{*,LU})$ is the HOMO (LUMO) on the donor molecule A and $\phi_B^{HO}(\phi_B^{*,LU})$ is the HOMO (LUMO) on acceptor molecule B. This integral may be approximated by a simple dipole [38,39] or even multipole [40–42] interaction energy. It is noted that a quantitative estimation of intermolecular coupling between closely packed molecules requires also the inclusion exchange and penetration terms [43–46]. We consider excitation energy transfer only between the ($a_{1u} \rightarrow 2e_g$) excited states for all investigated MPc's.[2] Because a_{1u} and $2e_g$ are essentially unaffected by the metal center (depicted in Fig. 6), the electronic coupling integral, described in Eq. (2), and therefore V_{DA} will be equal for all MPc's.

With respect to the analogy of the absorption and normalized fluorescence spectra (Fig. 5), F_{DA} is expected to be similar as well. Based on these perceptions k_D can assumed to be similar for all MPc's.

4.2. Implications of the excited state spectrum on the non-radiative deactivation

Non-radiative deactivation processes within molecules can be characterized by matrix elements derived from the time-dependent pertubation theory. Under the assumption of weak coupling, the wavefunctions ψ can be divided (Born–Oppenheimer approximation) in an electronic ϕ and a vibrionic χ part. Therefore, the rate for non-radiative deactivation k_{nr} can be written [47] as

$$k_{nr} \sim \frac{2\pi}{\hbar} \left\langle \phi^f | H' | \phi^i \right\rangle^2 \langle \chi_i | \chi_f \rangle^2 \rho_v, \tag{3}$$

where H' is the pertubation operator. In the case of internal conversion between states of equal multiplicity (which is the case here) it has been shown, that H' is the operator of the kinetic energy of the cores [47]. Based on Eq. (3) it becomes obvious that the excitation energies (Table 3) of the respective phthalocyanines must have a significant influence on the radiationless deactivation processes described by k_{nr}: As depicted in Fig. 8b the density of states

[1] Valid in vacuum deposited organic bilayer and bulk heterojunction solar cells.

[2] To split excitons at the donor–acceptor interface into free charge carriers it is widely accepted, that the present energetic offset between the HOMO of the donor (metal phthalocyanines) and the LUMO of the acceptor (C_{60}) have to be equal or somewhat larger than the exciton binding energy. Thus, only Q-band excitons are considered to be able to split at the MPc/C_{60} interface.

ρ_v in the final state increases with the size of the energy gap ΔE between the final and initial state. At the same time the electronic excitation energy which has to be absorbed by the lattice vibration is also rising. Thus, $\langle \chi_i | \chi_f \rangle^2$ decreases due to the lower overlap of the vibrational wavefunctions with different vibrational quantum numbers. Concerning the investigated metal phthalocyanines this means, that k_{nr} depends on the number as well as on the energetic difference of the LMEC-states lying in between the initially excited state and the ground state: As more LMEC-states are available and as closer their energetics are, k_{nr} will increase due to Eq. (3). Thus, FePc is expected to have the highest relaxation rate k_{nr} and ZnPc the lowest.

4.3. Relation between device performance and excited state spectrum

Exciton transport is in general characterized by the effective exciton diffusion length L_{ex}

$$L_{ex} = \sqrt{D \cdot \tau}. \quad (4)$$

The lifetime τ is related to k_{nr} as

$$\tau \sim \frac{1}{\sum_i k_{i,nr}}, \quad (5)$$

while D is directly proportional to k_D,

$$D \sim k_D. \quad (6)$$

Based on the presented experimental and theoretical results (*vide supra*) D is assumed to be similar while an increasing number of intermediate states leads to a decreasing τ depending on the metal phthalocyanine of interest. Obviously, the differences in lifetime τ will lead to different values of L_{ex} in the present MPc series. This is in agreement with experimental results [48–51]. Furthermore, the optimized thickness of the MPc layer in the device decreases in the series ZnPc → CuPc → NiPc → FePc which is another indication that L_{ex} decreases in same series, as less excitons are able to reach the donor–acceptor-interface.

Besides the specific exciton diffusion length L_{ex}, also the hole mobility μ is considered to have an influence on I_{sc} and the fill factor. Therefore, the electronic effects which affect the characteristic hole mobility still have to be elucidated; work in this regard is currently on going in our laboratories.

5. Conclusion

In summary a study on different metal phthalocyanines (MPc's with M = Zn, Cu, Ni, Fe) was presented in which the fundamental physical origin of their characteristic performance in organic solar cells was investigated under a structural, optical and electronic point of view. MPc/C_{60} based bilayer hetero-junction solar cells exhibited a clear dependence of the optimal layer thickness and overall performance on the employed MPc material. The origin of these differences were explored by AFM and high resolution XRPD measurements on powder and evaporated thin films. In the course of these measurements it was found, that all MPc's exhibit a similar thin film crystal structure. Furthermore, the relation between the known crystal structure of α-CuPc [18] and the molecular packing of vacuum deposited thin films was clarified.

The optical properties of the metal phthalocyanines were investigated by solid state fluorescence and absorption measurements. While the MPc molecules under study have similar absorption characteristics, they differ markedly by their fluorescence spectra. Based on this finding, the lowest excited states of the MPc series were explored by correlated multi-reference ab inito calculations. An increasing number of excited states is obtained energetically below the initially excited ligand-based π–π^* state (Q-band) going from ZnPc (zero) → CuPc with one → NiPc with two → FePc with over six excited states. These states arise from d–d excitations and ligand–metal exchange coupling. It is argued that an increasing number of intermediate states lead to increasing rates for non-radiative relaxation. This will directly affect the lifetime and therefore the diffusion lengths L_{ex} of photoelectrically active excitons in the present MPc series. Thus, the effect offers a straightforward explanation for the experimentally observed reduced device performances from ZnPc to FePc.

Acknowledgments

We acknowledge the financial support of the Fonds der chemischen Industrie (FCI) and the Bundesministerium für Bildung und Forschung (BMBF) within the project OPEG, Förderkennzeichen F13N9714. Furthermore we thank Erwin Thiel for the solid state fluorescence measurements. We would also like to thank Frank Neese for helpful discussions.

Appendix A. Sample preparation of the metal phthalocyanine/C_{60} bilayer hetero-junction (HJC) solar cells

To ensure a reproducible purity of the used phthalocyanines all compounds were gradient sublimed before they were used in devices. A bilayer phthalocyanine/C_{60} heterojunction cell architecture was used for all devices to guarantee a defined layer structure and a high reproducibility of the solar cell performance.

A prestructured ITO covered glass substrate with an active area of 31.5 mm^2 was exposed to UV-light during 30 min, to lower the ionisation potential (IP) of the ITO. The substrate was then transferred into a high vacuum evaporation chamber (2×10^{-6} mbar). At first the metal phthalocyanines were evaporated with rates of 2 Å/s and layer thicknesses of 10–60 nm. This was followed by a C_{60} layer (2 Å/s, 10–60 nm) and a 6 nm thick Bphen (4,7-diphenyl-1,10-phenanthroline) layer (0.6 Å/s). The active area of our device was defined by a 100 nm thick silver electrode (5 Å/s) which was evaporated on top of the organic layers. A schematic picture of the layer setup is depicted in Fig. 1b.

Appendix B. High resolution X-ray powder diffraction

B.1. Sample preparation and measurement setup

Fe, Ni, Cu and Zn-Phthalocyanine layers of 30 nm and 1 μm thickness were vacuum deposited (2×10^{-6} mbar) with a rate of 2 Å/s on precleaned ITO covered glass substrates. High resolution X-ray powder diffraction patterns of thin films were recorded at room temperature. A laboratory powder diffractometer (D-8, Bruker, Cu Kα_1 radiation from primary Ge(1 1 1) Johannson monochromator; Lynx-Eye position sensitive detector (PSD) with an opening angle of 3°) in Bragg–Brentano mode was used. The sample was loaded on a plexiglas sample holder with a 2 mm deep cavity of 32 mm diameter. The samples were aligned such to minimize sample height errors and rotated during measurement for better particle statistics. Data were generally taken in steps of 0.009° [2Θ] from 2.0°–62.0° [2Θ] at a scanning speed of 0.5°/min.

B.1.1. Sample height correction

To account for the small but (almost) unavoidable sample displacement error, a glass substrate with a sole ITO thin film was aligned carefully in a previously calibrated sample holder and used as reference standard. The (2 2 2) reflection as the strongest reflections of ITO turned out to be largely insensitive to peak shifts and could thus be used as a suitable reference for correcting the sample height error. This approach is based on the assumption that the position of the (2 2 2) reflection of ITO is constant throughout all samples under investigation which seemed to be reasonable [52]. The calculated cubic lattice parameter was fixed to 10.28104 Å. LeBail fits [24] using exclusively the (2 2 2) reflection of ITO for all samples containing ITO, immediately revealed individual sample displacement parameters and allowed the angular correction of the reflections of the different phthalocyanine samples.

B.2. Determination of domain size

The fundamental parameter (FP) approach [53] was used to describe the peak profile of our 1 μm and 30 nm thick evaporated MPc films using direct convolutions of wavelength distribution, the geometry of the diffractometer and the microstructural properties like domain size and microstrain. Due to the fact that the geometry of the Lynx-Eye position sensitive detector is not fully characterized by FP's, fine tuning of the available parameters was performed by using refined values of the FP's from a precise measurement of the NIST line profile standard SRM 660a (LaB_6) measured in a silicon (9 1 1) low background sample holder over the full 2Θ range of the diffractometer.

Appendix C. Estimating the grain size from the AFM images

The morphology of 30 nm thick films of different metal phthalocyanines vacuum deposited on ITO coated glass was investigated with an atomic force microscopy (AFM) with Si-tips (resonance frequency 68 kHz, force constant 1,3 N/m) used in tapping mode. As shown in Fig. 3, the used ITO is very smooth (RMS = 0.48 nm) but with height differences of up to 3 nm not completely flat. This influences the further film growth of the organic materials, resulting in dints in the Pc film (Fig. 3). All Pc's show a similar topography and their crystallite sizes are only slightly different. For estimating the grain size from the AFM images a threshold method was used. First, the images were flattened with a third grade polynomial fit. Only structures higher than the threshold level of the geometrical mean were taken into account and the average diameter d of their 2D projection was calculated.

Appendix D. Fluorescence measurement technique

Due to the in general low fluorescent quantum yield of the measured phthalocyanines the smallest and almost unavoidable amount of fluorescence light coming from impurities became significant. To get still a clear and reliable measurement signal the ZnPc and CuPc films were exposed with a 532 nm laser which describes a significant shift to the maximum absorption regime of the respective phthalocyanines. Using this technique we were able to avoid overlap coming from parasitaric impurities within the phthalocyanine films by shifting their fluorescence peaks to shorter wavelength than the fluorescence of the MPc's.

Appendix E. Theoretical methods

The metal basis set was triple-ζ quality with polarization functions (TZVP [54]). The ligand heavy atoms were treated with a split valence basis and polarization functions, while hydrogens do not carry polarization functions (SV(P) [54]). This basis set leads to overall 625 basis functions, and is expected to give qualitatively meaningful results in a correlated ab initio calculation.

Geometry optimizations were carried out under D_{4h} symmetry constraints at the B3LYP [55–57] density functional theory (DFT) level, using TURBOMOLE, v5.10 [58]. All molecules were optimized in the respective ground states that are indicated in the main text.

The multireference-configuration-interaction (MRCI) calculations were done with the the spectroscopy oriented CI (SORCI,[32]) procedure as implemented in ORCA [59].

The reference wavefunctions were built by the complete-active-space (CAS) technique, involving the relevant frontier orbitals n, containing m electrons – CAS(n,m) – of the molecule under study. In order to keep the MR-CI calculation tractable and balanced, we have chosen CAS(n,m) to be for ZnPc: CAS(2,3); CuPc: CAS(3,4); NiPc: CAS(8,7); FePc: CAS(8,7).

Following [32,60], the initial orbitals for the MR-CI calculation were quasi-restricted orbitals from an unrestricted DFT calculation, obtained at the B3LYP [55–57] level. This approach leads in the present case to the expected energetic order of the relevant orbitals (the metal d-block and the ligand a_{1u} and e_g orbitals), that were chosen to belong to the active space. We have also used Hartree–Fock orbitals as initial orbitals, however, this made

it necessary to re-order the relevant orbitals in the definition of the active space of the MR-CI procedure (see above). The energies of the resulting MR-CI excited states agrees between both alternatives to within 0.1 eV.

In all MRCI calculations, the thresholds T_{sel}, T_{pre} and T_{nat} defined previously [32] and introduced to enhance computational efficiency at small loss of accuracy were set to 10^{-6} Eh, 10^{-4} Eh and 10^{-5} Eh, respectively.

Appendix F. Supplementary data

Supplementary data associated with this article can be found, in the online version, at doi:10.1016/j.orgel.2009.11.016.

References

[1] C.W. Tang, Appl. Phys. Lett. 48 (1986) 183.
[2] P. Peumans, S. Uchida, S.R. Forrest, Nature 425 (2003) 158.
[3] S. Uchida, J. Xue, B.P. Rand, S.R. Forrest, Appl. Phys. Lett. 84 (2004) 4218.
[4] M. Hiramoto, M. Suezaki, M. Yokoyama, Chem. Lett. 3 (1990) 327.
[5] J. Drechsel, B. Männing, F. Kozlowski, M. Pfeiffer, K. Leo, Appl. Phys. Lett. 86 (2005) 244102.
[6] J. Xue, S. Uchida, B.P. Rand, S.R. Forrest, Appl. Phys. Lett. 85 (2004) 5757.
[7] I. Bruder, M. Karlsson, F. Eickemeyer, J. Hwang, P. Erk, A. Hagfeldt, J. Weis, N. Pschirer, Sol. Energy Mater. Sol. Cells 93 (2009) 1896.
[8] A.B.J. Parusel, S. Grimme, J. Porphyrins Phthalocyanines 5 (2001) 225–232.
[9] K. Toyota, J. Hasegawa, H. Nakatsuji, J. Phys. Chem. A 101 (1997) 446–451.
[10] N. Ishikawa, D. Maurice, M. Head-Gordon, Chem. Phys. Lett. 260 (1996) 178–185.
[11] J. Mack, M.J. Stillman, Coord. Chem. Rev. 219–221 (2001) 993–1032.
[12] J.O. Morley, M.H. Charlton, J. Phys. Chem. 99 (1995) 1928–1934.
[13] G. Ricciardi, A. Rosa, E.J. Baerends, J. Phys. Chem. A 105 (2001) 5242–5254.
[14] K.A. Nguyen, R. Pachter, J. Chem. Phys. 118 (2003) 5802–5810.
[15] M.-S. Liao, S. Scheiner, J. Chem. Phys. 114 (2001) 9780–9791.
[16] M.-S. Liao, J.D. Watts, M.-J. Huang, S.M. Gorun, T. Kar, S. Scheiner, J. Chem. Theory Comput. 1 (2005) 1201–1210.
[17] V.N. Nemykin, R.G. Hadt, R.V. Belosludov, H. Mizuseki, Y. Kawazoe, J. Phys. Chem. A 111 (2007) 12901–12913.
[18] P. Erk, Private Communication to Cambridge Crystallographic Data Center (CCDC reference code: CUPOCY14).
[19] S. Singht, S.K. Tripathi, G.S.S. Saini, Mater. Chem. Phys. 112 (2008) 793.
[20] S. Senthilarasu, Y.B. Hahn, S.H. Lee, J. Appl. Phys. 102 (2007) 043512.
[21] A.K. Debanath, S. Samanta, A. Singh, D.K. Aswal, S.K. Gupta, J.V. Yakhmi, S.K. Deshpande, A.K. Poswal, C. Sürgers, Physica E 41 (2008) 154.
[22] C.J. Brown. J. Chem. Soc. A (CCDC reference code: CUPOCY10) (1968) 2488.
[23] P. Erk, H. Hengelsberg, M.F. Haddow, R. van Gelder. Cryst. Eng. Comm. (CCDC reference code CUPOCY15) 6 (2004) 474.
[24] A. Le Bail, H. Duroy, J.L. Fourquet, Mater. Res. Bull. 23 (1988) 447.
[25] D. Raoufi, A. Kiasatpour, H.R. Fallah, A.S.H. Rozatian, Appl. Surf. Sci. 253 (2007) 9085.
[26] M.K. Debe, K.K. Kam, Thin Solid Films 186 (1990) 289.
[27] R. Resel, M. Ottmar, M. Hanack, J. Keckes, G. Leising, J. Mater. Res. 14 (2000) 934.
[28] O. Berger, W.-J. Fischer, B. Adolphi, S. Tierbach, V. Melev, J. Schreiber, J. Mater. Sci. Mater. Electron. 11 (2000) 331.
[29] P. Erk, H. Hengelsberg, M.F. Haddow, R. van Gelder, Cryst. Eng. Comm. 6 (78) (2004) 474.
[30] A. Hoshino, Y. Takenaka, H. Miyaji, Acta. Cryst. Sect. B B59 (2003) 393.
[31] M.G. Cory, M.C. Zerner, Chem. Rev. 91 (2001) 813–822.
[32] F. Neese, J. Chem. Phys. 119 (2003) 9428.
[33] A. Henriksson, B. Roos, M. Sundbom, Theor. Chim. Acta 27 (1972) 303–313.
[34] R. Ake, M. Gouterman, Theor. Chim. Acta 17 (1970) 408.
[35] P.S. Vincett, E.M. Voigt, K.E. Rieckhoff, J. Chem. Phys. 55 (1971) 4131.
[36] A. Szabo, N.S. Ostlund, Modern Quantum Chemistry: Introduction into Advanced Electronic Structure Theory, Dover, 1996.
[37] M. Klessinger, Elektronenstruktur organischer Molekle, VCH, 1982.
[38] T. Förster, Naturwissenschaften 6 (1946) 166.
[39] T. Förster, Ann. Phys. 2 (1948) 55.
[40] H. Wiesenhofer, D. Beljonne, G.D. Scholes, E. Hennebicq, J.L. Brdas, E. Zojer, Adv. Funct. Mater. 15 (2005) 155.
[41] D. Beljonne, J. Cornil, R. Silbey, P. Milli, J.L. Brdas, Adv. Funct. Mater. 112 (2000) 4749.
[42] E. Hennebicq, G. Pourtois, G.D. Scholes, L.M. Herz, D.M. Russell, C. Silva, S. Setayesh, A.C. Grimsdale, K. Müllen, J.L. Brédas, D. Beljonne, JACS 112 (2005) 4744.
[43] R.F. Fink, J. Pfister, A. Schneider, H. Zhao, B. Engels, Chem. Phys. 343 (2008) 353.
[44] R.F. Fink, J. Pfister, H.M. Zhao, B. Engels, Chem. Phys. 346 (2008) 275.
[45] D. Beljonne, C. Curutchet, G.D. Scholes, R.J. Silbey, J. Phys. Chem. B 113 (19) (2009) 6583.
[46] C.Y. Wong, C. Curutchet, S. Tretiak, G.D. Scholes, J. Chem. Phys. 130 (2009) 81104.
[47] M. Klessinger, J. Michl, Excited, States and Photochemistry of Organic Molecules, VCH, Weinheim, Cambridge, Newyork, 1995.
[48] P. Peumans, A. Yakimov, S.R. Forrest, J. Appl. Phys. 93 (7) (2003) 3693.
[49] Y. Terao, H. Sasabe, C. Adachi, Appl. Phys. Lett. 90 (2007) 103515.
[50] T. Stübinger, W. Brütting, J. Appl. Phys. 90 (2001) 3632.
[51] H.R. Kerp, E.E. van Faassen, Nord. Hydrol. 1 (1999) 1761.
[52] L. Kerkache, A. Layadi, E. Dogheche, D. Rémis, J. Phys. D 39 (2006) 184.
[53] R.W. Cheary, A.A. Coelho, J.P. Cline, J. Res. Natl. Inst. Stand. Technol. 109 (2005) 1.
[54] A. Schaefer, H. Horn, R. Ahlrichs, J. Chem. Phys. 97 (1992) 2571.
[55] A.D. Becke, Phys. Rev. A 38 (1988) 3098.
[56] A.D. Becke, J. Chem. Phys. 98 (1993) 5642.
[57] C. Lee, W. Yang, R.G. Parr, Phys. Rev. B 37 (1988) 785.
[58] R. Ahlrichs, M. Bär, M. Häser, H. Horn, C. Kölmel, Chem. Phys. Lett. 162 (1989) 165.
[59] F. Neese, ORCA – An Ab initio, Density Functional and Semiempirical Program Package, Version 2.4.41, Max-Planck Institute for Bioinorganic Chemistry, Mülheim an der Ruhr, Germany, 2005.
[60] N. Marom, L. Kronik, App. Phys. A 95 (2009) 165.
[61] M. Sumimoto, Y. Kawashima, K. Hori, H. Fujimoto, Dalton Transactions (2009) 5737.

Organic Electronics 11 (2010) 388–396

Contents lists available at ScienceDirect

Organic Electronics

journal homepage: www.elsevier.com/locate/orgel

Mixing of molecular exciton and excimer phosphorescence to tune color and efficiency of organic LEDs

Massimo Cocchi [a], Jan Kalinowski [b,*], Lisa Murphy [c], J.A. Gareth Williams [c], Valeria Fattori [a]

[a] Institute of Organic Synthesis and Photoreactivity, National Research Council of Italy (ISOF-CNR), I-40129 Bologna, Italy
[b] Gdańsk University of Technology, 80-233 Gdańsk, Poland
[c] Department of Chemistry, University of Durham, DH1 3LE, UK

ARTICLE INFO

Article history:
Received 30 July 2009
Received in revised form 5 November 2009
Accepted 5 November 2009
Available online 16 November 2009

Keywords:
Organic light-emitting diodes
Organic electroluminescence
Exciton phosphorescence
Excimer phosphorescence
White light-emitting diodes
Platinum
Luminescence

ABSTRACT

We report highly efficient, variable-color light-emitting diodes (LEDs) realized via mixing of molecular exciton and excimer phosphorescent emissions from a new organic phosphor platinum N^C^2^N-[1,3-di(4-methoxy-pyrid-2-yl)-4,6-difluorobenzene] chloride (PtL^{26}Cl), a member of the Pt(N^C^N) complex series, where N^C^N represents a cyclometallating tridentate ligand based on 1,3-dipyridylbenzene, *L*. PtL^{26}Cl-doped TCTA blends [TCTA = 4,4′,4″-tris(*N*-carbazolyl-triphenylamine)] have been used as either the low-concentration bluish-green (molecular) phosphorescence emitter or high-concentration red (excimer) phosphorescence emitter. By adjusting the relative amount of blue and red emissive species, the color of the light emission was tuned from bluish-green through green and white up to red. The concentration-optimized devices can easily reach high brightness up to B = 10,000 cd/m^2, achieving extremely high external quantum efficiency (EQE) up to 20% at low-current densities (<10^{-2} mA/cm^2) and up to 17% at B = 500 cd/m^2. High purity white light emission [CIE coordinates (x = 0.34, y = 0.35)] was realized at this B, QE = 11.5%, power efficiency of 6.8 lm/W and color rendering index (CRI) = 74, though CRI = 81 has been achieved with CIE coordinates (x = 0.42, y = 0.38). The reported performance data are among the best achievements reported for color and white emission organic LEDs.

© 2009 Elsevier B.V. All rights reserved.

1. Introduction

Organic light-emitting diodes (OLEDs) [1] have been intensively studied due to their potential in next generation full-color displays [2] and solid-state lighting [3–6]. Various strategies have been used to fabricate full-color displays. For example, fluorescent color-changing medium arrays were used to change blue OLED emission into red or green fluorescent colors [7]. Other approaches involve the use of patterned lateral red, green, and blue (RGB) emitters [8], stacked RGB emitters [9], patterns by photo-bleaching [10] or ink-jet printing [11]. Several routes have been employed to realize white light-emitting OLEDs (WOLEDs). Typically, the fabrication of stacked [4] or multilayer [12] LED structures with separated molecular emitters, that is, blue, green and red has been realized. However, the OLEDs with the most impressive characteristics are those based on a single emissive dopant, where molecular excitons are harnessed to form triplet excimers in addition to molecular excited states [13–17].

Electrophosphorescence from cyclometallated Pt(II) complexes has recently received broad attention due to their potential for tailoring the emission color and efficiency of organic LEDs [18–22]. Many of the Pt(II) complex blend-based emitters show two phosphorescence bands located in the bluish-green and red regions of the visible spectrum. Their contribution to the total emission output can be controlled by the concentration of the Pt(II) com-

* Corresponding author. Tel./fax: +48 (58) 664 6535.
E-mail addresses: cocchi@isof.cnr.it (M. Cocchi), kalino@polnet.cc (J. Kalinowski), j.a.g.williams@durham.ac.uk (J.A. Gareth Williams).

1566-1199/$ - see front matter © 2009 Elsevier B.V. All rights reserved.
doi:10.1016/j.orgel.2009.11.017

plex in a host matrix used for the preparation of blend emissive layers of the LEDs. This feature has been employed in the fabrication of very high efficiency organic white [16] and color [22] LEDs. Pursuing this strategy, we now report a significant improvement in efficiency and white color purity of organic LEDs based on a new metallo-organic phosphor, platinum N^C^2^N-[1,3-di(4-methoxy-pyrid-2-yl)-4,6-difluorobenzene] chloride (PtL^{26}Cl) – a new member of the Pt(N^C^N) complex series, where N^C^N represents a cyclometallating tridentate ligand based on 1,3-dipyridylbenzene, *L*. PtL^{26}Cl-doped TCTA blends [TCTA = 4,4′,4″-tris(*N*-carbazolyl-triphenylamine)] have been used as either the low-concentration bluish-green (molecular) phosphorescence emitter or high-concentration red (excimer) phosphorescence emitter. By adjusting the relative amount of blue and red emissive species, the color of the light emission was tuned from bluish-green through green and white up to red. The concentration-optimized devices can easily reach high brightness (up to 10,000 cd/m^2), and extremely high external quantum efficiencies (QE) of up to 20% achieved. High purity white light emission [the Commission Internationale de L'Eclairage (CIE) coordinates (x = 0.34, y = 0.35)] was realized at 500 cd/m^2, QE = 11.5%, power efficiency of 6.8 lm/W and color rendering index (CRI) of 74. The reported performance data are among the best performance achievements reported for color and white emission organic LEDs. Although a very high external QE (up to 34% at 1000 cd/m^2) has recently been achieved by improving light outcoupling of WOLEDs [23], the purity of their white light (x = 0.43, y = 0.49), with a lower CRI = 72 was much worse, placing these emitting devices beyond the warm incandescent lamp light (x = 0.41, y = 0.41) towards the red.

2. Experimental

2.1. OLED structures

In Fig. 1 the structure of the organic LEDs studied is schematically presented. The devices consist of an indium tin oxide (ITO) coated glass anode transparent to the light generated in the emitter layer (EML) which consists of a PtL^{26}Cl (x wt.%) – doped TCTA blend. Holes are injected from the ITO anode, and pass through (TPD:PC) and TCTA hole-transporting layers (HTL), and recombine in the EML with electrons that were injected from an Al/LiF cathode and transported through the electron transporting layer (ETL) of a triazole derivative (TAZ). The 10 nm-thick TCTA layer, characterized by a triplet exciton energy E_T of 2.85 eV, has been used to block triplet exciton transfer from the Pt complexes (E_T = 2.60–2.65 eV) to the non-radiative triplet of TPD (E_T = 2.45 eV). The 30 nm-thick layer of TAZ (E_T = 2.75 eV) plays a similar role of inhibiting quenching of the Pt complex triplet excitons at the cathode while at the same time blocking holes, both properties that enable the recombination process to be confined to a 30 nm-thick EML layer. Such a LED architecture allowed us to maximize its performance parameters (for general electronic mechanisms of organic LED function see e.g. Ref. [1]). The PtL^{26}Cl has been shown to reveal the best performance and all the presented OLEDs are based on this compound.

2.2. LED preparation and experimental procedures

LEDs were fabricated by growing a sequence of thin layers on clean glass substrates pre-coated with a 150 nm-thick layer of indium tin oxide (ITO) with a sheet resistance of 20 Ω per square. A 60 nm-thick (TPD:PC) blend hole-transporting layer was deposited on top of the ITO by spin coating from a 10 mg/ml dichloromethane solution at room temperature. All remaining organic layers were deposited in succession by thermal-evaporation under vacuum of $\sim 10^{-4}$ Pa, followed by high vacuum ($\sim 10^{-4}$ Pa) thermal-evaporation of the cathode layer consisting of 0.5 nm-thick LiF and by a 100 nm-thick Al cap. The EML was evaporated by co-deposition of the phosphor and TCTA to form a 30 nm-thick blend film. We have chosen a monomer/excimer emitting dopant PtL^{26}Cl (Fig. 1) from a group of highly efficient N^C^N-coordinated platinum (II) complex phosphors, PtL^nCl, where L^n represents cyclometallating tridentate ligands with various substituents in either the central phenyl ring (e.g. F atoms for both L^{22} and L^{26}) or in the pyridine rings (e.g. methyl for L^{23} and methoxy for L^{26}), and fabricated a four-layer LED. The photoluminescence (PL) quantum efficiency (QE) (φ_{PL}), emission lifetimes (τ) along with redox potentials of PtL^{26}Cl are summarized in Table 3. We note the unusually high red excimer phosphorescence quantum yield for neat films of PtL^{26}Cl (0.74), which probably exceeds that for the blue monomolecular phosphorescence of this complex in solution (0.71). Solid-state absorption and emission measurements were made using a Perkin–Elmer Lambda 9 UV/Vis/NIR spectrometer and a StellarNet spectroradiometer, respectively. The current–voltage characteristics were measured with a Keithley Source-Measure unit, model 236, under continuous operation mode, while the light output power was measured with an EG&G power meter. All measurements were carried out at room temperature under argon atmosphere and were reproduced for many runs, excluding any irreversible chemical and morphological changes in the devices. The performance of the emissive layer has been optimized by locating the EML between exciton blocking layers of TCTA and TAZ, the latter acting also as an electron transporting and hole-blocking layer.

2.3. Procedure for synthesis of the platinum phosphors

The platinum complexes PtL^nCl are readily prepared in one step from the respective ligands HL^n, in yields of up to 80%, upon treatment with K_2PtCl_4 in refluxing acetic acid. The ligands themselves are best accessed by cross-coupling procedures. For HL^{26}, a mixture of 4-methoxy-2-(tri-*n*-butyltin)pyridine (0.80 g, 2.02 mmol), 1,5-dibromo-2,4-difluorobenzene (0.25 g, 0.92 mmol), Pd(PPh$_3$)$_2$Cl$_2$ (30 mg, 3.8 μmol) and LiCl (0.27 g, 6.44 mmol) in toluene (6 mL) was degassed by five freeze–pump-thaw cycles, and then heated at reflux under an atmosphere of nitrogen gas for 72 h. After cooling to room temperature, saturated aqueous KF (10 mL) was added and the mixture stirred for 30 min.

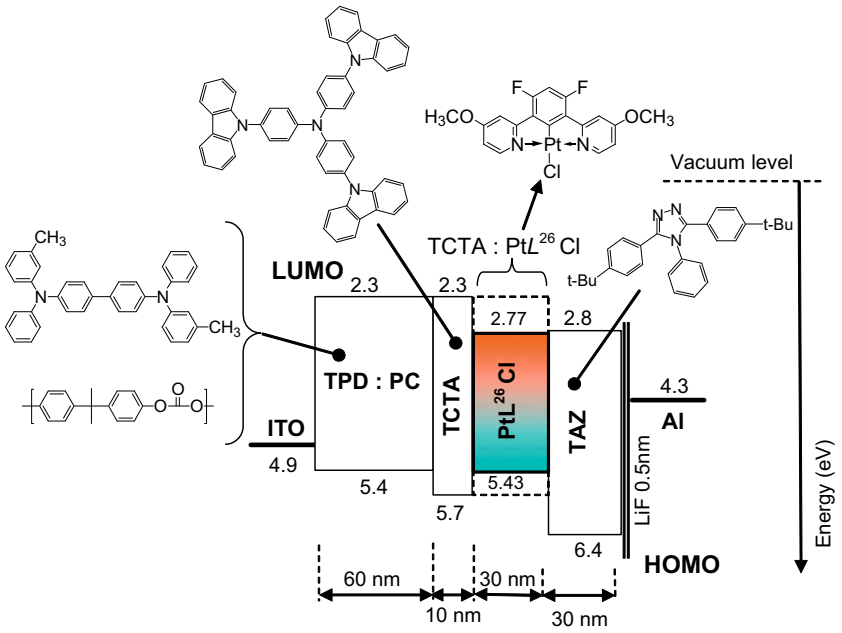

Fig. 1. The architecture of the LEDs manufactured, and molecular structures of the materials used. These are complemented by an energy level diagram shown for understanding the exciton and electronic traffic within the devices. The highest occupied molecular orbital (HOMO) obtained for each material corresponds to its ionization potential. The lowest unoccupied orbital (LUMO) is equal to the molecular electronic affinity, estimated from the reduction potential. The Fermi level positions for ITO and Al electrode contacts are added for completion. The positions of all the levels are indicated by the numbers in electronvolts relative to the vacuum level at energy zero.

The precipitated solid was removed by filtration and washed with water (25 mL) and toluene (30 mL). The filtrate was added to $NaHCO_3$ solution (10%, 50 mL) and the resulting mixture extracted with dichloromethane (2×100 mL). The organic phase was dried over $MgSO_4$, and the solvent was removed under reduced pressure to leave a pale brown residue. Purification by column chromatography (alumina, hexane/ethyl acetate, from 100/0 to 0/100) led to the desired product as a colourless solid (120 mg, 44%). $R_f = 0.35$ (alumina, hexane/ethyl acetate 60/40). NMR (500 MHz, $CDCl_3$) $\delta_H = 3.89$ (6H, s, OCH_3), 6.79 (2H, dd, $J = 5.5$ and 2.5, H^5), 7.00 (1H, t, $^3J_{F\text{-}H} = 11$, $H^{5\prime}$), 7.28 (2H, d, $J = 2.5$, H^3), 8.52 (2H, d, $J = 5.5$, H^6), 8.56 (1H, t, $^4J_{F\text{-}H} = 9.0$, $H^{2\prime}$). $\delta_C = 55.5$ (OCH_3), 105.2 (t, $^2J_{F\text{-}C} = 27$, $C^{5\prime}$), 108.9 (s, C^5), 110.7 (s, C^3), 124.7 (s, $C^{1\prime}$), 133.9 (s, $C^{2\prime}$), 151.1 (s, C^6), 154.2 (s, C^2), 160.7 (dd, $^1J_{F\text{-}C} = 255$, $^3J_{F\text{-}C} = 13$, $C^{4\prime}$), 166.2 (s, C^4). $\delta_F = -113.0$ (dd, $^3J_{F\text{-}H} = 11$, $^4J_{F\text{-}H} = 9.0$). HRMS (ES^+) $m/z = 329.1098$ ($M+H^+$); calc. for $C_{16}H_{10}$- $F_2N_2 = 329.1102$.

Platinum N^C^2^N-[1,3-di(4-methoxy-pyrid-2-yl)-4,6-difluorobenzene] chloride (PtL^{26}Cl) was prepared from a mixture of the ligand HL^{26} (30 mg, 0.091 mmol) and K_2PtCl_4 (38 mg, 0.091 mmol) in acetic acid (2 mL). The mixture was degassed by three freeze–pump-thaw cycles, and then heated at reflux under a nitrogen atmosphere for 72 h. The resulting precipitate was separated by centrifugation and washed successively with water, ethanol and diethyl ether (3×5 mL of each). The residue was extracted into dichloromethane, filtered, and the solvent removed under reduced pressure to give the product as a very pale yellow solid (21 mg, 44%). NMR (500 MHz, $CDCl_3$) $\delta_H =$ 3.98 (6H, s, OCH_3), 6.68 (1H, t, $^3J_{F\text{-}H} = 11$, $H^{5\prime}$), 6.78 (2H, dd, $^3J = 6.7$, $^4J = 3.0$, H^5), 7.39 (2H, d, $^3J = 3.0$, H^3), 9.08 (2H, d, $^3J = 6.8$, $^3J_{H\text{-}Pt(195)} = 39$, H^6). $\delta_F = -108.8$ (d, $^3J_{F\text{-}H} = 11$). MS (MALDI) $m/z = 557$, M^+; 522, ($M-Cl^+$).

3. Results and discussion

3.1. Electroluminescence spectra

Fig. 2 shows EL spectra and the CIE coordinates (x, y) of LED structures from Fig. 1 for different PtL^{26}Cl complex dopant concentrations. It is clear that a reduction in its concentration leads to a relative increase of the blue light emission band originating from the radiative decay of molecular triplet excitons of the isolated phosphorescent molecules of the Pt complex while increasing dopant concentration increases the contribution of the broad red light band emanating from the emission of triplet Pt complex excimers or aggregates that comprise two closely associated molecules. They have main maxima at $\lambda \approx 465$ and 620 nm, respectively. The EL spectrum of a neat film of the Pt complex (100%) is practically devoid of blue monomer emission, as in the case of OLEDs based on the unsubstituted parent complex PtL^1Cl, and simple derivatives [16,24]. Fig. 3 shows the voltage dependence of luminance for the devices with different PtL^{26}Cl concentrations. Luminance (B) increases monotonically with increasing dopant concentration (up to ca. 10,000 cd/m^2 for neat phosphor films), showing in all cases a tendency to saturation associated with high-voltage (high brightness) roll-off in the EL quantum efficiency [1]. A detailed examination of the B (V) characteristics shows a distinct increase in luminance between 25 and 35 wt.% PtL^{26}Cl concentrations except for

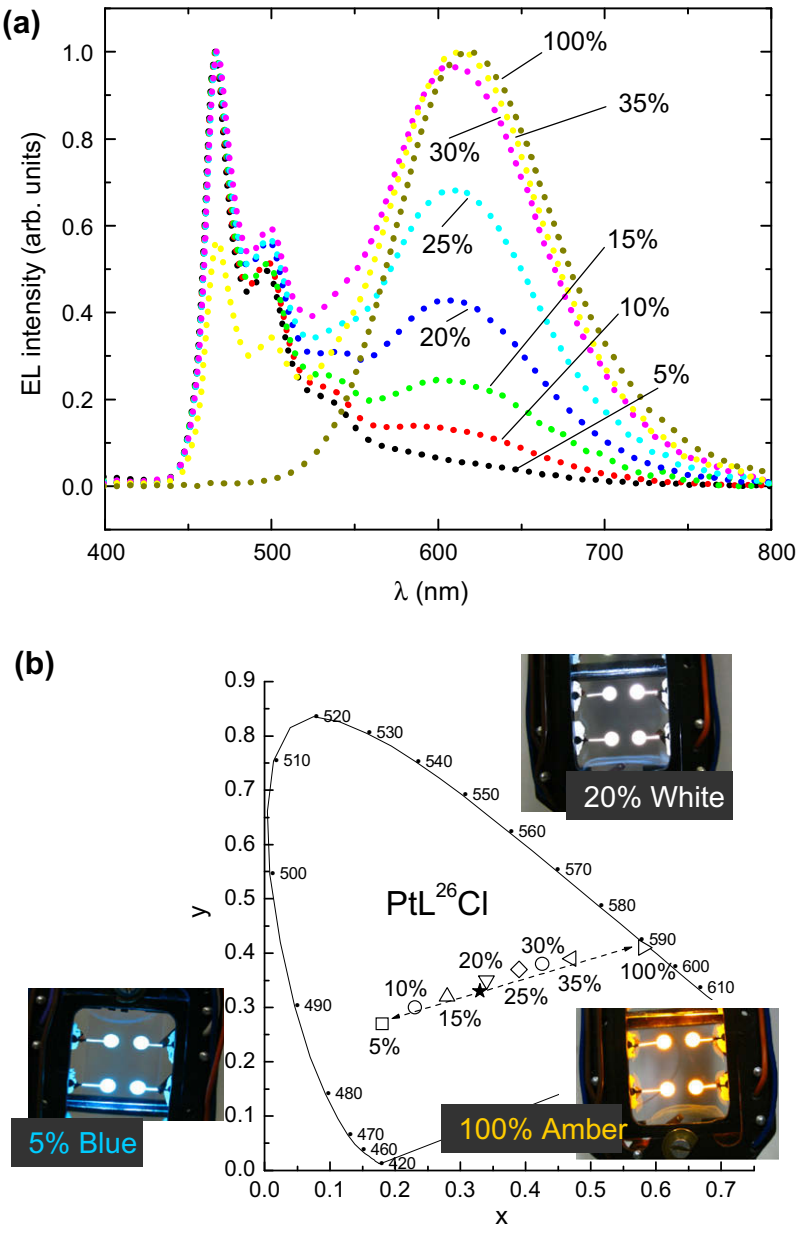

Fig. 2. EL spectra (a), and CIE diagram (b) for LEDs with emitters of varying concentrations of PtL^{26}Cl. At low concentrations of the phosphor the LEDs are "blue-biased" (dominated by emission from the molecular triplet excitons), at high phosphor concentrations the LEDs become "red-biased" being dominated by the emission from phosphor excimers. The blue emission band practically disappears for 100% phosphor emitter (neat PtL^{26}Cl films). The LED with a 20 wt.% content of the phosphor approaches closely a white light with CIE coordinates (0.33, 0.33). Examples of emission colors at various phosphor concentrations are given by photographs in the CIE diagram in part (b). (For interpretation of the references in colour in this figure legend, the reader is referred to the web version of this article.)

the highest voltage (>15 V) region, where, surprisingly, neat films reveal the highest light output.

3.2. Dimers vs excimers

The nature of bi-molecular emissive states is a challenging question concerning all planar organometallic platinum complexes. Are they excited states of dimers that pre-exist in the ground-state, or excimers (bi-molecular emissive species not having a bi-molecular ground-state)? Based on the close similarity of absorption and excitation spectra of neat PtL^{26}Cl films shown in Fig. 4, we believe that the long-wavelength broad EL bands at 620 nm, emanating from PtL^{26}Cl-based devices, have purely excimeric character. An important point to note here is that the QE and purity of white light (CIE coordinates) emanated from Pt complex-based LEDs depend on the substituents at the central ring and lateral rings of the Pt complex. The excel-

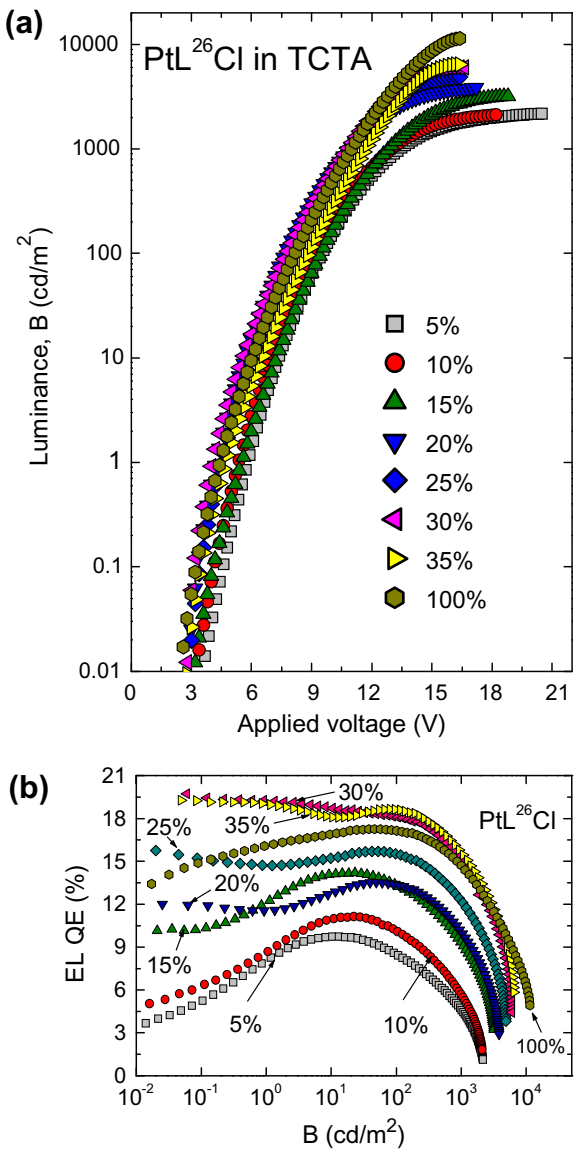

Fig. 3. Luminance (B) vs applied voltage (a) and EL QE vs B (b) at varying PtL^{26}Cl concentration in EML of devices from Fig. 1.

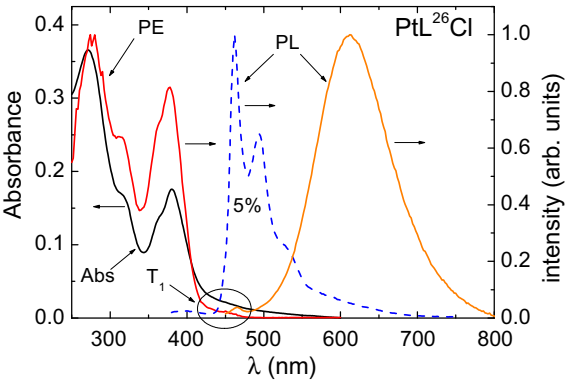

Fig. 4. Absorption (Abs), photoluminescence (PL) at λ_{exc} = 380 nm, and excitation (PE) detected at λ_{det} = 600 nm spectra of a 50 nm-thick film of pure PtL^{26}Cl. The PL spectrum at λ_{exc} = 350 nm of a 30 nm-thick TCTA film containing 5 wt.% of PtL^{26}Cl is reported for comparison (dashed line). The close similarity of Abs and PE spectra indicates the PL spectrum to be underlain by the excimer rather than dimer emission.

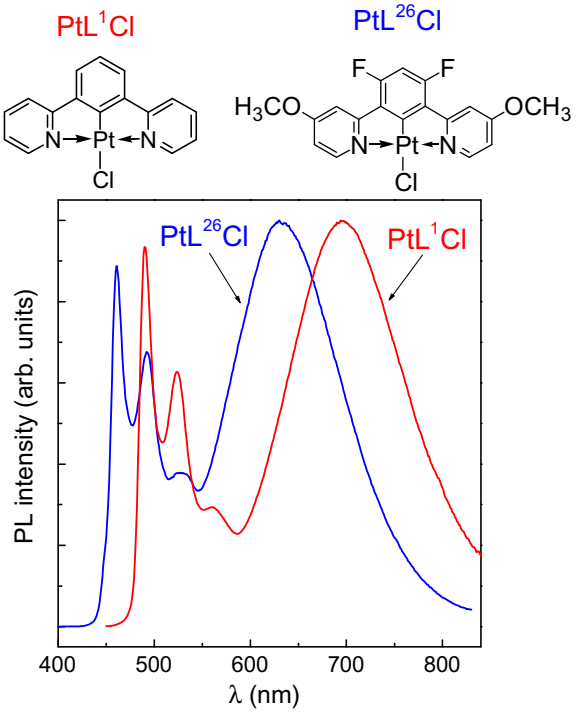

Fig. 5. PL spectra of a substituted (PtL^{26}Cl) and unsubstituted (PtL^{1}Cl) Pt(II) complex in solution (CH_2Cl_2) showing the effect of a blue shift due to the substituents. For explanation see text. (For interpretation of the references in colour in this figure legend, the reader is referred to the web version of this article.)

lent performance of the present complex PtL^{26}Cl-based LEDs (as reported in Section 3.3) is associated with the combination of fluorine atoms in the cyclometallating phenyl ring and methoxy substituents in the pyridyl rings leading to a blue shift in both molecular exciton and excimer emission, as shown in Fig. 5 in comparison with the unsubstituted Pt(II) complex, PtL^{1}Cl. Obviously, these substituents cause a rise in energy of the molecular excited state, which can be understood in terms of the frontier orbitals involved in the excited state, as obtained from recent TD-DFT calculations [25,26]. They show that the HOMO in this series of complexes is largely based on the metal and the cyclometallating ring, whereas the LUMO is essentially localized on the pyridyl rings. Thus, the electron-withdrawing influence of F atoms meta to the C–Pt bond will serve to lower the energy of the HOMO but not the LUMO. Conversely, the electron-donating methoxy groups will have the effect of raising the LUMO energy without significantly destabilizing the HOMO. The net effect is a substantial increase in the HOMO–LUMO gap, and a shift of the excited state to higher energy. The excimer is similarly destabilized and its emission maximum shifted away from the NIR, where energy is wasted in the case of PtL^{1}Cl.

Finally, we note that, in general, the bi-molecular excited triplet state is a result of excitonic and charge-transfer resonances [1]. The relation between their contributions to the function describing the overall excimer state and thus the excimer energy depend on the distance and mutual orientation of interacting molecules. The states with a negative CT-resonance energy component have the lowest energies [1]. The direct electron–hole recombination mechanism of the excimer formation in the EL favors the low-energy CT states to dominate the excimer character, observed as a red shift in the EL spectrum compared with that of PL [24]. This shift is not too big in case of PtL^{26}Cl (cf. Figs. 2 and 4), suggesting the exciton resonance to dominate the excimer structure under both optical and electrical excitation of the emission. On the other hand, the EL–PL maxima red shift of 80 nm has been ascribed to the difference between the spectral locations of the emission peaks originating from dimer and excimer in neat films of Pt(II) (2-(4′,6′-difluorophenyl) pyridinato-*N*,C^2) acetyl acetonate (FPt1) [27]. Since, however, the excitation and absorption spectra of solid FPt1 have not been reported, one cannot firmly distinguish the dimer emission from that of a second excimer or electromer [28]. Moreover, the absence of molecular exciton emission, reported for solid FPt1 [27], does not have to be a rule. Its occurrence may be expected in organic solids with large intermolecular separation distance (ca. 0.4 nm or so) and configurations impeding the formation of a facially oriented molecular pair.

3.3. OLEDs performance

The physical characteristics of PtL^{26}Cl-based LEDs are collected in Table 1 and Figs. 2 and 3. An apparent monotonic trend towards red CIE coordinates is accompanied by increasing external QE, power efficiency (PE), luminous efficiency (LE) and the color rendering index (CRI), following the concentration of the phosphor dopant except for the remarkable decrease in correlated color temperature (CCT). The emission color of all the low PtL^{26}Cl concentration emitter LEDs is blue–green-biased while the neat PtL^{26}Cl film emitter LEDs fall in the red region. The CIE coordinates for the LEDs of intermediate concentrations (10%, 15%, 20%, 25%, 30%) of PtL^{26}Cl in their emitters (0.23, 0.30), (0.28,0.32), (0.34,0.35), (0.39,0.37), (0.42,038), respectively, lie on the line joining blue–green to red in the CIE color diagram (see Fig. 2b), and show how varying the doping provides a simple way of tuning color over a wide range from white to amber-orange. The color of emission from each blend does not change significantly in the brightness range studied of [100–10,000] cd/m^2. The external EL QE ranges between 0.5% and 1.0% at low-current densities ($<10^{-4}$ mA/cm^2) for the lowest phosphor concentration (5%) and as high as 20% at low-current densities for optimized phosphor concentration of 30–35% with the power efficiency (PE) reaching 9.6 lm/W. We note that the external EL QE value of 20% corresponds to 100% (80%) internal EL QE for the commonly assumed light outcoupling factor 0.2 (0.25). The luminous efficiency (LE) falls in the range 10.7–30 cd/A for the 5 and 35 wt.% PtL^{26}Cl-doped emitter LEDs, respectively. The light turn-on voltage (0.01 cd/m^2) for all the devices was ca. 3 V and the operating voltage at 500 cd/m^2 was ca. 10 V (cf. Fig. 3a). Hence, the electrical properties are only slightly sensitive to the EML composition, and good performance is achieved for almost all the devices. The EL QE evolves with luminance showing typical roll-off at high luminance values (Fig. 3b).

The CRI quantifies the eye's ability to distinguish color under illumination by the light source. Thus, the LEDs with a higher phosphor dopant concentration, giving high CRI, can serve as a good starting point for the manufacture of white LEDs. Among a series of the devices characterized in Table 2, the 20%-doped device stands for the highest-purity white light. Its CIE coordinates ($x = 0.34$, $y = 0.35$) are very close to the pure white color defined by ($x = 0.33$, $y = 0.33$), but its CRI = 74, though high enough, is still far from the desired upper limit of 100. The CRI of our LEDs reaches a maximum high value of 81 at the 30 wt.% phosphor content in the emitter. However, this improvement of CRI is achieved at the expense of the white color purity of the device (0.42, 0.38) which, still being considered as white light, is shifted towards the warm incandescent lamp light ($x = 0.41$, $y = 0.41$). In Table 2, characteristics of selected most advanced WOLEDs are presented and compared with the present results. It is seen that the color purity, EL QE and CRI of our present 20%-doped emitter device fall in the two highest-purity white light OLEDs. However, since no data on efficiencies of the exciplex-driven WOLED reported in Ref. [31] are available, the overall performance advantage of one of these two devices cannot be assessed.

It is important from both device engineering and device physics perspectives to understand the mechanism

Table 1
OLED[a] performances[b]. Each device is listed by concentration (x) of the PtL^{26}Cl complex in the emitting layer. At ca. 500 cd/m^2.

PtL^{26}Cl complex x (wt.%)	Bias (V)	j (mA/cm^2)	QE (% ph/e)	PE (lm/W)	LE (cd/A)	CIE (x, y)	CCT (K)	CRI
5%	11.8	4.7	6.1	2.8	10.7	0.18, 0.27	–	–
10%	11.4	3.6	7.6	3.8	13.7	0.23, 0.30	–	–
15%	11.6	2.5	10.9	5.4	20.0	0.28, 0.32	8230	70
20%	9.8	2.5	11.5	6.8	21.3	0.34, 0.35	5190	74
25%	10	2.1	13.6	7.9	25.0	0.39, 0.37	3700	78
30%	9.8	1.7	16.6	9.6	29.5	0.42, 0.38	3100	81
35%	10.8	1.7	17.0	8.7	30.0	0.47, 0.39	2385	80
100%	10	1.8	16.0	8.1	27.7	0.58, 0.41	–	–

[a] OLED configuration: ITO/TPD75 wt.%:PC25 wt.% (50 nm)/TCTA (10 nm)/PtL^{23}Cl [x]:TCTA [100 − x](30 nm)/TAZ (30 nm)/LiF/Al (cf. Fig. 1).
[b] Driving voltage bias (V); current density (j); external quantum efficiency (QE); power efficiency (PE); luminous efficiency (LE); CIE coordinates; correlated color temperature (CCT); color rendering index (CRI).

Table 2
Most advanced performance characteristics of selected WOLEDs.

WOLED structure	φ_{ext} (% ph/e)	η_P (lm/W) (B) (cd/m^2)	CIE[a]	CRI[b]	Comments and references
Fluorescent/phosphorescent	34.0	81.0 (1000)	(0.43, 0.49)	72	Maximum values [23]
	11.0	22.1 (500)	(0.38, 0.41)	85	Values at 1 mA/cm^2 [29]
	18.4	23.8	(0.38, 0.41)	85	Maximum values [29]
Multiple phosphor-doped emitters	5.2	6.4	(0.37, 0.40)	83	Maximum values [13] (B is not specified)
Phosphorescent triple-doped	12.0	26.0 (100)	(0.43, 0.45)	80	Values at 10^{-3} mA/cm^2 (Ref. [30])
Phosphorescent triplet excimers	5.7	5.2 (500)	(0.40, 0.43)	81	Maximum values [15]
	15.5	9.5 (40)	(0.43, 043)	<60	Maximum values [16]
	18.1	11.8 (500)	(0.33, 0.38)	65	Values at ≈2 mA/cm^2 [22]
	11.5	6.8 (500)	(0.34, 0.35)	74	Values at 2.5 mA/cm^2 (this work)
Phosphorescent triplet excimer/exciplex	6.5	9.0 (500)	(0.46, 0.45)	90	Maximum values [17]
Exciplex emission with mixed acceptors	–	– (425)	(0.32, 0.35)	90.4	No data for φ_{ext} and η_P are reported (Ref. [31])
Phosphorescent with no emitter specified	Not reported	102 (1000)	Not specified	70	Not specified [32]

[a] CIE = Commission Internationale de l'Eclairage; ideal white light CIE coordinates are (x = 0.33, y = 0.33) and those for warm incandescent lamp light are (0.41, 041).
[b] CRI = color rendering index; for ideal white light CRI = 100.

Table 3
Photophysical and electrochemical parameters of the PtL^{26}Cl complex in solution, rigid matrices and neat solid film, at 295 K in argon and air atmospheres.

PtL^{26}Cl in	φ_{PL} (%) ± 5%	τ (μs)	E_p^{ox} (V) vs SCE[c]	E_p^{red} (V) vs SCE[c]
DCM solution (monomer)	71	7.8 (0.58)[b]	0.75	<−2.20 (?)
95% PMMA matrix (monomer)	53[a]	3.4 (3.4)[b]	–	–
95% TCTA matrix (monomer)	49[a]	3.4 (3.0)[b] 1.2	–	–
90% TCTA matrix (monomer + excimer)	54[d]	–	–	–
85% TCTA matrix (monomer + excimer)	56[d]	–	–	–
80% TCTA matrix (monomer + excimer)	60[d]	–	–	–
75% TCTA matrix (monomer + excimer)	62[d]	–	–	–
70% TCTA matrix (monomer + excimer)	64[d]	–	–	–
65% TCTA matrix (monomer + excimer)	67[d]	–	–	–
Neat film (excimer)	74[a]	(1.1)[b]	5.43[e]	2.77 (>2.5) (?)[f]

[a] Calculated using integrating sphere and the calculation method described in Ref. [34].
[b] τ For samples aerated.
[c] Electrochemical data in dimethyl sulfoxide (DMSO) solution owing to the low solubility in more usual solvents (DCM or MeCN). Measured using platinum working, reference and counter electrodes, and employing the ferrocene/ferrocenium coupled as an internal reference. Irreversible peak potentials are reported vs Saturated Calomel Electrode (SCE).
[d] Calculated as a sum of the monomer (M) and excimer (EX) quantum efficiencies according to: φ_{PL}(wt.% dopant) = $\varphi_{PL}^{(M)}$(5% dopant) × EL$^{(M)}$/EL$^{(tot)}$ + $\varphi_{PL}^{(EX)}$(100% dopant) × EL$^{(EX)}$/EL$^{(tot)}$. This is an approximation assuming the monomer (blue)-to-excimer (red) contribution ratio in PL to follow that for EL as in Fig. 2. EL intensities were taken suitably from the EL spectra as the blue band, red band and total under-curve areas.
[e] Highest occupied molecular orbital (HOMO) and lowest unoccupied molecular orbital LUMO levels (eV) as calculated from the redox potentials.
[f] Calculated employing the optical gap (E_O) as E(LUMO) = E(HOMO) + E_O = 5.43–2.66 = 2.77 eV. It correctly falls above the value of 2.5 eV – a lower limit predicted from the reduction potential (row 1). Its exact value could not be determined because the reduction wave of the complex is obscured by the solvent. Thus, this value is not certain as indicated by the question mark.

governing the enhancement in WOLEDs efficiency. To understand the general trend of the EL external quantum efficiency (EL EQE) increasing as PtL^{26}Cl concentration increases (see Table 1), we recall that the EL EQE (φ_{EL}) is simply proportional to the recombination probability (P_R) of holes injected from TCTA into the emission layer with electrons injected into it from TAZ (cf. Fig. 1) and to the total emission efficiency (φ_{PL}). Thus, $\varphi_{EL} = \xi P_R \varphi_{PL}$, where ξ is the light output coupling factor. Using the data of Tables 1 and 3, we find $\xi P_R(5\%) = 0.12$ and $\xi P_R(35\%) = 0.25$. From these numbers it is seen that a two fold increase of the product ξP_R when going from a 5% to a 35%-doped blend finds only partial correspondence in the increased PL efficiency, $\varphi_{PL}(35\%)/\varphi_{PL}(5\%) = 1.37$. Furthermore, if we reasonably assume ξ to be only a slightly varying function of the dopant concentration, the difference must be attributed to the concentration increasing recombination probability, P_R. This probability is given by [1]

$$P_R = \frac{1}{1 + (\tau_{rec}/\tau_t)} \quad (1)$$

where τ_{rec} is the recombination and τ_t the faster carrier transit time through the emitter layer, respectively. Assuming reasonably that hole mobility substantially exceeds electron mobility in the blend EMLs, we arrive at

$$\tau_{rec} = \frac{1}{\gamma n_e} \quad \text{and } \tau_t = \frac{d_{em}^2}{\mu_h U} \quad (2)$$

where τ_{rec} is the recombination time of holes captured by PtL^{26}Cl-located electrons with a second order recombination rate constant γ, the latter acting as negative recombination centers PtL^{26}Cl$^-$ of concentration n_e; τ_t is the hole transit time through the EML of thickness d_{em} dependent on its mobility, μ_h, and applied voltage, U. Obviously, increased concentration of the phosphor dopant increases n_e, but reduces μ_h. Consequently, the decreasing τ_{rec}-to-τ_t ratio in (1) leads to increasing P_R and, following it, increase in EL efficiency. For a concentration dopant high enough to make $\tau_{rec}/\tau_t \ll 1$, $P_R \to 1$ that is all injected holes recombine with injected electrons, the EL efficiencies tend to saturation as observed (Table 1).The situation changes with neat PtL^{26}Cl film emitters since electron mobility may be comparable with or even exceed the hole mobility in this molecular solid. Then, P_R may differ from unity by an amount reducing slightly EL efficiency at low and moderate current densities, but its enhancement can be expected at high current densities (high voltages). The latter may be due to the fact that only emissive excimers are generated in neat film EMLs, and these emissive species are subject to weaker quenching as compared with quenching of monomolecular excitons similar to the situation discussed earlier to understand the electric field effect on exciplex luminescence in electron donor–acceptor organic solid films [33]. Indeed, the luminance of neat PtL^{26}Cl film-based devices is greater than that for PtL^{26}Cl blend-based ones at high voltages as shown in Fig. 3a. A detailed investigation of the current density evolution of the EL QE at different concentrations of PtL^{26}Cl dopant is underway and will be reported in a forthcoming paper.

4. Concluding remarks

We have shown that by varying the concentration of a Pt(II) organic complex, PtL^{26}Cl, in blends of (TCTA:PtL^{26}Cl) used as single-dopant EMLs in four-layer LEDs, their performance parameters can be effectively tuned. The good color tuning from bluish-green to reddish-yellow has been attributed to the mixing of the molecular (blue) and excimer (red) phosphorescence, the emission from excited ground-state molecular aggregates shown to be disregarded. Amongst the series of fabricated LEDs, the 20 wt.% PtL^{26}Cl content EML-based device is a high purity white LED with CIE coordinates (0.34, 0.35) and CRI = 74, which render it one of the best achievements reported for WOLEDs. The external EL efficiency has been shown to follow the dopant content, reaching a maximum at concentrations between 30 and 35 wt.%. This correlation is explained in terms of increasing phosphorescence efficiency and electron–hole recombination probability within EMLs due to the dopant-induced increase of the negative PtL^{26}Cl$^-$ recombination centers and a reduction in the hole mobility. The extremely high external EL QE of ca. 20% has then been obtained at low-current densities, which corresponds to an internal EL QE of almost 100%. The composition of monomer and excimer emissions has shown an interesting impact on the overall emission output: the luminance of the neat PtL^{26}Cl film EML-based LED exceeds those for blend EML-based devices, the effect being attributed to the different sensitivity of monomer excitons and excimers to quenching processes operating effectively at large driving current densities.

Acknowledgements

This work was partly supported by the CNR project PM.P04.010 MACOL, the FIRB Projects LUCI and NODIS, and partly by the University of Durham (doctoral fellowship to LM) and E.U. COST-D35.

References

[1] J. Kalinowski, Organic Light Emitting Diodes: Principles, Characteristics, and Processes, Marcel Dekker, New York, 2005.
[2] T. Wakimoto, in: Z.H. Kafafi (Ed.), Organic Electroluminescence, CRC Taylor and Francis, Boca Raton, 2005 (Chapter 9).
[3] T. Jüstel, H. Nikol, C. Ronda, Angew. Chem. Int. Ed. 37 (1998) 3084.
[4] B.W. D'Andrade, S.R. Forrest, Adv. Mater. 16 (2004) 1585.
[5] A.R. Duggal, in: Z.H. Kafafi (Ed.), Organic Electroluminescence, CRC Taylor and Francis, Boca Raton, 2005 (Chapter 10).
[6] B.W. D'Andrade, Nature Photon. 1 (2007) 33.
[7] C. Hosokawa, E. Eida, M. Matsuura, F. Fukuoka, H. Nakamura, T. Kusumoto, SID 97 Dig. 1037 (1997).
[8] S. Miyaguchi, S. Ishizuka, T. Wakimoto, J. Funaki, Y. Fukuda, H. Kubota, K. Yoshida, T. Watanabe, H. Ochi, T. Sakamoto, M. Tsuchida, I. Ohshita, T. Thoma, J. SID 7 (1999) 221.
[9] P.E. Burrows, V. Khalfin, G. Gu, S.R. Forrest, Appl. Phys. Lett. 73 (1998) 435.
[10] J. Kido, K. Hongawa, K. Okuyama, K. Nagai, Appl. Phys. Lett. 64 (1994) 815.
[11] T. Shimoda, S. Kanbe, H. Kobayashi, S. Seki, H. Kiguchi, I. Yudasaka, M. Kimura, S. Miyashita, R.H. Friend, J.H. Burroughes, C.R. Towns, SID 99 Dig. 376 (1999) (May).
[12] J. Kido, M. Kiura, K. Nagai, Science 267 (1995) 1332.
[13] B.W. D'Andrade, M.E. Thompson, S.R. Forrest, Adv. Mater. 14 (2002) 147.
[14] V. Adamovich, J. Brooks, A. Tamayo, A.M. Alexander, P.I. Djurovich, B.W. D'Andrade, C. Adachi, S.R. Forrest, M.E. Thompson, New J. Chem. 26 (2002) 1171.
[15] E.L. Williams, K. Haavisto, J. Li, G.E. Jabbour, Adv. Mater. 19 (2007) 197.
[16] M. Cocchi, J. Kalinowski, D. Virgili, V. Fatori, S. Develay, J.A.G. Williams, Appl. Phys. Lett. 90 (2007) 163508.
[17] J. Kalinowski, M. Cocchi, D. Virgili, V. Fattori, J.A.G. Williams, Adv. Mater. 19 (2007) 4000.
[18] J.A.G. Williams, S. Develay, D.L. Rochester, L. Murphy, Coord. Chem. Rev. 252 (2008) 2596.
[19] V. Fattori, J.A.G. Williams, L. Murphy, M. Cocchi, J. Kalinowski, Photon. Nanostruct. Fundam. Appl. 90 (6) (2008) 225.
[20] X. Yang, Z. Wang, S. Madakuni, J. Li, G.E. Jabbour, Adv. Mater. 20 (2008) 2405.
[21] M. Cocchi, D. Virgili, V. Fattori, D.L. Rochester, J.A.G. Williams, Adv. Funct. Mater. 17 (2007) 285.
[22] M. Cocchi, J. Kalinowski, V. Fattori, J.A.G. Williams, L. Murphy, Appl. Phys. Lett. 94 (2009) 073309.
[23] S. Reineke, F. Lindner, G. Schwartz, N. Seidler, K. Walzer, B. Lüssem, K. Leo, Nature 459 (2009) 234.
[24] M. Cocchi, D. Virgili, V. Fattori, J.A.G. Williams, J. Kalinowski, Appl. Phys. Lett. 90 (2007) 023506.
[25] W. Sotoyama, T. Satoh, H. Sato, A. Matsuura, N. Sawatari, J. Phys. Chem. A 109 (2005) 9760.
[26] D.L. Rochester, S. Develay, S. Zalis, J.A.G. Williams, Dalton Trans. (2009) 1728.

[27] B. D'Andrade, S.R. Forrest, Chem. Phys. 286 (2003) 321.
[28] J. Kalinowski, J. Non-Cryst. Solids 354 (2008) 4170.
[29] Y. Sun, N.C. Giebink, H. Kanno, B. Ma, M.E. Thompson, S.R. Forrest, Nature 440 (2006) 908.
[30] B.W. D'Andrade, R.J. Holmes, S.R. Forrest, Adv. Mater. 16 (2004) 624.
[31] D. Wang, W. Lu, Z.S. Su, T.L. Li, B. Chu, D.F. Bi, L.L. Chen, W.M. Su, H. He, Appl. Phys. Lett. 89 (2006) 233511.
[32] Universal Display Corporation, Press Releases, 2008, <http://www.universaldisplay.com/downloads/Press%20Releases/2008/PANL_whitemilestone_FINAL.pdf>.
[33] J. Kalinowski, M. Cocchi, D. Virgili, V. Fattori, J.A.G. Williams, Chem. Phys. Lett. 432 (2006) 110.
[34] J.C. de Mello, H.F. Wittmann, R.H. Friend, Adv. Mater. 9 (1997) 230.

Organic Electronics 11 (2010) 397–406

Contents lists available at ScienceDirect

Organic Electronics

journal homepage: www.elsevier.com/locate/orgel

Utilizing surface plasmon polariton mediated energy transfer for tunable double-emitting organic light-emitting devices

Kun-Cheng Tien, Ming-Shiang Lin, You-Heng Lin, Chih-Hung Tsai, Ming-Hung Shiu, Ming-Chi Wei, Hsing-Chieh Cheng, Chun-Liang Lin, Hao-Wu Lin, Chung-Chih Wu *

Department of Electrical Engineering, Graduate Institute of Photonics and Optoelectronics, and Graduate Institute of Electronics Engineering, National Taiwan University, Taipei 10617, Taiwan, ROC

ARTICLE INFO

Article history:
Received 3 October 2009
Received in revised form 24 October 2009
Accepted 14 November 2009
Available online 20 November 2009

Keywords:
OLEDs
Surface plasmon polaritons
Double emission

ABSTRACT

In typical organic light-emitting devices (OLEDs), a significant portion of internally generated radiation is trapped into the surface plasmon polariton (SPP) modes, in general not accessible for external use. By thinning the metal electrode, the SPP modes can be coupled to the outside surface of the device. As such, one can recycle a portion of SPPs by capping the thinned metal electrode with an appropriate absorbing/re-emission medium, inducing SPP-mediated energy transfer and re-emission. Such an approach may be used for implementing double-emitting OLEDs with different emission colors on two sides and with a broad color tuning capability.

© 2009 Elsevier B.V. All rights reserved.

1. Introduction

Surface plasmon polaritons (SPPs) are guided electromagnetic waves propagating at the interface between a dielectric and a conductor, which arise via the coupling of the electromagnetic fields to oscillations of the conductor's electron plasma and are evanescently confined near the interface [1–8]. In typical organic light-emitting devices (OLEDs), emitters are located close enough to the metal electrode, and thus a large portion of internally generated radiation is trapped into SPP modes (20–40%, depending on the device structure) and is not available for external use [9,10]. Thus an effective approach/structure that is able to access/recycle SPP modes for external use and compatible with typical OLED fabrication is certainly desired.

In a conventional OLED with a thick top metal electrode, the SPP modes are mainly distributed from the bottom surface of the metal layer downward into the organic layer, therefore making it difficult to access/manipulate the SPP modes from the outside of the device. Some periodically corrugated structures were proposed previously to out-couple SPPs [11]; yet they in general are less compatible with typical OLED fabrication and also result in strong wavelength and angular dependence in emission characteristics. In extensive studies of SPP optics in recent years, it has been shown that by thinning the thickness of a metal layer, the originally independent SPPs on two sides of a metal layer could interact with each other, resulting in coupled SPPs that have modal field distributions spanning on two sides of the metal layer [5,6]. As such, by making OLEDs with thinner metal electrodes, SPPs of the devices could exhibit a significant field distribution outside the devices, giving a possibility to access/manipulate SPPs from outside of the device for external emission. In this work, we adopt such a principle to manipulate SPPs of OLEDs for external use. We performed electromagnetic simulation/analysis of the SPPs of OLEDs with thin metal electrodes and investigated double-emitting OLEDs with a wide range of color tunability.

2. Experimental

2.1. OLED device structures investigated

Two types of OLED devices were studied in this work (Fig. 1): one based on green-emitting OLEDs (Types-IA

* Corresponding author. Tel.: +886 2 33663636; fax: +886 2 23689178.
E-mail address: chungwu@cc.ee.ntu.edu.tw (C.-C. Wu).

1566-1199/$ - see front matter © 2009 Elsevier B.V. All rights reserved.
doi:10.1016/j.orgel.2009.11.018

and IB) and one based on blue-emitting devices (Type-II). The Type-I OLED device structures (Fig. 1) studied in this work were: glass substrate/ITO (120 nm)/m-MTDATA (30 nm)/α-NPD (20 nm)/Alq_3:C545T (1 wt.%, 20 nm)/Alq_3 (35 nm)/LiF (0.5 nm)/Al (1 nm)/Ag (*X* nm)/Alq_3 (80 nm, for Type-IA devices with non-doped capping) or Alq_3:DCJTB (1 wt.%, 80 nm, for Type-IB devices with doped capping). Indium–tin–oxide (ITO) was used as the bottom anode, 4,4′,4″-tris(3-methylphenylphenylamino)triphenylamine (m-MTDATA) as the hole-injection layer [12], α-naphthylphenylbiphenyl diamine (α-NPD) as the hole-transport layer [13], tris-(8-hydroxyquinoline) aluminum (Alq_3) doped with the fluorescent dye C545T [(10-(2-benzothiazolyl)-1,1,7,7-tetramethyl-2,3,6,7-tetrahydro-1H,5H,11H (1) benzopyrano (6,7,8-ij) quinolizin-11-one)] as the emitting layer [14,15], undoped Alq_3 as the electron-transport layer, thin LiF/Al as the electron injection layer [12], Ag as the top cathode, and non-doped or doped Alq_3 as the capping layer. The thickness of Ag cathode (*X* = 20, 30, 40, 50, 120 nm) was varied to investigate the SPP properties. The Alq_3 was used as the capping so that the dielectrics on both sides of the metal layer would have same/similar refractive indices to ensure effective generation of coupled SPP modes [4,5]. The 1 wt.% DCJTB [4-(Dicyanomethylene)-2-tert-butyl-6-(1,1,7,7-tetramethyljulolidin-4-yl-vinyl)-4H-pyran] doped in the Alq_3 capping is used to absorb the SPPs propagating in the capping layer for re-emission (i.e. recycling SPPs), thus inducing the donor–acceptor (C545T–DCJTB) energy transfer mediated by coupled SPPs across the metal layer [4]. The thickness of the electron-transport layer (undoped Alq_3) was adjusted in a way to increase fraction of internally generated radiation coupled into SPP modes and to make the SPP effects more easily observable [8,14].

The Type-II OLED device structure (Fig. 1) studied in this work was: glass substrate/ITO (120 nm)/m-MTDATA (30 nm)/α-NPD (20 nm)/ADN:perylene (1 wt.%, 20 nm)/Alq_3 (35 nm)/LiF (0.5 nm)/Al (1 nm)/Ag (*X* nm)/Alq_3:rubrene (1 wt.%, 80 nm), where the thickness of the Ag cathode was varied (*X* = 15, 20, 25, 30, 40, and 50 nm). The Type-II device structure is similar to that of Type-I, except that the emitting layer is replaced by blue-emitting ADN:perylene [where ADN is 9,10-di-(2-naphthyl) anthracene] and that the capping is replaced by Alq_3:rubrene. Therefore, the donor–acceptor system in the SPP-mediated energy transfer is switched from (C545T, DCJTB) to (perylene, rubrene).

2.2. Electromagnetic simulation of OLEDs

The optical model used for performing the analysis adopts a rigorous and classical electromagnetic model based on the equivalence between the emission of a photon due to an electrical dipole transition and the radiation from a classical electrical dipole antenna, which can take into account losses due to absorption and electromagnetic interaction with metals (e.g. SPPs) [14–20]. With plane-wave expansion of the dipole field, the full-vectorial electromagnetic fields generated by a radiation dipole embedded in a layered structure is calculated, from which the distribution of the radiation power into different plane-wave modes and the far-field radiation related to emission characteristics of an OLED are obtained [14–20]. In the plane-wave expansion, each plane-wave mode can be characterized by an in-plane wave vector k_t, where k_t is the component of the wave vector parallel to the layer surface. To model emission characteristics of a real OLED, one treats the emitting layer as an ensemble of mutually incoherent dipole radiators with distributions in dipole orientations (a random isotropic distribution in the present study), locations (assuming a decaying exponential distribution from the hole-transport layer/emitting layer interface into the emitting layer with an exciton diffusion length of 10 nm in the present study [21]), and frequencies (using the photoluminescence (PL) spectrum of the emitting layer as the intrinsic spectral distribution of the dipole radiators). It has been shown that the quantum efficiency of the emitter might influence the simulation results and the power dissipation into different modes [22]. The optical model adopted here indeed has included the influences of the optical structures on the quantum yields of the emitters and the internal quantum efficiencies of OLEDs. Yet, since the donor (C545T) used in this work has very high fluorescent quantum yield (0.95 in solution) [23], an emitter quantum efficiency of 100% is assumed for simplicity of the simulation. The total emission intensity *I* from the OLED as a function of the wavelength λ and the viewing angle θ (i.e. $I(\theta, \lambda)$, with θ measured relative to the surface normal) is then obtained by averaging contributions over these distributions.

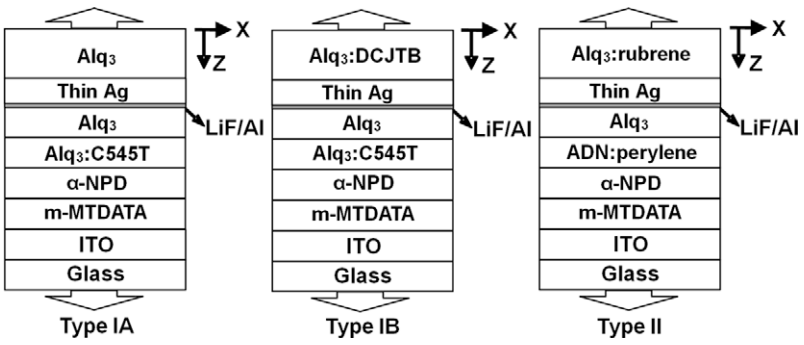

Fig. 1. Schematic device structures under investigation.

2.3. OLED fabrication and characterization

OLEDs were fabricated on the ITO-coated glass substrates with multiple organic layers sandwiched between the transparent bottom indium–tin–oxide (ITO) anode and the top metal cathode. The organic and metal layers were deposited by thermal evaporation in a vacuum chamber with a base pressure of $< 10^{-6}$ torr. The deposition rate of organic layers was kept at ~0.2 nm/s. The deposition system permitted the fabrication of the complete device structure in a single pump-down without breaking vacuum. The active area of the device was 1×1 mm^2.

Current–voltage–luminance (I–V–L) characterization of the devices was measured using an Agilent 4155B semiconductor parameter analyzer and a Si photodiode calibrated with Photo Research PR650. EL spectra of devices were collected by a calibrated CCD spectrograph. The total external quantum efficiencies of devices were determined from the measured angular dependence of emission intensity and spectra.

3. Results and discussion

3.1. Electromagnetic simulation of SPP modes in OLEDs

In the following, we use simulation results of Type-I devices (C545T-based devices) to illustrate characteristics of the SPP modes. Fig. 2a shows the calculated mode distributions (fraction of radiation coupled into different modes) of internally generated radiation (at 525 nm) as a function of k_t/k_0 (k_t is the in-plane component of the wavevector and

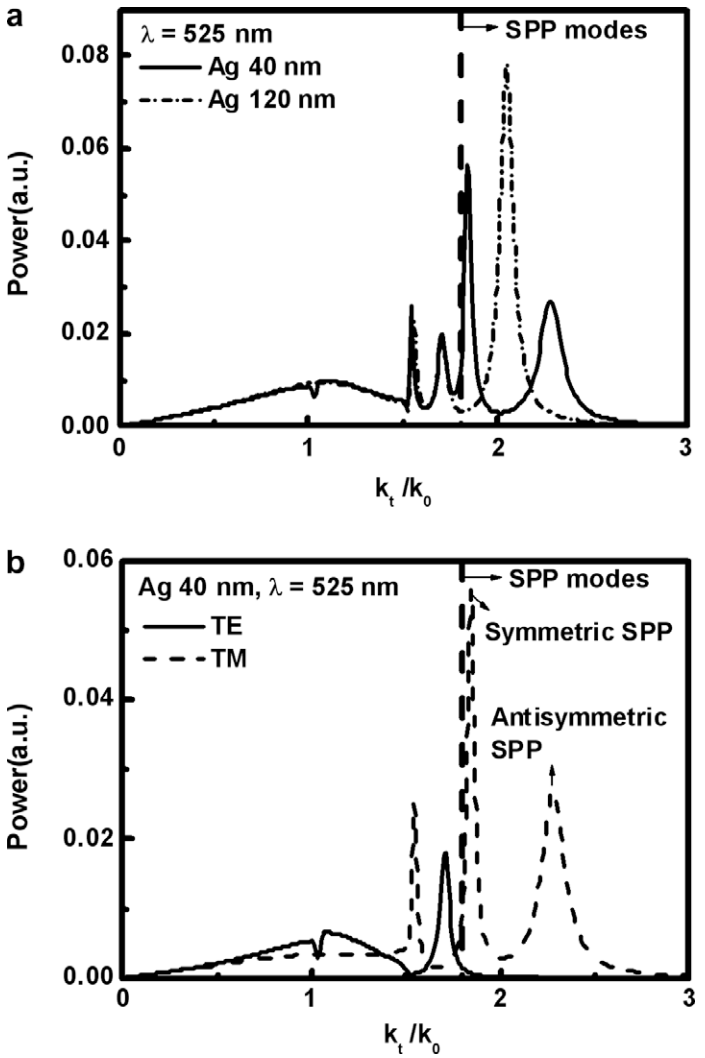

Fig. 2. (a) Calculated mode distributions (power dissipation) of internally generated radiation ($\lambda = 520$ nm) as a function of the normalized in-plane wavevector k_t/k_0 for a conventional OLED with thick Ag cathode (120 nm) and for a Type-I double-emitting OLED with thin Ag cathode (40 nm). (b) Calculated mode distributions (power dissipation) for the same Type-I double-emitting OLED with thin Ag cathode (40 nm), with TE and TM modes separated.

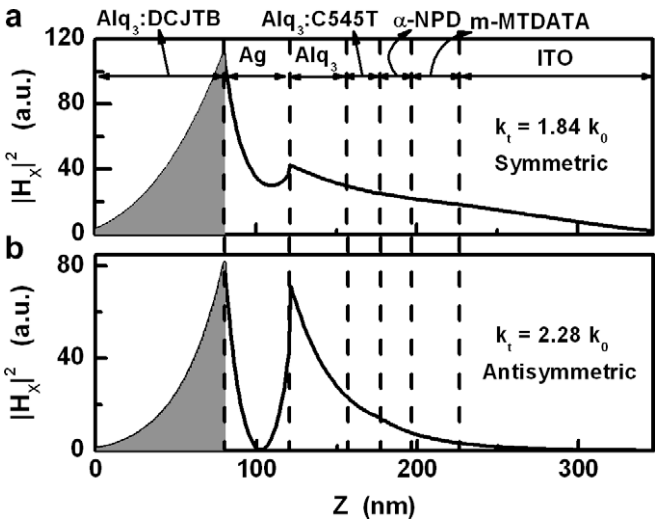

Fig. 3. The distributions of the field intensity for the (a) symmetric and (b) antisymmetric SPP modes of the Type-I double-emitting OLED with thin Ag cathode (40 nm), at the wavelength of 525 nm, and along the z-axis. The transverse magnetic field H_x is shown, since SPP modes are of TM nature.

k_0 is the free-space wavevector) from a conventional OLED with thick Ag cathode (i.e. 120 nm Ag) and from an OLED with thin Ag cathode (40 nm). With the confining nature of the SPPs, modes with $k_t/k_0 > 1.75$ (where $n \sim 1.75$ is the refractive index of the bounding medium of Alq_3 at 525 nm) are associated with the SPP modes [3,5]. The conventional OLED with the thick Ag cathode (120 nm) has only one major SPP mode peaking at $k_t = 2.05\ k_0$, which is the typical SPP having only one-side distribution (i.e. from the Ag/Alq_3 interface downward into the Alq_3). The OLED with thin Ag (40 nm), on the other hand, has two major SPP modes peaking at $k_t = 1.84\ k_0$, and $k_t = 2.28\ k_0$. These two modes, one with k_t lower than $2.05\ k_0$ and one with k_t higher than $2.05\ k_0$ indeed are the coupled SPP modes resulted from interaction and splitting of two one-side SPP modes (i.e. one above and one below the metal cathode) [4]. Further analyses on polarization properties (Fig. 2b) reveal that these coupled SPP modes associated with thin Ag are mainly of TM (transverse magnetic mode) nature, similar to conventional one-side SPP modes associated with the thick metal layer. The distributions of the field intensity for these two modes (transverse magnetic field H_x, since they are of TM nature) along the z-axis (from the Alq_3/air interface downward as shown in Fig. 1) are shown in Fig. 3a and b. From Fig. 3, it is seen that the mode at $k_t = 1.84\ k_0$ is of symmetric nature and the mode at $k_t = 2.28\ k_0$ is of antisymmetric nature (i.e. with a node located within the thin metal layer). Both modes span from the inside to the outside of the thin Ag cathode and exhibit significant distributions in the capping layer.

In Table 1, the peak k_t/k_0 values for symmetric SPP modes and antisymmetric SPP modes associated with different Ag thicknesses are listed. The peak k_t/k_0 values for these two types of SPP modes are splitted farther away from each other when the Ag thickness is reduced (that is, the coupling/interaction between SPPs on two sides of the metal layer increases).

Table 1
SPP characteristics of Type-I devices versus Ag thickness.

Ag (nm)	Symmetric SPP(k_t/k_0)	Antisymmetric SPP (k_t/k_0)	ET_{d-a} (%)
20	1.75	2.94	5.29
30	1.79	2.49	6.77
40	1.84	2.28	6.43
50	1.89	2.17	4.92

3.2. Color-tunable double-emitting devices: Type I

Since these symmetric or antisymmetric modes propagate horizontally and have rather long propagation lengths (of micrometer scale), in Type-IB devices, by doping into the capping layer a small amount of DCJTB dyes (e.g. 1 wt.%) whose absorption matches C545T emission, the SPPs in the capping can be effectively absorbed and then be re-emitted, thus recycling a portion of SPPs for external emission. In each of Fig. 4a–d, the (0°) EL spectra with relative intensities measured from the top side of the Type-IA device (with non-doped capping) and the Type-IB device (with doped capping) are compared for each of the Ag cathode thickness (20, 30, 40, 50 nm), respectively. Without DCJTB dopants in the capping, pure C545T emission is observed, while with DCJTB dopants in the capping, the emission combines both DCJTB and C545T emission. The observed DCJTB emission from the top side of Type-IB devices cannot not be completely due to re-absorption/re-emission of the directly out-coupled top (donor) emission, since for each Type-IB device C545T emission from the top side only drops slightly compared to those of Type-IA devices. Instead, the significant DCJTB emission from the top side is mainly due to recycled SPPs, which in some sense can be regarded as the SPP-mediated energy transfer from the C545T donor to the DCJTB acceptor and is a rather long-range energy-transfer process. Fig. 4e shows the (0°)

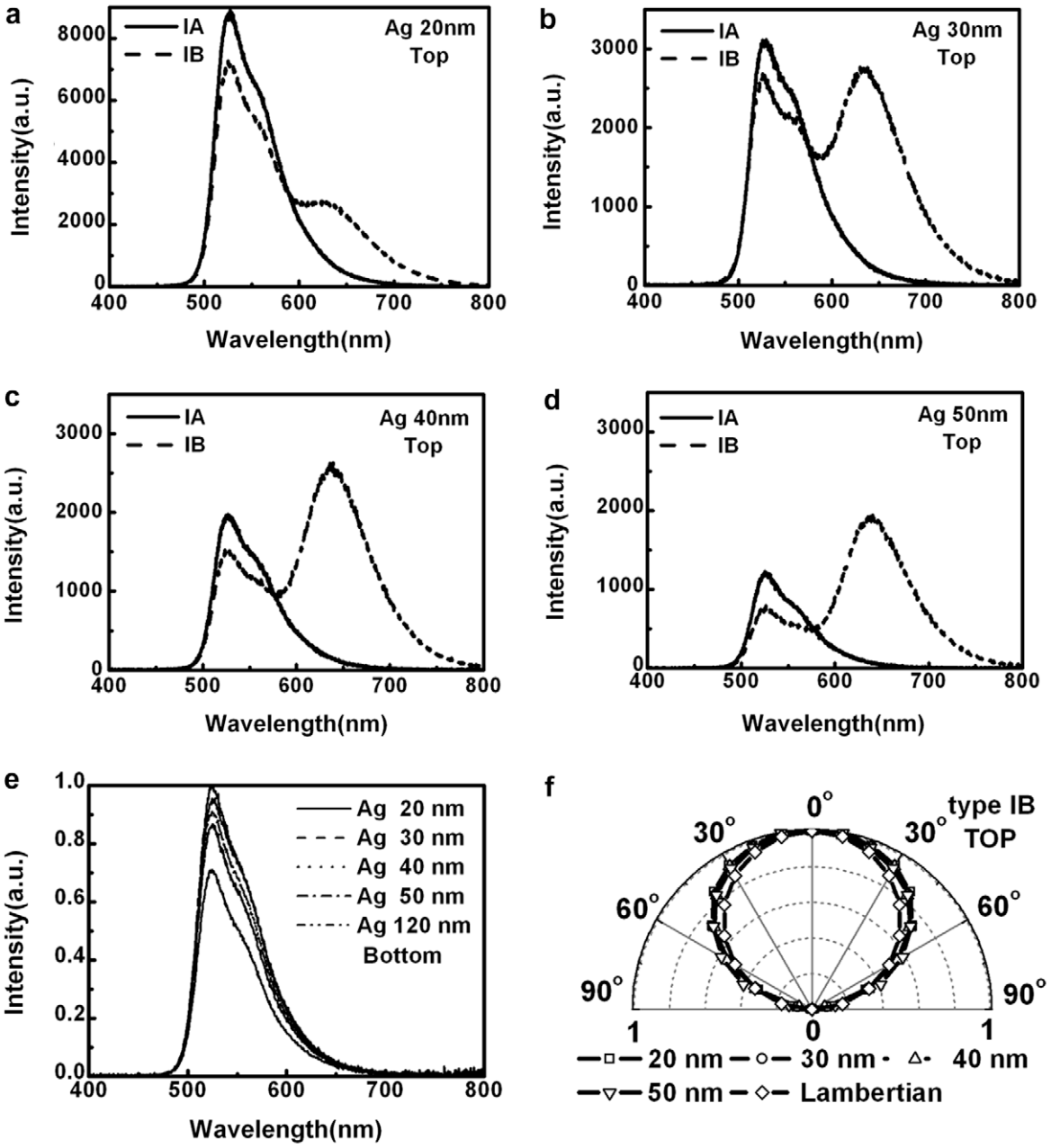

Fig. 4. The (0°) EL spectra with relative intensities measured from the top side of the Type-IA device (with non-doped capping) and the Type-IB device (with doped capping) are compared for each of the Ag cathode thickness: (a) 20, (b) 30, (c) 40, (d) 50 nm. (e) (0°) EL spectra with relative intensities for bottom emission of Type-IB devices with different Ag cathode thicknesses (20, 30, 40, 50 nm), compared to that of the conventional bottom-emitting device (Ag = 120 nm). (f) Polar plots of the top-emission intensity for Type-IB devices with different Ag cathode thicknesses (20, 30, 40, 50 nm), compared to the Lambertian pattern. For (a)–(f), measurements were performed at a current density of 100 mA/cm^2.

EL spectra with relative intensities for bottom emission of Type-IB devices (with doped capping) with different Ag cathode thicknesses (20, 30, 40, 50, 120 nm). The EL spectra are basically the same as those of Type-IA devices and are not dependent on the Ag thickness. Yet in general, the intensity of bottom emission (for both Types-IA and IB) drops gradually with reducing the Ag thickness, mainly due to lowered reflection of the Ag cathode. Fig. 4f shows the polar plots of the top-emission intensity for Type-IB devices (similar for Type-IA devices, data not shown), which are all nearly Lambertian regardless of the Ag thickness (since there is no strong microcavity structure in these devices).

In Type-IB devices, as the Ag thickness increases, the directly out-coupled top radiation (C545T emission) decays rapidly due to reduced transmission of the semi-transpar-

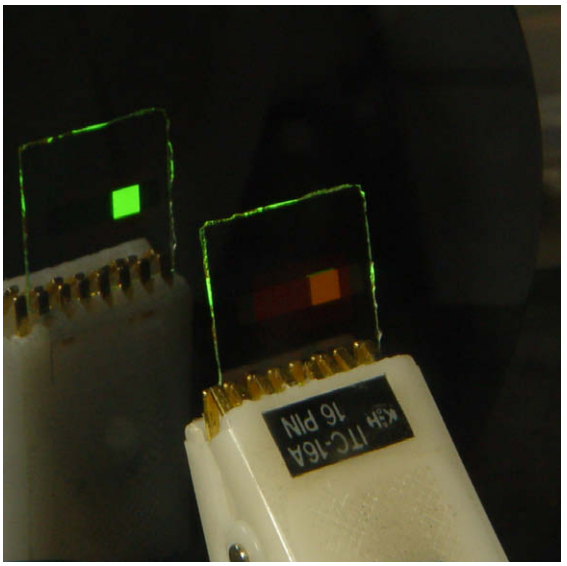

Fig. 5. Photo of a Type-IB double-emitting device with the Ag thickness of 40 nm (i.e. the device shown in Fig. 4c), where green emission is observed from the bottom side (the reflected image appearing in the reflecting mirror) and orange-like emission is observed from the top side. (For interpretation of the references in colour in this figure legend, the reader is referred to the web version of this article.)

ent cathode. Yet, interestingly the intensity of the SPP-recycled top emission (DCJTB emission) stays rather constant versus the Ag cathode thickness (which will be explained later in this section). As such, for the top emission, the ratio of the DCJTB emission relative to the directly out-coupled C545T emission rises when the Ag thickness increases, providing a capability of color tuning. Due to the capability to tune emission colors with the metal thickness, the SPP-mediated energy transfer can be used for implementing double-emitting OLEDs with different emission colors on two sides or with color tuning capability. For instance, Fig. 5 shows a photo of a Type-IB double-emitting device with the Ag thickness of 40 nm (i.e. the device shown in Fig. 4c), where green emission is observed from the bottom side (the reflected image appearing in the reflecting mirror) and orange-like emission is observed from the top side.

Fig. 6a and b shows the external quantum efficiencies for bottom emission and top emission of Type-IA devices (with non-doped capping), respectively. Fig. 6c and d shows the external quantum efficiencies for bottom emission and top emission of Type-IB devices (with doped capping), respectively. Magnitudes and trends of efficiencies (versus Ag thickness) for bottom emission of both Type-IA/Type-IB devices are basically same; yet they differ for top emission of Types-IA and IB devices. The top-emission quantum efficiency of Type-IA devices drops rapidly with increasing the Ag thickness, but the efficiency drop is more gradual for Type-IB devices. In Table 2, measured the quantum efficiencies of the bottom emission, the top emission, and the total emission (including both top and bottom emission) for both Type-IA/Type-IB devices are listed and are compared to those of the conventional bottom-emitting device (with Ag = 120 nm). All these efficiencies are also plotted in Fig. 7 as a function of the Ag thickness for comparison. For Type-IA devices (with non-doped capping), the total efficiency drops monotonically in reducing the Ag thickness. Yet for Type-IB devices (doped capping) enhanced total efficiency is observed for Ag = 50 and 40 nm, although the enhancement by up to 3% is modest. It however should be noticed that the present devices have not gone through thorough optimization yet. For instance, with changing the top mirror structure/property of the devices, the organic layer structures in the device should be modified accordingly for maximizing optical output. Preliminary analyses show that further enhancement should be achievable.

In Fig. 7, the measured quantum efficiencies are also compared with the calculated out-coupling efficiencies for top emission ($\eta_{device,top}$), bottom emission ($\eta_{device,bot}$) and total emission ($\eta_{device} = \eta_{device,top} + \eta_{device,bot}$). $\eta_{device,top}$ is calculated by $\eta_{device,top} = \eta_{d\text{-}out,top} + ET_{d-a} \times QY_a \times \eta_{a\text{-}out,top} + A_{d-a,direct} \times QY_a \times \eta'_{a\text{-}out,top}$. $\eta_{d\text{-}out,top}$ is the direct out-coupling efficiency for donor (C545T) top emission. By taking into consideration of the complex optical index (i.e. both n and k) of the DCJTB-doped Alq_3 capping, the $\eta_{d\text{-}out,top}$ for Type-IB devices would suffer ~10% decrease compared with $\eta_{d\text{-}out,top}$ for Type-IA devices due to direct absorption by acceptors, which is consistent with the experiment results shown in Fig. 4a–d). ET_{d-a} is the efficiency of the donor (C545T)-to-acceptor (DCJTB) energy transfer mediated by coupled SPPs for Type-IB devices (for instance, ~6.43% for the OLED with Ag = 40 nm, Table 1). QY_a is the emission quantum yield of the acceptor (1 wt.% DCJTB doped in the Alq_3 capping, ~70%). $\eta_{a\text{-}out,top}$ is the out-coupling efficiency for acceptor top emission (through SPP-mediated energy transfer). $A_{d-a,direct}$ is the efficiency of the donor (C545T)-to-acceptor (DCJTB) energy transfer through direct absorption for Type-IB devices ($\sim 0.1 \times \eta_{d\text{-}out,top}$). $\eta'_{a\text{-}out,top}$ is the out-coupling efficiency for acceptor top emission (through direct acceptor absorption). Since $\eta_{d\text{-}out,top}$ is much larger than $A_{d-a,direct} \times QY_a \times \eta'_{a\text{-}out,top}$, indeed it results in $\eta_{device,top} = \eta_{d\text{-}out,top} + ET_{d-a} \times QY_a \times \eta_{a\text{-}out,top} + A_{d-a,direct} \times QY_a \times \eta'_{a\text{-}out,top} \approx \eta_{d\text{-}out,top} + ET_{d-a} \times QY_a \times \eta_{a\text{-}out,top}$. In calculating ET_{d-a}, the emission properties of the donor emitter, the SPP modal field distribution, the propagation properties of the SPP modes, and the complex dielectric constants of related media are used. The calculated ET_{d-a} values (for C545T donor and DCJTB acceptor) for different Ag thicknesses are listed in Table 1, which are basically consistent with the variation of the DCJTB top-emission intensity versus Ag thickness shown in Fig. 4a to d. The ET_{d-a} values do not vary significantly versus the Ag thickness (20–40 nm) till the Ag thickness increases to 50 nm. Meanwhile, the transmission of thin Ag drops significantly when its thickness increases from 20 to 50 nm. These explain why the intensity of the SPP-recycled top emission (DCJTB emission) stays rather constant versus the Ag cathode thickness, in contrast with that of the directly out-coupled C545T top emission. On the other hand, $\eta_{device,bot}$ is calculated by $\eta_{device,bot} = \eta_{d\text{-}out,bot} + ET_{d-a} \times QY_a \times \eta_{a\text{-}out,bot}$, where $\eta_{d\text{-}out,bot}$ is the direct out-coupling efficiency for donor bottom emission, and $\eta_{a\text{-}out,bot}$ is the out-coupling efficiency for acceptor bottom emission. Since $\eta_{d\text{-}out,bot}$ is much larger than $ET_{d-a} \times$

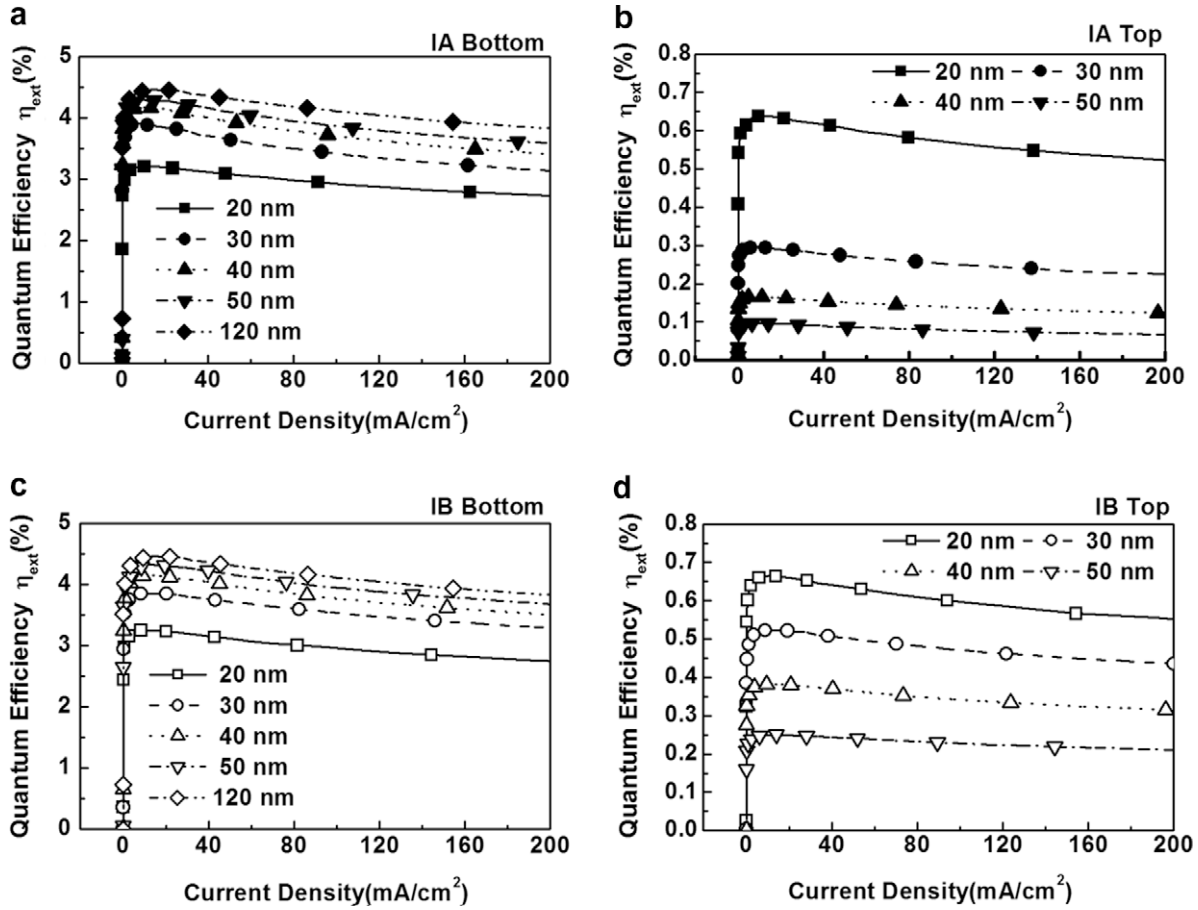

Fig. 6. (a) and (b) show the external quantum efficiencies for bottom emission and top emission of Type-IA devices (with non-doped capping), respectively. (c) and (d) show the external quantum efficiencies for bottom emission and top emission of Type-IB devices (with doped capping), respectively.

Table 2
The measured external quantum efficiencies of various devices. "Enhancement" indicates the ratio of the total efficiency of various devices relative to that of the conventional bottom-emitting device (Ag = 120 nm).

Ag (nm)	IA				IB			
	Bottom (%)	Top (%)	Total (%)	Enhancement	Bottom (%)	Top (%)	Total (%)	Enhancement
20	3.21	0.64	3.85	0.86	3.25	0.68	3.93	0.88
30	3.90	0.3	4.20	0.94	3.85	0.52	4.37	0.98
40	4.17	0.17	4.34	0.97	4.14	0.38	4.53	1.014
50	4.30	0.10	4.40	0.99	4.3	0.3	4.6	1.03
120	4.46	0.0	4.46	1.00	4.46	0.0	4.46	1.00

$QY_a \times \eta_{a\text{-out,bot}}$, ($\eta_{d\text{-out,bot}} \gg ET_{d-a} \times QY_a \times \eta_{a\text{-out,bot}}$), indeed it results in $\eta_{device,bot} = \eta_{d\text{-out,bot}} + ET_{d-a} \times QY_a \times \eta_{a\text{-out,bot}} \approx \eta_{d\text{-out,bot}}$. Thus in bottom emission of all Type-IB devices (Fig. 4e), the DCJTB acceptor emission (recycled SPP emission) is hardly visible. As can be seen in Fig. 7, overall rather good agreement between calculation and experiment results of efficiencies is obtained.

3.3. Color-tunable double-emitting devices: Type II

As has been demonstrated in the previous section, by varying the metal cathode thickness, the SPP-mediated energy transfer (or SPP recycling) can be used for implementing double-emitting OLEDs with different emission colors on two sides or with color tuning capability. As another instance of such implementation, in Type-II devices, by adopting a blue-emitting layer in the device (i.e. using the blue-emitting perylene dopant in ADN) and a yellow dopant (i.e. rubrene that can absorb perylene emission) in the capping, double-emitting devices with blue emission from the bottom side and white emission from the top side were realized.

In Fig. 8, the (0°) EL spectra measured from the top side of Type-II devices with different Ag cathode thick-

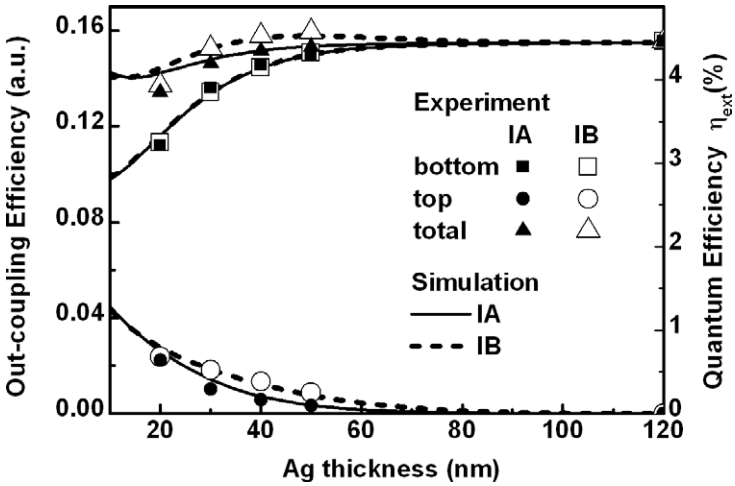

Fig. 7. The measured quantum efficiencies of the bottom emission, the top emission, and the total emission (including both top and bottom emission) as a function of the Ag cathode thickness for both Type-IA/Type-IB devices, compared with the calculated out-coupling efficiencies for top emission, bottom emission and total emission.

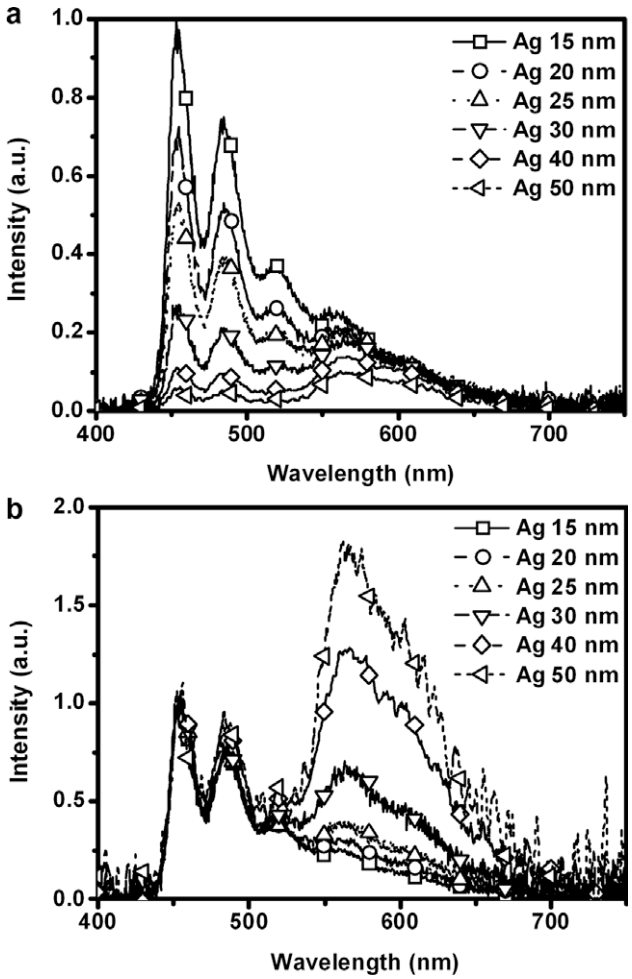

Fig. 8. The (0°) EL spectra measured from the top side of Type-II devices with different Ag cathode thicknesses (X = 15, 20, 25, 30, 40, and 50 nm) at a fixed current density: (a) with relative intensities, and (b) normalized to the blue perylene emission peak.

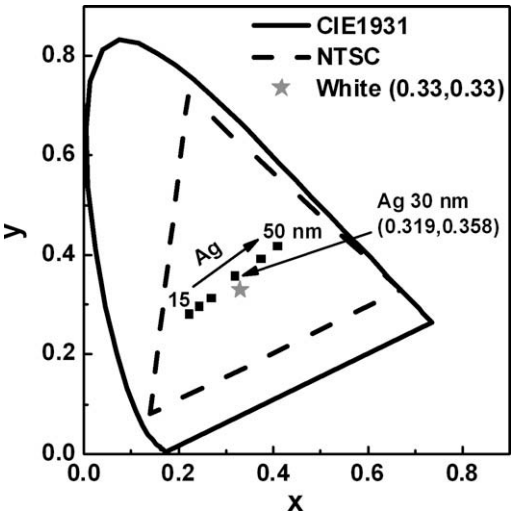

Fig. 9. 1931 CIE coordinates of top-emission EL of Type-II devices with different Ag cathode thicknesses (X = 15, 20, 25, 30, 40, and 50 nm).

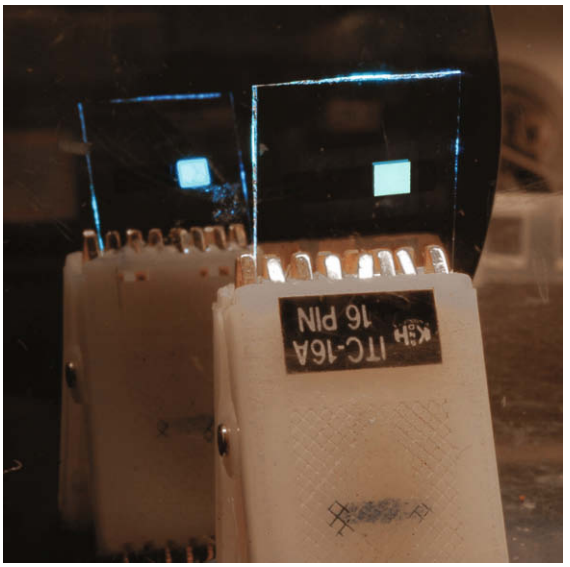

Fig. 10. Photo of the Type-II double-emitting device with the Ag thickness of 30 nm, where blue emission is observed from the bottom side (the reflected image appearing in the reflecting mirror) and white emission is observed from the top side. (For interpretation of the references in colour in this figure legend, the reader is referred to the web version of this article.)

nesses (X = 15, 20, 25, 30, 40, and 50 nm) are shown. Fig. 8a shows the EL spectra with relative intensities at a fixed driving current, while Fig. 8b shows the EL spectra normalized to the perylene emission peak. For the top emission of Type-II devices, the ratio of the yellow rubrene emission relative to the directly out-coupled blue perylene emission rises when the Ag thickness increases, yielding white emission with a wide range of complementary color compositions. Although the total top and bottom emission intensities decrease with increasing the Ag thickness (as in Type-I devices), yet it clear indicates the possibility of color tuning with this approach. Fig. 9 shows the 1931 CIE coordinates of top-emission EL of these Type-II devices, demonstrating that a wide range of white colors (from bluish white to yellowish white) can be tuned simply by adjusting the metal cathode thickness. In particular, the Type-II device with a Ag thickness of 30 nm gives CIE coordinates of $(x, y) = (0.319, 0.358)$, very close to the ideal equal-energy white at $(x, y) = (0.33, 0.33)$. Fig. 10 shows a photo of the Type-II double-emitting device with the Ag thickness of 30 nm, where blue emission is observed from the bottom side (the reflected image appearing in the reflecting mirror) and white emission is observed from the top side. Such a scheme of white emission has a particular advantage that the EL spectra/white color would not change with the driving currents/biases. These double-emitting OLEDs with color tunability may have some interesting applications, such as one single backlight panel for two touch pads requiring different backlight colors.

4. Conclusions

In typical OLEDs, a significant portion of internally generated radiation is trapped into the surface plasmon polariton modes, in general not accessible for external use. By thinning the metal electrode, the SPP modes can be coupled to the outside surface of the device. As such, one can recycle a portion of SPPs by capping the thinned metal electrode with an appropriate absorbing/re-emission medium, inducing SPP-mediated energy transfer and re-emission. Such an approach may be used for implementing double-emitting OLEDs with different emission colors on two sides and with a broad color tuning capability.

Acknowledgements

The authors would like to acknowledge financial support from National Science Council and Ministry of Economic Affairs of Republic of China.

References

[1] D. Sarid, Phys. Rev. Lett. 47 (1981) 1927.
[2] J.J. Burke, G.I. Stegeman, T. Tamir, Phys. Rev. B 33 (1986) 5186.
[3] H. Raether, Surface Plasmons, Springer, Berlin, 1988.
[4] P. Andrew, W.L. Barnes, Science 306 (2004) 1002.
[5] S.A. Maier, Plasmonics: Fundamentals and Applications, Springer-Verlag, 2007.
[6] L.H. Smith, J.A.E. Wasey, W.L. Barnes, Appl. Phys. Lett. 84 (2004) 2986.
[7] G.W. Ford, W.H. Weber, Phys. Rep. 113 (1984) 195.
[8] W.H. Weber, C.F. Eagen, Opt. Lett. 4 (1979) 236.
[9] C.-L. Lin, T.-Y. Cho, C.-H. Chang, C.-C. Wu, Appl. Phys. Lett. 88 (2006) 081114.
[10] T.-Y. Cho, C.-L. Lin, C.-C. Wu, Appl. Phys. Lett. 88 (2006) 111106.
[11] S. Wedge, J.A.E. Wasey, I. Sage, W.L. Barnes, Appl. Phys. Lett. 85 (2004) 182.
[12] Y. Shirota, Y. Kuwabara, H. Inada, T. Wakimoto, H. Nakada, Y. Yonemoto, S. Kawami, K. Imai, Appl. Phys. Lett. 65 (1994) 807.
[13] L.S. Hung, C.W. Tang, M.G. Mason, P. Raychaudhuri, J. Madathil, Appl. Phys. Lett. 78 (2001) 544.
[14] C.-L. Lin, H.-C. Chang, K.-C. Tien, C.-C. Wu, Appl. Phys. Lett. 90 (2007) 071111.

[15] C.-L. Lin, H.-W. Lin, C.-C. Wu, Appl. Phys. Lett. 87 (2005) 1–3.
[16] C.-C. Wu, C.-L. Lin, P.-Y. Hsieh, H.-H. Chiang, Appl. Phys. Lett. 84 (2004) 3966–3968.
[17] K.A. Neyts, J. Opt. Soc. Am. A 15 (1998) 962–971.
[18] W. Lukosz, R.E. Kunz, J. Opt. Soc. Am. 67 (1977) 1607–1615.
[19] J.E. Sipe, Surf. Sci. 105 (1981) 489–504.
[20] J.A.E. Wasey, W.L. Barnes, J. Mod. Opt. 47 (2000) 725–741.
[21] C.W. Tang, S.A. VanSlyke, C.H. Chen, J. Appl. Phys. 65 (1989) 3610.
[22] S. Nowy, B.C. Krummacher, J. Frischeisen, N.A. Reinke, W. Brutting, J. Appl. Phys. 104 (2008) 123109.
[23] K. Okumoto, H. Kanno, Y. Hamaa, H. Takahashi, K. Shibata, Appl. Phys. Lett. 89 (2006) 063504.

Organic Electronics 11 (2010) 407–411

Contents lists available at ScienceDirect

Organic Electronics

journal homepage: www.elsevier.com/locate/orgel

Highly efficient and low-cost top-emitting organic light-emitting diodes for monochromatic microdisplays

Guohua Xie [a], Qin Xue [a], Ping Chen [a], Chen Tao [a], Chunmei Zhao [a], Jianhua Lu [a], Zhaoxin Gong [a], Tianyu Zhang [a], Ran Huang [b], Huan Du [b], Wenfa Xie [a], Jingying Hou [a], Yi Zhao [a,*], Shiyong Liu [a,*]

[a] State Key Laboratory on Integrated Optoelectronics, College of Electronics Science and Engineering, Jilin University, 2699 Qianjin Street, Changchun 130012, People's Republic of China
[b] Institute of Microelectronics, Chinese Academy of Sciences, Beijing 100029, People's Republic of China

ARTICLE INFO

Article history:
Received 30 August 2009
Received in revised form 9 November 2009
Accepted 16 November 2009
Available online 20 November 2009

Keywords:
OLED microdisplay
Low cost
Electrical doping
Trapping

ABSTRACT

An efficient top-emitting organic light-emitting diode (TEOLED) achieving high luminance at very low voltage and enabling the integration of organic light-emitting diodes (OLEDs) with silicon-based driving circuits to realize high resolution and low power consumption OLED microdisplay is introduced. One of the key features is a p doped hole injecting layer (HIL) significantly reducing the driving voltage matching with that of silicon-based driving circuits without a high-voltage option. A well modulated interface is introduced to reduce the quenching of the excitons, and direct charge trapping effect in the emitter layer (EML) also play a role in balancing the charges in EML. We have demonstrated a TEOLED achieving a brightness of about 2500 cd/m^2 at 4 V and a maximum power efficiency of 28.8 lm/W at 1000 cd/m^2, which are ones of the best results of fluorescent emitters reported in literatures. Our OLED microdisplays without a high-voltage CMOS process show potentially low cost for commercial production.

© 2009 Elsevier B.V. All rights reserved.

1. Introduction

OLEDs have attracted intensive attention during the past two decades due to their potential applications in flat panel displays and lighting [1–5]. TEOLEDs have the advantage of easy integration with opaque substrates, such as silicon wafers with active matrix driving circuits [6–10]. TEOLEDs on CMOS substrates, including peripheral row and column driving part as well as pixel, contribute to the emergence of OLED microdisplays which have great promising applications in military and commercial productions. However, it's not easy to drive an OLED emitting enough brightness to the response of human eyes with the conventional logic MOSFET due to the difference of the driving voltage of these two components. One possible approach is to adopt a high-voltage CMOS process which requires additional mask steps to form the drift region to disperse the strong electric field [10]. In this approach, the additional mask steps entail process complexity and high cost [10]. An alternative approach is to reduce the driving voltage of OLEDs to match with that of conventional silicon-based active matrix circuits ($\leqslant$5 V). The introduction of the concept of electrical doping would reduce the driving voltage of OLEDs to be compatible with that of CMOS circuits. Recently, electrical doping [11] technology containing p doping or n doping or p–i–n structure was introduced in OLEDs to achieve low driving voltage and high power efficiency. Note that the devices with state-of-the-art performances were fabricated with p–i–n architectures [2,4,12–19].

In this paper, we report OLED microdisplays by introducing TEOLEDs, on CMOS substrates, with MoO_x ($2 < x < 3$) [20] p doping strategy accompanied with highly efficient fluorescent dye doped emitting layer to achieve

* Corresponding authors. Tel.: +86 431 85168242x8301.
E-mail addresses: zhaoyi2688@163.com (Y. Zhao), syliu@jlu.edu.cn (S. Liu).

1566-1199/$ - see front matter © 2009 Elsevier B.V. All rights reserved.
doi:10.1016/j.orgel.2009.11.019

low voltage and high power efficiency, aiming for low-cost mass production. We investigate the effect of MoO_x p doping. Due to this unique electrical doping strategy, which leads to the formation of charge transfer (CT) complexes and subsequently an increased conductivity in the injecting layer, we meet the requirement of driving an OLED with silicon-based CMOS circuits, which could be readily obtained from a foundry, without a high-voltage option.

2. Experimental

2.1. TEOLEDs fabrication and measurement

TEOLEDs on pristine 1-mm-thick Si substrates covered with 340 nm SiO_2 were fabricated in the same batch. All the materials were used as purchased. The OLED microdisplays shared common cathodes were fabricated in the same run with TEOLEDs except for the anodes. All the devices were transferred to the glove box (MBRAUN) and then encapsulated under a nitrogen atmosphere using slow setting two-part epoxy resin adhesives (Araldite Precision – Syringe Pack) mixed with Syringe A and Syringe B and covered with glass lids. The glue solidification process would take couples of hours. TEOLEDs were kept in the glove box till measured in air after a 24 h break with a PR650 spectrascan spectrometer and a Keithley 2400 programmable voltage–current source. The external quantum efficiency, weighted according to the response of the human eyes, was determined in an integrating sphere (Jm-3200, Jm-smart Technology) calibrated by a halogen lamp (Halostar, OSRAM).

2.2. Morphology characterization

An atomic force microscopy (SII NanoTechnology) and an Olympus BX51M model optical microscope equipped with a CCD camera were used to characterize the morphologies. The heat treatment processes were carried out in a low vacuum oven (DZF-6021, Yiheng Instruments). In the first half an hour, the temperature was maintained at 150 °C, and then cooled down to the ambient temperature for 6 h.

2.3. Chip fabrication

Here, CMOS refers to complementary metal oxide semiconductor, and MOSFET for metal oxide semiconductor field effect transistor. The 320 × 240 pixel silicon driving circuit, containing a novel three-transistor voltage-programmed pixel driver, was implemented using the standard 0.5 μm CMOS process (CSMC, Central Semiconductor Manufacturing Corporation), then a newly developed Ag chemical mechanical polishing (CMP) process. Both the 4 bit D/A converter and the pixel driver were implemented with pMOS devices. The pixel area was 28.4 × 28.4 μm^2 and the display area was 10.7 × 8.0 mm^2 with a diagonal of about 13 mm.

Fig. 1a presents a schematic illustration of our OLED microdisplay and a finished chip is shown in Fig. 1b after tape out in the wafer foundry. After a chemical mechanical polishing (CMP) process (Fig. 1d and e), the large steps at the pixel edges (not shown here) fabricated in the CMOS foundry would be smoothed for OLED fabrication.

3. Results and discussion

For comparison, we fabricated two kinds of TEOLEDs on silicon substrates without circuits and the structures are as follows: Si/SiO_2/Ag (60 nm)/MoO_x (2 nm)/4,4′,4″-tris (N-3-methylphenyl-N-phenyl-amino)triphenylamine (m-MTDATA) (45 nm)/N,N′-bis(naphthalene-1-yl)-N,N′-bis (phenyl)-benzidine (NPB) (5 nm)/tris(8-hydroxy-quinolinato)aluminium (Alq_3): 10-(2-benzothiazolyl)-1,1,7,7-tetramethyl-2,3,6,7-tetrahydro-1H,5H,11H-benzo[*l*]-pyrano[6,7,8-*ij*]quinolizin-11-one (C545T) (20 nm, 100:1)/4,7-diphenyl-1,10-phenanthroline (BPhen) (40 nm)/LiF (1 nm)/Al (2 nm)/Ag (20 nm), and Si/SiO_2/Ag (60 nm)/m-MTDATA:MoO_x (10 nm, 3:1)/m-MTDATA (35 nm)/NPB (5 nm)/Alq_3:C545T (20 nm, 100:1)/BPhen (40 nm)/LiF (1 nm)/Al (2 nm)/Ag (20 nm). Fig. 2 shows the brightness-voltage–current density characteristics of these two TEOLEDs. It is obvious that the one with MoO_x doped HIL shows better performance regarded to the luminance and current. TEOLED with MoO_x doped m-MTDATA reaches a luminance of about 2 cd/m^2 at 2.30 V, compared to that of 1 cd/m^2 at 2.35 V with MoO_x buffer. The luminance at 4 V for the one with MoO_x buffer and MoO_x doping, respectively, are 579 and 2500 cd/m^2. The shadow and the dash line in Fig. 2 indicate the output voltage range of our microdisplay driver with 2.0 V reference voltage of D/A convertor. The p doped device proves steeper brightness–voltage curve, which is the prerequisite to realize high gray-resolution image in OLED microdisplays. The benefits of our structures will be discussed in detail in the followings.

As known, a balanced injection of the carriers would improve the efficiencies and reduce the efficiency roll-off [21]. As shown in Fig. 3, we observed no efficiency loss in p doped TEOLED in spite of the imbalance injection of holes and electrons from counter electrodes according to our previous study of the single carrier devices [22]. While TEOLEDs without and with MoO_x doping show no difference in current efficiency (Fig. 3a), the p doped device exhibits significantly improved power efficiency (Fig. 3b), due to the reduction of driving voltage. A high power efficiency of 28.8 lm/W is achieved at a luminance of 1000 cd/m^2, compared to that of 22.7 lm/W at the same luminance for the one with MoO_x buffer. We ascribe these properties to the well modulated interfaces suppressing the quenching of the emitters and emitter doping-induced carrier trapping [23] reducing carrier imbalance in the EML. By introducing this MoO_x doping strategy, monochromatic green OLED microdisplays (see the inset of Fig. 3a) are demonstrated by using the TEOLED stacks mentioned above, while those with MoO_x buffer are too dim to be visible due to the unavoidable luminance loss on the rough CMOS substrate caused by the complicated chip processing.

The elimination of excess charge accumulation at the emitter's interfaces will reduce the quench of the excitons,

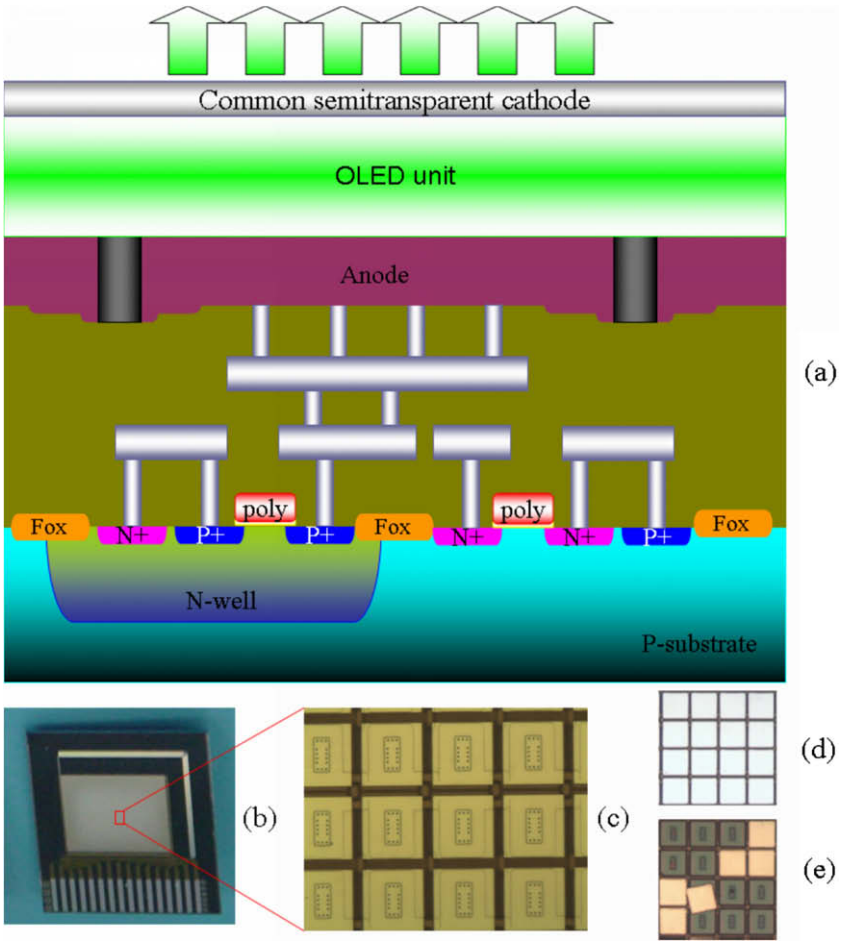

Fig. 1. (a) Schematic diagram of OLED microdisplay. (b) A chip from the foundry before CMP process. (c) a magnified view of the pixels. (d) pixels after Ag CMP process. (e) defects made to characterize the topography after CMP process.

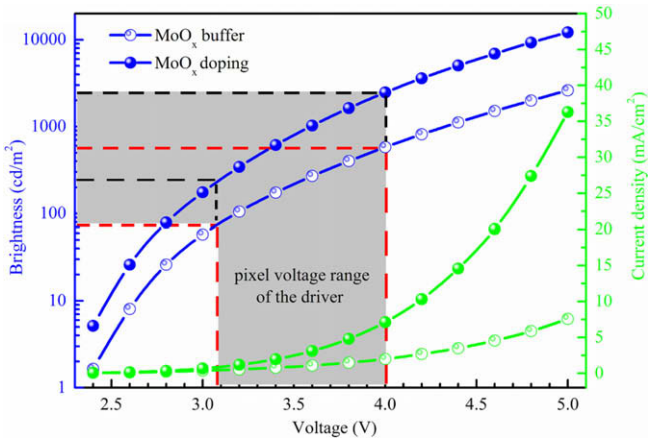

Fig. 2. Brightness–voltage–current density characteristics of the devices without and with MoO_x doping.

thereby maintain high efficiency at high luminance. The 5-nm-thick NPB also serves as an electron blocking layer (EBL) as its high lowest unoccupied molecular orbital (LUMO) level hinders electrons from reaching m-MTDATA and anode. Meanwhile, the EBL prevents excitons generated in the emission layer from drifting and diffusing into the highly conducting HIL where non-radiative quenching might occur [2]. We consider that the excess positive charges, due to efficient hole injection by p doping, tend to accumulate at the interface of m-MTDATA/NPB, but

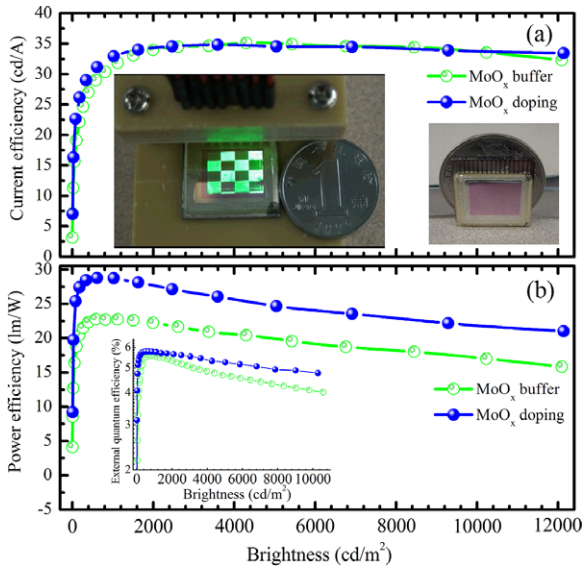

Fig. 3. (a) Current efficiency–brightness characteristics. (b) power efficiency–brightness characteristics of the devices with MoO_x buffer and MoO_x doping, respectively. The insets of (a) shows a snap of the unpackaged OLED microdisplay (left-hand side), on a home-made 16-pin probe testing platform, playing the ANSI [8] contrast ratio pattern, and a photograph of the chip with a coin of 1 Yuan RMB (right-hand side), respectively. The inset of (b) exhibits the external quantum efficiencies (5.6% for the one with MoO_x buffer and 5.8% for the one with MoO_x doping at a luminance of 1000 cd/m^2, respectively.).

not at the interface of NPB/EML. The thin NPB layer followed by the pristine m-MTDATA not only results in the energy level alignment but also dissipates the accumulated holes at the interface of EBL/EML. These conclusions are likely consistent with the result reported in the literature [24].

Another benefit of our structure is the highly efficient emitter, C545T, which also plays a role of hole and electron traps in Alq_3 [25–27]. The trapped holes will decrease free hole distribution in the EML, and hence a reduction of current density [26]. It is pointed out that imbalance between the numbers of holes and electrons in the EML are one of the sources of efficiency roll-off at high intensities [21]. By introducing electron transporting layer (ETL) BPhen owning relatively high electron mobility and low highest occupied molecular orbital (HOMO) level (as hole blocking layer, HBL) which can confines the excitons in the EML, we can avoid a vast imbalance of holes and electrons in the EML, in spite of the imbalance injection from the electrodes. In our structures, not only charge carrier trapping but also direct exciton recombination on the fluorescent dopants are responsible for the high efficiencies, and the energy transfer followed by Förster energy transfer process from the host molecule to the dopant molecule can also play a role.

In the stage of OLED microdisplays package for practical utility, wire-bond [28,29] is needed to connect to the external circuits on a holder. During the wire-bond process, the temperature of the substrate will rise, which might affect the reliability of OLEDs. Here, we demonstrated that MoO_x could also help to improve the stability of TEOLEDs. Apparent differences of the morphologies and topographies of 10 nm neat m-MTDATA and m-MTDATA doped with MoO_x on Ag (60 nm) after a heat treatment at 150 °C for half an hour, shown in Fig. 4, can be seen. The surface morphology of pristine m-MTDATA (Fig. 4c) is damaged by thermal annealing due to the crystallization. In contrast, that of MoO_x doped m-MTDATA (Fig. 4d) ap-

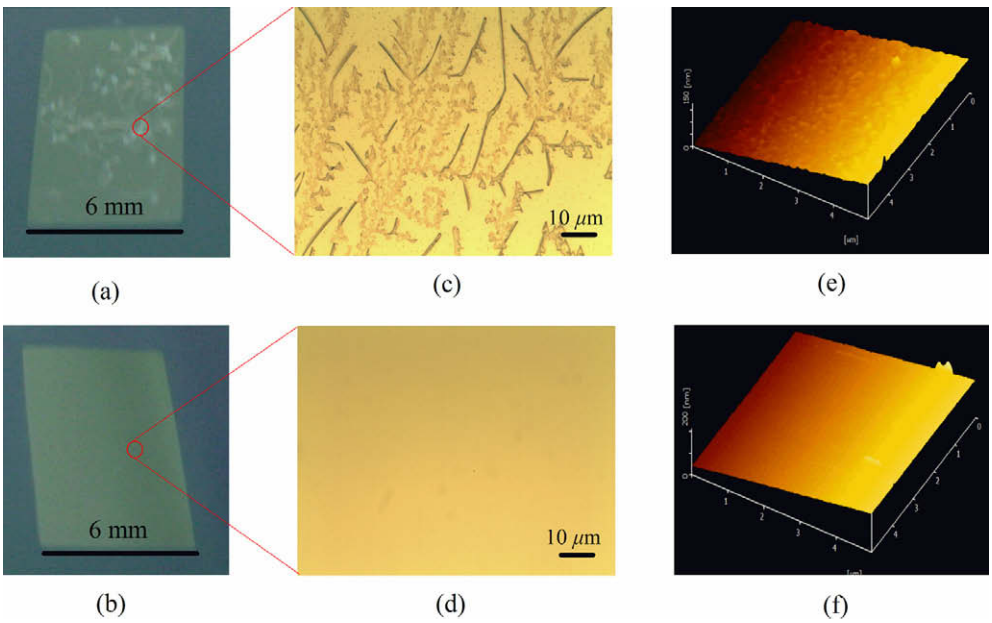

Fig. 4. (a and b) Photos of 10 nm pristine m-MTDATA and MoO_x doped m-MTDATA on 60 nm Ag on the Si/SiO_2 substrate, respectively. (c and d) microscopical images of the above two devices after annealing. (e and f) AFM topographic images of the above devices after annealing at 150 °C.

pears to be no significant change after annealing, which is consistent with the AFM measurement (Fig. 4f). This result suggests that MoO_x in m-MTDATA not only leads to an increase of the conductivity, but also contributes to an improvement of the stability of TEOLEDs.

4. Conclusions

In summary, we have succeeded in reducing the operating voltage of TEOLEDs emitting high brightness to below 5 V, resulting in the possibility of introducing cost-effective CMOS substrates without high-voltage option from the foundry. The high conductivity of the p doping layer contributes to a decrease in driving voltage as well as an increase in the reliability of TEOLEDs. The p doped TEOLED with highly efficient C545T fluorescent dye exhibits high brightness of 10,000 cd/m^2 at 4.9 V and a maximum power efficiency of 28.8 lm/W at 1000 cd/m^2. The highly conductive p doped layer also allows the introduction of thicker TEOLEDs, which effectively reduces pixel defect formation caused by electrical short circuits between the bottom and top electrodes, on the CMOS substrates with rough surfaces. OLED microdisplays are demonstrated by combining the low voltage and highly efficient TEOLED with MoO_x p doping layer. We speculate that a controlled n doping, a highly efficient phosphorescent emitter and a carefully designed outcoupling scheme will result in a higher power efficiency [14]. Low power consumption microdisplays based on the efficient TEOLEDs introducing the inexpensive and readily available MoO_x p dopant, combined with the mature and cheap CMOS technology, show potentially low cost for commercial use.

Acknowledgements

This work was funded by the National Key Basic Research and Development Program of China under Grant Nos. 2003CB314703 and 2010CB327701, and the National Natural Science Foundation of China (Grant Nos. 60977024, 60937001, 60876032, 60907013, 60706018 and 60906021). The authors gratefully acknowledge Huan Wang for AFM measurements, Linyuan Xin and Prof. Feng Li for technical assistance from Key Laboratory for Supramolecular Structure and Materials of Ministry of Education, Jilin University.

References

[1] Y. Sun, N.C. Giebink, H. Kanno, B. Ma, M.E. Thompson, S.R. Forrest, Nature 440 (2006) 908.
[2] M. Pfeiffer, S.R. Forrest, K. Leo, M.E. Thompson, Adv. Mater. 14 (2002) 1633.
[3] B.W. D' Andrade, S.R. Forrest, Adv. Mater. 16 (2004) 1585.
[4] S. Reineke, F. Lindner, G. Schwartz, N. Seidler, K. Walzer, B. Lüssem, K. Leo, Nature 459 (2009) 234.
[5] R. Meerheim, K. Walzer, G. He, M. Pfeiffer, K. Leo, Proc. SPIE 6192 (2006) 61920P.
[6] G.B. Levy, W. Evans, J. Ebner, P. Farrell, M. Hufford, B.H. Allison, D. Wheeler, H. Lin, O. Prache, E. Naviasky, IEEE J. Solid State Circ. 37 (2002) 1879.
[7] A.P. Ghosh, Proc. SPIE 4464 (2002) 1.
[8] D. Armitage, I. Underwood, S.-T. Wu, Introduction to microdisplays, John Wiley & Sons, Chichester, 2006.
[9] U. Voegl, D. Kreye, S. Reckziegel, M. Törker, C. Grillberger, J. Amelung, Proc. SPIE 6477 (2007) 647703.
[10] C.A. Lee, S.H. Jin, H.I. Kwon, I.W. Cho, J. Kong, C.J. Lee, M.W. Lee, J.W. Kyung, J.D. Lee, B.-G. Park, J. Inform. Display 5 (2004) 28.
[11] Here, we refer to p and n doping as "electrical doping" due to their impact on the conductivity of the carriers injecting or/and transporting layers. To avoid confusion with the admixture of emissive dyes with a host which is also denoted as doping, we refer to doping in emissive layer as "optical doping" which usually associates with the emissive colors and spectra.
[12] M. Pfeiffer, S.R. Forrest, X. Zhou, K. Leo, Org. Electron. 4 (2003) 21.
[13] G. He, M. Pfeiffer, K. Leo, M. Hofmann, J. Birnstock, R. Pudzich, J. Salbeck, Appl. Phys. Lett. 85 (2004) 3911.
[14] Q. Huang, K. Walzer, M. Pfeiffer, V. Lyssenko, G. He, K. Leo, Appl. Phys. Lett. 88 (2006) 113515.
[15] T. Matsushima, C. Adachi, Appl. Phys. Lett. 89 (2006) 253506.
[16] G. Schwartz, S. Reineke, K. Walzer, K. Leo, Appl. Phys. Lett. 92 (2008) 053311.
[17] T. Matsushima, C. Adachi, Appl. Phys. Lett. 92 (2008) 063306.
[18] R. Meerheim, R. NItsche, K. Leo, Appl. Phys. Lett. 93 (2008) 043310.
[19] S.Y. Kim, W.S. Jeon, T.J. Park, R. Pode, J. Jang, H.K. Kwon, Appl. Phys. Lett. 94 (2009) 133303.
[20] H. Kanno, N.C. Giebink, Y. Sun, S.R. Forrest, Appl. Phys. Lett. 89 (2006) 023503.
[21] N.C. Giebink, S.R. Forrest, Phys. Rev. B 77 (2008) 235215.
[22] G. Xie, Y. Meng, F. Wu, C. Tao, D. Zhang, M. Liu, Q. Xue, W. Chen, Y. Zhao, Appl. Phys. Lett. 92 (2008) 093305.
[23] F. Nüesch, D. Berner, E. Tutiscaron, M. Schaer, C. Ma, X. Wang, B. Zhang, L. Zuppiroli, Adv. Funct. Mater. 15 (2005) 323.
[24] M. Pfeiffer, K. Leo, X. Zhou, J.S. Huang, M. Hofmann, A. Werner, J. Blochwitz-Nimoth, Org. Electron. 4 (2003) 89.
[25] Q. Wang, J. Ding, Y. Cheng, L. Wang, D. Ma, J. Phys. D: Appl. Phys. 42 (2009) 065106.
[26] C.-C. Lee, M.-Y. Chang, P.-T. Huang, Y.C. Chen, Y. Chang, S.-W. Liu, J. Appl. Phys. 101 (2007) 114501.
[27] C.H. Jeong, J.T. Lim, M.S. Kim, J.H. Lee, J.W. Bae, G.Y. Yeom, Org. Electron. 8 (2007) 683.
[28] H.K. Charles, K.J. Mach, S.J. Lehtonen, A.S. Francomacaro, J.S. DeBoy, R.L. Edwards, Microelectron. Reliab. 43 (2003) 141.
[29] G. Harman, Wire Bonding in Microelectronics: Materials, Processes, Reliability and Yield, McGraw-Hill, 1997.

Organic Electronics 11 (2010) 412–418

Contents lists available at ScienceDirect

Organic Electronics

journal homepage: www.elsevier.com/locate/orgel

Efficient phosphorescent white OLEDs with high color rendering capability

Chih-Hao Chang [a], Kun-Cheng Tien [a], Chung-Chia Chen [a], Ming-Shiang Lin [a], Hsing-Chieh Cheng [a], Su-Hao Liu [a], Chung-Chih Wu [a,*], Jui-Yi Hung [b], Yuan-Chieh Chiu [b], Yun Chi [b,*]

[a] Department of Electrical Engineering, Graduate Institute of Photonics and Optoelectronics, and Graduate Institute of Electronics Engineering, National Taiwan University, Taipei 10617, Taiwan, ROC
[b] Department of Chemistry, National Tsing Hua University, Hsinchu, Taiwan 30013, Taiwan, ROC

ARTICLE INFO

Article history:
Received 2 November 2009
Received in revised form 12 November 2009
Accepted 19 November 2009
Available online 23 November 2009

Keywords:
Iridium
Osmium
Phosphorescence
White OLEDs
Color rendering index

ABSTRACT

By utilizing a newly developed deep-blue iridium complex along with efficient green and orange-red phosphors, we have successfully demonstrated efficient three-component phosphorescent white-emitting organic light-emitting devices (WOLEDs) with excellent performances. Such WOLEDs were based on the deep-blue phosphorescent OLEDs architecture with double emitting layers and double confining layers; portions of the deep-blue phosphors were selectively replaced with green and orange-red phosphors, thereby forming a structure with the green/orange-red emitting layers sandwiched between the two deep-blue emitting layers. Such three-component phosphorescent WOLEDs yielded a high color rendering index (CRI) of up to 94 and Commission Internationale de l'Eclairage (CIE) coordinates close to the ideal equal-energy white (0.33, 0.33). Furthermore, they exhibited rather stable colors and high CRI over a wide brightness range of 10^2–10^4 cd/m^2 and yielded electroluminescence efficiencies of up to 10.3%, 24.0 cd/A and 16.4 lm/W for the forward directions.

© 2009 Elsevier B.V. All rights reserved.

1. Introduction

With intrinsically high quantum efficiency, white-emitting organic light-emitting devices (WOLEDs) incorporating phosphorescent emitters have become the most promising candidates for meeting the stringent efficiency requirements in lighting applications [1,2]. For high-quality white-light illumination, WOLEDs with CIE$_{x,y}$ coordinates similar to those of the blackbody radiation (with a correlated color temperature (CCT) between 2500 K and 6500 K), and a color rendering index (CRI) above 80 are required [3]. While simply mixing two complementary colors can effectively produce white light, the CRI of such two-component WOLEDs are usually rather mediocre. Intuitively, the CRI can be enhanced by increasing the number of dopants to extend the spectral range of the electroluminescence (EL). For instance, in 2002, D'Andrade et al. demonstrated that the CRI of phosphorescent WOLEDs could be greatly improved from 50 to 83 by using three (red, green and greenish-blue) phosphorescent dopants instead of two complementary (red and greenish-blue) dopants [4]. As another example, in 2006, the same group combined blue fluorophors and red/green phosphors to generate white EL, in which deeper blue emission was obtained from the singlet emission of the fluorophors (to relax the requirement for the more challenging true-blue phosphors with high emission efficiencies) while red/green emission was obtained from the triplet emission of the phosphors [5]. In such hybrid WOLEDs, the CRI was improved to 85. In 2007, Schwartz et al. also successfully demonstrated high-CRI WOLEDs (CRI = 86) using a similar hybrid fluorophor/phosphor approach [6].

Although the hybrid fluorophor/phosphor approach has achieved certain success in raising the CRI of phosphor-incorporated WOLEDs, the inherent singlet/triplet branch-

* Corresponding authors. Tel.: +886 2 33663636; fax: +886 2 23689178 (C.-C. Wu).
E-mail addresses: chungwu@cc.ee.ntu.edu.tw (C.-C. Wu), ychi@mx.nthu.edu.tw (Y. Chi).

1566-1199/$ - see front matter © 2009 Elsevier B.V. All rights reserved.
doi:10.1016/j.orgel.2009.11.020

ing ratio in OLEDs may nevertheless still limit the color tuning, thereby reducing the CRI or resulting in color-efficiency tradeoffs for phosphor-incorporated WOLEDs. As such, the fabrication of WOLEDs using all red/green/blue phosphors is still highly desired, since it would yield the greatest flexibility in tuning the color of WOLEDs. Until recently, one of the major obstacles in implementing high-CRI three-component phosphorescent WOLEDs was the lack of efficient true-blue phosphors, giving insufficient light output in the shorter wavelength region. For instance, the adoption of the common greenish-blue phosphor FIrpic in the three-component phosphorescent WOLEDs generally yielded a warm white and a CRI of only up to ~80 due to deficient color rendering in the blue region [7], which would limit the applications of such WOLEDs in lighting. However, such deficiency may be compensated by adopting novel true-blue organic phosphors developed recently [8–10]. In this paper, through employment of a recently developed true-blue iridium phosphor $Ir(fppz)_2(dfbdp)$ together with efficient green/red phosphors in appropriate device architectures, we report three-component pure-white phosphorescent WOLEDs with CRI of up to 94 and with CIE coordinates close to the ideal equal-energy white emission (0.33, 0.33).

2. Experimental

2.1. Materials

We employed the deep-blue iridium phosphor, $Ir(fppz)_2(dfbdp)$ (Fig. 1a) [13], where fppzH and dfbdpH stand for 5-(2-pyridyl)-3-trifluoromethylpyrazole and (2,4-difluorobenzyl)diphenylphosphine, respectively. It has been shown that 2-pyridyl azole chromophores possess a very large intraligand $\pi\pi^*$ energy gap [11]. By reacting the chromophores with the third-row transition metals and the employment of appropriate ancillary chelates with sufficient $\pi\pi^*$ gaps, one can effect the isolation of a true-blue phosphors [12]. In our recent work [13,14], we have shown that the employment of non-conjugated ancillary chelates, such as the benzylphosphine chelate used in the present complex, not only greatly restricts their participation in the lowest-lying electronic transition but also enhances the coordination strength, leading to effective confinement of the lowest energy transition over the unique 2-pyridyl azole moiety and successful tuning of the phosphorescence toward authentic blue. Fig. 1b shows the photoluminescence (PL) spectrum of the heteroleptic Ir^{III} complex $Ir(fppz)_2(dfbdp)$ in CH_2Cl_2 solution. The lowest-energy PL peak locates at 431 nm, corresponding to a triplet energy of 2.87 eV. The PL spectrum clearly demonstrates its deep-blue phosphorescence, corresponding to $CIE_{x,y}$ of (0.162, 0.138) (Fig. 1c). It also exhibited rather high PL quantum yields when doped into the host materials used in this study [10]: 0.73 in 9-(4-tert-butylphenyl)-3,6-bis(triphenylsilyl)-9H-carbazole (CzSi, Fig. 2a) [15,16], and 0.58 in *p*-bis(triphenylsilyl) benzene (UGH2, Fig. 2a) [17].

On the other hand, the highly efficient green and red phosphors, tris(2-phenylpyridine)iridium(III) ($Ir(ppy)_3$) (Fig. 1a) and $Os(bpftz)_2(PPh_2Me)_2$ (Fig. 1a) [where bpftz stands for 3-trifluoromethyl-5-(4-tert-butyl-2-pyridyl) triazolate, PPh_2Me represents a monodentate phosphine ligand], were adopted in this study [18]. The widely used green phosphorescent emitter, $Ir(ppy)_3$, exhibits very high PL quantum efficiency (>90%) in wide-gap hosts [19]. On the other hand, the Os complex $Os(bpftz)_2(PPh_2Me)_2$ with high steric hindrance exhibits orange-red emission at around 603 nm, short excited-state lifetime (0.97 μs) and high PL quantum yield of ~90% in solution [20]. Fig. 1b shows their PL spectra along with those of the deep-blue complex $Ir(fppz)_2(dfbdp)$, while the corresponding CIE coordinates [(0.317, 0.616) for $Ir(ppy)_3$ and (0.624, 0.374) for $Os(bpftz)_2(PPh_2Me)_2$] are shown in Fig. 1c. The PL spectra of these B, G and R emitters cover most of the visible wavelengths, meaning that in principle, white emission with pure white colorant and high color rendering should be attainable with appropriate mixing of these phosphorescent emitters.

2.2. OLED fabrication

All synthesized compounds were subject to temperature-gradient sublimation under high vacuum before use. OLEDs were fabricated on the ITO-coated glass substrates with multiple organic layers sandwiched between the transparent bottom indium-tin-oxide (ITO) anode and the top metal cathode. The organic and metal layers were deposited by thermal evaporation in a vacuum chamber with a base pressure of $<10^{-6}$ torr. The deposition rate of organic layers was kept at ~0.2 nm/s. The deposition system permitted the fabrication of the complete device structure in a single pump-down without breaking vacuum. The active area of the device was 2×2 mm^2, as defined by the shadow mask for cathode deposition. Organic materials (other than phosphorescent emitters) and device structures used in this study are shown in Fig. 2a and b, respectively.

2.3. Device characterizations

Current–voltage–luminance (*I–V–L*) characterization of the devices was measured using an Agilent 4155B semiconductor parameter analyzer and a Si photodiode calibrated with Photo Research PR650. EL spectra of devices were collected by a calibrated CCD spectrograph. Total photon output from the device (either from the viewing direction or from all directions of the device) was measured in an integrating sphere containing a calibrated photodetector.

3. Results and discussion

For OLEDs incorporating deep-blue phosphors, one of the key challenges is the acquisition of effective device architectures. Deep-blue phosphors usually require large triplet energy hosts to prevent the reverse energy transfer from dopants to hosts [21]. Effective confinement of excitons in the emitting layer is also a critical issue. The excitons formed in the emitting layer would have high energy, and would therefore easily diffuse to adjacent layers and result in a decrease of the device efficiency or suffer

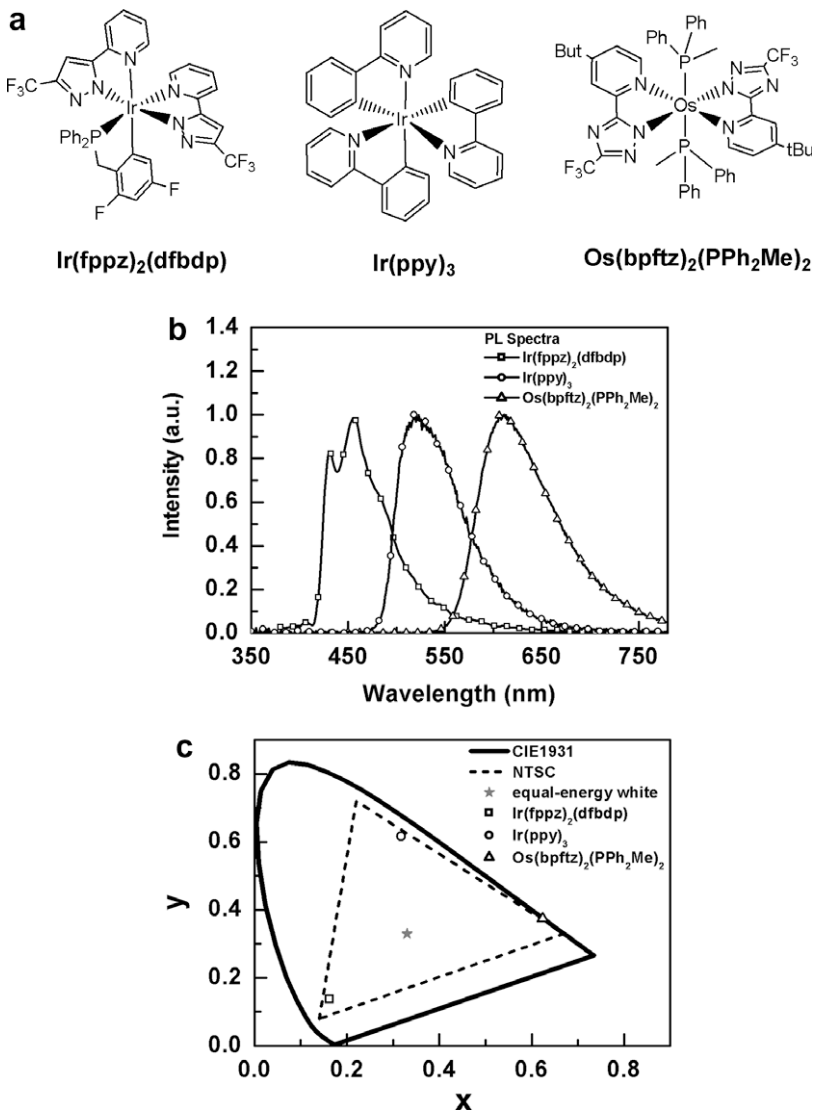

Fig. 1. (a) The structural drawings, (b) PL spectra, and (c) CIE coordinates of $Ir(fppz)_2(dfbdp)$, $Ir(ppy)_3$ and $Os(bpftz)_2(PPh_2Me)_2$ measured in CH_2Cl_2 solution.

from unwanted color degradation. Since the hosts of deep-blue phosphors generally have large triplet energy as well as larger HOMO/LUMO energy gaps, finding suitable blocking materials for exciton/carrier confinement is generally more difficult [22]. Besides, as with other OLEDs, charge balance is also important to ensure high efficiencies [23]. In this work, since we want to focus on WOLEDs incorporating deep-blue phosphors, prior investigations on the OLED structures incorporating the deep-blue phosphor $Ir(fppz)_2(dfbdp)$ deemed necessary.

For WOLEDs, device structures can be roughly classified into single- and multiple-emitting-layer (EML) architectures. The fabrication of WOLEDs with a single EML is usually difficult because the multiple dopants and the host have to be evaporated simultaneously with precise ratio control. Furthermore, the relative intensities of the different emissions might vary upon variation of the operational biases [24]. On the other hand, the device structure with multiple EMLs sometimes suffers from shifting of the recombination zone (RZ) upon increasing the biases [25]. As such, the buffer layer is often inserted between the EMLs to prevent the RZ shift and to stabilize the emission color [26,27]. However, the hindered carrier transport at the buffer layer might degrade the power efficiency. In this work, by using the developed deep-blue phosphorescent OLED device structure as a template, we implemented multiple-EML WOLEDs with pure white colorant and unprecedented high CRI value by selectively incorporating green and red phosphors, yet without inserting buffer layers between EMLs.

3.1. Blue OLEDs with different architectures

To prevent the back transfer of the triplet excitons from the deep-blue phosphors to the host material, the wide-gap materials, CzSi with a large triplet energy of 3.02 eV

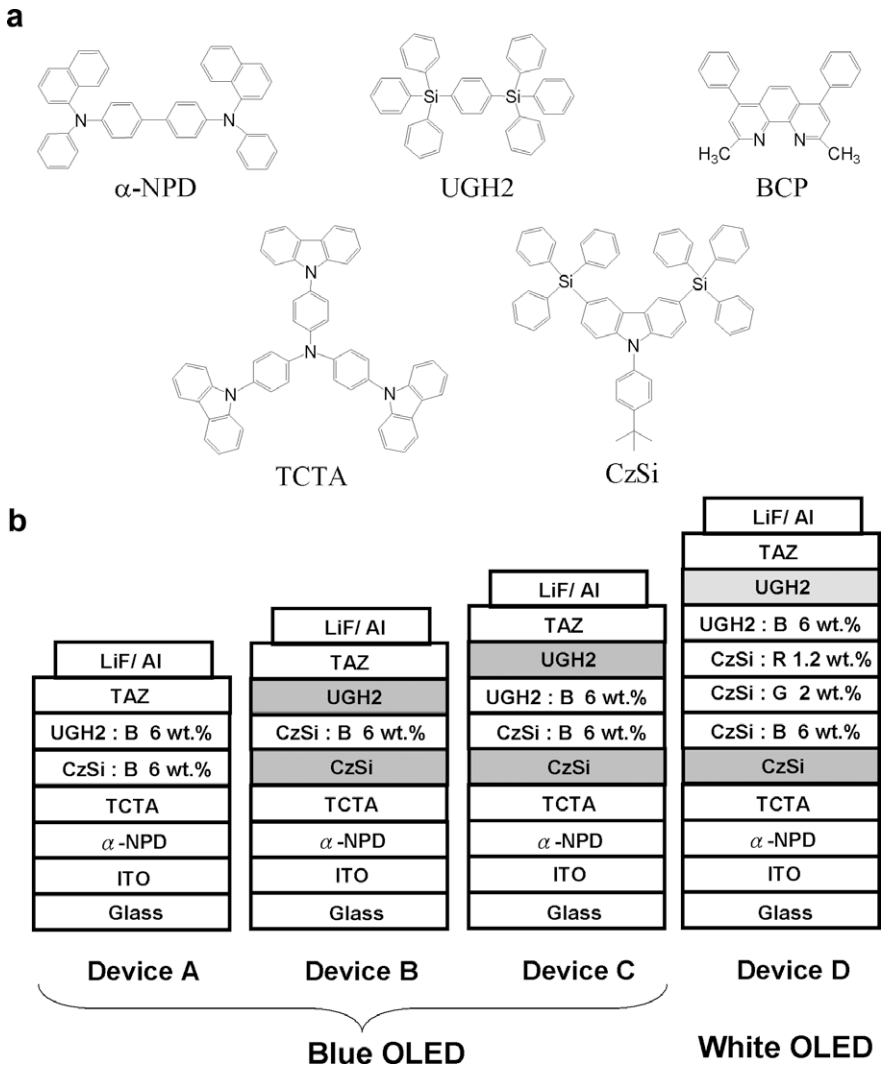

Fig. 2. (a) The structural drawing of materials used in OLEDs; and (b) schematic structures of blue and white OLEDs.

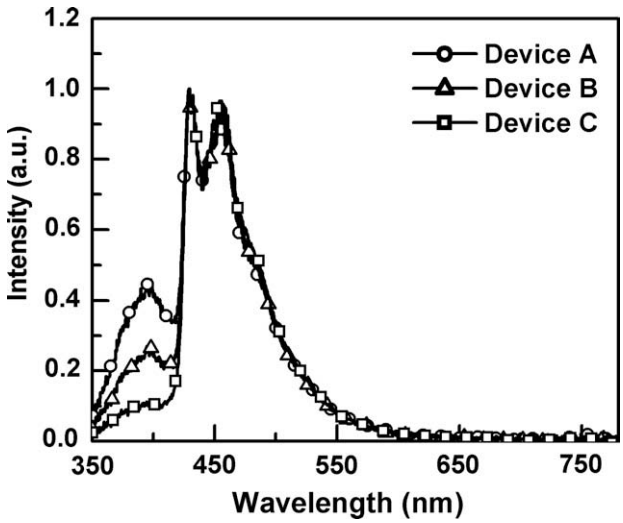

Fig. 3. EL spectra of Devices A–C at 1000 cd/m^2.

and UGH2 with a large triplet energy of 3.18 eV [15–17], were adopted as the hosts for the deep-blue phosphors. CzSi is of hole-transport nature, while UGH2 is of electron-transport nature [8]. Three different device architectures (Fig. 2b) for deep-blue OLEDs were investigated to examine the characteristics of carrier balance and carrier/exciton confinement. The first device structure (Device A) was composed of: ITO/α-NPD (30 nm)/TCTA (20 nm)/CzSi doped with 6 wt.% of $Ir(fppz)_2(dfbdp)$ (23 nm)/UGH2 doped with 6 wt.% of $Ir(fppz)_2(dfbdp)$ (3 nm)/TAZ (40 nm)/LiF (0.5 nm)/Al (150 nm). The second device (Device B) was composed of: ITO/α-NPD (30 nm)/TCTA (20 nm)/CzSi (3 nm)/CzSi doped with 6 wt.% of $Ir(fppz)_2(dfbdp)$ (23 nm)/UGH2 (2 nm)/TAZ (40 nm)/LiF (0.5 nm)/Al (150 nm). The third device (Device C) was composed of: ITO/α-NPD (30 nm)/TCTA (20 nm)/CzSi (3 nm)/CzSi doped with 6 wt.% of $Ir(fppz)_2(dfbdp)$ (23 nm)/UGH2 doped with 6 wt.% of $Ir(fppz)_2(dfbdp)$ (3 nm)/UGH2 (2 nm)/TAZ (40 nm)/LiF (0.5 nm)/Al (150 nm). In all these devices, 4,4′-bis[N-(1-naphthyl)-N-phenyl-amino]biphenyl (α-NPD) and 4,4′,4″-tris(carbazol-9-yl)-triphenylamine (TCTA) were used as the hole-transport layers (HTLs) [28], 3-(4-biphenylyl)-4-phenyl-5-(tert-butylphenyl)-1,2,4-triazole (TAZ) as the electron-transport layer (ETL) [29], LiF as the electron-injection layer [30], and aluminum as the cathode. The materials and device architectures are shown in Fig. 2.

In Device A, double emission layers (23-nm hole-transporting CzSi and 3-nm electron-transporting UGH2 doped with 6 wt.% $Ir(fppz)_2(dfbdp)$) were used to achieve balance between the hole and electron injection/transport and thus to shift the exciton formation zone away from the interfaces between the carrier-transport layers, taking advantage of the inherent physical nature of both CzSi and UGH2. Since the electron-transport capability of UGH2 is poorer than the hole-transport capability of CzSi, a relatively smaller thickness was used for the UGH2 emitting layer to avoid the degradation of device performances that may be induced by un-balanced carrier-transport properties. Device B consisted of a single emitting layer (23-nm hole-transporting CzSi doped with 6 wt.% $Ir(fppz)_2(dfbdp)$), and a thin layer of non-doped CzSi (3 nm) and UGH2 (2 nm) were inserted between the emission and hole-transport layers and between the emission and electron-transport layers, respectively. The hole-transporting CzSi possesses high-triplet-energy and is thus capable of blocking the high-energy triplet excitons (on the dopants) from migrating to TCTA (with a lower triplet energy than the dopant) [28]. On the other hand, the electron-transporting UGH2 with high-triplet-energy is expected to retard the high-energy triplet excitons (on the dopants) from migrating to TAZ (with a lower triplet energy than the dopant). For Device C, the double emission layers and the high-triplet-energy buffer layers on the two opposite sides of the emitting layers were simultaneously adopted for better confinement of triplet excitons and carriers.

Fig. 3 shows the EL spectra of these three blue-emitting devices. Device A exhibited EL predominantly from the deep-blue phosphor $Ir(fppz)_2(dfbdp)$, but a notable emission in the near-UV region was also observed, showing carrier recombination in the charge-transport layers (TCTA

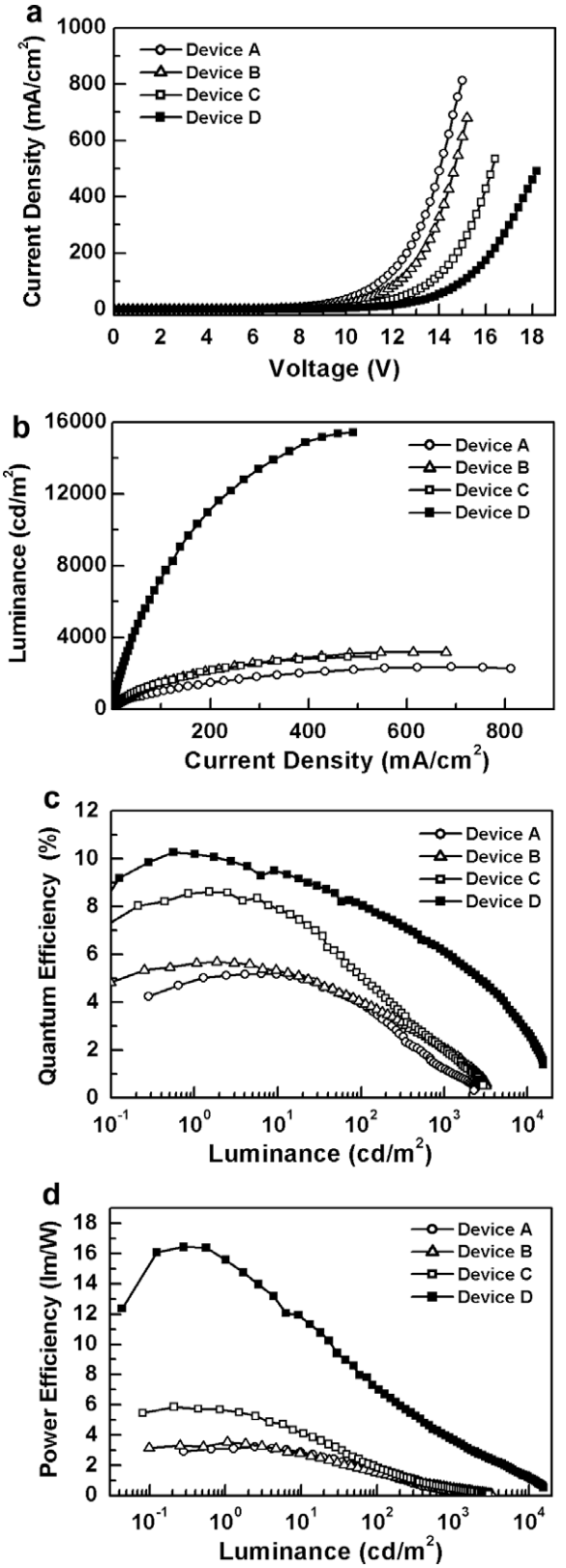

Fig. 4. (a) Current–voltage (*I–V*) characteristics, (b) luminance–current (*L–I*) characteristics, (c) external quantum efficiency versus luminance, and (d) power efficiency versus luminance for the Devices A–D.

and/or TAZ, both of which are known to exhibit near-UV emission at ~400 nm) [22]. With the employment of the two high-triplet-energy buffer layers on the opposite sides of the emitting layers (Devices B and C), the near-UV emission generated from TAZ or TCTA in Device A was significantly reduced. Such results indicated that the two buffer layers (confinement layers) could effectively hinder the carrier recombination in, or the exciton diffusion into, the charge-transport layers adjacent to the emitting layers.

The EL characteristics of the three blue-emitting devices are shown in Fig. 4, with quantitative data summarized in Table 1. The peak external quantum efficiencies for Devices A–C were 5.2%, 5.7% and 8.6%, respectively. Thus, Device C exhibited a significant efficiency improvement (1.5–1.7 times) in comparison with Devices A and B. Therefore, these results confirmed the effectiveness of the double emitting layer and double buffer layer structure for achieving efficient deep-blue electrophosphorescence.

3.2. WOLEDs with four emitting layers and double buffer layers

Based on the deep-blue phosphorescent OLED structure described in the previous section, we then studied the incorporation of green and red phosphors in the device structure to implement the desired white emission (Device D, Fig. 2b). The architecture of Device D consisted of four emitting layers and double confining layers: ITO/α-NPD (30 nm)/TCTA (20 nm)/CzSi (3 nm)/CzSi doped with 6 wt.% of $Ir(fppz)_2(dfbdp)$ (16 nm)/CzSi doped with 2 wt.% of $Ir(ppy)_3$ (3 nm)/CzSi doped with 1.2 wt.% of $Os(bpftz)_2(PPh_2Me)_2$ (4 nm)/UGH2 doped with 6 wt.% of $Ir(fppz)_2(dfbdp)$ (3 nm)/UGH2 (2 nm)/TAZ (40 nm)/LiF (0.5 nm)/Al (150 nm). The green-emitting phosphor $Ir(ppy)_3$ and the orange-red-emitting phosphor $Os(bpftz)_2(PPh_2Me)_2$ were selectively doped into portions of the CzSi emitting layer (replacing the deep-blue phosphor $Ir(fppz)_2(dfbdp)$), forming a structure with the green/orange-red emitting layers sandwiched between the two blue-emitting layers [CzSi doped with 6 wt.% of $Ir(fppz)_2(dfbdp)$ and UGH2 doped with 6 wt.% of $Ir(fppz)_2(dfbdp)$].

The EL characteristics of Device D are shown in Fig. 4 and the respective data are summarized in Table 1. The peak external quantum efficiency, luminance efficiency and power efficiency of Device D (along the forward viewing directions) were 10.3%, 24.0 cd/A and 16.4 lm/W, respectively. The efficiencies at the practical luminance of 100 cd/m^2 remained at around 8.0%, 17.4 cd/A and 7.0 lm/W, respectively. The maximum luminance reached 15,428 cd/m^2 at a driving voltage of 18.2 V. For lighting applications, the light emitted from all sections of the substrate can in principle be redirected to the forward direction via certain lighting fixtures; hence the total efficiency of the device was also characterized by using an integrating sphere setup [31]. The total quantum and power efficiency measured in the sphere were about 1.7 times larger than the forward viewing efficiency, which is consistent with previous reports [32]. Thus, the total peak external quantum efficiency and power efficiency were 17.5% and 27.9 lm/W, respectively. On closer inspection of Devices D, which was formed by replacing some deep-blue emitters in Device C with red and green emitters, one can clearly see the improvement of efficiency (vs. Device C efficiency). This efficiency enhancement might have resulted from the higher QY of red and green emitters than that of deep-blue emitters. Moreover, the relative higher driving voltage of Device D suggested that the lower-energy emitters (e.g. $Os(bpftz)_2(PPh_2Me)_2$) doped in Device D may have induced a significant amount of carrier trapping, which could in turn reduce the leakage of carriers into adjacent carrier-transport layers (e.g. TCTA and TAZ) and improve the carrier balance [20]. Indeed, comparison of the EL spectra of Devices D (Fig. 5a) and C (Fig. 3) revealed that the near-UV emission from TAZ or TCTA in Device D had reduced significantly.

The normalized EL spectra and corresponding CIE coordinates of Device D at different luminance levels are shown in Fig. 5, while quantitative data are summarized in Table 1. Device D exhibited a rather pure white emission with the CIE coordinates close to the ideal equal-energy white of (0.33, 0.33). Furthermore, the EL spectra and colors were stable at all brightness levels ranging from 10^2 to 10^4 cd/m^2, with the color variation (variation of the CIE coordinates) being as small as $\Delta(x,y) = (0.014, 0.028)$. The WOLEDs generated balanced white light over a wide range of brightness. The FWHM (full width at half maximum) of the EL spectra was measured as wide as ~210 nm at different luminance levels. Such wide EL emission effectively cover visible spectral region and largely enrich the color rendering capability. The maximum CRI of Device D

Table 1
EL characteristics of Devices A–D.

		Device A (blue)	Device B (blue)	Device C (blue)	Device D (white)
EQE (%)	Max.	5.2	5.7	8.6	10.3
	10^2 cd/m^2	3.9	4.0	5.1	8.0
Luminance efficiency (cd/A)	Max.	4.8	5.3	8.4	24.0
	10^2 cd/m^2	3.5	3.7	4.8	17.4
Power deficiency (lm/W)	Max.	3.2	3.6	5.9	16.4
	10^2 cd/m^2	1.6	1.5	1.9	7.0
Max. luminance	(cd/m^2) (V)	2270 (15.0 V)	3188 (15.0 V)	2942 (16.4 V)	15428 (18.2 V)
CIE coordinates/CRI/CCT (K)	10^2 cd/m^2	(0.155, 0.112)	(0.156, 0.115)	(0.156, 0.113)	(0.335, 0.367)/92/5410
	10^3 cd/m^2	(0.160, 0.117)	(0.157, 0.115)	(0.158, 0.119)	(0.322, 0.349)/94/5933
	10^4 cd/m^2	–	–	–	(0.328, 0.377)/90/5650

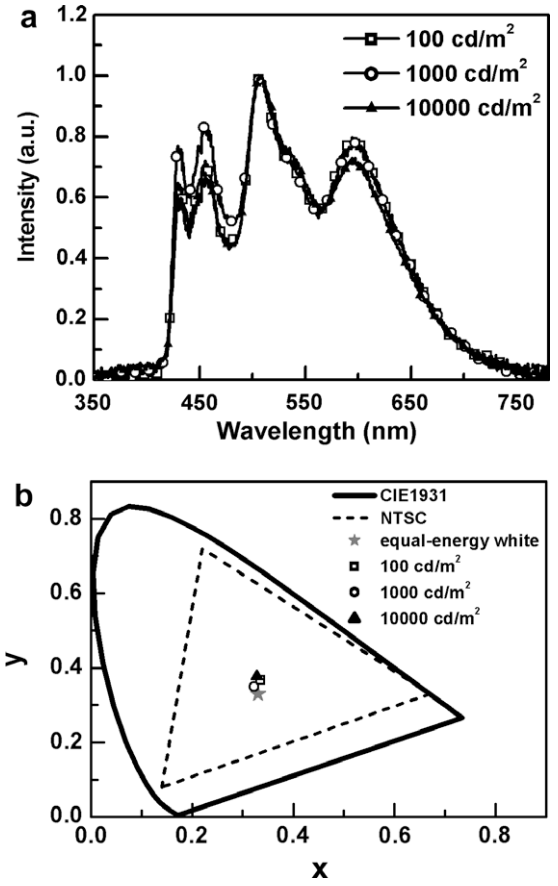

Fig. 5. (a) The normalized EL spectra of Device D at different luminance levels; and (b) CIE coordinates of Device D at different luminance levels.

reached as high as 94 (around the luminance of 1000 cd/m^2). It is also worth mentioning that the CRI remained above 90 throughout the wide brightness range of 10^2–10^4 cd/m^2 investigated.

4. Conclusions

In conclusion, by utilizing a newly developed deep-blue iridium complex along with tailor made green and orange-red phosphors, we successfully demonstrated efficient three-component phosphorescent WOLEDs with high color performances and stable colors. Such WOLEDs were based on the deep-blue phosphorescent OLED structure with double emitting layers and double confining layers; portions of deep-blue phosphors were then selectively replaced by green and orange-red phosphors, thereby forming a structure with the green/orange-red emitting layers sandwiched between the two deep-blue emitting layers. Such three-component phosphorescent WOLEDs yielded a high CRI of up to 94 and CIE coordinates close to the ideal white emission (0.33, 0.33). Furthermore, these devices exhibited stable colorant and high CRI over a wide brightness range of 10^2–10^4 cd/m^2 and yielded EL efficiencies of up to 10.3%, 24.0 cd/A and 16.4 lm/W for the forward directions.

Acknowledgement

The authors gratefully acknowledge the financial support from National Science Council and Ministry of Economic Affairs of Taiwan.

References

[1] S. Reineke, F. Lindner, G. Schwartz, N. Seidler, K. Walzer, B. Lüssem, K. Leo, Nature 459 (2009) 234–238.
[2] S.H. Eom, Y. Zheng, E. Wrzesniewski, J. Lee, N. Chopra, F. So, J. Xue, Appl. Phys. Lett. 94 (2009) 153303.
[3] B.W. D'Andrade, S.R. Forrest, Adv. Mater. 16 (2004) 1585–1595.
[4] B.W. D'Andrade, M.E. Thompson, S.R. Forrest, Adv. Mater. 14 (2002) 147–151.
[5] Y. Sun, N.C. Giebink, H. Kanno, B. Ma, M.E. Thompson, S.R. Forrest, Nature 440 (2006) 908–912.
[6] G. Schwartz, M. Pfeiffer, S. Reineke, K. Walzer, K. Leo, Adv. Mater. 19 (2007) 3672–3676.
[7] C.H. Chang, Y.J. Lu, C.C. Liu, Y.H. Yeh, C.C. Wu, J. Disper. Technol. 3 (2007) 193–199.
[8] C.H. Yang, Y.M. Cheng, Y. Chi, C.J. Hsu, F.C. Fang, K.T. Wong, P.T. Chou, C.H. Chang, M.H. Tsai, C.C. Wu, Angew. Chem. Int. Ed. 46 (2007) 2418–2421.
[9] C.F. Chang, Y.M. Cheng, Y. Chi, Y.C. Chiu, C.C. Lin, G.H. Lee, P.T. Chou, C.C. Chen, C.H. Chang, C.C. Wu, Angew. Chem. Int. Ed. 47 (2008) 4542–4545.
[10] Y.C. Chiu, J.Y. Hung, Y. Chi, C.C. Chen, C.H. Chang, C.C. Wu, Y.M. Cheng, Y.C. Yu, G.H. Lee, P.T. Chou, Adv. Mater. 21 (2009) 2221–2225.
[11] P.T. Chou, Y. Chi, Chem. Eur. J. 13 (2007) 380–395.
[12] J.K. Yu, Y.H. Hu, Y.M. Cheng, P.T. Chou, S.M. Peng, G.H. Lee, A.J. Carty, Y.L. Tung, S.W. Lee, Y. Chi, C.S. Liu, Chem. Eur. J. 10 (2004) 6255–6264.
[13] Y.H. Song, Y.C. Chiu, Y. Chi, Y.M. Cheng, C.H. Lai, P.T. Chou, K.T. Wong, M.H. Tsai, C.C. Wu, Chem. Eur. J. 14 (2008) 5423–5434.
[14] Y.C. Chiu, Y. Chi, J.Y. Hung, Y.M. Cheng, Y.C. Yu, M.W. Chung, G.H. Lee, P.T. Chou, C.C. Chen, C.C. Wu, H.Y. Hsieh, Appl. Mater. Interf. 1 (2009) 433–442.
[15] M.H. Tsai, H.W. Lin, H.C. Su, T.H. Ke, C.C. Wu, F.C. Fang, Y.L. Liao, K.T. Wong, C.I. Wu, Adv. Mater. 18 (2006) 1216–1220.
[16] M.H. Tsai, T.H. Ke, H.W. Lin, C.C. Wu, S.F. Chiu, F.C. Fang, Y.L. Liao, K.T. Wong, Y.H. Chen, C.I. Wu, Appl. Mater. Interf. 1 (2009) 567–574.
[17] X. Ren, J. Li, R.J. Holmes, P.I. Djurovich, S.R. Forrest, M.E. Thompson, Chem. Mater. 16 (2004) 4743–4747.
[18] Y.L. Tung, S.W. Lee, Y. Chi, Y.T. Tao, C.H. Chien, Y.M. Cheng, P.T. Chou, S.M. Peng, C.S. Liu, J. Mater. Chem. 15 (2005) 460–464.
[19] Y. Kawamura, K. Goushi, J. Brooks, J.J. Brown, H. Sasabe, C. Adachi, Appl. Phys. Lett. 86 (2005) 071104.
[20] C.H. Chang, Y.H. Lin, C.C. Chen, C.K. Chang, C.C. Wu, L.S. Chen, W.W. Wu, Y. Chi, Org. Electron. 10 (2009) 1235–1240.
[21] R.J. Holmes, S.R. Forrest, Y.J. Tung, R.C. Kwong, J.J. Brown, S. Garon, M.E. Thompson, Appl. Phys. Lett. 82 (2003) 2422–2424.
[22] C.H. Chang, C.C. Chen, C.C. Wu, C.H. Yang, Y. Chi, Org. Electron. 10 (2009) 1364–1371.
[23] C. Adachi, M.A. Baldo, M.E. Thompson, S.R. Forrest, J. Appl. Phys. 90 (2001) 5048–5051.
[24] B.W. D'Andrade, R.J. Holmes, S.R. Forrest, Adv. Mater. 16 (2004) 624–628.
[25] G. Cheng, Y. Zhang, Y. Zhao, Y. Lin, C. Ruan, S. Liu, T. Fei, Y. Ma, Y. Cheng, Appl. Phys. Lett. 89 (2006) 043504.
[26] S. Tokito, T. Iijima, T. Tsuzuki, F. Sato, Appl. Phys. Lett. 83 (2003) 2459–2461.
[27] C.L. Ho, W.Y. Wong, Q. Wang, D. Ma, L. Wang, Z. Lin, Adv. Funct. Mater. 18 (2008) 928–937.
[28] S. Reineke, G. Schwartz, K. Walzer, K. Leo, Appl. Phys. Lett. 91 (2007) 123508.
[29] J. Kido, C. Ohtaki, K. Hongawa, K. Okuyama, K. Nagai, Jpn. J. Appl. Phys. 32 (Pt. 2) (1993) L917–L920.
[30] L.S. Hung, C.W. Tang, M.G. Mason, Appl. Phys. Lett. 70 (1997) 152–154.
[31] S.R. Forrest, D.D.C. Bradley, M.E. Thompson, Adv. Mater. 15 (2003) 1043–1048.
[32] B.W. D'Andrade, J.J. Brown, Appl. Phys. Lett. 88 (2006) 192908.

Organic Electronics 11 (2010) 419–426

Contents lists available at ScienceDirect

Organic Electronics

journal homepage: www.elsevier.com/locate/orgel

Influence of nature of surface dipoles on observed photovoltage in dye-sensitized solar cells as probed by surface potential measurement

Shyam S. Pandey [a,*], Shohei Sakaguchi [a], Yoshihiro Yamaguchi [b], Shuji Hayase [a]

[a] Graduate School of Life Science and Systems Engineering, Kyushu Institute of Technology, 2-4 Hibikino, Wakamatsu-ku, Kitakyushu 808-0196, Japan
[b] Nippon Steel Chemical Co., Ltd., 46-80 Nakabaru, Sakinohama, Tobata-ku, Kitakyushu 804-8503, Japan

ARTICLE INFO

Article history:
Received 10 February 2009
Received in revised form 12 November 2009
Accepted 19 November 2009
Available online 26 November 2009

Keywords:
Surface potential
Interface
DCA
Dye dipole
Dye aggregation
Dye-sensitized solar cells

ABSTRACT

A contact free method of surface potential measurement using scanning Kelvin-probe microscopy (SKPM) was conducted to probe the nature of nanocrystalline TiO_2/dye interface. In combination with electrical measurements an effort has been made to establish a correlation between the nature of sensitizing dye and observed surface potential with open circuit voltage (Voc) after dye-sensitized solar cell (DSSC) fabrication. Effect of chenodeoxycholic acid (DCA) as co-adsorbent with dyes upon the enhancement of DSSC efficiency has been probed by SKPM, which revealed a positive shift of surface potential upon treatment of thin films of TiO_2 with DCA. The enhancement of DSSC performance upon DCA introduction has been explained by upward shift of TiO_2 conduction band edge leading to enhanced Voc along with the prevention of π-stacked aggregation resulting in enhanced short-circuit current density.

© 2009 Elsevier B.V. All rights reserved.

1. Introduction

Silicon solar cells are presently playing a pivotal role in harvesting the solar energy efficiently but their high cost of production is one of the major stumbling blocks towards their reach at common mass level as a clean energy substitute. Dye-sensitized solar cells (DSSC) are a cheap alternatives to silicon solar cells for efficient conversion of solar energy into electrical energy and has attracted the attention of material science community in the recent past [1,2]. Although, DSSC based on organic dyes giving a respectable photoconversion efficiency of 10–11% which is still lower than the efficiency obtained by silicon solar cells (20%) [3,4]. One of the most important and challenging factor attributed to the lower efficiency of the DSSC, is the narrower optical absorption window (400–800 nm) of organic dyes, which is narrower than the optical absorption window of crystalline silicon (500–1100 nm). Recently, Inakazu et al. have proposed the extension of optical absorption window by selective adsorption of two dyes on nanoporous titania under pressurized CO_2 atmosphere leading to the enhancement in photoconversion efficiency [5]. Over all photoconversion efficiency of a DSSC is basically decided by the short-circuit current density (Jsc), open circuit voltage (Voc) and fill factor (FF). There are reports about a number of organic dyes giving very high Jsc but over all poor photoconversion efficiency of the cell was mainly attributed to small observed Voc [6,7]. Voc plays an important role in controlling the photoconversion efficiency and is basically decided by the difference in the conduction band level of TiO_2 and potential of I_3^-/I^- redox couple in DSSCs. In an interesting report O'Regan and Gratzel [8] advocated the role of electron recombination in governing the Voc based on their transient photovoltage and photocurrent measurements in the DSSC.

Several approaches such as introduction of nitrogen containing heterocyclic additives like pyrimidine, alkyl pyridine, etc. [9,10], molecular modification of TiO_2 surface by dipolar carboxylic acid derivatives [11,12], coating of

* Corresponding author. Tel.: +81 93 695 6005; fax: +81 93 695 6000.
E-mail address: shyam@life.kyutech.ac.jp (S.S. Pandey).

1566-1199/$ - see front matter © 2009 Elsevier B.V. All rights reserved.
doi:10.1016/j.orgel.2009.11.021

TiO_2 surface with a very thin conformal overlayers of insulators like silica, alumina, strontium titanate, etc. [13–15], lithium intercalation of TiO_2 particulates [16] and introduction of chenodeoxycholic acid (DCA) [17] in electrolyte solution have been utilized to improve the Voc of DSSC. Kelvin probe method is a very sensitive non-invasive technique which finds versatile application in determining the relative work functions of metals and semiconductors by measuring the contact potential difference between a reference surface and a material under investigation. It has been successfully used to determine the band offsets in heterojunction solar cells [18], change in the work functions of the metal and semiconductors after molecular adsorption [19] and determination of work functions of organic molecular semiconductors like porphyrins, phthallocyanines and perrylenes [20].

Ruhle and Cahen [21] have extensively studied the conducting F-doped Tin oxide and nanocrystalline mesoporous TiO_2 interface using Kelvin probe method and reported a macroscopic band bending due to Fermi level equilibration. Organic sensitizing dyes used for the fabrication of DSSC possess some finite dipole moments and hence are supposed to create a band offsets after their attachment to TiO_2 surface, therefore, are expected to af-

a

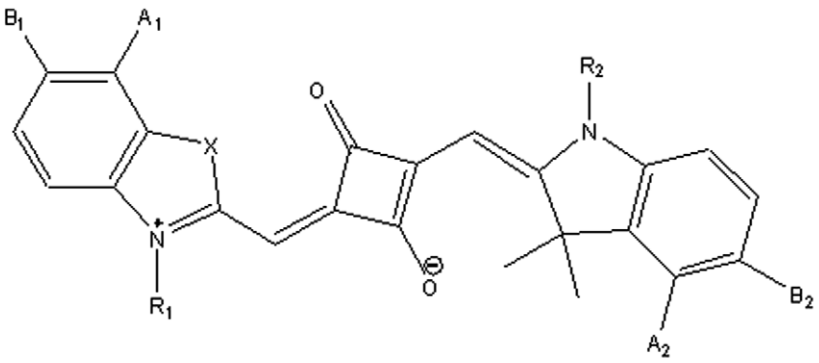

X	R_1	R_2	A_1, B_1	A_2, B_2	Dye
CMe_2	C_8H_{17}	C_2H_4 -COOH	Benzo	Benzo	SQ-A
CMe_2	$C_{18}H_{37}$	$C_{18}H_{37}$	H, -COOH	H, -COOH	SQ-B
CMe_2	C_4H_9	C_4H_9	H, -COOH	H, -COOH	SQ-C

b

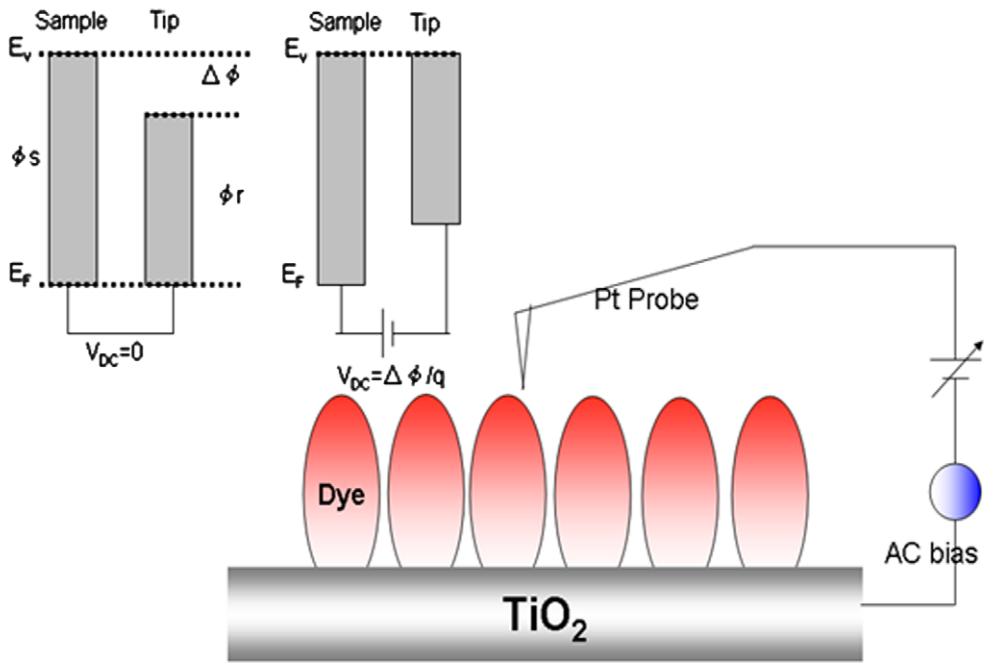

Fig. 1. (a) Structure of SQ dyes. (b) Schematics of SKPM measurement.

fect the Voc of the DSSC. Present article deals with the measurement of surface potentials of a number of sensitizing dyes adsorbed on to the nanocrystalline titania surface in order to delineate the dye surface potential with Voc. At the same time, the role of DCA in the enhancement of the photovoltage was also investigated since it is believed to suppress the back electron transfer or recombination [22].

2. Experiment

Ruthenium based two inorganic dyes N3 and N719 were purchased from Solaronics Corporation, Switzerland while organic dye NK3628 was purchased from Hayashibara Tokyo, Japan. Organic dyes D77 and D102 were purchased from Mitsubishi Paper Mills Company limited and used as supplied. Squaric acid based sensitizing dyes SQ-A, SQ-B and SQ-C used in the present study have been synthesized following the methods by Oswald et al. [23] and Matsui et al. [24]. Structures of these SQ dyes have been shown in Fig. 1(a).

To prepare samples for surface potential measurement by the Kelvin probe method, a thin layer of dense TiO_2 was applied on glass slides by spin coating followed by their calcination at 450 °C having film thickness of about 100 nm. Adsorption of the organic and inorganic sensitizing dyes on TiO_2 thin film was performed by dipping the calcinated titania coated glass slides in the ethanolic solution of the dyes (0.25 mM) for 3 h and 24 h respectively. To study the effect of DCA on Voc in the case of organic sensitizing dyes, it was dissolved in the similar solvent used for making the dye solution for its adsorption on the titania thin film. Surface potential measurement was performed using scanning Kelvin probe microscope (SKPM model JSPM 5200, JEOL Datum). Measurements were done in non-contact mode using a platinum probe for scanning under vacuum. First of all, surface potential of only TiO_2 thin film on glass was measured and its value was taken as reference followed by measurement of surface potential of dye adsorbed on titania film for comparison and study of influence of nature of dye adsorption on observed surface potential. Schematic representation of SKPM has been shown in Fig. 1(b).

DSSC were fabricated using Ti-Nanoxide D paste (Solaronix SA) which was coated on a Low E glass (Nippon Sheet Glass Co., Ltd.) by a doctor-blade. The substrate was then baked at 450 °C to fabricate TiO_2 layers of about 12 μm thickness. The substrate was dipped in a solution containing dye in the presence and/or absence of DCA. Concentration of DCA in the organic dye solution was 2.5 mM. A Pt sputtered SnO_2/F glass substrate was employed as the counter electrode. Electrolyte (WWS30) containing LiI (500 mM), iodine (50 mM), *t*-butylpyridine (580 mM), MeEtIm-DCA (ethylmethylimidazolium dicyanoimide) (4:6 wt/wt) (600 mM) in acetonitrile, was used to fabricate the DSSC. A Himilan film (Mitsui-DuPont Polychemical Co., Ltd.) of 25 μm thickness was used as a spacer. The cell area was 0.25 cm^2. Performance of the solar cells was evaluated using a metal mask on the solar cell in order to remove the effect of the optical reflection under the irradiation of 100 mW/cm^2 at AM 1.5.

The molecular dipole moments of the sensitizing dyes used in the present investigation were calculated after structural optimization of the dye using time dependent density functional theory (TD-DFT) calculations on Gaussian G03 program package with B3LYP functional and 6–311 g basis set.

3. Results and discussion

Fig. 2(a) shows the surface potential profile of sensitizing dyes adsorbed on a thin film of nanocrystalline TiO_2 measured using the Kelvin probe microscope. Considering

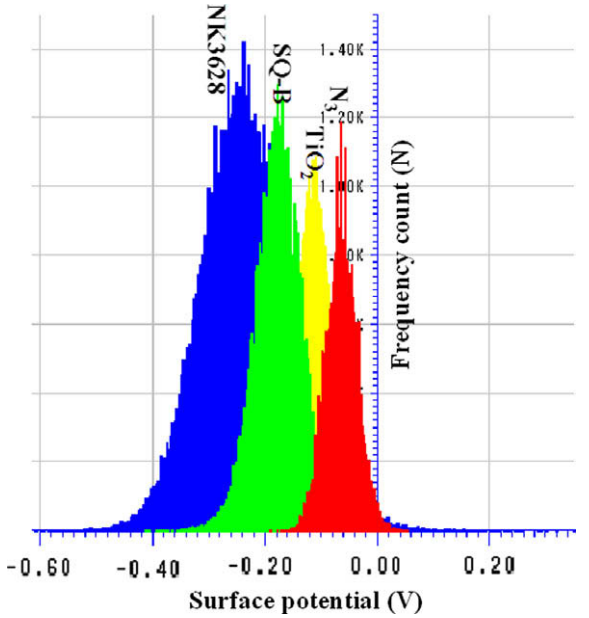

Fig. 2a. Surface potential histogram of inorganic and organic sensitizing dyes adsorbed on thin film of nanoporous TiO_2.

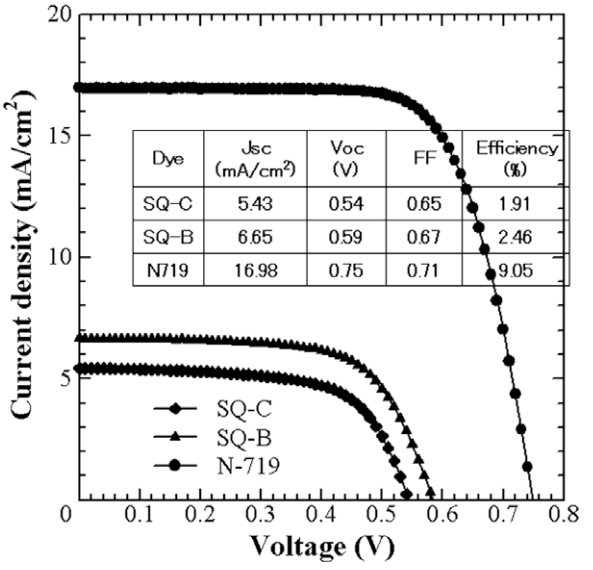

Dye	Jsc (mA/cm²)	Voc (V)	FF	Efficiency (%)
SQ-C	5.43	0.54	0.65	1.91
SQ-B	6.65	0.59	0.67	2.46
N719	16.98	0.75	0.71	9.05

Fig. 2b. Photovoltaic characteristics of DSSC based on organic (SQ-B, SQ-C) and inorganic (N-719) dyes.

the surface potential of bare TiO_2 surface as reference, a perusal of the surface potential profile corroborates that the work functions of organic and ruthenium based inorganic dyes differ distinctively. Surface potentials of organic dyes show a negative shift while ruthenium based inorganic dye N3 shows a positive shift of surface potential as compared to that of the reference TiO_2 surface. As shown in Fig. 2(b), experimentally observed value of Voc of the organic dyes SQ-B and SQ-C (0.59 V and 0.54 V) have been found to be lower than that of ruthenium based inorganic dye N-719 (0.75 V), which is also one of the reasons for their lower photoconversion efficiency. Zhan et al. reported appreciably very high short-circuit current density for the DSSC based on their newly synthesized organic dye but the cause of the observed lower photoconversion efficiency was attributed to very low Voc [25]. This indicates that probably nature of the adsorbed dye on the TiO_2 surface leads to differential shifting of the conduction band in the case of organic and inorganic dyes due to band alignment after dye adsorption.

This can be attributed to the formation of different kind of dipoles being formed at TiO_2/dye interface upon dye adsorption since these sensitizing dyes possess some finite dipole moments leading to differential nature of band alignments as shown schematically in Fig. 3. Ruthenium dye (N719) has relatively positive shift in the surface potential as compared to that of bare TiO_2 surface probably forms the negative dipole i.e. dipole moments pointed towards TiO_2 surface, shifting the TiO_2 conduction band edge upwardly leading to higher observed Voc. At the same time, lower Voc observed for the organic dyes could be explained considering formation of positive dipole by organic dye at TiO_2/dye interface. Similar trends of differential shifting of TiO_2 conduction band upon treatment of TiO_2 surface by organic carboxylic and phosphonic acids has also been reported by Ruhle et al. [11]. Passivation effect of metal/semiconductor junction by monolayer of polar organic molecules has also been investigated in detail by Vilan et al. [26] using the Kelvin probe method where they have emphasized that polar organic molecules led to the change of the barrier height of the junction systematically in the order of the dipole moments of the free molecules.

Using the Kelvin probe method, surface potentials of a number of ruthenium based inorganic and organic dyes adsorbed on TiO_2 surface were measured along with the fab-

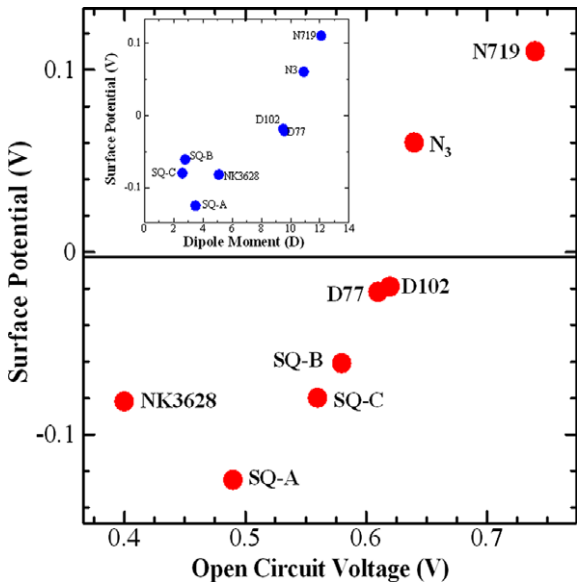

Fig. 4. Surface potential vs Voc for some sensitizing dyes. Surface potential shown here are potential with respect to bare TiO_2 surface measured as the reference. Inset shows relationship between calculated dipole moment and measured surface potential of dyes used in the present study.

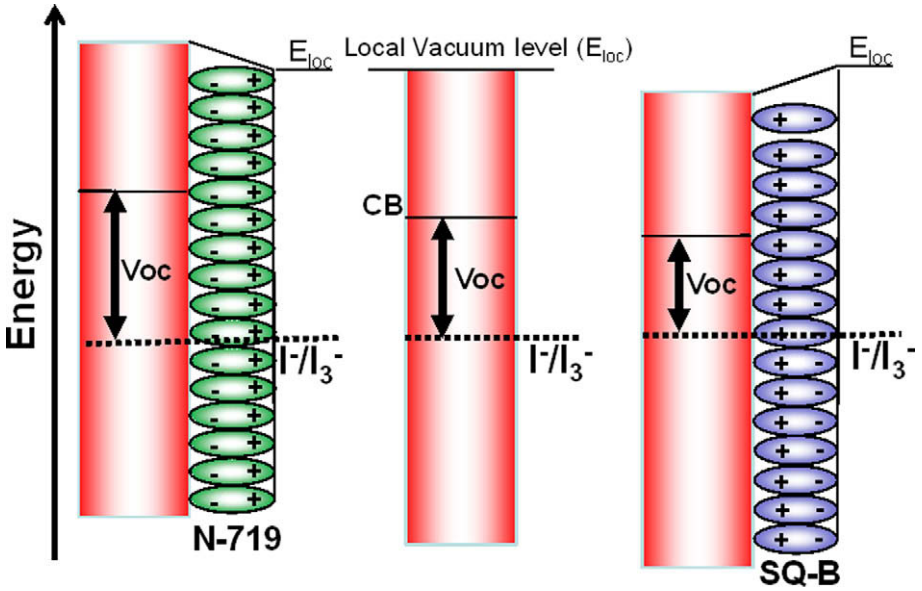

Fig. 3. Schematics of energy band diagram of nanoporous TiO_2/electrolyte interface with inorganic and organic dye adsorbed on thin TiO_2 film.

rication of DSSC and an effort was made to study the effect of surface potential on the observed Voc. Fig. 4 represents the effect of measured surface potential of dyes on the observed Voc. As can be seen clearly from this figure that dyes having high Voc (ruthenium based inorganic dyes) have the positive surface potential as compared to that of the reference surface potential of the nanoporous TiO_2 film. This positive shift in the surface potential of ruthenium dyes indicates that most likely the vicinity of TiO_2 is negative leading to the downward shift of the vacuum level of titania followed by an upward shift in the conduction band edge. Since Voc is governed by the difference in the conduction band of TiO_2 and redox energy level of I_3^-/I^- redox couple, this upward shift of conduction band edge leads to the higher observed Voc. In a similar manner, low Voc in the case of organic dyes can also be explained by downward shift of TiO_2 conduction band edge due to negative shift of surface potential by organic dyes as compared to that of bare TiO_2 surface. It is interesting to note that relatively positive shift in surface potential for both of the organic as well as inorganic dyes led to an increase in the observed Voc. Kruger et al. [27] have studied the effect of molecular dipole moment on the contact potential difference and emphasized that molecular species having higher dipole moment results into enhanced band bending at the interface.

To get further insight about the TiO_2/dye interface, we calculated the dipole moments of the dyes used in the present investigation after optimization of the dye structure using Gaussian G03 program package. Inset of Fig. 4 shows the correlation between the measured surface potential and calculated dipole moments of the dyes under investigation. A perusal of Fig. 4 (inset) indicates that dyes having higher dipole moment show relatively positive shift in the surface potential which could be attributed to the enhanced band bending at TiO_2/dye interface leading to higher observed Voc. Therefore, surface potential measurement using Kelvin probe method seems to be an important diagnostic tool to predict whether a given sensitizing dye will give higher/lower Voc prior to DSSC fabrication. At the same time it is also helpful to design an efficient dye giving positive shift in the surface potential.

A number of cholic acid derivatives have been frequently employed as co-adsorbent along with sensitizing dyes for the enhancement of efficiency of DSSC [28–31]. The exact role of cholic acid towards enhancement of DSSC performance is not yet completely clear, however, Kay and Gratzel [28] proposed the four possible roles played by cholic acid viz. (a) suppression of dye aggregation, (b) positive shift of the TiO_2 conduction band edge, (c) decrease in leakage current by adsorbed dyes and (d) tuning of redox potential of sensitizing dyes. Using various cyanine dyes Sayama et al. [32] have advocated the predominance of factor (c) as the key role played by the cholic acid for enhancement of their DSSC efficiency. On the other hand, Kopidakis et al. [33] emphasized that incorporation of DCA is associated with the upward shift of TiO_2 conduction band edge leading to enhancement of Voc and thus DSSC performance based on their transient photovoltage measurements.

To investigate the role of DCA on DSSC performance, surface potential measurement was conducted on thin nanoporous TiO_2 films in the presence and absence of DCA using the Kelvin probe method. Fig. 5 shows the surface potential profile of TiO_2 thin film in the presence and absence of DCA and clearly corroborates that there is a positive shift of surface potential in the presence of DCA as compared to reference surface potential of bare titania surface. This suggests that presence of DCA leads to the nega-

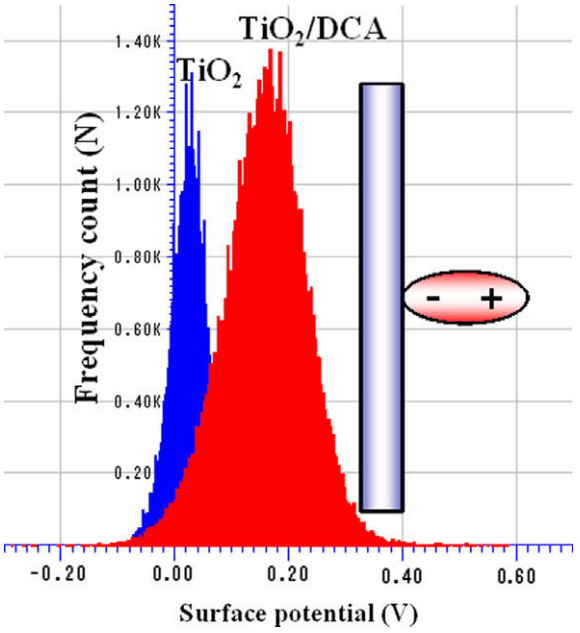

Fig. 5. Surface potential histogram of nanoporous titania film in the presence and absence of DCA.

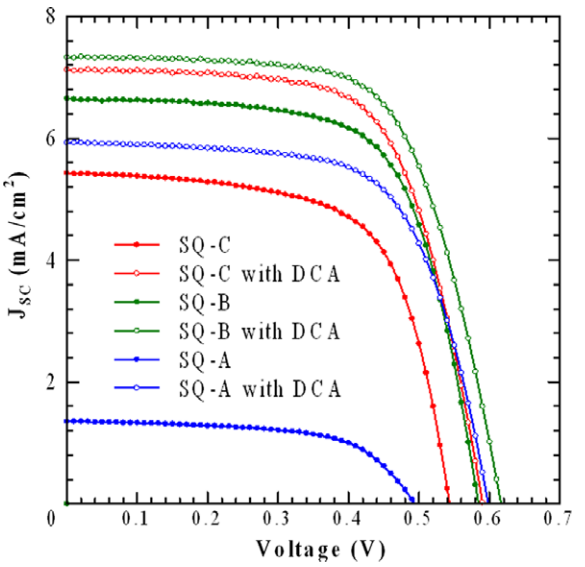

Fig. 6. Photovoltaic performance for DSSCs containing squaric acid based organic dyes in the presence and absence of DCA. Cell area 0.2115 cm^2, AM 1.5, 100 mW/cm^2.

tive shift of TiO_2 vacuum level followed by upward shift of its conduction band edge leading to the enhancement of Voc. Similar observation of enhancement of DSSC efficiency in the presence of DCA as co-adsorbent along with the Ruthenium dye has also been observed by Neale et al. [30] who emphasized the predominance of the shift of TiO_2 conduction band edge leading to overall improvement in the photovoltage.

To verify the role of DCA in efficiency enhancement of DSSC based on organic dyes as sensitizer, three squaric acid based organic dyes viz SQ-A, SQ-B and SQ-C have been utilized for the DSSC fabrication and their current–voltage (*I–V*) curve upon irradiation of 100 mW/cm^2 simulated solar light has been shown in Fig. 6. It clearly shows that introduction of DCA as co-adsorbent leads to the enhancement of cell efficiency by increasing both of the Voc and Jsc in the case of the all of the organic SQ dyes. A similar observation has also been made by Wang et al. [34] where both of Jsc and Voc were found to be increasing upon increase in the DCA concentration in the case of their coumarin based organic dyes.

A careful perusal of Fig. 6 clearly corroborates that although both Voc and Jsc are getting improved upon introduction of DCA in the case of the SQ dyes but improvement is much pronounced for the dye SQ-A as compared to that of SQ-B and SQ-C. To understand this observation, surface potential measurement using the Kelvin probe method was conducted upon thin films of nanoporous titania adsorbed with these dyes in the presence and absence of DCA. The measured surface potential profile of SQ dyes in the presence and absence of DCA has been shown in Fig. 7. As clearly evidenced by this figure, there was a marked positive shift of surface potential in the case of dye SQ-A as compared to that of SQ-B after introduction of DCA, which could probably be responsible for the pronounced enhancement of Voc for the sensitizing dye SQ-A.

Upon adsorption of dye in the presence of DCA there is a dynamic competition between the dye molecule and DCA for their attachment on the total available sites on the TiO_2 particle surface. Based on dye desorption studies, Neale et al. [35] have reported that adsorption of ruthenium dye in the presence of DCA led to the reduction of dye loading up to 60% and emphasized that even the reduction at such extent has not affected over all photovoltaic performance. A perusal of Figs. 5 and 7 indicates that the shift in the surface potential in the presence of DCA only was 0.13 V, while this shift was 0.06 V for SQ-B and 0.08 V for SQ-A in the presence of DCA. This indicates a differential competition of DCA for its attachment on TiO_2 surface in the presence of these dyes. Considering the 0.13 V shift associated with 100% adsorption by DCA molecules, the relative abundance of SQ-A and SQ-B in the presence of DCA, could be approximated to be 38% and 54%, respectively, which is in similar range as observed by Neale et al. Presence of relatively larger extent of DCA (62%) in the case SQ-A could be attributed to the formation of larger π-aggregates which probably hinders their attachment and favours the attachment for DCA molecules.

Another role of DCA has been reported to suppress the dye aggregation resulting into the suppression of charge recombination between the injected electrons and I_3^- ions of the electrolyte. Khazraji et al. have also emphasized that

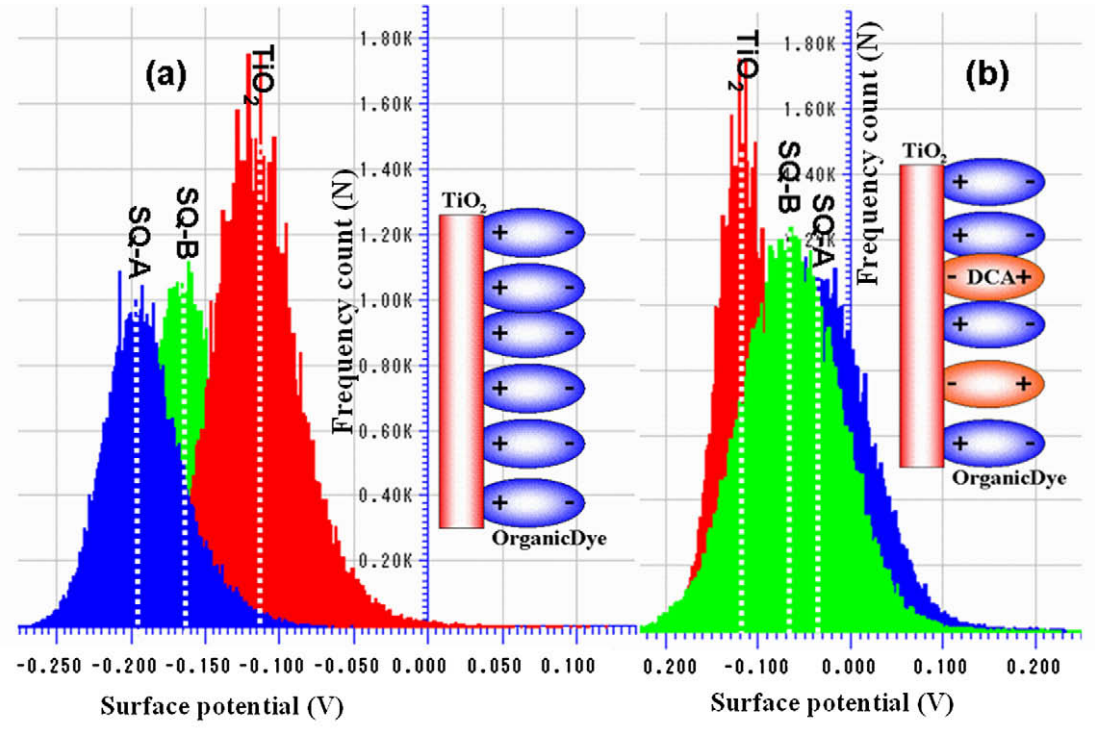

Fig. 7. Surface potential histogram of organic SQ dyes in the absence (a) and presence (b) of DCA.

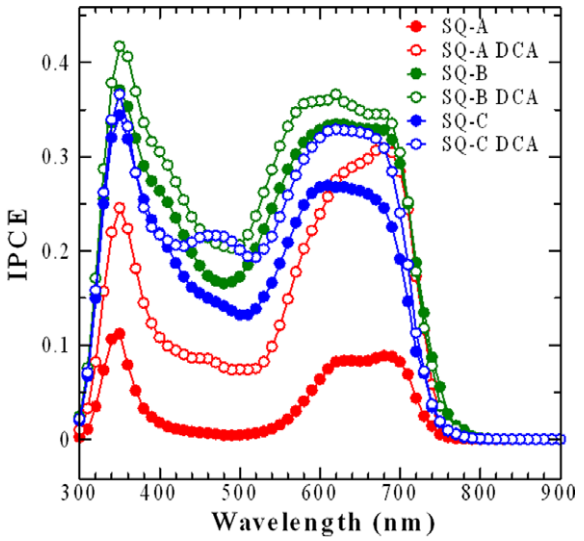

Fig. 8. IPCE as a function of the wavelength of incident monochromatic light for TiO_2 electrodes in the presence and absence of DCA for SQ dyes.

as compared to the dye aggregates, monomers can inject electrons to TiO_2 more efficiently [36]. A perusal of dye structures of SQ dyes as shown in Fig. 1(a) clearly indicates that SQ-A having increased aromatic ring is relatively prone to form π-stacked dye aggregates as compared to that of SQ-B where the reduced number of aromatic ring along with the very long alkyl chain (Octadecyl) resists the easy dye aggregation. In the presence of DCA these π-stacked aggregates get broken leading to facile electron injection yield and thus Jsc. Presumably this prevention of dye aggregation is responsible for the pronounced effect of DCA in the case SQ-A.

Incident photon to electron conversion efficiency (IPCE) as function of wavelength (action spectrum) is basically measured to evaluate the photoresponse of photoelectrode under investigation in the whole spectral region. Fig. 8 shows the action spectra of SQ dyes in the presence and absence of DCA. A perusal of action spectrum clearly indicates that there is a clear enhancement of IPCE maximum upon the introduction of DCA for all of the SQ dyes. Following a similar trend as observed in the *I–V* characteristics as shown in Fig. 6, there was pronounced enhancement of IPCE for SQ-A (9–31%) as compared to the IPCE enhancement for SQ-B (34–36%) in the presence of DCA. SQ-C having identical structure of SQ-B differing only in the length of alkyl substituent viz. butyl in place of octadecyl also shows relatively enhanced IPCE (27–33%) as compared to that of SQ-B upon DCA introduction. This further supports that inclusion of DCA leads to the breaking of π-stacked aggregates followed by facile electron injection resulting in to pronounced enhancement of Voc in the case of SQ-A.

4. Conclusions

It has been shown that surface potential measurements using SKPM is an important probing tool to get the initial idea about the Voc to be observed after DSSC fabrication. Lower Voc in the case of organic dyes under investigation has been attributed to the formation of positive dipole at TiO_2/dye interface leading to the negative shift of surface potential and downward shift of the conduction band edge of TiO_2 owing to a decrease in the overall observed Voc. The role of DCA in the enhancement of Voc by the upward shift of the titania conduction band edge has been clearly shown by surface potential measurement, which gives a positive shift after DCA introduction. The use of DCA as co-adsorbent with newly synthesized organic dyes SQ-A, SQ-B and SQ-C also give the positive shift in measured surface potential, which was much pronounced for dye SQ-A. This positive shift in the surface potential in the presence of DCA was also in accordance with the DSSC performance, where both of the Voc and Jsc were found to be increased after DCA incorporation. Pronounced improvement of device performance in the case of SQ-A as compared to that of SQ-B in the presence of DCA has been attributed to the enhanced shift of the surface potential and prevention of dye aggregation owing to its molecular structure.

Acknowledgements

This work has been partially supported by New Energy and Industrial Technology Organization (NEDO) under the Japanese Government. The authors (SSP) would like to thank the Fukuoka Industry Science and Technology (IST) Foundation for their financial support.

References

[1] B. O'Regan, M. Gratzel, Nature 353 (1991) 737.
[2] A. Hagfeldt, M. Gratzel, Acc. Chem. Res. 33 (2000) 269.
[3] M.K. Nazeeruddin, P. Pechy, M. Gratzel, Chem. Commun. (1997) 1705.
[4] A. Hagfeldt, M. Gratzel, Chem. Rev. 95 (1995) 49.
[5] F. Inakazu, Y. Noma, Y. Ogomi, S. Hayase, Appl. Phys. Lett. 93 (2008) 093304.
[6] Q.H. Yao, F.S. Meng, F.Y. Li, H. Tian, C.H. Huang, J. Mater. Chem. 13 (2003) 048.
[7] Z.S. Wang, F.Y. Li, C.H. Huang, Chem. Commun. (2000) 2063.
[8] B.C. O'Regan, S. Scully, A.C. Mayer, E. Palomares, J. Durrant, J. Phys. Chem. B 109 (2005) 4616.
[9] H. Kusama, H. Arakawa, J. Photochem. Photobiol. A 160 (2003) 171.
[10] H. Kusama, Y. Konishi, H. Sugihara, H. Arakawa, Sol. Energy Mater. Sol. Cells 80 (2003) 167.
[11] S. Ruhle, M. Greenshtein, S.G. Chen, A. Merson, H. Pizem, C.S. Sukenik, D. Cahen, A. Zaban, J. Phys. Chem. B 109 (2005) 18907.
[12] S. Sakaguchi, H. Ueki, T. Kato, T. Kado, R. Shiratuchi, W. Takashima, K. Kaneto, S. Hayase, J. Photochem. Photobiol. A 164 (2004) 117.
[13] E. Palomares, J.N. Clifford, S.A. Haque, T. Lutz, J.R. Durrant, J. Am. Chem. Soc. 125 (2003) 475.
[14] G.R.R.A. Kumara, K. Tennakone, V.P.S. Perera, A. Konno, S. Kaneko, M. Okuya, J. Phys. D: Appl. Phys. 34 (2001) 868.
[15] A. Kay, M. Gratzel, Chem. Mater. 14 (2002) 2930.
[16] Y. Harima, K. Kawabuchi, S. Kajihara, A. Ishii, Y. Ooyama, K. Takeda, Appl. Phys. Lett. 90 (2007) 103517.
[17] J.H. Yum, P. Walter, S. Huber, D. Rentsch, T. Gieger, F. Nuesch, F.D. Angelis, M. Gratzel, M.K. Nazeeruddin, J. Am. Chem. Soc. 129 (2007) 10320.
[18] M. Leibovitch, L. Kronik, B. Mishori, Y. Shapira, C.M. Hanson, A.R. Clawson, P. Ram, Appl. Phys. Lett. 69 (1996) 2587.
[19] R. Cohen, L. Kronik, A. Shanzer, D. Cahen, A. Liu, Y. Rosenwaks, J.K. Lorenz, A.B. Ellis, J. Am. Chem. Soc. 121 (1999) 10545.
[20] Y. Harima, K. Yamashita, H. Ishii, K. Seki, Thin Solid Films 366 (2000) 237.
[21] S. Ruhle, D. Cahen, J. Appl. Phys. 96 (2004) 1556.
[22] K. M Lee, V. Suryanarayanan, K.C. Ho, K.R.J. Thomas, J.T. Lin, Sol. Energy Mater. Sol. Cells 91 (2007) 1426.

[23] B. Oswald, L. Patsenker, J. Duschl, H. Szmacinski, O.S. Wolfbeis, E. Terpetsching, Bioconjugate Chem. 10 (1999) 925.
[24] M. Matsui, H. Mase, J.Y. Jin, K. Funabiki, T. Yoshida, H. Minoura, Dyes Pigments 70 (2006) 48.
[25] W.H. Zhan, W.J. Wu, J.L. Hua, Y.H. Jing, F.S. Meng, H. Tian, Tetrahedron Lett. 48 (2007) 2461.
[26] A. Vilan, J. Ghabboun, D. Cahen, J. Phys. Chem. B 107 (2003) 6360.
[27] J. Kruger, U. Bach, M. Gratzel, Adv. Mater. 12 (2000) 447.
[28] A. Kay, M. Gratzel, J. Phys. Chem. 97 (1993) 6272.
[29] P. Wang, S.M. Zakeeruddin, P. Comte, R. Charvet, H.B. Robin, M. Gratzel, J. Phys. Chem. B 107 (2003) 14336.
[30] N.R. Neale, N. Kopidakis, J. van de Lagemaat, M. Gratzel, A.J. Frank, J. Phys. Chem. B 109 (2005) 23183.
[31] K. Hara, Y. Dan-oh, C. Kasada, Y. Ohga, A. Shinpo, S. Suga, K. Sayama, H. Arakawa, Langmuir 20 (2004) 4205.
[32] K. Sayama, S. Tsukagoshi, T. Mori, K. Hara, Y. Ohga, A. Shinpo, Y. Abe, S. Suga, H. Arakawa, Sol. Energy Mater. Sol. Cells 80 (2003) 47.
[33] N. Kopidakis, N.R. Neale, A.J. Frank, J. Phys. Chem. B 110 (2006) 12485.
[34] Z.S. Wang, Y. Cui, Y. Dan-Oh, C. Kasada, A. Shinpo, K. Hara, J. Phys. Chem. C 111 (2007) 7224.
[35] N.R. Neale, N. Kopidakis, J. van de Lagemaat, M. Gratzel, A.J. Frank, J. Phys. Chem. B 109 (2005) 23183.
[36] A.C. Khazraji, S. Hotchandani, S. Das, P.V. Kamat, J. Phys. Chem. B 103 (1999) 4693.

Organic Electronics 11 (2010) 427–433

Contents lists available at ScienceDirect

Organic Electronics

journal homepage: www.elsevier.com/locate/orgel

Effect of hole transporting materials in phosphorescent white polymer light-emitting diodes

Dong-Hyun Lee [a], Yang-Peng Liu [a], Kyung-Hee Lee [a], Heeyeop Chae [a], Sung M. Cho [a,b,*]

[a] School of Chemical Engineering, Sungkyunkwan University, Suwon 440-746, Republic of Korea
[b] Advanced Materials and Process Research Center for IT, Sungkyunkwan University, Suwon 440-746, Republic of Korea

ARTICLE INFO

Article history:
Received 30 September 2009
Received in revised form 12 November 2009
Accepted 19 November 2009
Available online 26 November 2009

Keywords:
Polymer light-emitting diodes
Hole transporting material
Interlayer
TCTA

ABSTRACT

We have investigated the effect of hole transporting materials in phosphorescent white polymer light-emitting diodes. The doping of a hole transporting material TCTA (4,4′,4″-tris(N-carbazolyl)-triphenylamine) resulted in enhanced luminance and efficiency while the doping of other hole transporting materials degraded the device performance. The effect of hole transporting materials on the performance of the device has been explained with the triplet energy level, HOMO (highest occupied molecular orbital)/LUMO (lowest unoccupied molecular orbital) level, and hole mobility of the materials. The doping of TCTA into an emissive layer increased the maximum current efficiency by 43%. Simultaneous utilization of TCTA both as an interlayer and a dopant in an emissive layer has been found to enhance the device performance further. The optimized phosphorescent white polymer light-emitting device showed the current efficiency of 20.5 cd/A with the luminance of 1800 cd/m^2 at an operating voltage of 11.5 V.

© 2009 Elsevier B.V. All rights reserved.

1. Introduction

White organic light-emitting diodes (WOLEDs) have been studied due to their potential applications in full-color flat panel displays, back-lighting sources for liquid-crystal displays, and solid-state lighting [1–3]. High-efficiency WOLEDs are important since they can save electrical energy and have longer lifetime by reducing heat generation from the devices. In order to achieve highly efficient WOLEDs, multilayer structures have been commonly utilized to realize both the minimized electron/hole injection barriers and the optimized electron–hole balance in the devices. Highly efficient multilayer WOLEDs have been fabricated by vacuum deposition using various low molecular weight organic materials. In contrast, as another type of WOLEDs, white polymer light-emitting diodes (WPLEDs) utilize polymers instead of low molecular weight organic materials and have much simpler structures, e.g. single emissive layer since the structures can only be fabricated by solution processes which are difficult to avoid the dissolution of the layer underneath. As the result, WPLEDs have usually exhibited much lower efficiencies compared with multilayer WOLEDs with low molecular weight organic materials. In order to achieve white emission from polymer light-emitting diodes (PLEDs), single emissive layer structure with a polymer host such as PVK (poly(N-vinylcarbazole)) doped with two or three phosphorescent dyes has been studied most frequently. A WPLED with two or three iridium-cored phosphorescent dyes doped into PVK:OXD-7 (1,3-bis[(4-*tert*-butylphenyl)-1,3,4-oxadiazolyl]phenylene) matrix was reported to show the maximum luminous efficiency (LE) of 21.9 cd/A [4]. In the study, OXD-7 was included into the host PVK to facilitate electron transport. More recently, a WPLED with the maximum LE of 36.1 cd/A has been reported [5]. The device utilized a separate water/alcohol-soluble electron transport layer doped with Li_2CO_3 salt for efficient electron transport and hole blocking. The WPLED

* Corresponding author. Address: School of Chemical Engineering, Sungkyunkwan University, Suwon 440-746, Republic of Korea. Tel.: +82 31 2907251; fax: +82 31 2907272.
E-mail address: sungmcho@skku.edu (S.M. Cho).

1566-1199/$ - see front matter © 2009 Elsevier B.V. All rights reserved.
doi:10.1016/j.orgel.2009.11.022

has also been fabricated with PVK:OXD-7 matrix doped with two phosphorescent dyes. High-efficiency PLEDs reported to date have not utilized a small molecular hole transporting material other than PVK as a hole transporting polymer host. However, most of recent reports on WOLEDs with low molecular weight organic materials have proved the effectiveness of the inclusion of hole transporting TCTA in the device structure [6–10]. Since the hole transporting TCTA has relatively higher triplet energy level (2.8 eV) and lower HOMO level (5.9 eV) than those of most phosphorescent emitters, the inclusion of TCTA into the emissive layer or as an interlayer results in beneficial effect on the device performance [6,7].

In this study, we introduced a hole transporting TCTA into WPLEDs for the first time and investigated the effect of the introduction on the device performance. In order to examine the effect of TCTA in detail, we have compared the results with other hole transporting materials such as TPD (N,N′-diphenyl-N,N′-bis(3-methylphenyl)-1,1′-diphenyl-4,4′-diamine) and α-NPD (4,4′-bis[N-(1-naphthyl)-N-phenylamino]biphenyl). We have found the optimal concentration of TCTA in single emissive layer and also showed the effect of TCTA on the device performance when used as an interlayer.

2. Experimental details

For the preparation of WPLEDs, commercial ITO (indium tin oxide) glass substrates with a sheet resistance of 10 Ω/square were used. The ITO glass was cleaned by sonification in an isopropyl alcohol (IPA) and acetone, and finally rinsed in deionized water. The line pattern of ITO was prepared by conventional photolithography process. After the plasma treatment of ITO surface at 100 W oxygen plasma for 3 min, PEDOT:PSS (poly(3,4-ethylenedioxythiophene) doped with poly(styrene sulfonate); Baytron P AI4083) was spin-coated on the ITO surface to have the thickness of 40 nm and baked at 110 °C for 5 min. Subsequently, single emissive layer was spin-coated with a premixed organic solution to have the thickness of 50 nm. The organic solution was composed of a host PVK, an electron transporting OXD-7, a blue phosphorescent FIrpic (bis(3,5-difluoro-2-(2-pyridyl)phenyl-(2-carboxypyridyl)iridium)), a green phosphorescent Ir(mppy)$_3$ (tris(2-(4-toltyl)phenylpyridine)iridium), and a red phosphorescent Ir(piq)$_2$(acac) (bis (1-(phenyl)isoquinoline)-iridium acetylacetonate), which were dissolved in chlorobenzene solvent. The composition was pre-optimized and fixed in all experiments with 50:40:9.6:0.2:0.2 for PVK:OXD-7:FIrpic:Ir(mppy)$_3$:Ir(piq)$_2$(acac). For investigating the effect of hole transporting TCTA, TPD and α-NPD on the performance of the devices, some devices were fabricated using an organic solution in which TCTA, TPD, or α-NPD (0–10 wt.% of the amount of PVK) was added additionally to the premixed solution with the fixed composition. After the single emissive layer was formed, the layer was dried at 80 °C for 30 min. Finally, the device was completed by thermal evaporation at a pressure of 2×10^{-6} torr of lithium fluoride (LiF) and aluminum (Al), of which the thicknesses are 1 and 100 nm, respectively. In order to fabricate devices with a TCTA interlayer, a solution containing 0.5 wt.% TCTA in toluene was spin-coated on PEDOT:PSS surface. The interlayer was dried at 180 °C for 30 min on a hot plate prior to the spin coating of single emissive layer.

Active area of all fabricated devices was 9 mm^2 and all electrical measurements were performed under ambient condition without encapsulation. The current–voltage–luminance (*I–V–L*) characteristics were measured using a source measure unit (Keithley 2400) and using a luminance meter (Minolta CS100). The electroluminescence (EL) spectra and device efficiencies of the devices were recorded by using Minolta CS1000.

3. Results and discussion

In order to investigate the effect of hole transporting materials in single emissive layer PLED, we have tested three different materials of TCTA, TPD, and α-NPD. In the single emissive layer, the compositions of other constituents, PVK, OXD-7, FIrpic, Ir(ppy)$_3$, and Ir(piq)$_2$(acac) are fixed for a meaningful comparison of the hole transporting materials. Hole drift mobility of TCTA, TPD, and α-NPD is known to be 2.0×10^{-5}, 1.1×10^{-3}, 8.8×10^{-4} cm^2 V^{-1}s^{-1}, respectively [11], which means that the drift speed of holes in TCTA is the lowest when compared with those in TPD and α-NPD at a fixed electric field. By analyzing the *I–V–L* characteristics and efficiencies of the devices doped with a fixed amount of the materials, we could estimate how hole mobility affects the performance of the devices from the experimental results. As another factor to affect the device performance, the HOMO and LUMO levels of the hole transport materials are shown in Fig. 1a, along with those of other constituents in the device. An important thing

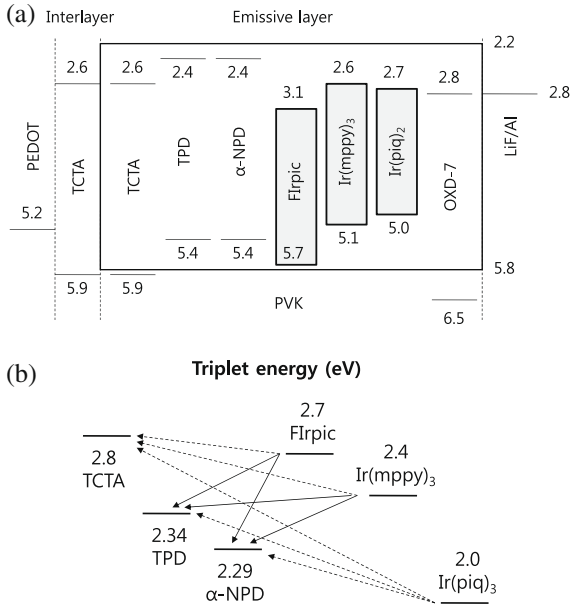

Fig. 1. (a) Energy level diagram showing HOMO/LUMO levels of constituent materials for the devices and (b) triplet energy levels (T_1) of hole transporting materials and phosphorescent emitters.

we can notice from the figure is the fact that the emission from FIrpic could be hindered upon the inclusion of TPD and α-NPD since the materials should act as competitive hole traps due to their higher HOMO levels than that of FIrpic. We think that it should be the reason why the previous studies reporting single layer PLEDs doped with FIrpic [4,5] have not utilized the hole transport materials other than the hole transporting host PVK in their devices. In single layer PLEDs doped with $Ir(mppy)_3$ only, however, the effective utilization of TPD and α-NPD has been reported in the literature [12,13]. Since HOMO levels of TPD and α-NPD are lower than that of $Ir(mppy)_3$, TPD and α-NPD do not act as efficient hole traps preventing the formation of excitons at the phosphorescent emitter. Moreover, higher hole mobility of TPD and α-NPD than that of the host PVK can enhance the performance of the devices upon the doping of the materials. Even though the hole mobility and HOMO/LUMO levels of the hole transporting materials can affect the device performance, the most important factor affecting the performance of the devices upon the utilization of hole transporting materials should be the triplet energy of the materials. The utilization of TPD and α-NPD has been examined with multilayer phosphorescent OLEDs doped with FIrpic or $Ir(mppy)_3$ in the literature [14,15]. They found that exciton energy could transfer from FIrpic or $Ir(mppy)_3$ to TPD and α-NPD since the triplet energies of the hole transporting materials are lower than those of FIrpic or $Ir(mppy)_3$. The triplet energies of hole transporting TCTA, TPD, α-NPD are 2.8 [7], 2.34 [14], 2.29 eV [14], respectively and the energies of phosphorescent FIrpic, $Ir(mppy)_3$, and $Ir(piq)_2(acac)$ emitters are 2.7 [14], 2.4 [6], 2.0 eV [16], respectively. As shown in Fig. 1b, it is expected

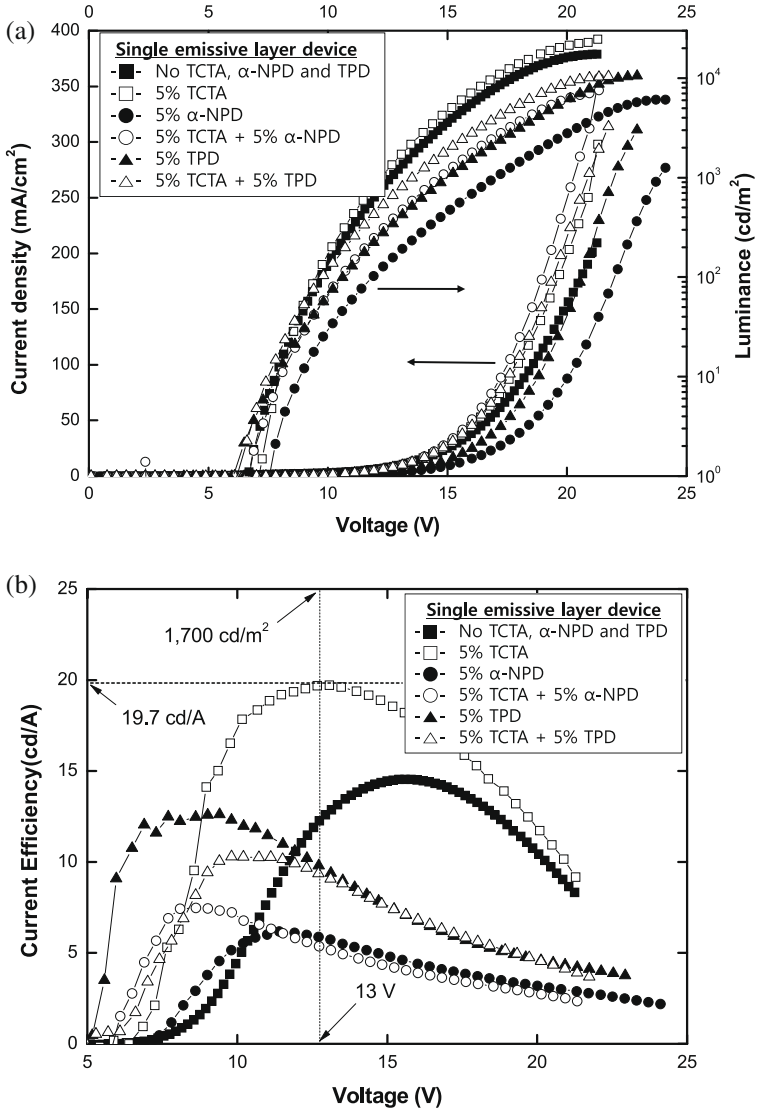

Fig. 2. (a) Current–voltage–luminance (*I–V–L*) curves of WPLEDs with different hole transporting materials and (b) current efficiency characteristics of the devices.

that low triplet energies of TPD and α-NPD should provide non-radiative paths for exciton quenching and reduce the phosphorescent light emission from FIrpic and $Ir(mppy)_3$. Since the triplet energy of TCTA is higher than those of three different phosphorescent emitters, however, TCTA is not expected to cause the exciton quenching. In addition, the lowest HOMO level of TCTA compared with those of other constituents could enhance the performance of the devices.

As expected, we indeed have found the reduced efficiency upon the doping of TPD or α-NPD into emissive layer as shown in Fig. 2a and b. On the other hand, the doping of TCTA into the emissive layer was found to increase the highest current efficiency by 43% along with the decrease in the voltage at the highest current efficiency as shown in Fig. 2b. The result indicates that TCTA confines the triplet excitons within the emissive layer effectively while TPD or α-NPD acts as centers for the excitons to be transferred readily. As shown in Fig. 2b, the devices singly doped with TPD or α-NPD exhibited the lower efficiencies compared with that of undoped device. Specially, the doping of α-NPD lowers the efficiency most significantly. We think that it is mainly because the triplet energy is the lowest for α-NPD. However, the doping of TCTA enhances both luminance and efficiency of the device due to the enhanced exciton confinement. The co-doping of TCTA with TPD or α-NPD results in the increases in the efficiency compared with the singly doped cases but the resulting efficiency still does not exceed that of undoped device. It is worth to mention that the voltages at the highest efficiencies are in order of TPD, α-NPD, and TCTA which is the same as in descending order for the hole mobilities of the three compounds. Since the hole mobility of PVK is $2.5 \times 10^{-6}\ cm^2\ V^{-1}s^{-1}$ [17] which is the lowest compared with those of TCTA,

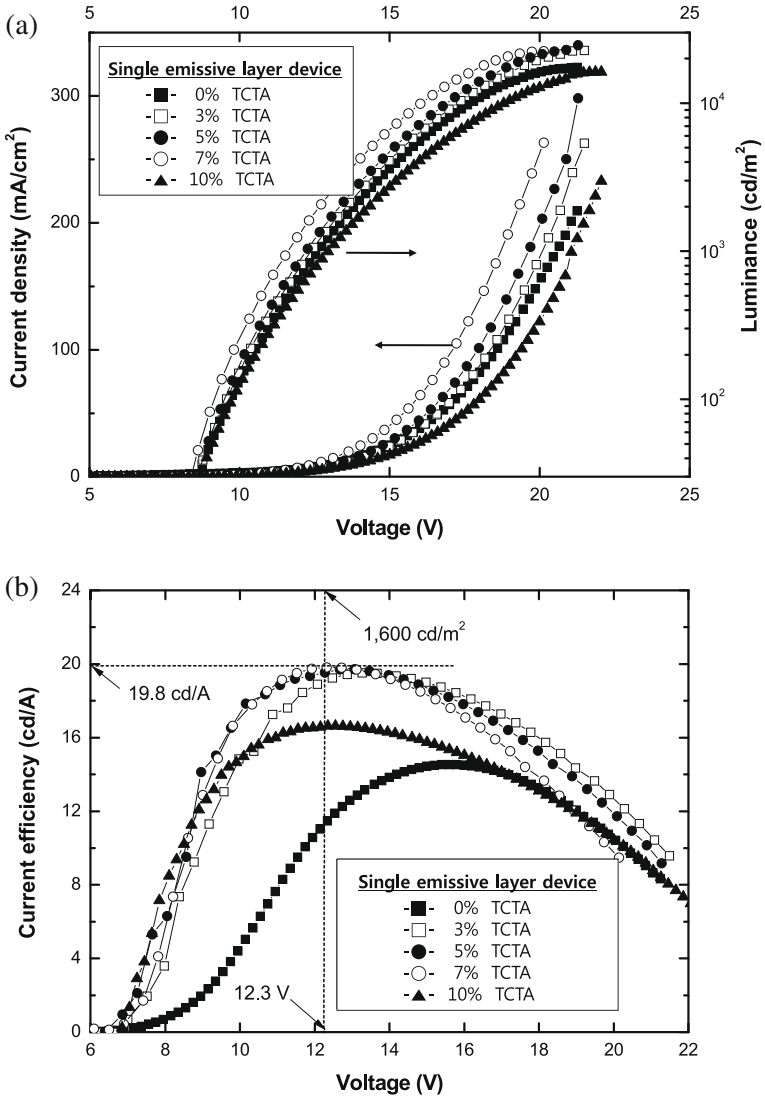

Fig. 3. (a) Current–voltage–luminance (*I–V–L*) curves of WPLEDs with different TCTA concentrations and (b) current efficiency characteristics of the devices.

TPD, and α-NPD, the voltage at the highest efficiency was found the highest for the undoped device. This result suggests that the addition of hole transport material in single layer PLEDs affect the operating voltages giving the highest efficiency of the devices due to their different hole mobility. Another thing to be noticed from Fig. 2a is that the current density is always higher whenever TCTA exists in the emissive layer. We attribute it to the lowest HOMO levels of TCTA close to that of PVK.

In order to optimize the concentration of TCTA, we have varied the TCTA concentration in single layer WPLEDs and measured the performance of the devices as shown in Fig. 3a and b. The highest efficiency was obtained at TCTA concentration of 7 wt.%. As can be seen from the figure, however, the highest efficiency of the devices with a TCTA concentration range from 5 to 7 wt.% was found close to be around 20 cd/A at a voltage around 12 V. The voltage giving the highest efficiency was found to decrease as the TCTA concentration increases. We attribute it to the fact that the hole mobility of TCTA is higher than that of PVK. After optimization, the voltage showing the highest efficiency was reduced from 13 to 12.3 V even though the

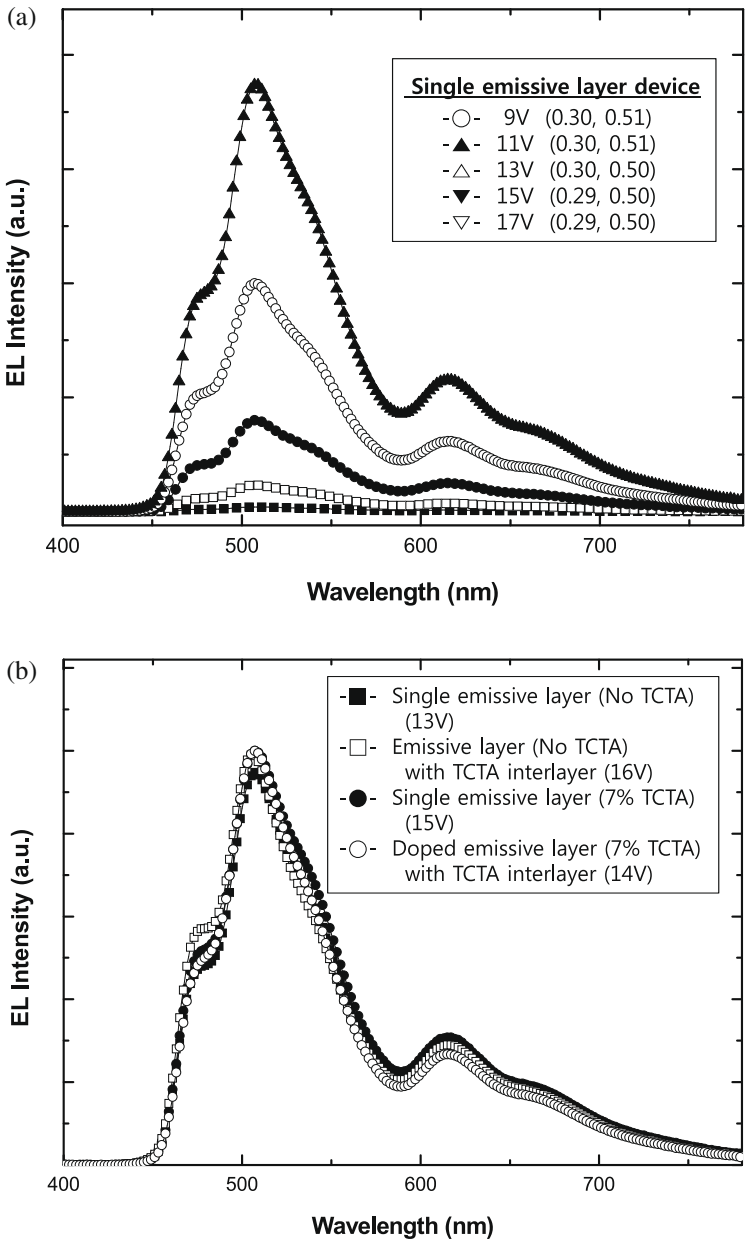

Fig. 4. (a) Electroluminescence spectra of WPLEDs with the 7 wt.% doping of TCTA and the corresponding color coordinates at different applied voltages and (b) electroluminescent spectra of WPLEDs of four different structures.

luminance and current efficiency were almost the same as shown in Figs. 2b and 3b. We have shown the EL spectra of the TCTA-doped single emissive-layer device in Fig. 4a. As the driving voltage increases, the spectra and color coordinate were not found changed significantly. The color coordinate was (0.30, 0.50) which corresponded to greenish white emission.

When TCTA is separated as an interlayer instead of the doping into the emissive layer as a hole transporting constituent, the role of TCTA can be examined more clearly. Since HOMO levels of TCTA and PVK are very close, the hole injecting property to the emissive layer should be almost the same. We expect that the difference in hole mobility between TCTA and PVK can give different device property. More importantly, the triplet exciton confinement given by TCTA interlayer enhances the device efficiency more pronouncedly than that by TCTA addition in the emissive layer. In the literature [6], TCTA interlayer has been introduced by a wet process to enhance the device efficiency greatly. The same experimental procedure was followed in this study.

We have measured the current efficiency to compare the performance between devices of different structures. In order to compare the device performance with the current efficiency, the emission spectra should be the same for all the devices in the comparison. We have fabricated four different kinds of devices which are the followings: (1) conventional single emissive-layer device without TCTA doping; (2) single emissive-layer device (without TCTA) with a TCTA interlayer; (3) TCTA-doped single emissive-layer device; (4) TCTA-doped emissive-layer device with a TCTA interlayer. We have measured the emission spectra for the devices and shown the data in Fig. 4b. As shown in the figure, the emission spectra were found almost the same for the four different devices.

As shown in Fig. 5a and b, the introduction of TCTA in the devices both as an interlayer and a co-dopant showed

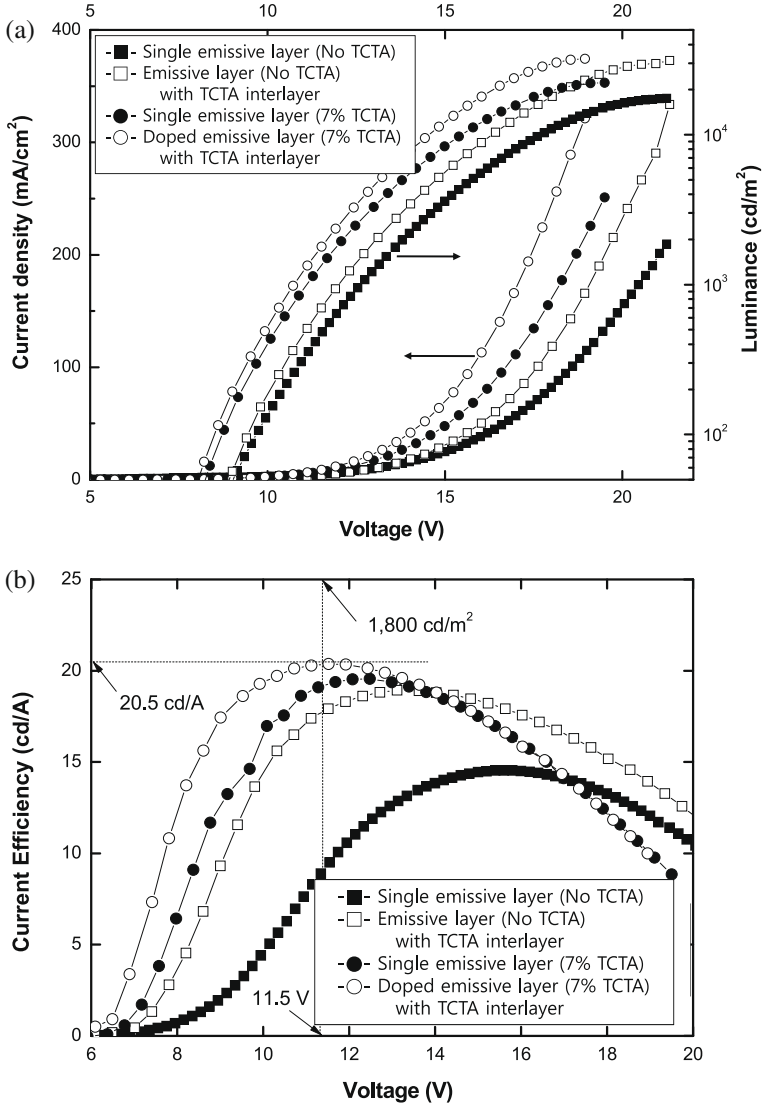

Fig. 5. (a) Current–voltage–luminance (*I*–*V*–*L*) curves of WPLEDs with a TCTA interlayer and (b) current efficiency characteristics of the devices.

the increase in the current efficiency of the devices. Relative to the current efficiency of the single emissive-layer device (without TCTA) without the interlayer, the utilization of TCTA as a co-dopant into the single emissive layer showed the higher increase in the current efficiency compared with the utilization of TCTA as an interlayer. Simultaneous utilization of TCTA both as an interlayer and as a dopant in the emissive layer can enhance the device performance further. The simultaneous utilization of TCTA is found to maximize the current efficiency. It should be mentioned here that the utilization of TCTA interlayer has not only increased the current efficiency but also increased the luminance significantly as shown in Fig. 5a. The optimized phosphorescent white polymer light-emitting device with TCTA showed the current efficiency of 20.5 cd/A with the luminance of 1800 cd/m^2 at an operating voltage of 11.5 V. The performance of WPLEDs in this study is comparable to the performance of previously reported WPLEDs [4,5] which showed the best efficiency to date.

4. Conclusions

We have investigated the effect of hole transporting materials in phosphorescent white polymer light-emitting diodes. The doping of a hole transporting material TCTA resulted in the enhanced luminance and efficiency while the doping of other hole transporting materials degraded the device performance. We have revealed that the doping of hole transporting TPD and α-NPD into an emissive layer gave a harmful effect on the device performance due to their low triplet energies compared with those of phosphorescent emitters. On the other hand, the utilization of TCTA as an interlayer or as a dopant in an emissive layer enhanced the luminance and current efficiency of the devices. The results were explained with the triplet energy level, HOMO/LUMO level, and hole mobility of the materials. The optimized phosphorescent white polymer light-emitting device showed the current efficiency of 20.5 cd/A with the luminance of 1800 cd/m^2 at an operating voltage of 11.5 V.

Acknowledgements

This research was supported by Basic Science Research Program through the National Research Foundation of Korea (NRF) funded by the Ministry of Education, Science and Technology (2009-0083540). This work was also partially supported by a grant from Gyeonggi Province through the GRRC (Gyeonggi Regional Research Center) program in Sungkyunkwan University.

References

[1] J. Kido, M. Kimura, K. Nagai, Multilayer white light-emitting organic electroluminescent device, Science 267 (1995) 1332–1334.
[2] B.W. D'Andrade, S.R. Forrest, White organic light-emitting devices for solid-state lighting, Adv. Mater. 16 (2004) 1585–1595.
[3] A. Misra, P. Kumar, M.N. Kamalasanan, S. Chandra, White organic LEDs and their recent advancements, Semicond. Sci. Technol. 21 (2006) 35–47.
[4] H. Wu, J. Zou, F. Liu, L. Wang, A. Mikhailovsky, G.C. Bazan, W. Yang, Y. Cao, Efficient single active layer electrophosphorescent white polymer light-emitting diodes, Adv. Mater. 20 (2008) 696–702.
[5] F. Huang, P.-I. Shih, C.-F. Shu, Y. Chi, A.K.-Y. Jen, Highly efficient polymer white-light-emitting diodes based on lithium salts doped electron transporting layer, Adv. Mater. 21 (2009) 361–365.
[6] J.J. Park, T.J. Park, W.S. Jeon, R. Pode, J. Jang, J.H. Kwon, E.-S. Yu, M.-Y. Chae, Small molecule interlayer for solution processed phosphorescent organic light emitting device, Org. Electron. 10 (2009) 189–193.
[7] S. Reineke, F. Lindner, G. Schwartz, N. Seidler, K. Walzer, B. Lussem, K. Leo, White organic light-emitting diodes with fluorescent tube efficiency, Nature 459 (2009) 234–238.
[8] A. Benor, S. Takizawa, P. Chen, C. Perez-Bolivar, P. Anzenbacher Jr., Dramatic efficiency improvement in phosphorescent organic light-emitting diodes with ultraviolet-ozone treated poly(3,4-ethylenedioxythiophene):poly(styrenesulfonate), Appl. Phys. Lett. 94 (2009) 1–3.
[9] J.-W. Kang, S.-H. Lee, H.-D. Park, W.-I. Jeong, K.-M. Yoo, Y.-S. Park, J.-J. Kim, Low *roll-off* of efficiency at high current density in phosphorescent organic light emitting diodes, Appl. Phys. Lett. 90 (2007) 223508-1–223508-3.
[10] G. Cheng, Y. Zhang, Y. Zhao, Y. Lin, C. Ruan, S. Liu, T. Fei, Y. Ma, Y. Cheng, White organic light-emitting devices with a phosphorescent multiple emissive layer, Appl. Phys. Lett. 89 (2006) 043504-1–043504-3.
[11] K. Mullen, U. Scherf, Organic Light Emitting Devices, Wiley-VCH, 2006.
[12] D.-H. Lee, J.S. Choi, H. Chae, C.-H. Chung, S.M. Cho, Highly efficient phosphorescent polymer OLEDs fabricated by screen printing, Displays 29 (2008) 436–439.
[13] X.H. Yang, D. Neher, Polymer electrophosphorescence devices with high power conversion efficiencies, Appl. Phys. Lett. 84 (2004) 2476–2478.
[14] J. Lee, N. Chopra, S.-H. Eom, Y. Zheng, J. Xue, F. So, J. Shi, Effects of triplet energies and transporting properties of carrier transporting materials on blue phosphorescent organic light emitting devices, Appl. Phys. Lett. 93 (2008) 123306-1–123306-3.
[15] K. Goushi, R. Kwong, J.J. Brown, H. Sasabe, C. Adachi, Triplet exciton confinement and unconfinement by adjacent hole-transport layers, J. Appl. Phys. 95 (2004) 7798–7802.
[16] S.H. Kim, J. Jang, J.Y. Lee, Improved efficiency in red phosphorescent organic light-emitting devices using double doping structure, Syn. Met. 157 (2007) 228–230.
[17] D.M. Pai, J.F. Yanus, M. Stolka, Trap-controlled hopping transport, J. Phys. Chem. 88 (1984) 4714–4717.

Organic Electronics 11 (2010) 434–438

Contents lists available at ScienceDirect

Organic Electronics

journal homepage: www.elsevier.com/locate/orgel

Solution processable lutetium phthalocyanine organic field-effect transistors

Nandu B. Chaure [a], Jose Luis Sosa-Sanchez [b,1], Andrew N. Cammidge [b], Michael J. Cook [b], Asim K. Ray [c,*]

[a] Department of Physics, University of Pune, Ganeshkhind, Pune 411007, India
[b] School of Chemistry, University of East Anglia, Norwich NR4 7TJ, UK
[c] The Wolfson Centre For Materials Processing, Brunel University, Uxbridge, Middlesex UB8 3PH, UK

ARTICLE INFO

Article history:
Received 26 October 2009
Received in revised form 19 November 2009
Accepted 20 November 2009
Available online 24 November 2009

Keywords:
Substituted bisphthalocyanines
Field-effect transistors
Semiconductors
Mobility

ABSTRACT

Spun films of novel thermotropic liquid crystalline lutetium bisphthalocyanine sandwich complexes substituted with sixteen octyl chains are employed as active organic semiconducting layers in the fabrication of organic field-effect transistors (OFET). When the device is annealed under vacuum at 70 °C, an increase in the field effect mobility in the saturated regime by a factor of five is observed while the threshold voltage is reduced to half the value obtained for as-deposited films. The annealed devices exhibit an increase in on/off ratio by two orders of magnitude. An improvement in performance of OFETs annealed above the crystal to mesophase transition temperature is consistent with atomic force microscopic images indicating increases in grain sizes and decreases in mean surface roughness of the organic bisphthalocyanine films.

© 2009 Elsevier B.V. All rights reserved.

1. Introduction

Metallated phthalocyanines (MPcs) are organometallic macrocycles that typically comprise the usually planar organic ligand (Pc^{2-}) and a metal ion or metalloid within the central cavity of the ring. Common examples are 1:1 complexes of ligand and a metal ion and particular compounds have found applications that include their use as commercial blue/green dyes and pigments, charge generators and carriers in electrophotography and laser printing [1], singlet oxygen photosensitisers for photodynamic therapy [2] and the active layer in a number of optical data recording systems [3]. Detailed studies of their electrical properties have given values for room temperature. Values of the electrical conductivity of undoped samples lie typically within the range 10^{-7} Scm^{-1} to 10^{-15} Scm^{-1} depending upon the polymorphic form of the sample [4]. Complexes of lanthanide metallated Pcs are interesting for a number of reasons. Examples include 2:1 complexes with Pcs, ($Ln^{(III)}Pc_2$), in which the metal ion is sandwiched between two Pc ligands [5,6]. The redox and electrochromic properties of the sandwich compounds have been much investigated [7] and the electrical properties of the so-called 'green' redox state are of particular interest because it is a neutral free radical structure. The conductivity of this free radical state of the lutetium complex, $Ln^{(III)}Pc_2$, has been especially well studied and results led to its description as the first organic semiconductor [8]. In particular, $Lu^{(III)}Pc_2$, and the scandium and tantalum analogues, have been investigated as the electroactive component of thin film field-effect transistors, the films being formed by vapour phase deposition methods [9]. $Lu^{(III)}Pc_2$, substituted with alkylthio groups are soluble in most common organic solvents and values of the dc conductivity were estimated to be in the range of 10^{-8} Scm^{-1} to 10^{-5} Scm^{-1} depending on alkyl chain lengths. The conductivity was also found to be sensitive to the presence of volatile organic compounds

* Corresponding author. Tel.: +44 0 1895 267794; fax: +44 0 1895269737.
E-mail address: asim.ray@brunel.ac.uk (A.K. Ray).
[1] Present address: Centro de Investigación en Dispositivos Semiconductores, Instituto de Ciencias, Benemérita Universidad Autónoma de Puebla.

1566-1199/$ - see front matter © 2009 Elsevier B.V. All rights reserved.
doi:10.1016/j.orgel.2009.11.023

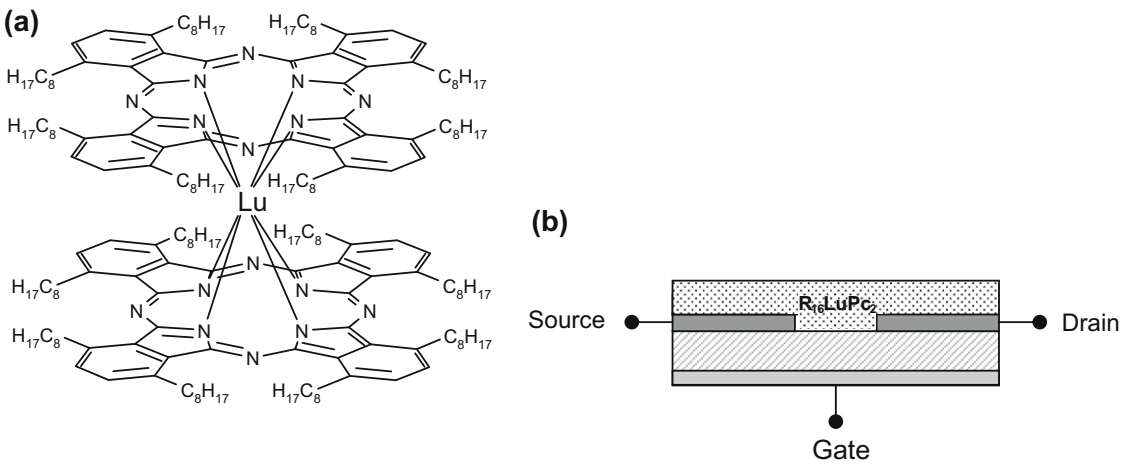

Fig. 1. (a) Structure of $R_{16}LuPc_2$. In this notation, each R refers to a C_8H_{11} (octyl) chain; and (b) schematic cross-sectional view of the bottom gated field-effect transistors used for measurements.

in the ppm range [10]. The conductivity of spun films of liquid crystalline alkyl-substituted dysprosium phthalocyanine $[(C_6S)_8Pc]_2Dy$ derivatives was dependent upon the heat treatment and exhibited directional anisotropy, values varying between 2.76×10^{-5} Scm^{-1} and 2.91×10^{-11} Scm^{-1} [11].

The present paper reports an investigation of the transistor properties of a novel derivative of $Lu^{(III)}Pc_2$. The compound bears eight octyl chains on each of the two rings, i.e. $R = C_8H_{17}$ in Fig. 1a, that render it soluble in organic solvents and we refer to it hereafter as $R_{16}LuPc_2$. The solubility enabled it to be deposited readily as films by the spin coating method [12], a methodology ideal for simple device fabrication [13]. As with similarly substituted 1:1 metallated Pcs [14], the presence of alkyl substituents on the new compound leads to thermotropic liquid crystal properties, in this case a mesophase is exhibited above 62 °C, which allows for a convenient low temperature annealing of the film structure. A bottom gated organic field-effect transistors (OFET) has been fabricated on heavily doped silicon substrates using spin coated films of $R_{16}LuPc_2$ molecules. The electrical behaviour of OFETs is studied with a view to determining the influence of annealing on the transistor characteristics. The surface morphology of the $R_{16}LuPc_2$ is found to be responsible for improvement of the device parameters when an OFET is heated at 70 °C above the crystal to mesophase transition temperature.

2. Experimental details

Heavily doped n-type silicon (1 0 0) wafers having resistivity of 5 μΩ m were covered with 250 nm thick plasma enhanced chemical vapour deposited silicon dioxide (SiO_2) as gate dielectric. Using photolithographic and sputtering techniques, the source and drain contacts were then prepared on the oxide layers in interdigitated gold (50 nm thick)/Cr (10 nm thick) electrode configurations. The octadecyltrichlorosolane (OTS) monolayer was self-assembled on the oxide layer by dipping the substrates in 1% solution of OTS in ethanol in order to improve the quality of the interface between the organic semiconductor and gate dielectric layers. As shown in Fig. 1b, the structure of the bottom-gated thin film organic transistors was then accomplished by depositing a ~100 nm thick $R_{16}LuPc_2$ film at room temperature as an active semiconducting layer on the gate dielectric with the electrode systems. The deposition technique used was to spin coat a small volume of the spreading solution of $R_{16}LuPc_2$ in chloroform (5 mg ml^{-1} concentration) at 2000 rpm for 30 s. The film thickness t was estimated to be 100 nm using the Dektak 6M stylus profilometer. Prior to the deposition of the organic layers, the transistor substrates were ultrasonically cleaned and degreased in acetone and iso-propanol and finally washed in Millipore Milli-Q (resistivity of 18 MΩ cm). The native oxide layer on the reverse side of the silicon wafer was removed by the dry etching method and a layer of Ga–In eutectic was then applied in order to form an ohmic gate terminal. The gate capacitance C_i per unit area of the oxide was estimated to be 9 nF cm^{-2}. Values of the transistor channel length L and W were found to be 10 μm and 2000 μm, respectively. Using a microprocessor controlled Keithley 93 I-V measurement system, the characteristics were obtained at room temperature and in air for the transistors consisting of as-deposited $R_{16}LuPc_2$ films. Measurements were repeated under identical conditions to examine the effects of thermal annealing on the transistor characteristics. For this purpose, the devices were heated to 70 °C in a tubular furnace under vacuum of $\sim 2 \times 10^{-7}$ torr and then gradually cooled down to room temperature at the rate of 1 °C min^{-1}. The surface morphology of the organic $R_{16}LuPc_2$ films was investigated in the tapping mode using a Nanoscope III multimode scanning probe microscope. The atomic force micoscopic images (AFM micrographs) of the $R_{16}LuPc_2$ surfaces were collected over a scan area of 5 × 5 μm for both as-deposited and annealed devices.

3. Results and discussion

The synthesis and structural characterisation of the compound $R_{16}LuPc_2$ will be reported elsewhere [15]. In

summary, the compound was prepared by reacting metal-free 1,4,8,11,15,18,22,25-octakis(octyl)phthalocyanine with lutetium acetate in an octanol solution using DBU as promoter. $R_{16}LuPc_2$ was shown to exhibit a crystal to columnar mesophase transition at 62 °C. The compound is soluble in various hydrocarbon solvents as well as chloroform, the solvent selected for spin coating the material as films.

The AFM micrographs in Fig. 2 show the spin coated deposition of fairly compact, significantly void-free organic $R_{16}LuPc_2$ active layers with uniform thickness and good film adhesion to the silicon substrates. The presence of randomly oriented disc like structures of dimensions between 50 nm and 100 nm was observed on the as-deposited $R_{16}LuPc_2$ film surface. The agglomeration of small size grains is apparent following heat treatment at 70 °C, i.e. at a temperature within the mesophase range exhibited by the compound in the form of bulk material. Following this annealing process, relatively large size clusters with dimensions of the order of 150–200 nm are formed. Values of the average surface roughness were found to have decreased from 30 nm for as-deposited films to 2.2 nm for annealed $R_{16}LuPc_2$ films.

A set of reproducible, hysteresis-free output characteristics are shown in Fig. 3 for both as-prepared and annealed $R_{16}LuPc_2$ field-effect transistors in terms of the drain-to-source current I_{DS} as a function of the drain-to-source voltage V_{DS} for different values of the gate voltage V_{GS} ($0V \leqslant V_{GS} \leqslant -50$ V). The output characteristics were typical of behaviour of a p-type OFETs operating in an accumulation mode. The conductance of the annealed devices was found to be greater than that of as-deposited devices. Values of 1.5 μA and 5 μA for the as-prepared and annealed devices, respectively indicate more than three times increase in the maximum saturation current at $V_{GS} = -50$ V over the same range of V_{DS}. Furthermore, the drain-to-source current in heat treated devices was found to saturate at a drain-to-source voltage lower than the corresponding value for the as-deposited devices.

The graph in Fig. 4 of $\sqrt{I_{DS}}$ as a function of V_G corresponding to $V_{DS} = -45$ V was found to be linear, giving the well known quadratic behaviour:

$$I_{DS(sat)} = \frac{W}{2L}\mu_{(sat)}C_i(V_{GS} - V_T)^2 \quad (1)$$

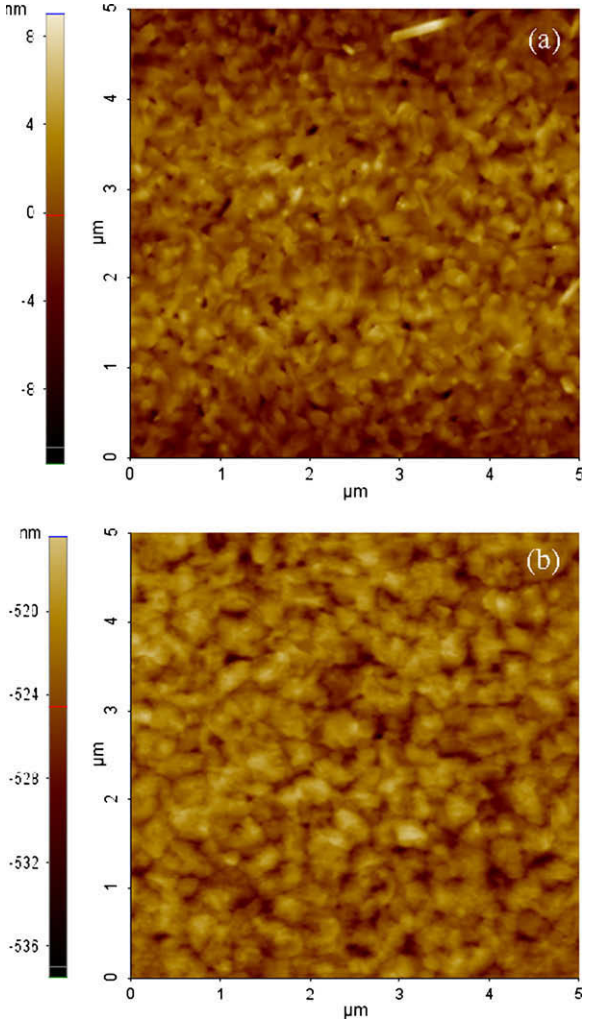

Fig. 2. Micrograph AFM images of (a) as-prepared and (b) annealed $R_{16}LuPc_2$ active layers.

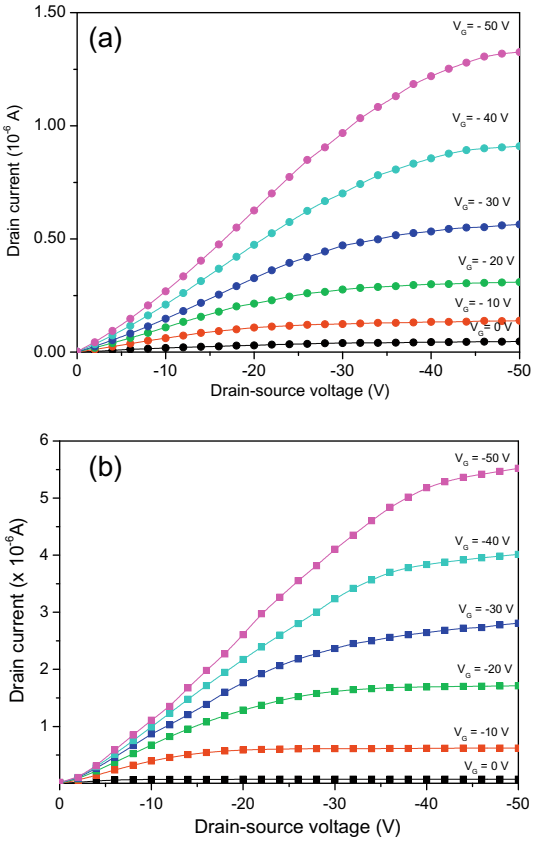

Fig. 3. Output characteristics: drain-to-source current (I_{DS}) as a function of the drain-to-source voltage (V_{DS}) at various drain-to-source voltages of channel length (L) 10 μm and channel width (W) 2000 μm.

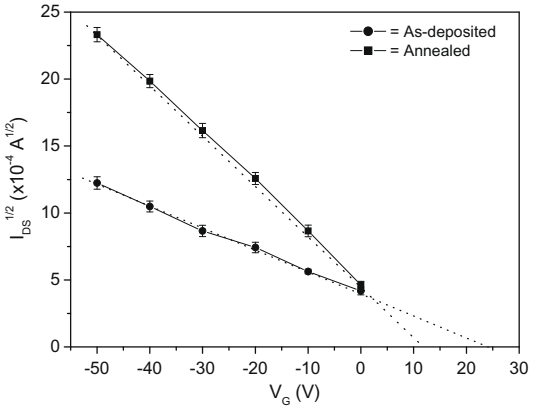

Fig. 4. The square root of drain current as a function of gate voltage in the saturation regime (V_{DS} = −45 V).

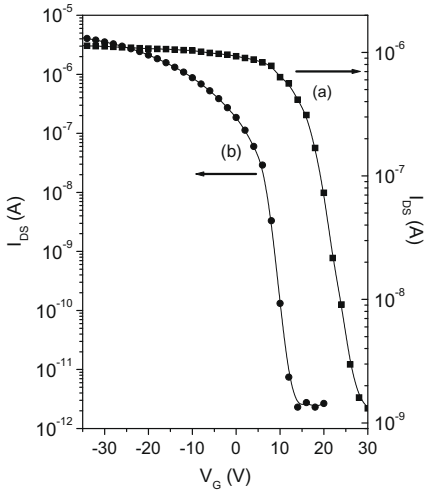

Fig. 5. Transfer characteristics: drain-to-source current (I_{DS}) as a function of gate-to-source voltage (V_G) recorded for (a) as-prepared and (b) annealed $R_{16}LuPc_2$ transistors. Drain-to-source voltage was kept constant at −45 V.

Values of the field effect mobility $\mu_{(sat)}$ in the saturated regime and threshold voltages V_T were estimated from the slope and the intercept at $I_{DS} = 0$ of the linear graphs, respectively. Values of the on/off current modulation ratio were estimated from the transfer characteristics in Fig. 5 in terms of the dependence of the drain-to-source current I_{DS} on the gate voltage V_{GS} at a fixed drain–source voltage of $V_{DS} = -45$ V. Calculations were performed for the transistors using both as-prepared and annealed $R_{16}LuPc_2$ active layers and the results were summarised in Table 1. Values of the mobilities are found to be two orders of magnitude higher than those recently reported for a lutetium (III) bisphthalocyanine derivative substituted with hexylthio groups [16].

The transistor parameters are believed to be dependent upon the $SiO_2/R_{16}LuPc_2$ interface and the grain boundaries in the polycrystalline $R_{16}LuPc_2$ films [17,18]. A value of 2.8×10^{12} cm^{-2} is obtained for the density N_t of traps at the interface between the as-deposited $R_{16}LuPc_2$ layer and the gate SiO_2 dielectrics using the equation [19]:

$$N_t = \left[\frac{S\log(e)}{\left(\frac{KT}{q}\right)} - 1\right]\frac{C_i}{q} \tag{2}$$

where k, T and q are the Boltzmann constant, the operating temperature and the electronic charge, respectively. S, the sub-threshold voltage swing defined as the voltage V_{GS} required to increase the drain-to-source current I_{DS} by a factor of 10 was calculated using the following equation:

$$S = \frac{dV_{GS}}{d(\log I_{DS})} \tag{3}$$

Values of S were found to be 3.8 V/decade and 1.6 V/decade from the transfer characteristics for as-deposited and heat treated transistors, respectively. A similar calculation for the annealed $R_{16}LuPc_2$ layer produced a reduced value of 1.4×10^{12} cm^{-2} for the density N_t of traps at the interface between the annealed $R_{16}LuPc_2$ and SiO_2 layers. The origin of this reduction of the interface traps may possibly attributed to the decrease in surface roughness of the annealed $R_{16}LuPc_2$ layer and the increase in the interfacial bonding between the active organic layer and the gate dielectric.

As observed earlier in AFM images in Fig. 2, the grain boundaries in the $R_{16}LuPc_2$ layer are expected to influence the transistor characteristics. The effect of grain-boundary potential barriers is usually explained in terms of the Levinson model which describes the dependence of the drain-to-source current (I_{DS}) in the linear regime on the density N_g of traps at the grain boundaries in the form [20]:

$$I_{DS} = \mu_0 V_{DS}\frac{W}{L}C_i V_G \exp\left(-\frac{q^3 N_g^2 t}{8\varepsilon_0\varepsilon kTC_i V_G}\right) \tag{4}$$

where μ_0 and ε are the trap free mobility and the dielectric constant of $R_{16}LuPc_2$, respectively. This model has been applied to determine charge transport in polycrystalline semiconductor thin films including organic films [21]. Fig. 6 shows the Levinson plots of $\ln(\frac{I_{DS}}{V_G})$ as a function of $\frac{1}{V_G}$ for the devices using both as-deposited and annealed $R_{16}LuPc_2$ films. Values of 1.2×10^{12} cm^{-2} and

Table 1
Summary of transistor parameters measured for as-prepared and annealed devices.

$R_{16}LuPc_2$ transistors	Mobility ($\mu_{(sat)}$) cm^2/Vs	On/off current ratio	Threshold voltage (V_T) V	Sub-threshold voltage (V/decade)	Interface trap density (cm^{-2})	Grain-boundary trap density (cm^{-2})
As-prepared	1.5×10^{-3}	$\sim 10^3$	−25	3.8	2.81×10^{12}	1.2×10^{12}
Annealed	8.0×10^{-3}	$\sim 10^5$	−12.5	1.6	1.40×10^{12}	7.6×10^{11}

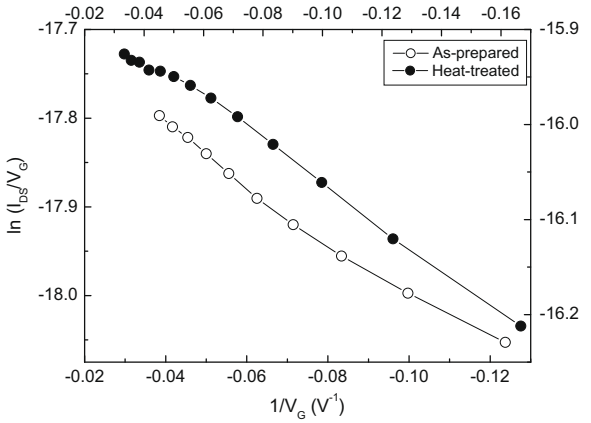

Fig. 6. Levinson plots of $\ln(I_{DS}/V_G)$ as function of $(1/V_G)$.

7.6×10^{11} cm^{-2} for N_g were obtained from the slopes of the best linear fits for as-deposited and annealed samples.

4. Concluding remarks

Organic thin film transistors have been fabricated using the solution processable spin coating technique for depositing newly synthesised the lutetium phthalocyanine complexes $R_{16}LuPc_2$. The improvement in transistor performance by annealing the devices at 70 °C under vacuum demonstrates the importance of heat treatment above the crystal to mesophase transition temperature. An increase in the value from 1.5×10^{-3} cm^2/Vs for as-deposited films to 8.0×10^{-3} cm^2/Vs for annealed films is achieved for the field effect mobility in the saturated regime. Simultaneously, the threshold voltage is reduced from −25 V for the as-deposited device to −12.5 V for the annealed device while the decrease in the sub-threshold voltage swing is observed from 3.8 V/decade to 1.6 V/decade for corresponding devices. The improved transistor parameters measured for heat treated devices are attributed to the reduction in effective grain boundaries, grain-boundary trap densities and a substantial decrease in the average surface roughness of the $R_{16}LuPc_2$ films.

Acknowledgement

We are grateful to Benemérita Universidad Autónoma de Puebla, México for offering travel grant to Professor Jose Luis Sosa-Sanchez.

References

[1] P. Erk, H. Hengelsberg, in: K.M. Kadish, K.M. Smith, R. Guilard (Eds.), The Porphyrin Handbook, vol. 19, Academic Press, San Diego, 2003, pp. 105–149.
[2] S. Ogura, K. Tabata, K. Fukushima, T. Kamachi, I. Okura, Development of phthalocyanines for photodynamic therapy, J. Porphyrins Phthalocyanines 10 (2006) 1116–1124.
[3] T. Shima, Y. Yamakawa, T. Nakano, J. Kim, J. Tominaga, Metal-free phthalocyanine layer prepared on read-only-memory disc for super-resolution readout, Jpn. J. Appl. Phys. Part 2 45 (2006) L1007–L1009.
[4] M. Hanack, D. Dini, in: K.M. Kadish, K.M. Smith, R. Guilard (Eds.), The Porphyrin Handbook, vol. 18, Academic Press, San Diego, 2003, pp. 251–280.
[5] R. Weiss, J. Fischer, in: K.M. Kadish, K.M. Smith, R. Guilard (Eds.), The Porphyrin Handbook, vol. 16, Academic Press, San Diego, 2003, pp. 171–246.
[6] M. Bouvet, in: K.M. Kadish, K.M. Smith, R. Guilard (Eds.), The Porphyrin Handbook, vol. 19, Academic Press, San Diego, 2003, pp. 38–103.
[7] S. Komorsky-Lovrić, F. Quentel, M. L'Her, F. Scholz, Voltammetry of microparticles of lutetium bisphthalocyanine, J. Solid State Electrochem. 12 (2008) 165–169.
[8] J. Simon, J.-J. André, Molecular Semicondcutors, Springer, Berlin, 1985.
[9] G. Guillaud, J. Simon, J.P. Germain, Metallophthalocyanines – gas sensors, resistors and field effect transistors, Coord. Chem. Rev. 178–180 (1998) 1433–1484.
[10] D. Atilla, N. Kilinc, F. Yuksel, A.G. Gurek, Z.Z. Ozturk, V. Ahsen, Synthesis, characterization, mesomorphic and electrical properties of tetrakis(alkylthio)-substituted lutetium(III) bisphthalocyanines, Synth. Met. 159 (1–2) (2009) 13–21.
[11] T. Basova, A.G. Gurek, V. Ahsen, A.K. Ray, Electrical properties of dysprosium phthalocyanine films, Org. Electron. 8 (6) (2007) 784–790.
[12] G.C. Bryant, M.J. Cook, C. Ruggiero, T.G. Ryan, A.J. Thorne, S.D. Haslam, R.M. Richardson, Structural study of spin-coated and LB films of monomeric and oligomeric phthalocyanines, Thin Solid Films 243 (1994) 316–324.
[13] B. Mukherjee, A.K. Ray, A.K. Sharma, M.J. Cook, I. Chambrier, A simply constructed lead phthalocyanine memory diode, J. Appl. Phys. 103 (2008) 074507.
[14] A.S. Cherodian, A.N. Davies, R.M. Richardson, M.J. Cook, N.B. McKeown, A.J. Thomson, J. Feijoo, G. Ungar, K.J. Harrison, Mesogenic behavior of some 1,4,8,11,15,18,22,25-octa-alkylphthalocyanines, Mol. Cryst. Liq. Cryst. 196 (1991) 103–114.
[15] J.L. Sosa-Sanchez, N.B. Chaure, A.K. Ray, D.L. Hughes, I. Chambrier, A.N. Cammidge, M.J. Cook, Synthesis, characterisation and thin film conductivity of a solution processible lutetium bis-phthalocyanine complex, in preparation.
[16] N.B. Chaure, T. Basova, A.K. Ray, A.G. Gurek, V. Ahsen, Memory effects in thin film organic transistor characteristics, J. Phys. D: Appl. Phys. 42 (12) (2009). Art. No. 125103.
[17] A.-L. Deman, I. Tardy, PMMA-Ta_2 O_5 bilayer gate dielectric for low operating voltage organic FETs, Org. Electron. 6 (2005) 78–84.
[18] S. Malik, A.K. Ray, A.K. Hassan, A.V. Nabok, Nanocomposite organic films on silicon, IEEE Trans. Nanotechnol. 2 (3) (2003) 149–153.
[19] Dhananjay, S.S. Cheng, C.Y. Yang, C.W. Ou, Y.C. Chuang, M.C. Wu, C.W. Chu, Dependence of channel thickness on the performance of In2 O3 thin film transistors, J. Phys. D: Appl. Phys. 41 (9) (2008). Art. No. 092006 2008.
[20] J. Levinson, F.R. Shepherd, P.J. Scanlon, W.D. Westwood, G. Este, M.J. Rider, Conductivity behavior in polycrystalline semiconductor thin film transistors, Appl. Phys. 53 (1982) 1193–1202.
[21] S. Verlaak, V. Arkhipov, P. Heremans, Modeling of transport in polycrystalline organic semiconductor films, Appl. Phys. Lett. 82 (5) (2003) 745–747.

Organic Electronics 11 (2010) 439–444

Contents lists available at ScienceDirect

Organic Electronics

journal homepage: www.elsevier.com/locate/orgel

Characterizing coherence lengths of organic light-emitting devices using Newton's rings apparatus

Chih-Hung Tsai, Kun-Cheng Tien, Ming-Che Chen, Kuei-Ming Chang, Ming-Shiang Lin, Hsing-Chieh Cheng, You-Heng Lin, Hong-Wei Chang, Hao-Wu Lin, Chun-Liang Lin, Chung-Chih Wu *

Department of Electrical Engineering, Graduate Institute of Photonics and Optoelectronics, and Graduate Institute of Electronics Engineering, National Taiwan University, Taipei, Taiwan 10617, ROC

ARTICLE INFO

Article history:
Received 20 November 2009
Accepted 22 November 2009
Available online 26 November 2009

Keywords:
OLEDs
Coherence
Newton rings
Interferogram

ABSTRACT

We investigated the temporal coherence properties of organic light-emitting devices (OLEDs) by characterizing their coherence lengths. The interferometry based on the Newton's rings apparatus was adopted to characterize the coherence lengths of various OLEDs, including non-doped/doped OLEDs and non-cavity bottom-emitting/cavity top-emitting OLEDs. The types of OLEDs investigated exhibit coherence lengths of 3–10 μm, depending on the device structures/emitters and spectral bandwidths of the OLED emission. OLEDs using emitting molecules with more limited number of allowed vibronic transitions give narrower-band and more coherent emission. Introducing the microcavity into the device structure to induce resonance also narrows the emission spectra and meanwhile increases the coherence length. Such information may be useful for modeling, design, and optimization of optical properties of OLEDs.

© 2009 Elsevier B.V. All rights reserved.

1. Introduction

Organic light-emitting diodes (OLEDs) are becoming increasingly important because of their applications in flat panel displays and lighting [1,2]. Along with the advancement of the OLED technology, demands in precise and detailed adjustment and optimization of optical properties of OLEDs are also increasing [3,4]. For OLEDs with multiple material layers, optical coherence properties of the devices influence various optical phenomena, such as interference, propagation, and distribution of radiation generated by the emitter. Thus, for optical modeling and designs of OLEDs, information regarding the coherence properties of OLEDs would become more essential and indispensible. Coherence properties of various Lambertian and non-Lambertian emitters/light sources had been studied conventionally [5]; yet only recently had people started to investigate coherence properties of OLEDs [6].

There are two kinds of optical coherence properties associated with a light source: temporal coherence and spatial coherence [7]. Temporal coherence is a measure of the phase correlation between different points along the propagation direction of a light wave [8]. Spatial coherence is a measure of the phase correlation between different points transverse to the propagation direction of a light wave [9]. Spatial coherence tells how uniform the phase of the wave front is. In recent studies of optical coherence of OLEDs, mainly the spatial coherence was reported [10]; yet the temporal coherence of OLED light sources has not been well investigated. In this work, we performed investigations on the temporal coherence properties of various OLEDs.

One typical parameter to characterize the temporal coherence of a light source is the coherence length [11]. The coherence length is the propagation distance from a light source to a point where the electromagnetic wave still maintains a specified degree of coherence (phase cor-

* Corresponding author. Tel.: +886 2 33663636; fax: +886 2 23689178.
E-mail address: chungwu@cc.ee.ntu.edu.tw (C.-C. Wu).

1566-1199/$ - see front matter © 2009 Elsevier B.V. All rights reserved.
doi:10.1016/j.orgel.2009.11.024

relation). In interference experiments, it corresponds to a maximal optical path difference at which two originally coherent beams can still exhibit distinguishable interference [12]. That is, within the coherence length of a light source, the interference of two beams from a same light source will remain detectable, but not distinguishable beyond the coherence length. In interference experiments with varying the optical path difference, in principle, the coherence length can be determined. In this work, by adopting interferometry based on the Newton's rings apparatus [13], we characterized the coherence lengths of various OLEDs.

2. Experimental

2.1. Newton's rings apparatus

The arrangement of the experiment setup is shown in Fig. 1. The setup was comprised of a light source O_1 (e.g. an OLED), the Newton's rings apparatus N_1, a silicon photodetector D_1, a motorized linear stage M_1, and two focusing lens (the convex L_1 and the parabolic lens L_2). The OLED emission was first collimated by the convex lens L_1 (with a focal length of 5 cm). Under the illumination of a collimated OLED emission, a series of concentric rings of interference induced by the Newton's rings apparatus would occur nearby. A parabolic lens L_2 was used to image such interference patterns near the apparatus onto a convenient surface for detection. A silicon photodiode detector D_1 mounted on the motorized linear stage M_1 was used to record the pattern of interference rings (i.e. the interferogram), upon moving the stage. A 0.3-mm-width slit was placed in front of the silicon photodiode for enhancing the measurement resolution. Upon moving the motorized linear stage with a velocity of 48 μm/s, the photodiode detected the variation of the light intensity and converted it into a current signal. A galvanometer with pico-ampere resolution was used to measure the current signal. A computer was used to control the motorized stage/the galvanometer and was used to record the data.

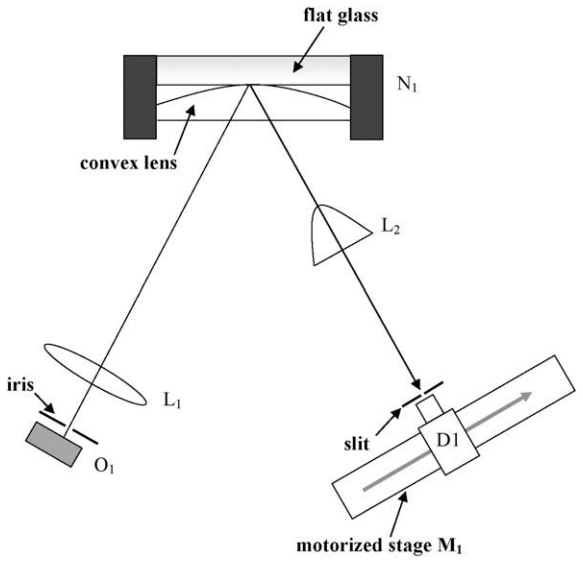

Fig. 1. The experiment setup used for characterizing the coherence lengths of light sources, based on the Newton's rings apparatus.

The Newton's rings apparatus in Fig. 1 was comprised of a long-focal-length convex lens and a flat glass surface, as shown in Fig. 2. It provided a continuous variation of the air gap between the convex and flat glass surfaces. As shown in Fig. 2, there are four surfaces (S_1, S_2, S_3, and S_4) in the Newton's rings apparatus. Under the illumination of a collimated OLED emission, mainly reflection beams from the two surfaces S_2 and S_3 (i.e. R_2 and R_3) would induce distinguishable interference. Reflection beams from the other two surfaces S_1 and S_4 (i.e. R_1 and R_4) would not contribute to the interference patterns, since the thicknesses of the glass plate and the convex lens are much larger than the coherence length of OLEDs studied in this work (of μm scale, as will be seen later).

As shown in Fig. 3, the two reflected beams from S_2 and S_3 will meet again (either in the real space in front of the air gap or virtually behind the air gap) and induce interference if the optical path difference is within the coherence length of the light source. As shown in Fig. 3, the interference would occur in a region near the air gap (i.e. the area F_1 as indicated in Fig. 3). As illustrated in Fig. 3, some interference occur in front of the air gap (e.g. P_1 and P_2) and form a real image of interference patterns; meanwhile some occur behind the air gap (e.g. P_3 and P_4) and indeed form a virtual image of interference patterns. Such interference patterns (i.e. Newton's rings, a series of alternately bright and dark concentric rings) formed near the air gap are called localized fringes [14]; in order to measure the interference patterns formed near the Newton's rings apparatus, it is necessary to project the image in the F_1 region onto a convenient detecting surface for recording.

2.2. OLED fabrication and characterization

OLEDs were fabricated on the ITO-coated or metal-coated glass substrates with multiple organic layers sandwiched between the bottom anode and the top metal cathode. Cleaned and UV-ozone-treated indium tin oxide (ITO) was used as the bottom anode for bottom-emitting OLEDs, while the reflective metal was used as the bottom

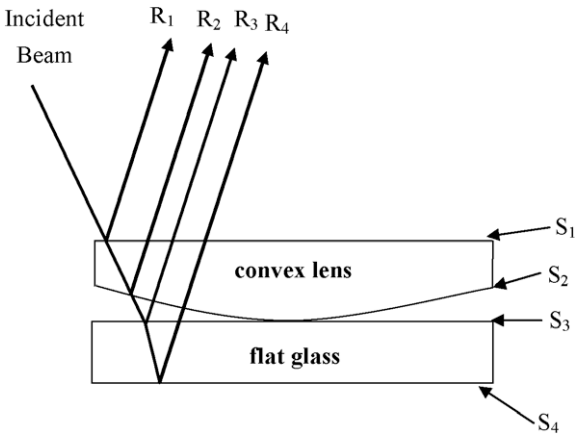

Fig. 2. Schematic illustration of the Newton's rings apparatus.

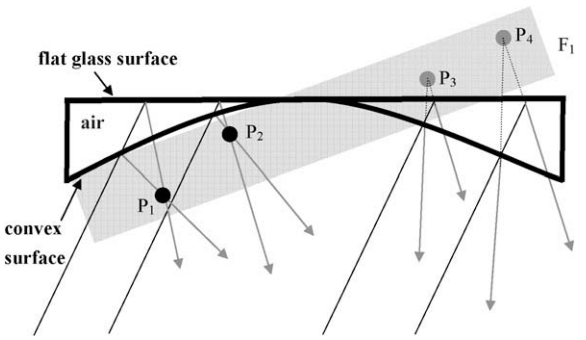

Fig. 3. Schematic illustration of the formation of localized interference fringes (Newton's rings) near the air gap of the Newton's rings apparatus.

anode for microcavity top-emitting OLEDs. All the organic and metal layers were deposited by thermal evaporation in a vacuum chamber with a base pressure of $<10^{-6}$ torr. The deposition rate of organic layers was kept at ~0.2 nm/s. The deposition system permitted the fabrication of the complete device structure in a single pump-down without breaking vacuum. The active area of the device was 2×2 mm^2, as defined by the shadow mask for cathode deposition. After the device deposition, the devices were encapsulated with a cover glass under dry nitrogen atmosphere. Electroluminescence (EL) spectra of devices were collected using a calibrated CCD spectrograph.

3. Results and discussion

3.1. OLED structures and characteristics

Three types of OLEDs (devices A, B, and C) were prepared for studies of coherence properties. These devices were all green-emitting OLEDs based on the typical tris-(8-hydroxyquinoline) aluminum (Alq_3) [15]. Their device structures were:

Device A: Glass/ITO/m-MTDATA (30 nm)/α-NPD (20 nm)/Alq_3 (60 nm)/LiF (0.5 nm)/Al (1 nm)/Ag (150 nm).
Device B: Glass/ITO/m-MTDATA (30 nm)/α-NPD (20 nm)/Alq_3:C545T (1 wt.%, 20 nm)/Alq_3 (40 nm)/LiF (0.5 nm)/Al (1 nm)/Ag (150 nm).
Device C: Glass/Ag (80 nm)/m-MTDATA:F_4-TCNQ (2 wt.%, 30 nm)/α-NPD (20 nm)/Alq_3:C545T (20 nm)/Alq_3 (30 nm)/LiF (0.5 nm)/Al (1 nm)/Ag (20 nm)/Alq_3 (70 nm).

Device A is an Alq_3 bottom-emitting OLED. Device B is an Alq_3 bottom-emitting OLED doped with the green dye C545T [10-(2-benzothiazolyl)-1,1,7,7-tetramethyl-2,3,6,7-tetrahydro-1H,5H,11H (1) benzopyrano (6,7,8-ij)quinolizin-11-one] [16]. Device C is a top-emitting microcavity OLED based on the Alq_3:C545T emitter [17]. The bottom-emitting OLEDs (Devices A and B) adopted the transparent ITO as the bottom anode and the thick Ag as the reflective top cathode, while the microcavity top-emitting OLED (Device C) used the thick Ag as the reflective bottom anode and the thin Ag as the semi-transparent top cathode. In the microcavity top-emitting OLED, the thin Ag cathode is further capped with a 70 nm Alq_3 to form a low-absorption high-reflection composite mirror for maximizing optical output of cavity OLEDs [18]. In these devices, the organic multilayer structure consists of un-doped 4,4′,4″-tris(3-methylphenylphenylamino)triphenylamine (m-MTDATA) or m-MTDATA doped with 2 wt.% of the p-type dopant tetrafluorotetracyano-quinodimethane (F_4-TCNQ) as the hole-injection layer [19], α-naphthylphenylbiphenyl diamine (α-NPD) as the hole-transport layer [20], un-doped Alq_3 or Alq_3 doped with C545T as the emitting layer, and un-doped Alq_3 as the electron-transport layer. Ultrathin layers of LiF (0.5 nm) and Al (1 nm) serve as the electron-injection layers [21,22]. For the microcavity top-emitting OLED (Device C), the resonant wavelength was set around the intrinsic emission peak wavelength of C545T by adjusting the thicknesses of organic layers and the capping layer. During the coherence length measurements, the devices were driven by a fixed dc bias.

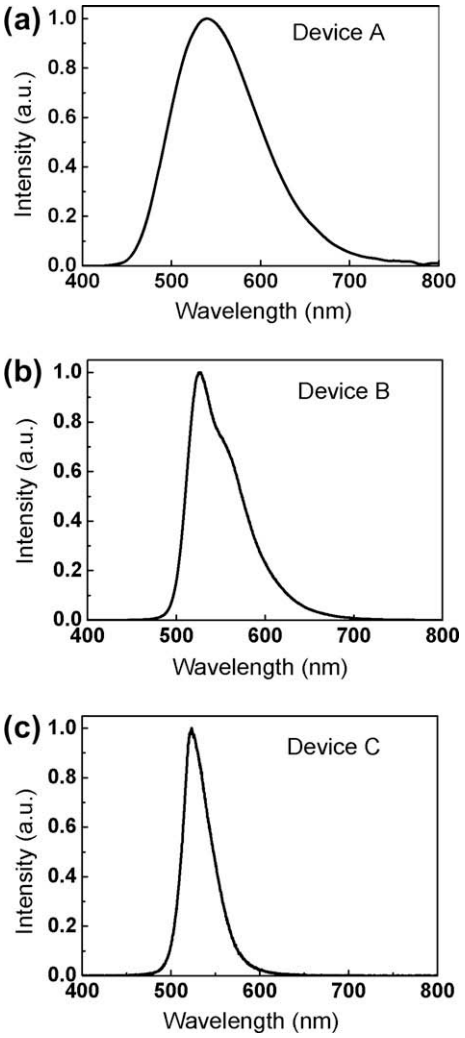

Fig. 4. EL spectra of the OLEDs under investigation: (a) Device A (FWHM ~110 nm), (b) Device B (FWHM ~60 nm), and (c) Device C (FWHM ~40 nm).

Fig. 4a shows the EL spectrum of un-doped Alq_3 Device A, which exhibits an EL peak at 540 nm and a full width at half maximum (FWHM) of ~110 nm, a typical broad-band emission of Alq_3. Fig. 4b shows the EL spectrum of the C545T-doped Device B, which exhibits an EL peak at 525 nm and a smaller FWHM of ~60 nm due to the narrower emission spectrum of the green dopant C545T. Fig. 4c shows the EL spectrum of microcavity top-emitting Device C (doped with C545T), which exhibits an EL peak at 523 nm and a further reduced FWHM of ~40 nm due to the microcavity effects induced by the microcavity structure.

3.2. Characterization of coherence lengths

In order to verify the effectiveness of the coherence length measurement using the Newton's rings apparatus we set up, we first used it to measure the coherence length of a commercial red LED based on $GaAs_{0.6}P_{0.4}$/GaP (model: 204URC, Everlight Electronics Co., Ltd.). The EL spectrum of the red LED is shown in Fig. 5a[1], which exhibits an EL peak at 665 nm and a full width at half maximum (FWHM) of ~24 nm. Then the LED was investigated by the Newton's rings apparatus. Upon illuminating the collimated LED emission onto the Newton's rings apparatus, a series of concentric rings of constructive and destructive interference, as shown in Fig. 5b, could be observed at the detecting surface (via the aid of a white paper). Fig. 5c shows the corresponding interferogram recorded by scanning the photodiode D_1 from the center of the concentric rings to the edge.

The Newton's rings (i.e. alternately bright and dark rings centered around a dark spot) are induced by interference of two beams reflected from surfaces S_2 and S_3, i.e. the curved convex surface and the adjacent flat glass surface. The dark spot at the center of the Newton's rings is associated with the contact point between the convex lens and the flat glass plate, at which the air gap is nearly zero but the two reflected beams S_2 from the convex surface and S_3 from the flat glass surface has a phase difference close to 180°. The bright rings are induced by constructive interference between these two reflected beams, while the dark rings are induced by destructive interference. The mth dark ring ($m = 1,2,3,\ldots$, excluding the central dark spot) from the center corresponds to the mth-order destructive interference (minimum) in the interferogram, which is associated with a phase difference of $(2m + 1)\pi$ and an optical path difference of $\Delta d = m\lambda$. The optical path difference of course increases with the air gap. As the air gap between surface S_2 and surface S_3 increases, the visibility of the interference fringes decreases due to reduced coherence between two reflected beams. The fringe visibility is defined as [23]:

$$V = \frac{I_{max} - I_{min}}{I_{max} + I_{min}}, \quad (1)$$

where I_{max} and I_{min} are the neighboring maximum (peak) and minimum (valley) in the interferogram. In principle, the coherence length can be defined as the optical path difference at which the interference fringe visibility drops to

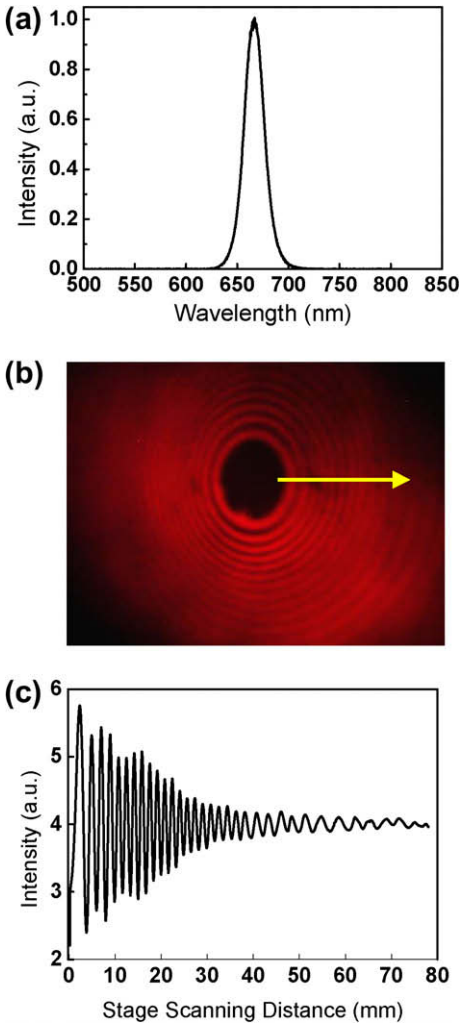

Fig. 5. (a) EL spectra of the $GaAs_{0.6}P_{0.4}$/GaP LED under investigation, (b) image of Newton's rings for emission of the $GaAs_{0.6}P_{0.4}$/GaP LED appearing at the detection surface, (c) the corresponding interferogram recorded at the detection surface. The arrow in (b) indicates the scanning path of the recording photodiode D_1.

1/e of the peak value [24]. In practical measurements of real light sources, when approaching the coherence length, the visibility may drop rapidly to nearly zero, and thus the coherence length may be alternatively/roughly defined as the optical path difference at which the interference fringe visibility drops to nearly zero [25]. Thus in the interferometry based on the Newton's rings apparatus, the coherence length of a light source like a LED or OLED could be estimated by counting the number of distinguishable interference rings in the interferogram and then multiplying the number with the major wavelength of the light source [26].

In Fig. 5c, about 32 minima can be distinguished in the interferogram. Thus the coherence length of this red LED is estimated to be about 21.3 μm (665 nm × 32). The coherence length determined this way is consistent with that of the same type of LED reported previously by other researchers [27], indicating the effectiveness and accuracy

[1] For interpretation of color in Fig. 5, the reader is referred to the web version of this article.

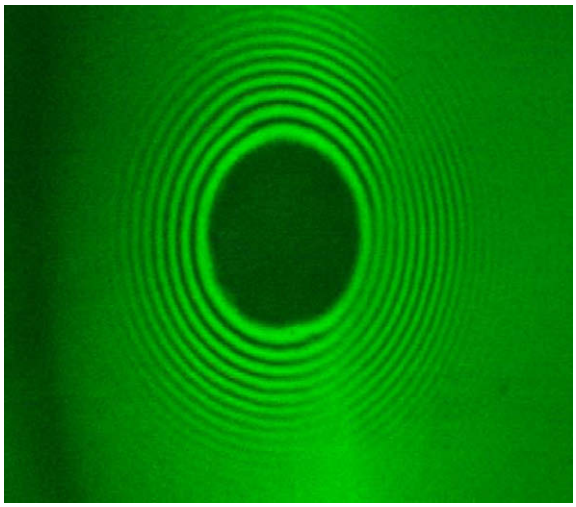

Fig. 6. Image of Newton's rings for emission the OLED under investigation (Device B) appearing at the detection surface.

of the current Newton's rings apparatus for determining the coherence length of a light source.

Similarly, Fig. 6 shows one example image of Newton's rings for one of the OLED light sources under investigation (Device B). Correspondingly, Fig. 7a–c show the corresponding interferograms for Device A, Device B, and Device C, respectively. In Fig. 7a, about six distinguishable minima can be observed in the interferogram of Device A, from which a coherence length of ~3.2 μm (540 nm × 6) is estimated. In Fig. 7b, about 14 distinguishable minima can be observed in the interferogram of Device B, from which a coherence length of ~7.4 μm (525 nm × 14) is estimated. In Fig. 7c, about 18 distinguishable minima can be observed in the interferogram of Device C, from which a coherence length of ~9.4 μm (523 nm × 18) is estimated.

The results show that the three types of OLEDs under investigation have coherence lengths of 3–10 μm, depending on the device structures/emitters and thus spectral bandwidth of the OLED emission. OLEDs with broader EL spectra appear to have longer coherence lengths. Such trend is consistent with that observed in various light sources. For example, in various lasers, the positive feedback and stimulated emission are induced by the cavity structures, resulting in highly coherent and spectrally narrowed emission. As such, the coherent lengths of various laser systems could range from tens of m (e.g. helium–neon laser) [28], to tens/hundreds of m (e.g. some semiconductor lasers) [29], to well over km (e.g. some fiber lasers) [30]. On the other hand, the less coherent and broader-bandwidth emitters like semiconductor LEDs have much smaller coherent lengths (micrometer scale, like the one shown in Fig. 5). Unlike the semiconductor LEDs whose emission mechanism is mainly band-edge emission, for OLEDs, the emission mechanism is mainly due to the radiative relaxation of excitons (molecular excited states generated by electrical excitation) [31]. The molecular exciton relaxation could occur via coupling different molecular vibration states (between electronic excited states and ground states) [32], usually resulting in much

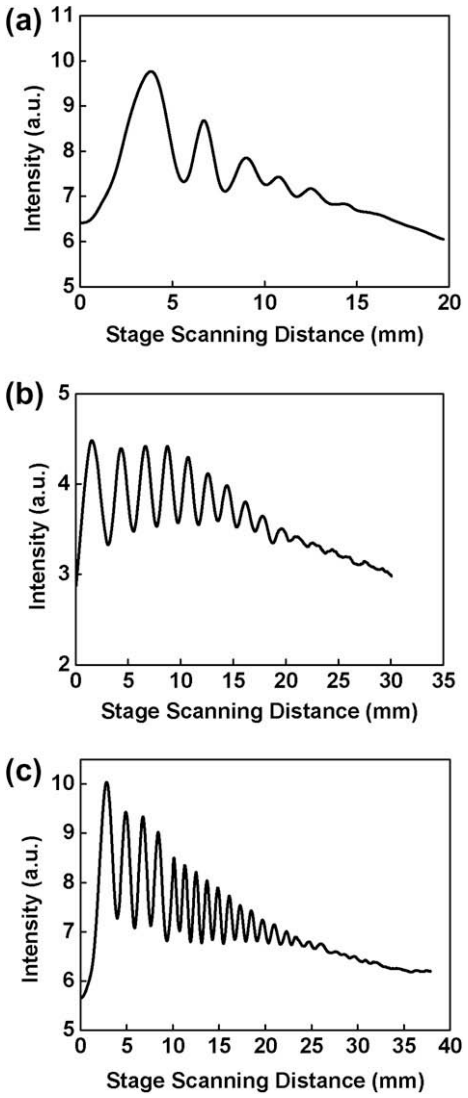

Fig. 7. Interferograms for emission of OLEDs in the Newton's rings experiment: (a) Device A, (b) Device B, (c) Device C.

broader-band and less coherent emission compared to the band-edge emission of semiconductor LEDs. For emitting molecules which inherently have more limited number of allowed vibronic transitions would naturally give narrower-band and more coherent emission. The emission and coherence characteristics of Device B (using narrower-band emitter C545T) vs. those of Device A (using broad-band emitter Alq_3) give a good example. When further introducing the microcavity into the device structure to induce resonance around some wavelengths, like in Device C, it is seen that the emission spectra could be further narrowed and meanwhile the coherence length is increased.

4. Conclusions

In conclusion, we performed investigations on the temporal coherence properties of OLEDs by characterizing

their coherence lengths. The interferometry based on the Newton's rings apparatus, which is convenient and effective, was adopted to characterize the coherence lengths of various OLEDs, ranging from non-doped to doped OLEDs and from non-cavity bottom-emitting to cavity top-emitting OLEDs. The results show that the types of OLEDs under investigation have coherence lengths of 3–10 μm, depending on the device structures/emitters and thus spectral bandwidths of the OLED emission. OLEDs using emitting molecules with more limited number of allowed vibronic transitions give narrower-band and more coherent emission. Introducing the microcavity into the device structure to induce resonance also narrows the emission spectra and meanwhile increases the coherence length. Such information may be useful for modeling, design, and optimization of optical properties of OLEDs.

Acknowledgements

The authors gratefully acknowledge the financial support from National Science Council and Ministry of Economic Affairs of Taiwan.

References

[1] M.A. Baldo, D.F. O'Brien, Y. You, A. Shoustikov, S. Sibley, M.E. Thompson, S.R. Forrest, Nature 395 (1998) 151.
[2] C.-J. Yang, C.-L. Lin, C.-C. Wu, Y.-H. Yeh, C.-C. Cheng, Y.-H. Kuo, T.-H. Chen, Appl. Phys. Lett. 87 (2005) 143507.
[3] C.-C. Liu, S.-H. Liu, K.-C. Tien, M.-H. Hsu, H.-W. Chang, C.-K. Chang, C.-J. Yang, C.-C. Wu, Appl. Phys. Lett. 94 (2009) 103302.
[4] C.-L. Lin, H.-C. Chang, K.-C. Tien, C.-C. Wu, Appl. Phys. Lett. 90 (2007) 071111.
[5] R.E. Shaffer, R.J. Comb, Appl. Spectroscopy 55 (2001) 1404.
[6] D. Hill, K. Leo, G. He, Q. Huang, Appl. Phys. Lett. 90 (2007) 101111.
[7] S. Yang, A.T. Hammack, M.M. Fogler, L.V. Butov, Phys. Rev. Lett. 97 (2006) 187402.
[8] C.R. Wheeler, R.D. Ramsier, P.N. Henrisken, Eur. J. Phys. 24 (2003) 443.
[9] W.H. Carter, A. Gamliel, E. Wolf, J. Mod. Opt. 41 (1994) 1973.
[10] K. Saxena, D.S. Mehta, R. Srivastava, M.N. Kamalasanan, Appl. Phys. Lett. 89 (2006) 061124.
[11] F.J. Duarte, L.S. Liao, K.M. Vaeth, Opt. Lett. 30 (2005) 22.
[12] A. Donges, Eur. J. Phys. 19 (1998) 245–249.
[13] A. Dobroiu, A. Alexandrescu, D. Apostol, V. Nascov, V. Damian, Proc. SPIE 4068 (2000) 342–347.
[14] D.W. Robinson, Appl. Opt. 22 (1983) 2169–2176.
[15] M.-T. Lee, C.-K. Yen, W.-P. Yang, H.-H. Chen, C.-H. Liao, C.-H. Tsai, C.H. Chen, Org. Lett. 6 (2004) 1241–1244.
[16] C.H. Chen, C.W. Tang, Appl. Phys. Lett. 79 (2001) 3711–3713.
[17] C.-L. Lin, H.-C. Chang, K.-C. Tien, C.-C. Wu, Appl. Phys. Lett. 90 (2007) 071111.
[18] C.-W. Chen, P.-Y. Hsieh, H.-H. Chiang, C.-L. Lin, H.-M. Wu, C.-C. Wu, Appl. Phys. Lett. 83 (2003) 5127.
[19] M. Pfeiffer, A. Beyer, T. Fritz, K. Leo, Appl. Phys. Lett. 73 (1998) 3202–3204.
[20] Y. Li, M.K. Fung, Z. Xie, S.-T. Lee, L.-S. Hung, J. Shi, Adv. Mater. 14 (2002) 1317–1321.
[21] C.-I. Wu, C.-T. Lin, Y.-H. Chen, M.-H. Chen, Y.-J. Lu, C.-C. Wu, Appl. Phys. Lett. 88 (2006) 152104.
[22] C.-L. Lin, H.-W. Lin, C.-C. Wu, Appl. Phys. Lett. 87 (2005) 021101.
[23] M.V. Klein, T.E. Furtak, Optics (1986) 520.
[24] J.R. Meyer-Arendt, Introduction to Classical and Modern Optics, 1984, p. 208.
[25] F.A. Jenkins, H.E. White, Fundamentals Opt. (1981) 277.
[26] H. Xie, Y. Peng, D. Meng, L. Jiang, Proc. SPIE 6028 (2005) 602825.
[27] J.-T. Li, J. Zhu, Z.-X. Wang, M. Li, J.-Y. Zhou, Chin. J. Lasers 32 (2005) 31–34.
[28] J.P. Mathieu, Optics (1975) 163–168.
[29] G.K. Ackermann, J. Eichler, Holography: A Practical Approach, 2007.
[30] C. Spiegelberg, J. Geng, Y. Hu, Y. Kaneda, S. Jiang, N. Peyghambarian, J. Lightwave Technol. 22 (2003) 57–59.
[31] C.W. Tang, S.A. VanSlyke, C.H. Chen, J. Appl. Phys. 65 (1989) 3610.
[32] L.S. Hung, C.W. Tang, M.G. Mason, P. Raychaudhuri, J. Madathil, Appl. Phys. Lett. 78 (2001) 544.

Organic Electronics 11 (2010) 445–449

Contents lists available at ScienceDirect

Organic Electronics

journal homepage: www.elsevier.com/locate/orgel

Formation of gap states and enhanced current injection efficiency in organic light emitting diodes incorporated with subphthalocyanine

Yu-Hung Chen [a], Yu-Jen Chang [a], Guan-Ru Lee [a], Jung-Hung Chang [a], I-Wen Wu [a], Jheng-Hao Fang [a], Shu-Han Hsu [a], Shun-Wei Liu [a], Chih-I Wu [a,*], Tun-Wen Pi [b]

[a] Department of Electrical Engineering and Graduate Institute of Photonics and Optoelectronics, National Taiwan University, Taipei, Taiwan 10617, People's Republic of China
[b] National Synchrotron Radiation Research Center, Hsinchu, Taiwan 30077, People's Republic of China

ARTICLE INFO

Article history:
Received 8 August 2009
Received in revised form 17 November 2009
Accepted 21 November 2009
Available online 26 November 2009

Keywords:
Hole injection
Photoemission
Subphthalocyanine

ABSTRACT

The improvement of current injection efficiency in organic light emitting diodes is demonstrated with incorporation of SubPc-doped NPB as hole injection layers. The photoemission spectra illustrate the presence of gap states and the occurrence of axial reaction on SubPc with NPB. Quantum chemistry calculation provides simulated valence-band spectra indicating that the formation of gap states is due to the HOMOs of new complexes created from the reaction of SubPc and NPB, which facilitate the hole injection at the anode interfaces.
© 2009 Elsevier B.V. All rights reserved.

1. Introduction

Organic light emitting diodes (OLEDs) receive great attention in recent years due to applications in lighting and future display technology [1]. In typical multi-layer OLEDs, carrier injection at anodes is a crucial issue in improvement of electrical characteristics. There are many techniques to enhance the hole injection efficiency, e.g. oxidation of ITO [2,3] and electrical doping of hole injection layers with oxidizing regents [4,5] or tetrafluoroteracyanoquinodimethane (F_4TCNQ) [6]. Among electrical doping materials, phthalocyanine derivatives (Pcs) are frequently studied due to some of their physical properties, such as high mobility in ordered thin films, self-assembling behaviors, and n-type doping effect by incorporating alkali atoms [7–9]. One of the pc-related compounds, chloro[subphthalocyaninato]boron(III) (SubPc), is also widely investigated for their non-linear optical property [10,11]. Some research groups have employed SubPc in photovoltaic devices to improve the solar cell performance, including open circuit voltage, power conversion efficiency, and quantum efficiency, owing to better energy level alignment at the abrupt junction of donor/acceptor interfaces [12,13]. In this paper, we report the enhanced current injection efficiency of OLEDs using SubPc-doped hole injection layers (HILs) and the studies of mechanisms leading to such improvement.

2. Experimental and theoretical method

In this study, OLEDs were fabricated with SubPc-doped *N,N′*-di(naphthalene-1-yl)-*N,N′*-diphenyl-benzidene (NPB) as HILs and the electrical characteristics of devices with various HILs were measured with Keithley 2636A. Compared to the metal oxides usually used in OLEDs as HILs, e.g. MoO_x and WO_3 [14], SubPc can be evaporated with stable deposition rate at relatively low temperature of about 220 °C. Photoemission experiments were performed at the National Synchrotron Radiation Research Center (NSRRC) in Hsinchu, Taiwan, Republic of China. The valence-band and core-level photoemission spectra were measured at U5 beamline, which can provide photons with energy range from 100 eV to 1000 eV [15]. Photoelectrons

* Corresponding author. Tel.: +886 939603591; fax: +886 2 33663683.
E-mail address: chihiwu@cc.ee.ntu.edu.tw (Chih-I Wu).

1566-1199/$ - see front matter © 2009 Elsevier B.V. All rights reserved.
doi:10.1016/j.orgel.2009.11.025

emitted from samples were collected with a 125 mm hemispherical analyzer in an UHV chamber. Procedures of sample preparation and organic material evaporation were described in the previous report [16].

To identify the origins of the gap states found in valence band, theoretical simulation with density functional theory methods were used to compute the molecular orbitals (MOs) and simulated density of states. The optimized geometric structures were obtained with the method of B3-LYP and the basis set of 6-31G, and the single-point energy was then applied to retrieve the detail information of molecular energy using Gaussian03 software [17]. The simulated valence-band spectra using calculated MOs was extracted via GaussSum [18] with full-width-at-half-maximum of 0.4 eV.

3. Results and discussion

A series of devices with SubPc-doped NPB as HILs were fabricated to investigate hole injection efficiency. The device structures are UV-ozone-cleaned indium tin oxide (ITO)/HIL (5 nm)/NPB (35 nm)/Alq3 (40 nm)/LiF (0.5 nm)/Al (150 nm). Various doping levels of SubPc in NPB were tested and thickness of HILs was optimized for best current density. The reference device was fabricated with MoO_x as the HIL for comparison. Fig. 1(a) shows the *J–V* characteristics of devices with different HILs in both linear and semi-log scales and the result reveals that the performance of SubPc-doped devices are all much improved. The device with 5–10% SubPc-doped NPB shows the best current injection efficiency as compared to those with other doping concentrations and is also superior to the devices with MoO_x, which has been widely used as HILs. At higher concentration of SubPc doped in NPB, the current density of devices decrease, which is probably due to the decrease of mobility of NPB with too many foreign molecules. Fig. 1(b)–(d) shows the luminance vs. voltage, luminous efficiency characteristics, and electroluminance (EL) spectra, respectively, of the devices with SubPc doped in NPB. As indicated from these data, the device with 5% SubPc-doped NPB also demonstrates the best brightness at the same voltage, whereas the luminance efficiency and EL spectra are almost the same for all devices. The results illustrate that SubPc doped in NPB promotes hole injection capability between ITO and NPB.

In order to identify the role of SubPc in NPB as HILs, photoemission experiments were carried out *in situ* at synchrotron radiation center. Fig. 2(a) shows the valence-band spectra of pristine NPB, pristine SubPc, and 1:1 mixture of these two molecules, respectively. The vicinity of HOMO regions are enlarged and shown in Fig. 2(b). For pristine NPB and SubPc, there is no detectable density of states within 1 eV below the Fermi level. However, states extended in the forbidden gap from HOMO to the Fermi level are emerged with mixing of NPB and SubPc. The formation of the gap states has been observed at the interface of the

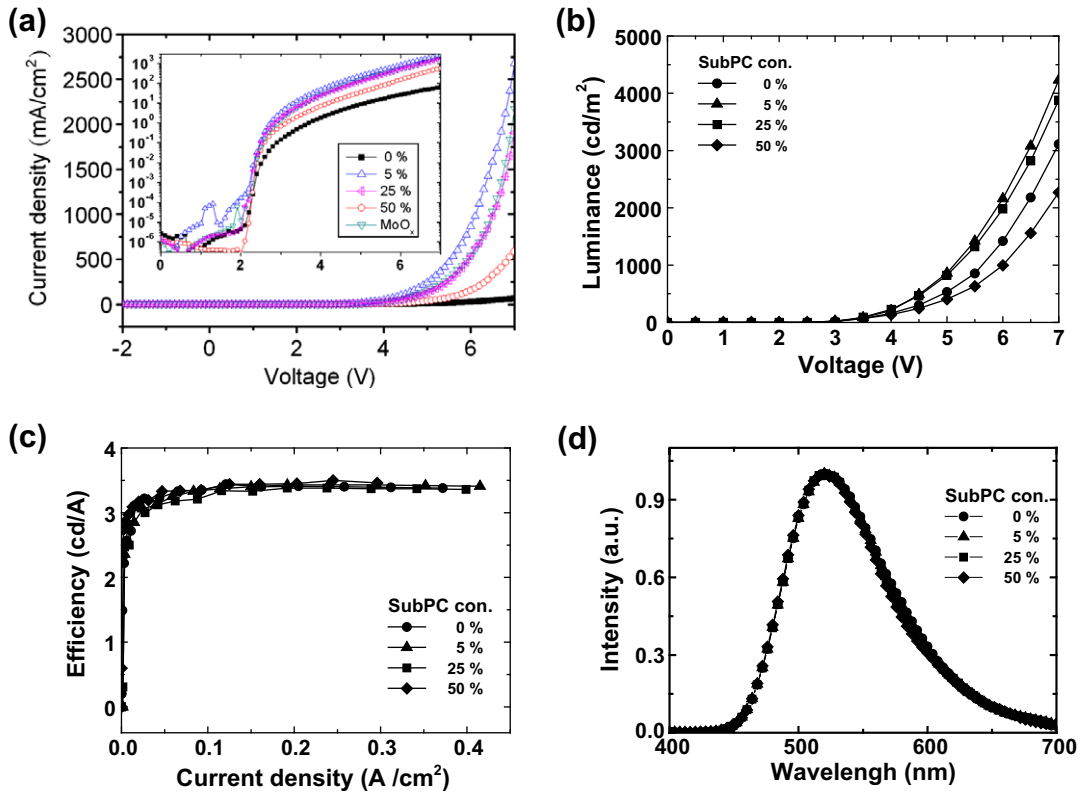

Fig. 1. (a) *J–V* characteristics, (b) luminance-voltage, (c) luminous efficiency, and (d) EL spectra of OLEDs with SubPc-doped NPB of different concentrations as HILs.

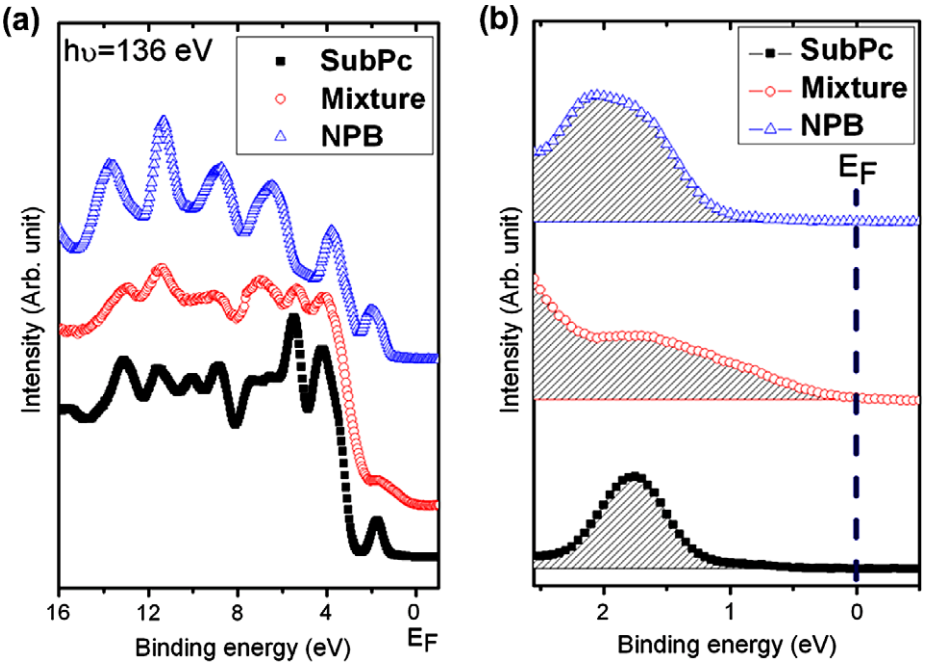

Fig. 2. (a) Valence spectra of pristine NPB and pristine SubPc, and NPB/SubPc mixture. (b) The region of HOMO near the Fermi level.

Pc-derivatives and metal electrodes [19–21]. However, the studies of interfaces between Pc-derivatives with other organic molecules are relatively sparse in literatures [22–25] and there is no report on the formation of gap states. These gap states between the HOMOs of the organic materials and the Fermi level at the anode interfaces could provide extra states for holes and facilitate the hole injection, resulting in the enhancement of current density of devices when SubPc is doped into NPB. To find out the origins of these gap states, the interfacial chemistry between NPB and SubPc was further studied with core-level photoemission spectra.

The carbon 1*s* and boron 1*s* core-level spectra of SubPc with incremental deposition of NPB were measured with excitation photon energy of 350 eV and 250 eV, respectively. In order to extract detailed chemical information from XPS, all the core-level spectra were subtracted by the Shirley background, and then analytically fitted with the Voigt profile. The carbon 1*s* core-level spectra of pristine SubPc shown at the bottom of Fig. 3(a) consists of four major features, which are similar to those of other Pc-derivatives from previous reports [26–28]. The main peak C1, at 284.8 eV, is attributed to the 18 carbon atoms in benzene rings and the next prominent peak C2, at 286.4 eV, is contributed by the remaining 6 pyrrole carbons. Whereas C3 and C4 peaks are the shake-up structures of carbon element in benzene and pyrrole rings, respectively. With as little as 0.5 angstroms of NPB deposition, the rapid smear of C2 component implies that the chemical reaction happens around the center of SubPc. The evolution of boron 1*s* core-level on SubPc substrates with NPB coverage is demonstrated in Fig. 3(b). The binding energy of boron 1*s* peak in pristine SubPc is 191.8 eV and a new feature appears at the low binding energy side with increasing NPB

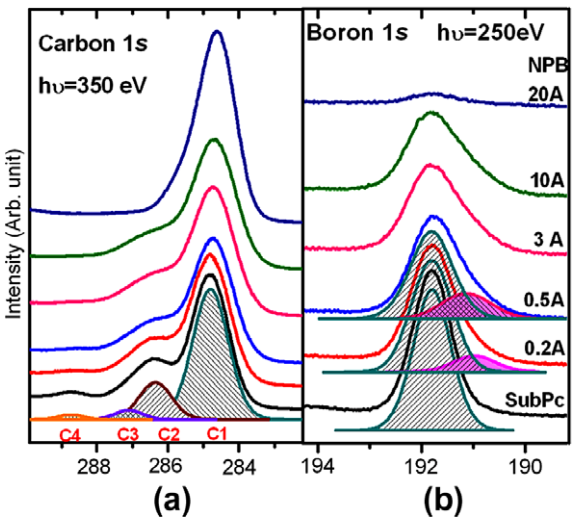

Fig. 3. (a) Carbon 1*s* core-level spectra of SubPc with incremental deposition of NPB. (b) Boron 1*s* core-level spectra of SubPc with incremental deposition of NPB.

coverage, which indicates that boron atoms in some of the SubPc molecules are gaining extra portion of electrons in the deposition process. The possible reaction of SubPc has been discussed and characterized into three categories: axial reactivity, peripheral reactivity, and ring expansion reaction [11]. From the result of core-level photoemission spectra, it can be assumed that the appearance of the new feature in boron 1*s* core-level is attributed to an axial reaction process on SubPc with deposition of NPB. The axial reaction in this case means that elimination of the axial ligand (chlorine) of SubPc forms a meta-stable

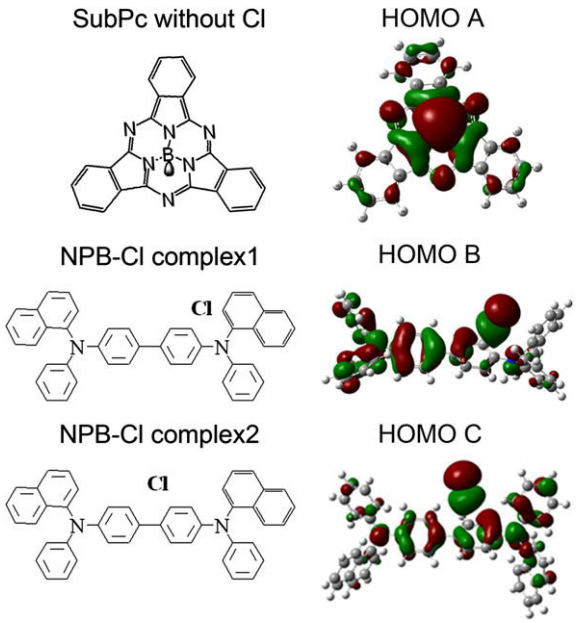

Fig. 4. Chemical structures of complexes resulting from the reaction of SubPc and NPB and their frontier molecular orbitals.

intermediate structure, with chlorine atoms detached from SubPc molecules [29]. Quantum chemistry calculation were then carried out to verify the occurrence of axial reaction and to identify the correlation between this reaction and the gap states detected in UPS experiments.

In axial reactivity, chlorine would dissociate from SubPc and form a new complex with NPB molecules. The calculated Gibbs free energy is about −440 kcal/mol if chlorine and NPB form a complex. A similar case can be found in Li and Alq_3 [30,31] or in $FeCl_3$ and NPB [32]. From energy calculation, two geometrical arrangements with similar energy would possibly be formed as chlorine-NPB complex. The molecular structures of these two chlorine-NPB complexes and a SubPc molecule with chlorine detached, which are the species in the NPB/SubPc mixed films, are shown on the left hand side of Fig. 4. The spatial distributions of HOMOs of these three species are shown on the right hand side of Fig. 4.

To investigate the correlation of molecular structures and electronic structures, the molecular energy levels and simulated valence-band spectra were calculated. Fig. 5(a) shows the simulated spectra of pristine NPB and SubPc, which agree fairly well with the experimental UPS results. The vertical bars under the simulated spectra are the molecular levels of single molecule. In both simulated and experimental data, we can see that there is no energy level within 1 eV below the Fermi level in either pristine SubPc or NPB. Fig. 5(b) is the re-drawn of Fig. 2(b) with calculated molecular energy levels shown under the associated experimental valence-band spectra. As shown in the spectrum of NPB-SubPc mixture in Fig. 5(b), there are three new energy levels at the top of valence band corresponding to HOMO A, HOMO B, and HOMO C in Fig. 4, respectively. From the comparison of calculated energy levels and experimental spectra, it is clear that the gap states are attributed to the HOMOs of the new complexes resulting from the axial reaction of SubPc with deposition of NPB.

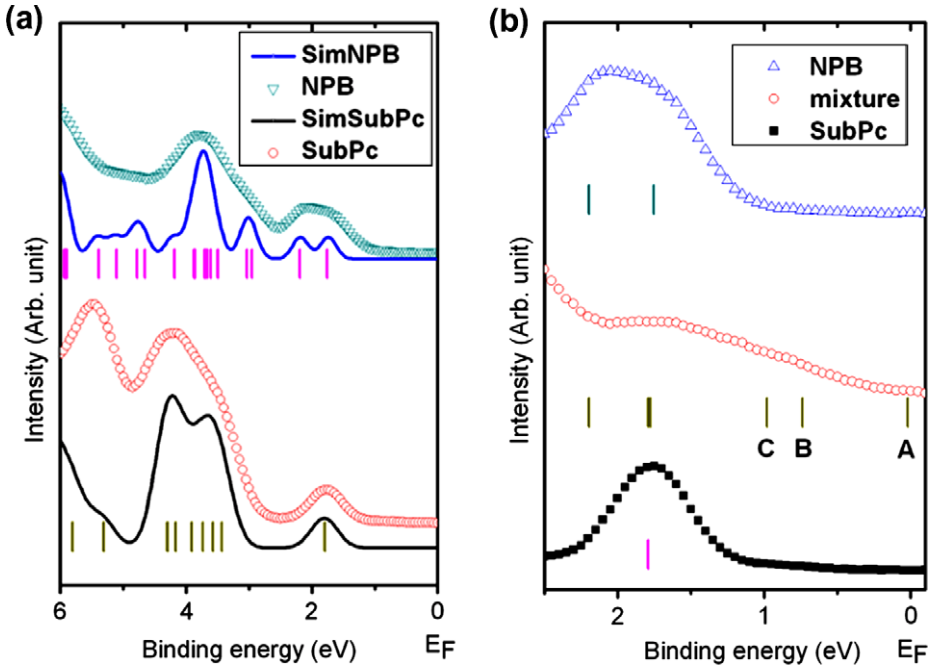

Fig. 5. (a) The experimental and simulated valence-band spectra of pristine NPB and SubPc. The vertical bars under the simulated spectra are the molecular levels of single molecule. (b) Comparison of experimental HOMO spectra and calculated molecular levels of pristine NPB, pristine SubPc, and NPB/SubPc, respectively.

4. Conclusion

In conclusion, we demonstrated the enhancement of current injection efficiency in OLEDs with incorporation of SubPc-doped NPB as HILs. The origins of enhanced current efficiency were investigated via photoemission spectroscopy and quantum chemistry calculation. The corresponding core-level spectra indicate the occurrence of axial reaction on SubPc with NPB. Furthermore, simulated valence-band spectra show that the formation of gap states is due to the HOMOs of new complexes created from the reaction of SubPc and NPB, which facilitate the hole injection at the anode interfaces.

Acknowledgements

This work was partially supported by the National Science Council, Republic of China, under contract No. NSC95-2745-M-002-011. We are also grateful to Computer and Information Networking Center, National Taiwan University for the support of high-performance computing facilities.

References

[1] C.W. Tang, S.A. Vanslyke, Appl. Phys. Lett. 51 (12) (1987) 913–915.
[2] C.C. Wu, C.I. Wu, J.C. Sturm, A. Kahn, Appl. Phys. Lett. 70 (11) (1997) 1348–1350.
[3] M.G. Mason, L.S. Hung, C.W. Tang, S.T. Lee, K.W. Wong, M. Wang, J. Appl. Phys. 86 (3) (1999) 1688–1692.
[4] C. Ganzorig, M. Fujihira, Appl. Phys. Lett. 77 (25) (2000) 4211–4213.
[5] D.B. Romero, M. Schaer, L. Zuppiroli, B. Cesar, B. Francois, Appl. Phys. Lett. 67 (12) (1995) 1659–1661.
[6] J. Blochwitz, M. Pfeiffer, T. Fritz, K. Leo, Appl. Phys. Lett. 73 (6) (1998) 729–731.
[7] M. de Wild, S. Berner, H. Suzuki, H. Yanagi, D. Schlettwein, S. Ivan, et al., Chem. Phys. Chem. 3 (10) (2002) 881–885.
[8] Z. Bao, A.J. Lovinger, A. Dodabalapur, Appl. Phys. Lett. 69 (20) (1996) 3066–3068.
[9] L. Yan, N.J. Watkins, S. Zorba, Y. Gao, C.W. Tang, Appl. Phys. Lett. 79 (25) (2001) 4148–4150.
[10] B. del Rey, U. Keller, T. Torres, G. Rojo, F. Agullo-Lopez, S. Nonell, et al., J. Am. Chem. Soc. 120 (49) (1998) 12808–12817.
[11] C.G. Claessens, D. Gonzalez-Rodriguez, T. Torres, Chem. Rev. 102 (3) (2002) 835–853.
[12] K.L. Mutolo, E.I. Mayo, B.P. Rand, S.R. Forrest, M.E. Thompson, J. Am. Chem. Soc. 128 (25) (2006) 8108–8109.
[13] H. Gommans, D. Cheyns, T. Aernouts, C. Girotto, J. Poortmans, P. Heremans, Adv. Funct. Mater. 17 (15) (2007) 2653–2658.
[14] L.S. Liao, W.K. Slusarek, T.K. Hatwar, M.L. Ricks, D.L. Comfort, Adv. Mater. 20 (2) (2008) 324–329.
[15] C.H. Ko, R. Klauser, D.H. Wei, H.H. Chan, T.J. Chuang, J. Synchrotron Radiat. 5 (1998) 299–304.
[16] T.W. Pi, T.C. Yu, C.P. Ouyang, J.F. Wen, H.L. Hsu, Phys. Rev. B 71 (20) (2005) 205310.
[17] M.J. Frisch, et al., Gaussian 03, Revision E.01, Gaussian, Inc., Wallingford, CT, 2004.
[18] Noel M. O'boyle, Adam L. Tenderholt, Karol M. Langner, J. Comput. Chem. 29 (5) (2008) 839–845.
[19] Y.L. Gao, L. Yan, Chem. Phys. Lett. 380 (3–4) (2003) 451–455.
[20] T. Schwieger, M. Knupfer, W. Gao, A. Kahn, Appl. Phys. Lett. 83 (3) (2003) 500–502.
[21] J.X. Tang, C.S. Lee, S.T. Lee, Appl. Surf. Sci. 252 (11) (2006) 3948–3952.
[22] S.T. Lee, Y.M. Wang, X.Y. Hou, C.W. Tang, Appl. Phys. Lett. 74 (5) (1999) 670–672.
[23] S.M. Tadayyon, H.M. Grandin, K. Griffiths, P.R. Norton, H. Aziz, Z.D. Popovic, Org. Elec. 5 (4) (2004) 157–166.
[24] S.W. Cho, K.H. Yoo, K. Jeong, C.N. Whang, Y. Yi, M. Noh, Appl. Phys. Lett. 91 (5) (2007) 052102.
[25] S.W. Cho, Y. Yi, M. Noh, M.H. Cho, K.H. Yoo, K. Jeong, et al., Synth. Met. 158 (13) (2008) 539–543.
[26] J. Ahlund, K. Nilson, J. Schiessling, L. Kjeldgaard, S. Berner, N. Martensson, et al., J. Chem. Phys. 125 (3) (2006) 034709.
[27] L. Zhang, H. Peisert, I. Biswas, M. Knupfer, D. Batchelor, T. Chasse, Surf. Sci. 596 (1–3) (2005) 98–107.
[28] K. Nilson, P. Palmgren, J. Ahlund, J. Schiessling, E. Gothelid, N. Martensson, et al., Surf. Sci. 602 (2) (2008) 452–459.
[29] N. Kobayashi, T. Ishizaki, K. Ishii, H. Konami, J. Am. Chem. Soc. 121 (39) (1999) 9096–9110.
[30] A. Curioni, W. Andreoni, J. Am. Chem. Soc. 121 (36) (1999) 8216–8220.
[31] R.Q. Zhang, W.C. Lu, C.S. Lee, L.S. Hung, S.T. Lee, J. Chem. Phys. 116 (20) (2002) 8827.
[32] J. Endo, T. Matsumoto, J. Kido, Jpn. J. Appl. Phys. 41 (3B) (2002) L358–L360.

Organic Electronics 11 (2010) 450–455

Contents lists available at ScienceDirect

Organic Electronics

journal homepage: www.elsevier.com/locate/orgel

A nano-indentation study of the reduced elastic modulus of Alq_3 and NPB thin-film used in OLED devices

Chien-Jung Chiang [a,*], Steve Bull [b], Chris Winscom [c], Andy Monkman [a]

[a] Institute of Photonic Materials, Department of Physics, Durham University, DH1 3LE, UK
[b] School of Chemical Engineering and Advanced Materials, University of Newcastle upon Tyne, NE1 7RU, UK
[c] Centre for Phosphor and Display Materials, The Wolfson Centre for Materials Processing, Brunel University, UXBRIDGE UB8 3PH, UK

ARTICLE INFO

Article history:
Received 14 September 2009
Received in revised form 19 November 2009
Accepted 20 November 2009
Available online 26 November 2009

Keywords:
OLED
Flexible OLED
Nano-indentation
Coated systems
NPB
Alq_3

ABSTRACT

Two of the commonly-used Organic Light Emitting Diode (OLED) materials tris-(8-hydroxyquinoline) aluminum (Alq_3) and *N*,*N*′-bis(naphthalen-1-yl)-*N*,*N*′-bis(phenyl)benzidine (NPB) are thermally evaporated as thin-films on two kinds of substrates with different hardness. By using nano-indentation techniques, the reduced elastic modulus of each of the coatings is measured. The data are carefully analysed through the standard Oliver and Pharr method, and the recently developed critical indentation depth method which takes the effect of the substrate more into account.

© 2009 Elsevier B.V. All rights reserved.

1. Introduction

Thin-films of organic luminescent molecules have been used in Light Emitting Diodes (LED) for two decades. Applications for lighting and small size displays are said to be approaching the cost and lifetime requirements of the electronics consumer market. Comparing their relatively low power consumption with other rivals such as inorganic LEDs in lighting or backlit liquid crystal devices in flat panel Liquid Crystal Displays (LCDs), the Organic Light Emitting Diode (OLED) distinguishes itself by having the potential to be mechanically flexible. Unlike LCDs and inorganic LEDs, OLEDs or printable polymer LEDs can be fabricated on a plastic substrate to make the device flexible, and amenable to roll-to-roll manufacture. It is therefore essential to understand how this rolling process might mechanically damage the multi-layer structured OLED, and studies towards this aim have appeared in the last 5 years. Most of these studies, however, have focused on what was estimated to be the most brittle layer in the structure – the commonly-used Indium Tin Oxide (ITO) layer as the anode [1,2]. However, study of the elasticity properties of the organic conducting and emissive layers is still rare in literature [3]; to obtain such information from a 100 nm thick thin-film is not a simple task. One method potentially able to perform this task is nano-indentation.

Nano-indentation has been used routinely in the mechanical characterization of thin-films and thin-surface layers in recent years [4]. The technique applies a programmed function of increasing and decreasing load to the surface of interest with an indenter of well-defined shape and continuously measures the indenter displacement. The advantage of this method is that mechanical information, such as elastic modulus, can be obtained through the analysis of the load–displacement behaviour alone with a coating of the material to be tested on a substrate made from different material. This makes it an ideal

* Corresponding author.
E-mail addresses: Chien-jung.chiang@durham.ac.uk (C.-J. Chiang), s.j.bull@newcastle.ac.uk (S. Bull), chris.winscom@brunel.ac.uk (C. Winscom), a.p.monkman@durham.ac.uk (A. Monkman).

1566-1199/$ - see front matter © 2009 Elsevier B.V. All rights reserved.
doi:10.1016/j.orgel.2009.11.026

tool for our task. The technique has been used to assess the elastic and plastic properties of micron thick coatings on a range of substrates but there are limitations in measuring the properties of much thinner coatings, particularly when elastic properties are required [5,6]. For coatings of a few hundred nano-metres thickness it has been suggested that extrapolating the properties determined at a range of peak loads or indenter displacements to zero load/depth can be used to determine the coating only properties. With high quality, sharp indenters it is possible to assess coatings down to 100 nm thick by this method [7]. This has been attempted in this study.

2. Experimental

Among all the small molecules used in OLEDs, tris-(8-hydroxyquinoline) aluminum (Alq_3) (Fig. 1a) and *N*, *N*′-bis(naphthalen-1-yl)-*N*,*N*′-bis(phenyl)benzidine (NPB) (Fig. 1b) are two of the most popular materials. Because of the relatively high stabilities of the structures during operation and good electrical conductivities, they can be found in almost every OLED device structure. Therefore it is reasonable to expect that they would be used in the flexible OLED devices, too. So it is important to understand their elastic characteristic. In order to evaluate the effect of the substrate [8], two different kinds of substrates were used: polyethylene terephthalate (PET) supplied from DuPont Teijin Films and standard silicon wafers. All the substrates were cleaned in an ultrasonic bath with acetone, and then isopropanol for 5 min each. The substrates were then loaded into the Kurt J. Lesker Spectros II Deposition System. The tested materials were deposited under a vacuum of 5×10^{-7} mbar. Finally, the samples with 100 nm of Alq_3, 200 nm of Alq_3 and 200 nm of NPD on three individual PET substrates and samples with 100 nm of Alq_3, 100 nm of NPD on two silicon wafers were prepared, respectively (see Table 1).

The Young's moduli of the samples were measured by standard nano-indentation techniques. For each material nano-indentation tests were performed under open loop, load and displacement control with maximum displacements (h_{max}) from 10 nm to 1000 nm using a Hysitron Triboindenter fitted with a sharp Berkovich diamond indenter (tip end radius ~50 nm). In open loop control the indentation loading and unloading segments were controlled by timed ramps whereas in the other loading schemes feedback loops were used to ensure that the desired peak loads and displacements were achieved. The indentation systems frame stiffness and the diamond tip shape was carefully calibrated with a fused silica test sample, using the standard Oliver and Pharr method [9], before and after measurements with no change in either recorded. Nano-indentation load (P) *vs.* displacement (h) curves were then recorded for each indent and only those where evidence of plastic deformation was observed (i.e. the loading and unloading curves are different) were used in the analysis of Young's modulus by the Oliver and Pharr method [9]. The indenter displacement is in fact made up of two components: the plastic depth of the indent, or contact depth, and the elastic deflection of the surface at the edge of the contact. The relationship between the contact depth (h_c) and the maximum displacement (h_{max}) can be determined from Eq. (1):

$$h_c = h_{max} - \varepsilon \frac{P_{max}}{S} \tag{1}$$

where, P_{max} is the maximum loading, and ε is a constant that depends on the shape of the indenter [10]. Empirical studies have shown that for a Berkovich indenter, the typical value of ε is about 0.75. S is the unloading stiffness, which comes from:

$$S = \frac{dP}{dh}\Big|_{h=h_{max}} = mB(h_{max} - h_f)^{m-1} \tag{2}$$

where, m and B are fitting parameters, and h_f is the final displacement after completely unloading.

In this approach, S, the initial slope of the unloading curve, can finally be used to determine the reduced elastic modulus of the sample (effectively from the recovery of the elastic deflection of the surface) based upon the Sneddon flat punch solution [11] and the following equation:

$$E_r = \frac{1}{\beta}\frac{\sqrt{\pi}}{2}\frac{S}{\sqrt{A}} \tag{3}$$

where, A is the contact area which can be deduced from h_c based upon an accurate knowledge of the tip end shape, and β is a constant also depends on the geometry of the indenter (β = 1.034 for the Berkovich indenter) [10].

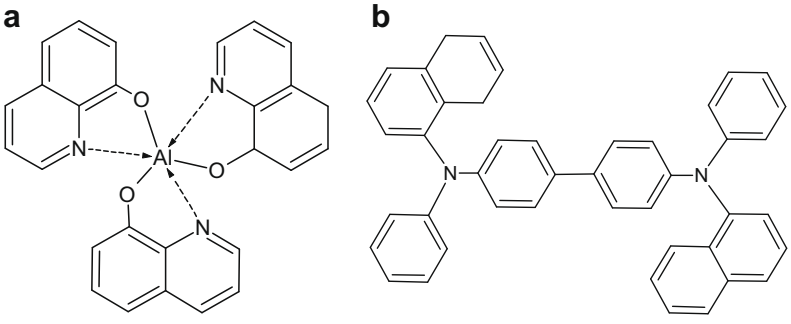

Fig. 1. (a) Structure of tris-(8-hydroxyquinoline) aluminum (Alq_3) and (b) *N*,*N*′-bis(naphthalen-1-yl)-*N*,*N*′-bis(phenyl)benzidine (NPB).

Table 1
Samples investigated.

Sample ID	Ia	Ib	Ic	IIa	IIb
Substrate material	PET	PET	PET	Silicon wafer	Silicon wafer
Substrate thickness/mm	0.1	0.1	0.1	1	1
Coating material	Alq3	Alq3	NPD	Alq3	NPD
Coating thickness/nm	100	200	200	100	100

3. Results and discussion

Fig. 2 shows one example of our load–displacement curve for the sample Ic obtained under open loop control at h_{max} = 475 nm. There is little difference to curves obtained by the other control schemes (load or displacement control) showing that time dependent deformation (creep viscoelasticity) is not significant in this sample. The load-unload curve shows the typical behaviour of a material undergoing a nano-indentation test. The initial slope (~4.4 μN/nm) of the unloading process is used to deduce the reduced elastic modulus of the coating material (in this case, NPB) at the specific h_c. There are a number of jumps (pop-ins) in the loading curve initially. These are most likely related to through-thickness cracking in the coating. Once the coating cracks it no longer supports as much load and the load support is transferred to the substrate – hence the behaviour is dominated by substrate deformation. The cracked coating will also have a lower effective Young's Modulus. The reason for the cracking is probably the mismatch in properties between substrate and coating; a lower Young's modulus substrate material will expand elastically more than the coating for a given contact stress and the as the coating tries to follow this expansion (because it is adhered to it) it is stretched beyond its fracture strain.

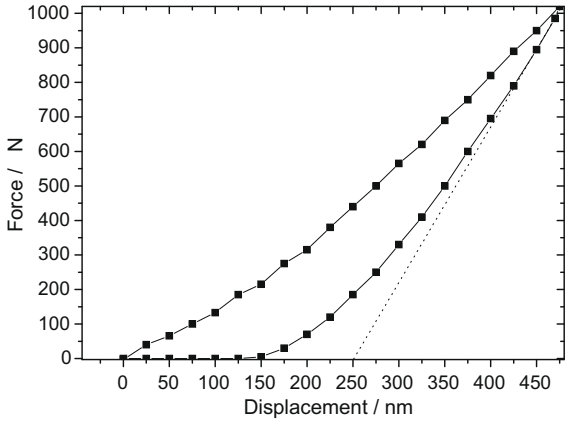

Fig. 2. Load–displacement curve for the 200 nm thick NPB coated on a PET film obtained under open loop control at maximum indenter displacement (h_{max}) = 475 nm.

The reduced elastic modulus of samples Ia, Ib and Ic against the contact depth are shown in Fig. 3a. It is clear that the Alq_3 coating has a greater stiffness than the NPD coating. Since the coating thicknesses of all the samples are ~100 nm all the values of reduced elastic modulus are expected to be affected by the substrate material. Therefore the value when the contact depth is extrapolated to zero should approximate the reduced elastic modulus of the coating layer deposited (ISO 14577-4 (2007)). From Fig. 3a, all the three samples have a Young's Modulus between 9 GPa and 13 GPa when h_c approaches zero. Fig. 3b, however, shows a completely different result when using a silicon wafer as the substrate. The reduced elastic modulus of Alq_3 and NPD are over 160 GPa and 100 GPa, respectively, as h_c approaches zero which seems too large for a molecular film. If we omit the data when h_c < 5 nm because of the effect of surface roughness, and do the extrapolation of the curve only between h_c = 5 nm and 10 nm as shown in Fig. 4, the reduced elastic modulus would become about 100 GPa (Alq_3) and 60 GPa (NPD). All the different reduced Young's moduli obtained from different substrate materials and different analysis methods are listed in Table 2.

There is a question about the validity of the data when h_c < 25 nm since the accuracy of the measurement depends

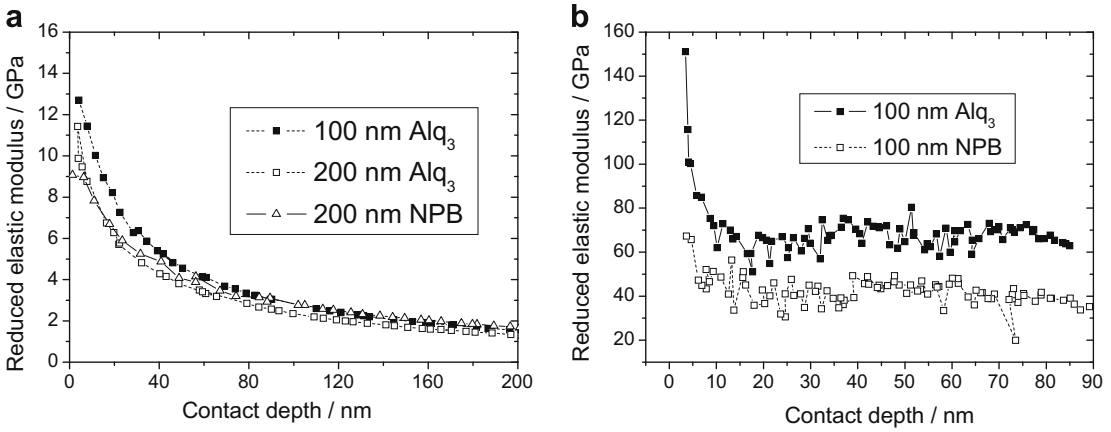

Fig. 3. Reduced elastic modulus against contact depth for the samples Ia, Ib and Ic (a) and of samples IIa and IIb (b).

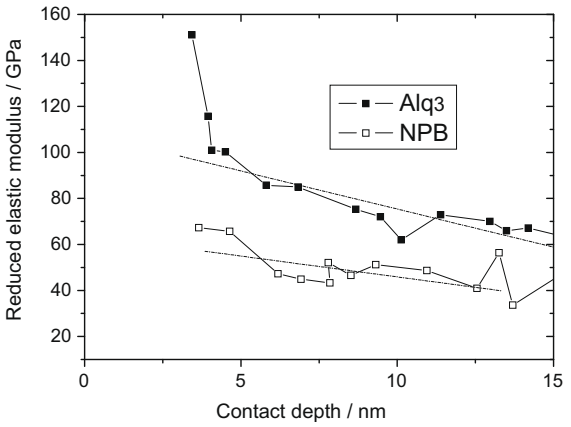

Fig. 4. Extrapolation to zero depth of the curve in Fig. 3b when considering the contact depth from 5 nm to 10 nm.

Table 2
Reduces elastic moduli of samples determined by different methods.

Reduced elastic modulus/GPa	Sample ID				
	Ia	Ib	Ic	IIa	IIb
Data analysis method					
Extrapolation to 0	13	12	9	100	60
Series of springs – Eq. (4)				123.5	61
Plateau in measured value as function of RID				70	40

on the relative indentation depth (RID, i.e. the penetration divided by the coating thickness). This is due to the fact that for a blunt conical indenter there is a transition from spherical contact to conical contact behaviour – for the Berkovich indenter used here this transition occurs at h_c = indenter radius/4, i.e. 12 nm and data at lower depths should be treated with caution as it has been shown that the contact modulus measured varies considerably with tip radius under spherical contact conditions [12]. The decrease in Modulus as h_c increases to 20 nm could be due to this but may also be due to the fracture of the thin coating. It is not likely that the measured values in this depth range are due to an increasing contribution from the substrate since the plateau in Modulus at greater contact depths is not equal to the Young's Modulus of the substrate.

When a coating/substrate system is compressed between the indenter and sample support the measured reduced elastic modulus can be regarded as a combination of springs in series via, to a first approximation,

$$\frac{1}{E_{reduced}} = \frac{1}{E_{indenter}} + \frac{1}{E_{substrate}} + \frac{1}{E_{coating}} \quad (4)$$

Given the indenter properties (E = 1141 GPa) and silicon wafer substrate properties (E = 130 GPa) and the plateau values of measured modulus above h_c = 20 nm using the Eq. (4), Alq_3 would have a Young's modulus of 124 GPa and NPD of 61 GPa which are similar to the values produced by extrapolation of the data to zero contact depth. This gives us some confidence in the measured values.

However, as mentioned previously, the ratio of the indenter tip end radius (IR) to the coating thickness (t) also plays an important role in nano-indentation data analysis [12]. For IR = t, the data can only be reliable when the penetration depth is equal to or greater than half the thickness of the coating material. For IR down to 0.1t, the reliable data can extend to RID = 0.05. If we use this concept to examine our experimental data, with the IR of the indenter about 50 nm, and the thickness of the small molecule coatings between 100 nm and 200 nm, the range would sit between IR = 0.25t and 0.5t. In such circumstances the critical RID to achieve reliable data would be 0.25 for the 100 nm coating and 0.125 for the 200 nm coating – i.e. the contact depth of 25 nm as identified above. The reduced elastic modulus of the samples is plotted against RID in Fig. 5a (Ia, Ib, Ic) and 5b (IIa, IIb). In both cases the reliability of the data at RID < 0.1 used in extrapolation to zero contact depth for coating property assessment is questionable and the Young's Modulus data should be determined by different methods to ensure good accuracy.

The fact that the measured Young's Modulus values do not converge to the Modulus of the substrate in either case shows that the indenter/coating/substrate system must be considered as a set of springs in series as described by Eq.

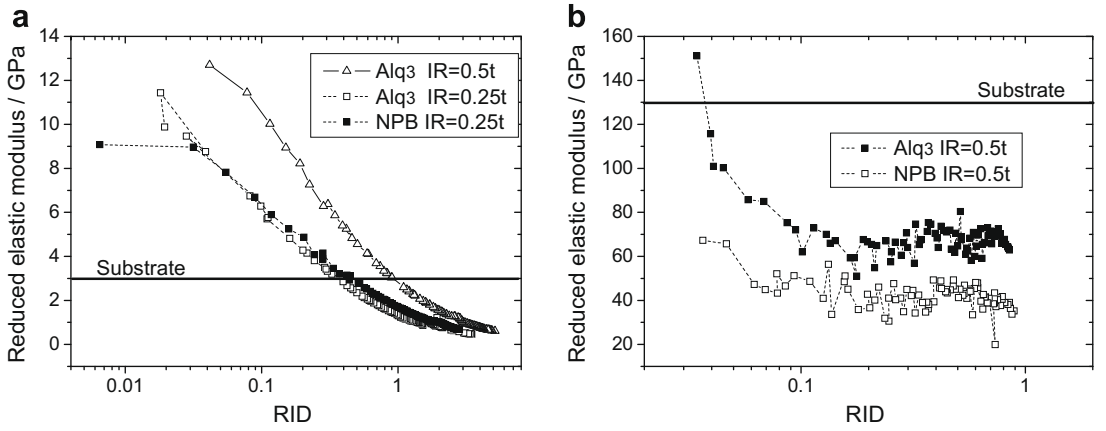

Fig. 5. Reduced elastic modulus against relative indentation depth (RID) for the samples Ia, Ib and Ic (a) and for samples IIa and IIb (b).

(4). It is well known that the properties of a low modulus gasket will dominate the elastic properties of a bolted joint and in a similar manner a low modulus coating or substrate will dominate the properties of the system. The load jumps in the loading curve show that through-thickness fracture occurs at very low loads and the coating stiffness will depend on such cracking. The cracks are approximately parallel to the loading direction during indentation and are expected to have a relatively small effect on the Young's Modulus measured in this direction. However, the Young's Modulus necessary for OLED bending calculations is that in the direction perpendicular to these cracks which could be dramatically affected by cracking. The knowledge of the strain to failure in the film, as well as the knowledge of the modulus of uncracked material would be necessary to determine the bending resistance of these materials.

In systems where the elastic properties of the coating are well known and the coating is deposited on a stiff and a polymer substrate (e.g. in the case of copper on sapphire and polyimide in Fig. 6) the analysis methods used here only give the correct Young's modulus for coatings on the stiff substrate. Thus for design purposes the properties of the films on a hard, stiff substrate should be used as these are more likely to be correct. The deposition of relatively stiff, stressed films on a polymeric substrate can lead to enhanced deformation of the substrate which cannot be accounted for by the simple, time-independent analysis that has been used here. Given the different results from the two substrates (Table 2), we note first that the density of the thin-film, or the way it is grown might be different when deposited onto different materials, and both the film density and the structure of the aggregation can alter the elastic response of the thin-film. The mobility of added species on polymer substrates is often low when compared to materials like silicon leading to the formation of less dense coatings with lower elastic moduli. Thus the properties on silicon may not be totally correct for the films deposited on PET but are a better first approximation to the real properties than the values measured on the PET substrate unless a better model is developed to account for substrate deformation during indentation.

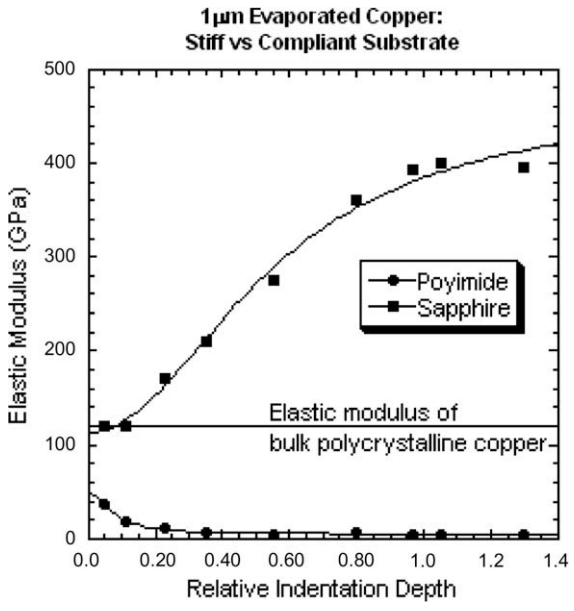

Fig. 6. Elastic modulus against relative indentation depth (RID) for the polycrystalline copper coated on softer (polyimide) and stiffer (sapphire) bases.

4. Conclusion

For such a thin coating on a compliant substrate (i.e. the samples Ia, Ib, Ic) it is difficult to completely filter out the effect of the substrate and there may be considerable scatter in the extrapolated modulus due to the quality of the data available for extrapolation. Fig. 5a actually show a monotonic increase in Reduced Modulus with relative indentation depth and there is considerable agreement between the samples with different coatings but the same thickness. An increase in coating thickness results in an increase in measured Reduced Modulus at a given depth which implies that differing substrate contributions have been recorded. However, on the silicon substrate there is much greater discrimination between the properties of the individual coatings as the results are dominated by the coatings rather than the substrate material.

To conclude, in this work the reduced elastic modulus of the Alq_3 and NPD thin-films used in the OLED devices are measured with different substrates using the nanoindentation method developed by Oliver and Pharr. Different methods of analysis have been applied. When measured on silicon, the reduced elastic modulus of Alq_3 and NPD are in the range of 60–120 GPa, which is similar to values obtained for amorphous carbonaceous coatings and heavily cross-linked materials where density is high. When the film is deposited on the PET film, however, the Young's Modulus is much smaller (~13 GPa) due to changes in film density and structure.

References

[1] S.K. Park et al., Mechanical stability of externally deformed indium-tin-oxide films on polymer substrates, Japanese Journal of Applied Physics Part 1-Regular Papers Short Notes & Review Papers 42 (2003) 623–629.
[2] G.P. Crawford (Ed.), Flexible flat panel displays, Wiley-SID Series in Display Technology, John Wiley & Sons, Ltd., Brown University, USA, 2005. pp, 99–120.
[3] C.-J. Chiang et al., Mechanical modeling of flexible OLED devices, Organic Electronics 10 (2009) 1268–1274.
[4] S.J. Bull, Nanoindentation of coatings, Journal of Physics D: Applied Physics 38 (2005) R393–R413.
[5] A.M. Korsunsky et al., On the hardness of coated systems, Surface & Coatings Technology 99 (1998) 171–183.
[6] J. Chen, S.J. Bull, A critical examination of the relationship between plastic deformation zone size and Young's modulus to hardness ratio in indentation testing, Journal of Materials Research 21 (2006) 2617–2627.
[7] J. Chen, S.J. Bull, On the factors affecting the critical indenter penetration for measurement of coating hardness, Vacuum 83 (2009) 911–920.
[8] A.A. Pelegri, X. Huang, Nanoindentation on soft film/hard substrate and hard film/soft substrate material systems with finite element analysis, Composites Science and Technology 68 (2008) 147–155.

[9] W.C. Oliver, G.M. Pharr, An improved technique for determining hardness and elastic-modulus using load and displacement sensing indentation experiments, Journal of Materials Research 7 (1992) 1564–1583.
[10] G.M. Pharr, Measurement of mechanical properties by ultra-low load indentation, Materials Science and Engineering A 253 (1998) 151–159.
[11] I.N. Sneddon, The relation between load and penetration in the axisymmetric business problem for a punch of arbitrary profile, International Journal of Engineering Science 3 (1965) 47–57.
[12] A.M. Korsunsky, A. Constantinescu, The influence of indenter bluntness on the apparent contact stiffness of thin coatings, Thin Solid Films 517 (2009) 4835–4844.

Organic Electronics 11 (2010) 456–462

Contents lists available at ScienceDirect

Organic Electronics

journal homepage: www.elsevier.com/locate/orgel

Step toward robust and reliable amorphous polymer field-effect transistors and logic functions made by the use of roll to roll compatible printing processes

Jean-Marie Verilhac [a,*], Mohamed Benwadih [a], Anne-Laure Seiler [a], Stephanie Jacob [a], Cecile Bory [a], Jacqueline Bablet [a], Marie Heitzman [a], Jamal Tallal [a], Lucian Barbut [a], Philippe Frère [b], Gilles Sicard [b], Romain Gwoziecki [a], Isabelle Chartier [a], Romain Coppard [a], Christophe Serbutoviez [a]

[a] CEA Liten, Printed Components Laboratory, 17 rue des Martyrs, 38054 Grenoble, France
[b] TIMA Laboratory, 46 Avenue Felix Viallet, 38031 Grenoble, France

ARTICLE INFO

Article history:
Received 30 September 2009
Received in revised form 19 November 2009
Accepted 21 November 2009
Available online 26 November 2009

Keywords:
Organic field-effect transistors
Amorphous semiconductor
Gravure printing
Screen printing

ABSTRACT

Printed organic electronic is believed to be one of the next major technological breakthroughs in the field of microelectronic. The use of high throughput standard graphic arts printing to process organic field-effect transistors (OFETs) opens promising perspectives for low cost, large area and flexible circuits. Nevertheless, these techniques are commonly known to produce relatively thick (>1 μm) layers and to require complex inks formulations composed of several additives. In this paper, we demonstrate that screen printing and gravure printing may be highly versatile and could be well appropriate to deposit organic semi-conducting layers. These fast "single step" processes combined with amorphous semi-conducting polymer give thin, uniform and reproducible layers. The performances of printed or spin-coated films are similar and lead to robust and reliable full printed transistors and logic functions. Moreover, the capability of screen printing and gravure to deposit small patterns of semiconductor is discussed. Lines and spaces down to 500 μm are reported without specific inks and tools optimizations.

© 2009 Elsevier B.V. All rights reserved.

1. Introduction

During the past decade, huge understanding of physical process in the field of organic field-effect transistors (OFET) [1] combined with tremendous progress on chemistry design and synthesis of solution-processed organic semiconductors [2], have led to demonstrations of high-performance solution-processed organic transistors with electrical properties and stability closed to amorphous Si [3–5]. One of the next challenges is now to demonstrate the robustness and reliability of OFETs to support the realization of circuits and active matrixes with several hundreds of connected transistors. The benefit of organic electronics is usually associated to the possibility to formulate inks that are compatible with conventional graphic arts printing processes. These techniques are well appropriate for large area, flexible substrate and for the high throughputs required to decrease production cost. When looking at the severe specifications in terms of thickness or resolution of the semi-conducting layers and also in term of viscosity of the associated formulations, the most intuitively adapted printing technique is inkjet. By the use of appropriate nozzle, small volumes of droplet from 100 pL down to 1 pL are afforded and have led to small pattern resolution down to few μm and thicknesses below

* Corresponding author.
E-mail address: verilhacjm@cea.fr (J.-M. Verilhac).

1566-1199/$ - see front matter © 2009 Elsevier B.V. All rights reserved.
doi:10.1016/j.orgel.2009.11.027

100 nm [6]. Another advantage of inkjet is the ability to generate patterns by digital proofing, without any physical mask, thus reducing the cycle time for prototyping and manufacturing. For these reasons, inkjet printing has been the most widely studied technique for the deposition of the organic semi-conducting layer and has demonstrated promising results. Nevertheless, this process suffers form relatively low deposition speed and low throughput capability compared to other printing techniques [7]. This could be detrimental when working on large area because it could generate non uniform drying of the layer and could lead to non homogenous transistors performances. Even if digital circuits may be tolerant enough to support small variations from transistor to transistor, it is obvious that the next generation of analogue circuits, used for example in sensors applications, will be highly sensitive to any deviations. To overcome this issue the use of high cadence printing techniques that afford a fast "single step" deposition similar to spin-coating process, are of interest. For this purpose, Offset printing, Pad printing, Gravure printing, Flexography or Screen printing may be well appropriate, but have been poorly studied [8–10]. This is mainly due to common statements coming from conventional graphic arts printing, such as printed layer thicknesses in the range of 1–10 μm, spatial resolution adapted for the human eye (∼100 μm) and high ink viscosity requirement [11]. In this paper, we aim to demonstrate that these techniques-namely, focusing on gravure printing and screen printing-could be highly versatile and that when combined with amorphous organic semiconductors, could yield to robust and reliable full printed transistors and circuits.

2. Material and methods

For the active semi-conducting layer, we use a triarylamine copolymer, proprietary polymer from Merck Chemicals, which is a well known family of air stable and solution-processed P-channel semiconductor [12]. The nonplanar conformation of the triarylamine prevents the polymer from crystallization. The lack of supramolecular order makes this class of semi-conducting material robust against the deposition and annealing processes. In the present report, we use a 3 wt% formulation of an amorphous polytriarylamine derivative in mesitylene. This formulation was deposited as blanket layer by an industrial semi-automatic screen printing apparatus from EKRA and by gravure printing with a Labratester I automatic tool from Schläfli. The bottom contacts staggered field-effect transistors performances have been compared with layer realized by spin-coating. T-shape gold source and drain contacts were patterned either by standard photolithography or by laser ablation on a plastic PEN substrate (Dupont Teijin) sputtered with 30 nm of gold. Laser ablation is a powerful tool for the realization of source and drain electrodes as it enables a single step direct patterning contrary to photolithography which requires several steps and is more time consuming. This technique is well adapted for roll to roll or sheet to sheet industrial manufacturing. In counterpart, laser ablation could damage the underlying layer – in our case the PEN substrate – which could be detrimental for the transistor performances. In this study, both photolithography and laser ablation are compared. The gold source and drain surface were cleaned with a Reactive Ion Etching oxygen plasma (Nextral) and subsequently treated with a 10^{-3}mol/L solution of pentafluorobenzene thiol (PFBT) in ethanol for 1 min and then rinsed with pure ethanol. Layers on top of the semiconductors are composed of a 1 μm thick low k perfluoropolymer dielectric layer (Cytop®) [13] inkjet printed with an Altadrop equipment from Altatech. Cytop formulations suffer from high viscosities (∼100 cPs) which make them poorly compatible with conventional inkjet printing processes. In our case, a dilute 0.7 wt% solution of Cytop in its solvent (CT-Solv.100 from Asahi Glass) was used. The solution was inkjetted with a single piezoelectric printhead from Microfab (60 μm diameter) drive at a voltage >80 V. Finally, a silver conductive gate (Cabot®) has been deposited by inkjet with a Dimatix printer. Each 5 × 5 cm test sheet is composed by 27 transistors with channel lengths of 50 μm and 100 μm and channel widths ranging from 500 μm to 2 mm.

AFM measurements were carried out in tapping mode with a Veeco dimension 3000. Ellipsometric measurements were done by a GESP 5 model apparatus made by SOPRA. Measures of tan (ψ) and cos (σ)-corresponding to the change of amplitude and phase of the reflection on the sample, which are specific to the sample, were done at 72° (for maximum intensity) and for a wide range of wavelength: from 250 nm to 800 nm, with an interval of 10 nm.

Electrical characterizations of the OTFTs were performed in air without encapsulation, using a HP4156 semiconductor analyzer combined with an automatic prober. Transistor parameters such as saturation mobility, threshold voltage and $I_{ON/OFF}$ ratio were extracted following the 1620™ IEEE standard test procedure.

3. Results and discussions

Recently, we have reported [14] that the thickness of amorphous semiconductor in top gate staggered transistors has a significant influence on the device properties such as the threshold voltage and the subthreshold slope. Variation of these parameters has been attributed to topological effect induced by the source and drain electrodes and by diffusion limited charge transport through the semiconductor bulk, respectively at low and high thickness regime. This result emphasizes the importance of thickness homogeneity in order to decrease the spread of device parameters within a sheet and from sheet to sheet. In this study, we target a semi-conducting layer thickness of 100 nm which is the optimum values, taking into account the 30 nm source and drain step height. For this purpose, we kept the low viscosity (∼10 cPs) of the 3 wt% formulation in mesitylene and we adapted the printing tools parameters in order to achieve 100 nm thick layers. Note that we observed previously [15,16] that the formulation viscosity may have a significant impact on the morphology of semi-crystalline polymers such as regioregular poly(3-hexylthiophene). In particular, higher solution viscosity

leads to poorer supramolecular organization. In the case of amorphous semi-conducting polymers, this argument is not relevant and this family of materials could be formulated in large range of inks viscosity without impacting the transistor performances.

Fig. 1 shows the calibration curves of the semiconductor thickness as a function of process parameters for spin-coating, gravure and screen printing. In the case of spin-coating, we used a 2 wt% formulation and we observe the well known dependence of thickness with rotating speed. For gravure and screen printing, we tuned the thickness by changing, respectively the cell density (number of lines/cm) and the squeegee pressure (N). We observe a linear dependence for both parameters. For screen printing, the thickness increases when increasing the squeegee pressure due to a higher volume of ink transferred through the meshes. In the case of gravure printing, higher cell density gives lower thickness. This could be explained as the cell depth/volume ratio increases when the cell density decreases which leads to higher dry film thickness. We evaluated the thickness non-uniformity of the semi-conducting layer on 5 × 5 cm substrate area by ellipsometric measurements. The results are listed in table 1. We obtained very uniform layers with typical standard deviation less then 5%, yielding a low spread of transistors performances within a sheet. Values from sheet to sheet are also very similar as could be seen from the two screen printed samples. This is not surprising as similarly to spin-coating, gravure and screen printing are fast deposition processes typically with speed in the range of several centimeters to meters per second. The fast coating combined with the use of high boiling point solvent such as mesitylene (BP = 160 °C) enable a homogenous drying process for all the printed area.

Fig. 2 shows Atomic Force Microscopy images of the treated PEN substrates and the amorphous polymer surface for all the deposition techniques investigated. The RMS roughness values are summarized in Table 1. The PEN substrate with gold source and drain patterned by photolithography or laser ablation was cleaned with an oxygen Reactive Ion etching plasma before Self-Assembled Monolayer (SAM) deposition. Gold cleaning such as oxygen plasma or UV-Ozone are well known to improve the quality of the SAM treatment [17]. Such plasma activation leads to a rough PEN surface with RMS ~ 20 nm. Deposition of the semi-conducting layer tends to planarize the surface and the roughness drops to RMS values of 5 nm, excepted for the gravure deposited layer for which we measure a value of 1.4 nm. This smoother surface in the case of gravure is not yet fully understood, and is still under investigation. The semi-conducting top surface does not show any evidence of periodic micro-patterning that may originated from the printing tools, such as gravure cells or screen meshes. This is due to the ink viscosity which is sufficiently

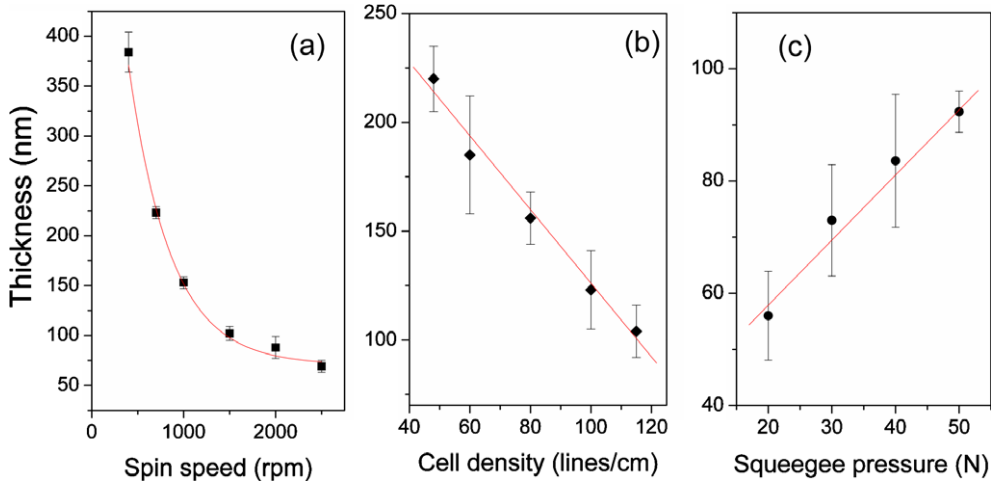

Fig. 1. Dependence of the semi-conducting layer thickness as a function of (a) the rotating speed (rpm) for the spin-coating deposition, (b) the Anilox cell density (lines/cm) for the gravure printing deposition and (c) the squeegee pressure (N) in the case of the screen printing deposition. The solution concentration in mesitylene is 2 wt% for the spin-coating and 3 wt% for the printing techniques.

Table 1
Summary of thickness, roughness and transistors performances for the various deposition techniques used for the semi-conducting layer.

Deposition technique	Source and drain patterning	Thickness[a] (nm)	Roughness (RMS) (nm)	Saturation mobility (cm^2/V s)	Threshold voltage V_T (V)	OFF current (A)	ON/OFF ratio
Spin-coating	Photolithography	123 +/− 3	4.7	0.026 +/− 0.003	−6.6 +/− 1.1	4×10^{-12}	8×10^4
Gravure	Photolithography	128 +/− 7	1.4	0.027 +/− 0.004	−8.9 +/− 1.6	3×10^{-12}	8×10^4
Screen printing	Photolithography	109 +/− 4	4.0	0.033 +/− 0.002	−6.6 +/− 1.1	3×10^{-12}	1×10^5
Screen printing	Laser ablation	112 +/− 3	5.0	0.036 +/− 0.002	−9.0 +/− 1.1	3×10^{-12}	2×10^4

[a] Ellipsometric measurement.

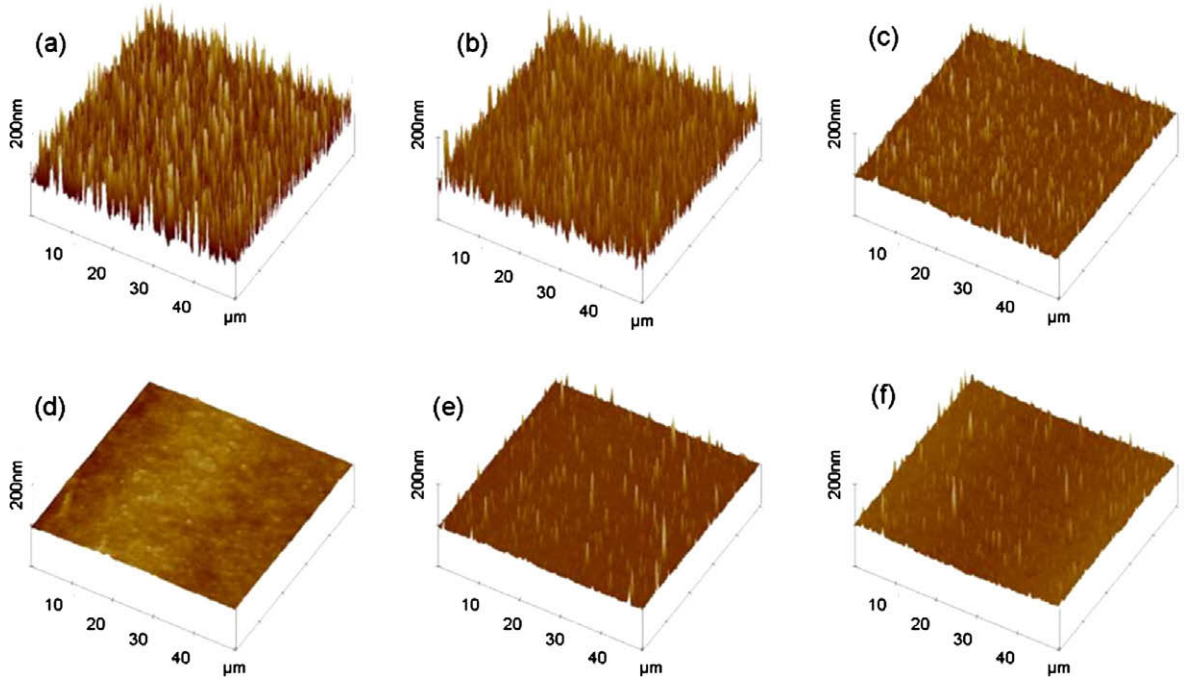

Fig. 2. AFM tapping mode (50 × 50 μm) of the PEN bare substrate after plasma treatment (a) source and drain made by photolithography, (b) source and drain made by laser ablation. AFM images of the semi-conducting layer surface deposited on the plasma treated PEN, by (c) spin-coating, (d) gravure printing, (e) screen printing (electrodes patterns by photolithography) and (f) screen printing (electrodes patterns by laser ablation).

low to spread the ink formulation on the substrate surface. In the staggered transistor geometry studied, the semiconductor surface roughness may have an impact on the transistor mobility [18]. In our case, we do not observe significant difference in mobility for the three deposition conditions used (Table 1). The average mobility taken from 27 transistors per sheet is ranging from 0.025 cm^2/V s to 0.035 cm^2/V s which is the current state of the art mobility for amorphous semi-conducting polymer [12]. Such a non dependence of the mobility with the semi-conducting roughness may be attributed to the presence of some randomly dispersed peaks (average height ~50 nm) which increase the RMS roughness values without impacting the charge carrier's transport at the semiconductor–dielectric interface.

Fig. 3a shows typical output and transfer characteristics of all printed transistors with amorphous semiconductor. The gold source and drain electrodes treated with a perfluorobenzene SAM give good ohmic contact for all the devices tested. The OFF current in the order of 1–10 pA is an indication of a poorly doped semi-conducting layer which is a specific feature of this class of amorphous polymer with high ionization potential and narrow density of states (DOS) [1,12]. Comparison of saturation mobility, threshold voltage (extracted in the saturation regime) and I_{ON}/I_{OFF} ratio are summarized in Table 1. It is remarkable to see that the transistors have similar properties for all the deposition techniques used. Moreover, no differences are observed between source and drain patterned by photolithography or laser ablation. The high stability of the transistors is shown in Fig. 3b. The devices have been cycled at room temperature between $V_{gs} = -40$ V and $V_{gs} = +5$ V with no noticeable degradation of the ON current or the $I_{ON/OFF}$ ratio over a 80 h period (more than 3 days without discontinuity). Moreover, small bias stress time of 1000 s with high gate bias ($V_G = -40$ V) and low drain bias ($V_{DS} = -1$ V) gave threshold voltage shift $\Delta V_T < 1.5$ V which is comparable with a-Si TFT [19]. Variation in ON and OFF current and the standard deviation mobility from on sheet to another is depicted in Fig. 3c and d. More than 50 sheets have been processed with the same transistor geometry and with the semi-conducting layer deposited independently by spin-coating, gravure or screen printing. The I_{ON}/I_{OFF} ratio is typically higher than 10^4 and the mobility could be fitted by a Gaussian law centered on 0.026 cm^2/V s with a width of 0.009 cm^2/V s. Subsequent technology optimization leads to a yield of functional transistors close to 100%. We believe that the robustness and reliability of this technology is due to a combination of appropriate fast deposition printing tools with the use of amorphous semi-conducting polymer. For example, in the case of high mobility transistors made with solution processed semi-conducting small molecules [3] or polymers [20], the deposition process could impact significantly the morphology and change the mobility by several orders of magnitude. The mobility of the triethylsilylethynyl anthradithiophene (TES-ADT) can vary by more than two orders of magnitudes when moving from amorphous to polycrystalline morphology [21]. Even in the polycrystalline form, the mobility could vary from 0.005 cm^2/V s to 0.36 cm^2/V s just by changing the crystal size [22]. This variety of crystalline materials may be more sensitive with the deposition process, and contrary to amorphous polymer, they will require specific optimizations of solvents

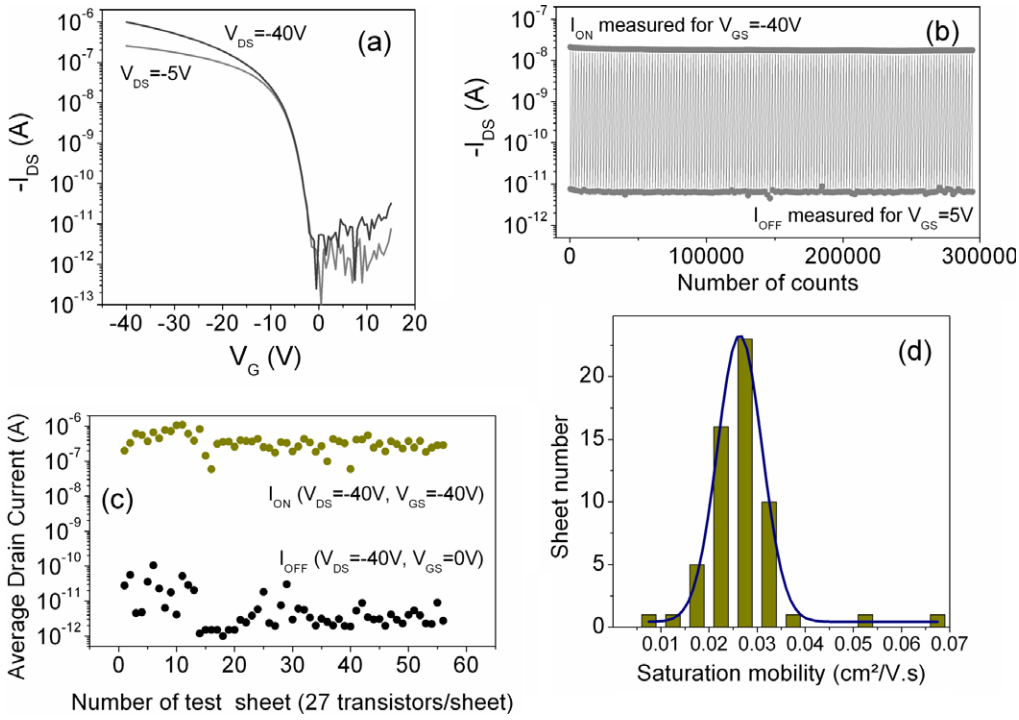

Fig. 3. (a) Typical transfer and output characteristics (L = 40 μm and W = 9 mm) of top gate staggered all printed transistors. (b) Operation stability of a device (L = 100 μm and W = 1 mm) driven by square-wave pulses V_{GS} = −40 V and + 5 V at 1 Hz (V_{DS} = −40 V and duty cycle of 10%). (c) Sheet to sheet variation (c) of the ON and OFF currents and (d) of the saturation mobility value (average values taken from 27 transistors per sheet).

formulation, surface treatment and annealing procedure to give their best properties.

In order to further demonstrate the good performances of our transistors, full printed unipolar basic logic functions such as organic inverters and ring oscillators, have been realized on PEN foil. In that case, the semi-conducting layer has been deposited by screen printing. An image of a five-stage ring oscillator is shown in the inset of Fig. 4b. The oscillators are made of connected inverters composed of drive OFET with channel length L = 40 μm and channel width W = 10 mm and a load OFET with channel length L = 40 μm and channel width W = 2 mm. The output characteristics of inverters behave properly with maximum gain values of 5 for V_{DD} = 40 V (Fig. 4a). The oscillation frequency (Fig. 4b) tends to increase with supply voltage up to a maximum frequency of 300 Hz at 50 V. The amplitude of the oscillations is rather low around 12 V for a supply voltage V_{DD} = 50 V. This is a typical feature of unipolar inverters. As the load transistor acts as a resistor, the current is never completely blocked and the residual small leakage current decreases the amplitude of the oscillations. Moreover, the choice of transistors W/L layout has not been optimized to reach the fastest switching of the circuits, many improvements may still be done in order to get higher performances.

The best improvement for organic circuits will be to switch from unipolar to complementary logic functions. Combination of P channel and N channel transistors leads to more robust circuits with higher gain and lower noise margin, static consumption and driving voltage [23]. Realization of such circuits implies the local patterning of each

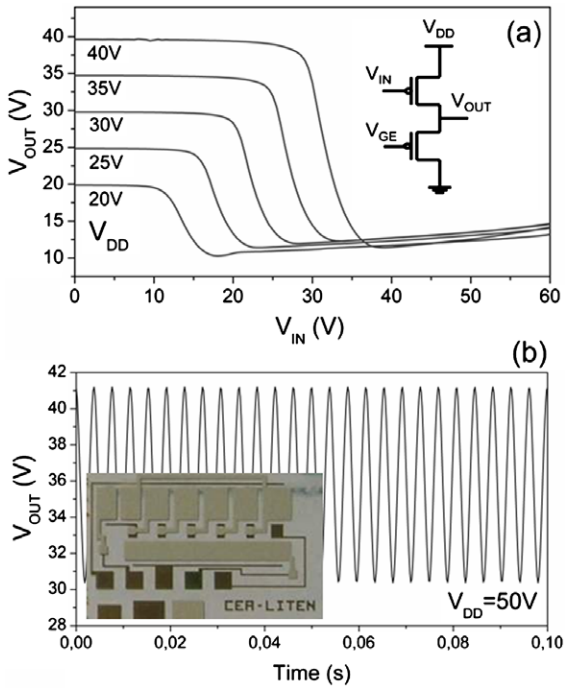

Fig. 4. (a) Output characteristics of (a) a unipolar P type inverters (V_{GE} = 0 V) for different V_{DD} values and (b) a fully printed five-stage ring oscillator (inset shows an image of the printed inverter).

semiconductor. In order to investigate the patterning capability of gravure and screen printing, we use specific anilox

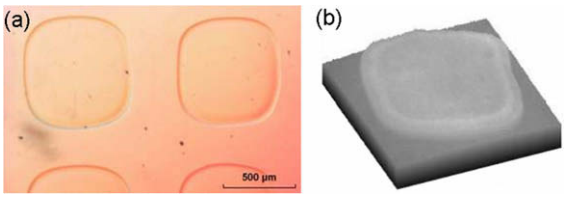

Fig. 5. (a) Image of the patterned semi-conducting layer. (b) 3D image of a printed pattern made with a fluorescence microscope (the coffee-stain effect could be seen at the edge of the pattern).

or screen with various lines of 500 µm to 5 mm and spaces ranging from 500 µm to 3 mm. The definition of the patterns and the minimum separation distance between them depend greatly on the nature of solvents, the substrate surface tension and the annealing process. The spatial resolution of the patterns is enhanced when the ink does not spread, which is generally favored by the use of low substrate surface tension and high solvent surface tension. Drying time and annealing temperature should also play a crucial role. For this study, all these parameters have not yet been optimized and we use the standard process conditions describe earlier to check the patterning capability of the screen printing and gravure printing processes. Fig. 5 shows images of semi-conducting square plot patterned by screen printing. The patterns are 750 × 750 µm and they are separated by 300 µm. The combination of solvent and surface treatment used leads to a small spread of the ink of around 200–300 µm from the targeted dimensions. This spread is independent of the pattern size which enables similar spatial resolution between patterns from various dimensions. Semi-conducting squares of 500 µm, 1 mm, 3 mm and 5 mm have been printed with same separation of 300 µm. This non desirable spread could be further reduced by working on ink and surface engineering. Although the resolution is isotropic for screen printing, the resolution of patterns made by gravure is slightly anisotropic, with the higher resolution normal to the drawing direction. Nevertheless, similar size and separation of the patterns have been found for screen and gravure printing techniques. They are also in the same order of what have been obtained with inkjet printing of such formulation. Most often, applications such as active matrix for electrophoretic display or organic circuits require currents in the order of µA to be operational. The use of mobility in the range of 0.03 $cm^2/V\,s$ implies to use W/L ratio above 30. Taking into account a medium channel length of 40 µm, this leads to channel width of around 1–2 mm and pattern area around 0.2 mm^2. This is in the capability offers by screen or gravure printing and it indicates that the patterning step with these techniques is not the limiting factor of the current technology. Moreover, taking into account that further process optimizations may lead to lower spatial resolution between printed patterns, this opens promising perspectives to increase the device density of organic circuits.

Another figure of merit of printed patterns is their 3D topography. In particular, when decreasing the size of the patterns, edge effect becomes a non negligible part of the area. For direct patterning, the difference of solvent evaporation rate in the center or at the edge of the deposited ink generates a gradient of concentration which gives higher thickness at the frontier of the patterns. This phenomenon-the so-called coffee-stain effect- is depicted in Fig. 5b for a printed pattern of amorphous polymer in mesitylene solvent and it is poorly dependent on the printed technique used. The border effect has a width around 100–200 µm and a thickness typically two or three times higher than in the center of the pattern. This smooth over-thickness could have detrimental effects for printed Organic Light Emitting Diodes (OLED) as it gives pixels with non homogenous brightness, but in the case of OFETs the impact is lower. Nevertheless, the coffee-stain effect could be reduced by the use of appropriate solvents formulation or substrate surface tension. Transistors made with direct patterning of the amorphous semiconductor gave identical performances ($\mu = 0.03 cm^2/V\,s$, I_{ON}/I_{OFF} ratio $>10^4$ and $V_T = -9$ V) than similar transistors with full sheet printed semi-conducting layer. These P channel transistors have been combined with N channel transistors in a full printed process flow and give efficient CMOS-like 5–11 stages ring oscillators.

4. Conclusions

In summary, we have demonstrated that standard industrial tools such as Gravure printing or Screen printing could be highly versatile. In particular, we showed that they could match the severe specifications required for the deposition of the semi-conducting layer in organic field-effect transistors. Low thickness of 100 nm with high uniformity has been reached without specific optimization of the ink formulation. We realized both blanket and direct patterning of the semiconductor material with lines and spaces around 500 µm. Further ways of optimization could still be investigated in order to achieve smaller spatial resolution. The combination of these fast single step printing techniques with amorphous semi-conducting polymer leads to robust and reliable full printed transistors, inverters and oscillators. The lack of supramolecular organization makes this family of materials almost process independent and well suited for the field of printed electronics. Nevertheless, their low mobility will limit the field of applications. In that sense, taking into account the semiconducting layer, strong efforts should be done on the development of high mobility ($>1\ cm^2/V\,s$) small molecules and polymers, in order to move toward high-performance transistors and circuits. Even if the feasibility of printed high mobility transistors has already been demonstrated, they show more pronounced sensitivity to process variations, and strong developments are still requested in order to reach acceptable reliability and uniformity on large area. This will go through a careful control of the crystal growth, as well as optimized ink formulation and stable roll to roll or sheet to sheet manufacturing processes.

Acknowledgements

This work was performed in the frame of the French state funded project PRINTRONICS. Authors want to thanks

Damien Boudinet and Stephane Altazin for helpful discussions.

References

[1] H. Sirringhaus, Adv. Mater. 17 (2005) 2411–2425.
[2] J.E. Anthony, M. Heeney, B.S. Ong, MRS Bull. 33 (2008) 698–705.
[3] R. Hamilton, J. Smith, S. Ogier, M. Heeney, J.E. Anthony, I. McCulloch, J. Veres, D.D.C. Bradley, T.D. Anthopoulos, Adv. Mater. 21 (2009) 1166–1171.
[4] R.A. Street, Adv. Mater. 21 (2009) 2007–2022.
[5] S.G.J. Mathijssen, M. Cölle, H. Gomes, E.C.P. Smits, B. De Boer, I. McCulloch, P.A. Bobbert, D.M. de Leeuw, Adv. Mater. 19 (2007) 2785–2789.
[6] T. Kawase, S. Moriya, C.J. Newsome, T. Shimoda, Jpn. J. Appl. Phys. 44 (2005) 3649–3658.
[7] H. Sirringhaus, C.W. Sele, T.V. Werne, C. Ramsdale, in: H. Klauk (Ed.), Organic Electronics, Wiley-VCH, Weinheim, Germany, 2006 (Chapter 12).
[8] A. Manuelli, A. Knobloch, A. Berns, W. Clemens, IEEE Polytronic Conf. (2002) 201.
[9] H. Yan, Z. Chen, Y. Zheng, C. Newman, J.R. Quinn, F. Dötz, M. Kastler, A. Facchetti, Nature 457 (2009) 679–686.
[10] A.C. Huebler, F. Doetz, H. Kempa, H.E. Katz, M. Bartzsch, N. Brandt, I. Hennig, U. Fuegmann, S. Vaidyanathan, J. Granstrom, S. Liu, A. Sydorenko, T. Zillger, G. Schmidt, K. Preissler, E. Reichmanis, P. Eckerle, F. Richter, T. Fischer, U. Hahn, Org. Electron. 8 (2007) 480–486.
[11] H. Kipphan, Handbook of Print Media, Springer, Berlin, 2001.
[12] W. Zhang, J. Smith, R. Hamilton, M. Heeney, J. Kirkpatrick, K. Song, S.E. Watkins, T. Anthopoulos, I. McCulloch, J. Am. Chem. Soc. 131 (2009) 10814–10815.
[13] J. Veres, S.D. Ogier, S.W. Leeming, D.C. Cupertino, S.M. Khaffaf, Adv. Funct. Mater. 13 (2003) 199–204.
[14] J.M. Verilhac, M. Benwadih, S. Altazin, S. Jacob, R. Gwoziecki, R. Coppard, C. Serbutoviez, Appl. Phys. Lett. 94 (2009) 143301.
[15] J.M. Verilhac, G. LeBlevennec, D. Djurado, F. Rieutord, M. Chouiki, J.P. Travers, A. Pron, Synth. Met. 156 (2006) 815–823.
[16] J.M. Verilhac, R. Pokrop, G. LeBlevennec, I. Kulszewicz-Bajer, K. Buga, M. Zagorska, S. Sadki, A. Pron, J. Phys. Chem. B 110 (2006) 13305–13309.
[17] W.-K. Kim, K. Hong, J.-L. Lee, Appl. Phys. Lett. 89 (2006) 142117.
[18] L.-L. Chua, P.K. Ho, H. Sirringhaus, R.H. Friend, Adv. Mater. 16 (2004) 1609–1615.
[19] N.B. Choi, D.W. Kim, H.S. Seo, C.D. Kim, H. Kang, M.J. Kim, I.J. Chung, Jpn. J. Appl. Phys. 46 (2007) 1333–1336.
[20] I. Mcculloch, M. Heeney, C. Bailey, K. Genevicius, I. Macdonald, M. Shkunov, D. Sparrowe, S. Tierney, R. Wagner, W.M. Zhang, M.L. Chabinyc, R.J. Kline, M.D. McGehee, M.F. Toney, Nature 5 (2006) 328–333.
[21] K.C. Dickey, J.E. Anthony, Y.-L. Loo, Adv. Mater. 18 (2006) 1721–1726.
[22] S.S. Lee, C.S. Kim, E.D. Gomez, B. Purushothaman, M.F. Toney, C. Wang, A. Hexemer, J.E. Anthony, Y.-L. Loo, Adv. Mater. 21 (2009) 3605–3609.
[23] R. Blache, J. Krumm, W. Fix, IEEE International Solid-State Circuits Conference 2009, Session 11, 208–209.

Organic Electronics 11 (2010) 463–466

Contents lists available at ScienceDirect

Organic Electronics

journal homepage: www.elsevier.com/locate/orgel

Interfacial and mechanical studies of a composite Ag–IZO–PEN barrier film for effective encapsulation of organic TFT

Kian Soo Ong *, Raymond Gan Ching Ruey, Eric Ou, Zhang Zheng, Doreen Lai Mei Ying

*Institute of Materials Research and Engineering, Agency for Science, Technology and Research (A*STAR), 3 Research Link, Singapore 117602, Singapore*

ARTICLE INFO

Article history:
Received 24 September 2009
Received in revised form 10 November 2009
Accepted 24 November 2009
Available online 2 December 2009

Keywords:
OTFT
Barrier film
Encapsulation
Bending test

ABSTRACT

A composite silver–indium zinc oxide (Ag–IZO) layer is deposited on a polyethylene naphthalate (PEN) film by DC and RF sputter respectively. Tof–SIMS and XPS studies showed that an interface was formed when Ag has successfully plugged into the softer layer of IZO forming a composite Ag-IZO layer to achieve a water vapor transmission rate (WVTR) of $\sim 1.6 \times 10^{-4}$ g/day/m^2. Poly (3-hexylthiophene) (P3HT) based organic thin-film transistors (OTFT) encapsulated with the Ag–IZO–PEN film kept in glove box and ambient condition are tested and shown that this film is capable to provide the OTFT with adequate protection against moisture and oxygen for more than 3600 h. Mechanical bending tests on the Ag–IZO film also revealed that it has only 0.9% increase in sheet resistance after 10,000 cycles of bending which make this barrier film very suitable for encapsulation of flexible OTFT devices.

© 2009 Elsevier B.V. All rights reserved.

1. Introduction

Organic thin-film transistors (OTFTs) have the potential application for use on low-cost electronic devices such as flexible solar cells, disposable electronic tags and flexible displays [1]. However, the performance of OTFTs and flexible electronic devices are adversely affected when exposure to various elements in the environment inclusive of light exposed, oxygen and moisture [2]. Therefore, in many applications, OTFTs need to be protected from these elements in the environment with an effective protecting barrier or encapsulation layer [3,4].

For low-cost OTFTs, a liquid-processable barrier layer would be preferable to lower manufacturing cost. But, additional 3–5 inorganic inter layers (e.g. Al_2O_3) are required to improve the gas and water permeability properties of such barrier layer.

In this paper, our barrier layer consists of a DC sputtered Ag and RF sputtered IZO on a PEN film. We measure the WVTR of the barrier film by calcium test [5–7] and study lifetime of the barrier film in relation to the on/off ratio of the encapsulated devices inside a nitrogen glove box and in air. Furthermore, we characterize the barrier film using Tof–SIMS and XPS to have more in-depth understanding on the formation of an interface between the Ag and the IZO and how this interface may affect the film's WVTR and bending properties. Ag is selected as part of the barrier component because its cost and properties is optimized as compared to Au and Al.

2. Materials and methods

2.1. Fabrication of P3HT OTFT

The bottom-gate, bottom-contact OTFT was fabricated as follows: first, 200 nm of SiO_2 gate dielectric was deposited on a heavily doped n-type silicon wafer. Second, the gold drain and source channels and electrodes were formed by thermal evaluation of gold through shadow mask. A thin layer of Chromium was used to provide the adhesion between the gold and the dielectric layers. The channel length/width (L/W) was 10 μm/2 mm. Third, the dielectric layer was treated with octadecyltrichlorosilane

* Corresponding author. Tel.: +65 68748362; fax: +65 68720785.
E-mail address: ks-ong@imre.a-star.edu.sg (K.S. Ong).

1566-1199/$ - see front matter © 2009 Elsevier B.V. All rights reserved.
doi:10.1016/j.orgel.2009.11.028

(OTS) to form a self-assembled monolayer (SAM). This SAM allows edge-on orientation of P3HT by replacing the hydroxyl groups at the SiO_2 surface with alkyl groups capable of attracting the hexyl side chains of P3HT [8]. Finally, the P3HT layer was spin-coated from a 0.08 wt.% chlorobenzene solution at 3500 rpm for 60 s, followed by 10 min of hot plate baking at 120 °C. The thickness of the P3HT is ~350 nm.

2.2. Encapsulation of P3HT OTFT

The Ag–IZO–PEN barrier film as fabricated at room temperature (~22 °C and substrate's temperature is <50 °C after sputtering process) as follows: First, 90 nm of IZO was sputtered on the PEN substrate by 75 W RF, 82 V_{bias}, Ar:H_2 is 10:1 sccm and process pressure of 3×10^{-3} torr. Second, 300 nm of Ag was sputtered on the IZO by 100 W DC, Ar 10 sccm and process pressure of 4.3×10^{-3} torr. Third, the film was adhered directly on the OTFT with a thin layer of adhesive. A UV curable epoxy sealant was then applied around the edges of the barrier film and cured under UV radiation for 20 s. This epoxy sealant is to enhance the adhesion between the barrier film and the silicon wafer. The encapsulation process was done in a Nitrogen filled glove box where the O_2 and H_2O were controlled below 2 ppm.

2.3. Characterization methods

The *I–V* characteristics of the devices were measured in air by an Agilent 4156C Precision Semiconductor Parameter Analyzer. The on/off ratio was directly extrapolated from the plot of log I_{ds} versus V_g at $V_{ds} = -40$ V, where I_{ds} is the drain–source current, V_g is the gate voltage and V_{ds} is the drain–source voltage. WVTR of the Ag–IZO–PEN barrier film was measured by calcium test conducted at 60 °C 90%RH. The interface of Ag–IZO composite barrier was studied using time of flight-secondary ion mass spectroscopy (Tof–SIMS, ION TOF SIMS IV) and X-ray photoelectron spectroscopy (XPS, ESCA-LAB-220i XL VG Scientific). Bending test was conducted on a 5 cm × 5 cm barrier film using a radius of curvature of 12.5 mm at 1 cycle per second. The sheet resistances (in Ohm/sq) of the barrier films were measurement by a four-pin probe of Loresta-EP tester after 1 k, 5 k, 10 k, 20 k and 60 k of bending cycles. The schematic diagram of the bending tester and the detail calculation of achieving 12.5 mm radius of curvature is described in detail else where [9,10].

3. Results and discussion

The calcium test of Ag–IZO–PEN was done at 60 °C 90%RH over a period of 1200 h. As shown in Fig. 1, the WVTR of 1.6×10^{-4} g/m^2/day was calculated from the slope of the plot of calcium conductance versus test duration. In contrast, this result was far better than the WVTR (by Mocon tester) of 0.8–1.2 and 0.65×10^{-2} m/m^2/day of the bare PEN and IZO coated PEN substrate respectively. This result is also comparable or better than other types of encapsulation layer such as PECVD deposited SiO_x–PEN

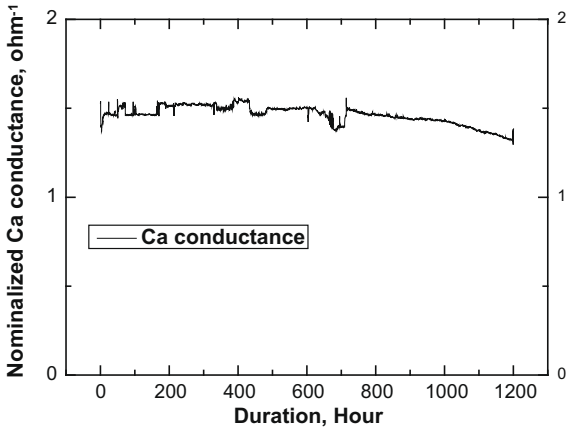

Fig. 1. Permeation rate of Ag–IZO–PEN film as a function of Ca conductance over the duration of 1200 h at 60 °C 90%RH.

(<5×10^{-3}) by Dennler et al. [11]. The improvement in WVTR is come from depositing a layer of Ag on top of the IZO layer.

In order to have better understanding of the contribution of the Ag layer to the barrier properties, we conducted Tof–SIMS and XPS analysis on the interface of Ag–IZO and the result is shown in Figs. 2 and 3 respectively. The Tof–SIMS depth profile of Ag has a distinguish peak immediately after the rise of the In, Zn and O depth profiles in which ZnAg and InAg profile formed a similar plateau as the Ag profile. The similar decay profile of Ag and InAg indicates that an interface is formed between Ag and IZO layer. This interface was formed during the sputtering of Ag onto the IZO surface and some Ag atoms penetrated and/or migrated into the IZO layers. The XPS scans on the same film confirmed that there is no doping or oxidation of Ag to the IZO layers but rather an Ag–IZO interface was formed between the pure Ag and IZO layer. As from the WVTR result, IZO alone has a high water permeation rate 6.5×10^{-2} g/m^2/day implies that this IZO layer is not sufficient to block the migration of water molecules to the other side of the layer [12]. It is most possible due to

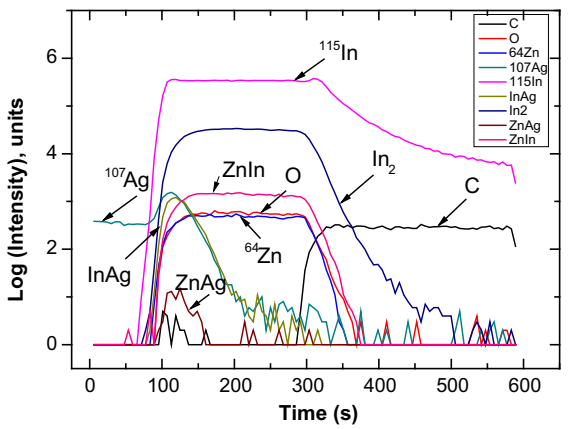

Fig. 2. Tof–SIMS depth profile of Ag–IZO–PEN film.

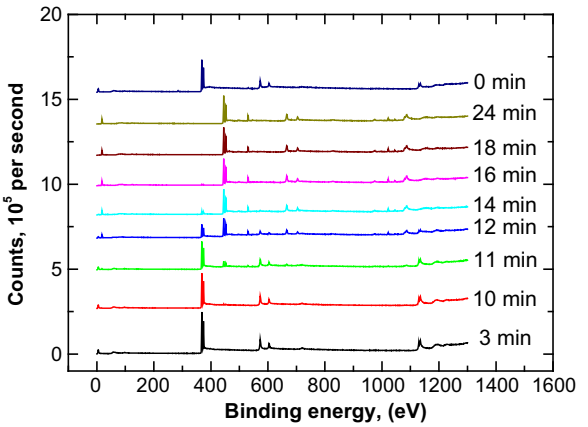

Fig. 3. XPS scan on the Ag–IZO–PEN film at various time intervals. The peak of Ag3d, In3d, Zn2p and O1s are 368.3 eV, 444.9 eV, 1022.2 eV and 530.3 eV respectively. Notice that the peak of Ag3d vanished at 16 min and In3d peak appeared after 10 min of Ar sputtering indicates that there is an interface at Ag and IZO layer.

vacancies between the IZO clusters (as shown in Fig. 4) still large enough that allow water permeation. The situation with the Ag–IZO film is different, as the Ag molecules are incorporated to the interstitial or grain boundaries of IZO forming a much denser interface which could reduce the migration of the water molecules much more effectively, hence the WVTR of the Ag–IZO–PEN film decreased to a value of 1.6×10^{-4} from the 6.5×10^{-2} of IZO–PEN. The atomic ratio plots showed in Fig. 5 further reveals the migration pattern of Ag in the IZO layer is homogenous and decrease gradually (~20% per minute of Ar sputtering during the XPS scan) as the sputter energy decreases with the distance from the sputter target during the Ag deposition process. Fig. 6 shows a schematic diagram of the formation of Ag–IZO interface. Smaller molecules such as H_2O which pass through the pin holes in the Ag layer are blocked by the denser Ag–IZO interface resulting in better barrier performance.

In order to further prove that our Ag–IZO–PEN barrier film is suitable for OTFT application, we fabricated and encapsulated the OTFT device as described in the earlier part of the paper. We measured and calculated the on/off ratio of the encapsulated devices in air and at the same time for the encapsulated devices kept inside the Nitrogen filled glove box. The change in on/off ratio versus the life time (in days) is showed in Fig. 7. The changes in on/off ratio of both samples (i.e. inside glove box and in air) did not varies (~50% higher than the initial value) significantly over the period of >3600 h show that the encapsulation of the Ag–IZO–PEN barrier film provide adequate protection against moisture for the sample kept in air so that its on/off performance over time was similar to that of samples kept in the N_2 glove box.

Finally, we also conduct a bending cycle testing to the Ag–IZO–PEN film and the result is comparable to other flexible substrate such as CNT–PEN [13]. From Fig. 8, only a 0.9% increase in sheet resistance was observed after 10,000 cycles of bending. We believe that the interlayer at the Ag–IZO interface helps to reduce the bending stress and preventing crack formation [14] of the barrier film during the bending cycles. More studies are still required to investigate the impact of bending test on the Ag–IZO interface such as any further migration of Ag into the IZO layer due to the mechanical interactions and the changes (if any) in the life time performance of the barrier film after bending stress.

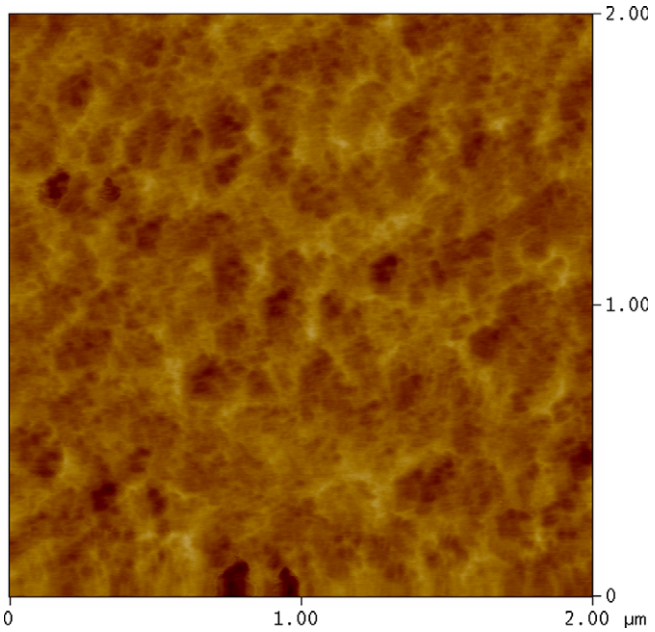

Fig. 4. AFM images of IZO–PEN shows the formation of IZO clusters and surface roughness (RMS) is 1.072 nm. The scan area is 2 μm × 2 μm.

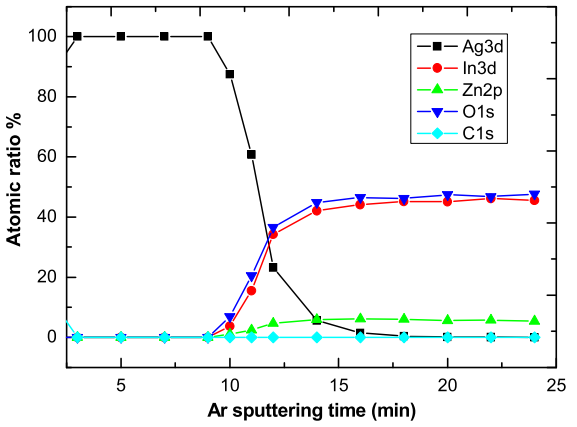

Fig. 5. XPS scan of Ag–IZO–PEN film showing the atomic ratio of Ag, In, Zn O and C within the Ag–IZO interface.

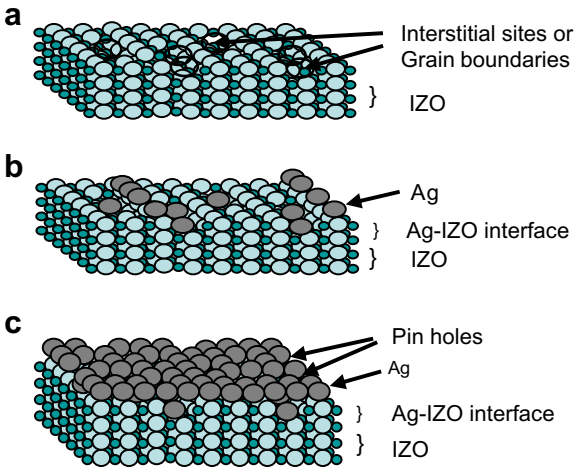

Fig. 6. Schematic diagram of the formation of Ag–IZO interface. a. Interstitial sites or grain boundaries at IZO layer; b. Ag molecules incorporated to the IZO layer to form Ag–IZO interface and c. formation of top Ag layer. Smaller molecules such as H_2O which pass through the pinholes in the Ag layer are blocked by the denser Ag–IZO interface.

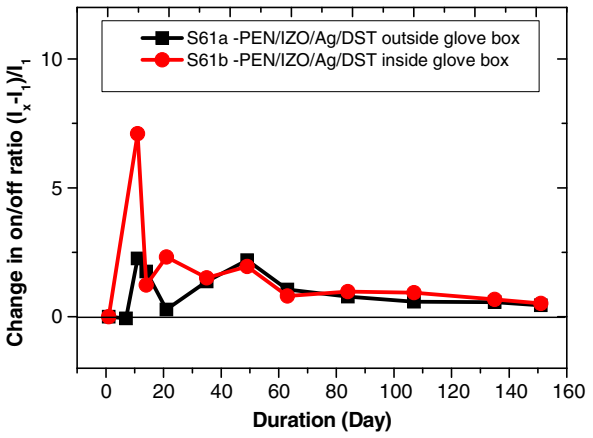

Fig. 7. The changes in on/off ratio of the encapsulated OTFT device, where I_1 denotes the initial on/off ratio of the device immediately after encapsulation and I_x denotes the on/off ratio of the same device after x days.

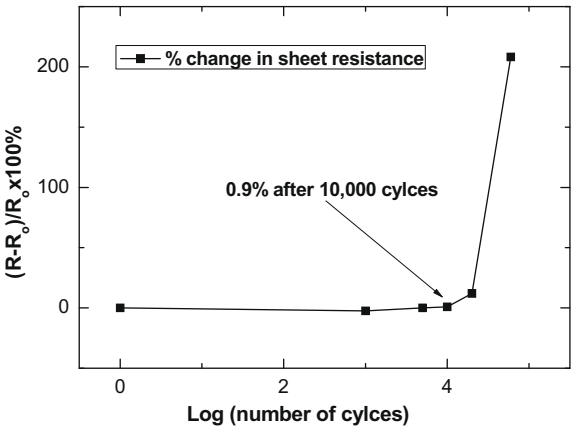

Fig. 8. Changes in sheet resistance of Ag–IZO–PEN film after bending cycles of 1 k, 5 k, 10 k, 20 k and 60 k of bending cycles.

4. Conclusions

We have fabricated an Ag–IZO–PEN barrier film for effective encapsulation of P3HT OTFT devices. The low water permeation rate of 1.6×10^{-4} g/m^2/day allows the device to survive more than 3600 h. Further investigation using Tof–SIMS and XPS reveals that there is a dense interlayer at the interface between the Ag and the IZO layers where the Ag atoms migrated into the IZO layer. This interface layer also helps to prevent and reduce the cracks formation when the film undergoes mechanical bending cycles. We will continue to investigate the possibilities of using different metal–metal oxide barrier films instead of inorganic–organic or metal oxide–organic barriers for flexible OTFT devices.

References

[1] Jay Lewis, Materials Today 9 (2006) 38–45.
[2] P.E. Burrows, G.L. Graff, M.E. Gross, P.M. Martin, M.K. Shi, M. Hall, E. Mast, C. Bonham, W. Bennett, M.B. Sullivan, Displays 22 (2001) 65–69.
[3] A.S. da Silva Sobrinho, G. Czeremuszkin, M. Latrèche, Journal of Vacuum Science and Technology 18 (2000) 149–157.
[4] A.G. Erlat, B.M. Henry, J.J. Ingram, D.B. Mountain, A. McGuigan, R.P. Howson, C.R.M. Grovenor, G.A.D. Briggs, Y. Tsukahara, Thin Solid Films 388 (2001) 78–86.
[5] R. Paetzold, A. Winnacker, D. Henseler, V. Cesari, K. Heuser, Review of Scientific Instruments 74 (2003) 5147–5150.
[6] A. Ranade, N.A. D'Souza, R.M. Wallace, B.E. Gnade, Review of Scientific Instruments 76 (2005) 013902.
[7] N. Kim, W.J. Postscavage Jr., B. Domercq, B. Kippelen, S. Graham, Applied Physics Letters 94 (2009).
[8] Christos D. Dimitrakopoulos, Patrick R.L. Malenfant, Advanced Materials (2002) 99–117.
[9] Kian Soo Ong, Jianqiao Hu, Roshan Shrestha, Fourong Zhu, Soo Jin Chua, Thin Solid Films 447 (2005) 32–37.
[10] Mark Dai Joong Auch, Kian Soo Ong, Guenther Ewald, Chua Soo-Jin, Thin Solid Films 417 (2002) 47–50.
[11] G. Dennler, C. Lungenschmied, H. Neugebauer, N.S. Sariciftci, M. Latrèche, G. Czeremuszkin, M.R. Wertheimer, Thin Solid Films 511–512 (2006) 349–353.
[12] Ahmet G. Erlat, Bernard M. Henry, Chris R.M. Grovenor, Andrew G.D. Briggs, Richard J. Chater, Yusuke Tsukahara, Journal of Physical Chemistry B 108 (2004) 883–890.
[13] Eric C.-W. Ou, Liangbing Hu, Gan Ching Ruey Raymond, Kian Soo Ong, Jisheng Pan, Zhang Zheng, Youngbae Park, David Hecht, Glen Irvin, Paul Drzaic, George Gruner, ACS Nano 3 (2009) 2258–2264.
[14] Yves Leterrier, Progress in Materials Science 48 (2003) 1–55.

Organic Electronics 11 (2010) 467–471

Contents lists available at ScienceDirect

Organic Electronics

journal homepage: www.elsevier.com/locate/orgel

Comparison of hole mobility in thick and thin films of a conjugated polymer

Salvatore Gambino, Ashu K. Bansal, Ifor D.W. Samuel *

Organic Semiconductor Centre, SUPA, School of Physics and Astronomy, University of St. Andrews, North Haugh, St. Andrews, Fife, KY16 9SS, United Kingdom

ARTICLE INFO

Article history:
Received 3 October 2009
Received in revised form 25 November 2009
Accepted 29 November 2009
Available online 3 December 2009

Keywords:
Charge transport
Mobility
Time of flight
Charge generation layer

ABSTRACT

The problem that conventional time of flight (TOF) mobility measurements are made on much thicker films than typically used in organic optoelectronic devices is investigated by comparing the mobility of thick and thin films of the poly(phenylenevinylene) based copolymer "SuperYellow". We report for the first time mobility values perpendicular to the substrate for this widely used material and find them to be of the order of 10^{-6}–10^{-7} cm^2/V s for both spin-coated and drop-cast films. A high photoluminescence quantum yield (PLQY) of 60 ± 5% is measured for both types of films. The results indicate a trade-off between PLQY and charge transport in poly(arylenevinylene)s. The insensitivity of the charge transporting and photophysical properties to the film preparation procedure and thickness is a desirable characteristic that may result from the bulky side groups of "SuperYellow".

© 2009 Elsevier B.V. All rights reserved.

1. Introduction

The time of flight (TOF) technique is one of the most widely used methods to study charge carrier drift mobility in low mobility materials such as organic semiconductors [1]. This technique has been successfully applied in a wide range of organic materials such as small molecules [2,3], polymers [4,5] and dendrimers [6,7] to study both hole and electron transport. An important feature of TOF is that it measures mobility in the direction perpendicular to the substrate. This direction is of crucial importance for optoelectronic devices such as organic light emitting diodes (OLEDs), organic solar cells (OSCs) and (in the future) electrically pumped lasers.

However, in such devices the organic semiconductors usually have a thickness of 100–200 nm, whereas the TOF method is normally applied to films of thickness several micrometers. The reason TOF is only used for relatively thick films is that charge carriers must begin from a well-defined region and so in conventional TOF the excitation light must be absorbed in a layer much thinner than the film thickness. However, it is known that photophysical properties are strongly influenced by choice of solvent and deposition conditions [8–10]. An important question arises of whether conventional TOF measurements are relevant to thin film devices such as OLEDs. In this work, we address this issue by comparing TOF measurements on both thick and thin films of the same material – the poly(phenylenevinylene) (PPV) based copolymer "SuperYellow". "SuperYellow" (SY) is a widely used yellow emitting copolymer that has successfully been employed in polymer light emitting devices such as PLED [11] and LEFET [12]. Previous studies of this material have focused only on its electroluminescence properties including material stability, and efficiency [13] but so far nothing has been reported about charge transport in the direction perpendicular to the substrate and its photoluminescence quantum yield, which are key parameters for understanding structure–property relations of materials and device operation.

A range of methods including steady state current–voltage measurements, dark-injection space charge limited current (DI-SCLC) [14,15], and charge extraction in a linearly increasing voltage (CELIV) [16,17] have been applied to study charge mobility in the direction perpendicular to the substrate in thin films. In the present work we use the charge generation layer (CGL) TOF technique to

* Corresponding author. Tel.: +44 1334463114; fax: +44 1334463104.
E-mail address: idws@st-and.ac.uk (I.D.W. Samuel).

1566-1199/$ - see front matter © 2009 Elsevier B.V. All rights reserved.
doi:10.1016/j.orgel.2009.11.030

measure thin films, and conventional TOF for thick films. In CGL-TOF a strongly absorbing layer is photoexcited, leading to charge injection into the test film [18,19]. We note that Bässler and co-workers [20], have used TOF and CGL-TOF technique to measure hole mobility on a PPV-ether, but the samples studied were a few microns thick, leaving open the question of whether the measurements were relevant to thin film devices.

2. Experimental

SuperYellow (PDY-132) was obtained from Merck and used as received, its molecular structure is shown in Fig. 1a. Lumogen Red (a perylene dye) was supplied by BASF and was used as the charge generation layer for CGL-TOF measurements. Films for both absorption and photoluminescence quantum yield (PLQY) measurements were prepared at the same time from the same solution, by dissolving SY in chlorobenzene at 5 mg/ml and spin coating onto quartz substrates in a glovebox. The spin speed was 2000 rpm giving a thickness of about 150 nm. The film PLQY was determined using a He–Cd laser operating at 442 nm to excite the sample in an integrating sphere purged by nitrogen, following the method of Greenham et al. [21].

For both TOF and CGL-TOF measurements, solutions of SY were made with concentrations of 10 mg/ml in chlorobenzene. Films for TOF measurements were drop cast onto an ITO substrate and left to dry overnight inside a glovebox. The resulting films had thicknesses in the range 4–8 μm, and were then transferred to an evaporator where under high vacuum a 30 nm semi-transparent aluminum film was deposited through a shadow mask to define an active area of approximately 6 mm^2. Films for the CGL-TOF measurements were spin-coated onto an ITO substrate at a speed of 1000 rpm, giving films of thickness close to 300 nm. The samples were then transferred to an evaporator where under high vacuum a 10 nm layer of Lumogen Red followed by 150 nm of aluminum was deposited through a shadow mask.

Both TOF and CGL-TOF measurements were performed at room temperature and in vacuum using 500 ps light pulses from a dye laser for excitation. For TOF measurements (Fig. 2a) the SY was excited at 470 nm through the semi-transparent Al layer. CGL-TOF measurements were performed by exciting the charge generation layer through the ITO and polymer layers (Fig. 2b). The excitation wavelength was 580 nm, which is the peak of the absorption spectrum of Lumogen Red (see Fig. 1b). At this excitation wavelength the SY is completely transparent. The HOMO of the Lumogen Red lies 6.2 eV from the vacuum level [22] enabling hole injection into the polymer layer (HOMO = −4.8 eV) [23].

In both cases the photogenerated packet of charge carriers is then swept through the device under an applied field, and the transit time (t_{tr}) measured using a digital storage oscilloscope (Tektronix TDS 3032). The aluminium electrode was biased positively and the photocurrent signal detected from the ITO. The applied bias led to the photogenerated electrons being removed from the device at the aluminium electrode and holes being swept across the device to be collected at the ITO electrode. Thus the

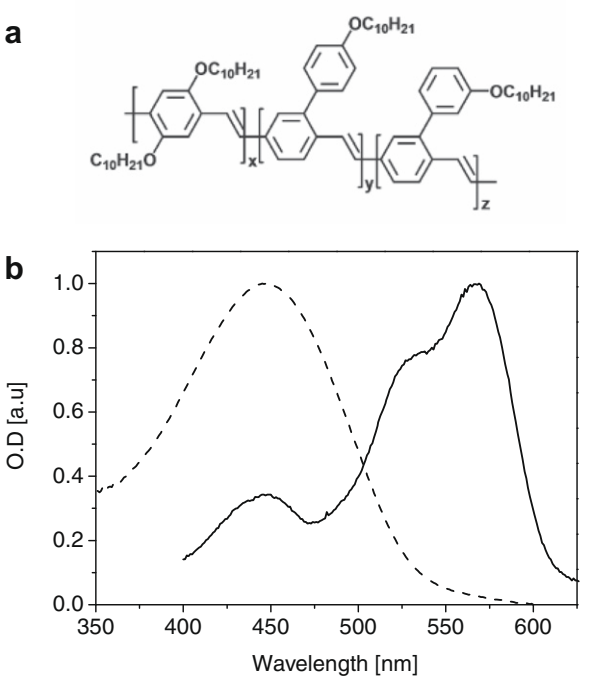

Fig. 1. (a) SuperYellow molecular structure. (b) Normalized SY (dashed line) and Lumogen Red (solid line) absorption spectra.

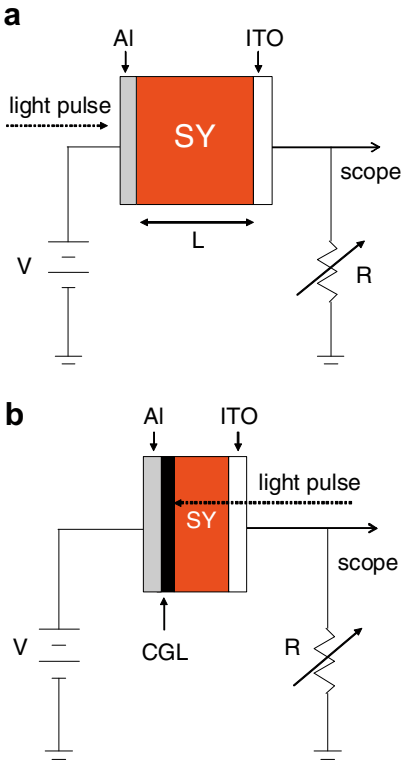

Fig. 2. Schematic of TOF set-up: (a) standard TOF configuration and (b) CGL-TOF configuration. SY denotes SuperYellow. CGL denotes charge generation layer.

measured photocurrent transients are hole currents. Hole mobilities, μ, were deduced from the transit times t_{tr} via the relation $\mu = d^2/(Vt_{tr})$ where d is the film thickness and V is the applied voltage. The time resolution is determined by the RC time constant of the measurement circuit, which was selected to be $\leqslant 20$ t_{tr}. The total charge injected into the film was kept around 2–3% CV in all cases, where C is the capacitance of the device and V is the applied voltage.

3. Results and discussion

Fig. 3a shows the hole photocurrent transient on a linear scale for a drop-cast film, at room temperature measured for an applied electric field $E = 4.2 \times 10^5$ V/cm. The signal has a distinct plateau indicative of non dispersive charge transport, followed by a shoulder and a long tail. The well defined change in the slope of the photocurrent transient allows a clear measurement of the transit time ($t_{tr} = 3.5 \times 10^{-3}$ s) which corresponds to the intersection of asymptotes to the plateau and the tail on a log–log plot. The transit time corresponds to a mobility of 5.4×10^{-7} cm^2/V s. The results of CGL-TOF measurements on the spin-coated sample are shown in Fig. 3b. The transit time (under the same experimental conditions of temperature and electric field) is 6.7×10^{-5} s which corresponds to a mobility of 1.2×10^{-6} cm^2/V s.

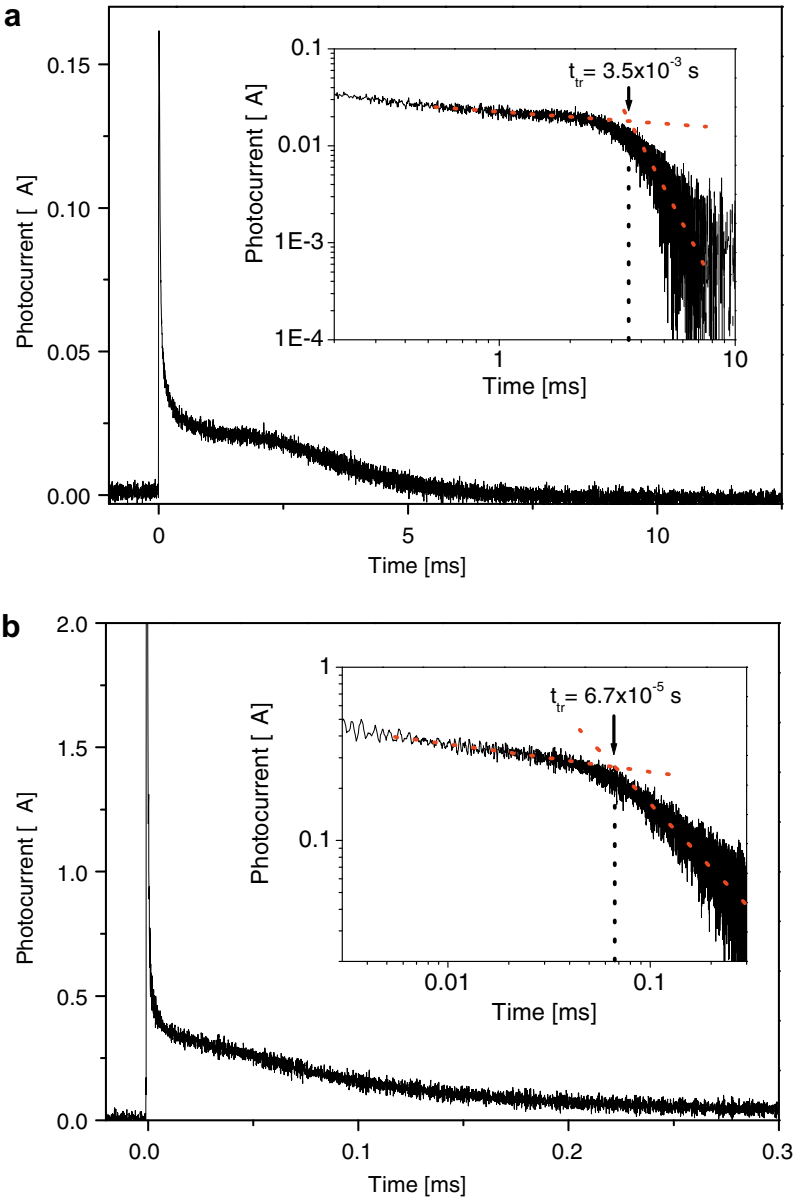

Fig. 3. SY room temperature hole photocurrent transient taken at an applied electric field $E = 4.2 \times 10^5$ V/cm. Data are plotted in both linear and log–log (inset) scale for (a) drop-cast film and (b) spin coated film.

Our measurements give the hole mobility in the direction perpendicular to the substrate, and we have studied its field dependence, as shown in Fig. 4. As the electric field is increased from 1.7×10^5 to 5.4×10^5 V/cm, the hole mobility increases from 5.6×10^{-7} to 6.7×10^{-7} cm^2/V s for the drop-cast film, and from 6.5×10^{-7} to 1.4×10^{-6} cm^2/V s for the spin-coated sample. Our results show that the casting conditions have only a modest effect on the mobility – although the spin-cast film has a stronger field-dependence of mobility, the mobility values for the two samples are within a factor of two of each other.

Variations in mobility values of over an order of magnitude or in charge transport behaviour, such as dispersive or non dispersive, have been observed in polymers of the PPV family as a result of molecular weight [24], solvents [25,26], side-chains [27,28], and annealing [29]. These differences are normally attributed to intrinsic factors, such as chain packing. However, extrinsic factors such as environmental conditions during sample fabrication, (air or in inert atmosphere), or chemical purity also have a marked impact on charge mobility [30,31]. In our study we have removed such factors by using the same high quality material from Merck, preparing samples in a glove box, and measuring them in vacuum for both thick and thin films. The non dispersive nature of the photocurrent transients also suggests the good chemical purity of the material under investigation [2].

Although recently hole mobility values up to 10^{-4} cm^2/V s have been reported for a PPV derivative polymer prepared by a precursor route [32], our mobility values are within the range of others polymers of the PPV family (10^{-6}–10^{-7} cm^2/V s) [28]. We have made a direct comparison by measuring MEH–PPV. Fig. 4 shows the results of TOF measurements on drop-cast films of MEH–PPV (~5 μm) made from a solution with concentration of 10 mg/ml in chlorobenzene and it can be seen that the hole mobility is an order of magnitude higher than for SY. This result shows that the very bulky sidegroups of SY do reduce charge mobility. It is also consistent with the observation of lower mobility in PPV copolymers than homopolymers [33].

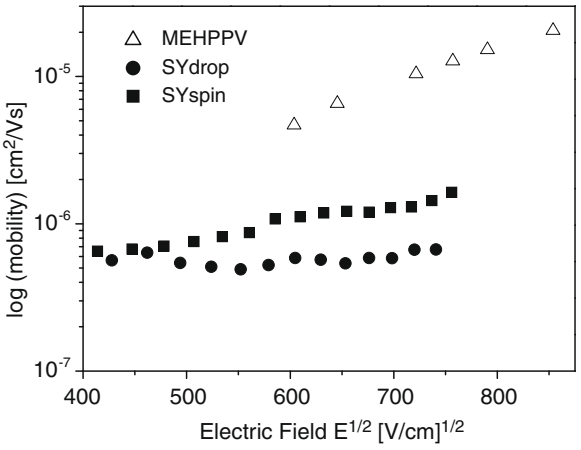

Fig. 4. Field dependent hole mobilities at room temperature. Filled symbols are experimental data for SuperYellow drop-cast film (circle) and spin coated film (square), also are shown MEH–PPV data (triangle) for a direct comparison.

It is also instructive to explore the impact of the sidegroups and film preparation conditions on the photoluminescence quantum yield. We measure the PLQY value of 60 ± 5%, for both types of film. This value is 4–5 times higher in the solid state than the reported values for the related homopolymers: 10–15% for MEH–PPV [21] and 12% for BEH-PPV [34], showing that the particularly bulky sidegroups of SY are effective in controlling intermolecular interactions which can quench photoluminescence. Our results show that SY has much higher PLQY, but much lower mobility than MEH–PPV. However overall SY has substantially better OLED performance than MEH–PPV. Single layer SY based OLEDs have been reported having an External Quantum Efficiency (EQE) of 5.3%, max Power efficiency of 10 lm/W and 11 cd/A [35]. Meanwhile similar single layer OLEDs based on MEH–PPV have shown EQE values of 1–2% and Luminous efficiency of 3 lm/W [36–38]. The above results show that high mobility is not essential for good OLED performance.

4. Conclusions

In summary, we have reported for the first time the charge mobility perpendicular to the film and photoluminescence quantum yield for drop-cast (thick) and spin-coated (thin) films of the widely used PPV copolymer SuperYellow. We find that TOF and CGL-TOF measurements on thick and thin films give similar mobilities in the range 10^{-7}–10^{-6} cm^2/V s, depending on the electric field. This suggests, in the case of this material, at least, conventional TOF measurements do give information relevant to the much thinner films used in devices. We find that the high photoluminescence quantum yield of 60% is achieved at the expense of reduced charge mobility, indicating a trade-off relevant to the development of organic optoelectronic devices. Our results suggest that the bulky side groups of SY cause a highly amorphous film to form over a wide range of preparation conditions, and therefore suggest that the use of such bulky sidegroups could be a useful strategy for the preparation of materials insensitive to processing conditions.

References

[1] P.M. Borsenberger, D.S. Weiss, In Organic Photoreceptors for Xerography, Marcel Dekker Inc., New York, 1998.
[2] G.G. Malliaras, Y. Shen, D.H. Dunlap, H. Murata, Z.H. Kafafi, Appl. Phys. Lett. 79 (2001) 2582.
[3] H.H. Fong, K.C. Lun, S.K. So, Chem. Phys. Lett. 353 (2002) 407.
[4] M. Redecker, D.D.C. Bradley, M. Inbasekaran, E.P. Woo, Appl. Phys. Lett. 73 (1998) 1565.
[5] A.R. Inigo, H.C. Chiu, W. Fann, Y.S. Huang, U.S. Jeng, T.L. Lin, C.H. Hsu, K.Y. Peng, S.A. Chen, Phys. Rev. B 69 (2004) 075201.
[6] J.M. Lupton, I.D.W. Samuel, R. Beavington, M.J. Frampton, P.L. Burn, H. Bässler, Phys. Rev. B 63 (2001) 155206.
[7] S. Gambino, S.G. Stevenson, K.A. Knights, P.L. Burn, Ifor D.W. Samuel, Adv. Funct. Mater. 19 (2009) 317.
[8] I.D.W. Samuel, G. Rumbles, C.J. Collison, S.C. Moratti, A.B. Holmes, Chem. Phys. 227 (1998) 75.
[9] T.-Q. Nguyen, R.C. Kwong, M.E. Thompson, B.J. Schwartz, Appl. Phys. Lett. 76 (2000) 2454.
[10] T.-Q. Nguyen, R.Y. Yee, B.J. Schwartz, J. Photochem. Photobiol. A: Chem. 144 (2001) 21.

[11] H.J. Bolink, E. Coronado, J. Orozco, M. Sessolo, Adv. Mat. 20 (2008) 79.
[12] E.B. Namdas, P. Ledochowitsch, J.D. Yuen, D. Moses, A.J. Heeger, Appl. Phys. Lett. 92 (2008) 183304.
[13] H. Spreitzer, H. Becker, E. Klunge, W. Kreuder, H. Schenk, R. Demandt, H. Schoo, Adv. Mat. 10 (1998) 1340.
[14] D. Poplavskyy, J. Nelson, J. Appl. Phys. 93 (2003) 341.
[15] D. Poplavskyy, J. Nelson, D.C.C. Bradley, Appl. Phys. Lett. 83 (2003) 707.
[16] G. Juska, K. Arlauskas, M. Viliunas, K. Genevicius, R. Österbacka, H. Stubb, Phys. Rev. B 62 (R16) (2000) 235.
[17] A.J. Mozer, N.S. Sariciftci, A. Pivrikas, R. Österbacka, G. Juska, L. Brassat, H. Bässler, Phys. Rev. B 71 (2005) 035214.
[18] P.M. Borsenberger, L. Pautmeier, H. Bässler, J. Chem. Phys. 95 (1991) 1258.
[19] P.M. Borsenberger, L.T. Pautmeier, H. Bässler, Phys. Rev. B 46 (1992) 12145.
[20] C. Im, H. Bässler, H. Rost, H.H. Hörhold, J. Chem. Phys. 13 (2000) 3802.
[21] N.C. Greenham, I.D.W. Samuel, G.R. Hayes, R.T. Phillips, Y.A.R.R. Kessener, S.C. Moratti, A.B. Holmes, R.H. Friend, Chem. Phys. Lett. 241 (1995) 89.
[22] S. Gambino, I.D.W. Samuel, H. Barcena, P.L. Burn, Org. Electron. 9 (2008) 220.
[23] J.S. Swensen, C. Soci, A.J. Heeger, Appl. Phys. Lett. 87 (2005) 253511.
[24] A.R. Inigo, H.C. Chiu, W. Fann, Y.S. Huang, U.S. Jeng, C.H. Hsu, K.Y. Peng, S.A. Chen, Synth. Met. 139 (2003) 581.
[25] A.R. Inigo, C.H. Tan, W. Fann, Y.S. Huang, G.Y. Perng, S.A. Chen, Adv. Mat. 13 (2001) 504.
[26] W. Geens, S.E. Shaheen, B. Wessling, C.J. Brabec, J. Poortmans, N.S. Sariciftci, Org. Electron. 3 (2002) 105.
[27] C. Vijila, B. Balakrisnan, C. Huang, Z.K. Chen, C.G. Zhen, M.D.J. Auch, S.J. Chua, Chem. Phys. Lett. 414 (2005) 393.
[28] C. Tanase, J. Wildeman, P.W.M. Blom, M.E. Mena Benito, D.M. de Leeuw, A.J.J.M. van Breemen, P.T. Herwing, C.H.T. Chlon, J. Sweelssen, H.F.M. Schoo, J. Appl. Phys. 97 (2005) 123703.
[29] C.H. Tan, A.R. Inigo, W. Fann, P.K. Wei, G.Y. Perng, S.A. Chen, Org. Electron. 3 (2002) 81.
[30] S. Gambino, Ph.D. Thesis, Universita' degli studi di Palermo, 2006.
[31] S.A. Choulis, Y. Kim, J. Nelson, D.D.C. Bradley, M. Giles, M. Shkunov, I. McCulloch, Appl. Phys. Lett. 85 (2004) 3890.
[32] M. Sims, S.M. Tuladhar, J. Nelson, R.C. Maher, M. Campoy-Quiles, S.A. Choulis, M. Mairy, D.D.C. Bradley, P.G. Etchegoin, C. Tregidgo, K. Suhling, D.R. Richards, P. Massiot, C.B. Nielsen, J.H.G. Steinke, Phys. Rev. B 76 (2007) 195206.
[33] C. Tanase, P.W.M. Blom, D.M. de Leeuw, E.J. Meijer, Phys. Stat. Solidi (a) 201 (2004) 1236.
[34] M.R. Anderson, G. Yu, A.J. Heeger, Synth. Met. 85 (1997) 1275.
[35] SuperYellow (PDY-132) Merck data sheet.
[36] D. Braun, A.J. Heeger, Appl. Phys. Lett. 58 (1991) 1982.
[37] J. Salbeck, Ber. Bunsenges. Phys. Chem. 100 (1996) 1666.
[38] G. Yu, Synth. Met. 80 (1996) 143.

Organic Electronics 11 (2010) 472–478

Contents lists available at ScienceDirect

Organic Electronics

journal homepage: www.elsevier.com/locate/orgel

Poly(aniline) doped with 5-formyl-2-furansulfonic acid: A humidity memory

Marja Vilkman [a,*], Kaisa Lehtinen [a], Tapio Mäkelä [b], Patrice Rannou [c], Olli Ikkala [d]

[a] VTT Technical Research Centre of Finland, Printable Electronics and Optics, P.O. Box 1000, FI-02044 VTT, Finland
[b] VTT Technical Research Centre of Finland, Micro- and Nanoelectronics, P.O. Box 1000, FI-02044 VTT, Finland
[c] Laboratoire d'Electronique Moléculaire, Organique et Hybride, UMR5819-SPrAM (CEA/CNRS/Univ. J. FOURIER-Grenoble I), INAC, CEA-Grenoble, 17, Rue des Martyrs, F-38054 Grenoble Cedex 9, France
[d] Helsinki University of Technology, Optics and Molecular Materials, P.O. Box 5100, FI-02015 TKK, Finland

ARTICLE INFO

Article history:
Received 2 September 2009
Received in revised form 25 November 2009
Accepted 29 November 2009
Available online 3 December 2009

Keywords:
Polyaniline
Humidity sensor
Irreversible
Functional dopant

ABSTRACT

We present a new concept for a humidity sensor based on doped poly(aniline) that shows irreversible changes of its sheet resistance and capacitance upon exposure to humid conditions, *i.e.* a humidity memory. Therein humidity triggers an irreversible dedoping process, which results in a phase separation and crystallization of the hydrated form of its protonating agent, as suggested by combining FT-IR and UV–Vis-NIR spectroscopies, optical microscopy, dc-conductivity, and frequency dependent capacitance measurements. We also introduce a simple concept to activate the sensor and to monitor it through non-contact capacitance measurements. We anticipate that the proposed concept could be implemented for functional packaging to qualitatively detect whether their contents have been exposed to humidity during their transportation and storage history.

© 2009 Elsevier B.V. All rights reserved.

1. Introduction

π-Conjugated polymers have attracted considerable interest as materials for organic and soft electronics [1–3], such as field-effect transistors [4–8], light-emitting diodes [9–13], photovoltaic cells [14–21], lasers [22–24], and sensors [25–27]. One of their advantages is that they can allow simple processing *e.g.* by printing and that several of their properties can be tuned by chemical modification of the polymer backbone, side-chains, or incorporating functional counter-ions [28]. For example, solubility or dispersibility in solvents [29–32] enables printing techniques to process semi-conducting or conducting poly(aniline), poly(thiophene), and poly(pyrrole). In their doped conducting state, the structural organization depends critically on the counter-ions, which have a major effect on the dc-conductivity [33–35] and mechanical properties, such as Young modulus and elongation at break [36]. Sensors for specific molecules or environmental conditions comprise one of the most promising applications of conducting polymers, enabling detection and monitoring of *e.g.* carbon dioxide gas [37], TNT vapor [38], moisture [39–42], temperature [43], and biological moieties, like antigens [44], glucose [45] or DNA [46]. Functionalization of the counter-ions provides one general strategy to construct efficient, reliable, specific, and yet simple sensors based on conducting polymers.

The characteristic response of doped PANI to humidity is an increased dc-conductivity, as water molecules absorbed from the surrounding atmosphere and those trapped within its semi-crystalline structure impact the conduction mechanism [47–51]. This enhancement is typically reversible, as dc-conductivity decreases again upon drying. This allows reversible moisture sensors that can measure the instantaneous prevailing moisture conditions [26,39–42]. On the other hand, guaranteeing the authenticity and quality of selected products is increasingly required in some high-end consumer applications. This requires follow-up of the storage and transportation history. For example, low moisture content may need to be demonstrated throughout the product history. In several com-

* Corresponding author. Tel.: +358 50 358 6644; fax: +358 20 722 7012.
E-mail address: marja.vilkman@vtt.fi (M. Vilkman).

1566-1199/$ - see front matter © 2009 Elsevier B.V. All rights reserved.
doi:10.1016/j.orgel.2009.11.031

monplace applications only qualitative but very simple indication of the history suffices without a need to know the exact level of humidity. Such a sensor could be denoted as a humidity memory; the sensor should remember if the package content has been exposed to moisture at any stage during transportation and storage. Only a few examples of such smart materials exist capable of irreversible moisture sensing, for example based on water absorption, which leads to increase in capacitance [52] or aggregation of dyes, which results in a change in fluorescence and absorption spectrum [53].

We present here a novel type of conducting poly(aniline) (PANI) complex, which utilizes a functional polar counter-ion that phase separates and crystallizes irreversibly due to humidity probably due to hydration, and therefore works as an irreversible humidity sensor, *i.e.* a humidity memory. Therefore it can sense whether the material has been exposed to humid conditions during its history. Thus it can be considered as a sensor analogue to an electrical WORM-type (write-once-read-many-times) memory [54–56]. The concept is based on a surprising observation that upon exposure to humidity, PANI doped with the 5-formyl-2-furansulfonic acid (FFSA: see Fig. 1a) protonating agent experiences irreversible loss in dc-conductivity, which is in contrast to the characteristic reversible increase of conductivity. Here, we will first explore the optimum degree of protonation, investigate the electrical and spectroscopic response to humidity, demonstrate a method to trigger and to read the memory, and finally propose tentative explanations for this complicated process.

2. Experimental

2.1. Materials

Panipol Ltd. (Finland) provided the emeraldine base (EB) form of PANI and it was used without further purification. The sodium salt of 5-formyl-2-furansulfonic acid (Na-FFSA, 98 %) was purchased from Chemos Ltd. and the formic acid (>98 %) from Riedel de Haën. The Dowex Marathon C cation-exchange resin, used for converting Na-FFSA in its sulfonic acid form (FFSA), was purchased from Aldrich.

2.2. Sample preparation

PANI-EB was dissolved in formic acid and the solution was filtered through a 1 μm filter. Na-FFSA was ion-exchanged to its acidic form (FFSA) in formic acid in order to use it as a protonating agent for PANI-EB. Complexation of PANI-EB and FFSA was performed immediately after the ion exchange procedure by combining the formic acid solutions of the corresponding starting materials to obtain PANI[FFSA]$_x$ ionic complexes, where x denotes the nominal ratio of the sulfonic acid group *vs.* nitrogen atom of the repeating units of PANI-EB (see Fig. 1). Samples were prepared with x = 0.1, 0.3, and 0.5. All the samples were spin-coated in a nitrogen glove box (oxygen and moisture levels below *ca.* 0.1 ppm) and subsequently the thin films were dried either in a vacuum oven (with a base pressure lower than *ca.* 10^{-2} mbar) or in a high vacuum oven (base pressure lower than *ca.* 10^{-7} mbar) at 60 °C for at least 48 h before performing the electrical measurements. The thicknesses of the thin films were measured with an Optical Profiler (Veeco) from dried films.

2.3. Electrical measurements

The dc-conductivity measurements were performed online with a digital multimeter (Keithley 2001) in an environmental chamber (Espec), in which relative humidity and temperature were simultaneously controlled. The sheet resistance R_s [Ω/□] was measured from spin-coated samples with a two-probe configuration, instead of using the conventional Valdes method [57,58] in which four probes are arranged in a collinear way, due to size restrictions imposed by the environmental chamber. The gold electrodes, spaced by a *ca.* 1 mm distance and allowing the measurement of R_s [Ω/□] were evaporated through a metal mask on a glass slide before spin-coating the thin films of conducting PANI[FFSA]$_x$.

2.4. UV–Vis-NIR spectroscopy

UV–Vis-NIR spectra of thin films spin-coated on microscope glass slides were recorded in the 275–1050 nm wavelength range using an AvaSpec-USB2 spectrophotometer (Avantes).

2.5. Fourier transform infrared (FT-IR) spectroscopy

The infrared spectra were obtained using a Nicolet 380 FT-IR spectrometer with an attenuated total reflection (ATR) setup. A minimum of 64 scans were averaged at a resolution of 2 cm^{-1}.

2.6. Optical microscopy

The optical microscopy pictures where taken with a digital camera connected to an optical microscope (Olympus BX60) utilizing the differential interference contrast (DIC) setup.

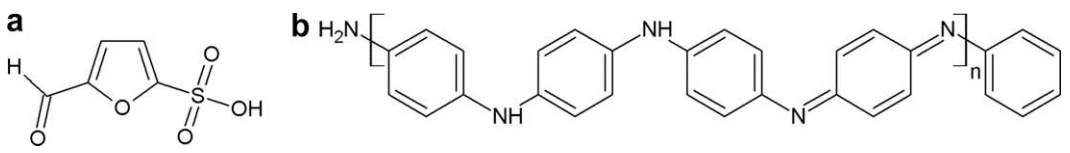

Fig. 1. Chemical structures of (a) 5-formyl-2-furansulfonic acid (FFSA) and (b) poly(aniline) in its Emeraldine Base (PANI-EB) state.

2.7. Capacitance

The frequency dependent capacitance of doped PANI[FFSA]$_x$ thin films was measured as a function of the elapsed time following the exposure of the sensor to humid conditions using two lateral electrodes and an AC LF-impedance analyzer (HP 4192A). The continuous capacitive measurements utilized two stationary aluminium electrodes attached on the outer side of the sensor element. Fig. 6a demonstrates how the sensor can be placed inside a package to allow detection by the non-contact capacitance measurements.

3. Results and discussion

Fig. 2a displays the response of the PANI[FFSA]$_x$ sheet resistance R_s to humid (RH = 50%) or dry (RH = 1%) air using films of *ca.* 70 nm thickness and different nominal doping ratios x = 0.1, 0.3, and 0.5. The films were kept in an environmental chamber with temperature and humidity control and the changes in the resistance were followed online. The nominally fully-doped case, *i.e.* PANI[FFSA]$_{0.5}$ containing one FFSA per iminic (—N=) sites of PANI-EB, showed the highest conductivity but only minor dependence on the humidity. Slightly reduced doping level, *i.e.* x = 0.3, allowed a clear humidity response while still showing a sufficiently high dc-conductivity level for a sensor. Very small doping levels (x = 0.1) showed very large dependence on humidity but the conductivity level was very low. Finally, an undoped PANI-EB thin film spin-coated from a formic acid solution was measured as a reference, also to ensure that formic acid can be removed from the films. Drying for 48 h at 60 °C in a vacuum oven was enough to essentially remove the formic acid, as the dc-conductivity remained out of the measuring range of our dc-conductivity setup and neither UV–Vis nor FT-IR spectroscopic investigations showed evidence of formic acid doping. To even more ascertain removal of the potential traces of formic acid, the samples were further dried in a high vacuum oven at 60 °C for several days maintained at a base pressure of *ca.* 10^{-7} mbar. Therefore, formic acid residuals cannot act as secondary protonation agents within the samples.

PANI[FFSA]$_{0.3}$ was chosen for detailed investigations due to its feasible combination of response to humidity and conductivity. Fig. 2b shows R_s as a function of the elapsed time after its initial contact with a 50% RH atmosphere at 25 °C using films of thicknesses of *ca.* 40 nm and 80 nm. First, the films were kept for a few hours under dry conditions at 25 °C, during which the sheet resistance did not essentially increase. Then, the films were transferred to a humidity chamber (50% RH and 25 °C), where the sheet resistance started to rapidly increase as a function of time. After 2 days at 50% RH we checked that the above-mentioned change was not reversible and we transferred the thin films back to the dry conditions (RH = 1%). This led to a small but abrupt increase of R_s, as is expected due to the generic classical response of conducting PANI-based materials upon decrease of humidity. Finally, the samples were again transferred to humid air (RH = 50%) where R_s values started to further rise (see Fig. 2b).

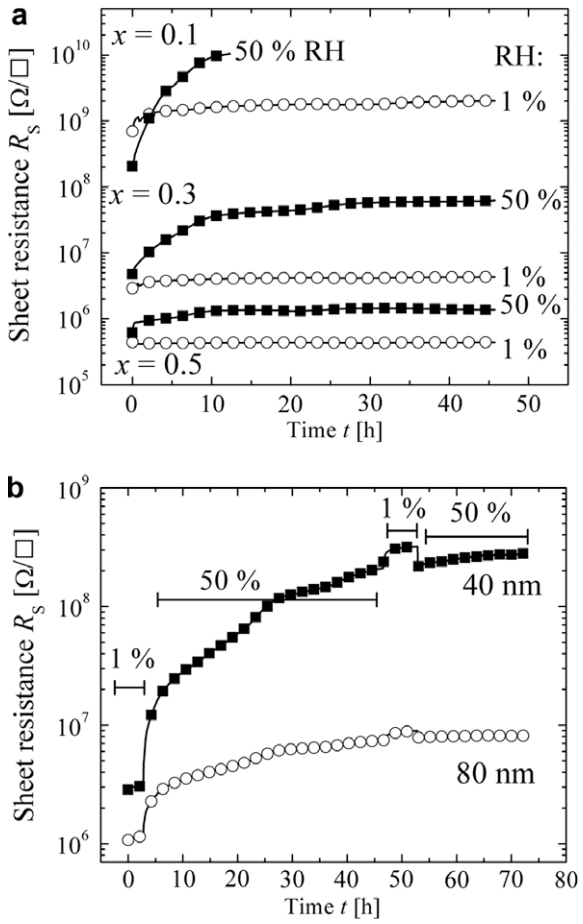

Fig. 2. Evolution of the sheet resistance R_s of thin films of PANI[FFSA]$_x$ as a function of the elapsed time after the initial contact with a humid atmosphere. (a) R_s for thin films of *ca.* 70 nm thickness with doping ratios x = 0.1, 0.3 or 0.5 under constant humidity. (b) R_s for PANI[FFSA]$_{0.3}$ when the humidity was switched between two constant values 1% and 50% at 25 °C using *ca.* 40 and 80 nm films. This indicates the irreversible nature of the conductivity loss due to exposure to humidity.

UV–Vis-NIR spectroscopy was used to investigate the effect of moisture on the electronic transport properties of PANI[FFSA]$_x$ thin films, as it allows sensitive optical probing of the state of doping and the polaron delocalization of doped PANI solutions [59] and thin films [60,61]. Conducting PANI shows three bands in its UV–Vis-NIR absorbance spectrum with maxima located at *ca.* 350, 420, and 800–880 nm [59,60]. They are related to π–π^*, polaron–π^*, and π–polaron electronic transitions, respectively. On the other hand, the UV–Vis spectrum of undoped PANI-EB shows two bands: one with a maximum at *ca.* 320–330 nm and second one with a maximum at *ca.* 600–650 nm [62], which are ascribed to its π–π^* and n–π^* electronic transitions, respectively. Fig. 3 shows the UV–Vis-NIR spectra of PANI[FFSA]$_{0.3}$ in the dried state and after a 3-day humidity treatment (50% RH and 25 °C) for thin films of thicknesses of *ca.* 40 nm and 80 nm. The films ex-

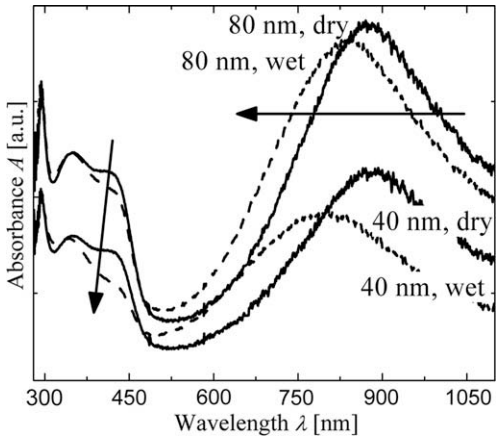

Fig. 3. UV–Vis-NIR spectra of PANI[FFSA]$_{0.3}$ thin films in their pristine states (solid line) and after a 3-day humidity treatment at 50% RH and 25 °C (dotted line) using two film thicknesses 40 nm and 80 nm. Do note that the black arrows are only guidelines for eyes.

posed to the humidity show a decrease of the intensity of the band associated with the polaron–π^* transition. This optical change happens concomitantly with a hypsochromic shift of the maxima of the band related to the π–polaron electronic transition of doped PANI, which moved from 875 nm to 835 nm, and from 875 nm to 790 nm for the two film thicknesses, 80 and 40 nm, respectively. These two spectral changes suggest humidity-induced partial dedoping, which further converts the doped PANI form into its semi-conducting PANI-EB one.

In optical microscopy, the dry PANI[FFSA]$_{0.3}$ films are structureless and homogeneously green whereas exposure to humidity leads to inhomogeneity where small crystal/particle-like dispersion emerges and the sample shows some bluish[1] color (see Fig. 4a). Even more striking effects take place when water is dropped directly on top of a PANI[FFSA]$_{0.3}$ film. After the water evaporation, large phase separated domains with sharp boundaries and edges are observed as well as strongly blue color (see Fig. 4b), which indicates PANI dedoping and suggests phase separation to form large crystals. The only available mechanism for phase separation is that the FFSA counter-ions form separate crystals and simultaneously PANI becomes at least partly dedoped. The conclusion would be that under dried conditions FFSA is bound to PANI due to protonation, whereas under humid conditions their mutual protonation interaction is suppressed allowing the phase separation. The latter phenomenon is not surprising due to the strong aggregation tendency of the relatively rigid PANI chains, if the binding strength of the additive becomes reduced. A question arises, what is the characteristic property of FFSA to promote this observed behavior. There have been numerous functionalized counter-ions already incorporated to protonate PANI [28,29,33–36]. Typically they have contained bulky or spacer-like groups to promote solubility or fusibility, thus

[1] For interpretation of color in Figs. 4 and 6, the reader is referred to the web version of this article.

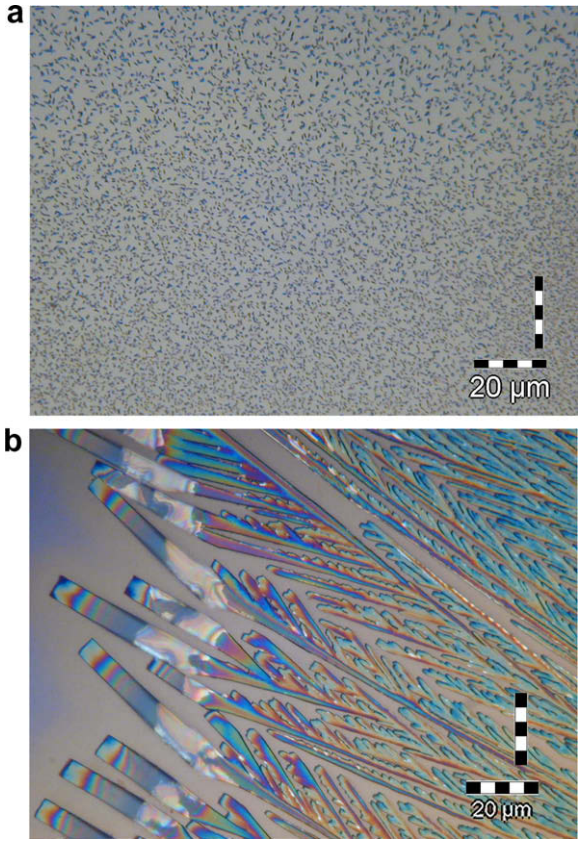

Fig. 4. Optical micrographs of a PANI[FFSA]$_{0.3}$ thin film spin-coated on a glass substrate showing phase-separated hydrated FFSA crystals resulting from (a) a few days humidity treatment in a humidity chamber [50% RH at 25 °C] or (b) the deposition of water on top of its free surface.

indirectly also promoting hydrophobicity. By contrast, FFSA contains five electronegative oxygen atoms and it is quite hydrophilic. Therefore, under humid conditions, it could be expected to easily trap water and to form hydronium salts instead of protonating PANI. In this case, the strong ionic interaction between PANI and FFSA is suppressed, as evident from UV–Vis-NIR (Fig. 3), and the hydrated FFSA phase separates as separate crystals.

In order to shed further light for the proposed mechanism, FT-IR spectroscopy was incorporated. Often in PANI complexes a detailed interpretation of FT-IR absorption has shown to be challenging, but in the present case we expected that the carbonyl >C=O band could be diagnostic [63], as it is known to be sensitive for hydrogen bond formation [64]. Accordingly, the strong FT-IR band of Na-FFSA near 1680 cm^{-1} is assigned to the carbonyl absorption, see Fig. 5b. Therein this band is particularly prominent, as each FFSA contains a carbonyl group. In agreement, in PANI[FFSA]$_{0.3}$ the band is smaller due to concentration effects. But interestingly, in wet PANI[FFSA]$_{0.3}$ the band is particularly narrow and centered at 1680 cm^{-1}, whereas in dry PANI[FFSA]$_{0.3}$ it is slightly down-shifted to 1677 cm^{-1} and it becomes considerably broadened towards lower wavenumbers. We suggest that this downshift in dry PANI[FFSA]$_{0.3}$ is due to hydrogen bonding of the hydrogen bond

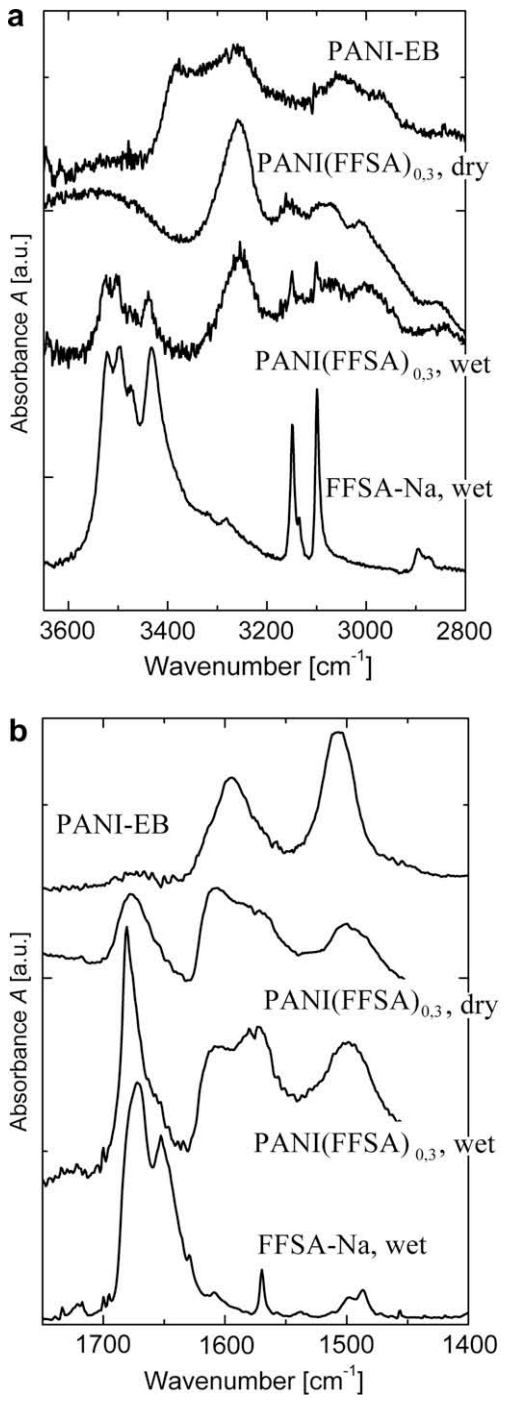

Fig. 5. FT-IR spectra of PANI[FFSA]$_{0.3}$ thin films in their dried states and after a 3-day humidity treatment at 50% RH and 25 °C, of PANI-EB thin films, and of FFSA-Na in the (a) 3600–2800 cm^{-1} and (b) 1750–1400 cm^{-1} wavenumber range.

accepting carbonyl group of FFSA to the secondary amines ≥N—H of the PANI backbones of the neighboring chains, as they are the only hydrogen bond donors available in large quantities. As UV–Vis-NIR, dc-conductivity, and the characteristic green color indicate that in the dried state the sulfonic acid groups protonate the iminic nitrogen groups, the FFSA molecules therefore connect two neighboring PANI chains by the ionic interaction at one end to the imines and hydrogen bond to the amines at the other end. This FFSA-induced networking between the PANI chains could also explain the slightly unexpected 1610 cm^{-1} peak in PANI[FFSA]$_{0.3}$, see Fig. 5b. In principle, the 1610 cm^{-1} band could originate from the furan rings of FFSA, but it is unlikely, since there is no such band in the FFSA-Na spectrum. Previously, the *ca.* 1610 cm^{-1} band has been assigned to a usually IR-inactive band of the quinoid ring, which can become active due to protonation-induced conformational changes [65]. Therefore we suggest that the band represents the quinoid rings of doped PANI, especially since the humidity-induced decrease in its intensity is in line with the suggested partial dedoping reaction, based on the electrical and UV–Vis-NIR measurements. Also in the previous literature, upshifting of the quinoid ring FT-IR band of a modified PANI chain has been presented (*e.g.* *N*-grafting of the PANI chain [62,66]).

Effect of humidity is considered next: in humid PANI[FFSA]$_{0.3}$ the carbonyl band of the FFSA dopant at 1680 cm^{-1} becomes sharp, suggesting suppression of hydrogen bonds. This would indeed be expected if the hydrated FFSA molecules phase separate and the hydrogen bonds to the PANI secondary amines are opened. Also, the intensity of the band at 1610 cm^{-1} decreases upon the humidity treatment, which could be expected if the FFSA-induced PANI-to-PANI connections are opened and the conformational stresses within PANI chains are relieved. Additionally, the spectrum of wet PANI[FFSA]$_{0.3}$ in Fig. 5a shows also that humidity initiates the formation of new bands, compared to the spectra of dry PANI[FFSA]$_{0.3}$: peaks located at 3150 cm^{-1} and 3101 cm^{-1} and bands in the 3400–3500 cm^{-1} wavenumber range. All of these bands are similar to the Na-FFSA spectrum. This also suggests that humidity triggers a partial dedoping reaction, after which the hydrated dopant phase separates from the PANI matrix and crystallizes.

Even if we expect that the above-mentioned humidity-induced phase separation concept is a plausible explanation for the observed effects, it still remains somewhat speculative. Therefore, for completeness, also other scenarios can be mentioned. The aldehyde (CHO) groups of FFSA might react with the secondary amine (—NH) groups of the PANI backbone through *e.g.* a Leuckart–Wallach reaction [67,68], leading to *N*-grafted PANI. Even though this reaction might explain the 1610 cm^{-1} peak, the irreversible nature of the suggested reaction conflicts with the results. The aldehyde group might also react with the primary amine (—NH$_2$) end-groups of the PANI chain to form a Schiff base [69]. This reaction would indeed lead to a moisture-sensitive bond [70,71], but since the breaking of the bond should not affect the conductivity significantly, it is not likely that this reaction is dominating the humidity-induced reaction leading to decreased dc-conductivity.

Based on the above observations, we finally demonstrate in the following that PANI[FFSA]$_x$ thin films can be used for electrically responsive active layers in sensors, which are sensitive to humidity and which report whether a package has been opened under humid conditions, see Fig. 6a. First, a PANI[FFSA]$_{0.3}$ thin film was spin-coated from a formic acid

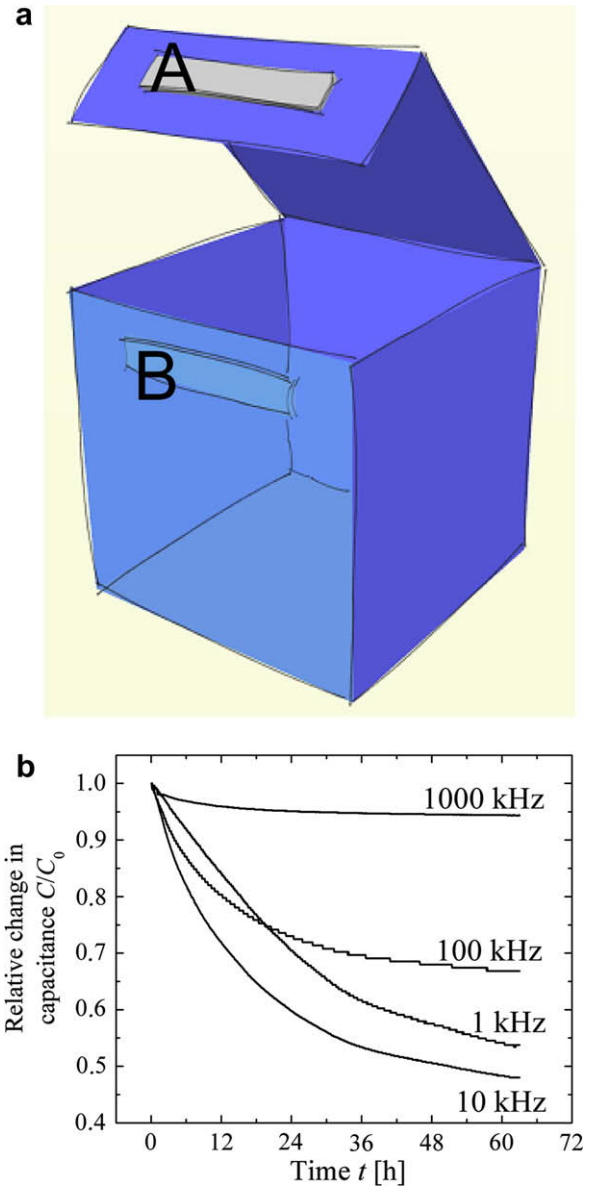

Fig. 6. (a) Schematic representation of the structure and the operating principle of the humidity memory as the seal of quality showing the adhesive tape (A) located on the lid and the PANI(FFSA) sensor (B) located inside the package. The sensor is activated when the protective layer (*i.e.* the tape) is peeled off. (b) Evolution of the reduced capacitance C/C_0 of PANI[FFSA]$_{0.3}$-based sensor (at four different frequencies) as a function of the elapsed time after its contact with the *ca.* 20% RH atmosphere of the VTT laboratory, in which the *ca.* 2.5 days tests were performed. Note that C_0 indicates the capacitance value before the activation of this humidity sensor.

solution onto a PET substrate (Melinex ST504) and dried in a vacuum oven at 60 °C for at least 48 h. Then, the samples were simply covered with a protective layer, consisting of a two-sided adhesive tape (3M 9415PC) having high and low adhesion sides, in order to protect the film against spurious humidity. The low adhesion side was pressed on the sensor element right after drying and the highly adhesive side was pressed against a paperboard, simulating a package lid. The sensor can be attached inside a package on the package wall opposing the package lid. Opening the package causes the low adhesion side to detach from the sensitive and electrically responsive PANI[FFSA]$_{0.3}$ layer. On the other hand, closing the lid does not attach the protective layer on the sensor anymore.

Moisture of the surrounding atmosphere triggers the dedoping of the conducting PANI[FFSA]$_{0.3}$ active layer of the sensor when the protecting layer is peeled off, impacting simultaneously its sheet resistance and capacitance. Due to the chosen design (see Fig. 6a), lateral electrodes on the outer side of the sensor advantageously enable a non-contact measurement of the capacitance through the package without the necessity of additional wiring. Fig. 6b shows the change in the reduced capacitance C/C_0 as a function of elapsed time after the activation of the sensor, which consisted of removing of the protective layer and exposure to a laboratory atmosphere showing a *ca.* 20% RH content. Fig. 6b demonstrates that the proposed capacitance measurement allows for simple yet unequivocal and precise follow-up of the dedoping reaction of this PANI[FFSA]-based humidity sensor, as water absorption usually causes an increase of the dielectric constant, which, in turn, leads to an increase of the capacitance value [42,52]. While the best responses achieved so far with the presently developed prototypical sensor are the ones obtained within the 1–100 kHz frequency range, one can easily anticipate that accurate capacitance measurements will become within reach with a portable meter, usually operating in the 0.1–100 kHz range, thanks to the easy control of the intrinsic dc-conductivity level (through the x doping ratio of the PANI[FFSA]$_x$ thin films) and of the film thickness of this conducting PANI-based humidity sensor.

4. Conclusions

We have presented a concept for an irreversible humidity sensor, *i.e.* a so-called humidity memory. PANI is partially protonated using a highly polar dopant 5-formyl-2-furansulfonic acid (FFSA), which upon humidity exposure phase separates from PANI, obviously due to hydration, and causes dedoping. Subsequently the sheet resistance increases and the capacitance decreases, as well as the PANI layer turns from light green to blue. The sensor detects and remembers any presence of moisture; however, the exact humidity level can not be quantitatively detected. Thus the sensor can be utilized in applications where it is enough to simply distinguish between completely dry and humid past conditions. The sensor can *e.g.* be attached to a package as a seal of quality, and we demonstrate activation when and only when the protective layer is peeled off. Sheet resistance or non-contact capacitive measurements allow humidity detection and easy operation. We expect that the concept can be tuned and generalized using other highly hygroscopic counter-ions.

Acknowledgements

We acknowledge Grants from National Technology Agency of Finland (Grant PAFU) and Academy of Finland.

We thank all PAFU project group members, Polymer Electronics team at VTT and Dr. Sami Nummelin for helpful discussions.

References

[1] D.R. Gamota, P. Brazis, K. Kalyanasundaram, J. Zhang, Printed Organic and Molecular Electronics, Kluwer Academic Publishers, Boston, 2004 (p. 695).
[2] S.R. Forrest, Nature 428 (2004) 911–918.
[3] M.A.M. Leenen, V. Arning, H. Thiem, J. Steiger, R. Anselmann, Phys. Status Solidi A 206 (2009) 588–597.
[4] Z. Bao, Adv. Mater. 12 (2000) 227–230.
[5] R.J. Kline, M.D. McGehee, J. Macromol. Sci. Polym. Rev. 46 (2006) 27–45.
[6] M.L. Chabinyc, J. Vac. Sci. Technol. B. 26 (2008) 445–457.
[7] B.S. Ong, Y. Wu, Y. Li, P. Liu, H. Pan, Chem. Eur. J. 14 (2008) 4766–4778.
[8] S. Allard, M. Forster, B. Souharce, H. Thiem, U. Scherf, Angew. Chem. Int. Ed. 47 (2008) 4070–4098.
[9] G. Hughes, M.R. Bryce, J. Mater. Chem. 15 (2005) 94–107.
[10] U. Mitschke, P. Bäuerle, J. Mater. Chem. 10 (2000) 1471–1507.
[11] I.F. Perepichka, D.F. Perepichka, H. Meng, F. Wudl, Adv. Mater. 17 (2005) 2281–2305.
[12] S.-H. Hwang, C.N. Moorefield, G.R. Newkome, Chem. Soc. Rev. 37 (2008) 2543–2557.
[13] A.C. Grimsdale, K.L. Chan, R.E. Martin, P.G. Jokisz, A.B. Holmes, Chem. Rev. 109 (2009) 897–1091.
[14] K.M. Coakley, M.D. McGehee, Chem. Mater. 16 (2004) 4533–4542.
[15] C.J. Brabec, N.S. Sariciftci, J.C. Hummelen, Adv. Funct. Mater. 11 (2001) 15–26.
[16] S. Günes, H. Neugebauer, N.S. Sariciftci, Chem. Rev. 107 (2007) 1324–1338.
[17] P.W.M. Blom, V.D. Mihailetchi, L.J.A. Koster, D.E. Markov, Adv. Mater. 19 (2007) 1551–1566.
[18] B.C. Thompson, J.M.J. Fréchet, Angew. Chem. Int. Ed. 47 (2008) 58–77.
[19] A. Hadipour, B. de Boer, P.W.M. Blom, Adv. Funct. Mater. 18 (2008) 169–181.
[20] G. Dennler, M.C. Scharber, C.J. Brabec, Adv. Mater. 21 (2009) 1323–1338.
[21] L.-M. Chen, Z. Hong, G. Li, Y. Yang, Adv. Mater. 21 (2009) 1434–1449.
[22] G. Kranzelbinder, G. Leising, Rep. Prog. Phys. 63 (2000) 729–762.
[23] U. Scherf, S. Riechel, U. Lemmer, R.F. Mahrt, Curr. Opin. Solid State Mater. Sci. 5 (2001) 143–154.
[24] I.D.W. Samuel, G.A. Turnbull, Chem. Rev. 107 (2007) 1272–1295.
[25] D.A. Bernards, R.M. Owens, G.G. Malliaras, Organic Semiconductors in Sensor Applications, Springer Series in Material Science, vol. 107, Springer, Berlin Heidelberg, 2008.
[26] B. Adhikari, S. Majumdar, Prog. Polym. Sci. 29 (2004) 699–766.
[27] S.W. Thomas, G.D. Joly, T.M. Swager, Chem. Rev. 107 (2007) 1339–1386.
[28] A. Pron, P. Rannou, Prog. Polym. Sci. 27 (2002) 135–190.
[29] Y. Cao, P. Smith, A.J. Heeger, Synth. Met. 48 (1992) 91–97.
[30] W.-Y. Zheng, R.-H. Wang, K. Levon, Z.Y. Rong, T. Taka, W. Pan, Macromol. Chem. Phys. 196 (1995) 2443–2462.
[31] M. Leclerc, K. Faïd, Adv. Mater. 9 (1997) 1087–1094.
[32] R.M. Walczak, J.K. Leonard, J.R. Reynolds, Macromolecules 41 (2008) 691–700.
[33] B. Dufour, P. Rannou, P. Fedorko, D. Djurado, J.-P. Travers, A. Pron, Chem. Mater. 13 (2001) 4032–4040.
[34] M. Tiitu, N. Volk, M. Torkkeli, R. Serimaa, G. ten Brinke, O. Ikkala, Macromolecules 37 (2004) 7364–7370.
[35] K. Lee, S. Cho, S.H. Park, A.J. Heeger, C.-W. Lee, S.-H. Lee, Nature 441 (2006) 65–68.
[36] B. Dufour, P. Rannou, D. Djurado, H. Janeczek, M. Zagorska, A. de Geyer, J.-P. Travers, A. Pron, Chem. Mater. 15 (2003) 1587–1592.
[37] K. Ogura, H. Shiigi, T. Oho, T. Tonosaki, J. Electrochem. Soc. 147 (2000) 4351–4355.
[38] A. Narayanan, O.P. Varnavski, T.M. Swager, T. Goodson, J. Phys. Chem. C 112 (2008) 881–884.
[39] B.Z. Lubentsov, O.N. Timofeeva, M.L. Khidekel', Synth. Met. 45 (1991) 235–240.
[40] S. Jain, S. Chakane, A.B. Samui, V.N. Krishnamurthy, S.V. Bhoraskar, Sens. Actuators B 96 (2003) 124–129.
[41] K. Ogura, H. Shiigi, M. Nakayama, A. Fujii, J. Electrochem. Soc. 145 (1998) 3351–3357.
[42] D. Li, Y. Jiang, Y. Li, X. Yang, L. Lu, X. Wang, Mater. Sci. Eng. C 11 (2000) 117–119.
[43] M. Vilkman, H. Kosonen, A. Nykänen, J. Ruokolainen, M. Torkkeli, R. Serimaa, O. Ikkala, Macromolecules 38 (2005) 7793–7797.
[44] A.I. Minett, J.N. Barisci, G.G. Wallace, React. Funct. Polym. 53 (2002) 217–227.
[45] W.J. Sung, Y.H. Bae, Anal. Chem. 72 (2000) 2177–2181.
[46] J. Wang, M. Jiang, Langmuir 16 (2000) 2269–2274.
[47] P.K. Kahol, A.J. Dyakonov, B.J. McCormick, Synth. Met. 89 (1997) 17–28.
[48] M. Angelopoulos, A. Ray, A.G. MacDiarmid, A.J. Epstein, Synth. Met. 21 (1987) 21–30.
[49] T. Taka, Synth. Met. 57 (1993) 5014–5019.
[50] H.H.S. Javadi, M. Angelopoulos, A.G. MacDiarmid, A.J. Epstein, Synth. Met. 26 (1988) 1–8.
[51] M. Nechtschein, C. Santier, J.P. Travers, J. Chroboczek, A. Alix, M. Ripert, Synth. Met. 18 (1987) 311–316.
[52] J.W. Fergus, T. Hsu, Meas. Sci. Technol. 16 (2005) 1255–1260.
[53] J. Kunzelman, B.R. Crenshaw, C. Weder, J. Mater. Chem. 17 (2007) 2989–2991.
[54] H.S. Majumdar, J.K. Baral, R. Österbacka, O. Ikkala, H. Stubb, Org. Electron. 6 (2005) 188–192.
[55] J. Lin, D. Ma, Appl. Phys. Lett. 93 (2008) 093505.
[56] J. Ouyang, C.-W. Chu, D. Sieves, Y. Yang, Appl. Phys. Lett. 86 (2005) 123507.
[57] L.B. Valdes, Proc. IRE. 42 (1954) 420–427.
[58] F.M. Smith, Bell Syst. Tech. J. 37 (1958) 171.
[59] Y. Xia, J.M. Wiesinger, A.G. MacDiarmid, A.J. Epstein, Chem. Mater. 7 (1995) 443–445.
[60] Y. Xia, A.G. MacDiarmid, A.J. Epstein, Macromolecules 27 (1994) 7212–7214.
[61] P. Rannou, B. Dufour, J.-P. Travers, A. Pron, D. Djurado, H. Janeczek, D. Sek, J. Phys, Chem. B 106 (2002) 10553–10559.
[62] W.-Y. Zheng, K. Levon, J. Laakso, J.-E. Öesterholm, Macromolecules 27 (1994) 7754–7768.
[63] D. Lin-Vien, N.B. Colthup, W.G. Fateley, J.G. Grasselli, The Handbook of Infrared and Raman Characteristic Frequencies of Organic Molecules, Academic Press, Inc., San Diego, 1991.
[64] M.M. Coleman, J.F. Graf, P.C. Painter, Specific Interactions and the Miscibility of Polymer Blends, Technomic Press, Lancaster, PA, USA, 1991. p. 495.
[65] Z. Ping, G.E. Nauer, H. Neugebauer, J. Theiner, A. Neckel, J. Chem. Soc., Faraday Trans. 93 (1997) 121–129.
[66] M.G. Mikhael, A.B. Padias, H.K. Hall Jr., J. Polym. Sci. Part A: Polym. Chem. 35 (1997) 1673–1679.
[67] O. Wallach, Ann 272 (1892) 99.
[68] E. Staple, E.C. Wagner, J. Org. Chem. 14 (1949) 559–578.
[69] T.T. Tidwell, Angew. Chem. Int. Ed. 47 (2008) 1016–1020.
[70] T. Okuyama, H. Shibuya, T. Fueno, J. Am. Chem. Soc. 104 (1982) 730–736.
[71] M.A.E.-D. El-Taher, J. Solut. Chem. 25 (1996) 401–410.

Organic Electronics 11 (2010) 479–485

Contents lists available at ScienceDirect

Organic Electronics

journal homepage: www.elsevier.com/locate/orgel

Arylamino-9,10-diphenylanthracenes for organic light emitting devices

Yong-Jin Pu *, Akinori Kamiya, Ken-ichi Nakayama, Junji Kido *

Department of Organic Device Engineering, Yamagata University, Yonezawa, Yamagata 992-8510, Japan

ARTICLE INFO

Article history:
Received 26 October 2009
Received in revised form 20 November 2009
Accepted 1 December 2009
Available online 16 December 2009

Keywords:
Organic light emitting diode
Hole transporting
Anthracene
Blue emitting
Arylamine

ABSTRACT

Hole-transporting arylamino-9,10-diphenylanthracene derivatives were synthesized by C–N cross coupling with palladium catalyst. The materials showed higher glass transition temperatures (135–177 °C) than that of a conventional hole-transporting material, *N*,*N*'-bis(naphthalen-1-yl)-*N*,*N*'-bis(phenyl)benzidine (NPD). The compounds all showed higher hole mobilities than that of NPD, with one of the compounds showing a much higher hole mobility of $\sim 1.0 \times 10^{-2}$ $cm^2 V^{-1} s^{-1}$. Tris-(8-quinolinolato) aluminum (Alq_3)-based green light emitting devices containing the arylamino-9,10-diphenylanthracene derivatives as hole transport layers were fabricated. The devices containing the anthracene derivatives showed lower driving voltages and higher efficiencies compared with those of the equivalent device containing NPD. The anthracene derivative with a dibenzofuran substituent was also used as the emitting material in a device. This device emitted blue light with high efficiencies of 5.0 lm/W and 6.3 cd/A at 4.0 V and 1000 cd/m^2, respectively.

© 2009 Elsevier B.V. All rights reserved.

1. Introduction

Organic light emitting devices (OLEDs) have attracted a great deal of attention because of their application in flat panel displays [1] and general lighting [2,3]. Since organic electroluminescence was first reported by Pope et al. from a single crystal of anthracene [4], thousands of π-conjugated molecules have been developed as charge transport and/or light emitting materials for OLEDs. Among these numerous compounds, 9,10-diphenylanthracene derivatives have played a leading role as host or emitting materials in highly efficient and long-lived state-of-the-art OLEDs [5–10]. 9,10-Diphenylanthracene itself shows strong blue emission but it has high crystallinity, which is a severe drawback for device stability in OLED applications. To make 9,10-diphenylanthracene amorphous, arylamino substituents were introduced and blue emission from OLEDs containing these arylamino-9,10-diphenylanthracene derivatives was reported [11,12]. Generally, arylamine groups increase the hole-transporting ability of the compounds [13], so arylamino-9,10-diphenylanthracene derivatives are expected to exhibit good hole transport properties. High hole mobility, in addition to a small hole injection barrier, is an important parameter in reducing the energy consumption of OLEDs because it reduces the required driving voltage. 9,10-Diphenylanthracene derivatives **1**–**6** containing bulky π-conjugated arylamino groups were synthesized. Their glass transition temperature, hole mobilities and performance as a hole-transporting material in OLEDs were investigated. The compound with a dibenzofuran substituent **5** exhibited high efficiency as a blue emitting material in OLEDs.

2. Results and discussion

2.1. Synthesis and thermal properties

Arylaminoanthracene derivatives **1**–**6** were synthesized by the Pd(0)-catalyzed C–N cross-coupling reaction of 9,10-bis(4-(phenylamino)phenyl)anthracene and an arylhalide (Scheme 1). Purification of the compounds was made difficult by their poor solubility in common organic solvents. Diethylfluorene-substituted compound **4** showed

* Corresponding authors.
E-mail addresses: pu@yz.yamagata-u.ac.jp (Y.-J. Pu), kid@yz.yamagata-u.ac.jp (J. Kido).

1566-1199/$ - see front matter © 2009 Elsevier B.V. All rights reserved.
doi:10.1016/j.orgel.2009.12.001

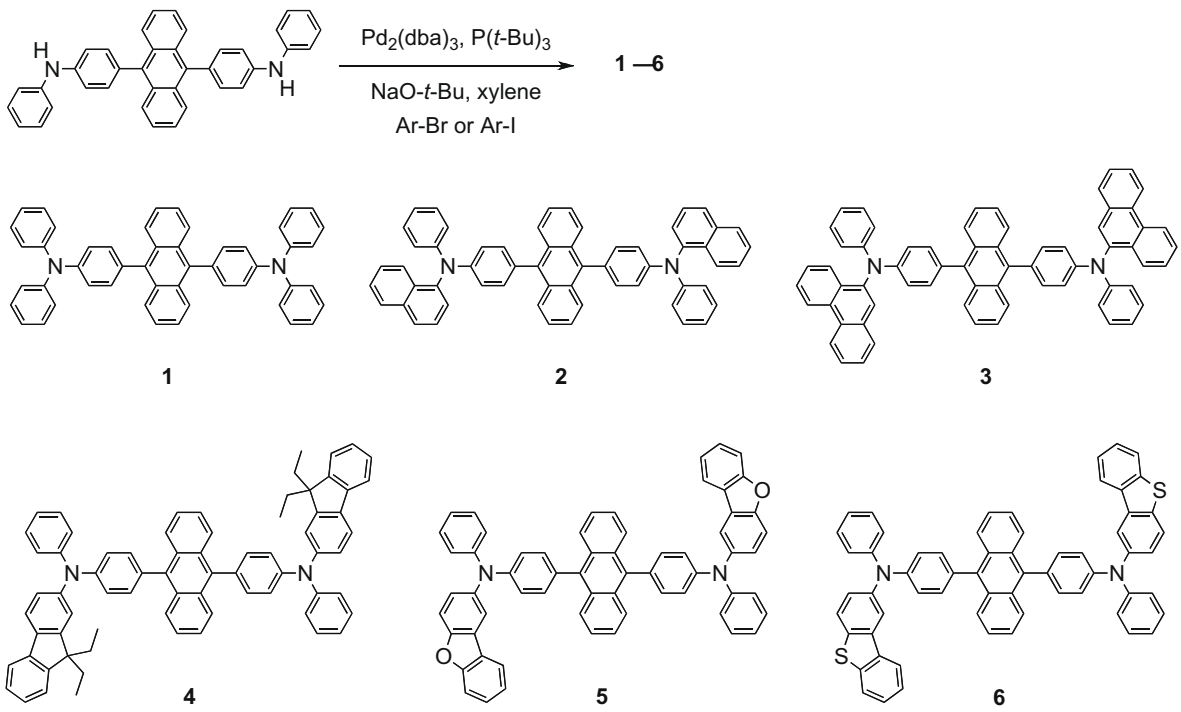

Scheme 1. Synthetic route and chemical structure of compounds **1**–**6**.

the best solubility in chloroform, and **1** and **2** were also soluble in chloroform. The compounds with bulky aryl groups (**3**, **5** and **6**) showed poor solubility, especially **3** which contained a bulky phenanthrene substituent. Only **3** was not able to be purified by column chromatography with chloroform; a solution of **3** in hot dichlorobenzene was passed through a short silica column to remove highly polar impurities. After column chromatography, all of the compounds were further purified by train sublimation with two heating zones at pressures under 5.0×10^{-2} Pa for **1** and **2**, and under 5.0×10^{-4} Pa for **3**–**6**. Thermogravimetric analysis (TGA) showed that the decomposition temperatures (T_d) with loss of 5 wt% of the compounds were over 400 °C. Differential scanning calorimetry thermograms of the compounds are shown in Fig. 1. The glass transition temperatures (T_g) of **2**–**6** (Table 1) were higher than the T_g of 100 °C of *N*,*N*'-bis(naphthalen-1-yl)-*N*,*N*'-bis(phenyl)benzidine (NPD). Compound 3 showed the highest T_g of 177 °C because of the bulky phenanthrene substituent. On the other hand, a T_g for 1, which has a symmetrical structure and simple phenyl substituent, was not observed in our experiment, probably because of its high crystallinity.

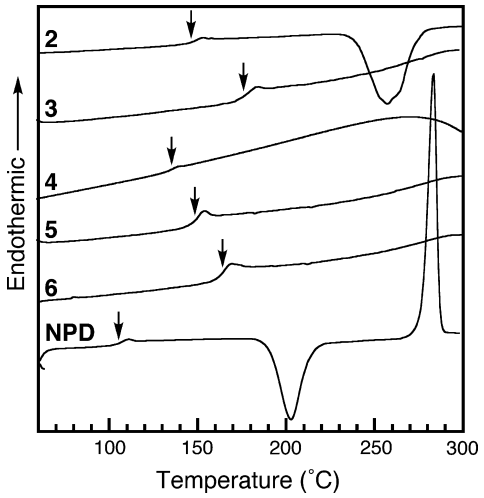

Fig. 1. DSC thermograms of the compounds.

2.2. Photophysical and electrochemical properties

UV absorption and PL spectra of solutions and films on a quartz substrate of **1**–**6** were measured (Fig. 2). All of the compounds except **4** showed three absorption peaks between 360 and 400 nm which were ascribed to the vibrational structure of the central anthracene moiety. All of the compounds **1**–**6** exhibited blue emission with wavelength maxima located around 480–490 nm. The PL quantum efficiency (PLQE) of 1 wt% doped polymethylmethacrylate (PMMA) films and neat films of the anthracenes were determined using an integrating sphere. All the compounds showed a high PLQE of around 80% in a diluted film, which suggests that these anthracene compounds should be useful as emitting dopants in OLEDs. The ionization potential (I_p) of each compound, which generally corresponds to the energy level of the highest occupied molecular orbital (HOMO), was measured by

Table 1
Thermal and optoelectrochemical properties of compounds **1–6**.

	T_g (°C)	T_d (°C)	UV/nm (log ε)		PL (nm)[a]	Φ (%)[b]	E_g (eV)[c]	I_p (eV)	E_a (eV)[d]
			Chloroform	Film					
1	–[e]	479	258 (4.91), 306 (4.70),360 (4.00), 380 (4.22),398 (4.28)	263, 306, 363, 384, 402	475 (468)	85 (30)	2.82	5.80	2.98
2	146	474	258 (5.03), 305 (4.67),360 (4.35), 379 (4.40),398 (4.39)	262, 305, 364, 383, 403	494 (482)	81 (26)	2.77	5.76	2.99
3	177	494	257 (5.30), 297 (4.70),361 (4.35), 378 (4.37),398 (4.33)	259, 299, 367, 383, 404	471 (470)	83 (41)	2.74	5.74	3.00
4	135	438	259 (5.03),339 (4.76), 398 (4.37)	262, 337, 404	489 (474)	70 (28)	2.73	5.67	2.94
5	147	511	253 (4.01), 260 (3.97),293 (3.80), 301 (3.86),315 (3.64),361 (3.18), 379 (3.28),398 (3.27)	254, 265, 293, 318, 301, 364, 384, 405	490 (483)	87 (34)	2.72	5.70	2.98
6	162	517	259 (5.14),311 (4.84),360 (4.21), 379 (4.34),398 (4.34)	261, 312, 364, 384, 404	488 (484)	84 (6)	2.75	5.68	2.93

[a] Chloroform solution (neat film).
[b] 1 wt% Doped PMMA film (neat film).
[c] Estimated from the onset of UV absorption of the film.
[d] E_g–I_p.
[e] Not detected between −30 and 400 °C.

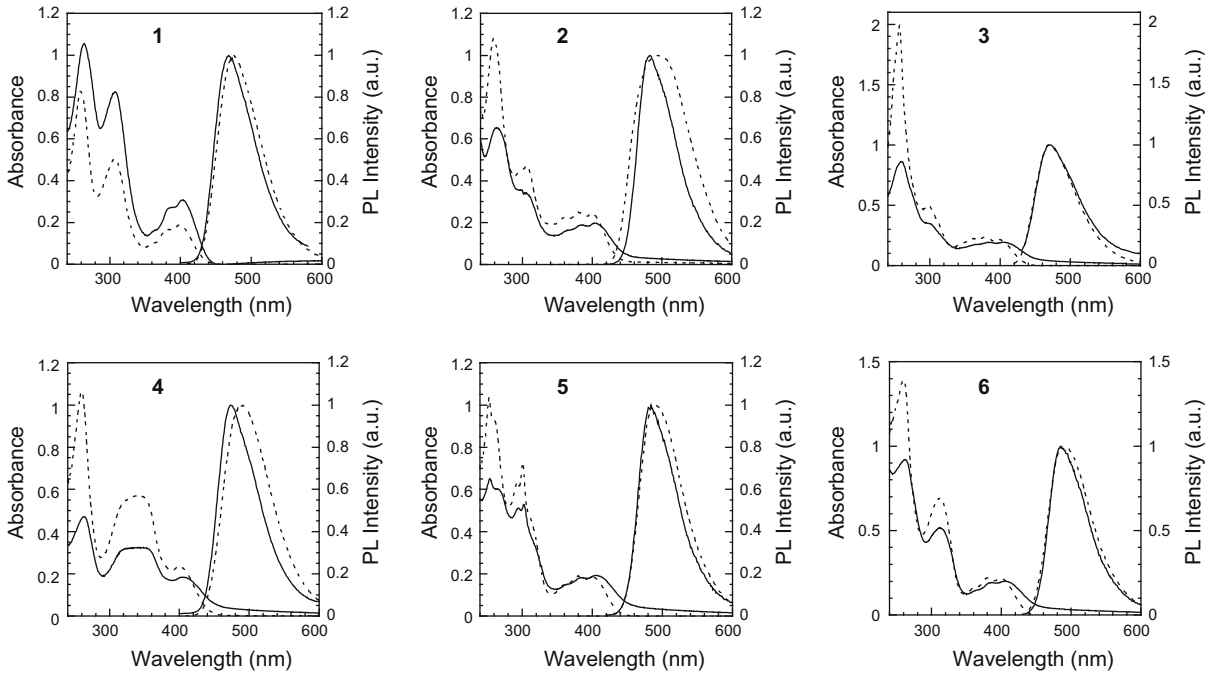

Fig. 2. UV–vis and PL spectra of chloroform solutions (dashed line) and films (solid line) of **1–6**.

photoelectron yield spectroscopy. The electron affinity (E_a), which generally corresponds to the energy level of the lowest unoccupied molecular orbital (LUMO), was tentatively estimated from the difference between I_p and the optical energy gap (E_g). All of the compounds showed similar I_p and E_a, meaning the HOMO and LUMO energy levels were almost independent of the attached substituents. The I_p of 1 was a little higher than the other compounds because its phenyl substituent is less electron-donating than the other aryl substituents.

2.3. Hole mobilities and OLED characteristics

The hole mobilities of the compounds were estimated by time-of-flight (TOF) measurements (Fig. 3). Compounds **1**, **3**, and **6** exhibited slightly higher mobilities of around 10^{-3} cm^2 $V^{-1}s^{-1}$ than that of NPD, and diethylfluorene-substituted **4** exhibited much a higher mobility of close to 10^{-2} cm^2 $V^{-1}s^{-1}$ (Fig. 4). The detailed condition and nondispersive photocurrents of **4** at 10 different electric fields are shown in Supporting information.

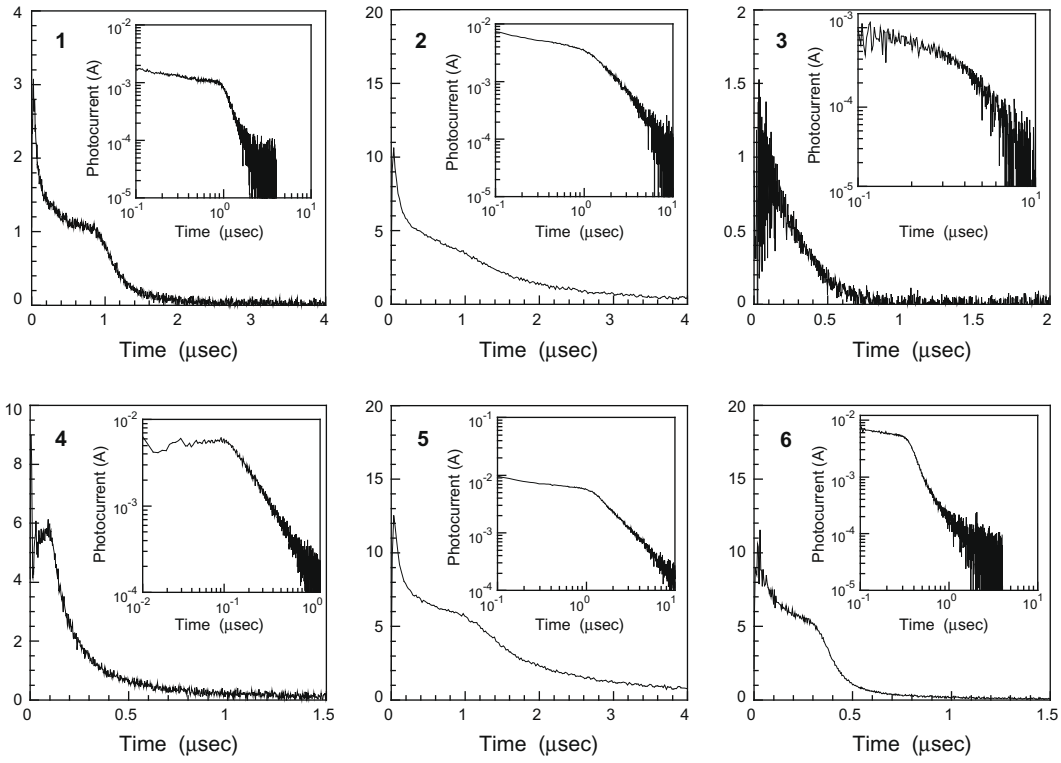

Fig. 3. Transient photocurrents obtained from TOF measurements. (Inset) Double logarithmic plot of the TOF data.

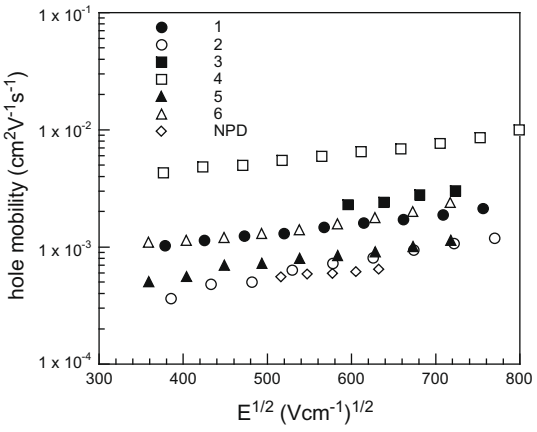

Fig. 4. Hole mobilities of compounds **1**–**6**.

OLEDs with the configuration of ITO/HTL: **1**–**6** or NPD (40 nm)/Alq_3 (60 nm)/LIF (0.5 nm)/Al (100 nm) were fabricated. The luminance–voltage and current density–voltage plots are shown in Fig. 5, and the device efficiencies are summarized in Table 2. OLEDs containing **1**–**6** showed comparable driving voltages and efficiencies to those of NPD. The OLED containing naphthalene-substituted **2** exhibited a lower driving voltage by 0.6 V and 1.4 times higher efficiency at 1000 cd/m^2 than those of the device containing NPD. No correlation between the device efficiency and the high hole mobility of the compounds was observed for these devices. The hole injections from ITO to the compounds should be poor because of their large I_ps, and those hole injection abilities mainly determined the device performance rather than the hole mobilities. To explain the device performance from the perspective of the materials in the HTL, the hole injection ability from ITO in a hole-only device has to be taken into account. Dibenzofuran-substituted **5** was used as a blue emitter in a device with the configuration of ITO/NPD (50 nm)/2-methyl-9,10-bis(naphthalen-2-yl)anthracene (MADN): 5 (10 wt%) (30 nm)/1,4-di(1,10-phenanthrolin-3-yl)benzene (DPB) (20 nm)/LiF (0.5 nm)/Al (100 nm). The device exhibited blue emission from **5**, with a maximum wavelength of 468 nm and Commission Internationale de L'Éclairage (CIE) chromaticity coordinates of (0.14, 0.21). The device efficiencies were as high as 5.0 lm/W and 6.3 cd/A at 1000 cd/m^2, meaning that these arylaminoanthracene derivatives could be useful as not only hole-transporting materials but also as blue emitting dopants in OLEDs. (Fig. 6).

3. Conclusion

Arylamino-9,10-diphenylanthracene derivatives were synthesized and purified by train sublimation. Their T_g ranged from 135 to 177 °C because of their bulky aryl substituents. The compounds all showed higher hole mobilities than that of NPD, and diethylfluorene-substituted **4** showed a much higher hole mobility of

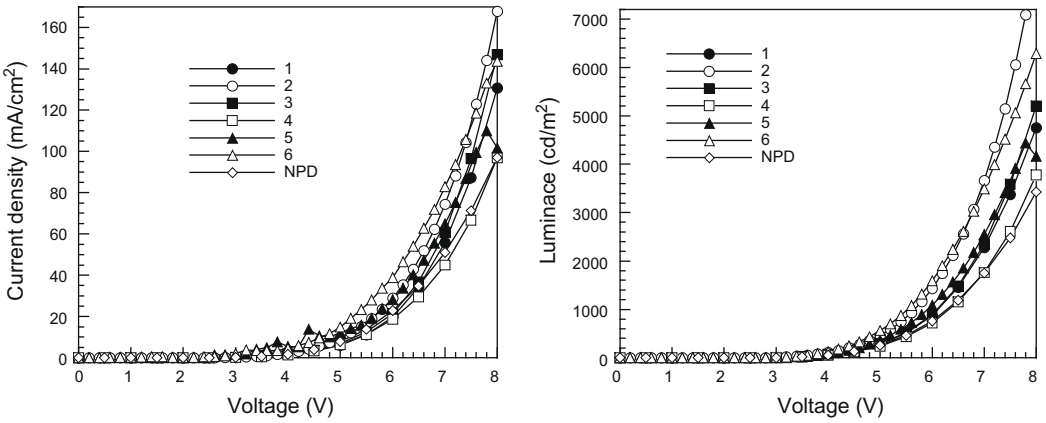

Fig. 5. Current density–voltage and luminance–voltage plots of the OLEDs containing **1**–**6** as the HTL.

Table 2
Device efficiencies at 100 cd m^{-2} and 1000 cd m^{-2}.

HTL	100 (cd m^{-2})				1000 (cd/m^2)			
	Voltage (V)	η_P (lm W^{-1})	η_C (cd A^{-1})	η_{EXT} (%)	Voltage (V)	η_P (lm W^{-1})	η_C (cd A^{-1})	η_{EXT} (%)
1	4.3	3.2	4.3	1.4	6.1	2.3	4.4	1.5
2	4.0	3.6	4.6	1.5	5.7	2.7	4.9	1.6
3	4.2	3.0	3.9	1.3	6.1	2.1	4.1	1.3
4	4.4	2.6	3.6	1.2	6.3	1.9	3.9	1.3
5	4.1	3.1	4.0	1.3	5.9	1.8	3.4	1.1
6	3.9	2.1	2.5	0.8	5.5	2.1	3.8	1.2
NPD	4.3	2.3	3.3	1.0	6.3	1.7	3.4	1.1
5 (EML)	3.3	4.9	5.1	3.3	4.0	5.0	6.3	4.0

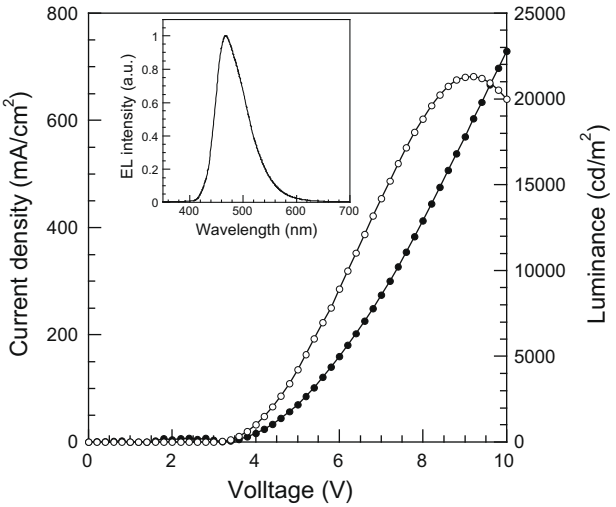

Fig. 6. Current density–voltage and luminance–voltage plots of the blue-emitting OLED containing **5** as the emitting dopant. (Inset) EL spectrum of the OLED.

$\sim 1.0 \times 10^{-2}$ cm^2 $V^{-1}s^{-1}$. Lower driving voltages and higher efficiencies compared with those of NPD were achieved in devices containing the anthracene derivatives as the HTL. Dibenzofuran-substituted **5** was also used as a blue emitting dopant, and a high device efficiency of 5.0 lm/W and blue emission of CIE (0.14, 0.21) was achieved.

4. Experimental

4.1. Characterization and OLED Fabrication

^{1}H NMR spectra were measured in deuterated solvents on a JEOL ECX 400 MHz spectrometer. Elemental analyses

were carried out by the Elemental Analysis Service, Yamagata University, Japan. Mass spectra were obtained on a JEOL JMS-K9 mass spectrometer. TGA was performed on a Seiko SII EXSTAR 6000 and TGA/DTA 62000 analyzers. DSC was performed on a Perkin–Elmer Diamond DSC7 calorimeter. Ionization potentials were measured on a photoelectron yield spectrometer (RIKEN KEIKI AC-3). UV–visible absorption spectra were recorded of solutions in chloroform or of film on quartz with a Shimadzu UV-3150 spectrometer. PL spectra were recorded using a Jobin Yvon Fluoromax-4 fluorometer. PL quantum efficiencies were measured on a Hamamatsu C9920–01 integral sphere system under nitrogen. TOF measurement was performed on OPTEL TOF-401 system with N_2 laser. OLEDs were fabricated on ITO-coated glass substrates, which were provided by AGC Display Glass Yonezawa Co., Ltd. and cleaned by ultrasonication sequentially in detergent, methanol, 2-propanol and acetone, then exposure to UV-ozone under ambient conditions for 20 min. Organic materials were deposited by thermal evaporation at pressures less than 2×10^{-4} Pa. Lithium fluoride and aluminum were deposited at a pressure less than 1×10^{-3} Pa through a shadow mask to form a cathode. The active area of each device is 2×2 mm^2. Layer thickness calibration was performed using a Dektak 3 surface profilometer. EL spectra were measured on a Hamamatsu PMA-11 photonic multichannel analyzer. The current–voltage characteristics and luminance of the OLEDs were measured using a Keithley 2400 Source Meter and Konica Minolta CS-200 chromameter, respectively. External quantum efficiencies were calculated assuming a Lambertian emission pattern and considering all spectral features in the visible region.

4.2. Synthesis

9,10-*bis*-(4-(Phenylamino)phenyl)anthracene was purchased from Wakayama Seika Kogyo Co., Ltd. All other compounds were purchased from a general chemical company or synthesized.

Compound ***1***: A mixture of 9,10-bis(4-(*N*-phenylamino)phenyl)anthracene (2.00 g, 3.90 mmol), bromobenzene (1.84 g, 11.7 mmol), sodium *t*-butoxide (1.12 g, 11.7 mmol), tris(dibenzylideneacetone)dipalladium (28 mg, 0.031 mmol), tri-*t*-butylphosphine (8 mg, 0.04 mmol) and xylene (200 cm^3) was heated at 100 °C under nitrogen for 15 h. The mixture was allowed to cool to room temperature, then the organic layer was washed with water, dried over magnesium sulfate and filtered. The solvent was removed and then the residue was purified by column chromatography on silica gel using *n*-hexane/chloroform (2:1), followed by train sublimation at 5.0×10^{-2} Pa with the zone temperatures set at 300 °C and 250 °C . Yield: 1.3 g, 51%. ^{1}H NMR (400 MHz, CD_2Cl_2, ppm) δ 7.08 (4H, td, J = 0.9, 7.25 Hz), 7.25–7.36 (24H, m), 7.40 (4H, dd, J = 3.2, 6.8 Hz), 7.84 (4H, dd, J = 3.2, 6.8 Hz). EI-MS m/z Calcd: 664.8. Found: 665. Anal. Calcd for $C_{50}H_{36}N_2$: C, 90.33; H, 5.46; N, 4.21. Found: C, 90.43; H, 5.54; N, 4.23.

Compound ***2***: **2** was prepared in the same manner as **1**, using 1-iodonaphthalene instead of bromobenzene. The residue was purified by column chromatography on silica gel using *n*-hexane/chloroform (3:2), followed by train sublimation at 5.0×10^{-2} Pa with the zone temperatures set at 330 °C and 310 °C . Yield: 0.63 g, 21%. ^{1}H NMR (400 MHz, CD_2Cl_2, ppm) δ 6.99 (2H, td, J = 1.4, 7.25 Hz), 7.20–7.61 (28H, m), 7.80 (4H, dd, J = 3.2, 6.8 Hz), 7.86 (2H, d, J = 8.2 Hz), 7.96 (2H, d, J = 8.6 Hz), 8.12 (2H, d, J = 8.2 Hz). EI-MS m/z Calcd: 765.0. Found: 765. Anal. Calcd for $C_{50}H_{40}N_2$: C, 91.07; H, 5.27; N, 3.66. Found: C, 91.05; H, 5.35; N, 3.62.

Compound ***3***: A mixture of 9,10-bis(4-(*N*-phenylamino)phenyl)anthracene (2.00 g, 3.90 mmol), 9-bromophenanthrene (3.01 g, 11.7 mmol), sodium *t*-butoxide (1.12 g, 11.7 mmol), tris(dibenzylideneacetone)dipalladium (28 mg, 0.031 mmol), tri-*t*-butylphosphine (8 mg, 0.04 mmol), and xylene (100 cm^3) was heated at 100 °C under nitrogen for 15 h. The mixture was allowed to cool to room temperature, and the organic layer was washed with water, dried over magnesium sulfate, and filtered. The solvent was removed and the residue was dissolved in hot dichlorobenzene. This solution was passed through a short silica column and then the solvent was removed. Finally, the product was purified by train sublimation at 5.0×10^{-4} Pa with the zone temperatures set at 327 °C and 317 °C. Yield: 0.57 g, 17%. ^{1}H NMR (400 MHz, CD_2Cl_2, ppm) δ 6.99–7.03 (2H, m), 7.24–7.39 (20H, m), 7.59–7.89 (16H, m), 8.23 (2H, d, J = 8.6 Hz), 8.75 (2H, d, J = 8.2 Hz), 8.81 (2H, d, J = 8.2 Hz). EI-MS m/z Calcd: 865.1. Found: 865. Anal. Calcd for $C_{66}H_{44}N_2$: C, 91.64; H, 5.13; N, 3.24. Found: C, 91.48; H, 4.83; N, 3.19.

Compound ***4***: **4** was prepared in the same manner as **1**, using 2-bromo-9,9-diethylfluorene instead of bromobenzene. The residue was purified by column chromatography on silica gel using *n*-hexane/chloroform (2:1), followed by train sublimation at 5.0×10^{-4} Pa with the zone temperatures set at 316 °C and 296 °C. Yield: 0.41 g, 11%. ^{1}H NMR (400 MHz, CD_2Cl_2, ppm) δ 0.39 (12H, t, J = 7.3 Hz), 1.99 (8H, q, J = 7.3 Hz), 7.08 (2H, td, J = 1.4, 6.9 Hz), 7.23–7.43 (30H, d, J = 8.2 Hz), 7.67–7.71 (4H, m), 7.88 (4H, dd, J = 3.2, 6.4 Hz). EI-MS m/z Calcd: 953.3. Found: 953. Anal. Calcd for $C_{72}H_{60}N_2$: C, 90.72; H, 6.34; N, 2.94. Found: C, 90.94; H, 6.34; N, 2.99.

Compound ***5***: **5** was prepared in the same manner as **1**, using 3-iododibenzofuran instead of bromobenzene. The residue was purified by column chromatography on silica gel using *n*-hexane/chloroform (3:2), followed by train sublimation at 5.0×10^{-4} Pa with the zone temperatures set at 320 °C and 290 °C. Yield: 0.63 g, 19%. ^{1}H NMR (400 MHz, CD_2Cl_2, ppm) δ 7.07 (2H, t, J = 7.02 Hz), 7.28–7.52 (26H, m), 7.58–7.61 (4H, m), 7.86–7.95 (8H, m). EI-MS m/z Calcd: 845.0. Found: 845. Anal. Calcd for $C_{62}H_{40}N_2O_2$: C, 88.13; H, 4.77; N, 3.32. Found: C, 88.05; H, 4.76; N, 3.29.

Compound ***6***: **6** was prepared in the same manner as **1**, using 3-iododibenzothiophene instead of bromobenzene. The residue was purified by column chromatography on silica gel using *n*-hexane/chloroform (3:2), followed by train sublimation at 5.0×10^{-4} Pa with the zone temperatures set at 340 °C and 324 °C. Yield: 0.38 g, 11%. ^{1}H NMR (400 MHz, CD_2Cl_2, ppm) δ 7.10 (2H, t, J = 7.02 Hz), 7.31–7.50 (26H, m), 7.84–7.90 (8H, m), 8.07–8.10 (4H, m). EI-MS m/z Calcd: 877.1. Found: 877. Anal. Calcd for $C_{62}H_{40}N_2S_2$: C, 84.90; H, 4.60; N, 3.19. Found: C, 84.85; H, 4.66; N, 3.19.

Acknowledgements

The authors thank AGC Display Glass Yonezawa Co., Ltd. for providing ITO substrates, and Wakayama Seika Kogyo Co., Ltd. for providing 9,10-*bis*-(4-(phenylamino)phenyl) anthracene.

Appendix A. Supplementary data

Supplementary data associated with this article can be found, in the online version, at doi:10.1016/j.orgel.2009.12.001.

References

[1] T. Urabe, T. Sasaoka, K. Tatsuki, J. Takaki, SID Int. Symp. Dig. Tech. 38 (2007) 161.
[2] F. So, J. Kido, P. Burrows, MRS Bull. 33 (2008) 663.
[3] S. Reineke, F. Lindner, G. Schwartz, N. Seidler, K. Walzer, B. Lüssem, K. Leo, Nature 459 (2009) 234.
[4] M. Pope, H.P. Kallmann, P. Magnante, J. Chem. Phys. 38 (1963) 2042.
[5] C. Adachi, T. Tsutsui, S. Saito, Appl. Phys. Lett. 56 (1990) 799.
[6] T.J. Boyd, Y. Geerts, J.K. Lee, D.E. Fogg, G.G. Lavoie, R.R. Schrock, M.F. Rubner, Macromolecules 30 (1997) 3553.
[7] T.J. Boyd, R.R. Schrock, Macromolecules 32 (1999) 6608.
[8] L. Wang, W.Y. Wong, M.F. Lin, W.K. Wong, K.W. Cheah, H.L. Tam, C.H. Chen, J. Mater. Chem. 18 (2008) 4529.
[9] V.V. Jarikov, D.Y. Kondakov, C.T. Brown, J. Appl. Phys. 102 (2007) 104908.
[10] Y.Y. Lyu, J. Kwak, O. Kwon, S.H. Lee, D. Kim, C. Lee, K. Char, Adv. Mater. 20 (2008) 2720.
[11] M. Tamano, T. Enokida, US Patent 5811834, 1997.
[12] K. Danel, T.H. Huang, J.T. Lin, Y.T. Tao, C.H. Chuen, Chem. Mater. 14 (2002) 3860.
[13] Y. Shirota, H. Kageyama, Chem. Rev. 107 (2007) 953.

Organic Electronics 11 (2010) 486–489

Contents lists available at ScienceDirect

Organic Electronics

journal homepage: www.elsevier.com/locate/orgel

Effect of host organic semiconductors on electrical doping

Jae-Hyun Lee, Dong-Seok Leem [1], Jang-Joo Kim *

Department of Materials Science and Engineering, Seoul National University, Seoul 151-742, Republic of Korea

ARTICLE INFO

Article history:
Received 11 October 2009
Received in revised form 14 November 2009
Accepted 1 December 2009
Available online 6 December 2009

Keywords:
Electrical doping
Organic semiconductor
Conductivity
Carrier density
Mobility

ABSTRACT

The effect of host organic semiconductors on electrical doping has been investigated. Electrical conductivities and carrier densities in various hosts are increased by doping with ReO_3. The degree of carrier generation by the *p*-doping is, however, different for different host organic semiconductors and depends on the energy difference between the HOMO level of the hosts and the Fermi energy level of the dopant ($\Delta E = E_{HOMO,host} - E_{F,dopant}$). The larger ΔE resulted in increased carrier generation. In contrast, hole mobilities were reduced by the doping if the organic semiconductors are heavily doped with a doping concentration of 25 mol%. The reduction of the mobilities is also different for different organic semiconductors and is not inversely proportional to the generated carrier densities.

© 2009 Elsevier B.V. All rights reserved.

1. Introduction

Electrical doping in organic semiconductors is an important technique to reduce the driving voltage and improve the power efficiency in organic light emitting diodes (OLEDs) and other organic electronic devices [1]. Electrical doping in charge transporting materials can reduce the contact resistance between the electrodes and organic materials and can enhance the electrical conductivity. Recently, various types of dopants have been developed for *n*- and *p*-doping in organic materials. Lithium in tris(8-quinolinolato)aluminum (Alq_3), cesium, cesium carbonate (Cs_2CO_3), rubidium carbonate (Rb_2CO_3) and cesium nitride (CsN_3) in 4,7-diphenyl-1,10-phenanthroline (BPhen) have been commonly used as *n*-type dopants [2–7]. Various combination of *p*-type dopants and host organic semiconductors have been reported to increase the conductivity of doped organic molecules, including tetrafluoro-tetracyano-quinodimethane (F_4-TCNQ) in 4,4′,4″-tris(*N*,*N*-diphenyl-amino)triphenylamine (TDATA), metal halides such as antimony pentachloride ($SbCl_5$) in *N*,*N*′-diphenyl-*N*,*N*′-bis(3-methylphenyl)-1,1′-biphenyl-4,4′-diamine (TPD), ferric chloride ($FeCl_3$) and copper iodide (CuI) in 1,4-bis[*N*-(1-naphthyl)-*N*′-phenylamino]-4,4′ diamine (NPB), and metal oxides such as tungsten oxide (WO_3) in 4,4′,4″-tris(*N*-(2-naphthyl)-*N*-phenyl-amino)-triphenylamine (2TNATA), vanadium oxide (V_2O_5), molybdenum oxide (MoO_3) and rhenium oxide (ReO_3) in NPB or *N*,*N*′-dicarbazolyl-4–4′-biphenyl (CBP) [8–17]. These papers observed that the *p*-dopants form CT complexes with the hole transporting organic materials to increase the conductivity [8–18]. In our previous report, we demonstrated that dopants having a larger work function are more effective in generating holes for a host [19]. To our best knowledge, however, there has been no systematic study on the effect of host materials on electrical conductivity, generation of carriers and carrier mobility by doping.

In this letter, we report the effect of host materials on the electrical conductivity of the doped semiconductors. We selected several hosts having different highest occupied molecular orbital (HOMO) levels to investigate the effectiveness of doping. ReO_3 was selected as the dopant since its work function is very high (>6 eV) [20]. We will demonstrate that higher carrier densities are generated in the host possessing higher lying HOMO level (smaller

* Corresponding author.
E-mail address: jjkim@snu.ac.kr (J.-J. Kim).
[1] Present address: Department of Chemistry, Imperial College-London, South Kensington Campus, London, UK.

1566-1199/$ - see front matter © 2009 Elsevier B.V. All rights reserved.
doi:10.1016/j.orgel.2009.12.002

absolute HOMO energy). In contrast, however, hole mobilities are reduced by doping in all the hosts when the doping concentration is very high.

2. Experimental

ReO_3 was used as the *p*-dopant and four different organic semiconductors of 2TNATA, NPB, 1,1-Bis-(4–methylphenyl)-aminophenyl-cyclohexane (TAPC), and CBP were used as the hosts. The doped organic layers were formed by the coevaporation of the dopant and each host by thermal evaporation in high vacuum. The doping concentration was controlled by the evaporation rate of the dopant in the range of 0.02∼0.32 Å/s under a constant evaporation rate of 2 Å/s for the organic hosts. The carrier density in the doped films was obtained from the capacitance–voltage (*C–V*) measurement of the metal-insulator-doped organic semiconductor (MIS) structure. A LiF (50 nm), doped organic semiconductor (50 nm) and an Ag electrode (50 nm) were successively deposited on indium tin oxide (ITO) coated glass substrates for the purpose. The *C–V* measurements were carried out by a 1260 impedance/gain-phase analyzer and a 1287 electrochemical interface (Solartron). Electrical conductivities of the doped films were measured using the four leads method. For the measurements, 1000×1000 μm^2 sized organic layers were thermally evaporated on a 200 nm thick SiO_2 covered *p*-type Si wafer. Then four strips of 50 nm thick gold electrodes were deposited on the organic layers. The size of the strip was 50×1100 μm^2 and the gap between the strips was 55 μm. The conductivity was measured using a Suss PM8 probe station with an Agilent 4155C semiconductor parameter analyzer. 50 nm thick doped organic films evaporated on glass substrates were used for the ultraviolet–visible–near infrared (UV–Vis–NIR) absorption measurement (Varian, Cary 5000).

From the references and the measured data by cyclic voltammetry in our laboratory, we confirmed the HOMO level of 5.0 eV for 2TNATA, 5.4 eV for NPB, 5.8 eV for TAPC and 6.0 eV for CBP, respectively [11,21,22]. The HOMO level of the hosts are located higher than the work functions of the ReO_3 (6.0 eV) based on the assumption that the Fermi level of a metal oxide dopant is the same as that of the bulk semiconductor [23]. Therefore, the hosts and the dopant are expected to form CT complexes in the doped films by transferring electrons from the host molecules to the dopant.

3. Results and Discussion

The formation of CT complexes can be easily detected by the appearance of new absorption peaks in the Vis–NIR region which are not shown by either component alone. Fig. 1a shows the difference in the UV–Vis–NIR absorption spectra between 25 mol% ReO_3 doped host films and undoped films. The additional peaks appeared in the doped films at 467 and 1226 nm for 2TNATA, 500 and 1352 nm for NPB, 455 and 691 nm for TAPC and 454 nm for CBP, respectively. These additional peaks are generated at the expense of the $\pi-\pi^*$ transition of undoped films, indicating that these peaks originated from the characteristic absorption peaks of the charge transfer complexes or the radical cation host molecules ($Host^+$) formed by doping [24]. The absorption intensities of the CT complexes increased with the doping concentration as shown in Fig. 1b. However, the intensity of the CT peaks becomes smaller as the HOMO level of the hosts becomes lower. ReO_3 doped 2TNATA showed the highest intensity of CT complex absorption in the full doping concentration range, followed by NPB, TAPC and CBP in sequence.

The carrier density generated by the doping was estimated by the *C–V* measurement using the MIS devices [25]. Details of the sample preparation and the carrier density measurements were described in a previous report [26]. The carrier density increased with an increase in the doping concentration of ReO_3, as shown in Fig. 2. Again, the host having a higher lying HOMO level generates a larger carrier density than the host with a lower lying HOMO level. For instance the ReO_3 doped 2TNATA film with a 25 mol % doping concentration has the higher carrier density of 6.2×10^{18} cm^{-3} than CBP films which have a carrier density of 7.3×10^{17} cm^{-3}. The charge generation efficiency, defined as the ratio of the carrier density to the number of dopant molecules in the doped films, is reduced in the following sequence: 2TNATA (3.8%) > NPB (0.75%) > TAPC (0.38%) > CBP (0.29%). These carrier generation efficiencies follow a similar trend as the absorption intensity of CT complexes (Fig. 1b). From Figs. 1 and 2, we could conclude that the hosts with higher HOMO levels result in higher doping efficiencies. In other words, a larger energy difference between the HOMO level of an organic host

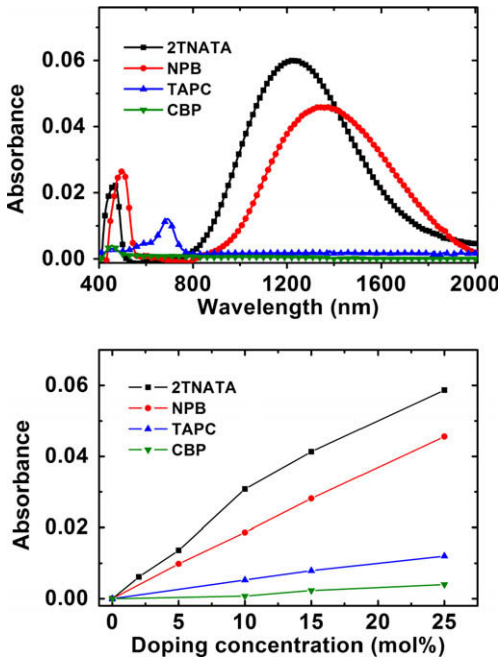

Fig. 1. (a) The difference in the absorption spectra between the 25 mol% ReO_3 doped film and undoped film. (b) The intensity of the CT complex absorption peak vs doping concentration for ReO_3 doped 2TNATA (square), NPB (circle), TAPC (triangle) and CBP (inverse triangle), respectively.

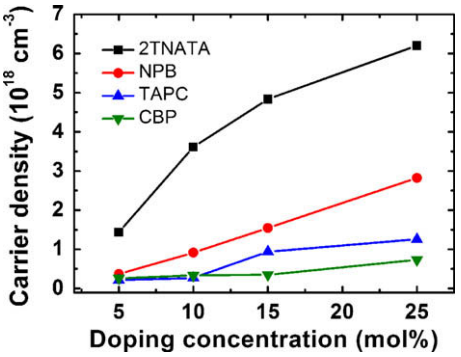

Fig. 2. Carrier density vs doping concentration for ReO_3 doped 2TNATA (square), NPB (circle), TAPC (triangle) and CBP (inverse triangle), respectively.

and the Fermi level of a *p*-dopant ($\Delta E = E_{HOMO,host} - E_{F,dopant}$) facilitates the formation of more CT complexes at the same doping concentration. These results are consistent with previous results of the energy difference of ΔE by using different *p*-dopants having different Fermi levels in a host [19]. This doping efficiency was calculated on the assumption that the dispersion of ReO_3 is the same for all the molecular films if the doping concentration is the same in each film. Even though there are good possibilities of the formation of dopant aggregates in the films, this assumption is expected to be valid in these systems since the chemical structure of all the hosts are based on the triphenylamine group [16,27].

In order to investigate the relationship between the carrier density and electrical conductivity, we measured the electrical conductivity of the doped films. The four leads method was used to measure the conductivity to avoid the problem of the contact resistance between the metal electrode and the organic layer in a sandwich type hole only device or in a two parallel electrodes structure [28]. The scheme of four leads measurement is shown in the inset of Fig. 3. During the primary current flows through the outer electrode i.e., between electrodes 1 and 4, we measured the voltage drop between the inner electrodes 2 and 3 with the small secondary current. The current density–electric field (*J*–*E*) characteristics of the 2TNATA, NPB, TAPC and CBP films doped with 25 mol% of ReO_3 are shown in Fig. 3. The linear region in the *J*–*E* graph corresponds to the region where the secondary current becomes negligible to the primary current and we could measure the conductivity from the slope in the region with negligible effect to the contact resistance.

The electrical conductivity and the mobility of doped and undoped films are shown in Fig. 4. The conductivity of the doped films is the highest for NPB, followed by 2TNATA, CBP and TAPC. This sequence was different from the trend of the generated carrier density by doping. This difference comes from the characteristics of the mobility of the doped organic semiconductors.

The mobility of a doped organic semiconductor is obtained from the following equation,

$$\mu_h = \frac{\sigma}{qN_h},$$

where σ is the conductivity, q is the electronic charge, and N_h is the carrier density. The measured conductivity by the four leads method and the carrier density by *C*–*V* measurement were used for the calculation. The mobility of ReO_3 doped host films are compared with that of the undoped host films in Fig. 4. The mobility of the undoped film was measured using the time-of-flight method. ReO_3 doped NPB has the highest mobility of 2.3×10^{-6} cm^2/Vs followed by CBP, TAPC and 2TNATA. These hole mobilities of the doped host films are 1∼2 orders of magnitude lower than the undoped host films.

The drift mobility of the doped NPB film with 25 mol % of ReO_3 is almost the same as the field effect mobility of the same film. The sample for the four leads method was directly used for the measurement of the field effect mobility. P doped Si substrate was used as the gate, and electrodes 2 and 3 as the source and drain electrodes, respectively. The channel length and width were 55 and 1000 μm, respectively. The hole mobility of the ReO_3 doped NPB film was measured to be 3.0×10^{-6} cm^2/Vs in the saturation region, which is almost the same as the previous drift mobility. The consistency of the separately measured hole mobilities of the ReO_3 doped NPB film confirms the validity of the con-

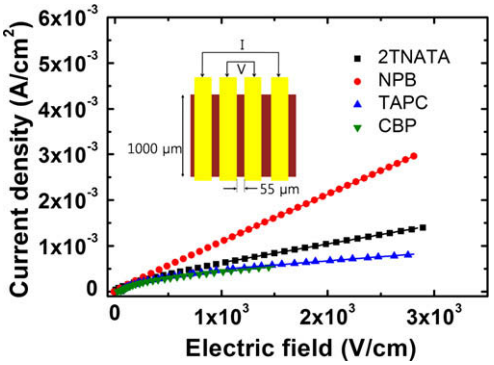

Fig. 3. The current density–electric field characteristics of devices with 25 mol% ReO_3 doped 2TNATA (square), NPB (circle), TAPC (triangle) and CBP (inverse triangle), respectively. Inset: scheme diagram of the four leads method.

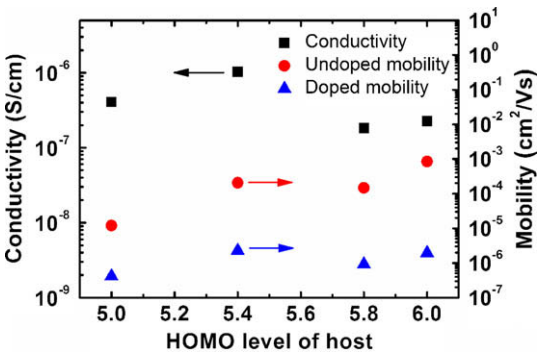

Fig. 4. The conductivity (square) and the mobility (triangle) of the films doped with 25 mol% ReO_3 and the mobility of the undoped films (circle) vs. the HOMO level of the organic hosts.

ductivity measured by the four leads method and of the carrier density by the *C–V* measurement.

The reduction of the hole mobilities by the doping observed in the system is consistent with the previous report in the F_4-TCNQ doped NPB system [29], but is contradictory to the F_4-TCNQ doped ZnPc system [30]. In F_4-TCNQ doped ZnPc, the mobility was increased from 3×10^{-4} to 1×10^{-3} cm^2/Vs as the doping concentration increased from 0.002 to 0.04 mol%. In contrast, the hole mobility was reduced from 1.6×10^{-5} to 4.3×10^{-6} cm^2/Vs when the same dopant F_4-TCNQ is doped into NPB with the doping concentration of 4 mol %. In our experiment, the doping concentration is even higher with 25 mol%.

The mobility of *p*-type dopant doped organic semiconductors could be interpreted by a form of charge transport in a disordered hopping system with the trap states correlating to the charged dopants. At a low doping concentration, generated hole carriers fill the trap states of intrinsic host organic materials to enhance the mobility of doped films. At a high doping concentration, however, large number of charged dopants form deep trap states to interrupt the hole transport. Different doping concentrations and different distributions of the density of states in disordered hopping systems could cause this contrary behavior of mobility depending on the doping concentration [31,32]. Therefore, in our results, it is reasonable to understand that the negatively charged dopant, ReO_3 reduced the mobility of holes in the doped organic semiconductors at the high doping concentration.

4. Conclusion

In summary, we investigated the host effect on the electrical properties of ReO_3 doped organic semiconductors such as 2TNATA, NPB, TAPC and CBP possessing different HOMO energy levels [CBP (6.0 eV) > TAPC (5.8 eV) > NPB (5.4 eV) > 2TNATA (5.0 eV)]. Through the UV–Vis–NIR spectroscopic measurements and the *C–V* measurements, we demonstrated that the doped host with a larger energy difference of $\Delta E = E_{HOMO,host} - E_{F,dopant}$ facilitates to form more CT complexes and a higher carrier density due to the doping. High doping of ReO_3 reduced the hole mobility for all the hosts. The degree of reduction, however, is different for different hosts and is not proportional to the generated carrier density in the hosts.

Acknowledgements

This research was supported by a grant (2009K000069) from Center for Nanoscale Mechatronics and Manufacturing, one of the 21st Century Frontier Research Programs and the WCU program which are both supported by the Ministry of Education, Science and Technology of Korea.

References

[1] J. Blochwitz, M. Pfeiffer, T. Fritz, K. Leo, Appl. Phys. Lett. 73 (1998) 729.
[2] J. Kido, T. Matsumoto, Appl. Phys. Lett. 73 (1998) 2866.
[3] G. He, M. Pfeiffer, K. Leo, M. Hofmann, J. Birnstock, R. Pudzich, J. Salbeck, Appl. Phys. Lett. 85 (2004) 3911.
[4] T. Hasegawa, S. Miura, T. Moriyama, T. Kimura, I. Takaya, Y. Osato, H. Mizutani, SID Int. Symp. Digest of Tech. Papers 35 (2004) 154.
[5] J.Y. Lee, K.S. Yook, S.O. Jeon, C.W. Joo, T.-W. Lee, T. Noh, H.-J. Yang, S.-K. Kang, IMID/IDMC/Asia display '08 Digest 38 (2008) 1319.
[6] D.-S. Leem, S.-Y. Kim, J.-J. Kim, M.-H. Chen, C.-I. Wu, Electrochem. Solid-State Lett. 12 (2009) J8.
[7] D.-S. Leem, J.-H. Lee, J.-J. Kim, J.-W. Kang, Appl. Phys. Lett. 93 (2008) 103304.
[8] X. Zhou, M. Pfeiffer, J. Blochwitz, A. Werner, A. Nollau, T. Fritz, K. Leo, Appl. Phys. Lett. 78 (2001) 410.
[9] C. Ganzorig, M. Fujihira, Appl. Phys. Lett. 77 (2000) 4211.
[10] J. Endo, T. Matsumoto, J. Kido, Jpn. J. Appl. Phys. 41 (2002) L358.
[11] J.-H. Lee, D.-S. Leem, J.-J. Kim, Org. Electron. 9 (2008) 805.
[12] C.-C. Chang, M.-T. Hsieh, J.-F. Chen, S.-W. Hwang, C.H. Chen, Appl. Phys. Lett. 89 (2006) 253504.
[13] X.L. Zhu, J.X. Sun, H.J. Peng, Z.G. Meng, M. Wong, H.S. Kwok, Appl. Phys. Lett. 87 (2005) 153508.
[14] T. Matsushima, C. Adachi, J. Appl. Phys. 103 (2008) 034501.
[15] T.J. Park, S.Y. Kim, W.S. Jeon, J.J. Park, R. Pode, J. Jang, J.H. Kwon, J. Nanosci. Nanotechnol. 8 (2008) 5606.
[16] M. Kröger, S. Hamwi, J. Meyer, T. Riedl, W. Kowalsky, A. Kahn, Org. Electron. 10 (2009) 932.
[17] D.-S. Leem, H.-D. Park, J.-W. Kang, J.-H. Lee, J.W. Kim, J.-J. Kim, Appl. Phys. Lett. 91 (2007) 011113.
[18] K.-H. Yim, G.L. Whiting, C.E. Murphy, J.J.M. Halls, J.H. Burroughes, R.H. Friend, J.-S. Kim, Adv. Mater. 20 (2008) 3319.
[19] J.-H. Lee, D.-S. Leem, H.-J. Kim, J.-J. Kim, Appl. Phys. Lett. 94 (2009) 123306.
[20] I.D. Baikie, U. Peterman, B. Lägel, K. Dirscherl, J. Vac. Sci. Technol. A 19 (2001) 1460.
[21] M. Aonuma, T. Oyamada, H. Sasabe, T. Miki, C. Adachi, Appl. Phys. Lett. 90 (2007) 183503.
[22] I.G. Hill, A. Kahn, J. Appl. Phys. 86 (1999) 4515.
[23] Q. Sun, B.K. Rao, P. Jena, D. Stolcic, Y.D. Kim, G. Gantefor, A.W. Castleman Jr., J. Chem. Phys. 121 (2004) 9417.
[24] P.J. Low, M.A.J. Paterson, D.S. Yufit, J.A.K. Howard, J.C. Cherryman, D.R. Tackley, R. Brook, B. Brown, J. Mater. Chem. 15 (2005) 2304.
[25] S. Grecu, M. Bronner, A. Opitz, W. Brütting, Synth. Met. 146 (2004) 359.
[26] J.-. Lee, D.-S. Leem, H.-J. Kim, J.-J. Kim, SID Int. Symp. Digest of Tech. Papers, (2009) P-161.
[27] S. Hamwi, J. Meyer, T. Winkler, T. Riedl, W. Kowalsky, Appl. Phys. Lett. 94 (2009) 253307.
[28] S. Roth, D. Carroll, One-Dimensional Metals, 2nd., Wiley-vch, 2003.
[29] T. Matsushima, C. Adachi, Thin Solid Films 517 (2008) 874.
[30] B. Maennig, M. Pfeiffer, A. Nollau, X. Zhou, K. Leo, P. Simon, Phys. Rev. B 64 (2001) 195208.
[31] V.I. Arkhipov, P. Heremans, E.V. Emelianova, H. Bässler, Phys. Rev. B 71 (2005) 045214.
[32] L. Ma, W.H. Lee, Y.D. Park, J.S. Kim, H.S. Lee, K. Cho, Appl. Phys. Lett. 92 (2008) 063310.

Organic Electronics 11 (2010) 490–497

Contents lists available at ScienceDirect

Organic Electronics

journal homepage: www.elsevier.com/locate/orgel

Long-lived persistent currents in poly(3-octylthiophene) thin film transistors

Petro Lutsyk [a,1], Krzysztof Janus [a,*], Mikołaj Mikołajczyk [a], Juliusz Sworakowski [a], Bogusław Boratyński [b], Marek Tłaczała [b]

[a] Institute of Physical and Theoretical Chemistry, Wrocław University of Technology, Wyb. Wyspianskiego 27, 50-370 Wrocław, Poland
[b] Faculty of Microsystem Electronics and Photonics, Wrocław University of Technology, Janiszewskiego 11/17, 50-372 Wroclaw, Poland

ARTICLE INFO

Article history:
Received 3 August 2009
Received in revised form 20 November 2009
Accepted 3 December 2009
Available online 11 December 2009

Keywords:
Persistent photocurrent
Light-induced memory effect
Poly(3-octylthiophene)
Field-effect transistor

ABSTRACT

Persistent post-photocurrents (PPC) have been studied in organic field-effect transistors (FET) made of thin films of regioregular poly(3-octylthiophene). The phenomenon occurs after illumination of FET with UV light. The drain-source current persisting after switching off the illumination is ca. three orders of magnitude higher than that in a virgin sample, and lasts for a long time. It may be erased by applying a negative potential to the gate electrode or by reversing the drain-source voltage. The magnitude and kinetic behaviour of the current depend on ambient atmosphere, particularly on the presence of O_2 molecules. The effect has been explained by formation of mobile O_2^- anions during irradiation. These slowly recombining anions are responsible for the occurrence of PPC. The effect may be used in opto-electronic switches.

© 2009 Elsevier B.V. All rights reserved.

1. Introduction

Rapidly growing interest in organic electronic devices has been due to current and emerging applications of organic materials as elements of organic light emitting diodes, organic field-effect transistors, etc. In particular, low-cost and easy high-volume production of thin film transistors (TFT) is possible using e.g. ink-jet printing technique [1,2]. Polymeric field-effect transistors (FET) have been developed using, in most cases, two types of semiconducting polymers – polyfluorenes and poly(3-alkylthiophene)s (PAT) [3]. In the case of substituted polythiophenes, the FET performance critically depends on the regioregularity of the polymer and its ordering at the polymer–insulator interface. High charge carrier mobilities, up to 0.1 $cm^2/(V\,s)$ were found only for poly(3-hexylthiophene) FET with the chains ordered edge-on to the surface [3]. This value is comparable with the mobility in amorphous silicon generally used in up-to-date TFT electronics. Nowadays, however, the major problem preventing a wider application of organic TFTs is not attaining higher mobilities but making these devices more stable and enduring [2,4].

One of the effects affecting operation of field-effect transistors is a persistent current following illumination of a FET structure. The post-illumination drain-source current does not return to its initial value but, instead, to a value some orders of magnitude higher. The decay, without an external stimulus, may take days. The phenomenon, referred to as persistent photoconductivity, or photo-induced memory effect has been observed in transistors made of both, inorganic and organic materials, and extensively studied as it may be interesting for development of photosensing transistors with ability of writing and erasing information. In this paper, we shall employ the name of persistent post-photocurrent (PPC).

Several explanations of the phenomenon have been offered, involving both, physical and chemical processes. For example, in silicon and GaAs [5,6], the effect of photo-in-

* Corresponding author. Tel.: +48 713204069; fax: +48 713203364.
E-mail address: krzysztof.janus@pwr.wroc.pl (K. Janus).
[1] Address: Institute of Physics, National Academy of Science of Ukraine, Prospekt Nauky 46, 03680 Kyiv, Ukraine.

1566-1199/$ - see front matter © 2009 Elsevier B.V. All rights reserved.
doi:10.1016/j.orgel.2009.12.003

duced persistence of current after illumination has been explained by a spatial separation of photogenerated charge carriers occurring at local potential barriers of point trapping centres and/or p–n junctions.

Appearance of PPC was also reported for poly(phenylene vinylene) [7,8] and interpreted invoking self-trapping of charge carriers and formation of polarons and bipolarons in the polymer. It was postulated that photocurrent in the polymer is predominantly carried by mobile polarons near the surface, while photogenerated charges are stored in long-lived bipolarons with low mobility within the bulk. The decay of PPC is limited by diffusion of bipolarons towards the surface of the film and dissociation into polarons.

The persistent current was also observed in poly(3-hexylthiophene) [9–12]. In Ref. [10], PPC was explained by electron trapping at Al donor sites because such an effect was detected only in samples with thin layer of Al deposited on top and/or bottom of the polymer. Dutta and Narayan [11] showed, however, that PPC exists in polythiophene without Al electrodes, being practically independent of intensity and duration of illumination. The persistent current has not been observed in FETs with the negatively biased gate while at zero or a positive gate voltage PCC lasted for hours [10–13]. The persistent current could be erased by applying a short pulse of negative voltage to the gate electrode [11–13]. The effect was attributed to negatively charged traps that effectively screened the gate voltage [11,12]. The same effect was observed in FETs made of low-molecular-weight tetrathiafulvalene derivatives [13] and interpreted as due to enhanced recombination of trapped electrons upon applying a negative gate voltage.

It has been well established that in vast majority of organic semiconductors charge transport is realized by holes. In these materials, molecular oxygen and oxidation products form traps for electrons [14]. Consequently, in p-type devices (such as all the devices mentioned above), electrons are efficiently localized on such species, inevitably present in the active materials. The situation is more complex in n-type devices. Here, a possibility of formation of electron traps by oxygen depends on position of the electron affinity of the impurity molecules relative to that of the host ones. n-Channel transistors may be much more robust to oxidation (or photooxidation) and as such be much more stable in air [15] giving the possibility of manufacturing photoresponsive FETs free of PPC. Such devices may act as very fast and reversible opto-electronic switches [16].

Although several papers have been devoted to study of PPC, the matter of this phenomenon remains unclear. The origin of slow current decay after switching off illumination and its recovery to the initial (pre-illumination) level after applying a gate voltage have not been explained. This work is a contribution to study of the kinetics of photocurrent and persistent post-photocurrent in an organic FET, aiming at explaining the origin of persistent current. We measured the kinetics of photocurrent and persistent current in the FETs made of regioregular poly(3-octylthiophene-2,5-diyl) (p3OT) (Fig. 1a), in various atmospheres and at several temperatures. The material was chosen as it shows promising FET characteristics and sensitivity to light with a high ratio of photocurrent to dark current (up to 10^4 [17,18] or even exceeding this value).

2. Experimental

Steady-state current–voltage characteristics, and the temporal behaviour of photocurrent and of persistent current, have been measured in FET made of p3OT. Thin films of molecular weight optimised ($M_n \sim 25{,}000$) [19,20] regioregular p3OT (Aldrich) were fabricated by spin coating (in ambient air, at 800 rpm) from chloroform solutions (concentration amounting to 2 mg/ml). The thicknesses of the films ranged between 20 and 50 nm, as measured with an atomic force microscope (AFM, NanoScope V, Veeco). Absorption spectra of the films on quartz substrates were measured using a Perkin–Elmer Lambda 20 UV–vis spectrophotometer.

Silicon/SiO_2 wafers (from CEMAT Silicon, Poland) with 200 nm thick thermal oxide were used as substrates for FET. The oxide was thinned by chemical etching in the areas where the source and drain multifinger electrodes were to be later deposited (Fig. 1b). The contact metalization was e-beam evaporated and defined by lift-off lithography. In this way, the surface of the substrate was planarized providing proper conditions for polymer deposition. The length and width of the FET channel were equal to 20 μm and 11.6 mm, respectively, and the surface capacitance was equal to 20 nF/cm^2.

The drain-source current was measured with a Keithley 6517A electrometer, the voltage source of the electrometer

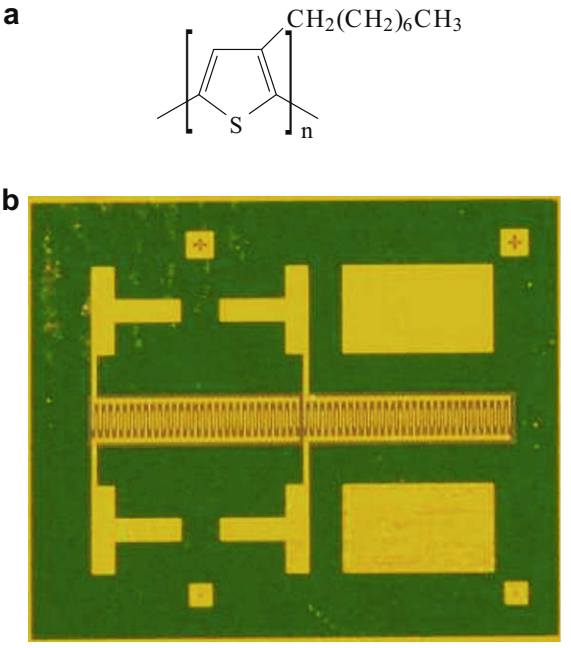

Fig. 1. (a) Molecular structure of poly(3-octylthiophene-2,5-diyl) (p3OT). (b) Top view of an Si/SiO_2/Au substrate used for fabrication of FETs. Dimensions of the substrate amount to 6×5 mm^2, $L = 20$ μm, $W = 11.6$ mm.

being used for supplying the drain-source voltage, U_{DS}. The gate-source voltage, U_{GS}, was supplied from a High Voltage Power Supply (Stanford Research Systems) equipped with a decade resistive voltage divider. The measurements of current–voltage and kinetic characteristics were performed in vacuum ($p < 0.02$ mbar). Additionally, some kinetic curves were measured in dry nitrogen atmosphere or in ambient air. The measurements were automatically controlled with LabView software. A ZXE-150 xenon lamp (Optel, Poland) equipped with an UV UG11 optical filter (with transmission band maximum at 335 nm) and quartz optical fibre were used for illumination of the samples.

The mobility of charge carriers, μ, threshold voltage, U_T, and on–off ratio have been calculated from the current–voltage characteristics. According to the conventional FET theory, μ can be calculated from the current–voltage dependencies

$$I_{DS} = \mu \frac{WC}{L}\left(U_{GS} - U_T - \frac{U_{DS}}{2}\right)U_{DS} \quad (1)$$

$$I_{DS} = \mu \frac{WC}{2L}(U_{GS} - U_T)^2 \quad (2)$$

where I_{DS} and U_{DS} stand for drain-source current and voltage, U_{GS} is gate-source voltage, L and W are length of channel (i.e. the distance between source and drain electrodes) and width of channel, respectively, and C stands for surface capacitance. Eqs. (1) and (2) apply to the linear section and to the saturation regime of the current–voltage characteristics, respectively.

3. Results

Current–voltage characteristics of TFT made of p3OT were measured for gate-source voltages ranging from −50 to 0 V (Fig. 2). A hysteresis of drain-source current vs. U_{GS} was observed, similar to that reported earlier [21]. The time necessary for the stabilisation of drain-source currents was found longer if subsequent curves were taken with increasing gate fields (i.e. taken with U_{GS} changed from 0 to −50 V), and the dependence of the saturation current on U_{GS} did not follow the quadratic dependence expected from Eq. (2). For decreasing gate fields (U_{GS} ranging from −50 to 0 V) the current in studied FETs stabilised sufficiently fast, and the saturation current quadratically depended on the gate voltage (Fig. 3). The faster the stabilisation, the better was the fit of measured characteristics with Eq. (2). Consequently, the characteristics were measured with the gate voltage changing from −50 to 0 V (Fig. 2).

The mobility of charge carriers determined from current–voltage characteristics measured on as-deposited samples in both, linear and saturation regime was about 10^{-4} cm^2/(V s), i.e., was one order lower than that reported previously [17,18]. The on–off ratio in saturation regime was in the range of $(0.5–1.0) \times 10^5$, threshold voltage was about −20 V (Fig. 3). The electrical parameters of as-deposited structures could be improved by a treatment of the samples with chloroform vapours [22]. Under illumination, the drain-source current in the off state substantially increased whereas the on current remained essentially unchanged. Consequently, the on–off ratio (in the saturation regime) decreased to about 10^2.

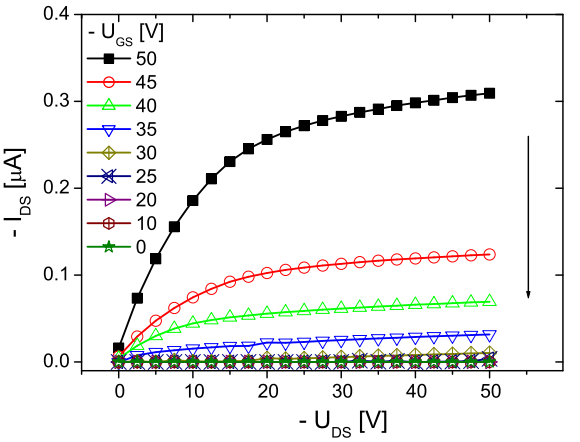

Fig. 2. Output dark current–voltage characteristics for p3OT FET, measured in vacuum. The arrow indicates the sequence of measurements of the characteristics.

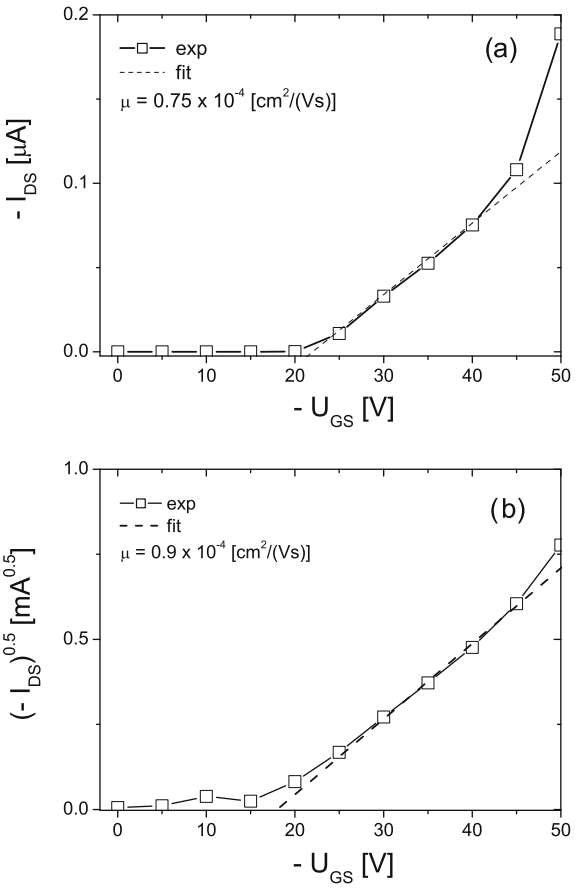

Fig. 3. Transfer current–voltage characteristics for p3OT FET, measured in the linear regime ($U_{DS} = -5$ V) (a) and in the saturation regime ($U_{DS} = -45$ V) (b), in vacuum. The broken lines show fits to the experimental curves using Eq. (1) in (a) and Eq. (2) in (b).

The temporal behaviour of the drain-source current following the illumination of the structure was examined in more detail. Upon illumination, the drain-source current rises within tens of seconds to reach a plateau. The magnitude of the effect depends primarily on the gate voltage and, to some extent, on ambient atmosphere: for example, if the measurements are carried out in air, at $U_{GS} = 0$ V and $U_{DS} = -40$ V the current increases by ca. six orders of magnitude (from pA up to μA level; Fig. 4), whereas at gate voltages lower than −10 V the increase does not exceed the factor of 4. In vacuum, during a prolongued illumination (15–30 min), the drain-source current increases to a maximum and then decreases very slowly (Fig. 5). At higher temperatures, the maximum appears at shorter times, and the decay is steeper. Such a maximum has not been found in samples measured in ambient atmosphere in spite of a prolongued illumination (Fig. 4). Measurements taken after the measuring chamber was flushed with nitrogen (i.e. after the concentration of oxygen was lowered to a fraction of mol. %) yield results qualitatively similar to those taken in ambient atmosphere, the magnitude of both photocurrent and the persistent current being, however, much lower.

After switching off the illumination, the current slowly decreases to the nA level (Figs. 4 and 5). The current does not return to the previous pA level, measured before the illumination, and lasts for more than 72 h (Fig. 4). The photocurrents and PPC measured in air are higher and the decays of PPC are slower than those measured in vacuum or in N_2 atmosphere as can be clearly seen from the data in Table 1. The dependencies of photocurrent and PPC on drain-source voltage (measured at 600 s after switching off the illumination) are linear for U_{DS} ranging between 0 and −75 V. The current is also temperature dependent: small changes of the magnitude of PPC are observed on increasing the temperature (Fig. 5). The measured decays are not monoexponential, and may be fitted with two exponentials for measurements taking up to ca. 3 h. Three exponents or stretched-exponential dependence [9] are required to fit the kinetics at longer times.

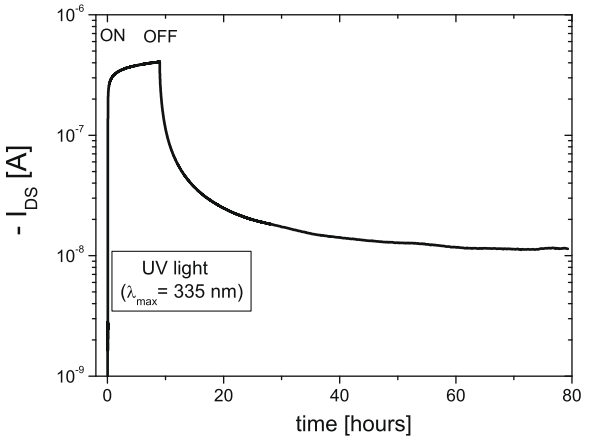

Fig. 4. Kinetics of photocurrent increase and of PPC decay, measured in ambient air. $U_{DS} = -40$ V, $U_{GS} = 0$ V.

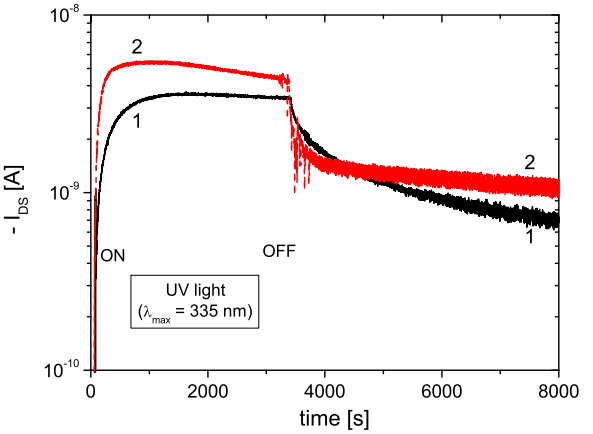

Fig. 5. Kinetics of photocurrent increase and PPC decay, measured in vacuum at 300 K (1) and 370 K (2). $U_{DS} = -30$ V, $U_{GS} = 0$ V.

The effect of the gate voltage on the behaviour of PPC was examined: the gate voltage was either set at 0 V or at a negative value and kept constant during the entire experiment, or pulses of voltage were applied to the gate at various times after switching off illumination. In the former case, we observed quantitative, but not dramatic, changes in the kinetics (compared to that measured at zero gate-source voltage), the latter procedure resulted in an irreversible decrease of the drain-source current to the pA level.

Contrary to the results presented in Refs. [11,12], we did observe PPC at $U_{GS} \leqslant 0$ V, i.e., in our samples the memory effect did not require keeping positive voltage on gate. The persistent current at $U_{GS} < 0$ V decays faster than that at $U_{GS} = 0$ V, merging into the dark current after a relatively short time.

The persistent current was quickly erased by applying a negative electrical potential to the gate electrode: in the experiment described below, U_{GS} was equal to 0 during illumination and a certain period after the illumination (cf. Fig. 6). After switching off the illumination, we observed a typical slow decay of PPC (Fig. 6, $300 < t < 500$ s). A positive voltage applied to the gate electrode did not erase PPC; just opposite, the persistent current slightly increased after setting $U_{GS} = 0$ again (Fig. 6, compare the magnitudes of current at 500 s and at 550 s). Application of $U_{GS} < 0$ resulted in an increase of the absolute value of the drain-source current but after setting $U_{GS} = 0$ again, the current returned to the low level of ca. 10^{-12} A (Fig. 6, $t > 1500$ s). The rate of erasing was found voltage-dependent: the higher negative voltage applied, the faster was the erase of PPC to the level from before illumination. For example, at $U_{GS} = -10$ V a few minutes and at $U_{GS} = -50$ V only few seconds are needed to completely reset the current. After erasing the persistent current with $U_{GS} < 0$ V, a subsequent biasing of the gate electrode with a positive potential does not affect the current, like before exposing the sample to illumination (Fig. 6, $25 \text{ s} < t < 75$ s).

The magnitude and temporal behaviour of PPC was found dependent on the way the experiment was carried out. After switching off the drain-source voltage for a short

Table 1
Dependencies of photocurrents and PPC on ambient atmospheres. All measurements were taken at $U_{DS} = -40$ V, $U_{GS} = 0$ V.

(μA)	Vacuum ($p < 0.02$ mbar)	Nitrogen	Air
Photocurrent (10 min after switching on the illumination)	0.10	0.10	0.40
Persistent post-photocurrent (10 min after switching off the illumination)	0.01	0.01	0.20

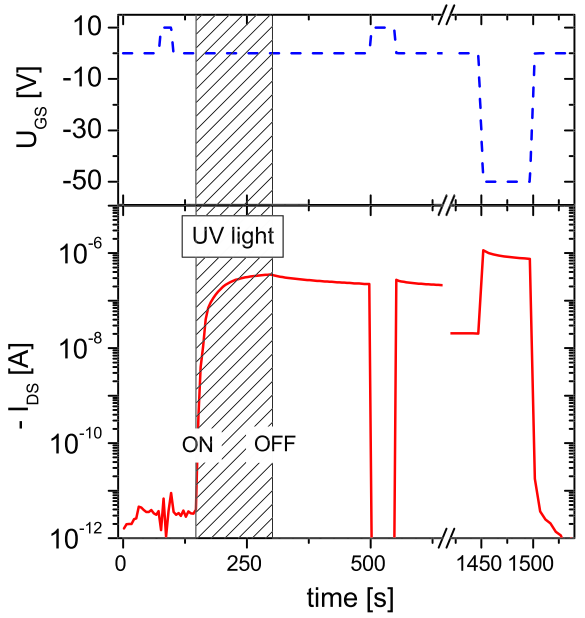

Fig. 6. Kinetics of photocurrent increase and PPC decay at various U_{GS}, measured in ambient air. $U_{GS} = 10$ V was applied in the time spans 25–75 s and 500–550 s; the illumination of sample was turned ON at 150 s and turned OFF at 300 s (striped area); $U_{GS} = -50$ V was applied between 1450–1500 s. $U_{DS} = -40$ V.

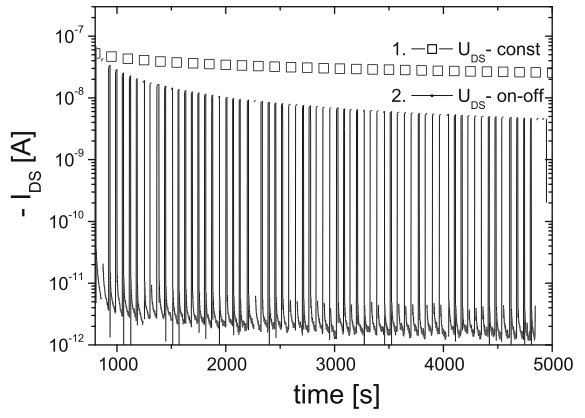

Fig. 7. Kinetics of PPC decay, measured in vacuum at constant $U_{DS} = -10$ V (1) and under periodically switched U_{DS} (2). The cycle in (2) consisted of 10 s at $U_{DS} = -10$ V, followed by 50 s at $U_{DS} = 0$ V.

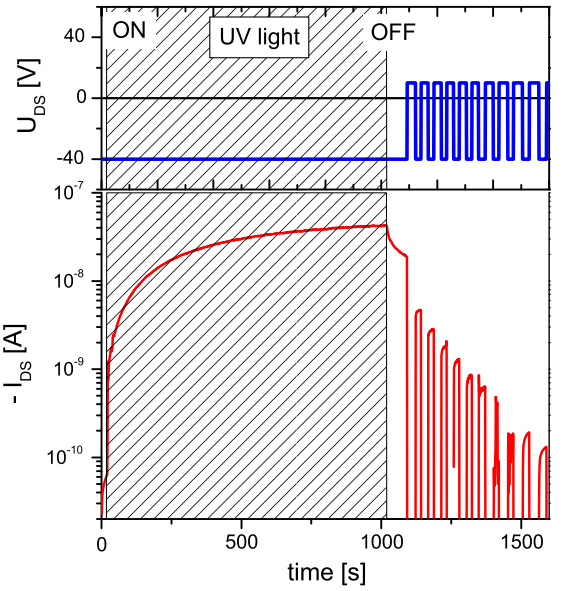

Fig. 8. Rapid erase of PPC induced by subsequent changes of U_{DS} polarity. $U_{GS} = 0$ V, $U_{DS} = -40$ V (during illumination) and -40 V or $+10$ V (after illumination). The period of illumination with UV light is marked with a striped pattern.

period of time (of the order of tens of seconds) and subsequent switching it on again, the persistent current was restored at a lower level. Periodic changes of U_{DS} resulted in a faster decay of PPC (Fig. 7). Reversing the sign of U_{DS} and switching it back also decreases the persistent current, the rate of decrease being faster for higher U_{DS} and for longer time of application of the reversed voltage. The persistent current could be completely erased after a few such cycles (Fig. 8).

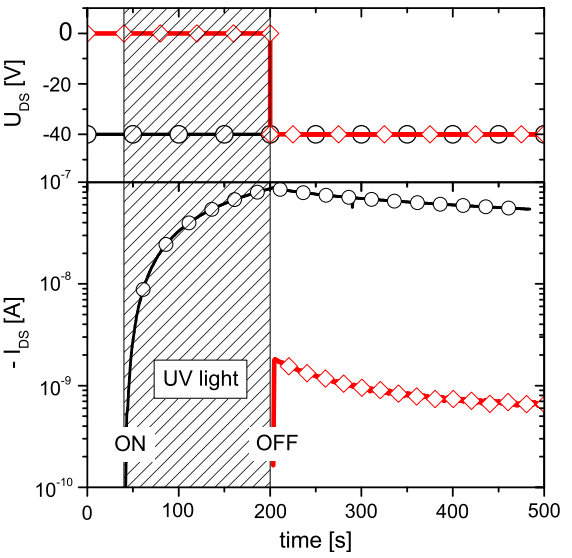

Fig. 9. Comparison of magnitude of PPC measured after biased (circles) and unbiased illumination (diamonds). $U_{GS} = 0$ V, during illumination $U_{DS} = -40$ V (biased) or 0 V (unbiased) and -40 V after illumination (in both cases). The period of illumination with UV light is marked with a striped pattern.

Illumination of an unbiased TFT prior to applying the drain-source voltage also resulted in the appearance of the persistent current, its value, however, was about two orders of magnitude lower than that observed after illumination of a biased sample (Fig. 9).

4. Discussion

The results shown in the preceding section demonstrate that both, the photocurrent and persistent post-photocurrent weakly depend on temperature (Fig. 5). Thus the thermal activation of trapped carriers is unlikely to be the main source of persistent current. On the other hand, the magnitude and the temporal behaviour of the photocurrent depend on the ambient atmosphere. A long illumination in ambient air or under reduced amount of oxygen resulted in a continuous increase of the current (possibly attaining a saturation beyond the time scale of our experiments), while in vacuum a maximum followed by a slow decrease was observed (Figs. 4 and 5). Photocurrents and persistent currents measured in vacuum or under a reduced concentration of oxygen, lower than those measured in air, evidence the doping of the polymer with molecules present in air, most probably with molecular oxygen. O_2 is omnipresent in organic materials even under ultrahigh vacuum, and, according to the literature, it is one of the most efficient dopants for p-type organic semiconductors, including polythiophenes [23–25]. A special feature of polythiophenes is a reversible enhancement of conductivity caused by illumination of samples in presence of O_2 [24–27], explained by formation of long-lived charge transfer complexes of oxygen with thiophene rings. The complexes of oxygen with polythiophene have an ionic character [23]. An evident influence of O_2 on persistent current was also observed in transient measurements for oxotitanium phthalocyanine [24], in which the post-photocurrent was found to persist after exposure of sample to O_2 atmosphere, while the current dropped to zero in vacuum.

Appearance of PPC in polythiophene has been explained [11,12] by the presence of electrons trapped on the polymer/insulator interface. The layer of immobile negatively charged species adds its own electric field to that originating from the gate potential. This model explains the similarity of the drain-source post-photocurrent at $U_{GS} = 0$ V and the current at $U_{GS} < 0$ V in the unilluminated sample. It fails, however to explain some phenomena observed in our experiments, for example vanishing of the PPC after a few subsequent changes of the sign of U_{DS} or appearance of a small PPC if the sample is illuminated under $U_{DS} = 0$ V. These phenomena can be simply explained assuming the presence of long-lived mobile ions created during illumination of the samples.

Our experiments indicate that the primary event, responsible for the behaviour of the samples under study (and, in particular, for the appearance of the persistent current) is the light-induced charge transfer, resulting in creation of holes on the polymer chains and of long-lived negatively charged small dopant molecules (most probably, O_2^-). The efficiency of creation of such pairs depends on the voltage, hence at $U_{DS} = 0$ V the concentration of charges should be low as is indeed the case in our experiments. Due to their small size, the negatively charged species are likely to be mobile in the polymer matrix, one could therefore expect their accumulation near the positive electrode until a steady-state has been reached. Note that this implies the build-up of a gradient of negatively charged molecular species. The dynamic equilibrium results from a competition of two driving forces: the electric field due to applied voltages (U_{DS} and U_{GS}) and the concentration gradient, the supply of ionic species being due to the illumination. Switching off the illumination (with the drain-source voltage still on) results in a decrease of the current: there is no supply of negative ions. The accumulated negative ions can discharge at the positive electrode being one of sources of the persistent current.

The persistent current can be erased by setting $U_{DS} = 0$ V (Fig. 7), by reversing the sign of U_{DS} (Fig. 8), or, finally, by applying a negative potential to the gate electrode (Fig. 6). In all cases, the effects can be rationalised taking into account a combination of drift and diffusion of mobile negative species and their following recombination with positive charges in the polymer or with the positive electrode.

The decay of PPC under $U_{DS} = 0$ V can be rationalised taking into account the diffusion of the negative species from the positive electrode area towards the bulk, followed by recombination. When the drain-source voltage is switched off, the persistent current vanishes. This feature confirms that there are no parasitic capacitor-discharge currents in studied FETs. In the absence of the external biasing field, the rate of recombination of the light-induced species is enhanced, they are, however, relatively long-lived and may exist without biasing voltage for a time extending up to a few hours. Re-application of U_{DS} effectively stops (or at least slows down) the diffusion of light-induced long-lived species, their concentration (and hence the persistent current), however, being lowered by the fast recombination during the period of $U_{DS} = 0$.

The reasoning presented above is supported by results of additional experiments: (i) illumination of TFT prior to applying U_{DS} and (ii) several inversions of the polarity of U_{DS} after illumination. As shown in Fig. 9, very low magnitude of persistent current in (i) points to the importance of the field-enhanced charge separation during illumination. The rapid decay of PPC in (ii) (Fig. 8) is a result of change in the direction of drift. Negative ions concentrated near the positive electrode after switching the polarity of U_{DS} move towards the bulk (both drift and diffusion currents) where they can recombine.

The most interesting phenomenon is a fast erasing of persistent current after applying a short pulse of negative potential to the gate electrode (Figs. 6 and 10), observed also by other authors in their studies of polythiophene FET [11,12]. The effect has been explained there by accumulation of polarons existing in the bulk of the poly(3-hexylthiophene) near the polymer–insulator interface, where the layer of negatively charged species was earlier formed. That caused rapid recombination and erasing of negatively charged layer screening the gate voltage. In our model, in which a gradient of concentration of mobile anions between drain and source is responsible for the appearance of PPC, the erasing effect may be explained in

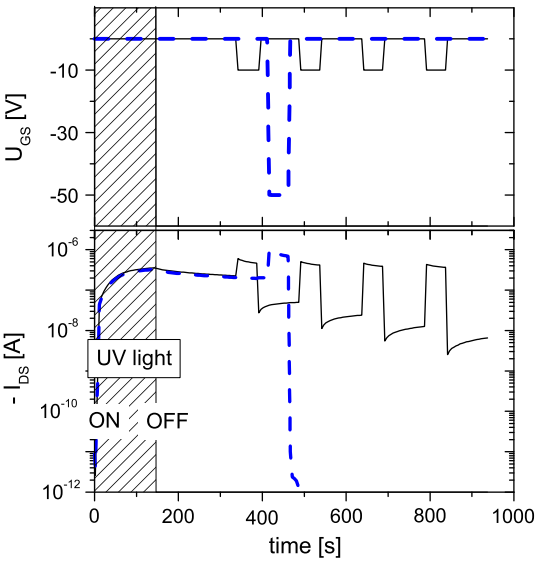

Fig. 10. Influence of U_{GS} on the kinetics of PPC erasing. $U_{DS} = -40$ V, $U_{GS} = 0$ V during illumination and was periodically switched to -10 V (solid line) or -50 V (dashed line) after illumination. The period of illumination with UV light is marked with a striped pattern.

the following way: When a negative gate voltage is applied, the transistor works in a usual way, i.e., a channel for positive carriers is formed between source and drain electrodes at the polymer–insulator interface in TFT. As a result, the current rises (cf. Fig. 6, 1450 s < t < 1500 s). Simultaneously, due to electric field originating from negative potential on gate electrode, the electric field gradient in the vicinity of source and drain electrodes drastically changes. This, together with diffusion, allows the negative ions to move into the bulk and recombine with positively charged polymer chains. The higher negative voltage is applied, the faster recombination occurs, resulting in erasing the persistent current (Fig. 10). Application of a positive gate potential decreases the measured I_{DS} current due to emptying of the channel. A temporary increase of PPC after switching off the gate voltage is the effect of discharging the gate – source and drain capacitance. The permanent post-photocurrent returns to its previous level after a few minutes.

It must be stressed, however, that the mechanism put forward in this paper, albeit explaining several features observed in our experiments, does not explain the magnitude of the persistent current: to maintain the measured currents for 3 days, ca. 10^{16} ions (i.e. ca. 10^{-8} moles of ions) should discharge – a number that by ca. one order of magnitude exceeds reasonable estimates. This means that the proposed mechanism of PPC, in our opinion, is not the only one operative in the poly(3-octylthiophene). Possibly, other mechanisms, postulated by other authors may contribute to a degree depending on the material, sample morphology, and experimental conditions.

5. Final remarks

A reversible opto-electronic switching with on–off ratio of about 10^6 has been observed in thin film field-effect transistor made of regioregular poly(3-octylthiophene). The turning on is realised by UV illumination, after which a long-lived persistent post-photocurrent occurs, and the switching off may be achieved upon applying a negative electrical potential to the gate electrode. The effect may be used in an opto-electronic memory device, where information is written optically and erased electrically in a reversible manner.

The origin of persistent post-photocurrent has been explained by formation of long-lived charge transfer polythiophene–oxygen complexes with their subsequent dissociation to negatively charged oxygen ions and holes on polythiophene chains. The gradient of negative ions formed at the positive electrode prevents fast decay of the current. Recombination of ions, that is erasing of persistent current, can be realised by changing the gradients of electric field near the source and drain electrodes either by applying negative voltage to the gate or by reversing drain-source voltage.

According to our model, the permanent post-photocurrent may occur in samples consisting of materials fulfilling two basic conditions: (i) the illumination results in the charge transfer and creation of well separated ionic pairs; (ii) the pairs are long-lived, one of the ionic species being mobile. In the case of poly(3-octylthiophene), the positive component of the pair are holes on the thiophene chains, the negative (mobile) one – single charged molecular oxygen. A similar scheme should also be operative for other poly(alkylthiophene)s as their energy levels do not differ much from those of poly(3-octylthiophene). One can presume that persistent post-photocurrent can be observed also in other classes of materials provided they fulfil the conditions mentioned above.

Acknowledgements

This work was supported by the Ministry of Science and Higher Education of Poland (Grant No. 3 T08E 084 30), and by the European Commission through the Human Potential Programme (Marie-Curie RTN BIMORE, Grant No. MRTN-CT-2006-035859). One of the authors (KJ) thanks Professor D.M. Taylor (University of Wales Bangor) and the British Council (Young Scientists Programme) for his stay in Bangor.

References

[1] H. Sirringhaus, C.W. Sele, T. Von Werne, C. Ramsdale, Manufacturing of organic transistor circuits by solution-based printing, in: H. Klauk (Ed.), Organic Electronics. Materials, Manufacturing and Applications, Wiley-VCH, Weinheim, 2007, pp. 294–322.
[2] D. Tobjörk, N.J. Kaihovirta, T. Mäkelä, F.S. Pettersson, R. Österbacka, Org. Electron. 9 (2008) 931–935.
[3] H. Sirringhaus, P.J. Brown, R.H. Friend, M.M. Nielsen, K. Bechgaard, B.M.W. Langeveld-Voss, A.J.H. Spiering, R.A.J. Janssen, E.W. Meijer, P. Herwig, D.M. de Leeuw, Nature 401 (1999) 685–688.
[4] G. Horowitz, Organic transistors, in: H. Klauk (Ed.), Organic Electronics. Materials, Manufacturing and Applications, Wiley-VCH, Weinheim, 2007, pp. 3–32.
[5] Ch. Lee, B.-Su Yoo, Chin. J. Phys. 28 (1990) 93–103.
[6] J. Kakalios, H. Fritzsche, Phys. Rev. Lett. 53 (1984) 1602–1605.
[7] C.H. Lee, G. Yu, A.J. Heeger, Phys. Rev. B 47 (1993) 15543–15553.
[8] V. Dyakonov, E. Frankevich, Chem. Phys. 227 (1998) 203–217.

[9] S. Dutta, K.S. Narayan, Phys. Rev. B 68 (2003) 125208.
[10] M. Ujimoto, W. Takashima, K. Kaneto, Thin Solid Films 499 (2006) 313–317.
[11] S. Dutta, K.S. Narayan, Adv. Mater. 16 (2004) 2151–2155.
[12] C.C. Chen, M.Y. Chiu, J.T. Sheu, K.H. Wei, Appl. Phys. Lett. 92 (2008) 143105.
[13] M. Mas-Torrent, P. Hadley, N. Crivillers, J. Veciana, C. Rovira, ChemPhysChem 7 (2006) 86–88.
[14] F. Gutman, L.E. Lyons, Organic Semiconductors, J. Wiley, New York, 1970.
[15] A.L. Briseno, S.C.B. Mannsfeld, P.J. Shamberger, F.S. Obuchi, Z. Bao, S.A. Jenekhe, Y. Xia, Chem. Mater. 20 (2008) 4712–4719.
[16] B. Mukherjee, M. Mukherjee, Y. Choi, S. Pyo, J. Phys. Chem. C 113 (2009) 18870–18873.
[17] K.S. Narayan, N. Kumar, Appl. Phys. Lett. 79 (2001) 1891–1893.
[18] M.J. Deen, M.H. Kazemeini, Proc. IEEE 93 (2005) 1312–1320.
[19] R.J. Kline, M.D. McGehee, E.N. Kadnikova, J. Liu, J.M.J. Frechet, M.F. Toney, Macromolecules 38 (2005) 3312–3319.
[20] J.-M. Verilhac, G. LeBlevennec, D. Djurado, F. Rieutord, M. Chouiki, J.-P. Travers, A. Pron, Synth. Met. 156 (2006) 815–823.
[21] S. Scheinert, T. Doll, A. Scherer, G. Paasch, I. Hörselmann, Appl. Phys. Lett. 84 (2004) 4427–4429.
[22] P. Lutsyk, K. Janus, unpublished results.
[23] M.S.A. Abdou, F.P. Orfino, Y. Son, S. Holdcroft, J. Am. Chem. Soc. 119 (1997) 4518–4524.
[24] L. Lüer, H.-J. Egelhaaf, D. Oelkrug, Opt. Mater. 9 (1998) 454–460.
[25] Ch.-Ch. Liu, Ch.-M. Yang, W.-H. Liu, H.-H. Liao, Sh.-Fu Horng, H.-F. Meng, Synth. Met. 159 (2009) 1131–1134.
[26] E.J. Meijer, A.V.G. Mangnus, B.-H. Huisman, G.W. 't Hooft, D.M. de Leeuw, T.M. Klapwijk, Synth. Met. 142 (2004) 53–56.
[27] S. Ogawa, T. Naijo, Y. Kimura, H. Ishii, M. Niwano, Jpn. J. Appl. Phys. 45 (2006) 530–533.

Organic Electronics 11 (2010) 498–502

Contents lists available at ScienceDirect

Organic Electronics

journal homepage: www.elsevier.com/locate/orgel

Letter

White phosphorescent polymer light-emitting devices based on a wide band-gap polymer derived from 3,6-carbazole and tetraphenylsilane

Gang Cheng [a], Teng Fei [b], Yi Zhao [a,*], Yuguang Ma [b,*], Shiyong Liu [a]

[a] State Key Laboratory on Integrated Optoelectronics, College of Electronic Science and Engineering, Jilin University, Changchun 130012, China
[b] State Key Laboratory of Supramolecular Structure and Materials, Jilin University, Changchun 130012, China

ARTICLE INFO

Article history:
Received 11 June 2009
Received in revised form 27 September 2009
Accepted 1 November 2009
Available online 2 December 2009

Keywords:
White emission
Light-emitting devices
Wide band-gap polymer
Phosphorescent complex

ABSTRACT

A wide band-gap polymer derived from 3,6-carbazole and tetraphenylsilane has been employed as a host for ternary phosphorescent iridium complexes in a white polymer light-emitting device (PLED). By studying both electroluminescence and photoluminescence of the doped polymeric light-emitting layer, it was found that both energy transfer and direct trapping attribute to the emission. Balanced white light with an external quantum efficiency of 4.26%, corresponding to a luminous efficiency of 8.55 cd/A and a power efficiency of 4.55 lm/W, as well as a color rendering index of 82 were achieved at 100 cd/m^2.

© 2009 Elsevier B.V. All rights reserved.

1. Introduction

White polymer light-emitting devices (PLEDs) have attracted increasing attention due to their advantage of allowing inexpensive solution processing technologies, such as spin-coating and ink-jet printing, which are more suitable for the preparation of large area displays and lighting sources [1]. To achieve high efficiency, host–guest systems are widely used in the emitting layer (EML) of PLEDs, due to the possibility of combining the advantages of high charge mobility of host polymers and high emission efficiency of guest dyes. Among various dyes employed, heavy metal complexes have shown theoretical 100% efficiency due to their efficient intersystem crossing from singlet to triplet excited states followed by relaxing through phosphorescence [2]. Therefore, the usage of this kind of phosphorescent dyes as emitters in white organic light-emitting devices based on both small molecular and polymeric hosts are intensively investigated. Compared to those based on small molecular hosts [3–6], white phosphorescent PLEDs are less efficient due to the deficiency of suitable polymeric hosts, which should have higher triplet energy than those of guest dyes, especially blue ones, to prevent backward energy transfer [7]. Although non-conjugated polymer poly(vinyl-carbazole) (PVK) has been used as a host in white PLEDs [8,9], it suffers from problems with charge injection and transport because of its non-conjugated nature. Therefore, the development of highly conductive conjugated polymers with high triplet energy is strongly desired. For this purpose, δ-Si structure has been introduced into conjugated polymers to interrupt the extended π-conjugation and achieve high values of triplet energy [10–14]. Complete energy transfers from the polymers to green phosphorescent dyes have been realized [10,11]. However, the triplet energy of this kind of polymers seems not high enough as hosts for blue phosphorescent dyes [12,14]. Recently, it was found that carbazole-based polymers with an interconnection of carbazole units in 3,6 positions have higher triplet energy than their 2,7-counterparts and are suitable hosts for green iridium complexes [15,16]. Based on these achievements, to realize a more suitable polymeric host for blue phosphorescent dyes, we have introduced δ-Si structure into a 3,6-carbazole based polymer and synthesized a wide band-gap poly-

* Corresponding authors. Fax: +86 43185168270 (Y. Zhao).
E-mail addresses: yizhao@jlu.edu.cn (Y. Zhao), ygma@jlu.edu.cn (Y. Ma).

1566-1199/$ - see front matter © 2009 Elsevier B.V. All rights reserved.
doi:10.1016/j.orgel.2009.11.029

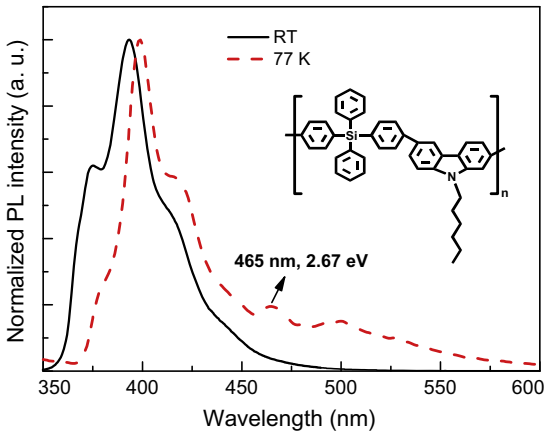

Fig. 1. Normalized PL spectra of P36HCTPSi in THF solution at RT and 77 K. Inset: chemical structure of P36HCTPSi.

mer, namely P36HCTPSi, as shown in the inset of Fig. 1. The synthesis and characterizations of this polymer have been reported elsewhere in detail [17]. From the onset of its absorption, a band gap of 3.26 eV has been estimated and a highest occupied molecular orbital (HOMO) level of 5.53 eV was calculated via cyclic voltammetry. Consequently, the lowest unoccupied molecular orbital (LUMO) energy level of 2.27 eV can be deduced. This wide band gap makes P36HCTPSi a possible candidate for a suitable host in white PLEDs.

In this paper, we demonstrate a white phosphorescent PLED based on P36HCTPSi, in which blue, green, and red phosphorescent dyes, bis[(4,6-difluorophenyl)pyridinato-N,C^2]-(picolinato)iridium (III) (FIrpic), *fac*-tris[2-(2-pyridyl-kN)-5-methylphenyl]iridium(III) [Ir(mppy)$_3$], and tris(1-phenylisoquinoline) iridium (III) [Ir(piq)$_3$] were respectively dispersed as an EML. In addition, monochromatic blue, green, and red PLEDs using single iridium complex doped P36HCTPSi as EMLs, were fabricated and characterized as well.

2. Experimental details

Devices consisting of ITO/PEDOT:PSS/EML/TPBI/LiF/Al were fabricated as follows; PEDOT:PSS was spin-coated onto cleaned ITO-coated glass substrate from its aqueous solution and then heated at 120 °C for 20 min to remove the residual water solvent at atmosphere. Doped P36HCTPSi was spin-coated from chlorobenze solution atop the PEDOT:PSS layer as an EML in a nitrogen-filled glove box. In the white device, the concentrations of P36HCTPSi, FIrpic, Ir(mppy)$_3$, and Ir(piq)$_3$ were respectively 5, 0.4, 0.04, 0.02 mg/ml, while in the monochromatic devices, the concentrations of host and guest were fixed at 5 and 0.4 mg/ml, respectively. After the spin-coating, all devices were transferred into a vacuum chamber immediately without exposure to the atmosphere. Inside the chamber, 40 nm-thick 2,2′,2″-(1,3,5-phenylene)tris(1-phenyl-1H-benzimidazole) (TPBI), 0.5 nm-thick LiF, and 200 nm-thick Al were in sequence deposited by thermal evaporation at a pressure of 4.0×10^{-4} Pa.

UV–visible absorption spectra were recorded on a UV-3100 spectrophotometer. Photoluminescent (PL) spectra were carried out with a RF-5301PC fluorometer. Atom force microscope (AFM) measurements in air were performed using a Solver scanning probe microscope (NT-MDT) in tapping mode. Electroluminescent (EL) spectra and Commission Internationale De ÍEclairage (CIE) coordination of these devices were measured by a PR650 spectrometer. The luminance–current density–voltage characteristics were recorded simultaneously with the measurement of the EL spectra by combining the spectrometer with a Keithley model 2400 programmable voltage–current source. All measurements were carried out at room temperature under ambient conditions.

3. Results and discussion

As has been reported in our previous paper [17], P36HCTPSi has a high thermal decomposition of 451 °C and a high glass transition of about 217 °C, indicating its good thermal stability. To estimate its triplet energy, PL spectra of P36HCTPSi in THF solution (10^{-5} M) at room temperature (RT) and 77 K were measured and compared in Fig. 1. The measurement was carried out with a RF-5301PC fluorometer with excitation at 330 nm. Compared with the spectrum at RT, where only fluorescent emission can be detected, a new emission band with a maximum peak at 465 nm appears, indicating that the triplet energy of the polymer might be around 2.67 eV [16,18]. This value is higher than that of FIrpic (2.62 eV) [19], the widely used blue phosphorescent emitter. Therefore, P36HCTPSi is expected to be a suitable host material for a full phosphorescent white PLED.

In order to testify this possibility, a white PLED respectively dispersing FIrpic (8 wt%), Ir(mppy)$_3$ (0.8 wt%), and Ir(piq)$_3$ (0.4 wt%) into P36HCTPSi host as red, green, and blue phosphorescent emitters was fabricated and characterized. Normalized EL spectra of this white device at differ-

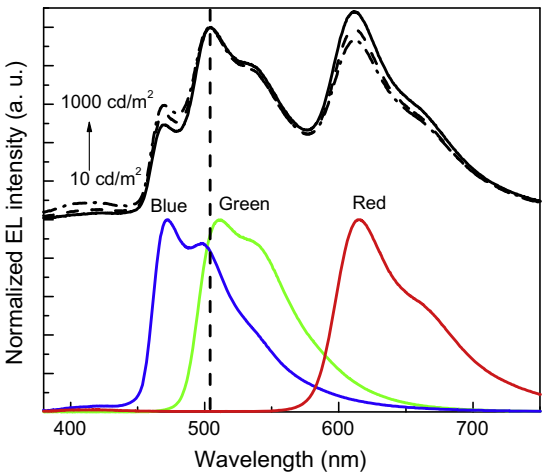

Fig. 2. Normalized EL spectra of the white PLED at 10, 100, and 1000 cd/m^2, as well as those of blue, green, and red devices at 100 cd/m^2. (For interpretation of the references to colour in this figure legend, the reader is referred to the web version of this article.)

ent luminance and those of the monochromatic devices at 100 cd/m^2 are compared in Fig. 2. Balanced emission is observed in the white device with three emission peaks at 469, 504, and 612 nm. According to the EL spectra of the monochromatic devices, the peaks at 469 and 612 nm are from the radioactive decay of FIrpic and Ir(piq)$_3$, respectively, while the one at 504 is an overlapped emission of FIrpic and Ir(mppy)$_3$ as indicated by the dashed line. It is worthy to note that a weak emission at around 415 nm becomes obvious at higher luminance, which can also be observed in the blue device, but not in green and red devices. To investigate the origin of this emission, PL spectrum of P36HCTPSi in film state and absorption spectra of FIrpic, Ir(mppy)$_3$, and Ir(piq)$_3$ in toluene were measured and shown in Fig. 3a. PL of P36HCTPSi with an main peak at 399 nm and a shoulder at round 415 nm shows better overlaps with the absorptions of Ir(mppy)$_3$ and Ir(piq)$_3$ than FIrpic, indicating more efficient Förster energy transfer from P36HCTPSi to Ir(mppy)$_3$ and Ir(piq)$_3$. Therefore, the incomplete energy transfer might be the main reason for the weak emission at 415 nm in the blue device. Since the concentration of FIrpic (8 wt%) is much higher than that of Ir(mppy)$_3$ (0.8 wt%) and
Ir(piq)$_3$ (0.4 wt%) in the white device, it is not surprised that this device shows a similar weak emission from the host like the blue one.

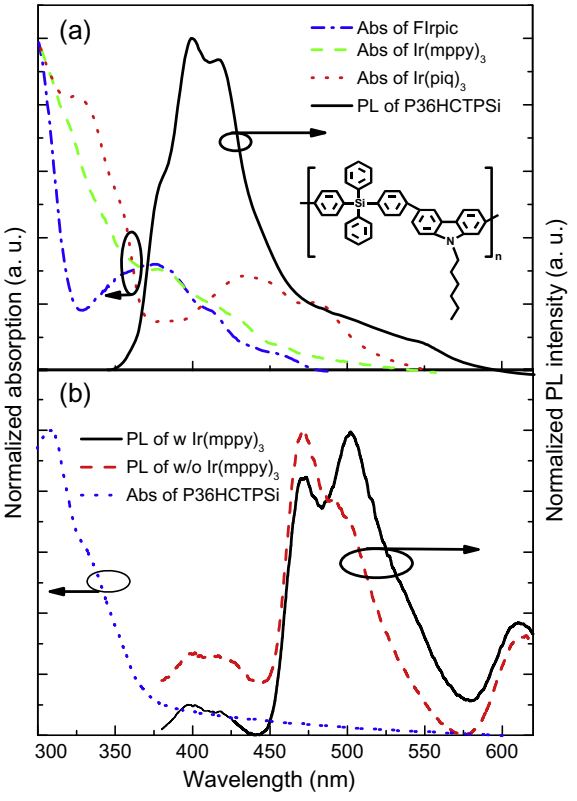

Fig. 3. (a) Normalized absorption spectra of FIrpic, Ir(mppy)$_3$, and Ir(piq)$_3$ in toluene and PL spectrum of P36HCTPSi in thin film; (b) Normalized absorption spectrum of P36HCTPSi in thin film and normalized PL spectra of blended films of P36HCTPSi (5 mg/ml):FIrpic (0.4 mg/ml):Ir(mppy)$_3$ (0.04 mg/ml):Ir(piq)$_3$ (0.02 mg/ml) and P36HCTPSi (5 mg/ml):FIrpic (0.4 mg/ml):Ir(piq)$_3$ (0.02 mg/ml).

To further investigate the mechanism behind the EL of the white device, blended films of P36HCTPSi (5 mg/ml):FIrpic (0.4 mg/ml):Ir(mppy)$_3$ (0.04 mg/ml):Ir(piq)$_3$ (0.02 mg/ml) and P36HCTPSi (5 mg/ml):FIrpic (0.4 mg/ml): Ir(piq)$_3$ (0.02 mg/ml) were spin-coated on glass substrates. The former has the same component as the EML of the white device, while Ir(mppy)$_3$ is absent in the latter. Normalized PL spectra of the blended films with and without Ir(mppy)$_3$ are shown in Fig. 3b, excited by radiation at a wavelength of λ = 330 nm, where P36HCTPSi has strong absorption (see Fig. 3b). Compared to the one without Ir(mppy)$_3$, PL of the film with Ir(mppy)$_3$ shows a increased intensity of Ir(piq)$_3$ and decreased intensities of P36HCTPSi and FIrpic, indicating energy transfers take place from both P36HCTPSi and FIrpic to Ir(mppy)$_3$, and successively to Ir(piq)$_3$. In addition, compared to EL of the white device shown in Fig. 1, PL of the film with Ir(mppy)$_3$ shows a stronger emission of P36HCTPSi and higher emission ratios of FIrpic/Ir(mppy)$_3$ and FIrpic/Ir(piq)$_3$, suggesting that direct charge trapping is involved in the EL process. According to the energy level diagram shown in Fig. 4, Ir(mppy)$_3$

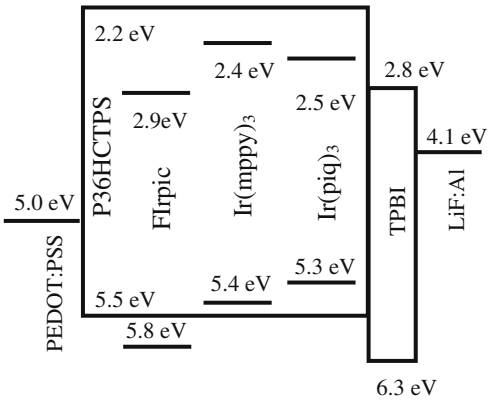

Fig. 4. Proposed energy diagram of the materials used in our devices.

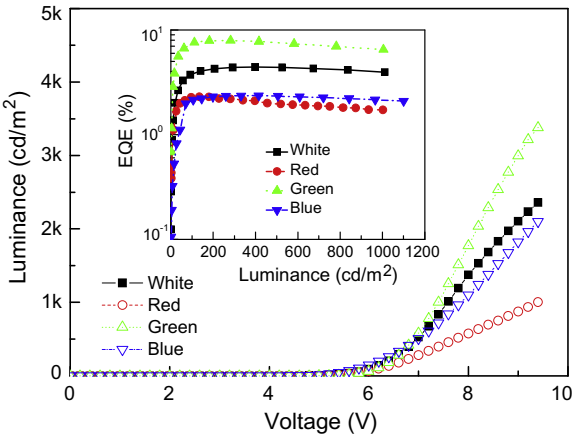

Fig. 5. Luminance–voltage characteristics of white, blue, green, and red devices; Inset: EQE-luminance curves of these devices. (For interpretation of the references to colour in this figure legend, the reader is referred to the web version of this article.)

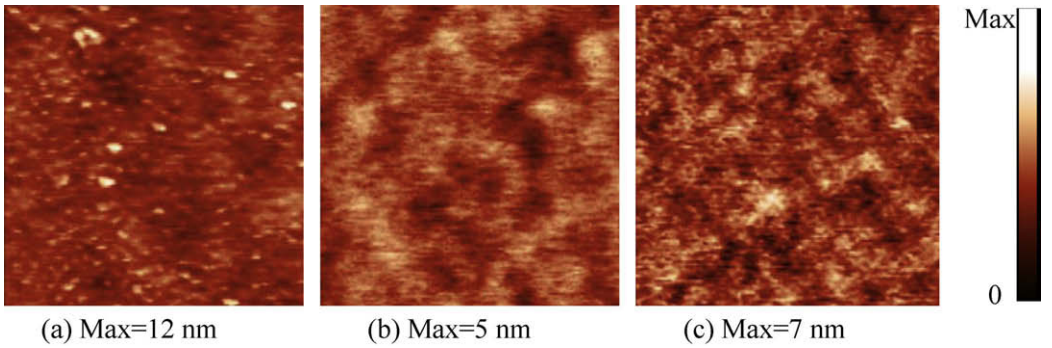

Fig. 6. AFM height imagines of P36HCTPSi films doped with (a) FIrpic, (b) Ir(mppy)$_3$, and (c) Ir(piq)$_3$, with concentration of 8 wt%. The size for all images is 2.5 × 2.5 μm.

and Ir(piq)$_3$ molecules in the polymer are traps for both holes and electrons, which facilitates the direct injection of both charges. For FIrpic molecules, on the other hand, only electrons can be trapped in. This might be another reason for the relatively stronger host emission in the blue device. As discussed previously in Fig. 3b, energy transfers occur in the white device from higher energy iridium complexes to lower energy ones, it is understandable that the concentration of FIrpic (8 wt%) is higher than a Ir(piq)$_3$ (0.4 wt%) by 20 times. The concentration of Ir(mppy)$_3$ (0.8 wt%), on the other hand, is only two times higher than Ir(piq)$_3$. To understand the relatively similar concentration of Ir(mppy)$_3$ and Ir(piq)$_3$, external quantum efficiency (EQE)-luminance curves of blue, green, and red devices are plotted in the inset of Fig. 5. The maximum EQE (7.9%) of Ir(mppy)$_3$ is much higher than those of FIrpic (2.4%) and Ir(piq)$_3$ (2.3%). This high EQE demands a lower concentration of Ir(mppy)$_3$ to achieve the balanced white emission. AFM measurements were applied on P36HCTPSi films doped with FIrpic, Ir(mppy)$_3$, and Ir(piq)$_3$ to investigate the relatively low efficiencies of blue and red devices. Herein, the doping concentration is 8 wt% in all films. As shown in Fig. 6, the morphology of Ir(mppy)$_3$ and Ir(piq)$_3$ doped films are quite homogeneous while slight phase-separation is observed in the FIrpic doped film, which might lower the efficiency of the blue device. For the red device, the low efficiency may be attributed to the poor match between the energy levels of P36HCTPSi and Ir(piq)$_3$ [20].

Luminance–voltage characteristics of these devices are shown in Fig. 5. Luminances of blue, green, red, and white devices at 9.4 V are 1000, 3300, 2100, and 2300 cd/m^2, respectively. Main performances at different luminance of the white device are listed in Table 1; EQE, luminous efficiency, power efficiency, and CRI at 100 cd/m^2 are 4.26%, 8.55 cd/A, 4.55 lm/W, and 82, respectively. CIE coordinates slightly vary from (0.40, 0.46) to (0.38, 0.45) with the increasing luminance from 10 to 1000 cd/m^2 because of the change of EL spectrum as shown in Fig. 1.

Table 1
Performances of the white device at difference luminance.

L[a] (cd/A)	EQE (%)	LE[b] (cd/A)	PE[c] (lm/W)	CIE coordinates (*x*, *y*)	CRI
10	1.37	2.79	1.75	0.40, 0.46	81
100	4.26	8.70	4.55	0.39, 0.45	82
1000	3.96	7.95	3.28	0.38, 0.45	82

[a] Luminance.
[b] Luminous efficiency.
[c] Power efficiency.

4. Conclusion

We demonstrated a white phosphorescent PLED by employing a wide band-gap polymer P36HCTPSi as a host material for blue, green, and red emission phosphorescent iridium complexes. Energy transfers from the host to guests and from higher energy iridium complexes to lower energy ones are observed. Direct trapping is found playing an important role in EL as well. In our white PLED, EQE, luminous efficiency, power efficiency, and CRI at 100 cd/m^2 are 4.26%, 8.55 cd/A, 4.55 lm/W, and 82, respectively.

Acknowledgements

The authors are grateful for financial support from the National Science Foundation of China (Grant Nos. 60906021, 60977024, 60876032, 60706018, 60907013, and 20834006), and the Ministry of Science and Technology of China (Grant Nos. 2009CB623605, 2010CB327701).

References

[1] R.H. Friend, R.W. Gymer, A.B. Holmes, J.H. Burroughes, R.N. Marks, C. Taliani, D.D.C. Bradley, D.A.D. Santos, J.L. Brédas, M. Lögdlund, W.R. Salaneck, Nature 397 (1999) 121.
[2] M.A. Baldo, D.F. O'Brien, Y. You, A. Shoustikov, S. Sibley, M.E. Thompson, S.R. Forrest, Nature 395 (1998) 151.
[3] B.W. D'Andrade, M.E. Thompson, S.R. Forrest, Adv. Mater. 14 (2002) 147.
[4] G. Cheng, Y.F. Zhang, Y. Zhao, Y.Y. Lin, C.Y. Ruan, S.Y. Liu, T. Fei, Y.G. Ma, Y.X. Cheng, Appl. Phys. Lett. 89 (2006) 043504.
[5] S.-J. Su, E. Gonmori, H. Sasabe, J. Kido, Adv. Mater. 20 (2008) 4189.
[6] Q. Wang, J.Q. Ding, D.G. Ma, Y.X. Cheng, L.X. Wang, X.B. Jing, F.S. Wang, Adv. Funct. Mater. 19 (2009) 84.
[7] S. Tokito, T. Iijima, Y. Suzuri, H. Kita, T. Tsuzuki, F. Sato, Appl. Phys. Lett. 83 (2003) 569.
[8] F. Huang, P.-I. Shih, C.-F. Shu, Y. Chi, A.K.-Y. Jen, Adv. Mater. 21 (2009) 361.
[9] Y.H. Xu, R.Q. Yang, J.B. Peng, A.A. Mikhailovsky, Y. Cao, T.-Q. Nguyen, G.C. Bazan, Adv. Mater. 21 (2009) 584.
[10] X. Zhang, C. Jiang, Y. Mo, Y. Xu, H. Shi, Y. Cao, Appl. Phys. Lett. 88 (2006) 051116.
[11] Y. Mo, R. Tian, W. Shi, Yong Cao, Chem. Commun. 2005 (2005) 4925.

[12] K.-F. Shao, X.-J. Xu, G. Yu, Y.-Q. Liu, L.-M. Yang, Chem. Lett. 35 (2006) 404.
[13] C.-H. Yang, K.-H. Fang, C.-H. Chen, I.-W. Sun, Chem. Commun. 2004 (2004) 2232.
[14] A. van Dijken, J.J.A.M. Bastiaansen, N.M.M. Kiggen, B.M.W. Langeveld, C. Rothe, A. Monkman, I. Bach, P. Stössel, K. Brunner, J. Am. Chem. Soc. 126 (2004) 7718.
[15] Y. Mo, X. Jiang, Y. Cao, Org. Lett. 9 (2007) 4371.
[16] Z. Wu, Y. Xiong, J. Zou, L.i. Wang, J. Liu, Q. Chen, W. Yang, J. Peng, Y. Cao, Adv. Mater. 20 (2008) 2359.
[17] T. Fei, G. Cheng, D.H. Hu, P. Lu, Y.G. Ma, J. Polym. Sci., Part A: Polym. Chem. 47 (2009) 4784.
[18] F.-C. Chen, G. He, Y. Yang, Appl. Phys. Lett. 82 (2003) 1006.
[19] B.W. D'Andrade, R.J. Holmes, S.R. Forrest, Adv. Mater. 16 (2004) 624.
[20] C.-H. Chien, F.-M. Hsu, C.-F. Shu, Y. Chi, Org. Electron. 10 (2009) 871.

Organic Electronics 11 (2010) 503–507

Contents lists available at ScienceDirect

Organic Electronics

journal homepage: www.elsevier.com/locate/orgel

Letter

Enhancement of performance for blue organic light emitting devices based on double emission layers

Qingjin Qi, Xiaoming Wu, Yulin Hua *, Qingchuan Hou, Musen Dong, Zhiyong Mao, Bin Yin, Shougen Yin

School of Materials Science and Engineering, Tianjin University of Technology, Tianjin 300384, China
Key Laboratory of Display Materials and Photoelectric Devices (Tianjin University of Technology), Ministry of Education, Tianjin 300384, China
Tianjin Key Lab for Photoelectric Materials and Devices, Tianjin 300384, China

ARTICLE INFO

Article history:
Received 16 September 2009
Received in revised form 26 November 2009
Accepted 29 November 2009
Available online 5 December 2009

Keywords:
Recombination region
Balance
Double emitting layers
OLED

ABSTRACT

Blue organic light emitting devices (OLEDs) with high efficiency were reported by the designing of double emission layers (DELs) and changing doping concentration of fluorescent material in DELs. The carrier injection in each emission layer was greatly improved with the aid of different doping concentration, which resulted in carriers' recombination with a well balance. The maximum current efficiency and power efficiency of the OLEDs were 18.99 cd/A and 11.63 lm/W at 2.0 mA/cm^2, respectively, and the maximum brightness of the optimum device was 40,040 cd/m^2 at 14 V. Consequently, besides a better color and efficiency stabilization, these devices with the DELs presented a higher current efficiency and brightness than the conventional devices with single emission layer (SEL) by more than 70%.

© 2009 Elsevier B.V. All rights reserved.

1. Introduction

White organic light emitting devices (WOLEDs) have been developed intensively in the past 20 years due to its great potential applications in large flat panel display and solid-state lighting [1–4]. There are two main methods to realize white light emitting including the mixture of red, green and blue three prime colors or blue and orange-yellow complementary colors. Apparently, blue light emitting plays a key role for the white light devices, which is still confronted with some problems such as low efficiency and short lifetime compared with other colors-emitting [5]. In order to improve the EL performance and optimize the structure of blue OLEDs, researchers have paid great attentions for this recently i.e., Divayana et al. reported a blue OLED with exciton-confining structure [6]. Jonghee Lee et al. demonstrated an adjustment of interlayer between transporting and emitting layer [7]. Bacsa et al. reported a multi-layer configuration for blue OLEDs [8]. In addition, double emitting layers structure was employed into blue OLEDs by utilizing phosphorescent materials doped in hosts, as a result, broadening carrier recombination zone in the EMLs and reducing carrier accumulation in the interface were achieved [9,10]. i.e. Meng-Ting Lee et al. described the blue OLEDs with double emission layers (DELs) through using same phosphorescent material doped in two different hosts, which achieved the current efficiency of 29.5 cd/A, and the power efficiency of 21 lm/W at 4.4 V [9]. However, the phosphorescent materials have some common drawbacks such as quenching phenomena of triplet–triplet excited states, and relatively short lifetime. Fluorescent materials can avoid these drawbacks efficiently, but its efficiency is lower compared with phosphorescent materials. Previously, our research group reported a single emitting layer (SEL) blue OLED doping with fluorescent material, which showed the current efficiency of 11.8 cd/A and brightness of 25,690 cd/m^2, respectively, [11]. Therefore, it is expected that the EL performances of blue

* Corresponding author. Address: Institute of Physical Material, Tianjin University of Technology, Nankai District, Tianjin 300384, PR China. Tel.: +86 022 60215378; fax: +86 022 60215226.
E-mail address: yulinhua@tjut.edu.cn (Y. Hua).

1566-1199/$ - see front matter © 2009 Elsevier B.V. All rights reserved.
doi:10.1016/j.orgel.2009.11.032

OLEDs doping with fluorescent materials would be enhanced efficaciously through employing DELs structure. By now, there is no any report that utilized the fluorescence DELs by using same host and same dopant with different doping concentration for the blue OLED.

In this paper, we demonstrated a high efficiency blue OLED with DELs, which was realized through modulating the doping concentration of the fluorescent material N-(4-((E)-2-(6-((E)-4-(diphenylamino)styryl)naphthalen-2-yl)vinyl)phenyl)-N-phenylbenzenamine(N-BDAVBi) in the host 4,4′-N,N′-dicarbazole-biphenyl(CBP) with wide band gap. Doping concentration is 2%, 5% and 8% in each emission layer. This novel structure of DELs could expand light-emitting region and improve carrier combination rate efficiently. Moreover, the EL performances of this device is better than those of SEL OLEDs doped with fluorescent materials, which has the satisfactory current efficiency of a high value closed to that of the OLEDs doped with phosphorescent materials.

2. Experimental

The device's structure and energy level diagram of DELs are shown in Fig. 1, N,N′-bis(naphthalen-1-yl)-N,N′-bis(phenyl)-benzidine(NPB) and 4,7-diphnenyl-1,10-phenanthroline(BPhen) were used as hole transport and electron transport materials, respectively. 4,4′-N,N′-dicarbazole-biphenyl(CBP) acted as the bipolar host material, and N-(4-((E)-2-(6-((E)-4-(diphenylamino)styryl)naphthalen-2-yl)vinyl)phenyl)-N-phenylbenzenamine(N-BDAVBi) acted as blue fluorescent material, respectively. And different doping concentration of N-BDAVBi with 8%, 5%, 2% doped in each emitting layer was shown in Fig. 1. All the organic layers were deposited onto a pre-cleaned ITO glass substrate with a sheet resistance of 20 Ω/sq, by thermal evaporation coating system at a pressure of about 2×10^{-4} Pa. Two light-emitting layers were deposited unsuccessively in twice during the process of thermal evaporation, which results in the EML I, EML II and their interface. From Devices A–F, the double EMLs were constructed by CBP:N-BDAVBi/CBP:N-BDAVBi, in which the doping concentration of EML I/EML II were 8%/8%, 5%/5%, 2%/2%, 8%/2%, 8%/5% and 5%/2%, respectively. The followed by a deposited LiF, which as a buffer layer, and an Al as cathode, all of the above step without breaking the vacuum. The deposition rates and thickness of the various layers were monitored using a quartz crystal oscillator. The evaporation rates were 0.1–0.3 nm/s for the each organic layer, and 1 nm/s for the LiF layer and Al cathode. The electroluminescent (EL) spectra and the brightness of the devices were measured with the PR650 spectra scan spectrometer. The current and current density versus voltage characteristics were measured simultaneously with the EL spectra by using the Keithley model 2400 programmable voltage–current source. And all of the records were carried out at room temperature.

3. Results and discussion

It was universally acknowledged that the mobility of holes transport materials is far greater than that of electron transport materials for general organic materials [12]. This unbalancedness will reduce the combination rate of electrons and holes in the light-emitting layers and lead to performance degradation for devices. In this report, we used NPB and BPhen as the hole and the election transport materials, respectively, for the balance of carrier injection in view of their similar mobility of each. As shown in Fig. 1, the highest occupied molecular orbital (HOMO) level is 5.4 eV, 5.9 eV and 5.3 eV for NPB, CBP and N-BDAVBi, respectively. An injection barrier about 0.5 eV appears at the NPB/CBP interface, which is unfavorable for holes injection into host material (CBP). Alternatively, an injection barrier about 0.1 eV at the NPB/N-BDAVBi interface promotes holes transport directly and may be trapped at the doping site. On the other hand, the lowest unoccupied

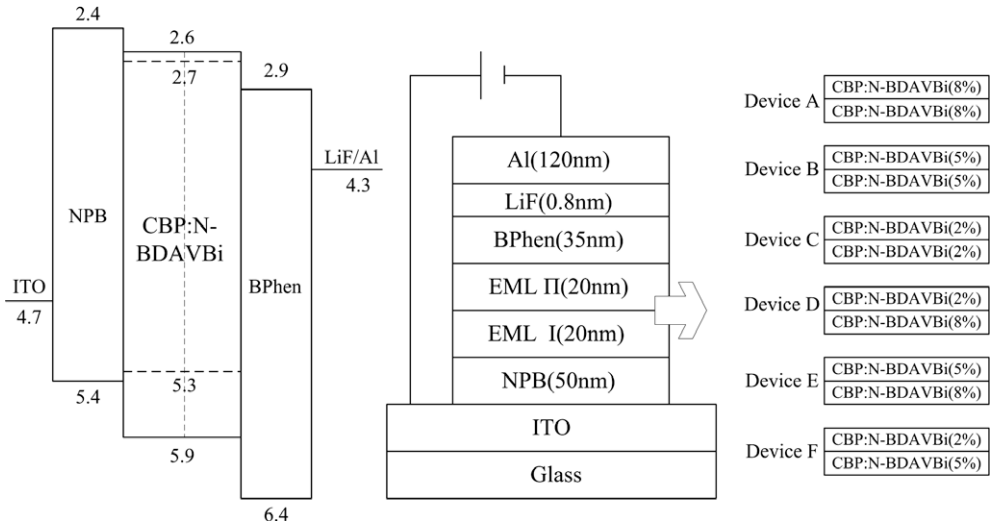

Fig. 1. Configurations of Devices A–F with DELs and the Energy level diagram of device (unit: eV).

molecular orbital (LUMO) level is 2.9 eV, 2.6 eV and 2.7 eV for BPhen, CBP and N-BDAVBi, respectively, and the energy barrier is about 0.3 eV (at the interface of BPhen/CBP) and 0.2 eV (at the interface of BPhen/N-BDAVBi). Therefore, electrons can be injected into host and dopant easily with a higher mobility [13]. In order to improve the carrier balance and the combination rate in the exciton region, we constructed DELs (Devices A–F). Firstly, we focused our work on the DELs with the same doping concentration in each light-emitting layer for each device, corresponding to the light-emitting layer's structure of the three devices presented below.

Device A: CBP: N-BDAVBi (20 nm, 8%)/CBP: N-BDAVBi (20 nm, 8%)
Device B: CBP: N-BDAVBi (20 nm, 5%)/CBP: N-BDAVBi (20 nm, 5%)
Device C: CBP: N-BDAVBi (20 nm, 2%)/CBP: N-BDAVBi (20 nm, 2%)

The dependence of current efficiency on current density, current density and brightness on voltage of devices were presented in Fig. 2a and b, respectively. It is derived that the current efficiency decreases with the increasing of current density, and the current density and brightness increases with the increasing of voltage for a certain doping concentration. The maximum current efficiency and brightness were about 10.1 cd/A and 26,750 cd/m^2 at 2.0 mA/cm^2, respectively, when the doping concentration is optimized to 8% (for both of EML I and EML II). There is a slight enhancement in brightness for the double emitting layer devices with the same doping concentration compared with the SEL devices reported by our group [11]. For Devices A–C, holes could easily across from EML I to EML II, and electrons could easily across from EML II to EML I for the double light-emitting layers with the high doping concentration in each emission layer, which would result in efficient combination for the holes and electrons in the light-emitting region. But holes could not easily inject into emitting layer due to the high barrier (NPB/CBP), especially for the case of the lower doping concentration. Therefore, high doping concentration was needed to reduce the barrier for the injection of holes in emission layer [12].

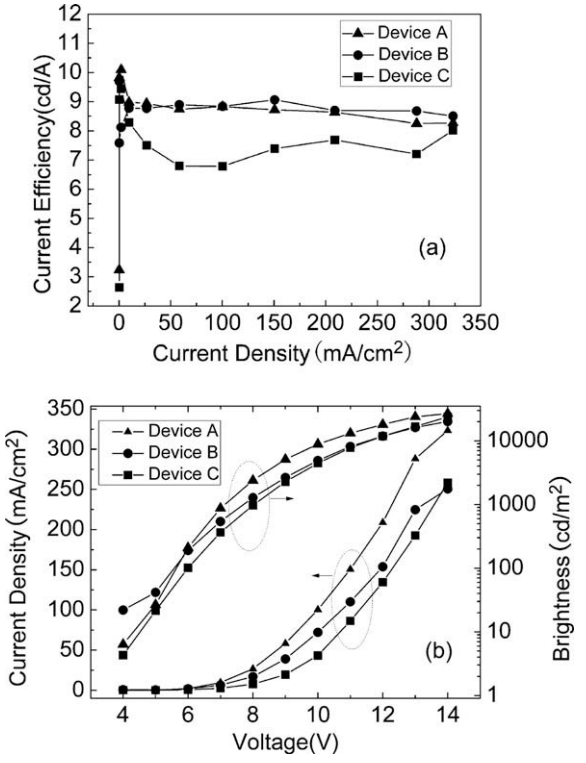

Fig. 2. Result for DELs Devices A–C, in each layer with the same doping concentration. (a) Dependence of current efficiency on current density. (b) Dependences of current density and brightness on voltage.

For the further consideration, the emitting layer with low doping concentration was considered as the assistant emitting region relative to the dominating emitting region which doped with a higher concentration. At the low driving voltage, the carriers could be easily injected into the assistant emitting region, which due to the superior mobility of hole than that of the electron in N-BDAVBi. For this reason, the carrier balance could be fulfilled and excitons combination rate could be enhanced in EML II. With the increase of the voltage, more electrons could be injected into the dominating emitting region to combine the holes to form the excitons in the EML I, which resulted in a better balance of the carriers in both EML I and EML II with high and low doping concentration, respectively, at a large range of driving voltage. This clue provides an optimal route that with high doping concentration (in EML I) and low doping concentration (in EML II) simultaneously to achieve excellent EL performance of these devices.

Nextly, we investigated the DELs doping with different concentration in each emission layer. EML configurations of the devices were demonstrated by followings.

Device D: CBP: N-BDAVBi (20 nm, 8%)/CBP: N-BDAVBi (20 nm, 2%)
Device E: CBP: N-BDAVBi (20 nm, 8%)/CBP: N-BDAVBi (20 nm, 5%)
Device F: CBP: N-BDAVBi (20 nm, 5%)/CBP: N-BDAVBi (20 nm, 2%)

Apparently, the introduction of the DELs using different doping concentration in each emission layer improves the device's EL performances significantly, which showed in Fig. 3a and b. It was worth to note that the EL performances of Devices D–F have been enhanced efficiently compared with those of Devices A–C, shown in Table 1, which presented the EL performances of all devices. The maximum current efficiency and brightness of Devices D–F were about 18.99 cd/A, 17.15 cd/A, 17.24 cd/A and 33,050 cd/m^2, 31,010 cd/m^2, 40,040 cd/m^2, respectively. Apparently, the efficiency was nearly 1.7 times higher than that of the SEL device. Additionally, In DELs devices, the current efficiency and brightness both were increased greatly with the increase of voltage (from 4.5 V to14 V), which is more quickly than the increasing trend in SEL device. With a higher current efficiency for Devices D–F, the recombina-

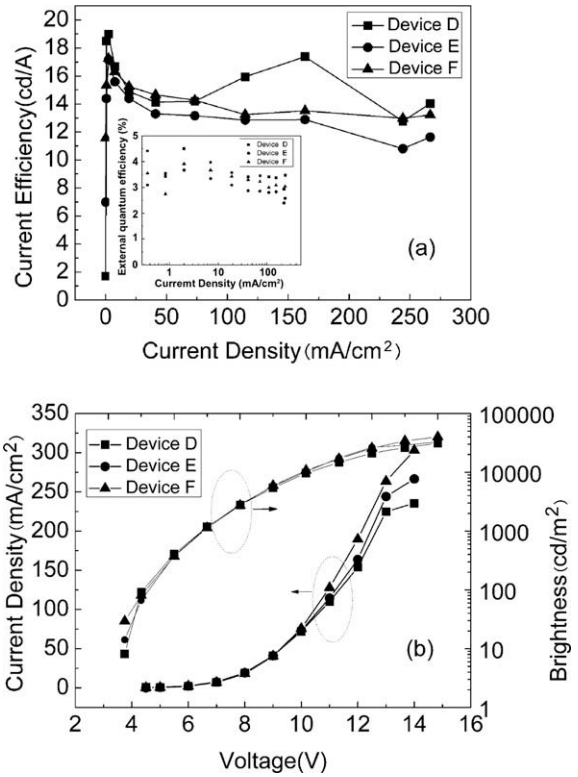

Fig. 3. EL performance for DELs Device D–F, in each layer with the different doping concentration. (a) Dependence of current efficiency on current density. (b) Dependences of current density and brightness on voltage. The insert of (a) exhibits external quantum efficiency on current density.

tion rate of two types of carriers was greatly improved, which could be mainly ascribed to the enhancement of carriers balance in the dominating and assistant regions at different driving voltage. With the increase of the driving voltage, the carriers' combination regions would be broadened and emitting light regions would be away from the cathode gradually [14], which could prevent accumulation of the excessive excitons around the cathode.

The enhancement of performances could be explained with the double emitting regions model. When the operating voltage was lower, the recombination between holes and electrons was only appeared in the interface of EML II/ETL as assistant emitting region due to their different mobility. But, when the operating voltage was increased, the electrons injected from cathode were further transferred to interface of EML I/EML II and the dominating emitting region with a larger width occurred with that the assistant emitting region moves to it gradually. As a result, the recombination rate of electrons and holes was further improved by comparing with the SEL devices which only have a narrower emitting region.

At a certain current density, it was obvious that current efficiency and brightness of the devices doped with varied concentration in EML I and EML II were higher than that of the device with same doping concentration in them. It was well known that more electrons and holes were recombined in else at a higher doping concentration, and the device performances could be enhanced to a certain extent. For the EML I and EML II with same doping concentration (about 8%) in which holes and electrons were accumulated in the assistant emitting region, on the contrary, only a little of holes and electrons were appeared in the dominating emitting region, so it is more difficult to achieve the effect of broading emitting region by doping with high concentration. Otherwise, although the device of DELs could obtain wider emitting region for the low doping concentration, but recombination rate of the holes and electrons was lower in the emitting region. So the EL performance of devices could not be obviously enhanced. In this work the different doping concentration adjusted in EMLs (Device F) were employed to avoid the accumulation of excitons farthest in the assistant emitting region and improve the recombination rate of excitons in the dominating emitting region. Fig. 3 showed that the optimization balance of excitons was realized through the lower doping concentration in the assistant emitting region (2%) and the higher doping concentration in dominating emitting region (8%), respectively. Therefore, the performances of devices were enhanced through optimizing doping concentration in the each EML. Furthermore, the stable current efficiency in the Devices D–F was achieved, which exhibited a high value at the high brightness in Fig. 3. Meanwhile, the insert of the Fig. 3a shows the external quantum efficiency (EQE%) of the Devices D–F with a stable efficiency characteristic at the driving voltage of 4.5–14 V. The photoelectric performances of all devices were shown in Table 1. Therefore, the current efficiency of Device D was

Table 1
the photoelectric performances of Devices A–F.

Device		EML I N-BDAVBi (wt.%)	EML II N-BDAVBi (wt.%)	Maximum current efficiency (cd/A)	Maximum brightness (cd/m^2)	Maximum EQE (%)	CIE coordinates at 6 V	From 6 V to 10 V current efficiency roll off (%)
Double emission layers	A	8	8	10.1	26,750	2.32	(0.164, 0.263)	12
	B	5	5	9.7	23,660	1.97	(0.158, 0.290)	16
	C	2	2	9.4	20,100	2.06	(0.149, 0.289)	28
	D	8	2	18.99	33,050	4.41	(0.161, 0.263)	15
	E	8	5	17.15	31,010	3.67	(0.169, 0.321)	21
	F	5	2	17.24	40,040	3.91	(0.162, 0.287)	17
Single emission layer		Reported in our previous work[11]		11.5	25,690		(0.148, 0.291)	

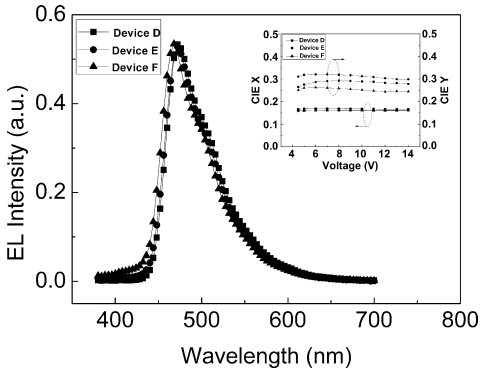

Fig. 4. Normalized EL spectra of Devices D–F at the driving voltage of 10 V. The CIE chromaticity of Devices D–F shown in the insert at the driving voltage of 4.5–14 V.

higher than that of others. This result may be owed to the superiority of DELs.

Fig. 4 showed the normalized EL spectra of the Devices D–F with different doping concentration of N-BDAVBi at 10 V, in which the dominant peaks locate at 472, 470 and 468 nm, respectively. Accordingly, the blue shift occurs in the dominant peaks from Device D to F. This could be explained that the recombination region would transferred from the EML II/ETL to the EML I/EML II, gradually, and the excitons could reduce the excessive accumulation around the EML II/ETL. Meanwhile, the EL intensity increase corresponding to the Devices D–F. The insert of Fig. 4 showed the CIE chromaticity of Devices D–F at which the operating voltage varies from 4.5 V to 14 V gradually, which presented the good color stability at different driving voltage.

4. Conclusions

In summary, a strategy to optimize and enhance the performance of blue OLED with the designing of double emission layers (DELs) and changing doping concentration of fluorescent material in DELs. Devices with the DELs structure can expand the light-emitting region efficiently compared with the single emitting layer devices. In addition, an optimal route of dominating emitting region with high doping concentration and assistant emitting region with low doping concentration was employed to balance the injection ration of holes and electrons at the interface of emission layers. A result shows that the EL performance of the DELs devices can be enhanced efficiently and color and efficiency stability could also be improved greatly. The maximum current efficiency and power efficiency of device were 18.99 cd/A and 11.63 lm/W at 2.0 mA/cm^2, respectively. Moreover, the maximum brightness of 40,040 cd/m^2 at 14 V was also achieved in the optimized device.

Acknowledgements

This work was supported by the National Natural Science Foundation of China (NSFC) (No. 60906022, 60876046), the Scientific Developing Foundation of Tianjin Education Commission (No. 20070805), the Tianjin Key Discipline of Material Physics and Chemistry Acknowledgements.

References

[1] Tang, S.A. VanSlyke, Appl. Phys. Lett. 51 (1987) 913.
[2] J. Tseng, R.C. Chiechi, F. Wudl, Y. Yang, Appl. Phys. Lett. 88 (2006) 093512.
[3] B.W. D'Andrade, S.R. Forrest, Adv. Mater. (Weinheim, Ger.) 16 (2004) 1585.
[4] M.T. Lee, J.S. Lin, M.T. Chu, M.R. Tseng, Appl. Phys. Lett. 93 (2008) 133306.
[5] Z.Q. Gao, B.X. Mi, C.H. Chen, K.W. Cheah, Y.K. Cheng, W.-S. wen, Appl. Phys. Lett. 90 (2006) 123506.
[6] Y. Divayana, X.W. Sun, B.J. Chen, Appl. Phys. Lett. 89 (2006) 173511.
[7] Jonghee Lee, Jeong-Ik Lee, Ki-Im Song, Su Jin Lee, Hye Yong Chu, Appl. Phys. Lett. 92 (2008) 203305.
[8] W.S. Bacsa, M. Schaer, L. Zuppiroli, J. Appl. phys. 84 (1998) 10.
[9] Meng-Ting Lee, Jin-Sheng Lin, Miao-Tsai Chu, Mei-Rurng Tseng, Appl. Phys. Lett. 94 (2009) 083506.
[10] H. Fukagawa, K. Watanabe, T. Tsuzuki, S. Tokito, Appl. Phys. Lett. 93 (2008) 133312..
[11] Yu Wang, Yulin Hua, Xiaoming Wub, Lijuan Zhang, Qingchuan Hou, Feng Guan, Nan Zhang, Shougen Yin, Xiaoman Cheng, Org. Electr. 9 (2008) 692–698.
[12] H.S. Bang, D.C. Choo, T.W. Kim, J.H. Park, J.H. Seo, Y.K. Kim, Mol. Cryst. Liq. Cryst. 498 (2009) 265–273.
[13] Byung Doo Chin, Soo-Hyeong Lee, Jai Kyeong Kim, Chang Hee Lee, in: Proc. SPIE, vol. 6333, 2006, pp. 633315–633318.
[14] Jun Yeob Lee, Ukjeon-dong, Suji-gu, Yongin, Gyeonggi, Mol. Cryst. Liq. Cryst. 498 (1) (2009) 131–139.

Organic Electronics 11 (2010) 509–513

Contents lists available at ScienceDirect

Organic Electronics

journal homepage: www.elsevier.com/locate/orgel

Top-gate-type ambipolar organic field-effect transistors with indium–tin oxide drain/source electrodes using polyfluorene derivatives

Hirotake Kajii *, Kyohei Koiwai, Youhei Hirose, Yutaka Ohmori

Center for Advanced Science and Innovation, Osaka University, 2-1 Yamada-oka, Suita, Osaka 565-0871, Japan

ARTICLE INFO

Article history:
Received 4 November 2009
Received in revised form 26 November 2009
Accepted 3 December 2009
Available online 11 December 2009

Keywords:
Ambipolar organic field-effect transistor
Polyfluorene
Top-gate
Light-emitting device

ABSTRACT

The characteristics of solution processed top-gate-type organic field-effect transistors (OFETs) with indium–tin oxide (ITO) drain/source electrodes using polyfluorene derivatives were investigated. An OFET with poly(9,9-dioctylfluorene) (F8) as an active layer, which contains only a fluorene backbone, exhibited ambipolar characteristics with hole and electron field-effect mobilities of approximately 10^{-3} cm^2 V^{-1} s^{-1}. All OFETs with fluorene derivatives exhibited ambipolar characteristics because the value of the work function of the ITO electrode is approximately in the middle between the highest occupied molecular orbital and lowest unoccupied molecular orbital levels of fluorene derivatives. Fluorene derivatives can conduct both holes and electrons. Ambipolar OFETs with F8 and a fluorene derivative doped in F8 can be applied to various color tunable light-emitting devices.

© 2009 Elsevier B.V. All rights reserved.

1. Introduction

Organic semiconductors have attracted considerable attention due to their simple and low-cost processing, and potential electronic and optoelectronic applications. In particular, they have demonstrated the possibility of electronic and optoelectronic devices fabricated by solution processing for large-area and flexible devices. Recently, organic field-effect transistors (OFETs) have been extensively studied in view of their applications to low-cost, large-area, flexible electronics [1–9]. High performance of organic field-effect transistors (OFETs) fabricated using highly crystalline organic materials have been realized; however, solution processing has still attention in simple fabrication process for large area devices. The characteristics of polymer devices fabricated by solution processing are strongly dependent on the self-organized structure. OFETs with various device structures have been reported to show ambipolar characteristics and light emission [8–18]. In particular, ambipolar materials are useful for fabricating OFETs, because they can be used either as a p-channel or a n-channel by changing the polarity of the gate voltage.

Poly(9,9-dioctylfluorene) (F8), which contains only a fluorene backbone, exhibits blue emission and various morphological behaviors [19–22]. Fluorene-type polymers have emerged as an important class of conducting polymers due to their efficient emission, high stabilities and relatively high mobility. Fluorene-type polymers also have the potential for full color emission via energy transfer to longer wavelength emitters in blends with other emissive materials.

For n-channel OFETs, the injected carrier is the electron, and therefore it is preferable for the source electrode work-function value to be lower. However, most metals with a low work-function (i.e. Ca, Li, Cs, etc.) are very sensitive to oxygen and moisture in the air, and thus it is difficult to fabricate and handle devices using these metals. Indium–tin oxide (ITO) is suitable for the electrode of organic devices such as organic light-emitting diodes and organic photovoltaics due to its optical transparency. The work function of ITO is relatively low.

* Corresponding author. Tel./fax: +81 6 6879 4213.
E-mail address: kajii@casi.osaka-u.ac.jp (H. Kajii).

1566-1199/$ - see front matter © 2009 Elsevier B.V. All rights reserved.
doi:10.1016/j.orgel.2009.12.004

In this study, we investigated the characteristics of top-gate type OFETs with ITO drain/source electrodes using polyfluorene derivatives. We also discuss ambipolar characteristics of OFETs and the application of light-emitting field-effect transistors by varying the gate voltage.

2. Experimental procedure

A top-gate structure, whose device has a gate electrode on the gate insulating layer, was employed for the OFETs based on polyfluorene derivatives. Poly(9,9-dioctylfluorene) (F8, Mw = 82k, ADS129BE) and poly[(9,9-dihexyl-2,7-(2-cyanodivinylene)-fluorenylenyl-2,7-diyl)] (CN-PDHFV, Mw = 20k, ADS127GE) purchased from American Dye Source Inc. were used as the organic layer without further purification. Fluorene copolymers of poly[(9,9-dioctylfluorenyl-2,7-diyl)-co-bithiophene] (F8T2, Mw = 52k) and poly[(9,9-dioctylfluorenyl-2,7-diyl)-co-(1,4-benzo-{2,1′,3}-thiadiazole)] (F8BT, Mw = 363k) were supplied by Sumitomo Chemical Co., Ltd. Fig. 1 shows the device structure and schematic energy level diagrams of F8, F8T2 and F8BT films. The energy levels of the highest occupied molecular orbitals (HOMOs) of polyfluorene derivatives were taken from previously published work [15,23,24]. The bandgap energy was simply estimated from the edge of the absorption spectrum. Polished ITO precoated on a glass substrate, obtained commercially, was used for the source and drain electrodes. Surface morphologies were observed by atomic force microscopy (AFM; JEOL, JSPM-5200). The average surface roughness of the ITO was estimated to be about 0.5 nm from the AFM image. The channel length and width were 0.1 and 2 mm, respectively. The substrate was degreased with solvents and cleaned in a UV ozone chamber. A semiconducting layer was formed by spin coating from a xylene solution onto patterned ITO electrodes, which served as source and drain electrodes, in air. The typical thickness of the semiconducting layer was approximately 50–70 nm. Organic layers were baked at 290 °C in a dry nitrogen glove box, and Poly(methyl methacrylate) (PMMA) was then used as a gate insulator on the active layer without intermixing. Using anhydrous *n*-butyl acetate as a solvent, a PMMA solution was spun onto an active layer and baked above 150 °C. The typical thickness of the gate insulator was approximately 600 nm. An Au gate electrode with a 30-nm thickness was vacuum evaporated at a background pressure of about 10^{-4} Pa onto the polymer gate insulating layer formed on the polyfluorene semiconducting layer. The deposition rate and thickness of the deposited electrode were monitored using a quartz crystal oscillator.

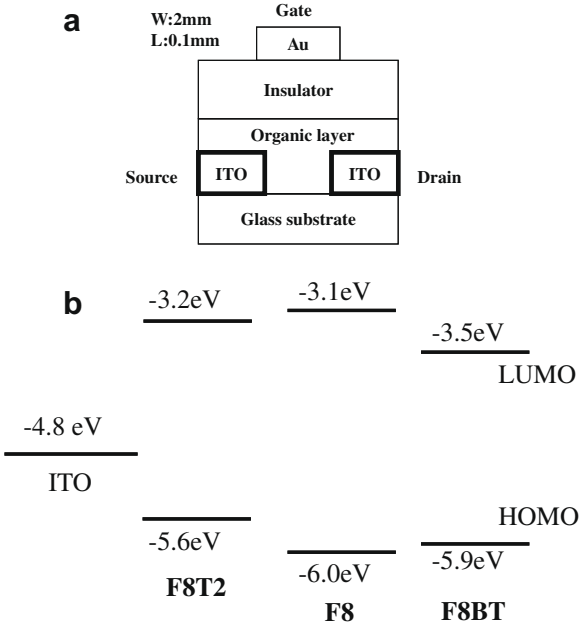

Fig. 1. (a) Device structure and (b) energy diagram of the materials used in this study.

After the deposition of the Au gate electrode, devices were exposed to air. Then, measurements of electrical characteristics of the OFETs were carried out at room temperature in a vacuum chamber with a background pressure of about 10^{-4} Pa after evacuation for more than 6 h. The current–voltage characteristics were obtained using 2400 and 6517 A source meters (Keithley). The electroluminescence (EL) output was measured using a photodiode (Hamamatsu Photonics). The EL spectra were measured using a photonic multichannel spectral analyzer (Hamamatsu Photonics PMA-11). For the measurement of EL spectra, the devices were covered with a glass plate and encapsulated by epoxy resin in an argon gas atmosphere to prevent oxidation of the electrode and the organic layer.

3. Results and discussion

Poly(9,9-dioctylfluorene) (F8), which contains only a fluorene backbone, exhibits blue emission and various morphological behaviors. Polyfluorene-based block copolymers of F8T2 with thiophene group as a hole transporter and F8BT with an electron-withdrawing group were used as hole- and electron-transport materials, respectively. The value of the work function of the ITO electrode is located approximately in the middle between the highest occupied molecular orbital (HOMO) and lowest unoccupied molecular orbital (LUMO) levels of fluorene derivatives, as shown in Fig 1b. Therefore, for top-gate type OFETs with fluorene derivatives as active layers, both holes and electrons can be expected to be injected from the ITO drain/source electrodes into the HOMO and LUMO levels of fluorene derivatives by applying a voltage.

It is well known in OFETs that charge carriers run a few nanometers around the insulator/semiconductor interface[25,26]. The OH groups at the interface between the polymer gate insulator and the organic active layer interfere with n-type carrier transport[8,9,15,18,27]. PMMA, which does not contain electron-trapping groups, such as OH, was used as a gate insulator.

Fig. 2a and b show the output characteristics of top-gate type OFETs with F8. For both the hole and electron enhancement modes, the drain–source current increased superlinearly at lower drain–source voltages. The injection barriers of both holes and electrons from ITO drain/source

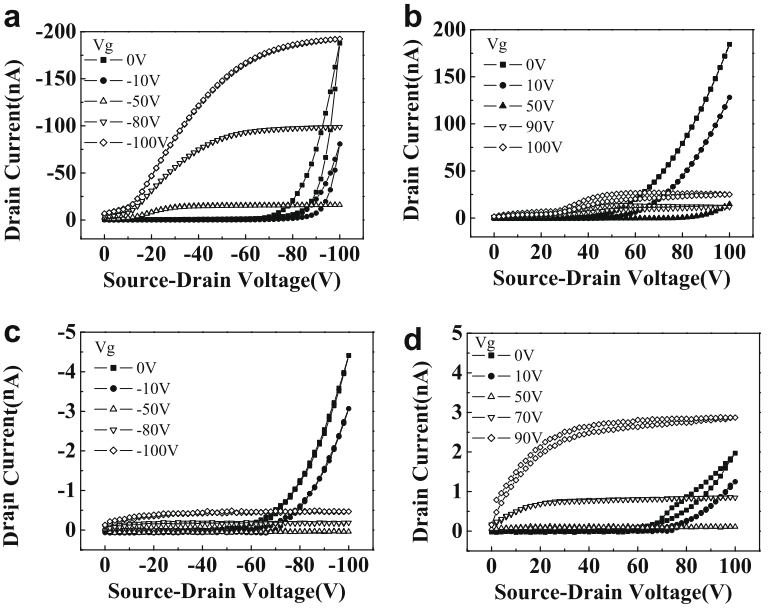

Fig. 2. Output characteristics of top-gate-type OFETs with (a and b) F8 and (c and d) CN-PDHFV, for different gate voltages in the hole and electron enhancement modes, respectively.

electrodes into the HOMO and LUMO levels are relatively high, more than 1 eV. These superlinear currents result from the relatively large contact resistance for both hole- and electron-injection. From measurements of drain–source current characteristics, shown in Fig. 2a, the saturation characteristics were typical for a p-channel OFET working in the accumulation mode. Output characteristics of the F8 device operated in the electron enhancement mode are shown in Fig. 2b. The leakage drain–source current increased superlinearly with drain–source voltage at lower gate voltages. Application of positive gate voltage suppressed this component, and typical saturation characteristics of an n-channel OFET were observed at high gate voltages. That is, ambipolar characteristics were obtained from the top-gate-type F8 device with ITO drain/source electrodes. Hysteresis was observed due to the charge trapping in the electron enhancement mode.

Fig. 3 shows transfer characteristics of top-gate-type OFETs based on F8. The hole mobility and threshold voltage of the top-gate type F8 device were estimated to be $\mu = 7.2 \times 10^{-4}\,cm^2\,V^{-1}\,s^{-1}$ and $V_{th} = -24$ V, respectively, at the drain-source voltage V_{DS} of −100 V. For n-channel OFET operation, the effective electron mobility and threshold voltage were estimated to be $\mu = 1.2 \times 10^{-3}\,cm^2\,V^{-1}\,s^{-1}$ and $V_{th} = 61$ V, respectively, at a drain-source voltage V_{DS} of 100 V. For the F8 device, the threshold voltage in the hole enhancement mode is lower than that in the electron enhancement mode because the hole injection barrier is lower than the electron injection barrier, as shown in Fig. 1b.

The LUMO level of CN-PDHFV with the electron-withdrawing cyano group to the vinylene bonds is lower than that of F8. For bottom-gate-type CN-PDHFV OFET with Ca drain/source electrodes, only n-channel characteristics have been reported [28]. By using the top-gate type OFET

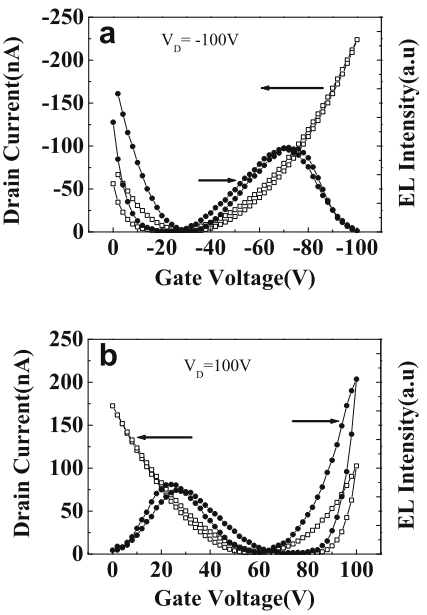

Fig. 3. Transfer characteristics and corresponding light output of the F8 device for different drain voltages of (a) −100 V and (b) 100 V.

structure with ITO electrodes, ambipolar characteristics were observed, as shown in Fig. 2c and d. It is to be noted that fluorene derivatives can conduct both holes and electrons. That is, fluorene polymers as transport materials for holes and electrons are thus essential in functionalizing electronic devices.

Transfer characteristics of top-gate-type OFETs based on F8T2 and F8BT are shown in Fig. 4a and b. For top-gate-type OFETs with F8T2 and F8BT as active layers,

ambipolar characteristics were also observed. As shown in Table 1, F8, F8T2 and F8BT devices exhibited ambipolar characteristics with both hole and electron field-effect mobilities of approximately 10^{-3} cm^2 V^{-1} s^{-1}. For devices with bottom-contact/top-gate geometry, charge injection can be expected to occur a large area away from the edge of electrodes and be aided due to the influence of the applied gate filed because the drain/source electrodes and the gate electrode were overlapped[15]. Although these devices with ITO source/drain electrodes have relatively large contact resistance, these carrier mobilities are in relative agreement with those of bottom-gate-type OFETs with Au and Ca drain/source electrodes for p- and n-channel OFETs measurements, respectively [8].

For the p-channel OFET characteristics, the threshold voltage of the F8T2 device was lower than that of the F8 device. This is because the injection barrier of holes from ITO drain/source electrodes into the HOMO level of F8T2 is relatively lower than that of F8. On the other hand, for n-channel OFET characteristics, the threshold voltage of OFET based on F8BT with an electron-withdrawing group was lower than that of the F8 device, because the injection barrier of electrons from ITO into the LUMO level of F8BT is relatively lower than that of F8. These results suggest that by OFET measurements using top-gate-type OFETs with ITO drain/source electrodes, the carrier transport characteristics in various polyfluorene derivatives can be characterized.

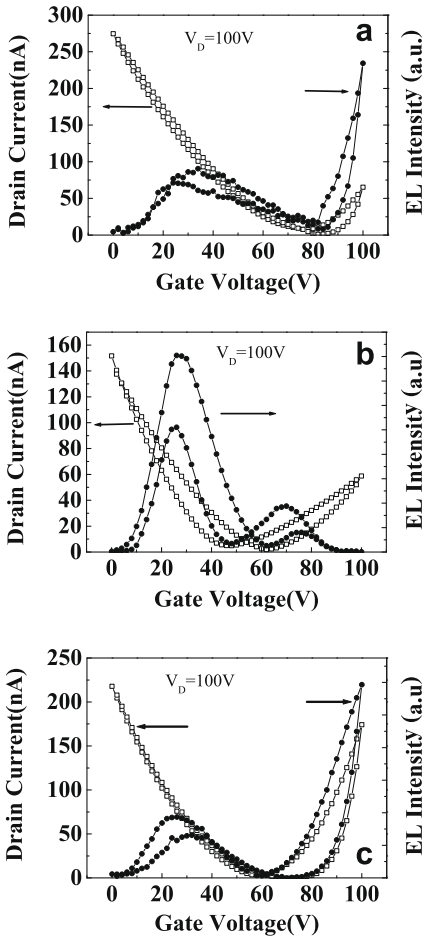

Fig. 4. Transfer characteristics and corresponding light output of (a) F8T2, (b) F8BT and (c) F8:F8BT devices for a positive drain voltage of 100 V.

For this ambipolar OFET with F8, blue light emission was observed by varying the gate voltage as shown in Figs. 3 and 5. A peak of EL intensity was observed when hole current dominated at gate voltages between 0 (−30) and 60 (−100) V. The EL intensity was at a minimum when the drain current reached a minimum. On the other hand, EL intensity increased with gate voltage when electron current dominated above approximately 60 (−20) V. The typical output power of devices was on the order of 10^{-1} nW. For ambipolar OFETs with F8BT and F8T2, yellow–green and yellow light emissions, respectively, from F8BT and F8T2 were also observed. It is to be noted that top-gate-type fluorene OFETs with ITO drain/source electrodes can be applied to light-emitting transistors.

For both the F8 and F8T2 devices, a peak of EL intensity was observed when hole current dominated as shown in Figs. 3 and 4a. The behavior of the gate voltage dependence of the EL intensity in the F8T2 device is the same as that in the F8 device. On the other hand, for an F8BT device, two EL intensity peaks were observed when either hole or electron currents dominated. In ambipolar OFETs, simultaneous electron and hole injection can be achieved by applying the gate voltages. For both F8 and F8T2 devices, the electrons cannot be injected easily in organic layer at lower gate voltages due to high injection barrier of electrons although the electron mobility is the same as the hole mobility as shown in Table 1. Therefore, EL intensity continued to increase at high gate voltages when the injected electrons increased with gate voltages. These results suggest that carrier transport of holes is predominant in our F8 and F8T2 devices.

The dye doping method is of practical importance because it allows for easy improvement in performance, such as color tunability. OFETs with 5 wt.% F8BT doped in F8 as an active layer also showed ambipolar characteristics as indicated in Fig. 4c. For an F8:F8BT device, white emission with a CIE coordinate of (0.34, 0.40) was obtained due to blue and yellow–green emission from F8 and F8BT. This emission mechanism from the F8:F8BT device can be interpreted in terms of the following two mechanisms. In the first mechanism, electrons and holes are injected from the source and drain electrodes, respectively, to the F8. As a result, excitons are formed on the F8 and excitonic energy is then effectively transferred to the F8BT by the Förster energy transfer process. In the second mechanism, injected holes and electrons are directly trapped on F8BT molecules; excitons are then formed after carrier recombination. As a result, the emission from F8BT molecules is obtained. The transfer characteristics of the F8:F8BT device are the same as those of the F8 device as shown in Fig. 4c. That is, for the F8:F8BT device, carrier transfer is still dominant in the F8 film. This result suggested that excitons are formed on the F8, and the excitonic energy transfers to the F8BT by the Förster energy transfer process, because the band gap of F8BT is lower than that of F8.

Table 1
HOMO and LUMO levels of fluorene derivatives, and field-effect mobility and threshold voltage obtained from polyfluorene OFET measurements.

Polymer	HOMO	LUMO	Field-effect mobility ($cm^2V^{-1}s^{-1}$)		Threshold voltage (V)	
	(eV)	(eV)	Hole	Electron	Hole	Electron
F8	6.0	3.1	0.7×10^{-3}	1.2×10^{-3}	−24	61
F8T2	5.6	3.2	1.0×10^{-3}	1.3×10^{-3}	−7	71
F8BT	5.9	3.5	0.8×10^{-3}	0.4×10^{-3}	−18	40
CN-PDHFV	6.0[28]	3.6[28]	0.7×10^{-5}	4×10^{-5}	−20	30

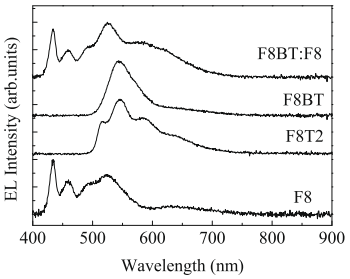

Fig. 5. EL spectra of the F8, F8BT, F8T2 and F8:F8BT devices.

4. Conclusions

We demonstrated the characteristics of solution processed top-gate type ambipolar polyfluorene OFETs with ITO drain/source electrodes. An OFET with F8 as an active layer, which contains only a fluorene backbone, exhibited ambipolar characteristics with hole and electron field-effect mobilities of approximately $10^{-3}\,cm^2\,V^{-1}\,s^{-1}$. All OFETs with fluorene derivatives exhibited ambipolar characteristics because the value of the work function of the ITO electrode is located approximately in the middle between HOMO and LUMO levels of fluorene derivatives. It is to be noted that fluorene derivatives can conduct both holes and electrons. By OFET measurements using top-gate type OFETs with ITO drain/source electrodes, carrier transport characteristics in various polyfluorene derivatives can be characterized. Ambipolar OFETs with F8, F8BT and F8T2 exhibited blue, yellow–green and yellow EL emissions, respectively, with varying gate voltage. For F8 and F8T2 devices, a peak of the EL intensity was observed when hole current dominated. On the other hand, for an F8BT device, two peaks of the EL intensity were observed when either hole or electron currents dominated. These results suggested that carrier transport of holes is predominant in the F8 and F8T2 films. White emission was also observed from an ambipolar OFET with 5 wt.% F8BT doped in F8 as an active layer. We thus demonstrated that top gate-type fluorene OFETs with ITO drain/source electrodes can be applied to light-emitting transistors.

Acknowledgements

This research was partially supported financially by Industrial Technology Research Grant Program in 2000 from New Energy and Industrial Technology Development Organization (NEDO) of Japan, and by the Ministry of Education, Culture, Sports, Science and Technology in Japan (MEXT) under a Grant-in-Aid for Scientific Research (A) #20246058, a Priority Area "Super-Hierarchical Structures" #19022020, under a grant for the Osaka University Global COE Program, "Center for Electronic Devices Innovation", and a Grant-in-Aid of Special Coordination Funds for Promoting Science and Technology. Authors thank Sumitomo Chemical Co. Ltd., for providing fluorene derivatives of F8T2 and F8BT.

References

[1] K. Kudo, D.X. Wang, M. Iizuka, S. Kuniyoshi, K. Tanaka, Synth. Met. 111–112 (2000) 11.
[2] H. Sirringhaus, T. Kawase, R.H. Friend, T. Shimoda, M. Inbasekaran, W. Wu, E.P. Woo, Science 290 (2000) 2123.
[3] K. Kaneto, W.Y. Lim, W. Takashima, T. Endo, M. Rikukawa, Jpn. J. Appl. Phys. 39 (2000) L872.
[4] T. Minakata, Y. Natsume, Synth. Met. 153 (2005) 1.
[5] M. Ando, M. Kawasaki, S. Imazeki, H. Sasaki, T. Kamata, Appl. Phys. Lett. 85 (2004) 1849.
[6] H. Kawaguchi, T. Someya, T. Sekitani, T. Sakurai, IEEE J. Solid-State Circuits 40 (2005) 177.
[7] T. Someya, Y. Kato, S. Iba, H. Kawaguchi, T. Sakurai, IEEE Trans. Electron Devices 52 (2005) 2502.
[8] L.L. Chua, J. Zaumseil, J.F. Chang, E.C.-W. Ou, P.K.-H. Ho, H. Sirringhaus, R.H. Friend, Nature 434 (2005) 194.
[9] T. Takenobu, S.Z. Bisri, T. Takahashi, M. Yahiro, C. Adachi, Y. Iwasa, Phys. Rev. Lett. 100 (2008) 066601.
[10] H. Tada, H. Touda, M. Takada, K. Matsushige, Appl. Phys. Lett. 76 (2000) 873.
[11] T. Yasuda, T. Goto, K. Fujita, T. Tsutsui, Appl. Phys. Lett. 85 (2004) 2098.
[12] C. Rost, S. Karg, W. Riess, M.A. Loi, M. Murgia, M. Mucccine, Appl. Phys. Lett. 85 (2004) 1613.
[13] J.S. Swensen, C. Soci, A.J. Heeger, Appl. Phys. Lett. 87 (2005) 253511.
[14] M.A. Loi, C. Rost-Bietsch, M. Murgia, S. Karg, W. Riess, M. Muccini, Adv. Func. Mater. 16 (2006) 41.
[15] J. Zaumseil, C.L. Donley, J.-S. Kim, R.H. Friend, H. Sirringhaus, Adv. Mater. 18 (2006) 2708.
[16] K. Yamane, H. Yanagi, A. Sawamoto, S. Hotta, Appl. Phys. Lett. 90 (2007) 162108.
[17] T. Sakanoue, M. Yahiro, C. Adachi, H. Uchiuzou, T. Takahashi, A. Toshimitsu, Appl. Phys. Lett. 90 (2007) 171118.
[18] T. Takahashi, T. Takenobu, J. Takeya, Y. Iwasa, Adv. Func. Mater. 17 (2007) 1623.
[19] Y. Ohmori, M. Uchida, K. Muro, K. Yoshino, Jpn. J. Appl. Phys. 30 (1991) L1941.
[20] M. Grell, D.D.C. Bradley, G. Ungar, J. Hill, K.S. Whitehead, Macromolecules 32 (1999) 5810.
[21] K. Asada, T. Kobayashi, H. Naito, Jpn. J. Appl. Phys. 45 (2006) L247.
[22] H. Kajii, D. Kasama, Y. Ohmori, Jpn. J. Appl. Phys. 47 (2008) 3152.
[23] Y. Hino, H. Kajii, Y. Ohmori, Thin Solid Films 499 (2006) 359.
[24] T. Hamasaki, T. Morimune, H. Kajii, S. Minakata, R. Tsuruoka, T. Nagamachi, Y. Ohmori, Thin Solid Films 518 (2009) 548.
[25] C. Tanase, E.J. Meijer, P.W.M. Blomd, D.M. de Leeuw, Org. Electron. 4 (2003) 33.
[26] M. Kiguchi, M. Nakayama, K. Fujikawa, K. Ueno, T. Shimada, K. Sakai, Jpn. J. Appl. Phys. 42 (2003) L1408.
[27] S. Fukuda, H. Kajii, H. Okuya, T. Ogata, M. Takahashi, Y. Ohmori, Jpn. J. Appl. Phys. 47 (2008) 1307.
[28] T. Yasuda, K. Fujita, T. Tssusui, Jpn. J. Appl. Phys. 43 (2004) 7731.

Organic Electronics 11 (2010) 514–520

Contents lists available at ScienceDirect

Organic Electronics

journal homepage: www.elsevier.com/locate/orgel

Modeling nanoparticle embedded organic memory devices

H. Houili [a], E. Tutiš [b], R. Izquierdo [a,*]

[a] Département d'Informatique, Université du Québec à Montréal, Case Postale 8888, Succursale Centre-Ville, Montréal, Canada QC H3C 3P8
[b] Institute of Physics, Bijenička Cesta 46, P.O. Box 304, HR-10000, Zagreb, Croatia

ARTICLE INFO

Article history:
Received 28 August 2009
Received in revised form 5 December 2009
Accepted 5 December 2009
Available online 21 December 2009

Keywords:
Organic semiconductor
Organic diode
Non-volatile resistive memory
Nanoparticle charging

ABSTRACT

We present a model for organic bistable devices (OBDs) embedded with metallic nanoparticles. The model takes into account charge transport through the organic material, field-dependent charge carrier mobility, and injection from the electrodes. The charge trapped by the nanoparticles induces space charge effects that reduce the electric field at the electrode and inhibit charge injection leading to the low conductivity state of the OBD. Between the two situations where the nanoparticles are neutral and charged with 15 units of charge, the ON-to-OFF ratio is more than two orders of magnitude. We also discuss the relevance of our model to various OBD devices in the literature.

© 2009 Elsevier B.V. All rights reserved.

1. Introduction

Non-volatile organic thin film memory devices are being explored as a replacement to flash memory or as an alternative to some devices in specific niches of applications. The latter include applications requiring some characteristics which are specific to organic semiconductor based devices, such as flexibility, low cost and large area [1,2]. Organic memory devices with different organic materials and device architectures were explored in the literature. Two types of devices were mainly studied;: single layer and three layer devices. Among single layer devices there are devices where the organic is a small molecule material or a polymer sandwitched between two metal electrodes [3,4], and devices with dispersed metal (usually gold) nanoparticles in the organic [2,5]. Then there are the devices where the nanoparticles are embedded between two layers of the organic material [6]. We refer to this device here as the three layer device. All these devices show bistability and switch reliably at a threshold voltage V_{th} between an OFF- and ON-states which correspond to the low and high impedance states. The memory state is retained for hours to days even when the bias voltage is suppressed.

The three layer device with the embedded metallic layer (Al cathode/AIDCN or Alq3/Al metal layer/AIDCN or Alq3/Al anode) has received considerable interest [5,6]. Although the experimental results seem to be reproducible, the parameters that control the device characteristics (e.g. the threshold voltage, the ON/OFF ratio, and erase voltage) remain still hard to determine accurately. In fact, those parameters depend most probably on the detailed structure of the intermediate metal layer and on the presence of impurities in the organic material. The middle metal layer must have a nominal thickness of 5–10 nm for the device to switch [5]. In fact, the metal layer must be granular (i.e. disconnected nanoparticles) in order to obtain bistability [2,5]. Recently, Wang et al. [7] reported a new method to achieve a good control of the nanostructured metal middle layer using self-assembled gold nanoparticles (NPs). The resulting OBDs show strong and highly reproducible electrical bistability. In fact, in this case, unlike in the case of the three layer devices where the nanostructured middle layer is produced by thermal evaporation, we have accurate data and control on the structure of the middle layer, such as the size of the nanoparticles and their density distribution.

* Corresponding author. Tel.: +1 514 987 3000x3307.
E-mail address: izquierdo.ricardo@uqam.ca (R. Izquierdo).

1566-1199/$ - see front matter © 2009 Elsevier B.V. All rights reserved.
doi:10.1016/j.orgel.2009.12.006

In addition to the recent results on organic semiconductor devices, electric bistability was already observed in inorganic device as early as 1960s [8,9]. The devices consisted of a thin oxide layer sandwiched between metal electrodes (e.g. cathode(Al)/insulator(SiO)/anode(Au)). However, in such case, the switching was observed only after applying a high voltage; the so called "forming process". Simmons and Verderber proposed a model (henceforth referred to as SV model) that accounted for all the experimental observations. In the SV model, the charge transport is due to tunneling between localized states in the SiO matrix. The space charge effects of the filled localized states (or traps), reduces the electric field at the electrode, which inhibits tunneling and results in an OFF-state. Based on the similarity of the observed characteristics between this device and the organic three layers device, Bozano et al. [10] suggested that the SV model could be applied to their organic devices. However, one can easily figure out that the direct application of the SV model to organic devices is confronted with many difficulties. For instance, transport takes place via tunneling from the electrodes to the localized states in the SV device. In the organic device no such tunneling between the electrodes and the middle metal layer is possible, as the organic layer thickness is more than 30 nm. Furthermore, the mobility of charge carriers in the organic layer should also be considered; unlike in the case of the insulating matrix in the SV device.

Wu et al. [11] attributed the mechanism of bistability in the three layer devices to the separation and storage of charge at the middle metal nanocluster layer, which subsequently induces charges through the organic layer. This process is similar to the field effect process in the channel of an organic transistor. However, it is unlikely that such a mechanism is able to increase the conductivity of the whole organic layer, which is some 30 nm thick. For instance, in organic field effect transistors, the channel where charge induction is effective is 1nm thick in spite of the very high gate polarization field. Moreover, simple electrostatic considerations lead to the conclusion that at maximum charge separation (permitted by the bias voltage) in the nanocluster, the induced charge region in the organic material is confined to the molecules in contact with the nanoparticles. Thus, most of the organic layer is not concerned by the induced charge enhanced conductivity. Additionally, according to that model, an insulating oxide layer around the nanocluster islands (or particles) is necessary in order to achieve charge separation, which is at the origin of the charge storage. Surprisingly, in a previous work, the same authors reported bistability and switching characteristics in a gold middle layer device [12]. In this case, it seems hard to accept the fact that the gold nanoclustered particles are surrounded by an oxide layer.

We should also emphasize here that, unlike the inorganic devices described above, the three layer device and the Wang et al. device, i.e. devices with metal nanoparticle inclusion, do not need forming before switching. We propose here a model that explains the bistability of the organic devices based on metal nanoparticle inclusion. Our model is based on the space charge effects of the charged nonoparticles, and takes into account the transport of carriers inside the organic layer and the injection from the electrodes. All the parameters used in the model correspond to the Wang device as described in Refs. [7,13].

2. Experimental device characteristics

To build our model we give here a summary of the device structure and the experimental results. More details can be found in the original publications [7,13]. The device is represented in Fig. 1, showing also the parylene nanopillars supporting the gold nanoparticles. There are two stable states in the *IV*-characteristics for which the corresponding value of current differs by three orders of magnitude (Fig. 2). The high current state is the ON-state and the low current state is the OFF-state. After fabrication, the devices is in the OFF-state. By increasing the applied voltage from zero, the device switches to the ON-state at a threshold voltage V_{th}. The current continues to increase until a voltage V_{max}, then follows a region of negative differential resistance (NDR) and finally the current increases again after a voltage V_{min}. If the voltage sweep scan do not pass V_{min} then the device will remain in ON-state and will keep this state after removing the applied voltage. The retention time is observed to be about several months. At an applied voltage of $V_{Off} > V_{min}$ the device switches back to the OFF-state.

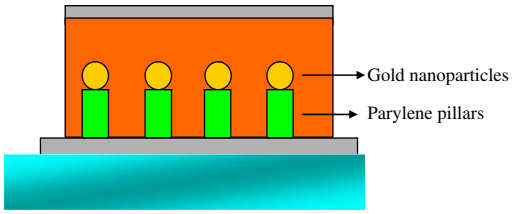

Fig. 1. Device structure: Al/Alq3:Au NPs/Al [7].

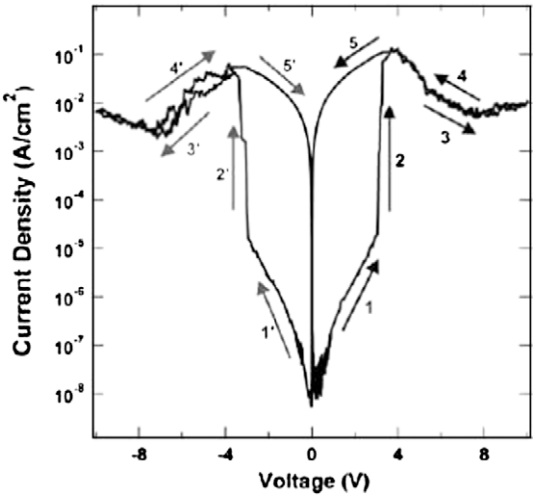

Fig. 2. *IV*-characteristics for the device shown in Fig. 1 [13].

3. One-dimensional device simulation

It has been reported previously in the literature that trapping of charges by impurities or trap levels can induce hysteresis and bistability. An example is the SV model mentioned above. Also in OLEDs [14], Brütting et al. concluded that trapped charges at the organic/organic interfaces of the multilayer diode were at the origin of the hysteresis observed in *IV* curves. We propose to study, as a first step, the trapping of charges in the metal nanocluster using a simulation model originally developed for multilayer organic light-emitting diodes [15]. Taking into account of the symmetrical structure in multilayer diodes, the model is one-dimensional and includes all the physical processes privailing in these devices like charge transport through the organic layer and between different layers, electron–hole recombination, and charge injection from the metal electrodes. Also included in the code is the electric field-dependence of the mobility of electrons and holes, which is an important feature of charge transport in organic semiconductors. There is no way, however, to introduce a middle metal layer because the simulation code considers charge transport only through hopping between molecular energy levels. Fortunatly, Bozano et al. [5] reported that replacing the metal middle layer with a CuPc layer preserves the bistability and the memory characteristics. Thus, we assume, instead of the middle metal layer, a uniform CuPc middle layer. Because the model is one-dimensional all the layers are uniform. Following reference [5], the device structure is thus: Al/Alq3(40 nm)/CuPc(5 nm)/Alq3(40 nm)/Al. Fig. 3 shows the resulting charge distribution (electrons and holes) at a bias voltage of 10 V. At low voltage (not shown), the injection of electrons is blocked due to the energy barrier at the cathode. At high voltage, bipolar injection occurs and the space charge effects of the trapped carriers in the CuPc layer (due to energy level offset) are important. The space charge effects of these trapped charges induces an additional electric field that influences both charge injection at the electrodes and charge transport due to mobility variations.

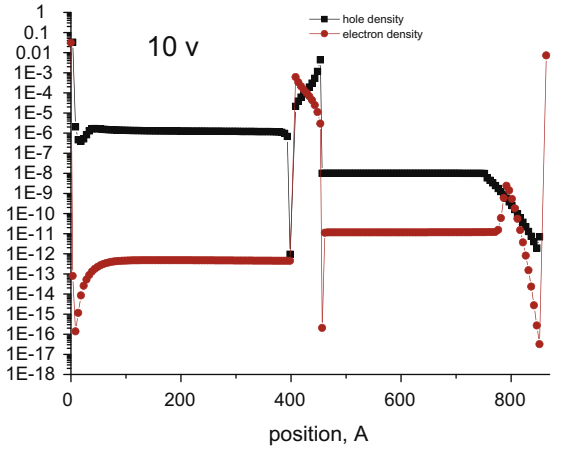

Fig. 3. Results of the 1D simulation giving the electron and hole density distributions in the device: ITO/Alq3/CuPc/Alq3/Al-LiF

The electric current calculated for two different initial states: without and with trapped charges in the CuPc layer, gave the same value. The only difference is the time required to reach equilibrium. Thus there is no bistable state. We checked, also, that even for the case of trapped charges the time to reach equilibrium is large but not enough to suggest a quasi-equilibrium state that might be compared to quasi-stable state. We conclude that trapping effects in 1D, i.e. same path for all carriers, cannot be at the origin of bistability. These findings support the experimental fact that devices with thick middle metal layers do not switch [5]. In fact, as mentionned in the introduction, the middle layer must be thin enough to form disconnected clusters or nanoparticles.

4. Drift-diffusion model

From the previous section it is now clear that to account for the disconnected nature of the middle metal layer we must consider a 2D model that includes two carrier paths: one through the middle layer i.e. the nanoparticles and the other in between the nanoparticles. The carriers following the first path change the charge of the metal nanoparticles, which will modify the distribution of the electric field through the device and affect the movement of the charge carriers that follow the second path.

We assume metallic NPs with a radius $R = 6$ nm as in Wang's devices. The amount of charge that can be captured or stored by the nanoparticle is limited by its capacitance. In fact, the charging energy for one electron on the nanoparticle with radius R is given by $E_c = e^2/2C$, where the capacitance is $C = 4\pi\epsilon_0\epsilon_r R$. $epsilon_r$ is the relative dielectric constant of the organic material. In our case, for a radius of 6nm we have $E_c = 0.034$ eV, a value which is comparable to the thermal energy at ambient temperature; $kT = 0.025$ eV. Thus at thermal equilibrium the mean charge on the nanoparticle is one electron (or hole). The electric field around the nanoparticle will change this limit as the potential drop on a distance comparable to the nanoparticle extension is already much bigger than the charging energy. In the literature, metallic nanoparticles with 12 nm diameter were reported to have a charge of 15 units [16], whereas 5 nm diameter nanoparticles were reported to have a charge of 4 units [17].

We consider monopolar (electron-only or hole-only) devices. We will justify our choice in the discussion below. The electron concentration in the device, ρ_n, is given by the continuity equation:

$$\frac{\partial}{\partial t}\rho_n - \nabla \cdot \mathbf{J} = 0, \tag{1}$$

with the electron current $\mathbf{J}$, given as the sum of the drift and diffusion currents:

$$\mathbf{J} = e\rho_n\mu_n\mathbf{F} + eD_n\nabla\rho_n. \tag{2}$$

The electric field, $\mathbf{F}$, is determined by the Poisson equation:

$$\nabla \cdot \mathbf{F} = -\frac{e}{\epsilon_0\epsilon_r}\rho_n, \mathbf{F} = -\nabla V, \tag{3}$$

where V is the electric potential and ϵ_r the relative dielectric constant of the organic material. The diffusion coefficient of electrons, D_n, and their mobility, μ_n, verify the Einstein relation:

$$D_n = \frac{\mu_n kT}{e}, \tag{4}$$

with k the Boltzmann constant and T the temperature. We assume the well established Poole–Frenkel law for the mobility of charge carriers in organic semiconductors: [18]

$$\mu_n(F) = \mu_0 \exp\left(\sqrt{\frac{F}{F_0}}\right). \tag{5}$$

We used finite elements method in order to solve these equations in 2D for the appropriate boundary conditions at the electrodes and the NP surface. The device thickness is 75 nm along the x-axis, which is the direction of the electric field. The perpendicular (lateral) dimension of the device (y-axis) has a length of 42 nm with only one nanoparticle. Periodic boundary conditions are then imposed on the y-direction to take into account the large extension of the device in that direction with respect to its thickness. Thus the surface density of the nanoparticles is 5.66×10^{10} cm^{-2}. The electrostatic potential on the electrodes is fixed by the applied bias whereas the electron concentration is determined through the carrier injection. We used Scott and Malliaras injection formula [19] which considers most of the effects inherent to metal/organic interfaces. The injection current is given by

$$J_{\text{inj}} = \frac{16\pi\epsilon_0\epsilon_r N_0 k^2 T^2}{e^2}\mu_n \exp\left(-\frac{\Delta}{kT}\right)\psi^2 f \exp\left(f^{1/2}\right), \tag{6}$$

where

$$\psi = f^{-1} + f^{-1/2} - f^{-1}\left(1 + 2f^{1/2}\right), \qquad f = \frac{e^3 F}{4\pi\epsilon_0\epsilon_r k^2 T^2}. \tag{7}$$

The density of sites (molecules) of the organic material at the interface with the metal is given by $N_0 = 0.46\times 10^{22}$ cm^{-3}, and the energy barrier at the cathode $\Delta = 0.5$ eV [15].

The equations of the model are solved for a fixed charge on the NPs. The model does not allow dynamic variation of the nanoparticle charge. In order to apply appropriate boundary conditions on the nanoparticle surface we consider the NP as a thin dielectric shell. The mobility of electrons inside the shell is taken sufficiently high in order to be consistent with the metallic conductivity of gold, whereas the dielectric constant is infinite as it should be for a metal. The boundary of the geometry is thus the inner boundary of the shell where the electron perpendicular current is set to zero. The electric potential on the inner boundary, V_{NP}, is derived from the nanoparticle charge, Q_{NP}, through the relation: $V_{\text{NP}} = Q_{\text{NP}}/C_{\text{NP}}$.

5. Results and discussion

Fig. 4, shows the resulting electron density distribution at an applied voltage of 2 V and zero charge on the NPs i.e. $Q_{\text{NP}} = 0$. We can see an almost uniform electron density and electric field. The observed current density is 0.6 A/cm^2. Consider now Fig. 5 which gives the electron density and the potential distribution for the same parameters as the previous figure except for the nanoparticle charge which is now $Q = 15$ units. We observe that the carrier density is greatly reduced between the NPs and the anode. The current density is 0.0018 A/cm^2. Therefore, from these results, we can attribute the OFF state of the device to charged nanoparticles, and ON-state to uncharged nanoparticles. The ON-to-OFF ratio is 300 which is comparable to Fig. 2. Higher ratio for higher NPs charge are obtained.

From the electric field distribution in the charged case (OFF-state) given in Fig. 6, the electric field magnitude in

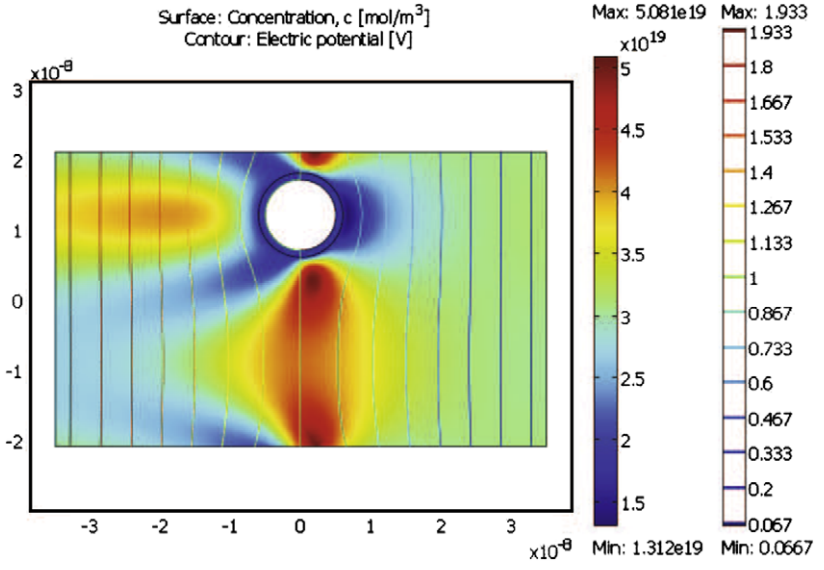

Fig. 4. Electric field distribution and electron concentration for a bias of 2 V and $Q_{NP} = 0$.

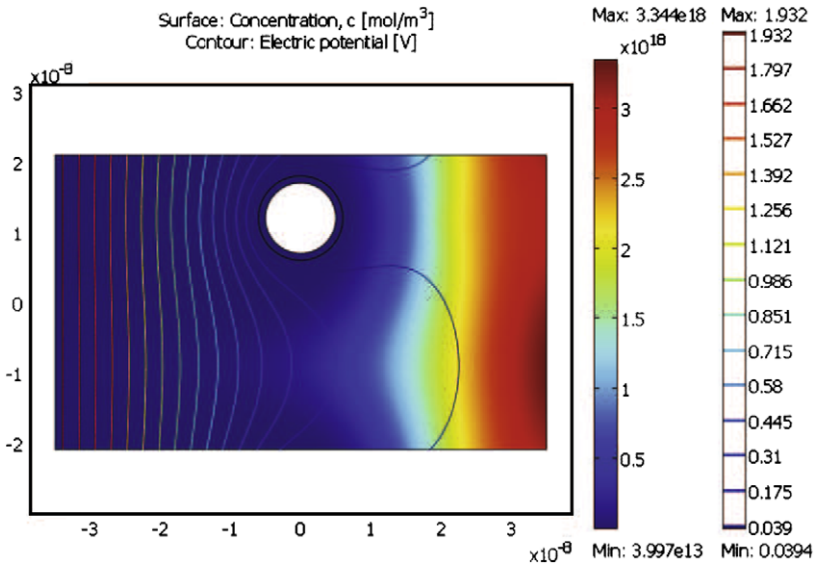

Fig. 5. Electric field distribution and electron concentration for a bias of 2 V and $Q_{NP} = 15$ units.

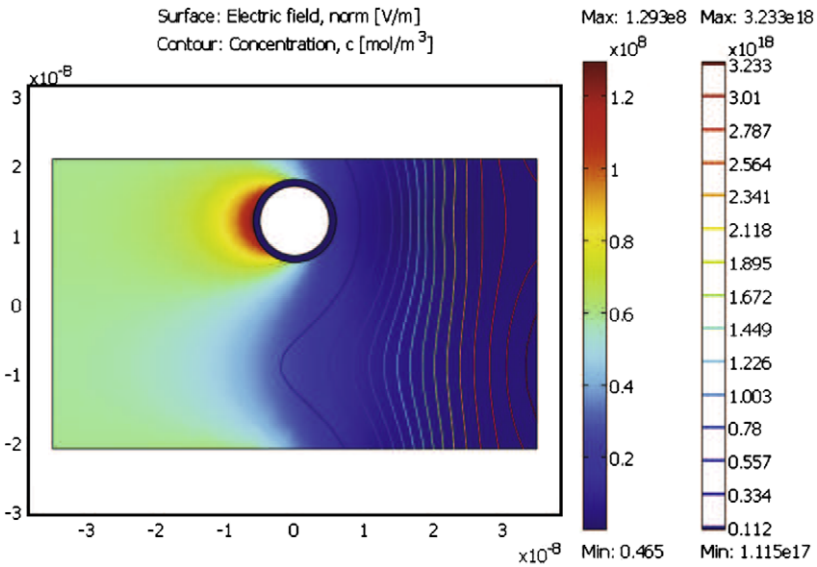

Fig. 6. Electric field distribution and electron concentration for a bias of 2 V and $Q_{NP} = 15$ units.

the part of the device between the cathode and the NPs, is several orders of magnitude lower than in the other part of the device between the NPs and the anode. Thus, due to the space charge effect of the nanoparticles (corresponding to OFF-state), the small electric field at the cathode reduces greatly the injection of electrons. This reduction of the injection is at the origin of the low current caracterizing the OFF-state. By measuring the electric potential at the middle metallic layer, the UCLA group [20] found that the potential drops essentially through one half of the device in the OFF-state. The corresponding electric field is thus very small, a fact which in agreement with the results of our model. A main feature of our model is that the OFF-state corresponds to charged nanoparticles. In this respect our model differs from some proposed models based on the assumption that the ON-state corresponds to charged nanoparticles [21,22]. In fact, these models treat the nanoparticles as traps in the organic material. When empty these traps reduce the transport as a consequence of trapping and de-trapping of charge carriers, whereas when they are filled the transport increases. What is surprising in those models is the fact that they neglect space charge effect of the traps/nanoparticles. With the exception of the SV model [9] in the case of inorganic devices, our model is the first to account correctly for this effect in the case of organic/nanoparticle devices. In fact, our calculation

above showed that at a reasonable charge state of the NPs the electric field is low enough to inhibit the charge injection from the electrodes. At the same time, the electric field is increased in the part of the device between the NPs and the anode. As the device is electron-only, this increase of field may only increase the mobility of electrons due to the field-dependence in the Poole–Frenkel law. However, from our results, no noticible increase in current is observed as the primary effect is the reduction of the number of electrons injected from the cathode.

A strong support to our model can be found in Fig. 3 of Ref. [22] concerning ITO/Alq_3/Al devices with MoO_3 nanoparticles. In fact, it was shown there that the magnitude of the current for the device without nanoparticles is comparable to the ON-current for the device with nanoparticles. This observation confirms that the ON-state corresponds to uncharged nanoparticles, whereas OFF-state corresponds to charged nanoparticles.

We now address our assumption of monopolar devices (electron-only or hole-only). Actually, devices with a single layer of an organic material present always an asymmetry with respect to electron injection from the cathode and hole injection from the anode. In our case, the barrier for electron injection is 1.3 eV whereas the barrier for hole injection is 1.5 eV, which makes the device essentially electron-only. With an ITO anode as in Ref. [22], the barrier for hole injection is 0.7 eV and the device is hole-only. The presence of both electrons and holes in the OBD device will not suppress entirely the switching but can reduce the ON-to-OFF ratio by orders of magnitude. This effect was reported in a nice experiment in Ref. [23] where the switching was observed for ITO/Alq_3/Al metal layer/Alq_3/Al device with an ON-to-OFF ratio of 10^4. With an additional PEDOT:PSS layer bewteen ITO and Alq3, which facilitates hole injection, the switching was still there but with an ON-to-OFF ratio of 10^2.

It is worth to note that the capacitance of the nanoparticles used so far is only valid for an isolated nanopraticle. The presence of the other nanoparticles and also the electrodes modify the value of the capacitance. Increasing the nanoparticle density to 2.83×10^{10} cm^{-2}, we obtained the same current and ON-to-OFF ratio as in Fig. 5 when the nanoparticle charge is $Q = 7$. This decrease of the nanoparticles charge means that the capacitance of the nanoparticles decreases due to the electrostatic influence between nanoparticles. Decreasing the nanoparticle radius will also decrease the capacitance and leads to the same effect. In contrast, the electrostatic influence of the electrodes increases the capacitance although the effect is much less pronounced. In fact for a thickness of 35 nm (the bias is set to 1V in order to have the same electric field) and nanoparticle density of 2.83×10^{10} cm^{-2} we obtained $Q = 7.5$.

In our OBD devices [7,13], after the fabrication process, the NPs are highly charged (Q_{OFF}) so that initially the device is in the OFF-state. When the applied voltage increases beyond the threshold voltage V_{th}, the electric field is high enough on the NP side facing the anode (see Fig. 6) to enable the escape of electrons from the NPs leading to ON-state with a low or zero charge. Then, the current increases with voltage until V_{max}. After the negative differential resistance (NDR) region, as the voltage increases beyond V_{min} the NPs are again charged so that OFF-state will be recovered. Depending on the voltage attained, the newly acquired charge of the NPs will determine the levels of the current in the OFF-state. Multi-OFF states are also observed in experiments [13]. The fact that once in the ON-state and when the voltage does not exceed V_{min}, the NPs do not get charged again when the potential drops below the threshold voltage is worth explaining. Clearly, this issue is related to the retention time. We suggest that this is related to the interface dipole between the metal and the organic material. In fact metal surfaces with plasma treatment present in general high electric dipoles at the interface with the organic [24]. When the NPs are highly charged (OFF-state), the dipole effect is negligible. When the NPs have a small charge then the effect of the dipole is to repel electrons (the negative part of dipole is in the organic material). Thus, in the ON-state, the NPs cannot be charged by electrons below the threshold voltage because of this repulsion. Thus, retention can be explained by this interface dipole. A quantitative approach to the latter point as well as the *IV*-characteristics cannot be obtained by the present model because the charge of the nanoparticles is fixed. We expect to account for these processes more quantitatively when we introduce the variation of the charge of the NPs. We are currently investigating a charging equation for the NPs which will account for the discharging effect of the electric field on one side of the nanoparticle and the charging due to current flow on the other side.

The device current–voltage characteristics as a function of temperature can give insights into the conduction mechanism. We emphasize however that this temperature dependence has essentially three contributions: (i) the temperature dependence on the injection current given, in our model, through Eq. (6), (ii) the temperature dependence of the carrier mobility through the parameters F_0 and μ_0 in Eq. (5) and (iii) the escape of electrons trapped in the nanoparticles. In its present state, our model, does not include the last two contribution. Although the mobility temperature dependence can be readily introduced, the temperature dependence of electron escape from the metal nanopraticles is related to the charging equation mentioned above. We believe that the last contribution is the most important origin of the current temperature dependence in OBDs. The experiment reported in Fig. 7 of Ref. [23] show that when increasing the temperature from 303 K to 333 K, the OFF-current increases by four orders of magnitude and joins the ON-current at a temperature of 373 K. Such an increase in OFF-current cannot be attributed to the Poole–Frenkel mobility nor to the temperature dependence of the injection current. In fact, using the 1D code described in Section 3, we calculated the current–voltage characteristics of the device without nanoparticles and found that even at 400 K the current increases by less than one order of magnitude. Thus the OFF-current increase in the experiment is essentially due to the fact that the nanoparticles have a small charge due to high escape rate of electrons at high temperature. Further evidence for this interpretation is the decrease of the threshold voltage when temperature increases (reported in the same experiment). In fact, at higher temperature the electric field for electron escape from the nanoparticle trap is lower.

The physical process described by our model applies also to the organic vertical transistor described in Ref. [25]. An electrode with a nano-aperture placed between source and drain electrodes serves as a gate. When biased positively it closes the transistor channel preventing the holes, which are injected from the source, from reaching the drain electrode. Compared with the OBD devices, the nanoparticles act like a floating gate.

As for the bistability of organic devices without nanoparticles or middle metal layer, we suggest there are other processes involved like filaments formation [26]. During the forming process, conductive filaments form through the organic layer giving the ON-state. At higher voltage, the filaments break due to Joule heating and OFF-state is recovered. We do not discard also the possibility that the space charge process described by our model and the filaments formation process coexist in organic OBDs with nanoparticles depending on the fabrication and operation methods. For instance, in the device of Ref. [22] it is almost certain that switching is due only to the space charge effect of the MoO_3 nanoparticles because the current of the device without nanoparticles is comparable to the ON-current. In contrast, the device of Ref. [23] with Aluminum middle layer involves probably the two switching mechanisms because the device without middle layer switches and its current is comparable to OFF-current as can be seen in Fig. 5 of the same reference.

6. Conclusion

We presented a model for the organic memory devices embedded with metallic nanoparticles. The high (ON) and low (OFF) current states of the device are accounted for through the charge states of the nanoparticles. As a consequence of this charge, the electric field at the injecting electrode is reduced leading to OFF-current. The ON-to-OFF ratio obtained is more than three orders of magnitude for an average of only 15 electrons on each nanoparticle for the OFF-state and zero charge for the ON-state. The devices described by our model do not need forming before switching and would give a current comparable to ON-current when the nanoparticles are not included. Even though for some OBD devices reported in the literature, there could be a different switching mechanism, our model demonstrates the importance of the space charge effects of the nanoparticles and the possibility to fabricate OBD devices that switch only through this mechanism.

Acknowledgments

Helpful discussions concerning the experimental results with Dr. H.P. Wang are here acknowledged. One of the authors, I.R., thanks NSERC, RESMIQ, and CQMF for support.

References

[1] J. Campbell Scott, L.D. Bozano, Adv. Mater. 19 (2007) 1452.
[2] Y. Yang, J. Ouyang, L. Ma, R.J.H. Tseng, C.W. Chu, Adv. Func. Mater. 16 (2006) 1001.
[3] A.K. Mahapatro, R. Agrawal, S. Ghosh, J. Appl. Phys. 96 (2004) 3583.
[4] F.L.E. Jakobsson, X. Crispin, M. Cölle, M. Büchel, D.M. de Leeuw, M. Berggren, Org. Electron. 8 (2007) 559.
[5] L.D. Bozano, B.W. Kean, M. Beinhoff, K.R. Carter, P.M. Rice, J.C. Scott, Adv. Func. Mater. 15 (2005) 1933.
[6] L. Ma, S. Pyo, J. Ouyang, Q. Xu, Y. Yang, Appl. Phys. Lett. 82 (2003) 1419.
[7] H.P. Wang, S. Pigeon, R. Izquierdo, R. Martel, Appl. Phys. Lett. 89 (2006) 183502.
[8] T.W. Hickmott, J. Appl. Phys. 33 (1962) 2669.
[9] J.G. Simmons, R.R. Verderber, Proc. Roy. Soc. A 301 (1967) 77.
[10] L.D. Bozano, B.W. Kean, V.R. Deline, J.R. Salem, J.C. Scott, Appl. Phys. Lett. 84 (2004) 607.
[11] J. Wu, L. Ma, Y. Yang, Phys. Rev. B 69 (2004) 115321.
[12] L. Ma, J. Liu, S. Pyo, Q. Xu, Y. Yang, Mol. Cryst. Liq. Cryst. 378 (2002) 185.
[13] H.P. Wang, S. Pigeon, R. Izquierdo, R. Martel, Mater. Res. Soc. Symp. Proc. 997 (2007) 9.
[14] W. Brütting et al., J. Appl. Phys. 89 (2001) 1704.
[15] H. Houili, E. Tutis, H. Lutjens, M.N. Bussac, L. Zuppiroli, Comput. Phys. Commun. 156 (2003) 108.
[16] D.S. Kim, D.S. Lee, C.G. Woo, M. Choi, J. Aerosol Sci. 37 (2006) 1876.
[17] W.L. Leong, P.S. Lee, S.G. Mhaisalkar, T.P. Chen, A. Dodabalapur, Appl. Phys. Lett. 90 (2007) 042906.
[18] G.G. Malliaras, Y. Shen, D.H. Dunlap, H. Murata, Z. Kafafi, Appl. Phys. Lett. 79 (2001) 2582;
S. Naka, H. Okada, H. Onnagawa, Y. Yamaguchi, T. Tsutsui, Synth. Metals 111–112 (2000) 331.
[19] J.C. Scott, G.G. Malliaras, Chem. Phys. Lett. 299 (1999) 115.
[20] J. He et al., J. Appl. Phys. 97 (2005) 064507.
[21] D.-I. Son, D.-H. Park, W.K. Choi, S.-H. Cho, W.-T. Kim, T.W. Kim, Nanotechnology 20 (2009) 195203.
[22] K.S. Yook, S.O. Jeon, C.W. Joo, J.Y. Lee, S.H. Kim, J. Jang, Org. Electron. 10 (2009) 48.
[23] V.S. Reddy, S. Karak, S.K. Ray, A. Dhar, Org. Electron. 10 (2009) 138.
[24] M. Castellani, I. Salzmann, P. Bugnon, S. Yu, M. Oehzelt, N. Koch, Appl. Phys. A 97 (2009) 1.
[25] N. Ohashi, M. Nakamura, N. Muraishi, M. Sakai, K. Kudo, IEICE Trans. Electron. E89-C (2006) 1765.
[26] G. Dearnaley, A.M. Stoneham, D.V. Morgan, Rep. Prog. Phys. 306 (1970) 1129.

Organic Electronics 11 (2010) 521–528

Contents lists available at ScienceDirect

Organic Electronics

journal homepage: www.elsevier.com/locate/orgel

Solution processed polymer tandem cell utilizing organic layer coated nano-crystalline TiO_2 as interlayer

Won-Suk Chung [a,c], Hyunjung Lee [a], Wonmok Lee [b,*], Min Jae Ko [a], Nam-Gyu Park [a], Byeong-Kwon Ju [c], Kyungkon Kim [a,*]

[a] Materials Science and Technology Division Solar Cell Research Center, Korea Institute of Science and Technology (KIST), Seoul 136-791, Republic of Korea
[b] Department of Chemistry, Sejong University, 98 Gunja-dong, Gwangjin-gu, Seoul 143-747, Republic of Korea
[c] Display and Nanosystem Lab, College of Engineering, Korea University, Seoul 136-701, Republic of Korea

ARTICLE INFO

Article history:
Received 14 June 2009
Received in revised form 8 November 2009
Accepted 5 December 2009
Available online 11 December 2009

Keywords:
Solar cells
Organic photovoltaics
Polymer tandem solar cells
Polymer solar cells
Titanium dioxide nanoparticles

ABSTRACT

A solution processed polymer tandem cell has been fabricated by utilizing organic layer coated TiO_2 nanoparticle (OL-TiO_2) as an interlayer. The crystalline phase of the OL-TiO_2 was anatase. The dispersed solution of the OL-TiO_2 showed high optical transparency and excellent film forming property. The top and bottom cell were clearly separated by the OL-TiO_2 interlayer without interlayer mixing, which was not observed for the tandem cell utilizing commercially available TiO_2 nanoparticle (N-TiO_2) as an interlayer. The conversion efficiency of a polymer tandem cell was enhanced from 1.43% to 3.44% by replacing the interlayer from N-TiO_2 to OL-TiO_2. The tandem cell performance was further enhanced by adjusting the thicknesses of the active layers in the subcells and adjusting the conductivity of the PEDOT:PSS layer in the bottom cell. The highest conversion efficiency of 3.66% was obtained from the tandem cell having the structure of ITO/Baytron P VP AI 4083/P3HT:PCBM (100 nm)/OL-TiO_2/Baytron PH 500/P3HT:PCBM (100 nm)/Al. In addition that, it was found that the OL-TiO_2 interlayer enhanced the stability of the tandem cell comparing to that of the single junction cell by the reduction of the oxygen diffusion to the bottom layer by the interlayer. It is expected that the performance of the tandem cell can be further enhanced by adopting efficient low band gap materials.

© 2009 Elsevier B.V. All rights reserved.

1. Introduction

The single junction solar cell has limitations to overcome Shockley–Queisser limitation because excess energy of the photons, absorbed with energies greater than the semiconductor band gap, are lost as heat and photons with energies less than the semiconductor band gap are not absorbed [1]. The tandem solar cell technology could be one way to overcome the limits of the single junction solar cell. However, it is difficult to fabricate polymer tandem solar cells because the previously deposited layer could be destroyed by the following solution process. Therefore, it is important to use a proper separation layer (or interlayer), which isolates two subcells. The interlayer protects the bottom cell as well as recombining the charge carriers from the subcells. There are several reports on the formation of the interlayer and middle electrode by the vacuum deposition method [2–7]. However, it is desirable to fabricate polymer tandem cells with all solution processes in terms of large area fabrication, the production cost and the high throughput. It is essential to develop solution processed interlayer materials to fabricate the polymer solar cell with solution process. Semiconducting metal oxides are thought to be promising candidates for the interlayer due to their optical transparency, electron mobility and chemical stability. Gilot et al., used ZnO nanoparticles/PEDOT interlayer for the

* Corresponding authors.
E-mail addresses: wonmoklee@sejong.ac.kr (W. Lee), kimkk@kist.re.kr (K. Kim).

1566-1199/$ - see front matter © 2009 Elsevier B.V. All rights reserved.
doi:10.1016/j.orgel.2009.12.007

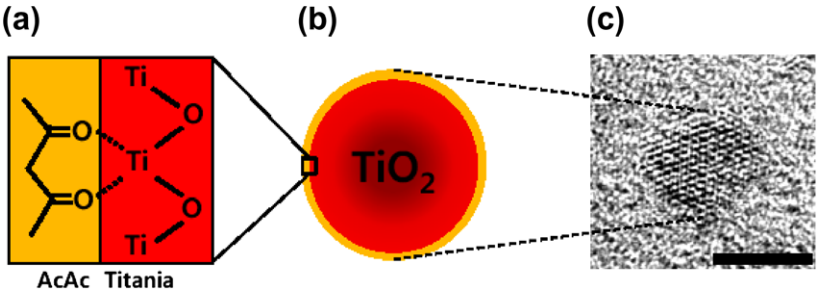

Fig. 1. Organic layer coated TiO_2 nanoparticle used in this study. (a,b) Schematic illustration of the nanoparticle surface where acetylacetone (AcAc) is bound to Ti exposed on the surface (c) HR-TEM image of an individual TiO_2 nanoparticle crystalline lattice. Scale bar represents 5 nm.

polymer tandem cell [8]. However, the neutral pH PEDOT was used for the interlayer instead of commercially available acidic PEDOT:PSS solution due to the chemical instability of the ZnO against the weak acid solution. Recently, Kim et al., successively fabricated solution processed polymer solar cells by utilizing the TiO_x/PEDOT:PSS interlayer, and the power conversion efficiency reached more than 6% under the 1 sun illumination condition [9]. Thought the TiO_x is promising interlayer material for the polymer tandem cell, the TiO_x layer formation needs a hydrolysis process, which might affect the throughput of the polymer tandem cell production and storage stability of the TiO_x solution is thought to be concerned. The nano-crystalline TiO_2 nanoparticle (NC-TiO_2) is possible candidate material for the interlayer due to their chemical stability, crystallinity and optical transparency. In this study, we fabricated polymer tandem solar cell by using NC-TiO_2 interlayer. Two types of NC-TiO_2 (TiO_2 nanoparticle with or without organic layer on the surface) were utilized as interlayer for the tandem cell. The effects of NC-TiO_2 interlayers on the performance of polymer tandem solar cell will be discussed.

2. Experimental

2.1. Materials and solutions

The P3HT and PCBM blended solution was used to form bulk-heterojunction active layers for the polymer tandem solar cell. The regioregular poly(3-hexylthiophene) (P3HT, Aldrich) and the fullerene derivative [6,6]-phenyl C_{61}-butyric acid methyl ester (PCBM, American Dye Source, Inc.) were dissolved in chlorobenzene with the weight ratio of 1:0.8, and used for active layer of subcells. Three kinds of PEDOT:PSS solutions (Baytron P VP AI 4083, Baytron P, and Baytron PH 500) were purchased from Baytron, H.C. Starck and diluted with methanol by 1:1 vol%. Two types of titanium oxide solution were prepared for the transparent interlayer in the polymer tandem cell. One is the solution that organic layer coated TiO_2 nanoparticles (OL-TiO_2) are dispersed in ethanol. The OL-TiO_2 were synthesized through the hydrolysis of titanium butoxide at 60 °C in the presence of acetylacetone as an organic modifier and p-toluene sulfonic acid as an acid catalyst [10,11]. The mean size and the crystallinity of particles were adjusted by tuning the ratio of reactants. As synthesized nanoparticles were precipitated in toluene, and redispersed in ethanol by 5 wt% which exhibited a transparent yellow color. The schematic diagram of OL-TiO_2 nanoparticle showing acetylacetone coordinated to TiO_2 at the nanoparticle surface and high resolution transmission electron microscope (HR-TEM) image of an individual nanoparticle are shown in Fig. 1. From the selected area electron diffraction (SAED) on TiO_2 nanoparticles and XRD data, it was confirmed that their crystalline structure of OL-TiO_2 was anatase. The other solution (N-TiO_2) was obtained from the dispersing the TiO_2 nanoparticles (F-6, Showa Denko, Japan) in ethanol by bead-mill. The particle size of the N-TiO_2 was about 15 nm.

2.2. Device fabrication and measurements

The polymer tandem solar cell structure used in this study is shown in the Fig. 2. The tin doped indium oxide (ITO) was used as bottom electrode (BE in Fig. 2) for the tandem cell. The patterned ITO/glass substrates were cleaned in an ultrasonic bath of isopropanol and acetone repeatedly, followed by a UV treatment for 20 min. For the hole injection layer of the bottom cell (HIL in Fig. 2), the PEDOT:PSS aqueous solution (Baytron P VP AI 4083, Baytron P, or Baytron PH 500) was spin-coated onto ITO substrates and dried in the vacuum oven at 120 °C for 10 min. The thickness of the HIL was approximately 40 nm. P3HT:PCBM solution was spun onto the HIL and dried in air at room temperature for 10 min to form a bottom active layer (BL in Fig. 2). Three different thicknesses (70, 100 and 200 nm) of the BL were prepared and the

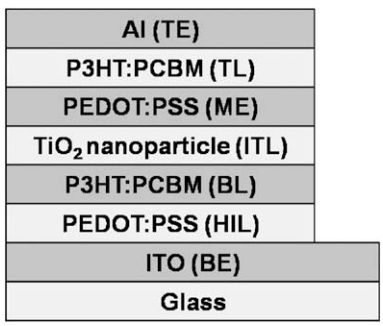

Fig. 2. The polymer tandem cell structure used in this study.

thickness of the layer was controlled by R.P.M of the spin coater. Subsequently, the interlayer (ITL in Fig. 2) for the tandem cell was formed by spinning the TiO_2 nanoparticle solution and drying at 60 °C for 10 min in the vacuum oven. The obtained thickness of the ITL was about 40 nm. Highly conductive PEDOT:PSS (Baytron PH 500, H.C. Starck) was used for the middle electrode (ME in Fig. 2). Since the surface of the ITL is hydrophilic, the aqueous PEDOT:PSS solution can be deposited on it. The same P3HT:PCBM solution was used for the formation of top active layer (TL in Fig. 2). Also, the thickness of the TL was varied from 70 to 200 nm. Finally, Al top electrode (TE in Fig. 2) was vacuum deposited in the base pressure of 2×10^{-6} torr. The thickness of the TE was about 80 nm. The deposited Al electrode area defines an active area of the device as 0.09 cm^2. The prepared tandem cells were directly annealed at 150 °C by a radiation heater for 10 min in the same thermal vacuum evaporator. The base pressure of the evaporator was maintained in the range of 2×10^{-6} to 7×10^{-6} torr.

Photocurrent–voltage measurements were performed on the tandem cells by using a Keithley model 2400 source measuring unit. A class-A solar simulator with a 150 W Xenon lamp (Newport) served as a light source, where its light intensity was adjusted by a NREL-calibrated mono Si solar cell, with a KG-2 filter, for approximately AM 1.5 G 1 sun light intensity. External quantum efficiency was measured as a function of wavelength from 300 to 800 nm using incident photo-to-current conversion system (IPCE) (PV measurements, Inc.). Calibration was performed using a silicon photodiode G425, which was NIST-calibrated as a standard. The atomic force microscopy (AFM) was used to investigate the surface morphology formed by TiO_2 nanoparticle solutions. The AFM measurements were carried out on an Asylum Research MFP-3D-SA AFM mounted on AC160-TS cantilever in noncontact mode. The cross-sectional image of the polymer tandem solar cell was taken with the Dual Beam FIB/SEM system (Nova 200, FEI Company), which allows sectional analysis for the cross-section of delaminated region.

3. Results and discussion

The device structure of the polymer tandem cell used in this experiment is glass/ITO (bottom electrode; BE)/PEDOT:PSS (hole injection layer; HIL)/P3HT:PCBM (bottom active layer; BL)/TiO_2 nanoparticle layer(interlayer; ITL)/PEDOT:PSS (PH 500) (middle electrode; ME)/P3HT:PCBM (top active layer; TL)/Al (top electrode; TE) (Fig. 2). Since this study focuses on the development of the TiO_2 nanoparticle interlayer, the same active layer (P3HT:PCBM) is used for the bottom and top cells.

Two different types of TiO_2 solutions have been examined for the formation of ITL of the polymer tandem cells. The commercially available TiO_2 nanoparticle (F-6, Showa Denko, Japan) was dispersed in ethanol solution (N-TiO_2 solution), and used for the ITL of a polymer tandem cell (TC-N). For the other solution, organic layer (acetylacetone, (AcAc)) coated TiO_2 nanoparticles (OL-TiO_2 solution) were used to form the ITL for another tandem cell (TC-OL). The

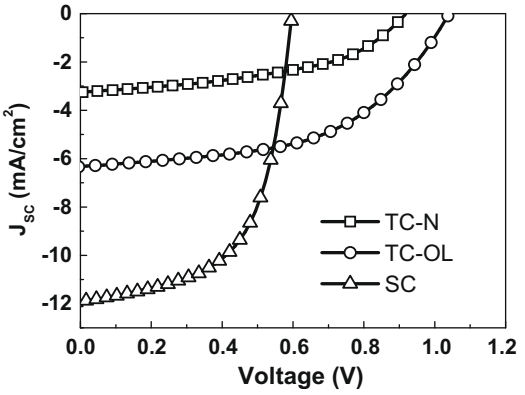

Fig. 3. Current density–voltage characteristics of single junction cell (SC) and tandem cells (TC-N and TC-OL) under the AM 1.5G 1 sun illumination.

N-TiO_2 solution had turbid milky color and precipitated after several days. Whereas, the OL-TiO_2 solution was highly dispersive, transparent and stable over six months without any precipitation.

Fig. 3 shows the current density–voltage characteristics of TC-N and -OL under the AM 1.5 1 sun illumination. The V_{OC} of TC-N (0.92 V) is higher than that of single junction cell (0.6 V). However, there is significant decrease in the J_{SC} and FF of TC-N compared to those of SC. The performance of the tandem cell was enhanced by replacing the interlayer from N-TiO_2 to OL-TiO_2. The V_{OC}, J_{SC} and FF of the tandem cell was increased from 0.92 V, 3.24 mA/cm^2 and 0.48 to 1.04 V, 6.33 mA/cm^2 and 0.52 by changing the interlayer, respectively. As a result, the power conversion efficiency of TC-OL was 3.44% which is 141% higher than that of TC-N (1.43%).

The surface of the interlayer was investigated using atomic force microscopy (AFM). AFM images were obtained after spinning the corresponding TiO_2 nanoparticle solutions on the P3HT:PCBM film. As shown in Fig. 4, large aggregations (ca. 150–300 nm) are observed from the film prepared from the N-TiO_2 solution. The inset of Fig. 4(a) reveals that large aggregations are composed of small nanoparticles (~20 nm). However, no notable aggregation was observed from the surface of the film prepared by the OL-TiO_2 solution (Fig. 4(b)). The RMS roughness of the OL-TiO_2 film was 4.5 nm, which is significantly lower than that of the N-TiO_2 film (87.4 nm). The height profiles of the corresponding film (Fig. 4(c) and (d)) clearly show the difference in the roughness between films. The height of the OL-TiO_2 film is around 10 nm and that of the N-TiO_2 film is in the range of 100–150 nm. However, small voids with size around 30 nm were observed from the OL-TiO_2 film. Those voids are thought to be formed during the solvent evaporation.

The focused ion beam (FIB) image of the TC-OL (Fig. 5(b)) shows the bottom and top cell are clearly separated by the OL-TiO_2/PEDOT:PSS interlayer. In contrast, the TC-N does not show a clear separation of subcells, and large voids (bright region) are observed where the N-TiO_2/PEDOT:PSS ITL is located (Fig. 5(a)). Based on the AFM and FIB experiments, it is believed that the dense

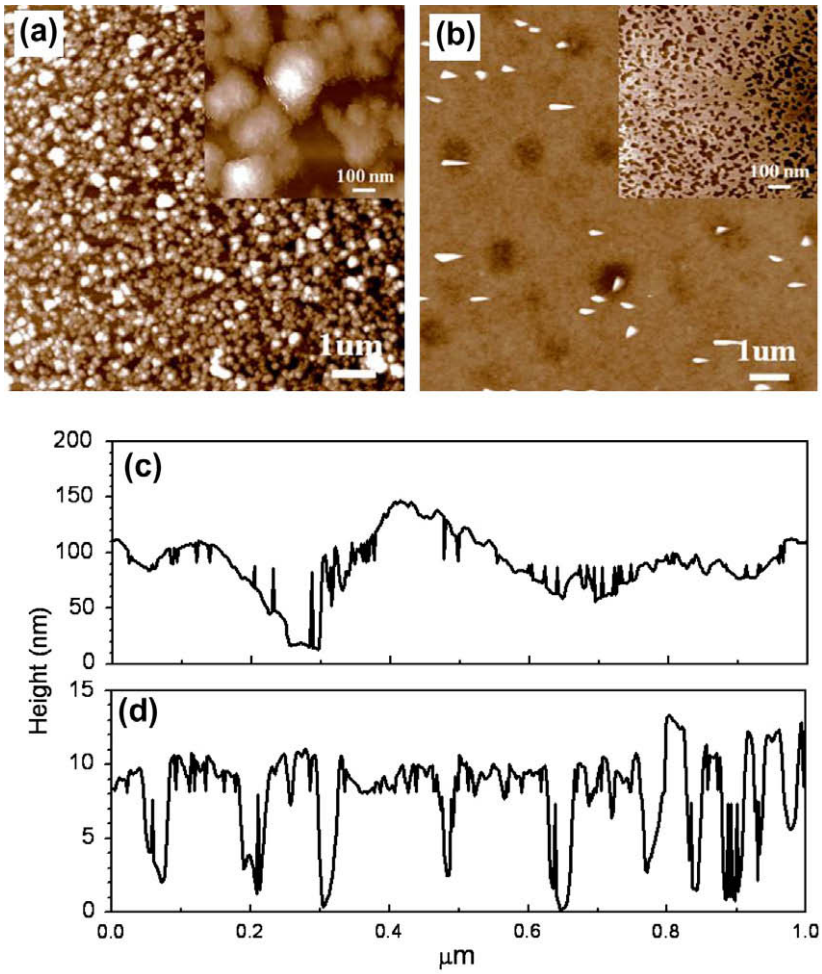

Fig. 4. (a) AFM image and (c) height profile of the film from N-TiO_2 solution, and (b) AFM image and (d) height profile of the film from OL-TiO_2 solution.

OL-TiO_2 interlayer helps the separation of subcell and forms better interfacial contact between the OL-TiO_2 and PEDOT:PSS layer. This implies that the recombination efficiency at the N-TiO_2/PEDOT:PSS interlayer will be significantly lower than that at the OL-TiO_2/PEDOT:PSS interlayer, which leads to voltage drop across the interface, and results in a lower V_{OC} of the TC-N [7].

These properties, however, were obtained after several repeated measurements under the 1 sun illumination. Fig. 6 shows the change in the photovoltaic properties of

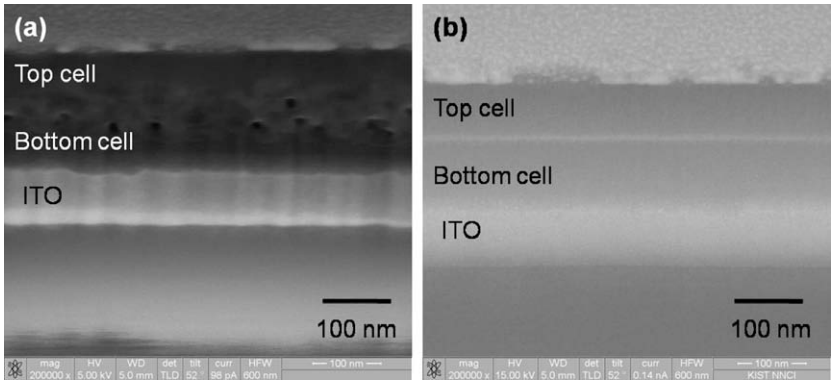

Fig. 5. The Focused Ion Beam (FIB) cross-sectional image of the polymer tandem cells (a) TC-N and (b) TC-OL.

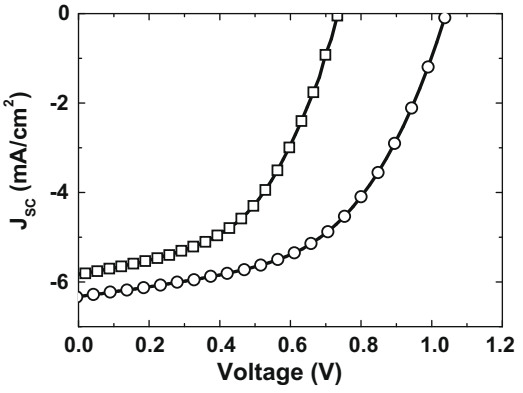

Fig. 6. Current density–voltage characteristics of a tandem cell utilizing OL-TiO_2 as interlayer before (square) and after (circle) AM 1.5G irradiation for 3 min.

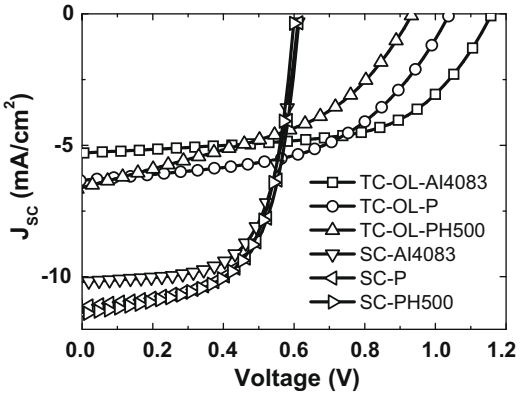

Fig. 7. Influence of hole injection layer conductivity on the current density–voltage characteristics of single cells and tandem cells.

the TC-OL after 3 min of 1 sun illumination. As shown in Fig. 5, the J_{SC} and V_{OC} were increased from 5.83 mA/cm^2 to 6.33 mA/cm^2 and from 0.73 V to 1.04 V after the illumination, respectively. It is reported that the non-ohmic contact between metal oxide and the PEDOT layer could reduce the V_{OC} of the tandem cell [8]. The ohmic contact between the interface can be achieved by increasing the conductivity of the metal oxide and it can be improved by exposing the UV light on the metal oxide [12]. Since there is UV portion in the AM 1.5 light, it is possible that conductivity of the TiO_2 film can be increased by the AM 1.5 illumination.

Although the V_{OC} of the tandem cell was significantly increased by using OL-TiO_2, the V_{OC} is still lower than the sum of the V_{OC} of the bottom and top cells. In the polymer tandem solar cell having the TiO_2/PEDOT:PSS interlayer, electrons from the bottom cell recombine with the hole from the top cell, at the TiO_2/PEDOT:PSS interface. If the bottom cell generates more photo-current than the top cell, the excess electrons cannot recombine with the hole from the top cell, and will be accumulated at the interface between the bottom cell and the interlayer. The electron accumulation will partially compensate the built-in voltage across the bottom cell until the photo-current from the bottom cell matches with that of the top cell [7]. Moreover, excess electrons could act as a resister inside the bottom cell and reduce the fill factor of the cell. This results in a reduced performance of the tandem cell.

It was reported that photo-generated holes can be collected from the area where ITO electrode is not deposited due to the conductivity of the PEDOT:PSS [13]. Based on the report, it is highly possible that the mismatch of J_{SC} value between the bottom and top cells depends on the conductivity of PEDOT:PSS, which is used in the bottom cell, and this becomes significant as the conductivity of the PEDOT:PSS layer is increased. The photovoltaic properties of the single and tandem cells were examined by changing the conductivity of the PEDOT:PSS layer. The three different conductivities of the PEDOT:PSS solution, Baytron P VP AI 4083 (σ = 0.0002–0.002 S/cm), Baytron P (max σ = 0.1–1 S/cm), and Baytron PH 500 (σ = 10–50 S/cm), were used for the hole transporting layer (HTL) of the bottom cell [14]. Hereafter, the tandem cell using Baytron P VP AI 4083, Baytron P and Baytron PH 500 as HTL for the bottom cell will be denoted as TC-OL-AI4083, TC-OL-P, and TC-OL-PH 500, respectively. As shown in Fig. 7 and Table 1, the J_{SC} of the single junction cell increased by increasing the conductivity of the PEDOT:PSS. This implies that the J_{SC} mismatch between the bottom and top cell of the tandem cell will be increased as the conductivity of PEDOT:PSS increases. The J_{SC} mismatch between subcells accommodates the charging of ITL and increase the internal resistance of the tandem cell, which resulted in the reduction of the V_{OC} and FF of the tandem cell. The J_{SC} of the tandem cell was decreased from 6.7 mA/cm^2 to 5.3 mA/cm^2 as the HTL of the bottom cell was changed from the highly conductive Baytron PH 500 (TC-OL-PH 500) to the less conductive Baytron P VP AI 4083 (TC-OL-AI4083). However the V_{OC} and FF of the TC-OL-AI4083 were significantly enhanced, in particular, the V_{OC} of the cell was almost doubled compared to that of the single junction cell. As a result, the power conversion efficiency of the TC-OL-AI4083 (3.66%) was 6%, and 37% higher than that of TC-OL-P and TC-OL-PH 500, respectively. Based on the experimental results, the conductivity of the PEDOT:PSS is considered to be closely related to J_{SC}, V_{OC} and FF in the tandem cells.

However, the J_{SC} value of the tandem cell was significantly lower than that of the single cell. In order to optimize the photo-current of the tandem cell, we varied the thickness of the active layers of the top and the bottom cell. First, the thickness of active layer of the top cell (TL) was varied while maintaining the thickness of active layer of the bottom cell (BL) at 100 nm. Table 2 summarizes the photovoltaic performance of the tandem cell and Fig. 8(a) shows their *I–V* curves. The J_{SC} of the tandem cell was increased from 4.88 to 5.91 mA/cm^2 as the thickness of the TL increased from 70 to 200 nm. The highest photo-current of 5.91 mA/cm^2 was obtained from the T3 and the value is 21% higher than that from the T1. The external quantum efficiency (EQE) for these tandem cells (Fig. 9(a)) are consistent with the J_{SC} result of the tandem cells. The EQE of the tandem cell was increased at around 400 and 600 nm as the thickness of the top cell increased. Whereas, no

Table 1
The dependence of HIL conductivity on the performances of single cells and tandem cells having OL-TiO_2 interlayer.

HIL	ITL	V_{OC} (V)	J_{SC} (mA/cm^2)	FF	Efficiency (%)
Baytron P VP AI 4083		0.61	10.17	0.65	4.04
Baytron P		0.62	11.14	0.63	4.32
Baytron PH 500		0.60	11.42	0.62	4.26
Baytron P VP AI 4083	Baytron PH 500	1.16	5.3	0.60	3.66
Baytron P	Baytron PH 500	1.04	6.33	0.52	3.44
Baytron PH 500	Baytron PH 500	0.93	6.69	0.43	2.67

Table 2
The dependence of active layer thickness on the performances of single cells and tandem cells having OL-TiO_2 interlayer.

Cell type	Active layer thickness (nm)	V_{OC} (V)	J_{SC} (mA/cm^2)	FF	Efficiency (%)
Single junction					
S1	70	0.63	8.55	0.63	3.39
S2	100	0.62	10.25	0.63	4.04
S3	200	0.60	11.19	0.55	3.71
Tandem					
T1	100 (bottom)/70 (top)	1.05	4.88	0.52	2.62
T2	100 (bottom)/100 (top)	1.16	5.3	0.60	3.66
T3	100 (bottom)/200 (top)	1.07	5.91	0.48	2.97
T4	70 (bottom)/100 (top)	1.00	5.95	0.42	2.44
T5	200 (bottom)/100 (top)	1.02	3.16	0.59	1.89

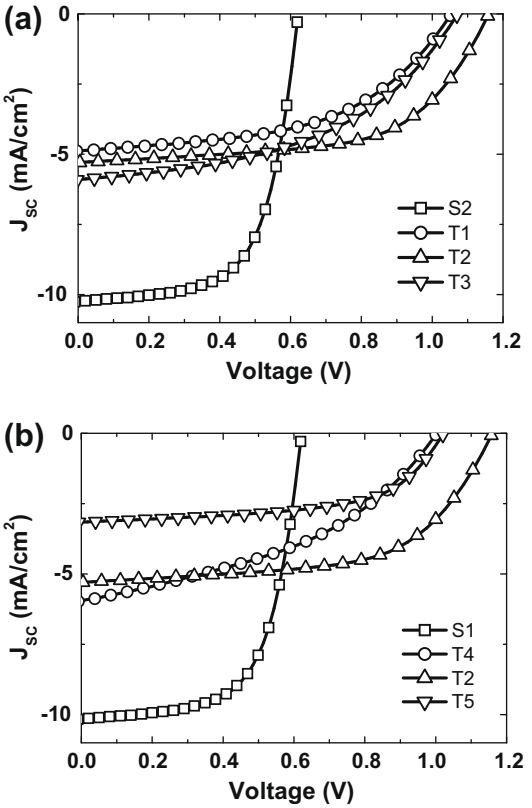

Fig. 8. The effects of varying the thickness of (a) top active layer (TL) and (b) bottom active layer (BL) on the current density–voltage characteristics of tandem cells. The detailed thicknesses of each active layer are listed in Table 2.

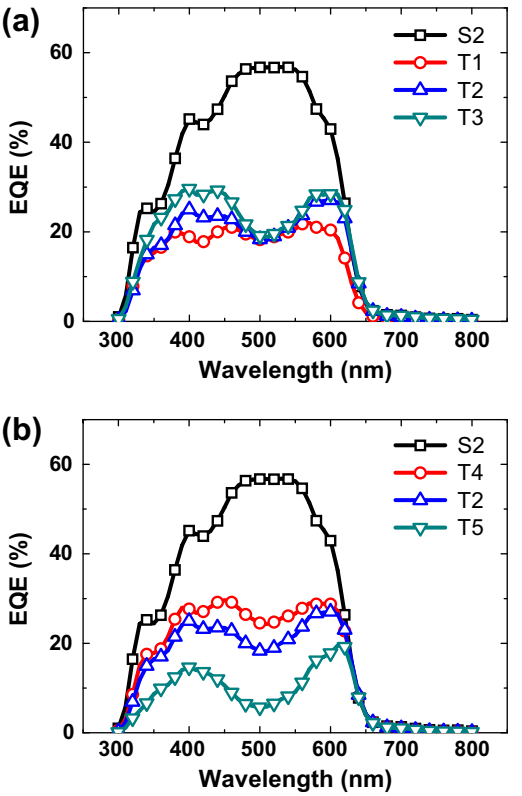

Fig. 9. External quantum efficiency (EQE) spectra of single cell and tandem cells with different active layer thickness of (a) the top cells and (b) bottom cells. The detailed thicknesses of each active layer are listed in Table 2.

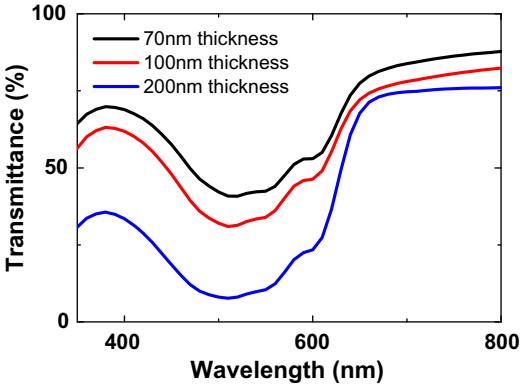

Fig. 10. Transmittance of P3HT:PCBM film with various thickness.

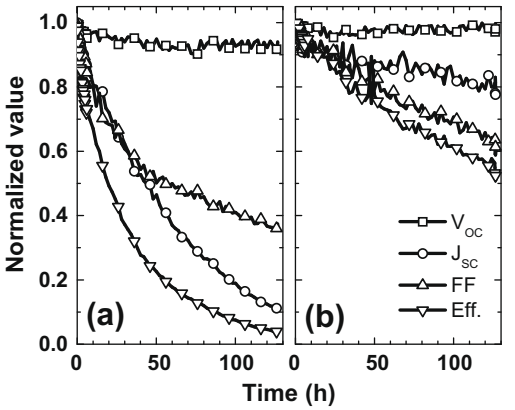

Fig. 11. Comparison of the cell stability under the 1 sun illumination for (a) a single cell (b) a tandem cell TC-OL. The stability test of the single and tandem cell were conducted without any passivation or glass encapsulation.

change in the EQE at 500 nm was observed by varying the thickness of the TL. This is related to the transmittance of the P3HT in the BL. The transmittance of 100-nm thick film of P3HT was about 30% at 500 nm (Fig. 10). This implies only 30% of incoming light of 500 nm wavelength can reach to the TL. Because P3HT has the largest molar extinction coefficient at the wavelength, thin layer of the TL (70 nm) is enough to absorb all the 500 nm light arriving on it. As a result, the EQE of the tandem cell at 500 nm is independent with the thickness of TL. On the other hand, the transmittance of the P3HT at around 400 and 600 nm is relatively higher than that at 500 nm due to the lower molar extinction coefficient. Because larger amount of 400 and 600 nm wavelength light reaches to the TL and P3HT in the TL has lower molar extinction coefficient at the wavelength, the EQE values of the tandem cell at the wavelengths are proportional to thickness of the TL.

For the next experiment, the thickness of the BL was varied while maintaining the thickness of active layer of the TL at 100 nm. The result of their photovoltaic performance and *I–V* curves are shown in Table 2 and Fig. 8(b). The J_{SC} of the tandem cell was increased from 3.16 to 5.95 mA/cm^2 as the thickness of BL decreased from 200 to 70 nm. The highest photo-current of 5.95 mA/cm^2 was obtained from the T4 and the value is 88% higher than that from the T5. The EQE of the tandem cell was inversely correlated with the thickness of BL without concerning the wavelength. Because the light arriving on the TL will be increased as decrease the thickness of BL. As a result of varying the thickness of active layer, the thinner BL (T4) or the thicker TL (T3) generated more photo-current than other tandem cells. Based on the experiments, it seems that the photo-current of our tandem cells are mainly determined by the photo-current generation from the top cell. However, the highest conversion efficiency was obtained from the tandem cell of T2 which has intermediate thickness (100 nm for the top and bottom cell). It is ascribed to the enhanced V_{OC} and FF of the T2 compare to the other tandem cells.

Interestingly, the tandem cell showed enhanced stability compared to the single cell (Fig. 11). The active layers of the cells were covered with commercial epoxy resin (Clear Epoxy, Dong Sung Uni. Tech. Co., Korea) in air before the light soaking test. The stability of the cells was monitored by continuous irradiation under a sulfur plasma lamp. The light intensity of the lamp was adjusted using a NREL-calibrated mono Si solar cell with a KG-2 filter, for approximately AM 1.5G 1 sun light intensity. The temperature of the testing chamber was approximately 35 °C. Fig. 10 compares the stability of the TC-4083 and the single junction cell, and it was found that there was 94% degradation after 125 h irradiation for the single junction cell, whereas the TC-OL-4083 maintained 56% of its initial efficiency. The degradation is mainly ascribed to the decreased J_{SC} and FF for both the single and tandem cells. The decline of the J_{SC} and FF of the single cell was much faster than that of the tandem cell. It is thought that the better stability of the tandem cell is ascribed to the dense TiO_2 nanoparticles interlayer, which can protect the active layer in the bottom cell from the oxygen. Similar results have been reported, where the stability of a cell was enhanced by utilizing the TiO_x as an electron transporting layer [15].

4. Conclusions

In conclusion, solution processed polymer tandem cells have been fabricated by utilizing the highly dispersive organic layer coated crystalline TiO_2 nanoparticles (OL-TiO_2)/PEDOT:PSS interlayer. The top and bottom cell were clearly separated by the interlayer without interlayer mixing, which was not observed for the tandem cell utilizing commercially available TiO_2 nanoparticle (N-TiO_2) for the interlayer. The conversion efficiency of the polymer tandem cell was enhanced from 1.43% to 3.44% by replacing the interlayer from N-TiO_2 to OL-TiO_2. The J_{SC} of the tandem cell was increased by decreasing the bottom layer thickness or increasing the top layer thickness. This implies that the photo-current of our tandem cells are mainly determined by the photo-current generation from the top cell. However, the highest conversion efficiency was obtained from the tandem cell having intermediate thickness (100 nm for the top and bottom cell) due to the enhanced V_{OC} and FF by minimizing the charging of the excess charge

carriers at the interlayer. Based on the V_{OC}, J_{SC} and FF of the tandem cell, it is thought that the OL-TiO_2 layer performs the role of interlayer in the tandem cell with little loss of J_{SC} and V_{OC}. In addition that, it was found that the OL-TiO_2 interlayer enhanced the stability of the tandem cell comparing to that of the single junction cell. It could be ascribed to the reduction of the oxygen diffusion to the bottom layer by the interlayer. We believe the highly dispersive OL-TiO_2 has several advantages for the solution processed polymer solar cell in terms of excellent film forming property, crystallinity, transparency, stability and processability. It is expected that the performance of the tandem cell can be further enhanced by adopting efficient low band gap materials to the bottom cell.

Acknowledgements

This research was supported by the New and Renewable Energy Program through the Korea Institute of Energy Technology Evaluation and Planning (KETEP) funded by the Ministry of Knowledge Economy (MKE) (008NPV08J010000) and KISTInternal Research Fund under the contract number of 2E20980. Also, Mr. W.-S. Chung thanks the IT R&D Program of MKE/KEIT (No. 2009-F-016-01) for the supporting.

Reference

[1] P. Wurfel, Physic of Solar Cells, Wiley-VCH, Weinhein, Germany, 2004.
[2] M. Hiramoto, M. Suezaki, M. Yokoyama, Chem. Lett. (1990) 327.
[3] A. Yakimov, S.R. Forrest, Appl. Phys. Lett. 76 (2000) 2650.
[4] G. Dennler, H.-J. Prall, R. Koeppe, M. Egginger, R. Autengruber, N.S. Sariciftci, Appl. Phys. Lett. 89 (2006) 073502.
[5] V. Shrotriya, E.H. Wu, G. Li, Y. Yao, Y. Yang, Appl. Phys. Lett. 88 (2006) 064104.
[6] K. Kawano, N. Ito, T. Nishimori, J. Skai, Appl. Phys. Lett. 88 (2006) 073514.
[7] A. Hadipour, B. de Boer, J. Wildeman, F.B. Kooistra, J.C. Hummenlen, M.G.R. Turbiez, M.M. Wienk, R.A.J. Janssen, P.W.M. Blom, Adv. Funct. Mater. 16 (2006) 1897.
[8] J. Gilot, M.M. Wienk, R.A.J. Janssen, Appl. Phys. Lett. 90 (2007) 143512.
[9] J.Y. Kim, K. Lee, N.E. Coates, D. Moses, T.-Q. Nguyen, M. Dante, A.J. Heeger, Science 317 (2007) 222.
[10] E. Kwak, W. Lee, N.-G. Park, J. Kim, H. Lee, Adv. Funct. Mat. 19 (2009) 1093.
[11] E. Scolan, C. Sanchez, Chem. Mater. 10 (1998) 3217.
[12] F. Verbakel, S.C.J. Meskers, R.A.J. Janssen, Appl. Phys. Lett. 89 (2006) 102103.
[13] M.-S. Kim, M.-G. Kang, L.J. Guo, J. Kim, Appl. Phys. Lett. 92 (2008) 133301.
[14] Product information of PEDOT:PSS (Baytron P VP AI 4083, P, PH 500) on CLEVIOS homepage. <http://www.clevios.com>, 2009.
[15] K. Lee, J.Y. Kim, S.H. Park, S.H. Kim, S. Cho, A.J. Heeger, Adv. Mater. 19 (2007) 2445.

Organic Electronics 11 (2010) 529–534

Contents lists available at ScienceDirect

Organic Electronics

journal homepage: www.elsevier.com/locate/orgel

Realization of highly efficient white polymer light-emitting devices via interfacial energy transfer from poly(*N*-vinylcarbazole)

Aiyuan Li [a], Yuanyuan Li [a], Wanzhu Cai [a], Guijiang Zhou [b,c], Zhao Chen [a], Hongbin Wu [a,*], Wai-Yeung Wong [b,*], Wei Yang [a], Junbiao Peng [a], Yong Cao [a]

[a] *Institute of Polymer Optoelectronic Materials and Devices, Key Lab of Specially Functional Materials, Ministry of Education, South China University of Technology, Guangzhou 510640, PR China*
[b] *Department of Chemistry and Centre for Advanced Luminescence Materials, Hong Kong Baptist University, Waterloo Road, Kowloon Tong, Hong Kong, PR China*
[c] *Department of Chemistry, Faculty of Science, Xi'an Jiao Tong University, Xi'an 710049, PR China*

ARTICLE INFO

Article history:
Received 27 October 2009
Received in revised form 4 December 2009
Accepted 4 December 2009
Available online 11 December 2009

Keywords:
White polymer light-emitting devices
Phosphorescence quenching
Poly(*N*-vinylcarbazole)

ABSTRACT

We report highly efficient white polymer light-emitting devices (WPLEDs) using a newly synthesized, deep-blue emitting fluorene-co-dibenzothiophene-S,S-dioxide copolymer as host, doped with two narrow-bandgap iridium complexes. Despite the low-lying triplet energy levels of the host, phosphorescent quenching by the polyfluorene copolymer host was significantly suppressed with poly(*N*-vinylcarbazole) (PVK) as hole-injecting, anode buffer layer. The energy transfer process had been studied via transient photoluminescence spectra and confirmed that PVK layer is responsible for the efficient electrophosphorescence in the devices. As a result of balanced red–green–blue (RGB) emission from the host and the triplet emitters, white emission with Commission Internationale de L'Eclairage (CIE) coordinates of (0.278, 0.312) was achieved, with a peak luminous efficiency of 15.1 cd A^{-1} and a color rendering index (CRI) of 79–86.

© 2009 Elsevier B.V. All rights reserved.

1. Introduction

White polymer light-emitting devices (WPLEDs) [1,2] have attracted intense attention due to their potential applications as backlight for liquid crystal displays as well as lighting sources. Despite the relatively lower efficiency when compared to its vapor deposition counterparts [3–6], WPLEDs based on solution processing technology have particular advantages, such as low-cost manufacturing and easy-processibility over large-area size by roll-to-roll printing technology. Several approaches towards WPLEDs have been reported, including multi-layer structure capable of red–green–blue (RGB) emission [7,8], polymer blends containing RGB emitting species with appropriate ratio [9], doping polymer host with RGB phosphorescent or fluorescent dopants [10–12], or white emitting single polymer [13–15]. Of these approaches, WPLEDs based on non-conjugated polymer host, i.e. poly(*N*-vinylcarbazole) (PVK) and phosphorescent dopants give the highest efficiency since these devices may convert 100% injected electrons into photons as they can utilize singlet as well as triplet excitons via Dexter energy transfer owing to strong spin–orbit coupling induced by the heavy atom effect [11,12,16,17].

In contrast, electrophosphorescent WPLEDs based on conjugated polymer host, such as polyfluorenes [18], usually suffer from inefficient energy transfer since the host may act as quenching sites for the triplet excited states due to their relatively low triplet energy level [19]. As a result, the application of blue and green emitting triplet emitters (with energy level higher than 2.3 eV) in such systems is limited. An alternative approach to address this problem is to use polyfluorenes/PVK mixed hosts [18], which had been shown to have good chemical compatibility and raised triplet energy level for the host polymer

* Corresponding authors. Tel.: +86 20 35902080; fax: +86 20 87110606 (H.-B. Wu), Tel.: +852 34117074; fax: +852 34117348 (W.-Y. Wong).
E-mail addresses: hbwu@scut.edu.cn (H. Wu), rwywong@hkbu.edu.hk (W.-Y. Wong).

1566-1199/$ - see front matter © 2009 Elsevier B.V. All rights reserved.
doi:10.1016/j.orgel.2009.12.008

blend, thus leading to efficient energy transfer from polyfluorenes to the iridium dyes. We report here a new approach to realize highly efficient WPLEDs using polyfluorenes as host, doped with green and red emitting iridium complexes, from a multilayer device structure in which PVK was used as the anode buffer layer. Recently, our group reported an enhanced green electrophosphorescent emission using polyfluorene as host via interfacial energy transfer from PVK [19]. Steady and transient PL spectra revealed that PVK buffer layer plays an important role in energy transfer process, and can thus minimize phosphorescent quenching by the polyfluorene copolymer host with superior device performance.

In this contribution, we demonstrate that this device structure can be utilized to fabricate highly efficient WPLEDs based on polyfluorenes host. Optimized device shows a peak luminous efficiency (LE) of 15.1 cd A^{-1} and a peak power efficiency (PE) of 8.4 lm W^{-1}, with Commission Internationale de L'Eclairage (CIE) coordinates of (0.278, 0.312) at 10 mA cm^{-2}. To our knowledge, the obtained efficiencies are one of the highest reported value for WPLEDs based on fluorescent polymer host materials.

2. Experimental

2.1. Materials

The molecular structures of the RGB emitters are shown in Scheme 1. A newly synthesized conjugated polymer PF-2,8FSO1 was selected as the host material and deep-blue

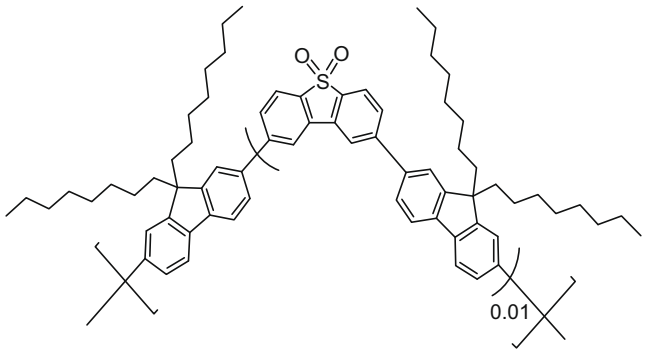

PF-2,8FSO1

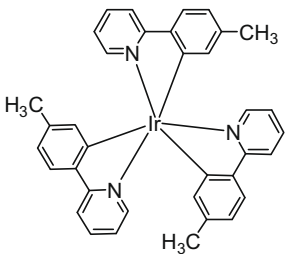

$Ir(mppy)_3$

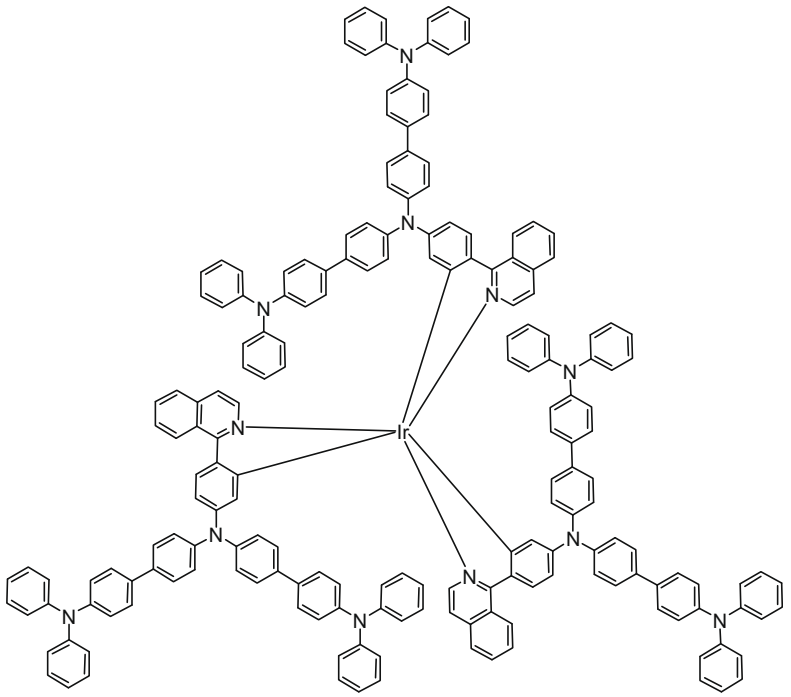

Ir-G2

Scheme 1. The molecular structures of the RGB materials used in this work.

emitters for the WPLEDs due to its high efficiency (with an external quantum efficiency (EQE) of 3.6% and a LE of 3.7 cd A^{-1}), deep-blue emitting properties and excellent spectral stability [20,9]. The two highly efficient electrophosphorescent narrow-bandgap iridium(III) complexes used for this study are $Ir(mppy)_3$ [2,21] for green emission and Ir-G2 [22] for red emission, respectively.

2.2. Device fabrication

The fabrication of the devices followed a well-established procedure [11]. Patterned indium tin oxide (ITO) coated glass with a sheet resistance of 15–20 ohm/square were cleaned by a surfactant scrub, then underwent a wet-cleaning process inside an ultrasonic bath, beginning with deionized water, followed by acetone and isopropanol. After oxygen plasma cleaning for 4 min, a 40-nm thick poly(3,4-ethylenedioxythiopene):poly(styrenesulfonate) (PEDOT:PSS) (Bayer Baytron 4083) anode buffer layer was spin-cast on the ITO substrate and then dried by baking in a vacuum oven at 80 °C overnight. A hole transporting layer of poly(*N*-vinylcarbazole) (PVK) with a thickness of 40 nm was deposited from chlorobenzene solution, then annealed at 100 °C on a hotplate for 10 min. The fluorescent host and phosphorescent guests were dissolved in *p*-xylene and chlorobenzene, respectively, then blended together to form targeted solution for the devices. The active layer, with thickness in the 40–50 nm range was spin-

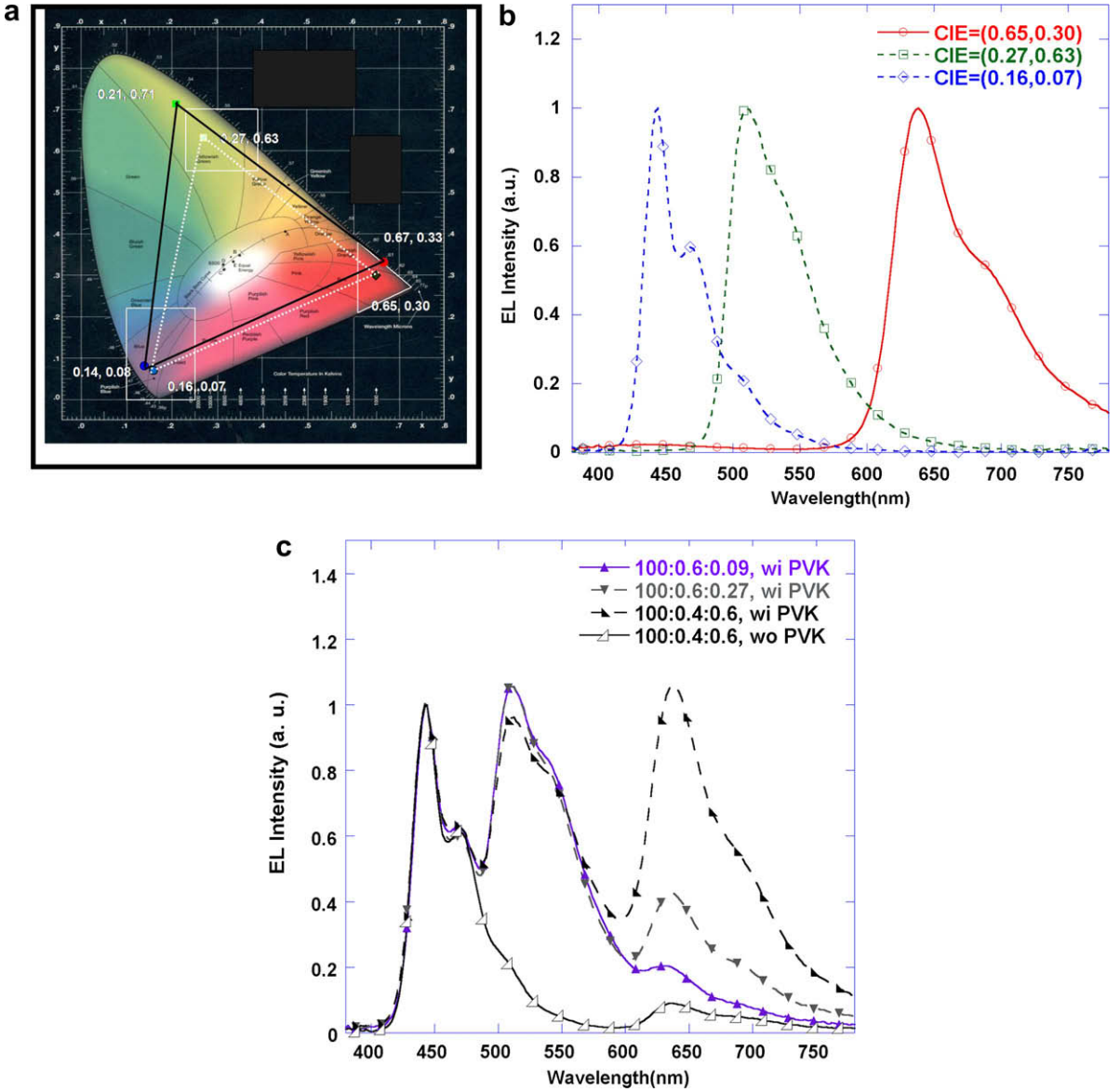

Fig. 1. (a) The emission color of the RGB devices shown in the 1931 CIE chromaticity diagram; (b) EL spectra of PF-2,8FSO1, $Ir(mppy)_3$ and Ir-G2 devices; (c) the normalized EL spectra of the devices with different blend ratio (PF-2,8FSO1 (100 wt%):$Ir(mppy)_3$ (*x* wt%):Ir-G2 (*y* wt%)) and the control device in which PVK interlayer is absent. All of the EL spectra were obtained at a current density of 10 mA cm^{-2}.

Table 1
Summary of device performance of the WPLEDs.

Device structure	Maximum LE (cd A^{-1})	Maximum EQE (%)	Maximum PE (lm W^{-1})	CIE coordinates	CRI
PEDOT/EML/Ba/Al	0.5	0.38	0.26	(0.170, 0.109)	–
PEDOT/PVK/EML/Ba/Al	10.6	6.3	4.9	(0.302, 0.367)	86
PEDOT/PVK/EML/PFN/Ba/Al	15.1	9.4	8.4	(0.278, 0.312)	79

coated atop of the PVK layer, and kept at the temperature of 100 °C for 30 min to remove the solvent residue. After that, a home-made water/alcohol soluble conjugated polymer, poly[(9,9-bis(3′-(*N*,*N*-dimethylamino)propyl)-2,7-fluorene)-alt-2,7-(9,9-dioctylfluorene)] (PFN) [23–25], was used as an electron injection layer (with a thickness of 20 nm) was spin-coated on the top of the resulting emissive layer. Finally, 4 nm barium and 100 nm aluminum layer were evaporated with a shadow mask at a base pressure of 3×10^{-4} Pa. The thickness of the evaporated cathode was monitored by a quartz crystal thickness/ratio monitor (Model: STM-100/MF, Sycon). The overlapping area between the cathode and anode defined a pixel size of 19 mm^2. Except for the deposition of the PEDOT layers, all the fabrication processes were carried out inside a controlled atmosphere of nitrogen dry-box (Vacuum Atmosphere Co.) containing less than 10 ppm oxygen and moisture. The current density–luminance–voltage (*J*–*L*–*V*) characteristic was measured using a Keithley 236 source-measurement unit and a calibrated silicon photodiode. The forward-viewing luminance was calibrated by a spectrophotometer (SpectraScan PR-705, Photo Research) and the forward-viewing LE was calculated accordingly. Throughout the whole manuscript, reported value of luminance and LE are for forward-viewing direction only. The external quantum efficiency (EQE) of electroluminescence (EL) was collected by measuring the total light output in all directions in an integrating sphere (IS-080, Labsphere). The photoluminescence (PL) spectra were recorded by a single-grating monochromator (Instaspec IV, Oriel Co.) equipped with a CCD detector, and EL spectra were collected by a PR-705 photometer. Time-resolved spectra were measured by fluorescence lifetime spectrometer (FLS-920, Edinburgh Instrument Ltd.).

3. Results and discussions

The 1931 CIE coordinates of the individual RGB devices in a single active layer configuration of ITO/PEDOT:PSS (40 nm)/RGB emissive layer/Ba(4 nm)/Al (100 nm) are (0.65, 0.30), (0.27, 0.63), and (0.16, 0.07), respectively. While the CIE coordinates of the primary RGB color system adopted by National Television System Committee (NTSC) for color TV are (0.67, 0.33) (R), (0.21, 0.71) (G) and (0.14, 0.08) (B), it can be clearly seen that the red and blue emitters match the NTSC standard very well (see Fig. 1a). Therefore, when WPLEDs based on these RGB emitters are used for flat panel displays, a wide color gamut (79%) is expected (Fig. 1a), close to that of other displays, such as liquid crystal displays (72%) and plasma displays (100%). From Fig. 1b, the EL spectra of the RGB devices cover the entire visible light spectrum from 400 to 700 nm. As a result, it is expected that white emission with very high color quality can be realized if emission of each color is carefully balanced.

To obtain white emission with high efficiencies, a series of devices with various doping concentrations were fabricated and evaluated [9,19], and the device performance of the obtained WPLEDs is summarized in Table 1 for comparison. Depending on the doping concentration of the red and green iridium complexes, the emission color of the WPLEDs can be tuned in a wide range (Fig. 1c). With a device configuration of ITO/PEDOT:PSS (40 nm)/PVK (40 nm)/PF-2,8FSO1 (100 wt%):Ir(mppy)$_3$ (*x* wt%):Ir-G2 (*y* wt%)

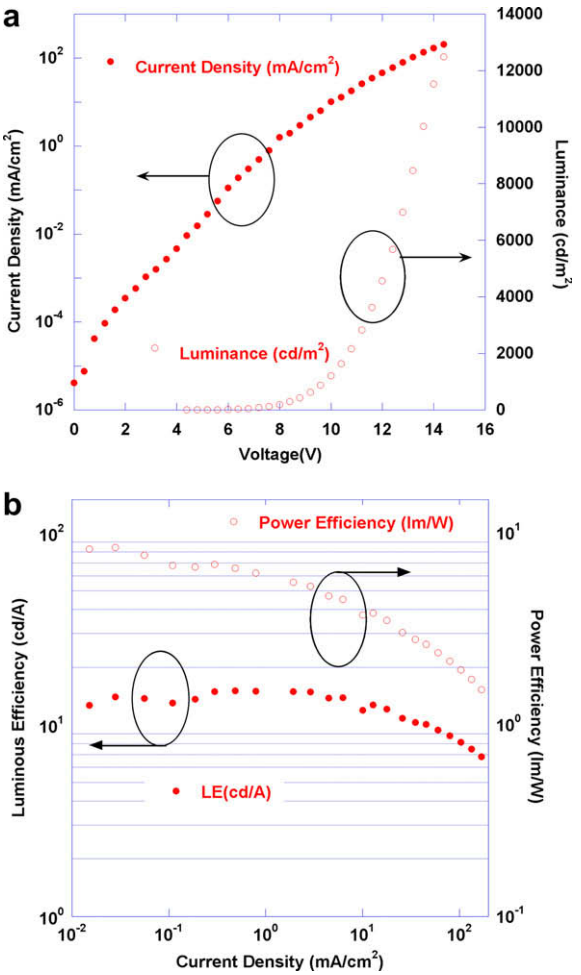

Fig. 2. (a) *J*–*L*–*V* and (b) LE–PE–*J* characteristics of a device with configuration of ITO/PEDOT:PSS (40 nm)/PVK (40 nm)/PF-2,8FSO1 (100 wt%):Ir(mppy)$_3$ (0.4 wt%):Ir-G2 (0.6 wt%) (40 nm)/PFN (20 nm)/Ba (4 nm)/Al (100 nm).

(40 nm)/cathode, it was found that when the blend ratio between PF-2,8FSO1:Ir(mppy)$_3$:Ir-G2 is fixed at 100:0.4:0.6, a white emission with a LE of 10.6 cd A^{-1} and CIE coordinates of (0.302, 0.367) was obtained at a current density of 10 mA cm^{-2}. Remarkably, the white emission has a high color rendering index (CRI) of 86. The device performance of WPLEDs can be further enhanced when a thin layer of alcohol/water-soluble polymer PFN [23–25] was incorporated as the electron injection layer at the cathode side. As a result of efficient electron injection and more balanced carrier transport, a nearly pure white emission was realized, with a peak LE of 15.1 cd A^{-1}, CIE coordinates of (0.278, 0.312) and a CRI of 79.

Fig. 2 shows typical *J*–*L*–*V* and LE–PE–*J* characteristics of an optimized WPLEDs. The turn-on voltage (defined as the voltage at a luminance of 1 cd m^{-2}) of the device is as low as 4.4 V, which can help to reduce power consumption and obtain high PE. As a result, a forward-viewing PE of 8.4 lm W^{-1} was reached at 5.2 V (i.e. at 0.03 mA cm^{-2}). It was found that high LE (over 10 cd A^{-1}) was retained over a wide range of *J* values, for example, from 0.01 to 60 mA cm^{-1}, corresponding to *L* between 1 and 6000 cd m^{-2}.

We note that for the control devices in which PVK interlayer is absent, only a degraded device performance was obtained, with a peak LE of 0.5 cd A^{-1} and a peak EQE of 0.38%. Furthermore, the green emission from Ir(mppy)$_3$ is hardly detected in this device (Fig. 1c), but an intense green emission can be observed in the devices with PVK interlayer. As reported by Wang et al., the triplet energy of the charge transport layer can have significant impact on the energy transfer quenching from the excited state of the Ir complexes and the subsequent device performance [26]. Since the triplet energy of Ir(mppy)$_3$ is 2.38 eV [27], and the triplet energy of the conjugated polymer is typically below 2.3 eV [28], so the inefficient Ir(mppy)$_3$ emission in the control device can be attributed to the energy back transfer from the triplet excitons on the Ir(mppy)$_3$ molecules to the low-lying triplet states of the polymer [19]. On the other side, with the presence of PVK interlayer, which have a triplet exciton with energy of 3.0 eV [29], exothermal energy transfer quenching from the excited state of the emitters can be avoided [26]. Furthermore, since the electrical excitation of the EL process in the devices is dominated by charge trapping mechanism (which can be inferred from the energy level of the device, characterized by deep hole traps with depths of 0.6 eV and densities of 10^{18} cm^{-3}) [2], we speculate that the recombination zone was located at the interface between the PVK layer and the emitting layer. Therefore, triplet exciton with energy of 3.0 eV was formed on PVK at the interface and can be readily transferred to the iridium dyes within a few nanometers via Förster or Dexter energy transfer, leading to efficient green and red electrophosphorescence, thus avoid the quenching from the excited state of the emitters to the triplet state of PF-2,8FSO1. In addition, due to different solubility of PVK in chlorobenzene and *p*-xylene, we can eliminate the possibility of intermixing at the interface which has also been addressed by the analysis on the cross section of the profile of the bilayer in our previous publication [19,30].

The role of the PVK layer can be further clarified by transient PL spectra. Fig. 3 shows the transient PL spectra of the films of PVK:Ir(mppy)$_3$ (2 wt%) (40 nm), PVK (40 nm)/PF-2,8FSO1:Ir(mppy)$_3$ (2 wt%) (40 nm) and PF-2,8FSO1:Ir(mppy)$_3$ (2 wt%) (40 nm), which are denoted as A, B, and C, respectively. When sample A was excited at 300 nm which is around the absorption peak of PVK, and the probe was fixed at the emission peak of Ir(mppy)$_3$ (~510 nm), a single exponential decay with a lifetime of 703 ns was recorded, which is consistent with our previous measurement [19]. In contrast, for sample C, in which the PVK layer is absent, when excited at the absorption peak of PF-2,8FSO1 at 375 nm, the phosphorescence decay is significantly faster (with τ_1 = 9.8 ns, valued 68% and τ_2 = 69 ns, valued 32%). This difference in the density of excited states can be attributed to the quenching by PF-2,8FSO1 due to the low-lying triplet energy level. More-

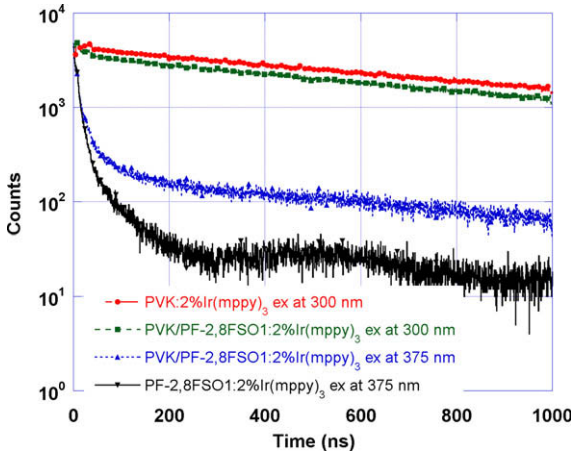

Fig. 3. Transient PL spectra of samples with configurations of PVK:Ir(mppy)$_3$ (2 wt%) (40 nm) (sample A), PVK (40 nm)/PF-2,8FSO1:Ir(mppy)$_3$ (2 wt%) (40 nm) (sample B), and PF-2,8FSO1:Ir(mppy)$_3$ (2 wt%) (40 nm) (sample C), excited at 300 nm and 375 nm, respectively.

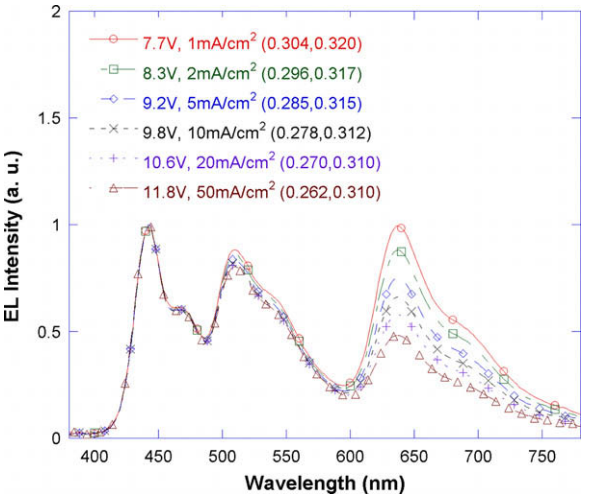

Fig. 4. The EL spectra of a typical WPLEDs upon variations of applied current density from 1 mA cm^{-2} to 50 mA cm^{-2}.

over, for sample B, when excited at 300 nm, a nearly single exponential decay with a lifetime of 795 ns (with a value of 99%) was observed, suggesting that the decay of the phosphorescence is not affected by PF-2,8FSO1. In contrast, when the same sample was excited at 375 nm, a much faster decay (with τ_1 = 12.9 ns, valued 43% and τ_2 = 285 ns, valued 57%) was found, representing a significant quenching of the phosphorescence.

In fact, our devices showed a voltage/current density-dependent emission color. Taking a device with PFN interlayer as an example, as shown in Fig. 4, as the applied current density increase from 1 mA cm^{-2} (corresponding to a luminance of 150 cd m^{-2}) to 50 mA cm^{-2} (corresponding to a luminance of 5000 cd m^{-2}), the CIE coordinates shift from (0.304, 0.320) to (0.262, 0.310). Color shift upon increasing current density is common in dopants based WOLED/WPLEDs, which was usually attributed to the facts that the doping concentration of narrow energy gap dopants are usually very low (not higher than 1 wt%), thus the possibility of charge trapping on such dopants or energy transfer from wide energy gap dopant will decrease as the low energy excited sites are saturated [18]. However, according to our estimate, in order to excite the all of the narrow gap iridium complex Ir-G2 in our devices, an injected current density of 10,000 mA cm^{-2} should be applied. In other words, the blue shift of color in our devices with increasing current density may not simply attribute to saturation of low energy excited sites. In fact, the color shift in our devices upon the change of applied current density (voltage) can be attributed to the competition between hole trapping on narrow gap iridium complex Ir-G2 sites and undisturbed hole transport across the emissive layer [31,32]. Endeavor for improvement of the EL spectral stability is on going in our group by adopting the concept of management of charges and excitons in the single active layer [33].

4. Conclusions

In summary, we have reported a white polymer light-emitting devices based on a newly synthesized conjugated polymer which dually functions as the host and the blue emitter, which can be blended with two phosphorescent materials $Ir(mppy)_3$ and Ir-G2 as the green and red emitters. By spin coating the emissive blend atop the PVK hole transporting layer, we obtained white emission with a luminous efficiency of 15.1 cd A^{-1}, and a good color quality (i.e. a CRI of 86). Our results demonstrate that with the presence of high-triplet-lying PVK, phosphorescent quenching by the polyfluorene copolymer host can be significantly avoided, thus highly efficient white emitting polymer light-emitting devices with very good color quality can be fabricated from a fluorescent host.

Acknowledgements

H.-B. Wu thanks the Ministry of Science and Technology Project (No. 2009CB623602) and the Natural Science Foundation of China (Project No. 60937001, and U0634003) and the China Postdoctoral Science Foundation (20060400215) for the financial support. W.-Y. Wong thanks the Hong Kong Research Grants Council (HKBU 202106) and the Hong Kong Baptist University (FRG2/08-09/111) for financial support.

References

[1] H.B. Wu, L. Ying, W. Yang, Y. Cao, Chem. Soc. Rev. 38 (2009) 3391.
[2] H.B. Wu, J.H. Zou, F. Liu, L. Wang, A. Mikhailovsky, G.C. Bazan, W. Yang, Y. Cao, Adv. Mater. 20 (2008) 696.
[3] Y. Sun, N.C. Giebink, H. Kanno, B. Ma, M.E. Thompson, S.R. Forrest, Nature 440 (2006) 908.
[4] S.-J. Su, E. Gonmori, H. Sasabe, J. Kido, Adv. Mater. 20 (2008) 4189.
[5] N. Chopra, J. Lee, Y. Zheng, S.-H. Eom, J.G. Xue, F. So, Appl. Phys. Lett. 93 (2008) 143307.
[6] C.-L. Ho, W.-Y. Wong, Q. Wang, D.-G. Ma, L.-X. Wang, Z. Lin, Adv. Funct. Mater. 18 (2008) 928.
[7] Y.H. Xu, J.B. Peng, Y.Q. Mo, Q. Hou, Y. Cao, Appl. Phys. Lett. 86 (2005) 163502.
[8] Y. Zhou, Q.J. Sun, Z.A. Tan, H.Z. Zhong, C.H. Yang, Y.F. Li, J. Phys. Chem. C 111 (2007) 6862.
[9] J.H. Zou, J. Liu, H.B. Wu, J.B. Peng, W. Yang, Y. Cao, Org. Electron. 10 (2009) 843.
[10] X. Gong, S. Wang, D. Moses, G.C. Bazan, A.J. Heeger, Adv. Mater. 17 (2005) 2053.
[11] D. An, J.H. Zou, H.B. Wu, J.B. Peng, W. Yang, Y. Cao, Org. Electron. 10 (2009) 299.
[12] H.B. Wu, G.J. Zhou, J.H. Zou, C.-L. Ho, W.-Y. Wong, W. Yang, J.B. Peng, Y. Cao, Adv. Mater. 21 (2009) 4181.
[13] G.L. Tu, Q.G. Zhou, Y.X. Cheng, L.X. Wang, D.G. Ma, X.B. Jing, F.S. Wang, Appl. Phys. Lett. 85 (2004) 2172.
[14] J.X. Jiang, Y.H. Xu, W. Yang, R. Guan, Z.Q. Liu, H.Y. Zhen, Y. Cao, Adv. Mater. 18 (2006) 1769.
[15] J. Liu, L. Chen, S.Y. Shao, Z.Y. Xie, Y.X. Cheng, Y.H. Geng, L.X. Wang, X.B. Jing, F.S. Wang, Adv. Mater. 19 (2007) 4224.
[16] W.-Y. Wong, C.-L. Ho, Coord. Chem. Rev. 253 (2009) 1709.
[17] W.-Y. Wong, C.-L. Ho, J. Mater. Chem. 19 (2009) 4457.
[18] T.-H. Kim, H.K. Lee, O.O. Park, B.D. Chin, S. Lee, J.K. Kim, Adv. Funct. Mater. 16 (2006) 611.
[19] Z. Chen, C.Y. Jiang, Q.L. Niu, J.B. Peng, Y. Cao, Org. Electron. 9 (2008) 1002.
[20] Y.Y. Li, H.B. Wu, J.H. Zou, L. Ying, W. Yang, Y. Cao, Org. Electron. 10 (2009) 901.
[21] H.Z. Xie, M.W. Liu, O.Y. Wang, X.H. Zhang, C.S. Lee, L.S. Hung, S.T. Lee, P.F. Teng, H.L. Kwong, H. Zheng, C.M. Che, Adv. Mater. 13 (2001) 1245.
[22] G.J. Zhou, W.Y. Wong, B. Yao, Z.Y. Xie, L.X. Wang, Angew. Chem. Int. Ed. 46 (2007) 1149.
[23] H.B. Wu, F. Huang, Y.Q. Mo, W. Yang, D.L. Wang, J.B. Peng, Y. Cao, Adv. Mater. 16 (2004) 1826.
[24] F. Huang, H.B. Wu, D.L. Wang, W. Yang, Y. Cao, Chem. Mater. 16 (2004) 708.
[25] H.B. Wu, F. Huang, J.B. Peng, Y. Cao, Org. Electron. 6 (2005) 118.
[26] Y. Wang, Appl. Phys. Lett. 85 (2004) 4848.
[27] H.H. Liao, H.F. Meng, S.F. Homg, W.S. Lee, J.M. Yang, C.C. Liu, J.T. Shy, F.C. Chen, C.S. Hsu, Phys. Rev. B 74 (2005) 245211.
[28] M. Sudhaker, P.I. Djurovich, T.E. Hogen-Esch, M.E. Thompson, J. Am. Chem. Soc. 125 (2003) 7796.
[29] J. Pina, J. Seixas de Melo, H.D. Burrows, A.P. Monkman, S. Navaratnam, Chem. Phys. Lett. 400 (2004) 441.
[30] J. Huang, Q. Liu, J.H. Zou, X.-H. Zhu, A.-Y. Li, J.-W. Li, S. Wu, J.B. Peng, Y. Cao, R.D. Xia, D.D.C. Bradley, J. Roncali, Adv. Funct. Mater. 19 (2009) 2978.
[31] M.C. Gather, R. Alle, H. Becker, K. Meerholz, Adv. Mater. 19 (2007) 4460.
[32] Q. Wang, J.Q. Ding, D.M. Ma, Y.X. Cheng, L.X. Wang, X.B. Jing, F.S. Wang, Adv. Funct. Mater. 19 (2009) 84.
[33] Q. Wang, J.Q. Ding, D.M. Ma, Y.X. Cheng, L.X. Wang, F.S. Wang, Adv. Mater. 21 (2009) 2397.

Organic Electronics 11 (2010) 535–538

Contents lists available at ScienceDirect

Organic Electronics

journal homepage: www.elsevier.com/locate/orgel

Cathodes comprising highly conductive poly(3,4-ethylenedioxythiophene): poly(styrenesulfonate) for semi-transparent polymer solar cells

Felix Nickel, Andreas Puetz, Manuel Reinhard, Hung Do, Christian Kayser, Alexander Colsmann *, Uli Lemmer

Light Technology Institute, Karlsruhe Institute of Technology (KIT), Engesser Strasse 13, 76131 Karlsruhe, Germany

ARTICLE INFO

Article history:
Received 4 November 2009
Received in revised form 1 December 2009
Accepted 8 December 2009
Available online 22 December 2009

Keywords:
Polymer solar cell
Polymer electrode
Semi-transparent
Doping
PEDOT:PSS

ABSTRACT

Semi-transparent polymer solar cells from a blend of poly-(3-hexylthiophene-2,5-diyl) and [6,6]-phenyl C_{61} butyric acid methyl ester (P3HT:PCBM) comprising a poly(3,4-ethylenedioxythiophene):poly(styrenesulfonate) (PEDOT:PSS) cathode and a vacuum deposited n-doped organic buffer layer have been realized. Among the investigated organic material systems for n-doping, the use of lithium doped bathophenanthroline (BPhen:Li) allowed for proper energy level alignment and subsequently for an open-circuit voltage $V_{oc} \approx 600$ mV. Upon deposition the PEDOT:PSS adheres selectively on the BPhen:Li buffer layer in order to form the laterally defined transparent cathode.

© 2009 Elsevier B.V. All rights reserved.

1. Introduction

Due to the recent progress in power conversion efficiencies to more than 5%, polymer solar cells have increasingly attracted attention [1–5]. Taking the absorption bands of organic materials into account, polymer solar cells open pathways to semi-transparent devices that can be used e.g. for façade-integrated photovoltaics. As a matter of principle such semi-transparent devices need two transparent but conducting contacts where indium tin oxide (ITO, workfunction $\Phi_a \approx 4.8$ eV) or highly conductive poly(3,4-ethylenedioxythiophene):poly(styrenesulfonate) (PEDOT:PSS, workfunction $\Phi_a \approx 5.2$ eV) [6–9] can be used to form the anode. However, the realization of a transparent and conducting cathode with a low work function is challenging. So far transparent cathodes have been realized by ultrathin metal layers [10], sputtered ITO [11] or by a combination of a lithiumfluoride (LiF) or lithium cobalt oxide ($LiCoO_2$) interlayers with an ultrathin aluminium cathode and a sputtered aluminium doped zinc oxide layer [12,13]. Utilizing a lamination process, semi-transparent organic photovoltaic devices comprising cathodes based on vapor phase polymerized PEDOT can be fabricated [14]. Another approach features the incorporation of zinc oxide nanoparticles below a PEDOT:PSS cathode [15]. In general, transparent cathodes can be fabricated from high work function materials in conjunction with n-doped buffer layers or an ultrathin low work function metal layer.

N-doped organic layers can be considered as standard buffer layers for vacuum deposited organic photovoltaic devices [16]. In particular alkali metal doping of electron transport materials is a well investigated material combination for organic optoelectronic devices [17,18], but also cationic dye doping (e.g. rhodamine B, RhB) of fullerenes or 1,4,5,8-naphthalenetetracarboxylic dianhydride (NTCDA) is a common approach [19,20].

In this work we demonstrate a semi-transparent polymer solar cell incorporating vacuum deposited lithium doped bathophenanthroline (BPhen:Li) buffer layers below a cathode from PEDOT:PSS.

* Corresponding author. Tel.: +49 721 608 8587; fax: +49 721 608 2590.
E-mail address: alexander.colsmann@kit.edu (A. Colsmann).

1566-1199/$ - see front matter © 2009 Elsevier B.V. All rights reserved.
doi:10.1016/j.orgel.2009.12.009

2. Experimental

In order to fabricate semi-transparent polymer solar cells following the architecture depicted in Fig. 1a ITO coated glass samples (Merck, $R_{\square} = 13\ \Omega/\square$) were structured in hydrochloric acid and solvent cleaned following established standard procedures. A 20 nm film of PEDOT:PSS (Clevios VP AI 4083) was spincast on the ITO anode followed by a 200 nm thick film from a blend of poly-(3-hexylthiophene-2,5-diyl) and [6,6]-phenyl C_{61} butyric acid methyl ester (P3HT:PCBM, 1:0.9 by weight, 40 mg/ml in *o*-dichlorobenzene). Then the samples were transferred to a vacuum chamber (10^{-7} mbar) where a 20 nm BPhen:Li layer with a molar ratio of 1:1 was co-deposited from effusion cells through a shadow mask followed by a thin layer of gold with a nominal thickness of 3 nm. At such small nominal thicknesses gold is known not to form a closed thin layer but clusters [21]. Finally, we spincast a 120 nm layer of highly conductive PEDOT:PSS (Clevios PH 750 with 5% dimethylsulfoxide) on top of the layer stack in order to form the transparent and conductive cathode. We determined the conductivity $\sigma \approx 570$ S/cm of the PEDOT:PSS formulation on a glass substrate previously [9]. Subsequently, the active area of the solar cell was determined by the cross section of the 12 mm wide ITO anode and the 2 mm wide PEDOT:PSS contact.

We found that PEDOT:PSS performs self patterning in a way that it only wets the BPhen:Li pads but not the P3HT:PCBM surface. This finding was substantiated by contact angle measurements between the respective PEDOT:PSS formulation and the surfaces under investigation. While the contact angle of the PEDOT:PSS formulation on P3HT:PCBM was determined to 99° ± 2° indicating very bad adhesion, it measured only 69° ± 6° on BPhen surfaces. This contact angle was further reduced by doping BPhen with lithium to 55° ± 3°. Gold clusters on top of both BPhen and BPhen:Li changed the contact angle to 70° ± 3° that is still well below the contact angle of PEDOT:PSS on P3HT:PCBM. The difference in contact angles can be attributed to different surface energies of P3HT:PCBM and the BPhen:Li/Au pads and explains the exclusive wetting of PEDOT:PSS on P3HT:PCBM.

For comparison, solar cells with vacuum deposited buffer layers based on BPhen:Li and the matrix-dopant systems C_{60}:RhB and NTCDA:RhB on top of the P3HT:PCBM bulk heterojunction followed by a 250 nm thick aluminium electrode were fabricated.

The current voltage characteristics of the solar cells were recorded with a source measure unit (Keithley 238). A spectrally monitored Oriel 300 W solar simulator was used to simulate the sunlight according to the ASTM-G173-03e1, AM 1.5 standard with an irradiation of 100 mW/cm^2 [22].

3. Results and discussion

On their way to the contact, electrons that were generated in the active layer, have to pass two interfaces that can potentially account for losses.

In order to minimize the losses at the first interface between the organic layer stack and the buffer layer we investigated different n-doped transport layers. From the range of material combinations for n-doping we chose the matrix-dopant systems C_{60}:RhB (molar 15:1), NTCDA:RhB (42:1) and BPhen:Li (1:1). From the *JV* curves of polymer solar cells comprising either of these n-doped layers and an aluminium cathode as depicted in Fig. 2 we conclude, that doped C_{60} and NTCDA do not form suitable buffer layers. The deep lying LUMOs of C_{60} ($E_{LUMO} = -4.3$ eV) and NTCDA ($E_{LUMO} = -4.5$ eV) and subsequently their even lower Fermi levels lead to reduced open-circuit voltages (V_{oc}) and hence to moderate power conversion efficiencies. In contrast, incorporating BPhen:Li ($E_{LUMO} \approx -3.0$ eV) as a buffer layer results in a $V_{oc} \approx 600$ mV being comparable to P3HT:PCBM solar cells with established standard architectures. Consequently, we further investigated BPhen:Li buffer layers for their use in semi-transparent organic solar cells.

In the next step we studied the electrical properties of the BPhen:Li/PEDOT:PSS interface in order to improve the conversion between the electron current in the BPhen:Li layer to a hole current in the PEDOT:PSS cathode. Therefore we investigated the *JV* curve of a bilayer pn-heterojunction (ITO/PEDOT:PSS/BPhen:Li/Al) with and without gold clusters between the organic layers. As depicted in Fig. 3 the vacuum deposited gold clusters improve the current through the pn-junction by about one to two orders of magnitude. This concept is similar to the concept of recombination zones that have been reported for organic tandem solar cells so far where noble metal clusters establish efficient recombination of charge carriers between two stacked and monolithically linked solar cells [23,24].

Taking both results into account, we built semi-transparent solar cells with a cathode from PEDOT:PSS and a BPhen:Li buffer layer. A typical *JV* curve of these devices is shown in Fig. 4 (solid line) together with the corresponding transmission spectrum (inset). We found a good device transmission $T = 50\%$ in the 650–700 nm regime, where

(a)

PEDOT:PSS	50 nm
Au clusters	3 nm
BPhen:Li	20 nm
P3HT:PCBM	200 nm
PEDOT:PSS	25 nm
ITO	125 nm
Glass	

(b)

Fig. 1. (a) Device architecture of the semi-transparent organic solar cells. (b) Photo of a semi-transparent solar cell.

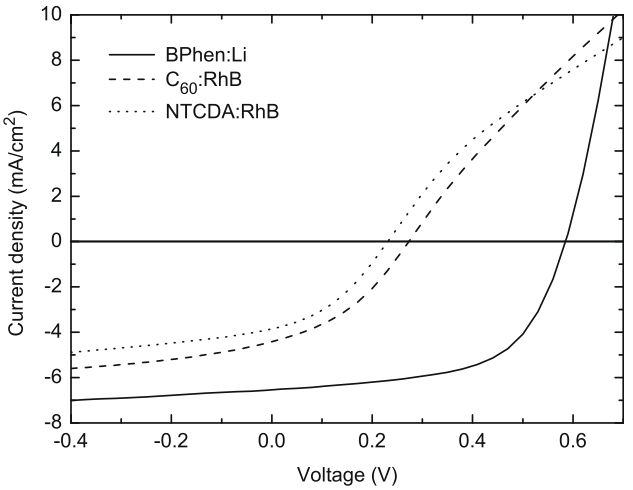

Fig. 2. *JV* curves of P3HT:PCBM solar cells incorporating n-doped buffer layers from C_{60}:RhB, NTCDA:RhB and BPhen:Li, respectively, as well as an aluminium cathode. Due to the energetically higher transport energy level of BPhen:Li compared to C_{60}:RhB and NTCDA:RhB, a higher $V_{oc} \approx 600$ mV can be achieved.

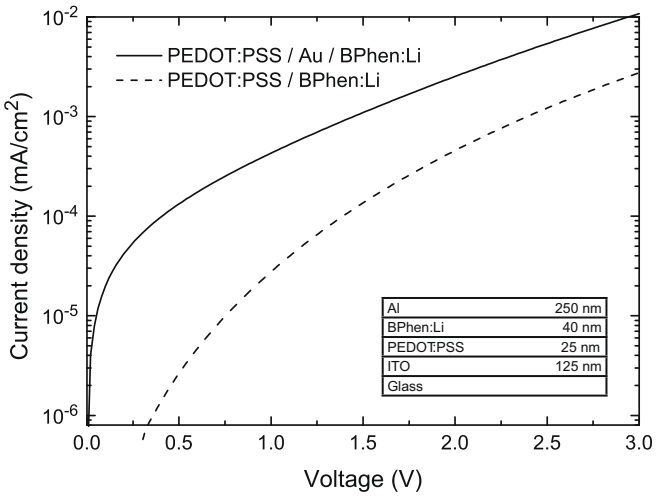

Fig. 3. *JV* curves of an ITO/PEDOT:PSS/BPhen:Li/Al bilayer device (dashed line). The current density through this pn-junction increases by about one to two orders of magnitude when gold clusters are introduced between the PEDOT:PSS and the BPhen:Li layer (solid line). Thus the resistance of this pn-junction decreases significantly. Inset: layer stack.

both the active layer and the electrodes exhibit only moderate absorption. Due to efficient photon harvesting of P3HT around 500 nm and of the fullerenes for wavelengths below 400 nm, the solar cell transmits only a small fraction of the sunlight in the lower wavelength part of the solar spectrum. The device $V_{oc} = 513$ mV is close to the maximum V_{oc} of about 600 mV that can usually be achieved with the absorber blend P3HT:PCBM when utilizing e.g. a calcium cathode. This indicates an ohmic contact between BPhen:Li and PEDOT:PSS due to proper energetic alignment of the respective transport levels. N-doping with lithium shifts the Fermi energy in BPhen towards the LUMO preventing electrons from dissipative energy losses upon recombination with holes in the PEDOT:PSS layer (work function $\Phi_a = 5.2$ eV).

The *JV* curve is affected by a high serial device resistance of 105 Ω cm^2 that can be derived from the reciprocal slope of the *JV* curve at higher voltages. We attribute this high serial device resistance to the moderate conductivity of the PEDOT:PSS cathode as compared to standard metal electrodes.

In order to examine the influence of the PEDOT:PSS lateral conductivity on the solar cell performance, we built devices with an additional thin gold layer on top of the PEDOT:PSS cathode. As derived from the *JV* curve of these devices in Fig. 4 (dashed line), the serial device resistance was reduced to 25 Ω cm^2, due to the gold layer supporting lateral conductivity. Consequently, the fill factor increased from 30% to 40%. At the same time, the V_{oc} of the device increased to 570 mV. This can be attributed to a smaller

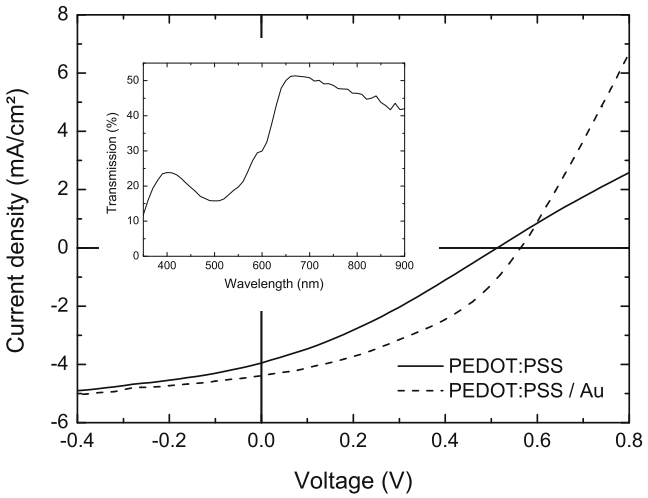

Fig. 4. *JV* curve of a semi-transparent organic solar cell comprising a PEDOT:PSS cathode and a BPhen:Li buffer layer (solid line). The device performance is strongly limited by the serial resistance of the PEDOT:PSS cathode. An additional gold layer on top of the PEDOT:PSS cathode reduces the device serial resistance by a factor 4 (dashed line). Inset: transmission spectrum of the semi-transparent device.

voltage drop along the PEDOT:PSS cathode. Although the device with the additional gold layer on top of the PEDOT:PSS was almost non-transparent, it can be concluded, that the limited lateral conductivity of PEDOT:PSS in this device architecture accounts partly for the moderate power conversion efficiency of 0.6% of the device.

4. Conclusion

In conclusion we have demonstrated semi-transparent organic solar cells comprising n-doped buffer layers and PEDOT:PSS cathodes. The material system BPhen:Li proved itself superior over cationic dye doped material systems in order to achieve open-circuit voltages as high as in conventional devices. Efficient current conversion between the electron current in the buffer layer and the hole current in the cathode was achieved by the incorporation of gold clusters between both layers.

Acknowledgements

The authors would like to acknowledge Erik Ahlswede, Jonas Hanisch and Michael Powalla (Zentrum für Sonnenenergie- und Wasserstoff-Forschung, Stuttgart, Germany) for many fruitful discussions, H.C. Starck for supplying PEDOT:PSS and the Deutsche Forschungsgemeinschaft (DFG) and the Federal Ministry of Education and Research (BMBF) for funding.

References

[1] W. Ma, C. Yang, X. Gong, K. Lee, A.J. Heeger, Adv. Funct. Mater. 15 (2005) 1617.
[2] J. Peet, J.Y. Kim, N.E. Coates, W.L. Ma, D. Moses, A.J. Heeger, G.C. Bazan, Nat. Mater. 6 (2007) 497.
[3] J. Hou, H.-Y. Chen, S. Zhang, G. Li, Y. Yang, J. Am. Chem. Soc. 130 (2008) 16144.
[4] S.H. Park, A. Roy, S. Beaupre, S. Cho, N. Coates, J.S. Moon, D. Moses, M. Leclerc, K. Lee, A.J. Heeger, Nat. Photonics 3 (2009) 297.
[5] K. Vandewal, K. Tvingstedt, A. Gadisa, O. Inganäs, J.V. Manca, Nat. Mater. 8 (2009) 904.
[6] S.I. Na, S.S. Kim, J. Jo, D.Y. Kim, Adv. Mater. 20 (2008) 4061.
[7] E. Ahlswede, W. Mühleisen, M.W. Bin Moh Wahi, J. Hanisch, M. Powalla, Appl. Phys. Lett. 92 (2008) 143307.
[8] A. Colsmann, F. Stenzel, G. Balthasar, H. Do, U. Lemmer, Thin Solid Films 517 (2009) 1750.
[9] H. Do, M. Reinhard, H. Vogeler, A. Pütz, M.F.G. Klein, W. Schabel, A. Colsmann, U. Lemmer, Thin Solid Films 517 (2009) 5900.
[10] J. Meiss, M.K. Riede, K. Leo, J. Appl. Phys. 105 (2009) 063108.
[11] R.F. Bailey-Salzman, B.P. Rand, S.R. Forrest, Appl. Phys. Lett. 88 (2006) 233502.
[12] J. Hanisch, E. Ahlswede, M. Powalla, Thin Solid Films 516 (2008) 7241.
[13] J. Hanisch, E. Ahlswede, M. Powalla, Eur. Phys. J. Appl. Phys. 37 (2007) 261.
[14] A. Gadisa, K. Tvingstedt, S. Admassie, L. Lindell, X. Crispin, M.R. Andersson, W.R. Salaneck, O. Inganäs, Synth. Met. 156 (2006) 1102.
[15] S.K. Hau, H.-L. Yip, J. Zou, A.K.-Y. Jen, Org. Electron. 10 (2009) 1401.
[16] K. Walzer, B. Maennig, M. Pfeiffer, K. Leo, Chem. Rev. 107 (2007) 1233.
[17] J. Huang, M. Pfeiffer, A. Werner, J. Blochwitz, K. Leo, S. Liu, Appl. Phys. Lett. 80 (2002) 139.
[18] A. Colsmann, J. Junge, T. Wellinger, C. Kayser, U. Lemmer, SPIE-Eur. Conf. Proc., Strasbourg 6192 (2006) 6195.
[19] B. Maenning, J. Drechsel, D. Gebeyehu, P. Simon, F. Kozlowski, A. Werner, F. Li, S. Grundmann, S. Sonntag, M. Koch, K. Leo, M. Pfeiffer, H. Hoppe, D. Meissner, N.S. Sariciftci, I. Riedel, V. Dyakonov, J. Parisi, Appl. Phys. A 79 (2004) 1.
[20] A.G. Werner, F. Li, K. Harada, M. Pfeiffer, T. Fritz, K. Leo, Appl. Phys. Lett. 82 (2003) 4495.
[21] J. Xue, S. Uchida, P. Rand, S.R. Forrest, Appl. Phys. Lett. 85 (2004) 5757.
[22] Standard Tables for Reference Solar Spectral Irradiances: Direct Normal and Hemispherical on 37° Tilted Surface, ASTM Standard G173-03e1, Book of Standards, vol. 14.04, doi:10.1520/G0173-03E01.
[23] J. Drechsel, B. Männig, F. Kozlowski, M. Pfeiffer, K. Leo, H. Hoppe, Appl. Phys. Lett. 86 (2005) 244102.
[24] A. Colsmann, J. Junge, C. Kayser, U. Lemmer, Appl. Phys. Lett. 89 (2006) 203506.

Organic Electronics 11 (2010) 539–543

Contents lists available at ScienceDirect

Organic Electronics

journal homepage: www.elsevier.com/locate/orgel

Aging of flat heterojunction zinc phthalocyanine/fullerene C_{60} organic solar cells

R. Lessmann *, Z. Hong, S. Scholz, B. Maennig, M.K. Riede, K. Leo

Institut für Angewandte Photophysik, Technische Universität Dresden, 01062 Dresden, Germany

ARTICLE INFO

Article history:
Received 15 November 2009
Received in revised form 7 December 2009
Accepted 9 December 2009
Available online 16 December 2009

Keywords:
Solar cell
Aging
Stability
C_{60}
ZnPc
Oxidation
Mass spectrometry
External quantum efficiency

ABSTRACT

This work addresses the long-term aging of organic solar cells based on a flat zinc phthalocyanine (ZnPc)/C_{60} heterojunction. We investigate both the typical degradation behavior of the short circuit current and of the saturated photocurrent, defined as $I(-1V)$. The latter remains constant after a relatively small initial decay, which is directly related to a substantial reduction of the contribution of excitons generated in C_{60} to the external quantum efficiency. Mass spectroscopy analysis of the organic material after aging revealed oxidized C_{60} and sub-products thereof. The reduction of $I(-1V)$ is thus attributed to the reaction of C_{60} molecules with oxygen impurities. The results strongly suggest that ZnPc/C_{60} photovoltaic cells are intrinsically very stable on a time scale of thousand of hours if such reactions are prevented.

© 2009 Elsevier B.V. All rights reserved.

1. Introduction

Efficient photovoltaic conversion in a heterojunction organic solar cell was first demonstrated by Tang [1] and have recently been more intensively investigated due to their potential as flexible, light-weight, and low-cost devices [2,3,5]. The main challenges in organic solar cell research are currently to improve the device efficiency and lifetime [6,7].

There are a number of reports which show that organic solar cells can be relatively stable. For instance, some dye sensitized solar cells exhibited no visible degradation operating at 75 °C over 7000 h [8], or only small changes even after 13,000 h under 400 Wm^{-2} [9]. A polymer solar cell using proprietary materials showed only a minor drop in short circuit current (I_{SC}) after 2000 h [10]. Several recent publications investigated the lifetime of polythiophene/PCBM bulk heterojunction cells [11–14,16]. For instance, all of them show that these polymer devices have an initial increase in efficiency that is related to a temperature effect [17] and morphological rearrangement of the bulk layer [14]. The degradation that follows the initial increase in efficiency is due to photo-oxidation of the polymer chain, reducing the absorption and the mobility [13]. The degradation is further related to the material of the top electrode [16]. It was also suggested, but not proven, that an increased roughness of the polymer surface takes place [14,15].

Small molecule based solar cells offer greater flexibility in the device stack over polymer and dye sensitized solar cells due to the easier deposition of multiple layers. However, lifetime data for complete encapsulated devices are still rare. In 1987, Manabe et al. produced a rather stable solar cell [18], that even had an improvement on I_{SC} over more than 600 h. Wang et al. compared different C_{60}/CuPc solar cells and showed that the devices live longer if C_{60} was moved far away from the Al electrode, leading to a shelf lifetime to half of its initial efficiency of 950 h [19].

* Corresponding author. Tel.: +49 351 463 34389; fax: +49 351 463 37065.
E-mail address: rudolf.lessmann@iapp.de (R. Lessmann).

1566-1199/$ - see front matter © 2009 Elsevier B.V. All rights reserved.
doi:10.1016/j.orgel.2009.12.010

High efficiency tandem solar cells were shown to be very stable with less than 3% of decrease in power conversion efficiency over 1000 h at 50 °C [20]. An extensive review of lifetime of organic solar cells is given in [21].

Non-encapsulated CuPc/C_{60} devices live only for a few minutes in air, in contrast to vacuum, where they are stable for at least several hours [22]. This is attributed to a strong degradation effect from oxygen with light assisted diffusion of oxygen. One of the main degradation processes for non-encapsulated devices is the quenching of excitons caused by anionic oxygen associated with C_{60} [23]. Molecular oxygen can diffuse through the whole device, in which the Al and Ag electrodes are only weak barriers [24–26]. Furthermore, oxygen causes a strong reduction in the electron mobility in C_{60} [27]. Modified electrodes and also a shift of the position of C_{60} layer further away from the Al electrode can improve device stability [11,19].

Yet, oxygen contamination acts an electron acceptor, causing p-doping of ZnPc, which improves the conductivity and lowers the barrier for hole injection/extraction to a diode anode such as Au or ITO [28,29]. Sobbi et al. extensively studied the stability of ZnPc in solution and film, concluding that ZnPc is very stable in the solid state [29].

Given the high known stability of ZnPc, this work focuses on the intrinsic stability of the C_{60} layers of the organic solar cell. In this paper, accurate measurements of solar cell electrical parameters are presented: I_{SC}, saturated photocurrent ($I(-1V)$), and fill factor (FF) of samples with a general device structure of glass/UV treated ITO (90 nm)/buffer layer/ZnPc (18 nm)/C_{60} (52 nm)/buffer layer/Al (100 nm). Table 1 summarizes all different device structures which are analyzed. Four modifications of anode and cathode are compared: structure A is the general structure using 4 nm ZnPc as cathode buffer layer. Structure B uses 4 nm ZnPc as cathode buffer layer and ITO modified with 1 nm Au followed by 1 nm of the proprietary organic dopant NDP2, which is comparable to the commonly used F_4-TCNQ [30]. Structure C is the general structure using 5 nm C_{60} doped with acridine orange base (AOB) as cathode buffer layer. Finally, structure D has a C_{60} layer doped with AOB and again the ITO is modified with 1 nm Au/1 nm NDP2. These systems were chosen due to their well known standard materials which allow for efficiencies up to 3.6% [31]. ZnPc is preferred over BCP or BPhen as buffer layer, due to its intrinsic higher thermal stability. It was previously shown that the BCP buffer can be replaced with CuPc or other materials [4], without compromising the device's performance, in house experiments have shown that ZnPc works as well. These layer sequences are building blocks for p–i–n solar cells, where the thin ZnPc and C_{60} layers are placed into the maximum of the optical field. The position of the absorption layers can be tuned by using transparent transport layers to achieve higher conversion efficiencies [5].

Table 1
List of the four different device structures, the value in brackets is the thickness in nm. The molar concentration of AOB in the AOB:C_{60} layer is 2%.

	Anode	Buffer	Donor	Acceptor	Buffer	Cathode
A	ITO(90)		ZnPc(18)	C_{60}(52)	ZnPc(4)	Al(100)
B	ITO(90)	Au(1)/ NDP2(1)	ZnPc(18)	C_{60}(52)	ZnPc(4)	Al(100)
C	ITO(90)		ZnPc(18)	C_{60}(52)	AOB:C_{60}(5)	Al(100)
D	ITO(90)	Au(1)/ NDP2(1)	ZnPc(18)	C_{60}(52)	AOB:C_{60}(5)	Al(100)

2. Experimental setup and methods

In total, 40 devices on 10 substrates (10 with each structure type) were prepared by vacuum deposition in a custom-made setup (Kurt J. Lesker Ltd.), of which four devices were left out due to short circuits or contact problems. Eight devices were stored in dark. The encapsulation is done on the wafer with a glass cover using the light curing sealant XNR5516 (Nagase GmbH). The samples are illuminated with blue light of 475 nm at 30 ± 7 mW/cm^2 using focused high power LEDs (LXHL-PB01, Philips GmbH). Blue LEDs were chosen as a compromise between light intensity and photon energy.

The LEDs are actively air cooled and their operation current is adjusted such that no significant (less than 4%) deviation of light intensity occurs during the experiment. Each LED is independently monitored using silicon photodiodes and the values of I_{SC} are corrected for the very small variation of illumination. The drawback of using LEDs is that the spectrum is very narrow and not related to the solar AM 1.5; nevertheless, the spectrum is very well defined and very stable over a very long time. The stability of this setup cannot be easily provided by conventional solar simulators.

The samples are aged under different temperatures, at 35 °C, 40 °C, 50 °C, 60 °C (also 63 °C for structure C and D). The temperatures are controlled by individual electronic controllers, using resistive heaters and digital thermometers with platinum film resistors (PT1000). The temperatures of all samples are calibrated with the same thermocouple reference with an experimental error smaller than ±0.5 °C.

The equation used to fit the transient measurements is a stretched exponential of type $A = A_0\exp[-(t/\tau)^{\beta}]$ [32], where A is the measured quantity, A_0 is the initial value at time $t_0 = 0$, t is the time (abscissa), τ is the decay constant, and β is the stretching factor [32]. The most straightforward value fitting procedure is the fitting of $I(-1V)$ and I_{SC} because of their direct relation to the generated charge. Using the stretched exponential $I_{SC}(t) = I_{SC}(t_0)\exp(-(t/\tau)^{\beta})$, the time for the I_{SC} decay to 50% of its initial value is $t_H = \tau(-\ln(0.5))^{1/\beta}$.

3. Experimental results

3.1. Electrical analysis

Device C is used to show the typical behavior of the ZnPc/C_{60} flat heterojunction device over time. The sample is aged with a substrate temperature of 50 ± 0.5 °C. The overall behavior of the main extracted parameters can be seen in the normalized transients in Fig. 1. At the end of the measurements, after 1200 h, the FF is around 0.25 and the I_{SC} is below 70% of its initial value. After the fast

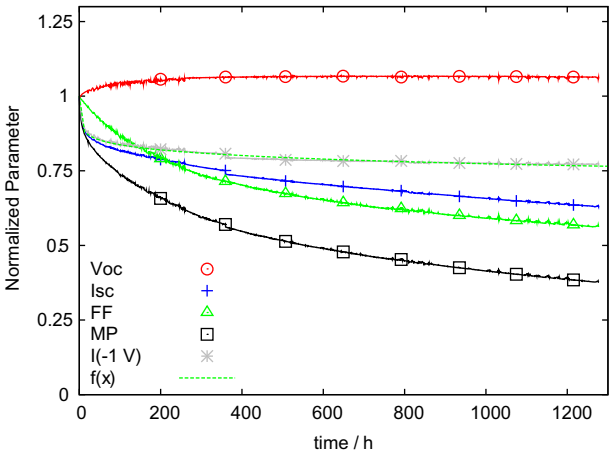

Fig. 1. Normalized values of characteristic parameters of a device with structure (C) aged at illumination of 475 nm and temperature of 50 °C. The initial values are: open circuit voltage (V_{OC}) = 0.41 V, short circuit current (I_{SC}) = -1.52×10^{-4} A (area = 6.2 mm^2), fill factor (FF) = 0.45, maximum power (MP) = -2.78×10^{-5} W, $I(-1V) = -1.13 \times 10^{-4}$ A. $f(x)$ is a stretched exponential shown fitted over $I(-1V)$. The fit parameters are $\tau = 4.8 \times 10^6$ h, $\beta = 0.16$ resulting in t_H = 485,736 h.

initial decay, the $I(-1V)$ remains remarkably constant. The observed time behavior of the normalized parameters is typical for all device structures, even for the device aged at 35 °C. Fig. 2 is an overview of the time to half of the initial value (t_H) of I_{SC}. The values obtained by fitting the $I(-1V)$ curves are scattered with no clear correlation to the experiment temperature. A reference device stored at room temperature in dark shows only minor changes in the I–V curve before and after the experiment, indicating that the observed degradation of the illuminated devices is photo- and thermically activated.

Fig. 3 shows the complete dynamics of the light I–V curve under aging conditions (T = 50 °C). The high current region (bright region, upper left corner) almost disappears after the first 200 h indicating a drastic increase in the series resistance. The broadening of the region with low current values (green and blue) shows how the I–V curve gets flatter and consequently the FF gets lower. The region of negative voltage remains almost unaffected. The inset shows the J–V curves of the first and the last measurement.

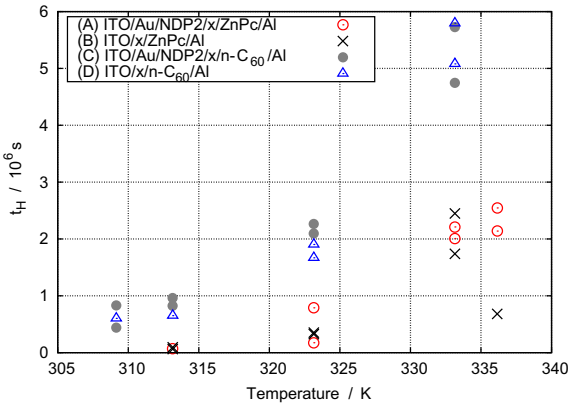

Fig. 2. Time to half (t_H) of initial short circuit current for the four different device structures. × Stands for the ZnPc (18 nm)/C_{60} (52 nm) bilayer.

The FF seems to be affected not only by the increase in series resistance, but also by the appearance of an 'S'-shape. This S-shape is related to an internal energy barrier for hole or electron transport [33]. During the accelerated aging experiment, the dark I–V curves (not shown) have a strongly reduced forward current compared to the first I–V curve. After 100 h, the exponent (n) from the current dependence on the applied voltage $I \propto V^n$ tends to 2 for the forward current. The voltage range of the I–V curve with this constant exponent ($n \sim 2$) increases over time. This is an indication of a space charge build up [34], probably due to low mobility in one or both main materials (ZnPc and C_{60}).

The characteristic values under AM1.5G of the reference device were V_{OC} = 0.49 V, J_{SC} = −6.5 mA, FF = 0.37, $I(-1V)/I_{SC}$ = 1.31 at the beginning of the experiment. At the end of the experiment, the values under AM1.5G were V_{OC} = 0.39 V, J_{SC} = −5.0 mA, FF = 0.29, $I(-1V)/I_{SC}$ = 1.42.

3.2. Chemical analysis

To address the material stability, additional 3 samples with structure A are analyzed with laser desorption/ionization time of flight mass spectrometry (LDI-TOF-MS, short LDI, as described elsewhere [35]). One sample is kept in the dark (1), this sample did not show any significant alteration of its I–V curve after 1200 h. Two samples are aged for 1000 h at 80 °C (2 and 3), one of these is further heated at T = 115 °C for 200 h (3), leading to a darkening of the sealant and subsequently to a complete loss of all photovoltaic characteristics. ZnPc and ZnPc + O are observed in the mass spectrum for positive charge. C_{60}, C_{60} + O, and C_{58} are observed in the negative spectrum. C_{56} and C_{54} signals are observed only for higher laser intensities. The ratio of intensities from ZnPc + O/ZnPc for the 3 characterized samples is: (1) > (2) ≃ (3). The ratio of ZnPc + O in the device leads to the conclusion that there are oxygen impurities in the fresh sample and, upon heating, ZnPc + O is

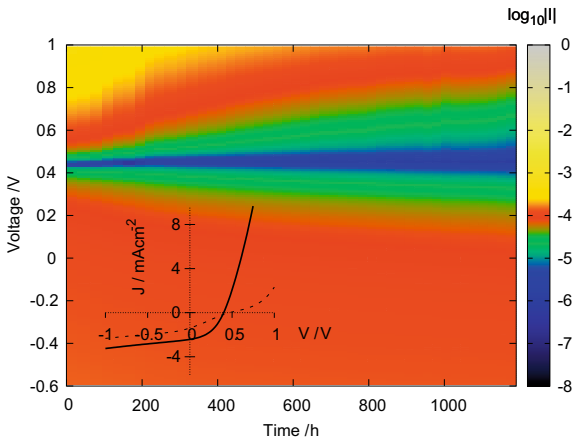

Fig. 3. Color map of $\log_{10}|I(V)|$ as function of time for a device with structure C illuminated at 475 nm and held at 50 °C. The inset shows the *J–V* curves at the beginning of the measurements initial (solid line) and after 1200 h (dashed line).

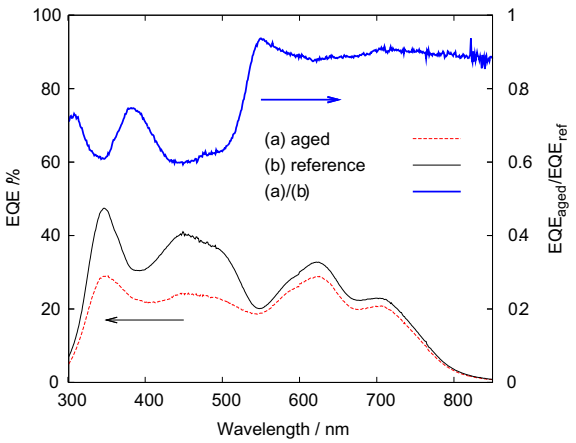

Fig. 4. EQE of device with structure (C), after aging (a) and reference (b). The ratio (a)/(b) is shown to emphasize the changes in the aged sample.

destroyed, either by losing the oxygen or by the fragmentation of the ZnPc part.

Stronger C_{60} + O and C_{58} signals are observed in the sample (2), indicating that the oxygen impurities are not reacted with C_{60} in the fresh sample. In sample (3) the oxidized C_{60} is probably reacted further to compounds with very low mass (such as CO_2).

The two obvious sources of oxygen contamination are the ITO and the organic materials. The ITO, used as anode, was treated with UV, then baked under vacuum at 100 °C for 1 h, and subsequently moved into nitrogen atmosphere, before loading the substrate into the deposition chamber. The organic materials were briefly exposed to air after the purification by sublimation, and afterwards always contained in nitrogen atmosphere. Most probably a joint contribution of oxygen from ITO and from ZnPc is responsible for the contamination. ZnPc and ZnPc + O cannot be separated by sublimation.

The thermal activation energies for the dark reaction described by Wohlers et al. [36] can be easily overcome by photoexcitation of C_{60} [37], creating two single or one double bonds in the form C_{60} > O (two different C atoms bound to one O atom) and C_{60}=O; and subsequently breaking the C_{60} cage into smaller molecules, which are stable only with an even number of C atoms [38]. It is likely that in the fresh sample, molecular oxygen is already available in the bulk and is partially reacted (1). Over time, atomic oxygen is created and reacts forming C_{60} + O which later dissociates in C_{58} (2). After further heating (3) the partially oxidized C_{60} or C_{58} further decomposes (CO_2), or polymerizes.

3.3. External quantum efficiency spectrum

Despite the changes in the ZnPc layer, the main loss in the I_{SC} is due to a reduction of the C_{60} contribution, most probably due to the illumination centered at 475 nm. Dividing the wavelength dependent external quantum efficiency (EQE) of the aged cell by the EQE of the reference cell (Fig. 4), it is seen that the main drop of I_{SC} comes from C_{60}. The normalized signal has a similar pattern to the EQE itself and the C_{60} contribution can be seen inverted, indicating that there is a much stronger degradation of C_{60} than of ZnPc. The major loss is the due to C_{60} layer, which is probably related to quenching or trapping effects of O_2 on excitons in C_{60}. The traps created upon aging have a negative effect on the charge carrier mobility. Nevertheless, there is also a loss in the ZnPc contribution, with a relatively weak signal change at around 600 nm to 700 nm. It is possible that the loss of the ZnPc part is due to decreasing of electron mobility in C_{60}, not necessary related to degradation in ZnPc film. This is consistent with the *I–V* after degradation. The degradation in ZnPc can thus be neglected in these devices.

3.4. Remarks

No clear correlation has been found between the changes in $I(-1V)$ and the aging temperature. If chemical reactions are related to $I(-1V)$, it can be concluded that main chemical reactions occur in the first 400 h of the experiment, after that time $I(-1V)$ remains practically constant showing that the materials are intrinsically very stable. The fact that I_{SC} and $I(-1V)$ have a fast initial drop can be explained by a photo-assisted process, in agreement with the literature [22]. Another interesting observation is that, besides the low active area, no sudden death (complete failure) occurred during the aging experiments, in any of the 36 devices.

4. Conclusions

In summary, we present detailed measurements of the aging of encapsulated organic solar cells under controlled temperature and illumination with blue LEDs for 1200 h. Transients show a fast initial degradation of I_{SC}, FF and $I(-1V)$. The decay of I_{SC} of the illuminated samples is temperature dependent. After the initial decay, $I(-1V)$ remains almost constant. The measurements indicate

materials degradation: Partially oxidized C_{60} and oxidized ZnPc degrade during the experiment as proven by LDI measurements. I_{SC} is strongly affected by loss of the current contribution from C_{60}, more than from ZnPc, as shown by EQE measurements. A common decrease of the EQE signal throughout the visible range can be ascribed to the effect of traps on charge transport, which is consistent with the decreased current under forward bias. On the other hand, the significant loss in blue range due to C_{60} can be explained by quenching of excitons in the C_{60} films. Therefore, degradation in ZnPc layer should be very limited or negligible. Our results shows that C_{60} and ZnPc are intrinsically very stable. ZnPc/C_{60} solar cells have the potential to be very stable on a time scale of many years, if reactions with oxygen are prevented.

Acknowledgements

R. Lessmann acknowledges CAPES-Brazil for the award of a scholarship. This work has been funded by the BMBF through the InnoProfile Project 03IP 602.

References

[1] C.W. Tang, Appl. Phys. Lett. 48 (1986) 183.
[2] G. Dennler, S. Bereznev, D. Fichou, K. Holl, D. Ilic, R. Koeppe, M. Krebs, A. Labouret, C. Lungenschmied, A. Marchenko, et al., Sol. Energy Mater. Sol. Cells 81 (2007) 947.
[3] M. Grätzel, Philos. Trans. R. Soc. London, Ser. A 365 (2007) 993.
[4] Z.R. Hong, Z.H. Huang, X.T. Zeng, Chem. Phys. Lett. 425 (2006) 62.
[5] K. Walzer, B. Maennig, M. Pfeiffer, K. Leo, Chem. Rev. 107 (2007) 1233.
[6] S.H. Park, A. Roy, S. Beaupré, S. Cho, N. Coates, J.S. Mon, D. Moses, M. Leclerc, K. Lee, A.J. Heeger, Nat. Photon. 3 (2009) 297.
[7] J.Y. Kim, K. Lee, N.E. Coates, D. Moses, T.Q. Nguyen, M. Dante, A.J. Heeger, Science 317 (2007) 222.
[8] O. Kohle, Adv. Mater. 9 (1997) 904.
[9] M.K.I. Senevirathna, Sol. Energy Mater. Sol. Cells 91 (2007) 544.
[10] S. Schuller, P. Schilinsky, J. Hauch, C.J. Brabec, Appl. Phys. A 79 (2004) 37.
[11] R. De Bettignies, J. Leroy, M. Firon, C. Sentein, Synth. Met. 156 (2006) 510.
[12] S.A. Gevorgyan, M. Jørgensen, F.C. Krebs, Sol. Energy Mater. Sol. Cells 92 (2008) 736.
[13] Y.M. Chang, W.F. Su, L. Wang, Sol. Energy Mater. Sol. Cells 92 (2008) 761.
[14] B. Paci, A. Generosi, V.R. Albertini, R. Generosi, P. Perfetti, R. De Bettignies, C. Sentein, J. Phys. Chem. C 112 (2008) 9931.
[15] J.W. Andreasen, S.A. Gevorgyan, C.M. Schlepütz, F.C. Krebs, Sol. Energy Mater. Sol. Cells 92 (2008) 793.
[16] M.O. Reese, A.J. Morfa, M.S. White, N. Kopidakis, S.E. Shaheen, G. Rumbles, D.S. Ginley, Sol. Energy Mater. Sol. Cells 92 (2008) 746.
[17] J.A. Hauch, P. Schilinsky, S.A. Choulis, R. Childers, M. Biele, C.J. Brabec, Sol. Energy Mater. Sol. Cells 92 (2008) 727.
[18] K. Manabe, S. Kusabayashi, M. Yokoyama, Chem. Lett. 16 (1987) 609.
[19] M.L. Wang, Q.L. Song, H.R. Wu, B.F. Ding, X.D. Gao, X.Y. Sun, X.M. Ding, X.Y. Hou, Org. Electron. 8 (2007) 445.
[20] R. Franke, B. Maennig, A. Petrich, M. Pfeiffer, Sol. Energy Mater. Sol. Cells 92 (2008) 732.
[21] M. Jørgensen, K. Norrman, F. Krebs, Sol. Energy Mater. Sol. Cells 92 (2008) 686.
[22] M. Rusu, J. Strotmann, M. Vogel, M.C. Lux-Steiner, K. Fostiropoulos, Appl. Phys. Lett. 90 (2007) 153511.
[23] J.W. Arbogast, A.P. Darmanyan, C.S. Foote, Y. Rubin, F.N. Diederich, M.M. Alvarez, S.J. Anz, R.L. Whetten, J. Phys. Chem. 95 (1991) 11.
[24] F.C. Krebs, K. Norrman, Prog. Photovolt. 15 (2007) 697.
[25] K. Norrman, N.B. Larsen, F.C. Krebs, Sol. Energy Mater. Sol. Cells 90 (2006) 2793.
[26] M. Lira-Cantu, K. Norrman, J.W. Andreasen, F.C. Krebs, Chem. Mater. 18 (2006) 5684.
[27] R. Könenkamp, G. Priebe, B. Pietzak, Phys. Rev. B 60 (1999) 11804.
[28] H.R. Kerp, K.T. Westerduin, A.T. van Veen, E.E. van Faassen, J. Mater. Res. 16 (2001) 503.
[29] A.K. Sobbi, D. Wöhrle, D. Schlettwein, J. Chem. So. Perkin Trans. 2 (1993) 481.
[30] K. Schulze, C. Uhrich, R. Schueppel, K. Leo, M. Pfeiffer, E. Brier, E. Reinold, P. Baeuerle, Adv. Mater. 18 (2006) 2872.
[31] T. Taima, S. Toyoshima, K. Hara, K. Saito, K. Yase, Jpn. J. Appl. Phys. Pt. 2 45 (2006) L217.
[32] G. Williams, D.C. Watts, T. Faraday Soc. 66 (1970) 80.
[33] C. Uhrich, R. Schuepel, A. Petrich, M. Pfeiffer, K. Leo, E. Brier, P. Kilickiran, P. Baeuerle, Adv. Funct. Mater. 17 (2007) 2991.
[34] A.R.V. Benvenho, R. Lessmann, I.A. Hummelgen, R.M.Q. Mello, R.W.C. Li, F.F.C. Bazito, J. Gruber, Mater. Chem. Phys. 95 (2006) 176.
[35] S. Scholz, K. Walzer, K. Leo, Adv. Funct. Mater. 18 (2008) 2541.
[36] M. Wohlers, A. Bauer, T. Rühle, F. Neitzel, H. Werner, R. Schlögl, Fullerenes, Nanotubes Carbon Nanostruct. 5 (1997) 49.
[37] G.H. Kroll, P.J. Benning, Y. Chen, T.R. Ohno, J.H. Weaver, L.P.F. Chibante, R.E. Smalley, Chem. Phys. Lett. 181 (1991) 112.
[38] H.W. Kroto, Nature 329 (1987) 529.

Organic Electronics 11 (2010) 544–551

Contents lists available at ScienceDirect

Organic Electronics

journal homepage: www.elsevier.com/locate/orgel

Dibenzo[b,d]thiophene based oligomers with carbon–carbon unsaturated bonds for high performance field-effect transistors

Chengliang Wang [a,c], Zhongming Wei [a,c], Qing Meng [a,c], Huaping Zhao [a], Wei Xu [a], Hongxiang Li [b,*], Wenping Hu [a,*]

[a] Beijing National Laboratory for Molecular Sciences, Key Laboratory of Organic Solids, Institute of Chemistry, Chinese Academy of Sciences, Beijing 100190, PR China
[b] Laboratory of Material Science, Shanghai Institute of Organic Chemistry, Chinese Academy of Sciences, Shanghai 200032, PR China
[c] Graduate University of Chinese Academy of Sciences, Beijing 100039, PR China

ARTICLE INFO

Article history:
Received 30 October 2009
Received in revised form 18 December 2009
Accepted 18 December 2009
Available online 24 December 2009

Keywords:
Thin film transistors
Organic semiconductors
Oligomer

ABSTRACT

Dibenzo[b,d]thiophene (**DBT**) based oligomers with carbon–carbon double and triple bonds were synthesized. Their thermal stability and energy levels were studied by thermal analyses, UV–vis absorption spectra and electrochemistry. Single crystals of 3,7-bis(phenylethynyl)dibenzo[b,d]thiophene (**BEDBT**) revealed the introduction of unsaturated bonds eliminated the steric repulsion between adjacent aromatic rings and **BEDBT** displayed planar structure in crystals. Thin film transistors of these compounds displayed typical *p*-type behaviour. The best performance was obtained from 3,7-distyryldibenzo[b,d]thiophene (**DSDBT**) on OTS modified substrates with mobility as high as 0.15 cm^2/Vs and on/off current ratio up to 10^8, one of the highest performance for **DBT** based oligomers.

© 2009 Elsevier B.V. All rights reserved.

1. Introduction

Organic field-effect transistors (OFETs) have attracted great interest because of their merits (low cost, could be fabricated on large scale and on flexible substrates) and potential applications in flexible electronic devices (roll-up displays, smart card, RFID and so on) [1–4]. The typical structure of OFETs includes source, drain and gate electrodes, an organic semiconductor layer, and a dielectrical layer. Among them, organic semiconductor layer is the key point to determine the performance of OFETs. Till now, much progress has been made to the design and synthesis of novel organic semiconductors for OFETs. Some organic semiconductors such as pentacene and heteroacenes with mobility larger than 0.5 cm^2/Vs have been reported [5–11]. The reason for the high performance of these fused ring organic semiconductors could be attributed to their large planar conjugated structures which would lead to large charge transfer integral and low reorganization energy. However, these fused ring compounds usually suffered tedious synthesis steps, complex purifications, low stabilities and solubilities. Studies have showed that oligomers would have good solubility and are easy to be modified to fit different applications, but oligomers usually exhibit low device performance because of their nonplanar structures caused by the steric repulsion between adjacent aromatic rings [12–17]. We and some researchers have reported, by introduction of carbon–carbon double [18–24] and triple bonds [25–32], planar conjugated oligomers which combined the merits of fused ring compounds and single bonds linked oligomers can be obtained. For instance, phenylvinylene oligomer [19] and its alkyl functionalized derivates [20] showed a maximum mobility of 1.3 cm^2/Vs; similar thiophenylvinylene oligomers [21] exhibited mobility up to 0.4 cm^2/Vs, seven times of its single bonds linked components [13,14]. Similar results have also been observed from the organic semiconductors with carbon–carbon triple bonds. For example, single crystals of 9,10-bisphenylethynyleneanthracene showed mobility as high as 0.73 cm^2/Vs [26]; the performances of transistors

* Corresponding authors.
E-mail addresses: lhx@mail.sioc.ac.cn (H. Li), huwp@iccas.ac.cn (W. Hu).

1566-1199/$ - see front matter © 2009 Elsevier B.V. All rights reserved.
doi:10.1016/j.orgel.2009.12.011

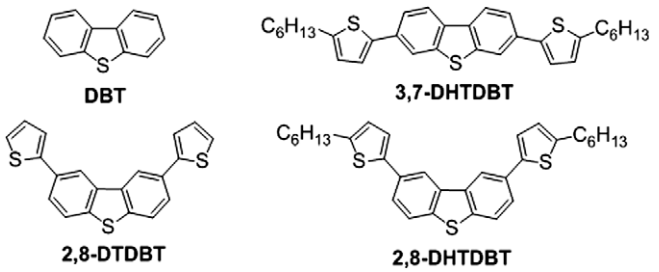

Scheme 1. The chemical structures of **DBT** and some of its single bonds linked oligomers.

of thiophene-phenyl cooligomers with carbon–carbon triple bonds was much better than those of their single bond components [25].

Dibenzo[b,d]thiophene (**DBT**, chemical structure see Scheme 1) is a commercial available chalcogenophene coumpound [33,34]. It has high ionization potential compared with anthracene, fluorene and carbazole which has conjugated planar structure and is commonly used as blocking unit in semiconductors. Additionally, the S atoms in **DBT** could introduce S···S and S···π intermolecular interactions which might facilitate charge transport. All of these merits suggested that **DBT** should be an ideal conjugated unit for organic semiconductors. In our previous work [34], we have observed single bonds linked **DBT** oligomer 3,7-bis(5′-hexylthiophene-2′-yl)dibenzothiophene (**3,7-DHTDBT**) displayed good transistor performance. In order to further investigate the application of **DBT** in organic semiconductors and the effect of carbon–carbon double and triple bonds to the performance of materials, herein two new 3,7-disubstituted **DBT** derivates, 3,7-bis(phenylethynyl)dibenzo[b,d]thiophene (**BEDBT**) and 3,7-distyryldibenzo[b,d]thiophene (**DSDBT**) were synthesized. Their physicochemical properties and charge transport characteristics were studied.

2. Results and discussion

The synthesis routes of **BEDBT** and **DSDBT** were outlined in Scheme 2. **BEDBT** were synthesized through modified Pd catalyzed Sonogashira coupling reaction [35]. **DSDBT** were synthesized through Heck reaction using $Pd(OAc)_2$ as catalyst [36]. **BEDBT** was easy to form crystals and was purified through recrystallization from toluene. **DSDBT** was obtained through column chromatography and further purified by vacuum sublimation. Both compounds were soluble in normal organic solvents such as CH_2Cl_2, THF, toluene and chlorobenzene, and totally characterized by ^1H NMR, MS and elementary analysis.

Single crystals of **BEDBT** suitable for X-ray diffraction (XRD) measurements were grown from toluene solution. As we expected, the single crystals of **BEDBT** revealed that it had nearly planar structure and belonged to a crystal system of monoclinic space group $P2_1$ with unit-cell parameters of $a = 11.666(2)$, $b = 7.6007(15)$, $c = 22.162(4)$ Å and $\beta = 94.89(3)°$. As showed in Fig. 1A, **BEDBT** adopted herringbone geometry in the crystals, and the herringbone angle was about 51.7°. Interestingly, adjacent **BEDBT** molecules along *a* axis formed Head-to-Head and Tail-to-Tail pairs (relative to S atoms). Fig. 1B showed the intermolecular interactions among neighbor molecules along *a* axis. S···H, S···π and C–H···π intermolecular interactions were found in Head-to-Head pairs, and only C–H···π intermolecular interactions existed in Tail-to-Tail pairs.

The thermal stabilities of **BEDBT** and **DSDBT** were characterized by thermogravimetric analysis (TGA). From their TGA curves (see Supplementary data), we could see **BEDBT** and **DSDBT** decomposed onset of 300 °C and 350 °C respectively, suggesting their good thermal stabilities. Fig. 2A showed the UV–vis absorption spectra of **BEDBT** and **DSDBT** in CH_2Cl_2 solution at the concentration of 10^{-5} M. The two compounds showed similar absorption peaks, but the maximum absorption of **DSDBT** was about 30 nm red shift than that of **BEDBT**, indicating a larger π-conjugation length of **DSDBT**. This phenomenon has also been observed by others [25,37]. The optical energy gaps estimated from UV–vis spectra were 3.35 and 3.1 eV for **BEDBT** and **DSDBT** respectively. The UV–vis absorption of vacuum deposited thin films of **BEDBT** and **DSDBT** were also tested to show the molecular arrangement in solids. They all showed very broad absorptions and the initial absorptions were red shifted compared with those of the solutions, indicating the ordered arrangements in solid states. The cyclic voltammetry of **BEDBT** and **DSDBT** in CH_2Cl_2 solutions at the concentration of 10^{-3} M were illustrated in Fig. 2B and C (using ferrocene (Cp_2Fe) as internal standard substance). The HOMO energy levels calculated from electrochemistry were −5.87 eV for **BEDBT** and −5.57 eV for **DSDBT** (the HOMO energy level of ferrocene was about −4.8 eV). The HOMO energy level of **BEDBT** was even lower than 2,8-disubstituted **DBT** derivatives 2,8-di(5'-hexyl-thiophen-2'-yl)-dibenzothiophene (**2,8-DHTDBT**, chemical structure see Scheme 1) reported in our previous work [33]. The lower HOMO energy level of **BEDBT** should be attributed to its short conjugated length (which was determined by UV–vis spectrum), the high ionic potential of **DBT** and the stronger electron-withdrawing effect of ethynylene group than that of the vinyl group. And this low HOMO energy level would cause carriers accumulation difficulty and charge injection barrier, which usually leads to low transistor performance. The energy gaps and HOMO/LUMO energy levels of **BEDBT** and **DSDBT** were summarized in Fig. 2D. The low HOMO energy levels suggested the good environmental stability of **BEDBT** and **DSDBT**.

The charge transport properties of **BEDBT** and **DSDBT** were examined to study their applications in OFETs. The

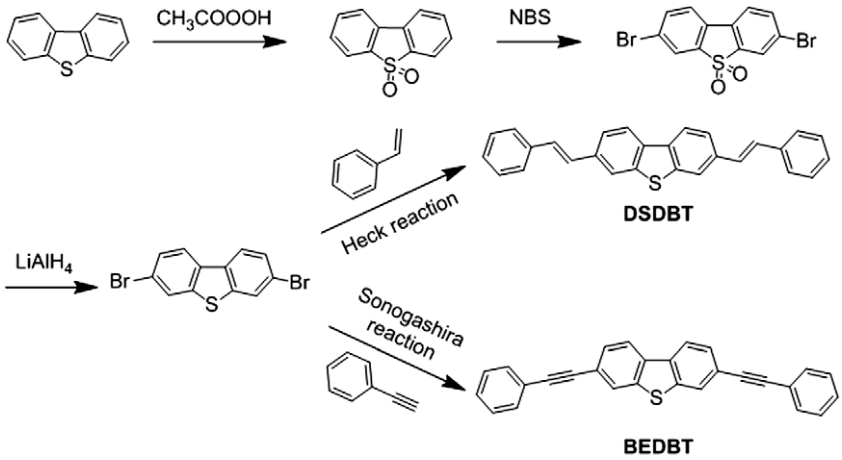

Scheme 2. Synthesis routes of **DSDBT** and **BEDBT**.

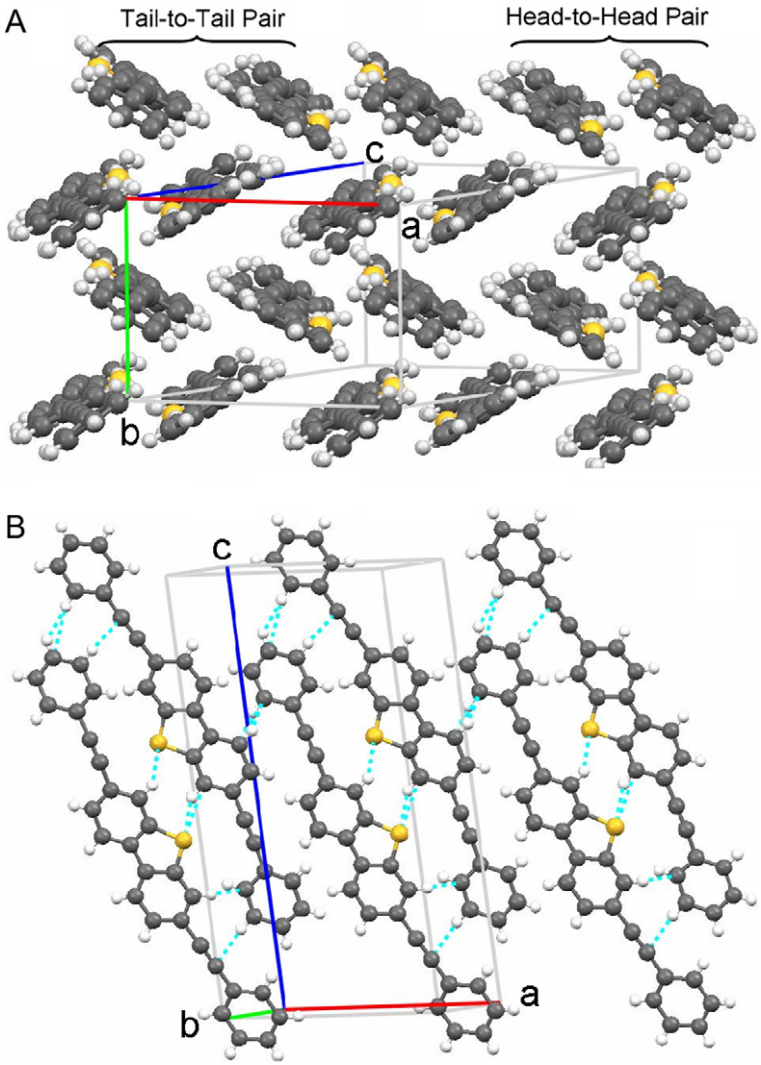

Fig. 1. (A) Packing diagram of **BEDBT**, (B) intermolecular interactions between Head-to-Head and Tail-to-Tail pairs along *a* axis in **BEDBT** crystals.

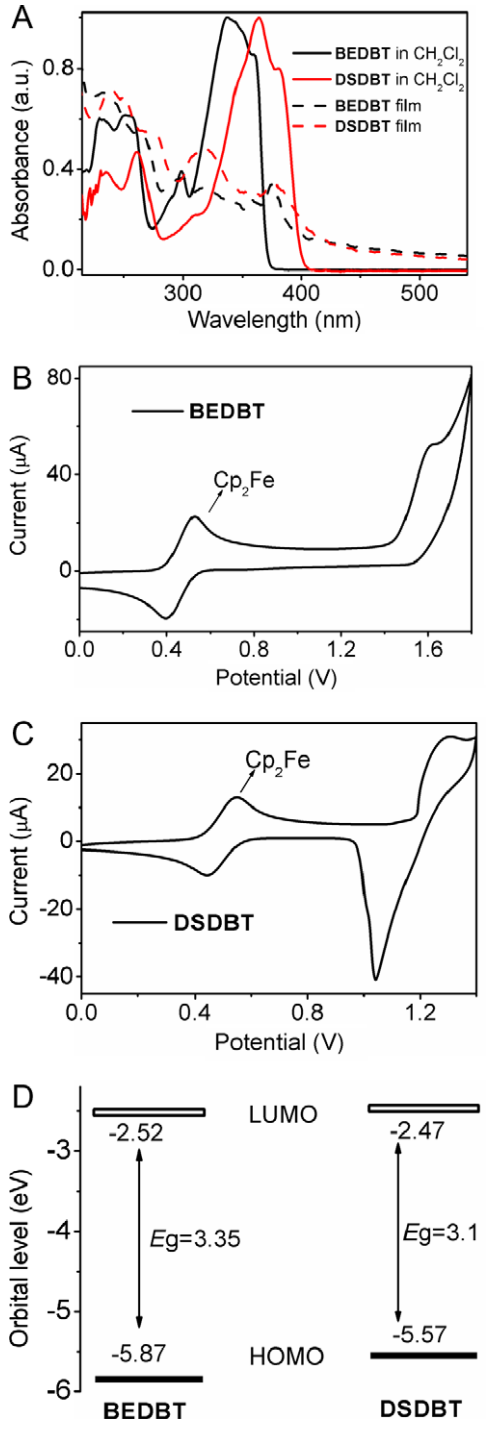

Fig. 2. (A) UV–vis absorption spectra, (B and C) cyclic voltammograms and (D) orbital levels of **BEDBT** and **DSDBT**.

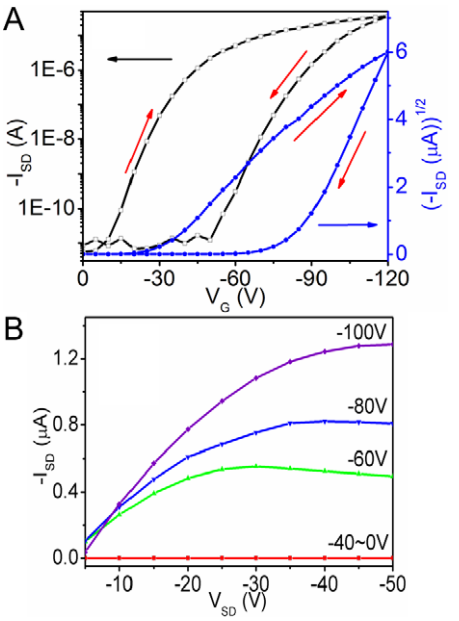

Fig. 3. (A) An example transfer with hysteresis loop (V_{DS} = −100 V) and (B) output curves of devices based on **DSDBT** films deposited on OTS modified SiO_2/Si substrates at 50 °C.

transistors were fabricated in top-contact mode using gold as the source and drain electrodes. The field-effect mobilities (μ) were calculated in the saturation regime according to the following equation: $I_D = \mu Ci(W/2L)(V_G - V_T)^2$, where I_D is the drain current, Ci is the capacitance per unit area of the gate dielectric, W and L are the channel width and length, respectively, V_G and V_T are the gate and threshold voltage, respectively. All the devices showed typical *p*-type channel FET performance under ambient conditions. Fig. 3 showed typical transfer and output curves of an example device obtained at 50 °C on octadecyltrichlorosilane (OTS) modified SiO_2/Si substrates using **DSDBT** as a semiconductor layer. The FET performance of **DSDBT** and **BEDBT** on different deposition temperature were summarized in Table 1. From Table 1, we could see the devices of **DSDBT** displayed mobility larger than 0.03 cm^2/Vs. And when the temperature of substrate increased (from 25 °C to 50 °C), the mobility of devices increased; further increasing the substrate temperature, the performance of devices decreased. The highest mobility of **DSDBT** could reach up to 0.15 cm^2/Vs, one of the highest mobility reported for **DBT** based oligomers. While scanning V_G from 0 to −120 V and then retraced scanning from −120 to 0 V at V_{DS} = −100 V, hysteresis behaviour was observed (Fig. 3A). This might be attributed to the instability of the oxidized species which was proved by the irreversible oxidations from the electrochemistry results. The performance of **BEDBT** devices was much lower compared with **DSDBT**, which was probably due to its lower HOMO energy level. The highest performance of **BEDBT** devices was obtained at T_{sub} = 25 °C.

In order to investigate the mobility-substrate temperature dependence, the morphologies and the structures of **DSDBT** and **BEDBT** films deposited at different substrate temperature were investigated by atomic force microscopy (Fig. 4 for **DSDBT** and Fig. 5 for **BEDBT**) and X-ray diffraction (Fig. 6) respectively. From the AFM images, we could see with the increase of substrate temperature, the grain size of **DSDBT** film increased. The step height of crystalline terrace layers at T_{sub} = 50 °C was about 2.2 nm (Fig. 4E, left)

Table 1
FET characteristics of **DSDBT** and **BEDBT** prepared by vacuum deposition on OTS modified SiO_2/Si substrates at different temperatures.

Entry	T_{sub} (°C)	μ_{max} (cm^2/Vs)	On/off ratio
DSDBT	25	0.039	4×10^6
	50	0.15	2×10^8
	100	0.06	3×10^7
BEDBT	25	1.3×10^{-4}	7×10^5
	50	8.0×10^{-5}	9×10^4

which was nearly equal to the simulated molecular length (about 2.24 nm) by minimized energy optimization (Fig. 4E, right), indicating that the **DSDBT** molecules grown layer-by-layer and took nearly perpendicular orientation on the substrate in the films. Further increasing the substrate temperature to 100 °C, larger grain was obtained. However, the continuity of the films became worse (see Supplementary data), and this should take the responsibility for the lower device performance at T_{sub} = 100 °C. From

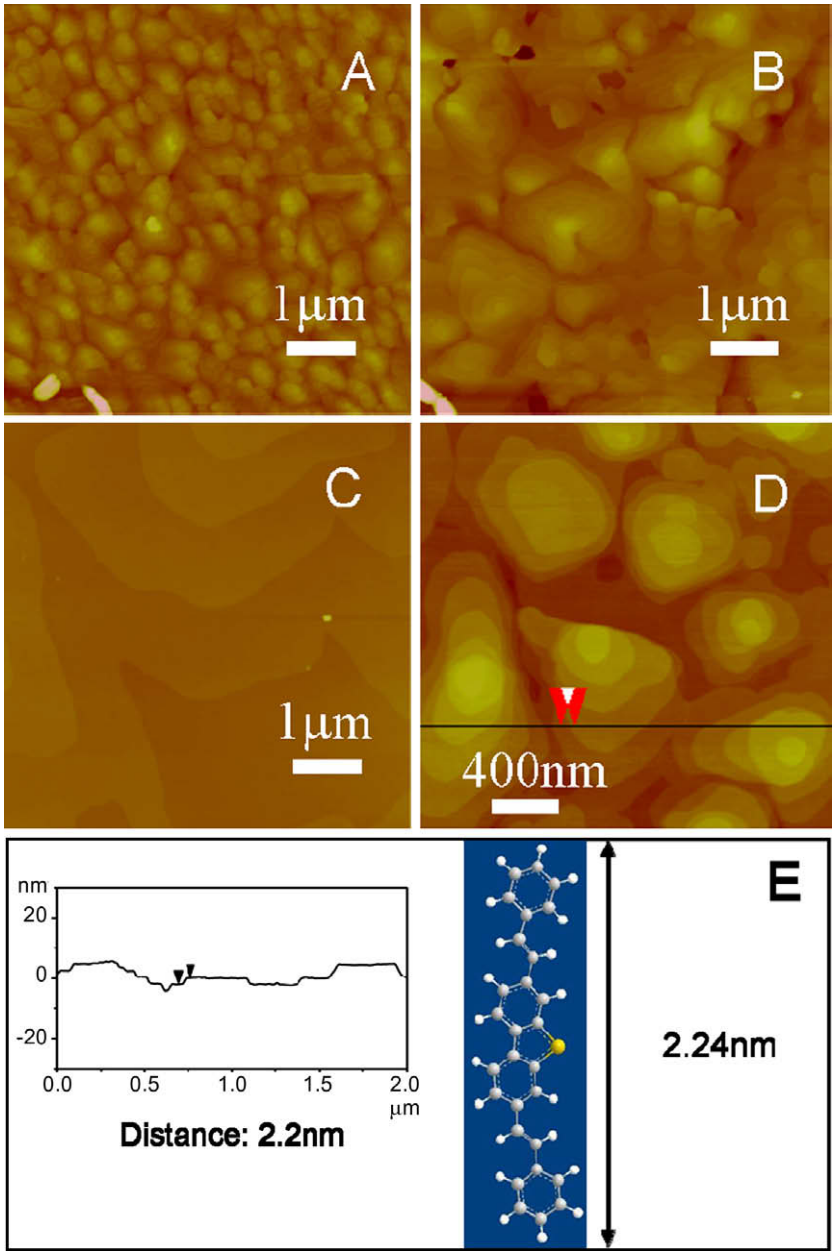

Fig. 4. (A–C) AFM images (5 × 5 μm) of thin films of **DSDBT** on OTS modified SiO_2/Si substrates at the substrate temperature of (A) 25 °C, (B) 50 °C, (C) 100 °C. (D) AFM images (2 × 2 μm) of **DSDBT** thin films on OTS modified SiO_2/Si substrate at the substrate temperature of 50 °C and (E) the step heights of crystalline terrace layers as measured by a section analysis along the line marked in (D) (left) and optimized model molecular structure (right).

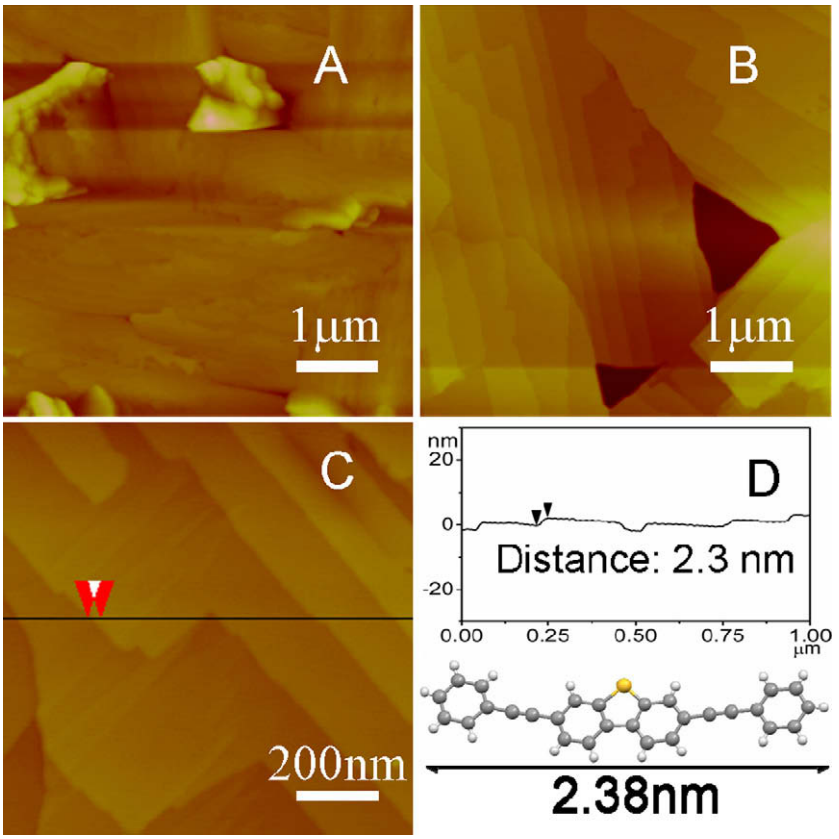

Fig. 5. (A and B) AFM images (5 × 5 μm) of **BEDBT** thin films on OTS modified SiO_2/Si substrates at the substrate temperature of (A) 25 °C, (B) 50 °C. (C) AFM images (1 × 1 μm) of **BEDBT** thin films on OTS modified SiO_2/Si substrates at the substrate temperature of 25 °C and (D) the step heights of crystalline terrace layers as measured by a section analysis along the line marked in (C) (top) and molecular structure in crystal (bottom).

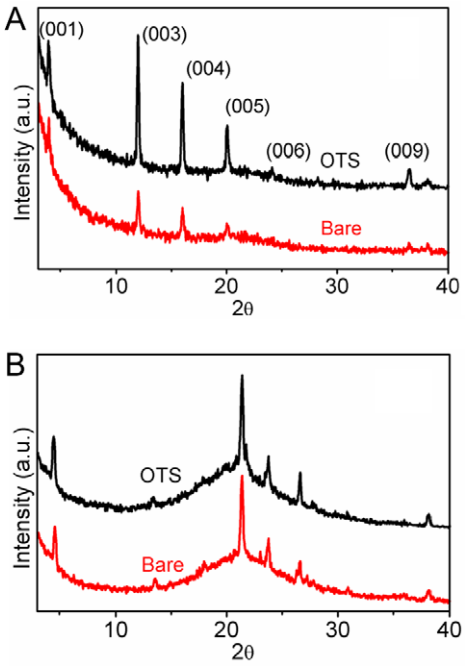

Fig. 6. XRD patterns of thin films of (A) **DSDBT** and (B) **BEDBT** on bare and OTS modified SiO_2/Si substrate at 25 °C.

the XRD patterns of **DSDBT** films (Fig. 6B), the *d*-spacing determined from their dominant peaks were 1.97 nm, closed to the simulated molecular length (2.24 nm), which also proved that the molecules were grown almost vertically to the substrates when deposited. **BEDBT** films exhibited similar results as **DSDBT**. When the substrate temperature increased to 50 °C, larger grains were obtained, but larger grain boundaries were also formed at the same time. The step height of layers of thin films determined from AFM results was about 2.3 nm (very close to the molecular length, Fig. 5D), suggesting **BEDBT** was grown layer-by-layer and nearly vertically on the substrate.

3. Conclusions

In summary, dibenzothiophene oligomers with carbon–carbon double and triple bonds were synthesized. TGA, UV–vis spectra and electrochemistry results indicated that both compounds had high stability and high oxidation resistance. Single crystal structure of **BEDBT** revealed that the introduction of carbon–carbon unsaturated bonds eliminated the steric repulsions between adjacent aromatic rings. Thin film transistors of these compounds exhibited typical *p*-channel performance. **DSDBT** displayed high FET performance with mobility up to 0.15 cm^2/Vs, and

on/off ratio as high as 10^8. The performance of **BEDBT** was much lower compared with **DSDBT**, which could be attributed to its smaller π-conjugated system and lower HOMO energy level. Further optimization of the devices, field-effect transistors based on solution-processed films and single crystals of these materials are underway.

4. Experimental

4.1. General

All reactants and solvents were purchased from commercial suppliers and used as received unless ultra noted. The reactant 3,7-dibromodibenzo[b,d]thiophene was synthesized using *N*-bromosuccinimide (NBS) as bromination reagent according to literature [34,38–39]. MS (EI) was recorded on a Shimadzu GCMS-QP2010 Plus mass spectrometer. ^{1}H NMR spectra were obtained on a Varian 400 MHz spectrometer in $CDCl_3$ with tetramethylsilane as an internal reference. Elemental analyses were performed on a Carlo Erba model 1160 elemental analyzer. UV–vis spectra were recorded on a Hitachi U-3010 spectrometer. Cyclic voltammograms were obtained on a CHI660C analyzer in a conventional three-electrode cell using a glassy carbon working electrode, a platinum wire counter electrode, an Ag/AgCl reference electrode and Bu_4NPF_6 as supporting electrolyte. X-ray diffraction (XRD) measurements for films were carried out on a *D*/max2500 instrument (Cu Kα radiation, $\lambda = 1.54056$ Å). XRD measurements for single crystals were carried out in the reflection mode using a Rigaku Saturn CCD area detector system (Mo Kα radiation, $\lambda = 0.71073$ Å). AFM images were obtained in air using a Digital Instruments Nanoscope III in tapping mode.

4.2. Materials synthesis

4.2.1. Synthesis of 3,7-distyryldibenzo[b,d]thiophene (*DSDBT*)

A 100 mL flask was charged with 3,7-dibromodibenzo-[b,d]thiophene (1.71 g, 5 mmol), PPh_3 (0.13 g, 0.5 mmol), $Pd(OAc)_2$ (0.112 g, 0.5 mmol) and dry Et_3N (20 mL). After the mixture was degassed three times and backfilled with N_2, styrene (5.2 g, 50 mmol) was added. The reaction solution was stirred at 100 °C for 3 days. The mixture was evaporated under reduced pressure. The residual solid was purified by chromatography on silica gel (petroleum ether:dichloromethane = 1:1) to provide **DSDBT** as light yellow powder (yield: 1.2 g, 62%). mp: >300 °C. MS (EI) *m*/*z*: 388 [M^+]. ^{1}H NMR (400 MHz, $CDCl_3$): 8.01 (d, 2H), 7.97 (s, 2H), 7.64 (d, 2H), 7.56 (d, 4H), 7.39 (t, 4H), 7.29 (t, 2H), 7.24 (d, 4H). Anal. calcd for $C_{28}H_{20}S$: C, 86.56; H, 5.19; found: C, 86.31; H, 5.28.

4.2.2. Synthesis of 3,7-bis(phenylethynyl)dibenzo[b,d]-thiophene (*BEDBT*)

A 100 mL flask was charged with 3,7-dibromodibenzo[b,d]thiophene (1.71 g, 5 mmol), $Pd(PPh_3)_2Cl_2$ (0.21 g, 0.3 mmol), CuI (0.115 g, 0.6 mmol), THF (30 mL) and aqueous 2-aminoethanol (2 M, 20 mL). After the mixture was degassed three times and backfilled with N_2, phenylacetylene (1.86 g, 18 mmol) was added. The reaction solution was stirred at 80 °C overnight. THF was removed, and the aqueous layer was extracted by CH_2Cl_2. The combined organic layer was evaporated under reduced pressure. The residual solid was purified by recrystallization from toluene to give **BEDBT** as white crystals (yield: 1.15 g, 60%). mp: 234 °C. MS (EI) *m*/*z*: 384 [M^+]. ^{1}H NMR (400 MHz, $CDCl_3$): 8.10 (d, 2H), 8.03 (s, 2H), 7.63 (d, 2H), 7.57 (m, 4H), 7.37 (m, 6H). Anal. calcd for $C_{28}H_{16}S$: C, 87.47; H, 4.19; found: C, 87.25; H, 4.29.

4.3. Device fabrication and electrical characterization

The SiO_2/Si substrates used were heavily doped *n*-type Si wafer with 500 nm-thick SiO_2 layer and capacitance of 7.5 nF/cm^2. After rinsed with conc. H_2SO_4/H_2O_2, water, and iso-propanol, they were surface modified with OTS. Before sublimation, the OTS modified substrates were rinsed with hexane, chloroform and iso-propanol successively. The organic semiconductors were deposited at a rate increasing gradually under a pressure of about 10^{-4} Pa to a final thickness of 50 nm determined by a quartz crystal monitor. The source and drain electrodes were deposited with gold by using shadow masks with W/L of ca. 48.2. Device characteristics were obtained with a Keithley 4200 SCS and Micromanipulator 6150 probe station in a clean and shielded box at room temperature in air.

Acknowledgements

This work was supported by National Natural Science Foundation of China (60771031, 60736004, 20571079, 20721061 and 50725311), Ministry of Science and Technology of China (2006CB806200, 2006CB932100) and Chinese Academy of Sciences.

Appendix A. Supplementary data

Supplementary data associated with this article can be found, in the online version, at doi:10.1016/j.orgel.2009.12.011.

References

[1] S.R. Forrest, Chem. Rev. 97 (1997) 1793.
[2] J. Zaumseil, H. Sirringhaus, Chem. Rev. 107 (2007) 1296.
[3] V. Coropceanu, J. Cornil, D.A. da Silva Filho, Y. Olivier, R. Silbey, J.-L. Brédas, Chem. Rev. 107 (2007) 926.
[4] A.J. Baca, J.-H. Ahn, Y. Sun, M.A. Meitl, E. Menard, H.-S. Kim, W.M. Choi, D.-H. Kim, Y. Huang, J.A. Rogers, Angew. Chem. Int. Ed. 47 (2008) 5524.
[5] Y.Y. Lin, D.J. Gundlach, S.F. Nelson, T.N. Jackson, IEEE Electron Device Lett. 18 (1997) 606.
[6] K. Xiao, Y. Liu, T. Qi, W. Zhang, F. Wang, J. Gao, W. Qiu, Y. Ma, G. Cui, S. Chen, X. Zhan, G. Yu, J. Qin, W. Hu, D. Zhu, J. Am. Chem. Soc. 127 (2005) 13281.
[7] M.L. Tang, S.C.B. Mannsfeld, Y.-S. Sun, H.A. Becerril, Z. Bao, J. Am. Chem. Soc. 131 (2009) 882.
[8] M.L. Tang, T. Okamoto, Z. Bao, J. Am. Chem. Soc. 128 (2006) 16002.
[9] K. Takimiya, H. Ebata, K. Sakamoto, T. Izawa, T. Otsubo, Y. Kunugi, J. Am. Chem. Soc. 128 (2006) 12604.
[10] T. Yamamoto, K. Takimiya, J. Am. Chem. Soc. 129 (2007) 2224.
[11] T. Okamoto, K. Kudoh, A. Wakamiya, S. Yamaguchi, Org. Lett. 7 (2005) 5301.
[12] M.L. Tang, M.E. Roberts, J.J. Locklin, M.M. Ling, H. Meng, Z. Bao, Chem. Mater. 18 (2006) 6250.

[13] H. Meng, F. Sun, M.B. Goldfinger, G.D. Jaycox, Z. Li, W.J. Marshall, G.S. Blackman, J. Am. Chem. Soc. 127 (2005) 2406.
[14] S. Ando, J.-I. Nishida, E. Fujiwara, H. Tada, Y. Inoue, S. Tokito, Y. Yamashita, Chem. Mater. 17 (2005) 1261.
[15] H. Meng, J. Zheng, A.J. Lovinger, B. Wang, P.G. Van Patten, Z. Bao, Chem. Mater. 15 (2003) 1778.
[16] K. Ito, T. Suzuki, Y. Sakamoto, D. Kubota, Y. Inoue, F. Sato, S. Tokito, Angew. Chem. Int. Ed. 42 (2003) 1159.
[17] D. Kumaki, T. Umeda, T. Suzuki, S. Tokito, Org. Electron. 9 (2008) 921.
[18] C. Videlot-Ackermann, J. Ackermann, H. Brisset, K. Kawamura, N. Yoshimoto, P. Raynal, A.E. Kassmi, F. Fages, J. Am. Chem. Soc. 127 (2005) 16346.
[19] H. Klauk, U. Zschieschang, R.T. Weitz, H. Meng, F. Sun, G. Nunes, D.E. Keys, C.R. Fincher, Z. Xiang, Adv. Mater. 19 (2007) 3882.
[20] H. Meng, F. Sun, M.B. Goldfinger, F. Gao, D.J. Londono, W.J. Marshal, G.S. Blackman, K.D. Dobbs, D.E. Keys, J. Am. Chem. Soc. 128 (2006) 9304.
[21] M.C. Um, J. Jang, J. Kang, J.P. Hong, D.Y. Yoon, S.H. Lee, J.J. Kim, J.I. Hong, J. Mater. Chem. 18 (2008) 2234.
[22] N. Drolet, J.-F. Morin, N. Leclerc, S. Wakim, Y. Tao, M. Leclerc, Adv. Funct. Mater. 15 (2005) 1671.
[23] L. Zhang, L. Tan, Z. Wang, W. Hu, D. Zhu, Chem. Mater. 21 (2009) 1993.
[24] J. Ronacali, Acc. Chem. Res. 33 (2000) 147.
[25] Q. Meng, J. Gao, R. Li, L. Jiang, C. Wang, H. Zhao, C. Liu, H. Li, W. Hu, J. Mater. Chem. 19 (2009) 1477.
[26] C. Wang, Y. Liu, Z. Ji, E. Wang, R. Li, H. Jiang, Q. Tang, H. Li, W. Hu, Chem. Mater. 21 (2009) 2840.
[27] W. Cui, X. Zhang, X. Jiang, H. Tian, D. Yan, Y. Geng, X. Jing, F. Wang, Org. Lett. 8 (2006) 785.
[28] V.A.L. Roy, Y.-G. Zhi, Z.-X. Xu, S.-C. Yu, P.W.H. Chan, C.-M. Che, Adv. Mater. 17 (2005) 1258.
[29] W. Zhao, Q. Tang, H.S. Chan, J. Xu, K.Y. Lo, Q. Miao, Chem. Commun. (2008) 4324.
[30] A. Marrocchi, M. Seri, C. Kim, A. Facchetti, A. Taticchi, T.J. Marks, Chem. Mater. 21 (2009) 2592.
[31] N.S. Baek, S.K. Hau, H.-L. Yip, O. Acton, K.-S. Chen, A.K.-Y. Jen, Chem. Mater. 20 (2008) 5734.
[32] C.P. Gerlach, T.W. Kelley, D.V. Muyres, New, High-Performance Acenyl Semiconductors, in: 227th ACS National Meeting, Anaheim, CA, 2004.
[33] B. Chawla, F.D. Sanzo, J. Chromatogr. 589 (1992) 271.
[34] J. Gao, L. Li, Q. Meng, R. Li, H. Jiang, H. Li, W. Hu, J. Mater. Chem. 17 (2007) 1421.
[35] M.S.M. Ahmed, A. Mori, Tetrahedron 60 (2004) 9977.
[36] H. Kang, G. Evmenenko, P. Dutta, K. Clays, K. Song, T.J. Marks, J. Am. Chem. Soc. 128 (2006) 6194.
[37] C. Videlot-Ackermann, J. Ackermann, K. Kawamura, N. Yoshimoto, H. Brisset, P. Raynal, A. El Kassmi, F. Fages, Org. Elecron. 7 (2006) 465.
[38] H. Sirringhaus, R.H. Friend, C. Wang, J. Leuninger, K. Müllen, J. Mater. Chem. 9 (1999) 2095.
[39] I.I. Perepichka, I.F. Perepichka, M.R. bryce, L.-O. Pålsson, Chem. Commun. (2005) 3397.

Organic Electronics 11 (2010) 552–557

Contents lists available at ScienceDirect

Organic Electronics

journal homepage: www.elsevier.com/locate/orgel

High-performing submicron organic thin-film transistors fabricated by residue-free embossing

Christoph Auner [a], Ursula Palfinger [a], Herbert Gold [a], Johanna Kraxner [a], Anja Haase [a], Thomas Haber [b], Meltem Sezen [b], Werner Grogger [b], Georg Jakopic [a], Joachim R. Krenn [a], G. Leising [c], Barbara Stadlober [a,*]

[a] Institute of Nanostructured Materials and Photonics, Joanneum Research GmbH, Franz-Pichlerstrasse 30, A-8160 Weiz, Austria
[b] Institute for Electron Microscopy, Graz University of Technology, Steyrergasse 17, A-8010 Graz, Austria
[c] Institute of Solid State Physics, Graz University of Technology, Petersgasse 16, A-8010 Graz, Austria

ARTICLE INFO

Article history:
Received 30 October 2009
Received in revised form 14 December 2009
Accepted 20 December 2009
Available online 29 December 2009

Keywords:
Organic thin-film transistors
Nanoimprint lithography
Hot Embossing
Submicron channel length

ABSTRACT

In this study, we report on an innovative residue-free nanoimprint lithography process for the patterning of submicron-spaced contacts, used as source and drain electrodes in downscaled organic thin-film transistors. The method is based on thermally initiated radical polymerization of a novel imprint resist whose outstanding chemical and physical properties are responsible for the excellent results in processability and structure transfer. In combination with a pretreated stamp the thermally curable resist enables residue-free imprinting, thus making etching obsolete. In addition, this process implies only moderate temperature budgets and it is eco-friendly due to a water-based lift-off. To validate the process, source and drain patterned submicron organic thin-film transistors with pentacene as the semiconductor were fabricated, which show excellent transistor behavior parameterized by a low switch-on voltage of $V_{so} = -3$ V, an on–off ratio of more than 10^5 and a charge carrier mobility of $\mu = 0.25$ cm^2/V s.

© 2009 Elsevier B.V. All rights reserved.

1. Introduction

Organic electronics has currently reached a stage of development in material properties, device understanding and reproducibility that allows aiming for more challenging applications than those realized today. Examples are flexible radio-frequency transponders, large-area read-out circuits for complex sensor networks, flexible high-density memories and large backplanes for high-resolution active-matrix displays [1]. In any of these products, organic thin-film transistors (OTFTs) and corresponding circuits are essential elements. Needless to say, more advanced applications make higher demands on the transistor circuit's performance. Required are higher cut-off frequencies, increased current levels, higher integration densities and decreased operation voltages. Like in "silicon world" adequate downscaling of the critical transistor dimensions, which are channel length, dielectric layer thickness and electrode overlap, is believed to improve all the above-mentioned performance parameters. In this regard, one of the main arguments for organic electronics comes into play that is the fabrication of circuits on flexible substrates over large areas with high throughput techniques. Without any doubt, advanced and flexible organic electronics generate a need for a high-resolution structuring technique that can easily be integrated in an in-line manufacturing environment. Once a nanoscale patterning technique shall be compatible with roll-to-roll (r2r) or sheet-to-sheet (s2s) fabrication, nanoimprint lithography (NIL) is an interesting alternative to the well-established but low-resolution standard printing techniques. Reasons for that are the

* Corresponding author. Tel.: +43 316 876 2721; fax: +43 316 876 2710.
E-mail address: barbara.stadlober@joanneum.at (B. Stadlober).

1566-1199/$ - see front matter © 2009 Elsevier B.V. All rights reserved.
doi:10.1016/j.orgel.2009.12.012

unrivalled high resolution (10 nm) typical for all imprinting techniques, the short process times due to a parallel pattern transfer enabling high-throughput, the straightforward implementation into a roller-based manufacturing facility and its universal applicability (for all types of structures, materials, devices and length scales) thus facilitating integration of components from different device classes (optical, electrical, photonic, sensory). The compatibility of nanoimprinting with r2r manufacturing was recently shown by Ahn et al. [2,3] on the basis of a metal wire-grid polarizer with 200 nm periodicity and by Jackson [4] by means of amorphous silicon-based backplanes for active-matrix displays using a roll-to-roll self-aligned imprint lithography technique.

There are some examples found in literature dealing with the fabrication of nanoscale OTFTs based on serial writing techniques such as e-beam lithography [5–9] but only few examples of submicron transistors fabricated on the basis of nanoimprint lithography [10–15]. Apart from one group that describes the fabrication of submicron-spaced electrodes via a combination of lamination and nanotransfer printing [15], most studies apply Hot Embossing (HE) [10–14]. In Hot Embossing the resist is heated above the glass transition temperature and cooled down again during the imprinting step. Although possessing a few disadvantages, Hot Embossing is the longest well-established technique and has already proven to be applicable in defining sub-micrometer channel lengths of OTFTs in a common gate configuration on rigid silicon substrates [10–13], as well as of fully patterned OTFTs on polyester film substrates and thin organic gate dielectrics [14]. One drawback of HE is the temperature budget of about 125 °C, which is unfavorable for low-cost flexible film substrates and can generate dimensional instabilities. Moreover, with HE a residual layer of the thermoplastic resist remains after the imprinting step and has to be removed by anisotropic etching. The reactive ion etch process is very undesirable because it is costly, hard-to-control, complicated to integrate in an in-line production and might be harmful for an organic layer underneath.

In this paper we describe the fabrication of submicron organic thin-film transistors in a bottom-gate configuration by a novel thermally initiated radical polymerization based nanoimprint lithography process (TIP-NIL). The TIP-NIL method relies on a novel imprint resist that provides residue-free nanoimprinting at moderate temperatures (90 °C) and can be lifted-off with water. Residue-free and lift-off capable TIP-NIL has a lot of advantages. On the one hand production costs are decreased due to the expendability of the etching step and the possibility to use standard Hot Embossing tools. On the other hand the usage of water for the lift-off increases environmental sustainability and process safety. Furthermore, an improvement of the functionality of imprinted bottom-gate OTFTs can be expected, since the reactive ion etching implies a high probability for damaging the underlying gate dielectric. Oxygen plasma etching of organic dielectrics is known to increase the gate leakage and the number of OH-groups acting as traps at the interface. All that qualifies TIP-NIL as a very powerful high-resolution patterning process for large-area fabrication of flexible organic electronics.

2. Fabrication

To demonstrate the huge potential of TIP-NIL, we have fabricated short-channel OTFTs with pentacene as the active semiconducting layer. For this purpose doped silicon wafers were used as the substrates thus forming the bottom-gate electrode covered by 100 nm thermal SiO_2 as the gate dielectric. The TIP-NIL step was used for the definition of the source and drain electrodes with a separation L in the range 0.9 μm < L < 2.4 μm. We used a home-made silicon stamp patterned by electron beam lithography. The e-beam resist pattern was permanently transferred into the silicon stamp by reactive ion etching (SF6-Ar) resulting in a final stamp depth of about 1 μm. After stripping the resist, an anti-sticking layer (perfluorchloroctyl–tricholorosilane) was applied onto the stamp.

The principle of the TIP-NIL process is illustrated in Fig. 1a. After application of the imprint resist on the substrate by drop coating the first step (A) is to align the silicon stamp roughly with respect to the substrate by means of an EVG 520 mask aligner. The aligned stamp is pressed into the low-viscous resist at low pressure, displacing the resist underneath the source–drain patterns completely (B). Curing is performed by a thermally initiated radical polymerization for up to 10 min at 90 °C. This results in a permanent transfer of the source–drain pattern into the resist. The curing time can be controlled by the initiator concentration. After removing the stamp (C), the source–drain material (30 nm gold) is applied onto the device either by e-beam or by thermal evaporation (D). The subsequent lift-off is performed by dissolving the resist with deionized water. This removes the gold layer on top of the resist while preserving it at the imprinted areas (E). An optical microscopy image of the device after the lift-off is shown in Fig. 1b illustrating the appearance of the source–drain electrodes. Finally, the active material (50 nm pentacene) is thermally evaporated to complete the transistor structure (F). In Fig. 1c an AFM phase image is displayed revealing a pentacene grain size of about 1.5 μm in the channel.

The key component of our TIP-NIL process for the patterning of submicron-spaced source and drain electrodes is a novel imprint resist that is curable by thermally initiated radical polymerization, is water soluble, low-viscous and is further referred to as TIP-NIL-ACMO. It is a blend of an acrylic resist and a thermal initiator. The actually applied special formulation is composed of acryloyl morpholine monomers (ACMO) mixed with 1.5 wt.% of the thermal initiator AIBN, yielding a low-viscous material. This low-viscose resist formulation exhibits outstanding properties during temperature-assisted imprinting. The residue-free imprint is additionally facilitated by an adjustment of the stamp's surface energy to maximize the contact angle, i.e. a high difference in polarity of resist and stamp. This was achieved by coating the silicon stamp with perfluorchloroctyl–tricholorosilane thus minimizing its polarity. Both properties, the low viscosity and the big difference in polarity, are required to achieve a residue-free imprint. In

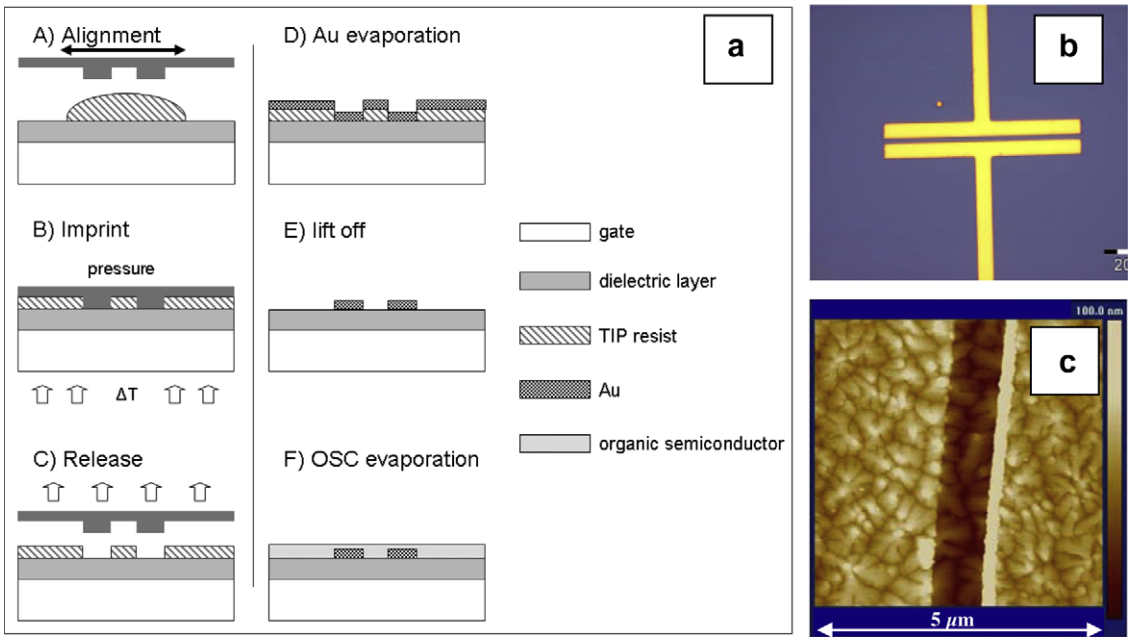

Fig. 1. (a) Scheme of the TIP-NIL process: A silicon stamp containing the source–drain structures is aligned roughly onto the substrate (A). The stamp is pressed into the resist thus completely displacing the resist under the source–drain structures (B). Subsequently, the resist is cured by thermal initiated polymerization. After the stamp removal (C) the source–drain material is evaporated onto the substrate (D). The imprint resist is dissolved with water, which leaves the metal source–drain electrodes well preserved (E). Finally, the sample is covered by the organic active layer, pentacene (F). (b) Image of the source and drain structures after the lift-off. (c) AFM topographic image (5×5 μm) of the pentacene layer formed on top of the contacts and in the channel (L = 900 nm).

addition, the treatment of the stamp facilitates its separation from the patterned imprint resist.

Of particular importance is the residue-free displacement of the TIP-NIL-ACMO enabling an etch-free process of manufacture. Furthermore, in comparison to HE, a lower temperature budget is needed to achieve a permanent pattern transfer since the thermal initiation of the polymerization starts at about 90 °C. This facilitates the usage of thermally sensitive flexible substrates and decreases processing times. Additionally, the cured resist is not heated over its glass transition temperature, therefore the cooling step before stamp removal becomes redundant and the production time is further shortened.

3. Microscopic characterization

To characterize the imprint result, the specimens were investigated by transmission electron microscopy. Post column energy filters were used for zero-loss imaging and elemental mapping. The cross section lamellae of the samples were prepared using a focused ion beam instrument (FIB) [16]. Fig. 2a shows a SEM image of a sample after the imprint step where a lamella has already been cut out. A TEM bright field image of the lamella is displayed in Fig. 2b, showing the troughs for the electrodes on the sides and the appearance of the resist (bright trapezoid) in the middle acting as place-holder for the channel. The organic layer of the resist can clearly be distinguished from the Si/SiO_2 substrate. In order to investigate whether the imprint is residue-free or not, a close-up of the region near the resist edge was analyzed by energy filtered TEM, which enables the distinction of materials according to their elemental composition. Fig. 2c represents an elemental map of the nitrogen distribution. Here, regions of materials containing nitrogen, such as TIP-NIL-ACMO, appear bright. It clearly reveals the limited spatial distribution of the imprinted TIP-NIL-ACMO layer in the channel region and its absence in the electrode areas. This is explicit evidence that the resist is displaced completely during the TIP-NIL process; no residue of the resist is observed in the imprinted areas. Thus, the specimen can directly be covered with gold without prior etching.

After lifting-off the gold layer on top of the TIP-NIL-ACMO resist by using deionized water, pentacene is thermally evaporated to finalize the transistor structure as shown in Fig. 3. Here, a cross section TEM image (Fig. 3a) and a corresponding scheme of the transistor (Fig. 3b) are presented. Additionally, one tear-off edge of an electrode is shown in Fig. 3c. As expected, the gold electrode is perfectly preserved in the imprinted region (right part of Fig. 3c), whereas it is gone in the channel where the TIP-NIL-ACMO was dissolved (left part of Fig. 3c). Thereby, it is proven that the introduced TIP-NIL route gives excellent downscaled transistor structures with respect to their appearance and therefore appropriate device characteristics are expected.

4. Electrical characterization

The electrical characterization of TIP-NIL fabricated OTFTs indeed reveals very good performance of devices

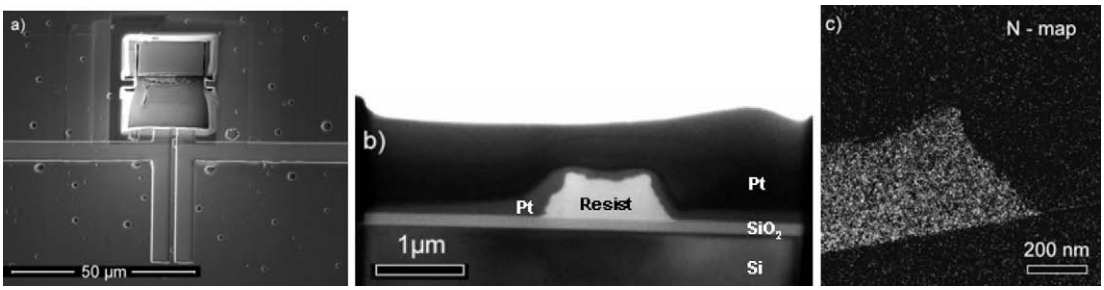

Fig. 2. A sample after the imprinting step: (a) SEM image of the cross section of a lifted-out FIB lamella. (b) A TEM zero-loss filtered bright field image of the cross section lamella, where the imprinted organic layer appears bright in-between the Si/SiO_2 and protective Pt layers. (c) An energy filtered TEM elemental map of nitrogen representing TIP-NIL-ACMO showing the edge of the channel. The resist can clearly be distinguished from all other involved materials.

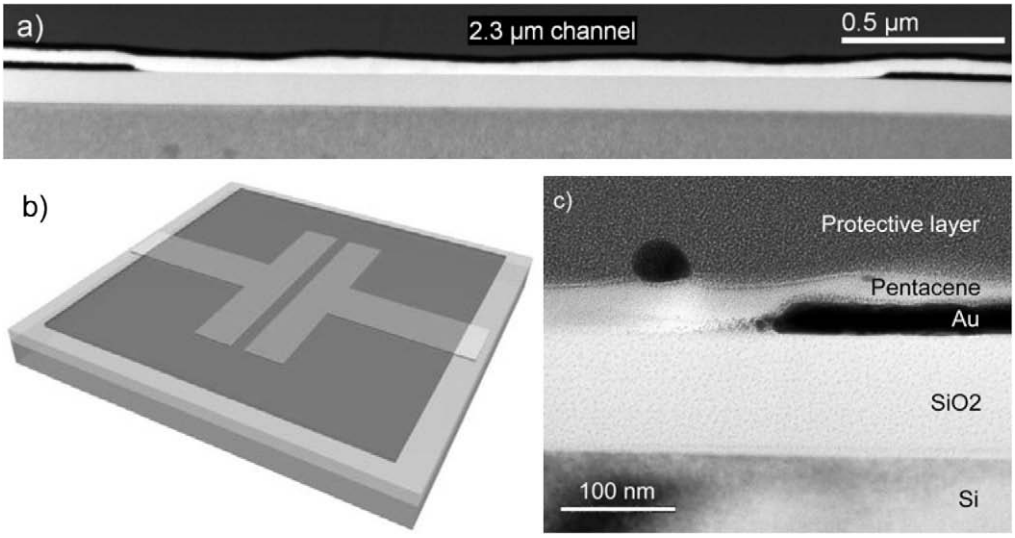

Fig. 3. A TEM zero-loss filtered bright field image of a cross section lamella of a completed transistor structure (a) and an according scheme (b). The gold electrode is well preserved at the imprinted areas and lifted-off elsewhere. A tear-off edge of an electrode is shown in (c).

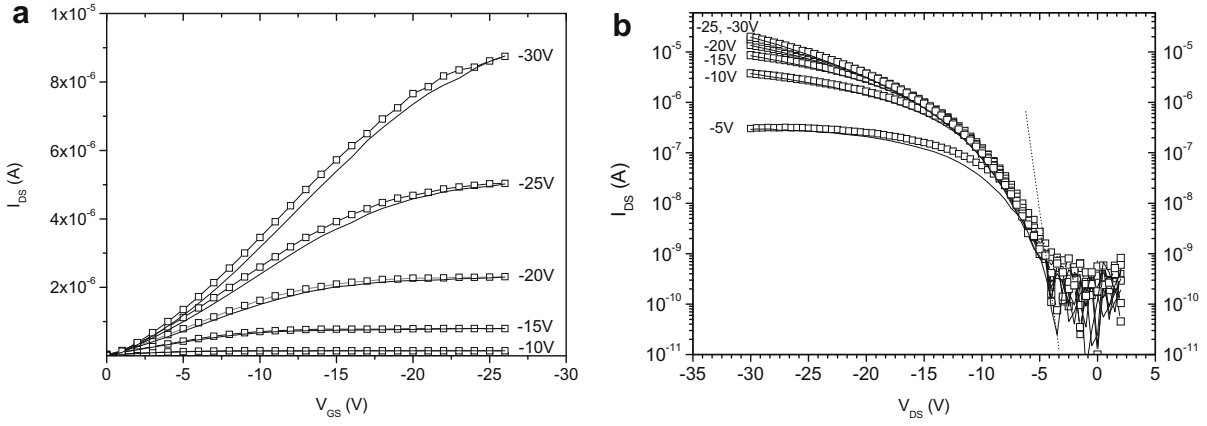

Fig. 4. $I(V)$-curves of a TIP-NIL fabricated OTFT with a channel length of 950 nm. (a) In the output characteristics the gate voltage is varied in steps of 5 V between $-5\ V \leqslant V_{GS} \leqslant -40\ V$ whereas (b) in the transfer characteristics the drain voltage is varied in steps of 5 V between $-5\ V \leqslant V_{DS} \leqslant -40\ V$. Lines with square symbols correspond to forward drain voltage sweep and solid lines to reverse drain voltage sweep.

with submicron channel lengths. In Fig. 4, the output and transfer characteristics of a device with a channel length $L = 950$ nm is displayed. In the $I_{DS}(V_{DS})$-curve clear saturation of the drain current is observed together with a small hysteresis between forward and reverse sweep which is typical for SiO_2 gate dielectrics [17] and is related to the existence of shallow interface traps. Accordingly, in the linear part of the $I_{DS}(V_{DS})$-curve at very small drain voltages a small curvature appears that probably stems from interface traps [18]. An influence of a contact resistance barrier is unlikely, since the morphology of the semiconductor on top of the gold contacts is similarly coarse as it is in the channel region. This indicates that carriers travelling to the accumulation layer only feel a small access resistance [12]. From the semi-logarithmic plot of the transfer curve $I_{DS}(V_{GS})$, a small onset voltage of $V_{so} = -3$ V, a subthreshold swing of $S = 1$ V/dec (corresponding to an interface trap density of about 5×10^{12} cm^{-2} eV^{-1}) [19], an on–off ratio of more than 10^5 and a charge carrier mobility $\mu = 0.25$ cm^2/V s is deduced. The high mobility is mainly a result of the coarse pentacene morphology in the channel being around the threshold for intragrain-dominated transport (grain size $\sim$1.5 μm) found earlier in long-channel SiO_2-based OTFTs [20].

The performance of TIP-NIL fabricated submicron OTFTs based on pentacene as the semiconductor and SiO_2 as the gate dielectric, is comparable to that one of the best devices fabricated earlier with Hot Embossing [12]. However, the latter always implies a hard-to-control reactive ion etch step. Moreover, in order to minimize contact resistance effects, a UV-ozone treatment of the hot embossed gold contacts was introduced for inducing a better growth of pentacene on top of the gold contacts and thus minimizing the access resistance [12]. With the TIP-NIL process all that appears to be obsolete.

5. Conclusion

In summary, we have fabricated well performing OTFTs with submicron channel lengths using an improved thermally initiated nanoimprinting process (TIP-NIL). The nanoimprinted OTFTs are comprised of pentacene as active semiconductor and SiO_2 as dielectric layer. With the novel TIP-NIL process, high performing devices with channel lengths down to 800 nm were fabricated showing complete drain current saturation, low switch-on voltages ($V_{so} = -3$ V) and a high charge carrier mobility ($\mu = 0.25$ cm^2/V s). The process is based on a specially formulated resist (TIP-NIL-ACMO) optimally adapted to fast and precise nanoimprinting of organic electronic components. TIP-NIL-ACMO allows a very fast thermal curing, which reduces the fabrication time decisively, thus enabling a high throughput. Exceptional is the absence of any residual layer of TIP-NIL-ACMO after the imprint step, making the etching step obsolete, which is a huge advantage for the whole process. Finally, TIP-NIL-ACMO allows a lift-off with deionized water, which is a big advantage with respect to ubiquitous availability, the potential for immediate recycling and environmental sustainability, resulting in a decrease of production costs and an increase of process safety. Overall, TIP-NIL has a huge potential as a high-resolution patterning process for large-area fabrication of flexible organic electronics in a roll-to-roll manufacturing environment.

Clearly, there are several further steps that have to be taken before residue-free TIP-NIL can be transferred to roll-to-roll fabrication of OTFTs, which are the usage of soft gate dielectrics and the problem of alignment of the nanoimprint stamp. Very recently we could show that UV-based nanoimprinting is successfully applicable in an etch-free process on fully patterned OTFTs with organic based gate dielectrics [21]. Similar results are also expected for the TIP-NIL process. Concerning the proper alignment of the nanoimprint tool to the sample one has to combine the imprint step with a technique for self-alignment of gate to source–drain level. Such developments are ongoing.

6. Methods

OTFTs: The OTFTs are based on SiO_2 as the gate dielectric and have coplanar bottom-gate device architecture with a W/L ratio of about 50. For substrates highly-doped silicon wafer with 100 nm thermally grown silicon dioxide are used.

Fabrication of contacts by nanoimprinting: The TIP-NIL patterning of the gold source–drain electrodes is done in an EVG 520 nano imprinting equipment. The imprint stamp is made of silicon patterned by electron beam lithography. The resist structures are permanently transferred into the silicon stamp by reactive ion etching (SF_6-Ar) resulting in a final depth of about 1 μm. After stripping, an anti-sticking layer (perfluorchloroctyl–tricholorosilane) is applied onto the stamp. The ACMO based TIP-NIL-resist is fabricated by a mixture of ACMO (acryloyl morpholine) by Rahn AG and 1.5 wt.% AIBN (by Aldrich) yielding a low-viscous material. The resist is applied on the substrate by drop coating. The curing is done at 90 °C for 10 min. A 30 nm thick gold layer is deposited by either e-beam or thermal evaporation. The lift-off is performed by dissolving the resist with deionized water. The 40 nm thick pentacene layer is thermally evaporated onto the sample in high-vacuum conditions at a rate of 0.2 nm/min for the first 5 nm and 0.8 nm/min for the remaining 35 nm.

FIB/SEM: Prior to the FIB/SEM investigations the specimens are covered with a 20 nm carbon layer to minimize charging of the sample. In the focused ion beam instrument Pt layers are grown by electron beam induced deposition (EBID) followed by ion beam assisted deposition (IBAD). These Pt layers protect the surface against incoming Ga ions during cutting out and milling the lamellas. The lamellas are transferred to a TEM grid and thinned down to several tens of nm.

TEM: The TEM investigations are performed using a Philips CM20 (S) TEM (twin lens) with a thermionic LaB_6 cathode operated at 200 kV equipped with a Gatan Imaging Filter (GIF 200). For energy dispersive X-ray spectroscopy an HPGe detector (Noran/Thermo Fisher Scientific) running under Noran System Six software is used. EELS and energy filtered TEM (EFTEM) are performed using a Gatan Imaging Filter (GIF) with a 1024 × 1024 CCD (YAG scintillator) at-

tached to the microscope. Elemental maps were calculated using three-window-technique.

Acknowledgment

Parts of this work were done within the NILaustria Cluster. The authors thank for financial support from Nanoinitiative Austria (FFG).

References

[1] For a review on applications and products see: H. Klauk (Ed.), Chapter 4 in Organic Electronics: Materials, Manufacturing and Applications, Wiley-VCH, Weinheim, Germany, 2006.
[2] S.H. Ahn, L.J. Guo, High-speed roll-to-roll nanoimprint lithography on flexible plastic substrates, Adv. Mater. 20 (2008) 2044–2049.
[3] S.H. Ahn, L.J. Guo, Large area roll-to-roll and roll-to-plate nanoimprint lithography: a step toward high-throughput application of continuous nanoimprinting, ACS Nano 3 (2009) 2304–2310.
[4] W.B. Jackson, Active-matrix backplanes produced by roll-to-roll self-aligned imprint lithography (SAIL), in: SID International Symposium Digest of Technical Papers 2008, vol. 39, p. 322.
[5] Y. Zhang, J.R. Patta, S. Ambily, Y. Shen, D.C. Ralph, G. Malliaras, 30 nm channel length pentacene transistors, Adv. Mater. 15 (2003) 1632.
[6] J. Collet, O. Tharaud, A. Chapoton, D. Vuillaume, Low-voltage, 30 nm channel length, organic transistors with a self-assembled monolayer as gate insulating film, Appl. Phys. Lett. 76 (2000) 1941.
[7] M. Leufgen, U. Bass, T. Muck, T. Borzenko, G. Schmidt, J. Geurts, V. Wagner, Optimized sub-micron organic thin-film transistors: the influence of contacts and oxide thickness, Synth. Met. 146 (2004) 341.
[8] L. Wang, D. Fine, T. Jung, D. Basu, H. von Seggern, A. Dodabalpur, Pentacene field-effect transistors with sub-10 nm channel lengths, Appl. Phys. Lett. 85 (2004) 1772.
[9] J.B. Lee, P. Chang, J.A. Liddle, V. Subramanian, Pentacene field-effect transistors with 10-nm channel lengths, IEEE Trans. Electron Dev. 52 (2005) 1874.
[10] X. Cheng, D. Li, L. Jay Guo, A hybrid mask-mould lithography scheme and its application in nanoscale organic thin film, Nanotechnology 17 (2006) 927–932.
[11] M.D. Austin, S.Y. Chou, Fabrication of 70 nm channel length polymer organic thin-film transistors using nanoimprint lithography, Appl. Phys. Lett. 81 (2002) 4431–4433.
[12] B. Stadlober, U. Haas, H. Gold, A. Haase, G. Jakopic, G. Leising, N. Koch, S. Rentenberger, E. Zojer, Orders-of-magnitude reduction of the contact resistance in short-cannel hot embossed organic thin film transistors by oxidative treatment of Au electrodes, Adv. Funct. Mater. 17 (2007) 2687–2692.
[13] A.P. Kam, J. Seekamp, V. Solovyev, C. Clavijo Cedeno, A. Goldschmidt, C.M. Sotomayor Torres, Nanoimprinted organic field-effect transistors: fabrication, transfer mechanism and solvent effects on device characteristics, Microelectron. Eng. 73–74 (2004) 809–813.
[14] U. Haas, H. Gold, A. Haase, G. Jakopic, B. Stadlober, Submicron pentacene-based organic thin-film transistors on flexible substrates, Appl. Phys. Lett. 92 (2007) 043511.
[15] J. Zaumseil, T. Someya, Z. Bao, Y.-L. Loo, R. Cirelli, J.A. Rogers, Nanoscale organic transistors that use source/drain electrodes supported by high-resolution rubber stamps, Appl. Phys. Lett. 82 (2003) 793–795.
[16] L.A. Giannuzzi, F.A. Stevie, Introduction to Focused Ion Beams, Springer, Berlin, 2004.
[17] S.G.J. Mathijssen, M. Kemerink, A. Sharma, M. Cölle, P.A. Bobbert, R.A.J. Janssen, D.M. De Leeuw, Charge trapping at the dielectric of organic transistors visualized in real time and space, Adv. Mater. 20 (2008) 975.
[18] P. Stallinga, H.L. Gomes, Modelling electrical characteristics of thin-film field-effect transistors II: effects of traps and impurities, Synth. Met. 156 (2006) 1316.
[19] M. Zirkl, A. Haase, A. Fian, H. Schön, C. Sommer, G. Jakopic, G. Leising, B. Stadlober, I. Graz, N. Gaar, R. Schwödiauer, S. Bauer-Gogonea, S. Bauer, Low-voltage organic thin film transistors with high-k nanocomposite gate dielectrics for flexible electronics and optothermal sensors, Adv. Mater. 19 (2007) 2241.
[20] A. DiCarlo, F. Piacenza, A. Bolognesi, B. Stadlober, H. Maresch, Influence of grain sizes on the mobility of organic thin-film transistors, Appl. Phys. Lett. 86 (2005) 263501.
[21] C. Auner, U. Palfinger, H. Gold, J. Kraxner, A. Haase, T. Haber, M. Sezen, W. Grogger, G. Jakopic, J.R. Krenn, G. Leising, B. Stadlober, Residue-free room temperature UV-nanoimprinting of submicron organic thin film transistors, Org. Electron. 10 (2009) 1466.

Organic Electronics 11 (2010) 558–563

Contents lists available at ScienceDirect

Organic Electronics

journal homepage: www.elsevier.com/locate/orgel

Electron transport along semiconducting polymer heterojunctions

Chuan Liu, Henning Sirringhaus *

Cavendish Laboratory, Madingley Road, Cambridge CB3 0HE, United Kingdom

ARTICLE INFO

Article history:
Received 4 September 2009
Received in revised form 20 December 2009
Accepted 21 December 2009
Available online 28 December 2009

Keywords:
Bilayer
Polymer transistors
Electron transfer
Recombination

ABSTRACT

Most conjugated polymer field-effect transistors rely on charge accumulation between an organic semiconductor and a gate dielectric. Much less use has been made of devices based on heterojunctions between two semiconducting polymers. Here we have realized ambipolar polymer field-effect transistors based on bilayers of two polyfluorene-based semiconducting polymers, poly(9,9-dioctylfluorene-*alt*-*N*-(4-butylphenyl)diphenylamine) and poly(9,9-dioctylfluorene-*alt*-benzothiadiazole). We show that the energy offset between the lowest unoccupied molecular orbitals of the two polymers of 1–1.5 eV is sufficient to confine electrons at the bi-layer interface for n-type operation. However, the transfer current–voltage characteristics exhibit an unusual plateau. This is shown to be due to hole charge trapping in donor-like states in the TFB layer during p-type operation.

© 2010 Elsevier B.V. All rights reserved.

1. Introduction

In organic field-effect transistors (OFETs) the choice of gate dielectric determines the charge transport properties in the thin accumulation layer formed at the interface between the organic semiconductor and the dielectric. Key factors for selecting an optimum gate dielectric are the dielectric breakdown strength, leakage current density and dielectric constant [1]. In particular, any charge transfer from the organic semiconductor into the dielectric will affect device performance and induce, for example, threshold/turn-on voltage shifts during operation [2]. It is important to understand under which conditions electrons in the lowest unoccupied molecular orbital (LUMO) states (or holes in the highest occupied molecular orbital (HOMO) states) of the organic semiconductor can transfer across the interface into trap states or, less likely, into the conduction/valence bands of the dielectric. This transfer can be induced by the gate field or illumination [2]. However, in most systems charge transfer across the interface cannot be studied systematically because it relies on the often poorly characterized trap state distribution of the polymer dielectric. In comparison, the density of states of many polymer semiconductors is known better. We can choose a series of semiconducting polymers with a well controlled energy offset between the HOMO or LUMO states of the two polymers, respectively, to study the interfacial charge transfer between two semiconducting polymers in bi-layer polymer transistor structures in which one of the polymers acts as the semiconductor and the other one as the gate dielectric. The energy offset can be tuned to a sufficiently small value such that interfacial charge transfer is expected to be more significant than in the case of the conventional semiconductor/dielectric structures. A potential application of such semiconducting polymer heterojunctions could be in electrically programmable and erasable memory devices. However, in this work we focus on a basic electrical characterization of such structures. Our main aim is to understand how charge transfer across the interface manifests itself in the electrical characteristics. A particularly interesting question is what energy offset is needed to essentially block charge transfer across the interface.

* Corresponding author.
E-mail address: hs220@cam.ac.uk (H. Sirringhaus).

1566-1199/$ - see front matter © 2010 Elsevier B.V. All rights reserved.
doi:10.1016/j.orgel.2009.12.013

2. Experimental section

2.1. Materials

Bi-layer heterojunction OFETs with vacuum sublimed small molecule organic semiconductors have been widely researched for ambipolar transistors and light emitting transistors [3–6]. Solution-processed polymer multilayers are much harder to fabricate due to problems with finding sufficiently orthogonal organic solvents. They have been successfully realized by various methods, primarily to enhance luminescence efficiency of organic light-emitting-diodes (OLEDs) [7,8]. In contrast, to the best of our knowledge bi-layer polymer OFETs have not been reported yet. Here, we have investigated bilayers based on combining two semiconducting polyfluorene copolymers. Poly(9,9-dioctylfluorene-*alt*-benzothiadiazole) (F8BT) [9] was used as a first semiconducting polymer layer in contact with the source–drain electrodes. F8BT exhibits stable ambipolar transistor characteristics with electron and hole mobilities of 10^{-4}–10^{-3} $cm^2\,V^{-1}\,s^{-1}$ in top-gate architectures with polymethylmethacrylate (PMMA) top-gate dielectric [10,11]. However, rather than depositing a PMMA dielectric directly on top of the F8BT layer we inserted a layer of poly(9,9-dioctylfluorene-*alt*-*N*-(4-butylphenyl)diphenylamine) (TFB) as an interfacial layer on top of the F8BT. Single-layer TFB transistors with PMMA dielectric do not exhibit electron transport owing to the low electron affinity of TFB, but exhibit stable p-type operation with hole mobilities of 10^{-4}–10^{-3} $cm^2\,V^{-1}\,s^{-1}$ and good stability in air [12]. The electron affinity of TFB is by more than 1 eV lower than that of F8BT and it should therefore be possible to induce an electron accumulation layer under positive gate bias at the internal bi-layer interface between F8BT and TFB.

2.2. Device fabrication

Both F8BT and TFB were obtained from Cambridge Display Technology (CDT) (F8BT, molecular weight M_n: 97 kg/mol; TFB, M_n: 55 kg/mol). The F8BT solutions were prepared with a concentration of 8 mg/ml in xylene and heated at 80 °C for 30 min before being filtered through a 0.45 μm pore size PTFE membrane syringe filter. The transistors for this study were fabricated in the top-gate/bottom-contact configuration, as illustrated in Fig. 1. 15–20 nm thick source/drain electrodes of thermally evaporated gold were patterned by photolithography on Corning glass substrates using an adhesion layer of vapour deposited 3-mercaptopropyltrimethoxysilane ($HS(CH_2)_3$-$Si(OCH_3)_3$). F8BT solutions were spin-cast at 2000 rpm in a nitrogen glove-box. The thickness of F8BT and TFB films was around 30 nm. TFB films spun from 10 mg/ml solution in xylene were fabricated on top of the F8BT layer by one of the two following methods: (1) TFB was spin coated on a Mica wafer and then floated off into de-ionised water. The glass substrate with the F8BT layer was then pushed onto the layer of TFB and removed such that the TFB layer attaches to the F8BT. (2) We also employed a "transfer-printing procedure" using elastomeric poly(dimethylsiloxane) (PDMS) stamps to transfer the TFB film onto the F8BT layer [8]. After the lamination of the TFB, the substrates were subsequently heated above 130 °C for 10 h in a nitrogen or vacuum atmosphere to remove any residual water. Then a layer of PMMA was spin coated on top from an 80 mg/ml solution in n-butyl acetate to form a 650 nm thick layer. A 25–30 nm Au top-gate electrode was finally evaporated through a shadow mask in a vacuum of 3×10^{-6} mbar. Transistor characteristics were measured in pulsed mode, i.e., only a short (∼ms) voltage pulse was applied to the gate electrode to diminish the effect of bias stress [13,14], using an Agilent 4145B Semiconductor Parameter Analyser (SPA) in inert N_2 atmosphere.

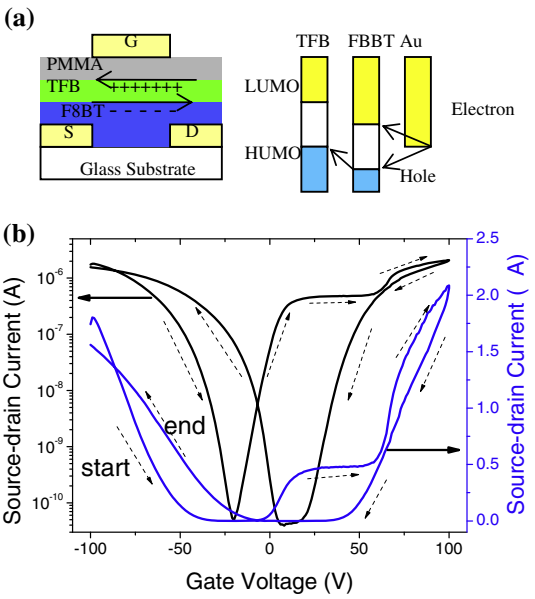

Fig. 1. (a): Cross-section of "F8BT/TFB/PMMA" FET together with a schematic energy diagram. The arrows indicate the expected charge transfer of electrons and holes under positive and negative gate voltages, respectively; (b): Transfer characteristics of a "F8BT/TFB/PMMA" transistor operated at $V_d = -100$ V with a channel length $L = 10$ μm and channel width $W = 1$ cm plotted on a logarithmic (black) and a linear current scale (blue). The dashed arrows show the direction of the voltage sweep. (For interpretation of the references to colour in this figure legend, the reader is referred to the web version of this article.)

3. Results and discussions

3.1. Transfer characteristics

The structure of the "F8BT/TFB/PMMA" transistors and the associated schematic energy diagram is shown in Fig. 1. Under negative gate voltage V_g holes can be injected from the gold electrodes into the F8BT layer and from there into the TFB layer. The accumulation layer for negative V_g is expected to be formed at the interface between the TFB and the PMMA. Because the ionisation potential of TFB ($I_p \approx 5.3$ eV) is lower than that of F8BT ($I_p \approx 5.8$ eV), there is no energy barrier for holes at the F8BT/TFB interface [9,12]. On the other hand, for positive V_g electrons are injected from the gold source/drain electrodes into the

F8BT. Because the electron affinity of TFB ($\chi \approx 2.3$ eV) is 1.2 eV higher than that of F8BT ($\chi \approx 3.5$ eV), there is a significant barrier for electron transfer across the interface. If this barrier is high enough to block electrons, the electron accumulation layer should be at the F8BT/TFB interface. In fact, it is straightforward to verify this from the electrical characteristics, since any electron current observed under positive gate voltage must arise from electron accumulation in F8BT, since TFB is not capable of transporting electrons. Therefore, we expect such bi-layer transistors to exhibit ambipolar behavior with electron mobilities similar to that of F8BT-only devices for positive gate bias and hole mobilities similar to that of TFB-only devices for negative gate bias.

The transfer characteristics of a transistor fabricated by the float-off technique are shown in Fig. 2. They confirm our expectation that the device is able to operate in ambipolar mode as the current rises for both negative and positive gate voltages. However, there are clear deviations from idealized ambipolar behavior. Most notably, the forward scan of V_g (from negative to positive voltages) exhibits a first threshold around $V_g = -20$ V at which the electron current starts to rise, but then a current plateau is reached between $0 < V_g < 50$ V. The electron current continues to rise only above a second threshold voltage above 50 V. On the backward scan (from positive to negative voltages) we observe a normal monotonous decrease of the electron current. Devices made by the two lamination techniques exhibited very similar characteristics and in the following we will focus on samples prepared by the float-off technique.

3.2. Dependence on starting point of gate voltage

To understand the origin of the unusual current plateau we investigated how the shape of the characteristics depends on the gate voltage range. When the maximum positive V_g of the scan was less than the second turn-on voltage around $V_g = 50$–60 V, the current on the backward scan decreased immediately, i.e., it did not retrace along the current plateau exhibiting a large hysteresis. The hole mobility extracted from the negative gate voltage region was 1.8×10^{-4} cm^2 V^{-1} s^{-1}, which is close to that of a single-layer TFB/PMMA device. The electron mobility extracted from the current rise above the second threshold using the equation for the saturated FET mobility was about 2×10^{-4} cm^2 V^{-1} s^{-1}, close to that extracted from a single layer "as spun" F8BT/PMMA device (the small reduction of capacitance induced by the TFB layer was taken into account). This indicates that the electron accumulation layer was indeed well confined at the interface between F8BT and TFB, and that an energy offset on the order of 1.2 eV between the LUMO of the two semiconducting polymers is sufficient to block electron transfer across the interface up to high gate voltages of 100 V. We have observed previously in p-type bi-layer polymer FETs with lower energy barrier at the heterointerface that gate voltage induced charge transfer across the interface manifests itself in a characteristic current saturation behavior of the transistor transfer curves at high gate voltages [15]. The behavior observed here is different. We will discuss the origin of the current plateau at intermediate gate voltages below, but at high gate voltage we observe clean electron accumulation at the F8BT/TFB interface with evidence for gate-induced charge transfer.

We observed similar current plateaus also in devices in which TFB was replaced with poly(9,9′-dioctylfluorene)-co-*bis*-N,N′-(4-butylphenyl)-bis-N,N′-phenyl-1,4-phenylenediamine (PFB) and poly(triarylamine) (PTAA), all of which have similar electronic structure and LUMO levels compared to TFB. Current plateaus were, however, not found for ambipolar devices in which TFB was replaced with a second laminated F8BT layer or a poly(9,9-dioctylfluorene-*alt*-bithiophene) (F8T2) film. Therefore, we can exclude that the effect might be due to residual moisture, impurities or other artefacts introduced by the lamination process [16,17]. We observed some variation in the shape of the current plateau from device to device. In most devices the current in this region was either saturated or increased very gently. In some devices the current was found

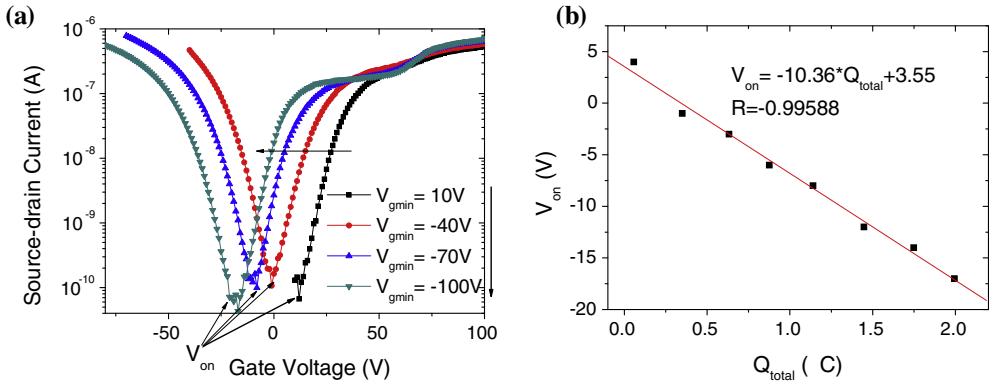

Fig. 2. (a) Transfer characteristics of an "F8BT/TFB/PMMA" device with channel length of 2 μm and channel width of 1 cm on a logarithmic current scale ($V_d = -60$ V). (b) Linear fit of V_{on} versus the total hole charges passed through the channel, estimated by integrating the current passed through the device during the p-type portion of the transfer scan. Black squares are values extracted from the integration of the transfer characteristics and the red line is a linear fit. The fitting parameters for slope, intercept and correlation coefficient (R) are listed. (For interpretation of the references to colour in this figure legend, the reader is referred to the web version of this article.)

to decrease slightly producing a "bump" shape. We note that the observed current plateau is distinct from the case of single-layer transistors with interface or bulk trap states, which have been reported to exhibit a shoulder in the sub-threshold region, but not current saturation observable on a linear current scale as seen here [17,18].

When the starting point of the forward gate voltage sweep V_{gmin} was moved to more negative gate voltage we observed pronounced changes in the transfer characteristics (Fig. 2a). When the V_g scan started at V_{gmin} = +10 V, i.e., the device was never operated in hole accumulation, the plateau in the electron regime was not present and the electron current increased monotonously above a turn-on voltage of 10–15 V. As V_{gmin} was set to more negative values, the current plateau became increasingly pronounced, and the plateau region extended from V_g = 20–60 V when the scan started from $V_g = -100$ V. The onset voltage V_{on} at which the first electron current rise was observed, i.e., the voltage at which the minimum in the transfer characteristics occurs (see Fig. 2), shifted from V_{on} = 12 V for scans starting at V_{gmin} = +10 V to $V_{on} = -15$ V for scans starting at $V_{gmin} = -100$ V. In contrast, the turn-on voltage for the second turn-on of the electron current remained almost unaffected.This result clearly suggests that the appearance of the plateau is caused by operating the device in hole accumulation prior to inducing the electron accumulation layer. We have found that V_{on} is in fact proportional to the total positive charge injected into the channel during the hole-accumulation portion of the transfer characteristics. This can be estimated by integrating the measured drain current I_d from $V_g = V_{gmin}$ to $V_g = V_{on}$. In the pulsed measurement mode used here, $Q_{htotal} = \sum_{V_g=V_{min}}^{V_g=V_{on}} Q(V_g) = Nt_{pulse}\sum_{V_g=V_{min}}^{V_g=V_{on}} I_d(V_g)$, where the constant N is number of applied pulses per gate voltage step and t_{pulse} is the time during which each gate voltage pulse is applied ($Nt_{pulse} \sim 0.04$ s). V_{on} is found to shift to more negative voltages linearly with the total hole charge passed through the channel: $\Delta V_{on} \propto Q_{htotal}$ (Fig. 2b). This suggests that the origin of the current plateau is the presence of deeply trapped charges that remain in the TFB layer after the hole operation. The number of trapped charges can be expected to be a fraction of the total hole charge passed through the device and the probability β that a particular charge injected into the device ends up being a trapped charge, was estimated to be $\beta = 2 \times 10^{-5}$ from the data in Fig. 2b using $\Delta V_{on} = -\beta Q_{total}/(C_i WL)$, where C_i is the capacitance of the PMMA gate dielectric per square centimeter, W is the channel width and L is the channel length. This relationship is similar to the photo-induced charge transfer across the interface between semiconducting rubrene and dielectric parylene, for which a linear relationship was also found between injected charges and integrated incident light intensity [2].

3.3. Proposed model

We would now like to provide a qualitative explanation for the observed current plateau in the device characteristics. Since V_{on} shifts to negative values with prolonged hole accumulation at the beginning of the transfer scan we assume that donor-like traps are responsible for the current plateau. A donor-like trap state, i.e., a donor level located near the HOMO level, is positively charged when not occupied by an electron and neutral when filled with an electron. Previous device simulation studies have shown that interface or bulk donor-like traps with energies below the mobile states result in shoulder-like features in the sub-threshold region of single-layer OFETs [17,18], but not in a pronounced current plateau on a linear current scale.Based on this assumption the dynamic process of the formation of the current plateau can be explained in terms of the energy diagram in Fig. 3. For simplicity, only a single level trap is considered here but the following discussion is also applicable to a distribution of traps, which is more likely in a polymer semiconductor. When holes are accumulated in the TFB in the p-type region of the I_d–V_g curve, some of them become trapped in positively charged donor-like trap states in the TFB bulk. The positive space charge of these trapped holes then aids the injection of electrons and formation of an electron accumulation layer when applying a positive gate bias. This explains the shift of V_{on} to more and more negative voltages with increasing Q_{htotal}. Once an electron accumulation layer is formed at the F8BT/TFB interface the quasi-Fermi level of electrons moves close to the LUMO of F8BT. Aided by the Coulombic attraction between the electrons and the trapped holes electrons begin to transfer from F8BT into TFB and recombine with the trapped holes in TFB. As a result the donor-like states are occupied and become neutral. This process keeps the mobile electron concentration at the F8BT/TFB interface from increasing until most trapped holes have recombined, and this results in the current saturation in the I_d–V_g curve. When most trapped holes have recombined raising the gate voltage above the second turn-on voltage then leads to a further increase of the electron concentration at the F8BT/TFB interface and the electron current rises again. Under conditions where no positive space charge in the TFB layer aids the charge transfer across the interface, the electron accumulation layer can be maintained at the F8BT/TFB interface up to the highest gate voltages applied, i.e., the electron current continues to rise up to gate voltages of +100 V. In the absence of the positive fixed charge of the trapped holes, the backward scan of the transfer characteristics is also normal as it is in

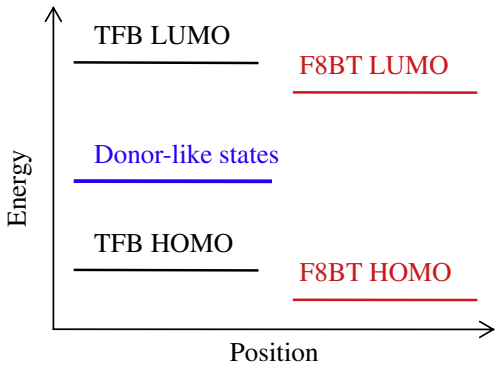

Fig. 3. Schematic energy diagram at the heterojunction with LUMO level and trap states in the bi-layer structure.

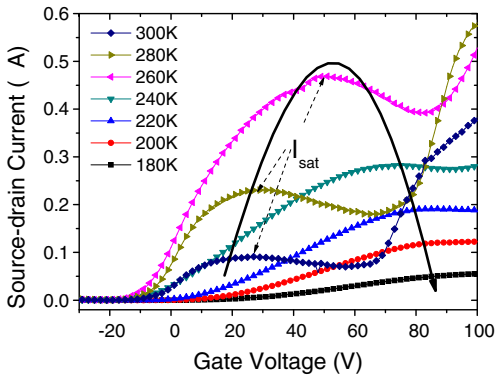

Fig. 4. Transfer characteristics of an "F8BT/TFB/PMMA" transistor measured at different temperatures (during cool down), with a channel length of 10 μm and channel width of 1 cm ($V_d = -100$ V), on a linear scale. The black arrow indicates how the height and position of the current plateau evolves with temperature.

single-layer devices, i.e., does not retrace the current plateau. The nature of the hole trap state in TFB and its energy in the bandgap of TFB is not known, and Fig. 3 is merely a schematic diagram. It is possible that some of the holes injected into the TFB film during hole accumulation might simply be hindered from transferring sufficiently fast back to the source–drain electrodes due to the energy barrier of around 0.5 eV between the HOMO levels of TFB and F8BT.

3.4. Temperature dependence

The dependence of the transfer curves on temperature is shown in Fig. 4. A value of −100 V was used for V_{gmin}. As the temperature (T) is reduced from 280 to 180 K, the current of the bi-layer transistors at high V_g (90–100 V) decreases monotonously in a similar way as that of single-layer F8BT transistors. However, the current observed in the plateau region exhibits clearly a non-monotonous temperature dependence. At 300 K the plateau current is about a factor of 4–5 lower than at 260 K. In the temperature region between 300 and 260 K the maximum current I_{sat} at which the source–drain current in the plateau region saturates or peaks increases with decreasing temperature. Below 260 K the plateau current then decreases with decreasing temperature and the plateau is in fact gradually lost. V_{on} remains relatively temperature independent between 300 and 240 K. The same non-monotonous temperature dependence was also observed when the device was heated up again. Five individual samples were measured and exhibited similar temperature dependence.

This temperature dependence could be explained in the following way. The initial rise of the plateau current with decreasing temperature indicates that the recombination of electrons in the F8BT with the trapped holes in the TFB is a thermally activated process. We have estimated an approximate activation energy on the order of 280 meV by fitting this narrow temperature regime to $I_{sat} \propto \exp(E_a/kT)$. This could be due to an energy barrier for electron injection into empty electronic states in the TFB, which electrons need to be injected into before they can reach/recombine with the holes trapped in the TFB. Such an energy barrier would reduce the rate of recombination during the transfer scan at lower temperatures and as a result lead to an increased plateau current. This behavior would be expected to be superimposed on the thermally activated temperature dependence of the field-effect mobility of F8BT. It appears that below 260 K the latter dominates.

4. Conclusions

We have investigated the current–voltage characteristics of ambipolar polymer FETs in which the active layer is a bilayer of two semiconducting polymers. We found that an energy offset on the order of 1.2 eV between the LUMO levels of the two polymers is sufficient to block electron transfer between the two polymers up to high gate voltages, such that an electron accumulation layer can be induced at the internal interface between the two polymers. The formation of such an electron accumulation layer is facilitated by the presence of positive holes trapped in donor-like states in the layer with the lower ionisation potential resulting in a negative shift of the turn-on voltage for electron accumulation. However, the presence of these positive holes also enables electrons to transfer across the interface and recombine with these holes, resulting in a plateau followed by another turn on region in the I_d–V_g curve in the electron accumulation regime.

The device investigated here could in principle be used as a memory device [19,20], and resembles somewhat in its operation a floating-gate memory transistor [21,22]. The procedure of injecting positive charges across the interface during the p-type operation of the device is equivalent to the "write" process in these memory devices, during which charges are stored in the floating-gate. The "read" process might correspond to recording the current at $V_g = 0$ V. By controlling the total number of holes flowing through the device during the write-process one could vary the information stored in the device. However, to use such devices for memory applications we need to understand better the nature of the hole trap states in the polymer and how the recombination process of electrons could be controlled to achieve suitably long retention times.

Acknowledgements

We would like to thank the Engineering and Physical Sciences Research Council (EPSRC) for funding, Cambridge Display Technology for supply of materials, as well as Matt Bird for helpful discussions.

References

[1] J. Veres, S.D. Ogier, S.W. Leeming, D.C. Cupertino, S.M. Khaffaf, Adv. Funct. Mater. 13 (2003) 199.
[2] V. Podzorov, M.E. Gershenson, Phys. Rev. Lett. 95 (2005) 16602.
[3] A. Dodabalapur, H.E. Katz, L. Torsi, R.C. Haddon, Science 269 (1995) 1560.
[4] B. Crone, A. Dodabalapur, Y.-Y. Lin, R.W. Filas, Z. Bao, A. LaDuca, R. Sarpeshkar, H.E. Katz, W. Li, Nature 403 (2000) 521.
[5] F. Dinelli, R. Capelli, M.A. Loi, M. Murgia, M. Muccini, A. Facchetti, T.J. Marks, Adv. Mater. 18 (2006) 1416.

[6] C. Rost, D.J. Gundlach, S. Karg, W. Rie, J. Appl. Phys. 95 (2004) 5782.
[7] J.-S. Kim, R.H. Friend, Appl. Phys. Lett. 87 (2005) 023506.
[8] K.H. Yim, Z. Zheng, Z. Liang, R.H. Friend, W.T.S. Huck, J.S. Kim, Adv. Funct. Mater. 18 (2008) 1012.
[9] A.J. Campbell, D.D.C. Bradley, H. Antoniadis, Appl. Phys. Lett. 79 (2001) 2133.
[10] J. Zaumseil, C.L. Donley, J.S. Kim, R.H. Friend, H. Sirringhaus, Adv. Mater. 18 (2006) 2708.
[11] Z. Zheng, K.H. Yim, M.S.M. Saifullah, M.E. Welland, R.H. Friend, J.S. Kim, W.T.S. Huck, Nano Lett. 7 (2007) 987.
[12] M. Redecker, D.D.C. Bradley, M. Inbasekaran, W.W. Wu, E.P. Woo, Adv. Mater. 11 (1999) 241.
[13] A. Salleo, T.W. Chen, A.R. Völkel, Y. Wu, P. Liu, B.S. Ong, R.A. Street, Phys. Rev. B 70 (2004) 11531.
[14] J.-F. Chang, H. Sirringhaus, Phys. Rev. B 76 (2007) 205204.
[15] C. Liu, H. Sirringhaus, J. Appl. Phys. (2010), in press.
[16] T. Junga, A. Dodabalapur, R. Wenz, S. Mohapatra, Appl. Phys. Lett. 87 (2005) 182109.
[17] S. Scheinert, G. Paasch, M. Schrödner, H.-K. Roth, S. Sensfu, Th. Doll, J. Appl. Phys. 92 (2002) 330.
[18] S. Scheinert, G. Paasch, T. Doll, Synth. Met. 139 (2003) 233.
[19] R.C.G. Naber, C. Tanase, P.W.M. Blom, G.H. Gelinck, A.W. Marsman, F.J. Touwslager, S. Setayesh, D.M. de Leeuw, Nat. Mater. 4 (2005) 243.
[20] R. Schroeder, L.A. Majewski, M. Voigt, M. Grell, IEEE Electron Dev. Lett. 26 (2005) 69.
[21] H.E. Katz, X.M. Hong, A. Dodabalapur, R. Sarpeshkar, J. Appl. Phys. 91 (2002) 1572.
[22] Th.B. Singh, N. Marjanović, G.J. Matt, N.S. Sariciftci, R. Schwödiauer, S. Bauer, Appl. Phys. Lett. 85 (2004) 5409.

Organic Electronics 11 (2010) 564–572

Contents lists available at ScienceDirect

Organic Electronics

journal homepage: www.elsevier.com/locate/orgel

Deep-blue phosphorescent iridium complexes with picolinic acid N-oxide as the ancillary ligand for high efficiency organic light-emitting diodes

Hoe-Joo Seo [a,1], Kyung-Mo Yoo [b,1], Myungkwan Song [c], Jin Su Park [c], Sung-Ho Jin [c], Young Inn Kim [c,*], Jang-Joo Kim [b,*]

[a] Department of Chemistry and Center for Plastic Information System, Pusan National University, Busan 609-735, Republic of Korea
[b] Department of Materials Science and Engineering and OLED Center, Seoul National University, Seoul 151-744, Republic of Korea
[c] Department of Chemistry Education, Interdisciplinary Program of Advanced Information and Display Materials, Center for Plastic Information System, Pusan National University, Busan 609-735, Republic of Korea

ARTICLE INFO

Article history:
Received 30 October 2009
Received in revised form 19 December 2009
Accepted 19 December 2009
Available online 29 December 2009

Keywords:
Phosphorescent organic light-emitting diodes (PhOLEDs)
Iridium complex
Deep-blue emitter
External quantum efficiency
Picolinic acid N-oxide ancillary ligand

ABSTRACT

A new series of highly efficient deep-blue phosphorescent Ir(III) complexes, $(F_2CH_3ppy)_2$-Ir(pic-N-oxide) **6** and $(F_2CF_3CH_3ppy)_2$Ir(pic-N-oxide) **7**, based on phenylpyridine (ppy) as the main ligand and picolinic acid N-oxide (pic-N-oxide) as the ancillary ligand, were synthesized for applications in phosphorescent organic light-emitting diodes (PhOLEDs). The photophysical, electrochemical, and electroluminescent (EL) properties of these substances were investigated. The energy levels of these substances were adjusted by the introduction of electron-donating and electron-withdrawing substituents on the ppy ligand. The Ir(III) complexes have high phosphorescent quantum yields as well as high thermal stability. High performance PhOLEDs fabricated using the Ir(III) complexes showed bright deep-blue emissions with the Commission Internationale de L'Eclairage (CIE) coordinates of (0.147, 0.210) at the current density of 0.1 mA/cm^2, and high external quantum (23.3%) and current (36.1 cd/A) efficiencies.

© 2009 Elsevier B.V. All rights reserved.

1. Introduction

Organic light-emitting diodes (OLEDs) are currently attracting great attention owing to their potential applications in full-color flat panel displays that serve as an efficient and low cost alternative to the widely used liquid crystal displays. An intense effort has been devoted to developing emitting materials and device structures for OLEDs in order to obtain higher efficiencies that are required for commercialization [1–4]. For commercial full-color OLEDs, materials that emit in the three basic color regions of blue, green, and red are required. Blue emitting materials are not only one of the major constituents in red-green-blue full-color displays, they also serve as the key emitting element for generating white light in combination with a complementary yellow color. As a result, explorations for new blue emitting materials that have higher performances remains one of the major challenges in this field.

Heavy-metal complexes, particularly those containing Ir(III), have been employed successfully in the construction of high efficiency phosphorescent organic light-emitting diodes (PhOLEDs) in displays and solid-state lighting [5–16]. In these systems, both triplet and singlet excitons are harvested as light by doping the phosphorescent emitters into charge-transporting hosts. Close to 100% internal quantum efficiencies have been reported for Ir(III) complexes in PhOLEDs [17–20]. Deep-blue Ir(III) complexes are needed in order to effectively reduce power consumption and increase the color gamut of full-color OLEDs. Importantly, the emission wavelengths of these complexes

* Corresponding authors.
E-mail addresses: yikim@pusan.ac.kr (Y.I. Kim), jjkim@snu.ac.kr (J.-J. Kim).
[1] H.J. Seo and K.M. Yoo made equal contribution to this paper.

1566-1199/$ - see front matter © 2009 Elsevier B.V. All rights reserved.
doi:10.1016/j.orgel.2009.12.014

can be readily tuned from red/green to sky blue by modification of the metal ligands. For example, emission from Ir(III) complexes can cover the whole visible region by simply modifying the 2-arylpyridine main ligand and the ancillary ligand [21]. However, in contrast to green and red phosphorescent complexes, the design and synthesis of deep-blue emitting Ir(III) complexes is a more challenging task [22–29].

Two strategies exist for creating phosphorescent Ir(III) complexes whose deep-blue emission is governed by the energy difference between the hightest occupied molecular orbital (HOMO) and lowest unoccupied molecular orbital (LUMO). The first involves low-lying the energy of the HOMO of the Ir(III) complexes [30–36]. 2-(2,4-Difluorophenyl)pyridine based Ir(III) complexes are good examples of the implimentation of this strategy. In these types of Ir(III) complexes, electron-withdrawing fluorines are introduced on the phenyl ring to cause an high HOMO energy. The second method relies on an high-lying the energy of the LUMO. This strategy has been used in the design of *fac*-Ir(F_2MeOppy)$_3$ [F_2MeOppy: 2-(2′,4′-difluorophenyl)-4-methoxypyridinato] and (F_2MeOppy)$_2$Ir(ptz) [ptz: 5-(2-pyridyl)tetrazolate], which emit at 464 nm [31] and 452 nm [37], respectively. The blue shift seen in these substances is ascribed to the effect of the strong electron-donating substituents at the 4-position of the pyridyl moiety low LUMO energy level. Several groups have demonstrated that phosphorescent wavelengths can be tuned in the blue to red region by functionalization of the main ligands of Ir-complexes with electron-withdrawing and electron-donating substituents [38–41].

Another important requirement for PhOLED applications is that the Ir(III) complexes have high phosphorescent quantum efficiencies. The physical properties, such as charge transfer character and solubility, of the Ir(III) complexes in heteroleptic Ir(III) complexes can be regulated through a proper choice of the ancillary ligand. Also, the nature of the ancillary ligand can profoundly effect the properties of lowest energy emitting excited state of the complex [42,43]. The electron density at the metal center can be controlled by the electron-donating or electron-withdrawing character of the ancillary ligand. The ground state electron density at the metal center governs the amount of metal to ligand charge transfer (MLCT) character that is mixed into the lowest energy electronic transition and, consequently, it governs both the emission wavelength and excited state radiative lifetime.

Despite the fact that significant work has been carried out in this area, efficient and stable deep-blue Ir(III) complexes are still rare. As a result, the design and synthesis of high performance, deep-blue Ir(III) complexes is a subject of great continuing [44,45]. Below, we describe the synthesis and properties of novel deep-blue emitting Ir(III) complexes **6** and **7** that have been designed by using the two strategies discussed above. Importantly, picolinic acid N-oxide (pic-N-oxide) is used for the first time in these complexes as the ancillary ligand. In addition, the complexes contain a methyl group at the 4-position of the pyridyl ring of the 2-(2,4-difluorophenyl)pyridine ligand **1** and the 2-(2′,4′-difluoro-3′-trifluoromethylphenyl)-4-methylpyridine ligand **3**. The combination of these substituents promotes an increase in the HOMO–LUMO energy gap, resulting in a hypsochromic shift compared to emission from the parent Ir(III) complex. PhOLEDs fabricated using these deep-blue Ir(III) complexes exhibit a maximum external quantum efficiency of 23.3% and deep-blue emission with the Commission Internationale de l'Eclairage (CIE) coordinates of (0.147, 0.210). To our best knowledge, the quantum efficiency is the highest among PhOLEDs emitting deep-blue color with the y value close to 0.2 in the CIE coordinate.

2. Results and discussion

The deep-blue emitting Ir(III) complexes ($F_2CH_3ppy)_2$-Ir(pic-N-oxide) **6** and ($F_2CF_3CH_3ppy)_2$Ir(pic-N-oxide) **7** (Scheme 1) were designed on the basis of considerations that include the ability to tune (1) HOMO–LUMO energy gaps by introduction of electron-donating and electron-withdrawing substituents into the phenylpyridine main ligand, and (2) electro-optical properties for enhanced PhOLED performance by modify the ancillary ligand. As a result, the target Ir(III) complexes **6** and **7** contain difluoro or difluoro and a trifluoromethyl group substituents on the phenyl group of the 2-phenyl-4-methylpyridine main ligand and pic-N-oxide as the ancillary ligand.

The procedure used to prepare the target Ir(III) complexes **6** and **7** involves coupling of $IrCl_3{\cdot}3H_2O$ with the main ppy ligand followed by introduction of the ancillary pic-N-oxide ligand (Scheme 1) [46]. In order to prepare the main ligand **3**, 2-(2′,4′-difluorophenyl)-4-methylpyridine (**1**, Fig. S1), prepared in 83% yield by employing a Suzuki coupling reaction between 2,4-difluorophenylboronic acid and 2-bromo-4-methylpyridine, was transformed to the iodo derivative **2** (Fig. S2) in 76% yield by sequential treatment with LDA and iodine. Reaction of **2** with (trifluoromethyl)trimethylsilane in the presence of CuI and KF gave 2-(2′,4′-difluoro-3′-trifluoromethylphenyl)-4-methylpyridine (**3**, Fig. S3) in 39% yield.

The cyclometalated Ir(III) μ-chloride bridged dimeric ($[(C\hat{}N)_2Ir(\mu\text{-}Cl)]_2$ complexes **4** and **5** were independently synthesized by reacting $IrCl_3{\cdot}3H_2O$ with an excess of the respective main ligands 2-(2′,4′-difluorophenyl)-4-methylphenylpyridine (**1**) and 2-(2′,4′-difluoro-3′-trifluoromethylphenyl)-4-methylpyridine (**3**) in 79–86% yields. Finally, replacment of the two bridging chlorides in **4** and **5** with pic-N-oxide produces the desired complexes ($F_2CH_3ppy)_2$-Ir(pic-N-oxide) **6** and ($F_2CF_3CH_3ppy)_2$Ir(pic-N-oxide) **7** in yields of *ca.* 50%. Ir(III) complexes **6** and **7** were purified by using silica gel column chromatography followed by multiple sublimation with a high vacuum, gradient temperatute train sublimation procedure. The structures, purities, and properties of the Ir(III) complexes **6** and **7** were determined by using ^{1}H NMR spectroscopy (Figs. S4 and S5), elemental analysis, differential scanning calorimetry (DSC), thermal gravimetric analysis (TGA), CV, UV–visible, and PL spectroscopy.

The thermal stabilities of the Ir(III) complexes **6** and **7** were evaluated using TGA and DSC under a nitrogen atmosphere. The 5% weight loss temperatures ($\Delta T_{5\%}$), recorded in Table 1, indicate that ($F_2CH_3ppy)_2$Ir(pic-N-oxide) **6** and

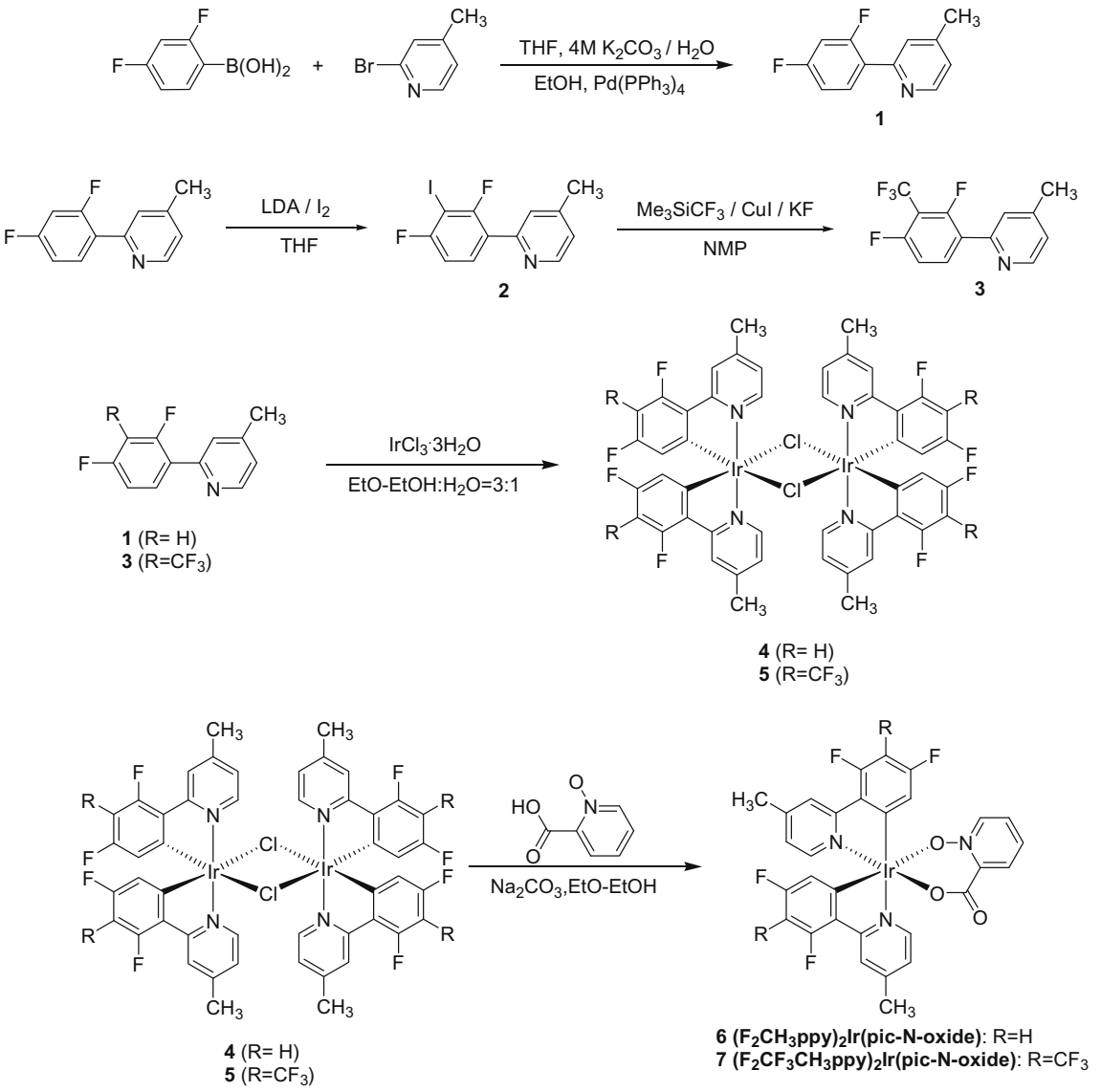

Scheme 1. Synthesis of Ir(III) complexes **6** and **7**.

Table 1
Thermal and photophysical property of Ir(III) complexes.

Complex	T_g [°C][a]	T_d [°C][b]	λ_{max} [nm][c]	HOMO [eV][d]	LUMO [eV][e]	τ[μs][f]	η_{PL} [%][g]
$(F_2CH_3ppy)_2Ir$(pic-N-oxide)	165	346	463, 491	−5.9	−3.0	1.46	67 ± 5
$(F_2CF_3CH_3ppy)_2Ir$(pic-N-oxide)	216	377	454, 482	−6.2	−3.2	1.48	80 ± 5

[a] T_g: glass transition temperature.
[b] T_d: decomposition temperature.
[c] λ_{max}: wavelengths of photoluminescence peaks.
[d] HOMO: highest occupied molecular orbital energy levels referenced to vacuum level.
[e] LUMO: lowest unoccupied molecular orbital energy levels referenced to vacuum level.
[f] τ: exciton lifetime when doped with 6 wt% in mCP film.
[g] η_{PL}: PL efficiency when doped with 6 wt% in mCP film.

$(F_2CF_3CH_3ppy)_2Ir$(pic-N-oxide) **7** have excellent thermal stabilities of 346 °C and 377 °C, since picolinic acid N-oxide ligand formed thermodynamically stable six membered ring with Ir(III) metal ion. The observations indicate that the Ir(III) complexes **6** and **7** have enhanced the rigidities that should prevent degradation of emitting layers of

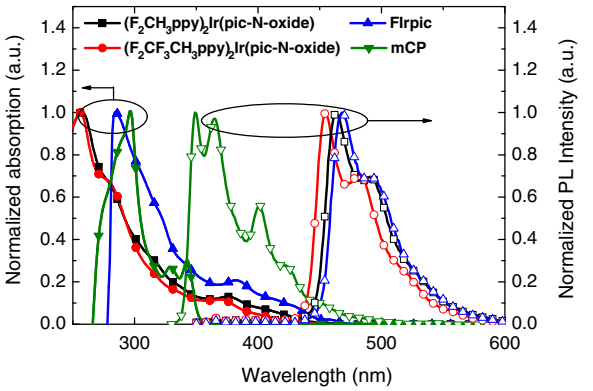

Fig. 1. Normalized absorption spectra (closed symbols) and PL spectra (open symbols) of $(F_2CH_3ppy)_2Ir$(pic-N-oxide) **6** (square), $(F_2CF_3CH_3ppy)_2$-Ir(pic-N-oxide) **7** (circle), FIrpic (up triangle), and mCP (down triangle).

PhOLEDs caused by the current-induced heat. The glass transition temperatures of Ir(III) complexes **6** and **7** are 165 and 216 °C, respectively. Importantly, the blue Ir(III) complex **7** that contains the trifluoromethyl substituent exhibits a higher thermal stability than the Ir(III) complex **6** which lacks this substituent.

The absorption spectra of the Ir(III) complexes $(F_2CH_3ppy)_2Ir$(pic-N-oxide) **6** and $(F_2CF_3CH_3ppy)_2Ir$(pic-N-oxide) **7** as well as FIrpic in dilute solutions (*ca.* 10^{-5} M in dichloromethane) and the absorption spectrum of mCP in film states are shown in Fig. 1 along with the PL spectra of the Ir(III) complexes and mCP. As is commonly seen with most Ir(III) complexes, the absorption spectra of these Ir(-III) complexes **6** and **7** can be divided into two regions [47,48]. The intense peaks in the short wavelength regions below 400 nm are assigned to spin-allowed $^1\pi$–π^* transitions that closely resemble those present in spectra of ppy main ligands (λ_{max}: 273 nm). The weaker absorption shoulders that appear above 400 nm are associated with charge transfer transitions [49]. The data suggest that substantial mixing takes place between ligand-based $^3\pi$–π^* states, spin forbidden metal to ligand charge transfer (^{3}MLCT) states, and higher-lying ^{1}MLCT transition states induced by the spin–orbit coupling effect [50,51]. The spin–orbit coupling is enhanced by the presence of closely-spaced π–π^* and MLCT states and the heavy-atom effect of Ir(III) center [52,53].

PL spectra were obtained on doped films of the Ir(III) complexes **6** and **7** in mCP with the concentrations of 8 wt.%. Optical band gaps of Ir(III) complexes **6** and **7**, deduced from the absorption edge of the absorption spectra, are 2.92 eV and 3.00 eV, respectively, both of which are larger than that of FIrpic (2.90 eV). The Ir(III) complexes **6** and **7** were found to emit intense deep-blue light, as shown in Fig. 1. The $(F_2CH_3ppy)_2Ir$(pic-N-oxide) **6** and $(F_2CF_3$-$CH_3ppy)_2Ir$(pic-N-oxide) **7** complexes exhibit maximum PL peaks at 463 nm and 454 nm, deriving predominantly from ligand-centered $^3\pi$–π^* excited states, that are blue shifted from the maximum peak of 468 nm arising from FIrpic. Triplet energy levels (T_1) are 2.65 eV for FIrpic, 2.68 eV for $(F_2CH_3ppy)_2Ir$(pic-N-oxide) **6**, and 2.73 eV for $(F_2CF_3CH_3ppy)_2Ir$(pic-N-oxide) **7**, respectively.

The PL efficiencies of mCP films doped with the Ir(III) complexes were determined using an integrating sphere with a He:Cd laser (λ: 325 nm and continuous wave) as the excitation light source. $(F_2CF_3CH_3ppy)_2Ir$(pic-N-oxide) **7** exhibits a very large PL quantum efficiency of 80 ± 5%, which is almost the same as FIrpic (87 ± 3%). In contrast, $(F_2CH_3ppy)_2Ir$(pic-N-oxide) **6** has a slightly lower PL efficiency of 67 ± 5%.

The transient PLs of the Ir(III) complexes, doped in mCP at a concentration of 6 wt.%, display single exponential decays, indicating that the bi-molecular interactions are negligible at this concentration (Fig. S6). Exciton lifetimes of the Ir(III) complexes were determined to be 1.46 μs and 1.48 μs for $(F_2CH_3ppy)_2Ir$(pic-N-oxide) **6** and $(F_2CF_3$-$CH_3ppy)_2Ir$(pic-N-oxide) **7**, respectively, values that are comparable to that of FIrpic (1.43 μs). The HOMO energy levels of the Ir(III) complexes, obtained by using CV measurements, are −5.9 eV for $(F_2ppy)_2Ir$(pic-N-oxide) **6** and −6.2 eV for $(F_2CF_3CH_3ppy)_2Ir$(pic-N-oxide) **7**. Both CVs are reversible and stable over repeated scans, implying that the Ir(III) complexes are stable under the oxidation conditions. By combining HOMO energy and optical band gap measurements, LUMO energy levels of −3.0 eV and −3.2 eV were determined for $(F_2CH_3ppy)_2Ir$(pic-N-oxide) **6** and $(F_2CF_3CH_3ppy)_2Ir$(pic-N-oxide) **7**, respectively. The higher electron density on the oxygen atom of N-oxide in pyridyl ring is expected to increase the energy level of LUMO and cosequently results in a blue-shifted emmision. Although the higher energy level of LUMO from the $(F_2CH_3ppy)_2Ir$(pic-N-oxide) **6** was observed, compared to that of FIrpic, the electron-withdrawing CF_3-group in $(F_2CF_3CH_3ppy)_2Ir$(pic-N-oxide) **7** makes both energy levels of HOMO and LUMO lower. This is primarily responsible for the blue-shift of an emission peak. The energy levels and the photophysical data for $(F_2CH_3ppy)_2Ir$(pic-N-oxide) **6** and $(F_2CF_3CH_3ppy)_2Ir$(pic-N-oxide) **7** are summarized in Table 1.

PhOLEDs were fabricated using the Ir(III) complexes **6** and **7** as dopants in mCP, selected as the host material because of its large spectral overlap with Ir(III) complexes **6** and **7** (Fig. 1) and higher triplet energy level than the Ir(III) complexes **6** and **7**. PhOLED with FIrpic as a dopant were also fabricated for comparison purposes. The PhOLEDs performance of these Ir(III) complexes **6**, **7**, and FIrpic are summarized in Table 2.

In Fig. 2 is shown the structures of the PhOLEDs and the energy levels of the compounds used in this study. The Type I PhOLEDs, fabricated on a clean glass substrate precoated with indium tin oxide (ITO), have the following components: ITO/4,4′,4″-tris(N-(2-naphthyl)-N-phenyl-amino)triphenylamine (2-TNATA) as a hole transporting layer (30 nm)/1,1-bis[(di-4-tolylamino)phenyl]cyclohexane (TAPC) (30 nm) as an electron blocking layer/mCP:8 wt.% dopant (20 nm)/*p*-bis(triphenylsilyl)benzene (UGH2):15 wt.% dopant (10 nm)/aluminium(III) bis(2-methyl-8-quinolinate)-4-phenylphenolate (BAlq) (40 nm) as the electron transporting layer/LiF (1 nm)/Al (100 nm). The PhOLEDs have dual emission layers in order to bring about a better balance between the electron and hole. mCP and UGH2 were selected as the *p*-host and the *n*-host, respectively. mCP has a large spectral overlap with Ir(III)

Table 2
EL performance of Ir(III) complexes.

Type	EML	EQE [%][a]	CE [cd/A][a]	PE [lm/W][a]	CIE [x, y][b]	EQE [%][c]	LE [cd/A][c]	PE [lm/W][c]	CIE [x, y][c]
I	FIrpic	22.6	42.8	27.5	0.151, 0.307	7.1	14.1	2.7	0.158, 0.322
I	$(F_2CH_3ppy)_2Ir$(pic-N-oxide)	19.6	34.5	22.6	0.161, 0.278	5.7	10.8	2.1	0.168, 0.291
I	$(F_2\ CF_3CH_3ppy)_2Ir$(pic-N-oxide)	21.4	31.6	14.3	0.149, 0.193	5.3	8.0	1.5	0.153, 0.200
II	$(F_2CF_3CH_3ppy)_2Ir$(pic-N-oxide)	23.3	36.1	17.3	0.147, 0.210	4.2	6.7	1.1	0.152, 0.221

[a] Maximum efficiency.
[b] Values collected at a current density of 0.1 mA/cm^2.
[c] Values collected at a current density of 20 mA/cm^2.

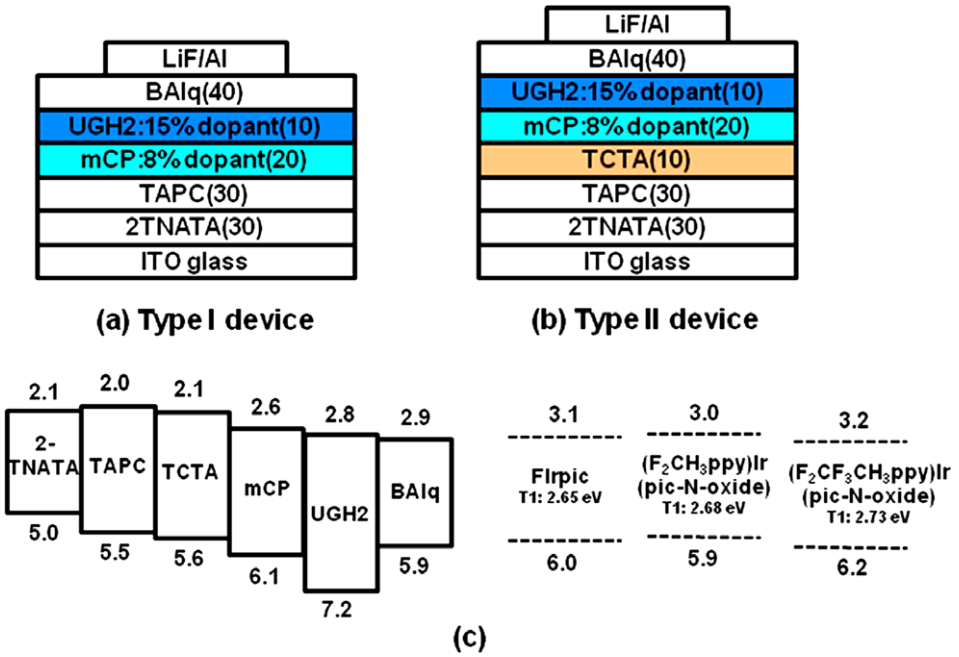

Fig. 2. Structures of the devices for (a) Type I and (b) Type II, and (c) energy levels of materials used in the study.

complexes **6** and **7** (Fig. 1) and as a result, it should promote efficient energy transfer. Both of the hosts have higher triplet energy levels than the Ir(III) complexes **6** and **7** in order to block triplet energy transfer from the Ir(III) complexes **6** and **7** to the hosts. UGH2 also works as an electron transport and exciton blocking layer. Concentrations of the Ir(III) complexes **6** and **7** were selected to be 8 wt.% in mCP and 15 wt.% in UGH2, respectively, which give optimal performances of the PhOLEDs.

Another type of $(F_2CF_3CH_3ppy)_2Ir$(pic-N-oxide) **7** derived PhOLED (Type II) was fabricated by adding a TCTA layer in an attempt to reduce accumulation of holes at HTL/EML interface. This PhOLED that has the following components: ITO/2-TNATA (30 nm)/TAPC (30 nm)/TCTA (10 nm)/mCP:8 wt.% **7** (20 nm)/UGH2:15 wt.% $(F_2CF_3CH_3ppy)_2Ir$(pic-N-oxide) (10 nm)/BAlq (40 nm)/LiF (1 nm)/Al (100 nm).

As shown in Fig. 3, current density–voltage–luminance curves (*J–V–L*) of the PhOLEDs prepared from FIrpic and $(F_2CH_3ppy)_2Ir$(pic-N-oxide) **6** are almost the same, indicating that the small energy differences in the HOMO and LUMO energy levels of the Ir(III) complexes **6** and **7** have little effect on charge transport. The turn-on voltage is slightly high (4.5 V) owing to the high injection barrier of holes from TAPC and low electron mobility in UGH2. The PhOLED doped with $(F_2CF_3CH_3ppy)_2Ir$(pic-N-oxide) **7** require a slightly higher driving voltage than those studied

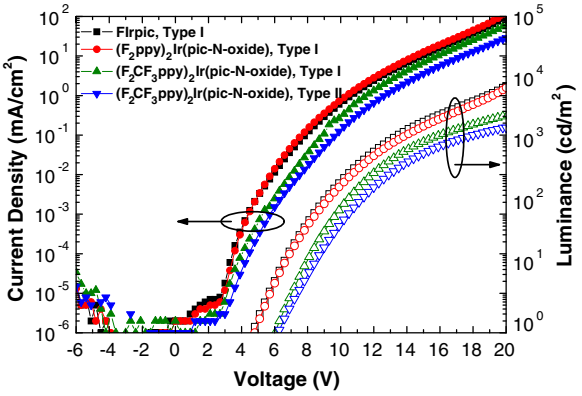

Fig. 3. Current density–voltage–luminance characteristics of the devices.

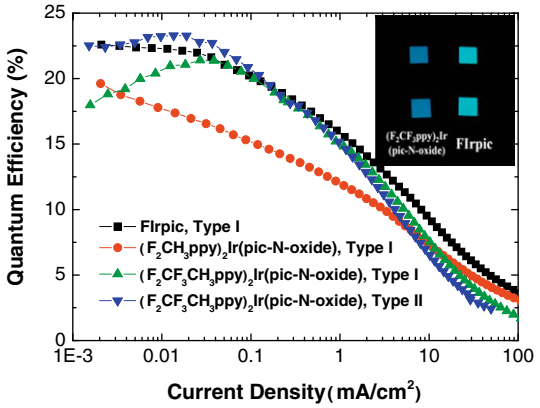

Fig. 4. External quantum efficiency of the devices. Inset: images of $(F_2CF_3CH_3ppy)_2Ir$(pic-N-oxide) **7** devices and FIrpic devices.

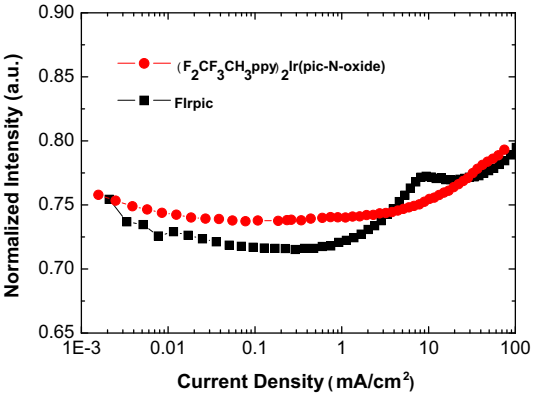

Fig. 5. Variation of relative peak intensity of longer wavelength vibronic peak to that of shortwavelength vibronic peak in EL spectra with increasing current.

previously most likely caused by the low HOMO and LUMO energy levels of the Ir(III) complexes **6** and **7**.

External quantum efficiencies of the PhOLEDs are displayed in Fig. 4. The Type I PhOLED doped with $(F_2CF_3CH_3ppy)_2Ir$(pic-N-oxide) **7** as the emitter has the very large maximum external quantum efficiency of 21.4%, which is very close to the reference FIrpic. Insertion of a 10 nm thick TCTA layer between the TAPC and mCP/$(F_2CF_3CH_3ppy)_2Ir$(pic-N-oxide) layers in the Type II device results in the even larger maximum external quantum efficiency of 23.3%.

The EL spectra of the PhOLEDs, especially at the low current density of 0.1 mA/cm^2, are the same as the solution PL spectra of the Ir(III) complexes **6** and **7**, displaying deep-blue emissions with Commission Internationale de l'Eclairage (CIE) coordinates of (0.149, 0.193) for the Type I and (0.147, 0.210) for the Type II devices, compared to a Type I device with FIrpic (0.151, 0.307) (Fig. S7). The emission color of the $(F_2CF_3CH_3ppy)_2Ir$(pic-N-oxide) **7** based PhOLED is compared with the FIrpic based PhOLED in the inset in Fig. 4, clearly displaying deep-blue color. The observed efficiencies and deep-blue emission demonstrate that these PhOLEDs have the best performance of any blue PhOLEDs studied to date with the *y* value close to 0.2 in the CIE coordinate. The PhOLEDs doped with $(F_2CH_3ppy)_2$-Ir(pic-N-oxide) **6** have a slightly lower maximum external quantum efficiency (19.6%) as a consequence of the lower PL quantum efficiency. The CIE coordinate of the $(F_2CH_3ppy)_2Ir$(pic-N-oxide) based PhOLED is (0.161, 0.278) at the current density of 0.1 mA/cm^2. All the PhOLEDs made using $(F_2CF_3CH_3ppy)_2Ir$(pic-N-oxide) **7** showed better performance for the Devices II structure than the Devices I, as listed in Table 2.

All the PhOLEDs prepared in this investigation show a large roll-off efficiencies with increasing current, which likely originates from a shift of the recombination zone as well as triplet–triplet and triplet-polaron annihilation at high current density [54]. The hypothesized existence of a recombination zone shift is supported by the observed variation of the emission spectra of the PhOLEDs with current density. The intensity ratios of the two vibronic peaks in the EL spectra of the dopants of $(F_2CF_3CH_3ppy)_2Ir$(pic-N-oxide) **7** ($I_{482\ nm}/I_{454\ nm}$) and FIrpic ($I_{491\ nm}/I_{463\ nm}$) are displayed in Fig. 5. The ratios increase with increasing current density above 1 mA/cm^2 for both PhOLEDs. The increasing ratio, associated with an intensified emission of the long wavelength vibronic peak with increasing current, suggests that the recombination zone shifts away from the Al electrode with increasing current. This roll-off can be minimized by a proper choice of electron and hole transporting, and host materials, as demonstrated for the FIrpic doped PhOLEDs.

3. Conclusions

Deep-blue emitting Ir(III) complexes containing electron density modulated phenylpyridine main ligands and a pic-N-oxide ancillary ligand have been synthesized. The new Ir(III) complexes are thermally and electrochemically stable and they have high photoluminescence efficiencies of over 80%. PhOLEDs fabricated using these Ir(III) complexes showed high external quantum (23.3%), current efficiencies (36.1 cd/A) and deep-blue emission with a CIE coordinate of (0.147, 0.210). Owing to these important characteristics, PhOLEDs prepared from these deep-blue Ir(III) complexes hold high potential for applications in display and solid-state lighting technologies.

4. Experimental

4.1. General information

All reagents and solvents were purchased from Adrich Chemical Co., Fluka and Alfa Aesar, and used without further purification. Anhydrous tetrahydrofuran (THF) was distilled over sodium and benzophenone under a nitrogen atmosphere. Silica column chromatography was performed using silica gel 60 G (particle size 5–40 μm, Merck Co.).

4.2. Synthesis of 2-(2′,4′-difluorophenyl)-4-methylpyridine (1)

2-(2′,4′-Difluorophenyl)-4-methylpyridine (1) was prepared by using a Suzuki coupling reaction between 2,4-difluorophenylboronic acid and 2-bromo-4-methylpyridine

[55]. 2-Bromo-4-methylpyridine (2.54 g, 20 mmol) and 2,4-difluorophenylboronic acid (3.47 g, 22 mmol) were dissolved in freshly distilled THF (100 mL) under nitrogen atmosphere. Potassium carbonate in water (10 mL, 2 M) and ethanol (2 mL) were added and the resulting mixture was cooled in a liquid nitrogen bath and thoroughly degassed. Tetrakis(triphenylphosphine)palladium(0) (1.2 g, 1 mmol) was added and the resulting mixture stirred at 70 °C for 24 h, cooled to room temperature, poured into water (100 mL), and extracted with diethyl ether (50 mL × 3 times). The combined organic layers were washed with water (50 mL) and brine (50 mL), dried over anhydrous magnesium sulfate, and concentrated *in vacuo* giving a residue, which was subjected to flash chromatography on silica gel using *n*-hexane/ethyl acetate as the eluent to yield **1** (3.41 g, 83%). ^{1}H NMR (300 MHz, $CDCl_3$, ppm): 8.55 (d, 1H, J = 4.8 Hz), 7.94 (td, 1H, J = 6.6, 10.5 Hz), 7.55 (s, 1H), 7.08 (d, 1H, J = 4.5 Hz), 6.89–7.01 (m, 2H), 2.41 (s, 3H).

4.3. Synthesis of 2-(2′,4′-difluoro-3′-iodophenyl)-4-methylpyridine (2)

2-(2′,4′-Difluoro-3′-iodophenyl)-4-methylpyridine (2) was prepared by using the published procedure [56]. 2-(2′,4′-Difluorophenyl)-4-methylpyridine (3.41 g, 16.6 mmol) was dissolved in freshly distilled THF (50 mL) under a nitrogen atmosphere. Lithium diisopropylamide (10 mL, 2 M) in *n*-hexane/THF was added dropwise to the solution at −78 °C and the mixture was stirred for 1 h. A solution of iodine (4.64 g, 18.3 mmol) in THF (20 mL) was added and the mixture was stirred for 3 h at −78 °C, warmed to room temperature, and poured into water (50 mL). The combined organic layers obtained by extraction with diethyl ether (50 mL × 3 times) was washed with saturated sodium thiosulfate (50 mL) and brine (50 mL), dried over anhydrous magnesium sulfate and concentrated *in vacuo* giving a residue which was subjected to flash chromatography on silica gel using *n*-hexane/ethyl acetate as the eluent to give **2** (4.18 g, 76%). ^{1}H NMR (300 MHz, $CDCl_3$, ppm): 8.57 (d, 1H, J = 4.8 Hz), 7.95 (td, 1H, J = 6.3, 8.7 Hz), 7.57 (s, 1H), 7.13 (d, 1H, J = 4.8 Hz), 6.99–7.05 (m, 1H), 2.42 (s, 3H).

4.4. Synthesis of 2-(2′,4′-difluoro-3′-trifluoromethylphenyl)-4-methylpyridine (3)

2-(2′,4′-Difluoro-3′-trifluoromethylphenyl)-4-methylpyridine (3) was prepared by using the published procedure [56]. A mixture of copper(I) iodide (6.00 g, 31.5 mmol) and anhydrous potassium fluoride (1.10 g, 19.0 mmol) was heated under reduced pressure while being gently shaken until the color changed to yellow. 2-(2′,4′-Difluoro-3′-iodophenyl)-4-methylpyridine (4.18 g, 12.6 mmol), 1-methyl-2-pyrrolidone (30 mL), and (trifluoromethyl)trimethylsilane (4 mL) were added to the mixture which was then vigorously stirred for 24 h at room temperature. The mixture was poured into aqueous ammonia (14%, 100 mL) and extracted with dichloromethane (50 mL × 3 times) to give an organic phase that was washed with water (50 mL) and brine (50 mL), dried over anhydrous magnesium sulfate and concentrated *in vacuo*. The residue was subjected to flash chromatography on silica gel using *n*-hexane/ethyl acetate as the eluent to give **3** (1.39 g, 39%). ^{1}H NMR (300 MHz, $CDCl_3$, ppm): 8.59 (d, 1H, J = 5.1 Hz), 7.98 (td, 1H, J = 6.3, 9 Hz), 7.60 (s, 1H), 7.17 (d, 1H, J = 4.8 Hz), 7.01–7.07 (m, 1H), 2.46 (s, 3H).

4.5. General procedure for the synthesis of (C^N)$_2$Ir(pic-N-oxide) complexes 6 and 7

The (C^N)$_2$Ir(pic-N-oxide) complexes were synthesized in two steps using standard method [5,57]. A solution of $IrCl_3{\cdot}3H_2O$ (0.70 g, 2 mmol) and 2.5 equivalents of the main ligand **1** or **3** in 2-ethoxyethanol/water (16 mL, 3:1 v/v) was stirred at 125 °C for 24 h, cooled to room temperature, and concentrated *in vacuo*. Washing the residue with ethanol gave rise to the dimeric iridium complexes $[(C^N)_2Ir(\mu\text{-}Cl)]_2$ **4** or **5**. After drying, the crude product was directly used for next step without further purification. A solution of either **4** or **5** (1 mmol), Na_2CO_3 (10 mmol) and 5 equivalents of pic-N-oxide in 2-ethoxyethanol (10 mL) was stirred at 130 °C under a nitrogen atmosphere for 20 h, cooled, and poured into water. Extraction with dichloromethane (30 mL × 3 times) gave an organic layer which was dried over anhydrous magnesium sulfate, and concentrated *in vacuo* giving a residue that was subjected to flash chromatography on silica gel using dichloromethane/methanol as the eluent to afford the desired Ir(III) complexes **6** and **7**, respectively.

4.5.1. Dimer iridium complex 4

Tetrakis[2-(2′,4′-difluorophenyl)-4-methylpyridine-C^2,N′]-bis(μ-chloro)diiridium(III) $[Ir(F_2CH_3ppy)_2Cl]_2$. Yellow solid. Yield: 86% (2.19 g). *Anal.* Calc. for $C_{48}H_{32}Cl_2F_8Ir_2N_4$: C, 45.32; H, 2.54; N, 4.40. Found: C, 46.12; H, 2.44; N, 4.46%.

4.5.2. Dimer iridium complex 5

Tetrakis[2-(2′,4′-difluorophenyl-3′-trifluoromethylphenyl)-4-methylpyridine-C^2,N′]-bis(μ-chloro)diiridium(III) $[Ir(F_2CF_3CH_3ppy)_2Cl]_2$. Yellow solid. Yield: 79% (2.41 g). *Anal.* Calc. for $C_{52}H_{28}Cl_2F_{20}Ir_2N_4$: C, 40.45; H, 1.83; N, 3.63. Found: C, 41.12; H, 1.72; N, 3.68%.

4.5.3. Iridium(III)bis[2-(2′,4′-difluorophenyl)-4-methylpyridinato-N,C$^{2'}$]picolinate N-oxide, (F_2CH_3ppy)$_2$Ir(pic-N-oxide) (6)

Yellow solid. Yield: 46%. (340 mg). ^{1}H NMR (300 MHz, $CDCl_3$, ppm): 8.55 (d, 1H, J = 5.7 Hz), 8.32 (d, 1H, J = 7.5 Hz), 8.10 (s, 1H), 8.04 (s, 1H), 7.93 (td, 1H, J = 1.5, 7.5 Hz), 7.77 (d, 1H, J = 5.4 Hz), 7.38–7.43 (m, 1H), 7.24 (d, 1H, J = 6.3 Hz), 7.00 (dd, 1H, J = 1.2, 5.7 Hz), 6.78 (dd, 1H, J = 1.2, 5.7 Hz), 6.34–6.50 (m, 2H), 5.85 (dd, 1H, J = 2.4, 8.7 Hz), 5.59 (dd, 1H, J = 2.4, 8.7 Hz), 2.55 (s, 6H). *Anal.* Calc. for $C_{30}H_{20}F_4IrN_3O_3$: C, 48.78; H, 2.72; N, 5.69. Found: C, 48.58; H, 2.91; N, 5.29%.

4.5.4. Iridium(III)bis[2-(2′,4′-difluoro-3′-trifluoromethylphenyl)-4-methylpyridinato-N,C$^{2'}$]picolinate N-oxide, ($F_2CF_3CH_3ppy$)$_2$Ir(pic-N-oxide) (7)

Yellow solid. Yield: 34% (297 mg). ^{1}H NMR (300 MHz, $CDCl_3$, ppm): 8.57 (d, 1H, J = 6.0 Hz), 8.35 (d, 1H, J = 7.2 Hz), 8.18 (s, 1H), 8.13 (s, 1H), 8.00 (td, 1H, J = 1.5,

7.8 Hz), 7.76 (d, 1H, J = 4.5 Hz), 7.49 (t, 1H, 5.7 Hz), 7.12 (d, 1H, J = 6.0 Hz), 6.90 (d, 1H, J = 6.3 Hz), 5.64 (d, 1H, J = 10.2 Hz), 5.69 (d, 1H, J = 10.8), 2.59 (s, 6H). *Anal.* Calc. for $C_{32}H_{18}F_{10}IrN_3O_3$: C, 43.94; H, 2.07; N, 4.80. Found: C, 44.18; H, 2.35; N, 4.57%.

4.6. Measurements of physical and electrochemical properties

UV–visible absorption spectra of **6** and **7** were recorded by using a Varian 5000 spectrophotometer. Photoluminescence (PL) spectra were measured with a He:Cd laser (λ: 325 nm, and continuous wave) as the excitation light source and a photomultiplier tube (PMT, Hamamatsu) with a monochromator (Acton Research Co., SpectraPro 2300i) as the detector. Cyclic voltammograms (CV) of the Ir(III) complexes were recorded by using a Princeton Applied Research (AMETEK VSP) potentiostat at room temperature on 0.1 M solutions of the Ir(III) complexes in acetonitrile or dichloromethane containing tetrabutylammonium perchlorate (Bu_4NClO_4) at a scan rate of 100 mV/s under nitrogen gas. Pt was used as the working and counter electrode and Ag/AgCl electrode as the reference electrode.

The PL efficiencies of doped films containing **6** and **7** were measured using the integrating sphere (Newport) with a He:Cd laser (λ: 325 nm, and continuous wave) as the excitation light source. The absolute PL efficiency measurement system was calibrated by using two standard lamps of LS-1-CAL calibrated light source and DH-2000 deuterium–tungsten halogen light source (Ocean Optics, Inc.). Transient photoluminescence of the phosphorescent dye doped films were measured using a Nd:YAG laser (λ: 355 nm, 10 Hz, and 9 ns pulse width) as the excitation light source and PMT (Hamamatsu) with a monochromator (Acton Research Co., SpectraPro 2300i) as the detector. The samples were kept in a vacuum chamber maintained at pressures under 10^{-3} Torr during the measurement.

4.7. Fabrication of the PhOLEDs using Ir(III) complexes 6 and 7

The PhOLEDs were fabricated by using thermal evaporation onto a cleaned glass substrate precoated with indium tin oxide (ITO) under a vacuum. Prior to organic layer deposition, the ITO substrates were exposed to UV-ozone flux for 10 min following degreasing in acetone and isopropyl alcohol. All of the organic layers were deposited by using thermal evaporation at a base pressure of $<5 \times 10^{-8}$ Torr. Current density–voltage–luminescence (J–V–L) characteristics of the PhOLEDs were measured simultaneously using a Keithley 2400 programmable source meter and SpectraScan PR650 (Photo Research). All the materials were purified using train sublimation before use.

Acknowledgement

This research was supported by a grant (2009K000069) from Center for Nanoscale Mechatronics and Manufacturing, one of the 21st Century Frontier Research Programs, which are supported by Ministry of Education, Science and Technology. This work was supported by the Korea Science and Engineering Foundation (KOSEF) grant funded by the Korea government (MEST) (No. M10600000157-06J0000-15710) and Strategic Technology under Ministry of Knowledge Economy of Korea.

Appendix A. Supplementary data

Supplementary data associated with this article can be found, in the online version, at doi:10.1016/j.orgel.2009.12.014.

References

[1] C.W. Tang, S.A. Van Slyke, Appl. Phys. Lett. 51 (1987) 913.
[2] R.H. Friend, R.W. Gymer, A.B. Holmes, J.H. Burroughes, R.N. Marks, C. Taliani, D.D.C. Bradley, D.A. Dos Santos, J.L. Bredas, M. Logdlund, W.R. Salaneck, W.R. Nature (London) 397 (1999) 121.
[3] R.J. Tseng, R.C. Chiechi, F. Wudl, Y. Yang, Appl. Phys. Lett. 88 (2006) 093512.
[4] B.W. D'Andrade, S.R. Forrest, Adv. Mater. 16 (2004) 1585.
[5] S. Lamansky, P. Djurovich, D. Murphy, F. Abdel-Razzaq, H.E. Lee, C. Adachi, P.E. Burrows, S.R. Forrest, M.E. Thompson, J. Am. Chem. Soc. 123 (2001) 4304.
[6] W. Zhu, Y. Mo, M. Yuan, W. Yang, Y. Cao, Appl. Phys. Lett. 80 (2002) 2045.
[7] X. Gong, J.C. Ostrowski, G.C. Bazan, D. Moses, A.J. Heeger, Appl. Phys. Lett. 81 (2002) 3711.
[8] K.R.J. Thomas, M. Velusamy, J.T. Lin, C.H. Chien, Y.T. Tao, Y.S. Wen, Y.H. Hu, P.T. Chou, Inorg. Chem. 44 (2005) 5677.
[9] W. Lu, B.X. Mi, M.C.W. Chan, Z. Hui, C.M. Che, N. Zhu, S.T. Lee, J. Am. Chem. Soc. 126 (2004) 4958.
[10] C.H. Huang, F.Y. Li, W. Huang, Introduction to Organic Light-Emitting Materials and Devices, Fudan University, Shanghai, China, 2005.
[11] M.A. Baldo, S. Lamansky, P.E. Burrows, M.E. Thompson, S.R. Forrest, Appl. Phys. Lett. 75 (1999) 4.
[12] Y.S. Park, J.W. Kang, D.M. Kang, J.W. Park, Y.H. Kim, S.K. Kwon, J.J. Kim, Adv. Mater. 20 (2008) 1957.
[13] D.M. Kang, J.W. Kang, J.W. Park, S.O. Jung, S.H. Lee, D. Park, Y.H. Kim, S.C. Shin, J.J. Kim, S.K. Kwon, Adv. Mater. 20 (2008) 2003.
[14] K.S. Yook, S.O. Jeon, C.W. Joo, J.Y. Lee, Appl. Phys. Lett. 93 (2008) 113301.
[15] J.J. Park, T.J. Park, W.S. Jeon, R. Pode, J. Jang, J.H. Kwon, E.S. Yu, M.Y. Chae, Org. Electron. 10 (2009) 189.
[16] J. Lee, J.I. Lee, K.I. Song, S.J. Lee, H.Y. Chu, Appl. Phys. Lett. 92 (2008) 133304.
[17] J. Brooks, Y. Babayan, S. Lamansky, P.I. Djurovich, I. Tsyba, R. Bau, M.E. Thompson, Inorg. Chem. 41 (2002) 3055.
[18] P.C. Wu, J.K. Yu, Y.H. Song, Y. Chi, P.T. Chou, S.M. Peng, G.H. Lee, Organometallics 22 (2003) 4938.
[19] D. Tanaka, Y. Agata, T. Takeda, S. Watanabe, J. Kido, Jpn. J. Appl. Phys. 46 (2007) L117.
[20] S.J. Su, E. Gonmori, H. Sasabe, J. Kido, Adv. Mater. 20 (2008) 4189.
[21] C. Yang, X. Zhang, H. You, L. Zhu, L. Chen, L. Zhu, Y. Tao, D. Ma, Z. Shuai, J. Qin, Adv. Funct. Mater. 17 (2007) 651.
[22] K. Dedeian, J. Shi, N. Shepherd, E. Forsythe, D.C. Morton, Inorg. Chem. 44 (2005) 4445.
[23] C.H. Yang, S.W. Li, Y. Chi, Inorg. Chem. 44 (2005) 7770.
[24] T. Sajoto, P.I. Djurovich, A. Tamayo, M. Yousufuddin, R. Bau, M.E. Thompson, Inorg. Chem. 44 (2005) 7992.
[25] H. Fukagawa, K. Watanabe, T. Tsuzuki, S. Tokito, Appl. Phys. Lett. 93 (2008) 133312.
[26] Y. Zheng, S.H. Eom, N. Chopra, J. Lee, F. So, J. Xue, Appl. Phys. Lett. 89 (2008) 2343.
[27] H. Jang, C.H. Shin, N.G. Kim, K.Y. Hwang, Y. Do, Synth. Met. 154 (2005) 157.
[28] S.Y. Kim, J.H. Kim, Y. Ha, S.H. Lee, J.H. Seo, Y.K. Kim, Curr. Appl. Phys. 7 (2007) 380.
[29] S.C. Lee, Y.S. Kim, Mol. Cryst. Liq. Cryst. 2491 (2008) 209.
[30] V. Adamovich, J. Brooks, A. Tamayo, A.M. Alexander, P.I. Djurovich, B.W. D'Andrade, C. Adachi, S.R. Forrest, M.E. Thompson, New J. Chem. 26 (2002) 1171.
[31] A.B. Tamayo, B.D. Alleyne, P.I. Djurovich, S. Lamansky, I. Tsyba, N.N. Ho, R. Bau, J. Am. Chem. Soc. 125 (2003) 7377.
[32] P. Coppo, E.A. Plummer, L.D. Cola, Chem. Commun. 2004 (1774).
[33] S.J. Yeh, M.F. Wu, C.T. Chen, Y.H. Song, Y. Chi, M.H. Ho, S.F. Hsu, C.H. Chen, Adv. Mater. 17 (2005) 285.

[34] C.H. Yang, Y.M. Cheng, Y. Chi, C.J. Hsu, F.C. Fang, K.T. Wong, P.T. Chou, C.H. Chang, M.H. Tsai, C.C. Wu, Angew. Chem. Int. Ed. 46 (2007) 2418.
[35] S.H. Kim, J. Jang, S.J. Lee, J.Y. Lee, Thin Solid Films 2517 (2008) 722.
[36] N.G. Park, G.C. Choi, Y.H. Lee, Y.S. Kim, Curr. Appl. Phys. 6 (2006) 620.
[37] L.L. Wu, C.H. Yang, I.W. Sun, S.Y. Chu, P.C. Kao, H.H. Huang, Organometallics 26 (2007) 2017.
[38] H.J. Bolink, E. Coronado, S.G. Santamaria, M. Sessolo, N. Evans, C. Klein, E. Baranoff, K. Kalyanasundaram, M. Gräetzel, Md.K. Nazeeruddin, Chem. Commun. (2007) 3276.
[39] P. Coppo, E.A. Plummer, L. De Cola, Chem. Commun. 2004 (1774).
[40] T. Sajoto, P.I. Djurovich, A.B. Tamayo, M. Yousufuddin, R. Bau, M.E. Thompson, R.J. Holmes, S.R. Forrest, Inorg. Chem. 44 (2005) 7992.
[41] Y. You, S.Y. Park, J. Am. Chem. Soc. 127 (2005) 12438.
[42] P.I. Kvam, M.V. Puzyk, K.P. Balashev, J. Songstad, Acta Chem. Scand. (1995) 49.
[43] K.P. Balashev, M.V. Puzyk, V.S. Kotlyar, M.V. Kulikova, Coord. Chem. Rev. 159 (1997) 109.
[44] C. Hosokawa, H. Higashi, H. Nakamura, T. Kusumoto, Synth. Met. (1997) 91.
[45] M. Matsuura, M. Funahashi, K. Fukuoka, H. Tokailin, C. Hosokawa, M. Edia, T. Kusumoto, Proc. IDW'97 (1997) 581.
[46] K.K.W. Lo, J.S.W. Chan, L.H. Lui, C.K. Chung, Organometallics 23 (2004) 3108.
[47] C.L. Ho, W.Y. Wong, G.J. Zhou, Z. Xie, L. Wang, Adv. Funct. Mater. 17 (2007) 2925.
[48] S.C. Lo, C.P. Shipley, R.N. Bera, R.E. Harding, A.R. Cowley, P.L. Burn, I.D.W. Samuel, Chem. Mater. 18 (2006) 5119.
[49] P.J.J. Hay, Phys. Chem. A 106 (2002) 1634.
[50] A.P. Wilde, K.A. King, R.J. Watts, J. Phys. Chem. 95 (1991) 629.
[51] M.C. Columbo, A. Hauser, H.U. Güdel, Top. Curr. Chem. 171 (1994) 143.
[52] Y. Wang, N. Herron, V.V. Grushin, D. LeCloux, V. Petrov, Appl. Phys. Lett. 79 (2001) 449.
[53] F.O. Garces, K.A. King, R.J. Watts, Inorg. Chem. 27 (1998) 3464.
[54] S. Reineke, K. Walzer, K. Leo, Phys. Rev. B 75 (2007) 125328.
[55] N. Miyaura, A. Suzuki, Chem. Rev. 95 (1995) 2457.
[56] S.Y. Takizawa, H. Echizen, J.I. Nishida, T. Tsuzuki, S. Yokito, Y. Yamashite, Chem. Lett. 35 (2006) 748.
[57] M. Nonoyama, Bull. Chem. Soc. Jpn. 47 (1974) 767.

Organic Electronics 11 (2010) 573–582

Contents lists available at ScienceDirect

Organic Electronics

journal homepage: www.elsevier.com/locate/orgel

The effect of molecule size and shape on free charge generation, transport and recombination in *all*-thiophene dendrimer:fullerene bulk heterojunctions

Attila J. Mozer [a,*], Chang-Qi Ma [b,*], Wallace W.H. Wong [c], David J. Jones [c], Peter Bäuerle [b], Gordon G. Wallace [a]

[a] *ARC Centre of Excellence for Electromaterials Science, Intelligent Polymer Research Institute, University of Wollongong, Australia*
[b] *Institute of Organic Chemistry II and Advanced Materials, Ulm University, Germany*
[c] *Bio21 Institute, The University of Melbourne, Building 102 (Level 4), 30 Flemington Road, Parkville, Victoria 3010, Australia*

ARTICLE INFO

Article history:
Received 18 September 2009
Received in revised form 21 December 2009
Accepted 22 December 2009
Available online 28 December 2009

Keywords:
Thiophene dendrimers
Bulk heterojunction solar cells
Charge mobility
Charge carrier lifetime

ABSTRACT

Charge mobilities of *all*-thiophene dendrimers were studied using the charge extraction by linearly increasing voltage technique (CELIV). Four dendrimers differing in size, shape and with and without trimethylsilyl (TMS) protecting groups have been compared yielding important structure–property correlations: The hole mobility of the dendrimers with 21 or 42 thiophene units was found to be very similar and around 10^{-5} cm^2 V^{-1} s^{-1}, indicating that shape and size of the studied dendrimers have little effect on their charge transport properties. Hole mobility is decreased by a factor of 3–10 by incorporation of TMS groups, which is attributed to the intrinsically slower electron transfer rates between the TMS-protected dendrimer molecules. Bulk heterojunction solar cells using 1:2 mixtures of the thiophene dendrimers and the electron acceptor [6,6]-phenyl-C_{61} butyric acid methyl ester ($PC_{61}BM$) were fabricated and their performances were analyzed. The decreased hole mobility in the blend, the unbalanced electron and hole mobility and a rather short charge carrier lifetime measured by charge extraction and transient absorption techniques are thought to be important factors that limit overall power conversion efficiency in theses devices. Improved free charge generation with increasing dendrimer size was observed, which was related to increased separation distance between electron and hole pairs.
© 2009 Elsevier B.V. All rights reserved.

1. Introduction

Conjugated polymer–fullerene bulk heterojunction (BHJ) solar cells represent one of the promising organic photovoltaic technologies due to their ease of solution-processing, low costs, and the potential of producing large-scale flexible devices [1]. The key component of a BHJ solar cell is the photoactive layer comprised of a conjugated polymer as electron donor and a soluble fullerene derivative as electron acceptor. In the blended film, nano-scale phase separation between donor and acceptor occurs providing sufficient donor–acceptor interface for charge separation [2,3]. Another particularly important issue in improving power conversion efficiencies of a BHJ solar cell is the efficiency of charge collection, which is governed by the product of mobility (μ) and free charge carrier lifetime (τ). Generally, high and balanced charge carrier mobilities and sufficiently long charge carrier lifetime are necessary to achieve efficient charge collection at the electrodes. Regioregular poly(3-hexylthiophene) (rr-P3HT) is considered as current benchmark for BHJ solar cells reaching external quantum efficiencies above 80% and a power conversion efficiencies up to 5.5% [4–8]. Copolymers in cooperation with electron accepting benzothiadiazole unit to form a

* Corresponding authors. Tel.: +61 02 42981429 (A.J. Mozer).
E-mail addresses: attila@uow.edu.au (A.J. Mozer), changqi.ma@uni-ulm.de (C.-Q. Ma).

1566-1199/$ - see front matter © 2009 Elsevier B.V. All rights reserved.
doi:10.1016/j.orgel.2009.12.016

push–pull structure were developed and showed excellent performance in BHJ solar cells application [9–13]. As an example, by using blends of a copolymer poly[N-9″-heptadecanyl-2,7-carbazole-alt-5,5-(4′,7′-di-2-thienyl-2′,1′,3′-benzothiadiazole) and $PC_{71}BM$ in cooperation with a TiOx buffer layer, power conversion efficiencies of more than 6% were achieved for solution processed BHJ solar cells [13].

In comparison to polymeric materials with linear conjugated chains, conjugated dendrimers represent a novel class of three dimensional macromolecules with shape-persistent and defined, monodisperse structures [14,15]. Due to their branched 3D structure, conjugated dendrimers usually have good solubility and film forming ability. More importantly, conjugated dendrimers are regarded as a class of organic materials with isotropic and homogenous properties, which could be beneficial for charge transport in solid films [15]. In this respect, several examples of semiconducting conjugated dendrimers were reported in literature, including: phenylenes, phenylene–ethenylenes and carbazole dendrimer or thiophene dendrimers [14,15].

Thiophene-based materials typically exhibit excellent charge transport properties. Therefore, 3D dendritic structures are of interest for applications in organic electronics. Since the development of the first *all*-thiophene dendrimers, which were reported by Advincula and coworkers [16,17] variation of oligothiophene-based dendrimers by changing core, branching units or position of oligothiophene blocks were developed by several research groups [18–23]. Aiming at increasing dimensionality and functionality of thiophene-based materials, our research group has recently developed a novel synthetic strategy in synthesizing large *all*-thiophene dendrimers [24]. Due to their defined chemical structures, these dendrimers serve as good model compounds for structure–property-performance relationship investigation. As an example, photovoltaic performance of BHJ solar cells using thiophene dendrimer as p-type semiconductor blended with n-type fullerene derivative [6,6]-phenyl-C_{61}-butyric acid methyl ester ($PC_{61}BM$) highly depended on the molecular structure [25]. All the reported thiophene dendrimer-based devices showed high open circuit voltages (V_{oc}) around 1.0 V, whereas the short circuit currents (J_{sc}) of these devices were limited by the light harvesting ability of the dendrimer films used and perhaps also by inefficient charge collection. The fill factor of all devices was found to be rather low (around 0.4) [25]. To clearly determine the origin of the limiting factors of performance of dendrimer-based BHJ solar cells, investigations on charge mobility and charge carrier lifetime is necessary. Despite the increasing number of reports on optoelectronic applications of conjugated dendrimers, there are only a few studies focused on detailed charge mobility and charge carrier lifetime measurements [23,26–29].

Herein we have investigated the charge transport properties of four different thiophene dendrimers varying in size, shape and protecting group in pristine films and also in their 1:2-blends with $PC_{61}BM$ using the photo-induced charge extraction by a linearly increasing voltage (photo-CELIV) technique. The lifetime of the reasonably mobile (free) charge carriers was determined in the dendrimer:$PC_{61}BM$ mixture using a delayed-field charge extraction technique and compared to transient absorption measurements, where the spectral decay of dendrimer cation radicals was optically monitored. The results are correlated with the molecular structure of the dendrimers, providing insights into designing the next generation of electro- and photoactive dendrimers with enhanced charge mobility.

2. Materials and methods

The dendrimers were synthesized according to previously published procedures [24,25].

The photovoltaic devices were prepared by spin-coating EL-grade PEDOT:PSS (Baytron P AI 4083) onto pre-cleaned, patterned indium tin oxide (ITO) substrates. The photoactive layer was deposited by spin-coating from a chlorobenzene solution with a total concentration of 25 mg/ml. Film thickness was determined by profilometry (Veeco Dektak 150+ Surface Profiler). The counter electrode of LiF (1 nm) and aluminum (100 nm) was deposited by vacuum evaporation at 5×10^{-6} mbar. The solar cells were illuminated at 100 mW cm^{-2} using 1 kW Oriel solar simulator with an AM 1.5G filter in air and *J–V* curves were measured using a Keithley 2400 source measurement unit. For accurate measurement, the light intensity was calibrated using a reference silicon solar cell (PV measurements Inc.) certified by the National Renewable Energy Laboratory. The devices with thick active layers (more than 200 nm) were fabricated in a similar device structure as mentioned above. To get a thick solid film, solution with concentration of 75 mg/ml was used.

Photo-CELIV measurements performed on sealed PV devices using the 2nd harmonics of a Q-switched Nd:YAG laser (10 Hz, INDI, Spectra-Physics) as the excitation source and voltage pulses applied using a function generator. The extraction currents were recorded using a 500 MHz Tektronix oscilloscope and a set of resistors. Delay time between the laser pulse and the voltage pulse was set using a digital delay generator. No effect of changing illumination side or sign of the applied voltage bias was observed for any of the samples indicating that the charge concentration prior to charge extraction was uniform throughout the thickness of the samples.

Transient absorption measurements were performed on the same PV devices characterized above using the 2nd harmonics of a Q-switched Nd:YAG laser (10 Hz, INDI, Spectra-Physics) as the pump and a pulsed Xe lamp, a band pass filter and a monochromator as the 890 nm probe. A 200 MHz Femto photoreceiver and 500 MHz oscilloscope was used to record the traces.

3. Results and discussion

3.1. Charge mobilities of all-thiophene dendrimers

The experimental arrangement of the photo-CELIV technique and the device architecture of a BHJ solar cell are schematically illustrated in Fig. 1. The photo-CELIV technique, in which charge carriers are photo-generated

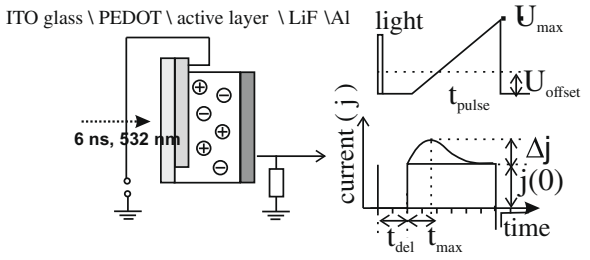

Fig. 1. Schematic representation of the experimental arrangement and pulse sequence of the photo-CELIV technique.

by a short laser pulse and then subsequently extracted by a linearly increasing voltage pulse, has been shown to be particularly useful for thin organic photodiodes and BHJ solar cells [30]. The main advantage is that this technique can be directly applied to thin organic diodes and operational solar cells without a need to change contacts, device geometry or the film thickness [31]. This is important because charge carrier drift mobilities in disordered organic materials may depend on a number of parameters, including electric field (E), temperature (T) [32] and charge carrier concentration (n) [33]. Various mobility techniques, therefore, tend to yield different mobility values that can be partially attributed to the different E and n regime they operate [34].

The chemical structures of the four thiophene dendrimers investigated here are displayed in Chart 1. The synthesis of these compounds and a detailed study on their BHJ solar cell device performance have been reported [24,25]. These four compounds have been selected to allow comparison of three of their main characteristics: (i) TMS-protected or non-protected structure (*42T-Si* vs. *42T*); (ii) dendrimer generation and size (*18T-Si* vs. *42T-Si*); (iii)

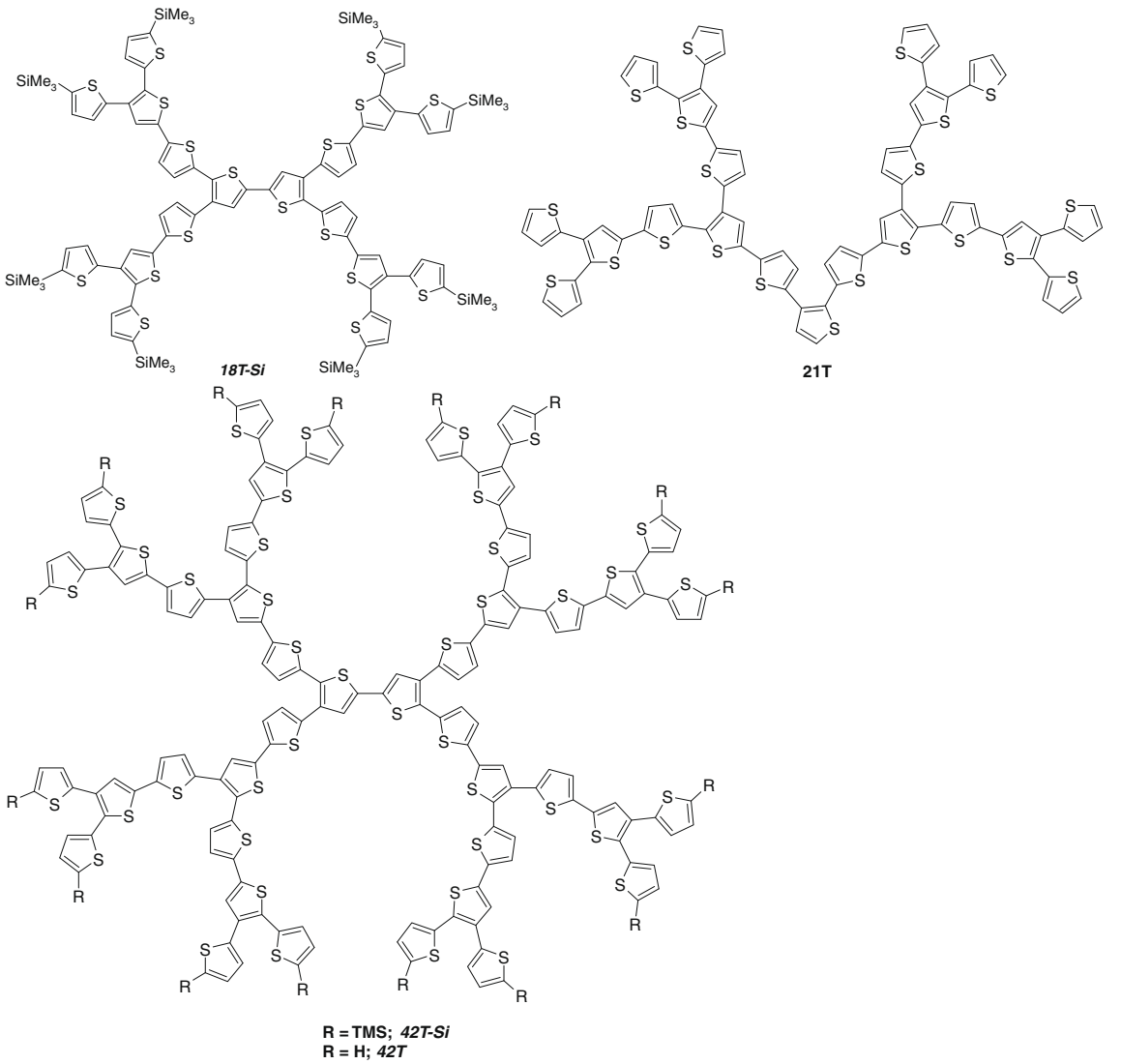

Chart 1. Chemical structure of *all*-thiophene dendrimers.

dendrimer shape (*21T* vs. *42T*). Thin films of the dendrimers were deposited onto PEDOT-covered ITO glass and sandwich-type diode structures were completed by evaporating thin LiF/Al electrodes (see Fig. 1). The devices were encapsulated with a glass slide bonded with UV-epoxy adhesive. The devices (active area 0.2 cm^2) were illuminated by 6 ns pulses at 532 nm of a Nd:YAG laser while they were held at open circuit by an externally applied offset bias. After a tunable delay time, a linearly increasing voltage pulse was applied and the current response was recorded using an oscilloscope and a set of resistors.

The recorded photo-CELIV current traces using 300 nm *21T* active layer are displayed in Fig. 2A and B. First, the delay time t_{del} between the light pulse and the voltage pulse was varied (Fig. 2A). The extraction maximum shifted to longer times with increasing delay time and the extraction current decreased. The former is indicative of a delay-time dependent mobility. A similar trend was observed previously for poly[2-methoxy-5-(3,7-dimethyloctyloxy)-1,4-phenylenevinylene] (MDMO-PPV) films and was attributed to dispersive (time dependent) relaxation of the charge carriers [35]. Charges could be extracted ~100 μs after charge generation indicative of their relatively long lifetime, which is comparable to other conjugated systems measured previously. Photo-CELIV traces recorded at fixed 12 μs delay time and at varying voltage rise speed $(A = U_{max}/t)$ are shown in Fig. 2B. The charge extraction peak is shifted to longer times due to the smaller applied voltages. Similar traces were recorded for all four dendrimers, and the mobility values calculated according to Eq. (1) are plotted in Fig. 3A and B

$$\mu = \frac{2d^2}{3At_{\max}^2\left[1 + 0.36\frac{\Delta j}{j(0)}\right]} \quad (1)$$

where d is the film thickness, t_{max} is the time at which the extraction current reaches its maximum value (Δj), and $j(0)$ is the capacitive current [36].

The extracted charge for all dendrimers were close to the capacitive charge CU ($(\Delta j \sim j(0))$ and was very similar for all samples.

No difference in the mobility or in its delay time dependence at shorter delay times was observed for the *21T* dendron and the *42T* dendrimer. The mobility values at very long delay times (>30 μs), where the extracted charge concentration is much lower due to recombination, were measured at increased charge carrier concentrations by increasing the laser intensity. This resulted in increased mobility reaching the values measured at shorter delay

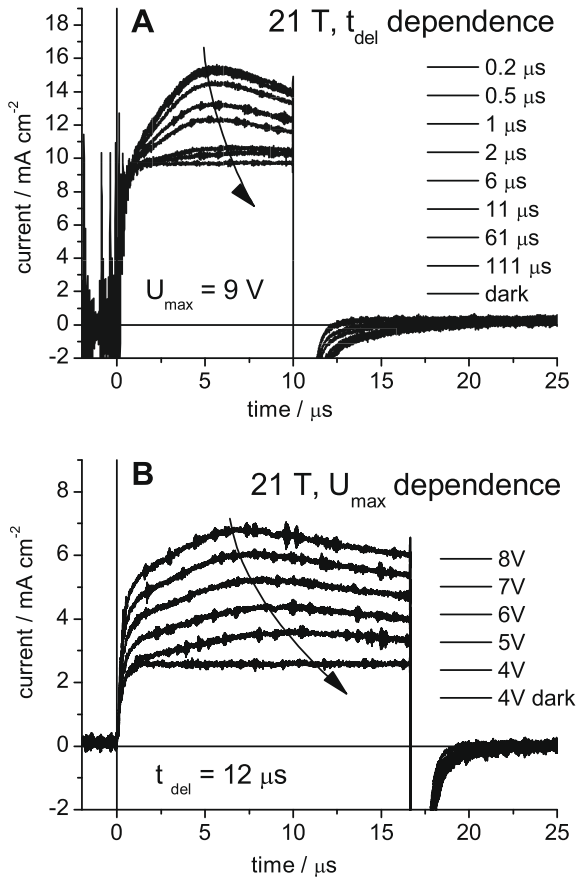

Fig. 2. Photo-CELIV current traces recorded at (A) various delay times and fixed voltage rise speed or (B) fixed delay time and various voltage rise speed.

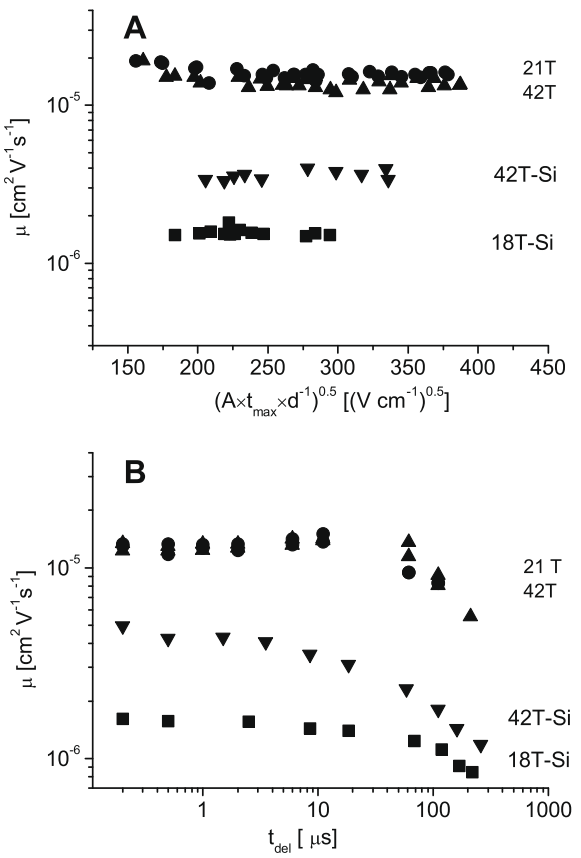

Fig. 3. Charge mobility of the (●) 21T, (▲) 42T, (▼) 42T-Si, (■) 18T-Si thiophene dendrimers (A) as a function of effective electric field at maximum extraction (B) vs. delay time.

times (<30 μs), suggesting that the drop of mobility at longer delay times in Fig. 3B is due to charge transport mediated by deep traps. The delay-time independent mobility at shorter delay times suggests that the shape and the size of the dendrimers without TMS protecting groups does not play a significant role. This is somewhat surprising, since *42T* has larger conjugated segments than *21T*, and correspondingly, the energy of the cation radicals depends on the size of the dendrimer. For example, the difference in the first oxidation potential of *42T* vs. *21T* is 0.22 eV [25]. Studies of excited state dynamics of a series of dendrimers with varying size showed a very rapid (200–300 fs) energy transfer of the photoexcitation to the longest conjugated segment [37]. Similarly, it is expected that at sufficiently long delay times (>200 ns, as measured using photo-CELIV), the charge cation radicals will be primarily localized on the longest conjugated segments. The very similar mobility (and its delay time dependence) of *21T* and *42T* is thought to be controlled by inter-dendrimer charge transfer rates between units located on the periphery rather than the conjugated core. We note that this result is in contrast to a previous mobility study, where a two order of magnitude increase in the field-effect mobility was observed in dendritic oligothiophenes having 25 and 65 thiophene units [23]. The following reasons may be responsible for this difference. Firstly, the charge carrier concentration is significantly higher in a field-effect configuration [33] and the direction of charge transport is alongside the substrate confined to the first couple of layers of the conjugated material near the gate dielectric surface [38,39]. Secondly, the peripheral groups in the oligothiophene dendrimers are linked through a benzene ring instead of the thiophene ring used in the *all*-thiophene dendrimers. The phenyl groups may promote better inter-dendrimer interaction as indeed reported in Ref. [23], therefore increasing the electronic coupling.

It is apparent that the TMS protecting groups significantly impedes mobility (*42T-Si*, *18T-Si* vs. *42T* and *21T*, see Fig. 3). The hole mobility decreased by a factor of 3–10 by the incorporation of the TMS groups at the periphery. The delay time dependence shows that the mobility is rather constant for all dendrimers till around 10 μs and then drops significantly at longer times. The fact that the mobility of the TMS-protected dendrimers is lower even at the shortest t_{del} indicates that it is intrinsic to their molecular structure. It is not due to higher concentration of traps or increased disorder, which is expected to play a role at longer delay times. The electronic structure of the dendrimers is not influenced noticeably by the TMS groups. Their UV–vis absorption and photoluminescence spectrum as well as their HOMO/LUMO energy levels are virtually identical [25]. Since these dendrimers should have a spherical shape with little interaction between them, we assume that charge hopping will predominantly occur at their interface. The insulating TMS groups located at this crucial interface may reduce the inter-dendrimer electronic coupling and lower the charge transfer rates between the molecules. Interestingly, the larger *42T-Si* exhibits larger mobilities than the *18T-Si*. It is known from concentration dependent ^{1}H NMR measurements [40], that *42T-Si* has more intensive intermolecular interactions than *18T-Si*, which results in increased electronic coupling and therefore reducing the insulating effect of the TMS groups.

Clearly, further studies that include a wider range of dendritic thiophene materials will be necessary to fully uncover the effect of molecular size and shape on their charge transport properties. Based on the comparison presented here, we propose that increased interaction enabling a direct coupling of the longest conjugated segments should significantly enhance their mobility. Moreover, introducing a largely asymmetrical dendrimer shape allowing molecular packing in proximity to the dendrimer core should be beneficial. A dendrimer shell containing electronic units with extended wavefunctions promoting electronic coupling between neighboring units is another modification that may increase charge mobility.

3.2. Charge mobility in the thiophene dendrimer:$PC_{61}BM$ (1:2 w/w) bulk heterojunctions

Our previous solar cell results showed that for thiophene dendrimers:PCBM blends the best weight ratio is

Table 2
Photovoltaic properties of dendrimer:PCBM 1:2 based bulk heterojunction solar cells.

Dendrimer	Thickness (nm)	J_{sc} (mA cm^{-2})	V_{oc} (mV)	*FF*	η (%)
18T-Si	105	1.49	753	0.29	0.32
21T	70	2.76	970	0.27	0.72
42T	75	5.19	950	0.32	1.57
42T-Si	105	2.21	922	0.29	0.58

Table 1
Charge mobility in dendrimer and dendrimer: $PC_{61}BM$ (1:2 w/w) mixtures measured by the photo-CELIV technique.

Dendrimer	Thickness (nm)	μ_h[a] (cm^2 V^{-1} s^{-1})	μ_h^{blend}[a] (cm^2 V^{-1} s^{-1})	μ_h/μ_h^{blend}
18T-Si	720	1.5×10^{-6}	1.7×10^{-7}	8.8
21T	260	1.5×10^{-5}	8.3×10^{-6}	1.8
42T	224	1.2×10^{-5}	3.0×10^{-6}	4
42T-Si	450	3.6×10^{-6}	2.8×10^{-7}	12.8
Dendrimer:$PC_{61}BM$ (1:2 w/w)	*d*	μ_h[a] (cm^2 V^{-1} s^{-1})	μ_e[a] (cm^2 V^{-1} s^{-1})	μ_e/μ_h
18T-Si: $PC_{61}BM$	525	1.7×10^{-7}	2.0×10^{-4}	1170
21T: $PC_{61}BM$	260	8.3×10^{-6}	N.A.	N.A.
42T: $PC_{61}BM$	235	3.0×10^{-6}	5.1×10^{-5}	17
42T-Si: $PC_{61}BM$	350	2.8×10^{-7}	1.1×10^{-4}	392

[a] At ~90,000 V cm^{-1} effective extraction field at extraction maximum.

1:2 by weight. Accordingly, the four thiophene dendrimers were mixed with $PC_{61}BM$ in a 1:2 ratio, and the performance of the photovoltaic devices were tested. The photovoltaic parameters including V_{oc}, J_{sc}, *FF* and power conversion efficiency η for 1:2 mixtures of dendrimer:$PC_{61}BM$ at various active layer thickness are shown in Table 2. Generally, the PV performance of the 1:2 mixtures shows similar trend to the previously reported 1:4 mixtures [25]. The lower J_{sc} and slightly lower *FF* of the devices shown here indicate that the fabrication of these cells may not be fully optimized particularly in terms of film thickness. All devices show high V_{oc}, moderate *FF* and somewhat limited J_{sc}. The best η of 1.6% is achieved for *42T*:$PC_{61}BM$ BHJ solar cell using 75 nm active layer. In the following, charge mobility and recombination is studied in these dendrimer: $PC_{61}BM$ (1:2 w/w) heterojunction primarily to understand the factors limiting efficiency in these devices.

First, charge mobility is determined using the photo-CELIV technique. As an example, Fig. 4 shows photo-CELIV transients for a *42T*:$PC_{61}BM$ (1:2) blend as a function of time delay (Fig. 4A) and voltage rise speed *A* at a fixed 12 μs time delay (Fig. 4B). Unlike in the pristine films, two extraction peaks are observed depending on t_{del}. At shorter delay times ($t_{del} < 0.5$ μs) a small extraction peak appears at around $t_{max} = 1$ μs, corresponding to a charge carrier mobility of around 5×10^{-5} $cm^2\,V^{-1}\,s^{-1}$. A second extraction peak, which is observable to up to several tens of μs time delays and corresponding to a much lower mobility value, is also observed. Similarly to the pristine dendrimer photo-CELIV curves, the time to reach extraction maximum t_{max} shifts to longer times with decreasing voltage rise speed (Fig. 4B).

Mobility values were calculated both from the first and the second extraction peaks and shown vs. the square root of the effective extraction field at extraction maximum in Fig. 5. We note that the sign of the charge carriers cannot be directly determined from the photo-CELIV transients shown here. We attribute the first extraction peak to electron transport in the $PC_{61}BM$ phase, and the second peak is assigned to the hole mobility in the thiophene dendrimer phase based on the following argument. The first peak is absent in the pristine dendrimer and its value is on the same order of magnitude as the reported values of electron mobility of the $PC_{61}BM$ phase in various donor:$PC_{61}BM$ mixtures. For example, it is around 10^{-4} $cm^2\,V^{-1}\,s^{-1}$ in the as cast P3HT:$PC_{61}BM$ 1:1 blend [41], and around 3×10^{-4} $cm^2\,V^{-1}\,s^{-1}$ in the MDMO-PPV:$PC_{61}BM$ 1:2 mixture [42,43]. Inganäs and coworkers have reported two extraction peaks in a series of fluorene–thiophene copolymer:$PC_{61}BM$ (1:4) mixtures and assigned the first peak to electron extraction with mobility values reaching 10^{-3} $cm^2\,V^{-1}\,s^{-1}$ [44]. The shape of the second extraction curve and the calculated mobility values are similar to the pristine dendrimer mobility values, therefore it is assigned to the hole mobility in the dendrimer phase.

The mobility values determined at an electric field of $E = 90{,}000$ $V\,cm^{-1}$, which corresponds to a typical value of extraction field in a dendrimer-based BHJ solar cell at short circuit conditions, are summarized in Table 1. Generally, hole mobilities for all dendrimers are reduced in their

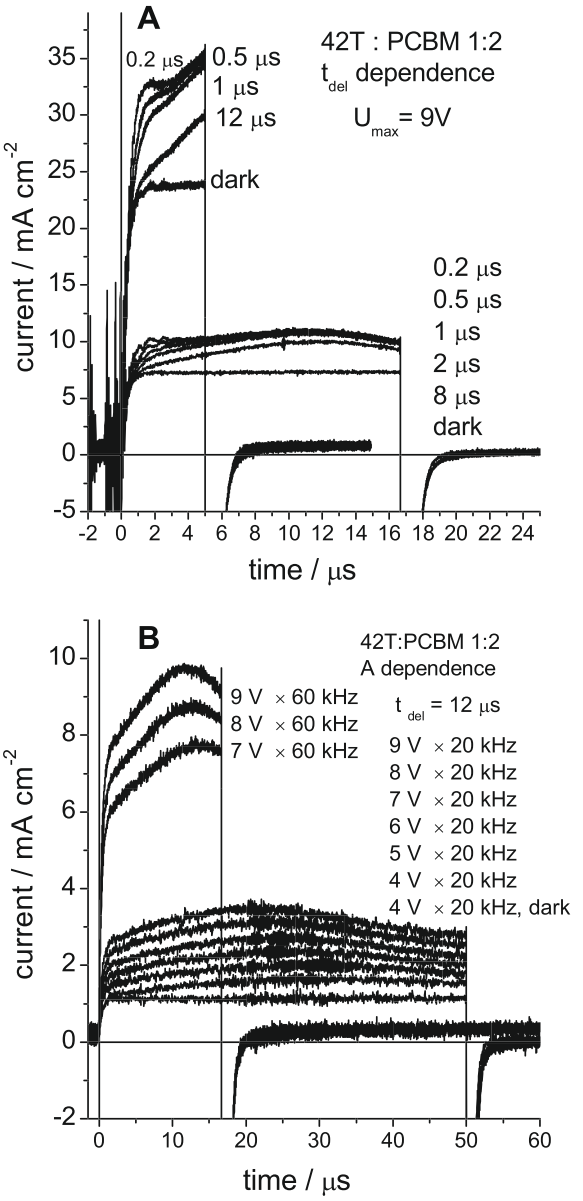

Fig. 4. Photo-CELIV current traces recorded at (A) various delay times and fixed voltage rise speed or (B) fixed delay time and various voltage rise speed (*A*) for *42T*:$PC_{61}BM$ (1:2) bulk heterojunction solar cells.

mixture with $PC_{61}BM$ (column μ_h/μ_h^{blend} in Table 1), but not to the same extent. The larger decrease of the hole mobility in the TMS-protected dendrimers is attributed to the smaller molecular molar ratio of the thiophene dendrimer to $PC_{61}BM$ due to their larger molecular weight. Increased interaction or the more extended π-conjugated system of the larger *42T-Si* (2.8×10^{-7} $cm^2\,V^{-1}\,s^{-1}$) may also contribute to its higher hole mobility in the blend in comparison to that of *18T-Si* (1.7×10^{-7} $cm^2\,V^{-1}\,s^{-1}$).

The hole mobilities in *21T*:$PC_{61}BM$ and *42T*:$PC_{61}BM$ mixtures did not drop so dramatically as compared to the TMS-protected dendrimer blends (1.8 and 4 times, respectively). Contrary to expectations, it is well known that the

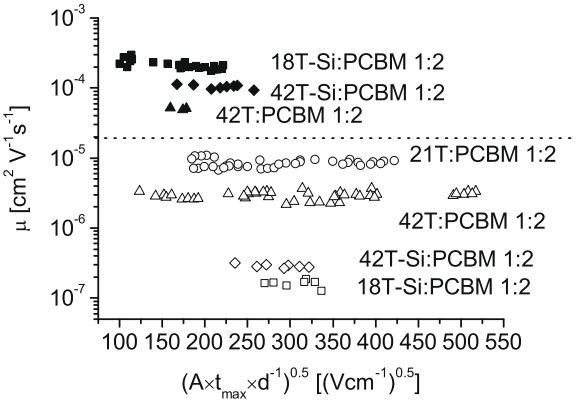

Fig. 5. Charge mobility in thiophene dendrimer/$PCB_{61}M$ 1:2 bulk heterojunctions calculated for the first (closed symbols) and second (open symbols) extraction peak using the photo-CELIV technique.

hole mobility in MDMO-PPV is *increased* quite significantly when mixed with $PC_{61}BM$ in a 1:4 ratio [42,43,45], which has recently been explained by the interpenetration of $PC_{61}BM$ molecules into the side-chain structure of MDMO-PPV [46]. It is evident that no such improvement is observed here. The less dramatic *decrease* in hole mobility of dendrimer *21T* may be related to its different size and shape. Although in pristine films no major difference was observed between *21T* and *42T* in the pristine films, mixing $PC_{61}BM$ (ratio 5–6 thiophene units to one $PC_{61}BM$ molecule) [25] may promote better alignment of the slightly asymmetric *21T* in the blend. We note that the AFM images of the films showed very smooth films with smooth surfaces confirming that an intimate mixture of the donor and acceptor is formed. No indication of large scale ordering or aggregation on the surface was observed. Also, the thiophene to $PC_{61}BM$ ratio is the same in *21T* and *42T* mixtures. Due to the inherently smaller cluster size (determined by the dendrimer size) of *21T*, a more uniform distribution of the thiophene units and $PC_{61}BM$ is possible, which may explain its slightly higher mobility in the blend.

The electron mobility in the dendrimer:$PC_{61}BM$ mixture (assigned to the first extraction peak in Fig 4A) decreases in the order of *18T-Si*, *42T-Si* and *42T*. We have observed a small extraction peak for *21T*:$PC_{61}BM$ at short delay times, but could not determine the mobility values because the first and second peaks overlapped. The reported electron mobility values in best performing conjugated donor:$PC_{61}BM$ heterojunctions are typically around 10^{-3} $cm^2\,V^{-1}\,s^{-1}$ in 1:4 donor:PCBM mixtures and slightly lower (around $3\times10^{-4}\,cm^2\,V^{-1}\,s^{-1}$) in 1:2 mixtures [41–44]. A morphology dependent electron mobility in annealed vs. as cast P3HT:PCBM 1:1 films has been also reported [41]. The observed very smooth surface morphology may suggest that the dendrimer and $PC_{61}BM$ could be well intermixed and no $PC_{61}BM$ crystallites are formed, which may be responsible for the somewhat lower electron mobility. As indicated in the Supplementary data Table 1, the TMS-protected dendrimers have higher molecular weight, which, at the same weight ratio of 1:2, results in almost twice as high $PC_{61}BM$ molar ratio in the blend. The higher molar ratio of $PC_{61}BM$ in the TMS-protected dendrimer films is proposed to be responsible for their higher electron mobility.

3.3. Charge carrier lifetime in thiophene dendrimer:$PC_{61}BM$ (1:2 w/w) mixtures

Free charge generation efficiency and charge carrier lifetime are crucial parameters influencing charge extraction. Free charge carrier lifetime in dendrimer:$PC_{61}BM$ mixtures were determined using (i) a delayed electric-field extraction technique [47]; or (ii) visible/NIR transient absorption spectroscopy. In the first case, similarly to the photo-CELIV technique, charges are photo-generated at open circuit conditions by 6 ns laser pulses and subsequently extracted by a square wave voltage pulse applied after a tunable delay time (see SI1). The concentration of the extracted charges is plotted vs. time delay and charge carrier lifetime is determined from the decay of the charge concentration. Using this charge extraction method, recombination of the reasonably mobile (free) charge carriers is monitored [48].

Charge extraction curves recorded at various delay times for *21T*:$PC_{61}BM$ and *42T*:$PC_{61}BM$ are shown in a logarithmic plot in Fig. 6A and B, respectively. The extraction current decreases gradually with increasing t_{del} due to recombination. The magnitude and shape of the extraction curve is quite different for these two dendrimer:$PC_{61}BM$ mixtures even at the shortest delay times. At longer delays, the extraction current decreases to the baseline indicating efficient charge extraction within the applied extraction pulse. The extraction currents were integrated and the extracted charge density normalized to the fraction of absorbed photons ($1–10^{-A}$, where A is the absorbance of the films at the 532 nm excitation wavelength) is plotted vs. delay time in Fig. 7A. The magnitude of the normalized extracted charge density is related to the yield of charge generation minus any fast component of the recombination kinetics, and possibly trapped charges that are not extracted within the applied extraction pulse. The decays in Fig. 7A, on the other hand, are related to the lifetime of the extracted charges. Clearly, all dendrimer:$PC_{61}BM$ films exhibit similar time-decays within the experimental certainty, therefore similar lifetimes. In our previous report, we found that J_{sc} of dendrimer:PCBM solar cells are linearly correlated to the light absorbing ability of the dendrimers [25]. In addition, herein we observed that extracted charge concentration normalized to the absorbed photon intensity for the *42T*:$PC_{61}BM$ and *42T-Si*:$PC_{61}BM$ mixtures was ~2× higher as compared to that of *18T-Si*:$PC_{61}BM$ and *21T-Si*:$PC_{61}BM$. The higher extracted charge concentration for the larger dendrimers is clearly not due to difference in charge mobility, since *42T* and *42T-Si* have quite different mobility yet same charge extraction yield. We propose that the increased extracted charge concentration is related to increased free charge generation yield, which depends on the dendrimer size. Photoluminescence quenching experiments, which are indicative of photoinduced electron transfer from the excited donor to the electron acceptor, show very similar and highly efficient quenching from all four excited dendrimer molecules to $PC_{61}BM$ (see SI 2). Initial charge separation may result in coulombically bound

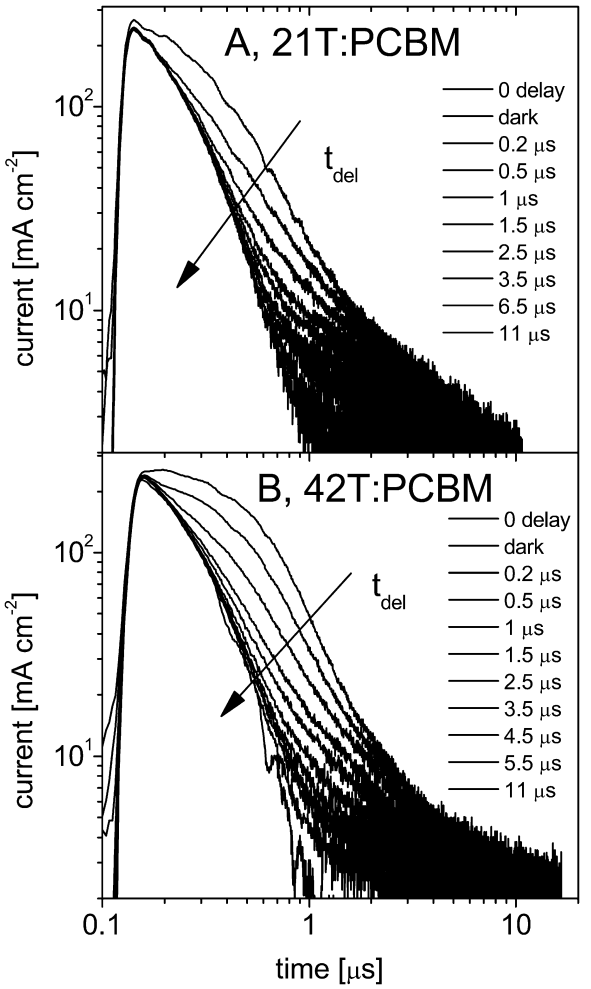

Fig. 6. Photocurrent transients recorded using a delayed-field charge extraction technique for (A) *42T*:$PC_{61}BM$ 1:2 and (B) *42T-Si*:$PC_{61}BM$ 1:2 mixtures. The arrow indicates increasing delay time between the light pulse and the square-shaped voltage pulse.

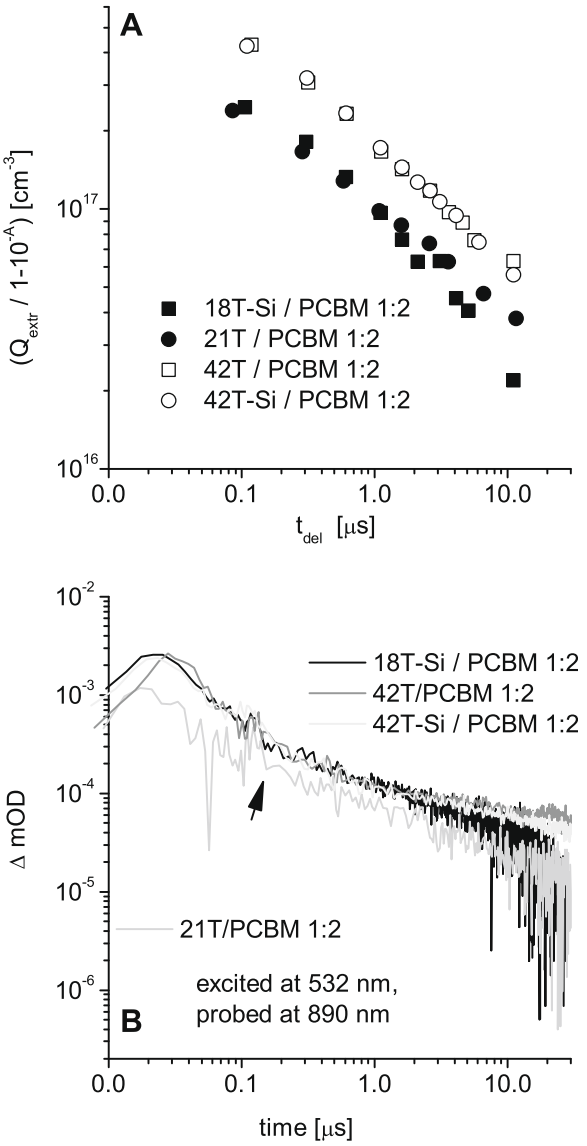

Fig. 7. Extracted charge normalized to the faction of absorbed excitation intensity $1–10^{-A}$ vs. delay time (A) and transient absorption traces recorded at 890 nm for various dendrimer:$PC_{61}BM$ blends (B).

electron and hole pairs. In such cases, the generation of free charge carriers (that are probed by charge extraction) is a secondary, thermally activated process. The generation of free charge carriers from the coulomb-coupled pairs depends on a number of parameters including temperature, initial charge separation distance between the electron and hole, mobility and the dielectric constant. All other parameters being very similar, we propose that the difference in charge separation distance, which itself related to the molecular size, controls the free charge generation efficiency in these dendrimer:$PC_{61}BM$ mixtures. Deibel et al. have performed a Monte-Carlo simulation of hopping transport of Coulomb-bound electron–hole pairs in an energetically disordered donor–acceptor blend system, which predicted an increased geminate electron–hole pair dissociation yield with increasing length of the conjugated segments [49].

Contrary to the charge extraction technique above, which measures the lifetime of the reasonably mobile (free) charge carriers, using transient absorption the time-decay of the charged radical ions was optically followed. We have performed visible pump/NIR probe transient absorption measurements on the dendrimer:$PC_{61}BM$ 1:2 films. The films were excited at 532 nm and the changes of the sample transmission were monitored at 890 nm with ~10 ns time resolution. According to previous photoinduced absorption studies [25], the signal at 890 nm in the dendrimer:$PC_{61}BM$ blends is due to absorption by dendrimer cation radicals. The recorded transient absorption signals are shown in Fig. 7B. The signal magnitude is related to the absorption coefficient of the cation radicals at 890 nm as well as their concentration, while the decays are related to their time dependent recombination. The curves all show biphasic decays: a fast component till ~100 ns and a second, power law decay extending to the recorded 30 μs time scale.

A comparison of Fig 7A and B provides an opportunity to compare charge recombination kinetics of mobile charge carriers and all of the optically monitored photo-generated holes within the same films. For e.g., in MDMO-PPV:PCBM blends [35] we have observed a bimolecular recombination law using charge extraction, while transient absorption measurements on the same system usually gave a power-law dependence [50,51]. This difference was explained by the fact that only reasonably mobile charges are extracted in the photo-CELIV, while all the charges including the deeply trapped ones are monitored optically. In the present manuscript, we have used a square-voltage-pulse delayed field extraction technique, which yields stronger extraction fields than used in CELIV. A similar power-law charge concentration decay was observed using this square-voltage-pulse technique in various other material combinations published to date, indicating its better suitability when the concentration decay in the presence of strong dispersion is studied [30,47].

The main difference is at the shorter <100 ns time delays, where the transient absorption shows an additional, fast component of the recombination. Such biphasic decay has been previously observed in a number of electron donor:acceptor systems [50,52] and has been attributed to the recombination of dissociated electron and holes in the presence of an exponential distribution of hole traps. The decays are characterized by signal decay half times $\tau_{1/2}$ in Fig. 7A and B. The $\tau_{1/2}$ values are similar between the charge extraction and the second component of the transient absorption decay and are around 0.7 μs, which is quite short as compared to other donor:acceptor systems. For example, measurements on MDMO-PPV:$PC_{61}BM$ 1:4 blends have yielded 3× longer effective lifetimes of around 2 μs [31]. The charge recombination appears to be faster in the blends as compared to the pristine dendrimers (see Fig. 3), which is thought to be related to the increased (electron) mobility enhancing recombination.

4. Conclusions

Charge mobilities of four *all*-thiophene dendrimers varying in size, shape and with or without TMS protecting groups have been studied using the photo-CELIV technique. No difference in charge mobility due to variation of size or shape of the dendrimer without TMS protecting groups has been observed between the dendrimer containing 21 or 42 thiophene units. It was also found that the incorporation of the TMS protecting groups significantly impedes mobility, which was attributed to the insulating effect of the peripheral TMS groups reducing charge transfer rates between neighboring dendrimer molecules. Charge carrier mobility is reduced when the dendrimers were mixed with the electron acceptor $PC_{61}BM$, but in varying extents depending on the molecular structure and the thiophene to $PC_{61}BM$ molar ratio. Very similar cation radical lifetimes (characterized by signal decay times $\tau_{1/2}$ of 0.7 μs) have been determined using a delay-field extraction technique and transient absorption spectroscopy, which together with the small hole mobility is expected to cause short hole drift lengths. Charge extraction measurements revealed significant molecular size dependence: 2× more charge could be extracted from the larger *42T* and *42T-Si* dendrimer:$PC_{61}BM$ mixture. This was attributed to higher free charge generation yield due to larger initial charge separation distance in the larger dendrimer molecules. Strategies to improve charge mobilities have been discussed, which includes the increase of molecular interaction between the neighboring dendrimers, introducing an asymmetric dendrimer shape and a stronger electronic coupling using modified dendrimer periphery.

Acknowledgements

The Australian Research Council is acknowledged for funding. AJM, GGW, WWHW and DJJ acknowledge the support from International Science Linkage Project CG 100059 (DIISR, Australia). CQM and PB would like to acknowledge DFG and DAAD for financial support. WWHW also thanks the Go8-DAAD research co-operation scheme for funding. The authors thank Professor Andrew B. Holmes (Bio21 Institute, The University of Melbourne) for his interest and support in this work, and Professor René A.J. Janssen and Dr. Martijn M. Wienk (Eindhoven University of Technology) for their helpful discussions. We thank CSIRO MHT for access to device fabrication equipment.

Appendix A. Supplementary data

Supplementary data associated with this article can be found, in the online version, at doi:10.1016/j.orgel.2009.12.016.

References

[1] B.C. Thompson, J.M.J. Fréchet, Polymer-fullerene composite solar cells, Angew. Chem. Int. Ed. 47 (2008) 58–77.
[2] C.J. Brabec, G. Zerza, G. Cerullo, S. De Silvestri, S. Luzzati, J.C. Hummelen, S. Sariciftci, Tracing photoinduced electron transfer process in conjugated polymer/fullerene bulk heterojunctions in real time, Chem. Phys. Lett. 340 (2001) 232–236.
[3] P.A. van Hal, S.C.J. Meskers, R.A.J. Janssen, Photoinduced energy and electron transfer in oligo(*p*-phenylene vinylene)-fullerene dyads, J. Appl. Phys. A: Mater. Sci. Process. 79 (2004) 41–46.
[4] P. Schilinsky, C. Waldauf, C.J. Brabec, Recombination and loss analysis in polythiophene based bulk heterojunction photodetectors, Appl. Phys. Lett. 81 (2002) 3885–3887.
[5] G. Li, V. Shrotriya, J. Huang, Y. Yao, T. Moriarty, K. Emery, Y. Yang, High-efficiency solution processable polymer photovoltaic cells by self-organization of polymer blends, Nat. Mater. 4 (2005) 864–868.
[6] W. Ma, C. Yang, X. Gong, K. Lee, A.J. Heeger, Thermally stable, efficient polymer solar cells with nanoscale control of the interpenetrating network morphology, Adv. Funct. Mater. 15 (2005) 1617–1622.
[7] X. Yang, J. Loos, S.C. Veenstra, W.J.H. Verhees, M.M. Wienk, J.M. Kroon, M.A.J. Michels, R.A.J. Janssen, Nanoscale morphology of high-performance polymer solar cells, Nano Lett. 5 (2005) 579–583.
[8] M.D. Irwin, D. Bruce Buchholz, A.W. Hains, R.P.H. Chang, T.J. Marks, p-Type semiconducting nickel oxide as an efficiency-enhancing anode interfacial layer in polymer bulk-heterojunction solar cells, Proc. Natl. Acad. Sci. 105 (2008) 2783–2787.
[9] D. Mühlbacher, M. Scharber, M. Morana, Z. Zhu, D. Waller, R. Gaudiana, C. Brabec, High photovoltaic performance of a low-bandgap polymer, Adv. Mater. 18 (2006) 2884–2889.
[10] J. Peet, J.Y. Kim, N.E. Coates, W.L. Ma, D. Moses, A.J. Heeger, G.C. Bazan, Efficiency enhancement in low-bandgap polymer solar cells by processing with alkane dithiols, Nat. Mater. 6 (2007) 497–500.
[11] L.H. Slooff, S.C. Veenstra, J.M. Kroon, D.J.D. Moet, J. Sweelssen, M.M. Koetse, Determining the internal quantum efficiency of highly efficient polymer solar cells through optical modeling, Appl. Phys. Lett. 90 (2007) 143506.

[12] N. Blouin, A. Michaud, M. Leclerc, A low-bandgap poly(2,7-carbazole) derivative for use in high-performance solar cells, Adv. Mater. 19 (2007) 2295–2300.
[13] S.H. Park, A. Roy, S. Beaupre, S. Cho, N. Coates, J.S. Moon, D. Moses, M. Leclerc, K. Lee, A.J. Heeger, Bulk heterojunction solar cells with internal quantum efficiency approaching 100%, Nat. Photon. 3 (2009) 297–302.
[14] S.C. Lo, P.L. Burn, Development of dendrimers: macromolecules for use in organic light-emitting diodes and solar cells, Chem. Rev. 107 (2007) 1097–1116.
[15] J. Roncali, P. Leriche, A. Cravino, From one- to three-dimensional organic semiconductors: in search of the organic silicon?, Adv Mater. 19 (2007) 2045–2060.
[16] C. Xia, X. Fan, J. Locklin, R.C. Advincula, A first synthesis of thiophene dendrimers, Org. Lett. 4 (2002) 2067–2070.
[17] C. Xia, X. Fan, J. Locklin, R.C. Advincula, A. Gies, W. Nonidez, Characterization, supramolecular assembly, and nanostructures of thiophene dendrimers, J. Am. Chem. Soc. 126 (2004) 8735–8743.
[18] S.A. Ponomarenko, S. Kirchmeyer, A. Elschner, B.H. Huisman, A. Karbach, D. Drechsler, Star-shaped oligothiophenes for solution-processible organic field-effect transistors, Adv. Funct. Mater. 13 (2003) 591–596.
[19] Y. Zhang, C. Zhao, J. Yang, M. Kapiamba, O. Haze, L.J. Rothberg, M.K. Ng, Synthesis, optical, and electrochemical properties of a new family of dendritic oligothiophenes, J. Org. Chem. 71 (2006) 9475–9483.
[20] W.J. Mitchell, N. Kopidakis, G. Rumbles, D.S. Ginley, S.E. Shaheen, The synthesis and properties of solution processable phenyl cored thiophene dendrimers, J. Mater. Chem. 15 (2005) 4518–4528.
[21] N. Kopidakis, W.J. Mitchell, J. van de Lagemaat, D.S. Ginley, G. Rumbles, S.E. Shaheen, W.L. Rance, Bulk heterojunction organic photovoltaic devices based on phenyl-cored thiophene dendrimers, Appl. Phys. Lett. 89 (2006) 103524-3.
[22] H. John, R. Bauer, P. Espindola, P. Sonar, J. Heinze, K. Müllen, 3D-hybrid networks with controllable electrical conductivity from the electrochemical deposition of terthiophene-functionalized polyphenylene dendrimers, Angew. Chem. Int. Ed. 44 (2005) 2447–2451.
[23] N. Negishi, Y. Ie, M. Taniguchi, T. Kawai, H. Tada, T. Kaneda, Y. Aso, Synthesis of dendritic oligothiophenes and their self-association properties by intermolecular π–π interactions, Org. Lett. 9 (2007) 829–832.
[24] C.-Q. Ma, E. Mena-Osteritz, T. Debaerdemaeker, M.M. Wienk, R.A.J. Janssen, P. Bäuerle, Functionalized 3D oligothiophene dendrons and dendrimers – novel macromolecules for organic electronics, Angew. Chem. Int. Ed. 46 (2007) 1679–1683.
[25] C.-Q. Ma, M. Fonrodona, M.C. Schikora, M.M. Wienk, R.A.J. Janssen, P. Bäuerle, Solution-processed bulk-heterojunction solar cells based on monodisperse dendritic oligothiophenes, Adv. Funct. Mater. 18 (2008) 3323–3331.
[26] S. Gambino, S.G. Stevenson, K.A. Knights, P.L. Burn, I.D.W. Samuel, Control of charge transport in iridium(III) complex-cored carbazole dendrimers by generation and structural modification, Adv. Funct. Mater. 19 (2009) 317–323.
[27] M. Guo, X. Yan, T. Goodson III, Electron mobility in a novel hyperbranched phthalocyanine dendrimer, Adv. Mater. 20 (2008) 4167–4171.
[28] S.-C. Lo, E.B. Namdas, C.P. Shipley, J.P.J. Markham, T.D. Anthopolous, P.L. Burn, I.D.W. Samuel, The synthesis and properties of iridium cored dendrimers with carbazole dendrons, Org. Electron. 7 (2006) 85–98.
[29] J.P.J. Markham, T.D. Anthopoulos, I.D.W. Samuel, G.J. Richards, P.L. Burn, C. Im, H. Bassler, Nondispersive hole transport in a spin-coated dendrimer film measured by the charge-generation-layer time-of-flight method, App. Phys. Lett. 81 (2002).
[30] R. Österbacka, A. Pivrikas, G. Juška, K. Genevičius, K. Arlauskas, H. Stubb, Mobility and density relaxation of photogenerated charge carriers in organic materials, Curr. Appl. Phys. 4 (2004) 534–538.
[31] A.J. Mozer, N.S. Sariciftci, L. Lutsen, D. Vanderzande, R. Österbacka, M. Westerling, G. Juska, Charge transport and recombination in bulk heterojunction solar cells studied by the photoinduced charge extraction in linearly increasing voltage technique, Appl. Phys. Lett. 86 (2005) 112104.
[32] V. Coropceanu, J. Cornil, D.A. daSilvaFilho, Y. Olivier, R. Silbey, J.L. Bredas, Charge transport in organic semiconductors, Chem. Rev. 107 (2007) 926–952.
[33] C. Tanase, E.J. Meijer, P.W.M. Blom, D.M. De Leeuw, Unification of the hole transport in polymeric field-effect transistors and light-emitting diodes, Phys. Rev. Lett. 91 (2003) 216601.
[34] A.J. Mozer, N. Sariciftci, Charge transport and recombination in donor-acceptor bulk heterojunction solar cells, in: J. Poortmans, V. Arkhipov (Eds.), Thin Film Solar Cells: Fabrication, Characterisation and Applications, John Wiley and Sons, West Sussex, 2006, pp. 387–426.
[35] A.J. Mozer, G. Dennler, N.S. Sariciftci, M. Westerling, A. Pivrikas, R. Österbacka, G. Juška, Time-dependent mobility and recombination of the photoinduced charge carriers in conjugated polymer/fullerene bulk heterojunction solar cells, Phys. Rev. B 72 (2005) 035217.
[36] G. Juška, K. Arlauskas, M. Viliūnas, J. Kočka, Extraction current transients: new method of study of charge transport in microcrystalline silicon, Phys. Rev. Lett. 84 (2000) 4946–4949.
[37] G. Ramakrishna, A. Bhaskar, P. Bäuerle, C.-Q. Ma, T. Goodson, Oligothiophene dendrimers as new building blocks for optical applications, J. Phys. Chem. A 112 (2008) 2018–2026.
[38] G. Horowitz, Organic thin film transistors: from theory to real devices, J. Mater. Res. 19 (2004) 1946–1962.
[39] A. Dodabalapur, L. Torsi, H.E. Katz, Organic transistors: two-dimensional transport and improved electrical characteristics, Science 268 (1995) 270–271.
[40] C.-Q. Ma, E. Mena-Osteritz, M. Wunderlin, P. Bäuerle, Synthesis and structure characterization of novel all-thiophene dendrons and dendrimers, Chem. Asian J., in preparation.
[41] V.D. Mihailetchi, H. Xie, B. De Boer, L.J.A. Koster, P.W.M. Blom, Charge transport and photocurrent generation in poly(3-hexylthiophene): methanofullerene bulk-heterojunction solar cells, Adv. Funct. Mater. 16 (2006) 699–708.
[42] V.D. Mihailetchi, J.K.J. van Duren, P.W.M. Blom, J.C. Hummelen, R.A.J. Janssen, J.M. Kroon, M.T. Rispens, W.J.H. Verhees, M.M. Wienk, Electron transport in a methanofullerene, Adv. Funct. Mater. 13 (2003) 43–46.
[43] S.M. Tuladhar, D. Poplavskyy, S.A. Choulis, J.R. Durrant, D.D.C. Bradley, J. Nelson, Ambipolar charge transport in films of methanofullerene and poly(phenylenevinylene)/methanofullerene blends, Adv. Funct. Mater. 15 (2005) 1171–1182.
[44] L.M. Andersson, F. Zhang, O. Inganäs, Bipolar transport observed through extraction currents on organic photovoltaic blend materials, Appl. Phys. Lett. 89 (2006) 142111.
[45] G. Dennler, A.J. Mozer, G. Juška, A. Pivrikas, R. Österbacka, A. Fuchsbauer, N.S. Sariciftci, Charge carrier mobility and lifetime versus composition of conjugated polymer/fullerene bulk-heterojunction solar cells, Org. Electron. 7 (2006) 229–234.
[46] A.C. Mayer, M.F. Toney, S.R. Scully, J. Rivnay, C.J. Brabec, M. Scharber, M. Koppe, M. Heeney, I. McCulloch, M.D. McGehee, Bimolecular crystals of fullerenes in conjugated polymers and the implications of molecular mixing for solar cells, Adv. Funct. Mater. 19 (2009) 1173–1179.
[47] T. Offermans, S.C.J. Meskers, R.A.J. Janssen, Time delayed collection field experiments on polymer: fullerene bulk-heterojunction solar cells, J. Appl. Phys. 100 (2006) 074509.
[48] T. Offermans, S.C.J. Meskers, R.A.J. Janssen, Electro-optical studies on MDMO-PPV:PCBM bulk-heterojunction solar cells on the millisecond time scale: trapped carriers, Org. Electron. 7 (2006) 213–221.
[49] C. Deibel, T. Strobel, V. Dyakonov, Origin of the efficient polaron-pair dissociation in polymer–fullerene blends, Phys. Rev. Lett. 103 (2009) 036402.
[50] I. Montanari, A.F. Nogueira, J. Nelson, J.R. Durrant, C. Winder, M.A. Loi, N.S. Sariciftci, C. Brabec, Transient optical studies of charge recombination dynamics in a polymer/fullerene composite at room temperature, Appl. Phys. Lett. 81 (2002) 3001–3003.
[51] A.F. Nogueira, I. Montanari, J. Nelson, J.R. Durrant, C. Winder, N.S. Sariciftci, C. Brabec, Charge recombination in conjugated polymer/fullerene blended films studied by transient absorption spectroscopy, J. Phys. Chem. B 107 (2003) 1567–1573.
[52] T.M. Clarke, A.M. Ballantyne, J. Nelson, D.D.C. Bradley, J.R. Durrant, Free energy control of charge photogeneration in polythiophene/fullerene solar cells: The influence of thermal annealing on P3HT/PCBM blends, Adv. Funct. Mater. 18 (2008) 4029–4035.

Organic Electronics 11 (2010) 583–588

Contents lists available at ScienceDirect

Organic Electronics

journal homepage: www.elsevier.com/locate/orgel

High performing doped cyanine bilayer solar cell

Bin Fan, Fernando Araujo de Castro, Jakob Heier, Roland Hany, Frank Nüesch *

Empa, Swiss Federal Laboratories for Materials Testing and Research, Laboratory for Functional Polymers, Überlandstr. 129, CH-8600 Dübendorf, Switzerland

ARTICLE INFO

Article history:
Received 6 November 2009
Received in revised form 21 December 2009
Accepted 22 December 2009
Available online 28 December 2009

Keywords:
Organic photovoltaics
Bilayer solar cell
Cyanine dye
Doping
Schottky junction

ABSTRACT

The advent of organic solar cells promises access to inexpensive solar electricity. Major advances in this thin film technology bear on biphasic and bicontinuous mesoscopic structures composed of an electron donor and acceptor material. Here, we demonstrate a high efficiency organic solar cell with simple planar bilayer architecture based on a soluble cyanine dye as electron donor and fullerene C_{60} as electron acceptor. Upon doping the trimethine cyanine layer and optimizing the device cathode, the cell reaches a power conversion efficiency of 2.0% under simulated AM1.5 solar irradiation. The external quantum efficiency approaches 80% at maximum and is among the highest reported in organic photovoltaic devices. Soluble cyanines are compatible with low-cost coating processes, adding to the merits of this class of photographic dyes for organic solar cell applications.

© 2009 Elsevier B.V. All rights reserved.

1. Introduction

Organic photovoltaics can be dated back to 1960, when Meier and Haus conceived a double layer device consisting of an electron donor and acceptor material, respectively [1]. In 1986 power efficiencies close to 1% were demonstrated by Tang using the same concept [2]. It is now well understood that photovoltaic action in bilayer devices relies on light absorption and subsequent formation of electronically excited states (excitons) that diffuse to the donor–acceptor interface where they are separated into positive and negative charge carriers. Most bilayer heterojunction devices suffer from a limited photoactive zone at the organic heterointerface, due to the rather small exciton diffusion length of typically 5–20 nm [3]. For thicker films, an important part of the organic layer just acts as light absorbing filter. Bulk-heterojunctions consisting of bicontinuous donor–acceptor microstructures bypass this difficulty [4]. Solution processed bulk-heterojunction devices presently constitute the most efficient organic photovoltaic devices with power conversion efficiencies up to 6.6% for polymers [5] and 4.4% for small molecules [6]. However, it is generally challenging to produce optimized meso-structures; while large structures will not suffice to dissociate all photogenerated excitons, very small phase dimensions are likely to hinder the separation of geminate electron–hole pairs formed after exciton ionization [7]. Alternatively, crystalline and pure organic materials having very high exciton diffusion lengths combine efficient charge carrier generation and transport in a bilayer device architecture. Exciton diffusion lengths exceeding 40 nm have indeed been realized for small evaporable molecules such as pentacene [8] and exhibit power conversion efficiencies of 2.1% [9].

Organic dyes with extraordinary high extinction coefficients offer yet another possibility to go around the constraints of small exciton diffusion length and modest charge transport, since ultrathin films could be applied in a planar bilayer fashion. Photographic polymethine dyes such as cyanines, merocyanines or squaraines are among the strongest light absorbers and were first developed as sensitizers in the photographic process [10]. They have also been successfully used in data storage devices [11], as fluorescent labels [12] and more recently in dye sensitized solar cells [13–15], where power conversion efficiencies ranging from 4% to 7% were achieved. There are only few examples of high efficiency solid organic solar cells

* Corresponding author. Tel.: +41 44 823 4740; fax: +41 44 823 4012.
E-mail address: frank.nueesch@empa.ch (F. Nüesch).

1566-1199/$ - see front matter © 2009 Elsevier B.V. All rights reserved.
doi:10.1016/j.orgel.2009.12.017

employing polymethine dyes. Merocyanine single layer Schottky barrier solar cells approaching a power conversion efficiency of 1% have long hold the world record [16]. Recently, vapor deposited squaraine dyes reached an efficiency of 3.1% [17]. Solution deposited donor–acceptor blends of a merocyanine dye and a squaraine dye revealed power conversion efficiencies of 1.7% [18] and up to 1.8% [19,20], respectively. Cationic cyanine dyes have received even less attention in organic solar cell construction. In previous work, soluble cyanine dyes were shown to act as electron donors and electron acceptors in planar heterojunction devices, though with poor efficiency [21]. The power conversion efficiency benchmark of 1% was achieved in subsequent work evidencing the importance of ameliorating charge transport in cyanine films [22]. Very recently, cationic and anionic heptamethine dyes showed promising near infrared sensitivity [23].

Here, we report on bilayer devices consisting of a soluble trimethine cyanine dye and C_{60}. We optimize the cell performance by oxidative doping of the cyanine layer and by adding a cathode buffer layer leading to a power conversion efficiency of 2.0% under standard solar irradiation and an outstanding external quantum efficiency approaching 80% at maximum. Hence, this classical cyanine dye employed as organic semiconductor in a bilayer solar cell architecture outperforms other soluble small molecules that have mostly been applied in bulk-heterojunction cells [24].

2. Experimental

1,1′-Diethyl-3,3,3′,3′-tetramethylcarbocyanine perchlorate (CyC) was synthesized based on a published procedure [25]. For further purification the cyanine dye was twice recrystallized in ethanol. Buckminster fullerene C_{60} (SES Research), poly(styrene sulfonate) doped poly(3,4-ethylenedioxythiophene) (PEDOT:PSS, Sigma–Aldrich) and tris-(8-hydroxyquinoline) aluminium (Alq_3, Sigma–Aldrich) were used without further purification. Etched indium tin oxide glass substrates (ITO, from AFC) were first cleaned in ozone, followed by ultrasonic cleaning in acetone, ethanol, soap and Milli-Q water, before being dried in a nitrogen flow.

Organic multilayer solar cell devices with ITO/PEDOT:PSS/CyC/C_{60}/Al architecture were deposited layer by layer on the clean conducting glass substrates. First, a 40 nm thick film of the hole conducting PEDOT:PSS film was spin coated on the ITO substrate, then heated to 120 °C for 12 min in order to remove residual water. The coated substrates were then transported into a nitrogen glove box to avoid exposure to oxygen and moisture. CyC was then spin coated from 1 wt% chlorobenzene solutions doped with various concentrations of $NOBF_4$ within the $NOBF_4$/CyC range from zero to 0.08 mol/mol. The doping concentration was adjusted by adding different amounts of $NOBF_4$ from a 0.01 M stock solution in acetonitrile to the cyanine solution in chlorobenzene.

For the subsequent vapor deposition steps, substrates were conveyed to a high vacuum deposition chamber directly linked to the glove box. A 40 nm thick C_{60} layer followed by a 60 nm thick aluminium electrode were vapor deposited at a pressure of 10^{-6} – 2×10^{-6} mbar. A total of eight solar cells with surface areas of 3.1 mm^2 and 7.1 mm^2 were produced on each conducting glass substrate to allow for some averaging. To improve the contact at the aluminium/C_{60} interface, a 2 nm thick Alq_3 film was vapor deposited on the C_{60} layer prior to aluminium cathode deposition. It has to be noted that from the PEDOT:PSS deposition on, all further fabrication steps occurred in inert atmosphere to avoid uncontrolled effects of water and oxygen uptake. Average film thicknesses were determined by profilometry (Ambios XP1) and absorption was measured using a Varian Cary 50 UV–vis spectrophotometer.

For solar cell characterization, the substrates were sealed in a vacuum tight box with current feedthroughs and an optical window. Current–voltage characteristics of the solar cells were measured by a Keithley 2400 source/measure unit in the dark and under simulated AM1.5 solar irradiation using the spectrum of a 300 W Xe lamp together with an AM1.5G filter set. The white light intensity P_{in} was calibrated in order to correspond to standard solar irradiation at 100 mW/cm^2 for full sun and 33 mW/cm^2 for 1/3 sun irradiation (see Supplementary material). Using a diaphragm, the irradiation spot was adjusted to match the surface of the solar cells. Open-circuit voltage (V_{OC}) and short-circuit current–density (J_{SC}) were obtained directly from the current–voltage characteristics. Power conversion efficiencies (PCE) were calculated as $PCE = FF \times V_{OC} \times J_{SC} \times P_{in}^{-1}$, where $FF = (J \times V)_{max} \times V_{OC}^{-1} \times J_{SC}^{-1}$ and $(J \times V)_{max}$ relates to the current–density and voltage measured at the maximum power point. A Cornerstone 130 monochromator (Oriel) was used together with the Xe lamp to measure the incident photon-to-current conversion efficiencies (IPCE). They were calculated as $IPCE = hc/\lambda e \times J_{SC} \times P_{in}^{-1}$ where h is Planck's constant, e is the elementary charge and λ is the monochromatic irradiation wavelength. Reflection losses at the solar cell substrate were not considered in the calculation. To verify the calibration of our characterization equipment, selected solar cells were also measured at the Laboratory for Photonics and Interfaces at the Swiss Federal Institute of Technology Lausanne (EPFL). For this purpose, cells were transported in a vacuum tight measurement box. The characteristics of all solar cell devices studied in this work are summarized in Table 1.

Electrical conductivity of the doped CyC films was measured by a standard four-probe method using a Keithley

Table 1
Photovoltaic performance of ITO/PEDOT:PSS/CyC/C_{60}/Al devices using pristine and doped CyC films. For doped cells, the $NOBF_4$/CyC concentration is 0.02 mol/mol. The photovoltaic parameters are measured under standard AM1.5 simulated solar irradiation, unless indicated. Usage of a 2 nm thin Alq_3 cathode buffer layer is also indicated.

	J_{SC} (mA/cm^2)	V_{OC} (V)	FF	η_P (%)
Pristine	0.96	0.24	0.18	0.04
Pristine + Alq_3	2.4	0.32	0.18	0.14
Doped	5.7	0.48	0.20	0.55
Doped + Alq_3	8.3	0.72	0.34	2.0
Doped + Alq_3[a]	2.8	0.71	0.43	2.6

[a] Measured at 1/3 of the simulated standard AM 1.5 irradiation intensity.

2400 source/measure unit. The glass substrates comprised four finger-like gold electrodes separated by a channel distance of 10 μm. The height of the fingers was measured to be 186 nm while the length of the finger-like structure was 1.18 cm. A current of 500 nA was applied at the outer electrodes, while the voltage was measured at the inner electrodes.

3. Results and discussion

The chemical structure of the trimethine cyanine dye (CyC) together with the energy level diagram of the other organic materials and electrodes used in the device construction are shown in Fig. 1. The hole conducting poly(3,4-ethylenedioxythiophene):poly(styrenesulfonate) (PEDOT:PSS) film (40 nm) and the CyC donor film (30 nm) were spin coated successively on top of a transparent indium tin oxide (ITO) substrate. Thereafter, the C_{60} acceptor film (40 nm) and the aluminium top electrode (60 nm) were deposited via thermal sublimation to form typical ITO/PEDOT:PSS/CyC/C_{60}/Al multilayer devices with an active area of 7.1 mm^2. To increase the conductivity of the donor layer, the cyanine was doped using nitrosonium tetrafluoroborate ($NOBF_4$). Oxidation of the cyanine dye is driven by the higher oxidation potential of NO^+, which in acetonitrile is 0.87 V vs. ferrocene/ferrocenium (Fc/Fc^+) as compared to 0.63 V vs. Fc/Fc^+ for the dye [26]. The merit of this doping agent is that the cyanine can be oxidized in solution in a controlled way. We first produced a concentrated $NOBF_4$ stock solution in acetonitrile where the NO^+ cation is stable for several hours. Small aliquots of the stock solution were then added to a 1 wt% cyanine solution in chlorobenzene, which turned out to be the best spin-coating solvent to form smooth doped films. To provide spectroscopic evidence of the doping process, CyC solutions were prepared with increasing doping concentrations up to a $NOBF_4$/CyC ratio of 2.2 mol/mol. While the monomer signature at 540 nm disappears with increasing $NOBF_4$ concentration, a clear cyanine dication peak at 483 nm emerges along with an isosbestic point at 500 nm (Fig. 2a). When thin films are produced from these solutions, the features are similar but no isosbestic point is observed due to the presence of dimers and aggregates in the solid (Fig. 2b). Full conversion of the cationic dye into its dication occurs at a $NOBF_4$/CyC molar ratio of 2 mol/mol. We believe the oxidation reaction to be quantitative and attribute the twofold excess needed for full conversion to the degradation of the $NOBF_4$ stock solution by water contamination.

Doping induces a steep rise of the short-circuit current J_{SC} going from 1 mA/cm^2 to 8 mA/cm^2 when the $NOBF_4$ concentration in the CyC solution is increased from zero to 0.02 mol/mol and unexpectedly decreases for higher doping concentrations (Fig. 3a). As we have verified by four-probe conductivity measurements, this behaviour is paralleled by the conductivity of the film reaching 2×10^{-6} S cm^{-1} at the optimum concentration of 0.02 mol/mol (Supplementary material, Fig. S2). We attribute this feature to film disruption upon aggregation of the charged cyanine dyes. At higher doping concentrations this behaviour is indeed observed by atomic force microscopy (Supplementary material, Fig. S4). The open-circuit voltage V_{OC} rises from 0.25 V to more than 0.6 V, similar to the current density, but stays rather constant for higher doping concentrations (Fig. 3b). Regarding the fairly low fill factor *FF* of about 0.2, it is independent of the doping concentration. At the optimum doping level of 0.02 mol/mol the power conversion efficiency (PCE) reaches 0.55% when measured at standard simulated AM1.5 solar irradiation which is an order of magnitude higher than 0.04% obtained for the undoped cyanine solar cell (Fig. 3c). The increase of photovoltaic performance upon oxidative doping corresponds to our previous findings using oxygen as doping agent [22]. In the latter work cyanine films were deposited from tetrafluoropropanol and solar cell efficiencies were typically around 0.1%. Photooxidative doping of the cyanine layer exposed at ambient atmosphere drastically increased the power conversion efficiency to 1.2% at 1/3 of the standard irradiation intensity. However, while the

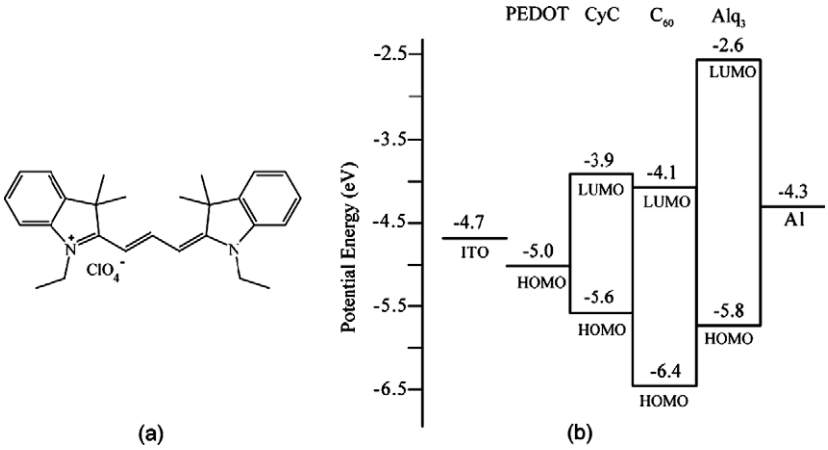

Fig. 1. Materials applied in our solar cells. (a) Molecular structure of trimethine cyanine CyC. (b) Energy diagram and solar cell architecture. The energy levels of the lowest unoccupied molecular orbitals (LUMO) and the highest occupied molecular orbitals (HOMO) of the organic semiconductors as well as the electrode work functions are taken from the literature [21,28].

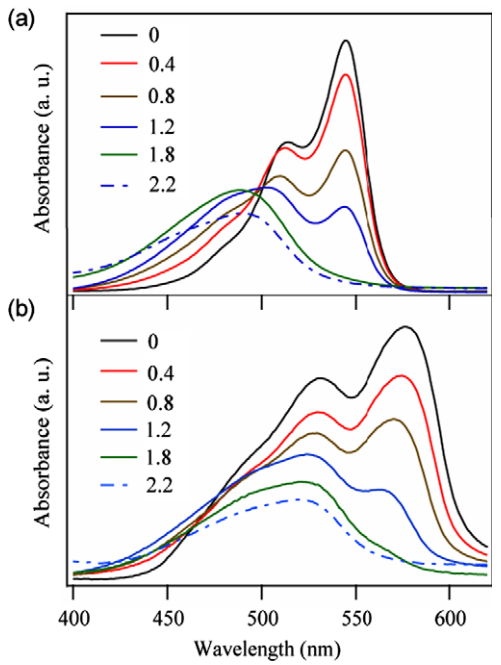

Fig. 2. Evolution of the UV–vis spectra upon doping with $NOBF_4$. (a) Solutions of identical CyC concentration doped with different amounts of $NOBF_4$. (b) Doped CyC films on a glass substrate spin coated from the respective solutions. The numbers indicate the different $NOBF_4$/CyC molar ratios.

photooxidative doping method partly destroys the CyC film and deteriorates the C_{60} layer, $NOBF_4$ doping provides a controlled and non-destructive way of adjusting conductivity in the cyanine film.

Despite the important rise in short-circuit current density, the power conversion efficiency of the device is limited by the marked "S-shape" in the current–voltage characteristics (Fig. 3c). This phenomenon has been reported for different organic solar cells and has been shown to originate from defects at the C_{60}/aluminium cathode interface [27]. Different methods have been proposed to achieve Ohmic contacts at the aluminium cathode implying annealing steps or various buffer layers. In $NOBF_4$ doped cyanine solar cells, annealing of the completed devices led to reduced device performance. Therefore we opted for the insertion of a 2 nm thin tris-(8-hydroxyquinoline) aluminium (Alq_3) buffer layer between C_{60} and aluminium [28]. As shown in Fig. 4a, the "S-shape" is largely reduced in the current–voltage characteristics of both the doped and undoped cell. We attribute the remaining small kink to the anode contact, since the aluminium cathode using the Alq_3 buffer layer is known to be Ohmic. In the same manner as for the devices lacking the Alq_3 buffer layer, doping induces an important shift of V_{OC} from 0.32 V to 0.72 V and gives rise to a dramatic short-circuit current increase from 2.4 mA/cm^2 to 8.3 mA/cm^2. Combining both a doped cyanine layer and a cathode buffer layer in the device construction results in fill factors of 0.43 and 0.34 at 1/3 sun and full sun irradiation, respectively. Consequently, we obtain high power conversion efficiencies of 2.6% (1/3 sun) and 2.0% (full sun).

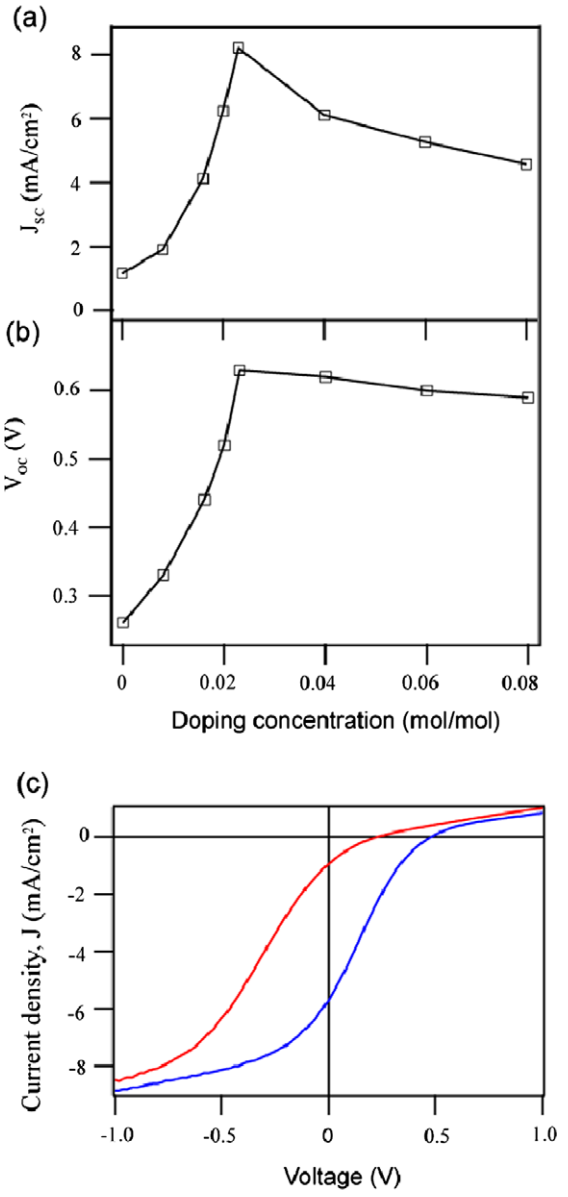

Fig. 3. Dependence of the photovoltaic parameters on the $NOBF_4$ doping concentration of the CyC film: (a) short-circuit current and (b) open-circuit voltage measured at 140 mW/cm^2, (c) current–voltage characteristics of devices using pristine CyC films (red) and doped CyC films with a $NOBF_4$/CyC molar ratio of 0.02 mol/mol (blue) and measured at 100 mW/cm^2 full sun irradiation. (For interpretation of the references to colour in this figure legend, the reader is referred to the web version of this article.)

One of the major benefits of doping the cyanine layer is obviously related to the intriguing rise in open-circuit voltage. The origin of the open-circuit voltage in planar heterojunction solar cells is not fully understood yet but was shown to be related to a combination of various device parameters, the most important being the difference between the quasi Fermi levels of electrons in the acceptor and holes in the donor material. Doping certainly lowers the quasi Fermi level of the holes in the cyanine layer [29]. To estimate the importance of this lowering on the

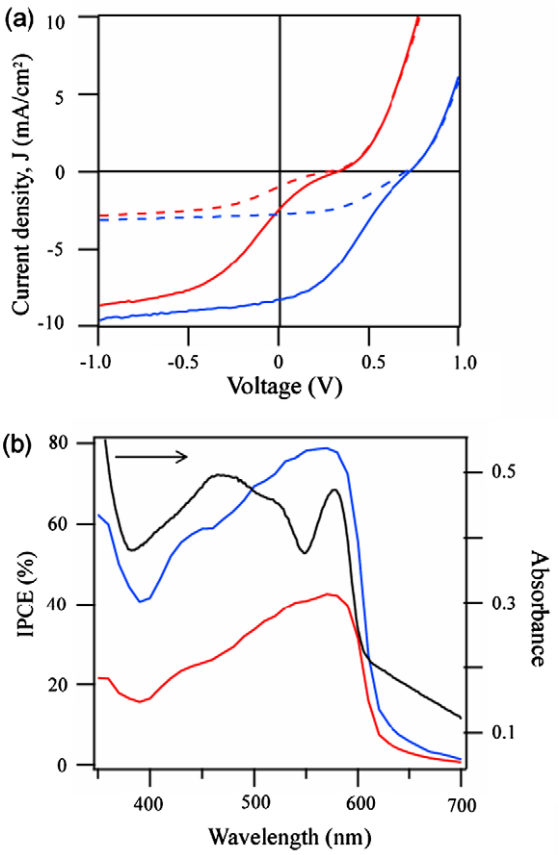

Fig. 4. Photovoltaic performance of solar cells having an Alq_3 cathode buffer layer. (a) Current–voltage characteristics for the pristine cells (red) and doped cells (blue) at full sun (solid line) and 1/3 sun simulated solar irradiation (dashed line). (b) Cell absorption (black) and IPCE curves for solar cells using a pristine CyC film (red) and a doped CyC film (blue). A $NOBF_4$ concentration of 0.02 mol/mol (blue) is used in the doped devices. (For interpretation of the references to colour in this figure legend, the reader is referred to the web version of this article.)

open-circuit voltage increase ΔV_{OC} the following expression can be easily derived (see Supplementary material):

$$\Delta V_{OC} = \frac{kT}{e} \ln\left(\frac{n_1 p_1}{n_0 p_0}\right) \quad (1)$$

Here p_0 and p_1 are the densities of photoinduced holes in the cyanine layer before and after doping, respectively, while n_0 and n_1 are the respective electron densities in the C_{60} layer, k is the Boltzmann constant, $T = 298$ K is the temperature and e is the elementary charge. Numerical evaluation of Eq. (1) then yields $\Delta V_{OC} = 0.10$ V (see Supplementary material), which is clearly inferior to the observed changes. Therefore, we have attributed the important change in open-circuit voltage to the creation of a Schottky junction at the PEDOT/CyC interface. As a consequence, the effective anode workfunction is lowered, thus the built-in field of the device is increased, which is corroborated by the change of 0.4 V in the onset voltage of the diode. Schottky barrier formation upon oxidative doping of the organic layer at the electrode interface has already been studied extensively [16,30,31]. More recently, p or n-doped transport layers deposited by controlled co-sublimation have been introduced in small molecule solar cells demonstrating the possibility of achieving photoactive pn- and pin-type heterojunctions [32,33].

Perhaps the most striking effect of doping the cyanine film is manifested in the photocurrent increase at short-circuit conditions. The incident photon-to-current conversion efficiency (IPCE) of doped and pristine CyC solar cells shows a maximum which corresponds to the cyanine absorption at 580 nm as well as a shoulder at 440 nm, which is attributed to the photoactivity of C_{60} (Fig. 4b). Doping improves the IPCE by a factor of two, reaching nearly 80% at maximum. This is astonishingly high given the modest solar cell absorbance of 0.47 at the maximum IPCE wavelength of 580 nm. In a simple model we can assume that incident light, being reflected by the aluminium cathode, penetrates twice through the photoactive layers thereby loosing 89% of its intensity. Accounting for additional reflection losses of 5–10% it follows that the monochromatic photon to electron conversion efficiency must be close to unity. This also means that the full cyanine layer has to be active in charge generation. As we have verified by varying the thickness of the CyC layer, a typical filter effect appears for thicker layers showing that doping is not leading to charge carrier generation in the bulk cyanine layer (Supplementary material, Fig. S3).

Unlike highly crystalline organic layers grown by physical vapor deposition, cyanine films are spin casted from solution and do not reveal large crystalline grains (Supplementary material, Fig. S4) provided with high exciton diffusion lengths. Possibly C_{60} diffuses into the cyanine layer leading to exciton dissociation and extraction of the electrons. Diffusion of C_{60} into conjugated polymer layers has already been observed [34]. On the other hand large cyanine aggregates may also be responsible for efficient exciton transport to the charge separating heterointerface. Indeed, we have recently found that CyC aggregates nucleate at the surface of a fullerene derivative, as it may at the C_{60} interface [35]. By all means, the very high monochromatic photon-to-current conversion efficiency indicates that electron–hole recombination processes are insignificant in our devices. As reported in previous work [36], cyanine counterions can diffuse across the donor–acceptor interface giving rise to surface dipoles. The latter could act as energy barrier for the recombination of photogenerated charges. Work is in progress to scrutinize this mechanism.

4. Conclusion

The present work demonstrates the full potential of soluble cyanine dyes used as solid organic semiconductors in solar cell devices. Solution doping of cyanines increases the conductivity of spin casted films and leads to efficient photovoltaic cells using simple bilayer heterostructure architecture. High power conversion efficiencies are achieved despite the rather narrow absorption spectrum of the cyanine dye. The results obtained lead the way to the application of related dyes harvesting solar light in other spectral

domains, particularly in the near-infrared domain. The fact that planar bilayer structures can be used obviates the need for tedious control of film morphology and therefore simplifies technological implementation. Importantly, this class of photographic dyes has been studied for more than a century. Large scale production of cyanine dyes is already occurring, which promises competitive materials prices for the emerging organic solar cell technology.

Acknowledgements

The authors would like to thank Prof. M. Grätzel for helpful discussions and advice. The Swiss Competence Center for Energy and Mobility CCEM-CH and "swisselectric research" are gratefully acknowledged for their financial support. Additional funding from the Swiss "Bundesamt für Energie" (BFE) is acknowledged. Dr. Thomas Geiger is acknowledged for dye synthesis.

Appendix A. Supplementary material

Supplementary data associated with this article can be found, in the online version, at doi:10.1016/j.orgel.2009.12.017.

References

[1] H. Meier, A. Haus, Angew. Chem., Int. Ed. 72 (1960) 631.
[2] C.W. Tang, Appl. Phys. Lett. 48 (1986) 183.
[3] T. Stübinger, W. Brütting, J. Appl. Phys. 90 (2001) 3632.
[4] G. Yu, J. Gao, J.C. Hummelen, F. Wudl, A.J. Heeger, Science 270 (1995) 1789.
[5] J. Hou, H.-Y. Chen, S. Zhang, R.I. Chen, Y. Yang, Y. Wu, G. Li, J. Am. Chem. Soc. 131 (2009) 15586.
[6] B. Walker, A.B. Tamayo, X.D. Dang, P. Zalar, J.H. Seo, A. Garcia, M. Tantiwiwat, T.Q. Nguyen, Adv. Funct. Mater. 19 (2009) 3063.
[7] P.K. Watkins, A.B. Walker, G.L.B. Verschoor, Nano Lett. 5 (2005) 1814.
[8] S. Yoo, W.J. Potscavage Jr., B. Domercq, S.-H. Han, T.-D. Li, S.C. Jones, R. Szoszkiewicz, D. Levi, E. Riedo, S.R. Marder, B. Kippelen, Solid-State Electron. 51 (2007) 1367.
[9] W.J. Potscavage Jr., S. Yoo, B. Kippelen, Appl. Phys. Lett. 93 (2008) 193308.
[10] T.H. James, in: The Theory of the Photographic Process, fourth ed., Macmillan, New York, 1977.
[11] H. Mustroph, M. Stollenwerk, V. Bressau, Angew. Chem., Int. Ed. 45 (2008) 2016.
[12] P.B. Sargent, Neuroimage 1 (1994) 288.
[13] J.-H. Yum, P. Walter, S. Huber, D. Rentsch, T. Geiger, F. Nüesch, F. De Angelis, M. Grätzel, M.K. Nazeeruddin, J. Am. Chem. Soc. 129 (2007) 10320.
[14] X. Ma, J. Hua, W. Wu, Y. Jing, F. Meng, H. Tian, W. Zhan, Tetrahedron 64 (2008) 345.
[15] K. Sayama, K. Hara, N. Mori, M. Satsuki, S. Suga, S. Tsukagoshi, Y. Abe, H. Sugihara, H. Arakawa, Chem. Commun. 13 (2000) 1173.
[16] A.K. Ghosh, T. Feng, J. Appl. Phys. 49 (1978) 5982.
[17] S. Wang, E.I. Mayo, M.D. Perez, L. Griffe, G. Wei, P.I. Djurovich, S.R. Forrest, M.E. Thompson, Appl. Phys. Lett. 94 (2009) 233304.
[18] N.M. Kronenberg, M. Deppisch, F. Würthner, H.W.A. Lademann, K. Deing, K. Meerholz, Chem. Commun. 48 (2008) 6489.
[19] F. Silvestri, M.D. Irwin, L. Beverina, A. Facchetti, G.A. Pagani, T.J. Marks, J. Am. Chem. Soc. 130 (2008) 17640.
[20] U. Mayerhöffer, K. Deing, K. Gruss, H. Braunschweig, K. Meerholz, F. Würthner, Angew. Chem., Int. Ed. 48 (2009) 8776.
[21] F. Meng, K. Chen, H. Tian, L. Zuppiroli, F. Nüesch, Appl. Phys. Lett. 82 (2003) 3788.
[22] B. Fan, R. Hany, J.E. Moser, F. Nüesch, Org. Electron. 9 (2008) 85.
[23] P.A. Bouit, D. Rauh, S. Neugebauer, J.L. Delgado, E. DiPiazza, S. Rigaut, O. Maury, C. Andraud, V. Dyakonov, N. Martin, Org. Lett. 11 (2009) 4806.
[24] M.T. Lloyd, J.E. Anthony, G.G. Malliaras, Mater. Today 10 (2007) 34.
[25] Z.-H. Peng, X.-F. Zhou, S. Carroll, H.J. Geise, B.-X. Peng, R. Dommisse, E. Esmans, R. Carleer, J. Mater. Chem. 6 (1996) 1325.
[26] T. Geiger, H. Benmansour, B. Fan, R. Hany, F. Nüesch, Macromol. Rapid Commun. 29 (2008) 651.
[27] D. Gupta, M. Bag, K.S. Narayan, Appl. Phys. Lett. 92 (2008) 093301.
[28] Q.L. Song, F.Y. Li, H. Yang, H.R. Wu, X.Z. Wang, W. Zhou, J.M. Zhao, X.M. Ding, C.H. Huang, X.Y. Hou, Chem. Phys. Lett. 416 (2005) 42.
[29] C. Uhrich, D. Wynands, S. Olthof, M.K. Riede, K. Leo, S. Sonntag, B. Maennig, M. Pfeiffer, J. Appl. Phys. 104 (2008) 043107.
[30] R. Gupta, S.C.K. Misra, B.D. Malhotra, N.N. Beladakere, S. Chandra, Appl. Phys. Lett. 58 (1991) 51.
[31] G.A. Chamberlain, T. Feng, J. Appl. Phys. 53 (1982) 6262.
[32] M. Pfeiffer, A. Beyer, B. Plönnigs, A. Nollau, T. Fritz, K. Leo, D. Schlettwein, S. Hiller, D. Wöhrle, Sol. Energy Mater. Sol. Cells 63 (2000) 83.
[33] C.K. Chan, W. Zhao, A. Kahn, I.G. Hill, Appl. Phys. Lett. 94 (2009) 203306.
[34] D.E. Markov, E. Amsterdam, P.W.M. Blom, A.B. Sieval, J.C. Hummelen, J. Phys. Chem. A 109 (2005) 5266.
[35] R. Steiger, R. Pugin, J. Heier, Colloid Surface B: Biointerface 74 (2009) 484.
[36] H. Benmansour, F.A. Castro, M. Nagel, J. Heier, R. Hany, F. Nüesch, Chimia 61 (2007) 787.

Organic Electronics 11 (2010) 589–593

Contents lists available at ScienceDirect

Organic Electronics

journal homepage: www.elsevier.com/locate/orgel

A novel *p*-dopant with low diffusion tendency and its application to organic light-emitting diodes

Ingmar Bruder [a], Soichi Watanabe [a], Jianqiang Qu [a], Imke B. Müller [a], Ralf Kopecek [a], Jaehyung Hwang [a], Jürgen Weis [b,*], Nicolle Langer [a,*]

[a] *BASF SE, Carl-Bosch-Str. 38, 67056 Ludwigshafen, Germany*
[b] *Max-Planck-Institut für Festkörperforschung, Heisenbergstraße 1, 70569 Stuttgart, Germany*

ARTICLE INFO

Article history:
Received 10 September 2009
Received in revised form 9 December 2009
Accepted 23 December 2009
Available online 4 January 2010

Keywords:
Organic electronics
Organic dopants
OLED
Diffusion
Lifetime

ABSTRACT

The novel *p*-dopant 2,3-di(*N*-phthalimido)-5,6-dicyano-1,4-benzoquinone (BAPD) was synthesized and compared to the state-of-the-art dopant F_4TCNQ. BAPD shows a higher evaporation temperature and thermal stability than F_4TCNQ, presumably due to its higher molecular weight and bulkiness. The efficiency of the host-to-dopant electron transfer as well as the diffusion characteristics of the *p*-dopants were investigated by ultraviolet photo emission spectroscopy (UPS) and X-ray photo emission spectroscopy (XPS). Although BAPD is a less strong *p*-dopant than F_4TCNQ, the lower diffusion tendency and higher thermal stability of this new class of dopants forms an attractive potential for the lifetime improvement of organic electronic devices.

© 2010 Elsevier B.V. All rights reserved.

1. Introduction

Organic light-emitting diodes (OLEDs) are expected to become the next-generation flat-panel displays and solid-state lighting devices because of their low power consumption, high brightness, high contrast and low costs [1–5]. For commercialization, OLEDs have to combine high power conversion efficiencies with long lifetimes. Therefore, highly efficient charge carrier injection and transport combined with a low driving voltage is required [6]. Hole-injection and transport can be enhanced by the introduction of an organic electron-accepting dopant [7–9] into an appropriate hole-transport layer (HTL). However, problematic issues still remain. Organic *p*-dopants such as F_4TCNQ have high vapor pressures due to their small molecular weight. Thus, these compounds tend to evaporate at very low temperatures complicating the control of the evaporation rate. Furthermore, it has been shown that small dopants tend to diffuse [10–12]. This diffusion precludes the fabrication of interface-only doped devices [10,12,13] because dopants tend to penetrate into other layers of the device and thereby change their composition and electrical properties. Hence, a change of the performance and lifetime of an OLED could be expected. In order to study the influence of the molecular weight and structure on the diffusion of the *p*-dopants in an OLED, a new *p*-dopant 2,3-di(*N*-phthalimido)-5,6-dicyano-1,4-benzoquinone (BAPD, Fig. 1a) was developed. The molecular weight of BAPD is higher than this of F_4TCNQ (M_{BAPD} = 448 g/mol, M_{F_4TCNQ} = 276 g/mol). Furthermore, the bulky structure of BAPD could lower the diffusion tendency. The calculated [14] electron affinity (EA) of BAPD is slightly lower (4.8 eV) than this of F_4TCNQ (5.0 eV).

2. Synthesis of BAPD

A mixture of 2,3-dichloro-5,6-dicyano-benzoquinone (33.4 g, 147.1 mmol) and potassium phthalimide (54.5 g, 294.2 mmol) in acetonitrile (500 ml) was stirred under

* Corresponding authors.
E-mail addresses: J.Weis@fkf.mpg.de (J. Weis), Nicolle.Langer@basf.com (N. Langer).

1566-1199/$ - see front matter © 2010 Elsevier B.V. All rights reserved.
doi:10.1016/j.orgel.2009.12.019

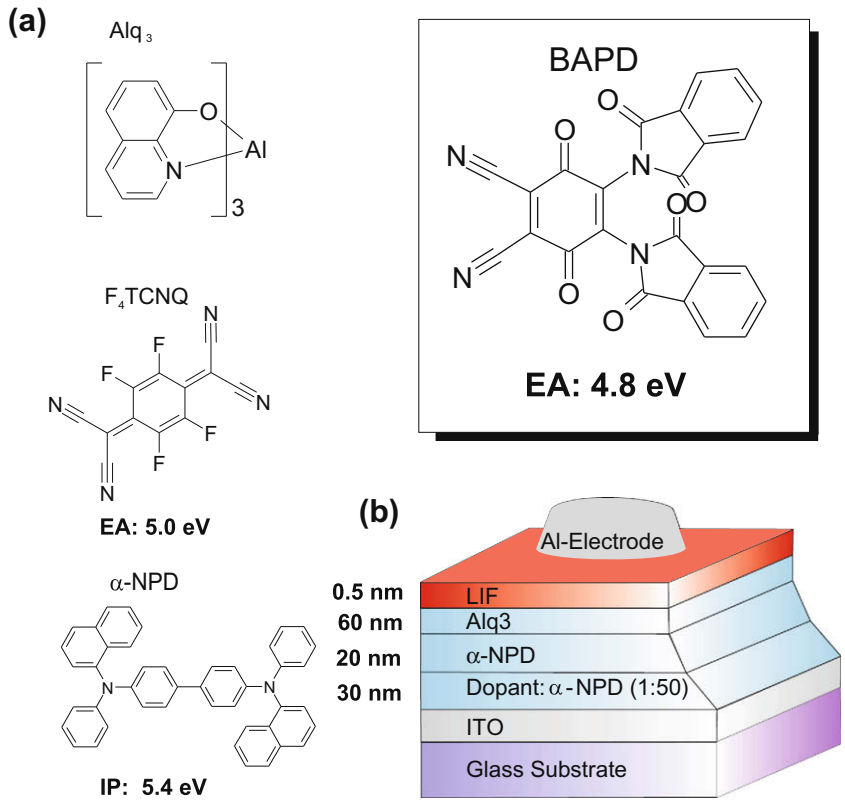

Fig. 1. (a) Chemical structure of the emitter Alq_3, *p*-dopants F_4TCNQ and BAPD with EA, HTL α-NPD with IP. (b) Schematic OLED device setup.

reflux for 12 h. The resulting deep brown suspension was filtrated. The solid was washed three times with warm water and one time with ethanol. After drying at 100 °C under vacuum, a yellow solid was obtained (9.3 g, 14%). ^{1}H NMR (D_2SO_4), δ = 7.6 ppm; Maldi-MS: m/z = 447.9. Before device fabrication, BAPD was purified by gradient zone sublimation.

3. Thermal stability and evaporation temperature

Due to the high molecular weight, BAPD evaporates at (150 ± 10) °C under a vacuum of 10^{-7} mbar. As a comparison, F_4TCNQ evaporates at (90 ± 10) °C at the same pressure. Since the thermal stability of the dopants is important for the processability, thermogravimetric analysis (TGAs) were made. Here, BAPD shows a higher thermal stability ((1 ± 0.4)% weight loss at 403 °C) than F_4TCNQ ((1 ± 0.4)% weight loss at 268 °C).

4. Doping and diffusion investigation by UPS and XPS

In order to understand the basic behavior of BAPD and F_4TCNQ in organic electronic devices, ultraviolet photo emission spectroscopy (UPS, He I, 21.22 eV) measurements were made. The doping strength of BAPD and F_4TCNQ was investigated on samples of type *A* (Figs. 2a and 2b): a 10 nm thick α-NPD layer, doped with 5 weight % of BAPD or F_4TCNQ, respectively. The HOMO level of a 30 nm undoped α-NPD layer acts as the reference (−1.52 eV below Fermi level ε_F). The stronger the dopant, the closer the HOMO level of sample type *A* will move to ε_F. The HOMOs of the BAPD- and F_4TCNQ-doped α-NPD layers are located at −0.89 and −0.57 eV with respect to ε_F. This means that BAPD acts as a *p*-dopant, but less strong than F_4TCNQ. This confirms the weaker electron-accepting properties of BAPD compared to F_4TCNQ, predicted by the lower calculated EA (*vide supra*).

Diffusion of dopants into the light-emitting layer of OLEDs could decrease their lifetime due to exciton quenching [15]. This quenching process is caused by the lower band gap of the radical anion of the dopant compared to the emitter. Therefore, the diffusivity of F_4TCNQ was investigated in comparison to BAPD with X-ray photo emission spectroscopy (XPS, Al Kα, 1486.6 eV) and UPS. In the XPS analysis, the F(1 s) core level intensities of a 10 nm thick pure F_4TCNQ layer, evaporated on a silicon wafer, were compared to samples in which this F_4TCNQ layer was covered by 30 nm of α-NPD. The measurements were carried out 24 h after the evaporation, in order to get a realistic picture of the diffusivity of the dopant. The amount of fluorine present on top of the 10 nm thick pure F_4TCNQ layer was measured to be (10.6 ± 0.3)%. When the F_4TCNQ layer was covered by 30 nm of α-NPD, only (0.2 ± 0.1)% of fluorine could be detected.

For BAPD, a comparable XPS investigation was difficult due to its elemental composition: In contrast to F_4TCNQ,

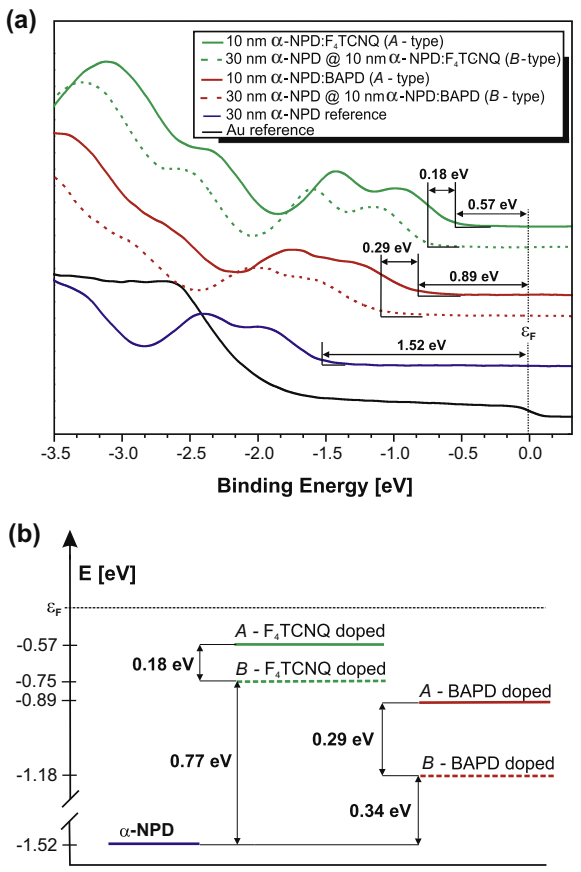

Fig. 2. UPS measurements of the HOMO level with respect to the Fermi level ε_F of (a) 5% homogeneously doped α-NPD layers (sample type *A*) in comparison to doped layers additionally covered by 30 nm of undoped α-NPD (sample type *B*). The respective cutoffs followed the HOMO shifts accordingly. The Fermi energy of the UPS measurement setup was calibrated with reference to gold. (b) Energy gap between ε_F and the HOMO of BAPD (F_4TCNQ)-doped *B*-type samples in relation to the doped *A*-type samples and the undoped α-NPD reference.

BAPD contains no atoms which make the molecule clearly distinguishable from the α-NPD surface.[1] To overcome this problem the diffusion of dopants was indirectly probed by UPS. This investigation was based on the fact, that UPS probes only the energetic conditions right at the surface [16].

Two types of samples were prepared: 10 nm thick 5% homogeneously doped α-NPD layers (sample type *A*, *vide supra*) and samples which doped layers were additionally covered by 30 nm of undoped α-NPD (sample type *B*, Fig. 2). As a reference an undoped 30 nm thick α-NPD layer was chosen. To relate the characteristic shifts (ε_F-HOMO) of the energy levels of sample type *A* and *B* (see Fig. 2) to the diffusivity of the respective dopants, one has to understand the relation of the Fermi energy ε_F to the doping density N_A within the samples:

[1] (4.6 ± 0.1)% of oxygen atoms were found by XPS on all samples, caused by the air exposure during the sample transfer into the measurement set up. Therefore, it was not possible to distinguish between oxygen included in the BAPD molecule and oxygen originated from the air exposure.

The electron density in the conduction band of an intrinsic semiconductor is given by

$$n(T) = 2\int_{E_{CB}}^{\infty} g_{\varepsilon}^{CB}(\varepsilon') f_{FD}(\varepsilon', \varepsilon_F, T)\, d\varepsilon', \tag{1}$$

where g_{ε}^{CB} is the normalized density of states in the conduction band and $f_{FD}(\varepsilon', \varepsilon_F, T)$ is the Fermi–Dirac distribution function. Congruently, the hole density created by thermal excitations are given by

$$p(T) = 2\int_{-\infty}^{E_{VB}} D_{\varepsilon}^{VB}(\varepsilon')[1 - f_{FD}(\varepsilon', \varepsilon_F, T)]\, d\varepsilon'. \tag{2}$$

At room temperature, the valence electrons of an *p*-doped semiconductor are rather excited into the acceptor states E_A of the *p*-dopant than into the conduction band of the semiconductor. Thus, the normalized density of states g_{ε}^{A} of the acceptor states E_A of the *p*-dopant determines the electron density and Eq. (1) changes to

$$n(T) = 2\int_{E_A}^{\infty} g_{\varepsilon}^{A}(\varepsilon') f_{FD}(\varepsilon', \varepsilon_F, T)\, d\varepsilon'. \tag{3}$$

It has been reported for F_4TCNQ-doped amorphous hole-transport layers, that small doping concentrations lead to deep acceptor states E_A [17]. Thus, the occupation probability of the respective states can be described in good approximation by Boltzmann statistics. Therefore, Eqs. (2) and (3) can be written as

$$n(T) = \underbrace{2\int_{E_A}^{\infty} g_{\varepsilon}^{A}(\varepsilon') \exp\left(-\frac{\varepsilon' - E_A}{k_B T}\right) d\varepsilon'}_{\equiv n_0(T)} \cdot \exp\left(-\frac{E_A - \varepsilon_F}{k_B T}\right), \tag{4}$$

$$p(T) = \underbrace{2\int_{-\infty}^{E_{VB}} g_{\varepsilon}^{VB}(\varepsilon') \exp\left(-\frac{E_{VB} - \varepsilon'}{k_B T}\right) d\varepsilon'}_{\equiv p_0(T)} \cdot \exp\left(-\frac{\varepsilon_F - E_{VB}}{k_B T}\right), \tag{5}$$

and are considered to be also qualitatively applicable to describe organics. Assuming a very narrow density of acceptor states g_{ε}^{A}, the integral in Eq. (4) is similar to the doping density N_A ($n_0(T) \approx N_A$). Since semiconductors are not charged, the relation $n(T) = p(T)$ is valid. Therefore, using Eqs. (4) and (5) the position of the Fermi level $\varepsilon_F(T)$ within the organic semiconductor can be derived to

$$\varepsilon_F(T) = \frac{E_A + E_{VB}}{2} + \frac{k_B T}{2} \ln \frac{p_0(T)}{N_A}. \tag{6}$$

If two samples (A and B) contains the same matrix molecule (in this case α-NPD) but different doping concentrations N_A^A and N_A^B of the same dopant, the energetic difference of their respective Fermi-levels $\varepsilon_F^A(T)$ and $\varepsilon_F^B(T)$ can be derived as

$$\varepsilon_F^A(T) - \varepsilon_F^B(T) = \frac{k_B T}{2} \ln\left(\frac{N_A}{N_B}\right). \tag{7}$$

Thus, the energetic difference of the Fermi-levels is only dependent on the respective doping densities.

If BAPD and F_4TCNQ would show the same diffusivity, the energy difference between the HOMO's of the respectively doped samples *A* and *B* should be identical according

to Eq. (7). BAPD sample *B* shows a difference of 0.29 eV compared to BAPD sample *A*, whereas F_4TCNQ sample *B* shows a difference of 0.18 eV compared to F_4TCNQ sample *A* (Fig. 2). This 0.11 eV larger shift for BAPD sample *B* indicates that the surface of the BAPD sample *B* is less *p*-doped than the respective F_4TCNQ sample *B*.

It has to be stated here, that in contrast to F_4TCNQ-doped samples, where we see a clear presence of fluorine in XPS, no diffusion of dopants for the BAPD case could also explain the discrepancy in Fermi level shift between F_4TCNQ and BAPD. In such cases, reported studies say, that the Fermi-levels of two organic layers are determined by dipole rather than band bending, i.e., flat bands [18,19]. The energy alignment mechanism on such interface is out of scope of our paper. However, in any case, our measurement verifies, that the dopant diffusivity of BAPD is smaller than that of F_4TCNQ.

5. Device fabrication and results

In order to investigate the potential of the new dopant, standard OLED devices [20] with a 2 weight % (wt%) *p*-doped α-NPD hole injection layer (HIL) and an Alq_3 emitter were prepared (Fig. 1b). The hole injection layer (HIL), consisting of F_4TCNQ or BADP doped into *N,N*-diphenyl-*N,N* '-bis(1-naphthyl)-1,1-biphenyl-4,4-diamine (α-NPD), was formed by vacuum co-evaporation on a precleaned indium tin oxide (ITO) substrate with a sheet resistance of 15 ohm/sq. On top of the HIL, organic layers were vacuum deposited at a base pressure of 1×10^{-7} mbar. α-NPD was deposited as the hole-transport layer (HTL), and aluminium tris(8-hydroxyquinoline) (Alq_3) was deposited as an electron-transporting emitting layer. Finally, LiF and aluminium were vacuum-deposited using a metal shadow mask to define an emitting area of 4.0 mm^2. After the cathode formation, the devices were encapsulated using UV-epoxy resin and a glass lid with desiccant under a dry nitrogen atmosphere (<1:0 ppm H_2O and O_2). Luminance and operational lifetime measurements were carried out at room temperature.

Here, the BAPD-doped device showed a slightly higher turn-on voltage (Fig. 3a), which is in agreement to the expected less efficient host-to-dopant electron transfer from α-NPD to BAPD compared to F_4TCNQ (*vide supra*). The current efficiency of the BAPD-doped device was slightly higher than the F_4TCNQ-doped device (3.6 and 2.6 cd/A at 500 cd/m^2, respectively), which could be due to a better charge-carrier balance in the diode. The diode lifetimes ($t_{1/2}$) were measured at a constant current density of 125 mA/cm^2. Under these conditions the BAPD device showed a lifetime of 140 h at an initial luminance of L_0 = 4800 cd/m^2 (see Fig. 3b). In contrast, the F_4TCNQ-doped device showed a shorter lifetime of 122 h at an initial luminance of L_0 = 3350 cd/m^2. Calculated with an extrapolation factor [21,22] n = 1.5, the lifetimes at an initial luminance of 500 cd/m^2 are estimated to be 4200 h for BAPD-doped devices and 2100 h for F_4TCNQ-doped devices, respectively. The improvement in device lifetime can be a result from the reduced diffusion of BAPD and/or from the better charge-carrier balance.

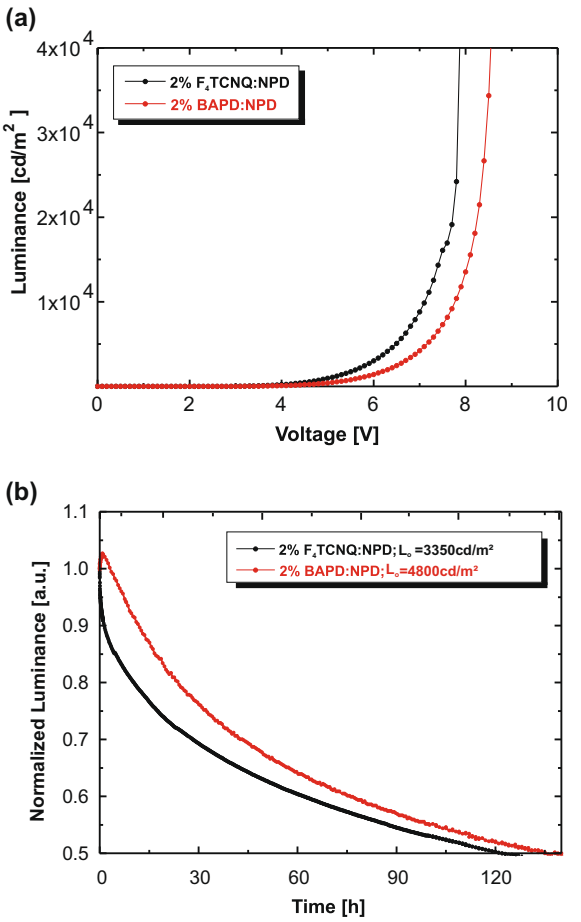

Fig. 3. (a) Luminance vs. bias voltage and (b) lifetimes of 5 wt% F_4TCNQ and BAPD doped α-NPD/Alq_3-based OLED devices. The lifetime measurement data was acquired based on a constant current density of 125 mA/cm^2 for both device types.

6. Conclusion

In summary, the novel *p*-dopant 2,3-di(*N*-phthalimido)-5,6-dicyano-1,4-benzoquinone (BAPD) was synthesized and compared to the state-of-the-art dopant F_4TCNQ. BAPD shows a significant higher evaporation temperature and thermal stability than F_4TCNQ. This can be an important advantage in handling and processing the material in mass-production. Furthermore, it was shown with precise UPS and XPS measurements, that the diffusion capability of BAPD was effectively lowered. Although BAPD is a less strong *p*-dopant than F_4TCNQ, the lower diffusion tendency and higher thermal stability of this new class of organic dopants forms an attractive potential for the lifetime improvement of organic electronic devices. Further improvements on the electron-accepting strength of this class of dopants are under way.

Acknowledgments

We acknowledge the financial support of the Bundesministerium für Bildung und Forschung (BMBF) within

the project OPEG, Förderkennzeichen F13N9714. Furthermore, we thank Sabine Hirth for the UPS/XPS measurements.

References

[1] C.W. Tang, S.A. VanSlyke, Appl. Phys. Lett. 51 (1987) 913.
[2] M.A. Baldo, D.F. O'Brien, Y. You, A. Shoustikov, M.E. Thompson, S.R. Forrest, Nature 395 (1998) 151.
[3] B. Geffroy, P. Roy, C. Prat, Polym. Int. 55 (2006) 572.
[4] T. Tsuzuki, N. Shirasawa, T. Suzuki, S. Tokito, Adv. Mater. 15 (2003) 1455.
[5] X. Gong, J.C. Ostrowski, D. Moses, G.C. Bazan, A.J. Heeger, Appl. Phys. Lett. 81 (2002) 3711.
[6] X. Zhou, J. Blochwitz, M. Pfeiffer, A. Nollau, T. Fritz, K. Leo, Adv. Funct. Mater. 11 (4) (2001) 310.
[7] J. Kido, T. Matsumoto, Appl. Phys. Lett. 73 (1998) 2866.
[8] B. Maennig, M. Pfeiffer, A. Nollau, X. Zhou, K. Leo, Phys. Rev. B 64 (2001) 195208.
[9] T. Matsushima, C. Adachia, Appl. Phys. Lett. 89 (2006) 253506.
[10] W. Gao, A. Kahn, J. Appl. Phys. 79 (2001) 4040.
[11] Z.Q. Gao, B.X. Mi, G.Z. Xu, Y.Q. Wan, M.L. Gong, K.W. Cheah, C.H. Chen, Chem. Commun. (2008) 117.
[12] W.C. Lin, W.B. Wang, Y.C. Lin, B.Y. Yu, Y.Y. Chen, M.F. Hsu, J.H. Jou, J.J. Shyue, Org. Electron. 10 (2009) 581.
[13] W. Gao, A. Kahn, Org. Electron. 3 (2002) 53.
[14] The calculated EA for F_4TCNQ (4.96 eV) using the BP86/def-TZVP COSMO = 4.5//BP86/def-SV(P) method implemented in TURBOMOLE [23–25] is in good agreement with the reported value obtained experimentally (5.24 eV) by ultraviolet photoemission spectroscopy (UPS) and inverse photoemission spectroscopy (IPES). For the experimental EA of F_4TCNQ; see: W. Gao, A. Kahn, Appl. Phys. Lett. 79 (2001) 4040–4042.
[15] K. Walzer, B. Maennig, M. Pfeiffer, K. Leo, Chem. Rev. 107 (2007) 1233.
[16] S. Hüfner, Photoelectron Spectroscopy Principles and Applications, Springer-Verlag, 2003.
[17] D. Ray, K.L. Narasimhana, J. Appl. Phys. 103 (2008) 093711.
[18] W. Gao, A. Kahn, Appl. Phys. Lett. 82 (26) (2003) 4816.
[19] S. Olthof, R. Meerheim, M. Schober, K. Leo, Phys. Rev. B 79 (2009) 245308.
[20] H. Aziz, Z.D. Popovic, N. Hu, A. Hor, G. Xu, Science 283 (1999) 1900.
[21] C. Féry, B. Racine, D. Vaufrey, H. Doyeux, S. Cinà, Appl. Phys. Lett. 87 (2005) 213502.
[22] K. Okumoto, H. Kanno, Y. Hamada, H. Takahashi, K. Shibata, Appl. Phys. Lett. 89 (2006) 013502.
[23] A. Schäfer, A. Klamt, D. Sattel, J.C.W. Lohrenz, F. Eckert, Phys. Chem. Chem. Phys. 2 (2000) 2187.
[24] R. Ahlrichs, M. Bär, M. Häser, H. Horn, C. Kölmel, Chem. Phys. Lett. 162 (1989) 165.
[25] A. Klamt, G. Schüürmann, J. Chem. Soc. 2 (1993) 799.

Organic Electronics 11 (2010) 594–598

Contents lists available at ScienceDirect

Organic Electronics

journal homepage: www.elsevier.com/locate/orgel

Interface trap level in top-contact pentacene thin-film transistors evaluated by displacement current measurement

Seiichi Suzuki, Yuhsuke Yasutake [1], Yutaka Majima *

Materials and Structures Laboratory, Tokyo Institute of Technology, 4259 Nagatsuta-cho, Yokohama 226-8503, Japan

ARTICLE INFO

Article history:
Received 9 December 2009
Accepted 25 December 2009
Available online 4 January 2010

Keywords:
Organic thin-film transistors
Displacement current measurements
Carrier injection
Interface trap
Pentacene

ABSTRACT

The interface trap level in top-contact pentacene thin-film transistors (TFTs) is obtained by displacement current measurement (DCM) during device operation at temperatures ranging from 260 to 340 K. The carrier injection voltage at the source electrode (V_{inj}) was measured from the displacement current and found to be independent of temperature, suggesting an Ohmic contact at the Au source electrode/pentacene interface. On the contrary, the threshold voltage (V_{th}) depended on the temperature. The interface trap level at the pentacene/gate dielectric interface was estimated as 36 meV from the temperature dependence of the interface trap density. By using the DCM method, it becomes possible to demonstrate the carrier injection and transport properties of top-contact pentacene TFTs.
© 2009 Elsevier B.V. All rights reserved.

1. Introduction

The device operation of organic thin-film transistors (OTFTs) is described by carrier injection at the source and the drain electrodes/organic thin-film interface and carrier transport in the channel at the organic thin-film/gate dielectric interface [1–4]. In top-contact OTFTs, carrier sheet formation at the organic thin-film/gate dielectric interface under the source and drain electrodes is related to both the carrier injection and the carrier transport properties, because the injected carriers accumulate as the carrier sheet and are then transported through the channel. Therefore, simultaneously measuring the carrier injection and carrier transport properties of OTFTs is important from the viewpoint of their practical use. Carrier injection properties have been investigated by Kelvin probe microscopy [5–7], four-terminal measurement [8,9], and displacement current measurement (DCM) [10–13]. DCM is a direct method that is used to probe the carrier motion, and therefore, it has been used to study the carrier injection properties in organic semiconductors having electrode/organic thin-film/dielectric/electrode sandwiched structures [12,13]. Recently, we developed a DCM method for top-contact OTFTs that expands the conventional DCM method to three-terminal devices under OTFT device operation [14,15].

In this study, we examine the interface trap level by the DCM method in top-contact pentacene TFTs during device operation. The carrier injection voltage at the source electrode (V_{inj}) and threshold voltage (V_{th}) are evaluated at temperatures ranging from 260 to 340 K. The interface trap level at the pentacene/gate dielectric interface is evaluated from the temperature dependence of the interface trap density.

2. Experimental

A schematic diagram of the DCM for top-contact OTFTs is shown in Fig. 1. Because we have already provided a detailed description of DCM for top-contact OTFTs in our previous paper [14,15], we only provide a brief outline here. The displacement current (I_{dis}) and channel current (I_{DS}) are evaluated from simultaneously measured source (I_S) and drain (I_D) currents under the application of a triangular-wave gate voltage (V_{GS}) and a constant drain voltage

* Corresponding author.
E-mail address: majima@msl.titech.ac.jp (Y. Majima).
[1] Present address: Graduate School of Arts and Sciences, University of Tokyo, Komaba, Meguro, Tokyo 153-8902, Japan.

1566-1199/$ - see front matter © 2009 Elsevier B.V. All rights reserved.
doi:10.1016/j.orgel.2009.12.020

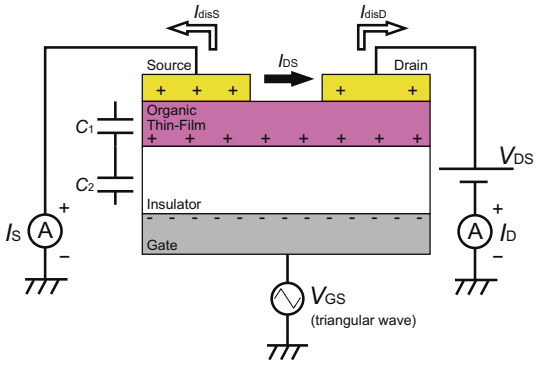

Fig. 1. Schematic diagram of displacement current measurements (DCMs) for top-contact organic thin-film transistors. Displacement current ($I_{dis} = I_{disS} + I_{disD}$) and channel currents ($I_{DS}$) are evaluated from simultaneously measured I_S and I_D under the application of a triangular-wave gate voltage (V_{GS}) and a constant drain voltage (V_{DS}). Capacitances C_1 and C_2 are the capacitance of the gate dielectric layer and the organic thin-film layer, respectively.

(V_{DS}). I_{dis} is obtained by differentiating the sum of the charges $Q_{S,D}$ that are stored on the source/drain electrodes $\sigma_{1S,1D}$ on the organic thin-film/gate dielectric interface $\sigma_{S,D}$ under the source/drain electrodes as

$$I_{dis} = -\frac{d(Q_S + Q_D)}{dt} = I_S + I_D, \tag{1}$$

where $Q_{S,D}$ are given by

$$\begin{aligned} Q_S &= (\sigma_{1S} + \sigma_S)S_S = \int_{t_S}^{t} (-I_S - I_{DS})dt, \\ Q_D &= (\sigma_{1D} + \sigma_D)S_D = \int_{t_D}^{t} (-I_D + I_{DS})dt. \end{aligned} \tag{2}$$

Here $S_{S,D}$ are the areas of the source/drain electrodes and $t_{S,D}$ is the time when $Q_{S,D}$ becomes zero. I_{dis} is re-expressed as

$$I_{dis} = -(C_S(t)S_S + C_D(t)S_D)\frac{dV_{GS}}{dt}, \tag{3}$$

where $C_{S,D}(t)$ is the effective capacitance between the gate electrode and the source/drain electrodes, respectively [15]. When the displacement current at the source electrode equals that at the drain electrode, I_{DS} is given by

$$I_{DS} = \frac{-I_S + I_D}{2}. \tag{4}$$

Pentacene OTFTs with an SiO_2/polyimide dual-gate dielectric structure were fabricated as follows [14–17]. An n^+-Si substrate was used as a gate electrode; SiO_2 (thickness: 90 nm, relative dielectric constant: $\varepsilon_r = 3.9$), was subsequently spin-coated on this substrate with a polyimide film (thickness: 40 nm, Nissan SUNEVER, Nissan Chemical Industries Ltd., Japan) [18,19]. Then, a pentacene thin-film (thickness: 30 nm, $\varepsilon_r = 3.2$, Sigma Aldrich, Japan) as an active electronic material was uniformly formed by physical vapor deposition through a shadow mask. Finally, source/drain gold electrodes were deposited by thermal evaporation through a shadow mask. The area of the pentacene thin-film was the same as the sum of the areas of the channel and source/drain electrodes, and the areas of the drain and source electrodes were both 8.9×10^{-3} cm^2. The channel length (L) was 11 μm, which was directly measured using an optical microscope, and the channel width (W) was 1.0 mm. The lengths (L_e) of the source and drain electrodes were both 0.89 mm, and the ratio of L/L_e was 1.2×10^{-2}. The displacement current is given by Eq. (1). The crystalline grain size of pentacene was measured to be 20–40 μm using a polarized optical microscope. Pentacene OTFTs were exposed to air after both the pentacene thin-film and gold source/drain electrodes were formed by evaporation. The pentacene OTFTs were annealed at 400 K for 9 h in nitrogen atmosphere before the measurements, and all measurements were conducted in nitrogen atmosphere. I_S and I_D were simultaneously measured using a digitizing storage oscilloscope (Hioki, 8855) under the application of a constant drain voltage (V_{DS}) and a triangular-wave gate voltage (V_{GS}) in the top-contact pentacene OTFTs. V_{GS} was applied as three cycles of triangular waves with an amplitude of 24 $V_{p\text{-}p}$ at 1 kHz. During all the measurements, V_{DS} was maintained at −12.9 V. Transfer curves were also measured using a conventional semiconductor parameter analyzer (Agilent 4156C). The measurements were performed at temperatures of 260, 280, 300, 320, and 340 K.

3. Results and discussion

Fig. 2 shows the experimental transfer curves (square-root of channel current ($\sqrt{I_{DS}}$) − V_{GS} and I_{dis} − V_{GS} characteristics) for temperatures ranging from 260 to 340 K. I_{DS} and I_{dis} were calculated from simultaneously measured I_S and I_D using Eqs. (1) and (4).

From the $\sqrt{I_{DS}} - V_{GS}$ characteristics in Fig. 2, the linear relationships between $\sqrt{I_{DS}}$ and V_{GS} were clearly observed, and the field-effect mobility μ and threshold voltage V_{th} were evaluated as 0.50, 0.60, 0.67, 0.78, and 0.97 cm^2/V s and −3.8, −3.4, −2.8, −2.3, and −0.69 V at temperatures of 260, 280, 300, 320, and 340 K, respectively. There existed peaks in the V_{GS} range between V_{th} and ~4 V at every temperature. This is because I_{disS} was not equal to I_{disD} in this V_{GS} range, as discussed in detail later.

Because carrier transport in the polycrystalline pentacene thin-film is thermally activated in the temperature range employed in this study, the field-effect mobility μ is given by $\mu = \mu_0 \exp(-\Delta/k_B T)$, where μ_0 is the prefactor field-effect mobility; Δ is the activation energy; and k_B is the Boltzmann constant [17]. Fig. 3 shows the Arrhenius plot of μ obtained from Fig. 2. The mobilities obtained by the two methods were identical at every temperature, and Δ was determined to be ~60 meV. This value is in good agreement with the reported value for the case of polycrystalline pentacene field-effect transistors [20].

From the $I_{dis} - V_{GS}$ characteristics in Fig. 2, I_{dis} had constant values of ±20 μA in the range of $-12 < V_{GS} < -7$ V and ±16 μA in the range of $5 < V_{GS} < 12$ V.

Because a pentacene thin-film acts as a p-type semiconductor, the carrier (hole) is fully injected from the interface of the pentacene/gold source and drain electrode at $V_{GS} = -12$ V, and the effective capacitance $C(t)$ in Eq. (3) consists of only the capacitance of the dual-gate dielectric

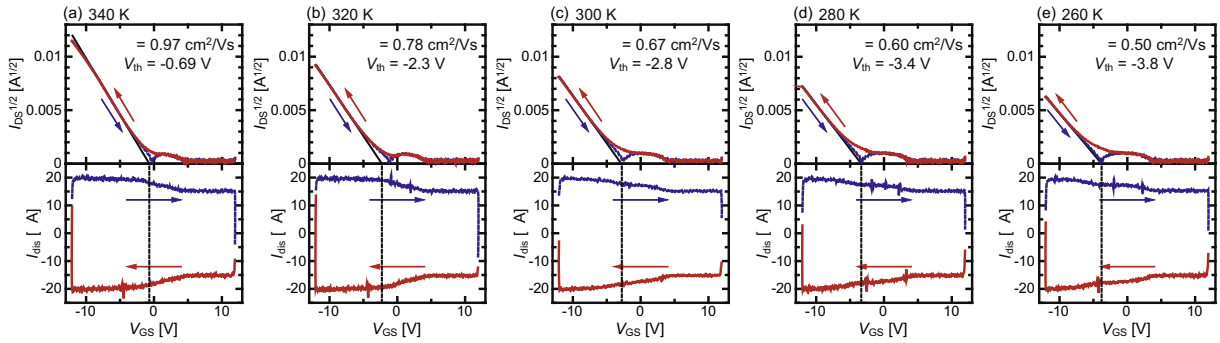

Fig. 2. Experimental $\sqrt{I_{DS}} - V_{GS}$ and $I_{dis} - V_{GS}$ characteristics at (a) 340, (b) 320, (c) 300, (d) 280, and (e) 260 K. Backward and forward gate voltage sweeps are plotted in red solid line and blue dashed line, respectively. (For interpretation of the references to colour in this figure legend, the reader is referred to the web version of this article.)

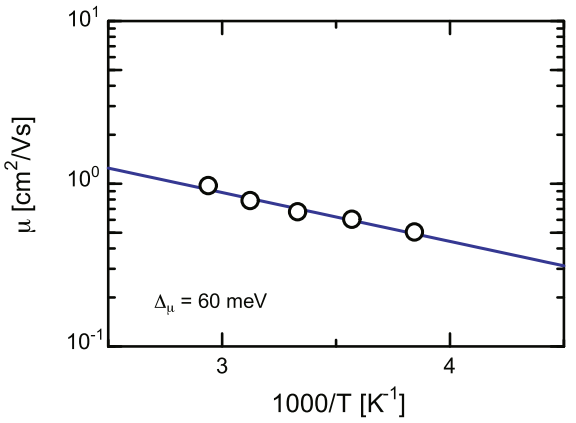

Fig. 3. Temperature dependence of field effect mobility μ.

layer (C_2). The calculated value of capacitance from the displacement current of 20 μA at $V_{GS} = -12$ V is 24 nF/cm^2, which is in good agreement with the theoretical capacitance C_2 of 25 nF/cm^2. On the other hand, the injection of carriers is inhibited in the range of $V_{GS} > V_{inj}$. In this case, the effective capacitance $C(t)$ is the series capacitance of the pentacene thin-film layer C_1 and C_2. The capacitance evaluated from the displacement current of 16 μA is 18 nF/cm^2; this value, too, corresponds well with the theoretical capacitance of $(1/C_1 + 1/C_2)^{-1} = 20$ nF/cm^2.

On comparing the temperature dependence of the $I_{dis} - V_{GS}$ characteristics shown in Fig. 2, different slopes were observed where the displacement current increases in the range $-3 < V_{GS} < 5$ V on the backward bias sweep; the slope increased at lower temperatures, and in particular, a two-step increase in I_{dis} was observed at 280 and 260 K for $-8 < V_{GS} < -4$ V and $-2 < V_{GS} < 4$ V, respectively. This discrepancy can be explained as follows.

Fig. 4 shows the temperature dependence of the $(I_S - I_c)$, $(I_D - I_c)$, and $(I_S - I_D)$ relationships in the backward bias sweeps of V_{GS}, where I_c is the displacement current at the source or drain electrode due to the series capacitance of the pentacene thin-film and the dual-gate dielectric of $(1/C_1 + 1/C_2)^{-1}$. $(I_S - I_c)$ begins increasing at a certain voltage corresponding to the charge injection voltage at the source electrode, V_{inj}, as indicated in each figure. V_{inj} is larger than V_{th}; therefore, the increase in I_S is attributed to carrier injection at the source electrode [14,15]. V_{inj} was evaluated to be 4.1, 4.5, 4.5, 4.4, and 4.6 V at 260, 280, 300, 320, and 340 K, respectively. The positive values of V_{inj} suggest that the gate dielectric is negatively charged.

Note that both V_{inj} and the shapes of I_S for $V_{th} < V_{GS} < V_{inj}$ were independent of temperature. Therefore, the interface of the pentacene thin-film and the Au source electrode interface was believed to be an Ohmic contact. A carrier sheet was formed smoothly at the interface between the pentacene and the gate dielectric below the source electrode at every temperature for $V_{GS} < V_{inj}$. Therefore, the carrier is ready to transport at the channel for $V_{GS} < V_{inj}$.

On the other hand, carrier sheet formation below the drain electrode is delayed and it has a temperature dependence because the $(I_D - I_c)$ relationship exhibited a temperature dependence; in Fig. 4, peaks appeared at around V_{th} at temperatures of 340 and 320 K, but no peaks were observed at lower temperatures. Because the direction of the displacement current at the drain electrode is negative and the channel current is positive, the peak around V_{th} in the $(I_D - I_c)$ relationship is due to the displacement current at the drain electrode side. At higher temperatures (320 and 340 K), the carrier sheet below the drain electrode spread faster than that at temperatures lower than 300 K. In Fig. 2, a two-step increase in I_{dis} was clearly observed at low temperatures. These results correspond well with the slow spread of the carrier sheet under the drain electrode.

The interface trap level is evaluated as follows. The temperature dependence of V_{th} and V_{inj} are shown in Fig. 5a. When there exists an interface trap at the channel, the interface trap densities directly depend on the threshold voltage and carrier injection voltage [21,22]. As carriers accumulate at the source electrode edge at $V_{GS} = V_{inj}$, the effective interface trap density is given by

$$\Delta N = \frac{C_2}{q}(-V_{th} + V_{inj}), \tag{5}$$

where q is the unit charge. The temperature dependence of the effective interface trap density is given by

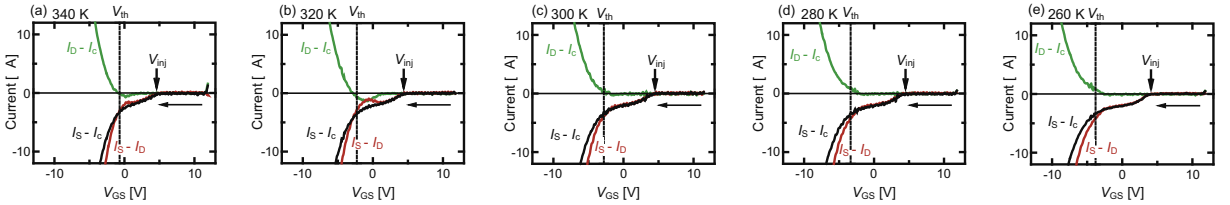

Fig. 4. Experimental $(I_S - I_c)$, $(I_D - I_c)$, and $(I_S - I_D)$ relationships in backward V_{GS} sweep, where I_c is the displacement current at the source or drain electrode due to the series capacitance of the pentacene thin-film and the dual-gate dielectric of $(1/C_1 + 1/C_2)^{-1}$ ($I_c = -7.6$ μA).

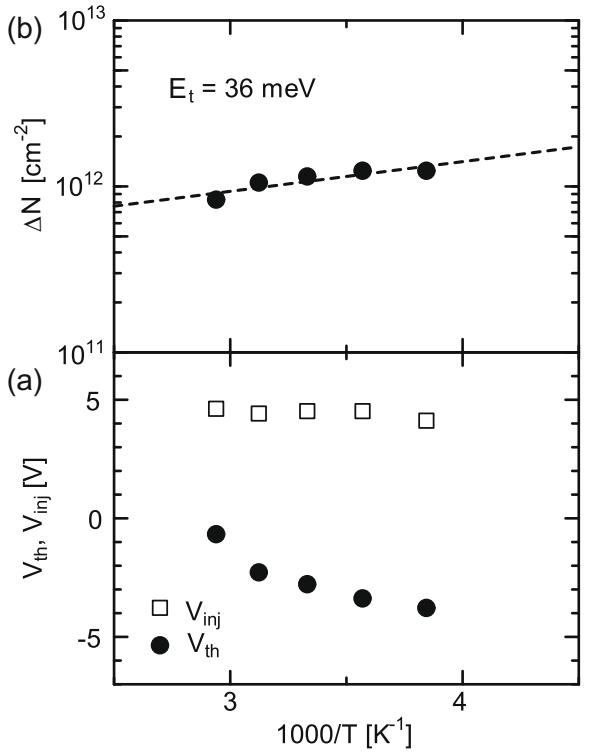

Fig. 5. (a) Temperature dependence of carrier injection voltage (V_{inj}) and threshold voltage (V_{th}). (b) Temperature dependence of effective interface trap density $\left(\Delta N = \frac{C_2}{q}(-V_{th} + V_{inj})\right)$.

$$\Delta N = N_t e^{\frac{E_t}{kT}}, \tag{6}$$

where N_t is the total concentration of the interface trap and E_t, the interface trap level [23]. Fig. 5b shows the temperature dependence of ΔN. From the slope of Fig. 5a, E_t is obtained as 36 meV, suggesting that a shallow interface trap exists at the interface between the pentacene and the gate dielectric. It should be noted that E_t is of the same order as the activation energy of the mobility (60 meV). The effect of the shallow interface trap appears only in the subthreshold region; however, it affects the closing of the channel and subthreshold swing. Consequently, the threshold voltage shift is due to the shallow interface trap, and a constant V_{inj} is due to Ohmic contact. These results provide us with information that can be used to understand the carrier injection and transport properties of top-contact pentacene TFTs.

4. Conclusions

The interface trap level in top-contact pentacene TFTs is demonstrated from the temperature dependence of the interface trap density as the difference between the threshold voltage and carrier injection voltage at the source electrode. The interface trap level has been evaluated as 36 meV, suggesting that the threshold voltage shift is due to a shallow interface trap. For the development of OTFTs, DCM for top-contact OTFTs is a simple and powerful technique to understand the carrier transport properties and carrier injection properties.

Acknowledgments

This study is partially supported by the Emergence of Highly Elaborated π-space and its Function; Grants-in-Aid for Scientific Research on Innovative Areas, MEXT, Japan; and the World Class University Program, Sunchon National University, Korea. One of the authors (S.S.) is supported as a JSPS research fellow.

References

[1] G. Horowitz, Adv. Mater. 10 (1998) 365–377.
[2] H. Sirringhaus, Adv. Mater. 17 (2005) 2411–2425.
[3] Y. Fujisaki, H. Sato, H. Fujikake, Y. Inoue, S. Tokito, T. Kurita, Jpn. J. Appl. Phys., Part 1 44 (2005) 3728–3732.
[4] K. Ueno, A. Abe, R. Onoki, K. Saiki, J. Appl. Phys. 98 (2005) 114503-1–114503-5.
[5] L. Bürgi, H. Sirringhaus, R.H. Friend, Appl. Phys. Lett. 80 (2002) 2913–2915.
[6] J.A. Nichols, D.J. Gundlach, T.N. Jackson, Appl. Phys. Lett. 83 (2003) 2366–2368.
[7] K.P. Puntambekar, P.V. Pesavento, C.D. Frisbie, Appl. Phys. Lett. 83 (2003) 5539–5541.
[8] V. Podzorov, S.E. Sysoev, E. Loginova, V.M. Pudalov, M.E. Gershenson, Appl. Phys. Lett. 83 (2003) 3504–3506.
[9] I. Yagi, K. Tsukagoshi, Y. Aoyagi, Appl. Phys. Lett. 84 (2004) 813–815.
[10] S. Egusa, N. Gemma, A. Miura, K. Mizushima, M. Azuma, J. Appl. Phys. 71 (1992) 2042–2044.
[11] S. Egusa, A. Miura, N. Gemma, M. Azuma, Jpn. J. Appl. Phys. 33 (1994) 2741–2745.
[12] S. Ogawa, Y. Kimura, H. Ishii, M. Niwano, Jpn. J. Appl. Phys. 42 (2003) L1275–L1278.
[13] S. Ogawa, T. Nijo, Y. Kimura, H. Ishii, M. Niwano, Appl. Phys. Lett. 86 (2005) 252104-1–252104-3.
[14] S. Suzuki, Y. Yasutake, Y. Majima, Jpn. J. Appl. Phys. 47 (2008) 3167–3169.
[15] Y. Majima, D. Kawakami, S. Suzuki, Y. Yasutake, Jpn. J. Appl. Phys. 46 (2007) L390–L393.
[16] H. Nishizawa, Y. Majima, Jpn. J. Appl. Phys. 45 (2006) L27–L29.
[17] D. Kawakami, Y. Yasutake, H. Nishizawa, Y. Majima, Jpn. J. Appl. Phys. 45 (2006) L1127–L1129.
[18] K.N. Narayanan Unni, S. Dabos-Signon, J.-M. Nunzi, J. Phys. D: Appl. Phys. 38 (2005) 1148–1151.

[19] J. Han, Z. Tan, K. Sato, M. Shikida, J. Micromech. Microeng. 14 (2004) 38–48.
[20] T. Minari, T. Nemoto, S. Isoda, J. Appl. Phys. 99 (2006) 034506-1–034506-5.
[21] P.J. McWhorter, P.S. Winokur, Appl. Phys. Lett. 48 (1986) 133–135.
[22] A. Bolognesi, M. Berliocchi, M. Manenti, A.D. Carlo, P. Lugli, K. Lmimouni, C. Dufour, IEEE Trans. Electron Dev. 51 (2004) 1997–2003.
[23] M.M. Mandoc, B. de Boer, G. Paasch, P.W.M. Blom, Phys. Rev. B 75 (2007) 193202-1–193202-4.

Organic Electronics 11 (2010) 599–603

Contents lists available at ScienceDirect

Organic Electronics

journal homepage: www.elsevier.com/locate/orgel

Active layer transfer by stamping technique for polymer solar cells: Synergistic effect of TiO_x interlayer

Dong Hwan Wang [a], Dae Geun Choi [b,*], Ki-Joong Lee [b], O. Ok Park [a,*], Jong Hyeok Park [c,*]

[a] Department of Chemical and Biomolecular Engineering (BK21 Graduate Program), Interdisciplinary Program for Polymers, Korea Advanced Institute of Science and Technology, 335 Gwahangno, Yuseong-gu, Daejeon 305-701, Republic of Korea
[b] Nano-Mechanical Systems Research Division, Korea Institute of Machinery & Materials (KIMM), 104, Jang-dong, Yuseong-gu, Daejeon 305-343, Republic of Korea
[c] Department of Chemical Engineering, Sungkyunkwan University, Suwon 440-746, Republic of Korea

ARTICLE INFO

Article history:
Received 27 October 2009
Received in revised form 24 December 2009
Accepted 27 December 2009
Available online 4 January 2010

Keywords:
Stamping technique
Photovoltaic devices
UV-curable resin
TiO_x interlayer

ABSTRACT

Several groups reported fabrication method of organic solar cells through a stamping technique by using PDMS mold. Although PDMS is a good stamp material, they have several problems in polymer transfer printing, especially when we use organic solvent (easily swollen). In this study, the polymer solar cells with an active layer of BHJ are successfully prepared via a simple imprinting transfer technique with help of UV-curable resin-coated polycarbonate (UV-PC) film. The transferred BHJ active layer from UV-PC film was perfectly retained at 220-nm thick on top of the PEDOT:PSS-coated ITO glass, and the device showed enhanced J_{sc} and device performance up to 3.19% after insertion of the TiO_x interlayer between the active layer and Al cathode. This unique imprinting transfer can be considered as an alternative approach to replace the spin-coating when the matters, pre-coated layers are affected by the solvent for next layer.

© 2010 Elsevier B.V. All rights reserved.

1. Introduction

Photovoltaic (PV) devices based on thin films from [6,6]-phenyl C61-butyric acid methyl ester (PCBM) and conjugate polymers of bulk-heterojunction (BHJ) have been extensively studied throughout the world due to their great potential applicability and the advantages of easy solution processability. They can be used as a flexible devices over large areas since solution-processable organic materials are adapted [1–6]. BHJ is considered more efficient than corresponding bilayer devices, since it would offer a high interfacial contact area between the donor and acceptor from the charge separation point of view. Thus BHJ make it possible to enhance charge carrier mobility, resulting in an increase of photocurrent density of polymer based PVs [7–10]. Recently, it is very common to use a single spin-coating process to prepare BHJ active layer. However, it is not proper to use the spin-coating process not only to fabricate photovoltaic modules with large areas but also to deposit the BHJ active layer to specific regions of the substrate [11,12].

Recently, Chu and Ho's group reported fabrication method for organic solar cells through a stamping technique [13]. Even though they used non-destructive solvent treatment method to spin-coat BHJ film on the top of PDMS surface this technique is still time-consuming process. In this study, it will be demonstrated that the active layer of BHJ polymer solar cells can be prepared via a simple transfer of active layer by stamping technique by using Norland Optical Adhesive 63 UV-curable resin based stamp without any surface pre-treatment. The BHJ film prepared from the imprinting transfer process has enough uniformity due to following fairly smooth silicon wafer substrate that it is comparable to with that from the spin-coating process.

* Corresponding authors.
E-mail addresses: lamcdg@kimm.re.kr (D.G. Choi), ookpark@kaist.ac.kr(O.O. Park), lutts@skku.edu (J.H. Park).

1566-1199/$ - see front matter © 2010 Elsevier B.V. All rights reserved.
doi:10.1016/j.orgel.2009.12.022

2. Experimental details

BHJ polymer solar cells from an imprinting technique with a UV-curable resin-coated polycarbonate (UV-PC) film were prepared sequentially by making the UV-curable film and fabricating the device. Fig. 1 shows the schematic diagram of the proposed device structure via active layer transfer by stamping technique with UV-PC film. First, a cleaned silicon wafer was treated by Trichloro-(1H,1H,2H,2H-perfluorooctyl) silane (FOTS) to reduce the surface energy, and then the self assembled monolayers (SAMs) were created to perform the imprinting process [14]. Norland Optical Adhesive 63 UV-curable resin was dropped on the flexible PC film and flattened with a common roller. Then the PC film was cured by UV and the silicon wafer was detached. The UV-PC film with very uniform morphology was realized and the maximum size was only dependent on the area of used silicon wafer. Fig. 2(a) shows the photograph of the UV-PC film. The active layer of BHJ composed of P3HT and PCBM from the chlorobenzene was spin-coated 900 rpm for 5 s of 220 nm thickness on the UV-PC film. Since the total UV-PC film has a few millimeter thickness, the UV-PC film can act as a well supporting substrate during the spin-coating process. Note that even though the spin-coating method was used to cover the active BHJ film on the UV-PC film as a model case in this study, the BHJ film can be also formed by spread method or spray method, both of which are suitable for the roll-to-roll process. Secondly, ITO glass was washed by organic solvents chloroform, acetone, and isopropanol to remove residual impurities. It was then exposed to oxygen plasma treatment for 10 min to reform the ITO surface. A hole transporting materials that is widely known for conducting polymer, poly(3,4-ethylene dioxythiophene:poly(styrene sulfonate) (PEDOT:PSS, Baytron P), was spin-coated up to ~40-nm thickness on the ITO. The PEDOT:PSS-coated ITO was thermal treated using a digital controllable hotplate for 5 min at 200 °C to evaporate the water. Then BHJ was transferred from the PC film to the continuously heated PEDOT:PSS-coated ITO substrate on a hotplate at 90 °C (Fig. 1). The UV-PC film with the active layer was attached to the heated substrate as shown in Fig. 2(c) and rubbed with cotton swabs to induce uniform force until the coated active layer from the UV-PC film was adhered to the heated substrate. The coated active layer from the UV-PC film was transferred to the PEDOT:PSS-coated ITO easily and reproducibly, when the stamping process was conducted with simple physical force at suitable temperature. After detaching the UV-PC film, the entirely transferred active layer onto the PEDOT:PSS-coated ITO could be observed as shown in Fig. 2(d). Then, the spin-coated TiO_x interlayer with ~3-nm thick was added on the active layer to increase the device performance [15]. Polymer solar cells as a reference device were prepared by the following steps. A spin-coated BHJ device with a solution consisting of poly(3-hexylthiophene)/[6,6]-phenyl C61-butyric acidmethyl ester (P3HT/PCBM) at a ratio of 1:0.6, the same as the former imprinting transferred BHJ film, was spin-coated on the top of PEDOT:PSS-coated ITO substrate that was washed

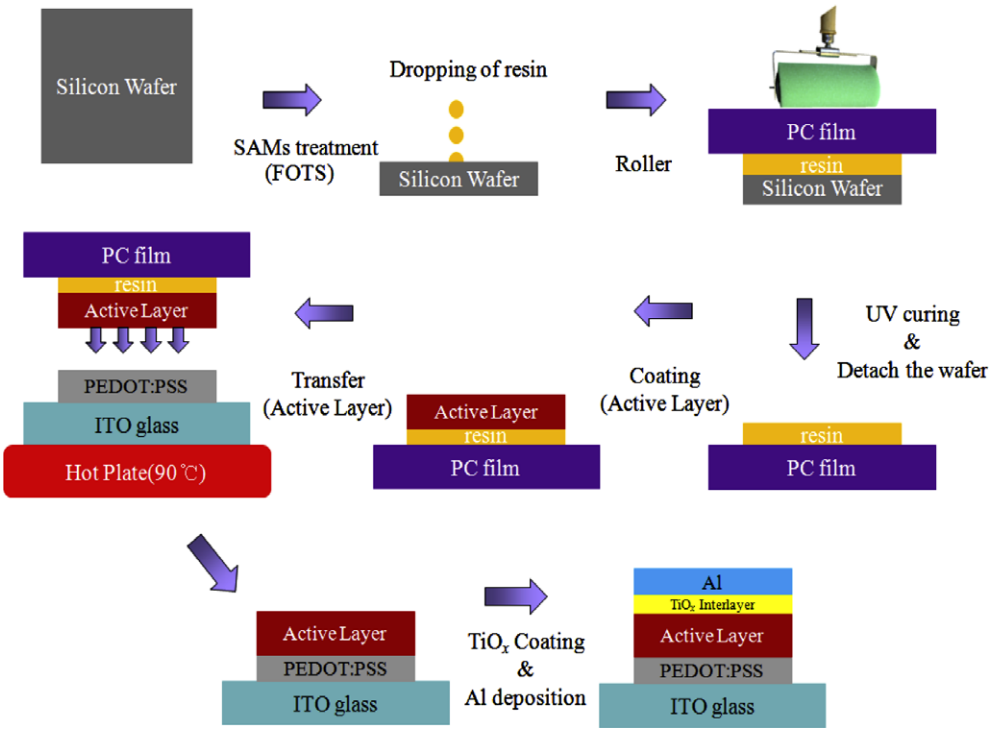

Fig. 1. Schematic diagram of the proposed device structure via an active layer transfer by stamping technique of the BHJ with a UV-curable resin-coated polycarbonate film.

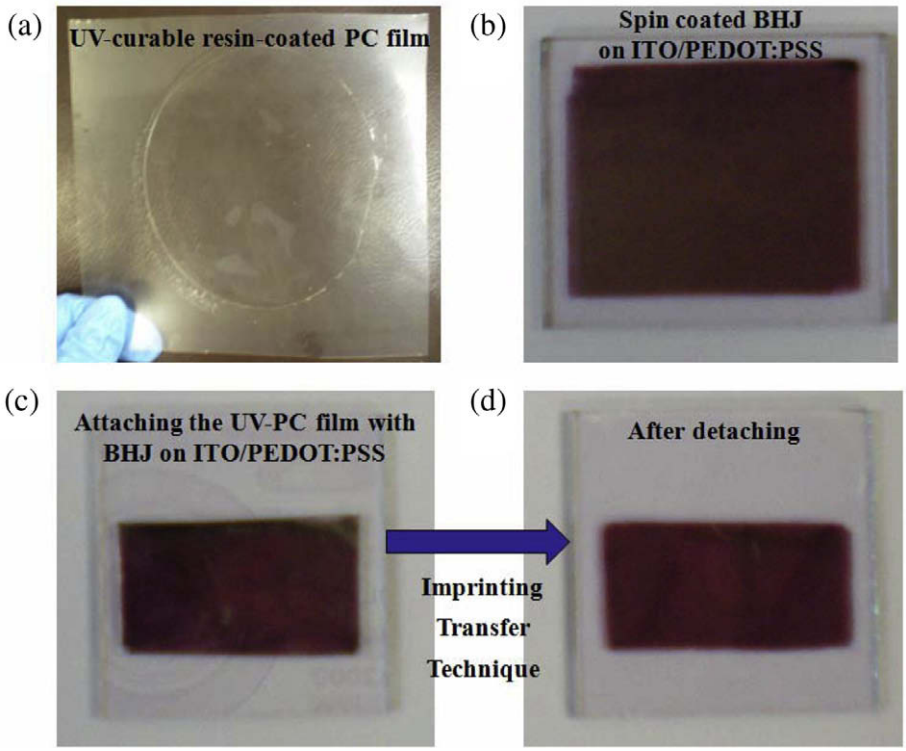

Fig. 2. (a) UV-curable resin-coated polycarbonate film, (b) spin-coated BHJ active layer on ITO/PEDOT:PSS substrate, (c) attaching the UV-PC film with BHJ active layer on ITO/PEDOT:PSS substrate, and (d) after detaching the UV-PC film with BHJ active layer on ITO/PEDOT:PSS substrate.

by the proper cleaning process. Next, TiO_x interlayer with ~3-nm thickness was added on the active layer with 2500 rpm for 30 s. Subsequently, an Al metal electrode with a 150 nm thickness was uniformly deposited under a pressure of 1.6×10^{-6} torr by thermal evaporator. Thermal annealing process was executed by directly placing the fabricated devices on a hotplate at 150 °C for 30 min. The active area device with the deposited Al electrode was confirmed in the range of 3–6 mm^2 by video microscope (SV-35). The photocurrent (J)–potential (V) curves were measured using a Oriel 91193, a 1000 W xenon lamp that served as the light source to the device. Its intensity was calibrated using a silicon reference cell (Fraunhofer ISE, Certificate No. C-ISE269) with an illumination rating of AM 1.5 by using a Keithley 2400 source measure unit.

3. Results and discussion

In order to confirm the morphologies of the device's BHJ, we investigated the AFM (Atomic Forced Microscope) images as shown in Fig. 3, which demonstrate the changing of surface morphology. Fig. 3(a) shows the spin-coated BHJ top-surface of 220-nm thick after the post annealing process. The RMS (root mean square surface roughness) value of the spin-coated BHJ surface is 17.1 nm. Fig. 3(c) shows the surface morphology of imprinting transferred BHJ film of 220-nm thick after the post annealing process. Interestingly, the RMS value of the imprinted BHJ is much lower as 2.2 nm. Fig. 4 shows the photocurrent (J)–potential (V) curves of devices with spin-coated BHJ film and imprinting transferred BHJ film. The spin-coated BHJ cell exhibits a conversion efficiency of 2.51%, whereas the imprinted BHJ cell exhibits 2.22%. In comparison to the spin-coated BHJ or imprinted BHJ, the short-circuit current (J_{sc}) decreased from 8.58 to 7.17 mA/cm^2, and the fill factor was not significantly changed, from 0.51 to 0.52. The decreased overall cell performance in the case of the imprinting method might be attributed to the lower surface roughness of the transferred active layer, which decreased the contact area between Al and the active layer. More roughened surface contacted with Al cathode can increase the cell performances [17]. On the other hand, the open circuit voltage (V_{oc}) of the imprinted BHJ cell increased from 0.57 to 0.60 since the smoother surface morphology leads to reduced series resistance at the BHJ/cathode interface and also better interfacial contact between ITO and BHJ from providing the regular force of the rubbing process [16]. Recently, our group showed that TiO_x interlayer inserted between the active layer and a metal cathode can enhance electron harvesting efficiency due to the more enhanced interfacial contact quality [16,18]. Fig. 4 also shows the J–V curves of devices prepared from two different methods with TiO_x interlayer. The spin-coated BHJ with TiO_x cell showed increased performance up to 2.98%. The critical factor of the increased efficiency was J_{sc}. The J_{sc} value of the spin-coated BHJ is 8.58 mA/cm^2 while the spin-coated BHJ with the TiO_x interlayer shows 9.14 mA/cm^2. The

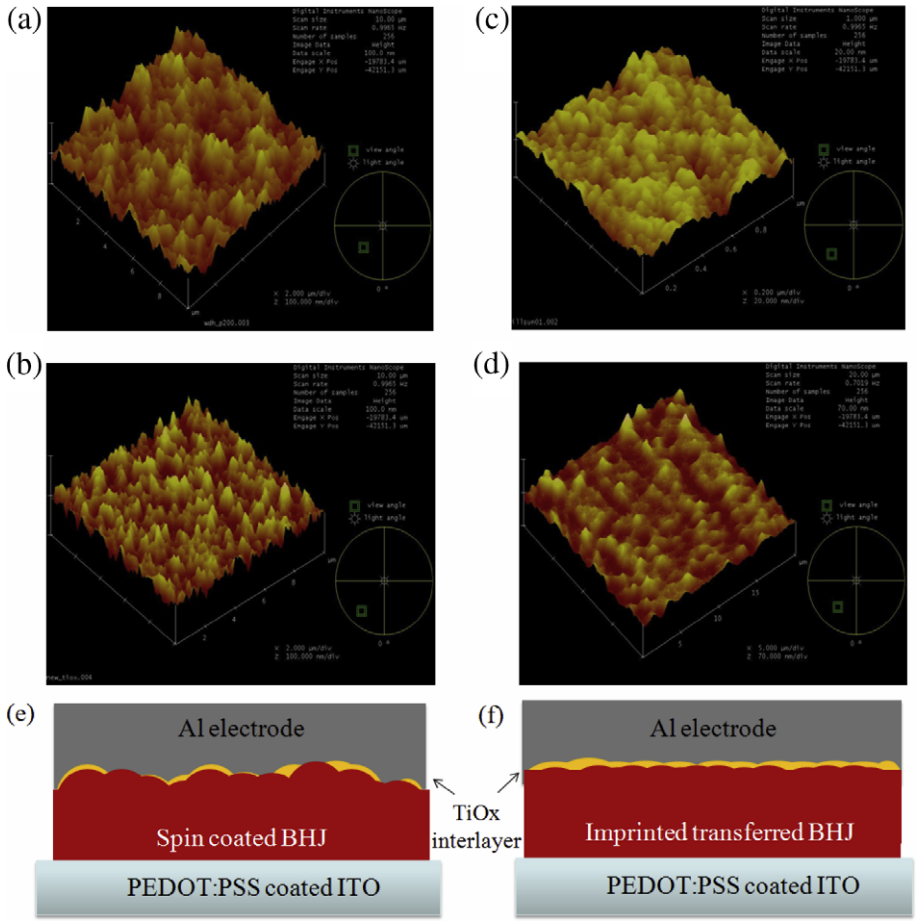

Fig. 3. (a) AFM 3D images of the spin-coated BHJ, (b) AFM 3D images of the spin-coated BHJ with TiO_x interlayer, (c) AFM 3D images of the imprinted transferred BHJ using UV-curable resin-coated polycarbonate film, (d) AFM 3D images of the imprinted transferred BHJ with TiO_x interlayer using UV-curable resin-coated polycarbonate film, (e) whole device sequential inner structure of spin-coated BHJ with TiO_x interlayer on the PEDOT:PSS-coated ITO, and (f) whole device sequential inner structure of imprinted transferred BHJ with TiO_x interlayer on the PEDOT:PSS-coated ITO.

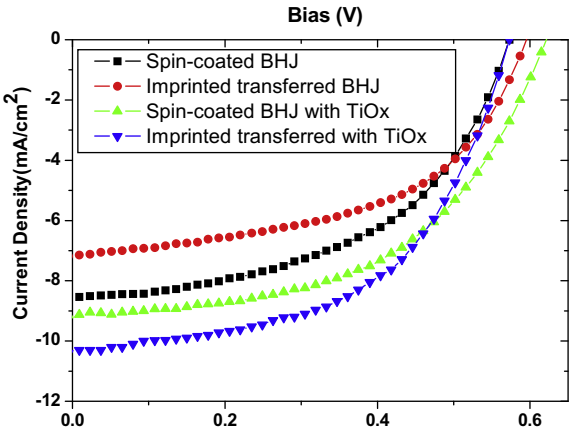

Fig. 4. *J–V* curves of devices with spin-coated BHJ or spin-coated BHJ with TiO_x and imprinted transferred BHJ or imprinted transferred BHJ with TiO_x interlayer. (-■- Spin-coated BHJ, -●- Imprinted transferred BHJ, -▲- Spin-coated BHJ with TiO_x interlayer, -▼- Imprinted transferred BHJ with TiO_x interlayer).

photocurrent value of the device with imprinting transferred BHJ is 7.17 mA/cm^2 while the imprinted transferred BHJ with the TiO_x interlayer shows 10.34 mA/cm^2 and 3.19%. Therefore, it suggests improved charge carrier harvesting since the TiO_x interlayer can serve a special role of hole blocking and as an electron transporting layer [15,18,19]. Interestingly, the effect of the TiO_x interlayer in the transferred system was much stronger than that of the spin-coated system. Generally, the effects of the TiO_x interlayer have been influenced by its thickness. Yoshikawa group reported that the conductivity of TiO_x is strongly influenced by its thickness [20]. Even though inserted TiO_x have shown various positive effects on cell performance and long-term stability the conductivity of 50-nm thick TiO_x film decreased to 1/5 value of 10-nm thick TiO_x film. Park's group and Yoshikawa group reposted the optimum thickness of TiO_x layer was between 3 and 5 nm [15,20]. As can be seen in Figs. 3(b) and S3, the RMS of the spin-coated BHJ surface with TiO_x interlayer is 13.4 nm, whereas, the imprinting transferred BHJ with TiO_x interlayer from Fig. 3(d) is 5.851 nm. When the surface roughness of the spin-coated systems with and without TiO_x

interlayer was compared, the surface roughness of the active film decreased after the insertion of the TiO_x interlayer. This means that the undulation surface might be covered by the TiO_x interlayer, and the thickness of the inserted TiO_x layer is not uniformed too, because the thin TiO_x layer is coated by following the pre-coated fluctuated active layer surface, as shown in Fig. 3(e). However, the morphology of imprinting transferred BHJ shows much lower RMS value, which means it had nearly flat surfaces due to the imprinting of the rubbing process. As shown in Fig. 3(f), this flat surface would help the formation of more uniform thickness of the TiO_x interlayer resulting in maximization of its positive functions. Therefore, we believe that this uniform surface morphology of the active layer prepared from the transfer by stamping technique can have more positive characteristics when the technique is combined with the TiO_x interlayer system.

4. Conclusions

It has been successfully demonstrated that the polymer solar cells with transferred BHJ film can be fabricated via a simple active layer transfer by stamping technique with help of a UV-curable resin-coated polycarbonate film. Due to the UV-curable resin that is not soluble in the organic solvent chlorobenzene, the BHJ film was coated on the flexible polymer substrate and then successfully transferred to the heated PEDOT:PSS-covered ITO glass substrate with smother surface. After inserting the TiO_x interlayer, the imprinting transferred BHJ device shows higher J_{sc} and better performance compared to the device with a spin-coated BHJ with TiO_x interlayer. This method will serve to the meaningful application of polymer solar cells fabricated by the imprinting process.

Acknowledgements

This work was supported by WCU (World Class University) program through the National Research Foundation of Korea funded by the Ministry of Education, Science and Technology (R32-2008-000-10142-0). This research was also partially supported by Basic Science Research Program through the National Research Foundation of Korea (NRF) funded by the Ministry of Education, Science and Technology (2009-0083540). One of the authors of KIMM (Choi) acknowledges the support from a grant (M102KN010001-08K1401-00210) from CNMM.

Appendix A. Supplementary data

Supplementary data associated with this article can be found, in the online version, at doi:10.1016/j.orgel.2009.12.022.

References

[1] M.K. Riede, T. Mueller, B. Maennig, K. Leo, K.O.S. Hvid, B. Zimmermann, M. Niggemann, A. Gombert, Appl. Phys. Lett. 92 (2008) 076101.
[2] A.J. Heeger, Angew. Chem. Int. Ed. 40 (2009) 2591.
[3] B.C. Thompson, J.M. Frechet, J. Angew. Chem. Rev. 47 (2008) 58.
[4] G. Dennler, M.C. Scharber, C.J. Brabec, Adv. Mater. 21 (2009) 1.
[5] C.J. Brabec, N.S. Sariciftci, J.C. Hummelen, Adv. Funct. Mater. 11 (2001) 15.
[6] J. Peet, M.L. Senatore, A.J. Heeger, Adv. Mater. 21 (2009) 1521.
[7] D.H. Wang, H.K. Lee, D.G. Choi, J.H. Park, O.O. Park, Appl. Phys. Lett. 95 (2009) 043505.
[8] P.W.M. Blom, V.D. Mihailetchi, L.J.A. Koster, D.E. Markov, Adv. Mater. 19 (2007) 1551.
[9] A.J. Moulé, K. Meerholz, Adv. Mater. 20 (2008) 240.
[10] M.C. Scharber, D. Mühlbacher, M. Koppe, P. Denk, C. Waldauf, A.J. Heeger, C.J. Brabec, Adv. Mater. 18 (2006) 789.
[11] T. Aernouts, T. Aleksandrov, C. Girotto, J. Genoe, J. Poortman, Appl. Phys. Lett. 92 (2008) 033306.
[12] V. Marin, E. Holder, M.M. Wienk, E. Tekin, D. Kozodaev, U.S. Schubert, Macromol. Rapid Commun. 26 (2005) 319.
[13] J.H. Huang, Z.Y. Ho, T.H. Kuo, D. Kekuda, C.W. Chu, K.C. Ho, J. Mater. Chem. 19 (2009) 4077.
[14] D.G. Choi, J.H. Jeong, Y.S. Shim, E.S. Lee, W.S. Kim, B.S. Bea, Langmuir 21 (2005) 9390.
[15] D.H. Wang, S.H. Im, H.K. Lee, J.H. Park, O.O. Park, J. Phys. Chem. C 113 (2009) 17286.
[16] C.J. Brabec, A. Cravino, D. Meissner, N.S. Sariciftci, T. Fromherz, M.T. Rispens, L. Sanchez, J.C. Hummelen, Adv. Funct. Mater. 11 (2001) 374.
[17] L. Han, N. Koide, Y. Chiba, A. Islam, R. Komiya, N. Fuke, A. Fukui, R. Yamanaka, Appl. Phys. Lett. 86 (2005) 213501.
[18] S.J. Yoon, J.H. Park, H.K. Lee, O.O. Park, Appl. Phys. Lett. 92 (2008) 143504.
[19] S.J. Park, A. Roy, S. Beaupre', S. Cho, N. Coates, J.S. Moon, D. Moses, M. Leclerc, K.H. Lee, A.J. Heeger, Nat. Photonics 3 (2009) 297.
[20] A. Hayakawa, O. Yoshikawa, T. Fujieda, K. Uehara, S. Yoshikawa, Appl. Phys. Lett. 90 (2007) 163517.

Organic Electronics 11 (2010) 604–612

Contents lists available at ScienceDirect

Organic Electronics

journal homepage: www.elsevier.com/locate/orgel

Asymmetric indolylmaleimides as non-dopant type red color emitting dyes

Ying-Shin Lee [a], Zhenghuan Lin [b,d], Yu-Yuan Chen [c], Ching-Yang Liu [c], Tahsin J. Chow [d,*]

[a] Department of Chemistry, National Central University, Jhongli, Taoyuan 300, Taiwan
[b] Department of Chemistry and Engineering, Huanghuai University, Zhumadian 463000, PR China
[c] Department of Applied Chemistry, Chinese Culture University, Taipei 111, Taiwan
[d] Institute of Chemistry, Academia Sinica, Taipei 105, Taiwan

ARTICLE INFO

Article history:
Received 1 September 2009
Received in revised form 28 December 2009
Accepted 29 December 2009
Available online 4 January 2010

Keywords:
Indolylmaleimide
Charge transfer emission
Non-dopant
Red luminescence
OLED

ABSTRACT

The photophysical properties of asymmetric indolylmaleimide derivatives (**4a–4f**) with a variety of aryl substituents at C(4) were analyzed. Their absorption spectra vary in the region of aryl substituents, whereas their emission spectra are nearly identical. The red emission is derived from a charge transfer transition along the indole-maleimide chromophore, which is not significantly disturbed by the introduction of a nearby aryl substituent at C(4). All compounds displayed intensive emissions both in solutions as well as in the form of solid films. Light emitting diodes (LED) were fabricated successfully by using the neat film of these materials as emitters. The performance of devices among the series varied slightly as a result of different film morphology. The best performance was found on the compound with a pyrene substituent, which exhibited optimal external quantum efficiency of 1.1%. This device could be turned on at 4 V and reached to optimal brightness of 9750 cd/m^2. The red color, according to the Commission Internationale de l'Eclairage (CIE) coordinates at (0.65, 0.34), was very close to pure red (0.67, 0.33).

© 2009 Elsevier B.V. All rights reserved.

1. Introduction

In the past decades active research investigations in bis-indolylmaleimides have revealed that these derivatives may exhibit multidisciplinary functionalities on diversified applications, such as biological activities for pharmaceutical applications [1] and luminescent properties for making organic light emitting diodes (OLEDs), etc. The structure of maleimides expresses a twofold symmetry when both substituents on the olefinic carbons are identical. Remarkable performances utilizing such type of symmetrical compounds as red color emitters in OLEDs have been done by Chow and Chen et al. [2,3]. It has been recognized, however, that maleimides containing a single substituent at C(3) may exhibit distinctively different physical properties from those of the symmetrical ones [4]. Through our works we have found that the characteristic red emission deriving from the asymmetrical derivatives is nearly as intensive as those of the symmetrical ones. The mono-substituted maleimide derivatives provide us an extra flexibility for modifying the structure of the second substituent at C(4), so that a tuning mechanism may be developed on this site. Either the chromaticity or intensity of the luminescence may become adjustable by the control of the second substituent. Report on unsymmetrical maleimides in this regard is not known to date, except a limited number of publications focusing on certain special pharmaceutical effects [5].

In this report a serial of asymmetric indolylmaleimide derivatives, in which an aromatic group is attached at C(4), are prepared. Their physical properties are discussed with a particular attention on their photo and electroluminescence (EL) characteristics. Maleimides are among the rare materials, which display intensive red emission even in the solid state, e.g., either in crystalline form or as neat film. Their high quantum efficiencies are attributed to their ready formation of an amorphous phase with a high glass-transition temperature. The asymmetric indolylmaleimides are expected to perform in a similar manner.

* Corresponding author. Tel.: +886 2 27898552; fax: +886 2 27884179.
E-mail address: tjchow@chem.sinica.edu.tw (T.J. Chow).

1566-1199/$ - see front matter © 2009 Elsevier B.V. All rights reserved.
doi:10.1016/j.orgel.2009.12.025

Successful fabrication of LEDs with these materials will light up a way toward future designs in luminescence sensors. A typical device made of asymmetric indolylmaleimide with a pyrene substituent, as shown in this report, can be turned on at 4.0 V with maximal intensity close to 10^4 cd/m^2.

2. Experimental section

2.1. General

Absorption spectra were taken on a Hewlett–Packard 8453 spectrophotometer and emission spectra on a Hitachi F-4500 fluorescence spectrophotometer. Infrared spectra were taken on a Perkin–Elmer L118-F000 FT-IR spectrometer. ^{1}H and ^{13}C NMR spectra were recorded on Bruker AV400, AV500, and AMX400 superconducting FT spectrometers. The signal of tetramethylsilane at δ 0.00 was used as an internal standard for both. Microanalyses were completed on a Perkin–Elmer 2400 elemental analyzer. Mass spectra were taken on a Joel JMS 700 double-focusing spectrometer, facilitated with fast atom bombardment (FAB) for sample ionization. Melting points of the compounds were uncorrected. Differential scanning calorimetry was done on a Perkin–Elmer DCS-7 instrument. The fluorescence quantum yields were determined in CH_3CN solutions at 293 K against Nile red as a reference (Φ_p = 0.78) [6]. Cyclic voltammetry measurements were carried out on a BAS 100B electrochemical analyzer equipped with a conventional three-electrode system, i.e., glassy carbon, platinum wire, and $Ag/AgNO_3$ as the working, counter, and reference electrodes, respectively. Degassed acetonitrile solution with 0.1 M tetra-*n*-butylammonium hexafluorophosphate was used as the electrolyte. E_{ox} and E_{red} data were measured with reference to a ferrocene (F_c) internal standard that was calibrated to +350 mV against a $Ag/AgNO_3$ reference electrode [7]. Measurements were taken at a scan rate of 100 mV s^{-1}. The aromatic boronic acids for the preparation of **4a**–**4f** were prepared according to the known procedures [8].

2.2. Device fabrication

Indium-tin oxide (ITO)-coated glass with a sheet resistance of <50 Ω was used as the substrate. Pretreatment of ITO includes a routine chemical cleaning using detergent and alcohol in sequence, followed by oxygen plasma cleaning. Thermal evaporation of organic materials was carried out using ULVAC Cryogenics at a chamber pressure of 10^{-6} Torr. Two types of devices were configured with ITO/NPB/dye/BCP/AlQ_3/LiF/Al (device A) and ITO/NPB/dye/TPBI/LiF/Al (device B), in which NPB, BCP, AlQ_3, TPBI, and *m*-MTDATA are 4,4′-bis[*N*-(1-naphthyl)-*N*-phenylamino]biphenyl, 2,9-dimethyl-4,7-diphenyl-1,10-phenanthroline, tris(8-hydoxyquinolinato)aluminum, 2,2′,2″-(1,3,5-benzenetriyl)tris(1-phenyl-1H-benzimidazole), and 4,4′,4″-tris(phenyl-*m*-methylphenylamino)triphenylamine, respectively. Current–voltage and light–intensity measurements were done on a Keithley 2400 source meter and a Newport 1835C optical meter equipped with a Newport 818-ST silicon photodiode, respectively. All measurements were completed under ambient conditions.

2.3. Synthesis of 3-bromo-4-(2′-methyl-3′-indolyl)-N-benzylmaleimide (*2*)

To a toluene (130 mL) solution of 2-methylindole (3.35 g, 25.50 mmol) was added MeMgCl (25.51 mmol, 9.87 mL) at an ice temperature under a nitrogen atmosphere, and the solution was warmed up gradually and heated to 60 °C for 1 h. A solution of 2,3-dibromo-*N*-benzylmaleimde (**1**, 8.00 g, 23.2 mmol) in toluene (10 mL) was then added to the above solution, and it was heated to reflux for 3 h. The solution was cooled to room temperature and diluted with ethyl acetate (100 mL). The solution was washed successively with 1 N aqueous HCl (150 mL), water (150 mL) and brine (150 mL). The solution was then dehydrated over anhydrous $MgSO_4$ and evaporated *in vacuo* to form a yellow residue. The crude product was purified by silica gel column chromatography with ethyl acetate/hexane (1:4) as an eluant to afford compound **2** in 68% yield (6.22 g, 15.8 mmol). ^{1}H NMR (CD_3COCD_3, 400 MHz): δ 2.51 (s, 3H), 4.81 (s, 2H), 7.06–7.10 (m, 1H), 7.12–7.16 (m, 1H), 7.28–7.30 (m, 1H), 7.33–7.36 (m, 2H), 7.38–7.43 (m, 3H), 7.47–7.49 (m, 1H), 10.78 (s, 1H). ^{13}C NMR (CD_3COCD_3, 125 MHz): δ 13.34, 41.99, 101.52, 110.99, 119.94, 120.45, 121.67, 126.66, 127.50, 127.84, 128.54, 136.09, 136.87, 138.41, 139.63, 165.86, 168.53, 205.14, 205.40. IR (KBr, cm^{-1}): 3381, 3061, 3033, 2928, 2360, 2340, 1773, 1709, 1624, 1610, 1458, 1430, 1396, 1351, 739, 431.

2.4. General procedure for synthesis of *3a*–*3f*

To a THF (20 mL) solution of **2** (2.00 g, 5.1 mmol) under a nitrogen atmosphere was added $Pd(PPh_3)_4$ (0.29 g, 0.25 mmol), and the mixture was stirred for 15 min. To the mixture was then added arylboronic acid (5.6 mmol) and aqueous Na_2CO_3 (2 M, 20 mL). Then the mixture was heated to 110 °C for 24 h. After cooled to room temperature, the mixture was diluted with ethyl acetate (20 mL) and followed by washing with water (30 mL) and brine (30 mL). It was then dehydrated over anhydrous $MgSO_4$ and dried *in vacuo*, forming a red residue. The crude product was purified by silica gel column chromatography with ethyl acetate/hexane (1:3) as an eluant to afford compounds **3a**–**3f**.

3-(2′-Methyl-3′-indoyl)-4-phenyl-*N*-benzylmaleimide (**3a**). Physical data of **3a** (yield 70%). ^{1}H NMR (CD_3COCD_3, 400 MHz): δ 2.25 (s, 3H), 4.83 (s, 2H), 6.82–6.86(m, 1H), 7.01–7.05 (m, 2H), 7.25–7.37 (m, 7H), 7.45–7.56 (m, 2H), 7.57–7.59 (m, 2H), 10.61 (s, 1H). ^{13}C NMR (CD_3COCD_3, 125 MHz): δ 13.37, 41.69, 102.63, 110.37, 120.07, 120.15, 121.84, 126.51, 127.55, 128.21, 128.54, 128.61, 129.05, 129.36, 130.28, 133.25, 134.04, 135.73, 136.94, 137.17, 170.63, 171.00. IR (KBr, cm^{-1}): 3396, 2362, 2342, 2091, 1771, 1760, 1748, 1734, 1697, 1650, 1637, 1492, 1474, 1458, 1431, 1399, 742, 694, 440. HRMS (*m*/*z*) calcd for $C_{26}H_{20}N_2O_2$: 392.1525 (M^+); found: 392.1526. LRMS (FAB, *m*/*z*): 392.1 (M^+, 100%), 307.2 (17), 154.1 (76), 136.2 (57), 107.2 (23).

3-(2′-Methyl-3′-indoyl)-4-(4″-biphenyl)-*N*-benzylmaleimide (**3b**). Physical data of **3b** (yield 47%). ^{1}H NMR (CD_3COCD_3, 400 MHz): δ 2.29 (s, 3H), 4.84 (s, 2H), 6.82–6.86 (m, 1H), 7.01–7.07 (m, 2H), 7.26–7.30 (m, 1H), 7.34–7.38 (m, 4H), 7.41–7.47 (m, 4H), 7.58–7.60 (m, 2H), 7.62–7.65 (m, 2H), 7.68–7.70 (m, 2H), 10.75 (s, 1H). ^{13}C NMR (CD_3COCD_3, 125 MHz): δ 12.84, 41.32, 102.42, 110.73, 119.60, 120.03, 121.36, 126.34, 126.66, 127.33, 127.65, 127.83, 128.47, 128.83, 129.82, 129.96, 132.88, 133.42, 136.41, 137.43, 137.80, 139.89, 141.06, 170.35, 170.85. IR (KBr, cm^{-1}): 3383, 3059, 3031, 2922, 2361, 2340, 1793, 1761, 1734, 1698, 1651, 1622, 1606, 1457, 1429, 1399, 746, 697, 452. HRMS (*m*/*z*) calcd for $C_{32}H_{24}N_2O_2$: 469.1910 ([M+H]$^+$); found: 469.1910. LRMS (FAB, *m*/*z*): 469.1 ([M+H]$^+$, 100%), 307.2 (17), 154.1 (36).

3-(2′-Methyl-3′-indoyl)-4-(1-naphthyl)-*N*-benzylmaleimide (**3c**). Physical data of **3c** (yield 62%). ^{1}H NMR (acetone-d_6, 400 MHz): δ 2.02 (s, 3H), 4.90 (s, 2H), 6.73–6.77 (m, 1H), 6.92–6.96 (m, 1H), 7.13–7.22 (m, 3H), 7.30–7.32 (m, 1H), 7.36–7.40 (m, 3H), 7.48–7.51 (m, 3H), 7.57–7.59 (m, 1H), 7.76–7.78 (m, 1H), 7.84–7.92, (m, 2H), 10.43 (s, 1H). ^{13}C NMR (acetone-d_6, 125 MHz): δ 12.74, 41.57, 119.59, 119.73, 121.23, 125.21, 125.72, 125.76, 125.82, 127.18, 127.38, 127.89, 128.27, 128.54, 128.73, 128.96, 129.40, 130.66, 133.63, 134.12, 135.95, 136.99, 137.50, 138.08, 170.43, 170.87. IR (KBr, cm^{-1}): 3419, 2361, 2340, 2090, 1793, 1760, 1748, 1733, 1698, 1649, 1635, 1490, 1458, 1429, 1398, 740, 698, 489. HRMS (*m*/*z*) calcd for $C_{30}H_{22}N_2O_2$: 443.1760 ([M+H]$^+$); found: 443.1753. LRMS (FAB, *m*/*z*): 443.2 ([M+H]$^+$, 100%), 154.1 (14).

3-(2′-Methyl-3′-indoyl)-4-(9-anthryl)-*N*-benzylmaleimide (**3d**). Physical data of **3d** (yield 50%). ^{1}H NMR (CD_3COCD_3, 400 MHz): δ 2.02 (s, 3H), 4.96 (s, 2H), 6.57–6.61 (m, 1H), 6.83–6.87 (m, 1H), 7.05–7.08 (m, 1H), 7.10–7.13 (m, 1H), 7.30–7.39 (m, 4H), 7.39–7.45 (m, 3H), 7.52–7.54 (m, 2H), 8.01–8.03 (m, 4H), 8.59 (s, 1H), 10.40 (s, 1H).^{13}C NMR (CD_3COCD_3, 125 MHz): δ 12.78, 41.76, 102.97, 110.46, 119.46, 121.11, 125.22, 126.01, 126.10, 127.22, 127.37, 127.76, 128.57, 128.68, 129.99, 131.39, 133.70, 135.75, 137.59, 138.17, 170.29, 170.85. IR (KBr, cm^{-1}): 3365, 3055, 2924, 2854, 2361, 2340, 1794, 1770, 1748, 1734, 1699, 1650, 1635, 1622, 1457, 1431, 1397, 734, 435. HRMS (*m*/*z*) calcd for $C_{34}H_{24}N_2O_2$: 493.1916 ([M+H]$^+$); found: 493.1908. LRMS (FAB, *m*/*z*): 493.1 ([M+H]$^+$, 72%), 154.1 (76).

3-(2′-Methyl-3′-indoyl)-4-(9-phenanthryl)-*N*-benzylmaleimide (**3e**). Physical data of **3e** (yield 62%). ^{1}H NMR (CD_3COCD_3, 400 MHz): δ 2.92 (s, 3H), 4.92 (s, 2H), 6.71–6.74 (m, 1H), 6.90–6.91 (m, 1H), 7.15–7.18 (m, 1H), 7.25–7.27 (m, 1H), 7.30–7.32 (m, 2H), 7.38–7.40 (m, 2H), 7.51–7.58 (m, 4H), 7.59–7.67 (m, 1H), 7.86–7.90 (m, 2H), 7.94 (s, 1H), 8.76 (d, J = 8.4 Hz, 2H), 10.41 (s, 1H). ^{13}C NMR (CD_3COCD_3, 125 MHz): δ 12.95, 41.70, 103.16, 110.60, 119.67, 119.87, 121.31, 122.65, 122.91, 126.16, 126.71, 126.91, 127.45, 127.63, 127.99, 128.60, 129.04, 130.24, 130.37, 131.15, 134.08, 135.99, 137.28, 137.52, 138.26, 170.51, 170.94. IR (KBr, cm^{-1}): 3423, 2360, 2339, 1793, 1771, 1748, 1733, 1698, 1650, 1636, 1474, 1457, 1428, 1397, 740, 429. HRMS (*m*/*z*) calcd for $C_{34}H_{24}N_2O_2$: 493.1916 ([M+H]$^+$); found: 493.1908. LRMS (FAB, *m*/*z*): 493.1 ([M+H]$^+$, 100%), 391.2 (16), 107.2 (47).

3-(2′-Methyl-3′-indoyl)-4-(1-pyrenyl)-*N*-benzylmaleimide (**3f**). Physical data of **3f** (yield 61%). ^{1}H NMR (CD_3COCD_3, 400 MHz): δ 2.08 (s, 3H), 4.95 (s, 2H), 6.64–6.68 (m, 1H), 6.85–6.89 (m, 1H), 7.12–7.16 (m, 2H), 7.30–7.34 (m, 1H), 7.38–7.42 (m, 2H), 7.53–7.55 (m, 2H), 7.89 (d, J = 9.3 Hz, 1H), 8.00–8.03 (m, 2H), 8.09–8.13 (m, 1H), 8.14–8.20 (m, 3H), 8.25–8.27 (m, 2H), 10.40 (s, 1H). ^{13}C NMR (CD_3COCD_3, 100 MHz): δ 13.27, 42.11, 103.49, 111.00, 120.16, 120.24, 121.74, 124.29, 124.70, 124.91, 125.33, 125.66, 125.77, 126.18, 126.28, 127.35, 127.41, 127.57, 127.78, 128.38, 128.71, 128.89, 129.06, 130.68, 131.12, 131.85, 134.52, 136.31, 137.31, 137.66, 138.69, 171.003, 171.56. IR (KBr, cm^{-1}): 3394, 3050, 2360, 2340, 1794, 761, 1749, 1734, 1699, 1650, 1636, 1623, 1457, 1428, 1397, 741, 455. HRMS (*m*/*z*) calcd for $C_{36}H_{24}N_2O_2$: 517.1916 ([M+H]$^+$); found: 517.1909. LRMS (FAB, *m*/*z*): 517.2 ([M+H]$^+$, 100%), 391.2 (5), 307.1 (6), 289.1 (5), 154.1 (33), 136.1 (21).

2.5. General procedure for the synthesis of ***4a–4f***

Compound **3** (1.40 g, 3.6 mmol) was mixed with NaOH (0.16 g, 4.0 mmol) in acetone (20 mL) under a nitrogen atmosphere, while the solution turned gradually from red to dark blue. To the mixture was added benzyl bromide (0.64 mL, 5.4 mmol), then the solution was stirred with a magnetic bar for 30 min, while the color tuned red. The mixture was stirred for another 1 h at room temperature. The reaction was quenched by the addition of water (500 mL), then was filtered. The filtrate was concentrated *in vacuo*, and the product was recrystallized from CH_2Cl_2 and hexane as red crystalline solids.

3-(2′-Methyl-*N*-benzyl-3′-indoyl)-4-(phenyl)-*N*-benzylmaleimide (**4a**). Physical data of **4a** (yield 78%). ^{1}H NMR (CD_2Cl_2, 400 MHz): δ 2.00 (s, 3H), 4.83 (s, 2H), 5.28 (s, 2H), 6.94–7.21 (m, 4H), 7.22–7.23 (m, 1H), 7.27–7.35 (m, 10H), 7.47–7.54 (m, 4H). ^{13}C NMR (CD_2Cl_2, 100 MHz): δ 12.17, 41.78, 46.75, 102.94, 109.57, 120.38, 120.45, 121.91, 125.95, 126.19, 127.50, 127.64, 128.30, 128.36, 128.63, 128.82, 129.13, 129.39, 130.47, 133.64, 134.26, 137.04, 137.07, 137.19, 138.32, 170.70, 170.99. IR (KBr, cm^{-1}): 3032, 2940, 2361, 1762, 1701, 1621, 1467, 1454, 1399, 1350, 739, 432. HRMS (*m*/*z*) calcd for $C_{33}H_{26}N_2O_2$: 482.1994 (M$^+$); found: 482.1986. LRMS (FAB, *m*/*z*): 482.2 (M$^+$, 100%), 307.1 (20), 136.1 (40). Anal. calcd for $C_{33}H_{26}N_2O_2$: C, 82.13; H, 5.43; N, 5.81, found: C, 82.01; H, 5.47; N, 5.93.

3-(2′-Methyl-*N*-benzyl-3′-indoyl)-4-(4″-biphenyl)-*N*-benzylmaleimide (**4b**). Physical data of **4b** (yield 75%). ^{1}H NMR ($CDCl_3$, 400 MHz): δ 2.12 (s, 3H), 4.84 (s, 2H), 5.31 (s, 2H), 6.97–7.04 (m, 3H), 7.10–7.13 (m, 1H), 7.20–7.21 (m, 1H), 7.26–7.30 (m, 1H), 7.33–7.35 (m, 4H), 7.37–7.41 (m, 3H), 7.43–7.46 (m, 2H), 7.50–7.52 (m, 6H), 7.62–7.64 (m, 2H). ^{13}C NMR ($CDCl_3$, 125 MHz): δ 12.57, 41.94, 46.84, 103.18, 109.46, 120.60, 120.74, 122.08, 125.97, 126.88, 126.94, 127.69, 128.78, 128.87, 129.76, 133.15, 133.42, 136.77, 137.29, 138.18, 140.15, 141.51, 170.73, 171.01. IR (KBr, cm^{-1}): 3032, 2938, 2362, 2342, 1762, 1700, 1618, 1456, 1418, 1398, 1350, 740, 425. HRMS (*m*/*z*) calcd for $C_{39}H_{30}N_2O_2$: 558.2307 (M$^+$); found: 558.2310. LRMS (FAB, *m*/*z*): 558.2 (M$^+$, 100%), 154.1 (25), 105.2 (10).

3-(2′-Methyl-*N*-benzyl-3′-indoyl)-4-(1″-naphthyl)-*N*-benzylmaleimide (**4c**). Physical data of **4c** (yield 76%). ^{1}H NMR ($CDCl_3$, 400 MHz): δ 1.63 (br, 3H), 4.93 (s, 2H), 5.08 (br, 2H), 6.54 (br, 2H), 7.04–7.15 (m, 7H), 7.30–7.40 (m, 4H), 7.46–7.60 (m, 6H), 7.53–7.81 (m, 2H). ^{13}C NMR ($CDCl_3$, 125 MHz): δ 11.99, 42.16, 46.44, 109.25, 120.16, 120.76, 121.97, 125.28, 125.48, 125.75, 125.91, 127.22, 127.74, 128.49, 128.68, 128.74, 128.88, 129.22, 129.82, 133.56, 136.39, 136.79, 136.91, 138.51, 170.71, 170.11. IR (KBr, cm^{-1}): 3060, 2361, 1762, 1701, 1650, 1619, 1455, 1420, 1397, 1351, 738, 697, 442. HRMS (*m*/*z*) calcd for $C_{37}H_{28}N_2O_2$: 533.2229 ([M+H]$^+$); found:533.2238. LRMS (FAB, *m*/*z*): 533.2 ([M+H]$^+$, 22%), 307.2 (45), 136.1 (56). Anal. calcd for $C_{37}H_{28}N_2O_2$: C, 83.43; H, 5.30; N, 5.26, found: C, 82.87; H, 5.39; N, 4.93.

3-(2′-Methyl-*N*-benzyl-3′-indoyl)-4-(9″-anthryl)-*N*-benzyl maleimide (**4d**). Physical data of **4d** (yield 76%). ^{1}H NMR ($CDCl_3$, 500 MHz): δ 1.60 (s, 3H), 4.98 (s, 2H), 5.01 (s, 2H), 6.34 (d, J = 8 Hz, 2H), 6.86–6.87 (m, 1H), 6.89–7.00 (m, 2H), 7.01–7.04 (m, 2H), 7.09–7.10 (m, 1H), 7.27–7.28 (m, 2H), 7.30–7.34 (m, 2H), 7.35–7.53 (m, 4H), 7.58 (d, J = 8 Hz, 2 H), 7.77 (d, J = 9 Hz, 2H), 7.94 (d, J = 9 Hz, 2H), 8.41 (s, 1H). ^{13}C NMR ($CDCl_3$, 125 MHz): δ 12.09, 42.30, 46.24, 109.17, 119.87, 120.73, 121.89, 124.23, 125.11, 125.19, 125.81, 128.74, 128.87, 129.29, 129.76, 131.31, 134.03, 136.36, 136.70, 136.87, 138.79, 139.60, 170.60, 170.97. IR (KBr, cm^{-1}): 3056, 2398, 2361, 2341, 1734, 1702, 1619, 1470, 1455, 1396, 1351, 732, 493. HRMS (*m*/*z*) calcd for $C_{41}H_{30}N_2O_2$: 582.2307 (M$^+$); found: 582.2300. LRMS (FAB, *m*/*z*): 583.1 ([M+H]$^+$, 100%), 391.3 (6), 289.1 (10), 136.2 (21). Anal. calcd for $C_{41}H_{30}N_2O_2$: C, 84.51; H, 5.19; N, 4.81, found: C, 84.07; H, 5.25; N, 4.93.

3-(2′-Methyl-3′-indoyl)-4-(9-phenanthryl)-*N*-benzylmaleimide (**4e**). Physical data of **4e** (yield 82%). ^{1}H NMR (CD_3COCD_3, 400 MHz): δ 1.63 (br, 3H), 4.95 (s, 2H), 5.04 (br, 2H), 6.48 (br, 2H), 7.03–7.19 (m, 7H), 7.30–7.34 (m, 1H), 7.37–7.40 (m, 2H), 7.50–7.66 (m, 7H), 7.85–7.91 (m, 2H), 8.59–8.63 (m, 2H). ^{13}C NMR (CD_3COCD_3, 125 MHz): δ 12.16, 42.24, 46.41, 109.34, 120.29, 120.88, 122.04, 122.54, 125.43, 126.55, 126.79, 127.67, 127.81, 128.68, 128.74, 128.94, 130.47, 130.62, 131.01, 133.91, 136.33, 136.59, 136.83, 136.93, 138.72, 170.77, 171.11. IR (KBr, cm^{-1}): 3061, 3032, 2939, 2361, 2341, 1761, 1702, 1619, 1469, 1453, 1397, 1350, 740, 432. HRMS (*m*/*z*) calcd for $C_{41}H_{30}N_2O_2$: 583.2386 ([M+H]$^+$); found:583.2386. LRMS (FAB, *m*/*z*): 583.2 ([M+H]$^+$, 100%), 391.3 (4), 289.2 (4), 154.1 (21), 107.2 (6). Anal. calcd for $C_{41}H_{30}N_2O_2$: C, 84.51; H, 5.19; N, 4.81, found: C, 84.15; H, 5.24; N, 4.75.

3-(2′-Methyl-*N*-benzyl-3′-indoyl)-4-(1-pyrenyl)-*N*-benzylmaleimide (**4f**). Physical data of **4f** (yield 84%). ^{1}H NMR ($CDCl_3$, 500 MHz): δ 1.30 (br, 3H), 4.97 (s, 2H), 5.02 (br, 2H), 6.29 (br, 2H), 7.02–7.03 (m, 4H), 7.30–7.34 (m, 1H), 7.37–7.40 (m, 2H), 7.58–7.60 (m, 3H), 7.74 (br, 3H), 7.96–8.01 (m, 3H), 8.05–8.07 (m, 3H), 8.14–8.20 (m, 2H). ^{13}C NMR ($CDCl_3$, 125 MHz): δ 12.01, 42.28, 46.39, 101.92, 103.88, 109.35, 119.61, 120.23, 120.89, 122.06, 124.42, 124.83, 124.98, 125.32, 125.60, 125.69, 126.08, 127.09, 127.29, 128.38, 138.78, 129.02, 130.09, 130.08, 130.59, 120.90, 131.11, 131.44, 131.86, 132.26, 134.23, 136.21, 136.56, 136.90, 137.03, 138.55, 170.87, 171.41. IR (KBr, cm^{-1}): 3034, 2936, 2362, 2339, 1761, 1700, 1618, 1470, 1455, 1396, 1350, 737, 431. HRMS (*m*/*z*) calcd for $C_{43}H_{30}N_2O_2$: 607.2386 ([M+H]$^+$); found: 607.2386. LRMS (FAB, *m*/*z*): 607.1 ([M+H]$^+$, 100%), 154.1 (20), 136.2 (14). Anal. calcd for $C_{43}H_{30}N_2O_2$: C, 85.12; H, 4.98; N, 4.62, found: C, 84.91; H, 5.31; N, 4.54.

3. Results and discussion

3.1. Synthesis and characterization

The synthesis of the asymmetric indolylmaleimide derivatives **4a**–**4f** is illustrated in Scheme 1. 3-Bromo-4-(2′-methyl-3′-indolyl)-*N*-benzylmaleimide (**2**) was synthesized in a yield of 68% by a substitution reaction of 3,4-dibromo-*N*-benzylmaleimide (**1**) [1a] with one equivalent of 2-methylindole in the presence of CH_3MgCl, and it was utilized as the pivotal compound in the following coupling reactions. The addition of the second substituent at C(4) was performed by a Suzuki coupling reaction with aromatic boronic acids, i.e., phenylboronic acid, 4-biphenylboronic acid, naphthalene-1-boronic acid, anthracene-9-boronic acid, phenathrene-9-boronic acid, and pyrene-1-boronic acid, respectively, to yield **3a**–**3f** in 47–70% yield. In ^{1}H NMR the hydrogens at methylene moieties appeared as a singlet at $\delta \sim 5.0$ ppm, whereas in ^{13}C field the carbonyl groups appeared at $\delta \sim 170$ ppm. The indolyl hydrogens in **3a**–**3f** were masked by alkylation with benzyl bromide in the presence of base. Compounds **4a**–**4f** were obtained as red color solids in yields of 75–84%. The additional substituents at C(4) of **4a**–**4f** hindered the rotation between the maleimide ring and the two aromatic substituents, so that line broadening in ^{1}H NMR spectra was appeared at both the methyl and methylene positions of indole. This phenomenon is more pronounced in **4c**, **4e** and **4f**, whereas the line broadening was weaker in **4d** due to the symmetrical geometry of anthracene group.

3.2. Physical properties

Compounds **4a**–**4f** exhibit three major absorption regions in the range of 260–550 nm (Fig. 1). The absorptions shorter than 300 nm are derived mainly from the local transitions of both indole π–π^* (major) and maleimide n–π^* (minor). The region between 300 and 400 nm comes from the π–π^* transitions on the second aryl substituents, while their exact positions depend on the nature of the aryl group. The broad featureless band on the longest wavelength side above 400 nm belongs to a charge transfer transition along the dipole from indole toward maleimide, which has been well documented in the literatures [4,9]. The emission spectra of all compounds **4a**–**4f** overlap heavily with each other (Fig. 1), which are essentially the same as those of the symmetrical bis(indolyl)maleimide. The lowest energy radiative transition is derived from a charge-separated dipole directing from the indolyl nitrogen group toward the maleimide carbonyl. Such a charge transfer (CT) transition normally exhibits a distinctive solvatochromic effect (ESI, S1, S2 and S3). A typical example is shown in Fig. 2, where an apparent blue shift can be seen in the emission spectra of **4b** along with the increasing of

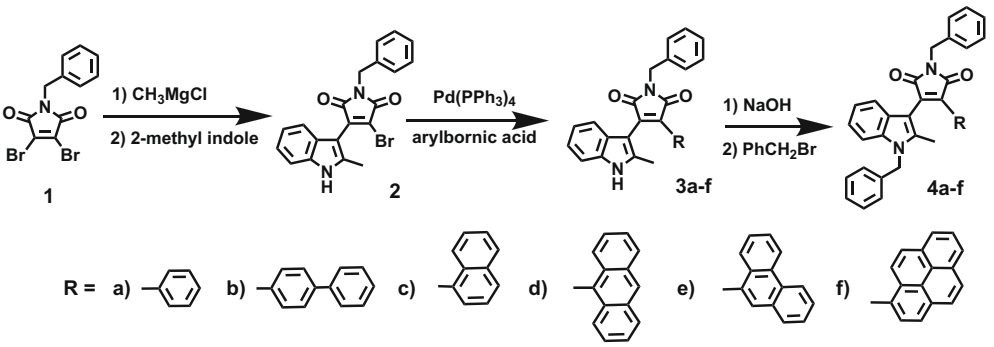

Scheme 1. The synthetic sequence of compounds **4a**–**4f**.

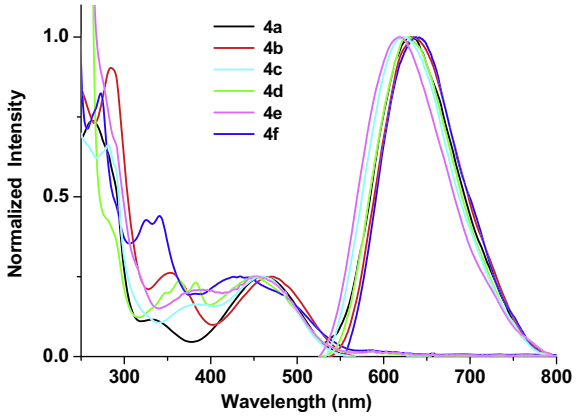

Fig. 1. Normalized absorption and emission spectra of compounds **4a**–**4f** in CH_2Cl_2. The emission spectra were obtained by irradiation at λ_{max} of the long wavelength absorption bands.

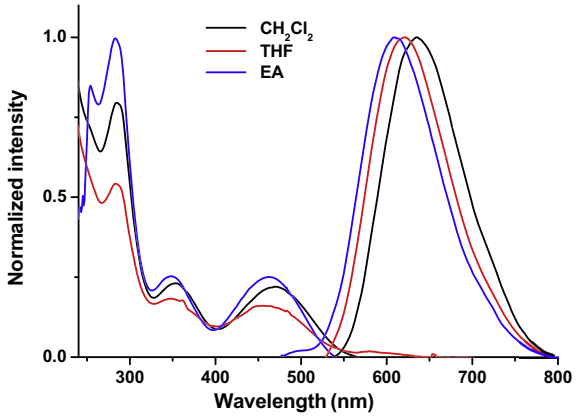

Fig. 2. Absorption and emission spectra of compound **4b** in different solvents.

solvent polarity. The red emissions with similar characteristics are found in all compounds **4a**–**4f**. A summary of their spectroscopic parameters is listed in Table 1.

The thermal stability of **4a**–**4f** was evaluated by differential scanning calorimetry (DSC). In a typical scan on a crystalline sample of compound **4d** (ESI S4), a sharp endothermic peak was detected at 251 °C, corresponding to the melting point (T_m) of the crystals. After cooling the same sample was heated again, yet a melting signal was not observed in the second scan. Nevertheless, a small endothermic hump at 98 °C was detected, which can be assigned to a glass-transition (T_g) temperature. The absence of T_m as well as the presence of T_g revealed the amorphous nature of solid films. All compounds **4a**–**4f** exhibited analogous glass-transition phenomena at considerable high temperatures, i.e., 63–109 °C (Table 1). The compact and round shape of these compounds is presumably responsible for the high T_g values. Red fluorescence was observable not only in solutions, but also in the solid state (ESI S5). This property provides an unusual advantage for the fabrication of LED devices in the form of neat films. In a common practice doping is usually necessary to avoid self-quenching in order to separate individual chromophores apart from each other.

Each compound showed two consecutive oxidative waves in dichloromethane by cyclic voltammetry (CV). The first wave at ca. 1.0 V corresponds to the oxidation of the indolyl group and second one at ca. 1.15 V is due to the aromatic substituent (Table 1). In the reductive sweep a single wave was observed at about −1.45 V by the reduction of maleimide moiety. The lowest unoccupied molecular orbital (LUMO) could be estimated by these redox potentials. The 0–0 transition energies were estimated at the interception of the absorption and emission spectra.

The physical nature of compound **4c** was further examined by semiempirical method AM1 implanted in Spartan software. In an optimized geometry the two aryl substituents at C(3, 4) are twisted from each other, while each maintains a dihedral angle of ca. 35° with respect to the central plane of maleimide. The irregular geometrical shape is favorable to the formation of amorphous solid during film preparation. Therefore high glass-transition temperatures (T_g) were detectable for all compounds (Table 1). As for their electronic configurations, the electron densities on the highest occupied molecular (HOMO) and the second highest occupied molecular orbital (SHOMO) are localized on the indolyl and naphthyl substituents, respectively (Fig. 3). The lowest energy transition from HOMO to LUMO (S_1 state) induces a charge separation between the indole and maleimide moieties. Charge recombination from S_1 to the ground state (S_0) results in an intensive red CT emission. It is interesting to find that the energy of this emission is only slightly perturbed by

Table 1
Physical data of compounds **4a**–**4f**.

	Abs (ε)[a] (nm ($M^{-1}cm^{-1}$))	PL (Φ_p)[a] (nm (%))	$E_{0\text{-}0}$[b] (eV)	E_{ox}[c] (V)	E_{red}[c] (V)	Band gap[d] (eV)	HOMO[e] (eV)	LUMO[f] (eV)	T_g/T_m (°C)
4a	462 (5.6×10^3)	630 (2.9)	2.28	1.01, 1.15	−1.45	2.46	−5.41	−3.13	63/158
4b	470 (6.1×10^3)	634 (4.9)	2.22	0.98, 1.12	−1.44	2.42	−5.38	−3.16	81/222
4c	460 (7.3×10^3)	620 (7.5)	2.28	0.99, 1.16	−1.48	2.47	−5.39	−3.11	83/225
4d	448 (7.0×10^3)	627 (6.8)	2.26	1.03, 1.18	−1.44	2.47	−5.47	−3.21	98/251
4e	459 (5.9×10^3)	617 (2.1)	2.22	1.01	−1.47	2.48	−5.45	−3.23	104/277
4f	433 (9.0×10^3)	634 (23.1)	2.22	0.99, 1.17	−1.44	2.43	−5.39	−3.17	109/193

[a] In CH_2Cl_2 at 293 K, quantum efficiency against Nile red ($\Phi_p = 0.78$) [6].
[b] Taken at the crossing point of the absorption and emission spectra.
[c] Fc/Fc+ at 0.35 V against $Ag/AgNO_3$ as the internal reference.
[d] Gap between E_{ox} and E_{red}.
[e] Calculated as $-(E_{ox} + 4.40)$ [10].
[f] Calculated as HOMO + band gap.

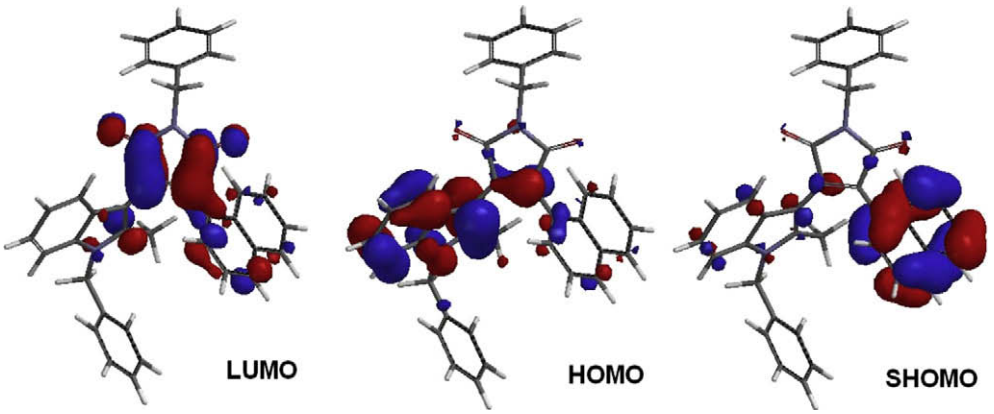

Fig. 3. Simulated frontier molecular orbitals of compound **4c**. From left to right are LUMO, HOMO, and SHOMO, respectively. The lowest energy transition from the first excited state, i.e., S_1 corresponding to HOMO → LUMO, is polarized from the indolyl substituent toward the central maleimide group. The transition involved the naphthyl moiety is at higher energy, and will transmit its energy rapidly through internal conversion to S_1. The simulation was performed by semiempirical method AM1 implanted in Spartan software.

adjacent aryl group, so that it explains the high similarity of PL spectra among all compounds **4a**–**4f**.

3.3. Device optimization

The electroluminescence of these materials was examined by the fabrication of LED devices. A typical lay-out of device configuration was ITO/HT/dye/ET/LiF/Al, whereas the hole transporter (HT) is either NPB or a combination of *m*-MTDATA/NPB, and the electron transporter (ET) is either TPBI or a pair of BCP/AlQ_3. A few selected combinations were compared in order to optimize the quantum yield as well as the purity of the red emission color. The parameters of devices made with compound **4a** in five trials I–V are given in Table 2. The ET material used in devices I and II was TPBI, while that in devices III–V was BCP/AlQ_3. The electroluminescence spectra of all devices are plotted in Fig. 4. A noteworthy feature in spectra I–IV is the presence of two emission bands, i.e., an extra peak appeared on the high energy side deriving from the emission of ET. Normally in the presence of TPBI the migration of holes can be blocked mostly at the film junction due to its exceptional low HOMO level (at −6.2 V). Therefore it functions both as an ET as well as a hole-blocker. However in the case of device I, a highly intensive band at 400 nm is observed, indicating holes have moved across the boundary into the bulk of TPBI. In certain occasions such dual emissions may be desired for the production of a white light [2,11]. However, in the present case we sought to reduce the hole leakage by inserting an additional layer of *m*-MTDATA between ITO and NPB to slow down the movement of holes. This new material is known to be capable of forming a highly uniform amorphous film, while its high HOMO level along with a moderate charge mobility can smooth the injection of holes [12]. With an additional layer of *m*-MTDATA, the quantum efficiency of device II was slightly improved. It was also clear that the intensity of 600 nm band was reduced to about half that of I (Fig. 4).

The HT material TPBI in devices III–V was replaced by a two-layer combination of BCP/AlQ_3. In this design AlQ_3 functioned as an electron injector and BCP a hole-blocker. The film thickness of **4a** in both III and IV was maintained 10 nm, while a layer of *m*-MTDATA was included in device IV. In the EL spectra of III and IV, a minor shoulder was found at peak maximum ca. 520 nm, which corresponded to the emission of AlQ_3. It was an evidence of a mild hole leakage from the emitting layer to the medium of ET. The improvement made by *m*-MTDATA in II and IV was some-

Table 2
Performance of electroluminescence devices made with **4a** as the emitting dye. The configuration of devices are listed in the following, with the thickness of films in nm embraced in the parentheses: I: ITO/NPB (40)/**4a** (10)/TPBI (40)/LiF (1)/Al (150); II: ITO/m-MTDATA (30)/NPB (20)/**4a** (30)/TPBI (40)/LiF (1)/Al (150); III: ITO/NPB (40)/**4a** (10)/BCP (10)/AlQ_3 (30)/LiF (1)/Al (150); IV: ITO/m-MTDATA (30)/NPB (20)/**4a** (10)/BCP (10)/AlQ_3 (30)/LiF (1)/Al (150); V: ITO/m-MTDATA (30)/NPB (20)/**4a** (30)/BCP (10)/AlQ_3 (30)/LiF (1)/Al (150).

Device type	Turn on (V)	L[a] (cd/m^2)	η_{ex}[b] (%)	η_l[c] (cd/A)	η_p[d] (lm/W)	CIE[e] (x, y)
I	4.5	690, 3030 (16)	0.50	0.69	0.25	0.40, 0.29
II	6.5	790, 2970 (22)	0.68	0.80	0.16	0.44, 0.27
III	4.5	520, 3390 (14)	0.28	0.50	0.20	0.55, 0.43
IV	5.0	540, 3450 (16)	0.30	0.54	0.16	0.57, 0.42
V	6.0	810, 3950 (18)	0.48	0.80	0.17	0.61, 0.39

[a] Intensity at 100 mA/cm^2, followed by the highest intensity at indicated voltage.
[b] External quantum efficiency.
[c] Luminance efficiency.
[d] Power efficiency.
[e] Commission Internationale de l'Eclairage 1931.

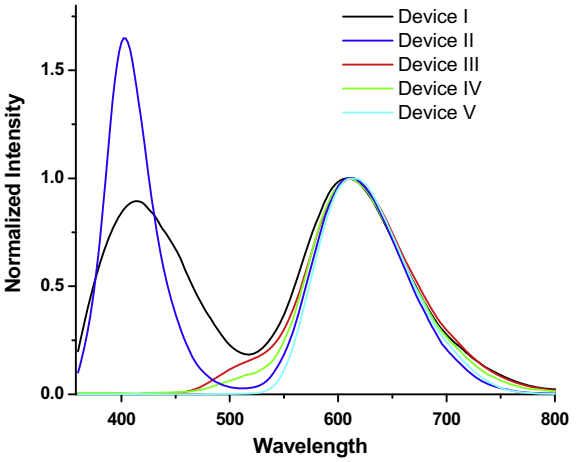

Fig. 4. EL spectra of **4a** fabricated in device types I–V. Intensity is normalized at 610 nm peak maximum.

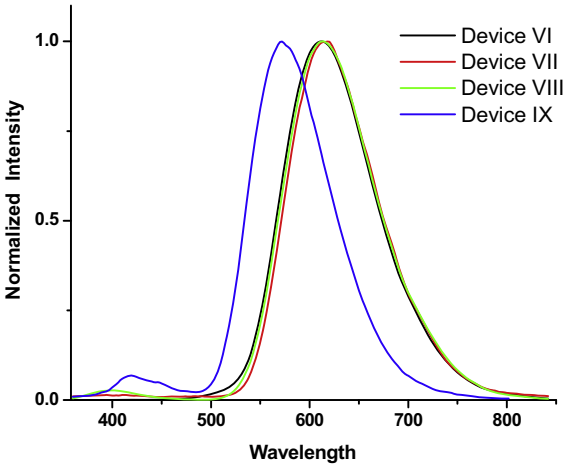

Fig. 5. EL spectra of **4c** fabricated in device types VI–IX. Intensity is normalized at peak maxima.

what limited. Although it is able to promote the light efficiency, however with an increased total thickness it also resulted to a higher turn-on voltage as well as a lower power efficiency comparing with those of I and II. A pure red emission was finally achieved by increasing the film thickness of **4a** from 10 nm to 30 nm. The EL spectrum of device IV, as shown in Fig. 4, exhibited a single emission band deriving from the maleimide.

Devices made with dye **4c** in different configurations were further examined with an optimized thickness of 30 nm. The ET materials in devices VI, VII, and VIII were composed of TPBI, BCP/AlQ_3, and BCP/TPBI, respectively. Their EL spectra are shown in Fig. 5, while each of them exhibits a single major emission nearly identical to each other. Hole leakage to ET is effectively blocked without noticeable side band. The light efficiency of these three devices was about 1%, with an optimal brightness in a range of 6000 cd/m^2 (Table 3). The CIE coordinate (Commission Internationale de l'Eclairage 1931) was located in the proximity of (0.6, 0.4), quite close to pure red color. The most unique feather in the fabrication of these devices was the use of neat films without doping. Devices made of neat films are relatively easier to fabricate and better in color stability especially under different operating conditions. For doped devices another factor need to be considered is the polarity of the host. For the charge transfer emission of **4a**–**4f**, the absorption maxima are quite sensitive to the influence of solvent. To illustrate the effect, a special device IX was made, in which dye **4c** was co-deposited in 5% weight ratio with CBP as a host material. This doped device performed with a remarkable light efficiency 4.5%, and an optimal brightness exceeding 1.2×10^4 cd/m^2. However, its emission maximum was blue shifted ca. 44 nm (from 615 to 571 nm) from those made of neat films as a result of the lower polarity of CBP. The CIE coordinate of device IX therefore was drifted to (0.47, 0.49), substantially away from pure red.

As concluded from above, a device of either type VI or type VII will be most suitable for producing a red emission, while the thickness of emitting films was kept in 30 nm. When the film is too thick, the turn-on voltage becomes higher and power efficiency reduced; yet when it is too thin, the color purity is lowered as a result of hole leakage. To comply with the above limitations, device type VII was selected for the fabrication using compounds **4b** and **4d**–**4f**. The EL spectra of these devices are shown in Fig. 6,

Table 3
Performance of electroluminescence devices made with **4c** as the emitting dye. The configuration of devices are listed in the following, with the thickness of films in nm embraced in the parentheses: VI: ITO/NPB (40)/**4c** (30)/TPBI (40)/LiF (1)/Al (150); VII: ITO/NPB (40)/**4c** (30)/BCP (10)/AlQ_3 (30)/LiF (1)/Al (150); VIII: ITONPB (40)/**4c** (30)/BCP (10)/TPBI (30)/LiF (1)/Al (150); IX: ITO/NPB (40)/**4c** (5%): CBP (40)/TPBI (40)/LiF (1)/Al (150).

Device type	Turn on (V)	L[a] (cd/m^2)	η_{ex}[b] (%)	η_l[c] (cd/A)	η_p[d] (lm/W)	CIE[e] (x, y)
VI	5.0	1110, 6040 (20)	0.67	1.11	0.31	0.59, 0.41
VII	4.5	930, 6250 (18)	0.54	0.93	0.26	0.58, 0.41
VIII	5.0	950, 5330 (17)	0.60	0.95	0.28	0.59, 0.40
IX	5.5	4450, 12530 (22)	1.51	4.45	0.82	0.47, 0.49

[a] Intensity at 100 mA/cm^2, followed by the highest intensity at indicated voltage.
[b] External quantum efficiency.
[c] Luminance efficiency.
[d] Power efficiency.
[e] Commission Internationale de l'Eclairage 1931.

and parameters of performance in Table 4. The emission spectra of **4a**–**4e** were found to be nearly identical, except **4f** which displayed a mild ~13 nm red shift with respect to others. Nevertheless this mild shift is consistent with its photoluminescence spectrum (Fig. 1).

The performance of devices of type VII fabricated for all the materials **4a**–**4f** can be depicted by both the L–V (Fig. 7) and η–J (Fig. 8) plots. Most devices displayed quantum efficiencies within the range of 0.4–0.6%, and maximal emission intensity 5500–6500 cd/m^2. The high similarity of these devices indicated that the variation of a C(4) substituent on maleimide does not influence their electrolumi-

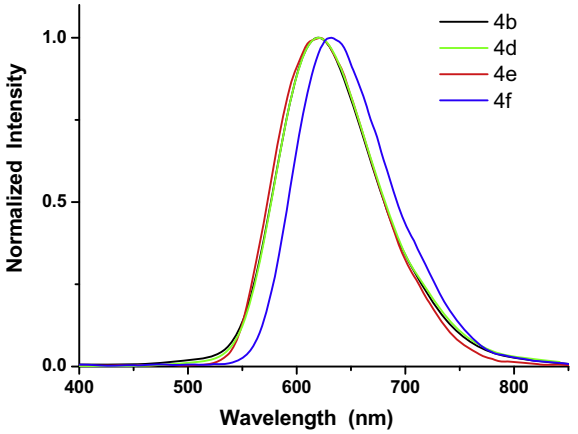

Fig. 6. EL spectra of device VIII using compounds **4b** and **4d**–**4f** as the emitters. A slight red shift is observed in the spectrum of **4f**.

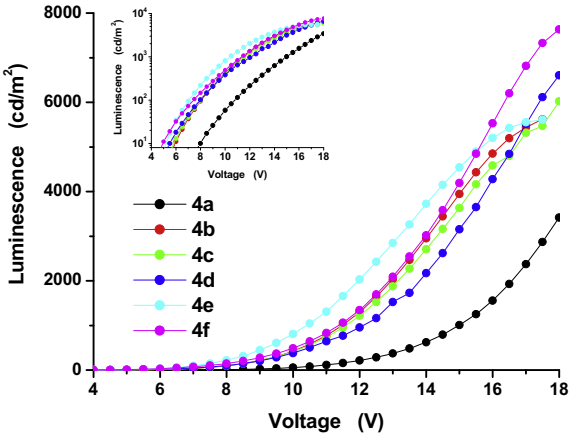

Fig. 7. Plot of luminescent intensity (L) versus applied voltage (V) of device VII using the neat film of compounds **4a**–**4f** as the emitter. The inset shows the plots of log(L) versus V, in which the turn voltages can be better illustrated.

Table 4
Performance of electroluminescence devices employing compounds **4b** and **4d**–**4f** as emitting materials. The configurations of devices VI and VII are the same as those in Table 3. The quantum efficiencies are recorded at 100 mA/cm^2.

Dye (device)	Turn on (V)	L[a] (cd/m^2)	η_{ex}[b] (%)	η_l[c] (cd/A)	η_p[d] (lm/W)
4b (VII)	4.5	870, 5618 (17)	0.60	0.87	0.24
4d (VI)	4.5	846, 6605 (17)	0.59	0.85	0.23
(VII)	4.5	1052, 7794 (18)	0.72	1.05	0.30
4e (VI)	4.5	696,5612 (17)	0.46	0.70	0.23
(VII)	4.5	824, 5976 (17)	0.54	0.83	0.29
4f (VI)	4.0	1068, 9750 (18)	1.06	1.07	0.40
(VII)	4.0	1088, 7634 (17)	1.08	1.09	0.30

[a] Intensity at 100 mA/cm^2, followed by the highest intensity at indicated voltage.
[b] External quantum efficiency.
[c] Luminance efficiency.
[d] Power efficiency.

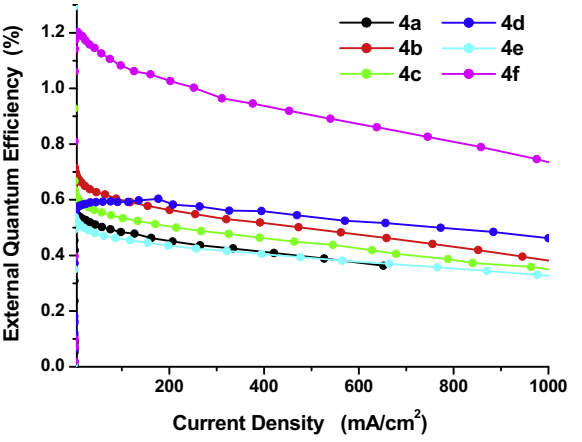

Fig. 8. External quantum efficiency (η) versus current density (J) plot of device VII using the neat film of compounds **4a**–**4f** as the emitter.

nescence significantly. Among all devices the one made with **4f** performed the best, which exhibited an optimal 1.2% quantum efficiency (Fig. 8), along with a maximal brightness close to 10,000 cd/m^2 (Fig. 7).

4. Conclusions

In summary, asymmetric indolylmaleimide derivatives with different aryl substituents at C(3) and C(4) were synthesized and applied successfully to the fabrication of OLED devices. These devices were made with neat films of the dyes, and exhibited stable red emission with CIE coordinate very close to pure red. This work has demonstrated that the unsymmetrical maleimide derivatives possess nearly the same spectroscopic properties as the symmetrical ones. It gives us a higher flexibility for the future design of red maleimide dyes. Other potential applications requires more complicated structures, such as ion sensors and solar cell materials, may also become feasible for maleimide derivatives.

Acknowledgements

This work was supported by Academia Sinica and the National Science Council of the Republic of China.

Appendix A. Supplementary data

Supplementary data associated with this article can be found, in the online version, at doi:10.1016/j.orgel.2009.12.025.

References

[1] (a) Y. Nishizuka, Nature 308 (1984) 693–698;
(b) S. Mahboobi, E. Eibler, M. Koller, S. Kumar KC, A. Popp, J. Org. Chem. 64 (1999) 4697;
(c) S. Mahboobi, I. Dechant, H. Reindl, H. Pongratz, A. Popp, D. Schollmeyer, J. Heterocycl. Chem. 37 (2000) 307.
[2] (a) T.S. Yeh, T.J. Chow, S.H. Tsai, C.W. Chiu, C.X. Zhao, Chem. Mater. 18 (2006) 832;;
(b) C.W. Chiu, T.J. Chow, C.H. Chuen, H.M. Lin, Y.T. Tao, Chem. Mater. 15 (2003) 4527;
(c) T.J. Chow, S.H. Tsai, C.W. Chiu, T.S. Yeh, Synth. Met. 149 (2005) 59;
(d) Y.P. Huang, S.-H. Tsai, D.-F. Huang, T.-S. Tsai, T.J. Chow, React. Funct. Polymer 67 (2007) 986.
[3] (a) L.H. Chan, Y.D. Lee, C.T. Chen, Macromolecules 39 (2006) 3262;
(b) W.C. Wu, H.C. Yeh, L.H. Chan, C.T. Chen, Adv. Mater. 14 (2002) 1072.
[4] (a) B.K. Kaletas, C. Mandl, G. Zwan, M. Fanti, F. Zerbetto, L.D. De Cola, B. Konig, R.M. Williams, J. Phys. Chem. A 109 (2005) 6440;
(b) B.K. Kaletas, H.C. Joshi, G. van der Zwan, M. Fanti, F. Zerbetto, K. Goubitz, L. De Cola, B. Konig, R.M. Williams, J. Phys. Chem. A 109 (2005) 9443.
[5] K. Dodo, M. Katoh, T. Shimizu, M. Takahashi, M. Sodeoka, Bioorg. Med. Chem. Lett. 15 (2005) 3114.
[6] N. Sarkar, K. Das, D.N. Nath, K. Bhattacharyya, Langmuir 10 (1994) 326.
[7] (a) J. Pommerehne, H. Vestweber, W. Guss, R.F. Mahrt, H. Bässler, M. Porsch, J. Daub, Adv. Mater. 7 (1995) 551;
(b) M. Thelakkat, H.W. Schmidt, Adv. Mater. 10 (1998) 219.
[8] G. Patrick, R. Matthias, Synthesis 5 (1996) 614.
[9] Q. Peng, Z. Lu, Y. Huang, M. Xie, D. Xiao, D. Zou, J. Mater. Chem. 13 (2003) 1570.
[10] S. Janietz, D.D.C. Bradley, M. Grell, C. Giebeler, M. Indasekaran, E.P. Woo, Appl. Phys. Lett. 73 (1998) 2453.
[11] Z. Lin, Y. -S. Wen, T.J. Chow, J. Mater. Chem. 19 (2009) 5141.
[12] (a) Y. Shirota, Y. Kuwabara, H. Inada, T. Wakimoto, H. Nakada, Y. Yonemoto, S. Kawami, K. Imai, Appl. Phys. Lett. 65 (1994) 807;
(b) Y. Shirota, J. Mater. Chem. 10 (2000) 1.

Organic Electronics 11 (2010) 613–617

Contents lists available at ScienceDirect

Organic Electronics

journal homepage: www.elsevier.com/locate/orgel

Aggregation-induced enhanced emission materials for efficient white organic light-emitting devices

Suijun Liu, Feng Li, Quan Diao, Yuguang Ma *

State Key Laboratory for Supramolecular Structure and Materials, Jilin University, Changchun 130012, PR China

ARTICLE INFO

Article history:
Received 23 November 2009
Received in revised form 29 December 2009
Accepted 29 December 2009
Available online 6 January 2010

Keywords:
Aggregation-induced enhanced emission
White organic light-emitting diode
Color stability
High performance
Non-doped

ABSTRACT

We demonstrated the first aggregation-induced enhanced emission (AIEE) materials for white organic light-emitting diodes (WOLEDs). AIEE properties of materials provide a possibility to turnaround the bad thermal effects to positive effects for device performance as WOLEDs working under the condition of the high brightness and high current density. The blue AIEE molecule **TDPVBi** shows high glass transition temperature (T_g) and special applicability for OLEDs, ca. enhanced smoothness as annealing its film. Constructing WOLED by combining both AIEE materials (**TDPVBi** and **CN-DPASDB**) results in devices with a maximum current efficiency of 7.9 cd A^{-1}, a maximum power efficiency of 6.2 lm W^{-1} and a maximum luminance of 25350 cd m^{-2}, respectively. The AIEE WOLED displays simplification in device fabrication and excellent color stability, which belongs to the best fluorescent WOLED reported.

© 2010 Elsevier B.V. All rights reserved.

1. Introduction

Recently white organic light-emitting diodes (WOLEDs) have attracted particular attention because they have the merits of low-cost fabrication process, high efficiency, ultra-thin thickness, light weight, planar light emitting and so on. They offer great potential applications in flat-panel displays, as well as next generation solid-state indoor light sources [1–8]. Generally, WOLEDs are required to have long-term stability as working at high brightness and high current density, thus device working at rigorous conditions becomes a crucial issue. For example the Joule heat may induce the change of chemical structure and morphology of active layer materials and makes the destroying of device. In this context, the materials with high glass transition temperature (T_g) and/or aggregation-induced enhanced emission (AIEE) properties are of special significance for WOLEDs, because they afford a possibility to turnaround the thermal effects ca. induced the aggregation to a positive effect for device performance. The AIEE materials combining with other approaches that are used to increase the device efficiency may be propitious to obtain long-term and color stable WOLEDs.

In the past few years, materials with AIEE properties have drawn more attention, because they possess our desired property that is enhanced emission from aggregate state. A few AIEE materials including silole derivatives [9,10], styrylbenzene derivatives [11,12], and others [13–15] have been developed by various research groups. Some of them have been used for EL device exhibiting excellent device performance [16]. Here we report two oligo(paraphenylene vinylene) derivatives exhibiting typical AIEE properties with very high emission efficiency in solid state as well as excellent thermal stability. AIEE compounds of 1,4-bis(α-cyano-4-diphenylaminostyryl)-2,5-diphenylbenzene (**CN-DPASDB**) and 2,5,2′,5′-tetrakis(2,2-diphenylvinyl)biphenyl (**TDPVBi**) (their structures shown in Fig. 1) emit orange and blue light, respectively. The white OLEDs are constructed by **CN-DPASDB** and **TDPVBi** light-emitting layers exhibiting a significant stability in color, as a result their Commission Internationale de l'Eclairage (CIE) coordinates have little shift with increasing the voltage after optimizing the structures. By our knowledge, this is the

* Corresponding author. Tel./fax: +86 431 85168480.
E-mail address: ygma@jlu.edu.cn (Y. Ma).

1566-1199/$ - see front matter © 2010 Elsevier B.V. All rights reserved.
doi:10.1016/j.orgel.2009.12.026

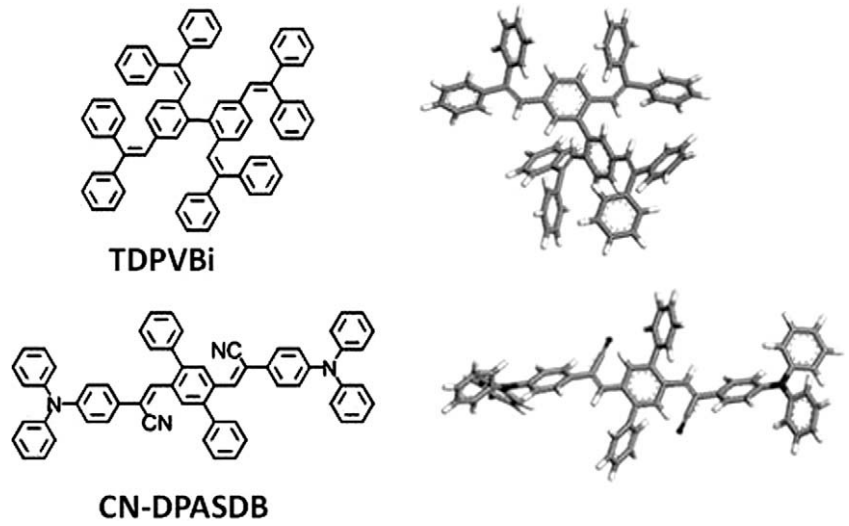

Fig. 1. The chemical structures of **TDPVBi** and **CN-DPASDB**. Sketch map of the 3D structure of **TDPVBi** and **CN-DPASDB** in the ground state, as predicted by molecular simulations.

first WOLEDs based on AIEE materials as the emitting layer. Herein we report the results.

2. Results and discussion

Fig. 2 shows the emission spectra of **CN-DPASDB** and **TDPVBi** in solution and solid state. **CN-DPASDB** in diluted THF solution emits orange light with peak wavelength of 583 nm and fluorescence efficiency of 9%. **TDPVBi** in diluted toluene solution emits blue light with peak wavelength of 464 nm and fluorescence efficiency of 11%, such fluorescence efficiencies of both compounds in solution are relatively lower compared with high fluorescent molecules ca. unsubstituted oligo(para-phenylene vinylene) distyrylbenzene (DSB) (fluorescence efficiency of 90% in solution). From the molecular configurations of **CN-DPASDB** and **TDPVBi** as shown in Fig. 1, the common characters of both molecules are non-planar and very twist molecular structure. The corresponding intramolecular motions ca. relative cis–trans isomerization of double bonds and free-rotation of end phenyl groups in solution may be the origin of weak fluorescence. In the solid state, the free-rotation occurring in both compounds in solution will be depressed due to intermolecular interaction, which is beneficial to enhanced fluorescent efficiency. The solid state fluorescence efficiency of **CN-DPASDB** and **TDPVBi** arrives at a very high value of 30%, and 80%, respectively, increasing up to 3–8 folds compared with their solutions.

Differential scanning calorimetry (DSC) analysis indicates that glass transition temperature (T_g) of **TDPVBi** is 110 °C, and no crystallization or phase transition occur upon heating beyond T_g. This suggests that the amorphous nature of the **TDPVBi** in condensed state, which may greatly benefit the formation of homogeneous and amorphous films through thermal evaporation. Atomic force microscopy (AFM) measurement indicates that the pristine vacuum deposition films of **TDPVBi** have a fairly smooth surface morphology with a root mean square (rms) roughness of 2.5 nm, and annealing for this film at 90 °C for 15 min makes surface more slippery with a rms roughness of 0.9 nm (detail shown in Fig. S1 in SEI). Such phenome-

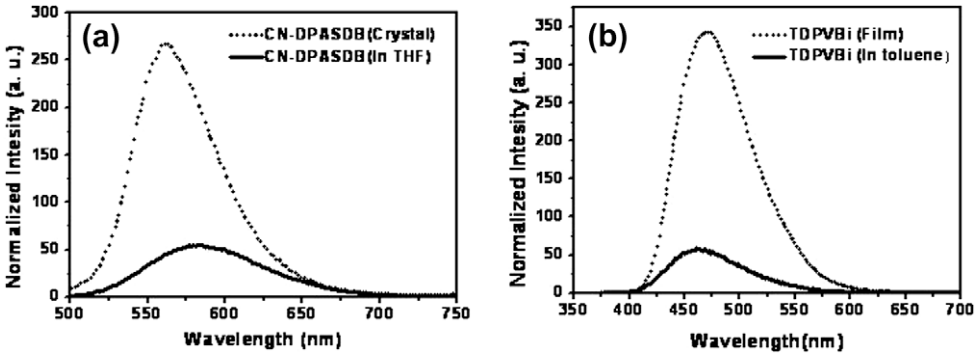

Fig. 2. (a) PL spectra of **CN-DPASDB** at room temperature in dilute THF solution (5×10^{-6} mol L^{-1}) and in crystal. (b) PL spectra of TDPVBi at room temperature in film on the quartz substrates and in dilute toluene solution (5×10^{-6} mol L^{-1}).

non should be related to enhance intermolecular interaction after annealing as the heating temperature is close to T_g, the molecules in film can adjust themselves to a suitable situation through free-rotation of end phenyl groups and the rotation of biphenyl core, which makes amorphous film of **TDPVBi** become more dense and rigid. **CN-DPASDB** is a crystalline material, but a film with smooth surface still can be obtained under a controlled vacuum deposition condition.

The devices performance based on **CN-DPASDB** and **TDPVBi** are characterized by utilizing a standard device with the structure of indium tin oxide (ITO)/N,N′-di-1-naphthyl-N,N′-diphenylbenzidine (NPB) (40 nm)/AIEE emitter layer (10–40 nm)/1,3,5-tri(phenyl-2-benzimidazolyl)-benzene (TPBi) (40–50 nm)/LiF (0.5 nm)/Al (100 nm). TPBi is chosen as the electron-transporting and hole-blocking layer because it has the much higher electron mobility than that of Alq_3 (the classic electron-transporting material) and relatively low highest occupied molecular orbital (HOMO) level [17]. The **CN-DPASDB** (10 nm) device shows the EL spectra with peak wavelength at 579 nm corresponding to the CIE coordinates of (0.50, 0.50), and EL spectra keeps unchanged when the driving voltage increases from 5 to 12 V. The turn-on voltage, maximum luminance and maximum luminescent efficiency are 5 V, 14667 cd m^{-2} and 4.0 cd A^{-1}, respectively (detail shown in Fig. 3). The performance of **CN-DPASDB** based device is better than that of the classic orange material ca. rubrene [18], while non-doped film fabrication of **CN-DPASDB** is relatively simple as compared with rubrene device in which rubrene must be doped into certain host materials due to their strong concentration quenching. So in the view of simplifying the fabrication process of OLED, **CN-DPASDB** is the suitable candidate to take the place of rubrene.

The OLED based on **TDPVBi** shows the blue emission (electroluminescent (EL) peak of 468 nm) with a CIE coordinates of (0.16, 0.21), maximum luminance exceeding 31170 cd m^{-2} and luminescent efficiency of 6.2 cd A^{-1} (detail shown in Fig. S3b in SEI). **TDPVBi** exhibits significantly improved film quality and thermal stability due to the cruciform structure compared with the classic blue-emitting material, 4,4′-bis(2,2-diphenylvinyl)-1,1′-biphenyl (**DPVBi**) and belongs to the best blue materials reported.

The non-doped WOLEDs with varied structure are fabricated (detail shown in Fig. S4a, S4d, S4g in SEI). These are the first demonstration of WOLEDs which are combined all by AIEE molecules with a high luminance and luminescent efficiency. A special design in WOLEDs is a very thin **CN-DPASDB** layer (0.1–0.5 nm) combining with a thick **TDPVBi** layer (20 nm), which is based on the consideration of the color match and the crystalline properties of **CN-DPASDB**. The very thin **CN-DPASDB** layer may decrease its crystalline effect. The device with the structure of ITO/NPB (50 nm)/**TDPVBi** (20 nm)/**CN-DPASDB** (0.5 nm)/TPBi (60 nm)/LiF (0.5 nm)/Al (100 nm) shows a high performance. Turn-on voltage, maximum luminance, maximum luminescent efficiency and maximum power efficiency are 3.5 V, 25350 cd m^{-2} (12.5 V), 7.9 cd A^{-1} (4.0 V), 6.2 lm W^{-1} (4.0 V), respectively. (detail shown in Fig. S4c(b) in SEI) Such device shows the CIE coordinate localized at white light zone at various voltages, the shift of CIE coordinate with driving voltages is significant, ca. CIE of (0.36, 0.38) at low voltage (4 V), and CIE of (0.24, 0.29) at high voltage (10 V) (detail shown in Fig. S4b(b) in SEI). Significant increase in blue spectra with increased voltage reflects a change of emitting region in device at high driving voltage. According to the theoretical analysis for multilayer OLED by Chen and Meng [19]. We can demonstrate that in this device the recombination is firstly concentrated on the orange **CN-DPASDB** layer at low voltages likely due to the relatively low electron mobility of **CN-DPASDB**, and then the recombination extends to the **TDPVBi** layer because the electric field strongly enhances the electron mobility as the voltage increases. An exchange of blue and orange emitting layer to construct a device with structure of ITO/NPB (50 nm)/**CN-DPASDB** (0.1 nm)/**TDPVBi** (20 nm)/TPBi (60 nm)/LiF (0.5 nm)/Al (100 nm), shows high device performance with a maximum luminance of 39790 cd m^{-2} (11.5 V) and maximum luminescent efficiency of 8.4 cd A^{-1} (6.0 V), (detail shown in Fig. S4f (b) in SEI) but blue spectra in such device are strongly suppressed, the CIE coordinates of the device is found to be located at the orange light zone (detail shown in Fig. S4e(b) in SEI). Such spectra behaviors are likely due to the energy transport between two emitting layer and/or shift of emission zone under device operation. Thus a thin layer of NPB (3 nm) is inserted between the **CN-DPASDB** and **TDPVBi** layers aiming at the balance of orange and blue emission. The optimized device structure of ITO/NPB (50 nm)/**CN-DPASDB** (0.1 nm)/NPB (3 nm)/**TDPVBi** (20 nm)/TPBi (60 nm)/LiF (0.5 nm)/Al (100 nm) shows the stable white emission and high device performance. From the energy level shown in Fig. 5, the lowest unoccupied molecular orbital (LUMO) level of NPB is −2.3 eV which is about 0.3 eV higher than that of **TDPVBi**, and exciton energy of NPB is 0.2 eV higher than that of **TDPVBi**, so the inserted NPB layer can play a role in partly block the electrons injection and energy transfer from blue **TDPVBi** layer to **CN-DPASDB** layer. From EL spectra of device shown in Fig. 4, the device shows excellent spectral stability, and CIE of (0.28, 0.35) at 4 V (2.9 cd m^{-2}) and (0.28, 0.34) at 11 V (17990 cd m^{-2}) localized at white light zone. Fig. 5 shows the luminance-voltage and luminescent efficiency–voltage characteristic of the device, respectively. The maximum luminance and the maximum luminescent efficiency of the device are 19450 cd m^{-2} (at 11.5 V) and 7.5 cd A^{-1} (at 6.5 V), respectively. As brightness of 1000 cd m^{-2}, the efficiency is 7.1 cd A^{-1}.

WOLEDs made of phosphorescent dyes have a high performance [20–23]. But phosphorescent dyes are not suitable for non-doped systems, which make the device process complex. Now reported best fluorescent WOLEDs showed the efficiency of 9.37 cd A^{-1}, 4.20 lm W^{-1} [24], and by utilizing a p-i-n structure efficiency arrive to 8.7 lm W^{-1} [25], but their color stability was not so good behaving a driving voltage depended spectra characteristics. There were up to nine organic layers in these WOLEDs which were too complex for practical application. The devices made by our AIEE materials are relatively simple in fabrication, which are combined by less than five organic layers. Currently, the blue materials are still the key com-

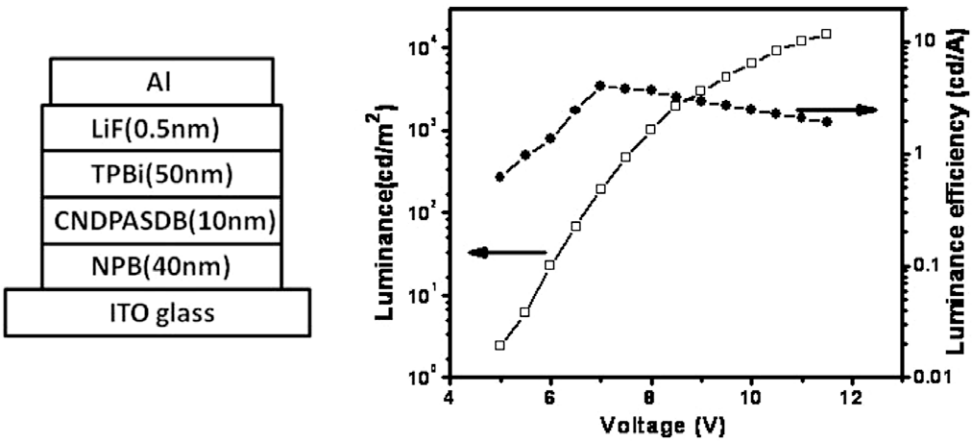

Fig. 3. The luminance-voltage and luminescent efficiency–voltage curves of the OLED based on **CN-DPASDB**.

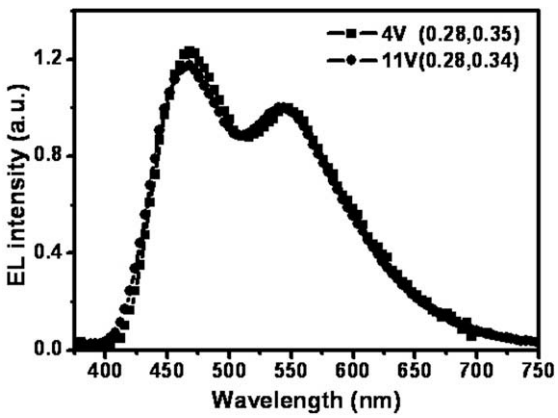

Fig. 4. The EL spectra and CIE coordinate of the WOLED at 4 V and 11 V.

ponent to determine the device performance in OLEDs, in this context, our AIEE blue material **TDPVBi**, which exhibit annealing induced more smooth surface morphology and enhanced PL intensity, provides the great potentials for the fabrication of stable device.

3. Experimental

3.1. Materials

The compounds, **CN-DPASDB** [26] and **TDPVBi** [27], were synthesized in our laboratory as previously reported. N,N′-di-1-naphthyl-N,N′-diphenylbenzidine (NPB), 1,3,5-tri(phenyl-2-benzimidazolyl)-benzene (TPBi) and lithium fluoride (LiF) were purchased commercially and used as the hole-transporting layer, electron-transporting layer, and electron-injection layer, respectively. They were used without purifying. The chemical structures of materials in this work are shown in Fig. 1.

3.2. Instruments

The indium tin oxide (ITO) coated glass substrates were cleaned in an ultrasonic bath with toluene, acetone, ethanol and deionized water, respectively, and then dried with nitrogen, finally irradiated in UV-ozone chamber. The organic materials were sequentially deposited onto the cleaned ITO coated glass substrate through thermal evaporation. The layer thickness of the deposited material was monitored in situ using an oscillating quartz thickness monitor. Finally a LiF buffer layer and Al cathode were deposited onto the organic films through a shadow mask. The background pressure of the chamber was under 10^{-6} Torr during the deposition process. The electroluminescent (EL) spectra and CIE coordinates of the devices were measured by using a PR 650 spectrometer. The luminance-voltage and current–voltage characteristics were measured simultaneously with a programmable Keithley 2400 voltage–current source. UV–vis absorption spectra were recorded on UV-3100 spectrophotometer. Fluorescence measurements were carried out with RF-5301PC instrument. The PL quantum efficiency of films were measured in an integrating sphere [28]. AFM images were recorded on a Seiko SPA 400 with an SPI 3800 probe station in tapping mode (dynamic force mode). All measurements were carried out at room temperature under ambient conditions.

4. Conclusion

In summary, the first AIEE materials based WOLEDs which showed simple device structure and high performance have been demonstrated by us. The blue AIEE molecule **TDPVBi** showed the special applicability for OLEDs, ca. enhanced smoothness as annealing its film. The blue and orange AIEE materials showed high EL performance, which are comparable with the classic blue material **DPVBi** and orange material rubrene. Combining both AIEE materials to construct WOLED exhibits a maximum current efficiency of 7.9 cd A^{-1}, a maximum power efficiency of 6.2 lm W^{-1} and a maximum luminance of 25350 cd m^{-2}, respectively. Important impress of the AIEE WOLED is its simplification in device fabrication and excellent color stability, which render such device the potential application as the solid-state indoor lighting sources.

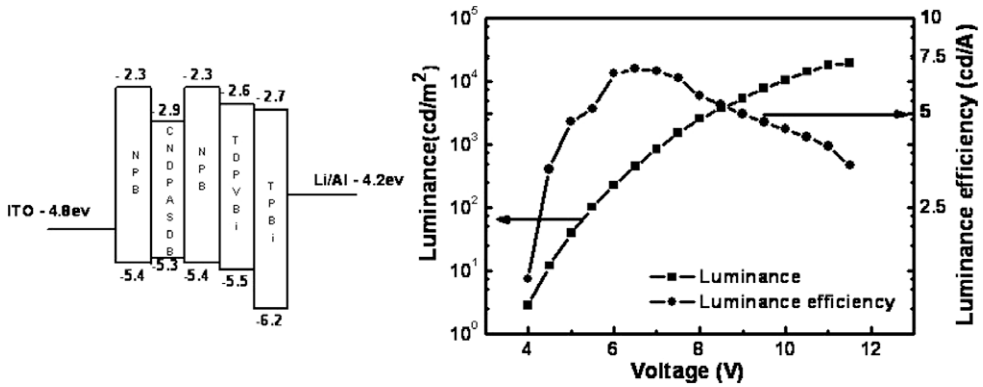

Fig. 5. The energy diagrams of the WOLED. The luminance–voltage characteristics and luminescent efficiency–voltage characteristics of the WOLED based on **TDPVBi** and **CN-DPASDB**.

Acknowledgment

We are grateful for financial support from National Natural Science Foundation of China (Grant Number 60706016), the Ministry of Science and Technology of China (Grant Number: 2009CB623605).

Appendix A. Supplementary data

Supplementary data associated with this article can be found, in the online version, at doi:10.1016/j.orgel.2009.12.026.

References

[1] B.W. D'Andrade, S.R. Forrest, Adv. Mater. 16 (2004) 1585–1595.
[2] Y. Sun, N.C. Giebink, H. Kanno, B. Ma, M.E. Thompson, S.R. Forrest, Nature 440 (2006) 908–912.
[3] G. Li, J. Shinar, Appl. Phys. Lett. 83 (2003) 5359–5361.
[4] X.-M. Yu, H.-S. Kwok, W.-Y. Wong, G.-J. Zhou, Chem. Mater. 18 (2006) 5097–5103.
[5] G. Schwartz, K. Fehse, M. Pfeiffer, K. Walzer, K. Leo, Appl. Phys. Lett. 89 (2006) 083509-1–083509-3.
[6] S.L. Lai, M.Y. Chan, M.K. Fung, C.S. Lee, S.T. Lee, Appl. Phys. Lett. 90 (2007) 203510-1–203510-3.
[7] L. Wang, M.-F. Lin, W.-K. Wong, K.-W. Cheah, H. Lam Tam, Z.-Q. Gao, C.H. Chen, Appl. Phys. Lett. 91 (2007) 183504-1–183504-3.
[8] B.D. Chin, J.K. Kim, O.O. Park, J. Phys. D: Appl. Phys. 40 (2007) 4436–4441.
[9] J.D. Luo, Z.L. Xie, J.W.Y. Lam, L. Cheng, H.Y. Chen, C.F. Qiu, H.S. Kwok, X.W. Zhan, Y.Q. Liu, D.B. Zhu, B.Z. Tang, Chem. Commun. (2001) 1740–1741.
[10] J.W. Chen, B. Xu, K.X. Yang, Y. Cao, H.H.Y. Sung, I.D. Williams, B.Z. Tang, J. Phys. Chem. B 109 (2005) 17086–17093.
[11] S.-J. Lim, B.-K. An, S.D. Jung, M.-A. Chung, S.Y. Park, Angew. Chem. Int. Ed. 43 (2004) 6346–6350.
[12] H.-C. Yeh, S.-J. Yeh, C.-T. Chen, Chem. Commun. (2003) 2632–2633.
[13] Z.X. Wang, H.X. Shao, J.C. Ye, L. Tang, P. Lu, J. Phys. Chem. B 109 (2005) 19627–19633.
[14] Y. Liu, X.T. Tao, F.Z. Wang, X.N. Dang, D.C. Zou, Y. Ren, M.H. Jiang, J. Phys. Chem. C 112 (2008) 3975–3981.
[15] Z.Q. Xie, B. Yang, W.J. Xie, L.L. Liu, F.Z. Shen, Y.G. Ma, J. Phys. Chem. B 110 (2006) 20993–21000.
[16] H.Y. Chen, W.Y. Lam, J.D. Luo, Y.L. Ho, B.Z. Tang, D.B. Zhua, M. Wong, H.S. Kwok, Appl. Phys. Lett. 81 (2002) 574–576.
[17] Y.Q. Li, M.K. Fung, Z.Y. Xie, S.T. Lee, L.S. Hung, J.M. Shi, Adv. Mater. 14 (2002) 1317–1321.
[18] T.-H. Liu, Y.-S. Wu, M.-T. Lee, H.-H. Chen, C.-H. Liao, C.H. Chen, Appl. Phys. Lett. 85 (2004) 4304–4306.
[19] C.-H. Chen, H.-F. Meng, Appl. Phys. Lett. 86 (2005) 201102-1–201102-3.
[20] B.W. D'Andrade, R.J. Holmes, S.R. Forrest, Adv. Mater. 16 (2004) 624–628.
[21] Y. Sun, N.C. Giebink, H. Kanno, B. Ma, M.E. Thompson, S.R. Forrest, Nature 440 (2006) 908–912.
[22] E.L. Williams, K. Haavisto, J. Li, G.E. Jabbour, Adv. Mater. 19 (2007) 197–202.
[23] Q. Wang, J.Q. Ding, D.G. Ma, Y.X. Cheng, L.X. Wang, X.B. Jing, F.S. Wang, Adv. Funct. Mater. 19 (2009) 84–95.
[24] H.S. Yang, Y.W. Shi, Y. Zhao, S.Y. Liu, Solid-State Electron. 52 (2008) 657–662.
[25] Y. Duan, M. Mazzeo, V. Maiorano, F. Mariano, D. Qin, R. Cingolani, G. Gigli, Appl. Phys. Lett. 92 (2008) 113304.
[26] Y.P. Li, F.Z. Shen, H. Wang, F. He, F. Li, Y.G. Ma, Chem. Mater. 20 (2008) 7312–7318.
[27] S.J. Liu, F. He, H. Wang, H. Xu, C.Y. Wang, F. Li, Y.G. Ma, J. Mater. Chem. 18 (2008) 4802–4807.
[28] Y. Kawamura, H. Sasabe, C. Adichi, Jpn. J. Appl. Phys. 43 (2004) 7729–7730.

Organic Electronics 11 (2010) 618–625

Contents lists available at ScienceDirect

Organic Electronics

journal homepage: www.elsevier.com/locate/orgel

Temperature-dependent ultra-thin polymer layer for low voltage organic thin-film transistors

Ting-Hsiang Huang, Hui-Chen Huang, Zingway Pei *

Department of Electrical Engineering, National Chung Hsing University, Taichung 40227, Taiwan, ROC

ARTICLE INFO

Article history:
Received 29 June 2009
Received in revised form 16 November 2009
Accepted 2 January 2010
Available online 12 January 2010

Keywords:
Low voltage OTFT
Organic dielectric
Random copolymer

ABSTRACT

In this article, a low voltage organic thin-film transistor (OTFT) was accomplished by using a random copolymer, poly(styrene-co-methyl methacrylate) (PS-r-PMMA), as the gate dielectric. The thickness of PS-r-PMMA polymer can be controlled well by thermal process and shows an ultra-thin property after toluene rinse. The thickness of PS-r-PMMA can be controlled in the range of 2–14 nm. By the densely packed copolymer brush, a leakage current as low as 10^{-9} A/cm^2 was obtained. By utilizing this polymer as gate dielectric, pentacene based organic thin-film transistor could be operated at 5 V with 0.1 cm^2/V s mobility and 0.27 V/dec subthreshold swing. In addition to good OTFT properties, the coating, annealing and removing sequential process of PS-r-PMMA ensure that this technique is compatible with the large area printing methods such as ink-jet printing and doctor blade coating. The random copolymer dielectric is therefore suitable for OTFT in large area printed flexible electronic applications.

© 2010 Elsevier B.V. All rights reserved.

1. Introduction

Research efforts devoted to polymer based microelectronic and optoelectronic devices have grown significantly in recent years. The advantages are low processing temperature which is compatible with the plastic substrates, simple processing steps that is potentially low cost, low elastic modulus which is flexible and deposition by printing process that could be produced in large area. Consumer products such as flexible display, radio frequency identification tag (RFID), smart cards, polymer solar cell and polymer sensors are therefore demonstrated [1–5]. Among all products, the organic thin-film transistor (OTFT) is no doubt the most important device. They are used not only as the logic circuit in sensors, RFID and smart cards but also the addressing and current source components in flexible display [30].

Although many efforts have been done to improve the properties of OTFTs, there are still some issues to be explored [6–8]. Main challenge is controlling the properties of the organic dielectric [9,10] which is printed in large area for low voltage OTFTs. Low voltage is essential for OTFTs, since the above-mentioned applications are portable products that have very limited energy capacity. Low driving voltage could save the usage of electrical power. Another is printing in large area with controlled properties. Both logic circuit and the active addressing circuit need OTFT performance with high uniformity. Very less thickness or interface properties variation could make those circuits unstable or even fail. For these requirements, the dielectric layer of OTFT must be well controlled and should have high uniformity over a large area.

One of the key factors that determine the driving voltage of a thin-film transistor is the capacitance of the gate dielectric layer expressed by the following equation:

$$Q_{ch} = C_i \times V \tag{1}$$

where Q_{ch} is the carrier density for channel, C_i is the density of the gate capacitance and V is the driving voltage.

* Corresponding author. Address: Department of Electrical Engineering, National Chung Hsing University, 250, Kuo Kuang Rd., Taichung 40227, Taiwan, ROC. Tel.: +886 4 22851549x801; fax: +886 4 22851410.
E-mail address: zingway@dragon.nchu.edu.tw (Z. Pei).

1566-1199/$ - see front matter © 2010 Elsevier B.V. All rights reserved.
doi:10.1016/j.orgel.2010.01.001

The density of capacitance can be further expressed as follows:

$$C_i = \frac{\varepsilon_o \varepsilon_r}{t} \quad (2)$$

where ε_o is permittivity of free space, ε_r is dielectric constant of the organic insulator and t is the thickness of the dielectric. Therefore, by Eq. (1), low driving voltage requires high gate capacitance. To achieve high capacitance for gate dielectric, by Eq. (2), there are two methods in general. One is adopting high dielectric constant material and the other is utilizing ultra-thin dielectric. High dielectric constant metal oxides such as HfO_2, Y_2O_3, Ta_2O_5, TiO_2 and Al_2O_3 [19–23] are not only popular for Si technology but also for the OTFTs. The metal oxides generally exhibit hydrophilic surface, higher roughness and fixed oxide charge in the dielectric layer. In addition, the metal oxides could not be deposited well by printing process in large area. However, the surface energy of gate dielectric greatly affects the morphology of organic semiconductor. Both small molecular and polymer organic semiconductor such as pentacene and polythiophene tend to form better film structures on the hydrophobic surface, leading to the higher mobility and better interface [11,12]. The roughness of the dielectric surface significantly influences the carrier transport mobility of OTFT [13,14], since the carriers scattering with the interface roughness will slow down the carrier transport velocity. These imply that the high dielectric constant metal oxides are not adequate materials for high quality and low voltage OTFTs in current situation even hybrid organic/inorganic material are used for higher mobility and better interfaces [24,25].

To obtain ultra-thin, robust and hydrophobic gate dielectric, techniques of self-assembled monolayer (SAM), are generally used [15–18]. The organic material for SAM, which is designed with several nanometers chain length, ensure that the OTFT could be operated in a voltage as low as ~1 V. The possibility of well packing of the SAM also keeps very low leakage current through the gate dielectric at high electrical field. Although SAM layer demonstrates the low voltage operational properties of OTFTs, it is hard to find demonstration of SAM in large area, which is the essential factor for low cost flexible electronics. This might be due to the inherent property of "monolayer". Any place between gate electrode and organic semiconductor without chemical bonding to the monolayer molecular will cause severe leakage current that might make the OTFT fail. Therefore, the basic requirements for gate dielectric are high capacitance, low current leakage, controlled thickness and fully printing compatibility.

In this work, an ultra-thin polymer dielectric layer with temperature-dependent thickness property for low voltage OTFTs was developed based on random copolymer. The random copolymer, poly(styrene-co-methyl methacrylate) (PS-r-PMMA), was studied well in the field of self-assembled nano-patterning [26–29]. In the nano-patterning, PS-r-PMMA was used as a surface modification layer for the following block copolymer layer. After thermal annealing, a very thin layer of PS-r-PMMA formed on the underlying surface, about several nanometers thick. The random polymer brushes ensured the coverage on the whole surface to restrict leakage current. Therefore, random copolymer such as PS-r-PMMA is suitable for the gate dielectric of low voltage OTFTs.

2. Experimental

2.1. Preparation of PS-r-PMMA dielectric

The PS-r-PMMA random copolymer (M_w = 100,000–150,000) solution was prepared by dissolving PS-r-PMMA in toluene in a concentration of 20 mg/ml. After stirring overnight, the PS-r-PMMA solution was either drop casted or spin coated on the Si substrate at 500 rpm for 60 s for material analysis. After coating, the PS-r-PMMA was thermally annealed at the temperatures varied from 130 to 190 °C for 12 h. By thermal annealing, the PS-r-PMMA polymers near the Si surface chemically bonded to the native oxide. After this bonding process, the sample was dipped in toluene, the residue PS-r-PMMA was dissolved and a sub-10 nm layer of PS-r-PMMA was formed.

For thin film characteristics, ellipsometer was used to measure the film thickness. For the accuracy of thickness measurement, the n and k parameters set in the ellipsometer were adjusted according a known thickness of rinsed PS-r-PMMA that was obtained from AFM image. Besides, scanning electron microscopy (SEM) and atomic force microscopy (AFM) were applied to observe the surface morphology.

2.2. OTFT fabrication

A bottom gate and top contact structure was applied to realize the PS-r-PMMA-based OTFT. A 100 nm thick aluminum was grown by thermal evaporation on the glass through a shadow mask as the gate electrode. Prior to the PS-r-PMMA coating, Al was illuminated by ultra-violet light (254 nm) for 30 min. In this step, a 7.5-nm-thick Al_2O_3 was grown on the Al surface. After coating, the PS-r-PMMA was thermally annealed at either 150 °C or 190 °C for 12 h and then removed the unattached chains by toluene. After ultra-thin PS-r-PMMA dielectric formation, the 40-nm-thick channel layer and 30-nm-thick source/drain electrodes were sequentially grown by thermal evaporation through associated shadow mask. Pentacene is used as the channel material and gold is used as the electrodes for source and drain. The electrical properties including leakage current of dielectric and current–voltage characteristics of OTFT were measured by a HP 4145A semiconductor analyzer. The capacitance measurements were carried out by 4284A impedance analyzer at 10 kHz. All electrical measurements were performed under dark and ambient environment.

3. Results and discussion

3.1. Physical properties of the PS-r-PMMA copolymer

Fig. 1a shows the schematic concept of the PS-r-PMMA thin film for large area application. While the PS-r-PMMA

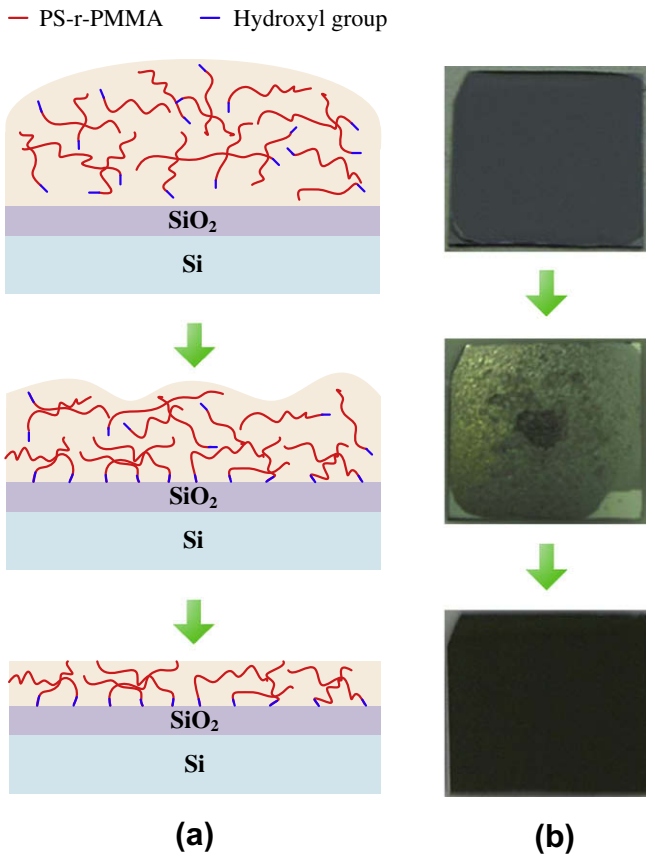

Fig. 1. The evolution of PS-r-PMMA dielectric material. (a) Schematic diagram of the formation mechanism from the solution to thin film. (b) Optical images for those process steps.

solution was casted on the native oxide layer, the copolymer chains stack with each other and distribute randomly in about 3 μm thick. After annealing the PS-r-PMMA (T_g = 101 °C) at the temperature above glass transition temperature (T_g) of both PS (T_g = 100 °C) and PMMA (T_g = 99 °C) in oxygen-free and humidity-free environment, the small amount of hydroxyl groups (OH^-) produced during the copolymer synthesis process will diffuse and react with the native oxide surface to from a chemical bond [26]. The un-bound PS-r-PMMA random copolymer chains are removable by toluene to form an ultra-thin and uniform dielectric film. Fig. 1b shows the evolution of PS-r-PMMA thin film observed by an optical microscope. The drop casted PS-r-PMMA solution was spread well over the entire Si substrate. After thermal annealing, the toluene evaporates and leaves a very rough PS-r-PMMA surface with irregular cavities that is a typical case in a large area printing process for dielectric films. After being rinsed by toluene, the irregular cavities and mounts were removed, obtaining a remarkable smooth surface of PS-r-PMMA film.

For further microscopic confirmation, Fig. 2a shows the SEM image of PS-r-PMMA film without toluene rinse in which many mounds and cavities were found. In contrast, after being rinsed by toluene for 30 s, large numbers of unattached PS-r-PMMA chains were taken away that mounds and cavities were removed as shown in Fig. 2b. The uniformity was significantly improved over the entire sample. After being rinsed in toluene, the thickness of the PS-r-PMMA film determined by the ellipsometer was reduced to nanometer regime. The scale bars in Fig. 2a and b are 100 μm and 100 nm, respectively. Fig. 2c and d shows the AFM topography image for the spin coated PS-r-PMMA film with and without rinse, respectively, in small scale. The pristine PS-r-PMMA layer showed a root mean square roughness (RMS) of 0.28 nm. After being rinsed in toluene, the smoother PS-r-PMMA surface with RMS roughness of 0.2 nm was found. Follow by optical microscopy, SEM image and AFM topography measurements, the toluene rinsed PS-r-PMMA film shows flat surface from macroscopic to microscopic. The results imply the possibility to grow better organic semiconductor on rinsed PS-r-PMMA. Fig. 2e and f shows the morphology of 40-nm-thick pentacene evaporated on the pristine and rinsed PS-r-PMMA and the pentacene grain sizes were 180 and 210 nm, respectively. Larger grains were found on flat PS-r-PMMA surface.

In addition to the smooth surface, the brush thickness of PS-r-PMMA can also be controlled. After complete film formation process, we divided each sample (2 cm × 2 cm) into nine regions (3 × 3 grid) and measured the thickness of these regions at once without considering swelling effect. Nine data from each condition were obtained for statistics analysis. Fig. 3a shows the relationship between the

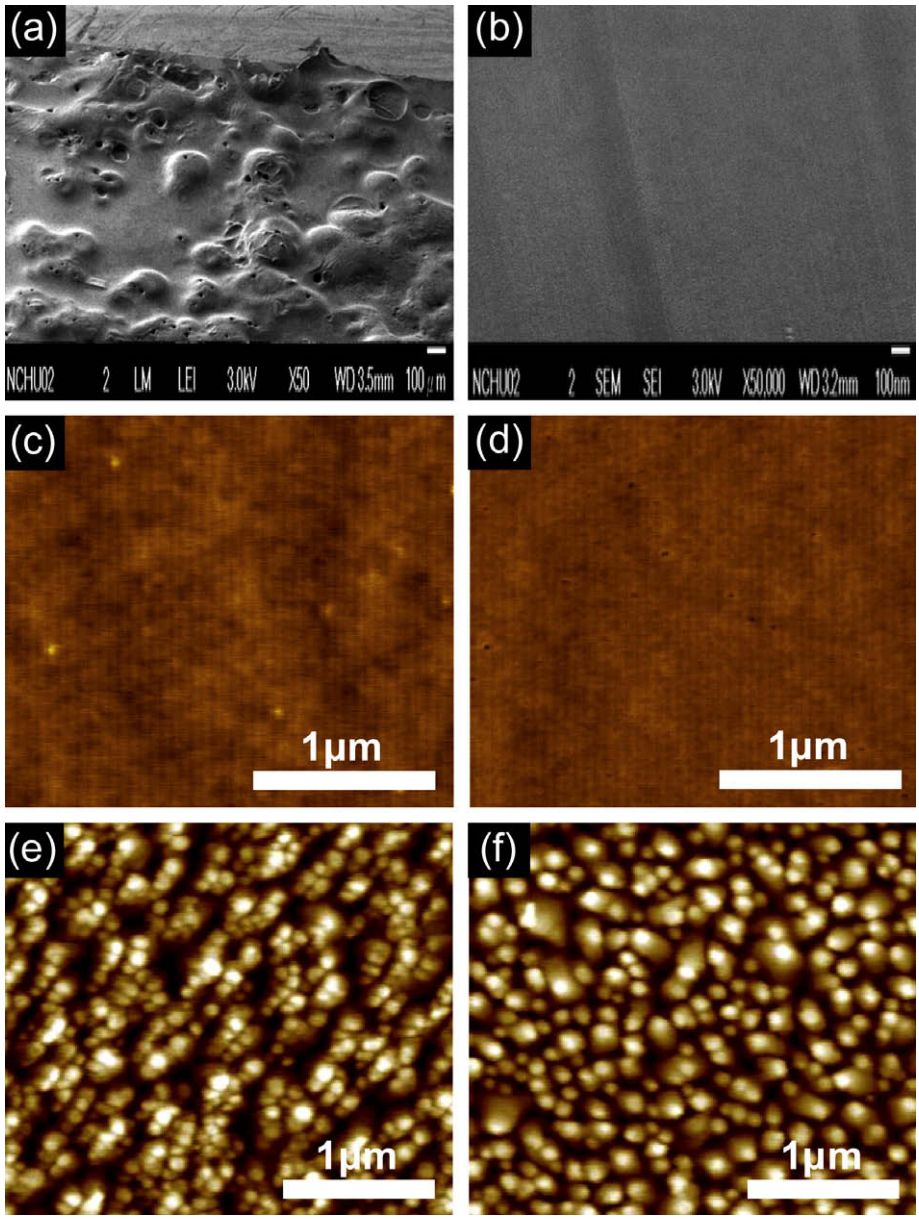

Fig. 2. The morphology of random copolymer dielectric material and organic semiconductor on it. (a) SEM image of PS-r-PMMA formed by drop casting. (b) PS-r-PMMA surface of drop casted PS-r-PMMA after toluene rinse. Tapping mode AFM images of spin coated PS-r-PMMA film (c) without toluene rinse and (d) with toluene rinse. Pentacene growth on (e) PS-r-PMMA without toluene rinse and (f) toluene rinsed PS-r-PMMA copolymer.

thickness and annealing conditions. Below 150 °C, the PS–PMMA film thickness was kept around 2–3 nm. At higher temperature, the thickness increased rapidly in the first 10 h and then kept around. The thickness of 10–14 nm and 6–8 nm were obtained for 190 and 170 °C annealed sample, respectively. This saturation in thickness can be explained by the following mechanism. The attached polymer chains will stretch to provide a high entropic barrier restricting the further adhesion of supplementary chains upon thermal annealing [26]. As the temperature increases further, sufficient thermal energy probably enhances the diffusion ability that would overcome the entropic barrier to attach on the hydrophilic oxide surface. If PS-r-PMMA did not strongly bond to the native oxide, the copolymer would be almost removed by toluene. Based on experimental results, the PS-r-PMMA thickness is temperature-dependent even after toluene rinsing. Therefore, we quoted the statements from the literature [26] and regard PS-r-PMMA chemically bond to silicon oxide.

Fig. 3b and c shows the schematic diagram for the PS-r-PMMA chain attachment on the oxide surface at low and high temperature, respectively. At low temperature, the thermal energy is not high enough to exceed entropic barrier for the unattached PS-r-PMMA chains so that only few

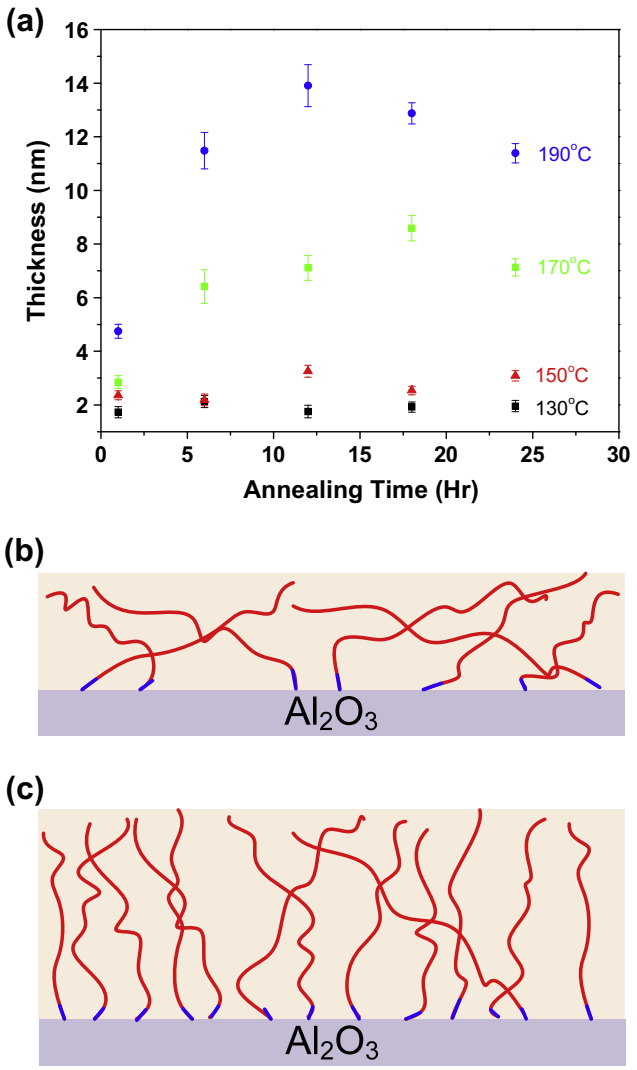

Fig. 3. Arrangement of PS-r-PMMA annealed at different temperatures. (a) Relationships between grafted layer thickness and annealing temperature. (b) The chains packed randomly at low temperature. (c) Contribution of line up effect strengthened the PS-r-PMMA chains and densely packed at high temperature.

polymer chains can reach and attach on the hydrophilic oxide surface. As a consequence, the long polymer chain laid along the oxide surface yields PS-r-PMMA film that is 2–3 nm thick. At high annealing temperature, 190 °C for instance, the grafting reaction occurs easily at surface due to enough thermal energy. The high-density PS-r-PMMA polymer chains attached on the oxide surface squeeze each other, causing the polymer chains to partly line up to form thicker film. The thickness of PS-r-PMMA therefore depends on chain stretching conditions and is controlled by thermal process.

3.2. Electrical properties of the PS-r-PMMA copolymer

The leakage current of PS-r-PMMA with metal–insulator–metal sandwich structure is presented in Fig. 4a. The leakage current was presented by current density and the contact area for the leakage current measurements was 0.04 cm^2. For pure polystyrene (PS), the current density raised up to 10^2 A/cm^2 at the electrical field of 1 MV/cm. Leakage current increases with raising the electric field and charge carriers easily transported through the pure polystyrene. For pure PMMA, the leakage current was in a range of 10^{-9}–10^{-7} A/cm^2 from 0.01 to 3 MV/cm. In contrast, the random copolymer PS-r-PMMA achieved an excellent leakage current density around 10^{-9} A/cm^2 and maintained at this order even in a strong electric field of 3 MV/cm. By comparing with pure PMMA and copolymer PS-r-PMMA, the remarkable leakage current reduction about two orders of magnitude was observed. This could be explained by the densely packed PS-r-PMMA film at high temperatures as depicted in Fig. 3c. During the annealing process, most of the PS-r-PMMA chains pack well that the defects existing in the organic insulator can be decreased and carriers hardly jump along the traps to form the leakage current.

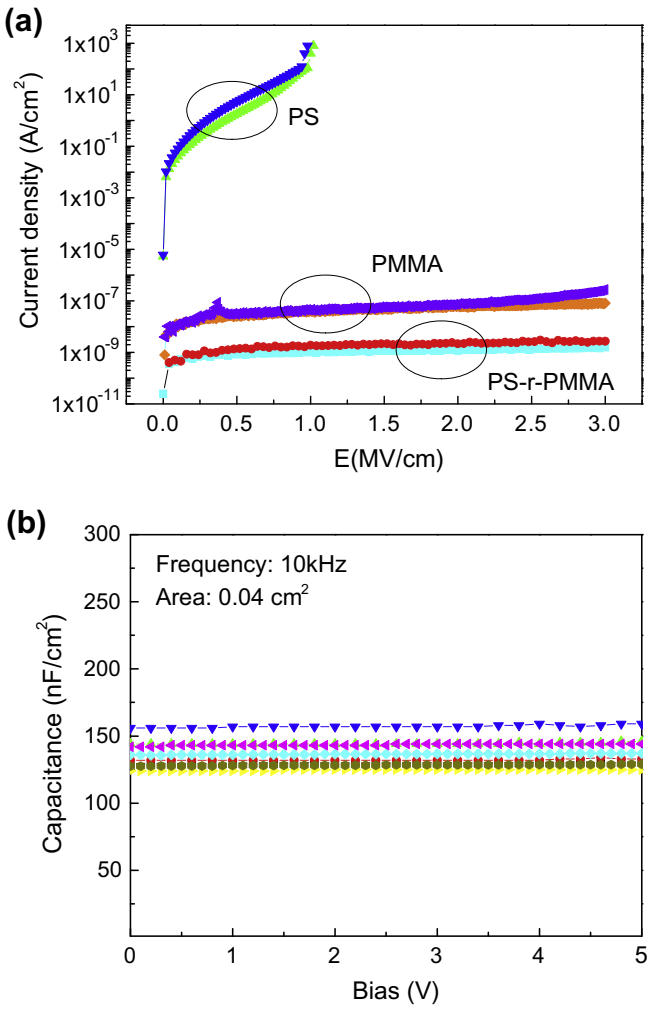

Fig. 4. Electrical properties of the PS-r-PMMA insulator. (a) Leakage current comparison between PS-r-PMMA, PS and PMMA. (b) Capacitance for 190 °C annealed PS-r-PMMA polymer film after toluene rinse.

The capacitance–voltage characteristics were measured for the PS-r-PMMA film with the metal–insulator–metal structure as shown in Fig. 4b. The capacitance density is in the range of 125–156 nF/cm^2. As a consequence of the high capacitance density and low leakage current density, the operation voltage was estimated around 5 V. In general, the channel carrier density of "on state" for TFT is about 10^{12}–10^{13} cm^{-2} that indicates charge density of 1.6×10^{-7}–1.6×10^{-6} C/cm^2. By applying this charge density and measured capacitance to Eq. (1), the operating voltage is estimated to be around 5 V, being compatible to silicon-based very large scale integration (VLSI) circuit technology at gate length of 1 μm [31].

3.3. Characteristics of OTFT with PS-r-PMMA dielectric

Fig. 5a shows the top contact structure of the PS-r-PMMA based OTFT by using pentacene as the channel material. Fig. 5b shows the chemical structure of PS-r-PMMA. To further investigate the surface energy of the PS-r-PMMA, the contact angle was shown in Fig. 5c. The water contact angle about 85° was obtained, thus indicating a hydrophobic surface after PS-r-PMMA coating. Fig. 6a and b illustrates the output and transfer characteristics of the OTFT with PS-r-PMMA annealed at 190 °C. The 5 V operation voltage was achieved. The mobility in which extracted from the saturation regime is ~0.1 cm^2/V s. The threshold voltage is −2.5 V and the subthreshold swing of 0.27 V/dec is obtained. The on/off current ratio is ~5000. In comparison, the transfer characteristics for OTFT with 150 °C annealing and original PS–PMMA film as dielectric layer are also depicted in Fig. 6c and d, respectively. By using 150 °C annealed PS-r-PMMA as the gate dielectric, even higher drain current at 5 V is obtained. The OTFT with PS-r-PMMA without rinse reasonably requires a voltage as high as 40 V to operate. For the environmental stability, PS-r-PMMA is not a hydroxyl-rich material, unstable effect of ambient oxygen and water on threshold voltage shift is not obvious. After polymer chains grafting on the native oxide, the intrinsic properties of PS

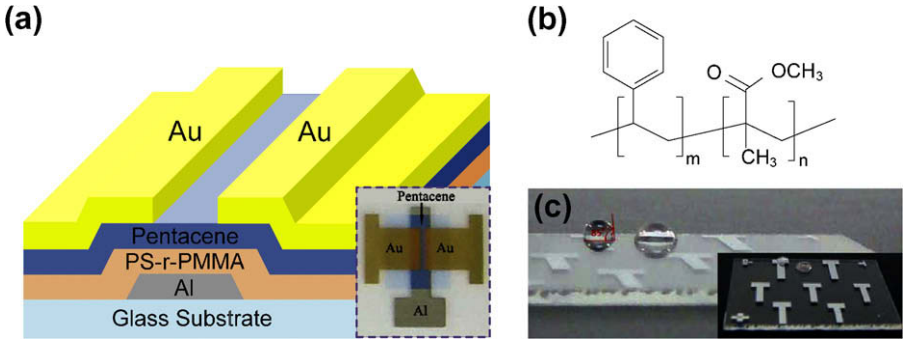

Fig. 5. (a) Schematic diagram of top contact OTFT with PS-r-PMMA dielectric and top view of the practical OTFT device. (b) Chemical structure of the PS-r-PMMA used in this research. (c) Water contact angle measurements comparing between Al_2O_3 and glass.

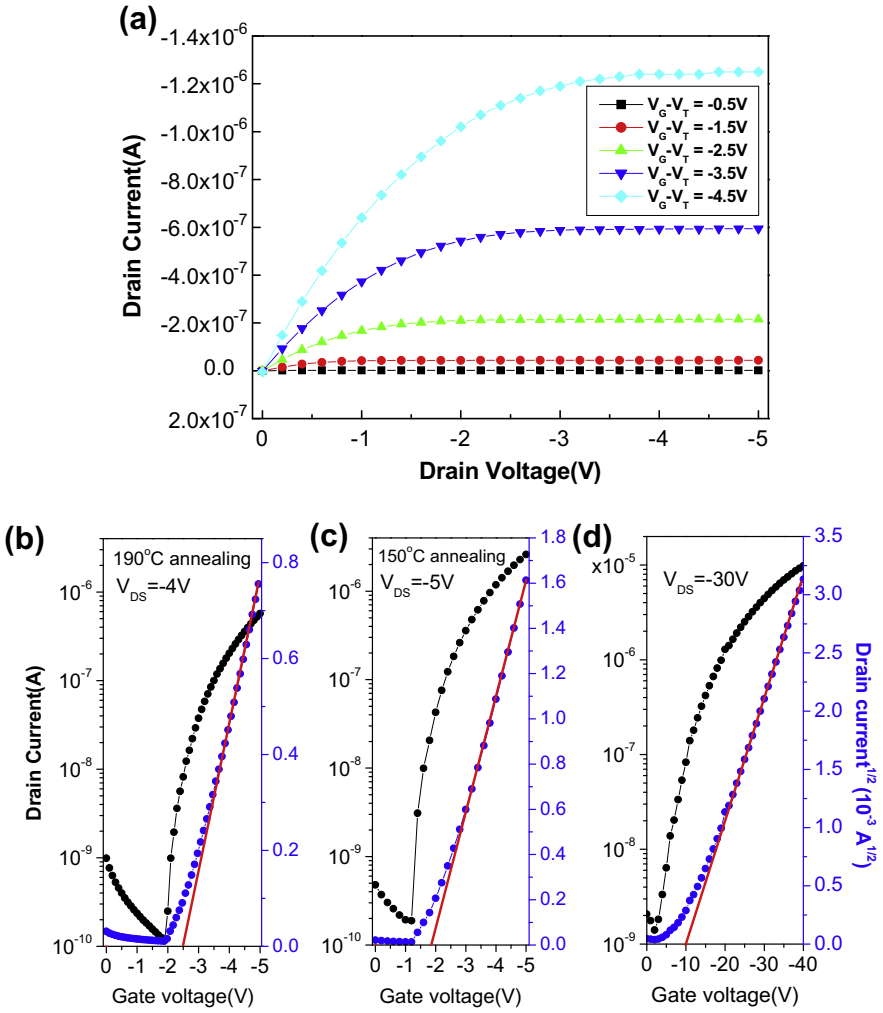

Fig. 6. Electrical characteristics of an OTFT with PS-r-PMMA copolymer insulator. (a) Output characteristics. Transfer characteristics of OTFT with various annealing temperature (b) 190 °C and (c) 150 °C after toluene rinse. (d) Transfer characteristics for OTFT with PS-r-PMMA insulator without rinsing toluene.

and PMMA do not affect the interface and bulk properties seriously in the ambient air and the hysteresis can be ignored.

The performance comparison with various annealed PS-r-PMMA are listed in Table 1. There is a noteworthy improvement in subthreshold swing by using ultra-thin

Table 1
Performance of pentacene based OTFT with various temperature annealed PS-r-PMMA dielectric layer.

Temperature (°C)	Rinse[a]	μ (cm^2/V s)	Vt (V)	On/off ratio	S.S ($V^{-1}dec^{-1}$)
190	Y	0.10	−2.5	10^3-10^4	0.27
150	Y	0.14	−1.9	10^4	0.29
190	N	0.07	−10	10^4	4.7

[a] After the dielectric layer annealed at appropriate temperature, the samples were rinsed with toluene for 30 s.

PS-r-PMMA as the OTFT gate dielectric. The surface is more regular for the ultra-thin PS-r-PMMA dielectric after toluene rinse than the original random coated PS-r-PMMA dielectric layer. Such a regular arrangement of chain performs a smooth surface for pentacene growth with less interface traps and high carrier mobility.

Moreover, relative small on/off current ratio of OTFT is observed. The phenomenon is attributed to the mobility of OTFT dominated by pentacene growth conditions. The purity of the pentacene and process temperature (substrate heating temperature) are regarded as the most important factors for a high quality channel layer. In this study, the 40-nm-thick pentacene channel layer was formed without substrate heating, leading to the mobility of ~0.1 cm^2/V s. Such a relatively low carrier mobility suppressed the channel current which associated with on/off current ratio. The other reason is regarded as the leakage current from the gate electrode. For the good PS-r-PMMA attachment and arrangement, the aluminum oxide played an important role. The AlO_x formed by UV treatment is not stable enough in the ambient air that oxygen molecules will release from the AlO_x surface. However, the lack of oxygen will lead to the PS-r-PMMA insufficient bonding or attachment during the annealing process. As the reason, we suggest other methods to form a robust and stable AlO_x such as oxygen plasma treatment to improve on/off ratio in the future [32].

4. Conclusions

In summary, we have demonstrated that the random copolymer such as PS-r-PMMA could have the potential in printable gate dielectric for low voltage OTFT. The print capability is evaluated by the casting, annealing and removing procedure which is compatible to ink-jet printing, slot-coating, screen printing, doctor blade and other printing methods. The developed dielectric also exhibits a temperature-dependent behavior in thickness which is controlled by thermal annealing. For the electrical properties, this random copolymer achieved well properties in low leakage current (~10^{-9} A/cm^2), smooth morphology and high capacitance density (~150 nF/cm^2). By applying this random copolymer to an OTFT as the gate dielectric, a small operation voltage as low as 5 V was obtained that is comparable to the real electronics in the VLSI technology of 1 μm technology node. In addition to 5 V operation, the PS-r-PMMA based OTFT exhibited subthreshold swing of 0.29 V/dec, threshold voltage of −1.9 V, I_{on}/I_{off} ratio of 10^4 and mobility of 0.14 cm^2/V s at process temperature of 150 °C.

Acknowledgement

The work was supported by National Science Council of Republic of China under grant NSC-97-2221-E-005-026.

References

[1] L. Zhou, S. Park, B. Bai, J. Sun, S.-C. Wu, T.N. Jackson, S. Nelson, D. Freeman, Yongtaek Hong, IEEE Electron. Dev. Lett. 26 (2005) 640.
[2] L. Zhou, A. Wanga, S.-C. Wu, J. Sun, S. Park, T.N. Jackson, Appl. Phys. Lett. 88 (2006) 083502.
[3] H. Sirringhaus, Adv. Mater. 17 (2005) 2411.
[4] G. Li, V. Shrotriya, J. Huang, Y. Yao, T. Moriarty, K. Emery, Y. Yang, Nat. Mater. 4 (2005) 864.
[5] Z.T. Zhu, J.T. Mason, R. Dieckmann, G.G. Malliaras, Appl. Phys. Lett. 81 (2002) 4643.
[6] H. Yan, Z. Chen, Y. Zheng, C. Newman, J.R. Quinn, F. Dötz, M. Kastler, A. Facchetti, Nature 457 (2009) 679.
[7] A. Benor, A. Hoppe, V. Wagner, D. Knipp, Org. Electron. 8 (2007) 749.
[8] L. Fumagalli, D. Natali, M. Sampietro, E. Peron, F. Perissinotti, G. Tallarida, S. Ferrari, Org. Electron. 9 (2008) 198.
[9] A. Facchetti, M.-H. Yoon, T.J. Marks, Adv. Mater. 17 (2005) 1705.
[10] M.-H. Yoon, C. Kim, A. Facchetti, T.J. Marks, J. Am. Chem. Soc. 128 (2006) 12851.
[11] W.S. Hu, Y.T. Tao, Y.J. Hsu, D.H. Wei, Y.S. Wu, Langmuir 21 (2005) 2260.
[12] R. Ruiz, D. Choudhary, B. Nickel, T. Toccoli, K.-C. Chang, A.C. Mayer, P. Clancy, J.M. Blakely, R.L. Headrick, S. Iannotta, G.G. Malliaras, Chem. Mater. 16 (2004) 4497.
[13] S.E. Fritz, T.W. Kelley, C.D. Frisbie, J. Phys. Chem. 109 (2005) 10574.
[14] J. Zhang, J.P. Rabe, N. Koch, Adv. Mater. 20 (2008) 3254.
[15] M. Halik, H. Klauk, U. Zschieschang, G. Schmid, C. Dehm, M. Schütz, S. Maisch, F. Effenberger, M. Brunnbauer, F. Stellacci, Nature 431 (2004) 963.
[16] H. Klauk, U. Zschieschang, J. Pflaum, M. Halik, Nature 445 (2007) 745.
[17] D.H. Kim, Y.D. Park, Y. Jang, H. Yang, Y.H. Kim, J.I. Han, D.G. Moon, S. Park, T. Chang, C. Chang, M. Joo, C.Y. Ryu, K. Cho, Adv. Funct. Mater. 15 (2005) 77.
[18] M.-H. Yoon, A. Facchetti, T.J. Marks, Proc. Natl. Acad. Sci. 102 (2005) 4678.
[19] O. Acton, G. Ting, H. Ma, J.W. Ka, H.-L. Yip, N.M. Tucker, A.K.-Y. Jen, Adv. Mater. 20 (2008) 3697.
[20] L. Manchanda, M. Gurvitch, IEEE Electron. Dev. Lett. 9 (1988) 180.
[21] C. Bartic, H. Jansen, A. Campitelli, S. Borghs, Org. Electron. 3 (2002) 65.
[22] L.A. Majewski, R. Schroeder, M. Grell, Adv. Mater. 17 (2005) 192.
[23] K.P. Pande, V.K.R. Nair, D. Gutierrez, J. Appl. Phys. 54 (1983) 5436.
[24] M. Zirkl, A. Haase, A. Fian, H. Schön, C. Sommer, G. Jakopic, G. Leising, B. Stadlober, I. Graz, N. Gaar, R. Schwödiauer, S. Bauer-Gogonea, S. Bauer, Adv. Mater. 19 (2007) 2241.
[25] D.K. Hwang, C.S. Kim, J.M. Choi, K. Lee, J.H. Park, E. Kim, H.K. Baik, J.H. Kim, S. Im, Adv. Mater. 18 (2006) 2299.
[26] P. Mansky, Y. Liu, E. Huang, T.P. Russell, C. Hawker, Science 275 (1997) 1458.
[27] B. Zhang, F.D. Blum, Macromolecules 36 (2003) 8522.
[28] O.K.C. Tsui, T.P. Russell, C.J. Hawker, Macromolecules 34 (2001) 5535.
[29] P.S. Jo, J. Sung, C. Park, E. Kim, D.Y. Ryu, S. Pyo, H.-C. Kim, J.M. Hong, Adv. Funct. Mater. 18 (2008) 1202.
[30] R.A. Street, Adv. Mater. 21 (2009) 2007.
[31] Y. Taur, E.J. Nowak, IEDM Tech. Dig. (1997) 215.
[32] M. Burghard, H. Klauk, K. Kern, Adv. Mater. 21 (2009) 2586.

Organic Electronics 11 (2010) 626–631

Contents lists available at ScienceDirect

Organic Electronics

journal homepage: www.elsevier.com/locate/orgel

Scaling limits of organic thin film transistors

A. Hoppe [a], D. Knipp [b,*], B. Gburek [a], A. Benor [b], M. Marinkovic [b], V. Wagner [a]

[a] Nano and Molecular Electronics Laboratory, Jacobs University Bremen, 28759 Bremen, Germany
[b] Electronic Devices and Nanophotonics Laboratory, Jacobs University Bremen, 28759 Bremen, Germany

ARTICLE INFO

Article history:
Received 22 November 2009
Received in revised form 1 January 2010
Accepted 2 January 2010
Available online 7 January 2010

Keywords:
Thin film transistors
Scaling behavior
Switching speed

ABSTRACT

The scaling behavior and the influence of the device geometry on the switching speed of organic thin film transistors were investigated. Thiophene transistors were characterized and the influence of contact effects and overlap capacitance was studied. Fundamental scaling limits of the switching frequencies were derived. The maximum transfer frequency is limited by the device design and the specific contact resistance between the drain/source electrode and the organic semiconductor. Finally, strategies will be presented how to realize organic transistors operating at frequencies of up to 100 MHz.

© 2010 Elsevier B.V. All rights reserved.

1. Introduction

Electronics based on organic materials has experienced unprecedented progress in recent years. The prospect of flexible, unbreakable, extremely low-weight electronics at relatively low cost has stimulated a lot of research and development on flexible display media [1], organic memories [2] and organic radio frequency identification (RFID) tags [3]. Progress in this field has been sustained by the synthesis of new materials [4], and the improvement of electronic devices [5–7]. In order to realize high performance organic integrated circuits the devices have to be electrically stable [1,3,8] and the switching frequency of the transistors should be as high as possible. High switching frequencies can only be achieved by using organic materials with high charge carrier mobilities and small or very small device dimensions [9,10]. When scaling down the transistor dimensions the channel length, the channel width and the thickness of the gate dielectric are reduced by a scaling factor $1/\kappa$ (see Fig. 1b). Scaling the device dimensions by $1/\kappa$ allows for lowering of the applied voltages by $1/\kappa$, while the electric field distribution within the device remains unchanged. As a result the overall current flow scales by $1/\kappa$, so that the power dissipation is reduced by $1/\kappa^2$. Therefore, the power dissipation per area of an integrated chip remains constant. The transfer frequency of the transistor scales by the scaling factor κ.

It has been demonstrated that the thickness of the gate dielectric of organic transistors can be reduced by using self-assembled monolayers (SAMs) as gate dielectric [11]. The channel length and channel width can be scaled down by using nano-patterning techniques like electron beam lithography, nanoimprint lithography or micro contact printing [12–14]. However, most of the realized short channel transistors exhibit a distinct drop of the device charge carrier mobility with decreasing channel length [14,15].

A basic introduction into the scaling behavior and the switching speed of field effect transistors is given in Section 2. The fabrication of the device structures will be given in Section 3. Afterwards the scaling behavior and the switching speed of organic thin film transistors will be described in Section 4. In particular the influence of contact effects on the scaling behavior and the overlap capacitance on the transfer frequency of organic transistor will be described. In Section 5 an upper limit of the transfer frequency will be derived for organic thin film transistors. Finally, a strategy will be presented how to overcome the existing scaling limits. The results will be summarized in Section 6.

* Corresponding author.
E-mail address: d.knipp@jacobs-university.de (D. Knipp).

1566-1199/$ - see front matter © 2010 Elsevier B.V. All rights reserved.
doi:10.1016/j.orgel.2010.01.002

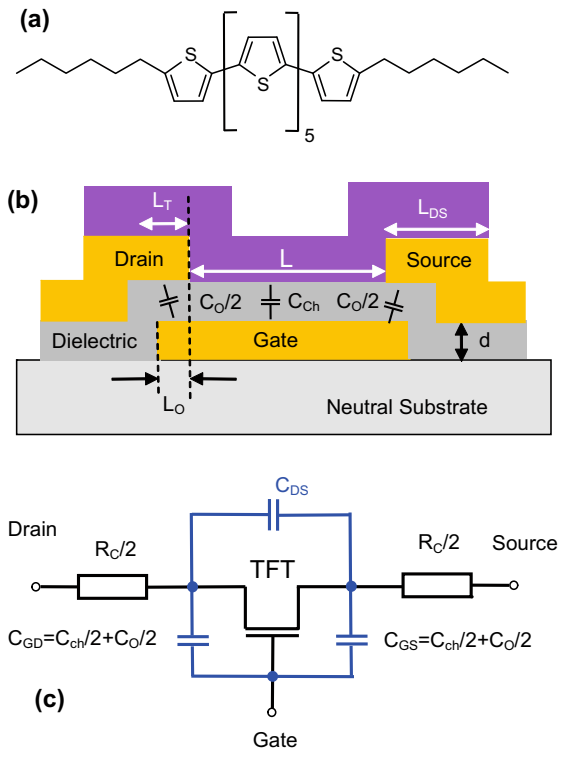

Fig. 1. (a) Molecular structure of dihexyl-7-thiophene (DH7T). (b) Cross section of an organic transistor realized in bottom gate configuration. (c) Equivalent circuit of a transistor including contact resistances and overlap capacitances.

2. Switching speed of field effect transistors

The transfer frequency defines the highest possible frequency at which the thin film transistor can be used as a current amplifier. The operating frequency of a field effect transistor is equal to the transfer frequency if the current gain is equal to unity, which means that the gate current of the transistor is equal to the transistor drain current [16,17]. The transfer frequency of an ideal field effect transistor is given by

$$f_T = \frac{1}{2\pi} \cdot \frac{g_m}{C_G W L}, \tag{1}$$

where g_m is the transconductance of the transistor [17]. C_G is the gate capacitance per unit area, W the channel width, and L the channel length. The product of the channel length and the channel width, WL, represents the channel area of the thin film transistor. The transconductance of the transistor is determined by $g_m = \partial I_{DS}/\partial V_{GS}$. The drain/source current of an organic transistor in the linear region of operation is given by

$$I_{DS} \approx C_G \cdot \frac{W}{L} \cdot \mu_{eff} \cdot V_{DS} \cdot (V_{GS} - V_T), \tag{2}$$

where μ_{eff} is the effective device mobility, V_{GS}, V_{DS}, and V_T are the gate/source voltage, the drain/source voltage, and the threshold voltage, respectively. After determining the transconductance, the transfer frequency in the linear region can be calculated by

$$f_T = \frac{1}{2\pi} \cdot \frac{\mu_{eff} V_{DS}}{L^2}. \tag{3}$$

The transfer frequency scales by $1/L^2$, so that a reduction of the channel length by one order of magnitude leads to an increase of the transfer frequency by two orders of magnitude.

3. Experimental

The measured transfer frequency was determined for organic thin film transistors. The cross section of an organic transistor structure is shown in Fig. 1b. The gold electrodes of the bottom gate coplanar transistor were realized by optical and electron beam lithography. The channel length of the transistors was varied from 50 nm to 50 μm. Optical and electron micrographs of the device are shown in Fig. 2.

In order to realize transistors with very short channel length down to 50 nm the devices were realized on a silicon substrate. The gate electrode of the transistors was not patterned resulting in relatively large overlap capacitance between the gate and the drain/source electrodes. An equivalent circuit of the transistor is shown in Fig. 1c.

The organic semiconductor used in this study was dihexyl-7-thiophene (DH7T), a soluble oligothiophene with seven thiophene units in the molecule (Fig. 1a). The semiconductor was evaporated at a substrate temperature of 190–195 °C in ultra-high vacuum at deposition rates of 0.2 nm/min. To improve the device performance, the silicon oxide dielectric was prior treated with a hexamethyldisilazane (HMDS) monolayer. All measurements were performed under ambient conditions after controlled cooling of the samples to room temperature. Further details on the device operation are given in Ref. [16]. Organic transistors based on DH7T exhibit high charge carrier mobilities exceeding 0.1 cm^2/Vs for long channel devices in air [18]. The measured transfer characteristic of the transistors with a short channel of 350 nm is shown in Fig. 3. The transistor exhibits a device charge carrier mobility of 0.02 cm^2/Vs.

4. Switching speed of organic thin film transistors

The measured transfer frequency as a function of the channel length is shown in Fig. 4. For simplicity only the channel length was scaled down in this experiment. For channel lengths from 5 to 50 μm the transfer frequency can be described by Eq. (3) and the transfer frequency scales by $1/L^2$. The transfer frequency maximum is reached for a channel length of approximately 1 μm. For transistors with a submicrometer channel length a drop of the transfer frequency is measured. The reduction is caused by the influence of parasitic resistors and parasitic capacitors on the device operation. Parasitic contact resistances at the drain and source electrodes of the transistor lead to a reduction of the effective charge carrier mobility and therefore to a drop of the transfer frequency. Furthermore,

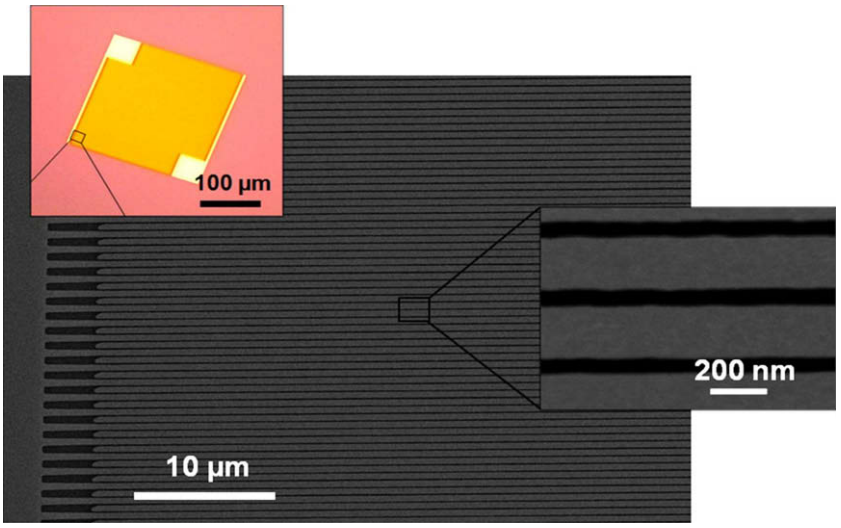

Fig. 2. Optical micrograph and SEM images of the drain and source electrodes of the bottom gate coplanar organic transistor.

the transfer frequency is reduced by the overlap capacitance between the drain/source electrodes and the gate electrode.

In the first step the influence of contact effects on the transfer frequency was investigated. In this case the expression for the transconductance in the linear regime has to be modified taking the influence of the contact effects on the drain current into account, which causes a voltage drop at the contacts resulting in a reduced effective drain/source voltage of the transistor. The drain/source current of an organic transistor is given by

$$I_{DS} \approx C_G \frac{W}{L} \cdot \mu_0 \frac{L}{L + W \cdot C_G \cdot R_C \cdot \mu_0 \cdot (V_{GS} - V_T)} \cdot V_{DS} \cdot (V_{GS} - V_T), \quad (4)$$

considering the influence of contact resistances [19]. The contact resistance R_C is equal to the sum of the drain and the source contact resistances. An equivalent circuit of the transistor including the contact resistances is shown in Fig. 1c. In order to compare the contact resistance of transistors with different device geometries the contact resistance is typically described by a normalized contact resistance, $r_C = R_C \cdot W$. After calculating the transconductance the transfer frequency can be determined by

$$f_T = \frac{1}{2\pi} \cdot \frac{\mu_0 \cdot V_{DS}}{[L + C_G \cdot r_C \cdot \mu_0 \cdot (V_{GS} - V_T)]^2}. \quad (5)$$

A similar expression can be derived for a transistor operating in the saturation region [16]. Based on the experimental data a normalized contact resistance of 3.5 kΩ cm was determined. The extracted value is consistent with contact resistances determined by fitting the channel dependent device charge carrier mobility of the DH7T organic transistors [18]. Lowering of the contact resistance leads to distinctly higher transfer frequencies of transistors with shorter channel lengths.

The contact resistance is affected by the contact geometry, the energy band alignment between the metal contact and the organic semiconductor. Furthermore, the structural order of the molecules in the vicinity of the drain and source contacts have a distinct influence on the band alignment and the contact resistance [19]. An expression for the contact resistance can be derived by considering the electric field distribution in the contact region. The current spreading under the contacts can be described by an ordinary 2nd order differential equation [20]. The equation provides a description of the charge spreading in a semiconductor film with lateral contacts. Solving the differential equation leads to an expression for the normalized contact resistance as a function of the transfer length, which is given by

$$r_C = \frac{\rho_C}{L_T} \cdot \coth\left(\frac{L_{DS}}{L_T}\right). \quad (6)$$

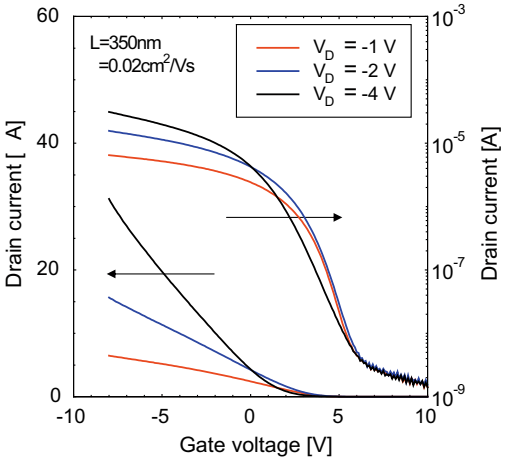

Fig. 3. Current voltage characteristic of a dihexyl-7-thiophene (DH7T) thin film transistor with a channel length of 350 nm.

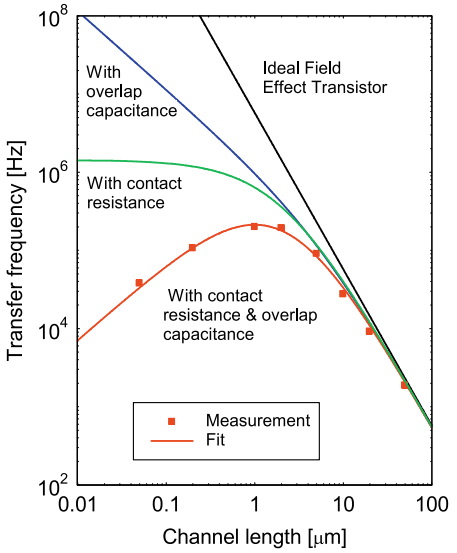

Fig. 4. Measured transfer frequency of a dihexyl-7-thiophene (DH7T) thin film transistor. The data was fitted by taking contact resistances and overlap capacitances between drain/source and gate electrode into account.

The transfer length, L_T, defines the critical distance over which most of the charge is transferred from the metal to the organic semiconductor. The transfer length is measured from the edge of the drain and the source electrodes (Fig. 1b). The transfer length is calculated by

$$L_T = \sqrt{\frac{\rho_C}{R_S}}. \tag{7}$$

The transfer length is determined by the specific contact resistance and the sheet resistance of the channel material. The parameter ρ_C describes the specific contact resistance between the drain/source electrode and the organic channel. The resistance R_S corresponds to the sheet resistance of the transistor channel. If the sheet resistance of the channel is high the transfer length will be small, so that most of the charges are injected close to the edge of the drain and source contacts. In this case the contact resistance is high. If the sheet resistance of the channel is small the transfer length will be large, so that the charges spread under the drain and source contacts. In this case the contact resistance is low. In the following calculation we assumed a uniform distribution of the charges in the channel, so that the sheet resistance is given by $1/R_S = L/W\,\partial I_{DS}/\partial V_{DS}$. This is a valid assumption since the thickness of the organic film is comparable to the thickness of the accumulation layer in the channel [34]. This leads to the following expression for the transfer length:

$$L_T = \sqrt{\rho C_G \mu_0 (V_G - V_T)}. \tag{8}$$

If the transistor operates in saturation a similar expression for the transfer length can be derived. If the length of the drain and source electrodes, L_{DS}, in Fig. 1b is significantly larger than the transfer length, L_T, the normalized contact resistance can be approximated by ρ_C/L_T resulting in the following expression for the normalized contact resistance

$$r_C \approx \frac{\rho_C}{L_T} = \sqrt{\frac{\rho_C}{C_G \mu_0 (V_G - V_T)}}. \tag{9}$$

As a consequence the contact resistance does not depend on the drain and source electrode length. However, the normalized contact resistance depends on the transfer length, which again depends on the charge carrier mobility and the applied voltages. Subsequently the contact resistance is gate voltage dependent, which is in very good agreement with experimental results of silicon and organic thin film transistors [21,22]. If the length of the electrodes is smaller than the transfer length the normalized contact resistance can be approximated by ρ_C/L_{DS}. Subsequently the normalized contact resistance depends on the contact geometry and a reduction of the drain and source electrode dimension leads to an increase of the normalized contact resistance. For the dihexyl-7-thiophene thin film transistors the transfer length was determined to be 1–5 μm, which means that most of the charges are injected in the organic semiconductor within a region of 1–5 μm from the edge of the drain and source contacts. The determined values for the transfer length are very similar to values obtained for other organic semiconductors like pentacene [23]. The sheet resistance of the transistor was determined to be 20–60 MΩ/□. The specific contact resistance is equal to 1–5 Ω cm^2. The determined values are comparable to the values determined for other organic thin film transistors with gold drain and source electrodes. Similar values of the transfer length can be expected for transistors with inkjet or microcontact printed drain and source electrodes [24,25].

In the following calculation it is assumed that the transfer length is smaller than the drain and source electrode length resulting in a normalized contact resistance that is independent on the geometry of the drain and source contacts. The transfer frequency can be expressed in terms of the transfer length by

$$f_T = \frac{1}{2\pi} \cdot \frac{\mu_0 V_{DS}}{(L + L_T)^2}. \tag{10}$$

In the next step the influence of the overlap capacitance on the transfer frequency is investigated. The equivalent circuit of the transistor including the overlap capacitance is shown in Fig. 1c. The overlap capacitance of conventional thin film transistors is determined by the registration of the drain/source and gate mask level. In the linear regime the gate/source and the gate/drain capacitances are equal to half of the channel capacitance plus half of the overlap capacitance, $C_{GS} = C_{ch}/2 + C_O/2$ and $C_{GD} = C_{ch}/2 + C_O/2$. The overlap capacitances between the drain and source contact, C_{DS}, can be neglected, since the capacitance is much smaller than the gate/source and gate/drain overlap capacitance.

The parameters C_{ch} and C_O are the channel and the overlap capacitances. The channel capacitance, C_{ch}, is given by $C_{ch} = C_G \cdot W \cdot L$, where C_G, is the gate capacitance per unit area and $W \cdot L$ the active channel area. The gate capacitance

per unit area is given by $C_G = \varepsilon_o \cdot \varepsilon_r/d$, where ε_0 is the dielectric permittivity of vacuum, and ε_r is the relative dielectric constants of the gate dielectric. The parameter d represents the thickness of the gate dielectric. The overlap capacitance is given by $C_O = 2C_G \cdot W \cdot L_O/2$, where $W \cdot L_O$ is the area in which the gate electrode is overlapped by the drain and the source electrode. The overlap capacitance is determined by the thickness of the gate dielectric and the technology used to pattern the electrodes of the transistor.

At unity current gain the gate current of a transistor corresponds to $2\pi\ f_T \cdot (C_{ch} + C_O)$ including the parasitic capacitances instead of just $2\pi\ f_T \cdot C_{ch}$. The expression taking the overlap capacitance into account $C_{ch}/(C_{ch}+C_o)$ can be substituted by $L/(L+L_o)$. Therefore, Eq. (10) has to be modified leading to the following expression for the transfer frequency:

$$f_T = \frac{1}{2\pi} \cdot \frac{\mu_0 V_{DS}}{L^2} \cdot \frac{L^2}{(L+L_T)^2} \cdot \frac{L}{L+L_O} \tag{11}$$

The equation can be divided in three terms, where the first term describes the ideal relationship between the transfer frequency and the channel length and the charge carrier mobility. The second terms can be considered to be a correction factor, which accounts for the influence of the contact effects on the transfer frequency. The influence of the contact effects on the transfer frequency is described by the transfer length. The third and last terms accounts for the influence of the overlap capacitance on the transfer frequency. The overlap effect is described by the overlap length between drain/source and gate electrodes. The influence of the contact resistance and the overlap capacitance on the transfer frequency is shown in Fig. 4. The DH7T transistor exhibits a maximum of the transfer frequency of 200 kHz. The experimental data can be described very well by the proposed equation taking the contact resistance and the overlap capacitance into account. A transfer length of 2–3 μm and an overlap length of 5 μm were determined by fitting the experimental data. If the overlap length would be reduced to zero the transistor would reach a transfer frequency of 2 MHz. The overlap length and the overlap capacitance are mainly determined by the alignment of the lithographic masks that define the drain/source and the gate electrodes. For transistors prepared by printing technologies the achievable transfer frequency might be significantly lower due to poor alignment of printed layers.

5. Scaling limits of organic thin film transistors

The influence of different charge carrier mobilities and specific contact resistances on the transfer frequency is shown in Fig. 5. It was assumed that the gate dielectric has a thickness of 50 nm, the drain source voltage is equal to −5 V and the overlap length was considered to be 2 μm. The transfer frequencies are plotted for charge carrier mobilities of 0.1 and 1 cm^2/Vs. The specific contact resistance was varied from 0.03 to 3 Ω cm^2. The measured experimental values of the specific contact resistances were equal to 0.2–0.8 Ω cm^2.

For long channels the transfer frequency is proportional to $1/L^2$ and determined by the first term of Eq. (11). In the

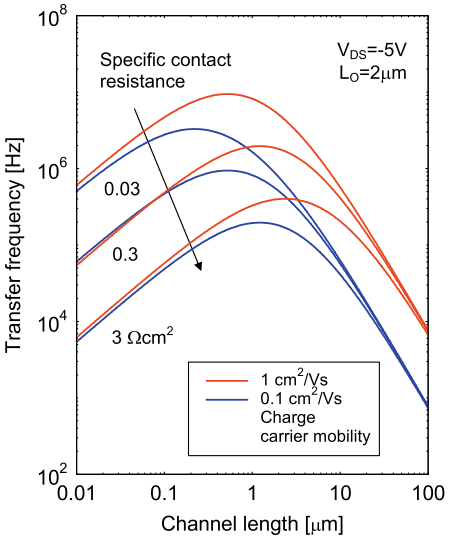

Fig. 5. Influence of the charge carrier mobility and the specific contact resistance on the transfer frequency of organic thin film transistors.

region of intermediate channel lengths the transfer frequency reaches its maxima. For shorter channels the transfer frequency drops due to the influence of the specific contact resistance. In the same region, the charge carrier mobility does not have an influence on the transfer frequency anymore. Based on Eq. (11) the channel length can be calculated at which the transfer frequency reaches its maxima. If the drain/source to gate overlap, L_O, is much larger than the transfer length, L_T, the optimal channel length would be equal to the transfer length, $L_{max} = L_T$. This is the case for most of the transistors fabricated on silicon oxide substrates or transistors prepared by inkjet printing, where the drain/source to gate overlap might be larger than the channel length. If the length of the drain/source to gate overlap is reduced to values comparable to the transfer length the maxima of the transfer frequency is reached for a channel length of

$$L_{max} \approx \frac{L_T}{2}. \tag{12}$$

This is the case for devices realized in this study. Based on Eq. (12) an optimal channel length of 1–5 μm can be calculated. If the overlap length can be reduced to values smaller than the transfer length, the channel length at which the transfer frequency reaches its maximum is given by

$$L_{max} \approx \sqrt{\frac{L_T L_O}{2}}. \tag{13}$$

In this case the highest transfer frequency is reached for channel lengths of 0.5–2 μm. Based on Eq. (12) an upper limit of the transfer frequency can be derived by

$$f_T^{max} \approx \frac{1}{2\pi} \cdot \frac{1}{\rho_C \cdot C_G} \cdot \frac{V_{DS}}{V_{GS} - V_T}. \tag{14}$$

The maximum of the transfer frequency does not depend on the charge carrier mobility and the channel length of the transistor. The transfer frequency is mainly deter-

mined by the specific contact resistance and the gate capacitance per unit area. Eq. (14) can be understood in the following way: During a switching cycle the gate capacitance has to be charged by the gate/source voltage. The charging process is ultimately limited by the contact resistance, which is described by the specific contact resistance. The experimental values of the specific contact resistance for the DH7T transistors were in the range of 0.2–0.8 $\Omega\,cm^2$. A reduction of the specific contact resistance by a factor 10–100 would lead to an increase of the transfer frequency by a factor of 10–100, so that transfer frequencies well above 50 MHz can be achieved [10]. The specific contact resistance can be minimized by selecting the best organic/metal material combination [18]. Furthermore, the interface property can be optimized and fine tuned by using self-assembled monolayers [19,26]. Alternatively the contact resistance can be minimized by doping of the contact region [27]. In order to minimize the overlap capacitance of thin film transistors self-alignment processes can be used [24,28]. Such processes are commonly used in the fabrication of amorphous or polycrystalline silicon thin film transistors realized on glass substrates [29,30]. In order to apply organic transistors in flexible displays or radio frequency identification tags addition requirements have to be fulfilled. The operating voltages of the transistors have to be low. To operate the organic transistor at low operating voltages the threshold voltage of the transistors has to be minimized. The threshold voltage is mainly determined by electronic defects in the organic film and the gate dielectric [31,32]. Organic transistors with low threshold voltages have been demonstrated allowing for the operation of organic transistors at only 2 V [33].

High transfer frequencies can only be achieved for transistors with high charge carrier mobility, low contact resistance, small overlap capacitance and short channel length. Very high transfer frequencies exceeding 50 MHz can only be realized for transistors with channel lengths of 500 nm or less. For such short channel lengths additional parasitic effects like short channel effects might have to be taken into account when describing the operation of the transistors. Further investigations are needed to study the operation of very short channel organic transistors.

6. Summary

The scaling behavior of organic thin film transistors was investigated. High transfer frequencies can be achieved by using short channel transistors with high charge carrier mobilities. However, the maximum of the transfer frequency is limited by contact effects and the overlap capacitance between drain/source and gate electrodes. The transfer frequency reaches a maximum if the channel length is comparable to half of the transfer length. An upper limit of the transfer frequency was derived which is determined by the specific contact resistance between the drain and source electrodes and the organic channel material. The charge carrier mobility does not affect the upper limit of the transfer frequency. Lowering of the contact resistances in combination with a self-aligned patterning process of the drain/source and gate electrodes will allow for the realization of integrated organic circuits operating at frequencies of up to 100 MHz.

References

[1] G.H. Gelinck, H.E.A. Huitema, E. van Veendaal, E. Cantatore, L. Schrijnemakers, J.B.P.H. van der Putten, T.C.T. Geuns, M. Beenhakkers, J.B. Giesbers, B.-H. Huisman, E.J. Meijer, E.M. Benito, F.J. Touwslager, A.W. Marsman, B.J.E. van Rens, D.M. de Leeuw, Nat. Mater. 3 (2004) 106–110.
[2] K.-J. Baeg, Y.-Y. Noh, J. Ghiem, S.-J. Kang, H. Lee, D.-Y. Kim, Adv. Mater. 18 (2006) 3179–3183.
[3] T.W. Kelley, P.F. Baude, C. Gerlach, D.E. Ender, D. Muyres, M.A. Haase, D.E. Vogel, S.D. Theiss, Chem. Mater. 16 (2004) 4413–4422.
[4] J.E. Anthony, J.S. Brooks, D.L. Eaton, S.R. Parkin, J. Am. Chem. Soc. 123 (2001) 9482.
[5] H. Sirringhaus, N. Tessler, R.H. Friend, Science 280 (1998) 1741.
[6] S. Steudel, K. Myny, V. Arkhipov, C. Deibel, S. De Vusser, J. Genoe, P. Heremans, Nat. Mater. 4 (2005) 597–600.
[7] N. Karl, in: R. Farchioni, G. Grosso (Eds.), Organic Electronic Materials, Springer, Berlin, 2001.
[8] A. Benor, A. Hoppe, V. Wagner, D. Knipp, Org. Electron. 8 (2007) 749–758.
[9] A. Hoppe, T. Balster, T. Muck, V. Wagner, Phys. Stat. Sol. 205 (3) (2008) 612.
[10] M. Kitamura, Y. Arakawa, Appl. Phys. Lett. 95 (2009) 023503.
[11] M. Halik, H. Klauk, U. Zschieschang, G. Schmid, C. Dehm, M. Schütz, S. Maisch, F. Effenberger, M. Brunnbauer, F. Stellacci, Nature 431 (7011) (2004) 963.
[12] S.Y. Chou, P.R. Krauss, P.J. Renstrom, Science 272 (5258) (1996) 85–87.
[13] Y. Xia, G.M. Whitesides, Angew. Chem. Int. Ed. 37 (1998) 550–575.
[14] M. Leufgen, A. Lebib, T. Muck, U. Bass, V. Wagner, T. Borzenko, G. Schmidt, J. Geurts, L.W. Molenkamp, Appl. Phys. Lett. 84 (2004) 9.
[15] L. Wang, D. Fine, T. Jung, D. Basu, H. von Seggern, A. Dodabalapur, Appl. Phys. Lett. 85 (2004) 1772.
[16] V. Wagner, P. Wöbkenberg, A. Hoppe, J. Seekamp, Appl. Phys. Lett. 89 (2006) 243515.
[17] M. Shur, Physics of Introduction to Electronic Devices, John Wiley & Sons, 1990.
[18] A. Hoppe, J. Seekamp, T. Balster, G. Götz, P. Bäuerle, V. Wagner, Appl. Phys. Lett. 91 (2007) 132115.
[19] A. Benor, D. Knipp, Org. Electron. 9 (2008) 209–219.
[20] D.K. Schroder, Semiconductor Material and Device Characterization, second ed., Wiley, New York, 1998.
[21] K.-Y. Chan, E. Bunte, H. Stiebig, D. Knipp, Semicond. Sci. Technol. 22 (2007) 1213–1219.
[22] H. Klauk, G. Schmid, W. Radlik, W. Weber, L. Zhou, C.D. Sheraw, J.A. Nichols, T.N. Jackson, Solid-State Electron. 47 (2003) 297–301.
[23] D. Belaineh, D. Knipp, V. Wagner, in press.
[24] Y.Y. Noh, N. Zhao, M. Caironi, H. Sirringhaus, Nat. Nanotechnol. 3 (1) (2008) 58.
[25] T. Sekitani, Y. Noguchi, U. Zschieschang, H. Klauk, T. Someya, Proc. Natl. Acad. Sci. 105 (13) (2008) 4976.
[26] P.V. Necliudov, M.S. Shur, D.J. Gundlach, T.N. Jackson, J. Appl. Phys. 88 (2000) 6594.
[27] C. Vanoni, S. Tsujino, T.A. Jung, Appl. Phys. Lett. 90 (2007) 193119.
[28] M. Ando, M. Kawasaki, S. Imazeki, H. Sasaki, T. Kamata, Appl. Phys. Lett. 85 (2004) 1849.
[29] I. Ryu, H.C. Kim, S.K. Kim, J. Jang, IEEE Electron Dev. Lett. 18 (1997) 272.
[30] W.S. Wong, E.M. Chow, R. Lujan, V. Geluz-Aguilar, M.L. Chabinyc, Appl. Phys. Lett. 89 (2006) 142118.
[31] G. Horowitz, R. Hajlaoui, H. Bouchriha, R. Bourguiga, M. Hajlaoui, Adv. Mater. 10 (12) (1999) 923.
[32] Knipp, J.E. Northrup, Adv. Mater. 21 (2009) 2511–2515.
[33] S. de Vusser, S. Steudel, K. Myny, J. Genoe, P. Heremans, Appl. Phys. Lett. 88 (2006) 162116.
[34] D. Knipp, A. Benor, V. Wagner, T. Muck, J. Appl. Phys. 101 (2007) 044504.

Organic Electronics 11 (2010) 632–640

Contents lists available at ScienceDirect

Organic Electronics

journal homepage: www.elsevier.com/locate/orgel

Highly efficient organic light-emitting diodes (OLEDs) based on an iridium complex with rigid cyclometalated ligand

Guanghui Zhang [a], Ho-Hsiu Chou [b], Xiaoqing Jiang [a], Peipei Sun [a,*], Chien-Hong Cheng [b,*], Yousuke Ooyama [c], Yutaka Harima [c]

[a] Jiangsu Key Laboratory of Biofunctional Materials, College of Chemistry and Environmental Science, Nanjing Normal University, Nanjing 210097, PR China
[b] Department of Chemistry, Tsing Hua University, Hsinchu 30043, Taiwan
[c] Department of Applied Chemistry, Graduate School of Engineering, Hiroshima University, Higashi-Hiroshima 739-8527, Japan

ARTICLE INFO

Article history:
Received 29 July 2009
Received in revised form 31 December 2009
Accepted 4 January 2010
Available online 11 January 2010

Keywords:
Phosphorescent OLEDs
Iridium complex
Rigid ligand
Excimer emission

ABSTRACT

A red-emitting iridium complex $(DMBA)_2Ir(acac)$ (DMBA = 5,6-dihydro-9,10-methylenedioxy benzo[c]acridine, acac = acetylacetone) containing rigid cyclometalated ligand DMBA was synthesized and its photophysical, electrochemical and electroluminescent properties were characterized. Organic light emitting devices utilizing the complex as dopant emitter were fabricated. When double hole-transporting layers were adopted, the brightness and efficiencies of electroluminescent devices were improved greatly. Based on the excimer emission, a maximum brightness of 66,312 cd m^{-2} at 15 V, together with a maximum external quantum efficiency of 17.7% at 5.0 V was achieved at a doping concentration of 5%. The result suggests that the introduction of a methylenedioxy group into the N-heterocycle of the cyclometalated ligand leads to higher-energy MLCT transitions and a blue shift of the photoluminescence spectrum.

© 2010 Elsevier B.V. All rights reserved.

1. Introduction

Research on organic light-emitting diodes (OLEDs) has been actively pursued in last two decades because of their numerous applications in flat-panel displays and lighting sources [1–3]. Since Forrest and Thompson's group reported the first example of electrophosphorescence at room temperature [4], phosphorescent OLED materials and devices have been intensively studied because of high external quantum efficiencies (EQEs) in their electroluminescence (EL) devices [5,6]. It has been widely accepted that the strong spin–orbit coupling induced by a heavy-metal ion, such as Ir, Pt, and Os promotes an efficient intersystem crossing (ISC) between the singlet and the triplet excited state manifold. Therefore, both singlet and triplet excitons can be harnessed and the strong electroluminescence with an internal efficiency theoretically approaching to 100% can be achieved. Of these phosphorescent materials, iridium complexes have been regarded as the most appropriate emitters because of their relative short lifetime and high quantum efficiency. The emission wavelength of iridium complexes can usually be tuned finely by the introduction of substituent groups with different electronic effects or variations of the conjugation system on ligands. We have reported two red emitters based on rigid quinoxaline derivative–Ir complexes, $Ir(DBQ)_2(acac)$ and $Ir(MDQ)_2(acac)$, and the OLEDs with very high external quantum efficiency and brightness (reached to 12.4% and 73,870 cd m^{-2}) were achieved [7]. Recently, $Ir(MDQ)_2(acac)$ was used for the fabrication of white OLEDs and a striking power efficiency of 124 lm W^{-1} corresponding to an EQE value of 46% was achieved [8]. In our recent work, a maximum brightness of 79,640 cd m^{-2}, together with a maximum EQE of 12.1%, was obtained by adopting rigid benzoimidazole derivative–Ir complex $(biio)_2Ir(acac)$ with a cyan emission [9]. Very recently, 4-phenylbenzoquinoline (PBQ) was used as cyclometalated ligand of the

* Corresponding authors. Tel./fax: +86 25 83598280.
E-mail addresses: sunpeipei@njnu.edu.cn (P. Sun), chcheng@mx.nthu.edu.tw (C.-H. Cheng).

1566-1199/$ - see front matter © 2010 Elsevier B.V. All rights reserved.
doi:10.1016/j.orgel.2010.01.003

complex $Ir(PBQ)_2(acac)$ and a high external quantum efficiency and brightness were achieved from the OLED based on this complex (14.6%, 61,693 cd m^{-2}) [10]. All of the above results provided evidences for our strategy that adopting rigid ligands of Ir complexes leads to high brightness and efficiencies of EL devices. As part of our ongoing efforts devoted to the development of phosphorescent emitters containing rigid ligands, we originally devised 5,6-dihydro-benzo[c]acridine (DBA) as cyclometalated ligand and pure red emission was achieved, but the maximum brightness and EQE of the EL device were 9540 cd m^{-2} and 4.66%, respectively, which were not so high as we expected [11]. In order to get better device performances, the optimization of the chemical structure and device structure was carried out in our lab.

In this work, we synthesized a novel Ir complex containing 5,6-dihydro-9,10-methylenedioxy benzo[c]acridine (DMBA) as cyclometalated ligand, and studied its photophysical and electrochemical properties. The EL devices utilizing this iridium(III) complex $(DMBA)_2Ir(acac)$ as a dopant emitter were then fabricated. After optimization of the device structure and doping concentration, high brightness and efficiencies were achieved, demonstrating our strategy that adopting Ir complexes containing 5,6-dihydrobenzo[c]acridine derivatives as rigid cyclometalated ligand leads to high performances of EL devices.

2. Experiments

Where necessary, reactions were carried out under nitrogen atmosphere. $TiCl_4$ was used after distillation. ^1H nuclear magnetic resonance (NMR) spectra were obtained on a Bruker AVANCE 400 spectrometer in $CDCl_3$ using tetramethylsilane (TMS) as an internal reference. Mass spectra (MS) were carried out on a VG-ZAB-HS instrument. Elemental analysis was performed on a Perkin–Elmer 240C elemental analyzer. UV–Vis absorption spectrum was recorded on a Varian Cary 50 UV–Vis spectrophotometer. Photoluminescence (PL) and electroluminescence (EL) spectra were measured on Hitachi F-4500 fluorescence spectrometer. Cyclic voltammetry (CV) measurements were carried out with a CHI660C electrochemical analyzer (CH instruments) at room temperature. Current, voltage, and light-intensity measurements were made simultaneously using a Keithley 2400 source meter and a Newport 1835-C optical meter equipped with a Newport 818-ST silicon photodiode.

2.1. Synthesis of the ligand DMBA

Concentrated sulfuric acid (1.5 mL) and 3,4-methylenedioxy-6-nitrobenzaldehyde (3.90 g, 20 mmol) were dissolved in acetic acid (40 mL). After cooled to 0 °C, 1-tetralone (2.92 g, 20 mmol) was then slowly added in it. The mixture was stirred at room temperature for 2 h. After setting aside for 48 h, the precipitate was filtered off and recrystallized from 95% ethanol to yield the pure product 2-(3,4-methylenedioxy-6-nitrobenzylidene)-1-tetralone.
$TiCl_4$ (2.2 mL, 20 mmol) was added dropwise using a syringe to a stirred suspension of zinc dust (2.6 g, 40 mmol) in anhydrous THF (30 mL) at room temperature under a dry nitrogen atmosphere. The mixture was refluxed for 2 h to form the low-valent titanium. Then the solution of 2-(3,4-methylenedioxy-6-nitrobenzylidene)-1-tetralone (1.6 g, 5 mmol) in THF (20 mL) was added slowly at room temperature. The mixture was stirred at room temperature over night under nitrogen atmosphere and then quenched with 10% HCl (50 mL) and the precipitate was collected and washed with sodium carbonate solution and water. The crude product was purified by recrystallization from ethanol followed by column chromatography on silica gel with dichloromethane and hexane (1:1, v/v) as eluent to furnish pure 5,6-dihydro-9,10-methylenedioxy benzo[c]acridine (DMBA) in 55% yield.

Yellow solid; m.p. 204–206 °C. ^1H NMR ($CDCl_3$, 400 MHz) δ: 8.50 (*d*, *J* = 7.6 Hz, 1H), 7.79 (*s*, 1H), 7.49 (*s*, 1H), 7.42 (*t*, *J* = 7.2 Hz, 1H), 7.35 (*t*, *J* = 7.6 Hz, 1H), 7.28 (*d*, *J* = 7.2 Hz, 1H), 7.01 (*s*, 1H), 6.30 (*s*, 2H), 3.09 (*t*, *J* = 6.0 Hz, 2H), 3.00 (*t*, *J* = 6.0 Hz, 2H). MS (%): *m*/*z* = 275 (100) [M^+], 274 (92.9) [M^+-1]. Anal. Calcd for $C_{18}H_{13}NO_2$: C, 78.53; H, 4.76; N, 5.09. Found: C, 78.73; H, 4.64; N, 5.16%.

2.2. Synthesis of the complex $(DMBA)_2Ir(acac)$

DMBA (2.2 mmol) was dissolved in 2-ethoxyethanol (10 mL) in a 50 mL round bottomed flask, then the solution of iridium trichloride (1.0 mmol) in 3.0 mL water was added. The mixture was stirred under nitrogen at 120 °C for 24 h and then cooled to room temperature. The precipitate was collected and washed with ethanol, acetone, and then dried in vacuum to give a cyclometalated Ir-chloro-bridged dimmer. Without further purification, the dimmer complex was used for the synthesis of corresponding mononuclear Ir complex. The dimmer complex, acetylacetone (2.0 mmol), and Na_2CO_3 (5.0 mmol) were dissolved in 2-ethoxyethanol (10 mL) and the mixture was then refluxed under nitrogen atmosphere for 12 h. After cooling to room temperature, the precipitate was filtered off and washed with water, ethanol, and ether. The crude product was purified by column chromatography on silica gel using dichloromethane and hexane (2:1, v/v) as eluent, then sublimated at 300–320 °C and 4×10^{-3} Pa to give the pure desired iridium complex $(DMBA)_2Ir(acac)$ as orange powder in 65% yield. ^1H NMR ($CDCl_3$, 400 MHz) δ: 8.08 (*s*, 2H), 7.71 (*s*, 2H), 7.01 (*s*, 2H), 6.64 (*d*, *J* = 7.2 Hz, 2H), 6.56 (*t*, *J* = 7.2 Hz, 2H), 6.33 (*d*, *J* = 7.6 Hz, 2H), 6.04 (*s*, 2H), 6.00 (*s*, 2H), 4.90 (*s*, 1H), 3.26–3.30 (*m*, 2H), 3.04–3.15 (*m*, 6H), 1.60 (*s*, 6H). Anal. Calcd for $C_{41}H_{31}IrN_2O_6$: C, 58.63; H, 3.72; N, 3.34. Found: C, 58.48; H, 3.85; N, 3.48.

2.3. Fabrication of the EL devices

The EL devices were fabricated by vacuum deposition of the materials at 10^{-4} Pa onto a clean glass that was precoated with a layer of indium tin oxide with a sheet resistance of 25 Ω square^{-1}. The deposition rate for the organic compounds was 0.1–0.2 nm s^{-1}. The cathode of LiF/Al was deposited by first evaporating LiF (1 nm) at a deposition rate of 0.01 nm s^{-1} and then evaporating aluminum (100 nm) at a rate of 0.1–0.2 nm s^{-1}. The cathode was then

capped with silver metal (100 nm) by evaporating silver at a rate of 0.3 nm s^{-1}.

3. Results and discussion

The rigid ligand DMBA was synthesized according to the synthetic procedure of DBA as we reported previously with some modifications (Scheme 1) [11]. Low-valent titanium reagent induced intramolecular reductive coupling reaction of 2-(3,4-methylenedioxy-6-nitrobenzylidene)-1-tetralone, which was obtained by an aldol condensation of 3,4-methylenedioxy-6-nitrobenzaldehyde and 1-tetralone catalyzed by sulfuric acid, afforded the ligand DMBA with moderate yield. The iridium complex $(DMBA)_2Ir(acac)$ was synthesized by a conventional two-step reaction from $IrCl_3{\cdot}3H_2O$ via Ir(III)-μ-chloro-bridged dimer complex [12,13]. The complex was characterized by ^1H NMR and elemental analysis.

The UV–Vis absorption and photoluminescence (PL) spectra of $(DMBA)_2Ir(acac)$ were shown in Fig. 1, and the photophysical data are summarized in Table 1. There are four major absorptions at 275, 375, 454, and 500 nm in the UV–Vis spectrum. Similar results were observed for many other iridium complexes [13–15]. The former two intense bands can be assigned to the allowed π–π^* transition of the DMBA ligand, whereas the later two absorptions are assigned to ^{1}MLCT (metal to ligands charge transfer) and ^{3}MLCT transitions. The ^{1}MLCT and ^{3}MLCT are not clearly resolved where a broad band is observed between 420 and 530 nm. The formally spin forbidden ^{3}MLCT at about 500 nm gains intensity by mixing with the higher lying ^{1}MLCT transition through the strong spin–orbit coupling of iridium atom. This mixing is strong enough in this Ir complex that the formally spin forbidden ^{3}MLCT has an extinction coefficient that is more than half that of the spin-allowed ^{1}MLCT transition. Compared with $(DBA)_2Ir(acac)$, the MLCT transitions of $(DMBA)_2Ir(acac)$ are higher in energy indicating an increase in energy separation between the metal *d*- and π^*-orbitals of the ligand. This may be due to the fact that the π^*-orbitals of DMBA are higher in energy than that of DBA, which may resulted from the introduction of a methylenedioxy group with a strong electron donating effect on the N-heterocyclic moiety [16,17].

Irradiating of dichloromethane solution of $(DMBA)_2Ir(acac)$ with 356 nm light led to strong photoluminescence at 572 nm. The PL quantum yield (Φ) was measured to be 0.40 using $Ir(ppy)_2(acac)$ (Φ = 0.34) [13] as reference. Compared with $(DBA)_2Ir(acac)$, a blue shift of 18 nm was observed. It is widely accepted that the lowest unoccupied molecular orbital (LUMO) predominantly locates at the N-heterocyclic part of the cyclometalated ligand and intro-

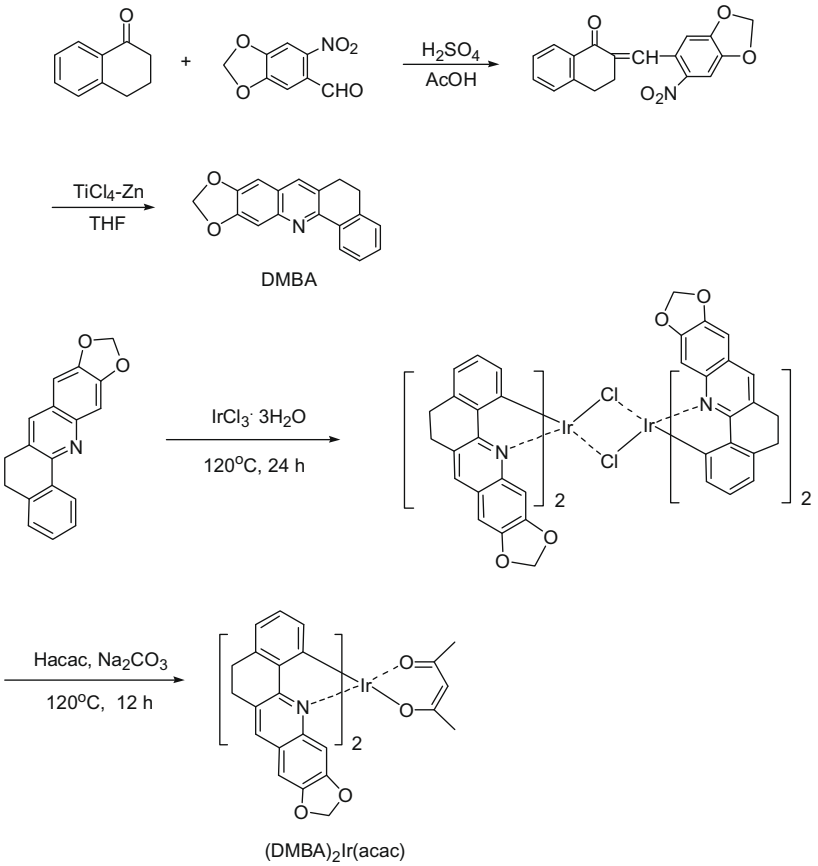

Scheme 1. Synthetic route of the ligand and the corresponding Ir complex.

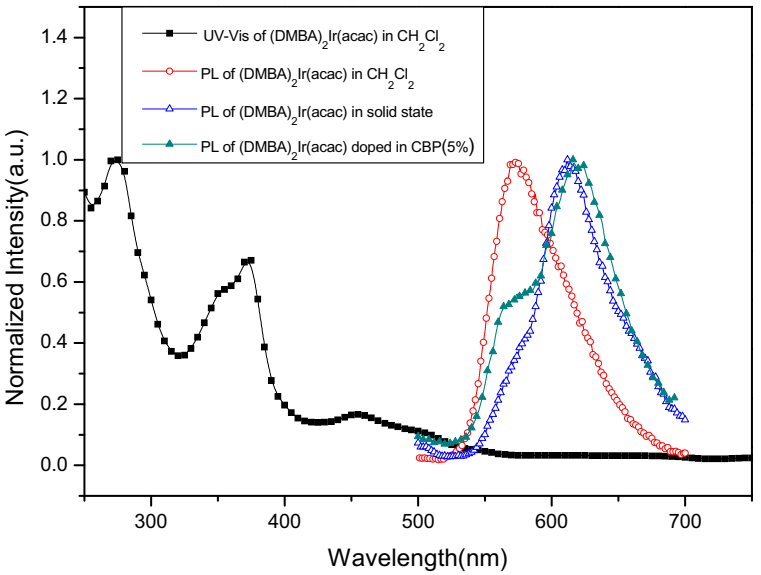

Fig. 1. UV–Vis and PL spectra of the complex $(DMBA)_2Ir(acac)$.

Table 1
Photophysical data of the iridium complexes.[a]

Complex	Absorption[b] λ_{max} (nm)	Emission[c]		Emission[d]		Quantum yield[e]
		λ_{max} (nm)	τ (μs)	λ_{max} (nm)	τ (μs)	
$(DMBA)_2Ir(acac)$	275, 375, 454, 500	572	0.207	572 612	0.018 0.034	0.40
$(DBA)_2Ir(acac)$[f]	275, 363, 463, 509	590				

[a] All data were collected at room temperature.
[b] Major absorption bands are listed.
[c] Measured in CH_2Cl_2 solution.
[d] Measured in the solid state.
[e] Obtained in CH_2Cl_2 using $Ir(ppy)_2(acac)$ as standard.
[f] Cited from literature [11].

duction of electron donating groups into the N-heterocycle (usually the pyridyl moiety) can raise the LUMO energy state of the corresponding Ir complex [16,17]. Hence, the energy gap will be enlarged and consequently lead to a PL hypsochromic shift. Compared with DBA, a methylenedioxy group with strong electron donating effect is introduced into the N-fused heterocycle, so a blue shift of 18 nm is rationalized, and this is consistent with the higher-energy MLCT transitions observed for $(DMBA)_2Ir(acac)$.

The emission spectrum of the complex in the solid state (powder sample) at room temperature is also presented in Fig. 1. Irradiation of $(DMBA)_2Ir(acac)$ with 480 nm light gave an orange-red emission with a peak wavelength of about 612 nm, namely a red shift of 40 nm relative to the solution spectrum. A non-obvious shoulder peak at about 572 nm was also observed. Face to face π–π interactions between aromatic molecules in the solid state often lead to a red-shifted luminescence and is typically ascribed to excimer formation. The square planar Pt complexes with excimer formation has been reported [18–22], while the influence of π stacking on the emission properties of octahedral Ir complex has also been depicted by Thompson [14] and Kang [23]. According to these previous reports, we presume that the red shift of the PL spectrum may be ascribed to excimer emission.

The emission lifetime of $(DMBA)_2Ir(acac)$ in CH_2Cl_2 solution at room temperature was measured to be 0.207 μs, which is shorter than 1.6 μs of $Ir(ppy)_2(acac)$ [14], but a little longer than 0.15 μs of *mer*-$Ir(ppy)_3$ [15]. The radiative (k_r) and non-radiative (k_{nr}) rate constant of $(DMBA)_2Ir(acac)$ were calculated to be 1.9×10^5 and 2.8×10^5, respectively, according to the equations $k_r = \Phi_{PL}/\tau$ and $\Phi_{PL} = k_r/(k_r + k_{nr})$ [15]. Previous report [18] showed that emission lifetimes are important evidences for excimer emission mechanism, so the solid state emission lifetimes at the wavelength of 572 and 612 nm were also measured in order to provide more evidences for the excimer emission mechanism. The measured life time of $\tau = 0.018$ μs of the emission at 572 nm, compared with 0.034 μs at 612 nm, is also consistent with excimer formation on $(DMBA)_2Ir(acac)$.

Cyclic voltammetry (CV) was employed to investigate the electrochemical behavior of $(DMBA)_2Ir(acac)$. The conventional three electrode configuration consists of a plati-

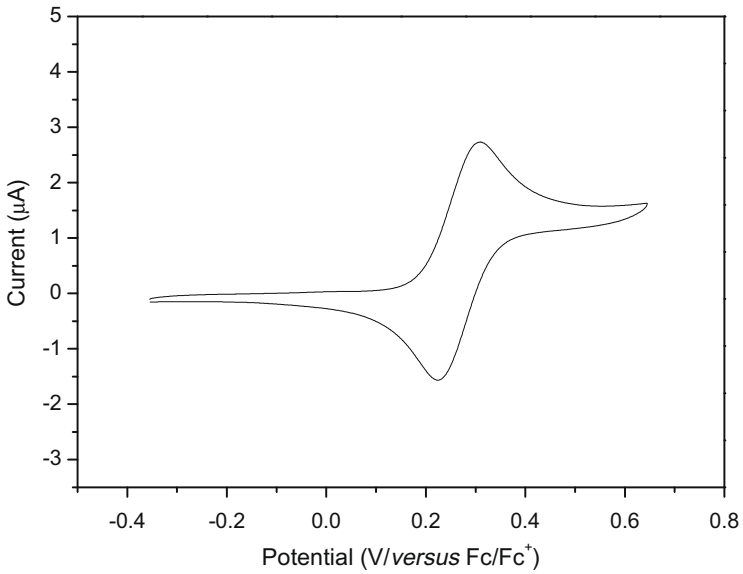

Fig. 2. Cyclic voltammogram of $(DMBA)_2Ir(acac)$.

num working electrode, a platinum wire auxiliary electrode, and a silver wire quasi-reference electrode. The ferrocene/ferrocenium couple was used as internal reference. The cyclic voltammogram was made in a one compartment glass cell in dichloromethane containing 10^{-3} M complex and 0.1 M tetra(*n*-butyl)ammonium hexafluorophosphate (*n*-Bu_4NPF_6) as a supporting electrolyte [24]. Fig. 2 depicts the cyclic voltammogram of the complex, where the potential is cycled at 50 mV s^{-1}.

The CV curve of this complex displayed a clean reversible one-electron oxidation wave at $E^{ox}_{1/2} = 0.27$ V versus Fc/Fc^+ couple reference indicating the good electrochemical stability of the complex. The oxidation process is usually considered as a metal-centered couple, i.e. Ir^{III}/Ir^{IV+} in the present complex, and the highest occupied molecular orbital (HOMO) energy level of the complex can be estimated according to the half-wave oxidation potential with regard to the energy level of the ferrocenium/ferrocene redox couple (being approximately 4.8 eV negative to the vacuum level [25]). The energy gap between HOMO and LUMO was obtained from the wavelength at the intersection of normalized absorption and emission spectrum. All the data are summarized in Table 2.

In order to study the electroluminescent properties of $(DMBA)_2Ir(acac)$, four devices (A–D) using this complex as dopant emitter were fabricated. These devices have the following structure: ITO/HTL/Ir:CBP/BCP/Alq. Either NPB (4,4′-bis[1-naphthylphenylamino]-biphenyl) or NPB together with TCTA (4,4′,4″-tris[*N*-carbazolyl]-triphenylamine) was used as the hole-transporting layer (HTL) and was first deposited on the indium tin oxide (ITO)-coated glass. CBP (4,4′-*N*,*N*′-dicarbozole biphenyl) as the host, and the complex $(DMBA)_2Ir(acac)$ as the dopant, were then deposited. A layer of BCP (2,9-dimethyl-4,7-diphenyl-1,10-phenanthroline) was used as the hole-blocker. Alq (tris(8-hydroxyquinolinato)aluminum) was used as electron transporting material, while LiF was used as electron-injection layer and Al was used as the cathode. The detailed structure of each device and key performance data are listed in Table 3; the molecular structures and energy level diagrams of the compounds used in the EL devices are presented in Fig. 3, and the data of energy levels of the related compounds are cited from literature [26,27]. The EL spectra and the brightness–voltage–current characteristics are shown in Figs. 4 and 5, respectively, while the external quantum efficiency–current density–current efficiency characteristics of the EL devices are presented in Fig. 6.

Device A was fabricated first, where NPB was used as the hole transporter and CBP doped with 7% $(DMBA)_2Ir(acac)$ as the emitting layer. This device emitted a red light with an emission maximum at 620 nm without any Alq contribution in the EL spectrum. An EQE of 7.6%, with a

Table 2
Electrochemical data of the complex $(DMBA)_2Ir(acac)$.

Complex	E_{onset} (V)[a]	$E_{1/2}$ (V)[b]	λ (nm)[c]	E_g (eV)[d]	HOMO (eV)	LUMO (eV)[e]
$(DMBA)_2Ir(acac)$	0.19	0.27	530	2.34	−5.07	−2.73

[a] Onset oxidation potential versus ferrocene/ferrocenium couple.
[b] Half-wave oxidation potential versus ferrocene/ferrocenium couple.
[c] Obtained from the wavelength at the intersection of absorption and emission spectrum.
[d] Calculated from the equation $E_g = hc/\lambda = 1241/\lambda$ (nm).
[e] Calculated via equation E_g = LUMO−HOMO.

Table 3
Structures and EL characteristics of the devices.[a]

Device[b]	Turn-on voltage (V)	L (cd m^{-2}, V)	η_{ext} (%, V)	η_c (cd/A, V)	η_p (lm/W, V)	CIE, 6 V (x, y)
A (7%)	4.5	15,100, 15.5	7.6, 4.5	12.6, 4.5	8.8, 4.5	(0.59, 0.39)
B (7%)	5.2	35,994, 13.5	10.9, 5.5	17.7, 5.5	13.4, 4.0	(0.62, 0.38)
C (5%)	6.6	66,312, 15.5	17.7, 5.0	35.7, 4.5	25.0, 4.5	(0.57, 0.42)
D (3%)	5.6	34,411, 14.5	14.3, 5.5	28.2, 5.5	20.7, 4.0	(0.58, 0.41)

[a] The data for brightness (L), external quantum efficiency (η_{ext}), current efficiency (η_c) and power efficiency (η_p) are the maximum values of the corresponding device. The turn-on voltages in all cases were defined as voltages corresponding to current densities of 1 mA cm^{-2}.
[b] The structure for device A: NPB (10 nm)/Ir:CBP (7%, 30 nm)/BCP (15 nm)/Alq (30 nm)/LiF (1 nm)/Al (100 nm); for devices B–D: NPB (10 nm)/TCTA (20)/Ir:CBP (x%, 30 nm)/BCP (10 nm)/Alq (50 nm)/LiF (1 nm)/Al (100 nm).

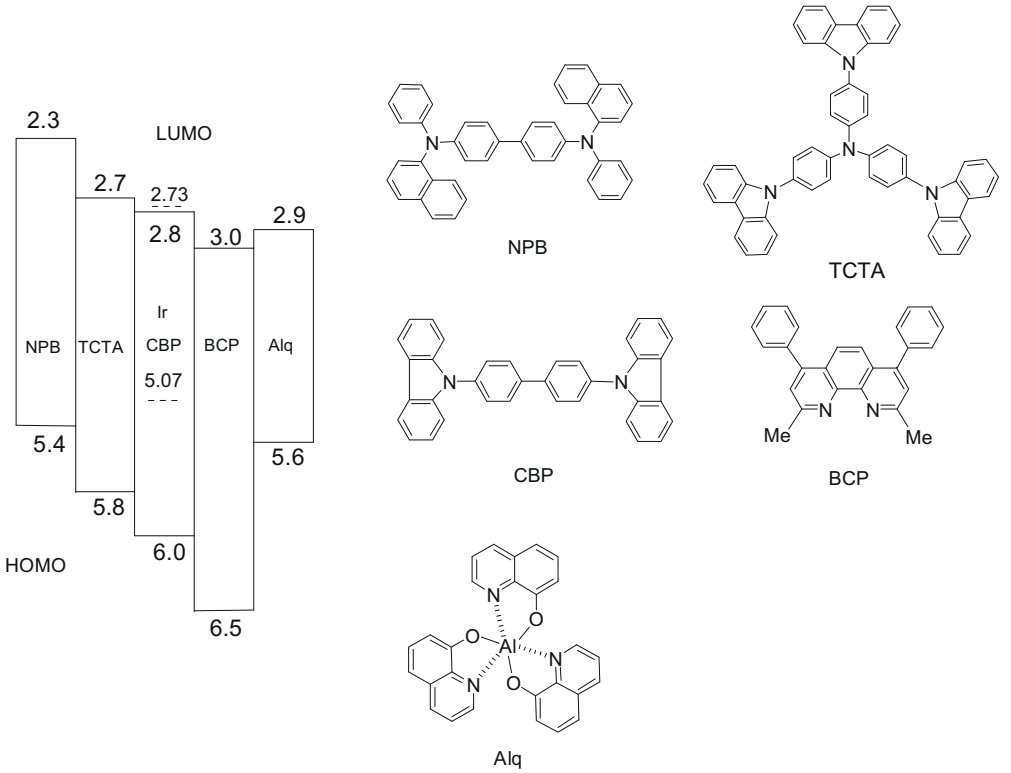

Fig. 3. Molecular structures and energy level diagrams of the compounds used in the devices.

current efficiency of 12.6 cd A^{-1}, power efficiency of 8.8 lm W^{-1} at 4.5 V, and a brightness of 15,100 cd m^{-2} at 15.5 V, were achieved. Compared with EL devices using $(DBA)_2Ir(acac)$ as dopant emitter with similar structure, device A showed a higher brightness and efficiency.

For further optimization of device structure, device B was fabricated, where NPB and TCTA were utilized together as the hole transporting materials. The thickness of BCP layer was reduced to be 10 nm, while the doping concentration was remained 7%. Considering the energy level, adding a layer of TCTA may help the transportation of holes from NPB to the emitting layer. As the results, an EQE of 10.9%, with a current efficiency of 17.7 cd A^{-1} at 5.5 V, a power efficiency of 13.4 lm W^{-1} at 4.0 V, and a brightness of 35,994 cd m^{-2} at 13.5 V, were achieved. The performance of device B was much better than that of device A, while the EL spectrum of device B remained almost the same, which thanks to the efficient holes and triplet excitons blocking effect of BCP. As a frequently used hole-blocker, BCP has a HOMO level of 6.5 eV deeper than that of the dopant complex (5.07 eV) and host material (6.0 eV), so the holes can be effectively blocked from the luminescent layer to Alq layer. An added benefit of the BCP layer is its higher triplet energy level of 2.5 eV [28] than the LUMO energy level of $(DMBA)_2Ir(acac)$, which efficiently blocks the diffusion of the dopant excitons. Based on the EL spectrum at an applied voltage of 6 V, Commission International de l'Eclairage (CIE) coordinates were calculated to be (0.62, 0.38), which were close to (0.59, 0.39) of device A.

The EL spectral shape of both devices A and B were similar to that of the powder sample and doped film emission spectra of $(DMBA)_2Ir(acac)$, where the emission peak at 620 nm may be the result of excimer emission, as we de-

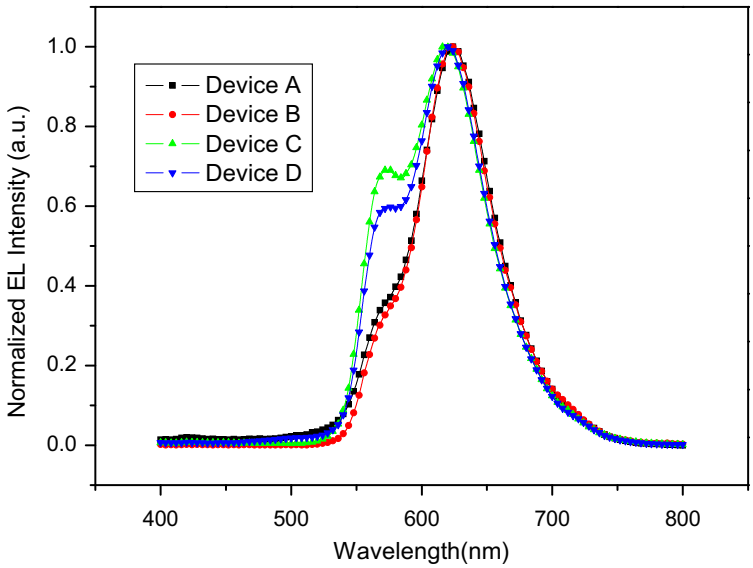

Fig. 4. EL spectra of devices A–D at a voltage of 6 V.

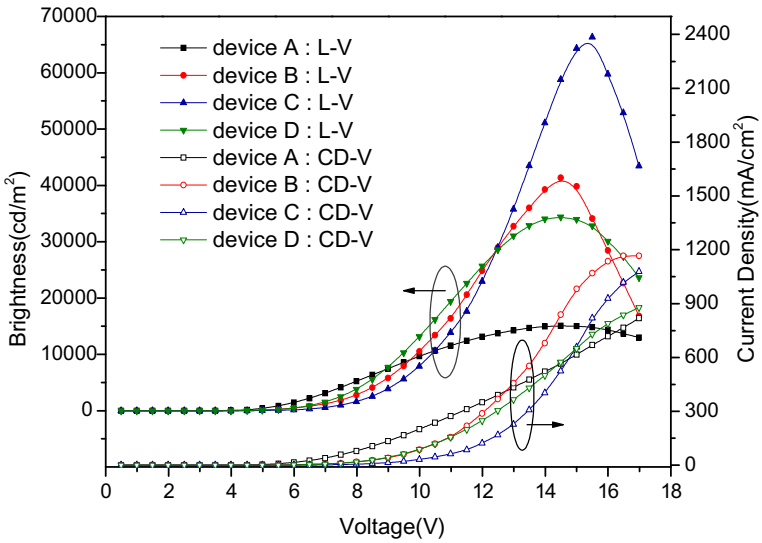

Fig. 5. The brightness–voltage–current characteristics of devices A–D.

scribed above, while the non-obvious shoulder peak at about 572 nm can be ascribed to monomer emission of $(DMBA)_2Ir(acac)$. To achieve efficient excimer emission from a doped layer, control of the dopant concentration is crucial, so devices C and D were fabricated with different doping concentration (5% and 3%, respectively). The structures of the devices C and D remained the same as device B.

The normalized EL spectra of devices B and C (inset) at various applied voltages are shown in Fig. 7. For device B, the shoulder peak at 572 nm becomes more obvious when the applied voltage increases. The relative intensity of the shoulder peak varies from 0.3 to 0.5, so the EL spectrum at 6 V is not a far cry from that of 12 V. For device C with a lower doping concentration of 5%, the shoulder peak becomes much more obvious where the relative intensity of the shoulder peak varies from 0.7 to 0.9. The emission spectrum depends on the applying voltage, but the CIE coordinates at different voltages do not change much since the main emission peak does not change. For device C, at the voltages of 6, 8, 10, and 12 V, the CIE coordinates were (0.57, 0.42), (0.56, 0.42), (0.56, 0.42), and (0.54, 0.43), respectively.

The lower doping concentration of device C improved the device performance, giving a maximum brightness of 66,312 cd m^{-2} at 15.5 V, an EQE of 17.7% at 5.0 V, a current efficiency of 35.7 cd A^{-1} and a power efficiency of 25.0 lm W^{-1}. This may be resulted from the effective prevention of triplet–triplet annihilation. It should be noted

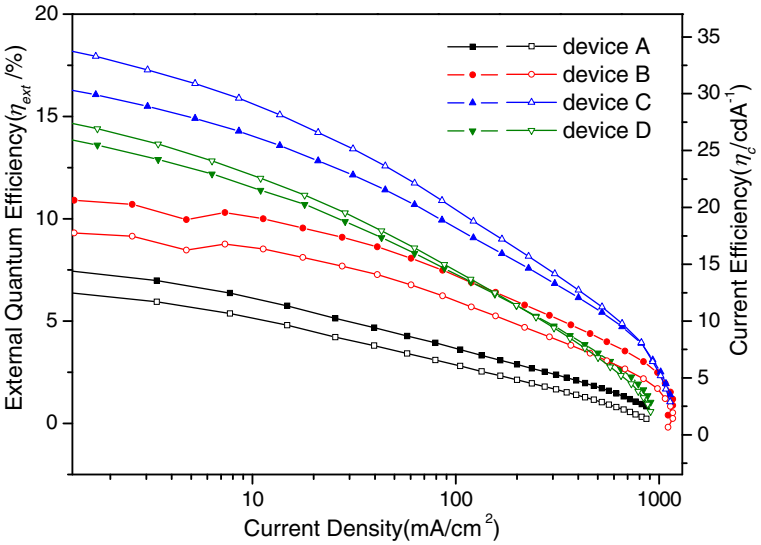

Fig. 6. External quantum efficiency–current density–current efficiency characteristics of the EL devices.

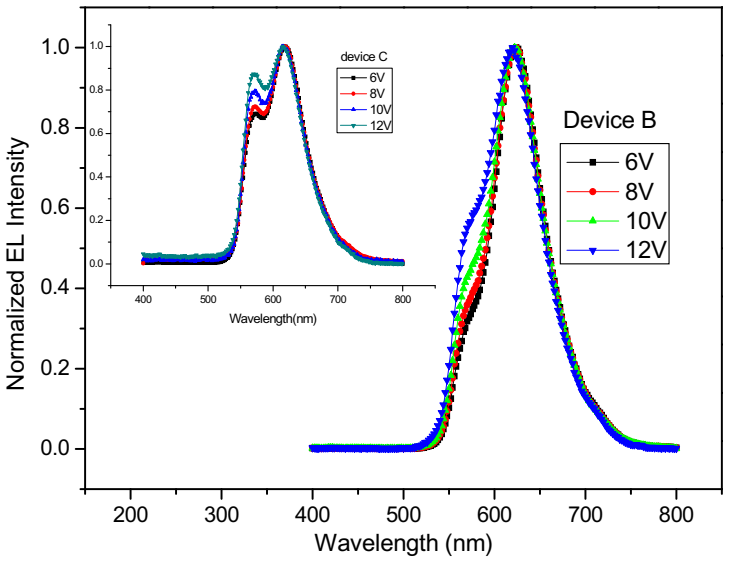

Fig. 7. EL spectra of devices B and C at various applied voltages (the inset shows the EL spectrum of device C).

that the LUMO energy level of $(DMBA)_2Ir(acac)$ is higher than the LUMO level of the CBP host (Fig. 3), which is similar to previous report [26]. The higher efficiency of device C may also be due to more balanced injection and transport of electrons and holes. Because the HOMO and LUMO levels of the dopant are higher than that of the host, the dopant complex will behave as hole traps and electron-scattering centers. As a result, a better recombination of electrons and holes in the emitting layer leads to a higher efficiency of the EL device. This result provides an example of highly efficient red-emitting OLEDs based on excimer emission of iridium(III) complex.

Device D was fabricated by using 3% $(DMBA)_2Ir(acac)$ as the dopant emitter. This device, respectively, achieved a maximum brightness of 34,411 cd m^{-2} at 14.5 V, EQE of 14.3%, current efficiency and power efficiency of 28.2 cd A^{-1} and 20.7 lm W^{-1}. The results are lower than that of device C but higher than that of devices A and B, so we can conclude that a doping concentration lower than 5% would be not profitable to the device performance.

4. Conclusions

The complex $(DMBA)_2Ir(acac)$ exhibits an orange emission in CH_2Cl_2 with a high quantum yield of 0.40 due to the adoption of rigid cyclometalated ligand, an orange-red emission in the solid state and doped thin film resulted

from the excimer formation. Good performances of the EL devices using the complex as dopant emitter can be achieved by optimization of the structure and doping concentration. When NPB and TCTA were used together as the hole transporting materials, the EL devices exhibit much higher brightness and efficiencies. Control of the doping concentration is crucial. A maximum brightness of 66,312 cd m^{-2} and a maximum EQE of 17.7% can be achieved at a doping concentration of 5%. This is a new successful example of our strategy for achieving highly efficient EL device by adopting rigid cyclometalated ligand for phosphorescent iridium complex as dopant emitter. Such a strategy shall provide useful guidelines for the future design and selection of highly phosphorescent materials for OLEDs. Further investigation on this series of complexes used for the fabrication of white OLEDs is currently in progress in our laboratory.

Acknowledgements

Financial supports from the National Natural Science Foundation of China (Project Nos. 20772057, 20773066, and 20972068), the Foundations for Excellent Postgraduate Students of Education Department of Jiangsu Province (No. CX09S_042Z), and Nanjing Normal University (No. 181200000242) are gratefully acknowledged.

References

[1] P.T. Chou, Y. Chi, Chem. Eur. J. 13 (2007) 380.
[2] M.S. Lowry, S. Bernhard, Chem. Eur. J. 12 (2006) 7970.
[3] W.S. Huang, C.W. Lin, J.T. Lin, J.S. Huang, C.W. Chu, Y.H. Wu, H.C. Lin, Org. Electron. 10 (2009) 594.
[4] M.A. Baldo, D.F. O'Brien, Y. You, A. Shoustikou, M.E. Thompson, S.R. Forrest, Nature 395 (1998) 234.
[5] E. Holder, B.M.W. Langeveld, U.S. Schubert, Adv. Mater. 17 (2005) 1109.
[6] Y. You, S.Y. Park, Dalton Trans. (2009) 1267.
[7] J.P. Duan, P.P. Sun, C.H. Cheng, Adv. Mater. 15 (2003) 224.
[8] S. Reineke, F. Lindner, G. Schwartz, N. Seidler, K. Walzer, B. Lüssem, K. Leo, Nature 459 (2009) 234.
[9] J.W. Hu, G.H. Zhang, H.H. Shih, X.Q. Jiang, P.P. Sun, C.H. Cheng, J. Organomet. Chem. 693 (2008) 2798.
[10] C.X. Li, H.H. Shih, X.Q. Jiang, P.P. Sun, Y. Pan, C.H. Cheng, Synth. Met. 159 (2009) 2070.
[11] C.X. Li, P.P. Sun, L.J. Yan, Y. Pan, C.H. Cheng, Thin Solid Films 516 (2008) 6186.
[12] M. Nonoyama, Bull. Chem. Soc. Jpn. 47 (1974) 767.
[13] S. Lamansky, P. Djurovich, D. Murphy, F. Adbel-Razzaq, H.E. Lee, C. Adachi, P.E. Burrows, S.R. Forrest, M.E. Thompson, J. Am. Chem. Soc. 123 (2001) 4304.
[14] S. Lamansky, P. Djurovich, D. Murphy, F. Adbel-Razzaq, R. Kwong, I. Tsyba, M. Bortz, B. Mui, R. Bau, M.E. Thompson, Inorg. Chem. 40 (2001) 1704.
[15] A.B. Tamayo, B.D. Alleyne, P. Djurovich, S. Lamansky, I. Tsyba, N.N. Ho, R. Bau, M.E. Thompson, J. Am. Chem. Soc. 125 (2003) 7377.
[16] I.R. Laskar, S.F. Hsu, T.M. Chen, Polyhedron 24 (2005) 189.
[17] L.L. Wu, C.H. Yang, I.W. Sun, S.Y. Chu, P.C. Kao, H.H. Huang, Organometallics 26 (2007) 2017.
[18] B.W. D'Andrade, J. Brooks, V. Adamovich, M.E. Thompson, S.R. Forrest, Adv. Mater. 14 (2002) 1032.
[19] X.H. Yang, Z.X. Wang, S. Madakuni, J. Li, G.E. Jabbour, Appl. Phys. Lett. 93 (2008) 193305.
[20] E.L. Williams, K. Haavisto, J. Li, G.E. Jabbour, Adv. Mater. 19 (2007) 197.
[21] B.W. Ma, P.I. Djurovich, M.E. Thompson, Coord. Chem. Rev. 249 (2005) 041914.
[22] G.J. Zhou, Q. Wang, C.L. Ho, W.Y. Wong, D.G. Ma, L.X. Wang, Chem. Commun. (2009) 3574.
[23] S. Jung, Y. Kang, H.S. Kim, Y.H. Kim, C.L. Lee, J.J. Kim, S.K. Lee, S.K. Kwon, Eur. J. Inorg. Chem. (2004) 3415.
[24] L.Q. Chen, H. You, C.L. Yang, D.G. Ma, J.G. Qin, Chem. Commun. (2007) 1352.
[25] F.I. Wu, H.J. Su, C.F. Shu, L. Luo, W.G. Diau, C.H. Cheng, J.P. Duan, G.H. Lee, J. Mater. Chem. 15 (2005) 1035.
[26] D.M. Kang, J.W. Kang, J.W. Park, S.O. Jung, S.H. Lee, H.D. Park, Y.H. Kim, S.C. Shin, J.J. Kim, S.K. Kwon, Adv. Mater. 20 (2008) 2003.
[27] M.H. Tsai, H.W. Lin, H.C. Su, T.H. Ke, C.C. Wu, F.C. Fang, Y.L. Liao, K.T. Wong, C.I. Wu, Adv. Mater. 18 (2006) 1216.
[28] V.I. Adamovich, S.R. Cordero, P.I. Djurovich, A. Tamayo, M.E. Thompson, B.W. D'Andrade, S.R. Forrest, Org. Electron. 4 (2003) 77.

Organic Electronics 11 (2010) 641–648

Contents lists available at ScienceDirect

Organic Electronics

journal homepage: www.elsevier.com/locate/orgel

Solution-processed organic films of multiple small-molecules and white light-emitting diodes

Dongdong Wang [a], Zhaoxin Wu [b,*], Xinwen Zhang [b], Bo Jiao [b], Shixiong Liang [b], Dawei Wang [c], Runlin He [d], Xun Hou [b]

[a] School of Science, Xi'an Jiaotong University, Xi'an 710049, PR China
[b] Key Laboratory for Physical Electronics and Devices of the Ministry of Education, School of Electronic and Information Engineering, Xi'an Jiaotong University, Xi'an 710049, PR China
[c] Department of Physics, University of Arkansas, Fayetteville, AR 72701, USA
[d] Firefly Lighting Co. Ltd, XiaMen 361009, PR China

ARTICLE INFO

Article history:
Received 3 September 2009
Received in revised form 4 December 2009
Accepted 4 January 2010
Available online 11 January 2010

Keywords:
Spin-coating molecular materials
Crystallization
White organic light-emitting devices
Mixed host

ABSTRACT

We investigated characteristics of solution-processed films of 4,4′-bis(2,2-diphenylvinyl)-1,1′-bibenyl (DPVBi), *N,N′*-bis(naphthalene-1-yl)-*N,N′*-bis(phenyl)-benzidine (NPB), and their blends, and it was found that the spin-coated films of NPB, and blends of NPB and DPVBi, though having lower densities, were more uniform than their vacuum-deposited counterparts. Using the spin-coated films of NPB:DPVBi as mixed host, doped with blue dye (4,4′-bis[2-(4-(*N,N*-diphenylamino)phenyl)vinyl]biphenyl) and yellow dye (5,6,11,12-tetraphenylnaphacene), new white organic light-emitting devices (WOLEDs) were demonstrated. The luminance (maximum luminance of 35822 cd/m^2), efficiency (5.3 lm/W (100 cd/m^2) and 8.3 cd/A (1000 cd/m^2)) and stability of these solution-processed devices are better than or equivalent to the vacuum-deposited one, which was expected as an alternative route to the fabrication of small-molecular WOLEDs, reducing the cost of devices and avoiding the complexities of the co-evaporation of multiple dopants and host materials in the vacuum deposition.

© 2010 Elsevier B.V. All rights reserved.

1. Introduction

White organic light-emitting devices (WOLEDs) have highly promising applications in areas such as full-color flat-panel displays, liquid–crystal-display backlighting and large area illumination. The white emission from WOLEDs are generally obtained by mixing complementary (e.g., blue and yellow or orange) or primary colors (red, green, and blue). Many approaches have been proposed to achieve white light emission, such as doping several dyes into one [1–4] or more emissive layers (EMLs) [5–7]. In WOLEDs with multiple EML structures, two or more EMLs are physically separated from each other. Thus the location of exciton recombination and the doping concentration [8] must be controlled carefully to obtain balanced white emission. This usually leads to a fabrication process of great complexity, poor reproducibility and high cost when the vacuum deposition technique is employed. Several methods and processes [9,10] have been reported to avoid the complexity of co-evaporation and/or reduce the manufacturing cost. Fusing organic solid solution is an effective method to avoid the complexity of co-evaporation process [9], where, the dopants are introduced prior to the device fabrication process through high-temperature and high-pressure fusion process. However, for this method to be possible, compatible material systems have to be found to match each other.

Solution processing of organic materials is another attractive technique for low-cost manufacturing device because it is easy to realize co-doping of several dopants and compatible with low-cost, large area manufacture technol-

* Corresponding author. Tel./fax: +86 29 82664867.
E-mail address: zhaoxinwu@mail.xjtu.edu.cn (Z. Wu).

1566-1199/$ - see front matter © 2010 Elsevier B.V. All rights reserved.
doi:10.1016/j.orgel.2010.01.004

ogy such as screen-printing, and inkjet printing [11]. In the past decades, organic materials in solution processing for fabricating devices are mainly polymers [12–15]. Alternatively, many solution-processible organic molecules were designed and synthesized to fabricate the light-emitting devices by spin-coating, such as dendritic molecules [16–18], oligomers [19], spiro-molecules [20,21], and binuclear metal chelates [22,23]. Recently, Lee et al. have also reported a spin-coated blue light-emitting devices based on 2-(t-butyl)-9,10-bis(2′-naphthyl) anthracene [24], which combines the simple materials of OLED and low-cost process of solution processing. Thus, it is desirable to develop solution-processed devices based on high-efficient molecular materials which films were usually made by vacuum-deposition.

In this paper, we investigated the characteristics of spin-coated films of DPVBi (4,4′-bis(2,2-diphenylvinyl)-1,1′-bibenyl), NPB (*N,N*′-bis(naphthalene-1-yl)-*N,N*′-bis(phenyl)-benzidine) and their blends, which were widely used in fabrication of OLEDs by vacuum-deposition. It was found that the spin-coated small-molecular films of NPB, and blends of NPB and DPVBi, though having lower densities, were more uniform than their vacuum-deposited counterparts. We demonstrate WOLEDs based on solution-processed films of the blends of NPB and DPVBi. In these WOLEDs, the white EML was formed by spin-coating a solution containing mixed hosts (MH) of NPB and DPVBi, blue dopant 4,4′-bis[2-(4-(*N,N*-diphenylamino)phenyl)-vinyl]biphenyl (DPAVBi) and yellow dye 5,6,11,12-tetraphenylnaphacene (rubrene). Besides avoiding complexity of co-evaporated process in vacuum deposition, these devices show high luminance and stable white-emitting under different driving voltages.

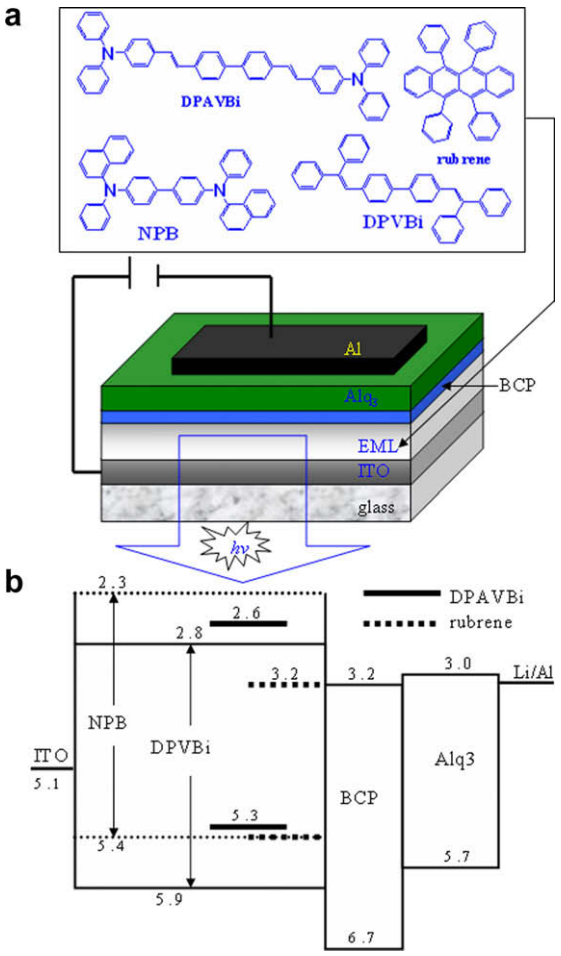

Fig. 1. (a) Chemical structures of the key materials used and structure of devices A–F, (b) schematic energy-level diagrams of devices A–F.

2. Spin-coated molecular films

The chemical structures of DPVBi, NPB, blue dye DPAVBi and yellow dye rubrene are shown in Fig. 1(a). The chlorobenzene was used as a solvent for dissolving these molecular materials. The solution-processed films of blends of NPB:DPVBi were fabricated as follows. The blends with NPB:DPVBi weight ratio of 0:10, 1:9, 1:4, 3:7, 2:3, 3:2, 4:1, 10:0 were first dissolved in chlorobenzene (~14 mg/ml), the solution was then spin-coated on indium tin oxide (ITO)-coated glass substrates to form a film with a thickness of 50 nm (1000 rpm). Finally, the spin-coated films were transformed to the oven for baking. Following previous reports [25], the spin-coated films are baked at 80 °C for 30 min in the oven to guarantee the removal of residual solvent of chlorobenzene in the spin-coated films. The surface morphology was investigated by AFM and 10× microscope objective with a numerical aperture of 0.3 (Nikon, Japan). The thickness and refractive indices of the films were measured by an ellipsometer.

Fig. 2 shows the microscope images of spin-coated films of NPB:DPVBi with different mixing ratios. Fig. 2(a)–(h) corresponds to NPB:DPVBi ratio of 0:10, 1:9, 1:4, 3:7, 2:3, 3:2, 4:1, and 10:0, respectively. Fig. 2(a) shows the spin-coated film of DPVBi, where significant crystallization and coagulation of DPVBi was observed. These effects are due to the low glass-transition temperature (T_g) of DPVBi (64 °C) during the annealing process [26]. If the NPB (10%) is blended with DPVBi (90%), however, crystallization of the spin-coating film of the blends was reduced as shown in Fig. 2(b). With the increasing NPB concentration in the blends, the crystallization of spin-coated film of the blends was further reduced as can be seen from Fig. 2(c) and (d). As the NPB concentration is increased to 40%, the crystallization and coagulation can no longer be observed (see Fig. 2(e)–(h)). The suppressing of the crystallization and coagulation of DPVBi can be attributed to two factors. One is that the NPB molecules in the blends function as defects and hence prevents the formation of an ordered crystal of DPVBi. This phenomenon is similar to a previous report [10], where the glass-transition temperature of NPD:rubrene was found to be higher than that of pure NPD(4,4′-bis[*N*-(1-naphthyl)-*N*-phenyl-amino]-biphenyl) because the doped rubrene serve as defects. The other is that a polymer with a high T_g was reported to effectively suppress the crystallization and coagulation of molecular material in molecularly doped polymers [27]. Since NPB has a T_g of about 95 °C, it is effective on preventing the crystallization and coagulation from happening in spin-

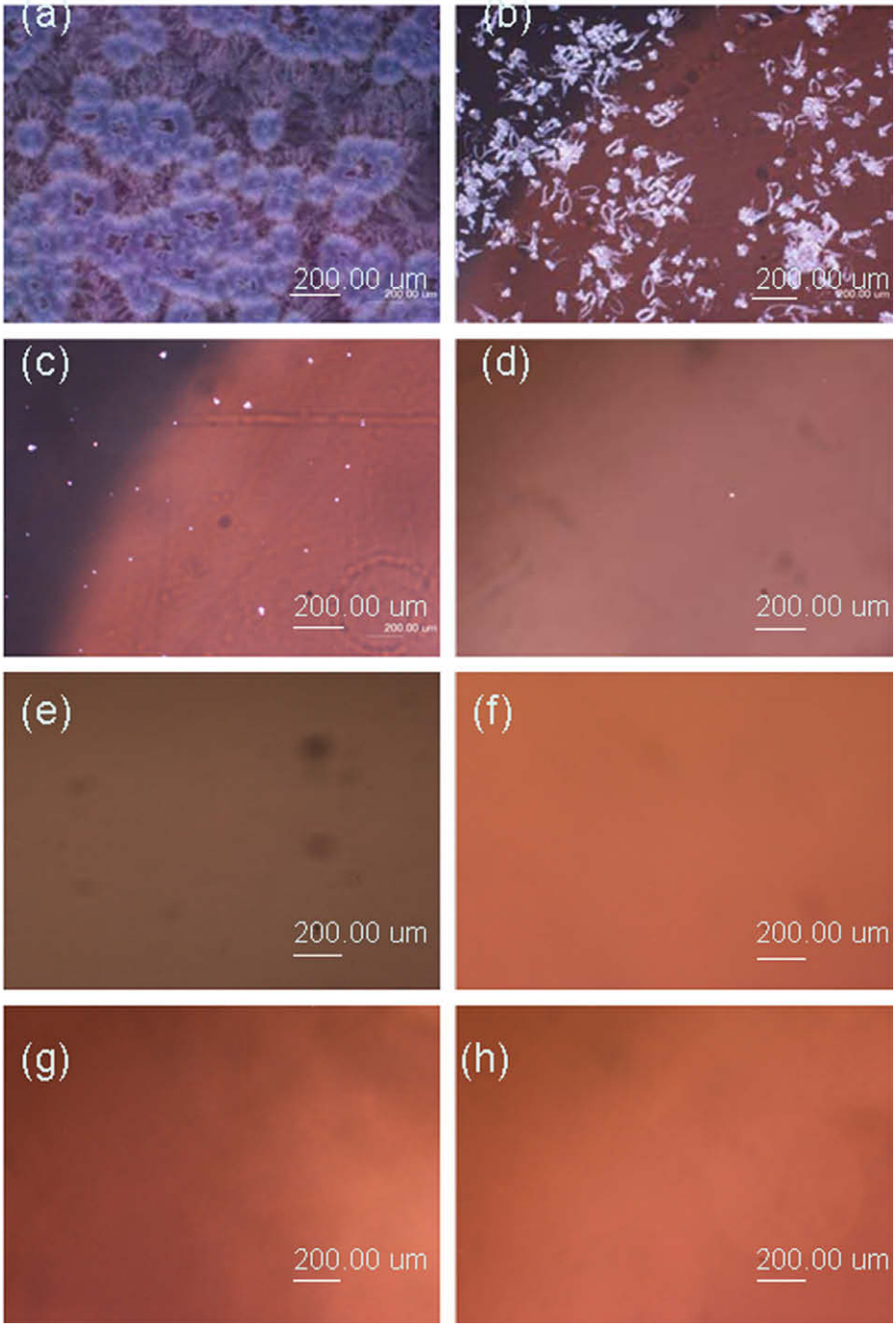

Fig. 2. The microscope images of organic films spin-coated on top of ITO. (a)–(h) Corresponding to NPB:DPVBi ratios of 0:10, 1:9, 1:4, 3:7, 2:3, 3:2, 4:1, and 10:0, respectively.

coated films and thus provides these films with better thermal stability.

Fig. 3 shows the surface morphology of spin-coated and vacuum-deposited films by atomic force microscopy (AFM). Fig. 3(a) is the surface of the ITO film, on which other organic materials were deposited or spin-coated. The root-mean-square of surface roughness (R_{RMS}) of ITO film is 1.51 nm. Fig. 3(b)–(f) is the surface morphology of spin-coated films of the blends with NPB:DPVBi ratios of 10:0, 3:7, 2:3, 3:2, and 4:1 (these films has no crystallization) on ITO film, which R_{RMS} of surface roughness is 0.319, 0.247, 0.254, 0.277, and 0.312 nm, and all the spin-coated films show a pin-free and smooth surface morphology. The surface morphology of vacuum-deposited films of NPB and NPB:DPVBi (3:2) were also shown in Fig. 3(g) and (h) with the R_{RMS} of 1.62 and 0.91 nm. The AFM investigations indicate that

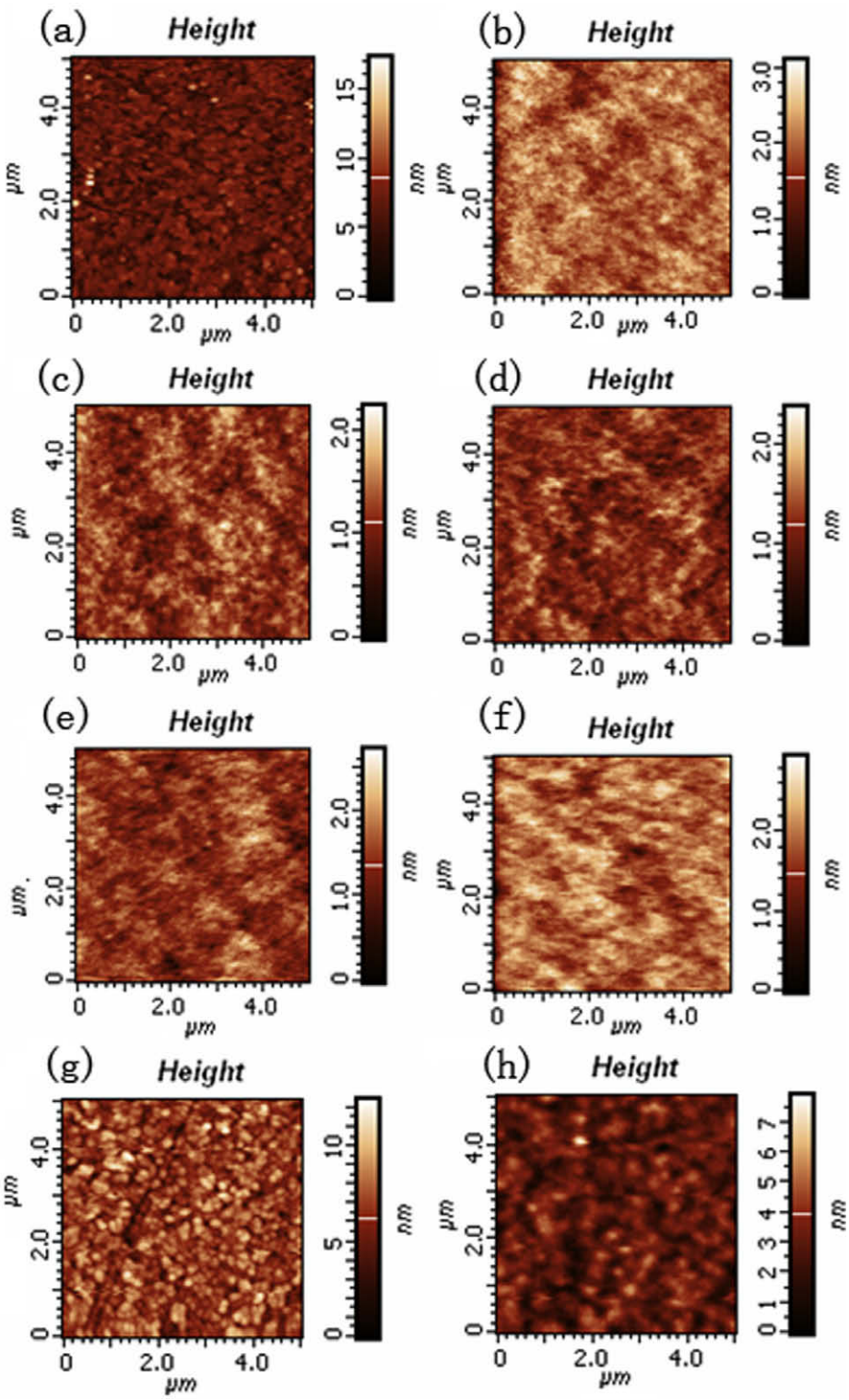

Fig. 3. The AFM images of ITO films (a) (R_{RMS} = 1.51 nm) and spin-coated films with NPB:DPVBi ratios of, (b) 10:0 (R_{RMS} = 0.319 nm), (c) 3:7 (R_{RMS} = 0.247 nm), (d) 2:3 (R_{RMS} = 0.254 nm), (e) 3:2 (R_{RMS} = 0.277 nm), (f) 4:1 (R_{RMS} = 0.312 nm), and the vacuum-deposited films with NPB:DPVBi ratios, (g) 10:0 (R_{RMS} = 1.62 nm) and (h) 3:2 (R_{RMS} = 0.91 nm) (scan size: 5 × 5 μm).

the spin-coated films of NPB, and NPB:DPVBi blends are more uniform than the vacuum-deposited ones.

The refractive indices of the spin-coated films can be obtained by spectroscopic ellipsometry, which can be used

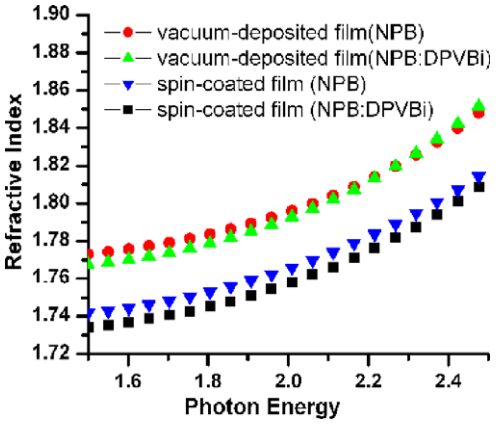

Fig. 4. The refractive indices of the spin-coated and vacuum-deposited films of NPB and the blends of NPB:DPVBi (3:2).

to evaluate the porosity of the films. The refractive index (n_f) of the film can expressed as $n_f = n_s(1-q) + n_p q$, where n_s and n_p are the mean indices of skeleton of the film and the pore space respectively, and q is the porosity, or the fractional volume of the pores in the film [28]. So the refractive index, n_f, is reversely in proportional to q, the porosity of films. Fig. 4 shows the refractive index of spin-coated films of NPB, the blends of NPB and DPVBi (3:2), and their vacuum-deposited counterparts. It was found that the refractive indices of spin-coated films of NPB and the blends of NPB and DPVBi (3:2) were smaller than those of vacuum-deposited counterparts. These showed that the spin-coated films were more porous and had lower density than the vacuum-deposited ones. How to deposit more dense molecular films by solution-processing will be a challenge in future research.

3. Fabrication and performances of WOLEDs

Based on spin-coated films of NPB:DPVBi, the device structure of WOLEDs in our experiments is ITO/EML (50 nm)/BCP (10 nm)/Alq_3 (30 nm)/LiF/Al. BCP (2,9-dimethyl-4,7-diphenyl-1,10-phenanthroline) is used as hole-blocking material and Alq_3 (tris(8-hydroxyquinoline)aluminum) as electron-transporting material. The spin-coated EML consist of MH doped with blue dye DPAVBi (4%) and yellow dye rubrene (0.27%) [29]. The composition of the EMLs used in six devices (labeled as A, B, C, D, E, and F) is summarized in Table 1. The six devices A, B, C, D, E, and F have different NPB:DPVBi weight ratios, which are 10:0, 4:1, 3:2, 2:3, 1:4, and 0:10, respectively. The details of device fabrication are as follows: (1) the chlorobenzene solution (~14 mg/ml) was spin-coated on clean patterned ITO-coated glass substrates to obtain a film of 50 nm thickness; (2) the spin-coated films of the devices A–D were annealed at 80 °C for 30 min and that of the devices E and F were annealed at 80 °C for 10 min to avoid the crystallization of spin-coated films; (3) the samples A–F were then loaded into a vacuum chamber to have the BCP hole-blocking layer (10 nm thickness), electron-transporting layer (30 nm thickness) and the cathode, LiF (0.6 nm)/Al (100 nm) deposited by thermal evaporation. The schematic energy-level diagram of the devices is shown in Fig. 1(b). The photoluminescence (PL) spectra of the films were measured with a fluorescence spectrophotometer (Fmax-4, JY Co.) and the absorption spectra were measured with UV3010 (Hitachi Co.). The electroluminescence (EL) spectra and CIE coordinates of the devices were measured by a spectrometer (PR650) and the current–voltage-luminescence characteristics were analyzed by Keithley 2602 source meter and Luminance meter.

The EL characteristics of devices A–F were summarized in Table 1. Fig. 5(a) and (b) shows their luminance–current density and current efficiency–luminance characteristics. Among all the devices, device C shows the best performances, it presents a power efficiency of 5.3 lm/W (100 cd/m^2) and current efficiency of 6.5 cd/A at a luminance of 1000 cd/m^2 and a maximum luminance of 35,822 cd/m^2 at 11.7 V. The luminance and current efficiency of the devices with MH (B–E) are higher than that with only NPB (device A) or DPVBi (device F). As we can see, device A shows a current efficiency of 3.83 cd/A (1000 cd/m^2) and a maximum luminance of 14,113 cd/m^2, while device F shows a current efficiency of 0.65 cd/A (1000 cd/m^2) and a luminance of 1476 cd/m^2.

The higher efficiency and luminance of devices B–E can be attributed to the blend of NPB and DPVBi used as MH, which effectively adjust the hole-injecting/transporting of devices by varying the ratio of the blend. DPVBi is a light-emitting material with intense fluorescence in the blue region [30], and NPB is widely used as a hole-transport material, whose hole mobility (10^{-4} cm^2 V^{-1} s^{-1}) is much higher than that of DPVBi and the hole-injecting bar-

Table 1
The composition of the EML and the EL characteristics of WOLEDs.

No.	Weight ratio				Performances		
	NPB	DPVBi	DPAVBi (*x*%)	Rubrene (*y*%)	Maximum luminance (cd/m^2)	Efficiency at 1000 cd/m^2	CIE (*x*,*y*)[a] 4 V/9 V
A	10	0	4	0.27	14,113	3.83	(0.315, 0.386)/(0.275, 0.336)
B	4	1	4	0.27	32,167	6.3	(0.292, 0.385)/(0.315, 0.387)
C	3	2	4	0.27	35,822	6.5	(0.305, 0.390)/(0.320, 0.392)
D	2	3	4	0.27	27,270	6.0	(0.306, 0.394)/(0.313, 0.388)
E	1	4	4	0.27	19,979	5.9	(0.262, 0.413)/(0.271, 0.356)
F	0	10	4	0.27	1476	0.65	(0.257, 0.360)/(0.278, 0.381)[a]
G[b]	3	2	4	0.27	23,466	8.3	(0.316, 0.405)/(0.309, 0.390)
H[b]	3	2	4	0.40	20,387	7.5	(0.310, 0.436)/(0.316, 0.426)

[a] The CIE coordinates at 6 V/12 V, respectively.
[b] Devices G and H have the structure as ITO/PEDOT:PSS/EML/BCP/Alq_3/LiF/Al.

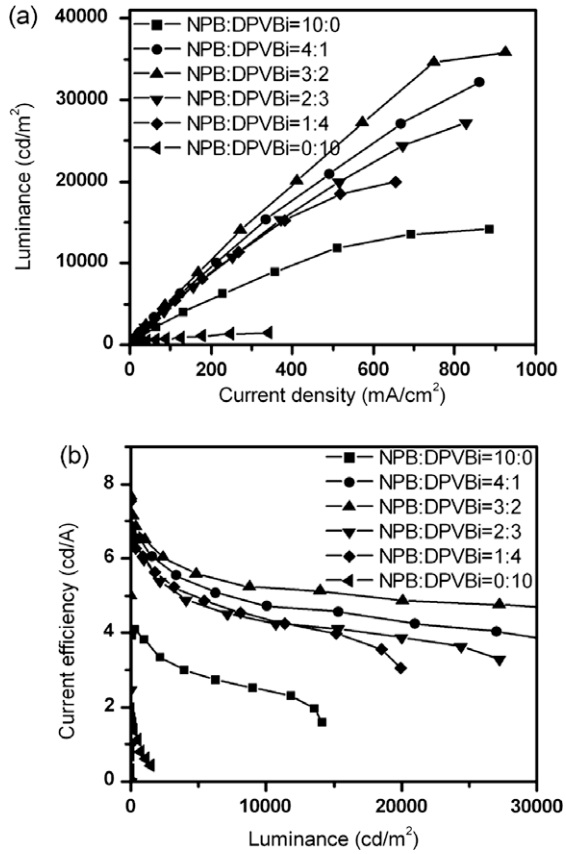

Fig. 5. (a) The luminance–current density and (b) current efficiency–luminance characteristics of the devices A–F.

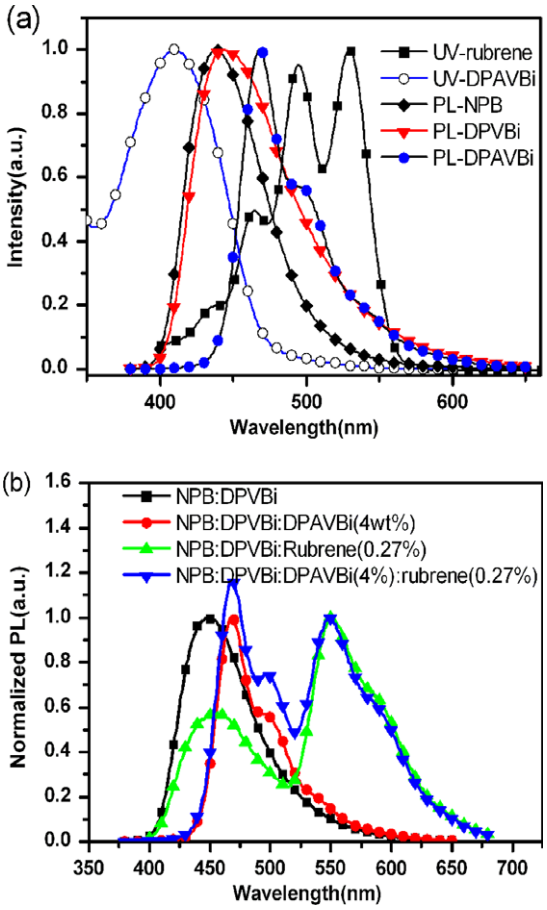

Fig. 6. (a) The UV absorption spectra of DPAVBi and rubrene in chlorobenzene solution and PL spectra of pure DPVBi, NPB, and 4% DPAVBi doped into PMMA film and (b) PL spectra of mixed film of NPB:DPVBi (3:2), DPAVBi (4%), rubrene (0.27%) and both DPAVBi (4%) and rubrene (0.27%) doped mixed film.

rier of NPB from ITO (0.3 eV) is lower comparing to DPVBi (0.8 eV) [30,31]. So the blend of NPB and DPVBi used as MH play the roles of both hole-transport layer (HTL) and EML in WOLEDs, and the hole injection and transport in WOLEDs can be adjusted by changing the ratio of NPB and DPVBi in EML, which could improve the balances of carriers (holes and electrons) in EML and achieve the high performance of devices.

In order to distinguish the energy-transfer processes in the EMLs of the WOLEDs, the absorption and PL spectra of the dyes, the MH and the dye-doped MH films are investigated. Fig. 6(a) shows the absorption spectra of DPAVBi and rubrene in chlorobenzene solution, and PL spectra of DPVBi, NPB and DPAVBi in films. In Fig. 6(a), there is a large spectral overlap between the fluorescent band of the MH (NPB:DPVBi) and the absorption bands of both DPAVBi and rubrene, which indicates that the lowest singlet-excited states in the MH can be energetically transferred to the dyes (DPAVBi or rubrene) via förster energy transfer. In addition, the spectra overlap between the fluorescent band of DPAVBi and the absorption band of rubrene suggests that the energy-transfer process between them can happen. Fig. 6(b) shows the PL spectra of the mixed NPB:DPVBi film (3:2), the DPAVBi (4%), rubrene (0.27%) and both DPAVBi (4%) and rubrene (0.27%) doped films. The excitation peak wavelength was at 350 nm for all the PL measurement. The DPAVBi and rubrene show a peak at 468 and 550 nm, respectively. In Fig. 6(b), no emission from the MH is observed in PL spectra of MH doped by DPAVBi, indicating that the energy in the excited MH molecule is completely transferred to DPAVBi with a doping concentration of 4%. On the other hand, a strong emission from MH is observed when the MH is doped with rubrene, suggesting the energy transfer from the MH to rubrene is incomplete with the doping concentration of 0.27%. When we doped both DPAVBi (4%) and rubrene (0.27%) in the MH, nearly comparable intensity of blue and yellow-emitting band are observed, which implies that the energy in the MH is shared by both dyes.

Fig. 7(a)–(d) shows the EL spectra of devices A–D under different applied voltages, where the EL intensity is normalized to the blue wavelength peak, and the CIE coordinates are shown in insets. As can be seen, the devices B–D with MH show quite stable CIE coordinates with various applied voltages. The CIE coordinates of device C change from (0.305, 0.390) at 4 V to (0.320, 0.392) at 9 V, in which the change of CIE coordinates is only (0.015, 0.002), while the CIE coordinates of device A with NPB as host shift from

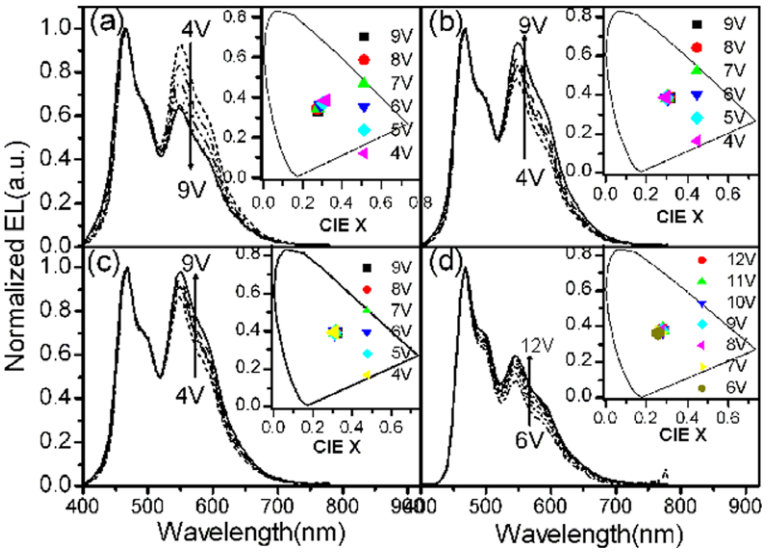

Fig. 7. The normalized EL spectra of the devices A–D and CIE coordinates in inset. (a)–(d) correspond to devices A–D, respectively.

(0.315, 0.386) to (0.275, 0.336), showing a change of (−0.040, +0.050). According to previous reports [32,33], the blueshift under increasing applied voltages in WOLEDs with lightly doped rubrene is attributed to the saturation effect of the rubrene molecules, which could account for the spectral variation of device A with NPB host doped with little amount of rubrene (only 0.27%). Therefore the stable color coordinates of devices B–D with MH are due to DPVBi in the blends that has an electron-transporting character [30,34], which transports electrons to the bulk of the EML effectively and consequently avoids the saturation effect of rubrene molecules. In addition, the role of BCP in WOLEDs is expected to prevent holes from entering electron-transporting layer and confine all the electron–hole pairs in the EML for efficient recombination, which also helps stabilize the color coordinates of WOLEDs.

The device performance of above device C still has room for improvement if we introduce a hole-injection layer such as poly(3,4-ethylenedioxythiophere):poly(styrene sulfonate) (PEDOT:PSS). Fig. 8(a) and (b) presented the comparison of efficiency and stability of solution-processed WOLEDs (device G) and the vacuum-deposited one (device H). The devices G and H have the same structure as ITO/PEDOT:PSS (50 nm)/EML (50 nm)/BCP (10 nm)/Alq_3 (30)/LiF (0.5)/Al(100 nm), in which the PEDOT:PSS was introduced as hole-injection layer, and EML consisted of the same ratio of NPB, DPVBi, DPAVBi, and rubrene as device C in Table 1. The water-dispersed PEDOT:PSS mixture was spin-coated on the top of ITO to form a film with a thickness of 50 nm. As for the solution-processed WOLEDs (device G), the fabrication of EML was the same as device C except the annealing condition is changed to be 130 °C for 15 min in the oven. As for the vacuum-deposited one (device H), the EML was formed by vacuum deposition of a solution-promixed deposition target with mixed hosts DPVBi and NPB doped with DPAVBi and rubrene [35]. In Fig. 8, device G shows a current efficiency of 8.3 cd/A at the luminance of 1000 cd/m^2 and an

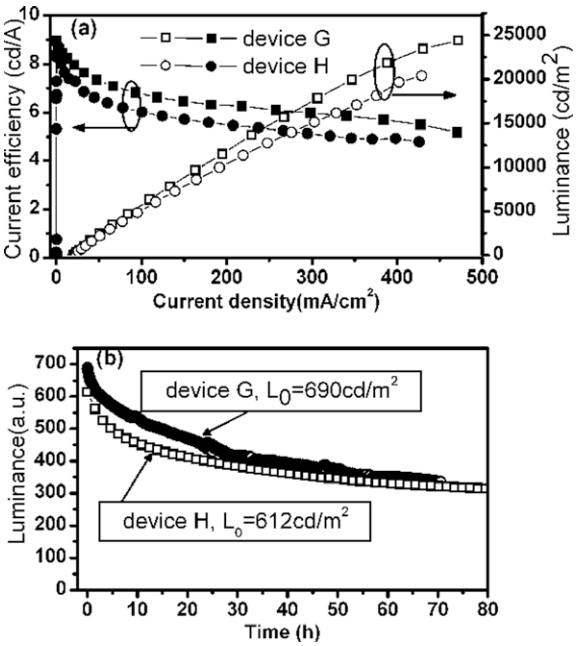

Fig. 8. (a) Current efficiency–luminance–current density characteristics of the devices G and H and (b) luminance decay versus time characteristic of devices G and H.

over 70 h lifetime with initial luminance of 690 cd/m^2, which were better than or equivalent to those of vacuum-deposited one, device H. In addition, the efficiency of device G was comparable to that of the vacuum-deposited multilayer WOLEDs based on the DPAVBi and rubrene as dopants in previous reports, in which the reported best efficiency is 7.7 cd/A (112 cd/m^2) [33] and 10.9 cd/A (10 mA/cm^2) [36]. So, solution-processed molecular films in our works provide a new route for the easy and simple

fabrication of WOLEDs without the sacrifice of device performance.

4. Conclusion

We have investigated solution-processed small-molecule films, such as DPVBi, NPB, and their blends. The more uniform films of NPB and the blends of DPVBi:NPB can be achieved by spin-coating, though having a lower density, in comparison with their vacuum-deposited counterparts. With the spin-coated films of DPVBi:NPB doped with DPAVBi and rubrene, which serves as the EML, a new WOLEDs were demonstrated. The solution-processed WOLEDs show the considerable efficiency and stability, which were prior or equivalent to the vacuum-deposited counterparts. Solution-processed small molecular films are expected to be a new route to fabricate their WOLEDs to reduce manufacture cost and avoid the complexity of the vacuum co-deposition process.

Acknowledgements

The authors are grateful to Ministry of Science and Technology of China (973 Program No. 2006CB921602), Program for New Century Excellent Talents of Ministry of Educations, the Technology Program of Shaanxi Province (No. 2006K04-c25) for financial support, and thanks for the financial support from Firefly Lighting Co. Ltd, in China.

References

[1] P.I. Shih, C.-F. Shu, Y.-L. Tung, Y. Chi, Appl. Phys. Lett. 88 (2006) 251110.
[2] J.-H. Jou, M.-H. Wu, C.-P. Wang, Y.-S. Chiu, P.-H. Chiang, H.-C. Hu, R.-Y. Wang, Org. Electron. 8 (2007) 735.
[3] Y. Duan, Y. Zhao, G. Cheng, W.L. Jiang, J. Li, Z.J. Wu, J.Y. Hou, S.Y. Liu, Semicond. Sci. Technol. 19 (2004) L32.
[4] B.W. D'andrade, R.J. Holmes, S.R. Forrest, Adv. Mater. 16 (2004) 624.
[5] Q. Wang, J.Q. Ding, D.G. Ma, Y.X. Cheng, L.X. Wang, X.B. Jing, F.S. Wang, Adv. Funct. Mater. 19 (2009) 84.
[6] F.W. Guo, D.G. Ma, L.X. Wang, X.B. Jing, F.S. Wang, Semicond. Sci. Technol. 20 (2005) 310.
[7] Y.R. Sun, N.C. Giebink, H. Kanno, B.W. Ma, M.E. Thompson, S.R. Forrest, Nature 440 (2006) 908.
[8] B.W. Drsquoandrade, M.E. Thompson, S.R. Forrest, Adv. Mater. 14 (2002) 147.
[9] Y. Shao, Y. Yang, Adv. Funct. Mater. 15 (2005) 1781.
[10] J.H. Jou, Y.S. Chen, C.P. Wang, Appl. Phys. Lett. 88 (2006) 193501.
[11] D.A. Pardo, G.E. Jabbour, N. Peyghambarian, Adv. Mater. 12 (2000) 1249.
[12] M. Granstrom, O. Inganas, Appl. Phys. Lett. 68 (1996) 147.
[13] X. Gong, W. Ma, J.C. Ostrowski, G.C. Bazan, D. Moses, A.J. Heeger, Adv. Mater. 16 (2004) 615.
[14] S.Z. Tokito, M. Suzuki, F. Sato, M. Kamachi, K. Shirane, Org. Electron. 4 (2003) 105.
[15] J. Huang, G. Li, E. Wu, Q. Xu, Y. Yang, Adv. Mater. 18 (2006) 114.
[16] M.H. Jonathan, N.G. Pillow, Ifor D.W. Samuel, Paul L. Burn, Adv. Mater. 11 (1999) 371.
[17] D. Anthopoulost, M.J. Frampton, E.B. Namdas, P.L. Burn, D.W.I. Samuel, Adv. Mater. 16 (2004) 557.
[18] J.Q. Ding, B.H. Zhang, J.H. Lu, Z.Y. Xie, L.X. Wang, X.B. Jing, F.S. Wang, Adv. Mater. 21 (2009) 1.
[19] R. Pudzich, J. Salbeck, Synth. Met. 138 (2003) 21.
[20] S.W. Culligan, Y. Geng, S.H. Chen, K. Klubek, K.M. Vaeth, C.W. Tang, Adv. Mater. 15 (2003) 1176.
[21] H. Fukagawa, K. Watanabe, S. Tokito, Org. Electron. 10 (2009) 798.
[22] J. Qiao, L.D. Wang, J.F. Xie, G.T. Lei, G.S. Wu, Y. Qiu, Chem. Commun. 5 (2005) 4560.
[23] A. Elschner, H.W. Heuer, F. Jonas, et al., Adv. Mater. 13 (2001) 1811.
[24] T.W. Lee, T.Y. Noh, O. Kwon, Adv. Funct. Mater. 19 (2009) 1625.
[25] Mathew K. Mathai, Vi-En Choong, Stelios A. Choulis, Benjamin Krummacher, Franky So, Appl. Phys. Lett. 88 (2006) 243512.
[26] P. Fenter, F. Schreiber, V. Bulovic, S.R. Forrest, Chem. Phys. Lett. 277 (1997) 521.
[27] H.S. Tada, K.J. Utsugi, Polym. Adv. Technol. 8 (1997) 443.
[28] K. Kinosita, M. Nishibori, J. Vac. Sci. Technol. 6 (1969) 730.
[29] The doping concentration of DPAVBi was optimized over the range of 2–7 wt% in NPB:DPVBi (80:20) structure for blue emission, and an optimal value is 4 wt%. For all of MH devices, the white emission can be obtained when the concentration of rubrene is 0.27 wt%.
[30] E.I. Haskal, Synth. Met. 91 (1997) 187.
[31] S.L. Lai, M.Y. Chan, M.K. Fung, C.S. Lee, S.T. Lee, Appl. Phys. Lett. 90 (2007) 203510.
[32] H.-H. Huang, S.-Y. Chu, P.-C. Kao, Y.-C. Chen, Thin Solid Films 516 (2008) 5669.
[33] C.-H. Hsiao, C.-F. Lin, J.-H. Lee, J. Appl. Phys. 102 (2007) 094508.
[34] G. Cheng, Y.F. Zhang, Y. Zhao, LS.Y. Liu, Y.G. Ma, Appl. Phys. Lett. 88 (2006) 083512.
[35] The solution-promixed deposition target was prepared as follow: the blends with NPB:DPVBi weight ratio of 3:2 doped with 4% DPAVBi and 0.4% rubrene were first dissolved in chloroform (~10 mg/ml), then the solution was transformed to the oven and baked at 80 °C for 30 min to remove the solvent chloroform. The same process can be found in the report of Jwo–Huei, Jou et al. (SPIE, 6999 (2008) 69992S).
[36] Y.-C. Tsai, J.-H. Jou, Appl. Phys. Lett. 89 (2006) 243521.

Organic Electronics 11 (2010) 649–657

Contents lists available at ScienceDirect

Organic Electronics

journal homepage: www.elsevier.com/locate/orgel

Improving efficiency of MEH-PPV/TiO_2 solar cells by lithium salt modification

D. Aaron R. Barkhouse [a,*], Hugh E. Bishop [a], Bernard M. Henry [a], Graham R. Webster [b], Paul L. Burn [c], Hazel E. Assender [a,*]

[a] Materials Department, University of Oxford, Parks Road, Oxford OX1 3PH, UK
[b] Department of Chemistry, University of Oxford, Chemistry Research Laboratory, Mansfield Road, Oxford OX1 3TA, UK
[c] Centre for Organic Photonics and Electronics, The University of Queensland, Chemistry Building, Queensland 4072, Australia

ARTICLE INFO

Article history:
Received 10 September 2009
Accepted 5 January 2010
Available online 13 January 2010

Keywords:
MEHPPV
Lithium
Hole mobility

ABSTRACT

The modification of MEH-PPV/TiO_2 photovoltaic devices with the lithium salt, Li[CF_3SO_2]$_2$N, is shown to result in a 40% increase in both the short-circuit current and fill factor while not affecting the open-circuit voltage. The power conversion efficiency of the modified devices is 1.05% under 80 mW/cm^2 simulated solar illumination, which is twice that of the control device without the salt and the highest reported to date for a polymer/TiO_2 solar cell. The increased performance is attributed to a large improvement in the hole mobility of the MEH-PPV, as measured by space-charge-limited current measurements, in the presence of the lithium salt. Modification of the devices with $LiClO_4$ is not as effective at improving device performance. Secondary ion mass spectroscopy measurements reveal that the poorer performance is due to a lower degree of Li diffusion into the polymer layer for $LiClO_4$ than for Li[CF_3SO_2]$_2$N.

© 2010 Elsevier B.V. All rights reserved.

1. Introduction

Conjugated polymers are attractive for use in organic photovoltaic devices because they are flexible, can be deposited from solution, and avoid the containment problems associated with the liquid electrolytes used in high-efficiency dye-sensitized solar cells (DSSCs). Although dye-sensitized solar cells are the most efficient variety of organic solar cell at present, polymer/electron transport material (ETM) devices are particularly attractive due to their simplicity and potential for low-cost processing. While the absorption coefficients of conjugated polymers are reasonably high ($\sim 10^5$ cm^{-1}) [1] their usefulness in devices has typically been limited by their relatively high exciton binding energies, the short exciton diffusion lengths ($\sim$10 nm) [2] and low hole mobilities ($\sim 10^{-7}$–10^{-4} cm^2/Vs) [3] with the latter due to their amorphous nature. The first two limitations can be overcome by blending the polymer with an electron accepting and transporting material (e.g. C_{60} or TiO_2), such that the distance excitons must travel to reach an appropriate interface and dissociate is reduced to the order of the exciton diffusion length [4]. Once separated, the charges must still traverse the thickness of the device in order to be collected and put to use, so it is desirable to increase the charge mobility of the polymer in order to get charges out more quickly and reduce recombination.

The lithium salt lithium bis(trifluoromethylsulfonyl)-amide (Li[CF_3SO_2]$_2$N or LiTFSI) has recently been shown to improve the hole mobility of the molecular hole transport material 2,2′,7,7′-tetrakis(*N*,*N*-di-*p*-methoxyphenylamine)-9,9′-spirobifluorene (Spiro-MeOTAD) [5], as well as improving the photovoltaic performance of various dye-sensitized [6–11] and organic/organic bilayer [12] solar cells. We have studied the effects of LiTFSI on charge

* Corresponding authors. Tel.: +44 1865 273781; fax: +44 1865 273789.
E-mail addresses: aaron.barkhouse@utoronto.ca (D.A.R. Barkhouse), hazel.assender@materials.ox.ac.uk (H.E. Assender).

1566-1199/$ - see front matter © 2010 Elsevier B.V. All rights reserved.
doi:10.1016/j.orgel.2010.01.005

transport in the polymer poly[2-(2-ethylhexyloxy)-5-methoxy-1,4-phenylenevinylene] (MEH-PPV), and on the performance of ITO/TiO_2/MEH-PPV/Au photovoltaic (PV) devices modified with LiTFSI using simple, solution-based procedures that are amenable to high-throughput fabrication techniques. By fitting the current–voltage data of ITO/MEH-PPV/Au hole-only diodes to a field-dependent space-charge-limited-current (SCLC) model, we find that the mobility of MEH-PPV can be increased by more than an order of magnitude by the addition of LiTFSI. We also find that the current and fill factor of PV devices can be increased by as much as 40% upon the addition of LiTFSI, resulting in a two-fold increase in device efficiency from 0.52% to 1.05% under 80 mW/cm^2 simulated solar illumination.

2. Results

2.1. Photovoltaic device performance – pre-treatment with LiTFSI

Three different device architectures were studied whereby the position of the lithium salt in the device was varied. In each case photovoltaic devices of the type ITO/TiO_2/MEH-PPV/Au were made, and their current–voltage (I–V) characteristics tested under 80 mW/cm^2 simulated solar illumination. The first device architecture involved treating the TiO_2 with the lithium salt before deposition of the polymer layer. Fig. 1 shows current–voltage curves for devices made with and without pre-soaking of the ITO/TiO_2 substrate in a 40 mg/ml LiTFSI/4-*t*-butylpyridine (tBP) solution (see Section 5 for details of fabrication and modification procedures). Lithium modification substantially improved the fill factor (FF) and short-circuit current (J_{sc}), with both increasing by 40%. The open-circuit voltage (V_{oc}) was not affected and remained at around 0.8 V. Devices with TiO_2 layers which had been soaked in neat tBP performed identically to the control devices, so the performance enhancement cannot be attributed to tBP. The highest power conversion efficiencies (η_{max}) obtained for individual control and lithium salt modified devices were 0.52% and 1.05%, respectively. For the lithium-modified device, this is the highest efficiency reported to date for a polymer/TiO_2 device. Fig. 2 shows the variation

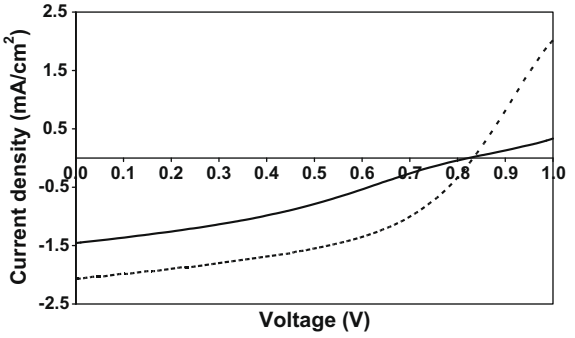

Fig. 1. Current–voltage curves of ITO/TiO_2/MEH-PPV/Au devices, under 0.8 sun simulated solar illumination, with (dashed line) and without (solid line) pre-treatment in a 40 mg/ml LiTFSI/tBP solution.

of the device performance parameters (J_{sc}, V_{oc}, FF, and η_{max}) with the concentration of LiTFSI in the soaking solution. The J_{sc} and FF increase with increasing salt concentration, before reaching a plateau at ~25 mg/ml. During this work we found that the maximum efficiency reached was strongly dependent on the batch of commercial Ti-Nanoxide used. For the device characteristics shown in Fig. 2 the cells were made from the same Ti-Nanoxide batch and the slightly lower efficiency may be due to it having a lower degree of crystallinity. Also, as device performance has been shown to be very sensitive to the thickness of the MEH-PPV layer for TiO_2/MEH-PPV bilayer devices [13], especially for an MEH-PPV layer thickness of roughly 40 nm, it is possible that small variations in the thickness of the MEH-PPV layer from one batch of devices to the next (even for devices cast at the same spin-speed from solutions of very similar concentration) might at least partially account for the difference in efficiency.

Kelly et al. showed that Li^+ adsorption onto TiO_2 can lower the energy of the conduction band and improve the injection yield from adsorbed dye molecules [14]. To determine whether this was the cause of the observed increase in current in our devices, we studied the photocurrent as a function of illumination wavelength. Fig. 3 shows the external quantum efficiency (EQE) of devices with and without pre-treatment with a 40 mg/ml LiTFSI/tBP solution. The maximum EQE value of 12% for the control device compares well with the value for similar devices reported in literature [1,15]. The maximum EQE of the lithium-modified device is a factor of 1.9 larger than that for the control device (Fig. 3a). If the increased current was the result of a downward shift in the TiO_2 conduction band allowing injection from vibrationally relaxed excited states in the polymer, then the increase in EQE should be greatest at long wavelengths, where absorbed photons would promote electrons to the lowest lying vibrational levels of the excited state. The spectra are qualitatively similar, as emphasized by the normalized EQE spectra, indicating that there is no shift in the onset of photocurrent generation (Fig. 3b). This suggests that any downward shift of the TiO_2 conduction band caused by Li^+ adsorption is not responsible for the observed increase in photocurrent, unlike the results of Kelly et al. This was not entirely unexpected, as there is already a substantial offset between the LUMO of MEH-PPV (3.0 eV) [13] and the conduction band level of TiO_2 (4.2 eV) [13], so a further increase in the offset caused by an interface dipole would not contribute significantly to exciton dissociation/charge injection.

2.2. Photovoltaic device performance – co-deposition of LiTFSI and MEH-PPV

The second device strategy utilized a blended film of the lithium salt and MEH-PPV. Fig. 4 shows the performance of ITO/TiO_2/MEH-PPV/Au devices made with an increasing amount of LiTFSI in the polymer spin-coating solution. A small amount of tBP was added as a co-solvent, as LiTFSI is not soluble in chlorobenzene. The addition of neat tBP to the polymer solution reduces the short-circuit current (J_{sc}) and open-circuit voltage (V_{oc}), possibly by creating a poorer solvent for the polymer and affecting the morphol-

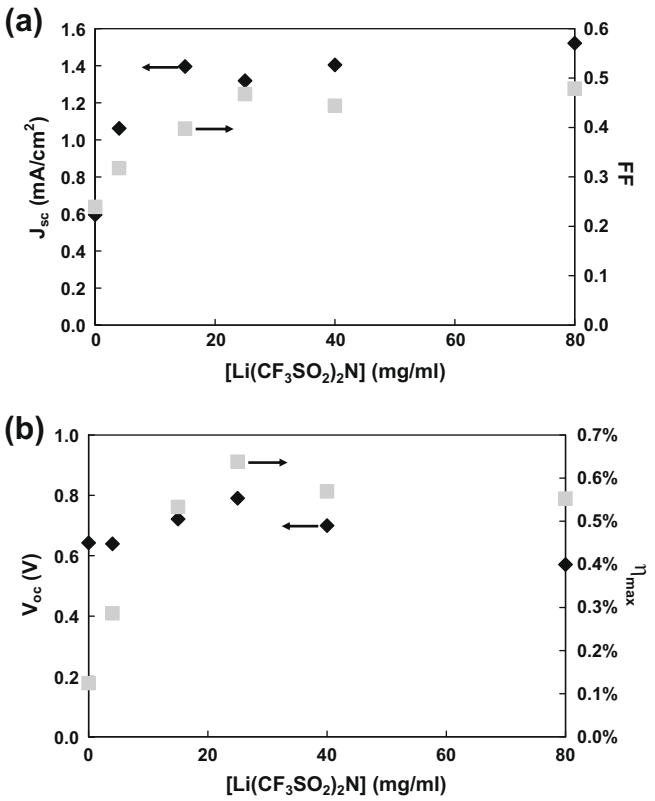

Fig. 2. Short-circuit current, fill factor (a), open-circuit voltage, and efficiency (b) of ITO/TiO_2/MEH-PPV/Au devices (under 0.8 sun simulated solar illumination) vs. concentration of LiTFSI in the pre-treatment solution.

ogy and transport properties of the polymer layer. Relative to devices with neat tBP added to the polymer solution, increasing the concentration of LiTFSI increases J_{sc} by 27% and FF by 49%, resulting in an 85% increase in η_{max} at the optimum concentration of 0.13 mg/ml LiTFSI in the spin-coating solution.

2.3. Photovoltaic device performance – post-treatment with LiTFSI

In the final device configuration the LiTFSI was deposited onto the MEH-PPV films before the completion of the cell with an Au contact. Fig. 5 shows the performance of these ITO/TiO_2/MEH-PPV/Au devices. As the concentration of LiTFSI in the spin-coating solution is increased, the J_{sc} and FF of the devices increase dramatically, and the V_{oc} is improved as well. It should be noted that these devices had an MEH-PPV layer thickness of 95 nm, more than double that for devices discussed above. This was necessary to avoid the introduction of partial shorts in the post-treated devices, but resulted in much lower efficiency in the control devices due to the increased series resistance of the thicker polymer layer. Fig. 6 shows the effect, on device performance, of varying the MEH-PPV layer thickness deposited prior to treatment with a LiTFSI/tBP spin-coating solution of fixed concentration of 40 mg/ml. It is clear that LiTFSI-modified devices with a thin MEH-PPV layer suffer from a low V_{oc} due to partial shorting, but the J_{sc} is independent of MEH-PPV thickness.

2.4. Photovoltaic device performance – pre- and post-treatment with $LiClO_4$

The next aspect of the study was to ascertain whether the counter anion played an important role in the improvement of cell performance. Devices were prepared with either a pre- or post-treatment with a $LiClO_4$/acetonitrile solution of different concentrations. It was found that when the TiO_2 was treated with the $LiClO_4$ solution the TiO_2 was slightly cloudy and when it was deposited onto the polymer it left a visible film on top of the MEH-PPV once the acetonitrile had evaporated, with the latter indicating re-crystallization of the salt and lack of incorporation into the polymer. Photovoltaic device results showed poor reproducibility for pre-treated devices, while the only effect following post-treatment with $LiClO_4$ was a decrease in FF with increasing $LiClO_4$ concentration. Washing the TiO_2 substrate with neat acetonitrile after soaking in the $LiClO_4$/acetonitrile solution (but before spin-coating the polymer) improved the device performance and reproducibility slightly, but the observed increase in photocurrent was much less than for LiTFSI treatment and it is not clear how much of the salt was washed away.

2.5. Hole mobility in MEH-PPV – effect of LiTFSI

To study the effect of LiTFSI on hole mobility in MEH-PPV, hole-only diodes of the type ITO/MEH-PPV/Au were fabricated, with a 40 mg/ml LiTFSI/tBP solution spun onto

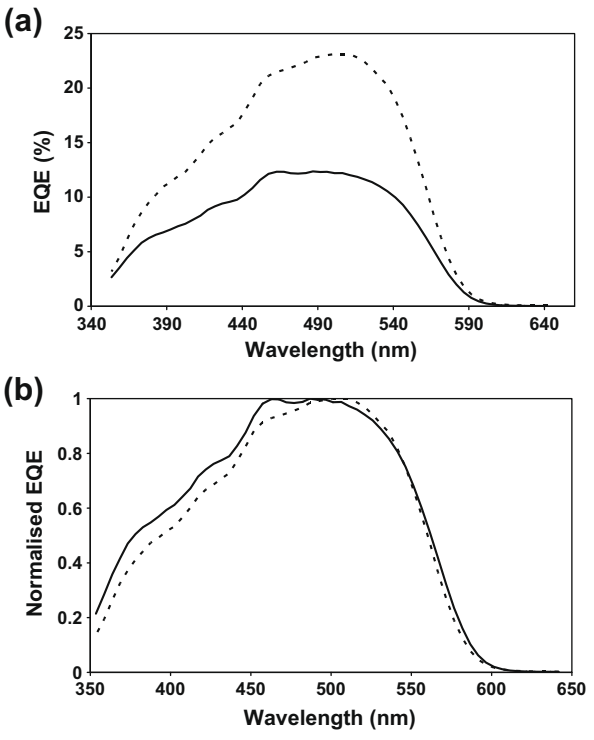

Fig. 3. External quantum efficiency vs. wavelength of ITO/TiO_2/MEH-PPV/Au devices pre-treated in 40 mg/ml LiTFSI/tBP solution, raw data (a) and normalized (b).

the ITO prior to MEH-PPV deposition. For space-charge-limited currents to be observed it was important to plasma treat the ITO electrode (prior to LiTFSI deposition) in order to create an ohmic contact with the polymer, as reported previously for poly(fluorene)-based polymers [16]. Fig. 7 shows the current–voltage characteristics of these devices after various pre-bias routines. The current in the devices was found to increase following a period of pre-bias at −5 V (a negative applied bias corresponds to driving Li^+ from the ITO contact into the polymer), and showed Poole–Frenkel (PF) type space-charge-limited current (SCLC) behavior. The hole mobility (μ_h) of the devices following pre-bias was therefore determined by fitting the *I–V* curves to a field-dependent SCLC model [17]:

$$J = \frac{9}{8}\varepsilon\varepsilon_0\mu_0 V^2 \exp\left(0.89\sqrt{\frac{E}{E_0}}\right)L^{-3}$$

Zero-bias capacitance measurements of the LiTFSI pre-treated devices studied here indicate that the dielectric constant increases from $\varepsilon_r = 3$ (before pre-bias) to as much as $\varepsilon_r = 20$ (after 2 min at −5 V). More extended pre-bias periods (greater than 2 min) did not increase the dielectric constant further. After 10 min at −5 V, the mobility of the pre-treated MEH-PPV reaches $\mu_h = 1.8 \times 10^{-6}$ cm^2/Vs, more than an order of magnitude higher than that of the control device. This increased mobility is consistent with previous reports in the literature, including a.c. impedance measurements showing increased conductivity in PPV which was 'doped' with $LiCF_3SO_3$ [18], and time-of-flight measurements on LiTFSI-modified Spiro-MeOTAD showing that LiTFSI does indeed improve hole mobility, rather than just increasing the carrier concentration in the hole transport material [5]. We note that if the current in our devices is in fact space-charge-limited, as suggested by the good fit to PF SCLC theory, then it is by definition independent of the equilibrium carrier density in the device, and is instead limited by the injected space charge.

Work on light-emitting electrochemical cells has shown that ion diffusion to the electrode interface can result in a large electric field at the interface [19]. In the cells of this study a larger electric field might aid exciton dissociation, providing an alternative explanation for our observed increase in current in LiTFSI-modified devices. However, it is unlikely that this is the case, as the MEH-PPV/TiO_2 interface has already been shown to be an efficient exciton dissociation site [13] due to the >1 eV difference between the MEH-PPV LUMO and the TiO_2 conduction band, which is at least double the exciton binding energy in MEH-PPV.

A related possibility for the improvement in determined hole mobility is that while there is a small barrier to charge extraction at the Au/MEH-PPV interface in control devices, doping of the polymer layer by the addition of LiTFSI serves to narrow this barrier, allowing improved hole extraction via tunneling. A similar effect has been observed for OLED structures containing ZnPc doped with F4-TCNQ [20]. However, due to the strong dependence of J_{sc} and FF on polymer layer thickness in our devices, as mentioned in Section 2.3, we believe that our devices are limited by bulk, rather than interfacial, series resistance prior to LiTFSI treatment.

2.6. Secondary ion mass spectroscopy (SIMS)

The distribution of lithium ions with depth within the devices was determined by SIMS depth profiling. Fig. 8 shows the distribution of positive ions throughout a control device (Fig. 8a) and a device which has been pre-treated with a 10 mg/ml solution of LiTFSI (Fig. 8b) as a function of sputtering time. The Ga signal is due to the sputtering of implanted primary ions. The polymer, TiO_2 and ITO layers are clearly delineated although the interfaces are broad because the outer polymer layer is not of a uniform thickness, as the spun polymer layer will tend to planarise the relatively rough TiO_2 surface. For the pre-treated device it is clear that lithium is present throughout the TiO_2 layer, and also appears to have migrated into the polymer. Indeed there is a substantial lithium signal from the surface of the polymer before there has been any significant erosion of the surface. The small lithium signal from the control is probably the result of some surface contamination. Fig. 9 shows the distribution of positive ions throughout a control device (Fig. 9a) and a device which has been post-treated with $LiClO_4$ (Fig. 9b). In this case the lithium signal of the post-treated device falls off well before the TiO_2 is reached, indicating that the lithium is confined to the near surface of the polymer. The residual tail in the lithium signal is probably an artifact resulting from a low intensity halo round the primary ion beam. Although the current in this halo is small it is strik-

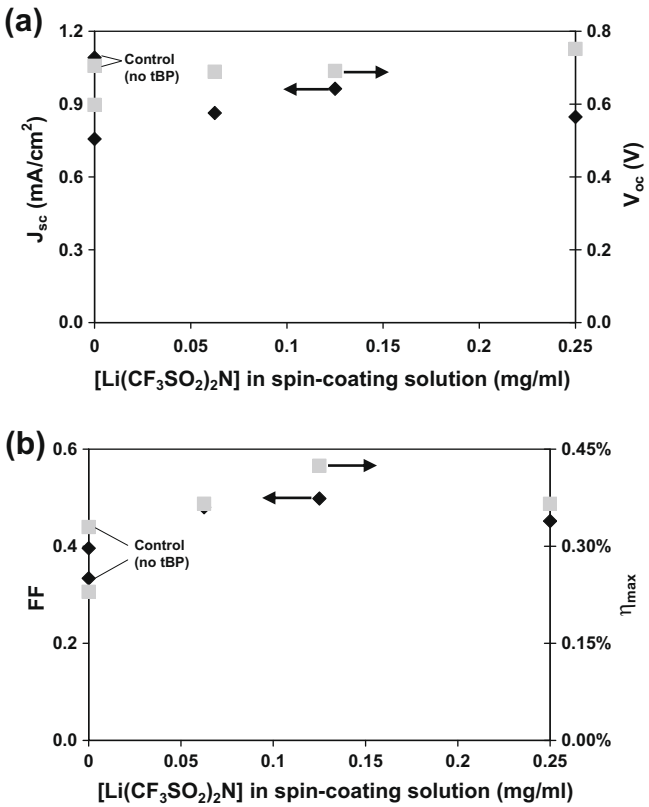

Fig. 4. Short-circuit current, open-circuit voltage (a), fill factor, and efficiency (b) of ITO/TiO_2/MEH-PPV/Au devices (under 0.8 sun simulated solar illumination) vs. concentration of LiTFSI in the MEH-PPV spin-coating solution (co-deposition).

ing the lithium rich surface outside the sputtered pit. There is also the possibility that a proportion of the mobile lithium atoms may migrate ahead of the sputtering front as a result of surface charging.

3. Discussion

The effect of LiTFSI on the performance of ITO/TiO_2/MEH-PPV/Au devices was found to depend on the concentration of LiTFSI as well as the procedure by which it is added to the device. When the ITO/TiO_2 substrate is pretreated with LiTFSI prior to MEH-PPV deposition, the J_{sc} and FF are improved and the V_{oc} is unaffected. According to recent models of device operation [21,22], this is consistent with an increase in hole mobility of the polymer. The increased hole mobility would result in a higher current due to reduced recombination, both under forward bias and zero applied bias, resulting in an increased short-circuit current, and also under small reverse bias, giving an improved fill factor. In the absence of additional contributions to the photocurrent following LiTFSI modification (e.g. from an increase in the exciton diffusion length), both Li-salt modified and control devices should have the same current under high forward bias due to field-assisted charge collection. Unfortunately this could not be verified experimentally as the injected current became much larger than the photocurrent at small forward biases, obscuring the region of the curve where the photocurrent of the modified and control devices should converge to a similar value.

When a small amount of LiTFSI/tBP was co-deposited with MEH-PPV, the tBP causes a decrease in J_{sc} and V_{oc}, which is compensated by the LiTFSI, resulting in a small improvement in device performance. The decrease in performance upon tBP addition could be due to the solution quality being degraded, resulting in a polymer morphology which is less favorable for hole and/or exciton transport, thereby reducing the J_{sc} by reducing the exciton diffusion length and/or increasing the series resistance of the MEH-PPV layer. A similar effect has been observed for MEH-PPV films cast from chlorobenzene (CB) vs. tetrahydrofuran, with the more open conformation of polymer chains in films cast from CB leading to higher mobilities [23]. Adding the LiTFSI counteracts the effect of the tBP by improving hole mobility in the polymer layer to overcome the detrimental effects of the tBP.

When the LiTFSI/tBP solution was spin-coated on top of the MEH-PPV layer, J_{sc} is found to be independent of the MEH-PPV thickness. This is also consistent with improved hole mobility, such that the series resistance of the polymer no longer limits the operation of the device. The FF is also improved, but thinner devices suffer from a low shunt resistance which reduces V_{oc}. The low shunt resistance could indicate over-doping of the polymer layer or

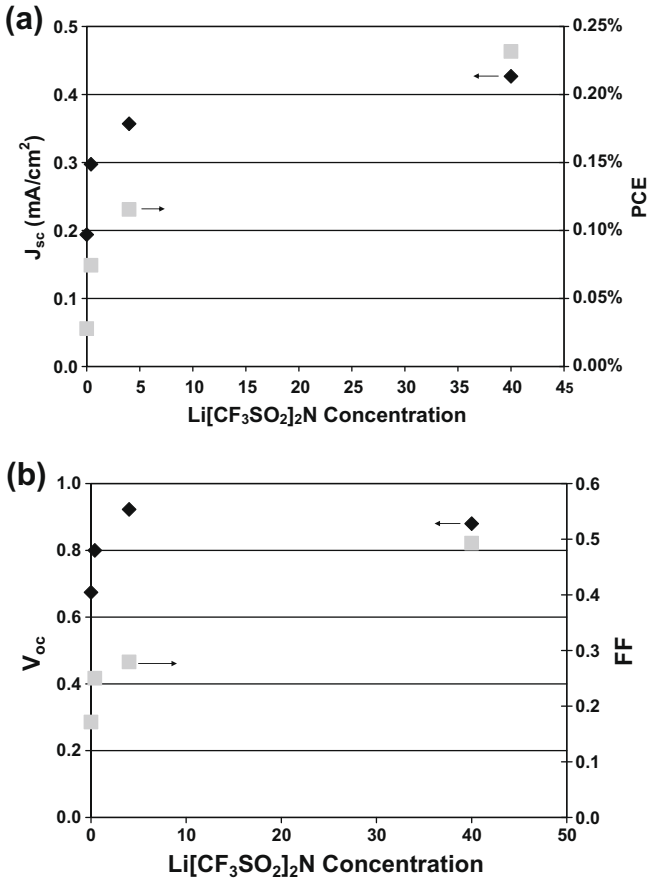

Fig. 5. Short-circuit current, efficiency (a), open-circuit voltage and fill factor (b) of ITO/TiO_2/MEH-PPV/Au devices (under 0.8 sun simulated solar illumination) vs. concentration of LiTFSI in the post-treatment spin-coating solution.

pinholes in the polymer layer leading to shorting through the device.

Thus, whether the LiTFSI is added to the TiO_2 layer, co-deposited with the MEH-PPV layer, or deposited on top of the MEH-PPV layer, the hole mobility of the polymer is improved. This is supported by measurements on SCLC hole-only diodes, which show that the conductivity of the polymer is greatly increased by spin-coating LiTFSI (from a tBP solution) at either the ITO or Au contact, and by SIMS experiments which indicate that lithium is present throughout the polymer layer in either case. $LiClO_4$ does not have the same effect on device performance, most likely because it recrystallizes rather than being absorbed into the polymer. This is supported by results of SIMS experiments which show that post-treatment with $LiClO_4$ does not result in the presence of lithium throughout the polymer layer. It should also be noted that any change to the conductivity of the TiO_2 cannot be responsible for the observed improvement in device performance. Doubling the thickness of the TiO_2 layer in control devices had no impact on device performance, indicating that the series resistance of the TiO_2 layer is small relative to that of the polymer layer. More importantly, SIMS measurements indicate that lithium is not present in the TiO_2 layer of post-treated devices, and therefore TiO_2 modification cannot account for their improved device performance.

While the mechanism underlying this improved hole mobility is unclear, a similar increase in hole mobility in TiO_2/dye/Spiro-MeOTAD devices has been reported [5], and was attributed to an effect equivalent to a broadening of the tail of the density of states. At high doping levels, Li^+ ions fill the deepest traps in the organic layer, while overlap between Coulomb wells of the accompanying anions reduces the barrier height for hole-hopping between these traps, increasing hole mobility. A similar effect may be responsible for the increased mobility reported here.

4. Conclusions

The performance of ITO/TiO_2/MEH-PPV/Au photovoltaic devices was improved by modification with LiTFSI. The best LiTFSI-modified devices exhibited a power conversion efficiency of 1.05% under 0.8 sun white light illumination, a world-leading efficiency for this type of device. Through a combination of hole-mobility measurements, SIMS experiments, and modeling results, the most likely mechanism behind the improved performance was found to be the increased hole mobility in the polymer leading to improved

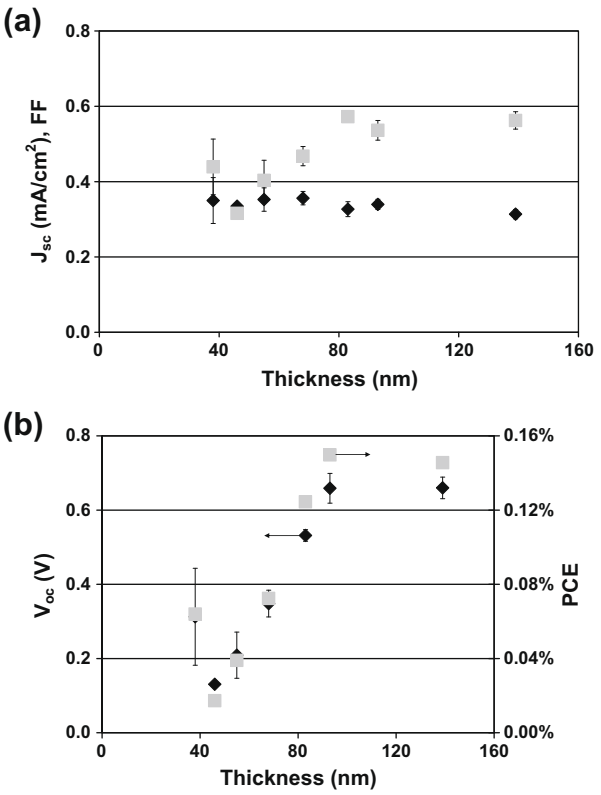

Fig. 6. Short-circuit current, fill factor (a), open-circuit voltage, and efficiency (b) of ITO/TiO_2/MEH-PPV/Au devices (under 0.8 sun simulated solar illumination) vs. MEH-PPV layer thickness for devices which have undergone post-treatment with a 40 mg/ml LiTFSI/tBP solution.

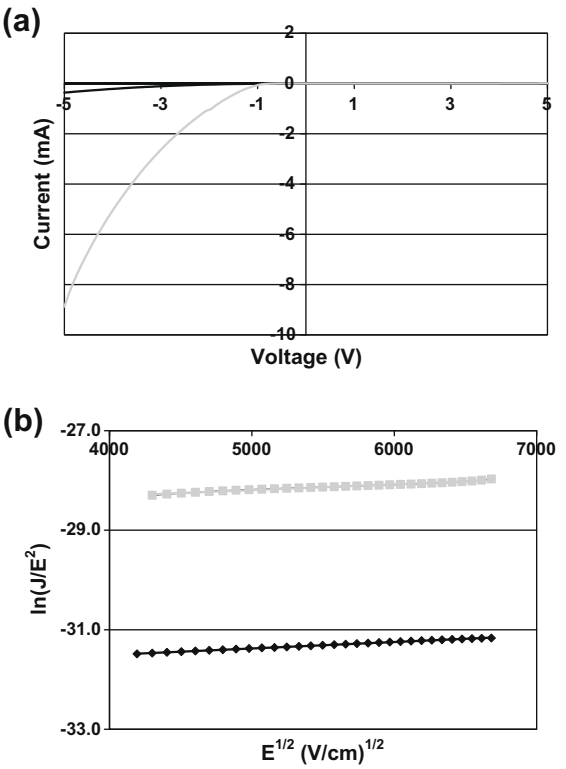

Fig. 7. (a) Current–voltage curves for ITO/MEH-PPV/Au hole-only diodes, which have been pre-treated with a 40 mg/ml LiTFSI/tBP solution, following various pre-bias routines. The curves are for 0 min (black dashed line), 5 min (solid black line), and 10 min (solid grey line) pre-bias at −5 V. The 0 min line coincides with the voltage axis in this figure. (b) Linear fit to field-dependent space-charge-limited current regime of current–voltage curves.

charge collection. $LiClO_4$ was not effective in increasing device performance, and this is believed to be due to a lower incorporation of lithium into the polymer due to re-crystallization of the salt following solution-based pre- or post-treatment. These results are exciting because the modification procedure(s) are simple, solution-based, and amenable to high-throughput processing. Also, the mechanism behind the improvement in device performance is not specific to this device architecture, opening up future avenues to explore for improving, e.g., bulk-heterojunction devices.

5. Experimental

5.1. Device fabrication

Photovoltaic devices with the structure ITO/TiO_2/MEH-PPV/Au were fabricated on patterned ITO glass. Porous TiO_2 layers were produced by the doctor blading technique. Solaronix Ti-nanoxide HT (Solaronix SA, Switzerland) was spread onto the patterned ITO substrate and sintered sequentially at 100 °C for 5 min, 300 °C for 10 min, and 500 °C for 45 min. The resulting film was 1.2 μm thick, with an average pore size of 9–10 nm as measured by gas sorption experiments [24]. MEH-PPV, which had an average $M_w = 5.4 \times 10^5$ and polydispersity of 20 or $M_w = 2.8 \times 10^5$ and polydispersity of 12, was deposited by spin-coating from a chlorobenzene solution. Unless otherwise specified, the spin-speed and solution concentration were chosen to give an MEH-PPV layer thickness of 35–40 nm. As no post-deposition sintering of the film was performed, polymer penetration into the TiO_2 pores was minimal, resulting in a bilayer rough-interface device architecture. Au contacts were evaporated under a vacuum of $\sim 10^{-6}$ mbar, to a thickness of 45 nm. ITO/MEH-PPV/Au hole-only diodes were fabricated as above, but without the TiO_2 deposition and sintering steps. In this case the ITO layer was also plasma-treated, in order to ensure ohmic contact with the MEH-PPV (HOMO = 4.9 eV [25]). The active area of each device was 6.25 mm^2.

5.2. Lithium modification

Three different lithium modification procedures were studied, which are termed pre-treatment, co-deposition, and post-treatment. Pre-treatment was done by soaking ITO/TiO_2 substrates in a solution of $Li[CF_3SO_2]_2N$ in 4-*t*-butylpyridine (tBP) prior to the deposition of the polymer layer. The substrates were immersed in the solution for

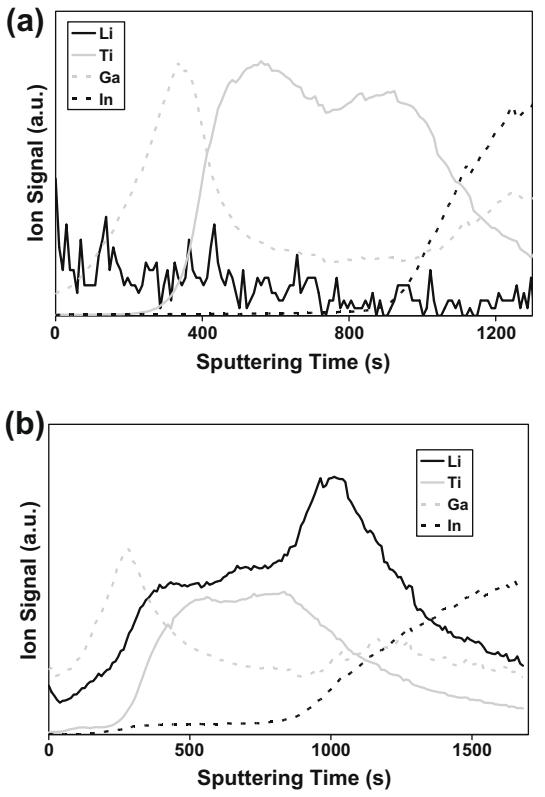

Fig. 8. Secondary ion mass spectroscopy data showing the distribution of lithium ions throughout an ITO/TiO_2/MEH-PPV device without (a) and with (b) pre-treatment in a 10 mg/ml solution of LiTFSI in tBP.

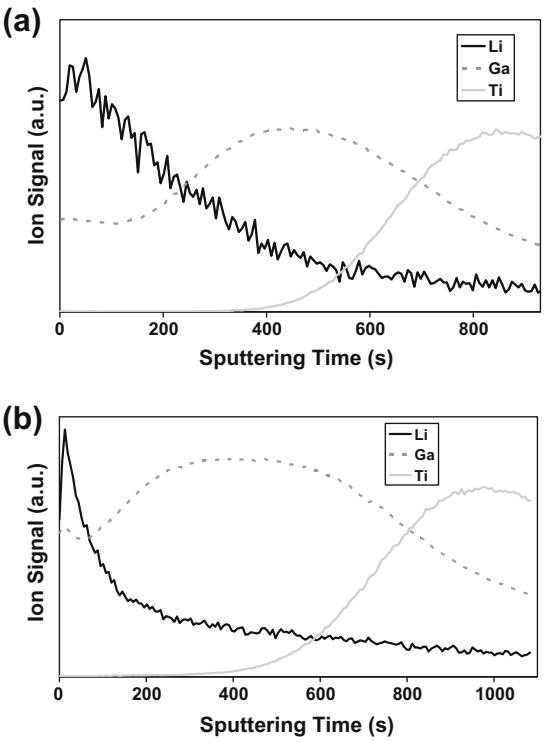

Fig. 9. Secondary ion mass spectroscopy data showing the distribution of lithium ions throughout an ITO/TiO_2/MEH-PPV device without (a) and with (b) post-treatment in a 2.5 mg/ml solution of $LiClO_4$ in acetonitrile.

20 min before being removed and the excess solvent blown off with a compressed air stream. The solution concentration was changed in order to vary the amount of $Li[CF_3SO_2]_2N$ adsorbed on the TiO_2 layer. Device fabrication then proceeded as described above. Pre-treatment of ITO/MEH-PPV/Au hole-only diodes was done by spin-coating a 40 mg/ml $Li[CF_3SO_2]_2N$/tBP solution onto ITO at 3000 rpm for 60 s. Co-deposition was done by adding a small amount of $Li[CF_3SO_2]_2N$/tBP solution to the MEH-PPV spin-coating solution. The concentration of the $Li[CF_3SO_2]_2N$ in the spin-coating solution was changed in order to vary amount of salt present in the resulting film. Post-treatment was performed by spin-coating a solution of $Li[CF_3SO_2]_2N$/tBP onto the polymer layer at 3000 rpm for 60 s prior to evaporation of the Au contacts.

5.3. Device testing

I–V measurements of devices were done using a Keithley 2400 digital multimeter controlled by in-house software created using LabVIEW. Devices were tested under 0.8 sun AM 1.5 illumination from a Xenon arc lamp solar simulator. A 420 nm cutoff long-pass UV filter was used, and devices were mounted in an Oxford Instruments cryostat and tested under a vacuum of 10 mTorr. Unless otherwise stated, results presented are average values from at least three devices.

5.4. EQE measurements

External quantum efficiency measurements were done using a CVI spectral products Xenon arc lamp, a CVI CM 110 monochromator and an Ocean Optics USB 2000 spectrometer with a cosine corrector. Devices were mounted in an Oxford instruments cryostat and tested under a vacuum of 10 mTorr.

5.5. SIMS measurements

SIMS profiles were recorded using a 20 keV gallium ion probe in conjunction with a quadrupole mass spectrometer, MM1212 (VG Scientific Ltd.) [26]. The ion beam was rastered over a 75 μm square with an electronic gate to eliminate wall effects.

Acknowledgements

The authors wish to thank The Toppan Printing Company for financial support. D.A.R. Barkhouse would also like to acknowledge the financial support of the Rhodes Trust and the Natural Sciences and Engineering Research Council of Canada.

References

[1] K.M. Coakley, M.D. McGehee, Photovoltaic cells made from conjugated polymers infiltrated into mesoporous titania, Applied Physics Letters 83 (2003) 3380–3382.

[2] J.M. Nunzi, Organic photovoltaic materials and devices, Comptes Rendus Physique 3 (2002) 523–542.
[3] P.W.M. Blom, V.D. Mihailetchi, L.J.A. Koster, D.E. Markov, Device physics of polymer:fullerene bulk heterojunction solar cells, Advanced Materials 19 (2007) 1551–1566.
[4] S. Gunes, H. Neugebauer, N.S. Sariciftci, Conjugated polymer-based organic solar cells, Chemical Reviews 107 (2007) 1324–1338.
[5] H.J. Snaith, M. Gratzel, Enhanced charge mobility in a molecular hole transporter via addition of redox inactive ionic dopant: implication to dye-sensitized solar cells, Applied Physics Letters 89 (2006) 262114.
[6] J. Kruger, R. Plass, L. Cevey, M. Piccirelli, M. Grätzel, High efficiency solid-state photovoltaic device due to inhibition of interface charge recombination, Applied Physics Letters 79 (2001) 2085–2087.
[7] Y. Harima, K. Yamashita, H. Ishii, K. Seki, Energy structures of molecular semiconductors contacting metals under air studied by the diffusion potential measurements and the Kelvin probe technique, Thin Solid Films 366 (2000) 237–248.
[8] S.A. Haque, T. Park, C. Xu, S. Koops, N. Schulte, R.J. Potter, A.B. Holmes, J.R. Durrent, Interface Engineering for solid-state dye-sensitized nanocrystalline solar cells: the use of ion-solvating hole-transporting polymers, Advanced Functional Materials 14 (2004) 435–440.
[9] D.B. Kuang, C. Klein, H.J. Snaith, J.-E. Moser, R. Humphry-Baker, P. Comte, S.M. Zakeeruddin, M. Grätzel, Ion coordinating sensitizer for high efficiency mesoscopic dye-sensitized solar cells: influence of lithium ions on the photovoltaic performance of liquid and solid-state cells, Nano Letters 6 (2006) 769–773.
[10] H.J. Snaith, S.M. Zakeeruddin, L. Schmidt-Mende, C. Klein, M. Grätzel, Ion-coordinating sensitizer in solid-state hybrid solar cells, Angewandte Chemie – International Edition 44 (2005) 6413–6417.
[11] U. Bach, D. Lupo, P. Comte, J.E. Moser, F. Weissörtel, J. Salbeck, H. Spreitzer, M. Grätzel, Solid-state dye-sensitized mesoporous TiO_2 solar cells with high photon-to-electron conversion efficiencies, Nature 395 (1998) 583–585.
[12] M.T. Lloyd, A.C. Mayer, A.S. Tayi, A.M. Bowen, T.G. Kasen, D.J. Herman, D.A. Mourey, J.E. Anthony, G.G. Malliaras, Photovoltaic cells from a soluble pentacene derivative, Organic Electronics 7 (2006) 243–248.
[13] A.J. Breeze, Z. Schlesinger, S.A. Carter, P.J. Brock, Charge transport in TiO2/MEH-PPV polymer photovoltaics, Physical Review B 64 (2001) 125205.
[14] C.A. Kelly, F. Farzad, D.W. Thompson, J.M. Stipkala, G.J. Meyer, Cation-controlled interfacial charge injection in sensitized nanocrystalline TiO_2, Langmuir 15 (1999) 7047–7054.
[15] L.H. Slooff, J.M. Kroon, J. Loos, M.M. Koetse, J. Sweelssen, Influence of the relative humidity on the performance of polymer/TiO_2 photovoltaic cells, Advanced Functional Materials 15 (2005) 689–694.
[16] A.J. Campbell, D.D.C. Bradley, Transient and steady-state space-charge-limited currents in polyfluorene copolymer diode structures with ohmic hole injecting contacts, Applied Physics Letters 76 (2000) 1734–1736.
[17] G.G. Malliaras, J.R. Salem, P.J. Brock, C. Scott, Electrical characteristics and efficiency of single-layer organic light-emitting diodes, Physical Review B 58 (1998) R13411–R13414.
[18] M. Esteghamatian, G. Xu, Effect of lithium doping on the conductivity of poly(*p*-phenylene vinylene), Synthetic Metals 63 (1994) 195–197.
[19] J.C. De Mello, N. Tessler, S.C. Graham, R.H. Friend, Ionic space-charge effects in polymer light-emitting diodes, Physical Review B 57 (1998) 12951–12963.
[20] W.Y. Gao, A. Kahn, Electronic structure and current injection in zinc phthalocyanine doped with tetrafluorotetracyanoquinodimethane: interface versus bulk effects, Organic Electronics 3 (2002) 53–63.
[21] C.M. Martin, V.M. Burlakov, H.E. Assender, D.A.R. Barkhouse, A numerical model for explaining the role of the interface morphology in composite solar cells, Journal of Applied Physics 102 (2007) 104506.
[22] R.A. Marsh, C. Groves, N.C. Greenham, A microscopic model for the behavior of nanostructured organic photovoltaic devices, Journal of Applied Physics 101 (2007) 083509.
[23] T.Q. Nguyen, V. Doan, B.J. Schwartz, Conjugated polymer aggregates in solution: control of interchain interactions, Journal of Chemical Physics 110 (1999) 4068–4078.
[24] Z. Xie, B.M. Henry, K.R. Kirov, H.E. Smith, A. Barkhouse, C.R.M. Grovenor, H.E. Assender, G.A.D. Briggs, G.R. Webster, P.L. Burn, M. Kano, Y. Tsukahara, Thin Solid Films 511 (2006) 523–528.
[25] R. Cervini, X.-C. Li, G.W.C. Spencer, A.B. Holmes, S.C. Moratti, R.H. Friend, Electrochemical and optical studies of PPV derivatives and poly(aromatic oxadiazoles), Synthetic Metals 84 (1997) 359–360.
[26] H.E. Bishop, D.P. Moon, P. Marriott, P.R. Chalker, Applications of a high spatial resolution combined AES/SIMS instrument, Vacuum 39 (1989) 929–939.

Organic Electronics 11 (2010) 658–663

Contents lists available at ScienceDirect

Organic Electronics

journal homepage: www.elsevier.com/locate/orgel

Organic field-effect transistors based on naphthyl end-capped divinylbenzene: Performance, stability and molecular packing

Hideaki Nagashima [a], Masatoshi Saito [a], Hiroaki Nakamura [a], Takeshi Yasuda [b,c,*], Tetsuo Tsutsui [d]

[a] Advanced Technology Research Laboratories, Idemitsu Kosan Co., Ltd., Sodegaura, Chiba 299-0293, Japan
[b] Exploratory Materials Research Laboratory for Energy and Environment, National Institute for Materials Science, Tsukuba, Ibaraki 305-0047, Japan
[c] PRESTO, Japan Science and Technology Agency, Chiyoda-ku, Tokyo 102-0075, Japan
[d] Institute for Materials Chemistry and Engineering, and Graduate School of Engineering Sciences, Kyushu University, Kasuga, Fukuoka 816-8580, Japan

ARTICLE INFO

Article history:
Received 30 July 2009
Received in revised form 5 January 2010
Accepted 5 January 2010
Available online 11 January 2010

Keywords:
Organic field-effect transistor
Organic semiconductor
Mobility
Air-stable

ABSTRACT

We synthesized naphthyl end-capped divinylbenzenes, in which naphthyl replaces phenyl as the substituent at the terminal positions of the oligo-*p*-phenylenevinylenes, and investigated the performance of organic field-effect transistors (OFETs), air stability and molecular packing in poly- and single-crystalline films. The OFETs exhibited field-effect hole mobility up to 0.21 $cm^2 V^{-1} s^{-1}$ when the organic semiconductor was evaporated on substrate at 90 °C. Field-effect mobility in air at a controlled temperature of 30 °C and high humidity of 80% was almost constant for a period of up to 220 days, indicating that the material is a very stable organic semiconductor in air.

© 2010 Elsevier B.V. All rights reserved.

1. Introduction

Organic field-effect transistors (OFETs) are attracting considerable attention due to their potential applications in optoelectronics, such as displays and integrated circuits [1–3]. Organic semiconducting materials with high field-effect mobility and remarkable environmental stability are critical for the fabrication of OFETs. In this regard, we recently characterized OFETs based on oligo-*p*-phenylenevinylene derivatives (OPVs) in which three phenylene rings are linked together with rigid vinylene units. In our previous reports, OFETs based on OPVs stored in air for one year showed good ambient stability [4] with field-effect hole mobility ranging from 0.024 to 0.17 $cm^2 V^{-1} s^{-1}$ [5–7]. To obtain higher carrier mobility without decreasing the chemical stability, it is crucial that the organic molecules be arranged in a specific molecular configuration.

Extended acenes such as tetracene and pentacene enhance the intermolecular overlap of organic semiconductors in the solid state and lead to high field-effect mobility. However, in contrast to their promising charge carrier transporting properties, the molecules are very reactive and environmentally unstable in air [4,8]. As a method to improve the air stability of organic semiconductors without decreasing the mobility, recent studies have shown that introducing naphthalene or anthracene terminal units to the oligothiophene leads to OFETs with high field-effect mobility and improved device stability under ambient conditions [9–11]. In line with this investigation, we synthesized naphthyl end-capped divinylbenzenes in which naphthyl replaces phenyl as the substituent at the terminal positions of OPVs and investigated the performance of OFETs, air stability and molecular packing in poly- and single-crystalline films.

2. Experimental details

To examine the effects of extending π-conjugation, we prepared two organic semiconductors: Nap-PV and CH_3-

* Corresponding author. Address: Exploratory Materials Research Laboratory for Energy and Environment, National Institute for Materials Science, Tsukuba, Ibaraki 305-0047, Japan. Tel.: +81 29 859 2850; fax: +81 29 859 2501.
E-mail address: YASUDA.Takeshi@nims.go.jp (T. Yasuda).

1566-1199/$ - see front matter © 2010 Elsevier B.V. All rights reserved.
doi:10.1016/j.orgel.2010.01.006

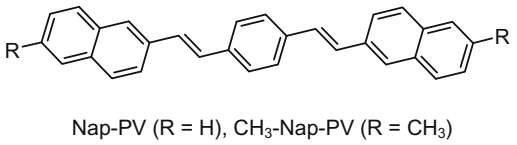

Fig. 1. Chemical structure of organic semiconductors used in this study.

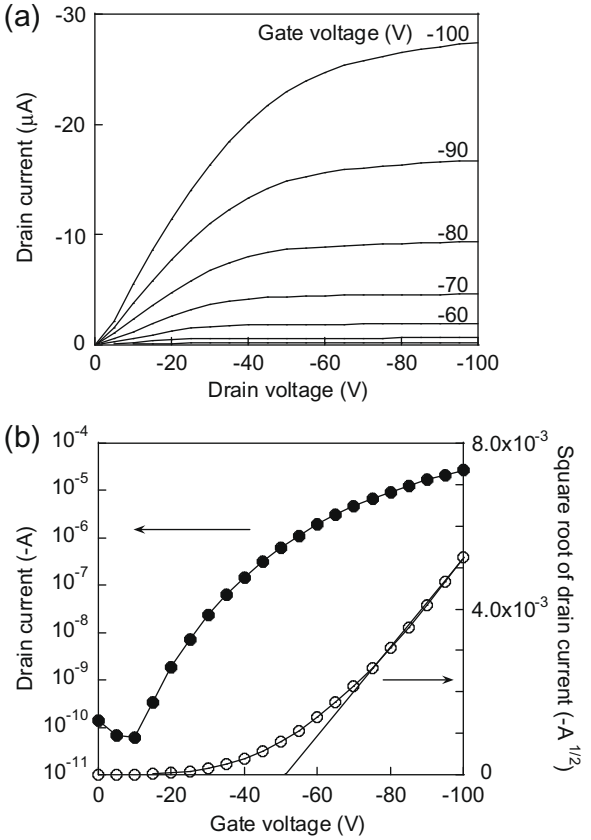

Fig. 2. (a) Plots of drain current versus drain voltage at various gate voltage values for OFETs using Nap-PV as organic semiconductor. (b) Plots of drain current (left) and square root of drain current (right) versus gate voltage at drain voltage of −100 V for the OFETs.

Nap-PV, which were end capped by naphthyl groups. The chemical structure of these compounds is shown in Fig. 1. The materials were synthesized by means of Horner–Wadsworth–Emmons reaction of corresponding aldehydes and tetraethyl *p*-xylylenediphosphonate [12]. These compounds were purified by train sublimation before use.

We fabricated OFETs having top-contact geometry [13]. An Au gate electrode was sputtered through a shadow mask onto a cleaned glass substrate to form 5-mm-wide, 30-nm-thick stripes. Poly(chloro-*p*-xylene) (Parylene-C) was subsequently deposited by thermal chemical vapor deposition at a thickness ranging from 800 to 1000 nm to serve as a gate insulator. The organic semiconductors were vacuum evaporated below 2×10^{-6} torr at a deposition rate of 0.05 nm/s and a thickness of 40–60 nm onto the substrate at room temperature (RT: around 23 °C) or higher (45–105 °C). A shadow mask with interdigitated configuration was attached to the film to form Au source–drain electrodes. The channel length L and width W were 75 μm and 5 mm, respectively. OFET measurement was conducted under vacuum conditions using an Agilent 4156C Precision Semiconductor Parameter Analyzer.

The highest occupied molecular orbital (HOMO) energy level of condensed matter was measured by photoelectron yield spectroscopy in air commercially available from Riken Keiki (AC-2) using vacuum-evaporated films on indium-tin-oxide electrodes.

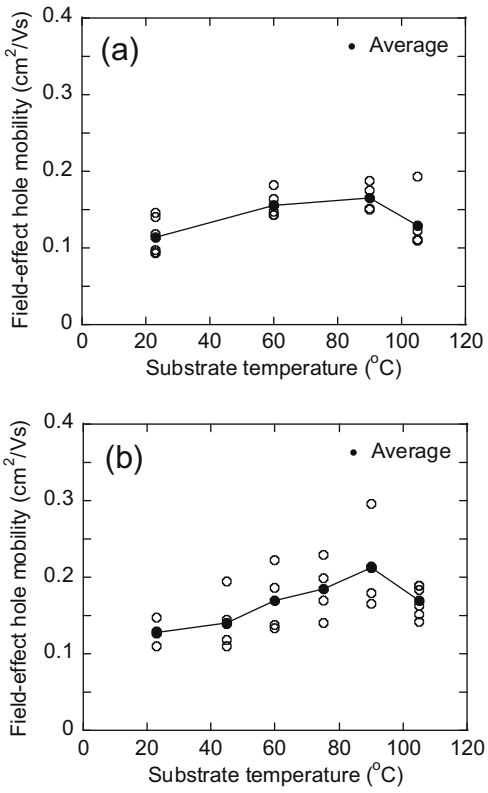

Fig. 3. Dependence of field-effect hole mobility of OFETs with (a) Nap-PV and (b) CH_3-Nap-PV on substrate temperature during evaporation.

Table 1
OFET characteristics (field-effect mobility, threshold voltage, and on/off current ratio) of organic semiconductors used in this study.

Compounds	Vacuum evaporated at RT			Vacuum evaporated at 90 °C		
	Field-effect mobility ($cm^2\ V^{-1}\ s^{-1}$)	Threshold voltage (V)	On/off ratio	Field-effect mobility ($cm^2\ V^{-1}\ s^{-1}$)	Threshold voltage (V)	On/off ratio
Nap-PV	0.11	−51	4.5×10^5	0.18	−51	6.7×10^5
CH_3-Nap-PV	0.11	−45	3.1×10^4	0.21	−39	1.0×10^6

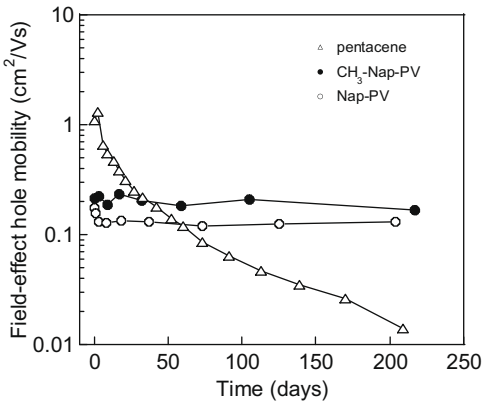

Fig. 4. Field-effect hole mobility plotted as a function of time of exposure to air at a controlled temperature of 30 °C and high humidity of 80%.

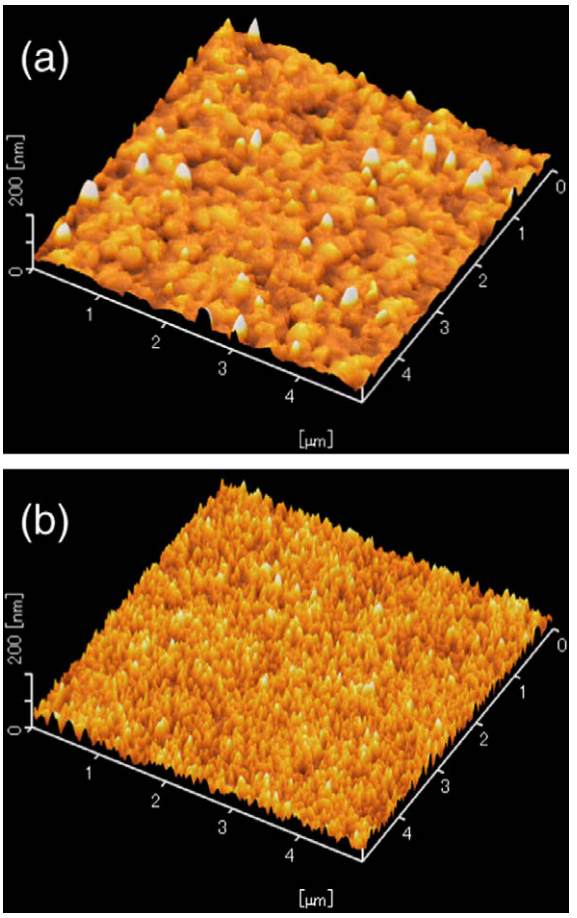

Fig. 5. AFM images of (a) Nap-PV and (b) CH_3-Nap-PV films vacuum-evaporated onto Parylene-C coated glass substrates held at room temperature.

Out-of-plane X-ray diffraction (XRD) measurement was carried out with a RINT2500 (Rigaku Corporation). Thin films of the material deposited onto Parylene-C coated Si wafers were analyzed by XRD using a standard θ–2θ scan with Cu-Kα radiation operated at 50 keV and 300 mA.

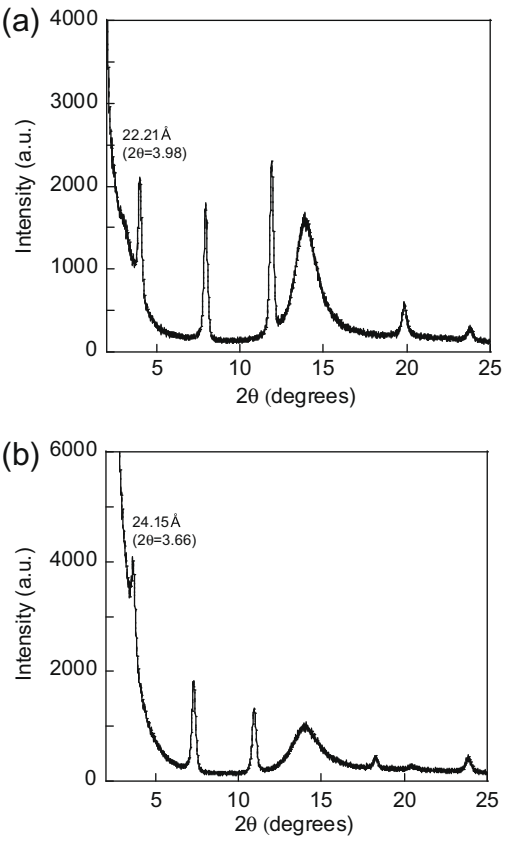

Fig. 6. X-ray diffraction pattern of θ–2θ scan of (a) Nap-PV and (b) CH_3-Nap-PV as a thin film vacuum-evaporated on Parylene-C coated Si wafers. The broad peak around $2\theta = 14°$ is attributed to the crystallinity of Parylene-C.

Single crystals of the organic semiconductors suitable for single-crystal X-ray analysis were obtained by the following procedure: the materials were placed inside the edge of glass tubes (630 mm in length and 28 mm in diameter). The tubes were evacuated and the air was replaced with nitrogen. The tubes were sealed under pressure of around 0.1 atm and then placed on an apparatus for train sublimation. The temperature was set to 240 °C near the source materials and 150 °C at the other edge. Single crystals typically appeared within 6 h.

XRD data on single crystals was collected by a Rigaku AFC10 diffractometer (Mo-Kα radiation, $\lambda = 0.71070$ Å, graphite monochromated). The structures were solved by direct methods [14]. Non-hydrogen atoms were refined anisotropically, and all hydrogen atoms were inserted at calculated positions. All calculations were performed using the crystallographic software package Crystal Structure Version 2.00.

The bandwidths formed by HOMO were calculated using the semiempirical intermediate neglect of differential overlap (INDO) method employed in Gaussian 03 [15]. Molecular coordinates of one-dimensional clusters were directly extracted from the experimental geometries determined by single-crystal X-ray analysis. Within the framework of the tight-binding theory, the bandwidths

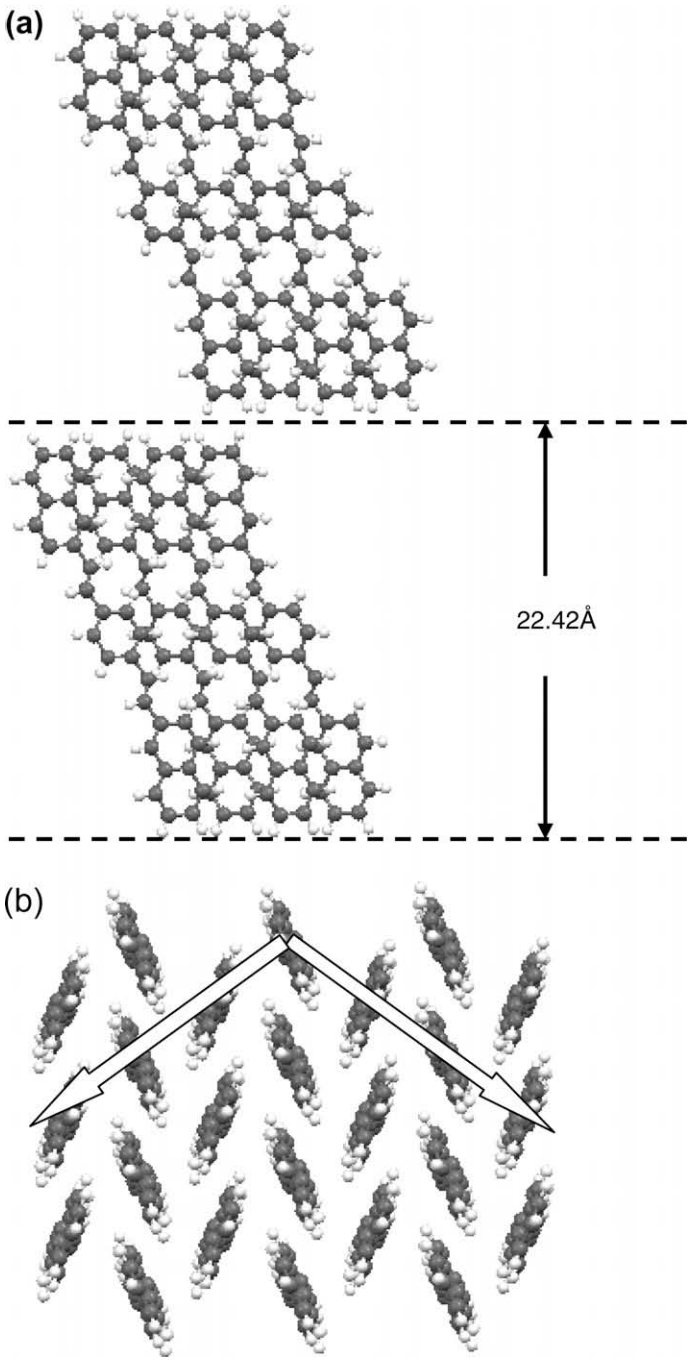

Fig. 7. (a) Single-crystal structure of Nap-PV and (b) illustration of herringbone packing structure as viewed down the long axis of a molecule. The arrows represent the T-shaped molecular arrangement.

were calculated as the extrapolation of the bandwidth versus $\cos(\pi/(N+1))$ plots to $\cos(\pi(N+1)) = 1$, where N is the number of molecules in the clusters [16].

3. Results and discussion

Fig. 2 shows the drain current–voltage relationships in the gate voltage range from 0 to −100 V for Nap-PV. The field-effect mobility is calculated using the standard analytic theory for metal–oxide–semiconductor field-effect transistors according to the following equation:

$$I_{D,sat} = \frac{WC_i}{2L}\mu(V_G - V_T)^2 \quad (1)$$

where $I_{D,sat}$ is the saturation drain current, C_i is the capacitance per unit area of the insulating layer, V_T is

the threshold voltage, V_G is the gate voltage, and μ is the field-effect mobility. The field-effect hole mobility and threshold voltage were calculated to be 0.11 $cm^2 V^{-1} s^{-1}$ and −51 V, respectively. The OFET characteristics (field-effect mobility, threshold voltage and on/off ratio) of Nap-PV and CH_3-Nap-PV evaporated on substrate at room temperature are summarized in Table 1. To further improve the performance of OFETs, organic semiconductors were vacuum evaporated on the Parylene-C coated substrate with an increase in substrate temperature [17–19]. Fig. 3 shows the dependence of field-effect mobility on the substrate temperature during the evaporation of organic semiconductors. The best performance was obtained when the temperature was set to 90 °C for both materials, and the field-effect mobility of CH_3-Nap-PV reached 0.21 $cm^2 V^{-1} s^{-1}$. The OFET characteristics of Nap-PV and CH_3-Nap-PV evaporated on the substrate at 90 °C are also summarized in Table 1. Compared with OPV field-effect mobility (0.024–0.17 $cm^2 V^{-1} s^{-1}$), that of CH_3-Nap-PV was slightly higher.

To study their stability, we stored OFETs with the organic semiconductors evaporated on substrate at 90 °C in air at a controlled temperature of 30 °C and high humidity of 80%. Field-effect mobility as a function of exposure time to air is shown in Fig. 4. The closed circles (CH_3-Nap-PV) and open circles (Nap-PV) were above 0.1 $cm^2 V^{-1} s^{-1}$ for a period of up to 220 days, indicating that both materials are a very stable organic semiconductor in air. On the other hand, the field-effect hole mobility of pentacene (open triangle) after 200 days is three orders of magnitude lower than the initial value.

The HOMO energy level of Nap-PV was found to be −5.50 eV. The introduction of two π-donating methyl groups to the skeleton raised the HOMO level of CH_3-Nap-PV to −5.38 eV. Our previous paper indicated that OFETs using organic semiconductors with a HOMO energy level below −5.20 eV show good ambient stability even after storage in air for one year [4].

The mobility of Nap-PV slightly decreased at the initial time in Fig. 4. Though the cause for the decrease is not clear, our observations of the degradation might be related to the adsorption of H_2O on the Nap-PV layer. The thin film morphology of Nap-PV (Fig. 5(a)) observed by atomic force microscope (AFM) was clearly different from that of CH_3-Nap-PV (Fig. 5(b)). So, when H_2O is adsorbed on the both films, increase in hole trap concentration or change of the morphology resulting in decrease of hole motilities [8] might occur more easily in the Nap-PV film compared to the CH_3-Nap-PV film.

Thin films of Nap-PV and CH_3-Nap-PV grown on Parylene-C coated Si substrates through thermal evaporation under vacuum showed only multiple (0 0 *l*) XRD patterns (Fig. 6). Sharply resolved diffraction peaks up to the fifth order indicate a highly ordered structure. The primary diffraction peaks appeared at 3.98° for Nap-PV and 3.66° for CH_3-Nap-PV, corresponding to *d*-spacing of 22.21 and 24.15 Å. These values correspond well to one-half the *c*-axis of 22.42 and 23.67 Å of Nap-PV and CH_3-Nap-PV, respectively, as determined by single-crystal X-ray analysis. These results suggest that the molecular assembly in the thin film is quite similar to that in bulk crystals: the molecules are oriented nearly orthogonally to the substrate as shown in Fig. 7(a), and the π-orbital direction in the film is parallel to the substrate, favorable for in-plane charge transport. Fig. 7(b) shows the crystal packing of Nap-PV projected along the long axis of a molecule. It is classified as a herringbone arrangement, similar to the crystal structure of pentacene and sexithiophene showing high field-effect mobility [3].

To clarify the origin of high field-effect hole mobility of Nap-PV and CH_3-Nap-PV, we performed semiempirical INDO calculations for the molecular geometries directly extracted from single-crystal analysis. HOMO bandwidths along the T-shaped molecular arrangement shown in Fig. 7(b) are calculated to be 211.3 and 244.7 meV for Nap-PV and CH_3-Nap-PV, respectively. This arrangement allows the formation of a two-dimensionally expanding electronic structure parallel to the *ab*-plane, which is responsible for the high field-effect hole mobility of Nap-PV and CH_3-Nap-PV even in the thin-film phase.

4. Conclusions

We have reported the performance of organic field-effect transistors (OFETs), air stability and molecular packing in poly- and single-crystalline films of naphthyl end-capped divinylbenzenes. High-performance OFETs were obtained when the organic semiconductor was evaporated on substrate at 90 °C. The field-effect hole mobility reached 0.21 $cm^2 V^{-1} s^{-1}$. Compared with that of OPVs (below 0.17 $cm^2 V^{-1} s^{-1}$), the field-effect mobility of CH_3-Nap-PV and Nap-PV is slightly higher. The field-effect mobility of the OFETs in air at a controlled temperature of 30 °C and high humidity of 80% was above 0.1 $cm^2 V^{-1} s^{-1}$ for a period of up to 220 days, indicating that the materials are a very stable organic semiconductor under air. XRD results suggest that the molecular assembly in the thin film is quite similar to that in bulk crystals: the molecules are oriented nearly orthogonally to the substrate and the π-orbital direction in the films is parallel to the substrate, favorable for in-plane charge transport.

Acknowledgment

We thank Mr. T. Ashimine of Kyushu University for the measurement of pentacene OFETs.

References

[1] D. Braga, G. Horowitz, Adv. Mater. 21 (2009) 1473.
[2] T.N. Ng, S. Sambandan, R. Lujan, A.C. Arias, C.R. Newman, H. Yan, A. Facchetti, Appl. Phys. Lett. 94 (2009) 233307.
[3] A.R. Murphy, J.M.J. Fréchet, Chem. Rev. 107 (2007) 1066.
[4] T. Ashimine, T. Yasuda, M. Saito, H. Nakamura, T. Tsutsui, Jpn. J. Appl. Phys. 47 (2008) 1760.
[5] T. Yasuda, M. Saito, H. Nakamura, T. Tsutsui, Appl. Phys. Lett. 89 (2006) 182108.
[6] T. Yasuda, M. Saito, H. Nakamura, T. Tsutsui, Chem. Phys. Lett. 452 (2008) 110.
[7] H. Nakamura, M. Saito, T. Kusumoto, T. Yasuda, T. Tsutsui, Appl. Phys. Express 1 (2008) 021802.
[8] Y. Qiu, Y. Hu, G. Dong, L. Wang, J. Xie, Y. Ma, Appl. Phys. Lett. 83 (2003) 1644.
[9] J.A. Merlo, C.R. Newman, C.P. Gerlach, T.W. Kelley, D.V. Muyres, S.E. Fritz, M.F. Toney, C.D. Frisbie, J. Am. Chem. Soc. 127 (2005) 3997.

[10] H. Tian, J. Shi, B. He, N. Hu, S. Dong, D. Yan, J. Zhang, Y. Geng, F. Wang, Adv. Funct. Mater. 17 (2007) 1940.
[11] H. Tian, J. Shi, D. Yan, L. Wang, Y. Geng, F. Wang, Adv. Mater. 18 (2006) 2149.
[12] J.J. Li, Name Reactions: A Collection of Detailed Reaction Mechanisms, second ed., Springer-Verlag, Berlin, 2003 (and references therein).
[13] T. Yasuda, K. Fujita, H. Nakashima, T. Tsutsui, Jpn. J Appl. Phys. 42 (2003) 6614.
[14] Crystal data of Nap-PV: monoclinic $P2_1/n$, $a = 5.9061(8)$ Å, $b = 7.4162(11)$ Å, $c = 44.846(5)$ Å, $\beta = 91.246(2)^\circ$, $V = 1963.83$ Å^3, $Z = 4$. Crystal data of CH_3-Nap-PV: orthorhombic, $a = 5.961(4)$ Å, $b = 7.336(6)$ Å, $c = 47.33(2)$ Å, $V = 2069.74$ Å^3, $Z = 4$. We decided the crystal structure of CH_3-Nap-PV as the space group of $Pca2_1$. However, the exact space group may be *Pbca* if CH_3-Nap-PV molecule has a symmetrical point in the crystal.
[15] M.J. Frisch et al., Gaussian 03, Revision C.02, Gaussian Inc., Wallingford, CT, 2004.
[16] J. Cornil, J.Ph. Calbert, J.L. Brédas, J. Am. Chem. Soc. 123 (2001) 1250.
[17] T. Yasuda, K. Kashiwagi, Y. Morizawa, T. Tsutsui, J. Phys. D: Appl. Phys. 40 (2007) 4471.
[18] Y. Yoshida, H. Takiguchi, T. Hanada, N. Tanigaki, E.-M. Han, K. Yase, J. Cryst. Growth 198/199 (1999) 923.
[19] M.E. Hajlaoui, F. Garnier, L. Hassine, F. Kouki, H. Bouchriha, Synth. Met. 129 (2002) 215.

Organic Electronics 11 (2010) 664–669

Contents lists available at ScienceDirect

Organic Electronics

journal homepage: www.elsevier.com/locate/orgel

Insulator MnO: Highly efficient and air-stable n-type doping layer for organic photovoltaic cells

Jiaxiu Luo, Lixin Xiao *, Zhijian Chen, Bo Qu, Qihuang Gong *

State Key Laboratory for Mesoscopic Physics and Department of Physics, Peking University, Beijing 100871, PR China

ARTICLE INFO

Article history:
Received 3 November 2009
Received in revised form 6 January 2010
Accepted 8 January 2010
Available online 11 January 2010

Keywords:
Organic photovoltaic
n-Type dopant
Air stability
MnO

ABSTRACT

The insertion of thin MnO layer between organic photoactive layer and metal electrode significantly improved the power conversion efficiency (PCE) and the air stability of organic photovoltaic cell (OPV). PCE (2.91%) was obtained by inserting 3-nm-thick MnO, higher than 0.91% for the device without MnO, and 2.59% for the device with 0.5-nm-thick LiF. In addition, the PCE of MnO device retained 28.42% of initial value after 2 weeks while the device without MnO dropped down to only 6.03% just after 2 days, even better than that of LiF device which dropped down to 7.29% of initial value after 2 weeks without encapsulation. Insulator MnO is promising to improve the electron transport and operation stability in OPVs.

© 2010 Elsevier B.V. All rights reserved.

1. Introduction

Organic photovoltaic cell (OPV) has been considered as the next promising generation of solar energy conversion device due to its advantage in the fabrication of large-area, cost-effective, flexible, low-weight organic films with high absorption coefficient [1], and even high exciton separation efficiency (nearly 90%) [2]. However, the power conversion efficiency (PCE) is still the major course and needed to be improved further. Although many efforts have been made to improve PCE, including efforts from materials to structure of devices [3,4], low efficient charge transport and injection (collection) are still the bottle-neck of the improvement of PCE.

The modification at the interface between organic active layer and electrodes has been found to be effective for charge collection in OPV, many strategies have been developed on it. In the aspect of indium tin oxide (ITO) anode, plasma and UV-ozone treatment, buffer layer, e.g., poly(3,4-ethylene dioxythiophene):poly(styrene-sulfonate) (PEDOT:PSS) [5], self-assembled mono-layers (SAMs) [6] or ultra-thin metal layer, e.g., Au, Pt [7] have been successfully used to modify the surface of it. Meanwhile, in the aspect of metal cathode especially aluminum (Al), ultrathin (less than 1.0 nm) LiF [8] is still the most effective buffer layer among the few options.

Besides the charge transport, the device operation stability is also crucial to the application of OPV. If the improvement of charge transport and operation stability can be carried out simultaneously, the fabrication will be simplified and cost-effective. Titanium oxide (TiO_x) could be used as hole blocking layer and optical spacer to improve PCE [9], and as shielding layer to prevent the intrusion of oxygen and humidity into the polymer layer [10], but the solution process may give change on the organic layer surface. Considering the results which were previously reported about the effect of MnO (manganese mono-oxide) in organic light-emitting device (OLED) [11], we introduced a thin layer (optimal thickness ~3.0 nm) insulator MnO between organic layer and metal cathode, and obtained higher PCE and longer operation lifetime in the air than the device without it, and even higher PCE and longer operation lifetime in the air than device with LiF as the n-type dopant.

* Corresponding authors. Tel.: +86 10 62754990; fax: +86 10 62756567 (L. Xiao).
E-mail addresses: xiao66@pku.edu.cn (L. Xiao), qhgong@pku.edu.cn (Q. Gong).

1566-1199/$ - see front matter © 2010 Elsevier B.V. All rights reserved.
doi:10.1016/j.orgel.2010.01.007

2. Experimental

The OPV devices were fabricated with traditional sandwich structure as follows: ITO/PEDOT:PSS/poly(3-hexylthiophene) (P3HT): [6,6]-phenyl-C_{61}-butyric acid methyl ester (PCBM)/Al (as the reference device), ITO/PEDOT:PSS/P3HT:PCBM/MnO/Al (hereafter referred to as MnO device), ITO/PEDOT:PSS/P3HT:PCBM/LiF/Al (hereafter referred to as LiF device). The pre-cleaned ITO/glass substrate (light-incident-side electrode) was spin coated with PEDOT:PSS aqueous solution at 3000 rpm, and dried at 200 °C for 5 min in air, and 15 min in vacuum subsequently. The P3HT:PCBM film was prepared from P3HT:PCBM orthodichlorobenzene solution (15 mg:12 mg/ml) at 600–800 rpm on top of the PEDOT:PSS layer, and then baked at 150 °C for 1 h in vacuum. The remaining parts of fabrication were just the same as OLED. Finally, MnO, LiF, Al were separately thermal deposited on top of the photoactive layer under a vacuum of 10^{-4} Pa. The thickness of organic layer, MnO, LiF and Al is around 90, x (x = 0, 1.5, 3.0, 6.0, and 10.0), 0.5 and 150 nm, respectively. The active area of the device in cathode area is 0.126 cm^2. The structure of device is shown in Fig. 1a. All the devices were fabricated under the same conditions without encapsulation, and there were no more annealing for the device after fabrication. The current density–voltage (I–V) characteristics were measured through Keithley 2611 source meter under dark and illumination with a solar simulator (Oriel 300 W) with AM 1.5G filter under a power of 100 mW/cm^2. The absorption was measured using a Lambda 950 UV/Vis spectrometer. All the measurements were performed at room temperature in ambient atmosphere.

3. Results and discussion

To explore the doping effect of MnO on the charge transporting of OPV, we investigated the device performance via inserting of thin MnO layer (0, 1.5, 3.0, 6.0, and 10.0 nm) between organic photoactive layer and metal electrode. As shown in the upper part of Fig. 2, the dark current of the device containing MnO was lower than that of the device without MnO (reference device), indicating that the insertion of MnO buffer layer can prevent the permeation defects from cathode metal evaporation, and then the leakage current was reduced. Therefore, exciton quenching was alleviated and the device performance was improved [12].

In addition, the MnO devices exhibited increase in short-circuit current (I_{sc}) and great enhancement in open-circuit voltage V_{oc} in the lower part of Fig. 2. The great enhancement in V_{oc} could be interpreted by the increase of shunt resistance (R_{sh}) resulted from the prevention of diffusion into organic layer from the cathode metal atoms with MnO buffer layer, which generally resulted in an enhancement on V_{oc} and fill factor (FF) [13]. The insertion of MnO to reduce *Schottky* barrier for charge transport and injection could also contribute to the enhancement of V_{oc}. The energy diagram of MnO device is shown in Fig. 1b. Within the MnO layer, a dipole layer might be formed at the interface to lead to energy level realignment as well as band bending to adjust electrical properties of device and optimize the electron collection process. Furthermore, the electron attenuation length of inorganic insulating interfacial layer is much longer than organic solid with Van der Waals interaction. From the view point of that, Wolf and Bassler [14] proposed that a thin inorganic insulator between organic semiconductor and metal electrode can enhance electron injection in OLED. Therefore, an enhancement of I_{sc} in OPV could also be deduced by inserting of MnO layer. The enhanced I_{sc} might also be due to the hole blocking of MnO resulting from its deep energy level (−6.5 eV) of the highest occupied molecular orbit (HOMO), as previously reported in OLED [11], to reduce the recombination of charge carriers.

The V_{oc} of MnO devices with different thickness was almost the same, while the I_{sc} was improved as the MnO

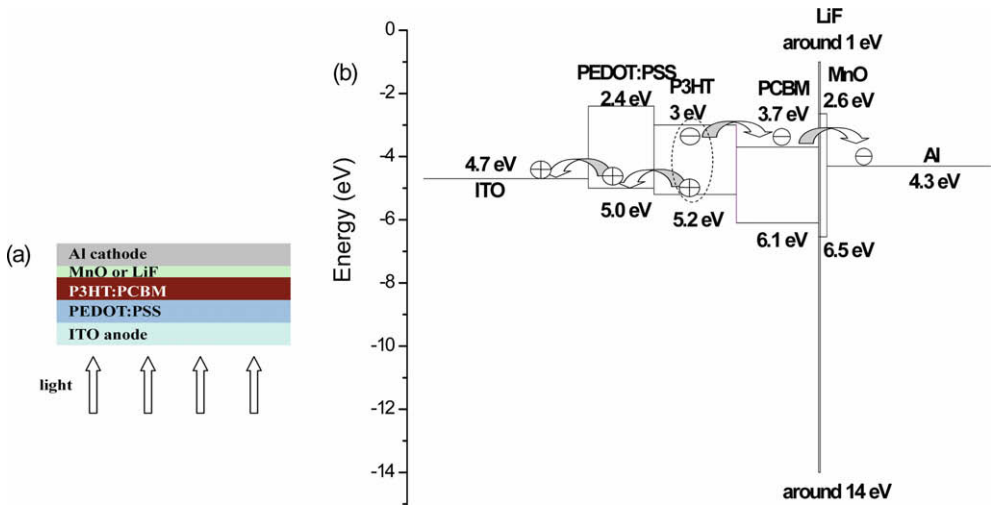

Fig. 1. (a) OPV structure; (b) energy level diagram of the OPV.

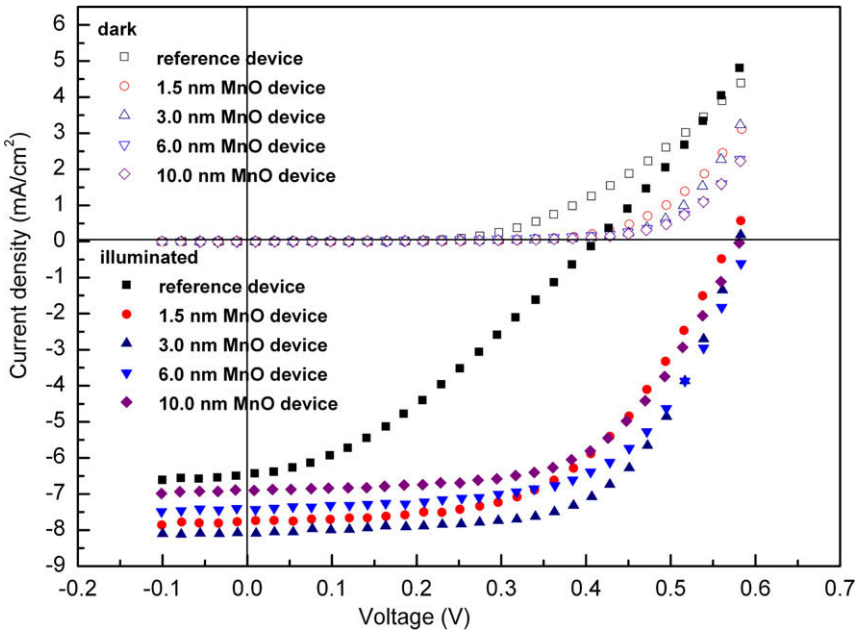

Fig. 2. *I–V* plot of devices with and without MnO in the dark and under illumination.

thickness initially increased from 1.5 to 3.0 nm, but it declined when the thickness increased further, which can be interpreted by a tunneling model as previously reported [11,15]. There exists an optimal thickness of an insulating buffer layer (3.0 nm in this study) which made the total barrier (both original energy barrier and the extra barrier introduced by insulating layer itself) lower to achieve more efficient electron transport and collection.

Owing to the enhancement of V_{oc} and I_{sc}, the PCE and FF of MnO device were higher than the reference one. Compared to the reference device, PCE of devices with 1.5, 3.0, 6.0, and 10.0 MnO increased up 62%, 82%, 76%, and 71%, respectively. There were 2.7-, 3.2-, 2.9-, and 2.6-folds enhancement for the FF of the devices with 1.5, 3.0, 6.0, and 10.0 MnO in comparison to the reference one as listed in Table 1. The higher FF of MnO devices was originated from the decrease of series resistance (R_s) denoted by the inverse slope of the *I–V* curves near V_{oc} and the increase of R_{sh} calculated from the inverse slope of the *I–V* curves at 0 V under illumination.

Moreover, MnO device (3.0 nm) showed even higher PCE than that of LiF device (the common efficient device) as shown in Fig. 3. The I_{sc} of LiF device was 7.46 mA/cm^2, while the I_{sc} of MnO device was increased to 8.05 mA/cm^2. The enhanced I_{sc} for MnO device might be due to the more efficient electron injecting of MnO than that of LiF as previously reported in OLED [11]. As shown in Table 1, the R_s of MnO device slightly decreased to 13 from 18 Ω cm^2 for LiF device, and the R_{sh} increased to 1931 Ω cm^2 from 1334 Ω cm^2 for LiF device. These indicate that less defects in MnO device is induced than in the LiF device. Although the R_s and R_{sh} could affect V_{oc} and FF, V_{oc} mainly depends on energy level arrangement of active materials and electrode work function as well as the interface properties. Comparing with LiF device, the organic active materials and the electrodes of MnO device were the same. Moreover, the mechanism of inserting MnO was similar with LiF to reduce *Schottky* barrier, which is almost the same in MnO and LiF devices, thus V_{oc} keeps the same value in both MnO and LiF devices. FF has the same situation, which also depends on the interface properties. Because FF strongly depends on recombination strength [16], in addition, the recombination situation was partly influenced by interface properties. Owing to the larger I_{sc}, the PCE of MnO device was increased to 2.91% from 2.59% for that of LiF device. These indicate that insulator MnO is more efficient n-type doping layer than LiF for OPVs.

Table 1
Performances of the resultant OPVs.

Device	Reference	LiF	1.5 nm MnO	3.0 nm MnO	6.0 nm MnO	10.0 nm MnO
V_{oc} (V)	0.41	0.58	0.57	0.58	0.60	0.59
I_{sc} (mA/cm^2)	6.43	7.46	7.74	8.05	7.41	6.91
FF	0.34	0.60	0.55	0.62	0.60	0.58
PCE (%)	0.91	2.59	2.43	2.91	2.64	2.35
R_s (Ω cm^2)	44	18	21	13	17	21
R_{sh} (Ω cm^2)	391	1334	1499	1931	2364	1827

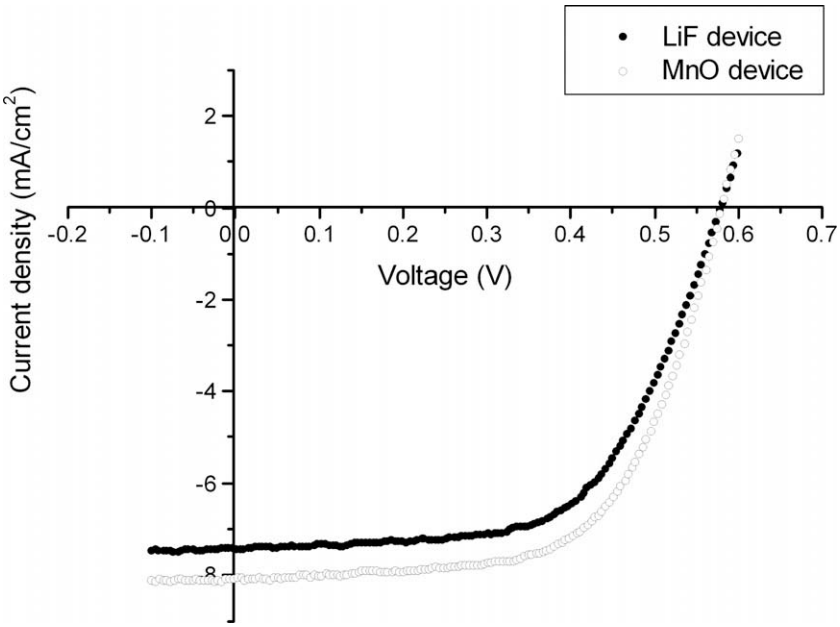

Fig. 3. *I–V* plot of LiF and MnO (3.0 nm) devices under illumination.

Table 2
Air stability of MnO (3.0 nm), LiF and reference devices.

PCE maintenance (%)	24 h	48 h	72 h	2 weeks
MnO (3.0 nm) device	81.58	72.63	66.84	28.42
LiF device	77.08	58.33	46.88	7.29
Reference device	51.72	6.03	2.91	0.02

Furthermore, the air stability of device can be improved by inserting a MnO layer. The air stability of device was investigated through the measuring of PCE maintenance of the MnO (3.0 nm) device, the LiF device and the reference device stored in ambient environment (80% RH) without encapsulation in the dark within 2 weeks. We observed the PCE of the MnO device still kept 28.42% of the initial

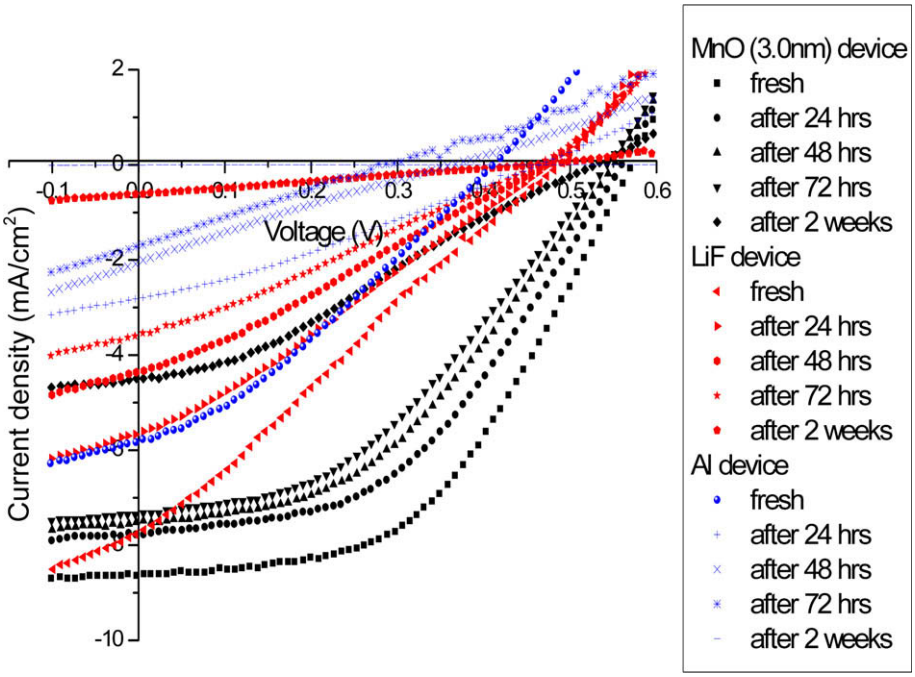

Fig. 4. *I–V* plot of MnO device, LiF device and reference device before and after air stability study.

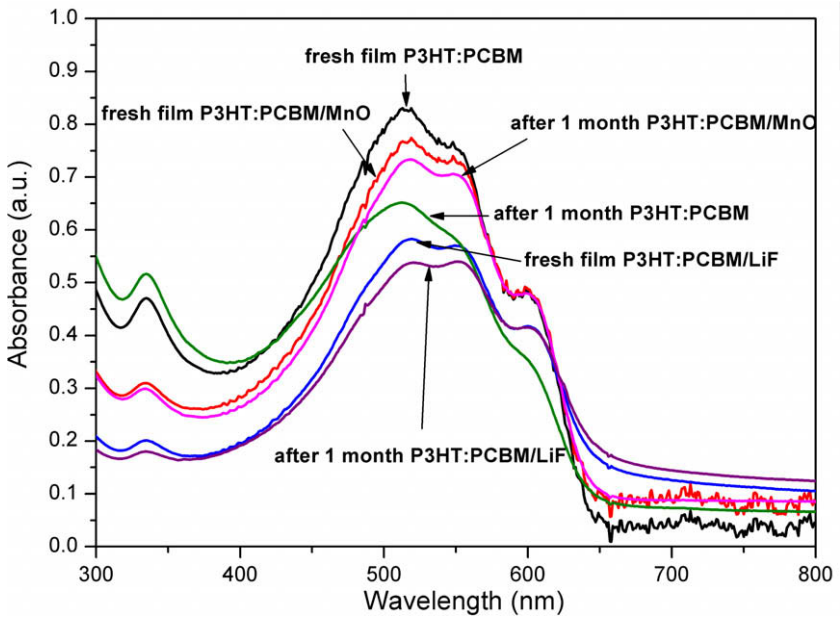

Fig. 5. The absorption spectra of P3HT:PCBM, P3HT:PCBM/MnO and P3HT:PCBM/LiF films (fresh and after 1 month).

value of fresh made device after 2 weeks, while the reference device dropped down to only 6.03% just after 2 days, and even the LiF device decreased to 7.29% of initial value after 2 weeks without encapsulation. The maintenance of PCE (ratio of after storage/fresh made device) is listed in Table 2, and the *I–V* curve before and after air stability study is shown in Fig. 4. These results indicate that the MnO device is the most air stable, even more stable than the LiF device.

To study the mechanism of MnO to prolong the lifetime of device, we investigated the air stability of absorption spectra of P3HT:PCBM film, P3HT:PCBM/MnO film (P3HT:PCBM covered with MnO) and P3HT:PCBM/LiF film (P3HT:PCBM covered with LiF) stored in ambient environment (80% RH) without encapsulation in the dark (Fig. 5). After 1 month, the intensity of the absorption band between 500 and 570 nm (the main absorption peak for the P3HT) of P3HT:PCBM film decreased the most (18.6–24.1%), while P3HT:PCBM/MnO film only decreased a little (0.8–5.5%). The decrease of absorption of P3HT:PCBM/LiF film (2.6–8.2%) is slightly more than that of P3HT:PCBM/MnO film, which is consistent with the air stability of device performance as stated above. The intensity decrease possibly related to the reduction of corresponding functional groups and the variation of inter-chain order degree of polymer which were resulted from photo- and thermo-oxidation [17,18]. The absorption of P3HT:PCBM/MnO film varied little after 1 month maybe due to the shielding effect of highly air-stable MnO. The MnO layer can protect organic layers from oxygen and humidity penetration which can decrease the conductivity of C_{60} film by several orders of magnitude [19]. We surmise that oxygen and humidity influence on the conductivity of PCBM (derivative of C_{60}) film should be in a comparable extent. There is also a probability that the trace water and organic solvent from spin-coating operation after annealing can be removed during MnO deposition [20]. These results implied that the operation stability of OPV can be improved by inserting of insulator MnO thin layer.

4. Conclusion

In summary, a facile way to fabricate air stable and highly efficient OPV with insulator MnO as n-type doping layer was devised. Not only the PCE, but also the air stability of OPV can be improved via inserting thin MnO layer between organic photoactive layer and metal electrode. The optimal thickness of MnO is 3.0 nm. A PCE of 2.91% was obtained by inserting 3-nm-thick MnO, which was even higher than the PCE of 2.59% for the device with 0.5-nm-thick LiF. Moreover, the PCE of MnO device maintained 28.42% of initial value after 2 weeks without encapsulation while the reference device without MnO dropped down to only 6.03% just after 2 days. The air stability of MnO device was even better than that of LiF device which dropped down to 7.29% of initial value after 2 weeks. Insulator MnO is promising to improve the electron transport and operation stability in OPVs.

Acknowledgements

This work was financially supported by the National Natural Science Foundation of China under Grant Nos. 60677002, 10674011, 10934001, 60878019 and 10821062, and the National Basic Research Program of China under Grant Nos. 2007CB307000 and 2009CB930504.

References

[1] S. Gunes, H. Neugebauer, N.S. Sariciftci, Chem. Rev. 107 (2007) 1324.
[2] V.D. Mihailetchi, H. Xie, B.d. Boer, L.J.A. Koster, P.W.M. Blom, Adv. Funct. Mater. 16 (2006) 699.

[3] R.C. Hiorns, E. Cloutet, E. Ibarboure, L. Vignau, N. Lemaitre, S. Guillerez, C. Absalon, H. Cramail, Macromolecules 42 (2009) 3549.
[4] J.Y. Kim, K. Lee, N.E. Coates, D. Moses, T.Q. Nguyen, M. Dante, A.J. Heeger, Science 317 (2007) 222.
[5] S.E. Saheen, C.J. Brabec, N.S. Sariciftci, F. Padinger, T. Fromberz, J.C. Hummelen, Appl. Phys. Lett. 78 (2001) 841.
[6] S. Khodabakhsh, B.M. Sanderson, J. Nelson, T.S. Jones, Adv. Funct. Mater. 16 (2006) 95.
[7] J.C. Bernede, L. Cattin, M. Morsli, Y. Berredjem, Sol. Energy Mater. Sol. Cells 92 (2008) 1508.
[8] C.J. Brabec, S.E. Shaheen, C. Winter, N.S. Sariciftci, P. Denk, Appl. Phys. Lett. 80 (2002) 1288.
[9] S.H. Park, A. Roy, S. Beaupre, S. Cho, N. Coates, J.S. Moon, D. Moses, M. Leclerc, K. Lee, A.J. Heeger, Nat. Photonics 3 (2009) 297.
[10] K. Lee, J.Y. Kim, S.H. Park, S.H. Kim, S. Cho, A.J. Heeger, Adv. Mater. 19 (2007) 2445.
[11] J. Luo, L. Xiao, Z. Chen, Q. Gong, Appl. Phys. Lett. 93 (2008) 133301.
[12] Q.L. Song, F.Y. Li, H. Yang, H.R. Wu, X.Z. Wang, W. Zhou, J.M. Zhao, X.M. Ding, C.H. Huang, X.Y. Hou, Chem. Phys. Lett. 416 (2005) 42.
[13] S. Han, W.S. Shin, M. Seo, D. Gupta, S. Moon, S. Yoo, Org. Electron. 10 (2009) 791.
[14] U. Wolf, H. Bassler, Appl. Phys. Lett. 74 (1999) 3848.
[15] Y.E. Kim, H. Park, J.J. Kim, Appl. Phys. Lett. 69 (1996) 599.
[16] L.J.A. Koster, V.D. Mihailetchi, P.W.M. Blom, Appl. Phys. Lett. 88 (2006) 52104.
[17] M. Manceau, A. Rivaton, J. Gardette, S. Guillerez, N. Lemaitre, Polym. Degrad. Stab. 94 (2009) 898.
[18] K. Kawano, C. Adachi, Adv. Funct. Mater. 19 (2009) 3934.
[19] R. Konenkamp, G. Priebe, B. Pietzak, Phys. Rev. B 60 (1999) 11804.
[20] S. Rait, S. Kashyap, P.K. Bhatnagar, P.C. Mathur, S.K. Sengupta, J. Kumar, Sol. Energy Mater. Sol. Cells 91 (2007) 757.

Organic Electronics 11 (2010) 670–676

Contents lists available at ScienceDirect

Organic Electronics

journal homepage: www.elsevier.com/locate/orgel

Durability under mechanical bending of the indium tin oxide films deposited on polymer substrate by thermionically enhanced sputtering

Y.F. Lan [a,*], W.C. Peng [b,1], Y.H. Lo [a,2], J.L. He [a,2]

[a] Department of Materials Science and Engineering, Feng Chia University, 100 Wenhwa Rd., Seatwen, Taichung City 40724, Taiwan
[b] TFT Int Engineering Department, AU Optronics Corporation, 1 JhongKe Rd., Central Taiwan Science Park, Taichung City 40763, Taiwan

ARTICLE INFO

Article history:
Received 8 September 2009
Received in revised form 6 January 2010
Accepted 7 January 2010
Available online 11 January 2010

Keywords:
Indium tin oxide
Polyethylene terephthalate
Sputtering
Thermionic enhancement
Mechanical durability

ABSTRACT

The emerging demand for flexible display panels has created a demand for coating techniques capable of depositing high-quality transparent conductive coatings (TCOs) on polymeric materials. This study demonstrates indium tin oxide (ITO) films deposited on polyethylene terephthalate (PET) substrates using a thermionic emission (TE) enhanced DC magnetron sputtering system to improve electrical and optical properties under static and dynamic mechanical bending.

Experimental results show that the ITO-coated PET specimen prepared with TE and without TE presents an average transmittance in the visible region of the spectrum of 83% and 70%, and an electrical resistivity of 4.5×10^{-4} and $1.7 \times 10^{-3}\,\Omega\,cm$, respectively. By contrast, the static bending test revealed that the critical radius of curvature (R_c) is 13.9 and 17.0 mm for the ITO-coated PET with and without TE. The dynamic bending test showed that the ITO-coated PET with TE is durable for more than 1200 cycles, while the corresponding number for the ITO-coated PET without TE is smaller than 50 cycles for the ITO-coated PET without TE. These results evidence that the ITO film deposited using the TE approach exhibits a higher degree of crystallinity and film adhesion than that deposited without TE. TE improves optical and electrical properties of the ITO coatings and their longer durability under mechanical bending.

© 2010 Elsevier B.V. All rights reserved.

1. Introduction

Indium tin oxide (ITO) films have been extensively applied in flat panel displays [1,2] and photovoltaic devices [3,4] as transparent conductive oxide (TCO) electrodes because of their low electrical resistivity and high optical transmittance. The emerging demand for flexible display panels has created a demand for coating techniques capable of depositing high-quality TCOs on polymeric materials to particularly achieve light-weight, compactness, impact tolerance [5,6] and mechanical bending durability [7,8]. Among commonly used polymeric materials, PET (polyethylene terephthalate) and PC (polycarbonate) have been considered as substrate materials for flexible displays because of their satisfactory optical transmittance and low material cost compared to other materials [9].

Modified sputter deposition techniques have directly obtained promising results to deposit ITO films on flexible substrates at a low deposition temperature. Yang [10] found a resistivity of $6.3 \times 10^{-4}\,\Omega\,cm$ and an average optical transmittance of 80% by utilizing an RF magnetron sputtering system with supplemental substrate biasing to deposit ITO film on PPA (polypropylene adipate) substrates. Kim [11] added negative cesium ions into a glow discharge sputtering system to impart additional energy into the growing ITO film, to achieve an electrical resistivity of $6.2 \times 10^{-4}\,\Omega\,cm$ and an average optical transmit-

* Corresponding author. Tel./fax: +866 4 24519053.
E-mail addresses: p9331075@fcu.edu.tw (Y.F. Lan), marspeng@auo.com (W.C. Peng), s823113@hotmail.com (Y.H. Lo), jlhe@fcu.edu.tw (J.L. He).
[1] Tel.: +866 3 5678787x5211; fax: +866 3 5665199.
[2] Tel./fax: +866 4 24519053.

1566-1199/$ - see front matter © 2010 Elsevier B.V. All rights reserved.
doi:10.1016/j.orgel.2010.01.008

tance of 87%. Hoshi and Kiyomura [12] accomplished an electrical resistivity of $3.5 \times 10^{-4}\,\Omega\,cm$ and an average optical transmittance over 80% by using an RF applied grid in the DC sputtering system to increase ion density. Our previous study also demonstrated a thermionic electron emission (TE) approach as a supplement to the DC sputtering system to obtain an ITO film with an electrical resistivity of $4.5 \times 10^{-4}\,\Omega\,cm$ and an average optical transmittance of 80% [13]. The TE approach can be utilized to deposit high-quality ITO deposition at relatively low substrate temperature with low-cost equipment. The quality of the film thus formed, in terms of electrical resistivity and optical transmittance, is improved by the increased crystallinity of the film under intense ion bombardment. However, thermal expansion and elastic properties for both TCO films and polymer substrates are very different, resulting in large mechanical stresses. A TCO film on a PET polymer substrate subjected to such stress cracks and eventually fractures, markedly reduces its electrical conductivity. Cairns et al. [14] investigated the mechanical properties of ITO films on a PET substrate, focusing on the cracking mechanism and its relationship to electrical properties. In addition, Fortunato et al. [15] also observed that ZnO:Al cracking under increasing strain increases its resistance. This result is consistent with similar studies of silicon oxide deposited on the PET substrate [16].

Most studies on the above subject have been performed using thin films on polymer substrates and have demonstrated initial cracking and the mechanism failure of electrical conductivity of thin films. The current authors' earlier study sought to obtain high-quality ITO films deposited by TE, and motivates this study. The goal of this study is to improve electrical response the ITO-coated PET under static and dynamic mechanical bending to improved crystallinity and the film adhesion through the TE technique which contributes to resist damage under mechanical action. This paper investigates the effect of mechanical bending of an ITO film deposited by DC magnetron sputtering on a PET substrate with and without TE. A discussion follows about the change in electrical resistance of ITO-coated PET specimens under a single static bending event and their durability under dynamic repeated bending.

2. Materials and methods

The schematic of the DC magnetron sputter system incorporating thermionic emission apparatus is shown in Fig. 1(a) and the filament assembly is shown in Fig. 1(b). The current study used a 0.6 mm diameter tungsten filament for electron emission. The filament was negatively biased to a voltage of −30 V relative to the coating chamber by a DC current power supply and resistively heated to generate electron emission current at 3 A. The ITO target used for sputtering was In_2O_3:SnO_2 = 90:10 (wt.%). The distance between the substrate and the target was 6 cm. ITO films deposited on the PET substrates with a 10 mm × 45 mm strip and 135 μm thick were used for the mechanical bending test, while the other samples with dimensions of 20 mm × 20 mm were used for microstructure analysis, adhesion measurement, optical transmittance and electrical resistivity measurement. The deposition was carried out in argon plasma at a pressure of 0.15 Pa. Table 1 lists deposition conditions as well as the substrate temperature measured by a thermometer placed on the substrate. Although no external heating was employed during deposition, the substrate temperature as exposed to the plasma increased to 50 and 90 °C, respectively without and with TE. Thermal radiation from the thermionic filament when employing TE caused a higher substrate temperature.

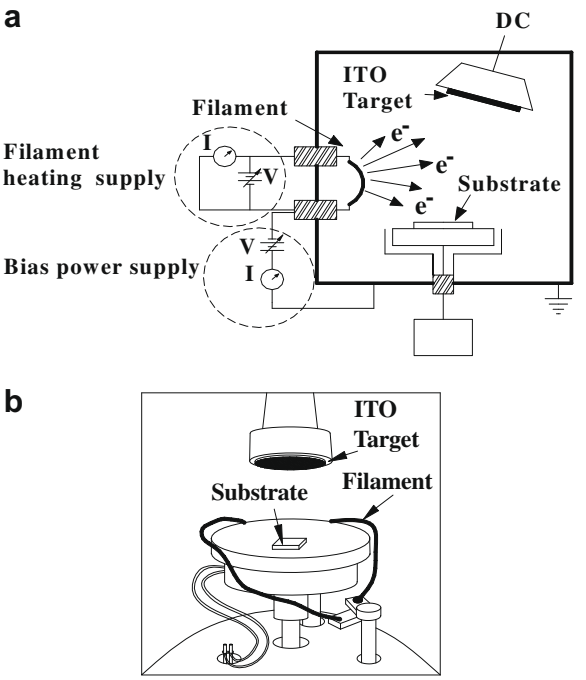

Fig. 1. Schematic diagram of: (a) the thermionic enhanced DC magnetron sputter system and (b) the filament assembly.

The crystal structure of deposited films was investigated by a grazing incident X-ray diffractometer (GIXD, Bruker D8 Discover, by CuK_α radiation) with a grazing incidence angle of 1°. Surface morphology of the deposited ITO films was observed using a field emission scanning electron microscope (FESEM, Hitachi S-4800). Optical transmittance of the ITO-coated PET specimen was measured using a UV–Visible spectrophotometer (Shimadzu UV-1601). Electrical resistivity of ITO-coated PET specimens was measured using a Four-Point Probe method (Quatek QT-50) and the carrier concentration and mobility were determined by an Ecopia Hall effect measurement system under a magnetic field of 0.55 T (Ecopia HMS-3000).

After deposition, film adhesion was measured using a crosscut tester, according to the ASTM D3359 standard [17]. The tester consisting of eleven blades within a pitch of 1 mm was used to scratch the coating vertically and horizontally for causing one hundred squares (crosshatching). A tape was attached onto the crosshatched surface then quickly ripped off from the specimen. The coating adhesion was rated by visually comparing the sample to a series of six levels depicted in the ASTM method. Subsequently,

Table 1
Deposition conditions for ITO films.

Target materials	ITO target (90 wt.% In_2O_3 – 10 wt.% SnO_2)	
Ar sputtering gas flow rate (sccm)	100	
Base pressure (Pa)	$<6.6 \times 10^{-4}$	
Working pressure (Pa)	0.15	
Substrate material	PET	
Target power setting (W)	80	
Thermionic condition	Without	With
Thermionic emission current (A)	0	3
Recorded target voltage (V)	259	253
Recorded target current (mA)	319	325
Deposition time (min)	4.5	4.0
Film thickness (nm)	150	150
Initial deposition temperature (°C)	Set at ambient	
Measured final deposition temperature (°C)	50	90

the mechanical bending test, consistent with the ASTM D1593 standard [18], was conducted on the coated sample, as shown in Fig. 2. During the test, the single-stroke distance and cycle times were controlled and recorded. The radius of curvature associated with each bending was then calculated based on the recorded stroke distance. The ITO-coated strip was placed with the ITO side upwards, and subjected to tensile stress under each bending. Both ends of the strip were electrically connected to an LCR meter. Static and dynamic tests were performed separately. In the static bending test, the sample was bent by controlling the stroke distance to obtain a designated radius of curvature (R) while electrical resistance of the ITO-coated specimen was recorded using the LCR meter. Progressively reducing the R value caused a sudden increase in electrical resistance of the ITO-coated PET specimen when cracks formed in the ITO film. The corresponding R value was defined as R_c (critical radius of curvature), which is the minimum bending radius of curvature that the ITO film can tolerate.

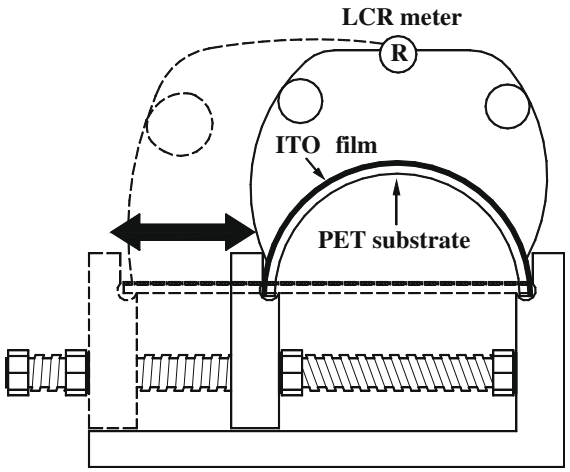

Fig. 2. A schema of the static and dynamic tester for the durability of the ITO-coated PET specimen.

The dynamic bending test was performed by repeatedly bending the sample at a constant R value of 18.6 mm. The electrical resistance and optical transmittance of the ITO-coated specimen were recorded after every 50 bending cycles. After performing the dynamic mechanical bending test, film morphology of the ITO-coated specimens was observed using the scanning electron microscope (SEM, Hitachi S-3000).

3. Results and discussion

3.1. Microstructure of the deposited ITO films

Fig. 3 shows the X-ray diffraction patterns and the corresponding cross sectional film morphologies of ITO-deposited specimens. The XRD pattern of ITO film deposited without TE shows an amorphous feature. In the case of the film deposited with TE, diffraction peaks of ITO (2 2 2), (4 0 0), (4 4 0) and (6 2 2) clearly demonstrate a crystalline structure in the deposited ITO film. The presence of the crystalline structure is likely due to the accompanying substrate temperature elevation and intensified plasma density when employing TE. Researches have previously reported that enhanced crystallinity of the ITO film deposited using TE mainly results from increased plasma density [13]. The ion flux toward the substrate promotes ion bombardment, enhancing surface migration of adatoms on the growing film. The literature has shown that increasing power density in an RF sputter system [19] and applying an RF biased grid [12] also enhances the crystallinity of deposited ITO films.

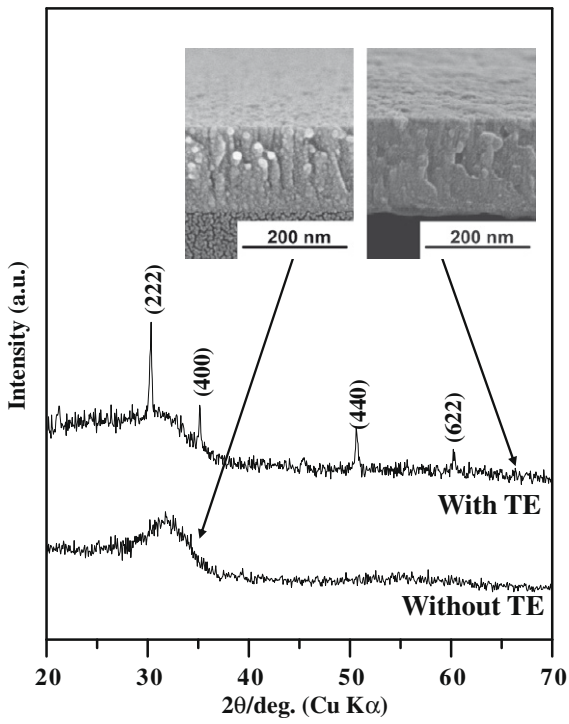

Fig. 3. X-ray diffraction patterns and cross sectional morphology (the inset) of ITO films deposited without and with TE.

Fig. 3 (inset) shows the corresponding SEM morphologies of the deposited ITO films without and with TE. The figure shows that the ITO film deposited without TE reveals a loosely packed feature while the ITO film deposited with TE exhibits a dense morphology. Intensified ion bombardment results in TE employment for a denser film. SEM observations agree with the result of XRD characterization.

3.2. Optical transmittance of the deposited ITO films

Table 2 presents the measured optical transmittance of ITO-coated specimens deposited without and with TE. The average optical transmittance in the 400–700 nm wavelength range is 70% and 83% respectively for the ITO films deposited without and with TE. Using TE obtains a significant transmittance increase of ITO film. For a thin film material, optical transmittance is governed by absorption, reflection and scattering, all of which depend on chemical composition, chemical bonding, crystal structure and discontinuities (impurities and defects). The ITO film, composed of indium, tin and oxygen atoms in a bixbyite structure [20], is a highly degenerated wide band gap semiconductor with band gap energy roughly between 3.5 and 4.3 eV. This results in high transmittance of ITO film in the visible region (1.7–3.1 eV). Unfortunately, defects including vacancies, line defects, grain boundaries, etc., exist in the deposited film. These discontinuities form scattering centers and are detrimental to film transparency. The higher transmittance observed for TE deposited film is attributed to fewer scattering effects and structural homogeneity resulting from a higher degree of crystallinity [21,22]. From the result of XRD characterization, improved optical transmittance for the film deposited with TE is attributed to an increased degree of film crystallinity.

3.3. Electrical resistivity of the deposited ITO films

Table 2 shows the electrical properties of ITO films deposited on PET substrates without and with TE. The ITO films deposited without and with TE have an electrical resistivity around 1.7×10^{-3} and $4.5 \times 10^{-4}\ \Omega$ cm, respectively. The ITO film deposited with TE also exhibits higher carrier concentration as well as a considerably higher carrier mobility. This demonstrates that TE employment favors the crystalline structure of the ITO film resulting in higher carrier concentration and mobility compared to the film deposited without TE. The higher carrier concentration is probably associated with a greater amount of Sn^{+4} activated as an effective donor in the crystalline structure; passive neutral Sn atoms are commonly found in amorphous ITO film [23]. With respect to the carrier mobility of the ITO film, previous reports [24,25] have discussed several electron scattering mechanisms that may influence the carrier mobility in the ITO thin film. These mechanisms include grain boundary scattering, ionized impurity scattering and neutral impurity scattering. The ITO film deposited with TE shares fewer extent of aforementioned carrier scattering events. However, it is believed that the enhanced carrier mobility of the ITO film deposited with TE predominantly governs the electrical resistivity of the deposited ITO film [26].

3.4. Adhesion of the deposited ITO films

Fig. 4 presents the SEM and optical microscopic (shown at the bottom-left corner) photographs of the ITO-coated PET specimens following the crosscut adhesion test. The darker regions in the SEM pictures are those of the delaminated ITO film whereas the lighter regions are those of the

Table 2
Optical transmittance and electrical properties of the ITO deposited specimen without and with TE.

Conditions	Average transmittance in 400–700 nm	Electrical property		
	T_{avg} (%)	ρ ($10^{-4}\Omega$ cm)	N (10^{20}/cm^3)	n (cm^2/V)
Without TE	70	17.0	5.1	5.9
With TE	83	4.6	7.5	18.1

ρ: Electrical resistivity, N: carrier concentration, μ: carrier mobility.

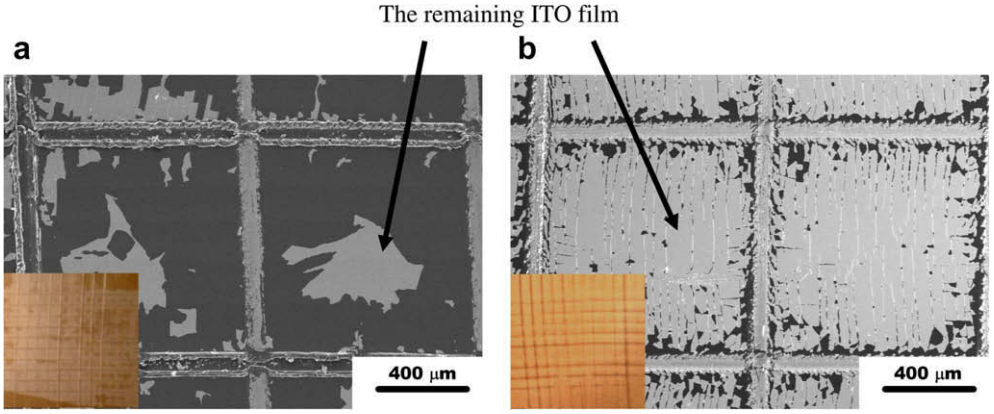

Fig. 4. SEM and optical microscopic photographs (insertion) of the ITO-coated PET specimens after crosscut film adhesion test (a) without and (b) with TE.

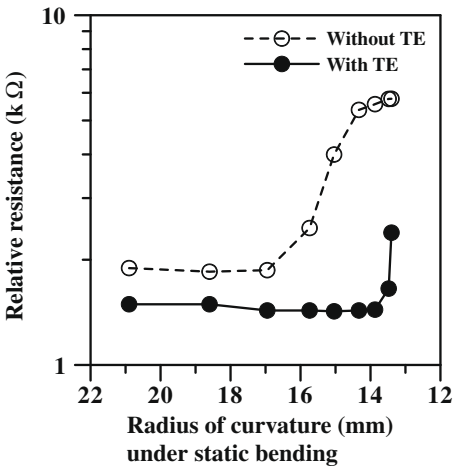

Fig. 5. Relative resistance as a function of bending radius of curvature for the ITO-coated PET specimens prepared without and with TE.

retained ITO film. Clearly, the ITO film deposited with TE, Fig. 4(b) was only damaged and delaminated in areas in which a shear force tore apart the ITO film and the PET substrate. In the remaining flat areas in Fig. 4(b), the ITO films remain on the PET surface but suffer from extensive parallel cracking. In contrast, either the flat regions or the shoulders of the scratch scars of ITO coatings on PET, presented in Fig. 4(a), were destroyed in the crosscut test. The adhesion classification of the ITO film deposited with TE and without TE is ASTM-4B and ASTM-0B, respectively, according to the ASTM standard [17]. The contribution to the increased film adhesion is debatable. The intensified ion bombardment, associated with TE supplement, apparently plays the role of removing surface contamination from the polymer substrate surface before the ITO coating is formed. Moreover, a substrate surface intensively bombarded with ions can be chemically activated and its surface wettability [27,28] physically increased, such that the initially grown film is strongly bonded to the substrate surface. However, thermal radiation generated by the TE filament may also increase the film adhesion by promoting the surface migration of adatoms. We therefore separately carried out an experiment by intentionally maintaining the substrate temperature at 90 °C (equivalent to the substrate temperature when TE is employed) when depositing ITO without using the TE technique. The result of the film adhesion test for the sample deposited without TE appears the same as those samples deposited at 50 °C without TE (no additional heating). This indicates that the additional thermal radiation effect of using TE to cause substrate temperature elevation to 90 °C did not show any observable influence on the film adhesion.

3.5. Mechanical bending durability of the deposited ITO films

Fig. 5 plots the result of static bending test on the ITO-coated PETs. The R_c values of ITO films deposited without and with TE are determined as 17.0 and 13.9 mm, respectively; above these values, the measured electrical resistance increases abruptly. This rapid increase in the electrical resistance of ITO film is caused by crack formation in the ITO films, which breaks the conduction path for the free carrier [29,30], shown in Fig. 6. The parallel cracks are formed in the ITO film deposited without TE, while the ITO film deposited with TE retains its integrity throughout the static bending test. Increased film adhesion by the TE supplement contributes to the increased bending resistance. Results of the static bending tests show that the TE supplement enables an ITO film that is deposited on the substrate to tolerate greater mechanical bending.

Fig. 7 plots the repeating dynamic bending test result of the ITO-coated PETs. The initial electrical resistance of an ITO film deposited without TE exceeds that of such a film deposited with TE. This result is consistent with the electrical resistivity measured using the Four-Point Probe, as presented in Table 2. A significant difference in electrical resistance between the ITO film deposited without and with TE is also found to be 10 kΩ. Electrical resistance value increases sharply from 3 to 10 kΩ in the case of the ITO deposited without TE, after the first 50 cycles. In contrast, the electrical resistance of ITO films deposited with TE does not observably change, even after over 1200 cycles. This finding indicates that the ITO film deposited with TE is more durable over mechanical bending cycles. The sharp increase in electrical resistance of the ITO film deposited without TE after the first 50 cycles is caused by rapid crack formation in the film, which releases bending stress. The roaming of free carriers in the ITO film drives the observed constant high electrical resistance. An ITO film that

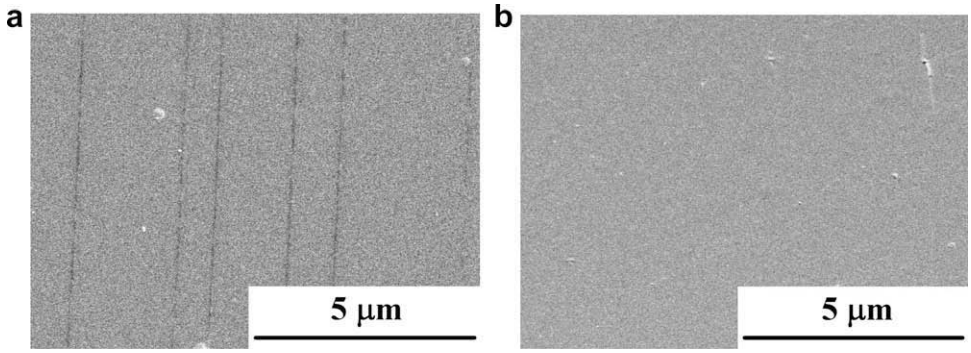

Fig. 6. SEM surface morphology of the ITO films deposited on PET substrates (a) without and (b) with TE after bending test.

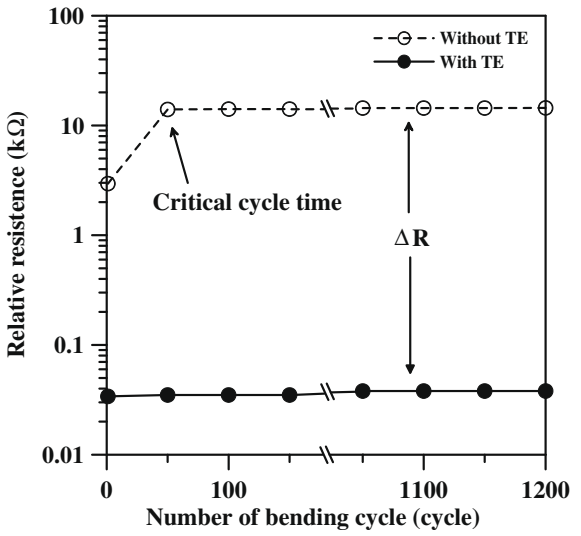

Fig. 7. Relative resistance as a function of bending cycle for the ITO-coated PET specimens deposited without and with TE.

strongly adheres to the PET substrate responds to repeated bending without cracking, retaining low electrical resistance through the test. Microscopically, the well-crystallized ITO film deposited with TE has a higher mechanical strength (than the amorphous ITO film deposited without TE), and thus better resists crack formation, and responds synergistically with the substrate because of strong film adhesion.

During dynamic bending, the electrical resistance and optical transmission of the deposited ITO film is also primarily concerned to resist. Fig. 8 shows the average transmittance of the ITO film deposited without and with TE through the dynamic bending test. The ITO-coated PET specimens prepared both without and with TE average transmittance value remain unchanged through the whole cyclic history, 70% and 83%, respectively. The only exception is that the transmittance of the ITO-coated PET specimens prepared without TE declines slightly after 800 cycles, perhaps because the substrate undergoes unrecoverable plastic deformation under the ITO coating after a certain number of cycles. The inset of the SEM image is Fig. 8 shows observations inside the crack of some fibers peeled off from the substrate matrix.

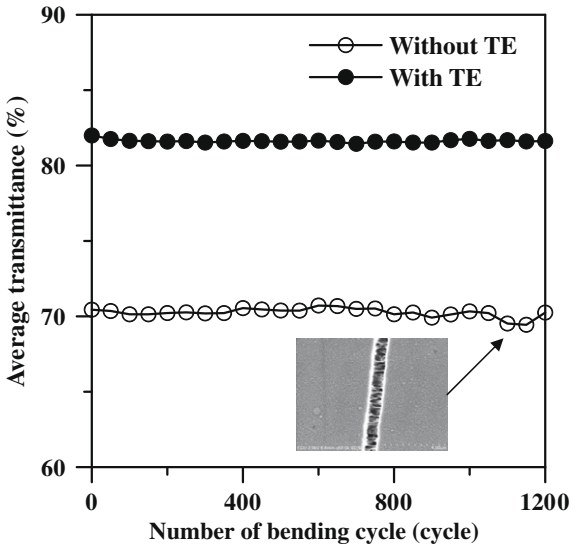

Fig. 8. Average optical transmittance of the ITO films deposited without and with TE as a function of bending cycle.

4. Conclusions

The current study involves the microstructure investigation of an ITO thin film, deposited on a flexible PET substrate by DC magnetron sputtering with thermionic emission enhancement. The microstructure explains enhanced durability of electrical and optical properties of the film under static and dynamic mechanical bending. The film deposited with TE has a higher average visible transmittance of 83%, compared to the ITO film deposited without the thermionic emission enhancement and a lower electrical resistivity of $4.5 \times 10^{-4}\,\Omega$ cm. A lower critical radius of curvature of 13.9 mm under static bending and a longer cycle time (over 1200 cycles) in the dynamic bending test are obtained in this study. In contrast, the ITO film deposited the without thermionic emission enhancement has an average optical transmittance of 70% and an electrical resistivity of $1.7 \times 10^{-3}\,\Omega$ cm. Its critical radius of curvature under static bending and the available cycle time in dynamic bending test are only 17.0 mm and fewer than 50 cycles, respectively. This work therefore concludes that thermionic emission enhancement not only enhances ITO film crystallinity for better optical transparency and electrical properties, but also significantly improves film adhesion on the PET substrate for stronger bending durability.

Acknowledgements

The authors appreciate Dr. Chin-Chiuan Guo in Chienkuo Technology University in Taiwan for generously offering four-point probe tester and Hall Effect measurement rig. This work was financial supported by the National Science Council of Taiwan under the grant NSC94-2216-E-035-004.

References

[1] S.H. Han, Y.H. Kim, S.H. Lee, M.H. Choi, J. Jang, D.J. Choo, Stable organic thin-film transistor in a pixel for plastic electronics, Org. Electron. 9 (2008) 1040–1043.
[2] C.G. Granqvist, A. Hultåker, Transparent and conducting ITO films: new developments and applications, Thin Solid Films 411 (2002) 1–5.
[3] S.K. Lee, N.S. Cho, J.H. Kwak, K.S. Lim, H.K. Shim, D.H. Hwang, C.J. Brabec, New low band-gap alternating polyfluorene derivatives for photovoltaic cells, Thin Solid Films 511–512 (2006) 157–162.
[4] S.K. Hau, H.L. Yip, J. Zou, A.K.Y. Jen, Indium tin oxide-free semi-transparent inverted polymer solar cells using conducting polymer as both bottom and top electrodes, Org. Electron. 10 (2009) 1401–1407.
[5] C. Guillen, J. Herrero, Comparison study of ITO thin films deposited by sputtering at room temperature onto polymer and glass substrates, Thin Solid Films 480 (2005) 129–132.

[6] M. Boehme, C. Charton, Properties of ITO on PET film in dependence on the coating conditions and thermal processing, Surf. Coat. Technol. 200 (2005) 932–935.
[7] C.J. Chiang, C. Winscom, S. Bull, A. Monkman, Mechanical modeling of flexible OLED devices, Org. Electron. 10 (2009) 1268–1274.
[8] M.C. Choi, Y. Kim, C.S. Ha, Polymers for flexible displays: from material selection to device applications, Prog. Polym. Sci. 33 (2008) 581–630.
[9] A.N. Banerjee, C.K. Ghosh, K.K. Chattopadhyay, H. Minoura, A.K. Sarkar, A. Akiba, A. Kamiya, T. Endo, Low-temperature deposition of ZnO thin films on PET and glass substrates by DC-sputtering technique, Thin Solid Films 496 (2006) 112–116.
[10] Z.W. Yang, S.H. Han, T.L. Yang, L. Ye, D.H. Zhang, H.L. Ma, C.F. Cheng, Bias voltage dependence of properties for depositing transparent conducting ITO films on flexible substrate, Thin Solid Films 366 (2000) 4–7.
[11] D. Kim, Influence of negative metal ion bombardment on the properties of ITO PET films deposited by dc magnetron sputtering, J. Non-Cryst. Solids 331 (2003) 41–47.
[12] Y. Hoshi, T. Kiyomura, ITO thin films deposited at low temperatures using a kinetic energy controlled sputter-deposition technique, Thin Solid Films 411 (2002) 36–41.
[13] Y.F. Lan, W.C. Peng, Y.H. Lo, J.L. He, Indium tin oxide films deposited by thermionic-enhanced DC magnetron sputtering on unheated polyethylene terephthalate polymer substrate, Mater. Res. Bull. 44 (2009) 1760–1764.
[14] D.R. Cairns, R.P. Witte II, D.K. Sparacin, S.M. Sachsman, D.C. Paine, G.P. Crawford, R.R. Newton, Strain-dependent electrical resistance of tin-doped indium oxide on polymer substrates, Appl. Phys. Lett. 76 (2000) 1425–1427.
[15] E. Fortunato, P. Nunes, A. Marques, D. Costa, H. Águas, I. Ferreira, M.E.V. sa Costa, M.H. Godinho, P.L. Almedia, J.P. Borges, R. Martins, Influence of the strain on the electrical resistance of zinc oxide doped thin film deposited on polymer substrates, Adv. Eng. Mater. 4 (2002) 610–612.
[16] Y. Leterrier, L. Boogh, J. Andersons, J.A.E. Mansons, Adhesion of silicon oxide layers on poly(ethylene terephthalate). 1. Effect of substrate properties on coating's fragmentation process, J. Polym. Sci. Pt. B – Polym. Phys. 35 (1997) 1449–1461.
[17] ASTM D3359, Standard test methods for measuring adhesion by Tape Test, American Society for Testing and Materials, 2002.
[18] ASTM D1593, Standard specification for nonrigid vinyl chloride plastic film and sheeting, American Society for Testing and Materials, 1999.
[19] P.F. Carcia, R.S. McLean, M.H. Reilly, Z.G. Li, L.J. Pillione, R.F. Messier, Influence of energetic bombardment onstress resistivity and microstructure of indium tin oxide films grown by radio frequency magnetron sputtering on flexible polyester substrates, J. Vac. Sci. Technol. A 21 (3) (2003) 745–751.
[20] D.R. Kammler, T.O. Mason, K.R. Poeppelmeier, Bulk phase relations conductivity, and transparency in novel bixbyite transparent conducting, J. Am. Ceram. Soc. 84 (2001) 1004–1009.
[21] Y. Hu, X. Diao, C. Wang, W. Hao, T. Wang, Effects of heat treatment on properties of ITO films prepared by rf magnetron sputtering, Vacuum 75 (2004) 183–188.
[22] D.S. Devi Amma1, V.K. Vaidyan, P.K. Manoj, Structural electrical and optical studies on chemically deposited tin oxide films from inorganic precursors, Mater. Chem. Phys. 93 (2005) 194201.
[23] H. Morikawa, M. Fujita, Crystallization and decrease in resistivity on heat treatment of amorphous indium tin oxide thin films prepared by dc Magnetron sputtering, Thin Solid Films 339 (1999) 309–313.
[24] H. Kim, C.M. Gilmore, A. Piqué, J.S. Horwitz, H. Mattoussi, H. Murata, Z.H. Kafafi, D.B. Chrisey, Electrical optical, and structural properties of indium-tin-oxide thin films for organic light-emitting devices, J. Appl. Phys. 86 (1999) 6451–6461.
[25] H.O. Lee, Electron scattering mechanisms in indium-tin-oxide thin films prepared at the various process conditions, Appl. Surf. Sci. 252 (2006) 3428–3435.
[26] J.S. Kim, J.W. Bae, H.J. Kim, N.E. Lee, G.Y. Yeon, K.H. Oh, Effects of oxygen radical on the properties of indium tin oxide thin films deposited at room temperature by oxygen ion beam assisted evaporation, Thin Solid Films 377 (2000) 103–108.
[27] Y. Nakamura, Y. Suzuki, Y. Watanabe, Effect of oxygen plasma etching on adhesion between polyimide films and metal, Thin Solid Films 290–291 (1996) 367–369.
[28] F. Sarto, M. Alvisi, E. Melissano, A. Rizzo, S. Scaglione, L. Vasanelli, Adhesion enhancement of optical coatings on plastic substrate via ion treatment, Thin Solid Films 346 (1999) 196–201.
[29] Y. Leterrier, L. Médico, F. Demarco, J.A.E. Månson, U. Betz, M.F. Escolà, M.K. Olsson, F. Atamny, Mechanical integrity of transparent conductive oxide films for flexible polymer-based displays, Thin Solid Films 460 (2004) 156–166.
[30] S.P. Gorkhali, D.R. Cairns, G.P. Crawford, Reliability of transparent conducting substrates for rollable displays: a cyclic loading investigation, J. Soc. Inform Display 12 (2004) 45–49.

Organic Electronics 11 (2010) 677–685

Contents lists available at ScienceDirect

Organic Electronics

journal homepage: www.elsevier.com/locate/orgel

The magneto conductance responses in polymer photovoltaic devices

Tsung-Hsun Lee [a], Bin Hu [b], Cheng-Lun Tsai [a], Ruei-Syuan Guan [c], Ten-Chin Wen [d], Tzung-Fang Guo [c,*], J.C.A. Huang [e,*]

[a] Department of Physics, National Cheng Kung University, Tainan 701, Taiwan
[b] Department of Materials Science and Engineering, University of Tennessee Knoxville, TN 37996, USA
[c] Institute of Electro-Optical Science and Engineering, Advance d Optoelectronic Technology Center, National Cheng Kung University, Tainan 701, Taiwan
[d] Department of Chemical Engineering, National Cheng Kung University, Tainan 701, Taiwan, ROC
[e] Department of Physics, Center for Micro/Nano Science and Technology, Institute of Innovations and Advanced Studies, National Cheng Kung University Tainan 701, Taiwan

ARTICLE INFO

Article history:
Received 9 September 2009
Received in revised form 7 January 2010
Accepted 8 January 2010
Available online 14 January 2010

Keywords:
Magneto conductance
Magneto resistance
Photovoltaics
Polymer
MC

ABSTRACT

This article studies the magneto conductance (MC) responses of regioregular poly(3-hexylthiophene) (P3HT)-based polymer photovoltaic devices. The net MC results of devices are the sum of the positive and negative MC effects. The positive MC effect is due to the increased population of the singlet polaron-pair (PP) states (of the high dissociation rate to charge carriers) under the magnetic field. The negative MC effect results from the decline on the triplet exciton–charge reactions to charge carriers (the mobility and concentration of triplet excitons are decreased by the magnetic field). The MC responses of P3HT-based photovoltaic devices can be manipulated by the applied magnetic field, the electrical bias, the built-in potential, and the interfacial dipole layer. An inversion in the MC response is observed at the electrical bias near the open-circuit voltage. In addition, blending of an electron acceptor material, [6,6]-phenyl C61-butyric acid methyl ester, in P3HT active layer quenches the photo-excited states at the donor–acceptor interface and results in distinct MC responses of photovoltaic cells, which probably are related to the features indicating the formation of inter-molecular charge–transfer complexes at donor–acceptor junction.
© 2010 Elsevier B.V. All rights reserved.

1. Introduction

Organic conjugated molecules/polymers have very unique properties [1–3], they can be used as organic semiconductors in fabricating novel electronic devices [4–9]. In addition, the electronic devices incorporating organic conjugated molecules/polymers as the active layers, exhibit strong magneto responses [10,11]. The output performance, such as the electroluminescence [10,12–14], resistance or conductance [10–16], and photocurrent [11,17–20] in organic/polymer diodes and photovoltaic (PV) cells can be modulated by the applied magnetic field, although the basic device configurations are composed of intrinsically non-magnetic components. The magneto responses of organic semiconductors would have new applications in organic electronics and spintronic devices. [21–24].

A large magneto resistance (MR) or magneto conductance (MC) response in organic/polymer light-emitting diodes (O/PLEDs) has been reported by many researchers, which is intimately associated with the threshold of light emission and the ambipolar injection of charge carriers [10,25]. While the organic/polymer diodes are operated at PV regime with illumination, the magnitude of photocurrent is varied with the applied magnetic field [11,17–20]. These results suggest that the dissociations and charge-reaction processes of the photo-excited states to the generation of free charge carriers are susceptible to changes by the applied magnetic field. The excited states, induced either electrically (in O/PLEDs) or optically (in PV

* Corresponding authors. Tel.: +886 6 2757575; fax: +886 6 2747995.
E-mail addresses: guotf@mail.ncku.edu.tw (T.-F. Guo), jcahuang@mail.ncku.edu.tw (J.C.A. Huang).

1566-1199/$ - see front matter © 2010 Elsevier B.V. All rights reserved.
doi:10.1016/j.orgel.2010.01.009

cells) in organic semiconductor layers, are essentially important to the MR or MC responses in organic/polymer diodes and PV cells [12,26–29].

The excited states (excitons) in the regioregular poly(3-hexylthiophene) (P3HT)-based polymer diodes are Coulombically bound electron–hole (e–h) pairs, commonly having a short range of the separation distance [27,30–33]. Those excitons may undergo a relaxation process to become the excited polaron-pairs (PP) states with a longer range of e–h separation distance than that of excitons. Fig. 1a illustrates the schemes for formation of intra- and inter-molecular excited PP states from excitons. Both the excitons and PP states are the excited states of conjugated organic molecules possessing singlet and triplet electronic configurations. The lifetime of the singlet and triplet PP states is shorter than that of the singlet and triplet exciton states [34,35]. The magnitude of exchange energy for the singlet/triplet excited states is exponentially decayed with respect to the e–h separation distance and is related to the energy difference between singlet and triplet states [30,31]. Accordingly, the status of the long-range (>1 nm) PP states having exchange energies of the order smaller than 10^{-3} meV is subjected to changes brought in by the applied magnetic field. Sakagughi et al. reported that the external magnetic field dependencies on the photodecomposition reaction in solution, which were attributed to the electronic Zeeman and hyperfine interactions in the intermediate radical pair [36]. The intersystem crossing process of singlet/triplet PP states as illustrated in Fig. 1b involves the spin orbital coupling (SOC) [37,38] and the hyperfine interaction (HFI) [19,27,39–41]. The population of singlet and triplet PP states can be modified by the external magnetic field, such as the changes of the splitting and difference of the energy states by Zeeman effect [19,27,28]. Since the photocurrent of P3HT-based diodes is the sum of "current flows" generated by the photo-excited states (excitons and PP states), any variations induced by an applied magnetic field on the distribution, dissociation, and charge-reaction processes of the singlet/triplet excited states (excitons and PP states) would certainly modulate the magnitude of photocurrent and MC response in PV devices [18,29]. In this manuscript, we studied how the change of the electrical bias and the device electrode influences the dissociation and charge-reaction processes of photo-excited states in P3HT-based polymer diodes. Increasing the applied magnetic field increases the distribution of singlet PP states and reduces the mobility of triplet excitons by Zeeman splitting [28,29]. The dissociation rate of the singlet PP states is higher due to the stronger ionic feature than that of triplet PP states, [19,42,43] which is accountable for an increase of free charge carriers and a positive MC effect. However, the decline of triplet exciton–charge reactions to charge carriers (reduce in mobility and concentration of triplet excitons), caused by the applied magnetic field [44–46], results in the decrease of free charge carriers and contributes to a negative MC effect. The net MC responses of the photovoltaic cells are the sum of positive and negative MC effects, in which the processes are schematically illustrated in Fig. 1c. Additionally, the MC responses are influenced by built-in electrical field of the diodes, which is tunable by varying the bias voltages

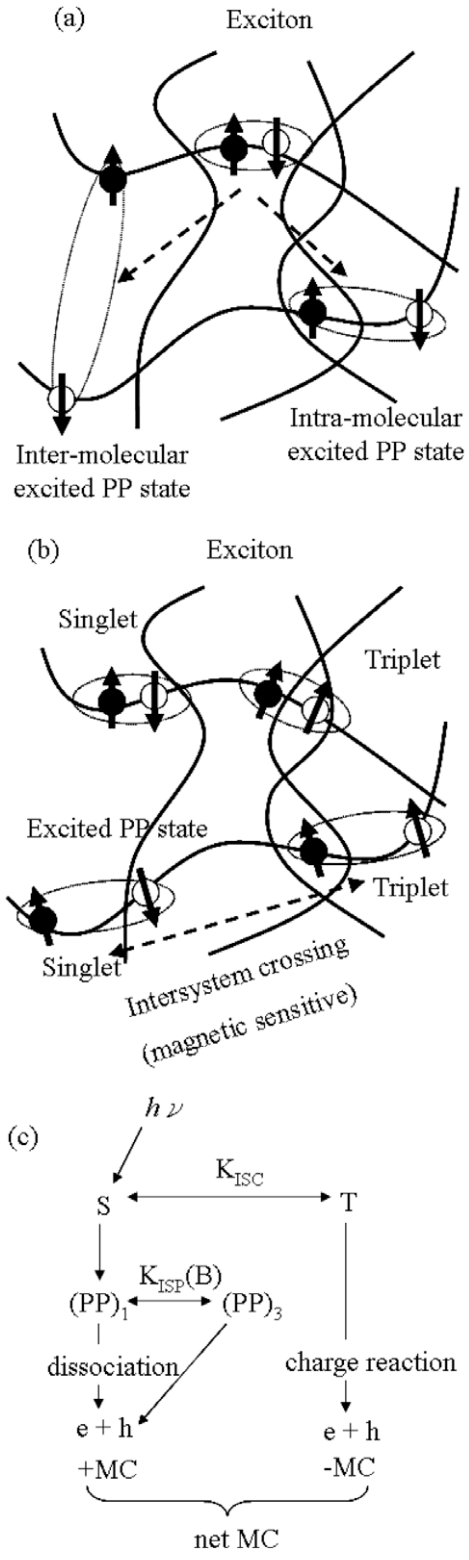

Fig. 1. (a) The formation of intra- and inter-molecular excited PP states from excitons. (b) The singlet and triplet electronic configurations of excitons and PP states. (c) A schematic drawing for the processes of the positive, negative and net MC responses. KISC represents the intersystem crossing process. KISP(B) represents the intersystem crossing process of PP state.

and the work function of electrodes. An inversion in MC response is observed at the electrical bias near the open-circuit voltage (V_{oc}). The magneto responses for inter-molecular charge–transfer complex states at the donor–acceptor interface are investigated by blending an electron acceptor material, [6,6]-phenyl C61-butyric acid methyl ester (PCBM), in P3HT as the active layer. The distinct MC features suggest the formation of inter-molecular charge–transfer complexes at donor–acceptor junction.

2. Experimental

The polymer diodes and photovoltaic devices are fabricated in a standard arrangement by sandwiching the active layer between a transparent electrode and a metal electrode. The transparent electrode is comprised of the cleaned indium–tin–oxide (ITO) covered glass substrate (RITEK Corp., 15 Ω/□) coated with poly (3,4-ethylenedioxythiophene) poly (styrenesulfonate) (PEDOT:PSS; Baytron P, Bayer AG, Germany) layer. Regioregular P3HT (98.5% electronic grade, Rieke Metals, Inc., USA) and PCBM (procured from Nano-C, USA) are dissolved in dichlorobenzene to yield the P3HT (20 mg/ml) and P3HT:PCBM (20:20 mg/ml) solutions. The active layers are obtained by spin-coating the solutions on the PEDOT:PSS/ITO/glass substrates at the drying process of the films in a slow-growth regime [47,48]. The thicknesses of P3HT and P3HT:PCBM films are approximately 160 ± 10 nm and 200 ± 10 nm, respectively [49]. Ca (40 nm) and Al (100 nm), as metal electrodes, are thermally deposited onto the surface of the active layer inside a vacuum chamber (4.0×10^{-6} h Pa).

A halogen lamp is used as the light source (80 mW/cm^2) to investigate the MC response of the photovoltaic cells in this study. The devices are encapsulated by the UV-curable epoxy with a cover glass and placed at the direction parallel

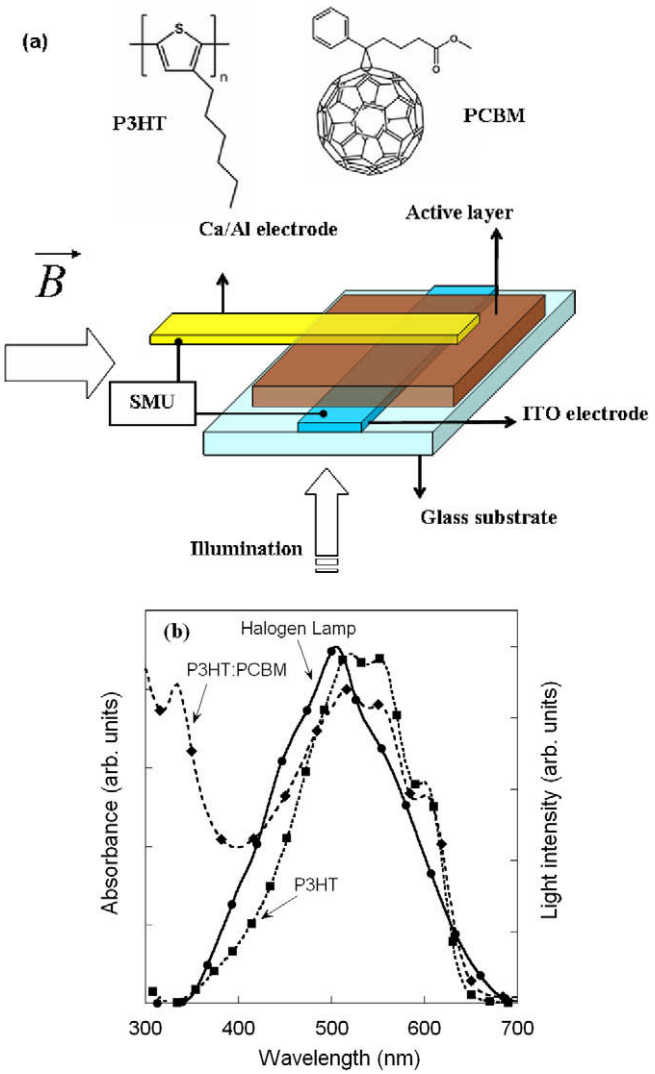

Fig. 2. (a) A schematic drawing that illustrates the device configuration, the measurement of MC responses for the polymer diodes under the applied magnetic field with illumination, and the chemical structures of P3HT and PCBM in this study. SMU represents the source measurement unit. (b) (●) The emission spectrum of halogen lamp and the absorption spectra of (■) P3HT and (♦) P3HT:PCBM films used in this studies.

to the magnetic field. In order to eliminate the influence due to drifting with different bias voltages, the MC curves are averaged, based on the approach reported by Desai et al. [13]. The MC magnitude presented in this manuscript is defined as;

$$\mathrm{MC} = \frac{\Delta I(B)}{I(0)} = \frac{I(B) - I(0)}{I(0)} \quad (1)$$

Where $I(B)$ and $I(0)$ are the current intensity of the photovoltaic cells with and without the applied magnetic field, respectively. All the measurements are performed at room temperature. The magneto conductance of polymer diodes in our study is found to be independent of external magnetic field's direction [20]. The schematic drawings of the device configuration, the measurement of MC responses for polymer diodes under the applied magnetic field with illumination, and the chemical structures of P3HT and PCBM in this study are illustrated in Fig. 2a and b presents the emission spectrum of halogen lamp and the absorption spectra of P3HT and P3HT:PCBM films used in this studies. The spectrum overlap are high for the emission of the halogen lamp and absorbance of P3HT and P3HT:PCBM films.

3. Result and discussion

3.1. Effect of applied magnetic field and device electrodes on MC responses

Fig. 3 presents the measured MC of the short-circuit current (I_{sc}, photocurrent measured at 0 V bias voltage) for devices with the configurations of ITO/PEDOT:PSS/P3HT/Al (P3HT/Al-device) and ITO/PEDOT:PSS/P3HT/Ca/Al (P3HT/Ca-device) with illumination. MC response of the I_{sc} for P3HT/Al-device is positive and sharply increased from 0% to 0.8% in the low magnetic field (<30 mT) and then gradually decreased as the applied magnetic field is increased. The MC of P3HT/Al-device is reduced to zero and inversed from positive to negative at the applied magnetic field near $B \sim 150$ mT, and is of $\sim -1.4\%$ at $B = 900$ mT. The positive

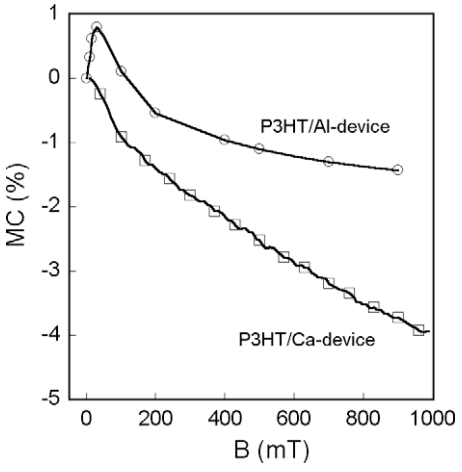

Fig. 3. MC curves of the I_{sc} (photocurrent measured at 0 V bias voltage) for P3HT/Al-device (○) and P3HT/Ca-device (□) with illumination by a halogen lamp (white light) at the intensity of 80 mW/cm^2.

and negative MC response of the I_{sc} for P3HT/Al-device is modulated by the applied magnetic field.

As illustrated in Fig. 1c, the singlet excitons (S) can dissociate into inter-molecular singlet PP states ($(PP)_1$) due to their lower binding energies towards the generation of photocurrent as compared to that of triplet excitons (T). The singlet PP states ($(PP)_1$) can partially convert into triplet PP states ($(PP)_3$) through the intersystem crossing process. Excitons and PP states in singlet and triplet configurations can be involved in the dissociation and charge-reaction processes to generate the photocurrent. In PP states, an external magnetic field can cause an external Zeeman splitting on triplet states and thus change the intersystem crossing if the external Zeeman splitting is greater than the internal Zeeman splitting. This suggests that an external magnetic field can increase the singlet/triplet population ratio in inter-molecular excited states (PP states) [50].

Kalinowski et al. reported the dissociation rates are different for singlet and triplet PP states ($k1 \gg k3$) due to the fact that singlet PP state has a stronger ionic character than triplets and therefore singlet PP states are stronger coupled with the ionic reaction products of separated holes and electrons [19]. Tandon et al. suggested both the original pair of polarons and the singlet exciton state are ionic in nature, whereas the triplet exciton is covalent [43,51]. Accordingly, the singlet PP states have higher dissociation rate than that of triplet PP states is reasonably assumed in our work.

Xu et al. also suggested that a low magnetic field (<30 mT) usually affects the formation rate of singlet/triplet PP states at the relaxation process of photo-excited excitons [18,29]. The increased distribution of singlet PP states by the applied magnetic field raises the I_{sc} (singlet PP states have a relatively higher dissociation rate for converting into free charge carriers than that of triplet PP states) [19,28], and contributes to a positive and sharply elevated MC response in the low magnetic field for P3HT/Al-device.

Although the initial excited states in P3HT by photo illumination are singlet based on the selection rule, the singlet excited states can be partially converted into triplet excited state through intersystem crossing caused by internal magnetic interaction from SOC and HFI. Both singlet and triplet excitons can exist in P3HT active layer under the illumination. The densities of triplet exciton of P3HT under illumination are about 77% as reported by Burrows et al. [52] for the study of $S1 \sim > T1$ intersystem crossing in pi-conjugated organic polymers. It is noticed that there is no heavy atoms in the system.

As the applied magnetic field is gradually increased, the decrease of triplet exciton–charge reactions causes a simultaneous reduction in the I_{sc} and accounts for a negative MC response. The exciton–charge reaction is essentially Coulombic interaction between an excited state and a trapped or free charge carrier [53,54]. The studies of phosphorescence and delayed fluorescence quenching effect indicate that the excitons can interact with trapped charge carriers to de-trap the charge carriers. [44,55,56] Alternatively, the triplet excitons can react with free charge carriers in organic materials to dissociate the

electron–hole pairs. [45,57] However, a magnetic field can decrease the reaction-rate constant by removing the triplet degeneracy and deducing the triplet mobility due to the external Zeeman splitting [26,28,39,55]. The triplet exciton–charge reactions can be decreased with magnetic field and yield a negative component in MC effect. Although the exciton–charge reactions of both singlet and triplet excitons can contribute the device current, the influence of the applied magnetic field on the exciton–charge reaction of the triplet excitons is more apparent, probably due to their longer diffusion length and sufficient contacts with charge carriers than those singlet excitons. It is assumed that the change on the exciton–charge reaction of the singlet excitons by the magnetic field is not comparable to that of the triplet excitons. The triplet exciton–charge reactions are decreased with magnetic field and yield a negative component in MC effect. The other possibility of the negative MC effect on I_{sc} is a reduction in the initial concentration of triplet excited states. An external magnetic field can increase singlet/triple population ratio in intermolecular excited states (PP states) by reducing the intersystem crossing within PP states [50], that would lead to a decrease in the population of triplet PP states and consequently in the concentration of triplet excitons. As a result, the current due to the exciton–charge reaction of triplet excitons should be decreased and contributed to the negative MC effect on I_{sc}. The magnetic field dependence of the I_{sc} for P3HT/Al-device can be attributed to the tradeoff between the distribution and dissociation of the singlet PP states (positive MC response) with the changes on the triplet exciton–charge reactions to charge carriers (negative MC response) under the influence of applied magnetic field.

While the Ca is used instead of Al as the metal electrode for P3HT-based polymer diode, the MC curve of P3HT/Ca-device is negatively increased with the applied magnetic field (unlike that of P3HT/Al-device), as show in Fig. 3. Since the interfacial barrier height at the polymer/metal junction is reduced by the low work function Ca electrode, P3HT/Ca-device has a better polymer/metal interface for the generation and collection of charge carriers than that of P3HT/Al-device, as applied for photovoltaic cells [58,59]. Alternatively, the high built-in potential of P3HT/Ca-device would accelerate the dissociation of the polaron-pair states in P3HT layer without the magnetic field that would improve the charge extraction. (The magnitudes of V_{oc} are ~0.25 and ~1.01 V for P3HT/Al-device and P3HT/Ca-device, respectively.) Noted that MC effect is defined by the current ratio with and without the magnetic field. The improvement of the charge extraction without the magnetic field did not contribute the MC response. Since most of the polaron-pair states probably are dissociated due to the higher built-in electrical field in P3HT/Ca-device, the exciton–charge reactions of triplet excitons would be the dominated mechanism. The charge reaction of triplet excitons are reduced as the applied magnetic field is increased, which decreases the overall photocurrent and hence results in net negative MC responses. The MC of P3HT/Ca-device is of ~−4.0% in an applied magnetic field of B = 1000 mT.

The devices with the configuration of ITO/PEDOT:PSS/P3HT/LiF/Ca/Al (P3HT/LiF/Ca-device) are also fabricated to investigate the influence of the additional dipole layer at P3HT/Ca interface on MC responses. Fig. 4 illustrates the MC curves of the I_{sc} for P3HT/LiF(X nm)/Ca-device with varied thicknesses of LiF layers. The measured MC responses of I_{sc} in an applied magnetic field of B = 1000 mT are of ~−4.0%, −2.9%, and −2.3% for P3HT/LiF(X nm)/Ca-device of X = 0, 1.5, and 5.0 nm, respectively. The magnitudes of MC responses decrease with increasing thickness of LiF layer. These results suggest that the additional dipole layer (LiF) functions as an electrical dipole field to accelerate the dissociation of the photo-excited states near (or diffused to) the polymer/metal junction, but lower the influence of the applied magnetic field on the triplet excitons. The inset of Fig. 4 presents the thickness of LiF layer versus MC response at B = 1000 mT and I_{sc} plots. The magnitudes of I_{sc} are increased with the thickness of interfacial dipole layer, which are of 0.007, 0.023, and 0.076 mA/cm^2 for P3HT/LiF(X nm)/Ca-device of X = 0, 1.5, and 5.0 nm, respectively, and are associated with the decreased magnitude of MC responses. The interaction of the photo-excited states with electrodes is important to determine the magnitude of I_{sc} and MC responses of P3HT-devices in our studies. Recent publications by Kalinowski et al. and Lei et al. had reported the photocurrent and device current are partially contributed by the exciton-induced injection of electrons [60,61]. MC responses of tri(8-hydroxyquinoline) aluminum (Alq3)-based diodes are possibly due to the magnetic field modulation of the stream of singlet excitons reaching the cathode as proposed by Kalinowski et al. [50].

3.2. The effect of electrical bias on MC responses

Fig. 5a presents the MC curves of P3HT/Ca-device with illumination at various bias voltages. The MC responses are of ~−4.0% for the P3HT/Ca-device biased at 0.00 and 0.50 V in an applied magnetic field of B = 1000 mT, and they significantly increase to ~−6.2% and ~−23.0% when

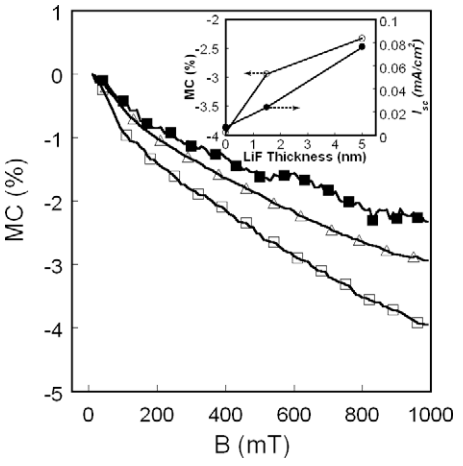

Fig. 4. MC curves of the I_{sc} (photocurrent measured at 0 V bias voltage) with illumination by a halogen lamp (white light) at the intensity of 80 mW/cm^2 for P3HT/LiF(X nm)/Ca-device at B = 1000 mT of X = (□) 0, (△) 1.5, and (■) 5.0. The inset presents the thickness of LiF layer versus (○) MC response at B = 1000 mT and (●) I_{sc} plots.

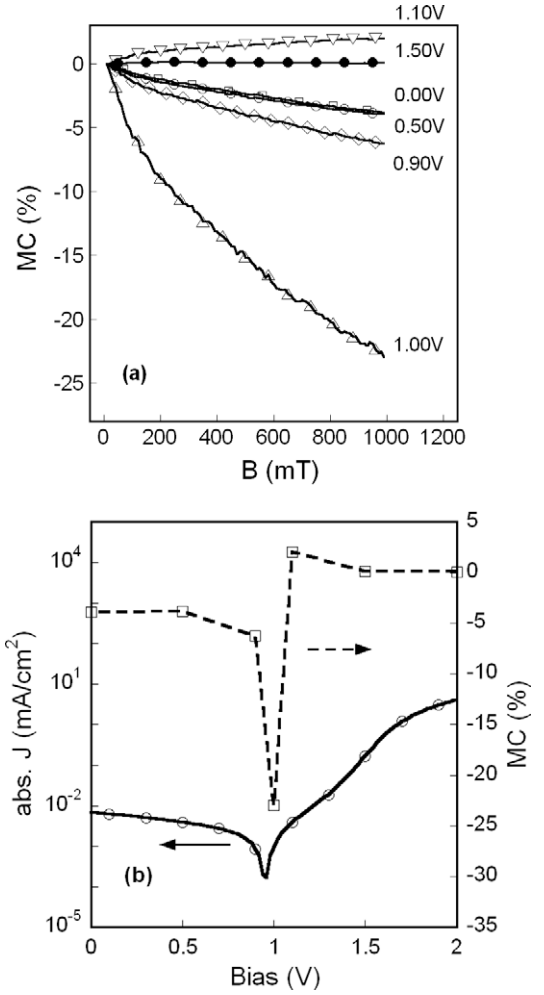

Fig. 5. (a) MC curves of P3HT/Ca-device with illumination by a halogen lamp (white light) at the intensity of 80 mW/cm^2 in the bias voltages of 0 V (○), 0.50 V (□), 0.90 V (◇), 1.00 V (△), 1.10 V (▽), and 1.50 V (●), (b). MC curve (□) of the P3HT/Ca-device with illumination versus bias voltage at B = 1000 mT and semi-logarithm current–voltage (J–V) plot (○).

the devices are biased at 0.90 and 1.00 V, respectively. However, the MC response is reversed from negative (∼−23.0% at 1.00 V) to positive (∼2.0% at 1.10 V) as the bias voltage was raised to 1.10 V and is almost vanished (<0.1%) at a bias voltage that exceeds 1.50 V. Fig. 5b plots the MC curve of the P3HT/Ca-device with illumination versus bias voltage and semi-logarithm current–voltage (J–V) plot at B = 1000 mT. The inversion of the MC curve is found at the bias voltage close to the V_{oc} in the semi-logarithm J–V plot.

The photo-excited states in P3HT active layer are the Coulombically bound e–h pairs. The Coulombic interaction of those excited e–h pairs is varied with the separation distance and is subjected to change with magnitude and direction of the internal (built-in electrical field: difference in the work function of two electrodes) and external (the applied bias) electrical fields. As the applied bias voltage of P3HT/Ca-device approaches V_{oc}, the influence of the built-in electrical field on the Coulombically bound e–h pairs is minimized, because the built-in electrical field is offset by the applied electrical bias (V–$V_{oc} \sim 0$). The internal and external electrical fields are of opposite directions at the bias regime in which the applied voltage is lower than the V_{oc}. As a result, the denominator $I(0)$ in Eq. (1) is nearly zero as the bias voltage approaches V_{oc}. Therefore, a drastic MC response (negative) as calculated by Eq. (1) at an applied bias voltage close to V_{oc} is observed as shown in Fig. 5a and b. However, the influence of the applied magnetic field on the I_{sc} at the electrical bias approaches V_{oc} should also be considered as a factor for the significant increase of MC responses. Noted that it requires the very delicate control to precisely measure the current (very small magnitude) at the effective electrical field of the device down to zero (V–$V_{oc} \sim 0$). The $I(0)$ and $I(B)$ for P3HT/Ca-device biased at the voltages, 0.90 and 1.00 V (very close, but not equal to V_{oc}), are of -8.51×10^{-4} and -7.98×10^{-4} mA/cm^2, 9.28×10^{-4} and 7.15×10^{-4} mA/cm^2, respectively. Although the device current at the bias voltage very close to the V_{oc} is small, the finite differences, $I(B) - I(0)$, of -0.53×10^{-4} and -2.13×10^{-4} mA/cm^2 correspond to the −6.2% and −23.0% of MC responses for the device biased at 0.90 and 1.00 V, respectively. These results probably suggest that the MC responses at the bias voltage close to V_{oc} (the effective voltage $V - V_{oc} \sim 0$) would be determined by the influence of the applied magnetic field on the photo-excited states, in which the mechanism for the decrease in exciton–charge reactions of the triplet excitons are eminent as mentioned in the previous paragraph and thus results in the maximum (negative) MC responses.

The injection of charge carriers occurs at the bias voltage larger than V_{oc}. Firstly, $I(0)$ is exponentially increased in this bias regime. Secondly, the excited states in P3HT active layer should include the electrical-induced excitons and PP states from the recombination of the injected and oppositely-charged carriers. Thirdly, the Coulombic interactions of those excited (photo- and electrical-induced) states may be reduced (or the average intercarrier distance of excited states is changed) by the external electrical field at the bias voltage larger than the V_{oc}, which affects strongly the energy gap between the singlet and triplet excited state and influences the mixing of the spin states. The increased distribution of singlet PP states under the influences of the magnetic field at the bias voltage larger than the V_{oc} probably contributes a positive MC response. The MC curve is positively increased and inversed from ∼−23.0% at 1.00 V to ∼2.0% at 1.10 V when B = 1000 mT. However, the MC response is almost suppressed as the current densities or bias voltages increase. This result can be interpreted by the current generated due to the formation and dissociation of excited states under the influence of external magnetic field only and accounts for a relatively small amount of the total current density. The denominator $I(0)$ is exponentially increased at the bias voltage larger than V_{oc}, which is responsible for a relatively small MC response based on the calculation in the Eq. (1). The above summaries fortify the assumption that the measured MC is basically associated with the interaction of excited states with the applied magnetic field and electrical bias.

3.3. Features of inter-molecular charge–transfer complexes on MC responses

Fig. 6 illustrates the MC curves of P3HT/Ca-device and P3HT:PCBM/Ca-device at the applied bias voltage, 2.00 and 0.70 V, respectively, larger than its V_{oc} without illumination. For the P3HT/Ca-device, a positively increased MC response is observed at the low magnetic field ($B < \sim 200$ mT), which is associated with the dissociation of electrical-excited PP states from the injected charge carriers (without illumination and the bias voltage large than V_{oc}) as facilitated by the applied electrical and magnetic field. However, the influence from the applied electrical and magnetic field on the total current density of P3HT/Ca-device reaches a saturated level at $B > \sim 400$ mT. Further increasing the applied magnetic field above ~400 mT did not enlarge the MC response and account for a flat MC curve as shown in Fig. 6.

Blending an electron acceptor, (PCBM), with P3HT as the active layer (a bulk-heterojunction conjugated system) effectively causes the charge separation of the excited states at the donor–acceptor (P3HT-PCBM) interface and therefore markedly changes the MC responses as illustrated in Fig. 6. The MC curve of P3HT:PCBM/Ca-device without illumination is almost inhibited (showing a flat line close to zero) at the low magnetic field from 0 to ~180 mT, but is positively increased with the applied magnetic field at $B > \sim 180$ mT. The observation of MC curves for the P3HT:PCBM/Ca-device in Fig. 6 confirms very well the characteristic features for the existence of the inter-molecular charge–transfer complexes at the donor–acceptor interface [29]. The dissociation of the inter-molecular charge–transfer complexes is interrupted by the strong Coulmbic interactions in donor–acceptor molecules at the low magnetic field. Therefore, the MC curve is almost zero and has a threshold of increase at $B \sim 180$ mT. The increased distribution of singlet inter-molecular charge–transfer complexes states due to the magnetic field dependent intersystem crossing by the applied magnetic field ($B > 180$ mT) raises the I_{sc} through the dissociation of singlet charge–transfer complex, which are responsible for the positively increased MC response of P3HT:PCBM/Ca-device.

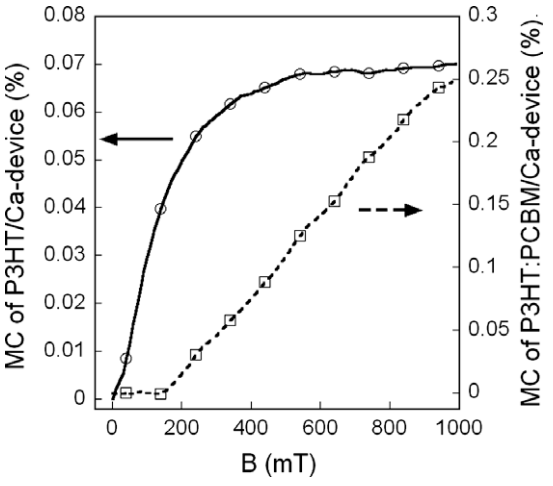

Fig. 6. MC curves of P3HT/Ca-device (○) and P3HT:PCBM/Ca-device (□) at the applied bias voltage, 2.00 and 0.70 V, respectively, larger than its V_{oc} without illumination.

Fig. 7a presents the MC curves of P3HT:PCBM/Ca-device with illumination at various bias conditions. Fig. 7b plots the MC curve of the P3HT:PCBM/Ca-device with illumination versus bias voltage and semi-logarithm J–V plot at $B = 1000$ mT. The MC curves presented in both the Figs. 7a and b have sharply increased (negatively) and inversed MC responses at the bias voltages near the V_{oc}. However, the magnitude of MC response for P3HT:PCBM/Ca-device is relatively low (<0.1%) as compared to that of P3HT/Ca-device (Fig. 5) at the applied bias lower than the V_{oc} (~0.59 V for P3HT:PCBM/Ca-device). This observation can be interpreted in terms of quenching most of the

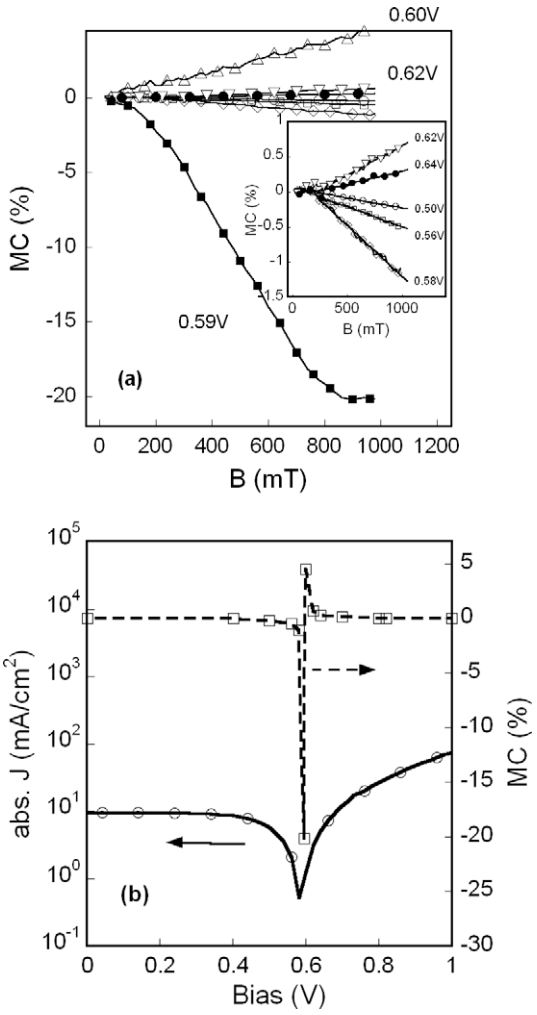

Fig. 7. (a) MC curves of P3HT:PCBM/Ca-device with the illumination by a halogen lamp (white light) at the intensity of 80 mW/cm^2 at bias voltages of 0.50 V (○), 0.56 V (□), 0.58 V (◇), 0.59 V (■), 0.60 V (△), 0.62 V (▽) and 0.64 V (●). The inset shows the MC curves at enlarged scale at the biased voltages of 0.50 V (○), 0.56 V (□), 0.58 V (◇), 0.62 V (▽) and 0.64 V (●). (b) MC curve (□) of the P3HT:PCBM/Ca-device with illumination versus bias voltage at $B = 1000$ mT and semi-logarithm current–voltage (J–V) plot (○).

photo-excited excitons and PP states (magnetic-sensitive) by the separation of oppositely-charged carriers at the P3HT-PCBM (donor–acceptor) interface. Consequently, the P3HT:PCBM/Ca-device has the low MC responses at the bias voltages lower than the V_{oc}. Nevertheless, the observed MC responses at $V < V_{oc}$ are negative and increased negatively with the applied magnetic field. We suggest that the negative MC responses are due to the reduced charge reactions of excitons in P3HT-PCBM/Ca-device by the applied magnetic field, in which the excitons probably are generated by the back transfer of the charge–transfer complex states at the high magnetic field. However, this assumption needs more investigations in detail. The sharply increased (negatively) MC response at bias voltage of 0.59 V in Figs. 7a and b is suggested to be due to the drastic reduction of the denominator $I(0)$ in Eq. (1), which is nearly zero at the bias voltage close to V_{oc}. The inset of Fig. 7a shows the MC curves at the enlarged scale as the biased voltages are nearby V_{oc}. Those curves have a threshold of MC response at the low magnetic field and are increased negatively or positively at the high magnetic field, which are associated with the presence of inter-molecular charge–transfer complexes in the donor–acceptor interface as discussed in the previous paragraph.

4. Conclusions

In conclusion, the mechanisms to interpret the MC responses for polymer photovoltaic devices made of P3HT and P3HT:PCBM as the active layers are presumably correlated with the influence of the applied magnetic filed and electrical bias on the photo- and electrical-excited states (excitons and PP states) and inter-molecular charge–transfer complexes of conjugated molecules. Our results have indicated that the MC responses can be modulated to yield positive, negative, and/or inverse effects by the photo illumination, the usage of different metal electrodes, interfacial dipole layer, the applied magnetic field and electrical bias, and the composition of polymer active layers. We regard the studies to change the excitation light intensity and wavelength would be essential to verify the origin of the device current (injected or photo-induced) in organic/polymer photovoltaic devices and further understand the mechanisms of MC responses [62]. This part of research is important and in progress at this time. As for P3HT:PCBM-based bulk-heterojunction photovoltaic cells, the charge–transfer complexes would be the critical excited states to influence the overall power conversion efficiency. The magnitude of photocurrent as well as the device performance can be further improved, if the dissociation of inter-molecular charge–transfer complexes is facilitated, probably by manipulating and optimizing the bulk-heterojunction and the polymer/electrode interfaces. The studies to understand the inter-molecular charge–transfer complex states in the active layer under the influence of applied magnetic field are currently underway.

Acknowledgments

The author Guo would like to thank the National Science Council (NSC) of Taiwan NSC96-2113-M-006-009-MY3, the Asian Office of Aerospace Research and Development (AOARD-09-4055), and NCKU Landmark project for financially supporting this research. The author Huang is grateful for the financial support from NSC under grant NSC96-2120-M-006-001.

Reference

[1] D. Braun, A.J. Heeger, Appl. Phys. Lett. 58 (1991) 1982.
[2] G. Yu, J. Gao, J.C. Hummelen, F. Wudl, A.J. Heeger, Science 270 (1995) 1789.
[3] A. Dodabalapur, H.E. Katz, L. Torsi, R.C. Haddon, Science 269 (1995) 1560.
[4] J. Kalinowski, J. Phys. D: Appl. Phys. 32 (1999) R179.
[5] L.S. Huang, C.W. Tang, M.G. Mason, Appl. Phys. Lett. 70 (1997) 152.
[6] S. Günes, H. Neugebauer, N.S. Sariciftci, Chem. Rev. 107 (2007) 1324.
[7] S.H. Li, Z. Xu, L. Ma, C.W. Chu, Y. Yang, Appl. Phys. Lett. 91 (2007) 083507.
[8] H. Sirringhaus, Adv. Mater. 17 (2005) 2411.
[9] T.H. Lee, J.C.A. Huang, G. L'vovich Pakhomov, T.F. Guo, T.C. Wen, Y.S. Huang, C.C. Tsou, C.T. Chung, Y.C. Lin, Y.J. Hsu, Adv. Funct. Mater. 18 (2008) 3036.
[10] Ö. Mermer, G. Veeraraghavan, T.L. Francis, Y. Sheng, D.T. Nguyen, M. Wohlgenannt, A. Köhler, M.K. Al-Suti, M.S. Khan, Phys. Rev. B 72 (2005) 205202.
[11] P. Desai, P. Shakya, T. Kreouzis, W.P. Gillin, Phys. Rev. B 76 (2007) 235202.
[12] J. Kalinowski, M. Cocchi, D. Virgili, V. Fattori, P. Di Marco, Phys. Rev. B 70 (2004) 205303.
[13] P. Desai, P. Shakya, T. Kreouzis, W.P. Gillin, N.A. Morley, M.R. Gibbs, J. Phys. Rev. B 75 (2007) 094423.
[14] F.J. Wang, H. Bässler, Z.V. Vardeny, Phys. Rev. Lett. 101 (2008) 236805.
[15] J.D. Bergeson, V.N. Prigodin, D.M. Lincoln, A.J. Epstein, Phys. Rev. Lett. 100 (2008) 067201.
[16] F.L. Bloom, W. Wagemans, M. Kemerink, B. Koopmans, Phys. Rev. Lett. 99 (2007) 257201.
[17] E. Frankevich, A. Zakhidov, K. Yoshino, Y. Maruyama, K. Yakushi, Phys. Rev. B 53 (1996) 4498.
[18] Z. Xu, B. Hu, J. Howe, J. Appl. Phys. 103 (2008) 043909.
[19] J. Kalinowski, J. Szmytkowski, W. Stampor, Chem. Phys. Lett. 378 (2003) 380.
[20] T.H. Lee, T.F. Guo, J.C.A. Huang, T.C. Wen, Appl. Phys. Lett. 92 (2008) 153303.
[21] Z.H. Xiong, D. Wu, Z.V. Vardeny, J. Shi, Nature 427 (2004) 821.
[22] M.N. Baibich, J.M. Broto, A. Fert, F.N. Van Dau, F. Petroff, P. Eitenne, G. Greuzet, A. Friederich, J. Chazelas, Phys. Rev. Lett. 61 (1988) 2472.
[23] G. Binasch, P. Grünberg, F. Saurenbach, W. Zinn, Phys. Rev. B 39 (1989) 4828.
[24] D. Chiba, M. Yamanouchi, F. Matsukura, H. Ohno, Science 301 (2003) 943.
[25] P. Desai, P. Shakya, T. Kreouzis, W.P. Gillin, J. Appl. Phys. 102 (2007) 073710.
[26] U.E. Steiner, T. Ulrich, Chem. Rev. 89 (1989) 51.
[27] E.L. Frankevich, A.A. Lymarev, I. Sokolik, F.E. Karasz, S. Blumstengel, R.H. Baughman, H.H. Hörhold, Phys. Rev. B 46 (1992) 9320.
[28] B. Hu, Y. Wu, Nature Mater. 6 (2007) 985.
[29] Z. Xu, B. Hu, Adv. Funct. Mater. 18 (2008) 2611.
[30] A. Kadashchuk, A. Vakhnin, I. Blonski, D. Beljonne, Z. Shuai, J.L. Brédas, V.I. Arkhipov, P. Heremans, E.V. Emelianova, H. Bässler, Phys. Rev. Lett. 93 (2004) 066803.
[31] G.D. Scholes, G. Rumbles, Nature Mater. 5 (2006) 683.
[32] H. Ohkita, S. Cook, Y. Astuti, W. Duffy, S. Tierney, W. Zhang, M. Heeney, I. McCulloch, J. Nelson, D.D.C. Bradley, J.R. Durrant, J. Am. Chem. Soc. 130 (2008) 3030.
[33] A.P. Monkman, H.D. Burrows, L.J. Hartwell, L.E. Horsburgh, I. Hamblett, S. Navaratnam, Phys. Rev. Lett. 86 (2001) 1358.
[34] H. Ohkita, S. Cook, Y. Astuti, W. Duffy, S. Tierney, W. Zhang, M. Heeney, I. McCulloch, J. Nelson, D.D.C. Bradley, J.R. Durrant, J. Am. Chem. Soc. 130 (2008) 3031.
[35] J.G. Müller, U. Lemmer, J. Feldmann, U. Scherf, Phys. Rev. Lett. 88 (2002) 147401.
[36] Y. Sakaguchi, H. Hayashi, S. Nagakura, Bull. Chem. Soc. Jpn. 53 (1980) 39.
[37] Y. Sheng, T.D. Nguyen, G. Veeraraghavan, Ö. Mermer, M. Wohlgenannt, Phys. Rev. B 75 (2007) 035202.
[38] Y. Wu, Z. Xu, B. Hu, J. Howe, Phys. Rev. B 75 (2007) 035214.

[39] V. Ern, R.E. Merrifield, Phys. Rev. Lett. 21 (1968) 609.
[40] R.P. Groff, R.E. Merrifield, A. Suna, P. Avakian, Phys. Rev. Lett. 29 (1972) 429.
[41] I.S. Kaulach, E.A. Silinsh, Phys. Stat. Sol. (b) 75 (1976) 247.
[42] M. Wohlgenannt, Z.V. Vardeny, J. Phys.: Condens. Matter 15 (2003) R83.
[43] K. Tandon, S. Ramasesha, S. Mazumdar, Phys. Rev. B 67 (2003) 045109.
[44] J. Levinson, S.Z. Weisz, A. Cobas, A. Rolon, J. Chem. Phys. 52 (1970) 2794.
[45] W. Helfrich, Phys. Rev. Lett. 16 (1966) 401.
[46] H. Killestreiter, H. Baessler, Chem. Phys. Lett. 11 (1971) 411.
[47] G. Li, V. Shrotriya, J. Huang, Y. Yao, T. Moriarty, K. Emery, Y. Yang, Nature Mater. 4 (2005) 864.
[48] T.F. Guo, T.C. Wen, G.L. Pakhomov, X.G. Chin, S.H. Liou, P.H. Yeh, C.H. Yang, Thin Solid Film 516 (2008) 3138.
[49] C.Y. Li, T.C. Wen, T.H. Lee, T.F. Guo, J.C.A. Huang, Y.C. Lin, Y.J. Hsu, J. Mater. Chem. 19 (2009) 1643.
[50] J. Kalinowski, M. Cocchi, D. Virgili, P.D. Marco, V. Fattori, Chem. Phys. Lett. 380 (2003) 710.
[51] M. Wohlgenannt, K. Tandon, S. Mazumdar, S. Ramasesha, Z.V. Vardeny, Nature 409 (2001) 494.
[52] H.D. Burrows, J.S. de Melo, C. Serpa, L.G. Arnaut, A.P. Monkman, I. Hamblett, S. Navaratnam, J. Chem. Phys. 115 (2001) 9601.
[53] H. Bouchriha, G. Delacote, P. Delannoy, M. Schott, J. Phys. 35 (1974) 577.
[54] J. Kalinowski, Organic Light Emitting Diodes: Principles, Characteristics, and Processes, M. Dekker, New York, 2000, pp. 107–114.
[55] I.V. Tolstov, A.V. Belov, M.G. Kaplunov, I.K. Yakuschenko, N.G. Spitsina, M.M. Triebel, E.L. Frankevich, J. Lumin. 112 (2005) 368.
[56] M. Pope, J. Burgos, N. Wotherspoon, Chem. Phys. Lett. 12 (1971) 140.
[57] M. Wittmer, I. Zschokke-Gränacher, J. Chem. Phys. 63 (1975) 4187.
[58] V.D. Mihailetchi, P.W.M. Blom, J.C. Hummelen, M.T. Rispens, J. Appl. Phys. 94 (2003) 6849.
[59] C.J. Brabec, A. Cravino, D. Meissner, N.S. Sariciftci, T. Fromherz, M.T. Rispens, L. Sanchez, J.C. Hummelen, Adv. Funct. Mater. 11 (2001) 374.
[60] J. Kalinowski, K. Szybowska, Org. Electron. 9 (2008) 1032.
[61] Y.L. Lei, Y. Zhang, R. Liu, P. Chen, Q.L. Song, Z.H. Xiong, Org. Electron. 10 (2009) 889.
[62] R. Signerski, J. Kalinowski, I. Koropecký, S. Nešpurek, Thin Solid Film 121 (1984) 175.

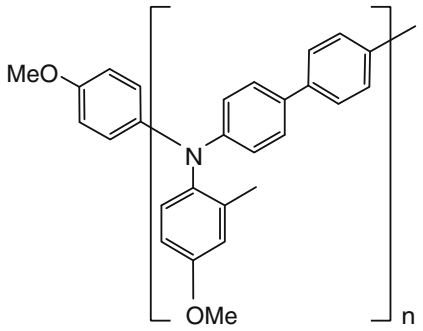

Fig. 1. Structure of poly(4,4-diphenyl-(4-methoxy-2-methyl-phenyl)-amine).

Table 1
Molecular weight data for PTAA polymers.

PTAA	M_n ($gmol^{-1}$)	Mw ($gmol^{-1}$)	PDi	HOMO (eV)	LUMO (eV)
1	5400	11,070	2.05	5.07	2.18
2	10,000	19,100	1.91	5.12	2.23
3	15,700	38,800	2.47	5.12	2.23
4	18,200	40,300	2.21	5.11	2.22

2.2. Solution preparation

Of 1% w/w stock solutions of PTAA in toluene were prepared and filtered using a 0.45 μm PTFE filter. Solutions of both single component and simple blends were prepared 24 h prior to device fabrication to allow complete mixing.

2.3. Devices fabrication

Discrete bottom-gate, top-contact organic field effect transistor (OFET) devices were fabricated on OTS treated heavily *n*-doped silicon wafers comprising a 3000 Å thermally grown gate oxide layer. Substrates were cleaned by sonication in de-ionised water for 15 min, then acetone for 15 min and finally methanol for 15 min, prior to immersion in a solution of 10 mM OTS in toluene for 20 min maintained at 60 °C. Substrates were then dried on a hot plate for 2 h at 150 °C in ambient conditions. PTAA solutions were drop cast on the substrate, and dried at room temperature under vacuum (0.1 mBar/60 min) to remove any entrapped solvent. Film quality for all measured devices was good with no evidence of pin holes or de-wetting from the substrate. Samples were drop cast on bare silica without OTS treatment or OTS treated silica were also thermally annealed for 1 h at 100 °C under reduced pressure of 0.1 mBar as indicated. Gold source and drain channel electrodes with a 60 μm channel length and 2 mm channel width were thermally evaporated, at 10^{-6} mBar at a rate of 0.5 nm/s until a layer thickness of 50 nm was obtained, yielding nine transistors per substrate.

2.4. Characterisation

Scanning Force Microscopy (SFM) was performed using an AFM XE100 (PSIA Inc, Seoul, Korea) in true non contact mode at 0.3 Hz. We used a commercial silicon cantilever with a nominal spring constant of about 40 N/m, whose resonant frequency was 325 kHz, the back of the cantilever being coated with aluminum to increase signal feedback. Topography as well as phase contrast images were recorded.

UV–vis absorption spectra of various compounds were recorded on a Varian Eclipse between 200 and 800 nm. Toluene solution sample were placed in quartz cuvettes (1 cm path) and baseline correction was done by subtracting the signal for pure solvent.

Cyclic voltammograms were recorded using a BASI cell system. Of 0.1% w/w solutions of PTAA in toluene was drop casted on platinum foil and left to dry before measuring against ferrocene. The electrochemical cell consists of a three electrodes system: Platinum wire as counter electrode, platinum foil covered in polymer as working electrode and silver/silver nitrate reference electrode. Of 0.1 M TBAHFP in acetonitrile was used as supporting electrolyte. Electrolyte was purged under nitrogen for 5 min prior to introduction of the PTAA coated platinum foil. After introduction the nitrogen purge was left on for 2 min until the measurement started.

DC characteristics of the devices were obtained using an E5270B 8 Slot precision measurement frame from Agilent Technology coupled to a 3 Agilent E5287A atto level High Resolution Module. Contacts were made using Karl Süss PH100 manual microprobes. Output characteristics were obtained at a constant gate voltage $V_G = -80$ V and transfer characteristics at a constant drain voltage $V_{sd} = -80$ V. From the slope of the square root of the drain current characteristic, we were able to calculate the saturated hole mobility (μ_{FET}) and the threshold voltage, according to the following equation:

$$I_D = \frac{\mu_{FET} W C_i}{2L}(V_G - V_T)^2 \quad (1)$$

where W is the width of the channel (2 mm), L the length of the channel (60 μm), C_i is the equivalent capacitance of the dielectric intercepting the channel and V_T the threshold voltage. Measurements were performed in air, in the dark under normal atmospheric pressure. In all cases when a transistor effect was measurable film quality was pinhole free leading to more than 70% responsive devices with a variation over the substrate of less than 20%.

3. Results and discussion

3.1. Optical and electrochemical properties

UV–vis absorption spectra and cyclic voltammograms were recorded for all PTAA samples the results being summarized in Table 1. The optical absorption and fluorescence spectra of PTTA solutions at a concentration of 10^{-4} M in toluene confirm no Stokes Shift with the slight peak broadening and more intense absorption at lower wavelength linked to the flexibility of the backbone chain of this particular PTAA derivative as shown in Figs. 2a and b. The onset of the absorption peak at 415 nm was well defined for all polymers and was used to calculate the value of the optical

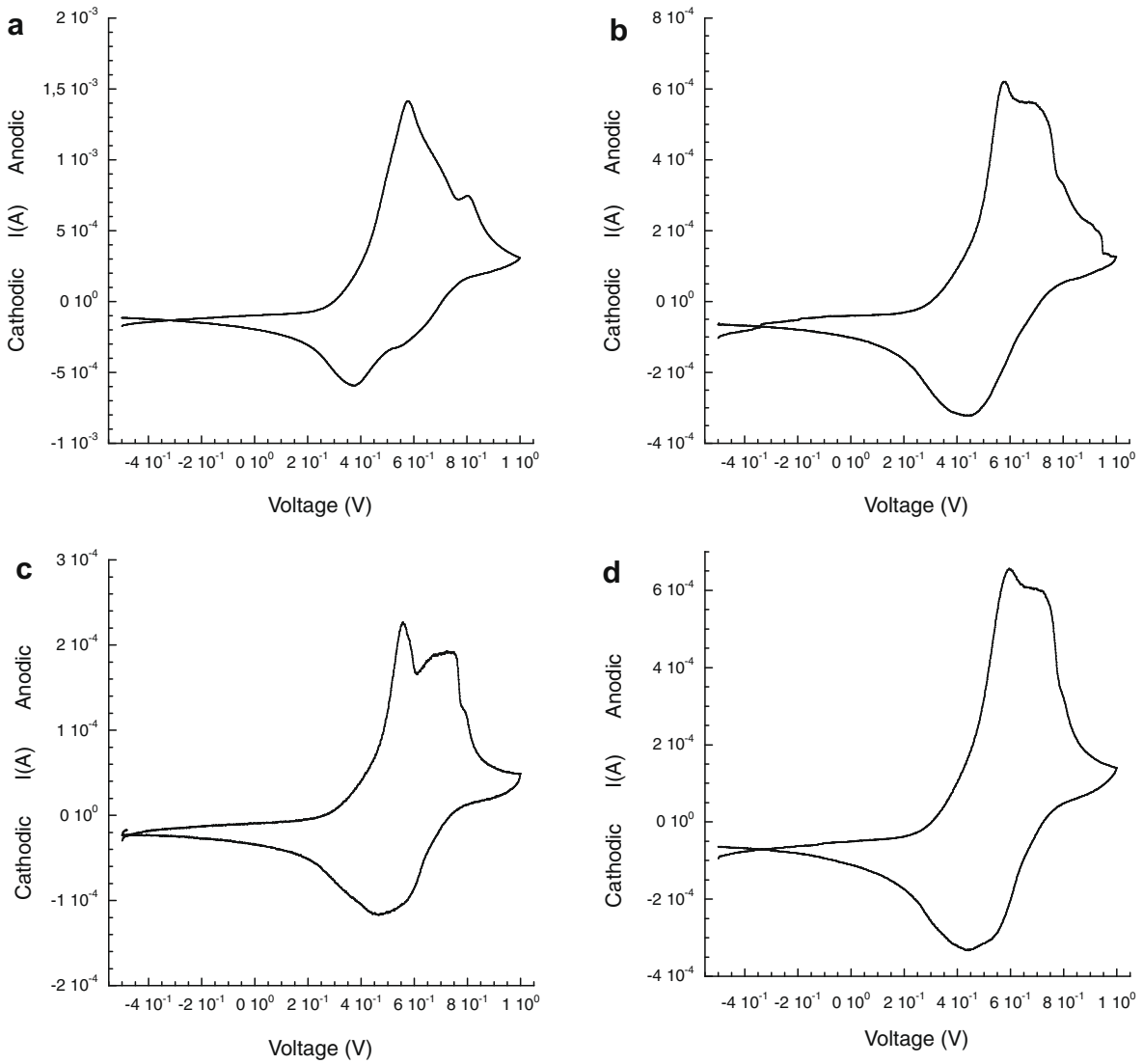

Fig. 2a. Cyclic voltamograms of (a) M_n = 5400, (b) M_n = 10,000, (c) M_n = 15,700 and (d) M_n = 18,200 as thin film deposited on platinum foil, in acetonitrile containing 0.1 M of tetrabutylammonium hexafluorophosphate.

band gap of the material, 2.89 eV. In our calculation we use the optical and electronic band gap to calculate the HOMO level of the material which shows only a weak molecular weight dependency at $M_n < 10{,}000$ gmol^{-1}. CV curves for PTAA 1–4 thin films, shown in Figs. 2a and b, are reproducible and stable upon cycling. Whilst samples in solution however do not exhibit a reversible characteristic [11] due to diffusion issues into the solid film [12], this does not restrict energy level determination since we use the formalism of Scharber et al. [13].

3.2. Electronic properties

The threshold voltage (0.4 ± 0.05 V), off current and on/off ratio were found to be independent of molecular weight with minimal current–voltage hysteresis as shown in Fig. 3 shows both the effect of PTAA molecular weight and surface treatment of mean saturated hole mobility. The insertion of an OTS SAM between the dielectric and the active semiconductor polymer increases the hole mobility by one order of magnitude independent of polymer molecular weight. Since the all polymer films by both optical and Atomic Force Microscopy were pinhole free and in the case of bare silica devices, wafers were cleaned and annealed prior to solution deposition and stored under dry vacuum to limit the adsorption of moisture and organic pollutants, the increase in mobility after insertion of the SAM layer is indicative of the rapid diffusion of oxygen and moisture through PTAA. Since both the threshold voltage and off current are independent of molecular weight this rules out any differences due to low molar mass ionic impurities [14]. Further indication of material purity across the range of polymers studied is shown in Fig. 3(a) and (b), where there is no difference in the minimal hysteresis. In all cases

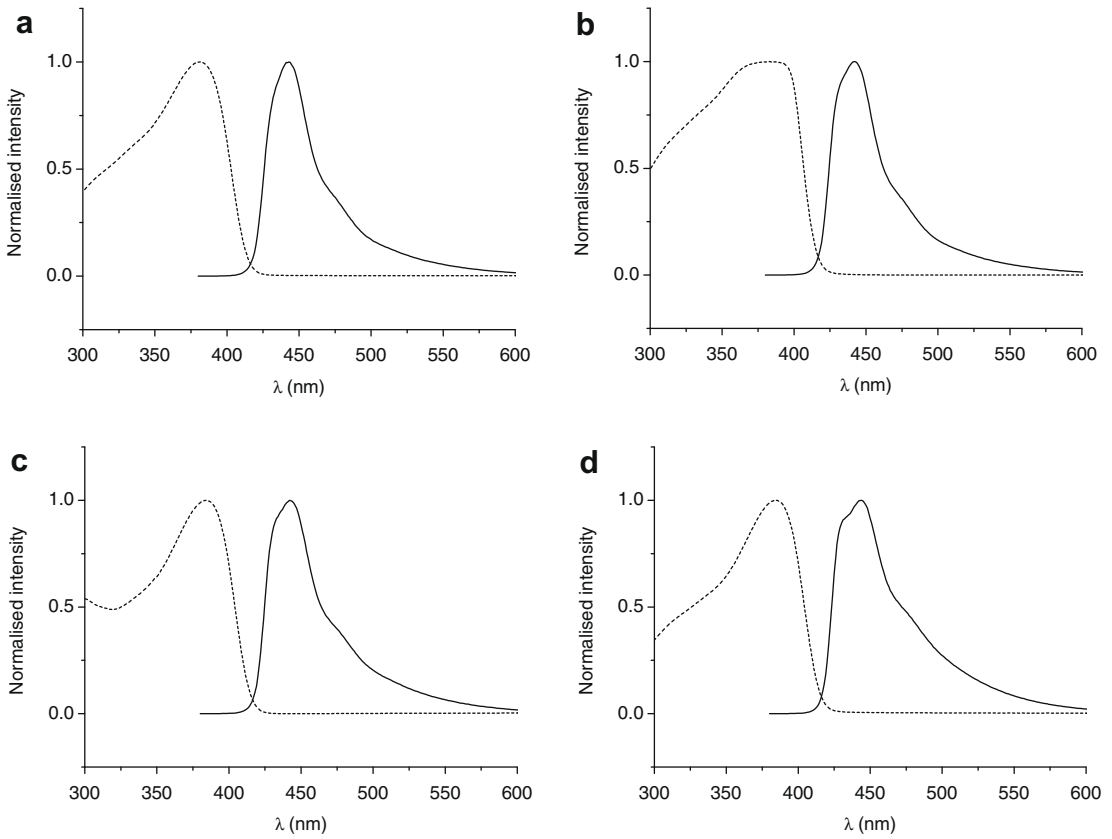

Fig. 2b. Absorption and fluorescence spectra of (a) M_n = 5400, (b) M_n = 10,000, (c) M_n = 15,700 and (d) M_n = 18,200 PTAA in solution of toluene. For more visibility, spectra have been normalized.

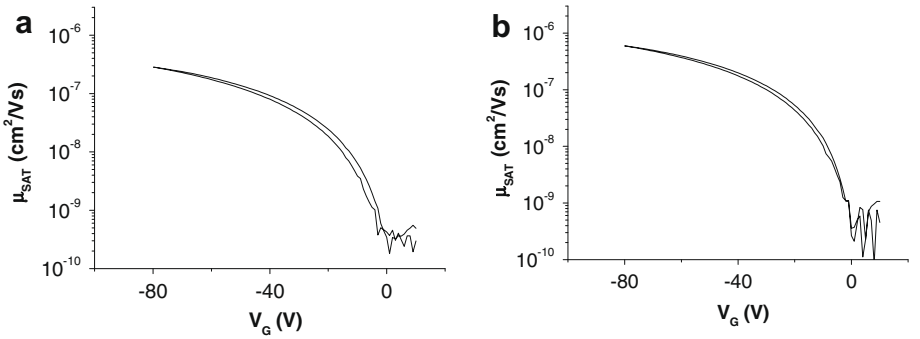

Fig. 3. Transfer characteristics in the saturated regime (V_{sd} = −80 V) for (a) PTAA 1 and (b) PTAA 4 on OTS treated silica.

on/off ratio was greater than 1000 and reproducible further confirming the absence of unwanted doping species. Annealing the dry polymer film has only a minor positive effect compared to film deposited on OTS at room temperature, lying within the 10% error margin and can be explained by the amorphous nature of the PTAA (see Fig. 4).

It is known that monomeric arylamine compounds can exhibit high mobility and that this value decreases sharply upon dimerisation and subsequent oligomerisation [15]. Here we report for the first time for low molar mass PTAA in the open literature [16] the increase in saturated hole mobility with increasing degree of polymerisation (DP) between 20 and 70 and the evidence of a plateau at around DP = 70, M_n = 20,000 gmol^{-1}. When a charge is generated on a polymer chain it is usually delocalized with the conjugation length being less than the degree of polymerisation, due to multiple defects present on a chain with the consequence that the charge is trapped in a 1D system if it cannot be delocalized further. Active transport in disordered

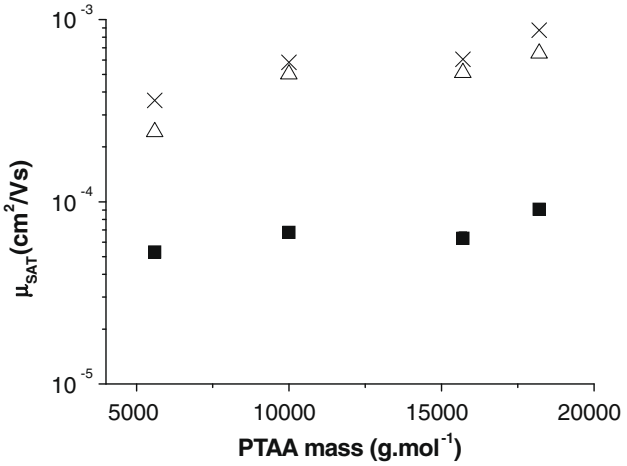

Fig. 4. Mean saturated hole mobility (μ_{FET}) of PTAA as a function of molecular weight for various deposition condition and post thermal annealing treatment (△, OTS treated silica; ■, bare silica; ×, OTS treated silica and post annealing.

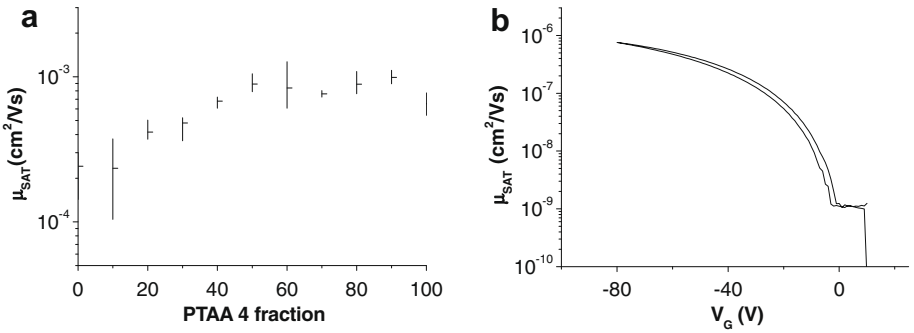

Fig. 5. (a) Mean saturated hole mobility (μ_{FET}) and (b) transfer characteristics in the saturated regime (V_{sd} = −80 V)on OTS treated silica of solution blends of PTAA 1 and PTAA 4.

systems is attributed mainly to charge hopping between polymer chains and in the case of high molecular weight polymers the conjugation length is statistically larger [9,17]. With decreasing polymer molecular weight the chain end density increases so lowering the saturated hole mobility. This is exacerbated in the case of poly(4,4-diphenyl-(4-methoxy-2-methyl-phenyl)amine) where the end caps give rise to *N*-triaryl sites with two *para*-methoxyphenyl substituted electron donating groups rather than the single *p*-methoxy-*o*-methylphenyl substitution that exists along the polymer chain.

Blends of PTAA 1 and PTAA 4 were drop cast onto OTS treated silica and the electronic properties determined, see Fig. 5. Dilution of high molecular weight PTAA 4 with low molecular weight PTAA did not result in the anticipated fall in saturated hole mobility, but in formulations having a PTAA 4 content >50 wt.%. Within the experimental error of the experiment there is evidence to suggest that indeed the performance of the blend is greater than that of either single component. Whilst the glass transition temperature of the PTAA polymers are extremely diffuse, making measurement impossible, we believe the improvement in electrical performance is due to improved polymer chain coalescence during the film formation process leading to a reduction in overall free volume within the film and so aiding charge hopping between the high molecular weight polymer chains [18].

4. Conclusions

The molecular weight of amorphous semiconductor PTAA polymer has an influence on the hole mobility on the saturated regime in bottom-gate top-contact thin film transistors. The best performances are found when the low and the high molecular weight PTAA are blended in equal ratio. Although the smallest molecular weight polymer exhibits a low mobility, it has a beneficial effect in terms of film coalescence and reduction in film free volume.

Acknowledgement

The authors would like to thank the UK DTI for financial support.

References

[1] S.-C. Lo, P.L. Burn, Chem. Rev. 107 (2007) 1097.

[2] (a) E. Menard, M.A. Meitl, Y. Sun, J.-U. Park, D.J.-L. Shir, Y.-S. Nam, S. Jeon, J.A. Rogers, Chem. Rev. 107 (2007) 1117;
(b) J. Zaumseil, H. Sirringhaus, Chem. Rev. 107 (2007) 1296;
(c) A.R. Murphy, J.M.J. Frechet, Chem. Rev. 107 (2007) 1066.
[3] (a) I. McCulloch, M. Heeney, C. Bailey, K. Genevicius, I. Macdonald, M. Shkunov, D. Sparrowe, S. Tierney, R. Wagner, W. Zhang, M.L. Chabinyc, R.J. Kline, M.D. McGehee, M.F. Toney, Nat. Mater. 5 (2006) 328;
(b) L. Wang, M.-H. Yoon, A. Facchetti, T.J. Marks, Adv. Mater. 19 (2007) 3252.
[4] (a) A.L. Briseno, S.C.B. Mannsfeld, M.M. Ling, S. Liu, R.J. Tseng, C. Reese, M.E. Roberts, Y. Yang, F. Wudl, Z. Bao1d, Nature 444 (2006) 913;
(b) H. Klauk, U. Zschieschang, J. Pflaum, M. Halik, Nature 445 (2007) 745.
[5] B.R. Saunders, M.L. Turner, Adv. Colloid Interf. Sci. 138 (2008) 1.
[6] (a) S.W. Thomas III, G.D. Joly, T.M. Swager, Chem. Rev. 107 (2007) 1339;
(b) A. Das, R. Dost, T. Richardson, M. Grell, J.J. Morrison, M.L. Turner, Adv. Mater. 19 (2007) 4018;
(c) M.-B. Madec, J.J. Morrison, V. Sanchez-Romaguera, M.L. Turner, S.G. Yeates, J. Mater. Chem. 19 (2009) 6750.
[7] (a) D.M. Wilson, S. Hoyt, J. Janata, K. Booksh, L. Obando, IEEE Sensors 1 (2001) 256;
(b) J. Locklin, Z. Bao, Anal. Bional. Chem. 384 (2006) 336.
[8] W. Zhang, J. Smith, R. Hamilton, M. Heeney, J. Kirkpatrich, K. Song, S.E. Watkins, T. Anthopoulos, I. McCulloch, J. Am. Chem. Soc. 131 (31) (2009) 10814.
[9] A. Zen, J. Pflaum, S. Hirschmann, W. Zhuang, F. Jaiser, U. Asawapirom, J. Rabe, U. Scherf, D. Neher, Adv. Funct. Mater. 14 (2004) 757.
[10] I.-W. Shen, M.C. McCairn, J.J. Morrison, M.L. Turner, Macromol. Rapid Commun. 28 (2007) 449–455.
[11] A.F.M. Barton, Handbook of Solubility Parameters and Other Cohesion Parameters, CRC Press, 1985.
[12] M. Horie, Y. Luo, J.J. Morrison, L.A. Majewski, A. Song, B.R. Saunders, M.L. Turner, J. Mater. Chem. 18 (43) (2008) 5230.
[13] M.C. Scharber, D. Mühlbacher, M. Koppe, P. Denk, C. Waldauf, A.J. Heeger, C.J. Brabec, Adv. Mater. 18 (2006) 789.
[14] G. Lloyd, M. Raja, I. Sellers, N. Sedghi, R. di Lucrezia, S. Higgins, B. Eccleston, Microelectron. Eng. 59 (2001) 323.
[15] (a) J. Veres, S. Ogier, S. Leeming, D. Cupertino, S. Khaffaf, Adv. Funct. Mater. 13 (2003) 199;
(b) E.T. Seo, R.F. Nelson, J.M. Fritsch, L.S. Marcoux, D.W. Leedy, R.N. Adams, J. Am. Chem. Soc. 88 (1966) 3498;
(c) R.F. Nelson, R.N. Adams, J. Am. Chem. Soc. 90 (1968) 3925.
[16] J. Veres et al., US2006/0155040 A1, 13 July 2006.
[17] A.J. Heeger, Faraday Discuss. Chem. Soc. 88 (1989) 203.
[18] Z. Wicks, Film Formation, Federation Series on Coatings Technology, 1986.

currents. Our vertical-type complementary organic inverter exhibited a transfer gain of up to −9 at a supply voltage (V_{DD}) of 4 V. To the best of our knowledge, this device is the first organic complementary inverter formed by integrating p- and n-channel OVTs.

2. Experimental

Fig. 1(a) and (b) display three-dimensional and circuit schematic representations, respectively, of the organic complementary inverter. Initially, a 30 nm-thick gold (Au) layer was deposited on a cleaned glass substrate to function as the collector electrode for the p- and n-channel OVTs. For the n-channel OVT, N,N′-dioctyl-3,4,9,10-perylenedicarboximide (PTCDI, ca. 98% purity, Sigma–Aldrich) was deposited on the Au layer to function as the collector layer. A 30 nm-thick aluminum (Al) strip was deposited on the collector layer to serve as the common-base electrode for the p- and n-channel OVTs. Next, a thin Al film (15 nm), to operate as the base electrode, was deposited on the strip. To decrease the OFF current, the sample was heated at 150 °C for 2 h [11]. A 100 nm-thick layer of C_{60} was thermally evaporated onto the thin Al layer to function as the emitter layer. A 30 nm-thick silver (Ag) layer was deposited onto the emitter layer of the n-channel OVT to behave as the emitter electrode. For the p-channel OVT, a 50 nm-thick layer of copper phthalocyanine (CuPc, Luminescence Technology) was thermally deposited onto the Au layer to smooth the surface morphology and then a 270 nm-thick layer of pentacene (ca. 98% purity, Luminescence Technology) was thermally evaporated to function as the collector layer. A thin Al film (10 nm) was then deposited and a lithium fluoride (LiF) layer (0.4 nm) was thermally evaporated to function as a hole injection enhancement layer. Next, a 20 nm-thick layer of N,N′-bis(naphthalen-1-yl)-N,N′-bisphenylbenzidine (NPB) was thermally evaporated to enhance the carrier energy. Pentacene was then thermally evaporated to form the 100 nm-thick emitter layer. Finally, a film of WO_3 (10 nm)/Al (30 nm) was deposited onto the emitter layer of the p-channel OVT to function as the emitter electrode. All the organic materials were used as received; they were thermally evaporated at a base pressure of 10^{-6} torr. The devices were patterned using a metal mask; the active area for both the p- and n-channel triodes was 0.04 cm^2. The current–voltage (I–V) characteristics of the devices were measured in the dark under a nitrogen (N_2) atmosphere using a Keithley 4200-SCS semiconductor parameter analyzer.

3. Results and discussion

In previous reports describing the performance of p- and n- channel OVTs [11,12], a p-channel OVT employing Au as the emitter electrode could be operated through voltage-driving under an apparent saturation region, although the ON current was much less than that of an n-channel OVT. This behavior was attributed to the longer mean free path of electrons in metal films than that of holes [13]; electrons have a lower probability of recombining at the metal base than do holes and, thus, a greater number of electrons could diffuse through the metal base layer into the collector layer. Therefore, to enhance the ON current of the p-channel OVT, we inserted a WO_3 layer

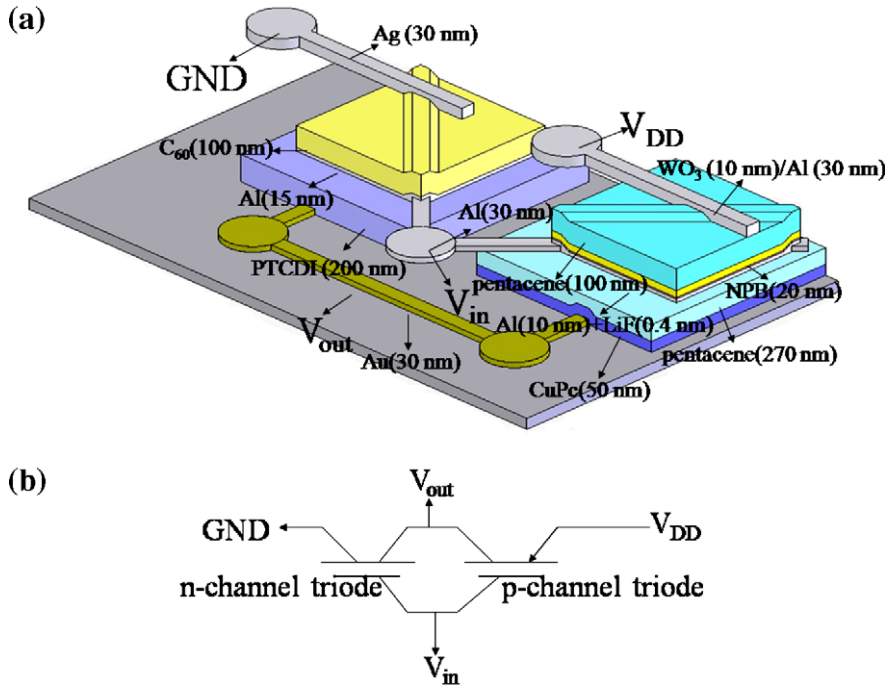

Fig. 1. (a) Three-dimensional and (b) circuit schematic representations of the organic complementary inverter.

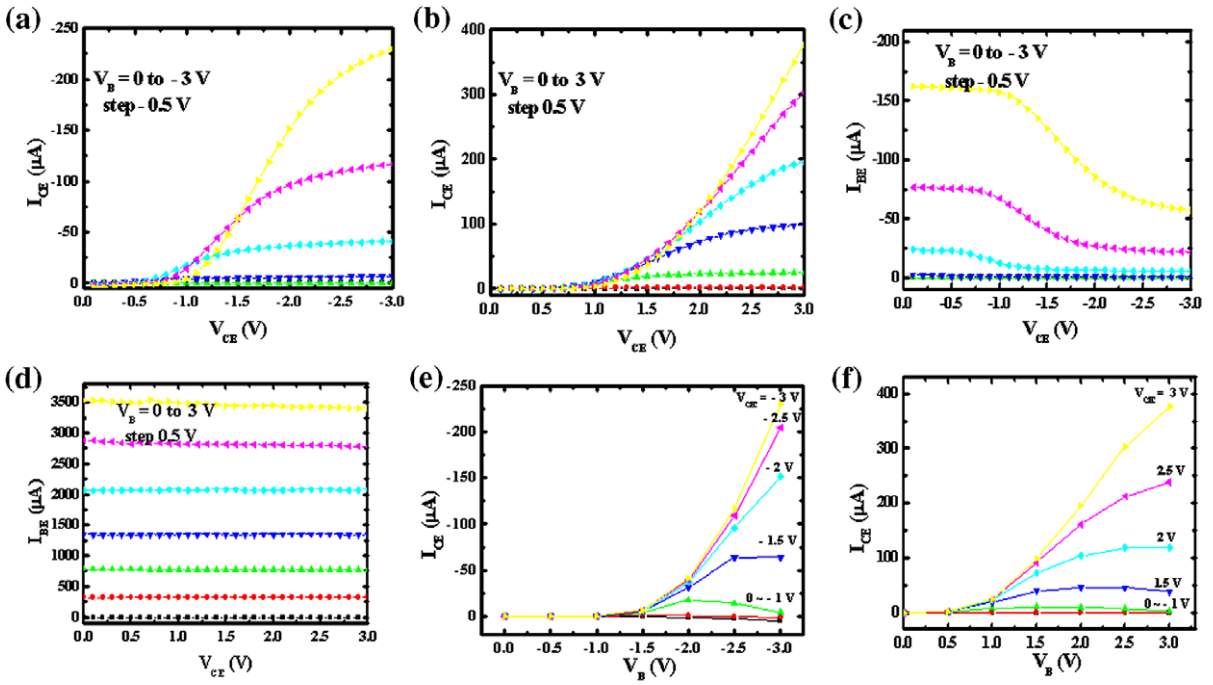

Fig. 2. (a) and (c) Collector-to-emitter current (I_{CE}) and the base current (I_{BE}) plotted with respect to the collector-to-emitter voltage (V_{CE}) for the p-channel organic triode at base voltages (V_B) ranging from 0 to −3 V at a step of −0.5 V. (b) and (d) I_{CE} and I_{BE} plotted with respect to V_{CE} for the n-channel organic triode at values of V_B ranging from 0 to 3 V at a step of 0.5 V. (e) and (f) the I_{CE} versus V_B characteristics of the p- and n-channel OVTs at V_{CE} ranging from 0 to −3 V at a step of −0.5 V and ranging from 0 to 3 V at a step of 0.5 V, respectively.

at the Al–pentacene junction to lower the barrier between the electrode and organic semiconductor and prevent the reaction and/or diffusion of the metal into the active layer [14,15]. Current matching between p- and n-channel OVTs is important for an effective complementary inverter. Fig. 2(a) and (c) display the collector-to-emitter current (I_{CE}) and base current (I_{BE}) with respect to the collector-to-emitter voltage (V_{CE}) of the p-channel OVTs and Fig. 2(b) and (d) display the I_{CE} and I_{BE} with respect to the V_{CE} of the n-channel OVTs. Fig. 2(e) and (f) display the I_{CE} versus the base voltage (V_B) characteristics of the p- and n-channel OVTs, respectively. Due to the carriers without large enough energy, most of carriers would become recombination current at the base electrode, as result of the lower current gain [14]. To enhance the current gain, there are two possible ways to decrease the carrier recombination at based electrode. One is that increasing the tunneling current by optimizing LiF thickness [16]. The other is that the enhancing the carrier energy by replacing NPB layer with the material with higher HOMO level. For the p-channel OVT, the ON current (V_B = −3 V), OFF current (V_B = 0 V), and turn-on voltage were −229 μA, −67.6 nA, and −0.8 V, respectively; for the n-channel OVT, these values were 377 μA (at V_B = 3 V), 86.9 nA (at V_B = 0 V), and 0.4 V, respectively. Owning to the OVTs composed of the EB and the CB diode, while the V_B was applied for zero, the most of the OFF current was caused by the leakage current of the CB diode. Therefore, the OFF current could be decreased by heating the device [11] or/and increasing the thickness of the CB diode. As the Fig. 1(e) and (f) shown, a leakage current exists at small V_{CE} bias. It was observed in organic and inorganic vertical-type triodes due to the asymmetry of the CB diode and the EB diode and unideal transport factor [12,17,18]. As the V_{CE} increasing, the I_{CE} would be appropriately small current or near zero and this V_{CE} was defined as the turn-on voltage. Although the ON current of the p-channel OVT could be increased by one order of magnitude, it remained somewhat less than that of the n-channel OVT. To further improve the performance of the p-channel OVT, we suspect that it would be necessary to insert a material possessing a higher energy level between the NPB layer and the thin Al layer to

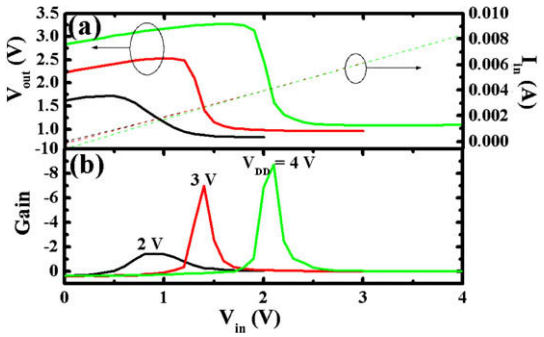

Fig. 3. (a) Measured transfer characteristics and input current (I_{in}) and (b) corresponding gain of an organic complementary inverter at supply voltages (V_{DD}) ranging from 2 to 4 V at a step of 1 V.

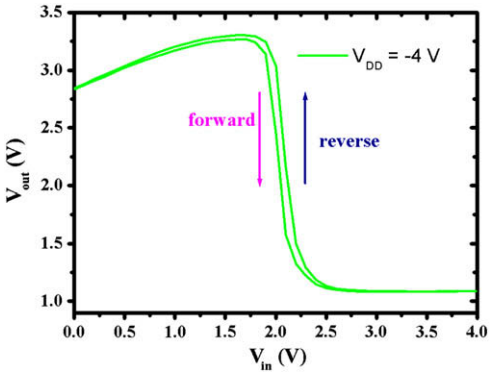

Fig. 4. Transfer characteristics in both forward and reverse directions for the complementary organic inverter at a value of V_{DD} of 4 V.

raise the carrier energy; such studies are currently under investigation.

Fig. 3 displays the transfer characteristics, the input current and corresponding gain of the complementary vertical-type organic triode in the supply voltage (V_{DD}) range from 2 to 4 V at a step of 1 V. The larger input current was caused by the base current of the OVT. Although the complementary inverter could be operated by the lower voltage, larger input current may consume more power. Besides, it was not beneficial to drive the next device in the integrated circuit application. Therefore, enhancing tunneling current or/and increasing carrier energy could decrease the input current and improve the power dissipation. In addition, the electrical characteristics of the complementary inverter, corresponding gain, was also worth discussing. The corresponding gain, defined as $-dV_{out}/dV_{in}$, increased gradually upon increasing the value of V_{DD}, reaching its highest value of −8.75 when V_{DD} was equal to 4 V. Relative to the corresponding resistance-load inverter [12], the complementary vertical-type organic triode exhibited an enhanced gain and a lower driving voltage. Fig. 4 displays the transfer characteristics for both the forward and reverse directions when V_{DD} was 4 V. In the ideal case, the OVTs would not employ the insulator and the complementary inverter would not exhibit the hysteresis phenomenon. Fig. 4 reveals only minor hysteresis, which presumably resulted from the presence of impurities in the organic materials, thereby trapping some carriers within the active layers. In addition to hysteresis phenomena, the noise margin is another important electronic characteristic. Fig. 4 reveals values for the noise margin low (N_{ML}) and noise margin high (N_{MH}) of 0.97 and 0.82 V, respectively [19]. These measured values are less than the theoretical values ($N_{MH} = N_{ML} = V_{DD}/2$), presumably because of (i) the current mismatch and larger OFF current in the p- and n-channel OVTs and (ii) the gradual shift in the turn-on voltage upon increasing the base voltage. The p-channel OVT operated under the linear region at the lower value of V_{in} of the inverter. A shift in the turn-on voltage would result in a change in the value of V_{out} upon increasing V_{in} and then a decrease in the values of N_{ML} and N_{MH}. We suspect that the electrical characteristics of the vertical-type complementary organic inverter would be improved further upon lowering the base currents, OFF currents and turn-on voltages of both OVTs.

4. Conclusions

In summary, we have fabricated the first organic complementary organic inverter incorporating p- and n-channel OVTs that could be operated at a low-voltage of 4 V to provide a corresponding gain of −9. Our results suggest that these OVTs have the same electronic applications as planar-type OTFTs – while displaying the advantageous properties of lower driving voltages and a faster operating frequencies.

Acknowledgement

This study was supported in part by the National Science Council, Taiwan, under Grants NSC 97-2628-E-007-026-MY2 and NSC 98-2221-E-001-002.

References

[1] B. Crone, A. Dodabalapur, Y.Y. Lin, R.W. Filas, Z. Bao, A. LaDuca, R. Sarpeshkar, H.E. Katz, W. Li, Nature (London) 403 (2000) 521.
[2] H. Klauk, U. Zschieschang, J. Pflaum, M. Halik, Nature (London) 445 (2007) 745.
[3] M.M. Ling, Z. Bao, P. Erk, M. Koenemann, M. Gomez, Appl. Phys. Lett. 90 (2007) 093508.
[4] T.D. Anthopoulos, D.M. deLeeuw, E. Cantatore, S. Setayesh, E.J. Meijer, C. Tanase, J.C. Hummelen, P.W.M. Blom, Appl. Phys. Lett. 85 (2004) 4205.
[5] J.H. Schon, S. Berg, Ch. Kloc, B. Batlogg, Science 287 (2000) 1022.
[6] H.E. Katz, A.J. Lovinger, J. Johnson, C. Kloc, T. Siegrist, W. Li, Y.Y. Lin, A. Dodabalapur, Nature 404 (2000) 478.
[7] H. Klauk, G. Schmid, W. Radlik, W. Weber, L. Zhou, D.C. Sheraw, J.A. Nichols, T.N. Jackson, Solid-State Electron. 47 (2003) 297.
[8] Y. Yang, A.J. Heeger, Nature 372 (1994) 344.
[9] S.H. Li, Z. Xu, L.P. Ma, Y. Yang, Appl. Phys. Lett. 91 (2007) 083507.
[10] K. Kudo, M. Iizuka, S. Kuniyoshi, K. Tanaka, Thin Solid Films 393 (2001) 362.
[11] K. Nakayama, S. Fujimoto, M. Yokoyama, Org. Electron. 10 (2009) 543.
[12] S.S. Cheng, Y.C. Chuang, D. Kekuda, C.W. Ou, M.C. Wu, C.W. Chu, Adv. Mater. 21 (2009) 1860.
[13] R.N. Stuart, F. Wooten, W.E. Spicer, Phys. Rev. Lett. 10 (1963) 7 (1963).
[14] S.S. Cheng, J.H. Chen, G.Y. Chen, D. Kekuda, M.C. Wu, C.W. Chu, Org. Electron. 10 (2009) 1636.
[15] M. Yi, S. Yu, C. Feng, T. Zhang, D. Ma, M.S. Meruvia, I.A. Hümmelgen, Org. Electron. 8 (2008) 311.
[16] C.Y. Yang, T.M. Ou, S.S. Cheng, M.C. Wu, S.Y. Lin, I.M. Chan, Y.J. Chan, Appl. Phys. Lett. 89 (2006) 183511.
[17] N. Chand, R. Fischer, H. Morkoc, Appl. Phys. Lett. 47 (1985) 313.
[18] A.F.J. Levi, T.H. Chui, Appl. Phys. Lett. 51 (1987) 984.
[19] K.C. Smith, A.S. Sedra, Microelectronic Circuits, Oxford, New York, 1998.

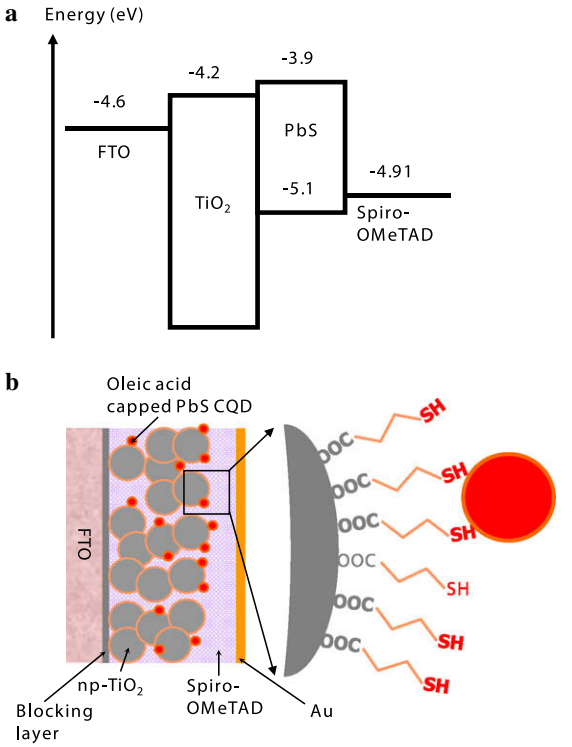

Scheme 1. Schematic of (a) band diagram and (b) device structure.

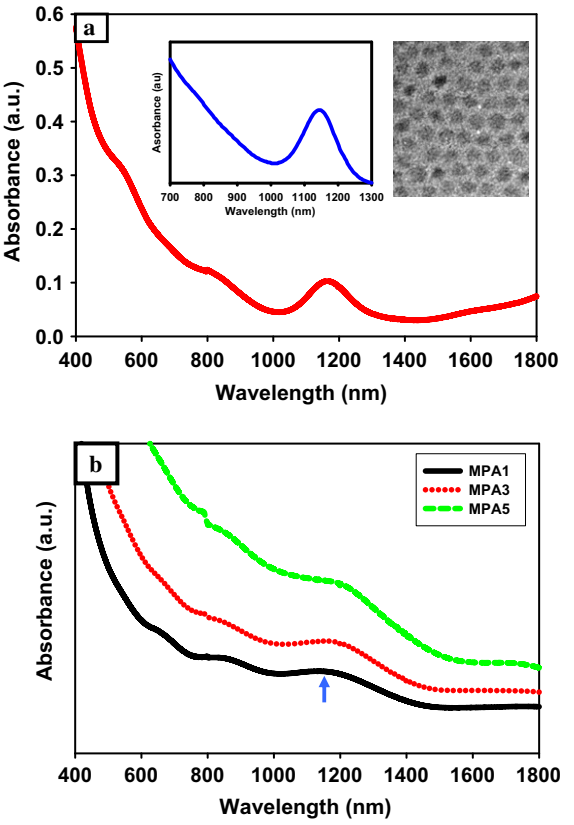

Fig. 1. Vis-NIR absorption spectra. (a) PbS CQD film deposited on a glass substrate; upper left inset: NIR absorption spectra of PbS CQDs in chloroform, upper right inset: TEM image, and (b) Vis-NIR absorption spectra of devices subjected to a different number of the dipping process.

In general, np-TiO_2 is used as a photoanode in dye-sensitized and hybrid solar cells because of its versatility, processability, high surface area, and easily controlled porosity. Further, it is very difficult to load a large amount of NIR PbS CQDs on a flat electrode material with low surface area. In addition, the single layer of CQDs on the electrode prevents rapid quenching of electron-hole recombination by a mutual interaction. To obtain a single layer of immobilized PbS CQDs on a np-TiO_2 surface, we treated the surface with a linker molecule, 3-mercaptopropionic acid (MPA). Scheme 1b shows a schematic diagram of the device structure used in this study. In a typical process, an approximately 50 nm-thick TiO_2 blocking layer is deposited on FTO (Fluorine doped Tin Oxide) glass (TEC15, USA) by the spray pyrolysis deposition (SPD) method using a 0.02 M solution of titanium diisopropoxide bis(acetylacetonate) so as to prevent direct contact between FTO and the hole-transport layer (HTL). Then, using a home-made TiO_2 (Degussa P25) paste, a 700 nm-thick np-TiO_2 layer is screen-printed on the blocking layer and sintered at 500 °C for 30 min. The surface of the np-TiO_2 layer is treated with MPA and the substrate is then dipped into a solution of PbS CQDs for 1 min, followed by washing in ethanol to remove the unattached PbS CQDs; this substrate is denoted "MPA1", where the number "1" shows that the substrate was dipped once for 1 min. Higher loadings are obtained by repeating the dipping process three and five times; the corresponding substrates are denoted "MPA3" and "MPA5", respectively. Next, following a recently published procedure [14], the PbS CQDs loaded np-TiO_2 layer is spin-coated with a 0.17 M solution of Spiro-OMeTAD dissolved in chlorobenzene containing ionic dopants lithium bis(trifluoromethylsulfonyl)imide salt (Li-TFSI) and tris(p-bromopheny)ammoniumyl hexachloroantimonate (N[p-C_6H_4Br)3$SbCl_6$). Finally, a 50 nm-thick gold electrode is deposited by thermal evaporation in a high vacuum. The device parameters such as current density are known to strongly depend on the sensitizer concentration. Hence, we ensure that more PbS CQD sensitizer is loaded onto the np-TiO_2 layer by increasing the number of repetitive dipping process. Further, oleic-acid-capped PbS CQDs were prepared by a hot colloidal synthetic method [15] and dispersed in hexane/*i*-propanol (1:0.8 v/v).

Fig. 1 shows the Vis-NIR absorption spectra of a pristine PbS CQDs film deposited on glass (Fig. 1a) and np-TiO_2 layers loaded with PbS CQDs by repeated dipping (Fig. 1b). The absorption peak of the pristine PbS CQD film appears distinctly at 1150 nm, as shown in Fig. 1a. The unchanged absorption peak position of the PbS CQDs loaded onto np-TiO_2 (Fig. 2b) indicates that these CQDs are physically spaced apart inside the matrix. The left inset in Fig. 1a also shows the characteristic absorption spectrum of PbS CQDs in chloroform. It is well known that the absorption peak position of PbS CQDs strongly depends on their size due to a strong quantum confinement effect [16]. The peak at 1180 nm corresponds to 4.5 nm-diameter PbS CQDs in

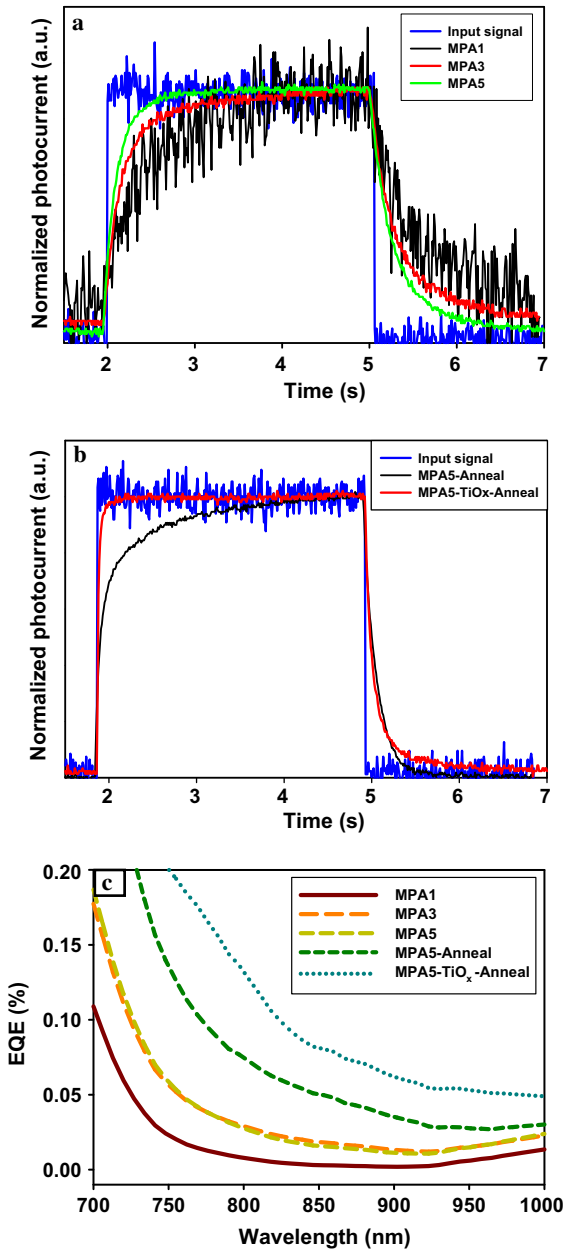

Fig. 2. Transient response time under illumination by 980 nm laser (power: 116 mW, modulation: 0.2 Hz). (a) Effect of the number of times the dipping process is repeated. (b) Effect of thermal annealing and TiO_x surface treatment/thermal annealing. (c) EQE in the NIR region.

the present case. The transmission electron micrograph (TEM) image (inset in Fig. 1a) also confirms the size, ~4.5 nm, and monodispersity of PbS CQDs. Under the consideration of the energy-level alignment between the LUMO (lowest unoccupied molecular orbital) of PbS CQDs synthesized by us and the conduction band of TiO_2 [16], we would expect efficient electron injection from the CQDs into the np-TiO_2 layer. Fig. 1b shows the Vis-NIR absorption spectra of MPA1, MPA3, and MPA5 np-TiO_2 substrates loaded with PbS CQDs. All absorption spectra were calibrated using an np-TiO_2 film without PbS CQDs so that PbS CQDs peaks could be obtained without any interference from the underlying np-TiO_2 layer. In this figure, the monotonic increase of the absorbance from MPA1 to MPA3 indicates an increase in the amount of PbS CQDs loaded into the pores of the np-TiO_2 layer. When the dipping process was repeated up to five times, the absorption steadily increased with the number of PbS CQDs adsorbed on the np-TiO_2 surface. However, further repetition of the dipping process could not result in any additional increase in the absorption peak; this indicates that no further increase was obtained in the amount of PbS CQDs adsorbed on the np-TiO_2 surface by repeating the dipping process for more than five times.

Fig. 2 shows the transient response time of the devices that were fabricated by repeating the dipping process for a different number of times; the transient response was obtained under illumination of 980 nm laser (power: 116 mW, modulation: 0.2 Hz). The transient response time was measured using a home-designed system consisting a 980 nm laser diode (Axcel AX-040: 116 mW), a modulator (Neos AOBD), a function generator (Tektronix CFG250), a photodiode (Newfocus), an oscilloscope (Yokogawa DL1702) and a multimeter (Keithley 2002). Both the rise and decay response times are very important because slow transient response time during either rise or decay determines the quality of a photodetector. In the present study, the rise-saturation time is shortened from ~2 s (for MPA1) to ~0.7 s (for MPA5) due to an increase in the number of generated charge carriers, as shown in Fig. 2a [17]. The long saturation time implies the existence of deep surface traps in np-TiO_2 and PbS CQD layers. Deep surface traps are filled preferentially by the generated charge carriers so that the rate of trap filling becomes faster as the number of charge carries increases [17]. From the external quantum efficiency (EQE) and photocurrent at 980 nm, it is confirmed that the number of charge carriers increased from device MPA1 to MPA5, as shown in Table 1. The EQE was also measured using a fully computerized home-designed system comprising a light source (300 W Xe lamp, Newport, 66902) with a monochromator (Newport cornerstone 260) and a multimeter (Keithley 2002). The slight difference in the EQE values for the photocurrent at 980 nm may be due to the different power levels of the EQE (0.1 mW) and the transient response equipment (116 mW) at 980 nm. We believe that the oleic-acid-capped PbS CQDs are almost insulating, and hence, the serial resistances of the devices pertaining to the loaded oleic-acid-capped PbS CQDs may increase with the number of times the dipping process is repeated [11,12]. Thus, the insulating layer of oleic-acid-capped PbS CQDs may hinder the transport of generated charge, increasing the decay time. The heat treatment of the MPA5 device at 110 °C for 1 min under ambient condition before spin-coating of spiro-OMeTAD increases the interfacial contact at the np-TiO_2/PbS CQDs layer; consequently, an increase in the EQE and the photocurrent of the device from 10 to 35 μA and 0.02% to 0.03% are observed as shown in Fig. 2c and Table 1, respectively. The slight decrease in the device resistance implies that the interfacial contact between np-TiO_2 and PbS CQDs is improved by annealing. Moreover, the transient decay time significantly shortened

Table 1
List of device characteristics.

Sample	MPA1	MPA3	MPA5	MPA5-anneal	MPA5–TiO_x-anneal
Cell resistance (MΩ)[a]	0.65	0.7	1	0.9	0.95
Photocurrent (μA)[b]	1	7.5	10	35	60

[a] Recorded by multimeter (Keithley 2002) in dark state.
[b] Under illumination of 980 nm laser (116 mW/cm^2).

when the rise-saturation time is increased. The shortened decay time seems to occur by efficient extraction of charge carriers from PbS CQDs, and the increased photocurrent results from improved interfacial contact. However, the net response time of the device is diminished owing to the retardation of the rise-saturation time over 2 s. During the process of annealing, the retardation of rise-saturation time may be attributed to the formation of extra traps caused by oxidation of PbS CQDs [18]. The formation and filling of surface traps can produce the asymmetric rise and decay transient response [17]. Further annealing at 110 °C after spin-coating of spiro-OMeTAD results in low efficiency. Apart from this, the introduction of a TiO_x interlayer between np-TiO_2/PbS CQDs and spiro-OMeTAD prevents and/or reduces the unwanted oxidation of PbS CQDs and also promotes the transportation of charge carries. In order to introduce a TiO_x interlayer, a methanolic solution of partially hydrolyzed titanium(IV) tetra-isopropoxide (10 mM) (Aldrich) was spin-casted on the np-TiO_2/PbS CQD layer and annealed at 110 °C for 1 min. An increase in the EQE (from 0.03% to 0.05%) and the photocurrent (from 35 to 60 μA) was observed by the introduction of the TiO_x interlayer followed by heat treatment. The significant shorting of rise-saturation time (Fig. 2b) in this case may be due to the generation of more charge carriers and/or decrease in the number of surface traps in the device.

In summary, a photovoltaic effect from the cell structure of np-TiO_2/PbS CQDs/spiro-OMeTAD is investigated in the NIR region. Oleic-acid-capped PbS CQDs were incorporated into np-TiO_2 with the help of a linker molecule (MPA). The amounts of PbS CQDs loaded into np-TiO_2 layer not only increase of EQE but also reduce the response time at NIR region. Further, the thermal annealing improves the interfacial contact between the np-TiO_2 layer and PbS CQDs, and hence, an increase in EQE and a shortening of the transient decay time are observed in an annealed system. However, the net response time is deteriorated by prolonged rise-saturation time due to the oxidation of PbS CQDs. Further, the insertion of a TiO_x interlayer followed by thermal annealing led to a further increase in the efficiency and reduction in the response time of the device system as the interlayer provides a pathway for easy transport of electrons and simultaneously decreases the oxidation of PbS CQDs. Further research is going on to improve and optimize the performance of the structure so that it can be used as an NIR photodetector.

Acknowledgements

This study was supported by a grant from the Fundamental R&D Program for Core Technology of Materials funded by the Ministry of Knowledge Economy, and by the Global Research Laboratory (GRL) Program through the National Research Foundation of Korea funded by the Ministry of Education, Science and Technology, Republic of Korea.

References

[1] K.H. An, B. O'Connor, K.P. Pipe, M. Shtein, Org. Electron. 10 (2009) 1152.
[2] C. Girotto, B.P. Rand, S. Steudel, J. Genoe, P. Heremans, Org. Electron. 10 (2009) 735.
[3] G. Hodes, J. Phys. Chem. C 112 (2008) 17778.
[4] R.D. Schaller, V.I. Klimov, Phys. Rev. Lett. 92 (2004) 186601.
[5] K.R. Choudhury, D.W. Song, F. So, Org. Electron. 11 (2010) 23.
[6] K.R. Choudhury, Y. Sahoo, T.Y. Ohulchanskyy, P.N. Prasad, Appl. Phys. Lett. 87 (2005) 073110.
[7] H.J. Lee, J.-H. Yum, H.C. Leventis, S.M. Zakeeruddin, S.A. Haque, P. Chen, S.I. Seok, M. Gratzel, M.K. Nazeeruddin, J. Phys. Chem. C 112 (2008) 11600.
[8] K.W. Johnston, A.G. Pattantyus-Abraham, J.P. Clifford, S.F. Myrskog, D.D. MacNeil, L. Levina, E.H. Sargent, Appl. Phys. Lett. 92 (2008) 15115.
[9] C.J. Karlsson, F.A.A. Olsson, D. Letalick, M. Harris, Appl. Opt. 39 (2000) 3716.
[10] J. Qian, K.-T. Yong, I. Roy, T.Y. Ohulchanskyy, E.J. Bergey, H.H. Lee, K.M. Tramposch, S. He, A. Maitra, P.N. Prasad, J. Phys. Chem. B 111 (2007) 6969.
[11] G. Konstantatos, L. Howard, A. Fischer, S. Hoogland, J. Clifford, E. Klem, L. Levina, E.H. Sargent, Nature 442 (2006) 180.
[12] J.P. Clifford, G. Konstantatos, K.W. Johnston, S. Hoogland, L. Levina, E.H. Sargent, Nature Nanotechnol. 4 (2009) 40.
[13] S. Hinds, L. Levina, E.J.D. Klem, G. Konstantatos, V. Sukhovatkin, E.H. Sargent, Adv. Mater. 20 (2008) 1.
[14] H.J. Lee, H.C. Leventis, S.-J. Moon, P. Chen, S. Ito, S.A. Haque, T. Torres, F. Nüesch, T. Geiger, S.M. Zakeeruddin, M. Grätzel, M.K. Nazeeruddin, Adv. Funct. Mater. 19 (2009) 2735.
[15] M.A. Hines, G.D. Scholes, Adv. Mater. 15 (2003) 1844.
[16] B.-R. Hyun, Y.-W. Zhong, A.C. Bartnik, L. Sun, H.D. Abruňa, F.W. Wise, J.D. Goodreau, J.R. Matthews, T.M. Leslie, N.F. Borrelli, ACS Nano 2 (2008) 2206.
[17] K. Schwarzburg, F. Willig, Appl. Phys. Lett. 58 (1991) 2520.
[18] M.I. Kamchatka, Y.M. Chashchinov, D.B. Chesnokova, Inorg. Mater. 37 (2001) 910.

Organic Electronics 11 (2010) 700–704

Contents lists available at ScienceDirect

Organic Electronics

journal homepage: www.elsevier.com/locate/orgel

Letter

Sensitization of organic photovoltaic cells based on interlayer excitation energy transfer

Musubu Ichikawa [a,b,*], Eiichi Suto [a], Hyeon-Gu Jeon [a], Yoshio Taniguchi [a]

[a] Functional Polymer Science Course, Faculty of Textile Science and Technology, Shinshu University, 3-15-1 Tokida, Ueda City, Nagano 386-8567, Japan
[b] Presto, Japan Science and Technology Agency (JST), 4-8-1 Honcho, Kawaguchi, Saitama 332-0012, Japan

ARTICLE INFO

Article history:
Received 9 September 2009
Received in revised form 14 December 2009
Accepted 25 December 2009
Available online 6 January 2010

Keywords:
Organic solar cells
Organic photovoltaic cells
Exciton transfer
Excitation transfer
Energy transfer
Förster resonant excitation transfer

ABSTRACT

We incorporated an additional *p*-type organic semiconductor layer (APL) between the anode and the phthalocyanine layer, which is an indispensable *p*-type semiconductor layer (IPL) in forming a *p*/*n* junction with a fullerene C_{60} layer. We used two thiophene/phenylene co-oligomers as the APL. The incorporation increases the short-circuit current density (J_{SC}) and enhances incident photon–current conversion efficiency (IPCE) over the wavelength region where the APL shows strong absorption. Combined dependence of the APL/IPL implies that Förster resonance excitation transfer is the main factor in J_{SC} and IPCE enhancements. We demonstrate clearly that the 'positive' hole injection barrier at the interface between the APL and the IPL impacts the smooth transportation of holes to the indium-tin-oxide anode. However, the small positive hole barrier of 0.1 eV has no noticeable influence on the fill factor of the current density versus voltage characteristic under photoirradiation, or on those devices with 'negative' hole barriers.

© 2009 Elsevier B.V. All rights reserved.

Organic photovoltaic (PV) cells have received a lot of attention because of their potential use in applications, such as in flexible solar cells, and the low-cost production of those applications [1]. The power conversion efficiency (PCE) of organic PV cells has been increasing [2–9], but further enhancements are required before being utilized in practical applications. To enhance the PCE, researchers must first increase the intensity of light absorption as well as broaden the available spectrum. In this context, tandem-stacking organic PV cells [7,10,11] is one viable option, because we can basically use four different organic semiconductors (two *p*-type and two *n*-type) in a tandem device, and each material would cover its own specific absorption spectrum [7,11]. However, in the case of tandem devices, performance matching between each cell is very important. For example, in the case of series-connected tandem PV cells, while the open-circuit voltage (V_{OC}) is the summation of each individual V_{OC}, the short-circuit current (J_{SC}) should be limited to the lowest J_{SC} in each cell [7]. Although balancing each cell is the key, matching the performance of each cell in the best state will be difficult. Here, we will demonstrate another method by which we can use three or more organic semiconducting materials, and in which all the materials contribute to light absorption and to the generation of charge carriers.

We introduced an additional *p*-type organic semiconductor layer (APL) into organic PV cells that have a single *p*/*n* junction. In this sense, the devices are not tandem, as shown in Fig. 1(a). The APL was located between an electrode and an indispensable *p*-type layer (IPL), which was directly connected to an *n*-type layer (NL). By tuning the energy difference between the bandgap energies of both *p*-type materials, an APL bandgap larger than that of the IPL could be achieved, and the APL exciton produced by optical absorption could be transferred to the IPL, resulting in the creation of additional IPL excitons. Essentially, there is no distinguishable difference between the two types of

* Corresponding author. Address: Functional Polymer Science Course, Faculty of Textile Science and Technology, Shinshu University, 3-15-1 Tokida, Ueda City, Nagano 386-8567, Japan. Tel.: +81 268 21 5498; fax: +81 268 21 5417.
E-mail address: musubu@shinshu-u.ac.jp (M. Ichikawa).

1566-1199/$ - see front matter © 2009 Elsevier B.V. All rights reserved.
doi:10.1016/j.orgel.2009.12.023

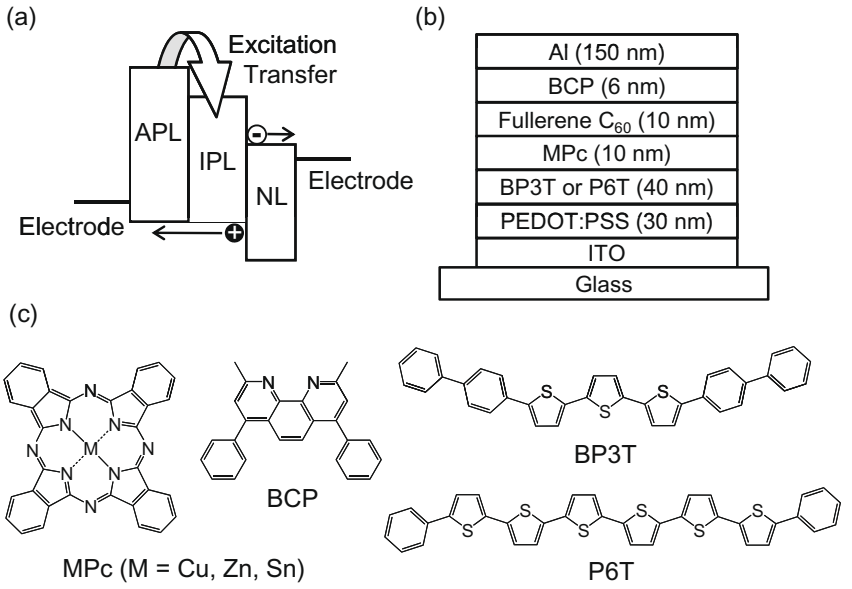

Fig. 1. (a) Conceptual energy diagram of PV cell proposed in this study, (b) sectional cell structure, and (c) structures of chemicals and their abbreviations used in this study.

IPL excitons produced by direct optical excitation and transfer, and consequently, the IPL exciton created by exciton transfer should also separate into charge carriers at the *p*/*n* junction in the same way. In short, by achieving interlayer excitation energy transfer between the APL and the IPL, PV cells can be sensitized by utilizing the light absorbed by the APL.

In relation to this work, Hidel et al. have reported the sensitization of organic PV cells by incorporating an 'antenna' layer [12]. The antenna layer was positioned externally between the cathode and the anode, and was coupled with an organic PV component based on energy transfer via surface plasmon polaritons (SPPs) through a thin Ag cathode. While the 15–20-nm thick Ag cathode successfully increased the quantum efficiency of energy transfer from the antenna, such a thin metal electrode leads to undesirable higher series resistances. The device proposed in the present study used an APL placed internally between the anode and the cathode as an antenna; it therefore requires no thin electrode with high resistivity. In addition, the SPP-based antenna required high photoluminescence (PL) efficiency [12], whereas the APL does not require high light emissivity. This is essentially because excitation transfer from the APL to the IPL is based on a common form of non-radiative excitation energy transfer, such as Förster resonance excitation transfer (FRET) and Dexter electron exchange excitation transfer [13,14].

Fig. 1(b) shows the schematic device structure employed in the present study, and Fig. 1(c) shows the chemical structures of the materials used. We used BP3T or P6T as the APL materials, and metallophthalocyanines (MPc; *M* = Cu, Zn, and Sn) as the IPL materials. APL materials should possess good hole-transporting ability, and (thiophene/phenylene) co-oligomers such as BP3T and P6T have been reported as having this ability [15–18]. The chemicals BP3T and P6T (Institute Research and Innovation), ZnPc and SnPc (Aldrich) and BCP (TCI) were purified by temperature-gradient train sublimation with Ar gas flow before use. We used C_{60}, purchased from Frontier Carbon (nanom purple SUH grade) and CuPc (for the organic light-emitting device) donated by Nippon Steel Chemicals, without further purification. We prepared the devices by depositing several materials sequentially onto commercially available indium-tin-oxide (ITO) coated glass substrates, which had sheet resistance of 15 Ω/square. To begin with, the substrates were washed with detergent water, pure water, and 2-propanol under ultrasonification and treated with O_2 plasma at a power of 50 W for 5 min. We prepared a poly(3,4-ethylenedioxythiophene) poly(styrenesulfonate) (PEDOT:PSS) layer on the substrates by spin-coating a commercially available formula (H.C. Starck, Clevios P Al 4083). We deposited several organic layers by thermal evaporation under vacuum (2.0×10^{-4} Pa) at a rate of 1 Å/s. Finally, the aluminium electrode was prepared on top of the organic layer stack by thermal evaporation in vacuum at a rate of 10 Å/s. Active areas of the cells were about 6 mm^2. We transferred the produced devices into a highly inert glove box (O_2 concentration 5 ppm; dew point < −50 °C) with no exposure to ambient conditions, and then mounted them in a small chamber, which had a quartz window, in the glove box. A source meter (Keithley 2410) measured their current density versus voltage (*J*–*V*) curves both with and without 100-mW/cm^2 artificial solar light irradiation of airmass 1.5 global (AM1.5G) from a Newport Oriel solar simulator (Model 91160) with an AM1.5G filter (Newport Oriel 81088) and a light-intensity stabilizer (Newport Oriel, Model 68945). The power density of irradiation was measured with a pyroelectric optical power meter (Ophir P3). We recorded the incident photon–current conversion efficiency (IPCE) spectra of the devices

with a digital multimeter (Advantest AD7461A) at zero bias, under monochromatic light irradiation from a light source (Bunko Keiki SM-25A); the intensity of the monochromatic light for each wavelength was measured with a calibrated silicon photodiode (Hamamatsu Photonics S1337-1010BQ). Surface morphologies of thin films were evaluated with a scanning probe microscope (Veeco, Dimension ICON) in tapping mode. Note that in this study we employed relatively thinner layers of MPc and C_{60} compared to other studies of organic PVs with MPc and/or C_{60}, because we aimed to determine exactly how the interlayer excitation energy transfer influences organic photovoltaic devices.

Fig. 2 shows the *J–V* curve of the BP3T/CuPc/C_{60} device that had a BP3T layer as the APL. The figure also shows the curve of another PV cell (CuPc/C_{60}) with no APL layer, as a reference. In the case of this control, we simply omitted the BP3T and the thicknesses of the other layers remained the same. As shown in the figure, placing the BP3T layer in front of the CuPc layer mainly enhanced J_{SC} but not V_{OC}. The PCE of the BP3T/CuPc/C_{60} device was 0.63%, much lower than that reported for CuPc/C_{60} planar junction-based PV cells [19], because we used thinner CuPc and C_{60} layers to evaluate the effectiveness of the APL. Fig. 3 shows the IPCE spectra of the two devices. The IPCE increases in the shorter wavelength region where BP3T has strong absorption, as shown in the inset of the figure. This result suggests that the BP3T exciton produced by optical absorption is transferred to the CuPc layer and that the CuPc exciton created by the transfer was converted to charge carriers at the interface of CuPc/C_{60}. It is possible that the sensitization resulted from a direct contact between BP3T and C_{60}, through defects in the CuPc layer because of the thinness of the layer; we will discuss this point later. Note that another increase occurs around 600 nm, which may not have been caused by the transfer. We are not sure why this other increase occurred, but we believe that the BP3T layer can prevent the CuPc exciton, produced by optical absorption, from quenching by the PEDOT:PSS layer.

Fig. 4 shows the IPCE spectrum of another cell using BP3T, in which we replaced CuPc with SnPc as the IPL (device structure abbreviated as BP3T/SnPc/C_{60}). We observed

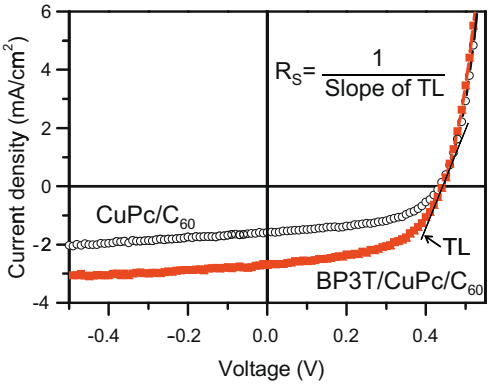

Fig. 2. *J–V* curves of PV cells with or without BP3T as the APL under 1 sun irradiation. TL: tangential line at V_{OC}.

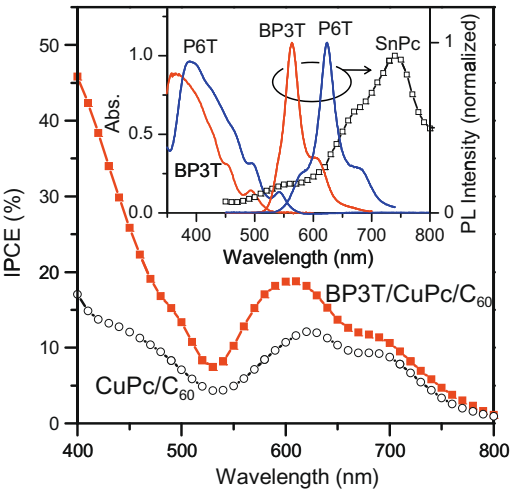

Fig. 3. IPCE spectra of PV cells with and without BP3T as the APL. Inset: absorption spectra of thin films of BP3T, P6T, and SnPc, and PL spectra of BP3T and P6T thin films. Thin films were deposited on quartz plates by thermal evaporation.

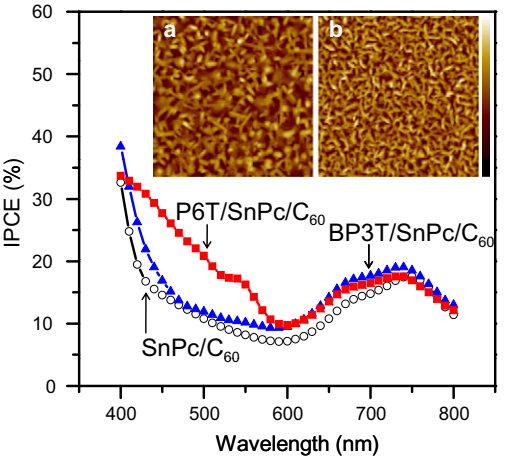

Fig. 4. IPCE spectra of SnPc-based PV cells incorporating BP3T (blue solid triangles), P6T (red solid squares) as the APLs, and a control cell (black open circles). The inset shows the surface morphologies of 40-nm thick BP3T (a) and P6T (b) layers deposited on a 40-nm thick PEDOT:PSS layer. The field size of both images are the same (1 μm × 1 μm) and the colour bar next to image (b) is the height scale: full scales of the bar for (a) and (b) are 58.5 nm and 48.7 nm, respectively. (For interpretation of the references to colour in this figure legend, the reader is referred to the web version of this article.)

no noticeable enhancement of IPCE due to light absorption by BP3T as compared to its reference device that contained no BP3T layer (SnPc/C_{60}). These devices include two heterojunctions: one is IPL/C_{60} and the other is APL/IPL. It would be believed that charge separation occurred in the case of the APL excitons at the APL/IPL interfaces possibly because the lowest unoccupied molecular orbital (LUMO) levels of BP3T and P6T are higher than those of the phthalocyanine (Pc) derivatives used [20]. If the sensitization by the APL occurred because of charge separation at the APL/IPL interface, the negative LUMO level of SnPc more than

CuPc should lead to more efficient charge separation in the case of the Marcus normal region [21]. However, no noticeable enhancement of IPCE due to BP3T occurred for the BP3T/SnPc device, as shown in Fig. 4. Consequently, the sensitization mechanism by the APL differs from the double exciton dissociation at both sides of a Pc layer reported by Sista et al. [22] and Zhang et al. [23]. There could essentially be a difficulty with this double exciton-dissociation in that the layer, both sides of which would contribute to exciton dissociations, would need to have sufficient charge carrier mobilities for both electron and hole.

On the other hand, a remarkable enhancement appeared from 400 to 550 nm in the case of the device with the P6T/SnPc/C_{60} structure. As shown in the inset of Fig. 4, the surfaces of both the BP3T and P6T layers were slightly rough as a result of the high crystalline nature of these materials, and the root-mean-square roughness (RMS) of the layers, each 40-nm thick, was 8.1 nm for BP3T and 7.6 nm for P6T. It is possible that these rough surfaces induce a fairly direct contact between the APL and C_{60}, through defects in the 10-nm thick IPL. However, no IPCE enhancement in the BP3T/SnPc/C_{60} system and the remarkable IPCE improvements in both BP3T/CuPc/C_{60} and P6T/SnPc/C_{60} systems, greatly refute that the APL mainly touches the C_{60} layer directly and causes the sensitizations when introducing the APLs.

The sensitized spectral region of the P6T/SnPc/C_{60} device increased in wavelength as compared to the BP3T/CuPc/C_{60} device, as shown in Figs. 3 and 4. This change occurred because P6T shows absorption in a larger wavelength region than BP3T, as shown in the inset of Fig. 3. Furthermore, P6T displays photoluminescence (PL) in a longer wavelength region than BP3T, and SnPc preferentially absorbs longer wavelength light than CuPc. Consequently, the overlap integral becomes large in the case of combined P6T and SnPc, where the overlap integral indicates a spectral overlap between the photoluminescence of an excitation energy donor and the absorption of an excitation energy acceptor. In addition, we observed clear sensitization due to P6T as the APL in the case of the P6T/CuPc/C_{60} cells, where there was a sufficient spectral overlap between the PL of P6T and the optical absorption of CuPc. From these results, we believe that it was probably the following scheme that increased IPCE: the BP3T or P6T layer in front of the Pc derivative layer absorbed the corresponding light, resulting in the formation of its exciton; the exciton was transferred to the back Pc derivative layer; and finally, the Pc exciton separated both the charge carriers at the Pc–C_{60} interface. The abovementioned spectral overlap dependence suggests that the mechanism of excitation transfer from front layer to back layer may be FRET. We are planning further studies to shed light on the mechanism of excitation transfer occurring in the cells; its quantum efficiency, including the determination of Förster radii between those thiophene derivatives and the phthalocyanines; and the intrinsic exciton diffusion lengths of those thiophenes.

It is worth noting that, while finalizing the present manuscript, Hong et al. reported an organic PV device with a pentacene/ZnPc/C_{60} multi-heterojunction [24]. The concept described in that literature is very similar to that in the present study, and they utilized pentacene as a sensitizer for a ZnPc/C_{60} heterojunction. They concluded that endothermic triplet energy transfer occurred between pentacene and ZnPc. Although both singlet and triplet energy transfers have the potential to sensitize by means of excitation transfer, what multiplicity of exciton is more advantageous in this sensitization needs to be discussed in the next stages of research. This is because a compromise between exciton lifetime and the reachable range of excitation transfer for the two types of excitons – singlet and triplet should be considered. In any case, an increase in both J_{SC} and IPCE, and moreover, an unchanged V_{OC} have been clearly observed in the present study as a result of singlet-exciton transfer between APL and IPL as discussed above.

Finally, we discuss the case where the hole generated at the p/n (Pc/C_{60}) junction is required to pass over the additional IPL–APL interface. Depending on the combination of materials, there is a hole injection barrier at the interface, and then the barrier probably affects hole transportation from the p/n junction to the electrode. We estimated the series resistance of a device from the inverse of the slope of the tangential line (TL) of the J–V curve at V_{OC}, as shown in Fig. 2. Fig. 5 summarizes the resistances of six devices with an APL, where the injection barrier of holes (ΔE_H) is defined as the energy difference between the highest occupied molecular orbital (HOMO) levels of the APL and the IPL [20]. Negative ΔE_H means that the hole is injected endothermically from the IPL to the APL. The resistance decreases gradually with decreasing ΔE_H, but increases rapidly when ΔE_H is positive. However, the fill factors (FF) of all the cells prepared are about 0.5 whether with or without the APL. In short, normalized FF for each device with the APL is almost 1 as shown in Fig. 5, where the normalized FF is defined as the ratio of FFs between PV cells using a certain Pc with and without each APL. This means that neither the large exothermic hole injection at the P6T/SnPc interface nor the small 'positive' hole injection barrier of

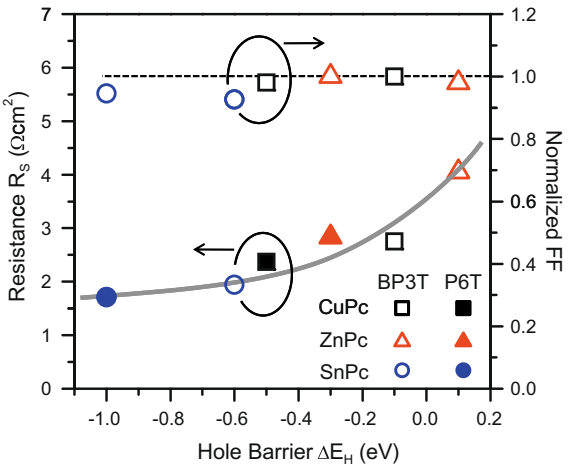

Fig. 5. Hole injection barrier ΔE_H dependence of R_S and normalized FF (see text) of all the devices with APLs obtained under photoirradiation. The thick grey line is a guide for the eye. ΔE_H was calculated from the difference in HOMO levels between the APL and the IPL for each cell.

0.1 eV at the BP3T/ZnPc interface influenced the charge collection through the APL/IPL interface. Furthermore, as one can see from the fairly good FFs of the cells, the entire devices show clear rectifying characteristics whether with or without APLs. Consequently, this concept would probably work well when we adjust the difference of the bandgaps of both the APL and the IPL and align their HOMO levels, appropriately.

In conclusion, we have demonstrated the sensitization of organic PV cells with a single *p*/*n* junction-based on interlayer excitation energy transfer. We incorporated an additional *p*-type semiconducting organic material layer (APL) between the PEDOT:PSS layer and a Pc layer, indispensable *p*-type semiconductor layer (IPL), to form a *p*/*n* junction with the C_{60} layer for generating charge carriers from excitons. Incorporating the APL led to sensitization of the IPCE, and the sensitized wavelength regions changed depending on the absorption spectra of the APL. The combination dependence of APL/IPL suggests that IPCE enhancements mainly result from Förster resonance excitation transfer (FRET). We demonstrated clearly that the 'positive' hole injection barrier at the APL–IPL interface has an impact on the smooth transportation of holes to the anode (indium-tin-oxide). The PV cells demonstrated here showed an insufficient PCE of below 1%, but we believe that this approach will lead to further improvements in the PCE of organic PV cells in the future. We are now working to incorporate more APLs for more efficient light collection with cascading excitation transfer toward the IPL.

Acknowledgements

This work was partly supported by CLUSTER (second stage) of the Ministry of Education, Culture, Sports, Science and Technology (MEXT), Japan. This work was also partly supported by JST PRESTO program.

References

[1] S.R. Forrest, Nature 428 (2004) 911.
[2] C.W. Tang, Appl. Phys. Lett. 48 (1986) 183.
[3] P. Peumans, S.R. Forrest, Appl. Phys. Lett. 79 (2001) 126.
[4] C.J. Brabec, N.S. Sariciftci, J.C. Hummelen, Adv. Funct. Mater. 11 (2001) 15.
[5] J. Xue, S. Uchida, B.P. Rand, S.R. Forrest, Appl. Phys. Lett. 84 (2004) 3013.
[6] A. Hayakawa, O. Yoshikawa, T. Fujieda, K. Uehara, S. Yoshikawa, Appl. Phys. Lett. 90 (2007) 163517.
[7] J.Y. Kim, K. Lee, N.E. Coates, D. Moses, T.-Q. Nguyen, M. Dante, A.J. Heeger, Science 317 (2007) 222.
[8] K. Sakai, M. Hiramoto, Mol. Cryst. Liq. Cryst. 491 (2008) 284.
[9] S. Wang, E.I. Mayo, M.D. Perez, L. Griffe, G. Wei, P.I. Djurovich, S.R. Forrest, M.E. Thompson, Appl. Phys. Lett. 94 (2009) 233304.
[10] M. Hiramoto, M. Suezaki, M. Yokoyama, Chem. Lett. 19 (1990) 327.
[11] J. Xue, S. Uchida, B.P. Rand, S.R. Forrest, Appl. Phys. Lett. 85 (2004) 5757.
[12] T.D. Heidel, J.K. Mapel, M. Singh, K. Celebi, M.A. Baldo, Appl. Phys. Lett. 91 (2007) 093506.
[13] T. Förster, Discuss. Faraday Soc. 27 (1959) 7.
[14] D.L. Dexter, J. Chem. Phys. 21 (1953) 836.
[15] M. Ichikawa, H. Yanagi, Y. Shimizu, S. Hotta, N. Suganuma, T. Koyama, Y. Taniguchi, Adv. Mater. 14 (2002) 1272.
[16] H. Yanagi, Y. Araki, T. Ohara, S. Hotta, M. Ichikawa, Y. Taniguchi, Adv. Funct. Mater. 13 (2003) 767.
[17] K. Nakamura, M. Ichikawa, R. Fushiki, T. Kamikawa, M. Inoue, T. Koyama, Y. Taniguchi, Jpn. J. Appl. Phys. 43 (2004) L100.
[18] S. Hotta, T. Katagiri, T. Yamao, K. Shimizu, H. Yanagi, M. Ichikawa, Y. Taniguchi, Int. J. Polym. Mater. 57 (2008) 515.
[19] J. Xue, B.P. Rand, S. Uchida, S.R. Forrest, Adv. Mater. 17 (2005) 66.
[20] Lowest unoccupied molecular orbital (LUMO)/highest occupied molecular orbital (HOMO) levels of the materials used in this study: −2.8/−5.1 (BP3T), −2.6/−4.7 (P6T), −3.5/−5.2 (CuPc), −3.4/−5.0 (ZnPc), −4.2/−5.7 (SnPc), and −4.5/−6.2 (C60). Unit of the levels is eV. We estimated HOMO and LUMO levels for BP3T and P6T from the ionization potential and the optical absorption edges of each thin-film. The others were from the literature.
[21] R.A. Marcus, Rev. Mod. Phys. 65 (1993) 599.
[22] S. Sista, Y. Yao, Y. Yang, M.L. Tang, Z. Bao, Appl. Phys. Lett. 91 (2007) 223508.
[23] G. Zhang, W. Li, B. Chu, L. Chen, F. Yan, J. Zhu, Y. Chen, C.S. Lee, Appl. Phys. Lett. 94 (2009) 143302.
[24] Z.R. Hong, R. Lessmann, B. Maennig, Q. Huang, K. Harada, M. Riede, K. Leo, J. Appl. Phys. 106 (2009) 064511.

ITO deposition, MoO_3 contributes to hole extraction and the suppression of electron leakage [9]. The effects of varying the MoO_3 layer thickness and cathode materials are also investigated.

To prepare both conventional and inverted devices shown schematically in Fig. 1, bare and ITO-coated glass substrates were cleaned by a standard solvent regimen followed by UV-ozone treatment [10]. Materials were deposited at a rate of 2 Å/s for metals, and 1 Å/s for purified organics and MoO_3 in a high-vacuum (base pressure < 4×10^{-7} Torr) thermal evaporation chamber. Prior to the deposition of the top contact, samples were transferred to a high purity N_2 ambient (<1 ppm H_2O and O_2) where a shadow mask defining arrays of 1-mm diameter circular openings was attached. The top ITO contact was sputter-deposited at a power of 40 W (0.2 Å/s) and a pressure of 2 mTorr using Ar plasma [11]. All deposition rates and thicknesses were measured by quartz crystal monitors and checked by variable-angle spectroscopic ellipsometry. Device performance was measured in air using a semiconductor parameter analyzer in the dark and under illumination from a 150 W Xe lamp with AM1.5G filters using standard procedures [12]. Lamp intensity was varied with neutral density filters and measured by an NREL-calibrated Si photodiode. A transfer-matrix formalism was used to simulate the optical field and absorption, and to predict the short-circuit current (J_{SC}) of the devices [1]. The absorption spectra of the materials were measured using a Lambda 1050 UV/Vis/NIR spectrophotometer.

Previously, conventional planar small-molecule OPVs lacking a BCP blocking layer have exhibited greatly reduced efficiency [13,14]; however, we find that SubPc/C_{60} devices with Al cathodes can achieve similar performance without BCP, yet is sensitive to the C_{60} layer thickness. The comparable performance is achieved when C_{60} is thick enough to prevent the excitons generated within a diffusion length of the donor–acceptor (DA) interface from migrating to the metal-C_{60} interface where they quench, yet is not too thick to negatively impact performance by increasing resistance or placing the peak optical absorption far from the DA interface. Under simulated, 1 sun AM1.5G illumination, the device with BCP (Device 1, Fig. 1) showed a responsivity ($R = J_{SC}/P_0$, where P_0 is the incident light intensity) of 0.048 ± 0.001 A/W, a fill factor FF = 0.63 ± 0.01, and V_{OC} = 1.10 ± 0.02 V, leading to a power conversion efficiency of η_P = 3.3 ± 0.1%, while the device without BCP (Device 2, Fig. 1) achieved η_P = 3.0 ± 0.2%, with R = 0.049 ± 0.001 A/W, FF = 0.61 ± 0.03 and V_{OC} = 1.01 ± 0.02 V.

To prevent damage to the donor during ITO deposition, a MoO_3 buffer layer was inserted into the following inverted structure: glass/Al 1000 Å/C_{60} 500 Å/SubPc 90 Å/MoO_3 100 Å/ITO 400 Å (Device 3 in Fig. 1). This device showed η_P = 0.86 ± 0.08%, with R = 0.032 ± 0.002 A/W, FF = 0.48 ± 0.01 and V_{OC} = 0.56 ± 0.02 V under 1 sun, AM1.5G illumination. For the inverted device, the ideality factor n = 2.0 ± 0.1, series resistance R_{SA} = 4.9 ± 0.1 Ω cm [2], and reverse saturation current density, $J_S = (2 \pm 1) \times 10^{-5}$ mA/cm^2, were obtained by fitting the dark current–voltage (J_D–V) characteristics with the modified Shockley equation [15].

The low V_{OC} of the inverted device is attributed to the lower work function of sputtered ITO (4.03 eV) as compared to commercially-deposited and UV-Ozone-treated ITO (4.7 eV) used in the conventional cell [11]. This decreases the built-in electric field (E_{bi}) from 1.2×10^7 V/m to 6.8×10^6 V/m for an ITO or sputtered ITO anode, respectively. Accumulated charge at the interface can result in an S-shaped J–V characteristic [16], which is not observed here. Therefore in calculating the electric field, we assume that all free carriers are depleted from the active region, and hence the field is uniform throughout the device. Without a sufficient E_{bi}, the charge separated pair that forms at the donor–acceptor interface on exciton dissociation is likely to recombine, leading to reduced J_{SC} and V_{OC}. This is also reflected by the increase in the ideality factor from 1.89 ± 0.06 for the conventional cell, to 2.0 ± 0.1 for the inverted cell, indicating a larger recombination current. The decreased fill factor is primarily due to the higher series resistance of the device, a result of the higher contact

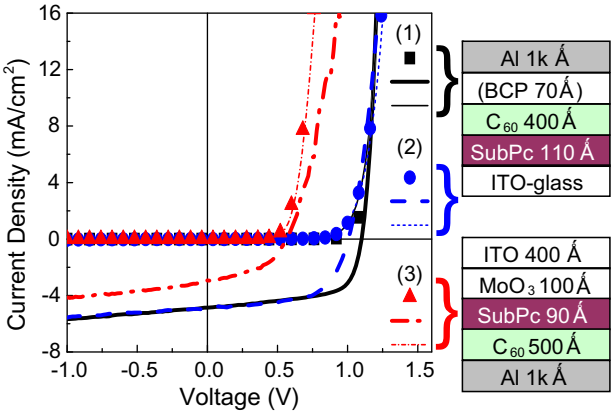

Fig. 1. Current density *vs*. voltage characteristics of conventional and inverted solar cells with the structure (1) indium tin oxide (ITO)-coated glass/SubPc 110 Å/C_{60} 400 Å/BCP 70 Å/Al 1000 Å in the dark (squares) and under 1 sun, AM1.5G simulated illumination (solid line); (2) ITO-coated glass/SubPc 110 Å/C_{60} 400 Å/Al 1000 Å in the dark (circles) and under 1 sun, AM1.5G simulated illumination (dashed line); and (3) glass/Al 1000 Å/C_{60} 500 Å/SubPc 90 Å/MoO_3 100 Å/ITO 400 Å in the dark (triangles) and under 1 sun, AM1.5G simulated illumination (dash-dotted line). Fits according to the theory in text are indicated by the thin solid line, short dashed line, and short dash-dotted line for devices (1), (2), and (3), respectively. The light is incident via ITO.

resistance of the C_{60}/Al interface compared to that of an Al/C_{60} interface.

To increase V_{OC}, a series of inverted devices was fabricated with varied MoO_3 layer thicknesses (t) from 100 Å to 700 Å, while using a low work function, 5 vol% Mg:Ag cathode. It was found that V_{OC} increases from 0.78 ± 0.02 V to 1.02 ± 0.02 V when t changes from 100 Å to 300 Å, and saturates for thicker MoO_3 films, as shown in Fig. 2(a). Consistent with optical simulations, the responsivity peaks at t = 300 Å, yielding η_P = 2.4 ± 0.2%, as shown in Fig. 2(b).

The measured absorption of MoO_3 films on quartz substrates is shown in Fig. 3. The absorption edge corresponds to the MoO_3 band gap [17] (E_g). It is found to increase by 0.43 eV as t increases from 100 Å to 300 Å, and saturates thereafter. The absorption edge is also influenced by optical interference. After subtracting this effect, the increase in E_g is approximately 0.3 eV over this range of thicknesses. It has been found previously that the work function of MoO_3 (Φ_{MoO_3}) increases logarithmically with the layer thickness [18]. The energy shift improves device performance by: (1) creating a greater difference between the LUMO of MoO_3 and SubPc, thereby reducing the electron leakage current, and (2) promoting band bending in the highest occupied molecular orbitals (HOMO) of SubPc at the SubPc/MoO_3 interface.

The parallel resistance, R_P, and the photocurrent density, J_{ph}, are found at J = 0 using [19]:

$$V_{OC} = \frac{nkT}{q} \ln\left[\frac{J_{ph}(V_{OC})}{J_S} + 1 - \frac{V_{OC}}{R_P J_S}\right]$$

where q is the electron charge, k is the Boltzmann constant, and T is the absolute temperature. Typically [9] $J_{ph}/J_S >> 1$ and $V_{OC}/R_P << J_{ph}$ (V), and hence V_{OC} depends logarithmically on J_{ph}/J_S. By assuming a constant J_{ph} (V) = J_{SC}, the calculated V_{OC} matches the experimental data for conventional cells, but overestimates that of the inverted cells by 10% (see Table 1 and Fig. 2(a), dashed line). This is likely due to the reduction in J_{ph} with increasing voltage, deviating from the assumption of a constant J_{ph}.

As inferred from the energy level diagram of the MoO_3/SubPc interface in the inset of Fig. 3, the increase in Φ_{MoO_3} with thickness reduces the energy difference between the valence band maximum of MoO_3 and the HOMO of SubPc, consequently producing steeper band bending when these materials are brought into contact. This favors hole extraction from SubPc to the contact, reflected by the decrease in the ideality factor with MoO_3 thickness changing from 100 Å to 500 Å (see Table 1). When the MoO_3 thickness reaches 700 Å, however, the increase in device resistance becomes dominant and the ideality factor increases again. The combined effects of the reduced electron leakage and enhanced hole extraction due to the presence of MoO_3 results in a maximum V_{OC} = 1.02 ± 0.02 V, close to that of the conventional device.

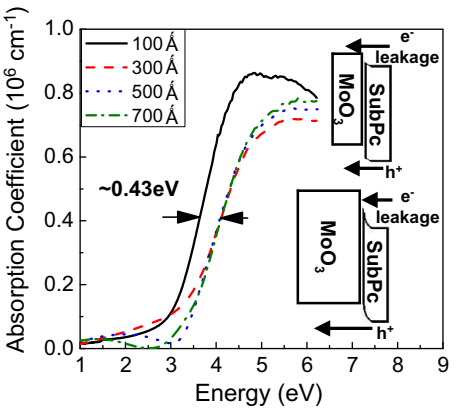

Fig. 3. Measured absorption spectra for 100 Å (solid lines), 300 Å (dashed lines), 500 Å (dash-dotted lines), 700 Å (short dashed lines) thick MoO_3 films on quartz substrates. *Inset*: Schematic band diagram of the MoO_3/SubPc interface for a MoO_3 thickness of t = 100 Å (upper) and 500 Å (lower).

Finally, the influence of the cathode work function (Φ_{Cat}) on performance was investigated, with results shown in Fig. 4. Values used for Φ_{Cat} are from Ref. [20]. Here, 1000 Å thick layers of Ag, Au, Al and Mg:Ag were used as cathodes, with MoO_3 t = 100 and 500 Å. For devices with t = 100 Å, V_{OC} increased significantly from 0.14 V to 0.91 V, while Φ_{Cat} decreased from 5.0 eV (Au) to 3.7 eV (Mg:Ag), as shown in Fig. 4(a). Different cathode optical

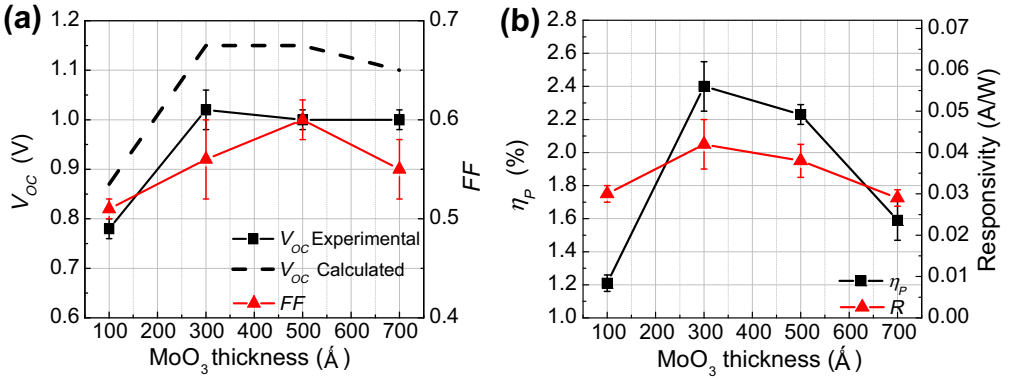

Fig. 2. Device characteristics measured under simulated 1 sun, AM1.5G illumination for the structure: glass/Mg:Ag 1000 Å/C_{60} 500 Å/SubPc 90 Å/MoO_3 t Å/ITO 400 Å where t = 100, 300, 500, and 700. (a) Measured open-circuit voltage, V_{OC} (squares), calculated V_{OC} (dashed lines), and fill factor, FF (triangles) *vs.* MoO_3 thickness. (b) Power conversion efficiency, η_P (squares), and responsivity R (triangles) *vs.* MoO_3 thickness.

Table 1
Inverted solar cell performance for the structure: glass/Mg:Ag 1000 Å/C_{60} 500 Å/SubPc 90 Å/MoO_3 t Å/ITO 400 Å under simulated 1 sun, AM1.5G illumination.

t (Å)	R (A/W)	V_{OC} (V)	V_{OC} (V) calculated	η_P (%)	n	J_S (mA/cm^2)
100	0.030	0.78	0.87	1.21 ± 0.05	2.6 ± 0.06	7.6×10^{-6}
300	0.042	1.02	1.15	2.4 ± 0.2	2.4 ± 0.04	3.6×10^{-8}
500	0.038	1.00	1.15	2.23 ± 0.06	2.4 ± 0.01	3.6×10^{-8}
700	0.029	1.00	1.10	1.6 ± 0.1	2.7 ± 0.01	4.0×10^{-7}

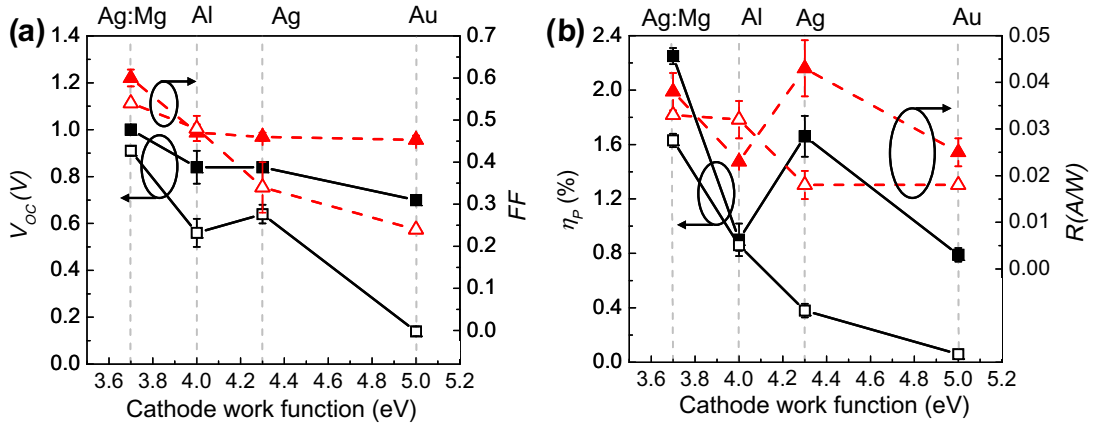

Fig. 4. The influence of cathode work function (Φ_{Cat}) on device characteristics under 1 sun, AM1.5G illumination. Sample structure: glass/cathode 1000 Å/C_{60} 500 Å/SubPc 90 Å/MoO_3 t Å/ITO 400 Å with cathode compositions of Mg:Ag, Al, Ag, Au and t = 100 Å (open symbols) and 500 Å (closed symbols). Cathode work functions (from Ref. [20]) are indicated by dashed vertical lines. (a) The dependence of FF (triangles and dashed lines) and V_{OC} (squares and solid lines) on Φ_{Cat}. (b) The dependence of η_P (squares and solid lines) and R (triangles and dashed lines) on Φ_{Cat}.

properties shift the optical field distribution, therefore changing the responsivity. The power conversion efficiency has a maximum at 2.23 ± 0.06% for Mg:Ag cathodes and t = 500 Å MoO_3 (see Fig. 4(b). The decrease in Φ_{Cat} results in an increased E_{bi} (from -1.9×10^7 V/m for Au to 1.2×10^7 V/m for Mg:Ag), leading to a higher V_{OC}. The built-in field for the Au-cathode devices is negative, giving rise to an increased electron leakage. Hence, the increase in t shows a much more dramatic impact on V_{OC} (from 0.91 V to 1.02 V for Mg:Ag and from 0.14 V to 0.7 V for Au). We conclude that to achieve a high-efficiency inverted cell, the electrodes must be chosen such that a sufficiently high E_{bi} is provided based on the energy levels of the photoactive layers and the contacts, and the electron leakage is effectively suppressed.

Note that there currently is disagreement as to the assignment of the energy levels of MoO_3. For example, there are reports that the conduction and valence band energies of MoO_3 are at E_C = 2.3 eV and E_V = 5.2–5.3 eV [21,22], while more recently, E_C = 6.7 eV and E_V = 9.7 eV [23] have been reported. Since photoelectron spectroscopy used to measure these energies is sensitive to factors such as surface conditions and the presence of inter-gap defect states, variations in source materials and sample preparation conditions may lead to this discrepancy. Previously [9], where the growth conditions were nearly identical as in this work, MoO_3 was used as an electron blocking layer in organic solar cells with transport properties similar to those from an organic (SubPc) blocking layer where its HOMO energy is 5.6 eV and its LUMO is at 3.6 eV. Therefore, we conclude that it is likely that the MoO_3 film reported here has E_C = 2.3 eV and E_V = 5.3 eV, consistent with earlier reports. This assignment is consistent with measurements made in our laboratory, and to be reported elsewhere.

In summary, 2.4 ± 0.2% power efficiency, inverted small molecule organic photovoltaic cells have been demonstrated. We have shown that an organic cathode buffer layer is not necessary in either conventional or inverted planar SubPc/C_{60} OPVs. The inverted device performance can be substantially improved by employing a compound MoO_3/ITO anode that suppresses electron leakage while maximizing the incident optical field intensity in the donor/acceptor interface region. The work function of layers adjacent to the donor or acceptor plays an important role in determining the V_{OC}.

Acknowledgements

The authors thank Dr. Ning Li, Michael Slootsky and Richard R. Lunt for helpful discussion, and the Defense Advanced Research Projects Agency (DARPA award No. W911NF-09-1-0034) and Global Photonic Energy Corp. for partial financial support.

References

[1] P. Peumans, A. Yakimov, S.R. Forrest, J. Appl. Phys. 93 (2003) 3693–3723.
[2] G. Parthasarathy, P.E. Burrows, V. Khalfin, V.G. Kozlov, S.R. Forrest, Appl. Phys. Lett. 72 (1998) 2138–2140.
[3] J. Meiss, N. Allinger, M.K. Riede, K. Leo, Appl. Phys. Lett. 93 (2008) 103311–103313.

[4] J. Meiss, M.K. Riede, K. Leo, J. Appl. Phys. 105 (2009) 063105–063108.
[5] J. Meiss, M.K. Riede, K. Leo, Appl. Phys. Lett. 94 (2009) 013303–013313.
[6] X. Tong, R.F. Bailey-Salzman, G. Wei, S.R. Forrest, Appl. Phys. Lett. 93 (2008) 173303–173304.
[7] C. Tao, S. Ruan, X. Zhang, G. Xie, L. Shen, X. Kong, W. Dong, C. Liu, W. Chen, Appl. Phys. Lett. 93 (2008) 193303–193307.
[8] H. Schmidt, H. Flugge, T. Winkler, T. Bulow, T. Riedl, W. Kowalsky, Appl. Phys. Lett. 94 (2009) 243302–243303.
[9] N. Li, B.E. Lassiter, R.R. Lunt, G. Wei, S.R. Forrest, Appl. Phys. Lett. 94 (2009) 023303–023307.
[10] C.C. Wu, C.I. Wu, J.C. Sturm, A. Kahn, Appl. Phys. Lett. 70 (1997) 1348.
[11] J. Xue, S.R. Forrest, J. Appl. Phys. 95 (2004) 1869–1877.
[12] V. Shrotriya, G. Li, Y. Yao, T. Moriarty, K. Emery, Y. Yang, Adv. Funct. Mater. 16 (2006) 2016–2023.
[13] H. Gommans, B. Verreet, B.P. Rand, R. Muller, J. Poortmans, P. Heremans, J. Genoe, Adv. Funct. Mater. 18 (2008) 3686–3691.
[14] C.Y. Kwong, A.B. Djurišić, P.C.C.A.W.K. Chan, Jpn. J. Appl. Phys. 43 (2004) 1305–1311.
[15] J. Xue, S. Uchida, B.P. Rand, S.R. Forrest, Appl. Phys. Lett. 84 (2004) 3013–3015.
[16] A. Kumar, S. Sista, Y. Yang, J. Appl. Phys. 105 (2009) 094512–094516.
[17] H.Y. Fan, Phys. Rev. 82 (1951) 900.
[18] Y. Kinoshita, R. Takenaka, H. Murata, Appl. Phys. Lett. 92 (2008) 243303–243309.
[19] B.P. Rand, D.P. Burk, S.R. Forrest, Phys. Rev. B 75 (2007) 115311–115327.
[20] M.A. Baldo, S.R. Forrest, Phys. Rev. B 64 (2001) 085201.
[21] F. Wang, X. Qiao, T. Xiong, D. Ma, Org. Electron. 9 (2008) 985–993.
[22] V. Shrotriya, G. Li, Y. Yao, C. Chu, Y. Yang, Appl. Phys. Lett. 88 (2006) 073503–073508.
[23] M. Kroger, S. Hamwi, J. Meyer, T. Riedl, W. Kowalsky, A. Kahn, Appl. Phys. Lett. 95 (2009) 123301–123303.

periodic corrugation to the angular and spectral emissions [19]. These processes, however, require either very high pressure and temperature or vacuum process for the fabrication of the structure. It was also not very clear whether the enhancement is originated from the PC effect or from the reflection from the corrugated metallic mirror or from the combined effects.

In this study, we report on corrugated OLEDs fabricated on polymer based PCs to enhance the light extraction. The photonic crystals are fabricated using ultraviolet (UV)–NIL process at room-temperature and low-pressure, thereby it can be applied in large-area imprinting and in roll-to-roll fabrication process. Improvement of the efficiency in the corrugated OLEDs is achieved due to the coupling of the PC effect on the polymer, anode and organic layers and the Bragg-diffraction effect by the corrugated metallic mirror. The corrugated OLEDs with various PC heights are fabricated and evaluated. FDTD calculation is carried out to understand the contribution of the coupling to PC and the reflection from the corrugated metallic mirror to light extraction.

2. Experimental

Corrugated green emitting OLEDs were fabricated on PC substrates and compared with a reference planar OLED without a PC structure. The fabrication process is schematically represented in Fig. 1. PC patterns in silicon stamps were transferred to the polymer layer on glass substrates using UV–NIL. The silicon stamps were fabricated via DUV lithography and RIE. The lattice constant and diameter of the holes are 530 nm and 265 nm, respectively, and the depths of the holes are controlled by etching time to get 15 nm, 50 nm, 65 nm, 80 nm and 100 nm. The PC patterns in the stamps have hexagonal lattice structures as shown in Fig. 2(a). The holes produce polymer circular pillars on the glass substrates by UV–NIL. OLEDs were fabricated on the PC substrates by successively depositing a 300-nm-thick IZO layer by sputtering, 60-nm-thick 2TNATA (4,4′,4″-Tris(N-(2-naphthyl)-N-phenyl-amino)-triphenylamine) as a hole injection layer, 20-nm-thick NPB (N,N′-diphenyl-N,N′-bis(1,1′-biphenyl)-4,4′-diamine) as a hole transporting layer, 60-nm-thick Alq_3 (tris-(8-hydroxyquinoline)-aluminum) as an emitting and electron transporting layer and 100-nm-thick LiF/Al as a cathode by thermal evaporation under high vacuum ($\leqslant 10^{-7}$ torr), respectively. The current–voltage characteristics and the light-output power of the devices were measured using a Keithley 237 source measurement unit and a photodiode (Newport Model 818-UV) connected to an optical power meter (Newport Model 1835-C).

3. Results and discussion

Fig. 2 shows the cross-sectional images of the fabricated PC structure of a stamp (a) and corrugated OLEDs (b–f). The images were obtained using high-resolution (field emission) ion imaging with dual-beam focused-ion-beam (DB–FIB) microscope (NOVA200). The images show multi-layers consisting of the PC structures of the resin and the corrugated IZO, organic and aluminum layers. The OLEDs with pillar heights (corrugation depths) of 15 nm and 50 nm have perfectly conformal layers with the imprinted polymer pattern. On the other hand, the OLEDs fabricated on the PC substrates with the pillars higher than 65 nm (Fig. 2d–f) showed cracks in the IZO layer and voids at the interface between the IZO and the organic layers. Void formation leads to unstable current distribution, resulting in a considerable decrease in the light emitting efficiency. Deposition of organic layers on the cracked IZO layer leads to the formation of sharp edges in the crevices, leading to high leakage current as described later. Therefore these high PCs have larger electrical negative effect than optical advantage.

Fig. 3 displays the current–voltage (J–V) characteristics of the devices. The turn-on voltages of all the devices are

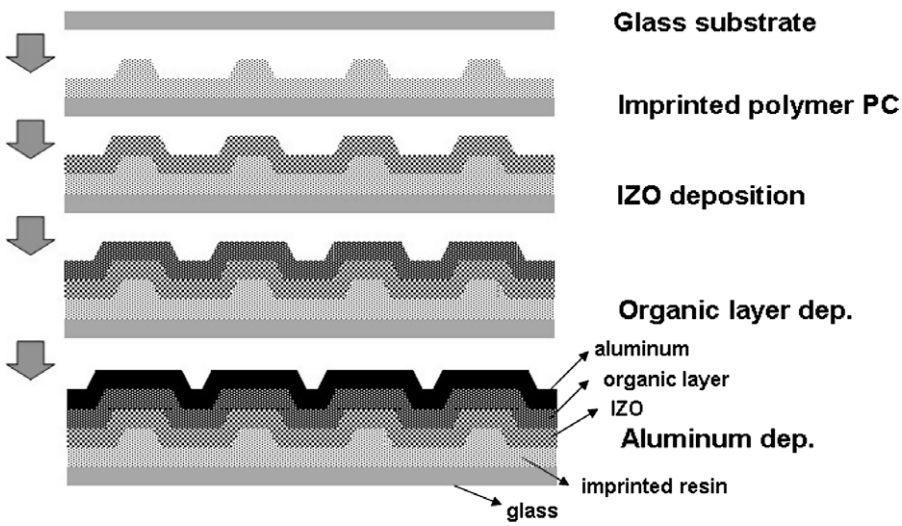

Fig. 1. Fabrication process of corrugated OLEDs.

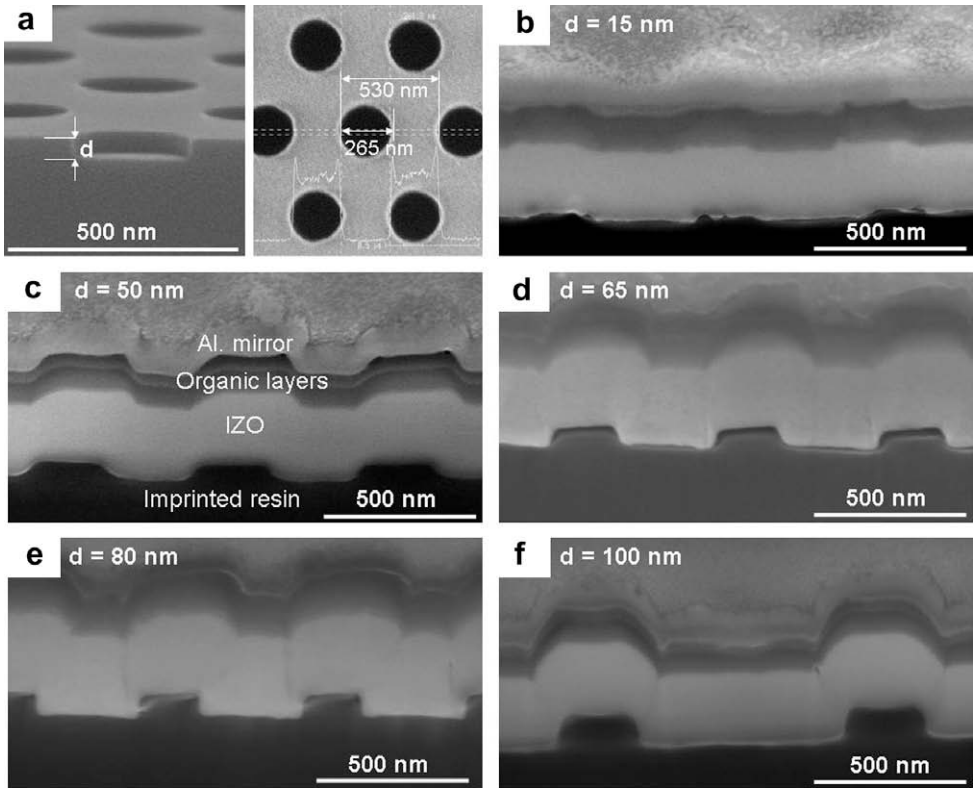

Fig. 2. SEM image of one of the stamps used in the UV–NIL process (a), and DB–FIB images of the cross-sections of fabricated corrugated OLED samples with (b) 15 nm corrugation depth, (c) 50 nm corrugation depth, (d) 65 nm corrugation depth, (e) 80 nm corrugation depth and (f) 100 nm corrugation depth.

approximately 3 V. It is interesting to note, however, that higher pillars in the PC substrate result in higher current densities at a same voltage, and it is consistent with previous reports [13]. This is another important advantage of corrugated OLEDs to reduce the operating voltage and to improve the power efficiency. This phenomenon can be explained by the increase of the interface area of the layers and by the enhancement of the electric-field intensity of the corrugated anode [14].

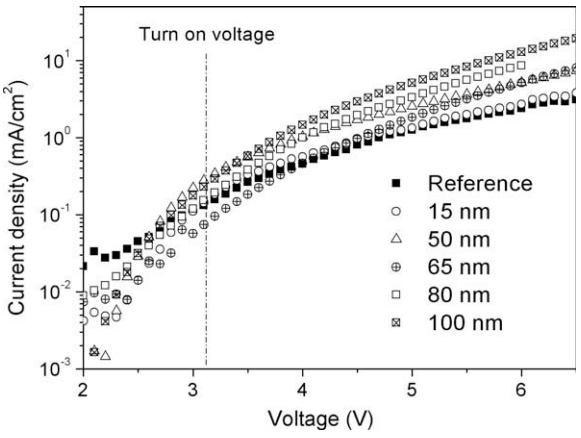

Fig. 3. Voltage–current characteristics of the corrugated OLEDs with different corrugation depths.

The electroluminescence (EL) intensities of the OLEDs were measured using an integrating sphere (Labsphere Co., 6″ in diameter). The devices were attached to a port on the integrating sphere where the glass side faced the inside of the integrating sphere. A 20 mm hole in diameter was used as the port to collect all the forward emitted light including the diffracted light, which is larger than the active area (3×3 mm^2) of the devices. All the devices including the reference OLED were characterized using the same system. Fig. 4 shows the efficiency enhancement with respect to the current density and the electrical input power density. Forty nine percentage enhancement of the light extraction with respect to the current density was obtained from the device having the corrugation depth of 50 nm. The improvement of the power efficiency is even higher. Remarkably high improvement of 93% was achieved with 50 nm pillars resulting from the decrease of the operating voltage as shown in Fig. 3. In our previous study, the improvement in the light extraction was 50% for SPC–OLED with a corrugation depth of 265 nm having identical lattice constant and diameter [15]. The improvement in the power efficiency was almost the same as the luminous (current) efficiency, as there was no reduction in the operating voltage because of the existence of a planarization layer below the ITO layer. The superior power efficiency and the simple fabrication method of the corrugated OLEDs demonstrate that they are practically more meaningful than the SPC–OLED. However, too high pillars resulted in uneven charge distribution and light emission

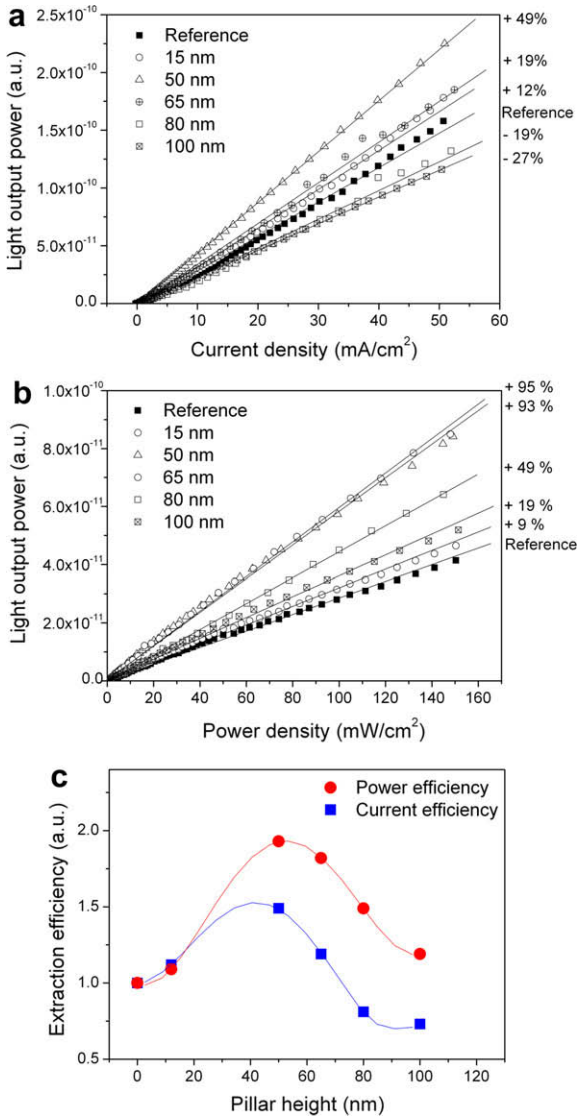

Fig. 4. (a) Light-output power versus current density, (b) light-output power versus electrical input power density and (c) the relative extraction efficiencies with respect to corrugation depth normalized to the OLEDs without pillars.

induced from the uneven electrode as shown in Fig. 5. The corrugated OLED fabricated on a 100 nm high PC structure is not able to emit light uniformly. This effect may also accelerate the degradation of the OLED.

The variation of emission spectrum and intensity with viewing angle were measured using a rotating stage and optical fiber at the current of 1 mA and are shown in Fig. 5(b–d).The reference OLED with planar substrate shows little change in the emission spectra and Lambertian pattern of emission intensity with viewing angle as expected. In contrast the OLED with the corrugation depth of 50 nm showed regularly fluctuated spectra and intensity with the angle [19]. Thereby the far-field radiation of the 50 nm corrugated OLED gets a profile similar to the shape of tulip as depicted in Fig. 5(d). The radiation profile of 10 nm-PC OLED is almost the same as the Lambertian emission, but the diffraction wings are getting more apparent as the pillar height increases. In this way, the intensity at the angle about 30° gets stronger and its shape becomes close to a butterfly wing which is consistent with our previous research [15].

Device lifetime can be a significant issue in corrugated OLEDs because of the possibility of non-uniform film thickness, electric field distribution and current. It is true for large corrugation depth of 100 nm as displayed in Fig. 5(a). Non-uniform distribution of emission intensities is apparent. In contrast, however, emission intensity of the OLED with the corrugation depth of 50 nm is uniform over the emission area. Moreover, the leakage current at low voltage is very low as displayed in Fig. 3. These facts imply that the film thickness and the current are rather uniform without significant concentrated electric field if the corrugation depth is less than certain value, which turns out to be 50 nm in this study. Further study on the effect of corrugation depth on the device stability is going on and will be reported later.

4. FDTD Analysis

In a corrugated OLED, as seen in Fig. 2, the corrugation depth of the PC layers and the metal grating can be considered as identical. However, as a future study, using certain planarization techniques, (such as sol–gel of high refractive index materials like TiO_2 or ZnO) according to the thickness of the coating layer and number of sol–gel steps a complete planarization can be attained as well as a partial planarization. In other words, PC layers of the anode and organic layers can be designed to have a different corrugation depth from that of to the metal grating. Therefore, it is important to have an insight on the relation of the corrugation depth with Bragg-diffraction and Bragg-reflection efficiencies, separately. Three sets of 3 dimensional (3D) FDTD simulations were performed using the structures shown in the inset of Fig. 6. The first structure has a flat anode surface on a planarized PC layer, i.e., single-layer PC structured OLED having the effect of only Bragg-diffraction. The second set of the simulations was performed for the corrugated OLED with no polymer PC structure to estimate the effect of the Bragg-reflection only. In this structure, the Bragg-diffraction effect on the anode and the organic layers must be negligible as the refractive index difference between the organic layers and the anode is very small. Finally, the simulations were performed for the multi-layer corrugated OLEDs. Corrugation depth was varied as a parameter in the simulations. Gaussian dipole sources were assumed to be located at the interface of NPB/Alq_3 with random distribution of dipole orientation. The number of dipoles was kept the same for all the structures in order to compare the extraction efficiencies from pure PC effect and Bragg-diffraction even though the surface area of the emission layer in corrugated OLEDs increases as the corrugation depth increased.

Fig. 6 shows the result of simulations in which the improvement in the light extraction is compared in terms of corrugation depths. In the single-layer PC structured OLEDs, the light extraction efficiency increases linearly as

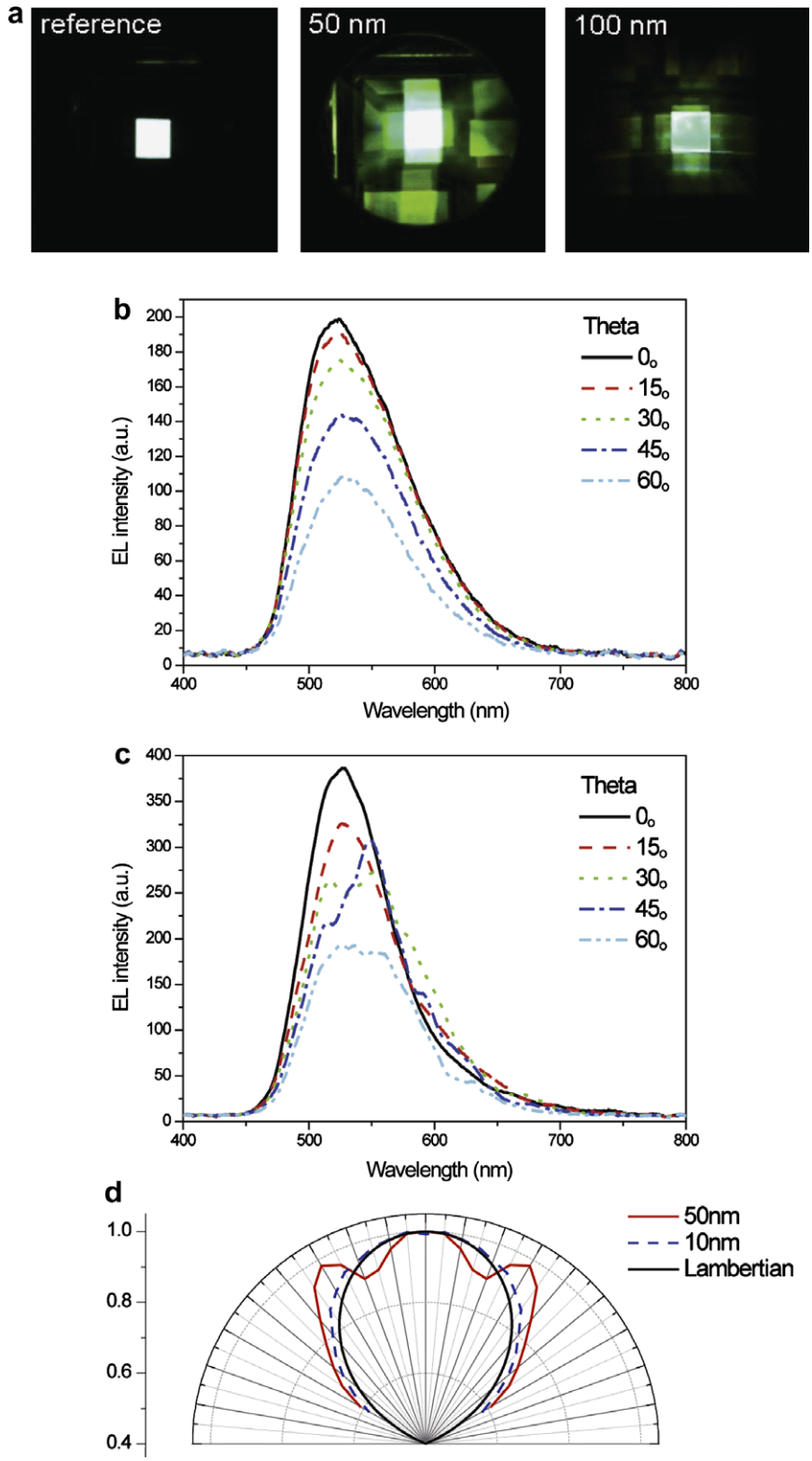

Fig. 5. (a) Photographs of the reference OLED and corrugated OLEDs with pillar heights of 50 nm and 100 nm, the angular emission characteristics of OLEDs with (b) planar and (c) 50 nm corrugated substrates and (d) the radiation profiles.

the corrugation depth increases. This result indicates that large portion of emitted light can be extracted using high pillars if there is a method to fill up a gap with a high refractive and transparent material avoiding any void or defect.

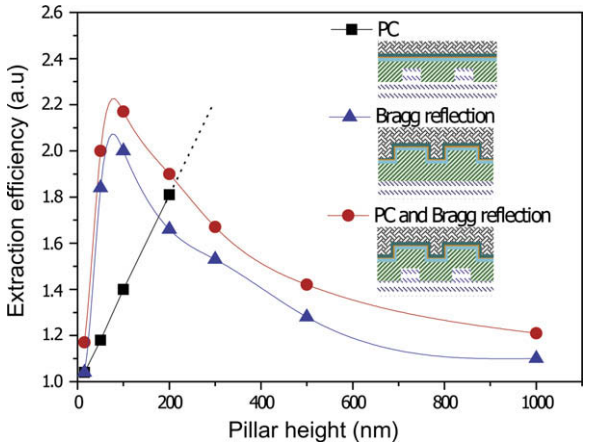

Fig. 6. Simulated relative light extraction efficiency versus the corrugation depth for three different structures shown in inset.

This is an expected result in accordance with previously reported findings [16]. The simulations were limited to corrugation depth below 300 nm in this device as the thickness of the anode was 300 nm. In the second case where the Bragg-reflection is the main factor in the improvement of the efficiency, the increase in the efficiency is substantial even at the corrugation depth of 50 nm and it reaches a peak value at the corrugation depth of 100 nm. Interestingly enough, however, the enhancement of the light extraction efficiency begins to decrease as the corrugation depth exceeds 100 nm. This simulation result can be explained as follows. When the corrugation depth exceeds a certain value, the deeper metal pit causes random phased electromagnetic waves due to multi-reflection and diffraction from the metal surface and side walls. Energy absorption by the surface plasmon from the metal surface leads to the reduction of the light extraction as well. These factors reduce the amount of Bragg-reflected light waves, resulting in less improvement of efficiency [21]. The light extraction in the third structure was further enhanced by the PC structure. The enhancement of extraction is dominated by the Bragg-reflection from the corrugated organic and metallic layers if the height of nanostructure is below 100 nm. Combined effect of light extraction becomes the maximum at the corrugation depth of 100 nm. This result suggests that further improvement of the light extraction than 49% achieved in this experiment is possible by using the corrugated OLEDs with the corrugation depth of 100 nm if we can prevent the formation of cracks and sharp edges in IZO layer, thereby to have good electrical contact.

5. Conclusions

High-efficiency corrugated OLEDs were fabricated on PC structured substrates using UV–NIL process at room-temperature and low-pressure. The Bragg-diffraction effect on the PCs of substrate, anode and organic layers and the Bragg-reflection from the corrugated metal mirror result in high light extraction efficiency even with a sub-100 nm corrugation depth. Furthermore the corrugated anode structure reduces the operating voltage. As a result, 93% enhancement of the power efficiency was obtained from an OLED even with a very shallow corrugation depth of 50 nm compared to the reference OLED with planar structure. The roles of corrugated metal mirror and PC layers on the efficiency enhancement were separately examined through FDTD analyses. The analyses showed that the increase in the efficiency reaches a peak value at a critical corrugation depth of 100 nm and the major enhancement comes from the Bragg-reflection by the corrugated metal mirror.

Acknowledgments

This research was supported by a grant (2009K000069) from Center for Nanoscale Mechatronics & Manufacturing, one of the 21st Century Frontier Research Programs, which are supported by Ministry of Education, Science and Technology, KOREA. In addition, the authors are grateful to Dr. Se-Heon Kim from the Department of Physics, KAIST for his constructive comments regarding the results of the FDTD simulations.

References

[1] G. Gu, D.Z. Garbuzov, P.E. Burrows, S. Venkatesh, S.R. Forrest, M.E. Thompson, Opt. Lett. 22 (1997) 396.
[2] N.C. Greenham, R.H. Friend, D.D.C. Bradley, Adv. Mater. 6 (1994) 491.
[3] C.F. Madigan, M.H. Lu, J.C. Sturm, Appl. Phys. Lett. 76 (2000) 1650.
[4] J.J. Wierer, M.R. Krames, J.E. Epler, N.F. Gardner, M.G. Craford, J.R. Wendt, J.A. Simmons, M.M. Sigalas, Appl. Phys. Lett. 84 (2004) 3885.
[5] R. Windisch, P. Heremans, A. Knobloch, P. Kiesel, G.H. Dohler, B. Dutta, G. Borghs, Appl. Phys. Lett. 74 (1999) 2256.
[6] I. Schnitzer, E. Yablanovitch, C. Canau, T.J. Gmitter, A. Scherer, Appl. Phys. Lett. 63 (1993) 2174.
[7] T. Tsutsui, M. Yahiro, H. Yokogawa, Adv. Mater. 13 (2001) 1149.
[8] R.H. Jordan, L.J. Rothberg, A. Dodabalapur, R.E. Slusher, Appl. Phys. Lett. 69 (1996) 1997.
[9] A. Kock, E. Gornik, M. Hauser, K. Beinstingl, Appl. Phys. Lett. 57 (1990) 2327.
[10] J.M. Lupton, B.J. Matterson, I.D.W. Samuel, M.J. Jory, W.L. Barnes, Appl. Phys. Lett. 77 (2000) 3340.
[11] T. Kim, P.O. Leisher, A.J. Danner, R. Wirth, K. Streubel, K.D. Choquette, IEEE Photonics Technol. Lett. 18 (2006) 1876.
[12] Y.C. Kim, S.H. Cho, Y.W. Song, Y.J. Lee, Y.H. Lee, Y.R. Do, Appl. Phys. Lett. 89 (2006) 173502.
[13] K. Ishihara, M. Fujita, I. Matsubara, T. Asano, S. Noda, H. Ohata, A. Hirasawa, H. Nakada, N. Shimoji, Appl. Phys. Lett. 90 (2007) 111114.
[14] M. Fujita, T. Ueno, K. Ishihara, T. Asano, S. Noda, H. Ohata, T. Tsuji, H. Nakada, N. Shimoji, Appl. Phys. Lett. 85 (2004) 5769.
[15] S. Jeon, J.W. Kang, H.D. Park, J.J. Kim, J.R. Youn, J. Shim, J.H. Jeong, D.G. Choi, K.D. Kim, A.O. Altun, S.H. Kim, Y.H. Lee, Appl. Phys. Lett. 92 (2008) 223307.
[16] Y.J. Lee, S.H. Kim, J. Huh, G, H. Kim, Y.H. Lee, S.H. Cho, Y.C. Kim, Y.R. Do, Appl. Phys. Lett. 82 (2003) 3779.
[17] A.M. Adawi, R. Kullock, J.L. Turner, C. Vasilev, D.G. Lidzey, A. Tahraoui, P.W. Fry, D. Gibson, E. Smith, C. Foden, M. Roberts, F. Qureshi, N. Athanassopoulou, Org. Electron. 7 (2006) 222.
[18] S. Fan, P.R. Villeneuve, J.D. Joannopoulos, E.F. Schubert, Phys. Rev. Lett. 78 (1997) 3294.
[19] U. Geyer, J. Hauss, B. Riedel, S. Gleiss, U. Lemmer, M. Gerken, J. Appl. Phys. 104 (2008) 093111.
[20] P.A. Hobson, S. Wedge, J.A.E. Wasey, I. Sage, W.L. Barnes, Adv. Mater. 14 (2002) 1393.
[21] C.J. Yates, I.D.W. Samuel, P.L. Burn, S. Wedge, W.L. Barnes, Appl. Phys. Lett. 88 (2006) 161105.

2. Experimental

2.1. Syntheses and characterization of compounds

Unless otherwise noted, all chemicals were obtained from commercial suppliers and used without further purification. ^{1}H NMR spectra were measured in deuterated solvents on a JEOL ECX 400 MHz spectrometer. Elemental analyses were carried out by the Elemental Analysis Service, Yamagata University, Japan. Thermal gravimetric analysis (TGA) was performed on Seiko SII EXSTAR 6000 and TGA/DTA 6200 analyzers. Differential Scanning Calorimetry (DSC) was performed on a Perkin–Elmer Diamond DSC calorimeter. Ionization potentials were measured with a photoelectron spectrometer surface analyzer (RIKEN KEIKI AC-3). UV–visible absorption spectra were recorded of solutions in chloroform or films on quartz with a Shimadzu UV-3150 spectrometer. PL spectra were recorded on a Jobin Yvon Fluoromax-2 fluorometer. PL quantum efficiencies were measured on a Hamamatsu C9920-01 integral sphere system under nitrogen.

Compound **2**: A mixture of 2,7-dibromo-9,9-diethylfluorene (**1**) (22.8 g, 60.0 mmol), carbazole (5.01 g, 30.0 mmol), copper (11.4 g, 180 mmol) and potassium carbonate (25.2 g, 180 mmol) in *o*-dichlorobenzene (200 ml) was stirred under reflux for 24 h under a nitrogen atmosphere. After cooling to room temperature, the mixture was poured into water and then extracted with toluene. The combined organic phases were washed with brine and dried over $MgSO_4$. The crude mixture was purified by column chromatography on silica gel (chloroform/hexane = 1/3) affording **2** (8.61 g, 61.6%) as a white solid. ^{1}H NMR (400 Mz, $CDCl_3$, ppm) δ 0.44 (6H, t, J = 7.4 Hz), 2.02–2.07 (4H, m), 7.26–7.32 (2H, m), 7.39–7.45 (4H, m), 7.49–7.55 (4H, m), 7.64 (1H, d, J = 8.8 Hz), 7.89 (1H, d, J = 8.8 Hz), 8.16 (1H, d, J = 7.8 Hz).

BCzBF: A mixture of **2** (4.20 g, 9.00 mmol), bis(pinacolato)diboron (2.00 g, 15.0 mmol), $PdCl_2$(dppf) (0.183 g, 0.225 mmol), and potassium acetate (2.21 g, 22.5 mmol) in DMSO (350 ml) was stirred at 80 °C for 8 h under a nitrogen atmosphere. After cooling the solution to room temperature, **2** (3.80 g, 6.00 mmol), $PdCl_2$(dppf) (0.183 g, 0.225 mmol) and 2 M aqueous potassium carbonate (10 ml, 5.0 eq) were added and the mixture was stirred at 80 °C under nitrogen overnight. The mixture was cooled to room temperature and then the product was extracted with chloroform and washed with water, brine and dried over $MgSO_4$. The crude mixture was purified by column chromatography on silica gel (chloroform/hexane = 1/2), giving BCzBF as a yellow solid. The product was further purified by train sublimation. Yield: 2.08 g, 35.4%. ^{1}H NMR (400 Mz, $CDCl_3$, ppm) δ 0.53 (12H, t, J = 7.4 Hz), 2.08–2.23 (8H, m), 7.30–7.34 (6H, m), 7.42–7.46 (6H, m), 7.53–7.59 (4H, m), 7.69 (2H, s), 7.75 (2H, d, J = 7.4 Hz), 7.75 (2H, d, J = 8.1 Hz), 7.96 (2H, d, J = 7.5 Hz), 8.18 (4H, d, J = 8.0 Hz). Elemental Anal. Calcd for $C_{58}H_{48}N_2$: C, 90.12; H, 6.26; N, 3.62. Found C, 89.93; H, 6.26; N, 3.56%.

Compound **3**: A mixture of **1** (5.89 g, 15.5 mmol), diphenylamine (1.31 g, 7.75 mmol), $Pd(OAc)_2$ (34.8 mg, 0.155 mmol), 1,1′-bis(diphenylphosphino)ferrocene (0.687 g, 1.24 mmol) and sodium *tert*-butoxide (1.49 g, 23.4 mmol) in toluene (60 ml) was stirred under reflux for 24 h under a nitrogen atmosphere. After cooling to room temperature, the mixture was poured into water and then extracted with toluene. The combined organic phases were washed with brine and dried over $MgSO_4$. The product was purified by column chromatography on silica gel (chloroform/hexane = 1/3), affording **3** (2.09 g, 57.6%) as a white solid. ^{1}H NMR (400 Mz, $CDCl_3$, ppm) δ 0.35 (6H, t, J = 6.5 Hz), 1.9 (4H, t, J = 7.8 Hz), 7.00 (3H, t, J = 7.3 Hz), 7.06 (1H, s), 7.10 (4H, d, J = 7.3 Hz), 7.21–7.27 (4H, m), 7.39–7.47 (3H, m), 7.52 (1H, d, J = 8.2 Hz).

BDABF: A mixture of **3** (1.20 g, 2.56 mmol), bis(pinacolato)diboron (0.541 g, 2.13 mmol), $PdCl_2$(dppf) (60.0 mg, 0.0768 mmol) and potassium acetate (0.627 g, 6.39 mmol) in DMSO (60 ml) was stirred at 80 °C for 5 h under a nitrogen atmosphere. After cooling the solution to room temperature, **3** (0.80 g, 1.70 mmol), $PdCl_2$(dppf) (0.04 g, 0.0510 mmol) and 2 M aqueous potassium carbonate (5.5 ml, 5.0 eq) were added and the mixture was stirred at 80 °C under nitrogen overnight. The mixture was cooled to room temperature and then the product was extracted with chloroform and washed with water, brine and dried over $MgSO_4$. The product was purified by column chromatography on silica gel (chloroform/hexane = 1/2), giving BDABF (0.880 g, 53.2%) as a yellow solid. The product was further purified by train sublimation. Yield: 0.801 g, 47.9%. ^{1}H NMR (400 Mz, $CDCl_3$, ppm) δ 0.42 (12H, t, J = 7.32 Hz), 1.9–2.1 (8H, m), 7.00–7.07 (6H, m), 7.13 (10H, d, J = 8.1 Hz), 7.23–7.28 (8H, m), 7.55–7.69 (8H, m). Elemental Anal. Calcd for $C_{58}H_{52}N_2$: C, 89.65; H, 6.75; N, 3.61. Found C, 89.65; H, 6.82; N, 3.48%.

Compound **4**: *n*-Butyl lithium (1.6 M, 49.3 ml, 78.9 mmol) was added to a stirred solution of **1** (30.0 g, 78.9 mmol) in dry THF (500 ml) under a nitrogen atmosphere at −78 °C. After stirring for 0.5 h, trimethylchlorosilane (11.1 ml, 94.7 mmol) was added. The mixture was warmed to room temperature, then the product was extracted with chloroform and washed with water, brine and dried over $MgSO_4$. The crude mixture was purified by column chromatography on silica gel (hexane) to give **4** (27.6 g, 93.7%) as a colorless oil. ^{1}H NMR (400 Mz, $CDCl_3$, ppm) δ 0.28–0.35 (15H, m), 1.95–2.06 (4H, m), 7.41–7.46 (4H, m), 7.48 (1H, d, J = 7.5 Hz), 7.56 (1H, d, J = 8.7 Hz), 7.65 (1H, d, J = 7.3 Hz).

Compound **5**: *n*-Butyl lithium (1.6 M, 55.3 ml, 88.7 mmol) was added to a stirred solution of **1** (27.5 g, 73.8 mmol) in dry THF (500 ml) under a nitrogen atmosphere at −78 °C. After stirring for 0.5 h, trimethylchlorosilane (27.2 ml, 133 mmol) was added. The mixture was cooled to room temperature, then the product was extracted with chloroform and washed with water, brine and dried over $MgSO_4$. The crude mixture was purified by column chromatography on silica gel (hexane) followed by recrystallization from toluene/ethanol = 1/4 to give **5** (21.9 g, 52.0 mmol) as a white solid. ^{1}H NMR (400 Mz, $CDCl_3$, ppm) δ 0.26–0.32 (15H, m), 1.4 (12H, s), 2.0–2.1 (4H, m), 7.45 (1H, s), 7.49 (1H, d, J = 7.3 Hz), 7.70 (2H, d, J = 7.3 Hz), 7.75 (4H, s), 7.8 (1H, d, J = 7.3 Hz).

Compound **6**: A mixture of **2** (5.68 g, 12.2 mmol), **5** (6.14 g, 14.6 mmol), $Pd(PPh_3)_4$ (0.28 g, 0.244 mmol) and 2 M aqueous potassium carbonate (5.00 g, 36.6 mmol) in toluene (60 ml) and ethanol (30 ml) was stirred under reflux for 24 h under nitrogen. After cooling to room temperature, the mixture was poured into water and then extracted with toluene. The combined organic phases were washed with brine and dried over $MgSO_4$. The crude mixture was purified by column chromatography on silica gel (chloroform/hexane = 2/3), affording **6** (6.32 g, 76.1%) as a white solid. ^{1}H NMR (400 Mz, $CDCl_3$, ppm) δ 0.33 (9H, s), 0.42 (6H, t, J = 7.3 Hz), 0.51 (6H, t, J = 7.4 Hz), 2.0–2.2 (8H, m), 7.28–7.35 (2H, m), 7.44–7.56 (8H, m), 7.63–7.74 (5H, m), 7.80 (1H, d, J = 7.8 Hz), 7.86 (1H, d, J = 8.2 Hz), 7.95 (1H, d, J = 7.8 Hz), 8.19 (2H, d, J = 7.8 Hz).

Compound **7**: A mixture of **6** (6.50 g, 9.55 mmol) and iodine monochloride (1 M in CH_2Cl_2, 10.5 ml, 10.5 mmol) in CH_2Cl_2 (80 ml) was stirred at 0 °C for 1 h under nitrogen. After cooling to room temperature, the mixture was poured into water and then extracted with toluene. The combined organic phases were washed with brine and dried over $MgSO_4$. The crude mixture was purified by column chromatography on silica gel (chloroform/hexane = 1/3), affording **7** (4.60 g, 65.6%) as a white solid. ^{1}H NMR (400 Mz, $CDCl_3$, ppm) δ 0.40 (6H, t, J = 7.8 Hz), 0.51 (6H, t, J = 7.8 Hz), 2.0–2.2 (8H, m), 7.28–7.35 (2H, m), 7.44 (4H, d, J = 4.2 Hz), 7.50 (1H, d, J = 3.2 Hz), 7.53–7.71 (8H, m), 7.76 (1H, d, J = 7.8 Hz), 7.77 (1H, d, J = 7.8 Hz), 7.85 (1H, d, J = 7.8 Hz), 7.95 (2H, d, J = 7.8 Hz).

CzDABF: A mixture of **7** (3.50 g, 4.77 mmol), diphenylamine (1.21 g, 7.16 mmol), $Pd_2(dba)_3$ (34.9 mg, 0.0382 mmol), tri(*tert*-butyl)phosphine (0.0114 ml, 0.0477 mmol) and sodium *tert*-butoxide (0.688 g, 7.16 mmol) in toluene (60 ml) was stirred under reflux for 24 h under nitrogen. After cooling to room temperature the mixture was poured into water and then extracted with toluene. The combined organic phases were washed with brine and dried over $MgSO_4$. The crude mixture was purified by column chromatography on silica gel (chloroform/hexane = 1/2), affording *CzDABF* (2.17 g, 58.7%) as a white solid. The product was further purified by train sublimation. Yield: 0.801 g, 51.7%. ^{1}H NMR (400 Mz, $CDCl_3$, ppm) δ 0.44 (6H, t, J = 7.0 Hz), 0.51 (6H, t, J = 6.8 Hz), 1.9–2.2 (8H, m), 7.00–7.07 (3H, m), 7.14 (5H, d, J = 7.2 Hz), 7.25–7.30 (6H, m), 7.44 (4H, d, J = 3.6 Hz), 7.53–7.72 (8H, m), 7.85 (1H, d, J = 8.2 Hz), 7.94 (1H, d, J = 7.8 Hz), 8.17 (2H, d, J = 7.8 Hz). Elemental Anal. Calcd for $C_{58}H_{50}N_2$: C, 89.88; H, 6.50; N, 3.61. Found C, 89.75; H, 6.51; N, 3.58%.

2.2. Device fabrication and characterization

Light emitting devices were fabricated on indium tin oxide (ITO) coated glass substrates, which were prepared by ultrasonication sequentially in detergent, methanol, 2-propanol and acetone, then exposed to UV-ozone under ambient conditions for 15 min. MoO_3, Cs, rubrene and the bipolar materials were deposited by thermal evaporation at less than 1×10^{-4} Pa. Finally, the aluminum cathode was deposited through a shadow mask at less than 1×10^{-4} Pa. The active area of each device is 2 mm × 2 mm. Layer thickness calibration was performed using a Dektak 3 surface profilometer. The EL spectra were measured on a Hamamatsu PMA-11 photonic multichannel analyzer. The current–voltage (I–V) characteristics and luminance of the devices were measured using a Keithley 2400 Source Meter and Konica Minolta CS-200 chromameter, respectively. External quantum efficiencies were calculated assuming a Lambertian emission pattern and considering all spectral features in the visible region.

3. Results and discussion

Scheme 1 shows the synthetic routes to the carbazole and/or diphenylamine substituted-difluorene derivatives. Monocarbazolyl compound **2** was synthesized by an Ullmann coupling reaction between **1** and carbazole. After synthesis of the boronic ester derivative of **2** by the reaction of *bis*-(pinacolato)diboron and **1** with a palladium catalyst, dicarbazolyl compound BCzBF was synthesized successively in the same pot, *via* palladium-catalyzed Suzuki coupling of **2** with the boronic ester derivative of **2**. **3** was synthesized by palladium-catalyzed C–N coupling between **1** and diphenylamine. BDABF was synthesized in the same manner as BCzBF. In the synthesis of CzDABF, the coupling reaction between **2** and the boronic ester of **3** and the coupling reaction between **3** and boronic ester **2** gave a small amount of BCzBF or BDABF, respectively, as byproducts because of a homocoupling side reaction. These byproducts are difficult to remove from CzDABF because of their similar structure and polarity. Therefore, CzDABF was synthesized using a different route. **6** was obtained from a coupling reaction between **2** and **5**, then reacted with ICl to form **7**. Finally, a diphenylamine group was introduced to **7**, giving CzDABF.

TGA showed that the decomposition temperatures (T_d) with loss of 5 wt.% of the compounds were over 400 °C. The glass transition temperatures (T_g) of BDABF and CzDABF determined by DSC were higher than 100 °C. On the other hand, a T_g for BCzBF, which has a symmetrical structure and rigid carbazole substituents, was not observed in our experiment, probably because of its high crystallinity.

The UV absorption and PL spectra of the compounds were measured in the solution state and in the film state on a quartz substrate (Table 1). Absorption and PL maxima exhibited red shifts as the number of diphenylamine groups increased, suggesting that the electron donating diphenylamine group reduced the HOMO (highest occupied molecular orbital)–LUMO (lowest unoccupied molecular orbital) gap of the compounds. The ionization potentials (I_p) of the compounds were measured by ultraviolet photoelectron yield spectroscopy under atmospheric conditions. The I_p increased as the number of diphenylamine groups increased because diphenylamine moieties are better at donating electron density than carbazole moieties, which increases the HOMO energy level. Tentative electron affinity (E_a) values were estimated from the difference between I_p and the optical energy gap obtained from the edge of the UV absorption of the films. As the number of diphenylamine groups increased, the E_a of the compounds decreased and the I_p increased. DFT calculations

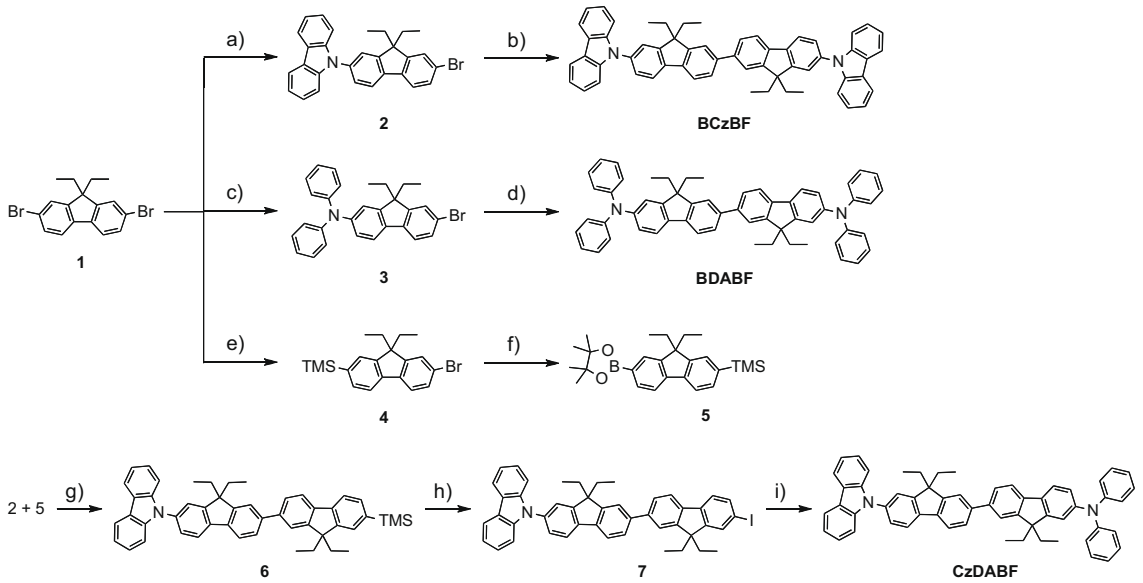

Scheme 1. Synthetic route to the bipolar compounds. (a) carbazole, Cu, K_2CO_3, dichlorobenzene, 180 °C, 20 h, (b) (i) Pd(dppf)Cl_2, KOAc, bis(pinacolato)diboron, DMF, 80 °C 3 h; (ii) **2**, Pd(dppf)Cl_2, K_2CO_3, 80 °C, 20 h, (c) diphenylamine, Pd(OAc)$_2$, 1,1′-bis(diphenylphosphino)ferrocene, NaO-*t*-Bu, toluene, reflux, 20 h, (d) (i) Pd(dppf)Cl_2, KOAc, bis(pinacolato)diboron, DMF, 80 °C 3 h; (ii) **3,** Pd(dppf)Cl_2, K_2CO_3, 80 °C 20 h, (e) (i) *n*-BuLi, −78 °C 1 h; (ii) $(CH_3)_3SiCl$, −78 °C to r.t., 20 h, (f) (i) *n*-BuLi, −78 °C 1 h; (ii) 2-isopropoxy-4,4,5,5-tetramethyl-1,3,2-dioxaborolane, −78 °C to r.t., 9 h, (g) Pd$(PPh_3)_4$, K_2CO_3 *aq*., toluene, ethanol, reflux, 20 h, (h) ICl, dichloromethane, 0 °C, 1 h, (i) $Pd_2(dba)_3$, tri(*t*-butyl)phosphine, NaO-*t*-Bu, toluene, reflux, 24 h.

Table 1
Thermal and optoelectrochemical properties and charge mobilities of the bipolar compounds.

	T_g (°C)	$T_{d5\%}$ (°C)	UV[a] (nm)	PL[a] (nm)	I_p (eV)	E_a[b] (eV)	E_g^{OPT}[a] (eV)	HOMO[c] (eV)	LUMO[c] (eV)	μ_h ($cm^2V^{-1}s^{-1}$)	μ_e ($cm^2V^{-1}s^{-1}$)
BCzBF	N.D.	477	350, 297	425	5.98	2.89	3.09	5.51	1.85	2.3×10^{-3}	1.5×10^{-3}
BDABF	106	417	380, 310	452	5.57	2.69	2.88	5.16	1.72	1.0×10^{-3}	N.D.
CzDABF	126	447	377, 299	449	5.76	2.79	2.93	5.02	1.58	1.3×10^{-4}	1.3×10^{-3}

[a] Neat film.
[b] $E_a = I_p - E_g^{OPT}$.
[c] Obtained from DFT calculations using B3LYP 6311+G(d,p)//631G(d).

showed that the HOMO energy levels of BCzBF and BDABF are delocalized over the whole molecule, while the HOMO of CzDABF is localized on the diphenylamine and bifluorene units. On the other hand, the LUMOs of all three compounds are localized on the bifluorene unit (Fig. S1). HOMO and LUMO levels estimated from the calculations were consistent with the values obtained experimentally for I_p and E_a.

The charge transport properties of the compounds were investigated by the TOF transient photocurrent technique at room temperature (Fig. 1). The carrier transit times were determined from the folding point in the double-logarithmic plots of the data (insets in Fig. 1). The hole mobilities of all three compounds were high, comparable to the mobilities of common hole transporting materials [15]. BDABF did not exhibit a photocurrent during measurement of electron mobility. On the other hand, BCzBF and CzDABF showed sufficient electron photocurrent to determine their electron mobilities. The electron mobilities of these two compounds were as high as their hole mobilities, and much higher than the electron mobility of 10^{-6}–10^{-7} $cm^2V^{-1}s^{-1}$ of the well-known electron transporting material, *tris*-(8-hydroxyquinoline) aluminum (Alq_3). These results demonstrate that the diphenylamine group increased the hole transport ability of bifluorene, while the carbazole group gave the compound bipolar charge transport abilities. The bipolar charge transport properties of these carbazole compounds are consistent with previously reported bipolar compounds such as CBP [9].

Fig. 2 shows the current density–voltage (*J*–*V*) characteristics of the hole-only devices containing *p*-doped bipolar compounds (ITO/bifluorene:MoO_3 50 mol% (120 nm)/Au) and undoped bifluorene (ITO/bifluorene (120 nm)/Au). While the undoped hole-only devices exhibited low current densities, the current density of the *p*-doped hole-only devices increased considerably in an Ohmic manner. The conductivities of the *p*-doped devices at 4.0×10^5 Vcm^{-1} were 1.5×10^{-6} Scm^{-1}, 1.7×10^{-6} Scm^{-1} and 1.1×10^{-6} Scm^{-1} for BCzBF, BDABF and CzDABF, respectively. Similarly, electron-only devices containing

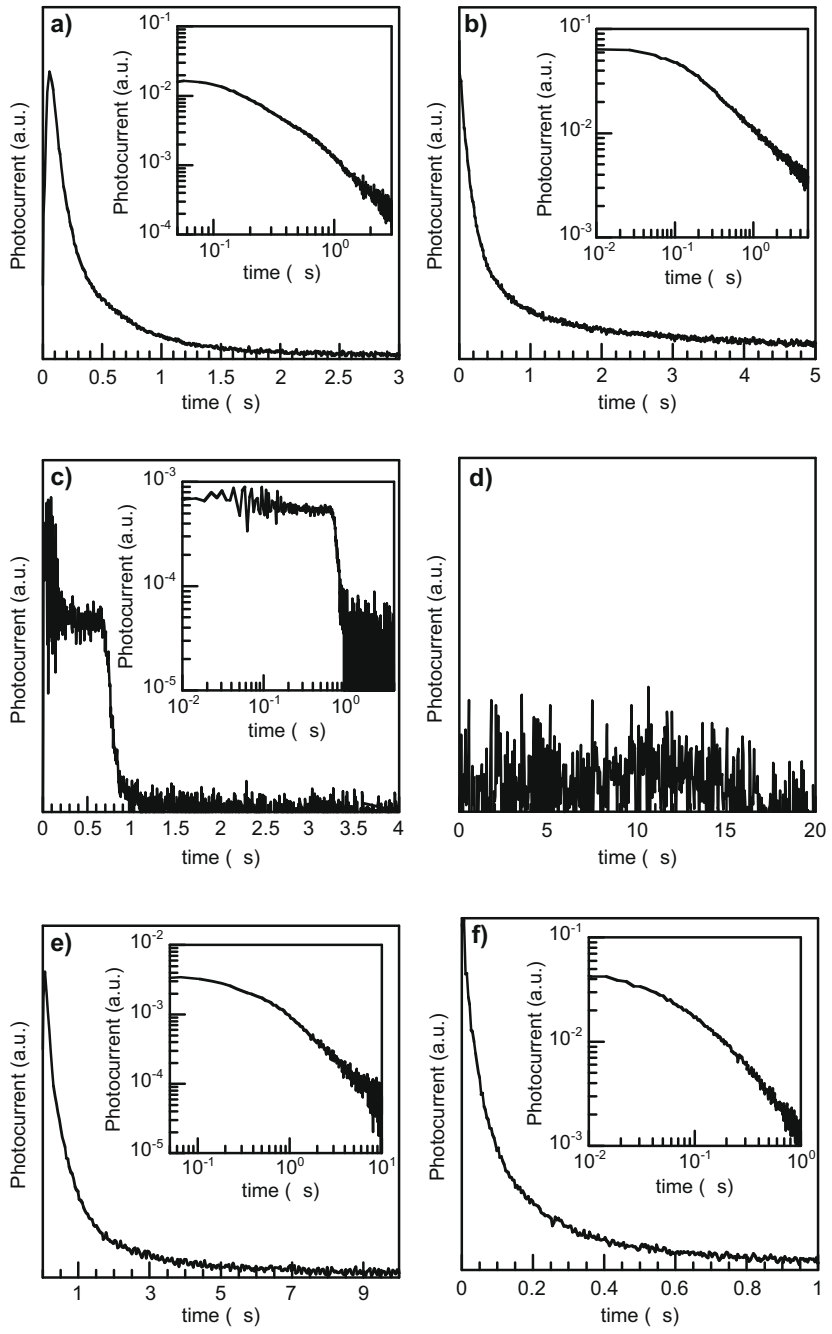

Fig. 1. Time-of-flight (TOF) transients of the bipolar compounds: (a) BCzBF, hole, $E^{1/2}$ = 700 (V/cm)$^{1/2}$, d = 3.0 μm. (b) BCzBF, electron, $E^{1/2}$ = 700 (V/cm)$^{1/2}$, d = 8.0 μm. (c) BDABF, hole, $E^{1/2}$ = 700 (V/cm)$^{1/2}$, d = 3.0 μm. (d) BDABF, electron, $E^{1/2}$ = 700 (V/cm)$^{1/2}$, d = 3.0 μm. (e) CzDABF, hole, $E^{1/2}$ = 700 (V/cm)$^{1/2}$, d = 3.0 μm. (f) CzDABF, electron, $E^{1/2}$ = 700 (V/cm)$^{1/2}$, d = 3.0 μm.

n-doped bipolar compounds (ITO/BCP (10 nm)/bifluorene:Cs 30 wt.% (120 nm)/Au) and undoped bipolar compounds (ITO/BCP (10 nm)/bifluorene (100 nm)/Au) were fabricated. The Cs-doped electron-only devices exhibited conductivities that were seven orders of magnitude higher than the undoped electron-only devices. At 4.0×10^5 Vcm^{-1}, the conductivities of the *n*-doped electron-only devices were 4.7×10^{-6} Scm^{-1}, 1.0×10^{-6} Scm^{-1} and 1.2×10^{-6} Scm^{-1} for BCzBF, BDABF and CzDABF, respectively. These results demonstrate that the bifluorene compounds have small enough I_p to be *p*-doped and E_a to be *n*-doped effectively, in addition to their bipolar charge transport ability in an undoped state.

OLEDs with a homo-junction structure were fabricated containing BCzBF and CzDABF with the device configurations: device I = ITO/bifluorene:MoO_3 (50 mol%, 20 nm)/

bifluorene (80 nm)/bifluorene:Cs (30 wt.%, 20 nm)/Al (80 nm) and device II = ITO/bifluorene:MoO_3 (50 mol%, 20 nm)/bifluorene (10 nm)/bifluorene: rubrene (20 wt.%, 60 nm)/bifluorene (10 nm)/bifluorene: Cs (30 wt.%, 20 nm)/Al (80 nm). Fig. 4a shows the PL spectra of the bipolar compounds and the EL spectra of the OLED. The EL spectra of device I did not correspond to the PL spectra of the bipolar compounds. This might be caused by absorption in the blue region by a radical species in the doped layers or exciplex emission in the interface between the doped and undoped layers. External quantum efficiencies (EQE) of device I were low at around 0.5% at 100 cd m^{-2} (Table 2). The low EQE of these devices were probably caused by the lack of an energy barrier between the layers making charge recombination poor and exciton quenching caused by the close proximity of doped layers to the emission zone. Device II was fabricated with rubrene doped into the emission layer to efficiently trap carriers and undoped bifluorene layers between the emission layer and the doped layers to prevent quenching. For device II, only yellow emission derived from

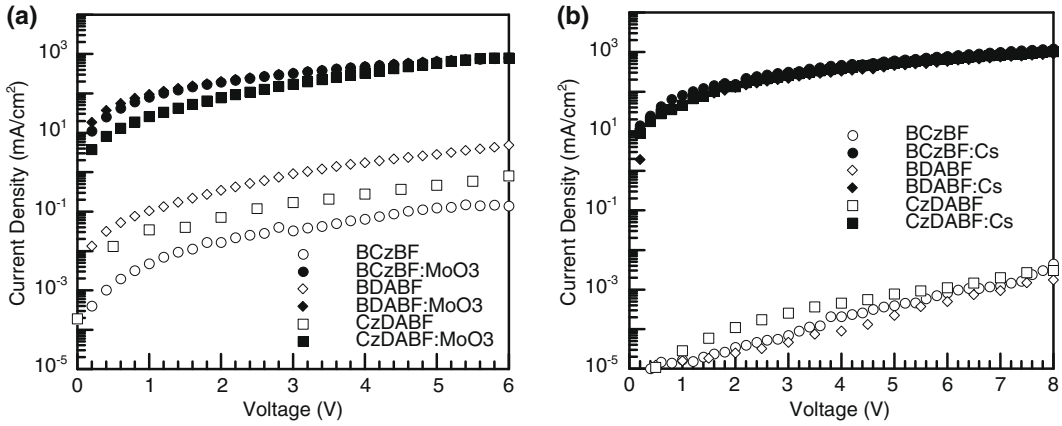

Fig. 2. Current density–voltage characteristics of (a) hole-only devices (ITO/bifluorene or bifluorene:MoO_3 (120 nm)/Au) and (b) electron-only devices (ITO/BCP (10 nm)/bifluorene or bifluorene:Cs (100 nm)/Al).

Table 2
Turn-on voltage at 1 cd m^{-2} and efficiencies at 100 cd m^{-2} and 1000 cd m^{-2} of OLEDs containing bipolar compounds.

EML	V_{on} (V)	100 cd m^{-2}				1000 cd m^{-2}			
		Voltage (V)	P.E. (lm W^{-1})	C.E. (cd A^{-1})	E.Q.E. (%)	Voltage (V)	P.E. (lm W^{-1})	C.E. (cd A^{-1})	E.Q.E. (%)
BCzBF	3.0	5.5	0.68	1.2	0.56	8.8	0.27	0.75	0.37
BCzBF:rubrene	3.8	7.0	2.9	6.5	2.1	10.4	1.4	4.5	1.5
CzDABF	3.0	5.2	0.76	1.3	0.49	8.2	0.32	0.84	0.35
CzDABF:rubrene	3.1	4.6	3.1	4.6	1.5	6.9	1.5	3.4	1.1

P.E., power efficiency; C.E., current efficiency; E.Q.E., external quantum efficiency.

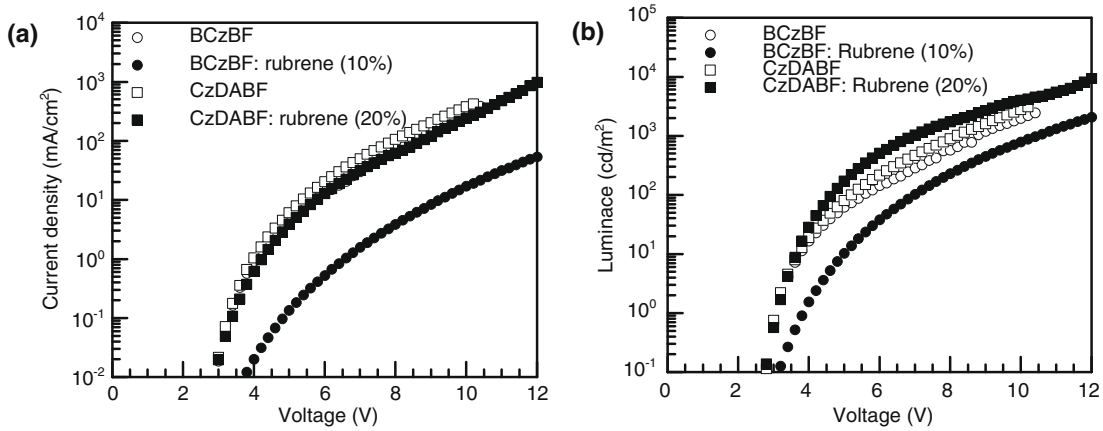

Fig. 3. (a) Current density–voltage and (b) luminance–voltage characteristics of OLEDs.

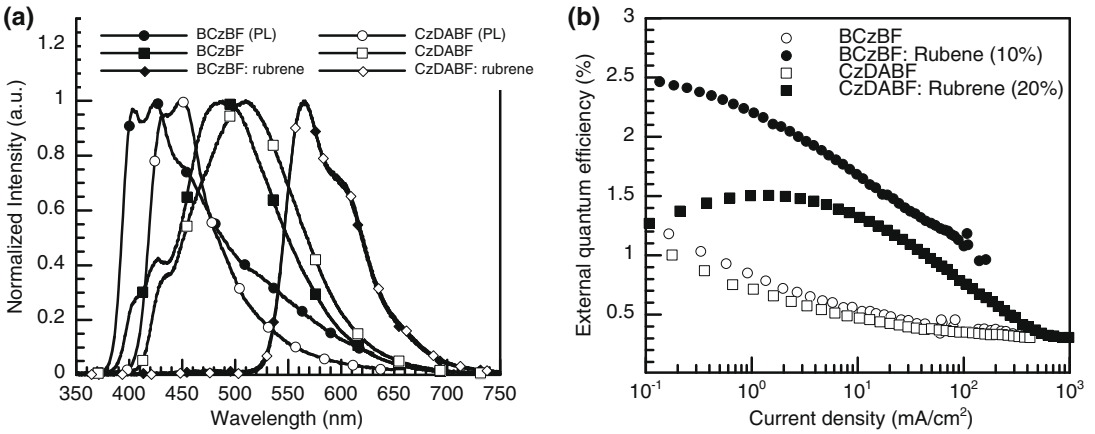

Fig. 4. (a) EL spectra and (b) quantum efficiency–current density characteristics of OLEDs containing the bipolar compounds.

rubrene was observed (Fig. 4a). Although the driving voltages increased compared to those of device I because of carrier trapping by rubrene (Fig. 3a), device II exhibited higher EQEs than that of device I (Fig. 4b). The maximum EQE of 1.5% for device II containing CzDABF is consistent with the theoretical EQE of 1.35% estimated from the PL quantum yield of 27% of 20 wt.% rubrene in CzDABF. Doping concentrations of rubrene of less than 20 wt.% increase the PL quantum yield, but incomplete carrier trapping causes emission from the bifluorene host and results in lower overall EQE. The homo-junction structure of the OLEDs was expected to extend the lifetimes of the devices because of a lack of organic interfaces but the lifetime measurements did not show an improvement over typical device structures. Further detailed investigations are under way and will be presented in the future.

4. Conclusion

Bipolar fluorene compounds were synthesized by palladium-catalyzed C–C and C–N coupling reactions. The energy levels of these compounds were related to the number of carbazole and diphenylamine groups. TOF measurements demonstrated that these compounds have bipolar charge transport abilities. Hole mobilities were as high as that of NPD and electron mobilities were much higher than that of Alq_3. These bifluorene compounds have small enough I_p to be *p*-doped and E_a to be *n*-doped. Hole- and electron-only devices containing these compounds with *p*-type doping with MoO_3 and *n*-type with Cs showed Ohmic current density–voltage characteristics. OLEDs with a homo-junction structure containing these bipolar compounds as the emitting material exhibited poor efficiencies. Addition of rubrene as an emitting material into these devices improved the EQEs to 1.5–2.0%.

Appendix A. Supplementary data

Supplementary data associated with this article can be found, in the online version, at doi:10.1016/j.orgel.2010.01.010.

References

[1] R.F. Service, Science 310 (2005) 1762.
[2] F. So, J. Kido, P. Burrows, MRS Bulletin 33 (2008) 663.
[3] Z.Y. Ge, T. Hayakawa, S. Ando, M. Ueda, T. Akiike, H. Miyamoto, T. Kajita, M.A. Kakimoto, Adv. Funct. Mater. 18 (2008) 584.
[4] Y.D. Sun, L. Duan, P. Wei, J. Qiao, G.F. Dong, L.D. Wang, Y. Qiu, Org. Lett. 11 (2009) 2069.
[5] S.Y. Takizawa, V.A. Montes, P. Anzenbacher, Chem. Mater. 21 (2009) 2452.
[6] S.L. Tao, L. Li, J.S. Yu, Y.D. Jiang, Y.C. Zhou, C.S. Lee, S.T. Lee, X.H. Zhang, O.Y. Kwon, Chem. Mater. 21 (2009) 1284.
[7] Y.L. Liao, C.Y. Lin, Y.H. Liu, K.T. Wong, W.Y. Hung, W.J. Chen, Chem. Commun. (2007) 1831.
[8] J.Y. Shen, X.L. Yang, T.H. Huang, J.T. Lin, T.H. Ke, L.Y. Chen, C.C. Wu, M.C.P. Yeh, Adv. Funct. Mater. 17 (2007) 983.
[9] C. Adachi, R. Kwong, S.R. Forrest, Org. Electron. 2 (2001) 37.
[10] H. Tsuji, C. Mitsui, Y. Sato, E. Nakamura, Adv. Mater. 21 (2009) 1.
[11] T. Mori, A. Oda, J. Kido, in: The 56th Spring Meeting, The Japan Society of Applied Physics and Related Societies, 2006, p. 1395 (Extended Abst.).
[12] J. Kido, T. Matsumoto, Appl. Phys. Lett. 73 (1998) 2866.
[13] S. Tokito, K. Noda, Y. Taga, J. Phys. D: Appl. Phys. 29 (1996) 2750.
[14] S. Watanabe, N. Ide, J. Kido, Jpn. J. Appl. Phys. 46 (2007) 1186.
[15] S.B. Lee, T. Yasuda, M.J. Yang, K. Fujita, T. Tsutsui, Mol. Cryst. Liq. Cryst. 405 (2003) 67.

complex series (PtL^{26}Cl), where N^C^N represents a 1,3-di(2-pyridyl) benzene-based tridentate ligand, *L*. We focus on its generally non-monotonous drive current evolution which appears to vary with the Pt(II) complex concentration. Although such a non-monotonous evolution has already been observed in other systems (for an overview see Ref. [1]), the main interest had been in the ELQE roll-off reflecting various processes that quench the emissive states and/or their precursors at large current densities [10,11]. Recently, it was realized and illustrated experimentally on a few examples of molecular exciton EL [1,12] that the importance of another process had been overlooked in the past: the current (voltage)-enhanced recombination efficiency leading often to the substantial ELQE increase seen particularly well in the lower driving current densities regime. The purpose of this work is to establish unified approach to and universal description of the current dependence of the ELQE within the whole current densities range accessible for OLEDs including their emission simultaneously from both monomolecular and bi-molecular excited states, and to critically compare the results with experiment based on the high performance data obtained here for PtL^{26}Cl emitter LEDs treated as a distinctive example.

2. Experiment

The originally synthesized, highly phosphorescent platinum N^C^2^N-[1,3-di(4-methoxy-pyrid-2-yl)-4,6-difluorobenzene] chloride (PtL^{26}Cl)-doped (4,4′,4″-tris(*N*-carbazolyl-triphenylamine) (TCTA) blends have been used as either the low-concentration bluish-green (molecular exciton), high-concentration red (excimer) or concentration-optimized white (molecular exciton + excimer) emitters with the phosphorescence yield between 0.49 and 0.74 for low-concentration and neat film EMLs, respectively. Our LED structures ITO/TPD75 wt%:PC25 wt% (60 nm)/TCTA(10 nm)/TCTA($100-x$)wt%:PtL^{26}Cl*x*wt% (30 nm)/TAZ(30 nm)/LiF/Al, were fabricated by casting a sequence of thin layers on clean glass substrates pre-coated with a 150 nm-thick layer of indium tin oxide (ITO) with a sheet resistance of 20 Ω per square. A 60 nm-thick diamine derivative (TPD):polycarbonate (PC) blend hole-transporting layer (HTL) was deposited on top of the ITO glass by spin coating from a 10 mg/ml dichloromethane solution at room temperature. All remaining organic layers were deposited in succession by thermal-evaporation under vacuum of $\sim 10^{-6}$ hPa, followed by high vacuum ($\sim 10^{-6}$ hPa) thermal-evaporation of the cathode layer consisting of 0.5 nm-thick LiF and by a 100 nm-thick Al cap. The EML was evaporated by co-deposition of the phosphor and TCTA to form a 30 nm-thick blend film. Holes are injected from the ITO anode, and pass through (TPD:PC) and TCTA hole-transporting layers, and re-combine with electrons that were injected from a Al/LiF cathode and transported through the electron transporting layer (ETL) of a triazole derivative, TAZ. The 10 nm-thick TCTA layer has been used to block triplet exciton transfer from the Pt complexes to the non-radiative triplet of TPD. The 30 nm-thick layer of TAZ plays a similar role of inhibiting quenching of the Pt complex triplet excitons at the cathode while at the same time blocking holes, both properties that enable the recombination process to be confined to a 30 nm-thick EML [6]. Resulting LED architecture allowed us to maximize its performance parameters (for general mechanisms of organic LED function see e.g. Ref. [1]).

3. Results

The EL spectra of the LEDs based on different concentrations of PtL^{26}Cl blended with TCTA as EMLs, along with the phosphor concentration dependent relative contribution of the monomer and excimer emissions, are shown in Fig. 1. Like in other PtL^{x}Cl-based emitter LEDs [6] the EL spectra constitute of two, monomer blue and excimer reddish-yellow (amber), bands, the amber band component increasing with complex concentration up to reddish only emission from PtL^{x}Cl neat films. Fig. 2 shows the EL external quantum efficiency (QE) as a function of the driving current density (j) for a series of LEDs at varying concentration dopant emitters. The essential information in the figure is: (i) an increase of the QE with increasing current in the

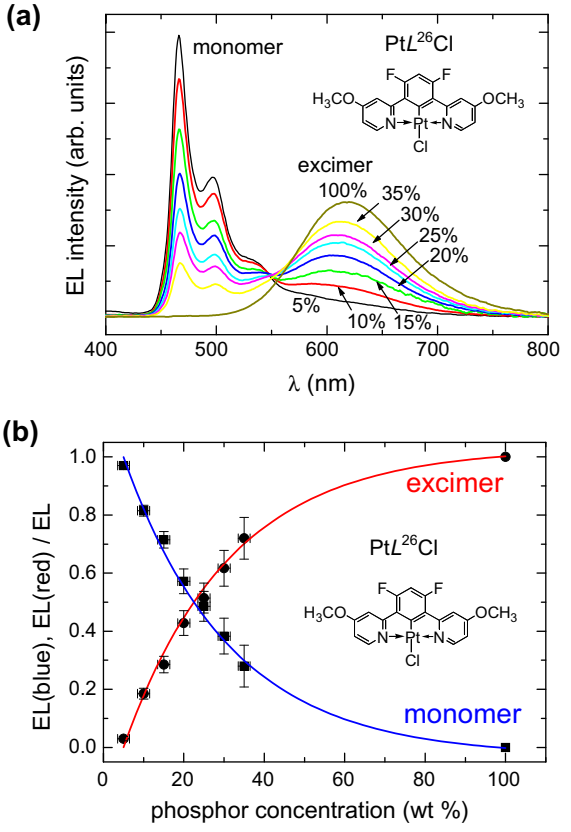

Fig. 1. (a) EL spectra of the device studied with different concentrations of the phosphor (PtL^{26}Cl) as indicated in the figure. (b) The relative contributions of the monomer blue and excimer red emission band components (EL_{blue}, EL_{red}) to the total EL emission (EL) as a function of the phosphor concentration in the EML (taken suitably as the blue part, red part and total spectrum under-curve area ratios). (For interpretation of the references to color in this figure legend, the reader is referred to the web version of this article.)

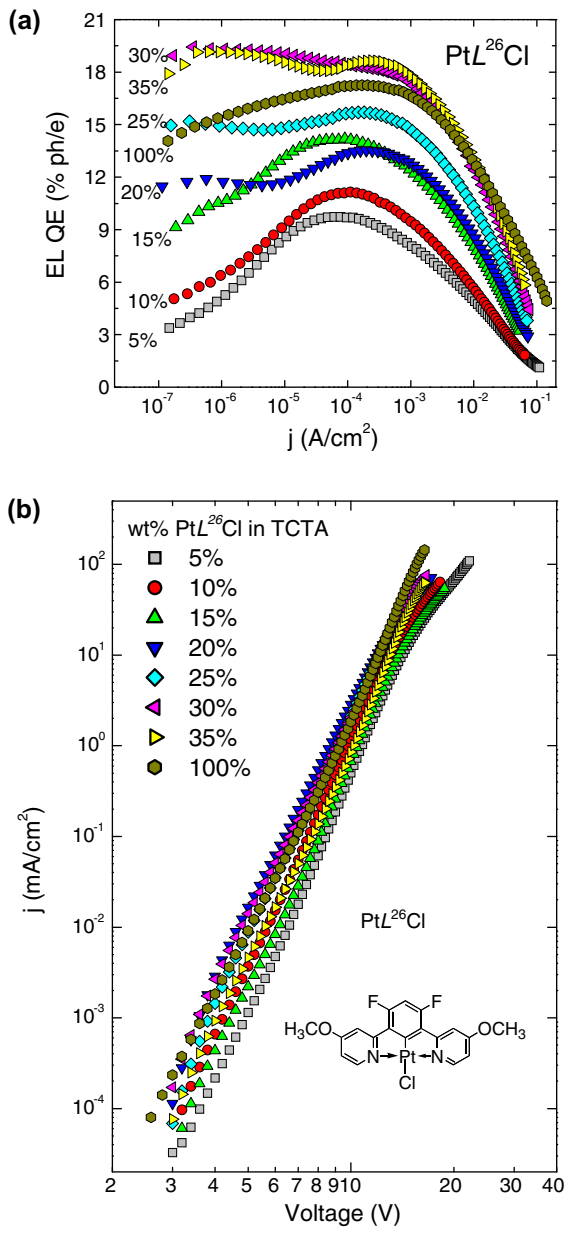

Fig. 2. (a) External EL quantum efficiency (EL QE) of PtL^{26}Cl emitter-based LEDs as a function of the driving current and parametric in the concentration (c in wt%) of PtL^{26}Cl in their emitting layers. Note a distinctive change in the curve shape, accompanying the phosphor content. (b) Current–voltage characteristics of the same LEDs.

low-current regime for the dopant concentration below 15 wt%, (ii) a maximum or a bump in the moderate-current regime whose position varies slightly with the PtL^{x}Cl content in the EML, (iii) a drop at large current densities, (iv) an enormous increase of the EL QE with phosphor concentration tending to saturation at 30–35 wt%, where it reaches 20% (photon/electron) corresponding to almost 100% of the internal QE – the upper limit of the LED performance, (v) an excess of the light output for neat PtL^{x}Cl over blend EMLs at the highest current densities accessible.

4. Modeling

We determine the external EL QE from the general expression representing all electronic processes involved in creation and fate of n different excited states, modified by the phosphor concentration, c:

$$\varphi_{EL}^{(ext)}(c) = P_R(c)P_d \sum_{i=1}^{n} \xi_i(c)\,\varphi_i^{PL}(c)P_{qi}(c)P_{si} \qquad (1)$$

Here, $\xi_i(c)$ (<1) is the light output coupling factor accounting for LED optical side modes escaping of usual front face detected EL light flux and dependent on the LED's material composition, their architecture as well as their operation conditions, φ_i^{PL} is the quantum efficiency of the radiative decay of excited state i created in the electron-hole recombination process, which is commonly identified with the photoluminescence (PL) quantum efficiency. The fundamental message of Eq. (1) is that the ELQE is a result of the superposition of four independent processes operating in the LED at the same time, and represented by the factors

$$P_R = (1+\tau_r/\tau_t)^{-1}, \quad P_d = (1+\tau_c/\tau_d)^{-1},$$
$$P_{qi} = (1+\tau_{0i}/\tau)^{-1}, \quad 0 \leqslant P_{si} \leqslant 1 \qquad (2)$$

which account for the probability of the formation of a charge pair (CP) state (P_R), its dissociation avoidance (P_d), and escape of a quenching process by the final emissive i state (P_{qi}), irrespective of the type of emissive material and LED architecture. The P_{si} stands for the probability of creation of a singlet or triplet ith emitting state. They are defined by spin multiplicity and a set of time constants characterizing the formation and decay of various electronic species as depicted in a scheme presented in Fig. 3. These are: the charge carriers encounter (recombination) time (τ_r), effective transit time of charges out of the recombination zone (τ_t) corresponding to the maximum of the monomolecular decay rate constant of electrons $(\tau_t^e)^{-1}$, and holes $(\tau_t^h)^{-1}$, $(\tau_t)^{-1} = (\tau_t^e)^{-1} + (\tau_t^h)^{-1}$, dissociation time of CP states (τ_d), formation time of an emissive state (T_1) ≡ charge pair internal capture time (τ_c), intrinsic lifetime of the emissive state (τ_0) and its lifetime (τ) triggered

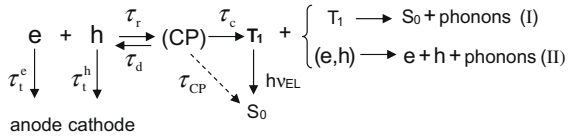

Fig. 3. The kinetic scheme illustrating formation of emissive states (T_1) in the recombination process of electrons and holes injected at the electrical contacts (e + h). Naturally, the emissive state is preceded by an intermediate state of a coulombically-correlated charge pair (CP). In general, CP can also directly decay to the ground molecular state (S_0) either in a radiative or radiationless transition with a time constant τ_{CP}. The radiative decay of T_1 produces the only optical emission called electroluminescence ($h\nu_{EL}$) if τ_{CP} is much longer than charge capture time (τ_c). For description of other time constants see text. The yield of the radiative decay can be reduced by (T_1 + T_1) (I) and (T_1 + e and/or h) (II) interactions. We note that here the emissive state (T_1) stands for either the first monomolecular triplet exciton or excimer triplet state, and factor P_{si} = 1 ($P_{s1} = P_{s2}$) since due to the heavy Pt atom a strong spin-orbit coupling transforms all singlet into triplet states.

off by the exciton–exciton ($T_1 + T_1$) and exciton-charge carrier interactions (T_1 + e and/or h).

The analytic treatment rests upon the assumption that all the above time constants can be related to physical observables of the current density, j, electric field strength, F, organic layers thickness, d, and independently determined parameters including carriers mobility (μ_e, μ_h), the (CP)-dissociation rate constant, η, dielectric permittivity, ε, and the intrinsic lifetime of the emissive species, τ_0:

$$\tau_r = (\gamma n)^{-1}, \quad \tau_t^{e,h} = d/\mu_{e,h}F, \quad \tau_c/\tau_d = \tau_c \nu_0 \eta(F), \quad \tau_0/\tau = \tau_0 j/\varepsilon_0 \varepsilon F \tag{3}$$

We consider the carrier motion to be dominated by the hole hopping for all emitters, $\tau_t \approx \tau_t^h$, except for neat films forming ambipolar conductive organic layers. Consequently, the τ_r-to-τ_t ratio for blend emitters can be approximated by $\tau_r/\tau_t = (8/9)(\mu_{e,h}/\mu_{eff}) j_{SCL}/j \approx (8/9) j_{SCL}/j$ obtained with $j_{SCL} = (9/8)\mu_{eff}\ \varepsilon_0\varepsilon F^2/d \approx (9/8)\mu_h \varepsilon_0 \varepsilon F^2/d$ and $\mu_{eff} \approx \mu_h$ standing for the effective charge carriers mobilities under double injection, and assuming the second order recombination rate constant, $\gamma = e(\mu_e + \mu_h)/\varepsilon_0\varepsilon$, to obey the Langevin recombination mechanism [1] between balanced concentration ($n = j/e(\mu_e + \mu_h)F$) of electrons and holes within the EML. The electron (hole) mobility is assumed to obey the ubiquitous dependence $\mu_{e,h}(F) = \mu_{e0,h0} \exp(\beta_{\mu_e,\mu_h} F^{1/2})$, where $\mu_{e0,h0}$ is the zero-field limit of the mobility and the scaling factor β_{μ_e,μ_h} is determined by the energetic and positional disorder of the material, the dielectric constant and the temperature [1,13]. To be correct one has to note that such defined β_{μ_e,μ_h} (as determined from charge carrier mobility experiments) differs from that included in the formula for j_{SCLC} by a factor 0.89 which is due to the approximations made in its derivation [14,15]. The magnitude of this factor which is close to unity does not alter the scaling coefficient to a significant degree and the final results fall in the experimental error and the accuracy of the fitting procedure. The τ_0/τ ratio follows from the general steady-state kinetic equation for the density of T_1 states, taking into account ($T_1 + T_1$) and [T_1 + (e,h)] exciton annihilation processes (see Fig. 3):

$$\frac{dT_1}{dt} \cong \frac{j}{ew} - \gamma_{TT} T_1^2 - \gamma_{Tq} n T_1 = 0 \tag{4}$$

where 'w' is the width of the recombination zone, and γ_{TT} and γ_{Tq} are the second order ($T_1 - T_1$) and ($T_1 - q$) annihilation rate constants, respectively. The effective lifetime imposed by these interactions is given by $\tau^{-1} = \gamma_{TT} T_1 + \gamma_{Tq} n$ and the analytic solution of Eq. (4) by

$$T_1 = -\frac{\gamma_{Tq}}{\gamma_{TT}} \frac{j}{e\mu F} + \frac{1}{2\gamma_{TT}} \sqrt{\left(\frac{\gamma_{Tq} j}{e\mu F}\right)^2 + \frac{4\gamma_{TT} j}{ew}} \tag{5}$$

If the ($T_1 - q$) interaction becomes the dominating quenching process, as observed recently for Ir(III)-tetrazolate phosphors [12], $\tau^{-1} \approx \gamma_{Tq} j/e\mu F$ or $\tau^{-1} \approx j/\varepsilon_0\varepsilon F$ for slow triplets quenched by mobile holes, allowing Langevin relation to be applied for $\gamma_{Tq} \approx e\mu_h/\varepsilon_0\varepsilon$. This is a rough approximate expression resulting from the general definition of $\gamma_{Tq} = 4\pi R_{eff}(D_T + D_h)$, where D_T and D_h are the diffusion coefficients of triplet and a hole, respectively, and R_{eff} is the exciton effective capture distance (see e.g. Ref. [16]). This definition bases on the premise that the triplet quenching reaction is controlled by the diffusion motion of mutually approaching triplet and hole like that in the case of the recombination of two oppositely charged carriers which is called Langevin recombination process. Since in our emissive layers the triplets are well localized on PtL^{26}Cl molecules a natural assumption is that $D_T \ll D_h$, reducing γ_{Tq} to $4\pi R_{eff} D_h$. The R_{eff} is not exactly known and can vary between one up to 10 intermolecular spacings (~2–20 nm) dependent on the charge separation (dipole moment) on the dopant molecule, thus the local dielectric constant. To simplify the calculations we assumed R_{eff} to be somewhere within the upper limit of this range that is approaching the Coulomb radius $R_C = e^2/4\pi\varepsilon_0\varepsilon kT$ like in the e–h recombination process. Consequently, it could be roughly approximated by $\gamma_{Tq} \approx e\mu_h/\varepsilon_0\varepsilon$ which means that the triplet-charge carrier interaction rate constant is comparable with that for the second order e–h recombination rate constant. Being aware of this simplifying approximation, we point out that an expected lower value of R_{eff} ($<R_C$) would not change the character of the function $\tau(j)$ and consequently EL QE (j). Possible differences in values of some other fitting parameters might be expected due to variation of R_{eff}. This will be considered as a refinement to be made in our works being underway. We note that PtL^{26}Cl triplet exciton transfer within their blends with TCTA is impeded due to the triplet energy mismatch for these blend components (2.65 eV vs. 2.85 eV, respectively). This is the case expressed by τ_0/τ in Eq. (3).

In order to examine the validity of Eq. (1), the mechanism of the field-assisted (CP)-dissociation process must be established in addition. In contrast to the dissociation of molecular excitons when the primary step formation of nearest-neighbor charge transfer state controls the field dependence of the dissociation rate, the dissociation quantum efficiency of CPs is governed by the separation ability of CP associated with field-dependent diffusion of a carrier in the Coulombic field of the countercharge, and can be expressed by [17],

$$\eta(F) = \frac{\sin h(e\delta F/kT)}{A + \sin h(e\delta F/kT)} \tag{6}$$

where δ is the hopping distance of the carrier and $A = (\tau_c^{-1} + \tau_{CP}^{-1})\tau_d(F = 0)$. This is the field-dependent CP dissociation efficiency to be inserted in (3) along with a standard frequency factor ν_0.

We use Eqs. (2) to calculate the ELQE (1) taking into account two emissive states ($T_1^{(n)}$, n = 1,2), monomer (n = 1) and excimer (n = 2), created with different proportions dependent on the dopant concentration. In general, more emissive states ($n > 2$) can contribute to the LED's emission (see e.g. Ref. [7]). For simplicity we assume $\xi_1 = \xi_2 = \xi = 0.3$ a typical value for OLEDs. We take the measured values of τ_{01} = 3.4 μs, τ_{02} = 1.3 ± 0.3 μs, and $\varphi_1^{PL}(5\ wt\%) = 0.53$, $\varphi_2^{PL}(100\ wt\%) = 0.74$ which vary with the dopant concentration as follows from the blue and red component contributions to the EL shown in Fig. 1b, $\varphi_1^{PL}(c) = \varphi_1^{PL}(5\ wt\%) \times$ [EL(blue)/EL] and $\varphi_2^{PL}(c) = \varphi_2^{PL}(100\ wt\%) \times$ [EL(red)/EL]. In Fig. 4 we display the j dependence of the three of the

probability factors defined by Eq. (2) taking into account Eqs. (3) and (6) for different phosphor concentrations in the LED EMLs. The displayed curves have been obtained by suitable parametrization procedures in order to fit the experimental data in Fig. 4a. We find that the j dependence of $P_R(j)$ can be approximately modeled by the current evolution of the ratio $(j_{SCL}/j)_m$ at different dopant concentrations c_m ($m = 1,2,3,4$), j_{SCL} being calculated employing a Poole–Frenkel type field-dependent mobility with a field independent prefactor varying with dopant concentration, $\mu_{eff0} = \mu_{h0}(c_1) = 6.5 \times 10^{-12}$, through $\mu_{h0}(c_2) = 1.4 \times 10^{-12}$, $\mu_{h0}(c_3) = 2 \times 10^{-14}$ to $\mu_{h0}(c_4) = 1.9 \times 10^{-13}$ cm^2/Vs and $\beta_{\mu h}$ from 7×10^{-3}, through 8.5×10^{-3}, 10^{-2} up to 1.35×10^{-2} (cm/V)$^{1/2}$ for respective c_m, and j taken from experiment (Fig. 2b). The low values of the zero-field mobilities may create an impression of very low mobility in emissive layers under working conditions of the LEDs studied. However, taking into account its Poole-Frenkel type field dependence with the fitted values of the scaling factors one comes to the mobility values comparable with those of other organic complex-doped blends. For example, our μ_h ($F = 8 \times 10^5$ V/cm) $= \mu_{h0} \exp(\beta_{\mu h} F^{1/2}) = 1.9 \times 10^{-13} \exp(1.35 \times 10^{-2} \times 9 \times 10^2) \approx 3.3 \times 10^{-7}$ cm^2/Vs, the value comparable with those measured for other blends (e.g. $\sim 10^{-8} - 10^{-7}$ cm^2/Vs for electrons and holes in Ir(ppy)$_3$ doped CBP films at electric fields above 10^5 V/cm [18]). Furthermore, we note that j at a given voltage differs at different c_m and for all dopant concentrations: though it shows a strong increase with applied voltage, it cannot be strictly described by a power dependence within the whole range of V, characteristic of the volume-controlled double injection currents in the presence of exponentially distributed in energy charge traps [1]. Thus, the capacitor charge related to the unit volume ($\varepsilon_0 \varepsilon F/d$) may be lower than the average concentration of the total charge in the sample ($j/\Theta\mu_{eff}F$; Θ-the free-to-trapped charge concentration ratio), indicating substantial j deviation towards injection-limited currents. It is clearly seen in the current evolution of the j_{SCL}-to-j ratio (Fig. 4c), which largely exceeds unity for the 5%-doped sample at the lowest current densities. To fit the $P_d(j)$ we used Eq. (6) with $\delta_1 = 1.02$, $\delta_2 = 1.06$, $\delta_3 = 1.22$ and $\delta_4 = 1.20$ nm, and $(\tau_c \nu_0)_m = 6.5$, 9, 10 and 8 for $m = 1,2,3,4$, respectively. One would expect δ to reflect the distance between molecules forming hopping sites for the carriers. For $m = 1,2$ these correspond exactly to the intermolecular distance between TCTA molecules, $\delta(\text{nm}) = 10^7 (M/c_m \rho N_A)^{1/3}$, where $M = 741$ g/mol is its molecular weight, $\rho \approx 1.2$ g/cm^3- typical density of organic films, and $N_A = 6 \times 10^{23}$/mol is the Avogadro's number. The fit numbers δ_m for $m = 3,4$ differ from the intermolecular distance between molecules of PtL^{26}Cl ($M = 558$ g/mol), 1.37 and 0.91 nm, respectively, that suggests progressive clustering of dopant molecules. An excess of the current in neat films of the phosphor relative to the blends is observed in the high voltage range applied. This suggests the effect of increased carrier (electrons and holes) transport parameters (μ_0 and β_μ), being partly a consequence of the decreased distance between carrier molecular hopping sites. Finally, the $P_{qn}(j)$ curve has been reconstructed based on the experimental dependence of j [$(V/d) = F$] (Fig. 2b) and independently determined τ_{01} and τ_{02} for

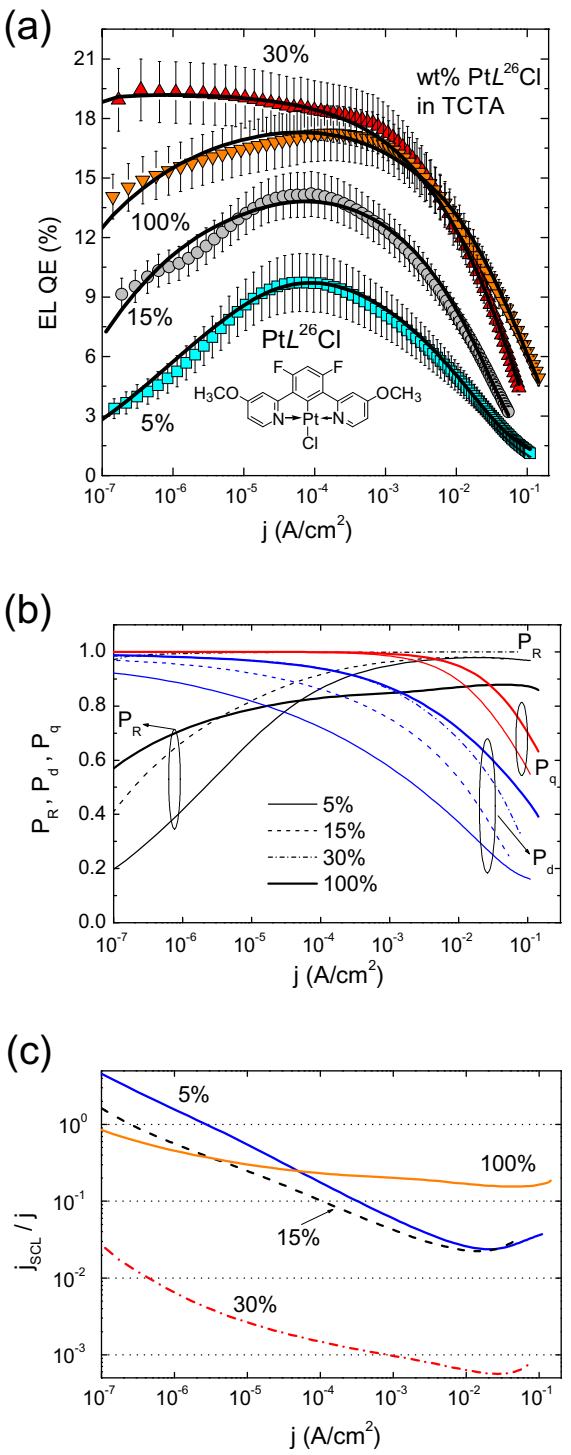

Fig. 4. (a) Selected experimental (figure points) and theoretical curves based on the current evolution of P_R, P_d and P_q from part (b) (solid lines) external ELQE vs. device current density for the devices with four different concentrations of PtL^{26}Cl as indicated in the figure (cf. Fig. 2). (b) The recombination (P_R), dissociation evasion (P_d), and quenching escape (P_q) probabilities defined by Eqs. (2) as a function of current density at different dopant concentrations, $c_1 = 5$ wt%, $c_2 = 15$ wt%, $c_3 = 30$ wt% and $c_4 = 100$%. The values of fitting parameters are given in the text. (c) The calculated space-charge-limited hole (hole + electron) current/measured current ratio (j_{SCL}/j) vs. j.

monomer and excimer microemitters as given above. A dielectric constant $\varepsilon = 3$, typical for organic solids, has been assumed and the carriers pathway identified with total device thickness $d = 130$ nm. Such a choice of d assumes the carrier mobility to be an average over all four layers of the device and makes the carrier transition time to approach its lower limit, but the alternation of d does not affect the functional shape of the $P_R(F)$ and QE(j) curves. An apparent difference in neat film emitters characteristics (Figs. 2 and 4) must be associated with the increased role of electrons. Their injection barrier from TAZ ETL of electronic affinity of ca. 2.8 eV into emitter is here reduced due to its greater electronic affinity (ca. 2.77 eV) as compared with that of ca. 2.3 eV for the emitter dominating material (TCTA) in blends. It is reasonable to assume their substantial role in electrical transport with $(\tau_t)^{-1} = (\tau_t^e)^{-1} + (\tau_t^h)^{-1} \neq (\tau_t^h)^{-1}$. The μ_{eff} becomes a combination of μ_e and μ_h, different for the SCL and plasma flow conditions [1,19], but still fitting to the Poole–Frenkel type field mobility dependence $\mu_{\text{eff}}(F)$ can be possible with μ_0 and β_μ corresponding to the combined electron and hole transport parameters. They apparently differ from their counterparts for TCTA and explain differences in optoelectrical characteristics of (PtL^{26}Cl doped TCTA) blend and neat film PtL^{26}Cl emitters-based LEDs. In addition, the increased molecular packing and negligible contribution of the monomer emission in the latter lead to higher values of P_d and P_q (Fig. 4b) resulting in the increased QE at the largest current densities as shown in Figs. 2a and 4a.

5. Discussion and conclusions

The good reproduction of the experimental data on the driving current evolution of the ELQE for PtL^{26}Cl-based LEDs strongly suggests that the underlying approach to the quantum efficiency of organic LEDs is within the experimental accuracy correctly described in this work, at least for practically accessible range of current densities. Our analysis indicates that increasing current leads not only to quenching of excited states imposed by growing exciton–exciton and exciton-charge carrier (P_q) interactions accompanied by their or their precursors field-assisted dissociation (η included in P_d) but at the same time may lead to increasing recombination probability (P_R) of injected carriers for low (<15 wt%) phosphor content. It has become clear that of these three factors only P_R can be an increasing function of the current (j) as long as its field (F) dependence is more steep than the space-charge-limited one carrier dominating current (j_{SCL}). Its constant value is expected if $j(F) \sim j_{\text{SCL}}(F)$, and goes to unity for $j_{\text{SCL}} \ll j$. We note that increasing P_R can be related to a decreasing current leakage invoked to explain the low-current regime QE(j) increase in earlier experiments on Ir complex-based OLEDs [20]. While both P_d and P_q by their definition decrease with the driving current (applied electric field), though almost invisible at low-current densities, a maximum of the ELQE is expected at a certain current ($j = j_{\max}$). It moves towards higher values at higher (>15 wt%) dopant contents, which reflects the increasing role of electrons in the current and sets the carrier flow at which the increasing recombination rate becomes suppressed by quenching processes. For the same reason no low-current increase of the ELQE is observed for high dopant content blend emitters. Electrons and holes are expected to have very different scaling factors ($\beta_{\mu e}$, $\beta_{\mu h}$) in their field-dependent mobilities – what is clearly confirmed from the fitting procedures for blend and neat film-based emitters. Instead of an increase a mild fall down to a dramatic roll-off of the ELQE (j) dependence at low values of the driving current in high dopant content blend emitters is observed. Some recent publications indicate the essential role of the recombination rate on the QE (j) dependence for color OLEDs based on single monomolecular exciton emission centers [12,21]. This work extends these previous analyses to multi-center emissive OLEDs and includes their premises by replacing a qualitative discussion of the (HTL/ETL)/EML energy barrier effects and carrier transport properties of each layer material [21] by a quantitative description that relates the recombination and transit times of the carriers to physical observables. We present a generalized formula for analyzing experimental data that accurately describes the current evolution of QE in OLEDs independent of their architecture. Our approach shows how the recombination probability can be expressed by the measured current and charge transport parameters. The latter, if not available from experiment, can be determined in a way that an optimal overall fit QE(j) is obtained.

Acknowledgements

This work was supported in part by the CNR project PM.P04.010 MACOL, the FIRB Projects LUCI and NODIS, and by the European COST Project No. D35-0010-05.

References

[1] J. Kalinowski, Organic Light Emitting Diodes: Principles, Characteristics and Processes, Marcel Dekker, New York, 2005.
[2] J.A.G. Williams, S. Develay, D.L. Rochester, L. Murphy, Coord. Chem. Rev. 252 (2008) 2596.
[3] M. Cocchi, D. Virgili, V. Fattori, D.L. Rochester, J.A.G. Williams, Adv. Funct. Mater. 17 (2007) 285.
[4] V. Fattori, J.A.G. Williams, L. Murphy, M. Cocchi, J. Kalinowski, Photonics Nanostruct. Fundam. Appl. 6 (2008) 225.
[5] X. Yang, Z. Wang, S. Madakuni, J. Li, G.E. Jabbour, Adv. Mater. 20 (2008) 2405.
[6] M. Cocchi, J. Kalinowski, V. Fattori, J.A.G. Williams, L. Murphy, Appl. Phys. Lett. 94 (2009) 073309.
[7] J. Kalinowski, M. Cocchi, D. Virgili, V. Fattori, J.A.G. Williams, Adv. Mater. 19 (2007) 4000.
[8] M. Cocchi, J. Kalinowski, D. Virgili, V. Fatori, S. Develay, J.A.G. Williams, Appl. Phys. Lett. 90 (2007) 163508.
[9] M. Cocchi, D. Virgili, V. Fattori, J.A.G. Williams, J. Kalinowski, Appl. Phys. Lett. 90 (2007) 023506.
[10] M.A. Baldo, C. Adachi, S.R. Forrest, Phys. Rev. B 62 (2000-II) 10967.
[11] J. Kalinowski, W. Stampor, J. Mężyk, M. Cocchi, D. Virgili, V. Fattori, P. Di Marco, Phys. Rev. B 66 (2002) 235321.
[12] M. Cocchi, J. Kalinowski, S. Stagni, S. Muzzioli, Appl. Phys. Lett. 94 (2009) 083306.
[13] J. Sworakowski, Braz. J. Phys. 29 (1999) 318.
[14] P.N. Murgatroyd, J. Phys. D: Appl. Phys. 3 (1970) 151.
[15] W. Brütting, S. Berleb, A.G. Mückl, Org. Electron. 2 (2001) 1.

[16] J. Kalinowski, J. Mężyk, F. Meinardi, R. Tubino, M. Cocchi, D. Virgili, J. Chem. Phys. 128 (2008) 124712.
[17] J. Kalinowski, W. Stampor, P. Di Marco, J. Chem. Phys. 96 (1992) 4136.
[18] S.B. Lee, T. Yasuda, M.J. Yang, K. Fujita, T. Tsutsui, Mol. Cryst. Liq. Cryst. 405 (2003) 67.
[19] M.A. Lampert, P. Mark, Current Injection in Solids, Academic Press, New York, London, 1970.
[20] B.W. D'Andrade, M.E. Thompson, S.R. Forrest, Adv. Mater. 14 (2002) 147.
[21] J. Yoon, I. Park, Appl. Phys. Lett. 93 (2008) 193303.

P3HT:PCBM solar cell are still being reported. However, the relatively large band gap of P3HT, limits the fraction of solar spectrum that can be harvested, and the relatively small energy difference between the LUMO of PCBM and HOMO of P3HT, results in a lower open circuit voltage (V_{oc}). Therefore, the band gap of the polymer and the HOMO must be decreased in order to achieve the organic solar cells with high PCE. In this context, research efforts have been focused on the design and synthesis of new donor and acceptor materials with high carrier mobility and strong absorption in visible and near infrared region of solar spectrum [10–14], as well as device processing [15–18] fabrication [19–22] and architecture design [2,23–25].

A number of groups have investigated solution processed BHJ solar cells based on conjugated small molecules as donors and fullerene derivatives as acceptors. To date, the PCE ranging from 0.3% to 2.5% have been reported for the devices based on small molecules [26–31]. Recently, PCE of approximately 3.0% has been reported on solar cells based on low band gap small molecule blended with PCBM [32]. The efficiency based on small molecules is still low compared to either thermally deposited bi-layer small molecules solar cells [33–36], or polymer based solar cells. Despite of the low PCE attained by these solar cells, conjugated small molecules offer several advantages such as higher electron and hole mobilities due to better molecular ordering, over polymeric materials, making them promising materials for the solution processed solar cells. The most important advantage of conjugated small molecules is that they do not suffer from batch to batch variation, broad molecular weight distribution and difficult synthesis and purification methods, as it is for polymer counterpart.

In this investigation, we report the fabrication and characterization of single layer BHJ devices, based on conjugated alternating phenylenevinylene copolymer **P**:PCBM active layer with different weight ratio, deposited at different substrate temperatures. It was found that the optimum photovoltaic (PV) performance observed with the **P**:PCBM (1:3) deposited at 65 °C and PCE of ~1.14% which is further improved up to 1.28%, when the TiO_2 layer is incorporated in between the BHJ layer and the Al electrode. The PV device based on **P**:PCBM and **BTD-TNP**:**PPI** BHJs exhibits PCE about 2.68%, which has been further improved up to 2.91% when the TiO_2 layer was inserted between the active layer and the top Al electrode followed by thermal annealing. The increase in the PCE has been attributed to the improved photon absorption, better charge transportation in the device, induced by the incorporation of TiO_2 layer and thermal annealing. The PCE of thermally annealed single and bi-layer BHJ with TiO_2 layer is approximately 1.67% and 3.5%, respectively.

2. Results and discussion

2.1. Optical and electrochemical properties of materials

The synthesis of the conjugated alternating phenylenevinylene copolymer **P** [37], the small molecule **BTD-TNP** [38] and the perylene–pyrene bisimide (**PPI**) [39] has been reported elsewhere. Fig. 1 shows the chemical structures of these materials and PCBM.

Fig. 2 shows the UV–visible absorption spectra copolymer **P**, PCBM, **BTD-TNP** and **PPI** thin films. The copolymer **P** thin film shows a broad absorption band from 320 nm to 480 nm with absorption peak around 450 nm and onset around 620 nm. The small molecule **BTD-TNP** shows an absorption band from 600 to 680 nm and its absorption is extended up to 790 nm. The single layer films of copolymer **P**:PCBM, and **BTD-TNP**:**PPI** shows the absorption bands in different wavelength regions i.e. 420–560 nm and 550–750 nm for **P**:PCBM and **BTD-TNP**:**PPI**, respectively. The bi-layer blend film, however, showed continuous solar absorption spectra from 400 to 750 nm, arising from both BHJ layers.

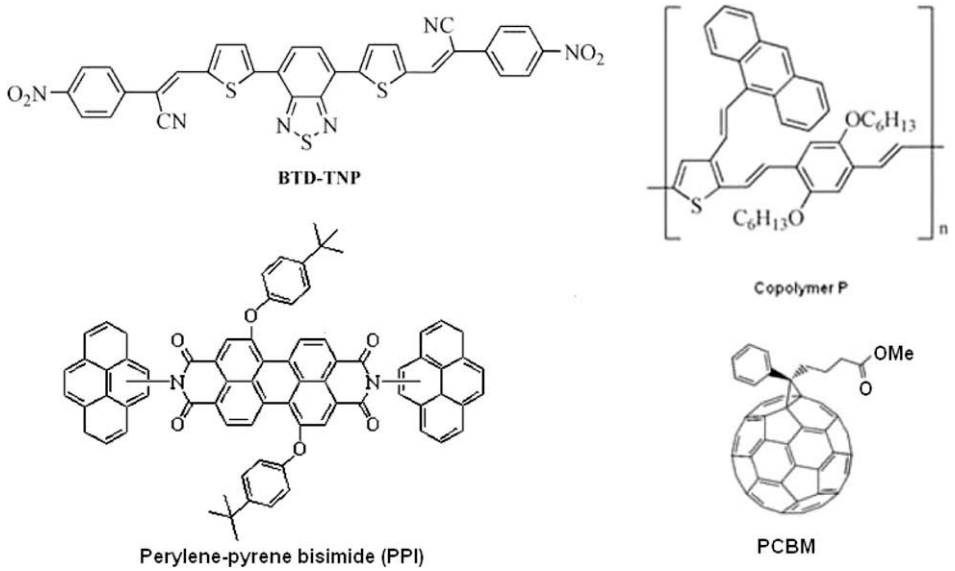

Fig. 1. Chemical structures of **BTD-TNP**, copolymer **P**, perylene–pyrene bisimide (**PPI**) and PCBM.

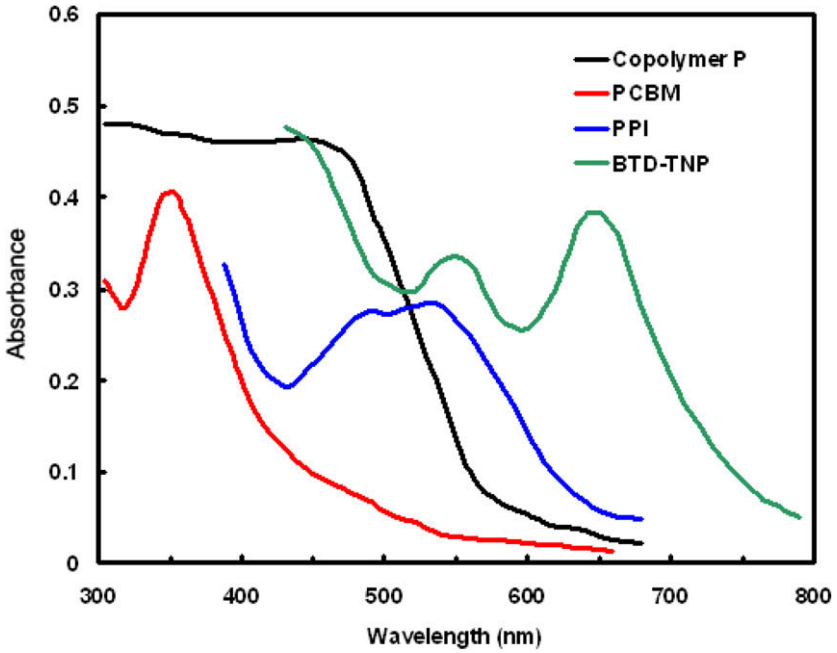

Fig. 2. UV–visible optical absorption spectra of copolymer **P**, PCBM, **PPI** and **BTD-TNP**.

The electrochemical cyclic voltammetry was performed to determine the highest occupied molecular orbital (HOMO) and lowest unoccupied molecular orbital (LUMO) energy levels of **P**, **BTD-TNP**, PCBM and **PPI**. The HOMO and LUMO energy levels were calculated according to the following equations [40]:

$$E_{HOMO} = -(E_{ox} + 4.71)\text{eV}$$

and

$$E_{LUMO} = -(E_{red} + 4.71)\text{eV},$$

where E_{ox} and E_{red} are the onset oxidation and reduction potential vs. Ag/AgCl, respectively, observed in cyclic voltammogram. The potentials were internally calibrated using Ag/AgCl redox couple, which is estimated to have an oxidation potential of −4.71 eV vs vacuum. The values of HOMO and LUMO energy levels and the band gap of the above materials, estimated from the cyclic voltammetry (CV) data, are listed in Table 1.

Table 1
Estimated values of highest occupied molecular orbital and lowest unoccupied molecular orbital energy levels and band gap of materials from cyclic voltammetry data.

Material	E^{ox}_{onset} (V)	E^{red}_{onset} (V)	E_{HOMO} (eV)	E_{LUMO} (eV)	$E_g = E_{HOMO} - E_{LUMO}$ (eV)
Copolymer **P**	0.49	−1.71	−5.20	−3.00	2.20
BTD-TNP	0.49	−1.31	−5.10	−3.40	1.70
PPI	1.04	−1.01	−5.75	−3.70	2.05
PCBM	–	–	−6.30	−3.90	2.40

*2.2. Photovoltaic properties of copolymer **P**:PCBM single layer BHJ device*

We have optimized the fabrication conditions of the device based on copolymer **P**:PCBM blend in terms of substrate temperature and blend ratio, before investigating the bi-layer BHJ PV device. Fig. 3a shows a schematic representation of a single layer BHJ solar cell based on a blend of **P** and PCBM. The energy level diagram for the materials involved in the single layer BHJ device is also shown in Fig. 3b. Since the HOMO and LUMO of **P** are by 1.2 and 1.0 eV higher than the corresponding energy levels of PCBM, the **P** and PCBM act as donor and acceptor, respectively. In view of interface morphology of thin BHJ films for solar cells, we have investigated the temperature effect on the performance for solar cells prepared by spin casting warm **P**:PCBM blend onto ITO/PEDOT:PSS substrates at different temperatures over 30–70 °C. Since the thickness of the photoactive layer affects the short circuit photocurrent of the device, we have kept the temperature of both blend solutions and substrate the same to slow down the evaporation rate, in order to control the film morphology. We have kept the thickness of all active layers almost constant to compare the PV properties of the devices. The thickness of the active layer deposited at different substrate temperatures was kept constant by controlling the viscosity of blend and spinning rate during the spin coating of the layer onto the substrate. The current–voltage (J–V) characteristics of the devices based on copolymer **P**:PCBM (1:3 weight ratio) under illumination intensity of 100 mW/cm^2 at different temperatures are shown in Fig. 4a. The variation of the PCE of the PV device with the substrate temperature is shown in the Fig. 4b. It seems from Fig. 4a that the

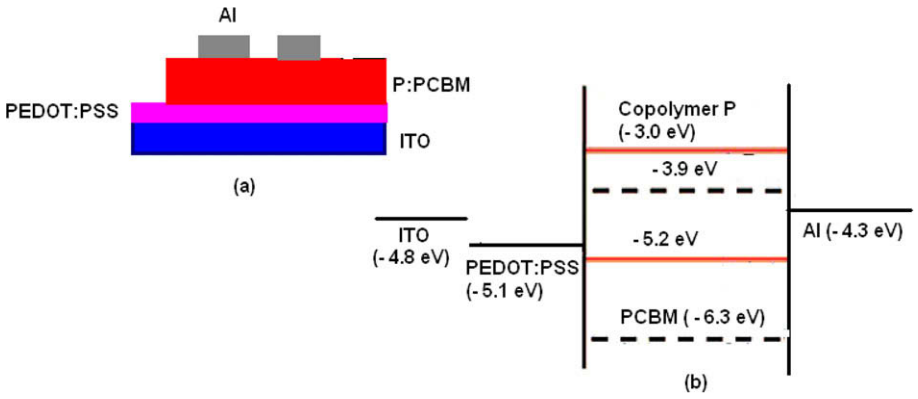

Fig. 3. A schematic representation of the device configuration (a) a bulk heterojunction solar cell based on copolymer **P**:PCBM and (b) the associated energy level diagram.

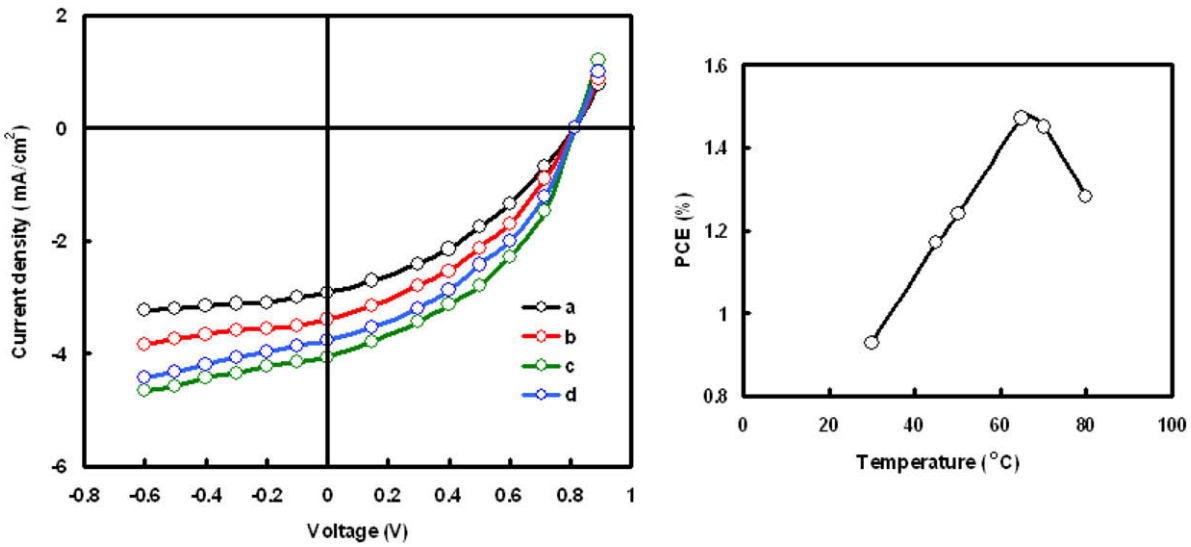

Fig. 4. (a) Current–voltage characteristics of ITO/PEDOT:PSS/Copolymer **P**:PCBM (1:3 by wt)/Al device at different substrate temperatures (a) 30 °C, (b) 45 °C, (c) 65 °C and (d) 80 °C. (b) Variation of power conversion efficiency (PCE) with substrate temperature.

substrate temperature affects mainly the J_{sc}, while the V_{oc} remains unchanged. Consequently the PCE increased continuously from 0.93% to 1.14% by increasing the substrate temperature from room temperature to 65 °C. Since copolymer **P** was spin cast from a warm DCB solution (70 °C), it could be crystallized quickly with defects upon contracting the substrate at lower temperatures. However, the copolymer **P** macromolecules in the bulk volume could take a long time to be crystallized during the slow film formation as the boiling point of DCB is as high as 180 °C. The defect rich copolymer **P** crystalline domains at the interface with ITO/PEDOT:PSS layer may act as trap site to reduce the overall hole mobility of **P** across the PV active film. The decrease in hole collection efficiency induced by the interfacial defects is proportional to the decrease in the substrate temperature. The observed decrease in PCE above 60 °C is probably due to the relatively faster evaporation of the solvent, which in turn, led to fast crystallization of **P** with introduced defects into the bulk film. Therefore, the optimized ITO substrate temperature for spin coating **P**:PCBM for a warm DCB solvent seemed to be 65 °C. All the devices described thereafter have been fabricated on the ITO/PEDOT:PSS substrate at 65 °C. Since the PCE of the device is maximum when the substrate temperature is about 65 °C, which is almost the same temperature of the warm blend solution, the change in PCE is only due the substrate temperature.

After optimizing the conditions for the device fabrication, we have further investigated the BHJ solar cells based on single layer copolymer **P**:PCBM blends with different weight ratio of 1:0.5, 1:1, 1:2, 1:3 and 1:4. The measured *J–V* characteristics (Fig. 5) show a strong dependence of the PV response on the copolymer **P**:PCBM wt. ratios. The observed increase in PCE with increasing **P**:PCBM wt. ratio results from an enhanced electron mobility associated with an increased PCBM content within the blend [41].

The decrease in PCE observed at 1:4 wt. ratio in **P**:PCBM blend is most probably due to the over suppressed hole transport induced by relatively nanoscale clusters of **P** in active layer and/or increased PCBM sites for charge recom-

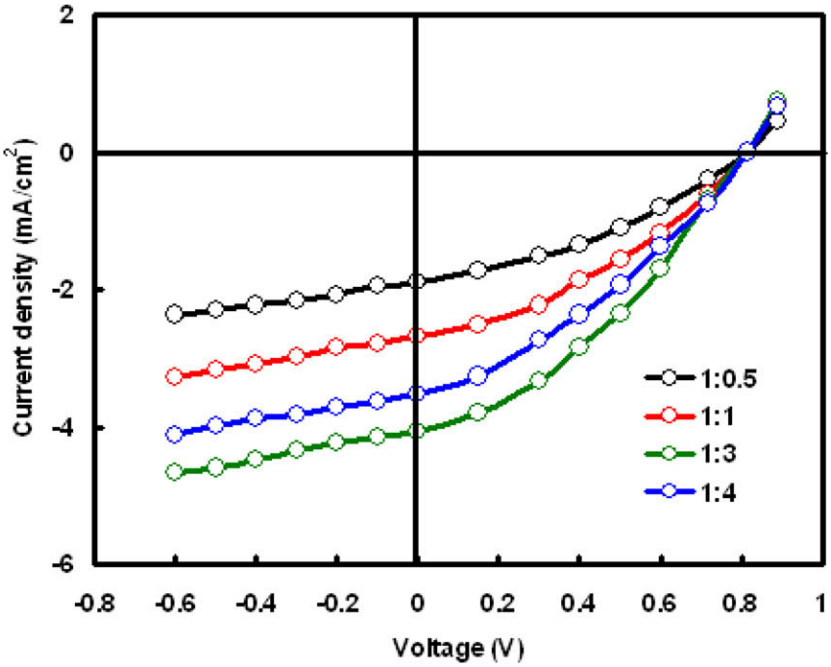

Fig. 5. Current–voltage characteristics of ITO/PEDOT:PSS/Copolymer **P**:PCBM/Al device with different weight ratio of Copolymer **P** to PCBM at substrate temperature 70 °C.

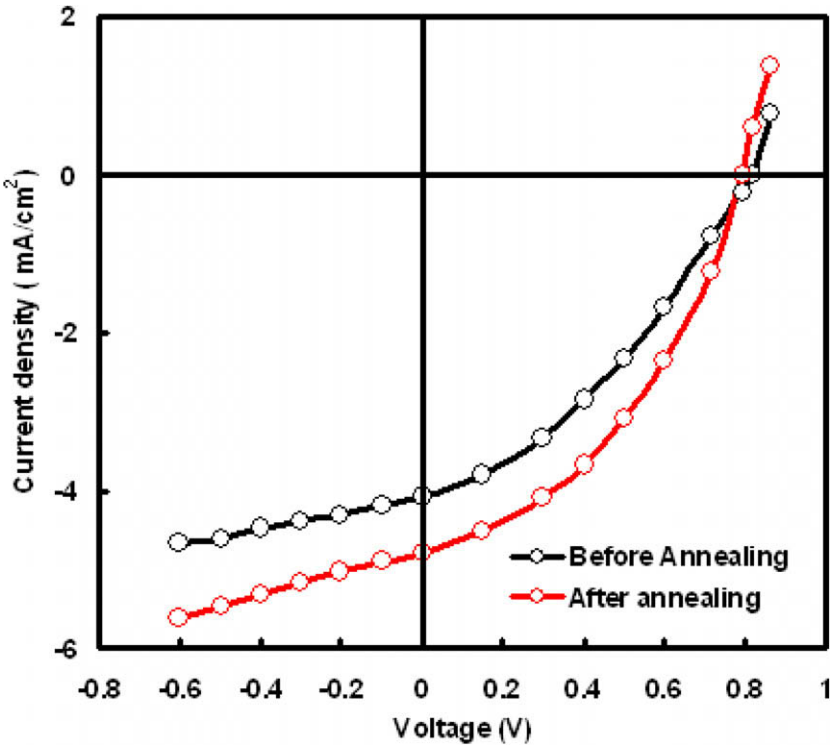

Fig. 6. Effect of thermal annealing on the current–voltage characteristics of ITO/PEDOT:PSS/Copolymer **P**:PCBM/Al device under illumination.

bination. The diluted solar absorption associated with the relatively reduced amount of copolymer **P** in the blend layer may also be contributing to the reduction in PCE. Therefore, we have used 1:3 weight ratio for **P** to PCBM deposited at substrate temperature of 65 °C for further investigation.

Fig. 6 shows the *J–V* characteristics for PV devices based on copolymer **P**:PCBM (1:3 wt. ratio) before and after thermal annealing at 100 °C for 20 min. It is found that the V_{oc} of ITO/PEDOT:PSS/**P**:PCBM/Al device remains almost unchanged while its J_{sc} slightly increased and fill factor (FF) significantly increased from 0.34 to 0.38 upon thermal annealing. In polymer solar cells, the FF is determined by the product of charge carrier lifetime and mobility. Therefore, the improved FF and J_{sc} is attributed to an enhanced charge transport due to the formation of large copolymer **P** crystalline domains in blend layer induced by thermal annealing. It is also found that the thickness of the blend film is decreased upon thermal annealing. This means that the molecular packing density of the as cast film is low. Therefore, all molecular interactions between the **P** domain, PCBM and **P**-PCBM domain are insufficient. Thermal annealing of the blend leads to an increase in the packing density, i.e. the distance between all molecules is narrowed and consequently, the efficiencies of exciton dissociation and charge transport are improved. Moreover, the annealing of the blend layer reduces the free volume and density of defects at the interface to facilitate the hole transport.

Charge carrier mobilities in donor/acceptor BHJ thin film play an important role on the performance of the organic PV devices [42,43]. We have fabricated the hole only device having structure ITO/PEDOT:PSS/**P**:PCBM/Au using the as cast annealed **P**:PCBM blends and the *J–V* characteristics in dark were measured. The hole mobility in the blend has been estimated using the SCLC model [42]. It is found that the hole mobility has been increased from 3.2×10^{-5} to 8.6×10^{-5} cm^2/V s upon the thermal annealing. The increase in the hole mobility also support our conclusion about the reduction in the free volume and density of defects at the interface. The enhancement in the photocurrent may also be attributed to the balanced charge transport in the device due to the improved hole mobility in copolymer **P** domain.

In addition to the enhanced hole transport, it is also essential to improve the electron transport in the PV device to achieve higher PCE. It has been already reported that the PCE has been improved, when a TiO_2 layer was inserted into the P3HT:PCBM blend in the PV device based on P3HT:PCBM [25]. This is due to the fact that the TiO_2 is a good electron transporting material, since its LUMO level is lower than that of PCBM and also very close to the work function of Al. We have also incorporated a thin TiO_2 layer into our copolymer P:PCBM devices. The *J–V* characteristics of the device are shown in Fig. 7a and the PV parameters are shown in Table 2. The as cast ITO/PEDOT:PSS/copolymer **P**:PCBM (1:3)/TiO_2/Al device showed a relatively enhanced PCE with respect to its counterpart without TiO_2. This was attributed to improved electron transport in the device with its LUMO level (−4.4 eV) lower than that of PCBM (−3.9 eV) (as shown in Fig. 7b). The subsequent thermal annealing also led to further enhanced performance with PCE about 1.67%, which once again is due to the formation of polycrystalline domains in the active layer.

To model the *J–V* characteristics of the copolymer **P**:PCBM solar cells, the BHJ of active layer of copolymer **P**:PCBM can be considered to be a single virtual semiconductor with HOMO and LUMO equivalent to those of **P** and PCBM, respectively, and having electron and hole mobilities equal to electron mobility of PCBM and hole mobility of **P**. When two electrode materials are brought to intimate contact with the active organic layer, the Fermi level alignment takes place and electron diffuse from the cathode to anode. Fig. 8a represents schematically the energy levels of the materials used in BHJ layer. Fig. 8b represents schematically the energy level diagram of the system

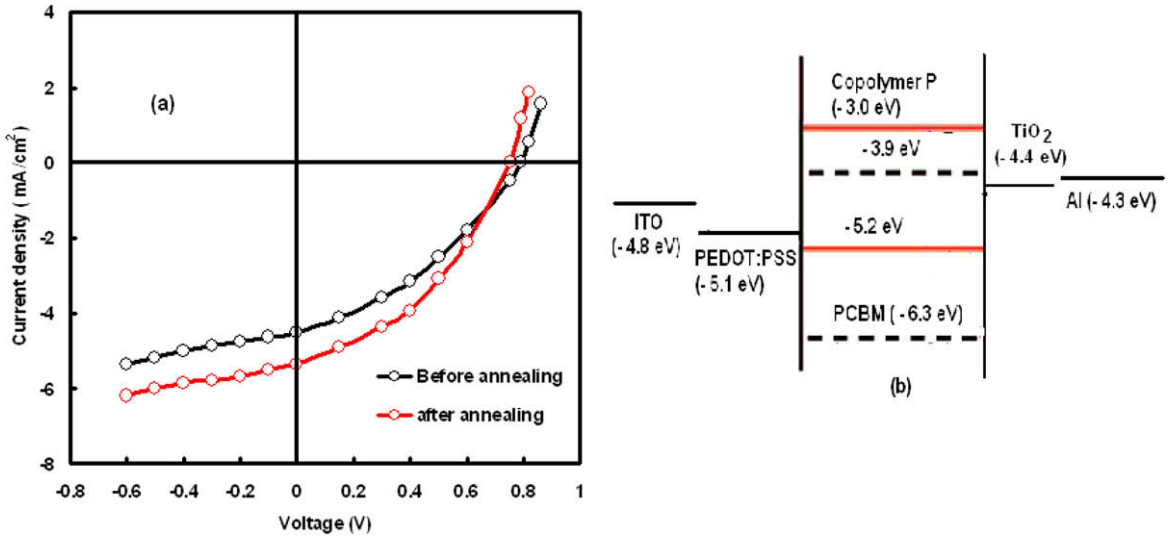

Fig. 7. (a) Current–voltage characteristics of ITO/PEDOT:PSS/Copolymer **P**:PCBM/TiO_2/Al device. (b) Energy band diagram of the device.

Table 2
Photovoltaic properties of the single layer and bi-layer bulk-heterojunction solar cells based on copolymer **P**:PCBM(1:3) and **BTD-TNP**:**PPI** (1:2 wt.%) with and without TiO_2 before and after post-annealing.

Compositions of active layer	J_{sc} (mA/cm^2)	V_{oc} (V)	FF	PCE (η) (%)
P:PCBM(1:3)	4.07	0.82	0.34	1.14
P:PCBM(1:3) (annealed)	4.80	0.80	0.38	1.46
P:PCBM(1:3)/TiO_2	4.51	0.79	0.36	1.28
P:PCBM(1:3)/TiO_2 (annealed)	5.35	0.76	0.41	1.67
BTD-TNP:**PPI** (1:2)	3.67	0.78	0.42	1.20
P:PCBM (1:3)/**BTD-TNP**:**PPI** (1:2)	7.20	0.81	0.46	2.68
P:PCBM (1:3)/**BTD-TNP**:**PPI** (1:2) (annealed)	7.80	0.78	0.49	2.98
P:PCBM (1:3)/**BTD-TNP**:**PPI** (1:2)/TiO_2	7.60	0.80	0.48	2.91
P:PCBM (1:3)/**BTD-TNP**:**PPI** (1:2)/TiO_2 (annealed)	8.80	0.78	0.51	3.50

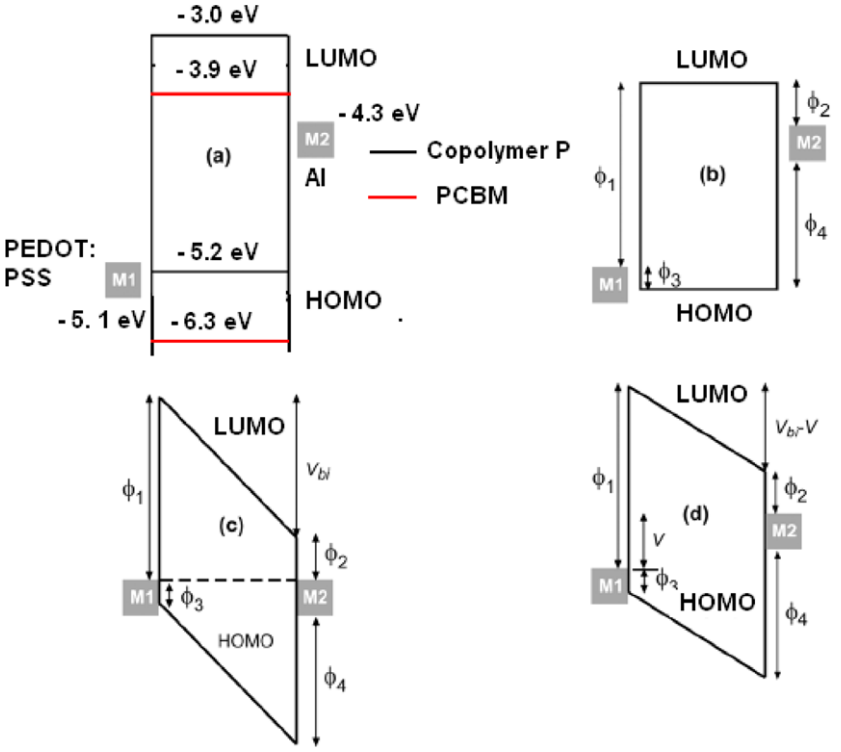

Fig. 8. Schematic energy diagrams (a) of the PEDOT:PSS/copolymer **P**:PCBM/Al device before the materials are brought to intimate contact, (b) of the virtual semiconductor (the blend of copolymer **P** and PCBM is assumed to be a single virtual semiconductor) before it is brought to intimate contact with electrodes, (c) of the system when the semiconductor is brought to intimate contact with electrode materials and (d) represents the situation when a forward bias voltage V is applied to the device.

with a virtual semiconductor before the intimate contact. Fig. 8c shows the situation when the virtual semiconductor has been brought to intimate contact with the contacting electrodes to formulate the device. The mathematical simulations show that in thermal equilibrium the electric field in the device is equal to V_{bi}/d, which reduces to $(V_{bi} - V)/d$, when forward bias of voltage V, is applied to the device. Fig 8d describes the situation when the forward bias is applied to the device.

We have calculated the J–V characteristics of the ITO/PEDOT:PSS/PPAT:PCBM/Al device in dark and under illumination using the model development by Kumar et al. [44] for BHJ devices. In this model they have solved the continuity equation including both drift and diffusion of charge carriers using a constant electric field in dark and under illumination and obtained the analytical expressions for J–V characteristics. The dark current in the device can be expressed as

$$J = \frac{q^2 D_n N_c (V_{bi} - V + JAR_s)\exp(-\phi_1/nkT)}{dnkT\left[1 - \exp\left(\frac{-q(V_{bi}-V+JAR_s)}{nkT}\right)\right]} \times \left(\exp\left(\frac{q(V - JAR_s)}{nkT}\right) - 1\right) + \frac{V - JAR_s}{R_p A}, \quad (1)$$

where n is the diode ideality factor, A is the cross section area, R_s and R_p are the series and parallel resistance, respectively, D_n is diffusion coefficient, N_c effective density

of state, ϕ_1 is the electron injection barrier at anode and d is the thickness of the organic layer.

Under illumination the J–V characteristics can be given as

$$J = \frac{q^2 D_n N_c (V_{bi} - V + JAR_s)\exp(-\phi_1/nkT)}{dnkT\left[1-\exp\left(\frac{-q(V_{bi}-V)+JAR_s}{nkT}\right)\right]} \times \left(\exp\left(\frac{q(V-JAR_s)}{nkT}\right)-1\right) + \frac{V-JAR_s}{R_p A} - J_{ph}(V), \qquad (2)$$

where J_{ph} is the photogenerated current. The photocurrent is determined by the light generated charge carriers due to the photon absorption by the active layer that reaches the appropriate electrodes with their lifetime (τ). The velocity of the charge carriers is determined by their mobility and internal electric field. At higher internal electric field all the generated charge carriers within the bulk of the device will contribute to the photocurrent, while at lower internal electric fields, only the generated charge carriers in the vicinity of the electrodes are collected by the electrodes.

Fig. 9 shows the comparison of the calculated and experimental J–V characteristics of the device. When a forward bias (negative at Al electrode) is applied to the device, electrons are injected into the LUMO of PCBM and holes are injected into the HOMO of copolymer **P**. In the copolymer **P**:PCBM BHJ, the copolymer **P** and PCBM form the different percolated paths for hole and electron, respectively, in which the electrons and holes transport easily towards the electrodes. Therefore, the electrons and holes move in PCBM and copolymer **P** channels, respectively. The two currents are added to each other in order to get the overall current in the device. The theoretical values of the current in dark and under illumination were estimated using Eqs. (1) and (2), respectively. The values of parameters used here are: $\phi_1 = 1.2$ eV, $\phi_2 = 0.9$ eV for holes $T = 300$ K, $\mu = 2.2 \times 10^{-5}$ cm^2/Vs, $R_s = 20\ \Omega$, $A = 25$ mm^2, $d = 100$ nm, $\varepsilon = 3.5$, $N_c = N_v = 10^{19}$ cm^3, $V_{bi} = 0.70$ V, and $R_p = 2.0 \times 10^4\ \Omega$ for dark and $R_p = 3.5 \times 10^3\ \Omega$ under illumination. As it can be seen from Fig. 9, the calculated J–V characteristics of the devices in both dark, as well as under illumination follow closely the experimental results. Therefore, we conclude that the model based on drift and diffusion current at constant electric field is valid for our BHJ device.

2.3. Photovoltaic properties of solar cells based on two bulk heterojunction layers

We have used copolymer **P**:PCBM and **BTD-TNP**:**PPI** BHJs for fabrication of solar cells. Fig. 10 shows the normalized optical absorption spectra of a bi-layer film of copolymer **P**:PCBM/**BTD-TNP**:**PPI**. The bi-layer film shows a continuous absorption from 350 nm to 780 nm arising from both BHJ layers.

In order to get more information about the photocurrent generation, we have measured the incident photon to current efficiency (IPCE) of the devices. The values of IPCE have been estimated using the following expression:

$$\text{IPCE}\ (\%) = 1240\, J_{sc}/\lambda P_{in}, \qquad (3)$$

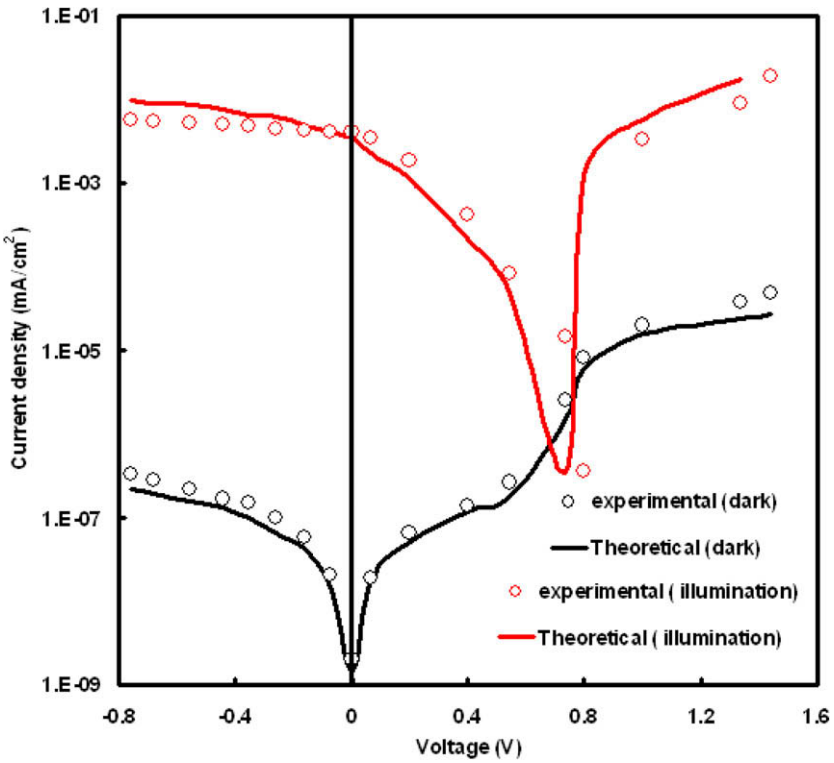

Fig. 9. Calculated and experimental J–V characteristics of an ITO/PEDOT:PSS/copolymer **P**:PCBM (1:3 wt. ratio)/Al device in dark and under illumination.

where J_{sc} (mA/cm^2) is the short circuit photocurrent, P_{in} mW/cm^2 and λ (nm) is the illumination intensity and wavelength of the monochromatic light. Fig. 11 shows the IPCE spectra of the PV devices employed with different active layers. It can be seen from the IPCE spectra of each device, that it closely resembles the absorption spectra of the blend used in the device. The bi-layer BHJ devices shows the improved IPCE in comparison to that the single

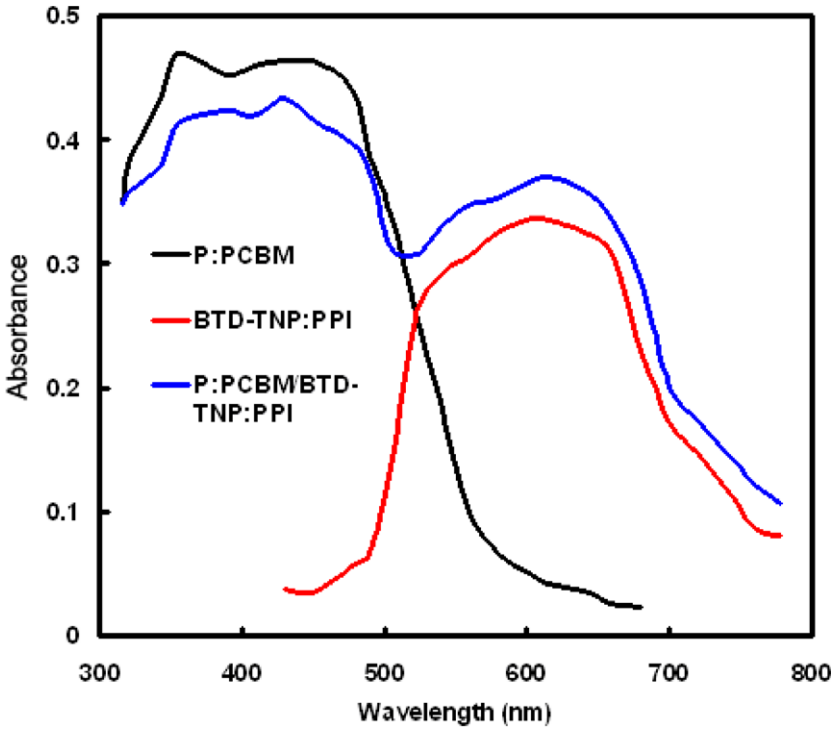

Fig. 10. Optical absorption spectra of copolymer **P**:PCBM, **BTD-TNP**:**PPI** and their bi-layer thin films.

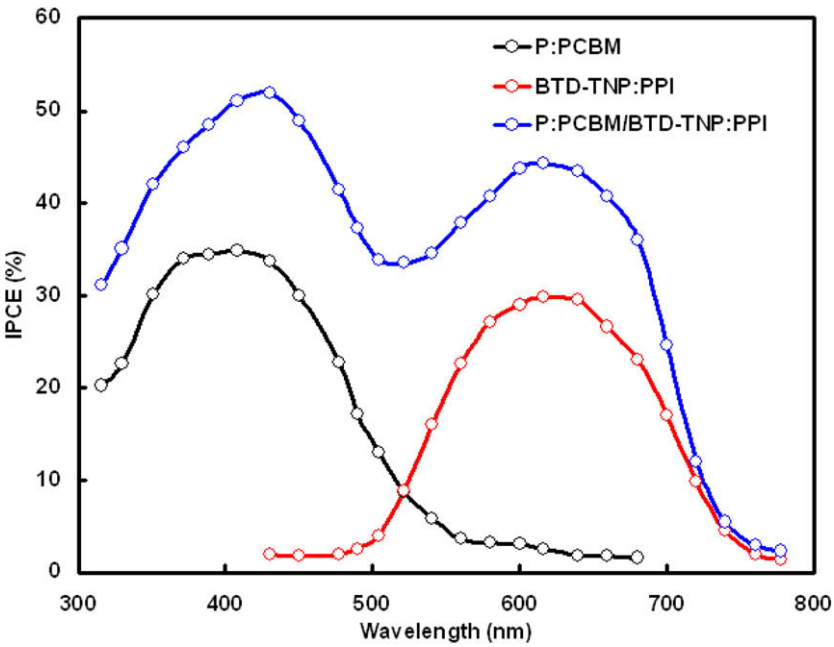

Fig. 11. IPCE spectra of photovoltaic devices using different photoactive layers.

layer BHJ devices. This increase in the IPCE was attributed to the improvement in the light harvesting and enhanced charge transport.

The *J–V* characteristics of ITO/PEDOT:PSS/**P**:PCBM/**BTD-TNP**:**PPI**/Al bi-layer heterojunction devices are shown in Fig. 12 and PV parameters are listed in Table 2. The single **P**:PCBM layer and bi-layer solar cells exhibit similar V_{oc} and bi-layer device showed a much higher J_{sc} and PCE. In general, the J_{sc} is determined by the product of photoinduced charge carrier density and the charge carrier mobility [1], as given by $J = nq\mu E$, where n is the charge carrier density, q is the electronic charge, μ is the mobility of charge carrier, and E is the electric field. The observed higher value of J_{sc} in the bi-layer BHJ device is attributable to the increased number of photo induced charge carriers by extended absorption to the solar photons in longer wavelength region. The schematic energy level diagram of the bi-layer BHJ solar cells fabricated from **P**:PCBM and **BTD-TNP**:**PPI** blend with and without TiO_2 layer is shown in Fig. 13. As the HOMO of **P** is at higher energy level than that of **BTD-TNP**, holes from the second layer can effectively pass through the first layer to the anode. The higher value of J_{sc} in bi-layer BHJ may also be due to the increased electric field induced by the additional electric forces related to the concentration gradient of charge carriers across the bi-layer heterojunction. This effect minimizes also the charge recombination.

The incorporation of TiO_2 layer between the active layer and Al electrode further increases the J_{sc} and PCE which is attributed to the increased electron transport in the device as we have discussed earlier. The formation of large polycrystalline domains of copolymer **P** in the first layer induced by the thermal annealing also increased the PCE of both devices with and without TiO_2 layer.

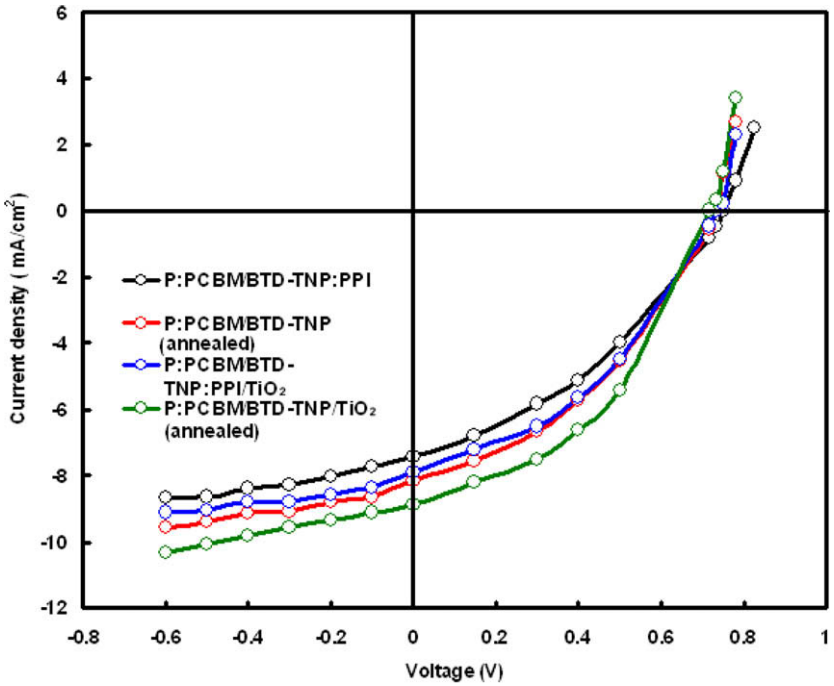

Fig. 12. Current–voltage characteristics of bi-layer BHJ photovoltaic devices with and without TiO_2 (as cast and annealed).

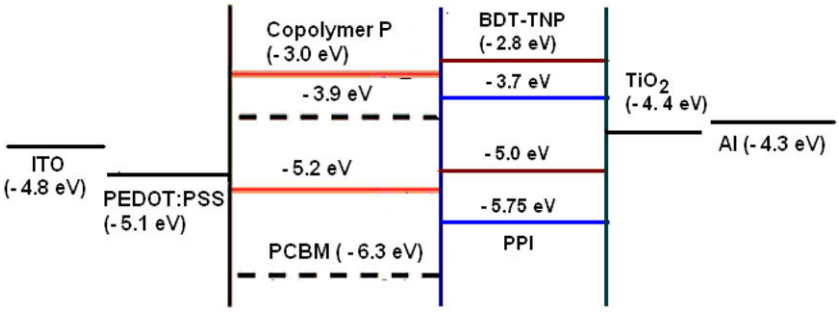

Fig. 13. Schematic energy band diagram of the bi-layer device based on two bulk-heterojunction layer with TiO_2 layer inserted before Al electrode.

In organic solar cells, the photocurrent generation is governed by two main factors [45]: (i) the fractional number of the absorbed photons in the active layer (relative to the total flux of photons from solar spectrum) and (ii) the incident photon to carrier collection efficiency defined as the fraction of collected carriers per absorbed photons. It is observed that in both single layer BHJ and bi-layer BHJ devices, the photocurrent increases when the TiO_2 layer is inserted between the active layer and the top Al electrode. The TiO_2 layer acts as an optical spacer and hole blocker [46] between the photoactive layer and the top Al electrode. The TiO_2 layer redistributes the light intensity within the active layer by changing the optical interference between the incident light and reflected light from Al electrode [47]. This mechanism leads to an increase in the fraction of light absorbed in active layer. In addition, the hole blocking feature of TiO_2 layer also enable the efficient electron collection without a significant increase in series resistance [46].

3. Conclusions

In conclusion, we have fabricated a single layer BHJ device with copolymer **P** and PCBM composites with different wt ratio of **P** to PCBM deposited at different substrate temperatures. It was observed that the single layer BHJ with 1:3 wt ratio shows the optimum PCE of about 1.14% which is further improved upon thermal annealing. The bi-layer BHJ PV device having structure ITO/PEDOT:PSS/**P**:PCBM/**BTD-TNP**:**PPI**/Al shows a PCE of approximately 2.68% which is further improved up to 2.98% upon thermal annealing. This increase was attributed to the enhancement in the hole transport due to the increased crystalline nature of copolymer **P** upon thermal annealing. The incorporation of TiO_2 layer into the active organic layer and the top Al electrode improves the PCE in both single and bi-layer BHJ devices. This increase in PCE is attributed to the enhanced photon absorption, due to the constructive optical interference between the incident light and the reflected light from the Al electrode and also to the hole blocking nature of TiO_2 layer that improves the electron transport. The increase PCE upon thermal annealing has been attributed to the improvement in the hole transport in the device.

4. Experimental

UV–visible spectra of the materials in thin film were recorded on a Beckman DU-640 spectrometer with spectrograde THF. The cyclic voltammetry of materials was performed on a potentiostat–Galvanostat (PGSTAT 30 Autolab, ECO-Chemie, Netherland) in acetonitrile solution (0.1 M) of 4-tert-butylpyridine (TBP) at room temperature. A glassy carbon electrode coated with a thin film of copolymer **P** or **BTD-TNP** or PCBM was used as the working electrode. Pt and Ag wire were used as the counter electrode and quasi reference electrodes, respectively.

All the devices were prepared on indium tin oxide (ITO) coated glass substrates. The substrates were cleaned with detergent, de-ionized water, acetone and isopropyl alcohol successively for 15 min and then dried in an oven. A thin film of PEDOT:PSS (40 nm) was spin cast onto ITO coated glass from aqueous solution. The substrates were dried at 80 °C for 20 min and then cooled up to room temperature. For single layer BHJ devices, the copolymer **P** and PCBM mixture was prepared by co-dissolving **P** and PCBM in 1,2-dichlorobenzene (DCB) at 65 °C. The thin films of copolymer **P**:PCBM blend with different weight ratio were prepared by spin coating a warm solution (60 °C) of blend onto ITO/PEDOT:PSS coated glass substrates and then dried at 60 °C in air. Al metal electrode was deposited on the top of **P**:PCBM blend film to complete the device having structure ITO/PEDOT:PSS/**P**:PCBM/Al. Likewise, another single layer BHJ devices based on **BTD-TNP**:**PPI** blends were prepared by same method as discussed above. The ITO/PEDOT:PSS/**P**:PCBM/TiO_2/Al device was fabricated by the deposition of TiO_2 paste on the top of **P**:PCBM layer before the deposition of Al electrode.

For the bi-layer BHJ devices, the **P**:PCBM (from dichlorobenzene solvent) layer was deposited on the top of ITO/PEDOT:PSS followed by drying at 60 °C for 1 h. The **BTD-TNP**:**PPI** (from chloroform solvent) was then spin cast on the top of **P**:PCBM layer and then dried again at 60 °C for 1 h. Finally, the Al electrode was deposited on the top of active layer by the thermal vacuum evaporation method. The device ITO/PEDOT:PSS/Copolymer **P**:PCBM/**BTD-TNP**:**PPI**/TiO_2/Al was fabricated the by inserting the TiO_2 layer before the deposition of Al electrode. The post-annealing of some devices was conducted by heating at 100 °C for 5 min followed by cooling up to room temperature.

The *J–V* characteristics of the devices in dark as well as under illumination intensity of 100 mW/cm^2, were obtained using a Keithley electrometer equipped with built in power supply. A 100 W halogen lamp was used as light source. The intensity of the illumination was measured with lux meter. The IPCE spectra of the device were calculated by illuminating the device with a halogen lamp using monochromator and measuring the resulting current with Keithley electrometer under short circuit conditions. The fabrication and characterization were performed under ambient conditions.

References

[1] S. Gunes, H. Neugebauer, N.S. Sariciftci, Chem. Rev. 10 (2007) 1324.
[2] J.Y. Kim, K. Lee, N.E. Coates, D. Moses, T.Q. Nguyen, M. Dante, A.J. Heeger, Science 317 (2007) 222.
[3] I. Gur, N. Fromer, C.P. Chen, A. Kanarkas, A.P. Alivisatos, Nano Lett. 7 (2007) 409.
[4] M. Reyes-Reyes, K. Kim, J. Dewald, R. Lopez-Sandoval, A. Avadhanula, S. Curran, D.L. Caroll, Org. Lett. 7 (2005) 5749.
[5] Y. Kim, S. Cook, S.M. Tuladhar, S.A. Choulis, J. Nelson, J.R. Durrant, D.D.C. Bradley, M. Giles, I. McCullough, C. Ha, M. Ree, Nat. Mater. 5 (2006) 197.
[6] W. Ma, C.Y. Yang, X. Gong, K. Lee, A.J. Heeger, Adv. Funct. Mater. 15 (2005) 1617.
[7] M. Reyes-Reyes, K. Kim, D.L. Carroll, Appl. Phys. Lett. 87 (2005) 083506/1.
[8] S.H. Park, A. Roy, S. Beaupre, S. Cho, N. Coates, J.S. Moon, D. Moses, M. Leclerc, K. Lee, A.J. Heeger, Nat. Photon. 3 (2009) 297.
[9] M.C. Scharber, D. Muhlbacher, M. Koppe, P. Denk, A. Waldauf, A.J. Heeger, C.J. Brabec, Adv. Mater. 18 (2006) 789.
[10] W.-Y. Wong, X.-Z. Wang, Z. He, A.B. Djurisic, C.-T. Yip, K.-Y. Cheung, H. Wang, C.S.K. Mak, W.-K. Chan, Nat. Mater. 6 (2007) 521.

[11] M. Koppe, M. Scharber, C. Brabec, W. Duffy, M. Heeney, I. McCulloch, Adv. Funct. Mater. 17 (2007) 1371.
[12] Z. Zhu, D. Waller, R. Gaudiana, M. Morana, D. Muhlbacher, M. Scharber, C. Brabec, Macromolecules 40 (2007) 1981.
[13] S.A. Backer, K. Sivula, D.F. Kavulak, J.M.J. Frechet, Chem. Mater. 19 (2007) 2927.
[14] Y. Yao, C. Shi, G. Li, V. Shrotriya, Q. Pei, Y. Yang, Appl. Phys. Lett. 89 (2006) 153507/1.
[15] J. Peet, J.Y. Kim, N.E. Coates, W.L. Ma, A.J. Moses, A. Heeger, G.C. Bazan, Nat. Mater. 6 (2007) 497.
[16] C.J. Ko, Y.K. Lin, F.C. Chen, Adv. Mater. 19 (2007) 3520.
[17] G. Li, Y. Yao, H. Yang, V. Shrotriya, Y. Yang, Adv. Funct. Mater. 17 (2007) 1636.
[18] T. Kietzke, R.Y.C. Shin, D.A.M. Egbe, Z.-K. Chen, A. Sellinger, Macromolecules 40 (2007) 4424.
[19] D. Vak, S.S. Kim, J. Jo, S.H. Oh, S.I. Na, J. Kim, D.Y. Kim, Appl. Phys. Lett. 91 (2007) 081102/1.
[20] J. Huang, G. Li, Y. Yang, Adv. Mater. (2008), <http://www3.interscience.wiley.com/cgi-bin/fulltext/117881983/PDFSTART>.
[21] S.S. Kim, S.I. Na, J. Jo, G. Tae, D.Y. Kim, Adv. Mater. 19 (2007) 4410.
[22] C.N. Hoth, A. Choulis, P. Schilinsky, C.J. Brabec, Adv. Mater. 19 (2007) 3973.
[23] J. Gilot, M.M. Wienk, R.A.J. Janssen, Appl. Phys. Lett. 90 (2007) 143512/1.
[24] A. Hadipour, B. de Boer, J. Wildeman, F.B. Kooistra, J.C. Hummelen, M.G.R. Turbiez, M.M. Wienk, R.A.J. Janssen, P.W.M. Blom, Adv. Funct. Mater. 16 (2006) 1897.
[25] J.Y. Kim, S.H. Kim, H.-H. Lee, K. Lee, W. Ma, X. Gong, A.J. Heeger, Adv. Mater. 18 (2006) 572.
[26] M.T. Lloyd, A.C. Mayer, S. Subramanian, D.A. Mourney, D.J. Herman, A. Bapat, J.E. Anthony, G.G. Malliaras, J. Am. Chem. Soc. 129 (2007) 9144.
[27] M.L. Sun, L. Wang, X.-H. Zhu, D. Du, R. Liu, W. Yang, Y. Cao, Sol. Energy Mater. Sol. Cells. 91 (2007) 1681.
[28] C. He, Q. He, X. Yang, G. Wu, C. Yang, F. Bai, Z. Shuai, L. Wang, Y.J. Li, Phys. Chem. C 111 (2007) 8661.
[29] A.B. Tamayo, B. Walker, T.Q.J. Nguyen, Phys. Chem. C 112 (2008) 11545.
[30] C. He, Q. He, Y. Yi, G. Wu, F. Bai, Z. Shuai, Y. Li, J. Mater. Chem. 18 (2008) 4085.
[31] H. Kageyama, H. Ohishi, M. Tanaka, Y. Ohmori, Y. Shirota, Appl. Phys. Lett. 94 (2009) 063304/1.
[32] A.B. Tamayo, X.D. Dang, B. Walker, J. Seo, T. Kent, T.Q. Nguyen, Appl. Phys. Lett. 94 (2009) 103301/1.
[33] K. Schulze, C. Uhrich, R. Schueppel, K. Leo, M. Pfeiffer, E. Brier, E. Reinold, P. Baeuerle, Adv. Mater. 18 (2006) 2872.
[34] K.L. Mutolo, E.I. Mayo, B.P. Rand, S.R. Forrest, M.E. Thompson, J. Am. Chem. Soc. 128 (2006) 8108.
[35] M.Y. Chan, S.L. Lai, M.K. Fung, C.S. Lee, S.T. Lee, Appl. Phys. Lett. 90 (2007) 023504/1.
[36] P. Peumans, S. Uchida, S.R. Forrest, Nature 425 (2003) 158.
[37] J.A. Mikroyannidis, M.M. Stylianakis, P. Suresh, G.D. Sharma, Sol. Ener. Mater. Sol. Cells 93 (2009) 1792.
[38] P. Suresh, P. Balraju, G.D. Sharma, J.A. Mikroyannidis, M.M. Stylianakis, ACS Appl. Mater. Interf. 1 (2009) 1370.
[39] J.A. Mikroyannidis, M.M. Stylianakis, M.S. Roy, P. Suresh, G.D. Sharma, J. Power Source 194 (2009) 1171.
[40] J. Hou, Z. Tan, Y. Yan, Y. He, C. Yang, Y. Li, J. Am. Chem. Soc. 128 (2006) 4911.
[41] H. Hoppe, M. Niggemann, C. Winder, J. Kraut, R. Hiesgh, A. Hinsch, D. Meissner, N.S. Sariciftci, Adv. Funct. Mater. 14 (2004) 1005.
[42] M.M. Mandoc, L.J.A. Koster, P.W.M. Blom, Appl. Phys. Lett. 90 (2007) 133504/1.
[43] C. Deibel, A. Wagenpfahl, V. Dyakonov, Phys. Status Solidi (RRL) 2 (2008) 175.
[44] P. Kumar, S.C. Jain, V. Kumar, S. Chand, R.P. Tandon, J. Phys. D: Appl. Phys. 42 (2009) 055102/1.
[45] C. Winder, N.S. Sariciftci, J. Mater. Chem. 14 (2004) 1077.
[46] S. Cho, J. Yuen, J.Y. Kim, K. Lee, A.J. Heeger, S. Lee, Appl. Phys. Lett. 92 (2008) 063505/1.
[47] L.H. Slooff, S.C. Veenstra, J.M. Kroon, D.J.D. Moet, J. Sweelssen, M.M. Koetse, Appl. Phys. Lett. 90 (2007) 143506/1.

crystal, to overcome the conductivity mismatch problem of injecting spins from a metallic ferromagnet into a semiconductor [12,13].

Here we present, for the first time, FETs of 5,6,11,12-tetraphenylnaphthacene (rubrene, $C_{42}H_{28}$) single-crystals with high-quality, ferromagnetic Co electrodes and Al_2O_3 tunnel barriers, that can be used for carrier injection without spin randomization. Although the device layout, well-controlled interface, and choice of materials seem ideal for realizing the spin-valve effect, it has remained elusive in our devices so far. Possible reasons are discussed towards the end of the paper, and are expected to evoke both theoretical and experimental follow-up.

Fig. 2a is a photograph of one of our devices, showing the Co/Al_2O_3 electrodes (light bars) underneath a piece of rubrene single-crystal. Cobalt electrodes were chosen for two reasons. First, the reported workfunction of bare Co aligns favorably with the HOMO of rubrene [4], which should help in maximizing the amount of carriers injected from the electrodes into the semiconductor via tunneling (rather than thermal activation over a Schottky barrier). Second, technological processes are known, that allow the realization of a controlled and very thin Al_2O_3 layer on top of the Co film, acting at the same time as a well-defined tunnel barrier and as a protective layer against oxidation of the ferromagnet which is crucial, since CoOx is known to possess antiferromagnetic correlations, which would cause spin-flip scattering, randomizing the carrier spin during the injection. The Co electrodes (16 nm thick) are defined by photolithography on a highly doped Si/SiO_2 (300 nm) wafer and covered with a 2.5 nm Al_2O_3 tunnel barrier. The high-quality, pin-hole-free Al_2O_3 film is formed by plasma oxidation of Al evaporated on top of Co without breaking the UHV (10^{-10} Torr). This Al_2O_3 tunnel barrier prevents the Co electrodes from oxidation and helps to overcome the conductivity mismatch, as mentioned above. After lift-off with acetone, the electrodes are thoroughly cleaned in an oxygen plasma to ensure no resist is left. This is essential, as demonstrated by independent photon emission spectroscopy measurements [14]. Directly after this a rubrene single-crystal is electrostatically laminated on top of the electrodes. The lamination process yields uniform contact without air gaps, bubbles or interference fringes [6]. Similar single-crystal FET geometries were studied before in the case of non-ferromagnetic electrodes [6,8,9].

In order to verify the critical features of our device, we first performed the experiments described below. A Co/Al_2O_3/NiFe(permalloy) magnetic tunnel junction (MTJ [15], see inset of Fig. 1a) was used to check the quality of the Co/Al_2O_3 electrodes after exposure to air, acetone and oxygen plasma cleaning. To mimic the FET device fabrication process, the calibrated 2.0 nm thick Al film (resulting in a 2.5 nm thick layer of Al_2O_3) on top of the Co film (both grown in UHV) is first plasma oxidized for 10 min, exposed to air, covered with photoresist, cleaned by acetone and isopropanol, and oxidized again for 10 min to remove photoresist remnants and clean the bottom electrode. The MTJ is completed by evaporating the NiFe top electrode in UHV again. The magnetoresistance of a representative MTJ thus fabricated, is shown in Fig. 1a. We observe a clear hysteresis and a magnetoresistance (*MR*) of 16%, very close to the value of clean interfaces produced without breaking the vacuum (also shown in Fig. 1a), implying the good quality of the Al_2O_3 tunnel barrier (protecting the underlying Co from oxidation) and its robustness under our FET fabrication process. The realization of air-exposed FM electrodes in an organic spin-valve structure has been demonstrated before [16], but here an additional (and essential) cleaning step is used to remove any organic contaminations.

For spin valves, the ability to reverse the magnetization of the injector and detector electrodes independently is essential [1]. Therefore, the switching fields of both electrodes need to be sufficiently different. The magnetization of the 16 nm Co layer is in plane, and its switching field depends on the ratio between length and width. The switching fields H_{sw} of the Co/Al_2O_3 electrodes for different electrode widths d were determined from test samples with an ensemble of electrodes (see right inset of Fig. 1b), using the same fabrication procedure and substrate as for the FET devices. Hysteresis curves measured in a vibrating sample magnetometer (VSM) clearly reveal sharp switching fields, as shown in the left inset of Fig. 1b for the case of a test sample containing an ensemble

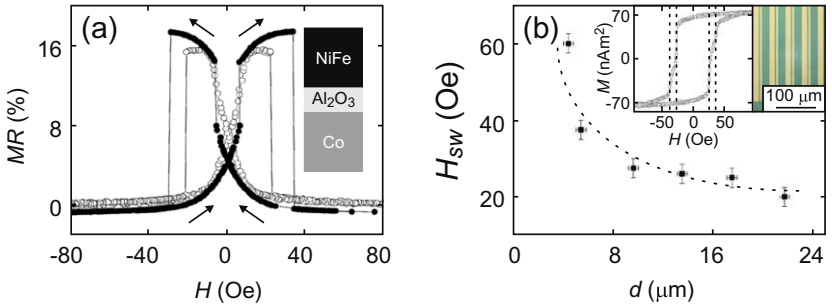

Fig. 1. Electrode characterization. (a) Magnetoresistance *MR* vs. magnetic field *H* for Co/Al_2O_3(~2.5 nm)/NiFe(15 nm) magnetic tunnel junctions (MTJs, inset). Data shown for a MTJ with 16 nm Co layer treated with photoresist, acetone and IPA (open circles) and an untreated one with a 8 nm Co layer (solid dots). *MR* is defined as $(R - R_P)/R_P$, with R_P the resistance for parallel magnetization of the Co and NiFe layers at large magnetic fields. Arrows denote the sweep directions. Different switching fields due to difference in Co layer thickness. (b) Switching field H_{sw} vs. electrode width d for Co/Al_2O_3 (16 nm/2.5 nm) electrodes. The dotted line is a guide to the eye. Left inset: Magnetization *M* vs. magnetic field *H* for electrodes with a width of 5.4 and 13.5 ± 0.4 μm. The switching field H_{sw} for the two widths is denoted by the dashed lines. Right inset: Ensemble of electrodes for H_{sw} measurements.

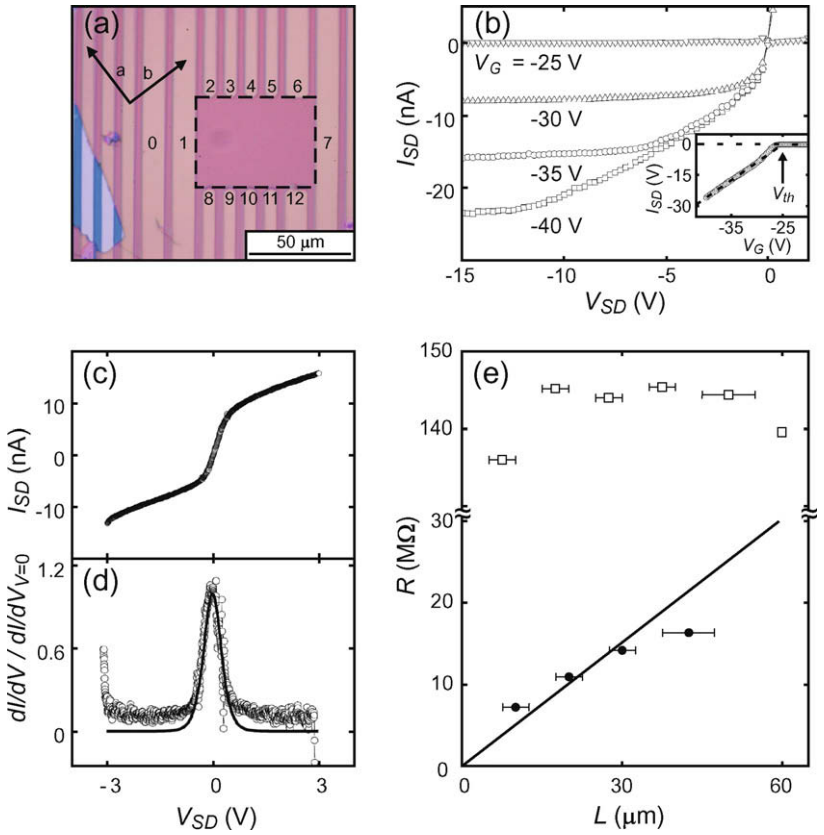

Fig. 2. Single-crystal FET device. (a) Photograph of the rubrene single-crystal (partly) overlapping with Co/Al_2O_3 electrodes (numbered 0–12; other electrodes not used). Electrodes 1, 6, 7 and 12 have 12 ± 0.4 μm width, 2–5 and 8–11, 6.5 ± 0.4 μm. The doped Si substrate is used as back gate. The active device area is denoted by the dashed rectangle, with channel length $L = 60$ μm and width $W = 50$ μm. The crystal axes *a* and *b* (the latter corresponding to the highest mobility) are denoted by the arrows. (b) Source–drain current I_{SD} vs. voltage V_{SD}(electrodes 1 and 7) for different gate voltages V_G. Inset: I_{SD} vs. V_G for $V_{SD} = -10$ V. The threshold voltage $V_{th} = -25$ V is indicated by the arrow. (c) Zoom-in around $V_{SD} = 0$ V($V_G = -40$ V) for the measurements in (b). (d) Normalized differential conductance $dI/dV / dI/dV_{V=0}$ vs. V_{SD}. The line is a fit to the derivative of Eq. (1). (e) Resistance *R* vs. channel length *L* for two-terminal measurements (open squares) for $V_{SD} = -1$ V and 4-terminal measurements (solid dots) for $I_{SD} = -1$ nA (linear regime, $V_G = -40$ V for all measurements). The solid line is a fit to Eq. (3).

of electrodes with two different widths (5.4 and 13.5 ± 0.4 μm). From these VSM measurements the switching field as a function of electrode width is derived, see Fig. 1b. H_{sw} strongly depends on electrode width for $d < 10$ μm, but saturates for wider electrodes.

The multi-terminal single-crystal device of Fig. 2a is characterized using different measurement configurations, and the main characteristics have been reproduced in multiple devices. The negative Si back gate voltage (used to induce holes) is expected to be screened by the Co/Al_2O_3 electrodes, i.e. the charge accumulation should be much lesser on top of the electrodes than at the crystal/SiO_2 interface in between the electrodes. To confirm this, a voltage of −10 V was applied between electrode 0 and 7 for a gate voltage of −40 V. No current larger than 10^{-11} A was measured. We conclude that, although current between adjacent electrodes can flow over the full crystal width, for non-adjacent electrodes there is only a current path through the non-contacted region (channel width $W = 50$ μm, channel length $L = 60$ μm) denoted by the dashed lines in Fig. 2a. Using electrodes 1–12, 2- and 4-terminal measurements are performed. The multi-terminal layout is also suitable for measuring spin accumulation in the so-called non-local geometry [17].

For 2-terminal measurements, the source–drain voltage V_{SD} is applied over electrodes 1 and 7, and the resulting current I_{SD} is measured using the same electrodes. Different contact combinations are discussed later on. I_{SD}–V_{SD} curves for different gate voltages V_G are shown in Fig. 2b. The typical gate leakage current in our devices is $I_{leak} < 10^{-11}$ A. The threshold voltage V_{th} is −25 V (inset of Fig. 2b), obtained from extrapolating the I_{SD}–V_G curves for large V_G (linear regime) to $I_{SD} = 0$. This value is relatively high, and might be related to hole trapping at the SiO_2/single-crystal interface or incomplete lamination of the crystal to the substrate.

The weak gate dependence around $V_{SD} = 0$ V implies that the device resistance is contact-dominated [8,9], as discussed in more detail below. The contact-dominated behavior is expected, since we have a tunnel barrier on top of the Co electrodes. The reasonable contact quality without a large hole injection barrier is demonstrated by

the linearity at $V_{SD} = 0$ V, as can be seen in Fig. 2c [18]. The overall non-linear shape around $V_{SD} = 0$ (see Fig. 2c) can be described by a back-to-back diode model [8]

$$I_{b-b} = I_0 \tanh\left(\frac{eV_{SD}}{2\eta k_B T}\right), \quad (1)$$

where I_0 is the saturation current, η the diode ideality factor, k_B the Boltzmann constant and T the temperature. The normalized differential conductance, obtained by numerical differentiation of the data, can be fitted by the derivative of Eq. (1), as shown in Fig. 2d. The small offset is explained by the fact that I_0 is weakly bias dependent, contrary to what is assumed in the derivation of Eq. (1). We obtain a value $\eta = 7.7 \pm 0.2$, as compared to $\eta = 1$ for an ideal Schottky diode. This high value demonstrates that although Schottky barrier formation plays a role in our devices, tunneling is important [19] and holes are indeed injected in the single-crystal through the tunnel barrier. Temperature-dependent measurements should give more insight into the height of the Schottky barriers.

In the linear regime, the usual FET relation applies

$$I_{SD} = \frac{W}{L}\mu C_i (V_G - V_{th}) V'_{SD}, \quad (2)$$

where C_i the capacitance of the gate insulator per unit area and μ the carrier mobility. Note that V'_{SD} is the voltage drop over the conducting channel, excluding the voltage drop over the electrodes. The channel resistance R_{ch} is determined from 4-terminal measurements. Current is driven between electrodes 1 and 7, the voltage drop is measured using the intermediate electrodes, to study the channel resistance as a function of length, see Fig. 2e (solid dots). Note that the square resistance $R_\square \sim 25\ \mathrm{M\Omega/\square}$ is $\sim 10^3$ times the quantum resistance. By rewriting Eq. (2), R_{ch} is given by

$$R_{ch} = \frac{L}{WC_i(V_G - V_{th})}\frac{1}{\mu}. \quad (3)$$

Fitting to Eq. (3), we extract a hole mobility of $0.25\ \mathrm{cm^2(Vs)^{-1}}$. The relatively low mobility is attributed to contaminations in the starting material (only one purification cycle is used) and the rather long period (∼weeks) between crystal growth and device fabrication. Although the crystals are stored in a nitrogen environment, oxidation cannot completely be ruled out [20]. Optimization of these factors has proven to result in typically 1–10 $\mathrm{cm^2\,(Vs)^{-1}}$ mobilities [21].

The 2- and 4-terminal resistance measurements are compared in Fig. 2e, where the difference is explained by the contact resistance. The normalized contact resistance R_cW of $0.28\ \mathrm{M\Omega\,cm}$ (used in 2D devices) dominates the 2-terminal resistance, as concluded before. This is much higher than contact resistances found for nickel oxide electrodes ($0.1 - 1\ \mathrm{k\Omega\,cm}$) [10] and cobalt oxide electrodes (10–200 $\mathrm{k\Omega\,cm}$) [8]. The high contact resistance in our devices can be explained by the Al_2O_3 tunnel barrier, and implies that charge is injected through the tunnel barrier, as intended.

In spite of the seemingly ideal choices for the spin injecting and detecting interfaces, we have not been able to unambiguously demonstrate a spin-valve effect in our FETs. This could have several reasons. First of all, the spin relaxation time τ_{sf} may be not as long as expected. Based on EPR studies [22], we have assumed a lower bound of 1 μs for τ_{sf}. Using $\lambda_{sf} = \sqrt{D\tau_{sf}}$, where λ_{sf} is the spin relaxation length, D the diffusion constant, and the Einstein relation $D = \mu k_B T/e$, gives $\lambda_{sf} > 1\ \mu\mathrm{m}$, comparable to the present device dimensions. Recently, even much larger values (∼ mm) were predicted for rubrene single-crystals [23]. However, if τ_{sf} is significantly shorter, we should make the channels shorter and/or use crystals with higher mobility. We cannot exclude that τ_{sf} is temperature dependent as well and is longer at lower temperatures. Devices similar to those demonstrated here, with shorter channel length, will provide a well-controlled experimental platform to investigate the conditions for the occurrence of spin injection in organic semiconductors.

In conclusion, we have succeeded to realize well-defined tunnel barriers between ferromagnetic electrodes and organic single-crystals. The high-quality tunnel barrier should allow for spin injection without randomization. This, in combination with the observed FET functionality, provides us with necessary conditions for demonstrating a spin-valve FET. Similar devices are also expected to shine light on the spin relaxation time in organic semiconductors and the underlying physical mechanisms.

Acknowledgements

We thank J.G.M. Sanderink, A.S. Molinari, B.C. Min, R. Jansen, S.P. Dash, T. Banerjee and D.N. Reinhoudt for fruitful discussions and help. This work is part of WGvdW's VIDI research program 'Organic materials for spintronic devices', financially supported by the Netherlands Organization for Scientific Research (NWO) and the Technology Foundation STW.

References

[1] G.A. Prinz, Physics Today 48 (1995) 58;
G.A. Prinz, Science 282 (1998) 1660;
S.A. Wolf et al., Science 294 (2001) 1488.
[2] R. Farchioni, G. Grosso, Organic Electronic Materials, Springer-Verlag, Berlin, 2001;
G. Cuniberti, G. Fagas, K. Richter (Eds.), Introducing Molecular Electronics, Springer-Verlag, Berlin, Heidelberg, 2005;
H. Klauk (Ed.), Organic Electronics: Materials, Manufacturing and Applications, Wiley-VCH, Weinheim, 2006.
[3] W.J.M. Naber, S. Faez, W.G. van der Wiel, J. Phys. D: Appl. Phys. 40 (2007) R205.
[4] V.A. Dediu, L.E. Hueso, I. Bergenti, C. Taliani, Nature Mat. 8 (2009) 707.
[5] S. Sanvito, A.R. Rocha, J. Comput. Theor. Nanosci. 3 (2006) 624.
[6] R.W.I. de Boer, M.E. Gershenson, A.F. Morpurgo, V. Podzorov, Phys. Stat. Sol. (a) 201 (2004) 1302.
[7] V. Podzorov, E. Menard, A. Borissov, V. Kiryukhin, J.A. Rogers, M.E. Gershenson, Phys. Rev. Lett. 93 (2004) 086602.
[8] A.S. Molinari, I. Gutiérrez, I.N. Hulea, S. Russo, A.F. Morpurgo, Appl. Phys. Lett. 90 (2007) 212103.
[9] A.S. Molinari, G. Lezama, P. Parisse, T. Takenobu, A.F. Morpurgo, Appl. Phys. Lett. 92 (2008) 133303.
[10] I.N. Hulea, S. Russo, A. Molinari, A.F. Morpurgo, Appl. Phys. Lett. 88 (2006) 113512.
[11] C.L. Dennis, C.V. Tiusan, J.F. Gregg, G.J. Ensell, S.M. Thompson, IEE Proc.–Circuits Devices Syst. 152 (2005) 340;
S. Sugahara, IEE Proc.–Circuits Devices Syst. 152 (2005) 355.
[12] G. Schmidt, D. Ferrand, L.W. Molenkamp, A.T. Filip, B.J. van Wees, Phys. Rev. B 62 (2000) R4790.
[13] A. Fert, H. Jaffrès, Phys. Rev. B 64 (2002) 184420.

[14] M. Grobosch, C. Schmidt, W.J.M. Naber, W.G. van der Wiel, M. Knupfer, Synthetic Metals, in press, 2009, doi:10.1016/j.synthmet.2009.09.014.
[15] J.S. Moodera, L.R. Kinder, T.M. Wong, R. Meservey, Phys. Rev. Lett. 74 (1995) 3273.
[16] G. Szulczewski, H. Tokuc, K. Oguz, J.M.D. Coey, Appl. Phys. Lett. 95 (2009) 202506.
[17] M. Johnson, R.H. Silsbee, Phys. Rev. Lett. 55 (1985) 1790.
[18] N. Kawasaki, Y. Ohta, Y. Kubozono, Appl. Phys. Lett. 91 (2007) 123518.
[19] S.M. Sze, K.K. Ng, Physics of Semiconductor Devices, Wiley, New Jersey, 2007.
[20] C. Kloc, K.J. Tan, M.L. Toh, K.K. Zhang, Y.P. Xu, Appl. Phys. A 95 (2009) 219.
[21] A.F. Stassen, R.W.I. de Boer, N.N. Iosad, A.F. Morpurgo, Appl. Phys. Lett. 85 (2004) 3899;
I.N. Hulea, S. Fratini, H. Xie, C.L. Mulder, N.N. Iossad, G. Rastelli, S. Ciuchi, A.F. Morpurgo, Nat. Mat. 5 (2006) 982.
[22] V.I. Krinichnyi, Synth. Met. 108 (2000) 173.
[23] J.H. Shim, K.V. Raman, Y.J. Park, T.S. Santos, G.X. Miao, B. Satpati, J.S. Moodera, Phys. Rev. Lett. 100 (2008) 226603.

sophisticatedly manufactured from a very fine capillary glass tube having a tip diameter of <1 μm.

In contrast to top-down process, Tessler et al. reported a bottom-up approach for conducting polymer patterning based on a hydrophobic SAM formed on a 80 nm thick TiO_2-covered substrate [12]. The SAM exposed to UV light through the photomask became hydrophilic due to the photocatalytic effect of TiO_2 in the exposed regions and enabled the solution-deposition of the conducting polymer via dewetting from the hydrophobic regions during subsequent spin-casting. However, this technique requires a thin TiO_2 layer for the photocatalytic reaction with SAM at a humidity of ca. 40%. Other dewetting techniques had hydrophobic regions defined by microcontact printing for ~3 μm patterning [13] and electron-beam lithography for a 500 nm transistor channel length [14]. However, it should be noted that electron-beam lithography is costly and time-consuming process for large-area applications.

In this work, we propose a hybrid process that combines conventional photolithography and local surface energy modification through hydrophobic treatment in order to fabricate the conducting polymer source/drain electrodes of poly(3-hexylthiophene) (P3HT) organic field-effect transistors (OFETs). This technique is then applied to the fabrication of nanoscale conducting polymer patterns using photoresist (PR) templates, where nanoscale resist features are produced by holographic lithography.

2. Experimental section

2.1. Selective surface energy treatment for microscale polymer patterning

The proposed fabrication process is shown in Fig. 1. In brief, a 50 nm thick silicon oxide (SiO_2) surface on a heavily doped n-type silicon substrate was successively cleaned with acetone, ethyl alcohol, and deionized water in an ultrasonic bath. For the initial hydrophilic surface modification, an oxygen plasma treatment was carried out at 300 W for 60 s. A positive tone PR (AZ-6612, Clariant) solution was spin-coated on the substrate at 2800 rpm for 30 s

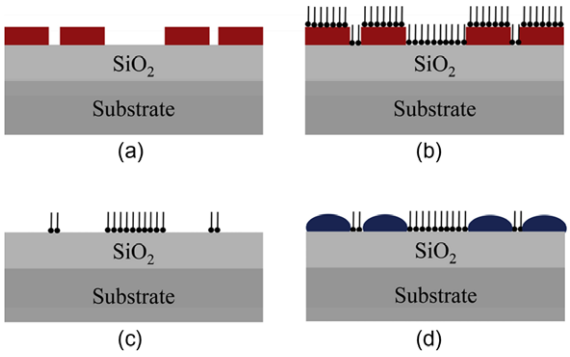

Fig. 1. Schematic of conducting polymer patterning using selective surface modification. (a) Photoresist patterns from conventional photolithography and the subsequent development process. (b) OTS attachment to the exposed substrate surface by self-assembly. (c) After removal of the PR patterns. (d) Conducting polymer solution dispersion; only hydrophilic regions are wet.

and then baked at 100 °C for 1 min. A UV light (λ = 365 nm) irradiated the PR film for 6.7 s through a clear-field photomask on which the desired patterns had been chromium-deposited. After development process, a gentle oxygen plasma treatment was performed at 100 W for 30 s in order to remove any residual PR layer under the trenches and generate hydroxyl groups at the exposed surfaces, which anchor the hydrophobic molecules during the SAM treatment.

The substrate with the PR patterns was immersed into an octadecyltrichlorosilane solution (OTS; 1.5 wt.% in toluene) for 5 min. At above 1.5 wt.%, aggregated OTS molecules were observed in all of the exposed regions. At less than 1.5 wt.%, the wettability contrast did not provide sufficient definition, especially for the 5 μm channel length, resulting in current leakage between the source and drain electrodes. During the OTS SAM coating, the head groups ($-SiCl_3$) reacted with the hydroxyl groups on the substrate surface in the trenches via siloxane linkage, and the alkyl chains underwent van der Waals interaction between each other with the hydrocarbon tail groups ($-CH_3$) exposed to the air, thereby rendering the surface hydrophobic nature. The substrate was then baked at 120 °C for 10 min to remove any residual toluene solvent. After PR pattern removal by acetone soaking for 5 min in an ultrasonic bath, the protected regions underneath the PR patterns remained hydrophilic during the photolithography process and the subsequent OTS treatment. Thus, a substrate with locally varied surface energies was achieved and subsequently utilized for spontaneous polymer patterning.

As a conducting polymer solution, we adopted the aqueous poly(3,4-ethylene-dioxythiophene):poly(styrene sulfonate) (PEDOT:PSS) polymer solution (1:2.5 by weight, 1 wt.% solid content, BAYTRON®, PH 500) due to its excellent processing ability, as well as its conducting, transparent, and thin film characteristics. Recent studies have shown that the conductivity of PEDOT:PSS can be dramatically increased with no loss in optical transparency through the addition of a small amount of diethylene glycol dopant [15,16]. In this experiment, diethylene glycol was mixed with PEDOT:PSS (1:10 by volume), and the solution was then dropped and dragged on the specially treated substrate using the doctor-blade method with a razor edge; there were no notable effects of blading direction relative to the feature geometries. The solution was dewetted by the hydrophobic regions and was thus spontaneously confined in the hydrophilic regions during spreading. Next, the sample was left in air for 2 min to allow the solvent to evaporate; at this time the polymer solution contracted, reducing the surface energy, which resulted in contours with sharp edges at the corners. Finally, the conducting polymer patterns were heated at 110 °C for 10 min to increase the conductivity for subsequent use as the source and drain electrodes of OFETs.

2.2. Nanoscale polymer patterning

Laser interference lithography (i.e., holographic lithography) was used to fabricate nanoscale periodic PR patterns because it can produce nanoscale features with ease. In brief, a diluted positive PR (AZ6612, Clariant) with

a thinner (AZ1500, Clariant) (volume ratio = 1:2) was spin-coated to a 150-nm thickness on a clean substrate that had previously been coated with hexamethyldisilazane (HMDS; above 98%, Fluka). Next, one-beam interference lithography method was utilized at an incident angle (θ) of 7.18 to fabricate repeated PR line patterns having a line-width of 290 nm at a 1.3 μm pitch size. A UV laser beam from the He–Cd ion laser (325 nm) was then passed through a spatial filter consisting of several lenses and a pin hole (10 μm diameter) in the end, where diffraction-limited beam enhancement occurs; this enhanced beam was projected onto the angle bracket where the sample holder and Lloyd mirror were placed perpendicular to each other. The PR was exposed to light for 50 s, equivalent to a dose of 30 mJ/cm^2, with a sinusoidal intensity owing to the constructive and destructive interference between the two split beams, one directly from the laser and the other reflected from the Lloyd mirror.

A specific pitch size was determined by $\Lambda = \lambda/2\sin\theta$, where θ is the incident angle, Λ is the pitch size of the pattern, λ is the laser wavelength, and the exposure time was optimized for the specific line width. After laser exposure, a developing process was performed by dipping the entire substrate into MIF 300 solution for 30 s and then rinsing with deionized water.

However, the solution-based SAM coating method used for microscale features did not work well for the nanoscale PR features due to the incomplete wetting to such confined areas caused by trapped air bubbles that prevented direct contact of the solution to the bottom of the exposed substrate surface between the PR features. Therefore, we applied a hydrophobic treatment in vapor phase using a tridecafluoro-1,1,2,2-tetrahydrooctyltrichlorosilane (Gelest Inc., CF_3–$(CF_2)_5$–$(CH_2)_2$–$SiCl_3$), which is commonly used as an anti-sticking material for the stamp surface treatment in nanoimprint lithography [17]. Perfluorocarbon-based trichlorosilanes have been reported to significantly decrease the stiction and friction of surfaces compared to hydrocarbon-based surface coatings [18].

A substrate with nanoscale PR features was loaded into a custom-built glass vacuum chamber and then pumped down to 10^{-3} torr. Then the pump was isolated from the chamber and the vapor of the hydrophobic material was then introduced into the chamber through a needle valve. The container of the hydrophobic agent solution was kept at 80 °C in order to maintain sufficient vapor pressure; this process was kept for 10 min at a static pressure of 0.3 torr. Next, the valve supplying the vapor of the hydrophobic material was closed and a second needle valve connected to a container partially filled with DI water was opened to allow water vapor into the chamber. The chamber was maintained for another 10 min at a total pressure of 0.8 torr in order to cross-link the neighboring attached molecules via a condensation reaction. Such a condensation reaction can produce a dense network within the monolayer on the substrate surface [19]. Finally, the chamber was again pumped down to a pressure 10^{-3} torr and the cycle was repeated twice more.

After removing the PR patterns with acetone, the polymer solution was cast on the substrate with locally different surface energies by using a multi-step spin-coating method; 1000 rpm for 10 s, 3000 rpm for 20 s, and 5000 rpm for 20 s.

3. Results and discussion

3.1. Surface energy measurement

To investigate the surface energy variation at each process step, the contact angle was measured with water at room temperature and then converted into surface energy using the Good–Girifalco–Fowkes–Young (G–G–F–Y) equation [20]:

$$(1+\cos\theta)\gamma_{LV} = 2(\gamma_{SV}\mathbf{V}_{LV})^{1/2}$$

where γ_{LV} is the surface tension of the test liquor (water; 72.8 dyne/cm), θ is the contact angle, and γ_{SV} is the surface energy of the medium of interest. Table 1 presents the results of contact angle measurements and their corresponding calculated surface energies at each step.

The initial surface treatment with oxygen plasma gas produced a very hydrophilic surface with a contact angle of 2.2°, equivalent to a high surface energy of 89.8 mN/m. The contact angle of the exposed substrate surface after development increased to a value of 14.2°. The surface became hydrophobic after application of the OTS SAM coating, attaining a contact angle of 97.7°, equivalent to a surface energy of 16.8 mN/m; this region was thermodynamically stable such that the surface is unlikely to react to other chemical elements.

The initial hydrophilic nature of the region under the PR pattern remained after PR removal, though the value increased to 26.8° due to the instability of the surface Si–OH groups with time. During the sequential processes for PR patterning and removal, the increase in contact angle is associated with a decrease in hydroxyl group coverage on the surface through the dehydration reaction between two neighboring hydroxyl groups, leading to the formation of a siloxane (Si–O–Si) bond [21]. The contact angle was 15° immediately after PR removal, and increased to 26.8° after 10 min in air. As such, polymer solution dispersion was completed within 10 min after PR removal. This selective surface engineering drives the spontaneous patterning of the conducting polymer solution, covering energetically unstable surfaces of hydrophilic regions with a high surface energy.

Table 1
Contact angle measurement and corresponding surface energy calculated at each step.

Experimental process		Contact angle (°)	Surface energy (mN/m)
Initial oxygen plasma treatment		2.2	89.8
Exposed area	After development	14.2	87.1
	After OTS treatment	97.7	16.8
Protected area	After PR pattern removal	26.8	80.5
On PEDOT:PSS film		7.6	19.7

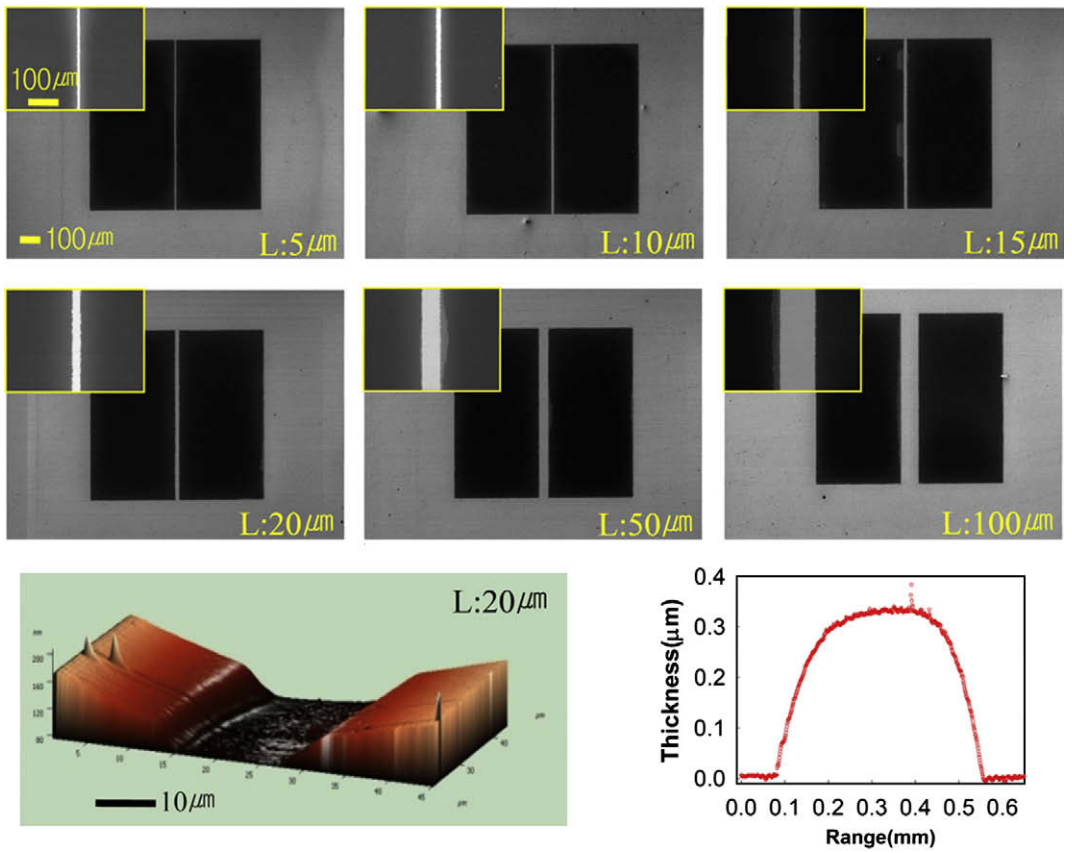

Fig. 2. (a) FE-SEM images of the conducting polymer source/drain electrodes with channel lengths from 5 to 100 μm. (b) AFM image of the surface morphology at the 20 μm gap. (c) Surface profile of a 500 μm wide conducting polymer electrode.

The contact angle of the DEG-PEDOT:PSS film deposited on the hydrophilic region was also measured using water. Water was dropped through a syringe and wet the DEG-PEDOT:PSS film at a contact angle of 7.6°, corresponding to a surface energy of 89 mN/m. This illustrates that the DEG-PEDOT:PSS solution has a high affinity to water, which is driving force for spontaneous wetting in the localized hydrophilic regions.

3.2. Results of microscale polymer patterning

Fig. 2a presents SEM images of conducting polymer patterns (500 μm × 1000 μm) at gaps ranging from 5 to 100 μm. The polymer patterns exactly reproduce the corresponding photomask patterns via the proposed patterning method. The solution wets the pre-determined hydrophilic areas. The significant outcomes are that the gap is clearly defined along the 1000 μm length even at 5 μm gap and that no cracks are observed within the polymer patterns.

Fig. 2b shows the AFM image of the surface morphology of the 20 μm gap, where it can be seen that the conducting polymer solution is well confined at the hydrophilic region at that resolution during dispersion. Fig. 2c represents the thickness profile of the polymer pattern measured by surface profiler (Alpha-Step IQ, KLA Tencor); the polymer electrode has a maximum thickness of 380 nm at the center. When a liquid interfaces with air, the molecules at the interface have a higher energy than that of the interior molecules; therefore, the eventual curvature of the thickness profile shown in the figure is formed to minimize the surface area and thereby reduce its surface energy.

These conducting polymer patterns were subsequently used as the source/drain electrodes in OFET devices. Using the four-point probe method, the conductivity of the conducting polymer pattern was measured to be ca. 400×10^2 S/cm. The polymer electrodes for the bottom contact OFETs (BC-OFET) were fabricated on top of a 50-nm thick gate insulating layer of silicon oxide that was grown on the heavily doped n-type silicon substrate. A prior study investigating the surface-treatment effects on the performance of OFETs indicated that OTS treatment of the gate dielectric layer increased the crystallinity of the semiconducting active material and hence carrier mobility [22]. In our case, as the exposed silicon oxide surface between the source/drain polymer electrodes was already coated with OTS during the selective hydrophobic treatment, 1 wt.% of P3HT solution in chloroform was spin-coated without further treatment and then baked at 125 °C for 20 min inside a nitrogen glove box.

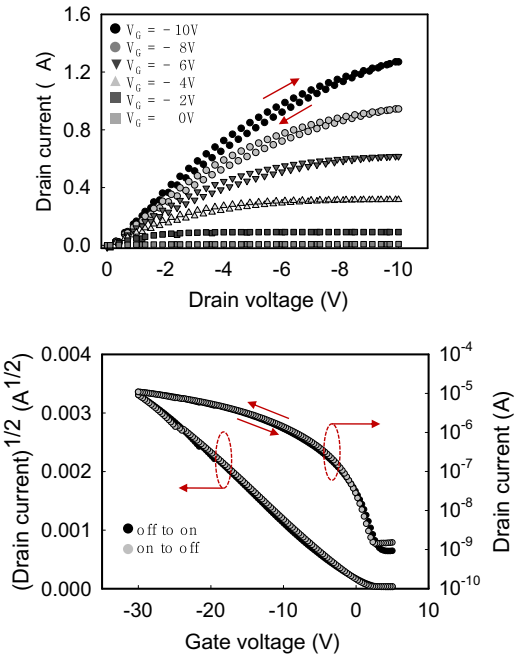

Fig. 3. (a) Output curves and (b) transfer characteristics, swept in both directions, of the P3HT OFFTs with the PEDOT:PSS source/drain electrodes fabricated using the selective surface engineering technique with channel width/length of 1000 and 5 μm, respectively.

Fig. 3a shows the typical transistor output curve at gate voltages from 0 to −10 V of BC-OFETs for a channel width/length of 1000 μm/5 μm. Fig. 3b shows the corresponding transfer characteristics in both forward and reverse scan and the calculated field-effect mobility and the threshold voltage are obtained from plots of the square root of $|I_D|$ in the saturation region at $V_D = -30$ V as a function of V_G (from +5 V to −30 V). All the measurements were performed in a nitrogen glove box. The output curves demonstrate a slight hysteresis phenomenon due to the hydroxyl groups at the surface of SiO_2 gate dielectric layer inherently remained after the selective surface treatment. The hydroxyl groups in the semiconducting materials or at the interface are reported to act as charge trapping sites, being negatively charged, and cause the hysteresis depending on the amount of hydroxyl groups [23]. Impurities such as moisture, oxygen and mobile ions also bring about large hysteresis in the device characteristics [24]. However, as the OFETs were fabricated and measured in dried nitrogen atmosphere in this experiment, the hysteresis was not noticeable, especially in transfer characteristics at the scan from $V_G = 5$ to −30 V and back to 5 V.

The charge carrier mobility in the saturation region is determined by the equation:

$$|I_D| = \frac{W}{2L}\mu C_i (V_G - V_T)^2$$

where C_i is the capacitance per unit area of gate insulator (50-nm thick silicon oxide, 69 nF/cm^2), W/L is the ratio of channel width to channel length, V_T is the threshold voltage, and μ is the charge carrier mobility of the OFET. For our device, the charge carrier mobility was calculated to be 1.4×10^{-3} cm^2/V s at a threshold voltage of 0.2 V and an on/off current ratio of 1.2×10^4. With increasing the channel length, the mobility was enhanced to 2.5×10^{-2} cm^2/V s ($L = 100$ μm) due to the reduced short channel effect.

Our device performance is comparable to other transistors with PEDOT:PSS conductive electrodes fabricated by different methods. For instance, Cho et al. reported transistors having ink-jet printed source/drain electrodes that were fabricated using a modified PEDOT:PSS solution (channel lengths from 25 to 150 μm) on P3HT film [25]. The devices had an average carrier mobility of 6.0×10^{-3} cm^2/V s in the saturation region regime ($V_d = -80$ V), V_T of 6 V, and on/off current ratio of 10^3. In addition, Azumi group demonstrated the microcontact printing of PEDOT:PSS solution as the source/drain electrodes for a channel length of 12 μm on P3HT film, with a carrier mobility of 1.7×10^{-3} cm^2/V s, and an on/off current ratio of 6.0×10^4 [26].

3.3. Nanoscale polymer line patterning

Fig. 4a shows the SEM image of separate PR line patterns after development with a linewidth of 290 nm, spacing of 1 μm, and a thickness of 120 nm, which was fabricated using an interference lithography technique. Its corresponding AFM image (Fig. 4b) illustrates a PR template ready for the local surface energy treatment.

After hydrophobic treatment in vapor phase, several trials using the doctor-blade method for polymer solution dispersion ended up with no polymer patterning at such a tiny scale; the solution covered the whole substrate because the generated solution film was too thick to be confined into the nanoscale hydrophilic line areas. Instead, a multi-step spin-coating method was utilized to produce nanoscale polymer patterns. Preliminary experiments with single-step casting at a low spin speed generated polymer coverage over the entire substrate similar to the doctor-blading results; at a high speed, all the polymer solution was spinned off before the substrate surface was wetted. Therefore, the spin speed was stepwise increased in order to provide a relaxation period to allow the polymer solution to equilibrate to the local surface energy.

Fig. 4c shows that the polymer line patterns are well matched with the feature size of the PR template; 292 nm wide lines at 1 μm spacing. However, some polymer residue can still be seen between the polymer lines in the AFM image (Fig. 4d). The cross-sectional surface profile (Fig. 4e) illustrates that 30 nm thick polymer nanolines were generated by using the multi-step spin-coating method.

4. Conclusions

In summary, a new process for conductive polymer patterning that combines conventional photolithography and self-assembly monolayer deposition of a hydrophobic material was proposed. As the regions protected by the

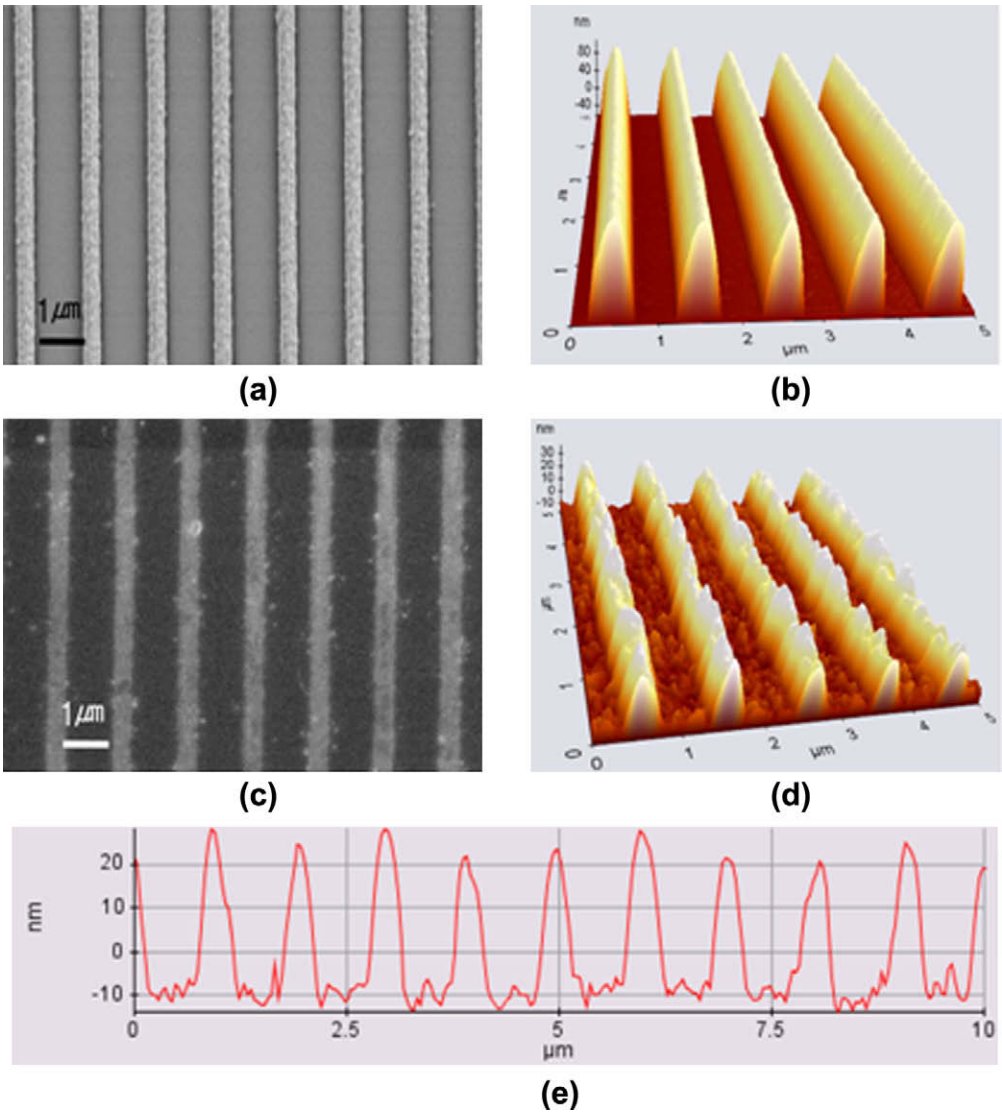

Fig. 4. (a) FE-SEM image of the nanoscale PR features produced by holographic lithography and (b) its corresponding AFM image. (c) FE-SEM and (d) AFM images of the nanoscale polymer line patterns with a width of 292 nm at 1 μm spacing produced by using the polymer template of (a). (e) Cross-sectional surface profile of the polymer line patterns.

photoresist patterns remained hydrophilic following the photoresist removal, a chemically patterned substrate with locally different surface energies was generated. Based on this process, we fabricated P3HT organic semiconducting field-effect transistors using the PEDOT:PSS source/drain electrodes formed by selective dewetting. The device showed a comparable transistor performance to previous devices: a field-effect mobility of 1.4×10^{-3} $cm^2/V\,s$; a threshold voltage of 0.2 V; and on/off current ratio of 10^4 at a 5 μm channel length. In addition, the polymer solution effectively wetted the nanoscale hydrophilic regions, predetermined by holographic lithography and subsequent selective hydrophobic treatment in vapor phase. As a result, nanoscale polymer lines with a linewidth of 292 nm at 1 μm spacing were reliably fabricated by the multi-step spin-coating method. In the near future, it is expected that this technique could be applied to solution-processible plastic electronics.

Acknowledgements

This work was partially supported by the Ministry of Knowledge Economy (MKE), Korea through a project of the Research Consortium for R2R printed RFID tags and the System IC 2010 project from the Ministry of Commerce, Industry and Energy (MCIE), Korea. This work was also supported by the Korea Science and Engineering Foundation (KOSEF) grant (No. R15-2008-006-03002-0, CELA NCRC), and the Program for Integrated Molecular System at GIST.

References

[1] G.P. Crawford, Flexible Flat Panel Displays, Wiley, 2005, pp. 156–158.
[2] D. Kumar, R.C. Sharma, J. Eur. Polym. 34 (1998) 1053–1060.
[3] E. Menard, M.A. Meitl, Y. Sun, J.U. Park, D.J.L. Shir, Y.S. Nam, S. Jeon, J.A. Rogers, Chem. Rev. 107 (2007) 1117–1160.
[4] M.L. Renak, G.C. Bazan, D. Roitman, Adv. Mater. 9 (1997) 392–395.
[5] M.H. Jung, H. Lee, Langmuir 24 (2008) 9825–9831.
[6] D. Li, L.J. Guo, Appl. Phys. Lett. 88 (2006) 063513.
[7] K.X. Steirer, J.J. Berry, M.O. Reese, M.F.A.M. Hest, A. Miedaner, M.W. Liberatore, R.T. Collins, D.S. Ginley, Thin Solid Films 517 (2009) 2781–2786.
[8] J.H. Lim, C.A. Mirkin, Adv. Mater. 14 (2002) 1474–1477.
[9] J.H. Na, S.H. Kim, N.S. Kang, J.W. Yu, C. Im, B.D. Chin, Int. Meeting Inf. Display 8 (2008) 1638–1641.
[10] J.U. Park, M. Hardy, S.J. Kang, K. Barton, K. Adair, D.K. Mukhopadhyay, C.Y. Lee, M.S. Strano, A.G. Alleyne, J.G. Georgiadis, P.M. Ferreira, J.A. Rogers, Nat. Mater. 6 (2007) 782–789.
[11] T. Sekitani, Y. Noguchi, U. Zschieschang, H. Klauk, T. Someya, PNAS 105 (2008) 4976–4980.
[12] E. Avnon, Y. Paz, N. Tessler, Appl. Phys. Lett. 94 (2009) 013502.
[13] C.R. Kagan, T.L. Breen, L.L. Kosbar, Appl. Phys. Lett. 79 (2001) 3536–3538.
[14] J.Z. Wang, Z.H. Zheng, H.W. Li, W.T.S. Huck, H. Sirringshaus, Nat. Mater. 3 (2004) 171–176.
[15] X. Crispin, F.L.E. Jakobsson, A. Crispin, P.C.M. Grim, P. Andersson, A. Volodin, C. Haesendonck, M. Auweraer, W.R. Salaneck, M. Berggren, Chem. Mater. 18 (2006) 4354–4360.
[16] K. Tvingstedt, O. Inganäs, Adv. Mater. 19 (2007) 2893–2897.
[17] G.Y. Jung, Z. Li, Wei Wu, Y. Chen, D.L. Olynick, S.Y. Wang, W.M. Tong, R.S. Williams, Langmuir 21 (2005) 1158–1161.
[18] U. Srinivasan, M.R. Houston, R.T. Howe, R.J. Maboudian, Microelectromech. Syst. 7 (1998) 252–260.
[19] B.C. Bunker, R.W. Carpick, R.A. Assink, M.L. Thomas, M.G. Hankins, J.A. Voigt, D. Sipola, M.P. Beor, G.L. Gulley, Langmuir 16 (2000) 7742–7751.
[20] F.M.J. Fowekes, Phys. Chem. 66 (1962) 382.
[21] B. Liberelle, X. Banquy, S. Giasson, Langmuir 24 (2008) 3280–3288.
[22] S.C. Lim, S.H. Kim, J.H. Lee, M.K. Kim, D.J. Kim, T. Zyung, Synth. Met. 148 (2005) 75–79.
[23] S.W. Lee, B.W. Koo, J.H. Shin, E.K. Lee, H.J. Park, H.S. Kim, Appl. Phys. Lett. 88 (2006) 162109.
[24] D.K. Schroder, Semiconductor Material and Device Characterization, second ed., Wiley, 1998 (Chapter 6).
[25] J.A. Lim, J.H. Cho, Y.D. Park, D.H. Kim, M. Hwang, K. Cho, Appl. Phys. Lett. 88 (2006) 082102.
[26] A. Takakuwa, R. Azumi, Jpn. J. Appl. Phys. 47 (2008) 1115–1118.

the versatile Suzuki coupling polymerization reaction, leading to fluorene-based polymers with additional functional components. To this end, various comonomers such as thiophene derivatives [7], benzothiadiazole [8], phenoxazine [9], triphenylamine [9,10], carbazole [11], quinoxaline, quinoline [12], triphenylamine-based hydrazone derivatives [13] and triazine, oxadiazole and cyano-substituted phenylene [14] have been incorporated into the polymer main chains or side chains. Although the addition of copolymerized monomer units can lead to a relatively large luminous efficacy, up to approximately 10 cd/A (see below), their role is not well understood [15]. It is generally agreed that their introduction can result in more "balanced" electron and hole contributions to the total current density [15]. However, it is still an issue of current debate whether their introduction then improves the recombination efficiency (as a result of more equal injected electron and hole current densities) or the light-outcoupling efficiency (as a result of a shift of the recombination profile to a region more close to the device centre where electrode quenching is less strong).

For the specific case of OLEDs based on fluorene-based polymers of the Sumation LUMATION™ blue series, containing copolymerized hole-transporting units (HTUs), Coehoorn et al. argued that the HTUs facilitate hole injection from the commonly used poly(3,4-ethylenedioxythiophene):poly(styrenesulphonic acid) (PEDOT:PSS) anode into the highest occupied molecular orbital (HOMO) states of the polymer [16]. Although this leads to more balanced electron and hole contributions to the total current density, the balance was still found to be voltage-dependent, resulting in a distinct maximum in the voltage dependence of the luminous efficacy and external quantum efficiency. From a device modeling study, it was argued that the efficiency maximum was predominantly due to a maximum in the recombination efficiency; the shape of the recombination profile was found to be only weakly dependent on the voltage. Similarly, Laquai and Hertel observed an efficacy maximum for OLEDs based on blue-emitting spirobifluorene polymers containing HTUs [17]. For the two concentrations of triarylamine HTUs studied, the maximum efficacy was found to be strongly different. In their analysis, the authors interpreted this as an effect of the different hole mobilities in these systems, affecting the position of the recombination zone within the light-emitting layer, and thereby the light-outcoupling efficiency.

So far, studies of the effects of the introduction of comonomers in blue light-emitting fluorene-based polymers on the OLED device performance have focused on materials containing one single type of comonomer [2–8,10–17]. In this paper, we present the results of a systematic study of OLEDs based on blue-emitting fluorene copolymers that contain *two different types of comonomers* with similar optical energy gaps but with different contributions to the hole mobility. This allows us to change the hole mobility either by changing the concentration of HTUs of one type, or by changing the ratio of HTUs of both types without changing the overall HTU concentration. The effect of the hole mobility can thus be studied in two independent ways. The luminous efficacies for some of the copolymers studied are shown to be high in comparison to those that were reported in the literature for devices based on other fluorescent fluorene-based OLED systems. Absolute measurements of the photoluminescence quantum efficiency (PLQE) of all examined materials are performed, which allows us to distinguish the effects on the luminous efficacy due to charge carrier mobility changes and due to changes of the radiative decay probability when varying the monomer concentration. As in the previous studies referred to above, again a maximum in the voltage-dependent efficacy is found. The position of the efficacy maximum and the efficacy at the maximum (corrected for the PLQE) are shown to be determined both by the hole mobility. By varying the hole mobility, it is therefore possible to tune the voltage dependence of the efficacy such that at the desired brightness the power conversion efficiency is optimal.

It is found that the observed voltage dependence of the efficacy can be understood well from a recently developed drift–diffusion device model [18]. The model takes advantage of recent developments in the field of OLED device physics, which have elucidated the roles of charge carrier diffusion [19,20], energetic disorder [21–23], and charge carrier injection [24]. It is considered more realistic than the drift-only device model used in Ref. [16], from which it was argued that the efficacy maximum is mainly due to the voltage dependence of the recombination rate (see above). The analysis shows that the presence of an efficacy maximum can already be explained from the voltage dependence of the light-outcoupling efficiency, but that the recombination efficiency also affects the shape of the efficacy curves, in particular at small voltages.

In Section 2, an overview is given of the copolymers studied and of the luminous efficacies measured for OLEDs based on these materials. The results of more in-depth studies of the energy level structure and of the PLQE are given in Section 3. In Section 4, current–voltage curves measured for separate unipolar (hole-only and electron-only) devices are presented and analyzed. An analysis of the composition dependence of the measured voltage dependence of the luminous efficacy using the results of device simulations is given in Section 5. Section 6 contains the conclusions. In the Appendix, details are given concerning the polymer synthesis, the device fabrication and the measurement methods employed in Sections 2 and 3.

2. Polymer structures and OLED device performance

The structure of the fluorene copolymers synthesized for this study is given in Fig. 1(a). The polymers consist of two different fluorene monomers, A and B, and two amine comonomers, C and D, with concentrations x_A = 50 - mol-%, $x_B = (50 - x_C - x_D)$ mol-%, x_C and x_D, respectively. The use of two different fluorene monomers increases the solubility and enhances the degree of structural disorder, so that the layers obtained from spin coating may be characterized as fully amorphous. The compositions of the 10 copolymers studied are given in Fig. 1(b). Details of the synthesis method, and of the device fabrication and optical measurements discussed below, are given in the Appendix.

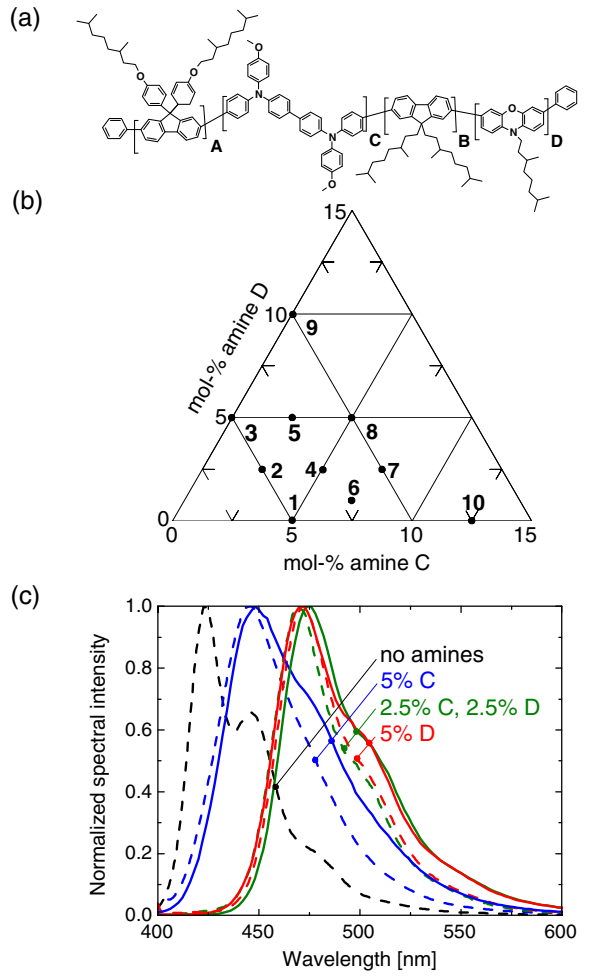

Fig. 1. (a) Structure of the fluorene copolymers described in this paper, comprising the fluorene monomers A and B and aromatic amine comonomers C and D (top). (b) Diagram showing the concentration of the comonomers C and D for the 10 copolymers studied. Horizontal lines connect points with equal values of x_D, from $x_D = 0$ (baseline, mol-% C axis) to $x_D = 0.15$ (top of the diagram). Lines parallel to the mol-% D axis connect points with equal values of x_C, from $x_C = 0$ at the mol-% D axis to $x_C = 0.15$ at the lower-right vertex of the diagram. (c) Normalized electroluminescence (EL) spectra (full, at $V = V_{max}$) and photoluminescence (PL) spectra (dashed) for copolymers **1**–**3**. Also the PL spectrum for a copolymer without amine co-monomers but with a random sequence of fluorene monomers A and B is included.

From a study of the electronic structures of the 10 copolymers using cyclic voltammetry, it follows that in all cases the hole mobility is due to hopping between the C and D guest monomers, whereas the electron mobility is due to hopping between conjugated polyfluorene segments. The ionization potentials were determined in solution and yielded estimated HOMO levels of 5.3 ± 0.1 eV with respect to the vacuum level. These values are comparable to those reported in the literature for comparable fluorene copolymers [6,25,26]. The ionization potential is smaller than in the polyfluorene host (5.8 eV). Previous studies by Doi et al. [2] and Spreitzer et al. [3] showed that incorporating guest sites with a reduced ionization potential into a host material with a (much) higher ionization

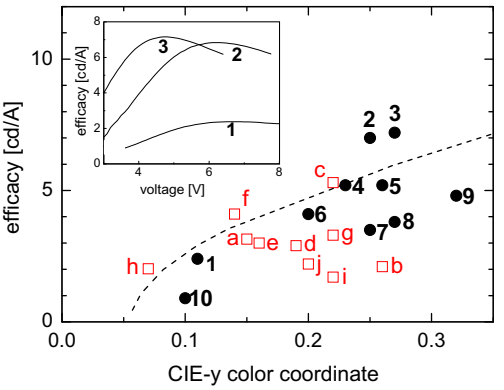

Fig. 2. Maximum luminous efficacy for the single layer OLEDs studied in this paper (full circles, see Fig. 1(b)) and for fluorescent fluorene-based copolymers, oligomers and/or single molecules, taken from the literature [3] (empty squares), as a function of the CIE(1931)-*y* coordinate. The dashed curve gives (in arbitrary units) the increase in luminous efficacy with increasing CIE-*y* coordinate which would be expected in the case of equal internal quantum efficiencies (see text). The inset shows the luminous efficacy of OLEDs based on fluorene copolymers **1**–**3** as a function of the applied voltage.

potential yields a critical guest concentration mobility below which the guest sites act as hole traps, and above which transport of holes proceeds predominantly via these sites. For all polymers investigated in this paper, with at least 5 mol-% of aromatic amines, the hole transport is in the second regime. The electron affinities were measured in film and gave estimated lowest molecular orbital (LUMO) levels of 2.1 ± 0.1 eV. The LUMO level coincides with the LUMO level of the polyfluorene host material, for which the single-particle HOMO–LUMO energy gap is known to be 3.6 ± 0.1 eV from X-ray photoelectron-spectroscopy and ultraviolet photoelectron-spectroscopy on poly(9,9-dioctylfluorene) [27].

For each copolymer studied a large number of nominally identical OLEDs were fabricated with the following stack structure: ITO (100 nm)/PEDOT:PSS (100 nm)/light-emitting polymer (LEP, 80 nm)/barium (5 nm)/aluminum (100 nm). Measurements of the perpendicular electroluminescence (EL) spectra showed a slight variation of the emission color, as shown in Fig. 1(c) for copolymers **1**–**3** (full lines). The color varies from blue for copolymers **1** and **10** containing only comonomer C to blue–green for copolymer **9**, containing the largest fraction of comonomer D. The small difference in optical gaps for amines C and D is within the error margin of the determination of the HOMO and LUMO energies. The difference may also be in part due to a slightly different exciton binding energy.

Measurements of the voltage dependence of the luminous efficacy, η_L, showed excellent reproducibility. For all polymers studied, η_L revealed a maximum, $\eta_{L,max}$, at a distinct value of the voltage, V_{max}. In Fig. 2, the full circles give for each copolymer $\eta_{L,max}$ as a function of the CIE-*y* coordinate of the EL spectrum measured at $V = V_{max}$. The CIE-*x* coordinate was almost equal for all polymers, *viz.* 0.14–0.15. For the LEP layer thicknesses studied (80 nm), almost no voltage dependence of the emission color was found, in all cases less than 0.01 CIE-*y* units. In the inset, the voltage

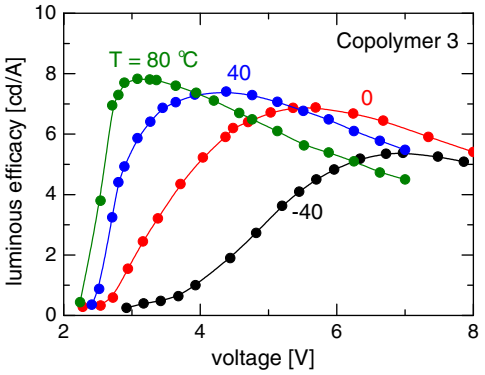

Fig. 3. Luminous efficacy of OLEDs based on copolymer 3 (5 mol-% amine D) as a function of the voltage, measured at various temperatures.

dependence of η_L is shown for the copolymers **1**–**3**. The figure shows that $\eta_{L,max}$ is strongly dependent on the amount and type of aromatic amine guest comonomer. For example, the value of $\eta_{L,max}$ of copolymer **3** is more than a factor of 2 larger than that of copolymer **8**, with essentially the same CIE-*y* coordinate. The variation can only in part be attributed to the varying eye-sensitivity to the EL spectrum, as may be concluded from a comparison with the trend shown by the dashed curve. The curve gives the effective eye-sensitivity (in arbitrary units) as a function of the CIE-*y* coordinate, based on a wavelength shifted EL spectrum of one selected material. The shape of the dashed curve was found to remain essentially identical when using the actual EL spectra of the copolymers **1**–**10**.

The luminous efficacy of the copolymers **2** and **3** may be considered high in comparison to the other copolymers studied here and to other fluorescent fluorene-based OLED systems that were reported in literature (open squares in Fig. 2, see figure caption). We note that higher efficacies, up to ~10.3 cd/A, were reported by Gohda et al. [28k]. However, in their study an additional 20 nm thick interlayer is included in between the PEDOT:PSS and the fluorene-based LEP layer which may be expected to positively affect the light-outcoupling efficiency by shifting the recombination away from the anode layer, thereby reducing electrode quenching. We find that the values of the maximum efficacy and of V_{max} show a significant temperature dependence, as shown in Fig. 3 for copolymer **3**. At 80 °C, $\eta_{L,max}$ has increased to almost 8 cd/A, observed at V_{max} = 3.0 V. A qualitatively similar temperature dependence of the efficacy curves was found for copolymer **2**. No (copolymer **2**) or only a weak (copolymer **3**) temperature dependence of the emission color in the maximum were observed. For copolymer **3**, the CIE-*y* coordinate decreased by 0.03 from −40 °C to +80 °C, whereas the CIE-*x* coordinate did not change. Therefore, the observed increase of the efficacy at $V = V_{max}$ can not be attributed to an increased eye-sensitivity to the emitted spectrum.

For all polymers studied, the observed ionization energies (5.3 ± 0.1 eV) are very close to the work function of PEDOT:PSS (~5.2 eV). Efficient hole injection is thus expected to take place for all devices studied. Therefore, the observed deviations of the maximum luminous efficacy from the variation in the eye-sensitivity, given by the dashed line in Fig. 2, are not related to differences in the injection efficiency. We demonstrate in this paper that the main factor which determines the voltage dependence of the luminous efficacy curves shown in Figs. 2 and 3 is the hole mobility. For that purpose, we first analyze in more detail in the next section the composition dependence of the external quantum efficiency.

3. Analysis of the external quantum efficiency

Fig. 4(a) shows in a way complimentary to Fig. 2 that the observed trends in the maximum luminous efficacy cannot be explained fully from the composition dependence of the eye-sensitivity to the EL spectrum. The figure gives the composition dependence of the external quantum efficiency (EQE, η_{EQE}) at $V = V_{max}$. The value of $\eta_{EQE,max}$ is largest for the copolymers **2** and **3**, with a 5 mol-% aromatic amine concentration, *viz.* up to 4.1 ± 0.2% for copolymer **2**. With increasing amine concentration, $\eta_{EQE,max}$ decreases. For copolymer **9**, with 10 mol-% of amine D, $\eta_{EQE,max}$ is lower by approximately 30%. And at comparable concentrations of amine C, $\eta_{EQE,max}$ has already dropped by a factor of ~3.

For fluorescent OLEDs, the EQE may be expressed as

$$\eta_{EQE} = \eta_{rec} \times \eta_S \times \eta_{rad} \times \eta_{oc}, \quad (1)$$

with η_{rec} the recombination efficiency, i.e. the fraction of injected charge carriers that actually recombine to form an exciton, η_S the fraction of singlet excitons formed upon recombination, η_{rad} the radiative decay probability of the singlet excitons, and η_{oc} the light-outcoupling efficiency. As a first step in our investigation of the cause of the variation of η_{EQE}, we study the photoluminescence quantum efficiency (PLQE, η_{PL}) of each copolymer in film.

The PLQE was measured using 80 nm polymer films spin coated on glass, using the integrating sphere method [29–31]. By carrying out the experiments for thin films on glass, instead of using the OLED devices, microcavity effects on the light absorption and emission related to the presence of metallic electrodes were avoided. Details are given in the Appendix. Examples of measured PL spectra are included in Fig. 1(c), for copolymers **1**–**3** and for a copolymer containing no HTUs but based on a random mixture of fluorene units as described in Section 2. A small red-shift is observed when going from copolymer **1** (5% C) to copolymer **2** (2.5% C, 2.5% D), corresponding to a photon energy difference of ~0.15 eV, similar to the shift observed in the EL spectra for these copolymers. We believe that the radiative decay of excitons in all copolymers (**2**–**9**) which contain amine D takes preferentially place at these amines, or from a charge transfer state involving these amines. As shown in Fig. 4(b), η_{PL} is found to be in between 42% and 59%. The systematic experimental error, predominantly in the system calibration, is approximately 5–10%. For a film of the reference fluorene homopolymer poly(9,9-dioctylfluorene) (PFO), spin coated from toluene (1% by weight solution), we measured η_{PL} = 52%. Ariu et al. reported η_{PL} = 53% for films of this material, spin coated from chloroform solution [32]. For comparison, Kanicki et al.

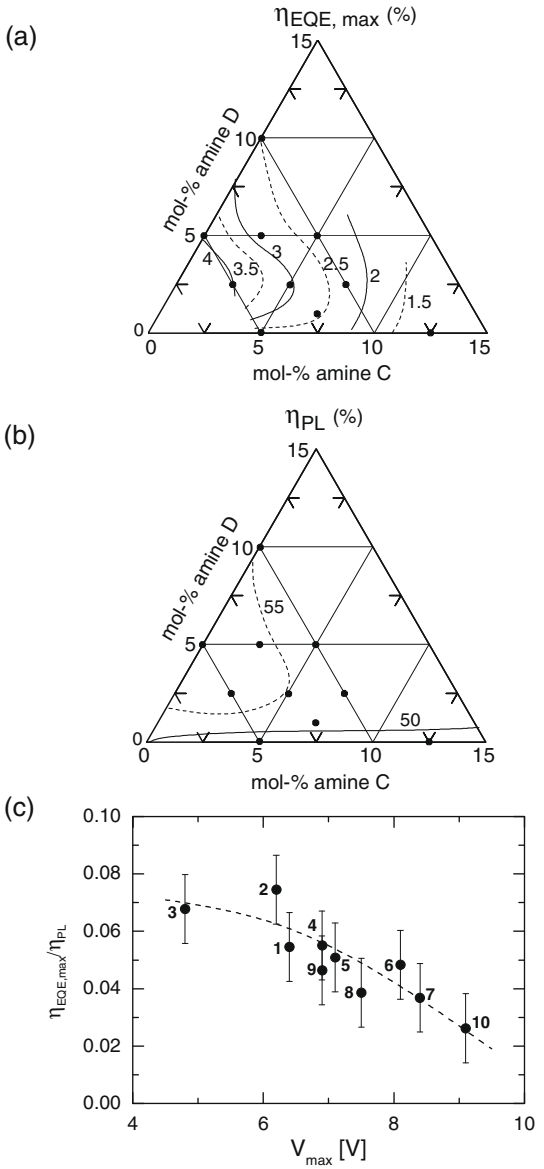

Fig. 4. (a) Composition dependence of the maximum EQE. (b) Composition dependence of the PLQE. (c) Ratio of the EQE the PLQE as a function of V_{max}, for copolymers **1**–**10**. The dashed line is a guide-to-the-eye. In figures (a) and (b), the contour lines are guides to the eye, and are based on data given in Table 1 (Appendix).

reported η_{PL} = 31% for a blue light-emitting polymer of the Dow Chemical Corp. [26] and Coehoorn et al. reported η_{PL} = 60% for a Sumation LUMATION™ blue series fluorene-based copolymer [16].

The effect on the PLQE of introducing the aromatic amine comonomers C or D into the fluorene backbone is, at the concentrations considered, at most 10%. The observation that in some cases the PLQE exceeds that of PFO may be a consequence of an increase in structural and/or energetic disorder, limiting the exciton diffusion length. The use of fluorene monomers of two different types (A and B) and the introduction of amine comonomers into the fluorene backbone is expected to reduce the quenching that Ariu et al. related to the ordered PFO β-phase [32]. Furthermore, the slightly smaller optical gap on amine D is also expected to impede exciton diffusion. At high amine D concentrations, their beneficial effect on the PLQE is reduced as a result of concentration quenching. Energy transfer to quenching sites is then facilitated by the small average distance between the amines. In the literature, also other mechanisms for concentration quenching have been described [33–36].

Neglecting microcavity effects, which can give rise to an enhancement of the radiative decay probability of singlet excitons (see e.g. Ref. [16]), we may employ η_{PL} as a first estimate of η_{rad}. It follows from Eq. (1) that the ratio η_{EQE}/η_{PL} will then reveal how in the absence of non-radiative decay processes in the polymer the EQE would vary with the composition and voltage. Interestingly, the value of η_{EQE}/η_{PL} at $V = V_{max}$ is found to be quite strongly related to the value of V_{max}, irrespective of the detailed composition, as may be seen from Fig. 4(c). We regard this as a key result obtained from this work. The figure shows that $\eta_{EQE,max}/\eta_{PL}$ decreases with increasing V_{max}.

A qualitatively similar result is obtained from the voltage dependence of the luminous efficacy at different temperatures, measured for all copolymers, when assuming that the PLQE is only weakly temperature dependent. In Fig. 3 the results for copolymer **3** were given. We have not measured the temperature dependence of η_{PL}, so that making a quantitative comparison with the results given in Fig. 4(c) is not possible. If η_{PL} would be temperature independent, the temperature dependent values of V_{max} and $\eta_{EQE,max}/\eta_{PL}$ as obtained using Fig. 3 would essentially coincide with the composition-dependent data points indicated in Fig. 4(c). However, we can presently not exclude that this agreement is somewhat fortuitous. First, η_{PL} may decrease slightly with increasing temperature, as has been observed for other organic semiconductors [37]. Second, the increase of $\eta_{EQE,max}$ with increasing temperature is for this specific polymer slightly (but at most a few percent) higher than that of $\eta_{L,max}$, in view of the small observed blue-shift of the emission (see Section 2).

4. Current density in unipolar devices

A subsequent step towards the understanding of the observed composition and temperature dependent systematics in the voltage dependence of the EQE is made by studying the *J*–*V* characteristics of selected unipolar devices. In Fig. 5, the current–voltage (*J*–*V*) characteristics of single-carrier hole-only (HO) and electron-only (EO) devices are shown for copolymers **1**–**3** (from top to bottom). For HO devices, a cathode consisting of thermally evaporated Pd (100 nm) was used instead of Ba–Al, to prevent electron injection. For EO devices the ITO/PEDOT:PSS anode was replaced with a thermally evaporated 30 nm thick Al layer. The *J*–*V* curves of the HO and EO devices were corrected for a small Ohmic leakage current and for the built-in voltage [16] ($V_{bi,h} \approx 1.0$ V and $V_{bi,e} \approx 0.65$ V, respectively). The figure shows that for all three polymers the *J*–*V* curves of the EO devices (dotted) are approximately

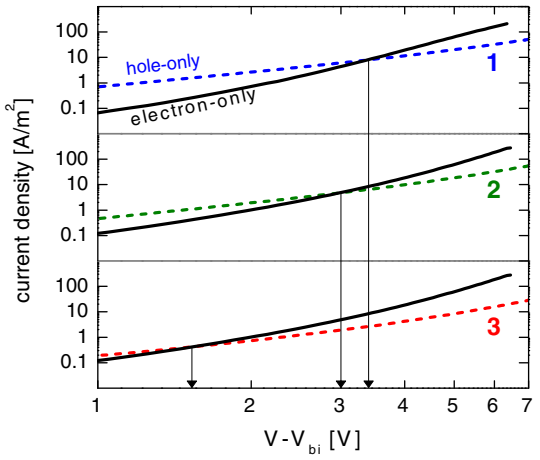

Fig. 5. Current–voltage characteristics of single-carier hole-only and electron-only devices with 80 nm layers of copolymers **1**–**3**, respectively. The arrows indicate the values of V_{cross}.

equal, but that at any voltage, the current density in the HO devices (dashed) decreases from polymer **1** to polymer **3**. The slopes of the EO curves are larger than those of the HO curves, but start off at a lower current density. As a consequence, the voltage at which the two built-in voltage corrected curves cross, V_{cross}, shifts from polymer **1** to polymer **3** to smaller values.

The strong composition dependence of the hole mobility is consistent with the role of the amines as hole-transporting units, in between which hopping takes place. The current density in HO devices depends therefore on the specific amine (C or D), as shown in Fig. 5. The figure also shows that this dependence is not necessarily gradual. The hole mobility decreases less strongly from copolymer **1** (only C) to copolymer **2** (2.5% C, 2.5% D) than from copolymer **2** to copolymer **3** (5% D). The current density measured at small voltages is indicative of a hole mobility difference of a factor ~4 between polymers **1** and **3**.

The relatively weak composition dependence of the current density in the EO devices is consistent with the point of view that the LUMO states are predominantly of a fluorene-character. Therefore, they are not or only weakly affected by copolymerization with the HTUs, of which the electron affinities are smaller than that of the polyfluorene host. The electron injection and mobility are thus expected to be only weakly dependent of the polymer composition.

5. Model for the voltage and composition dependence of the luminous efficacy

5.1. Composition dependence of the position of the efficacy maximum

Within a simplified picture of the transport, recombination and light-outcoupling processes, the voltage V_{cross} at which the current densities in HO and EO devices are equal might be used to estimate the voltage, V_{max}, at which in a double-carrier device the efficacy maximum is obtained. At that voltage, the hole and electron current densities are optimally balanced so that, as argued in the Introduction, the recombination efficiency and the light-outcoupling efficiency are expected to be quite optimal. Fig. 6(a) (closed circles) shows that this picture is very useful: the measured values of the voltage difference $V_{max} - V_{bi,dc}$ are surprisingly close to the measured values of the voltage V_{cross}. $V_{bi,dc}$, the built-in voltage for the double-carrier devices, is taken equal to 3 V for all three systems. We note that we regard the effective built-in voltages, used for obtaining V_{cross} for the single-carrier devices and used for obtaining the built-in voltage corrected voltage $V_{max} - V_{bi,dc}$, as relatively insensitive to the specific copolymer used, but that the uncertainty of each of the values of the built-in voltage used is several tenths of an eV. Therefore, the trend in the relative positions of the data points for the three copolymers is more significant than the close correspondence of the absolute values of V_{max} $V_{bi,dc}$ to those of V_{cross}. Furthermore, we note that the fact that in the double-carrier devices the onset of the emission is observed at voltages slightly below the voltage $V_{bi,dc}$ = 3 V (see the inset in Figs. 2 and 3) is consistent with the results of drift–diffusion OLED device modeling (see below).

The simple picture presented above explains why V_{max} increases with increasing hole mobility, but it does not yet explain why the EQE then tends to decrease (as shown in Fig. 4(c)). Also, it does not yet clarify the separate effects of the recombination efficiency and the light-outcoupling efficiency on the luminous efficacy. Furthermore, one might wonder why this picture appears to be so well applicable to the systems considered, as (i) the electron and hole mobility functions are expected to be quite different as a result of the different character of the intrinsic electronic states in between which hopping takes place, (ii) electron transport in large energy gap semiconducting polymers is often affected by the presence of (extrinsic) trap states [22,23], and (iii) an electron transport study for a similar system has revealed that there is a sizeable electron injection barrier (of at least ~0.5 eV [16]).

5.2. OLED device model

In order to develop a better understanding of the detailed shapes of the efficacy curves, including the trend in the luminous efficacy at $V = V_{max}$, we have carried out an exploratory device modeling study. The electron and hole mobility are assumed to be due to hopping in a Gaussian density of states. The mobility is then a function of the carrier density and the electric field, as described by Pasveer et al. [38]. To be specific, we have assumed widths of the Gaussian density of states equal to 0.13 eV (holes) and 0.07 eV (electrons). In addition, for electrons an exponential trap density of states with a width of 0.18 eV was assumed. The parameter choice was based on the results of a recent study of hole transport in a similar blue-emitting polyfluorene-based copolymer [21] and on the results of an electron transport study of the same material [23]. The electron and hole site densities were taken equal to 6×10^{26} m^{-3}, the electron trap density was taken equal to 1×10^{24} m^{-3}, and the electron injection barrier at the cathode was taken to be 0.7 eV. The voltage dependence of the current density and the recombination profiles were

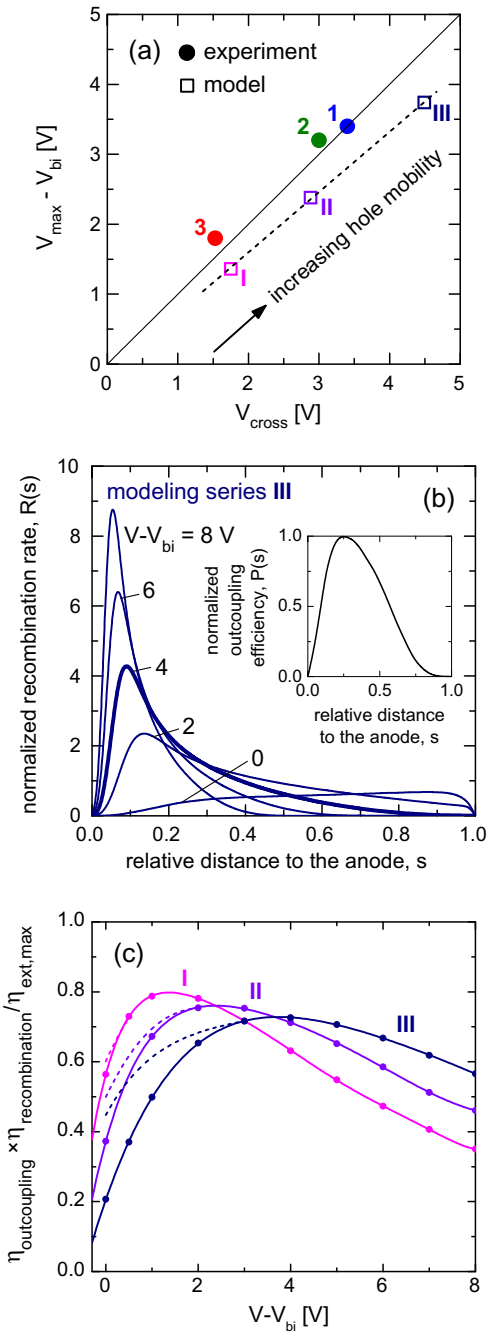

Fig. 6. Results of OLED device modeling. (a) Calculated voltages at which the EQE is maximal as a function of the voltage at which the current densities in the corresponding single-carrier devices cross (squares; both voltages are corrected for the built-in voltage), and the experimental results for copolymers **1**–**3** (spheres). (b) Calculated normalized recombination profiles for modeling series III and (inset) calculated normalized outcoupling efficiency as a function of the position in the device. (c) Calculated normalized product of the outcoupling and recombination efficiences for each modeling series (full curves, see Eq. (2)) and calculated normalized outcoupling efficiency (dashed curves).

calculated using a drift–diffusion-recombination model within which the electron and hole mobility functions are included as described above. The recombination is described as a bimolecular process, with a local recombination rate described by the (standard) Langevin formula. The calculations also include recombination of free holes with trapped electrons; however, for the systems and conditions studied the contribution from such processes is found to be only minor. Technical details concerning the method are given in Ref. [18]. The calculations were performed for L_{LEP} = 80 nm thick devices, with T = 298 K. We emphasize that the actual parameter values are expected to depend on the specific polymer, but that determining the precise composition dependence would be beyond the scope of this paper.

By taking appropriate values of the hole (electron) mobilities in the zero field and zero carrier density limits, $\mu_{0,h}$ ($\mu_{0,e}$), the device model leads to a similar crossing of the HO and EO current–voltage curves as shown in Fig. 5. In order to mimic the transport in devices containing polymers **1**–**3**, we have calculated the voltage dependence of the current density and of the recombination profiles for three different values of $\mu_{0,h}$, while keeping all other parameters fixed. The use of this simplified approach is motivated (i) by the clear indication obtained from Fig. 5 that a single composition-dependent parameter determines the device performance of all devices and (ii) by the results of the separate studies of hole and electron transport, discussed in Section 4, which indicate that the hole mobility constitutes this composition-dependent parameter. A first series of calculations (I) was carried out using a value of $\mu_{0,h}$ which led to crossing EO and HO curves at a voltage V^{I}_{cross} = 1.75 V above the built-in voltage, equal to the experimental value of V_{cross} for copolymer **3**. Two other series of calculations (II and III) were carried out for values of $\mu_{0,h}$ which were a factor 2.5 and 6.25 larger, leading to V^{II}_{cross} = 2.88 and V^{III}_{cross} = 4.49 V, respectively.

5.3. Model predictions of the voltage dependence of the luminous efficacy

For all three values of $\mu_{0,h}$ chosen, voltage-dependent normalized recombination profiles, $R(s, V)$ with $s \equiv x/L_{LEP}$, were calculated using the drift–diffusion-recombination model described in the previous subsection. The normalization is such that the integral is equal to the recombination efficiency, which may be defined as $\eta_{rec} \equiv (J_{h,anode} - J_{h,cathode})/J$. Here, $J_{h,anode}$ and $J_{h,cathode}$ are the hole current densities at the anode and cathode, respectively. As an example, Fig. 6(b) shows the normalized recombination profiles obtained for the modeling series III, calculated for values of $V - V_{bi,dc}$ ranging from 0 to 10 V. The figure shows that at small voltages, close to V_{bi}, the recombination profile is quite broad and most intense near the cathode. With increasing voltage the profile becomes narrower, with a peak which shifts to a location close to the anode. Qualitatively, this peak shift can be explained as a result of the steeper increase of the injected electron current density with increasing voltage, as compared to the increase of the hole current density.

In order to analyze the effect of the peak shift on the device efficiency, we make use of the position-dependent outcoupling efficiency curve, $P(s)$, as calculated for

blue-emitting polyfluorene–copolymer-based OLEDs with an equal layer stack structure, equal layer thicknesses and almost the same CIE emission color point as that of polymers **2** and **3** [16]. The calculations were performed using a well-established optical microcavity outcoupling model which includes the effects of exciton quenching and of the enhanced radiative decay rate near metallic electrodes [39]. The function $P(s)$ is normalized with respect to its peak value, and is given as an inset in Fig. 6(b). The product of the recombination efficiency and the outcoupling efficiency is then equal to

$$\eta_{rec} \times \eta_{oc} = \eta_{ext,max} \times \int_0^1 R(s,V)P(s)ds \quad (2)$$

where $\eta_{ext,max}$ is the external quantum efficiency which would be obtained if complete recombination would take place in a zone with infinitesimal thickness at the most optimal position in the device. The integral indicates to what extent the efficiency is less than the highest possible value for the device structure and emission spectrum considered, due to a non-ideal recombination efficiency and a non-ideal shape of the recombination profile. Fig. 6(c) shows for each modeling series the value of this integral as a function of the voltage, corrected for the built-in voltage (full curves). It also shows the ratio of this integral and the recombination efficiency ("normalized outcoupling efficiency", dashed curves), which gives the effect of the non-ideal shape of the recombination profile on the EQE. For each series of calculations we find that $\eta_{rec} = 1$ around and above V_{cross} (so that the full and dashed curves coincide) but that η_{rec} decreases at small voltages. The injected electron current density is then very small, so that not all injected holes recombine. Nevertheless, there is even some recombination at voltages below V_{bi}, resulting from the effects of charge carrier diffusion and energetic disorder [18]. The built-in voltage can therefore not be determined directly from the electroluminescence onset. For series III, the efficacy maximum is located at ~4 V above the built-in voltage. Fig. 6(b) shows that the corresponding recombination profile (thick curve) has its peak already quite close to the anode. As a result of the broad and asymmetric shapes of the outcoupling efficiency curve and the recombination profiles, the efficacy maximum is not located at the voltage at which the maximum of the recombination profile coincides with the maximum of the outcoupling efficacy curve.

The calculated voltage shift of the efficacy maximum with increasing hole mobility, shown in Fig. 6(c), is consistent with the experimental results. This may be seen from Fig. 6(a), within which the squares give the dependence of the calculated values of $V_{max} - V_{bi,dc}$ on the calculated values of V_{cross}. The effect of a change of the hole mobility on V_{cross} is found to be essentially equal to the effect on V_{max}. It is not surprising that there is no strict one-to-one correspondence between the calculated values of $V_{max} - V_{bi,dc}$ and V_{cross}, as this relationship is determined by the detailed values of the materials and device parameters, including the optical constants and thicknesses of the non-emissive layers. Furthermore, it may be seen from Fig. 6(a) that the experimentally observed difference between the peak voltages for polymers **1** and **3** (~1.6 V) can be understood as the result of a difference in the hole mobilities of approximately a factor of 4, in good agreement with the mobility difference estimated from the *J–V* curves (see Section 4). Studies of the current density in HO devices based on polymers **4**–**10** (not shown) confirm that the mobility increases with increasing monomer concentration, consistent with the picture discussed above that these units function as transport sites. It is then expected from the model that an increase of the monomer concentration results in an increase of V_{max}, as is indeed found experimentally (see Table 1).

Fig. 6(c) also provides answers to the questions posed in Section 5.1. It elucidates the separate roles of the light-outcoupling and recombination efficiencies and explains why the EQE tends to decrease with increasing V_{max}, i.e. with increasing hole mobility. For the three values of $\mu_{0,h}$ considered, the effect is due to a decrease of the degree of ideality of the shape of the recombination profile at $V = V_{max}$. For larger values of the hole mobility ($\mu_{0,h}$ at least a factor 5–10 larger than taken for modeling series III), it is expected that the EQE at V_{max} is also reduced as a result of a finite recombination efficiency. This might explain the rather fast decrease of the EQE with increasing V_{max} at large values of V_{max}, revealed by Fig. 4(c) and suggested (less directly) as well by Fig. 3.

The model discussed above was used in order to explain the observed trends. More quantitative modeling of the EQE would require making several refinements, such as a separate determination of the mobility functions for all materials and the use of separate optical outcoupling modeling for all materials (taking the (small) effects of the material dependence of the emission spectrum into account). Making such refinements is beyond the scope of this paper. It will then be possible to deduce the value of the fraction of singlet excitons formed. The experimental results presented in this paper do not indicate a strong dependence of η_S on the system studied.

5.4. Optimizing the luminous efficacy of OLEDs

From the analysis given above, it can be derived how blue-emitting fluorene polymers containing copolymerized hole-transporting amine monomers can be designed in a rational way for different OLED-applications. The

Table 1
Material parameters and OLED device properties of fluorene copolymers **1**–**10** (see Fig. 1(b) for the composition).

Copolymer	CIE-(x, y) (EL)	V_{max} V	$\eta_{L,max}$ cd/A	η_{PL} %	$\eta_{EQE,max}$ %
1	(0.15, 0.11)	6.4	2.4	44	2.4
2	(0.14, 0.25)	6.2	7.0	55	4.1
3	(0.14, 0.27)	4.8	7.2	59	4.0
4	(0.14, 0.23)	6.9	5.2	58	3.2
5	(0.14, 0.26)	7.1	4.6	55	2.8
6	(0.14, 0.20)	8.1	4.1	58	2.8
7	(0.14, 0.25)	8.4	3.5	57	2.1
8	(0.15, 027)	7.5	3.8	57	2.2
9	(0.15, 0.32)	6.9	4.8	54	2.5
10	(0.15, 0.10)	9.1	0.9	42	1.1

copolymer which is most optimal for a certain application is the material for which the power efficiency is largest at the required brightness level. The brightness level is proportional to the current density times the reduction of the efficiency due to a non-ideal shape of the emission profile and recombination efficiency, given by the factor $f_1 \equiv \eta_{oc} \times \eta_{rec}/\eta_{ext,max}$ shown in Fig. 6(c). The power efficiency is proportional to the same factor, multiplied by the factor $f_2 \equiv V_{gap}/V$ which gives the power loss resulting from the use of a voltage which is larger than the voltage corresponding to the single-particle energy gap, V_{gap}.

In Fig. 7, the full curves show for the three series of calculations carried out above the dependence of the power efficiency on the brightness. The brightness was taken equal to $C \times f_1 J$, with a proportionality factor $C = 27.5$ cd/A as obtained in Ref. [16] for emission from for similar blue-emitting polyfluorene–copolymer-based OLEDs, i.e. assuming for calculating the light-outcoupling the same optical stack as in Section 5.3. The power efficiency is expressed with respect to the ideal power efficiency, obtained when $f_1 = f_2 = 1$, using $V_{gap} = 3$ V. The brightness scale obtained coincides well with the actually observed range of brightnesses at $V = V_{max}$, which varies from $\sim$100 cd/m^2 for copolymer **3** to $\sim$13,000 cd/m^2 for copolymer **10**. The figure reveals clearly that the optimal polymer composition depends on the required brightness. For small-brightness applications, within which the OLED is operated at a voltage not far above V_{gap} (such as in some lighting and signage applications), making use of a copolymer with a relatively small hole mobility is most optimal (series I). On the other hand, for high-brightness applications within which the OLED is operated at a voltage well above V_{gap} (such as in passive matrix displays) using a copolymer with a relatively large hole mobility is more optimal (series III).

The maximum possible power efficiency could be enlarged by further lowering of the hole mobility (e.g. by adapting the chemical nature of the HTUs), as may be seen from the dashed curve in Fig. 7. It shows the modeling results for a hole mobility which is a factor of 2.5 smaller than for curve I, all other modeling parameters being equal. The increase of the maximum is due to (i) a slight further increase of the maximum value of the ratio $f_1 \equiv \eta_{oc} \times \eta_{rec}/\eta_{ext,max}$, to approximately 0.85, and (ii) a further decrease of V_{max}, to approximately 0.8 V above V_{bi}. It is evident from the figure that this would only be useful when only very small brightnesses are needed. Upon further reducing the hole mobility, V_{max} approaches V_{bi}, so that the energy drop across the devices approaches the energies of the emitted photons. The device then approaches the thermodynamic limit, where device modeling should include not only recombination but also charge carrier generation. Although a theoretical model for the latter process has been developed recently [18], its application to the presently studied devices would be beyond the scope of this work. Lowering the hole mobility could be realized by adapting the chemical nature of the HTUs, but also by lowering their concentration. For the specific polymers studied, the maximum of the external quantum efficiency is obtained at the boundary of the composition range investigated. It is expected that for slightly smaller amine concentrations even slightly higher values of η_{EQE} are obtained, at smaller values of V_{max}. However, the brightness obtained at the maximum will then also decrease, limiting the practical applicability. We note that an enhanced power efficiency at higher brightnesses could be obtained by enhancing the hole and electron mobilities. An enhancement by the same factor would give rise to a shift of the brightness at which the power efficiency is highest by the same factor, without a change in shape of the curves.

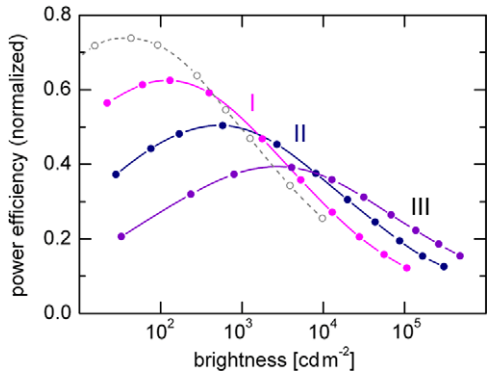

Fig. 7. Calculated dependence of the normalized power efficiency on the brightness, for OLEDs with hole mobilities which increase in steps of a factor 2.5 from small (dashed curve) to large (curve III). The $J(V)$ and efficiency data used for obtaining curves I–III have been calculated from the device simulations described in Section 5.3. The power efficiency is expressed with respect to the value that would be obtained for emission from the most optimal position in the emissive layer, at a voltage equal to V_{gap}. The approach used for obtaining an absolute brightness scale has been described in the text.

We have focused in this study on 80 nm LEP layer thicknesses, motivated by the observation of a maximum in the light-outcoupling efficiency close to this thickness as determined by microcavity interference effects (see e.g. Ref. [41]). This was confirmed by a study of the LEP layer thickness variation of the luminous efficacy carried out for devices based on copolymer **2**. With decreasing LEP layer thickness, the electron current density in single-carrier devices increases more rapidly than the hole current density, which is a well-known consequence of the presence of electron traps. As a result, V_{max} decreases. In principle, the higher current density at a given voltage and the smaller value of V_{max} could be used for obtaining a higher power efficiency at high brightnesses. However, reducing the LEP layer thickness to a value well below 80 nm, in order to accomplish this, is in practice hampered by the much smaller processing window, related to the occurrence of extrinsic defects.

6. Summary and conclusions

We have investigated the functioning of OLEDs based on blue and blue–green emitting fluorene polymers containing copolymerized aromatic amine comonomers which act as hole-transporting units and emitters. For that purpose, we have systematically synthesized and characterized a series

of 10 blue-emitting fluorene copolymers that contain two different types of comonomers (amines C and D) with similar optical energy gaps but with different contributions to the hole mobility. For all copolymers, the external quantum efficiency *versus* voltage curves are found to display a distinct maximum (at a voltage V_{max}). After correction for a small composition dependence of the radiative decay probability, an increase V_{max} is found to be accompanied by a decrease of the maximum efficiency. Also, V_{max} is found to increase systematically with increasing hole mobility. By making use of a numerical device model, it is shown that the voltage dependence of the efficiency curves can be understood as a result of a composition dependence of the hole mobility only. A voltage-dependent shift of the recombination profile across the emissive layer, leading to a voltage dependence of the light-outcoupling efficiency, is found to be the most important factor determining the shape of the efficiency curves.

The analysis shows how blue-emitting fluorene polymers containing copolymerized HTUs can be designed in a rational way for OLEDs applied under different conditions. At small (high) brightness levels, the most optimal power efficiency is obtained by the use of polymers with small (high) hole mobilities. The model provides insight in the functioning of OLED materials studied earlier in the literature, such as the blue-emitting polyfluorene-based polymer of the Sumation LUMATIONTM blue series mentioned in the Introduction. For OLEDs with the same device structure as used here (data point *i* in Fig. 2), $V_{max} \approx 11$ V and $\eta_L = 3.3$ cd/A were found [16]. The analysis presented in this paper explains, at least in part, why for this material the maximum efficiency is smaller than for polyfluorene-based copolymers with a smaller hole mobility. We conclude that for the class of OLED materials studied the voltage dependence of the efficiency can be tuned such that the power efficiency at the required brightness level is optimized.

Acknowledgements

The authors gratefully acknowledge the Dutch Polymer Institute for their financial support. We also acknowledge E.H.A. Beckers, N.M.M. Meulendijks-Kiggen (TNO Science and Industry), A.J.M. van den Biggelaar (Philips Research Laboratories), J.S. Wilson, M. Kilitziraki and H.C.A. Rooms (Holst Centre) for helpful discussions, support and measurements. The research by SLMvM was supported by NanoNed, a national nanotechnology program coordinated by the Dutch Ministry of Economic Affairs. The work of SH and RAHJK forms part of the research program of the Dutch Polymer Institute (DPI), project #437.

Appendix A. Experimental details

The fluorene copolymers were synthesized by the well-known Suzuki coupling method [40]. Into a toluene solution of $X-R-X$ (1 equiv), $Y-R'-Y$ (1 equiv), where R and R' are fluorene and/or arylamine segments and X and Y are halogen or boronate groups, catalytic amounts of $Pd(PPh_3)_4$ and a 20% aqueous solution of tetraethyl ammonium hydroxide were added. The copolymers were end-capped with (4,4,5,5-tetramethyl-1,3,2-dioxaborolyl)benzene. A schematic drawing of fluorene copolymer **2** is given in Fig. 1 with A 2,7-bis(4,4,5,5-tetramethyl-1,3,2-dioxaborolyl)-9,9-bis(4-[3,7-dimethyl-octyloxy]phenyl)fluorene, B 2,7-dibromo-9,9-bis(3,7-dimethyloctyl)-fluorene, C N,N′-bis(4-bromophenyl)-N,N′-bis(4-methoxyphenyl)-benzidine, and D 3,6-dibromo-N-(3,7-dimethyloctyl)phenoxazine. The reaction mixture was stirred at 110 °C overnight in an inert atmosphere (nitrogen flow). The organic layer was separated and washed with 2 wt-% NaCN aqueous solution to remove the catalyst residue. The organic layer was also washed with demi-water before drying with $MgSO_4$. The polymer was fractionated and precipitated in methanol. With a polydispersity in the range 1.4–2.4, the polymers have a weight-average molecular weight $\bar{M}_w$ in the range 130–680 kg/mol.

In order to estimate the HOMO and LUMO energy levels of the copolymers, cyclic voltammetry cycles were recorded in solution or in film. The cyclic voltammetry (CV) data were measured with a CHI 660A model from CH Instruments. The polymer films were deposited onto a platinum wire electrode and placed in an electrolyte solution of $TBAPF_6$ (0.1 M) in CH_3CN to measure the reduction potentials. For oxidation potential measurements in solution, the same configuration was used, however, the indicated compounds were dissolved (typically 0.1 mg) in dichloromethane as a solvent with 0.1 M of $TBAPF_6$. The potentials were measured relative to an Ag/Ag^+ reference electrode (scan rate was typically 0.1–1.0 V/s) and referenced to the first oxidation potential of Fc (~0.35 V). The oxidation potential of the Fc/Fc^+ relative to vacuum level was taken as 4.7 V [42]. The oxidation potentials of the copolymers were converted into ionization potentials using Fc/Fc^+ as the reference potential. The ionization potential (I_p) and electron affinity (E_a) were derived from the half-height oxidation and reduction potentials of the reversible scans and were related to the vacuum energy scale.

Light-emitting diodes were fabricated at Philips Research Laboratories in Eindhoven by spin coating polymers from toluene solution (1 wt-%) with film thicknesses of 80 ± 5 nm onto glass substrates under ambient conditions. Onto the OLED substrates with ~100 nm thick ITO (Indium–Tin–Oxide) coating a commercially obtained PEDOT:PSS dispersion (HC Starck, Baytron P VP AI 4083) was spin coated to yield approximately 100 nm thick films after drying. Barium and aluminum were thermally evaporated at reduced pressure to yield approximately 5 and 100 nm thick films, respectively. Following evaporation, the devices were hermetically sealed. The surface area of the pixels that were investigated was 9 mm^2. For single-carrier hole-only devices, a cathode consisting of thermally evaporated Pd (100 nm) was used. For electron-only devices the ITO/PEDOT:PSS anode was replaced with a thermally evaporated 30 nm thick Al layer.

The OLED layer thicknesses were derived from the geometric capacitance that was determined by dynamic capacitance measurements (Schlumberger gain/phase analyser 1260 SI) in the frequency range of 10 Hz–1 MHz and the bias range of −4 to 0 V. The AC variation on top of the

DC bias was 0.03 V. The dielectric constants of the different copolymers were determined by comparing the layer thickness of freshly prepared devices at 10–20 positions on the 6″ substrate with the geometric capacitance. The built-in voltages for the double-carrier and single-carrier hole-only devices were also determined by differential capacitance measurements in the frequency range of 100 Hz–10 kHz and the bias range of 0–3 V. The AC variation on top of the DC bias was 0.03 V. For the electron-only devices, the built-in voltage was taken from Ref. [16]. Photocurrent measurements were used to determine the built-in voltage.

Current (I) *versus* voltage (V) and luminance (L) *versus* voltage curves of 9 mm^2 OLED devices were measured using a Keithley Model 2400 general-purpose sourcemeter. Measurements at a high current density were carried out in a pulse-mode, in order to avoid heating of the devices. During the I–V–L cycle, the brightness was monitored by a calibrated photodiode, calibrated with a Konica Minolta LS-100 luminance meter, that was mounted orthogonally to the OLED that was connected to a Keithley Model 6517A electrometer/high-resistance meter. The EL spectra were measured using a spectroradiometer (Photo Research PR-705 camera), mounted orthogonally to the OLED plane. The EQE was then obtained by taking the ratio of the photon flux detected by the camera divided by the current density in the OLED, assuming that the brightness and spectral shape are independent of the viewing angle (Lambertian emission).

Solid-state fluorescence quantum yield measurements were determined using the integrating sphere method [29–31]. Thin polymer films with a thickness of 80 ± 2 nm were by spin coating from a toluene solution (1 wt-%) onto a glass substrate. The polymer films were excited under nitrogen flow with monochromatic light with a wavelength of 406 nm stemming from an ArKr laser (Beamlok 2080, Spectra-Physics Lasers Inc.). The fluorescence response in the wavelength range 350–800 nm was recorded by a Shamrock SR-163 spectrometer (Andor) that was linked to the integrated sphere by an optical fibre. The optical path from integrating sphere to CCD camera was calibrated by a DH-2000 Ocean Optics calibration lamp. Table 1 contains an overview of various device parameters for the 10 copolymers studied, obtained from the EL and PL experiments.

References

[1] M. Fukuda, K. Sawada, K. Yoshino, Jpn. J. Appl. Phys. 28 (1989) L1433;
M. Uchida, Y. Ohmori, C. Morishima, K. Yoshino, Synth. Met. 57 (1993) 4168;
Y. Ohmori, M. Uchida, K. Muro, K. Yoshino, Jpn. J. Appl. Phys. 30 (1991) L1941;
M. Fukuda, K. Sawada, K. Yoshino, J. Polym. Sci. (A) 31 (1993) 2465.

[2] S. Doi, C. Sekine, Y. Tsubata, M. Ueda, T. Noguchi, T. Ohnishi, J. Photopolym. Sci. Technol. 16 (2003) 303.

[3] H. Spreitzer, H. Becker, E. Breuning, A. Falcou, K. Treacher, A. Büsing, A. Parham, P. Stößel, S. Heun, J. Steiger, Proc. SPIE 4800 (2003) 16.

[4] W. Wu, M. Inbasekaran, M. Hudack, D. Welsh, W. Yu, Y. Cheng, C. Wang, S. Kram, M. Tacey, M. Bernius, R. Fletcher, K. Kiszka, S. Munger, J. O'Brien, Microelectron. J. 35 (2004) 343.

[5] L. Akcelrud, Program. Polym. Sci. 28 (2003) 875.

[6] M. Redecker, D.D.C. Bradley, M. Inbasekaran, W.W. Wu, E.P. Woo, Adv. Mater. 11 (1999) 241.

[7] W. Yang, Y. Niu, C. Liu, Q. Hou, J. Huang, R. Yang, X. Zeng, Y. Cao, Synth. Met. 135–136 (2003) 183.

[8] Q. Hou, Y.H. Niu, W.B. Huang, W. Yang, R.Q. Yang, M. Yuan, Y. Cao, Synth. Met. 135–136 (2003) 185.

[9] M. Inbasekaran, Y. Cheng, S. Gaynor, M. Hudack, C. Wang, D.M. Welsh, W. Wu, US Patent 6916902, 2005; M. Inbasekaran, M.T. Bernius, W. Wu, J.J. O'Brien, Patent WO/2000/46321.

[10] S. Grigalevicius, L. Ma, Z.-Y. Xie, U. Scherf, J. Polym. Sci. A 44 (2006) 5987.

[11] M. Bernius, M. Inbasekaran, E. Woo, W. Wu, L. Wujkowski, Thin Solid Films 363 (2000) 55;
M. Bernius, M. Inbasekaran, E. Woo, W. Wu, L. Wujkowski, J. Mater. Sci.: Mater. Electron. 11 (2000) 111.

[12] S. Wang, Y.Q. Liu, X.W. Zhan, G. Yu, D.B. Zhu, Synth. Met. 137 (2003) 1153.

[13] M.-J. Park, J.-H. Leeb, D.-H. Hwang, Curr. Appl. Phys. 6 (2006) 752.

[14] D. Zeng, J. Chen, Z. Chen, W. Zhu, J. He, F. Yu, H. Huang, H. Wu, C. Liu, S. Ren, J. Du, J. Sun, E. Xu, A. Cao, Q. Fang, Macromol. Rap. Commun. 28 (2007) 772.

[15] M. Inbasekaran, E. Woo, W. Wu, M. Bernius, L. Wujkowski, Synth. Met. 111–112 (2000) 397;
L.C. Palilis, D.G. Lidzey, M. Redecker, D.D.C. Bradley, M. Inbasekaran, E.P. Woo, W.W. Wu, Synth. Met. 111–112 (2000) 159;
B. Liu, W.-L. Yu, Y.-H. Lai, W. Huang, Chem. Mater. 13 (2001) 1984;
J.-I. Lee, H.Y. Chu, H. Lee, J. Oh, L.-M. Do, T. Zyung, J. Lee, H.-K. Shim, ETRI J. 27 (2005) 182;
D. Vak, S.J. Shin, J.-H. Yum, S.-S. Kim, D.-Y. Kim, J. Lumin. 115 (2005) 109;
N.C. Yang, S.M. Lee, Y.M. Yoo, J.K. Kim, D.H. Suh, J. Polym. Sci. (A) 42 (2004) 1058;
J. Lee, B.-J. Jung, S.K. Lee, J.-I. Lee, H.-J. Cho, H.-K. Shim, J. Polym. Sci (A) 43 (2005) 1845;
E. Lim, B.-J. Jung, H.-K. Shim, Macromolecules 36 (2003) 4288;
Q. Sun, X. Zhan, C. Yang, Y. Liu, Y. Li, D. Zhu, Thin Solid Films 440 (2003) 247;
R.-F. Chen, Q.-L. Fan, S.-J. Liu, R. Zhu, K.-Y. Pu, W. Huang, Synth. Met. 156 (2006) 1161.

[16] R. Coehoorn, S.I.E. Vulto, S.L.M. van Mensfoort, J. Billen, M. Bartyzel, H. Greiner, R. Assent, Proc. SPIE 6192 (2006) 61920O.

[17] F. Laquai, D. Hertel, Appl. Phys. Lett. 90 (2007) 142109.

[18] R. Coehoorn, S.L.M. van Mensfoort, Phys. Rev. B 80 (2009) 085302.

[19] N.I. Craciun, J.J. Brondijk, P.W.M. Blom, Phys. Rev. B 77 (2008) 035206.

[20] S.L.M. van Mensfoort, R. Coehoorn, Phys. Rev. B 78 (2008) 085207.

[21] S.L.M. van Mensfoort, S.I.E. Vulto, R.A.J. Janssen, R. Coehoorn, Phys. Rev. B 78 (2008) 085208.

[22] M.M. Mandoc, B. de Boer, G. Paasch, P.W.M. Blom, Phys. Rev. B 75 (2007) 1932022.

[23] S.L.M. van Mensfoort, J. Billen, S.I.E. Vulto, R.A.J. Janssen, R. Coehoorn, Phys. Rev. B 80 (2009) 033202.

[24] J.J.M. van der Holst, M.A. Uijttewaal, R. Balasubramanian, R. Coehoorn, P.A. Bobbert, G.A. de Wijs, R.A. de Groot, Phys. Rev. B 79 (2009) 085203.

[25] I. Grizzi, C. Foden, S. Goddard, C. Towns, Mater. Res. Soc. Symp. Proc. 771 (2003) L1.7.1.

[26] J. Kanicki, S.-J. Lee, Y. Hong, C.-C. Su, J. SID 13/12 (2005) 993.

[27] L.S. Liao, C.S. Lee, S.T. Lee, M. Inbasekaran, W.W. Wu, in: W.R. Salaneck et al. (Eds.), Conjugated Polymer and Molecular Interfaces, Marcel Dekker, New York, 2002, pp. 401–441 (Chapter 12).

[28] (a) Ref. [3];
(b) H.J. Bolink, L. Cappelli, E. Coronado, I. Recalde, Adv. Mater. 18 (2006) 920;
(c) S. Tao, Z. Peng, X. Zhang, P. Wang, C.-S. Lee, S.-T. Lee, Adv. Funct. Mater. 15 (2005) 1716;
(d,e) C.D. Müller, A. Falcou, N. Reckefuss, M. Rojahn, V. Wiederhirn, P. Rudati, H. Frohne, O. Nuyken, H. Becker, K. Meerholz, Nature 421 (2003) 830;
(f) D. Gebeyehu, K. Walzer, G. He, M. Pfeiffer, K. Leo, J. Brandt, A. Gerhard, P. Stößel, H. Vestweber, Synth. Met. 148 (2005) 205;
(g) Ref. [16];
(h) E. Wang, C. Li, Y. Mo, Y. Zhang, G. Ma, W. Shi, J. Peng, W. Yang, Y. Cao, J. Mater. Chem. 16 (2006) 4133;
(i) Ref. [26];
(j) Ref. [2];
(k) T. Gohda, Y. Kobayashi, K. Okano, S. Inoue, K. Okamoto, S. Hashimoto, E. Yamamoto, H. Morita, S. Mitsui, M. Koden, SID Symp. Digest Tech. Papers 37 (2006) 1767.

[29] J.C. de Mello, H.F. Wittmann, R.H. Friend, Adv. Mater. 9 (1997) 230.

[30] L.-O. Pålsson, A.P. Monkman, Adv. Mater. 14 (2002) 757.

[31] A.R. Johnson, S.-J. Lee, J. Klein, J. Kanicki, Rev. Sci. Instrum. 78 (2007) 096101.
[32] M. Ariu, D.G. Lidzey, M. Sims, A.J. Cadby, P.A. Lane, D.D.C. Bradley, J. Phys.: Condens. Matter 14 (2002) 9975.
[33] P. Sreearunothai, A.C. Morteani, I. Avilov, J. Cornil, D. Beljonne, R.H. Friend, R.T. Phillips, C. Silva, L.M. Herz, Phys. Rev. Lett. 96 (2006) 117403.
[34] J.G.S. Ramon, E.R. Bittner, J. Chem. Phys. 126 (2007) 18101.
[35] T.J. Chuang, R.J. Cox, K.B. Eisenthal, J. Am. Chem. Soc. 86 (1974) 6828.
[36] T.J. Chuang, K.B. Eisenthal, J. Chem. Phys. 59 (1973) 2140.
[37] See e.g. Fig. 11 in M. Segal, M.A. Baldo, R.J. Holmes, S.R. Forrest, Z.G. Soos, Phys. Rev. B 68 (2003) 075211.
[38] W.F. Pasveer, J. Cottaar, C. Tanase, R. Coehoorn, P.A. Bobbert, P.W.M. Blom, D.M. de Leeuw, M.A.J. Michels, Phys. Rev. Lett. 94 (2005) 206601.
[39] K. Neyts, J. Opt. Soc. Am. A 15 (1998) 962;
H. Greiner, O.J.F. Martin, Proc. SPIE 5214 (2004) 249.
[40] B. Ruhstaller et al., SID Symp. Digest Tech. Papers 38 (2007) 1686.
[41] N. Miyara, A. Suzuki, Chem. Rev. 95 (1995) 2457.
[42] J.O.M. Bockris, S.U.M. Khan, Surface Electrochemistry, A Molecular Level Approach, Kluwer Academic/Plenum Publishers, New York, 1993.

ring-opening metathesis, reversible addition fragmentation chain transfer and nitroxide mediated polymerizations [22–26]. Recently, the GRIM approach has been associated with the ring-opening polymerization (ROP) of D,L-lactide [27]. Extending this family of block copolymers with other lactones would yield interesting materials, especially by polymerizing ε-caprolactone (CL) onto RRP3HT segment since poly(ε-caprolactone) (PCL) is: (1) crystallizable (in contrast to other segments copolymerized with P3HT, such as poly(methacrylate)s [22]); (2) miscible with a number of other polymer compounds (such as poly(vinyl chloride), poly(ethylene chloride), poly(styrene-*co*-acrylonitrile),...); (3) removable by hydrolysis, and; (4) biocompatible. The capacity of PCL to be miscible blended with various commercial polymers over a wide range of composition (in contrast to polylactide blocks) opens the way for interesting compatibilization of a P3HT matrix by using P3HT/PCL block copolymers, whatever their topology. PCL is therefore a valuable partner for RRP3HT for improved compatibility and for potential bio-applications.

Here, we report on the stepwise synthesis of diblock and triblock copolymers by controlled polymerization of ε-caprolactone from (di)hydroxyl-terminated RRP3HT, see Scheme 1. Such copolymers are inherently expected to self-assemble in the solid-state; the resulting nanoscale morphologies in thin deposits are studied via atomic force microscopy (AFM) and correlated with the charge transport properties in field-effect transistor configuration.

2. Experimental section

2.1. Synthesis

α-bromo poly(3-hexylthiophene): Into a flask under a nitrogen atmosphere containing 2-bromo-3-hexyl-5-iodothiophene (1.18 g, 3.15 mmol), dry THF (15.0 mL) was added via a syringe, and the mixture was stirred at 0 °C. i-PrMgCl (2.0 M solution in THF, 1.08 mL, 3.15 mmol) was added via a syringe, and the mixture was stirred at 0 °C for 0.5 h. A suspension of Ni(dppp)Cl_2 (18 mg, 0.03 mmol) in THF (5.0 mL) was added to the mixture via a syringe at 0 °C, and then the mixture was stirred at room temperature. After the reaction mixture was stirred for 1 day, a 5 N HCl aqueous solution was quickly added to quench the reaction. The mixture was stirred for 0.5 h more, then precipitated in cold MeOH. The product was washed with MeOH yielding a purple solid, >98.5% rr-HT-P3HT. Yield = 69%; UV ($CHCl_3$, nm): 445; IR (cm^{-1}): 819 (C–H

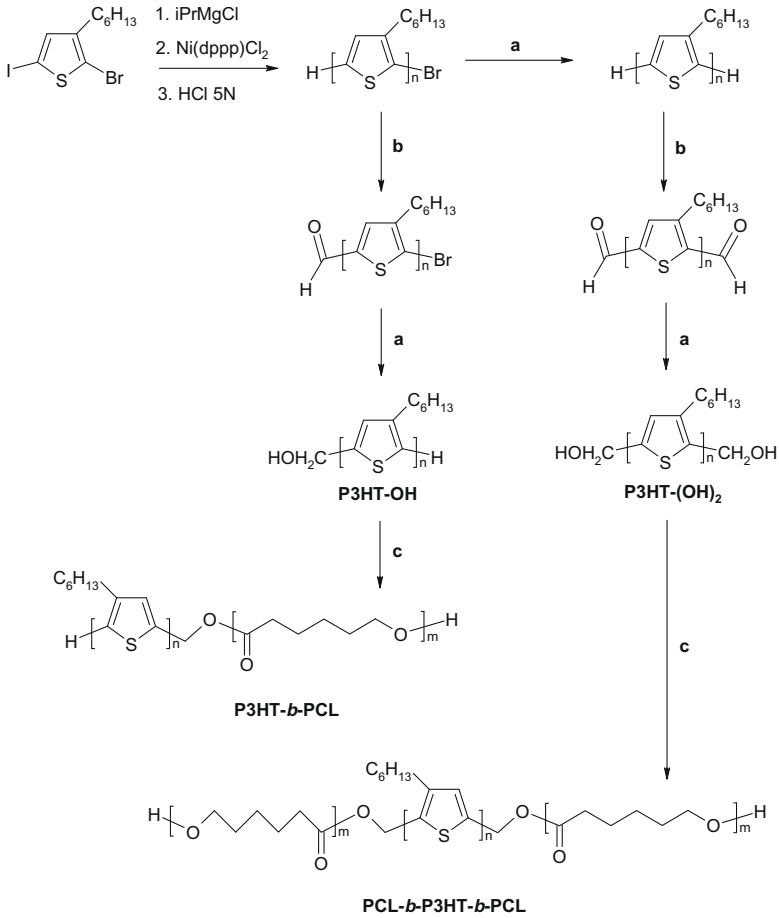

Scheme 1. Comparative routes leading to diblock (P3HT-*b*-PCL) and triblock (PCL-*b*-P3HT-*b*-PCL) copolymers. Reagents a: $LiAlH_4$/HCl, b: 1. $POCl_3$/DMF, 2. CH_3COONa/H_2O, and c: CL/$SnOct_2$.

aromatic out-of-plane) and I_{sym}/I_{asym} = 6, characteristic of rr-HT-P3HT; ^{1}H NMR (300 Hz, $CDCl_3$): 6.98 (s, 1H), 2.80 (t, ^3J = 7.5 Hz, 2H), 1.71 (quint, 2H), 1.34 (m, 6H), 0.91 (t, ^3J = 6.4 Hz, 3H); GPC analysis: M_n = 4450 g/mol; PDI = 1.17. **Formyl-de-hydrogenation of α-bromo poly(3-hexylthiophene):** H-P3HT-Br (M_n = 3700, PDI = 1.17) (300 mg, 0.071 mmol) was dissolved in anhydrous toluene (80 mL) under N_2. N,N-Dimethylformamide (1 mL, 13 mmol) and $POCl_3$ (0.7 mL, 7.6 mmol) were added. The reaction was carried out first at 75 °C for 50 h. The solution was cooled down to room temperature, followed by the adding of a saturated aqueous sodium acetate solution. The reaction mixture was stirred for another 2 h. The polymer was precipitated in cold methanol and washed with water, then methanol. Yield = 94%; GPC analysis: M_n = 4800 g/mol; PDI = 1.17; ^{1}H NMR (300 Hz, $CDCl_3$): M_nNMR = 5400 g/mol. **Reduction of α-bromo, ω-formyl poly(3-hexylthiophene):** HOC-P3HT-Br (M_n = 3500, PDI = 1.23; 200 mg, 0.057 mmol) was dissolved in anhydrous THF (80 mL), under N_2. $LiAlH_4$ 1 M solution in THF (0.5 mL) was then added. The reaction was then kept stirring at room temperature for 1.5 h. HCl (1 N, 1 mL) was then added to quench the excess of $LiAlH_4$. The polymer was precipitated in methanol and washed with water then methanol. After drying in vacuum, 190 mg of CH_2OH-P3HT-Br was obtained. Yield = 95%; GPC analysis: M_n = 5100 g/mol; PDI = 1.22; ^{1}H NMR (300 Hz, $CDCl_3$): M_n NMR = 5400 g/mol. **Synthesis of poly(3-hexylthiophene)-*b*-poly(ε-caprolactone):** In a previously dried and nitrogen-purged 25 mL round-bottom flask equipped with a three-way stopcock and a rubber septum, 0.43 ml of CL (3.92 mmol) and 3.3 ml of dried toluene were added to freshly dried 0.5 g of hydroxyl-P3HT (0.098 mmol). The reaction mixture was gently heated to 110 °C until complete dissolution of P3HT before adding a 0.2 M solution of $Sn(Oct)_2$ (0.2 mL, 0.039 mmol, $[OH]_0/[Sn(Oct)_2]_0$ = 2.5, final concentration of CL = 1 M). After 15 h at 110 °C, the reaction was cooled down and stopped by adding dropwise an aqueous HCl solution (1 mol L^{-1}). The copolymer was then precipitated from cold methanol yielding a brown solid. Yield = 76% (m = 704 mg); ^{1}H NMR (300 Hz, $CDCl_3$): M_nPCL = 2300 g/mol; Conversion in PCL = 50.4% (M_n in PCL expected = 40 × 114 = 4560 g/mol); GPC analysis: M_nGPC = 6500 g/mol; PDI = 1.23. A detailed description of the materials, synthesis steps and characterization techniques is given in the Supporting information.

2.2. Atomic force microscopy

Sub-monolayer deposits were prepared by solvent casting on freshly-cleaved muscovite mica or silicon oxide substrates from dilute solutions (0.05–0.5 g L^{-1}); the solvent was slowly evaporated at room temperature in a solvent-saturated atmosphere. Thicker, homogeneous films were prepared by spin-coating the solutions onto silicon oxide or glass substrates (spinning speed from 2500 to 4000 rpm, solution concentration = 1.0 g L^{-1}). AFM studies were carried out in Tapping-Mode with Multimode Nanoscope IIIa or Nanoscope V microscopes (Veeco) operating in air at room temperature, using microfabricated silicon cantilevers with a spring constant of around 30 N m^{-1} (TESP, Veeco). Images of different areas of the samples were collected and Nanoscope image processing software was used for image analysis.

2.3. FET fabrication and characterization

The FET devices consist in a thermally-grown 200 nm-thick SiO_2 gate dielectric on top of a doped n^{++}-type Si gate electrode. Gold source and drain electrodes were used, and the devices were fabricated either in bottom-contact (100 nm-thick electrodes, channel length of 5 or 10 μm) or top-contact (channel length of 50 μm) configurations. Homogeneous thin films of the (co)polymers were prepared by spin-coating a 1.0 g L^{-1} solution (at 2500 rpm) onto the silicon oxide gate dielectrics. The devices were then tested in a glove box under nitrogen atmosphere and the electrical characteristics were measured on a probe station with a Keithley 4200 semiconductor parametric analyzer. The charge mobility has been estimated from the saturation regime (at source-drain voltage of −60 V), see the description in Refs. [35,40–44] for instance.

3. Results and discussion

3.1. Synthesis of (co)polymers

The key-step for the controlled generation of these novel architectures is the synthesis of perfectly controlled (di)hydroxyl-terminated regioregular P3HT. The first method considered for the synthesis of P3HT-OH consisted in the hydroboration/oxidation reaction of previously synthesized vinyl-terminated P3HT, as recently reported by McCullough et al. (Route A, Scheme 2) [28]. However, the expected P3HT-OH compound was systematically contaminated by ca. 10 wt.% of non-hydroxylated P3HT [23,29] (see Supporting information, SI) leading upon ring-opening polymerization of ε-caprolactone (CL) to a mixture of P3HT-*b*-PCL and P3HT and requiring intensive purification by fractionation. Comparatively, the formyl-dehydrogenation of the α-bromo P3HT protic end-group (Route B) was successfully performed by a Vilsmeier reaction leading to α-bromo, ω-formyl P3HT characterized by a recovering yield of 94% [23,29]. The evolution of the reaction was followed by MALDI-ToF analysis until complete transformation of the α-bromo P3HT to α-bromo, ω-formyl P3HT (Fig. S2) allowing us to recover a 100% formyl end-capped structure. After completion of the reaction, both the formyl and the bromide end-groups were reduced by $LiAlH_4$ yielding the expected P3HT-OH with a narrow molecular weight distribution (polydispersity index = 1.22) and a recovering yield of 95% (see SI, Fig. S3). It is worth noting that the global yield of the polymerization and the post-polymerization end-group modification processes reached 62%. Such a high yield, together with the fact that the recovered P3HT-OH is 100% functionalized by a hydroxyl group, represents a relevant progress in the field. Dihydroxyl-terminated P3HT (P3HT-$(OH)_2$) was also obtained by the same procedure but starting with a reduction reaction of α-bromo P3HT by $LiAlH_4$ (Total recovering yield: 58%,

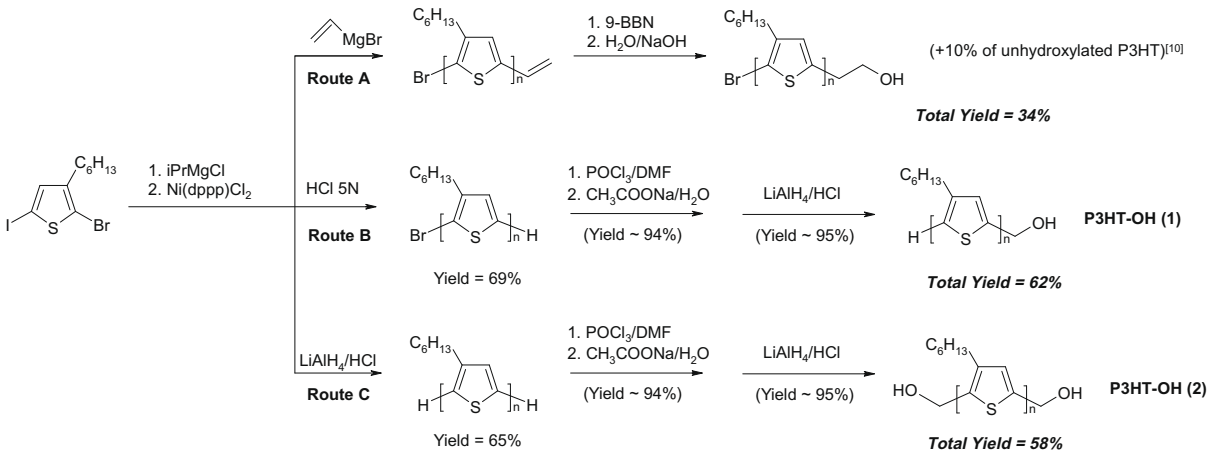

Scheme 2. Comparative routes leading to (di)hydroxyl-terminated P3HT. Route A: hydroboration/oxidation of α-bromo, ω-vinyl P3HT [10]. Routes B and C: vilsmeier oxidation/reduction of (α-bromo) P3HT.

Route C, Scheme 2, Fig. S4). The molecular characterization of representative P3HT is described in Table 1.

These homopolymers were used as the starting materials for the synthesis of di- and triblock copolymers shown in Scheme 1. Tin(II)octoate ($Sn(Oct)_2$) was used to catalyze the controlled ROP of CL from the hydroxyl-end-groups(s) of P3HT macroinitiators [30]. Both P3HT-OH and P3HT-$(OH)_2$ were thus treated with $Sn(Oct)_2$ in toluene with an initial hydroxyl/Sn molar ratio of 2.5. CL was then added and the polymerization was carried out in toluene at 110 °C with an initial monomer concentration of 1 M and an initial $[CL]_0/[OH]_0$ molar ratio of 40. After a reaction time of 15 h, the copolymers were recovered by precipitation (see SI); the PCL molecular weights (M_n), as estimated from ^1H NMR, are 1900 and 3200 g/mol for P3HT-*b*-PCL and PCL-*b*-P3HT-*b*-PCL, respectively (Table 1). These values are in good agreement with the expected molecular weights taking into account the monomer conversion and initial monomer-to-initiator molar ratios. Size exclusion chromatography traces of the copolymers were all monomodal with polydispersity indices below 1.2 (Table 1 and SI).

3.2. Microscopic morphology in thin deposits

The micro- and nano-scopic morphology of thin deposits of the (co)polymers was investigated by atomic force microscopy (AFM) in intermittent-contact mode. Thin deposits have been prepared by drop-casting or spin-coating onto various substrates starting from good solvents for both P3HT and PCL blocks (e.g., tetrahydrofuran, toluene or chlorobenzene). Thin deposits of the studied compounds all show a fibrillar (nanowire-like) morphology (see AFM images in Fig. 1). This is observed for both sub-monolayer deposits (Fig. 1c and Fig. 1e, where the substrate surface appears dark) and for thicker deposits (Fig. 1a,b,d) prepared by drop-casting, in which the fibrils extend up to a few μm and arrange in lamellae. Films prepared by spin-coating from the same solvent (tetrahydrofuran) also show entangled fibrillar structures (Fig. 1f), indicative that the fibrillar assembly occurs even with a very rapid solvent evaporation process (spinning speed >2500 rpm). Indeed, this fibrillar morphology is typical from the (crystalline) assembly of RRP3HT into π-stacked assemblies, as observed and described for highly regioregular poly(thiophene)s and other conjugated (co)polymers thin deposits prepared with the same methods [31,32]. In these fibrils, P3HT molecules have extended conjugated backbones, with their long axis perpendicular to the π-stacking direction (the fibril axis). The fibrils arrange in lamellae due to interdigitation of alkyl groups perpendicularly to the backbone axis with a lamellar thickness of 1.7 nm, as observed using (Grazing Incidence) X-ray Diffraction measurements [33–34], which is in agreement with the fibril thickness measured here. This is further supported by the measured width of the fibrils, which

Table 1
Molecular characteristics and FET properties of the synthesized RRP3HT and their corresponding PCL-based copolymers.

Compound	M_nP3HT (g/mol)[a]	M_nPCL (g/mol)[a]	M_nGPC (g/mol)[b]	PDI[b]	μ[d] ($cm^2\ V^{-1}\ s^{-1}$)	$I_{on/off}$[d]
P3HT-OH	5400[c]	–	5100	1.22	–	–
P3HT-*b*-PCL	6000	1900	6500	1.23	1.1×10^{-5}	$\sim 1 \times 10^3$
P3HT-$(OH)_2$	7400[c]	–	8700	1.16	6.0×10^{-5}	$\sim 3 \times 10^3$
PCL-*b*-P3HT-*b*-PCL	7900	3200	12100	1.15	4.6×10^{-4}	$\sim 2 \times 10^4$

[a] Absolute molar masses as determined by ^1H NMR analysis.
[b] Relative molar masses as determined by gel permeation chromatography in THF at 35 °C using PS standards.
[c] Molar masses obtained by ^1H NMR analysis have been calculated after confirmation of the number of hydroxyl-end-groups by MALDI-Tof.
[d] Charge mobilities μ and current on/off ratios $I_{on/off}$ have been estimated from the transfer characteristics of top-contact FET devices.

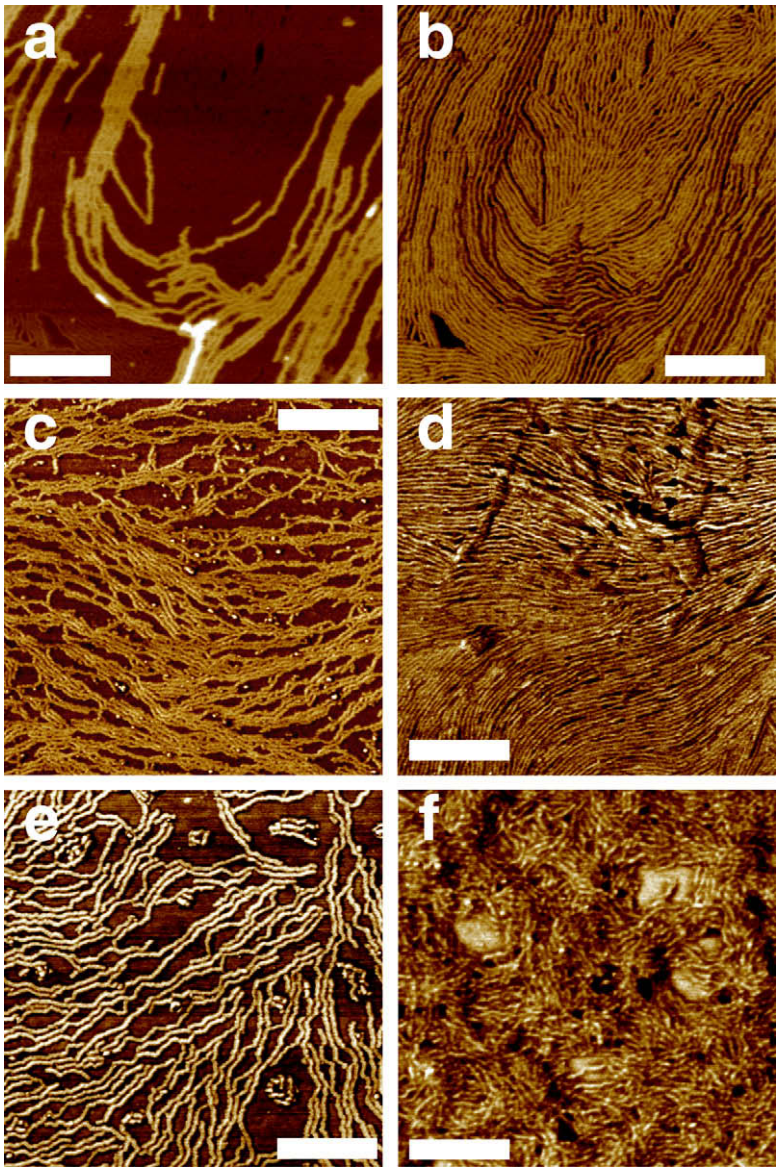

Fig. 1. AFM images of thin deposits from tetrahydrofuran of (a–b) P3HT-OH (a: height; b: phase); (c–d) P3HT-*b*-PCL (phase images, c: sub-monolayer deposit; d: thick film); (e–f) PCL-*b*-P3HT-*b*-PCL (phase images, e: sub-monolayer deposit; f: spin-coated film). The white scale bar is 250 nm-long.

correlates with the length of the P3HT conjugated backbone [35]: the measured widths are 11 ± 2 nm for P3HT-OH and 17 ± 2 nm for PCL-*b*-P3HT-*b*-PCL, while the estimated lengths of fully-extended P3HT backbones are 12.6 and 18.4 nm in average, respectively [36]. Note that, for the P3HT-*b*-PCL and PCL-*b*-P3HT-*b*-PCL block copolymers, adjacent fibrils (in bright) are close to each other, and appear to be separated by narrow dark bands in the phase images (for instance, compare Fig. 1b and Fig. 1e). This, together with the fact that the measured fibrils width is close to the length of the extended P3HT backbone, indicates that the PCL segments are very likely in a compact conformation in between the P3HT assemblies. Indeed, the PCL segments have a quite low degree of polymerization in these block copolymer structures (e.g. 20 monomer units in average in the diblock copolymer), which seems not sufficient to induce crystallization of PCL. If we consider a coiled conformation of the PCL segments, the estimated radius of gyration would be around 1.3–1.6 nm (in the di- and tri-block copolymers), i.e. around 3 nm in diameter [36]. All these results suggest that the self-assembly of the these block copolymers is driven by the ordering of the RRP3HT backbones (intra-lamellar π-stacking of conjugated backbones and inter-lamellar interdigitation between alkyl groups) rather than by the assembly of the PCL segments, which are very likely in a coiled configuration in between the P3HT fibrils [37].

3.3. Charge transport properties in field-effect transistors

Field-effect transistors (FET) were fabricated in bottom-gate configuration, with a gate dielectric layer made of SiO_2 on top of a heavily doped silicon (n^{++}) gate electrode. Thin films of the (co)polymers were deposited by spin-coating on the SiO_2 from chlorobenzene solutions because this deposition process leads to flat, homogeneous thin films suitable for FET fabrication (thickness $\sim 20 \pm 5$ nm and RMS roughness (over 1 μm^2) of about 2 nm, as measured with AFM). The devices were tested with gold source and drain electrodes either in top-contact or bottom-contact configurations, in the accumulation regime of hole transport (negative source-gate voltages) since holes are the major charge carriers in P3HT structures using this device architecture. Here we report results for top-contact FET devices, which show more reproducible FET characteristics using these preparation conditions [38]. Examples of transfer and output characteristics are shown in Fig. 2. For all (co)polymers, the output characteristics (source-drain current I_{ds} versus source-drain voltage V_{ds} at various gate voltages V_{gs}) show good saturation behavior, and the curves display typical characteristics of P3HT films using this preparation method [2,39]. From the transfer characteristics, we observe that the threshold voltages are close to 0 V, and the current on/off ratios are on the order of 10^3–10^4 (see Table 1). All these results show that the studied compounds behave as semiconducting polymers with low level of doping. The charge carrier mobilities μ, estimated in the saturation regime (i.e., from the slope of the plot of I_{ds} versus $V_{gs}^{1/2}$ at source-drain voltage $V_{ds} = -60$ V), are listed in Table 1. The μ values are in the range of 10^{-5}–10^{-3} $cm^2\,V^{-1}\,s^{-1}$; this is quite low compared to the highest mobilities reported for polymer FETs, which are on the order of 0.1–1 $cm^2\,V^{-1}\,s^{-1}$ for thiophene-based or thienothiophene-based polymers [40–42]. This difference can be attributed to the low molecular weight of the P3HT-based polymers studied here (maximum 7600 g/mol, corresponding to about 46 hexylthiophene units). Indeed, it has been shown that FETs made of low molecular weight fractions of P3HT show lower charge carrier mobilities: for $M_n < 10000$ g/mol, the charge mobility estimated in the same manner is $\sim 10^{-5}$–10^{-4} $cm^2\,V^{-1}\,s^{-1}$. For higher molecular weight fractions (10000 g/mol $< M_n <$ 40000 g/mol), μ is up to 10^{-2} $cm^2\,V^{-1}\,s^{-1}$. This difference has been attributed to the existence of charge transport pathways along longer chains connecting crystalline domains in the film and/or the more planar conformations in films of high molecular weight RRP3HT [43–44]. Surprisingly, we observe that the triblock copolymer film displays the highest value (around 0.5×10^{-3} $cm^2\,V^{-1}\,s^{-1}$), i.e. one order of magnitude higher than that of the corresponding P3HT homopolymer (0.6×10^{-4} $cm^2\,V^{-1}\,s^{-1}$) despite the fact that P3HT represents only about 60% by weight. This difference is not related to a molecular weight difference of the P3HT sequence, see Table 1. In our interpretation, it origi-

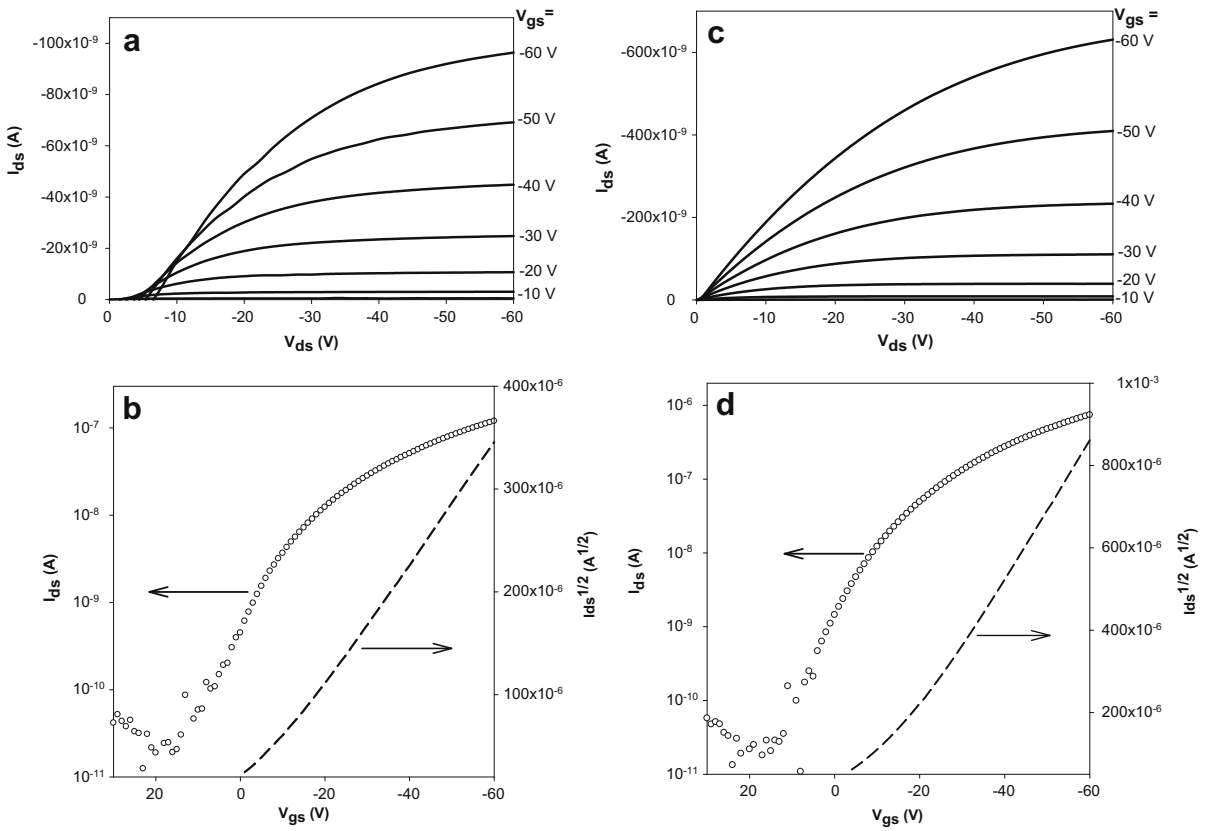

Fig. 2. Output (top) and transfer (bottom) characteristics of top-contact FET devices made of P3HT-$(OH)_2$ (a,b) and PCL-*b*-P3HT-*b*-PCL (c,d) as active layers.

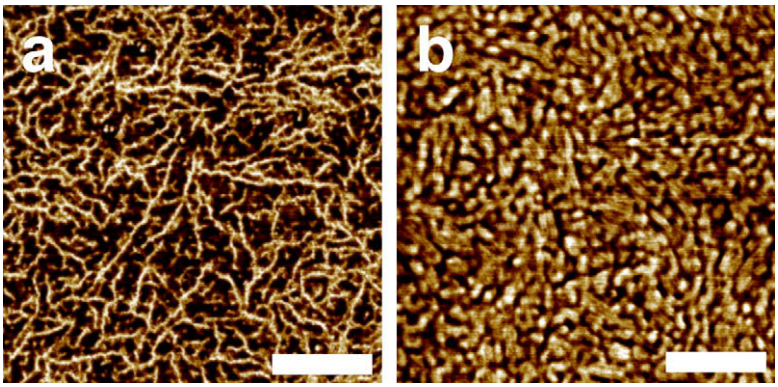

Fig. 3. AFM phase images of the active layer within the FET channel of (a) PCL-*b*-P3HT-*b*-PCL, and (b) P3HT-$(OH)_2$. The white scale bar is 250 nm-long.

nates from a difference in structural order within the thin films and/or interface with the electrodes. AFM measurements on the active layer in the channel of FET devices (see Fig. 3) reveal that films of PCL-*b*-P3HT-*b*-PCL show a higher degree of fibrillar order than pure P3HT-$(OH)_2$. The fibrils are relatively long in the case of PCL-*b*-P3HT-*b*-PCL (few hundreds nm-long) compared to the assemblies of P3HT-$(OH)_2$, which are confined in tens of nm-wide granular domains. In FET devices made of pure RRP3HT, it has been shown that films made of μm-long fibrillar structures lead to higher performances (i.e., charge mobility and current on/off ratio) than untextured, non-crystallized films, demonstrating that the fibrils act as efficient "conduits" for the charge transport in FET (in which the channel length is typically a few μm-long) [33]b,[35,39]. The higher degree of fibrillar order in PCL-*b*-P3HT-*b*-PCL spin-coated films is likely due to the tendency of this copolymer to phase-separate on the nanoscale, which probably forces the P3HT segments to be more in registry with each other and therefore leads to straight and long P3HT fibrils separated by small PCL domains. The higher charge carrier mobility observed here for the triblock copolymer also suggests that the charge transport is one-dimensional (along each fibril) rather than inter-fibrillar (bi-dimensional) in these materials [45], since in the case of the triblock copolymer film, the P3HT fibrils are surrounded by the PCL segments on each side, which are likely to insulate the π-conjugated systems of adjacent fibrils from each other.

4. Conclusions

In summary, we have described a well-controlled synthesis method for the design of poly(thiophene) block copolymers. Each reaction step has been carefully followed, making it possible to recover the target compounds in high yields without tedious purification steps. Regioregular P3HT homopolymers and P3HT-PCL block copolymers self-assemble into well-defined fibrillar structures. The charge transport properties of these (co)polymers have been characterized in FETs, showing characteristics of good quality organic semiconductors, with charge carrier mobilities in the range of 10^{-5}–10^{-3} $cm^2\,V^{-1}\,s^{-1}$. Interestingly, the copolymer PCL-*b*-P3HT-*b*-PCL shows higher charge mobility than the corresponding pure P3HT block, which is attributed to a higher degree of long-range fibrillar structures favored by nanophase separation. Since P3HT can be chemically doped after the self-assembly process and the lateral dimensions can be tuned by controlled synthesis of the polymer segments, these copolymers could be suitable materials for fabricating conducting nanowires insulated from each other. Moreover, the possibility of removing the PCL segments by hydrolysis shows potential for designing nano-sized pores (in between RRP3HT segments) [27] that could then be filled with electron acceptor molecules, which would be of interest for designing organic photovoltaic diodes with improved performances thanks to fine-control over the nanoscale morphology.

Acknowledgments

The authors thank the financial support from the Wallonia Region, the European Commission (FSE, FEDER), the National Fund for Scientific Research (F.R.S.-FNRS), and the Belgian Federal Science Policy Office (PAI 6/27). J.D. is Research Fellow and M.S., O.C, Ph.L., P.G. are Research Associates of the F.R.S.-FNRS. M.S. thanks Prof. Alan J. Heeger for a research stay in his group at University of California Santa Barbara and Drs. Jonathan D. Yuen, Shinuk Cho, and Daniel Moses for their kind help and enlightening discussions.

Supporting Information. Details of the synthesis and characterization are available from the authors or online on http://www.sciencedirect.com.

Appendix A. Supplementary data

Supplementary data associated with this article can be found, in the online version, at doi:10.1016/j.orgel.2010.01.016.

References

[1] I. Osaka, R.D. McCullough, Acc. Chem. Res. 41 (2008) 1202.
[2] (a) Z. Bao, A. Dodabalapur, A.J. Lovinger, Appl. Phys. Lett. 69 (1996) 4108;
(b) Z. Bao, A.J. Lovinger, Chem. Mater. 11 (1999) 2607.
[3] (a) H. Sirringhaus, P.J. Brown, R.H. Friend, M.M. Nielsen, K. Bechgaard, B.M.W. Langeveld-Voss, A.J.H. Spiering, R.A.J. Janssen,

E.W. Meijer, P. Herwig, D.M. de Leeuw, Nature 401 (1999) 685;
(b) A. Facchetti, Mater. Today 10 (2007) 28.
[4] W.L. Ma, C.Y. Yang, X. Gong, K. Lee, A.J. Heeger, Adv. Funct. Mater. 15 (2005) 1617.
[5] Y. Kim, S. Cook, S.M. Tuladhar, S.A. Choulis, J. Nelson, J.R. Durrant, D.D.C. Bradley, M. Giles, I. McCulloch, C.S. Ha, M. Ree, Nat. Mater. 5 (2006) 197.
[6] J.Y. Kim, K. Lee, N.E. Coates, D. Moses, T.Q. Nguyen, M. Dante, A.J. Heeger, Science 317 (2007) 222.
[7] S. Gunes, H. Neugebauer, N.S. Sariciftci, Chem. Rev. 107 (2007) 1324.
[8] A.C. Mayer, S.R. Scully, B.E. Hardin, M.W. Rowell, M.D. McGehee, Mater. Today 10 (2007) 28.
[9] K. Sivula, Z.T. Ball, N. Watanabe, J.M.J. Fréchet, Adv. Mater. 18 (2006) 206.
[10] S.P. Economopoulos, C.L. Chochos, V.G. Gregoriou, J.K. Kallitsis, S. Barrau, G. Hadziioannou, Macromolecules 40 (2007) 921.
[11] J.H. Zou, L.W. Liu, H. Chen, S.I. Khondaker, R.D. McCullough, Q. Huo, L. Zhai, Adv. Mater. 20 (2008) 2055.
[12] Z.Y. Zhou, X.W. Chen, S.J. Holdcroft, Am. Chem. Soc. 130 (2008) 11711.
[13] F. Ouhib, A. Khoukh, J.B. Ledeuil, H. Martinez, J. Desbrieres, C. Dagron-Lartigau, Macromolecules 41 (2008) 9736.
[14] C.R. Craley, R. Zhang, T. Kowalewski, R.D. McCullough, M.C. Stefan, Macromol. Rapid Commun. 30 (2009) 11.
[15] S.A. Jenekhe, X.L. Chen, Science 283 (1999) 372.
[16] H.-A. Klok, S. Lecommandoux, Adv. Mater. 13 (2001) 1217.
[17] M. Lee, B.-K. Cho, W.-C. Zin, Chem. Rev. (2001) 101.
[18] D.M. Vriezema, J. Hoogboom, K. Velonia, K. Takazawa, P.C.M. Christianen, J.C. Maan, A.E. Rowan, R.J.M. Nolte, Angew. Chem., Int. Ed. 42 (2003) 772.
[19] B.W. Messmore, J.F. Hulvat, E.D. Sone, S.I.J. Stupp, Am. Chem. Soc. 126 (2004) 14452.
[20] B.D. Olsen, R.A. Segalman, Mater. Sci. & Eng. R-Reports 62 (2008) 37.
[21] J.S. Liu, E. Sheina, T. Kowalewski, R.D. McCullough, Angew. Chem., Int. Ed. 41 (2001) 329.
[22] M.C. Iovu, R. Zhang, J.R. Cooper, D.M. Smilgies, A.E. Javier, E.E. Sheina, T. Kowalewski, R.D. McCullough, Macromol. Rapid Commun. 28 (2007) 1816.
[23] M.C. Iovu, M. Jeffries-El, E.E. Sheina, J.R. Cooper, R.D. McCullough, Polymer 46 (2005) 8582.
[24] M.C. Iovu, E.E. Sheina, R.R. Gil, R.D. McCullough, Macromolecules 38 (2005) 8649.
[25] M.C. Iovu, C.R. Craley, M. Jeffries-EL, A.B. Krankowski, R. Zhang, T. Kowalewski, R.D. McCullough, Macromolecules 40 (2007) 4733.
[26] G. Sauvé, R.D. McCullough, Adv. Mater. 19 (2007) 1822.
[27] B. Boudouris, W.C.D. Frisbie, M.A. Hillmyer, Macromolecules 41 (2008) 67.
[28] M. Jeffries-El, G. Sauvé, R.D. McCullough, Macromolecules 38 (2005) 10346.
[29] J.S. Liu, R.D. McCullough, Macromolecules 35 (2002) 9882.
[30] A. Duda, S. Penczek, A. Kowalski, J. Libiszowski, Macromol. Symp. 153 (2000) 41.
[31] Ph. Leclère, M. Surin, P. Brocorens, M. Cavallini, F. Biscarini, R. Lazzaroni, Mater. Sci. & Eng. R-Reports 55 (2006) 1.
[32] F.J.M. Hoeben, P. Jonkheijm, E.W. Meijer, A.P.H.J. Schenning, Chem. Rev. 105 (2005) 1491.
[33] (a) J.A. Merlo, C.D.J. Frisbie, Phys. Chem. B 108 (2004) 19169;
(b) J.A. Merlo, C.D.J. Frisbie, Polym. Sci. B 41 (2003) 2674.
[34] (a) S. Hugger, R. Thomann, T. Heinzel, T. Thurn-Albrecht, Colloid Polym. Sci. 282 (2004) 932;
(b) H.C. Yang, S. Park, D. Kim, K. Oh, S. Magonov, K. Cho, T. Chang, Z. Bao, C.Y. Ryu, Polym. Prepr. 44 (2003) 333;
(c) H. Yang, T.J. Shin, L. Yang, K. Cho, C.Y. Ryu, Z. Bao, Adv. Funct. Mater. 15 (2005) 671;
(d) H.C. Yang, T.J. Shin, Z. Bao, C.Y. Ryu, J. Polym. Sci., Part B: Polym. Phys. 45 (2007) 1303.
[35] (a) M. Surin, Ph. Leclère, R. Lazzaroni, J.D. Yuen, G. Wang, D. Moses, A.J. Heeger, S. Cho, K. Lee, J. Appl. Phys. 100 (2006) 33712;
(b) S. Cho, K. Lee, J.D. Yuen, G. Wang, D. Moses, A.J. Heeger, M. Surin, R. Lazzaroni, J. Appl. Phys. 100 (2006) 33712.
[36] The fully-extended length of RRP3HT chains is estimated by multiplying the average degree of polymerization N by the length of a monomer unit l (0.387 nm), taking into account the head-to-tail linkage of RRP3HT. The radius of gyration of the PCL coil is estimated with $R_g = l \times (N/6)^{1/2}$, with l being 0.85 nm in *trans-trans* conformation.
[37] Note that ultrathin deposits of pure PCL in the same conditions show dendritic structures with about 10 nm-thick crystalline lamellae (unpublished results). See also: V.H. Mareau, R.E. Prud'homme, Macromolecules 38 (2005) 398.
[38] When tested on several FETs, we observe that bottom-contact FETs show less reproducible properties than top-contact FETs (e.g. some of the output characteristics of bottom-contact FETs display discontinuities in the I–V curves). These differences between the two types of devices likely arise from different interface morphologies at the gold electrodes-semiconducting (co)polymer thin film.
[39] J.F. Chang, B.Q. Sun, D.W. Breiby, M.M. Nielsen, T.I. Solling, M. Giles, I. McCulloch, H. Sirringhaus, Chem. Mater. 16 (2004) 4772.
[40] G.M. Wang, J. Swensen, D. Moses, A.J. Heeger, Appl. Phys. 93 (2003) 6137.
[41] D.M. DeLongchamp, R.J. Kline, E.K. Lin, D.A. Fischer, L.J. Richter, L.A. Lucas, M. Heeney, I. McCulloch, J.E. Northrup, Adv. Mater. 19 (2007) 833.
[42] I. McCulloch, M. Heeney, M. Chabinyc, L.D. DeLongchamp, R.J. Kline, M. Coelle, W. Duffy, D. Fischer, D. Gundlach, B. Hamadani, R. Hamilton, L. Richter, A. Salleo, M. Shkunov, D. Sporrowe, S. Tierney, W. Zhong, Adv. Mater. 21 (2009) 1091.
[43] (a) R.J. Kline, M.D. McGehee, E.N. Kadnikova, J.S. Liu, J.M.J. Fréchet, Adv. Mater. 15 (2003) 1519;
(b) R.J. Kline, M.D. McGehee, E.N. Kadnikova, J.S. Liu, J.M.J. Fréchet, M.F. Toney, Macromolecules 38 (2005) 3312.
[44] (a) A. Zen, J. Pflaum, S. Hirschmann, W. Zhuang, F. Jaiser, U. Asawapirom, J.P. Rabe, U. Scherf, D. Neher, Adv. Funct. Mater. 14 (2004) 757;
(b) P. Schilinsky, U. Asawapirom, U. Scherf, M. Biele, C.J. Brabec, Chem. Mater. 17 (2005) 2175.
[45] J.D. Yuen, R. Menon, N.E. Coates, E.B. Namdas, S. Cho, S.T. Hannahs, D. Moses, A.J. Heeger, Nat. Mater. 8 (2009) 572.

between the donor and acceptor, which gives influence to exciton dissociation and charge transport and/or collection [10,14]. In order to control the blend morphology, various methods have been developed, among which thermal annealing [8,10,15–18], and vapor annealing [9,19,20] are frequently adopted. Although these fabrication protocols lead to an optimum morphology, it is challenging to apply these methods to practical fabrications. Thermal annealing is not compatible with the use of flexible substrates with low glass transition temperature, and solvent vapor annealing is not suitable for real roll-to-roll processes for the dangers of solvent vapor [21,22]. Recent years, several groups have devoted themselves to modifying the blend morphology by annealing-free approaches. One of these approaches is the addition of "unfriendly" solvents such as t-butanol, anisole and so on into the P3HT solution [23,24]. In mixed solution, P3HT chains tend to accumulate and form crystalline aggregates owing to the poor solubility. However the increased aggregate size of P3HT shortens the solution's shelf lifetime [25] and restrains the mixing of blends. Therefore, it is necessary to create new processing procedures for the development of flexible low-cost PSCs with high performance. Since the first report on additive to improve the device performance by Bazan and co-workers [26], lots of researches have focused their attention on this subject. Sariciftci and co-workers pointed out solar cells fabricated with additive shown red-shifted absorption and an increased optical absorption coefficient; meanwhile, the charge carrier mobility and carrier equilibrium mobility were also improved [27]. While Heeger and coworkers put their attention on investigating the mechanism of the modified morphology via introduction of a small concentration of additive, they interpreted that the modified morphology was attributed to the selective solubility as well as the difference of boiling points between host solvent and additive, such that the additive prevents isolated fullerene molecules from being dissolved throughout polymer phases and leaves more room for P3HT to undergo the crystallization process during the film-forming process [28,29]. However, the mechanism only concerns the role that the additive plays during the film-forming process and it gives no explanation on how the scale of phase segregation is tuned by the additive.

In this work, the role of the additive is revealed by combining the crystallization process of P3HT and the phase separation kinetics of P3HT/PCBM blends. Results show there are two different roles that the additive plays in the solution and during the film-forming process, respectively. First, the *n*-dodecylthiol improves the aggregation state of P3HT chains in the solution, which facilitates the coil-to-rod transformation, a premise condition for P3HT crystallization, and thus gives an enhancement of crystalline ability to P3HT. Secondly, *n*-dodecylthiol diminishes the influence of PCBM on the P3HT molecular interaction which benefits the P3HT crystallization, and the enhanced P3HT crystallinity reduces the PCBM amount resided in the amorphous regions of P3HT, then promotes the aggregation of PCBM which tunes the scale of phase segregation during the film-forming process. Thus, an increased P3HT crystallinity and a commensurate scale of phase separation balancing for exciton dissociation and charge transport and/or collection are finally obtained by adjusting the amount of additive, which results in an almost threefold increase in device efficiencies when the volume fraction of additive is 2.0% compared with reference devices without any additive in the photoactive layer as a consequence. Our conclusion suggests that an important characteristic of adding the additive is to promote the dispersion of P3HT in solution rather than the aggregation of P3HT, which gives rise to an increase of the solution's shelf lifetime and benefits the application of industrial mass production.

2. Experimental section

2.1. Materials

Regioregular HT-HT P3HT (>98.5%; HT: head-to-tail; Mw = 68 kDa) was purchased from Nichem Fine Technology Co. Ltd. PCBM (99.0%) was purchased from Solenne Co. Ltd. *n*-Dodecylthiol was purchased from Sigma–Aldrich Co. Ltd. Chlorobenzene was purchased from Beijing Chemical, China. All used as received.

2.2. Sample preparation

Samples for Dynamic light scattering analysis were prepared by dissolving P3HT in chlorobenzene to form a 10 mg ml^{-1} solution. The solution was sat for 12 h at r.t. Followed by blending with different volume fraction of *n*-dodecylthiol. Solutions for measurement were filtered with 450 nm PTFE membrane. The solution for spin-coating was prepared as followings: P3HT was first dissolved in chlorobenzene to make 10 mg ml^{-1} solution, followed by blending with *n*-dodecylthiol after 12 h, then PCBM (8 mg ml^{-1}) was added into the solution. The solution was stirring for 3 h prior to use.

2.3. Fabrication of solar cells

The solar cell devices used here were prepared on glass/ITO substrates. The substrates were cleaned by ultrasonic treating in detergent and deionized water then dried at 110 °C for 40 min. 40-nm-thick poly(ethylenedioxythiophene):poly(styrenesulfonate) (PEDOT:PSS, Baytron P4083) layer was spin-coated on the ITO glass and dried at 120 °C for 30 min. 90-nm-thick active layer was then deposited by spin-coating P3HT/PCBM blends under an inert atmosphere. Finally, the samples were transferred into an evaporator, 1-nm-thick LiF and 100-nm-thick Al electrodes were deposited by evaporation, respectively. The active surface area of typical device is 0.12 cm^2.

2.4. Characterization

UV–vis absorption spectroscopy (UV–vis): Solution and solid-state UV–vis absorption spectra were recorded with a Lambda 750 spectrometer (Perkin–Elmer, Wellesley, MA).

Grazing incidence X-ray diffraction (GIXD): GIXD patterns were obtained on Bruker D8 Discover Reflector (k = 1.78897 Å, Co source) under 40 kV and 40 mA tube

current. The X-ray profile was recorded from 3° to 30° with a step of 0.04° using automatic slits.

Atomic force microscope (AFM): The surface morphology of the films was characterized by SPA300HV equipped with a SPI3800N Probe Station (Seiko Instruments Inc., Japan) in tapping mode.

Transmission electron microscope (TEM): TEM was performed on JEOL JEM-1011 transmission electron microscope under 100 kV.

Dynamic light scattering (DLS): DLS of P3HT aggregates in solution was performed using a light scattering goniometer (BI200-SM, Brookhaven Instruments) equipped with a digital autocorrelator (BI-9000 AT, Brookhaven Instruments) and an Ar ion laser (Model 95, Lexel Laser, Inc.).

Viscosity measurement: Viscosity measurements were carried out with ARES G2 rotational rheometer. For all presented measurements, the P3HT/chlorobenzene (10 mg/ml) solution with and without *n*-dodecylthiol was fed into the cylinder rheometer and measured under constant angular shear frequency ($\omega = 1\ S^{-1}$) at 25 °C.

Photoluminescence spectroscopy (PL): PL emission spectrum was recorded with Hitachi F-4500 spectrophotometer equipped with a 150 W xenon lamp at room temperature.

Device parameter measurements: Current density–voltage (*J–V*) curves of the photovoltaic devices under white light illumination were measured using a computer-controlled Keithley 236 source meter.

3. Results and discussion

3.1. Modify the film morphology by the addition of n-dodecylthiol

The addition of *n*-dodecylthiol to P3HT/PCBM solution prior to spin-coating was found to significantly enhance the P3HT self-organization ability. The self-organization ability can be defined as the process of transformation from disorder to order, known as crystallizing, which can be divided into two mechanism-controlled processes: intrachain mechanism of coil-to-rod transformation to form lamellae, and interchain mechanism of lamellae stacking into ordered structure as suggested by Hotta and co-workers [30]. Thus, the self-organization ability could be viewed as the tendency of P3HT crystallizing into ordered structure. This enhanced self-organization ability led to improved P3HT crystallinity and intensified phase separation extent of P3HT/PCBM in films.

The enhanced self-organization ability of P3HT was confirmed by UV–vis absorption spectra. The UV–vis absorption spectra of the P3HT/PCBM blend films with and without *n*-dodecylthiol are shown in Fig. 1(A). Two bands of peaks are clearly indexed: one is the peak around 334 nm which corresponds to the absorption PCBM, the other is a broad peak consisting of a main absorption at 520 nm and two vibronic shoulder absorptions at 558 nm and 607 nm, which represents the contribution of P3HT. The shoulder mentioned above was not distinguishably observed for the as-produced film (without additive in solution). After adding of *n*-dodecylthiol, the two vibronic

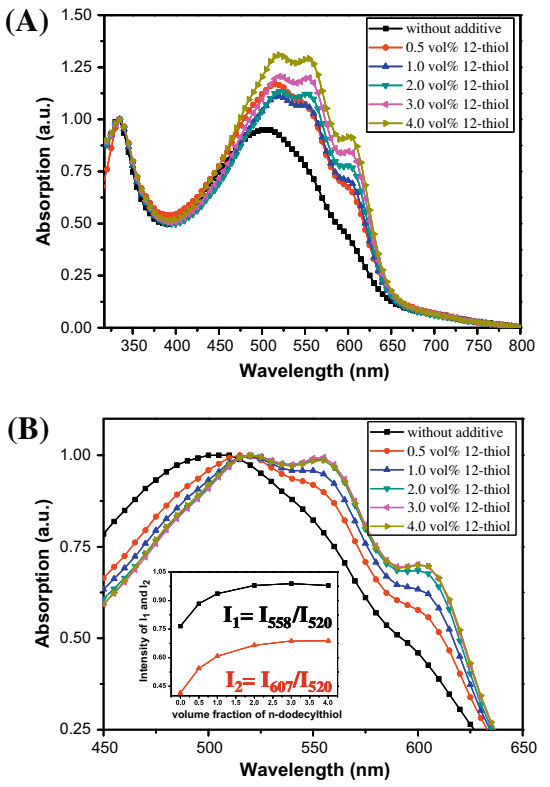

Fig. 1. (A) Absorption spectra for P3HT/PCBM blend films with different volume fraction (0.5%, 1.0%, 2.0%, 3.0% and 4.0%) of *n*-dodecylthiol. (B) Magnified image normalized at the maximum absorbance of the specified regions; Inset is the change trends of $I_1$and I_2, $I_1 = I_{558}/I_{520}$; $I_2 = I_{607}/I_{520}$; I_{520}, I_{558}, I_{607} represent the intensity of the peak located at 520 nm, 558 nm and 607 nm, respectively.

shoulder absorptions became visible. It is well known that the shoulder at 558 nm is attributed to the absorption of extended conjugation of P3HT in the solid-state [31] and the other one at 607 nm comes from the interchain stacking of P3HT [32]. Increasing the concentration of *n*-dodecylthiol from 0% to 4.0%, the ratios of peak intensity I_1 and I_2 (To quantitatively compare the aggregating state of P3HT, the spectra with different *n*-dodecylthiol content were normalized according to the peak intensity around 520 nm, and $I_1 = I_{558}/I_{520}$; $I_2 = I_{607}/I_{520}$; I_{520}, I_{558}, I_{607} represent the intensity of the peak located at 520 nm, 558 nm and 607 nm, respectively.) increased gradually as shown in the inset of Fig. 1(B). The change trends of I_1 and I_2 suggested the increased planarization and stabilization of P3HT chains, and the enhanced ordered packing of P3HT backbones resulted from the interchain π–π stacking, respectively [33]. At the same time, the intensity of the absorption band associated with P3HT also increased, which was attributed to the enhanced absorption coefficient of the film due to the growth of P3HT crystals promoted by the enhanced P3HT self-organization ability [18,34].

The enhanced P3HT self-organization ability after the addition of *n*-dodecylthiol aided the evolution of a well-ordered P3HT crystallite was also proved by the GIXD result

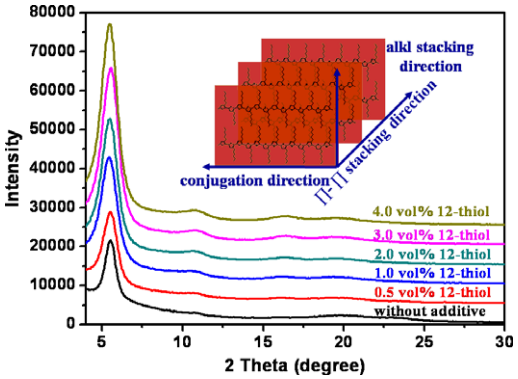

Fig. 2. GIXD spectra for P3HT/PCBM films deposited from different volume fraction of *n*-dodecylthiol. The inset shows the structure and orientation of the thiophene crystallites.

as shown in Fig. 2. All films showed an intense (1 0 0) diffraction peak at $2\theta = 5.4°$, corresponding to an ordered lamellar structure with an interlayer spacing, which was formed by parallel stacks of P3HT main chains that were separated by the alkyl side chains, as shown in the inset of Fig. 2 [22]. The intensity of the peak at $2\theta = 5.4°$ was proportional to the number of P3HT crystalline nanodomains and, in a certain view point, to the crystallinity of the investigated samples when the films had same area and thickness [35]. Judging from the increasing intensity of this peak with the amount of *n*-dodecylthiol, an increased crystallinity of P3HT could be traced, which resulted from the enhanced self-organization ability due to the addition of *n*-dodecylthiol. However, diffraction peaks caused by PCBM were barely seen in the diffractogram of the blend films both with and without *n*-dodecylthiol. Thus, adding of *n*-dodecylthiol only promoted the crystallization of P3HT but had little influence on the crystallization of PCBM.

Bright-field TEM which has been used to directly reveal the phase segregation in composite P3HT:PCBM films was used in our experiment. The TEM images of the P3HT/PCBM blend film were shown in Fig. 3. The dark areas of the images were thought to be PCBM-rich domains because of their relative higher electron scattering density as compared with P3HT [10]. As-produced film (Fig. 3(a)) was apparently homogeneous and the phase separation between P3HT and PCBM could hardly be distinguished. After the addition of *n*-dodecylthiol, fibrillar P3HT crystals, which were relatively brighter as compared to the background, became longer and its number also increased. In addition, the PCBM-rich domains grew up gradually, suggesting an intensified phase separation after adding *n*-dodecylthiol.

Based on the above observations, the conclusion that adding *n*-dodecylthiol to P3HT/PCBM blend system could improve the self-organization ability of P3HT to form crystallites and increase the scale of phase segregation was strongly confirmed. However, the thing we mostly care about is the mechanism behind these phenomena.

3.2. Mechanism for improving the P3HT crystallinity and enhancing the P3HT/PCBM phase separation extent

In this section, a proposed mechanism was put forward to explain the improved self-organization ability of P3HT and the enhanced scale of phase segregation. Experiments showed that these phenomena should be attributed to two functions of *n*-dodecylthiol in different stages: (1) reduced the P3HT chains entanglement in solution, which promoted the P3HT self-organization ability and thus benefited the crystallization of P3HT; (2) diminished the influence of PCBM on the P3HT molecular interaction, and promoted the aggregation of PCBM to form phase segregation during the film-forming process.

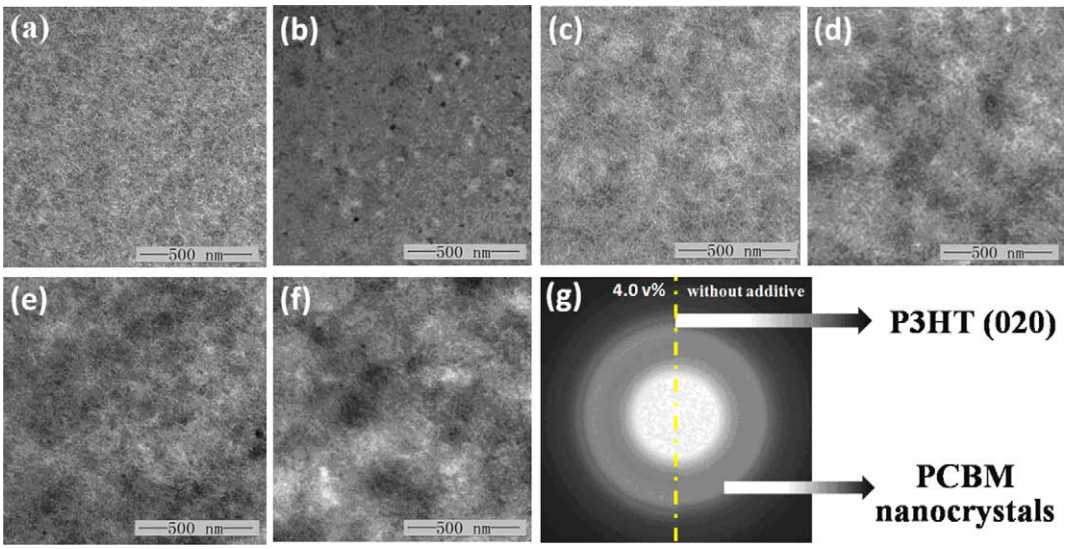

Fig. 3. TEM images of P3HT/PCBM blend films with different volume fraction of *n*-dodecylthiol: (a) 0.0%, (b) 0.5%, (c) 1.0%, (d) 2.0%, (e) 3.0% and (f) 4.0%. SAED patterns (g) obtained from P3HT/PCBM films with 0.0% and with 4.0% *n*-dodecylthiol.

3.3. Reducing the extent of entanglement among P3HT chains in solution

As is well known, it is not easy for P3HT to self-organize during the crystallizing process because of the strong chains entanglement [36]. Clarifying the effects of chains entanglement on aggregation and/or crystallization of P3HT is quite necessary for further understanding the mechanism of additive in this case. In order to exactly present the aggregation states of P3HT in solution, P3HT/chlorobenzene solution with and without additive were investigated by DLS and UV–vis. The DLS result of P3HT/clorobenzene solution showed two peaks in Fig. 4(A). The aggregation state of P3HT in solution has been investigated in recent years, the experimental results indicated the presence of two coexisting phases: P3HT in solution and P3HT in aggregates [30]. So the peak centered at 6.5 nm should be assigned to the scattering signal of P3HT single chain, the other one centered at 170 nm corresponded to the signal of P3HT aggregates. The aggregates were actually in amorphous state, because no absorption peak at 607 nm was observed in the combining UV–vis detection (Fig. 4(B)) [37]. After the addition of *n*-dodecylthiol, the dispersion of P3HT chains in chlorobenzene was improved. As shown in Fig. 4(A), the averaged size of P3HT aggregates reduced from 170 nm to 134 nm and 75 nm after adding 2.0% and 4.0% *n*-dodecylthiol, respectively. Whereas the peak position of single P3HT chains remained unchanged, but its intensity increased which hinted more single P3HT chains were obtained.

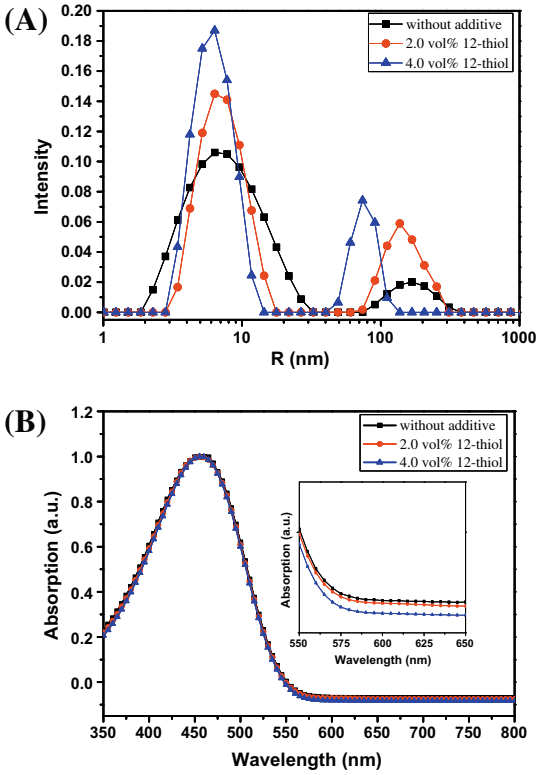

Fig. 4. (A) DLS spectra for P3HT/chlorobenzene solutions with different volume fraction of *n*-dodecylthiol. (B) Absorption spectra for P3HT/chlorobenzene solutions with different volume fraction of *n*-dodecylthiol. The insets show magnified images of the specified regions.

The influence of the additive on the solution viscosity was also investigated. The viscosity of P3HT/chlorobenzene solution is 1.12 cp, it reduced to 1.05 cp after the *n*-dodecylthiol (has higher viscosity than chlorobenzene) was added. The decrease amplitude was 6.25% (Table 1). As we know, the interaction among polymer chains affects the solution viscosity. A viscosity decrease of the solution means the physical cross-linking among the polymer chains reduced, i.e., the polymer coils have a tendency to not interact with each other [25]. After *n*-dodecylthiol was added, the entanglements among polymer chains became disentangled. As a result, some of P3HT chains escaped from the amorphous aggregates and randomly distributed as single molecule or smaller aggregate in the solution, which resulted in a reduced viscosity.

The changed states of P3HT in solution had a profound effect on the crystallinity of P3HT film. As we can see from Fig. 5(A), red-shifts in parallel with more pronounced vibronic peaks in P3HT film absorption spectra were observed after the addition of *n*-dodecylthiol, which was attributed to the enhanced self-organization ability of P3HT. As a result, P3HT formed crystallites more easily and thus resulted in a high absorption coefficient. Meanwhile, more intensive peaks in GIXD of P3HT films (Fig. 5(B)) also indicated higher crystallinity of P3HT after the addition of *n*-dodecylthiol. AFM height images of P3HT films with different amount of *n*-dodecylthiol were also shown in Fig. 5(C). The film casted from the solution contained *n*-dodecylthiol showed more fibrillar P3HT crystals running across the surface and had higher rms value. All these data demonstrated that the reduced P3HT aggregate size and the increased number of P3HT single chains after the addition of *n*-dodecylthiol in solution could enhance the crystallinity of P3HT.

It has been elucidated that the crystallization of P3HT is fundamentally driven by a single chain mechanism. A coil-to-rod transformation in P3HT main chain conformation followed by interchain π–π stacking is thought to be the precondition toward crystallization [30]. Consequently, rod-like rigid conformation of P3HT is quite necessary for production of crystallinity P3HT films. However, the chains entanglement certainly reduces the mobility of P3HT and thus hinders its coil-to-rod transformation. While *n*-dodecylthiol mixed with chlorobenzene could aid the dispersion of P3HT molecules. As a result, some of P3HT chains

Table 1
Viscosity of chlorobenzene (CB), *n*-dodecylthiol (12-thiol), P3HT/chlorobenzene solution (P3HT/CB, the concentration of P3HT was 10 mg/ml) and P3HT/chlorobenzene/*n*-dodecylthiol solution (P3HT/CB/12-thiol, the volume fraction of *n*-dodecylthiol was 4.0% and the concentration of P3HT was 10 mg/ml).

	CB	12-Thiol	P3HT/CB	P3HT/CB/12-thiol
Viscosity (25 °C cp)	0.73	2.53	1.12	1.05

The viscosity of chlorobenzene and *n*-dodecylthiol are from Handbook of Chemistry and Physics, 82th ed.

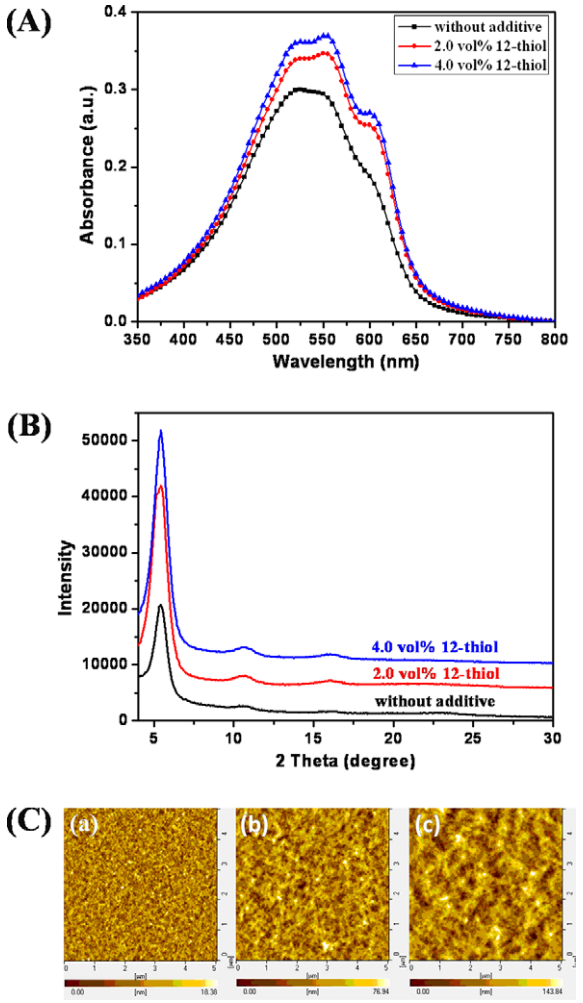

Fig. 5. (A) Absorption spectra and (B) GIXD spectra for P3HT films deposited from different volume fraction of *n*-dodecylthiol. (C) Tapping mode AFM height images of P3HT/PCBM blend films with different volume fraction of *n*-dodecylthiol: (a) 0.0%, (b) 2.0% and (c) 4.0%. The root-mean-square value is (a) 2.85 nm, (b) 13.22 nm and (c) 26.67 nm, respectively.

escaped from the amorphous aggregates and randomly distributed as single molecules or smaller aggregates in the solution. This speculation has been supported by DLS and in Fig. 4(A). Both the peak intensity of the aggregates and of the single chains were enhanced after adding *n*-dodecylthiol to solution, suggesting that some of the original larger-size aggregates transformed into more small aggregates and more single chains, which was also consist with the viscosity measurements. Due to the decreased extent of chains entanglement, P3HT single chains gained more freedom in rotation or motion, and also gave rise to the possibility of coil-to-rod transformation. In addition, with the evaporation of chlorobenzene, the fraction of *n*-dodecylthiol increased. Owning to the low solubility of P3HT in it (Table 2) (the solubility of P3HT and PCBM were obtained using the method depicted by Yang et al. [38]), P3HT would be promoted to aggregate to avoid the solvent.

Table 2
Boiling points, vapor pressure and P3HT, PCBM solubility of chlorobenzene and *n*-dodecylthiol.

Solvent	Boiling points (°C)	Vapor pressure at 25 °C (Pa)	S_{P3HT} (mg/ml)	S_{PCBM} (mg/ml)
Chlorobenzene	132	1573	>20.0	>20.0
n-Dodecylthiol	266–283	1	<0.2	1.8

Boiling points and vapor pressure are from Handbook of Chemistry and Physics, 82th ed.

During this process, the P3HT with rod conformation would get π–π stacking and then formed microcrystalline. The fraction of the polymer in the ordered aggregated phase is determined by the fraction of P3HT chains with rod conformation state at a given temperature [30]. Thus, the reduced entanglement extent among P3HT chains caused by the addition of *n*-dodecylthiol promoted the crystallinity of P3HT.

3.4. Diminishing the influence of PCBM and enhancing the phase segregation extent during the film-forming process

In P3HT/PCBM blend system, PCBM aggregation and phase separation extent during the film-forming process also played crucial role in energy conversion efficiency. In this case, *n*-dodecylthiol selectively dissolved PCBM and had a relative higher boiling point compared with chlorobenzene. These differences caused a change in phase separation kinetics of P3HT/PCBM blend system. The addition of *n*-dodecylthiol in P3HT/PCBM blend would enhance the discrepancy in precipitation sequence between P3HT and PCBM. During the film-forming process, chlorobenzene evaporated first, then P3HT precipitated prior to PCBM and formed aggregates. Due to the easiness of conformation transition and without the disturbance of PCBM, the P3HT crystallinity would be enhanced [34], i.e., the ratio of amorphous P3HT reduced. The Debye–Scherrer rings observed in the selected area electron diffraction (SAED) of P3HT shown in Fig. 4(G) confirmed the enhanced crystallinity of P3HT after the addition of *n*-dodecylthiol, which was consistent with the crystallinity change of P3HT after annealing treatment by Loos and co-workers [39]. While in P3HT/PCBM composite film, PCBM resided only in the amorphous P3HT domains [40]. So the enhanced P3HT crystallinity decreased the amount of PCBM in it after the addition of *n*-dodecylthiol, which resulted in a large scale of phase separation. When the volume fraction of *n*-dodecylthiol increased, this phenomenon was intensified and consequently a larger scale of phase separation was obtained.

3.5. Optimizing the n-dodecylthiol content for high performance photovoltaic devices

Photovoltaic devices based on P3HT/PCBM blend films with different *n*-dodecylthiol content were made according to standard ITO/PEDOT:PSS/P3HT:PCBM/LiF/Al architecture. The current density–voltage (*I*–*V*) curves of the devices are shown in Fig. 6(A). The open-circuit voltage

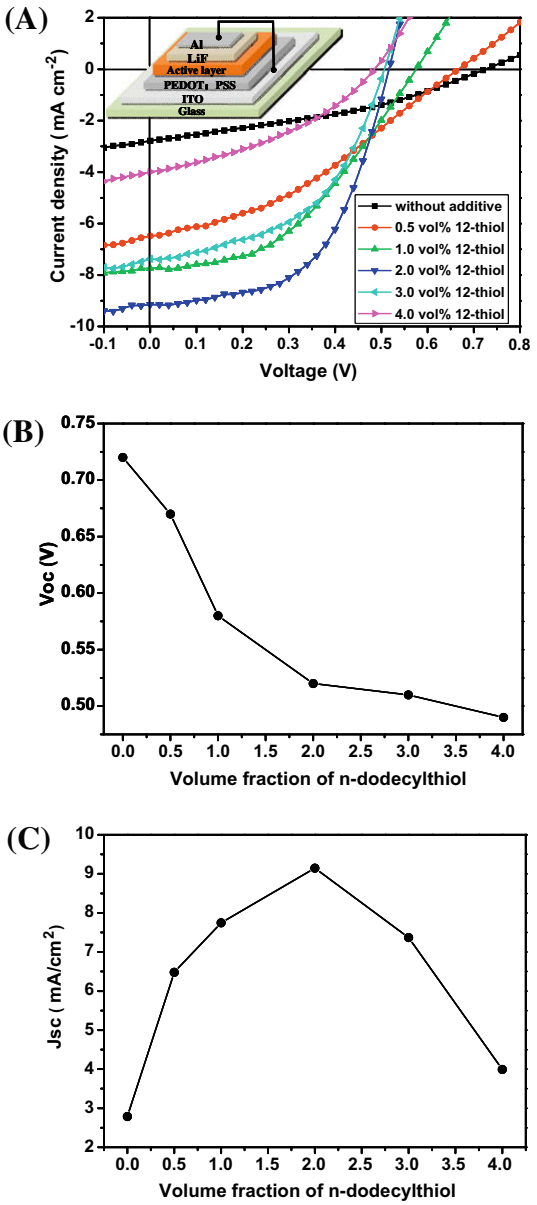

Fig. 6. (A) *I–V* curves for devices processed from P3HT/PCBM with different volume fraction of *n*-dodecylthiol under AM 1.5 illumination. Inset shows the structure of the organic solar cell. (B) Plot of V_{oc} and (C) J_{sc} vs. *n*-dodecylthiol content under AM 1.5G illumination.

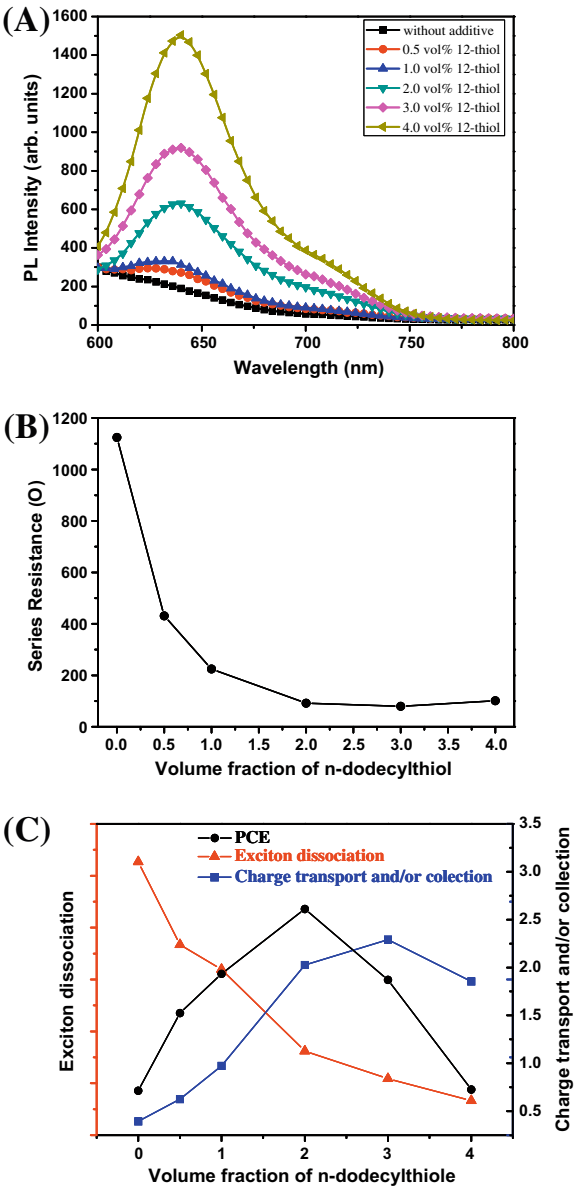

Fig. 7. (A) Photoluminescence (PL) quenching of P3HT/PCBM films with different volume fraction of *n*-dodecylthiol. Intensities of the spectra have been normalized according to the excitation at 520 nm. (B) Plot of series resistance vs. *n*-dodecylthiol content under AM 1.5G illumination. (C) Plots of exciton dissociation efficiency, carrier transport and/or collection efficiency, and PCE vs. *n*-dodecylthiol content under AM 1.5G illumination.

(V_{OC}) dropped monotonically with *n*-dodecylthiol content (Fig. 6(B)) from 0.68 V to 0.49 V. Generally, V_{oc} of polymer solar cells is dominated by the difference in energy levels between the HOMO of donor and the LUMO of the acceptor [20]. The addition of *n*-dodecylthiol increased the P3HT conjugation length on average, as a result decreased the HOMO energy level of P3HT, which resulted in decreasing in V_{oc} for the photovoltaic device. Unlike V_{oc}, the short-circuit current density (J_{sc}) presented a quite different changing mode against *n*-dodecylthiol content as shown in Fig. 6(C). An up-down mode with peak value of 9.1 mA cm^{-2} at 2.0% content was presented. A better fitting with solar emission spectrum and an improved charge transport after adding *n*-dodecylthiol may partially account for the improvement of J_{sc}. However, when the volume fraction of *n*-dodecylthiol beyond 2.0%, it would contaminate the J_{sc} for a large phase separation which was not suit for the exciton dissociation. To investigate the relationship between phase separation extent and exciton dissociation, photoluminescence was conducted

by exciting at 520 nm. The photoluminescence intensity increased with *n*-dodecylthiol as shown in Fig. 7(A), indicating that fewer excitons were able to diffuse to the interface before returning to base. In other view of point, the average interface distance between P3HT and PCBM turned out to be longer [41] as concluded above. The enhanced phase separation extent played a negative role for exciton dissociation, but benefited the charge transport and/or collection. The series resistance of the device calculated from the *I*–*V* curve in dark (Fig. 7(B)) decreased significantly after adding *n*-dodecylthiol, which is a signal of the efficiency of charge transport and/or collection [42]. A relative larger scale in phase separation would reduce the probability of charge recombination during charge transport and/or collection [20,43]. To establish the relationship between the device performance and the size of phase separation, plot of PCE vs. *n*-dodecylthiol content was made and shown in Fig. 7(C). Two other curves which represent exciton dissociation ability (the reciprocal of intensity of PL) and charge transport and/or collection ability (the reciprocal of series resistance), respectively, were also shown. At low volume fraction of *n*-dodecylthiol (<2.0%), corresponding to the small-scale phase separation, the PCE was limited by poor charge transport and/or collection, and charges were more likely to meet an opposite charge to recombine before reaching the electrode. While at high volume fraction of *n*-dodecylthiol (>2.0%), corresponding to large scale phase separation, exciton dissociation was impeded. When *n*-dodecylthiol was 2.0%, corresponding to intermediate-scale phase separation, an optimum balance between exciton dissociation and charge transport and/or collection was obtained, resulting in a PCE peak value of 2.61%, which was almost threefold increase in device efficiencies compared with reference devices without any additive in the photoactive layer as a consequence. This phenomenon is consistent with the dynamical Monte Carlo modelling of organic solar cells [44].

4. Conclusions

In this work, *n*-dodecylthiol was added to P3HT/PCBM solution to improve the P3HT crystallinity and enhance the P3HT/PCBM phase separation. It was shown that *n*-dodecylthiol played important role both in the solution and during the film-forming process. In solution, *n*-dodecylthiol reduced the P3HT chains entanglement which facilitated the P3HT coil-to-rod transformation and enhanced the P3HT crystallinity. During the film-forming process, due to the introduction of *n*-dodecylthiol, the P3HT crystallinity was enhanced, and it reduced the PCBM amount which dissolved in the amorphous regions of P3HT, then promoted the aggregation of PCBM, which contributed to the controlled scale of phase segregation. On these bases, an increased P3HT crystallinity and a commensurate scale of phase separation balancing for exciton dissociation and charge transport and/or collection were finally obtained by adjusting the amount of *n*-dodecylthiol, which resulted in an almost threefold increase in device efficiencies when the volume fraction of additive is 2.0% compared with reference devices without any additives in the photoactive layer as a consequence.

Acknowledgements

This work was financially supported by the National Natural Science Foundation of China (20621401, 20834005), the Chinese Academy of Sciences (KJCX2-YW-M11) and the Ministry of Science and Technology of China (2009CB930603, 2009CB623604).

References

[1] P.W.M. Blom, V.D. Mihailetchi, L.J.A. Koster, D.E. Markov, Advanced Materials 19 (2007) 1551.
[2] S. Gunes, H. Neugebauer, N.S. Sariciftci, Chemical Reviews 107 (2007) 1324.
[3] B.C. Thompson, J.M.J. Frechet, Angewandte Chemie-International Edition 47 (2008) 58.
[4] F.C. Krebs, Organic Electronics 10 (2009) 761.
[5] S.H. Eom, S. Senthilarasu, P. Uthirakumar, S.C. Yoon, J. Lim, C. Lee, H.S. Lim, J. Lee, S.H. Lee, Organic Electronics 10 (2009) 536.
[6] C.W. Tang, Applied Physics Letters 48 (1986) 183.
[7] J.J.M. Halls, C.A. Walsh, N.C. Greenham, E.A. Marseglia, R.H. Friend, S.C. Moratti, A.B. Holmes, Nature 376 (1995) 498.
[8] W.L. Ma, C.Y. Yang, X. Gong, K. Lee, A.J. Heeger, Advanced Functional Materials 15 (2005) 1617.
[9] G. Li, V. Shrotriya, J.S. Huang, Y. Yao, T. Moriarty, K. Emery, Y. Yang, Nature Materials 4 (2005) 864.
[10] X.N. Yang, J. Loos, S.C. Veenstra, W.J.H. Verhees, M.M. Wienk, J.M. Kroon, M.A.J. Michels, R.A.J. Janssen, Nano Letters 5 (2005) 579.
[11] G. Dennler, N.S. Sariciftci, R. Schwodiauer, S. Bauer, H. Reiss, Journal of Materials Chemistry 16 (2006) 1789.
[12] H. Hoppe, N.S. Sariciftci, Journal of Materials Research 19 (2004) 1924.
[13] Y.H. Chang, S.R. Tseng, C.Y. Chen, H.F. Meng, E.C. Chen, S.F. Horng, C.S. Hsu, Organic Electronics 10 (2009) 741.
[14] H. Xin, F.S. Kim, S.A. Jenekhe, Journal of the American Chemical Society 130 (2008) 5424.
[15] L.H. Nguyen, H. Hoppe, T. Erb, S. Gunes, G. Gobsch, N.S. Sariciftci, Advanced Functional Materials 17 (2007) 1071.
[16] Y. Kim, S.A. Choulis, J. Nelson, D.D.C. Bradley, S. Cook, J.R. Durrant, Applied Physics Letters 86 (2005).
[17] F. Padinger, R.S. Rittberger, N.S. Sariciftci, Advanced Functional Materials 13 (2003) 85.
[18] Y. Kim, S. Cook, S.M. Tuladhar, S.A. Choulis, J. Nelson, J.R. Durrant, D.D.C. Bradley, M. Giles, I. McCulloch, C.S. Ha, M. Ree, Nature Materials 5 (2006) 197.
[19] Y. Zhao, Z.Y. Xie, Y. Qu, Y.H. Geng, L.X. Wang, Applied Physics Letters 90 (2007) 43504.
[20] G. Li, Y. Yao, H. Yang, V. Shrotriya, G. Yang, Y. Yang, Advanced Functional Materials 17 (2007) 1636.
[21] S. Berson, R. De Bettignies, S. Bailly, S. Guillerez, Advanced Functional Materials 17 (2007) 1377.
[22] Y.M. Chang, L. Wang, Journal of Physical Chemistry C 112 (2008) 17716.
[23] S. Samitsu, T. Shimomura, S. Heike, T. Hashizume, K. Ito, Macromolecules 41 (2008) 8000.
[24] A.J. Moule, K. Meerholz, Advanced Materials 20 (2008) 240.
[25] M. Koppe, C.J. Brabec, S. Heiml, A. Schausberger, W. Duffy, M. Heeney, I. McCulloch, Macromolecules 42 (2009) 4661.
[26] J. Peet, C. Soci, R.C. Coffin, T.Q. Nguyen, A. Mikhailovsky, D. Moses, G.C. Bazan, Applied Physics Letters 89 (2006) 252105.
[27] A. Pivrikas, P. Stadler, H. Neugebauer, N.S. Sariciftci, Organic Electronics 9 (2008) 775.
[28] Y. Yao, J.H. Hou, Z. Xu, G. Li, Y. Yang, Advanced Functional Materials 18 (2008) 1783.
[29] J.K. Lee, W.L. Ma, C.J. Brabec, J. Yuen, J.S. Moon, J.Y. Kim, K. Lee, G.C. Bazan, A.J. Heeger, Journal of the American Chemical Society 130 (2008) 3619.
[30] S. Rughooputh, S. Hotta, A.J. Heeger, F. Wudl, Journal of Polymer Science Part B-Polymer Physics 25 (1987) 1071.
[31] N. Kiriy, E. Jahne, H.J. Adler, M. Schneider, A. Kiriy, G. Gorodyska, S. Minko, D. Jehnichen, P. Simon, A.A. Fokin, M. Stamm, Nano Letters 3 (2003) 707.

[32] H. Sirringhaus, P.J. Brown, R.H. Friend, M.M. Nielsen, K. Bechgaard, B.M.W. Langeveld-Voss, A.J.H. Spiering, R.A.J. Janssen, E.W. Meijer, P. Herwig, D.M. de Leeuw, Nature 401 (1999) 685.
[33] P.J. Brown, D.S. Thomas, A. Kohler, J.S. Wilson, J.S. Kim, C.M. Ramsdale, H. Sirringhaus, R.H. Friend, Physical Review B 67 (2003) 64203.
[34] T. Erb, U. Zhokhavets, G. Gobsch, S. Raleva, B. Stuhn, P. Schilinsky, C. Waldauf, C.J. Brabec, Advanced Functional Materials 15 (2005) 1193.
[35] H.C. Yang, T.J. Shin, L. Yang, K. Cho, C.Y. Ryu, Z.N. Bao, Advanced Functional Materials 15 (2005) 671.
[36] R.H. Colby, M. Rubinstein, J.L. Viovy, Macromolecules 25 (1992) 996.
[37] J. Clark, C. Silva, R.H. Friend, F.C. Spano, Physical Review Letters 98 (2007) 206406.
[38] L.G. Li, H.W. Tang, H.X. Wu, G.H. Lu, X.N. Yang, Organic Electronics 10 (2009) 1334.
[39] S.S. van Bavel, E. Sourty, G. de With, J. Loos, Nano Letters 9 (2009) 507.
[40] J.Y. Kim, D. Frisbie, Journal of Physical Chemistry C 112 (2008) 17726.
[41] A.L. Ayzner, D.D. Wanger, C.J. Tassone, S.H. Tolbert, B.J. Schwartz, Journal of Physical Chemistry C 112 (2008) 18711.
[42] C.J. Ko, Y.K. Lin, F.C. Chen, Advanced Materials 19 (2007) 3520.
[43] A.R. Campbell, J.M. Hodgkiss, S. Westenhoff, I.A. Howard, R.A. Marsh, C.R. McNeill, R.H. Friend, N.C. Greenham, Nano Letters 8 (2008) 3942.
[44] P.K. Watkins, A.B. Walker, G.L.B. Verschoor, Nano Letters 5 (2005) 1814.

that this behavior is very different from that of a vacuum-deposited film of pentacene with no side chains, showing an increased behavior of the mobility with increasing T_a [10]. The annealing effect is found to suppress both the development of the cracks and the increase of the off-current with time in air under ambient pressure. It is suggested that the cracks act as trapping sites of moisture and/or oxygen for the off-current flow.

A top contact FET structure, shown in Fig. 1, was used in our study. A solution-processed polymer showing the low current leakage and negligible hysteresis, poly(4-vinylphenol) (PVP) mixed with methylated poly(melamine-co-formaldehyde) (MMF) of 125 wt.% as a cross-linker [11], was selected as a gate insulator. The PVP with MMF, dissolved in propylene glycol methyl ether acetate (PGMEA) in 10 wt.%, was spin-coated on the top of the pre-patterned ITO gate electrode, baked at 100 °C for 1 min to remove any residual PGMEA, and subsequently baked for 5 min at 200 °C to produce thermal cross-linking in the PVP layer. The thickness of the cross-linked PVP film was about 540 nm and the capacitance per unit area was 6.4 nF/cm^2. A solution of the TIPS-pentacene, dissolved in 1,2-dichlorobenzene (1,2-DCB) in 1.0 wt.%, was drop-casted on the top of the PVP insulator and was baked at 60 °C for 1 min to evaporate the 1,2-DCB solvent. The baking temperature of 60 °C is known to improve the crystallinity of the TIPS-pentacene film itself [6]. It should be noted that the cross-linked PVP layer is chemically inert against the 1,2-DCB solvent used for the TIPS-pentacene. The source and drain electrodes were prepared on the TIPS-pentacene film using gold (Au) at the deposition rate of 0.1 nm/s. The thickness of the Au electrode was 80 nm. The length (L) and the width (W) of the channel were 50 and 2000 μm, respectively. The fabricated TIPS-pentacene FETs were annealed up to 150 °C to examine the mobility enhancement, the crack development and the resulting morphological change, and the crystallinity in the TIPS-pentacene film. After thermal annealing, the TIPS-pentacene FETs were stored in air under atmospheric pressure for 4000 h to determine how the electrical properties of the TIPS-pentacene FETs change with time. The electrical measurements were carried out using a semiconductor parameter analyzer (HP4155A) at room temperature.

We first describe the crack development and the crystallinity of the TIPS-pentacene film prepared on the cross-linked PVP insulator as a function of the annealing temperature T_a. As shown in the optical microscopic (OM) images in Fig. 2, it is clear that no cracks were developed when annealed at temperatures below 60 °C. As T_a increases further beyond 60 °C, cracks were developed and more propagated. This may result from the inelastic stress built up during the thermal annealing above 60 °C. In contrast to a vacuum-deposited pentacene film [10], the cracks are naturally developed in the TIPS-pentacene film due to the existence of side chains irrespective of the mismatch in thermal expansion between the pentacene film and a gate dielectric layer. This is clear from the fact that no considerable difference between the cracks developed on a cross-linked PVP in our case and those on an inorganic SiO_2 [8] was observed although the thermal expansion coefficients of the two materials are much different (by a factor of 10) from each other [12]. Like other typical polymers with side chains [13,14], the side chains in the TIPS-pentacene are expected to be affected by the thermal treatment than the main backbone. This implies that the type of side chains is very important to suppress the development of cracks during thermal annealing and to increase the solubility of the pentacene derivatives in common organic solvents.

Fig. 2 shows that the X-ray diffraction (XRD) peak intensities along the (0 0 1) direction in the TIPS-pentacene films baked initially at 60 °C as a function of T_a. As T_a increases, the (0 0 1) diffraction peak increases and reaches a maximum at T_a = 60 °C and then decreases. Our XRD results indicate that the highest ordered state was obtained when the TIPS-pentacene film was annealed at 60 °C. This may result from the evaporation of any residual 1,2-DCB solvent and the relaxation of any mechanical strain in the TIPS-pentacene film, producing structurally more ordered arrangement of the TIPS-pentacene molecules, during the annealing process. The resultant high crystallinity is directly related to the large mobility of the TIPS-pentacene FET. The inset shows typical series of (0 0 l) diffraction peaks of the TIPS-pentacene film annealed at 60 °C, in which the well-defined and sharp diffraction peaks also represent the existence of highly ordered domains in the TIPS-pentacene film [7]. The decrease in the (0 0 1) diffraction peak for the TIPS-pentacene films annealed above 60 °C was accompanied by the crack development. Based on the crystallinity of the TIPS-pentacene film in relation to the crack development, the optimum value of T_a is determined to be 60 °C in this study.

We now examine how the electrical properties of our TIPS-pentacene FETs are influenced by the thermal annealing which is closely related to the crack development. Fig. 3a and b shows the output characteristic curves and

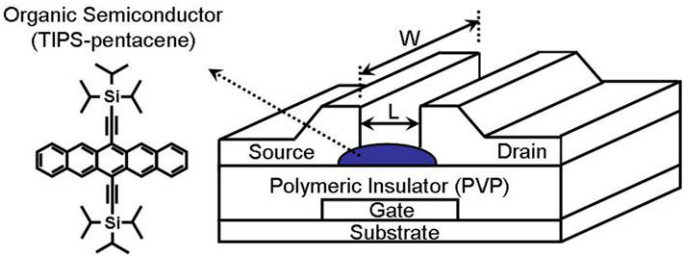

Fig. 1. The chemical structure of a soluble organic semiconductor, TIPS-pentacene, and the schematic diagram of our TIPS-pentacene FET with a solution-processed polymer insulator. The channel length and the channel width are denoted by L and W, respectively.

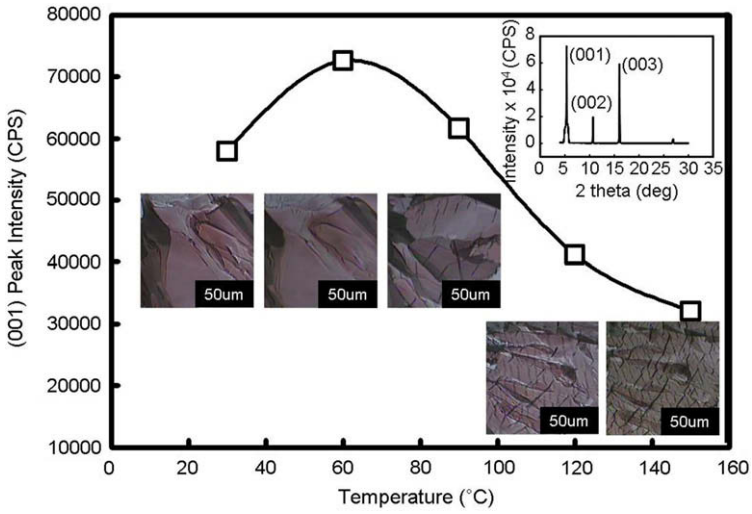

Fig. 2. The peak intensities of the X-ray diffraction along (0 0 1) and the corresponding optical microscopic images of the TIPS-pentacene films annealed at various temperatures. The inset shows typical series of the X-ray diffraction peaks observed in the TIPS-pentacene films annealed at 60 °C.

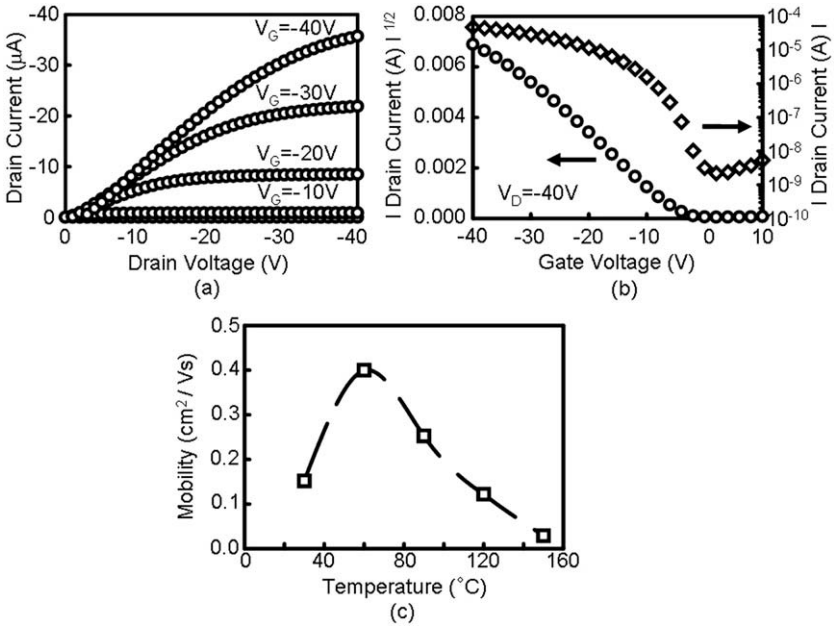

Fig. 3. (a) The output characteristic curves of our TIPS-pentacene FETs annealed at 60 °C, (b) the corresponding transfer characteristic curves, and (c) the field-effect mobility of each TIPS-pentacene FET as a function of the annealing temperature. The data at the drain voltage of −40 V were used for obtaining the mobility in each TIPS-pentacene FET.

the corresponding transfer characteristic curves of our TIPS-pentacene FETs annealed at the optimum value of T_a = 60 °C, respectively. From the characteristic curves, the field-effect mobility was determined to be 0.401 cm^2/V s. Note that without the help of an extra passivation layer and the optimization of the work function [6], and blending of the TIPS-pentacene [15], the high value of about 0.401 cm^2/V s has not been attained so far in a TIPS-pentacene FET fabricated on a solution-processed polymer gate insulator.

The annealing temperature (T_a) dependence of the field-effect mobility is shown in Fig. 3c. The mobility for the as-prepared TIPS-pentacene FET case was 0.152 cm^2/V s, and that annealed at T_a = 60 °C was 0.401 cm^2/V s. For T_a above 60 °C, the mobility decreases as low as 0.029 cm^2/V s at T_a = 150 °C due to the appearance of thermal cracks in the TIPS-pentacene film. This behavior does not exist in thermally-deposited films of pentacene with no side chains but a simple increased behavior is observed with

increase in the annealing temperature [10]. The on–off current ratio varies from 9×10^3 to 3×10^4 depending on T_a.

Let us investigate the thermal annealing effect on the stability of our TIPS-pentacene FETs in terms of the field-effect mobility and the off-current with time. Three different types of the TIPS-pentacene FETs (with no thermal treatment, annealed at 60 °C, and annealed at 150 °C) were studied at three different storage times of 0, 600, and 4000 h in air under atmospheric pressure. The OM images, taken after 4000 h, showing the morphology for each case were presented in Fig. 4a–c. In the non-annealed TIPS-pentacene FET, the cracks that did not exist initially were developed in time while in the annealed cases, no considerable change in the morphology was observed irrespective of the presence of the cracks. It is clear from Fig. 4d that after 4000 h, the mobility value for the non-annealed TIPS-pentacene FET decreases drastically by about 90% from 0.152 to 0.011 $cm^2/V\,s$ while the mobility values of the annealed cases decrease rather slowly by about 50% from 0.401 to 0.205 $cm^2/V\,s$ for $T_a = 60$ °C and from 0.029 to 0.016 $cm^2/V\,s$ for $T_a = 150$ °C. This implies that in relation to the cracks, the annealing effect plays a critical role in the stability of the TIPS-pentacene FETs. It is found that the thermal treatment at the optimum value of $T_a = 60$ °C avoids the crack development and enhances the crystallinity in the TIPS-pentacene film. This is why the TIPS-pentacene FET annealed at 60 °C exhibits the highest mobility (0.401 $cm^2/V\,s$) and the best stability in time among the three types of the TIPS-pentacene FETs we studied.

Fig. 4e shows both the relative change of the off-current and the resulting on–off current ratio with time for three different devices to address the temporal degradation in relation to the cracks. After 4000 h stored in air under atmospheric pressure, the values of the off-current for the TIPS-pentacene FETs with cracks shown in Fig. 4a and c increase as large as 80 times while the value for the TIPS-pentacene FET annealed at the optimum value of $T_a = 60$ °C, showing no cracks, increases by about a factor of 10. From the fact that the moisture and/or oxygen diffused into an organic semiconductor film deteriorate the electric properties of the FETs [16–18], it is reasonable to conclude that the physicochemical adsorption of air and/or moisture onto the cracks dictates primarily the long-term stability of the TIPS-pentacene FETs with time. After 4000 h, the on–off current ratio for the TIPS-pentacene FET annealed at the optimum value of $T_a = 60$ °C is on the order of 10^3, while that for the non-annealed case is below 10^2.

In summary, we demonstrate how the thermal annealing affects the mobility enhancement, the development of cracks and the resultant degradation mechanism of the electrical properties, and the temporal stability of the TIPS-pentacene FETs fabricated on a single, solution-processed polymer insulator. The annealing process at the optimum temperature of 60 °C results in the highest field-effect mobility of 0.401 $cm^2/V\,s$ among the TIPS-pentacene FETs we studied. Such high value has not been obtained so far in the TIPS-pentacene FET having a solution-processed polymer insulator without an additional buffer layer or a blending process. It is found the annealing effect suppresses both the development of the cracks and the increase of the off-current with time in the ambient environment. The cracks act as trapping sites of moisture and/or oxygen for the off-current flow and thus deteriorate the electrical performances of the TIPS-pentacene FET. Finally, further studies on the structural arrangement of side chains of the TIPS-pentacene in relations to the cracks as a function of temperature and the nature of the solvent used will provide a scientific platform for developing all solution-processed printed electronics.

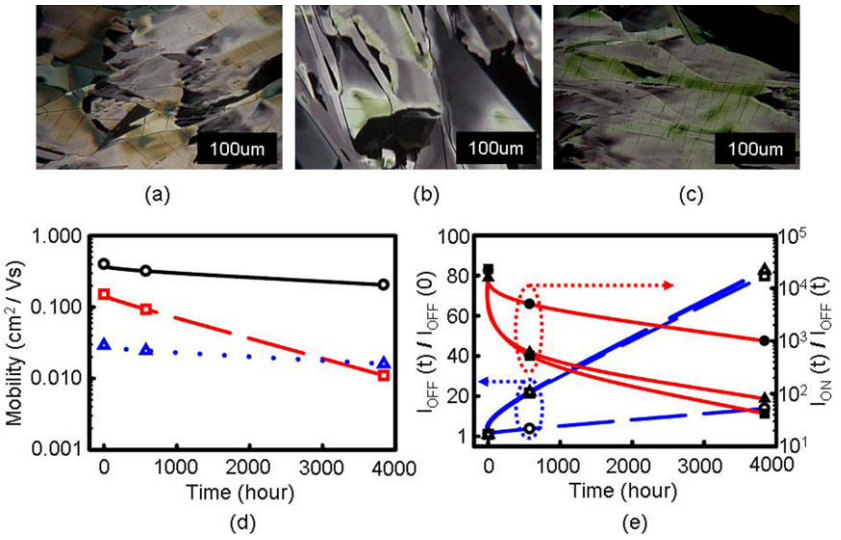

Fig. 4. The optical microscopic images, taken after 4000 h stored in air under atmospheric pressure, of the TIPS-pentacene film, (a) without the thermal treatment, (b) annealed at 60 °C, (c) annealed at 150 °C and (d) the field-effect mobility of each case as a function of the storage time. Open squares (dashed line), open circles (solid line), and open triangles (dotted line) represent the non-annealed case, the annealed case at 60 °C, and the annealed case at 150 °C, respectively, (e) the relative change of the off-current (open symbols) and the resulting on–off current ratio (filled symbols) of each case as a function of the storage time in the ambient environment.

Acknowledgement

This work was supported by Korea Ministry of Knowledge Economy through the System IC-2010 Project.

References

[1] T.N. Jackson, Y.Y. Lin, D.J. Gundlach, H. Klauk, IEEE J. Sel. Top. Quantum Electron. 4 (1998) 100.
[2] C.D. Dimitrakopoulos, P.R.L. Malenfant, Adv. Mater. 14 (2002) 99.
[3] Y.Y. Lin, D.J. Gundlach, S.F. Nelson, T.N. Jackson, IEEE Elect. Device Lett. 18 (1997) 606.
[4] Y. Kato, S. Iba, R. Teramoto, T. Sekitani, T. Someya, H. Kawaguchi, T. Sakurai, Appl. Phys. Lett. 84 (2004) 3789.
[5] S.K. Park, J.E. Anthony, D.A. Mourey, T.N. Jackson, Appl. Phys. Lett. 91 (2007) 063514.
[6] S.H. Lee, M.H. Choi, S.H. Han, D.J. Choo, J. Jang, S.K. Kwon, Org. Electron. 9 (2008) 721.
[7] S.I. Shin, J.H. Kwon, H. Kang, B.K. Ju, Semicond. Sci. Technol. 23 (2008) 085009.
[8] J. Chen, C.K. Tee, J. Yang, C. Shaw, M. Shitein, J. Anthony, D.C. Martin, J. Polym. Sci., Polym. Phys. 44 (2006) 3631.
[9] J. Chen, J. Anthony, D.C. Martin, J. Phys. Chem. B 110 (2006) 16397.
[10] S.J. Kang, M. Noh, D.S. Park, H.J. Kim, C.N. Whang, C.H. Chang, J. Appl. Phys. 95 (2004) 2293.
[11] S.C. Lim, S.H. Kim, J.B. Koo, J.H. Lee, C.H. Ku, Y.S. Yang, T. Zyung, Appl. Phys. Lett. 90 (2007) 173512.
[12] S. Yamagata, Y. Yanagase, Y. Kokubun, Jpn. J. Appl. Phys. 43 (2004) 5766.
[13] S.A. Chen, J.M. Ni, Macromolecules 25 (1992) 6081.
[14] K. Nakane, T. Yamashita, K. Iwakura, F. Suzuki, J. Appl. Polym. Sci. 74 (1999) 133.
[15] R. Hamilton, J. Smith, S. Ogier, M. Heeney, J.E. Anthony, I. McCulloch, J. Veres, D.D.C. Bradley, T.D. Anthopoulos, Adv. Mater. 21 (2009) 1166.
[16] Y. Qiu, Y. Hu, G. Dong, L. Wang, J. Xie, Y. Ma, Appl. Phys. Lett. 83 (2003) 1644.
[17] A. Benor, A. Hoppe, V. Wagner, D. Knipp, Org. Electron. 8 (2007) 749.
[18] Y. Wu, P. Liu, S. Gardner, B.S. Ong, Chem. Mater. 17 (2007) 221.

fabricate a device of ZnO nanorod/semiconductor polymer heterostructure by a simple process, and ZnO EL with ultraviolet (UV) at 380 nm is detected under forward bias.

2. Experimental setup

The procedure for device fabrication is as follows. First, we cleaned the indium tin oxide (ITO) glass using acetone, ethanol, and deionized water sequentially. In the ZnO nanorod synthesis process, zinc acetate dehydrate solution was used as the seeding layer and spin-coated on the ITO glass substrate for subsequent growth of nanorods. Then, it was baked at 350°C for 20 min at ambient pressure. The hydrothermal reaction solution for ZnO nanorod fabrication was prepared by mixing 25 mM zinc nitrate hexahydrate ($Zn(NO_3)_2{\cdot}6H_2O$) and 25 mM hexamethylenetriamine ($C_6H_{12}N_4$) in 200 ml of deionized water in a glass beaker. During growth, the glass beaker was placed in an electrically heated thermostatic water bath and maintained at 92°C for 15 min. Subsequently, the sample was removed from solution and washed with ethanol and deionized water repeatedly and baked for 30 min at ambient pressure. A p-type polymer poly [2-methoxy-5-(2-ethylhexyloxy)-1,4-phenylenevinylene] (MEH-PPV) was dissolved in chloroform with a concentration of 5 mg/mL and then spin-coated on as-grown ZnO nanorod layers at a rotation speed of 1000 rpm (rotations per minute). This low rotation speed is intended to provide a smooth surface for subsequent thin film deposition. About 100 nm of Al film was deposited by thermal evaporation under high vacuum conditions at 2×10^{-4} Pa. A schematic diagram of the device and energy levels is shown in Fig. 1. In our experiment, a forward bias on the device denotes that the ITO is used as anode and Al as cathode. Device testing consists of measuring the EL spectrum at different DC bias voltages and of measuring the current–voltage–light power (*I–V–L*) characteristics with a system comprising an ACTON 150 CCD spectrometer, a Keithley 2410 electrometer and a Newport 1830-C Optical Power Meter Mainframe controlled by a computer. All of these tests were carried out at room temperature and in ambient atmosphere.

3. Results and discussion

The morphology of the ZnO nanorods was observed by field emission scanning electron microscopy (SEM). From the SEM pictures shown in Fig. 2(a), we can observe a ZnO nanorod array grown primarily aligned along the per-

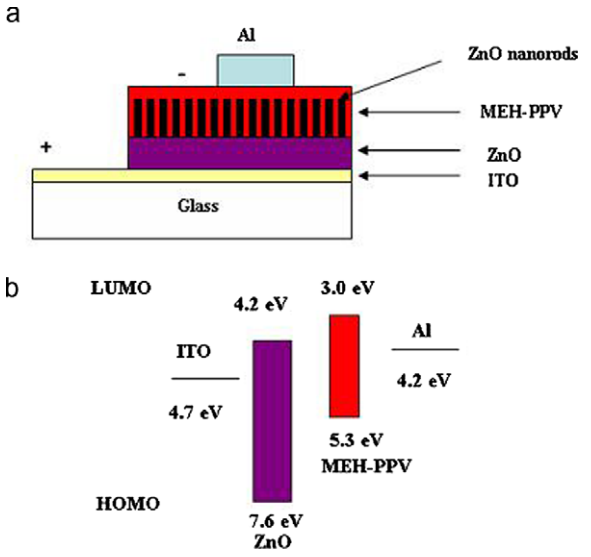

Fig. 1. Schematic diagram (a) and energy levels (b) of the ZnO nanorods/MEH-PPV heterostructure.

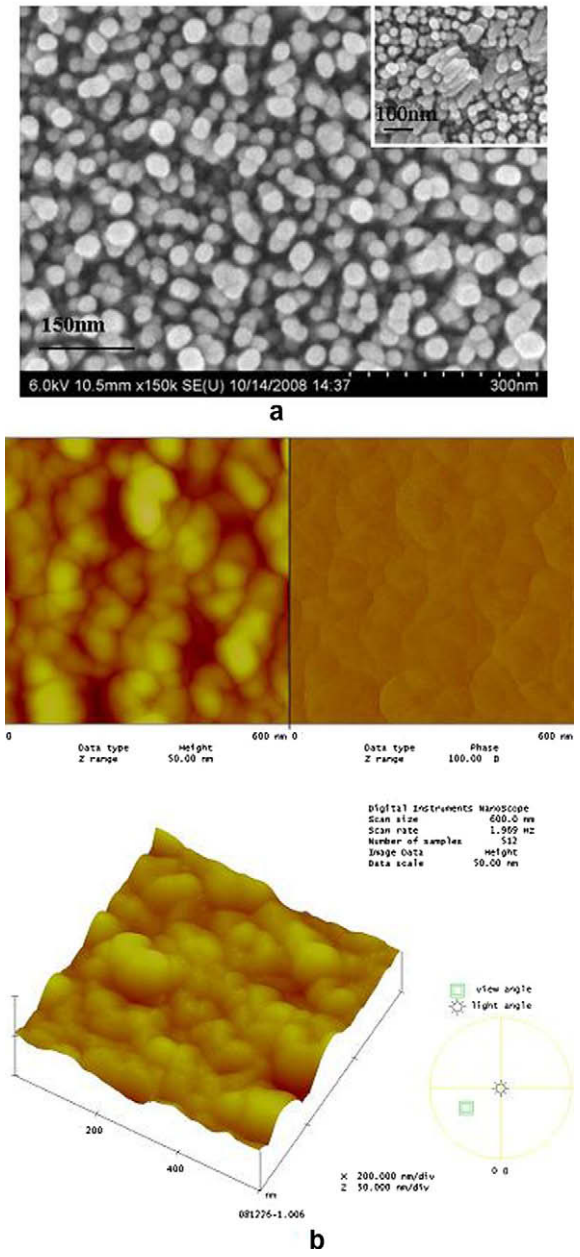

Fig. 2. (a) Top view of ZnO nanorods on ITO glass. Inset: top view of some fallen ZnO nanorods. (b) AFM picture of ZnO nanorods/MEH-PPV.

pendicular direction of the ITO substrate. The average height and diameter of the nanorods are about 130 nm and 30 nm, respectively. If the polymer layer of MEH-PPV is coated onto the nanorods as shown in Fig. 1, some MEH-PPV molecules should fill the space in between nanorods. It looks like the ZnO nanorods are encircled by MEH-PPV molecules. The thickness of MEH-PPV should be enough to cover all nanorods in order to prevent current leakage from ZnO nanorods to the Al electrode directly. This can be proved by atomic force microscopy (AFM) pictures as shown in Fig. 2(b). After coating with MEH-PPV, the roughness is a few nanometers and there is no phase separation according to the phase picture in Fig. 2(b). This means that all ZnO nanorods are completely covered with MEH-PPV.

Although the ultraviolet emission of ZnO excited by light has been detected, it is difficult to observe under an electric field. Even when it is observed, the intensity is very weak. The reason is that p-type doping of ZnO has remained a challenge. Nominally undoped ZnO typically exhibits n-type conductivity due to asymmetric doping limitations and the possibility of holes getting compensated by intrinsic donors, such as zinc interstitials and oxygen vacancies. So it is difficult to realise p-type ZnO doping with high quality and reproducibility. Now, different groups still continue their efforts in these researches to obtain more effective p-type ZnO. Hsu et al. reported that p-type ZnO can be prepared by a hydrothermal method by adjusting the properties of the seed layer [7]. Light emitting diodes based on n-GaN/p-ZnO have been fabricated and UV emission under forward bias was observed. In addition, devices based on p-ZnO/n-type organic materials were also prepared. The UV emission of ZnO is weak in these devices. The problem is that the stability of p-ZnO requires further study in this report. In order to obtain UV emission properties of ZnO, a lot of researchers have applied other p-type semiconductors, for example, Si, GaN, ZnTe, $SrCu_2O_2$, SiC, etc., to substitute p-ZnO to make the light emitting diodes. Only a few kinds of diodes have emitted UV light under a DC bias [11–13]. Meanwhile, some researchers use organic materials to prepare ZnO/polymer heterojunctions devices. Könenkamp et al. prepared a kind of LED with ZnO nanowires/polymer heterojuctions, and detected the electroluminescence at 384 nm [9,14]. Then Chang et al. also realised 383 nm electroluminescence in ZnO nanowires/polymer heterojuctions [10]. In these studies, the process for preparing the LED is almost the same. Firstly, a layer of organic insulator was spin-coated on a layer of ZnO nanowires or rods, and then the organic insulator was removed from the nanowires or rods. Afterwards, a p-type organic luminescence material was spin-coated. The UV emission of ZnO is weaker than defect emissions of ZnO in these reports. In our experiments, we fabricated ZnO nanorod/polymer heterostructure LEDs in which no insulator material is used to fill the space between nanorods. When the forward bias is 28 V, UV emission of ZnO at 380 nm is prominent and better than that of other similar reported LED devices [7,9,10,14]. All results of our experiments demonstrate that UV emission devices can be fabricated by a simple method based on ZnO nanorods/polymer heterostructures.

Fig. 3(A) shows the EL spectra of the ZnO nanorod/polymer heterostructure LED under different forward biases. When the forward bias is 22 V, the EL spectrum shows emission with multiple peaks at 380 nm, 580 nm, 610 nm, and 747 nm, respectively. When the DC bias voltage is increased, the EL intensity increases but the spectrum shape is not changed further. In order to make these emission peaks clearly distinguishable, the EL spectrum at 28 V is fitted to a Gaussian function, as shown in Fig. 3(B). It is clear that except for emissions at 380 nm, 580 nm, 610 nm, and 747 nm, there is a peak at around 640 nm. The emission at 380 nm is the band edge emission of ZnO nanorods and the emission at 580 nm with a shoulder at 610 nm is due to the exciton emission of MEH-PPV. According to the literature [9], emissions at 640 nm and 747 nm correspond to the defect emission of ZnO. With an increase in voltage, the intensity of the 380 nm line increases faster than other emissions along with increasing voltage. When the voltage reaches 28 V, the ZnO band edge emission becomes predominant and stronger than other emissions, and the full width at half maximum of this emission is 25 nm. In addition, defect emissions of ZnO nanorods is observed clearly at long wavelengths. To

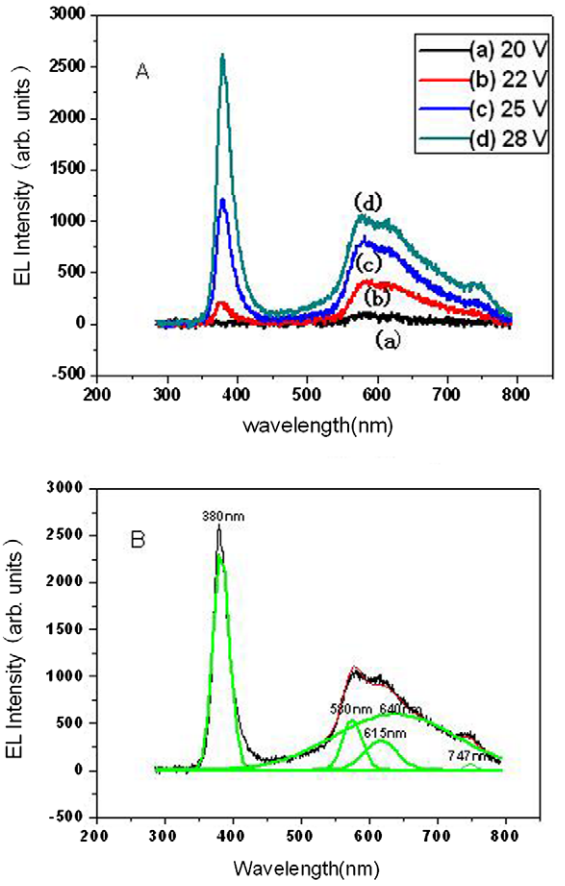

Fig. 3. (A) EL spectrum at different applied voltages of the ZnO nanorod/polymer heterostructure. (B) EL spectrum at 28 V after Gaussian fitting.

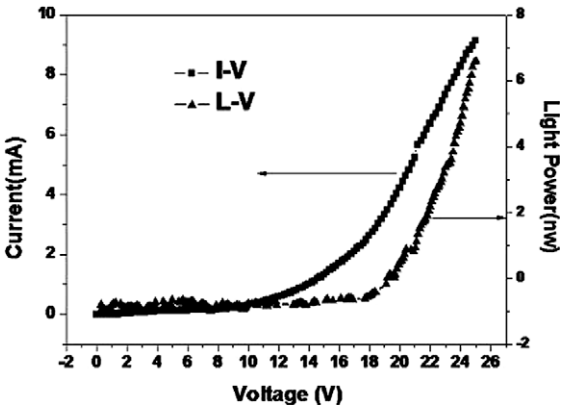

Fig. 4. Current–voltage–light power (380 nm) characteristics of the ZnO nanorod/polymer heterostructure.

summarise, the emissions of ZnO is stronger than that of MEH-PPV. However, under reverse bias no emissions are observed.

Fig. 4 shows the *I–V* characteristics of the ZnO nanorod LED. This structure demonstrates well-behaved and stable rectifying diode behaviour. According to the *I–L–V* characteristics, the luminescence increases faster than current at high voltages. It is concluded that the emission efficiency at high voltage is improved compared with the phenomenon at low voltage.

Fig. 1(b) shows the energy band structure of the device under forward bias. When the voltage is low, only the exciton emission of MEH-PPV is detected. As we know, the exciton emission of organic materials is due to carrier injection from both sides. The electron is injected from Al into the MEH-PPV layer and holes are injected from the ZnO nanorods. It has been reported that ZnO nanorods synthesised by hydrothermal methods display ambipolar charge transport [15]. Using bottom contact field-effect transistor structure, ZnO nanorods exhibit electron and hole mobilities up to 3.2 and 2.1$cm^2\ V^{-1}\ s^{-1}$, respectively. The hole mobility of ZnO nanorods is far larger than the electron mobility of MEH-PPV (about $10^{-5}\ cm^2\ V^{-1}\ s^{-1}$). So carriers recombine preferentially in the MEH-PPV layer at low applied voltage, and then excitons are formed in MEH-PPV and give the emission at 580 nm. Along with the increase of the applied voltage, band edge emission at 380 nm and defect emissions at 640 nm and 747 nm from ZnO nanorods are observed. But, at the beginning, the intensity at 380 nm is lower than that at 640 nm and 747 nm. Increasing the applied voltage results in band bending in MEH-PPV. So a carrier tunnelling process becomes possible. Electrons in the Al electrode tunnel through the MEH-PPV layer directly into the defect states of the ZnO nanorods under a relatively low electric field. Holes in the ITO electrode tunnel to the valence band of the ZnO nanorods. These holes recombine with electrons in defect states and give stronger defect emissions at a relatively low applied voltage. When the applied voltage is higher, the tunnelling of electrons and holes is more effective; in particular more electrons tunnel into the conduction band of the ZnO nanorods. The recombination of electrons in the conduction band and holes in the valence band give rise to band edge emission, which is enhanced faster than other emissions with increases in applied voltage. Moreover, the barrier between the valence band of ZnO and HOMO of MEH-PPV (as shown in Fig. 1(b) is enough to accumulate and confine holes in the ZnO nanorods. Therefore, the band edge emission of the ZnO nanorods is detected and competes with and exceeds other emissions. Again, this is proved by the *I–V–L* measurement. As seen from Fig. 4, the emission at 380 nm increases faster at high voltage than at low voltage. At the same time, although the exciton emission of MEH-PPV increases too, its enhancement is nevertheless lower than the ZnO nanorod emissions because of the fact that more electrons tunnel directly into ZnO nanorods from the Al electrode. So there are fewer carriers in MEH-PPV than in the ZnO nanorods.

Under reverse bias, no emission is observed. Although electrons and holes could be injected into the ZnO nanorods from the ITO electrode and into MEH-PPV from the Al electrode, they are confined within the ZnO nanorods and MEH, respectively, because of the barrier. The LUMO potential of MEH-PPV is higher than the conduction band potential of the ZnO nanorods, and the valence band potential of the ZnO nanorods is lower than that of HOMO of MEH-PPV. So it is difficult for electrons to transfer to a higher potential and holes to a lower potential under reverse bias. This results in a carrier imbalance in both ZnO and MEH-PPV. In such a case, exciton recombination emission of MEH-PPV or band edge emission of ZnO is difficult to realise in two layers.

4. Conclusion

In conclusion, a ZnO nanorod inorganic/organic heterostructure LED was prepared. A band edge ultraviolet emission peak at 380 nm, and defect emission from ZnO at 640 nm and 747 nm were detected. In addition, the typical exciton emission of MEH-PPV was measured. At low voltage, the emissions of MEH-PPV and defect emission of ZnO are clear and band edge emission is weak. At higher voltage, the band edge emission of ZnO is prominent and stronger than other emissions. The full width at half maximum of the 380 nm emission is 25 nm. Under high forward bias, the tunnelling of carriers results in stronger 380 nm emission. Under reverse bias, there is no emission. Because the ZnO nanorods were fabricated at low temperature, this ZnO-based LED offers a low-cost process in the field of UV LEDs.

Acknowledgements

The authors express their thanks to the NSFC (10974013, 10774013, 60825407, and 10804006), RFDP (20070004024 and 20070004031), the Beijing NOVA program (2007A024) and the 111 Project (B08002).

References

[1] Q.-X. Yu, B. Xu, Q.-H. Wu, Y. Liao, G.-Z. Wang, R.-C. Fang, H.-Y. Lee, C.-T. Lee, Optical properties of ZnO/GaN heterostructure and its

near-ultraviolet light-emitting diode, Appl. Phys. Lett. 83 (2003) 4713–4715.
[2] Ü. Özgür, Ya.I. Alivov, C. Liu, A. Teke, M.A. Reshchikov, S. Doğan, V. Avrutin, S.-J. Cho, H. Morkoç, A comprehensive review of ZnO materials and devices, J. Appl. Phys. 98 (2005) 041301-1–041301-103.
[3] J.B. Baxter, F. Wu, E.S. Aydil, Growth mechanism and characterization of zinc oxide hexagonal columns, Appl. Phys. Lett. 83 (2003) 3797–3799.
[4] C.X. Xu, X.W. Sun, C. Yuen, B.J. Chen, S.F. Yu, Z.L. Dong, Ultraviolet amplified spontaneous emission from self-organized network of zinc oxide nanofibers, Appl. Phys. Lett. 86 (2005) 011118-1–011118-3.
[5] G.T. Du, W.F. Liu, J.M. Bian, L.Z. Hu, H.W. Liang, X.S. Wang, A.M. Liu, T.P. Yang, Room temperature defect related electroluminescence from ZnO homojunctions grown by ultrasonic spray pyrolysis, Appl. Phys. Lett. 89 (2006) 052113-1–052113-3.
[6] A. Javey, S.W. Nam, R.S. Friedman, H. Yan, C.M. Lieber, Layer-by-layer assembly of nanowires for three-dimensional, multifunctional electronics, Nano Lett. 7 (2007) 773–777.
[7] Y.F. Hsu, Y.Y. Xi, K.H. Tam, A.B. Djurišić, J. Luo, C.C. Ling, C.K. Cheung, A.M.C. Ng, W.K. Chan, X. Deng, C.D. Beling, S. Fung, K.W. Cheah, P.W.K. Fong, C.C. Surya, Undoped p-type zno nanorods synthesized by a hydrothermal method, Adv. Funct. Mater. 18 (2008) 1020–1030.
[8] S. Zhao, Z. Xu, F. Zhang, W. Jiang, J. Huang, Y. Wang, X. Xu, Schematic design of a complex thin-film luminescent screen usable for vacuum fluorescent and field emission display, Opt. Lett. 32 (5) (2007) 2094–2096.
[9] R. Könenkamp, R.C. Word, M. Godinez, Ultraviolet electroluminescence from zno/polymer heterojunction light-emitting diodes, Nano Lett. 5 (2005) 2005–2008.
[10] C.-Y. Chang, F.-C. Tsao, C.-J. Pan, G.-C. Chi, H.-T. Wang, J.-J. Chen, F. Ren, D.P. Norton, S.J. Pearton, Electroluminescence from ZnO nanowire/polymer composite p–n junction, Appl. Phys. Lett. 88 (2006) 173503-1–173503-3.
[11] Y.I. Alivov, J.E. Van Nostrand, D.C. Look, M.V. Chukichev, B.M. Ataev, Observation of 430 nm electroluminescence from ZnO/GaN heterojunction light-emitting diodes, Appl. Phys. Lett. 83 (2003) 2943–2946.
[12] H. Ohta, K. Kawamura, M. Orita, M. Hirano, N. Sarukura, I. Hosono, Current injection emission from a transparent p–n junction composed of p-$SrCu_2O_2$/n-ZnO, Appl. Phys. Lett. 77 (2000) 475–477.
[13] A. Kudo, H. Yanagi, K. Ueda, H. Hosono, H. Kawazoe, Y. Yano, Fabrication of transparent p–n heterojunction thin film diodes based entirely on oxide semiconductors, Appl. Phys. Lett. 75 (1999) 2851–2853.
[14] R. Könenkamp, R.C. Word, C. Schlegel, Vertical nanowire light-emitting diode, Appl. Phys. Lett. 85 (2004) 6004–6006.
[15] C.-Y. Wong, L.-M. Lai, S.-L. Leung, V.A.L. Roy, E.Y.-B. Pun, Ambipolar charge transport and electroluminescence properties of ZnO nanorods, Appl. Phys. Lett. 93 (2008) 023502–023503.

of the long sublimation tube, it is essential to control the temperature gradient of the long sublimation tube very carefully for an efficient purification process.

With this technique, however, usually one cannot get a sufficient purity through just one purification process, and needs a couple of purifying processes to get a sufficiently high purity of target materials. Consequently, it consumes long time and a lot of source materials inefficiently [16,20]. After a couple of sublimation purification, one can get only 50% or less from the first source materials. These drawbacks become more serious problems in the view point of low cost devices which is one of the most important competitive merits of organic electronic devices. Therefore, the improvement of the purifying efficiency is urgently needed for the realization of low-cost and high-performance organic electronic devices.

Our research group has already reported a modified sublimation purification system using arrays of partitions [21]. By installing arrays of partitions in the sublimation tube, the HPLC purity of 1,3-bis[2-(2,2′-bipyridine-6yl)-1,2,4-oxadiazol-5yl] benzene (Bpy-OXD) was increased from 99.37% to 99.73%. This increase of purity resulted in lowering the driving voltage of EL device (for luminance of 1000 cd/m^2) as large as 1 V (from 4.7 V to 3.9 V), and increasing the lifetime of device 1.5 times longer (from 50 h to 79 h). In that system, however, some inherent problems exist and hinder us in commercializing as an efficient purification system. One is the difficulty of extracting the purified materials from the array of partition. Although the final yield was almost the same with that of a conventional method, it is very difficult and time-consuming to extract the purified materials deposited on the array of partition, especially on the junction parts between partitions. Another problem is the existence of undivided region by partitions – the surface of glass tube – which is almost the same state with the conventional method.

In this paper, we report a highly efficient sublimation purification system using baffles with orifices to solve those problems mentioned above. The purity and the effective yield of purified materials were improved simultaneously by introducing baffles with orifices in the sublimation glass tube.

2. Experimental

2.1. New purification system

The new sublimation purification system developed in this study was shown schematically in Fig. 1. There are two heaters; one is for the sublimation of materials and set on the high-temperature (T_h) region (Heater 1, 10 cm in length), and the other is for temperature gradient of long glass tube which is set on the low-temperature (T_l) region where purified materials are deposited (Heater 2, 20 cm in length). The sublimation tube is a 70 cm long quartz tube (40 mm in external diameter, 2 mm in thickness), and the pressure in the tube was controlled 1 Pa or 80 Pa with an Ar gas (99.9999%) flow.

Several pieces of baffles (32 mm in diameter) with orifices were inserted between inner glass tubes (32 mm in diameter), and they were attached each other tightly enough to prevent leakage of purified materials through joint chinks between inner tubes and baffles. Two groups of baffles were introduced separately in T_l region and T_h region, respectively. The number of baffles, hence the interval between baffles, was changed from 0 to 2 or 3 (20 mm and 10 mm intervals, respectively) in T_h region. The intervals between baffles in T_l region were also changed from 20 mm to 50 mm. Baffles were installed very carefully not to align orifices straightly between neighbored ones. A photograph of Fig. 1b shows the set of three pieces of baffles in T_h region and 50 mm interval in T_l region.

We have used mainly two kinds of baffles with different orifices; one has two orifices (10 mm in diameter) and another four (7 mm in diameter), as shown in Fig. 1c. We have also used two kinds of materials for the baffles; stainless steel (SS) and quartz. The percentage of open areas (orifices) is about 25%, and the thickness is 2 mm for all kinds of baffles.

We have also modified the source boat to be a similar shape with the inner glass tube having a narrow orifice on the rear side to prevent a reverse flow of sublimed materials as shown in Fig. 1a and b. Several pieces of glass tubes whose diameter is the same with the inner glass tube were installed on the rear of the source boat up to the gas

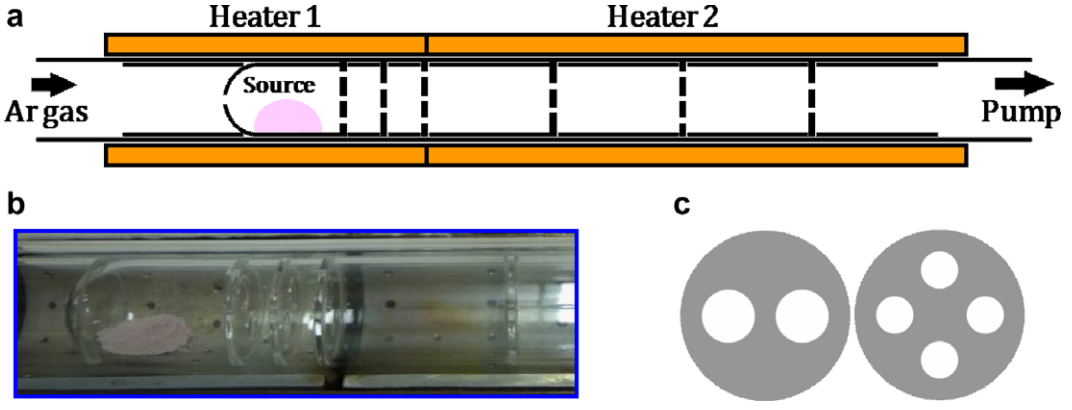

Fig. 1. (a) A schematic illustration of the new sublimation purification system where baffles with orifices are inserted between inner glass tubes. (b) An example of set-up of the new purification system; three pieces of baffles in T_h region and 50 mm interval in T_l region. 90° twisted installing of baffles by turns not to align orifices straightly between neighbored ones is worthy of notice. (c) Representative two kinds of baffles with two and four orifices.

inlet for the guidance of Ar gas into the source boat through a narrow orifice. Otherwise most of Ar gas flow outside of the source boat not into it because of a narrow orifice of the source boat, which resulted in two times longer sublimation time.

2.2. Evaluation of purification efficiency

For the evaluation of purification efficiency of a new purification system, we used three organic materials; bathocuproine (BCP, TCI, 97%), tris(8-hydroxyquinolinato) aluminum(III) (Alq_3, TCI, >95%) and 1,3-bis[2-(2,2′-bipyridine-6yl)-1,2,4-oxadiazol-5yl]benzene (Bpy-OXD, Hodogaya Chemical Co., Ltd., >99%), whose molecular structures are shown in Fig. 2. We have purified these materials under various conditions by changing the interval between baffles inserted in T_l region and/or by changing the number of baffles inserted in T_h region with various kinds of baffles described at the previous section, and compared the purification efficiency with that of conventional method.

As the factors for purification efficiency, we have evaluated and compared the purity (for BCP and Bpy-OXD) and the yield (for Alq_3 and BCP) of purified materials. For the evaluation of the purity factor, we have measured the melting point (T_m) of purified materials with the differential scanning calorimetry (DSC, Seiko Instruments, DSC6200, 2 °C/min heating condition). We have also compared the driving voltages to get 10 mA/cm^2 (V_{10J}) and 100 mA/cm^2 (V_{100J}) of EL devices whose structure is shown in Fig. 2d schematically; all of the materials used in this study are electron transport materials, and used as the electron transport layer (ETL) in the EL devices. In general, T_m goes up and driving voltage of EL device goes down as the purity is increased [7,19,22,23]. For Bpy-OXD, we have also checked the HPLC purity and compared with the results of T_m and driving voltages. The measurement condition of HPLC is as follow: column: Inertsil ODS-2 (5 μm, 4.6 × 250 mm), carrier: CH_3CN/0.05% TFA = 4/6, rate: 0.9–1.0 ml/min, temp.: 40 °C, det.: 254 nm. For the evaluation of the yield factor of purified materials, we have extracted carefully all of materials deposited at T_l region which is divided by a fixed length, and made it as the total yield. Among them, we have made the yield from a fixed section (50 mm length from the start of T_l region) as the effective yield. And then we have calculated the ratio of the effective yield (R_{EY}) by dividing the effective yield with the total yield.

3. Result and discussion

3.1. Yield

For the understanding of the effect of introducing baffles on yield, we have compared the total yield and the effective yield of purified BCP under various purification conditions, and some representative results are shown in Fig. 3, and summarized in Table 1. When we compared

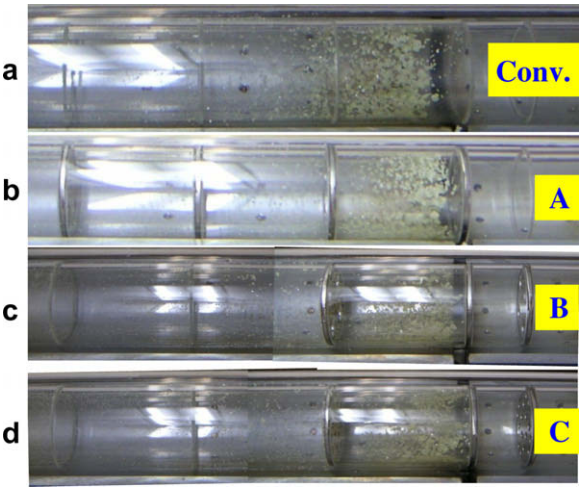

Fig. 3. Some representative results of purification of BCP under various purifying conditions; (a) a conventional method without introducing baffles, (b) introducing baffles only in T_l region, (c) introducing baffles with four orifices in both of T_h and T_l regions, and (d) the same setting with (c) except the number of orifices of baffles (16 orifices).

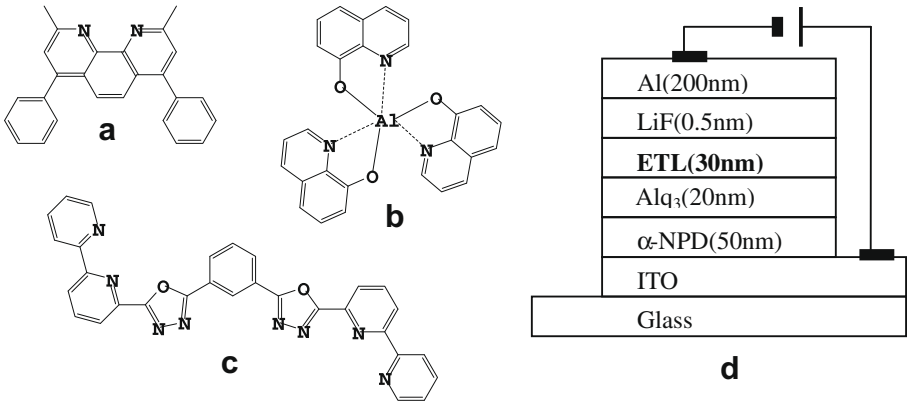

Fig. 2. Molecular structures of (a) bathocuproine (BCP), (b) tris(8-hydroxyquinolinato) aluminum(III) (Alq_3), (c) 1,3-bis[2-(2,2′-bipyridine-6yl)-1,2,4-oxadiazol-5yl] benzene (Bpy-OXD) and (d) EL device structure used in this study. All of purified materials were used to make the electron transport layer (ETL).

Table 1
Summary of the yield data of purified BCP under various conditions which are shown in Fig. 3.

Condition	Total yield[a] (%)	Effective yield[b] (%)	R_{EY}[c] (%)
Conv.	86.49	**63.35**	**73.25**
A	84.58	**66.06**	**78.10**
B	86.72	**68.34**	**78.80**
C	87.09	**67.77**	**77.82**

[a] The quantity of BCP set in the source boat was 0.5 g.
[b] A yield from the first glass tube with 50 mm length.
[c] R_{EY} = (effective yield/total yield) × 100.

the total yield, we cannot get any relation between the total yield and the purification condition. In some conditions the total yield was increased compared with the conventional method, and in another conditions the yield was decreased. However, when we compared the effective yield – yield from the first glass tube with 50 mm length where is considered to collect the highest purity materials – it was found that the effective yield was increased by introducing baffles in all conditions. These increases became clearer by comparing R_{EY}, as shown in Table 1. In a conventional method, R_{EY} was about 73%, and it was increased up to about 78% by introducing baffles. If we consider that yields from the first baffle in T_l region were about 8% which are not concluded in the effective yields, these increases are much more meaningful.

This result strongly suggests that the purified materials are deposited more concentrated region by introducing baffles, which means that purified materials can be extracted from narrower region. This may be related not only to the efficiency of extraction but also to the purity of extracted materials since more pure materials can be deposited on narrower region.

To elucidate the effect of introducing baffles on the yield more clearly, we have changed the intervals between baffles in T_l region, and investigated whether there are any relations with the effective yield. The results with Alq_3 are summarized in Fig. 4 and Table 2. The intervals were controlled to be from 50 mm to 20 mm (Fig. 4b–e), and compared with a conventional method (Fig. 4a). At first, when we compare the effective yield from the marked region by two blue lines whose width is about 13 cm, it seems that there is not any relation between the intervals and the effective yield. However, when we look at the R_{EY}, it is clear that the R_{EY} is increased as the intervals are shortened. Considering 13 cm is quite broad region in this purification system, this clear relation between the intervals and the R_{EY} affords proof of the effect of introducing baffles on the yield mentioned above. When we compare the width of region where 50% yield was obtained, we can grasp this effect even more clearly. As shown in Fig. 4, yield 50% lines were shifted to T_h region as the intervals were shortened, which means that purified materials were deposited more compactly by introducing baffles and the deposition region was narrowed as the intervals was shortened.

In this section, it was clearly described that baffles introduced in T_l region make purified materials deposited on more concentrated region which was revealed with increased R_{EY} value.

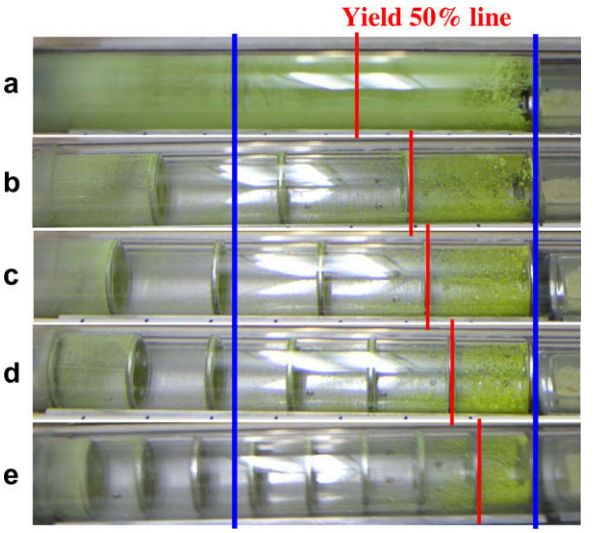

Fig. 4. Results of purification of Alq_3 (a) with a conventional method (without baffles), and (b–e) with the new system under different intervals between baffles; (b) 50 mm, (c) 40 mm, (d) 30 mm, and (e) 20 mm. The width of marked region by two blue lines is about 13 cm. Red lines represent the place to where 50% yield was extracted from the start. (For interpretation of the references to color in this figure legend, the reader is referred to the web version of this article.)

Table 2
Summary of the yield data of purified Alq_3 under various conditions with different intervals between baffles which are shown in Fig. 4.

Interval (mm)	Total yield[a] (%)	Effective yield[b] (%)	R_{EY}[c] (%)
No	74.88	71.92	**96.05**
50	73.43	70.65	**96.21**
40	72.33	69.90	**96.64**
30	77.88	75.48	**96.91**
20	74.64	72.73	**97.44**

[a] The quantity of Alq_3 set in the source boat was 1.0 g.
[b] A yield from the marked region of about 13 cm length.
[c] R_{EY} = (effective yield/total yield) × 100.

3.2. Purity

To evaluate the effect of introducing baffles on the purity clearly, we have used Bpy-OXD which is relatively easy to get HPLC purity data and to compare another data such as T_m and driving voltages of EL devices. It is also possible to compare this new purification system with the former one of our research group because it was also used in the former purification system.

All of results for Bpy-OXD were summarized in Table 3. We have used two kinds of baffles; QA has two orifices and QB four which are shown in Fig. 1c, and both of them are made of quartz. We have purified Bpy-OXD with introducing two or three baffles in T_h region – totally four kinds of sets; QA2, QA3, QB2, QB3 – and compared the purity data of them with those of non-purified (raw) one. We have also purified with a conventional method (without baffles, No or Conv.), and compared it with the above data. In all case, the purified materials were extracted from the first inner glass tube of T_l region with a length of 50 mm. The inter-

Table 3
Summary of the purity data of various Bpy-OXDs. The relations between T_m and the driving voltage, HPLC purity were also shown in Fig. 6 graphically.

Baffles	# of baffles	T_m (°C)	HWHM (°C)	V_{10J} (V)	V_{100J} (V)	HPLC purity (%)
Raw		**257.34**	1.76	**3.97**	**6.56**	**99.27**
No		**261.83**	1.32	**3.71**	**6.00**	**99.80**
QA	2	**262.43**	1.13	**3.29**	**5.53**	**99.95**
	3	**262.14**	1.22	**3.41**	**5.67**	**99.81**
QB	2	**262.40**	1.17	**3.52**	**5.74**	**99.95**
	3	**262.39**	1.25	**3.59**	**5.71**	**99.93**

vals of baffles in T_l region were also fixed as 50 mm. The yields of purified Bpy-OXD have shown the same tendency with those of mentioned in the former section, and are not mentioned in this section any more.

At first, we have checked the melting point (T_m) of purified materials with DSC, and the results were shown in Fig. 5. T_m was measured from a point of intersection of two tangent lines of DSC curves, as shown in Fig. 5. The value of half width at half maximum (HWHM) of the peak was also calculated. The right half parts of all peaks are almost the same with each other, and we calculated only the left part of HWHM. In general, T_m goes up and HWHM becomes narrow as the purity gets higher [22]. As summarized in Table 3, T_m was increased abruptly and HWHM also got narrow after purification. These behaviors show us that the material purity was increased by the purification process definitely. The most important thing is that all of the materials purified with introducing baffles have higher T_m and smaller HWHM than those of material purified by a conventional method even though the differences are not so remarkable.

We have also made EL devices of purified Bpy-OXDs with a device structure shown in Fig. 2, and compared their driving voltages to get 10 mA/cm^2 (V_{10J}) and 100 mA/cm^2 (V_{100J}). As shown in Fig. 6a together with T_m graphically, V_{10J} and V_{100J} show almost the same tendencies with T_m. These changes of V_{10J} and V_{100J} show us another strong evidence of increased purity by introducing baffles in T_h region.

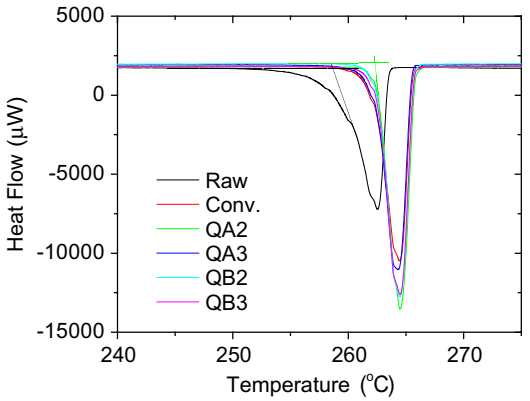

Fig. 5. DSC curves of purified Bpy-OXDs with various purifying conditions which are defined by the color of line. The detailed conditions are explained in the text. Two tangent lines for the raw material and QA2 were also shown by dotted lines with the same colors with the main curves, which were drawn for measuring T_m. (For interpretation of the references to color in this figure legend, the reader is referred to the web version of this article.)

Finally, we have measured HPLC purity of all purified Bpy-OXDs. The purity of the raw material before purification is 99.27%. After purification with a conventional method, the purity is increased to 99.80%. By introducing baffles, the purity is increased more largely up to 99.95% (QA2 and QB2). This purity increase comes to be more obvious when we compare the decrement of the impurities; percentage of the decrease of impurity content after the purification against the raw material. For a conventional method, the decrement is 72.6% (from 0.73% to 0.20%). For the new system, the decrement is increased up to 93.2% (from 0.73% to 0.05%). This is very striking value because we can get only 92.5% value at the best after twice purifications by a conventional method even when we apply the same decrement for the second purification cycle. Generally, it becomes more difficult to eliminate impurities from purer materials, and we can expect the decrement value of the second purification cycle to be smaller than that of the first cycle. Consequently, the decrement value of 93.8% is even more meaningful and cannot be easily attained even we make purification twice with a conventional method. This value is also far better than that of the former purification system we have reported before although the purity of the starting material was somewhat different. The former system showed only 71.8% decrement (from 0.96% to 0.27%) [21]. This large difference can be a strong evidence that this new purification system has been improved greatly by solving the problems of the former system mentioned in Section 1. The main solution may be the full separation of deposition area of purified materials by introducing baffles.

It is also valuable to mention that the tendency of T_m (accordingly the driving voltage of EL devices) is almost the same with that of HPLC purity, as shown in Fig. 6b. This means that we can compare the purity of materials indirectly by comparing T_m and/or the driving voltages of EL devices instead of HPLC measurement. Because most of organic electronic materials are not easily soluble in general organic solvents, it is difficult to measure the purity directly by HPLC. In that case, we can estimate the purity of purified materials indirectly by comparing the T_m and/or the device performance made of it.

In this section, it was clearly described that the purity of purified materials was increased largely by introducing baffles in T_h region. The impurity decrement becomes 93.2% value by introducing baffles which is expected to be better than that of twice purified ones by a conventional method.

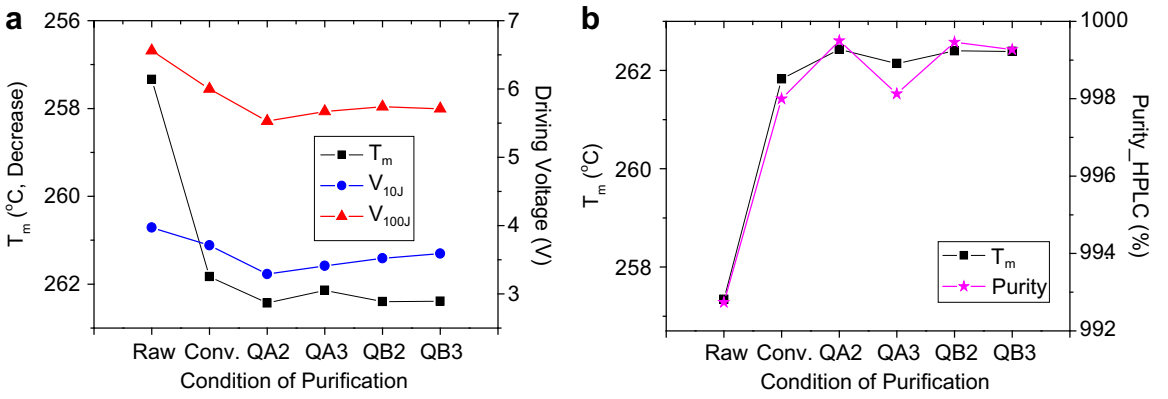

Fig. 6. Graphical summaries of (a) T_m and two driving voltages (V_{10J} and V_{100J}), and (b) T_m and HPLC purity. Note that the lines in graphics are just for visual guidance.

3.3. Comparison with a conventional method

As described in the previous two sections, the yield and the purity of the new purification system are enhanced largely comparing with a conventional method. It seems, however, that we need much more intuitive evidence for the enhancement of purification efficiency of this new system. For this purpose, we have repeated the purification of BCP three times with a conventional method, and compared its yield (from the first 50 mm glass tube) and purity with those of purified one just once by the new purification system (QB2 condition). The results are summarized in Table 4.

At first, the yield of purified BCP was decreased as the purification is repeated, and the final yield after repeating three times was 14.9%. This means that we can get just 0.15 g of purified BCP from 1 g source BCP after repeated purification three times. This result shows us that how serious the wasting materials is in repeating purification. On the other hand, the yield of the new system was 64.5%, and is reasonable value considering only 0.5 g BCP set in the source boat.

We have checked the driving voltages of EL devices made of purified BCPs. Surprisingly, the driving voltage was increased after the 2nd purification [24]. It was lowered again largely after the 3rd purification, but it was still higher than the value for purified one by QB2 condition. This result means that the purity of BCP purified three times by a conventional method is still lower than that of BCP purified just once by the new system. When we consider the yield simultaneously, this result shows us very clearly and intuitively how efficient this new purification system is. We can get at least four times larger quantity of purified materials – even the purity is much higher – by using this new purification system instead of a conventional method.

Table 4
Summary of the yield and the purity data of multiple purified BCP with a conventional method, and purified BCP with the new system under QB2 condition.

Condition	Yield (%)	Relative yield[a] (%)	V_{10J} (V)	V_{100J} (V)
Raw	–	–	**8.97**	**12.49**
1st	70.8[b]	–	**7.65**	**11.50**
2nd	57.8	37.8	**10.89**	**13.93**
3rd	47.9	**14.9**	**7.59**	**11.52**
QB2	**64.5**[c]	–	**7.45**	**11.03**

[a] Calculated against the BCP quantity set at the 1st cycle.
[b] Yield from about 1.0 g.
[c] Yield from about 0.5 g.

3.4. Discussion

It was clearly demonstrated that the purifying efficiency (both of the yield and the purity) has been improved in the new sublimation purification system. This improvement is definitely due to introducing baffles in the sublimation tube. In this section, we want to discuss what kinds of mechanisms work to improve the purifying efficiency by just introducing baffles with orifices.

At first, the dominant mass transport mechanism is diffusion in this system because the pressure is controlled to be 1 Pa or 80 Pa with an Ar gas flow. In this pressure condition, the mean free path (l) of sublimed materials will be from a few millimeters to several tens of micrometers [25,26]. Because both of the diameter of orifices in baffles and the intervals between baffles are larger than l, we do not need consider the effusion process. Actually, it is still unclear for the present what the exact role of baffles is, but at least three kinds of mechanisms are under consideration and acceptable quite reasonable ones.

The first is that the collision of sublimed materials with baffles can enhance the collapse of clusters into individual molecules which can result in promotion of impurity separation from target materials. In principle, materials are sublimed and deposited in a molecular state in sublimation purification method. However, it is well known that materials are diffused not only in a molecular state but also in a cluster form in a real purification system. If there is an impurity molecule in the cluster, that impurity will be deposited on the same region with target materials. In this new purification system, clusters can undergo frequent collision with baffles and glass tubes, and be collapsed into smaller clusters or even into individual molecules. These

collapses of clusters can promote the separation of impurities from the target material, and result in increase of the purity of deposited materials.

The second is that the travelling distance of sublimed materials unto deposition points can be extended by introducing baffles. Sublimed materials which may be directly diffused unto deposition region without baffles can collide with baffles and change its diffusion direction and result in the increase of travelling distance. Because there are a few baffles at least and the orifices are not aligned straightly each other, the collision of sublimed materials with baffles can be occurred very often, and the travelling distance may be increased very largely. This increase of travelling distance can lead to the enhanced separation of impurities from target materials.

The third is that baffles installed in T_l region can suppress the efflux of purified materials out of the extraction region. Some of purified target materials can be flowed out of the extraction region and grow far away from the sublimation region together with impurities, which is one of the serious causes of lowering the purification yield. Baffles installed in T_l region can block such efflux of purified materials and return them into the extraction region, which can increase the effective yield. Such a role of baffles installed in T_l region may be related not only to the effective yield but also to the purity of extracted materials as mentioned in Section 3.1.

4. Summary

We have developed a highly efficient sublimation purification system using baffles with orifices in the sublimation tube. It was described that baffles introduced in T_l region made purified materials deposited on more concentrated region which was revealed with increased R_{EY} value. It was also clearly demonstrated that the purity of purified materials was increased largely by introducing baffles in T_h region. The impurity decrement increased up to 93.2% by introducing baffles from 72.6% in a conventional method, which is expected to be better than that of twice purified ones by a conventional method. From the results of multiple purification of BCP by a conventional method, it was also proved that one can get at least four times larger quantity of purified materials – even the purity is much higher – by using this new purification system instead of a conventional method. This improvement of purifying efficiency by introducing baffles in the sublimation tube was discussed briefly with three kinds of possible functions of baffles; collapsing clusters into individual molecules, extending travelling distance, and suppressing the efflux of purified materials.

Acknowledgement

This work was supported by CLUSTER (the second stage) of Ministry of Education, Culture, Sports, Science and Technology, Japan. The authors would like to give special thanks to Mr. Norimasa Yokoyama and to whom it may concerned of Hodogaya Chemical Co., Ltd. for offering lots of Bpy-OXD and for measuring HPLC purities of various Bpy-OXD samples. This paper is dedicated to the first principal, Chotaro Harizuka, on the occasion of 100th anniversary of Faculty of Textile Science and Technology, Shinshu University.

References

[1] C. Wöll (Ed.), Physical and Chemical Aspects of Organic Electronics: From Fundamentals to Functional Devices, Wiley-VCH, Weinheim, 2009 (Chapter 25).
[2] H. Klauk (Ed.), Organic Electronics: Materials, Manufacturing and Applications, Wiley-VCH, Weinheim, 2006 (Chapter 2).
[3] S.R. Forrest, Nature 428 (2004) 911.
[4] J.R. Sheats, J. Mater. Res. 19 (2004) 1974.
[5] A.R. Murphy, J.M.J. Fréchet, Chem. Rev. 107 (2007) 1066.
[6] K. Kato, T. Mori, Mol. Cryst. Liq. Cryst. 471 (2007) 53.
[7] W. Brütting (Ed.), Physics of Organic Semiconductors, Wiley-VCH, Weinheim, 2005 (Chapter 4).
[8] M. Pope, C.E. Swenberg, Electronic Processes in Organic Crystals and Polymers, Oxford University Press, New York, 1999 (Chapter II).
[9] V. Coropceanu, J. Cornil, D.A. da Silva Filho, Y. Olivier, R. Silbey, J.-L. Brédas, Chem. Rev. 107 (2007) 926.
[10] H.J. Wagner, R.O. Loutfy, C.-K. Hsiao, J. Mater. Sci. 17 (1982) 2781.
[11] H.E. Kats, L. Torsi, A. Dodabalapur, Chem. Mater. 7 (1995) 2235.
[12] D. Wöhrle, L. Kreienhoop, G. Schnurpfeil, J. Elbe, B. Tennigkeit, S. Hiller, D. Schlettwein, J. Mater. Chem. 5 (1995) 1819.
[13] O.D. Jurchescu, J. Baas, T.T.M. Palstra, Appl. Phys. Lett. 84 (2004) 3061.
[14] R.F. Salzman, J. Xue, B.P. Rand, A. Alexander, M.E. Thompson, S.R. Forrest, Org. Electron. 6 (2005) 242.
[15] L.B. Roberson, J. Kowalik, L.M. Tolbert, C. Kloc, R. Zeis, X. Chi, R. Fleming, C. Wilkins, J. Am. Chem. Soc. 127 (2005) 3069.
[16] S.R. Forrest, Chem. Rev. 97 (1997) 1793.
[17] W. Warta, R. Stehle, N. Karl, Appl. Phys. A 36 (1985) 163.
[18] C.-Y. Liu, A.J. Bard, Chem. Mater. 12 (2000) 2353.
[19] D.A. Pardo, N. Peyghambarian, G.E. Jabbour, Jpn. J. Appl. Phys. 40 (2001) 4922.
[20] H. Klauk (Ed.), Organic Electronics: Materials, Manufacturing and Applications, Wiley-VCH, Weinheim, 2006 (Chapter 9).
[21] H.-G. Jeon, M. Inoue, N. Hiramatsu, M. Ichikawa, Y. Taniguchi, Org. Electron. 9 (2008) 903.
[22] K. Yamamoto, M. Momota, H. Kitamura, K. Narita, Anal. Sci. 12 (1996) 893.
[23] B. Geffroy, P. Le Roy, C. Prat, Polym. Int. 55 (2006) 572.
[24] This result is somewhat similar to the result of ZnPc purification reported in Ref. [12], where ZnPc purified three times show rather lower device performance than that of twice purified one.
[25] P.W. Atkins, Physical Chemistry, fourth ed., Oxford University Press, Great Britain, 1993 (Chapter 24).
[26] See also the table in <http://en.wikipedia.org/wiki/Mean_free_path> where some typical mean free path values for different pressures are listed.

DP-DTT (**2**) exhibit excellent p-channel transport with hole mobilities of 0.42 cm^2/Vs [10a]. However, n-channel **DTT**-based semiconductors have been unknown until recently [11]. One approach to realizing electron transport in OTFTs is to functionalize p-channel semiconductors with strong electron-withdrawing and/or perfluorinated substituents, such as fluoro- [7a], perfluoroalkyl- [7b,12], perfluoroaryl- [7c,13], carbonyl- [14], cyano- [15], and trifluoromethylphenyl- [16] groups. Perfluorobenzoyl (COC_6F_5)-substituted quarter thiophenes (**DFCO-4T**) exhibit especially high electron mobilities of 0.45 cm^2/Vs for vapor-deposited films and 0.21 cm^2/Vs for solution-cast films [14a].

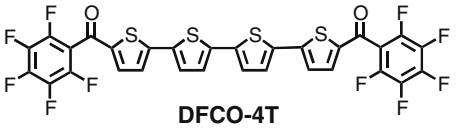

Following a similar molecular design strategy, we partly communicated synthetic approaches to several **DTT**-based compounds and their physicochemical properties [11]. Initial TFT results showed that two of these materials are n-channel semiconductors with electron mobilities of 10^{-3}–0.03 cm^2/Vs, and these were the first reports on **DTT**-based semiconductors. Although perfluorophenyl-substituted **DFP-DTT** (**3**) has been reported [17], its OTFT performance has not been explored. Herein, we report in full on the synthesis, characterization, and OTFT performance of **DTT**-based (**3**–**10**) organic semiconductors with appropriate electron-withdrawing groups, as shown in Fig. 1.

2. Experimental section

2.1. Materials and methods

All chemicals and solvents were of reagent grade and were obtained from Aldrich, Arco, or TCI Chemical Co. Solvents for reactions (toluene, benzene, ether, and THF) were distilled under nitrogen from sodium/benzophenone ketyl, and halogenated solvents were distilled from CaH_2. ^1H and ^{13}C NMR spectra were recorded on a Bruker 500, 300, or a Bruker DRX-200 instrument. Chemical shifts for ^1H and ^{13}C spectra were referenced to solvent peaks. ^{19}F NMR spectra were referenced to external $CFCl_3$. Differential scanning calorimetry (DSC) was carried out on a Mettler DSC 822 instrument, and calibrated with a pure indium sample at a scan rate of 10 K/min. Thermogravimetric analysis (TGA) was performed on a Perkin–Elmer TGA-7 thermal analysis system using dry nitrogen as a carrier gas at a flow rate of 40 mL/min. The UV–Vis absorption and fluorescence spectra were obtained using JASCO V-530 and Hitachi F-4500 spectrometers, respectively, and all spectra were measured in a specified solvent at room temperature. The IR spectra were obtained using a JASCO FT/IR-4100 spectrometer. Differential pulse voltammetry experiments were performed with a CH Instruments model CHI621C Electrochemical Analyzer. All measurements were carried out at a specified temperature with a conventional three-electrode configuration consisting of a platinum disk working electrode, an auxiliary platinum wire electrode, and a non-aqueous Ag reference electrode. The supporting electrolyte was 0.1 M tetrabutylammonium hexafluorophosphate ($TBAPF_6$) in a specified dry solvent. All potentials reported are referenced to an Fc^+/Fc internal standard (at +0.6 V). Elemental analyses were performed on a Heraeus CHN–O-Rapid elemental analyzer. Mass spectrometric data were obtained with a JMS-700 HRMS instrument. Prime grade silicon wafers (p^+-Si) with ~300 nm (±5%) thermally grown oxide (from Montco Silicon) were used as device substrates. Preparation of **DTT** (**1**) and **TTA** (via one-pot [1 + 1 + 1] synthesis), **DFB-DTT** (**4**), **FBB-DTT** (**5**), **DB-DTT** (**6**), and **DT-DTT** (**9**) as well as X-ray crystal structure determinations of compounds **4**, **5**, and **6** see supporting information of Ref. [11].

2.2. Synthesis

2.2.1. One-pot [2 + 1] synthesis of dithieno[2,3-b:3′,2′-d]thiophene (DTT; 1)

Under nitrogen at −78 °C, 2.5 M *n*-BuLi (48 mL in hexanes, 0.12 mol) was slowly added to an ether solution

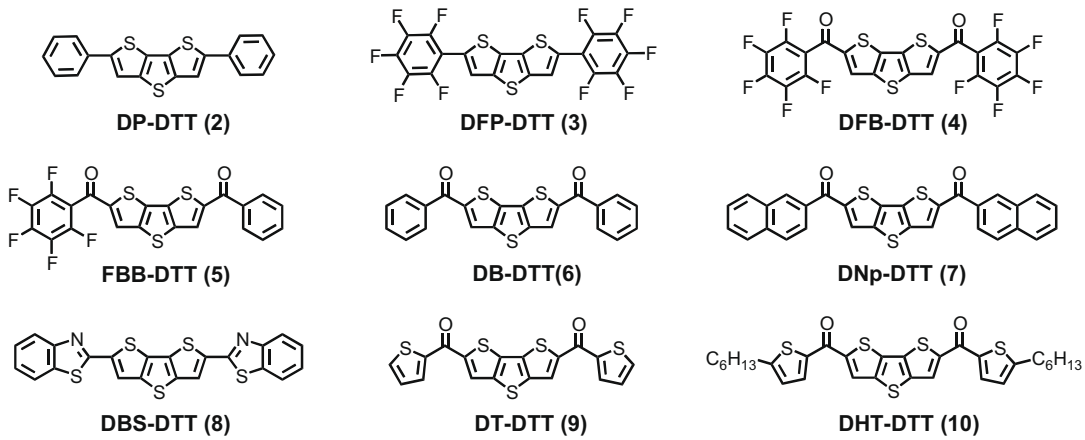

Fig. 1. Chemical structures of dithieno[2,3-b:3′,2′-d]thiophene (**DTT**) derivatives employed in this study.

(48 mL) of 3-bromothiophene (12 mL, 0.12 mol), and the mixture was stirred for 40 min. This solution was then warmed to 0 °C to vacuum remove C_4H_9Br, and then ether (48 mL) was added. (Note: without removing C_4H_9Br, 3-butyl-S-thiophene will be generated as a major side product after the S addition in the next step.) At −78 °C, sulfur (1.92 g, 0.06 mol) was added into this ether solution, stirred for 30 min, warmed to 0 °C, and stirred for another 30 min. p-Toluenesulfonyl chloride (TsCl, 11.42 g, 0.06 mol) was added to this solution at 0 °C, stirred for 30 min, then warmed up to 40 °C for 4 h. Next, at 0 °C, 2.5 M *n*-BuLi (52.8 mL in hexanes, 0.132 mol) was slowly added to this mixture, stirred for 30 min, and then refluxed for 1 h. $CuCl_2$ (18.32 g, 0.138 mol) was added to this mixture at 0 °C, stirred for 1 h, warmed to room temperature, and stirred overnight. Solids were removed by filtration, and the organic + ether portion was collected, and then chromatographed (silica gel; hexanes as the eluent). The **DTT** product was recrystallized from hexanes as light-yellow powder to give a total of 2.94 g in a yield of ~25.0%. ^{1}H NMR ($CDCl_3$): δ 7.36 (*d*, *J* = 5.4 Hz, 2H, 2,6-CH), 7.29 (*d*, *J* = 5.1 Hz, 2H, 3,5-CH).

2.2.2. One-pot [1 + 1 + 1] synthesis of pentathienoacene (PTA) [5a]

Follow the one-pot [1 + 1 + 1] synthetic procedure [11], 3-bromothieno[3,2-b]thiophene [18] was employed to give pentathienoacene (**PTA**) [5a] as yellow–orange powder in 12% yield. ^{1}H NMR (300 Hz; DMSO-d_6): δ 7.68 (*d*, *J* = 5.1 Hz, 2H, *CH*), 7.43 (*d*, *J* = 5.1 Hz, 2H, CH).

2.2.3. Synthesis of DP-DTT(2) [10a] and DFP-DTT (3) [19]

Under nitrogen at 0 °C, *n*-BuLi (2.5 M, 0.87 mL in hexanes, 2.18 mmol) was added to a 20 mL ether solution of **DTT** (0.195 g, 0.99 mmol) and the mixture was stirred at this temperature for 1 h. Tri-*n*-butylstannyl chloride (0.60 mL, 2.18 mmol) in 10 mL ether was then added into the mixture and stirred for 30 min at 0 °C. The mixture was then stirred at room temperature for 12 h. Ether was next removed under vacuum and 10 mL toluene solution of dry bromopentafluorobenzene (0.30 mL, 2.11 mmol) as well as 20 mL toluene solution of tetrakis(triphenylphosphine)palladium (50 mg, 0.04 mmol) were added and the mixture was refluxed for 24 h. Water was added to quench the reaction and the solid product was collected/filtered and was washed with hexanes, which was further purified by gradient sublimation at a pressure of $<10^{-4}$ Torr, giving a bright-yellow solid **DFP-DTT** (**3**; 259 mg) in a yield of 49.2%. ^{1}H NMR ($CDCl_3$): δ 7.77, ^{19}F NMR ($CDCl_3$): δ −139, −154, and −161.

DP-DTT (2) [10a] was prepared ~50% yield via similar procedure except using C_6H_6Br in the coupling reaction.

2.2.4. Synthesis of DNp-DTT (7)

Under nitrogen, $AlCl_3$ (6.47 g, 47.8 mmol) was added to a 100 mL CS_2 solution of **DTT** (0.939 g, 4.78 mmol) and 2-naphthalenecarbonyl chloride (2.03 g, 10.5 mmol), and the mixture was stirred at 40 °C for 3 days. Water was then added to quench the reaction, and the solid product was washed with ether and ethyl acetate, which was then purified by gradient sublimation at a pressure of $<10^{-4}$ Torr, giving a bright-yellow solid (0.736 g) in a yield of 30%. ^{1}H NMR ($CDCl_3$): δ 8.46, (s, 1H), 8.02–7.94 (m, 4H), 7.98 (s, 1H), 7.66–7.62 (m, 2H), 7.55–7.52 (m, 2H). ^{13}C NMR ($CDCl_3$): not sufficiently soluble to obtain a spectrum. Anal. calcd. for $C_{30}H_{16}O_2S_3$: C, 71.40; H, 3.20; S, 19.06. Found: C, 71.58; H, 2.98; S, 19.38. Orange crystals of the title compound suitable for X-ray diffraction were obtained by slow diffusion of hexanes into CH_2Cl_2 solution. The molecular structure of **7** has been confirmed by X-ray diffraction as shown in Fig. 4 (cif file of **7** is in SI).

2.2.5. Synthesis of DBS-DTT (8)

Under nitrogen, 3 eq. of 2-aminothiophenol (0.25 g, 1.96 mmol) was added to a 50 mL C_6H_5Cl solution of **DTT**-$(COCl)_2$ (0.21 g, 0.65 mmol, generated from **DTT**-$(COOH)_2$ with $SOCl_2$) and the mixture refluxed for 3 days. The desired solid product was collected by filtration, washed with ether, and then purified by gradient sublimation at pressures of $<10^{-4}$ Torr, giving a bright-yellow solid (0.13 g) in a yield of 42%. ^{1}H NMR ($C_2D_2Cl_4$): not sufficiently soluble to obtain a spectrum. Anal. calcd. for $C_{22}H_{10}N_2S_5$: C, 57.11; H, 2.18; N, 6.05, S, 34.65. Found: C, 56.55; H, 2.25; N, 5.96, S, 34.19. MS (FAB) *m*/z) calcd. for $C_{22}H_{10}N_2S_5$: 462 (M^+). Found: 462.

2.2.6. Synthesis of DHT-DTT (10)

Under nitrogen, a CH_2Cl_2 solution of **DTT**-$(COCl)_2$ (0.35 g, 1.1 mmol), 2-hexylthiophene (0.39 g, 2.3 mmol), and $AlCl_3$ (1.47 g, 11.0 mmol) was stirred at room temperature for 2 days. Water was added to quench the reaction and the solvent was removed under vacuum. The solid product was collected by filtration and washed with ether. The product was purified by gradient sublimation at pressures of $<10^{-4}$ Torr, giving a bright-yellow solid (0.22 g) in a yield of 35%. ^{1}H NMR ($CDCl_3$): δ 8.12 (s, 2H), 7.81 (d, *J* = 3.9 Hz, 2H), 6.91 (*d*, *J* = 3.9 Hz, 2H), 2.90 (*t*, *J* = 7.5 Hz, 4H), 1.75 (m, 4H), 1.42 – 1.30 (m, 12H), 0.90 (*t*, *J* = 7.5 Hz, 6H) Anal. calcd. for $C_{30}H_{32}O_2S_5$: C, 61.60; H, 5.51; S, 27.41. Found: C, 61.8; H, 5.82; S, 27.11. MS (EI) *m*/z) calcd. for $C_{30}H_{32}O_2S_5$: 584(M^+). Found: 584.

2.3. X-ray crystal structure determinations of compounds 3 and 7 [20]

The chosen crystal was mounted on a glass fiber. Data collection for compound **3** was carried out on a Bruker Smart Apex CCD diffractometer and compound **7** on a Nonius Kappa CCD diffractometer with Mo radiation (λ = 0.71073 Å) at 100(2) K and 200(2) K, respectively. After data collection, the frame was integrated and absorption correction was applied. The initial crystal structure was solved by direct methods, the structure solution was expanded through successive least-squares cycles, and the final solution was determined. All of the non-hydrogen atoms were refined anisotropically. Hydrogen atoms attached to carbon atoms were fixed at calculated positions and refined using a riding mode. Crystal data, data collection, and refinement parameters are summarized in Table S1.

2.4. Film deposition and characterization

All p^+-Si/SiO_2 substrates were cleaned via sonication in absolute ethanol for 3 min and then by oxygen plasma treatment for 5 min (20 W, 0.5 Torr). For the SiO_2 coating layer, –$SiMe_3$ groups were introduced using hexamethyldisilazane (HMDS) and were deposited by placing the clean SiO_2 substrates in a N_2-filled chamber saturated with HMDS vapor for 48–72 h. All of the semiconducting materials were vacuum deposited at $\sim 6 \times 10^{-6}$ Torr ($\sim$500 Å, 0.2–0.3 Å/s) at the preset deposition temperatures (T_D). Thin films of organic semiconductors were analyzed by atomic force microscopy (AFM) (JEOL-5200 Scanning Probe Microscope) in the tapping mode, scanning electron microscopy (Hitachi S-4800 FE-SEM), and wide angle θ–2θ X-ray diffraction (XRD) (Rigaku ATXG) using monochromated Cu K_α radiation. For TFT device fabrication, top-contact electrodes ($\sim$70 nm) were deposited by evaporating gold ($\sim 1 \times 10^{-6}$ Torr) through a shadow mask with a channel length (L) of 100 μm and a channel width (W) of 5000 μm.

3. Results and discussion

3.1. Synthesis

Since the key building block is the **DTT** core, a convenient, efficient, and cheap one-pot [2 + 1] synthesis of **DTT** was explored. Our new route from inexpensive, commercially available materials dispenses with the requirement for expensive bis(phenylsulfonyl)sulfide, and results in **DTT** in a much shorter synthetic time [21]. For this one-pot [2 + 1] synthesis, 3-bromo-thiophene (2 eq.) was first lithiated with *n*-BuLi (2 eq.), followed first by S_8 (1 eq.) and then by TsCl (1 eq.) additions, as shown in Scheme 1. Without isolating the product, the crude mixture was dilithiated with *n*-BuLi and ring closure was achieved with $CuCl_2$. Finally, **DTT** was isolated in a yield of about 25%. An alternative one-pot [1 + 1 + 1] synthesis of **DTT** was also achieved and offered a higher yield (about 30%). The former [2 + 1] route is simpler, but the latter [1 + 1 + 1] route enables the synthesis of fused thiophenes with more rings (e.g., pentathienoacene (**PTA**) was obtained in 12% yield) [5a] and asymmetric fused thiophenes (e.g., **DS-DTT**) that are not feasible using previous methods, as shown in Scheme 2 [11].

The synthesis of functionalized dithieno[2,3-b:3′,2′-d]thiophene was achieved and is shown in Schemes 3–6. Perfluorophenyl and perfluorobenzoyl functionalization of the **DTT** core should result in good candidates of n-channel semiconductors **3** (**DFP-DTT**) [17] and **4** (**DFB-DTT**). Since the electronic performance of **3** has not been examined, it was explored via the Stille coupling of the **DTT** core with C_6F_5Br in $\sim$49% yield as shown in Scheme 3, which is comparable to the Suzuki coupling method. For comparison **DP-DTT** (**2**) [10a] was also achieved via similar synthetic route. Preparation of **4** was explored using three different routes shown in Scheme 4. Route I, via the double deprotonation of **DTT** and then double acylation, provided the most efficient path to **4** (36% yield). Route II, via the thermal acylation of **DTT**, produced the double acylation product **4** in a yield of <30% with a considerable amount of mono-acylated **FB-DTT**

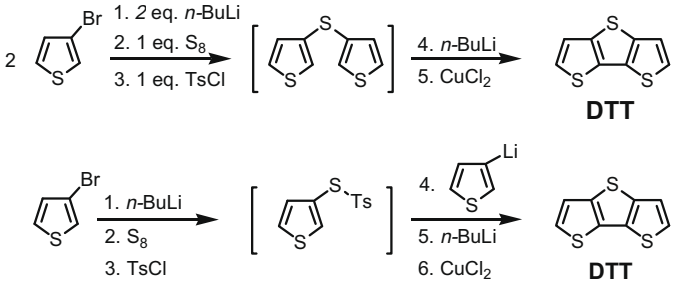

Scheme 1. One-pot [2 + 1] and [1 + 1 + 1] syntheses of the **DTT** core.

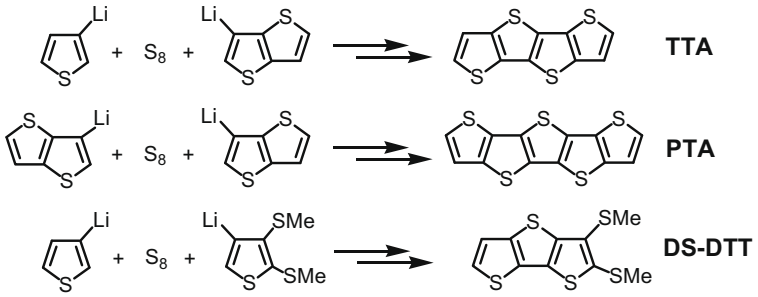

Scheme 2. One-pot syntheses of tetrathienoacene (**TTA**), pentathienoacene (**PTA**) and asymmetric **DTT**.

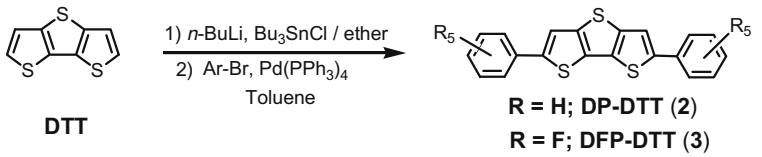

Scheme 3. Synthetic route to **DP-DTT (2)** and **DFP-DTT** (**3**).

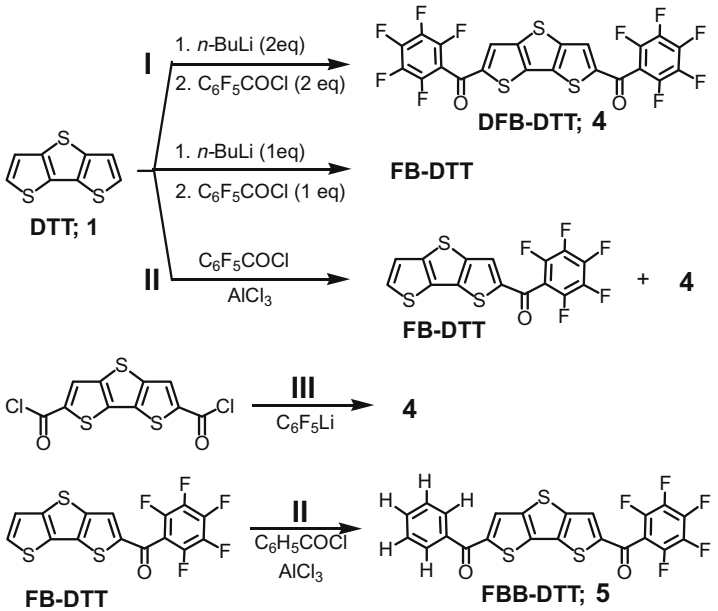

Scheme 4. Synthetic routes to **DFB-DTT** (**4**) and **FBB-DTT** (**5**).

side product, even after refluxing for one week. Presumably, compound **4** could also be generated from route III**,** the reverse of route I; however, a yield of less than 10% was obtained. Unprecedentedly, since mono-acylated **FB-DTT** could also be obtained as the major product (>80%) via mono-deprotonation of **DTT** with 1 eq. of *n*-BuLi and then mono-acylation with 1 eq. C_6F_5COCl, asymmetric **FBB-DTT** (**5**) was developed from the thermal mono-acylation of **FB-DTT** with benzoyl chloride via route II in a yield of 57% as shown in Scheme 4. Benzoyl-, 2-naphthylcarbonyl (Np-), and 2-thienoyl-substituted derivatives **6**, **7**, and **9** were also obtained in good yields via Route II (shown in Scheme 5). **DBS-DTT** (**8**) and **DHT-DTT** (**10**) can be obtained from refluxing **DTT**-$(COCl)_2$ [22] with 2-aminothiophenol and 2-hexylthiophene in a yield of ~40%, as shown in Scheme 6.

3.2. Thermal and optical properties

For these DTT derivatives, differential scanning calorimetry (DSC) scans exhibit a sharp endotherm above 214 °C, and thermogravimetric analysis plots demonstrate weight loss (5%) only on heating above 241 °C, as summarized in Table 1. For compounds **4**–**6**, lower melting points and lower weight loss temperatures were observed for **DTT** derivatives with a greater number of perfluorophenyl groups, which indicates a higher volatility contributed by the F-substituents, as reported in the literature [23]. Similar trend was observed for **DFP-DTT** (**3**) compared to its non-fluorinated derivative **DP-DTT** (**2**) [10a].

The optical absorption spectra of **DTT**s **2**–**10** in *o*-$C_6H_4Cl_2$ are significantly red-shifted compared to **1** (λ_{max} ~300 nm), as shown in Fig. 2, and the **DTT**s with the

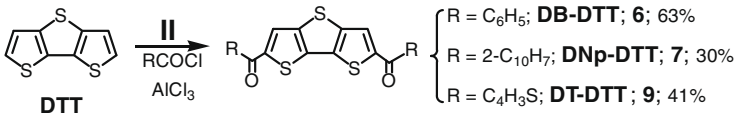

Scheme 5. Synthetic routes to **DTT**s (**6**, **7**, and **9**).

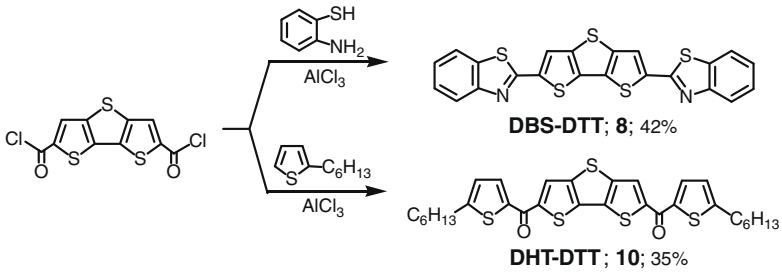

Scheme 6. Synthetic routes to **DTT**s (**8** and **10**).

Table 1
Thermal, optical absorption, and electrochemical data for compounds **2**–**10**.

Compound	DS C T_m (°C)	TGA (°C; 5%)	UV–Vis[b] λ_{max} (nm)	Reductive potential (V)[c]	Oxidative potential (V)[c]	ΔE_{gap} (eV)	
						(UV)[b]	(DPV)[c]
2	290[a]	394[a]	374	−1.95	1.21	3.00	3.17
3	258	270	367	−1.62	1.64	3.07	3.26
4	214	241	403, 383	−0.81	2.16	2.89	2.97
5	239	265	399, 382	−1.00	2.07	2.93	3.07
6	262	298	395, 378	−1.12	1.96	2.94	3.08
7	291	384	384, 399	−1.14	1.93	2.91	3.06
8	262	388	441, 417	−1.46	1.47	2.69	2.93
9	320	342	406, 391	−1.06	1.93	2.85	2.99
10	238	334	409, 399	−1.12	1.88	2.84	3.00

[a] See Ref. [10a].
[b] In *o*-$C_6H_4Cl_2$.
[c] By DPV in *o*-$C_6H_4Cl_2$ at 25 °C (using ferrocene/ferrocenium as internal standard at +0.6 V).

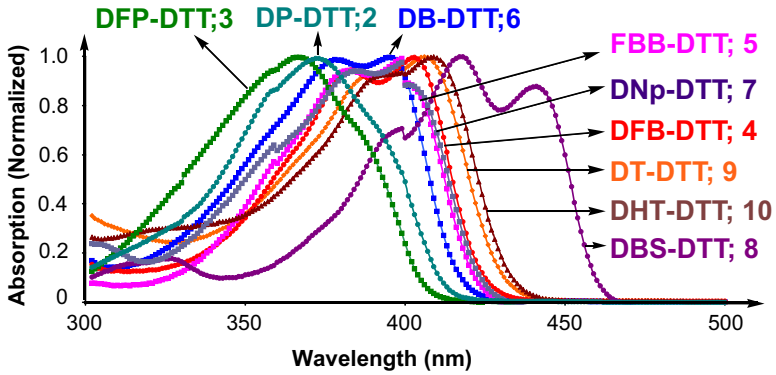

Fig. 2. Optical spectra of **DTT**s (**2**–**10**) in *o*-$C_6H_4Cl_2$ solution.

carbonyl substituents exhibit further red-shifted absorptions (λ_{max} >400 nm) than those without carbonyl substituents **DP-DTT** and **DFP-DTT** (λ_{max} ~360 nm). For compounds **4**–**6**, note that the absorption is slightly red-shifted in the compound having the greater number of F atoms. This result is in line with established substituent group directing effects [6c,24]. Compared to benzoyl-substituted **6**, more π-electron delocalization is observed for the 2-naphthylcarbonyl (**7**), and 2-thienoyl-substituted thienyl (**9**/**10**) or benzothiazolyl (**8**) substituted compounds, giving the latter the lowest energy gap among the compounds in this study. This result indicates delocalization extending from the **DTT** core to the two benzothiazolyl substituents. The HOMO–LUMO energy gaps calculated from the onset of the optical absorption (2.6–3.1 eV) increase in the order: **8** < **9** ≈ **10** < **4** < **7** < **5** < **6** < **2** < **3**, as shown in Table 1.

The photooxidative stability of the **DTT** derivatives was investigated by monitoring the absorbance decay at λ_{max} of **2**–**10** in aerated $CHCl_3$ solutions exposed to white light (fluorescent lamp) at room temperature. Under these conditions for 4–5 days, no decomposition is observed for any of these compounds, demonstrating the favorable stability of these materials.

3.3. Electrochemical characterization

Differential pulse voltammograms (DPVs; using ferrocene/ferrocenium as internal standard at +0.6 V) of **DTT**s **2**–**10** were recorded in dichlorobenzene at 25 °C, and the resulting reductive and oxidative potentials are summarized in Table 1 [25]. As expected, the non-carbonyl substituted **DTT**s exhibit the largest band gap of all the compounds in this study revealing relatively small -electron delocalization. Furthermore, the electron affinity increases with an increase in the number of fluoroaryl rings, where fluoroaryl substitution in **DFP-DTT** (**3**) strongly lowers both the HOMO and LUMO energies compared to those in **DP-DTT** (**2**). Similar trend was observed for **DFB-DTT** (**4**) compared to its non-fluorinated derivative **DB-DTT** (**6**) and half fluorinated asymmetric **FBB-DTT** (**5**). The HOMO–LUMO energy gaps obtained from the DPV data are 2.97 eV for **DFB-DTT**, 3.07 eV for **FBB-DTT**, and 3.08 eV for **DB-DTT** (Fig. 3; assuming ferrocene/ferrocenium oxidation at 4.8 eV) and the ordering is consistent with that obtained by optical absorption data. Compared to compound **6**, the HOMO and LUMO energies of the 2-naphthylcarbonyl (**7**), thienyl- (**9**) and hexylthienyl- (**10**) substituted compounds showed no significant change. In contrast, the benzothiazolyl substitution in compound **8** strongly shifts both the HOMO and LUMO levels to higher values, causing the compound to exhibit the most extensive π-electron delocalization among the **DTT** series with the smallest band gap (about 2.93 eV) [26]. Overall, the electrochemically-derived HOMO–LUMO energy gaps are ranked in the order **8** < **4** < **9** ≈ **10** < **7** < **5** < **6** < **2** < **3** (Table 1), which is consistent with the values obtained from optical spectroscopy.

3.4. Crystal structure

The diffraction-derived crystal structures of compounds **3** and **7** are shown in Figs. 4 and 5, and the crystal structure data are summarized in Table S1 [27]. Similar to **DFCO-4T** [14], compound **3** with F-substituents on both ends exhibits intramolecular and intermolecular ortho-F (perfluorophenyl)-H (DTT core) contacts [28], as shown in Fig. 4A and B. Like other non-carbonyl diaryl substituted DTTs [10], compound **3** exhibits typical herringbone packing with an interplanar angle of ~43.7° and the perfluorophenyl groups are only slightly deviated at angles of ~11° to the DTT core (Fig. 4B). The distances between the planar DTT cores are ~3.60 Å (Fig. 4B) with the shortest sulfur–sulfur distance of ~3.48 Å (Fig. 4C). Similar to compounds **4**, **5**, and **6**, the functionalized 2-naphthylcarbonyl moieties in compound **7** are not coplanar with the **DTT** cores, but are with a less acute torsional angles of about 36.4° (Fig. 5C) [29]. However, without the H–F intermolecular interactions, the molecular packings are considerably different for compound **7** (compared to **4** and **5**). Compound **7** exhibits typical herringbone structure (Fig. 5D) and adopt an edge-to-face packing motif [30] with an smaller interplanar angle of ~23.0° for **7** (Fig. 5E) [31] with the shortest sulfur–sulfur distance of ~3.25 Å (Fig. 5D). Comparing the carbonyl substituted DTT derivatives **4**–**6**, the distances

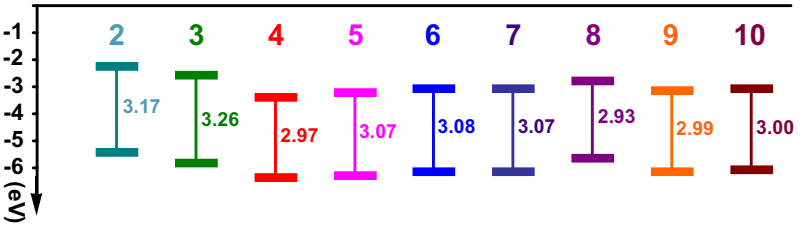

Fig. 3. The electrochemically-derived HOMO and LUMO energy levels of **DTT**s **2**–**10**.

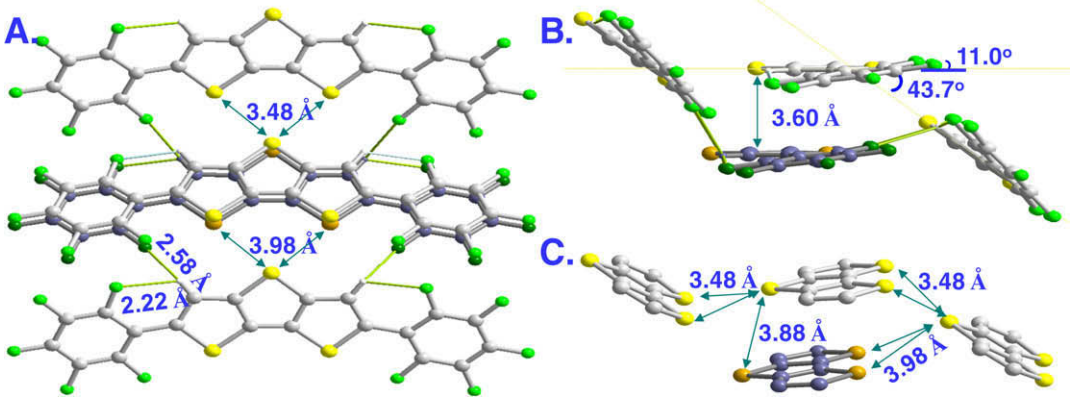

Fig. 4. Single-crystal structure of compound **3**. (A) Top view. Intramolecular (2.22 Å) and intermolecular (2.58 Å) F–H interactions between **DTT** cores. (B) Side view. The two **DTT** units with a 3.60 Å planar distance and an interplanar angle of 43.7 °. (C) S–S distances in **DTT**s.

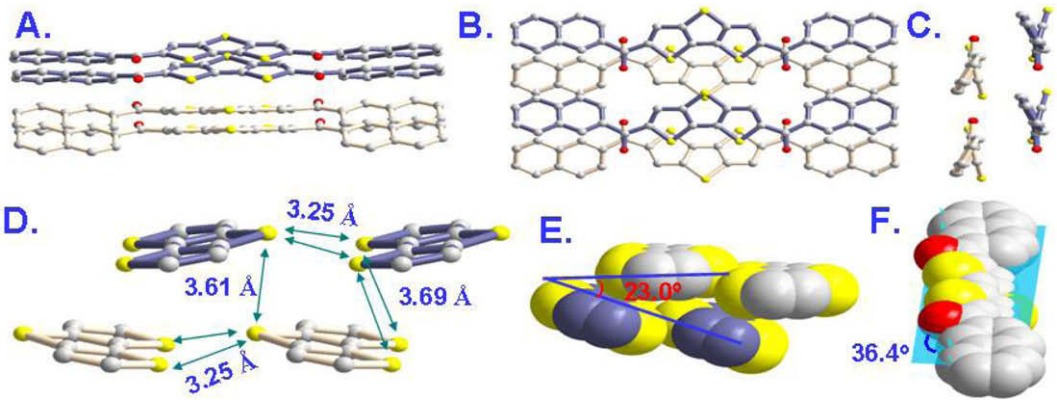

Fig. 5. Single-crystal structure of **7**. (A) Front view of **7**. (B) Top view. (C) Side view. (D) **DTT** cores with a herringbone arrangement and the S–S distances in **DTTs.** (E) **DTT** cores with an interplanar angle of 23.0°. (F) 2-Naphthyl with a torsional angle of about 36.4° to the **DTT** core.

between the planar DTT cores and the shortest S–S distances among DTT cores are **5** (~3.50 Å) < **6** (3.68 Å) < **4** (3.74 Å) and **5** (3.20 Å) < **6** (3.23 Å) < **4** (3.42 Å), respectively, demonstrating the tightest molecule-packing of **5** in the solid state, which is in accord with the OTFT device performance trends (*vide infra*).

3.5. Thin-film transistor characterization

Top-contact/bottom gate OTFT devices were fabricated by vacuum deposition (5×10^{-6} Torr) of each compound on bare and HMDS-treated SiO_2/p^+-Si substrates at preset deposition temperatures (T_D). Gold source and drain contacts were patterned by thermal evaporation using shadow masks that gave a channel length of 100 μm and a width of 5000 μm. The TFT properties were tested under positive or negative gate bias under vacuum to explore the major charge carrier types and device performance. TFT data are summarized in Table 2, and representative transfer and output plots are shown in Fig. 6.

Devices fabricated with **DTT**-based compounds all exhibit TFT activity, with compounds **3–5** performing as n-channel semiconductors, and the rest of the compounds performing as p-channel semiconductors. Derived field-effect mobilities of the **DTT** derivatives strongly depend upon both the dielectric surface treatment and the deposition temperature (T_D). In general, enhanced device performance is observed at higher deposition temperatures and on HMDS-treated SiO_2 substrates. Compounds **3–5** exhibit electron mobilities as high as 0.07, 0.002 and 0.03 cm^2/Vs, respectively. Compound **4** is active both under vacuum ($\mu = 3 \times 10^{-5}$–0.002 cm^2/Vs) and under ambient conditions ($\mu = 1 \times 10^{-4}$ cm^2/Vs), exhibiting high current on/off ratios of 10^5–10^6. Compounds **3** and **5**, on the other hand,

Table 2
Majority charge carrier types, field-effect mobilities (μ, cm^2/Vs),[a] current on/off ratios (I_{on}/I_{off}), and threshold voltages (V_T, V) for thin-film OTFTs fabricated by vacuum deposition of compounds **3–10** on bare and HMDS-treated p^+-Si/SiO_2 substrates at the indicated deposition temperatures (T_D, °C). Device performance measured under vacuum unless otherwise indicated.

Compound	Polarity	T_D	Bare			HMDS		
			μ	$I_{on}:I_{off}$	V_T	μ	$I_{on}:I_{off}$	V_T
3	N	25	3×10^{-4}	10^5	+74	0.07	10^7	+62
		50	3×10^{-4}	10^5	+62	0.06	10^7	+54
4	N	25	3×10^{-5}	10^4	+74	0.002	10^5	+35
		25[b]	Not active			1×10^{-4}	10^5	+28
5	N	25	4×10^{-6}	10^4	+60	0.003	10^7	+46
		70	3×10^{-6}	10^4	+38	0.03	10^7	+31
6	P	25	3×10^{-4}	10^6	−66	0.001	10^6	−65
		70	0.006	10^7	−66	0.005	10^7	−49
		90	0.01	10^7	−40	0.01	10^7	−53
7	P	25	Not active			3×10^{-5}	10^3	−66
		90	0.001	10^7	−45	0.004	10^6	−67
8	P	25	5×10^{-6}	10^5	−17	0.005	10^5	−24
		70	4×10^{-6}	10^4	−18	0.008	10^7	−26
		90	4×10^{-4}	10^5	−10	0.01	10^5	−23
9	P	25	Not active			1×10^{-5}	10^4	−58
		70	2×10^{-4}	10^6	−50	1×10^{-5}	10^5	−64
10	P	25	3×10^{-6}	10^4	−77	6×10^{-6}	10^5	−78
		50	1×10^{-5}	10^5	−76	4×10^{-6}	10^5	−77

[a] Device performance is the averaged value of at least four samples. (Standard deviation between devices is <10%.)
[b] Measured in ambient.

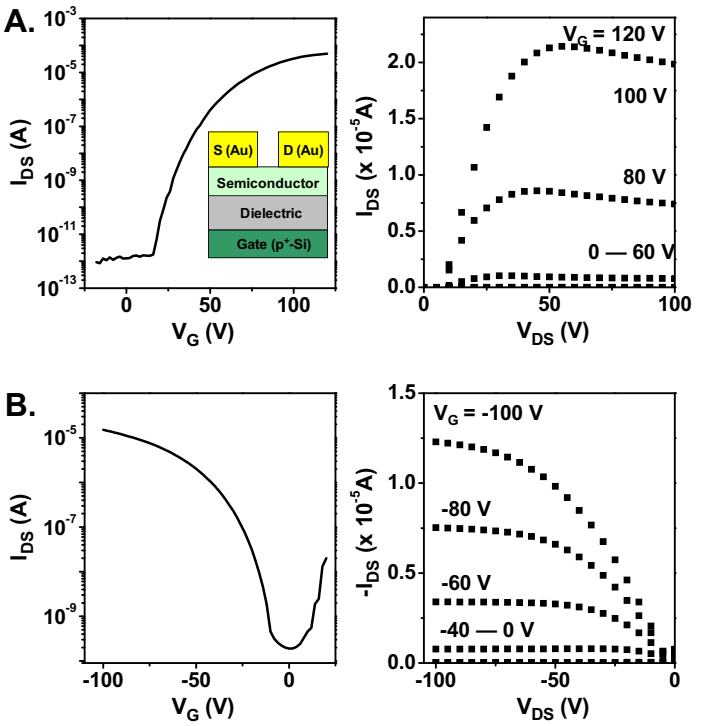

Fig. 6. OTFT plots of devices fabricated with compounds **3** and **8** on HMDS-treated SiO_2 substrates. (A) Transfer (V_{DS} = 100 V) and output plots of **3** (T_D = 25 °C), (B) transfer (V_{DS} = −100 V) and output plots of **8** (T_D = 90 °C). The general OTFT device structure (inset).

are only active under vacuum. Compound **3** exhibits the highest electron mobility, 0.07 cm^2/Vs, of all the **DTT** derivatives on HMDS-treated SiO_2 substrates (T_D = 25 °C) with an I_{on}/I_{off} of ~10^7 (Fig. 6A). The end-substitution with electron-withdrawing perfluorophenyl groups promotes majority carrier sign inversion in this family, as previously demonstrated for other materials [13]. The non-fluorinated **DTT** derivatives **6**–**10** exhibits p-channel transport with hole mobilities of 4×10^{-6}–0.01 cm^2/Vs. Among the p-channel **DTT**-based compounds, **6** and **8** exhibit relatively high mobilities, up to 0.01 cm^2/Vs, with I_{on}/I_{off} of 10^5–10^7 on HMDS-treated SiO_2 substrates (Fig. 6B). For these compounds, there is a clear correlation between μ and T_D, which is also evident in the XRD and AFM characterization data (*vide infra*). The other **DTT** (**7**, **9**, and **10**) derivatives exhibit relatively low hole mobilities of 4×10^{-6}–0.004 cm^2/Vs and I_{on}/I_{off} of 10^3–10^7.

3.6. Thin-film microstructure and morphology

Vacuum-deposited film crystallinity and morphology are known to affect TFT performance. Thin-film microstructures and morphologies for this new class of materials were studied by θ–2θ XRD, AFM, and SEM. X-ray diffraction experiments provide useful information to understand the crystallinity of the semiconductors as thin films and the molecular orientation relative to the substrate surface. In general, high crystallinity and preferential alignment of the π-conjugated core (perpendicular to the dielectric surface) are beneficial to efficient charge transport between the source and drain electrodes. In this study, conventional $\theta/2\theta$ scans were utilized to obtain out-of-plane *d*-spacings in the vacuum-deposited thin films on HMDS-treated Si/SiO_2 substrates at various T_Ds. The thicknesses of all films were determined to be 50–70 nm by profilometry. Representative XRD scans are shown in Fig. 7, and the data are presented in Table 3.

The $\theta/2\theta$ out-of-plane XRD scans show that all of compounds except **4** and **10** were highly textured and exhibit high intensities with multiple reflections (Fig. 7). For all of the films except compound **6** (*vide infra*), a single set of diffraction peaks is observed without the presence of any reflections corresponding to π–π stacking distances, and *d*-spacing values are estimated from the nominal (1 0 0) reflection peaks as 18.2–24.4 Å, suggesting the presence of a crystalline polymorph where the majority of the molecules have an edge-on orientation with respect to the substrate surface, with the π–π stacking direction roughly parallel to the substrate surface. This molecular orientation promotes in-plane charge transport from the source to the drain. Compounds **3**–**8** (except **4**) exhibit strong XRD peak intensities and multiple reflections, consistent with good TFT mobility, as described above. Compound **10** with poor TFT mobility exhibits only a single Bragg reflection, indicating low film texturing. This low texturing is possibly due to hindered molecular packing by the *n*-hexyl side groups. Interestingly, films of compound **4**, having reasonable carrier mobility (⩽0.002 cm^2/Vs), also exhibits only a single reflection and modest peak intensity. This indicates the presence of an interface mismatch between the HMDS-

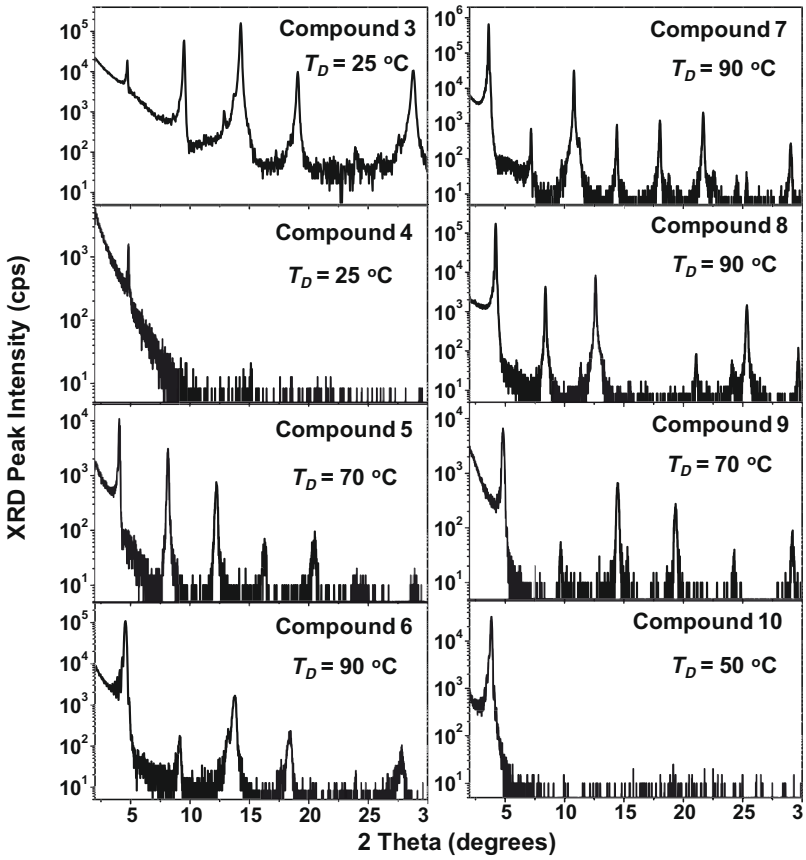

Fig. 7. Representative θ–2θ XRD scans on a logarithmic scale of **DTT** (**3**–**10**) films vapor-deposited at the indicated T_Ds on HMDS-treated SiO_2 substrates.

Table 3
The reflections and *d*-spacings calculated from (1 0 0) reflection for vacuum-deposited films of compounds **3**–**10** on HMDS-treated SiO_2 substrates at the indicated T_Ds.

Compound	Reflections	T_D (°C)	2θ (°) (1 0 0)	*d*-spacing (Å)
3	100–600	25, 50	4.70	18.8
4	100	25	4.84	18.2
5	100–700	25, 70	4.06	21.7
6	100–600	25–90	4.57	19.2–19.5
7	100–800	25, 90	3.61	24.4
8	100–700	25–90	4.20	21.0
9	100–600	25, 70	4.80	18.4
10	100	25, 50	3.83	23.0

treated SiO_2 dielectric and the fluorinated semiconductor layers, which prevents ordered crystal growth in the semiconductor layer. Similar results have been observed for end-fluorinated perylene- and naphthalene-based compounds [1c,32].

Since the TFT performance for several compounds is quite sensitive to the deposition temperature (*vide supra*), T_D-dependent XRD patterns were also examined. Fig. 8A shows field-effect mobilities and XRD data for films of compound **8** on HMDS-treated substrates at various T_Ds. As shown, there is a clear correlation between mobility values and XRD peak intensity. Note that XRD peak position for compound **8** films does not change at different T_Ds. Similar behavior is also observed for compound **5**-based TFTs (not shown). Interestingly, compound **6**-derived films show somewhat different XRD patterns. As the T_D increased, the XRD peak intensity for compound **6** films decreases slightly (Fig. 8B). However, the XRD peak position shifts to slightly higher angle, from $2\theta = 4.53°$ to 4.60°, at higher T_D values, suggesting some structural reorganization (from 19.5 to 19.2 Å of *d*-spacing). Enhanced mobility at higher T_D values for compound **6**-based TFTs appears to be associated with this reduced *d*-spacing.

Since microstructure characterization at the dielectric-semiconductor interface, where charge transport in TFTs occurs, is challenging by conventional techniques, we studied the morphology of the semiconductor surfaces via AFM and SEM, assuming that the microstructure at the surface conveys information about the underlying microstructure at the interface. From the film morphologies, it is clear that the film growth patterns depend significantly on the substrate temperature and surface treatment, which are strongly correlated with the device performance (*vide supra*). Figs. 9 and S1 show representative surface morphologies of the films of compounds **3**–**10**. For example, films exhibit ribbon-like grains (compounds **4** and **5** at 25 °C), plate-like faceted films (**3**, **5**–**8** at high T_D), or small grains (compounds **9** and **10**).

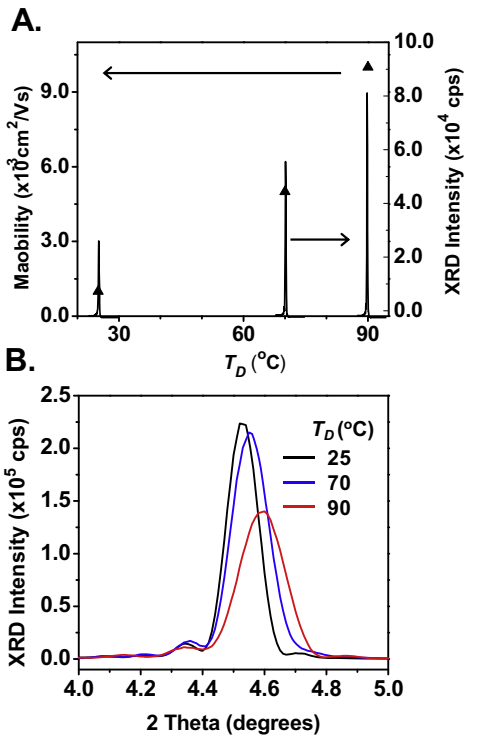

Fig. 8. (A) Field-effect mobilities and XRD ($\theta/2\theta$ scan; $2\theta = 3–6°$) data for compound **8**-based TFTs on HMDS-treated SiO_2 substrates at the indicated T_Ds. (B) XRD ($\theta/2\theta$ scan) data ($2\theta = 4–5°$) for compound **6**-derived films on bare SiO_2 substrates grown at the indicated T_Ds.

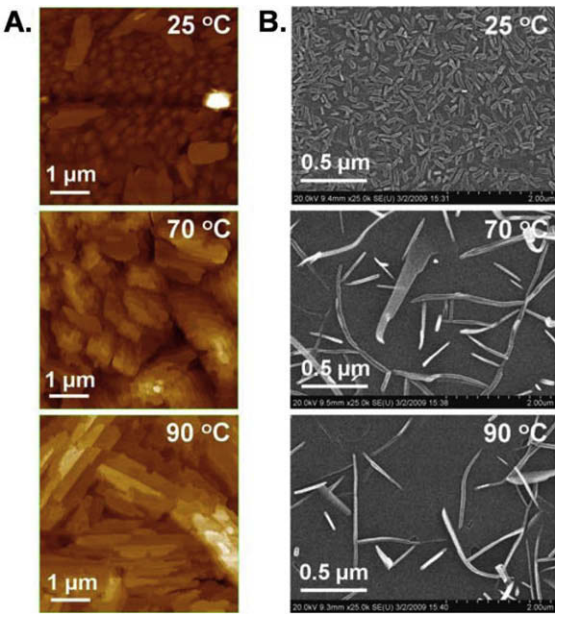

Fig. 9. (A) AFM images ($5 \times 5\ \mu m^2$) of films from compound **6** on bare SiO_2 substrates grown at the indicated T_Ds. (B) SEM images of films from compound **8** on HMDS-treated SiO_2 substrates grown at the indicated T_Ds.

Similar to the XRD patterns, AFM images also show a strong dependence of film morphology on the T_Ds and a correlation with the device performance. Fig. 9A and B shows AFM and SEM images of the films from compounds **6** and **8**, respectively, grown at different T_Ds. The films from compound **6** on bare SiO_2 substrates exhibit small grains with a few plate-like grains at $T_D = 25$ °C, but much larger, well-faceted grains are observed at higher T_Ds, as assessed by AFM (Fig. 9A). Films from compound **8** on HMDS-treated SiO_2 substrates show similar behavior, with lower T_D samples having small grains at $T_D = 25$ °C, but large crystal-like grains protruding from the film surface at higher T_Ds. The large highly-crystalline surface microstructural features exhibited by both compounds at the higher deposition temperature correlates well with the enhanced TFT performance. Similar T_D-dependent morphological change is also observed for compounds **3**, **5**, and **7** (Fig. S1).

4. Conclusions

Convenient, efficient, cost-effective, one-pot [2 + 1] and [1 + 1 + 1] synthesis of DTT were achieved that enables the efficient realization of a new **DTT**-based semiconductor series for organic thin-film transistors (OTFTs). Perfluorophenyl and perfluorobenzoyl substitutions are found to be effective in promoting n-channel transport. Diperfluorophenyl **DFP-DTT** (**3**), diperfluorobenzoyl **DFB-DTT** (**4**), and asymmetric **FBB-DTT** (**5**) films exhibit n-type transport with mobilities as high as 0.07 cm^2/Vs [33]. Compared to **DFCO-4T** [14a], the lower mobilities can be ascribed to the larger interplanar π–π separation distances (3.74 Å for **4** and 3.56 Å for **5** vs. 3.5 Å for **DFCO-4T**) caused by non-negligible F···H interactions in compounds **4** and **5** [34]. Interestingly, the intermolecular H···F interactions in asymmetric compound **5**, the compound having the shortest interplanar DTT core distances in this study, reveal the potential utility of this asymmetric design for other n-channel systems. In contrast, the non-fluorinated aryl carbonyl substituted **DTT** derivatives exhibit exclusively p-type transport, with the greatest hole mobility of 0.01 cm^2/Vs, observed for **DB-DTT** (**6**) and **DBS-DTT** (**8**). The carrier mobilities are found to be strongly dependent on the substrate deposition temperatures and surface treatments, and these **DTT**-based OTFTs exhibit excellent ambient stability over many months (near 1 year). These results provide new information about the structural characteristics of **DTT**-based semiconductors and the advantages of using this stable core for designing more soluble derivatives.

Acknowledgements

We thank the National Science Council, Taiwan, Republic of China (Grant Numbers NSC98-2628-M-008-003, NSC97-2113-M-008-003, and NSC98-2627-E-006-003) and Industrial Technology Research Institute of Taiwan for support. Financial assistance for this research was partially provided by the NSF-MRSEC program through the Northwestern Materials Research Center (DMR-0520513).

Appendix A. Supplementary data

Supplementary data associated with this article can be found, in the online version, at doi:10.1016/j.orgel.2010.01.022.

References

[1] (a) For recent discussions of this topic, see: C. Kim, A. Facchetti, T.J. Marks, Science 318 (2007) 76;
(b) A.R. Murphy, J.M.J. Frechet, Chem. Rev. 107 (2007) 1066;
(c) B.A. Jones, A. Facchetti, M.R. Wasielewski, T.J. Marks, J. Am. Chem. Soc. 129 (2007) 15259;
(d) J.E. Anthony, Chem. Rev. 106 (2006) 5028.

[2] (a) For recent studies, see: H. Yan, Z. Chen, Y. Zheng, C. Newman, J.R. Quinn, F. Dotz, M. Kastler, A. Facchetti, Nature 457 (2009) 679;
(b) M.L. Tang, S.C.B. Mannsfeld, Y.-S. Sun, H.A. Becerril, Z. Bao, J. Am. Chem. Soc. 131 (2009) 882;
(c) N. Kobayashi, M. Sasaki, K. Nomoto, Chem. Mater. 21 (2009) 552;
(d) Y. Didane, G.H. Mehl, A. Kumagai, N. Yoshimoto, C. Videlot-Ackermann, H. Brisset, J. Am. Chem. Soc. 130 (2008) 17681;
(e) S. Subramanian, S.K. Park, S.R. Parkin, V. Podzorov, T.N. Jackson, J.E. Anthony, J. Am. Chem. Soc. 130 (2008) 2706;
(f) M.L. Tang, A.D. Reichardt, N. Miyaki, R.M. Stoltenberg, Z. Bao, J. Am. Chem. Soc. 130 (2008) 6064.

[3] (a) D.H. Kim, D.Y. Lee, H.S. Lee, W.H. Lee, Y.H. Kim, J.I. Han, K. Cho, Adv. Mater. 19 (2007) 678;
(b) Y. Li, Y. Wu, P. Liu, Z. Prostran, S. Gardner, B.S. Ong, Chem. Mater. 19 (2007) 418;
(c) T.W. Kelly, P.F. Baude, C. Gerlach, D.E. Ender, D. Muyres, M.A. Hasse, D.E. Vogel, S.D. Theiss, Chem. Mater. 16 (2004) 4413.

[4] (a) I. Mcculloch, M. Heeney, C. Bailey, K. Genevicius, I. Macdonald, M. Shkunov, D. Sparrowe, S. Tierney, R. Wagner, W. Zhang, M.L. Chabinyc, R.J. Kline, M.D. Mcgehee, M.F. Toney, Nat. Mater. 5 (2006) 328;
(b) Y. Wu, P. Liu, S. Gardner, B.S. Ong, Chem. Mater. 17 (2005) 221;
(c) A.R. Murphy, J.M.J. Frecht, P. Chang, J. Lee, V. Subramanian, J. Am. Chem. Soc. 126 (2004) 1596.

[5] (a) K. Xiao, Y. Liu, T. Qi, W. Zhang, F. Wang, J. Gao, W. Qiu, Y. Ma, G. Cui, S. Chen, X. Zhan, G. Yu, J. Qin, W. Hu, D. Zhu, J. Am. Chem. Soc. 127 (2005) 13281;
(b) Y. Liu, Y. Wang, W. Wu, Y. Liu, H. Xi, L. Wang, W. Qui, K. Lu, C. Du, G. Yu, Adv. Funct. Mater. 19 (2009) 1;
(c) H.H. Fong, V.A. Pozdin, A. Amassian, G.G. Malliaras, D.M. Smilgies, M. He, S. Gasper, F. Zhang, M. Sorensen, J. Am. Chem. Soc. 130 (2008) 13202;
see examples in Ref. [9].

[6] (a) M.M. Payne, S.R. Parkin, J.E. Anthony, C.-C. Kuo, T.N. Jackson, J. Am. Chem. Soc. 127 (2005) 4986;
(b) J.G. Laquindanum, H.E. Katz, A.J. Lovinger, J. Am. Chem. Soc. 120 (1998) 664;
(c) M.-C. Chen, C. Kim, S.-Y. Chen, Y.-J. Chiang, M.-C. Chung, A. Facchetti, T.J. Marks, J. Mater. Chem. 18 (2008) 1029.

[7] (a) Y. Sakamoto, T. Suzuki, M. Kobayashi, Y. Gao, Y. Fukai, Y. Inoue, F. Sato, S. Tokito, J. Am. Chem. Soc. 126 (2004) 8138;
(b) A. Facchetti, M. Mushrush, M.-H. Yoon, G.R. Hutchison, M.A. Ratner, T.J. Marks, J. Am. Chem. Soc. 126 (2004) 13859;
(c) M.-H. Yoon, A. Facchetti, C.E. Stern, T.J. Marks, J. Am. Chem. Soc. 128 (2006) 5792;
(d) M.-H. Yoon, C. Kim, A. Facchetti, T.J. Marks, J. Am. Chem. Soc. 128 (2006) 12851;
(e) Z. Wang, C. Kim, A. Facchetti, T.J. Marks, J. Am. Chem. Soc. 129 (2007) 13362;
(f) D. Shukla, S.F. Nelson, D.C. Freeman, M. Rajeswaran, W.G. Ahearn, D.M. Meyer, J.T. Carey, Chem. Mater. 20 (2008) 7486.

[8] (a) M. Mushrush, A. Facchetti, M. Lefenfeld, H.E. Katz, T.J. Marks, J. Am. Chem. Soc. 125 (2003) 9414;
(b) M.-H. Yoon, S.A. DiBenedetto, A. Facchetti, T.J. Marks, J. Am. Chem. Soc. 127 (2005) 1348;
(c) A. Dodabalapur, Mater. Today 9 (2006) 24.

[9] (a) For 3 fused ring review see: T. Ozturk, E. Erdal Ertasb, O. Mert, Tetrahedron 61 (2005) 11055;
(b) . For 5 fused ring example see:X. Zhang, A.P. Cote, A. Matzger, J. Am. Chem. Soc. 127 (2005) 10502;
(c) . For 6 fused ring example see:T. Okamoto, K. Kudoh, A. Wakamiya, S. Yamaguchi, Org. Lett. 7 (2005) 5301;
(d) . For 7 fused ring example see:M. He, F. Zhang, J. Org. Chem. 72 (2007) 442.

[10] (a) Y. Sun, Y. Ma, Y. Liu, Y. Lin, Z. Wang, Y. Wang, C. Di, K. Xiao, X. Chen, W. Qiu, B. Zhang, G. Yu, W. Hu, D. Zhu, Adv. Funct. Mater. 16 (2006) 426;
(b) Y. Sun, Y. Liu, Y. Ma, C. Di, Y. Wang, W. Wu, G. Yu, W. Hu, D. Zhu, Appl. Phys. Lett. 88 (2006) 242113;
(c) C. Hunziker, X. Zhan, P.A. Losio, H. Figi, O. Kwon, S. Barlow, P. Gunter, S.R. Marder, J. Mater. Chem. 17 (2007) 4972;
(d) L. San Miguel, W.W. Porter III, A.J. Matzger, Org. Lett. 9 (2007) 1005;
(e) X.-C. Li, H. Sirringhaus, F. Garnier, A.B. Holmes, S.C. Moratti, N. Feeder, W. Clegg, S.J. Teat, R.H. Friend, J. Am. Chem. Soc. 120 (1998) 2206;
(f) J. Li, F. Qin, C.M. Li, Q. Bao, M.B. Chan-Park, W. Zhang, J. Qin, B.S. Ong, Chem. Mater. 20 (2008) 2057.

[11] M.-C. Chen, Y.-J. Chiang, C. Kim, Y.-J. Guo, S.-Y. Chen, Y.-J. Liang, Y.-W. Huang, T.-S. Hu, G.-H. Lee, A. Facchetti, T.J. Marks, Chem. Commun. (2009) 1846.

[12] (a) A. Facchetti, M. Mushrush, H.E. Katz, T.J. Marks, Adv. Mater. 15 (2003) 33;
(b) A. Facchetti, M.-H. Yoon, C.L. Stern, G.R. Hutchison, M.A. Ratner, T.J. Marks, J. Am. Chem. Soc. 126 (2004) 13480;
(c) A. Facchetti, Y. Deng, A. Wang, Y. Koide, H. Sirringhaus, T.J. Marks, R.H. Friend, Angew. Chem. Int. Ed. 39 (2000) 4547.

[13] (a) A. Facchetti, M.-H. Yoon, C.L. Stern, H.E. Katz, T.J. Marks, Angew. Chem. Int. Ed. 42 (2003) 3900;
(b) S.E. Koh, B. Delley, J.E. Medvedeva, A. Facchetti, A.J. Freeman, T.J. Marks, M.A. Ratner, J. Phys. Chem. B 110 (2006) 24361.

[14] (a) J.A. Letizia, A. Facchetti, C.L. Stern, M.A. Ratner, T.J. Marks, J. Am. Chem. Soc. 127 (2005) 13476;
(b) X. Cai, C.P. Gerlach, C.D. Frisbie, J. Phys. Chem. C 111 (2007) 452.

[15] (a) B.A. Jones, A. Facchetti, T.J. Marks, M.R. Wasielewski, Chem. Mater. 19 (2007) 2703;
X. Cai, M.W. Burand, C.R. Newman, D.A. Da Silva Filho, T.M. Pappenfus, M.M. Bader, J.-L. Bredas, K.R. Mann, C.D. Frisbie, J. Phys. Chem. B 110 (2006) 14590;
(c) T. Jung, B. Yoo, L. Wang, B.A. Jones, A. Facchetti, M.R. Wasielewski, T.J. Marks, A. Dodabalapur, Appl. Phys. Lett. 88 (2006) 183102.

[16] (a) S. Ando, R. Murakami, J. Nishida, H. Tada, Y. Inoue, S. Tokito, Y. Yamashita, J. Am. Chem. Soc. 127 (2005) 14996;
(b) S. Ando, J. Nishida, H. Tada, Y. Inoue, S. Tokito, Y. Yamashita, J. Am. Chem. Soc. 127 (2005) 5336.

[17] T. Kazuo, N. Naoto, O. Tetsuo, Synthesis 10 (2005) 1589.

[18] Y. Mazaki, K. Kobayashi, Tetrahedron Lett. 30 (1989) 3315.

[19] **DFP-DTT** (**3**) was prepared via Suzuki coupling reaction, see Ref. [17]. Stille coupling route could also provide the title compound in comparison yield.

[20] X-ray crystal structure determinations of compounds **4**, **5**, and **6** are given in the supporting information of Ref. [11].

[21] (a) F. De Jong, M.J. Janssen, J. Org. Chem. 36 (1971) 1645;
(b) F. Allared, J. Hellberg, T. Remonen, Tetrahedron Lett. 43 (2002) 1553;
J. Frey, A.D. Bond, A.B. Holmes, Chem. Commun. (2002) 2424.

[22] Generated in situ by refluxing DTT-$(COOH)_2$ in $SOCl_2$ for 6 h.

[23] See similar examples in Ref. [12].

[24] This can be ascribed by the increased molecular polarity of the compounds substituted by these F groups. H.Z. Chen, M.M. Ling, X. Mo, M.M. Shi, M. Wang, Z. Bao, Chem. Mater. 19 (2007) 816.

[25] (a) Measured with a Pt working electrode in an o-dichlorobenzene solution using 0.1 mol dm-3 Bu4NPF6 as the supporting electrolyte. Y. Sakamoto, T. Suzuki, M. Kobayashi, Y. Gao, Y. Fukai, Y. Inoue, F. Sato, S. Tokito, J. Am. Chem. Soc. 126 (2004) 8138;
(b) N. Jun-ichi Nishida, D. Kumaki, S. Tokito, Y. Yamashita, J. Am. Chem. Soc. 128 (2006) 9598.

[26] Benzothiazolyl (BS) derivatives tend to form coplanar arrangement, for example see Y.-C. Chang, Y.-D. Chen, C.-H. Chen, Y.-S. Wen, J.T. Lin, H.-Y. Chen, M.-Y. Kuo, I. Chao, J. Org. Chem. 73 (2008) 4608. In contrast, the carbonyl substituents to the DTT cores are with 30°–55° dihedral angels.

[27] For crystal structures of compounds **4**, **5**, and **6**, see SI in Ref. [11].

[28] The intra- and inter-molecular F–H interactions was also observed in other fluorophenyl thiophenes, for examples, see D.J. Crouch, P.J. Skabara, M. Heeney, I. McCulloch, S.J. Coles, M.J. Hursthouse, Chem. Commun. (2005) 1465.

[29] For **DFCO-4T** in Ref. [14], the twist angles are slightly larger (about 60.3°) than the **DTT** derivatives. The twisted angles are about ~52°/53°, 30°/55°, and 45° for **4**, **5**, and **6**, respectively, see Ref. [11].

[30] For compounds **4** and **5**, the arrangement of the **DTT** cores adopt a nearly face-to-face packing motif, see SI in Ref. [11].
[31] For **6**, the interplanar angle is 36.5°.
[32] H.E. Katz, J. Johnson, A.J. Lovinger, W. Li, J. Am. Chem. Soc. 122 (2000) 7787.
[33] Ambipolar transport in these **DTT** materials was not observed.
[34] In addition to the larger intermolecular core distance, the less conjugation of **DTT**s may be responsible for the lower mobilities.

the semiconductor thickness. This finding showed that the charge transport in these systems takes place mainly in the first two monolayers close to the insulator/semiconductor interface [3].

While those crystalline vacuum-deposited oligothiophene films are well-established, well-studied model systems showing highly ordered layer-by-layer growth and high charge carrier mobilities [4–6], low-cost production requires semiconductors which are soluble in solvents and can therefore be fast and easily processed by methods like drop-casting, spin-coating, dip-coating or printing. These requirements are fulfilled by several polymers of the thiophene material class, the polythiophenes. One of the best-known materials of this class is regio-regular poly-(3-hexylthiophene) (rr-P3HT), which is soluble in several solvents, therefore processable wet-chemically, and shows comparably high charge carrier mobility [7].

Unlike the above-mentioned small oligothiophene molecules deposited by evaporation in vacuum, the long polythiophene chains processed from solution do not show such high ordering [8,9]. Several studies have been performed on the dependence of the charge carrier mobility on the P3HT film thickness [10–13]. They were performed on silicon substrates with the silicon serving as common gate electrode and a silicon oxide layer serving as gate insulator on which source and drain electrodes as well as the P3HT were deposited. Contrary to this bottom-gate setup, a top-gate structure with spin-coated gate insulator on top of the P3HT layer is often used in plastic devices, where the insulator thus serves also as encapsulation of the P3HT layer, which otherwise shows rapid degradation of its electric qualities within minutes or hours.

Increasing mobility μ with increasing P3HT layer thickness was found for thin layers in bottom-gate transistors on silicon substrates. Sandberg et al. presume that because of interfacial strain, thin layers/monolayers are poorly ordered whereas the presence of a highly ordered bulk in thicker films causes an ordering effect in the interfacial layer [12]. This reordering is obviously completed at a thickness of ca. 20 nm, where Wang et al. found a constant charge carrier mobility after a strong increase with thickness for thinner layers [13]. Further deposition of the polymer to even higher thickness does not have a big effect on the interface layers any more. As the charge transport takes place mainly in the part of the semiconductor adjacent to the gate insulator, the charge carrier mobility remains fairly constant with further increased thickness.

The interface between semiconductor and insulator is known to play a crucial role in OFET performance [14]. In OFETs fabricated on silicon substrates P3HT is processed on the smooth surface of silicon oxide. In our devices however, the interface between insulator and semiconductor, at which the charge transport is presumed to take place, is the one between the upper side of the P3HT layer and the organic insulator deposited on top of it. Thus possible changes in the P3HT surface roughness, e.g. with increasing layer thickness, would directly affect the charge transport properties. Knipp et al. showed that in bottom-gate pentacene OFETs the charge carrier mobility of a device with a rough surface of the gate dielectric was more than one order of magnitude lower than in a film deposited on a smooth surface, while all other parameters remained the same [15]. In a more quantitative study, also on evaporated pentacene layers, Steudel et al. investigated the relation between the rms value of the SiO_2 surface and the charge carrier mobility in OFETs produced on this surface and also found a strong mobility decrease with increasing rms value [16]. A similar result was found by Jung et al. [17] with spin-coated polythiophenes on SiO_2 and could be related to the grain size variation with surface roughness. Therefore, the thickness dependence of the P3HT charge carrier mobility determined in silicon-based bottom-gate devices cannot be transferred to the top-gate device setup and was investigated in the present study with the organic insulator poly(methyl methacrylate) (PMMA).

As typical for disordered systems, P3HT shows non-constant, gate-voltage dependent mobility. This manifests itself in the linear regime by a non-linear shape of the transfer curves. Nevertheless in most studies, charge carrier mobilities are determined by linear fits in a very limited voltage range, often at extreme voltages, to obtain larger mobility values. Mobilities obtained in this way are difficult to compare since the selected voltage regime matters. Furthermore, valuable physical information is lost, as the exponent of the gate-voltage dependence of the charge carrier mobility reflects the width of the density of localized states, in which the charge transport takes place via hopping from one state to another. Therefore, in this study the transfer curves are fitted according to the Vissenberg–Matters model [18], allowing us to use the complete transfer curves over the entire measurement range and to extract the threshold voltage, the charge carrier mobility at a certain gate-voltage and the exponent of its variation with the gate-voltage, which allows us to calculate the width of the exponential density of states.

2. Experimental

The organic field-effect transistors (OFETs) were produced on poly(ethylene terephtalate) (PET) foils. The transistors were built in a bottom-contact configuration with top-gates. The setup is shown in the upper left of Fig. 1. 30 nm thick gold source and drain electrodes were structured by optical (UV) lithography. Each sample contained 45 transistors, among them 12 transistors with equal geometry, i.e. a channel length L of 20 μm and a channel width W of 20 mm. These transistors were used for the statistical analysis presented here.

As organic semiconductor, regio-regular poly-(3-hexylthiophene) (rr-P3HT, Fig. 1, lower left) from BASF, Germany with a molecular weight of 40,000 g/mol and a regioregularity of 94% was used. It was spin-coated onto the samples at 2000 rpm from solutions in chloroform ($CHCl_3$) filtered through a 450 nm filter. Solutions with different concentrations of P3HT, ranging from 0.02 wt.% to 2.0 wt.%, were taken for spin-coating to obtain different film thicknesses. After one minute of heating at 90 °C, the gate insulator was spin-coated on top. Poly(methyl methacrylate) (PMMA, Fig. 1, lower right) from Evonik industries, Germany, with a molecular weight M_w of 1250 kD

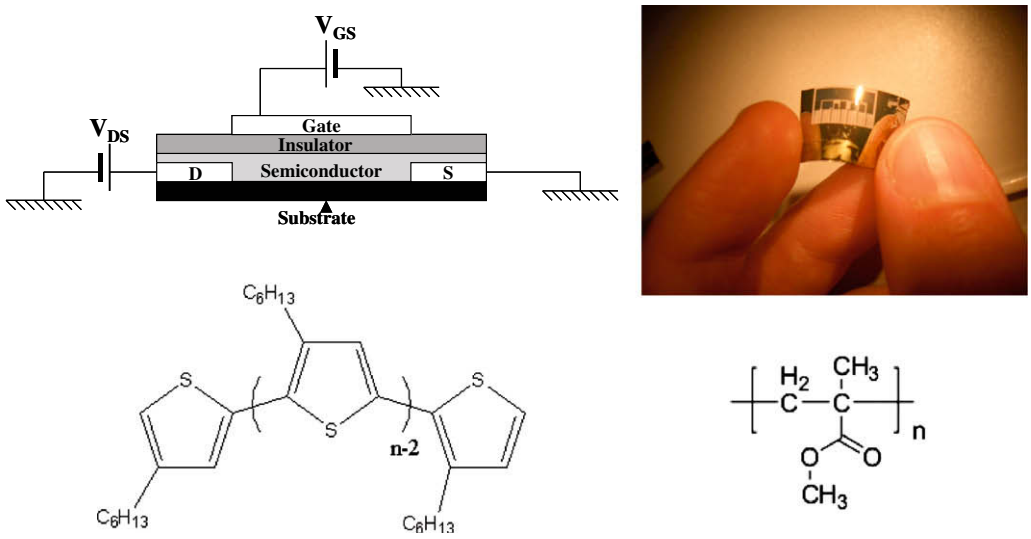

Fig. 1. Top: schematic view (left) and photo of OFET in bottom-contact and top-gate configuration produced on flexible and transparent plastic substrates; bottom: chemical structure of regio-regular poly-(3-hexylthiophene) (rr-P3HT, left) and poly(methyl methacrylate) (PMMA, right).

was used in a 5 wt.% solution in methyl-ethyl-ketone and spin-coated at 2000 rpm, yielding a layer of (860 ± 10) nm thickness. Remaining solvents were baked out during 5 min at 60 °C. The top-gate electrodes of gold (thickness (50 ± 5) nm) were deposited through a shadow mask in an argon sputter coater. Transfer and output curves were taken by measurements in darkness in ambient air (21 °C, 34% relative humidity) in a probe station where the source, drain and gate electrodes were contacted by needles. The thickness of the P3HT semiconductor layers was measured by a *Dektak* profilometer and confirmed by atomic force microscopy (AFM). Exemplary capacitance measurements with two gold rectangles produced on the same sample templates on the source/drain and on the gate level, respectively, confirmed the thickness measurements. The layer thicknesses were determined to be 3, 10, 12, 17, 21, 39, 53, 88, and 216 nm.

Exemplary transfer (taken in the linear regime at $V_{DS} = -1$ V) and output curves of the transistor devices can be seen in Fig. 2. Hardly any hysteresis is observed at all. The shape is typical for polymeric transistors, with a power law dependence of the mobility on the gate-voltage [19]. This results in an increasing slope with higher, i.e. more negative, gate-source voltage, which cannot be described by a simple linear fit consistent with the standard gradual channel approximation. Therefore, we used the Vissenberg–Matters model for charge transport in highly disordered systems [18]. It assumes charge transport to take place via variable range hopping between localized states in the tail of an exponential density of states (DOS)

$$N(E) = \frac{N_t}{\sigma} \exp\left(\frac{E}{\sigma}\right) \quad \text{for } E \leqslant 0 \tag{1}$$

with the total number of tail states N_t and the width of the DOS σ. For one given temperature T, the charge carrier mobility μ is then related to the gate-voltage V_{GS} in an exponential correlation:

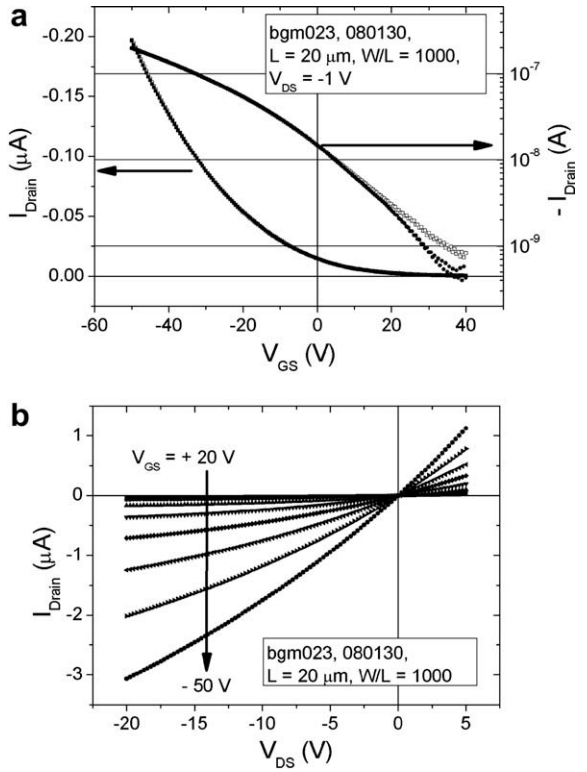

Fig. 2. Transfer curve (a) and output curves (b) taken from a transistor with a P3HT layer thickness of 21 nm. The mobility increases by a power law with the gate-source voltage. The exponent is found to be 2.4, the threshold voltage V_{th} is 44 V. Filled symbols show the forward measurements (from positive to negative voltage), open symbols the reverse measurements.

$$\mu = \mu_0 \left(\frac{V_{GS} - V_{th}}{V_{aa}}\right)^{\gamma} \tag{2}$$

μ_0 is the charge carrier mobility at $V_{GS} - V_{th} = V_{aa}$, where V_{aa} is an adequately chosen constant. According to the Vissenberg–Matters model, the exponent γ of the gate-voltage dependence is directly related to the width of the exponential DOS σ and thus to the disorder of the system by

$$\gamma = 2\left(\frac{\sigma}{k_B T} - 1\right) \quad (3)$$

where k_B is Boltzmann's constant. Data analysis in this way contains thus additional physical information compared to linear fits in a limited voltage range, the data obtained are clearly defined and allow for easier comparison with other data. The fits reproduce the whole transfer curves over the entire voltage range measured, as can be seen in Fig. 3.

Highest charge carrier mobilities of up to 1×10^{-2} cm^2/(Vs) are observed, which are high values for P3HT transistors for the given induced carrier density in the channel. Publications report of mobilities beyond 0.1 cm^2/(Vs) on e.g. silicon substrates determined at high gate-voltages (60 V) and oxide thickness of 200 nm or less [20,21], which corresponds to an electric field of 5 MV/cm, for higher carrier densities than are used in the present study. Our gate-source voltage of −50 V at 860 nm insulator thickness corresponds to a reasonable electric field of around 500 kV/cm. Applications at operation voltages of 10 V or lower would then require a reasonable insulator thickness below 170 nm.

When exposed to air, P3HT field-effect transistors usually show a rapid decrease in device performance. The charge carrier mobility μ decreases within minutes and falls by an order of magnitude after one day only. This makes not encapsulated P3HT OFETs inappropriate for most applications. In our devices, however, the P3HT layer is encapsulated by the insulator layer and therefore protected against air and humidity. No decrease of charge carrier mobility has been observed even for transistors produced more than four months ago. This shows that PMMA encapsulation is suitable for the protection of P3HT layers.

Fig. 4a shows the average values and standard deviation of the charge carrier mobility μ_0 for the $L = 20\mu$m transistors of nine different samples with nine different P3HT

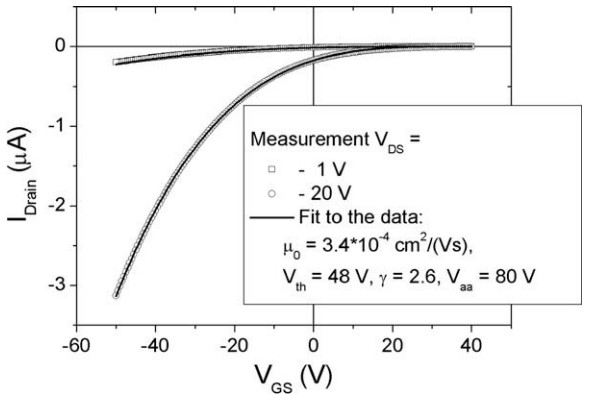

Fig. 3. Fits according to the Vissenberg–Matters model to transfer curves from the same transistor as in Fig. 2. The fits reproduce the curves over the entire voltage range which was measured, V_{GS} from +50 to −50 V, in the linear regime (V_{DS} = −1 V) as well as at V_{DS} = −20 V.

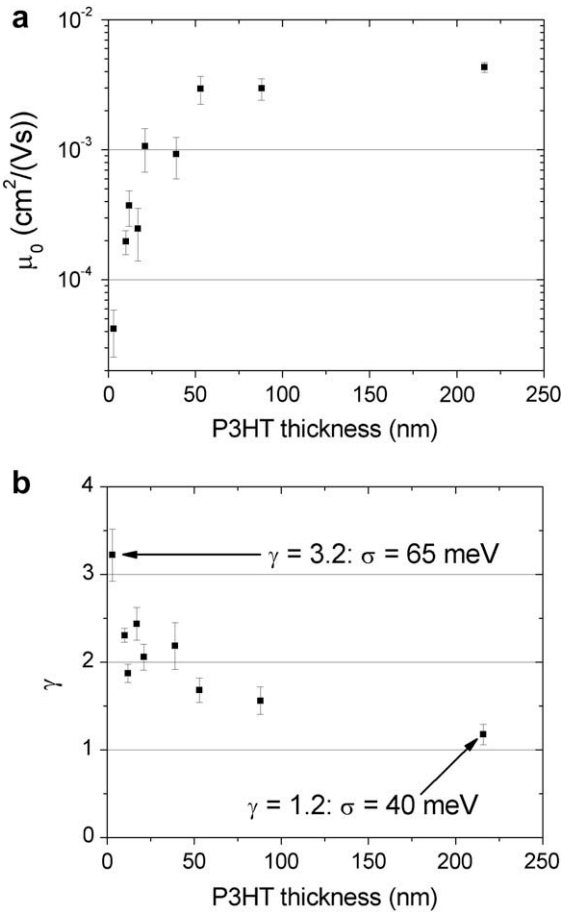

Fig. 4. (a) Charge carrier mobilities μ_0 (at V_{aa} = 80 V) and (b) exponent γ obtained for the L = 20 μm transistors, plotted over the thickness of the P3HT semiconductor layer. Each data point represents the average and standard deviation of 12 transistors with the same device geometry on the same substrate. The overall number of transistors shown is thus 108.

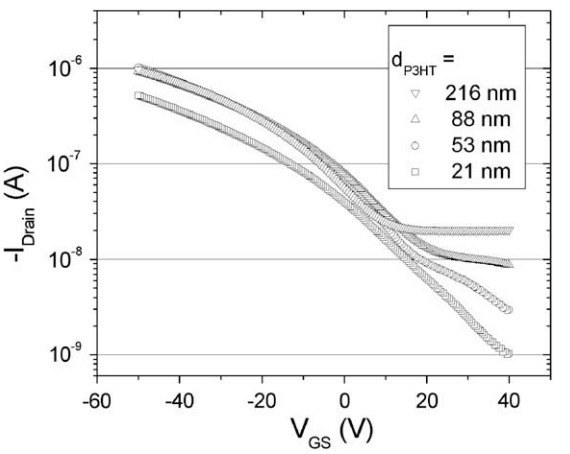

Fig. 5. Comparison of logarithmically plotted transfer curves of devices with different P3HT thickness depicting the constant on-current but increasing off-current in devices with more than 50 nm thickness.

layer thicknesses between 3 and 216 nm. As experiments with P3HT transistors processed by dip-coating have shown, a single monolayer of P3HT corresponds to a thickness of about 2 nm [11,22]. While for the smallest thickness of 3 nm, obtained by spin-coating a 0.02 wt.% solution, a low charge carrier mobility of just $\mu_0 = (4.2 \pm 1.7) \times 10^{-5}$ cm^2/(Vs) was obtained, at a film thickness of 21 nm the mobility increased by more than one order of magnitude to $\mu_0 = (1.1 \pm 0.4) \times 10^{-3}$ cm^2/(Vs). For films with thicknesses higher than 50 nm, a saturation of the mobility value at 3×10^{-3} cm^2/(Vs) was observed. In devices with thicker active layer, like the ones with 88 and 216 nm P3HT thickness, no significant increase of on-current and mobility is observed any more. The devices even show worse quality in the sense that the off-current is increased by more than one order of magnitude with further growing layer thickness as seen in Fig. 5. This is due to the fact that the positive voltage applied at the top-gate can only deplete a thin layer next to the interface whereas not entirely depleted regions still enable bulk current flow in the thicker films due to the residual doping level. Hence there is an optimum active layer thickness just below 50 nm in our top-gate transistors, which combines high charge carrier mobility with low off-currents.

Part (b) of Fig. 4 shows the average and standard deviation of the mobility exponent γ in dependence of the semiconductor thickness. The exponent strongly decreases from 3.2 at 3 nm thickness down to less than 2 in thicknesses above 40 nm. For even bigger thickness, the change is much less dramatic. While from these values of γ the width of the exponential density of states was determined to be 40 meV ($\gamma = 1.2$) for the thickest film, it increases up to 65 meV ($\gamma = 3.2$) in the thin films of 3 nm thickness. The reduced mobility in these thin films can thus directly be related to higher electronic disorder.

Phase contrast AFM measurements were taken to verify if the observed electronic disorder is related to the structural order of the film. Fig. 6 shows exemplarily the phase contrast images (3×3 μm^2) of a 10 nm thick film spin-coated from 0.05 wt.% solution in chloroform and of a 50 nm thick film spin-coated from 0.7 wt.% solution. Indeed, it is observed that the thicker film is much more ordered, exhibiting larger grain sizes. According to Fourier transformation of the data, the average correlation length in the phase contrast image of the thicker film is ca. 150 nm compared to 80 nm in the left image of the thinner film.

3. Conclusion

P3HT transistors in top-gate configuration with PMMA as gate insulator were successfully produced on flexible and transparent plastic foils as substrate. The electrical characteristics were analyzed according to the Vissenberg and Matters model for charge transport in disordered systems taking into account the gate-voltage dependence of the charge carrier mobility, which is directly related to the width of the DOS and thus the disorder of the system. High charge carrier mobility μ of up to 10^{-2} cm^2/(Vs) was obtained at $V_{GS} = -50$ V for a 860 nm insulator. Due to the encapsulation of the P3HT semiconductor by the insulator, the device performance remained stable during months. Low operation voltages of 10 V are expected with decrease of the insulator thickness. This active layer thickness dependence study shows a strong mobility increase with thicker P3HT layer in the regime of a few nm, up to a saturation around 50 nm. Further increase in thickness does not improve the mobility, but deteriorates the device performance by increasing the off-current. The mobility increase is accompanied by a decrease of the exponent γ of the gate-voltage dependence of the mobility. The observed thickness dependence of the mobility is thus explained by poor ordering in very thin films and improved ordering at 40–50 nm, while further increase of thickness does not affect the film order. Phase contrast AFM images confirm the better ordering of thicker P3HT films.

Acknowledgements

The authors acknowledge financial support by PolyIC GmbH & Co., KG, Fürth, Germany, in the frame of the Ma-

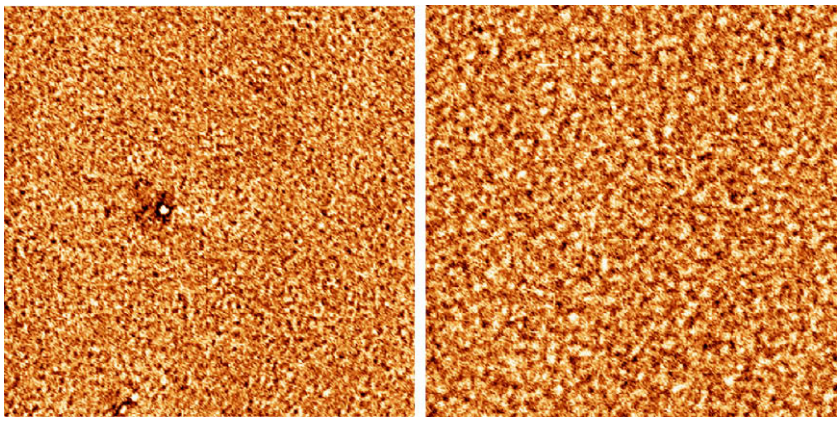

Fig. 6. AFM phase contrast images (3×3 μm^2) of the surface of a 10 nm thick P3HT film on a silicon wafer, spin-coated from 0.05 wt.% solution in chloroform (left), and of a 50 nm thick film spin-coated from 0.7 wt.% solution (right).

DriX project of the German Bundesministerium für Bildung und Forschung (BMBF).

References

[1] G. Horowitz, J. Mater. Res. 19 (2004) 1946.
[2] C.D. Dimitrakopoulos, D.J. Mascaro, IBM J. Res. Dev. 45 (2001) 11.
[3] T. Muck, J. Fritz, V. Wagner, Appl. Phys. Lett. 86 (2005) 232101.
[4] H. Katz, A. Lovinger, J. Laquindanum, Chem. Mater. 10 (1998) 457.
[5] M. Halik, H. Klauk, U. Zschieschang, G. Schmid, S. Ponomarenko, S. Kirchmeyer, W. Weber, Adv. Mater. 15 (2003) 917.
[6] A. Hoppe, J. Seekamp, T. Balster, G. Götz, P. Bäuerle, V. Wagner, Appl. Phys. Lett. 91 (2007) 132115.
[7] H. Sirringhaus, P.J. Brown, R.H. Friend, M.M. Nielsen, K. Bechgaard, B.M.W. Langeveld-Voss, A.J.H. Spiering, R.A.J. Janssen, E.W. Meijer, P. Herwig, D.M. de Leeuw, Nature 401 (1999) 685.
[8] H. Sirringhaus, P.J. Brown, R.H. Friend, M.M. Nielsen, K. Bechgaard, B.M.W. Langeveld-Voss, A.J.H. Spiering, R.A.J. Janssen, E.W. Meijer, Synth. Met. 111–112 (2000) 129.
[9] A. Salleo, Mater. Today 10 (2007) 38.
[10] H. Jia, S. Gowrisanker, G.K. Pant, R.M. Wallace, B.E. Gnade, J. Vac. Sci. Technol. A 24 (2006) 1228.
[11] A.N. Aleshin, H. Sandberg, H. Stubb, Synth. Met. 121 (2001) 1449.
[12] H.G.O. Sandberg, G.L. Frey, M.N. Shkunov, H. Sirringhaus, R.H. Friend, Langmuir 18 (2002) 10176.
[13] G. Wang, T. Hirasa, D. Moses, A.J. Heeger, Synth. Met. 146 (2004) 127.
[14] N. Benson, M. Schidleja, C. Melzer, R. Schmechel, H. von Seggern, Appl. Phys. Lett. 89 (2006) 182105.
[15] D. Knipp, R.A. Street, A.R. Völkel, Appl. Phys. Lett. 82 (2003) 3907.
[16] S. Steudel, S. De Vusser, S. De Jonge, D. Janssen, S. Verlaak, J. Genoe, P. Heremans, Appl. Phys. Lett. 85 (2004) 4400.
[17] Y. Jung, R.J. Kline, D.A. Fischer, E.K. Lin, M. Heeney, I. McCulloch, D.M. DeLongchamp, Adv. Funct. Mater. 18 (2008) 742.
[18] M.C.J.M. Vissenberg, M. Matters, Phys. Rev. B 57 (1998) 12964.
[19] M. Estrada, A. Cerdeira, J. Puigdollers, L. Reséndiz, J. Pallares, L.F. Marsal, C. Voz, B. Iñiguez, Solid State Electron. 49 (2005) 1009.
[20] G. Wang, J. Swensen, D. Moses, A.J. Heeger, J. Appl. Phys. 93 (2003) 6137.
[21] J.-F. Chang, B. Sun, D.W. Breiby, M.M. Nielsen, T.I. Sölling, M. Giles, I. McCulloch, H. Sirringhaus, Chem. Mater. 16 (2004) 4772.
[22] A. Ivanov, A. Hoppe, V. Wagner, in: Proceedings of 5th Organic Electronics Conference, Frankfurt, 2007.

core [9]. It was found that the "bricklayer" structure showed much better TFT performance than the "slipped-stacked" structure, and that the bulkiness of the substituents (relative to the molecular size) which produced the bricklayer structure was required to fall within a narrow range; If the size of the substituents was too large or too small, a "slipped-stacked" or "herringbone" structure occurred, which showed poorer TFT performance. Based on this strategy, many small molecules yielding promising TFT performances have been developed [10–12].

In 2007, our group reported the development of promising *TIPS* anthracene derivatives (*TIPSAnts*) using the anthracene moiety in place of pentacene [13]. Anthracene is much more stable with respect to Diels–Alder reactions, and this stability prevents butterfly dimer decomposition, improves processability, and yields high crystallinity [14–16]. Small molecules containing *TIPSAnt* showed promising optical, electrochemical, and crystalline properties that resulted in moderate charge-carrier mobilities. However, to achieve higher TFT performances, further improvements were required. Because *TIPSAnt* contains dibromo moieties, it can serve as a soluble oligomer core for aromatic coupling reactions. The synthetic functionalities of *TIPSAnt* led to the development of a variety of new *TIPSAnt*-based small molecules.

Recently, we reported single crystal TFT performances of *TIPSAnt* derivatives by incorporating naphthalene and bithiophene moieties as counterparts of *TIPSAnt* [17]. Device performance was increased by increasing the molecular surface area available for π-stacking overlap. However, *TIPSAntNa* and *TIPSAntBT* single crystals showed only a "slipped-stacked" structure.

In this paper, we report three new small molecules based on *TIPSAnt*, 2,6-bis(thiophene-2′-yl)-9,10-bis(triisopropylsilylethynyl)anthracene (*TIPSAntT*), 2,6-bis(benzo[b]thiophene-2′-yl)-9,10-bis(triisopropylsilylethynyl)anthracene (*TIPSAntBeT*), and 2,6-bis(5′-phenyl-thiophene-2′-yl)-9,10-bis(triisopropylsilylethynyl)anthracene (*TIPSAntPT*). We systematically designed these new small molecules to elucidate the relationship between thin-film structure and TFT device performance for aromatic end-capped *TIPSAnt* derivatives. Thiophene, benzothiophene, and phenyl thiophene were used as end cappers for the *TIPSAnt* series. Two structural factors were considered: (1) the increase in the rigidity caused by fusing the aromatic rings, and (2) the increase in the effective π-stacking area of the "bricklayer" structure. We performed a comparative study to investigate the relationship between the molecular structures and TFT performances by measuring the thermal, optical, electrochemical, crystalline, and morphological properties of these molecules. This study demonstrated, for the first time, that the preparation of a "bricklayer" stacking structure using a *TIPSAnt* derivative yields high TFT performance.

2. Experimental

2.1. Instruments and reagents

^{1}H and ^{13}C NMR spectra were recorded on a Bruker AVANCE 400 spectrometer with tetramethylsilane as an internal reference. For the NMR measurements, chloroform-d ($CDCl_3$) was used as the solvent for the materials except *TIPSAntBeT* (1,1,2,2,-tetrachloroethane-d_2). Elemental analysis was performed using EA-1110-FISONS elemental analyzer. UV–vis spectra were measured by using a Jasco V-530 UV/vis Spectrometer. Thermogravimetric analysis (TGA) measurement was performed under nitrogen atmosphere at a heating rate of 10 °C/min using TA Q500 instrument, and the differential scanning calorimetric (DSC) measurement was made using TA Q100 instrument operated under nitrogen atmosphere. Cyclic voltammetry (CV) measurement was performed on an AUTOLAB/PGSTAT12 at room temperature with a three-electrode cell in a solution of 0.1 M tetrabutylammonium tetrafluoroborate (TBABF4) in anhydrous acetonitrile at room temperature under nitrogen gas with a scan rate of 50 mV/s. The working electrode was the oligomer coated platinum, the counter electrode was a platinum wire, and the reference electrode was $Ag/AgNO_3$ (0.10 M) which was separated by a diaphragm. The measurements were calibrated using ferrocene as a standard. The single crystal for X-ray analysis was typically grown from hexane and chlorobenzene. Analyses were performed on a Bruker SMART Apex II X-ray Diffractometer. Data have been submitted as .cif files. AFM (Multimode IIIa, Digital Instruments) operating in tapping-mode was used to image surface morphology of our semiconductor. Synchrotron X-ray diffraction analyses of PAT4 films were performed at the 10C1 beam line (wavelength ≈1.54 Å) of the Pohang Accelerator Laboratory (PAL). Top-contact OTFTs were fabricated on a common gate of highly n-doped silicon with a 300 nm thick thermally grown SiO_2 dielectric layer. Substrates were modified with octyltrichlorosilane from a toluene solution for 2 h at room temperature. Films of organic semiconductor were spin-coated at 2000 rpm from 0.7 wt.% chloroform or chlorobenzene solution, with nominal thickness 45 nm. Gold source and drain electrodes were evaporated on the top of semiconductor (100 nm). For all measurements, we used channel lengths (L) of 150 μm and channel widths (W) of 1500 μm. Electrical characteristics of the TFTs were measured in air using both Keithley 236 source/measure units. The carrier mobility was calculated in the saturation regime from the slope of a plot of the square root of the drain current versus gate voltage (V_G) by fitting the data to the following equation: $I_{DS} = (WC_i/2L)\mu(V_G - V_T)^2$, where I_{DS} is the drain current, μ is the carrier mobility and V_T is the threshold voltage. For single crystal TFTs, saturated chlorobenzene solution of the small molecules was slowly evaporated at room temperature on OTS-modified SiO_2 substrates. After 1 or 2 days, well-defined rod-type single crystals were obtained and gold electrode was patterned onto the single crystals by thermal evaporation with thickness of 100 nm. Width and length of the channels were calculated from optical microscopy (OM) images. The thickness of single crystals was measured using an alpha stepper (Alpah Step 500, Tencor).

Chemical reagents were purchased from Aldrich Chemical Co. and were used without further purification. Solvents with analytical-grade were used during the whole experiments, and all chemicals were used without further purification. 2,6-Dibromo-9,10-bis-(triisopropylsilylethy-

nyl)anthracene (*TIPSAnt*) [13], 2-pinacolborylthiophene (1a) [18], and 2-(4′,4′,5′,5′-tetramethyl-1′,3′,2′-dioxaborolane)benzo[b]thiophene (1b) [19], 5-phenyl-1-tributyl stannyl thiophene (1c) [20] were synthesized according to the reported procedures.

2.2. Synthesis

2.2.1. Synthesis of 2,6-Bis(thiophene-2′-yl)-9,10-bis(triisopropylsilylethynyl)anthracene (TIPSAntT)

Into 150 mL two-neck flask were added *TIPSAnt* (1 g, 1.43 mmol) and 2-pinacolborylthiophene (1a) (0.66 g, 3.16 mmol) in 15 mL of anhydrous toluene. Catalytic amount of tetrakis(triphenyl phosphine)palladium(0) was transferred into the mixture in dry box. Subsequently, (2 M Na_2CO_3) sodium carbonate (0.76 g, 7.21 mmol) deaerated for 30 min and the phase transfer catalyst, Aliquat®336 (0.29 g, 0.72 mmol) in toluene purged under nitrogen for 1 h was transferred via cannula. The reaction mixture was stirred at 90 °C for 3 days and cooled to room temperature. Then, the reaction mixture was poured into saturated sodium bicarbonate solution and extracted with EA. The organic layer was washed with brine, and then dried over anhydrous $MgSO_4$. The crude product was column chromatographed with hexane and MC mixture as the eluent, and then crystallized from hexane and MC to yield *TIPSAntT* (0.72 g, 71.0%) as bright orange crystal. ^{1}H NMR ($CDCl_3$, ppm) δ = 8.84 (d, 2H), 8.60 (d, 2H), 7.87 (dd, 2H), 7.53 (d, 2H), 7.37 (d, 2H), 7.14 (dd, 2H), 1.31 (m, 42H). ^{13}C NMR ($CDCl_3$, ppm) δ = 144.31, 132.57, 132.49, 132.19, 128.25, 127.92, 125.79, 125.72, 123.99, 122.97, 118.53, 105.28, 103.10, 19.00, 11.55. Anal. calcd for $C_{44}H_{54}S_2Si_2$: C, 75.15%; H, 7.74%; S, 9.12%. Found: C, 74.73%; H, 7.58%; S, 8.99%.

2.2.2. Synthesis of 2,6-bis(benzo[b]thiophene-2′-yl)-9,10-bis(triisopropylsilylethynyl)anthracene (TIPSAntBeT)

Into 150 mL two-neck flask were added *TIPSAnt* (1 g, 1.43 mmol) and 2-(4′,4′,5′,5′-tetramethyl-1′,3′,2′-dioxaborolane)benzo[b] thiophene (1b) (0.86 g, 3.31 mmol) in 20 mL of anhydrous toluene. Catalytic amount of tetrakis(triphenyl phosphine)palladium(0) was transferred into the mixture in dry box. Subsequently, (2 M Na_2CO_3) sodium carbonate (0.76 g, 7.21 mmol) deaerated for 30 min and the phase transfer catalyst, Aliquat®336 (0.29 g, 0.72 mmol) in toluene purged under nitrogen for 1 h was transferred via cannula. The reaction mixture was stirred at 90 °C for 3 days and cooled to room temperature. Then, the reaction mixture was poured into saturated sodium bicarbonate solution and extracted with MC. The organic layer was washed with brine, and then dried over anhydrous $MgSO_4$. The crude product was column chromatographed with hexane and MC mixture as the eluent, and then crystallized from chlorobenzene to yield *TIPSAntBeT* (0.63 g, 55.1%) as bright orange crystal. ^{1}H NMR (1,1,2,2-tetrachloroethane-d_2 at 100 °C, ppm) δ = 9.06 (s, 2H), 8.74 (d, 2H), 8.05 (d, 2H), 7.93 (d, 2H), 7.86 (d, 2H), 7.83 (s, 2H), 7.41 (m, 4H), 1.44 (m, 42H). ^{13}C NMR (1,1,2,2-tetrachloroethane-d_2 at 100 °C, ppm) δ = 144.34, 141.05, 140.35, 133.07, 132.98, 132.83, 128.25, 126.00, 124.85, 124.84, 124.77, 123.89, 122.46, 121.02, 119.35, 106.50, 103.41, 19.10, 12.01. Anal. calcd for $C_{52}H_{58}S_2Si_2$: C, 77.75%; H, 7.28%; S, 7.98%. Found: C, 77.24%; H, 7.02%; S, 7.68%.

2.2.3. Synthesis of 2,6-bis(5′-phenyl-thiophene-2′-yl)-9,10-bis(triisopropylsilylethynyl)anthracene (TIPSAntPT)

To a 150 mL two neck round-bottom flask equipped with a stir bar under N_2 was added *TIPSAnt* (0.60 g, 0.86 mmol) and 5-phenyl-1-tributylstannyl thiophene (1c) (1.16 g, 2.58 mmol). Tris(dibenzylideneacetone)dipalladium (0.016 g, 0.017 mmol) and tri-o-tolyphosphine (0.021 g, 0.069 mol) was transferred into the mixture in dry box. Subsequently anhydrous toluene (20 mL) was added and purged under nitrogen for 30 min. The reaction mixture was stirred at 120 °C for 3 days and cooled to room temperature. Then, solvent was evaporated with rotary evaporator and dried at vacuum. The crude product was column chromatographed with hexane and MC mixture as the eluent, and then crystallized from hexane and chlorobenzene to yield *TIPSAntPT* (0.56 g, 75.7%) as bright orange crystal. ^{1}H NMR ($CDCl_3$, ppm) δ = 8.86 (d, 2H), 8.59 (d, 2H), 7.91 (dd, 2H), 7.66 (dd, 4H), 7.49 (d, 2H), 7.41 (t, 4H), 7.35 (d, 2H), 7.30 (t, 2H), 1.32 (m, 42H). ^{13}C NMR ($CDCl_3$, ppm) δ = 144.39, 143.44, 134.24, 132.60, 132.35, 132.22, 128.99, 127.90, 127.67, 125.58, 125.28, 124.94, 124.23, 122.79, 118.51, 105.29, 103.13, 19.04, 11.61. Anal. calcd for $C_{56}H_{62}S_2Si_2$: C, 78.63%; H, 7.31%; S, 7.50%. Found: C, 78.52%; H, 7.28%; S, 7.52%.

3. Results and discussion

3.1. Synthesis of the small molecules

The soluble oligomer core, *TIPSAnt*, was synthesized according to procedures developed previously [13]. The bromo groups of *TIPSAnt* enabled coupling of the molecules to a variety of borolanylaryl or stannylaryl molecules, for example, acene, thiophene, or fluorene derivatives. In the present work, we chose thiophene, benzothiophene, and phenyl thiophene for *TIPSAntT*, *TIPSAntBeT*, and *TIPSAntPT*, respectively, as counterparts of *TIPSAnt*. Aromatic end cappers (1a–1c) were easily synthesized via well-known lithiation methods. *TIPSAntT* and *TIPSAntBeT* were synthesized via a Suzuki coupling reaction, and *TIPSAntPT* was synthesized via a Stille coupling reaction with high yields, as shown in Scheme 1. To achieve high purity, we purified the molecules by column chromatography, followed by several consecutive recrystallizations. The products were bright orange highly crystalline solids. The relative solubilities of the resulting products were as follows: *TIPSAntT* > *TIPSAntPT* > *TIPSAntBeT*. *TIPSAntT* showed good solubility in common organic solvents, such as THF, toluene, and chloroform, whereas *TIPSAntBeT* was soluble only in hot chlorobenzene. *TIPS* groups improved the solubility of the π-conjugated rings, but as the molecular size and rigidity increased, the solubility of the molecules decreased. The compounds were characterized by ^{1}H NMR, ^{13}C NMR, and elemental analysis.

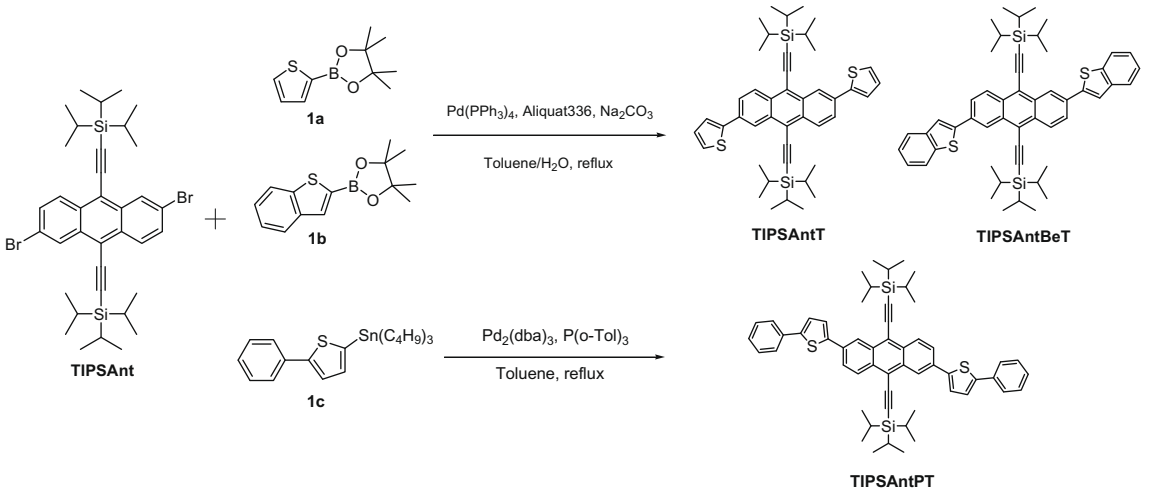

Scheme 1. Syntheses of the small molecules.

3.2. Thermal properties

The thermal stabilities of the small molecules were characterized by thermogravimetric analysis (TGA) under a nitrogen atmosphere. *TIPSAntT* exhibited good thermal stability, with a decomposition temperature, based on 5% weight loss (T_{d5}), of 355 °C, whereas *TIPSAntBeT* and *TIPSAntPT* exhibited excellent thermal stabilities, showing a T_{d5} of 416° and 420 °C, respectively. The larger molecular weights of *TIPSAntBeT* and *TIPSAntPT* may have contributed to their improved thermal stabilities. The thermal transitions of the small molecules were studied by differential scanning calorimetry (DSC) under a nitrogen atmosphere. *TIPSAntT* exhibited liquid crystalline properties, with the first endothermal peak at 173 °C and the second endothermal peak at 290 °C, and corresponding exothermal peaks at 140 °C and 220 °C. *TIPSAntBeT* and *TIPSAntPT* exhibited similar transition behavior, with major melting endotherms at 209 and 304 °C, and corresponding crystallization exotherms upon cooling at 206 and 262 °C. All peaks were significant and reversible, without the presence of additional thermal transitions. From these thermal responses, we concluded that the small molecules were highly crystalline and should form well-ordered thin films when deposited onto a substrate. DSC results are shown in Fig. 1.

3.3. Optical properties

The UV–vis absorption spectra of the small molecules were recorded both in solution (chlorobenzene) and in film states, as shown in Fig. 2. The UV–vis data for the small molecules is summarized in Table 1. All small molecules showed good absorption properties, with vibronic structures in both solution and film states. In both the solution and film states, the absorption spectra of the small molecules showed relative red-shifts as follows: *TIPSAntT* < *TIPSAntBeT* < *TIPSAntPT*. The largest red-shift in the absorption spectrum of *TIPSAntPT* suggested the presence of increasing electron delocalization along the main chain due to more extensive conjugation. The lowest energy transitions in the film states were more red-shifted (18–37 nm) than those in solution states for all small molecules (see Δ2nd Max in Table 1). The intensities of the lowest energy transitions were also larger in the film states compared to the intensities in the solution states. The red-shifts and increased intensities demonstrated extended π-conjugation and substantially more intermolecular ordering within the 2D stacking of the small molecules in the film state. The most striking red-shift, observed for *TIPSAntPT* (37 nm), indicated that this molecule has the strongest intermolecular interactions. The existence of strong interactions between the π-conjugated systems of neighboring molecules in the solid state is desirable for good TFT device performance.

3.4. Electrochemical properties

To investigate the electrochemical stability and the charge transport properties of the small molecules, we carried out cyclic voltammetry (CV) measurements on thin films of the small molecules, summarized in Table 2. The small molecules showed reversible waves for both p-doping and n-doping processes. The oxidation potentials E_{ox} (p-doping) for *TIPSAntT*, *TIPSAntBeT*, and *TIPSAntPT* were 0.99, 1.13, and 0.96 V, respectively. The relatively high oxidation potentials for *TIPSAnts*, compared to *TIPS* pentacene (380 mV), [21] resulted in better oxidation stability of the materials. The highest occupied molecular orbital (HOMO) levels of *TIPSAntT*, *TIPSAntBeT*, and *TIPSAntPT* were estimated to be −5.39, −5.53, and −5.36 eV, respectively, using the previously reported empirical equation [22]. The observation that *TIPSAntBeT* had the lowest HOMO was attributed to reduced delocalization along the backbone through the introduction of a fused aromatic unit, benzothiophene. The delocalization of electrons from the benzothiophene unit onto the backbone was less favorable than from a single thiophene and benzene ring, due to the larger resonance stabilization energy of the fused ring [23]. It is worth noting that among the three materials, the

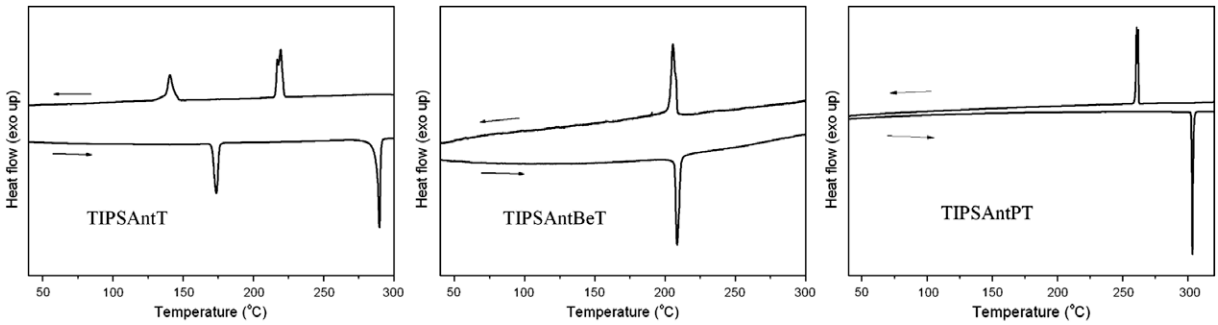

Fig. 1. DSC scans of the small molecules.

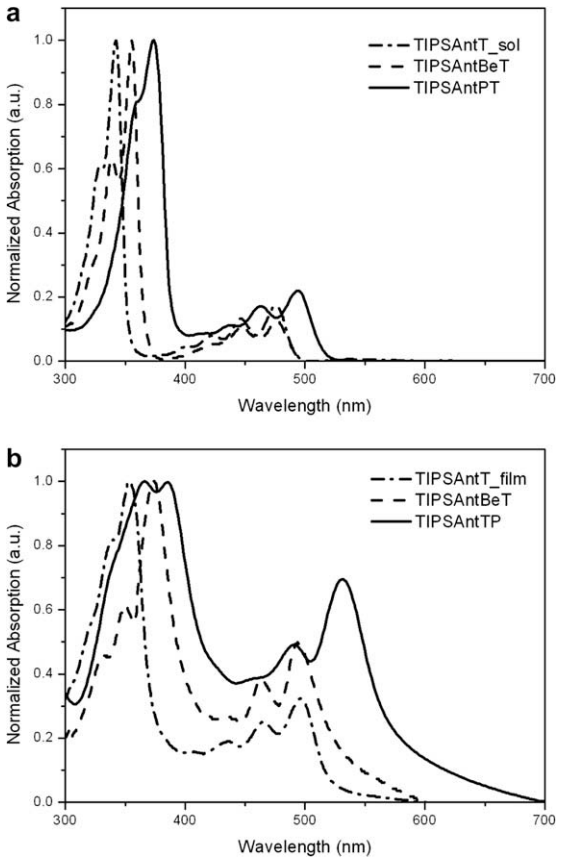

Fig. 2. UV–vis absorption of the small molecules. (a) In a chlorobenzene solution (b) in the spin-coated film state.

HOMO level of *TIPSAntPT* provided the best match to the work function of gold metal [24]. As a result, hole injection from the gold source electrode in p-type thin-film transistors composed of *TIPSAntPT* was expected to be the most efficient among the three materials. In contrast, the lowest lying HOMO level of *TIPSAntBeT* would be expected to increase the hole injection barrier between the gold electrodes and the *TIPSAntBeT* film. The relative band gaps of *TIPSAnts*, calculated from CV measurements and the onset of absorption in the film states, decreased in the order *TIPSAntT* > *TIPSAntBeT* > *TIPSAntPT*, as summarized in Table 2.

Table 1
UV–vis absorption properties of the small molecules.

λ_{max}	UV_sol[a]	UV_film[b]	Δ1st Max[c]	Δ2nd Max[d]
TIPSAntT	342, 475	353, 496	11	21
TIPSAntBeT	357, 476	373, 494	16	18
TIPSAntPT	373, 494	366, 531	−7	37

[a] In chlorobenzene solution.
[b] Spin-coated thin film from chlorobenzene solution.
[c] The 1st maximum peak difference between solution and film states around 340–370 nm.
[d] The 2nd maximum peak difference between solution and film states around 470–530 nm.

The low band gap of *TIPSAntPT* was attributed to the extended conjugation system of the material, which benefited from the long conjugation length of the main chain, as described in Section 3.3.

3.5. X-ray crystallography

Crystallographic analysis allows for the rapid screening of potential OTFT materials. Single crystals of small molecules, easily grown from hexane and chlorobenzene, were analyzed by X-ray crystallography.

Fig. 3 shows the π-stacking structures of the small molecules in single crystals. All of the molecules showed face-to face molecular interactions similar to our previous results [13]. The interplanar distances in the three molecules were almost identical: 3.54, 3.55, and 3.54 Å for *TIPSAntT*, *TIPSAntBeT*, and *TIPSAntPT*, respectively. Single crystals of *TIPSAntT* and *TIPSAntBeT* showed "slipped-stacked" structures similar to that previously reported for *TIPSAnts* [13,17], as shown in Fig. 3b and d. However, single crystals of *TIPSAntPT* showed a "bricklayer" structure, as shown in Fig. 3f. How the *TIPSAnt* columns interdigitate determines whether a "slipped-stacked" or "bricklayer" structure is formed. When *TIPSAntT* of *TIPSAntBeT* columns packed together, each conjugated core in one column adjoined two TIPS groups in an adjacent column to form a "slipped-stacked" structure, as shown in Fig. 3a and c. For *TIPSAntPT*, by contrast, the bulky phenyl groups prevented the conjugated cores of the *TIPSAntPT* molecules in one column from adjoining the two *TIPS* groups in an adjacent column. As a result, the conjugated cores of *TIPSAntPT* molecules in one column adjoined the conjugated cores of molecules in

Table 2
Electrochemical properties of the small molecules.

	E_{ox} (mV)[a]	E_{red} (mV)[a]	HOMO (eV)[b]	LUMO (eV)[b]	E_g (eV)	E_{g_opt} (eV) [c]
TIPSAntT	990	−1680	−5.39	−2.72	2.67	2.38
TIPSAntBeT	1130	−1310	−5.53	−3.09	2.44	2.36
TIPSAntPT	960	−1440	−5.36	−2.97	2.39	2.18

[a] E_{ox}, and E_{red} stand for the oxidation potential and the reduction potential, respectively.
[b] HOMO = $-(E_{ox} + 4.4)$ eV, LUMO = $-(E_{red} + 4.4)$ eV.
[c] Optical bandgap derived from UV–vis onset.

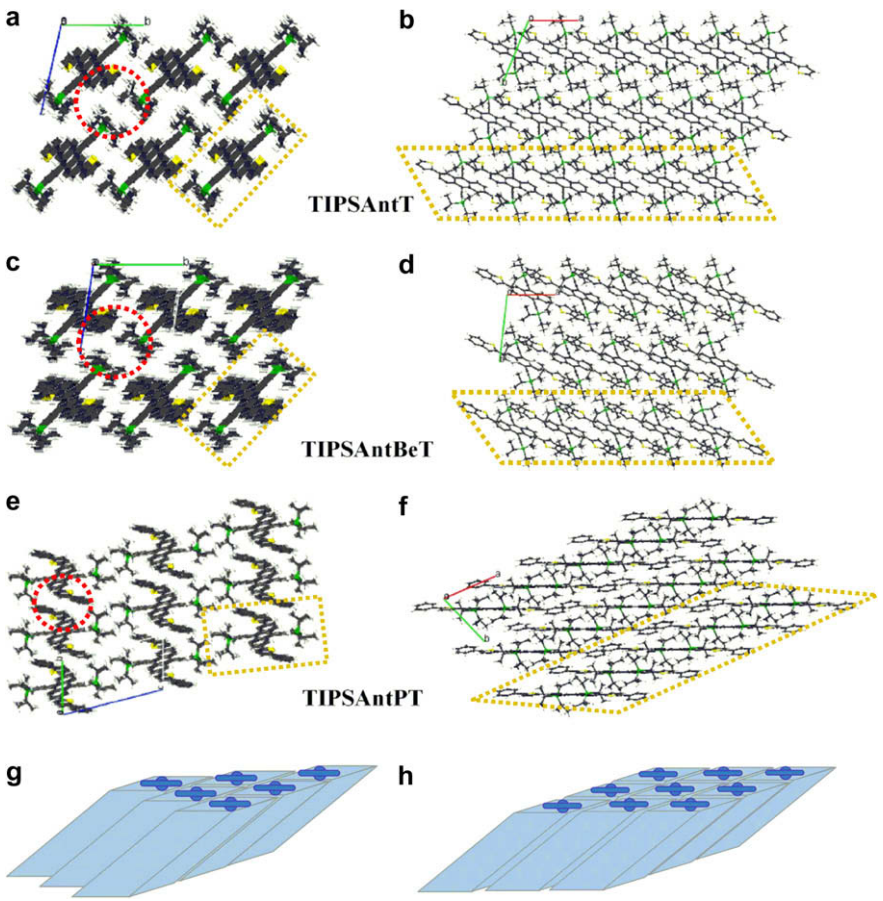

Fig. 3. Single crystal structures of (a and b) *TIPSAntT* and (c and d) *TIPSAntBeT*, which show "slipped-stacked" structures, and (e and f) *TIPSAntPT*, which shows a "bricklayer" structure. (a, c and e): view down crystallographic *a* axis, (b, d, and f): view down crystallographic *c* axis. Schematic figures of columns of *TIPSAnts* stacks: (g) for *TIPSAntT* and *TIPSAntBeT*, and (h) for *TIPSAntPT*. Yellow dotted squares indicate columns of *TIPSAnts* stack and red dotted circles indicate adjoining areas between adjacent columns. (For interpretation of the references to colour in this figure legend, the reader is referred to the web version of this article.)

adjacent columns, resulting in a "bricklayer" structure, as shown in Fig. 3e. *TIPSAntPT* is the first *TIPSAnt* derivative to yield a "bricklayer" stacking structure. In Fig. 3g and h, the *TIPSAnt* columns and the adjoining areas between adjacent columns are indicated by yellow and red dotted lines, respectively.

Fig. 4 shows the area of π-overlap between a molecule and above adjacent molecules of *TIPSAnt* derivatives. (The area of π-overlap with below adjacent molecules was omitted for clarity.) When bulkier substituents were incorporated into the conjugated core, the area of π-overlap increased. As a result, *TIPSAntBeT* had a larger π-overlap area than *TIPSAntT*. Only *TIPSAntPT* showed an additional area of π-overlap with adjacent molecules due to the "bricklayer" stacking structure. This additional area of π-overlap significantly improved the charge-carrier mobility.

3.6. TFT performances

Top-contact OTFTs were fabricated on a common gate of highly n-doped silicon with a 300 nm thick thermally grown SiO_2 dielectric layer. Substrates were modified with

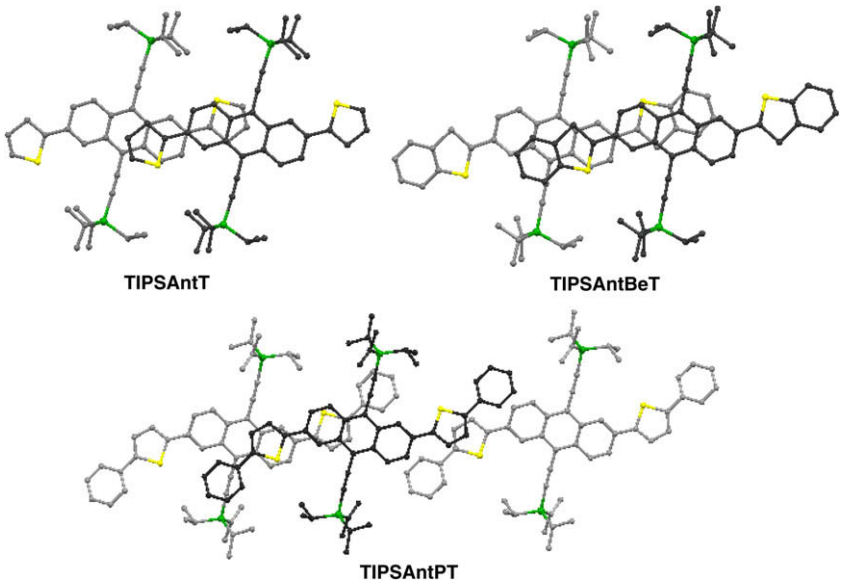

Fig. 4. Overlap of the molecules (dark-shaded molecules) along with their closest neighbors in the plane above the molecule (light-shaded molecules).

octyltrichlorosilane (OTS) by incubation in a toluene solution of OTS for 2 h at room temperature. Films of the organic semiconductors were spin-coated at 2000 rpm from a 0.5 wt.% chloroform solution of *TIPSAntT* and *TIPSAntPT*, and chlorobenzene for *TIPSAntBeT*, due to solubility limitations. All of the TFT results were obtained in ambient air condition and the devices did not show any unstable problems. As shown in Fig. 5, the TFT devices of all molecules showed typical p-channel responses and good saturation behavior. The TFT performances of *TIPSAnts* are summarized in Table 3. *TIPSAntPT* showed the most improved TFT performance among the three molecules, with an average mobility of 0.063 cm^2/Vs, on/off ratio of 4×10^5, and threshold voltage (V_T) of −4.0 V. *TIPSAntPT* showed an order of magnitude larger charge-carrier mobility than *TIPSAntT*, most likely because of the "bricklayer" structure of the film. *TIPSAntBeT*, however, showed a lower mobility than *TIPSAntT*. Although a larger area of π-overlap was observed, as shown in Fig. 4, *TIPSAntBeT* exhibited decreased mobility on account of its poorer solubility and higher crystallinity arising from the rigid benzothiophene. In addition, high crystallinity increased the number of hole-trapping sites at the interface between the OTS monolayer and the *TIPSAntBeT* film. If there were too many hole-trapping sites, a very large negative gate bias would be required to swing the polymer into hole accumulation mode, by inducing a high threshold voltage, V_T. The low HOMO level of *TIPSAntBeT* also produced a hole injection barrier. As a result, V_T of *TIPSAntBeT* (−28.7 V) was much larger than V_T for the other small molecules. The trend in TFT performance among the three small molecules corresponded with the morphological properties, which are discussed in the next section.

Single crystal TFTs based on the small molecules were fabricated because single organic crystals allow the facile investigation of the intrinsic material parameters that determine charge transport efficiency [25,26]. In particular, single crystals of functionalized pentacene reportedly yielded high mobilities because they were largely free from grain boundaries and molecular disorder, and, thus, overlap of the π-orbitals was enhanced [27]. A saturated chlorobenzene solution of the small molecules was slowly evaporated at room temperature onto OTS-modified SiO_2 substrates. After 1 or 2 days, well-defined rod-type single crystals were obtained, and gold electrodes were patterned onto the single crystals by thermal evaporation. The width and length of the channels were calculated from optical microscopy (OM) images. OM images of single crystal TFTs and a schematic device structure are shown in Fig. 6 The mobility trend for single crystal devices was the same as that of the film devices (*TIPSAntBeT* < *TIPSAntT* < *TIPSAntPT*). As expected, the highest TFT performances, showing a mobility of 0.12 cm^2/Vs, were achieved from one-dimensional (1D) single crystalline *TIPSAntPT* microribbons. The improved performance arose from the highly efficient π-orbital overlap of the "bricklayer" structure of the *TIPSAntPT* single crystals. *TIPSAntT* also grew as 1D single crystalline microribbons, resulting in a high mobility, but the less efficient π-orbital overlap of the "slipped-stacked" arrangement of *TIPSAntT* single crystals resulted in a lower mobility than was observed for *TIPSAntPT* single crystals. In contrast, *TIPSAntBeT* grew as three-dimensional (3D) polyhedron single crystals with a larger thickness than *TIPSAntPT*. (The thickness of single crystals was 80 and 200 nm for *TIPSAntPT* and *TIPSAntBeT*, respectively, measured with an Alpha Step 400, Tencor.) In single crystal TFTs, 1D or 2D microrods showed much higher TFT performance than 3D polyhedra because 3D polyhedra have difficulties contacting the gold electrodes [28,29]. As a result, the mobility of *TIPSAntBeT* single crystals was poor. TFT results of single crystals of the *TIPSAnt* derivatives are summarized in Table 3. We are currently working on improving device performances including operational stability and we will publish the results elsewhere.

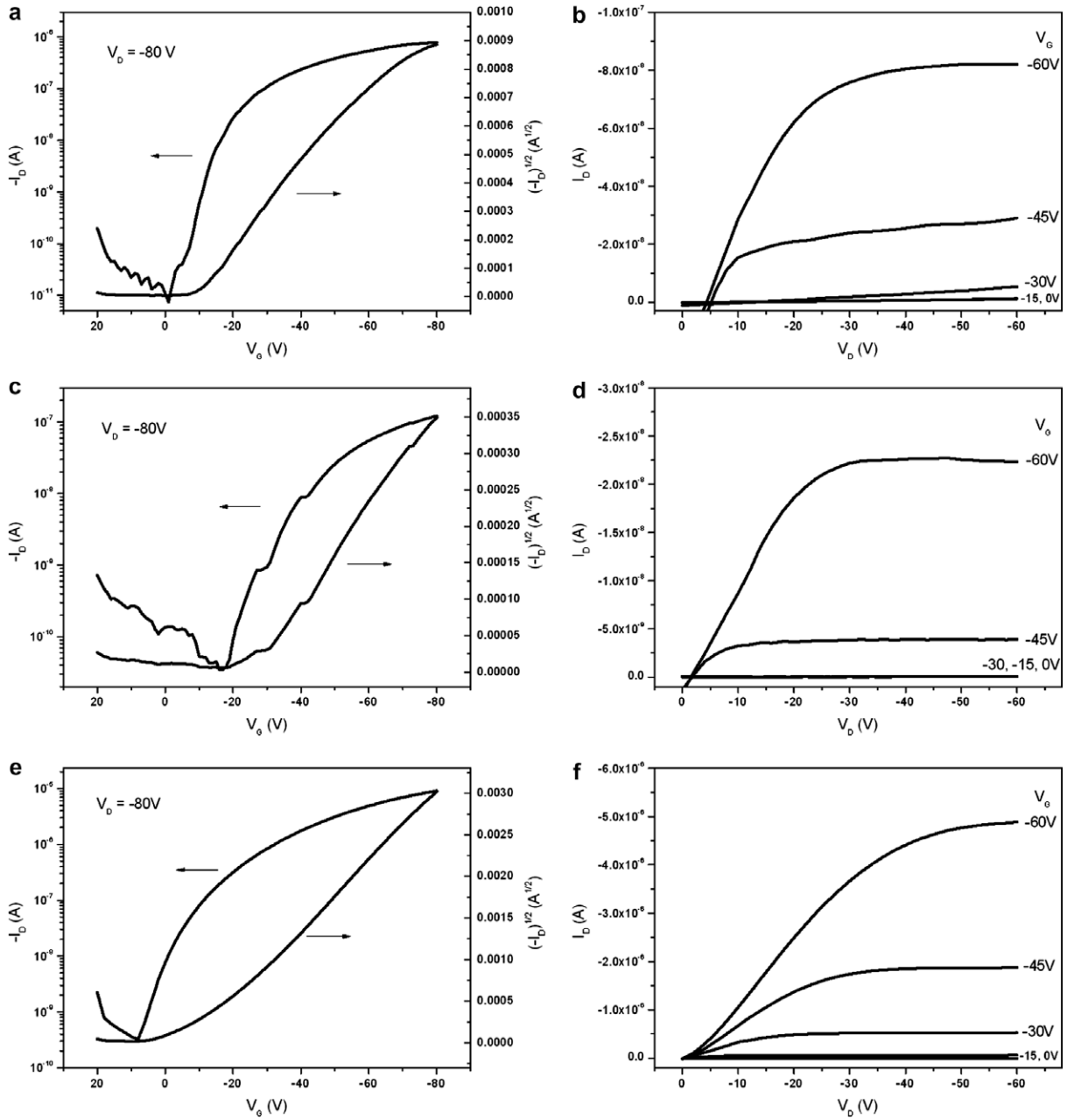

Fig. 5. Transfer characteristics and output characteristics of *TIPSAntT* (a and b), *TIPSAntBeT* (c and d), and *TIPSAntPT* (e and f).

3.7. Morphological properties

We performed atomic force microscopy (AFM) measurements to further investigate the relationship between molecular alignment in films and device performance as AFM provides the thin-film morphologies in micrometer scales to hundreds of nanometer scales. As shown in Fig. 7c, *TIPSAntPT* showed film morphologies dominated by 2D growth after spin-casting, due to the strong electronic interactions in the "bricklayer" π-stacking structure. Each crystalline domain connected smoothly in the as-cast film, yielding devices with high TFT hole mobilities based on *TIPSAntPT*. In contrast, *TIPSAntT* and *TIPSAntBeT* underwent 3D film growth, as shown in Fig. 7a and b, due to the limited π-overlap in the "slipped-stacked" structures. *TIPSAntBeT*, especially, showed poor substrate coverage, with the needle-like crystallites produced due to poor solubility. The high crystallinity also led to a very low mobility and high V_T. The rotational invariance of the fused benzothiophene in the backbone facilitated the adoption of a low energy backbone conformation, promoting the formation of highly ordered crystalline domains.

Out-of-plane and in-plane mode X-ray diffraction (XRD) spectra of films of the molecules were measured,

Table 3
TFT performances of the small molecules.

	Film			Single crystal		
	Mobility (cm^2/Vs)	I_{on}/I_{off}	V_T (V)	Mobility (cm^2/Vs)	I_{on}/I_{off}	V_T (V)
TIPSAntT	0.0039	6×10^4	−11.2	0.059	5×10^3	−24.1
TIPSAntBeT	0.0013	7×10^3	−28.7	0.0067	3×10	−8.5
TIPSAntPT	0.063	4×10^5	−4.0	0.12	2×10^2	−6.1

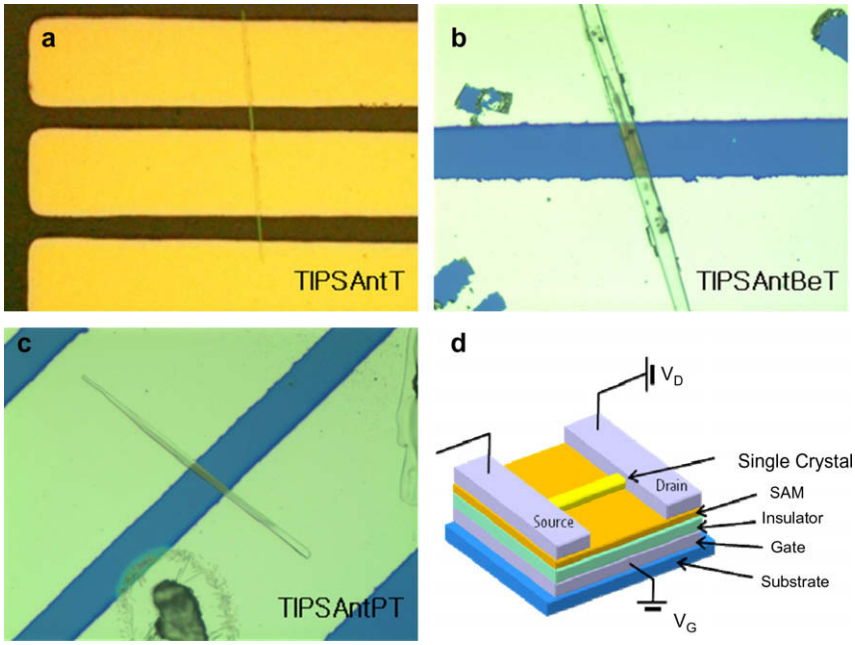

Fig. 6. Optical microscopy images of single crystal TFTs of (a) *TIPSAntT*, (b) *TIPSAntBeT*, and (c) *TIPSAntPT*. (d) Schematic device structure of single crystal TFTs.

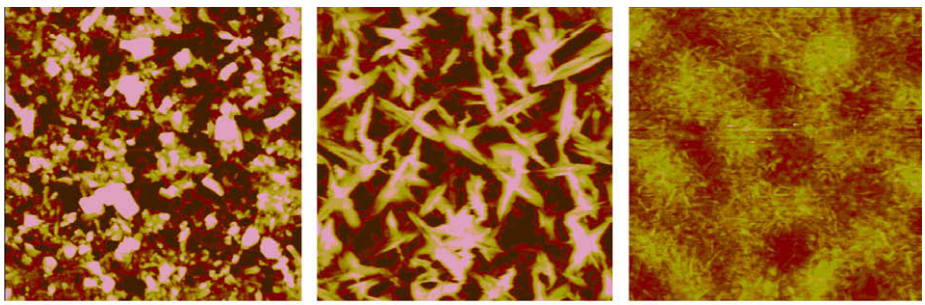

Fig. 7. AFM images (5μ × 5μ).

as shown in Fig. 8. The *TIPSAntT* film showed the lowest degree of crystallinity, exhibiting no specific ordering in the peaks of the out-of-plane mode XRD. Although a (0 1 0) peak was observed in the in-plane mode XRD of the *TIPSAntT* film, the interlayer spacing *d* was 4.28 Å, which is the largest spacing measured among the three molecules, indicating less effective intermolecular π-stacking. In contrast, *TIPSAntBeT* films showed highly crystalline properties, with (1 0 0), (2 0 0), and (3 0 0) reflections in the out-of-plane mode XRD indicating well-organized intraplanar lamella-like structures oriented normal to the substrate. The molecular length of the *TIPSAnt* derivatives along the *TIPS* axis was 16.7 Å, as determined by X-ray crystallography. The *d* spacing of the (1 0 0) peak was 14.9 Å, which implied that *TIPSAntBeT* molecules were aligned perpendicular to the substrate, with respect to

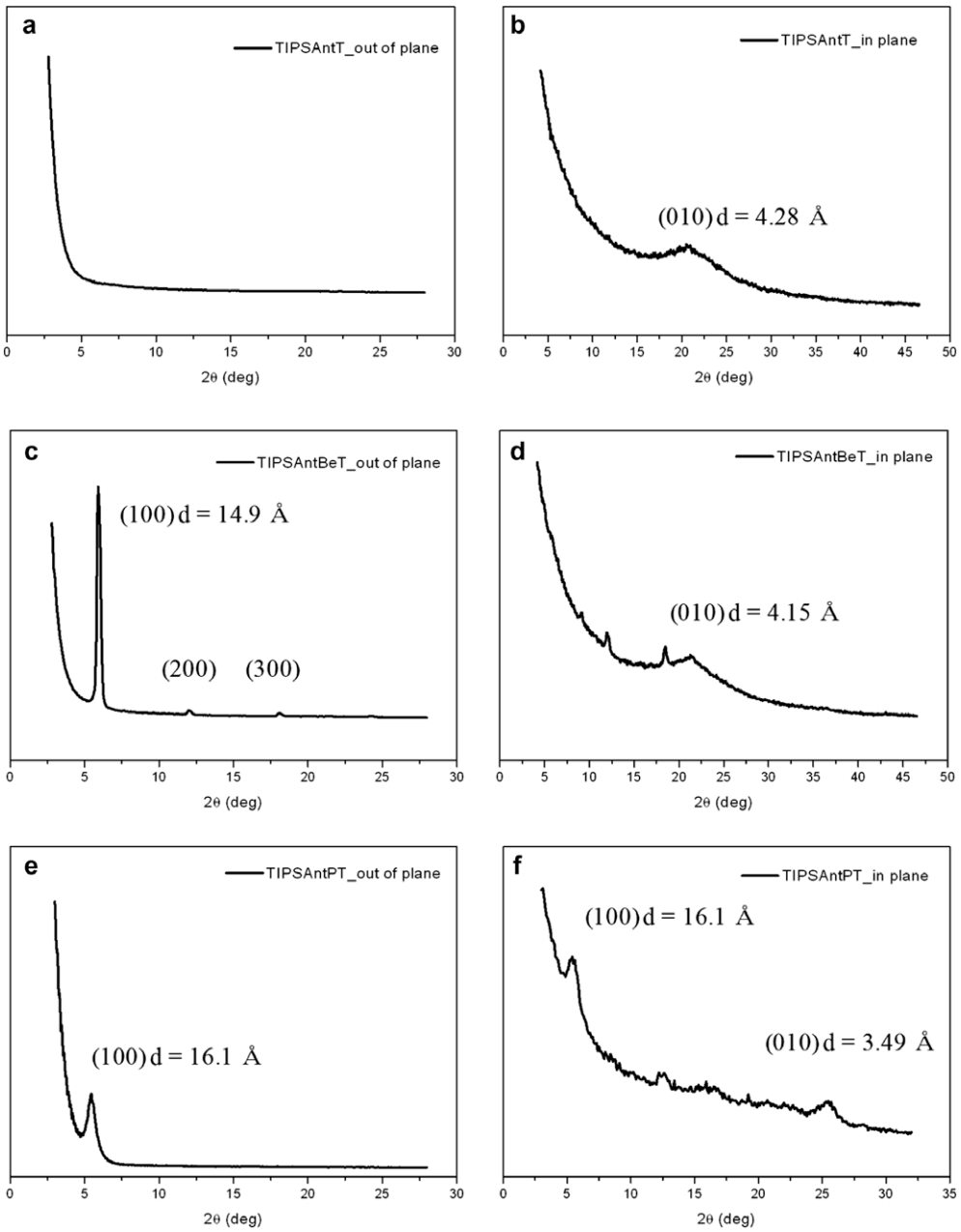

Fig. 8. XRD patterns (a) *TIPSAntT*_out of plane, (b) *TIPSAntT*_in-plane, (c) *TIPSAntBeT*_out of plane, (d) *TIPSAntBeT*_in-plane, (e) *TIPSAntPT*_out of plane, and (f) *TIPSAntPT*_in-plane.

the *TIPS* axis, with a tilt angle of 27°. Although the (0 1 0) peak in the in-plane mode XRD of the *TIPSAntBeT* films showed a closer interlayer *d* spacing of 4.15 Å, the high crystallinity of the *TIPSAntBeT* films resulted in poorer device performances than *TIPSAntT*. The high crystallinity of the *TIPSAntBeT* probably arose from a π-overlap area that was larger than that of *TIPSAntT*, as expected from X-ray crystallography. *TIPSAntPT* films showed the most promising XRD results in both out-of-plane and in-plane mode XRD experiments. The *d* spacing of the (1 0 0) peak was 16.1 Å, implying that *TIPSAntPT* was aligned more perpendicularly to the substrate along the *TIPS* axis than was *TIPSAntBeT*, with a smaller tilt angle of 15°. When the molecules were aligned perpendicular to the substrate, the π-overlap between adjacent molecules was maximized, and carrier transport could occur more effectively. In-plane XRD of *TIPSAntPT* showed a (0 1 0) peak that indicated the interlayer *d* spacing of 3.49 Å. This value was very close to the interplanar distances (3.54 Å) determined by X-ray crystallography measurements, indicating highly effective π-orbital overlap due to the "bricklayer" structure.

4. Conclusions

We synthesized three new *TIPSAnt* derivatives and carried out comparative studies among these three molecules to investigate the relationship between the molecular structures and TFT performances. Only *TIPSAntPT* showed a "bricklayer" stacking structure that resulted in a high charge-carrier mobility of 0.063 cm^2/Vs in the film state and 0.12 cm^2/Vs in the single crystal state. This result agreed well with the AFM and XRD findings. Although the rigidity of the substituents and large area of π-overlap resulted in high crystallinity for the *TIPSAntBeT*, the lack of solubility and the needle-like crystalline films reduced the device performance. These results provide valuable insight into the design of new small molecules for solution-processable OTFTs.

Acknowledgements

This research was supported by a grant (F0004011-2008-31) from the Information Display R&D Center, one of the 21st century Frontier R&D Programs funded by the Ministry of Commerce, Industry, and Energy of the Korean Government. We gratefully acknowledge Dr. J.-H. Kim and Dr. S.K. Lee for assistance with XRC measurements.

References

[1] A.R. Murphy, J.M.J. Frechet, Chem. Rev. 107 (2007) 1066.
[2] H.E. Katz, Chem. Mater. 16 (2004) 4748.
[3] B.S. Ong, Y.L. Wu, Y.N. Li, P. Liu, H.L. Pan, Chem. Eur. J. 14 (2008) 4766.
[4] S. Allard, M. Forster, B. Souharce, H. Thiem, U. Scherf, Angew. Chem. Int. Ed. 47 (2008) 4070.
[5] A.R. Murphy, J.M.J. Frechet, P. Chang, J. Lee, V. Subramanian, J. Am. Chem. Soc. 126 (2004) 1596.
[6] H. Sirringhaus, Adv. Mater. 17 (2005) 2411.
[7] M.M. Payne, S.R. Parkin, J.E. Anthony, C.C. Kuo, T.N. Jackson, J. Am. Chem. Soc. 127 (2005) 4986.
[8] K.C. Dickey, J.E. Anthony, Y.L. Loo, Adv. Mater. 18 (2006) 1721.
[9] J.E. Anthony, D.L. Eaton, S.R. Parkin, Org. Lett. 4 (2002) 15.
[10] S. Subramanian, S.K. Park, S.R. Parkin, V. Podzorov, T.N. Jackson, J.E. Anthony, J. Am. Chem. Soc. 130 (2008) 2706.
[11] M.L. Tang, A.D. Reichardt, T. Siegrist, S.C.B. Mannsfeld, Z.N. Bao, Chem. Mater. 20 (2008) 4669.
[12] M.L. Tang, A.D. Reichardt, N. Miyaki, R.M. Stoltenberg, Z. Bao, J. Am. Chem. Soc. 130 (2008) 6064.
[13] J.H. Park, D.S. Chung, J.W. Park, T. Ahn, H. Kong, Y.K. Jung, J. Lee, M.H. Yi, C.E. Park, S.K. Kwon, H.K. Shim, Org. Lett. 9 (2007) 2573.
[14] K. Fukui, C. Nagata, T. Yonezawa, K. Morokuma, Bull. Chem. Soc. Jap. 34 (1961) 230.
[15] M. Manoharan, F.D. Proft, P. Geerlings, J. Chem. Soc. Perkin Trans. 2 (2000) 1767.
[16] K.H. Jung, S.Y. Bae, K.H. Kim, M.J. Cho, K. Lee, Z.H. Kim, D.H. Choi, D.H. Lee, D.S. Chung, C.E. Park, Chem. Commun. (2009) 5290.
[17] D.S. Chung, J.W. Park, J.H. Park, G.H. Kim, H.S. Lee, D.H. Lee, H.K. Shim, S.K. Kwon, C.E. Park, J. Mater. Chem. 20 (2010) 524.
[18] Y. Dienes, S. Durben, T. Karpati, T. Neumann, U. Englert, L. Nyulaszi, T. Baumgartner, Chem. Eur. J. 13 (2007) 7487.
[19] A.J. Sandee, C.K. Williams, N.R. Evans, J.E. Davies, C.E. Boothby, A. Kohler, R.H. Friend, A.B. Holmes, J. Am. Chem. Soc. 126 (2004) 7041.
[20] J.J. Li, K.G. Carson, B.K. Trivedi, W.S. Yue, Q. Ye, R.A. Glynn, S.R. Miller, D.T. Connor, B.D. Roth, J.R. Luly, J.E. Low, D.J. Heilig, W.X. Yang, S.X. Qin, S. Hunt, Bioorg. Med. Chem. 11 (2003) 3777.
[21] C.R. Swartz, S.R. Parkin, J.E. Bullock, J.E. Anthony, A.C. Mayer, G.G. Malliaras, Org. Lett. 7 (2005) 3163.
[22] R. Cervini, X.C. Li, G.W.C. Spencer, A.B. Holmes, S.C. Moratti, R.H. Friend, Synth. Met. 84 (1997) 359.
[23] I. Mcculloch, M. Heeney, C. Bailey, K. Genevicius, I. Macdonald, M. Shkunov, D. Sparrowe, S. Tierney, R. Wagner, W.M. Zhang, M.L. Chabinyc, R.J. Kline, M.D. Mcgehee, M.F. Toney, Nat. Mater. 5 (2006) 328.
[24] H. Meng, J. Zheng, A.J. Lovinger, B.C. Wang, P.G. Van Patten, Z.N. Bao, Chem. Mater. 15 (2003) 1778.
[25] V. Podzorov, E. Menard, A. Borissov, V. Kiryukhin, J.A. Rogers, M.E. Gershenson, Phys. Rev. Lett. 93 (2004) 86602.
[26] J.Y. Lee, S. Roth, Y.W. Park, Appl. Phys. Lett. 88 (2006) 252106.
[27] V. Podzorov, S.E. Sysoev, E. Loginova, V.M. Pudalov, M.E. Gershenson, Appl. Phys. Lett. 83 (2003) 3504.
[28] J.A. Lim, H.S. Lee, W.H. Lee, K. Cho, Adv. Funct. Mater. 19 (2009) 1515.
[29] C.L. Wang, Y.L. Liu, Z.Y. Ji, E.J. Wang, R.J. Li, H. Jiang, Q.X. Tang, H.X. Li, W.P. Hu, Chem. Mater. 21 (2009) 2840.

also applied as etch resist to pattern silver [4–6], copper [7–10], and palladium [11]. The first implementation of microcontact printing in organic electronics was presented by Rogers and coworkers [12]. Microcontact printing allows for the realization of radio frequency identification tags and flexible displays [13]. The use of a standard gold etching solutions (e.g., potassium iodide/iodine solution, KI/I_2) is not possible, since the thiol SAMs cannot withstand the standard etching solution.

The major advantage of using printed thiol SAMs as etch resist is that the method can be applied to pattern microstructure over large areas. However, the method exhibits also some disadvantages. Only thin metal films can be patterned by the method since the etching solution exhibits a relatively poor selectivity between the thiol SAM and the metal film. Furthermore, the etching solution (ferri/ferrocyanide) is not compatible with standard chemicals used in semiconductor processing. Thus, an alternative and environmental friendly approach was developed, which allows for patterning of thicker coinage metals with a good selectivity while being environmental friendly and compatible with etching solution commonly used in semiconductor processing. The developed approach is based on using thiol self-assembled monolayers as a selective dewetting agent rather than an etch resist. A basic introduction to microcontact printing of self-assembled monolayers is given in Section 2. The use of thiol based self-assembled monolayer was dewetting agents is described in Section 3. The process was used to pattern gold electrodes of organic thin-film transistors. The device fabrication and characterization is discussed in Section 4, before summarizing the work in Section 5.

2. Microcontact printing of thiol self-assembled monolayers

A solution of an eicosanethiol (ECT, $CH_3(CH_2)_{19}SH$) SAM was used as "ink" for the surface engineering of the gold films. Thiol molecules like ECT consist of a radical or alkyl group, which is terminated with a thiol (–SH) group. The head group of the thiol molecules forms a bond with the cleaned gold surface, i.e., S–Au bond. Prior to deposition of the gold films, the substrates were cleaned by isopropanol. The gold films were prepared on oxidized silicon wafers, flexible polyethelene terephthalate (PET) foils and glass substrates. The gold films were deposited by electron beam evaporation. To improve the adhesion of the gold films on the substrates a 3 nm titanium layer was deposited prior the evaporation of the gold films. The regions covered by the ECT SAMs are hydrophobic, whereas the unexposed regions stay hydrophilic. The surface wetting behaviours of the two regions were characterized by water contact angle measurements. Complete wetting is observed in the hydrophilic areas, whereas the hydrophobic regions exhibit contact angles in the range of 110–114°. Such patterned SAMs cause a physicochemical modification of the gold surface, and allows the surface properties of the material to be controlled independently from the bulk properties. The presence of the long radical chains allows the SAM to be used as a surface wetting agent.

3. Thiol self-assembled monolayers as dewetting agents

The use of a ferri/ferrocyanide as an etching solution does not comply with standard chemicals used in semiconductor processing. To avoid using such a hazardous etching solution a new and environmental friendly patterning method was developed. The route to pattern is shown in Fig. 1.

In this case the thiol self-assembled monolayer is used as a selective wetting agent rather than an etch resist or etch mask. In the first step the thiol SAM is microcontact printed on a cleaned gold surface. An elastomeric stamp is used to print alkyl thiol SAMs over gold or silver films on flexible and rigid substrates. The stamps were prepared by casting an elastomeric material, polydimethylsiloxane (PDMS), against a relief structure (master). Afterwards the elastomer was cured at 70 °C for 2 h and removed from the master. Prior to microcontact printing the gold surfaces were cleaned by using a NH_4OH solution and UV/ozone treatment, respectively. An ~2 mM solution of eicosanethiol, ECT ($CH_3(CH_2)_{19}SH$) in acetone was used as "ink" for the printing process. Before printing the self-assembled molecules on the metal surfaces, the alkyl thiol molecules were spin coated on the PDMS stamp at 1000 rpm for 1 min. During the printing process, the stamp was brought in conformal contact with the substrate, so that the self-assembled molecules are transferred from the stamp to the substrate in the regions of contact. The printing of the SAMs was carried under ambient conditions in a clean room. The surface properties of the metal films were characterized by water contact angle measurements.

The area covered with the thiol SAMs turns hydrophobic, whereas the uncovered areas stay hydrophilic. Such patterned surface modification allows for selective wetting of polymers or resists over the prepatterned surfaces [14]. The polymer wets the hydrophilic regions of the substrates, whereas the hydrophobic regions remain uncoated. In the study, poly-methyl methacrylate (PMMA) was used to selectively wet the gold surface. The polymers were either dip or spin coated. The polymers form a film in the hydrophilic region of the substrate, whereas the hydrophobic regions stay uncoated. Subsequently, the dried patterned polymers were used as etch mask to pattern the gold film by potassium iodide/iodine (KI/I_2) etching solution (3:10 of KI/I_2:H_2O etching solution). The KI/I_2 solution etches away the gold film together with the SAMs. The SAM does not have to be removed by a UV ozone treatment or oxygen plasma. The titanium film was removed by a sulphuric acid solution, after patterning the gold film.

The electrodes were patterned on oxidized silicon wafers and glass. Structures down to 500 nm were patterned by this approach. The resolution was limited by the dimensions of the elastomeric stamp used for the microcontact printing process, which was patterned by optical lithography. The use of electron beam lithography should allow for patterning of stamps with smaller features. A titanium layer was used as adhesion layer for the gold film. The titanium film was used to improve the adhesion of the gold film on the glass substrates and the silicon wafers. Since the KI/I_2 solution does not attack the resist pattern the pat-

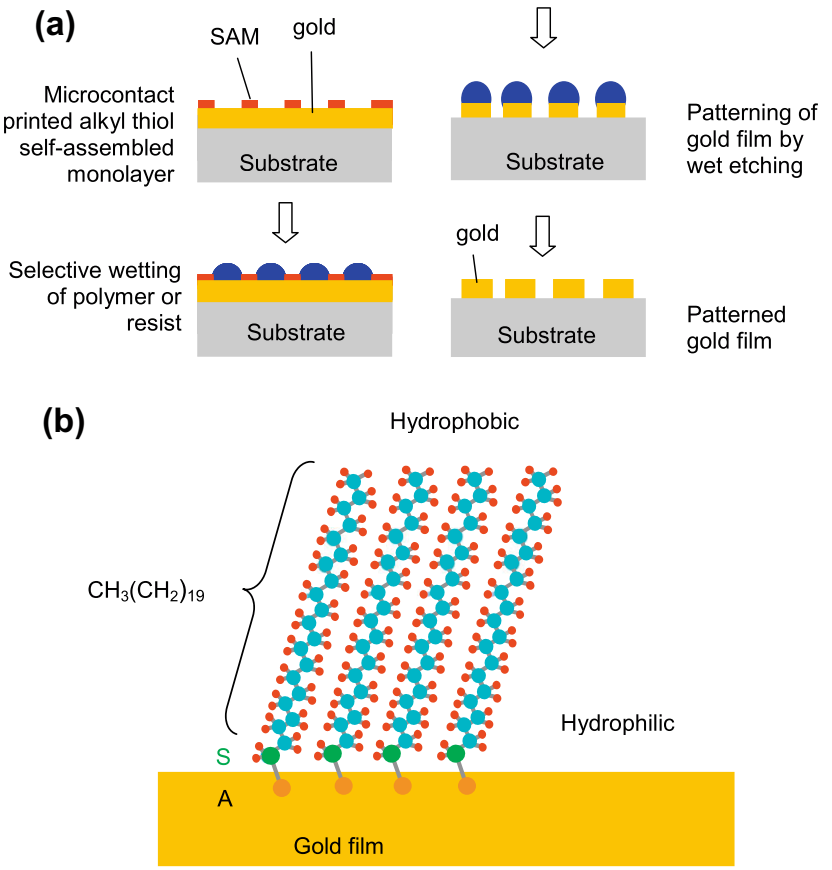

Fig. 1. Patterning of gold by microcontact printing of thiol based SAMs. The thiol based SAMs acts as selective surface wetting agent for a polymer or resist. The gold or silver films were patterned by a potassium iodide/iodine (KI/I_2) etching solution.

terning process is not limited to thin metal films. The same patterning experiments were repeated for silver electrodes which are typically used as electrodes in thin-film solar cells [15,16]. The results of the experiments were comparable to the results on gold surfaces.

The same patterning procedure was also applied to pattern gold structures on flexible plastic foils. Patterned gold structures on a 2 cm × 2 cm large polyethylene terephthalate (PET) plastic foil are shown in Fig. 2.

Therefore, the method allows for combining the advantages of a low cost printing process with the advantages of conventional semiconductor processing. In the following section the approach was used to fabricate drain and source electrodes of organic thin-film transistors (OTFTs). The cross section of the thin-film transistor is shown in Fig. 3b. Atomic force microscope images of pentacene films prepared on gold electrodes are shown in Fig. 4. The electrodes prepared by contact printing (b) and optical lithography (a). The pentacene crystals are large in the channel region (brown region) and distinctly smaller on top of the gold electrodes (yellow region). The edges of the electrodes are clearly visible in the AFM images. A comparison of the resolution between the electrodes patterned by optical lithography (a) and microcontact printing (b) shows that the resolution of the microcontact printing process is comparable to optical lithography.

4. Organic transistors with printed drain and source electrodes

The cross section of an organic thin-film transistor is shown in Fig. 3b. The OTFTs were fabricated on highly doped silicon wafers. Transistors with channel lengths down to 2 μm were realized by the patterning approach. The insulator of the transistors consists of 100 nm silicon oxide. Before depositing the organic semiconductor, pentacene, the silicon oxide gate dielectric and the gold electrodes were treated by hexadimethylsilazane (HMDS). The organic semiconductor layer, pentacene (Fig. 3a), was deposited by organic molecular beam deposition (OMBD) [17]. The organic film has a deposited at a deposition rate of 0.5 Å/s resulting in thickness of 30 nm and the film. The source material was two times sublimation purified before depositing the molecules at a base pressure of 5×10^{-6} Pa. The films were prepared at a constant substrate temperature of 70 °C. The source temperature was kept constant at 275 °C while depositing the pentacene films. The pentacene films consist of pentacene crystals with an average diameter of 1 μm. The diameter of the crystals is typical for pentacene films prepared on a HMDS treated silicon oxide film [17].

The transfer characteristic of a pentacene transistor is shown in Fig. 5. The length and width of the transistor

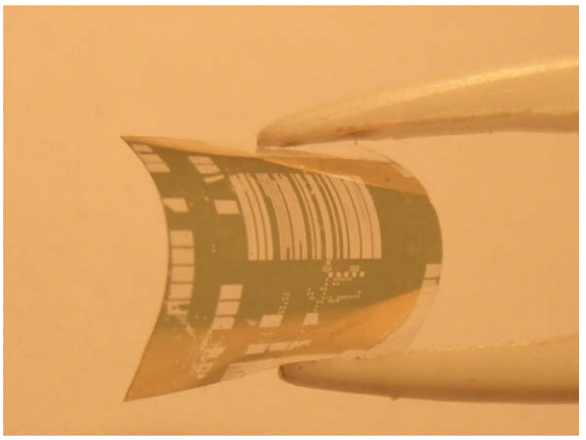

Fig. 2. Patterned gold test structures on a 2 cm × 2 cm large polyethelene terephthalate (PET) plastic foil. The structures were patterned by a combination of microcontact printing of an eicosanethiol SAMs, selective surface wetting/dewetting and wet chemical (KI/I_2 solution) etching. The dark regions represent the patterned gold region, whereas the bright regions exhibit the plastic foil.

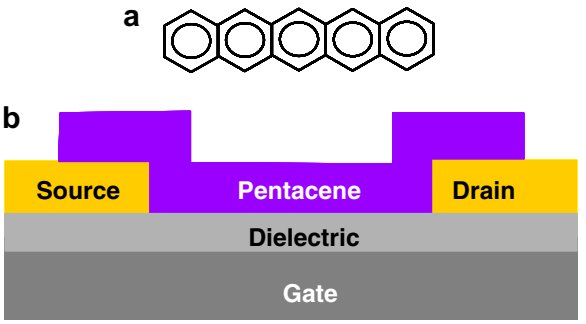

Fig. 3. Molecular structure of pentacene (a) and schematic cross section of a pentacene thin-film transistor (b). The source and drain electrodes were patterned by microcontact printing of an eicosanethiol SAMs, selective surface wetting/dewetting and wet chemical (KI/I_2 solution) etching.

channel were 60 μm and 4000 μm. The transistor exhibits a carrier mobility of 0.3 $cm^2/V\,s$ and threshold voltage of −1.0 V. The on/off ratio is $\sim 10^6$ at a gate voltage of −10 V and the subthreshold slope is 0.3 V/decade.

For transistors with shorter channel length the charge charier mobility drops down to 0.05 $cm^2/V\,s$. The drop of the charge carrier mobility is caused by the influence of contact effects that limit the charge carrier mobility for short channel behaviour [17–19]. Such behaviour is common for short channel organic thin-film transistors. The drain current of a thin-film transistor in the linear region is described by

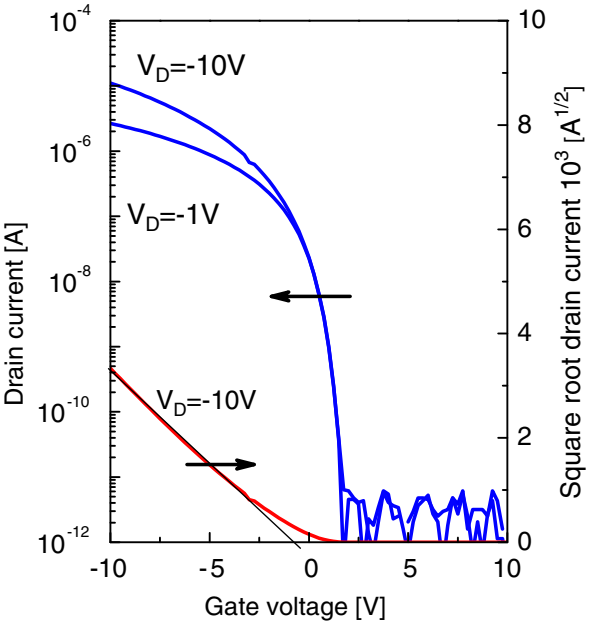

Fig. 5. Transfer characteristics of a pentacene TFT with drain and source contacts fabricated by a combination of microcontact printing of an eicosanethiol SAMs, selective surface wetting/dewetting and wet chemical (KI/I_2 solution) etching. The length and width of the transistor channel were 60 μm and 4000 μm.

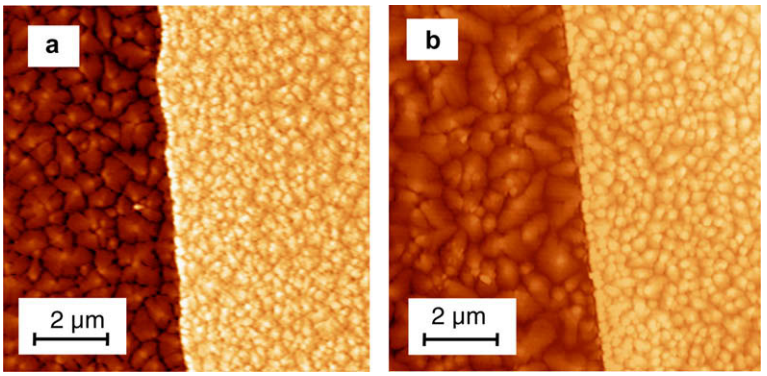

Fig. 4. Atomic force microscope (AFM) image of pentacene films prepared on a silicon dioxide dielectric treated with a hexamethyldisilazane (HMDS) self-assembled monolayer (SAM) and a gold drain/source electrode (yellow region). The drain/source electrodes were patterned by optical lithography (a) and microcontact printing (b). (For interpretation of the references to colour in this figure legend, the reader is referred to the web version of this article.)

Table 1
Measured transistor parameters and device parameters determined by using a transistor model that includes the contact resistance. The parameters are listed for transistors with printed drain and source electrodes (bottom) and transistors with electrodes patterned by optical lithography (top). The device parameters listed on the left (right) side were determined for device operation in the linear (saturation) region.

		Extracted device parameters		
		Charge carrier mobility ($cm^2/V\,s$)	Threshold voltage (V)	Contact resistance ($k\Omega\,cm$)
Transistor with electrodes patterned by optical lithography	Measurement	0.4/0.42	−1.2/−1.0	–
	Transistor model incl. contacts	0.41/0.42	−2.4/−1.1	0.93/1.3
Transistor with electrodes patterned by microcontact printing	Measurement	0.33/0.30	−2.5/−1.0	–
	Transistor model incl. contacts	0.35/0.32	−3.0/−1.5	2.0 / 3.2

$$I_D = \frac{W}{L} C_G \cdot \mu_{dev} \cdot V_D \cdot \left(V_G - V_T - \frac{V_D}{2} \right) \quad (1)$$

where W and L are the width and the length of the channel. C_G is the gate capacitance per unit area, and V_G, V_D and V_T are the gate, drain and threshold voltages, respectively. μ_{dev} is the device charge carrier mobility. The transistor operates in the linear region if $V_D < V_G - V_T$.

In order to account for the influence of the contacts on the drain current the drain voltage V_D and gate voltage V_G, in Eq. (1) are replaced by $V_D - I_D(R_D + R_S)$, and $V_G - I_D R_S$, where R_D and R_S are the drain and source contact resistances, which are expected to be equal. The term "$V_D - I_D(R_D + R_S)$" represents the actual voltage drop across the channel of the transistor. Thus, the drain current can be described by

$$I_D = \frac{W}{L} C_G \mu_0 \frac{L}{L + C_G \mu_0 r_C \left(V_G - V_T - \frac{V_D}{2} \right)} V_D \cdot \left(V_G - V_T - \frac{V_D}{2} \right) \quad (2)$$

where μ_0 is defined to be the intrinsic charge carrier mobility of the transistor and r_C the normalized contact resistance, $r_C = W(R_D + R_S)$. In the following the modified transistor model was used to determine the intrinsic charge carrier mobility, the threshold voltage and the normalized contact resistance of the pentacene thin-film transistor patterned by microcontact printing and optical lithography. The extracted device parameters are listed in Table 1. The parameters were determined for the linear region of operation (listed on the left side) and the saturation region (listed on the right side). The performance of the transistors with printed drain and source contacts is comparable to values published in literature [17–19].

5. Summary

A universal patterning approach was proposed that combines the advantages of a low cost printing process with the advantages of conventional semiconductor processing. The approach combines microcontact printing of thiol SAMS with selective surface dewetting/wetting. The printed regions turn hydrophobic, while the unprinted regions stay hydrophilic. The hydrophilic/hydrophobic patterns were used to selectively deposit polymers or resists on the substrates. Subsequently, the patterned polymer is used as etch resist and the bare regions of the gold films were patterned or etched by a KI/I_2 etching solution. The patterning method is environmental friendly as compared to commonly used microcontact printing approaches that apply ferri/ferrocyanide etchants. Furthermore, the method also allows for patterning of thick metal films, which is not possible by using thiol SAMs as etch resist. The method allows for patterning of electrodes over large area and flexible substrates. Organic thin-film transistor with electrodes fabricated by the method showed a performance comparable to transistors fabricated with conventional lithography. Similarly, the method can also be applied for patterning of electrodes of other organic or inorganic electronic devices on rigid or flexible substrates.

References

[1] B. Bhushan, Springer Handbook of Nanotechnology, Springer-Verlag, Berlin, Germany, 2004 (Chapter 5).
[2] Y. Xia, E. Kim, G.M. Whitesides, Angew. Chem., Int. Ed. (Reviews) 37 (1998) 550.
[3] A. Kumar, H.A. Biebuyck, N.L. Abbott, G.M. Whitesides, J. Am. Chem. Soc. 114 (1992) 9188.
[4] Y. Xia, E. Kim, G.M. Whitesides, J. Electrochem. Soc. 143 (1996) 1070.
[5] P. Fenter, P. Eisenberger, J. Li, N. Camillone III, S. Bernasek, G. Scoles, T.A. Ramnanarayanan, K.S. Liang, Langmuir 7 (1991) 2013.
[6] A. Dhirani, M.A. Hines, A.J. Fisher, O. Ismail, P. Guyot-Sionnest, Langmuir 11 (1995) 2609.
[7] Y. Xia, E. Kim, M. Mrksich, G.M. Whitesides, Chem. Mater. 8 (1996) 601.
[8] H. Keller, P. Sirnak, W. Schrepp, J. Dembowski, Thin Solid Films 244 (1994) 799.
[9] M. Itoh, K. Nishihara, K. Aramaki, J. Electrochem. Soc. 142 (1995) 3696.
[10] J.B. Schlenoff, M. Li, H. Ly, J. Am. Chem. Soc. 117 (1995) 12528.
[11] T.R. Lee, P.E. Laibinis, J.P. Folkers, G.M. Whitesides, Pure Appl. Chem. 63 (1991) 821.
[12] J.A. Rogers, Z. Bao, A. Makhija, Adv. Mater. 11 (9) (1999) 741–745.
[13] J.A. Rogers, Z. Bao, K. Baldwin, A. Dodabalapur, B. Crone, V.R. Raju, V. Kuck, H. Katz, K. Amundson, J. Ewing, P. Drzaic, Proc. Nat. Acad. Sci. 98 (9) (2001) 4835–4840.
[14] A. Benor, V. Wagner, D. Knipp, J. Vac. Sci. Technol. B 25 (2007) 1321.
[15] R. Brendel, Thin-Film Crystalline Silicon Solar Cells – Physics and Technology, Wiley-VCH, Weinheim, 2003.
[16] R. Dewan, D. Knipp, J. Appl. Phys. 106 (2009) 074901.
[17] A. Benor, D. Knipp, Org. Electron. 9 (2008) 209–219.
[18] P.V. Necliudov, M.S. Shur, D.J. Gundlach, T.N. Jackson, Solid-State Electron. 47 (2) (2003) 259–262.
[19] H. Klauk, G. Schmid, W. Radlik, W. Weber, L. Zhou, C.D. Sheraw, J.A. Nichols, T.N. Jackson, Solid-State Electron. 47 (2003) 297–301.

In case (2), polymer gate insulators generally give a clockwise hysteresis from a more complex origin. By introducing a cooperative hydrophilic/hydrophobic dielectric bilayer structure, it was pointed out that hysteresis with polymer gate insulator was bulk related rather than interface related, which was quite different from SiO_2 dielectric [15]. The positive shift of the threshold voltage in clockwise hysteresis loop is probably due to the negatively trapped charges inside the gate dielectric, which were injected from the gate electrode [16]. The bulk trapped electrons induce extra holes in the channel and result in larger drain current during the bias sweep loop, contributing to clockwise hysteresis [7]. To provide solid evidence for gate electron injection mechanism, various thickness SiO_2 buffer layer was added in between polymer insulator and gate electrode, which was effective to block electrons [9]. As the SiO_2 thickness increased, the clockwise hysteresis decreased, disappeared, and finally changed to anti-clockwise direction. This concluded the co-existence of bulk and interface effects. The bulk effect dominated first when SiO_2 thickness was not enough to block electron injection from the gate. As the SiO_2 layer was grown to a certain thickness, bulk and interface effects offset each other, showing non-visible hysteresis. When the thickness was enough to block all the electron injection from the gate, the interface effect dominated and anti-clockwise hysteresis appeared.

Case (3) is caused by the slow polarization in the bulk of the organic dielectric. Polar groups inside the dielectric can reorient and make the drain current lap the bias sweep, resulting in a clockwise hysteresis [6,8,10,17]. Under a negative gate bias, migration of impurity ions in the polymer can make a similar effect [18].

Polar group is believed to be responsible for the hysteresis behavior [7,8]. Many research groups tried to reduce the concentration of polar groups in polymer films by using thermal and photo curing process [19,20]. Various cross-linking reactions have been proposed and some of them are proved to be efficient to diminish hysteresis loop [7,8,19].

Low-operating voltage OFET is another concern during recent years. Reduction in the operating voltage of organic transistors is important for successful implementation in low-power electronics [21,22]. To achieve low-voltage operation, one method is to increase the dielectric constant of the gate insulator. A great deal of attention has been focused on high-*k* inorganic/smooth organic bilayer structures in recent years [23,24]. A second way to achieve low-voltage operation is to make ultrathin dielectric, like self-assembled monolayer [21,25] and multilayer [26]. It was also demonstrated that ion-gel could be used as a gate insulating material for OFETs [27]. A single organic layer dielectric through a solution process at a comparably low temperature such as spin coating or printing is desirable to reduce the processing cost [28]. Only a dielectric with very low leakage and high dielectric strength can be used for ultra thin dielectric for low-voltage operation.

In this report, we used cross-linkable polyacrylate copolymer (PA) as a gate insulator. Various curing temperatures on dielectrics were investigated and hysteresis free metal–insulator–semiconductor (MIS) capacitors and OFETs were tested. By downscaling the thickness of the dielectric, an OFET was tested for low-voltage operation.

2. Experimental

The cross-linkable solution was made with a co-solvent of methyl-3-methoxy propionate (MMP, 30%) and methyl ethyl diglycol (MEDG, 60%) and 10 wt% PA (MW ~ 9000, sample name: PB-174-binder, supplied by LG Chem. Co. Ltd.). The molecular structures and related molar ratio of each repetitive units of the random copolymer PB-174-binder were displayed in Fig. 1a. The film was spin-coated with the solution onto piranha cleaned p-type (for MIS capacitors) and n-type heavily doped (for metal–insulator–metal structures and OFETs) silicon wafers at 3000 rpm for 1 min inside the high purity Ar-filled glove box. And then the film was baked in an annealing furnace for 30 min at various temperatures of 170, 200, and 230 °C to study the temperature effects on the film properties and device performance. The unbaked and baked films were correspondingly referred to as PA, PA170, PA200, and PA230. It was expected that cross-linking reaction as shown in Fig. 1b occurred during the bake. Pentacene, which was purchased from Aldrich Chemical Co., was deposited onto the gate dielectric using an organic molec-

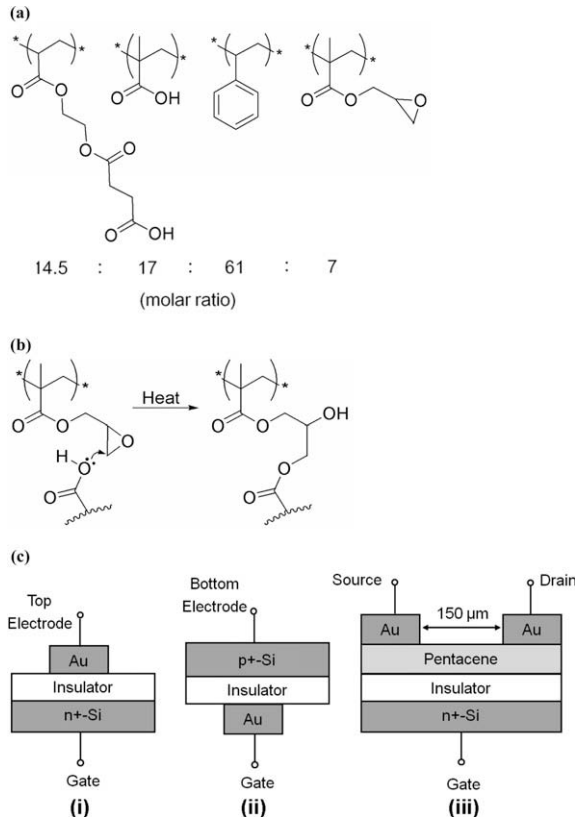

Fig. 1. (a) Repetitive units in PA copolymers and the corresponding molar ratios, (b) mechanism of cross-linking reaction between functional groups and (c) schematic of the device geometries of (i) Au/PA/n+-Si MIM structure, (ii) Au/PA/p−Si MIS capacitor and (iii) top-contact/bottom-gate OFET.

ular beam deposition system at a rate of 0.2–0.3 Å/s and at a substrate temperature of 50 °C. The thickness of the pentacene layer was 60 nm for OFETs and for morphology study with AFM. For metal–insulator–metal (MIM) structures and MIS capacitors, Au top electrode was deposited with evaporation through a shadow mask to make a circular dot area of 8.02×10^{-4} cm^2. For OFETs, Au electrodes were deposited in an evaporator and patterned by a shadow mask with a channel width of 1500 μm and a channel length of 150 μm. The device geometries of Au/insulator/n+Si (MIM structure), Au/insulator/p−Si (p−Si MIS capacitor), and top-contact pentacene OFETs are shown in Fig. 1c.

Fourier Transform Infrared (FT-IR) (Nicolet 700) spectra of the solid films were recorded in a transmission mode. Contact angle measurements were conducted using a contact angle goniometer (Model DSA-10, Krüss Co. Ltd.). Thickness was measured using a Woolham Co. VASE32 ellipsometer. Capacitance–voltage (*C–V*) characteristics of the MIS capacitors were measured to study the hysteresis behavior, using HP 4284A Precision LCR meter (Agilent Tech.) at 1 MHz. To study the roughness of the dielectric surface as well as pentacene morphology, atomic force microscopy (AFM), Dimension™ 3100 microscope (Digital Instruments) was used. The in-plane X-ray diffraction (XRD) was carried out at the 3C2 X-ray scattering beam line of the Pohang Light Sources (PLS), Pohang Accelerator Laboratory (PAL). The electrical performance of MIM structures and OFETs were characterized with a HP5270A (Agilent Tech.).

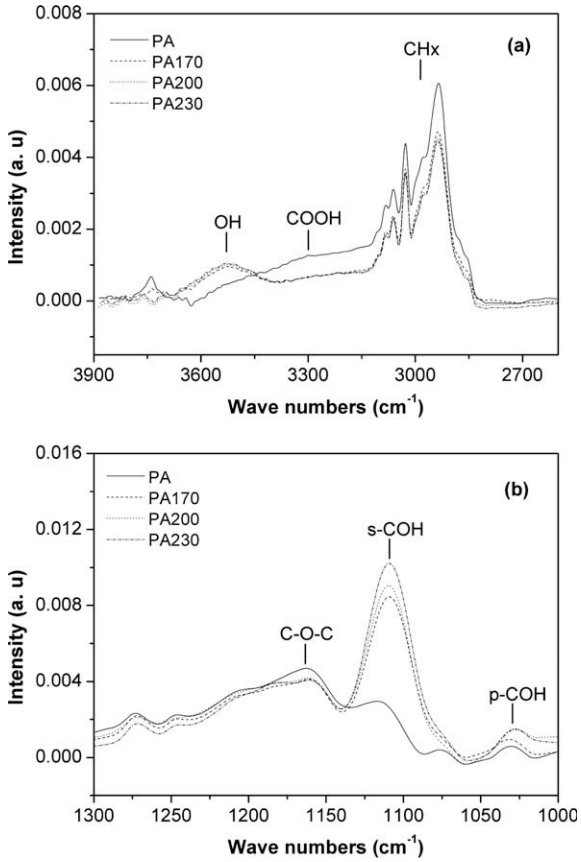

Fig. 2. FT-IR spectra of PA films cross-linked at various temperatures (a) O–H and C–H vibrations at high wave numbers and (b) C–O vibrations at low wave numbers.

3. Results and discussion

3.1. Properties of PA and pentacene films

FT-IR absorption spectra were recorded to monitor the progress of the cross-linking reaction. In Fig. 2a, the bands centered at 3530 and 2940 cm^{-1} were attributed to OH and CH_x groups, respectively, and the broad peak between 3500 and 3000 cm^{-1} was from COOH groups. The reduction in COOH broad absorption peak and the emerging of OH peaks suggested a successful cross-linking reaction with the mechanism demonstrated in Fig. 1b. The reduction of CH_x peak intensity in baked films showed the removal of the residue solvent from the film. In Fig. 2b, bands at low wave numbers were assigned to C–O vibration peaks from COOR (1162 cm^{-1}), secondary C–OH (s-COH, 1112 cm^{-1}) and primary C–OH (p-COH, 1030 cm^{-1}). The increase of p-COH and s-COH intensity at elevated temperatures suggested more intense reaction. p-OH and s-OH are major and minor products of the reaction as demonstrated in Fig. 1b. Due to the bulk hindrance effect, the acid groups tended to attack the less substituted side of epoxide in the nucleophilic substitution reaction, and thus s-COH product was preferred to p-COH groups. The COOR peak (C–O–C) intensity reduction from PA (untreated) to cured dielectrics indicated removal of the solvent.

Surface energy of the dielectric surface, which was reported to affect the pentacene crystallinity and mobility of OFETs [29], was determined from the contact angle measurements using distilled water and diiodomethane as a probe liquid. As shown in Fig. 3, the contact angles with polar probe liquid of water were 81.6°, 76.8°, 77.0° and 78.1° on PA, PA170, PA200 and PA230 films. The high contact angle on PA might be from the residual solvent which is less polar. With the residual solvent, aging effect might also drive the polar functional group into the dielectric bulk under the force of surface energy reduction [30]. Contact angles with non-polar probe liquid of diiodomethane showed a more obvious trend, with the values of 32.0°, 35.0°, 36.1° and 36.5° on PA, PA170, PA200 and PA230 films. Surface energy values were then calculated from the contact angles of the two probe liquids, as displayed in Table 2. Among the dielectric films, the lowest surface energy of the PA230 film was possibly because the reaction removed more COOH group as confirmed with FT-IR. The surface roughness was very small as shown in Fig. 4 and its contribution to the contact angle may be negligible.

AFM images of the insulator surface were captured to understand if the insulator surface has a significant influence on the growth mode of pentacene. Smooth dielectric films were obtained in all cases with root-mean-square (RMS) roughness of dielectrics all less than 0.5 nm (see Fig. 4a–d), which was negligible to affect the pentacene deposition mode [19]. Fig. 4e–h show AFM images of

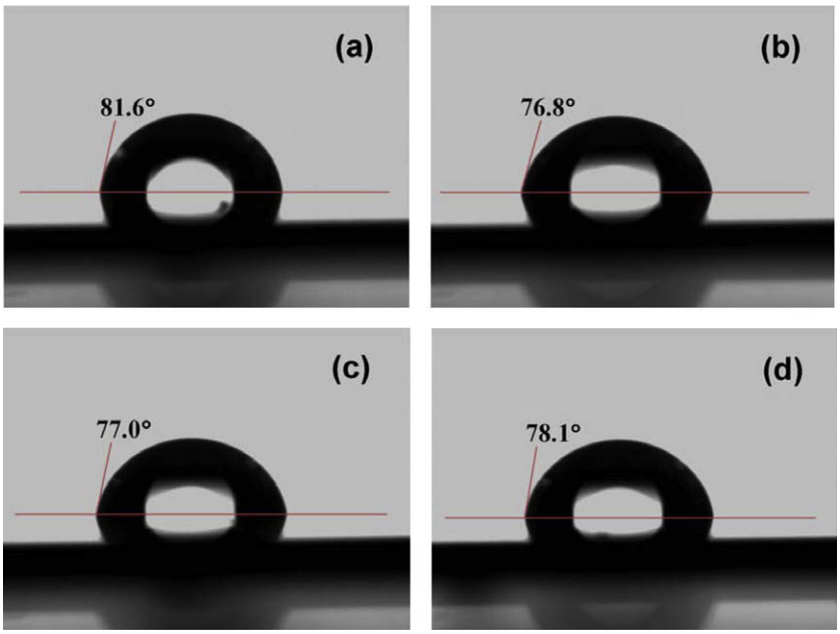

Fig. 3. Images of water drops on (a) PA, (b) PA170, (c) PA200 and (d) PA230.

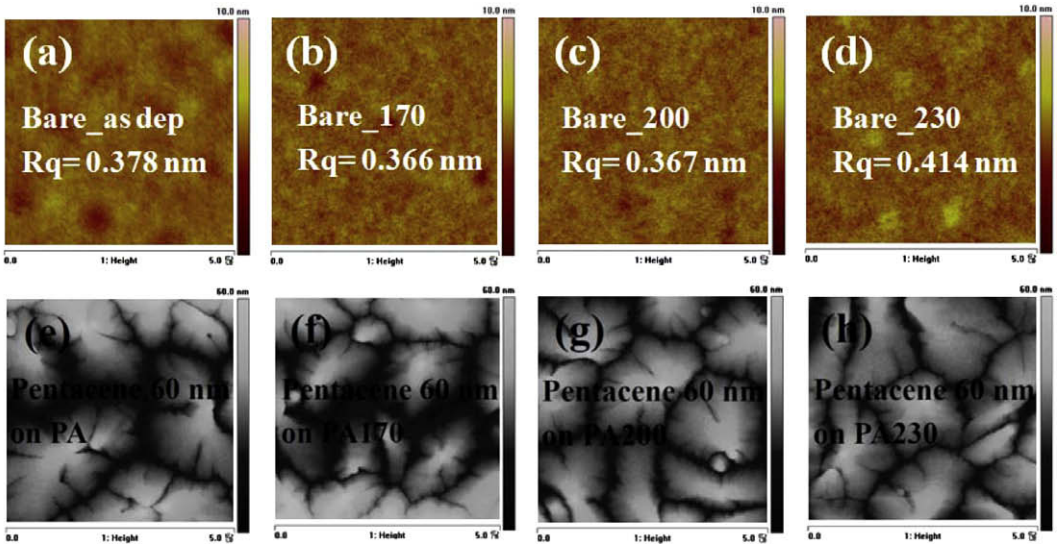

Fig. 4. AFM images (5×5 μm^2) of dielectric surfaces of (a) PA, (b) PA170, (c) PA200 and (d) PA230, and 60 nm pentacene films grown on (e) PA, (f) PA170, (g) PA200 and (h) PA230.

60 nm pentacene films, which were deposited on PA, PA170, PA200 and PA230, respectively. The pentacene grains are compactly stacked on PA200 and PA230, while wide and deep gaps emerged between grain boundaries in PA and PA170, as shown in the dark areas in Fig. 4e–h. The grain boundaries are thought to be interfacial trap sites which can disrupt the charge transport in the organic semiconductors [31]. The RMS roughness of the pentacene films, which was from the difference in peak-to-valley depth, showed values of 11.8, 10.3, 8.71 and 7.16 nm for PA, PA170, PA200 and PA230, indicating that a flatter topology could be obtained with PA cured at a relatively higher temperature.

Fig. 5 shows the XRD patterns of 60 nm pentacene films deposited on top of various polymer gate dielectrics at a moderate deposition temperature of 50 °C. In the spectra, first pentacene peak (0 0 1) at $2\theta = 5.74°$ represents thin film phase, while triclinic bulk phase peak is not visible in our spectra. This diffraction angle corresponds to the vertical periodicity of the 15.4 Å layer-by-layer spacing [32], indicating that the molecules were standing nearly perpendicular to the substrate and formed perfectly

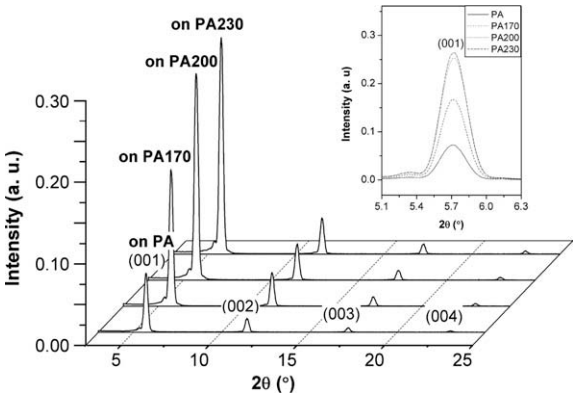

Fig. 5. XRD patterns of 60 nm pentacene films deposited on the gate dielectric of PA, PA170, PA200 and PA230 (bottom), and an overlap of (0 0 1) peaks (up).

packed structure. Because of the anisotropy in the electrical transport in pentacene domains, it is important to know how the crystalline regions are oriented relative to the substrate. To more accurately compare the crystallinity of the pentacene layer, the full width at half maximum (FWHM) values as well as the peak intensity was obtained. The peaks showed a quite similar FWHM value of ~0.26°, but quite different peak intensities. The (0 0 1) peak intensity of PA, PA170, PA200 and PA230 was inserted in Fig. 5. Since the FWHM was nearly the same for all samples, intensity of XRD peaks represented the crystallinity. It was reported that higher μ is closely related to the (0 0 1) plain crystallinity [33], while the best crystallinity was observed in the pentacene thin film on PA230.

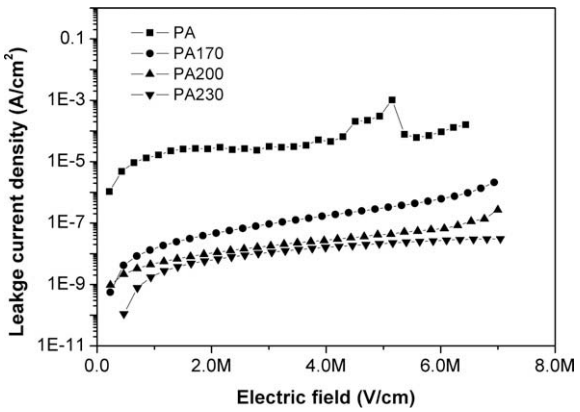

Fig. 6. Current density–electric field (J–E) characteristics of Au/PA/n+Si MIM structures.

3.2. I–V characteristics of MIM structures

An important concern with the gate dielectric material is the dielectric strength and the gate leakage. Fig. 6 displays the leakage current density through the dielectric layer as a function of the applied electric field. Under the low electric field, there are free ions that can be accelerated by the field and induce a current, which will be saturated after a certain voltage and give a constant current, as shown in the linear region of the curves. An increase in the leakage current in a higher electric field is caused by ion avalanche, which is generally explained by the Townsend discharge mechanism. Except PA, breakdown was not observed below ~7 MV/cm, and the PA230 showed the lowest leakage $\sim 5 \times 10^{-9}$ A/cm^2 at the electric field of 1 MV/cm. Table 1 compares the leakage current density values of existing cross-linked polymeric, hybrid, and inorganic dielectrics [4,20,22,34–41]. Pure polymeric gate insulators always give high leakage current density and low dielectric strength, and thereafter not listed in the table. PA230 showed desirable dielectric strength and low leakage, superior to most organic dielectrics and comparable to inorganic dielectrics such as Al_2O_3 ($E_{BD} \sim 7.9$ MV/cm). Note that ~7 MV/cm is the upper limit of our equipment, and no dielectric breakdown was observed under this electric field. The high dielectric strength may attribute to the linear chain structure and the soft side groups of PA polymer, which may contribute to a dense film with less air in the free volume, and reduce the possibility to dielectric breakdown. Curing is also an essential process for the use of polymers as gate dielectrics if a high breakdown field and a low gate leakage current are to be achieved [20]. The process further reduces the free volume

Table 1
Dielectric properties of various gate insulators.

Ref.	Polymer	Method	k[a]	E_{BD}[b] (MV/cm)	J[c] (A/cm^2)	Year
Current work	PA230	SC[d]	~3	>7	5×10^{-9}	Cur. work
[4,22]	CL-PVP	SC	3.6–6	2–6	10^{-8}	2002–2005
[34]	CL-PVA	SC	~6.6	~2	7×10^{-8}	2006
[20]	CL-PVCN	SC	3.18	>2	2×10^{-8}	2008
[35]	CL-PMMA	SC	3.5	>4	4×10^{-7}	2009
[36]	BCB	SC	2.65	>3	$\sim 10^{-8}$	2004
[37]	Hyb. resin	SC	3.1 (100 kHz)	~5	4.1×10^{-9}	2007
[38,39]	SiO_2	TG[e]	3.8–3.9	~12	$\sim 10^{-9}$	2004–2008
[40,41]	Al_2O_3	Anodized	9–11	3–8	$<10^{-9}$	2003–2004

[a] k is dielectric constant under 1 MHz if not specially indicated.
[b] E_{BD} is the abbreviation of break down electric field of a gate insulator or dielectric strength.
[c] J represents the leakage current density value at 1 MV/cm.
[d] SC is the abbreviation of spin coating.
[e] TG is the abbreviation of thermal growth.

in which ionized molecules can migrate. Organic polymers are especially prone to this partial discharge breakdown mechanism, because high temperature in the discharges readily causes degradation to carbon and gaseous products, and the process is often accelerated by the reaction of ozone and other active species formed in the gaseous discharges. Since the dielectric strength of PA polymer is very high and there was not a breakdown in the electrode, possibilities of thermal breakdown and electromechanical breakdown were excluded.

3.3. C–V characteristics of MIS capacitors

Typical *C–V* scans from depletion (positive gate bias) to accumulation region (negative gate bias) were carried out using Au/PA/p−Si MIS capacitors with various dielectrics, and the gate bias was swept back to check the amount of hysteresis originating from the bulk or interface charge trapping, as shown in Fig. 7. The negative shift of the depletion region could be explained by the positive fixed charge on the insulator/semiconductor interface as demonstrated by the following equation

$$V_{FB} = \phi_{MS} - \frac{Q_{SS}}{C_i}, \quad (1)$$

where ϕ_{MS} is the metal–semiconductor work function difference and Q_{SS} is the equivalent fixed oxide charges [42]. The defects and dangling bonds on p−Si wafer surface could induce positive fixed charge, which is responsible for the negative shift of the flat band voltage as indicated in Eq. (1). Since the fixed charge does not change with the gate voltage sweep, it just horizontally shifts *C–V* curve without changing its shape, and thus has little effect on the hysteresis behavior.

For a negative bias on the gate, two phenomena can happen (1) hole from the semiconductor can be injected into the oxide giving rise to a negative flat band voltage shift ($-\Delta V_{FB}$) and (2) electrons from the gate electrode can be injected into the oxide, giving rise to a positive shift (ΔV_{FB}) [43]. The clockwise hysteresis ($+\Delta V_{FB}$) is thus correlated with the electron injection from the gate. Electron

Table 2
Electrical characteristics of the gate dielectrics cross-linked at different temperatures.

Samples	C_{max} (pF)	k	γ (J/cm^2)	Mobility (cm^2/V s)	I_{on}/I_{off}	ΔV_{th} (V)	SS (V/dec)	N_{trap} ($\times 10^{11}$)	N_{trap}^{max} ($\times 10^{12}$)
PA	20.1	4.39	43.4	0.32	5×10^3	1.92	2.44	2.02	4.15
PA170	16.2	3.27	42.8	0.37	10^4	1.41	2.01	1.37	3.12
PA200	15.2	3.05	42.2	0.56	6×10^4	0.28	1.39	0.28	2.23
PA230	14.5	2.88	41.8	0.60	10^5	0.17	1.22	0.16	1.96

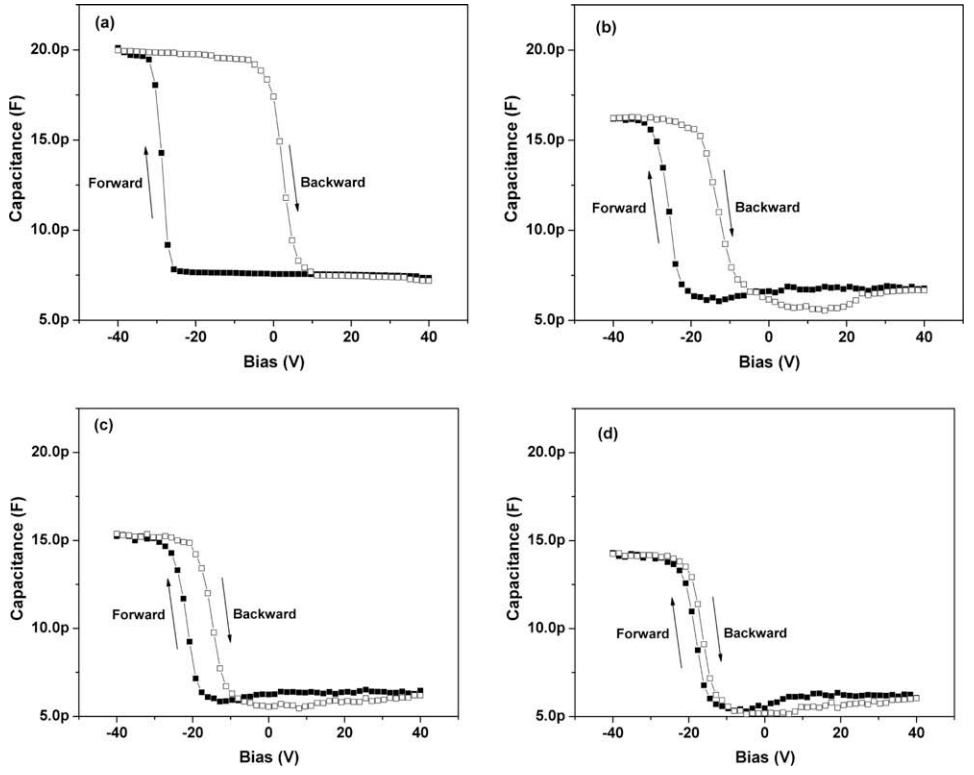

Fig. 7. Capacitance–voltage (*C–V*) characteristics of Au/PA/p−Si MIS capacitors with (a) PA, (b) PA170, (c) PA200 and (d) PA230.

injection from the gate and trapping in the dielectric is responsible for the hysteresis behavior under negative gate bias as was observed in many other polymeric gate dielectrics. Hysteresis characterized by flat band voltage shift (ΔV_{FB}) was calculated to be 30.4, 12.8, 6.5 and 1.7 V for PA, PA170, PA200 and PA230 capacitors, respectively. The difference in the flat band voltage is due to the trapped charges in the gate capacitor with a capacitance/area equal to C_i [42].

$$\Delta V_{FB} = -\frac{\Delta Q_{SS}}{C_i}. \tag{2}$$

If the trapping sites are evenly distributed in the dielectric film, the amount of hysteresis caused by electron trapping can be expressed as

$$\Delta V_{FB} = -\int_0^{t_i} \frac{\rho}{\varepsilon_0 \varepsilon} x \mathrm{d}x, \tag{3}$$

where ρ is the electron trap density across the dielectric layer, ε_0 is permittivity in vacuum, and ε is permittivity of the dielectric [44]. If the OH or residue carboxylic acid groups act as a electron trap, positive voltage shift during the *C*–*V* scan should be linearly decreased with the decrease in the density of the charge traps, and it matches well with the maximum amount of charge trapping, as evaluated in the later part with inverse subthreshold slope (*SS*). Linear relationship has been found between OH contents and hysteresis gap in the *C*–*V* curve [44]. Cross-linking reaction proved to be an efficient tool for hysteresis removal [19]. Compared with the calculated trapping density in the latter part, electron injection and trapping could be a major factor for hysteresis, while evidence for dipole reorientation and mobile ions were less obvious.

The maximum capacitance (C_{max}) values were 20.1, 16.2, 15.2 and 14.5 pF for PA, PA170, PA200 and PA230 capacitors and the *k* values were calculated to be 4.39, 3.27, 3.05 and 2.88 for each sample from

$$C_{max} = \varepsilon_0 A \frac{k}{t}. \tag{4}$$

Here, *k* is the dielectric constant, *t* is the thickness of the dielectric film and *A* is the capacitance area, and ε_0 is the permittivity in vacuum. Smaller amount of polar groups, such as COOH, made *k* and C_{max} smaller [45]. After annealing, capacitance can increase due to the decrease in the film thickness from 155.3 nm (PA) to 142.0 nm (PA230) but this effect was small.

3.4. Organic field-effect transistors

Top-contact pentacene OFETs were fabricated utilizing PA, PA170, PA200 and PA230 as a gate dielectric on n+-Si wafer. Their transfer and output characteristics are shown in Fig. 8 and Fig. 9, respectively. μ of the OFET was calculated in the saturation regime from a plot of the square root of the drain current versus V_G by fitting data to the equation [19],

$$I_{D,sat} = \frac{W}{2L} \mu C_i (V_G - V_{th})^2. \tag{5}$$

Here, $I_{D,Sat}$ is the drain current in the saturated regime, *W*/*L* is the channel width/length, V_G is the gate voltage, and V_{th} is the threshold voltage.

Table 2 displays the electrical data of OFETs with as deposited and cured PA dielectrics under an operating voltage of −20 V. PA230 device exhibited the best performance, with μ of ~0.60 $cm^2/V\,s$, $I_{on}/I_{off} \sim 10^5$, and a low SS of 1.22 V/dec. The relatively better μ might attribute to the effective curing of the film to reduce polar groups as monitored by FT-IR results. This enabled pentacene to

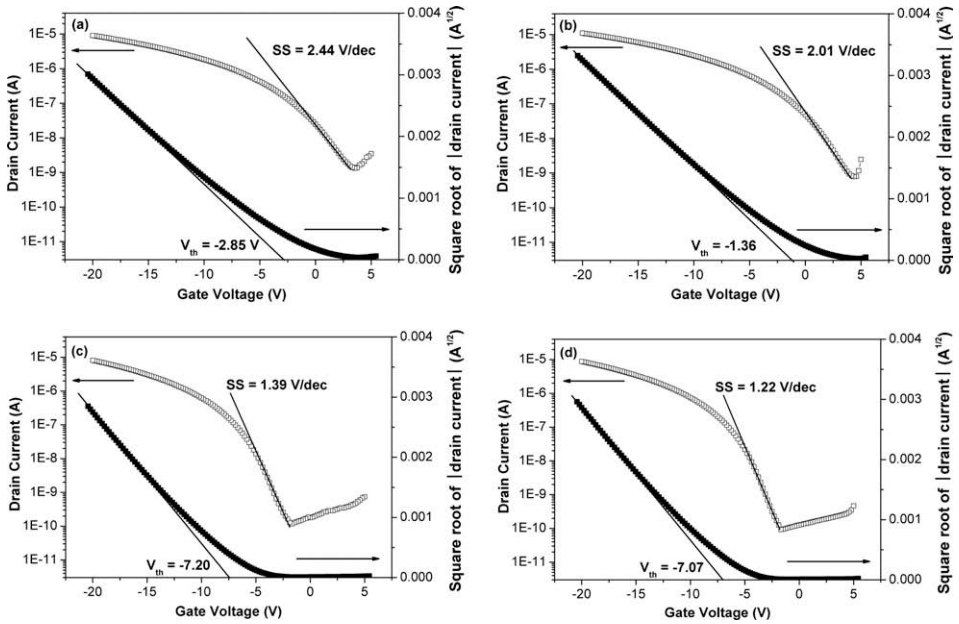

Fig. 8. Transfer characteristics of OFETs with different dielectrics (a) PA, (b) PA170 (c) PA200 and (d) PA230.

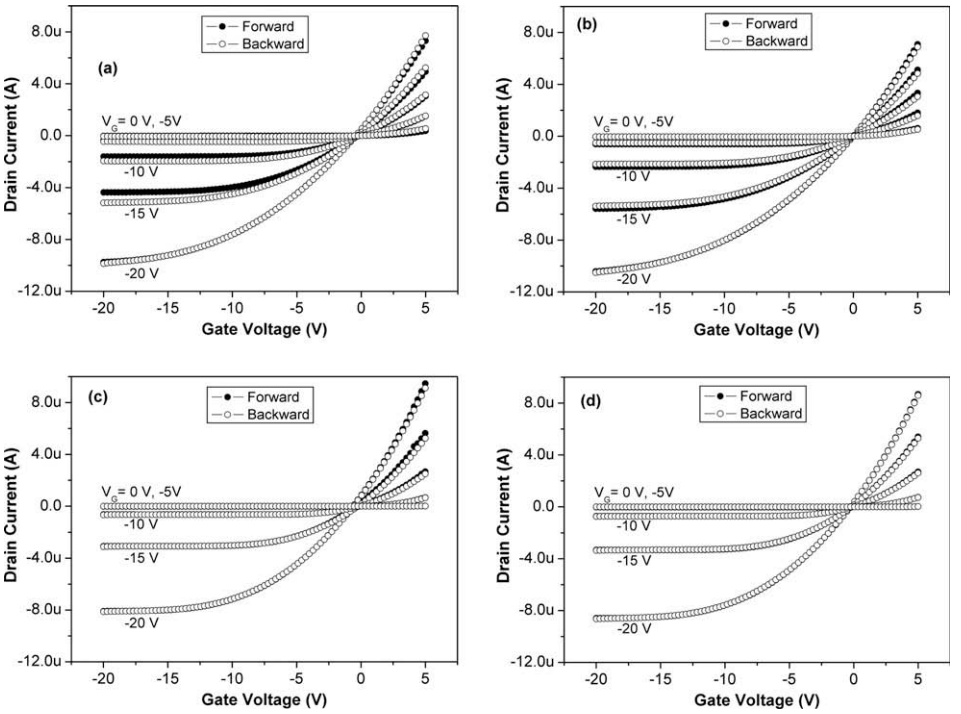

Fig. 9. Output characteristics of OFETs with (a) PA, (b) PA170 (c) PA200 and (d) PA230.

deposit under a layer-by-layer mode (as evidenced by XRD result) to form a dense film, in which the π–π conjugation made more effective hole transport. At the same time, the cross-linking reactions could provide the dielectric films with better insulating properties and devices with higher I_{on}/I_{off}. Optimized cross-linking condition also eliminated the charge traps inside and on the surface of the gate insulator, permitting the sharpest SS. The SS controls the voltage swing required for a transistor to turn from off to on, and it should be as low as possible [28]. High SS is a drawback of organic transistors, resulting from a combination of low gate-dielectric capacitance, low breakdown voltage, and high parasitic capacitances at the insulator/semiconductor interface.

The μ, I_{on}/I_{off} and SS were 0.56 $cm^2/V\,s$, 6×10^4, 1.39 V/dec for PA200 device, 0.37 $cm^2/V\,s$, 10^4, 2.01 V/dec for PA170 device, and 0.32 $cm^2/V\,s$, 5×10^3, 2.44 V/dec for PA transistor. As can be seen in Table 1, better cross-linked dielectric film could contribute to a better electrical performance, and significant improvement was observed for PA170 to PA200 OFETs. However, only slight enhancement in electrical property was observed from PA200 to PA230 devices, suggesting that the curing condition was optimized.

Fig. 9 shows that the saturation source–drain current is −8 to −10 μA under an operating voltage of −20 V. Although the PA and PA170 devices showed relatively higher output current of ∼−10 μA, the unreliable behavior of the hysteresis loop made the devices less attractive.

We estimated the density of the trapped charges in the device using

$$N_{trap}^{max} \approx \left[\frac{qS\log(e)}{kT} - 1\right]\frac{C_i}{q} \quad (6)$$

$$N_{trap} \approx \frac{C_i \Delta V_{th}}{q}, \quad (7)$$

where q is electronic charge, S is the (reciprocal) SS in V/dec, k is Boltzmann's constant and C_i is the capacitance/area of the gate dielectric. Eq. (6) estimates an upper limit of trapped charges [46]. In Eq. (7), the threshold voltage shift was due to the trapped charges in the gate capacitor [28].

The significant improvements in SS can be attributed to the decreased charge trap density at the pentacene/dielectric interface. Using Eq. (6), we estimate an upper limit of the trapped charge density to be $4.15 \times 10^{12}\,cm^{-2}$, $3.12 \times 10^{12}\,cm^{-2}$, and $2.23 \times 10^{12}\,cm^{-2}$ for PA, PA170, and PA200 devices, respectively. Using Eq. (7), we estimated the trapped charge density in PA, PA170, and PA200 to be $2.02 \times 10^{11}\,cm^{-2}$, $1.37 \times 10^{11}\,cm^{-2}$, and $2.8 \times 10^{10}\,cm^{-2}$, respectively. The consistency of ΔV_{FB}, trapped charge density and upper limit of charge trapping confirms the charge injection and trapping as the major origin of hysteresis. PA230 device showed least trapped charge density of $1.6 \times 10^{10}\,cm^{-2}$ (N_{trap}) and $1.96 \times 10^{12}\,cm^{-2}$ (N_{trap}^{max}), which shows that the trap states have been significantly reduced by cross-linking reaction at 230 °C. The hysteresis of the output curves was also diminished with annealing at an elevated temperature as shown in Fig. 9. There was a large difference between forward and backward output curves with PA, while the difference became negligible with PA230.Because of the high dielectric strength, the 230 °C baked thin PA film (∼89 nm) could

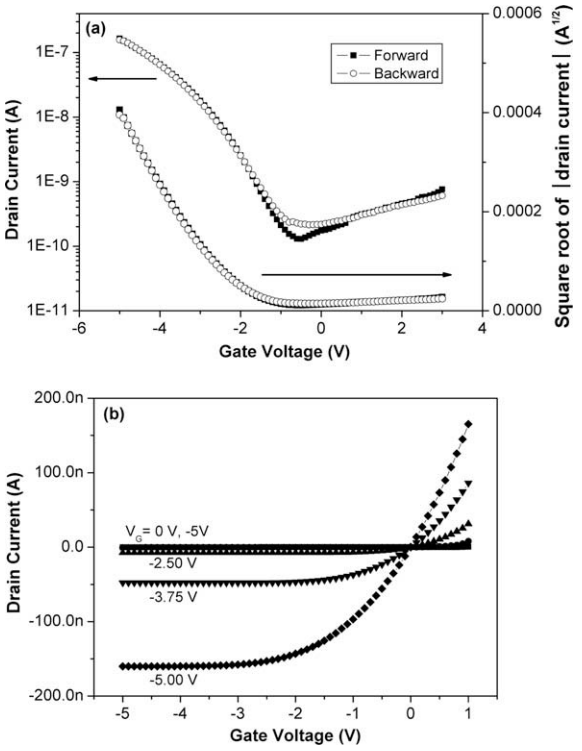

Fig. 10. (a) Transfer and (b) output characteristics of PA230–OFET operated at −5 V.

be used as a dielectric in OFET to improve C_i and to make low-voltage operation possible. Transfer and output characteristics are displayed in Fig. 10. Under −5 V operation, the device gave a drain current of −0.2 μA. The μ, I_{on}/I_{off} and SS were ~0.2 cm^2/V s, 10^3, 0.87 V/dec. Note that the W/L ratio is 10, and output current could be further improved by modifying W/L ratio.

4. Conclusions

We have reported newly fabricated hysteresis-free pentacene field-effect transistors with a polyacrylate copolymer gate insulator, and the effect of the cross-linking temperature was investigated. An elevated temperature of 230 °C enabled an effective cross-linking reaction in PA, and produced a high dielectric strength thin film and negligible hysteresis behavior was achieved in device operation. μ of 0.6 cm^2/V s, on/off current ratio of ~10^5, and inverse subthreshold slope as low as 1.22 V/dec were obtained with −20 V drain voltage. High dielectric strength made it possible to downscale the dielectric thickness, and a thin PA–OFETs could be operated at a low voltage of −5 V.

Acknowledgments

This research was supported by the Korea Science and Engineering Foundation (KOSEF) through the National Research Laboratory Project and Polymer Gel Cluster group of the Korean government. The author Wentao Xu is grateful to the Pohang Accelerator Laboratory for providing the synchrotron radiation source at the 3C2 beamlines used in this study, and Hyunjin Park, researcher at NCNT for supporting AFM analysis.

References

[1] M.E. Roberts, S.C.B. Mannsfeld, N. Queraltó, C. Reese, J. Locklin, W. Knoll, Z. Bao, Proc. Natl. Acad. Sci. USA 105 (2008) 12134.
[2] L. Wang, D. Fine, D. Sharma, L. Torsi, A. Dodabalapur, Anal. Bioanal. Chem. 384 (2006) 310.
[3] C.D. Dimitrakopoulos, D.J. Mascaro, IBM J. Res. Dev. 45 (2001) 11.
[4] H. Klauk, M. Halik, U. Zschieschang, G. Schmid, W. Radlik, W. Weber, J. Appl. Phys. 92 (2002) 5259.
[5] A. Facchetti, M.-H. Yoon, T.J. Marks, Adv. Mater. 17 (2005) 1705.
[6] G. Gu, M.G. Kane, Appl. Phys. Lett. 92 (2008) 053305.
[7] S.C. Lim, S.H. Kim, J.B. Koo, J.H. Lee, C.H. Ku, Y.S. Yang, T. Zyung, Appl. Phys. Lett. 90 (2007) 173512.
[8] D.K. Hwang, K. Lee, J.H. Kim, S. Im, J.H. Park, E. Kim, Appl. Phys. Lett. 89 (2006) 093507.
[9] C.A. Lee, D.-W. Park, K.-D. Jung, B.-J. Kim, Y.C. Kim, J.D. Lee, B.G. Park, Appl. Phys. Lett. 89 (2006) 262120.
[10] D.K. Hwang, M.S. Oh, J.M. Hwang, J.H. Kim, S. Im, Appl. Phys. Lett. 92 (2008) 013304.
[11] L.-L. Chua, J. Zaumseil, J.-F. Chang, E.C.W. Ou, P.K.H. Ho, H. Sirringhaus, R.H. Friend, Nature 434 (2005) 194.
[12] S.H. Kim, H. Yang, S.Y. Yang, K. Hong, D. Choi, C. Yang, D.S. Chung, C.E. Park, Org. Electron. 9 (2008) 673.
[13] D. Li, E.-J. Borkent, R. Nortrup, H. Moon, H. Katz, Z. Bao, Appl. Phys. Lett. 86 (2005) 042105.
[14] Z.-T. Zhu, J.T. Mason, R. Dieckmann, G.G. Malliaras, Appl. Phys. Lett. 81 (2002) 4643.
[15] S.Y. Park, M. Park, H.H. Lee, Appl. Phys. Lett. 85 (2004) 2283.
[16] T. Jung, A. Dodabalapur, R. Wenz, S. Mohapatra, Appl. Phys. Lett. 87 (2005) 182109.
[17] H.E. Katz, X.M. Hong, A. Dodabalapu, R. Sarpeshkar, J. Appl. Phys. 91 (2002) 1572.
[18] M. Egginger, M. Irimia-Vladu, R. Schwödiauer, A. Tanda, I. Frischauf, S. Bauer, N.S. Sariciftci, Adv. Mater. 20 (2008) 1018.
[19] T.-W. Lee, J.H. Shin, I.-N. Kang, S.Y. Lee, Adv. Mater. 19 (2007) 2702.
[20] J. Jang, S.H. Kim, S. Nam, D.S. Chung, C. Yang, W.M. Yun, C.E. Park, J.B. Koo, Appl. Phys. Lett. 92 (2008) 143306.
[21] M. Halik, H. Klauk, U. Zschieschang, G. Schmid, C. Dehm, M. Schütz, S. Maisch, F. Effenberger, M. Brunnbauer, F. Stellacci, Nature 431 (2004) 963.
[22] M.-H. Yoon, H. Yan, A. Facchetti, T.J. Marks, J. Am. Chem. Soc. 127 (2005) 10388.
[23] O. Acton, G. Ting, H. Ma, J.W. Ka, H.-L. Yip, N.M. Tucker, A.K.-Y. Jen, Adv. Mater. 20 (2008) 3697.
[24] F.-Y. Yang, K.-J. Chang, M.-Y. Hsu, C.-C. Liu, Org. Electron. 9 (2008) 925.
[25] H. Klauk, U. Zschieschang, J. Pflaum, M. Halik, Nature 445 (2007) 745.
[26] M.-H. Yoon, A. Facchetti, T.J. Marks, Proc. Natl. Acad. Sci. USA 102 (2005) 4678.
[27] J.H. Cho, J. Lee, Y. Xia, B. Kim, Y. He, M.J. Renn, T.P. Lodge, C.D. Frisbie, Nat. Mater. 7 (2008) 900.
[28] W. Xu, S.-W. Rhee, J. Mater. Chem. 19 (2009) 5250.
[29] S.Y. Yang, K. Shin, C.E. Park, Adv. Funct. Mater. 15 (2005) 1806.
[30] K. Shin, S.Y. Yang, C. Yang, H. Jeon, C.E. Park, Org. Electron. 8 (2007) 336.
[31] A. Bolognesi, M. Berliocchi, M. Manenti, A. Di Carlo, P. Lugli, K. Lmimouni, C. Dufour, IEEE Trans. Electron Dev. 51 (2004) 1997.
[32] C. Kim, A. Facchetti, T.J. Marks, Adv. Mater. 19 (2007) 2561.
[33] C. Kim, A. Facchetti, T.J. Marks, Science 318 (2007) 76.
[34] Y. Jang, D.H. Kim, Y.D. Park, J.H. Cho, M. Hwang, K. Cho, Appl. Phys. Lett. 88 (2006) 072101.
[35] Y.-Y. Noh, H. Sirringhaus, Org. Electron. 10 (2009) 174.
[36] L.-L. Chua, P.K.H. Ho, H. Sirringhaus, R.H. Friend, Appl. Phys. Lett. 84 (2004) 3400.
[37] C.G. Choi, B.-S. Bae, Org. Electron. 8 (2007) 743.
[38] S. Franssila, Introduction to Microfabrication, John Wiley & Sons Ltd., England, 2004. pp. 59–60.
[39] A. Boogaard, R. Roesthuis, I. Brunets, A.A.I. Aarnink, A.Y. Kovalgin, J. Holleman, R.A.M. Wolters, J.Schmitz, in: Proc. 11th Annual Workshop on Semiconductor Advances for Future Electronics and Sensors (SAFE), Veldhoven, the Netherlands, 2008, p. 452.

[40] L.A. Majewski, M. Grell, S.D. Ogier, J. Veres, Org. Electron. 4 (2003) 27.
[41] L.A. Majewski, R. Schroeder, M. Grell, J. Phys. D Appl. Phys. 37 (2004) 21.
[42] D.K. Schroder, Semiconductor Material and Device Characterization, third ed., John Wiley & Sons, New Jersey, 2004. pp. 336–338.
[43] S.-J. Kim, M.-S. So, M.C. Suh, H.K. Chung, Jpn. J. Appl. Phys. 44 (2005) L1414.
[44] S. Lee, B. Koo, J. Shin, E. Lee, H. Park, H. Kim, Appl. Phys. Lett. 84 (2006) 162109.
[45] M. Na, S.-W. Rhee, Org. Electron. 7 (2006) 205.
[46] A. Rolland, J. Richard, J.-P. Kleider, D. Mencaraglia, J. Electrochem. Soc. 140 (1993) 3679.

of donor unit and the bulkiness of side group of the acceptor unit. Although several research groups have synthesized TQ-based low-bandgap copolymers and reported the photovoltaic properties of those copolymers, the molecular weights of the copolymers were very low because of the lack of solubility, and therefore the power conversion efficiencies were below 0.7% [17,20–23].

Herein we report the synthesis and characterization of a new class of donor–acceptor alternating copolymers comprising 3-hexylthiophene (3HT) unit and TQ derivatives as electron-donating and electron-withdrawing unit, respectively. The optical and electrochemical properties of the copolymers and the performance of the copolymers/PCBM BHJ solar cells are reported.

2. Experimental

2.1. Materials

All reagents were obtained from Aldrich unless otherwise specified and used as received. Tetrahydrofuran (THF) was dried over sodium/benzophenone under nitrogen and freshly distilled before use. Hexane was dried over calcium hydride under nitrogen and freshly distilled before use. 5,6-Diamino-4,7-di(4-hexylthien-2-yl)-2,1,3-benzothiadiazole (**2**), 6,7-dimethyl-4,9-di(4-hexylthien-2-yl)[1,2,5]-thiadiazolo[3,4-*g*]quinoxaline (**3b**), and 6,7-dimethyl-4,9-di(5′-bromo-(4-hexylthien-2-yl))[1,2,5]-thiadiazolo[3,4-*g*]quinoxaline (**4b**) were synthesized by following the literature method [24]. [6,6]-Phenyl-C_{61}-butyric acid methyl ester (PCBM) was obtained from Nano-C. Poly(3,4-ethylenedioxythiophene):poly(styrene sulfonate) (PEDOT:PSS) (Baytron P VP AI 4083) was purchased from H.C. Stark and passed through a 0.45 μm PES syringe filter before spin-coating.

2.2. Synthesis

2.2.1. 2,5-Bistrimethylstannyl-3-hexylthiophene (*1*)

3-Hexylthiophene (5.0 g, 0.03 mol) and tetramethylethylenediamine (TMEDA) (13.5 ml, 3.0 equiv) were added into 150 ml of anhydrous hexane. After cooled to −78 °C with isopropanol/dry ice bath, *t*-BuLi (52.4 ml, 3.0 equiv) was added dropwise to the solution over 30 min. After the cooling bath was removed, the reaction mixture was stirred at room temperature for 48 h under nitrogen atmosphere. Then the reaction mixture was cooled back down to −78 °C, and the reaction solution was stirred overnight at room temperature after 92.0 ml of trimethyltinchloride solution (3.0 equiv) was added. The product mixture was washed with saturated solution of $NaHCO_3$, water, and brine, then dried over anhydrous $MgSO_4$ and filtered. After evaporation of the solvent under reduced pressure, the residue was further purified by flash chromatography on silica gel (99:1 hexane/triethylamine as eluent), yielding viscous light yellow liquid as a product. Yield: 12.44 g (85%). ^{1}H NMR (300 MHz, $CDCl_3$): δ (ppm) 7.21 (t, 1H), 2.56 (t, 2H), 1.60 (t, 2H), 1.52–1.41 (m, 6H), 0.86 (t, 3H), 0.43–0.30 (m, 18H). ^{13}C NMR (75 MHz, $CDCl_3$): δ (ppm) 151.88, 143.79, 137.82, 137.61, 32.77, 32.19, 31.55, 29.48, 22.08, 13.73, −8.18. Anal. Calcd for $C_{16}H_{32}S_1Sn_2$ (%): C, 38.91; H, 6.48; S, 6.50. Found (%): C, 38.92; H, 6.47; S, 6.49.

2.2.2. 6,7-Diphenyl-4,9-di(4-hexylthien-2-yl)[1,2,5]-thiadiazolo[3,4-g]quinoxaline (*3a*)

To a suspension of 5,6-diamino-4,7-di(4-hexylthien-2-yl)-2,1,3-benzothiadiazole (0.815 g, 1.64 mmol) in 80 ml of acetic acid, 1,2-diphenyl-1,2-ethanedione (0.862 g, 4.1 mmol) was added in one portion. When the mixture was stirred at room temperature for 8 h, green-colored precipitate was obtained. The precipitate was filtered, washed thoroughly with methanol, and then dried in vacuum to afford green powder as product. Yield: 1.01 g (92%). ^{1}H NMR (300 MHz, $CDCl_3$): δ (ppm) 8.86 (d, 2H), 7.83 (d, 4H), 7.44 (m, 6H), 7.30 (d, 2H), 2.80 (t, 4H), 1.78 (m, 4H), 1.48–1.35 (m, 12H), 0.93 (t, 6H). ^{13}C NMR (75 MHz, $CDCl_3$): δ (ppm) 153.11, 152.12, 143.23, 138.37, 135.80, 135.38, 135.04, 130.94, 130.79, 129.87, 128.27, 121.53, 32.01, 29.82, 29.37, 28.90, 22.91, 14.07. Anal. Calcd for $C_{40}H_{40}N_4S_3$ (%): C, 71.41; H, 5.95; N, 8.33; S, 14.31. Found (%): C, 71.14; H, 5.96; N, 8.30; S, 14.55.

2.2.3. 6,7-Diphenyl-4,9-di(5′-bromo-(4-hexylthien-2-yl))-[1,2,5]-thiadiazolo[3,4-g]quinoxaline (*4a*)

The compound **3a** (0.890 g, 1.32 mmol) was dissolved in 40 ml of THF, to which *N*-bromosuccinimide (NBS) (0.483 g, 2.71 mmol) was added in the dark. After stirring the mixture at room temperature for 3 h, the solvent was removed under reduced pressure. The residue was purified by column chromatography on silica gel (1:3 chloroform/hexane as eluent) to yield the dark-green product. Yield: 0.804 g (74%). ^{1}H NMR (300 MHz, $CDCl_3$): δ (ppm) 8.79 (d, 2H), 7.70 (d, 4H), 7.45 (m, 6H), 2.80 (t, 4H), 1.78 (m, 4H), 1.50–1.35 (m, 12H), 0.93 (t, 6H). ^{13}C NMR (75 MHz, $CDCl_3$): δ (ppm) 153.02, 150.77, 141.79, 137.45, 135.22, 134.29, 134.03, 130.85, 129.44, 127.69, 119.78, 118.25, 31.87, 29.88, 29.59, 28.71, 22.66, 13.89. Anal. Calcd for $C_{40}H_{38}N_4S_3Br_2$ (%): C, 57.83; H, 4.58; N, 6.75; S, 11.59. Found (%): C, 57.98; H, 4.65; N, 6.52; S, 11.79.

2.2.4. Poly(3-hexylthiophene-alt-6,7-diphenyl-4,9-bis-(4-hexylthien-2yl)-[1,2,5]thiadiazolo[3,4-g]quinoxaline (P(3HT-PhTDQ))

Under nitrogen atmosphere, monomer **1** (102.0 mg, 0.206 mmol) and **4a** (171.3 mg, 0.206 mmol) were dissolved in 10 ml of anhydrous 1,2-dichlorobenzene. The solution was flushed with N_2 for 20 min, and then 7.2 mg of $Pd(PPh_3)_2Cl_2$ was added. After the reaction mixture was stirred at 130 °C for 48 h, the polymer was precipitated by addition of 70 ml of methanol. The crude product was filtered through a Soxhlet thimble, and then subjected to Soxhlet extraction with methanol, hexane, acetone, and chloroform. The polymer was recovered from the chloroform fraction by rotary evaporation as dark green solid. Yield: 107.7 mg (63%). ^{1}H NMR (300 MHz, $CDCl_3$): δ (ppm) 9.18–8.80 (m, 2H), 7.75 (s, 4H), 7.33 (d, 6H), 7.20–6.93 (m, 1H), 3.01–2.54 (m, 6H), 1.98–1.60 (m, 6H), 1.58–1.21 (m, 18H), 0.98–0.65 (m, 9H). Anal. Calcd for $C_{50}H_{52}N_4S_4$ (%): C, 71.75; H, 6.22; N, 6.70; S, 15.34. Found (%): C, 71.46; H, 6.22; N, 6.67; S, 15.41.

2.2.5. Poly(3-hexylthiophene-alt-6,7-dimethyl-4,9-bis-(4-hexylthien-2yl)-[1,2,5]thiadiazolo[3,4-g]quinoxaline (P(3HT-MeTDQ))

The polymerization process was the same as that of P(3HT-PhTDQ), except that the monomer **4b** was used instead of **4a**. Yield: 62.5 mg (55%). ^{1}H NMR (300 MHz, $CDCl_3$): δ (ppm) 9.10–8.71 (m, 2H), 7.36–7.02 (m, 1H), 3.04–2.49 (m, 12H), 1.98–1.66 (m, 6H), 1.58–1.33 (m, 18H), 1.02–0.68 (m, 9H). Anal. Calcd for $C_{40}H_{48}N_4S_4$ (%): C, 67.39; H, 6.74; N, 7.86; S, 18.01. Found (%): C, 67.35; H, 6.78; N, 7.75; S, 17.96.

2.3. Measurement

The chemical structures of materials used in this study were identified by ^{1}H NMR and ^{13}C NMR (Avance DPX-300). Elemental analysis was performed on EA1110 (CE Instrument) elemental analyzer. Molecular weight and its distribution were measured by gel permeation chromatography (PL-GPC 50 Integrated GPC System, Polymer Laboratories) equipped with a refractive index detector using THF as eluent, where the columns were calibrated against standard polystyrene samples. The optical absorption and photoluminescence spectra were obtained by UV–vis–NIR spectrophotometer (Lambda 850, Perkin-Elmer) and fluorescence spectrometer (814, Photon Technology International), respectively. Cyclic voltammetry experiments were carried out on potentiostat/galvanostat (Model 273 A, EG&G Princeton Applied Research) in an electrolyte solution of 0.1 M tetrabutylammonium hexafluorophosphate (Bu_4NPF_6) in dichloromethane. Three-electrode cell was used for all experiments. Platinum wires (Bioanalytical System Inc.) were used as both counter and working electrodes, and silver/silver ion (Ag in 0.1 M $AgNO_3$ solution, Bioanalytical System Inc.) was used as a reference electrode.

2.4. Fabrication of photovoltaic devices

Polymer solar cells were fabricated on ITO glass cleaned by stepwise sonication in acetone and IPA, followed by O_2 plasma treatment for 10 min. The substrate was spin-coated with PEDOT:PSS at 4500 rpm for 1 min and annealed at 120 °C for 30 min to yield 40 nm thick film. A mixture of polymer and PCBM were dissolved in anhydrous chlorobenzene (30 mg/ml), and spin-coated on the top of the ITO/PEDOT:PSS film at 800 rpm for 60 s. The typical thickness of the active layer was 70–80 nm. LiF (0.5 nm) and Al (100 nm) were evaporated under vacuum lower than 10^{-6} Torr on the top of active layer through a shadow mask. The effective area of one cell was ca. 4 mm^2. The current–voltage (J–V) curve of the device was obtained on a computer-controlled Keithley 4200 source measurement unit under AM 1.5G (100 mW/cm^2) simulated by an Oriel solar simulator (Oriel 91160A). The light intensity was calibrated using a NREL-certified photodiode prior to each measurement. The external quantum efficiency (EQE) was measured using a Polaronix K3100 IPCE measurement system (McScience) where the light intensity at each wavelength was calibrated with a standard single-crystal Si cell.

3. Results and discussion

3.1. Synthesis and characterization

We synthesized alternating copolymers for preparation of low-bandgap polymers. The synthetic routes for preparation of the monomers and polymers are shown in Fig. 1. We used the palladium-catalyzed Stille coupling reaction to synthesize alternating copolymers of 3HT and TQ derivatives which are electron-donating and electron-withdrawing unit, respectively. At first, 3HT was dilithiated with 3 equiv amount of t-BuLi and TMEDA, followed by reaction with trimethyltin chloride to yield 2,5-bistrimethylstannyl-3-hexylthiophene (**1**). In a separate experiment, the comonomer **4a** was synthesized by condensation reaction of diamino compound with 1,2-diphenyl-1,2-ethanedione, followed by bromination with NBS in THF. Stille coupling of **1** with **4a** or **4b** resulted in the corresponding polymers, P(3HT-PhTDQ) and P(3HT-MeTDQ), with moderate yield. The polymers are highly soluble in common organic solvents, such as chloroform, toluene, and THF at room temperature. The number-average molecular weight (M_n) and polydispersity index (PDI) of P(3HT-PhTDQ) are 7200 and 1.6, respectively, and those of P(3HT-MeTDQ) are 11,100 and 1.5, respectively.

3.2. Optical properties

The optical absorption spectra of the two polymers in chloroform solutions and films on glass substrate are shown in Fig. 2a and b, respectively. Both of two polymers have broad absorption from visible to infrared region. The lower energy absorption peaks of P(3HT-PhTDQ) and P(3HT-MeTDQ) in solution are 784 nm and 703 nm, respectively. As expected, the broad and longer wavelength absorption of the polymers is attributed to the intermolecular charge transfer induced by the donor–acceptor structure of the 3HT and TQ units. When the maximum absorption of polymers in solution is compared with that in solid state (Fig. 2a vs. b), it reveals that the maximum absorption wavelengths (λ_{max}) of the two polymers are red-shifted in solid state by 76 nm and 30 nm, respectively, indicating that polymer chains are associated in solid state. The optical bandgaps (E_g(opt)) as determined from the onset of the absorption spectra of P(3HT-PhTDQ) and P(3HT-MeTDQ) are 1.02 eV and 1.35 eV, respectively. Particularly, the bandgap of P(3HT-PhTDQ) is lower than that of P(3HT-MeTDQ) because the electron-withdrawing phenyl group in P(3HT-PhTDQ) makes the TQ unit more electron-deficient while the electron-donating methyl group in P(3HT-MeTDQ) weakens the electron-withdrawing power of TQ unit. Since it has generally been accepted that the strong electron-withdrawing power of acceptor unit results in a decrease of bandgap for alternating copolymer, our results are very consistent with the prediction and other reports [11,25].

Fig. 3 compares photoluminescence (PL) spectra of P(3HT-MeTDQ) and P(3HT-MeTDQ)/PCBM composite in solid state. P(3HT-MeTDQ) shows strong PL with a maximum at 990 nm whereas P(3HT-PhTDQ) does not show

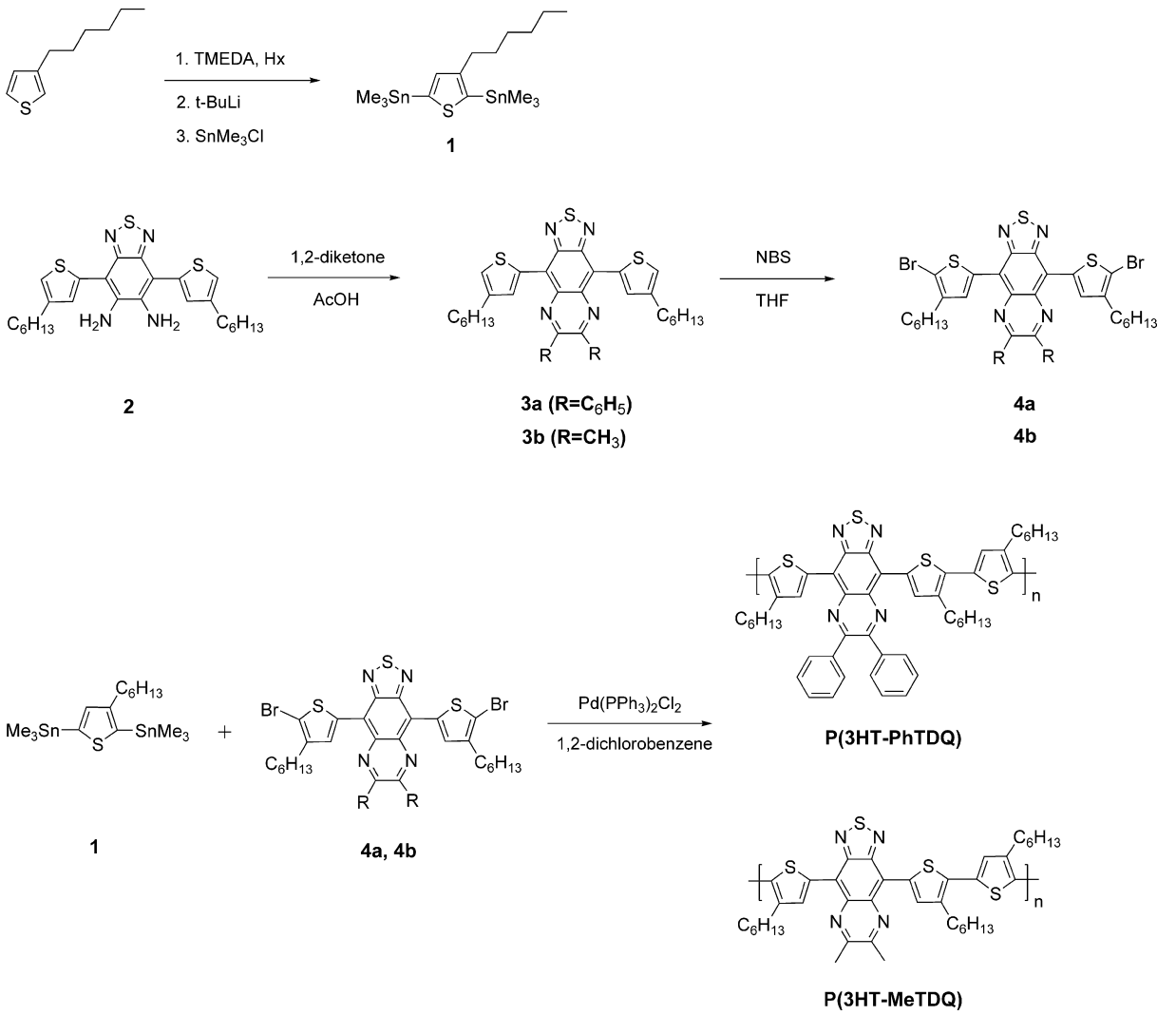

Fig. 1. Synthetic route of alternating copolymers.

PL below 1000 nm wavelength. The PL intensity of P(3HT-MeTDQ) is largely quenched by addition of PCBM, indicating that the charge transfer takes place effectively from the polymer to PCBM.

3.3. Electrochemical properties

The electrochemical data of all the polymers were obtained from the oxidation and reduction cyclic voltammograms, as shown in Fig. 4, and are summarized in Table 1. The onset oxidation and reduction potential of P(3HT-PhTDQ) are 0.38 eV and −0.48 eV (vs. Ag/Ag^+), respectively, and those of P(3HT-MeTDQ) are 0.52 eV and −0.65 eV (vs. Ag/Ag^+). The HOMO energy levels of the polymers can be calculated using the equation: HOMO = $-[E_{ox} - E_{1/2}(\text{ferrocene}) + 4.8]$ V, where E_{ox} is the onset oxidation potential of polymer and $E_{1/2}$(ferrocene) is the onset oxidation potential of ferrocene vs. Ag/Ag^+. The LUMO energy levels can be estimated by using the equation: LUMO = $-[E_{red} - E_{1/2}(\text{ferrocene}) + 4.8]$ V, where E_{red} is the onset reduction potential of polymer. The calculated HOMO and LUMO energy levels of P(3HT-PhTDQ) are −4.82 eV and −3.94 eV, and those of P(3HT-MeTDQ) are −4.96 eV and −3.79 eV, respectively, from which the electrochemical bandgaps (E_g(ec)) for each polymer can be determined. It is noted that the E_g(ec) values of the copolymers are smaller than their corresponding values of E_g(opt). It has generally been accepted that a LUMO–LUMO offset of 0.3–0.4 eV is necessary for efficient electron transfer from polymer to PCBM [26]. Since the LUMO energy level of PCBM has the value ranging between −4.0 and −4.3 eV [27,28], the LUMO–LUMO offset between P(3HT-MeTDQ) and PCBM is larger than 0.3 eV and therefore it is expected that exciton can be easily dissociated at the interface between P(3HT-MeTDQ) and PCBM, whereas the LUMO–LUMO offset between P(3HT-PhTDQ) and PCBM is small, and thus the charge separation is difficult to occur. Furthermore, the HOMO energy level of P(3HT-PhTDQ) is

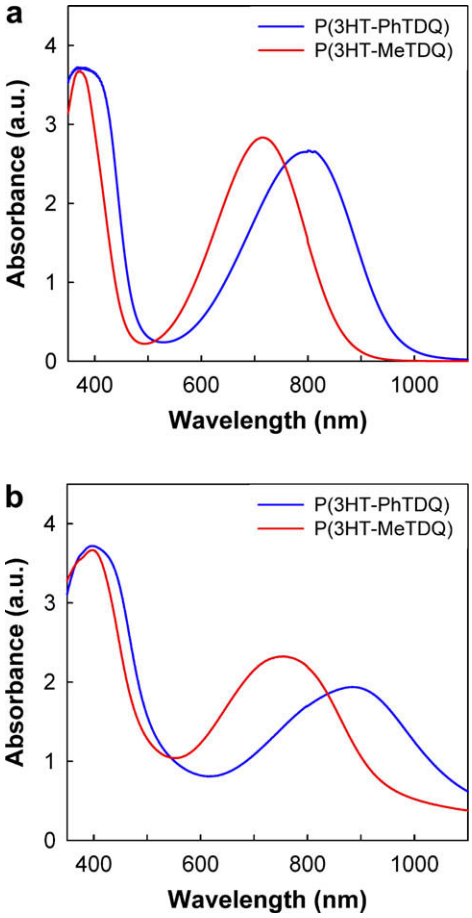

Fig. 2. UV–vis–NIR absorption spectra of the copolymers in chloroform (a) and in film (b).

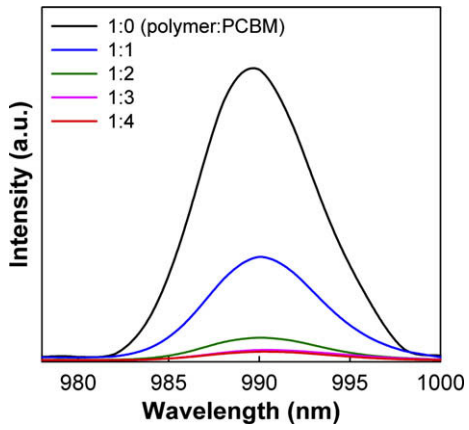

Fig. 3. Photoluminescence spectra of P(3HT-MeTDQ) and P(3HT-MeTDQ):PCBM composite films.

higher than that of PEDOT:PSS (−5.0 eV), while the HOMO energy level of P(3HT-MeTDQ) is almost the same as that of PEDOT:PSS, indicating that holes can be easily transported from P(3HT-MeTDQ) to PEDOT:PSS whereas holes can be trapped at the interface between P(3HT-PhTDQ) and PEDOT:PSS. Consequently, it can be expected that P(3HT-MeTDQ) is better candidate for active material in photovoltaic device.

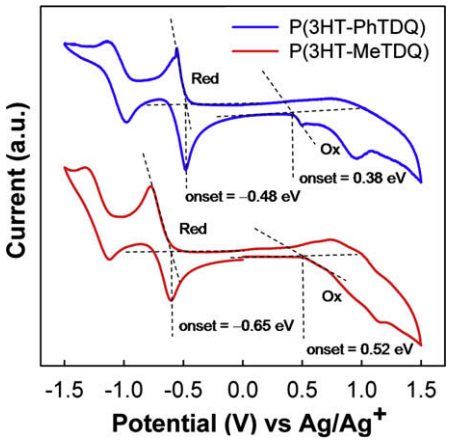

Fig. 4. Cyclic voltammograms of P(3HT-MeTDQ) and P(3HT-PhTDQ).

3.4. Photovoltaic properties

The polymer solar cells were fabricated with layered configuration of glass/ITO/PEDOT:PSS/polymer:PCBM/LiF/Al. The current–voltage characteristics of photovoltaic devices with two different polymers, P(3HT-PhTDQ) and P(3HT-MeTDQ), are shown in Fig. 5, and the photovoltaic parameters of open circuit voltage (V_{oc}), short circuit current (J_{sc}), fill factor (FF), and power conversion efficiency (PCE) are summarized in Table 2. When the PCEs of P(3HT-MeTDQ) are compared with those of P(3HT-PhTDQ), it reveals that the PCEs of P(3HT-MeTDQ) are higher than those of P(3HT-PhTDQ). It should be noted here that P(3HT-MeTDQ) device reaches 0.48% of PCE at the mixing ratio of 1:2 (polymer:PCBM) with V_{oc} = 0.58 V, J_{sc} = 1.58 mA/cm^2, and FF = 0.53. The values of V_{oc} and FF of P(3HT-MeTDQ) are comparable to or slightly higher than those of other TQ-based polymer solar cells [17,20–23], while the J_{sc} value is lower than others. When the external quantum efficiencies (EQE) of P(3HT-PhTDQ) and P(3HT-MeTDQ) are compared (Fig. 6), P(3HT-MeTDQ) exhibits 7.3% efficiency at 700 nm while P(3HT-PhTDQ) shows very low efficiency. This can be explained by the small offset of LUMO levels of P(3HT-PhTDQ) and PCBM, which implies that only a small fraction of the absorbed photons is dissociated at the polymer/PCBM interface.

It is important to optimize the morphology of active layer for achieving high efficiency. The AFM image of P(3HT-MeTDQ):PCBM blend film shows smooth and homogeneous film surface without exhibiting any characteristic feature of phase separation, as can be seen in Fig. 7a and b. This homogeneous morphology may cause low current density because it does not provide the pathway for charge carriers to pass through. It has recently

Table 1
Optical and electrochemical properties of polymers.

Sample	Absorption		E_g(opt)[a] (eV)	HOMO (eV)	LUMO (eV)	E_g(ec)[b] (eV)
	λ_{max}($CHCl_3$) (nm)	λ_{max}(film) (nm)				
P(3HT-PhTDQ)	784	860	1.02	−4.82	−3.94	0.88
P(3HT-MeTDQ)	703	733	1.35	−4.96	−3.79	1.17

[a] Determined from the onset of UV–vis–NIR absorption spectra.
[b] Calculated from the cyclic voltammetry.

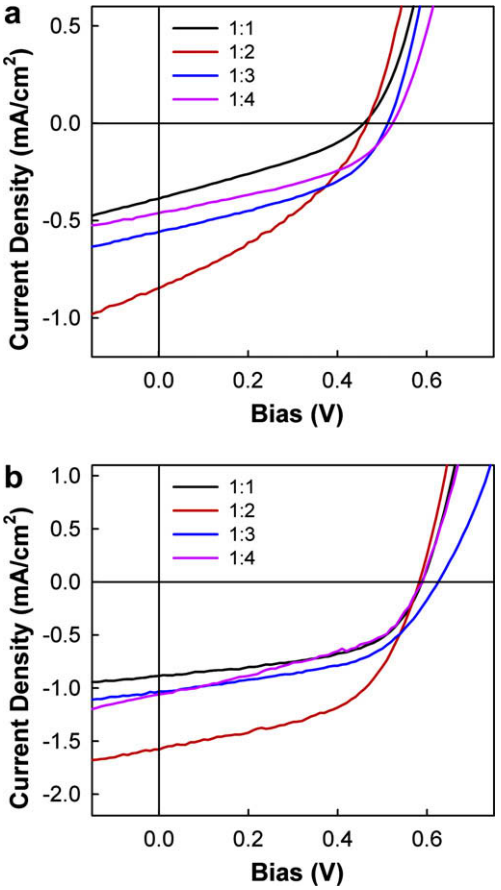

Fig. 5. Current–voltage characteristics of photovoltaic devices based on P(3HT-PhTDQ) (a) and P(3HT-MeTDQ) (b) with different mixing ratio of copolymer to PCBM by weight.

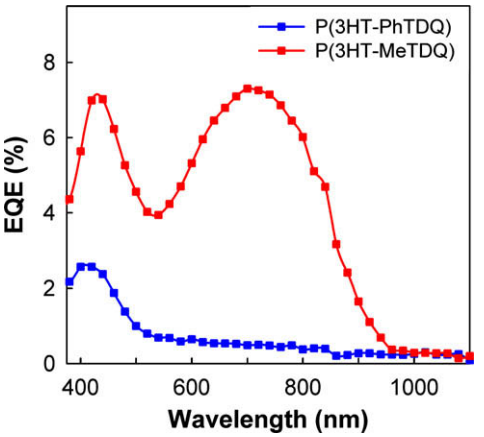

Fig. 6. External quantum efficiency spectra of polymer/PCBM solar cells.

been reported that the morphology of active layer can be effectively modified by the use of specific additives [29–32]. Peet and coworkers [29] have demonstrated that addition of 1,8-octanedithiol (ODT) to polymer:PCBM composite induces phase separation of active layer and thereby improves the PCE of BHJ solar cells. Accordingly, when we add 5 vol.% of ODT to chlorobenzene solution of P(3HT-MeTDQ):PCBM (1:2 w/w), the morphology of active layer shows a phase-separated structure, as shown in Fig. 7c and d. When the surface roughness and phase morphology of film with addition of ODT are compared with those of film without ODT, as shown in Fig. 7, it is realized that the surface roughness of film with ODT is larger than the film without ODT and that the film morphology with ODT exhibits more phase-separated structure as compared to the film without addition of ODT.

Table 2
Photovoltaic parameters of devices testing under standard AM 1.5G conditions.

Polymer	Polymer:PCBM	Solvent	V_{oc} (V)	J_{sc} (mA/cm²)	FF	PCE (%)
P(3HT-PhTDQ)	1:1	CB	0.46	0.39	0.32	0.06
	1:2	CB	0.47	0.85	0.36	0.14
	1:3	CB	0.51	0.56	0.43	0.12
	1:4	CB	0.52	0.46	0.42	0.10
P(3HT-MeTDQ)	1:1	CB	0.59	0.89	0.54	0.28
	1:2	CB	0.58	1.58	0.53	0.48
	1:3	CB	0.63	1.03	0.51	0.33
	1:4	CB	0.59	1.06	0.44	0.28
	1:2	CB/ODT	0.55	4.64	0.50	1.27

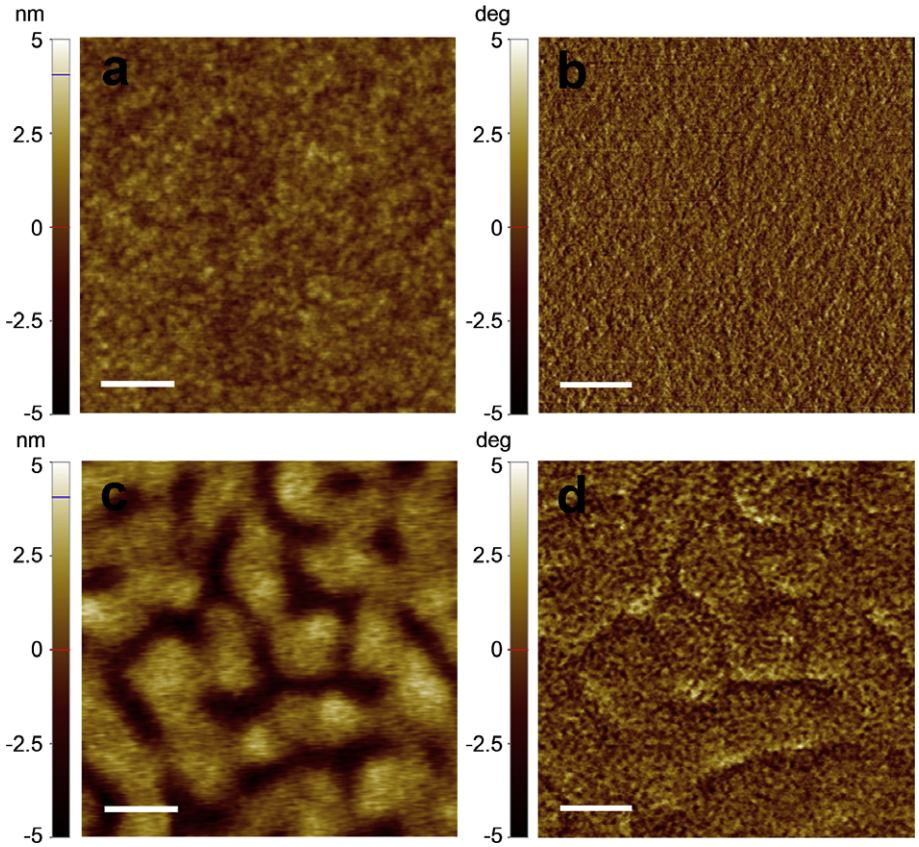

Fig. 7. AFM images of P(3HT-MeTDQ):PCBM (1:2 weight ratio) thin films cast from chlorobenzene (a, height; b, phase), and chlorobenzene with 1,8-octanedithiol as an additive (c, height; d, phase). Scale bars are 150 nm.

To investigate the effect of phase-separated morphology on the charge transport property, we measured hole and electron mobilities from the space charge limited current (SCLC) J–V curve obtained in the dark for hole-only device (ITO/PEDOT:PSS/P(3HT-MeTDQ):PCBM/Au) and electron-only device (Al/P(3HT-MeTDQ:PCBM)/Al) (Fig. 8). The SCLC behavior can be analyzed using the Mott–Gurney law [33]: $J = (9/8)\varepsilon\mu(V^2/L^3)$, where ε is the static dielectric constant of the medium, μ is the carrier mobility, $V = V_a - V_{bi}$ (V_a, the applied bias; V_{bi}, the built-in potential due to the difference in electrical contact work functions), and L is the layer thickness. When the hole and electron mobilities of the device with ODT, determined from the slope of plot of $J^{1/2}$ vs. V, are compared with those of the device without ODT, it is found that both the hole and electron mobilities of the device with ODT are enhanced compared to those of the device without ODT: the hole mobility increases from 6.37×10^{-6} to 2.30×10^{-5} cm^2/Vs; the electron mobility increases from 1.10×10^{-5} to 3.60×10^{-5} cm^2/Vs. This can be attributed to effective formation of phase-separated structure induced by the addition of ODT, which leads to better connectivity of each phase.

Fig. 9 compares J–V curves of devices with and without ODT, from which V_{oc}, J_{sc}, FF, and PCE are determined (Table 2). The PCE of the device with ODT (1.27%) is much higher than that of device without ODT (0.48%). Particularly, the addition of ODT causes a large increase in J_{sc}, because polymer/PCBM composite is phase-separated in nanometer scale as ODT is added, which provides effectively the pathway for charge carriers to pass through the active layer. On the other hand, the photovoltaic performance of P(3HT-PhTDQ) device is not improved by addition of ODT, indicating that the low PCE of the device is attributed mainly to the small difference between LUMO energy levels of the polymer and PCBM.

4. Conclusion

We have synthesized two types of 3-hexylthiophene-thiadiazoloquinoxaline alternating copolymers via the Stille coupling polymerization. Introduction of three hexyl side groups in a repeating unit results in highly soluble polymers with moderate molecular weight. The copolymers exhibited a wide range of optical absorption up to near-IR region. The device fabricated with P(3HT-MeTDQ) shows the PCE of 1.27%, one of the highest values among the TQ-based copolymers, when a small amount of ODT is added to polymer/PCBM composite. Our results demonstrate that P(3HT-MeTDQ) is a potential candidate for application of near-IR absorbing polymer solar cells.

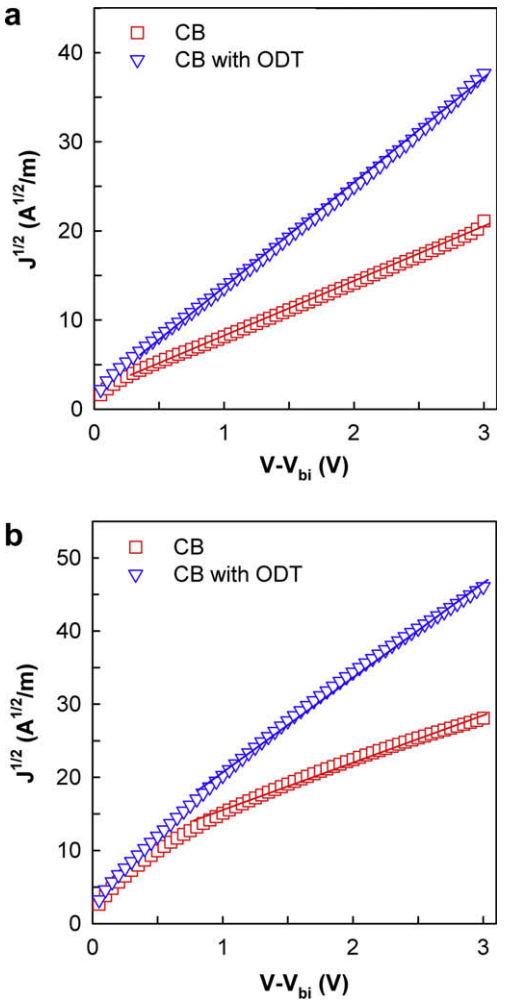

Fig. 8. Dark *J–V* characteristics for hole-only (a) and electron-only (b) devices of P(3HT-MeTDQ):PCBM (1:2 w/w) fabricated using different processing solvents. The solid lines are the best linear fit of the data points.

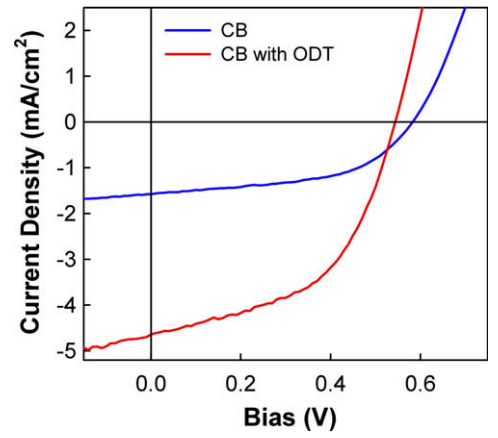

Fig. 9. Current–voltage characteristics of photovoltaic devices of P(3HT-MeTDQ):PCBM (1:2 w/w) fabricated using different processing solvents.

Acknowledgement

The authors thank the Ministry of Education, Science and Technology (MEST), Korea for financial support through the Global Research Laboratory (GRL) program.

References

[1] G. Yu, J. Gao, J.C. Hummelen, F. Wudl, A.J. Heeger, Science 270 (1995) 1789.
[2] C.J. Brabec, N.S. Sariciftci, J.C. Hummelem, Adv. Funct. Mater. 11 (2001) 15.
[3] K.M. Coakley, M.D. McGehee, Chem. Mater. 16 (2004) 1924.
[4] V.D. Mihailetchi, L.J.A. Koster, P.W.M. Blom, C. Melzer, B. de Boer, J.K.J. van Duren, R.A.J. Janssen, Adv. Funct. Mater. 15 (2005) 795.
[5] H. Xin, G. Ren, F.S. Kim, S.A. Jenekhe, Chem. Mater. 20 (2008) 6199.
[6] G. Li, V. Shrotriya, J. Huang, Y. Yao, T. Moriarty, K. Emery, Y. Yang, Nat. Mater. 4 (2005) 864.
[7] W. Ma, C. Yang, X. Gong, K.H. Lee, A.J. Heeger, Adv. Funct. Mater. 15 (2005) 1617.
[8] A. Dhanabalan, J.K.J. Van Duren, P.A. Val Hal, J.L.J. Van Dongen, R.A.J. Janssen, Adv. Funct. Mater. 11 (2001) 255.
[9] M.M. Wienk, M.G.R. Turbiez, M.P. Struijk, M. Fonrodona, R.A.J. Janssen, Appl. Phys. Lett. 88 (2006) 153511/1.
[10] E. Bundgaard, F.C. Krebs, Sol. Energy Mater. Sol. Cells 91 (2007) 954.
[11] N. Blouin, A. Michaud, D. Gendron, S. Wakim, E. Blair, R. Neagu-Plesu, A. Belletete, G. Durocher, Y. Tao, M. Leclerc, J. Am. Chem. Soc. 130 (2008) 732.
[12] S.H. Park, A. Roy, S. Beaupre, S. Cho, N. Coates, J.S. Moon, D. Moses, M. Leclerc, K. Lee, A.J. Heeger, Nat. Photon 3 (2009) 297.
[13] H.-Y. Chen, J. Hou, S. Zhang, Y. Liang, G. Yang, Y. Yang, L. Yu, Y. Wu, G. Li, Nat. Photon 3 (2009) 649.
[14] M. Karikomi, C. Kitamura, S. Tanaka, Y. Yamashita, J. Am. Chem. Soc. 117 (1995) 6791.
[15] Y. Zhu, C.-T. Yen, S.A. Jenekhe, W.-C. Chen, Macromol. Rapid. Commun. 25 (2004) 1829.
[16] Y. Zhu, R.D. Champion, S.A. Jenekhe, Macromolecules 39 (2006) 8712.
[17] W. Wang, E. Perzon, W. Mammo, F. Oswald, S. Admassie, N.-K. Persson, F. Langa, M.R. Andersson, O. Inganäs, Thin Solid Films 511 (2006) 576.
[18] M.-H. Lai, C.-C. Chueh, W.-C. Chen, J.-L. Wu, F.-C. Chen, J. Polym. Sci. A Poly. Chem. 47 (2009) 973.
[19] S. Zhang, Y. Guo, H. Fan, Y. Liu, H.-Y. Chen, G. Yang, X. Zhan, Y. Liu, Y. Li, Y. Yang, J. Polym. Sci. A Poly. Chem. 47 (2009) 5498.
[20] M. Chen, E. Perzon, M.R. Andersson, S. Marcinkevicius, S.K.M. Jönsson, M. Fahlman, M. Berggren, Appl. Phys. Lett. 84 (2004) 3570.
[21] X. Wang, E. Perzon, F. Oswald, F. Langa, S. Admassie, M.R. Andersson, O. Inganäs, Adv. Funct. Mater. 15 (2005) 1665.
[22] H. Yi, R.G. Johnson, A. Iraqi, D. Mohamad, R. Royce, D.G. Lidzey, Macromol. Rapid. Commun. 29 (2008) 1804.
[23] A.P. Zoombelt, M. Fonrodona, M.M. Wienk, A.B. Sieval, J.C. Hummelen, R.A.J. Janssen, Org. Lett. 11 (2009) 903.
[24] M. Sun, L. Wang, X. Zhu, B. Du, R. Liu, W. Yang, Y. Cao, Sol. Energy Mater. Sol. Cells 91 (2007) 1681.
[25] C.-Y. Yu, C.-P. Chen, S.-H. Chan, G.-W. Hwang, C. Ting, Chem. Mater. 21 (2009) 3262.
[26] A.P. Zoombelt, M. Fonrodona, M.G.R. Turbiez, M.M. Wienk, R.A.J. Janssen, J. Mater. Chem. 19 (2009) 5336.
[27] M.S. White, D.C. Olson, S.E. Shaheen, N. Kopidakis, D.S. Ginley, Appl. Phys. Lett. 89 (2006) 143517.
[28] M.D. Irwin, D.B. Buchholz, A.W. Hains, R.P.H. Chang, T.J. Marks, Proc. Natl. Acad. Sci. USA 105 (2008) 2783.
[29] J. Peet, J.Y. Kim, N.E. Coates, W.L. Ma, D. Moses, A.J. Heeger, G.C. Bazan, Nat. Mater. 6 (2007) 497.
[30] Y. Yao, J.H. Hou, Z. Xu, G. Li, Y. Yang, Adv. Funct. Mater. 18 (2008) 1783.
[31] A.J. Moulè, K. Meerholz, Adv. Mater. 20 (2008) 240.
[32] A.J. Moulè, A. Tsami, T.W. Brunnagel, M. Foster, N.M. Kronenberg, M. Scharber, M. Koppe, M. Morana, C.J. Brabec, K. Meerholz, U. Scherf, Chem. Mater. 20 (2008) 4045.
[33] M.A. Lampert, P. Mark, Current Injection in Solids, Academic Press, New York, 1970.

but it is not sufficient for large area applications. The conductivity of 1000 S/cm has been reported for the case of PEDOT by using vapor phase polymerization [12]. However, the process is not suitable for printing process.

As a deposition method of PEDOT:PSS for S/D electrodes ink jet printing has been considered to be an appropriate technology due to its efficient material usage. But its resolution is limited to 20–50 μm due to the statistical variations of droplets positioning and the spreading of droplets on the substrate [13]. This is not sufficient in defining S/D electrodes for the practical applications of OTFTs.

Especially, on a hydrophobic dielectric layer such as polyvinylphenol (PVP) it is difficult to define a fine and continuous pattern with the aqueous PEDOT:PSS because the hydrophilic PEDOT:PSS aggregates on the hydrophobic PVP. Thus, the aqueous PEDOT:PSS layer needs to be heated on substrate during the printing process in order to prevent aggregation of PEODT:PSS droplets on the PVP. However, the heating can result in the shrinkage of the plastic substrate, inducing alignment errors. Moreover, the droplets, which were dropped on the wrong positions, were immediately dried by heating and thus it was difficult to obtain fine patterns. Therefore, an alternative method of ink jet printing needs to be developed for patterning the aqueous PEDOT:PSS on the hydrophobic PVP layer that can be carried out at room temperature. The oxygen plasma process was frequently applied to change the surface energy of hydrophobic film [14]. For instance oxygen plasma was applied to define 5 μm channel length by etching polyimide film and changing surface energy of glass substrate [15]. However, the articles about patterning of the aqueous PEDOT:PSS ink on the hydrophobic PVP were rarely found.

In this work, we developed ink jet printing process for PEDOT:PSS for S/D electrodes of OTFTs. As an appropriate organic compound glycerol was chosen to enhance conductivity of PEDOT:PSS, and a controlled amount of glycerol was figured out to maximize the conductivity as well as to adjust the ink viscosity suitable for ink jet printing. As a result the conductivity of PEDOT:PSS was drastically enhanced to be suitable for S/D electrode of OTFTs. Additionally to avoid the aggregation problems of the aqueous PEODT:PSS on the hydrophobic PVP an ink jet printing technology was also developed by combining oxygen plasma treatment instead of heating. Moreover, the pattern shape was improved when a leveling agent was added. Finally, it was found that the electrode resistance, corresponding to sum of the contact resistance and the series resistance of electrode itself, of the modified PEDOT:PSS to pentacene was comparable to that of Au electrode. It implies that the expensive Au vacuum process can be replaced by the ink jet printing with the PEDOT:PSS.

2. Experimental procedure

The glycerol (from Aldrich) was mixed with PEDOT:PSS (from Bayer AG, Baytron ph 500) and the solution was stirred for 3 h. It is named by G-PEDOT:PSS for convenience. The amount of glycerol was controlled to maximize the conductivity and to make ink viscosity suitable for ink jet printing simultaneously. The surface tensions of the inks were measured by using K9ET (Kruss, Gremany). The curing temperature and time were also optimized to obtain high conductivity by measuring the resistivity with various temperatures and times. The resistivity was measured by a four-point-probe (CMT-Series, AIT). The solvent damage test on the G-PEDOT:PSS film was performed by putting it into various solvents for 5 min, such as water, acetone, anisole, chloroform, which are frequently used as solvents for the soluble semiconductors.

In order to overcome the aforementioned problem, such as the discontinuity in the PEDOT:PSS line that appeared when patterned on the PVP dielectric, the hydrophobic surface of a specific area on PVP was changed to be hydrophilic by treating the area with oxygen plasma. The plasma process was carried out under various conditions, and finally figured out the suitable parameters such as the oxygen flow rate being 3 sccm and the inductively coupled plasma power being 100 W for 5 min. The specific area was defined by the photolithography process. The photoresist was stripped off after the oxygen plasma treatment, and then PEDOT:PSS ink was dropped on the area by ink jet nozzle with a diameter of 50 μm. The geometrical characteristics were examined by a 3-Dimensional (3D) profiler (NV-E1000 Nano system). Several leveling agents were also tested to completely fill the area right up to the corners with the ink.

Test chips, which contained thirty-six OTFTs with the various channel length, were fabricated to investigate the electrical properties of the G-PEDOT:PSS ink for S/D electrodes. Test chips using Au and the pristine PEDOT:PSS electrode were also made for comparison. The bottom gate and bottom S/D contact structure were employed. PVP was used for gate dielectrics and pentacene for semiconductors. The details of the process can be found in other studies [16,17]. All of the processes were carried out in class 1000 clean room in order to minimize the particle contamination. The transfer and output characteristics of OTFTs were measured by a semiconductor parameter analyzer (Keithley SCS-4200). The series resistance of electrodes and the contact resistance were also measured and compared to that of the Au electrodes.

3. Results and discussion

The conductivity of the PEDOT/PSS was strongly dependent on the properties and structure of the additive organic compounds. Among the various organic compounds, glycerol was chosen, which is believed to act as a plasticizer and increased the chain mobility of the polymer. The addition of glycerol helped in not only improving the conductivity and surface wetting properties, but also in avoiding any nozzle clogging problems and in improving the reliability of ink jet printing due to its high boiling point [18].

The resistivity strongly depended on the amount of glycerol, as shown in Fig. 1a, in which the G-PEDOT:PSS film was cured at 120 °C for 20 min. The pristine PEDOT:PSS produced resistivity of 12.9 Ω cm. The resistivity of the G-PEDOT:PSS drastically decreased as the amount

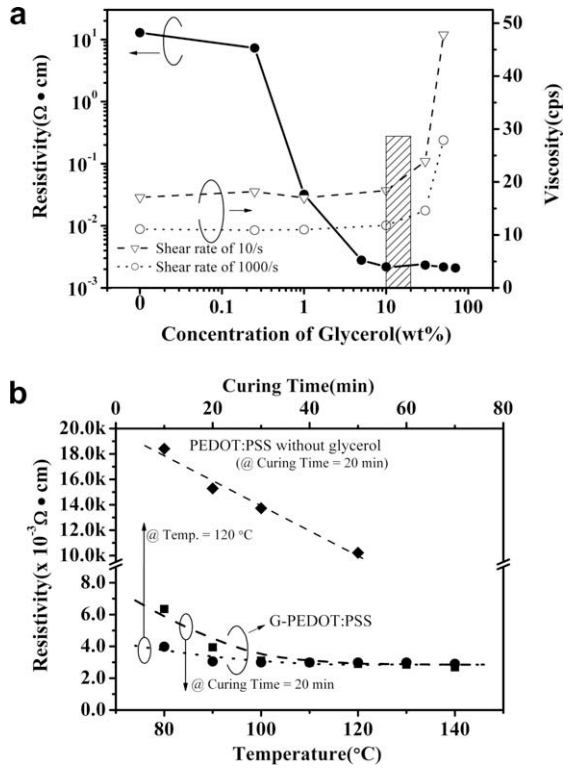

Fig. 1. (a) The resistivity and the viscosity variation of PEDOT:PSS according to the amount of glycerol, (b) The resistivity variation of the G-PEDOT:PSS, which was mixed with glycerol, according to the curing temperature and curing time.

of glycerol increased, and it reached the minimum value of about $2.2 \times 10^{-3}\ \Omega$ cm at 10 wt.% of glycerol.

The viscosity of the G-PEDOT:PSS also changed with the amount of glycerol, as shown in Fig. 1a. The viscosity rapidly increased when the amount of glycerol increased to above 20 wt.%. The viscosity needed to be <20 cps for reliable jetting to occur without any nozzle clogging problems [19]. Therefore, the optimum amount of glycerol was found to be about 10–20 wt.%, as shown in the shaded range in Fig. 1a. This leads to resistivity of $2.2 \times 10^{-3}\ \Omega$ cm, which corresponded to 450 S/cm, and changed the viscosity of the ink to be <20 cps.

The resistivity also varied with the curing temperature and time as well, as shown in Fig. 1b. It decreased as the temperature and the time increased, where it reached the minimum value of $2.2 \times 10^{-3}\ \Omega$ cm at 120 °C and 20 min. In addition the G-PEDOT:PSS film exhibited strong chemical resistance against the organic solvents such as acetone, anisole, and chloroform, which are frequently used as solvents for soluble semiconductors. The resistivity of G-PEDOT:PSS was not changed even after immersing it into the solvents for 5 min. Therefore, the subsequent semiconductor process, which uses strong solvents, can be performed on the G-PEDOT:PSS S/D electrodes.

In order to define S/D electrodes, the G-PEDOT:PSS ink was dropped on the plasma-treated PVP area, as shown in Fig. 2b. The channel length of 10 μm was well defined.

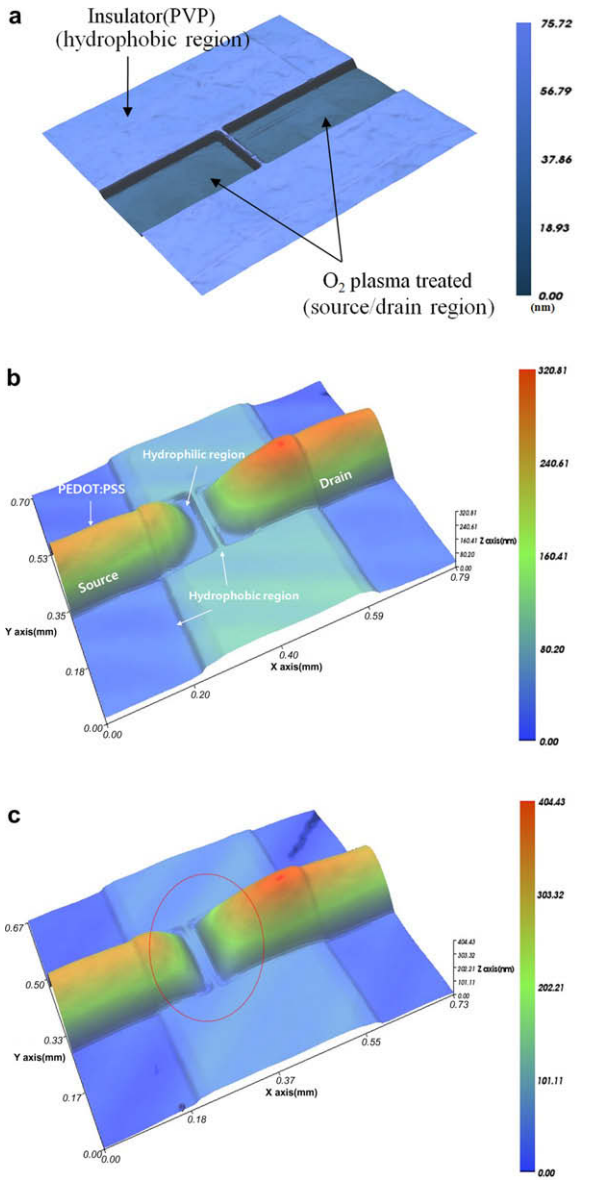

Fig. 2. (a)The 3D image of S/D electrode area on PVP dielectric treated by oxygen plasma; the S/D area was slightly etched off by 30 nm depth, (b) the 3D image of S/D electrode using the G-PEDOT:PSS without, and (c) with a leveling agent. By adding a leveling agent the ink was well spread up to the corners, forming a good shape.

The droplets that were dropped outside of the defined area due to the statistical variation of droppings moved and were confined into the area due to the surface energy difference between the plasma-treated and the non-treated area. In addition, the plasma-treated area was slightly etched off by ~30 nm, as shown in Fig. 2a, and it acted as a kind of bank to tightly keep the ink inside of the area, and thus the confinement was more enhanced.

However, the G-PEDOT:PSS did not completely fill the area right up to the corners, as shown in the 3D profiler image of Fig. 2b, even though the surface property changed after the oxygen treatment. After screening a wide range

of ink recipes, we found that additives of low surface energy solved the current problem. We chose poly(dimethylsiloxane)-based leveling agent (EFKA 3030, Ciba Co.), which is able to effectively reduce the surface energy and help the spreading of the ink in aqueous system. As expected, the modified ink decreased the surface tension significantly from 70.2 to 49.6 mN/m. It is generally known that fluorinated compounds also lower surface energy, but none of this kind was found to be suitable in our case. After ink jet printing, surface energy modified ink spreads uniformly to the corners of the designated area, as shown in Fig. 2c. From this, we can say that surface energy of the ink needs to be modified in ink jet printing and that uniform spreading can be achieved by selecting a proper additive.

The transfer and output characteristics of OTFTs, with the G-PEDOT:PSS, as well as the pristine PEDOT:PSS and the Au S/D electrodes are depicted in Fig. 3 for comparison. The performance parameters, such as field effect mobility and threshold voltage, were extracted from the transfer curves by comparing it with the following equation in the saturation region, and are summarized in Table 1:

$$I_{DS} = \frac{W}{2L}\mu C_G (V_G - V_T)^2 \quad (1)$$

where I_{DS} is the saturation drain current, W is the channel width, L is the channel length, μ is the field effect mobility, C_G is the capacitance of the PVP gate dielectric, V_G is the gate voltage, and V_T is the threshold voltage. The capacitance of the PVP gate dielectric that was measured at 1 MHz was 9.1 nF/cm^2, which was used to extract the parameters.

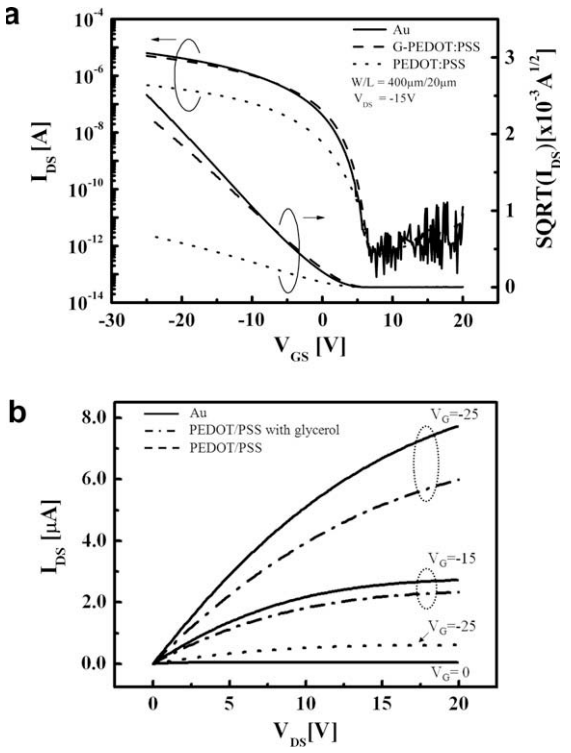

Fig. 3. (a) The transfer characteristics and (b) the output characteristics of pentacene OTFTs using the various S/D electrodes such as the pristine PEDOT:PSS (without glycerol) and the G-PEDOT:PSS (with glycerol) and Au as well (W = 400 μm and L = 20 μm).

Table 1
The performance parameters of pentacene OTFTs with the various S/D electrodes.

Parameter	PEDOT/PSS (without glycerol)	G-PEDOT/PSS (without glycerol)	Au
Mobility (cm^2/Vs)	0.01	0.13	0.16
Threshold voltage (V)	1.9	2.3	1.0
Subthreshold slop (V/dec)	0.98	0.58	0.83
I_{on}/I_{off} current ratio	7.8×10^5	5.6×10^6	1.6×10^7
Off state current (pA/μm)	0.002	0.002	0.003

According to Table 1, the performance of OTFTs that used the pristine PEDOT:PSS without glycerol was worse than the other two OTFTs that used the G-PEDOT:PSS and Au electrodes. The field effect mobility of the pristine PEDOT:PSS was about 0.01 cm^2/V s, which was 10× smaller than the others. Meanwhile, the field effect mobility of the G-PEDOT:PSS electrodes was similar to that of the Au electrodes, which was about 0.1 cm^2/V s. Such field effect mobility difference seems to be originated from the resistance of materials that were used for S/D electrodes. However, in Eq. (1), the resistance was not considered, so that the field effect mobility of the three OTFTs that were extracted from Eq. (1) was different from each other, even though they should have been equal because they used the same semiconductor and dielectric.

The resistance effect is especially clear in the high drain current region, as shown in Fig. 3a, where I_{on} at $V_{GS} = -25$ V of the pristine PEDOT:PSS was 10× smaller than the other two materials. In the output characteristics of Fig. 3b in the small V_{DS} region near 0 V, the drain current linearly increased with V_{DS}, reflecting an ohmic contact.

Let's consider the resistance that is associated with the electrode materials. The total resistance of OTFTs, where R_T consists of three components, is like the following:

$$R_T = (R_S + R_C) + R_{CH} = R_E + R_{CH} \quad (2)$$

where R_S is the series resistance of the electrode itself, R_C is the contact resistance between the electrode and pentacene, and R_{CH} is the channel resistance of pentacene. Here we define a new term electrode resistance R_E, which corresponds to the sum of R_S and R_C, to consider the large series resistance. In transfer length method (TLM) [20], which is frequently applied to extract the contact resistance, the measured R_C is actually equal to the above R_E because R_S is not separated from R_C but included into the measured R_C. For the case of metal electrodes the R_E can be assumed to be equal to R_C because R_S is negligible. However, for PEDOT:PSS with a non-negligible R_S the measured R_C should be considered to be the R_E instead of R_C alone.

The electrode resistance R_E and the channel resistance R_{CH} of the OTFTs in Fig. 3, where the channel width W was equal to 400 μm and the channel length L to 20 μm, were extracted by TLM measurement and compared in Fig. 4. The R_{CH} and the R_E of all OTFTs decreased as the gate

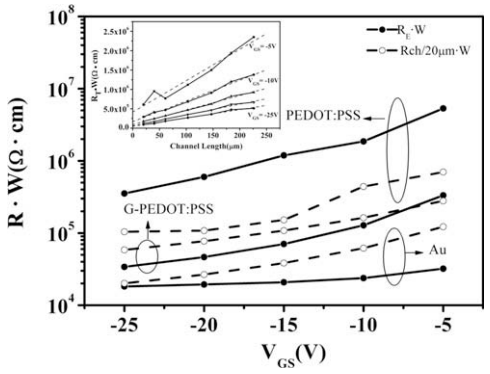

Fig. 4. The comparison of the normalized electrode resistance R_E W, corresponding to sum of contact R_C and series resistance R_S of electrode, and channel resistance $R_{CH}{\cdot}W$ (L = 20 μm) of S/D electrode using Au, G-PEDOT:PSS, and PEDOT:PSS. The inset is $R_T{\cdot}$W of G-PEDOT:PSS.

voltage increased toward negative bias direction since the channel carrier density became larger and the carrier injection enhanced as the gate voltage increased.

The R_{CH}'s were expected to be equal because the OTFTs used the same semiconductor material but they exhibited somewhat difference. We estimated that the difference was caused by the experimental variation as well as the different process history, where Au electrode was fabricated by lift-off meanwhile PEDOT:PSS meanwhile G-PEDOT:PSS electrode were treated by oxygen plasma.

The R_E's produced severe difference depending on the electrode materials. For PEDOT:PSS the R_E was much larger than its R_{CH} so that R_E limited the drain current. It was the cause of small current as mentioned previously. For G-PEDOT:PSS and Au the R_{CH} was larger than their R_E's so that R_{CH} limited current. However, the R_E's were not negligible comparing with R_{CH}'s. Especially, for Au it was equal to its R_{CH} at $V_{GS} = -25$ V. Therefore, the R_E's were also important factors to limit the currents.

The effect of the R_E on drain current will be clear by comparing the injection efficiency as figure-of-merit. The contact injection efficiency η is expressed by Eq. (3) [21] and depicted in Fig. 5 with respect to channel length and gate voltage as well

$$\eta = \frac{R_{CH}}{R_{CH} + R_E} \tag{3}$$

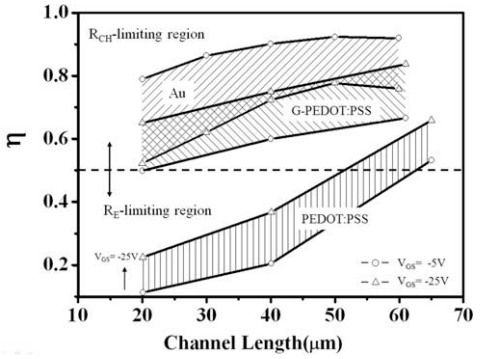

Fig. 5. The comparison of contact injection efficiency $\eta = \frac{R_{CH}}{R_{CH}+R_E}$ of S/D electrode using Au, G-PEDOT:PSS, and PEDOT:PSS.

The η was varied with channel length and gate voltage. The η of PEDOT:PSS was much smaller than the other two devices by exhibiting <0.5 in the most of channel length, meaning that R_E limited current; R_E-limiting electrode. For G-PEDOT:PSS and Au the η was larger than 0.5 in all channel length, meaning that R_{CH} limited current; R_{CH}-limiting electrode as a good contact. The η of G-PEDOT:PSS was overlapped with that of Au in a certain gate voltage region, implying that the injection efficiency of G-PEDOT:PSS is comparable to Au in the gate voltage region. However, at L = 20 μm and $V_{GS} = -25$ V the η of both electrodes approached to 0.5, and expected to be <0.5 when L was smaller than 20 μm and V_{GS} larger than −25 V, entering into R_E-limiting region. In Fig. 3a three OTFTs were in the R_E-limiting region when biased at $V_{GS} = -25$ V. Therefore, the R_E was also an important factor to limit the drain current along with the R_{CH} at $V_{GS} = -25$ V.

As shown in Eq. (2) the R_E consists of R_S and R_C. The series resistance R_S of the pristine PEDOT:PSS electrode was about 2 MΩ/□, which is about $10^4\times$ larger than that of the G-PEDTO:PSS (290 Ω/□) and $10^7\times$ larger than that of the Au electrode (0.3 Ω/□). Thus, the voltage drop on R_S of the pristine PEDOT:PSS electrode became non-negligible so that the R_S would be the main reason of $10\times$ smaller current of PEDOT:PSS than the others. Therefore, the R_E of PEDOT:PSS is mostly determined by the large R_S in the case of PEDOT:PSS.

The R_E of G-PEDOT:PSS was about 30 kΩ cm at $V_{GS} = -25$ V as shown in Fig. 4, which was $10\times$ smaller than that of the article [22], where it was 360 kΩ cm at $V_{GS} = -80$ V for polymer semiconductors. By the way the R_E was comparable to R_E = 20 kΩ cm of Au although the R_S of G-PEDOT:PSS was $10^3\times$ larger than that of Au. The reason can be found in the contact resistance R_C. The R_C determines the injection property of carriers from the electrodes into the semiconductors, which was parameterized by an energy barrier ϕ_B at the contact interface. According to articles [23], the energy barrier of PEDOT:PSS is 0.25 eV, which is smaller than 0.85 eV of Au. Especially, it has been reported that PEDOT:PSS formed a p-doped interface layer, resulting in a low energy barrier [22,24–26]. If it is true for G-PEDOT:PSS, the small energy barrier of G-PEDOT:PSS results in a smaller R_C than that of Au. Therefore, the electrode resistance R_E of G-PEDOT:PSS consists of the larger R_S and the smaller R_C than Au, resulting in the slightly larger than or comparable to that of Au, which has the smaller R_S and the larger R_C than that of G-PEDOT:PSS, as shown in Fig. 4.

According to Fig. 5 the R_E of G-PEDOT:PSS should be reduced further for the application to short channel <20 μm, resulting in the η to be larger than 0.5 as a good contact. There might be two ways to reduce R_E, such as selection of the proper organic additives to reduce R_S or surface treatment employing dipole layer to reduce R_C [27–29].

4. Conclusion

A solution process for the S/D electrodes of OTFTs was developed by using the polymer PEDOT:PSS as a material and ink jet printing for patterning. The conductivity of the PEDOT:PSS was improved to 450 S/cm by adding a con-

trolled amount of glycerol, 10–20 wt.%, which also made ink jet printing suitable in terms of viscosity, which was <20 cps. The ink was patterned on S/D electrode area, which was predefined by photolithography and oxygen plasma, in order to make the area more hydrophilic distinguishing from the other hydrophobic area. The shape of the G-PEDOT:PSS electrode improved with the addition of a leveling agent. The OTFTs with the G-PEDOT:PSS electrodes produced the electrode resistance of 30 kΩ cm at $V_G = -25$ V and the field effect mobility of 0.13 cm^2/V s, which were similar to those of the Au electrodes. However, for short channel applications the electrode resistance need to be further reduced.

Acknowledgement

This research was supported by a Grant (F0004020) from Information Display R&D Center, one of the Knowledge Economy Frontier R&D Program funded by the Ministry of Knowledge Economy of Korean government.

References

[1] F. Zhang, M. Johansson, M.R. Andersson, J.C. Hummelen, O. Inganas, Adv. Mater. 14 (2002) 662.
[2] H.J. Snaith, H. Kenrick, M. Chiesa, R.H. Friend, Polymer 46 (2005) 2573.
[3] T. Aernouts, P. Vanlaeke, W. Geens, J. Poortmans, P. Heremans, S. Borghs, R. Martens, R. Andriessen, L. Leenders, Thin Solid Films 451–452 (2004) 22.
[4] Y. Cao, G. Yu, C. Zhang, R. Menon, A.J. Heeger, Synth. Met. 87 (1997) 171.
[5] L. Groenendaal, F. Jonas, D. Freitag, H. Pielartzik, J.R. Reynolds, Adv. Mater. 12 (2000) 481.
[6] F. Xue, Y. Su, K. Varahramyan, IEEE Trans. Electron Dev. 52 9 (2005) 1982.
[7] D. Li, L.J. Guo, Appl. Phys. Lett. 88 (2006) 063513.
[8] J.Y. Kim, J.H. Jung, D.E. Lee, J. Joo, Synth. Met. 126 (2002) 311.
[9] J. Ouyang, C.W. Chu, F.C. Chen, Q. Xu, Y. Yang, Adv. Funct. Mater. 15 (2) (2005) 203.
[10] S.L. Lai, M.Y. Chan, M.K. Fung, D.S. Lee, S.T. Lee, Mater. Sci. Eng. B 104 (2003) 26.
[11] J. Ouyang, Q. Xu, C.W. Chu, Y. Yang, G. Li, J. Shinar, Polymer 45 (2004) 8443.
[12] B. Winther-Jensen, K. West, Macromolecules 37 (2004) 4538.
[13] H. Kipphan, Handbook of Print Media: Technologies and Producion Methods, Springer, New York, 2001.
[14] H.Y. Choi, S.H. Kim, J. Jang, Adv. Mater. 16 (8) (2004) 732.
[15] H. Sirringhaus, T. Kawase, R.H. Friend, T. Shimoda, M. Inbasekaran, W. Wu, E.P. Woo, Science 290 (2000) 2123.
[16] M.W. Lee, C.K. Song, J. Korean Phys. Soc. 47 (2005) 111.
[17] M.W. Lee, C.K. Song, J. Korean Phys. Soc. 54 (2009) 514.
[18] C.N. Hoth, S.A. Choulis, P. Schilinsky, C.J. Brabec, Adv. Mater. 19 (2007) 3973.
[19] B.J. Gans, P.C. Duineveld, U.S. Schubert, Adv. Mater. 16 (3) (2004) 203.
[20] P.V. Necliudov, M.S. Shur, D.J. Gundlach, T.N. Jackson, Solid-State Electron. 47 (2003) 259.
[21] Y, Shen, A.R. Hosseini, M.H. Wong, G.G. Malliaras, Chem. Phys. Chem. 5 (2004) 16.
[22] M. Barret, S. Sanaur, P. Collot, Org. Electron. 9 (2008) 1093.
[23] A. Kahn, N. Koch, W. Gao, J. Polym. Sci., Polym. Phys. 41 (2003) 2529.
[24] J.Z. Wang, J.F. Chang, H. Sirringhaus, Appl. Phys. Lett. 87 (2005) 083503.
[25] A.C. Fou, O. Onitsuka, M. Ferreira, M.F. Rubner, J. Appl. Phys. 79 (1996) 7501.
[26] A.C. Arias, M. Granstrom, D.S. Thomas, K. Petritsch, R.H. Friend, Phys. Rev. B 60 (1999) 3930.
[27] M. Kawasaki, S. Imazeki, M. Ohe, M. Ando, Jpn. J. Appl. Phys. 47 (2008) 6247.
[28] D.J. Yun, D.K. Lee, H.K. Jeon, S.W. Rhee, Org. Electron. 8 (2007) 690.
[29] S.A. Dibenedetto, A. Facchetti, M.A. Ratner, T.J. Marks, Adv. Mater. 21 (2009) 1407.

[16–18]. The solid-state electron affinity (EA) of $Mo(tfd)_3$ is 5.6 eV [18], which is large enough to *p*-dope a number of hole-transport materials including pentacene, which has the solid-state ionization energy (IE) of 5.1 eV [19]. Within Koopmans' approximation, EA is the difference between vacuum level (E_{vac}) and the lowest unoccupied molecular orbital (LUMO) energy level, whereas IE is the difference between vacuum level and the highest occupied molecular orbital (HOMO) level. In other words, the LUMO level of $Mo(tfd)_3$ is 0.5 eV lower in energy than the HOMO of pentacene, making an electron transfer from a pentacene molecule to the molecular dopant energetically favorable.

Top-contact OFET device structures with Au source/drain electrodes and large channel lengths (25–200 μm) are used in this study. Effects of channel length scaling are studied in devices with doped contacts and undoped (with only a 50 nm pentacene layer) reference OFETs. In contrast to most previous studies where pristine dopant films were deposited with the control of lateral [11] or vertical [14] position of the dopant layer, in our study, a 10 nm co-evaporated (1:1 ratio, from different crucibles) layer of $Mo(tfd)_3$ and pentacene was deposited under the metal electrodes and above the 50 nm pentacene layer for the selective doping in OFETs. $Mo(tfd)_3$ doping in the OFETs resulted in improved μ and V_{TH} values as well as a significant reduction in contact resistance.

2. Device fabrication and electrical characterization

OFETs were fabricated on heavily doped *n*-type silicon substrates (also serving as gate electrodes) with 200 nm thick thermally grown SiO_2 as the gate dielectric in a top contact configuration. Ti/Au (10 nm/100 nm) metallization on the backside of the substrate was carried out to further enhance the gate electrical contact. First, the substrates were cleaned by O_2 plasma for 3 min to make the SiO_2 surface hydrophilic. Surface treatment with octadecyltrichlorosilane (OTS) (5 mM in toluene) was performed by soaking the substrates in the OTS solution for 17 h in a N_2-filled glove box. The substrates were then rinsed with toluene and annealed at 60 °C for 5 min. The capacitance density of the OTS-treated SiO_2 was measured and found to have a value of 16.2 nF/cm^2. Pentacene (Sigma–Alrich), purified using gradient zone sublimation, was deposited (50 nm) on the substrates by vacuum sublimation without any active substrate heating. For doped devices, a 10 nm-thick layer of a 1:1 mixture of $Mo(tfd)_3$ (synthesized according to the literature [20]) and pentacene was co-evaporated, followed by deposition of 60 nm Au, through a shadow mask to define the source/drain electrodes. For undoped reference devices, Au was directly deposited on top of the pentacene layer. Devices were not exposed to normal ambient after loading in the glove box for OTS treatment. Fig. 1(a) shows the cross-sectional device structure of a standard OFET with a single pentacene layer. Such devices are referred to as reference OFETs. Fig. 1(b) shows the cross-sectional device structure of OFETs in which an additional co-evaporated layer (pentacene + $Mo(tfd)_3$, ratio 1:1) was deposited on top of the pentacene layer through the same shadow mask used to deposit the top electrodes. Such devices are referred to as contact-doped OFETs. The chemical structures of pentacene and $Mo(tfd)_3$ are also shown in Fig. 1.

The samples were transferred in an air-tight vessel, without being exposed to atmospheric conditions, into another N_2-filled glove box (O_2, H_2O < 0.1 ppm) for electrical testing. The electrical measurements were performed using an Agilent E5272A source/monitor unit. Output (I_{DS} vs. V_{DS}) and transfer (I_{DS} vs. V_{GS}) characteristics were measured for the devices, and μ and V_{TH} were measured in the saturation regime from the highest slope of $|I_{DS}|^{1/2}$ vs. V_{GS} plots using the saturation region current equation for standard transistors. For the study of stability under a constant bias, the time-dependent decay of I_{DS} was tested in the saturation regime ($V_{GS} = V_{DS} = -30$ V) for 1 h.

3. Results and discussion

Devices with channel width $W = 1000$ μm and various channel lengths ($L = 25$, 50, 100, and 200 μm) were characterized to obtain values of the hole mobility in saturation (μ_{sat}), V_{TH}, current on/off ratio (I_{on}/I_{off}), and sub-threshold

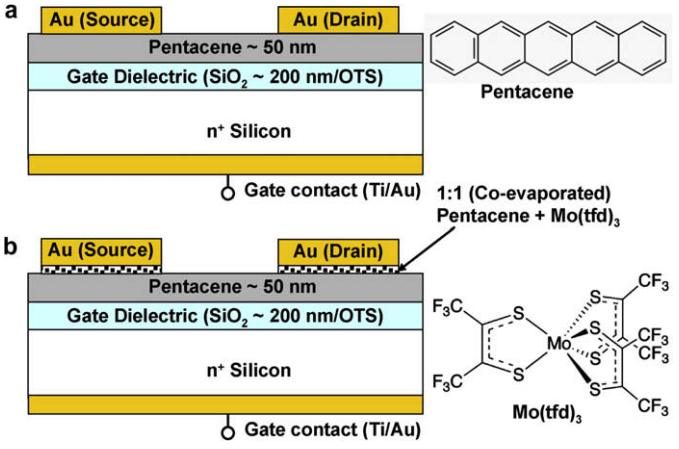

Fig. 1. Device structures of a reference top-contact pentacene OFET (a) and that of a device in which the contact region under the source and drain electrodes has been doped with $Mo(tfd)_3$ (b); chemical structures of pentacene and $Mo(tfd)_3$ are shown on the right.

slope (*SS*). Table 1 summarizes the performance parameters with $W = 1000$ μm and $L = 25$, 50, 100 and 200 μm for a total 13 reference devices and 14 contact-doped devices with μ, V_{TH} and $I_{on/off}$ averaged over 3 or 4 devices for each device geometry. Fig. 2(a) and (b) shows the comparison of output and transfer characteristics of contact-doped vs. reference devices for $W/L = 1000$ μm/200 μm, whereas Fig. 2(c) and (d) shows the same comparison for the smallest L in our study ($W/L = 1000$ μm/25 μm). Fig. 2(e) and (f) shows the plots for the comparison of μ_{sat} and V_{TH}. As can be seen from the results, I_{DS} in the contact-doped devices increases by 28% for devices with $W/L = 1000$ μm/200 μm and 50% for devices with $W/L = 1000$ μm/25 μm. On the other hand, the values of the *SS* and $I_{on/off}$ decrease in the contact-doped devices. The drop in $I_{on/off}$ is essentially due to the increase in I_{off} in the devices, which is higher for the devices with smaller channel L ($\sim 10^{-10}$ A for 1000 μm/200 μm, and $\sim 10^{-9}$ A for 1000 μm/25 μm). The $I_{on/off}$ is on the order $\sim 10^4$ or higher in the contact-doped OFETs in the studied range ($L = 25$–200 μm), which indicates that this technique can be suitable for applications where higher drive currents are desired at the cost of a moderate increase in power dissipation in the "off" state. Apart from the changes in the electrical parameters such as μ, V_{TH} $I_{on/off}$, and *SS*, the next important parameter to look at is contact resistance (R_C).

As explained in the literature [14], carrier injection from the Au contact to the semiconductor in the contact region can be separated into two processes: interface charge injection from the metal contact to the semiconductor and the vertical charge transport through the pentacene film to the channel. Hence, the contact resistance R_C is generally divided into two parts: a contribution from the interface resistance (R_{int}), and a contribution from the vertical bulk resistance (R_{bulk}) which results from the transport region between the electrode interface and the conduction channel near the semiconductor/gate dielectric interface [14]. Selective doping near the electrode interface is expected to mainly decrease R_{int} due to a reduction in the energy barrier height for carrier injection from the metal electrode to the semiconductor due to the band bending associated with the doping near that interface.

To better understand the effect of doping on R_C, the R_C values for each type of device were extracted using a transmission line method (TLM) based on the dependence of the current–voltage characteristics on L. A set of devices with L ranging from 25 μm to 200 μm and a fixed $W = 1000$ μm was used to calculate the R_C at a low V_{DS} of −3 V for V_{GS} values ranging from −15 V to −30 V. In the linear regime, the overall device resistance R_{on} can be considered to be the sum of the channel resistance R_{ch} and the total contact resistance R_C, as already explained in the literature [21–23]. The width-normalized contact resistance ($R_C W$) was estimated by extrapolating $R_{on}W$ to $L = 0$ μm using the y intercept of plots of $R_{on}W$ vs. L, which are shown in Fig 3(a) and (b) for reference and contact-doped OFETs, respectively. The $R_C W$ for different V_{GS} for both types of devices are plotted in Fig. 3(c). The $R_C W$ for contact-doped

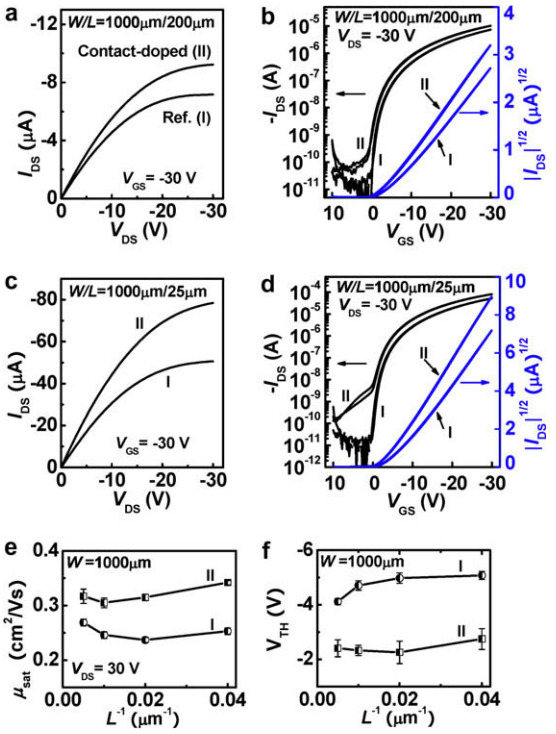

Fig. 2. Comparison of output and transfer characteristics of reference (I) and contact-doped (II) pentacene OFETs with $W/L = 1000$ μm/200 μm (a and b), and with $W/L = 1000$ μm/25 μm (c and d); (e) dependence of μ_{sat} on L^{-1}; and (f) dependence of V_{TH} on L^{-1} for both types of OFETs.

Table 1
Summary of the electrical parameters of reference (13 devices) and contact-doped OFETs (14 devices) with $W = 1000$ μm and $L = 25$, 50, 100, and 200 μm. Average values and standard deviations for devices were obtained by averaging over three or four devices with identical geometry fabricated on the same substrate.

Device (W/L)	μ (cm^2/Vs)	V_{TH} (V)	$I_{on/off}$	*SS* (V/dec)
Reference (13 devices)				
1000 μm/25 μm (3 dev.)	0.253 (±0.004)	5.1 (±0.2)	5×10^6	0.59 (±0.04)
1000 μm/50 μm (3 dev.)	0.237 (±0.005)	5.0 (±0.2)	2×10^6	0.58 (±0.02)
1000 μm/100 μm (4 dev.)	0.246 (±0.006)	4.7 (±0.2)	1×10^6	0.49 (±0.04)
1000 μm/200 μm (3 dev.)	0.269 (±0.006)	4.1 (±0.1)	7×10^5	0.36 (±0.07)
Contact-doped (14 devices)				
1000 μm/25 μm (3 dev.)	0.342 (±0.004)	2.8 (±0.4)	2×10^4	1.43 (±0.13)
1000 μm/50 μm (4 dev.)	0.315 (±0.006)	2.3 (±0.4)	1×10^4	1.59 (±0.07)
1000 μm/100 μm (4 dev.)	0.305 (±0.009)	2.3 (±0.2)	1×10^4	1.46 (±0.06)
1000 μm/200 μm (3 dev.)	0.317 (±0.013)	2.4 (±0.3)	2×10^5	0.73 (±0.02)

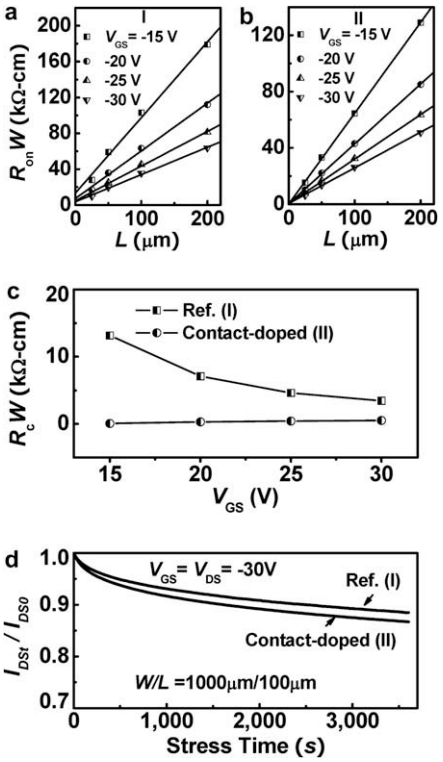

Fig. 3. Values of $R_{on}W$ obtained at various values of V_{GS} for different channel lengths for reference (I) (a), and contact-doped (II) (b) OFETs; (c) plot of R_CW as a function of V_{GS} for both types of devices; (d) decay of drain-source current for $V_{GS} = V_{DS} = -30$ V measured continuously over a period of 1 h.

devices is significantly lowered compared to reference OFETs. In the strong accumulation regime ($V_{GS} = -30$ V), it is lowered from ~3.4 kΩ-cm for reference to ~0.5 kΩ-cm for contact-doped devices.

Fig. 3(d) shows the time-dependent decay of I_{DS} under a continuous dc bias stress with $V_{GS} = V_{DS} = -30$ V measured over 1 h for both types of devices with the geometry $W/L = 1000\ \mu m/100\ \mu m$. The decay of the current measured in these experiments is nearly identical for the two types of devices. The current decays to 90–85% of its initial value after one hour. These results show that the reduction in R_C in contact-doped OFETs could be achieved without compromising the electrical stability under a continuous bias stress, which is very important for the reliable operation of organic devices and circuits.

4. Summary and conclusion

In summary, the electrical performance of *p*-channel pentacene OFETs could be improved by selectively doping the organic semiconductor region beneath the source/drain electrodes with $Mo(tfd)_3$. The doping with $Mo(tfd)_3$ yielded a small increase in μ, a reduction in V_{TH}, and a significant reduction in R_CW (from 3.4 kΩ-cm to 0.5 kΩ-cm at $V_{GS} = -30$ V). In contrast to previous studies performed in short channel OFETs [13,14], these improvements in electrical performance were achieved while maintaining large current on/off ratios and good electrical stability under continuous bias stress. These advances are important for the design of future backplanes for displays and other organic-based circuits.

Acknowledgements

The authors would like to thank Prof. Antoine Kahn from Princeton University for helpful discussions. This material is based upon work supported in part by Solvay S.A., by the STC Program of the National Science Foundation under Agreement No. DMR-0120967, and by the Office of Naval Research (Grant No. N00014-04-1-0120). This work was performed in part at the Microelectronics Research Center at Georgia Institute of Technology, a member of the National Nanotechnology Infrastructure Network, which is supported by NSF (Grant No. ECS-03-35765).

References

[1] A. Dodabalapur, Z. Bao, A. Makhija, J.G. Laquindanum, V.R. Raju, Y. Feng, H.E. Katz, J. Rogers, Appl. Phys. Lett. 73 (1998) 142.
[2] P.F. Baude, D.A. Ender, M.A. Haase, T.W. Kelley, D.V. Muyres, S.D. Theiss, Appl. Phys. Lett. 82 (2003) 3964.
[3] G.H. Gelinck, H.E.A. Huitema, E. Van Veenendaal, E. Cantatore, L. Schrijnemakers, J. Van der Putten, T.C.T. Geuns, M. Beenhakkers, J.B. Giesbers, B.H. Huisman, E.J. Meijer, E.M. Benito, F.J. Touwslager, A.W. Marsman, B.J.E. Van Rens, D.M. De Leeuw, Nat. Mater. 3 (2004) 106.
[4] L.S. Zhou, A. Wanga, S.C. Wu, J. Sun, S. Park, T.N. Jackson, Appl. Phys. Lett. 88 (2006) 083502.
[5] S. Kim, S.J. Choi, M. Jang, Y.K. Choi, Appl. Phys. Lett. 95 (2009) 063508.
[6] W.Y. Gao, A. Kahn, J. Appl. Phys. 94 (2003) 359.
[7] C.K. Chan, A. Kahn, Q. Zhang, S. Barlow, S.R. Marder, J. Appl. Phys. 102 (2007) 014906.
[8] K. Walzer, B. Maennig, M. Pfeiffer, K. Leo, Chem. Rev. 107 (2007) 1233.
[9] X.H. Zhang, S.P. Tiwari, B. Kippelen, Org. Electron. 10 (2009) 1133.
[10] D. Braga, G. Horowitz, Adv. Mater. 21 (2009) 1473.
[11] Y. Abe, T. Hasegawa, Y. Takahashi, T. Yamada, Y. Tokura, Appl. Phys. Lett. 87 (2005) 153506.
[12] C. Vanoni, S. Tsujino, T.A. Jung, Appl. Phys. Lett. 90 (2007) 193119.
[13] C. Vanoni, T.A. Jung, S. Tsujino, Appl. Phys. Lett. 94 (2009) 253306.
[14] F. Fujimori, K. Shigeto, T. Hamano, T. Minari, T. Miyadera, K. Tsukagoshi, Y. Aoyagi, Appl. Phys. Lett. 90 (2007) 193507.
[15] K. Tsukagoshi, F. Fujimori, T. Minari, T. Miyadera, T. Hamano, Y. Aoyagi, Appl. Phys. Lett. 91 (2007) 113508.
[16] O. Zeika, A. Werner, H. Hartmann, S. Willmann, PCT Appl. WO 061517 (2008).
[17] Y.B. Qi, T. Sajoto, M. Kröger, A.M. Kandabarow, S. Barlow, E.-G. Kim, L. Wielunski, L.C. Feldman, R.A. Bartynski, J.-L. Bredas, S.R. Marder, A. Kahn, Chem. Mater. 22 (2010) 524.
[18] Y.B. Qi, T. Sajoto, S. Barlow, E.G. Kim, J.L. Bredas, S.R. Marder, A. Kahn, J. Am. Chem. Soc. 131 (2009) 12530.
[19] C.K. Chan, A. Kahn, Appl. Phys. A-Mater. Sci. Process. 95 (2009) 7.
[20] A. Davison, R.H. Holm, R.E. Benson, W. Mahler, Inorg. Synth. 10 (1967) 8.
[21] E.J. Meijer, G.H. Gelinck, E. van Veenendaal, B.H. Huisman, D.M. de Leeuw, T.M. Klapwijk, Appl. Phys. Lett. 82 (2003) 4576.
[22] J. Zaumseil, K.W. Baldwin, J.A. Rogers, J. Appl. Phys. 93 (2003) 6117.
[23] Z. Bao, J. Locklin, Organic Field-effect Transistors, CRC Press, Boca Raton, 2007.

These compounds were found to exhibit a high external quantum efficiency of 4.6% and a pure deep blue emission with CIE coordinates (0.154, 0.078) [29]. In other research in this area, Yamashita's group used an indenopyrazine derivative, difluoro-diindeno[1,2-b;1′,2′-e]pyrazine-6,12-dione, as the channel material in an n-type OTFT, with excellent results (mobility, 0.17 cm^2/Vs; on/off ratio, 10^7) [30]. Indenopyrazine is therefore gaining recognition in optoelectronics as a potentially useful core structure for a new family of organic functional materials. However, if indenopyrazine derivatives with enhanced performance suitable for diverse optoelectronics applications are to be developed, more systematic studies of their structures and properties must be conducted.

In a previous study, we hypothesized that the π–π^* stacking of molecules in the thin-film state due to the plate-like molecular structure of indenopyrazine would give rise to a reduction in its fluorescence yield and a bathochromic effect on its emission wavelength. To remove this effect, we introduced short alkyl groups at the 6- and 12-positions of indenopyrazine and a bulky *m*-terphenyl side group at positions 2 and 8. An OLED device based on the resulting molecule was found to exhibit excellent characteristics, with high efficiency and a pure deep blue color [29]. In this study, we investigated the effects on the optical and electroluminescence properties of varying the substitution position of the side groups (Scheme 1). In particular, we examined the bulky *m*-terphenyl substitution positions 2 and 8 (*meta* positions), 1 and 7 (*ortho* positions), and 3 and 9 (*para* positions).

Although varying the substitution positions of side groups on emitting cores offers important information about the intrinsic properties of the molecules, it is difficult to change the side group substitution positions for most emitting cores (*e.g.* fluorene, bifluorene and anthracene) [9–28]. In this study, however, varying the substitution pattern was facilitated by the use of bromo-indanones with Br substituted at positions 4, 5, and 6 as the starting compounds. This procedure enabled the facile synthesis of three compounds in which *m*-terphenyl is substituted at the *ortho*, *meta*, and *para* positions: 6,6,12,12-tetraethyl-1,7-bis-[1,1′;3′,1″]terphenyl-4′-yl-6,12-dihydro-diindeno[1,2-b;1′,2′-e]pyrazine (*o*-TP-EPY), 6,6,12,12-tetraethyl-2,8-bis-[1,1′;3′,1″]terphenyl-4′-yl-6,12-dihydro-diindeno[1,2-b;1′,2′-e]pyrazine (*m*-TP-EPY), and 6,6,12,12-tetraethyl-3,9-bis-[1,1′;3′,1″]terphenyl-4′-yl-6,12-dihydro-diindeno[1,2-b;1′,2′-e]pyrazine (*p*-TP-EPY).

2. Experimental

2.1. Synthesis of o-, m-, and p-TP-EPY

The compounds *o*-, *m*-, and *p*-TP-EPY were synthesized following literature procedures [29]: to 2,8-dibromo-6,6,12,12-tetraethyl-6,12-dihydro-diindeno[1,2-b;1′,2′-e]pyrazine (1 g, 1.9 mmol) and 4,4,5,5-tetramethyl-2-[1,1′;3′,1″]terphenyl-4′-yl-[1,3,2]dioxaborolane (1.49 g, 4.19 mmol) in a 500 mL round-bottomed flask under a nitrogen atmosphere were added $Pd(OAC)_2$ (0.042 g, 0.19 mmol), tricyclohexylphosphine (0.053 g, 0.19 mmol) and toluene. The temperature was then increased to 50 °C, and tetraethylammonium hydroxide (13.5 mL, 19.0 mmol, 20 wt.% in water) was added. Stirring was continued at this temperature and the reaction was monitored by TLC. When the reaction was complete, the product was extracted with water and toluene. The organic extract was dried over anhydrous $MgSO_4$ and filtered, after which the solvent removed in vacuo. The resulting crude mixture was passed through a short column of silica with THF as the eluent and then recrystallized from THF to obtain *m*-TP-EPY as a white solid. The purification method of *o*- and *p*-TP-EPY was same as *m*-TP-EPY.

2.1.1. Synthesis of 6,6,12,12-tetraethyl-1,7-bis-[1,1′;3′,1″] terphenyl-4′-yl-6,12-dihydro-diindeno[1,2-b;1′,2′-e]pyrazine (o-TP-EPY)

The final yield was 1.06 g, 68%. ^{1}H NMR (500 MHz, $CDCl_3$): δ (ppm) 8.00–7.99 (d, 2H), 7.74–7.72 (m, 6H), 7.59 (d, 2H), 7.48–7.45 (t, 4H), 7.41–7.36 (m, 12H), 7.16–7.14 (m, 4H), 7.08 (s, 2H), 2.10 (m, 2H), 1.85 (m, 2H), 1.74 (m, 2H), 1.62 (m, 2H), 0.27–0.20 (m, 6H), −0.51 to −0.60 (m, 6H). ^{13}C NMR (500 MHz, $CDCl_3$): 162.7, 152.5, 145.4, 141.5, 141.1, 140.9, 139.0, 138.4, 134.1, 131.7, 130.7, 129.6, 129.1, 128.2, 127.8, 127.4, 126.9, 126.5, 125.0, 120.4, 56.2, 30.6, 30.1, 8.9, 8.8, 7.8. FT-IR (KBr cm^{-1}): 3056, 2961, 2928, 2873, 1599, 1486, 1469, 1456, 1400, 1367, 1291, 1244, 1204, 1182, 1103, 1076, 1030, 776, 755, 742, 698. HRMS Calcd for $C_{62}H_{53}N_2$ $(M+H)^+$, 825.4209, found: 825.4229.

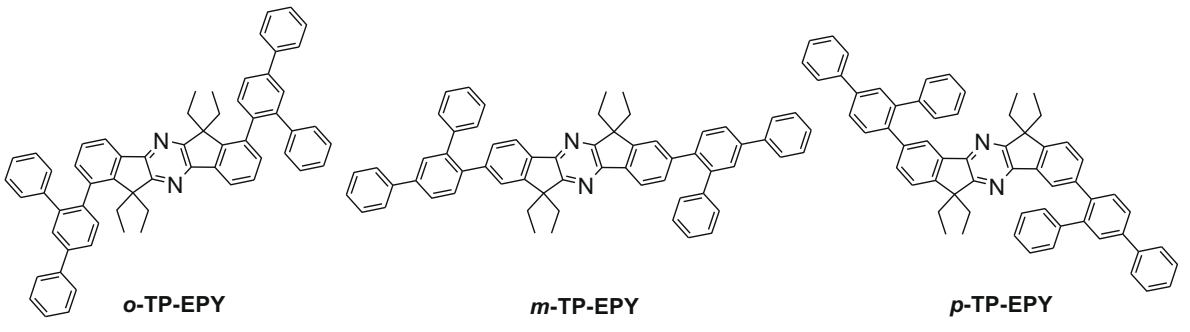

Scheme 1. Chemical structures of *o*-, *m*-, and *p*-TP-EPY.

2.1.2. Synthesis of 6,6,12,12-tetraethyl-3,9-bis-[1,1′;3′,1″] terphenyl-4′-yl-6,12-dihydro-diindeno[1,2-b;1′,2′-e]pyrazine (p-TP-EPY)

The final yield was 0.89 g, 57%. ^{1}H NMR (500 MHz, THF-d_8): δ (ppm) 8.09–7.76 (s, 2H), 7.76–7.75 (m, 8H), 7.71–7.69 (d, 2H), 7.46–7.43 (t, 4H), 7.35–7.34 (t, 2H), 7.27–7.22 (m, 6H), 7.19–7.15 (m, 6H), 7.04–7.03(d, 4H), 2.47–2.28 (m, 4H), 2.06–1.99 (m, 4H), 0.38–0.36 (t, 12H). ^{13}C NMR (300 MHz, $CDCl_3$): 162.9, 152.4, 148.0, 141.7, 141.3, 140.9, 140.7, 140.6, 139.8, 139.5, 131.7, 131.3, 130.2, 129.4, 129.0, 128.0, 127.6, 127.3, 126.8, 126.3, 122.4, 122.2, 53.8, 31.3, 8.8. FT-IR (KBr cm^{-1}): 3055, 3025, 2962, 2919, 2874, 2853, 1599, 1486, 1462, 1442, 1317, 1288, 1233, 1178, 1124, 895, 826, 763, 748, 697, 486, HRMS Calcd for $C_{62}H_{53}N_2$ (M+H)$^+$, 825.4209, found: 825.4214.

2.1.3. Synthesis of 1,7-dibromo-6,6,12,12-tetraethyl-6,12-dihydro-diindeno[1,2-b;1′,2′-e]-pyrazine (1c)

2.1.3.1. 4-Bromo-2,3-dihydro-2-(hydroxyimino)indene-1-one (1a). The yield was 79%. ^{1}H NMR (300 MHz, acetone-d_6): δ (ppm) 11.90 (s, 1H), 7.95–7.92 (d, 1H), 7.79–7.76 (d, 1H), 7.50–7.45 (t, 1H), 3.76 (s, 2H).

2.1.3.2. 1,7-Dibromo-6,12-dihydro-diindeno[1,2-b;1′,2′-e]pyrazine (1b). The yield was 56%. ^{1}H NMR (300 MHz, $CDCl_3$): δ (ppm) 8.17–8.15 (d, 2H), 7.65–7.63 (d, 2H), 7.45–7.42 (d, 2H), 4.02 (s, 4H).

2.1.3.3. 1,7-Dibromo-6,6,12,12-tetraethyl-6,12-dihydro-diindeno[1,2-b;1′,2′-e]pyrazine (1c). The yield was 38%. ^{1}H NMR (500 MHz, $CDCl_3$): δ (ppm) 8.08–8.05 (d, 2H), 7.58–7.56 (d, 2H), 7.32–7.29 (t, 2H), 2.72–2.55 (m, 4H), 2.37–2.29 (m, 4H), 0.27–0.24 (t, 12H). ^{13}C NMR (500 MHz, $CDCl_3$): 163.0, 152.2, 145.9, 142.5, 142.3, 134.1, 133.9, 129.4, 129.3, 128.5, 120.4, 120.2, 119.8, 57.5, 57.4, 28.3, 8.8. Fab$^+$-MS *m*/*e*: 526.

2.1.4. Synthesis of 3,9-dibromo-6,6,12,12-tetraethyl-6,12-dihydro-diindeno[1,2-b;1′,2′-e]pyrazine (3c)

2.1.4.1. 6-Bromo-2,3-dihydro-2-(hydroxyimino)indene-1-one (3a). The yield was 77%. ^{1}H NMR (300 MHz, acetone-d6): δ (ppm) 11.83 (s, 1H), 7.89–7.85 (m, 2H), 7.64–7.61 (d, 1H), 3.82 (s, 2H).

2.1.4.2. 3,9-Dibromo-6,12-dihydrodiindeno[1,2-b:1,2-e]pyrazine (3b). The yield was 53%. ^{1}H NMR (300 MHz, $CDCl_3$): δ (ppm) 8.37–8.36 (s, 2H), 7.64–7.60 (d, 2H), 7.54–7.38 (d, 2H), 4.04 (s, 4H).

2.1.4.3. 3,9-Dibromo-6,6,12,12-tetraethyl-6,12-dihydro-diindeno[1,2-b;1′,2′-e]-pyrazine (3c). The yield was 63%. ^{1}H NMR (500 MHz, CDCl3): δ (ppm) 8.23–8.21 (s, 2H), 7.58–7.56 (d, 2H), 7.33–7.26 (d, 2H), 2.33–2.28 (m, 4H), 2.06–2.02 (m, 4H), 0.38–0.33 (t, 12H), ^{13}C NMR(300 MHz, CDCl3): 163.1, 151.8, 148.5, 141.1, 132.3, 124.9, 124.6, 121.7, 54.1, 31.2, 8.7. Fab$^+$-MS *m*/*e*: 526.

2.2. Measurements

The structures of the synthesized compounds were characterized by using NMR, FT-IR, and fast-atomic bombardment (FAB) mass spectrometry. ^{1}H and ^{13}C NMR spectra were recorded on Bruker Avance 300 and Avance 500 spectrometers. The FT-IR spectra were recorded on a Thermo Electron Nicolet IR-200 spectrometer. FAB-mass spectra were recorded on a JEOL, JMS-AX505WA, HP5890 series II. The melting temperatures (T_m), glass-transition temperatures (T_g), crystallization temperatures (T_c), and degradation temperatures (T_d) of the compounds were measured by carrying out differential scanning calorimetry (DSC) under a nitrogen atmosphere with a DSC2910 (TA Instruments) and thermogravimetric analysis (TGA) with a SDP-TGA2960 (TA Instruments). The optical absorption spectra were obtained with a HP 8453 UV–Vis–NIR spectrometer. A Perkin Elmer luminescence spectrometer LS50 (xenon flash tube) was used for photo- and electroluminescence spectroscopy. The redox potentials of the compounds were determined with cyclic voltammetry (CV) by using a WBCS 3000 system with a scanning rate of 100 mV/s. We used a synthetic material coated ITO as the working electrode, a saturated Ag/$AgNO_3$ reference electrode, and acetonitrile (AN) with 0.1 M tetrabutylammonium perchlorate (TBAP) as the electrolyte. Ferrocene was used for potential calibration and for reversibility criteria.

2.3. Fabrication of the OLEDs

All organic layers were deposited under 10^{-6} Torr, with a rate of deposition of 1 Å/s to give an emitting area of 4 mm^2. In these devices, 4,4′,4″-tris(N-(2-naphthyl)-N-phenyl-amino)-triphenylamine [2-TNATA] was used as the hole injection layer, N,N′-bis(naphthalen-1-yl)-N,N′-bis(phenyl)benzidine [NPB] and 4,4′,4″-tri(N-carbazolyl)triphenylamine [TCTA] were used as the hole transporting and exciton blocking layers, respectively, and 8-hydroxyquinoline aluminum [Alq_3] was used as the electron transporting layer [31]. The LiF and aluminum layers were continuously deposited under the same vacuum conditions. The device structures were ITO/2-TNATA (30 nm)/NPB (10 nm)/TCTA (10 nm)/*o*- or *m*- or *p*-TP-EPY (30 nm)/Alq_3 (30 nm)/LiF (1 nm)/Al (200 nm). The current–voltage (I–V) characteristics of the fabricated EL devices were obtained with a Keithley 2400 electrometer. Light intensity was obtained with a Minolta CS-1000A.

2.4. Computational details

The HOMO and LUMO energy levels of the indenopyrazine derivatives were optimized by using the DMol^3 program of Materials Studio 4.3®, which carries out quantum mechanical calculations with density functional theory (DFT). The Perdew, Burke and Ernzerhof (PBE) functional and double numeric polarization basis set was used in the calculations. The structures were optimized by using delocalized internal coordinates; to confirm that each optimized conformation was the minimum structure we performed numerical frequency analysis.

3. Result and discussion

3.1. Synthesis and characterization

The indenopyrazine derivatives were synthesized according to literature procedures [29]. As shown in Scheme 2, we used bromo-indanones with Br substituted at positions 4, 5, and 6 as the starting compounds. In the first step, the oximes (1a, 2a, 3a) were synthesized via the reaction with isoamylnitrile dropped in under acid conditions. The oximes were then cyclized to synthesize the key intermediate dibromo-indenopyrazines (1b, 2b, 3b) with bromine present at the *ortho*, *meta*, and *para* positions in high yield (overall yield approximately 40%). Since the 6- and 12-position carbons of the synthesized dibromo-indenopyrazines are acidic, these carbons were capped with four ethyl groups (1c, 2c, 3c), and then the tetraethylated dibromo-indenopyrazines were coupled with a borated *m*-terphenyl group by carrying out Suzuki Ar–Ar coupling reactions. This procedure enabled the facile synthesis of *o*-, *m*-, and *p*-TP-EPY, in which *m*-terphenyl is substituted at the *ortho*, *meta*, and *para* positions respectively. The structures of the synthesized compounds were characterized by using NMR, FT-IR, and FAB-mass analysis.

3.2. Optical and electrochemical properties

The UV–visible absorption (Abs) spectra and photoluminescence (PL) spectra for the solution states of *o*-, *m*-, and *p*-TP-EPY are shown in Fig. 1, and the spectral features are summarized in Table 1. The PL quantum yields of the solution states of *m*-TP-EPY, *p*-TP-EPY, and *o*-TP-EPY were determined to be 73%, 61%, and 42%, respectively. As shown in Fig. 1, *the Abs peaks* of *o*-TP-EPY and *p*-TP-EPY were found to be blue-shifted 17 and 15 nm with respect to that of *m*-TP-EPY. In the PL spectra, the maxima for *o*-TP-EPY (411 nm) and *p*-TP-EPY (415 nm) were blue-shifted 26 and 22 nm, respectively with respect to that of *m*-TP-EPY at 437 nm, thereby moving these spectra from the blue region to the violet region. These findings suggest that changing the substitution position alters the intrinsic optical properties of the molecule.

These phenomena were also observed for the thin-film states, as shown in Fig. 2: *the Abs peaks* of *o*-TP-EPY (389 nm) and *p*-TP-EPY (390 nm) are blue-shifted 19 and 18 nm with respect to that of *m*-TP-EPY (408 nm), and the PL spectra maxima of *o*-TP-EPY (418 nm) and *p*-TP-EPY (426 nm) are blue-shifted 25 and 17 nm, respectively with respect to that of *m*-TP-EPY at 443 nm. Moreover, the minute differences of 6–11 nm between the PL spectral values of the solution and thin-film states for each derivative indicate that the short alkyl chains (ethyl) at carbon positions 6 and 12 of indenopyrazine and the *m*-terphenyl side groups on the aromatic rings effectively suppress the π–π^* stacking of the molecules regardless of whether the substitution pattern is *ortho*, *meta*, or *para*. In addition, the full widths at half maximum (FWHMs) of the PL spectra for the thin-film state are 43 nm for *o*-TP-EPY and *p*-TP-EPY, but 54 nm for *m*-TP-EPY. The sharper spectra of *o*-TP-EPY and *p*-TP-EPY probably arise because these molecules have fewer electron transition states than *m*-TP-EPY.

The energy bands, and the highest occupied molecular orbital (HOMO) and lowest unoccupied molecular orbital (LUMO) levels of *o*-, *m*-, and *p*-TP-EPY were estimated with cyclic voltammetry (CV) and through absorption edge analysis by using a plot of ($h\nu$) vs. $(\alpha h\nu)^2$, where α, h, and ν are the absorbance, Planck's constant, and the frequency of light; the results are summarized in Table 1 [23]. The HOMO levels of *o*-TP-EPY and *p*-TP-EPY are 6.13 and 6.07 eV, respectively, which are slightly lower by 0.10

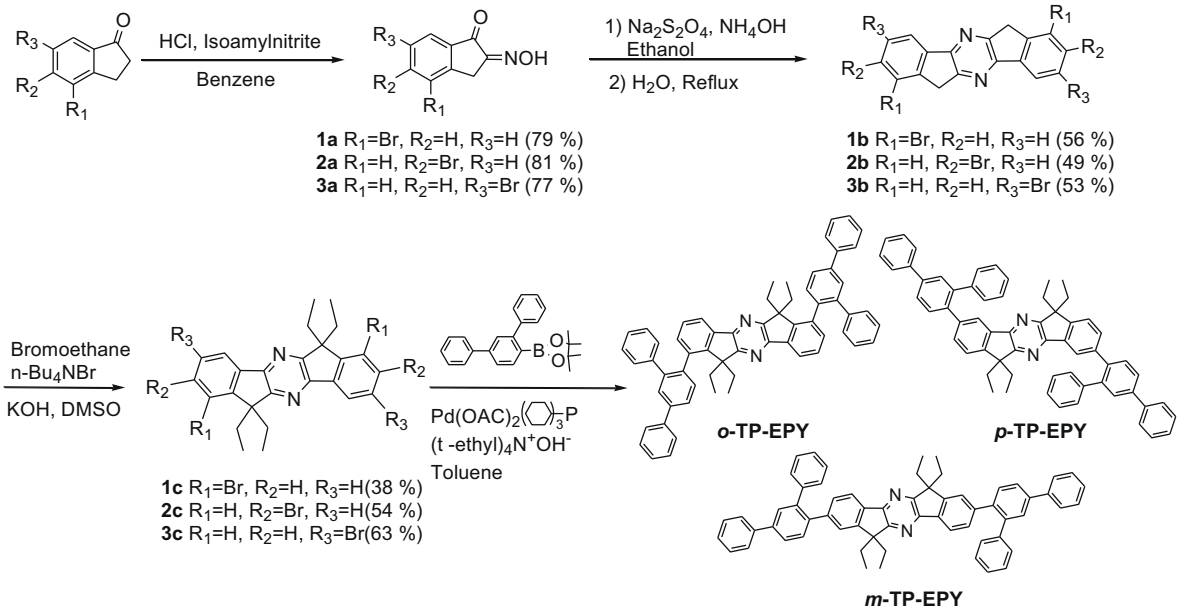

Scheme 2. Synthetic routes for *o*-, *m*-, and *p*-TP-EPY.

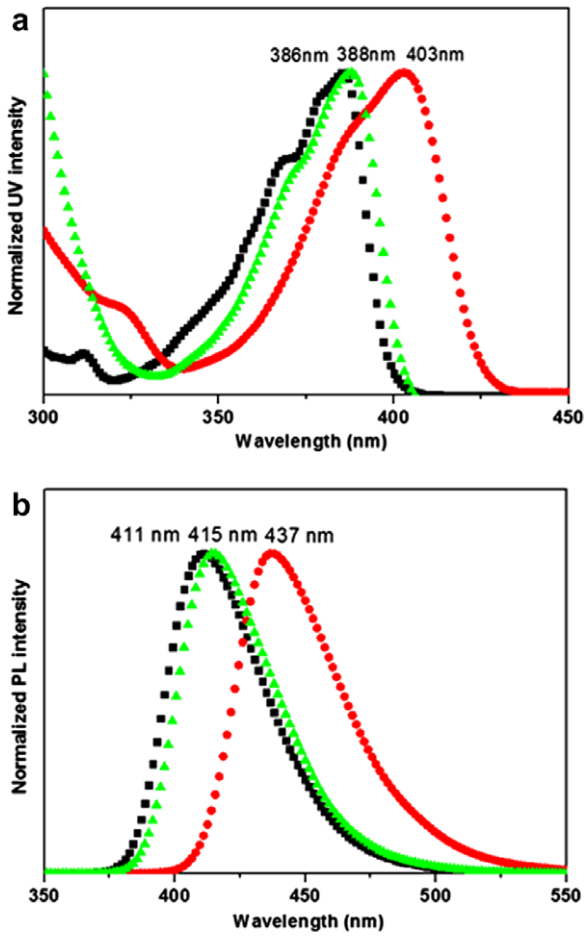

Fig. 1. Normalized UV and PL spectra of *o*-TP-EPY (■), *m*-TP-EPY (●), and *p*-TP-EPY (▲) in $CHCl_3$ (1.00×10^{-5} M) solution.

and 0.04 eV, respectively than the HOMO level of *m*-TP-EPY at 6.03 eV. The band gaps of *o*-TP-EPY and *p*-TP-EPY were found to be 0.21 and 0.24 eV wider, respectively than that of *m*-TP-EPY.

3.3. Theoretical calculations

In an attempt to theoretically explain the observed variations in the optical and electronic properties of the indenopyrazine core system with the substitution position of the *m*-terphenyl side group, we performed frontier molecular orbital calculations to determine the electron density distributions of ethyl indenopyrazine (EIP-core), and *o*-, *m*-, and *p*-TP-EPY (Fig. 3). The structures of the indenopyrazine derivatives were optimized by using the DMol[3] program of Materials Studio 4.3®, which carries out quantum mechanical calculations with density functional theory (DFT). The Perdew, Burke and Ernzerhof (PBE) functional and double numeric polarization basis set was used in the calculations [32–34]. The most remarkable result obtained from the molecular orbital analysis is that the lobe of the orbital at the junction points of the *ortho* and *para* positions of the EIP-core and side groups is smaller than the lobe of the orbital at the junction point of the *meta* position, in both the HOMO and LUMO as shown in Fig. 3. In particular, a node was found at the junction points of the *ortho* and *para* positions for the HOMO and the LUMO. Therefore, whereas there is an extension of the conjugation in *m*-TP-EPY from the EIP-core to the *m*-terphenyl group, the nodes observed for *o*-TP-EPY and *p*-TP-EPY indicate that these molecules are less conjugated than *m*-TP-EPY. This difference in conjugation means that the energy gaps decrease in the order *o*-TP-EPY > *p*-TP-EPY > *m*-TP-EPY, as shown in Table 1. In addition, this trend explains the spectral phenomena shown in Fig. 1, such as the larger blue shift in the *Abs* and PL spectra induced by substitution of the *m*-terphenyl group at the *ortho* and *para* positions, and the wider band gaps. These findings establish that the π-conjugation of the indenopyrazine derivatives can be adjusted by placing side groups at the node or lobe of the electron distribution of the indenopyrazine core system (Fig. 3(a)). Thus, in efforts to develop optoelectronics devices based on π-conjugated molecules, physical characteristics such as their optical and electronic properties can be systematically controlled according to the electron density distribution of the orbital at the position where the side group attaches to the molecular core.

3.4. Thermal properties

The thermal properties of the synthesized substances were determined by using thermogravimetric analysis (TGA) and differential scanning calorimetry (DSC). The results are summarized in Table 2. The T_m values of the synthesized *o*-, *m*-, and *p*-TP-EPY derivatives were found to be 365, 338, and 317 °C, respectively, which are more than 110 °C higher than the T_m of the commercial blue luminous material 4,4′-bis(2,2-diphenylvinyl)-1,1′-biphenyl (DPVBi),

Table 1
Optical and electrical properties of the synthesized compounds.

	UV_{max}[a] (nm)	PL_{max}[a] (nm)	Q.Y[b] (%)	UV_{max}[c] (nm)	PL_{max}[c] (nm)	FWHM[c]	HOMO (eV)	LUMO (eV)	ΔE_{exp}[d] (eV)	ΔE_{cal}[e] (eV)
o-TP-EPY	386	411	42	389	418	43	6.13	3.02	3.11	2.56
m-TP-EPY	403	437	73	408	443	54	6.03	3.16	2.87	2.38
p-TP-EPY	388	415	61	390	426	43	6.07	2.99	3.08	2.53

[a] Solution in $CHCl_3$ (1.00×10^{-5} M).
[b] Q.Y. (quantum yield) was measured by using a calibrated integrating sphere system [38,39].
[c] Film on glass.
[d] Experimental band gaps.
[e] Band gaps obtained with frontier molecular orbital calculations.

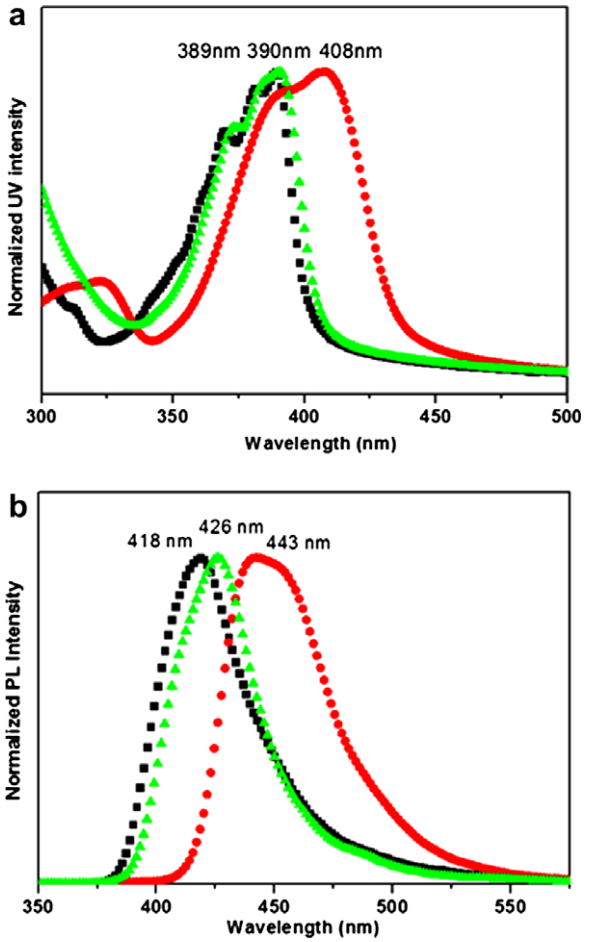

Fig. 2. Normalized UV–Vis and PL spectra of thin-films of *o*-TP-EPY (■), *m*-TP-EPY (●), and *p*-TP-EPY (▲).

which is 204 °C. The T_g values of *m*-TP-EPY and *p*-TP-EPY are 129 and 127 °C, respectively, which are approximately twice as high as that of DPVBi, 64 °C [29]. In the case of a thin-film of *m*-TP-EPY, the average surface roughness (R_a) measured with atomic force microscopy (AFM) was found to undergo almost no change in comparison to that of a DPVBi film after storage at 65 °C for 24 h [29]. Improved lifetimes of the synthesized substances in OLED devices are anticipated [35].

3.5. Electroluminescence properties

To determine whether the changes with substitution position in the intrinsic molecular properties are reflected in OLED (a representative optoelectronics device) performance, non-doped OLED devices were fabricated with the synthesized compounds as the emitting material layer (EML). The results are summarized in Table 3 and Fig. 4. The most important observation is that the electroluminescence (EL) spectra of *o*-TP-EPY and *p*-TP-EPY have maxima at 419 and 423 nm, respectively, which are blue-shifted 21 and 17 nm with respect to the peak for *m*-TP-EPY at 440 nm (see Fig. 4). This trend in the EL spectra is

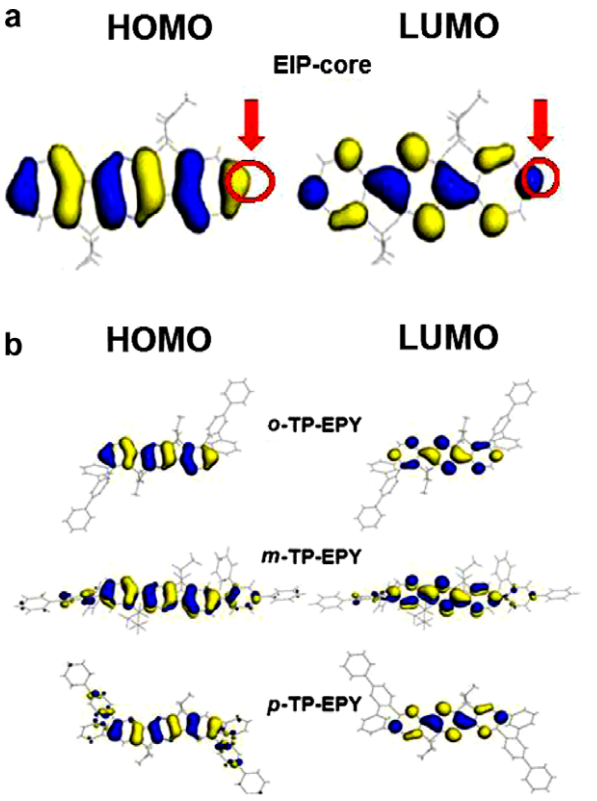

Fig. 3. Electronic density distributions of the frontier molecular orbitals (HOMO and LUMO) of the EIP-core (a), and of *o*-, *m*-, and *p*-TP-EPY (b).

Table 2
Thermal properties of *o*-, *m*-, and *p*-TP-EPY.

	T_g (°C)	T_c (°C)	T_m (°C)	T_d (°C)
o-TP-EPY	–	–	365	403
m-TP-EPY	129	167	338	441
p-TP-EPY	127	165	317	442

in good agreement with the shifts from the blue region to the violet region observed in the PL spectra of the thin-films. In addition, the EL spectra of *o*-TP-EPY and *p*-TP-EPY are sharper than the *m*-TP-EPY EL spectrum, as reflected in the FWHMs (43 and 42 nm for *o*-TP-EPY and *p*-TP-EPY, respectively, compared to 47 nm for *m*-TP-EPY). Such narrow emission spectra can result in pure colors, which is advantageous for emitting materials. In terms of the Commission Internationale de l'Eclairage (CIE) coordinates, the *y*-axis values of *o*-TP-EPY and *p*-TP-EPY are 0.068 and 0.063 that is, closer to the violet region than the value of 0.078 for *m*-TP-EPY. These CIE coordinates show that adjusting the π-conjugation by varying the junction position of the side group attached to the indenopyrazine core system changes the optical and electronic properties, and that such changes can be exploited in OLEDs. The EL devices were found to exhibit power efficiencies and external quantum efficiencies (EQE). in the ranges 0.16–0.9 lm/W and 1.2–4.6%, respectively, at 10 mA/cm^2 (see Table 3). The EQE of the *m*-TP-EPY device

Table 3
EL performances of multi-layered devices with the synthesized emitters. Device: ITO/2-TNATA (30 nm)/NPB (10 nm)/TCTA (10 nm)/*o*- or *m*- or *p*-TP-EPY (30 nm)/Alq_3 (30 nm)/LiF (1 nm)/Al (200 nm) at 10 mA/cm^2.

Compounds	Volt (V)	L.E.[a] (cd/A)	P.E.[b] (lm/W)	E.Q.E.[c] (%)	EL_{max} (nm)	FWHM[d] (nm)	CIE[e] (x,y)
o-TP-EPY	8.8	0.41	0.16	1.27	419	43	(0.175, 0.068)
m-TP-EPY	8.2	2.13	0.90	4.61	440	47	(0.157, 0.079)
p-TP-EPY	8.7	0.59	0.24	1.88	423	42	(0.173, 0.063)

[a] Luminescence efficiency.
[b] Power efficiency.
[c] External quantum efficiency.
[d] FWHM (full width half maximum).
[e] 1931 Commission Internationale de l'Eclairage/NTSC (National Television System Committee): CIE (0.14, 0.08).

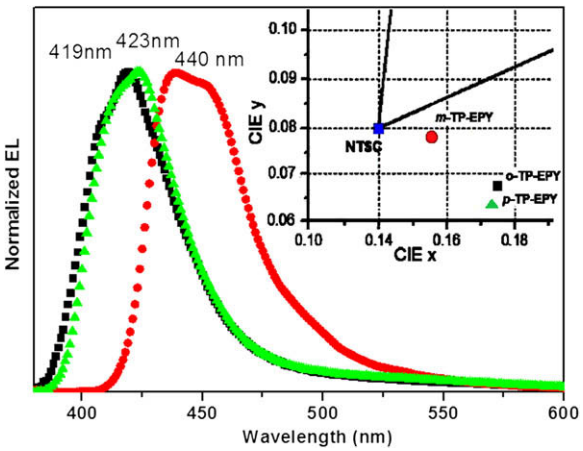

Fig. 4. EL spectra of *o*-TP-EPY (■), *m*-TP-EPY (●), and *p*-TP-EPY (▲) in OLED devices. The inset shows the CIE (*x*, *y*) coordinates of the *o*-, *m*-, and *p*-TP-EPY devices.

was 4.61%, which is 3.6 and 2.4 times the values for *o*-TP-EPY (1.27%) and *p*-TP-EPY (1.88%), respectively. This difference can be explained by the following two factors. First, *m*-TP-EPY has a higher PL quantum yield (73%) compared to *o*-TP-EPY (42%) and *p*-TP-EPY (61%). Second, *o*-TP-EPY and *p*-TP-EPY exhibit wider band gaps (3.11 and 3.08 eV) than *m*-TP-EPY (2.87 eV), making carrier injection difficult in OLED devices based on *o*-TP-EPY and *p*-TP-EPY. These factors caused the EL efficiency of *o*-TP-EPY and *p*-TP-EPY to be lower than that of *m*-TP-EPY. The EQE for *p*-TP-EPY, 1.88%, is superb; the excellent violet emitting materials presented previously, F_2PA and CBP, have EQE values of 1.95% and 1.25%, respectively [36,37].

4. Conclusions

New indenopyrazine derivatives with bulky *m*-terphenyl side groups substituted at the *ortho*, *meta*, or *para* junction positions were successfully synthesized. There are larger blue shifts in the *Abs* and PL spectra of *o*-TP-EPY and *p*-TP-EPY than in those of *m*-TP-EPY for both the solution and thin-film states, resulting in violet PL emission. These findings are consistent with the results of our molecular calculations, which indicate that the side group position on the indenopyrazine core, in particular whether the side group coincides with a node or lobe in the orbital structure, affects the π-conjugation of the molecule and hence alters the optical properties. These changes in optical properties are reflected in the behavior of the non-doped OLED devices fabricated using the synthesized compounds. In particular, the device containing *p*-TP-EPY (high T_g, 127 °C) was found to exhibit excellent properties: an EL spectrum with a peak at 423 nm for violet emission at CIE coordinates (0.173, 0.063) and an EQE of 1.88%.

Acknowledgements

This research was supported by a grant (Catholic Univ.) from the Fundamental R&D Program for Core Technology of Materials funded by the Ministry of Knowledge Economy (MKE), Republic of Korea. This work was supported by the National Research Foundation of Korea (NRF) grant funded by the Korea government (No. 20090080199). This study was supported by the Research Fund, 2009 The Catholic University of Korea (M2009B000200181).

References

[1] C.W. Tang, S.A. Van Slyke, Appl. Phys. Lett. 51 (1987) 913.
[2] M.A. Baldo, M.E. Thompson, S.R. Forrest, Nature 403 (2000) 750.
[3] J. Li, T.J. Marks, Chem. Mater. 20 (2008) 4873.
[4] F. Liang, Q. Zhou, Y. Cheng, L. Wang, D. Ma, X. Jing, F. Wang, Chem. Mater. 15 (2003) 1935.
[5] H. Choi, C. Baik, S.O. Kang, J.J. Ko, M.S. Kang, Md.K. Nazeeruddin, M. Grätzel, Angew. Chem. 120 (2008) 333.
[6] N.S. Baek, S.K. Hau, H.L. Yip, O. Acton, K.S. Chen, A.K.Y. Jen, Chem. Mater. 20 (2008) 5734.
[7] H.E. Katz, Chem. Mater. 16 (2004) 4748.
[8] F. Ebel, W. Deuschel, Chem. Ber. 89 (1956) 2794.
[9] Y.J. Pu, M. Higashidate, K.i. Nakayama, J. Kido, J. Mater. Chem. 18 (2008) 4183.
[10] L. Ying, Y. Xu, W. Yang, L. Wang, H. Wu, Y. Cao, Org. Electron. 10 (2009) 42.
[11] R. Grisorio, C. Piliego, P. Fini, P. Cosma, P. Mastrorilli, G. Gigli, G.P. Suranna, C.F. Nobile, J. Phys. Chem. C 112 (2008) 7005.
[12] J.H. Ahn, C. Wang, I.F. Perepichka, M.R. Bryce, M.C. Petty, J. Mater. Chem. 17 (2007) 2996.
[13] Z. Wang, H. Shao, J. Ye, L. Zhang, P. Lu, Adv. Funct. Mater. 17 (2007) 253.
[14] S. Tao, Z. Peng, X. Zhang, P. Wang, C.S. Lee, S.T. Lee, Adv. Funct. Mater. 15 (2005) 1716.
[15] A. Haldi, A. Kimyonok, B. Domercq, L.E. Hayden, S.C. Jones, S.R. Marder, M. Weck, B. Kippelen, Adv. Funct. Mater. 18 (2008) 3056.
[16] S.H. Lee, T. Nakamura, T. Tsutsui, Org. Lett. 3 (2001) 2005.
[17] S. Ye, Y. Liu, C. Di, H. Xi, W. Wu, Y. Wen, K. Lu, C. Du, Y. Liu, G. Yu, Chem. Mater. 21 (2009) 1333.
[18] P.I. Shih, C.H. Chien, C.Y. Chuang, C.F. Shu, C.H. Yang, J.H. Chen, Y. Chi, J. Mater. Chem. 17 (2007) 1692.
[19] C. Poriel, J.J. Liang, J.R. Berthelot, F. Barrière, N. Cocherel, A.M.Z. Slawin, D. Horhant, M. Virboul, G. Alcaraz, N. Audebrand, L. Vignau, N. Huby, G. Wantz, L. Hirsch, Chem. Eur. J. 13 (2007) 10055.

[20] C.H. Chen, F.I. Wu, C.F. Shu, C.H. Chien, Y.T. Tao, J. Mater. Chem. 14 (2004) 1585.
[21] C.H. Wu, C.H. Chien, F.M. Hsu, P.I. Shih, C.F. Shu, J. Mater. Chem. 19 (2009) 1464.
[22] C.H. Chien, C.K. Chen, F.M. Hsu, C.F. Shu, P.T. Chou, C.H. Lai, Adv. Funct. Mater. 19 (2009) 560.
[23] S.K. Kim, B. Yang, Y. Ma, J.H. Lee, J.W. Park, J. Mater. Chem. 18 (2008) 3376.
[24] B. Yang, S.K. Kim, H. Xu, Y.I. Park, H. Zhang, C. Gu, F. Shen, C. Wang, D. Liu, X. Liu, M. Hanif, S. Tang, W. Li, F. Li, J. Shen, J.W. Park, Y. Ma, ChemPhysChem 9 (2008) 2601.
[25] S.K. Kim, Y.I. Park, I.N. Kang, J.W. Park, J. Mater. Chem. 17 (2007) 4670.
[26] P.I. Shih, C.Y. Chuang, C.H. Chien, E.W.G. Diau, C.F. Shu, Adv. Funct. Mater. 17 (2007) 3141.
[27] J. Shi, C.W. Tang, Appl. Phys. Lett. 80 (2002) 3201.
[28] M.X. Yu, J.P. Duan, C.H. Lin, C.H. Cheng, Y.T. Tao, Chem. Mater. 14 (2002) 3958.
[29] Y.I. Park, J.H. Son, J.S. Kang, S.K. Kim, J.H. Lee, J.W. Park, Chem. Commun. (2008) 2143.
[30] T. Nakagawa, D. Kumaki, J. Nishida, S. Tokito, Y. Yamashita, Chem. Mater. 20 (2008) 2615.
[31] C.C. Wu, Y.T. Lin, K.T. Wong, R.T. Chen, Y.Y. Chien, Adv. Mater. 16 (2004) 61.
[32] B.J. Delley, Chem. Phys. 113 (2000) 7756.
[33] J.P. Perdew, K. Burke, M. Ernzerhof, Phys. Rev. Lett. 77 (1996) 3865.
[34] B.J. Delley, Chem. Phys. 92 (1990) 508.
[35] H. Aziz, Z.D. Popovic, Chem. Mater. 16 (2004) 4522.
[36] K. Okumoto, Y. Shirota, Chem. Mater. 15 (2003) 699.
[37] L. Zou, V. Savvate'ev, J. Booher, C.H. Kim, J. Shinar, Appl. Phys. Lett. 79 (2001) 2282.
[38] C.C. Wu, W.Y. Hung, T.L. Liu, L.Z. Zhang, T.Y. Luh, J. Appl. Phy. 93 (2003) 5465.
[39] J.C. Mello, H.F. Wittmann, R.H. Friend, Adv. Mater. 9 (1997) 230.

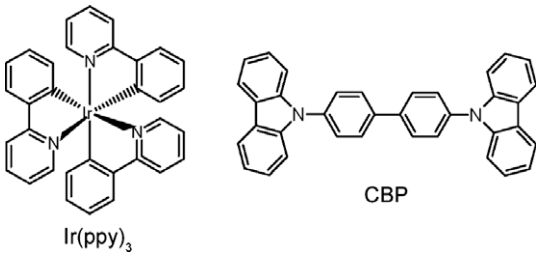

Fig. 1. The chemical structures of $Ir(ppy)_3$ and CBP.

as indicated below, injection of holes from the MoO_x film is quite significant and we can still observe well-defined transistor output characteristics.

Fig. 2a shows the output characteristics of a TFT with 100% of $Ir(ppy)_3$ at room temperature (292 K). Well-defined *p*-type current–voltage curves can be observed. Applying the standard expressions of

$$I_D = \frac{W}{L}\mu_{LIN}C_i\left[V_D(V_G - V_T) - \frac{V_D^2}{2}\right] \quad (1)$$

$$I_D = \frac{W}{2L}\mu_{SAT}C_i(V_G - V_T)^2 \quad (2)$$

one can extract the hole mobility of $Ir(ppy)_3$ [15]. In Eqs. (1) and (2), W (=9 mm) and L (=50 μm) are the channel width and length, respectively; C_i is the capacitance of gate dielectric per unit area; V_T is the threshold voltage; V_G and V_D are the gate bias and the potential difference across the *S*/*D* electrodes, respectively; μ_{LIN} and μ_{SAT} are the field effect (FE) mobility extracted from the linear and saturation regions, respectively. The results are $\mu_{LIN} = 9.5 \times 10^{-6}\ cm^2\ V^{-1}\ s^{-1}$, and $\mu_{SAT} = 1.7 \times 10^{-5}\ cm^2\ V^{-1}\ s^{-1}$. These values fall into the range of mobility values that are typical for an amorphous organic hole transporter for OLED applications. For example, when NPB, one of the most widely used amorphous organic hole transporters in OLEDs, was measured with the same method, a FE mobility of $2.4 \times 10^{-5}\ cm^2\ V^{-1}\ s^{-1}$ was obtained in the saturation region [10]. Judging from the values of the hole mobility, one can also view $Ir(ppy)_3$ as a rather good organic hole transporter.

Fig. 2b shows the output characteristics of pristine film of CBP. Despite the rather large HOMO value of CBP (~5.8 eV), one can still observe well-behaved output characteristics of a typical TFT. The result is consistent with recent reports that MoO_x films possess a work function approaching 6 eV and thus facilitate the injection of holes into the CBP film [16]. Using the same analysis as outlined for $Ir(ppy)_3$, we obtained $\mu_{LIN} = 1.2 \times 10^{-5}\ cm^2\ V^{-1}\ s^{-1}$, $\mu_{SAT} = 1.5 \times 10^{-5}\ cm^2\ V^{-1}\ s^{-1}$ for CBP in the linear and saturation, respectively.

In a POLED, $Ir(ppy)_3$ is most often present as a dopant in CBP rather than a host [5–7]. Therefore, it would be interesting to study a film of $Ir(ppy)_3$-doped CBP film. The TFT characteristics of such a film consisting of 20% $Ir(ppy)_3$ doped into CBP is shown in the inset of Fig. 3. Compared to the pristine (100%) $Ir(ppy)_3$ film, the output current I_D

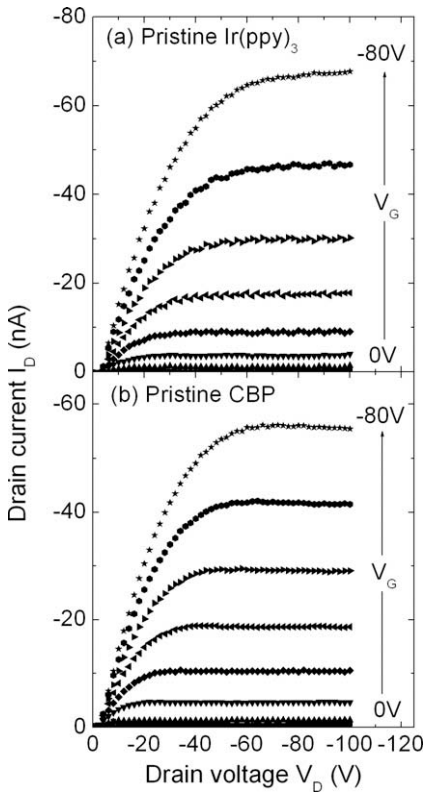

Fig. 2. Output characteristics of top contact OTFTs with 100 nm of (a) $Ir(ppy)_3$ and (b) CBP at 292 K. The gate voltages increase in steps of −10 V starting from 0 V to −80 V.

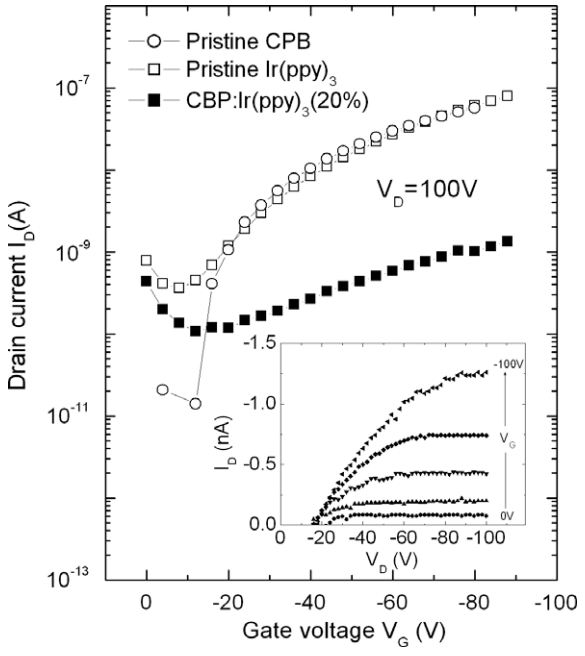

Fig. 3. Transfer characteristics of OTFT with 100 nm of pristine $Ir(ppy)_3$ (□), CBP:$Ir(ppy)_3$ (20%) (■) and pristine CBP (○). The inset shows the output characteristics of a TFT with CBP:$Ir(ppy)_3$ (20%).

for the doped film is substantially lowered. The extracted FE mobility in the saturation region is $\mu_{SAT} = 1.7 \times 10^{-7}\,cm^2\,V^{-1}\,s^{-1}$. The value is two orders of magnitude smaller than the pristine Ir(ppy)$_3$ film. Due to the large HOMO difference between CBP and Ir(ppy)$_3$, it is unlikely that holes can be injected into the CBP molecules directly. Instead, holes are expected to be directly injected to the dopant molecules Ir(ppy)$_3$ from the source electrode. Once injected, holes are expected to hop among the dopant molecules rather than the host. So, it is expected the hole mobility will decrease if the doping concentration is reduced. Following this line of thought, we doped the CBP film with lower concentrations (e.g. 10%) of Ir(ppy)$_3$. However, the signals were barely detectable and no reliable mobility values can be obtained. Fig. 3 is a summary of the room temperature transfer characteristics of the samples used in this study. Pristine films of Ir(ppy)$_3$ or CBP have well-defined transfer characteristics. In contrast, when Ir(ppy)$_3$ acts as a dopant in CBP, the output hole current is substantially reduced.

Having established Ir(ppy)$_3$ all by itself is a good hole transporter, we explore its conductivity mechanism further by measuring the temperature dependent characteristics. The results were then analyzed by the Gaussian disorder model (GDM) that is widely employed to describe hopping conduction in amorphous organic materials [17]. In the GDM, an amorphous organic material is treated as an ensemble of transporting sites for hopping conduction. The carrier mobility is field and temperature dependent. The GDM can be described as follows [17]:

$$\mu(F,T) = \mu_\infty \exp\left[-\left(\frac{2\sigma}{3kT}\right)^2\right] \exp\left\{CF^{\frac{1}{2}}\left[\left(\frac{\sigma}{kT}\right)^2 - \Sigma^2\right]\right\} \quad (3)$$

F, T, and k are the applied electric field, the absolute temperature and the Boltzmann constant; μ_∞ is the high temperature limit of mobility, and C is a constant. The energetic disorder σ can be interpreted as the width of Gaussian distribution of DOS of energy for the transporting sites; the positional disorder Σ describes the geometric randomness of the material. At low field ($F \to 0$), the second exponential term in Eq. (3) approaches 1, and thus, $\mu(0,T) \sim \exp[-4/9(\sigma/kT)^2]$. So, a semi-log plot of low field mobilities vs $1/T^2$ should yield a straight line. The slope of this line can be used to extract σ. Following this idea, we plot the FE mobilities extracted in low field region, i.e. the linear region in Fig. 2a. The results are shown in Fig. 4 as hollow squares. The solid line is the best fit to the TFT data. The extracted σ for Ir(ppy)$_3$ in an OTFT is 88 meV. The result is quite comparable to the data obtained from the FE mobility measurements of other amorphous organic hole transporters, such as phenylamine compounds (e.g. NPB) [10,11,18]. In those cases, the extracted σ are in the range 80–90 meV.

Beside pristine Ir(ppy)$_3$, we have, in addition, studied the temperature dependent transport of pristine CBP and Ir(ppy)$_3$-doped CBP (20%). The results are shown in Fig. 4. The extracted σ and μ_∞ of pristine CBP are 95 meV and $7.3 \times 10^{-3}\,cm^2\,V^{-1}\,s^{-1}$, respectively. The extracted μ_∞ for Ir(ppy)$_3$-doped CBP is substantially reduced by two orders of magnitude to about $5.0 \times 10^{-5}\,cm^2\,V^{-1}\,s^{-1}$. The reduction in μ_∞ indicates the increase in charge hopping distance in the Ir(ppy)$_3$-doped CBP film.

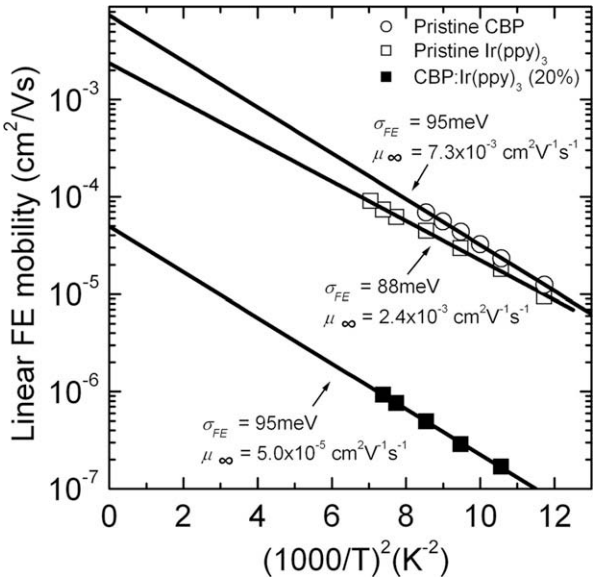

Fig. 4. Linear FE mobilities vs $(1/T)^2$ for Ir(ppy)$_3$ (□), CBP (○) and CBP:Ir(ppy)$_3$ (20%) (■). The energetic disorder and the high temperature limit of mobilities can be extracted from the plot. The straight lines are the best fits to the data.

The present report describes the hole transport behaviors of Ir(ppy)$_3$ and Ir(ppy)$_3$-doped CBP. However, it has direct relevance for explaining device operation and optimization. As Ir(ppy)$_3$ possesses significant hole mobility, it can potentially act directly as hole transporting component in a POLED. Furthermore, due to its relatively small HOMO value of ~5.2 eV, it can either function as a hole injection material itself and/or the target for hole injection from the anode. One recent demonstration shows, indeed, it is possible to have direct hole injection from the anode into Ir(ppy)$_3$-doped CBP [19,20]. With this realization, one can eliminate the hole-injection layer in a POLED and simplify device structure.

Finally, we want to emphasize the advantage of using TFT technique to study carrier transport in amorphous organic electronic materials. In principle, only a few monolayers (~10 nm) are required to form a complete conducting channel in an organic TFT [10]. In contrast, much thicker organic films are needed for other experimental techniques, e.g., time-of-flight or admittance spectroscopy [21–23]. Thus, TFT technique can provide a powerful platform for mobility determination when the material under investigation is in limited quantity.

Acknowledgements

Supports of this research by the Research Committee of Hong Kong Baptist University and the Research Grant Council of Hong Kong under grant #HKBU211006E and 211209E are gratefully acknowledged.

References

[1] C.W. Tang, S.A. VanSlyke, Appl. Phys. Lett. 51 (1987) 931.
[2] G. Horowitz, J. Mater. Res. 19 (2004) 1946.
[3] P. Peumans, A. Yakimov, S.R. Forrest, J. Appl. Phys. 93 (2003) 3693.
[4] H. Yersin (Ed.), Highly Efficient OLEDs with Phosphorescent Materials, Wiley, Berlin, 2007.
[5] T. Sajoto, P. Djurovich, A.B. Tamayo, J. Oxgaard, W.A. Goddard III, M.E. Thompson, J. Am. Chem. Soc. 131 (2009) 9813.
[6] M.A. Baldo, D.F. O'Brien, Y. You, A. Shoustikov, S. Sibley, M.E. Thompson, S.R. Forrest, Nature 395 (1998) 151.
[7] M.A. Baldo, S. Lamansky, P.E. Burrows, M.E. Thompson, S.R. Forrest, Appl. Phys. Lett. 75 (1999) 4.
[8] S.C. Tse, K.C. Kwok, S.K. So, Appl. Phys. Lett. 89 (2006) 262102.
[9] M.E. Kondakova, T.D. Pawlik, R.H. Young, D.J. Giesen, D.Y. Kondakov, C.T. Brown, J.C. Deaton, J.R. Lenhard, K.P. Klubek, J. Appl. Phys. 104 (2008) 094501.
[10] C.H. Cheung, K.K. Tsung, K.C. Kwok, S.K. So, Appl. Phys. Lett. 93 (2008) 083307.
[11] C.H. Cheung, K.C. Kwok, S.C. Tse, S.K. So, J. Appl. Phys. 103 (2008) 093705.
[12] W.J. Song, S.K. So, L.L. Cao, Appl. Phys. A 72 (2001) 361.
[13] C.H. Cheung, W.J. Song, S.K. So, Org. Elect. 11 (2010) 89.
[14] T. Matsushima, Y. Kinoshita, H. Murata, Appl. Phys. Lett. 91 (2007) 253504.
[15] S.M. Sze, Physics of Semiconductor Devices, Wiley, New York, 1981.
[16] M. Kroger, S. Hamwi, J. Meyer, T. Riedl, W. Kowalsky, A. Kahn, Org. Elect. 10 (2009) 932.
[17] H. Bässler, Phys. Stat. Sol. B 175 (1993) 15.
[18] T.P.I. Saragi, T.F. Lieker, J. Salbeck, Adv. Funct. Mater. 16 (2006) 966.
[19] Z.W. Liu, M.G. Helander, Z.B. Wang, Z.H. Lu, Org. Electron. 10 (2009) 1146.
[20] Z.W. Liu, M.G. Helander, Z.B. Wang, Z.H. Lu, Appl. Phys. Lett. 94 (2009) 113305.
[21] K.K. Tsung, S.K. So, Appl. Phys. Lett. 92 (2008) 103315.
[22] S.W. Tsang, S.K. So, J.B. Xu, J. Appl. Phys. 99 (2006) 013706.
[23] S. Ishihara, T. Okachi, H. Naito, Thin Solid films 518 (2009) 452.

characteristics. A built-in potential has been found and evaluated to describe the charge distribution at the p–p junction interface. Finally, the interface electronic structure was depicted to explain the ambipolar charge transport behavior.

Oxotitanium phthalocyanine (TiOPc) is an intrinsic molecular semiconductor that has a special electrical behavior depending on measuring ambient, which is electron-type in inert ambient and hole-type in air [11]. This trait makes it to be an excellent probe-molecule to investigate charge-carrier transport behavior in organic semiconductor. Copper phthalocyanine (CuPc) is a classical semiconductor defined as hole-type material, which possesses high chemical and thermal stability that are attractive for practical application [12]. Moreover, they belong to the same phthalocyanine family holding good molecular compatibility that is especially important for bilayer heterojunction devices. Based on the above reasons, we prepared organic p–p junction composed of CuPc/TiOPc.

2. Experiment

OFET devices with top contact were fabricated according to the following procedure (Fig. 1a). Heavily doped n-type silicon wafers (0.01–0.15 Ω cm) were acted as gate electrode and substrate. A layer of silicon dioxide (SiO_2) film with unit capacitance of 10 nF/cm^{-2} was served as gate insulator by thermal oxidation covered on the substrate. The OTS thin film acts as the modified layer covered on the surface of SiO_2 by inserting the substrate to OTS solution (chloroform as solvent, 2 mM) for 1 day. The wafers were ultrasonically cleaned with acetone, isopropyl alcohol, and ultra purified water, respectively. TiOPc with 5 nm and CuPc with 15 nm were deposited in succession at a base pressure of $(4–5) \times 10^{-4}$ Pa at a rate of 1 Å s^{-1} (it is recorded by quartz crystal oscillate), while the substrates were held at 200 °C. Subsequently to prepare the source/drain electrodes, 15 nm Au and 30 nm Al films were evaporated through shadow masks defining channel width of 3800 μm and length of 180 μm, respectively. The introduction of Al film could effectively protect Au layer from measured probe. Furthermore, organic metal–oxide–semiconductor (MOS) structures (Fig. 1b) and diodes were also fabricated and held with the same conditions described above. All organic source samples were purchased from Sigma–Aldrich without further purification. *IV* and *C–V* characteristics were performed at room temperature in air by Agilent 4155C and E4980A, respectively.

3. Results and discussion

OFET devices with top contact and the corresponding organic metal–oxide–semiconductor (MOS) structures were fabricated according to the description in experimen-

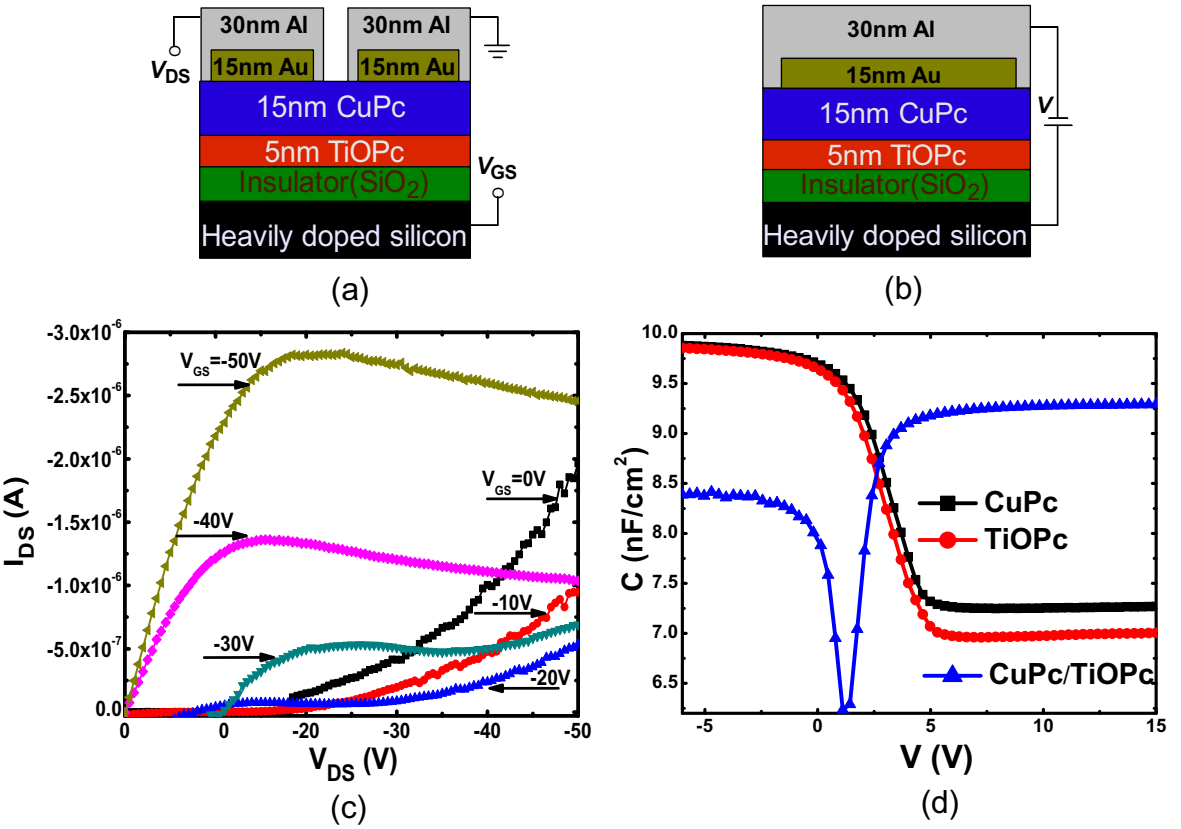

Fig. 1. Schematic cross-section of CuPc/TiOPc heterojunction. (a) FETs and (b) MOS structures. (c) Ambipolar characteristics of CuPc/TiOPc FETs. (d) Capacitance as a function of gate voltage for TiOPc, CuPc, and CuPc/TiOPc MOS structures at 1 kHz.

tal section shown in Fig. 1a and b. Gold with high work function (i.e., 5.1 eV) and Aluminum with low work function (i.e., 4.3 eV) were deposited to act as source/drain electrodes so that both electron and hole can be injected to organic semiconductors. Furthermore, the added Al thin film can effectively avoid damage by measuring probe because it is harder than Au film. The double active layers were prepared by combination TiOPc and CuPc, TiOPc deposited as the bottom layer and CuPc as the upper layer. In this case, CuPc actually also act as a prevent layer to protect TiOPc from air. Fig. 1c shows the output curves of CuPc/TiOPc-based transistors. By applying gate voltage (V_{GS}) from 0 to −20 V, the source-drain current (I_{DS}) displayed a drop step by step by scanning drain voltage (V_{DS}) from 0 to −50 V. It was attributed to electron-current, which was depleted by continuously increasing V_{GS}. The device show diode like curves at the low V_{GS}, which presents a typical ambipolar FET feature [13]. A current inversion appeared when V_{GS} was −30 V, and linear and saturation regions were observed at V_{GS} from −30 to −50 V. This indicated hole current has emerged and simultaneously electron-current has been full depleted. As a result, typical ambipolar behavior has been observed in FET.

For further clarifying bi-carrier transport, *C–V* characteristics of MOS structures were presented in (Fig. 1d). The applied frequency was 1 kHz. Note that the *C–V* properties of MOS have an apparent dependence on measuring frequency. When applying a low frequency region (i.e., <100 Hz), interface state will result in inversion phenomenon and decreased accumulation capacitance. Therefore, high frequency (1 kHz) should be used during *CV* measurement for excluding interface state effects. Furthermore, *CV* curves of single-layer TiOPc and single-layer CuPc were inserted for comparison. Firstly, single hole-only charge process was found in single-layer TiOPc and single-layer CuPc MOS structures by scanning bias from −6 to +15 V. Accumulation and depletion regions for hole current may be clearly observed at negative and positive bias, respectively. This represented holes dominated in TiOPc or CuPc and the inversion mode was not appeared. In respect of double-layer junction MOS, holes were firstly accumulated at the bias range of −5–0 V, then it were gradually depleted in the bias range of 0–1 V, finally an inversion region emerged that meant electron-current has dominated and accumulated in diode. Moreover, the capacitance of junction diode at hole accumulation region was smaller than that of single-layer devices. It is probably due to the accumulated holes at the CuPc layer, the introduction of TiOPc has formed double gate insulators that resulted in a low capacitance. It may be described by $C_h = \varepsilon\varepsilon_0 S/d$, assuming to be the same ε (dielectric constant) for TiOPc and SiO_2, in this case the increase of thickness of insulator led to lower capacitance [12]. Here, ε_0 and d are the vacuum permittivity, and dielectric layer thickness, respectively. As a result, two kinds of current types including holes and electrons have been demonstrated from p–p type CuPc/TiOPc junction.

For further ascertaining the electrical structures of junction interface, the corresponding diode characteristics were provided (Fig. 2a), the inset is diode configuration. To single-layer diodes (TiOPc or CuPc), symmetrical current at forward and reverse bias implied two electrodes (Heavily doped Si and Au) have a good contact behavior with TiOPc or CuPc for charge injection and extraction. However, the rectifying characteristic (rectifying ratio is 20) was found from the CuPc/TiOPc junction diode. This result revealed that the rectification came from the interface of two semiconductors and a built-in electric field (E_{bi}) was existence. From the rectifying direction, E_{bi} directed from CuPc to TiOPc. Fig. 2b shows the resistance–voltage curves of CuPc/TiOPc diode, in which diode resistance (R_d) represented bulk resistance (R_b) for single-layer TiOPc and CuPc devices in contrast to R_d represented a sum of R_b and junction resistance (R_j) for double-layer CuPc/TiOPc device. Considering junction diode, the R_d was 0.82 kΩ at forward bias and 17 kΩ at reverse bias. Under reverse bias, the applied bias mainly dropped at the interface and R_j dominated in R_d. In this case, E_{bi} was gradually strengthened with the increase of bias that led to an increase of R_j. The R_d reached a saturate value of 17 kΩ at a reverse bias of −0.3 V. As applying forward bias, the R_d was sharply decreased at a bias range from 0 to 0.47 V due to the E_{bi} was gradually weakened. The R_j was counteracted when applied bias was larger than 0.47 V. At this time, R_j fully represented R_b with 0.82 *k*Ω.

Moreover, the *C–V* Properties of diodes were presented to clarify the above *I–V* results. Fig. 2c shows the *C–V* characteristics of junction diode in the frequency of 1 kHz. A peak capacitance was observed when the applied voltage reached 0.47 V. This value revealed that the built-in potential (V_{bi}) was approximately 0.47 V that shows good consistent with *IV* measuring result deduced by Anderson's model equations [14,15]:

$$C_j = A\sqrt{\frac{q\varepsilon_s N_A N_D}{(N_A + N_D)}}(V_{bi} - V)^{-\frac{1}{2}} \quad (1)$$

where q is the electronic charge, ε_s is the dielectric constant of semiconductors. N_D and N_A are the doping densities of in TiOPc and CuPc, respectively. V_{bi} and V are built-in electric voltage and applied voltage. From this equation, the capacitance (C_j) exhibits a peak value when V_{bi} is equal to V. Moreover, charge transport mechanism in organic junction was studied by simulating *IV* characteristics using the following equation:

$$I = I_0\left[\exp\left(\frac{qV}{nkT}\right) - 1\right] \quad (2)$$

where I_0 refers to reverse bias the saturation current, k is the Boltzmann constant, T is the temperature. n is an ideality factor for general Shockley theory. By setting n was 13.2, we can observed that the simulation results are well match for the experiment results (Fig. 2d). It herein needs to point out that the ideality factors have a strong dependence on temperature that is inconsistent with the conventional Shockley theory [15].

Based on *IV* and *CV* analysis, we depicted the energy level diagram of CuPc/TiOPc as shown in (Fig. 3a). Their Fermi levels are aligned when put TiOPc and CuPc together under thermal equilibrium condition. The highest occupied molecular orbit (HOMO) of CuPc bends upward to accumulate holes and the lowest unoccupied molecular orbit

(LUMO) of TiOPc bends downward to accumulate electrons, which cause ambipolar transport behavior in FETs. Thus an E_{bi} is formed with direction from CuPc to TiOPc. ΔE_{HOMO} and ΔE_{LUMO} were the band offsets for two semiconductors, respectively. The V_{bi} is a sum of V_{D1} and V_{D2}, which is also equal to the difference of bulk Fermi levels between two semiconductors. The HOMO and LUMO data for CuPc and TiOPc can be found from elsewhere [16]. Finally, schematic diagrams of charge distribution were provided to describe the transformation of carriers' distribution from two single-layer films to an organic p–p junction shown in Fig. 3b. It should be noted that all unique characteristics for organic junction come from charge migration by the alignment of Fermi level. Based on the above analysis, we can deduce the accumulated charge are transported in different layers that electron and hole is flowed in TiOPc and CuPc layer, respectively. In this case, hole-transport in CuPc should be influenced by TiOPc film morphology. The film roughness of bottom layer and crystalline structure match of two films play key roles for ambipolar transport. In current work, both TiOPc and CuPc has phthalocyanine ring as ligand that possess similar crystalline growth mode, which result in good film compatibility. As a result, we believe that the match of interface electric structure and film morphology are two important respects to realize ambipolar transport.

Recent progress displayed that organic semiconductors have native capability for transport both electron and hole [17]. The key factor is how to offer proper interface for both electron and hole accumulation at a single device. Moreover, localized states at the interface often acts as charge trap to impede the form of conductive channel in OFET. Therefore, the functional interface should be introduced to develop ambipolar devices. Several effective methods including of modifying gate insulator or using polymer insulator (i.e., PVA) with OH-group have been proved to easily realize for ambipolar transport [18,19]. Therefore, organic heterojunction may also be considered to offer a

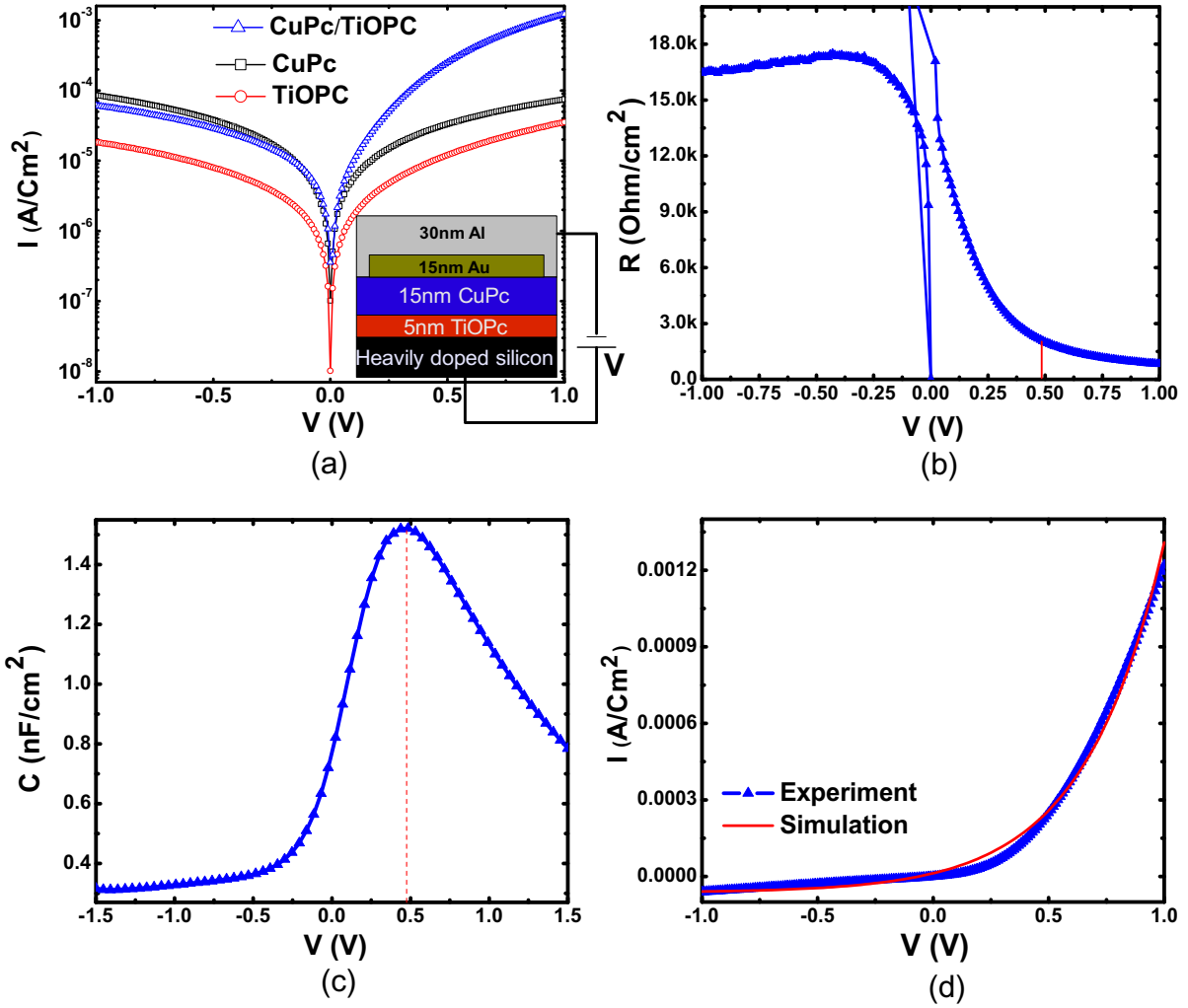

Fig. 2. (a) Current–voltage curves of the TiOPc, CuPc, and CuPc/TiOPc heterojunction diodes in semi-log scale. The inset gives the diode configuration. (b) Resistance–voltage and (c) capacitance–voltage curves of CuPc/TiOPc diode. (d) The simulation and experiment results of current–voltage characteristics of CuPc/TiOPc diode.

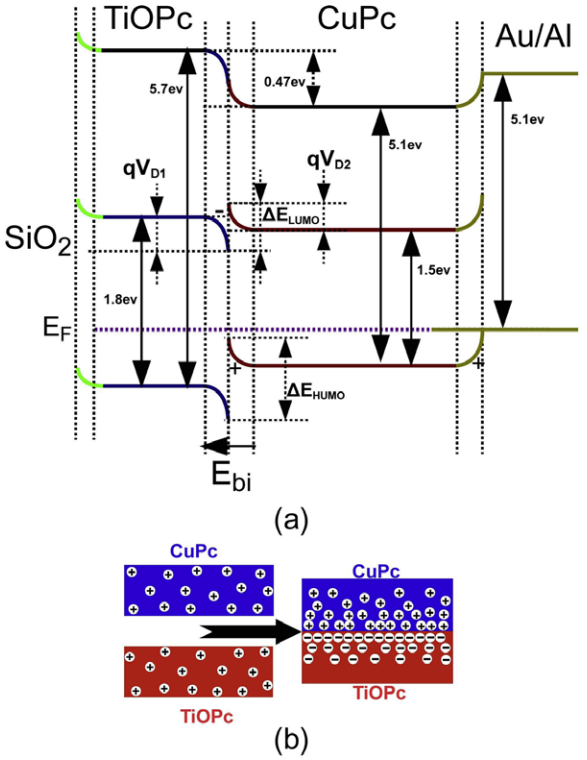

Fig. 3. (a) Schematic energy band diagram for Au/CuPc/TiOPc/SiO_2 used in FETs under equilibrium ($V_G = 0$) condition. (b) Illustration of the mobile carriers' distribution at the heterojunction interface of CuPc and TiOPc under zero bias conditions.

new interface for the accumulation of either electron or hole. In respect of organic heterojunction, the film quality of bottom layer including of surface roughness, surface energy, chemical properties, crystalline structure etc. will influence on charge-type and transport capability.

4. Conclusion

In summary, ambipolar charge transport has been demonstrated in CuPc/TiOPc junction by *IV* and *CV* FET measurements. A built-in electric field was confirmed by diode analysis. Its direction and electric potential were also addressed. All results indicated that both electrons and holes are located at the interface of p–p junction and can be driven by external electric field. Therefore, bi-carrier transport may be realized based on two conventional defined p-type materials. Current studies will be helpful for fundamental comprehensions on the charge transport in organic junction.

Acknowledgements

This research was supported by the National Natural Science Foundation of China (60806007), and Science and Technology Commission of Shanghai Municipality Program (08DZ1140702, 08520511200).

References

[1] C.W. Tang, Appl. Phys. Lett. 48 (1986) 183.
[2] C.W. Tang, S.A. VanSlyke, Appl. Phys. Lett. 51 (1987) 913.
[3] J. Wang, H.B. Wang, X.J. Yan, H.C. Huang, D.H. Yan, Appl. Phys. Lett. 87 (2005) 093507.
[4] E.J. Meijer, D.M. De Leeuw, S. Setayesh, E. Van Veenendaal, B.H. Huisman, P.W.M. Blom, J.C. Hummelen, U. Scherf, T.M. Klapwijk, Nat. Mater. 2 (2003) 678.
[5] C. Rost, D.J. Gundlach, S. Karg, W. Riess, J. Appl. Phys. 95 (2004) 5782.
[6] H.B. Wang, J. Wang, H.C. Huang, X.J. Yan, D.H. Yan, Org. Electron. 7 (2006) 369.
[7] H. Alves, A.S. Molinari, H.X. Xie, A.F. Morpurgo, Nat. Mater. 7 (2008) 574.
[8] J.W. Shi, H.B. Wang, D. Song, H. Tian, Y.H. Geng, D.H. Yan, Adv. Funct. Mater. 17 (2007) 397.
[9] H.B. Wang, X.J. Wang, B. Yu, Y.H. Geng, D.H. Yan, Appl. Phys. Lett. 93 (2008) 113303.
[10] J.H. Seo, G.S. Chang, R.G. Wilks, C.N. Whang, K.H. Chae, S. Cho, K.-H. Yoo, A. Moewes, J. Phys. Chem. B 112 (2008) 16266.
[11] H. Tada, H. Touda, M. Takada, K. Matsushige, Appl. Phys. Lett. 76 (2000) 873.
[12] Z. Bao, A.J. Lovinger, A. Dodabalapur, Appl. Phys. Lett. 69 (1996) 3066.
[13] S. Cho, J. Yuen, J.Y. Kim, K. Lee, A.J. Heeger, Appl. Phys. Lett. 90 (2007) 063511.
[14] J. Sun, B.N. Pal, B.J. Jung, H.E. Katz, Org. Electron. 10 (2009) 1.
[15] K. Harada, A.G. Werner, M. Pfeiffer, C.J. Bloom, C.M. Elliott, K. Leo, Phys. Rev. Lett. 94 (2005) 036601.
[16] J.F. Li, S.H. Su, K.S. Hwang, M. Yokoyama, J. Phys. D: Appl. Phys. 40 (2007) 2435.
[17] J. Zaumseil, H. Sirringhaus, Chem. Rev. 107 (2007) 1296.
[18] L.L. Chua, J. Zaumseil, J. Chang, E.C.W. Ou, P.K.H. Ho, H. Sirringhaus, R.H. Friend, Nature 434 (2005) 194.
[19] T.B. Singh, F. Meghdadi, S. Günes, N. Marjanovic, G. Horowitz, P. Lang, S. Bauer, N.S. Sariciftci, Adv. Mater. 17 (2005) 2315.

2. Experimental

2.1. Materials

1-Iodo-2-bromobenzene, *n*-butyllithium (n-BuLi), chlorodiphenylphosphine, *N*-bromosuccinimide, naphthalene-1-boronic acid, tetrakis(triphenylphosphine)palladium(0), potassium carbonate, 2,7-dibromo-9-fluorenone were purchased from the Aldrich Chem. Co. and used without further purification. Hydrogen peroxide was obtained from the Duksan Sci. Co. and used without further purification. Tetrahydrofuran (THF) was distilled over sodium and calcium hydride.

2.2. Synthesis

The synthetic route of SPPO21 is shown in Scheme 1. The synthesis of 1-(2-bromophenyl)naphthalene (**1**) and 2,7-dibromospiro[fluorene-7,11′-benzofluorene] (**2**) was described in a previous work [9].

2.3. 2,7-Bis(diphenylphosphino)spiro[fluorene-7,11′-benzofluorene] (*3*)

2,7-Dibromospiro[fluorene-7,11′-benzofluorene] (0.97 g, 1.85 mmol) was dissolved in THF. The solution was cooled to −78 °C and n-BuLi (10 M in hexane, 0.46 mL) was slowly added dropwise. The solution was stirred for 3 h and then a solution of chlorodiphenylphosphine (1.02 g, 4.62 mmol) was added under an argon atmosphere. The resulting mixture was gradually warmed to ambient temperature and quenched with methanol. The mixture was extracted with dichloromethane, and the combined organic layers were dried over magnesium sulfate, filtered and evaporated at a reduced pressure. The white powder that was obtained was purified using column chromatography.

2.4. 2,7-Bis(diphenylphosphoryl)spiro[fluorene-7,11′-benzofluorene] (SPPO21)

A mixture of 2,7-bis(diphenylphosphino)spiro[fluorene-7,11′-benzofluorene] (0.845 g, 1.14 mmol), dichloromethane (10 mL), and 2 mL of 30% hydrogen peroxide was stirred overnight at room temperature. The organic layer was separated and washed with dichloromethane and water. The extract was dried through evaporation to produce a white solid, which was further purified using column chromatography with a final yield of 0.74 g.

SPPO21 yield 83%. T_g 135 °C. ^{1}H NMR (200 MHz, $CDCl_3$): δ 8.75–8.71 (d, 1H), 8.34–7.30 (d, 1H), 7.95–7.84 (m, 3H), 7.70–7.41 (m, 15H), 7.35–7.20 (m, 12H), 7.13–7.06 (d, 2H) 6.73–6.69 (d, 2H). MS (FAB) *m/z* 767 [(M+1)+].

2.5. Characterization

The ^{1}H nuclear magnetic resonance (NMR) was obtained using a Varian 200 (200 MHz) spectrometer. The photoluminescence (PL) spectra were recorded on a fluorescence spectrophotometer (HITACHI, F-7000), and the ultraviolet–visible (UV–vis) spectra were obtained using a UV–vis spectrophotometer (Shimadzu, UV-2501PC). The transition temperature measurements for SPPO21 were carried out using a differential scanning calorimeter (DSC, Mettler DSC 822) at a heating rate of 10 °C/min under a nitrogen atmosphere. The low and high resolution mass spectra were recorded using a JEOL, JMS-AX505WA spectrometer in the FAB (fast atom bombardment) mode. The energy levels were measured using cyclic voltammetry (CV). Atomic force microscopic (AFM) measurements were performed on the evaporated SPPO21 film in order to study the morphological stability of the film.

2.6. Device fabrication

A basic device configuration of indium tin oxide (ITO, 150 nm)/N,N′-diphenyl-N,N′-bis-[4-(phenyl-m-tolyl-amino)-phenyl]-biphenyl-4,4′-diamine (DNTPD, 60 nm)/N,N′-di(1-naphthyl)-N,N′-diphenylbenzidine (NPB, 20 nm)/4,4′,4″-tris(N-carbazolyl)triphenylamine (TCTA, 10 nm)/SPPO21: iridium(III) bis(2-phenylquinoline) acetylacetonate ($Ir(pq)_2acac$, 30 nm, ×%)/2,9-dimethyl-4,7-diphenyl-1,10-phenanthroline (BCP, 5 nm)/tris(8-hydroxyquinoline) aluminum (Alq_3, 20 nm)/LiF(1 nm)/Al(200 nm) was used for the device fabrication. Various doping

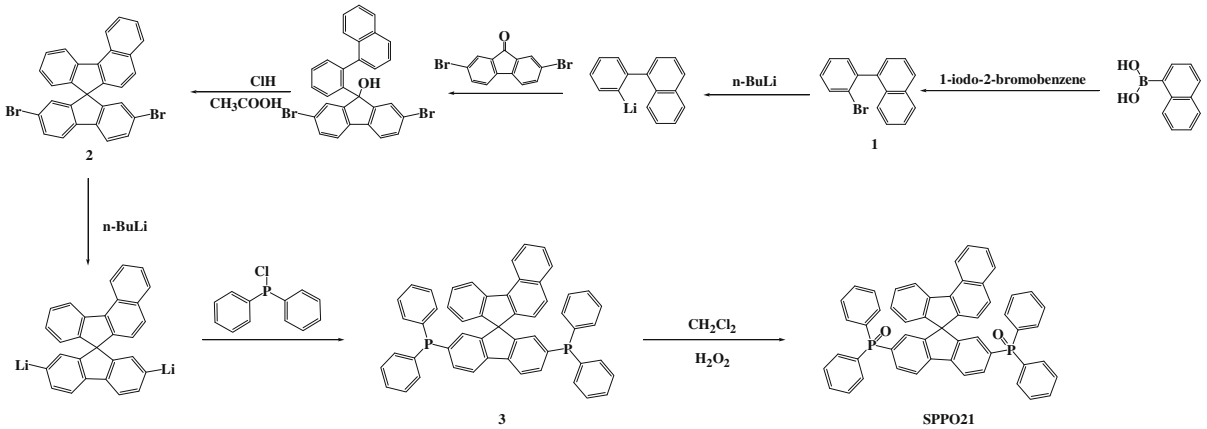

Scheme 1. Synthetic scheme of the SPPO21.

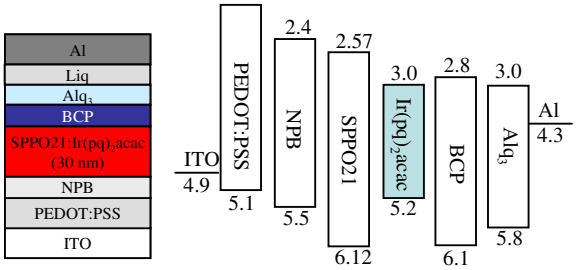

Fig. 1. Device structures of the red PHOLEDs and energy level diagram of the devices.

concentrations of 1% (device I), 2% (device II), 3% (device III), 5% (device IV) and 10% (device V) were used for the red emitting layer. The device structures of the red PHOLEDs are shown in Fig. 1. The photoluminescence (PL) measurements were carried out for $Ir(pq)_2acac$ doped SPPO21 using a fluorescence spectrophotometer. $Ir(pq)_2acac$ doped solid films with the same doping concentration as the red devices were fabricated for the PL measurements. The current density–voltage–luminance and electroluminescence (EL) characteristics of the red PHOLEDs were measured using a Keithley 2400 source measurement unit and a CS 1000 spectroradiometer. The external quantum efficiency was calculated from the EL spectra, luminance and current density. Lambertian distribution of the light emission was assumed in the calculation of the quantum efficiency and the light emission in the forward direction was measured.

3. Results and discussion

SPPO21 was synthesized through the phosphonation reaction of dibromospirobenzofluorene with chlorodiphenylphosphine. Dibromospirobenzofluorene was effectively prepared through the reaction of dibromofluorenone with 2-bromobiphenyl followed by lithiation and dehydration [9]. The synthetic yield of SPPO21 was 83%, and after purification using column chromatography, the purity of SPPO21 was over 99%. The synthetic scheme of SPPO21 is shown in Scheme 1. SPPO21 was fully characterized using ^1H NMR, high performance liquid chromatography, differential scanning calorimetry and high resolution mass spectrometry.

SPPO21, containing a spirobenzofluorene unit and two diphenylphophine units, was used as the electron transporting host material for the red phosphorescent dopant. The spirobenzofluorene moiety has good thermal and morphological stability because of its rigid benzofluorene unit [9]. Additionally, the spirobenzofluorene unit has a triplet bandgap of 2.4 eV, and can be applied as a molecular backbone for the host in red PHOLEDs. The phosphine oxide group isolates the core structure and has electron withdrawing characteristics because of its polarity [10,11]. Therefore, the electron transport properties of the molecule were enhanced by the phosphine oxide group and SPPO21 was an efficient electron transport type host material. Additionally, the energy levels of SPPO21 were effectively managed by the two electron withdrawing phosphine oxide units for efficient electron injection.

Fig. 2 shows the UV–vis and PL spectra of SPPO21. The PL spectra were obtained at both room temperature and 77 K in order to measure the triplet bandgap of SPPO21. SPPO21 exhibited strong absorption peaks at 297 and 340 nm, which corresponded to the absorption of the spirobenzofluorene unit. On the other hand, the diphenylphosphine oxide group did not greatly contribute to the optical absorption. A bandgap of 3.55 eV was calculated for SPPO21 using the absorption edge of the UV–vis spectrum. A PL emission peak was observed at 417 nm because of the wide bandgap of SPPO21. A low temperature PL spectrum was also obtained at 77 K, and the triplet emission peak of SPPO21 was detected at 533 nm with a triplet bandgap of 2.32 eV.

The CV measurements showed that SPPO21 had a HOMO level of 6.12 eV, and a lowest unoccupied molecular orbital (LUMO) of 2.57 eV as well a triplet bandgap of 2.32 eV, which was suitable for transferring energy to red emitting $Ir(pq)_2acac$ (triplet bandgap of 2.2 eV). Therefore, SPPO21 can be used as the host in the $Ir(pq)_2acac$ doped device.

SPPO21 had a spirobenzofluorene core structure with a twisted fluorene and benzofluorene backbone, which was advantageous for amorphous and thermally stable film formation. Additionally, the diphenylphosphine oxide unit that was connected to the spirobenzofluorene backbone structure also improved the thermal stability because of the polar phosphine oxide group and the phenyl group that was attached to the phosphine oxide unit. Therefore, SPPO21 had a high glass transition temperature of 135 °C.

The surface morphology of the evaporated SPPO21 film was analyzed using AFM in order to study the film stability of SPPO21. The AFM measurements were carried out for a pristine SPPO21 film and an SPPO21 film that was thermally treated at 100 °C for 2 h. The AFM images of SPPO21 are shown in Fig. 3. SPPO21 formed a stable amorphous film with a surface roughness of 0.12 nm. The surface morphology of the SPPO21 film did not change even after thermal treatment at 100 °C for 2 h, and the surface roughness of the SPPO21 film baked at 100 °C was 0.14 nm. Therefore, SPPO21 can effectively be used as a thermally stable host material in organic light-emitting diodes. The stability of the amorphous film was caused by the twisted structure

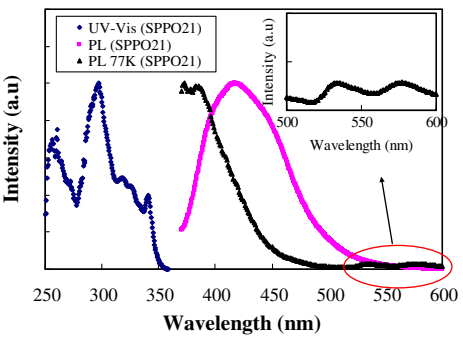

Fig. 2. UV–vis and PL spectra of SPPO21.

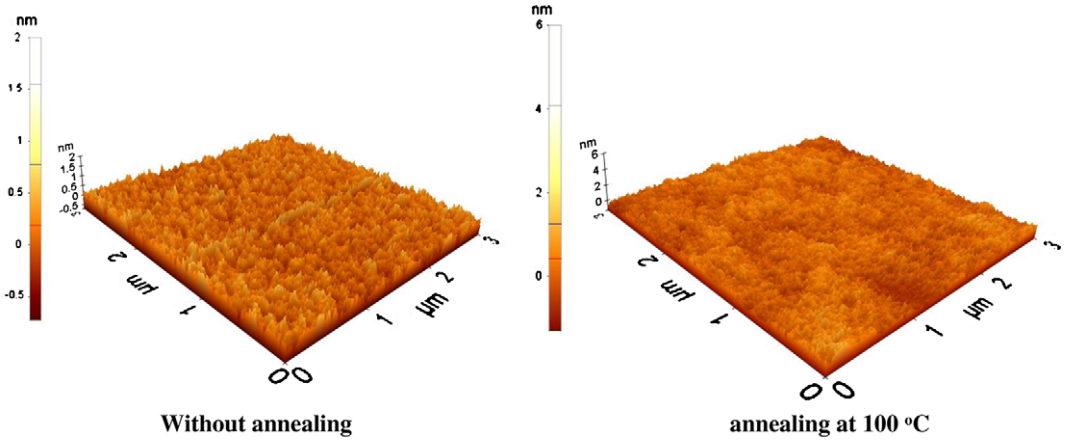

Fig. 3. Atomic force microscopic pictures of the SPPO21 without thermal treatment and after thermal treatment at 100 °C.

of the spirofluorene–benzofluorene core and the two diphenylphosphine oxide units.

The device performances of the red PHOLEDs were studied with respect to the doping concentration of Ir(pq)$_2$acac in order to evaluate the performance of SPPO21 as a host material for red PHOLEDs. Fig. 4 shows the current density–voltage–luminance curves of the red PHOLEDs with different doping concentrations. The current density of the red PHOLEDs increased as the doping concentration increased, and the highest current density was obtained for the red PHOLED with the highest doping concentration. SPPO21 had a HOMO/LUMO level of 6.12/2.57 eV, whereas the HOMO/LUMO of Ir(pq)$_2$acac was 5.2/3.0 eV in the energy level diagram (Fig. 1), corresponding to a HOMO/LUMO level difference of 0.92/0.43 eV between the SPPO21 and Ir(pq)$_2$acac. The large HOMO level gap between SPPO21 and Ir(pq)$_2$acac induced significant hole trapping by the dopant, and electrons were also trapped by the dopant because of the LUMO level gap of 0.43 eV [12]. Therefore, the charge trapping was critical to the current density, and the intermolecular hopping between the dopant materials dominated the charge transport behavior of the SPPO21 device, resulting in high current densities in the highly doped devices.

The luminance of the SPPO21 red PHOLEDs was high at a doping concentration of 3% despite the low current density, indicating a high recombination efficiency in device III. The low luminance of devices I and II was caused by their low current densities. Additionally the luminance of devices IV and V was low because of the low recombination efficiency of the holes and electrons.

Fig. 5 shows the quantum efficiency and current efficiency of the SPPO21 based red PHOLEDs. Device II exhibited the highest quantum efficiency at high luminance (>400 cd/m^2), whereas the quantum efficiency of device I

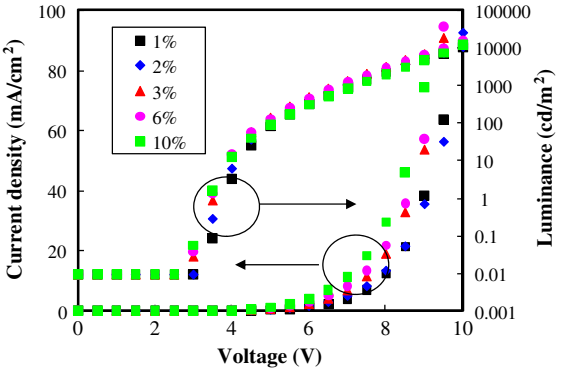

Fig. 4. Current density–voltage–luminance curves of the red PHOLEDs with the SPPO21 host according to the doping concentration of the Ir(pq)$_2$acac.

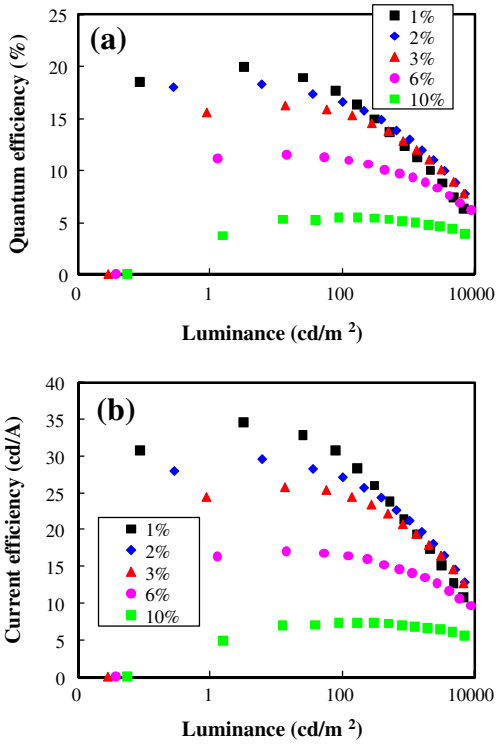

Fig. 5. Quantum efficiency (a) and current efficiency (b) of the red PHOLEDs with the SPPO21 host according to the doping concentration of the Ir(pq)$_2$acac.

was higher than the other devices at low luminance (<400 cd/m^2). The maximum quantum efficiencies of devices I and II were 20% and 18.3%, respectively, whereas the quantum efficiencies at 1000 cd/m^2 were 12.1% and 13.1%, respectively. The quantum efficiency of the SPPO21 device was higher than the SPPO2 that was reported earlier [13]. The external quantum efficiency of device I was the same as the theoretical external maximum quantum efficiency of 20%. However, the quantum efficiency was significantly reduced in devices IV and V. The maximum quantum efficiencies of devices IV and V were only 11.5% and 5.4%, respectively. The quantum efficiency of the SPPO21 based red PHOLEDs was optimized at a very low doping concentration of 1% or 2%. The current efficiency showed the same tendency. However, the reason for this observation was unknown. Therefore, the PL spectra of the Ir(pq)$_2$acac doped SPPO21 films and the EL spectra of the fabricated red PHOLEDs were examined at various doping concentrations.

Fig. 6 shows the PL spectra of the Ir(pq)$_2$acac doped SPPO21 films at different doping concentrations of Ir(pq)$_2$acac. The PL emission of the pure SPPO21 film was observed at around 400 nm with a maximum peak at 405 nm, and the Ir(pq)$_2$acac PL emission was detected at 605 nm. The Ir(pq)$_2$acac doped SPPO21 films exhibited PL peaks for both SPPO21 and Ir(pq)$_2$acac at doping concentrations below 6%, whereas the Ir(pq)$_2$acac doped SPPO21 films exhibited only the Ir(pq)$_2$acac emission at higher doping concentrations above 6%. Therefore, the energy transfer from the SPPO21 host to Ir(pq)$_2$acac was not complete at low doping concentrations. At 6% doping the SPPO21 emission was completely absorbed by Ir(pq)$_2$acac. However, the PL intensity of Ir(pq)$_2$acac was not as strong in the 6% doped SPPO21 film as the others despite the complete energy transfer from SPPO21 to Ir(pq)$_2$acac. The PL intensity of the emitter doped film is affected by the luminescence concentration quenching, which is governed by the doping concentration [14–16]. The concentration quenching rate constant was dependent on R^{-6}, where R is the average distance between dopant molecules. The average distance between Ir(pq)$_2$acac decreased according to the following relationship, $R = [(\text{molecular density in film}) \times (\text{mol\% of the dopant in a film})]^{-1/3}$ [16], and R decreased below 3.0 nm in the 3% doped film. The Förster radius of the phosphorescent emitter doped film was estimated to be below 3 nm [16–18]. Therefore, the concentration quenching was serious above a doping concentration of 3%, resulting in a decrease in the PL intensity. The highest PL intensity was obtained at a doping concentration of 2% because of the small concentration quenching, even though the SPPO21 emission was not completely quenched by the dopant. The low PL intensity at 1% doping was caused by the incomplete energy transfer, whereas the low intensity at 3% doping was caused by the concentration quenching.

The PL intensity of the film was well correlated with the quantum efficiency of the red PHOLEDs. The high efficiency was obtained for device II at a 2% doping concentration, and the efficiency decreased as the doping concentration increased. Even though other factors affected the quantum efficiency of the EL devices, these results proved that the PL emission was critical to the quantum efficiency of the SPPO21 based red PHOLEDs.

Fig. 7 shows the EL spectra of the SPPO21 based red PHOLEDs. The red PHOLEDs exhibited main emission peaks at around 600 nm and the emission peaks were red-shifted at higher doping concentrations because of the intermolecular dipole–dipole interaction that was caused by the short distance between the dopant molecules at high doping concentrations. The main emission peak shifted from 596 nm at 1% doping to 612 nm at 10% doping.

Comparing the PL spectra of the films and the EL spectra of the devices, device I did not show any host emission in the PL spectrum of the 1% doped film. All of the SPPO21 emissions were not absorbed by the 1% doped Ir(pq)$_2$acac in the PL excitation, but the host emission disappeared in the EL emission because of the hole and electron trapping by the Ir(pq)$_2$acac in the energy level diagram of the host and dopant. The excitons were generated not only in the host but also in the dopant because of the charge trapping caused by the large energy level difference between the host and dopant materials. Both the excitons that were formed in the host through the transfer of energy to the dopant and the excitons that were generated in the dopant directly emitted. Therefore, both the energy transfer and the charge trapping were parts of the main mechanism for the light emission in the SPPO21 based red PHOLEDs. The contribution of the charge trapping on the light emission was significant in the highly doped device, but the concentration quenching had a negative effect on the

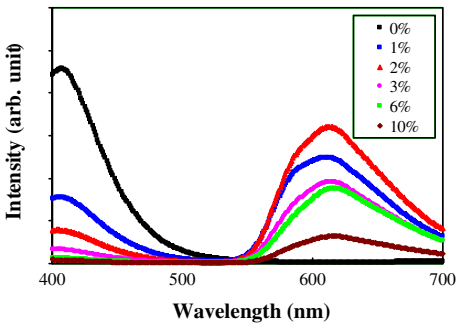

Fig. 6. Photoluminescence spectra of the SPPO21: Ir(pq)$_2$acac film according to the doping concentration of the Ir(pq)$_2$acac.

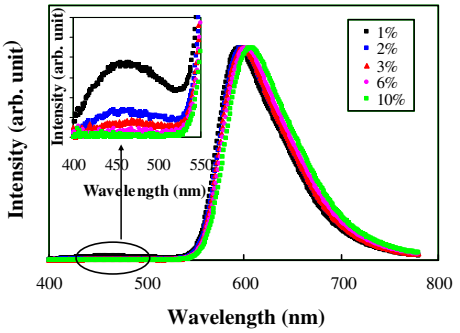

Fig. 7. Electroluminescence spectra of the red OLEDs with the SPPO21 host according to the doping concentration of Ir(pq)$_2$acac.

quantum efficiency. On the other hand, the energy transfer dominated the light emission and the charge trapping compensated for the incomplete energy transfer in the devices with low doping concentrations. Therefore, a high quantum efficiency over 20% was achieved in the SPPO21 based red PHOLEDs.

Even though SPPO21 did not exhibit an emission at 405 nm, a weak emission was detected at 465 nm in the EL spectra of the red PHOLEDs at low doping concentrations. The intensity of the emission weakened at higher doping concentrations and was not observed in device V. An expanded image of the emission peak is shown in Fig. 7 as an inset. This emission peak was caused by the exciplex of TCTA and SPPO21, which was confirmed by the PL emission of the mixed film of TCTA and SPPO21. The electron donating aromatic amine group in TCTA and the strong electron withdrawing phosphine oxide group combined to make the excited complex [19,20]. The TCTA hole transport layer and the SPPO21 host formed the exciplex at the interface, which emitted a weak peak at 465 nm. The exciplex formation was facilitated by the electron accumulation and overflow at the interface between the SPPO21 host and TCTA. Fewer electrons were trapped by the dopant in the red PHOLEDs with lower doping concentrations, leading to better electron transport through the SPPO21 emitting layer. Therefore, more electrons accumulated at the interface and were injected into the TCTA layer in device I, resulting in a relatively strong exciplex emission. The exciplex emission was responsible for the large efficiency roll-off in the red PHOLEDs with low doping concentrations in Fig. 5. A previous report showed that the charge leakage is critical to the efficiency roll-off, and confirming the results that were obtained in this work [21]. The efficiency roll-off decreased as the intensity of the 465 nm peak decreased.

4. Conclusions

The device performances of the red PHOLEDs with the phosphine oxide based SPPO21 host were studied, and a high external quantum efficiency of 20% was achieved. The device performances were optimized at a low doping concentration because of the little concentration quenching, energy transfer and charge trapping. SPPO21 exhibited a high quantum efficiency and low optimum doping concentration making it an effective host material for red PHOLEDs, and therefore, the SPPO21 host material exhibited potential for use in future display and lighting applications.

Acknowledgement

The present research was conducted by the research fund of Dankook University in 2009.

References

[1] J.Y. Lee, J.H. Kwon, H.K. Chung, Org. Electron. 4 (2003) 143.
[2] T. Tsuji, S. Kawami, S. Miyaguchi, T. Naijo, T. Yuki, S. Matsuo, H. Miyazaki, SID Int. Symp. Digest Technol. Pap. 35 (2004) 900.
[3] H. Kanno, K. Ishikawa, Y. Nishio, A. Endo, C. Adachi, K. Shibata, Appl. Phys. Lett. 90 (2007) 123509.
[4] W.S. Jeon, T.J. Park, S.Y. Kim, P. Pode, J. Jang, J.H. Kwon, Org. Electron. 10 (2009) 240.
[5] A. Tsuboyama, H. Iwawaki, M. Furugori, T. Mukaide, J. Kamatani, S. Igawa, T. Moriyama, S. Miura, T. Takiguchi, S. Okada, M. Hoshino, K. Ueno, J. Am. Chem. Soc. 125 (2003) 12971.
[6] M.A. Baldo, M.E. Thompson, S.R. Forrest, Pure Appl. Chem. 71 (1999) 2095.
[7] Y. Kawamura, S. Yanagida, S.R. Forrest, J. Appl. Phys. 92 (2002) 87.
[8] J.Y. Lee, Appl. Phys. Lett. 89 (2006) 223517.
[9] S.O. Jeon, Y.M. Jeon, J.W. Kim, C.W. Lee, M.S. Gong, Org. Electron. 9 (2008) 522.
[10] P.E. Burrows, A.B. Padmaperuma, L.S. Sapochak, P. Djurovich, M.E. Thompson, Appl. Phys. Lett. 88 (2006) 183503.
[11] A.B. Padmaperuma, L.S. Sapochak, P.E. Burrows, Chem. Mater. 18 (2006) 2389.
[12] S. Lamansky, R.C. Kwong, M. Nugent, P.I. Djurovich, M.E. Thompson, Org. Electron. 2 (2001) 53.
[13] S.O. Jeon, K.S. Yook, C.W. Joo, J.Y. Lee, Org. Electron. 10 (2009) 998.
[14] Y. Kawamura, K. Goushi, J. Brooks, J.J. Brown, H. Sasabe, C. Adachi, Appl. Phys. Lett. 86 (2005) 071104.
[15] X. Gong, J.C. Ostrowski, D. Moses, G.C. Bazan, A.J. Heeger, Adv. Funct. Mater. 13 (2003) 439.
[16] Y. Kawamura, J. Brooks, J.J. Brown, H. Sasabe, C. Adachi, Phys. Rev. Lett. 96 (2006) 017404.
[17] I. Tanaka, Y. Tabata, S. Tokito, J. Appl. Phys. 99 (2006) 073501.
[18] G. Ramos-Ortiz, Y. Oki, B. Domercq, B. Kippelen, Phys. Chem. Chem. Phys. 4 (2002) 4109.
[19] S.A. Jenekhe, J.A. Osaheni, Science 265 (1994) 765.
[20] Y. Yang, Q. Pei, Appl. Phys. Lett. 70 (1997) 1926.
[21] S.H. Kim, J. Jang, K.S. Yook, J.Y. Lee, Appl. Phys. Lett. 92 (2008) 023513.

luminescence efficiency of organic semiconductors with the high electron mobility of inorganic oxides.

In this context, recent work by Glezos et al. [11] has shown that a member of the class of polyoxometalates (POMs) [12], a class of soluble inorganic molecular oxides whose diverse chemistry allows for facile tuning of their structural, optical and electronic properties [13], exhibits a high electron mobility of $\sim 4 \times 10^{-3}$ cm^2/V s (in PMMA at 1:1 w/w) [11] and has a low lying conduction-band edge located at ≈4.0 eV (taking into account solid-state polarization effects and assuming an exciton binding energy of ≈0.3 eV) [14,15]. In addition, electron transport studies in polyoxometalate layers showed efficient electron transport in very thin structures [16]. These characteristics make it a very appealing candidate for use as an EIL in HyLEDs. Furthermore, its hydrophilic nature, in contrast to the hydrophobic character of the conjugated emissive polymer layer, allows its facile spin-casting from water or alcohol-based solvents without disrupting the emissive layer morphology.

Here we report *for the first time* the use of a commercially available, solution-processable inorganic anionic polyoxometalate (POM) molecular oxide (namely, the Keggin structure phosphotungstic acid $(PW_{12}O_{40})^{3-}$) [11] as a novel EIL in HyLEDs. A thin-POM layer, with a LUMO level lying between that of the emissive polymer and the Fermi level of Al, provides an intermediate step for facilitating and enhancing electron injection from Al to the polymer LUMO, when inserted between the emissive layer and Al. This results in a lowered turn-on voltage and a significant decrease of the operating voltage as well as a significant increase in the maximum current density and luminance, improving the overall performance of the HyLEDs.

2. Experimental

Both reference and HyLEDs were fabricated on oxygen plasma-cleaned indium tin oxide (ITO) coated glass substrates. Poly(3,4-ethylenedioxythiophene):poly(styrenesulfonate) (PEDOT:PSS, obtained from Aldrich) was used as an anode interfacial layer to improve hole injection. The ~70 nm thick PEDOT:PSS layer was spin-cast from an aqueous solution and then annealed in air at 130 °C for 15 min. Next, an ~70 nm thick layer of the light-emitting green-yellow (YE) polyfluorene copolymer poly[(9,9-dioctylfluorenyl-2,7-diyl)-co-(1,4-benzo-{2,1′,3}-thiadiazole)] (ADS233YE, obtained from American Dye Source Inc.) was spin-cast on PEDOT-PSS from a 8 mg/ml chloroform solution. Prior to spin-coating, the polymer solution was filtered using a 0.20 μm PTFE filter. After spin-coating, the emissive layer was annealed at 85 °C for 10 min in air. In order to enhance electron injection, a thin-POM layer was deposited from a methanol solution on the polymer film to serve as the EIL in the HyLED configuration. Note that methanol is an orthogonal solvent with regard to the polymer (no dissolution of the polymer film was observed). By varying the concentration of the POM solution from 0.2–1 wt.%, the thickness of the EIL varied between ~2 and 10 nm. Finally, a 150 nm thick Al layer was deposited by thermal evaporation (at $\sim 5 \times 10^{-5}$ mbar) through a shadow mask (defined active area of 12.56 mm^2). The thickness of the polymer and the POM films was measured with an Ambios XP-2 profilometer and a M2000 Woolam ellipsometer, respectively. Current density–voltage characteristics were measured with a Keithley 2400 source-measure unit. Luminance and electroluminescence (EL) spectra were recorded with an Ocean Optics USB 2000 fiber optic spectrophotometer, assuming a Lambertian emission profile (for luminance measurements). Photovoltaic mode measurements were recorded under ~70 mW cm^{-2} solar light illumination simulated from a Hg–Xe lamp and a AM 1.5G filter. Surface morphology and structure of POM, YE and YE/POM bilayer films was investigated with a Veeco atomic force microscope (AFM). All measurements were carried out in air at room temperature.

3. Results and discussion

The Keggin structure of the anionic $(PW_{12}O_{40})^{3-}$ tungsten polyoxometalate (POM) along with the device architecture of a representative HyLED studied in this work and its corresponding energy diagram are shown in Fig. 1a and b and c, respectively. The device configuration is ITO (100 nm)/PEDOT-PSS (70 nm)/YE (70 nm)/POM (*x* nm)/Al (150 nm), where POM is used as a thin EIL and ETL to modify the YE/Al interface. Reference devices without POM were also fabricated for direct comparison. Fig. 2 shows atomic force microscopy (AFM) surface morphology images of (a) a 20 nm thick POM film (b) a 70 nm thick YE film (c) a YE(70 nm)/POM(2 nm) bilayer film and (d) a YE(70 nm)/POM(10 nm) bilayer film, all deposited on quartz glass substrates. POM forms an inhomogeneous and nanostructured film surface with an RMS roughness of ~5 nm and some features extending up to 40 nm in height (even larger than the nominal film thickness). In contrast, the surface of the YE polymer film is amorphous and relatively smooth with an RMS roughness of ~0.6 nm and very few features up to a few nm in height (peak to peak difference of 6 nm). The surface of the polymer/POM bilayer film, exhibits a POM solution concentration dependent number of rather well-defined nanorod-type features up to 15 nm high (shown as bright nanorod domains protruding from the surface with a diameter between 10 and 100 nm), more likely attributed to the presence of POM nanoparticle clusters spontaneously growing and regularly distributed on the polymer surface. This behavior is not unexpected if we consider that POM nanoparticles have a diameter of ~1 nm [11], thus deeming unlikely the formation of a continuous homogeneous film of POM in the thickness range between 1 nm and a few nm by spin-coating from very low concentration solutions (<1 wt.%) in polar solvents. An interesting aspect though is that these nanocluster domains grow in size (both in diameter and height) and also increase in number, therefore increasing the polymer film coverage, with an increase of the POM concentration solution. The mean POM nanocluster diameter is calculated to be ~50 nm. Moreover, the surface RMS roughness of the bilayer films is increased up to ~1.5 nm. This picture is supported by SEM imaging coupled with EDX-analysis (data not shown here)

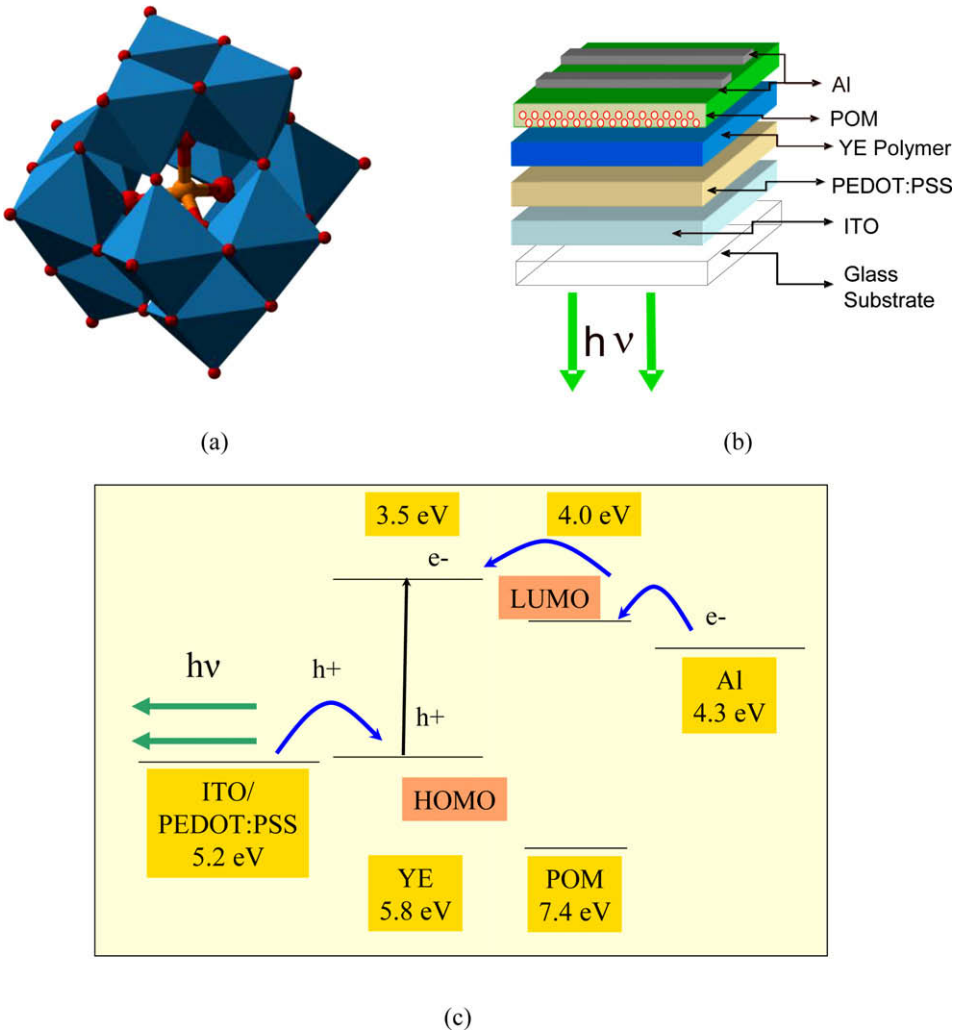

Fig. 1. (a) Keggin structure of the $(PW_{12}O_{40})^{3-}$ tungsten polyoxometalate (POM). The P atom occupies its center while the W atoms occupy the centers of the regular polyhedra and the O atoms are at the vertices. (b) Schematic architecture of the fabricated HyLED and (c) corresponding energy diagram.

which also indicate that POM nanoclusters with variable diameter and height are rather randomly distributed across the YE surface.

The difference in the surface topography and coverage between the POM film on glass and the POM onto the YE polymer film as well as the inhomogeneities present in either case as seen upon comparing Figs. 2a, c and d, respectively, may be a result of the different wetting conditions of this polar hydrophilic molecule on the two surfaces. We note however that although the heterogeneous coverage of POM on the YE film surface may contribute to an increased leakage current flow, the increased interfacial nanostructured area of POM with Al – as a result of the nanocluster presence – is expected to be beneficial for charge injection due to the high local electric field present in the vicinity of these surface POM domains.

The influence of the POM EIL and, in particular, its thickness on the current density versus voltage (J–V) and luminance versus voltage (L–V) characteristics of the YE-based PLEDs is shown in Figs. 3 and 4, respectively. A detailed description of the device performance characteristics is shown in Table 1. Reference PLEDs exhibit a turn-on voltage (for $L \approx 10$ cd m^{-2}) of 5.5 V, reach a luminance of ~1000 cd m^{-2} at 7.5 V and a maximum current density and luminance of ~1350 A m^{-2} and ~4150 cd m^{-2}, respectively, at 13 V. The maximum luminous current and power efficiency are 3.2 cd A^{-1} and 1 lm W^{-1} at ~3500 cd m^{-2}, typical of single-layer polyfluorene-benzothiadiazole (F8BT) based PLEDs with an Al cathode [17]. HyLEDs with a 2 nm thick POM EIL turn-on at 4 V (~1.5 V lower than the reference PLEDs), reach 1000 cd m^{-2} at 6.5 V and also exhibit a decrease in their maximum operating voltage as they reach a maximum current density and luminance of ~4400 A m^{-2} and ~5300 cd m^{-2}, respectively, at 12 V. An increase of the maximum current density by a factor of ~2.5 is demonstrated, with a smaller increase in the maximum luminance, which indicates a substantial increase of electron injection and the corresponding electron current (as also suggested by the steep exponential rise of the HyLED J–V–L characteristics above the turn-on voltage).

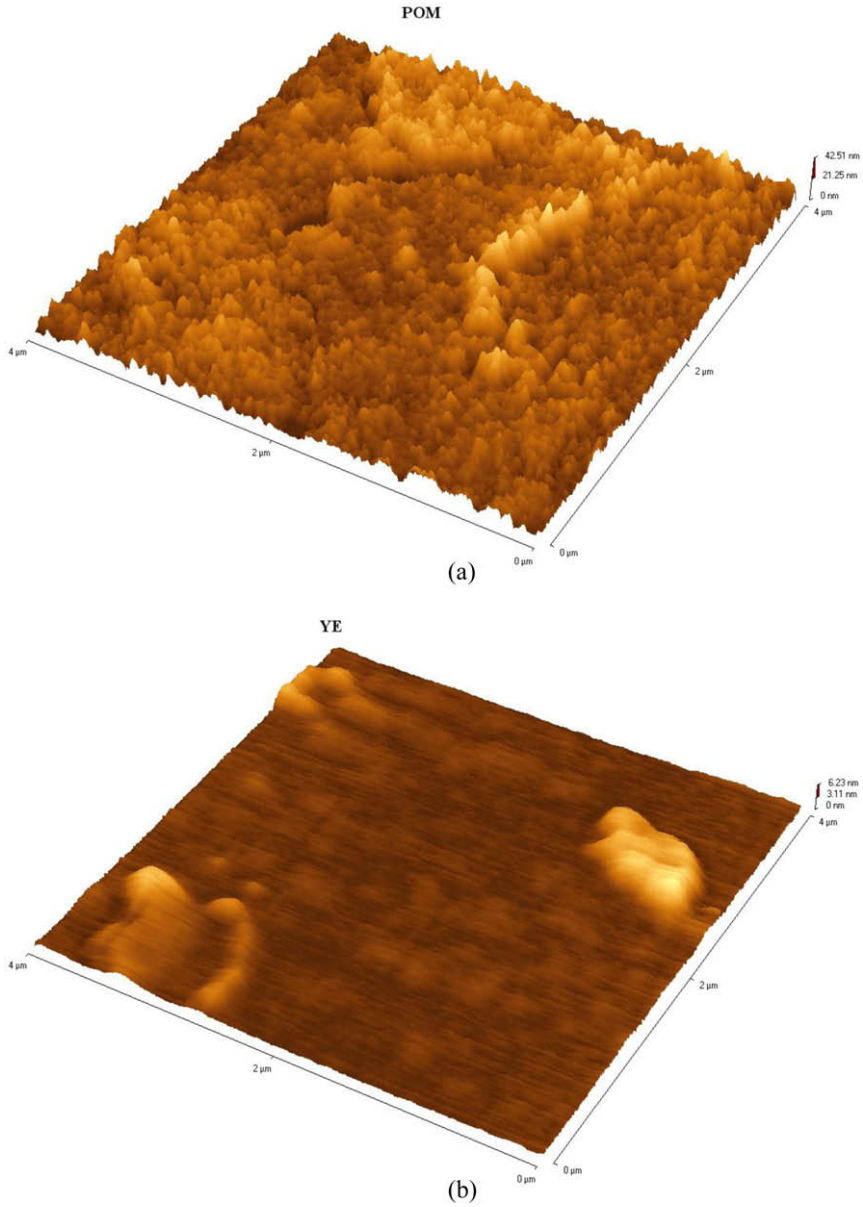

Fig. 2. 4 × 4 μm 3D AFM topographic images of (a) a 20 nm thick POM film on glass (b) a 70 nm thick YE film and (c) and (d) YE/POM bilayer films with a POM thickness of 2 and 10 nm, respectively. A larger interfacial contact area with increased surface roughness was observed when POM was inserted at the YE/Al interface.

Note that the inset of Fig. 3 shows the *J–V* characteristics plotted on a logarithmic scale (for the current) from where the presence of leakage current below the turn-on voltage can be identified. Both reference PLEDs and HyLEDs show high leakage current, regardless of the POM thickness that may be attributed to film heterogeneities. However, it appears than the insertion of a POM layer somewhat reduces the leakage current and that the use of a very thin-POM nanoclustered layer results in the lowest leakage current and a better diode behavior.

The maximum luminous current and power efficiency of the HyLEDs reach ~1.7 cd A^{-1} and 1.2 lm W^{-1} at ~120 and 10 cd m^{-2}, respectively. The small decrease in the HyLED current efficiency suggests that the charge balance in the reference devices is not improved upon insertion of the POM EIL. This is mainly attributed to the predominantly electron transporting character of the YE copolymer which results in electrons being the majority carriers in single-layer F8BT-based PLEDs [18–20]. However, the maximum power efficiency of the HyLED is slightly enhanced due to the significant lowering of its operating voltage. Upon increase of the POM thickness to ~10 nm, a slight increase of both the turn-on voltage to 4.5 V and the operating voltage (for $L \approx 1000$ cd m^{-2}) to 7.3 V is ob-

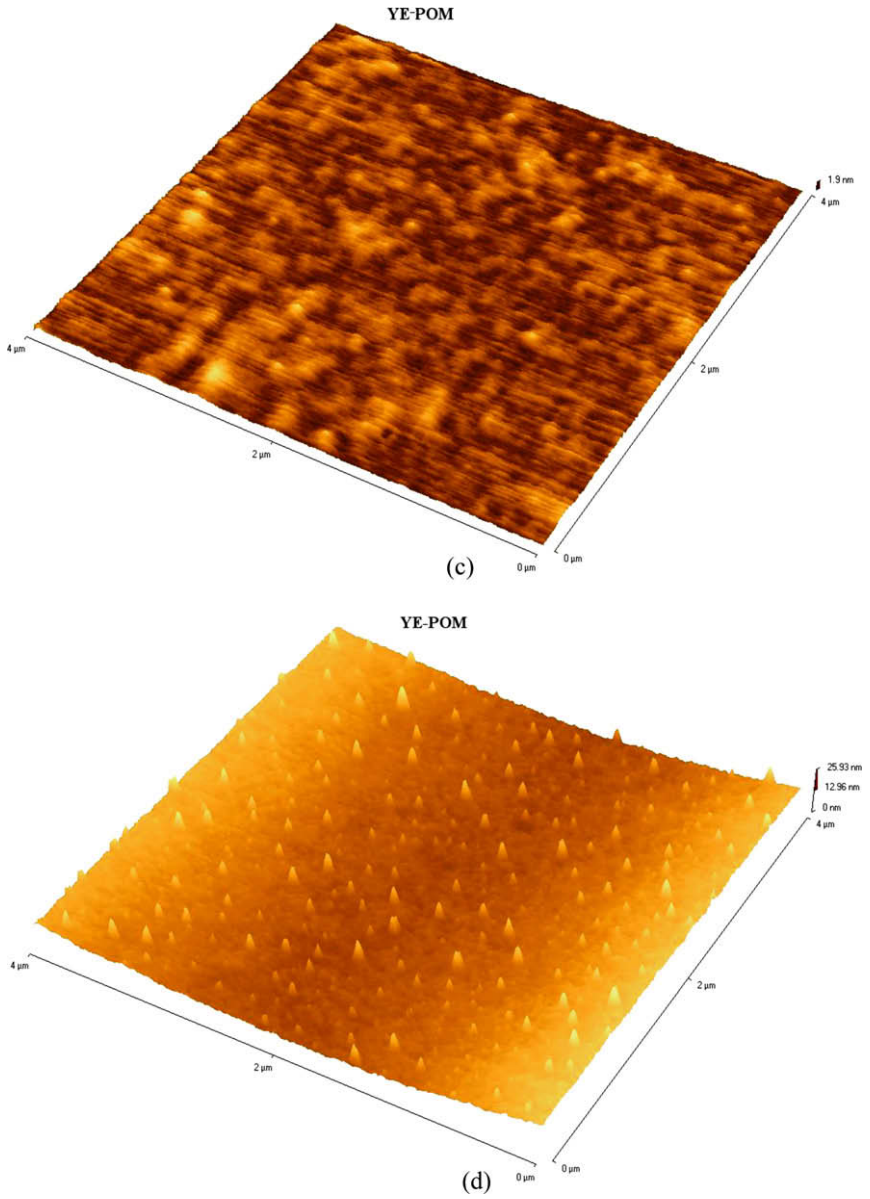

Fig. 2 (*continued*)

served (compared to 4 and 6.5 V, respectively, for the 2 nm thick EIL HyLED). Both values are still slightly lower though than those of the reference PLED. The maximum current and power efficiency reach 1 cd A^{-1} and 0.4 lm W^{-1}. Their decrease compared to those of the ~2 nm thick EIL-modified HyLED may be attributed to interference effects as a result of the increased distance of the recombination/emission zone from the cathode or to increased leakage current flow through the thicker EIL. Note that no appreciable change in the reference PLED EL spectrum was found upon insertion of the POM EIL layer. Green-yellow emission with a peak at ~540 nm, characteristic of F8BT [17] was observed, which indicates that charge recombination and exciton formation takes place inside the emissive layer, most likely away from the YE/POM interface due to the high electron mobility of the YE polymer and the electron-dominated character of the HyLEDs [21]. The relatively independent HyLED performance on the EIL thickness suggests that most of the applied electric field drops across the emitting layer and that the electron conductivity of POM is not a limiting factor in device performance, at least for thin EILs. Therefore, key limiting step for low voltage operation is the electron injection at the Al/YE interface. As the anode interface has the same structure, these improvements clearly indicate that an increased electron injection is responsible for the improved device operation of the thin-POM EIL-modified HyLEDs. The introduction of a thin-POM EIL reduces the turn-on

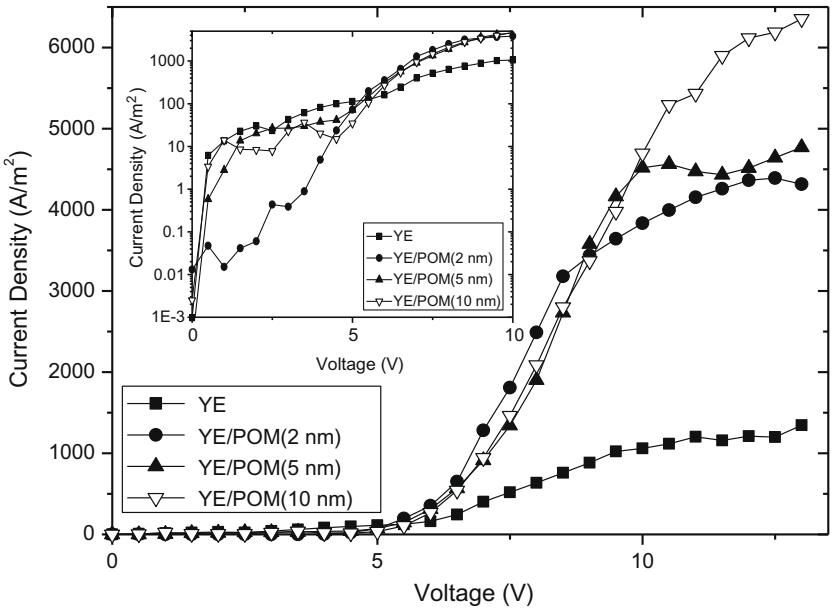

Fig. 3. Current density–voltage (J–V) characteristics of reference and HyLEDs for different POM thicknesses. A notable increase in the current density is demonstrated upon using a very thin-POM layer as EIL. The inset shows log(J)–V characteristics where the presence of leakage current, below the turn-on voltage, is seen.

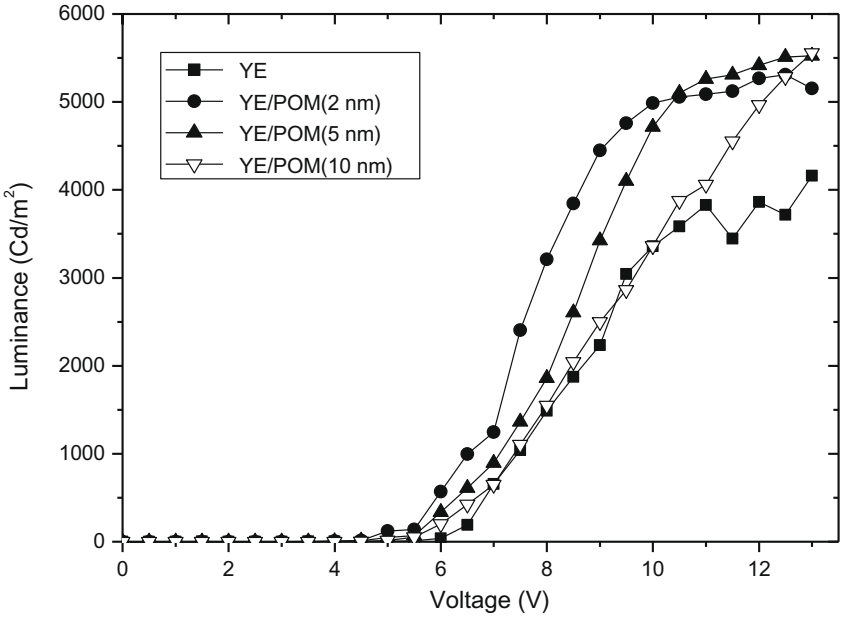

Fig. 4. Luminance–voltage (L–V) characteristics of reference and HyLEDs as a function of the POM layer thickness. Also, a notable increase in the luminance is demonstrated upon using a very thin-POM layer as EIL.

and operating voltage and enhances the maximum current density, luminance and luminous power efficiency (for a thin EIL), at the expense though of a decrease in the luminous current efficiency. The enhanced device operation is primarily attributed to the favorable position of the LUMO of POM that is situated at ≈4.0 eV, between the LUMO of YE (≈3.5 eV) [17] and the Al Fermi level (≈4.3 eV), thus acting as an intermediate step to reduce the energetic barrier height at the YE/Al interface and facilitate electron injection to the LUMO of YE. The nanostructured YE/POM surface and the high electron mobility of POM is also expected to further enhance the HyLED performance. n-Type

Table 1
Device performance characteristics of both reference PLEDs and HyLEDs with various POM thicknesses.

POM thickness (nm)	Turn-on voltage (V) (at 10 cd m^{-2})	Voltage (V) (at 100 cd m^{-2})	Voltage (V) (at 1000 cd m^{-2})	Maximum current density (A m^{-2}) (at voltage [V])	Maximum luminance (cd m^{-2}) (at voltage [V])	Maximum luminous current efficiency (cd A^{-1}) (at luminance [cd m^{-2}])	Maximum luminous power efficiency (lm W^{-1}) (at luminance [cd m^{-2}])
0	5.5	6.2	7.5	1348 (13)	4161 (13)	3.2 (3500)	1.0 (3500)
2	4.0	5.2	6.5	4366 (12)	5267 (12)	1.7 (120)	1.2 (10)
5	4.5	5.3	7.1	4771 (13)	5525 (13)	1.2 (5416)	0.6 (336)
10	4.7	5.7	7.3	6355 (13)	5556 (13)	0.9 (5556)	0.4 (202)

doping of POM upon spontaneous electron transfer from Al may also contribute in reducing the contact resistance and improving injection. Enhanced electron injection followed by facile transfer to the polymer LUMO results then in increased current flow as well as faster electron–hole recombination rate. Note that although the POM interlayer may act as a hole blocking layer (due to the very large Δ(HOMO) offset at the YE/POM interface) reducing hole leakage current, it may also increase electron leakage current, due to its nanostructured surface and increased roughness, thus contributing to the much higher current densities observed in the HyLEDs.

To further support the argument that the origin of the improved device performance is mainly related to changes in the energetics at the polymer/Al interface upon modification with the POM EIL, photovoltaic measurements were carried out to determine the open circuit voltage (V_{oc}). Its value reflects the built-in potential upon contact with the electrodes (for Ohmic contacts, it will be equal to the difference between the work-functions of PEDOT:PSS and Al). J–V curves were recorded under AM 1.5 G solar illumination (~70 mW cm^{-2}) and are presented in Fig. 5. The comparison of the V_{oc}'s of the devices with and without the POM EIL shows that a significant increase to ~1.27 V (compared to ~0.87 V for the reference device) is noted when a thin (<10 nm) POM film is used as an EIL. Attributing the ~0.4 V increase in V_{oc} to an enhanced built-in potential is also supported by the corresponding dark J–V characteristics where a higher 'compensation' voltage of ~0.3 V (defined as the voltage at which the internal field is cancelled by the external field) is observed for the HyLED (not shown here). This ~0.4 V increase of the built-in potential is suggestive of either pinning of the Fermi level of Al close to the LUMO of POM or decrease of the Al effective work-function. It is also noted that the high surface polarity of POM could lead to a favorable surface potential and further enhance electron injection as previously suggested for a ZnO modified ITO-F8BT interface [22]. The enhanced built-in field present in the HyLED results in a lowering of the effective electron injection barrier and therefore in an increased electron injection and charge recombination rate with a corresponding decrease of the operating voltage and an increase of both the maximum current density and luminance. Finally we note that, although POM is an n-type inorganic molecular oxide that could non-radiatively quench YE excitons due to its larger electron accepting ability and affinity, the similar short circuit photocurrent of the POM-modified HyLED with that of the YE PLED suggests otherwise. This observation along with the similar photoluminescence intensities measured for both YE and YE/POM films (not shown here) strongly suggests that no significant charge generation, due to exciton quenching (electron transfer to POM), takes place at the YE/POM interface. This is in contrast to other oxide/polymer interface based HyLEDs (for example, F8BT/TiO_2 based HyLEDs) where exciton quenching at this interface has been identified as a key exciton loss mechanism [22]. However, we have observed POM composition dependent PL and EL quenching in blends of YE and POM (data not shown here) suggestive of photoinduced electron transfer from the polymer excited state to the LUMO of POM and charge (electron) transfer between the two components that reduces exciton confinement in the polymer phase, respectively, and we will report these results in a future publication.

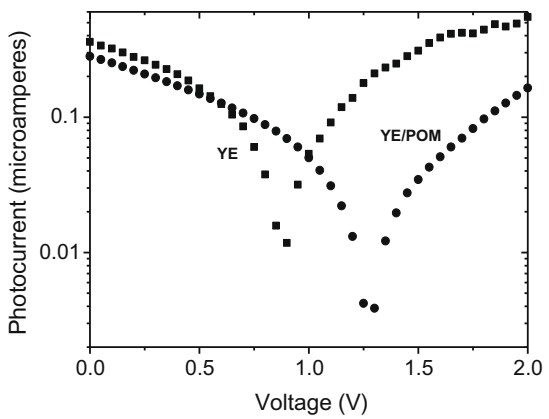

Fig. 5. Photocurrent density–voltage (AM1.5G, 70 mW cm^{-2}) characteristics of a reference and a HyLED. Photovoltaic open circuit voltage (V_{oc}) measurements reveal an increased built-in potential and, therefore, a reduced electron injection barrier height when POM is inserted at the YE/Al interface.

4. Summary

In summary, we have reported the use of a water soluble polyoxometalate (POM) inorganic molecular oxide for the formation of a novel thin (<10 nm), efficient electron injection layer (spin-cast from methanol, an orthogonal solvent with regard to the polymer layer underneath) be-

tween the emissive polymer layer and an Al cathode, and demonstrated improved performance HyLEDs based on the yellow-green emitting poly[(9,9-dioctylfluorenyl-2,7-diyl)-co-(1,4-benzo-{2,1′,3}-thiadiazole)] (YE) copolymer. Upon inserting this layer, a reduced turn-on and operating voltage combined with a significant increase in the maximum attainable current density and luminance were obtained in the HyLEDs. The superior electron injection characteristics was primarily attributed to the reduced effective electron injection barrier height at the POM-modified YE/Al interface, as suggested by the increased built-in potential directly measured with photovoltaic open circuit voltage measurements. This proof-of-concept demonstration elucidates polyoxometalate compounds as a versatile, emerging new class of efficient electron injection/transport molecular materials for high performance air-stable HyLEDs.

References

[1] T. Komoda, N. Ide, J. Kido, J. Light Vis. Environ. 32 (2008) 75.
[2] T.M. Brown, R.H. Friend, I.S. Millard, D.J. Lacey, J.H. Burroughes, F. Cacialli, Appl. Phys. Lett. 79 (2001) 174.
[3] F. Laquai, G. Wegner, H. Bässler, Phil. Trans. R. Soc. A 365 (2007) 1473.
[4] L.S. Hung, C.W. Tang, M.G. Mason, Appl. Phys. Lett. 70 (1997) 152.
[5] H.E. Katz, A.J. Lovinger, J. Johnson, C. Kloc, T. Siegrist, W. Li, Y.-Y. Lin, A. Dodabalapur, Nature 404 (2000) 478.
[6] H.J. Bolink, E. Coronado, D. Repetto, M. Sessolo, Appl. Phys. Lett. 91 (2007) 223501.
[7] S.A. Haque, S. Koops, N. Tokmoldin, J.R. Durrant, J.S. Huang, D.D.C. Bradley, E. Palomares, Adv. Mater. 19 (2007) 683.
[8] N. Tokmoldin, N. Griffiths, D.D.C. Bradley, S.A. Haque, Adv. Mater. 21 (2009) 1.
[9] L. Wang, B. Liang, F. Huang, J. Peng, Y. Cao, Appl. Phys. Lett. 89 (2006) 151115.
[10] Y. Jin, G.C. Bazan, A.J. Heeger, J.Y. Kim, K. Lee, Appl. Phys. Lett. 93 (2008) 123304.
[11] N. Glezos, P. Argitis, D. Velessiotis, C.D. Diakoumakos, Appl. Phys. Lett. 83 (2003) 488.
[12] M.T. Pope, A. Muller, Angew. Chem., Int. Ed. Engl. 30 (1991) 34.
[13] D.-L. Long, E. Burkholder, L. Cronin, Chem. Soc. Rev. 36 (2007) 105.
[14] A. Hiskia, A. Mylonas, E. Papaconstantinou, Chem. Soc. Rev. 30 (2001) 62.
[15] D. Velessiotis, N. Glezos, V. Ioannou-Sougleridis, J. Appl. Phys. 98 (2005) 084503.
[16] A.M. Douvas, E. Makarona, N. Glezos, P. Argitis, J.A. Mielczarski, E. Mielczarski, ACS Nano 2 (2008) 733.
[17] H.J. Bolink, E. Coronado, D. Repetto, M. Sessolo, E.M. Barea, J. Bisquert, G. Garcia Belmonte, J. Prochazka, L. Kavan, Adv. Funct. Mater. 18 (2008) 145.
[18] H. Yan, B.J. Scott, Q. Huang, T.J. Marks, Adv. Mater. 16 (2004) 1948.
[19] Q. Niu, Y. Zhou, L. Wang, J. Peng, J. Wang, J. Pei, Y. Cao, Adv. Mater. 20 (2008) 964.
[20] M. Shakutsui, H. Matsuura, K. Fujita, Org. Electron. 10 (2009) 834.
[21] M.C. Gather, M. Flammich, N. Danz, D. Michaelis, K. Meerholz, Appl. Phys. Lett. 94 (2009) 263301.
[22] D. Kabra, M.H. Song, B. Wegner, R.H. Friend, H.J. Snaith, Adv. Mater. 20 (2008) 2008.

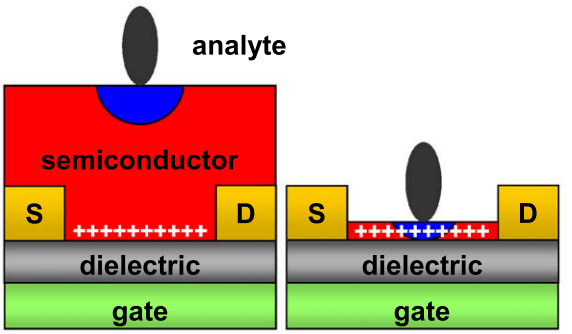

Fig. 1. Schematic representation of the operation principle of a SAMFET sensor. The transistor consists of an organic semiconductor, a source and drain electrode, a gate dielectric and a gate. A conducting channel is formed at the semiconductor gate dielectric interface. On the left side, analyte molecules are absorbed on top of a thick semiconductor layer. The current modulation is limited by the thickness of the semiconductor. The electrostatic interactions are stronger when the distance between the analyte and the channel is decreased. Hence a monolayer thick semiconductor (right) yields the ultimate sensing performance.

detection of NO. The operation principle is elucidated in Fig. 1. The left side shows a standard organic field-effect transistor consisting from top to bottom of an organic semiconductor, a source and drain electrode, a gate dielectric and a gate. Upon applying a bias to the gate, charge carriers are accumulated at the gate dielectric-semiconductor interface. A conducting channel is formed with a thickness of approximately 1–2 nm [12]. Analyte molecules absorbed on top of the semiconductor can modulate the charge transport in the channel by electrostatic interactions. However, it has been demonstrated by Huang et al. [13] that the sensitivity of such a sensor is dependent on the thickness of the active layer. The response of organic transistors to nerve agent simulants increased dramatically with decreasing layer thickness, due to the strong distance dependence of the electrostatic interactions. Torsi et al. [14] have reported chiral sensors and argue that the sensing is restricted to the conducting channel. The sensitivity did not increase with decreasing layer thickness but this could be due to the granular nature of the semiconducting films. Finally, sensitivity enhancement of up to an order of magnitude has been reported in transistors by using ultra thin semiconducting films [15]. Hence a semiconductor of only one monolayer thickness should yield the most sensitive gas sensor, as shown in Fig. 1 on the right.

A SAMFET has recently been reported by Smits et al. [16]. The monolayer consists of molecules with a semiconducting quinquethiophene core and an aliphatic spacer that is attached to the gate dielectric with a monofunctional anchoring group. The chemical structure of chloro[11-($5''''$-ethyl-$2,2':5',2'':5'',2''':5''',2'''':5''''$-quinque thien-5-yl)undecyl]dimethylsilane is shown in the inset of Fig 2. The SAMFETs were fabricated on heavily doped *n*-type Si wafers, acting as common gate electrode, with a 1000 nm thermally oxidized SiO_2 layer as gate dielectric. Gold source and drain electrodes were defined by conventional photolithographic methods, resulting in ring transistors with a channel length of 10 μm and a width

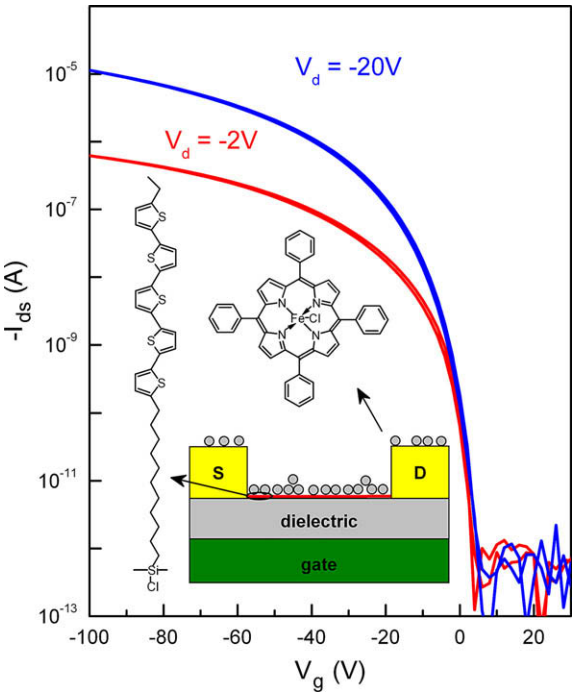

Fig. 2. Transfer characteristics of a typical SAMFET in vacuum with a 1 μm SiO_2 gate dielectric in the linear and saturated regime. The device exhibited *p*-type behavior with a pinch off voltage around 0 V. The inset shows a schematic cross-section of the SAMFET sensor. The chemical structures of the SAM molecule (left) and the NO receptor Fe(TPP)Cl (above) are shown.

of 2500 μm. Semiconducting monolayers were self-assembled from a toluene solution on a HF activated SiO_2 dielectric, as described previously [16]. The SAMFETs were annealed in vacuum at 110 °C for one hour to remove residual water and solvents. Electrical measurements were performed under vacuum using an Agilent 4155B semiconductor parameter analyzer. Possible gate bias stress effects in the electrical measurements were prevented by using a short integration time of less than 1 ms per step. A typical transfer curve is presented in Fig. 2. The mobility is about 0.01 cm^2/Vs and the current modulation six decades, in good agreement with previous reports.

The response of the SAMFETs was measured by admitting small amounts of NO, diluted in nitrogen carrier gas, to the closed chamber. The gas pressure in this static system was used to calculate the partial NO concentration at 1 bar. The response of the SAMFET itself to NO is indistinguishable from random drift of the threshold voltage. To make the SAMFET specific for NO, a porphyrin receptor was used. Porphyrins are known to bind NO in *e.g.* biological systems [17]. Here we used iron^{III} tetraphenylporphyrin chloride (Fe(TPP)Cl, Sigma Aldrich), that was previously used to detect NO in solution with a molecular controlled semiconductor resistor [18]. In the ideal case this receptor is grafted on, or incorporated into, the monolayer. Here, to demonstrate the concept, we used a thin spin coated film. The porphyrin receptor was dissolved in toluene, 1.6 mg/ml, and thin layers were spin coated at 800 rpm. The films

are only 10 nm thick and they contain a lot of pinholes. Therefore the diffusion of the nitric oxide is not limiting the detection rate. The addition of porphyrin on the SAMFET had no significant influence on the performance of the SAMFET. The chemical structure and the device layout are schematically depicted in the inset of Fig. 2.

The transfer curve of the SAMFET with the porphyrin shifts upon exposure to NO. We observe that the field-effect mobility remains unaffected; the only effect is a change in the threshold voltage towards positive gate bias. This clearly points to an increase of fixed negative interface charges upon exposure to NO. However, the reaction is not instantaneous, the threshold voltage shifts with time. A typical example is presented in Fig. 3. A possible reason might be the slow supply of negatively charged minority carriers needed to convert NO into NO_x^-, an effect that is presently under study. The threshold voltage shift takes about half an hour to saturate. Hence, in order to arrive at a dose response curve, the transfer curves were measured 30 min after NO exposure. To exclude any influence of competing charging effects, the threshold voltage of the SAMFET was monitored in the absence of NO. This measurement did not reveal a change of threshold voltage in time. The response to NO of the SAMFET without porphyrin was also investigated. These reference measurements are shown in Fig. 3. Only the combination of the SAMFET and the receptor in NO atmosphere yields a shift in threshold voltage.

We made many sensors and investigated the response to NO. Fig. 3 discussed above showed a typical measurement for 2.7 ppm NO. Concentrations in the ppm regime can reproducibly be detected. In exceptional cases however a much higher sensitivity has been measured. An example is presented in Fig. 4 where the transfer curves measured in the linear regime are presented on a linear scale as a function of the NO concentration. The transfer

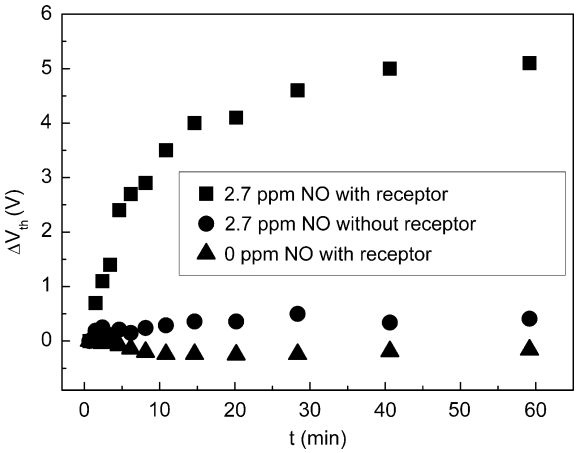

Fig. 3. The response of the SAMFET sensor as a function of time for a fixed NO concentration (2.7 ppm). The threshold voltage shifts towards more positive voltages and saturates after approximately 30 min. Reference measurements of the SAMFET without the porphyrin in NO (2.7 ppm) and the SAMFET with porphyrin in absence of NO are included. Only the combination of the SAMFET and the receptor in NO shows a threshold voltage shift that stands out over random drift.

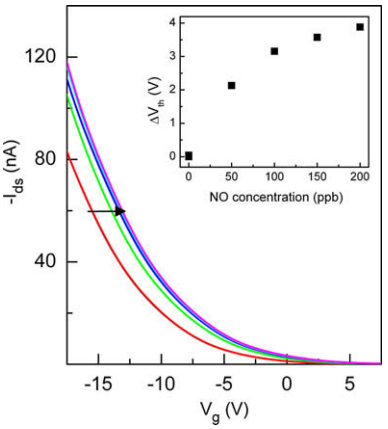

Fig. 4. Linear plot of the transfer characteristics of the SAMFET sensor. The measurements performed in vacuum and nitrogen were identical. The transfer curve measured 30 min after exposure is shifted towards positive values for increasing NO concentrations. The inset shows the threshold voltage shift as a function of NO concentration. The detection limit is as low as sub 100 ppb NO.

curve systematically shifts to positive gate biases with increasing NO content. The relative threshold voltage shift, ΔV_{th}, was determined by taking the gate biases yielding a fixed source drain current of 60 nA, as indicated by the arrow in Fig. 4. The shifts are used to construct a dose response curve. The inset shows the threshold voltage shift as a function of the NO concentration. The dose response curve shows that with the SAMFET sensor ppb concentrations of NO can be detected. The achieved sensitivity compares favorably with an earlier reported detection limit of an NO sensor based on a field-effect transistor [19].

The magnitude of the shift and the functional dependence such as the apparent saturation at high NO content are not yet quantitatively understood. Various operation mechanisms have been reported. For instance Fe(TPP)Cl has been attached to functionalised GaAs surfaces [18]. The current was measured upon exposure to NO in aqueous buffer solution. The current did increase with NO content. The change in current was explained as originating from a change in dipole moment of the Fe(TPP)Cl complex. However a threshold voltage shift in a field-effect transistor cannot be explained with only a change in surface dipole moment [20]. A different reaction mechanism was proposed by Lin and Farmer [21]. In solution NO forms a complex with Fe(TPP), NO–Fe(TPP). Catalytic reaction of this nitrosyl-complex with free NO then yields amongst others NO_2 which is known to cause a shift in threshold voltage [22] presumably by formation of negative surface charges. Recently, ZnO chemiresistors have been functionalised with a comparable iron(III)porphyrin, *viz.* ferriprotoporphyrin IX chloride [23]. NO could be detected down to the ppm range. The operation is reported to be due to electron transfer from ZnO to the receptor. In summary, iron porphyrins could selectively react towards NO, but the microscopic mechanism is unknown.

The selectivity of the SAMFET sensor versus other vapors was investigated. Preliminary experiments show that the sensor is not sensitive to a variety of gases. No threshold

voltage shift was observed for non-oxidizing agents as toluene (8 ppm), methanol (%) and ammonia (2 ppm). Even for oxidizing agents as O_2 and SO_2 the threshold voltage shift is negligible showing the selectivity of the porphyrin towards these gases. Reversibility of the sensor after NO detection was also examined. Full recovery of the sensor is achieved by annealing under vacuum conditions at 110 °C for 1 h. Under those conditions the threshold voltage returns to its pristine value. Our explanation is that the threshold voltage shift upon NO exposure is due to the formation of NO_x^-. At elevated temperature the equilibrium shifts to neutral nitrogen oxides that subsequently desorb from the surface. This could explain the full reversibility. A major problem still to be resolved is that a significant spread in the NO response was found for the numerous investigated SAMFET sensors. The differences can be due to imperfections in the monolayer, variations in the porphyrin converter deposition, or parasitic reactions with residual water. The latter becomes more important at lower NO content. The parameter spread is the focus of current research.

In summary, the response of a field-effect sensor is dominated by the electrostatic interactions between analyte and the conducting channel. In a self-assembled monolayer field-effect transistor the semiconductor is only one molecule thick, making it highly suited for sensing applications. SAMFETs sensors were fabricated using iron porphyrin as a specific receptor for the biomarker NO. The transfer curve systematically shifts to positive gate biases with increasing NO content. Dose response curves were obtained by plotting the threshold voltage shift as a function of NO concentration. High sensitivity was demonstrated by detecting parts per billion concentrations NO.

Acknowledgements

We gratefully acknowledge technical assistance from T. Geuns and financial support from the Zernike Institute for Advanced Materials, The Dutch Organization for Scientific Research (NWO) and from the EC (Project ONE-P No. 212311).

References

[1] I. Gaillard, S. Rouquier, D. Giorgi, Olfactory receptors, Cell. Mol. Life Sci. 61 (2004) 456–469.
[2] F. Rock, N. Barsan, U. Weimar, Electronic nose: current status and future trends, Chem. Rev. 108 (2008) 705–725.
[3] K.J. Albert, N.S. Lewis, C.L. Schauer, G.A. Sotzing, S.E. Stitzel, T.P. Vaid, D.R. Walt, Cross-reactive chemical sensor arrays, Chem. Rev. 100 (2000) 2595–2626.
[4] B.I. Jugdutt, The Role of Nitric Oxide in Heart Failure, Kluwer Academic Publishers, Boston, Massachusetts, 2004.
[5] J.L. Puckett, S.C. George, Partitioned exhaled nitric oxide to non-invasively assess asthma, Respir. Physiol. Neurobiol. 163 (2008) 166–177.
[6] T. Nagano, T. Yoshimura, Bioimaging of nitric oxide, Chem. Rev. 102 (2002) 1235–1269.
[7] A. Ciszewski, G. Milczarek, Electrochemical detection of nitric oxide using polymer modified electrodes, Talanta 61 (2003) 11–26.
[8] O. Kuzmych, B.L. Allen, A. Star, Carbon nanotube sensors for exhaled breath components, Nanotechnology 18 (2007) 375502.
[9] M. Gill, G.R. Graff, A.J. Adler, R.A. Dweik, Validation study of fractional exhaled nitric oxide measurements using a handheld monitoring device, J. Asthma 43 (2006) 731–734.
[10] J.T. Mabeck, G.G. Malliaras, Chemical and biological sensors based on organic thin-film transistors, Anal. Bioanal. Chem. 384 (2006) 343–353.
[11] L. Torsi, A. Dodabalapur, Organic thin-film transistors as plastic analytical sensors, Anal. Chem. 77 (2005) 380A–387A.
[12] C. Tanase, E.J. Meijer, P.W.M. Blom, D.M. de Leeuw, Local charge carrier mobility in disordered organic field-effect transistors, Org. Electron. 4 (2003) 33–37.
[13] J. Huang, J. Sun, H.E. Katz, Monolayer-dimensional 5,5′-bis(4-hexylphenyl)-2,2′-bithiophene transistors and chemically responsive heterostructures, Adv. Mater. 20 (2008) 2567–2572.
[14] L. Torsi, G.M. Farinola, F. Marinelli, M.C. Tanese, O.H. Omar, L. Valli, F. Babudri, F. Palmisano, P.G. Zambonin, F. Naso, A sensitivity-enhanced field-effect chiral sensor, Nat. Mater. 7 (2008) 412–417.
[15] R.D. Yang, T. Gredig, C.N. Colesniuc, J. Park, I.K. Schuller, W.C. Trogler, A.C. Kummel, Ultrathin organic transistors for chemical sensing, Appl. Phys. Lett. 90 (2007) 263506.
[16] E.C.P. Smits, S.G.J. Mathijssen, P.A. van Hal, S. Setayesh, T.C.T. Geuns, K. Mutsaers, E. Cantatore, H.J. Wondergem, O. Werzer, R. Resel, M. Kemerink, S. Kirchmeyer, A.M. Muzafarov, S.A. Ponomarenko, B. de Boer, P.W.M. Blom, D.M. de Leeuw, Bottom-up organic integrated circuits, Nature 455 (2008) 956–959.
[17] J.A. McCleverty, Chemistry of nitric oxide relevant to biology, Chem. Rev. 104 (2004) 403–418.
[18] D.G. Wu, G. Ashkenasy, D. Shvarts, R.V. Ussyshkin, R. Naaman, A. Shanzer, D. Cahen, Novel NO biosensor based on the surface derivatization of GaAs by "hinged" iron porphyrins, Angew. Chem. Int. Ed. 39 (2000) 4496–4500.
[19] F. Marinelli, A. Dell'Aquila, L. Torsi, J. Tey, G.P. Suranna, P. Mastrorilli, G. Romanazzi, C.F. Nobile, S.G. Mhaisalkar, N. Cioffi, F. Palmisano, An organic field effect transistor as a selective NOx sensor operated at room temperature, Sens. Actuat. B 140 (2009) 445–450.
[20] S.K. Possanner, K. Zojer, P. Pacher, E. Zojer, F. Schuerrer, Threshold voltage shifts in organic thin-film transistors due to self-assembled monolayers at the dielectric surface, Adv. Funct. Mater. 19 (2009) 958–967.
[21] R. Lin, P.J. Farmer, O atom transfer from nitric oxide catalyzed by Fe(TPP), J. Am. Chem. Soc. 123 (2001) 1143–1150.
[22] A. Das, R. Dost, T. Richardson, M. Grell, J.J. Morrison, M.L. Turner, A nitrogen dioxide sensor based on an organic transistor constructed from amorphous semiconducting polymers, Adv. Mater. 19 (2007) 4018–4023.
[23] C.C. Liu, J.H. Li, C.C. Chang, Y.C. Chao, H.F. Meng, S.F. Horng, C.H. Hung, T.C. Meng, Selective real-time nitric oxide detection by functionalized zinc oxide, J. Phys. D: Appl. Phys. 42 (2009) 155105.

the performance of OSCs based on other high performance electron donor materials [12,13]. These results may have been obtained due to unsatisfactory phase separation between the polymer donor and the fullerene acceptor, or due to the relatively low bulk charge carrier mobility of PQT-12. Recently, several selenium analogs of polythiophenes have been reported for optoelectronic applications, with higher mobilities than their sulfur analogs. For example, regioregular poly(3-hexylselenophene) (P3HS) [14], poly(9,9′-*n*-dioctylfluorene-alt-biselenophene) (F8Se2) [15], and poly(5,5′-bis(3-dodecylthiophene-2-yl)2-2′-biselenophene) (PDT2Se2) [16] revealed an order of magnitude larger field-effect mobility than their analogs, P3HT, poly(9,9-dioctylfluorene-co-bithiophene) (F8T 2), and PQT-12, when used as active layers in OFETs. Photovoltaic performance was also reported for the P3HS:PCBM blend [15]. In those reports, although the system was not optimized, high photovoltaic performances similar to those of a P3HT:PCBM device under identical conditions were obtained, indicating enhanced electron donor characteristics for the selenophene analogs.

In this paper, we describe the use of a selenium analog of PQT-12, PDT2Se2, blended with PCBM, as an electron donor material for BHJ photovoltaic cells. The blend ratio was optimized, yielding a PCE of 1.4% under AM 1.5 G illumination, 100 mWcm^{-2}, for a blend ratio of 1:4 w/w PDT2Se2:PCBM. This PCE is higher than the PCE reported for the PQT-12:PCBM system. A variety of structural and morphological analysis techniques were employed to predict the optimal fabrication conditions for this system. In addition, the space charge limited current (SCLC) behavior of both PDT2Se2 and PQT-12 sandwiched cells was characterized at several temperatures.

2. Results and discussion

The charge transport characteristics of PDT2Se2 and PQT-12 polymer thin films were compared by measuring the temperature-dependent SCLC behavior of the films. For hole-only currents, ITO/PEDOT:PSS/polymer/Au devices were fabricated. Fig. 1 shows the experimental *J–V* characteristics of hole-only devices made from PQT-12 and PDT2Se2 (film thickness, L = 120 nm) at several temperatures. SCLC behavior is described by the Mott–Gurney equation: [17]

$$J = \frac{9}{8}\varepsilon\varepsilon_0\mu\frac{E^2}{d} \tag{1}$$

where, J is the current density, ε_0 is the permittivity of a vacuum, ε is the relative permittivity of the polymer, μ is the mobility, E is the electric field, and d is the thickness of the layer. By fitting the experimental *J–E* curves to this equation and extrapolating to $E = 0$, we obtained the zero-field mobility, μ_0, and the temperature dependence of μ_0, as shown in Fig. 1. Although this law describes *J–V* characteristics at the low electric field limit, in the presence of larger electric fields it is generally observed that the value of J tends to be larger than is predicted by the above equation (Fig. 1). In such cases, the charge carrier mobility, μ, is not constant for a given electric field, but rather is described by the Poole–Frenkel equation [18],

$$\mu = \mu_\infty \exp\left(\frac{E_A}{k_T}\right)\exp(\gamma(T)\sqrt{E}) \tag{2}$$

where, μ_∞ is the mobility in the limit $T \to \infty$ and $E \to 0$, E_A is the activation energy, k is the Boltzmann constant, γ is the electric field coefficient for mobility, and E is the applied electric field. The dependence of the mobility on the electric field is generally observed for doped polymers, conjugated polymers, and organic glasses [19,20]. Therefore, we required a new *J–E* relationship that includes the effect of a non-constant field-dependent μ. Combining Eqs. (1) and (2), we obtained a relation for $J/E^{1/2}$ vs. $E^{1/2}$, which describes a linear relationship between log $(J/E^{1/2})$ and log $(E^{1/2})$ with coefficient γ:

$$\frac{J}{E^2} = \frac{9\epsilon\epsilon_0}{8d}\exp\left(-\frac{E_A}{kT}\right)\exp(\gamma(T)\sqrt{E}) \tag{3}$$

Fitting the experimental data to this combined equation yielded the electric field coefficients, γ, and the temperature dependence of these quantities for PQT-12 and PDT2Se2. The obtained values are plotted in Fig. 2, using the value of μ_0 obtained previously (Fig. 1). These results show that the substitution of a selenophene in place of a

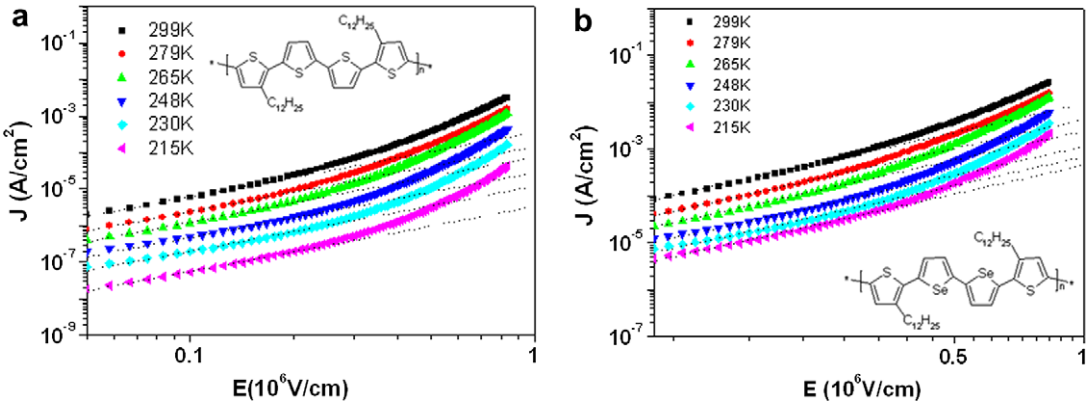

Fig. 1. Temperature-dependent *J–V* characteristics of (a) PQT-12 and (b) PDT2Se2 hole-only devices. The dashed line indicates the prediction of the SCLC model. The chemical structures of PQT-12 (a) and PDT2Se2 (b) are shown in the inset.

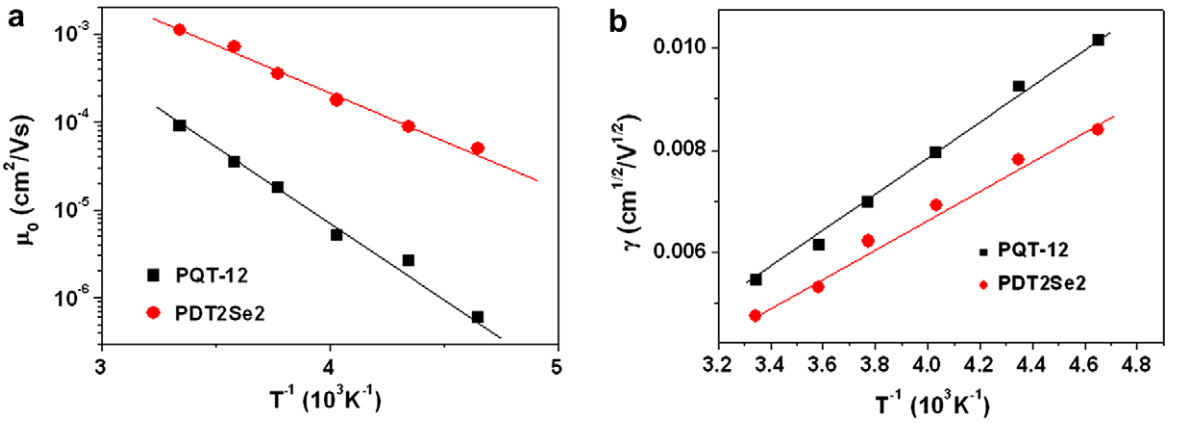

Fig. 2. Temperature dependence of (a) the zero-field mobility and (b) the electric field coefficient of PQT-12 and PDT2Se2. The straight lines indicate fits to the combined equation (Eq. (3)), as described in the manuscript.

polythiophene increased the (zero-field) mobility by an order of magnitude and decreased the temperature dependence of the mobility, or activation energy, which was determined by the trap distribution (E_A = 140 meV for PQT-12 and 92 meV for PDT2Se2). Likewise, both the field- and temperature-dependence of the mobility, γ, were lower in PDT2Se2 than in PQT-12. This behavior could be explained by Bässler's charge carrier hopping model in disordered organic semiconductors [21,22]. Systems with a large degree of energetic disorder have high energy barriers between adjacent hopping cites. High energy barriers create mobilities that are strongly dependent on the electric field, because the electric field can compensate for the energy barrier along the direction of charge carrier hopping. The temperature dependence of γ is also related to the energetic disorder, because the energy barrier between adjacent hopping cites may be difficult to overcome at lower temperatures. This behavior would be maximized in highly disordered systems. Therefore, the higher mobility and lower field dependence, activation energy, and temperature dependence of γ in PDT2Se2, relative to PQT-12, imply a lower degree of energetic disorder in PDT2Se2. Lower energetic disorder arises, structurally, from more effective interchain π–π overlap in PDT2Se2, generated by the introduction of the electron-rich selenophene. The values obtained for the activation energy and γ of PDT2Se2 were similar to those reported previously for poly(*p*-phenylene vinylene) derivatives [23,24].

To take advantage of the relatively high mobility and efficient π–π overlap in PDT2Se2, we fabricated photovoltaic cells by blending this polymer with PCBM and compared the results with those of PQT-12. Fig. 3 shows the UV–Vis absorption and photoluminescence spectra of the spin-coated films of homo PDT2Se2 and blended films. The absorption spectra of both films showed a maximum at 565 nm and a shoulder around 620 nm, indicative of a well-ordered inter-molecular packing structure. A trailing edge appeared in the near-IR region of the spectrum, resulting in an optical band gap of approximately 1.85 eV, which was slightly lower than the band gaps for P3HT and PQT-12 [1,10]. The electrochemical measurements revealed HOMO and LUMO levels of −5.1 eV and

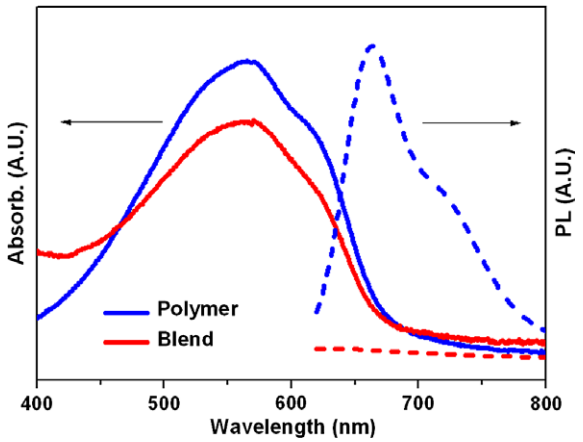

Fig. 3. UV–Vis absorption and PL spectra of spin-coated films of the PDT2Se2 homopolymer and a blend with PCBM.

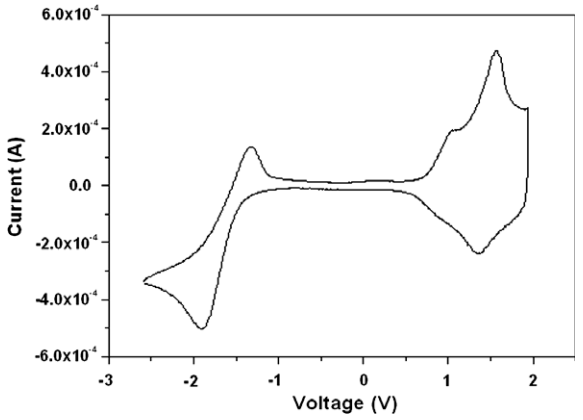

Fig. 4. Cyclic voltammogram of the spin-coated PDT2Se2.

−2.95 eV, respectively, yielding an electrochemical band gap of 2.15 eV (Fig. 4). The HOMO of PDT2Se2 was shifted slightly to lower values, by 100–200 meV, relative to that

of P3HT. Because there is a linear relationship between the donor-HOMO and acceptor-LUMO energy differences and the open circuit voltage (V_{OC}) of the bulk heterojunction devices [25], larger values of V_{OC} for PDT2Se2-based cells were expected. Efficient charge separation at the donor–acceptor interface requires an offset of ~0.3 eV between the donor-LUMO and acceptor-LUMO levels [26]. This energy level matching was present in the PDT2Se2:PCBM blend. Photoluminescence measurements on several films showed the effective quenching of PDT2Se2 emission due to the presence of PCBM in the film (Fig. 3). Quenching was attributed to a sufficient LUMO level difference between the donor and acceptor and the optimal morphology of the phase separation in blended films.

The *J–V* characteristics of the PQT-12:PCBM and PDT2Se2:PCBM blend (ratio from 1:1 to 1:4)-based photovoltaic cells are shown in Fig. 5, and the device performance parameters are summarized in Table 1. The best photovoltaic performances were obtained from blend ratios of 1:4 for both PQT-12 and PDT2Se2 cells, with a V_{OC} of 0.66 V, short circuit current (I_{SC}) of 2.7 mA cm^{-2}, fill factor (FF) of 29%, PCE of 0.53% for PQT-12:PCBM and with a V_{OC} of 0.69 V, short circuit current (I_{SC}) of 4.3 mA cm^{-2}, fill factor (FF) of 47%, PCE of 1.4% for PDT2Se2:PCBM, respectively. In accordance with the expectations from the HOMO level of PDT2Se2, a relatively large V_{OC} was obtained compared with those of PQT-12. (The V_{OC} of P3HT-based cells was <0.65 V. [26]) Although these photovoltaic parameters were still very low compared to conventional P3HT:PCBM based solar cells, it clearly shows that PDT2Se2 is much better electron donor material for photovoltaic cell than PQT-12, [13] Structural analyses were carried out to understand much better performances of PDT2Se2 compared to PQT-12 and their blend ratio dependence, by employing XRD recorded in grazing-incidence geometry. Fig. 6 shows out-of-plane XRD patterns of both homo polymers and polymer:PCBM blends with various ratios. Interestingly, diffraction spectra of both polymers are shifted to lower angle by blending with PCBM compared to their homo polymers. This inter-molecular expansion can be attributed to intercalation of the PCBM molecules between the side chains of the polymers [2]. One of the notable differences between two polymers is that PDT2Se2 shows significant decrease in the Bragg peak intensity by adding PCBM, while PQT-12:PCBM blend still shows intense peaks even for blend ratio of 1:4. In the case of PDT2Se2, no signatures of crystalline were observed for blend ratios of 1:3 and 1:4, implying the presence of a highly amorphous polymer lamellar structure. This means that the presence of excess fullerene effectively suppressed the crystallization of PDT2Se2 while PQT-12 could retain high crystalline nature. This structural difference can be attributed to two points. First, the molecular interactions for PDT2Se2-PCBM and PQT-12-PCBM are different. The surface energy of PCBM (34.2 mJ/m^2) is similar to that of PDT2Se2 (35.97 mJ/m^2) rather than that of PQT-12 [27]. (37.85 mJ/m^2) Therefore, more similar surface energies of PDT2Se2–PCBM resulted in rather homogeneous blends and low crystalline well-mixed films. Second, PQT-12 has highly interdigitated structure while PDT2Se2 does not have such highly interdigitated structure as can be shown from XRD results. The interlamellar backbone spacing in PDT2Se2 was determined from the Bragg equation to be 2.28 nm, which is longer than the spacing in PQT-12, 1.85 nm. Considering that the side chain length of C12 is about 1.6 nm, it is clear that the side chain of PDT2Se2 has lower degree of interdigitation than that of PQT-12. Therefore, crystalline structure of PDT2Se2 can be more easily disturbed by PCBM addition, leading to homogeneous state in blend system. Structural difference was also reflected in the morphology as shown in Fig. 7. Excellent miscibility between PDT2Se2 and PCBM was observed for

Table 1
Effects of PCBM content on I_{SC}, V_{OC}, FF and PCE of PQT-12:PCBM and PDT2Se2:PCBM blends.

	PQT-12/PCBM				PDTSe2/PCBM			
Blend ratio	1:1	1:2	1:3	1:4	1:1	1:2	1:3	1:4
Eff. (%)	0.26	0.31	0.37	0.53	0.76	0.9	1.4	1.36
J_{SC} (mA/cm^2)	2	2.2	2.2	2.7	3	3.4	4.3	4.3
V_{OC} (V)	0.53	0.53	0.64	0.66	0.63	0.64	0.67	0.69
FF (%)	25	27	27	29	40	40	47	46

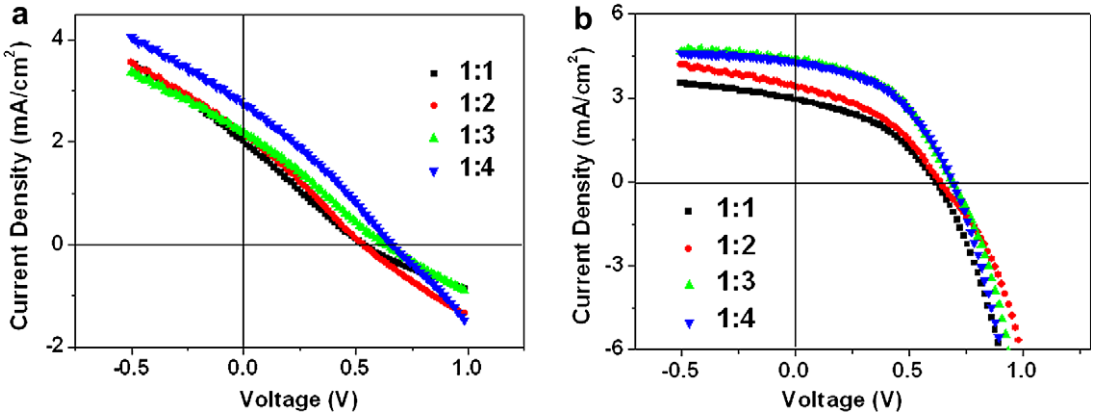

Fig. 5. Current density–voltage (*J–V*) characteristics of photovoltaic devices composed of (a) PQT-12:PCBM and (b) PDT2Se2:PCBM under 100 mW/cm^2 white light illumination.

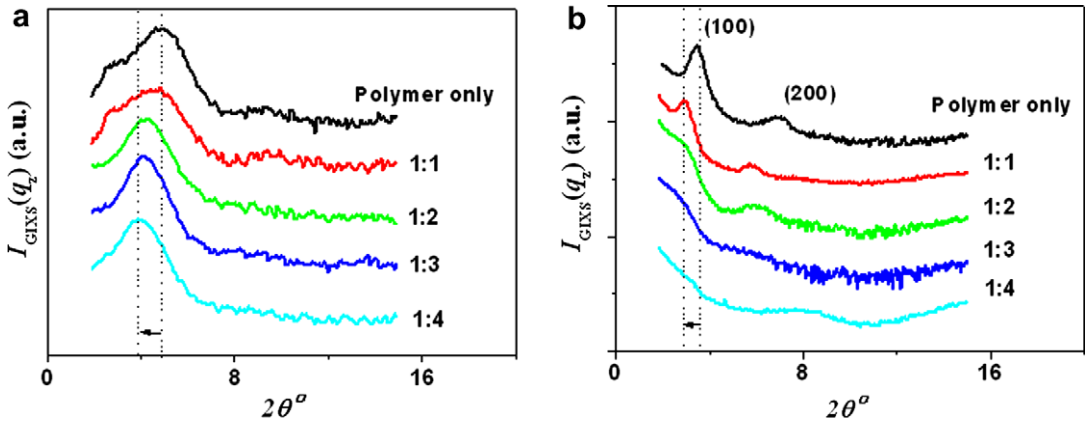

Fig. 6. GIXD images of thin films composed of the homopolymer and blends with PCBM of (a) PQT-12 and (b) PDT2Se2.

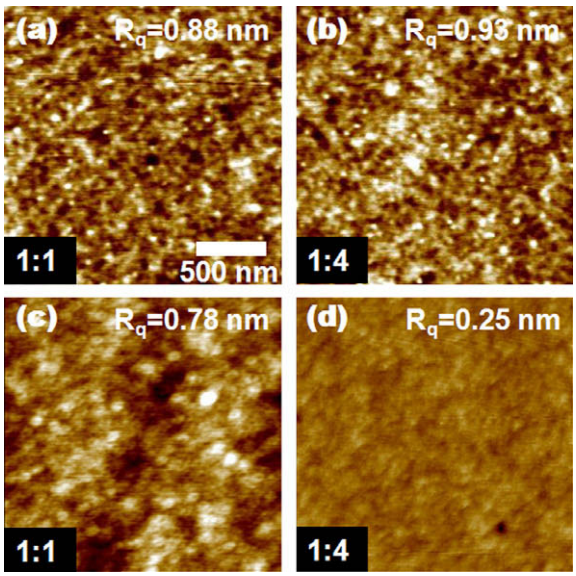

Fig. 7. AFM height images of the top surface of PQT-12:PCBM blend with ratio of (a) 1:1, (b) 1:4 and PDT2Se2:PCBM blend with ratio of (c) 1:1 and (d) 1:4.

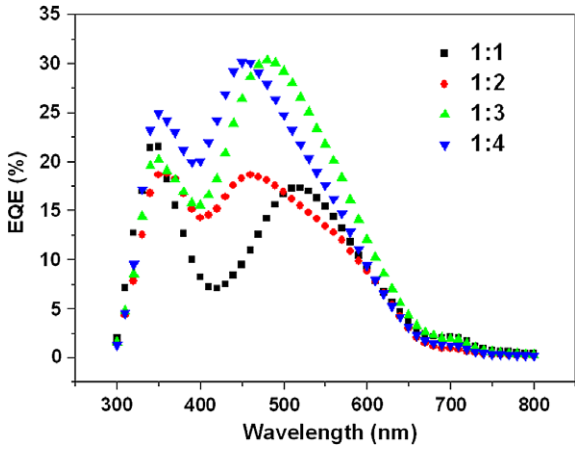

Fig. 8. IPCE spectra of PDT2Se2:PCBM devices with blend ratios of 1:1, 1:2, 1:3, and 1:4.

blend ratio of 1:4, with a low r.m.s. roughness of <0.3 nm while all the PQT-12:PCBM blends (Fig. 7(a) and (b)) and PDT2Se2:PCBM 1:1 blend (Fig. 7(c)) show large-scale phase separation with r.m.s roughness of >0.7 nm. Nanostructures that are optimized for efficient photovoltaic effects should fulfill two criteria: first, the phase separation should be small, comparable to the exciton diffusion length of 10 nm [28,29], to ensure charge separation at the donor–acceptor interface; second, a percolating pathway for both hole and electron charge carriers must exist for the transport of carriers to the respective harvesting electrode [24]. In other words, PDT2Se2:PCBM with blend ratio 1:4 has the domain sizes comparable to the exciton diffusion length (~10 nm), enabling sufficient donor–acceptor interfacial area. Formation of effective morphology by adding excess fraction of PCBM in PDT2Se2:PCBM system can also be observed by IPCE spectra as shown in Fig. 8. The spectral response extends from about 300 nm to 700 nm, indicating that both donor and acceptor contribute to the photocurrent. In terms of EQE, PDT2Se2:PCBM blend film with excess fraction of PCBM showed high EQE over 30%, showing good coincidence with previously obtained photovoltaic parameters, especially with J_{SC}. Therefore, we can see that the use of an excess weight fraction of PCBM in the PDT2Se2:PCBM BHJ system effectively suppress the domain size of the crystalline PDT2Se2 and generate homogeneous nanoscale phase separation, resulting in better photovoltaic performance compared to PQT-12:PCBM BHJ system. Unlike the P3HT:PCBM blend system, in which thermal annealing could be used to optimize the morphology, thermal annealing of the both PQT-12:PCBM and PDT2Se2:PCBM blend system at temperatures above 100 °C induced macrophase separation and a remarkable decrease in the photovoltaic performance. This behavior resulted from increased diffusive motion of the PCBM molecules within the polymer matrix, due to the significantly larger interchain spacings of both polymers, as described earlier [30].

3. Conclusion

PDT2Se2 blended with PCBM was investigated as an electron donor material for BHJ OSCs. This blend showed a higher bulk mobility and lower energetic disorder, as confirmed by temperature-dependent SCLC analysis. In contrast with P3HT:PCBM devices, PDT2Se2:PCBM devices showed optimum performances when an excess of PCBM was used, due to the large free volume present between the side chains of the polymer backbone. The PCE of an OSC composed of a blend of PDT2Se2 and PCBM (1:4, w/w) reached 1.4% under A.M. 1.5 G illumination, 100 mW cm^{-2}. This PCE was higher than those achievable using the PQT-12:PCBM system. Because the photovoltaic performance of this blend was much lower than the performance of P3HT:PCBM, further optimization is required.

4. Experimental

PDT2Se2 and PQT-12 were synthesized via Stille and oxidative coupling, as described previously [16]. PCBM (99%) used in this study was obtained from Aldrich. The PDT2Se2:PCBM blend solutions (weight ratios of 1:1, 1:2, 1:3, 1:4) were prepared in chlorobenzene at a concentration of 20 mg/mL. After cleaning the pre-patterned ITO-coated glass, PEDOT–PSS (Baytron P TP AI 4083, Bayer AG) was spin-coated to a thickness of 30–50 nm and annealed at 120 °C (for 60 min) in air. The active layer was spin-coated onto the PEDOT:PSS layer for 60 s to a thickness of 100 nm. Finally, lithium quinolate (Liq.) (0.6 nm)/Al (100 nm) cathodes were thermally deposited. The current density–voltage (*J–V*) characteristics were measured using Keithley 4200 source/measure units in the dark and under AM 1.5 G solar illumination (Oriel 1 kW solar simulator) with respect to the reference cell PVM 132 (calibrated at the National Renewable Energy Laboratory, NREL, at an intensity of 100 mW/cm^2).

UV–Vis and photoluminescence (PL) measurements were carried out on a UV–Vis–NIR spectrophotometer (Cary 5000: Varian Co. and FR 6500, JASCO CO.). Cyclic voltammetry measurements of the polymer films were performed on a BAS 100 B/W electrochemical analyzer in acetonitrile, with 0.1 M tetrabutylammonium perchlorate (Bu_4NClO_4) as the supporting electrolyte, at a scan rate of 100 mV/s. The potentials were measured against an Ag/AgCl reference electrode with ferrocene as the internal standard. The onset potentials were determined from the intersection of the tangents to the rising current and to the background current of the cyclic voltammogram. GIXD studies were performed using the 4C1 and 4C2 beam lines at the Pohang Accelerator Laboratory (PAL). The measurements were carried out with a sample-to-detector distance of 136 mm. Data were typically collected for ten seconds using an X-ray radiation source of λ = 0.138 nm with a 2D charge-coupled detector (CCD) (Roper Scientific, Trenton, NJ, USA). X-ray diffraction analysis for the one-dimensional diffraction pattern was performed at the 10C1 beam line (wavelength ~1.54 Å) at the (PAL).

AFM (Multimode IIIa, Digital Instruments), operated in tapping mode, was used to image the surface morphology of the photoactive layer.

Acknowledgments

This work was supported by a grant (F0004010-2008-31) from the Information Display R&D Center, one of the 21st Century Frontier R&D Program funded by the Ministry of Knowledge Economy of Korean Government and Basic Science Research Program through the National Research Foundation of Korea (NRF) funded by the Ministry of Education, Science and Technology (2009-0084786) and (2009-0079630).

References

[1] A.J. Moulé, K. Meerholz, Adv. Funct. Mater. 19 (2009) 3028.
[2] A.C. Mayer, M.F. Toney, S.R. Scully, J. Rivnay, C.J. Brabec, M. Scharber, M. Koppe, M. Heeney, I. McCulloch, M.D. McGehee, Adv. Funct. Mater. 19 (2009) 1173.
[3] Y.-T. Chang, S.-L. Hsu, M.-H. Su, K.-H. Wei, Adv. Mater. 21 (2009) 2093.
[4] C.-P. Chen, S.-H. Chan, T.-C. Chao, C. Ting, B.-T. Ko, J. Am. Chem. Soc. 130 (2008) 12828.
[5] J. Peet, J.Y. Kim, N.E. Coates, W.L. Ma, D. Moses, A.J. Heeger, G.C. Bazan, Nat. Mater. 6 (2007) 497.
[6] (a) J.Y. Kim, K. Lee, N.E. Coates, D. Moses, T.-Q. Nguyen, M. Dante, A.J. Heeger, Science 317 (2007) 222;
(b) J.Y. Kim, S.H. Kim, H.-Ho Lee, K. Lee, W. Ma, X. Gong, A.J. Heeger, Adv. Mater. 18 (2006) 572.
[7] W. Ma, C. Yang, X. Gong, K. Lee, A.J. Heeger, Adv. Funct. Mater. 15 (2005) 1617.
[8] M.D. Irwin, D.B. Buchholz, A.W. Hains, R.P.H. Chang, T.J. Marks, PNAS 105 (2008) 2783.
[9] Y.O. Wu, P. Liu, B.S. Ong, T. Srikumar, N. Zhao, G. Botton, S.P. Zhu, Appl. Phys. Lett. 86 (2005) 142102.
[10] B.S. Ong, Y. Wu, P. Liu, S. Gardner, Adv. Mater. 17 (2005) 1141.
[11] B.S. Ong, Y. Wu, P. Liu, S. Gardner, J. Am. Chem. Soc. 126 (2004) 3378.
[12] P. Vemulamada, H. Gong, T. Kietzke, A. Sellinger, Org. Electron. 9 (2008) 661.
[13] G. Wantz, F. Lefevre, M.T. Dang, D. Laliberte, P.L. Brunner, O.J. Dautel, Sol. Energy Mater. Sol. Cells 92 (2008) 558.
[14] (a) A.M. Ballantyne, L. Chen, J. Nelson, D.D.C. Bradley, Y. Astuti, A. Maurano, C.G. Shuttle, J.R. Durrant, M. Heeney, W. Duffy, I. McCulloch, Adv. Mater. 19 (2007) 4544;
(b) M. Heeney, W. Zhang, D. Crouch, D. Sparrowe, R. Hamilton, S. Higgins, P. Skabara, I. McCulloch, Chem. Commun. (2007) 5061.
[15] Y.M. Kim, E. Lim, I.-N. Kang, B.-J. Jung, J. Lee, B.W. Koo, L.-M. Do, H.-K. Shim, Macromolecules 39 (2006) 4081.
[16] H. Kong, D.S. Chung, I.-N. Kang, J.-H. Park, M.-J.I.H. Jung, C.E. Park, H.-K. Shim, J. Mater. Chem. 19 (2009) 3490.
[17] H.C.F. Martens, P.W.M. Blom, H.F.M. Schoo, Phys. Rev. B 61 (2000) 7489.
[18] P.W.M. Blom, M.J.M. de Jong, M.G. Munster, Phys. Rev. B 55 (1997) R656.
[19] D.M. Pai, J. Chem. Phys. 52 (1970) 2285.
[20] W.D. Gill, J. Appl. Phys. 43 (1972) 5033.
[21] H. Bässler, Phys. Status Solidi B 175 (1993) 15.
[22] A.J. Mozer, N.S. Sariciftci, A. Pivrikas, R. Ősterbacka, G. Juška, L. Brassat, H. Bässler, Phys. Rev. B 71 (2005) 035214.
[23] P.W.M. Blom, M.J.M. de Jong, S. Breedijk, Appl. Phys. Lett. 71 (1997) 930.
[24] L. Bozano, S.A. Carter, J.C. Scott, G.G. Malliaras, P.J. Brock, Appl. Phys. Lett. 74 (1999) 1132.
[25] G. Dennler, M.C. Scharber, T. Ameri, P. Denk, K. Forberich, C. Waldauf, C.J. Brabec, Adv. Mater. 20 (2008) 579.
[26] G. Dennler, M.C. Scharber, C.J. Brabec, Adv. Mater. 21 (2009) 1323.
[27] The surface energies of various films were determined from a geometric mean equation using the contact angles of distilled water and diiodomethane probe liquids.
[28] M. Theander, A. Yartsev, D. Zigmantas, V. Sundström, W. Mammo, M.R. Andersson, O. Inganäs, Phys. Rev. B 61 (2000) 12957.
[29] J.E. Kroeze, T.J. Savenije, M.J.W. Vermeulen, J.M. Warman, J. Phys. Chem. B 107 (2003) 7696.
[30] B.C. Thompson, B.J. Kim, D.F. Kavulak, K. Sivula, C. Mauldin, J.M.J. Fréchet, Macromolecules 40 (2007) 7425.

oligoquinoline derivatives [12] have been developed and subsequent attempts made to improve their EL properties. Among them, many researchers continuously strive to develop new, high efficient blue emitters because such derivatives provide excellent thermal- and electrochemical stabilities, as well as desirable photoluminescent properties [6]. For example, Park et al. have reported anthracene derivatives bearing bulky side groups with an excellent external quantum efficiency (EQE) of 7.18% and CIE coordinates of (0.156, 0.088) [13]. Additionally, anthracene derivatives bearing non-planar diarylsilyl groups with high EQE (6.3%) and good CIE coordinates (0.142, 0.149) have been reported by Char and coworkers [14]. In these studies, the bulky substituents provide steric hindrance that prevents intermolecular interactions and reduces self-quenching effects, leading to improved electroluminescent (EL) performance. These studies, as along with others [15], suggest that the structural features of the emitting materials are an important factor in EL performance. Meanwhile, the charge balance in the emitting layer is also a crucial factor towards improving EL performance. However, there have been few systematic studies on blue-emitting materials based on anthracene derivatives with different electronic properties and thus, charge transporting properties.

In this paper, we report highly efficient blue light-emitting materials based on the 10-naphthylanthracene core unit containing heteroaromatic moieties with different electronic properties: 2-(10-(naphthalen-2-yl)anthracen-9-yl)pyridine (**1**); 1-(10-(naphthalen-2-yl)anthracen-9-yl)isoquinoline (**2**); 9-(3-(10-(naphthalen-2-yl)anthracen-9-yl)phenyl)-9H-carbazole (**3**); 9-(4-(10-(naphthalen-2-yl)anthracen-9-yl)phenyl)-9H-carbazole (**4**); 9-(4-(10-(naphthalen-1-yl)anthracen-9-yl)phenyl)-9H-carbazole (**5**); 9-(4′-(10-(naphthalen-2-yl)anthracen-9-yl)biphenyl-4-yl)-9H-carbazole (**6**); 9-(4′-(10-(naphthalen-1-yl)anthracen-9-yl)biphenyl-4-yl)-9H-carbazole (**7**) (Scheme 1). In materials **1**–**4** and **6**, electron-withdrawing groups such as pyridine [16] and isoquinoline [17], and electron-donating groups such as carbazolylphenyl and carbazolylbiphenyl [18,19] were introduced into the 10-(naphthalen-2-yl)anthracene core to test the effects of anthracene side groups with different electronic properties on EL perfor-

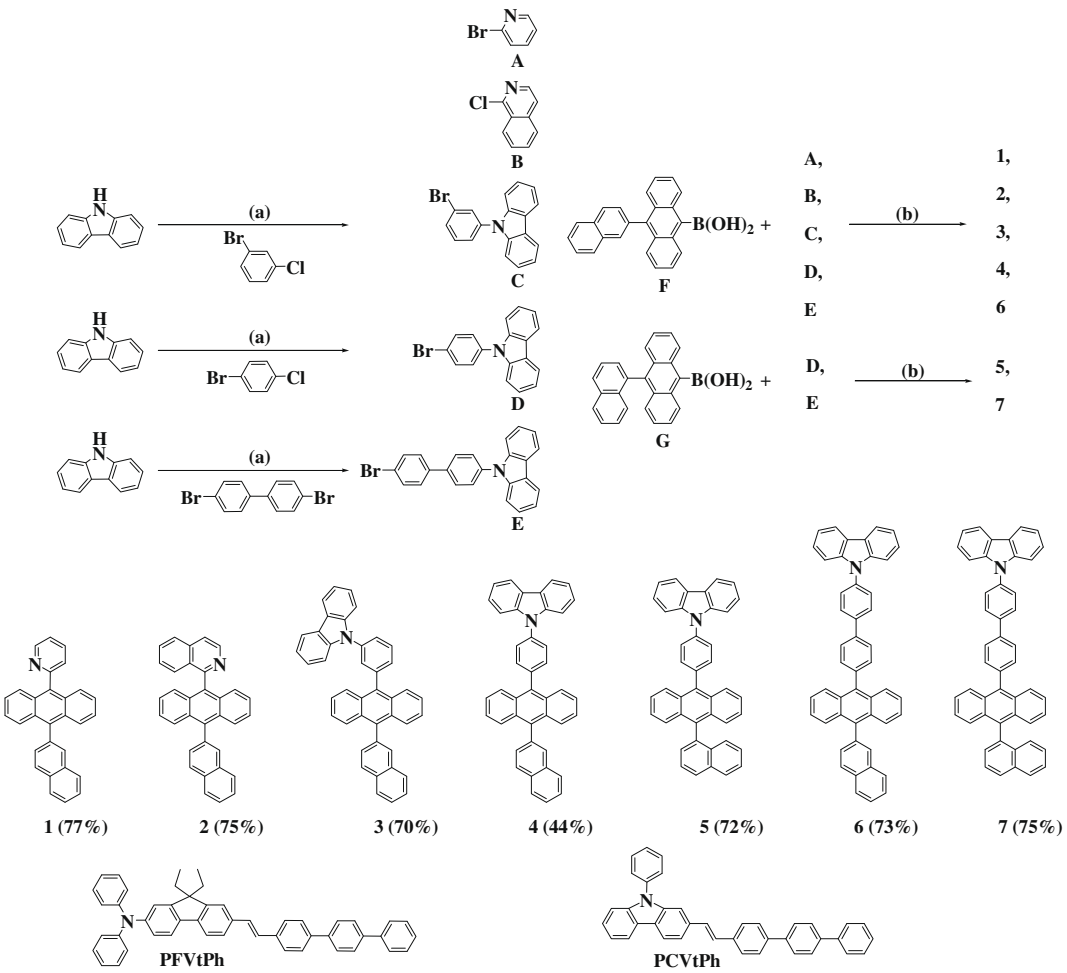

Scheme 1. Molecular structures and synthetic routes of new host materials (**1–7**). *Conditions*: (a) Cu, 18-Crown-6, K_2CO_3, 1,2-Dichlorobenzene, reflux, 24 h; and (b) $Pd(PPh_3)_4$, 2.0 M Na_2CO_3, toluene/EtOH, reflux, 4 h.

mance. Blue materials **5** and **7** bore a 10-(naphthalen-1-yl)anthracene core, instead of 10-(naphthalen-2-yl)anthracene, to study the differences in the EL performances between the 1- and 2-naphthylanthracene derivatives.

To investigate the EL properties of materials **1**–**7**, multilayered OLEDs were fabricated using these blue materials as the emitting layer (non-doped) and host material for 4′-[2-(2-diphenylamino-9,9-diethyl-9H-fluoren-7-yl)-vinyl]-*p*-terphenyl (**PFVtPh**) [20] and 3-(N-phenylcarba zol)vinyl-*p*-terphenyl (**PCVtPh**) [21] (doped). As will be demonstrated below, devices using materials **1**–**7** exhibited highly efficient blue emissions.

2. Experimental details

2.1. Materials and measurements

Carbazole, 1-bromo-3-iodobenzene, 1-bromo-4-iodobenzene, 4,4′-dibromobiphenyl, 2-bromopyridine (**A**), and 1-chloroisoquinoline (**B**) were used as received from Aldrich (City, State, Country) or TCI (City, State, Country). The 9-(3-bromophenyl)-9H-carbazole (**C**) [22], 9-(4-bromophenyl)-9H-carbazole (**D**) [23], 9-(4′-bromobiphenyl-4-yl)-9H-carbazole (**E**) [24], 9-(2-naphthyl)anthracene-10-boronic acid (**F**) [25], 9-(1-naphthyl)anthracene-10-boronic acid (G) [25], 4′-[2-(2-diphenylamino-9,9-diethyl-9H-fluoren-7-yl)vinyl]-*p*-terphenyl (**PFVtPh**) [20], and 3-(N-phenylcarbazol)vinyl-*p*-terphenyl (**PCVtPh**) [21] were synthesized as reported previously. All solvents were dried using standard procedures and all reagents were used as received from commercial sources, unless otherwise stated. All reactions were performed under a N_2 atmosphere.

The ^{1}H- and ^{13}C-NMR were recorded on a Varian Unity Inova 300Nb spectrometer. All FT-IR spectra were recorded using a Bruker VERTEX70 FT-IR spectrometer. Elemental analysis (EA) was measured using an EA 1108 spectrometer. Low- and high-resolution mass spectra were measured using a Jeol JMS-600 spectrometer in the EI mode and a JMS-T100TD (AccuTOF-TLC) in the positive ion mode.

2.2. General procedure for the Suzuki cross-coupling reaction

The 10-(naphthalen-2-yl)anthracen-9-yl-boronic acid (1.2 mol) or 10-(naphthalen-1-yl)anthracen-9-yl-boronic acid (1.2 mol) and the corresponding aryl halide derivatives (1.0 mol), $Pd(PPh_3)_4$ (0.04 mol), aqueous 2.0 M Na_2CO_3 (10.0 mol), ethanol, and toluene were mixed in a flask and refluxed for 4 h. After the reaction finished, the reaction mixture was extracted with ethyl acetate and washed with water. The organic layer was dried with anhydrous $MgSO_4$ and filtered with silica gel. The solution was then evaporated and the crude product re-crystallized from CH_2Cl_2/EtOH.

2.2.1. 2-(10-(Naphthalen-2-yl)anthracen-9-yl)pyridine (1)

Yield: 77%. ^{1}H-NMR (300 MHz, $CDCl_3$) [δ ppm]: 8.94 (d, J = 4.5 Hz, 1H), 8.07–7.90 (m, 5H), 7.71 (d, J = 8.4 Hz, 2H), 7.62–7.53 (m, 6H), 7.47 (td, J = 1.2, 6.2 Hz, 1H), 7.37–7.23 (m, 4H). ^{13}C-NMR (75 MHz, $CDCl_3$) [δ ppm]: 158.8, 150.5, 138.2, 136.8, 136.6, 135.6, 133.6, 133.0, 130.5, 130.4, 130.2, 130.0, 129.9, 129.6, 128.5, 128.4, 128.3, 128.2, 128.1, 127.4, 127.1, 126.7, 126.5, 126.4, 125.8, 125.4, 122.7. FT-IR [ATR]: ν = 3050, 1739, 1586, 1468, 785, 762, 748 cm^{-1}. MS(EI$^+$) m/z 381 (M$^+$). Anal. calcd for $C_{29}H_{19}N$: C 91.31, H 5.02, N 3.67; found: C 91.23, H 5.02, N 3.72.

2.2.2. 1-(10-(Naphthalen-2-yl)anthracen-9-yl)isoquinoline (2)

Yield: 75%. ^{1}H-NMR (300 MHz, $CDCl_3$) [δ ppm]: .8.86 (dd, J = 1.1, 5.9 Hz, 1H), 8.12–7.88 (m, 6H), 7.77–7.68 (m, 3H), 7.65–7.57 (m, 3H), 7.43–7.21 (m, 8H). ^{13}C-NMR (75 MHz, $CDCl_3$) [δ ppm]: 160.5, 143.3, 138.5, 136.8, 136.7, 136.6, 133.6, 133.0, 130.7, 130.6, 130.4, 130.3, 129.9, 129.7, 128.6, 128.5, 128.4, 128.3, 128.2, 128.1, 128.0, 127.9, 127.5, 127.2, 126.7, 126.5, 126.0, 125.4, 120.7. FT-IR [ATR]: ν = 3015, 1738, 1585, 1500, 761, 744 cm^{-1}. MS(EI$^+$) m/z 431 (M$^+$). Anal. calcd for $C_{33}H_{21}N$: C 91.85, H 4.91, N 3.25; found: C 91.73, H 4.95, N 3.19.

2.2.3. 9-(3-(10-(Naphthalen-2-yl)anthracen-9-yl)phenyl)-9H-carbazole (3)

Yield: 70%. ^{1}H-NMR (300 MHz, $CDCl_3$) [δ ppm]: 8.14 (d, J = 7.8 Hz, 2H), 8.06 (dd, J = 4.2, 5.4 Hz, 1H), 8.02–7.96 (m, 2H), 7.90–73 (m, 8H), 7.64–7.57 (m, 6H), 7.42 (t, J = 7.7 Hz, 4H), 7.35–7.29 (m, 4H). ^{13}C-NMR (75 MHz, $CDCl_3$) [δ ppm]: 141.2, 140.8, 138.1, 137.6, 136.6, 136.5, 136.0, 133.5, 132.9, 130.4, 130.3, 130.2, 130.1, 130.0, 129.8, 129.6, 129.5, 128.4, 128.3, 128.2, 128.1, 128.0, 127.4, 126.8, 126.6, 126.4, 126.2, 126.1, 125.7, 125.4, 123.7, 120.5, 120.3, 110.0. FT-IR [ATR]: ν = 3060, 1739, 1598, 1478, 763, 747 cm^{-1} MS(EI$^+$) m/z 545 (M$^+$). Anal. calcd for $C_{42}H_{27}N$: C 92.45, H 4.99, N 2.57; found: C 92.19, H 5.03, N 2.51.

2.2.4. 9-(4-(10-(Naphthalen-2-yl)anthracen-9-yl)phenyl)-9H-carbazole (4)

Yield: 44%. ^{1}H-NMR (300 MHz, $CDCl_3$) [δ ppm]: 8.22 (d, J = 7.8 Hz, 2H), 8.09 (d, J = 8.4 Hz, 1H), 8.05–8.01 (m, 2H), 7.95–7.92 (m, 1H), 7.86 (t, J = 9.0 Hz, 4H), 7.76 (t, J = 8.3 Hz, 4H), 7.69 (d, J = 8.1 Hz, 2H), 7.66–7.60 (m, 3H), 7.52 (td, J = 1.2, 7.8 Hz, 2H), 7.45 (td, J = 1.4, 7.6 Hz, 2H), 7.38–7.33 (m, 4H). ^{13}C-NMR (75 MHz, $CDCl_3$) [δ ppm]: 141.0, 138.4, 137.5, 137.2, 136.6, 136.3, 133.6, 133.0, 132.9, 130.4, 130.3, 130.1, 129.6, 128.3, 128.2, 128.1, 127.4, 127.1, 126.9, 126.6, 126.4, 126.2, 125.6, 125.4, 123.7, 120.6, 120.3, 110.1. FT-IR [ATR]: ν = 3062, 1739, 1598, 1479, 771, 749 cm^{-1}. MS(EI$^+$) m/z 545 (M$^+$). Anal. calcd for $C_{42}H_{27}N$: C 92.45, H 4.99, N 2.57; found: C 92.25, H 5.04, N 2.58.

2.2.5. 9-(4-(10-(Naphthalen-1-yl)anthracen-9-yl)phenyl)-9H-carbazole (5)

Yield: 72%. ^{1}H-NMR (300 MHz, $CDCl_3$) [δ ppm]: 8.22 (d, J = 7.5 Hz, 2H), 8.09 (d, J = 8.1 Hz, 2H), 8.04 (d, J = 8.1 Hz, 2H), 7.89 (d, J = 9.0 Hz, 2H) 7.86–7.82 (m, 2H), 7.80–7.69 (m, 4H), 7.60 (d, J = 6.6 Hz, 1H), 7.55–7.48 (m, 5H), 7.44 (d, J = 6.3 Hz, 1H), 7.40 (d, J = 5.1 Hz, 1H), 7.35 (d, J = 7.5 Hz, 1H), 7.30–7.22 (m, 4H). ^{13}C-NMR (75 MHz, $CDCl_3$) [δ ppm]: 141.1, 138.5, 137.4, 136.9, 135.8, 134.0, 133.8, 133.1, 130.9, 129.5, 128.5, 128.4, 127.5, 127.2, 127.0, 126.9, 126.6, 126.3, 125.9, 125.7, 125.6, 123.8, 120.7, 120.4, 110.2. FT-IR [ATR]: ν = 3061, 1597, 1479,

781, 740 cm^{-1}. MS(EI^+) m/z 545 (M^+). Anal. calcd for $C_{42}H_{27}N$: C 92.45, H 4.99, N 2.57; found: C 92.55, H 5.00, N 2.43.

2.2.6. 9-(4′-(10-(Naphthalen-2-yl)anthracen-9-yl)biphenyl-4-yl)-9H-carbazole (6)

Yield: 73%. ^{1}H-NMR (300 MHz, $CDCl_3$) [δ ppm]: 8.19 (d, J = 7.8 Hz, 2H), 8.10 (d, J = 8.7 Hz, 1H), 8.03–8.00 (m, 4H), 7.97–7.95 (m, 3H), 7.86–7.83 (m, 2H), 7.77–7.73 (m, 3H), 7.67–7.56 (m, 6H), 7.54(s, 1H), 7.48 (dd, J = 1.2, 6.9 Hz, 2H), 7.43 (dd, J = 1.2, 7.2 Hz, 1H), 7.40–7.31 (m, 6H). FT-IR [ATR]: v = 3058, 2360, 1600, 1479, 815, 741 cm^{-1}. MS(FAB^+) m/z 621 (M^+). HRMS-TOF (M^++H) Anal. calcd for $C_{48}H_{32}N$ 622.2535: found: 622.2508. Anal. calcd for $C_{48}H_{31}N$: C 92.72, H 5.03, N 2.25; found: C 92.52, H 5.03, N 2.25.

2.2.7. 9-(4′-(10-(Naphthalen-1-yl)anthracen-9-yl)biphenyl-4-yl)-9H-carbazole (7)

Yield: 73%. ^{1}H-NMR (300 MHz, $CDCl_3$) [δ ppm]: 8.20 (d, J = 7.8 Hz, 2H), 8.09 (d, J = 7.8 Hz, 1H), 8.05–8.01 (m, 2H), 8.00–7.92 (m, 3H), 7.87 (d, J = 8.7 Hz, 2H), 7.76–7.73 (m, 3H), 7.71–7.66 (m, 2H), 7.60 (d, J = 6.0 Hz, 1H), 7.56–7.53 (m, 3H), 7.50–7.45 (m, 4H), 7.41–7.38 (m, 2H), 7.35 (d, J = 6.9 Hz, 2H), 7.30 (d, J = 7.8 Hz, 2H), 7.26–7.22 (m, 2H). FT-IR [ATR]: v = 3047, 1626, 1453, 819, 746 cm^{-1}. MS(FAB^+) m/z 621 (M^+). HRMS-TOF (M^++H) Anal. calcd for $C_{48}H_{32}N$ 622.2535: found: 622.2522. Anal. calcd for $C_{48}H_{31}N$: C 92.72, H 5.03, N 2.25; found: C 92.66, H 5.03, N 2.21.

2.3. Physical measurements

The UV–Vis absorption and photoluminescence spectra of the newly designed host materials were measured in a CH_2Cl_2 solution (10^{-5} M) using a Shimadzu UV-1650PC and an Amincobrowman series 2 luminescence spectrometer. Fluorescent quantum yields were determined in the CH_2Cl_2 solution at 293 K against 9,10-diphenylanthracene as the standard (Φ = 0.90) [26]. The ionization potentials (or highest occupied molecular orbital (HOMO) energy levels) of the compounds were measured with a low-energy photo-electron spectrometer (Riken-Keiki, AC-2). Lowest unoccupied molecular orbital (LUMO) energy levels were estimated by subtracting the energy band gap from the HOMO energy levels. The energy band gap was determined by the on-set absorption energy from the absorption spectra of the materials. Thermal properties were measured using thermogravimetric analysis (TGA) (DTA-TGA, TA-4000) and differential scanning calorimeter (DSC) (Mettler Toledo; DSC 822) under N_2 at a heating rate of 10 °C/min. A heat-cool-heat method was used with an initial heating rate of 10 °C/min and rapidly quenched-cooled into liquid nitrogen and a final heating rate of 10 °C/min.

2.4. OLED fabrication and measurement

For fabricating OLEDs, indium-tin-oxide (ITO) thin films coated on glass substrates were used, which were 30 Ω square of the sheet resistivity and 100 nm thick. The ITO-coated glass was cleaned in an ultrasonic bath by the following sequence: acetone, methyl alcohol, distilled water, and stored in isopropyl alcohol for 48 h and dried with a N_2 gas gun. The substrates were treated by O_2 plasma under 2.0×10^{-2} torr at 125 W for 2 min [27]. All organic materials and metals were deposited under high vacuum (5×10^{-7} torr). The OLEDs were fabricated in the following sequence: ITO/4,4′-bis(*N*-(1-naphthyl)-*N*-phenylamino) biphenyl (NPB) (50 nm)/Blue-emitting materials (**1–7**) (30 nm)/4,7-diphenyl-1,10-phenanthroline (Bphen) (30 nm)/lithium quinolate (Liq) (2 nm) /Al (100 nm), NPB as the hole-transporting layer, Bphen as the electron-transporting layer, and Liq:Al as the composite cathode. The current density (J), luminance (L), luminous efficiency (LE), and CIE chromaticity coordinates of the OLEDs were measured with a Keithly 2400, Chroma meter CS-1000A. Electroluminance was measured using a Roper Scientific Pro 300i.

3. Results and discussion

3.1. Thermal properties

The thermal properties of **1–7** were measured by thermogravimetric analysis (TGA) and differential scanning calorimeter (DSC), and are listed in Table 1. The decomposition temperatures (T_d; corresponding to 5% weight loss)

Table 1
Optical properties of new host materials (**1–7**).

Compound	$T_d/T_g/T_m$ (°C)[a]	UV_{max} (nm)[b]	PL_{max} (nm)[b]	PL_{max} (nm)[c]	FWHM (nm)[d]	HOMO/LUMO (eV)	E_g (eV)	Φ[e]
1	320/95/278	375	431	432	59	−5.73/−2.67	3.06	0.75
2	343/127/298	375	418	442	57	−5.79/−2.71	3.08	0.57
3	370/129/312	376	419	443	52	−5.87/−2.76	3.11	0.73
4	386/153/272	377	427	449	54	−5.80/−2.70	3.10	0.76
5	364/154/325	375	421	434	54	−5.89/−2.78	3.11	0.78
6	467/157/417	377	427	440	54	−5.85/−2.77	3.08	0.70
7	416/168/384	376	420	443	52	−5.98/−2.87	3.11	0.70
MADN	397[f]/120[f]/255[f]	377	425	447[f]	54	−5.50[f]/−2.50[f]	3.0[f]	0.54

[a] T_d: the decomposition temperature (5% loss weight), T_g: the glass-transition temperature, T_m: the meting temperature.
[b] CH_2Cl_2 solution (10−5 M).
[c] Thin film.
[d] FWHM in solution.
[e] Using 9,10-diphenylanthracene as a standard; λ_{ex} = 360 nm (Φ = 0.90 in CH_2Cl_2).
[f] Ref. [10].

of all compounds were between 320 and 461 °C, indicating that thermal stability increases relative to the size of the substitution groups at the 10-position of the anthracene molecules. Moreover, **4** and **6**, having *para*-positioned carbazole and 2-naphthalene, exhibited a T_d higher than **3**, **5**, and **7** with *meta*-positioned carbazole or 1-naphthalene. Notably, the T_d of **6** was 60 °C higher than that of **4**. The glass temperatures (T_g) were observed for compounds **1**–**7** at 95, 127, 129, 153, 154, 157, and 158 °C, respectively, with DSC in the second heating scans. These results clearly reveal that compounds **4**–**7** possess good thermal stability, very desirable characteristic for OLEDs stability. Additionally, most compounds showed melting temperatures higher than 270 °C.

3.2. Optical properties

The optical properties for all compounds are summarized in Table 1. Fig. 1a shows the emission spectra of the blue materials (**1–7**), with the maximum emission peaks ranging from 418 to 431 nm in the deep-blue region. There was a slight blue-shift in the PL spectra of **5** and **7** compared to **4** and **6,** as well as **2** and **3** compared to **1** and **4**, respectively. This is likely due to a decrease in the π-conjugation length through the steric hindrance between 1-naphthalene and anthracene. Their full width at half maximum (FWHM) values ranged from 52 to 59 nm. The overall quantum yields of all compounds, with the exception of **2**, were high values (Φ = 0.70–0.78). As such, these compounds make excellent candidates for use as efficient blue-emitting materials in OLEDs. As shown in Fig. 1b, the emission spectra in the thin films of **1**–**7** are red-shifted compared to those in the CH_2Cl_2 solution, owing to the solid-state effect [28].

From the spectra overlap between the absorption of **PFVtPh** and the emission of materials **1**–**7**, as shown in Fig. 1a, sufficient energy transfer from **1**–**7** to **PFVtPh** through a Förster energy transfer was expected, indicating that materials **1**–**7** acted as good host materials in OLED devices using **PFVtPh** as a dopant.

3.3. Estimation of the HOMO and LUMO energy levels

The HOMO energy levels of these materials were estimated by an AC-2 photoelectron spectrometer, indicating a HOMO energy level variation of −5.73 to −5.98 eV for **1**–**7**. The lowest unoccupied molecular orbital (LUMO) energy levels calculated by subtraction of the optical band gaps from the HOMO energy levels were between −2.67 and −2.87 eV, as shown in Fig. 2.

The optical energy band gaps (E_g) of **1–7** ranged from 3.06 to 3.11 eV, as determined from the absorption spectra. These compounds possessed higher energy band gaps than those of **PFVtPh** (2.82 eV) and **PCVtPh** (3.10 eV), implying that energy transfer from materials **1**–**7** to **PFVtPh** and **PCVtPh** through a Förster energy transfer was expected, indicating them as good host materials in OLED devices using **PFVtPh** as a dopant. Furthermore, employment of cyclic voltammetry (CV), using a three-electrode cell with ferrocene as the internal standard, allowed for estimation of the electrochemical behavior of **1** and **4**. During the anodic scan in acetonitrile, **4** exhibited a reversible oxidation process at 0.92 V $\left(E^{OX}_{1/2}\right)$, with an onset potential of 0.88 V. Upon the cathodic scan, a reversible reduction potential $\left(E^{red}_{1/2}\right)$ of −2.19 V, together with an onset potential of −2.08 V, was detected. However, **1**, with the electron-deficient pyridine moiety, exhibited an irreversible oxidation process with an $\left(E^{OX}_{onset}\right)$ value of 0.81 V, while the reversible reduction process indicated values of $\left(E^{red}_{1/2}\right)$ of −2.18 V, respectively. These observations demonstrated that introduction of an electron-rich carbazole unit in **4** moderately increased the oxidation potential, while only slightly changing its reduction potential. On the basis of the onset potentials of oxidation, the respective HOMO levels of **1** and **4** could be estimated to be 5.61 and 5.68, with regard to ferrocene (4.80 eV below vacuum). The electrochemical results are consistent the estimation of HOMOs energy levels by an AC-2 photoelectron spectrometer.

Interestingly, among materials **1**–**7**, material **1**, with the pyridine moiety (−5.73 eV), had the highest HOMO energy

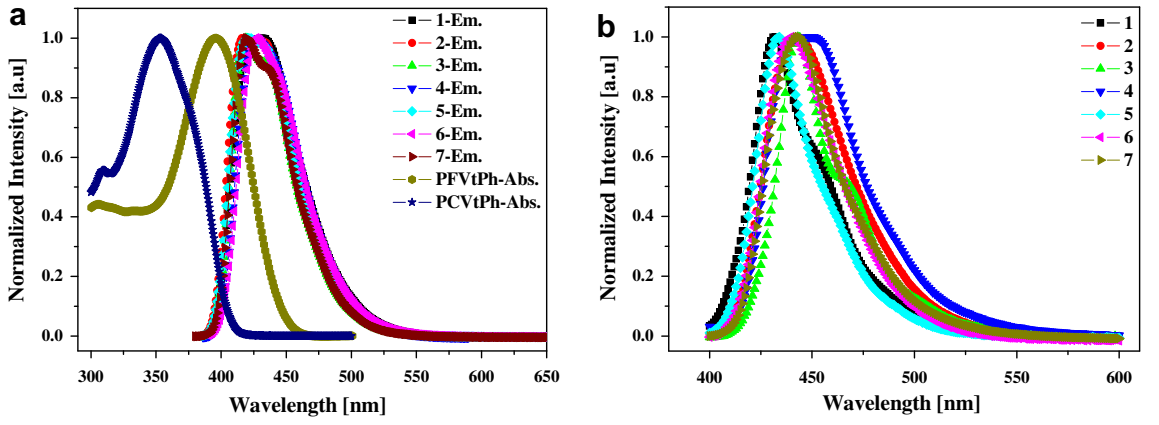

Fig. 1. (a) Emission spectra of host materials (**1**–**7**) and absorption spectra of dopant materials (**PFVtPh** and **PCVtPh**) in CH_2Cl_2; and (b) Emission spectra of **1**–**7** in thin film.

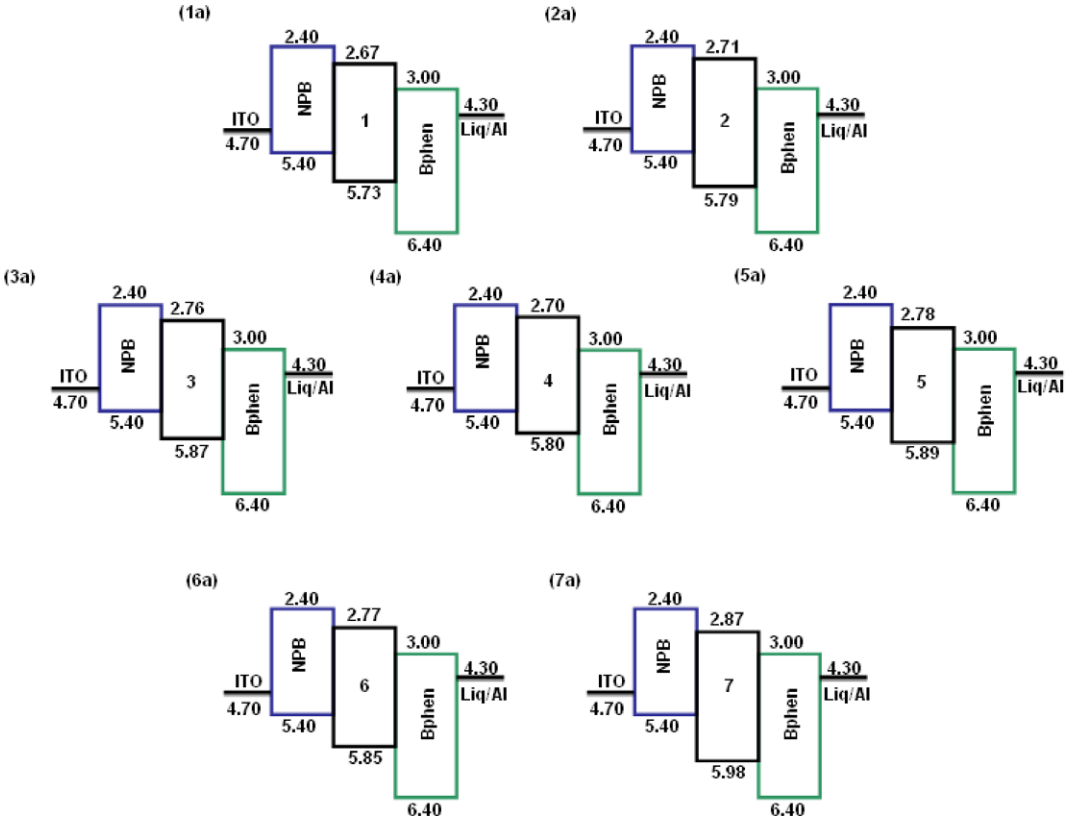

Fig. 2. Energy diagrams of non-doped devices **1a–7a**.

level. In order to investigate the origin of this observation, materials **1–4** were calculated using DFT calculations with a 6-31G* basis set level [29]. The respective highest occupied molecular orbital (HOMO) energy levels of **3** and **4** (both −5.211 eV) were lower than **1** (−5.101 eV) and **2** (−5.129 eV). This discrepancy can be explained by the HOMO shapes. The electron distributions of the HOMOs are shown in Fig. 3. In the HOMOs for **3**, **4**, the electrons are distributed over the anthracene, carbazole, and phenyl moieties, while in HOMOs **1** and **2**, the electrons are relatively localized over the anthracene moiety. Accordingly, the HOMOs for **3** and **4** show more delocalized electrons compared with **1** and **2**, and as such, the HOMO energies of **3** and **4** are lower than those of **1** and **2**.

3.4. Electroluminescence properties

The EL spectra of devices **1a–7a** showed deep-blue emissions with respective peaks at 441–454 nm, Fig. 4.

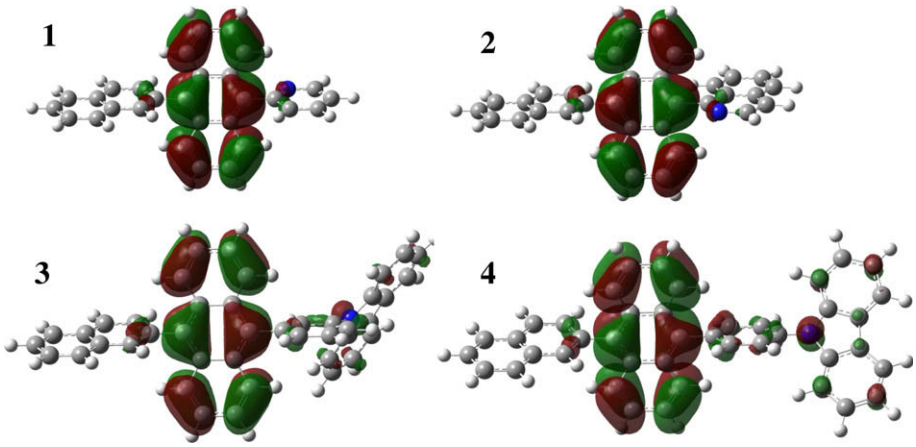

Fig. 3. The B3LYP/6-31G* calculated HOMOs for **1–4**.

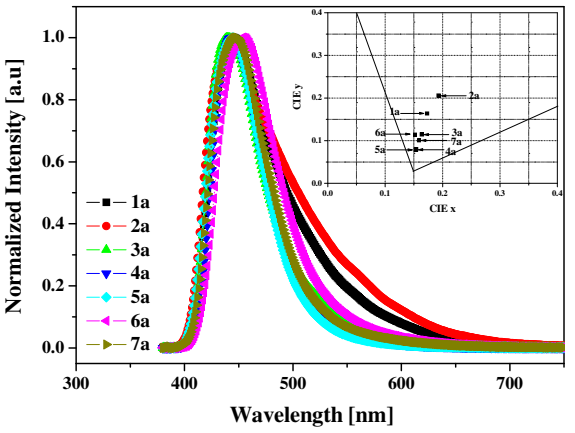

Fig. 4. EL spectra and the CIE coordinates at 8.0 V of non-doped devices **1a–7a**.

Interestingly, the EL spectra of devices **3a–7a**, using emitting materials with an electron-donating group (*N*-arylcarbazole), showed a narrower full-width at half maximum (FWHM) (ca. 16–34 nm) over devices **1a–2a**, using emitting materials with an electron-withdrawing group (pyridine, isoquinoline). Assumedly, in devices **3a–7a**, excimer and exciplex formations involving emitting materials are reduced since the *N*-aryl carbazole-substituted naphthylanthracene derivatives prevent intermolecular interactions. The red-shift emissions observed in devices **1** and **2** may not only be due to the excimer from the intermolecular interactions, but also derived from the exciplex in the device interfaces due to the miss-matched energy levels. Moreover, the CIE *x* and *y* coordinates of devices **3a** (0.164, 0.115), **4a** (0.154, 0.080), **5a** (0.153, 0.079), **6a** (0.152, 0.114), and **7a** (0.159, 0.101) were lower than devices **1a** (0.173, 0.164) and **2a** (0.193, 0.206) because of the narrow FWHM. In particular, the CIE coordinates of device **5a** (0.153, 0.079) were very close to the NTSC blue standard of (0.14, 0.08).

Fig. 5 shows the luminance–voltage–current density (*L–V–J*), luminous efficiencies (LE), power efficiencies (PE), and external quantum efficiencies (EQE) of devices **1a–7a**, respectively. The EL properties of devices **1a–7a** are summarized in Table 2, with all devices showing low turn-on voltages no greater than 4.5 V. The molecular structure and electronic properties of the blue materials can be correlated with device performances. First, devices **3a–7a**, using emitting materials with an electron-donating group (*N*-arylcarbazole), showed improved EL efficiencies, compared with devices **1a–2a** using emitting materials with an electron-withdrawing group (pyridine, isoquinoline). In devices **1a–2a**, excimer and exciplex formations involving emitting materials, appeared as shown in the EL spectra in Fig. 4. Presumably, these would contribute

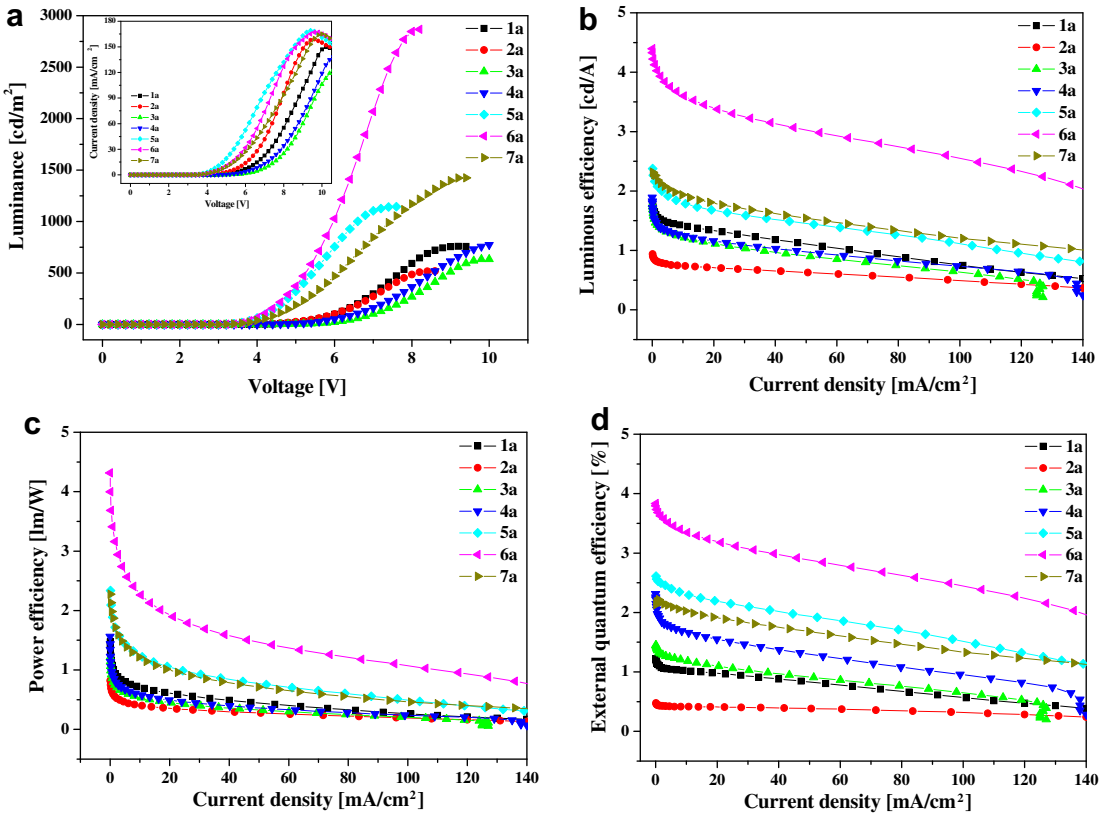

Fig. 5. (a) *L–V–J* characteristics; (b) luminous efficiencies; (c) power efficiencies; and (d) external quantum efficiencies as a function of current density for the devices **1a–7a**.

Table 2
EL performance characteristic of the devices **1a–7a** (non-doped).

Device	V_{on} (V)[a]	λ_{max}^{EL}, FWHM (nm)[b]	L (cd/m^2)[c]	J (mA/cm^2)[c]	LE (cd/A)[d/e/f/g]	PE (lm/W)[d/e/f/g]	EQE (%)[d/e/f/g]	CIE (x, y)[h]
1a	3.8	445, 74	759	150	1.78/1.33/1.45/1.18	1.47/0.61/0.76/0.49	1.22/0.98/1.03/0.88	(0.173, 0.164)
2a	3.6	444, 89	519	159	0.94/0.71/0.73/0.47	0.82/0.35/0.38/0.18	0.48/0.41/0.41/0.30	(0.193, 0.206)
3a	4.5	441, 58	634	127	1.78/1.12/1.25/0.85	1.21/0.45/0.56/0.30	1.45/1.11/1.21/0.86	(0.164, 0.115)
4a	4.1	444, 55	773	147	1.90/1.16/1.27/0.95	1.56/0.49/0.60/0.35	2.31/1.55/1.69/1.26	(0.154, 0.080)
5a	3.0	444, 58	1144	157	2.38/1.67/1.92/1.58	2.33/1.05/1.43/0.92	2.61/2.19/2.40/2.10	(0.153, 0.079)
6a	3.2	454, 64	2860	154	4.40/3.40/3.93/3.52	4.31/1.92/2.94/2.13	3.83/3.20/3.57/3.29	(0.152, 0.114)
7a	3.1	447, 61	1425	136	2.31/1.80/2.03/1.73	2.27/1.00/1.39/0.90	2.27/1.91/2.09/1.85	(0.159, 0.101)
MADN	4.0	442, 55	954	154	1.35/1.08/1.13/0.96	1.01/0.48/0.56/0.37	1.65/1.45/1.52/1.29	(0.153, 0.080)

[a] Turn-on voltage at 1 cd/m^2.
[b] Emission maximum and FWHM of EL emission spectra.
[c] Maximum luminance and current density.
[d] Maximum values.
[e] At 20 mA/cm^2.
[f] At 100 cd/m^2.
[g] At 500 cd/m^2.
[h] Commission Internationale de L'Énclairage (CIE) coordinates at a 8.0 V.

to the reduced EL properties of devices **1a–2a** by a self-quenching effect. Interestingly, the EL performances of device **2a** are much worse than those of device **1a**. In the EL spectra in Fig. 4, the FWHM of device **2a** was wider than that of device **1a**. This observation indicates that excimer and exciplex formations in device **2a** are severe and thus, lead to the reduced EL efficiencies of device **2a**, as compared with device **1a**. In addition, the lower quantum yield of material **2** relative to material **1** could partially contribute to the reduced EL efficiencies of device **2a**, as compared with device **1a**.

Among devices **3a–7a** with an electron-donating group (*N*-arylcarbazole), device **6a** exhibited excellent EL performances; its luminous efficiency, power efficiency, and external quantum efficiency reached 4.40 cd/A, 4.31 lm/W, and 3.83% (3.40 cd/A, 1.92 lm/W, and 3.20% at 20 mA/cm^2), respectively. The EL efficiencies of device **6a** were twice as high as the common blue host material MADN. Compared to device **6a**, using emitting material **6** with a 2-naphthyl group at the 9-position of the anthracene core, device **7a**, using emitting material **7** with a 1-naphthyl group at the 9-position of the anthracene core, showed reduced EL efficiencies. Material **7** had HOMO and LUMO energy levels lower than material **1**, as shown in Table 1. These data imply that the hole-injection into the emitting layer of device **7a**, using **7**, was less effective than device **6a**, using **6**, because of the smaller barrier between the NPB (−5.4 eV) and **6** (−5.85 eV) than **7** (−5.98 eV). However, electron-injection into the emitting layer of device **7a**, using **7**, was more effective than device **6a**, using **6**, because of the smaller barrier

Table 3
EL performance characteristic of the devices **1b–7c** (doped).

Device	V_{on} (V)[a]	λ_{max}^{EL}, FWHM (nm)[b]	L (cd/m^2)[c]	J (mA/cm^2)[c]	LE (cd/A)[d/e/f/g]	PE (lm/W)[d/e/f/g]	EQE (%)[d/e/f/g]	CIE (x, y)[h]
1b	2.9	464, 68	11750	205	10.35/10.24/10.03/10.32	8.77/6.06/8.29/7.37	5.70/5.66/5.44/5.66	(0.163, 0.240)
2b	5.2	463, 75	2804	76	5.20/5.15/4.50/5.07	1.87/1.54/1.72/1.63	2.80/2.78/2.36/2.71	(0.173, 0.270)
3b	3.6	458, 62	5785	247	6.26/5.49/6.24/5.89	4.44/2.38/3.92/2.99	4.05/3.53/4.04/3.80	(0.156, 0.201)
4b	3.1	456, 58	6698	251	6.96/6.38/6.96/6.70	6.13/3.21/4.97/3.90	4.81/4.47/4.81/4.65	(0.153, 0.179)
5b	2.9	457, 59	8265	165	8.09/7.76/8.04/7.91	8.01/4.45/6.64/5.65	5.67/5.49/6.64/5.58	(0.150, 0.176)
6b	2.8	462, 63	7474	168	8.60/7.86/8.59/8.36	8.38/4.48/7.11/5.70	5.30/4.86/7.11/5.17	(0.155, 0.213)
7b	2.8	460, 59	8442	188	8.10/7.18/8.07/7.60	8.30/4.14/6.67/5.19	5.58/5.02/6.67/5.29	(0.148, 0.183)
1c	4.2	454, 97	716	39	2.99/2.15/2.34/2.10	2.13/0.75/1.02/0.71	1.74/1.35/1.44/1.33	(0.182, 0.211)
2c	3.3	451, 92	785	75	2.11/1.42/1.54/1.32	1.95/0.57/0.73/0.47	1.08/0.93/0.95/0.89	(0.182, 0.200)
3c	3.4	436, 61	1313	260	2.59/1.91/2.17/1.84	2.04/0.93/1.26/0.87	2.44/2.00/2.23/1.93	(0.159, 0.102)
4c	3.8	442, 55	1385	260	2.78/1.83/2.09/1.75	2.57/0.93/1.26/0.83	2.96/2.33/2.48/2.14	(0.154, 0.087)
5c	3.2	448, 63	1709	176	2.96/2.08/2.34/2.03	3.09/1.28/1.75/1.23	2.31/1.92/2.08/1.90	(0.175, 0.118)
6c	3.2	456, 64	2609	157	4.46/3.23/3.87/3.27	4.37/1.74/2.90/1.83	3.60/2.78/3.27/2.85	(0.157, 0.132)
7c	3.0	452, 64	1806	200	3.92/2.05/2.36/2.00	4.40/1.28/1.77/1.21	3.33/2.29/2.54/2.24	(0.153, 0.097)

[a] Turn-on voltage at 1 cd/m^2.
[b] Emission maximum and FWHM of EL emission spectra.
[c] Maximum luminance and current density.
[d] Maximum values.
[e] At 20 mA/cm^2.
[f] At 100 cd/m^2.
[g] At 500 cd/m^2.
[h] Commission Internationale de L'Énclairage (CIE) coordinates at a 8.0 V.

between the Bphen (−3.0 eV) and **7** (−2.87 eV) than **6** (−2.77). Presumably, the higher hole-injection barrier of device **7a** could play a crucial factor in the reduced EL efficiencies of device **7a**, due to the larger energy differences in the HOMO energy levels (0.14 eV) than the LUMO energy levels (0.10 eV) between **6** and **7**. In addition, compared to devices **6a**, devices **3a–5a** possessed reduced EL efficiencies. In these cases, there are no significant differences between the HOMO–LUMO energy levels, the quantum efficiencies, and the degree of molecular aggregation between materials **6** and **3–5**. Presumably, the changes of carrier mobility and carrier recombination rate in the emitting layers of the devices by subtle structural changes in emitting materials, would play important roles in variation of the EL efficiencies of devices.

In order to enhance EL efficiencies, these host materials (**1–7**) were doped with blue dopant materials (**PFVtPh** and **PCVtPh**) at 8% in the same device structure, respectively. The EL properties of devices **1b–7c** are summarized in Table 3. Notably, the EL efficiencies of the **b** devices, using

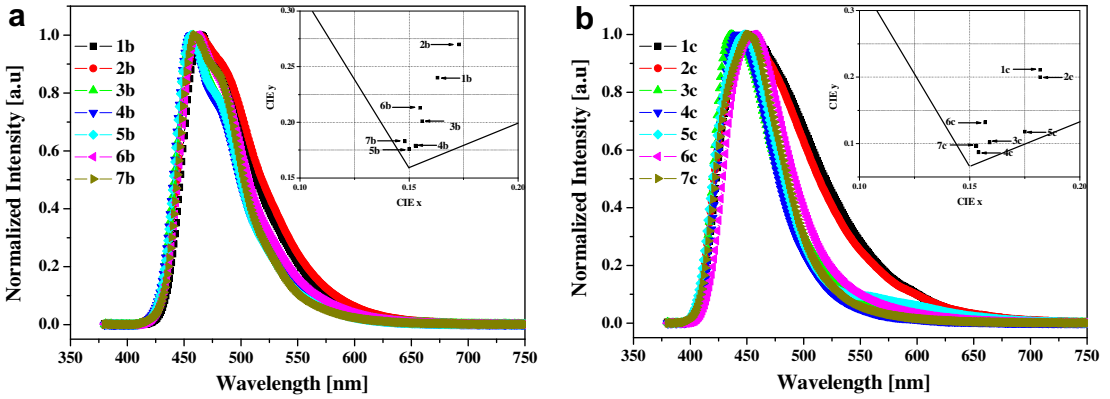

Fig. 6. EL spectra and CIE coordinates at 8.0 V of the doped devices; (a) **1b–7b**; and (b) **1c–7c**.

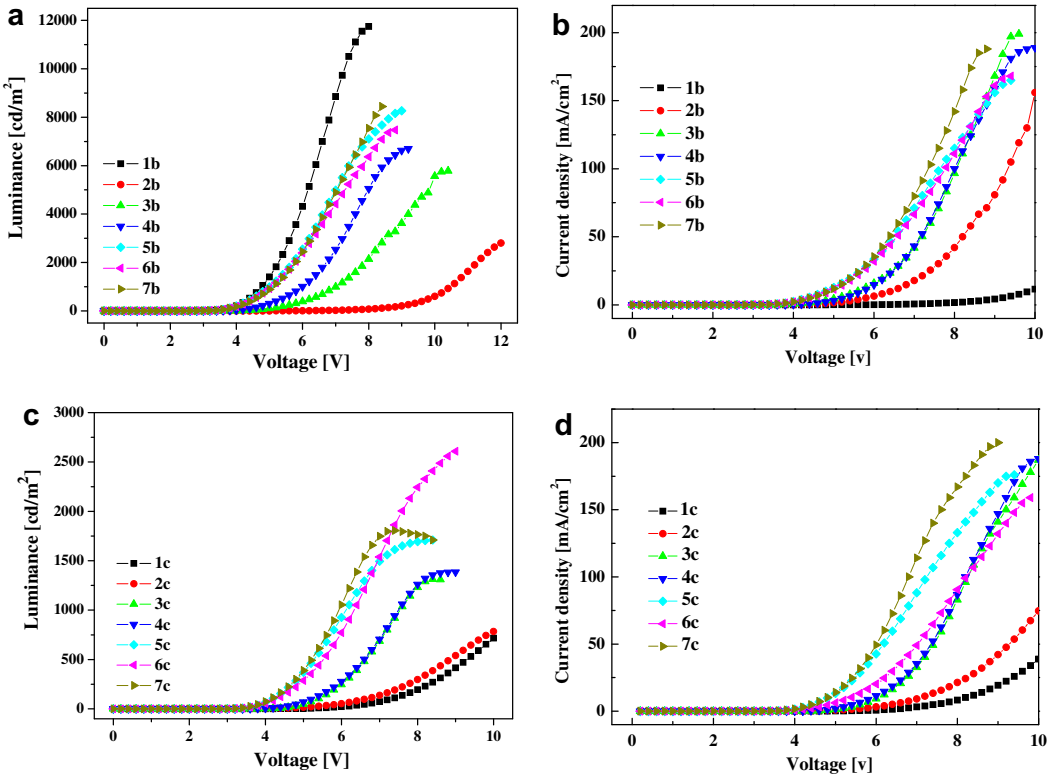

Fig. 7. *L–V–J* characteristics of the doped devices; (a) and (b) **1b–7b**; (c) and (d) **1c–7c**.

PFVtPh as a dopant, were more effective than those of the **c** devices that employed **PCVtPh** as a dopant. The electroluminescence in the host-dopant system can occur by the Förster-type energy transfer from the host to dopant [9]. It can be seen from Fig. 1a that the emission spectra of the host materials (**1–7**) overlapped better with the absorption spectra of **PFVtPh** than those of **PCVtPh**, demonstrating that **PFVtPh** can effectively accept energy from the host materials (**1–7**) by a Förster-type energy transfer and lead to improved EL efficiencies.

Fig. 6 shows the EL spectra of the **b** (8 wt.% **PFVtPh**-doped) and **c** devices (8 wt.% **PCVtPh**-doped). When dopant-doped, the devices using **3–7** also showed narrow bandwidths, as well as reduced CIE *x* and *y* coordinates when compared with the devices using **1** and **2**. The luminance–voltage–current density (*L–V–J*), luminous efficiencies, external quantum efficiency and power efficiency of the doped devices (**1b–7c**) are shown in Figs. 7 and 8, respectively. Compared to the corresponding non-doped devices, all **b** devices using **PFVtPh** as a dopant showed much improved EL efficiencies, while the CIE-coordinates were red-shifted. This indicates that the EL emissions of the **b** devices originate from the emissions of dopants **PFVtPh** by a Förster-type energy transfer between the dopant and the corresponding hosts. The variation of the CIE coordinates would contribute to the differences in the solvation state in solid-state devices using different hosts. Among the devices, **1b** with the CIE coordinates (0.160, 0.240) had an excellent EL performance; its luminous efficiency, power efficiency, and external quantum efficiency reached 10.35 cd/A, 8.77 lm/W, and 5.70% (10.24 cd/A, 6.06 lm/W, and 5.66% at 20 mA/cm^2), respectively. In addition, the maximum EQE of devices **5b–7b** were greater than 5%, a known theoretical limit. The CIE coordinates of devices **5b–7b** were (0.150, 0.176), (0.155, 0.213), and (0.148, 0.183), respectively. Thus, devices **1b**, **5b**, **6b**, and **7b** exhibited highly efficient sky-blue emissions. Intriguingly, performances of the **b** devices showed the complicated correlation with molecular structure of the blue hosts in the emitting layer. Presumably, in devices **b**, the various host materials would affect carrier balance in the emitting layers of the devices, which play important roles in EL efficiencies of the devices [30]. These effects would lead the variation of the EL efficiencies of devices **b**, there are no the significant differences in the quantum yields, HOMO–LUMO energy levels, and the overlap of the absorption spectra of **PFVtPh** with emission spectra of hosts **1–7**.

Devices **c** showed deep-blue emissions in spite of the lower EL efficiencies, compared with devices **b**. Particularly, devices **4c**, **6c**, and **7c** exhibited efficient deep-blue emissions with a maximum EQE of 2.96, 3.60, and 3.33%, respectively. The CIE coordinates of devices **4c**, **6c**, and **7c** were (0.154, 0.087), (0.157, 0.132), and (0.153, 0.097), respectively. In the **c** devices, the energy transfer from hosts to dopant **PCVtPh** was inefficient, as shown in Fig. 1. In these systems, the inefficient confinement of the

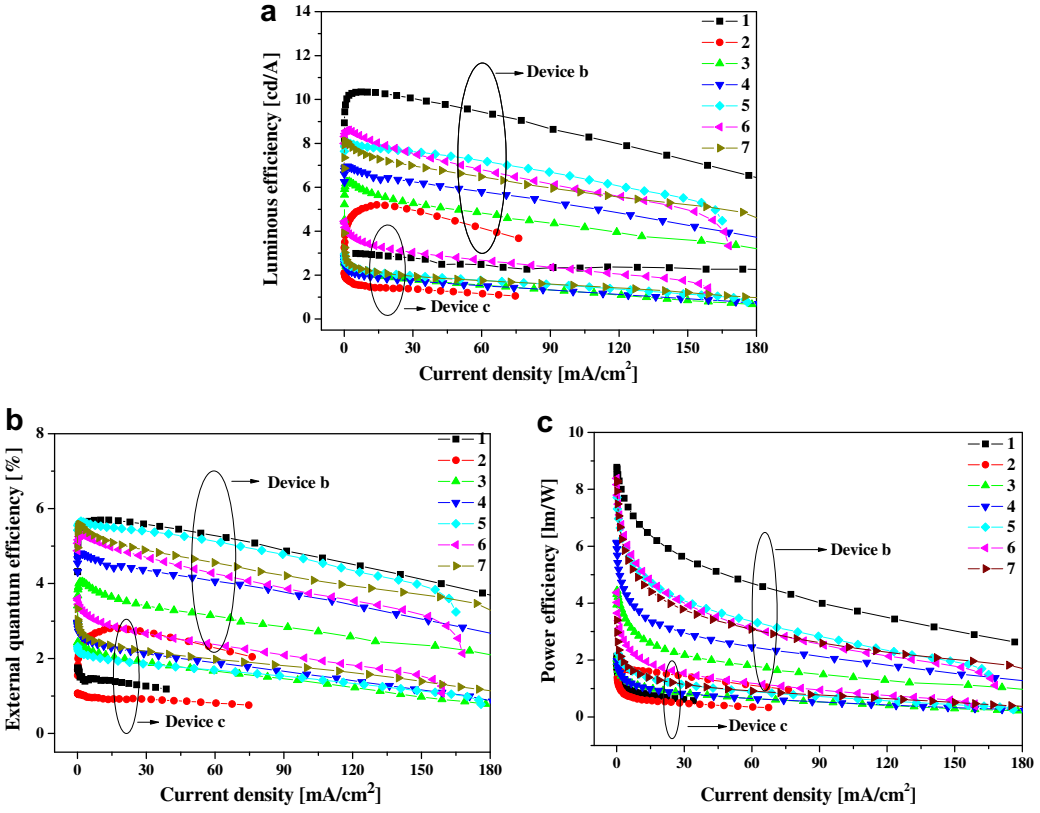

Fig. 8. (a) Luminous efficiencies; (b) external quantum efficiencies; and (c) power efficiencies as a function of current density for the doped devices (**1b–7c**).

excitons in dopant **PCVtPh** was due to the ineffective energy transfer between hosts and dopant **PCVtPh** [31]. Thus the **c** devices exhibited not only an emission of dopant **PCVtPh,** but also hosts **1**–**7**. This notion could be supported from the similar trend in the EL efficiencies between non-doped **a** devices and **PCVtPh**-doped **c** devices. For example, among the **c** devices, device **6c** exhibited the best EL efficiencies. Additionally, devices **3c–7c** showed improved EL efficiencies when compared with devices **1c–2c**. In addition, compared to device **6c** and **1c**, device **7c** and **2c** showed improved EL efficiencies, respectively. However, in contrast to the **c** devices, there were no clear correlations with the EL efficiencies between devices **a** and **b** as shown above. These observations indicate that the EL emissions of the hosts themselves would contribute to the emissions of the **c** devices. In addition, the contribution of the exciplexes between hosts **1**–**7** and dopant **PCVtPh,** to the emissions of the **c** devices cannot be excluded [32].

4. Conclusion

In conclusion, a series of new blue-emitting materials based on 10-naphthylanthracene derivatives with attached side-groups of varying electronic properties have been designed and synthesized *via* a Suzuki cross-coupling. We have demonstrated that the physical and electroluminescent properties are affected by the introduction of electron-withdrawing (pyridine, isoquinoline) and electron-donation groups (*N*-arylcarbazole) into the 10-naphthylanthracene core. Device **6a** (non-doped OLEDs) exhibited excellent electroluminescent performance (4.40 cd/A, 4.31 lm/W, and 3.83%), nearly twice that of MADN. In particular, device **5a** showed an efficient deep-blue emission with a maximum external quantum efficiency of 2.61% and CIE coordinates of (0.153, 0.079), very close to the NTSC blue standard of (0.14, 0.08). Using **1** as a host material for the **PFVtPh** blue dopant material, device **1b** showed high EL efficiencies with 10.35 cd/A, 8.77 lm/W, and 5.70% (10.24 cd/A, 6.06 lm/W, and 5.66% at 20 mA/cm^2). Moreover, using **4** as a host for the **PCVtPh** blue dopant, device **4c** exhibited efficient deep-blue emissions with a maximum external quantum efficiency of 2.96% and CIE coordinates of (0.154, 0.087), very close to the NTSC blue standard of (0.14, 0.08). This study demonstrates that these blue-emitting materials with the 10-naphthylanthracene core have sufficient potential for OLED display or lighting applications.

Acknowledgements

S. S. Y. acknowledges the financial support by Basic Science Research Program through the NRF funded by the Ministry of Education, Science and Technology (20090073679). J. Y. L. acknowledges the financial support by the NRF Grant (No. R11-2007-012-03002-0).

References

[1] C.W. Tang, S.A. Van Slyke, C.H. Chen, J. Appl. Phys. 65 (1989) 3610.
[2] C. Adachi, T. Tsutsui, S. Saito, Appl. Phys. Lett. 55 (1989) 1489.
[3] J. Kido, M. Kimura, K. Nagai, Science 267 (1995) 1332.
[4] C. Hosokawa, H. Higashi, H. Nakamura, T. Kusumoto, Synth. Met. 91 (1997) 3.
[5] M. Matsuura, M. Edia, M. Funahashi, K. Fukuoka, H. Tokailin, C. Hosokawa, T. Kusumoto, Proc. IDW'97 (1997) 581.
[6] Y.H. Kim, D.C. Shin, S.H. Kim, C.H. Ko, H.S. Yu, Y.D. Chae, S.K. Kwon, Adv. Mater. 13 (2001) 1690.
[7] C. Hosokawa, H. Higashi, H. Nakamura, T. Kusumoto, Appl. Phys. Lett. 67 (1995) 3853.
[8] K.C. Wu, P.J. Ku, C.S. Lin, H.T. Shih, F.I. Wu, M.J. Huang, J.J. Lin, I.C. Chen, C.H. Cheng, Adv. Funct. Mater. 18 (2007) 67.
[9] S.J. Lee, J.S. Park, K.J. Yoon, Y.I. Kim, S.H. Jin, S.K. Kang, Y.S. Gal, S.W. Kang, J.Y. Lee, J.W. Kang, S.H. Lee, H.D. Park, J.J. Kim, Adv. Funct. Mater. 18 (2008) 3922.
[10] J. Luo, Y. Zhou, Z.-Q. Niu, Q.-F. Zhou, Y. Ma, J. Pei, J. Am. Chem. Soc. 127 (2007) 11314.
[11] Z.Q. Gao, Z.H. Li, P.F. Xia, M.S. Wong, K.W. Cheah, C.H. Chen, Adv. Funct. Mater. 17 (2007) 3194.
[12] C.J. Tonzola, A.P. Kulkarni, A.P. Gifford, W. Kamonsky, S.A. Jenekhe, Adv. Funct. Mater. 17 (2007) 863.
[13] S.-K. Kim, B. Yang, Y. Ma, J.-H. Lee, J.-W. Park, J. Mater. Chem. 18 (2008) 3376.
[14] Y.-T. Lyu, J. Kwak, O. Kwon, S.-H. Lee, D. Kim, C. Lee, K. Char, Adv. Mater. 20 (2008) 2720.
[15] S.W. Wen, M.T. Lee, C.H. Chen, J. Display Technol. 1 (2005) 90.
[16] T. Yamamoto, T. Maruyama, Z.-H. Zhou, T. Ito, A. Fukuda, K. Kubota, J. Am. Chem. Soc. 116 (1994) 4832.
[17] N. Saito, T. Kanbara, Y. Nakamura, T. Yamamoto, K. Kubota, Macromolecules 27 (1997) 657.
[18] K.R.J. Thomas, J.T. Lin, Y.T. Tao, C.W. Ko, Adv. Mater. 12 (2000) 1949.
[19] K.R.J. Thomas, J.T. Lin, Y.T. Tao, C.W. Ko, J. Am. Chem. Soc. 123 (2000) 9409.
[20] Y.S. Kwon, K.H. Lee, G.Y. Kim, J.H. Seo, Y.K. Kim, S.S. Yoon, J. Nanosci. Nanotechnol. 9 (2009) 7056.
[21] K.H. Lee, Y.S. Kwon, L.K. Kang, G.Y. Kim, J.H. Seo, Y.K. Kim, S.S. Yoon, Synth. Met. 159 (2009) 2603.
[22] S.-J. Su, H. Sasabe, T. Takeda, J. Kido, Chem. Mater. 20 (2008) 1691.
[23] S.H. Kim, J. Jang, S.J. Lee, J.Y. Lee, Thin Solid Films 517 (2008) 722.
[24] M. Nomura, Y. Shibasaki, M. Ueda, K. Tugita, M. Ichikawa, Y. Taniguchi, Synth. Met. 148 (2005) 155.
[25] L. Wang, W. Wong, M. Lin, W. Wong, K. Cheah, H. Tam, C.H. Chen, J. Mater. Chem. 18 (2008) 4549.
[26] D.F. Eaton, in: J.C. Scaiano (Ed.), In Handbook of Organic Photochemistry, vol. I, CRC Press, Boca Raton, FL, 1989.
[27] C.C. Wu, J.C. Sturm, A. Khan, Appl. Phys. Lett. 70 (1997) 1348.
[28] J. Salbeck, F. Weissörtel, N. Yu, J. Baner, H. Bestgen, Synth. Met. 91 (1997) 209.
[29] M.J. Frisch, G.W. Trucks, H.B. Schlegel, G.E. Scuseria, M.A. Robb, J.R. Cheeseman, J.A. Montgomery, T. Vreven, Jr., K.N. Kudin, J.C. Burant, J.M. Millam, S.S. Iyengar, J. Tomasi, V. Barone, B. Mennucci, M. Cossi, G. Scalmani, N. Rega, G.A. Petersson, H. Nakatsuji, M. Hada, M. Ehara, K. Toyota, R. Fukuda, J. Hasegawa, M. Ishida, T. Nakajima, Y. Honda, O. Kitao, H. Nakai, M. Klene, X. Li, J.E. Knox, H.P. Hratchian, J.B. Cross, C. Adamo, J. Jaramillo, R. Gomperts, R.E. Stratmann, O. Yazyev, A.J. Austin, R. Cammi, C. Pomelli, J.W. Ochterski, P.Y. Ayala, K. Morokuma, G.A. Voth, P. Salvador, J.J. Dannenberg, V.G. Zakrzewski, S. Dapprich, A.D. Daniels, M.C. Strain, O. Farkas, D.K. Malick, A.D. Rabuck, K. Raghavachari, J.B. Foresman, J.V. Ortiz, Q. Cui, A.G. Baboul, S. Clifford, J. Cioslowski, B.B. Stefanov, G. Liu, A. Liashenko, P. Piskorz, I. Komaromi, R.L. Martin, D.J. Fox, T. Keith, M.A. Al-Laham, C.Y. Peng, A. Nanayakkara, M. Challacombe, P.M.W. Gill, B. Johnson, W. Chen, M.W. Wong, C. Gonzalez, J.A. Pople, Gaussian 03, Revision B05, Gaussian, Inc., Pittsburgh, PA, 2003.
[30] N. Matsumoto, T. Miyazaki, M. Nishiyama, C. Adachi, J. Phys. Chem. C 113 (2009) 6261.
[31] C. Adachi, R.C. Kwong, P. Djurovich, V. Adamovich, M.A. Baldo, M.E. Thompson, S.T. Forrest, Appl. Phys. Lett. 79 (2001) 2082.
[32] D. Kolosov, V. Adamovich, P. Djurovich, M.E. Thompson, C. Adachi, J. Am. Chem. Soc. 124 (2002) 9945.

encountered serious problems in that phase-mixing and/or small grains become heavy in film growth on a metal electrode. Thus, investigation of the electrical properties of PbPc thin films is a challenge from the viewpoint of both film growth and measurement technique.

In the present study, we examine nano-scale current–voltage (I–V) characteristics of monoclinic single-phase PbPc films using two recently developed methods: top-contact nanometre-spaced electrodes (nano-gap) fabricated by angle-controlled shadow-masking method [16] and point-contact current-imaging atomic force microscopy (PCI-AFM) [17–21]. The results indicate low resistivity at low electric field and space-charge limited-current (SCLC) behaviour at high electric field. These properties are different from those obtained by long-distance measurements using conventional micrometre-spaced electrodes (micro-gap).

2. Methods

Configurations of the thin films and electrodes for I–V measurements with micro-gap, nano-gap and PCI-AFM are illustrated schematically in Fig. 1a–c, respectively. The micro-gap, which is a commonly used method for I–V measurements, has two planar top-contact electrodes separated by a gap of d_{micro} = 60 μm formed by the conventional mask technique. As the gap is two orders greater than the grain size of PbPc thin films prepared in this experiment, the electrical properties would involve grain boundary effects. In contrast, as shown in Fig. 1b, the distance of nano-gap electrodes d_{nano} = 45 nm is one order smaller than grain size, and so I–V measurement using the nano-gap could considerably eliminate grain boundary effects. Despite the discriminating capability of the nano-gap method, it is less well utilised for I–V measurements due to the requirement that the nano-gap electrodes should be fabricated without degradation of organic layers. Indeed, conventional nano-fabrication methods, including electron-beam lithography and/or resist processes, cause serious deterioration and are not suitable for organic materials. In our experiments, the requirements are satisfied by angle-controlled shadow evaporation using specially designed apparatus with sample support at a distance of 500 mm from the evaporator to reduce thermal radiation [16].

As mentioned above, the nano-gap is a useful method to reduce the grain boundary effect. The results, however, still reflect only averaged data including large numbers of grains due to the long line edges of the electrodes. To determine the intrinsic electrical properties of PbPc, the AFM-based method is necessary for spatially-resolved conduction measurement. For this purpose, contact-mode operation with a conductive cantilever is typically adopted for current mapping. The contact-mode is a simple method but has problems of sample degradation because organic and/or nano-scale materials are easily damaged by lateral scanning during tip-sample contact. In contrast, intermittent contact-mode (so-called tapping mode) can reduce sample damage, but is inadequate to make sufficient electrical contact between the tip and sample to measure I–V characteristics.

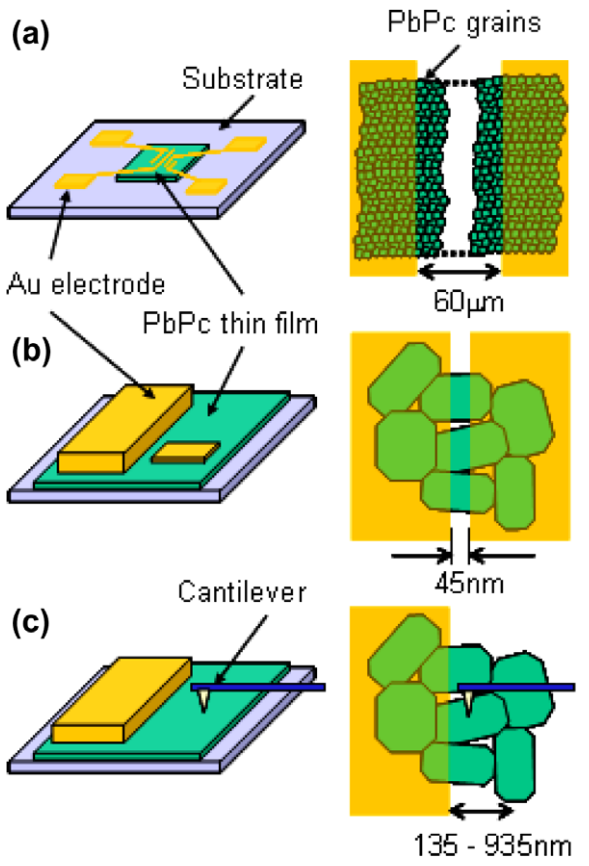

Fig. 1. Electrode configurations. Schematic illustrations of electrodes used to obtain I–V characteristics. (a) The micro-gap electrode is placed on PbPc thin films with top-contact geometry. Two planar Au electrodes are apposed in parallel with a gap distance of d_{micro} = 60 μm and edge length of 3 mm. The gap distance and edge length are far greater than the grain size of both monoclinic (500 nm) and amorphous (80 nm) thin films. Accordingly, the electrical properties measured using the micro-gap electrode are influenced by the grain boundary. (b) The configuration of the nano-gap electrode is similar to that of the micro-gap electrode except for the dimensions. The gap distance is d_{nano} = 45 nm and edge length was 5 μm. The gap distance is less than the grain size of PbPc thin films but the edge length is far greater than the grain size. Thus, the effects of grain boundary on electrical measurements are markedly reduced but still not fully excluded. (c) PCI-AFM measurements are conducted using a planar Au electrode half-covering a surface of PbPc ultra-thin film. The edge length is 10 mm, which is equivalent to the size of the sample substrate. The other electrode is a Pt-coated tip mounted on an AFM cantilever. By choosing the tip position, I–V measurements through a single-grain of PbPc crystal could be performed. The distance between the planar electrode edge and the tip apex is variable in the range from 135 nm to 935 nm for current mapping and I–d analysis.

Point-contact current-imaging atomic force microscopy (PCI-AFM) provides a solution to those problems in current mapping for delicate nano-materials without degradation. PCI-AFM is a combination of tapping-mode scan for topographic observation and point-contact for I–V measurements [17]. The tapping-mode scan is interrupted at preset pixels and the tip is then contacted to the sample with well-controlled loading force without lateral motion.

This procedure achieves simultaneous acquisition of topographic and current images with complete spatial conformity while scanning of a frame. The *I–V* measurement using PCI-AFM is a two-probe measurement between a planar electrode and a PtIr-coated tip. Accordingly, the measured *I–V* characteristics involve contact resistance. The contact resistance, however, can be estimated by analysis of numerous *I–V* data at each pixel with various distances between the tip and electrode [18]. As a result, PCI-AFM measurements can reveal intrinsic electrical properties of single-grain PbPc nano-crystals without contact resistance.

3. Experimental

3.1. PbPc thin film preparation and analysis

Substrates used were two-sided polished sapphire (0 0 0 1) (Shinkosha) and the surfaces of the substrates were prepared with Ar+ sputtering (bias potential, 500 V; ion current, 8.6 mA; Ar pressure, 9×10^{-2} Pa; 3 min) to eliminate contamination and scratches from polishing. PbPc powder (80% dye content) (Sigma–Aldrich) was purified by sublimation three times under a vacuum (10^{-4} Pa). The purified PbPc was deposited on the substrate by thermal evaporation using a shutter-equipped Knudsen-cell at 250–300 °C under a background pressure of 10^{-6} Pa during deposition, and the substrates were heated at 150 °C using a tungsten heater with monitoring using a thermocouple in contact with the substrate surface. The deposition rate and film thickness, which were determined using a quartz crystal microbalance, were 1 nm/min and 25 nm, respectively. The deposited PbPc thin films were stored in air under desiccant condition for two weeks before *I–V* measurements. This period is long enough to saturate carrier doping with oxygen because the conductivity increase was observed only within several hours from the breaking the vacuum after the film deposition.

The crystal structure of the PbPc thin film were examined by $\theta-2\theta$ X-ray diffraction using an X-ray diffractometer (X'Pert-Pro MRD; Philips) with Cu Kα line (0.154 nm). The X-ray beam was induced at 45 kV and 40 mA, and an X-ray mirror, which was assembled by grades shaped parabolic, was used as an incident beam conditioner. The divergence slit was fixed at 1/8° to maintain a beam width of 375 μm.

The surface morphology of the films was observed by atomic force microscopy (SPA-300HV; Seiko), with tapping mode, in air at room temperature. The force constant of the cantilever (SI-DF20; Seiko) was 4.5 N/m and resonant frequency was about 142 kHz.

3.2. Micro-gap electrode fabrication

Micro-gap electrodes were fabricated by thermal evaporation under a background pressure of 10^{-5} Pa. Au (99.95%) was deposited on the PbPc film with a metal (SUS 304) mask (Fuji Seimitsu Co.). The thickness of the mask was 100 μm and the width and length of slits were 6 μm and 3 mm, respectively, and the interval of the slits was 6 mm.

3.3. Nano-gap electrode fabrication

Nano-gap electrodes were fabricated by angle-controlled shadow-masking thermal deposition using a homemade chamber under a vacuum pressure of 10^{-7} Torr. Sample substrate was put in place at a distance of 500 mm from evaporation source to prevent heating of the sample surface by thermal irradiation. The Au layer must be deposited at a slow speed of 0.15–0.3 nm s^{-1} to avoid particle generation and surface diffusion. Such careful procedures contribute to reduction in the degradation of PbPc thin films and realize light effect of contact resistance to the total resistance. In fact, the contact resistance can be estimated less than 0.1 MΩ by the results of PCI-AFM measurements (see Section 3 in Supplementary material).

The fabrication procedure of the nano-gap consisted of two steps of Au deposition. First, the Au layer was deposited on the sample surface half-hidden by a small piece of Si(1 0 0) wafer. The wafer edge cleaved along a crystal axis is extremely sharp and enables fabrication of a sharp edge on the Au electrode. A second opposite electrode (second Au layer) was deposited with a metal mask, which had a pattern of lines and pads for electrical connections. The edge length (width of line) of the nano-gap was 5 μm. In the second deposition, the direction of the deposition angle was controlled to be oblique against the first-layer to form a shadow. The nano-gap distance dnano was estimated as:

$$d = h(1/\tan\theta_2 - 1/\tan\theta_1),$$

where h was the height of the first-layer electrode, and θ_1 and θ_2 were the angle of the first-layer electrode and the oblique deposition angle of the second-layer electrode, respectively. Using this equation, gap distance was controlled by changing the thickness of the first-layer electrode and the oblique angle in the fabrication process of the second-layer electrode. The thicknesses of the first- and second-layer electrodes were 80 and 30 nm, respectively, as measured with a quartz thickness monitor. The oblique angle for second-layer deposition was set to 30°. The nano-gap distance between the first- and second-layer electrodes was measured as 45 nm. These two electrodes are not equivalent due to the difference of contact condition. However, this nonequivalence is not so large that the electrical asymmetry has little influence on the analysis of *I–V* characteristics (see S1 in Supplementary data). A detailed description for nano-gap fabrication was reported previously [16].

3.4. Electrical measurement

The *I–V* measurements for micro- and nano-gap junctions were performed in air using a semiconductor characterisation system (4200; Keithley) at a delay and hold time of 0.5 s and 0.1 s, respectively. The scan ranges and steps were from −10 to 10 V in 0.5-V steps for micro-gap junctions, from −5 to 5 V in 0.05-V steps and from −15 to 15 V in 0.5-V steps for nano-gap junctions of monoclinic

and amorphous films, respectively. In the case of measurement of monoclinic films in nano-gap junctions, narrow scan range and slow scan rate were required to prevent field-induced migration and leakage generation. In all *I–V* measurements, hysteresis induced by the charging effect and irreversible structure changes were not observed. The detail of time response on *I–V* measurements are discussed in the Section 3 of Supplementary data.

3.5. Point-contact current-imaging atomic force microscopy (PCI-AFM)

PCI-AFM measurement was performed in air by a scanning probe microscope (JSPM-4200; JEOL) equipped with two function generators (WF1946; NF Corporation). Platinum-coated cantilevers (NSCS-12/Pt; MikroMasch) were used for current detection, and their force constant and resonant frequency were 4.5 N/m and about 150 kHz, respectively. A gold electrode was deposited on half of the area of a monoclinic PbPc ultra-thin film surface using the same apparatus that was used for nano-gap electrode. Topographic and current images were obtained simultaneously. In the tapping-mode scan, the feedback was active and the cantilever was oscillated at a resonant frequency of 150 kHz. When the tip met the preset positions for *I–V* measurements, the lateral scan was interrupted and the feedback was frozen. During the time when the feedback system was deactivated, the cantilever excitation stopped, and the tip was proceeded to make an electric contact with a preset loading force. The applied bias voltage was then swept and the *I–V* characteristics were stored in the memory. The time response of *I–V* measurement was enough fast to avoid transient effect (see Section 3 in Supplementary data). After *I–V* curve acquisition, the tip-sample separation was re-set to the former position, the feedback system was reactivated, and tapping-mode scan was restarted. These alternate operations were performed continuously, and both the topographical data and the *I–V* data were obtained at 128 points lengthwise and crosswise (total: 16,384 points). Current images were formed by extracting current data at a chosen bias voltage from *I–V* curves corresponding to each pixel. For analysis of the *I–V* curve, the current–voltage characteristic at the tip-electrode distance was the average of over 10 data points, which were extracted from a PCI-AFM current image at the points of the same tip-electrode distance. For *I–d* analysis, the current data were obtained by averaging the values at over 30 points with the same tip-electrode distance for noise reduction at large *d* (low current condition). The detailed experimental procedure was reported previously [17].

4. Results and discussion

4.1. Micro- and nano-gap measurements

Using the methods described above, the electrical properties of PbPc thin films are investigated on the nanometre scale. For this purpose, the growth of highly-ordered single-phase monoclinic-crystalline PbPc thin films is achieved by thermal deposition at 150 °C on an Ar^+-sputtered sapphire (0 0 0 1) substrate with well-optimised conditions [22]. Fig. 2a shows the molecular arrangement in the monoclinic PbPc crystal. The PbPc molecule has a quadrangular pyramidal structure and its central Pb atom is out of the molecular plane. Due to this asymmetrical structure, the PbPc molecules form a monoclinic crystal with a large unit cell that includes four columns oriented in alternate directions. The X-ray diffraction pattern of the PbPc film shows only (2*l*, 0, 0) peaks for monoclinic PbPc crystals, as shown in Fig. 2b. This result indicates that the films were grown with their *a*-axis normal to the substrate surface as a single-phase and formation of the triclinic phase was completely suppressed. This *a*-axis orientation of monoclinic PbPc crystal is also obvious from the AFM observation in Fig. 2c. This AFM image indicates Frank-van der Merwe type growth with the step of 1.3 nm in height corresponding to the half unit cell dimension of the monoclinic PbPc crystal along the *a*-axis.

To clarify the effects of electrode distance on observed electrical properties, conventional micro-gap methods are used for *I–V* curve measurements. Fig. 3a shows AFM topography and an *I–V* curve (inset) for monoclinic PbPc thin films. The average grain size of this film is 500 nm, which is two orders smaller than the distance between micro-gap electrodes. For this sample, the *I–V* characteristics indicate a featureless linear relationship with $\rho_{micro} = 1.1 \times 10^5\ \Omega m$, where ρ_{micro} is apparent resistivity involving the effect of grain boundaries, contact resistance at electrodes and any other imperfections. This value is of the same order as those reported for Zn phthalocyanine [23] and Cu phthalocyanine crystalline films [6,24].

To examine the influence of crystallinity and morphology on the electrical properties, amorphous PbPc thin films are also studied in comparison with monoclinic samples. The amorphous PbPc thin films prepared by deposition at room temperature show no peaks on X-ray diffraction analyses (not shown) and consist of small spherical grains 80 nm in diameter, as shown in Fig. 3b. Although amorphous PbPc thin films show markedly different crystallinity and morphology from monoclinic films, the *I–V* characteristics of the amorphous PbPc (inset in Fig. 3b) also shows a featureless linear relationship similar to the monoclinic samples, and the apparent resistivity of $8.8 \times 10^5\ \Omega m$ was only one order higher than that of monoclinic films.

The nano-gap method brings a marked change to observed *I–V* characteristics. Fig. 4a and d shows non-linear *I–V* curves for both monoclinic and amorphous PbPc thin films obtained by the nano-gap method. These non-linear characteristics are quite different from the linear relationship observed by micro-gap measurements. This difference may be attributable to the strong electric field applied by narrow-spaced nano-gap electrodes. Furthermore, the nano-gap measurement is also effective in eliminating the number of grain boundaries, which is a causal factor of the potential drop between electrodes. In fact, whereas the micro-gap spacing of 60 μm is much greater than the grain sizes of both monoclinic and amorphous PbPc films (500 nm and 80 nm, respectively), the 45-nm separation of the nano-gap is shorter than the both grain sizes. Thus,

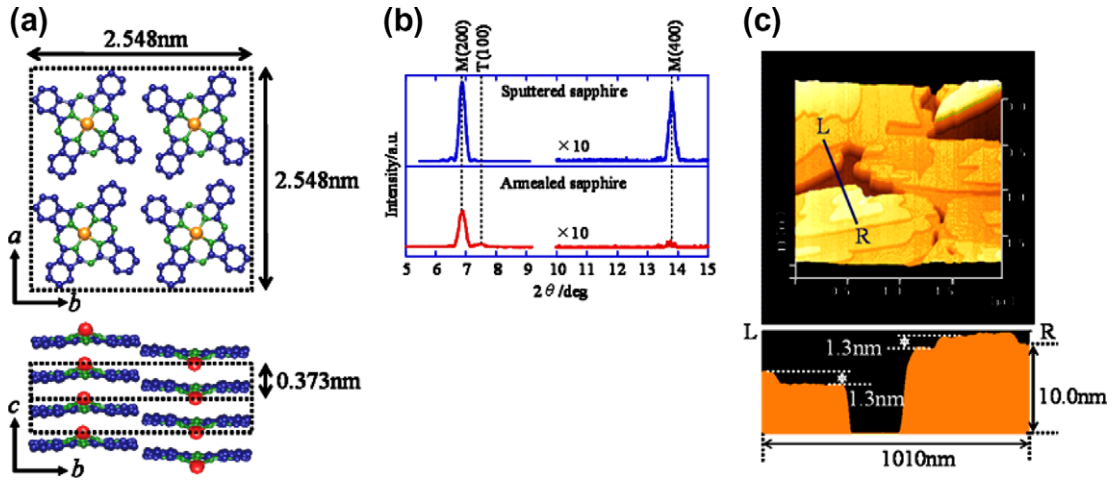

Fig. 2. Single-phase monoclinic PbPc thin film. (a) Molecular arrangement in the monoclinic PbPc crystal. The PbPc molecule has a quadrangular pyramidal structure and its central Pb atom is out of the molecular plane. Due to this asymmetrical structure, the PbPc molecules form a monoclinic crystal with a large unit cell including four columns oriented in alternative directions. (b) The X-ray diffraction pattern of the PbPc films. M and T indicate monoclinic and triclinic phases, respectively. In comparison with the growth on an annealed sapphire (0 0 0 1) surface, the films grown on Ar^+-sputtered sapphire (0 0 0 1) shows only (2*l*, 0, 0) peaks for monoclinic PbPc crystals indicating that the crystal has an orientation with the *a*-axis normal to the substrate surface as a single-phase and the formation of the triclinic phase is completely suppressed. (c) AFM image and line profiles of monoclinic PbPc film surface. The image indicates Frank-van der Merwe type growth with steps of 1.3 nm corresponding to the half unit cell dimension of the monoclinic PbPc crystal along the *a*-axis.

the electrical field affecting each grain in nano-gap measurement is far stronger than that in micro-gap measurement. Therefore, analysis based on various field functions was attempted for the non-linear *I*-*V* characteristics. To examine conduction mechanisms exhibiting non-linear electrical properties, the *I*-*V* data in Fig. 4a and d are analysed as shown in Fig. 4b and c for monoclinic PbPc thin films and Fig. 4e and f for amorphous films.

Fig. 4b shows two distinct regions in log *I*–log *V* plots for a monoclinic PbPc thin film. At low voltages, the slope was 1.0 indicating a linear relationship. The apparent resistivity of $\rho_{nano} = 1.9 \times 10^3\ \Omega m$ found in this region is two orders of magnitude lower than that obtained by the micro-gap method. This suggests that the resistivity obtained by micro-gap measurements reflects electrical properties not of the intrinsic monoclinic PbPc crystal but of the grain boundaries. With increasing bias voltage, the slope in Fig. 4b changes to 5.3 signifying the power law with a distinct transition bias at 3.0 V. Such behaviour is often observed in sandwich junctions of organic semiconductors and can be explained by the space-charge limited-current (SCLC) mechanism with an exponential distribution of trap levels [25,26].

In contrast to monoclinic films, the log *I*–log *V* plot for the amorphous film does not exhibit any meaningful relationship, as shown in Fig. 4e. Thus, neither linear relationship at low field nor SCLC mechanism at high electric field is appropriate for amorphous PbPc and another conduction model should be considered. Poole–Frenkel conduction model is often applied to non-linear electrical behaviour for amorphous semiconductors [27]. To examine the adequacy of this model for amorphous PbPc thin films, a log (I/E)–$E^{1/2}$ plot is shown in Fig. 4f. The plot shows the linear relationship for amorphous PbPc film throughout the whole bias region suggesting relevance of the Poole–Frenkel model. This result implies that electrical conduction is dominated by the field-assisted thermal excitation of localised carriers [28] reflecting the presence of a large numbers of trap sites around the Fermi level in the amorphous PbPc thin films.

As mentioned above, the nano-gap method clarifies the difference in electrical properties between monoclinic and amorphous PbPc thin films, despite the lack of remarkable differences on analysis using micro-gap methods. Moreover, the resistivity measured by the nano-gap method at low electric field is two or three orders of magnitude lower than that obtained by the micro-gap method. These results suggest that the presence of grain boundaries between electrodes obscures the observation of intrinsic electrical properties. Accordingly, it is a logical conclusion that the electrical measurement for a single-grain is required to obtain essential electrical properties of monoclinic PbPc crystals.

4.2. Point-contact current imaging

Electrical measurements of single-grain monoclinic PbPc crystals are conducted by PCI-AFM for ultra-thin PbPc films. For single-grain measurement, it is necessary that the sample is thin enough to avoid layered accumulation of multiple grains. The samples used here satisfy this requirement, as shown by AFM topography in Fig. 5 where the bare surface of the substrate can be seen behind the grains with an average thickness of 10 nm. A perpendicular stack of PbPc grains is rarely observed in such ultra-thin films. In this sample, certain grains are contiguous to a gold electrode placed at the left side in the image. Such grains are included in the scan areas of PCI-AFM measurements to obtain single-grain *I*–*V* characteristics, as represented by the dashed line in the AFM image. In addition, the scan-

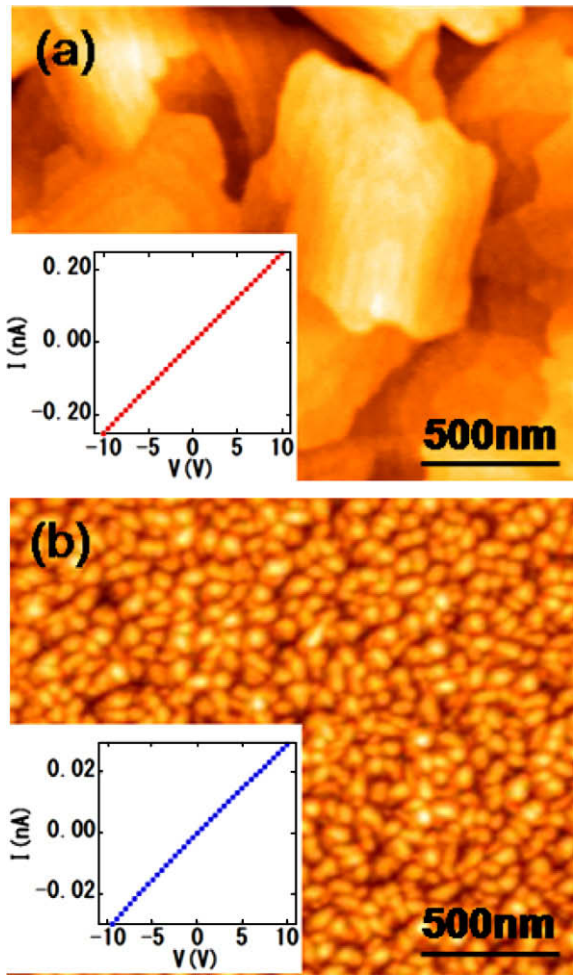

Fig. 3. Surface morphology and micro-gap *I–V* characteristics. (a) AFM topography of monoclinic polycrystalline PbPc thin film. The grain size is ca. 500 nm. The *I–V* curve of this monoclinic PbPc thin film obtained using the micro-gap electrode is shown in the inset. The *I–V* curve for the monoclinic PbPc shows linear characteristics with apparent resistivity of $\rho_{micro} = 1.1 \times 10^5\ \Omega m$. (b) AFM topography of amorphous PbPc thin film. Spherical grains 80 nm in diameter are shown in the image. The *I–V* curve of this amorphous PbPc thin film obtained with the micro-gap electrode is shown in the inset. The *I–V* curve for amorphous PbPc shows linear characteristics similar to that of the monoclinic sample, but the apparent resistivity is $\rho_{micro} = 8.8 \times 10^5\ \Omega m$, which is one order higher than that in the case of monoclinic PbPc.

ning area is at least 50 nm from the edge of the planar gold electrode to prevent Au atom migration under the high electric field between the tip and electrode. The actual closest tip-electrode distance during the scan is estimated to be ca. 135 nm.

Simultaneously obtained topography and current image of a PbPc thin film are shown in Fig. 6a and b, respectively. The current image is obtained with a bias voltage of 5.0 V. In comparison with topography, the current image gives sharp contrast and is sensitive to the surface conditions of the tip and sample. While topography retains constant smoothness and resolution for the whole scan area, the current image shows discontinuity around the centre due to abrupt changes in noise level. This may be attributable to removal of insulating contamination at the tip surface during the scan.

The line profiles of the topography and the current image are shown in Fig. 6c and d along lines A and B, respectively. Between the points p and q on line A (Fig. 6c), there are no PbPc grains and the insulating substrate surface is exposed. In this region, the line profile of the current image indicates constant values around 10^{-2} nA in a position-independent manner. These observations imply that the value indicates the noise level of PCI-AFM measurement using this apparatus. The following analyses are based upon this detection limit. The profile along line B (Fig. 6d) shows the effect of the grain boundary on electrical conduction. A distinct drop is observed in the current profile at point *r*, where a grain boundary can be seen in the topographic image (Fig. 6b). This is direct evidence why nano-gap measurements provide different electrical properties from those of micro-gap measurements.

4.3. Distance-dependent electrical characteristics

As mentioned above, the presence of the grain boundary is captured by PCI-AFM. Therefore, measurements using only the inside region of single-grain PbPc crystals are suitable for quantitative analysis of position-dependent electrical characteristics. Fig. 7a shows the electrical properties of single-grain PbPc crystals at tip-electrode distances of $d = 135$, 204, 286 and 443 nm. The observed *I–V* curves can be divided into two regions by analysis based on log *I*–log *V* plots: a low bias region showing a slope of 1.0 indicating a linear *I–V* relationship, and a high bias region above 0.6 V showing an increase in upward curvature with increasing bias voltage reflecting higher-order *I–V* characteristics. This behaviour, which is the transition from linear to SCLC conduction with increasing electric field, is consistent with the results of nano-gap measurements. Furthermore, in Fig. 7b, log *I*–log *d* plots at a bias voltage of 5.0 V clearly show a power law with the order of −2.79 demonstrating the adequacy of SCLC-type conduction [26].

On the basis of the simple theory that the transition voltage from linear to SCLC reflects field strength in the material, the transition voltage in PCI-AFM measurement with the distance range of $d = 135$–443 nm should be larger than that of nano-gap measurement with $d = 65$ nm. However, in actual measurements, the transition in PCI-AFM measurement occurs only around 0.6 V, which is quite low in comparison with the transition voltage of 3 V in nano-gap measurements. This anomaly can be attributed to the difference in trap density between the two methods. In the case of nano-gap measurement, many grain boundaries between electrodes and the trap site at the boundary should be filled by charge before the transition from linear to SCLC conduction. In contrast, such trap levels in PCI-AFM measurements are lower in comparison with those of nano-gap measurement because PCI-AFM can be used to determine the electrical properties for single-domain crystals. As a result, the low transition voltage in single-grain measurement by PCI-AFM reflects the pri-

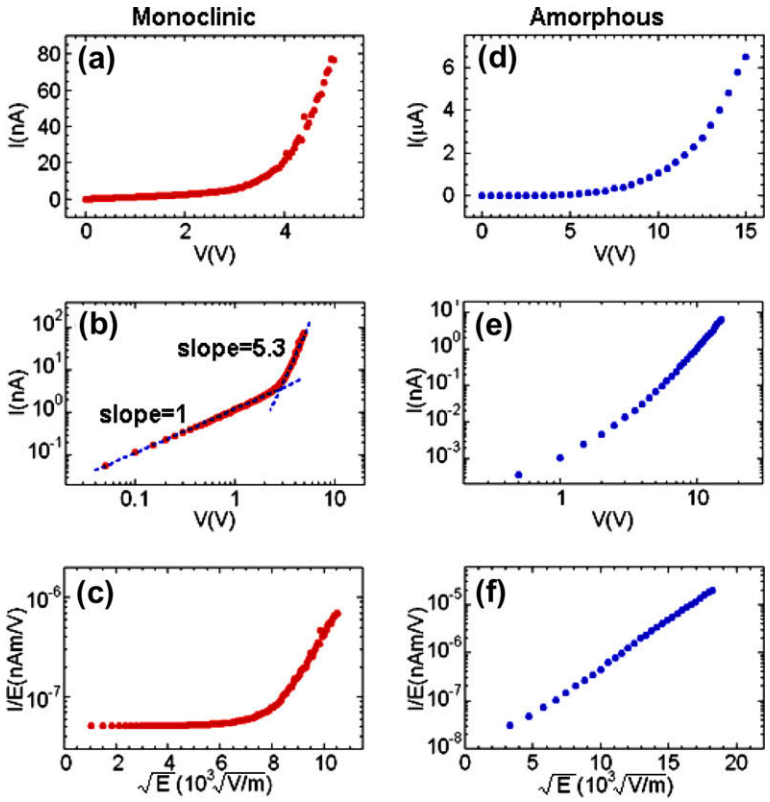

Fig. 4. Nano-gap *I–V* characteristics. (a) The *I–V* curve representing the non-linear relationship for monoclinic PbPc thin films obtained using the nano-gap electrode at room temperature. (b) The log *I*–log *V* plot shows two distinct linear regions with a distinct transition at 3.0 V. At low voltages, the slope is 1.0, indicating a linear *I–V* relationship with apparent resistivity of 1.9×10^3 Ωm. At high bias voltages, the slope is 5.3 signifying the power law of a space-charge limited-current (SCLC) mechanism. (c) The log (I/E)–$E^{1/2}$ plot shows a non-linear curve indicating that the Pool–Frankel model is inadequate for monoclinic PbPc thin films. (d) The *I–V* curve indicates a non-linear relationship for amorphous PbPc thin films obtained with the nano-gap electrode at room temperature. (e) The log *I*–log *V* plot shows the non-linear relationship without any distinct transition. SCLC or other models based on power law are inappropriate for amorphous PbPc thin films. (f) The log (I/E)–$E^{1/2}$ plot shows a linear curve indicating that the Pool–Frankel model is adequate for amorphous PbPc thin films.

mary change from linear to SCLC conduction with low trap site density.

Position-dependent electrical measurements of single-grain crystals by PCI-AFM provide further insight into nano-scale conduction. Fig. 7c shows a resistance–distance (*R–d*) curve plot at $V = 0.16$ V. At such a low bias voltage, the *I–V* characteristics are linear as shown in Fig. 7a. In general, a linear *I–V* curve indicates ohmic conduction, which in turn indicates a linear increase in resistance with increasing tip-electrode distance. However, Fig. 7c shows that the resistance increases at an accelerating pace with increasing tip-electrode distance. This distance dependence implies that the electron transport at low voltages is not ohmic. The *R–d* curve can be fitted by $R(d) = R_0 + A\exp(d/d_0)$, where R_0 is the sum of contact resistances at the interfaces between the electrodes and PbPc crystal. From the fitting, R_0 is 0.5 MΩ that is so small as to not affect the resistivity analysis. This exponential distance dependence suggests that there is a great deal of randomness for electron transport even in a single-grain crystal because only the hopping conduction through periodic and isopotential sites allows linear distance dependence [29].

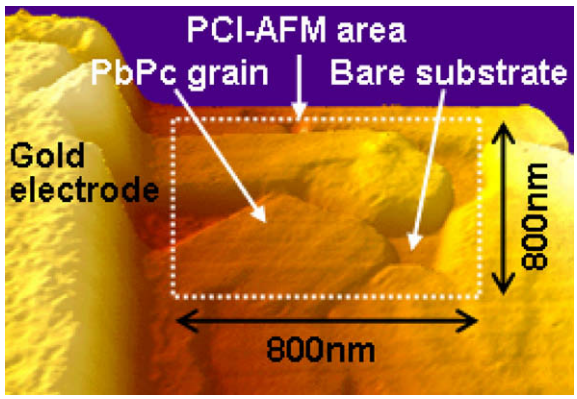

Fig. 5. Ultra-thin PbPc film for single-grain PCI-AFM measurements. AFM topography of ultra-thin monoclinic polycrystalline PbPc film used for single-grain PCI-AFM measurements. The image shows the bare surface of the substrate behind the grains. The PbPc layers are only 10 nm in thickness. A perpendicular stack of PbPc grains is rare and unexpected accumulation of multiple grains is inhibited in the ultra-thin film. Grains connected to the Au electrode are included in the scan areas of PCI-AFM measurements to obtain single-grain *I–V* characteristics, as represented by the dashed line. The scanning area is kept 135 nm from the edge of the planar gold electrode to prevent Au atom migration under the high electric field between the tip and electrode.

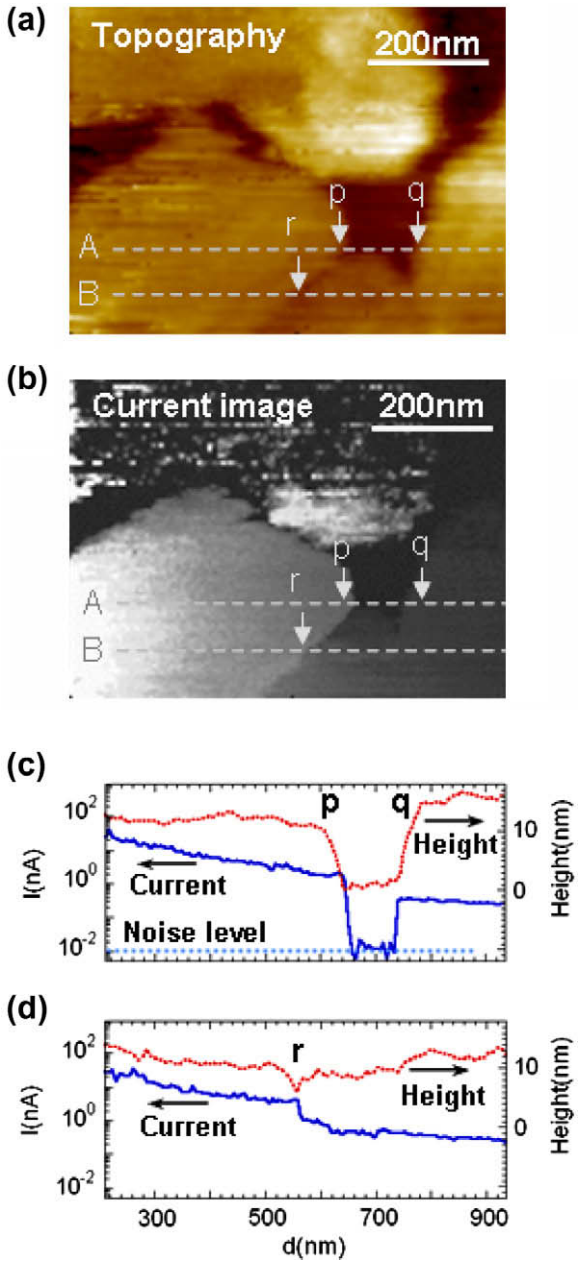

Fig. 6. Spatially-resolved electrical properties of single-grain PbPc by PCI-AFM. (a) Topography of monoclinic polycrystalline PbPc ultra-thin films obtained by PCI-AFM observation. (b) Current image corresponding to the topography. This current image is constructed from the current data at 5.0 V extracted from the *I*–*V* spectra acquired during the topography scan. The bright contrast in the grayscale figure indicates high current. The current is reduced from left to right side reflecting the location of the Au planar electrode on the left outside of the figure. (c) Line profiles of the topography and the current image along line A. Between points p and q on line A, there are no PbPc grains and the insulating substrate surface is exposed. In this region, the line profile of the current image shows a constant value of 10^{-2} nA with no position dependence. This value indicates a noise level (detection limit) of the PCI-AFM apparatus. (d) Line profiles of the topography and the current images along line B shows the effect of the grain boundary on electrical conduction. A distinct drop is observed in the current profile at point r, where a grain boundary could be seen in the topographic image.

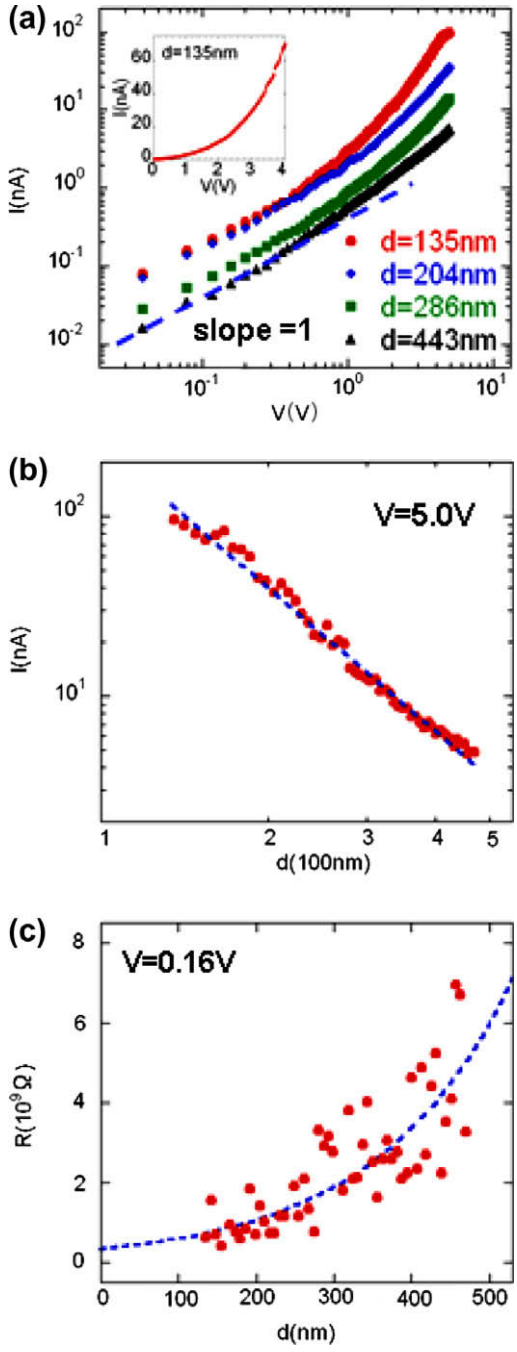

Fig. 7. Distance-dependent electrical characteristics of single-grain PbPc. (a) The *I*–*V* curve at electrode-tip distance d = 204 nm shows a non-linear curve for the overall voltage region (see inset). The log *I*–log *V* curve at d = 135–443 nm. At low voltages of less than 1 V, the slopes are 1.0 indicating a linear *I*–*V* relationship, regardless of d. The slopes became steeper with increasing voltage above 1 V, suggesting the transition from linear conduction to SCLC. (b) The log *I*–log d curve at bias voltage of 5.0 V. The plots indicate that the current is proportional to the −2.79 power of the distance over the full electrode-tip distance range indicating the SCLC mechanism. (c) *R*–d curve at V = 0.16 V shows non-linear behaviour where the resistance increased at an accelerating pace with increasing tip-electrode distance. The resistance–distance plots can be fitted by $R(d) = R_0 + A\ \exp(d/d_0)$, where R_0 is contact resistance at the interfaces between electrode and PbPc crystal.

Despite the considerable randomness mentioned above, distance-differential resistivity on the nano-scale is quite low in comparison with apparent resistivity values measured by other methods. The distance-differential resistivity $\rho_{diff} = 1 \times 10\,\Omega m$ is determined by PCI-AFM measurement at $d = 200$ nm, whereas the apparent resistivities obtained by other methods are considerably higher as follows: $\rho_{nano} = 1.9 \times 10^3$ and $\rho_{micro} = 1.1 \times 10^5\,\Omega m$ for nano-gap and micro-gap measurements of monoclinic thin films, respectively, and $\rho_{bulk} = 10^2\,\Omega m$, where ρ_{bulk} is for bulk single-crystal measurements. The high resistivity for thin films can be attributed to the presence of the grain boundary as discussed above. In particular, it is notable that ρ_{diff} taken by PCI-AFM measurement for single grains is lower than ρ_{bulk} using bulk crystal. This result implies that the resistivity on the nano-scale cannot be estimated using Ohm's law on the basis of bulk crystal measurement.

5. Conclusion

Here, we have demonstrated the reduction of nano-scale resistivity for PbPc monoclinic polycrystalline films using two recently developed nano-scale measurement techniques: nano-gap electrodes and PCI-AFM. These measurements, where electrode distances are narrower than the PbPc grain size, show quite different electrical properties from the results obtained by conventional micro-gap measurements. The comparison of micro-gap and nano-gap measurements indicates that the conduction in PbPc thin films is highly limited at the grain boundary and current-imaging by PCI-AFM exposed the potential drop at the grain boundary directly. These results indicate distinct advantages of the nano-gap and PCI-AFM methods. In particular, detailed analysis of current–distance characteristics using PCI-AFM provides new insight into nano-scale conduction for single-grain PbPc crystals, in which the low distance-differential resistivity indicates the potential of nano-structured organic materials for electrical applications.

Acknowledgement

This work was partially supported by Japan Society for the Promotion of Science (JSPS), Grant-in-Aid for Exploratory Research (20656005).

Appendix A. Supplementary data

Supplementary data associated with this article can be found, in the online version, at doi:10.1016/j.orgel.2010.02.011.

References

[1] A. Petrović, G. Bratina, Appl. Phys. Lett. 94 (2009) 123301.
[2] C. Hamann, A. Mrwa, Int. J. Electron. 73 (1992) 1039.
[3] Th. Frauenheim, C. Hamann, M. Müller, Phys. Status Solidi A 86 (1984) 735.
[4] A. Ahmad, R.A. Collins, Thin Solid Films 217 (1992) 75.
[5] J.C. Hsieh, C.J. Liu, Y.H. Ju, Thin Solid Films 322 (1998) 98.
[6] K. Kudo, T. Sumitomo, K. Hiraga, S. Kuniyoshi, K. Tanaka, Jpn. J. Appl. Phys. Part 1 36 (1997) 6994.
[7] K. Ukei, Acta Crystallogr., Sect. B 29 (1973) 2290.
[8] A. Miyamoto, K. Nichogi, A. Taomoto, T. Nambu, M. Murakami, Thin Solid Films 256 (1995) 64.
[9] L. Ottaviano, L. Lozzi, S. Santucci, S.D. Nardo, M. Passacantando, Surf. Sci. 392 (1997) 52.
[10] K. Ukei, K. Takamoto, E. Kanda, Phys. Lett. A 45 (1973) 345.
[11] Y. Iyechika, K. Yakushi, I. Ikemoto, H. Kuroda, Acta Crystallogr., Sect. B 38 (1982) 766.
[12] H. Yasunaga, K. Kojima, H. Yohda, K. Takeya, J. Phys. Soc. Jpn. 37 (1974) 1024.
[13] A.K. Ray, S.M. Tracey, A.K. Hassan, IEE Proc.-Sci. Meas. Technol. 146 (1999) 205.
[14] T.S. Shafai, R.D. Gould, Int. J. Electron. 69 (1990) 3.
[15] A. Ahmad, R.A. Collins, Phys. Status Solidi A 123 (1991) 201.
[16] Y. Otsuka, Y. Naitoh, T. Matsumoto, W. Mizutani, H. Tabata, T. Kawai, Nanotechnology 15 (2004) 1639.
[17] Y. Otsuka, Y. Naitoh, T. Matsumoto, T. Kawai, Jpn. J. Appl. Phys. 41 (2002) L742.
[18] Y. Otsuka, Y. Naitoh, T. Matsumoto, T. Kawai, Appl. Phys. Lett. 82 (2003) 1944.
[19] A. Terawaki, Y. Otsuka, H. Lee, T. Matsumoto, H. Tanaka, T. Kawai, Appl. Phys. Lett. 86 (2005) 113901.
[20] H. Tanaka, T. Yajima, T. Matsumoto, Y. Otsuka, T. Ogawa, Adv. Mater. 18 (2006) 1411.
[21] R. Tsunashima, Y. Noda, Y. Tatewaki, S. Noro, T. Akutagawa, T. Nakamura, T. Matsumoto, T. Kawai, Appl. Phys. Lett. 93 (2008) 173102.
[22] S. Tabuchi, H. Tabata, T. Kawai, Surf. Sci. 571 (2004) 117.
[23] A.M. Saleh, A.K. Hassan, R.D. Gould, J. Phys. Chem. Solids 64 (2003) 1297.
[24] C. Park, Y.D. Hyun, S.-T. Kim, Y.W. Park, Sens. Actuators, B 30 (1996) 23.
[25] A. Rose, Phys. Rev. 97 (1955) 1538.
[26] M.A. Lampert, Rep. Prog. Phys. 27 (1964) 329.
[27] J. Furlan, Z. Gorup, A. Levstek, S. Amon, J. Appl. Phys. 94 (2003) 7604.
[28] H. Kahnt, F. Schirrmeister, Phys. Status Solidi B 115 (1983) 171.
[29] R.L. McCreery, Chem. Mater. 16 (2004) 4477.

film characteristics, and correlate the material properties with MFM device performance. These results demonstrate that through careful film processing this material may be a promising solution for a non-volatile memory element for flexible electronics.

2. Experimental

Metal–Ferroelectric–Metal capacitors were fabricated as follows. P(VDF-TrFE) copolymer powder with 70/30 mol ratio (Hisense Electronics Co., China) was dissolved in 2-butanone without further purification as 3 and 4 wt.%, respectively. Chromium and gold (10/100 nm) were e-beam evaporated on a silicon substrate with a Si_3N_4 buffer layer as the bottom contact, and patterned using photolithography. Copolymer films (154 and 210 nm) were then spin-coated on the Cr/Au contact from the 3 and 4 wt.% solutions, followed by drying and annealing at 65 °C, 118 °C, 133 °C, 144 °C and 156 °C (T_m is approximately 148 °C) for 2 h in a vacuum oven (pressure was approxi-

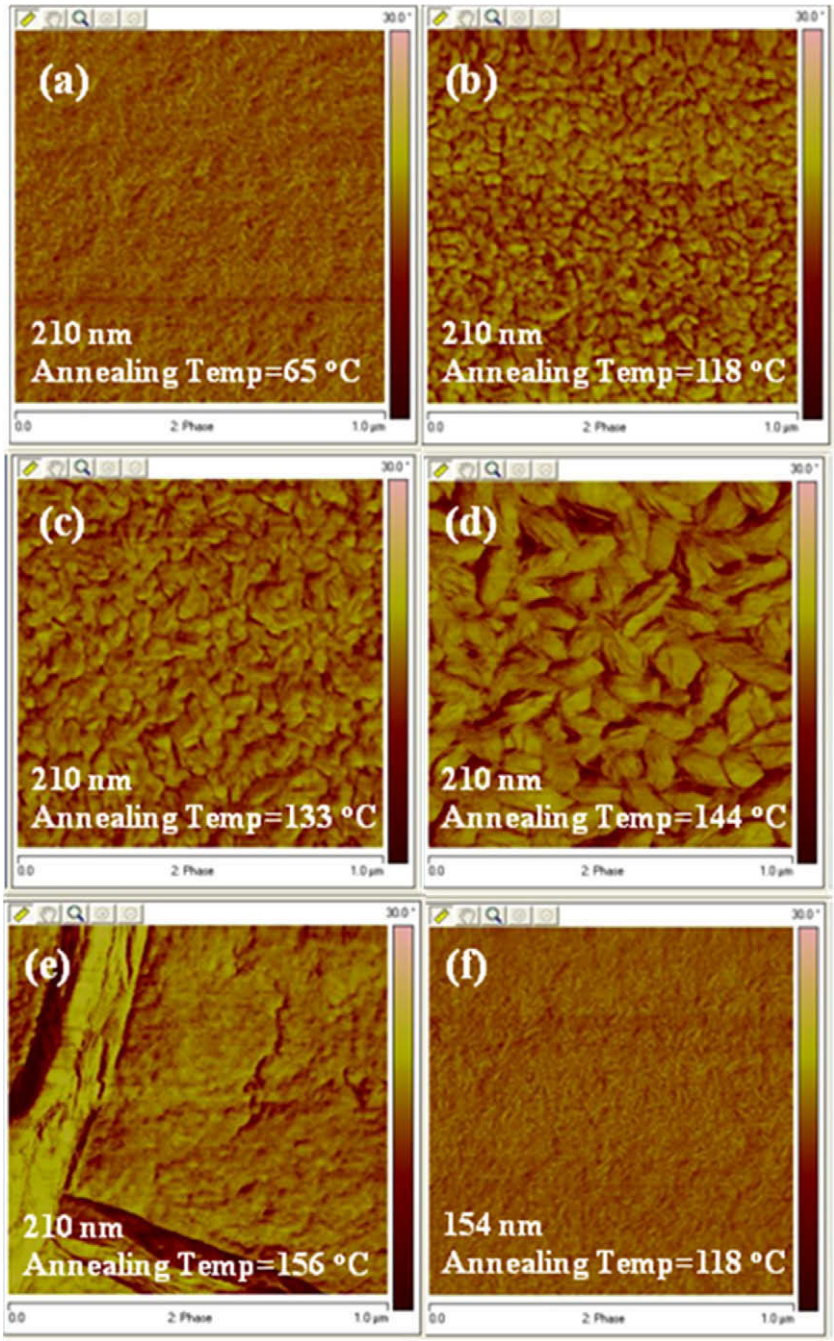

Fig. 1. (a)–(e) AFM phase images of 210 nm P(VDF-TrFE) films annealed from 65 °C to 156 °C and (f) shows 154 nm film annealed at 118 °C for comparison.

mately 20 Torr). All the samples were then left in the vacuum oven to slowly cool down to room temperature in order to maximize their grain size. Gold was thermally evaporated and photolithography patterned on the copolymer film as the top contact. The area of the MFM capacitors ranged from 0.0003 cm^2 to 0.0025 cm^2. The electrical performance was characterized using Capacitance–Voltage (HP4284, Agilent), Displacement Current–Voltage (Keithley 4200 semiconductor parameter analyzer), and Displacement Charge Density–Voltage (virtual ground circuit, RT66B, Radiant Technology). Film thicknesses were determined using a profilometer (Dektak), surface morphology was studied using Atomic Force Microscopy (AFM, DM09 Veeco), crystallinity was measured using thin film X-ray diffraction (XRD, Rigaku), and molecular bonding and orientation were characterized using Fourier-transform infrared reflection–absorption spectroscopy (FT-IR, Magna-IR 560, Nicolet). The ferroelectric β phase increases with annealing temperature. We demonstrate that high polarization and low leakage current can be achieved by annealing at, or slightly above T_c, whereas annealing at higher temperature, but below the melting temperature increases leakage current.

3. Results and discussions

To correlate the film's physical and chemical characteristics with device performance, P(VDF-TrFE) films were studied before top electrode deposition. We studied the microstructure, surface morphology, crystallinity and molecular phase configuration. Fig. 1a–e shows the AFM phase images (tapping mode) of 210 nm films annealed at temperatures ranging from 65 °C to 156 °C. Films annealed at 65 °C, below the Curie temperature (T_c = 118 °C), show a smooth surface with relatively small grain size (Fig. 1a). As the annealing temperature increases near, and above T_c (Fig. 1b and c), the polymer grain size increases, as expected. Films annealed at 144 °C (just below T_m = 148 °C) show the largest grain size (approximately 180 nm long) (Fig. 1d). Annealing at temperatures above T_m at 156 °C, results in films with a completely different morphology. This is due to film re-crystallization during cooling [11,16]. We also compare 154 nm (Fig. 1e) with 210 nm films (Fig. 1b) annealed using the same conditions. While the thinner films follow the same trend as thicker films (Fig. 2a), it can be seen that the thinner film shows smaller grains, even though the films are annealed using the same conditions and temperature. This indicates that P(VDF-TrFE) crystallization is a function of not only the annealing temperature, but also film thickness, and demonstrates that annealing has to be optimized for each film thickness. The evolution of film roughness as a function of annealing temperature and film thickness is shown in Fig. 2b. It is well known that P(VDF-TrFE) copolymer is a polycrystalline material, and that its ferroelectric response is attributed to the β phase (all-trans), which shows a rod-like shape with a relatively rough surface [15]. Fig. 2b shows a clear increase in the Root-Mean-Square (RMS) roughness as a function of annealing temperature, suggesting the presence of the β phase. Although higher annealing temperature favors

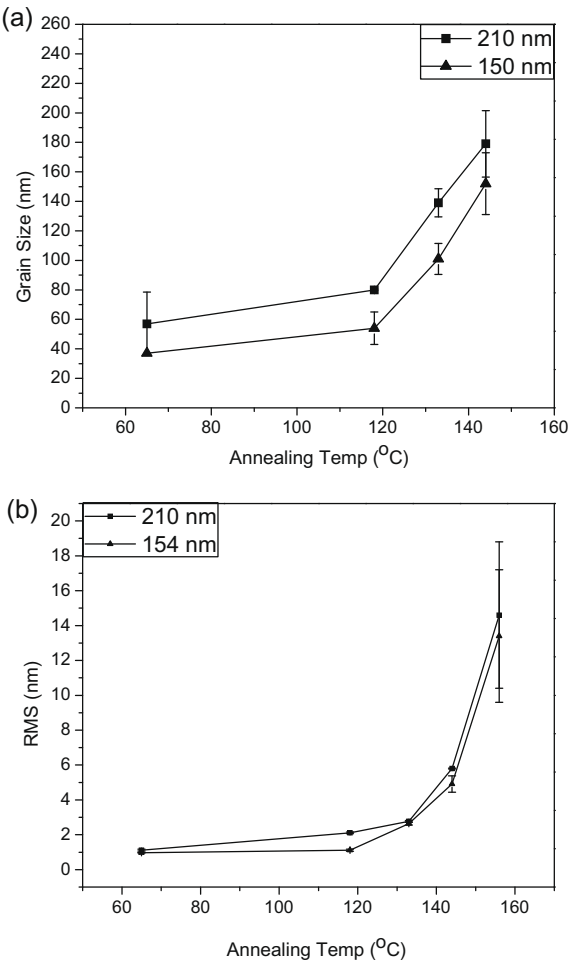

Fig. 2. (a) Average β phase crystallite grain size of 210 nm and 154 nm film at different annealing temperature treatment below T_m. (b) Surface roughness (RMS) of 210 nm and 154 nm films at different annealing temperatures.

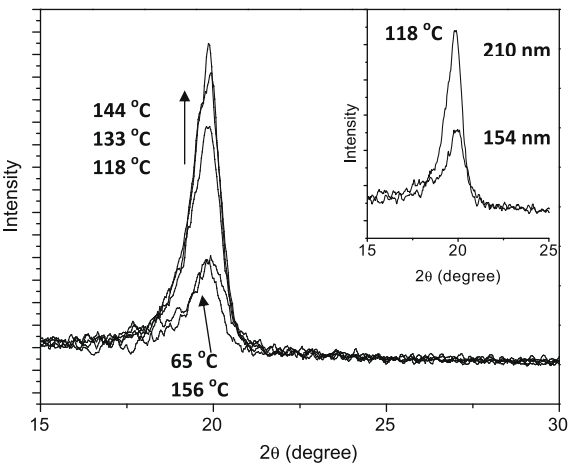

Fig. 3. XRD of 210 nm P(VDF-TrFE) films annealed at different temperatures. Inset shows both of the 210 nm and 154 nm films annealed at 118 °C.

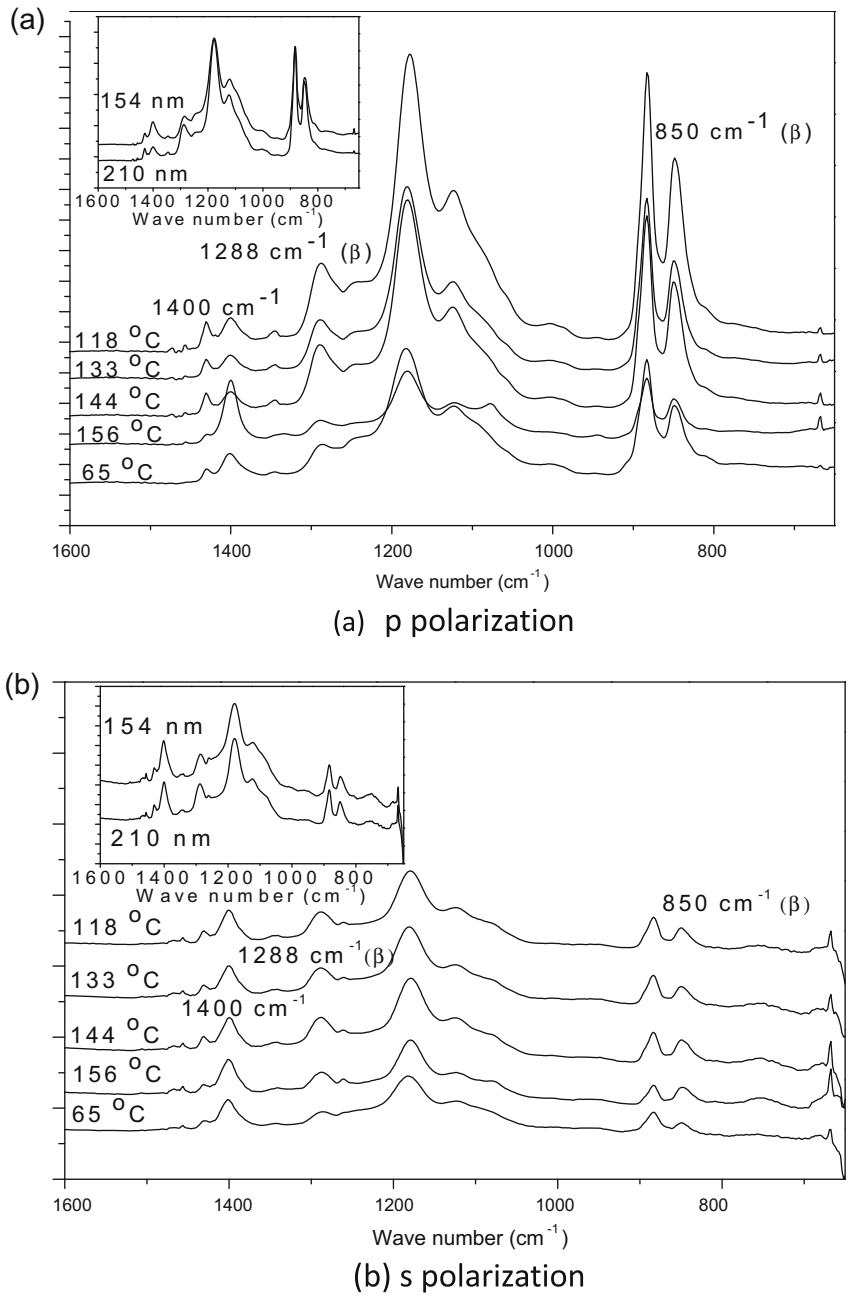

Fig. 4. (a) p Polarization (for molecular dipole interaction with direction perpendicular to substrate) and (b) s polarization (for molecular dipole interaction with direction parallel to substrate) of FT-IR of 210 nm P(VDF-TrFE) films annealed at different temperatures. Inset shows both of the 210 nm and 154 nm films annealed at 118 °C.

larger crystallites, it also increases surface roughness, which could result in increased leakage current. The RMS roughness increases from 1.1 nm to 14.6 nm for 210 nm films and from 1.0 nm to 13.4 nm for 154 nm films, as shown in Fig. 2.

Fig. 3 shows XRD results for the 210 nm films annealed at different temperatures. The sharp peak at $2\theta = 19.9°$ is assigned to the (1 1 0) and (2 0 0) orientations, and is attributed to the ferroelectric β phase. The diffraction angle of this peak does not change with the annealing conditions, indicating similar inter-chain spacing for all the annealing conditions [17]. The inter-planar distance was calculated to be approximately 4.5 Å, in agreement with an earlier report [10]. Higher annealing temperatures, but below T_m, produces more intense diffraction peaks, indicating a higher degree of crystallinity. Annealing above T_m causes a dramatic reduction in the peak intensity for the (1 1 0) and (2 0 0) peaks, which suggests a change in the crystalline

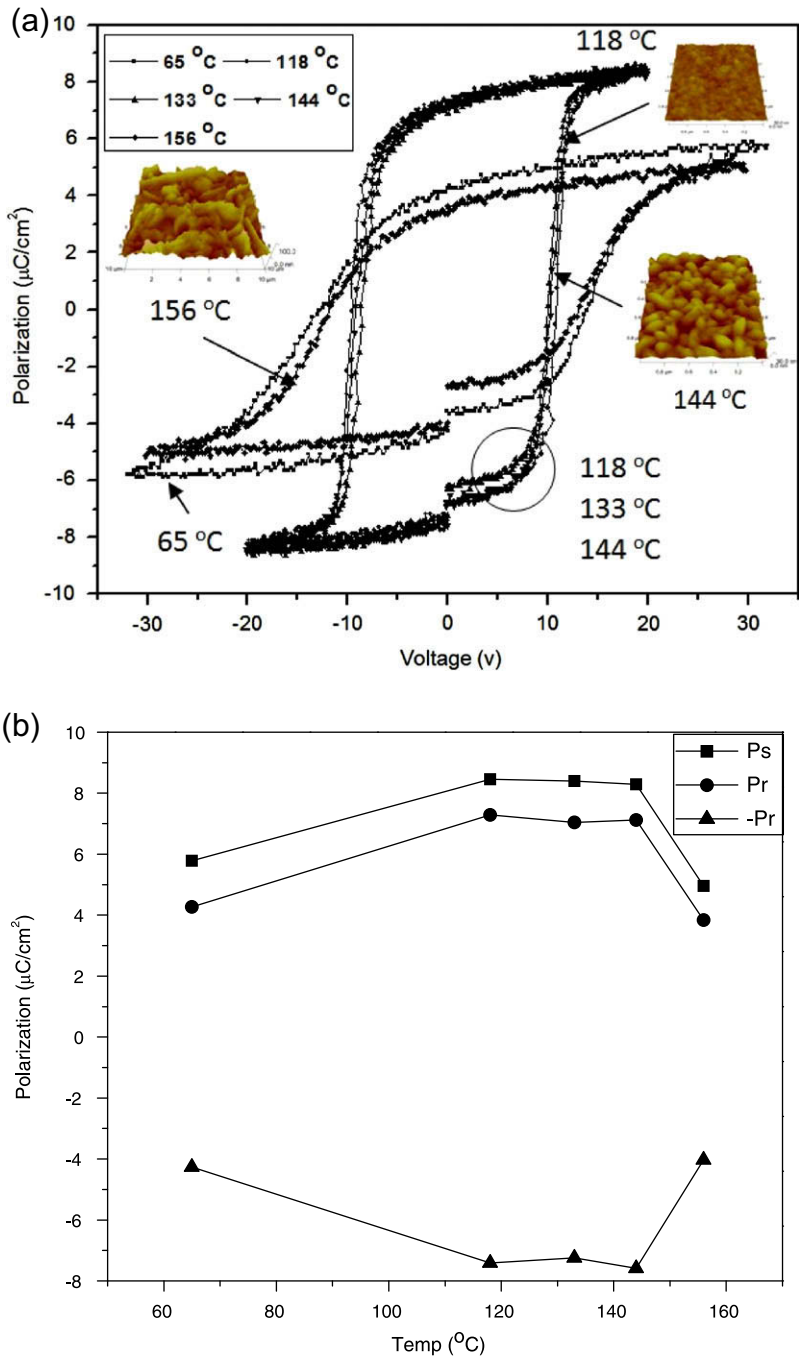

Fig. 5. (a) Hysteresis loops of 210 nm P(VDF-TrFE) copolymer films annealed at different temperatures. Inset AFM images show the morphologies of corresponding temperature annealed devices. (b) Saturation and remanent polarizations at different temperatures.

characteristics of the films, with a likely reduction in the ferroelectric β phase. The 154 nm films follow a similar trend. The 210 nm film shows a higher degree of crystallinity, as shown in the inset of Fig. 3.

Polarized FT-IR is used to characterize the localized chain orientation and configuration of the P(VDF-TrFE) films. We use the fact that the different P(VDF-TrFE) phases have different responses to the external electromagnetic field associated with FT-IR spectroscopy [18]. The large dipoles in P(VDF-TrFE) strongly interact with the applied IR electric field when the field is perpendicular to the dipole direction. Fig. 4a shows the FT-IR results (from 1600 cm^{-1} to 650 cm^{-1}) for 210 nm thick films annealed at different temperatures. IR with the electric field component parallel to the plane of the substrate (p polarization) is used for this measurement. The 1288 cm^{-1} and

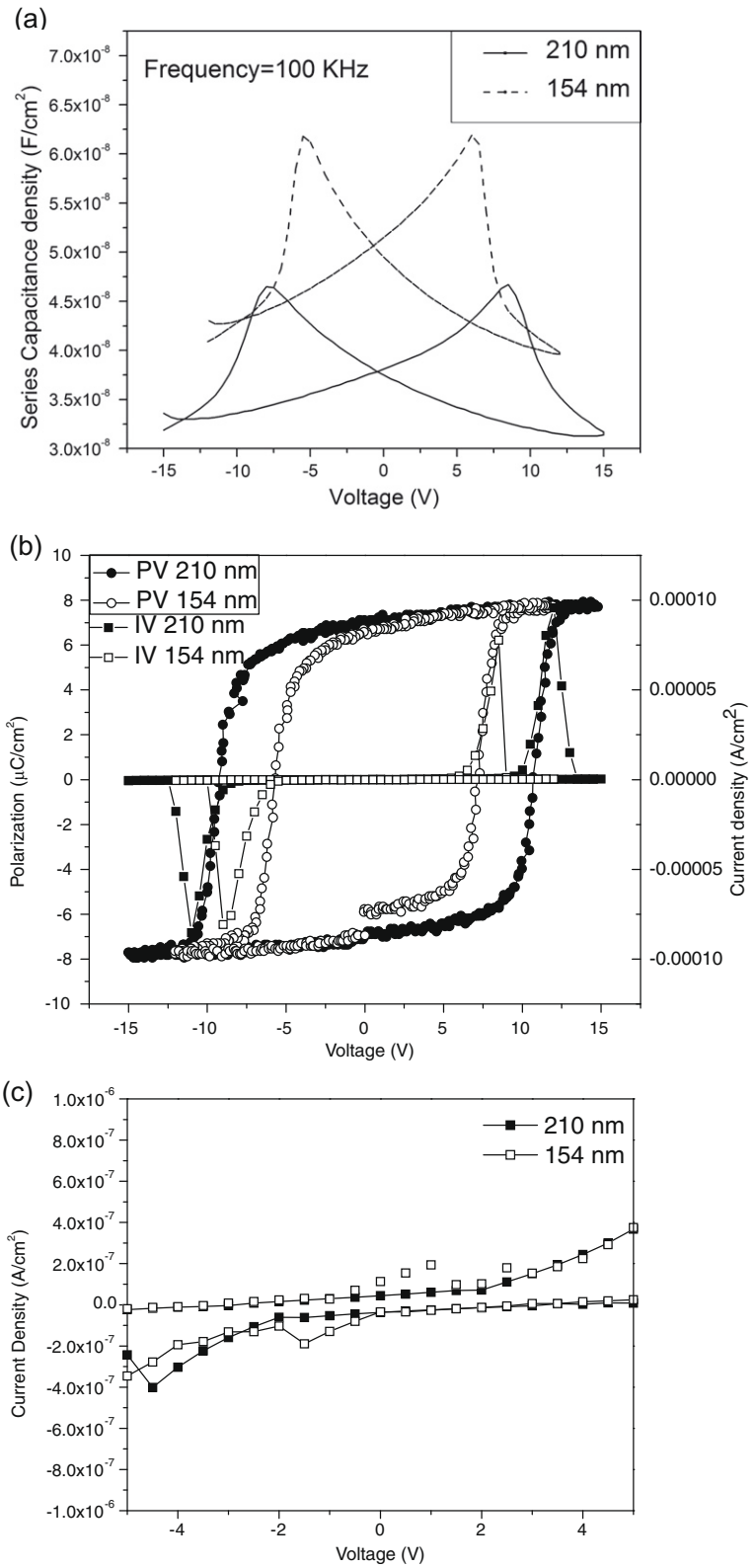

Fig. 6. (a) *C–V* measured at 100 kHz, (b) *P–V* and *I–V* data and (c) Leakage current for low voltage sweep for 210 nm and 154 nm P(VDF-TrFE) MFM devices annealed at 118 °C.

850 cm^{-1} bands are assigned to CF_2 symmetric stretching characteristics of the β phase, with three or more trans sequence of isomers [19]. These IR absorption bands indicate transition dipole moments μ parallel to the polar *b* axis [9]. For samples annealed at 118 °C, 133 °C and 144 °C, these two absorption bands can be clearly seen, indicating that the *b* axis of the copolymer film is perpendicular to the substrate. For the samples annealed at 65 °C and 156 °C, these two bands are relatively weak, indicating that the *b* axis is tilted away from the direction normal to the surface. Moreover, the 1400 cm^{-1} band (the wagging vibration of CH_2), which has μ parallel to the polymer chain *c* axis, increases for the film annealed above T_m, indicating that a significant portion of the copolymer chain tilts vertically, which is undesirable for vertical polarization [20]. In contrast, s polarized (the electric field component is perpendicular to the substrate) IR spectra of samples annealed at low temperature (Fig. 4b) show a large absorption ratio between 1400 cm^{-1} and 1288 cm^{-1} bands, indicating the strong wagging vibration of CH_2 along the *c* axis, and confirming that most of the copolymer chains are oriented parallel to the substrate when the films are annealed below T_m.

The electrical performance of the devices with area of 0.0005 cm^2 was evaluated after fabrication as a function of annealing conditions and film thickness. The Polarization–Voltage (*P*–*V*) hysteresis loops (1 Hz) for 210 nm MFM devices with different annealing temperatures measured at room temperature are shown in Fig. 5a. For devices annealed at 65 °C, PV shows a saturation polarization (P_s) of 5.8 μC/cm^2 and a remanent polarization (P_r) of 4.3 μC/cm^2 with a coercive voltage (V_c) of approximately 13.3 V (corresponding to a coercive field E_c = 0.63 MV/cm). These data are for a voltage sweep from −32 V to 32 V (*E* field of −1.52 MV/cm to 1.52 MV/cm). The low polarization and high V_c are consistent with a low concentration of the ferroelectric β phase, as confirmed by the AFM, FT-IR and XRD results. When the annealing temperature is increased to 118 °C, the polarization increases sharply, with a concurrent decrease of V_c. The *P*–*V* loops show a typical square shape with P_s, P_r and V_c of 8.5 μC/cm^2, 7.4 μC/cm^2 and 10.2 V, respectively. This corresponds to an E_c of approximately 0.5 MV/cm (measured at ±20 V for a field of ±0.95 MV/cm). These results are in agreement with previous reports [21]. The polarization saturates and the hysteresis loops remain almost constant as the annealing temperature increases to 133 °C and 144 °C. This saturation demonstrates that, although the grain size is different for each of these temperatures, annealing these films at 118 °C is enough to achieve acceptable ferroelectric performance. As the annealing temperature increases above T_m to 156 °C, P_s and P_r decrease, while V_c increases. This indicates the tilted chain orientation and a reduction of the ferroelectric β phase. This is also in agreement with changes in morphology seen with AFM, XRD and FT-IR. The discontinuities at the origin of the hysteresis loops are due to non-switchable polarization, as reported in Ref. [22].

P_s, P_r and $-P_r$ for the different annealing temperatures are plotted in Fig. 5b. While most of the polarization of P(VDF-TrFE) originates from the β phase, the β phase crystal orientation also impacts polarization [20]. The data suggest that annealing at temperatures equal to or slightly above T_c is sufficient to align the β phase dipole moment (μ) perpendicular to the substrate, which is the requirement for high P_s and P_r and low V_c. Although annealing at temperatures higher than T_c, but below T_m favors a higher degree of crystallinity with larger grains, the increased film roughness (Fig. 2) might be an issue for leakage current. The high surface roughness will cause a non-uniform electric field, with the concomitant increase in leakage current in the film. This will result in devices with lower electrical stability. Therefore, the best annealing temperature is at, or just above T_c.

Fig. 6 shows the *C*–*V*, *P*–*V* and *I*–*V* plots for 210 nm and 154 nm films annealed at 118 °C. Hysteresis was measured at ±15 V and ±12 V, respectively. Fig. 6a shows peak capacitance densities of 47 nF/cm^2 (210 nm) and 62 nF/cm^2 (154 nm), measured at 100 kHz. The dielectric constants of the films with the two thicknesses show similar values, between 7.8 and 11 depending on the measurement voltage, slightly higher than the value reported in the literature [21], probably due to the improved annealing treatment. The polarizations were measured to be 7.7 μC/cm^2 and 7.0 μC/cm^2 for P_s and P_r with a peak switching current of approximately 85 μA/cm^2 (Fig. 6b). The leakage current is lower than 5×10^{-7} A/cm^2 before the electric field reaches E_c (Fig. 6c). The maximum polling slope (d*P*/d*V*) of the two thicknesses of the devices shows similar values and the coercive field is consistent, indicating similar switching behavior. This indicates that film orientation might be more important that grain size. For the same annealing conditions, thicker films show larger grains, but the electrical performance of the films is similar for different thicknesses.

4. Conclusion

The transition of the β phase crystallite and the rearrangement of the molecular chain orientation to favor vertical ferroelectric polarization can be achieved with thermal annealing at or just above T_c. The polarization of the MFM devices after bias tends to saturate as annealing temperature increases. Higher annealing temperature (but below T_m) results in films with larger grains, higher degree of crystallinity and increased roughness, but less effect on molecular chain orientation. Annealing above the T_m, results in a shift of molecular chain orientation, degraded β phase crystallization and decreased polarization. Thicker films produce larger grains and a higher degree of crystallinity, however, the polarization does not increase because it is more related to molecular orientation. When reducing the thickness of the film, the annealing process needs to be optimized to reach high polarization as well as smooth surface morphology. We conclude that annealing at or slightly above T_c for the P(VDF-TrFE) copolymer is optimal to achieve maximum polarization and low leakage, and is compatible with low temperature substrates for flexible electronics applications.

Acknowledgements

The authors thank the Army Research Laboratory (ARL) for partial financial support of this project. We would also

like to thank Dr. Eric Forsythe of ARL for very helpful discussions regarding non-volatile memory integration.

References

[1] R.C.G. Naber, C. Tanase, P.W.M. Blom, G.H. Gelinck, A.W. Marsman, F.J. Touwslager, S. Setayesh, D.M. de leeuw, Nat. Mater. 4 (2005) 243.
[2] R.C.G. Naber, P.W.M. Blom, A.W. Marsman, D.M. de Leeuw, Appl. Phys. Lett. 85 (2004) 2032.
[3] G.H. Gelinck, A.W. Marsman, F.J. Touwslager, S. Setayesh, D.M. de Leeuw, R.C.G. Naber, P.W.M. Blom, Appl. Phys. Lett. 87 (2005) 092903.
[4] S. Gowrisanker, M.A. Quevedo-Lopez, H.N. Alshareef, B.E. Gnade, S. Venugopal, R. Krishna, K. Kaftanoglu, D.R. Allee, Org. Electron. 10 (2009) 1217.
[5] L. Pauling, The Nature of the Chemical Bonding, third ed., Cornell University Press, Ithaca, NY, 1960, p. 644.
[6] S. Fujisaki, H. Ishiwara, Y. Fujisaki, Appl. Phys. Lett. 90 (2007) 162902.
[7] A. Salimi, A.A. Yousefi, J. Polym. Sci.: Part B: Polym. Phys. 42 (2004) 3487.
[8] H.S. Xu, G. Shanthi, V. Bharti, Q.M. Zhang, Macromolecules 33 (2000) 4125.
[9] Z.J. Hu, M.W. Tian, B. Nysten, A. Jonas, Nat. Mater. 8 (2009) 62.
[10] T. Yamada, T. Kitayama, J. Appl. Phys. 52 (1981) 6859.
[11] W.P. Li, Y.J. Zhu, D.Y. Hua, P.Q. Wang, X.R. Chen, J. Shen, Appl. Surf. Sci. 254 (2008) 7321.
[12] T. Yamada, T. Ueda, T. Kitayama, J. Appl. Phys. 52 (1981) 948.
[13] K. Urayama, M. Tsuji, D. Neher, Macromolecules 33 (2000) 8269.
[14] I. Lazareva, Y. Koval, P. Müller, K. Müller, K. Henkel, D. Schmeisser, J. Appl. Phys. 105 (2009) 054110.
[15] R.C.G. Naber, B. de Boer, P.W.M. Blom, D.M. de Leeuw, Appl. Phys. Lett. 87 (2005) 203509.
[16] F.J. Baltá Calleja, A. González Arche, T.A. Ezquerra, C. Santa Cruz, F. Batallán, B. Frick, E. López Cabarcos, Adv. Polym. Sci. 108 (1993) 1.
[17] H.S. Xu, X.B. Liu, X.R. Fang, H.F. Xie, G.B. Li, X.J. Meng, J.L. Sun, J.H. Chu, J. Appl. Phys. 105 (2009) 034107.
[18] K.J. Kim, N.M. Reynolds, S.L. Hsu, Macromolecules 22 (1989) 4395.
[19] N.M. Reynolds, K.J. Kim, C. Chang, S.L. Hsu, Macromolecules 22 (1989) 1092.
[20] Y.J. Park, S.J. Kang, C. Park, K.J. Kim, H.S. Lee, M.S. Lee, U.I. Chung, I.J. Park, Appl. Phys. Lett. 88 (2006) 242908.
[21] K.H. Lee, G. Lee, K. Lee, M.S. Oh, S. Im, Appl. Phys. Lett. 94 (2009) 093304.
[22] A.K. Tagantsev, I. Stolichnov, E.L. Colla, N. Setter, J. Appl. Phys. 90 (2001) 1387.

ordered structure of the active layer [10–12]. The composition of the P3HT:PCBM active layer, i.e. the relative ratio of each polymer, also influences the microstructure of the active layer and consequently the performance of the OSCs [9,12]. Several research groups have reported that the optimized morphologies and photovoltaic (PV) performances occurred at a 1:1 ratio of the P3HT:PCBM (50 wt.% of P3HT) composites [11,13]. Recently, reports have shown that the use of a low composition (1:0.8–0.7 ratio of P3HT:PCBM) of PCBM resulted in a PCBM cluster free structure and thermally stable devices [1,14]. Although there have been several reports about the effect of the composite ratio on the performance of the OSCs mostly with the optical and electrical properties [9,12–14], further studies are required in order to understand the relationship between the properties and the microstructure of the active layer associated with phase separation depending on the ratio of P3HT:PCBM and the OSCs performance.

In this study, the effect of the P3HT:PCBM composition in the active layer was studied by varying the composite ratio of P3HT from 20 to 80 wt.%. The optical properties and microstructure of the active layer and the correlation with the device performance were explored.

2. Experimental

Regioregular P3HT (Rieke Metals, Inc.) and PCBM (Nano-C) were used for the active layer as purchased without any further purification. P3HT and PCBM were separately dissolved in chlorobenzene (30 mg/ml for each solution) and stirred at 60 °C for 1 h. These solutions were mixed with different weight ratios of: 20, 30, 40, 50, 60, 70, and 80 wt.% of P3HT. The substrate for the OSCs, the indium tin oxide (ITO; 10 Ω/square) coated glass substrate, was cleaned in an ultrasonic bath with deionized water, acetone and isopropyl alcohol for 15 min each, and then cleaned with UV–ozone for 10 min. The poly(3,4-ethylenedioxythiophene):poly(styrenesulfonate) (PEDOT:PSS; Baytron P VP AI 4083, H.C. Stark), used as an anodic buffer layer, was spin coated at 6000 rpm for 10 s and baked at 130 °C for 10 min. The P3HT:PCBM photoactive layer was spin coated on the PEDOT:PSS at 4000 rpm for 5 s. The thicknesses of the buffer and active layers were 30 nm and 70 nm, respectively, as measured using a surface profiler (alpha-step 500). The Al (100 nm) cathode was thermally evaporated through a shadow mask defining active area of 0.1 cm^2. Thermal annealing was conducted at 150 °C in an oven for 10 min under ambient N_2. The entire fabrication process was conducted in an air environment except for thermal annealing.

An UV/visible spectrophotometer (Shimadzu UV-1601) was used to characterize the absorption properties of the P3HT:PCBM layer. The crystallization of the active layer was analyzed using X-ray diffraction (XRD; Mac Science, Cu Kα wavelength of 1.54056 Å). The phase separation and resulting microstructure were observed using optical microscopy and field-emission transmission electron microscopy (FE-TEM; JEM-2100F, JEOL). For the TEM analysis, the specimens were prepared by floating the active layers onto the deionized water and then picking them up with a Cu grid. The current density versus voltage (J–V) characteristics were measured with a Keithley 236 source measurement unit and a solar simulator (Yamashita denso) under an AM 1.5 G (100 mW/cm^2) irradiation intensity. The total incident light intensity was calibrated with a pyranometer (Eko MS-802) and a standard reference silicon solar cell.

3. Results and discussion

Fig. 1 shows the UV/visible absorption spectra of the P3HT:PCBM active layer with different concentration ratios. A previous reports showed that the maximum absorption wavelengths (λ_{max}) of PCBM molecules are almost constant regardless of the amount of the PCBM composite or ordering of the active layer [9,15,16]. In this study, the intensity of the PCBM absorption spectra (~330 nm) increased without any shift in the wavelength as the composition of PCBM increased. On the other hand, as the composition of P3HT increased, the absorption spectra of P3HT between 450 and 650 nm gradually increased, was broader as well as more vibronic, and red-shifted. The λ_{max} of the P3HT peak were at 437, 461, 482, 495, 507, 512 and 515 nm for 20, 30, 40, 50, 60, 70 and 80% of P3HT, respectively. The shift of absorption peaks to higher energy indicates an increasing density of conformational defects, equivalent to non-plarnarity, and causes loss of conjugation [17]. Moreover, the absorption shoulder at ~610 nm which is assigned to interchain interactions became bigger and more pronounced. Since the thickness of the active layer was kept the same (~70 nm) for the all of the samples, the increased, broadened, red-shifted and pronounced absorption peaks of P3HT were attributed not only to the increased composite ratio but also to the closer chain packing of P3HT which resulted from strong interchain interactions [9,12,17,18].

The XRD analysis in Fig. 2 depicted the crystallization of P3HT, which was represented by the peak intensity and the

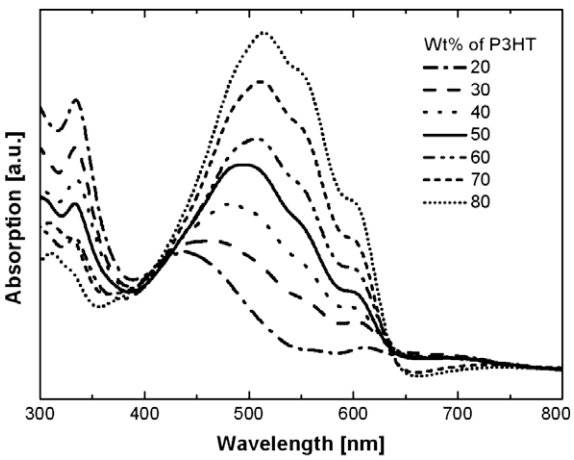

Wt% of P3HT [%]	20	30	40	50	60	70	80
P3HT λ_{max} (nm)	437	461	482	495	507	512	515

Fig. 1. UV/visible absorption spectra of the active layer with various composite ratios of P3HT:PCBM after thermal annealing at 150 °C for 10 min in a N_2 flow oven.

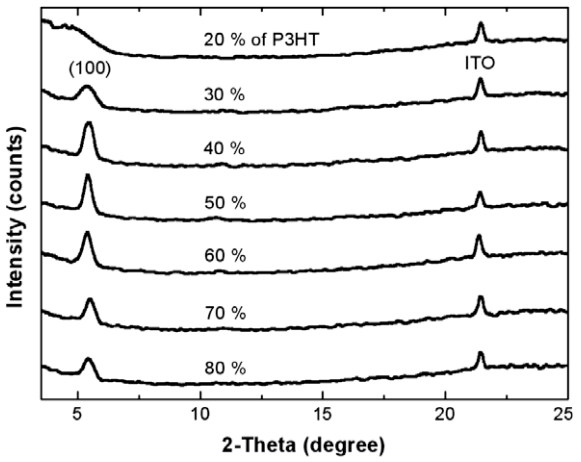

Fig. 2. XRD pattern of the active layer with various composite ratios of P3HT:PCBM.

full width at the half maximum (FWHM) intensity of the peak. The peak intensity of P3HT (100) gradually increased with increasing P3HT composition from 20% to 50%. One remarkable observation was that further increase of the P3HT composition exceeding 60% results in a gradually reduced peak intensity. The size of the crystallites was calculated from the broadening of a peak in the diffraction pattern with Scherrer's equation;

$$\tau = \frac{K\lambda}{\beta \cos\theta}$$

From the XRD peak intensity results, the calculated sizes of the crystallites gradually increased with increasing P3HT composition from 20% to 50%, and further increasing the P3HT composition above 60% reduced the crystallite size.

Comparing the absorption and XRD data, the absorption of P3HT continually increased and red-shifted with increasing P3HT composition which indicated closer chain packing at higher compositions. On the other hand, the diffraction peak of the P3HT (1 0 0) phase increased until 50 wt.% of P3HT and then decreased upon further increase of the P3HT composition. The results of the XRD denote the volume fraction of the π-conjugated planes of P3HT (1 0 0) with lamella oriented normal to the substrate [12,18]. Therefore, both results can be summarized as follows. The interchain packing of P3HT within the crystallized phase improved with increasing P3HT composition, but the volume fraction of the P3HT (1 0 0) phase normal to substrate increased until a P3HT composition of 50% and decreased at higher compositions.

The phase separation and microstructure of the active layer was directly characterized by optical microscopy and TEM. The phase contrast optical microscopy images in Fig. 3 show the macroscopic morphology of the active layer. Overgrown clusters resulting from local diffusion and crystallization of PCBM were observed in the active layers with P3HT compositions of 20, 30, and 40%, and their size and density reduced as the composition of P3HT increased. No PCBM clusters were found at higher P3HT compositions. Previous reports showed that the thermal annealing of the P3HT and PCBM composite film leads to the formation of overgrown PCBM clusters when the PCBM composition exceeds 50% [16,19,20].

Fig. 4 shows the FE-TEM images of various ratios of the P3HT:PCBM layer. For 20% of P3HT in Fig. 4(a), the P3HT rich (bright domains) and PCBM rich (dark domains) regions were barely distinctive compared to the higher compositions of the layer. For the layer with 30–50% of P3HT in Fig. 4(b–d), the phase separation was clear, and P3HT formed a fiber structure embedded in the PCBM matrix. The difference in the microstructures of the phase separated P3HT and PCBM was minimal though the composition varies from 30 to 50% in these TEM images. The TEM images were believed to be obtained in the regions without any PCBM overgrown clusters as shown in the optical micrographs. Therefore it was concluded that almost the same fraction of P3HT and PCBM formed the similar phase separated morphologies and the remaining PCBM formed overgrown clusters. The phase separated microstructure noticeably became blurred and eventually randomized

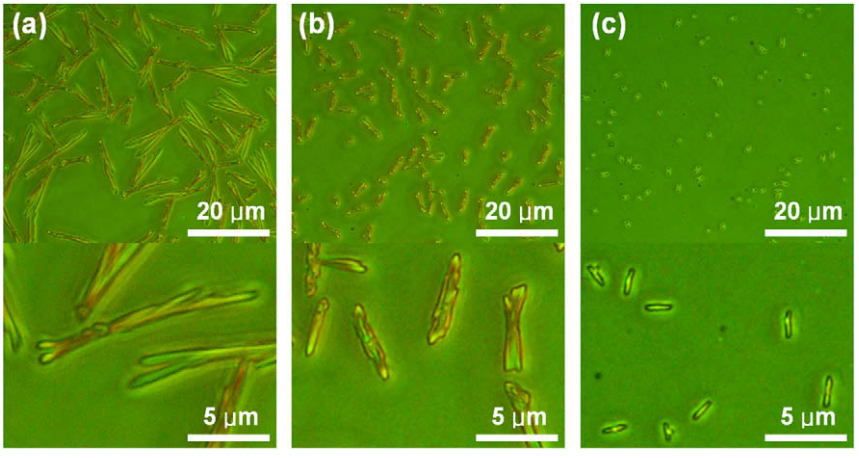

Fig. 3. Phase contrast optical microscope images of the active layer with various composite ratios of P3HT:PCBM; (a) 20%, (b) 30%, (c) 40% of P3HT.

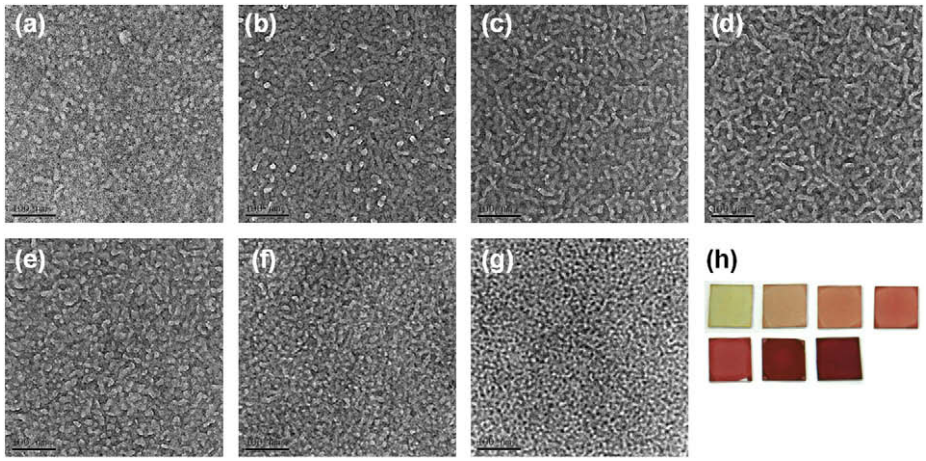

Fig. 4. Bright field TEM images of the active layer with various composite ratios of P3HT:PCBM; (a) 20%, (b) 30%, (c) 40%, (d) 50%, (e) 60%, (f) 70%, (g) 80% of P3HT; scale bar; 100 nm. (h) Photographs of the films with a sample size 20 mm × 20 mm; from the left 20, 30, 40, and 50% on the top and 60, 70, and 80% of P3HT on the bottom.

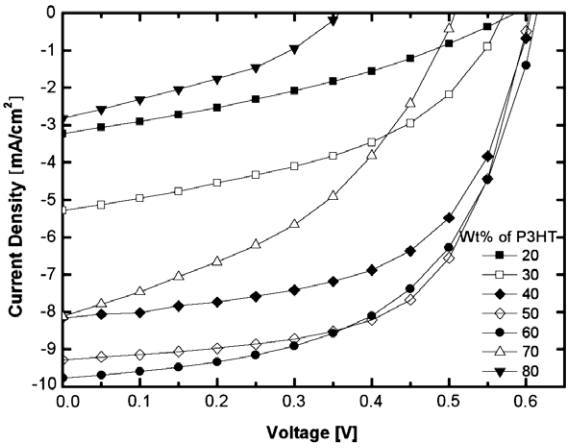

Fig. 5. The characteristics of the OSCs with various composite ratios of the P3HT:PCBM active layer; *J–V* curve for the best efficiency devices.

without clear fiber phases when increasing the P3HT composition above 60% in Fig. 4(e–g), which was in accordance with the XRD results. A previous report showed that the pure P3HT molecules form fibrillar structures even at room temperature [4]. Therefore, the disordering of P3HT in Fig. 4(e–g) was evidently caused by the small amount of PCBM molecules added to the P3HT matrix. Yang et al. suggested that the PCBM molecules deteriorate the ordering of P3HT by disrupting the chain packing and also by reducing the conjugation length of the polymer [12]. For the high P3HT composition regime in Fig. 4(e–g), the PCBM molecules did not likely crystallize because of the small amount of them present, which led to a lower probability of the molecules meeting for crystallization to take place in the given annealing conditions. Rather, the PCBM molecules hindered the crystallization of the P3HT phases because they were dispersed in the P3HT phases. As a result, a less ordered phase separated structure formed in the high P3HT composition layer.

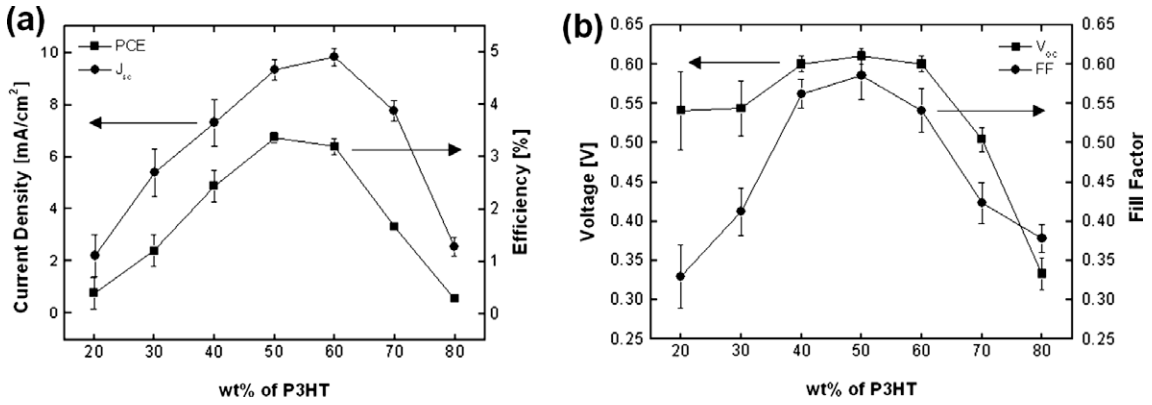

Fig. 6. Statistical data for the device parameters derived from each type of device with various composite ratios of the P3HT:PCBM active layer; (a) J_{sc} and PCE, (b) V_{oc} and FF.

Table 1
Summary of the statistical data for the device parameters derived from each type of device with various composite ratios of the P3HT:PCBM active layer.

Wt% of P3HT	20	30	40	50	60	70	80
J_{sc} (mA/cm^2)	2.21	5.40	7.33	9.35	9.84	7.78	2.56
V_{oc} (V)	0.54	0.54	0.6	0.61	0.60	0.50	0.33
FF	0.33	0.41	0.56	0.59	0.54	0.42	0.38
PCE (%)	0.40	1.20	2.44	3.37	3.20	1.66	0.29

Fig. 5 shows the current density–voltage (J–V) characteristics of the OSCs with various composite ratios of the P3HT:PCBM active layer. More than ten individual devices were fabricated and measured at each P3HT:PCBM composition. Fig. 6 and Table 1 show the statistical data of the device parameters. The device with 20% of P3HT exhibited very poor PV performances with a short circuit current density (J_{sc}) of 3.23 mA/cm^2, fill factor (FF) of 0.34, open circuit voltage (V_{oc}) of 0.58 V, and PCE of 0.63%. Moreover, the devices at this composition had a large variation in the device-to-device performance due to the large amount of PCBM overgrown clusters present (see Fig. 3). The PV performances depending on the P3HT:PCBM composition agreed well with the ordering of the P3HT phase and the phase separation as discussed in the XRD and TEM results. The J_{sc}, FF, PCE, and Voc all remarkably increased as the composition of P3HT increased from 20% to 50% because of the improved absorption of the incident light and the charge transportation property of the highly ordered P3HT fibers. Further increasing the P3HT composition from 60% to 80% degraded the PV performances even with the increased absorption at the high P3HT composition layer. This degradation in the PV performance was caused by degraded ordering of P3HT, the deficient PCBM molecules that accepted the generated electrons, and the deteriorated phase separation of the blurred heterojunction. Finally, the best PCE of 3.4% was obtained with reproducible performances from the device with the 50% P3HT composition layer.

4. Conclusion

The effect of the composite ratio of P3HT and PCBM on the PV performance of the OSCs was investigated in the BHJ structure. The UV/visible absorption and XRD results denoted that the interchain packing of crystallized P3HT improved with increasing P3HT composition, while the volume fraction of the P3HT (1 0 0) phase that was normal to the substrate increased until a P3HT composition of 50% and decreased at higher compositions. From the TEM analysis, P3HT and PCBM formed a heterojunction with the P3HT fiber structures as well as the PCBM overgrown clusters through phase separation when the PCBM composition exceeds 50 wt.%. Uniform phase separation, which formed P3HT fibers in the PCBM matrix without overgrown clusters, was obtained at a 50% P3HT and 50% PCBM composition. As the P3HT composition exceeded 50%, the fibril structures of P3HT were collapsed by the PCBM molecules, which hindered the crystallization of the P3HT phase. The optimized PV performance of the OSCs was achieved at an active layer composition of 50% P3HT and 50% PCBM with a maximum PCE of 3.4%.

Acknowledgment

This work was supported by the Grant No. (ROA-2006-000-10274-0) from the National Research Laboratory Program of the Korea Science and Engineering Foundation.

References

[1] W. Ma, C. Yang, X. Gong, K. Lee, A.J. Heeger, Adv. Funct. Mater. 15 (2005) 1617.
[2] H. Sirringhaus, P.J. Brown, R.H. Friend, M.M. Nielsen, K. Bechgaard, B.M.W. Langeveld-Voss, A.J.H. Spiering, R.A.J. Janssen, E.W. Meijer, P. Herwig, D.M. de Leeuw, Nature 401 (1999) 685.
[3] C.N. Hoth, S.A. Choulis, P. Schilinsky, C.J. Brabec, Adv. Mater. 19 (2007) 3973.
[4] H. Yang, S.W. LeFevre, C.Y. Ryu, Z. Bao, Appl. Phys. Lett. 90 (2007) 172116.
[5] K.M. Coakley, M.D. McGehee, Chem. Mater. 16 (2004) 4533.
[6] Y. Yao, J. Hou, Z. Xu, G. Li, Y. Yang, Adv. Funct. Mater. 18 (2008) 1783.
[7] A. Zen, M. Saphiannikova, D. Neher, J. Grenzer, S. Grigorian, U. Pietsch, U. Asawapirom, S. Janietz, U. Scherf, I. Lieberwirth, G. Wegner, Macromolecules 39 (2006) 2162.
[8] Y. Kim, S.A. Choulis, J. Nelson, D.D.C. Bradley, S. Cook, J.R. Durrant, J. Mater. Sci. 40 (2005) 1371.
[9] V. Shrotriya, J. Ouyang, R.J. Tseng, G. Li, Y. Yang, Chem. Phys. Lett. 411 (2005) 138.
[10] J. Jo, S.-S. Kim, S.-I. Na, B.-K. Yu, D.-Y. Kim, Adv. Funct. Mater. 19 (2009) 866.
[11] X. Yang, J. Loos, S.C. Veenstra, W.J.H. Verhees, M.M. Wienk, J.M. Kroon, M.A.J. Michels, R.A.J. Janssen, Nano Lett. 5 (2005) 579.
[12] G. Li, Y. Yao, H. Yang, V. Shirotriya, G. Yang, Y. Yang, Adv. Funct. Mater. 17 (2007) 1636.
[13] D. Chirvase, J. Parisi, J.C. Hummelen, V. Dyakonov, Nanotechnology 15 (2004) 1317.
[14] S.-H. Jin, B.V.K. Naidu, H.-S. Jeon, S.-M. Park, J.-S. Park, S.C. Kim, J.W. Lee, Y.-S. Gal, Sol. Energy Mater. Sol. Cells 91 (2007) 1187.
[15] W.-H. Baek, H. Yang, T.-S. Yoon, C.J. Kang, H.H. Lee, Y.-S. Kim, Sol. Energy Mater. Sol. Cells 93 (2009) 1263.
[16] A. Swinnen, I. Haeldermans, M. Ven, J. D'Haen, G. Vanhoyland, S. Aresu, M. D'Olieslaeger, J. Manca, Adv. Funct. Mater. 16 (2006) 760.
[17] S. Hotta, S.D.D.V. Rughooputh, A.J. Heeger, Synth. Met. 22 (1987) 79.
[18] Y. Kim, S. Cook, S.M. Tuladhar, S.A. Choulis, J. Nelson, J.R. Durrant, D.D.C. Bradley, M. Giles, I. Mcculloch, C.-S. Ha, M. Ree, Nat. Mater. 5 (2006) 197.
[19] T.J. Savenije, J.E. Kroeze, X. Yang, J. Loos, Adv. Funct. Mater. 15 (2005) 1260.
[20] L. Goris, A. Poruba, A. Purkrt, K. Vandewal, A. Swinnen, I. Haeldermans, K. Haenen, J.V. Manca, M. Vaněček, J. Non-Cryst. Solids 352 (2006) 1656.

able improvement of the conductivity and work function of the material. Furthermore, efforts have also been made to modify the PEDOT:PSS by low-electron energy [18] and adding anionic surfactants [19]. Recently, a simpler and efficient way for the electronic property modification of the material has been achieved using a UV–ozone treatment at ambient conditions [20–22]. This method showed a significant increase in the work function and enhancement of electrical conductivity of the PEDOT:PSS. Surprisingly, the potential of this easy and versatile method for the improvement of fluorescent OLEDs has not yet been investigated in detail. The present study therefore focuses on investigating the role of device architecture and duration of the UV–ozone exposure required for work function tuning to achieve balanced charge injection and optimum power efficiency in fluorescent OLEDs.

In this study, the fluorescent OLEDs selected to study the effect of UV–ozone exposure on the device efficiency are two green-emitting fluorescent devices of the following configuration; Device I – Indium tin oxide (ITO)/PEDOT:PSS (38 nm)/*N*,*N*-di(naphthalene-1-yl)-*N*,*N*′-diphenylbenzidine [α-NPD] (50 nm)/tris(8-quinolinolato) aluminum [Alq_3] (40 nm)/CsF (1 nm)/Al (100 nm); and Device II – ITO/PEDOT:PSS (38 nm)/α-NPD (40 nm)/Alq_3:1% C545T (30 nm)/Alq_3 (30 nm)/CsF (1 nm)/Al (100 nm). In both Devices I and II, the PEDOT:PSS layer was exposed to UV–ozone treatment from 0 min to 12 min in two minute intervals. The efficiency of the OLEDs whose PEDOT:PSS layer are treated by UV–ozone exposure are compared with the OLEDs fabricated without the UV–ozone exposure (control). Furthermore, the effect of the UV-exposure time on physical and/or chemical modification of the polymer related to charge injection and the device efficiency is discussed in relation to the device physics of charge injection.

2. Device fabrication

A cross section of the OLEDs (Device I and Device II) and the materials utilized as hole-transporting and emissive layers in device fabrication are shown in Fig. 1. As an anode, ITO (20 Ω/) on a glass substrate was used. In the first step, the ITO/glass substrate was cleaned by a detergent followed by ultrasonic bath in acetone and isopropanol. Following the wet cleaning, the sample was dried with nitrogen gas and exposed to UV–ozone dry cleaning for 20 min. Then, an aqueous solution of PEDOT:PSS (Baytron P VP AI 4083) was filtered using a 0.2 μm syringe filter and subsequently spin-coated at 3000 rpm onto a precleaned substrate. After the PEDOT:PSS spin coating, the film was annealed at 120 °C under ambient conditions for 10 min to remove water from the polymer film. The thickness of the dry PEDOT:PSS film is ∼ 38 ± 5 nm. Next, the PEDOT:PSS layer was exposed to UV–ozone (PSD-UV, Novascan, IA, USA) for time ranging from 0 to 12 min. Following the PEDOT:PSS deposition, the organic materials were deposited by resistive evaporation.

The organic layers, α-NPD and Alq_3, were deposited at a deposition rate of ∼2 Å/s. The source materials were purified by sublimation before deposition. To improve a better electron charge injection or device performance of the OLEDs, a 1 nm CsF was deposited after the deposition of the electron transport layer, Alq_3. The cathode realized by shadow mask deposition of aluminum without breaking the vacuum. The cathode thickness and pixel area is 100 nm with 0.04 cm^2, respectively. The resulting OLEDs electroluminescence characteristics were measured using Hamamatsu Photonic C9920-22 system containing a Keithley 2400 source-meter, an integrated sphere and a multichannel analyzer PMA-12. The electroluminescent

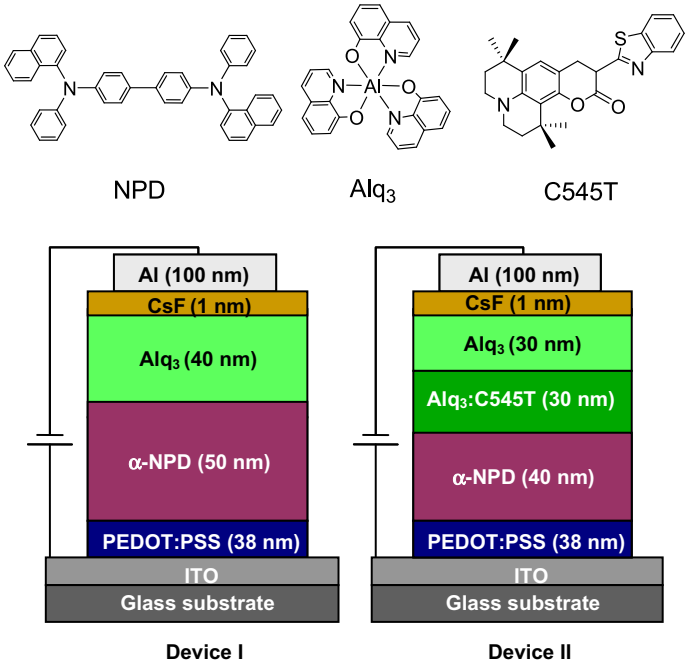

Fig. 1. Molecular structure of the transport and emitting layers used for the device fabrication (top), and the architectures of Device I and Device II (bottom).

characterizations were made in glove box under nitrogen atmosphere so as to protect the device degradation by oxygen or moisture.

3. Results

First, the effect of the UV–ozone exposure on surface property of the PEDOT:PSS was studied. PEDOT:PSS was spin-coated onto a silicon wafer substrate, which displays low surface roughness compared to ITO–glass substrate. To maintain the consistency of the process, the wafer was cleaning, spin-coated and treated with UV–ozone exactly in the same way used for the ITO substrate used in device fabrication. Fig. 2 presents the surface profilometry characterization of the PEDOT:PSS on a silicon wafer exposed to 8 min UV–ozone vs. the un-exposed, which was

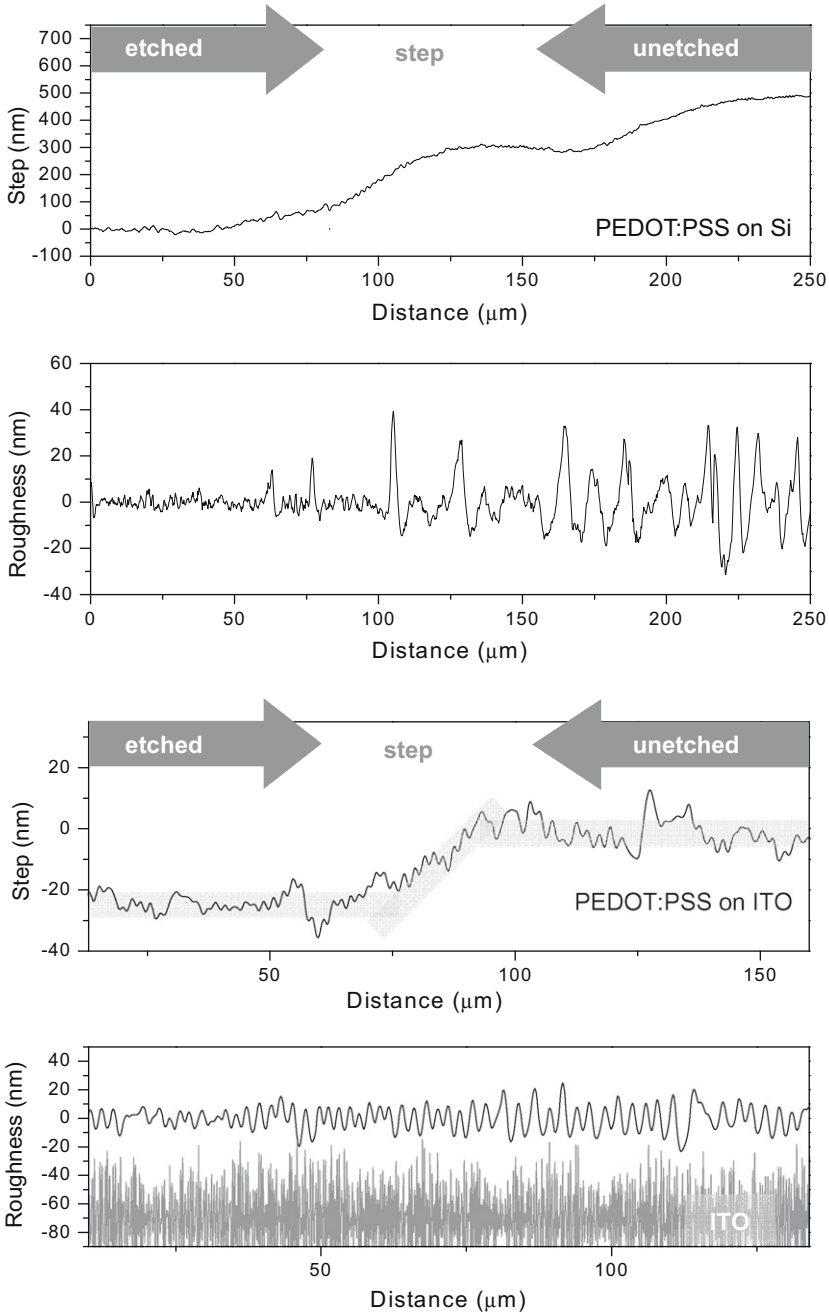

Fig. 2. Surface profilometry measurements of PEDOT:PSS on a silicon wafer (top and second panels) and PEDOT:PSS on an ITO-covered glass (third and bottom panels). Top panel: The step between the etched (left) and unetched (right) region (covered by a shadow mask) indicates approx. 150 nm of etching. Second panel: The etched regions shows lower surface roughness compared to the un-etched film. Third panel: the step between the etched (left) and unetched (right) region (covered by a shadow mask) indicates approx. 17 nm of etching. Bottom: The etched region shows lower surface roughness compared to the un-etched film, both regions show lower surface roughness than the ITO-covered glass substrate.

covered by a shadow mask during the UV–ozone treatment. The UV–ozone exposure resulted with two obvious changes, etching and decreased roughness of the polymer film. The scanning surface profilometry measurements across the exposed and un-exposed regions on of the polymer film showed a clearly observable step in the polymer thickness due to etching. For example, the UV–ozone exposure of the PEDOT:PSS on the silicon wafer for 8 min resulted in reduction of the thickness of the polymer film from 316 nm to ~155 nm, which corresponds to approx. 50% etching. Furthermore, the average roughness of the film was decreased from ~20 nm without the exposure to ~10 nm after the 8 min exposure. Similar effect was also observed for exposures shorter than 8 min, however, with a smaller effect on film thickness and roughness. Similarly, it is expected that both effects, etching and decreased surface roughness, will be observed for UV–ozone exposed PEDOT:PSS film on ITO substrate. On the ITO substrate, the PEDOT:PSS film deposited in the exactly same manner was only 37–39 nm thick. This is presumed to be due to the different wettability of the silicon vs. ITO. Here, the step from 37–39 nm to 20–22 nm after 8 min. of treatment, which corresponds to approx. 46% reduction in the PEDOT:PSS thickness, was observed.

The study of the etching effect and roughness was done using a silicon wafer rather than ITO because the roughness of the ITO is close to the thickness of the polymer film, which precludes accurate observation of the surface features. Unfortunately, the difference in surface chemistry of the silicon wafer vs. ITO and the attendant differences in surface energy and polymer–substrate interaction result also in a large difference of the polymer film thickness and compactness. Thus, the known conditions used to deposit a 38 ± 5 nm thick PEDOT:PSS film on ITO yield a ~310 nm film on a Si wafer. Importantly, the PEDOT:PSS is etched more on Si than on ITO, presumably as a result of a different ozone penetration depth and the fact that the wafer reflects the UV light used for etching. The etching study on Si is presented here only to illustrate the two factors that we believe are universal for the UV–ozone process: The etching and decrease in the surface roughness.

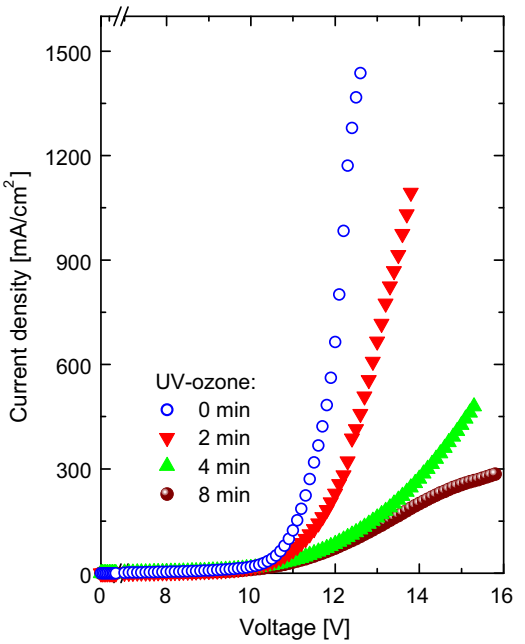

Fig. 3. Current density–voltage (*J–V*) characteristics of a fluorescent OLED utilizing PEDOT:PSS treated with UV–ozone for 0, 2, 4 and 8 min. The configuration of the Device II is ITO/PEDOT:PSS (38 nm)/α-NPD (40 nm)/Alq_3:1% C545T (30 nm)/Alq_3 (30 nm)/CsF (1 nm)/Al (100 nm).

Secondly, the effect of UV–ozone treatment on fluorescent OLEDs performance and its potential applicability to fabrication of the devices were performed by characterization of the OLED devices fabricated at different time of UV–ozone exposure of PEDOT:PSS (HIL) from 0 to 12 min. The electrical properties of the OLEDs were studied together with the optical characteristics. Fig. 3 shows the current density–voltage (*J–V*) characteristics of OLEDs (Device II) using PEDOT:PSS treated with UV–ozone for 0, 2, 4 and 8 min. As one can see, the UV–ozone exposure has a significant effect on charge injection, which decreases with extended UV–ozone exposure. Similar trend in the *J–V* characteristics was also observed for OLEDs regardless of the changes in the configuration. Because the treatment affects the hole injection from the PEDOT:PSS anode, the injection efficiency [3] was studied using a hole-only device with configuration of ITO/PEDOT:PSS (38 nm)/ α-NPD (70 nm)/CsF (1 nm)/Al (100 nm). The data from the hole-only device show that the injection efficiency dramatically decreases, e.g. at 8 V from 0.014 for untreated anode to 0.001 at 8 min of UV–ozone exposure, which corresponds to a thirteen-fold decrease.

In addition to the effect of the UV–ozone exposure on the thickness of the polymer film and the charge injection of the polymer by the exposure, we have also studied the potential effect of UV–ozone exposure time on the shape of the electroluminescent spectra of the devices. Fig. 4 shows that there is no appreciable change in the shape of the EL spectra as a result of the UV–ozone treatment.

Fig. 5a shows the external quantum efficiency (EQE) vs. current density dependence recorded for Device I. It shows that the use of UV–ozone treatment of the PEDOT:PSS layer has a positive effect on the electroluminescence characteristics of the device as well as the duration of exposure required for optimal performance. The EQE of the device improved from 1.15% to 1.55% for the duration of UV–ozone treatment from 0 min to 4 min. After 4 min of the treatment, the EQE drops off significantly. To get a more detailed insight into the phenomenon, the power efficiency of the improved devices by UV–ozone exposure were compared with the control device wherein the HIL was left untreated.

Fig. 5b shows the corresponding power efficiency vs. current density characteristics of the devices for 0, 2 and 4 min of UV–ozone exposure and the resulting increase in the device power efficiencies, which was found to increase from 1.05 lm/W at 0 min to 2.7 lm/W after a 4 min exposure with a maximum luminance of 37,000 cd/m^2. Thus, the maximum power efficiency of the devices was improved by more than 100%. Similarly to the EQE, the power efficiency decreases with a UV–ozone treatment

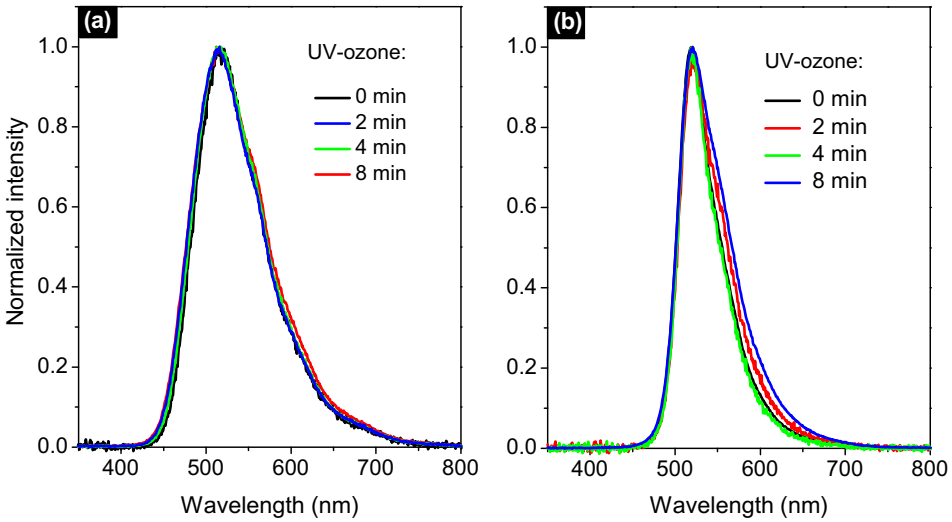

Fig. 4. Electroluminescence spectra of Device I (a) and Device II (b) at 0 min, 2 min, 4 min and 8 min of UV–ozone exposure.

prolonged beyond 4 min. Both the EQE and power efficiency measurements of Device I show that the optimal performance is achieved at 4 min of UV–ozone treatment.

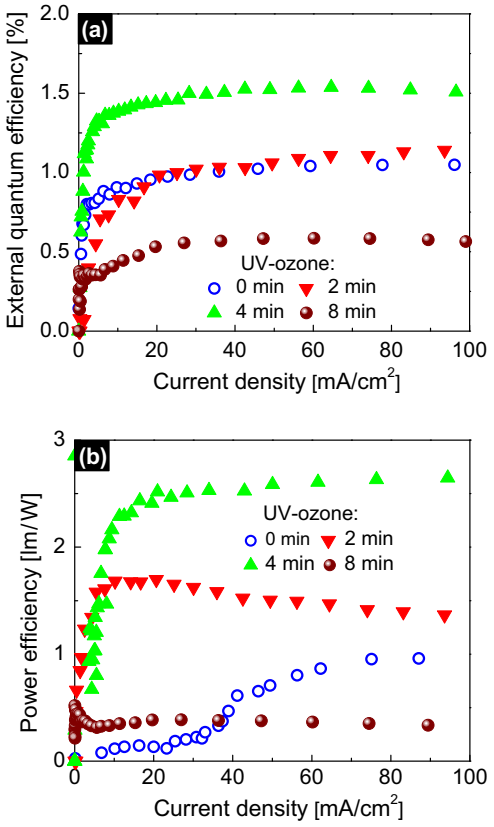

Fig. 5. EQE–current density (a) and power efficiency–current density (b) characteristics of Device I at 0 min, 2 min, 4 min and 8 min of UV–ozone exposure.

It was also observed that the corresponding current efficiency of the device has peaked at 4 min of the treatment with 4.6 cd/A that increased from 3.1 cd/A at 0 min. The UV–ozone treatment affects the turn-on voltage of the device from 3.5 V for the control device with untreated PEDOT:PSS layer to 2.6 V of for the 4 min of the UV–ozone exposure.

The UV–ozone treatment method was also tested to Device II with optimized emissive layer comprising highly emissive dopant C545T (fluorescence quantum yield ~0.95) in the emissive layer. Due to the strongly emitting dopant (quantum yield of C545T is more than twice higher, compared to the neat Alq_3 in Device I) even in the unoptimized HIL, Device II displays a relatively high performance [14]. The electroluminescence characteristics of the Device II are shown in Fig. 6. Fig. 6a shows the dependence of EQE on current density. Here, the use of UV–ozone exposure increases the EQE, which reached its maximum at 8 min and a further increase in the UV–ozone exposure of the PEDOT:PSS tends to reduce the performance of the device. The EQE of the Device II is improved from 4.0% for the untreated (control) device to 5.5% at 8 min exposure. Importantly, the control device reached 4.0% EQE at very high current density (>50 mA/cm^2) while the optimized Device II (8 min treatment) reached its maximum EQE at a low current density of 0.4–0.8 mA/cm^2. Similarly, the power efficiency of Device II was also improved, Fig. 6b. Specifically, the power efficiency of Device II increased from 4.10 lm/W for untreated (control) device to 8.24 lm/W fabricated using the UV–ozone treated PEDOT:PSS layer for 8 min. Once again, this corresponds to a 100% improvement in power efficiency. The maximum power efficiency in Device II with 8 min UV–ozone treatment was achieved at current density of 0.4–0.8 mA/cm^2, which corresponds to a respectable luminous output of 66–140 cd/m^2. The corresponding maximum current efficiency of the device increased following a similar trend and increased from 14.5 cd/A at 0 min to 19.5 cd/A at 8 min.

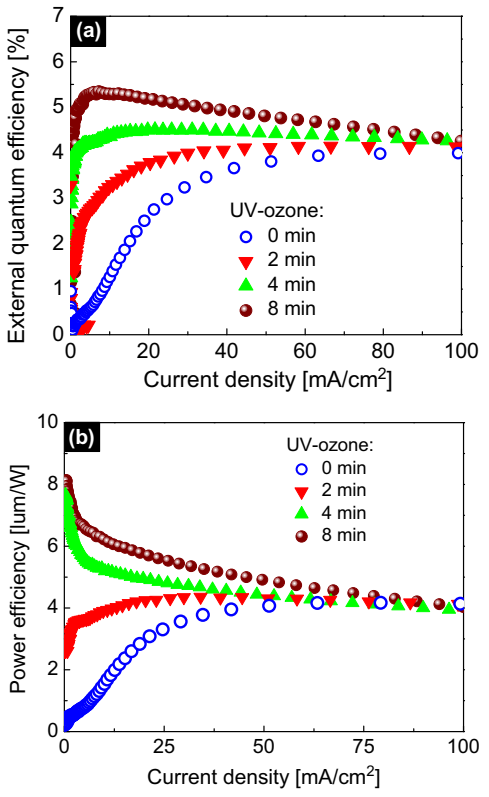

Fig. 6. EQE–current density (a) and power efficiency–current density (b) characteristics of Device II at 0 min, 2 min, 4 min, and 8 min UV–ozone exposure.

In both types of devices, it was observed that the value of maximum luminance is reduced with the increased UV–ozone exposure. For example, in Device II, the maximum luminance was 74,000 cd/m^2 for the untreated (control) device and 22,100 cd/m^2 for 8 min of UV–ozone treatment. However, upon UV–ozone treatment Device II achieves maximum luminous efficiency at significantly lower overall charge carrier density in the device available for recombination. Here, it is important to note that the luminance in either Device I at 4 min or Device II at 8 min satisfies the device requirement in display application while showing improved device efficiency. Thus, from the devices characterization results, a general comparable device efficiency improvement was observed for both Device II and Device I alike.

In addition to the electroluminescence characteristics of the OLEDs, we have also investigated the effect of changing the order of the process steps of UV–ozone exposure and annealing the PEDOT:PSS on the morphology of the polymer film and devices performance. The standard fabrication process utilizes spincoating, drying, annealing and UV–ozone treatment. The performance of these devices fabricated using the reversed order of the annealing and UV–ozone steps was found comparable to the devices fabricate using the standard process and no further improvements in the resulting devices were observed. Note, that all the devices described here were fabricated by the standard process based on the annealing of the PEDOT:PSS followed by UV–ozone exposure.

4. Discussion

The improvement of the electroluminescence efficiency of OLEDs by improving and balancing of charge injection is a crucial factor for fabrication of efficient devices. In particular, the PEDOT:PSS, a HIL material deposited by solution method at ambient condition is important material in the OLEDs, organic photovoltaics (OPVs) and other organic–electronic devices. Hence, the development of methods for tuning its electrical properties is highly desirable. In the realm of OLEDs, the requirement on the HIL is high work function, reduced charge trapping defects and smoother surface (reduced roughness) with low occurrence of pinhole defects [20]. The data obtained in this study show that UV–ozone exposure imparts such properties to the PEDOT:PSS HIL. Particularly, the surface profilometry measurements indicate that the surface roughness is dramatically reduced as a result of the UV–ozone treatment. Furthermore, when compared to the control devices fabricated without the UV–ozone treatment, the increase of the OLED performance suggests that the UV–ozone treatment improved balanced charge injection has been achieved. The study also indirectly proves the change in work function of the polymer film by UV–ozone exposure. This finding is in agreement with recent studies carried out using X-ray photoelectron spectroscopy (XPS) and Raman spectroscopy, which indicated that the use of UV–ozone exposure results in an increase in the work function by at least 0.2 eV [20] and at most 0.25 eV [21] with enhancement of electrical conductivity of the material. This increase in conductivity originates from a decrease in the number of the charge trapping related defects and the formation of linear or expanded polymer chain coil conformation [21]. Thus, the increase in the PEDOT:PSS layer work function, which resulted in better utility of injected charges, seems to be the main reason for the improved device efficiency of the OLEDs with UV–ozone treated PEDOT:PSS layer.

Our measurements indicate that an optimum UV–ozone exposure is required for the best device efficiency. The efficiency of the device first increases with prolonged UV–ozone exposure up to a certain critical time (i.e., 4 min and 8 min for Device I and Device II, respectively), after which the charge injection efficiency decreases. The decrease in charge injection efficiency seems to have originated from the UV–ozone induced increase in the work function of the polymer. The change in the performance of the OLEDs for different time of the UV–ozone exposure indicates that balanced charge injection of the HIL is dependent on the exposure time of the PEDOT:PSS. This is presumably due to the different composition of the emissive layers, which each require different PEDOT:PSS work function to achieve the balance in charge injection and optimal charge recombination in the respective emissive layers. The change in work function as a function of the time of UV–ozone exposure has two regimes: First,

the work function increases with time and then it saturates at a certain critical time [20]. Thus, we believe the untreated (control) devices showed a reduced performance simply due to its low (native) work function, as compared to the exposed cases. Similarly, the low performance in the devices that fabricated using the PEDOT:PSS treated for duration lower than critical time would be due to the insufficient increase in the work function and perhaps also due to insufficient time for complete oxidation of the material to induce an effective balanced charge injection. The change of the work function saturates after a certain critical time of UV–ozone exposure. Based on the device performance results, the work function seems to reach saturation after 4 min, as Device II showed performance improvement at 8 min, which indirectly showed that there is an increase of the work function after 4 min. Also, the improved performance of the device might have come from the reduced surface roughness and possible enhanced interface compatibility between the PEDOT:PSS (HIL) and α-NPD (HTL) as a result of the UV–ozone exposure. Furthermore, due to a mild erosion of the HIL surface and possible changes to HIL–HTL adhesion cannot be excluded. However, we reason that changes in the PEDOT:PSS surface, either chemical (oxidation) and or physical (reduced roughness), are not likely the main reason for the OLED performance improvement. This is because such changes would uniformly affect both the Device I and Device II as they have the same interface of injection, i.e., PEDOT:PSS/α-NPD. In other words, while the roughness of the polymer film is improved at 8 min than at 4 min, the best device performance is at 4 min for Device I while it is at 8 min for Device II, and this difference in time of exposure is related to the charge balanced issue which is controlled by the UV–ozone induced tuning or shift of the work function. Thus, the improvements in the device efficiency of the devices by the UV–ozone exposure, related to the change/increase in the work function, seems to be mainly originated from the oxidation and/or oxygenation of the PEDOT:PSS. The increase in the work function accompanied by decreased surface roughness is a significant factor in device performance improvement. It could be argued that the improved performance might be due to the change in polymer film thickness (5–10 nm) upon etching. However, a study by Zhou et al. [23] on PEDOT:PSS layer thickness in a device architecture similar to Device I indicates that the OLEDs employing different thicknesses of the HIL exhibited very similar performance. Thus, the variation in the PEDOT:PSS thickness due to UV–ozone exposure is not the reason for such a marked improvement in the performance of the devices. However, it should be noted that a UV–ozone exposure prolonged beyond a critical time increases the chance of creating pinhole defects due to excessive etching and device failure, while the change in work function saturates and does not provide further benefit.

We believe that the present easy-to-do inexpensive method that allows for improvement in device efficiency offers a promising avenue for improving low-cost devices for practical applications and is complimentary to the previous efforts made in enhancing the efficiency of the fluorescent OLEDs [14–16].

5. Summary

The application of a mild UV–ozone treatment of PEDOT:PSS HIL in the controlling of balanced charge injection and the device efficiency improvement of fluorescent OLEDs were investigated. Comparative measurements of the device characteristics with and without UV–ozone treated PEDOT:PSS layer were carried out. The study shows that the use of UV–ozone treatment of PEDOT:PSS improves the OLEDs power efficiency by at least 100%. It has also been found that the performance of OLEDs is dependent on the UV–ozone exposure time and that the exposure to achieve maximum device performance varies with the device configuration. The improved efficiency is due to the controlled increase in the work function and reduced roughness of the PEDOT:PSS as a result the UV–ozone induced oxidation of the material. Using the UV–ozone treatment of the PEDOT:PSS, the power efficiency of the Alq_3-based Device I was improved from 1.05 lm/W without the treatment to 2.7 lm/W at 4 min. Device II, which utilizes green coumarin C545T dopant and Alq_3 as a host for the emissive layer was improved from 4.1 lm/W without the treatment to 8.24 lm/W at 8 min. The improved efficiency of the devices is mainly obtained through the efficient balanced charge injection as a result of tuning the work function of the HIL brought about by the UV–ozone exposure. The surface profilometry study confirms that the UV–ozone oxidation etching of the PEDOT:PSS layer change the morphology or roughness of the PEDOT:PSS layer. Therefore the method addresses the two important conditions in the device fabrication, improved roughness and enhanced work function, and an impact on device performance improvements. In summary, this simple and versatile method can be used to improve the performance of OLED devices without a need for further instrumentation or advanced device architectures. As such, this method could be useful in fabrication of inexpensive large scale OLEDs without significant impact to the overall cost.

Acknowledgments

This work was supported by the Air Force Office of Scientific Research (AFOSR) (FA9550-05-1-0276 to P.A.), the State of Ohio (WCI-PVIC) and BGSU. The authors are also thankful to Dr. Fengyu Li for his help with surface SEM characterization.

References

[1] T.A. Skotheim, J. Reynolds, Handbook of Conducting Polymers, third ed., CRC Press, Taylor and Fransis, Boca Raton, FL, USA, 2007.
[2] G.G. Wallace, P.R. Teasdale, G.M. Spinks, L.A.P.K. Maguire, Conductive Electroactive Polymers: Intelligent Materials Systems, second ed., CRC Press, Taylor and Fransis, Boca Raton, FL, USA, 2002.
[3] Z. Kafafi, Organic Electroluminescence, CRC Press, Taylor and Fransis, Boca Raton, FL, USA, 2005.
[4] F. Faupel, C. Dimitrakopoulos, A. Kahn, C. Wöll, Reviews-organic electronics, Special Section of J. Mater. Res. 19 (2004) 1887.
[5] S.R. Forrest, Nature 428 (2004) 911.
[6] P. Anzenbacher Jr., V. Montes, S. Takizawa, Appl. Phys. Lett. 93 (2008) 163302.
[7] M.A. Baldo, D.F. O'Brien, M.E. Thompson, S.R. Forrest, Phys. Rev. B 60 (1999) 14422.

[8] W. Helefrich, W.G. Schneider, J. Chem. Phys. 44 (1966) 2902.
[9] P.K.H. Ho, J.-S. Kim, J.H. Burroughes, H. Becker, S.F.Y. Li, T.M. Brown, F. Cacialli, R.H. Friend, Nature 404 (2000) 481.
[10] Y. Cao, I.D. Parker, H. Yu, C. Zhang, A.J. Heeger, Nature 397 (1999) 414.
[11] J.S. Wilson, A.S. Dhoot, A.J.A.B. Seeley, M.S. Kahn, A. Köhler, R.H. Friend, Nature 413 (2001) 828.
[12] H.Y. Chen, W.Y. Lam, J.D. Luo, Y.L. Ho, D.B. Zhu, M. Wong, H.S. Kwonk, Appl. Phys. Lett. 81 (2002) 574.
[13] Y. Duan, M. Mazzeo, V. Maiorano, F. Mariano, D. Qin, R. Cingolani, G. Gigli, Appl. Phys. Lett. 92 (2008) 113304.
[14] K. Okumoto, H. Kanno, Y. Hamaa, H. Takahashi, K. Shibata, Appl. Phys. Lett. 89 (2006) 063504.
[15] J.-H. Lee, Y.-H. Ho, T.-C. Lin, C.-F. Wu, J. Electrochem. Soc. 154 (2007) 226.
[16] S. Chen, X. Li, W. Xie, Y. Zhao, C. Li, S. Liu, Thin Solid Films 516 (2008) 3364.
[17] M. Petrosino, P. Vacca, R. Miscioscia, G. Nenna, C. Minarini, A. Rubino, Proc. SPIE 6593 (2007) 659310.
[18] A.W. Denier van der Gon, J. Birgerson, M. Fahlman, W.R. Salaneck, Org. Electron. 3 (2002) 111.
[19] B. Fan, X. Mei, J. Ouyang, Macromolecules 41 (2008) 5971.
[20] C. Tengstedt, A. Kanciurzewska, M.P. Jong, S. Braun, W.R. Salaneck, M. Fahlman, Thin Solid Films 515 (2006) 2085.
[21] Y.-J. Lin, F.-M. Yang, C.-Y. Huang, W.-Y. Chou, J. Chang, Y.-C. Lien, Appl. Phys. Lett. 91 (2007) 092127.
[22] A. Benor, S. Takizawa, P. Chen, C.P. Bolívar, P. Anzenbacher Jr., Appl. Phys. Lett. 94 (2009) 193301.
[23] Y. Zhou, Y. Yuan, J. Lian, J. Zhang, H. Pang, L. Cao, X. Zhou, Chem. Phys. Lett. 427 (2006) 394.

with an agate mortar to obtain a corresponding sample with a smaller average grain size. Samples for photoluminescence (PL) measurements were prepared by pressing powder of the materials into aluminum cans to form tablets of 4 mm in diameter and 1 mm in thickness. Special cares have been devoted to make the powder in the tablets as densely packed as possible. Nevertheless, it is expected that due to the different crystal sizes and shapes, the packing densities of samples can be slightly different. Intensities of the UCL spectra so measured are thus not straightly quantitative. Hence, when comparing the absolute PL intensities of different samples, there can be small variations due to different packing densities.

XRD spectra were measured using a Siemens D5005 diffractometer with Cu-Kα radiation (λ = 1.5418 Å). Field emission scanning electron microscopy (FE-SEM) was carried out on a Hitachi S-4800 electron microscope. UCL spectra were measured under excitation of continuous 980 nm semiconductor laser with a maximum power of 2 W at an area of 0.01 cm^2. A Spectrometer with Spex 1403 photomultiplier with a boxcar averager was used to record the spectra. Conventional single photon PL spectra of crystalline samples under continuous 325 nm He–Cd laser were recorded by a UV-Laboratory Raman Infinity (n°9/35 INF, made by Jobin Yvon Company) with a resolution of 2 cm^{-1}. For comparison, PL measurements were also carried out on spin-coated thin film of polymethylmethacrylate (PMMA) doped with 0.1 wt.% rubrene and 0.5×10^{-3} M rubrene chloroform solution. The PL decay curves were measured by a two channel TEKTRONIX TDS-3052 oscilloscope and a Spectrometer with Spex 1403 photomultiplier under excitation of a 980 nm OPO laser and a 355 nm YAG:Nd^{3+} laser. The response time of the measurement system is about 30 ns and the lifetime shorter than 100 ns could not be exactly measured and overestimated with an error about several tens nanoseconds.

Fig. 1 shows X-ray diffraction (XRD) spectra of the four different rubrene powder samples. The main peaks in the XRD spectrum of Ru-1 can be indexed to the (0, 0, 2) and (0, 0, 6) planes of orthorhombic rubrene crystal [17]. Intensities of the (0, 0, 4) and the (0, 0, 8) peaks are much lower than those of (0, 0, 2) and (0, 0, 6). Besides the (0, 0, 2n) peaks, XRD spectra of Ru-2 and Ru-3 also show peaks corresponding to the (2, 0, 0), (2, 2, 0), (3, 1, 1), and (4, 2, 0) planes of a face-centered cubic (FCC) structure. It can also be seen that the (0, 0, 2) peak of the orthorhombic phase in Ru-2 and Ru-3 not only have lower relative intensities, but also be widened. The XRD results suggest that Ru-1 contains pure orthorhombic phase with a highly preferred orientation, while both Ru-2 and Ru-3 consist of orthorhombic and FCC phases. XRD spectrum of Ru-4 is virtually the same as that of Ru-1 which confirms that the grinding did not change the crystal structure. In addition, through comparing the intensities and widths of the diffraction peaks, it is concluded that Ru-1 and Ru-3 have the highest and the lowest crystallinity, respectively.

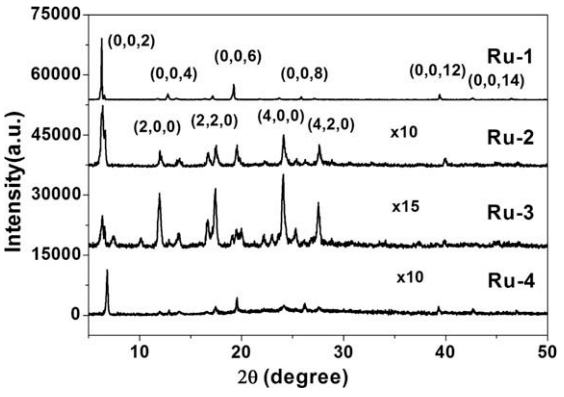

Fig. 1. XRD patterns of crystalline samples Ru-1, Ru-2, Ru-3, and Ru-4.

SEM images of the four crystalline samples are shown in Fig. 2. It can be seen that these samples have distinctly different crystal shapes and crystal sizes, which are about 40 μm, 15–30 μm, 10–20 μm, and 20 μm for Ru-1, Ru-2, Ru-3, and Ru-4, respectively. Crystalline features (sharp angles and edges, etc.) can be clearly observed in all samples. From SEM photographs, we can see that Ru-4 and Ru-1 have similar morphologies. It appears that the grinding of Ru-1 has broken the longer crystals into particles of smaller aspect ratios. On the other hand, Ru-2 and Ru-3 are respectively dominated by plate-like and short-rod crystals.

Fig. 3 shows UCL spectra of the four samples at room-temperature (RT) under the illumination of 980 nm laser. It can be seen that Ru-1 and Ru-3 give the highest and lowest UCL intensities, respectively. As mentioned in the experimental section, possible differences in packing densities of four samples might influence UCL intensities. However, when the conventional PL spectra (Fig. 4) of the four samples (which are exactly the same samples used for the UCL measurements) are compared, it can be seen that Ru-1 has lower PL intensity than Ru-2 and Ru-3. These results suggest that the possible packing density differences should not be a dominating factor on the relative UCL and conventional PL intensities of Ru-1, Ru-2, and Ru-3. On the other hand, as shown in Fig. 1, Ru-1 has a strong (0, 0, 2) texture. Hence, the highly preferred (0, 0, 2) orientation might be a possible cause for the highest UCL intensity. To check this, UCL intensities of Ru-1 were measured again upon tilting the samples to different angles with respect to the incident beam. No obvious change in UCL intensity has been observed. This suggests that the crystal orientation should not influence the UCL intensity.

Fig. 1 shows that Ru-1 consists purely orthorhombic phase, while Ru-2 and Ru-3 are mixtures of orthorhombic and FCC phases. The UCL intensity increases with the ratio of orthorhombic phase to FCC phase. Under the hypothesis that the orthorhombic phase gives the higher UCL intensity than the FCC phase, the UCL intensity order of Ru-1 > Ru-2 > Ru-3 can be consistently explained. Furthermore, Ru-1 has higher UCL (Fig. 3) and conventional PL (Fig. 4) intensities than Ru-4. This suggests that a larger grain size should increase both the UCL and conventional PL. One possible reason for this is stronger scattering effect in the sample with smaller grain size. It should also be pointed out that the UCL peak position of Ru-3 (594 nm) differs obviously from that (610 nm) of the other three samples, and the reasons are not clear.

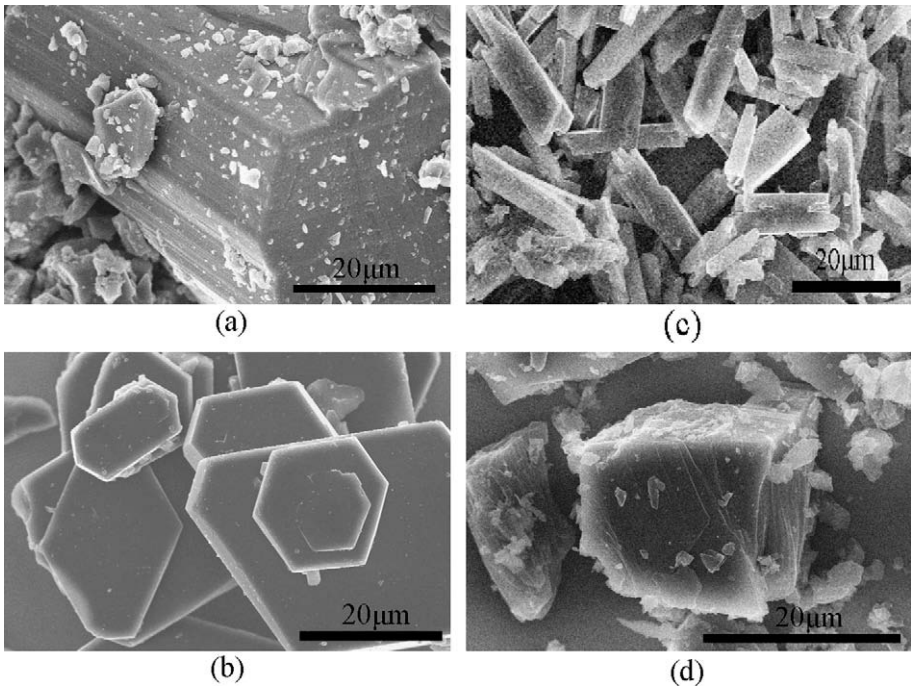

Fig. 2. SEM photographs of Ru-1 (a), Ru-2 (b), Ru-3 (c), and Ru-4 (d) samples.

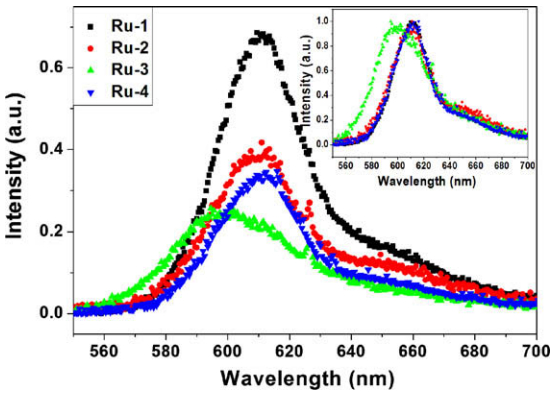

Fig. 3. UCL spectra of Ru-1, Ru-2, Ru-3, and Ru-4 at RT. Inset: Unitary UCL spectra of all samples at RT.

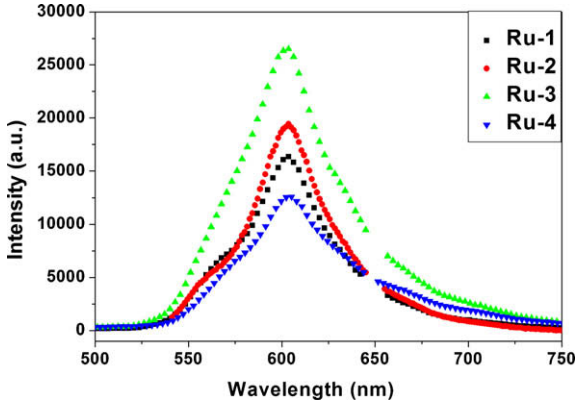

Fig. 4. Single photon emission spectra of samples Ru-1, Ru-2, Ru-3, and Ru-4 (λ_{ex} = 325 nm). Since the intense 650 nm laser line of He–Cd laser overlapped in the spectra, the spectra were drawn after the subtraction of 650 nm line.

Besides the influence of crystal phases and grain size on the difference of UCL intensities at RT, chemical impurities, structural defects, and reabsorption of fluorescence were also taken into account because these factors are related to the luminescence properties of crystal materials [18]. In our work, all samples were sublimed twice at 10^{-6} torr, so that the effect of chemical impurity could be ignored. The samples with lower crystallinity (Ru-2 and Ru-3) and the grinded sample (Ru-4) must have more structural defects than Ru-1. On the other hand, the blue-shift of photo-absorption and the red-shift of the emission peak of rubrene single crystal comparing with Rubrene solution were observed [19], which will lead to the suppression of reabsorption of fluorescence and the increase of fluorescence intensity. Therefore, quasi-single sample Ru-1 shows the highest UCL intensities at RT.

Fig. 5 shows the UCL spectra of the four samples at 77 K. It can be seen that the relative intensities of the samples are similar to those at RT (Fig. 3). One major difference from RT spectra is that the emission bands in all samples shift to shorter wavelength. At low temperature the oscillation of molecular crystal lattice mitigates so that the emission bands shift to higher energy [20].

Fig. 6 shows the dependence of the integral UCL intensity of Ru-1 on the excitation power density at RT and 77 K. At both temperatures, the UCL integral intensities show

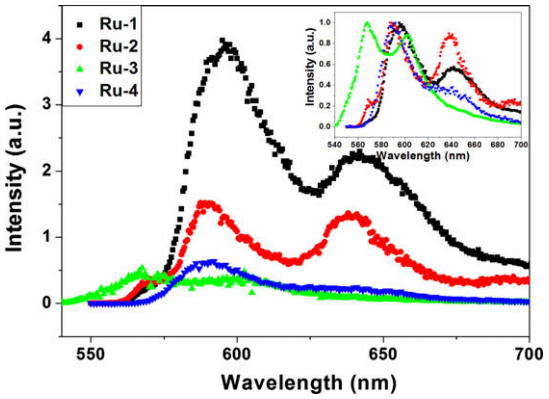

Fig. 5. UCL spectra of Ru-1, Ru-2, Ru-3, and Ru-4 at 77 K. Inset: Unitary UCL spectra of all samples at 77 K.

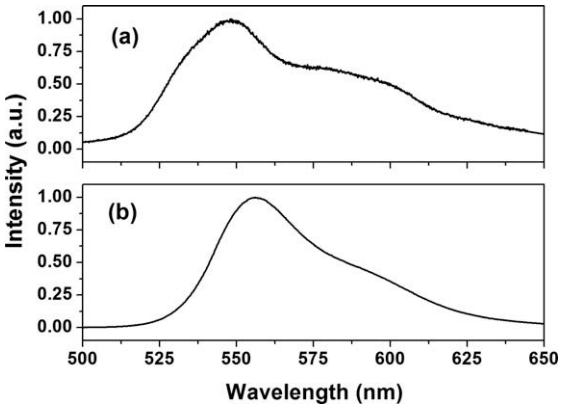

Fig. 7. Single photon emission spectra of 0.1wt.% rubrene dispersed PMMA film by spin-coated from chloroform solution (a) and 0.5×10^{-3} M rubrene chloroform solution (b) (λ_{ex} = 325 nm).

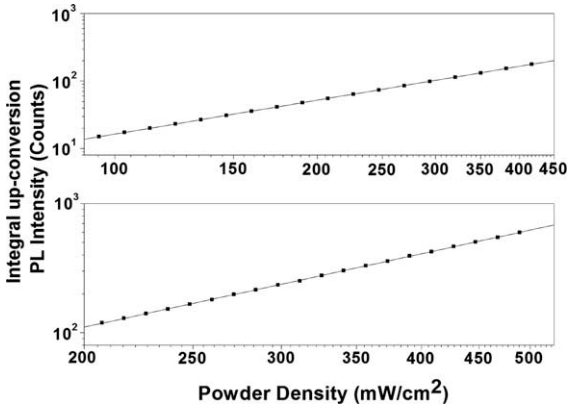

Fig. 6. The dependence of the integral UCL intensity of Ru-1 on the excitation power density of 980 nm laser at RT (a) and 77 K (b).

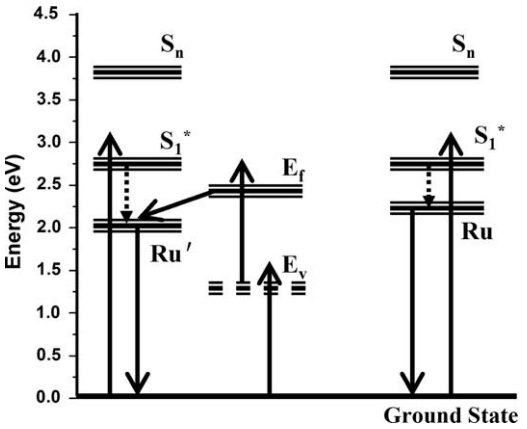

Fig. 8. The schematic level diagram of single- and two-photon emission and the energy transfer processes in UCL. S_1^*: The excited singlet state corresponding to UV laser illumination, E_f: The final state that is the second photon arrives, Ru: The energy level of single photon emission, Ru′: The energy level of UCL.

power law relationships to the excitation power density. The slopes of the fitted straight lines for RT and 77 K are 1.67 and 1.88, respectively, indicating that the UCL of rubrene crystal belongs to TPA process [21].

We also have measured UCL of 0.1 wt.% rubrene dispersed in PMMA film by spin-coated from their chloroform solution and 0.5×10^{-3} M rubrene chloroform solution under excitation of 980 nm laser. However, no UCL was observed; while the film and solution show conventional yellow PL around 550 nm upon illumination of 325 nm laser (Fig. 7). The distance between rubrene molecules in crystalline materials is expected to be much closer so that a stronger intermolecular interactional force produces. It is considered that the interaction between rubrene molecules in crystal is much stronger than that of dispersed rubrene molecules in solid matrix or in solution [19,22]. In other word, there should be no excitonic state corresponding to UCL emission level (610 nm) in rubrene film or solution [19]. Therefore, rubrene dispersed PMMA film or solution samples could not give UCL emission under excitation of 980 nm laser, but isolated rubrene molecules can be excited by 325 nm UV light, as shown in the right of Fig. 8.

In order to deeply investigate the mechanism of UCL process, we measured the decay curves of UCL and conventional PL of crystalline rubrene, and fitted the two lifetimes according to the equation: $y = A_1 * e^{-x/t_1} + A_2 * e^{-x/t_2}$. The results were t_1 = 68 ns (A_1 = 0.80346), t_2 = 472 ns (A_2 = 0.07556) and t_1 = 43 ns (A_1 = 9.99468), t_2 = 506 ns (A_2 = 0.02116) for up-conversion and conventional PLs, respectively. Considering the spectra of up-conversion and conventional PLs, we attribute the shorter lifetime and the longer lifetime to 610 nm emission and 650 nm emission, respectively, because the longer lifetime component presents a little proportion. The 650 nm emission is attributed to the emission of rubrene crystals which exist in small amounts in rubrene samples and this emission is the result of molecular interactions that is similar to the 610 nm emission [22]. Meanwhile, when excited by pulse laser, we can not capture the spectra of up-conversion

and conventional emissions of crystalline rubrene using our spectral measurement system even though we can see the bright light with our eyes, therefore the 610 nm emission should be less than the response time of our system (30 ns). That is, the lifetime of UCL is similar to that of single photon emission. The spectra in Figs. 3–5 were obtained under excitation of continuous 980 nm semiconductor laser and 325 nm He–Cd laser.

Considering that the lifetime of UCL through TTA is far longer than that of single photon emission, we think that the UCL process of crystalline rubrene would be arisen from TPA rather than from TTA. Under excitation of 980 nm infrared laser, as there are no sensitizers in the system, there must be a virtual state with a short lifetime (of the order of a few femto-seconds) playing a very important role in TPA process. As infrared light passes through crystalline rubrene molecules, the virtual state may form and exist for a very short duration [23–25]. If a second photon arrives before this virtual state decayed, TPA can result. The probability of TPA scaling with the square of the light intensity leads to a highly localized photon excitation. Therefore, TPA involves the concerted interaction of both photons that combine their energies, and then produces an electronic excitation similar to that conventionally caused by a single photon of a correspondingly shorter wavelength. Differing from single-photon absorption, the probability is squarely proportional to the incident intensity, as proved by Fig. 5 [23]. In crystalline rubrene, the second photon arriving level, also named as the final level (E_f), lies at 2.51 eV. After absorbed two 980 nm photons, UCL occurs through energy transfer from E_f to UCL level (2.03 eV), as shown in the left of Fig. 8. More detail mechanism for our UCL system is under studying.

UCL of crystalline rubrene samples under excitation of 980 nm infrared laser was demonstrated. It is interesting that it needs no assistance of any sensitizing materials. The UCL intensity increases as the proportion of orthorhombic crystal phase increases. Up-conversion quantum efficiency up to 0.19% was observed at RT in a sample with high phase purity of orthorhombic crystal. A large grain size appeared to have positive influences, while crystal orientation was observed to have little influence on the UCL intensity. UCL was not observed in all non-crystalline rubrene samples. The UCL is attributed to the excitonic state via stronger intermolecular interaction in the crystalline rubrene. It is well-known that most reported organic up-conversion lasers were in solutions which can limit certain applications [26], therefore, this special UCL system could be used to design new up-conversion optical systems.

Acknowledgements

This work was supported by the National Natural Science Foundation of China (Grant No. 10604054 and 60878027), Pillar Project in Burea of Science & Technology of Changchun city (08KZ24), and Knowledge Innovation Project of The Chinese Academy of Sciences (KJCX2-YW-M11).

References

[1] A. Mukherjee, Appl. Phys. Lett. 62 (1993) 3423.
[2] J.D. Bhawalkar, N.D. Kumar, C.F. Zhao, P.N. Prasad, J. Clin. Med. Surg. 37 (1997) 510.
[3] G.S. He, G.C. Xu, P.N. Prasad, B.A. Reinhardt, J.C. Bhatt, A.G. Dillard, Opt. Lett. 20 (1995) 43.
[4] B.H. Cumpston, S.P. Ananthavel, S. Barlow, D.L. Dyer, J.E. Ehrlich, L.L. Erskine, A.A. Heikal, S.M. Kuebler, I.Y.S. Lee, D.M. Maughon, Nature 51 (1999) 398.
[5] M.G. Mayer, Ann. Phys. 9 (1931) 273.
[6] R. Schroeder, W. Graupner, U. Scherf, B. Ullrich, J. Chem. Phys. 116 (2002) 3449.
[7] C. Bauer, B. Schnabel, E.B. Kley, U. Scherf, H. Giessen, R. Mahrt, Adv. Mater. 14 (2002) 673.
[8] R.R. Islangulov, D.V. Kozlov, F.N. Castellano, Chem. Commun. 30 (2005) 3776.
[9] W. Zhao, F.N. Castellano, J. Phys. Chem. A. 110 (2006) 11440.
[10] S. Baluschev, T. Miteva, B. Minch, V. Yakutkin, G. Nelles, A. Yasuda, G. Wegner, J. Appl. Phys. 101 (2007) 023101.
[11] P.E. Keivanidis, S. Baluschev, T. Miteva, G. Nelles, U. Scherf, A. Yasuda, G. Wegner, Adv. Mater. 15 (2003) 2095.
[12] F. Laquai, G. Wegner, C. Im, A. Busing, S. Heun, J. Chem. Phys. 123 (2005) 074902.
[13] S. Baluschev, F. Yu, T. Miteva, S. Ahl, A. Yasuda, G. Nelles, Nano Lett. 12 (2005) 2482.
[14] D. Hertel, H. Bässler, R. Guentner, U. Scherf, J. Chem. Phys. 115 (2001) 10007.
[15] A. Gerhard, H. Bässler, J. Chem. Phys. 117 (2002) 7350.
[16] S. Baluschev, V. Yakutkin, G. Wegner, T. Miteva, G. Nelles, A. Yasuda, S. Chernov, S. Aleshchenkov, A. Cheprakov, Appl. Phys. Lett. 90 (2007) 181103.
[17] E. Menard, A. Marchenko, V. Podzorov, M.E. Gershenson, D. Fichou, J.A. Rogers, Adv. Mater. 18 (2006) 1552.
[18] R. Katoh, K. Suzuki, A. Furube, M. Kotani, K. Tokumaru, J. Phys. Chem. C. 113 (2009) 2961.
[19] A. Saki, S. Seki, T. Takenobu, Y. Iwasa, S. Tagawa, Adv. Mater. 20 (2008) 920.
[20] V.M. Agranovich, G.F. Bassani, J. Knoester, G.C. La Rocca, A.M. Kamchatnov, M. Hoffmann, V.I. Yudson, D.G. Lidzey, in: V.M. Agranovich, D. Taylor (Eds.), Thin Films and Nanostructures: Electronic Excitations in Organic Based Nanostructures, Amsterdam, 2003, pp. 1–96.
[21] Y.Q. Lei, H.W. Song, L. Yang, L. Yu, Z. Liu, J. Chem. Phys. 123 (2005) 174710.
[22] X.H. Zeng, D.Q. Zhang, L. Duan, L.D. Wang, G.F. Dong, Y. Qiu, Appl. Surf. Sci. 253 (2007) 6047.
[23] K.D. Belfield, K.J. Schafer, Y. Liu, X. Ren, E. Stryland, J. Phys. Org. Chem. 13 (2000) 837.
[24] D.I. Lee, T. Goodson III, J. Phys. Chem. B. 110 (2006) 25582.
[25] F. Terenziani, C. Katan, E. Badaeva, M. Blanchard-Desce, Adv. Mater. 20 (2008) 4641.
[26] G.S. He, L. Yuan, P.N. Prasad, A. Abbotto, A. Facchetti, Opt. Commun. 140 (1997) 49.

resistance of 12 Ω/□. The substrates were ultrasonically cleaned in acetone, ethanol and de-ionized water, by which most of the ITO surface organic contaminants were removed. The surface of ITO gate electrode was then treated in an Ar plasma prior to depositions of the insulating layer. A radio frequency (r.f.) capacitively-coupled plasma (CCP) with a pressure of 0.1 Torr, Ar flow rate of 10 sccm, and r.f. main power of 100 W was used for surface treatment of the ITO gate electrode. Without breaking vacuum after the plasma surface treatment, plasma polymerized methyl methacrylate (ppMMA) insulting layer was then deposited, where a MMA monomer (Sigma–Aldrich Co.) was used. Plasma polymerization of the ppMMA dielectric layers was done again using the r.f. CCP equipment. Details of the plasma polymerization equipment were described elsewhere [10]. The ppMMA was deposited under following experimental condition: main power of 200 W, bias power of 20 W, system pressure of 0.5 Torr, Ar flow rate of 30 sccm, and deposition time of 10 min. The thickness of the ppMMA film was measured by field emission-scanning electron microscope (FE-SEM; Hitachi, S-4300) and found to be about 100 nm. A 60 nm-thick-pentacene (Sigma–Aldrich Co.) active channel layer, and 100 nm-thick-Au source/drain electrodes layer were then deposited using thermal evaporation technique. The Au source/drain electrodes were patterned on pentacene layer through a shadow mask. The OTFT devices had inverted staggered structures of Au/pentacene/ppMMA/ITO.

Film composition, surface morphology, and electrical properties of the ppMMA were investigated using Fourier transform infrared spectroscopy (FTIR; Bruker Optics, Vertex 80v) in vacuum, contact angle measurements (Erma Inc.), X-ray diffraction (XRD; Rigaku, D/Max 2200V/PC), atomic force microscope (AFM; Digital instrument, Nanoscope Mutimode IVa) and capacitance–voltage analysis (*C–V*, Keithley 590), respectively. For investigating performance of the OTFTs, current–voltage (*I–V*) characteristics according to applied voltage change were measured by a source measurement unit (Keithley 236) combined with another source measurement unit (Keithley 2400).

Fig. 1a shows FTIR spectrum for the ppMMA thin film. The FTIR spectra of the ppMMA and conventional spin-coated poly methyl methacrylate (PMMA) are consistent with similarly processed materials in Ref. [7], which identifies chemical similarities and dissimilarities of the two materials. Functional groups such as C–O, C=O, and CH are observed. The ppMMA thin film exhibits strong bands at 1730 cm^{-1} corresponding to the poly dimethylketene-like vinyl ester structure. Additionally, the C=C and CH stretches at 1460 and 1386 cm^{-1} are also evident. In the ppMMA, plasma polymer was formed in a cross-linked 3D network which is typical in plasma polymerization. This is indicated by the differences between the characteristic absorption peaks of ppMMA and solution processed PMMA, suggesting significant amount of fragmentation and rearrangement in the plasma deposition process. Inset in the Fig. 1a is AFM image of the surface of ppMMA gate dielectric. The surface roughness of a 100 nm-thick-ppMMA on ITO-coated glass was characterized and showed good root mean square roughness of about 0.24 nm. Fig. 1b shows a cross-sectional SEM image of the OTFT device. The surface energy of the ppMMA dielectric was about 45 mJ/m^2, which was similar to that of pentacene (42–48 mJ/m^2), which suggests that it might be possible to develop more efficient OTFTs channel by matching the surface energy of the ppMMA dielectric and the pentacene [11,12].

Fig. 2 shows the reflective XRD patterns and AFM image of 60 nm-thick-pentacene layer grown on ppMMA dielectric. XRD and AFM experiments were performed in order to investigate the effects of the surface properties of the gate dielectric on the surface morphology of pentacene. The structure of pentacene layer was elucidated by XRD in reflection mode at 20 kV, 20 mA and Cu Kα radiation (λ = 1.5406 Å) with a coupled (θ–2θ) scans configuration. The corresponding XRD pattern contains a series of sharp (0 0 k) peaks indicating that the pentacene film is highly ordered. The first peak at 5.7° (the thin-film phase) corresponds to a lattice parameter of 15.6 Å. The AFM images of pentacene layer on ppMMA reveal a dendritic structure

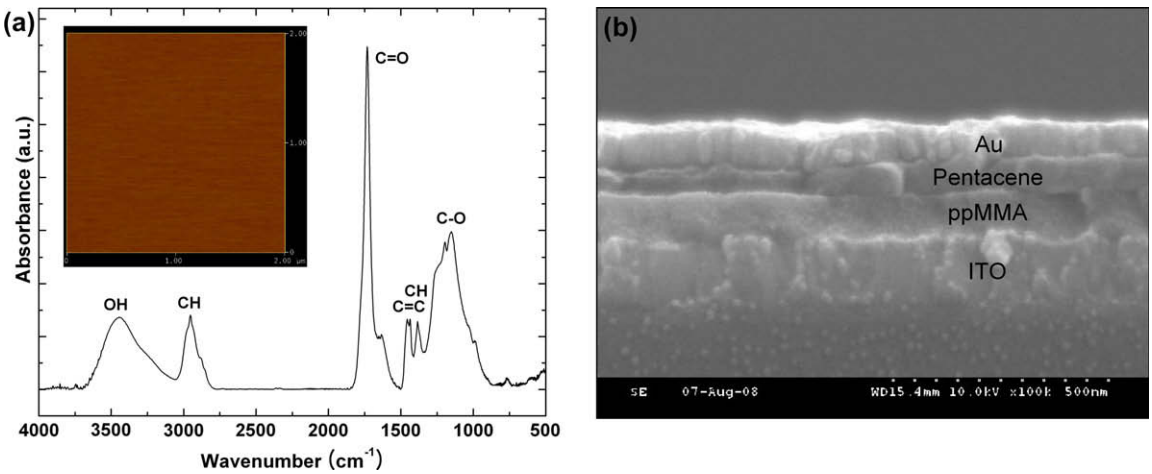

Fig. 1. (a) FTIR spectrum of ppMMA. Inset: AFM image (2 μm × 2 μm) of the surface of ppMMA gate dielectric. (b) SEM image of the OTFT device on a side view.

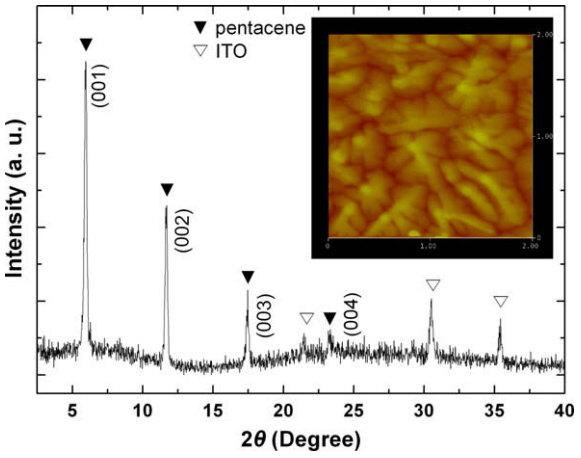

Fig. 2. X-ray diffraction pattern of the pentacene deposited on a ppMMA dielectric. Inset: the AFM image (2 μm × 2 μm) of the pentacene grown on a ppMMA dielectric.

with a grain size of ~1 μm. The data suggest a robust and pinhole-free ppMMA film, where the growth morphology of pentacene was similar to those prepared on other polymer substrates [13].

One of the main problems of OTFT devices is the occurrence of hysteresis. Although they are very often ignored in the literature, Gu et al. [14] described hysteresis effect for MIS capacitors based on pentacene and attributed them to carrier trapping or migration of dopants [15]. Fig. 3a shows the *C*–*V* characteristics (100 kHz) of a MIS device with a 100 nm-thick ppMMA in dark at room temperature. The normalized capacitance (C/C_{MAX}) was ranged to be within 1.00 and 0.80 when voltage was applied from −20 to 20 V. *C*–*V* characteristics in accumulation–depletion region were investigated using the MIS structure, and gate bias was swept back to check the amount of hysteresis origination from bulk or interface charge trapping. Very small hysteresis was observed in the *C*–*V* curves, which is due to low carrier trapping in MIS capacitor by non-solvent process and cross-linked polymerization deposition [16,17]. Dielectric constant *k* of the ppMMA layer was obtained with the following equation: [18]

$$k = C\frac{d}{\varepsilon_0 A}$$

where *C* (1.37 nF) is capacitance of the ppMMA dielectric, *d* and *A* are the ppMMA thickness (100 nm) and the dot area (0.04 cm^2), ε_0 is permittivity in vacuum (8.85×10^{-14} F cm^{-1}), respectively. According to the calculation, we obtained a higher dielectric constant ($k = 3.86$) for the ppMMA in an ITO–ppMMA–Au (MIM) sandwich structure, in contrast to the conventional PMMA layers ($k = 2.5$–2.9) in Ref. [3]. Jang et al. [4] described a correlation between device field-effect mobility and permittivity of dielectric materials. The higher field-effect mobility for dielectrics with higher dielectric constants may be due to increases the number of hole carriers at the semiconductor–dielectric interface. To investigate the potential of ppMMA as gate dielectric, we checked whether their leakage current density is sufficiently low by testing the corresponding ITO–ppMMA–Au (MIM) devices. Fig. 3b shows the current density–electric field (*J*–*E*) curve of the ppMMA insulator on ITO, and in particular the leakage behavior of the ppMMA dielectric. The ppMMA appeared to have quite a good dielectric strength of ~2 MV/cm based on a minimum leakage current density of $\sim 10^{-8}$ A/cm^2 even though its total thickness was only 100 nm. This might be caused by the pinhole-free ppMMA dielectric with highly cross-linked structure. Fig. 4 shows *I*–*V* characteristics of the

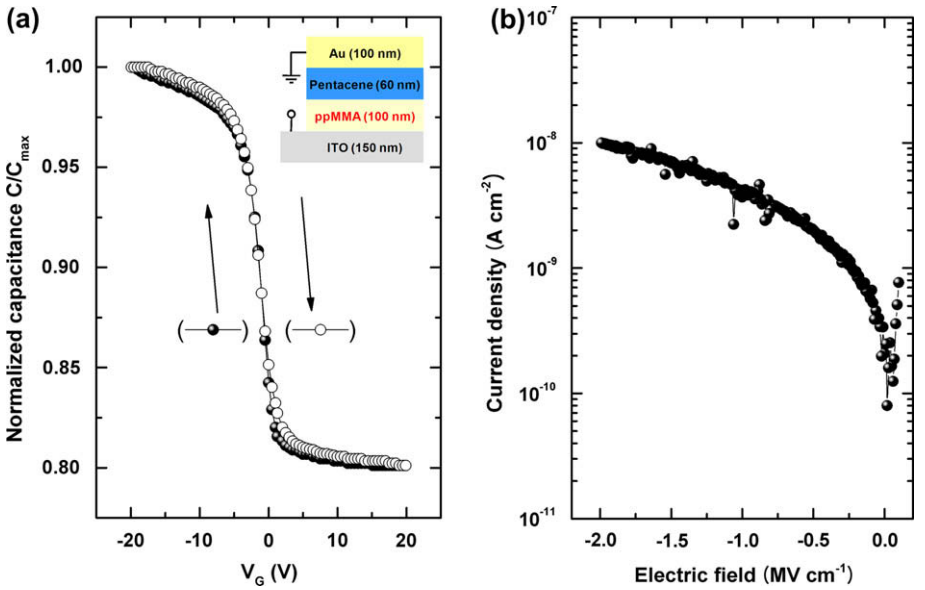

Fig. 3. *C*–*V* and *J*–*E* characteristics: (a) *C*–*V* characteristics of ITO–ppMMA–pentacene–Au (MIS) capacitor at ac signal frequency (100 kHz). The bias voltages were swept from −20 to +20 (○) and from +20 to −20 (●). Inset: schematic cross-section of the MIS device. (b) *J*–*E* characteristics of ITO–ppMMA–Au (MIM) device.

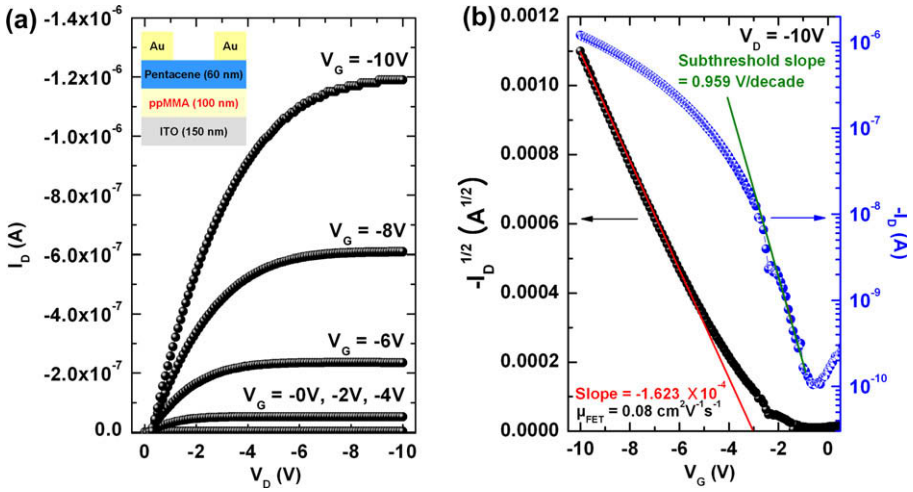

Fig. 4. Current–voltage (I–V) characteristics of OTFT device with inverted staggered structure of ITO/ppMMA/pentacene/Au: (a) drain current–drain voltage (output) characteristics of OTFT devices. Inset: schematic cross-section of the OTFT device; (b) drain current–gate voltage (transfer) characteristics of OTFT devices.

OTFT device with a 100 nm-thick-ppMMA layer in dark at room temperature: (a) typical output I_D–V_D curve at applied step gate voltages (−2 V); (b) transfer I_D–V_G curve at fixed −10 V drain voltage. The I–V characteristics were measured for the OTFT device with channel length of 100 μm and channel width of 2000 μm. From these data, average field-effect mobility was calculated in the saturation current regime (V_D = −10 V) by equation which are derived in threshold voltage V_{TH} and field-effect mobility μ: [18]

$$I_{Dsat} = \frac{W}{2L} C_i \mu (V_G - V_{TH})^2$$

where W and L are channel width and length, C_i is capacitance per unit area of the ppMMA insulators, V_G and V_{TH} are gate and threshold voltage, and μ is field-effect mobility. The OTFT devices with the ppMMA insulator was found to have a field-effect mobility of 0.08 ± 0.02 $cm^2\,V^{-1}s^{-1}$ in the saturation region, a lower threshold voltage of −3 ± 0.15 V, a lower sub-threshold slope of 0.959 ± 0.05 V/decade, and an on/off current ratio (I_{on}/I_{off}) of 1.0×10^4 ± 0.10, respectively. This combination of favorable properties demonstrated that the OTFT can be operated successfully at voltages ~10 V.

An OTFT device with inverted staggered structure of Au/pentacene/ppMMA/ITO was fabricated. Proposed plasma polymerization method could be applied to a completely dry process for the OTFT fabrication, which offers a one-step and compatible process with conventional methods. The OTFT with the ppMMA dielectric could be operated with a lower operation voltage of −10 V. It was demonstrated in this report that the 100 nm-thick-ppMMA dielectric thin film could be used to obtain an OTFT device with favorable electrical properties and performance of the OTFT device could be significantly improved. Plasma polymerization method has the benefits of polymer gate dielectrics including potentially high capacitive coupling, and shadow mask patterning and in situ dry processing with large-area flexible substrates.

Acknowledgments

This work was supported by the *Regional Innovation Center for Environmental Technology of Thermal Plasma* (RIC-ETTP) at the INHA University designated by MKE (2009).

References

[1] H. Klauk, Organic Electronics, Wiley-VCH Verlag, 2006 (Chapter 2–3).
[2] D.K. Hwang, K. Lee, J.H. Kim, S. Im, C.S. Kim, H.K. Baik, J.H. Park, E. Kim, Appl. Phys. Lett. 88 (2006) 243513.
[3] J.H. Park, D.K. Hwang, J. Lee, S. Im, E. Kim, Thin Solid Films 515 (2007) 4041–4044.
[4] Y. Jang, D.H. Kim, Y.D. Park, J.H. Cho, M. Hwang, K. Cho, Appl. Phys. Lett. 87 (2005) 152105.
[5] M. Halik, H. Klauk, U. Zschieschang, G. nter Schmid, C. Dehm, M. Schutz, S. Maisch, F. Effenberger, M. Brunnbauer, F. Stellacci, Nature 431 (2004) 963–966.
[6] H. Sirringhaus, T. Kawase, R.H. Friend, T. Shimoda, M. Inbasekaran, W. Wu, E.P. Woo, Science 290 (2000) 2123–2126.
[7] C. Zhang, J. Wyatt, D.H. Weinkauf, Polymer 45 (2004) 7665–7671.
[8] Y. Vickie Pan, Ernesto Z. Barrios, Denice D. Denton, J. Polym. Sci. Part A: Polym. Chem. 36 (1998) 587–602.
[9] S. Morita, J. Tamano, S. Hattori, M. Ieda, J. Appl. Phys. 51 (1980) 3938.
[10] J.S. Lim, P.K. Shin, Appl. Surf. Sci. 253 (2007) 3828–3833.
[11] Y. Jang, D.H. Kim, Y.D. Park, J.H. Cho, M. Hwang, K. Cho, Appl. Phys. Lett. 88 (2006) 072101.
[12] M. Yoshida, S. Uemura, T. Kodzasa, T. Kamata, M. Matsuzawa, T. Kawai, Synth. Met. 137 (2003) 967–968.
[13] S.Y. Yang, K. Shin, C.E. Park, Adv. Funct. Mater. 15 (2005) 1806–1814.
[14] G. Gu, Michael G. Kane, James E. Doty, Arthur H. Firester, Appl. Phys. Lett. 87 (2005) 243512.
[15] S.C. Lim, S.H. Kim, J.B. Koo, J.H. Lee, C.H. Ku, Y.S. Yang, T. Zyung, Appl. Phys. Lett. 90 (2007) 173512.
[16] J.M. Kim, J.W. Lee, J.K. Kim, B.K. Ju, J.S. Kim, Y.H. Lee, M.H. Oh, Appl. Phys. Lett. 85 (2004) 6368–6370.
[17] T. Miyadera, T. Minari, K. Tsukagoshi, H. Ito, Y. Aoyagi, Appl. Phys. Lett. 91 (2007) 013512.
[18] N. Arora, MOSFET Models for VLSI Circuit Simulation Theory and Practice, Springer, New York, 1993.

polymers under AM 1.5G illumination, a maximum PCE of 1.9% was achieved in an OPV cell with an active layer composition of 1:8 in PGREEN: $PC_{60}BM$ ([6,6]-phenyl-C61 butyric acid methyl ester) blends.

Here, we report on several pathways to improve and optimize the key device parameters including short-circuit current (J_{SC}), open-circuit voltage (V_{OC}) and fill factor (*FF*) via the use of $PC_{70}BM$ (to increase the J_{SC}), bis-$PC_{60}BM$ (to increase the V_{OC}), and MoO_3 interlayer (to increase the *FF*). Three different active layers consisting of blends of PGREEN with $PC_{60}BM$, $PC_{70}BM$, and bis-$PC_{60}BM$ sandwiched between an ITO anode and a LiF/Al cathode were used in this study. In addition, MoO_3 is introduced as an anode interlayer to replace the commonly used poly(3,4-ethylenedioxythiophene):poly(styrenesulfonate) (PEDOT-PSS) anode interlayer. Fig. 1 shows the repeat unit structure for the polymer employed and the energy level diagram of the solar cell components used in this study.

To fabricate OPV cells with a PEDOT:PSS interlayer, a thin layer (30 nm) of PEDOT:PSS was spin coated on top of a pre-cleaned ITO coated glass substrate. For cells with a MoO_3 interlayer, a thin film (10 nm) of MoO_3 was thermally evaporated on the ITO substrate under a vacuum of 10^{-6} torr. For the PEDOT:PSS cell, a 115 nm thick bulk-heterojunction active layer was spin-casted from a solution of PGREEN and $PC_{60}BM$ (1:8) prepared using chlorobenzene as the solvent. Subsequently, the active layer was annealed at 70 °C for 45 min, and a LiF/Al cathode (1/100 nm) was thermally evaporated onto the active layer material. The annealing temperature (70 °C) used for all devices reported in this work. Each device has an active area of 0.04 mm^2. The current density was measured as a function of voltage with a 150 W ozone free Newport xenon arc lamp in conjunction with a Keithley 4200 semiconductor parameter analyzer. Solar measurements were done under AM 1.5G, 1000 W/m^2 illumination conditions. External quantum efficiency of OPV cells as a function of wavelength were measured using a calibrated silicon photodiode in conjunction with a lock-in amplifier.

Fig. 2a shows the current density–voltage (*J–V*) characteristics of the PGREEN devices with different fullerene acceptors and different interfacial layers, measured under simulated solar illumination. First, we investigate the effect of $PC_{70}BM$ on the performance of the PGREEN cell. We found that the optimum blend composition (PEDOT:PSS/PGREEN:$PC_{70}BM$/LiF-Al) has a PGREEN:$PC_{70}BM$ blend ratio of 1:6; higher in polymer content when compared to the $PC_{60}BM$-based cells [16]. The device exhibits a J_{SC} value of 7.01 mA/cm^2, a V_{OC} value of 0.8 V and a *FF* value of 51%. Compared to the PEDOT:PSS cell with $PC_{60}BM$ as an acceptor, a 52% enhancement in PCE (Table 1) was observed. The major enhancements in the $PC_{70}BM$ cell are due to enhancements in short-circuit current and fill factor. The external quantum efficiencies of the PGREEN-

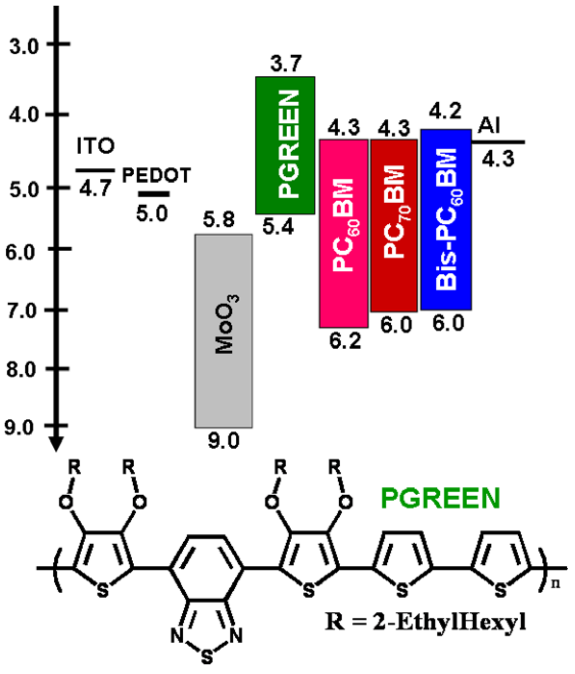

Fig. 1. A schematic diagram showing energy levels of the donor polymer, acceptor PCBM, buffer layer materials and electrodes, along with the repeat unit structure of PGREEN.

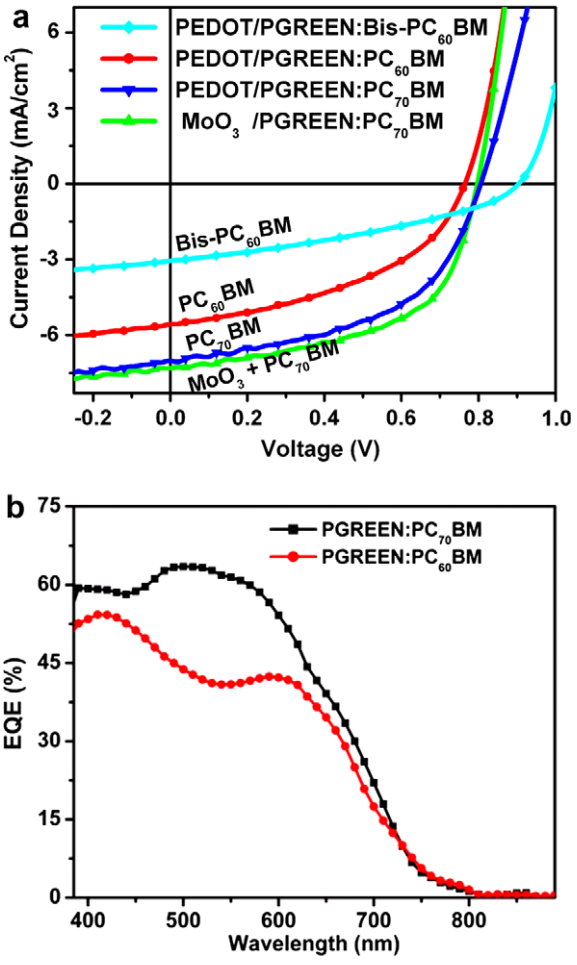

Fig. 2. (a) The *J–V* curve of a PGREEN polymer solar cell under AM 1.5 conditions and (b) external quantum efficiency (EQE) of PGREEN/$PC_{60}BM$ and PGREEN/$PC_{70}BM$.

Table 1
Photovoltaic parameters of PGREEN solar cell devices.

PV devices	J_{SC} (mA/cm^2)	V_{OC} (V)	*FF* (%)	PCE (%)	R_S (Ω cm^2)
PEDOT/PGREEN:$PC_{60}BM$/LiF-Al	5.56	0.77	44	1.90	24.52
MoO_3/PGREEN:$PC_{60}BM$/LiF-Al	5.38	0.77	51	2.12	15.88
PEDOT/PGREEN:$PC_{70}BM$/LiF-Al	7.01	0.80	51	2.89	22.78
MoO_3/PGREEN:$PC_{70}BM$/LiF-Al	7.32	0.79	56	3.22	14.64
PEDOT/PGREEN:bis-$PC_{60}BM$/LiF-Al	3.05	0.90	37	1.01	57.47

fullerene films with $PC_{70}BM$ and $PC_{60}BM$ are shown in Fig. 2b. Here, the $PC_{70}BM$ cell exhibits only one broad absorption band with a maximum at 475 nm whereas the $PC_{60}BM$ cell exhibits two broad-band absorptions with two absorption maxima. In addition, we also observed that the color of the $PC_{70}BM$ cell is brown as opposed to the asparagus green ($PC_{60}BM$ device)[16] due to the strong absorption of $PC_{70}BM$ in the blue-green region. Here, the absorption of $PC_{70}BM$ fills the transmission window of the PGREEN polymer [16,17] leading to the single broad absorption band. The external quantum efficiency (EQE) of the PGREEN-$PC_{70}BM$ device resembles its absorption spectrum, yielding a maximum value of 60% at 570 nm. This value is 11% higher than that of the $PC_{60}BM$ cell and illustrates the importance of the $PC_{70}BM$ phase in both light absorption and transport.

Next, we examine the effect of bis-$PC_{60}BM$ on the BHJ PGREEN OPV cells (PEDOT:PSS/PGREEN:bis-$PC_{60}BM$/LiF-Al). Bis-$PC_{60}BM$ has a higher lying LUMO energy [12] and is expected to give a larger V_{OC} value. Here, we found that an optimum blend ratio for the PGREEN:bis-$PC_{60}BM$ photoactive layer is 1:8, identical to that found for $PC_{60}BM$. As shown in Fig. 2, we do observe the overall V_{OC} enhancement in the bis-$PC_{60}BM$ cells to 0.90 V, as compared to 0.77 V for the $PC_{60}BM$ cells [12]. It should be noted that despite this increase in $V_{OC,}$ the overall performance of the OPV cells decreases due to significant reduction in J_{SC} and *FF*, resulting in a PCE of 1.01%.

To study the anode interface effect, first we replaced the anode interface layer PEDOT:PSS by MoO_3 for the PGREEN:$PC_{60}BM$ device with the optimum blend composition of 1:8. We observe the fill factor and PCE increase from 44% to 51%, and 1.90% to 2.12%, respectively (Table 1). The enhancement in fill factor is mainly due to a decrease in the series resistance (R_S) (Table 1) of the MoO_3 cell. Similar effects have been observed previously for other polymer and small molecule based devices [15–18]. To understand the effect of the MoO_3 interlayer, we have previously reported on the interface electronic structure of the MoO_3 interlayer by photoelectron spectroscopy, and observed that the MoO_3 interlayer exhibits an *n*-type alignment [18,19] (Fig. 1). Recently, the same behavior (*n*-type) of MoO_3 was also reported by Kröger et al. [20]. Furthermore, there is a 2 eV shift in the vacuum level resulting in band bending at the MoO_3/electroactive layer interface [18]. The resulting built-in electric field leads to an enhancement in hole extraction from the electroactive layer to the anode, leading to a reduction in the cell series resistance (Table 1).

The PGREEN:$PC_{70}BM$ PV cell with a MoO_3 interlayer exhibits the highest PCE of 3.22% and the corresponding cell has a J_{SC} value of 7.32 mA cm^{-2}, a V_{OC} value of 0.79 V and a *FF* value of 56% at an optimized blend composition of 1:6. This corresponds to a 69% enhancement in PCE compared with the $PC_{60}BM$ cell with a PEDOT:PSS interlayer. Relative to the PEDOT:PSS cell, the PCE's of both of the $PC_{60}BM$ and $PC_{70}BM$ cells having the MoO_3 interlayer were enhanced by 12% due to an enhancement in the fill factor.

In order to gain insight into the mechanisms behind the enhancement in EQE and short-circuit current, we carried out charge carrier transport studies on hole-only carrier devices. Here, the hole-only device has the following device structure: ITO/PEDOT/Active Layer/Pd [21] with either a pristine PGREEN or a PGREEN-$PC_{70}BM$ or $PC_{60}BM$ blend as the active layers at their optimum ratios (Fig. 3) reported above. Space-charge limited (SCL) currents were observed in these devices. From the current density–voltage (*J*–*V*) results, we determine that the hole mobility of the neat PGREEN polymer is $\sim 10^{-7}$ cm^2 V^{-1} s^{-1} which is low compared with the electron mobility in the PCBM ($\sim 10^{-3}$ cm^2 V^{-1} s^{-1}) [22]. This difference in electron and hole mobilities results in unbalanced charge transport in the BHJ photovoltaic cells. On the other hand, blending the copolymers with an optimized large proportion of PCBM leads to a significant increase in hole current as shown in Fig. 3 leading to an enhancement of hole mobility (4×10^{-5} cm^2 V^{-1} s^{-1}) in the polymer blend. The better charge balance leads to a higher short-circuit current, higher fill factor, and hence higher power conversion efficiency in these devices. Blending PGREEN with $PC_{70}BM$

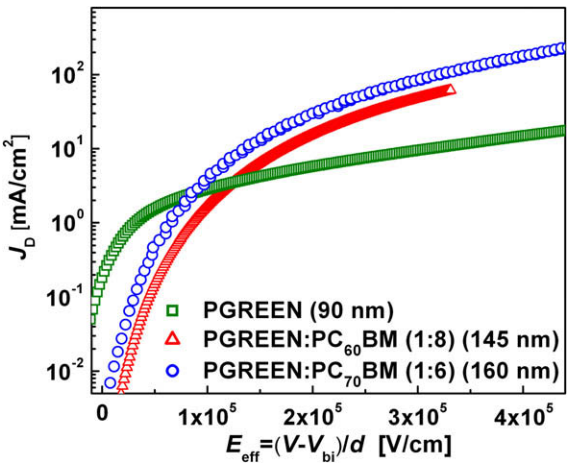

Fig. 3. The current densities for hole-only devices (ITO/PEDOT/Active Layer/Pd) of PGREEN, PGREEN:$PC_{60}BM$ and PGREEN:$PC_{70}BM$ as a function of the effective electric field.

leads to further enhancement of hole mobility of $9 \times 10^{-5}\,cm^2\,V^{-1}\,s^{-1}$. $PC_{70}BM$ also gives rise to enhanced light absorption in the visible window (480–550 nm) which fills the transmission window of the PGREEN polymer. The improved absorption and enhanced hole mobility of the PGREEN/$PC_{70}BM$ polymer blend, along with the enhanced hole extraction attributed to the MoO_3 interlayer, results in a 69% overall improvement in the OPV power conversion efficiency relative to the standard device which employs PEDOT/PSS with $PC_{60}BM$.

In conclusion, we have demonstrated a 69% improvement in the performance of PGREEN PV device using the electron acceptor $PC_{70}BM$ along with MoO_3 interface layer. The enhanced device performance is attributed to the combined effect of improved light absorption, enhanced charge transport in the active layer and efficient charge collection at the interface layer. While a significant enhancement of open-circuit voltage was observed in the bis-$PC_{60}BM$ cells, the overall power conversion efficiency decreases due to substantial decrease in short-circuit current and fill factor.

Acknowledgements

We gratefully acknowledge Sestar, LLC, the AFOSR (FA9550-09-1-0320) and the DOE (DE-FG02-07ER46464) for the financial support for this work.

References

[1] S. Gunes, H. Neugebauer, N.S. Sariciftci, Chem. Rev. 107 (2007) 1324.
[2] G. Dennler, M.C. Scharber, C.J. Brabec, Adv. Mater. 21 (2009) 1.
[3] M. Helgesen, R. Søndergaard, F.C. Krebs, J. Mater. Chem. 20 (2010) 36.
[4] F.C. Krebs, Sol. Energy Mater. Sol. Cells 93 (2009) 394.
[5] F.C. Krebs, S.A. Gevorgyan, J. Alstrup, J. Mater. Chem. 19 (2009) 5442.
[6] G. Li, V. Shrotriya, J.S. Huang, Y. Yao, T. Moriarty, K. Emery, Y. Yang, Nat. Mater. 4 (2005) 864.
[7] B.C. Thompson, J.M.J. Fréchet, Angew. Chem., Int. Ed. 47 (2008) 58.
[8] J. Hou, H.-Y. Chen, S. Zhang, G. Li, Y. Yang, J. Am. Chem. Soc. 130 (2008) 16144.
[9] E. Wang, L. Wang, L. Lan, C. Luo, W. Zhuang, J. Peng, Y. Cao, Appl. Phys. Lett. 92 (2008) 033307.
[10] Y. Liang, Y. Wu, D. Feng, S.-T. Tsai, H.-J. Son, G. Li, L. Yu, J. Am. Chem. Soc. 131 (2009) 56.
[11] Y. Yao, C. Shi, G. Li, V. Shrotriya, Q. Pei, Y. Yang, Appl. Phys. Lett. 89 (2006) 153507.
[12] M. Lenes, G.-J.A.H. Wetzelaer, F.B. Kooistra, S.C. Veenstra, J.C. Hummelen, P.W.M. Blom, Adv. Mater. 20 (2008) 2116.
[13] V. Shrotriya, G. Li, Y. Yao, C.-W. Chu, Y. Yang, Appl. Phys. Lett. 88 (2006) 073508.
[14] M.D. Irwin, D.B. Buchholz, A.W. Hains, R.P.H. Chang, T.J. Marks, Proc. Natl. Acad. Sci. 105 (2008) 2783.
[15] D.Y. Kim, G. Sarasqueta, F. So, Sol. Energy Mater. Sol. Cells 93 (2009) 1452.
[16] J. Subbiah, P.M. Beaujuge, K.R. Choudhury, S. Ellinger, J.R. Reynolds, F. So, ACS Appl. Mater. Interfaces 1 (2009) 1154.
[17] P.M. Beaujuge, J. Subbiah, K.R. Choudhury, S. Ellinger, T.D. McCarley, J.R. Reynolds, F. So, Chem. Mater., in press.
[18] D.Y. Kim, J. Subbiah, G. Sarasqueta, F. So, H. Ding, Irfan Y. Gao, Appl. Phys. Lett. 95 (2009) 093304.
[19] J. Subbiah, D.Y. Kim, M. Hartel, F. So, Appl. Phys. Lett. 96 (2010) 063303.
[20] M. Kröger, S. Hamwi, J. Meyer, T. Riedl, W. Kowalsky, A. Kahn, Org. Electron. 10 (2009) 932.
[21] V.D. Mihailetchi, L.J.A. Koster, P.W.M. Blom, C. Melzer, B. de Boer, J.K.J. van Duren, R.A.J. Janssen, Adv. Funct. Mater. 15 (2005) 795.
[22] V.D. Mihailetchi, J.K.J.V. Duren, P.W.M. Blom, J.C. Hummelen, R.A.J. Janssen, J.M. Kroon, M.T. Rispens, W.J.H. Verhees, M.M. Wienk, Adv. Funct. Mater. 13 (2003) 43.

violet (UV) curing of the gate dielectric will result in hysteresis-free OTFTs [18].

In this study, thermal cross-linking of the reactive –OH groups with an organosilane, p-tolyltrimethoxysilane (TTMS), is used to eliminate the presence of –OH groups; the TTMS serves as the thermal cross-linking agent. Our earlier studies showed that a thermally cross-linked PVP film was unable to serve as the dielectric because it was not chemically compatible when the subsequently deposited materials used to form the other OTFT device layers. UV cross-linked PVP-*co*-PMMA combined with a thermally cross-linked polysiloxane top layer and gold electrodes along with regioregular polythiophene used as the semiconductor has been reported to increase the on/off ratio by about two orders of magnitude [19].

In this work, the thermal cross-linking of a single layer of PVP-*co*-PMMA by the new agent TTMS is shown to yield a dielectric film that results in a significantly higher on/off ratio, i.e., on the order of 10^6. The material systems studied include bis(triisopropylsilylethynyl) (TIPS), PVP-*co*-PMMA and conductive ink that are chemically and mechanically compatible and are solution processable using traditional graphic arts printing (e.g. screen, gravure, flexography).

2. Experiment – processing

Polyimide film was used as the substrate. The gate was formed from 50 nm thick aluminum deposited by E-beam evaporation. Solutions of the dielectric were prepared with the cross-linking agent TTMS in TTMS/PVP-*co*-PMMA at ratios of 0.1/1, 0.25/1, 0.5/1, 1/1, 1.5/1, and 2/1 by weight; TTMS was added into basic solutions having 20% (wt.%) PVP-*co*-PMMA in 1-methoxy propanol acetate (PMA). The dielectric solution was spin-coated onto the substrate. The coated film was cured at 200 °C for 1 h in a convection oven. Source and drain electrodes were deposited on the cross-linked dielectric film by screen printing using silver (Ag) conductive ink, followed by curing of the Ag electrodes at 100 °C for 15 min in an oven. Finally, 2% (wt.%) TIPS in toluene solution was deposited in the channel between the source/drain (S/D) by drop casting. The channel length and channel width for the OTFT devices were 100 and 5000 μm, respectively.

The electrical characteristics of the OTFTs were measured at room temperature using a Keithley 4200 Semiconductor Characterization System when placed in a dark box purged with nitrogen. Thermogravimetric analysis (TGA) (CAHN TG-131) was used to examine the thermal properties of the solutions having different ratios. Cross-sectional views of the resulting devices and the thickness of the dielectric film were studied with scanning electron microscopy (SEM; JEOL JSM-6320F). X-ray photoelectron spectroscopy (XPS) was performed to investigate the chemical composition of the dielectric surface using a Kratos AXIS-165 with a monochromatic Al Kα (1486.6 eV) X-ray source.

3. Results and discussion

Fig. 1 shows the capacitance of films formed from solutions prepared with different TTMS/PVP-*co*-PMMA ratios.

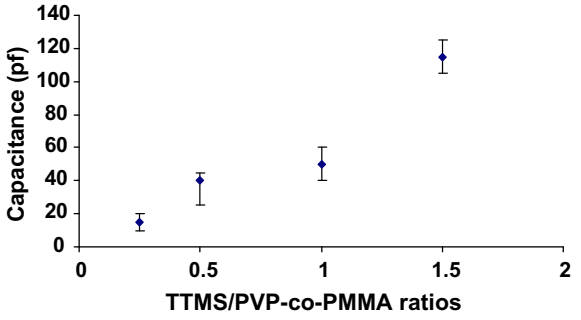

Fig. 1. Capacitance data for the OTFT devices fabricated with different TTMS/PVP-PMMA ratios of 0.25/1, 0.5/1, 1/1, and 1.5/1 by weight.

Increasing TTMS/PVP-*co*-PMMA ratios are shown to yield films with increasing capacitance. This is indicative of decreasing film thickness, because thinner films are made with lower viscosity solutions; thinner films are achieved when more TTMS is added, while keeping the spin coating conditions constant. However, there are two notable exceptions. In the cases of the TTMS/PVP-*co*-PMMA ratio being of 0.0/1 and 0.1/1, the leakage current between the gate electrode and the S/D electrodes was excessive and, therefore, no capacitance data was obtained. The leakage current of the noncross-linked PVP-*co*-PMMA film is apparently the result of dielectric film dissolution by the metal ink solvent used for fabrication of the S/D electrodes. It appears that the dielectric film underneath the electrodes was chemically modified by the solvent in the metal ink used for the printed source and drain which subsequently resulted in shorting to the gate electrode (Fig. 2a). Indeed, when assessing the OTFT device fabricated with a noncross-linked film, no dielectric layer was observed; the entire dielectric film was apparently dissolved as shown in Fig. 2a. The SEM image of the cross-section of the device with TTMS/PVP-*co*-PMMA ratio of 0.1/1 shows the source and drain penetrating the dielectric film at several locations (Fig. 2b) since the amount of TTMS is not sufficient to obtain optimal cross-linking of the PVP-*co*-PMMA. In comparison, Fig. 2c shows that the dielectric film resulting from the TTMS/PVP-*co*-PMMA ratio of 1/1 has a uniform thickness. On the other hand, for the film formed from a TTMS/PVP-*co*-PMMA ratio of 2/1, excess TTMS appears to have created pinholes as it evaporated during the thermal cross-linking process in the oven. The printed S/D electrodes are found to short with the gate electrode through those pinholes and therefore no capacitance values were recorded.

Fig. 3 shows the transfer characteristics of OTFTs with dielectric cross-linked films and different TTMS/PVP-*co*-PMMA ratios. Gate voltage sweeps were performed from +20 to −60 V at a bias voltage of −40 V. The field-effect mobility (μ) can be calculated from the transfer curve in the saturated regime, and it was calculated to be between 0.002 and 0.003 cm^2/V s. The threshold voltage is found to be between the range of 0 and 10 V; the highest threshold voltage of ~10 V was obtained with the device made by using the 1.5/1 TTMS/PVP-*co*-PMMA ratio. This device also had the lowest on-current, e.g., below 10^{-7}, compared to those of the other transistors made with TTMS/PVP-*co*-

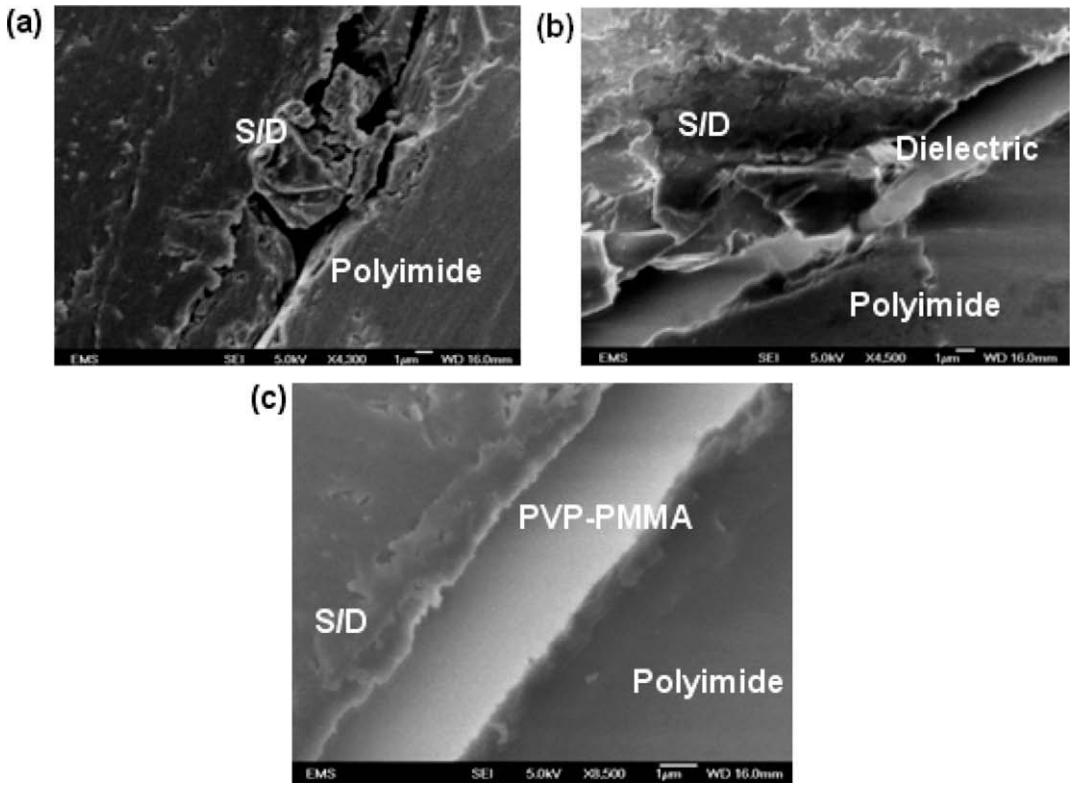

Fig. 2. SEM images of cross-sections of OTFT devices with dielectric layers formed using different ratios: (a) TTMS/PVP-*co*-PMMA: 0/1, i.e., uncross-linked dielectric film; (b) TTMS/PVP-*co*-PMMA: 0.1/1; (c) TTMS/PVP-*co*-PMMA: 1/1.

PMMA ratios of 0.25/1, 0.5/1, and 1.0/1. Also, the surface morphology of the dielectric with TTMS/PVP-*co*-PMMA ratio of 1.5/1 appeared to have greater roughness than those of the others which could be attributed to greater evaporation of TTMS during the device fabrication (Fig. 4). The coarser surface may provide increased nucleation sites for the semiconductor crystal which results in more grain boundaries in the film. Several studies have concluded that device performance deteriorates when organic semiconductors have high populations of grain boundaries [20–25].

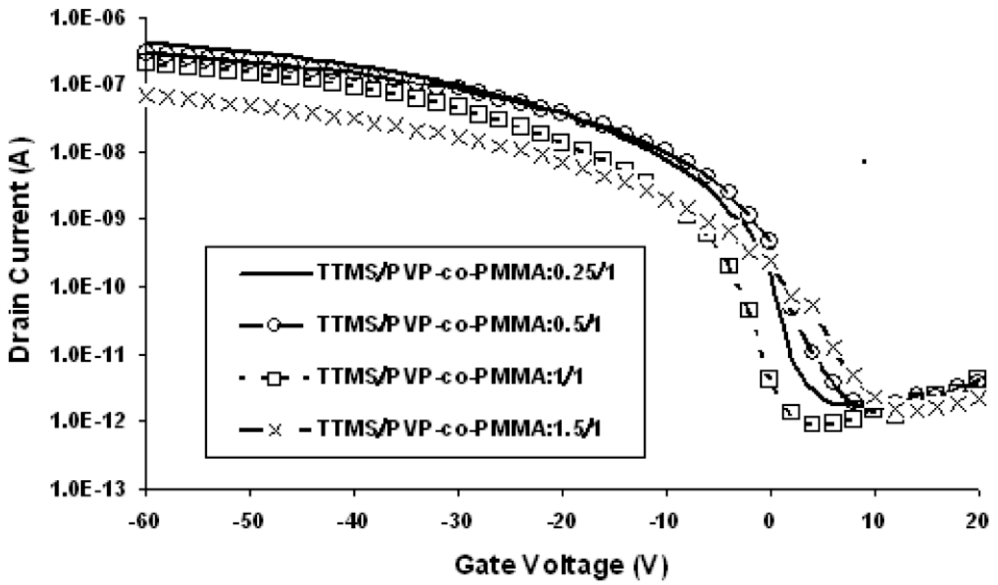

Fig. 3. Transfer curves for the OTFTs with the dielectric film cross-linked with TTMS at different ratios of TTMS/PVP-*co*-PMMA from 0.25/1 to 1.5/1.

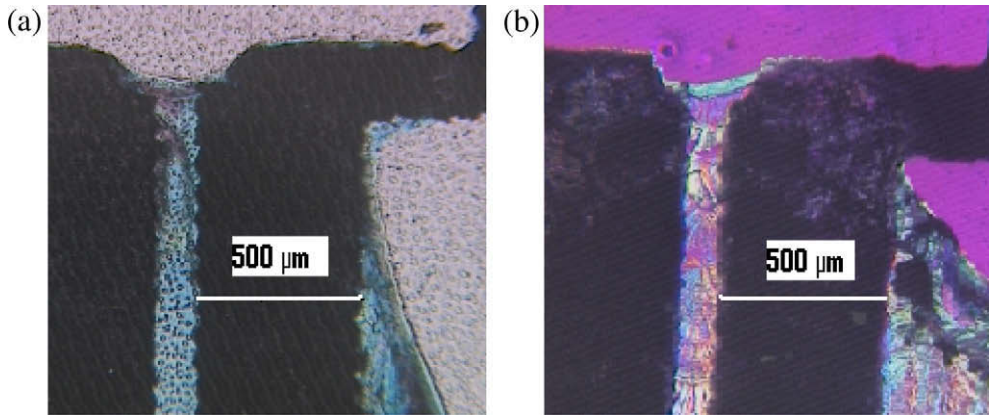

Fig. 4. Optical images of the top view of a bottom contact OTFT, *S* and *D* width is 500 μm, channel length is 100 μm, (a) dielectric with the TTMS/PVP-*co*-PMMA ratio of 1.5/1; (b) dielectric with the TTMS/PVP-*co*-PMMA ratio of 0.5/1.

TGA analyses of pure PVP-*co*-PMMA and TTMS show that the decomposition point for PVP-*co*-PMMA is above 300 °C, while TTMS evaporates at about 200 °C (Fig. 5a and b). Therefore, during thermal cross-linking at 200 °C, noncross-linked PVP-*co*-PMMA would remain in the film while the excess TTMS would begin to evaporate. Moreover, TGA studies for dielectric films with different TTMS/PVP-*co*-PMMA ratios indicate that the mass of the dielectric remains constant during thermal cross-linking at 200 °C (Fig. 5c). Thus, our TGA results shown in Fig. 5 suggest that higher amounts of TTMS should be added into the dielectric solution in order to assure optimal cross-linking

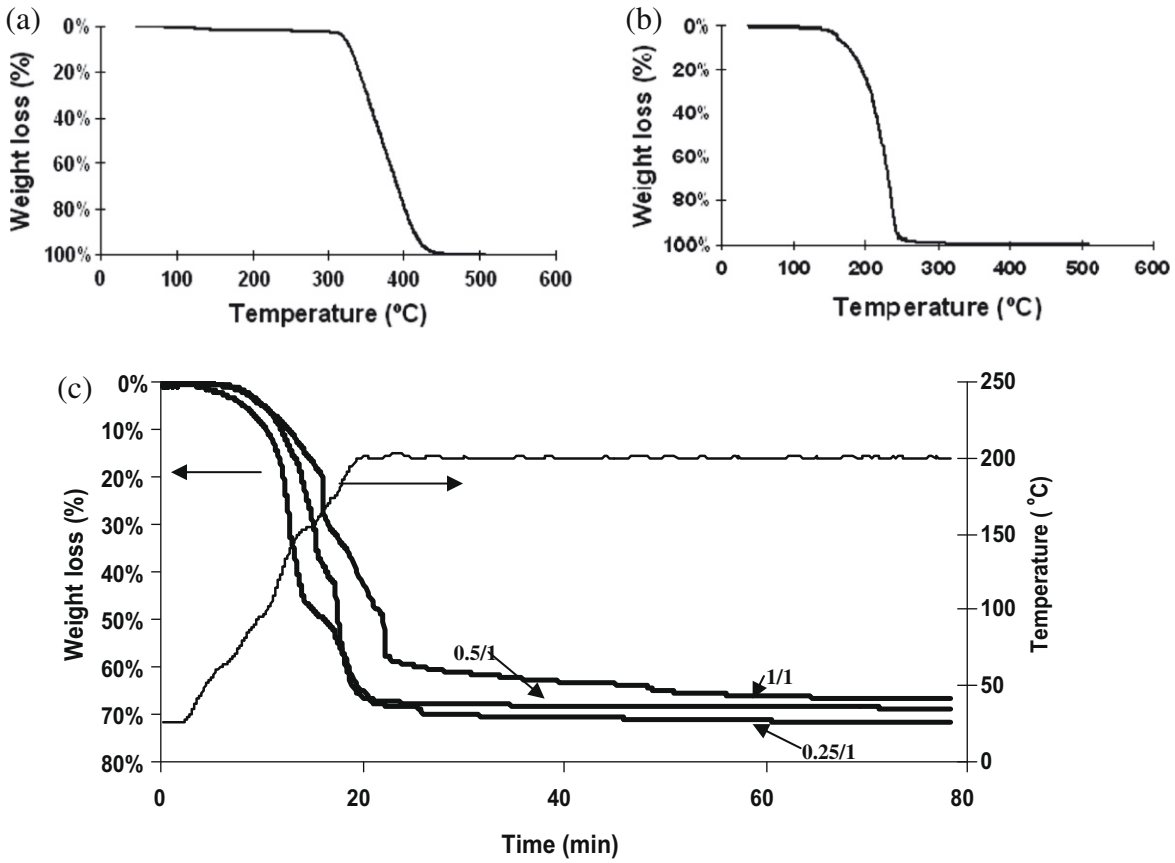

Fig. 5. TGA analyses for (a) pure PVP-*co*-PMMA; (b) pure TTMS; (c) dielectric solutions with TTMS/PVP-*co*-PMMA ratios of 0.25/1, 0.5/1, and 1/1, respectively, in (a) and (b), weight loss is recorded by increasing temperature to 500 °C, in (c), weight loss is recorded by increasing temperature to 200 °C first, then temperature is kept at 200 °C for 1 h.

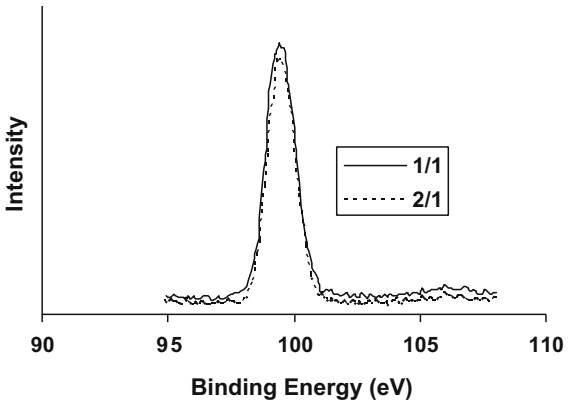

Fig. 6. XPS characterization for Si 2p of the dielectric with the TTMS/PVP-*co*-PMMA ratios of 1/1 and 2/1, respectively.

of the resulting dielectric film. The rough surface of the dielectric film formed with TTMS/PVP-*co*-PMMA ratio of 1.5/1 (Fig. 4a) indicates that higher roughness of the dielectric surface is caused by greater TTMS evaporation. Therefore, the proposed optimal TTMS/PVP-*co*-PMMA ratio window for these systems is 0.25/1–1.0/1.

XPS characterization was used to provide chemical information for the surface of the dielectric films. Data in Fig. 6 includes Si 2p XPS spectra that suggest dielectric films with TTMS/PVP-*co*-PMMA ratio of 1/1 have similar chemical composition to that with a ratio of 2/1, at least within the 6–8 nm from the surface that can be probed with XPS, although the latter samples have twice as much TTMS in the solutions used and the silicon peak contribution is only provided by TTMS. Therefore, the similar chemical composition of TTMS/PVP-*co*-PMMA samples manifested at two distinctly different ratios of TTMS and PVP-*co*-PMMA suggests that there is an optimal ratio for the reaction between TTMS and PVP-*co*-PMMA, while excess TTMS is removed via evaporation.

4. Summary – conclusions

In order to eliminate –OH groups in the final processed dielectric film, thermal cross-linking of PVP-*co*-PMMA is proposed. It was demonstrated that PVP-*co*-PMMA could be thermally cross-linked with a new cross-linking agent, TTMS, and that the OTFT field-effect mobility was similar to that of OTFTs fabricated with UV cross-linked PVP-*co*-PMMA. The optimal TTMS/PVP-*co*-PMMA ratio was found to be in the range of 0.25/1–1.0/1. Moreover, the thermally cross-linked dielectric film was chemically and mechanically compatible with the metal ink formulation used to fabricate the screen printed source and drain. The results of this study demonstrate that OTFTs can be fabricated using all-solution processed materials on a flexible polymeric substrate with sufficient electrical performance for a variety of applications e.g., displays, sensors, and memories.

Acknowledgment

The authors would like to thank the Motorola Research Center for funding this research.

References

[1] C.D. Dimitrakopoulos, D.J. Mascaro, Organic thin-film transistors: a review of recent advances, IBM J. Res. Dev. 45 (1) (2001) 11–27.
[2] J.M. Shaw, P.F. Seidler, Organic electronics. Introduction, IBM J. Res. Dev. 45 (1) (2001) 3–9.
[3] R. Forrest Stephen, The path to ubiquitous and low-cost organic electronic appliances on plastic, Nature 428 (6986) (2004) 911–918.
[4] H. Sirringhaus, T. Kawase, R.H. Friend, et al., Science (Washington, DC) 290 (5499) (2000) 2123–2126.
[5] A.C. Arias, S.E. Ready, R. Lujan, et al., All jet-printed polymer thin-film transistor active-matrix backplanes, Appl. Phys. Lett. 85 (15) (2004) 3304–3306.
[6] Th Birendra Singh, Niyazi Serdar Sariciftci, Progress in plastic electronics devices, Ann. Rev. Mater. Res. 36 (2006) 199–230.
[7] P. Syed Abthagir, Young-Geun Ha, Eun-Ah You, et al., Studies of tetracene- and pentacene-based organic thin-film transistors fabricated by the neutral cluster beam deposition method, J. Phys. Chem. B 109 (50) (2005) 23918–23924.
[8] Do Hwan Kim, Hwa Sung Lee, Hoichang Yang, et al., Tunable crystal nanostructures of pentacene thin films on gate dielectrics possessing surface-order control, Adv. Funct. Mater. 18 (9) (2008) 1363–1370.
[9] S. Kobayashi, T. Nishikawa, T. Takenobu, et al., Control of carrier density by self-assembled monolayers in organic field-effect transistors, Nat. Mater. 3 (5) (2004) 317–322.
[10] M.C. Kwan, K.H. Cheng, P.T. Lai, et al., Improved carrier mobility for pentacene TFT by NH_3 annealing of gate dielectric, Solid-State Electron. 51 (1) (2007) 77–80.
[11] Joseph. E. McDermott, Matthew McDowell, Ian G. Hill, et al., Organophosphonate self-assembled monolayers for gate dielectric surface modification of pentacene-based organic thin-film transistors: a comparative study, J. Phys. Chem. A 111 (49) (2007) 12333–12338.
[12] Y.Y. Lin, D.J. Gundlach, S.F. Nelson, et al., Stacked pentacene layer organic thin-film transistors with improved characteristics, IEEE Electron Dev. Lett. 18 (12) (1997) 606–608.
[13] D.J. Gundlach, Y.Y. Lin, T.N. Jackson, et al., Pentacene organic thin-film transistors – molecular ordering and mobility, IEEE Electron Dev. Lett. 18 (3) (1997) 87–89.
[14] Marcus Halik, Hagen Klauk, Ute Zschieschang, et al., High-mobility organic thin-film transistors based on alpha, alpha-didecyloligothiophenes, J. Appl. Phys. 93 (5) (2003) 2977–2981.
[15] Hagen Klauk, Marcus Halik, Ute Zschieschang, et al., High-mobility polymer gate dielectric pentacene thin film transistors, J. Appl. Phys. 92 (9) (2002) 5259–5263.
[16] Sangyun Lee, Bonwon Koo, Joonghan Shin, et al., Effects of hydroxyl groups in polymeric dielectrics on organic transistor performance, Appl. Phys. Lett. 88 (16) (2006) 162101–162103.
[17] Sang Chul Lim, Seong Hyun Kim, Jae Bon Koo, et al., Hysteresis of pentacene thin-film transistors and inverters with cross-linked poly(4-vinylphenol) gate dielectrics, Appl. Phys. Lett. 90 (17) (2007) 173511–173513.
[18] Se-Jin Choi, Ju-Hyung Kim, Hong H. Lee, Deep-UV curing of poly(4-vinyl phenol) gate dielectric for hysteresis-free organic thin-film transistors, IEEE Electron Dev. Lett. 30 (5) (2009) 454–456.
[19] Ping Liu, Yiliang Wu, Yuning Li, et al., Enabling gate dielectric design for all solution-processed, high-performance, flexible organic thin-film transistors, J. Am. Chem. Soc. 128 (14) (2006) 4554–4555.
[20] Sang Mi Cho, Seung Hoon Han, Jun Hee Kim, et al., Photoleakage currents in organic thin-film transistors, Appl. Phys. Lett. 88 (7) (2006) 071101–071103.
[21] A. Di Carlo, F. Piacenza, A. Bolognesi, et al., Influence of grain sizes on the mobility of organic thin-film transistors, Appl. Phys. Lett. 86 (26) (2005) 263501–263503.
[22] Gilles Horowitz, Tunneling current in polycrystalline organic thin-film transistors, Adv. Funct. Mater. 13 (1) (2003) 53–60.
[23] Seung-Yeon Kwak, Chaun Gi Choi, Byeong-Soo Bae, Effect of surface energy on pentacene growth and characteristics of organic thin-film transistors, Electrochem. Solid-State Lett. 12 (8) (2009) G37–G39.
[24] Vincenzo Vinciguerra, Manuela La Rosa, Donata Nicolosi, et al., Modeling the gate bias dependence of contact resistance in staggered polycrystalline organic thin film transistors, Org. Electron. 10 (6) (2009) 1074–1081.
[25] T. Yamada, T. Hasegawa, M. Hiraoka, et al., Control of film morphology and its effects on subthreshold characteristics in dibenzotetrathiafulvalene organic thin-film transistors, Appl. Phys. Lett. 92 (23) (2008) 233301–233303.

methods since the solvent can damage the organic semiconductor [16].

In this work, we introduce an external pressure sensible organic thin film transistor (OTFT) by soft-contact lamination. After forming two bottom electrodes and one roof electrode separately on the bridge-structured PDMS mold by thermal deposition of gold (Au), two bottom electrodes of the mold were used as source and drain electrodes in OTFT structure via soft-contact lamination. Then, the roof electrode between source and drain electrodes could play a role to control the effective channel length of OTFT through the PDMS deformation by the external pressure. Since the device performance was similar to the piezoelectric effect, the output current could be controlled through the pressure applied to the device.

2. Experimental

2.1. Overall device structure

The overall structure of the laminated OTFT is shown in Fig. 1. Pentacene was used as an organic semi-conducting layer, and a PDMS mold was replicated from a silicon master mold. Au electrodes were then deposited onto the PDMS mold by thermal evaporation through a shadow mask. Subsequently, the PDMS mold containing the Au electrodes was laminated on the substrate, which was composed of the gate electrode, dielectrics, and pentacene as shown in Fig. 1(a).

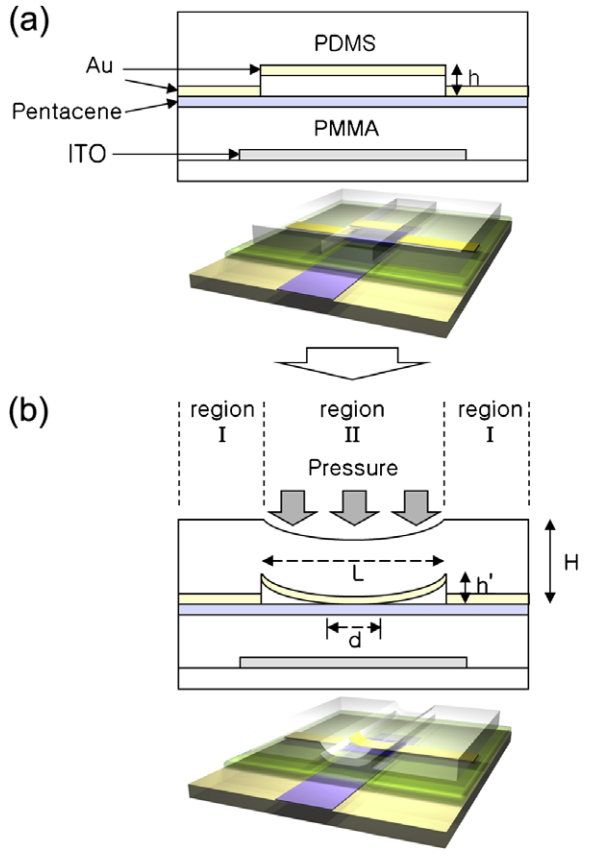

Fig. 1. Schematic illustrations of the soft-contact laminated OTFTs (a) without the external load and (b) with the external load. Under the external load, the area over which the pressure was applied was divided into two regions (region I and region II).

2.2. Preparation of Au electrode on the PDMS mold

Silicon master mold with a long protruding line, which was 35 μm high and 1 mm wide, was prepared. Polydimethylsiloxane (PDMS) (Sylgard 184, Dow Corning) prepolymer and its curing agent were mixed at a weight ratio of 10:1. The PDMS mixture was then poured onto the silicon master mold and thermally cured at 60 °C in a vacuum oven for 2 h. After thermal curing, the cured PDMS mold was peeled off from the master mold, and a shadow mask with a 1 mm wide line was aligned perpendicularly to the channel of the PDMS mold. An Au electrode (70 nm) was thermally evaporated onto the sample at the speed of 15–20 Å/s.

2.3. Preparation of the substrate

Transparent ITO coated glass was successively cleaned by sonication in acetone and isopropyl alcohol. An ITO film was then patterned by photography and a wet etching process. Onto ITO patterned glass, 10 wt.% of poly(methylmethacrylate) (PMMA) in toluene was spin-coated at a speed of 3000 rpm for 30 s. The PMMA-coated sample was moved to a hot plate and annealed at 100 °C for an hour on a hot stage. A pentacene film (100 nm) was then deposited onto the PMMA-coated substrate at a speed of 0.5–1 Å/s by thermal evaporation. All the processes, except for the thermal evaporation of pentacene, were done in an air environment.

2.4. Performance measurement

Pressure was applied onto the OTFT by a push–pull gauge with a rectangular tip (1 × 1 cm). Electric sources from a semiconductor parameter analyzer were connected to the ITO electrode and Au electrodes on the OTFT with probe tips. The characteristic curves of the devices were measured by a semiconductor parameter analyzer (Keithely Instruments Inc., 4200-SCS), and the capacitances of dielectrics were measured using an LCR meter (Agilent 4980A).

3. Results and discussion

Typical OTFT characteristics were observed after laminating the Au-deposited PDMS mold onto the pentacene-deposited substrate. If gate bias was not applied, no output current could be observed between the source–drain electrodes because the Au line on the PDMS mold was disconnected by anisotropic metal evaporation as shown in Fig. 1(a). Due to the low Young modulus and the elastic properties of PDMS, the roof of the PDMS mold was deformed by the external load when pressure was applied on the PDMS mold. If the external load on the PDMS mold was high enough, the Au line on the deformed roof of the PDMS mold reached the pentacene inside the channel.

The contact length, d, increased as the external pressure on the PDMS increased, and the output current also increased as the contact length increased. Contact between the Au line and the pentacene layer due to the external force contributed to the increase in the output current through the channel because of the conducting properties of Au. Consequently, it could be expected that this contact between the Au line and the pentacene layer reduced the active section of pentacene, from which electrons were transferred through. Electrons were transported more efficiently through the Au than the pentacene layer because of the relatively less electric resistance of Au. In other words, the actual channel length of pressed OTFT became $L - d$ because the potential difference between both the ends of the contacted Au line is negligible compared with the potential drop along the channel.

To investigate this contact effect more clearly, an additional experiment was performed. An Au line that was 1 mm in width was deposited on a flat PDMS substrate through a shadow mask. Then, to insert the Au line between the source–drain electrodes of OTFT, it was laminated on the complete OTFT structure which had a channel length of 2 mm. No external pressure was applied after the insertion of the Au line inside the channel. In this case, since the conformal contact between the OTFT and the PDMS substrate could be achieved without any external pressure via soft-contact lamination method, the actual channel length of 1 mm and the 2-fold of output current compared to the OTFT with the channel length of 2 mm were expected. Consequently, the output current of the device with the inserted Au line was increased by 90% compared to that with the 2 mm channel length, and it showed that the metal line when in contact with the pentacene layer was charged with an electric current. This result clearly demonstrated that electrons moved through the contacted Au electrode on the semi-conducting layer when the laminated device was pressed.

Fig. 2 shows the field-effect transistor characteristics of the laminated OTFT under various external pressures. As shown in Fig. 2(a) and (b), the gate voltage was scanned from +20 V to −120 V with −1 V step at a fixed source–drain voltage of −120 V. When the external pressures of 0, 0.2, 0.4, and 0.6 N/mm^2 were applied to the laminated OTFT device, the values of the on-current were 5.1, 10.3, 25.1, and 56.2 μA, whereas the values of the off-current were 1.5, 1.7, 0.9, and 0.6 nA, respectively. Besides the on- and off-currents, the values of the threshold voltage were 20.2, 20.1, 22.1, and 25.4 V, respectively. Fig. 2(c) and (d) also shows the drain current versus source–drain voltage at a fixed gate voltage at external pressures of 0 and 0.6 N/mm^2, respectively. Most notable was the increase in the on-current of OTFT as the external pressure was increased, while significant changes were not observed in the off-current and the threshold voltage. In the same manner, the values of the on/off ratio also increased as the external pressure was increased.

In OTFTs, if contact resistance is negligible, the drain current can be typically expressed as

$$I_D = \frac{WC_i}{2L}\mu_e(V_G - V_T)^2 \quad (1)$$

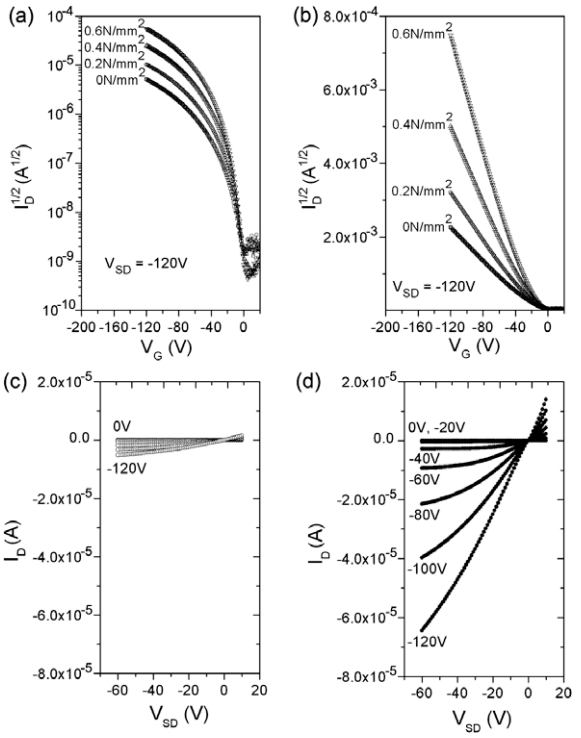

Fig. 2. Characteristics of the laminated OTFT under various external loads (from 0 to 0.6 N/mm^2). Transfer characteristics of the device at a fixed source–drain voltage of −120 V (a) in log scale and (b) in square-root scale. Output characteristics of the device with the external pressures of (c) 0 N/mm^2 and (d) 0.6 N/mm^2, respectively.

where I_D is the drain current, W and L are the channel width and length, respectively, μ_e is the effective mobility, C_i is the capacitance per unit area, V_G is the gate voltage, and V_T is the threshold voltage. In this work, OTFT characteristics were obtained from the same device, and the plot of total resistance of the device versus channel length which is measured by a microscope is nearly linear. It is known that the channel resistance is more dominant than the contact resistance when the channel length is over 10 μm [17], and the contact resistance of OTFT with the soft-contact laminated electrodes is more than an order of magnitude smaller than that with the evaporated Au electrodes [13]. In this experiment, contact resistance exists when holes move from pentacene to Au and from Au to pentacene across the interface between pentacene and Au. However, the channel lengths measured by microscope were much longer than 10 μm and the plot of total resistance of the device versus channel length which is measured by a microscope is nearly linear. Therefore, the constant charge carrier mobility of pentacene could be expected regardless of the external pressure, and it is assumed that the contact resistance between the pentacene and the Au layer containing the channel is negligible. Based on the assumption that the charge carrier mobility of pentacene does not change in the saturated region when the device is pressed, the effective channel length, L_{eff}, can be calculated from the experimental values of I_D and V_G. Without any external pressure, this OTFT device pro-

vided a charge carrier mobility of 0.27 $cm^2 V^{-1} s^{-1}$ as calculated through Eq. (1), because the values of L, W, and C_i of the device were 0.1 cm, 0.1 cm, and 3.8 nF cm^{-2}, respectively. The values of L_{eff} under the external pressures of 0.2, 0.4, and 0.6 N/mm^2 can be calculated using this constant charge carrier mobility and the experimental characteristics as shown in Fig. 3. The values of L_{eff} were determined to be 495, 127, and 82 μm under the external pressures of 0.2, 0.4, and 0.6 N/mm^2, respectively. Therefore, the theoretical values of the contact length between the Au line and the pentacene layer under the external pressures of 0.2, 0.4, and 0.6 N were 505, 803, and 918 μm, respectively.

While the laminated devices were pressed with an external pressure, the area over which the external pressure was applied can be divided into two regions (region I and region II), as shown in Fig. 1. During the application of an external pressure, the height of the posts, which support the roof of PDMS mold, h, was compressed to a height, h', in region I, and the roof of the PDMS mold was bent in region II using a uniform external force. Assuming that deformations in region I and region II are independent and there was no lateral expansion of the PDMS when the PDMS mold was exposed to the external pressure, a simple model describing the contact length can be considered. If it is assumed that the compression in region I and the bending in region II occur independently, the value of h' in region I can be easily calculated. A stable silicone rubber has a unique flexibility ($G \sim 1$ MPa = 1 N/mm^2) at room temperature. For simple extension and uni-axial compression, the rubber-elastic stress–strain relation can be expressed as follows [18]:

$$F_{ce} = A_R G\left(\delta - \frac{1}{\delta^2}\right) \tag{2}$$

where F_{ce} is the applied compressive or extensive force, A_R is the area of the rubber on which the force is applied, and δ is the rubber's extension ratio $\left(\delta = 1 + \frac{h-h'}{h}\right)$. Considering that $P = F_{ce}/A_R$, Eq. (2) can be rearranged as follows:

$$G\delta^3 - P\delta^2 - G = 0 \tag{3}$$

and the values of δ, which vary according to the external pressure, can be calculated by Eq. (3). By using these calculated values of δ, the values of h' can also be obtained.

As shown in Fig. 1, the bending of the PDMS bridge, which was supported by the compressed posts, occurred in region I. If it is assumed that the compression of PDMS is negligible in region II, a simply supported beam model with a uniform load [19] can be applied to region II. The moment of inertia can be set as $I = \frac{zy_1^3}{12}$ and

$$y(x) = -\frac{u}{24EI}\left(x^4 - 2Lx^3 + L^3x\right) \tag{4}$$

where u is the uniform load on the bridge, z is the width of the bridge and E is Young's modulus of PDMS. Considering that $u = P \cdot z$ and $y_1 = H - h$, Eq. (4) can be simplified to $y(x) = -\frac{P}{2E(H-h)^3}(x^4 - 2Lx^3 + L^3x)$. To calculate the value of x_1 such as $y(x_1) + h' = 0$, Eq. (4) can be also simplified as follows:

$$2h - h\delta - \frac{P}{2E(H-h)^3}\left(x^4 - 2Lx^3 + L^3x\right) = 0 \tag{5}$$

The contact length can be defined as the distance between x_1 and x_2, which intersects the pentacene layer as illustrated in Fig. 3(a). By considering the symmetric deformation of the PDMS roof, the contact length, d, becomes $L - 2 \cdot x_1$. Therefore, the value of the contact length, d, which varies according to the external pressure, can be obtained using Eqs. (3) and (5).

In this study, the experimental values of h, L, H, G, and P were 0.035 mm, 1 mm, 1 mm, 0.7 MPa, and 0.7 MPa, respectively. From these values, the contact length, d, versus the external pressure can be plotted as shown in Fig. 3(b). At an external pressure of 0.14 N/mm^2, the roof of the PDMS mold was initially brought into contact with the pentacene layer, and the contact length was then increased dramatically up to an external pressure of 0.3 N/mm^2. If the external pressure exceeded this range, the increasing rate of the contact length versus the external pressure decreased. The contact lengths measured by the inverted microscope (open circle), and calculated from the output current data using Eq. (1) (solid symbol) are shown in Fig. 3(b). The graph calculated from Eqs. (3) and (5) (solid line) was also compared to the data obtained from the experiments.

The external pressure sensing on a real time scale is shown Fig. 4. Each point was scanned at the stated intervals of 1 s, and various external pressures, which depended on time, were applied to the laminated OTFT. Due to the elastic property of the PDMS, the laminated OTFT returned to its initial shape after the external pressure was released.

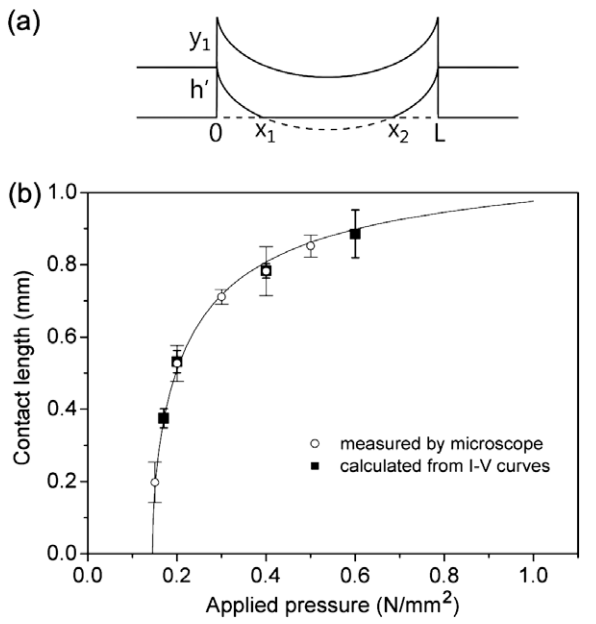

Fig. 3. (a) Schematic illustration of the contact length, which was defined as the distance between x_1 and x_2 and intersects the pentacene layer. (b) Three different types of PDMS deformation, which were the inverse operated values obtained from the output data using Eq. (1) (solid symbol), the calculated values by simple modeling from Eqs. (3) and (5) (solid line) and the experimentally measured values from the microscope (open circle). The sizes of error bars are ±5% for both solid symbols and the open circles.

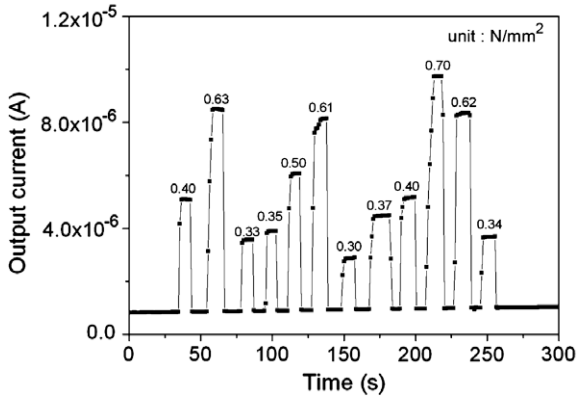

Fig. 4. Sensing of the external load on a real time scale. Source–drain voltage and gate voltage were −40 V and −50 V, respectively. The numbers in the figure means pressure applied onto the device and the output currents of the device under 0.4 N/mm^2 at different times were almost same.

The current output increased when an external pressure was applied, and the current was in proportion with the magnitude of the external pressure. Furthermore, the output currents of the device, which was exposed to the same external pressure of 0.4 N/mm^2 at different times, were almost same as shown in Fig. 4. The first and the second output currents were 5.10 and 5.16 μA, respectively. When the pressures are 0.33, 0.35, and 0.34 N/mm^2, output currents were 3.56, 3.89, and 3.68 μA, respectively. Therefore, these results suggest that the output current, which depends on the magnitude of the external pressure, and the laminated OTFT also have reversibility that restores the output current to the non-contact condition after the external pressure was released. Although the sensitivity of the device was low, it can be improved by controlling the thickness of the laminating mold or the Young modulus of the mold. A further study would be required to enhance the pressure sensitivity.

4. Conclusions

In conclusion, a pressure dependent output current-controllable OTFT was fabricated by soft-contact lamination. Soft-contact lamination provided OTFT with a new functionality, and the source–drain currents were controllable by changing the contact area of the electrodes on the semi-conducting layer, which corresponded to the external pressures applied to the device, without changing any of the semi-conducting material properties. As the external pressure on the device was varied from 0 to 0.6 N/mm^2, the source–drain current increased by 11-fold, from 5.1 to 56.1 μA, whereas the off-current and threshold voltage were almost fixed. Comparing the contact lengths calculated by three different methods, which were (a) the inverse operation from the output current data using Eq. (1), (b) the simple beam modeling using Eqs. (3) and (5), and (c) the experimental measurement by the microscope, the results obtained were very similar to each other. Reversible and time-durable operations of the device could also be achieved. Consequently, a new functionality was added to OTFTs via soft-contact lamination due to the elastic properties of the PDMS molds. Furthermore, these pressure dependent devices, which have an OTFT structure, hold a great promise for their use in fabricating novel piezoelectric-like devices or in various applications such as touch screens and flexible devices in the display field.

Acknowledgements

This work was supported by the Korea Research Foundation (KRF) Grant funded by the Korea Government (MEST) (No. 2009-0068479) and this research was supported by the Kyungwon University Research Fund in 2009.

References

[1] J. Yoon, A.J. Baca, S.-I. Park, P. Elvikis, J.B. Geddes, L. Li, R.H. Kim, J. Xiao, S. Wang, T.H. Kim, M.J. Motala, B.Y. Ahn, E.B. Duoss, J.A. Lewis, R.G. Nuzzo, P.M. Ferreira, Y. Huang, A. Rockett, J.A. Rogers, Nat. Mater. 7 (2008) 907.
[2] H.C. Ko, M.P. Stoykovich, J. Song, V. Malyarchuk, W.M. Choi, C.-J. Yu, J.B. Geddes, J. Xiao, S. Wang, Y. Huang, J.A. Rogers, Nature 454 (2008) 748.
[3] J.N. Tey, I.P.M. Wijaya, Z. Wang, W.H. Goh, A. Palaniappan, S.G. Mhaisalkar, I. Rodriguez, S. Dunham, J.A. Rogers, Appl. Phys. Lett. 94 (2009) 013107.
[4] T.-W. Lee, J. Zaumseil, S.H. Kim, J.W.P. Hsu, Adv. Mater. 16 (2004) 2040.
[5] I. Manunza, A. Sulis, A. Bonfiglio, Appl. Phys. Lett. 89 (2006) 143502.
[6] G. Darlinski, U. Böttger, R. Waser, H. Klauk, M. Halik, U. Zschieschang, G. Schmid, C. Dehm, J. Appl. Phys. 97 (2005) 093708.
[7] Y. Xia, G.M. Whitesides, Angew. Chem., Int. Ed. 37 (1998) 550.
[8] K.J. Lee, M.J. Motala, M.A. Meitl, W.R. Childs, E. Menard, A.K. Shim, J.A. Rogers, Ralph G. Nuzzo, Adv. Mater. 17 (2005) 2332.
[9] T.-W. Lee, J. Zaumseil, Z. Bao, J.W.P. Hsu, J.A. Rogers, Proc. Natl. Acad. Sci. USA 101 (2004) 429.
[10] V.C. Sundar, J. Zaumseil, V. Podzorov, E. Menard, R.L. Willett, T. Someya, M.E. Gershenson, J.A. Rogers, Science 303 (2004) 1644.
[11] M.A. Unger, H.-P. Chou, T. Thorsen, A. Scherer, S.R. Quake, Science 288 (2000) 113.
[12] N.Y. Lee, Y.S. Kim, Macromol. Rapid Commun. 28 (2007) 1995.
[13] J. Zaumseil, K.W. Baldwin, J.A. Rogers, J. Appl. Phys. 93 (2003) 6117.
[14] D.A. Bernards, T. Biegala, Z.A. Samuels, J.D. Slinker, G.G. Malliaras, S.F. Torres, H.D. Abruna, J.A. Rogers, Appl. Phys. Lett. 84 (2004) 3675.
[15] J. Zaumseil, T. Someya, Z. Bao, Y.L. Loo, R. Cirelli, J.A. Rogers, Appl. Phys. Lett. 82 (2003) 793.
[16] J. Kim, D.-Y. Khang, J.-H. Kim, H.H. Lee, Appl. Phys. Lett. 92 (2008) 133307.
[17] P.V. Necliudov, M.S. Shur, D.J. Gundlach, T.N. Jackson, Solid-State Electron. 47 (2003) 259.
[18] J.C. Lötters, W. Olthuis, P.H. Veltink, P. Bergveld, Microsyst. Technol. 3 (1997) 64.
[19] R. Huston, H. Josephs, in: Practical Stress Analysis in Engineering Design, third ed., CRC Press, Boca Raton, FL, USA, 2008 (Chapter 9).

they have received particular attention as in the context of bulk-heterojunction solar cells. For example, Morin and co-workers described the synthesis of a variety of new poly(2,7-carbazoles) [14]. In a later effort, the first photovoltaic device derived from poly(*N*-alkyl-2,7-carbazole), which has a power conversion efficiency (PCE) of 0.6%, was described by Müllen and co-workers [15].

In recent years, considerable interest has grown in the area of low-band gap polymers owing to their applications in organic solar cell devices as an active layer for light absorption and charge generation [16–18]. High power conversion efficiencies (PCEs) are key goal for solar applications since these values determine how much electrical energy is produced by absorbed photons. One strategy to improve PCE is to employ well designed and readily synthesized low-band gap polymers, which have improved overlap of the polymer absorption spectrum with the standard solar spectrum under AM 1.5G. One successful approach that has been used to design these polymers takes advantage of vinylene linkages in π-conjugated systems. Based on this design principal, a number of polymers have been prepared which, in comparison to conventional π-conjugated polymers, have low the band gaps in the range of 0.3–0.5 eV [19]. Another advantage arising from the introduction of vinylene units is that it serves as a good method to create planar molecules with extended π-conjugation lengths. This is a consequence of the relatively small dihedral angle that exists between vinylene and aryl groups that leads to an increase in the absorption maxima of the material [20]. Finally, different monomer units can be easily introduced into the polymer in order to fine tune electronic properties.

We have previously described the preparation of novel vinylene based, π-conjugated polymers, including the alkyloxyphenoxy and 1,3,4-oxadiazole-substituted PPVs, poly(9,9-dioctylfluorenyl-2,7-vinylene) (PFV), PFV-*co*-MEH-PPV, highly luminescent poly(*m*-SiPh-PV) derivatives, highly branched poly(PDOT-PV), poly(PDOT-PV-*co*-*m*-SiPh-PV), poly($3OC_1OC_{10}$-PV), and poly($3OC_1O$-C_{10}-PV-*co*-*m*-SiPh-PV) [21–27].

In this effort, repeating vinylene units were introduced between the 2- and 7-positions of the carbazole main chain by using the Gilch polymerization procedure [28]. The substances prepared in this effort include poly(*N*-(3,4-bis(decyloxy)phenyl)carbazolyl-2,7-vinylene) (PCzV) and its copolymer with MEH-PPV segment, poly[*N*-(3,4-bis(decyloxy)phenyl)carbazolyl-2,7-vinylene)-*co*-{2-methoxy-5-(2-ethylhexyloxy)-1,4-phenylenevinylene}] [PCzV-*co*-MEH-PPV]. These polymers possess many attractive properties, such as high molecular weights, low polydispersities and ready purification. To enhance the solubilities and electronic properties of the derived poly(carbazolyl-2,7-vinylene), a meta and para bis-decyloxyphenyl groups were incorporated on the carbazole nitrogen atoms. The addition of vinylene units along the 2,7-carbazole backbone is expected to tune the highest occupied molecular orbital (HOMO) level of π-conjugated polymers as well as improve the electro-optical properties. The preparation of these polymers along with an analysis of their thermal, optical, electrochemical, and photovoltaic properties are described below.

2. Experimental

2.1. General information

^{1}H NMR spectra were recorded on a Varian Mercury Plus 300 MHz spectrometer and the chemical shifts were recorded in ppm units with chloroform as the internal standard. UV–visible and the emission spectra were recorded with a JASCO V-570 and Hitachi F-4500 fluorescence spectrophotometers. Measurements of solid state emissions were carried out by supporting each film on a quartz substrate, which was mounted to receive front-face excitation at an angle of less than 45°. Each polymer film was excited with several portions of the visible light from a xenon lamp. The molecular weight and polydispersity of the polymer were determined by using gel permeation chromatography (GPC) using a PLgel 5 μm MIXED-C column on an Agilent 1100 series liquid chromatography system with THF as an eluent and calibration with polystyrene standards. Thermal analyses were carried out on a Mettler Toledo TGA/SDTA 851, DSC 822 analyzer under N_2 atmosphere at a heating rate of 10 °C/min. Cyclic voltammetry (CV) was carried out in a 0.1 M solution of tetrabutylammonium hexafluorophosphate ($TBPAPF_6$) in benzene:acetonitrile (1.5:1 v/v) [29] using a CHI600C voltammetric analyzer at a potential scan rate of 100 mV/s. Each polymer film was applied to a Pt disc electrode (0.2 cm^2) by dipping the electrode into the polymer solution. A platinum wire was used as the counter electrode, and $Ag/AgNO_3$ electrode was used as the reference electrode.

2.2. Materials

Sodium nitrite, copper cyanide, potassium cyanide, catechol, iodine, iodic acid, copper powder, RED-Al, methanesulfonyl chloride, triethylamine, potassium *tert*-butoxide, 4-*tert*-butylbenzyl bromide, tetrahydrofuran (THF), and *N*,*N*-dimethylacetamide were purchased from Aldrich Co. and used without further purification unless otherwise noted. Solvents were dried and purified by fractional distillation over sodium/benzophenone and handled in a moisture-free atmosphere. Column chromatography was performed using silica gel (Merck, 250–430 mesh).

2.3. Synthesis of 2,7-dicyanocarbazole (**4**)

To a solution of 2,7-diaminocarbazole (**3**) (2 g, 10 mmol) and hydrochloric acid (10 mL) in distilled water (100 mL) was added dropwise an aqueous solution of sodium nitrite (1.66 g, 24 mmol). The resulting solution was stirred for 2 h at 0 °C. Aqueous sodium carbonate was added at 0 °C to bring the pH to 7 (solution A). To a solution of copper cyanide (3.63 g, 40.56 mmol) in distilled water was added a solution of potassium cyanide (2.64 g, 40.56 mmol) in distilled water at room temperature (solution B). To this mixture in an ice bath was added solution A at 0 °C. After being stirred overnight at room temperature, the formed precipitate was removed by filtration. The precipitate was washed with distilled water before being

repeatedly triturated with acetone. The triturate was concentrated in vacuo to give a solid which was dissolved in ethyl acetate. Filtration followed by concentration of the filtrate gave a crystalline solid which was recrystallized from ethanol to give 0.54 g. Yield: 25%, ^{1}H NMR (acetone-d_6, δ ppm): 11.3 (br, 1H), 8.46–8.43 (d, 2H, aromatic protons), 8.06 (s, 2H, aromatic protons), 7.62–7.59 (d, 2H, aromatic protons). ^{13}C NMR (acetone-d_6, δ ppm): 141.01, 126.10, 123.48, 123.16, 120.16, 116.85, 110.75.

2.4. Synthesis of 1,2-bis(decyloxy)benzene (**5**)

To a solution of catechol (15 g, 135 mmol) in 1-bromodecane (83.7 mL, 404.7 mmol) and DMF (150 mL) was added potassium carbonate (74.58 g, 539.6 mmol). The mixture was stirred at 60 °C for 24 h. and concentrated in vacuo to give a residue which was subjected to flash chromatography on silica gel using ethyl acetate:hexane (1:10) as an eluent. This yielded 50.6 g (96%) of **5**. ^{1}H NMR ($CDCl_3$, δ ppm): 6.92 (s, 4H, aromatic protons), 4.05 (t, 4H, α-protons of decyloxy position), 1.93–1.78 (m, 4H, β-protons of decyloxy position), 1.61–1.25 (br, 28H, aliphatic protons), 0.92–0.89 (m, 6H, aliphatic protons). ^{13}C NMR ($CDCl_3$, δ ppm): 149.25, 121.02, 113.97, 69.21, 32.07, 29.68, 29.47, 26.20, 22.84, 14.24.

2.5. Synthesis of 1,2-bis(decyloxy)-4-iodobenzene (**6**)

To a solution of 1,2-bis(decyloxy)benzene (**5**) (20 g, 52 mmol) in acetic acid (600 mL) was added water (200 mL) at 40 °C. Sulfuric acid (16 mL) and iodine (6.768 g, 26.67 mmol) were added and the resulting mixture was stirred at 44 °C. Iodic acid (1 g, 5.68 mmol) was added three times during a 40 min period. After cooling, the mixture was extracted with diethyl ether, washed with aqueous sodium carbonate and saturated brine, dried over anhydrous $MgSO_4$ and concentrated in vacuo to give a the crystalline residue which was recrystallized from ethanol to yield 18.65 g (71%) of **6**. ^{1}H NMR ($CDCl_3$, δ ppm): 7.20–7.12 (s, 2H, aromatic protons), 6.64–6.60 (d, 1H, aromatic protons), 3.97–3.88 (t, 4H, α-protons of decyloxy position), 1.83–1.75 (m, 4H, β-protons of decyloxy position), 1.60–1.27 (br, 28H, aliphatic protons), 0.91–0.86 (m, 6H, aliphatic protons). ^{13}C NMR ($CDCl_3$, δ ppm): 149.80, 129.86, 123.68, 122.54, 115.64, 82.63, 69.45, 32.07, 29.52, 29.17, 26.10, 22.86, 14.31.

2.6. Synthesis of 9-(3,4-bis(decyloxy)phenyl)carbazole-2,7-dicarbonitrile (**7**)

To a solution of 2,7-dicyanocarbazole (**4**) (1 g, 5 mmol) and 1,2-bis(decyloxy)-4-iodobenzene (**6**) (7.13 g, 13.8 mmol) in *N*,*N*-dimethylacetamide (60 mL) was added copper powder (2 g, 31 mmol) and potassium carbonate (2.1 g, 15 mmol) under a N_2 atmosphere. The mixture was stirred at 160 °C for 12 h, diluted with distilled water, and extracted with methylene chloride. The methylene chloride extracts were dried over anhydrous $MgSO_4$ and concentrated in vacuo giving a residue, which was subjected to flash chromatography on silica gel using chloroform as an eluent. This gave 0.56 g (20%) of **7**. ^{1}H NMR ($CDCl_3$, δ ppm): 8.26–8.23 (d, 2H, aromatic protons on carbazole), 7.68 (s, 2H, aromatic protons on carbazole), 7.61–7.58 (d, 2H, aromatic protons on carbazole), 7.13–7.08 (d, 1H, aromatic proton on benzene), 7.02–6.96 (dd, 1H, aromatic proton on benzene), 6.94–6.91(d, 1H, aromatic proton on benzene), 4.16–4.11 (dt, 4H, α-protons of decyloxy position), 1.97–1.80 (m, 4H, β-protons of decyloxy position), 1.57–1.22 (br, 28H, aliphatic protons), 0.92–0.83 (m, 6H, aliphatic protons). ^{13}C NMR ($CDCl_3$, δ ppm): 149.81, 148.05, 141.09, 135.71, 127.53, 122.84, 120.77, 116.91, 116.80, 114.08, 112.82, 105.59, 98.32, 69.48, 32.05, 29.61, 29.30, 26.26, 22.73, 14.30.

2.7. Synthesis of 9-(3,4-bis(decyloxy)phenyl)carbazole-2,7-dicarboxylic acid (**8**)

A mixture of 9-(3,4-bis(decyloxy)phenyl)carbazole-2,7-dicarbonitrile (**7**) (2 g, 3 mmol) in ethanol (50 mL) containing sodium hydroxide (30%, 30 mL) was stirred at 110 °C for 24 h. After hydrochloric acid was added to bring the pH below 7, a portion of the water and ethanol were removed by concentration in vacuo. The resulting mixture was stirred at 120 °C for 3 h, cooled and filtered. The precipitate was dried under reduced pressure to yield 1.99 g (94%) of **8**. ^{1}H NMR (DMSO-d_6, δ ppm): 8.43–8.40 (d, 2H, aromatic protons), 7.91–7.87 (d, 4H, aromatic protons), 7.27–7.21 (t, 2H, aromatic protons), 7.16–7.12 (d, 1H, aromatic proton), 4.12–3.96 (dt, 4H, α-protons of decyloxy position), 1.83–1.65 (m, 4H, β-protons of decyloxy position), 1.52–1.09 (br, 28H, aliphatic protons), 0.91–0.0.81 (q, 6H, aliphatic protons). ^{13}C NMR (DMSO-d_6, δ ppm): 177.60, 162.22, 149.53, 147.48, 141.97, 137.67, 130.18, 121.41, 114.56, 109.57, 108.64, 103.25, 96.12, 71.66, 38.16, 28.33, 25.82, 22.58, 18.64, 13.62.

2.8. Synthesis of (9-(3,4-bis(decyloxy)phenyl)carbazole-2,7-diyl)dimethanol (**9**)

To a solution of 9-(3,4-bis(decyloxy)phenyl)carbazole-2,7-dicarboxylic acid (**8**) (2 g, 3 mmol) in benzene (90 mL) was added sodium bis(2-methoxyethoxy)aluminum hydride (RED-Al) (18.7 mL, 62.2 mmol). The mixture was stirred at 100 °C for 24 h. Ice-water was added after hydrochloric acid was added to make the solution acidic. Extraction with chloroform gave an extract that was dried over anhydrous $MgSO_4$ and concentrated in vacuo to give a residue which was subjected to flash chromatography on silica gel using chloroform:ethyl acetate (9:1) as an eluent. This gave 1.30 g (68%) of **9**. ^{1}H NMR ($CDCl_3$, δ ppm): 8.11–8.09 (d, 2H, aromatic protons on carbazole), 7.34 (s, 2H, aromatic protons on carbazole), 7.29–7.26 (d, 2H, aromatic protons on carbazole), 7.05–7.04 (m, 2H, aromatic protons on benzene), 6.99–6.98 (d, 1H, aromatic proton on benzene), 4.83–4.81 (d, 4H, $-CH_2OH$), 4.13–3.94 (dt, 4H, α-protons of decyloxy position), 1.94–1.77 (m, 4H, β-protons of decyloxy position), 1.58–1.19 (br, 28H, aliphatic protons), 0.92–0.83 (q, 6H, aliphatic protons). ^{13}C NMR ($CDCl_3$, δ ppm): 167.88, 162.92, 161.15, 142.61, 139.19, 124.08, 122.54, 120.06, 119.12, 112.50, 109.43, 94.32, 66.48, 65.18, 32.10, 29.55, 29.04, 26.15, 22.92, 14.33.

2.9. Synthesis of 9-(3,4-bis(decyloxy)phenyl)-2,7-bis(chloromethyl)carbazole (**10**)

To a solution of (9-(3,4-bis(decyloxy)phenyl)carbazole-2,7-diyl)dimethanol (**9**) (1 g, 2 mmol) in methylene chloride (100 mL) was added methanesulfonyl chloride (0.50 mL, 6.48 mmol) and triethylamine (0.90 mL, 6.48 mmol). The resulting mixture was stirred for 48 h at room temperature, diluted with water and extracted with chloroform. The extracts were dried over anhydrous $MgSO_4$ and concentrated in vacuo giving a residue which was subjected to flash chromatography on silica gel using chloroform as an eluent to yield 0.51 g (48%) of **10**. ^{1}H NMR ($CDCl_3$, δ ppm): 8.12–8.09 (d, 2H, aromatic protons on carbazole), 7.387.26–8.09 (m, 4H, aromatic protons on carbazole), 7.11–7.08 (q, 2H, aromatic protons on benzene), 7.0 (s, 1H, aromatic proton on benzene), 4.80–4.67 (s, 4H, CH_2Cl), 4.14–3.97 (dt, 4H, α-protons of decyloxy position), 1.93–1.82 (m, 4H, β-protons of decyloxy position), 1.57–1.19 (br, 28H, aliphatic protons), 0.99–0.86 (q, 6H, aliphatic protons). ^{13}C NMR ($CDCl_3$, δ ppm): 150.11, 149.02, 142.04, 135.71, 129.66, 122.84, 120.85, 120.77, 119.80, 114.08, 112.82, 110.29, 69.49, 47.33, 32.08, 29.63, 29.31, 26.26, 22.86, 14.31.

2.10. Synthesis of poly[N-(3,4-bis(decyloxy)phenyl)-carbazolyl-2,7-vinylene)-co-{2-methoxy-5-(2-ethylhexyloxy)-1,4-phenylenevinylene}] [PCzV-co-MEH-PPV] (**13**)

A potassium *tert*-butoxide solution (1.84 mL of a 1.0 M solution in THF) was added dropwise by using a syringe pump over a 15 min period to a 0 °C solution of 9-(3,4-bis(decyloxy)phenyl)-2,7-bis(chloromethyl)carbazole (**10**) (100 mg, 0.15 mmol) and 1,4-bis(chloromethyl)-2-(2-ethylhexyloxy)-5-methoxybenzene (**12**) (51 mg, 0.15 mmol) in freshly distilled THF (12 mL) under N_2 atmosphere. The solution was stirred at 0 °C for 50 min and cooled. End capping was performed by the addition of 3–4 drops of 4-*tert*-butylbenzyl bromide followed by stirring for 15 min at room temperature. The solution was poured into methanol and the precipitate was removed by filtration. After carrying out successive Soxhlet extractions, the polymer was obtained by pouring the solution into methanol. The resulting product 13 (49 mg, 38%) was obtained by drying reduced pressure. ^{1}H NMR ($CDCl_3$, δ (ppm): 8.19–6.70 (br, 13H, aromatic and vinylic protons), 4.26–3.29 (br, 9H, α-protons of alkoxy position), 2.03–0.86 (br, 53H, aliphatic protons). Anal. Calcd. for PCzV-*co*-MEH-PPV: C, 78.72; H, 9.32; N, 0.21. Found: C, 75.70; H, 9.13; N, 0.17.

The homopolymer, poly(*N*-(3,4-bis(decyloxy)phenyl)-carbazolyl-2,7-vinylene) (PCzV) was synthesized by using a method that is similar to that used to prepare PCzV-*co*-MEH-PPV.

PCzV: 1H NMR ($CDCl_3$, δ ppm): 8.12–7.94 (br, 2H, aromatic protons), 7.57–7.36 (br, 4H, aromatic protons), 7.18–6.79 (br, 5H, aromatic and vinylic protons), 4.23–3.48 (br, 4H, α-protons of decyloxy position), 1.95–0.68 (br, 38H, aliphatic protons). Anal. Calcd. for PCzV: C, 82.85; H, 9.21; N, 2.42. Found: C, 77.96; H, 9.12; N, 2.22.

2.11. Solar cell fabrication and measurements

Bulk-heterojunction solar cells used to measure photovoltaic properties were constructed as follows. Each glass substrate was coated with a transparent ITO electrode (110 nm thick, 10–20 Ω/sq sheet resistance). The ITO-coated glass substrates were ultrasonically cleaned with detergent, deionized water, acetone, and isopropyl alcohol. The layer of 40 nm thick PEDOT:PSS (H.C. Stack, PH500) was spin-coated onto the pre-cleaned and UV-ozone treated ITO substrates. The spin-coated film was baked in air at 150 °C for 30 min. For fabrication of the active layers composed of interconnected networks of electron donor and acceptor, 1,2-dichlorobenzene and chloroform (1:1 wt.%) solutions of the synthesized polymer (10 mg/mL) and $PC_{61}BM$ (15 mg/mL) were shaken at room temperature for 12 h. The polymer and $PC_{61}BM$ blends was then prepared by mixing the two solutions and subsequent shaking for 12 h. Filtration using a 0.45 μm PTFE (hydrophobic) syringe filter gave the polymer blends with a ratio of the electron donor to the $PC_{61}BM$ as an electron acceptor of 1:3, 1:4, 1:5, and 1:6 wt/wt, respectively. The TiO_x precursor solution (1 wt.%) was spin-casted (4000 rpm) onto the active layer with thickness of *ca.* 10 nm and heated at 80 °C for 10 min in air. After being subjected to vacuum (5×10^{-6} Torr), the Al electrodes with thickness around 100 nm were deposited. The top metal electrode area, comprising the active area of the solar cells, was found to be 4 mm^2. Performance of the solar cells were measured using a AM 1.5G solar simulator (Oriel 300 W) at 100 mW/cm^2 light illumination after adjusting the light intensity using Oriel power meter (model No. 70260 which was calibrated using laboratory standards that are traceable to the National Institute of Standards and Technologies, USA). Current density–voltage (*I–V*) curves were recorded using a standard source measurement unit (Keithley 236). All fabrication steps and characterization measurements were performed in an ambient environment without a protective atmosphere. Thickness of the thin films was measured using a KLA Tencor Alpha-step IQ surface profilometer with an accuracy of ±1 nm.

3. Results and discussion

3.1. Synthesis and characterization

The synthetic routes used for preparation of the monomer and the polymers are shown in Scheme 1. Syntheses of the poly(carbazolyl-2,7-vinylene) derivatives, although not often straightforward [30], were accomplished starting with 4,4′-dinitro-2-biphenylamine and employing a sequence involving the known intermediates 4,4′-dinitro-2-azidobiphenyl (**1**), 2,7-dinitrocarbazole (**2**), and 2,7-diaminocarbazole (**3**) [31].

In order to introduce chloromethyl units into the 2- and 7-position of carbazole, the dicyano derivative **4** is generated by using a diazotation-cyanide substitution route. To improve the processibility of the poly(carbazolyl-2,7-vinylene) derivatives, the bulky didecyloxyphenyl pendant group is introduced at the nitrogen atom of carbazole

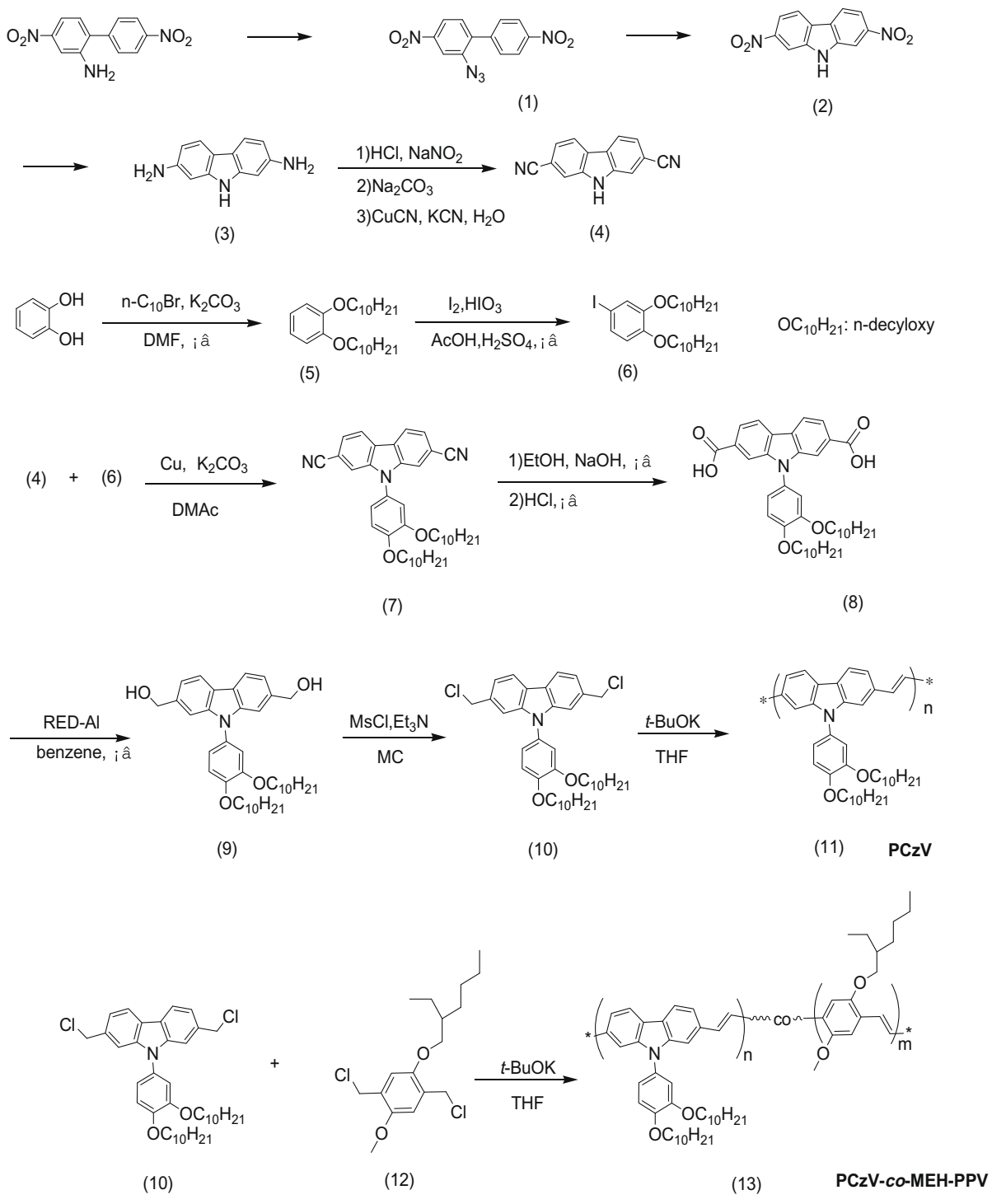

Scheme 1.

backbone. For this purpose, the ortho-hydroquinone derivative **5** is produced by using the Williamson ether synthesis method through reaction of *n*-decyl bromide and catechol. Iodination of **5** yields the iodo-arene **6**, whose coupling reaction with carbazole **4** produces **7**, which contains two decyloxy groups at the *m*- and *p*-positions of the *N*-phenyl position. Hydrolysis of the dicyano compound (**7**) affords the dicarboxylic acid **8**, which undergoes reduction with RED-Al in benzene to yield diol **9**. The corresponding dichloride **10** is then produced from **9** by treatment with

methane sulfonyl chloride. PCzV and PCzV-*co*-MEH-PPV are synthesized by using the Gilch polymerization method. Homopolymerization of 9-(3,4-bis(decyloxy)phenyl)-2,7-bis(chloromethyl)carbazole (**10**) and copolymerization with 1,4-bis(chloromethyl)-2-(2-ethylhexyloxy)-5-methoxybenzene (**12**) [32] are carried out with an excess of potassium *tert*-butoxide in dry THF under a N_2 atmosphere. This is followed by the addition of 3–4 drops of 4-*tert*-butylbenzyl bromide in order to end-cap the polymer chain. The polymers, formed in this manner, were found to be completely soluble in organic solvents such as chloroform, 1,2-dichlorobenzene, and THF. The high solubility of these polymers is an important requirement for device fabrication. To improve photovoltaic performance, the resulting polymers were purified by using Soxhlet extraction with different solvents, including methanol, acetone and finally chloroform, in order to remove the unreacted monomers, impurities, and oligomers.

Implementation of this procedure results in the production of highly purified and the narrowly polydispersed polymers. Molecular structures of the monomer and the resulting polymers were characterized by using ^{1}H-, and ^{13}C NMR spectroscopy, and elemental analysis. The chloromethyl protons of monomer **10** at 4.80–4.67 ppm disappear during the polymerization reaction and new vinylic proton resonances appear at 7.18–6.79 ppm together with the carbazole protons in PCzV and PCzV-*co*-MEH-PPV. The composition ratio of PCzV-*co*-MEH-PPV is calculated from the integration ratios of the 8.19–6.70 ppm and 4.26–3.29 ppm peaks in the ^{1}H NMR. ^{1}H NMR peak area calculations show that the actual composition of PCzV-*co*-MEH-PPV is 30:70 wt.%. Table 1 contains a summary of the polymerization results in the form of molecular weight, polydispersity, and thermal characteristics of PCzV and PCzV-*co*-MEH-PPV.

The weight-average molecular weight (M_w) and the polydispersity of the PCzV and PCzV-*co*-MEH-PPV were found to be 38,600, 1.60 and 79,900, 2.05, respectively.

Table 1
Polymerization results, thermal and electro-optical properties of PCzV and PCzV-*co*-MEH-PPV.

		PCzV	PCzV-*co*-MEH-PPV
$M_w \times 10^4$[a]		3.86	7.99
PDI[a]		1.60	2.05
DSC (T_g)[b]		95	78
TGA[c]		407	377
Abs (nm)	Solution	381,403	489
	Film[d]	386,417	499
PL (nm)	Solution	467,492	556,596
	Film[d]	482,510	585,631
E_g[e] (eV)		2.50	2.07

[a] M_w and PDI of the polymers were determined by GPC using polystyrene standards.
[b] Determined by DSC at a heating rate of 10 °C/min under N_2 atmosphere.
[c] TGA was measured at temperature of 5% weight loss for the polymers.
[d] Measured in the thin film onto the quartz substrate.
[e] Band gap estimated from the onset wavelength of the optical absorption.

3.2. Thermal, optical and electrochemical properties of the polymers

The thermal behaviors of the polymers were investigated by using DSC and TGA thermograms. PCzV and PCzV-*co*-MEH-PPV have glass transition temperatures (T_g) of 95 and 78 °C, respectively, and these polymers have good thermal stabilities with a 5% weight loss temperature at 407 and 377 °C under N_2 atmosphere. PCzV exhibits a higher thermal stability than the PCzV-*co*-MEH-PPV and both polymers have higher thermal stabilities than dialkyloxy-substituted PPVs or poly(9,9-dialkylfluorene)s [33,34]. The high T_g values and thermal stabilities of PCzV and PCzV-*co*-MEH-PPV indicate that these polymers can be used for the fabrication of bulk-heterojunction solar cells without complications associated with deformation or degradation during operation of the solar cells.

Fig. 1 is shown the normalized UV–visible absorption spectra (Fig. 1a) of the PCzV and PCzV-*co*-MEH-PPV in chloroform solutions and in thin films. The absorption spectrum of the PCzV contains two broad peaks at 381 nm and 403 nm in the solution state and at 386 nm and 417 nm in the thin film state. The peaks at *ca.* 400 nm correspond to the carbazole chromophore. The absorption spectrum of the PCzV-*co*-MEH-PPV has a maximum at 489 nm in the solution state and at 499 nm in the thin film state. Both absorption bands in thin film states are slightly red-shifted by *ca.* 10 nm compared to the solution state owing to interactions between the polymer chains. The optical band gaps (E_g), calculated from the onset of the absorption of the PCzV and PCzV-*co*-MEH-PPV, are 2.50 eV and 2.07 eV, respectively. The wavelength of the absorption peaks and the optical band gaps of the PCzV and PCzV-*co*-MEH-PPV are summarized in Table 1. Photoluminescent (PL) spectra of PCzV in chloroform solution and in the thin film state are shown in Fig. 1b. The spectrum of homopolymer PCzV has PL peaks at *ca.* 467 nm and 492 nm in the solution state and at 482 nm and 510 nm in the thin film state. The PL spectrum of the PCzV-*co*-MEH-PPV has maxima at 556 nm and 596 nm in the solution state and at 585 nm and 631 nm in the thin film state. The disappearance of PL emission from PCzV in the PCzV-*co*-MEH-PPV copolymer indicates that efficient energy transfer takes place from the wide band gap PCzV segment to the small band gap MEH-PPV segment. Thus, the transfer of exciton energy from the PCzV segment to the MEH-PPV segment occurs mainly along the polymer chain and intermolecular energy transfer occurs in the PCzV-*co*-MEH-PPV.

To investigate the charge injection and transport properties of PCzV and PCzV-*co*-MEH-PPV and to determine the energies of their highest occupied (HOMO) and lowest unoccupied (LUMO) molecular orbitals, redox measurements were carried using CV. The HOMO energies of PCzV and PCzV-*co*-MEH-PPV for the standard ferrocene/ferrocenium (4.8 eV) are found to be 5.29 eV and 5.34 eV, respectively. The respective LUMO energies, calculated based on the HOMO energies and the band gaps determined by using UV spectroscopic analysis spectra, for PCzV and PCzV-*co*-MEH-PPV are found to be 2.79 eV and 3.27 eV, respectively. The energy band diagrams of PCzV, PCzV-*co*-

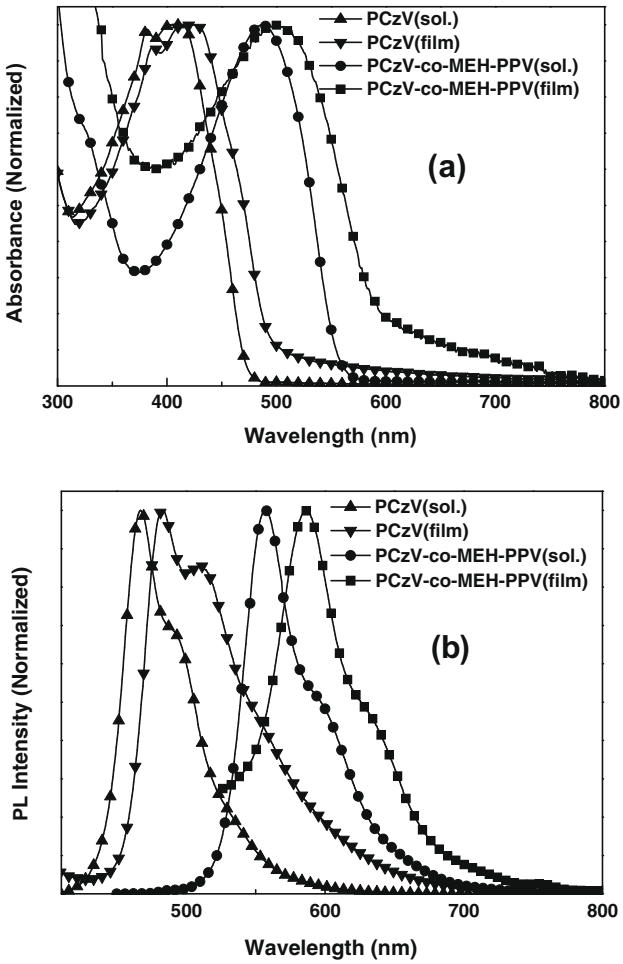

Fig. 1. UV–visible absorption (a) and PL emission (b) spectra of PCzV and PCzV-*co*-MEH-PPV.

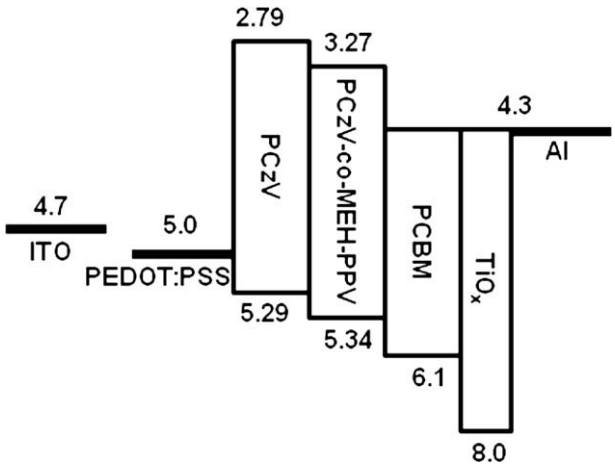

Fig. 2. Energy level diagram of the components of the bulk-heterojunction solar cell.

MEH-PPV and PCBM are shown in Fig. 2. The energies of these electron donors are well-matched to those of $PC_{61}BM$ as an electron acceptor. Photogeneration of charge in most of π-conjugated polymers is not very efficient since there recombination of two charge carriers is always involved. However, a consideration of the high LUMO energies of

PCzV and PCzV-*co*-MEH-PPV and the corresponding low HOMO energy level of $PC_{61}BM$ leads to the prediction that charge transfer will take place at the interface of these materials.

3.3. Solar cell properties of the polymers

Bulk-heterojunction solar cells were fabricated using PCzV and PCzV-*co*-MEH-PPV as electron donors and $PC_{61}BM$ as an electron acceptor. The photovoltaic cell structures are as follow: ITO/PEDOT:PSS/polymer:$PC_{61}BM$/TiO_x (10 nm)/Al (100 nm). We also used solution processable TiO_x [35–37] between the active layer and the metal cathode as a hole blocking and electron transporting layer [38,39]. The energy level of TiO_x matches the work function of Al well. Many research groups have obtained best photovoltaic performances through optimization of the ratios of electron donor polymers to the electron acceptor $PC_{61}BM$ [40,41]. The charge balance generally depends on the thickness of the active layer and the amount of $PC_{61}BM$ in the polymer blended active layer. In this effort, we probed the effect of the ratios of PCzV and $PC_{61}BM$ on photovoltaic performance using a 1,2-dichlorobenzene and chloroform mixed solvent system. The current density–voltage (*J*–*V*) characteristics of solar cells, fabricated with 1:3, 1:4, 1:5 and 1:6 ratios of polymer to $PC_{61}BM$, under AM 1.5G illumination, are shown in Fig. 3 and summarized in Table 2.

Fig. 3a is shown the *J*–*V* characteristics of PCzV with different ratios of $PC_{61}BM$. Open-circuit voltages (V_{oc}) of bulk-heterojunction solar cells are closely related to the energy difference between the HOMO level of the electron donor and the LUMO level of the electron acceptor. The V_{oc} of all solar cells we constructed are almost identical, but higher short-circuit current densities (J_{sc}) and a higher fill factors (FF) are observed with increasing $PC_{61}BM$ content in the blended active layer. The best photovoltaic performance of 0.57% was seen for a solar cell fabricated using a 1:6 ratio of PCzV:$PC_{61}BM$. For reference, the PCE of a cell made using a 1:3 ratio of PCzV:$PC_{61}BM$ (1:3 wt/wt) is 0.26%.

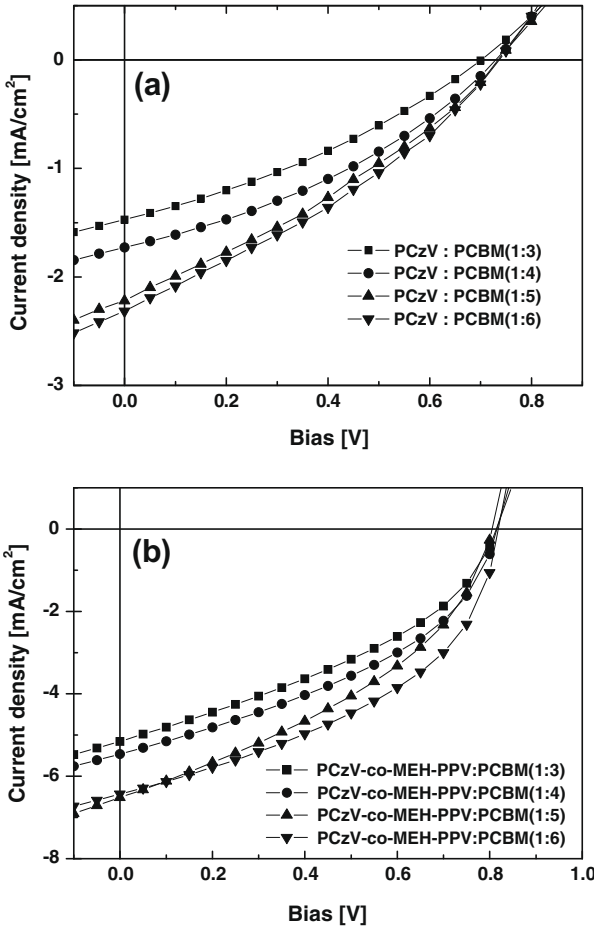

Fig. 3. Current density–voltage characteristic of PCzV (a) and PCzV-*co*-MEH-PPV (b) bulk-heterojunction solar cells containing different ratios of $PC_{61}BM$.

Table 2
Solar cell performance of PCzV and PCzV-*co*-MEH-PPV as electron donor sand $PC_{61}BM$ as the electron acceptor in ITO/PEDOT:PSS/polymer:$PC_{61}BM$/TiO_x/Al devices.

Active layer (polymer:$PC_{61}BM$)	V_{oc} (V) [a]	J_{sc} (mA/cm^2)[b]	FF (%)[c]	PCE (%)[d]
PCzV:$PC_{61}BM$ (1:3 wt/wt)	0.70	1.47	25	0.26
PCzV:$PC_{61}BM$ (1:4 wt/wt)	0.73	1.72	24	0.30
PCzV:$PC_{61}BM$ (1:5 wt/wt)	0.73	2.22	31	0.51
PCzV:$PC_{61}BM$ (1:6 wt/wt)	0.73	2.31	34	0.57
PCzV-*co*-MEH-PPV:$PC_{61}BM$ (1:3 wt/wt)	0.81	5.16	38	1.60
PCzV-*co*-MEH-PPV:$PC_{61}BM$ (1:4 wt/wt)	0.81	5.46	41	1.81
PCzV-*co*-MEH-PPV:$PC_{61}BM$ (1:5 wt/wt)	0.80	6.52	39	2.04
PCzV-*co*-MEH-PPV:$PC_{61}BM$ (1:6 wt/wt)	0.82	6.43	44	2.31

[a] V_{oc}, open-circuit voltage.
[b] J_{sc}, short-circuit current density.
[c] FF, fill factor.
[d] PCE, power conversion efficiency.

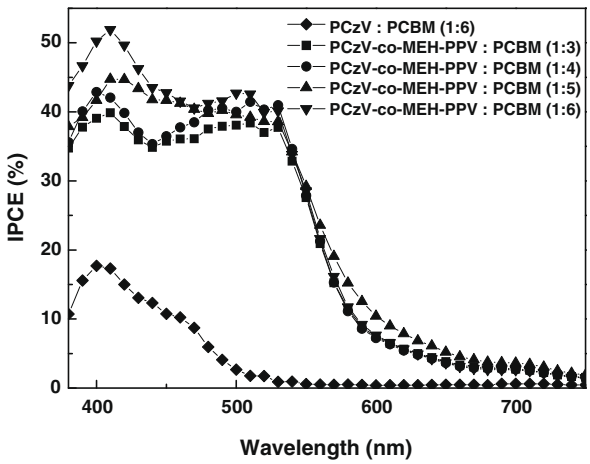

Fig. 4. IPCE spectra of PCzV and PCzV-*co*-MEH-PPV bulk-heterojunction solar cells containing different ratios of $PC_{61}BM$.

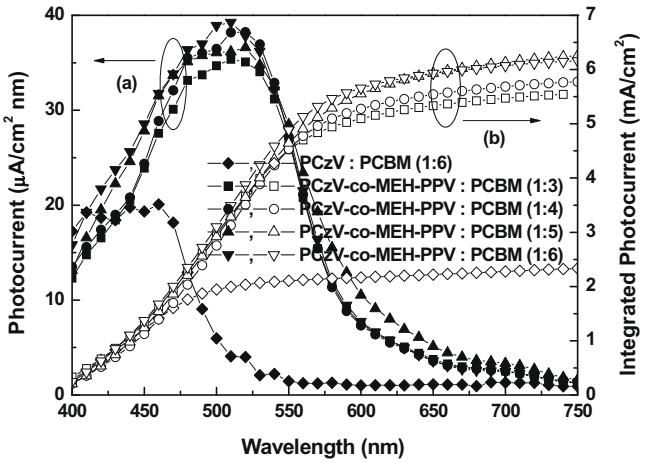

Fig. 5. (a) Photocurrents obtained using data from Fig. 4. (b) The total solar photocurrent obtained by integrating the curves shown in plots a.

Owing to the higher energy difference (1.04 eV) between the HOMO of PCzV-*co*-MEH-PPV and LUMO of $PC_{61}BM$ relative to that of PCzV and $PC_{61}BM$ (0.99 eV), the V_{oc} of PCzV-*co*-MEH-PPV:$PC_{61}BM$ solar cells are higher than those of the PCzV:$PC_{61}BM$ solar cells. The PCzV-*co*-MEH-PPV:$PC_{61}BM$ derived solar cells have similar photovoltaic performances as the PCzV:$PC_{61}BM$ cells (see Fig. 3b). The solar cell fabricated with 1:6 ratio of PCzV-*co*-MEH-PPV and $PC_{61}BM$, with TiO_x with V_{oc} of 0.82 V, J_{sc} of 6.43 mA/cm^2, FF of 44%, and PCE of 2.31%, displays the highest photovoltaic performance when compared with the solar cells arising from PCzV and $PC_{61}BM$.

Incident photon to current conversion efficiency (IPCE) spectra of the bulk-heterojunction solar cells fabricated with PCzV-*co*-MEH-PPV and $PC_{61}BM$ as active layers, recorded in the wavelength region between 380 nm and 750 nm, are shown in Fig. 4. In IPCE spectra of bulk-heterojunction solar cells, the shape of peak around 400 nm was enhanced with increasing amount of the $PC_{61}BM$. In order to easily understand, we measured absorption spectra of the PCzV-*co*-MEH-PPV, $PC_{61}BM$ and PCzV-*co*-MEH-PPV:$PC_{61}BM$ solutions (see Fig. S1). $PC_{61}BM$ showed a strong absorption peak at 340 nm and small peaks located at 400–600 nm. However as increasing the blending ratio of $PC_{61}BM$ content in PCzV-*co*-MEH-PPV and $PC_{61}BM$ solutions, the strong absorption peak of $PC_{61}BM$ showed at 340 nm and the absorption peak of PCzV-*co*-MEH-PPV was gradually reduced. It should be indicated that this makes it possible for the $PC_{61}BM$ molecules to penetrate into the PCzV-*co*-MEH-PPV polymer chains. Thus, the peak in IPCE spectra around 400 nm arises from the absorption of $PC_{61}BM$ and PCzV-*co*-MEH-PPV. As increasing the $PC_{61}BM$ content, more $PC_{61}BM$ molecules are embedded into the PCzV-*co*-MEH-PPV polymer chains, which was in favor of the generation and transport of charge carriers in the $PC_{61}BM$ phase. A maximum IPCE of 17% was observed in the case of the pristine PCzV homopolymer bulk-heterojunction solar cell at a wavelength of 410 nm. As increasing the MEH-PPV content in PCzV-*co*-MEH-PPV copolymers, IPCE also increases considerably and reaches a maximum of 52% at 410 nm and broadened up to 650 nm for a bulk-heterojunction solar cell comprised of a 1:6 ratio (wt/wt) of PCzV-*co*-MEH-PPV:$PC_{61}BM/TiO_x$. This finding may be a result of an increase of the charge-carrier mobility in the active layer and, thus, an increase in light absorption in the solar cell active layer promoted by a high amount of $PC_{61}BM$. This factor also contributes to the increased PCE of PCzV-*co*-MEH-PPV:$PC_{61}BM$ solar cells.

Integrated photocurrent curves were obtained by integrating IPCE spectra in the wavelength region between 400 nm and 750 nm (see Fig. 5). The J_{sc} value, determined from the overlap integral of the IPCE curve and the standard AM 1.5 G solar emission spectrum, is in excellent agreement with the measured photocurrent density. The error of J_{sc} and the integrated photocurrent is 5–7%, which is in the 5–10% range often seen in these values [42]. Therefore, a negligible spectral mismatch exists between the solar simulator used in this study and standard AM 1.5 G sunlight.

4. Conclusions

A new class of high molecular weight poly(*N*-(3,4-bis(decyloxy)phenyl)carbazolyl-2,7-vinylene) (PCzV) and its copolymers with an MEH-PPV have been prepared by using the Gilch polymerization procedure. PCzV and PCzV-*co*-MEH-PPV exhibit high glass transition temperatures and are easily spin casted onto the ITO substrates. Bulk-heterojunction solar cells with ITO/PEDOT:PSS/polymer:$PC_{61}BM/TiO_x$/Al configurations were fabricated with PCzV and PCzV-*co*-MEH-PPV as electron donors and $PC_{61}BM$ as the electron acceptor. The solar cells are comprised of 1:3, 1:4, 1:5 and 1:6 ratios of polymer to $PC_{61}BM$. The PCE values of the solar cells were found to increase with increasing $PC_{61}BM$ content and a maximum PCE of 2.31% (J_{sc} = 6.43 mA/cm^2, V_{oc} = 0.82 V, FF = 44%) is observed for the cell prepared from a 1:6 ratio (wt/wt) of PCzV-*co*-MEH-PPV:$PC_{61}BM$.

Acknowledgements

This work was supported by the Korea Science and Engineering Foundation (KOSEF) Grant funded by the

Korea Government (MEST) (R11-2008-088-01-003-0) and also by the Korea Energy Management Corporation (KEMCO) under the New and Renewable Energy R&D Grant (2008-N-PV08-02).

Appendix A. Supplementary data

Supplementary data associated with this article can be found, in the online version, at doi:10.1016/j.orgel.2010.03.024.

References

[1] S. Qiu, P. Lu, X. Liu, F. Shen, L. Liu, Y. Ma, J. Shen, Macromolecules 36 (2003) 9823.
[2] A.C. Grimsdale, K.L. Chan, R.E. Martin, P.G. Jokisz, A.B. Holmes, Chem. Rev. 109 (2009) 897.
[3] Q. Pei, Y. Yang, J. Am. Chem. Soc. 18 (1996) 7416.
[4] M. Ranger, D. Rondeau, M. Leclerc, Macromolecules 30 (1997) 7686.
[5] K. Faid, R. Cloutier, M. Leclerc, Macromolecules 26 (1993) 2501.
[6] R.D. McCullough, Adv. Mater. 10 (1998) 93.
[7] J.F. Morin, M. Leclerc, Macromolecules 35 (2002) 8413.
[8] H. Yi, A. Iraqi, M. Stevenson, C.J. Elliott, D.G. Lidzey, Macromol. Rapid Commun. 28 (2007) 1155.
[9] G. Zotti, G. Schiavon, S. Zecchin, J.F. Morin, M. Leclerc, Macromolecules 35 (2002) 2122.
[10] J.V. Grazulevicius, P. Strohriegl, J. Pielichowski, K. Pielichowski, Prog. Polym. Sci. 28 (2003) 1297.
[11] S. Wakim, B.R. A, Y. Tao, M. Leclerc, Polym. Rev. 48 (2008) 432.
[12] N. Blouin, A. Michaud, M. Leclerc, Adv. Mater. 19 (2007) 2295.
[13] N. Blouin, M. Leclerc, Account. Chem. Res. 41 (2008) 1110.
[14] N. Leclerc, A. Michaud, K. Sirois, J.F. Morin, M. Leclerc, Adv. Funct. Mater. 16 (2006) 1694.
[15] J. Li, F. Dierschke, J. Wu, A.C. Grimsdale, K. Müllen, J. Mater. Chem. 16 (2006) 96.
[16] M. Svensson, F. Zhang, S.C. Veenstra, W.J.H. Verhees, J.C. Hummelen, J.M. Kroon, O. Inganäs, M.R. Andersson, Adv. Mater. 15 (2003) 988.
[17] M. Catellani, B. Boselli, S. Luzzati, C. Tripodi, Thin Solid Films 403 (2002) 66.
[18] C.J. Tripodi, C. Winder, N.S. Winder, J.C. Winder, A. Winder, P.A. Winder, R.A.J. Winder, Adv. Funct. Mater. 12 (2002) 709.
[19] A. Winder, J. Winder, Chem. Commun. (1998) 2081.
[20] Y. Winder, J. Winder, Y. Winder, J. Phys. Chem. A 109 (2005) 7197.
[21] J.H. Winder, H.S. Winder, W. Winder, Y.S. Gal, J.H. Park, S.H. Jin, J. Polym. Sci. Part A – Polym. Chem. 38 (2000) 4185.
[22] S.H. Jin, S.Y. Kang, I.S. Yeom, J.Y. Kim, S.H. Park, K.H. Lee, Y.S. Gal, H.N. Cho, Chem. Mater. 14 (2002) 5090.
[23] S.H. Jin, H.J. Jin, J.Y. Kim, K. Lee, S.P. Lee, D.K. Moon, H.J. Lee, Y.S. Gal, Macromolecules 35 (2002) 7532.
[24] S.H. Jin, S.Y. Kang, M.Y. Kim, U.C. Yoon, J.Y. Kim, K.H. Lee, Y.S. Gal, Macromolecules 36 (2003) 3841.
[25] S.H. Jin, M.Y. Kim, J.Y. Kim, K. Lee, Y.S. Gal, J. Am. Chem. Soc. 126 (2004) 2474.
[26] H.S. Jeon, S.K. Lee, E.J. Lee, S.M. Park, S.C. Kim, S.H. Jin, Y.S. Gal, J.W. Lee, C. Im, Macromolecules 40 (2007) 4794.
[27] J.S. Park, M. Song, K.J. Yoon, I.A. Shin, M.J. Lee, T.I. Ryu, S.H. Jin, Y.S. Gal, J.W. Lee, Macromolecules 41 (2008) 6696.
[28] H.G. Gilch, L.J. Wheelwright, Polym. Sci. Part A – Polym. Chem. 4 (1966) 1337.
[29] J.M. Hancock, A.P. Gifford, Y. Zhu, Y. Lou, S.A. Jenekh, Chem. Mater. 18 (2006) 4924.
[30] J.F. Morin, M. Leclerc, D. Adès, A. Siove, Macromol. Rapid Commun. 26 (2005) 761.
[31] J.F. Morin, M. Leclerc, Macromolecules 34 (2001) 4680.
[32] P.L. Burn, A. Kraft, R. Baigent, D.D.C. Bradley, A.R. Brown, R.H. Friend, R.W. Gymer, A.B. Holmes, R.W. Jackson, J. Am. Chem. Soc. 115 (1993) 10117.
[33] C. Xia, R.C. Advincula, Macromolecules 34 (2001) 5854.
[34] J.L. Kim, J.K. Kim, H.N. Cho, D.Y. Kim, C.Y. Kim, S.I. Hong, Macromolecules 33 (2000) 5880.
[35] J.Y. Kim, S.H. Kim, H.H. Lee, K.H. Lee, M. Wanli, G. Xiong, A.J. Heeger, Adv. Mater. 18 (2006) 572.
[36] S.H. Park, A. Roy, S. Beaupre, S. Cho, N. Coates, J.S. Moon, D. Moses, M. Leclerc, K. Lee, A.J. Heeger, Nat. Photon. 3 (2009) 297.
[37] K. Lee et al., Adv. Mater. 19 (2007) 2445.
[38] S. Cho et al., Appl. Phys. Lett. 92 (2008) 063505.
[39] A. Hayakawa, O. Yoshikawa, T. Fujieda, K. Uehara, S. Yoshikawa, Appl. Phys. Lett. 90 (2007) 163517.
[40] W. Ma, C. Yang, X. Yang, K. Lee, A.J. Heeger, Adv. Funct. Mater. 15 (2005) 1617.
[41] G. Li, V. Shrotriya, J. Huang, Y. Yao, Y. Yang, Nat. Mater. 4 (2005) 864.
[42] O.K. Varghese, C.A. Grimes, Sol. Energy Mater. Sol. Cells 92 (2008) 374.

Table 1
The emission spectra (nm) of donors (C–H, M–H, and Q–H) calculated by TD-B3LYP/6-31G(d) method using Turbomole suite.

Molecules	TD-B3LYP/6-31G(d)	Experiment
C–H	317.2	350[a]
M–H	261.4	
Q–H	311.4	

[a] Ref. [19], measured in acetonitrile at 298 K under nitrogen atmosphere.

excited states properties of this type of porphyrin derivatives. The moieties of C (carbazole), M (N,N-dimethyl-phenyl), and Q (2,3,6,7-tetrahydro-1H,5H-pyrido[3,2,1-*ij*]quinoline) are chosen as energy transfer donors because of their wide application in red OLEDs [16,17,1]. Moreover, their emission peaks are in the region of 300–350 nm (predicted by TDDFT/B3LYP/6-31G(d) using Turbomole suite [18] in Table 1), which are similar with the fluorescence spectra of fluorene arms [11]. Accordingly, these moieties are linked to meso-sites of the porphyrin ring, that is, 5,15-di(R)porphyrin, 5,10,15,20-tetra(R)porphyrin, and Zn-5,10,15,20-tetra(R)porphyrin, namely, DCP, TCP, and ZCP (where R = C); DMP, TMP, and ZMP (where R = M); DQP, TQP, and ZQP (where R = Q), as shown in Scheme 1. The main aim of this work is twofold: (1) to testify if these porphyrin derivatives have TB energy transfer features; (2) to reveal the origin of their improved efficiency as red light-emitting materials. In addition, the experimental synthesized compounds such as tetraphenylporphyrin (TPP), 5,15-difluorenylporphyrin (DFP), 5,10,15,20-tetrafluorenylporphyrin (TFP), and Zn-5,10,15,20-tetrafluorenylporphyrin (FPZ) [15] will be used for comparative studies. This work is expected to provide valuable insight into the structure–photophysical property relationship for designing efficient red emitters with TB energy transfer features.

2. Computational methods

Recent studies [20–22] had confirmed that DFT theory can predict relatively accurate electronic structure for porphyrins derivatives. So, the DFT-B3LYP [23–25] level of theory with 6-31G(d) basis set was employed to optimize the ground-state geometries of 5,15-di(R)porphyrin, 5,10,15,20-tetra(R)porphyrin, and Zn-5,10,15,20-tetra(R)porphyrin, where R = carbazole, N,N-dimethyl-phenyl, and 2,3,6,7-tetrahydro-1H,5H-pyrido[3,2,1-*ij*]quinoline, as well as their ions structures. The free based porphyrin (FBP), Zn porphyrin (ZnP), and di-substituted porphyrins (DCP, DMP, and DQP) were optimized with D_{2h}, D_{4h}, and C_i symmetry constraint, respectively. Tetra-substituted porphyrins (TCP, TMP, TQP, and TPP) and Zn-chelated porphyrins (ZCP, ZMP, and ZQP) were restricted with C_{2h} point group constraint. On the basis of these optimized geometries, the ionization potentials (IP), electron affinity (EA), hole extraction potentials (HEP), electron extraction potentials (EEP), and reorganization energy (λ) [26] were calculated by the method as described in Refs. [15,27]. On the basis of the optimized ground-state geometries, the absorption spectra of these compounds were predicted by the TD-DFT//B3LYP/6-31G(d) method. This kind of calculation level had been proven to be reliable for porphyrin derivatives [15,23,24].

In order to facilitate the computation for large molecules, the lowest singlet excited-state (S_1) geometries of studied complexes were optimized by singlet configuration interaction CIS [28] with 3-21G(d) basis sets, which had been proved to be suitable for model the excited states of porphyrin derivatives [29]. Based on our previous report

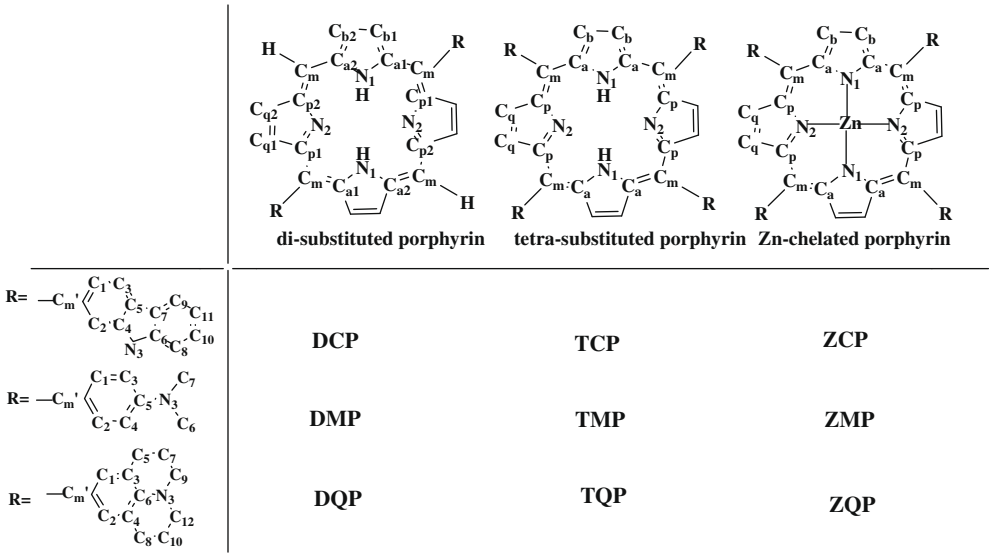

Scheme 1. The studied porphyrin derivatives: 5,15-di(R)porphyrin, 5,10,15,20-tetra(R)porphyrin, and Zn-5,10,15,20-tetra(R)porphyrin, namely, DCP, TCP, and ZCP (where R = carbazole); DMP, TMP, and ZMP (where R = N,N-dimethyl-phenyl); DQP, TQP, and ZQP (where R = 2,3,6,7-tetrahydro-1H,5H-benzo[*ij*]puinolizine), together with the schematic structures of porphyrins fragment and meso-substitutions.

[15], it was found that the TDHF/6-31G(d) method, in combination with the CIS level, was suitable for predicting the emission spectra of the type of porphyrin derivatives. Therefore, the emission spectra were obtained by TD-HF/6-31G(d) at the excited-states structures. All these calculations were performed on the SGI origin 2000 server, using Gaussian 03 program package [30].

3. Results and discussions

3.1. Ground-state geometry properties

The optimized geometries of porphyrin derivatives are illustrated in Fig. 1, and the labeling schemes are depicted in Scheme 1. The main optimized geometric parameters of studied compounds in the ground state are summarized in Table 2 (see Table S1 in Supporting information for details).

Fig. 1(b) illustrates that the porphyrin rings in studied compounds are essentially planar, while the meso-arms are not coplanar with the porphyrin rings. As shown in Table 2(a), the inter-ring dihedral angle $\alpha(C_{a1}–C_m–C_{m'}–C_1)$ between meso-arms and porphyrin ring is quite large (62.6° for DCP, 59.2° for DMP, and 59.9° for DQP). This may ascribe to the steric repulsions between two hydrogen atoms bound to the carbon atoms C_{b1} (or C_{q2}) and C_1 (or C_2). It is noteworthy that the large inter-ring dihedral angle preserves respective character of donor and acceptor, which is the typical structure feature of energy-transfer systems [31]. In addition, Table 2(a) also collects the main geometries of di-substituted porphyrins (DCP, DMP, and DQP) are similar with the experimentally synthesized compound DFP [15]. For example, the $C_{a1}–C_{b1}$, $C_{a1}–N_1$, $C_{a1}–C_m$, and $C_{p1}–C_m$ bond lengths of DCP, DMP and DQP deviate only by 0.001 Å from DFP, except for the $C_{m'}–C_m$ bond length. The natural bond orbital (NBO) analyses for these complexes give us a good explanation for the above results. According to the NBO analyses, the charge population of C, M, Q, and fluorenyl moieties is 0.0163, 0.033, 0.0354, and 0.0148 a.u. [15], respectively. Obviously, the electron-donation abilities of M and Q are better than those of C and fluorenyl groups. So, the bond length $C_{m'}–C_m$ of DMP and DQP are shortened by 0.004 Å from those of DCP and DFP.

Similarly, as given in Table 2(b), the main geometric parameters of tetra-substituted porphyrins and Zn-chelated porphyrins are consistent with referenced compounds TFP [15] and FPZ [15], respectively. Comparing with the tetra-substituted porphyrins, the $C_a–C_b$ and $C_p–N_2$ bond lengths of Zn-chelated porphyrins are elongated by 0.011 Å, while the $C_p–C_q$ bond length of Zn-chelated porphyrins is contracted by ca. 0.015 Å. The inter-ring dihedral angle $\alpha(C_a–C_m–C_{m'}–C_1)$ is 68.6°, 65.6°, 66.5°, 69.6°, 66.8°, and 67.6° for TCP, TMP, TQP, ZCP, ZMP, and ZQP, respectively. It is obvious that all the studied compounds have the typical structure feature of energy-transfer systems [31]. As shown above, there are small geometrical differences between theoretical design and experimentally synthesized molecules. It indicates that DCP, DMP, DQP, TCP, TMP, TQP, ZCP, ZMP, and ZQP should have similar electronic and optical properties with reference compounds [15].

3.2. Geometry properties of ionic-state molecules

According to our previous report [15], the internal reorganization energy (λ) for hole transfer can be calculated as followings:

$$\lambda_{hole} = \lambda_+ + \lambda_1 = [E^+(A) - E^+(A^+)] + [E(A^+) - E(A)] \quad (1)$$

E^+ and E represent the energies of the cation and neutral species in their lowest energy geometries, respectively, while (A^+) and (A) denote the structures of them. As shown in Eq. (1), the λ couples with the structure changes in the ionization process. Herein, all the ionic and neutral geometries of studied compounds are optimized by DFT//B3LYP/6-31G(d) method. And the calculated bond lengths of them are listed in Table S1 in Supporting information. Table S1 clearly shows that the largest variations between the ionic and corresponding neutral structures of DCP, DMP, and DQP are similarly with each other. Similarly, for tetra-substituted porphyrins and Zn-chelated porphyrins, the largest variations between the ionic and corresponding neutral compounds do not change with the changes of meso-substituents. Therefore, we only take DCP, TCP, and ZCP as examples. The deviations of bond lengths between their ionic and neutral geometries are depicted in Fig. 2. As shown in Fig. 2, the localizations of structural change mainly focus on porphyrin ring. Take DCP as an example, the $C_m–C_{m'}$ (labeled 15) bond length has remarkable change in the cationic state, while the $C_{a1}–C_m$ (labeled 5), $C_{p2}–N_2$ (labeled 11), and $C_{p1}–C_m$ (labeled 13) bond lengths change significantly in the anionic state. In addition, as depicted in Fig. 2, the bond lengths in meso-substituents change remarkably in the ionization process. As given in Table S1, the change of bond length $N_3–C_5$ is 0.023, 0.021, 0.025, 0.019, 0.019, and 0.016 Å for DMP^+, DMP^-, TMP^+, TMP^-, ZMP^+, and ZMP^-, respectively. And the bond length $N_3–C_6$ changes 0.027, 0.017, 0.020, 0.013, 0.020, and 0.013 Å for DQP^+, DQP^-, TQP^+, TQP^-, ZQP^+, and ZQP^-, respectively. Apparently, the involved meso-substituents can influence the internal reorganization energy, which will be further testified in Section 3.5.

3.3. Frontier molecular orbitals

Gouterman's four orbitals (HOMO−1, HOMO, LUMO, and LUMO+1 orbitals) [32] has been used as an essential standard on explaining the abundance chemistry properties of porphyrins. The plots of HOMOs of studied compounds are drawn in Fig. 3. And the energies and symmetries of the frontier molecular orbitals of these compounds are shown in Fig. 4 (detailed data are listed in Table S2 in Supporting information). The local density of states (LDOS) of porphyrin ring and meso-substituents are shown in Fig. 5. In addition, according to the LDOS analysis, the contribution of C_m to HOMO in studied compounds is listed in Table 3.

Recently, Otsuki and co-workers [33] have demonstrated that the Dexter-type energy transfer can explain the major parts of TB energy transfer, whereas the Förster-type energy transfer process accounts for only minor part of TB energy transfer. The Dexter mechanism can be

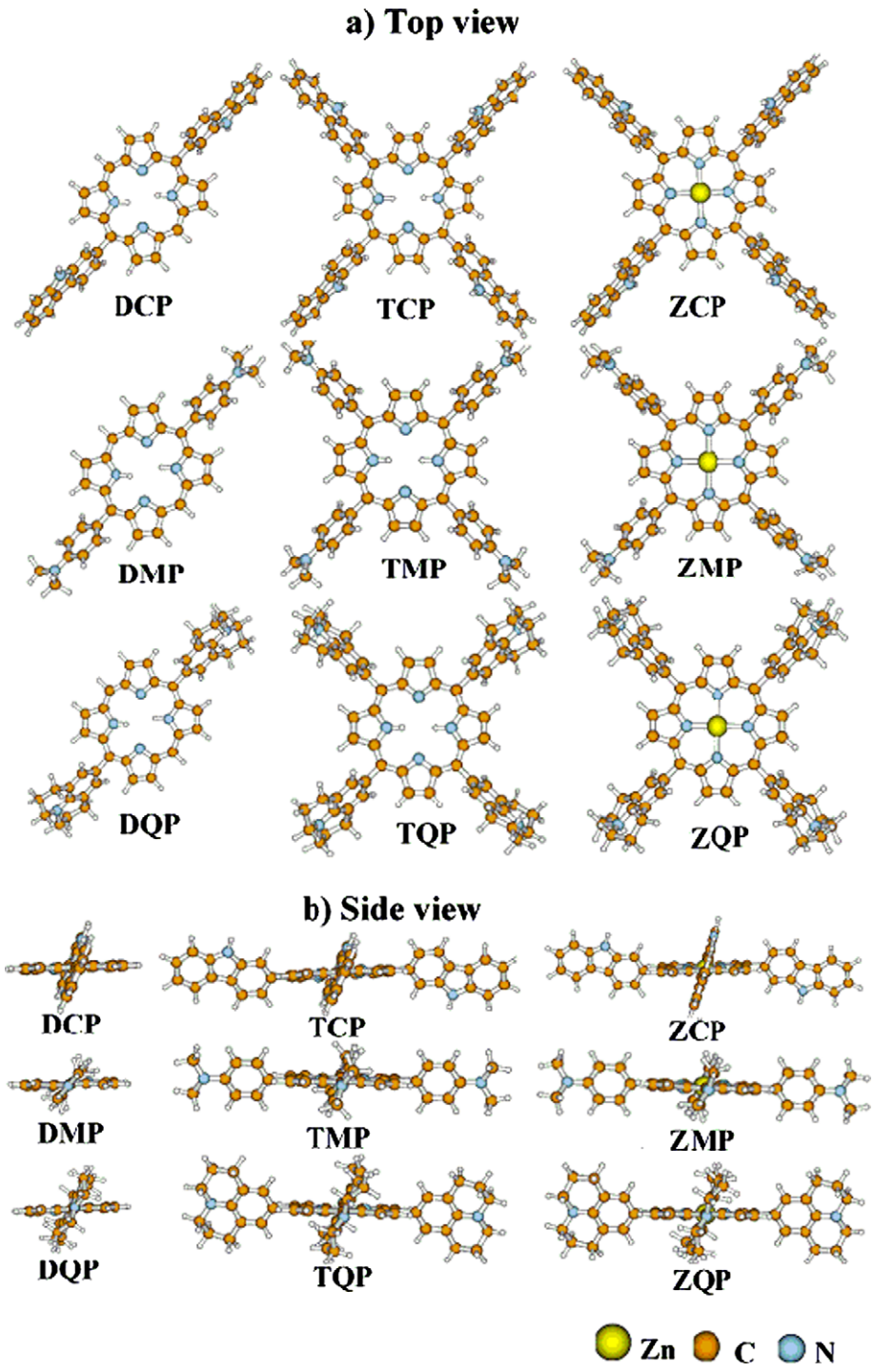

Fig. 1. (a) Front view and (b) side view of the optimized structures of studied compounds obtained by DFT//B3LYP/6-31G(d).

considered as an electron exchange process [34], thus the rate of Dexter-type energy transfer is sensitive to the nature of frontier orbitals. As a guiding principle [34], a stronger electronic interaction between the donor (meso-substituent) and acceptor (porphyrin) is acknowledged when HOMO is heavily populated at the C_m (as C_m is the connection bridge of donor and acceptor), whereas a weaker interaction is expected when HOMO has virtually no electron density at the C_m. As shown in Fig. 3, the HOMO of FBP with b_{3u} symmetry is heavily populated at the C_m, while the HOMO of ZnP is node on the C_m. After meso-substituents are added, the HOMOs of di- (a_u symmetry),

Table 2
Selected bond lengths and bond angles for studied compounds, and referenced compounds (DFP, TFP, and FPZ) [15].

	Di-substituted porphyrins							
	DFP [15]	DCP	DMP	DQP				
(a)								
Bond length (Å)								
C_{a1}–C_{b1}	1.436	1.436	1.435	1.435				
C_{a2}–C_{b2}	1.433	1.433	1.433	1.433				
C_{a1}–N_1	1.375	1.375	1.376	1.376				
C_{a2}–N_1	1.373	1.373	1.373	1.373				
C_{a1}–C_m	1.408	1.407	1.409	1.409				
C_{a2}–C_m	1.394	1.394	1.394	1.394				
C_{p1}–C_{q1}	1.462	1.462	1.462	1.462				
C_{p2}–C_{q2}	1.457	1.457	1.457	1.457				
C_{p1}–N_2	1.366	1.366	1.366	1.366				
C_{p2}–N_2	1.363	1.363	1.363	1.363				
C_{p1}–C_m	1.415	1.414	1.416	1.416				
C_{p2}–C_m	1.399	1.399	1.399	1.399				
$C_{m'}$–C_m	1.494	1.494	1.490	1.490				
Bond angles (°)								
$\alpha(C_{a1}–C_m–C_{p1})$	123.3	123.3	122.9	122.9				
$\alpha(C_{b1}–C_{a1}–C_m)$	128.5	128.5	128.5	128.5				
$\alpha(C_{p1}–N_2–C_{p2})$	105.6	105.6	105.7	105.7				
Dihedral angles (°)								
$\alpha(C_{b1}–C_{a1}–C_m–C_{p1})$		176.5	172.0	176.2				
$\alpha(C_{a1}–C_m–C_{m'}–C_1)$	61.9	62.6	59.2	59.9				
	Tetra-substituted porphyrins				Zn-chelated porphyrins			
	TFP [15]	TCP	TMP	TQP	FPZ [15]	ZCP	ZMP	ZQP
(b)								
Bond length (Å)								
C_a–C_b	1.434	1.434	1.434	1.434	1.445	1.445	1.444	1.444
C_a–N_1	1.377	1.377	1.377	1.377	1.377	1.378	1.378	1.378
C_a–C_m	1.406	1.405	1.407	1.407	1.407	1.406	1.408	1.407
C_b–C_b		1.369	1.370	1.370		1.360	1.361	1.361
C_p–C_q	1.460	1.460	1.459	1.459	1.445	1.445	1.444	1.444
C_p–N_2	1.367	1.367	1.367	1.367	1.378	1.378	1.378	1.378
C_q–C_q		1.354	1.354	1.354		1.361	1.361	1.361
C_p–C_m	1.412	1.412	1.413	1.413	1.407	1.407	1.408	1.408
C_m–C_m	1.498	1.499	1.496	1.496	1.499	1.500	1.496	1.497
N_2–Zn					2.043	2.044	2.044	2.042
N_1–Zn					2.043	2.042	2.043	2.044
Bond angles (°)								
$\alpha(C_a–C_m–C_p)$	125.3	125.3	125.1	125.0	124.7	124.7	124.5	124.5
$\alpha(C_b–C_a–C_m)$	126.7	126.7	126.9	126.6	124.3	124.5	124.1	124.3
$\alpha(C_p–N_2–C_p)$	110.7	105.5	105.5	105.5	106.5	106.5	106.5	106.6
Dihedral angles (°)								
$\alpha(C_b–C_a–C_m–C_p)$		175.3	179.6	174.4		179.4	175.6	175.8
$\alpha(C_a–C_m–C_{m'}–C_1)$	67.8	68.6	65.6	66.5	69.1	69.6	66.8	67.6

tetra- (b_u symmetry), and Zn-chelated porphyrins (b_u symmetry) have large electron density on the C_m. It indicates that our studied compounds have strong electron interaction, that is, the Dexter-type energy transfer process dominates in our designed compounds. Furthermore, as listed in Table 3, the contribution of C_m to HOMO of di-substituted porphyrins decreases as: DCP(49.12%) > DMP(39.32%) > DQP(33.73%). Similarly, the contributions of C_m to HOMO of TCP and ZCP are larger than those of TQP, TMP, ZQP, and ZMP. It is evident that the C moiety has importantly influence on the character of HOMOs, indicating that the Dexter-type energy transfer can easily occur in DCP, TCP, and ZCP. Consequently, we can predict with some confidence that DCP, TCP, ZCP would have higher efficiency than the others as red light-emitting materials, which will be further testified in Section 3.5.

Brédas et al. experimentally estimated the HOMO and LUMO energies by using an empirical formula based on the onset of the oxidation and reduction peaks measured by cyclic voltammetry [35]. The preliminary hole/electron injection properties of the materials are usually estimated by the values of HOMO/LUMO, in accord with the work function values of cathode/anode. Normally, the hole-transport materials with the higher value of HOMO should lose their electrons more easily, while the electron-transport materials with lower value of LUMO should accept electrons more easily. In this study, the calculated HOMO and LUMO energies obtained by DFT/B3LYP/6-31G(d) are

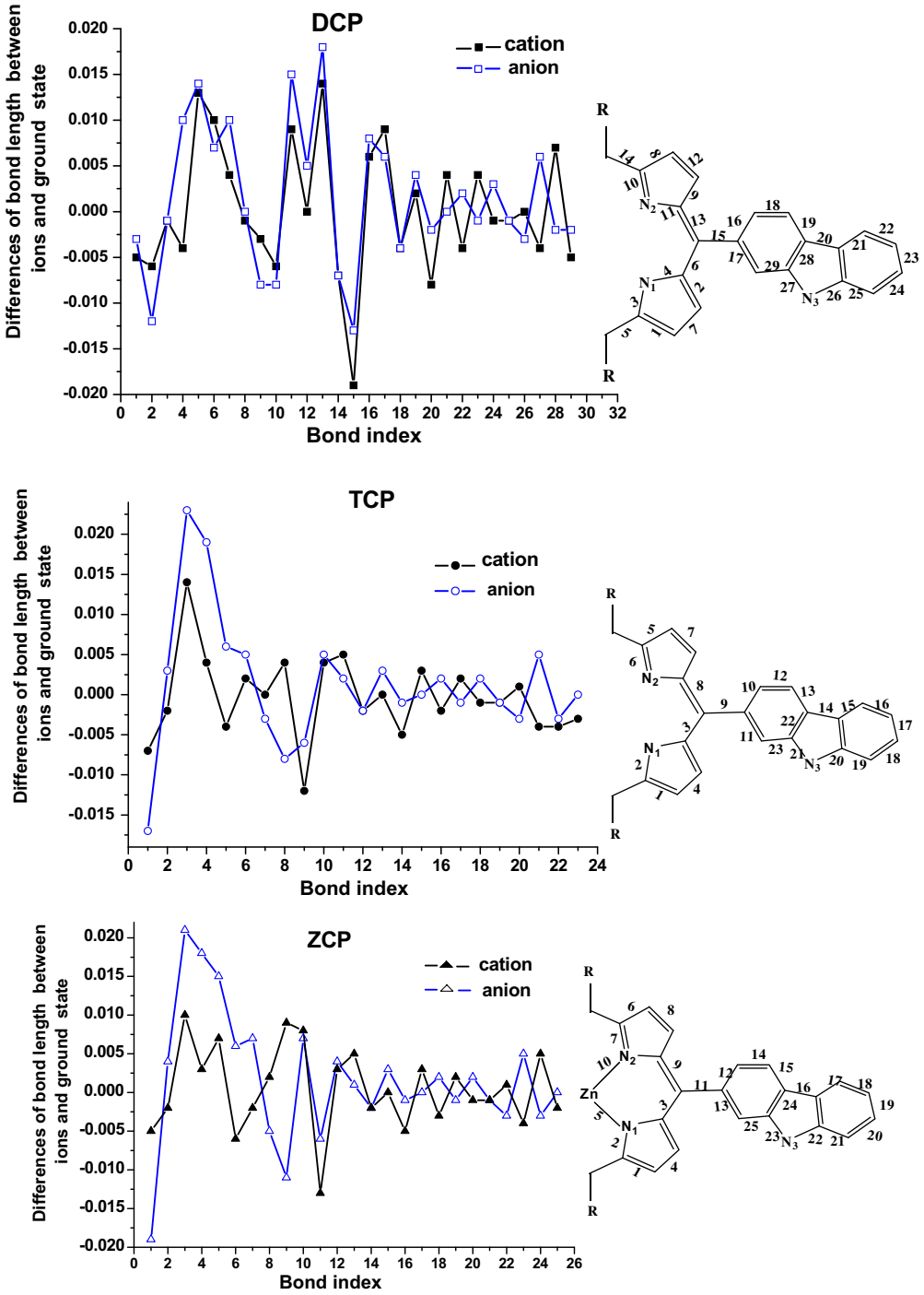

Fig. 2. The bond lengths deviates between the ionic and neutral structures of DCP, TCP, and ZCP. The atom numbers of studied compounds are labeled in Scheme 1.

listed in Table S2. As listed in Table S2, the HOMO and LUMO levels for TCP, DMP, TMP, ZMP, DQP, TQP, and ZQP are −4.79 and −2.13, −4.58 and −1.97, −4.30 and −1.76, −4.39 and −1.69, −4.50 and −1.94, −4.23 and −1.71, and −4.31 and −1.64 eV, respectively. Obviously, they are higher than the HOMO and LUMO energy levels of FBP (εHOMO, −5.15 eV and εLUMO, −2.24 eV), ZnP (εHOMO, −5.21 eV and εLUMO, −2.14 eV), TPP (εHOMO, −4.91 eV and εLUMO, −2.20 eV) DFP [15] (εHOMO, −4.94 eV and εLUMO, −2.24 eV), TFP [15] (εHOMO, −4.83 eV and εLUMO, −2.17 eV), and FPZ [15] (εHOMO, −4.91 eV and εLUMO, −2.10 eV). It suggests that the hole injection

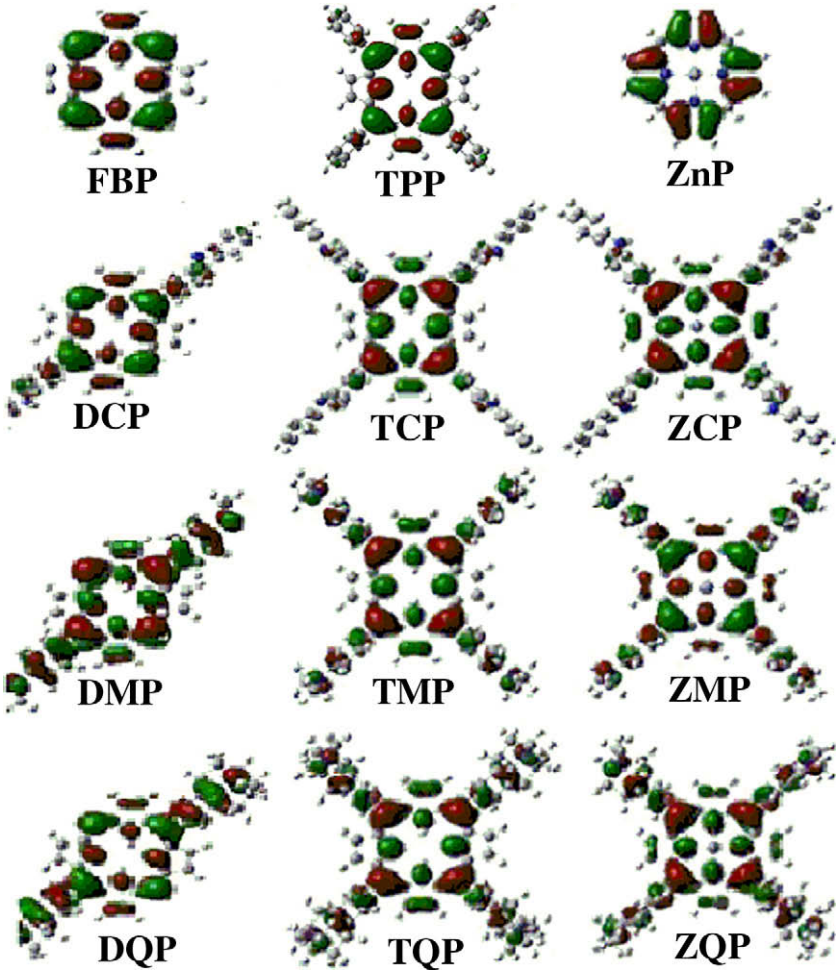

Fig. 3. The plots of HOMOs for studied compounds.

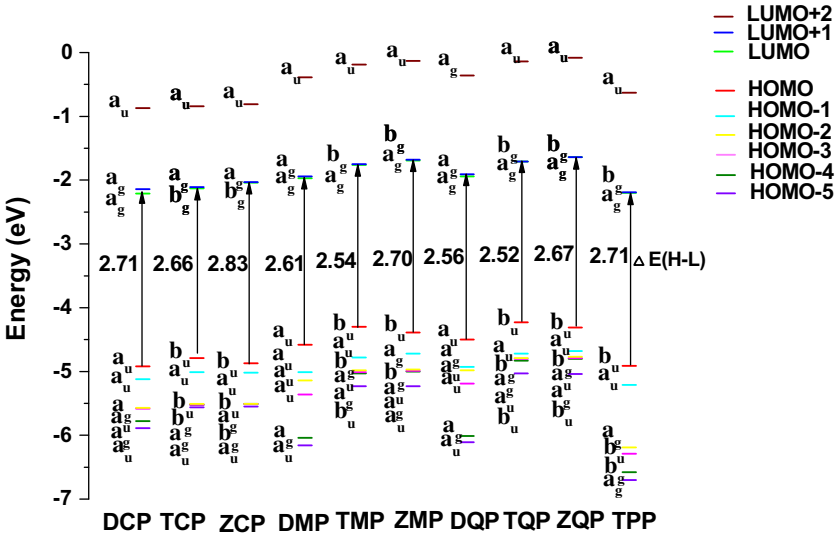

Fig. 4. Energies (eV) and symmetry of the frontier orbitals and energy gaps ΔE(H–L) of studied compounds.

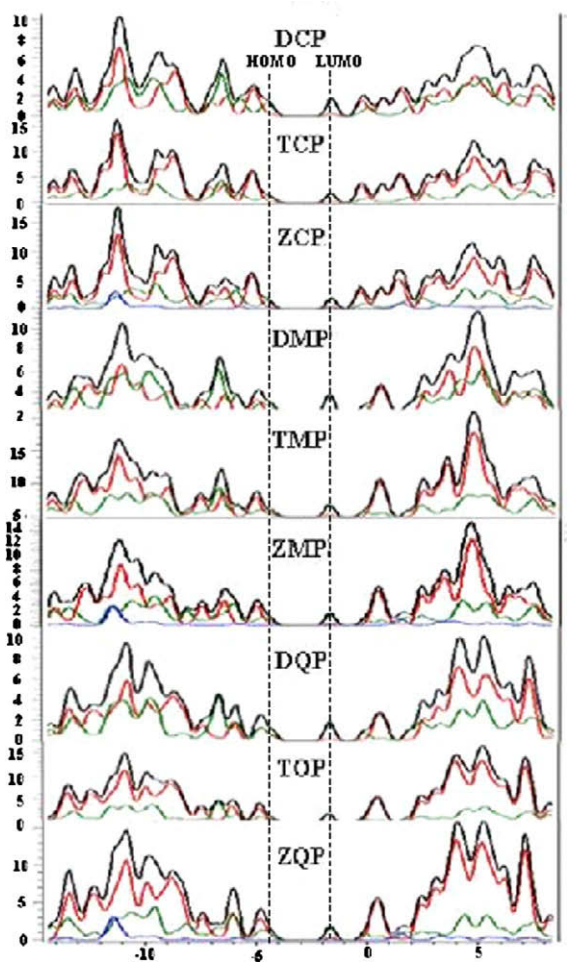

Fig. 5. The density of states (DOS) of all studied porphyrins. The black, red, green, blue lines stand for the local density of states (LDOS) of the total, meso-substitutions, porphyrin, and Zn (For interpretation of the references to colour in this figure legend, the reader is referred to the web version of this article.).

abilities of porphyrin derivatives are effectively enhanced by introducing these meso-substitutions. Furthermore, the HOMO energies of DCP, TCP, ZCP match well with the work function values of ITO (−4.8 eV), again indicating that these compounds have good hole injection ability [36].

The frontier MOs of these porphyrin derivatives are not entirely consistent with the common Gouterman four-orbital model. As drawn in Fig. 4, the LUMOs and LUMO+1s of studied molecules are nearly degenerate, and they are well separated from other unoccupied orbitals. However, the HOMOs and HOMO−1s of them are not degenerate any more, and the energy gaps between the HOMO−1s and other occupied orbitals become narrow. Take the $\Delta E_{(\mathrm{HOMO}-2)-(\mathrm{HOMO}-1)}$ energy gap for example, it is 0.45, 0.50, 0.49, 0.13, 0.20, 0.25, 0.05, 0.07, and 0.09 eV of DCP, TCP, ZCP, DMP, TMP, ZMP, DQP, TQP, and ZQP, respectively. The examination on the local density of states (LDOS) of different regions in studied molecules gives some clues for this phenomenon. As plotted in Fig. 5, the HOMO−1s, LUMOs and LUMO+1s of these porphyrin derivatives are mainly contributed by P-rings (drawn in red[1] line) with more than 80% compositions (except for HOMO−1 of DQP), however, the HOMOs of them are dominantly composed of the meso-substituents and P-rings. Clearly, their HOMOs energies are more sensitive to the meso-substituents than those of LUMOs. Similarly, as drawn in Fig. 5, the meso-substituents contribute near 90% to theirs HOMO−2s, HOMO−3s, HOMO−4s, and HOMO−5s, leading to narrow energy gaps between these inner occupied orbitals and corresponding HOMO−1s.

3.4. Absorption and fluorescence spectra analysis

TDDFT//B3LYP/6-31G(d) has been employed to investigate the absorption spectra of studied compounds in this work. Based on the calculated results (the absorption wavelength spectra, excitation energy, oscillator strength, and main configurations are listed in Table S3 in Supporting information), simulated electronic absorption spectra plots of porphyrin derivatives are shown in Fig. 6.

As depicted in Fig. 6, a shoulder peak at the high energy region (250–350 nm) has been observed in these porphyrin derivatives. Furthermore, the fluorescence spectra of these donors (C–H, M–H, and Q–H) are in the region of 300–350 nm, as listed in Table 1. Obviously, there is good overlap between the absorption band of energy transfer acceptors (DCP, DMP, DQP, TCP, TMP, TQP, ZCP, ZMP, and ZQP) and the fluorescence peak of corresponding donors (C–H, M–H, and Q–H). Thus, from the point of view of Förster-type energy transfer mechanism, the TB energy transfer process can easily occur in studied compounds.

Interestingly, as listed in Table S3(a), the Q bands for FBP are composed of two weak absorption peaks (oscillator strengths (f) < 0.0001 for 543.8 nm and oscillator strengths (f) < 0.0001 for 507.2 nm). And Table S3(b) also shows that ZnP has relative weak Q band (oscillator strengths (f) = 0.0008 for 510.2 nm). Now, we will take ZnP as an example to explore the reasons of its weak Q bands. For ZnP, the Q band at 510.2 nm is assigned to the two lowest excitation energy states (S_1 and S_2). The S_1 state is constructed by two transitions of (−0.50) $a_{1u} \rightarrow e_g$ and (0.51) $a_{2u} \rightarrow e_g$. And S_2 state consists of the (−0.50) $a_{2u} \rightarrow e_g$ and (0.51) $a_{1u} \rightarrow e_g$ transitions. It is obviously that the Q bands are expressed by sign-reversed superposition of two configurations and the weights of the configuration are equal. Consequently, the transition dipole moment is canceled out, which results in very weak intensity in Q bands. After introducing the meso-substitutions, as listed in Table S3(c)–(k), the oscillator strength (f) of the Q bands for these compounds are intensified. Take ZMP as an example (listed in Table S3(h)), the S_1 state consists of the superior (0.59) $b_u \rightarrow b_g$ and inferior (−0.40) $a_u \rightarrow a_g$ transitions, while S_2 state is descripted by two configurations, (0.58) $b_u \rightarrow a_g$, and (0.42) $a_u \rightarrow b_g$ transitions. Obviously, there is less complete cancellation of the transition dipole moments, so the Q bands of ZMP are intensified [37]. In addition to the

[1] For interpretation of color in Fig. 5, the reader is referred to the web version of this article.

Table 3
The contribution of C_m to HOMO in studied compounds based on the LDOS analysis.

	DCP	TCP	ZCP	DMP	TMP	ZMP	DQP	TQP	ZQP
C_m (%)	49.12	47.39	48.95	39.32	40.07	39.52	33.73	36.70	35.27

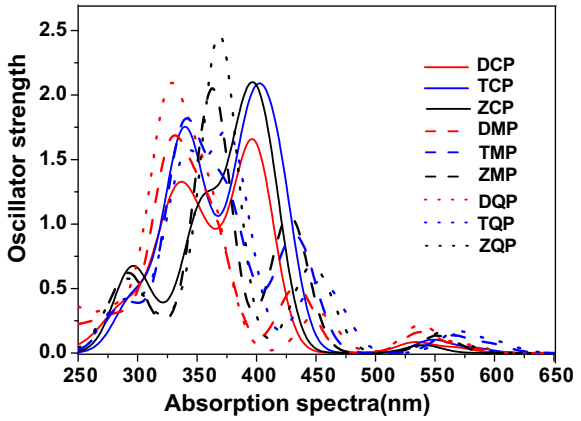

Fig. 6. The absorption spectra of studied compounds obtained by TDDFT//B3LYP/6-31G(d) method.

intensified oscillator strength, the slight red-shifts of the absorption spectra compared with corresponding bands of FBP and ZnP have been observed, which are caused by reducing energy of one-electron transition from the meso-substitutions. In addition, as listed in Table S3, inner occupied molecular orbitals (energies lower than the energy of HOMO) are involved in one-electron transitions for the B bands of studied compounds. It agrees with the analyses of molecular orbital energy in Section 3.3.

Our previous work [15] found that the TDHF method can successfully predict the fluorescence spectra of porphyrin derivatives in contrast to the corresponding experiments. Thus TDHF/6-31G(d) method has been employed to simulate the fluorescence spectra in this work. The obtained emission wavelengths, oscillator strengths, and main configurations for all the studied compounds are listed in Table 4. It is found that the fluorescence spectra of DCP, DMP, and DQP are similarly with each other. And for tetra- and Zn-chelated porphyrins, their fluorescence spectra are hardly influenced by introduced different substituents. But, as listed in Table 4, the fluorescence spectra of di-, tetra-, as well as Zn-chelated porphyrins are significantly different from each other. Taking DCP, TCP, and ZCP for examples, the fluorescence spectrum of TCP is 735.01 nm, while the fluorescence spectra of DCP and ZCP blue shift about 10 and 60 nm from that of TCP, respectively, which are in good agreement with the tendency of the fluorescence spectra of DFP, TFP, and FPZ [15]. The examination of the main orbital transitions associated with these emission wavelengths will give reasonable explanation for this phenomenon. As listed in Table 4, the main orbital transitions of all these emission wavelengths are from HOMO to LUMO. Fig. 4 shows the HOMO–LUMO gaps (ΔE_{H-L}) of DCP, TCP, and ZCP are 2.71, 2.66, and 2.83 eV, respectively. Clearly, the ΔE_{H-L} decreases as: ZCP > DCP > TCP, so the fluorescence wavelength of them increases as ZCP < DCP < TCP.

3.5. Charge injection and transport properties as well as exciton binding energy

The charge injection and transport rate, and balance as well as exciton confinement in the device are the main factors in determining the operating voltage and luminance efficiency of OLEDs. Normally, the lower IP value indicates a higher ease of injection of holes from ITO to hole-transport layer (HTL); and the higher EA value corresponds to the better ease of electron injection from cathode to electron-transport layer (ETL). Thus, in this report, IP and EA are employed to evaluate the energy barrier of injection holes and electrons, respectively.

The motilities of hole and electron are investigated by reorganization energy (λ) based on the Marcus theory [26], which has been widely applied to assess the ability of charge mobility [15,27,38]. Usually, smaller λ and more balance hole and electron reorganization energy (λ_{hole} and $\lambda_{electron}$) will result in higher efficient charge transport.

For OLEDs, the first phase is to inject electrons and holes into the organic functional film from the cathode and anode, respectively, which is also the key stage. Take TPP as an example, although it has smaller λ_{hole} and $\lambda_{electron}$ values (0.10 and 0.21 eV, as listed in Table 5), the fluorescence quantum yield of TPP is still low (0.12) [39]. The poor injection abilities of electrons and holes for TPP (its higher IP and lower EA values) may be the main factors. Hence, it is essential to evaluate the energy barrier for injection holes and electrons. The calculated IP and EA values of studied compounds are listed in Table 5, together with referenced compounds [15]. Table 5 shows that M- (DMP, TMP, and ZMP) and Q-substituted porphyrins (DQP, TQP, and ZQP) display improved IP values, which are lower than referenced compounds (DFP, TFP, and FPZ) and two widely-used hole materials in OLEDs (4,4′-bis(1-naphthylphenylamino) biphenyl (NPB) [40] and 4,4′-bis(phenyl-m-tolylamino) biphenyl (TPD) [40]). And the IP values of the compounds with same meso-substituents decrease as: di-substituted porphyrins > Zn-chelated porphyrins > tetra-substituted porphyrins. Consequently, the hole injection abilities increase in the following sequence: ZnP > FBP [15] > DFP [15] > DCP > FPZ [15] > ZCP > TFP [15] > TCP > DMP > DQP > ZMP > TMP > ZQP > TQP. In addition, Table 5 also shows DCP, TCP, and ZCP have similar EA values with referenced compounds [15]. And the values of EA are increased as ZCP < DCP < TCP, which suggests that ability of accepting an electron increase in the same sequence.

The next stage of OLEDs is electron and hole transport in the light-emitting layer. As listed in Table 5, though FPZ has much better charge transfer balance than that of TPP, the

Table 4
Emission wavelength (nm), and oscillator strength (f) calculated by TDHF/6-31G(d) method for all the meso-substituted porphyrins.

	TDHF/6-31G(d)				
	Wavelength (nm)	f	E_{Flu} (eV)	MO/character (coefficient)	
DCP	721.5	0.0241	1.72	HOMO → LUMO (0.76686)	HOMO−1 → LUMO+1 (−0.67447)
TCP	735.0	0.0170	1.69	HOMO → LUMO (0.76466)	HOMO−1 → LUMO+1 (−0.68436)
ZCP	661.2	0.0321	1.88	HOMO → LUMO (0.75460)	HOMO−1 → LUMO+1 (0.61111)
DMP	723.0	0.0168	1.72	HOMO → LUMO (0.76054)	HOMO−1 → LUMO+1 (−0.67381)
TMP	737.1	0.0086	1.68	HOMO → LUMO (0.75991)	HOMO−1 → LUMO+1 (−0.68771)
ZMP	660.7	0.0200	1.88	HOMO → LUMO (0.75005)	HOMO−1 → LUMO+1 (−0.61576)
DQP	723.0	0.0163	1.73	HOMO → LUMO (0.75730)	HOMO−1 → LUMO+1 (−0.66797)
TQP	735.1	0.0131	1.69	HOMO → LUMO (0.76416)	HOMO−1 → LUMO+1 (0.69097)
ZQP	660.6	0.0191	1.88	HOMO → LUMO (0.74992)	HOMO−1 → LUMO+1 (−0.61470)
TPP	733.9	0.0173	1.69	HOMO → LUMO (0.76684)	HOMO−1 → LUMO+1 (0.68701)

Table 5
The ionization potentials (IPs), electron affinities (EAs), extraction potentials (HEP/EEP) and reorganization energies (λ), and exciton binding energy (E_b) for studied complexes (in eV).

	IP (V)	HEP	EA (V)	EEP	λ_{hole}	$\lambda_{electron}$	$\lvert\lambda_{hole} - \lambda_{electron}\rvert$	E_b
FBP [15]	6.48	6.42	0.87	1.09	0.06	0.22	0.16	
ZnP	6.58	6.49	0.78	1.00	0.09	0.23	0.14	
DCP	5.94	5.77	1.14	1.34	0.17	0.20	0.03	0.99
TCP	5.68	5.47	1.17	1.32	0.21	0.15	0.06	0.97
ZCP	5.77	5.56	1.06	1.30	0.21	0.24	0.03	0.94
DMP	5.61	5.31	0.85	1.05	0.30	0.20	0.10	0.90
TMP	5.20	4.93	0.76	0.94	0.27	0.18	0.09	0.86
ZMP	5.29	4.94	0.64	0.90	0.35	0.26	0.09	0.82
DQP	5.48	5.12	0.84	1.03	0.36	0.19	0.17	0.83
TQP	5.09	4.79	0.72	0.94	0.30	0.22	0.08	0.83
ZQP	5.18	4.78	0.62	0.88	0.40	0.26	0.14	0.79
TPP	5.96	5.86	1.10	1.31	0.10	0.21	0.11	1.03
DFP [15]	5.97	5.80	1.17	1.37	0.17	0.20	0.03	0.98
TFP [15]	5.73	5.54	1.20	1.43	0.19	0.23	0.04	0.96
FPZ [15]	5.86	5.61	1.07	1.33	0.25	0.26	0.01	0.93
NPB [40]	5.60							
TPD [40]	5.58							
Alq_3 [41]						0.276		

fluorescence quantum yield of FPZ (0.05) [11] is still smaller than TPP (0.12) [39]. This is maybe due to the lower charge transfer rate of FPZ than that of TPP. Obviously, fast transfer rates are very important to practical OLEDs. Therefore, the λ_{hole} and $\lambda_{electron}$ of studied compounds are computed and shown in Table 5. As listed in Table 5, the values of λ_{hole} of C-substituted porphyrins (DCP, TCP, and ZCP) are much smaller than those of M- and Q-substituted porphyrins, suggesting that the hole transport rates of C-substituted porphyrins are higher than those of M- and Q-substituted porphyrins. Table 5 also shows that the $\lambda_{electron}$ of TCP, TMP, and DQP is 0.15, 0.18, and 0.19 eV, respectively, which is much smaller than that of tris(8-hydroxyquinoline) aluminum (Alq_3) [41] ($\lambda_{electron}$ = 0.276 eV, which is conventional electron-transport materials). Hence, these studied compounds are expected to be good electron-transport materials from the standpoint of λ. Furthermore, as the λ_{hole} increases, the $\lambda_{electron}$ values of studied compounds increase by the same magnitude. Thus the balance of the charge carriers is enhanced in studied compounds. It will effectively increase the probability of confined excitons in the light-emitting layer. It is noteworthy that DCP, TCP, and ZCP have the almost same rates in the transportation between hole and electron transport as DMP, TMP, ZMP, DQP, TQP, and ZQP. Consequently, DCP, TCP, and ZCP are anticipated to be highly efficient red emitters with great commercial potential.

In addition, as reported in our previous work, the carrier transport rate and transport balance of DFP are better than TFP, however, the fluorescence quantum yield of DFP (0.17) is smaller than TFP (0.24). Besides that, DFP has worse charge injection ability than TFP. The exciton binding energy (E_b), the energy required to destroy a exciton, should be another important factor responsible for the fluorescence efficiency. Very recently, E_b has been investigated by our group and computed by the following formula [38] (in eV):

$$E_{Flu} = \Delta E_{H-L} - E_b \quad (2)$$

where E_{Flu} is the excitation energy and ΔE_{H-L} is the energy differences of the HOMO and LUMO. Accordingly, the E_b values of studied compounds are computed and given in Table 5. Table 5 shows the value of E_b of TFP is smaller than that of DFP, indicating that TFP is easier to destroy the hole–electron excitions than DFP, thus the fluorescence quantum yield of TFP is higher than that of DFP. Table 5 also shows the E_b of all studied compounds are smaller than that of TPP, especially for TMP, ZMP, DQP, and ZQP, which indicates these compounds are easy to destroy the hole–electron excitons. Taking into account the changes

of IP, EA, λ and E_b, it is found that TCP and ZCP have faster carrier injection and transport rate, better transport balance, and relatively smaller exciton binding energy than other molecules. Therefore, our calculations predict that TCP and ZCP would be very promising red emitting materials with high fluorescence quantum yield, which is agree with the analysis in Section 3.3.

4. Conclusions

Our B3LYP calculations predict the electronic and photophysical properties of porphyrins derivatives with energy transfer donors at meso-positions. The calculated results show that the TB energy transfer character from fragments C, M, and Q to corresponding acceptors, has been detected in some extent by the three following properties: (1) the large inter-ring dihedral angles $\alpha(C_a–C_m–C_{m'}–C_1)$, which preserves the respective character of donor and acceptor; (2) heavily electron density populated at the C_m atoms in theirs HOMO orbitals, which indicates that these compounds should have strong electron interaction; (3) large overlap of the absorption band of studied compounds and the fluorescence emission peak of corresponding donors. Furthermore, the compounds with TB energy transfer characters have higher HOMO energies and smaller ionization potentials (IP) than these properties of referenced compounds (DFP, TFP, and FPZ). And the HOMO energies of DCP, TCP, ZCP well match with the work function values of ITO (−4.8 eV). And TCP and ZCP have faster carrier injection and transport rate, better carrier transport balance, and relatively smaller exciton binding energy than other molecules in the studied molecules, rendering great potential of these red emitting materials with high fluorescence quantum yield in the development of red OLEDs. Thus, if TCP and ZCP can be prepared and isolated, we predict that they will be proven to be highly efficient red light-emitting materials.

Acknowledgements

This work is supported by the National Natural Science Foundation of China (Nos. 20673045 and 20973078) and the Open Project of State Key Laboratory of Supramolecular Structure and Materials of Jilin University (No. SKLSSM200716).

Appendix A. Supplementary data

Supplementary data associated with this article can be found, in the online version, at doi:10.1016/j.orgel.2010.03.019.

References

[1] X.H. Zhang, B.J. Chen, X.Q. Lin, O.Y. Wong, C.S. Lee, H.L. Kwong, S.T. Lee, S.K. Wu, Chem. Mater. 13 (2001) 1565.
[2] C.T. Chen, Chem. Mater. 16 (2004) 4389.
[3] T. Virgili, D.G. Lidzey, D.D.C. Bradley, Adv. Mater. 12 (2000) 58.
[4] M.A. Baldo, D.F. O'Brien, Y. You, A. Shoustikov, S. Sibley, M.E. Thompson, S.R. Forrest, Nature 395 (1998) 151.
[5] V. Bulovic, A. Shoustikov, M.A. Baldo, E. Bose, V.G. Kozlov, M.E. Tompson, S.R. Forrest, Chem. Phys. Lett. 287 (1998) 455.
[6] Y. Hamada, H. Kanno, T. Tsujioka, H. Takahashi, T. Usuki, Appl. Phys. Lett. 75 (1999) 1682.
[7] X.T. Tao, S. Miyata, H. Sasabe, G.J. Zhang, T. Wada, M.H. Jiang, Appl. Phys. Lett. 78 (2001) 279.
[8] W.C. Wu, H.C. Yeh, L.H. Chan, C.T. Chen, Adv. Mater. 14 (2002) 1072.
[9] B.S. Li, J. Li, Y.Q. Fu, Z.S. Bo, J. Am. Chem. Soc. 126 (2004) 3430.
[10] B.S. Li, X.J. Xu, M.H. Sun, Y.Q. Fu, G. Yu, Y.Q. Liu, Z.S. Bo, Macromolecules 39 (2006) 456.
[11] C.O. Paul-Roth, G. Simonneaux, C. R. Chimie 9 (2006) 1277.
[12] R.G. George, M. Padmanabhan, Polyhedron 22 (2003) 3145.
[13] S. Speiser, Chem. Rev. 96 (1996) 1953.
[14] G.S. Jiao, L. Thoresen, K.H. Burgess, J. Am. Chem. Soc. 125 (2003) 14668.
[15] X.-F. Ren, A.-M. Ren, J.-K. Feng, C.-C. Sun, J. Photochem. Photobiol. A: Chem. 203 (2009) 92.
[16] F. Nüesch, D. Berner, E. Tutiš, M. Schaer, C. Ma, X. Wang, B. Zhang, L. Zuppiroli, Adv. Funct. Mater. 15 (2005) 323.
[17] R.M. Adhikari, R. Mondal, B.K. Shah, D.C. Neckers, J. Org. Chem. 72 (2007) 4727.
[18] R. Ahlrichs, M. Bär, H.P. Baron, R. Bauernschmitt, S. Böcker, P. Deglmann, M. Ehrig, K. Eichkorn, S. Elliott, F. Furche, F. Haase, M. Häser, H. Horn, C. Hättig, C. Huber, U. Huniar, M. Kattannek, A. Köhn, C. Kölmel, M. Kollwitz, K. May, C. Ochsenfeld, H. Öhm, H. Patzelt, O. Rubner, A. Schäfer, U. Schneider, M. Sierka, O. Treutler, B. Unterreiner, M.V. Arnim, F. Weigend, P. Weis, H. Weiss, Turbmole V5-7, University of Karlsruhe, Germany, since 1988.
[19] S.M. Bonesi, R. Erra-Balsells, J. Lumin. 93 (2001) 51.
[20] E.J. Baerends, G. Ricciardi, A. Rosa, S.J.A. van Gisbergen, Coord. Chem. Rev. 230 (2002) 5.
[21] K.A. Nguyen, R. Pachter, J. Chem. Phys. 114 (2001) 10757.
[22] Y.-H. Zhang, W.-J. Ruan, Z.-Y. Li, Y. Wu, J.-Y. Zheng, Chem. Phys. 315 (2005) 201.
[23] A.D. Becke, Phys. Rev. A 38 (1988) 3098.
[24] A.D. Becke, J. Chem. Phys. 98 (1993) 5648.
[25] C. Lee, W. Yang, R.G. Parr, Phys. Rev. B 37 (1988) 785.
[26] R.A. Marcus, N. Sutin, R.A. Marcus, N. Sutin, Biochim. Biophys. Acta 811 (1985) 265.
[27] Y.L. Liu, J.K. Feng, A.M. Ren, J. Comput. Chem. 28 (2007) 2500.
[28] J.B. Foresman, M. Head-Gordon, J.A. Pople, M.J. Frisch, J. Phys. Chem. 96 (1992) 135.
[29] A.A. Jarzęcki, T.G. Spiro, J. Phys. Chem. A 109 (2005) 421.
[30] M.J. Frisch, G.W. Trucks, H.B. Schlegel, G.E. Scuseria, M.A. Robb, J.R. Cheeseman, J.A. Montgomery Jr., T. Vreven, K.N. Kudin, J.C. Burant, J.M. Millam, S.S. Iyengar, J. Tomasi, V. Barone, B. Mennucci, M. Cossi, G. Scalmani, N. Rega, G.A. Petersson, H. Nakatsuji, M. Hada, M. Ehara, K. Toyota, R. Fukuda, J. Hasegawa, M. Ishida, T. Nakajima, Y. Honda, O. Kitao, H. Nakai, M. Klene, X. Li, J.E. Knox, H.P. Hratchian, J.B. Cross, V. Bakken, C. Adamo, J. Jaramillo, R. Gomperts, R.E. Stratmann, O. Yazyev, A.J. Austin, R. Cammi, C. Pomelli, J.W. Ochterski, P.Y. Ayala, K. Morokuma, G.A. Voth, P. Salvador, J.J. Dannenberg, V.G. Zakrzewski, S. Dapprich, A.D. Daniels, M.C. Strain, O. Farkas, D.K. Malick, A.D. Rabuck, K. Raghavachari, J.B. Foresman, J.V. Ortiz, Q. Cui, A.G. Baboul, S. Clifford, J. Cioslowski, B.B. Stefanov, G. Liu, A. Liashenko, P. Piskorz, I. Komaromi, R.L. Martin, D.J. Fox, T. Keith, M.A. Al-Laham, C.Y. Peng, A. Nanayakkara, M. Challacombe, P.M.W. Gill, B. Johnson, W. Chen, M.W. Wong, C. Gonzalez, J.A. Pople, Gaussian 03, Revision B.04, Gaussian, Inc., Pittsburgh, PA, 2003.
[31] G.S. Jiao, L.H. Thoresen, T.G. Kim, W.C. Haaland, F. Gao, M.R. Topp, R.M. Hochstrasser, M.L. Metzker, K. Burgess, Chem. Eur. J. 12 (2006) 7816.
[32] M. Gouterman, J. Chem. Phys. 30 (1959) 1139.
[33] J. Otsuki, Y. Kanazawa, A. Kaito, D.-M. Shafiqul Islam, Y. Araki, O. Ito, Chem. Eur. J. 14 (2008) 3776.
[34] D.L. Dexter, J. Chem. Phys. 21 (1953) 836.
[35] J.L. Brédas, R. Silbey, D.S. Boudreaux, R.R. Chance, J. Am. Chem. Soc. 105 (1983) 6555.
[36] W.L. Jia, X.D. Feng, D.R. Bai, Z.H. Lu, S. Wang, G. Vamvounis, Chem. Mater. 17 (2005) 164.
[37] C. Weiss, in: D. Dolphin (Ed.), The Porphyrins, vol. III, Academic Press, New York, 1978.
[38] X.-Q. Ran, J.-K. Feng, A.-M. Ren, W.-C. Li, L.-Y. Zou, C.-Ch. Sun, J. Phys. Chem. A 113 (27) (2009) 7933.
[39] J.W. Owens, R. Smith, R. Robinson, M. Robins, Inorg. Chim. Acta 279 (1998) 226.
[40] B.C. Lin, C.P. Cheng, Z.P.M. Lao, J. Phys. Chem. A 107 (2003) 5241.
[41] B.C. Lin, C.P. Cheng, Z.Q. You, C.P. Hsu, J. Am. Chem. Soc. 127 (2005) 66.

significantly degraded by directly depositing organic semiconductor onto the NPs, due to the improper alignment and undesirable orientation of the organic molecules subsequently grown on the dielectric/NPs surfaces. This condition can be improved by introducing a self-assembled monolayer (SAM) of thiol molecules onto the metal NPs before the deposition of the organic semiconductor layer [9]. It has been observed that pentacene thin films deposited on bare gold NPs tend to crystallize with the long molecular axes lying parallel to the substrate, whereas those deposited on thiol-modified gold substrates tend to crystallize with the long molecular axis of pentacene oriented vertically on the substrates [14].

In this work, we demonstrate, for the first time, that the memory window of pentacene OFET-based organic memory device can be significantly enhanced by adjusting the location of silver NPs embedded in the pentacene layer. In contrast with the conventional structure where the nanoparticles are placed directly onto the dielectric [9], we applied a sandwiched structure by placing the Ag NPs in between two pentacene layer. The memory window (i.e. shifting of the threshold voltage) can be controlled by varying the location of Ag NPs. Our findings show that the memory windows of the devices increase with the increasing thickness of the first pentacene layer, and a maximum memory window of 90 V is obtained in the pentacene (15 nm)/Ag NPs(5 nm)/pentacene (25 nm) configuration. The current device can be performed *in situ* in a single run, thus eliminating the process of thiol molecules SAM for metal NPs deposition and permits more reproducible device preparations.

2. Experimental

The schematic of the bottom-gate memory device structure used in this work is shown in Fig. 1(a). The devices were fabricated on highly-doped *n*-type Si substrates, with 300-nm thick thermally-grown SiO_2 as the gate dielectric. Substrates were cleaned by regular substrate cleaning procedures, including sonication under DI water with soap, followed by cleaning in DI water, acetone, isopropanol, acetone and isopropanol. After that, the substrates were exposed to an ozone plasma for 15 min and immediately functionalized with a self-assembled monolayer of octadecyltrichlorosilane (OTS) by immersing the substrate in OTS/hexane solution (1:500 v/v%).

Pentacene thin films, silver NPs and silver drain–source contacts were thermally evaporated at a base pressure of 1×10^{-7} Torr. Transistor devices with three types of structures were fabricated in this work (listed in Table 1). For type A devices, 40 nm of pentacene thin films were thermally evaporated on OTS-treated substrates, followed by the deposition of 50-nm thick silver drain–source electrodes through a mechanical shadow mask. For type B devices, OTS treatment was done after the deposition of nominally 5-nm thick Ag layers on the substrates, followed by the growth of 40 nm pentacene thin films and electrodes. For type C devices, the device configuration was in the form of pentacene/Ag NPs/pentacene. The thickness of the first and the second pentacene layers were varied such that the total thickness of the pentacene layers was 40 nm. Here, OTS treatment was done before the first pentacene layer in order to align the pentacene molecules vertically on the substrate, which is different from the thiol molecule SAM for the metal NPs as described in Refs. [9,15]. The Ag layers among type B and type C devices were maintained at a nominal thickness of 5 nm. It has been confirmed by the scanning electron microscopy (SEM) images that the as-deposited 5-nm silver films were discontinuous and isolated NPs were formed, as shown in Fig. 1(b) and (c). The channel lengths (L) and widths (W) of all devices were 50 μm and 1000 μm, respectively. The

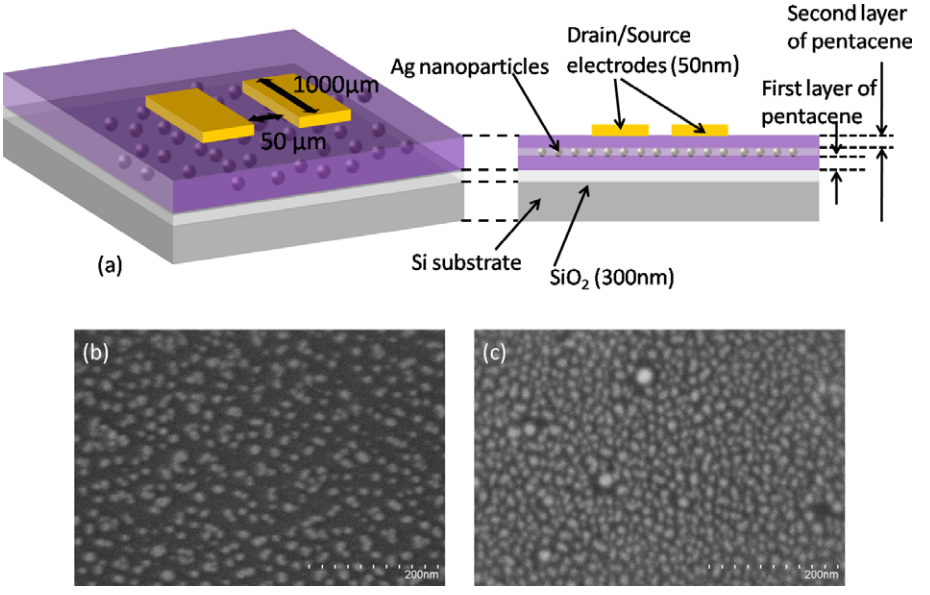

Fig. 1. (a) Schematic for pentacene/Ag NP/pentacene transistor memory devices; SEM image of Ag NPs on (b) SiO_2 and (c) 15-nm pentacene bottom layer. The calculated areal density of the silver nanoparticles on the SiO_2 and pentacene are 1.2×10^{11} cm^{-2} and 3.3×10^{11} cm^{-2}, respectively.

Table 1
Memory properties of type A, B and C devices (Pen = pentacene).

Device type	Structure	V_{th1} (V)	V_{th2} (V)	ΔV_{th} (V)	Trap density ($\times 10^{12}$ cm^{-2})	Mobility (cm^2 V^{-1} s^{-1})	On/off ratio
A	Pen(40)	−10	−15	5	0.35	0.296	10^4–10^5
B	Ag(5)/Pen(40)	−20	−50	30	2.08	0.005	10^2
C5	Pen(5)/Ag(5)/Pen(35)	5	−50	55	3.82	0.008	10^2
C10	Pen(10)/Ag(5)/Pen(30)	26	−52	78	5.40	0.021	10^2
C15	Pen(15)/Ag(5)/Pen(25)	30	−60	90	6.24	0.100	10^2–10^3

output and double-sweep transfer characteristics of the transistors were measured by two LabVIEW-controlled Keithley 2400 sourcemeters under dark and ambient conditions.

3. Results and discussion

The output and transfer characteristics for devices A, B and C15 (referring to pentacene (15 nm)/Ag NPs (5 nm)/pentacene (25 nm)) are shown in Fig. 2(a)–(f). For device A, the output curves are measured with the gate voltage (V_g) varied from 0 V to −60 V (Fig. 2(a)). The output curves exhibit a typical p-channel field-effect transistor behavior, and the field-effect mobility (μ) in the saturation region is obtained by the following equation [16]:

$$I_{ds} = \frac{\mu W C_i}{2L}(V_g - V_{th})^2 \quad (1)$$

I_{ds} is the drain–source current, C_i is the capacitance per unit area of the dielectric layer, and V_{th} is the threshold voltage. The threshold voltage of a device is determined by the x-axis intercept of the tangent of $I_{ds}^{0.5}$ against V_g curve. The carrier mobility for device A is measured to be 0.3 cm^2 V^{-1} s^{-1}, as listed in Table 1. With the drain–source voltage (V_{ds}) maintained at −60 V, when the gate bias sweeps between +60 V and −100 V with either increasing or decreasing V_g, an on/off ratio of 10^4–10^5 is measured and very small hysteresis is obtained (Fig. 2(b)). The hysteresis effect in the type A device can be attributed to the defects at the interface between the SiO_2 and pentacene [17,18]. It is important to mention that all of the measurements were performed in dark at ambient conditions, shortly after the devices were taken out of the thermal evaporation chamber. These procedures helped to minimize potential degradation effects.

For type B device where the Ag NPs were deposited at the interface between the SiO_2 and pentacene, I_{ds} drops significantly as compared with device A (Fig. 2(c)). The lower I_{ds} value is possibly due to the altered morphology of the pentacene thin film by the NPs, which leads to a reduced mobility [3,15]. On the other hand, if a 15-nm thick pentacene is deposited before the deposition of the Ag NPs (device C15), the I_{ds} (Fig. 2(e)) is almost two orders higher than that in device B. It suggests the first few monolayers of pentacene, which dominates on the transport properties of the OFET, are largely unaffected by the deposition of silver NP layer [19]. The hysteresis properties of type B and C devices were investigated by cyclic sweeping of V_g (i.e. from positive to negative and then back from negative to positive). The memory window of the device is defined as the difference of the threshold voltages in the two V_g sweeping direction, i.e. $\Delta V_{th} = V_{th1} - V_{th2}$. For type B device, with Ag NPs embedded at the SiO_2/pentacene interface, a memory window of 30 V is obtained (Fig. 2(d)). In contrast, if Ag NPs are located between two pentacene layers, a memory window as high as 90 V for the C15 device is achieved (Fig. 2(f)), which is three times higher compared with device B. The dependence of ΔV_{th} on V_{ds} is investigated by varying V_{ds} from −5 V to −60 V, and the results are plotted in Fig. 2(g). It can be noted that the memory window remains constant when V_{ds} is varying, which agrees with the observations in Ref. [4]. The carrier mobility of the memory device is also an important parameter, because it governs the operation speed of the memory device. The mobility in the saturation region for C15 device is 0.100 cm^2 V^{-1} s^{-1}, which is almost 20 times higher than that for type B device (0.005 cm^2 V^{-1} s^{-1}), suggesting the good performance of C15 device while comparing with the type B device.

To further investigate the hysteresis phenomena in type C devices, we varied the position of silver NPs by changing the thickness of the bottom pentacene layer while maintaining the total thickness of the pentacene. As summarized in Table 1, the memory window of the type C devices increases with thicker bottom pentacene layer, from 55 V for device C5 to 90 V for device C15. The enhancement of the memory window is attributed to the increasing charge trap density, as the deposited Ag atoms can penetrate into the pentacene layer, forming dopant-like traps [20,21]. To test this hypothesis, the morphology of silver NPs in device B and C15 are shown in Fig. 1(b) and (c), and the areal densities of Ag NPs as evaluated by image processing in MATLAB are 1.2×10^{11} cm^{-2} and 3.3×10^{11} cm^{-2}, respectively. The areal density of Ag NPs can be compared with the number of trapped charges Δn, which can be calculated by [22],

$$\Delta n = \frac{\Delta V_{th} \cdot C'}{e} \quad (2)$$

Because the Ag NPs was deposited above the bottom pentacene layer, so the capacitance of the pentacene should be considered. Therefore, the capacitance per unit area in the current device was obtained by $\frac{1}{C'} = \frac{1}{C_{SiO_2}} + \frac{1}{C_{pen}}$, C_{SiO_2} and C_{pen} are the capacitance per unit area of the SiO_2 and pentacene, respectively. As shown in Table 1, the charge trap density increases with thicker bottom pentacene layer, which agrees with the larger Ag nanoparticle densities observed in the SEM images. For device C15, the number of trapped charges is 6.24×10^{12} cm^{-2}, which represents each Ag NP contributes to around 20 trap states. The trap densities in the current OFET memory devices are comparable to that in inorganic ZnO thin-film transistor

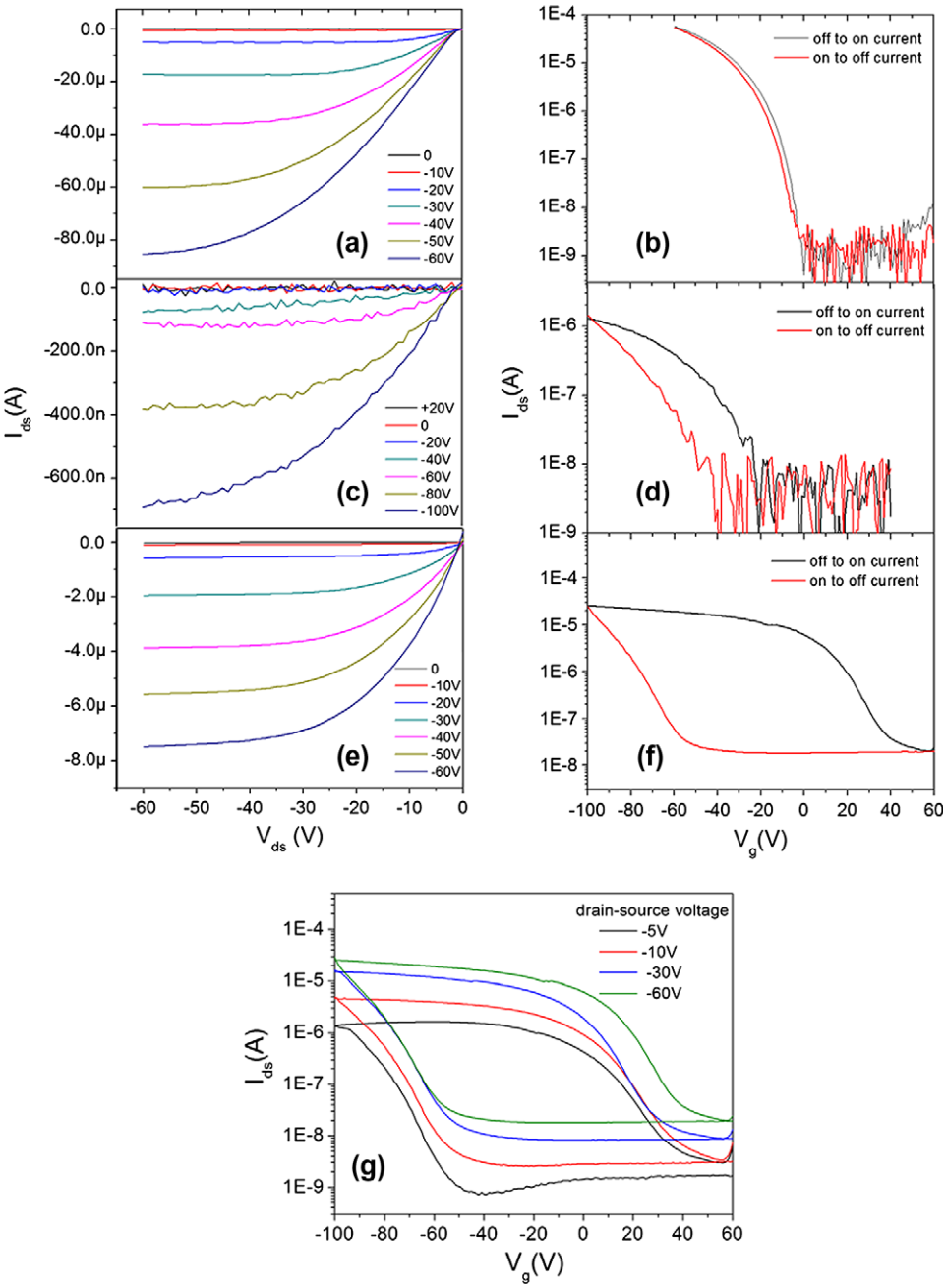

Fig. 2. Output characteristic curves (left column) and transfer curves (right column) for type A device [(a) and (b)], type B device [(c) and (d)] and C15 devices [(e) and (f)]; (g) shows the memory windows of device C15 under different source–drain voltage and no significant variation in the memory windows can be observed.

memory with Ag NPs embedded in the gate insulator/ZnO interface [23].

The memory effect obtained in the current devices is due to the trapping and detrapping of charges. It has been shown that these traps can either be electron or hole traps [24–26]. In order to identify the nature of the traps in our devices, drain current–time measurements are performed in device C15, and the results are shown in Fig. 3(a). During the measurements, the gate voltage is kept at different initial values V_{g0} (−20 V and −40 V) for 100 s, and is switched to $V_g = -30$ V for another 100 s. V_{ds} is maintained at −30 V throughout the whole measurement, and the value of I_{ds} is monitored. To ensure that the device starts at the same initiate state for each measurement, an initialization routine is conducted with $V_g = +60$ V for 60 s at the beginning of each measurement before V_{g0} is imposed on the device. As shown in Fig. 3(a), when the gate voltage is switched from a more negative value ($V_{g0} = -40$ V) to

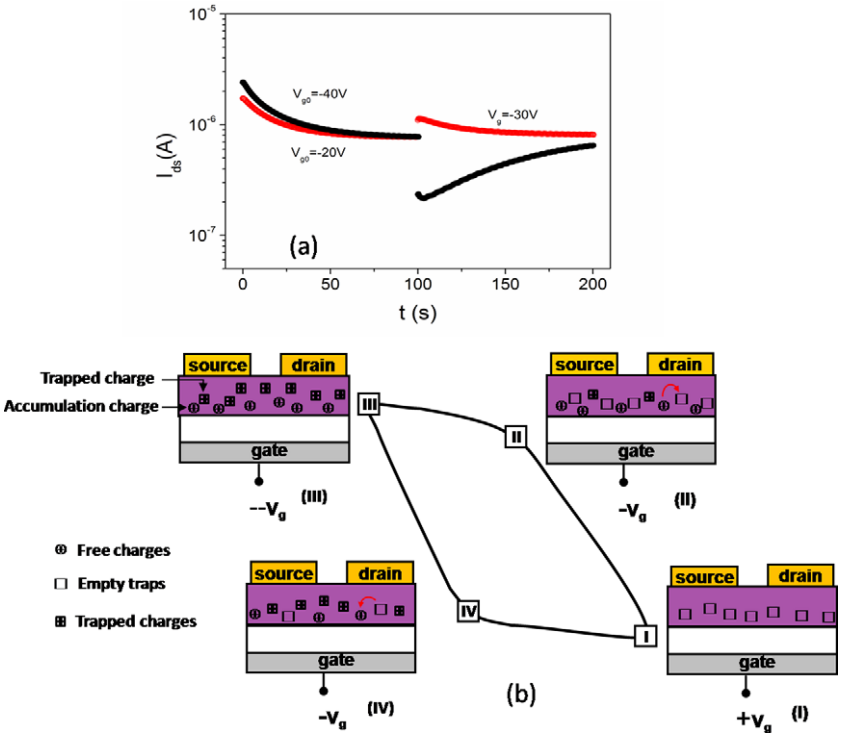

Fig. 3. (a) Current–time measurement with different V_g. (b) schematics for different trap states at different V_g sweeping directions ((⊕) free holes; (□) empty traps; (⊞) trapped holes; red arrow indicate charge trap and detrap directions).

−30 V, the current does not stay constant but increase with time. However, when the gate voltage is switched from a less negative value (−20 V) to V_g = −30 V, the current decreases with time. This response of the I_{ds} under different bias condition provide evidence that the traps in the current memory devices are predominantly hole traps. When V_g switches from −40 V to −30 V, the increasing current is due to the release of the trapped holes which can only be held at more negative V_g [16,27,28]. If electron traps dominate the observed hysteresis, I_{ds} should stay constant because the traps are emptied at more negative gate value, and no electrons can be released after switching to a less negative V_g [29].

A potential mechanism which explains the measured memory effect is provided as follows. When a large negative V_g is applied, holes are injected into the traps, and these trapped charges generate an internal electric filed opposite to the applied gate voltage, causing the screening effect. Therefore a higher negative V_g is required to turn on the device, resulting in a shift of threshold voltage to a more negative value [30,31]. Similarly, when a large positive V_g is applied, holes would be detrapped from the trap centers. Such trapping and detrapping processes result in the shift of transistor threshold voltage, hence forming the memory window. The drain–source current at different V_g sweeping directions are further explained by the schematic diagram as shown in Fig. 3(b). At the beginning of the sweeping cycle, a large positive gate bias is applied to the device and the traps are emptied (state I). During the positive to negative sweep direction (from state I to II), more and more holes would be trapped at the trap centers. When the trapped centers are filled up by the holes, the screening effect will become important and further increase the magnitude of V_g would not cause a significant increase of free holes and the drain–source current (state II–III). During the negative to positive sweep (from state III to IV), the trapped holes would released slowly and more holes are still in trap centers [18,27,29], therefore the drain–source current contributed from the free holes decrease significantly (state IV).

4. Conclusions

In summary, we demonstrated a novel OFET-based memory devices based on the Ag NPs embedded into pentacene layers. By varying the location of the Ag NPs, the memory effect was adjustable and the maximum memory window of 90 V has been obtained, which is a 300% improvement compared with the conventional structure where Ag NPs are directly deposited on silicon dioxide. The increased memory effect results from different trap densities induced by the Ag NPs, and hole trap mechanism is found to dominate the hysteretic behavior. By comparing the deposited Ag NPs density on the pentacene, it can be estimated that each nanoparticle contributes to around 20 traps states. This structure demonstrates potential for memory applications in organic thin-film transistors and integrated circuits.

Acknowledgements

This work is supported by research grants (Grant Nos. 1-ZV43 and 1-ZV4H) from Hong Kong Polytechnic University. Funding from HKSAR through UGC grant (Grant No. PolyU 5112/08E) is also acknowledged.

References

[1] J.C. Scott, L.D. Bozano, Adv. Mater. 19 (2007) 1452.
[2] C.D. Dimitrakopoulos, P.R.L. Malenfant, Adv. Mater. 14 (2002) 99.
[3] W. Wang, J. Shi, D. Ma, IEEE Trans. Electron. Dev. 56 (2009) 1036.
[4] W. Wu, H. Zhang, Y. Wang, S. Ye, Y. Guo, C. Di, G. Yu, D. Zhu, Y. Liu, Adv. Funct. Mater. 18 (2008) 2593.
[5] T. Sekitani, T. Yokota, U. Zschieschang, H. Klauk, S. Bauser, K. Takeuchi, M. Takamiya, T. Sakurai, T. Someya, Science 326 (2009) 1516.
[6] R.C.G. Naber, C. Tanase, P.W.M. Blom, G.H. Gelinck, A.W. Marsman, F.J. Touwslager, S. Setayesh, D.M. De Leeuw, Nat. Mater. 4 (2005) 243.
[7] Y.J. Park, H.J. Jeong, J. Chang, S.J. Kang, C. Park, J. Semicond. Technol. Sci. 8 (2008) 51.
[8] W.L. Leong, P.S. Lee, A. Lohani, Y.M. Lam, T.P. Chen, S. Zhang, A. Dodabalapur, S.G. Mhaisalkar, Adv. Mater. 20 (2008) 2325.
[9] C.W. Tseng, Y.T. Tao, J. Am. Chem. Soc. 131 (2009) 12441.
[10] T. Nakajima, Y. Takahashi, S. Okamura, T. Furukawa, J. Appl. Phys. 48 (2009) 09KE04.
[11] P. Wurfel, I.P. Batra, Phys. Rev. B 8 (1973) 5126.
[12] R.C.G. Naber, K. Asadi, P.W.M. Blom, D.M. De Leeuw, Adv. Mater. 21 (2009) 1.
[13] W.L. Leong, N. Maehwes, S. Mhaisalkar, Y.M. Lam, T. Chen, P.S. Lee, J. Mater. Chem. 19 (2009) 7354.
[14] W.S. Hu, Y.T. Tao, Y.J. Hsu, D.H. Wei, Y.S. Wu, Langmuir 21 (2005) 2260.
[15] C. Novembre, D. Guérin, K. Lmimouni, C. Gamrat, D. Vuillaume, Appl. Phys. Lett. 92 (2008) 103314.
[16] T.B. Singh, N. Marjanoviæ, G.J. Matt, N.S. Sariciftci, R. Schwödiauer, S. Bauer, Appl. Phys. Lett. 85 (2004) 5409.
[17] J.W.H. Smith, I.G. Hill, J. Appl. Phys. 101 (2007) 044503.
[18] M. Egginger, S. Bauer, R. Schwödiauer, H. Neugebauer, N.S. Sariciftci, Monatsh. Chem. 140 (2009) 735.
[19] M. Mottaghi, G. Horowitz, Org. Electron. 7 (2006) 528.
[20] J.H. Cho, D.H. Kim, Y. Jang, W.H. Lee, K. Ihm, J.-H. Han, S. Chung, K. Cho, Appl. Phys. Lett. 89 (2006) 132101.
[21] J. Lin, D.G. Ma, J. Appl. Phys. 103 (2008) 024507.
[22] K. Baeg, Y. Noh, J. Ghim, S. Kang, H. Lee, D. Kim, Adv. Mater. 18 (2006) 3179.
[23] D. Gupta, M. Anand, S.W. Ryu, Y.K. Choi, S.H. Yoo, Appl. Phys. Lett. 93 (2008) 224106.
[24] H. Lin, Z. Pei, Y. Chan, IEEE Electr. Dev. Lett. 28 (2007) 569.
[25] M.B. Madec, D. Crouch, G.R. Llorente, T.J. Whittle, M. Geoghegan, S.G. Yeates, J. Mater. Chem. 18 (2008) 3230.
[26] D.K. Hwang, K. Lee, J.H. Kim, S. Im, J.H. Park, E. Kim, Appl. Phys. Lett. 89 (2006) 093507.
[27] C. Ucurum, H. Goebel, F.A. Yildirim, W. Bauhofer, W. Krautschneider, J. Appl. Phys. 104 (2008) 084501.
[28] T. Ikoma, B. Jeppsson, Jpn. J. Appl. Phys. 12 (1973) 1011.
[29] G. Gu, M.G. Kane, J.E. Doty, A.H. Firester, Appl. Phys. Lett. 87 (2005) 243512.
[30] L. Zhen, W. Guan, L. Shang, M. Liu, G. Liu, J. Phys. D: Appl. Phys. 41 (2008) 135111.
[31] M.F. Mabrook, Y. Yun, C. Pearson, D.A. Zeze, M.C. Petty, Appl. Phys. Lett. 94 (2009) 173302.

when an inorganic gate insulator is applied. For example, it was observed in the pentacene/SiO_2 interface where hydroxyl (OH) group was proved to provide electron traps [23]. Ambient moisture diffusion into the interface between the pentacene and the gate dielectric [24] layer along with impurities, defects as well as grain boundaries in semiconductor [25,26] also act as charge traps. A clockwise hysteresis is also associated with a polymeric gate insulator, and is often induced by the charge injection from the gate electrode and trapping inside the dielectric [27]. The dielectric bulk trapped electrons induce more holes in the channel and result in larger drain current during the bias sweep loop, contributing to clockwise hysteresis [28]. Lee et al. added SiO_2 buffer layer in between polymer insulator and gate electrode and proved the evidence of the electron injection from the gate electrode into the dielectric [21]. Additionally, residual dipole or mobile ions cause slow polarization in the bulk of the organic dielectric. The dipole reorientation process makes the drain current fall behind the bias sweep and a clockwise hysteresis appears [29]. Under a negative gate bias, migration of ions from internal impurities in polymer can also induce a similar effect [30].

Another advantage of the polymeric insulator is its flexibility [6] and flexible OFETs have been reported by many groups on a polymer substrate such as poly ethylene terephthalate (PET) and poly ethylene naphthalate (PEN) with a conductive organic electrode (PEDOT:PSS) and a polymer insulator (PVP, PVA, PS) [31–33]. On the other hand, stainless steel substrate is one of the flexible substrates with high corrosion resistance, high conductivity and thermal stability [34,35]. Its excellent thermal conductivity as a metal is helpful for the thermal management of the organic device. Through chemical mechanical polishing (CMP) process, a stainless steel substrate can have smooth enough surface to serve as a gate electrode [36].

In this report, OFETs were fabricated using a cross-linkable high-*k* CEP/PMMF blend with various mixing ratios as a dielectric to achieve OFETs with low voltage, low hysteresis operation with high μ and steep inverse subthreshold slope (SS). Stainless steel substrate was studied as a gate electrode and as a substrate to fabricate flexible devices. Electrical performance of OFETs on N+Si and stainless steel were also compared and bending effect on the device performance was studied.

2. Experimental

Fig. 1a and b shows the molecular structure of CEP (cyanoethylated pullulan) and PMMF [poly(methylated melamine-co-formaldehyde)] and the structure after cross-linking. Fig. 1c shows the schematic of MIM (metal–insulator–metal) structure, MIS (metal–insulator–semiconductor) capacitor and a top-contact pentacene OFET. The cross-linkable solution was prepared in a co-solvent (*N*,*N*′-dimethylformamide:acetonitrile 1:1) with 5 wt.% CEP ($M_w \sim 489{,}000$, Shin Etsu Chemical Co.) and various amount of PMMF (Aldrich, $M_n \sim 511$). PMMF/CEP ratios were set at 10%, 30%, 50%, and 70% to study the effect of the cross-linker content on the film properties and device performances. The solid films were formed with spin coating on piranha cleaned p-type (for MIS capacitors) or heavily doped n-type (for MIM structures and OFETs) silicon wafers at 3000 rpm for 1 min inside the high purity Ar-filled glove box. The film was annealed for 1 h inside a vacuum oven at 200 °C. The baked films were referred to as CEPM10, CEPM30, CEPM50 and CEPM70 for each PMMF content. After forming the dielectric, a 60 nm thick pentacene active layer (Aldrich Chemical Co., without purification) was deposited in a thermal evaporator with a deposition rate of 0.2–0.3 Å/s at a substrate temperature of 50 °C. Then 70 nm thick Au source and drain electrodes were deposited through a shadow mask, using the thermal evaporator; the device channel length and width are 150 and 1500 μm, respectively. For MIM structures and MIS capacitors, Au top (or bottom) electrodes were deposited with evaporation through a shadow mask to make a circular dot area of 8.02×10^{-4} cm^2.

Fourier Transform Infrared (FT-IR) spectra of solid films were recorded in a transmission mode with Nicolet 6700. Contact angle measurements were conducted using Model CA-A face contact angle meter (Kyowa Kaimenkagaku Co., Ltd.). Ultraviolet photoelectron spectroscopy (UPS) was used to calculate the work functions of the gate electrodes. The thickness of CEPM films were measured by ellipsometry. Capacitance–voltage (*C*–*V*) characteristics of the MIS capacitors were measured using HP 4284A Precision LCR meter (Agilent Tech.) at 1 MHz. The electrical characteristics of the pentacene FETs were measured using HP 5270A (Agilent Tech.) in a dark box under ambient conditions. To study the roughness of the dielectric surfaces, as well as pentacene morphology, atomic force microscopy (AFM) was adopted using a Dimension™ 3100 microscope (Digital Instruments). The in-plane X-ray diffraction (XRD) was carried out at the 3C2 X-ray scattering beamline of the Pohang Light Sources (PLS) at Pohang Accelerator Laboratory (PAL).

3. Results and discussion

3.1. Properties of CEPM and pentacene films

FT-IR spectra of the solid film in Fig. 2 were recorded in a transmission mode to monitor the chemical changes in the cross-linking reaction as demonstrated in Fig. 1b. The observed band between 3100 and 2800 cm^{-1} was assigned to the C–H (CH_x) stretching vibrations. As the PMMF content increased, slightly thicker film was obtained from higher material concentration, giving more intense CH_x peak. In contrast, O–H stretching vibration peak intensity centered at 3480 cm^{-1} decreased from the OH group removal through cross-linking. The contact angle of deionized water on the film surface was measured as summarized in Table 1 [37].

AFM images of the insulator surface were obtained as shown in Fig. 3a–d. The film became rougher when more PMMF content was added with root-mean-square (RMS) roughness from 0.35 to 1.27 nm, which affected pentacene morphology. AFM images of 60 nm thick pentacene films on different dielectrics are displayed in Fig. 3e–h. The pentacene grain size showed decreasing trend from CEPM10 to CEPM70 because the surface roughness becomes a more

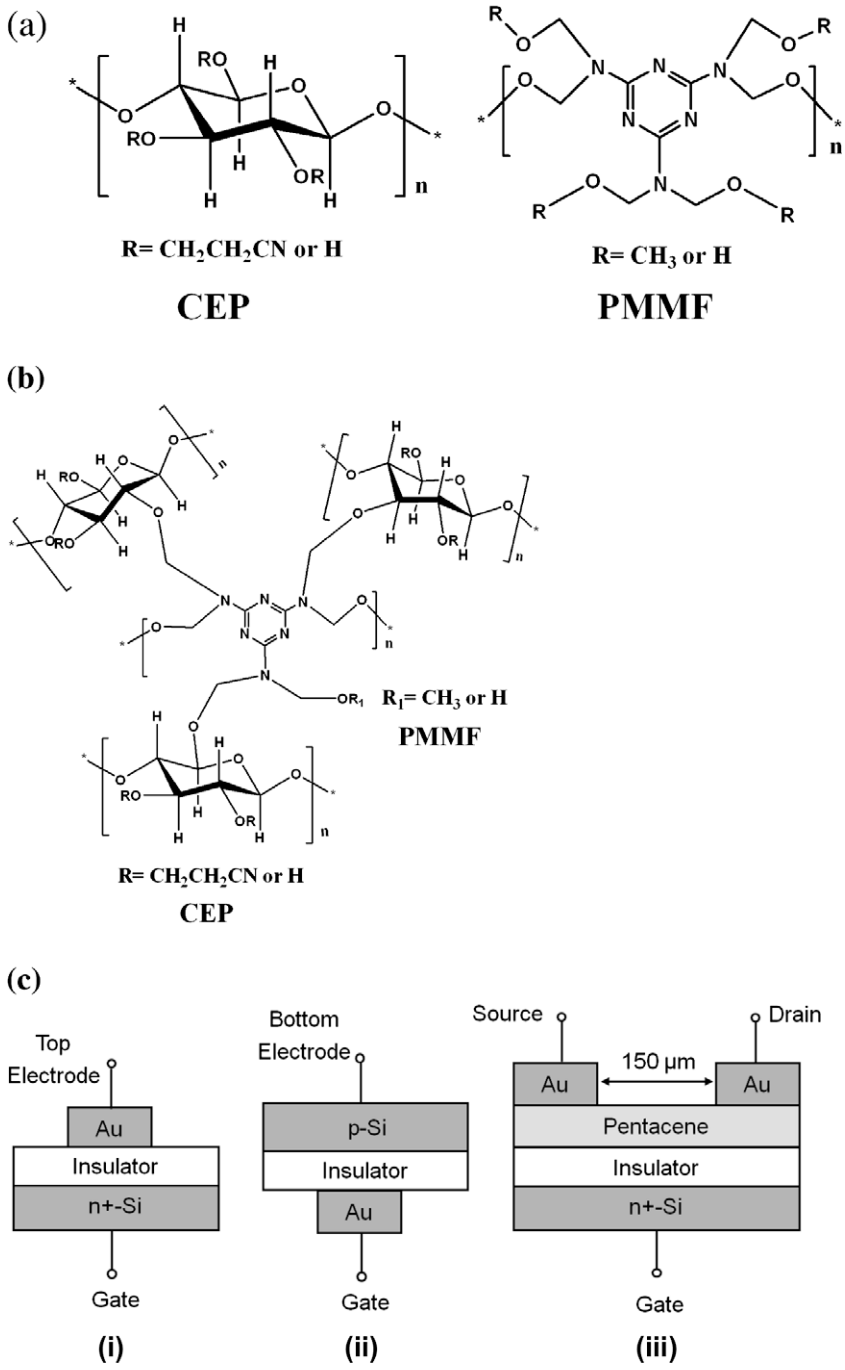

Fig. 1. (a) Chemical structures of CEP and PMMF, (b) structure formed by cross-linking CEP polymer with PMMF, and (c) schematic of the device geometries of (i) Au/CEPM/n+-Si MIM structure, (ii) Au/CEPM/p-Si MIS capacitor and (iii) top-contact/bottom-gate OFET.

effective factor than surface polarity. Although pentacene morphology would be affected, the RMS roughness below 1.51 nm was reported to have little effect on other gate dielectric properties such as capacitance and surface polarity, and so on μ [38].

XRD peak was recorded for 60 nm pentacene film to investigate the molecular ordering in a symmetric reflection coupled θ–2θ arrangement with a synchrotron radiation X-ray source. Fig. 4 exhibits a series of XRD patterns corresponding to the (0 0 l) planes of the thin-film phase of pentacene, and indicates that the ordering of layered structure of pentacene depends on the PMMF contents, which may determine μ of OFET devices [39]. Vacuum evaporated pentacene thin films typically consist of two

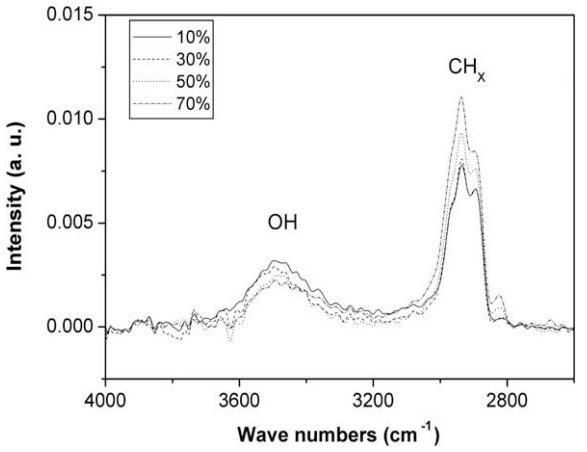

Fig. 2. FT-IR spectra of dielectrics in transmittance mode for CEPM10, CEPM30, CEPM50, and CEPM70.

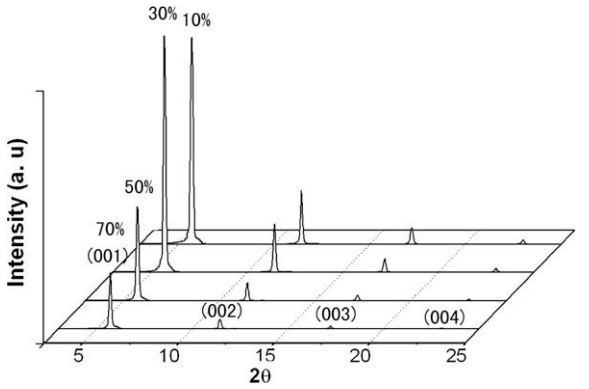

Fig. 4. XRD patterns of 60 nm pentacene films deposited on the gate dielectric of CEPM10, CEPM30, CEPM50, and CEPM70.

crystallographic phases, single crystal phase (bulk phase) and thin-film phase. Dimitrakopoulos et al. found the new pentacene phase with d_{001} of 15.4 Å, which is different from the well-known single crystal phase ($d_{001} \sim 14.1$ Å) [40]. Since pentacene molecules stand vertically on a substrate in thin-film phase, better charge transport and higher mobility can be expected. The surface polarity dependent crystallinity of pentacene on CEPM30 (high contact angle) vs. that of CEPM10, CEPM50, and CEPM70 (low contact angles) correlates well to the improvement in μ of OFETs with CEPM30 vs. other dielectrics as will be discussed in the later part of this paper.

Table 1
Thickness, contact angles, and parameters extracted from *C–V* characteristics.

PMMF/CEP (%)	Thickness (nm)	C.A. (°)	C_i (nF/cm^2)	k	ΔV_{FB} (V)
10	206.9	64.0	60.9	15.2	2.9
30	211.2	68.0	52.5	13.4	0.3
50	224.6	64.4	42.3	11.9	0.3
70	251.4	63.0	35.5	10.7	0.5

3.2. MIM structures and MIS capacitors

The leakage current density and gate voltage (*J–V*) characteristics of CEPM dielectrics are presented in Fig. 5. The

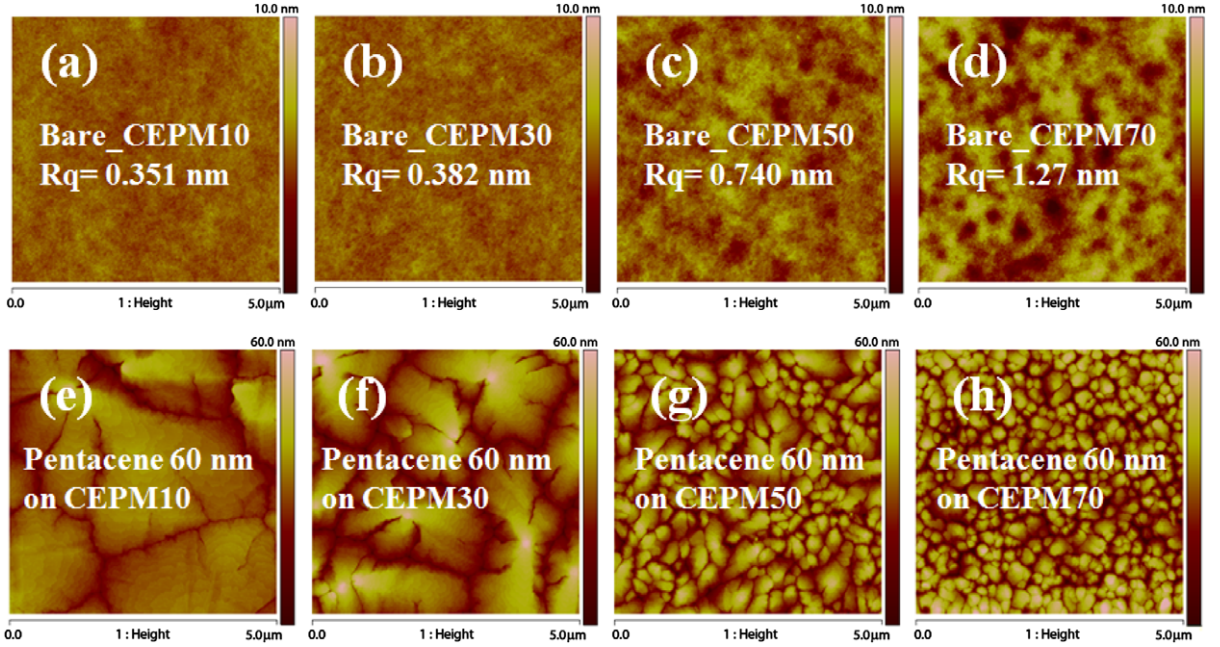

Fig. 3. 5 × 5 μm^2 AFM images of dielectric surface, (a) CEPM10, (b) CEPM30, (c) CEPM50, and (d) CEPM70, and 60 nm pentacene films grown on (e) CEPM10, (f) CEPM30, (g) CEPM50, and (h) CEPM70.

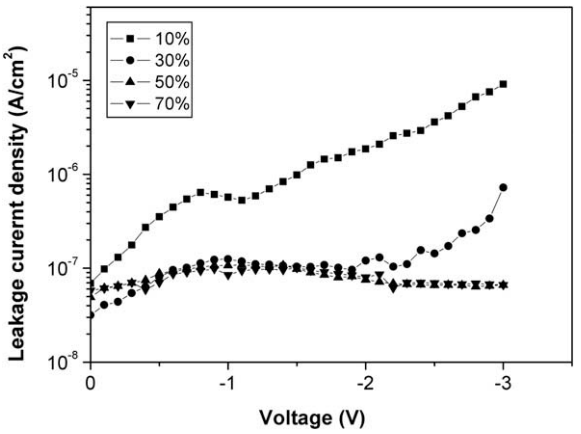

Fig. 5. *J–V* characteristics of Au/CEPM/n+-Si MIM structures with CEPM10, CEPM30, CEPM50, and CEPM70.

leakage current density of CEPM10 is as high as 10^{-5} A/cm^2 at an applied voltage of -3 V, while CEPM50 shows the leakage current density by more than two orders of magnitude lower to 5×10^{-8} A/cm^2. The significant reduction in the leakage current density from CEPM10 to CEP50 is likely from a better-formed net structure via a more effective cross-linking reaction. The tiny increase of leakage in CEPM70 indicates an excess of curing agent amount, and extra cross-linking agent might negatively affect on the film robustness, since PMMF itself cannot form a smooth film.

C–V characteristics of the Au/CEPM/p-Si MIS capacitors were measured to comparably study the hysteresis behavior at 1 MHz, and parameters are summarized in Table 1. The MIS capacitors with CEPM30 and CEPM50 showed negligible hysteresis behavior as measured by ΔV_{FB}, as shown in Table 1. This might attribute to effective removal of charge traps in the dielectrics, as will be discussed in a later part in this paper. The capacitance density (C_i) are 60.9, 52.5, 42.3, and 35.5 (nF/cm^2) for CEPM10, CEPM30, CEPM50, and CEPM70, respectively. The capacitance density is related to *k* value and the thickness of the dielectric, as indicated in the following equation [7],

$$C_i = \varepsilon_o \frac{k}{t} \quad (1)$$

In this equation, *k* is dielectric constant, *t* is thickness of the dielectric film, and ε_o is the permittivity of vacuum. Both thicker films from 206.9 nm for CEPM10 to 251.4 nm for CEPM70, and the lower *k* values from 15.2 to 10.7 lowered the capacitance. The change in *k* values attributes to the addition of different amount of low-*k* component PMMF, as expected from the following power–law relationship [41],

$$k^\beta = k_1^\beta + (1-\varphi)k_2^\beta \quad (2)$$

where *k*, k_1, and k_2 are the dielectric constants of cross-linked film and that of the two components, respectively. φ is the volume fraction of component one and β is a parameter representing the shape and orientation of the filler, which is in the range of [−1, 1] [42]. CEP/PMMF system possessing more low-*k* PMMF component tends to give lower *k* value.

3.3. Organic field-effect transistors

Top contact OFETs were fabricated by sequentially evaporating pentacene and Au through shadow masks

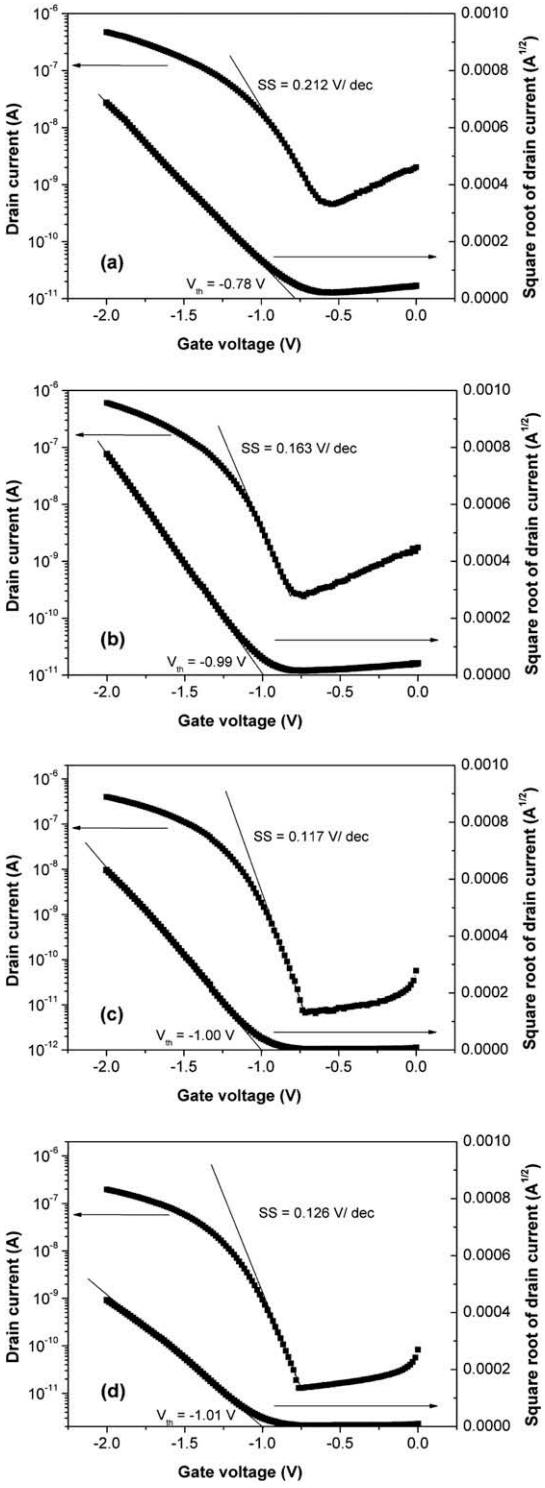

Fig. 6. Transfer characteristics (2 V operation) of OFETs with different dielectrics (a) CEPM10, (b) CEPM30, (c) CEPM50, and (d) CEPM70.

Table 2
Transistor characteristics with gate dielectrics cross-linked with various PMMF amounts.

V_{op} (V)	PMMF/CEP (%)	μ (cm^2/V s)	I_{on}/I_{off}	V_{th} (V)	ΔV_{th} (V)	SS (V/dec)	N_{trap} ($10^{10}/cm^2$)	N_{trap}^{max} ($10^{11}/cm^2$)
2	10	0.78	1.0×10^3	−0.78	0.17	0.212	6.47	9.55
2	30	2.16	2.4×10^3	−0.99	0.10	0.163	3.28	5.57
2	50	1.83	5.0×10^4	−1.00	0.01	0.117	0.264	2.48
2	70	0.91	1.5×10^4	−1.01	0.03	0.126	0.666	2.51
3	10	0.83	1.5×10^3	−0.77	0.27	0.450	10.3	24.6
3	30	1.77	2.0×10^4	−0.86	0.06	0.153	1.97	5.03
3	50	1.07	3.0×10^5	−0.92	0.01	0.066	0.264	0.245
3	70	0.66	1.3×10^4	−0.98	0.15	0.133	3.33	2.67

onto the cross-linked dielectrics. As can be observed from the device characteristics in Fig. 6, high quality devices with operating voltages as low as −2 V were achieved by employing the CEPM dielectrics. Electrical parameters are extracted from the following equations [31,43], and summarized in Table 2.

$$I_{D,sat} = \frac{W}{2L}\mu C_i (V_G - V_{th})^2 \quad (3)$$

$$S \equiv dV_G/d(\log I_{SD}) \quad (4)$$

Here, $I_{D,Sat}$ is the drain current in the saturated regime, W/L is the channel width/length, μ is the mobility, V_G is the gate voltage, and V_{th} is the threshold voltage. Also S is the inverse subthreshold slope (SS) and I_{SD} is the current between source and drain at a given gate voltage.

OFET-CEPM30 shows the highest μ of 2.16 cm^2/V s under a 2 V operation. OFET-CEPM30 showed on/off current ratio (I_{on}/I_{off}) of 2.4×10^3, SS of 0.163 V/dec, and V_{th} shift (ΔV_{th}) of 0.10 V. Although an relatively high μ value has been achieved with OFET-CEPM30, the other electrical parameters are not as good as OFET-CEPM50, which has a μ of 1.83 cm^2/V s $I_{on}/I_{off} \sim 5.0 \times 10^4$, a low SS of 0.117 V/dec, and small ΔV_{th} of 0.01 V. The improvement of the I_{on}/I_{off} using 50% PMMF is from the decrease in leakage current density as shown in Fig. 5.

The significant SS difference attributes to a decreased charge trap density at the pentacene/dielectric interface and inside the insulator. We estimated the upper limit of the charge trap density in the devices using Eq. (5) [44]

$$N_{trap}^{max} \approx \left[\frac{qS\log(e)}{kT} - 1\right]\frac{C_i}{q} \quad (5)$$

Here q is the electronic charge, k is Boltzmann's constant, and C_i is the capacitance/area of the gate dielectric. Using Eq. (5), we estimate an upper limit of trapped charge (N_{trap}^{max}) to be $9.55 \times 10^{11}/cm^2$, $5.57 \times 10^{11}/cm^2$, $2.48 \times 10^{11}/cm^2$, and $2.51 \times 10^{11}/cm^2$ for CEPM10, CEPM30, CEPM50, and CEPM70 devices, respectively. The consistency of charge traps and contact angle measurements strengthens the arguments that the origin of the hysteresis is from charge injection and trapping, which can be minimized by suitable amount of cross-linking agent. The SS change is also in consistency with the ΔV_{th}, which is another measure of trap states (N_{trap}), as compared in Fig. 7c and Table 2.

OFET-CEPM10 exhibits μ of 0.78 cm^2/V s, I_{on}/I_{off} of 1×10^3, a SS of 0.212 V/dec, and ΔV_{th} of 0.17 V. One factor for the low μ was high polarity of the dielectric surface as measured by contact angles of deionized water, which interacted with pentacene modules when growing film. Another very important reason was the high leakage (recorded with transfer characteristic, 1.44×10^{-7} A at −2 V) of the polymer film, which is almost one third of the on current (4.72×10^{-7} A), causing significant degradation of μ.

Fig. 8d shows the comparative trends of dielectric constant and on current of the transfer curves. Higher dielectric constant generally gives higher capacitance, which might generate a higher on current, while the low on current of OFET-CEPM10 is because of the high leakage current density and low μ.

All the above trends were observed more clearly under 3 V operation, as summarized in Table 2. Especially, the OFET-CEPM50 showed high I_{on}/I_{off} of 3×10^5, ΔV_{th} as low as 0.01 V and very sharp SS value of 0.066 V/dec, which might be the lowest SS value with polymer gate insulator to date. This exceeded our previous report approaching the theoretical minimum of 0.057 V/dec [20].

3.4. Flexible devices and lower voltage operations

To probe the possibility of utilizing CEPM-OFETs in flexible displays, stainless steel substrate was used as a gate substrate. The bending test was conducted with the device bended along the channel direction by attaching the substrate on the out-surface of a glass arc, whose diameter was 4.5 cm. Electrical characteristics were obtained with the bended device. The process has been described in detail in another paper [36]. As shown in Fig. 8a and b, only a slight degradation in μ and I_{on}/I_{off} was observed during the bending test showing a good mechanical robustness of the polymeric cross-linked gate insulator. By comparing the curves from stainless-OFET and N+Si-OFET, a positive V_{th} shift was observed. In this sense, stainless steel substrate not only provides flexibility, but also improves the V_{th}. As can be observed in Fig. 8a, stainless-OFET-CEPM50 gives higher on current, and better I_{on}/I_{off}, which attributes to the positively shifted V_{th}. UPS spectra of bare N+-Si and stainless steel substrate gates were taken to calculate work functions, as shown in Fig. 9. The work function data were obtained from the following equation [45,46],

$$\phi = h\upsilon(= 21.2\ \text{eV}) - E_{cutoff} + E_{Fermi} \quad (6)$$

where ϕ, E_{cutoff}, and E_{Fermi} are the work function, secondary electron cutoff and Fermi level, respectively. The photon

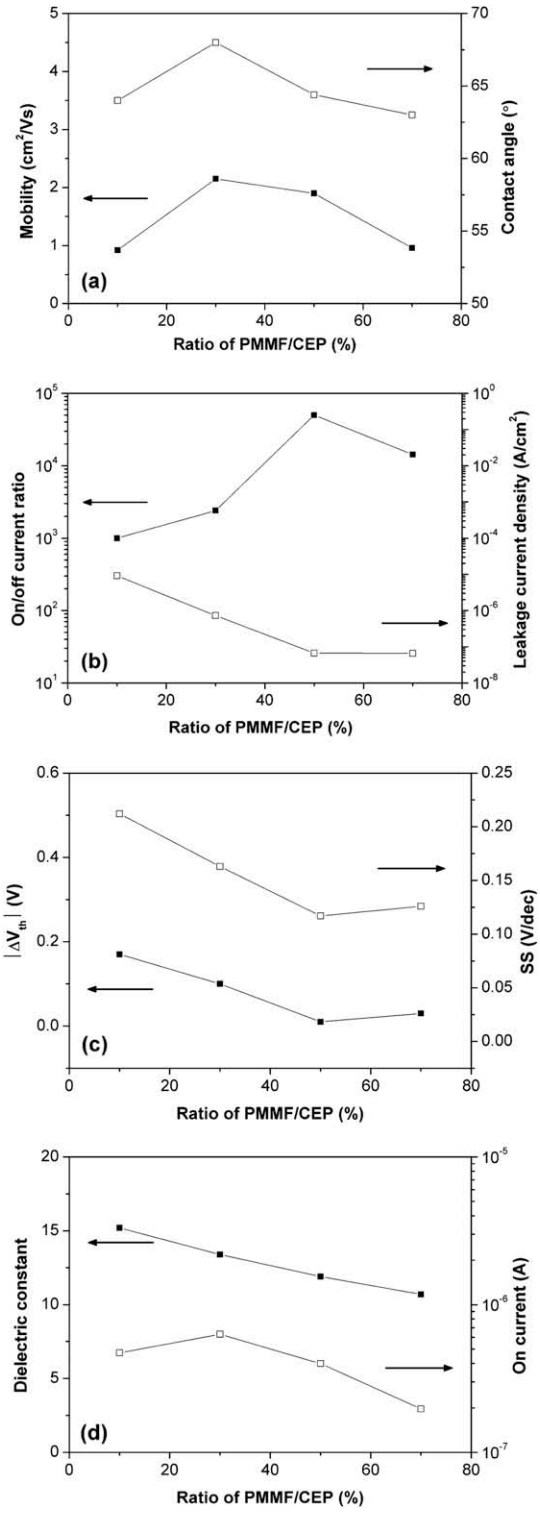

Fig. 7. (a) Plot of the mobility (■) and contact angle (□) vs. PMMF/CEP ratio, (b) I_{on}/I_{off} (■) and leakage current density at −3 V (□) vs. PMMF/CEP ratio, (c) plot of the $|\Delta V_{th}|$ (■) and SS (□) vs. PMMF/CEP ratio and (d) plot of the dielectric constant (■) and on current (□) vs. PMMF/CEP ratio.

energy of the UPS light source (helium I irradiation) is 21.2 eV. The work function increase from 4.29 to 4.53 eV

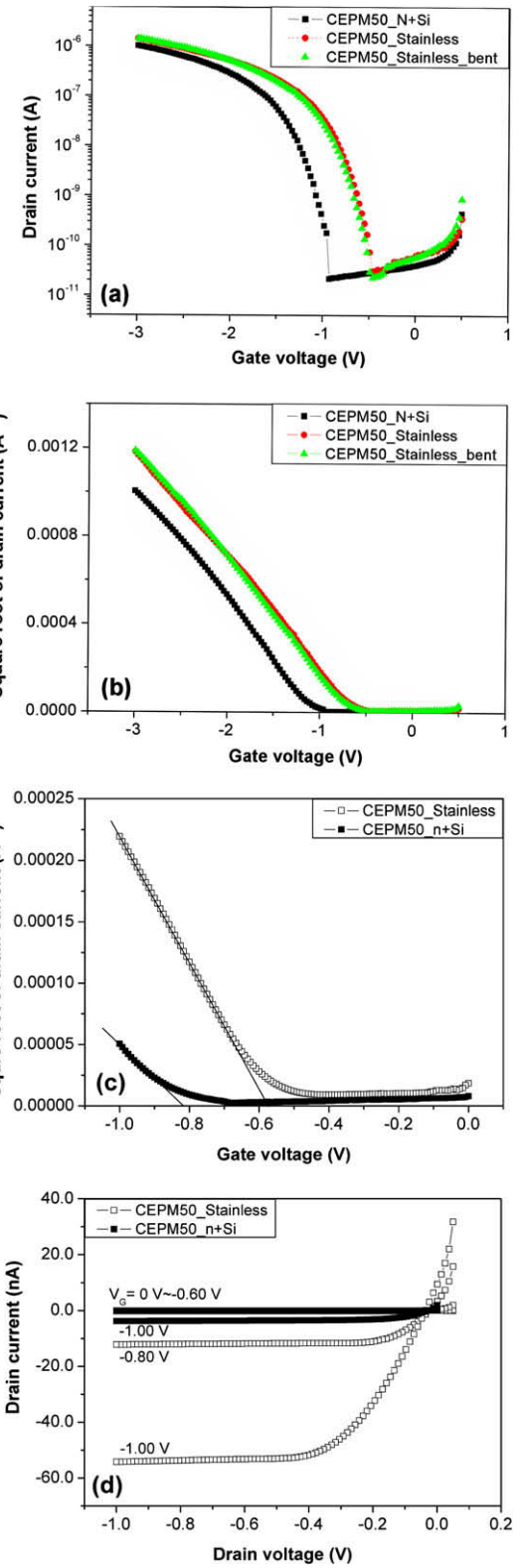

Fig. 8. Electrical characteristics of low-voltage operated OFETs on N+-Si and stainless steel substrate, (a) comparison of transfer curves, (b) square root of drain current vs. gate voltage, (c) V_{th} shift with 1 V operation and (d) output characteristics comparison with 1 V operation.

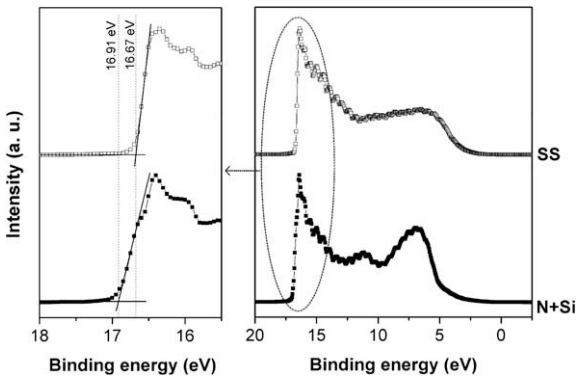

Fig. 9. UPS spectra of N+Si and stainless steel substrates surfaces.

for N+-Si and stainless steel substrate gives comparably positive V_{th} shift, as has been discussed in detail in some literature [47–49].

The slight positive V_{th} shift may have negligible effect if the operating voltage is high, while in a low-voltage operation, the effect would be quite obvious to improve the output current. In the case of low-voltage operation, if the V_{th} is too close to the maximum of the gate voltage sweep, the device cannot be operated well. The improvement in V_{th} becomes essential to improve the drain current. Fig. 8c and d show significant improvement in V_{th} and output curves for -1 V operation by changing N+Si to stainless steel substrate. The lower μ in N+Si device was caused by the very small difference between V_{th} (-0.83 V) and the maximum of the gate voltage sweep range (-1 V).

4. Conclusions

OFETs were fabricated using spin-coated CEP/PMMF blend at various ratios as a gate dielectric. The high-k polymer CEP was thermally cured at 200 °C by the cross-linking agent PMMF. The highest μ was obtained using OFET-CEPM30, while the best I_{on}/I_{off}, SS and reliability with the smallest hysteresis were obtained with OFET-CEPM50. The electrical performance was improved with the low surface wettability, low leakage current density of dielectric films, as well as the good crystallinity of pentacene thin films. In low-voltage operation of 1 V, devices on stainless steel substrate showed much better electrical performance than on an N+-Si substrate. It was due to the V_{th} shift, which resulted from the higher work function of the stainless steel gate electrode. The thin-film devices showed good electrical properties even with bending at considerable angles. These results indicate that cross-linked high-k dielectric is a promising candidate for low cost, low power consumption, reliable and flexible electronics.

Acknowledgment

This research was supported by the Korea Science and Engineering Foundation (KOSEF) through the National Research Laboratory Project and Polymer Gel Cluster group of the Korean government.

References

[1] B. Crone, A. Dodabalapur, Y.Y. Lin, R.W. Filas, A. Bao, A. Laduca, R. Sarpeshkar, H.E. Katz, W. Li, Nature 403 (2000) 521.
[2] C.D. Dimitrakopoulos, D.J. Mascaro, IBM J. Res. Dev. 45 (2006) 11.
[3] M.E. Roberts, S.C.B. Mannsfeld, N. Queraltó, C. Reese, J. Locklin, W. Knoll, Z. Bao, Proc. Natl. Acad. Sci. USA 105 (2008) 12134.
[4] H. Klauk, M. Halik, U. Zschieschang, G. Schmid, W. Radlik, W. Weber, J. Appl. Phys. 92 (2002) 5259.
[5] R. Schroeder, L.A. Majewski, M. Grell, Adv. Mater. 16 (2004) 633.
[6] M.E. Roberts, N. Queraltó, S.C.B. Mannsfeld, B.N. Reinecke, W. Knoll, Z. Bao, Chem. Mater. 21 (2009) 2292.
[7] A. Facchetti, M.-H. Yoon, T.J. Marks, Adv. Mater. 17 (2005) 1705.
[8] H. Klauk, U. Zschieschang, J. Pflaum, M. Halik, Nature 445 (2007) 745.
[9] M. Halik, H. Klauk, U. Zschieschang, G. Schmid, C. Dehm, M. Schütz, S. Maisch, F. Effenberger, M. Brunnbauer, F. Stellacci, Nature 431 (2004) 963.
[10] C.D. Dimitrakopoulos, S. Purushothaman, J. Kymissis, A. Callegari, J.M. Shaw, Science 283 (1999) 822.
[11] C.D. Dimitrakopoulos, I. Kymissis, S. Purushothaman, D.A. Neumayer, P.R. Duncombe, R.B. Laibowitz, Adv. Mater. 11 (1999) 1372.
[12] C.D. Dimitrakopoulos, P.R. Duncombe, B.K. Furman, R.B. Laibowitz, D.A. Neumayer, S. Purushothaman, US patent, 1999, 5981970.
[13] J. Collet, D. Vuillaume, Appl. Phys. Lett. 73 (1998) 2681.
[14] M.-H. Yoon, A. Facchetti, T.J. Marks, Proc. Natl. Acad. Sci. USA 102 (2005) 4678.
[15] O. Acton, G. Ting, H. Ma, J.W. Ka, H.-L. Yip, N.M. Tucker, A.K.-Y. Jen, Adv. Mater. 20 (2008) 3697.
[16] S.H. Kim, S.Y. Yang, K. Shin, H. Jeon, J.W. Lee, K.P. Hong, C.E. Park, Appl. Phys. Lett. 89 (2006) 183516.
[17] J. Lee, M.J. Panzer, Y. He, T.P. Lodge, C.D. Frisbie, J. Am. Chem. Soc. 129 (2007) 4532.
[18] J.H. Cho, J. Lee, Y. Xia, B. Kim, Y. He, M.J. Renn, T.P. Lodge, C.D. Frisbie, Nat. Mater. 7 (2008) 900.
[19] M.-H. Yoon, H. Yan, A. Facchetti, T.J. Marks, J. Am. Chem. Soc. 127 (2005) 10388.
[20] W. Xu, S.-W. Rhee, J. Mater. Chem. 19 (2009) 5250.
[21] C.A. Lee, D.-W. Park, K.-D. Jung, B.-J. Kim, Y.C. Kim, J.D. Lee, B.G. Park, Appl. Phys. Lett. 89 (2006) 262120.
[22] D.K. Hwang, M.S. Oh, J.M. Hwang, J.H. Kim, S. Im, Appl. Phys. Lett. 92 (2008) 013304.
[23] L.-L. Chua, J. Zaumseil, J.-F. Chang, E.C.W. Ou, P.K.H. Ho, H. Sirringhaus, R.H. Friend, Nature 434 (2005) 194.
[24] G. Gu, M.G. Kane, Appl. Phys. Lett. 92 (2008) 053305.
[25] D. Li, E.-J. Borkent, R. Nortrup, H. Moon, H. Katz, Z. Bao, Appl. Phys. Lett. 86 (2005) 042105.
[26] Z.-T. Zhu, J.T. Mason, R. Dieckmann, G.G. Malliaras, Appl. Phys. Lett. 81 (2002) 4643.
[27] T. Jung, A. Dodabalapur, R. Wenz, S. Mohapatra, Appl. Phys. Lett. 87 (2005) 182109.
[28] S.C. Lim, S.H. Kim, J.B. Koo, J.H. Lee, C.H. Ku, Y.S. Yang, T.H. Zyung, Appl. Phys. Lett. 90 (2007) 173512.
[29] H.E. Katz, X.M. Hong, A. Dodabalapu, R. Sarpeshkar, J. Appl. Phys. 91 (2002) 1572.
[30] M. Egginger, M. Irimia-Vladu, R. Schwödiauer, A. Tanda, I. Frischauf, S. Bauer, N.S. Sariciftci, Adv. Mater. 20 (2008) 1018.
[31] B.C. Shekar, J. Lee, S.-W. Rhee, Korean J. Chem. Eng. 21 (2004) 267.
[32] Y. Yang, J. Yoon, S.H. Kim, K. Hong, D.S. Chung, K. Heo, C.E. Park, M. Ree, Appl. Phys. Lett. 92 (2008) 243305.
[33] T. Sekitani, Y. Kato, S. Iba, H. Shinaoka, T. Someya, T. Sakurai, S. Takagi, Appl. Phys. Lett. 86 (2005) 073511.
[34] A. Sari, K. Kaygusuz, Renew. Energy 28 (2003) 939.
[35] M.G. Kang, N.G. Park, K.S. Ryu, S.H. Chang, K.J. Kim, Sol. Energy Mater. Sol. Cells 90 (2006) 574.
[36] D.-J. Yoon, S.-H. Lim, T.W. Lee, S.-W. Rhee, Org. Electron. 10 (2009) 970.
[37] F.M. Fowkes, in: R.L. Patrick (Ed.), Treatise on Adhesion and Adhesives, Marcel Dekker, New York, 1967, p. 352.
[38] K. Shin, S.Y. Yang, C. Yang, H. Jeon, C.E. Park, Org. Electron. 8 (2007) 336.
[39] C. Kim, C. Facchetti, T.J. Marks, Science 318 (2007) 76.
[40] C.D. Dimitrakopoulos, A.R. Brown, A. Pomp, J. Appl. Phys. 80 (1996) 2501.

[41] Y.-L. Liu, M.-H. Fangchiang, J. Mater. Chem. 19 (2009) 3643.
[42] M.G. Todd, F.G. Shi, IEEE Trans. Dielectrics Electrical Insulation 12 (2005) 601.
[43] T.-W. Lee, J.H. Shin, I.-N. Kang, S.Y. Lee, Adv. Mater. 19 (2007) 2702.
[44] A. Rolland, J. Richard, J.-P. Kleider, D. Mencaraglia, J. Electrochem. Soc. 140 (1993) 3679.
[45] D. Cahen, A. Kahn, Adv. Mater. 15 (2003) 271.
[46] S.-W. Rhee, D.-J. Yun, J. Mater. Chem. 18 (2008) 5437.
[47] W.T. Wondmagegn, R.J. Pieper, Mater. Res. Soc. Symp. Proc. 1115 (2009) H05–H71.
[48] D. Rechem, S. Latreche, C. Gontrand, Pramana – J. Phys. 72 (2009) 587.
[49] M. Liess, D. Chinn, D. Petelenz, J. Janata, Thin Solid Films 286 (1996) 252.

of the metal complex emitter in the polymer host must be improved.

Chemical modification of the phosphorescent green iridium(III) complex *fac*-tris(2-phenylpyridyl)iridium(III) [Ir(ppy)$_3$], which has been shown to have a high photoluminescence efficiency and relatively short radiative lifetime, has led to some improvement in the solubility. For example, methylation of Ir(ppy)$_3$ on the ligand phenyl ring at the position *para* to the ligand pyridyl ring, i.e. tris[2-(4-tolyl)pyridyl]iridium(III), [Ir(mppy)$_3$], enhances the solubility. However, although the solubility is improved, this approach still does not fully prevent the aggregation of the emissive molecules. This is due to Ir(mppy)$_3$ still having only poor to at best moderate solubility in organic solvents commonly used for processing polymer hosts such as toluene and chlorobenzene. The range of concentrations that the complex is used as a guest in a polymer host in which a uniform dispersion is achieved is therefore quite limited. Moreover, the low solubility of Ir(mppy)$_3$ makes it difficult to accurately control the doping concentrations and the long mixing time required for dissolution makes the fabrication process rather time-inefficient.

Dendrimer OLEDs offer the advantages of combining the high efficiency of small molecule OLEDs and the solution processing properties of polymer OLEDs [5,6]. High efficiency dendrimer OLEDs have been achieved when the dendrimer layer has been deposited by spin-coating, and an evaporated electron-transport layer has been used [7–9]. Lately, blade coating has shown potential as an alternative processing method to spin-coating and ink-jet printing. It also opens up the possibility of multi-layer OLEDs, in which all the layers are deposited by solution processing [10] without the use of post UV-cured polymerization of soluble cross-linkable precursors [11]. In general multi-layer structures are required to balance electron and hole currents for achieving highly efficient OLEDs.

In this Letter we use highly soluble dendrimers, p-G1-Ir and m-G1-Ir, as the light-emitting guest (chemical structures shown in Fig. 1c). The host is a mixture comprised of poly(9-vinylcarbazole) (PVK), and charge-transport materials, *N,N′-diphenyl-N,N′*-[bis(3-methylphenyl)]-[1,1′-biphenyl]-4,4′-diamine (TPD) and 2-(4-biphen-4′-yl)-5-(4-*tert*-butylphenyl)-1,3,4-oxadiazole (PBD) [12]. The p-G1-Ir and m-G1-Ir dendrimers consist of a *fac*-tris(2-phenylpyridyl)iridium(III) [Ir(ppy)$_3$] core, first generation biphenyl-based dendrons, and 2-ethylhexyloxy surface groups [13,14]. The synthesis of the dendrimers has been previously reported [15]. As shown in Fig. 1c, the difference between p-G1-Ir and m-G1-Ir is that p-G1-Ir has the dendron attached on the ligand phenyl ring *para* to the pyridyl ring whereas m-G1-Ir has the dendron attached on the ligand phenyl ring *meta* to the pyridyl ring [7,15,16]. Unlike most phosphorescent emitters based on small molecules, the phosphorescent dendrimers have superb solubility in common organic solvents due to the surface groups attached to the distal ends of the dendrons. In addition, the dendrons act as rigid spacers that reduce the intermolecular interactions of the emissive cores that can cause luminescence quenching [5,6,17]. Indeed, there is dramatic difference in solubility between the dendrimers used and Ir(mppy)$_3$. The solubility of p-G1-Ir is more than

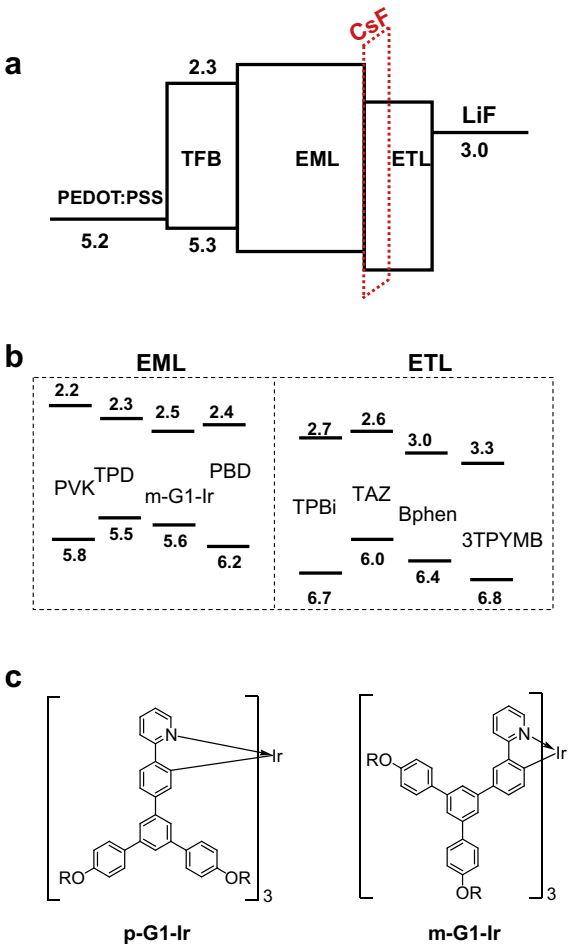

Fig. 1. (a) Schematic diagram of the OLED structures employed. The cathodes are CsF/Al for the devices without the ETL and LiF/Al for those with the ETL. (b) Energy diagram of the materials in this work, the numbers are in eV. (c) Structures of p-G1-Ir and m-G1-Ir.

10 wt.% both in toluene and chlorobenzene, whereas Ir(mppy)$_3$ is less than 0.5 wt.% in chlorobenzene and it is virtually insoluble in toluene. Bi-layer OLEDs with CsF/Al cathode and tri-layer OLEDs with an electron-transport layer (ETL) and a more stable LiF/Al cathode were fabricated with the dendrimers as the guest in a PVK:TPD:PBD blend host. The electron transport materials were deposited by a newly developed blade-coating method to avoid dissolution [10]. The ETL materials studied included 1,3,5-tris(*N*-phenylbenzimidazol-2-yl)benzene (TPBi), 3-(4-biphen-4′-yl)-4-phenyl-5-(4-*tert*-butylphenyl)-1,2,4-triazole (TAZ), 4,7-diphenyl-1,10-phenanthroline (Bphen), and tris-[3-(3-pyridyl)mesityl]borane (3TPYMB). High efficiencies were achieved for dendrimer weight concentrations of up to 33% with easy concentration control and instant dissolution during fabrication. An efficiency of 38 cd/A (at 5 V) and luminance of 27,000 cd/m^2 (at 14.5 V) were obtained in the bi-layer devices prepared by blade coating. Although direct comparison is not possible as different host materials have different solubility for the studies, current device efficiencies are higher than

those previously reported for similar bi-layer device fabricated from spin-coating [18]. In addition, the amount of dendrimer used in the emissive layer is less than that of previous reports, making the blade-coating fabrication more cost effective.

2. Experimental

Fig. 1 shows the OLED device structures used in the study. To fabricate the OLEDs, the indium-tin-oxide (ITO) substrate was first precleaned in deionized water with detergent, which was purchased from Alconox, and then UV–ozone treated. In order to use the blade-coating technique it was necessary to have large ITO substrates (7 cm × 8 cm). A 50 nm poly(3,4-ethylenedioxythiophene) poly(styrenesulfonate) (PEDOT:PSS, CLEVIOS™ P VP AI 4083) was then spin-coated onto the ITO substrate and annealed at 100 °C for 40 min in vacuum. To improve hole injection in the devices [19,20], poly[(9,9-dioctylfluorenyl-2,7-diyl)-*co*-(4,4′-{*N*-[4-*s*-butylphenyl]}diphenylamine)] (TFB) in toluene (1 wt.%) was blade-coated on top of the PEDOT:PSS and spin-rinsed with toluene after annealing at 180 °C for 40 min in vacuum to leave a TFB layer with thickness of about 5 nm. The light-emitting solution was prepared by mixing host solution, PVK:PBD:TPD in chlorobenzene (2 wt.%), and dendrimer guest solution, dendrimer in toluene (2 wt.%), and then blade-coated onto the TFB layer to give a 70 nm thick 'light-emitting' film. In the blend system, dendrimer:PVK:TPD:PBD, the ratio of TPD:PBD was fixed at 9:24 and the ratio of dendrimer:PVK was tuned. The ratios of p-G1-Ir:PVK were 1:66, 2:65, 6:61, 13:54, and 33:34. The ratios of m-G1-Ir:PVK were 2:65, 6:61, 13:54, and 33:34. The emissive layer was annealed at 80 °C for 60 min in vacuum. To complete the devices without an electron-transport layer, a 2 nm layer of CsF was deposited, followed by a 100 nm capping layer of Al. The latter two layers were deposited using thermal evaporation at a pressure of 10^{-6} Torr. For the devices with electron-transport layers, TPBi, TAZ, Bphen, and 3TPYMB, were dissolved in *n*-butanol (0.5 wt.%) and blade-coated on top of the emissive layer (dendrimer:TPD:PBD:PVK with a ratio of 6:9:24:61) to give thicknesses of order 20 nm [12]. Dissolution between the ETL and emissive layer was avoided by using the newly developed blade-coating method with *n*-butanol as the solvent. A thin (≈1 nm) layer of LiF was evaporated under the pressure of 10^{-6} Torr and covered with a 100 nm of Al to form the cathode and complete the devices. The active area of each pixel was 4 mm^2. *I–L–V* characteristics were measured with a Keithley 2400 source meter with the light output integrated with a PR650 photometer. PVK with a molecular weight (M_w) of 1,100,000 was purchased from Sigma–Aldrich. TPD, PBD, TPBi, TAZ, BPhen, and 3TPYMB were obtained from Luminescence Technology Corp, and TFB was purchased from American Dye Source.

3. Results and discussion

Figs. 2 and 3 show the bi-layer device characteristics and emission spectra based on p-G1-Ir and m-G1-Ir, respectively, and using CsF/Al as cathode. In general, the

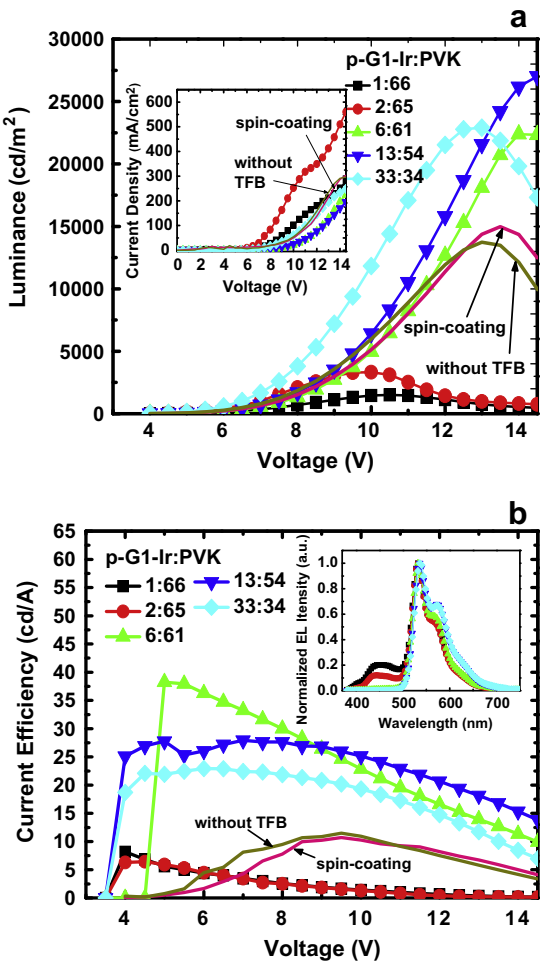

Fig. 2. Device performance of p-G1-Ir:PVK:TPD:PBD. (a) The luminance and the inset is the current density *versus* voltage. (b) The current efficiency *versus* voltage and the inset shows the electroluminescent spectra at 1000 cd/m^2. The ratio of TPD:PBD was fixed at 9:24. The performance of the device without TFB layer is indicated by dark yellow line, while the performance of the device fabricated by spin-coating instead of blade coating is indicated by pink line. (For interpretation of the references to colour in this figure legend, the reader is referred to the web version of this article.)

luminance and efficiency were not high at low dendrimer doping concentrations in the PVK (i.e. 1:66 and 2:65 with a fixed ratio of TPD:PBD of 9:24). This could be due to the fact that there were not enough emitters in the host to harvest the excitons, which is supported by the emission spectra where there is blue emission from the host (Fig. 2b). The blue emission at the wavelengths near 400 nm can be attributed to the TPD or PVK host while the broad emission peaking at 470 nm may originate from the $(TPD + PBD-)^*$ exciplex [12]. Interestingly, the blue emission from m-G1-Ir based devices is not as obvious as those of p-G1-Ir at the same doping concentration (2:65) (Fig. 3). Given that the two dendrimers have exact the same molecular weights and the same dendrimer doping concentrations, the smaller amount of blue emission from the (2:65) device could be due to the different shape of the dendrimers. The different shape results from the dendrons

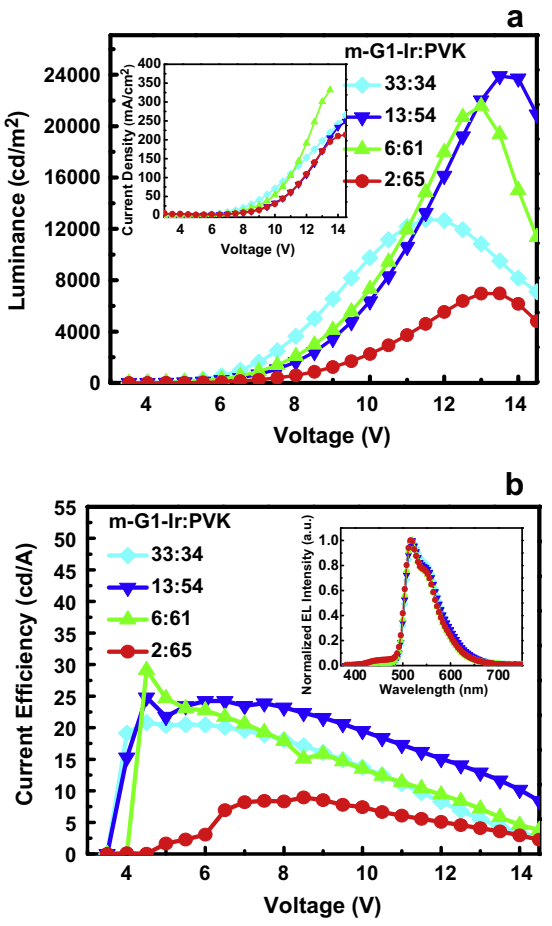

Fig. 3. Device performance of the m-G1-Ir:PVK:TPD:PBD. (a) The luminance and the inset shows the current density *versus* voltage. (b) The current efficiency *versus* voltage and the inset is the electroluminescent spectra at 1000 cd/m^2. The ratio of TPD:PBD was fixed at 9:24.

being attached to different positions on the ligand phenyl ring of the emissive core, which in turn could give rise to a different film morphology. The fact that m-G1-Ir has a larger effective hydrodynamic radii is evidence of the difference in shape between the two materials [15].

Both the luminance and efficiency significantly increased as the dendrimer concentrations increased above the ratio of 6:9:24:61 [dendrimer:TPD:PBD:PVK (TPD:PBD:PVK = host)]. The peak luminance of 22,900 cd/m^2 (at 13 V), 27,000 cd/m^2 (at 14.5 V), and 22,380 cd/m^2 (at 14 V) was achieved for p-G1-Ir:PVK with blending ratios of 33:34, 13:54, and 6:61, respectively. The current efficiency was around 22–38 cd/A for the mixing ratios of dendrimer:PVK between 33:34 and 6:61, showing that the dendrimers can be used in rather high blending concentrations due to the uniform distribution in the emissive layer with less aggregation and self-quenching. The highest external quantum efficiency is 10.2% at 5 V with a brightness of 50.1 cd/m^2 for p-G1-Ir:PVK at ratio of 6:61. Such excellent dispersion in the polymer host is attributed to the good solubility of the dendrimers in comparison to small molecule iridium(III) complexes.

While the efficiency of device with a p-G1-Ir:PVK ratio of 6:61 reaches up to 40 cd/A, it drops rapidly as the voltage increases. In contrast, the devices with a p-G1-Ir:PVK ratio of 13:54 keeps a high efficiency at high luminance. In fact the ratio 13:54 of dendrimer:PVK was found to be the optimum ratio for both dendrimers in the host. For OLEDs with higher dendrimer concentrations, although the dispersion is still good, some level of self-quenching sets in causing a slight reduction in the efficiency.

The significance of the blade-coating method can be understood from the performance of the device fabricated by spin-coating. The concentration ratio of p-G1-Ir:PVK is 6:61. As shown in Fig. 2, the luminance and current efficiency are low for the device fabricated by spin-coating. The peak luminance of 14,980 cd/m^2 was achieved at 13.5 V, and the maximum current efficiency of 10.7 cd/A was achieved at 9.5 V. This inferior performance may result from the layer-to-layer dissolution while using spin-coating technique or due to a completely different film morphology being formed. The layer-to-layer dissolution can be prevent by adopting the blade-coating technique as described in previous work [10]. The need for the TFB layer is

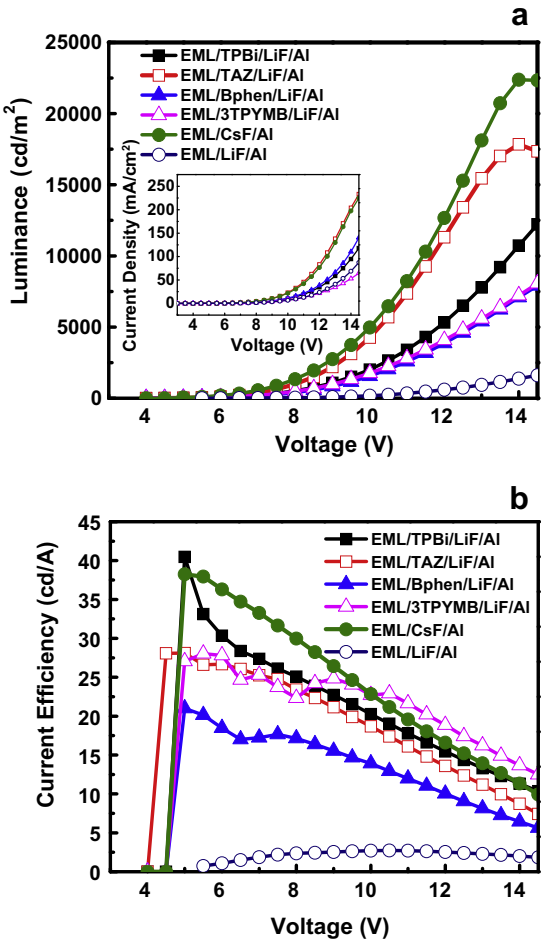

Fig. 4. The results of the multi-layer p-G1-Ir:PVK:TPD:PBD devices with ETL materials, TPBi, TAZ, Bphen, and 3TPYMB. (a) The luminance and the inset is the current density *versus* voltage. (b) The current efficiency *versus* voltage.

also shown in Fig. 2. For the device without TFB hole-transporting and electron-blocking layer, the peak luminance of 13,730 cd/m^2 was achieved at 13 V, and the maximum current efficiency of 11.5 cd/A was achieved at 9.5 V. The superior performance of the device with TFB layer results from the fact that more holes can be injected.

Fig. 4 shows the performance of the devices with TPBi, TAZ, Bphen, and 3TPYMB as the electron-transport layers and p-G1-Ir as the emitter. The ratio of dendrimer:TPD:PBD:PVK was 6:9:24:61. The results were compared with those without the electron-transport layer. Of the tri-layer devices, the device with TAZ shows the highest luminance as it and PBD have highest electron affinities [most stable Lowest Unoccupied Molecular Orbital (LUMO) energies] and this leads to more efficient electron injection into the light-emitting layer. However, the overall efficiency of TAZ devices is slightly lower than those containing TPBi. The device that had a LiF/Al cathode had a maximal efficiency of 40 cd/A (at 5 V with external quantum efficiency = 10.8% and brightness of 19 cd/m^2) and maximal luminance of 17,840 cd/m^2 (at 14 V). This difference probably arises from the fact that while the TAZ has the higher electron affinity it is a poorer hole blocking material than TPBi (see energy diagram Fig. 1b). In general the electron-transport layer in combination with LiF/Al cathode shows similar performance to devices with CsF/Al cathode but the latter devices tend to be less stable to the moisture. Without the electron-transport layer, the LiF/Al cathode has poorer electron injection capability and this may be due to a poor metal/organic interface leading to relatively low efficiencies (Fig. 4). The blade-coated layer of the electron transport materials therefore has a similar effect as with the equivalent vacuum deposited layers. Importantly, there is no dissolution of the emissive layer observed while blade coating the electron-transport layer.

4. Conclusion

In conclusion, we demonstrate that the good solubility of phosphorescent dendrimer emitters allows the formation of a dispersion of the dendrimers in a polymer host. The uniform dispersion enabled OLEDs with high efficiency and luminance to be achieved with a wide range of emitter concentrations because of low level of intermolecular quenching of the phosphorescence. The good compatibility of the phosphorescent dendrimers and the polymer host indicates that it is crucial to add functional groups to enhance the solubility when designing solution processable triplet emitters for use in blends. Importantly, all solution processed multi-layer OLEDs without layer-to-layer dissolution can be fabricated using the blade-coating technique. Blade-coating phosphorescent dendrimers show promise for the development of large-area and low-cost lighting emitting applications.

Acknowledgements

This work was supported by the National Science Council of the Republic of China (NSC NO. 97-3114-M-009-002, NO. 97-2628-M-009-016) and Professor Paul L. Burn is recipient of an Australian Research Council Federation Fellowship (Project Number FF0668728).

References

[1] S.R. Forrest, Nature 428 (2004) 911.
[2] M.A. Baldo, D.F. O'Brien, Y. You, A. Shoustikov, S. Sibley, M.E. Thompson, S.R. Forrest, Nature 395 (1998) 151.
[3] C. Adachi, M.A. Baldo, M.E. Thompson, S.R. Forrest, J. Appl. Phys. 90 (2001) 5048.
[4] M. Ikai, S. Tokito, Y. Sakamoto, T. Suzuki, Y. Taga, Appl. Phys. Lett. 79 (2001) 156.
[5] S.-C. Lo, P.L. Burn, Chem. Rev. 107 (2007) 1097.
[6] P.L. Burn, S.-C. Lo, I.D.W. Samuel, Adv. Mater. 19 (2007) 1675.
[7] S.-C. Lo, N.A. Male, J.P.J. Markham, S.W. Magennis, P.L. Burn, O.V. Salata, I.D.W. Samuel, Adv. Mater. 14 (2002) 975.
[8] S.-C. Lo, R.E. Harding, S.G. Stevenson, R.N. Bera, P.L. Burn, I.D.W. Samuel, Adv. Funct. Mater. 18 (2008) 3080.
[9] G. Zhou, W.Y. Wong, B. Yao, Z. Xie, L. Wang, Angew. Chem. Int. Ed. 46 (2007) 1149.
[10] S.R. Tseng, H.F. Meng, K.C. Lee, S.F. Horng, Appl. Phys. Lett. 93 (2008) 153308.
[11] X.H. Yang, D.C. Muller, D. Neher, K. Meerholz, Adv. Mater. 18 (2006) 948.
[12] X.H. Yang, D. Neher, Appl. Phys. Lett. 84 (2004) 2476.
[13] J.P.J. Markham, S.-C. Lo, S.W. Magennis, P.L. Burn, I.D.W. Samuel, Appl. Phys. Lett. 80 (2002) 2645.
[14] E.B. Namdas, T.D. Anthopoulos, I.D.W. Samuel, M.J. Frampton, S.-C. Lo, P.L. Burn, Appl. Phys. Lett. 86 (2005) 161104.
[15] S.-C. Lo, E.B. Namdas, P.L. Burn, I.D.W. Samuel, Macromolecules 36 (2003) 9721.
[16] J.P.J. Markham, I.D.W. Samuel, S.-C. Lo, P.L. Burn, M. Weiter, H. Bassler, J. Appl. Phys. 95 (2004) 438.
[17] S.-C. Lo, T.D. Anthopoulos, E.B. Namdas, P.L. Burn, I.D.W. Samuel, Adv. Mater. 17 (2005) 1945.
[18] T.D. Anthopoulos, J.P.J. Markham, E.B. Namdas, J.R. Lawrence, I.D.W. Samuel, S.-C. Lo, P.L. Burn, Org. Electron. 4 (2003) 71.
[19] S.A. Choulis, V.E. Choong, M.K. Mathai, F. So, Appl. Phys. Lett. 87 (2005) 113503.
[20] J.S. Kim, R.H. Friend, I. Grizzi, J.H. Burroughes, Appl. Phys. Lett. 87 (2005) 023506.

Table 1
Summary of the outcoupling efficiency and conditions of the simulation in the literature.

Groups (or authors)	OCEs, % (maximum)	Condition
Adachi et al. [1]	22	Under the fixed thickness of organic and ITO layers
Tessler [4]	20	Under the fixed thickness of organic and ITO layers
Ziebarth and McGehee [5]	36 (x = 75 nm)	Glass/ITO (150 nm)/PEDOT (80 nm)/Polymer(x)/Ca (5 nm)/Ag (50 nm)
	52 (x = 250 nm)	Only the thickness of the polymer layer was varied. Considered only the emission from dipoles oriented along the plane (TE mode)
Smith et al. [6]	25.8	Glass/ITO (100 nm)/dendrimer based on Ir-G1 (145 nm)/Al
	25.8	Glass/ITO (100 nm)/Alq_3 (130 nm)/Al
	33.7	Glass/ITO (100 nm)/MEH-PV (110 nm)/Al with preferred dipole orientation parallel to the plane (TE mode)
Lin et al. [7]	22	Under the fixed structure except the thickness of HTL
Mulder et al. [8]	30	Glass/ITO (160 nm)/PEDOT (30 nm)/TPD (50 nm)/Mcp:Firpic (6%, 20 nm)/BCP (40 nm)/LiF/Al (100 nm). Under the fixed thickness of all organic layers and the ITO layer
Celebi et al. [9]	22	Glass/ITO/PEDOT/TPD (50 nm)/Alq_3 (20 nm)/BCP (50 nm)/Mg:Ag (100 nm)/Ag (20 nm)
Krummacher et al. [10]	20	Glass/ITO (115 nm)/HTL (203 nm)/EBL (10 nm)/EML (7 nm)/HBL (10 nm)/ETL(x)/Ag (200 nm). Only the thickness of the ETL was varied
	20	Glass/ITO (140 nm)/PEDOT:PSS (30 nm)/TPD (80 nm)/Alq_3(x)/Ca (15 nm)/Al (100 nm) Only the thickness of the Alq_3 was varied
Nowy et al. [11]	23.0	Air/ITO (50 nm)/Alq_3 (160 nm)/Ca (15 nm)/Al
	25.8	Air/ITO (50 nm)/Alq_3 (160 nm)/Ag (similar structure with top emission device)
Our research	32.8	Systematic variation of the thickness of the ITO and the organic layer, and the location of emission zone

the OCEs of the conventional OLEDs, the microcavity structure has not been systematically varied to cover all possible states such as the position of the emission zone and the thicknesses of the ITO and organic layers. The analyses were done with either fixed thicknesses of both the ITO and organic layers [1,4,9] or with a fixed ITO thickness [6,7,10,11]. Especially, the thickness of the ITO layer was fixed in all the analyses because the effect of the thickness of the ITO layer on OCEs has not been considered in previous works.

In this paper, we systematically varied the location of the emission zone and the thicknesses of the organic layer and the ITO layer independently to calculate the maximum OCE in bottom emission OLEDs. This analysis will demonstrate that maximum outcoupling efficiencies over 27% and 30% are achievable if thin ITO layers in the range of 50–70 nm and 50–100 nm are used for blue and green phosphorescent OLEDs, respectively. Even higher efficiencies of 29% for blue and 31.6% for green can be obtained if we use thicker organic layers supporting two antinodes suggesting that phosphorescent OLEDs can have much higher external quantum efficiency than 20%.

To investigate the OCE of bottom emission OLEDs, a few assumptions are made. First, the device has a layered structure and is modeled as a simple one dimensional (1D) weak microcavity consisting of a thick reflective cathode, an organic layer, an ITO layer and a semi-infinite glass as shown in Fig. 1. Most efficient OLEDs have multiple organic layers consisting of the hole injection, hole transporting, emitting, electron blocking, electron transporting and electron injection layers. Accounting for all the layers in the calculation of the OCE requires too much computational time and is not necessary because the refractive indices of organic semiconductors are not significantly different for the materials commonly used in the devices. Therefore, the simplification of the multiple layers by a single emission layer does not degrade this optical calculation at all. Second, the dipole radiators are

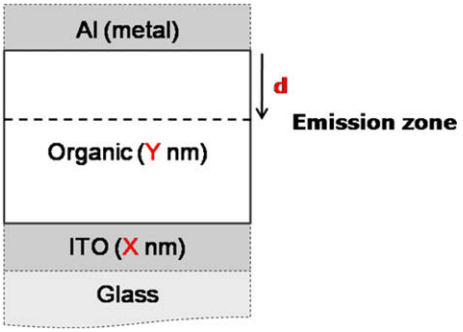

Fig. 1. Schematic diagram of the device structure for optical modeling. Parameters of x, y, and d are the thickness of ITO and the organic layer, and the position of emission zone, respectively.

imbedded in the layered structure as a sheet and their orientations are randomly distributed. Random distribution of the dipoles is in good agreement with experimental results for amorphous small molecular systems [13,14,19–23,28]. The sheet dipole approximation is also not a limitation of this calculation. Any distribution of excitons in a real device can be easily accounted for by the weighted integration of the calculated OCEs based on the sheet dipole approximation. Third, the intrinsic PL quantum yields of the phosphorescent dyes are assumed to be 100%. This assumption is reasonable for Ir(p-py)$_3$ in CBP or Firpic in mCP [1,29].

In the classical theory of radiation, the normalized damping rate of oscillating electric dipoles is proportional to the dissipated power of the dipoles [30]. Therefore, we calculated the normalized damping rate of the dipole radiators in the 1D microcavity as a function of the wavelength, the thicknesses of the organic and ITO layers, and the position of the emission zone. The total radiated power from the dipole radiators at each wavelength is described in detail elsewhere [17–19,22] and is given by

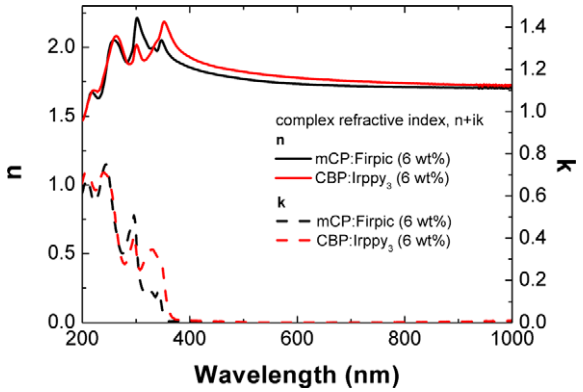

Fig. 2. Complex refractive indices spectra of Firpic doped mCP layer for blue (black line), and 6 wt.% Ir(ppy)$_3$ doped CBP for green (red line). Refractive indices were measured by a spectroscopic ellipsometer. (For interpretation of the references to colour in this figure legend, the reader is referred to the web version of this article.)

$$R(\lambda, y, d) = \int_0^{\infty} \mathrm{Re}[S(u, \lambda, x, y, d)]du \tag{1}$$

where $R(\lambda, t, d)$ is the radiated power from a dipole radiator which is a function of the wavelength λ, the ITO thickness x, the thickness of organic layer y and the distance of the emission zone from the cathode d. S is the electric field which is affected by an optical environment. Re[S] is the real part of S, representing the normalized damping rate, and u is the parallel component of the wavenumber k to the emissive layer. Detailed procedure of the derivation of Re[S] can be found in Refs. [21–23,26].

The electric field coupled to various optical modes can be classified by the parallel component of the wavenumber u. If $0 \leqslant u \leqslant k_{air}$ the electromagnetic field will be coupled to the radiation mode escaping to the air where k_{air} is the wavenumber of the air. The outcoupling efficiency or the light extraction efficiency, η_{out}, which is defined as the ratio of the surface emitted light to the total emitted light from the dipole radiators is described as follows:

$$\eta_{out}(x, y, d) = \frac{\int_{400}^{700} I_{PL}(\lambda) \int_0^{k_{air}} \mathrm{Re}[S(u, \lambda, x, y, d)]du d\lambda}{\int_{400}^{700} I_{PL}(\lambda) d\lambda} \Bigg/ \frac{\int_{400}^{700} I_{PL}(\lambda) \int_0^{\infty} \mathrm{Re}[S(u, \lambda, x, y, d)]du d\lambda}{\int_{400}^{700} I_{PL}(\lambda) d\lambda} \tag{2}$$

where I_{PL} is the PL spectrum of the emissive layer under consideration in free space.

We selected the blue and green PhOLEDs for the analyses where iridium(III) bis[(4,6-difluorophenyl)pyridinato-N,C$^{2'}$]picolinate (Firpic) doped in *N*,*N*′-dicarbazolyl-3,5-benzene (mCP) and *fac*-tris(2-phenylpyridine) iridium

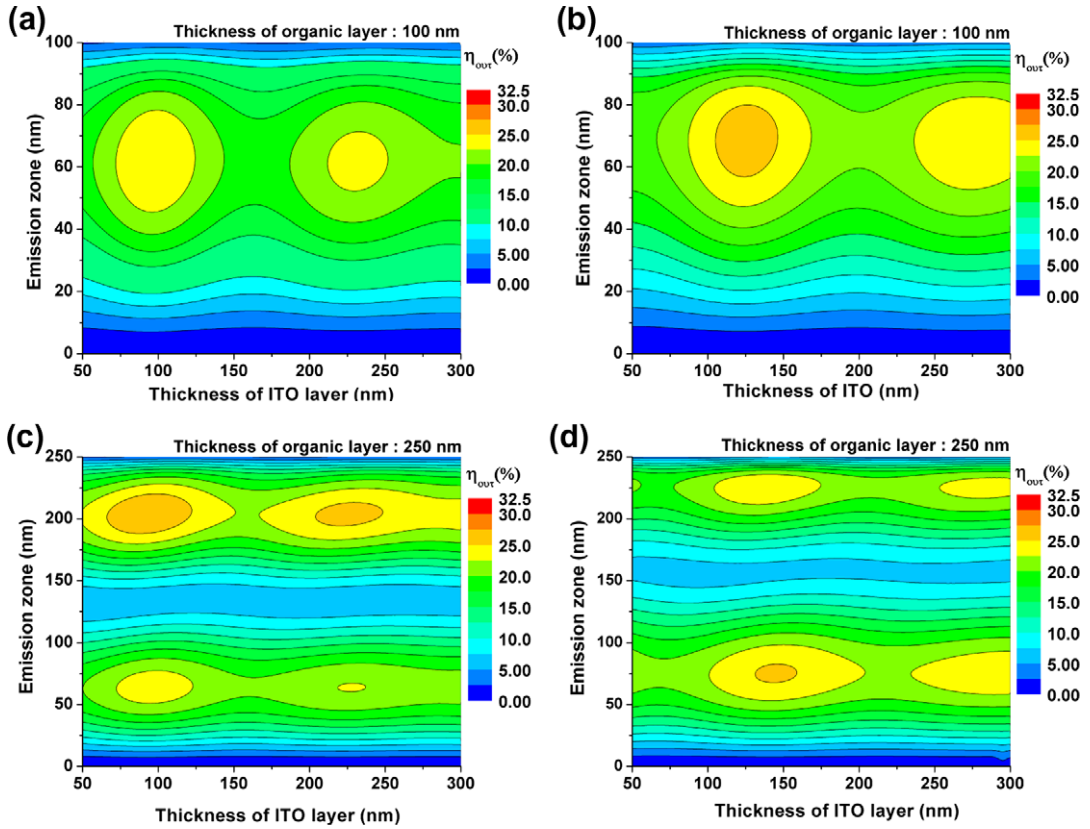

Fig. 3. Contour plots of outcoupling efficiency as a function of thickness of ITO and emission zone for selective thickness of organic layers: (a) 100 nm for blue, (b) 100 nm for green, (c) 250 nm for blue and (d) 250 nm for green. (For interpretation of the references to colour in this figure legend, the reader is referred to the web version of this article.)

($Ir(ppy)_3$) doped in *N*,*N*′-dicarbazolyl-4–4′-biphenyl (CBP) were used as the emitting layer, respectively. Both dopants are known to have almost 100% PL quantum yield [1,28]. Doping concentration was 6 wt.% in the organic layers. The complex refractive indices of the organic layers for the simulation were measured by a spectroscopic ellipsometry and are shown in Fig. 2 [31]. The refractive index of $Ir(ppy)_3$ in CBP is larger than Firpic in mCP in the visible region. The refractive indices of ITO layer and Al were taken from Refs. [32–34].

The calculated OCEs of the OLEDs are represented as contour plots in Fig. 3 as functions of ITO thickness and the location of emission zone for the blue and green OLEDs with two different thicknesses of the organic layers. The OCEs are significantly changed as the location of the emission zone changes. The OCEs increase from zero at $d = 0$ due to the quenching by the metal layer to the maximum at the antinode position of the electric field coming from the interference effect. Further movement of the emission zone from the metal cathode reduces the OCE due to the reduced electric field and increased interaction with ITO. If the organic layer is much thicker to support the second antinode as shown in Fig. 3(c) and (d), the distribution of OCEs has two peaks now. Proper selection of the thickness of the organic layers will result in higher OCEs at the second antinode than the first antinode because it is farther apart from the metal electrode to reduce the dipole-metal interaction.

The OCEs are also affected by the thickness of the ITO even though it is less extent than the position of the emission zone. The OCEs oscillate from 20% to 25% with increasing ITO thickness when the emission zone is located at the antinode position. This oscillation is coming from the interference effect of the reflected light from the ITO layer. The effect of the ITO thickness is less than the effect of the position of the emission zone because the reflection by the ITO layer is smaller than the reflection of the metal cathode. The maximum OCEs are obtained when the structure satisfies the resonance condition of the emitted light. When the thickness of the organic layer is 100 nm, which is a thickness commonly used in OLEDs, the maximum OCEs are 25.6% and 26.1% for blue and green OLEDs, respectively. It is worthwhile to note that maximum OCEs are obtained when the thicknesses of the ITO layer are 95 and 125 nm for blue and green OLEDs, respectively, if the thickness of the organic layer is 100 nm. The thicknesses are thinner than the widely used thickness of 140–160 nm in OLEDs. OLEDs with a 100 nm thick organic layer and 140–160 nm thick ITO layers result in maximum OCEs of 20 ± 2% for blue and 22 ± 2% for green which are consistent with previous theoretical results [1,15].

The maximum OCE for a given ITO thickness and an organic layer thickness can be obtained by varying the emission zone in the device. By repeating the procedure for different thicknesses of the ITO and organic layers, we can now get the contour plots of the maximum OCEs as functions of the thickness of the ITO layer and the thickness of the organic layer shown in Fig. 4(a) and (b) for the blue and green PhOLEDs, respectively. These figures clearly show that the OCEs in normal bottom emission OLEDs can be as high as 30% in green OLEDs and 27% in blue OLEDs if the first antinode is used, e.g., when the thickness of the organic layer is thinner than 200 nm. OCEs over 30% can be achieved with an ITO layer thinner than 100 nm for the green OLED. The blue OLEDs require a thinner organic and ITO layer than the green OLEDs as expected. The ITO layer must be thinner than 80 nm to get the OCE over 26% from the blue OLED. The EQEs can be even higher if the emission zone is located in the second antinode in the thicker OLEDs because of the smaller coupling to surface plasmon polariton mode and evanescent field. EQEs of 29% and 31.6% are possible for the blue and green OLEDs, respectively. The parameters that achieve the maximum OCEs are summarized in Table 2. It must be noted that the high efficiencies are obtained by using much thinner ITO layers and thicker organic layers than normally used in OLEDs. In fact, most recent high efficiency

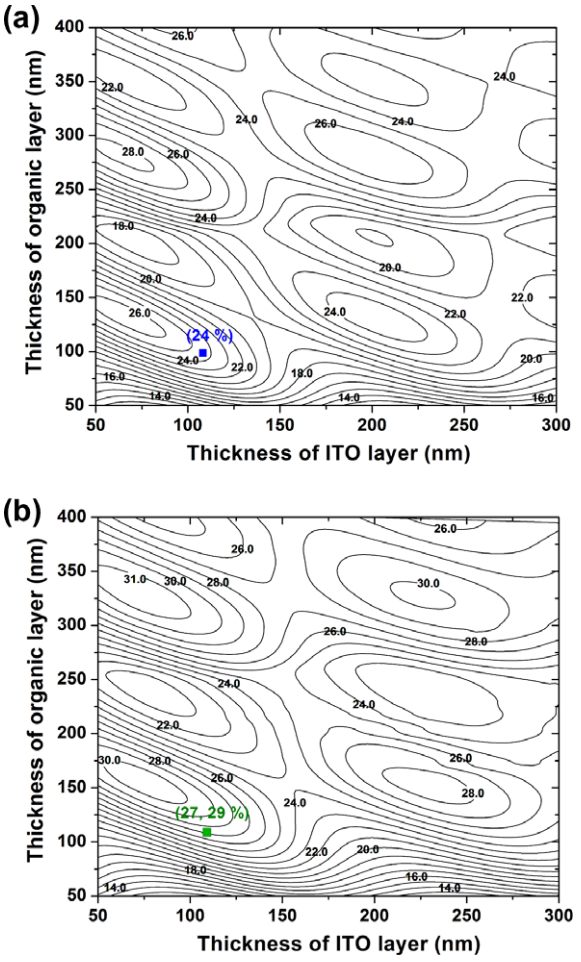

Fig. 4. Contour plot of the maximum outcoupling efficiency as a function of thickness of the organic and ITO layers where the position of the emission zone is varied within the organic layer to get the maximum outcoupling efficiency at given thicknesses of the organic and ITO layers: (a) blue and (b) green PhOLEDs [*Note:* The scatters in figures are the external quantum efficiencies referenced from published papers; Ref. [24] (green square in (b) (29% of EQE)), Ref. [25] (blue square in (a), and green square in (b) (27% of EQE))]. (For interpretation of the references to colour in this figure legend, the reader is referred to the web version of this article.)

Table 2
The values of the parameters achieving the maximum outcoupling efficiency for blue and green devices.

	1st antinode		2nd antinode	
	Blue	Green	Blue	Green
	27.3	30.4	28.9	31.6
Organic layer thickness (nm)	132	155	285	330
ITO thickness (nm)	67	75	65	75
Emission zone (nm)	68	75	207	242

OLEDs have adopted thinner ITOs ranging from 70 to 110 nm [24,25,27]. The EQEs of recent high efficiency OLEDs are compared to the calculated results in the figures. The experimental EQEs are very close to the maximum OCEs predicted by the analysis. These results indicate that the devices are well designed to satisfy the optical conditions for the location of the emission zone and the electron–hole balance.

Variation of the maximum OCEs through altering the thicknesses of the ITO layers can be easily understood by analyzing the coupling ratio of the dissipated power of the emitted light to various optical modes shown in Fig. 5 which are calculated along the ridge line of the first antinode in Fig. 4. There are discontinuities in the graphs when the ITO layer begins to support the waveguide mode (critical thickness for waveguiding in the ITO layer) so that the power dissipated in the organic and ITO layers shows rapid change at the expense of the surface plasmon polaritons mode at the thicknesses. It is clear that coupling to the glass substrate is almost constant if the ITO layer is thinner than the critical thickness of the ITO layer for waveguiding. Therefore, the variation of the OCEs is originated from the variation of the power dissipation to the organic, ITO and metal layers with the thickness of the ITO layer.

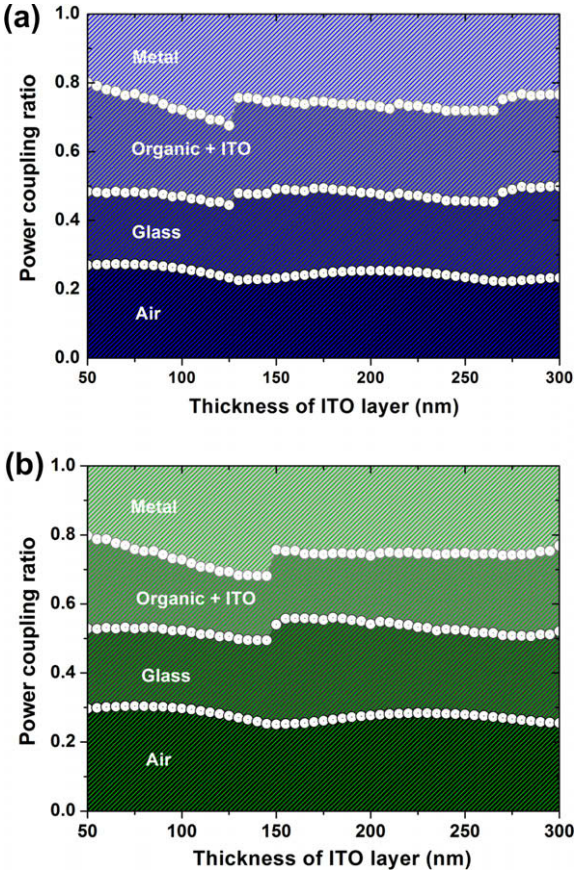

Fig. 5. Power coupling ratio of the dissipated power from emissive dipoles coupled to various optical modes for (a) blue and (b) green phosphorescent OLEDs. (For interpretation of the references to colour in this figure legend, the reader is referred to the web version of this article.)

In conclusion, we have systematically analyzed the outcoupling efficiencies of OLEDs. The green and blue phosphorescent OLEDs based on $Ir(ppy)_3$ doped CBP layer and Firpic doped mCP layer were used as examples, respectively. Emphasis was given to the effect of the thickness of the ITO layer on the OCEs. OCEs over 30–32% and 27–29% are possible for green and blue OLEDs, respectively, in contrast to the common belief of 20–22%. The high efficiencies are achievable with thinner ITO layers, 100 nm and 80 nm for green and blue PhOLED, respectively. If the ITO layer is 150 nm thick, the maximum OCE is about 22% which is consistent with previous results. Our theoretical OCEs are very much consistent with the external quantum efficiencies of recent high efficiency OLEDs. Even though our analysis was based on specific devices, the OCEs obtained in this analysis must be quite general for OLEDs since the refractive indices of organic semiconductors are not so much different from each other.

Acknowledgement

This study was supported by a Grant (2009K000069) from the Center for Nanoscale Mechatronics & Manufacturing, one of the 21st Century Frontier Research Programs and the WCU program (R31-2008-000-10075-0) funded by the Ministry of Education, Science and Technology.

References

[1] C. Adachi, M.A. Baldo, M.E. Thompson, S.R. Forrest, J. Appl. Phys. 90 (2001) 5048.
[2] C. Adachi, M.A. Baldo, S.R. Forrest, App. Phys. Lett. 77 (2000) 904.
[3] N.C. Greenham, R.H. Friend, D.D.C. Bradley, Adv. Mater. 6 (1994) 491.
[4] N. Tessler, Appl. Phys. Lett. 77 (2000) 1897.
[5] J.M. Ziebarth, M.D. McGehee, J. Appl. Phys. 97 (2005) 064502.
[6] L.H. Smith, J.A.E. Wasey, I.D.W. Samuel, W.L. Barnes, Adv. Funct. Mater. 15 (2005) 1839.
[7] C.L. Lin, T.Y. Cho, C.H. Chang, C.C. Wu, Appl. Phys. Lett. 88 (2006) 081114.
[8] C.L. Mulder, K. Celebi, K.M. Milaninia, M.A. Baldo, Appl. Phys. Lett. 90 (2007) 211109.
[9] K. Celebi, T.D. Heidel, M.A. Baldo, Opt. Express 15 (2007) 1762.
[10] B.C. Krummacher, S.N. Nowy, J. Frischeisen, M. Klein, W. Brutting, Org. Electron. 10 (2009) 478.
[11] S. Nowy, B.C. Krummacher, J. Frischeisen, N.A. Reinke, W. Brutting, J. Appl. Phys. 104 (2008) 123109.
[12] V. Bulović, V.B. Khalfin, G. Gu, P.E. Burrows, D.Z. Garbuzov, S.R. Forrest, Phys. Rev. B 58 (1998) 3730.
[13] M.-H. Lu, J.C. Sturm, Appl. Phys. Lett. 78 (2001) 1927.
[14] M.-H. Lu, J.C. Sturm, J. Appl. Phys. 91 (2002) 595.
[15] A. Chutinan, K. Ishihara, T. Asano, M. Fujita, S. Noda, Org. Electron. 6 (2005) 3.
[16] A. Badano, J. Kanicki, J. Appl. Phys. 90 (2001) 1827.
[17] R.R. Chance, A. Prock, R. Silbey, Adv. Chem. Phys. 37 (1987) 1.
[18] W.L. Barnes, J. Mod. Opt. 45 (1998) 661.

[19] J.A.E. Wasey, W.L. Barnes, J. Mod. Opt. 47 (2000) 725.
[20] C.C. Wu, C.L. Lin, P.Y. Hsieh, H.H. Chiang, Appl. Phys. Lett. 84 (2004) 3966.
[21] C.L. Lin, C.H. Chang, K.C. Tien, C.C. Wu, Appl. Phys. Lett. 90 (2007) 071111.
[22] W.I. Jung, S.Y. Kim, J.-J. Kim, J.-W. Kang, Chem. Phys. 355 (2009) 25 (PL).
[23] L.H. Smith, J.A.E. Wasey, W.L. Barnes, Appl. Phys. Lett. 84 (2004) 2986.
[24] D. Tanaka, H. Sasabe, Y.J. Li, S.J. Su, T. Takeda, J. Kido, Jpn. J. Appl. Phys. 46 (2006) L10.
[25] S.J. Su, T. Chiba, T. Takeda, J. Kido, Adv. Mater. 20 (2008) 2125.
[26] N. Chopra, J. Lee, Y. Zheng, S.H. Eom, J. Xue, F. So, Appl. Phys. Lett. 93 (2008) 143307.
[27] J. Lee, J.I. Lee, J.Y. Lee, H.Y. Chu, Org. Electron. 10 (2009) 1529.
[28] J.-S. Kim, P.K.H. Ho, N.C. Greenham, R.H. Friend, J. Appl. Phys. 88 (2000) 1073.
[29] Y. Kawamura, K. Goushi, J. Brook, J.J. Brown, H. Sasabe, C. Adachi, App. Phys. Lett. 86 (2005) 071104.
[30] K.G. Sullivan, D.G. Hall, J. Opt. Soc. Am. B 14 (1997) 1160.
[31] Refractive indices were measured by KRISS (Korea Research Institute of Standards and Science).
[32] R.A. Synowicki, Thin Solid Films 313–314 (1998) 394.
[33] Y.S. Jung, Thin Solid Films 467 (2004) 36.
[34] D.Y. Smith, E. Shiles, M. Inokuti, The optical properties of metallic aluminum, in: E.D. Palik (Ed.), Handbook of Optical Contents of Solids, Academic Press, 1985.

the inset of Fig. 1. Poly(3-hexylthiophene) (PAT6):6,6-phenyl-C_{61}-butyric acid methyl ester (PCBM):NaPc/FWCNT composites were obtained by mixing PAT6 and PCBM (weight ratio = 1:1) with NaPc/FWCNT in 1,2-dichlorobenzene. The photo-sensitive region was fabricated by spin-coating PAT6:PCBM:NaPc/FWCNT on indium tin oxide (ITO)-coated glass substrate followed by the deposition of Al contact layer by thermal evaporation.

A well-dispersed individual NaPc/FWCNT hybrid was observed in transmission electron microscopy (TEM, Fig. 1, Hitachi 8000). Organic molecules are densely attached on FWCNT by π–π stacking. The π–electronic interaction between NaPc and FWCNT facilitates packing NaPc fine crystallites onto the sidewall instead of columnar aggregates [11,12]. Thus, the rough organic layer prevents the formation of bundled nanotubes, which improves the solubility and processibility of FWCNT in organic solvents. A well-regulated microstructure is promisingly advantageous to electron transfer between NaPc and FWCNT.

The ultraviolet–visible–near-infrared (UV–vis–NIR) absorption spectra (SHIMADZU UV-3100FS) of (a) NaPc and (b) NaPc/FWCNT in tetrahydrofuran (THF) are shown in Fig. 2. NaPc solution exhibits a strong absorption band in UV region with a board shoulder from 600 to 900 nm centered at 705 nm stemming from Q bands of the annulation of benzene [13]. NaPc/FWCNT solution (Fig. 2b) shows a new shoulder at 1028 nm with the band edge at 1150 nm and a board band of NaPc molecules with the maximum at 701 nm. The red-shifted band in the near-infrared region is attributed to the conjugation extension and charge delocalization. The planar aromatic NaPc molecules were uncovalently adsorbed onto the sidewall of CNT with delo-

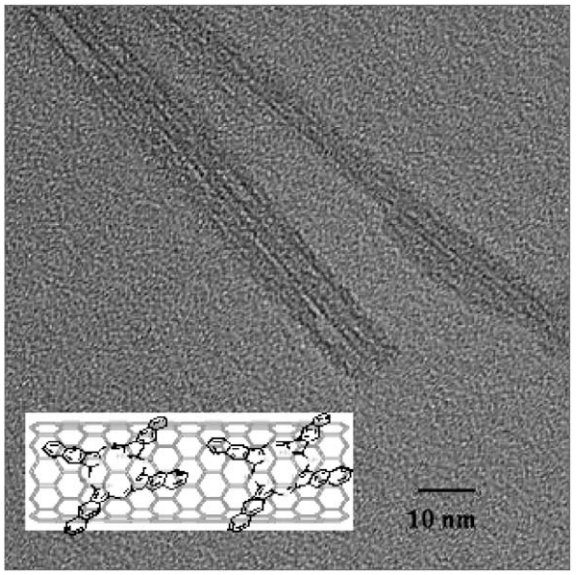

Fig. 1. TEM image of NaPc/FWCNT film. The inset shows NaPc packing onto the sidewall of a FWCNT by π–π stacking.

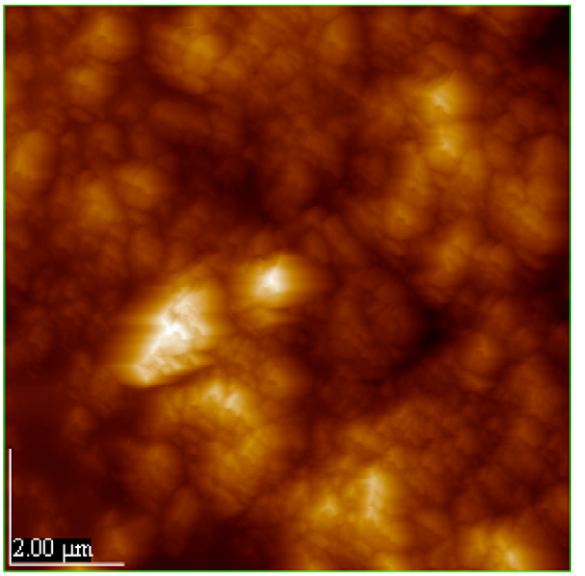

Fig. 3. AFM image of PAT6:PCBM:NaPc/FWCNT film.

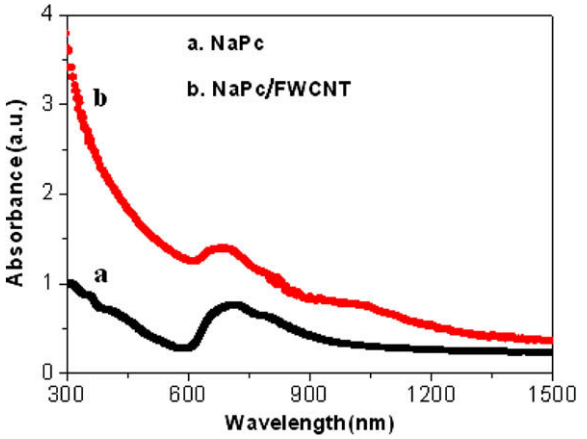

Fig. 2. UV–vis–NIR absorption spectra of (a) NaPc and (b) NaPc/FWCNT in THF.

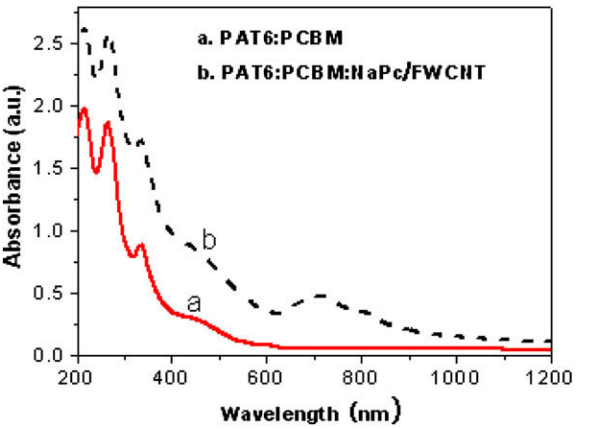

Fig. 4. UV–vis–NIR absorption spectra for (a) PAT6:PCBM film and (b) PAT6:PCBM:NaPc/FWCNT film.

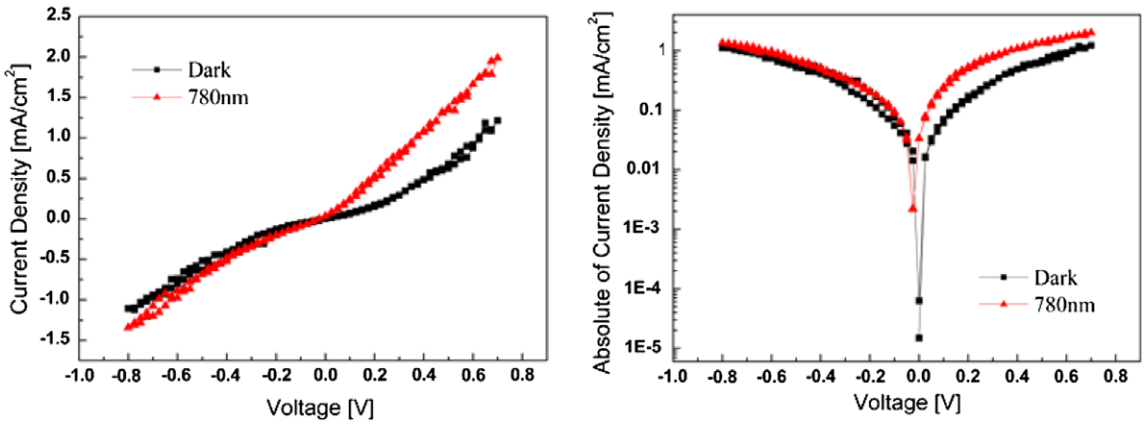

Fig. 5. *I–V* characteristics of devices using PAT6:PCBM:NaPc/FWCNT film as photo-sensitive region under dark and illumination at 780 nm.

calized π-conjugated system by π–π stacking. The red-shifted absorption in the electronic energy state with NaPc molecules in close proximity to the surface of FWCNT indicates the conjugated interaction between NaPc and FWCNT.

The surface morphology of PAT6:PCBM:NaPc/FWCNT film (∼150 nm, r.m.s. = 2.0–3.0 nm) was observed by atomic force microscopy (AFM, JEOL JSPM-5200). Fig. 3 shows a continuous film of low roughness without spherical crystallites or islands of aggregate. Compared with single NaPc or PCBM, this co-deposition produces significant changes film consistent with decreased intermolecular interaction of amorphous mixed film [11]. This microstructure greatly enlarges the donor–acceptor interface within the diffusion length of the exciton generation for charge dissociation.

Fig. 4 presents optical absorption spectra of (a) PAT6:PCBM and (b) PAT6:PCBM:NaPc/FWCNT films by spin-coating. PAT6:PCBM shows a strong absorption band in high energy region. Both two peaks at 280 and 340 nm are attributed to electronic transition of PCBM, and the shoulder centered around 440 nm stems from PAT6. PAT6:PCBM:NaPc/FWCNT film exhibits a board absorption band with a maximum of 710 nm and edge at around 1100 nm. This near-infrared absorption was assigned to the conjugated extension of NaPc/FWCNT. Our previous research founded that the device of ITO/NaPc-MWCNT-P3HT/Al exhibited nearly twice higher photocurrent in the near-infrared region (700–800 nm) than that without MWCNT due to efficient charge transfer and mobility [14]. The marked increase in the photocurrent and photovoltaic performance offers a great promise to detect near-infrared light.

Near-infrared optical response of ITO/PAT6:PCBM:-NaPc/FWCNT/Al device was investigated. *I–V* curve characteristic under dark and illumination at 780 nm (power density of 295 mW/cm^2) was obtained using an electrometer of Keithley 6514 with a DC power supply of Advantest R6145. The plot in Fig. 5 shows that the photocurrent of the devices increases at any voltage upon the illumination of near-infrared light at 780 nm due to efficient exciton absorption of PAT6:PCBM:NaPc/FWCNT film. Near-infrared optical response indicates that photo-generated charges induced by the creation and dissociation of carriers can be conducted to the reverse electrode leading to the evident photocurrent. Moreover, the magnitude of increase in photocurrent is higher than that of the bias amplitude. Uniform blending NaPc/FWCNT hybrid with P3HT:PCBM enable the exciton diffusion to the interface before the recombination and the continuous paths for photo-generated charge transport to the electrode forming the photocurrent. Field dependent dissociation of carriers at the interface results in the enhancement of photocurrent at high bias magnitude [15], because more carrier are pulled out leaving space for the dissociation, which, in contrast, is hindered by charge confinement at low bias. Illumination of NaPc/FWCNT hybrid using near-infrared light results in the generation of the enhanced photocurrent. Near-infrared optical response was attributed to efficient exciton absorption and charge transfer at the interface.

In conclusion, a NaPc/FWCNT hybrid was prepared by packing NaPc crystallites onto the sidewall by π–π stacking. Individual-dispersed NaPc/FWCNT is advantageous to charge transfer. A continuous PAT6:PCBM:NaPc/FWCNT film shown in AFM enlarges donor–acceptor interface. The near-infrared band of PAT6:PCBM:NaPc/FWCNT film with the edge at 1100 nm stems from the conjugation extension by π–π stacking. Devices exhibits the photocurrent illuminated by near-infrared light at 780 nm due to the efficient exciton absorption and charge transfer at the interface. Results offer a great potential to design a highly efficient NOD using CNT-conjugated dye hybrid.

Acknowledgments

This work was partly supported by the National Natural Science Foundation of China (No. 50873074) and the Key Project of Chinese Ministry of Education (No. 108029). Authors would like to thank Jie Liu group in the Department of Chemistry, Duke University for FWNT supply.

References

[1] F. Yang, S.R. Forrest, ACS Nano 2 (2008) 1022.

[2] L.C. Palilis, P.A. Lane, G.P. Kushto, B. Purushothaman, J.E. Anthony, Z.H. Kafafi, Org. Electron. 5 (2008) 747.
[3] J. Kalinowski, Opt. Mater. 30 (2008) 792.
[4] W.J. Shin, J.Y. Lee, J.C. Kim, T.H. Yoon, T.S. Kim, O.K. Song, Org. Electron. 9 (2008) 333.
[5] B.P. Rand, X.G. Xue, F. Yang, S.R. Forrest, Appl. Phys. Lett. 87 (2005) 233508.
[6] Y.Y. Feng, X.H. Ju, W. Feng, H.B. Zhang, Y.W. Cheng, J. Liu, A. Fujii, M. Ozaki, K. Yoshino, Appl. Phys. Lett. 94 (2009) 123302.
[7] Y.D. Park, J.A. Lim, J.A. Yunseok, M. Hwang, H.S. Lee, D.H. Lee, H.J. Lee, J.B. Baek, K. Cho, Org. Electron. 9 (2008) 317.
[8] J. Arranz-Andres, W.J. Blau, Carbon 46 (2008) 2067.
[9] M.S. Arnold, J.D. Zimmerman, C.K. Renshaw, X. Xu, R.R. Lunt, C.M. Austin, S.R. Forrest, Nano Lett. 9 (2009) 3354.
[10] Y.Y. Feng, H.B. Zhang, Y. Hou, T.P. McNicholas, D.N. Yuan, S.W. Yang, L. Ding, W. Feng, J. Liu, ACS Nano 2 (2008) 1634.
[11] P. Sullivan, S. Heutz, S.M. Schultes, T.S. Jones, Appl. Phys. Lett. 84 (2004) 1210.
[12] X.Q. Zhang, Y.Y. Feng, S.D. Tang, W. Feng, Carbon 48 (2010) 211.
[13] N. Kobayashi, S. Nakajima, H. Ogata, T. Fukuda, Chem. Eur. J. 10 (2004) 6294.
[14] W. Feng, Y. Li, Y.Y. Feng, J. Wu, Nanotechnology 17 (2006) 3274.
[15] J.A. Barker, C.M. Ramsdale, N.C. Greenham, Phys. Rev. B 67 (2003) 075205.

state and hence a net spin of 1/2 for $V(TCNE)_x$ [10]. Thus, the material can be described as a fully spin-polarized semiconductor. $V(TCNE)_x$ thus offers many of the advantages of the traditional organic semiconductors used in organic spintronics [11], but also include fully spin-polarized transport levels that should further aid both spin injection and transport. Hence, we propose a new hybrid organic spin valve design where $V(TCNE)_x$ is a spin-transporting *and* spin-filtering material sandwiched between two ferromagnetic (FM) metal contacts, see Fig. 1(a) and (b), in contrast to the previously proposed design where the $V(TCNE)_x$ layer functions as the soft magnet (spin detector) in Fig. 1(c) [12]. The new design makes use of the fully spin-polarized transport levels of $V(TCNE)_x$ that are expected to both enhance and preserve the injected spin polarization from the FM contacts. This spin valve could operate in a variety of modes with, e.g., a traditional soft and hard FM design or two identical FM contacts. The former situation would enable four different resistances to be obtained, see Fig. 1(b), whereas the latter would provide only the standard on/off functionality (Fig. 1(a)) but have the advantage of using only one FM metal in the fabrication process.

As spin injection and detection in a spintronic device occurs at the FM/organic/FM interfaces, the quality of those are of crucial importance. The organic film is generally fragile and depositing a metallic material on top of it often introduces substantial damage, making the contact poorly defined. The FM atoms (or clusters) might penetrate into the organic film and chemically react with the organic molecules [15]. The magnetic properties of the FM top contact is highly dependent on the roughness of the substrate [13], which is known to be rather high of an organic surface [14], and of course of the interaction with the substrate as well. Besides, the layer between the two FMs has to be thin enough so the spins do not flip before they reach the spin detector FM [3].

In this paper X-ray photoelectron spectroscopy (XPS) and near edge X-ray absorption fine structure spectroscopy (NEXAFS) results on the Ni/$V(TCNE)_x$ interface are reported in comparison with XPS results the Ni/TCNE interface model system.

2. Materials and methods

$V(TCNE)_x$ thin films (<100 Å) were prepared by a method based on physical vapor deposition, PVD [6]. The vanadium metal (purity 99.9%) was deposited using a portable Omicron® PVD source and were allowed to react with TCNE in room temperature, forming thin films on sputter-cleaned Au substrates. Thin films (~50 Å) of pristine TCNE were deposited on sputter-cleaned Au substrates at −160 °C. The base pressure in the chamber was in the high 10^{-10} mbar range and the pressure was in the low 10^{-8} mbar range during preparation of both types of films. Nickel was deposited by an Omicron® PVD source in small steps, ranging from a (sub)monolayer (~5 Å) to a multilayer (~20 Å).

The Ni/$V(TCNE)_x$ interface was studied *in situ* using XPS and NEXAFS (performed in the partial electron yield method) at beamline D1011 of the MAX-II storage ring at the synchrotron radiation facility MAX-lab in Lund, Sweden. The end-station is equipped with a SES-200 electron energy analyzer and the base pressure of the system is low 10^{-9} mbar. The energy calibration was performed such as errors of the monochromator and the analyzer were taken into consideration.

Preparation and XPS of Ni/TCNE as well as preparation and additional XPS of Ni/$V(TCNE)_x$ were performed in the

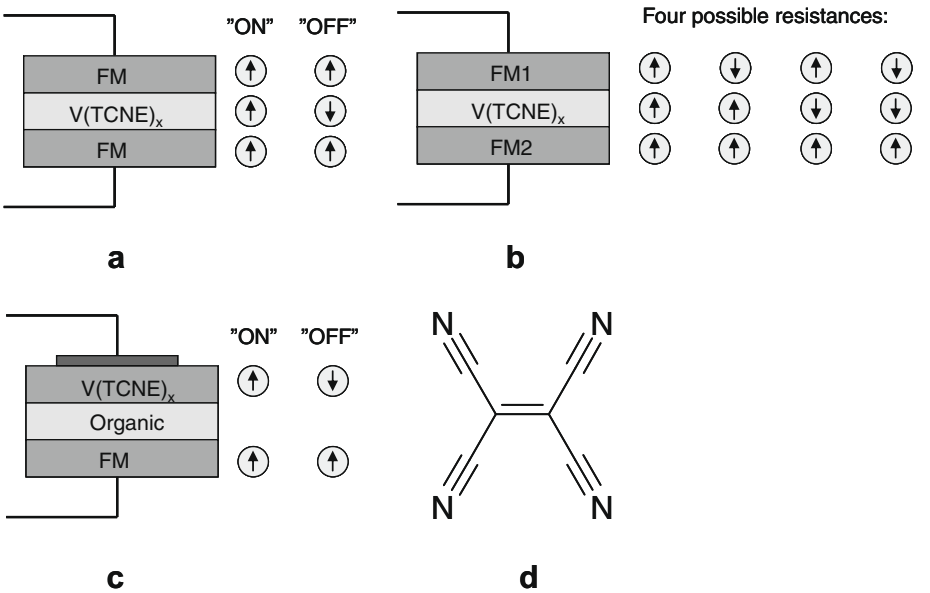

Fig. 1. Different spin valve designs and their possible resistances. (a) $V(TCNE)_x$ sandwiched between two identical FM contacts. (b) $V(TCNE)_x$ sandwiched between two different FM contacts. (c) $V(TCNE)_x$ and a FM contact sandwiching an organic semiconductor. Since $V(TCNE)_x$ is a semiconductor, a metallic contact on top of $V(TCNE)_x$ is needed. (d) The chemical structure of TCNE.

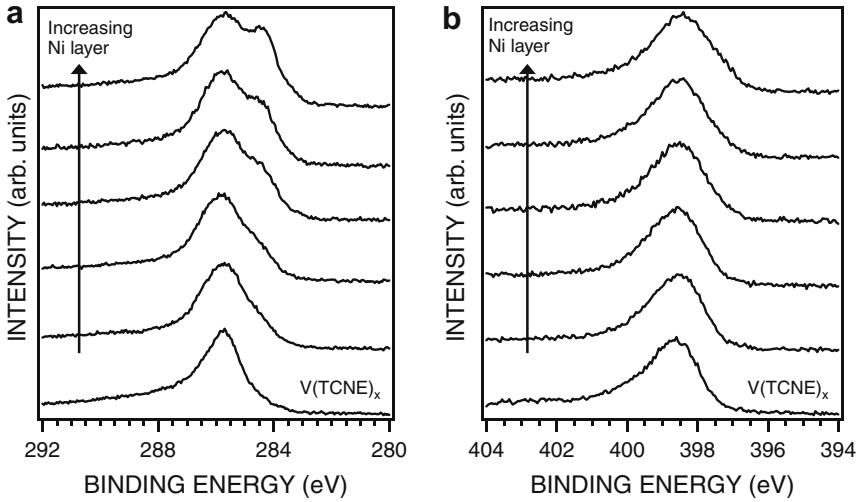

Fig. 2. Core levels upon increasing Ni deposition on $V(TCNE)_x$. The spectra are shifted with respect to pristine $V(TCNE)_x$. (a) C(1s), taken at photon energy 400 eV. (b) N(1s), taken at photon energy 720 eV.

home laboratory using a Scienta® ESCA 200 spectrometer. X-ray photoelectron spectroscopy (XPS) were performed using monochromatized Al(K_α) X-rays at $h\upsilon = 1486.6$ eV. The Ni/$V(TCNE)_x$ and Ni/TCNE interfaces were prepared under the same conditions in the home laboratory as in MAX-lab.

3. Results

3.1. Ni/$V(TCNE)_x$ interface

The features in the C(1s) spectrum (Fig. 2(a), bottom spectrum) of pristine $V(TCNE)_x$ has previously been assigned to a main peak located at 285.9 eV and a shake-up on its higher binding energy side [7]. Depending on preparation method there might also be a shoulder on the lower binding energy side (at ~284 eV) of the main peak, originating from residual by-products from the chemical reaction between the precursors [7]. For $V(TCNE)_x$ prepared by the PVD technique this shoulder is not present since only pure vanadium and TCNE are used in the film preparation [6]. However, an excess of metal upon PVD preparation gives a low binding energy feature, which was explained by metal binding to the vinyl bridge of TCNE [6,16]. Upon increasing Ni, a shoulder on the low binding energy side of C(1s) emerges. When the sample is tilted with respect to the detector, making the measurement more surface sensitive, the shoulder becomes even more pronounced (not shown here).

The N(1s) core level (Fig. 2(b), bottom spectrum) of pristine $V(TCNE)_x$ has its main feature at 398.5 eV. It origins from high to low binding energy from, a shake-up, vanadium-coordinated nitrogen and uncoordinated nitrogen, the latter responsible for the asymmetric N(1s) peak [7]. Given that the V^{2+} in $V(TCNE)_x$ is known to coordinate to six nitrogen atoms, some must remain uncoordinated since each TCNE molecule contains four nitrogen [17]. Upon increasing Ni coverage, the N(1s) spectra are modified on the lower binding energy side of the main peak. However, the changes are not as evident as for C(1s) and are seen only as a broadening of the N(1s) core level. When the sample is tilted, as described above, the broadening of the N(1s) core level becomes even more obvious. The V(2p) core level (spectra not shown here) remains unchanged upon increasing Ni.

The C K-edge of pristine $V(TCNE)_x$ (Fig. 3(a)) has its absorption onset located at 284 eV, originating from a transition to the LUMO of $V(TCNE)_x$ [9,18]. When Ni is deposited on $V(TCNE)_x$, the absorption onset decreases in intensity. The same occurs for the N K-edge (Fig. 3(b)), which has its absorption onset at 397 eV [18]. The V L-edge (not shown here) remains unchanged upon Ni deposition.

3.2. Ni/TCNE interface

The C(1s) core level of pristine TCNE is located at 287.4 eV (Fig. 4(a), bottom spectrum). The asymmetry of the C(1s) peak originates from cyano and vinyl carbon which differs with 0.4 eV only [19]. Upon increasing Ni deposition two new features appear on the lower binding energy side of C(1s). The new features are slightly more pronounced when making the measurements more surface sensitive, but their relative intensity is still significantly lower at the corresponding multilayer coverage compared to Ni/$V(TCNE)_x$, suggesting a more extended interface region for Ni/TCNE.

The N(1s) core level (Fig. 4(b)) of pristine TCNE is found at 400.1 eV. Since there is only one type of nitrogen present in TCNE, the peak is symmetric and well defined. Upon increasing the thickness of the Ni layer, a new feature on the low binding energy side appears. It mimics C(1s) in that the feature is more distinct when the measurements are performed more surface sensitive. The new features appear at the same deposition step for both C(1s) and N(1s) core levels.

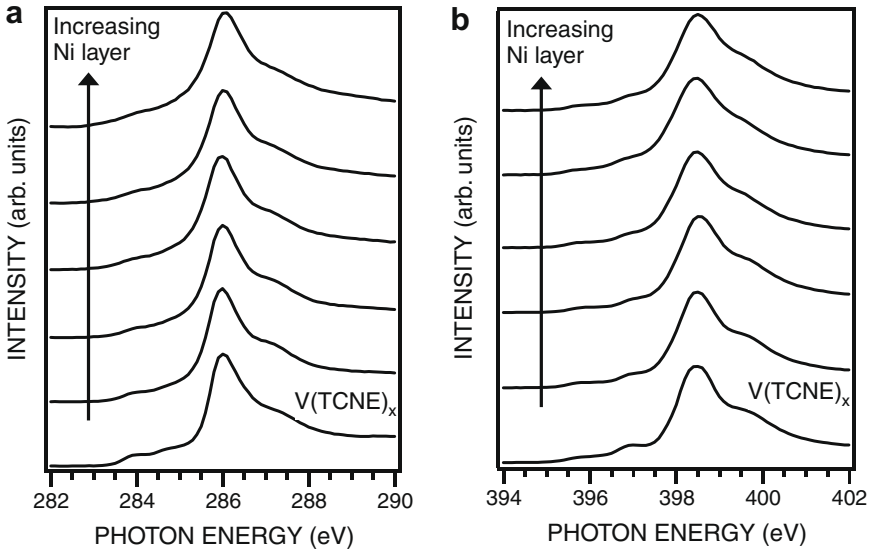

Fig. 3. NEXAFS spectra upon increasing deposition of Ni on $V(TCNE)_x$. (a) C K-edge. (b) N K-edge.

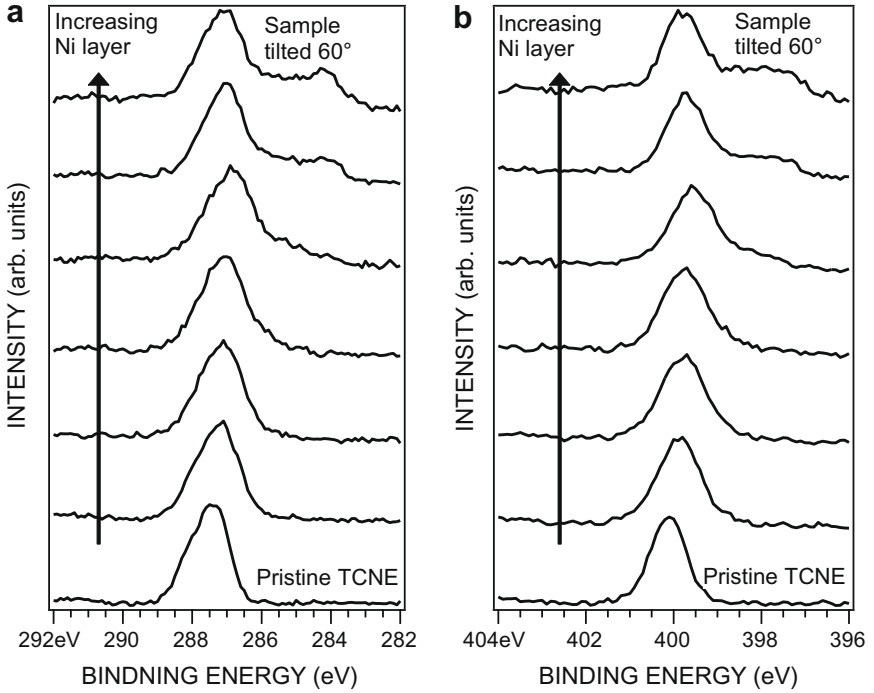

Fig. 4. Core levels upon increasing Ni deposition on pristine TCNE. The spectra are measured with respect to the Fermi level energy. (a) C(1s). (b) N(1s). The two topmost spectra of C(1s) and N(1s), respectively, are taken at the same Ni thickness, but the sample position with respect to the detector is different in order to make the measurements of the topmost of all spectra more surface sensitive.

4. Discussion

Both the XPS and NEXAFS results clearly show chemical interaction between Ni and TCNE. As the V(3d) core levels and V L-edge remain unaffected by Ni there is no vanadium-nickel interaction. Hence, the possible binding situations that can occur are cyano groups bonded to Ni, vinyl groups bonded to Ni, or a combination of both bonded to Ni. Studies of similar systems (π-conjugated organic materials with vinyl- and cyano groups forming interfaces with transition metal atoms) [20] showed that the transition metal preferentially bond to the cyano group but also that the vinyl group is an option. The Ni/TCNE system indicate an interaction where both the carbon and nitrogen atoms

simultaneously are affected by the Ni deposition and furthermore that two different new peaks appear in the C(1s) core level as the interface forms. This suggests that Ni attacks both the vinyl and the cyano groups of the TCNE molecule. The evolution of the C(1s) and N(1s) core levels upon Ni deposition for the $V(TCNE)_x$ is quite different, however. The C(1s) core level shows only one strong new peak appearing with a weak low binding energy shoulder upon Ni deposition. The N(1s) core level undergoes a broadening but does not display the new extended low-bonding energy feature of Ni/TCNE. This suggests that the Ni interaction with $V(TCNE)_x$ occurs mainly at the vinyl linkage of TCNE. The likely explanation for the difference is that most of the cyano groups of $V(TCNE)_x$ are coordinated to vanadium ions and hence not available as reaction sites. The distinct peak closest to the original C(1s) core level feature in Figs. 2(a) and 4(a) are thus assigned to vinyl carbon – nickel bonds and the weak shoulder in Fig. 2(a) (second new peak in Fig. 4(a)) are assigned to cyano group – nickel bonds, the latter producing the new low binding energy feature in the N(1s) core level spectra of Fig. 4(a). The evidence for lesser Ni diffusion into the $V(TCNE)_x$ as compared to TCNE is likely an affect of the compactness of the $V(TCNE)_x$ films obtained from PVD fabrication [6].

The Ni induced disruption of the vinyl linkage (and non-coordinated cyano groups) greatly modifies the LUMO of $V(TCNE)_x$ (as evident from the sharp decrease in intensity of the C and N K-edge absorption edges). This will increase the electron injection barrier as well as degrade the magnetic property of the interface region. Hence, a Ni/$V(TCNE)_x$ contact, and in extension probably any FM transition metal contact, is not optimal for use in a spin valve based on $V(TCNE)_x$. In conventional organic electronics, inserting a buffer layer between the top contact and the organic layer has been widely adopted in order to eliminate the risk of chemical interaction between the layers and hence improve the device performance [21,22]. This approach has recently successfully been adopted in spintronics devices, as well [23]. The results above indicate that a buffer layer between $V(TCNE)_x$ and Ni should be employed in design and fabrication of devices based on $V(TCNE)_x$.

5. Conclusions

In this paper a new hybrid organic spin valve design, i.e. FM/$V(TCNE)_x$/FM, is proposed, where the semiconducting $V(TCNE)_x$ layer delivers both spin-transporting *and* spin-filtering functionality. The electronic structure of the Ni/$V(TCNE)_x$ interface was investigated by means of XPS and NEXAFS and the results were interpreted together with XPS studies of the Ni/TCNE model system. $V(TCNE)_x$ and Ni interact chemically at the interface and both the cyano (that are not coordinated to V) and the vinyl groups participating in the reaction while vanadium remains unaffected. The interface region is fairly abrupt with no significant Ni diffusion into the $V(TCNE)_x$. The disruption of the vinyl linkage (and non-coordinated cyano groups) greatly modify the former LUMO of $V(TCNE)_x$ which will increase the electron injection barrier as well as degrade the magnetic network at the surface. These results indicate the need for a buffer layer between $V(TCNE)_x$ and Ni, and in extension most likely for any FM contact in the FM/$V(TCNE)_x$ structure.

Acknowledgements

The Surface Physics and Chemistry division is supported by the Swedish Research Council (Project Grant and Linneus Center) and the Knut and Alice Wallenberg Foundation.

References

[1] S.A. Wolf, D.D. Awschalom, R.A. Buhrman, J.M. Daughton, S.V. Molnár, M.L. Roukes, A.Y. Chtelkanova, D.M. Treger, Science 294 (2001) 1488.
[2] S.A. Wolf, D. Treger, A. Chtchelkanova, MRS Bullet. 31 (2006) 400.
[3] W.J.M. Naber, S. Faez, W.G. van der Wiel, J. Phys. D: Appl. Phys. 40 (2007) R205.
[4] A.J. Epstein, MRS Bullet. 28 (2003) 492.
[5] J.M. Manriquez, G.T. Yee, R.S. McLean, A.J. Epstein, J.S. Miller, Science 252 (1991) 1415.
[6] E. Carlegrim, A. Kanciurzewska, P. Norblad, M. Fahlman, Appl. Phys. Lett. 92 (2008) 163308.
[7] C. Tengstedt, M.P. de Jong, A. Kanciurzewska, E. Carlegrim, M. Fahlman, Phys. Rev. Lett. 96 (2006) 057209.
[8] M.P. de Jong, C. Tengstedt, A. Kanciurzewska, E. Carlegrim, W.R. Salaneck, M. Fahlman, Phys. Rev. B 75 (2007) 064407.
[9] E. Carlegrim, A. Kanciurzewska, M.P. de Jong, C. Tengstedt, M. Fahlman, Chem. Phys. Lett. 452 (2008) 173.
[10] J.B. Kortright, D.M. Lincoln, R.S. Edelstein, A.J. Epstein, Phys. Rev. Lett. 100 (2008) 257204.
[11] V.A. Dediu, L.E. Hueso, I. Bergenti, C. Taliani, Nat. Mater. 8 (2009) 707.
[12] A.J. Epstein, V.N. Prigodin, Polymer-, organic-, and molecular-based spintronic devices, US patent application 20030001154, 2003.
[13] I. Bergenti, A. Riminucci, E. Arisi, M. Murgia, M. Cavallini, M. Solzi, F. Casoli, V. Dediu, J. Magn. Magn. Mater. 316 (2007) 987.
[14] F. Zhang, Z. Xu, D. Zhao, S. Zhao, W. Jiang, G. Yuan, D. Song, Y. Wang, X. Xu, J. Phys. D 40 (2007) 4485.
[15] Y.Q. Zhan, M.P. de Jong, F.H. Li, V. Dediu, M. Fahlman, W.R. Salaneck, Phys. Rev. B 78 (2008) 045208.
[16] P. Bhatt, A. Kanciurzewska, E. Carlegrim, M. Kapilashrami, L. Belova, K.V. Rao, M. Fahlman, J. Mater. Chem. 19 (2009) 6610.
[17] D. Haskel, Z. Islam, J. Lang, C. Kmety, G. Srajer, K.I. Pokhodnya, A.J. Epstein, J.S. Miller, Phys. Rev. B 70 (2004) 054422.
[18] E. Carlegrim, B. Gao, A. Kanciurzewska, M.P. de Jong, Z. Wu, Y. Luo, M. Fahlman, Phys. Rev. B 77 (2008) 1.
[19] G. Beamson, D. Briggs, High Resolution XPS of Organic Polymers, Wiley, New York, 1992.
[20] M. Fahlman, W.R. Salaneck, S.C. Moratti, A.B. Holmes, J.L. Brédas, Chem. Eur. J. 3 (1997) 286.
[21] L.S. Hung, C.W. Tang, M.G. Mason, Appl. Phys. Lett. 70 (1997) 152G.
[22] G. Greczynski, M. Fahlman, W.R. Salaneck, J. Chem. Phys. 114 (2001) 8628.
[23] V. Dediu, L.E. Hueso, I. Bergenti, A. Riminucci, F. Borgatti, P. Graziosi, C. Newby, F. Casoli, M.P. de Jong, C. Taliani, Y. Zhan, Phys. Rev. B 78 (2008) 115203.

present study, we investigate the device characteristics of OFETs with Au electrodes modified with SAMs of 1-alkanethiol molecules, and show that such OFETs exhibit anomalous hysteretic output characteristics. The hysteresis can be reasonably explained by the structural change of the SAMs, which is caused by the application of an electric field parallel to the alkyl chain of the SAM molecules. This result implies the realization of the electrical detection of electrically-stimulated SAM switching, and should provide a useful contribution toward the development of molecular switches.

2. Experimental details

About 50 nm thick Au source/drain electrodes with 5 nm thick adhesion layers of Cr were formed on a highly-doped Si substrate covered with a 400 nm thick thermal oxide layer. Prior to electrode formation, the substrate surface was treated to impart hydrophobicity by a conventional hexamethyldisilazane treatment [6]. The substrate with formed electrodes was then submerged into a 0.01 M ethanol solution of 1-alkanethiol to form SAMs on the Au electrodes. After the SAM formation, the substrate was rinsed with pure ethanol and ultrasonicated for 1 min to desorb physisorbed 1-alkanethiol molecules on the SAMs. The molecules forming the semiconductor channel of the OFET were then deposited through a metal shadow mask. Although electrical shorts in SAMs are often formed upon vapor deposition of metals onto SAMs [7], a soft molecular layer deposited onto the SAM-modified electrode can avoid such damage in this study. The constructed device (Fig. 1) had a channel length of 30 μm and a channel width of 3 mm. FET characteristics were measured at room temperature under dark, high vacuum conditions.

C_{60} and pentacene molecules were used for the semiconductor channels. Both n-type C_{60} FETs and p-type pentacene FETs exhibited similar results. Although all the experimental results presented were obtained using C_{60} FETs, the discussion is also valid for hole transport.

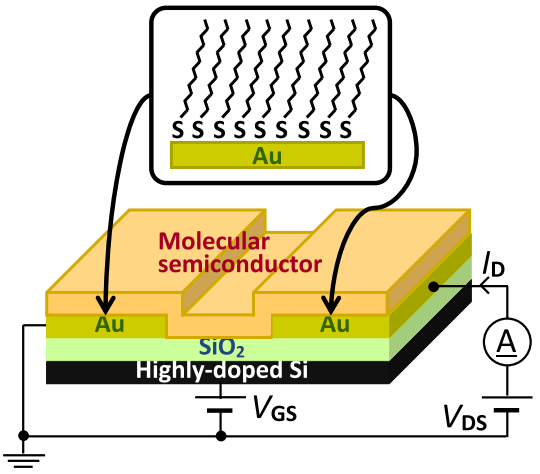

Fig. 1. Schematic diagram of the FET structure used in this study. The surfaces of the Au source/drain electrodes were modified with 1-alkanethiol SAMs. I_D, V_{DS}, and V_{GS} denote the drain current, drain voltage, and gate voltage, respectively.

3. Results

Fig. 2 shows (a) transfer (drain current, I_D, versus gate voltage, V_{GS}) and (b) output (I_D versus drain voltage, V_{DS}) characteristics of a C_{60} FET. SAMs of 1-dodecanethiol ($C_{12}H_{25}SH$; C12) molecules were formed on the Au electrodes by substrate immersion for 12 h. The voltage sweep rate used was 0.25 V/s. The transfer characteristics display a hysteresis where the I_D values for the forward sweep of V_{GS} from 0 to 120 V are higher than those for the backward sweep from 120 to 0 V. Such hysteretic behavior has been widely observed for OFETs and is interpreted as a carrier-trapping effect where carrier traps are gradually formed in the channel and trapped charges screen the gate electric field [8]. However, the output characteristics display an anomalous reversed hysteresis where the forward sweep I_D values are smaller than the backward ones, which was not observed for a C_{60} FET without SAMs on the electrode surfaces. Although this type of hysteresis can be observed in FETs with ferroelectric gate insulators that exhibit slow polarization, the present device has a conventional gate dielectric of SiO_2. Furthermore, the same type of hysteresis should also be observed in the transfer characteristics if the hysteresis is due to the ferroelectric characteristics of the gate insulator. Thus, it is concluded that the anomalous hysteresis originates from the SAM insertion into the metal–organic interface.

In order to clarify the difference between the transfer and output curves, the order of voltage application was investigated. To measure the transfer characteristics, V_{DS} is firstly set and then V_{GS} is swept, and vice versa for the output characteristics. Fig. 3 shows the time evolution of

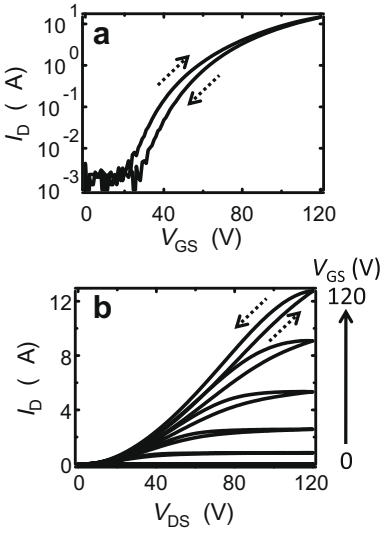

Fig. 2. (a) Transfer ($I_D - V_{GS}$) and (b) output ($I_D - V_{DS}$) characteristics of a C_{60} FET with Au source/drain electrodes modified with SAMs of 1-dodecanethiol molecules by substrate immersion in an ethanol solution of the SAM molecules for 12 h. The voltage sweep rate was 0.25 V/s. The dashed arrows indicate the voltage sweep directions.

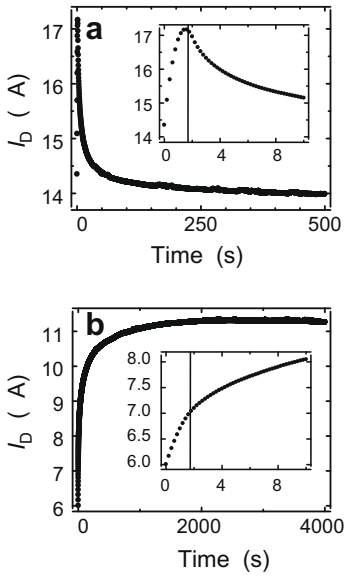

Fig. 3. Time evolution of I_D for a C_{60} FET identical to that used for Fig. 2, immediately after application of V_{DS} and V_{GS}. Data were acquired using two types of voltage-application orders to mimic the (a) transfer ($V_{DS} \rightarrow V_{GS}$) and (b) output ($V_{GS} \rightarrow V_{DS}$) characteristics. The firstly-applied voltages (V_{DS} for (a) and V_{GS} for (b)) were set to 120 V by gradually increasing at a rate of 0.1 V/s. After setting the first voltages, the second voltages (V_{GS} for (a) and V_{DS} for (b)) were set to 120 V at a rate of 10 V/s. Insets enlarge the first 10 s of the evolution. The first 1.8 s denoted by the solid lines can be considered as the response time of the measurement circuits, including the FET itself.

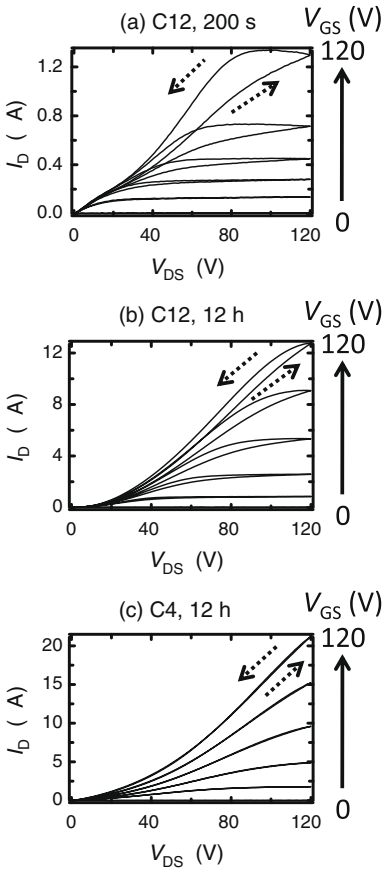

Fig. 4. Output characteristics of C_{60} FETs with Au source/drain electrodes modified with SAMs of (a and b) 1-dodecanethiol ($C_{12}H_{25}SH$; C12) and (c) 1-butanethiol (C_4H_9SH; C4) molecules by substrate immersion in an ethanol solution of the SAM molecules for (a) 200 s and (b and c) 12 h. The C_{60} FET used for (b) is identical to that used for Figs. 2 and 3. The voltage sweep rate was 0.25 V/s. The dashed arrows indicate the V_{DS} sweep directions.

I_D with two types of voltage-application order to mimic the transfer and output characteristics. Firstly-applied voltages (V_{DS} for Fig. 3(a) and V_{GS} for Fig. 3(b)) were set to 120 V by gradually increasing the absolute value at a rate of 0.1 V/s. After 1200 s to set the first voltages, the second voltages (V_{GS} for Fig. 3(a) and V_{DS} for Fig. 3(b)) were set to 120 V using a rate of 10 V/s. The time evolution curves of Fig. 3 were recorded immediately after the second-voltage applications. The first 1.8 s can be considered as a response time of the measurement circuits including the OFET itself. Fig. 3(a) mimics the transfer characteristics by application of voltages in the order of V_{DS} and V_{GS}. After the response time, I_D decreases with time, which accounts for the hysteresis observed in Fig. 2(a). On the other hand, Fig. 3(b) mimics the output characteristics by application of voltages in the order of V_{GS} and V_{DS}, and shows an increase in I_D. This is the same tendency as that observed in Fig. 2(b). These results indicate that the application of V_{DS}, which forms an electric field almost parallel to the alkyl chains of 1-alkanethiol molecules, causes the anomalous hysteresis where I_D is larger in the backward V_{DS} sweep than that in the forward sweep.

To clarify the reason for such a hysteresis, the effects of surface density and alkyl-chain length of SAM molecules were examined. Fig. 4 shows the output characteristics of three devices with different molecular species or different average surface densities of SAM molecules. The average surface density was varied by changing the substrate immersion period in an ethanol solution of SAM molecules. The self-assembly of 1-alkanethiol molecules on Au(1 1 1) surfaces is known to be almost complete within several minutes, but that on polycrystalline Au films is slower and the immersion period of 200 s employed for the device shown in Fig. 4(a) should result in an incomplete monolayer [9]. To confirm this, water contact angles were measured with Au films modified using the same conditions as those for Fig. 4. The measured values were 97° (C12, 200 s; Fig. 4(a)), 105° (C12, 12 h; Fig. 4(b)) and 100° (1-butanethiol (C_4H_9SH; C4), 12 h; Fig. 4(c)). A shorter period of SAM formation resulted in a lower water contact angle, which confirms incomplete coverage (or defective structure) of the SAM on the Au film surface. In addition, the shorter alkyl-chain length resulted in a lower angle. This result may reflect the fact that short chains cause rather defective SAMs, due to weak inter-chain interaction. All three devices display the same-type hysteresis with larger I_Ds in the backward sweeps, as shown in Fig. 4, although the hysteresis observed for the device employing C4 SAMs is too small to be clearly observed. The results show that lower density and longer chains of SAM molecules cause a larger hysteresis.

4. Discussion

The structure of 1-alkanethiol SAMs is stabilized by van der Waals interaction between the alkyl chains. The lower density of the SAM molecules corresponds to a larger separation between the alkyl chains and should lead to weaker interaction between them. The larger hysteresis observed for the device with lower-density SAMs can be interpreted as weaker inter-chain interaction, i.e., the less-stabilized SAM structure causes a larger hysteresis. Thus, the hysteresis very likely originates from a structural change of the SAMs. The most probable form of structural change is a V_{DS}-induced order–disorder transition of the SAM structure. Such switching behavior of SAMs caused by an applied electric field has been observed as a change in the wettability of a surface modified with a 16-mercapto-hexadecanoic acid SAM [10]. The electric field pulls hydrophilic terminal groups toward the substrate surface and the SAM-modified surface can become hydrophobic [11]. During the order–disorder transition, the ordered phase stabilized by the van der Waals interaction between the alkyl chains is broken, and each alkanethiol molecule no longer stands on the surface. The observed hysteresis is a current-increasing type, where I_D was higher during the backward sweep of V_{DS} than I_D during the forward sweep. There are two possible mechanisms that can link the structural change with the current increase.

Charge carrier conduction through alkanethiol SAMs is understood as a tunneling of the carriers through alkyl chains [12]. The alkyl tunneling barrier should be narrower in the disordered phase of SAMs than that of the ordered phase with standing alkanethiol molecules. The transition to a disordered phase may form a space between the SAM-modified electrode and the C_{60} active layer. The tunneling current is proportional to $\exp(-\beta d)$, where β is the decay constant and d is the width of the tunneling barrier. The reported values of β for alkyl chains and vacuum are approximately 1.2 and 2.3 $Å^{-1}$ [13], respectively. Therefore, the simple replacement of alkyl chains with vacuum should decrease the tunneling current through the interface, which is opposite to the observed hysteresis. However, if the movement of C_{60} molecules occurs simultaneously to fill the space formed by the tilting of SAM molecules, then the structural change results in a simple narrowing of the tunneling barrier and an increase in the drain current.

A possible mechanism other than tunneling-barrier narrowing is a change in the Schottky barrier height at the interface between the Au electrode and the C_{60} active layer. A recent theoretical calculation predicts that the work function change of electrodes by SAM modification $\Delta\Phi$, is proportional to $\cos\theta$, where θ is the tilt angle of the SAM molecules from the surface normal [14]. This indicates that the tilting of SAM molecules lowers the $\Delta\Phi$ value. $\Delta\Phi$ reported for clean polycrystalline Au films with 1-alkanethiol SAMs is approximately -1.2 eV, and is roughly independent of the alkyl-chain length [15]. However, in the present case, no special care was taken to clean the Au surface before the SAM formation, so that the Au surface is most likely contaminated. Electric dipoles formed at the interface between a contaminated metal and molecular layer are smaller than those for clean metal-molecular layer interfaces [16]. The $\Delta\Phi$ value of our interfaces was around -0.2 eV [17]. Therefore, considering the work function of a polycrystalline Au film (5.1 eV [18]) and the minimum energy of the conduction band derived from the lowest unoccupied molecular orbital of C_{60} molecules (4.6 eV, which is calculated from the threshold ionization energy of 6.17 eV [19] and an optical band gap of ca. 1.6 eV, assuming a crystalline thin film [20]), the electron injection barrier at the interface between the C_{60} active layer and the SAM-modified Au electrodes is expected to be around 0.3 eV. This value should be higher and I_D should decrease when tilting of the SAM molecules occurs. Therefore, it is concluded that the lowering of $\Delta\Phi$ cannot explain the observed current-increasing hysteresis.

The previous discussion suggests that the anomalous hysteresis observed in OFETs with source/drain electrodes modified with 1-alkanethiol SAMs occurs by tunneling-barrier narrowing induced by V_{DS}. However, the microscopic cause of the switching behavior is still unclear, because the application of V_{DS} can provide two types of stimuli; an electric field and an electric current. An electric field couples with the polar groups or the electric dipole of the SAM molecules, and such a coulombic force can change the structure of the SAMs. For an electric current, an electron has the ability to excite inter- and/or intra-molecular vibrations by inelastic tunneling through the alkyl chains, and the excited inter-chain vibrations can break the ordered phase SAM structure. A FET is a switching device that can turn off the electric current through it; therefore, by employing the FET structure, it is possible to apply an electric field without electric current flow (see the low-V_{GS} region of Fig. 2(a)). To measure the time evolution in Fig. 3(a), V_{DS} was firstly set to 120 V with a rate of 0.1 V/s (in total 1200 s to set V_{DS}) and then V_{GS} was set to 120 V with a rate of 10 V/s, in order to mimic the measurement of the transfer characteristics. Application of both V_{DS} and V_{GS} is necessary to turn on the device. Therefore, for this measurement, only an electric field was applied before an electric current started to flow. The decrease in I_D after the setting of V_{GS} in Fig. 3(a) indicates that the structural switching of SAMs was almost finished within 1200 s before the setting of V_{GS}. On the other hand, Fig. 3(b) shows the time evolution immediately after the application of V_{DS} and the structural change evolved at the same time. Fig. 3(b) also shows that the I_D increase was almost completed within several hundred seconds, which supports that the structural switching was almost finished within 1200 s before V_{GS} application when acquiring the data of Fig. 3(a). Therefore, the structural switching of SAMs is thought to be induced by an electric field. Naturally the I_D values in Fig. 3(a), where the switching was largely completed, are higher than those in Fig. 3(b), where the switching had just started.

Finally, it should be noted that the shapes of the hysteretic curves, in particular Fig. 4(a), show gate-voltage dependence. Generally, larger hystereses were observed with higher gate voltages. Higher V_{GS} values induce higher concentration of charge carriers in the channel, which

indicates that larger hystereses appear with larger currents. The current increase by SAM switching can be interpreted as tunneling-barrier narrowing. The tunneling current is proportional to $\exp(-\beta d)$. If the barrier width is reduced from d to $d-t$ and the tunneling current changes from I_i to I_f, then an increase in the tunneling current $I_f - I_i$, is expressed as $I_i[\exp(\beta t) - 1]$. This means that the current increment should be larger with larger currents, i.e., with higher V_{GS} values. Although the current through the device is not wholly determined by tunneling through the alkyl chains of SAMs, this can cause the gate-voltage dependence of the hysteretic behavior. However, the shape of the hysteretic curves is determined by two competing effects; in addition to the current increase by the SAM switching, current decrease by the gate bias stress should also be taken into account. The latter effect also depends on V_{GS}; higher V_{GS} values cause larger bias stresses. The sparser SAM (Fig. 4(a)) should increase the relative contribution of the former effect, due to the less-stabilized SAM structure, and thus the gate-voltage dependence of the hysteresis is clearly observed in Fig. 4(a). In the case of denser SAMs (Fig. 4(b) and (c)), the relative contribution of the former effect is less and as a consequence the gate-voltage dependence becomes less apparent.

5. Conclusions

The device properties of n-type C_{60} FETs with Au source/drain electrodes modified with 1-alkanethiol SAMs were investigated and were found to exhibit anomalous hysteretic output characteristics, where the I_D values in the forward sweep of V_{DS} from 0 to 120 V were smaller than those in the backward sweep of V_{DS} from 120 to 0 V. This is opposite to the generally observed hysteresis induced by the carrier-trapping effect [8], where the I_Ds in the forward sweep are larger than those in the backward sweep. Measurements on FETs employing different SAM densities and different alkyl-chain lengths showed that FETs with lower density and/or longer length SAM molecules display a larger hysteresis, which indicates that the hysteresis is caused by tunneling-barrier narrowing accompanied by the structural change of the SAMs, most probably an order–disorder transition of the SAM structure [11]. From time evolution measurements of I_D immediately after the application of V_{DS}/V_{GS}, an electric field parallel to the alkyl chains of the SAM molecules, V_{DS}, was found to induce switching behavior. It should be noted that p-type pentacene FETs also displayed the anomalous hysteresis, which indicates that the phenomenon occurs in both electron- and hole-transport systems.

The SAM modification of source/drain electrodes is an effective method to achieve energy level matching at the interface between electrodes and a molecular active layer, and thus gain effective charge injection from the electrodes into the molecular layer. The present study has revealed the occurrence of anomalous hysteretic behavior in OFETs with SAM-modified electrodes and has yielded important information for analysis of the operation of OFETs. Particular attention should be paid to OFETs that have source/drain electrodes modified with low-density/long-chain SAMs. Furthermore, there is a possibility that the anomalous hysteresis could cancel out the hysteresis caused by the charge-trapping effect. This could be achieved by tuning the density and length of SAM molecules on source/drain electrodes.

Exploiting the self-assembly of molecules to realize basic electronic components will pave the way for molecular-scale electronics [4]. The anomalous hysteresis found in this study is indicative of the switching of SAMs induced by electrical stimulation. Such electrically-stimulated switching of SAMs has been observed as a change in the wettability of a gold surface modified with a 16-mercapto-hexadecanoic acid SAM [10]. However, in order to realize an electric molecular switch, it is necessary to tune the electric conductance using an electrical method. Recently, the reliable conductance switching of SAMs has been achieved by the optically induced isomerization of diarylethene molecules [21]. On the other hand, the present result indicates the electrical detection of electrically-stimulated switching, which should have significant implications with respect to achieving a future molecular switch.

Generally, microscopic probing techniques such as scanning probes [22] and break junctions [23] are used to assess molecular-scale electronic junctions. However, the microscopic conductance of the junctions, i.e., single molecule conductance, typically varies by many orders of magnitude, but SAMs provide an average conductance of many molecules and may offer a more reliable assessment of the junction [24]. In addition, SAMs can amplify molecular-level conformational switching to macroscopically measurable changes by the synergistic molecular reorientation of ordered molecules [10]. Therefore, the anomalous hysteretic behavior observed in the present study can be regarded as a manifestation of molecular-level conformational switching by an electric field, which was amplified through the synergistic switching of ordered molecules forming the SAM, and was finally detected as a macroscopic change in I_D.

Acknowledgements

The authors acknowledge Takayuki Nagano, Yohei Ohta, and Naoko Kawasaki for their experimental assistance. This work was partly supported by a Grant-in-Aid for Young Scientists (B) (Grant No. 20710071) from the Ministry of Education, Culture, Sports, Science and Technology of Japan.

References

[1] G.D. Alton, Surf. Sci. 175 (1986) 226.
[2] H. Ishii, K. Sugiyama, E. Ito, K. Seki, Adv. Mater. 11 (1999) 605.
[3] M.L. Sushko, A.L. Shluger, Adv. Mater. 21 (2009) 1111.
[4] G.M. Whitesides, B. Grzybowski, Science 295 (2002) 2418.
[5] T. Nishikawa, S. Kobayashi, T. Nakanowatari, T. Mitani, T. Shimoda, Y. Kubozono, G. Yamamoto, H. Ishii, M. Niwano, Y. Iwasa, J. Appl. Phys. 97 (2005) 104509.
[6] L.-L. Chua, J. Zaumseil, J.-F. Chang, E.C.-W. Ou, P.K.-H. Ho, H. Sirringhaus, R.H. Friend, Nature 434 (2005) 194.
[7] B.C. Haynie, A.V. Walker, T.B. Tighe, D.L. Allara, N. Winograd, Appl. Surf. Sci. 203–204 (2003) 433.
[8] P.V. Pesavento, R.J. Chesterfield, C.R. Newman, C.D. Frisbie, J. Appl. Phys. 96 (2004) 7312.
[9] M. Kawasaki, T. Sato, T. Tanaka, K. Takao, Langmuir 16 (2000) 1719.

[10] J. Lahann, S. Mitragotri, T.-N. Tran, H. Kaido, J. Sundaram, I.S. Choi, S. Hoffer, G.A. Somorjai, R. Langer, Science 299 (2003) 371.
[11] S. Vemparala, R.K. Kalia, A. Nakano, P.J. Vashishta, Chem. Phys. 121 (2004) 5427.
[12] B. Mann, H.J. Kuhn, Appl. Phys. 42 (1971) 4398.
[13] L.A. Bumm, J.J. Arnold, T.D. Dunbar, D.L. Allara, P.S. Weiss, J. Phys. Chem. B 103 (1999) 8122.
[14] M.L. Sushko, A.L. Shluger, Adv. Funct. Mater. 18 (2008) 2228.
[15] D.M. Alloway, M. Hofmann, D.L. Smith, N.E. Gruhn, A.L. Graham, R. Colorado Jr., V.H. Wysocki, T.R. Lee, P.A. Lee, N.R. Armstrong, J. Phys. Chem. B 107 (2003) 11690.
[16] M. Grobosch, M. Knupfer, Adv. Mater. 19 (2007) 754.
[17] H.B. Michaelson, J. Appl. Phys. 48 (1977) 4729.
[18] T. Nagano, M. Tsutsui, R. Nouchi, N. Kawasaki, Y. Ohta, Y. Kubozono, N. Takahashi, A. Fujiwara, J. Phys. Chem. C 111 (2007) 7211.
[19] N. Sato, Y. Saito, H. Shinohara, Chem. Phys. 162 (1992) 433.
[20] D. Faiman, S. Goren, E.A. Katz, M. Koltun, N. Melnik, A. Shames, S. Shtutina, Thin Solid Films 295 (1997) 283.
[21] N. Katsonis, T. Kudernac, M. Walko, S.J. van der Molen, B.J. van Wees, B.L. Feringa, Adv. Mater. 18 (2006) 1397.
[22] X.D. Cui, A. Primak, X. Zarate, J. Tomfohr, O.F. Sankey, A.L. Moore, T.A. Moore, D. Gust, G. Harris, S.M. Lindsay, Science 294 (2001) 571.
[23] M.A. Reed, C. Zhou, C.J. Muller, T.P. Burgin, J.M. Tour, Science 278 (1997) 252.
[24] H.B. Akkerman, P.W.M. Blom, D.M. de Leeuw, B. de Boer, Nature 441 (2006) 69.

investigated the feasibility of air atomizing spray technology for large-area/low-cost fabrication of organic electronic and optoelectronic thin-film devices based on solution-processable polythiophene derivatives. There, a manually operated airbrush was utilized to fabricate different devices while comparing electrical and electro-optical characteristics, as well as film morphology and roughness of spray-coated devices to those of spin-coated ones with similar structure [8].

In this article we present a detailed investigation on the layer formation process during spray deposition of organic thin-films and its relation to solution properties and process parameters. By considering layer formation to be a stacking of individual droplets onto the substrate followed by partial merging between adjacent ones, we are able to correlate deposition conditions to the electrical and electro-optical characteristics of fabricated devices. Other than in previously reported research activities, we apply the technological framework developed here not only to the fabrication of organic photovoltaic devices, but also to the fabrication of organic thin-film transistors. This work clearly demonstrates the feasibility of this deposition technology for the fabrication of diverse organic electronic and optoelectronic devices independent of substrate material and geometry.

2. Materials and methods

Spray technology is used in a wide variety of applications such as surface coating, humidification, combustion and many more. Each application area requires different spray nozzles to fulfill the specified criteria and achieve the desired results. The layers deposited here were sprayed by an air atomizing nozzle. This type of nozzles provides, along with ultrasonic spray nozzles, the finest degree of atomization. It is worth mentioning that ultrasonic spray nozzles have also been successfully applied to the deposition of active layers [9] and hole-selective contacts [10] in organic photovoltaic devices. For our static test system, a commercially available automatic air atomizing spray gun (Krautzberger GmbH, Germany) was used. All ink containing parts of the spray gun are resistant to organic solvents and are therefore suitable for the desired application. Fig. 1(a) shows a schematic drawing of the test setup, indicating the vertical arrangement of nozzle and substrate. The spray gun contains an internal pneumatic control system which is activated by an electromechanical 3/2-way valve connected to a timer for precise spray time adjustment. Other spray gun settings that were varied to obtain the desired spray characteristics are material flow rate, atomizing gas (N_2) pressure and nozzle-to-sample distance. The performance of any kind of spray nozzle is strongly dependent on its size and geometry as well as on the physical properties of the liquid being atomized and the gaseous medium surrounding the droplets. For air-assisted nozzles the diameter of the orifice is the most significant dimension for atomization. Here a nozzle with 0.5 mm orifice diameter was chosen. The physical properties of the liquid being atomized have a direct effect on the flow and spray characteristics in a spray nozzle. Density, viscosity and surface tension are among the most critical fluid properties. As most liquids exhibit only minor differences in density, the significance of this property for atomization is rather low. However, higher density tends to result in a larger average droplet size. An increased viscosity tends to hinder any natural instabilities leading to fluid breakup, which results in a delayed disintegration and increased average droplet size in the spray. Surface tension plays a very important role because it represents the force resisting the formation of new surface area. Hence it affects the droplet size as well as the spray angle. Fluids with higher surface tension tend to produce sprays with an increased average droplet size and a decreased spray angle. In addition, boiling point and vapor pressure of solvents are of great significance for the drying behavior of droplets in a spray and hence the process of layer formation. The three solvents used in the work presented here are toluene, p-xylene and o-dichlorobenzene (Merck KGaA, Germany) having boiling points of 110.6 °C, 138.3 °C and 180.5 °C, respectively.

In all our experiments the atomizing gas pressure was kept below 1 bar in order to achieve a reasonable spray pattern and prevent the gas flow from pushing away the droplets already on the substrate before completely drying. Depending on the solution to be deposited, i.e. polymer and solvent type, the nozzle-to-sample distance can only be varied within a certain range. One can distinguish between three regimes: wet, intermediate and dry [3]. In the wet regime, the nozzle-to-sample distance is low resulting in the formation of a wet polymer layer on top of the substrate, hence producing inhomogeneous layers with no real thickness control. On the other hand, in the dry regime, when the nozzle-to-sample distance is high, the entire solvent is evaporated before reaching the sample and a polymer powder is formed. The intermediate regime is the one more suitable for the deposition of organic thin films. In this regime, homogeneous layers can be formed and the thickness can be precisely controlled by adjusting the spray time. It is important to mention, that the evaporation rate of the atomized liquid, and hence the different deposition regimes, is strongly dependent on the properties of the chosen solvent (e.g. boiling point and vapor pressure) as well as the droplet size achieved for a given set of process parameters.

The general device architectures for the organic photodetectors and thin-film transistors fabricated are illustrated in Fig. 1(b) and (c), respectively. For the fabrication of the organic photodetectors, ITO-electrodes with the desired structure were patterned on glass by conventional photolithography. The structured ITO-glass substrates were then cleaned by sonication in acetone and isopropanol in sequence. PEDOT:PSS aqueous dispersion (CLEVIOS™ P VP CH 8000) was deposited by spin coating at 2000 rpm for 20 s and then dried on a hot plate at 150 °C for 15 min. The active layer of the device consisted of a blend of regioregular poly(3-hexylthiophene-2,5-diyl) (P3HT) (Rieke Metals Inc.) and [6,6]-phenyl C61 butyric acid methyl ester (PCBM) (Solenne B.V.) as donor and acceptor materials, respectively. The P3HT:PCBM (1:1) blend was deposited from a solution of 0.5 wt% concentration in the different solvents. All samples were then placed

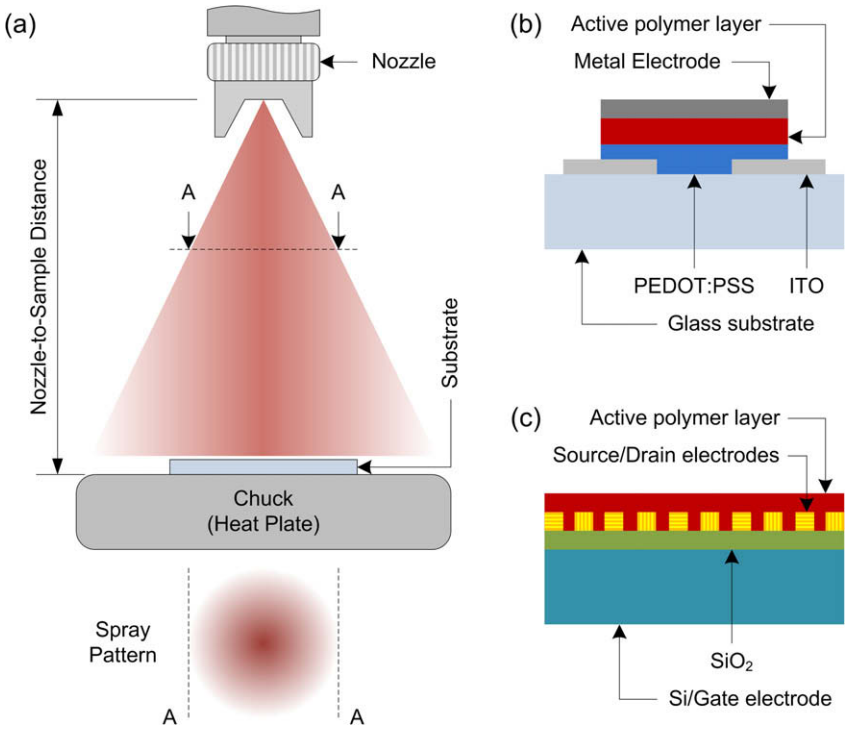

Fig. 1. (a) Illustration of the implemented experimental setup for spray deposition, showing the basic components and the resulting spray pattern while indicating the vertical arrangement of nozzle and substrate. (b) General layout of an organic photodetector showing the layer stack comprising two organic layers sandwiched between two electrodes. (c) General layout of an organic thin-film transistor showing a single organic layer deposited onto an interdigitated electrode structure. For both device types the active polymer layer was spray-coated.

again on a hot plate for annealing at 140 °C for 15 min. Finally, a LiF(1 nm)/Al(120 nm) cathode was thermally evaporated on top. The active area of each diode was defined by the ITO-electrode to be 25 mm^2. Organic thin-film transistors were fabricated on highly p-type doped Si wafers, on which a 45 nm thick SiO_2 layer was thermally grown. An interdigitated electrode structure (IDES) consisting of a 2 nm thick Ti layer (to promote Au adhesion on Si) followed by a 45 nm Au layer was evaporated on top of the SiO_2. The spacing formed between the source and drain contacts of this interdigitated structure was chosen to be 20 μm. Regioregular P3HT was used as a semiconductor for the channel of our p-type TFT and was deposited on top of the sample from a solution of 0.5 wt% concentration in xylene. Device fabrication was finalized by an annealing step at 120 °C for 10 min. Note that all organic layers were deposited in ambient conditions, only annealing steps and device encapsulation were performed in an inert gas atmosphere inside a glove box.

3. Results and discussion

Operating in the intermediate regime, the process of layer formation can be thought of as a process of successively stacking individual droplets onto the substrate at a certain rate. In the following we will discuss experimental results supporting this idea and correlating it to the performance of fabricated devices. By the correct choice of process parameters the effect of dissolving previously deposited droplets by new ones can be significantly minimized. This allows the fabrication of devices with more complicated layer stacks from the same solvent. However, if droplets arriving at the substrate are too dry, it can be assumed that a large portion of these droplets form separate domains and that charge transport across domain boundaries is impeded. For this reason, droplets arriving at the substrate surface should still be wet to an extent allowing a minimum of merging between individual droplets. Spray deposition from low boiling point solvents shows a higher sensitivity to process parameters and ambient condition variations due to a narrower intermediate regime and hence suffers from poor reproducibility. The lower evaporation rate of high boiling point solvents makes the deposition process less sensitive and easier to control over a larger parameter space. In order to ensure an optimal merging between droplets, we introduce a deposition approach in which we operate within the wet regime while heating up the substrate in order to speed up the drying of wet droplets arriving at the substrate. This approach allows the formation of dry layers with good thickness control over time, enhancing at the same time reproducibility, especially of devices deposited from low boiling point solvents (e.g. toluene). The substrate heating during deposition is a very important parameter which still has to be carefully optimized. Our investigations showed that, as a rule of thumb, the substrate temperature should be close to the boiling point of the used solvent. This turned out to be valid also for spray deposition of the conducting poly-

mer PEDOT:PSS (aqueous dispersion), which confirmed the applicability of our deposition approach to other organic conducting and semiconducting material systems in different types of solvents.

Fig. 2(a) shows a comparison of the IV-characteristics of four spray-coated organic photodetectors (OPDs) D1, D2, D3 and D4 where a dichlorobenzene based P3HT:PCBM blend was sprayed for 10, 15, 20 and 25 s, respectively. Each device was measured under dark and illuminated (halogen light source with 100 mW/cm^2) conditions. A clear decrease of the dark current density can be observed for longer spray durations, i.e. higher layer thickness, leading to an increase in the on/off-ratio of the respective OPD. Sample D4 exhibits a dark current density as low as 3.8×10^{-5} mA/cm^2 and an on/off-ratio of 8.2×10^4 at -1 V bias. This low dark current density is remarkable considering the relatively large active area of our devices compared to the ones reported by Tedde et al. [6]. Due to the increased layer thickness however, the series resistance rises from 81 Ω/cm^2 for D1 to 155 Ω/cm^2 for D4, leading to a decrease in the forward current density. Nevertheless, we are still able to achieve around one order of magnitude higher forward current densities at +2 V, with respect to devices presented by Tedde et al. [6]. This indicates an enhanced charge transport in layers prepared using our deposition approach. Due to the extremely high surface roughness, which depending on spray parameters can be above 100 nm [8], precise layer thickness measurement using profilometry or atomic force microscopy become rather meaningless. To be able to quantify the layer thickness and gain an idea about its dependence on the spray duration, optical transmission measurements on spray deposited layers were performed and the absorption spectrum of the blend material was calculated from reference measurements carried out on spin-coated layers of known thickness. An absorption coefficient of approx. 1×10^5 cm^{-1} at a wavelength of 510 nm (P3HT absorption peak), which corresponds to values found in literature [11], was then used to estimate the thickness of spray deposited layers. Note that the value obtained from this calculation represents an averaged absorption thickness over the illuminated area of about 25 mm^2, which is on a significantly larger scale than that of the individual droplets. The estimated layer thickness was then plotted versus

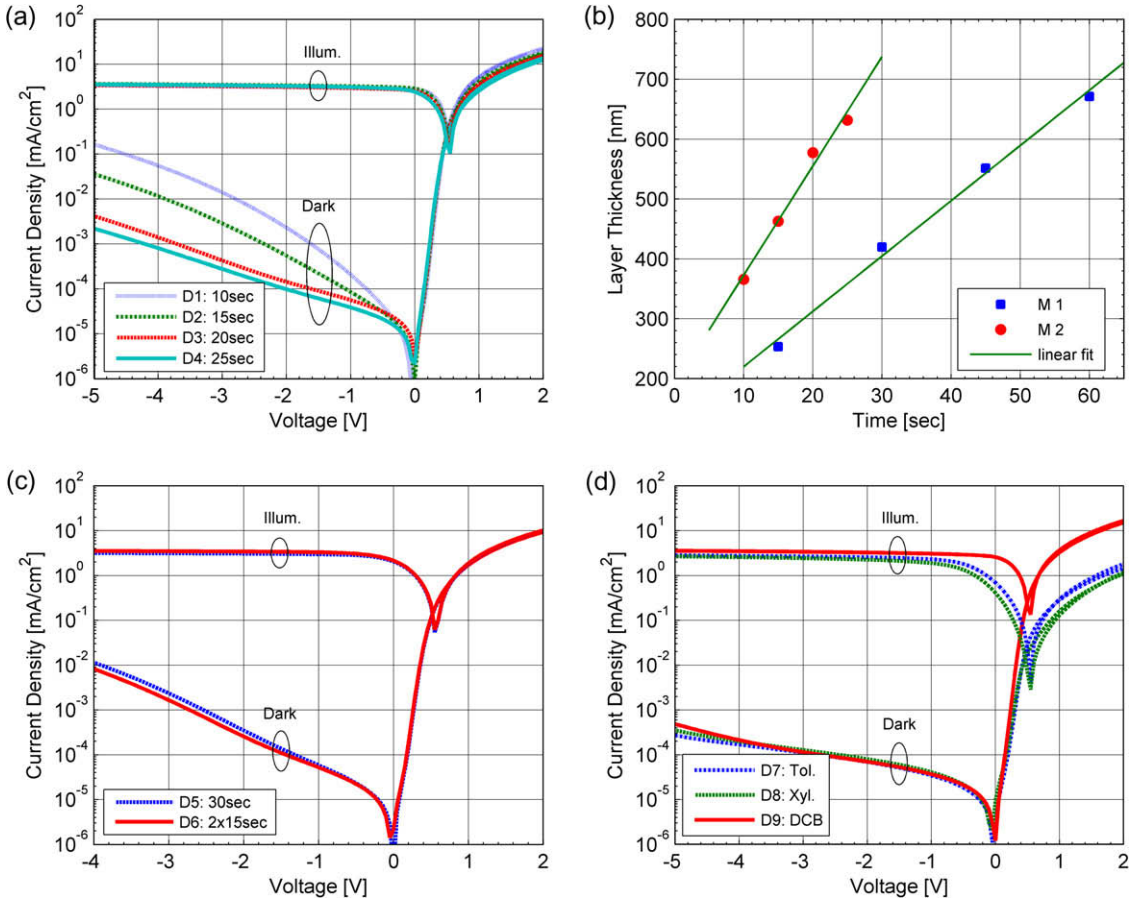

Fig. 2. (a) Comparison of the IV-characteristics of four spray-coated OPDs D1, D2, D3 and D4 with a P3HT:PCBM blend sprayed for 10, 15, 20 and 25 s, respectively. (b) An estimated layer thickness calculated from transmission measurements of spray-coated layers plotted versus spray duration. M1 and M2 indicate two different material flow rates, where M2 > M1. (c) IV-characteristics of devices fabricated by depositing the blend as a single coat of 30 s spray duration for the first device D5 and as a double coat of 15 s spray duration each for the second device D6. (d) IV-characteristics of three devices (D7, D8 and D9) representing the best device obtained from each of the three solvents, toluene, xylene and dichlorobenzene.

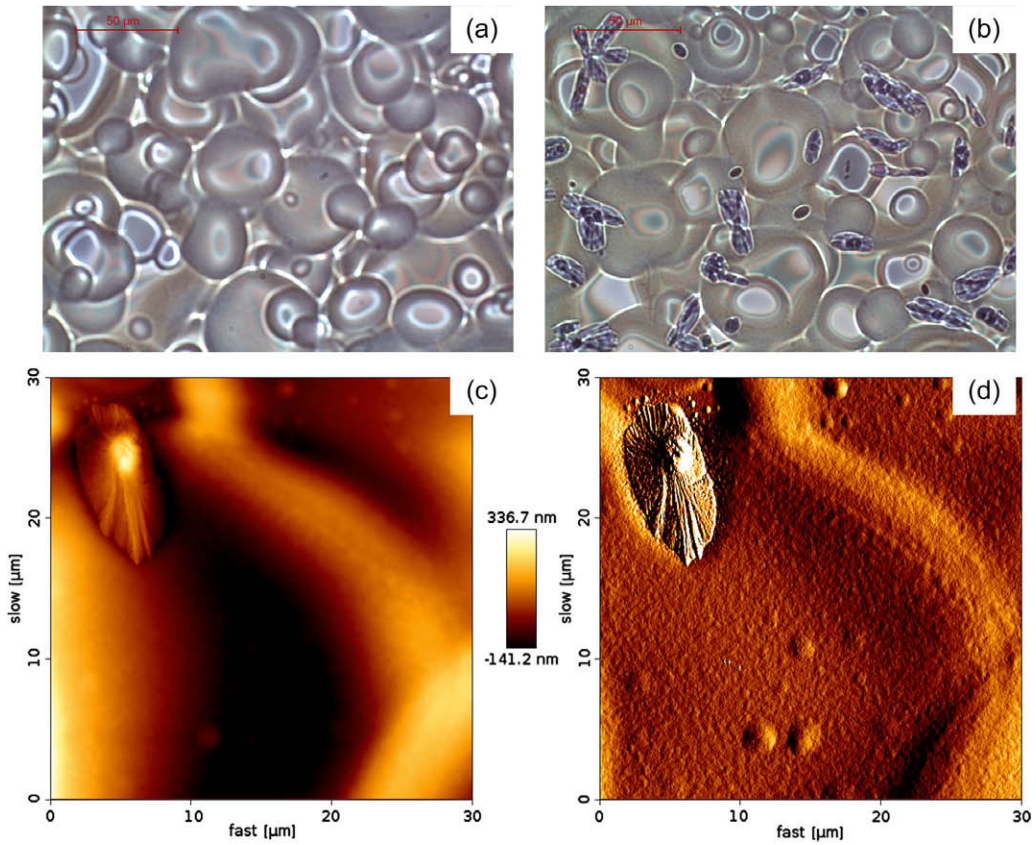

Fig. 3. (a) Microscopic image of a spray deposited blend layer. Individual droplets can be distinguished and a pinhole-free layer is built up by the successive stacking of such droplets. (b) Microscopic image of the same layer after a thermal annealing step, which reveals the formation of the typical and well-known PCBM crystalline structures. (c) AFM height image of the spray-coated P3HT:PCBM layer after annealing, visualizing the huge height differences existing. (d) An error image of the same area, clarifying the contours of the individual droplets and indicating the formation of a PCBM crystalline structure across their boundaries.

spray duration and is shown in Fig. 2(b). M1 and M2 indicate two different material flow rates, where M2 is higher than M1. The four measurement points shown for M2 in the figure correspond to the four devices shown in Fig. 2(a). By fitting a line through the measurement points it becomes clear that for the correct choice of spray parameters, the layer thickness exhibits a linear dependence on the spray duration over a wide range. In order to further verify the suggested description of the layer formation process, we examined single-coat and multiple-coat deposition. For this purpose two OPDs were fabricated, in which the P3HT:PCBM layer was deposited as a single coat of 30 s spray duration for the first device D5 and as a double coat of 15 s spray duration each for the second device D6. The IV-characteristics of both devices are plotted in Fig. 2(c), showing almost identical behavior with only small discrepancy, which lies within the usual fabrication uncertainty and can therefore be neglected, confirming results already obtained by Tedde et al. [6] and further supporting the suggested description of the layer formation process.

Single layers as well as complete OPDs presented so far were deposited from a dichlorobenzene based P3HT:PCBM solution. The reasons for preferring a high boiling point solvent were already discussed at the beginning of this section. Nevertheless, it is possible to fabricate devices with reasonable performance from other solvents, such as toluene and xylene. Due to the different behavior of each solvent when sprayed, most process parameters have to be entirely readjusted for each solvent. This makes a direct comparison between devices fabricated from different solvents rather misleading. Instead, we present the best device obtained out of each solvent, while applying only necessary changes to spray settings. For the same reason, we preferred to fix the substrate temperature used for spray deposition of the P3HT:PCBM blends to 150 °C for all three solvents discussed in this article. Fig. 2(d) shows the IV-characteristics of three devices (D7, D8 and D9) fabricated from three different solvents. All three devices exhibit low dark current densities of around 4×10^{-5} mA/cm^2 and an on/off-ratio between 4.6×10^4 and 8.4×10^4 at -1 V bias, while maintaining a dark current density as low as 4.6×10^{-4} mA/cm^2 and an on/off-ratio of 7.8×10^3 even at -5 V bias in case of D9. At low reverse bias (below -1 V) and under forward bias however, the dichlorobenzene based device shows significantly higher current density, which is up to one order of magnitude higher than for the other two devices at a bias voltage

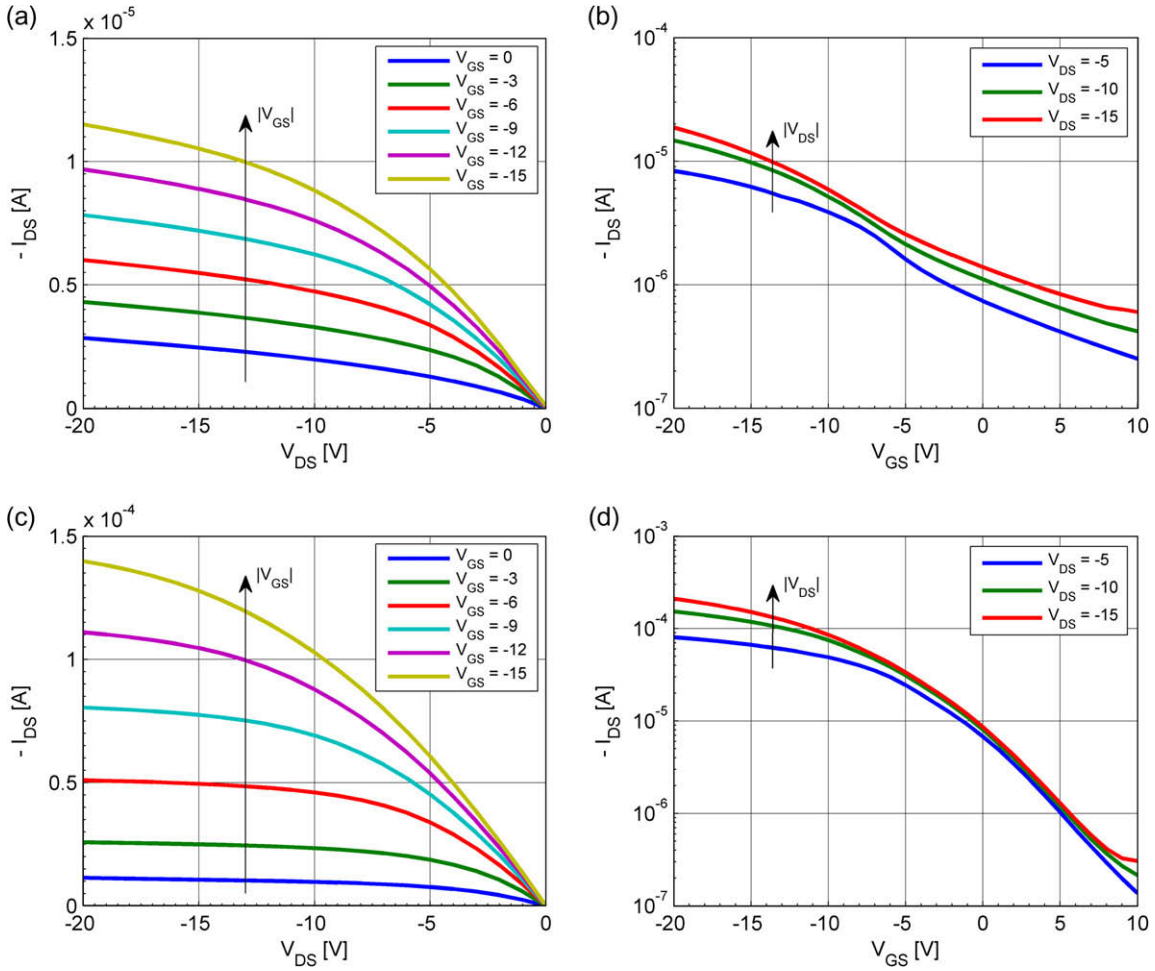

Fig. 4. (a) Output characteristics ($I_D V_{DS}$) of a device where the active polymer was deposited in the wet regime on a heated substrate forming a dry layer and (b) the corresponding transfer characteristics ($I_D V_{GS}$). (c) Output characteristics ($I_D V_{DS}$) of a device fabricated using a wet deposition approach and (d) the corresponding transfer characteristics ($I_D V_{GS}$). A field effective mobility of approx. 1.1×10^{-3} cm^2/V s can be calculated for the wet deposited device, which is about one order of magnitude higher than for the other.

above +1 V. In addition to that, the best results of devices prepared from a dichlorobenzene based solution were easier to obtain, less sensitive to variations in the process parameters and hence showed a much higher reproducibility.

Based on the linear relation of layer thickness and spray duration as well as the similarity between single-coat and multiple-coat deposition, we can confirm our view of the layer formation process proposed at the beginning of the article. This is further supported by examining microscopic images of spray deposited blend layers, as shown in Fig. 3(a). In this image individual droplets can be distinguished and a pinhole-free layer is built up by the successive stacking of such droplets. Spreading and deformation of droplets upon impact on the substrate could also be observed in other optical and atomic force microscopy images, which are not shown here. Droplets, which are originally assumed to be spherical, are deformed into more disk-like structures of increased diameter and heightened boundaries. This deformation is typical for spray deposited layers and is expected to depend on the droplet velocity at impact and solvent properties such as surface tension. Topography investigations carried out on spray deposited layers by atomic force microscopy reveal an extremely high surface roughness on a scale larger than the average droplet dimensions. Despite this high surface roughness, the results presented above demonstrate state of the art OPDs fabricated by spray deposition. On a sub-micrometer scale, a surface topography similar to spin-coated layers can be observed, which was suggested to indicate a similar nano-morphology and hence be one of the reasons for the good device performance [8]. Hoth et al. observed no significant difference in the ideality factor measured for spray-coated and doctor-bladed devices. This was explained by a rather comparable distribution of the donor and acceptor interfaces throughout the bulk of the heterojunction, again indicating a similar nano-morphology [7]. Taking a closer look on optical microscopy images of the same spray deposited layer shown in Fig. 3(a), this time however after the thermal annealing step usually performed for all devices, reveals the formation of the typical PCBM crystalline structures well known from the anneal-

ing of spin-coated P3HT:PCBM layers [12–14]. Such an image is shown in Fig. 3(b). It is interesting to notice that the crystallization of PCBM does not seem to be confined only within individual droplets, but is rather randomly distributed and can occur across the droplet boundaries as well. The existence of such crystalline structures reaching even over several droplets indicates that individual droplets in a spray-coated layer can behave to a certain extent as a continuous layer depending on the degree of merging between droplets during deposition and do not necessarily act as isolated domains. This picture is consistent with our proposed view of the layer formation process and gives another possible explanation for the competitive device performance of spray-coated OPDs. Fig. 3(c) shows an AFM height image of the spray-coated P3HT:PCBM layer after annealing measured in contact mode. There a crystalline PCBM structure can be seen while visualizing the huge height differences existing in a spray-coated layer. An error image of the same area is shown in Fig. 3(d), clarifying the contours of the individual droplets and the formation of the PCBM crystal across their boundaries.

Spray technology was also used to fabricate other classes of organic thin-film devices, such as organic light emitting diodes (OLED) based on MEH-PPV as the light emitting polymer and organic thin-film transistors (OTFT) based on P3HT as the p-type semiconducting polymer. Here we will present some of the results obtained for the OTFTs fabricated using spray deposition. First devices were prepared using exactly the same approach as for the OPDs, meaning that the polymer was deposited in the wet regime on a heated substrate forming a dry layer. The measured output characteristics ($I_D V_{DS}$) of this kind of device are shown in Fig. 4(a) along with the corresponding transfer characteristics ($I_D V_{GS}$) shown in Fig. 4b. Upon examination of these plots, one can clearly observe a transistor-like behavior with saturating drain current. The drain current of such spray-coated OTFT is about one order of magnitude lower than what is usually expected from devices of the same structure fabricated using other deposition techniques. This is also reflected in an extracted field effective mobility of approx. 1.02×10^{-4} cm^2/V s. Further, an on/off-ratio of only 5.8×10^{1} can be achieved. The lower mobility may not be surprising if the process of layer formation is taken into account, where the droplets arriving at the substrate are immediately dried. Such a fast growth of the active layer is known to have a negative effect on the mobility of OTFTs [15,16]. By operating the spray gun in the wet regime without heating the substrate, a wet layer of P3HT is formed on top of the substrate. This wet layer is then left to dry for some time, thereby introducing more time for reorganization. The inhomogeneous P3HT layer resulting from this deposition approach does not cause any additional problems. This is due to the fact that the P3HT layer thickness does not play an important role in device performance as long as it is sufficiently thick to allow the formation of a channel between source and drain contacts. By applying this deposition approach, the layer formation process becomes comparable to processes such as drop casting and dip coating, where a slow growth of the layer is achieved. Fig. 4(c) shows the output characteristics of an OTFT fabricated using the wet deposition approach. There significantly higher currents of up to 140 μA at −20 V drain bias and −15 V gate bias can be observed. The field effective mobility calculated from the transfer characteristics of such devices, plotted in Fig. 4(d), is approx. 1.1×10^{-3} cm^2/V s and an on/off-ratio of 5.8×10^{2} can be measured at −5 V drain bias.

4. Conclusion

In conclusion, we implemented a simple and low-cost spray-coating test setup using a commercially available automatic air atomizing spray gun. Using this setup we could successfully fabricate different classes of organic thin-film devices exhibiting performances comparable to ones fabricated using other deposition technologies. The technological framework developed based on the deposition approach presented here proved to enhance controllability of the process and reproducibility of the fabricated devices. For the correct choice of process parameters, the layer formation process can be thought of as a process of successively stacking individual droplets onto the substrate at a certain rate. Further, microscopy investigations indicated that individual droplets in a spray-coated layer can behave to a certain extent as a continuous layer depending on the degree of merging between droplets during deposition and do not necessarily act as isolated domains. Gaining insight into the layer formation process and correlating it to device performance represents an important step towards the realization of arbitrary shaped organic electronic devices fabricated by spray deposition.

References

[1] S.R. Forrest, The path to ubiquitous and low-cost organic electronic appliances on plastic, Nature 428 (2004) 911–918.
[2] S. Gunes, H. Neugebauer, N.S. Sariciftci, Conjugated polymer-based organic solar cells, Chem. Rev. 107 (2007) 1324–1338.
[3] D. Vak, S. Kim, J. Jo, S. Oh, S. Na, J. Kim, D. Kim, Fabrication of organic bulk heterojunction solar cells by a spray deposition method for low-cost power generation, Appl. Phys. Lett. 91 (2007) 081102–081103.
[4] R. Green, A. Morfa, A.J. Ferguson, N. Kopidakis, G. Rumbles, S.E. Shaheen, Performance of bulk heterojunction photovoltaic devices prepared by airbrush spray deposition, Appl. Phys. Lett. 92 (2008) 033301–033303.
[5] C. Girotto, B.P. Rand, J. Genoe, P. Heremans, Exploring spray coating as a deposition technique for the fabrication of solution-processed solar cells, Sol. Energy Mat. Sol. Cells 93 (2009) 454–458.
[6] S.F. Tedde, J. Kern, T. Sterzl, J. Fürst, P. Lugli, O. Hayden, Fully spray coated organic photodiodes, Nanoletters 9 (2009) 980–983.
[7] C.N. Hoth, R. Steim, P. Schilinsky, S.A. Choulis, S.F. Tedde, O. Hayden, C.J. Brabec, Topographical and morphological aspects of spray coated organic photovoltaics, Org. Electron. 10 (2009) 587–593.
[8] A. Abdellah, D. Baierl, B. Fabel, P. Lugli, G., Scarpa, Exploring spray technology for the fabrication of organic devices based on poly(3-hexylthiophene), in: Proc. 9th IEEE Conference on Nanotechnology IEEE-NANO-2009, 2009, pp. 831–934.
[9] K.X. Steirer, M.O. Reese, B.L. Rupert, N. Kopidakis, D.C. Olson, R.T. Collins, D.S. Ginley, Ultrasonic spray deposition for production of organic solar cells, Sol. Energy Mat. Sol. Cells 93 (2009) 447–453.
[10] K.X. Steirer, J.J. Berry, M.O. Reese, M.F. van Hest, A. Miedaner, M.W. Liberatore, R. Collins, D.S. Ginley, Ultrasonically sprayed and inkjet printed thin film electrodes for organic solar cells, Thin Solid Films 517 (2009) 2781–2786.
[11] Y. Kim, S. Cook, S.M. Tuladhar, S.A. Choulis, J. Nelson, J.R. Durrant, D.D.C. Bradley, M. Giles, I. McCulloch, C. Ha, M. Ree, A strong regioregularity effect in self-organizing conjugated polymer films and high-efficiency polythiophene:fullerene solar cells, Nat. Mater. 5 (2006) 197–203.

[12] E. Klimov, W. Li, X. Yang, G.G. Hoffmann, J. Loos, Scanning near-field and confocal Raman microscopic investigation of P3HT–PCBM systems for solar cell applications, Macromolecules 39 (2006) 4493–4496.
[13] A. Swinnen, I. Haeldermans, M. vande Ven, J. D'Haen, G. Vanhoyland, S. Aresu, M. D'Olieslaeger, J. Manca, Tuning the dimensions of C60-based needlelike crystals in blended thin films, Adv. Funct. Mat. 16 (2006) 760–765.
[14] M. Campoy-Quiles, T. Ferenczi, T. Agostinelli, P.G. Etchegoin, Y. Kim, T.D. Anthopoulos, P.N. Stavrinou, D.D.C. Bradley, J. Nelson, Morphology evolution via self-organization and lateral and vertical diffusion in polymer:fullerene solar cell blends, Nat. Mater. 7 (2008) 158–164.
[15] J. Chang, B. Sun, D.W. Breiby, M.M. Nielsen, T.I. Solling, M. Giles, I. McCulloch, H. Sirringhaus, Enhanced mobility of poly(3-hexylthiophene) transistors by spin-coating from high-boiling-point solvents, Chem. Mater. 16 (2004) 4772–4776.
[16] J. Park, S. Lee, H.H. Lee, High-mobility polymer thin-film transistors fabricated by solvent-assisted drop-casting, Org. Electron. 7 (2006) 256–260.

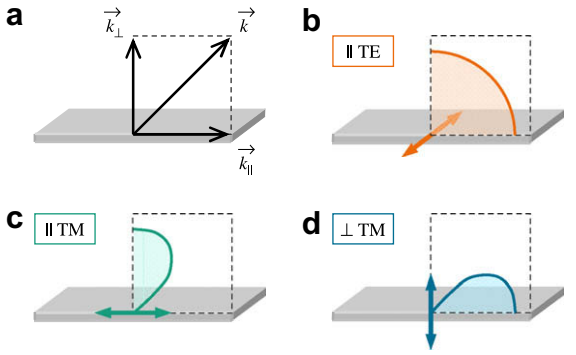

Fig. 1. (a) The wave-vector k (representing the direction of observation or measurement) and its two components in the directions parallel ($k_{||}$) and perpendicular ($k_{\perp}$) to the interfaces of the layered system are shown. The orientations of the dipole transition moments (arrows) of the three orthogonal dipoles ||TE (b), ||TM (c), and ⊥TM (d), with respect to the layered system are also illustrated. The indicated schematics of the internal radiation patterns of the dipoles correspond to those in the homogenous, infinite emissive material and are distorted in the presence of the interfaces of the layered system.

the corresponding polarization of the emitted radiation (transverse-electric "TE", transverse-magnetic "TM"); the direction of measurement or observation is represented by the wave-vector k [see Fig. 1 (a)].

Two major effects need to be pointed out when discussing the relevance of the emitter orientation in OLEDs: First, perpendicularly oriented active sites emit most power in the direction parallel to the interfaces [see Fig. 1(d)], and not in the desired perpendicular direction. Second, different interference conditions with the surrounding multilayer system apply to the fields of the three basic orthogonal dipoles. Consequently, the orientation of the emissive sites in the light-emitting material has a major impact on the device performance and overall efficiency [6,7]. Most common and optimized OLEDs stacks are designed in order to enhance the emission of parallel dipoles as this allows extracting most power to the outside medium air. This optimized stack architecture tends to trap almost all light generated by perpendicularly oriented dipoles inside the layered system or the substrate glass. As s result, the optical outcoupling efficiency for emitters with isotropic orientation is ~1/3 lower than for exclusively parallel oriented emitters. In the past, the external quantum efficiency (EQE) of devices was frequently used as a starting point to estimate internal properties of OLEDs such as the singlet-triplet generation ratio in the emissive material or the internal luminescence quantum efficiency q [6,8,9]. Because the orientation of the emissive sites strongly affects the optical outcoupling efficiency, it has to be known precisely for such estimates to be meaningful.

The orientation of the emissive sites in spontaneously emitting materials utilized in OLEDs is determined by the molecular morphology of the particular material. Considering *polymeric* materials deposited from solution by spin-coating, the polymer chains usually align in the plane of the film and the emissive sites tend to adopt this preferential orientation, as indicated by various photoluminescence (PL) and Raman studies [4,9–11]. Still, the chromophore could be attached to a polymer side-chain rather than to the backbone, which would cancel any orientation-correlation suggested from the spin-coating process. For a long time, vacuum deposited *small-molecule* materials were believed to have no preferred emitter orientation due to their rather isotropic, small molecular structure. Only recently, strong birefringence accompanied by a preferred parallel orientation of the transition dipole moments in vacuum deposited small molecular films was observed in PL investigations and attributed to the increased molecular length of the molecules [12].

In general, PL experiments suffer from the fact that the initially photo-generated excited states are not necessarily equal to those in EL operation [9]. Furthermore, the molecular orientation might depend on the exact deposition conditions and post-processing techniques [13]. Consequently, an *in situ* investigation of the orientation of the dipole transition moment in electrical operation is desirable.

In this study we propose and demonstrate a general method to determine the orientation of the emissive dipole moments in OLEDs *in situ* via optical characterization. The method is based on two main ideas. First, a special OLED stack is utilized, where the distance between the emissive sites and the metallic cathode is well adapted. Due to constructive interference, the contribution of perpendicularly oriented dipoles to the radiation pattern in air is optically enhanced. Second, these perpendicular dipoles contribute to TM polarized light emission only. Consequently, the TE polarized emission can be utilized to investigate the profile of the emission zone and the internal electroluminescence spectrum independent of the emitter orientation. Subsequently analyzing the radiation pattern with TM polarization allows quantifying the contributions form parallel and perpendicular emitters. In general, the method can be applied to all classes of emissive materials for OLEDs, including *small-molecule* and *dendrimer* materials. However, in the present study we apply it to a *polymeric* emitter material and show that the actual orientation of the emissive sites must be described by a superposition of both, parallel and perpendicular components.

2. Method

2.1. Optical modeling

The angular (θ, angle to the layered system normal) and spectral (λ, wavelength) radiation pattern of an emitter inside the OLED stack is simulated assuming a continuously oscillating dipole source [5]. The dipoles electromagnetic fields in the system are evaluated using a transfer-matrix formulation of the well known Green's function model by Chance et al. [14]. For further details on the generation of the dipole fields see Ref. [15] and references therein. In order to ensure normalization of the power emitted from the dipole in the layered system, we utilize the equivalence between the probability for spontaneous emission of a photon via a dipole transition and the radiated power of a classical dipole source in the corresponding layered system [5]. By this means, the so-called microcavity effect or rather the influence of OLED stack on the rate of emission can be regarded [3].

At this point it is worth noting that all calculations are performed with a self-developed software tool. Each layer within the OLED stack is assumed to have smooth, parallel interfaces and a certain thickness. The interaction between materials and radiation is regarded by the wavelength-dependent complex refractive index ($n + i\kappa$, with refractive index n and extinction coefficient κ). The emissive material is treated as loss-free when simulating the light generation process [5], whereas the complex refractive index is used to describe light propagation through the emissive layer and all other layers of the multilayer system utilizing a transfer-matrix method [16]. *Polymeric* as well as *small-molecule* materials are likely to exhibit birefringent optical properties [10,12], having different optical properties in the plane of the film ($n_{||}$, $\kappa_{||}$) and normal to the plane ($n_{\perp}$, $\kappa_{\perp}$). This optical birefringence and its dispersion can be fully accounted for in our simulations, based on previous approaches [4,17].

In real OLED devices the emissive material can be treated as an ensemble of incoherent radiators [18], where distributions in (a) emitter location, (b) dipole orientation, and (c) wavelength-dependent spectral intensity account for (a) the profile of the emission zone, (b) the distribution of emitter orientation, and (c) the internal EL spectrum. Finally, the emission pattern from the OLED $P(\theta,\lambda)$ can be obtained by an incoherent superposition of all single emitter contributions. By this means, $P(\theta,\lambda)$ corresponds to the experimentally accessible radiant intensity of a device.

2.2. Basic measurement approach

As illustrated in Fig. 1, any particular orientation of the emissive dipole moment can be decomposed into the three orthogonal dipoles (||TE, ||TM, ⊥TM). Parallel dipole moments contribute to both TE and TM polarized radiation, whereas perpendicular moments emit TM polarized radiation only [5,15]. Consequently, polarization dependent measurements allow the separation of the contributions from parallel and perpendicular dipoles. One basic idea for our measurement is to analyze the TE polarized radiation at first and determine the internal EL spectrum as well as the profile of the emission zone. This step is independent of the dipole orientation, since perpendicular dipole moments do not contribute to TE polarized radiation [19]. Keeping the internal EL spectrum and emission zone fixed while analyzing TM polarized radiation, the emitter orientation remains the only unknown parameter, which can be adjusted to match TM experiment and simulation.

In order to sense perpendicular dipoles in the TM polarized optical far-field of an OLED, their contributions to the radiation pattern must be sufficiently large compared to the TM polarized contributions arising from parallel dipoles. Here, we take advantage of the fact that the three orthogonal electrical dipoles interfere in different ways with the surrounding layered system. Additionally, they exhibit intrinsically distinct radiation patterns [5], which are schematically indicated in Fig. 1. Furthermore, the propagation through the surrounding layered system is polarization-dependent. As a result, the contribution of the three orthogonal dipoles to the far-field radiation pattern and to the device efficiency is significantly different.

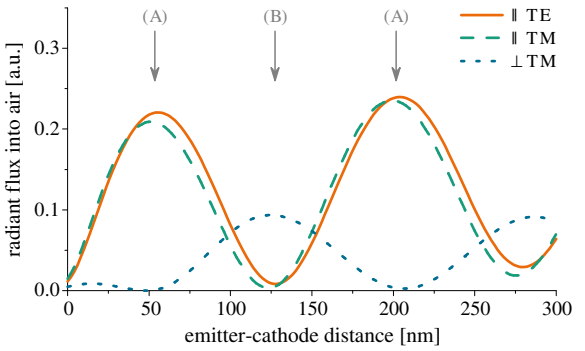

Fig. 2. As a measure for the contribution to the OLEDs far-field radiation pattern, the calculated radiant flux at λ = 500 nm is shown as a function of the emitter–cathode distance for the three single dipoles ||TE (line), ||TM (dashed), and ⊥TM (dotted) embedded in the OLED stack depicted in Fig. 3 but with 300 nm EML thickness. Evidently, parallel and perpendicular dipoles experience opposite interference conditions. In common, optimized OLEDs the emissive sites are placed around positions (A) to ensure a large optical outcoupling efficiency for parallel dipoles. However, position (B) is favorable for the detection of contributions from perpendicular transition moments in the optical far-field.

This is particularly evident in bottom emitting OLED structures where the emitter interacts with its reflected field from the metallic cathode and the interference conditions depend on the emitter-cathode distance.

As a measure of the far-field contribution, the radiant flux (i.e. emitted intensity into air integrated over all emission angles) at λ = 500 nm of the three orthogonal dipoles embedded in an OLED stack (300 nm emissive layer thickness, see Fig. 3 for details of the stack) was calculated as a function of the emitter–cathode distance (see Fig. 2). Evidently, the emission from parallel and perpendicular emitters experiences opposite interference conditions. This might be surprising at first, because one might expect that the difference in phase shift of approximately π (at moderate emission angles) upon reflection of TE and TM polarized light at the cathode results in a different interference behavior for TE and TM radiation. However, the typical character of dipole emission has to be taken into account as well, i.e. the interference behavior additionally depends on the initial phase relation of the relevant electromagnetic fields emitted by the dipoles in the *backward* direction towards the cathode and the *forward* direction towards the OLED substrate. The *forward* and *backward* emitted electric TE fields of a parallel oriented dipole (||TE) oscillate in phase initially. In case of the magnetic TM fields, there is a π phase difference for a parallel emitter (||TM), but an in-phase-behavior for perpendicularly oriented dipoles (⊥TM) [20]. Combining both effects (the phase difference due to cathode reflection and the initial phase relation of the emitted fields) results in a similar interference behavior for the TE and the TM waves of parallel dipoles (||TE, ||TM) while the interference effects of the radiation from perpendicularly oriented emitters are shifted by π (⊥TM). This π phase shift corresponds to a discrepancy in the emitter–cathode distance of a quarter wavelength $\lambda/(4n_{EM})$, where n_{EM} is the refractive index of the emissive material. Thus, at emitter–cathode distances where parallel emitters experience constructive interfer-

ence, destructive interference emerges for perpendicularly oriented emitters and vice versa. Constructive interference of parallel dipoles is expected at emitter–cathode distances of $1\cdot\lambda/(4\,n_{EM})$, $3\cdot\lambda/(4\,n_{EM})$, ..., and constructive interference of perpendicular dipoles occurs at emitter–cathode distances of $2\cdot\lambda/(4n_{EM})$, $4\cdot\lambda/(4\,n_{EM})$, ... The rigorous numerical simulation predicts slightly displaced positions of interference maxima and minima as the imperfect cathode mirror induces a non-ideal phase shift. Although the considerations above are strictly valid only for single, small emission angles θ, minor deviations occur when the radiant flux is analyzed (see Fig. 2).

In our case the optimum emitter position for an efficient OLED stack emitting preferentially into air would be around 50 nm or around 200 nm (positions (A) in Fig. 2) where parallel dipole contributions experience constructive interference. At these positions the perpendicular contributions undergo destructive interference. Consequently, the distribution of the dipole moment orientation is almost impossible to be obtained using standard, efficient OLED geometries, because virtually all light generated by perpendicularly oriented emitters is trapped inside the OLED stack. In contrast, changing the emitter–cathode distance by $\approx\lambda/(4n_{EM})$ to about 125 nm (position (B) in Fig. 2) yields a large far-field contribution from perpendicular dipole moments accompanied by weaker outcoupling of the radiation from parallel dipoles. This is the desired case for the present measurement.

It is worth noting that Fig. 2 illustrates the typical misery for light-emitting materials with isotropic emitter orientation: at the position for optimal outcoupling almost all light from perpendicular dipoles is trapped inside the OLED stack. Thus, nearly one third of the intrinsically emitted light is lost to the multilayer system.

2.3. Experimental

The calculations summarized in Fig. 2 are based on a monochromatic emitter localized at a single position within the emissive layer. However, most real OLEDs exhibit an expanded emission zone and a broad emission spectrum. Therefore, the interference contrast reduces and the intensity difference between TM radiation from parallel and perpendicular dipoles decreases in comparison to Fig. 2.

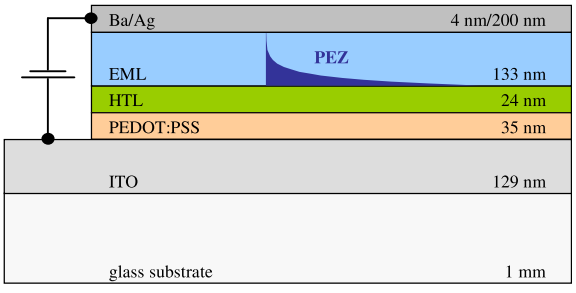

Fig. 3. The structure of the OLED utilized in this study and the exponentially decaying profile of the emission zone (PEZ) are schematically shown.

In order to still observe radiation from perpendicular dipoles in the optical far-field, the emission zone must be relatively well confined and the distance of the emissive sites to the cathode must be well adapted. In *small-molecule* OLEDs the emissive layer (EML) can be made very thin and the emitter–cathode separation can be adjusted via the thickness of an additional electron transport layer. *Polymeric* OLEDs can exhibit a confined emission zone at the anode sided interface of the EML if the emissive material is electron-dominated [2]. Accordingly, changing the EML thickness corresponds to a variation of emitter–cathode distance in this case.

We followed the latter approach in our study utilizing a *polymeric* OLED. A sketch of the OLED stack used is depicted in Fig. 3. The organic layers PEDOT:PSS (35 nm, Clevios P AI4083), hole transport layer [21] (HTL, 24 nm), and blue emitting conjugated polymer [2] (EML, 133 nm) were deposited by spin-coating on commercial glass substrates pre-coated with indium tin oxide (ITO, 129 nm). The HTL was crosslinked to immobilize the material prior to the deposition of the EML [22]. Finally, a thermally evaporated cathode of Barium (Ba, 4 nm) and Silver (Ag, 200 nm) capped the stack. For the approach described here, the EML thickness was adjusted to 133 nm in order to match the desired interference criterion around the mean wavelength of the internal EL spectrum of the emissive material.

The prerequisite for any optical simulation concerning OLEDs is the knowledge of the *passive* optical properties of the layered system, i.e. the materials complex refractive indices and layer thicknesses. The complex refractive indices of the thin film materials were determined by a dispersion-model-free approach utilizing reflection–transmission-spectroscopy of single supported films [1]. This measurement revealed that the emissive material is birefringent and that the magnitude of birefringence is wavelength-dependent. However, the material properties are well described by a uniaxial refractive index model. In the wavelength-range of interest (400 – 650 nm) the measured complex refractive indices are given in the Appendix for completeness. In order to determine the layer thicknesses, several additional reference stacks were fabricated and analyzed by profilometry as well as by reflection–transmission spectroscopy [1]. By this means we were able to measure the thickness of each layer to an accuracy of ±2 nm.

The internal luminescence quantum efficiency q of the emissive material enters the simulation when evaluating the relative emission rates for parallel and perpendicular transition moments [3]. Because the investigated material is a fluorescent polymer, the q-value represents the fluorescence quantum efficiency for a radiative transition from the excited singlet state into the ground state of the material. Note that charge carrier spin statistics, or rather the ratio of generated excited singlet and triplet states, is not included in the q-value. However, q plays a minor role for the present investigation because (a) the relative emission rates for parallel and perpendicular dipoles are not essentially different from unity for the distance of the emissive sites to the cathode of about 133 nm and (b) the materials q-value does not influence the interference

conditions of the emissive sites [19]. Nevertheless, we determined the q-value of the emitter material to be $q = 0.27 \pm 0.05$ in electrical operation [3] and take all associated effects into account in the present analysis.

In order to access the optical far-field, polarized angular radiation patterns are recorded utilizing a rotational stage and a fiber-spectrometer. The resulting experimental data have an accuracy of $\Delta\lambda < 5$ nm and $\Delta\theta < 0.5°$ as well as an intensity uncertainty below 2%.

3. Results and discussion

3.1. TE-polarization: internal EL spectrum and profile of the emission zone

Perpendicularly oriented dipoles do not contribute to TE polarized radiation. Consequently, only parallel dipole moments need to be considered when analyzing the TE emission pattern. By fitting the simulated TE polarized far-field radiation pattern to the experimental data across the whole spectral (λ = 400–650 nm) and angular (θ = 0°–90°) range, the internal EL spectrum of the emissive material and the profile of the emission zone can be deduced. For this analysis, the spectral characteristics of the far-field radiation pattern hold information about the internal EL spectrum [Fig. 4(f)], which was found to be identical to the previously determined PL spectrum [2] within the precision of the measurement. Furthermore, the angular characteristics of the emission pattern are related to the interference conditions at the position of the emissive sites and provide information about the emission zone. In a previous study, we have provided direct evidence for electron-dominated current in the emissive material and the former data indicated that the emission is exclusively generated within a about 10 nm wide sheet at the EML-HTL interface [2]. However, in the present study the emission pattern can be modeled satisfactorily only when assuming an exponentially shaped profile at the anode sided interface of the EML with an 1/e-width of (10 ± 2) nm, in agreement with Ref. [2].

Measured and modeled TE polarized emission patterns are shown in Fig. 4 (a–e) for representative constant emission angles ($\theta = 0°$, $\theta = 72°$) and emission wavelengths (λ = 450 nm, λ = 500 nm, λ = 550 nm). Perfect coincidence between experiment and simulation over the whole angular and spectral range is found, suggesting a high quality of the measurement and the theoretical model. The spectral emission in forward direction (Fig. 4(a), $\theta = 0°$) and into oblique emission angles (Fig. 4(b), $\theta = 72°$) is considerably suppressed for spectral components around 500 nm due to the desired destructive interference of parallel dipole contributions. Furthermore, as a result of the pronounced interference conditions at the position of the emissive sites, the angular radiation characteristics deviate from a Lambertian emission significantly [see Fig. 4(c–e)]. Still, the remarkably modulated behavior can be reproduced well by the simulation in the whole spectral range of emission. In fact, this pronounced angular characteristic allows for an accurate determination of the profile of the emission zone (PEZ). As an example, Fig. 5 shows the expected angular emission pattern at λ = 500 nm for a slightly narrower emission zone (Fig. 5(a), PEZ-width = 8 nm) and for a slightly broader emission zone (Fig. 5(b), PEZ-width = 12 nm). In both cases, there is a significant disagreement between simulated and experimental data, indicating a nanometer accuracy for the measurement of the emission zone. Similarly, the measured angular emission characteristics cannot be modeled accurately assuming any other emission zone which is of a different qualitative shape but still physically meaningful, e.g. a Gaussian profile centered at the HTL-LEP interface. Solely an exponential profile leads to a satisfactorily agreement between simulated and experimental data.

In result, the internal EL spectrum and the profile of the emission zone of the emissive material are disclosed. Both *active* material properties will be kept fixed for any further analysis.

3.2. TM-polarization: emitter-orientation

At this stage the only parameter remaining unknown is the distribution of the emissive sites in the emissive material, or rather the relative amount of perpendicular dipoles contributing to the radiation pattern. As pointed out above, the analysis will be most sensitive to contributions of perpendicular emitters in those spectral ranges where the parallel emitter contributions undergo destructive interference. Here, the OLEDs microcavity was designed to match this criterion at a wavelength of around 500 nm.

Fig. 6 shows the measured TM polarized emission pattern for representative constant emission angles ($\theta = 60°$, $\theta = 72°$) and emission wavelengths (λ = 450 nm, λ = 500 nm, λ = 550 nm), accompanied with the simulated emission pattern assuming contributions from *parallel dipole moments only*. In comparison to the simulations shown in Fig. 4, no assumption and no parameter has been changed; the polarization of the radiation is the only difference between Fig. 4 and Fig. 6. The emission in forward direction ($\theta = 0°$) arises from parallel dipoles only and the two polarization states TE and TM cannot be distinguished at $\theta = 0°$. Accordingly, there is perfect coincidence between measured and modeled emission in forward direction (Fig. 6(c–e) for $\theta = 0°$), similar to the TE polarization (Fig. 4). Regarding oblique emission angles on the contrary, the simulated emission spectra [Fig. 6(a and b)] and angular radiation pattern [Fig. 6 (c–e)] significantly underestimate the measured TM-emission in the wavelength range 450 nm $\leqslant \lambda \leqslant$ 550 nm. This clearly indicates missing contributions from perpendicular dipole moments in the calculation. It is worth noting, that the discrepancies are of a qualitative nature and cannot be compensated by simply scaling the datasets. Still, there are spectral regions (λ < 450 nm and λ > 550 nm) where the TM radiation characteristics can be modeled quite accurately assuming parallel dipoles only. These correspond to spectral ranges outside of the desired interference criterion, i.e. with too few perpendicular emitter contributions with respect to the emission caused by parallel active sites. This reflects the situation found in common, optimized OLEDs where the perpendicular dipole contributions are "invisible" in

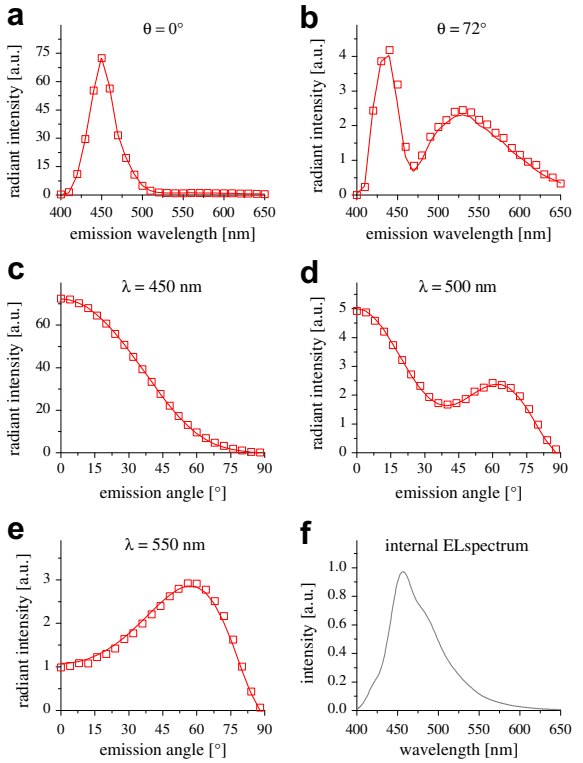

Fig. 4. The measured TE radiation pattern (squares) is shown for representative constant emission angles (a), (b) and emission wavelengths (c–e). By corresponding reverse simulations (lines), the internal EL spectrum of the emissive material (f) and the profile of the emission zone (not shown) were deduced.

the optical far-field relative to the rather intense emission from parallel dipoles.

In contrast, *including perpendicular dipole moments* into the simulation, the measured TM polarized emission pattern can be modeled accurately across the whole spectral and angular range (see Fig. 7). The simulated data in Fig. 7 correspond to a fraction of $p_{\perp} = (0.07 \pm 0.02)$ perpendicular dipoles, provided that $p_{||} = 1.00$ parallel dipoles contribute to the radiation pattern. The uncertainty of ±0.02 arises equally from the error in the width of the profile of the emission zone and the uncertainty of the refractive index measurement for the perpendicular refractive index. In other words, 93.5% parallel and 6.5% perpendicular dipole moments generate the radiation pattern of the *polymeric* emissive material. Assuming that the orientation of the emissive dipole moments follows a Gaussian distribution, this result means that the dipoles stagger around the preferred parallel direction with an 1/e-angle of about ±22°. Note that the isotropic emitter orientation commonly associated with *small-molecule* emissive materials corresponds to a fraction of 66.7% parallel and 33.3% perpendicular dipole moments.

Finally, it is worth recapitulating the parameters entering the calculation and how they were acquired: (a) the *passive* optical properties of the layered system (material refractive indices and layer thicknesses) were determined by separate spectroscopic methods [1], (b) the q-value of

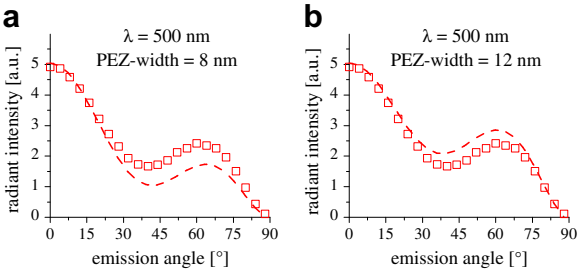

Fig. 5. Measured TE polarized angular emission characteristics at $\lambda = 500$ nm (squares) and corresponding simulations (dashed) assuming a slightly narrower (a) and slightly broader (b) emission zone. The discrepancies illustrate the high accuracy of the profile of the emission zone (PEZ) determination (see Fig. 4(d), corresponding to a PEZ-width of 10 nm).

the emissive material has been measured in a previous study [3], and (c) the *active* parameters internal EL spectrum and profile of the emission zone were known from the analysis of the TE radiation pattern and were kept fixed. The amount of perpendicular dipole moments contributing to the radiation pattern then remained the only free parameter for the reverse simulation of the TM polarized emission. We note that the resulting perfect coincidence between experimental and modeled TE and TM radiation patterns across the whole spectral and angular range can only be achieved with this dataset of *passive* and *active* properties of the layered system and the emissive material, respectively. Changing the input-parameters beyond their confidence intervals would result in significant qualitative discrepancies between measurement and simulation.

4. Conclusions

In summary, we have presented a general method for the *in situ* determination of the emitter orientation in OLEDs. We applied the method to a *polymeric* emissive material and deduced the orientation of the emissive dipole moments from measurements of the optical far-field of OLEDs in electrical operation. According to our results, the radiation pattern is generated by a fraction of 93.5 % parallel and 6.5 % perpendicular dipole moments. By this means we were able to proof the existence of perpendicular dipole moments in polymeric OLEDs. This measurement was basically enabled by an adapted OLED stack with an unusual emitter–cathode separation which increased the visibility of perpendicular dipole transition moments in the optical far-field. Commonly used, more efficient OLED device architectures prevent the determination of emitter orientation from the far-field pattern, because only parallel emitters contribute significantly to the emission into air.

In general, the presented method can be applied to all classes of OLED emissive materials. It is noteworthy that for the present study the emissive material is assumed to consist of one emissive species with an intrinsic spectrum independent of the dipole orientation. However, without loss of generality different molecular moieties can be mod-

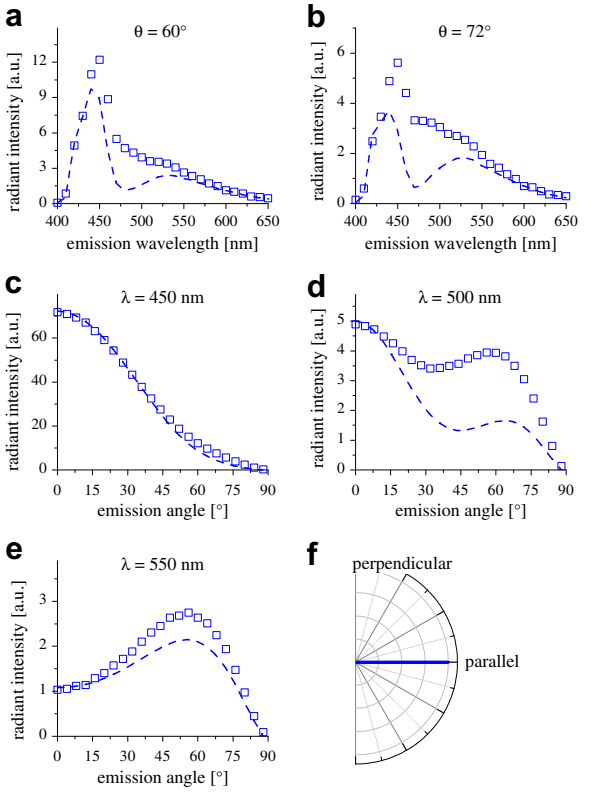

Fig. 6. The measured TM radiation pattern (squares) is shown for representative constant emission angles (a), (b) and emission wavelengths (c–e). The corresponding reverse simulations (dashed lines) are performed assuming parallel emitters only (f). The discrepancies indicate the missing contribution from perpendicular dipoles.

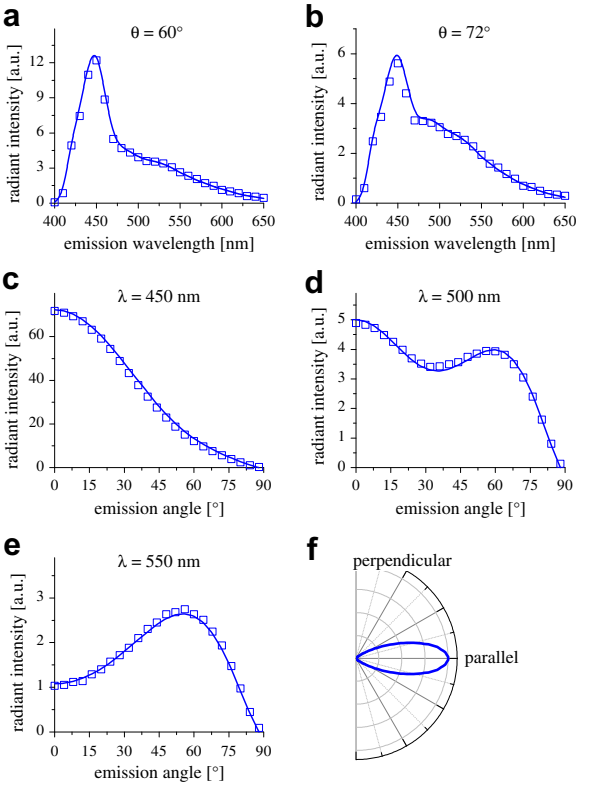

Fig. 7. The measured TM radiation pattern (squares) is shown for representative constant emission angles (a), (b) and emission wavelengths (c–e). The experimental data is identical to that in Fig. 6. The reverse simulations (lines) assume a fraction of 93.5 % parallel and 6.5 % perpendicular dipoles, corresponding to a Gaussian distribution where the dipoles stagger around the preferred parallel direction with an 1/e-angle of ±22° (f). Orientation of emissive dipoles in OLEDs: quantitative *in situ* analysis.

eled as a superposition of an appropriate number of emissive species with different emission spectra and orientation distributions. Provided the emission spectra are sufficiently distinct, the present approach can be extended to analyze all emitters individually. For this purpose additional OLED stacks featuring adapted ETL thicknesses might be required. Relevant examples worth noting here are three color white emitting polymer blends investigated previously [23,24] and polyfluorene, known to exhibit a rich phase behavior with significant impact on the emissive spectral characteristics [25].

The knowledge of the actual dipole orientation is a fundamental prerequisite to any precise quantitative simulation of the optical performance of OLEDs and to an accurate quantification of potential loss channels as well as to approaches to optimize the optical outcoupling efficiency of OLEDs. Moreover, estimates on internal emitter properties (singlet/triplet-ratio or internal luminescence quantum efficiency q) that start form external device measures (like the EQE) should be supported by precise information about the emitter orientation. Furthermore, the presented method could assist the development of new materials that exhibit a preferred parallel orientation of emissive species and thus promise higher optical outcoupling efficiencies.

Acknowledgements

The authors acknowledge financial support from the German Federal Ministry of Education and Research (BMBF) through the HOBBIT-project (FKZ 13N8951, FKZ 13N8952).

Appendix A

An approximation of refractive index n and extinction coefficient κ within the wavelength interval $\lambda = 400$–650 nm is (x = wavelength/100 nm): substrate: $n = 1.5 + 0.62/x^2$, $\kappa = 0$; ITO: $n = 1.3 + 2.6/x$, $\kappa = 0.03 - 0.01x + 0.001x^2$; PEDOT:PSS: $n = 1.42 + 0.66/x$, $\kappa = 0.07 - 0.031x + 0.004x^2$; HTL: $n = 1.57 + 0.2/x + 0.04/(x - 3.8)$, $\kappa = 0$; EML: $n_{||} = 1.42 + 1.7/x + 0.015/((x - 4.16)^2 + 0.03)$, $\kappa_{||} = 0.736 \cdot \exp[-((x - 4)/0.17)^2]$, $n_{\perp} = 1.51 + 0.2/x + 0.003/((x - 4.16)^2 + 0.03)$, $\kappa_{\perp} = 0.135 \cdot \exp[-((x - 4)/0.17)^2]$. The accuracy of the method used to determine these values [1] is about $\Delta n_{||} \approx 0.01$, $\Delta k_{||} \approx 0.001$, $\Delta n_{\perp} \approx 0.05$, and $\Delta k_{\perp} \approx 0.02$. The metal cathode was described by the Silver optical properties taken from [26], neglecting the presence of the thin electron injection layer Barium. This approach has proven

to yield consistent results here, but might need to be confirmed for other cathode preparation conditions.

References

[1] M. Flämmich, N. Danz, D. Michaelis, A. Bräuer, M.C. Gather, J.H.-W.M. Kremer, K. Meerholz, Dispersion-model-free determination of optical constants: application to materials for organic thin film devices, Appl. Opt. 48 (8) (2009) 1507–1513.

[2] M.C. Gather, M. Flämmich, N. Danz, D. Michaelis, K. Meerholz, Measuring the profile of the emission zone in polymeric organic light-emitting diodes, Appl. Phys. Lett. 94 (26) (2009) 263301-1–263301-3.

[3] M. Flämmich, M.C. Gather, N. Danz, D. Michaelis, K. Meerholz, *In situ* measurement of the internal luminescence quantum efficiency in organic light-emitting diodes, Appl. Phys. Lett. 95 (26) (2009) 263306-1–263306-3.

[4] J.A.E. Wasey, A. Safonov, I.D.W. Samuel, W.L. Barnes, Effects of dipole orientation and birefringence on the optical emission from thin films, Opt. Commun. 183 (1–4) (2000) 109–121.

[5] K.A. Neyts, Simulation of light emission from thin-film microcavities, J. Opt. Soc. Am. A 15 (4) (1998) 962–971.

[6] J.-S. Kim, P.K.H. Ho, N.C. Greenham, R.H. Friend, Electroluminescence emission pattern of organic light-emitting diodes: implications for device efficiency calculations, J. Appl. Phys. 88 (2) (2000) 1073–1081.

[7] L.H. Smith, J.A.E. Wasey, I.D.W. Samuel, W.L. Barnes, Light out-coupling efficiencies of organic light-emitting diode structures and the effect of photoluminescence quantum yield, Adv. Funct. Mater. 15 (11) (2005) 1839–1844;
S. Nowy, B.C. Krummacher, J. Frischeisen, N.A. Reinke, W. Brütting, "Light extraction and optical loss mechanisms in organic light-emitting diodes: Influence of the emitter quantum efficiency", J. Appl. Phys. 104 (12) (2008) 123109-1–123109-9.

[8] N.C. Greenham, R.H. Friend, D.D.C. Bradley, Angular dependence of the emission from a conjugated polymer light-emitting diode: implications for efficiency calculation, Adv. Mater. 6 (6) (1994) 491–494;
B.C. Krummacher, S. Nowy, J. Frischeisen, M. Klein, W. Brütting, Efficiency analysis of organic light-emitting diodes based on optical simulation, Org. Electron. 10 (3) (2009) 478–485.

[9] H. Becker, S.E. Burns, R.H. Friend, Effect of metal films on the photoluminescence and electroluminescence of conjugated polymers, Phys. Rev. B 56 (4) (1997) 1893–1905.

[10] D. McBranch, I.H. Campbell, D.L. Smith, J.P. Ferris, Optical determination of chain orientation in electroluminescent polymer films, Appl. Phys. Lett. 66 (10) (1995) 1175–1177;
C. Soci, D. Comoretto, F. Marabelli, D. Moses, Anisotropic photoluminescence properties of oriented poly(*p*-phenylene-vinylene) films: effects of dispersion of optical constants, Phys. Rev. B 75 (7) (2007) 075204-1–075204-11.

[11] S.H. Garrett, J.A.E. Wasey, W.L. Barnes, Determining the orientation of the emissive dipole moment associated with dye molecules in microcavity structures, J. Mod. Opt. 51 (15) (2004) 2287–2295;
M.C. Gather, D.D.C. Bradley, an improved optical method for determining the order parameter in thin oriented molecular films and demonstration of a highly axial dipole moment for the lowest energy π–π^* optical transition, Adv. Funct. Mater. 17 (3) (2007) 479–485;
S.M. King, H.L. Vaughan, A.P. Monkman, Orientation of triplet and singlet transition dipole moments in polyfluorene, studied by polarised spectroscopies, Chem. Phys. Lett. 440 (4–6) (2007) 268–274.

[12] D. Yokoyama, M. Moriwake, C. Adachi, Spectrally narrow emissions at cutoff wavelength from edges of optically and electrically pumped anisotropic organic films, J. Appl. Phys. 103 (12) (2008) 123104-1–123104-13;
D. Yokoyama, A. Sakaguchi, M. Suzuki, C. Adachi, Horizontal orientation of linear-shaped organic molecules having bulky substituents in neat and doped vacuum-deposited amorphous films, Org. Electron. 10 (1) (2009) 127–137.

[13] H.-W. Lin, C.-L. Lin, C.-C. Wu, T.-C. Chao, K.-T. Wong, Influences of molecular orientations on stimulated emission characteristics of oligofluorene films, Org. Electron. 8 (2–3) (2007) 189–197.

[14] R.R. Chance, A. Prock, R. Silbey, Molecular fluorescence and energy transfer near interfaces, Adv. Chem. Phys. 37 (1978) 1–67.

[15] N. Danz, R. Waldhäusl, A. Bräuer, R. Kowarschik, Dipole lifetime in stratified media, J. Opt. Soc. Am. B 19 (3) (2002) 412–419.

[16] C.C. Katsidis, D.I. Siapkas, General transfer-matrix method for optical multilayer systems with coherent, partially coherent, and incoherent interference, Appl. Opt. 41 (19) (2002) 3978–3987.

[17] P.C. Clemmow, The plane wave spectrum representation of electromagnetic fields, Pergamon Press, 1966.

[18] N. Danz, J. Heber, A. Bräuer, R. Kowarschik, Fluorescence lifetimes of molecular dye ensembles near interfaces, Phys. Rev. A 66 (6) (2002) 063809-1–063809-7.

[19] As a result of considering the influence of the layered system on the rate of emission and the internal luminescence quantum efficiency q of the emissive material, there is a constant multiplicative factor to all TE contributions which is depending on the orientation of the emissive sites, i.e. depending on perpendicular dipoles as well. However, because this factor is constant to all TE contributions there is no influence on the TE interference conditions.

[20] This behavior corresponds to the change of signs in Eqs. (17) and (18) of Ref. [15].

[21] P. Zacharias, M.C. Gather, M. Rojahn, O. Nuyken, K. Meerholz, New crosslinkable hole conductors for blue-phosphorescent organic light-emitting diodes, Angew. Chem., Int. Ed. Engl. 46 (23) (2007) 4388–4392.

[22] N. Rehmann, C. Ulbricht, A. Köhnen, P. Zacharias, M.C. Gather, D. Hertel, E. Holder, K. Meerholz, U.S. Schubert, Advanced device architecture for highly efficient organic light-emitting diodes with an orange-emitting crosslinkable iridium(III) complex, Adv. Mater. 20 (1) (2008) 129–133;
M.C. Gather, R. Jin, J. de Mello, D.D.C. Bradley, K. Meerholz, Highly-efficient solution-processed phosphorescent multi-layer organic light-emitting diodes investigated by electromodulation spectroscopy, Appl. Phys. B 95 (1) (2009) 113–124.

[23] C.A. Wächter, N. Danz, D. Michaelis, M. Flämmich, S. Kudaev, A.H. Bräuer, M.C. Gather, K. Meerholz, Intrinsic OLED emitter properties and their effect on device performance, Proc. SPIE 6910 (2008) 691006-1–691006-11.

[24] A. Köhnen, K. Meerholz, M. Hagemann, M. Brinkmann, S. Sinzinger, Simultaneous color and luminance control of organic light-emitting diodes for mood-lighting applications, Appl. Phys. Lett. 92 (3) (2008) 033305-1–033305-3.

[25] A.J. Cadby, P.A. Lane, H. Mellor, S.J. Martin, M. Grell, C. Giebeler, D.D.C. Bradley, M. Wohlgenannt, C. An, Z.V. Vardeny, Film morphology and photophysics of polyfluorene, Phys. Rev. B 62 (23) (2000) 15604–15609.

[26] E.D. Palik, Handbook of Optical Constants of Solids, Academic Press, 1991.

fluorene) (PFO) based devices, relying on the evolution of electromodulation spectrum with the applied dc voltage. Screening of the applied electric field was observed in the presence of a low work function (Ba) cathode, which was supposed to be due to strong electron injection and accumulation at the anode interface [3]. In this paper, we investigate poly (9,9-di-(2-ethylhexyl)-9*H*-fluorene-2,7-vinylene)) (PFV) based devices with a relatively high work function (Al) cathode by electroabsorption (EA) spectroscopy to probe the effect of PEDOT:PSS on built-in voltage, and compare the experimental results with those obtained previously on PFO. In a second part, the thermally stimulated current (TSC) technique was used to probe the trapped charge density in poly (9,9-dihexylfluorene-co-*N*,*N*-di(9,9-dihexyl-2-fluorenyl)-*N*-phenylamine) (PF-*N*-Ph) based devices. First results show that this technique is adequate to characterize electron or hole trap levels that could be created deliberately close to the anode, or the cathode, respectively.

2. Experimental overview

Devices with an active area of 10 mm^2 were fabricated by successively spin coating an ITO anode with a 40–50 nm thick layer (2000 rpm, 60 s) of PEDOT:PSS (Baytron P VP AI4083, H.C. Starck), followed by a layer of polyfluorene. ITO coated glass substrates (VisionTek Systems Ltd.) were previously cleaned in successive ultrasonic baths of distilled water, ethanol and acetone. After drying in nitrogen atmosphere, they were treated by UV ozone before use. A 100 nm thick layer of poly (9,9-di-(2-ethylhexyl)-9*H*-fluorene-2,7-vinylene)) (PFV, Sigma–Aldrich) or a 70–80 nm thick layer of poly (9,9-dihexylfluorene-co-*N*,*N*-di(9,9-dihexyl-2-fluorenyl)-*N*-phenylamine) (PF-*N*-Ph) was deposited by spin coating. Their chemical structures are shown in Fig. 1. Finally, a 100 nm aluminium cathode was evaporated under high vacuum conditions ($<10^{-4}$ Pa) and the devices were encapsulated with a glass coverlid using a UV-cured epoxy resin.

Electromodulation spectroscopy was proposed [4] to probe internal electric field in organic components due to the inadequacy of conventional techniques for thicknesses lower than 5 μm [5]. This consists in applying to the device a combined ac modulation and dc operating voltage and measuring changes in the transmission (T) of a probe beam (150 W xenon lamp, Oriel) through the active layer(s) using phase sensitive lock-in detection (SR830, Stanford Research). The light beam entered the sample through the glass substrate with a 45° angle of incidence, and was detected after double transmission and reflection on the back aluminium electrode. Provided that the origin of the electromodulation signal is Stark effect (it is then called electroabsorption), theory predicts that the fractional change in transmission $-\Delta T/T$ is proportional to the third order dc Kerr nonlinear susceptibility and the square of the electric field. One can deduce that the differential transmission is then modulated at both the 1st and 2nd harmonic frequencies in accordance with the following equations:

$$-\frac{\Delta T}{T}(1\omega) \propto \mathrm{Im}\,\chi^3(\lambda) E_{dc} E_{ac} \cos(\omega t) \quad \text{1st harmonic}$$

$$-\frac{\Delta T}{T}(2\omega) \propto \mathrm{Im}\chi^3(\lambda) E_{ac}^2 \cos(2\omega t) \quad \text{2nd harmonic}$$

Under conditions of low carrier injection, the bulk electric field E_{dc} is related to the dc component of the applied voltage V_{dc} by $E_{dc} = (V_{dc} - V_{BI})/d$, where V_{BI} is the built-in voltage and d is the thickness of the layer. V_{BI} is thus the applied voltage at which the first harmonic (1ω) EA spectrum is cancelled.

To examine the change induced by the presence of interface states, which may be the origin of electron trapping at the anode side, TSC experiments were used to determine the traps in devices [6–8]. The measurements were carried out using a cryostat whose temperature was controlled by an Oxford ITC 503 unit. A Keithley 230 programmable voltage source coupled with a Keithley 617 electrometer was used for monitoring the TSC spectra.

Two similar types of structures have been fabricated which differ by the presence of PEDOT:PSS layer. ITO/PEDOT:PSS/PFV/Al and ITO/PFV/Al structures have been investigated by EA spectroscopy. ITO/PEDOT:PSS/PF-*N*-Ph/Al and ITO/PF-*N*-Ph/Al structures have been investigated by TSC technique.

3. Results and discussion

Fig. 2 shows the first harmonic electromodulation spectrum of an ITO/PFV/Al device for different applied dc voltages ranging from −3 to 1 V. The signal is composed of two broad peaks, centred at approximately 385 and 465 nm, respectively, and with opposite signs. The increase of the

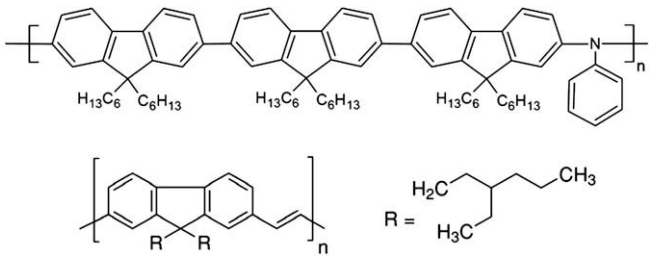

Fig. 1. Chemical structures of polyfluorene derivatives used in this study: poly (9,9-dihexylfluorene-co-*N*,*N*-di (9,9-dihexyl-2-fluorenyl)-*N*-phenylamine) and poly (9,9-di-(2-ethylhexyl)-9*H*-fluorene-2,7-vinylene), respectively.

applied dc bias does not modify the shape of the 465 nm peak, which is not clear for the 385 nm peak. The origin of the 385 nm could be a combination of Stark effect and effects that might arise from photogenerated charges [9]. We, therefore, focused on the low energy (465 nm) peak and verified the linear variation of the 1ω signal and the quadratic variation of the 2ω signal with V_{ac}, in agreement with the electroabsorption theory. As shown in the inset of Fig. 2, the extent of the electroabsorption spectrum [10] can be correlated with the PFV absorption range. Interestingly, one can measure an electroabsorption spectrum for $V_{dc} = 0$ V, which proves the existence of an internal built-in electric field.

Fig. 3 shows the first harmonic electromodulation spectrum of an ITO/PEDOT:PSS/PFV/Al device for different applied dc voltages ranging from −3 to 3 V. The signal is very similar in shape to that of Fig. 2, although a ∼8 nm wavelength shift was noticed that we could not explain.

In Fig. 4, the evolution of the low-energy peak as a function of applied dc bias was reported. A linear variation was obtained in agreement with the theoretical prediction of electroabsorption. The different slopes observed for ITO/PFV/Al and ITO/PEDOT:PSS/PFV/Al devices are due to different values of V_{ac} used for measurements. Built-in voltages deduced from Fig. 4 are 1 and 1.9 V, respectively.

The current–voltage characteristics presented in the inset of Fig. 4 show a strong reduction of the threshold voltage when using PEDOT:PSS. This voltage, above which a large double injection occurs, passes from approximately 10–15 to 3–4 V. Obviously, this result can be attributed to the anode modification. However, the 0.9 V increase of built-in voltage is inconsistent with the work function difference between ITO and PEDOT:PSS. Approximate values of 4.9 eV for ITO and 5.2 eV for PEDOT:PSS have been measured by Kelvin probe and supplied by H.C. Starck, respectively. Interestingly, the values of built-in voltages measured in the presence or not of PEDOT:PSS are very similar to those measured in PFO-based devices [3]. According to Lane et al. [11], the addition of a PEDOT:PSS layer leads to a pinning of the Fermi level of the anode to the HOMO of the active layer. Indeed, the built-in voltage was found to be nearly equal to the difference between the PFO ionization potential (5.8 eV) and the approximate value of aluminium work function (4.1 eV). Our results are in accordance with this theory, considering the ionization potential of PFV (5.73 eV) [12]. The hypothesis of the accumulation of negative charges at the PEDOT:PSS/polyfluorene interface may thus be generalized to various polyfluorene derivatives, which motivated the following investigation of trapped charges in PF-*N*-Ph based devices by an alternative method, namely the TSC technique.

Fig. 5 shows TSC characteristics measured on ITO/PEDOT:PSS/PF-*N*-Ph/Al diode with different charging voltages: $V_C = -6, -4, -2, +2, +3, +4, +5, +6$ V. The TSC spectra intensity increased with the applied voltage as observed in trap measurements of OLEDs, indicating that the trap filling depends on the bias condition [13]. A large width peak, which appears distributed in the temperature range (100–280 K), is clearly observed. Furthermore, the intensity of the peaks is lower for negative applied voltages compared to that obtained in diodes biased with positive applied voltages. All the peaks cannot be clearly distinguished because of their overlapping. However, with a reverse voltage, two peaks are observed with the following relaxation temperatures $Tm \sim 150$ K and $Tm \sim 200$ K. With a forward applied voltage higher than 3 V, two shoulders appear clearly at $Tm \sim 125$ K and $Tm \sim 250$ K in addition to these two peaks, indicating that additional trapped charges are released. The TSC peaks are denoted as A, B, C, and D.

Due to the overlapping of TSC peaks (A, B and C), TSC spectra display broad peaks and hence the position of the individual peaks and theirs trap parameters could not be clearly determined. For resolving TSC spectra, we obtained the activation energy E_T of each peak by the initial rise

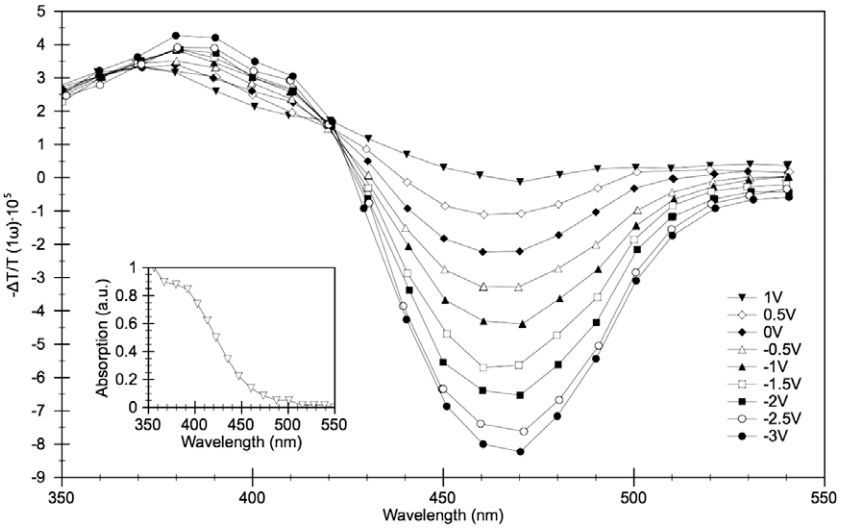

Fig. 2. 1 kHz first harmonic (1ω) electroabsorption spectra of an ITO/PFV (100 nm)/Al structure at various applied dc reverse biases. Inset: absorption spectrum of a PFV film in the visible range.

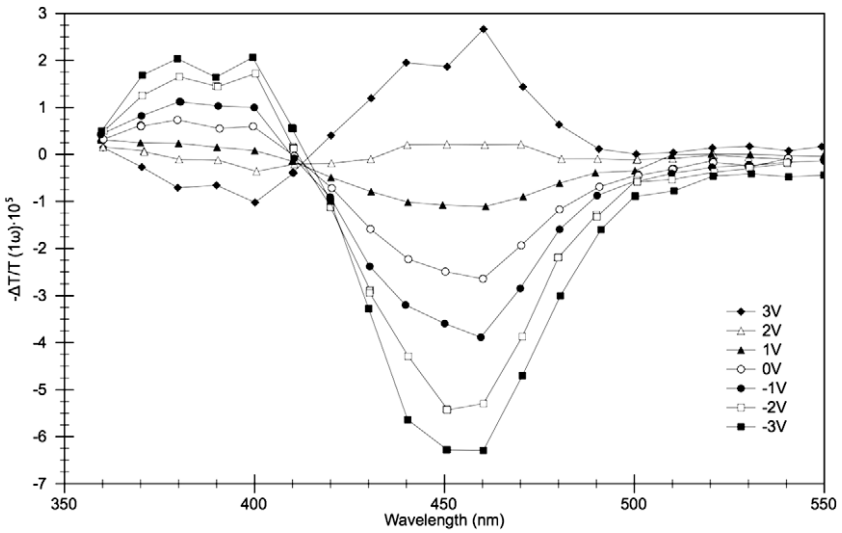

Fig. 3. First harmonic (1ω) electroabsorption spectra of an ITO/PEDOT:PSS (50 nm)/PFV (100 nm)/Al structure at various applied dc biases. 0.3 V rms modulation bias of frequency 1 kHz was used.

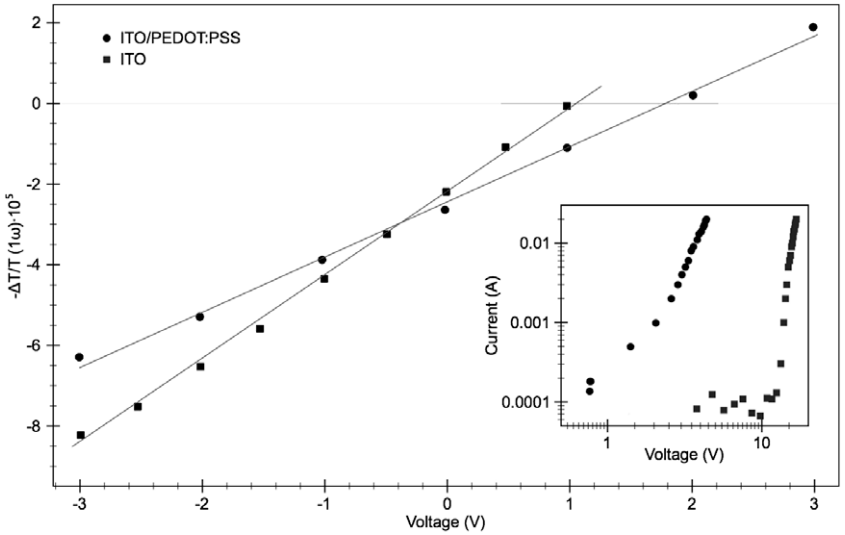

Fig. 4. Variation of the electroabsorption signal at 465 and 457 nm as a function of the applied dc bias for the ITO/PFV (100 nm)/Al and ITO/PEDOT:PSS (50 nm)/PFV (100 nm)/Al structures, respectively. Their current–voltage characteristics are presented in the inset.

method and its density by the measurement of the corresponding TSC intensity. Each individual component has been then computed from Cowell and Woods' relation [14] knowing its determined activation energy E_T and its peak position obtained by measuring the TSC spectra with different charging voltages. Next, by subtracting the computed spectrum from the experimental one, we obtained step by step, the values of activation energy of those peaks whose position could be identified by varying the applied voltage as explained previously.

In the inset of Fig. 5, the current–voltage characteristic of ITO/PEDOT:PSS/PF-*N*-Ph/Al at $T = 300$ K is reported. The diode shows a turn-on voltage of $V_{TO} \sim 4$ V. Peaks A and D depend strongly on the applied voltage, and appear when $V_C > V_{TO}$ suggesting that they are minority-like traps. Furthermore, at high temperatures (>300 K), we note the onset of an additional peak labelled E, which is visible in both directions.

Fig. 6 shows the decomposition of TSC spectra obtained with $V_C = +6$ V using the fitting curve to evaluate the activation energy and the trap density. The decomposition of TSC spectra obtained with $V_C = +6$ V is reported in the inset of Fig. 6. It is noted that the intensities of the peaks are lower in reverse direction than in forward direction. The decomposition of TSC spectrum with $V_C = -6$ V shows that the intensities of peaks A and D are smaller than that of peaks B and C suggesting that the latter is related to the injection of majority carrier, while at $V_C = +6$ V, peaks A

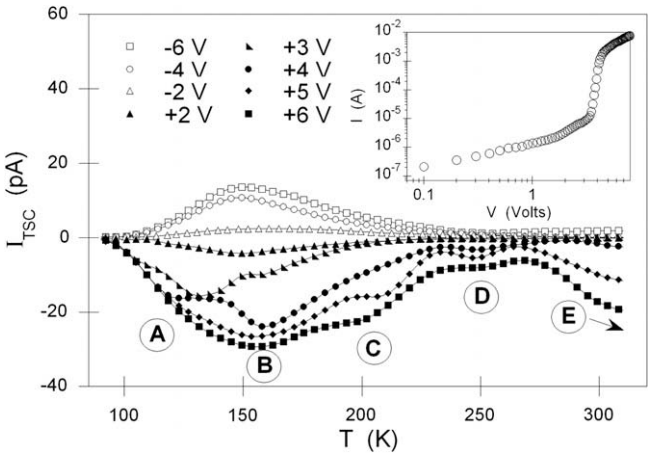

Fig. 5. TSC spectra recorded in an ITO/PEDOT/PF-*N*-Ph/Al diode using the following parameters: T_H = 300 K, β = 0.1 K/s, with different charging voltages: V_C = −6, −4, −2, +2, +3, +4, +5, +6 V. Inset is *I–V* characteristics of ITO/PEDOT/PF-*N*-Ph/Al structure measured at *T* = 300 K.

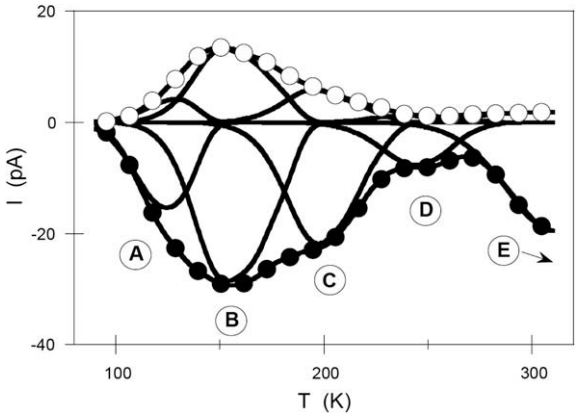

Fig. 6. Resolution of the TSC spectrum obtained with the following parameters: T_H = 300 K, β = 0.1 K/s, V_C = +6 V (●) and V_C = −6 V (○) by using the computed curves from the Cowell and Woods' relation [14] with the activation energies determined from the Arrhenius plots.

and D have stronger intensity indicating that they are related to minority carriers. As peak E is not entirely visible, we could not identify clearly its type (electron or hole traps). The trap parameters determined from the decomposition analysis are summarized in Table 1. Note the trap density of the level E represents the inferior limit because the corresponding TSC peak is not entirely visible. The density of traps has been measured at an applied voltage of +6 V.

In order to observe the influence of the hole injection layer on the defect formation, ITO/PF-*N*-Ph/Al diodes have been investigated by TSC technique. Fig. 7 shows the TSC characteristics measured on ITO/PF-*N*-Ph/Al and ITO/PEDOT:PSS/PF-*N*-Ph/Al diodes with a charging voltage of V_C = 6 V. We note that peaks A, B, E are present in both devices whereas peaks C and D are only observed in ITO/PEDOT:PSS/PF-*N*-Ph/Al diode. The inset of Fig. 7 shows the current–voltage characteristic, measured at *T* = 300 K, indicating a turn-on voltage of V_{TO} = 8.5 V. By comparing *I–V* measured in both structures of diodes, we note that the density of current is lower in ITO/PF-*N*-Ph/Al diode

Table 1
Summary of the trap parameters in ITO/PEDOT:PSS/PF-*N*-Ph/Al and ITO/ PF-*N*-Ph/Al diodes.

Peak	*T* (K)	ITO:PEDOT:PSS/PF-*N*-Ph/Al		ITO/PF-*N*-Ph/Al	
		E_T (eV)	N_T (cm^{-3})	E_T (eV)	N_T (cm^{-3})
A	124	0.13	2.4×10^{16}	0.13	1.5×10^{16}
B	153	0.22	6.1×10^{16}	0.23	3.4×10^{16}
C	198	0.33	4.4×10^{16}	–	–
D	247	0.45	1.5×10^{16}	–	–
E	>320	0.59	$>2.7 \times 10^{16}$	0.57	$>1.5 \times 10^{16}$

whereas the turn-on voltage is higher than that of ITO/PEDOT:PSS/PF-*N*-Ph/Al diode because of the absence of the PEDOT:PSS layer which favours hole injection from the anode into the active layer.

Peaks A, B, E are present in both devices. By using the decomposition technique, the trap parameters related to peaks A, B, E observed in ITO//PF-*N*-Ph/Al diode have been determined and are reported in Table 1.

Types A, B, E traps observed in both devices have similar activation energies indicating that they have a similar origin. The density of traps is measured for V_C = +6 V. We can note that the trap density measured in ITO/PF-*N*-Ph/Al diode is lower than those determined in ITO/PEDOT:PSS/PF-*N*-Ph/Al diode. As observed in *I–V* characteristics, the density of current is higher for ITO/PEDOT:PSS/PF-*N*-Ph/Al diodes due to the presence of PEDOT:PSS that favours hole injection. Consequently, more charges are injected into the active layer and hence more charges are trapped. As types C and D traps are not detected in ITO/PF-*N*-Ph/Al diodes, their formation are therefore related to the presence of the PEDOT:PSS layer, confirming the hypothesis previously formulated [3].

4. Conclusion

We have investigated the modifications of the interface formed between a PEDOT:PSS layer and the active polymer in polyfluorene derivative (PFV and PF-*N*-Ph) based diodes.

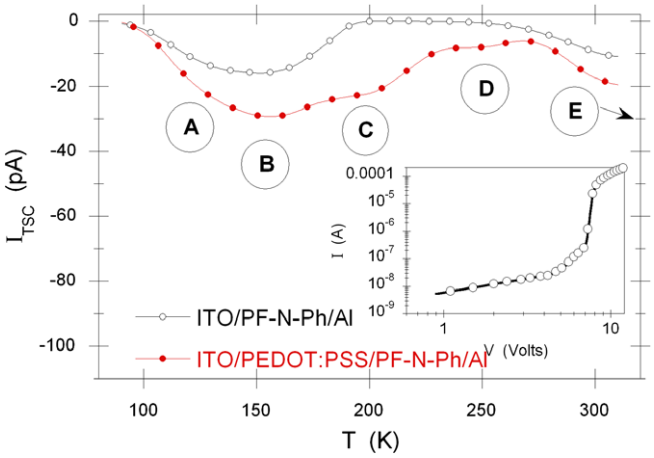

Fig. 7. TSC spectra recorded in ITO/PEDOT/PF-*N*-Ph/Al (●) and ITO/ PF-*N*-Ph/Al (○) diodes using the following parameters: T_H = 300 K, β = 0.1 K/s, with V_C = +6 V. Inset is *I*–*V* characteristics of ITO/PF-*N*-Ph/Al structure measured at *T* = 300 K.

By using two different spectroscopic techniques, which are complementary, we showed that the PEDOT:PSS/PF contact layer acts as an electron trapping surface, favouring accumulation of negative charges and thus an additional electric field at the interface. The presence of such a field modifies the electroabsorption spectrum of the diodes, as experimentally observed. Quantitative characterization of the trap centres has been performed using the TSC technique on diodes with and without a PEDOT:PSS layer, and the evidence of additional trap level creation induced by the PEDOT:PSS layer was clearly brought out. TSC is therefore proposed as a tool for deeper investigation of charge trapping at the electrodes. The data of the trap parameters could be used in future studies for modelling the charge injection from the anode of different devices, taking into account the PEDOT:PSS layer.

References

[1] H. Klauk, Organic Electronics: An Industrial Perspective, Wiley-VCH, 2006.
[2] S. Kirchmeyer, K. Reuter, Scientific importance, properties and growing applications of poly (3,4-ethylenedioxythiophene), J. Mater. Chem. 15 (2005) 2077–2088.
[3] P.J. Brewer, J. Huang, P.A. Lane, A.J. deMello, D.D.C. Bradley, J.C. deMello, Influence of poly (3,4-ethylenedioxythiophene)-poly (styrenesulfonate) in polymer LEDs, Phys. Rev. B 74 (2006) 115202–115208.
[4] I.H. Campbell, J.P. Ferraris, T.W. Hagler, M.D. Joswick, I.D. Parker, D.L. Smith, Measuring internal electric fields in organic light-emitting diodes using electroabsorption spectroscopy, Polym. Adv. Technol. 8 (1997) 417–423.
[5] M.A. Noras, Charge Detection Methods for dielectrics – Overview, Trek Application Note, Number 3005, 2003 (http://www.trekinc.com).
[6] R. Chen, Y. Kirsh, Pergamon, Analysis of Thermally Stimulated Processes, Pergamon Press Ltd., Oxford, 1981 (Chapter 1).
[7] J. Van derschueren, J. Gasiot, in: P. Braunlich (Ed.), Thermally Stimulated Relaxation in Solids, Springer Verlag, 1979 (Chapter 4).
[8] R.W. Haisty, Effect of illumination time on thermally stimulated currents in semi-insulating GaAs, Appl. Phys. Lett. 10 (1967) 31–35.
[9] V. Bodrozic, M. Roberts, N. Phillips, J.H. Burroughes, S. Mian, F. Cacialli, The influence of subgap features in the electromodulation and built-in voltage measurements of polyfluorene blue light-emitting diodes with anodic charge injection layers, J. Appl. Phys. 101 (2007) 084507–084516.
[10] E. Jalviste, N. Ohta, Theoretical foundation of electroabsorption spectroscopy: selfcontained derivation of the basic equations with the direction cosine method and the Euler angle method, J. Photochem. Photobiol. C 8 (2007) 30–46.
[11] P.A. Lane, P.J. Brewer, J. Huang, D.D.C. Bradley, J.C. deMello, Elimination of hole injection barriers by conducting polymer anodes in polyfluorene light-emitting diodes, Phys. Rev. B 74 (2006) 125320–125327.
[12] D.H. Hwang, J.D. Lee, J.M. Kang, S. Lee, C.H. Lee, S.H. Jin, Synthesis and light-emitting properties of poly (9,9,di-n-octylfluorenyl-2,7-vinylene) and PPV copolymers, J. Mater. Chem. 13 (2003) 1540–1545.
[13] A.G. Werner, J. Blochwitz, M. Pfeiffer, K. Leo, Field dependence of thermally stimulated currents in Alq_3, J. Appl. Phys. 90 (2001) 123–126.
[14] T.A.T. Cowell, J. Woods, The evaluation of thermally stimulated current curves, Brit. J. Appl. Phys. 18 (1967) 1045–1051.

5-dioctyl-2,5-dihydropyrrolo [3,4-] pyrrole-1,4-dione] PCBTDPP, one of the best in this new class of low-bandgap polymers [11,12], in bulk heterojunction (BHJ) solar cells (OPV). Our preliminary measurements demonstrated a PCE of 1.6% from this class of materials [11]. Through further optimizations of the active layer thickness, donor/accepter loading ratio, and the selection of solvent, we have improved PCE from 1.6% to 3.2% when PCBTDPP is blended with $PC_{70}BM$.

Solar cells were fabricated using blends of PCBTDPP and $PC_{60}BM$ or $PC_{70}BM$ in different solvents and/or ratios and at various spin coating rates to reach desired active layer parameters. Precleaned indium tin oxide (ITO) coated glass substrates were used as anode. Poly(3,4-ethylenedioxythiophene):poly(sterenesulfonate) (PEDOT:PSS) was spin coated at 7000 rpm for 60s and baked for 1 h at 120 °C, as hole transport layer. After cooling down to room temperature, active layers with desired ratio and thickness were spin coated on top of the PEDOT:PSS layers. Finally, a lithium fluoride (LiF)/aluminium (Al) cathode was thermally evaporated through a shadow mask under high vacuum. The active area of the solar cell is 1 cm^2.

Scheme 1 presents the chemical structure of PCBTDPP and the energy level diagram of the BHJ solar cells.

The photovoltaic performances of those solar cells were tested under AM 1.5G irradiation of 100 mW cm^{-2}, which was calibrated using a KG5 filter covered silicon photovoltaic solar cell traceable to the National Renewable Energy Laboratory (NREL).

2. Experimental results

The thin film UV–Vis absorption spectra of pristine (PCBTDPP), $PC_{60}BM$ and $PC_{70}BM$ are shown in Fig. 1.

The pure PCBTDPP film exhibits two main absorption bands in the visible range, one in the wavelength range of 332–483 nm and the other in 502–760 nm, leaving an absorption minimum around 500 nm. As compared to $PC_{60}BM$, $PC_{70}BM$ has significantly higher absorption in the spectral range of 400–600 nm, complementary to the absorption minimum of PCBTDPP, making $PC_{70}BM$ a better electron donor material for use with PCBTDPP in BHJ solar cells.

Fig. 2 shows the external quantum efficiency (EQE) spectra of the solar cells composed of PCBTDPP blended with $PC_{60}BM$ and $PC_{70}BM$. The measured devices in each case were fabricated with the best weight ratio and thickness of active layer for $PC_{60}BM$ and $PC_{70}BM$, respectively. The EQE of $PC_{60}BM$-based device shows a maximum of 34% at 665 nm with a drastic decrease around 500 nm, which is consistent with the absorption data discussed in Fig. 1. On the other hand, the $PC_{70}BM$-based device demon-

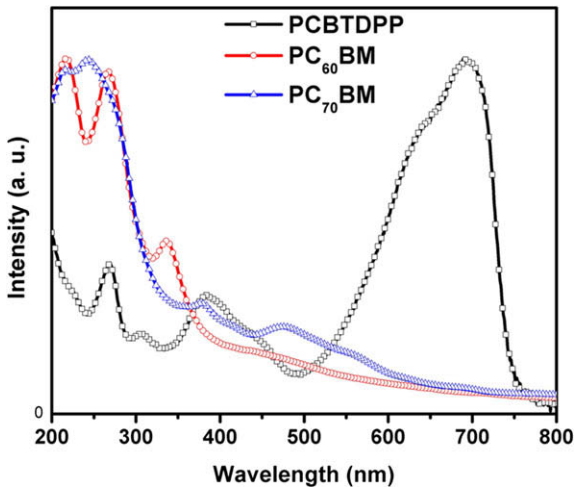

Fig. 1. UV–visible absorption spectra of PCBTDPP, $PC_{60}BM$ and $PC_{70}BM$ films.

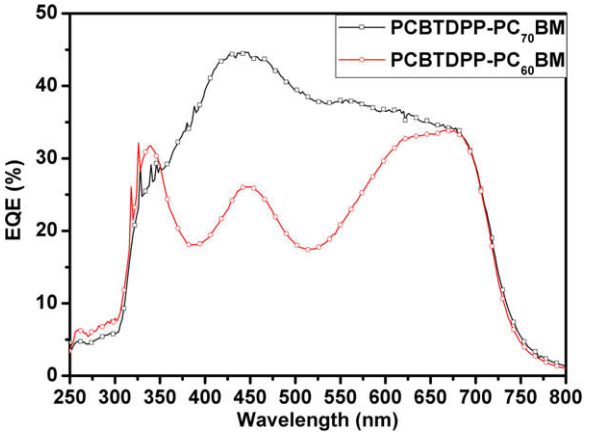

Fig. 2. EQE spectra of PCBTDPP blended with $PC_{60}BM$ (1:3) and $PC_{70}BM$ (1:3) devices.

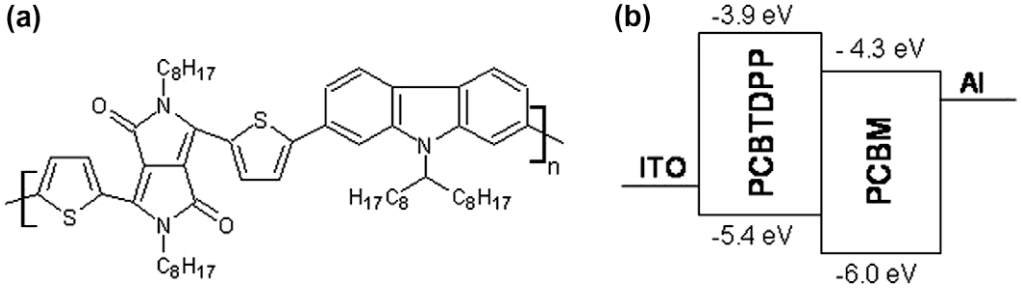

Scheme 1. (a) Chemical structure of PCBTDPP. (b) Energy band diagram of the BHJ solar cell (PCBTDPP: PCBM).

strates increased EQE across the whole visible spectral range, with a maximum of 45% at 450 nm, which indicates that the $PC_{70}BM$ is a much better acceptor than $PC_{60}BM$ for use with PCBTDPP. All the following optimizations will be done with this acceptor.

In order to optimize the ratio, thickness, and morphology of PCBTDPP:$PC_{70}BM$ bulk heterojunction films and study their effects on the device performance, solar cells using this couple with different weight ratios (1:2, 1:3, 1:4), thicknesses (from 60 to 130 nm) were fabricated with different organic solvents, and tested using standard solar cell characterization procedures.

First, we tested the effect of the PCBTDPP:$PC_{70}BM$ ratio on the device performance (Table 1). With increasing $PC_{70}BM$ ratio, the open-circuit voltage remained the same for all devices, but the short-circuit current density increased from 6.7 mA/cm^2 to 7.9 mA/cm^2 when the ratio was increased from 1:2 to 1:3. It is known that higher acceptor ratio ($PC_{60}BM$ or $PC_{70}BM$) favours the formation of a phase separated interpenetrated network with sizable domains [13], which in turn favours effective charge separation. However, the current decreased again to 6.5 mA/cm^2 when the ratio was increased up to 1:4. The impact of the donor ratio on the fill factor is also obvious. The maximum value was obtained with a ratio of 1:3. It is clear that the concentration of $PC_{70}BM$ in the blend has a strong impact on J_{sc} and the FF. For the PCBTDPP:$PC_{70}BM$ system, the best ratio is 1:3. Too high a $PC_{70}BM$ ratio will not only lead to lower J_{sc} and fill factor, but also a lower V_{oc}. Janssen et al. have already shown that saturating the active layer with $PC_{70}BM$ leads to a decrease in the J_{sc} and fill factor due to phase separation [14].

Table 1
Best performance parameters of BJH solar cell with PCBTDPP:$PC_{70}BM$ composites of different weight ratios under AM1.5G illumination of 100 mW cm^{-2}.

(PCBTDPP:$PC_{70}BM$)	J_{sc} (mA/cm^2)	V_{oc} (V)	FF (%)	η (%)
1:2	6.7	0.8	41	2.2
1:3	7.9	0.8	47	3.0
1:4	6.5	0.8	40	2.0

Table 2
Performance parameters of PCBTDPP:$PC_{70}BM$ (1:3) BJH solar cells of different thicknesses made with different solvents under AM1.5G irradiation of 100 mW cm^{-2}.

Active layers solvents	Thickness (nm)	J_{sc} (mA/cm^3)	V_{oc} (V)	FF (%)	η (%)
$CHCl_3$	70	2.2	0.74	45	0.7
	83	3.7	0.73	35	0.9
	90	4.8	0.72	35	1.2
	110	2.8	0.73	40	0.8
CB	80	6.2	0.79	48	2.3
	90	6.8	0.79	47	2.5
	100	5.2	1.79	46	1.9
	110	4.6	1.79	46	1.7
ODCB	74	7.7	0.80	46	2.8
	90	8.6	0.80	47	3.2
	105	8.1	080	45	2.9
	130	7.8	0.80	42	2.6

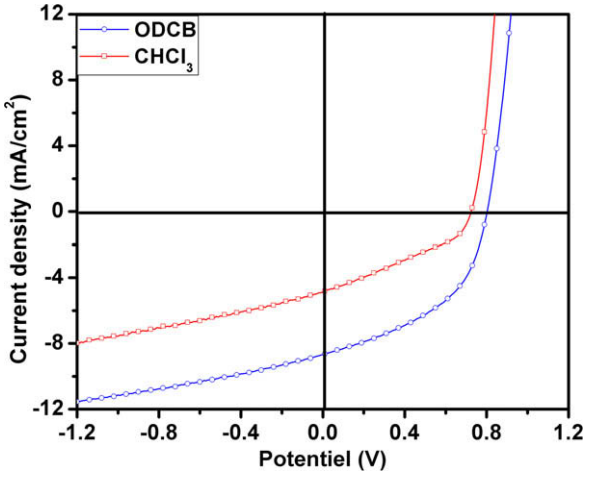

Fig. 3. *J–V* characteristics of ITO/PEDOT:PSS/PCBTDPP:3$PC_{70}BM$/LiF/Al devices with an active layer prepared by using $CHCl_3$ or ODCB as solvent. The active layers have the same thickness of 90 nm.

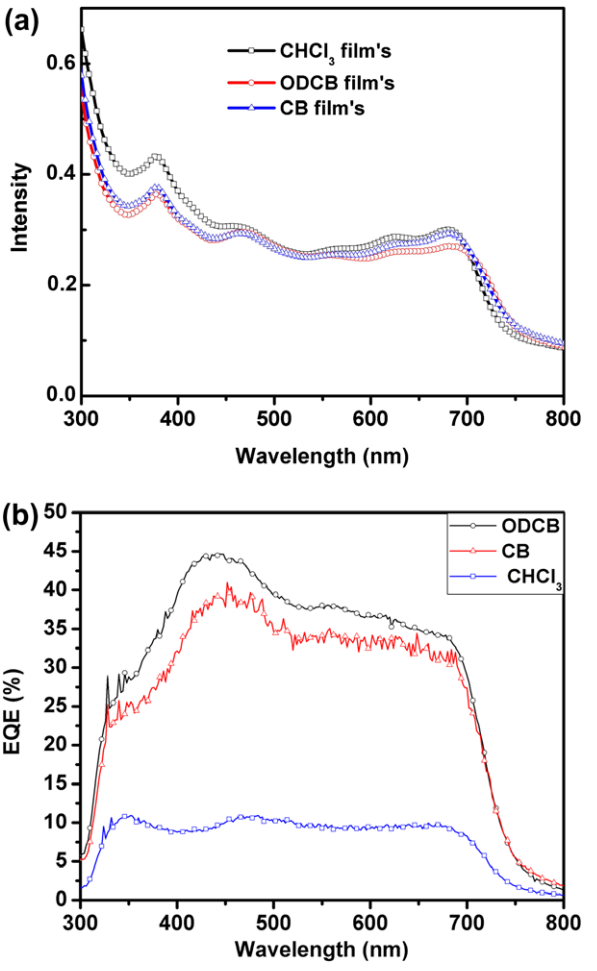

Fig. 4. (a) UV–vis absorption of PCBTDPP:$PC_{70}BM$ films prepared using different solvents; (b) External quantum efficiency (EQE) spectra of corresponding PCBTDPP:$PC_{70}BM$ solar cells.

The choice of electron donor and acceptor materials for use in BJH devices and their loading ratio is the first important step towards solar cell optimization. The choice of solvents is another important step [15]. It has a strong impact on the nano-scale morphology of the active layer, which plays an important role in the performance of solar cells [16] and OFETs [17].

In order to study the solvents effect on the morphology of the active layer and the solar cell performance, thin films of PCBTDPP:PCBM (1:3) blend were prepared using non-aromatic and aromatic solvents.

Table 2 summarizes the photocurrent densities of the solar cells in which the active layers were prepared with different solvents. Non-aromatic (chloroform ($CHCl_3$)) and aromatic (chlorobenzene (CB), and 1,2-Orthodichlorobenzene (ODCB)) solvents were used to study the solvent effect. Different active layer thicknesses were realised by using different spin rate in order to study the thickness effect on the photovoltaic performance of these devices.

The best device prepared using chloroform as solvent has a power conversion efficiency $\eta = 1.2\%$, a short-circuit current density $J_{sc} = 4.8$ mA/cm^2, an open-circuit voltage $V_{oc} = 0.72$, and a fill factor FF = 35%. The devices prepared using chlorobenzene as solvent show higher performance with $\eta = 2.5\%$, $J_{sc} = 6.8$ mA/cm^2, $V_{oc} = 0.79$ Volt, and FF = 47%. The devices prepared by using ODCB as solvent demonstrate the best performance with $\eta = 3.2\%$, $J_{sc} = 8.6$ mA/cm^2, $V_{oc} = 0.80$ V, and FF = 47%. The I–V curves of devices prepared using $CHCl_3$, and ODCB are shown in Fig. 3. Through this device optimization process, our PCBTDPP based solar cells have improved ~100% in power conversion efficiency as compared to our initial result 1.6%

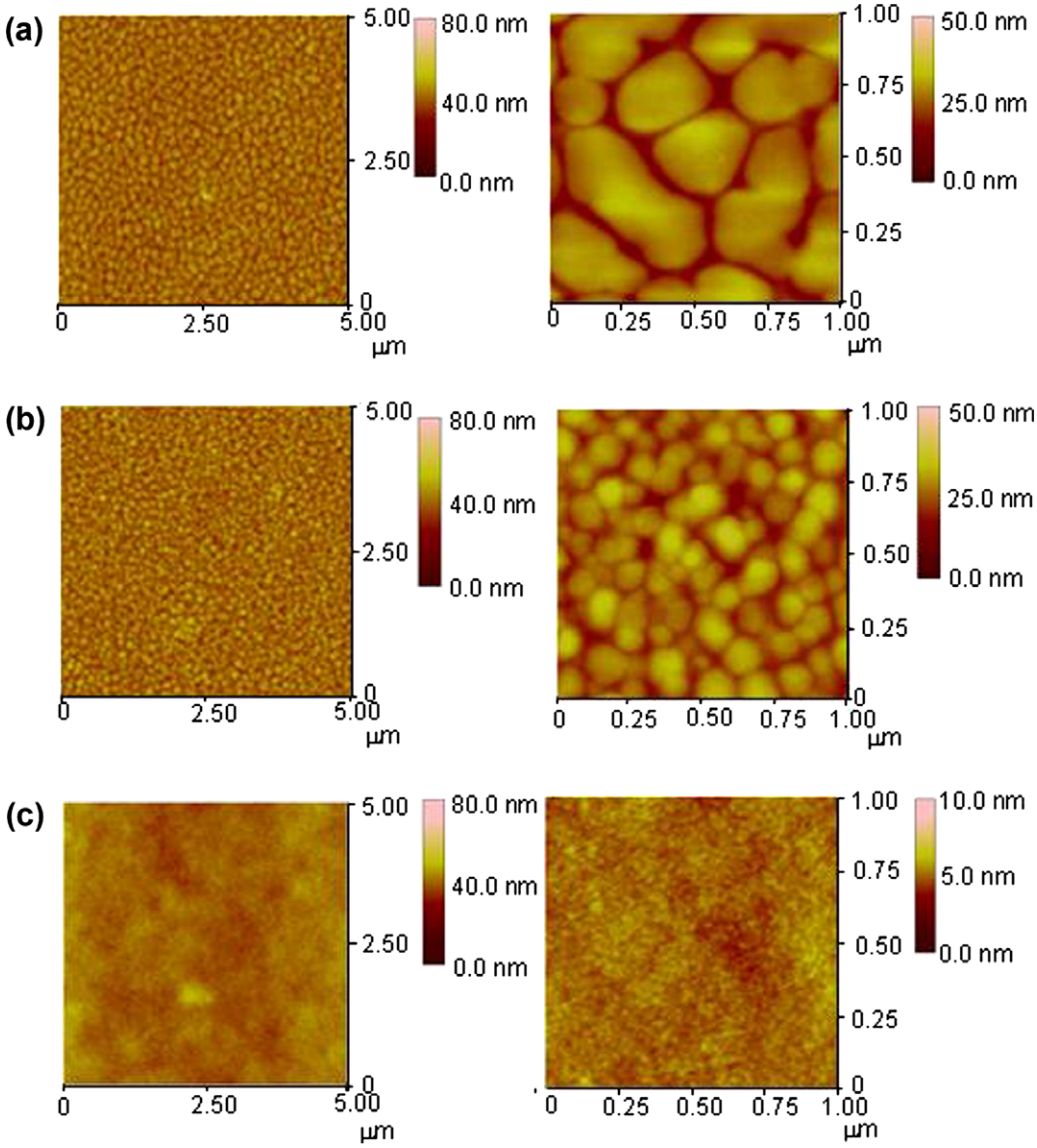

Fig. 5. 5×5 µm and 1×1 µm AFM images of PCBTDPP:3PC$_{70}$BM blend films spin-cast from different solvents: $CHCl_3$ (a), CB (b), and ODCB (c). These pictures are taken from active layers of the best devices obtained for each solvent.

[11], and ~40% as compared to the results reported recently by Zhou et al. (2.26%) using a similar polymer with different side chain [12]. This improvement can be attributed to the increased light absorption by replacing $PC_{60}BM$ with $PC_{70}BM$, as well as the optimized donor/acceptor ratio and active layer thickness.

The best values of the fill factor up to 45% were obtained when aromatic solvent (ODCB or chlorobenzene) was used, and the fill factor remains reasonably high up to an active layer thickness of 130 nm. In contrast, when chloroform was used as solvent, the average FF is less than 40%. The best values of short-circuit current were obtained at an active layer thickness of 90 nm in each case, independent of the solvent choice. The best V_{oc} values were obtained when chlorobenzene or ODCB was used as solvent. The V_{oc} decreased dramatically when chloroform was used, the same as other photovoltaic parameters, indicating that non-aromatic solvent is not preferred for making PCBTDPP based devices.

From the data shown in Table 2, we can conclude that for PCBTDPP:$PC_{70}BM$ (1:3) devices, the best film thickness is around 90 nm for maximum efficiency, and ODCB is preferred for active layer preparation.

The better performance of the devices prepared by ODCB is attributed to the optimized nano-scale morphology of the bulk heterojunction film with an average domain size around 20 nm. The most noticeable improvements in device performance are the fill factor and short-circuit current density, which are known as parameters directly dependant on the nano-scale morphology.

The external quantum efficiency (EQE) of a photovoltaic cell is given by the ratio between the number of electrons produced in the outer circuit and that of incident photons on the device. Fig. 4 compares the EQE spectra of PCBTDPP:$PC_{70}BM$ solar cells prepared with different solvents, as discussed above. The device prepared using ODCB as solvent shows the best overall EQE, which has the slowest drying rate among the three. The highest monochromatic EQE values for devices prepared using ODCB or CB are 44% and 41%, respectively. While that of the device prepared using chloroform is less than 22%. These results confirmed that even if we optimize the acceptor and donor ratio and the active layer thickness, it is also necessary to use the right solvent for the active layer preparation.

The surface morphology of PCBTDPP:$PC_{70}BM$ (1:3) active layers prepared using the three solvents was investigated by the atomic force microscopy (AFM). The tapping mode AFM images of the film prepared using chloroform (Fig. 5) show over-sized grain structures ~140 nm, indicating a large scale phase separation. The domains size is too large for efficient exciton dissociation. The surface morphology of the film spin cast from chlorobenzene is well-defined and the domain size is much smaller, ~50 nm. The situation improves even further when 1.2-dichlorobenzene is used as solvent, the film show much finer grain sizes (20–30 nm) with better organization and uniformity. This best organization observed on AFM pictures is in agreement with the solar cell performance. This indicates that the choice of solvent for active layer preparation is a crucial factor to get the optimum film morphology in order to realize the best device performance [18,19].

3. Conclusion

In this work, we have demonstrated how to control the nano-scale morphology of PCBTDPP:$PC_{70}BM$ bulk heterojunction by choosing right solvent, and donor/acceptor ratio. For this particular material, aromatic solvents deliver better device performance. AFM study connects the high device performance to better and organized phase-separated domains which provides an optimized *D–A* interface for efficient exciton dissociation and continuous electron and hole conducting channels necessary for efficient charge transport between electrodes. By replacing $PC_{60}BM$ with $PC_{70}BM$, we have significantly increased the light absorption in the spectral region where the PCBTDPP absorption is at minimum, and thus improved the short-circuit current density. With these optimization steps, we have improved the PCE from 1.6% in our previous study [11] to 3.2%.

Acknowledgments

This work was supported by the Sustainable Development Technology Canada (SDTC) program. The authors acknowledge Raluca Movileanu for the AFM measurements.

References

[1] G. Dennler, M.C. Scharber, C.J. Brabec, Polymer-fullerene bulk-heterojunction solar cells, Adv. Mater. 21 (2009) 1323–1338.
[2] S. Allard, M. Forster, B. Souharce, H. Thiem, U. Scherf, Organic semiconductors for solution-processable field-effect transistors (OFETs), Angew. Chem., Int. Ed. 47 (2008) 4070–4098.
[3] S.W. Thomas, G.D. Joly, T.M. Swager, Chemical sensors based on amplifying fluorescent conjugated polymers, Chem. Rev. 107 (2007) 1339–1386.
[4] R.B. Aïch, N. Blouin, A. Bouchard, M. Leclerc, Electrical and thermoelectric properties of poly(2,7-carbazole) derivatives, Chem. Mater. 21 (2009) 751–757.
[5] J. Roncali, Molecular engineering of the band gap of π-conjugated systems: facing technological applications, Macromol. Rapid Commun. 28 (2007) 176–1775.
[6] E. Bundgaard, F.C. Krebs, Low band gap polymers for organic photovoltaics, Sol. Energy Mater. Sol. Cells 91 (2007) 954–985.
[7] S.H. Park, A. Roy, S. Beaupre, S. Cho, N. Coates, J.S. Moon, D. Moses, M. Leclerc, K. Lee, A.J. Heeger, Bulk heterojunction solar cells with internal quantum efficiency approaching 100%, Nat. Photonics 3 (2009) 297–302.
[8] N. Blouin, A. Michaud, D. Gendron, S. Wakim, E. Blair, R.N. Plesu, M. Bellette, G. Durocher, Y. Tao, M. Leclerc, Toward a rational design of poly(2,7-carbazole) derivatives for solar cells, J. Am. Chem. Soc. 130 (2008) 732–742.
[9] L. Burgi, M. Trubiez, R. Pfeiffer, F. Bienewald, H.J. Kirner, C. Winnewisser, High-mobility ambipolar near-infrared light-emitting polymer field-effect transistors, Adv. Mater. 20 (2008) 2217–2224.
[10] Y. Zou, D. Gendron, R. Neagu-Plesu, M. Leclerc, Synthesis and characterization of new low-bandgap diketopyrrolopyrrole-based copolymers, Macromolecules 42 (2009) 6361–6365.
[11] Y.P. Zou, D. Gendron, R.B. Aïch, A. Najari, Y. Tao, M. Leclerc, A high-mobility low-bandgap poly(2,7-carbazole) derivative for photovoltaic applications, Macromolecules 42 (2009) 2891–2894.
[12] E. Zhou, S. Yamakawa, K. Tajima, C. Yang, K. Hashimoto, Synthesis and photovoltaic properties of diketopyrrolopyrrole-based donor−acceptor copolymers, Chem. Mater. 21 (2009) 4055–4061.
[13] S. ALem, R. Bettignies, J.-M. Nunzi, M. Cariou, Efficient polymer-based Interpenetrated network photovoltaic cells, Appl. Phys. Lett. 12 (2004) 2178–2180.
[14] J.K.J. van Duren, X. Yang, J. Loos, C.W.T. Bulle-Lieuwma, A.B. Sieval, J.C. Hummelen, J.R.A. Janssen, Relating the morphology of poly(p-phenylene vinylene)/methanofullerene blends to solar-cell performance, Adv. Funct. Mater. 14 (2004) 425–434.

[15] S. Barrau, V. Andersson, F. Zhang, S. Masich, J. Bijleveld, M.R. Andersson, O. Inganäs, Nanomorphology of bulk heterojunction organic solar cells in 2D and 3D correlated to photovoltaic performance, Macromolecules 42 (2009) 4646–4650.
[16] F. Zhang, K.G. Jespersen, C. Björström, M. Svensson, M.R. Andersson, V. Sundström, K. Magnusson, E. Moons, A. Yartsev, O. Inganäs, Influence of solvent mixing on the morphology and performance of solar cells based on polyfluorene copolymer/fullerene blends, Adv. Funct. Mater. 16 (2006) 667–674.
[17] Z. Bao, A. Dodabalapur, A-J. Lovinger, Soluble and processable regioregular poly(3-hexylthiophene) for thin film field-effect transistor applications with high mobility, Appl. Phys. Lett. 69 (1996) 4108–4110.
[18] J.F. Chang, B. Sun, D.W. Breiby, M.M. Nielsen, T.I. Solling, M. Giles, L. McCulluch, H. Sirringhaus, Enhanced mobility of poly(3-hexylthiophene) transistors by spin-coating from high-boiling-point solvents, Chem. Mater. 16 (2004) 4772–4776.
[19] L.M. Chen, Z. Hong, G. Li, Y. Yang, Recent progress in polymer solar cells: manipulation of polymer: fullerene morphology and the formation of efficient inverted polymer solar cells, Adv. Mater. 21 (2009) 1434–1449.

2. Experimental

2.1. Materials and measurements

9H-fluoren-9-one, *n*-butyllithium (*n*-BuLi), triethyl borate and chlorodiphenylphosphine (Aldrich Chem. Co.) were used without further purification. 2,2′-Dibromobiphenyl (TCI Chem. Co.), hydrogen peroxide (Duksan Sci. Co.) and sodium hydrogen carbonate (Junsei Chem. Co.) was used as received. Tetrahydrofuran was distilled over sodium and calcium hydride.

The ^{1}H nuclear magnetic resonance (NMR) was recorded on a Varian 200 (200 MHz) spectrometer. The photoluminescence (PL) spectra were recorded on a fluorescence spectrophotometer (HITACHI, F-7000) and the ultraviolet–visible (UV–Vis) spectra were obtained using a UV–Vis spectrophotometer (Shimadzu, UV-2501PC). The differential scanning calorimeter (DSC) measurements were performed on a Mettler DSC 822e under nitrogen at a heating rate of 10 °C/min. The low and high resolution mass spectra were recorded using a JEOL, JMS-AX505WA spectrometer in FAB mode. The energy levels were measured with a cyclic voltametry.

2.1.1. Synthesis of 4-bromo-9,9′-spirobifluorene (**1**)

2,2′-Dibromobiphenyl (11.00 g, 35.25 mmol) was dissolved in THF (70 mL) in the 250 ml two-neck flask. The solution was cooled to −78 °C and *n*-BuLi (10 M in hexane, 4.23 mL) was added dropwise slowly. The whole solution was stirred at −78 °C for 3 h, followed by addition of a solution of 9H-fluoren-9-one (7.62 g, 42.30 mmol) in THF (40 mL) under argon atmosphere. The solution was gradually warmed to ambient temperature and quenched by saturated, aqueous $NaHCO_3$ (110 mL). The solution was extracted with dichloromethane. The combined organic layers were dried over magnesium sulfate, filtered, and evaporated under reduced pressure. The white powdery product was obtained and the crude product was placed in other two-necked flask, and dissolved in acetic acid (300 mL). Catalytic amount of aqueous HCl (30 mL) was then added and the whole solution was refluxed for 12 h. After cooling to ambient temperature, purification by column chromatography with a mixed solvent of dichloromethane and *n*-hexane as an eluent gave a white powder.

Yield 50%. T_g 66 °C. ^{1}H NMR (200 MHz, $CDCl_3$): δ 8.68–8.65 (d, 1H), 7.86–7.82(d, 2H), 7.53–7.34 (m, 3H), 7.26–6.63 (m, 15H). ^{13}C NMR ($CDCl_3$), δ 150.9, 148.3, 147.7, 141.1, 140.3, 139.2, 132.5, 131.6, 128.4, 127.8, 127.4, 126.8, 126.4, 123.8, 123.5, 122.9, 122.2, 122.0, 119.9, 118.9, 116.0 ppm. MS (FAB) *m*/*z* 395 [(M + 1)+].

2.1.2. 9,9′-Spirobifluorene-4-yldiphenylphosphine (**2**)

The 4-bromo-9,9′-spirobifluorene (1.00 g, 2.53 mmol) was put into the THF (20 mL) solvent in the 100 ml two-neck flask. The solution was cooled to −78 °C and *n*-BuLi (10 M in hexane, 0.3 mL) was added dropwise slowly. The whole solution was stirred for additional 3 h, followed by addition of a solution of chlorodiphenylphosphine (0.67 g, 3.04 mmol) under argon atmosphere. The resulting mixture was gradually warmed to ambient temperature and quenched by methanol (7 mL). The mixture was extracted with dichloromethane. The combined organic layers were dried over magnesium sulfate, filtered, and evaporated under reduced pressure. The white powdery product was obtained to 0.25 g (19%).

2.1.3. 4-Diphenylphosphine oxide-spiro[fluorene-9,9′-fluorene] (SPPO11)

A solution of 4-diphenylphosphine oxide-9,9′-spirobifluorene (0.25 g, 0.49 mmol), dichloromethane (50 mL), and hydrogen peroxide (10 mL) were stirred overnight at room temperature. The organic layer was separated and washed with dichloromethane and water. The extract was evaporated to dryness affording a white solid, which was further purified by column chromatography to yield 0.24 g of chemically pure SPPO11.

Yield: 96%. T_m: 314 °C. ^{1}H NMR (200 MHz, $CDCl_3$): δ 8.68–8.64 (d, 1H), 7.85–7.71(M, 6H), 7.52–7.49 (m, 6H), 7.40–7.14 (m, 4H), 7.11–6.61 (m, 8H). ^{13}C NMR ($CDCl_3$), δ 150.4, 150.2, 148.1, 147.7, 144.9, 141.2, 139.3, 133.5, 133.3, 132.9, 132.6, 132.2, 132.0, 130.9, 128.7, 128.5, 128.2, 127.8, 127.4, 126.8, 125.5, 125.4, 124.7, 123.7, 123.0, 122.2, 120.0, 118.9 ppm. MS (FAB) *m*/*z* 517 [(M + 1)+].

2.1.4. OLED fabrication and measurement

A basic device configuration of indium thin oxide (ITO)/poly-3,4-ethylenedioxythiophene:polystyrenesulfonate (PEDOT:PSS)/*N*,*N*′-di(1-naphthyl)-*N*,*N*′-diphenylbenzidine (NPB) (20 nm)/*N*,*N*′-dicarbazolyl-3,5-benzene (mCP) (10 nm)/**SPPO11**:FIrpic (30 nm, 10%)/2,9-dimethyl-4,7-diphenyl-1,10-phenanthroline (BCP, 5 nm)/tris(8-hydroxyquinoline) aluminium (Alq_3) (20 nm)/LiF (1 nm)/Al (100 nm) was used to evaluate the SPPO11 as a host for the blue PHOLEDs. The doping concentration of the FIrpic was optimized at 10% and it was fixed in all devices. The blue PHOLED with the **SPPO11** as the electron transport layer instead of the BCP/Alq_3 was also fabricated and the simple blue PHOLED without the BCP/Alq_3 was prepared as the simple device. In addition, the blue PHOLED with the 2-diphenylphosphine oxide-9,9′-spirobifluorene (**SPPO1**) was fabricated to study the effect of the substitution position of the diphenylphosphine oxide on the device performances of the blue PHOLEDs. Device structures of the blue PHOLEDs are shown in Fig. 1. The devices were encapsulated with CaO and a glass lid after cathode deposition. Current density (*J*)–voltage (*V*)–luminance (*L*) characteristics and electroluminescence (EL) spectra of the devices were measured with Keithley 2400 source measurement unit and Minolta CS 1000A spectroradiometer.

3. Results and discussion

The synthesis of the 4-bromospirobifluorene which was an intermediate compound of the SPPO11 was difficult because the bromination of the spirobifluorene leads to the substitution at 2 position of the spirobifluorene. Therefore, few compounds with a substituent at the 4 position of the spirobifluorene were synthesized [13,14]. One way to synthesize the 4-bromospirofluorene is to use

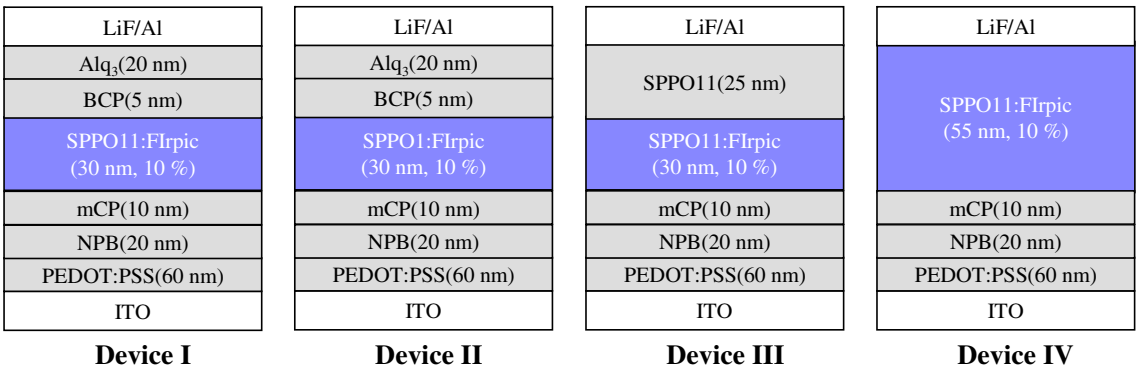

Fig. 1. Device structures of the blue PHOLEDs with the SPPO11 and SPPO1 hosts.

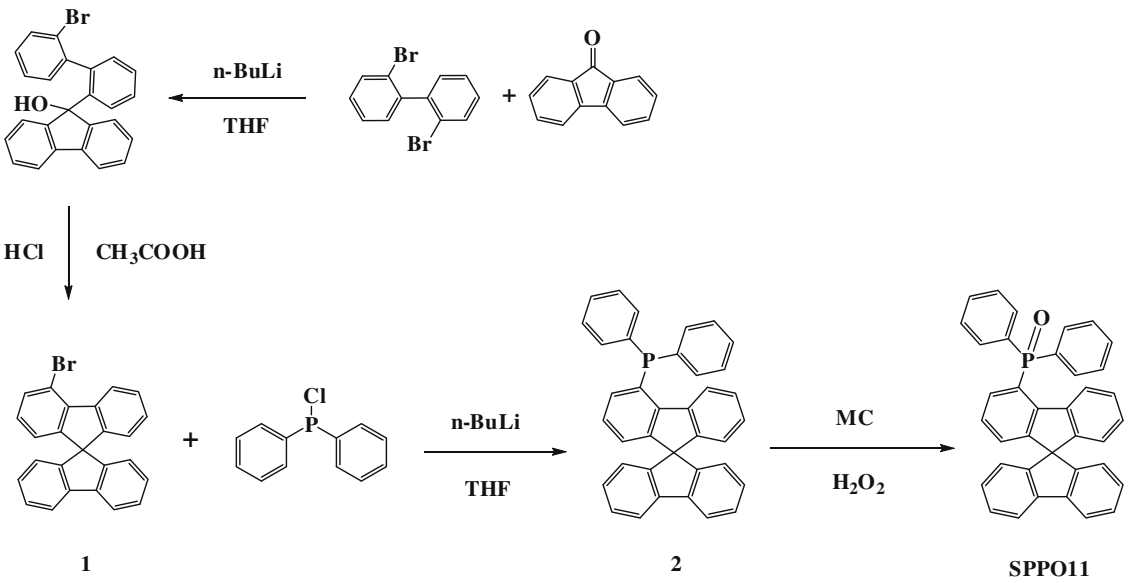

Scheme 1. Synthetic route of SPPO11.

Table 1
Physical properties of the SPPO11 and SPPO1.

		Optical analysis		Thermal analysis		Electrical analysis			
		Absorption (nm)	Emission (nm)	T_g (°C)	T_m (°C)	HOMO (eV)	LUMO (eV)	Bandgap (eV)	E_T (eV)
SPPO11	Solution	308, 322	346	127	314	6.57	2.82	3.75	2.78
	Solid	310, 325	353						
SPPO1	Solution	308, 316	339	96	236	6.55	2.73	3.82	2.77
	Solid	309, 319	353						

2,2′-dibromobiphenyl. As shown in the Scheme 1, the 2,2′-dibromobiphenyl was reacted with *n*-BuLi followed by the reaction with fluorenone. The use of 1 equivalent of *n*-BuLi resulted in the lithiation of only one bromo unit of the two bromo substituents in the 2,2′-dibromobiphenyl. Therefore, the reaction of the mono-lithiated 2,2′-dibromobiphenyl with the fluorenone followed by dehydration lead to the synthesis of the 4-bromo-9,9′-spirobifluorene. This synthetic route is very simple to prepare the 4-bromo-9,9′-spirobifluorene. The 4-bromo-9,9′-spirobifluorene was reacted with chlorodiphenylphosphine through the lithiation and then dehydrated by hydrogen peroxide, yielding the SPPO11.

The physical properties of the SPPO11 were compared with those of the SPPO1 to investigate the effect of the diphenylphosphine oxide substitution position on the physical properties. Physical properties of the SPPO11 and SPPO1 are summarized in Table 1 and Fig. 2. The UV–Vis absorption and PL emission peaks of the SPPO11 were similar to those of the SPPO1, but the red shift of

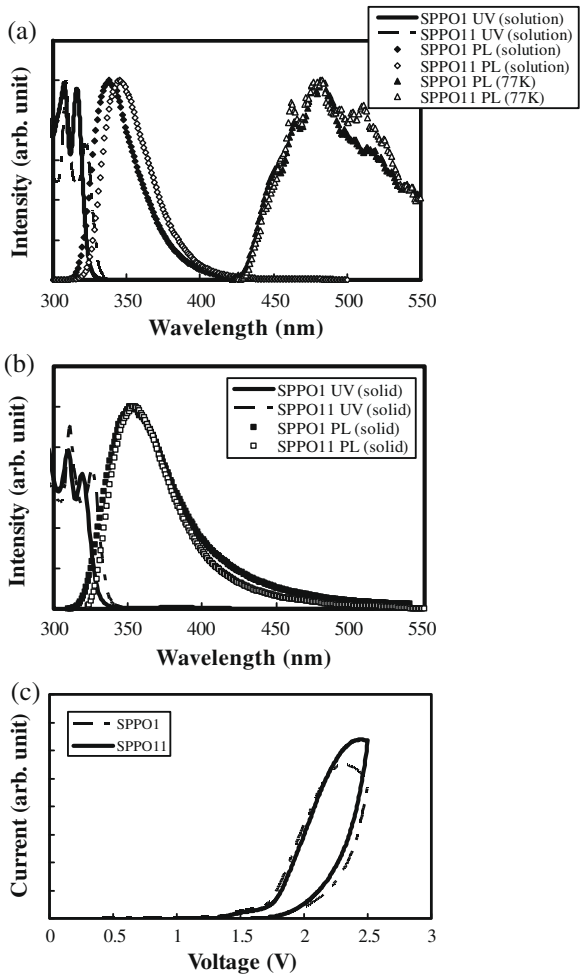

Fig. 2. UV–Vis, PL spectra and CV data of the SPPO1 and SPPO11 (a) UV–Vis and PL in solution, (b) UV–Vis and PL in solid state, (c) CV.

the UV–Vis absorption and PL emission were observed. The absorption peak around 308 nm was the same in the SPPO1 and SPPO11, but the absorption peak around 320 nm was red shifted in the SPPO11 by about 6 nm. The emission peak was also shifted to long wavelength in the SPPO11. In the solid film case, the UV absorption peak was similar to that of the solution except for the slight red shift of the absorption peak, while the emission peak was different. The emission peak of the SPPO11 was in the long wavelength range in solution, but the peak position of the emission peak in the solid film was similar. This is closely related with the geometrical structure and molecular orbital distribution of the SPPO1 and SPPO11 in Fig. 3. The molecular packing of the SPPO11 is difficult due to the steric hindrance of the diphenylphosphine oxide at 4 position of the spirobifluorene, resulting in less molecular interaction in solid state. Therefore, the peak position of the PL emission of the SPPO1 and SPPO11 was similar. In addition, the emission peak of the SPPO11 was narrower than that of the SPPO1 due to the suppressed molecular interaction in solid state.

The highest occupied molecular orbital (HOMO) and the lowest unoccupied molecular orbital (LUMO) distribution of the SPPO11 and the SPPO1 were studied to understand the physical properties of the SPPO1 and SPPO11 at molecular level and they are shown in Fig. 3. Density functional theory (DFT) calculations for host materials were carried out using a suite of Gaussian 03 program to understand the observed properties of the materials at the molecular level. The nonlocal density functional of Becke's 3-parameters employing Lee–Yang–Parr functional (B3LYP) with 6-31G* basis sets was used for the calculation [15]. The HOMO was distributed over the spirobifluorene unit of the SPPO11 and SPPO1, while the LUMO was localized in the fluorene group connected to the diphenylphosphine oxide. Comparing the HOMO distribution, both the SPPO11 and SPPO1 showed uniform orbital distribution, resulting in similar HOMO level. There was only 0.02 eV HOMO level difference between the SPPO1 and the SPPO11. In the LUMO case, the LUMO of the SPPO11 was localized in the fluorene unit connected to the diphenylphosphine oxide, while the LUMO of the SPPO1 was rather dispersed. The LUMO of the SPPO1 was distributed over the diphenyl unit in the diphenylphosphine oxide as well as the fluorene unit. The diphenyl unit in the diphenylphosphine oxide is an isolated unit as the conjugation through the phosphine oxide unit cannot be extended due to the tetrahedral structure of the phosphine oxide. Therefore, the electrons in the diphenyl unit are isolated and the LUMO level is shifted upward from the vacuum level due to lack of conjugation. The phenyl group is less conjugated than the spirobifluorene group, leading to the upward LUMO level shift. This LUMO level shift results in the large bandgap in the SPPO1 compared with SPPO11. Even though there is steric hindrance in the SPPO11, the geometrical structure of the spirobifluorene core was not affected by the position of the diphenylphosphine oxide.

The different substitution position of the diphenylphosphine oxide also affects thermal properties of the SPPO1 and SPPO11 and the T_g of the SPPO11 was improved significantly by the substitution of the diphenylphosphine oxide at 4 position of the spirobifluorene. The T_g depends on the molecular rigidity of the backbone structure and the steric hindrance of the molecule. Comparing the molecular rigidity of the molecule, the SPPO11 and the SPPO1 have the same rigid spirobifluorene core structure with the diphenylphosphine oxide unit. The difference between the SPPO11 and the SPPO1 is the steric hindrance between the diphenylphosphine oxide unit and the spirobifluorene core. The rotation of the diphenylphosphine oxide in the SPPO11 is limited due to the steric hindrance of the diphenyl unit with the spirobifluorene unit as the diphenyl unit and the fluorene unit is in plane. However, the rotation of the diphenylphosphine oxide in the SPPO1 is not hindered by the spirobifluorene group as the diphenylphosphine oxide group is out of plane with the spirobifluorene group. The steric hindrance suppressed the free rotation of the diphenylphosphine oxide group, increasing the T_g of the SPPO11.

The high T_g induced by the steric hindrance improved the morphological stability of the SPPO11. Fig. 4 shows the optical microscopic pictures of the SPPO11 and SPPO1

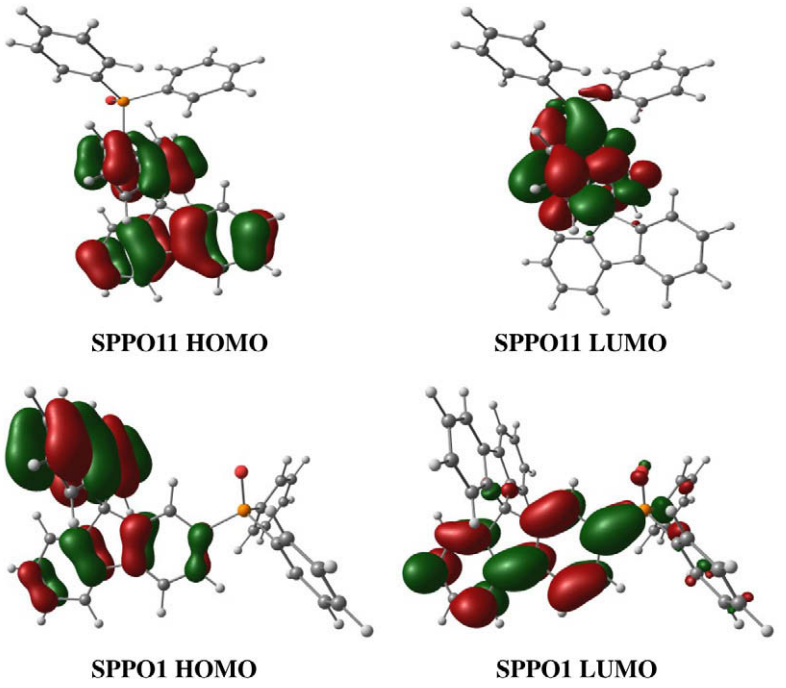

Fig. 3. Molecular simulation results of the SPPO11 and SPPO1.

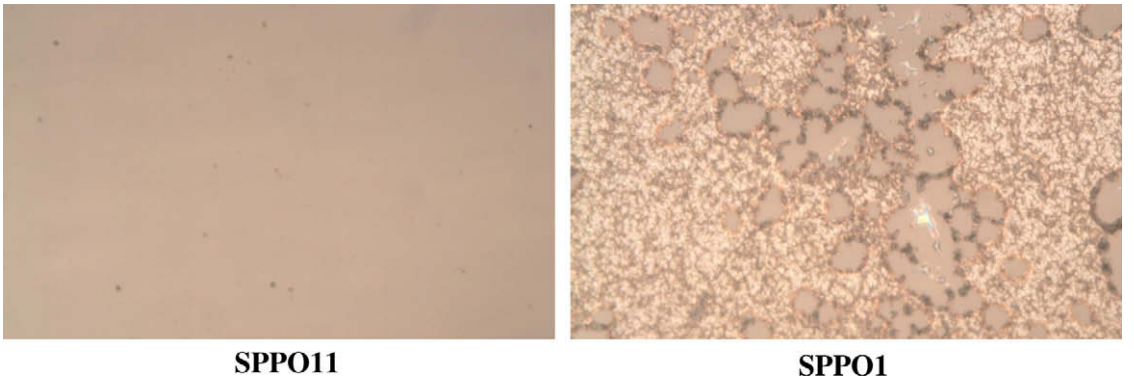

Fig. 4. Optical microscopic pictures of the SPPO11 and SPPO1 after thermal treatment at 80 °C for 10 min.

film after thermal treatment at 80 °C for 10 min on glass substrate. The crystallization of the SPPO1 was serious after thermal treatment and most of the film was crystallized. However, the SPPO11 film maintained the amorphous film morphology of the thermally deposited film even after thermal treatment. This indicates that the steric hindrance of the SPPO11 suppress the crystallization.

Electron only devices of the SPPO11 and SPPO1 were fabricated to compare the effect of substitution position on the electron injection. Fig. 5 shows the current density–voltage curves of the electron only devices of the SPPO11 and SPPO1. The device structure of the electron only devices was ITO (150 nm)/SPPO1 or SPPO11 (100 nm)/LiF (1 nm)/Al (100 nm). The electron current density of the SPPO11 was higher than that of the SPPO1,

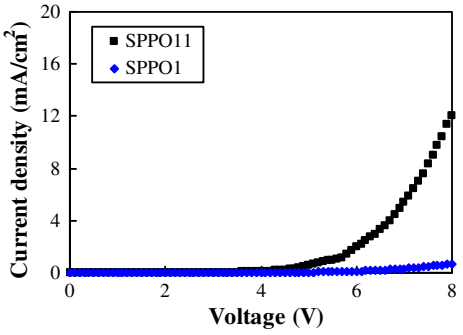

Fig. 5. Current density–voltage curves of the electron only devices of the SPPO11 and SPPO1.

indicating that the SPPO11 is better than the SPPO1 in terms of electron density. The electron density is determined by the LUMO level and electron mobility of the materials. The LUMO of the SPPO11 was 2.82 eV, while the LUMO of the SPPO1 was 2.73 eV. There was 0.09 eV energy level difference between the SPPO11 and the SPPO1. The LUMO level of the SPPO11 is better for electron injection than that of the SPPO1, leading to high electron density. In addition, the high electron mobility of the SPPO11 is also responsible for the high electron density of the SPPO11. The electron mobility of the SPPO1 was 5×10^{-4} cm^2/V s, while that of the SPPO11 was 7×10^{-4} cm^2/V s.

The triplet bandgap of the SPPO11 was 2.78 eV and it was similar to that of the SPPO1. The triplet bandgap of 2.77 eV is wide enough for energy transfer to the FIrpic dopant and the SPPO11 was evaluated as the host for the FIrpic. The device performances of the SPPO11 blue device (device I) were optimized by changing the doping concentration of the FIrpic and were compared with those of the SPPO1 (device II). The doping concentration of the FIrpic in the device I was optimized at 10%.

The *J*–*V*–*L* curves of the SPPO11 and SPPO1 blue PHOLEDs are shown in Fig. 6. The *J* and *L* of the SPPO11 device were higher than those of the SPPO1 device. The high *J* and *L* of the SPPO11 device are due to the efficient electron injection as shown in the electron only device data in Fig. 5. The electron density of the SPPO11 device was increased, resulting in the increase of the *J* and *L* of the SPPO11. The high *L* of the SPPO11 device indicates that more electron injection generates more excitons in the emitting layer.

The quantum efficiency and power efficiency of the SPPO11 and SPPO1 devices are shown in Fig. 7. The quantum efficiency of the SPPO11 device was higher than that of the SPPO1 device and a maximum quantum efficiency of 17.2% was obtained at 200 cd/m^2 compared with 15.6% of the SPPO1 device. The current efficiency was as high as 35.3 cd/A in the SPPO11 device. The high quantum efficiency of the SPPO11 device can be explained by the high electron density in the emitting layer. The hole injection from the ITO to the SPPO11 emitting layer is efficient as the multilayer structure of PEDOT:PSS/NPB/mCP was used as the hole transport layer. Therefore, holes can be effectively injected from the ITO to the SPPO11 emitting layer and more electron injection can balance the holes and electrons in the emitting layer, improving the quantum efficiency of the SPPO11 device. The high quantum efficiency and low driving voltage of the SPPO11 device also enhanced the power efficiency and a high power efficiency of 26.0 lm/W was obtained in the SPPO11 device.

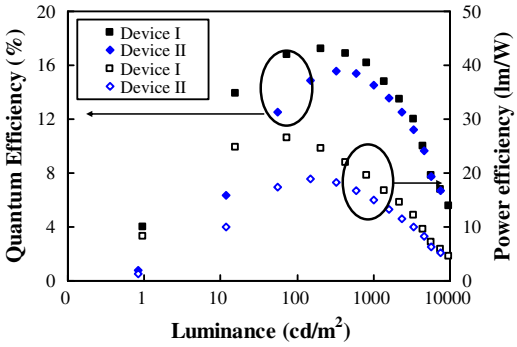

Fig. 7. Quantum efficiency and power efficiency curves of the blue PHOLEDs with SPPO11 and SPPO1 hosts.

The device performances of the SPPO11 device was further optimized by changing the device structure of the SPPO11 devices. A device with the SPPO11 as an electron transport layer instead of the BCP/Alq_3 (device III) and a device with SPPO11:FIrpic emitting layer without any electron transport layer (device IV) were fabricated. Figs. 8 and 9 shows the *J*–*V*–*L* and efficiency–*L* curves of the device I, device III and device IV. The current density and luminance were increased in the device III, while they were reduced in the device IV compared with device I. The high current density of the device III can be explained by the reduced interfacial trap at the interface. Device III had no interface between the emitting layer and the electron transport layer because the SPPO11 was used as both the host and the electron transport layer. Therefore, there was no interfacial energy barrier and interfacial traps, increasing the electron density in the emitting layer. The increased electron density in the emitting layer enhances

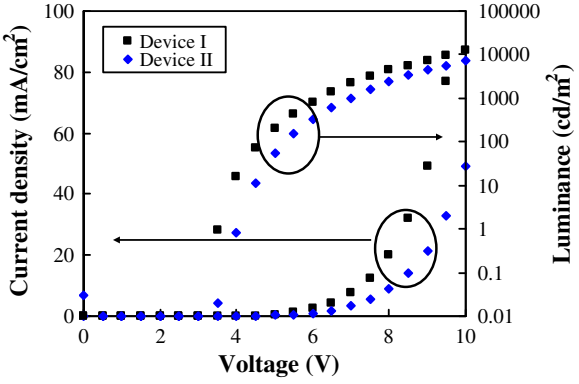

Fig. 6. Current density–voltage–luminance curves of the blue PHOLEDs with SPPO11 and SPPO1 hosts.

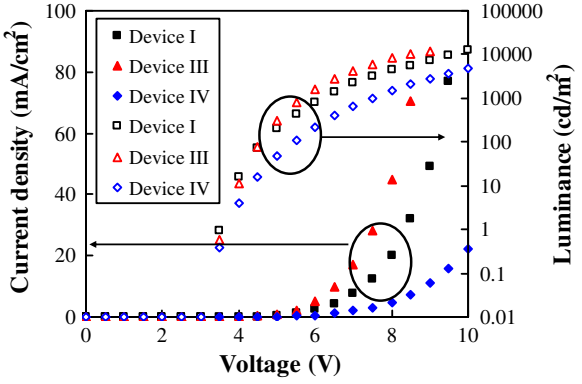

Fig. 8. Current density–voltage–luminance curves of the blue PHOLEDs with the SPPO11 as a host material according to the device structure.

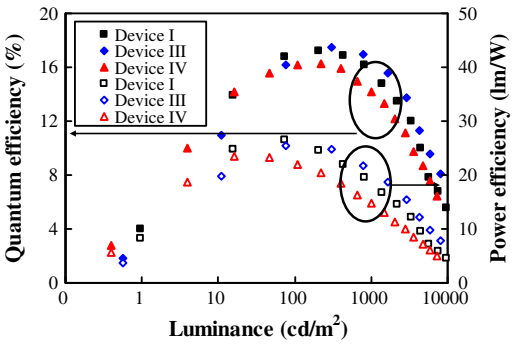

Fig. 9. Quantum efficiency and power efficiency curves of the blue PHOLEDs with the SPPO11 as a host material according to the device structure.

the quantum efficiency of the device III. A quantum efficiency of 17.5%, a current efficiency of 35.6 cd/A and a power efficiency of 24.7 lm/W were achieved at 300 cd/m^2 in the device III.

The current density was reduced in the device IV without the SPPO11 electron transport layer. The reduction of the current density is due to the electron trapping by the FIrpic dopant material. The LUMO level of the FIrpic was 3.2 eV compared with 2.82 eV of the SPPO11. The LUMO level difference between the SPPO11 and FIrpic induces electron trap by the FIrpic dopant, decreasing the current density of the device IV. The reduced electron density in the device IV has negative effect on the charge balance in the emitting layer, resulting in rather low quantum efficiency and power efficiency compared with device I.

4. Conclusions

In conclusion, the substitution of the diphenylphosphine oxide at 4 position of the spirofluorene was better than the substitution at 2 position in terms of thermal stability and electron injection. The SPPO11 could be effectively synthesized through the simple synthetic route for the synthesis of the 4-bromo-9,9′-spirobifluorene and high quantum efficiency was achieved in the device with the SPPO11 host. Therefore, the 4-bromo-9,9′-spirobifluorene can be used as an intermediate compound for the synthesis of thermally stable organic semiconductor materials for organic electronics applications.

Acknowledgement

This work was supported by 2009 Dankook university project for funding RICT.

References

[1] J.Y. Lee, J.H. Kwon, H.K. Chung, Org. Electron. 4 (2003) 143.
[2] R.J. Holmes, S.R. Forrest, Y.-J. Tung, R.C. Kwong, J.J. Brown, S. Garon, M.E. Thompson, Appl. Phys. Lett. 82 (2003) 2422.
[3] R.J. Holmes, B.W. D'Andrade, S.R. Forrest, X. Ren, J. Li, M.E. Thompson, Appl. Phys. Lett. 83 (2003) 3818.
[4] X. Ren, J. Li, R.J. Holmes, P.I. Djurovich, S.R. Forrest, M.E. Thompson, Chem. Mater. 16 (2004) 4743.
[5] M.H. Tsai, H.W. Lin, H.C. Su, T.H. Ke, C.C. Wu, F.C. Fang, Y.L. Liao, K.T. Wong, C.I. Wu, Adv. Mater. 18 (2006) 1216.
[6] M.F. Wu, S.J. Yeh, C.T. Chen, H. Murayama, T. Tsuboi, W. Li, I. Chao, S. Liu, J.K. Wang, Adv. Funct. Mater. 17 (2007) 1887.
[7] A.B. Padmaperuma, L.S. Sapochak, P.E. Burrows, Chem. Mater. 18 (2006) 2389.
[8] S.O. Jeon, K.S. Yook, C.W. Joo, J.Y. Lee, Appl. Phys. Lett. 94 (2009) 013301.
[9] E. Polikarpov, J.S. Swensen, N. Chopra, F. So, A.B. Padmaperuma, Appl. Phys. Lett. 94 (2009) 223304.
[10] J. Li, P.I. Djurovich, B.D. Alleyne, M. Yousufuddin, N.N. Ho, J.C. Thomas, J.C. Peters, R. Bau, M.E. Thompson, Inorg. Chem. 44 (2005) 1713.
[11] S.H. Kim, J. Jang, S.J. Lee, J.Y. Lee, Thin Solid Films 517 (2008) 722.
[12] K.S. Yook, S.O. Jeon, C.W. Joo, J.Y. Lee, Org. Electron. 10 (2009) 170.
[13] X. Cheng, G.H. Hou, J.H. Xie, Q.L. Zhou, Org. Lett. 6 (2004) 2381.
[14] F. Steuber, J. Staudigel, M. Stossel, J. Simmerer, A. Winnacker, H. Spreitzer, F. Weissortel, J. Salbeck, Adv. Mater. 12 (2000) 130.
[15] M.J. Frisch, G.W. Trucks, H.B. Schlegel, G.E. Scuseria, M.A. Robb, J.R. Cheeseman, J.A. Montgomery, T. Vreven Jr., K.N. Kudin, J.C. Burant, J.M. Millam, S.S. Iyengar, J. Tomasi, V. Barone, B. Mennucci, M. Cossi, G. Scalmani, N. Rega, G.A. Petersson, H. Nakatsuji, M. Hada, M. Ehara, K. Toyota, R. Fukuda, J. Hasegawa, M. Ishida, T. Nakajima, Y. Honda, O. Kitao, H. Nakai, M. Klene, X. Li, J.E. Knox, H.P. Hratchian, J.B. Cross, C. Adamo, J. Jaramillo, R. Gomperts, R.E. Stratmann, O. Yazyev, A.J. Austin, R. Cammi, C. Pomelli, J.W. Ochterski, P.Y. Ayala, K. Morokuma, G.A. Voth, P. Salvador, J.J. Dannenberg, V.G. Zakrzewski, S. Dapprich, A.D. Daniels, M.C. Strain, O. Farkas, D.K. Malick, A.D. Rabuck, K. Raghavachari, J.B. Foresman, J.V. Ortiz, Q. Cui, A.G. Baboul, S. Clifford, J. Cioslowski, B.B. Stefanov, G. Liu, A. Liashenko, P. Piskorz, I. Komaromi, R.L. Martin, D.J. Fox, T. Keith, M.A. Al-Laham, C.Y. Peng, A. Nanayakkara, M. Challacombe, P.M.W. Gill, B. Johnson, W. Chen, M.W. Wong, C. Gonzalez, J.A. Pople, Gaussian 03, Revision B05, Gaussian Inc., Pittsburgh, PA, 2003.

encountered in the formation of SAMs because of lateral siloxane crosslinking. On the other hand, for polymer dielectrics it has been demonstrated that they can be used to optimize the pentacene film growth mode, control the film morphology, and understand the relationship between surface viscoelasticity of polymers and device performance [14,16,17]. However, their device performances are still lower than SAM-modified devices.

Polystyrene (PS) is a low-cost thermoplastic polymer, which is transparent and can form uniform thin films. When it is spin-coated onto the SiO_2/Si substrate, the pendant phenyl groups tend to be oriented toward the film surface normal, independent of casting solvent, molecular weight, and film thickness [18]. The benzene ring orientation on the surface can potentially be used to facilitate ordered growth of semiconductors such as pentacene and, thus, provide a more efficient transistor channel than that on the SiO_2 surface. So far, the highest achievable mobility using PS as a dielectric layer is ~0.8 cm^2/V s due to imperfectly oriented benzene rings at the PS film surface that cannot effectively control the top-layer pentacene order [17].

Previously, Fischer et al. reported that the surface of a spin-coated PS film showed a rather disordered arrangement of phenyl groups which have a 30° tilt angle from surface [18]. After annealing at 120 °C, these phenyl groups became ordered at the PS/air interface and tilted away from the surface normal in an angular range near 57° [19]. Such a surface can create a good template to orient layers of molecular semiconductors on top and facilitate charge transport near the interface of semiconductor/dielectric. This inspires us to explore the use of thermally treated PS thin film to modify the pentacene/SiO_2 interface for achieving high-performance OTFT devices.

In this article, the tilt angle of PS's phenyl groups and the surface energy of PS films are changed by thermal annealing at 80 and 120 °C. Pentacene films were deposited onto the PS films (about 10 nm thickness) with different phenyl ring tilt angles. We found that pentacene formed a highly crystalline film with larger grain sizes and better connectivity on the PS films with the flatter orientation of phenyl groups. Carrier mobility up to 4 cm^2/V s and a large on/off current ratio of $>10^7$ could be achieved from the resulting OTFTs. These are among the highest values reported for the pentacene-based OTFTs.

2. Experimental

The sum frequency generation (SFG) spectra of PS films were obtained by overlapping visible and tunable IR laser pulses (25 ps) in time and space at incidence angles of 72° and 61.5°, respectively. The visible beam with a wavelength of 532 nm was delivered by an EKSPLA Nd:YAG laser operating at 50 Hz, which was also used to pump an EKSPLA optical parametric generation/amplification and difference frequency unit based on barium borate and $AgGaS_2$ crystals to generate tunable IR laser radiation from 1000 to 4000 cm^{-1}. The spectral resolution in the C–H stretching region was 1 cm^{-1} for the visible and IR lasers. Both beams were only mildly focused and had a diameter of approximately 1 mm at the sample. The energy for each beam was 150 μJ per pulse. The SFG signal generated at the sample was then analyzed by filters and a monochromator, detected with a gated photomultiplier tube and stored in a computer. The spectra were collected with 200 shots per data point in 4 cm^{-1} increments. For a given sample, the SFG measurements were repeated at least three times and the collected spectra were averaged to produce the final spectra presented in this work. Spectra were collected using ssp and sps (sum, visible, and infrared) polarization combinations. The SFG spectra were normalized by the product of the IR and visible pump beam intensities.

OTFTs were fabricated with a top-contact configuration (Fig. 2a) according to the following procedure. A heavily doped n-type silicon wafer and 300 nm thick layer of thermally grown SiO_2 (Montco Semiconductors) were used as the gate and gate insulator, respectively. The substrates were cleaned in water, acetone and isopropyl alcohol (IPA). Then, the PS (Aldrich, molecular weight: 280,000, glass transition temperature: 100 °C) buffer layer was spin-coated onto the surface of SiO_2 and the thickness was measured to be about 10 nm by AFM. After that, the substrates were placed into a vacuum oven and baked about 30 min at different temperatures (80 and 120 °C) under vacuum. Pentacene (Aldrich without further purification) was deposited onto the substrates by high vacuum evaporation at a rate of 0.4 Å s^{-1} from a resistively heated quartz crucible at 4×10^{-7} Torr to achieve a total film thickness of 50 nm, and subsequently Au films (50 nm) as drain and source electrodes were deposited onto the organic layer through a shadow mask. For a typical device, the channel length (L) and width (W) of the OTFT were 55 and 1550 μm ($W/L = 28$), respectively, thus, creating a series of OTFTs investigated in our experiments. All devices were characterized with an Agilent 4155B semiconductor parameter analyzer under ambient conditions without any precautionary measures being taken to isolate the devices from exposing to ambient oxygen and moisture. The morphologies of organic semiconductor films were investigated using a Digital Instruments nanoprobe atomic force microscope (AFM) in contacting mode at room temperature. Tips were etched silicon tips with a typical resonant frequency of 300–350 kHz. X-ray reflectivity was measured using a Siemens D5000 XRD with Cu-Kα radiation. Advancing contact angle values of water were measured and surface energies were calculated using the Young equation [20].

3. Results and discussion

Fig. 1 displays SFG spectra of polystyrene films (untreated and thermally treated at 80 and 120 °C) taken with ssp (upper panel) and sps (lower panel) polarization combination. The fitting routine for the SFG data [21] used the following expression for the SFG intensity [22]:

$$I_{\mathrm{SFG}} \propto |\chi^{(2)}|^2 = \left| \chi^{(2)}_{\mathrm{NR}} e^{i\phi} + \sum_v \int_{-\infty}^{\infty} \frac{A_v e^{i\phi_v} e^{-[\omega_L - \omega_v/\Gamma_v]^2}}{\omega_{\mathrm{IR}} - \omega_L + i\Gamma_L} d\omega_L \right|^2 . \quad (1)$$

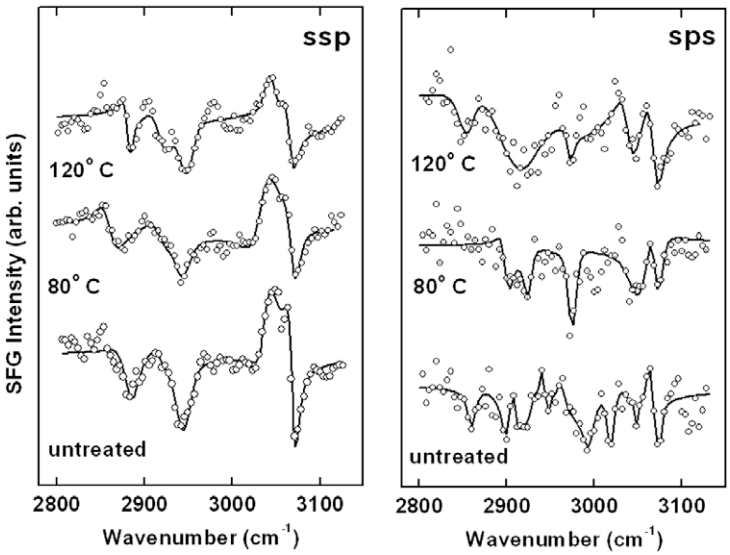

Fig. 1. SFG spectra (open circles) of polystyrene films untreated and thermally treated at 80 and 120 °C collected with ssp (upper panel) and sps (lower panel) polarization combination. Fits of Eq. (1) to the data are also shown (solid lines). The spectra were offset for clarity of presentation.

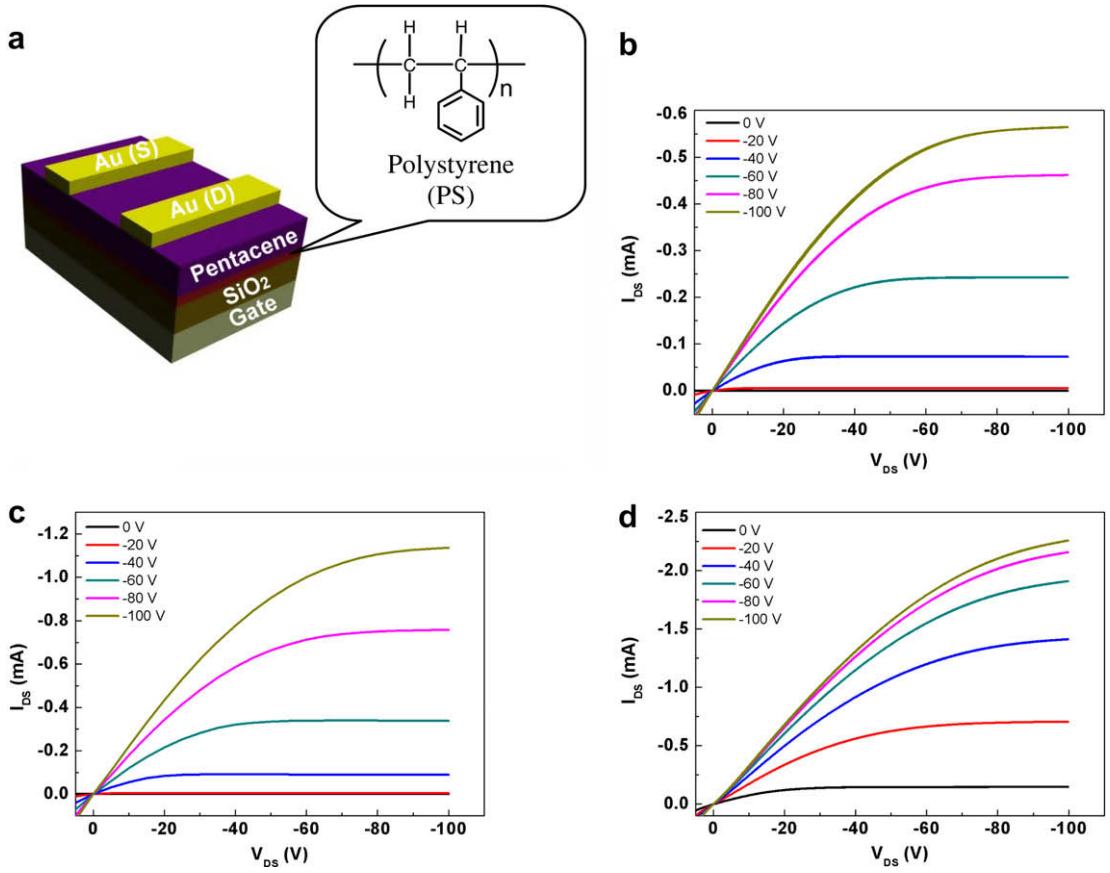

Fig. 2. Molecular structure of PS and the cross-sectional view of OTFTs (a) and output characteristics of pentacene TFTs with PS buffer layer untreated (b) and thermally treated at different temperatures: (c) 80 °C and (d) 120 °C.

Here, $\chi^{(2)}_{NR}$ is the second order non-linear susceptibility of the non-resonant background, A_v is the strength of the vth vibrational mode, ϕ denotes the phase of the respective mode, and ω_{IR} refers to the frequency of the incident IR

field. The integral is over Lorentzian lines, centered at ω_L and a width Γ_L, having a Gaussian distribution. In the fits, the Lorentzian line widths were set to 2 cm^{-1} and Γ_v was allowed to vary since the two contributions to the total line width could not be separated within the accuracy of the measurements. The ssp spectra are dominated by resonances near 3043 and 3068 cm^{-1}. The feature at 3043 cm^{-1} is assigned to ring mode υ_{7b}, while the latter mode can be unequivocally assigned to the υ_2 phenyl ring C–H stretching mode [23–25]. A shoulder near 2922 cm^{-1} is commonly associated with the asymmetric CH_2 stretching mode (d^-) of the polystyrene backbone [26–28]. The sps SFG spectra consist of weak but discernible features related to the υ_{7a} and υ_2 phenyl ring modes, as well as the d^- methylene mode. A quantitative analysis of the effect of film annealing on the orientation of the phenyl rings can be performed by evaluating the intensity ratios of selected features in the ssp and sps spectra [27]. The details of this calculation have been reported elsewhere and we will discuss the method only briefly here [29–31]. Following the procedure and notation described in Refs. [27,32], we have analyzed the intensities for the most prominent spectral feature, the υ_2 mode, in ssp and sps spectra to determine the molecular susceptibility ratio

$$\frac{\langle\beta_i\rangle_{xzx}}{\langle\beta_i\rangle_{xxz}} = \frac{A_i^{sps}F^{ssp}}{A_i^{ssp}F^{sps}}. \quad (2)$$

Here, β_i are the resonant molecular hyperpolarizabilities, A_i are the oscillator strengths according to Eq. (1), F are the Fresnel factors for given polarization combinations, and $\langle\rangle$ denotes a distribution over the tilt (Θ) angles against the surface normal and twist (ψ) angles about the molecular axis. The intensity ratio can be used to calculate molecular tilt angles for a given trial orientational distribution. We have assumed a delta function for Θ (i.e. uniform tilt angle for all phenyl rings) and an isotropic average of ψ. For the tilt angle calculation, we have to make assumptions about the molecular hyperpolarizability β_{ijk} of the υ_2 mode. Due to the C_{2v} symmetry of the υ_2 ring mode and low cross section for out-of-plane Raman polarizability we consider only β_{aac} and β_{ccc} [33]. In accord with published procedures based on density functional theory (DFT) and bond additive polarizability calculations we have assumed $\beta_{aac} = 0.86\beta_{ccc}$ (a, b, c denote the coordinates in the molecular frame with c in line with the 1′–4′ axis of the phenyl ring) and 0 for all other elements of the hyperpolarizability tensor β_{ijk} [27]. Based on these assumptions we can calculate the molecular tilt angle using:

$$\frac{(r-2)\sin^2\Theta}{r + r\cos^2\Theta + 2\sin^2\Theta} = \frac{A_i^{sps}F^{ssp}}{A_i^{ssp}F^{sps}}. \quad (3)$$

with $r = \beta_{aac}/\beta_{ccc}$. The refractive indices for air, silicon dioxide and polystyrene used to calculate the Fresnel factors were $n_{air} = 1$, $n_{SiO_2} = 1.45$ and $n_{PS} = 1.53$, respectively. The resulting intensity ratios, Fresnel factors, and hyperpolarizability ratios are summarized in Table 1 along with the resulting tilt angles. The determined tilt angles were 27°, 39° and 62° for the film untreated and thermally treated at 80 and 120 °C, respectively (the uncertainty of these values is ±5° which is a combination of the errors of the intensity ratios, the Fresnel factors and uncertainties of the value for r). The determined tilt angles clearly show the orientation of the phenyl group changes significantly due to the thermal treatment. The relative phase of the resonant and the non-resonant contributions are closely related to the molecular orientation. It has been elegantly shown for phenylsiloxanes on Si/SiO_2 that relative phases comparable to those observed here are related to phenyl groups pointing away from the surface [27]. Thus, we can conclude that the rings are oriented away from the surface with a mostly upright orientation for the film untreated, and that they assume a strongly tilted configuration after annealing. The low tilt angle value for the film without thermal treatment is in good agreement with NEXAFS studies of very thin polystyrene films. In this study, Stöhr and Samat report a tilt angle value of 30° [34]. The strongly tilted orientation observed after the 120 °C treatment has been reported by many groups. The majority of SFG studies of the orientation of annealed polystyrene report a flat orientation of the phenyl ring with respect to the surface [27,35]. Interestingly, the tilt angle value for the 80 °C-annealed film is in-between the 120 °C-annealed and unannealed surface. It is possible that the reorientation within the polystyrene film is thermodynamically restricted by the lower process temperature.

The contact angles and surface energies of the PS films untreated and thermally treated at different temperatures are listed in Table 2. The water contact angle of PS films without thermal treatment is about 102.6°, which is comparable to previous results [36]. When the thermal treatment temperature is increased, the water contact angle decreases, dropping to 95.8° for the film treated at 120 °C. The surface energy of the PS film without thermal treatment is about 36.7 mJ/m^2 while that of PS film treated at 120 °C is 48.5 mJ/m^2. Thus, as the phenyl groups of PS tilt away from the interface normal, the surface energy increases. The surface energy of pentacene was reported to be 47.4 mJ/m^2 [37]. Therefore, annealing the PS film at

Table 1
SFG results for the studied polystyrene films untreated and thermally treated at 80 and 120 °C.

Film treatment temperature (°C)	A^{sps}/A^{ssp}	F^{ssp}/F^{sps}	$\langle\beta_i\rangle_{xzx}/\langle\beta_i\rangle_{xxz}$	Θ
120	0.37	0.93	0.34	62°
80	0.23	0.93	0.21	39°
Untreated	0.13	0.93	0.12	27°

Table 2
Contact angle and surface energy of PS films untreated and thermally treated at 80 and 120 °C and electrical parameters (saturation region) of the devices based on them.

Temperature (°C)	Water contact angle (°)	γ_s (mJ/m²)	μ (cm²/V s)	V_T (V)	On/off ratio
Untreated	102.6 ± 1.0	36.7	0.8	40	10^8
80	97.9 ± 0.9	44.6	2.0	26.4	10^8
120	95.8 ± 0.9	48.5	4.0	6.5	10^7–10^8

120 °C results in a flatter phenyl group orientation with respect to the surface and a surface energy that is comparable in value to that of pentacene. Matching the surface energy of the dielectric to pentacene is known to enhance device performance, especially the charge carrier mobility [37,38].

Pentacene TFTs with top-contact geometry were fabricated as shown in Fig. 2a and PS buffer layers were untreated and thermally treated at 80 and 120 °C, respectively. Devices were tested in air and in a dark environment at room temperature. The output and transfer characteristics of devices are shown in Figs. 2 and 3. All devices exhibited good p-type TFT behaviors and the current–voltage characteristics conform well to the conventional transistor model in both linear and saturated regimes. The maximum saturation current at each gate voltage increased markedly with the increased thermal treating temperature which is consistent with previous studies [39]. The mobilities of the devices in the saturated regime were extracted from the following equation:

$$I_{DS} = C_i \mu (W/2L)(V_{GS} - V_T)^2 \quad (4)$$

where I_{DS} is the drain current, C_i is the capacitance per unit area of the gate dielectric layer, and V_{GS} and V_T are the gate voltage and threshold voltage, respectively. The field-effect mobilities of the devices were calculated from the linear fit of the square root of I_{DS} versus V_{GS} in the saturated regime. V_T was determined by extrapolating the linear section of the square root of I_{DS} versus V_{GS} to $I_{DS} = 0$. Table 2 summarizes OTFT electrical parameters in both linear and saturation regions, including carrier mobilities, on/off current ratios, and threshold voltages. It can be clearly observed that the carrier mobility of the devices is dependent on the thermal treatment temperatures of the PS films. For the devices based on the PS film untreated, carrier mobility of ca. 0.8 $cm^2/V\,s$, a threshold voltage about 40 V and on/off ratio of about 10^8 in the saturation region are observed which are similar to those of previous devices [14,17]. For the device using the PS film treated at 80 °C, the carrier mobility reaches 2.0 $cm^2/V\,s$, an increase of more than 2×, and the threshold voltage is reduced down to 26.4 V. When the PS thermal treatment temperature was increased to 120 °C, the performance of the devices is enhanced with a mobility of ~4.0 $cm^2/V\,s$, a large on/off ratio about 10^7–10^8, and a low threshold voltage about 6.5 V. This is among the best results reported for pentacene-based OTFTs. Thus, higher-temperature thermal treatments of PS thin film that produces a flat orientation of phenyl groups and then a decrease in surface energy leads to better device performance (higher carrier mobility and lower threshold voltage). This could be ascribed to better matched surface energies between pentacene and phenyl groups at the surface of PS film that results in formation of a highly crystalline pentacene film with good interconnection [15,38].

To clarify the origin of the enhanced OTFT performance, it is important to investigate the difference of nucleation, film growth, morphology and crystallinity of pentacene deposited onto the different PS films. The surface roughness of the gate dielectric can significantly affect the nucleation of deposited pentacene molecules, its thin-film growth, and eventually the device performance [40]. Thus, we first investigated the surface roughness of PS films. The atomic force microscopy (AFM) images of PS films with different thermal treatments on SiO_2 showed a very similar topography with smooth surface (as shown in Fig. 4). The root-mean-square (RMS) roughness is 0.2–0.3 nm for the films untreated and treated at 80 and 120 °C. These results are consistent with the RMS of the thermally growth SiO_2 ($R_q \approx 0.4$ nm) [39]. Therefore, the difference among pentacene morphologies and device parameters can be mainly attributed to the nature of PS–pentacene interface, since the surface roughness of the PS films are almost identical. Fig. 5 shows the AFM images of pentacene films deposited onto different PS films. During the initial stages of pentacene film growth, numerous large two-dimensional islands were formed on the untreated PS film and no conglomerated island structures could be observed. As the thickness of deposited pentacene films continued to increase, the islands grew both vertically and laterally, and eventually coalesced. With the higher-temperature treated PS films, the pentacene films were inclined to lateral growth of the grain. The step height of islands was about 2.4–4.8 nm, which

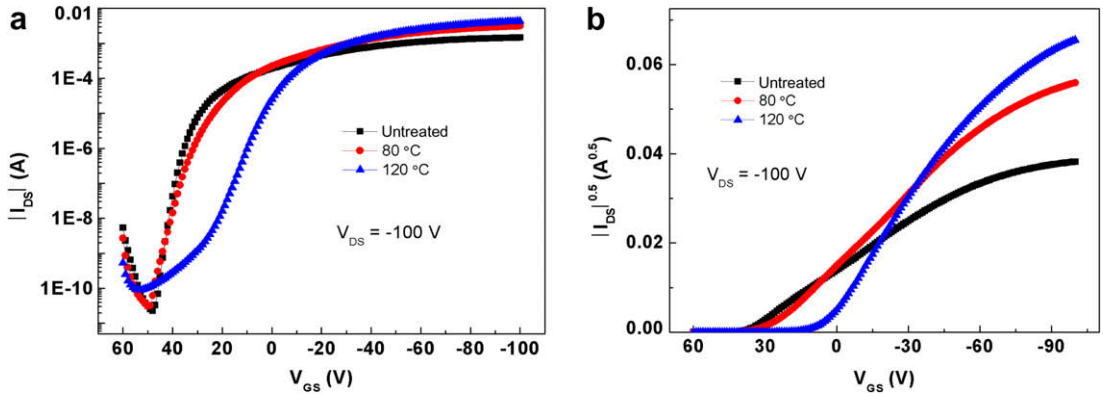

Fig. 3. $\log_{10}(|I_{DS}|)$ versus V_{GS} (a) and $|I_{DS}|^{1/2}$ versus V_{GS} (b) characteristics of pentacene TFTs with PS buffer layer untreated and thermally treated 80 and 120 °C.

corresponds to the thickness of 2–3 monolayers, considering the long axis of pentacene molecule [41]. For pentacene film deposited on PS (after thermal treatment at 80 and 120 °C), the predominant interconnection between the grains was observed at a thickness of ~2 nm. However, for the pentacene film deposited on untreated

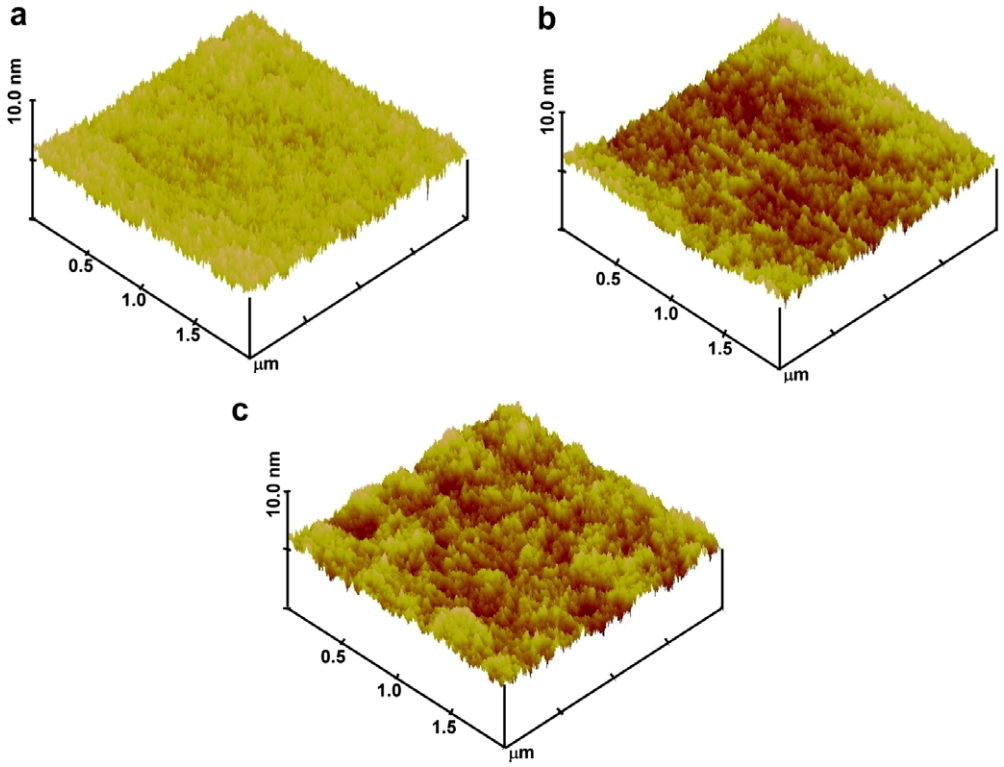

Fig. 4. AFM images of the surface of PS thin films untreated (a) and thermally treated at (b) 80 °C and (c) 120 °C. All images are 2 μm × 2 μm in size.

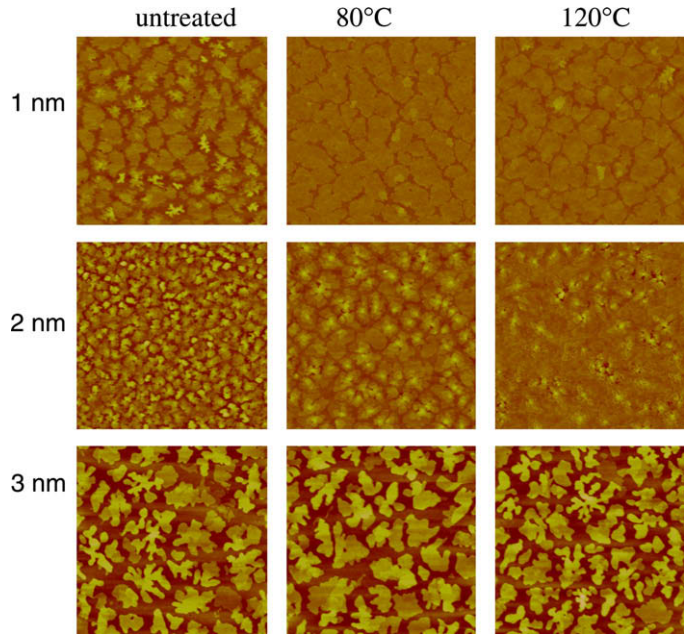

Fig. 5. AFM images at various thicknesses during the initial stages of pentacene film growth on PS films untreated and thermally treated 80 and 120 °C. All images are 5 μm × 5 μm in size.

PS, no connection between grains could be observed until the thickness of pentacene film reached 3 nm. This thickness value is lower than those reported for pentacene deposited on top of SAMs or other polymer dielectrics [15,39]. The low film thickness needed to form interconnected pentacene grains on the surface is attributed to the flat orientation of underlying phenyl groups at the surface of PS films and then the good connection between pentacene grains facilitates efficient charge transport [15]. Similar results were observed for devices made with an ordered octadecyltrichlorosilane (ODTS) SAM treated SiO_2 surface [15].

To investigate the crystalline phase and crystallinity of the deposited pentacene films, X-ray diffraction (XRD) measurements were performed. The X-ray patterns of the scans for 50 nm thick pentacene films deposited onto PS/SiO_2 are shown in Fig. 6. Only (0 0 l) reflections can be observed for all of the pentacene films, indicating that all pentacene nanocrystals in the pentacene films are oriented with their (0 0 l) phases parallel to the PS film [42,43]. For all the pentacene films, all peaks corresponding to (0 0 l) planes come from the substrate-induced thin-film phase with the same interlayer spacing of 15.4 Å, while the peaks corresponding to bulk phase with a vertical periodicity of 14.5 Å are not observed in our XRD patterns. It indicates that the pentacene molecules on PS films are apparently affected by the interaction with PS surface, because the thin-film phase is surface-induced and energetically less stable compared to the bulk phase [44]. Dimitrakopoulos et al. reported that the coexistence of thin-film and bulk phases can cause high defect densities in the pentacene films, leading to lower mobilities in devices [45]. Furthermore, the diffraction peak intensities increase with increasing annealing temperature of the PS films, indicating the crystallinity of the deposited pentacene films is increased at higher temperatures. This result showed that the flat orientation of phenyl groups on the surface of PS film tends to lead to the formation of higher crystallinity pentacene films, which in turn, facilitates better charge transport.

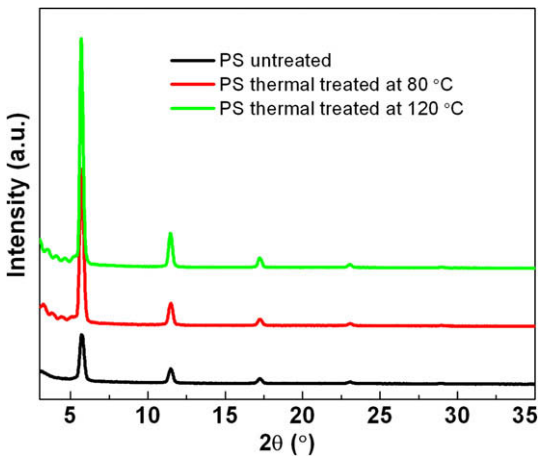

Fig. 6. XRD patterns of pentacene films on PS thin films untreated and thermally treated at 80 and 120 °C.

4. Summary

SFG results showed that the phenyl groups of polystyrene thin films untreated and thermally treated at 80 and 120 °C point away from the PS surface normal with tilt angles of 27°, 39° and 62°, respectively. The phenyl groups' flat orientation in PS films annealed at higher temperatures results in a higher surface energy of the PS films. OTFTs with an untreated and thermally treated PS buffer layer between SiO_2 and organic semiconductors were also fabricated. The device's performance is proportional to the thermal treatment temperature, viz. OTFTs based on the PS film with a flat orientation of the phenyl groups resulted in higher device performance. AFM and XRD results showed that a more highly oriented and crystalline pentacene film was grown on PS films with flatter phenyl group orientations. These pentacene films also had better interconnection between the crystalline domains. The devices with the PS films thermally treated at 120 °C exhibit the highest performance, producing a mobility of 4.0 cm^2/V s, an on/off current ratio of $\sim 10^7$–10^8, and a threshold voltage of about 6.5 V in the saturation region.

Acknowledgements

This work is supported by the NSF-STC Program under the Agreement Number MR-0120967. T.W. thanks the Deutsche Forschungsgemeinschaft for a research fellowship and A.K.-Y. Jen thanks the Boeing-Johnson Foundation for financial support.

References

[1] B.K. Crone, A. Dodabalapur, R. Sarpeshkar, A. Gelperin, H.E. Katz, Z. Bao, J. Appl. Phys. 91 (2001) 10140.
[2] C.D. Dimitrakopoulos, P.R.L. Malenfant, Adv. Mater. 14 (2002) 99.
[3] H. Sirringhaus, Nat. Mater. 2 (2003) 641.
[4] H.E.A. Huitema, G.H. Gelinck, J.B.P.H. van der Putten, K.E. Kuijk, C.M. Hart, E. Cantatore, P.T. Herwig, A.J.J.M. van Breemen, D.M. de Leeuw, Nature 414 (2001) 599.
[5] K. Xiao, Y. Liu, T. Qi, W. Zhang, F. Wang, J. Gao, W. Qiu, Y. Ma, G. Cui, S. Chen, X. Zhan, G. Yu, J. Qin, W. Hu, D. Zhu, J. Am. Chem. Soc. 127 (2005) 13281.
[6] Y. Wang, H. Wang, Y. Liu, C. Di, Y. Sun, W. Wu, G. Yu, D. Zhang, D. Zhu, J. Am. Chem. Soc. 128 (2006) 13058.
[7] Y. Lin, D.J. Gundlach, S.F. Nelson, T.N. Jackson, IEEE Trans. Electron Devices 18 (1997) 606.
[8] H. Usta, G. Lu, A. Facchetti, T.J. Marks, J. Am. Chem. Soc. 128 (2006) 9034.
[9] O. Acton, G. Ting, H. Ma, J.W. Ka, H.-L. Yip, N.M. Tucker, A.K.-Y. Jen, Adv. Mater. 20 (2008) 3697.
[10] C. Di, G. Yu, Y. Liu, X. Xu, D. Wei, Y. Song, Y. Sun, Y. Wang, D. Zhu, J. Liu, X. Liu, D. Wu, J. Am. Chem. Soc. 128 (2006) 16418.
[11] M.L. Swiggers, G. Xia, J.D. Slinker, A.A. Gorodetsky, G.G. Malliaras, R.L. Headrick, Brian T. Weslowski, R.N. Shashidhar, C.S. Dulcey, Appl. Phys. Lett. 79 (2001) 1300.
[12] F.-J. Meyer zu Heringdorf, M.C. Nakamura, R.M. Tromp, Nature 412 (2001) 517.
[13] Y. Wang, Y.Q. Liu, Y.B. Song, S.H. Ye, W.P. Wu, Y.L. Guo, C.A. Di, Y.M. Sun, G. Yu, W.P. Hu, Adv. Mater. 20 (2008) 611.
[14] C. Kim, A. Facchetti, T.J. Marks, Science 318 (2007) 76.
[15] H.S. Lee, D.H. Kim, J.H. Cho, M. Hwang, Y. Jang, K. Cho, J. Am. Chem. Soc. 130 (2008) 10556.
[16] C. Kim, A. Facchetti, T.J. Marks, Adv. Mater. 19 (2007) 2561.
[17] P.S. Jo, J. Sung, C. Park, E. Kim, D.Y. Ryu, S. Pyo, H.-C. Kim, J.M. Hong, Adv. Funct. Mater. 18 (2008) 1202.
[18] D.A. Fischer, G.E. Mitchell, A.T. Yeh, J.L. Gland, Appl. Surf. Sci. 133 (1998) 58.
[19] S. Wild, L.L. Kesmodel, G. Apai, J. Phys. Chem. B 104 (2000) 3179.

[20] D.K. Owens, R.C. Wendt, J. Appl. Polym. Sci. 13 (1969) 1741.
[21] F.G. Moore, K.A. Becraft, G.L. Richmond, Appl. Spectrosc. 56 (2002) 1575.
[22] C.D. Bain, J. Chem. Soc. Faraday Trans. 91 (1995) 1281.
[23] D.C. Duffy, P.B. Davies, J. Phys. Chem. 99 (1995) 15241.
[24] G. Varsanyi, in: L. Lang (Ed.), Assignments for Vibrational Spectra of Seven Hundred Benzene Derivatives, vols. 1.1, 1.2, 2, Adam Hilger, London, 1974.
[25] L.D. Bellamy, The Infra-red Spectra of Complex Molecules, third ed., Lowe & Brydone, Thetford, Norfolk, 1975.
[26] K.S. Gautam, A.D. Schwab, A. Dhinojwala, D. Zhang, S.M. Dougal, M.S. Yeganeh, Phys. Rev. Lett. 85 (2000) 3854.
[27] K.A. Briggman, J.C. Stephenson, W.E. Wallace, L.J. Richter, J. Phys. Chem. B 105 (2001) 2785.
[28] A. Opdahl, G.A. Somorjai, Langmuir 18 (2002) 9409.
[29] X. Zhuang, P.B. Miranda, D. Kim, Y.R. Shen, Phys. Rev. B 59 (1999) 12632.
[30] D. Zhang, J. Gutow, K.B. Eisenthal, J. Phys. Chem. 98 (1994) 13729.
[31] C. Hirose, H. Yamoto, N. Akamatsu, K. Domen, J. Phys. Chem. 97 (1993) 10064.
[32] C.S.C. Yang, P.T. Wilson, L.J. Richter, Macromolecules 37 (2004) 7742.
[33] D.H. Whiffen, Proc. Phys. Soc. 69A (1956) 375.
[34] J. Stöhr, M.G. Samat, J. Electron. Spectrosc. Relat. Phenom. 98 (1999) 189.
[35] P.T. Wilson, L.J. Richter, W.E. Wallace, K.A. Briggman, J.C. Stephenson, Chem. Phys. Lett. 363 (2002) 161.
[36] Y. Li, J.Q. Pham, K.P. Johnston, P.F. Green, Langmuir 23 (2007) 9785.
[37] T.-S. Huang, Y.-K. Su, P.-C. Wang, Appl. Phys. Lett. 91 (2007) 092116.
[38] W.Y. Chou, C.W. Kuo, H.L. Cheng, Y.R. Chen, Appl. Phys. Lett. 89 (2006) 112126.
[39] S.Y. Yang, K. Shin, C.E. Park, Adv. Funct. Mater. 15 (2005) 1806.
[40] D. Knipp, R.A. Street, A. Völkel, Appl. Phys. Lett. 82 (2003) 3907.
[41] H. Yanagisawa, T. Tamaki, M. Nakamura, K. Kudo, Thin Solid Films 464 (2004) 398.
[42] H.S. Lee, D.H. Kim, J.H. Cho, Y.D. Park, J.S. Kim, K. Cho, Adv. Funct. Mater. 16 (2006) 1859.
[43] C.C. Mattheus, G.A. de Wijs, R.A. Groot, T.T.M. Palstra, J. Am. Chem. Soc. 125 (2003) 6323.
[44] H. Yoshida, K. Inaba, N. Sato, Appl. Phys. Lett. 90 (2007) 181930.
[45] C.D. Dimitrakopoulos, A.R. Brown, A. Pomp, J. Appl. Phys. 80 (1996) 2501.

stability and higher mobility values than their organic counterparts. Oxide semiconductors also can be process at low-temperatures and are compatible with flexible substrates. Therefore, they are an attractive alternative to electron transport organic semiconductors for the realization of hybrid circuits based on complementary metal-oxide semiconductor technology. To date, there are only few reports of hybrid complementary circuits [6–8]. On flexible substrates, Oh et al. [6] recently demonstrated complementary inverters on polyethersulfone (PES) substrates using ZnO and pentacene channels with the same aspect ratio. Following this hybrid approach, these inverters showed the highest reported static gain of 100 V/V at a switching threshold voltage of 5 V with a supply voltage of 7 V. Although not provided in the paper, unbalance noise margins can be expected in such inverters. Furthermore, ZnO films are polycrystalline even when deposited at room temperature, leading to channels with grain boundaries that deteriorate the TFT stability, uniformity, and performance [9]. On the other hand, pentacene/*a*-IGZO complementary inverters only have been reported on rigid substrates [7] with gains of 56 V/V with supply voltage of 7 V but at a switching threshold voltage of 2.8 V. Unbalanced noise margins can also be expected in that case.

Here, we report on hybrid pentacene/*a*-IGZO complementary inverters composed of TFTs with different channel aspect ratios fabricated on flexible PES substrates. We propose a method to find the switching threshold voltage based on the resistance of the *p*- and *n*-channel TFTs, discuss the conditions for an optimum supply voltage, and propose a method for its estimation. With this method, we demonstrate hybrid complementary inverters that combine a high gain of 130 V/V at V_D = 25 V with a switching threshold voltage (V_M) of 12.5 V that allows high and balanced values of noise margins with values of 84% the theoretical maximum.

2. Device fabrication and electrical characterization

Hybrid inverters were fabricated with a bottom gate and top-contact source and drain electrode geometry, as shown in Fig. 1a. First, a tri-layer of Ti(7 nm)/Au(70 nm)/Ti(7 nm) was deposited using electron-beam (e-beam) at room temperature on flexible PES substrates (*i*-components) through a shadow mask. A 300 nm-thick Si_3N_4 gate dielectric layer was deposited by PECVD at 180 °C. A 30 nm-thick *a*-IGZO (Ga_2O_3:In_2O_3:ZnO = 1:1:2 mol%) active layer was then deposited by rf sputtering at a low-temperature of 90 °C using a power of 125 W, a working pressure of 6 mTorr, and an O_2/Ar (1/20) atmosphere using a shadow mask. Then, a 50 nm-thick layer of pentacene was deposited using thermal evaporation with a substrate temperature of 25 °C and an initial pressure of 2×10^{-8} Torr. Prior to thermal evaporation, pentacene was purified using gradient zone sublimation. Finally, Au(25 nm)/Al(25 nm) source/drain electrodes were deposited through a shadow mask over the pentacene and *a*-IGZO channels. Complementary inverter circuits, as shown in Fig. 1b, were constructed using *p*-channel pentacene and *n*-channel *a*-IGZO TFTs with a channel length of L = 180 μm and channel widths of W^p = 4000 μm and W^n = 400 μm, respectively. A picture of the flexible inverters is shown in Fig. 1c. The use of Au source/drain electrodes is expected to yield balanced electron and hole injection since, in both cases, the energy barrier for charge injection is ~0.6 eV [10,11]. The channel width ratio of W^n/W^p = 10, was selected to compensate for: (1) differences in electron and hole mobility; and (2) differences in the threshold voltage. The gate electrodes were patterned for both TFTs and served as the input voltage (V_{IN}) of the inverter circuit.

The current–voltage characteristics of independent *p*- and *n*-channel TFTs, fabricated on the same substrate with the same channel aspect ratio as those used in the complementary inverter, are shown in Fig. 2a–d. The transfer and

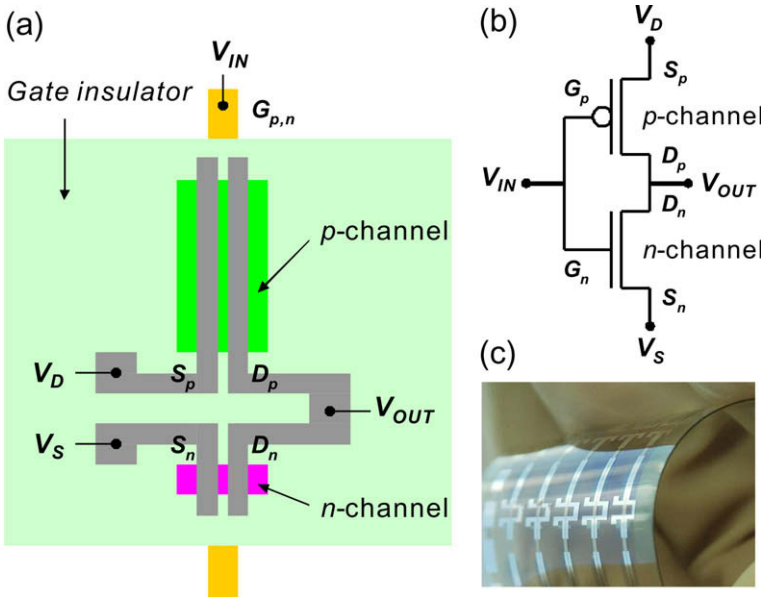

Fig. 1. (a) Schematics of the hybrid complementary inverter fabricated on a PES substrate with pentacene and *a*-IGZO as active channel layers. (b) Complementary inverter circuit diagram. (c) Photograph of complementary inverters on PES.

output characteristics of all TFTs were measured using an Agilent E5272A medium-power source/monitor unit connected to a probe station. The transfer curves and leakage currents measured for both forward and reverse gate biases are shown in Fig. 2a (*p*-channel) and Fig. 2b (*n*-channel). A saturation mobility of 0.13 cm^2/Vs and a threshold voltage of −10.3 V were obtained for pentacene TFTs. These values are comparable with the ones found in pentacene/Si_3N_4 TFTs on rigid substrates [12]. The small hysteresis in these TFTs, also found on rigid substrates, is due to a shift in the threshold voltage which is attributed to trapping at the pentacene/Si_3N_4 interface. The use of passivation layers is expected to significantly improve the hysteresis characteristics of these pentacene TFTs [2] without significantly affecting the properties of the *a*-IGZO channel. The *n*-channel *a*-IGZO TFT shows a saturation mobility of 3.8 cm^2/Vs and a threshold voltage of 13.6 V with negligible hysteresis. On rigid substrates, higher mobility values have been obtained because differences in processing conditions are expected to yield *a*-IGZO films with a slightly different stoichiometry than previously obtained. Higher mobility values are expected upon further optimization of the deposition process. The output curves shown in Fig. 2c (*p*-channel) and Fig. 2d (*n*-channel) exhibit good linearity at low drain-to-source voltage (V_{DS}) despite the relatively large energy barrier for charge injection.

3. Experimental method and analysis of complementary inverter

The static performance of an inverter is evaluated by its static gain and noise margin values. Achieving high and balanced noise margin values is necessary for reliable circuit operation in complex logic circuits such as ring oscillators. The noise margin, is limited by the steepness of the transition and by the position of the switching threshold voltage ($V_M = V_{IN} = V_{OUT}$). Highest values of noise margins are found when the ideal condition $V_M = 0.5V_D$ is met, hence when $V_M = V_{IN} = 0.5V_D = V_{OUT}$. However, the value of V_{IN} at which this transition occurs is generally not $0.5V_D$. The actual value of V_M depends on the range of V_D. A complementary inverter can be modeled by two series-connected voltage-dependent variable resistors. In general, for a given supply voltage, V_D, V_M corresponds to the input voltage that makes equal the resistance of the *n*-channel TFT ($R_{TN} = V_{DS}/I_{DS}$) and the *p*-channel TFT ($R_{TP} = -V_{DS}/-I_{DS}$). Note that R_{TN} and R_{TP} can be extracted from independent TFTs either from the output characteristics through the condition $V_{GS} = V_{DS}$ (as shown in Fig. 2c and d), or by directly measuring I_{DS} in a TFT with shorted gate and drain electrodes ($V_{GS} = V_{DS}$). Fig. 3 shows the values of R_{TN} and R_{TP}, extracted by following the first approach, for different values of $V_{GS} = V_{DS}$. Also note that the conventional analytical equation used to find V_M, derived from the MOSFET square law model, assumes that the mobility and threshold voltage remain constant during operation [13,14]. However, in organic or oxide TFTs, this analytical approach may not always hold true. An accurate calculation of V_M would require a fitting procedure to get the functional dependence of the mobility and threshold voltage as a function of V_{GS} and V_{DS}. In contrast, the proposed method does not require any fitting parameters, such as mobility or threshold voltage, and

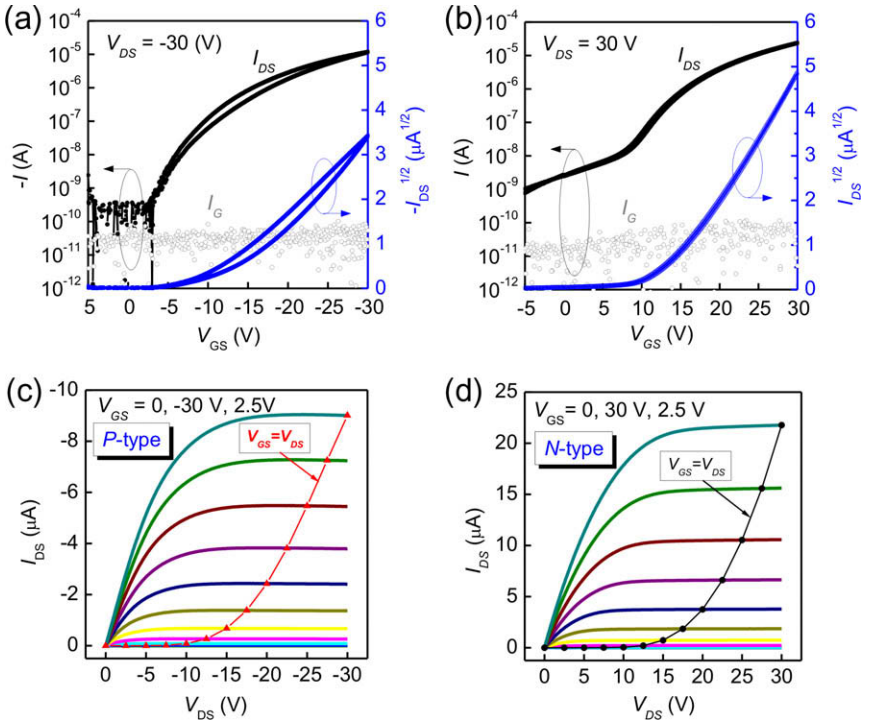

Fig. 2. Representative (a) hysteresis transfer and (c) output characteristics of pentacene TFTs with $L = 180$ μm and $W^p = 4000$ μm. Representative (b) hysteresis transfer and (d) output characteristics of *a*-IGZO TFTs with $L = 180$ μm and $W^n = 400$ μm.

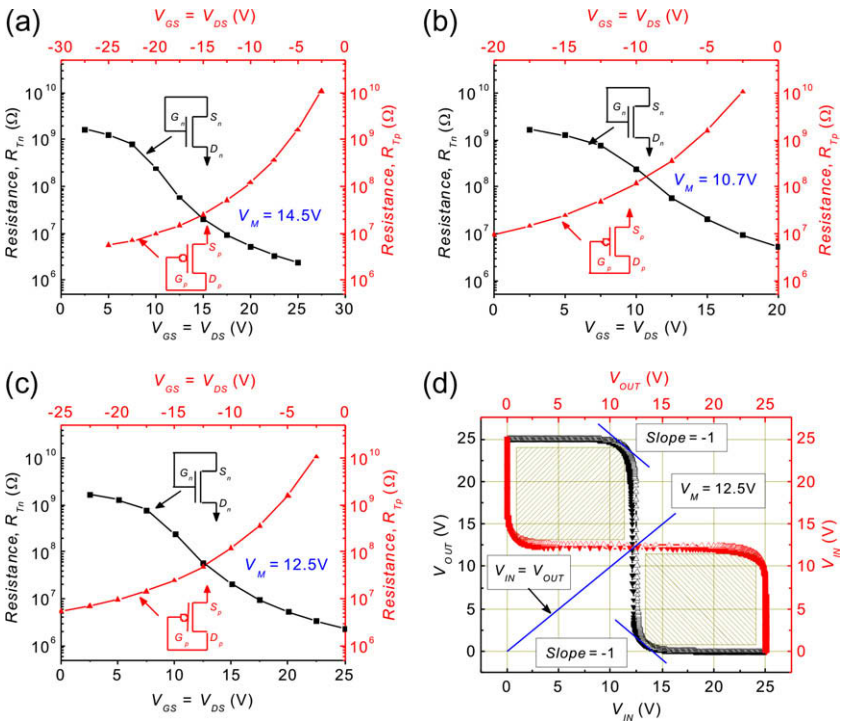

Fig. 3. Total resistance of pentacene *p*-channel and *a*-IGZO *n*-channel TFTs at $V_{GS} = V_{DS}$ by sweeping V_{GS} from (a) 0 V to ±30 V (positive for *n*-channel TFT, negative for *p*-channel TFT), (b) 0 V to ±20 V, and (c) 0 V to ±25 V (Insets show schematics of *n*- and *p*-channel TFT at $V_{GS} = V_{DS}$). (d) Bi-stable hysteresis voltage transfer characteristics at $V_D = 25$ V.

in principle requires just a pair of measurements of R_{TN} and R_{TP} as a function of $V_{GS} = V_{DS}$.

As mentioned earlier, to achieve balanced noise margins it is important to find the optimum value of V_D, such that $V_M = 0.5V_D$. To find the optimum range for V_D, a graphical solution is proposed as follows: (1) first, for a given range of $V_{DS} \in [0, \pm V_D]$ ($+V_D$ for the *n*-channel TFT and $-V_D$ for the *p*-channel TFT), the value of V_M is calculated as previously described; (2) if $V_M \neq 0.5V_D$ the range of V_{DS} needs to be adjusted. As shown in Fig. 3a, if $V_M < 0.5V_D$, then V_D needs to be decreased and the procedure start over again until $V_M = 0.5V_D$ is found. Correspondingly, as shown in Fig. 3b, if $V_M > 0.5V_D$, V_D needs to be increased and the procedure repeated until the condition $V_M = 0.5V_D$ is found. Fig. 3c shows the values of R_{TN} and R_{TP} extracted following this procedure for V_{DS} [0,±25 V], the range where $V_M = 0.5V_D = 12.5$ V. Note that testing at different V_D values is not really necessary once the output characteristics are measured for a large enough range of $V_{GS} = V_{DS}$. This is because the values of I_{DS} and consequently R_{TN} and R_{TP} can be interpolated from the output characteristics of the *n*- and *p*-channel TFTs. Therefore, the absolute value of the difference of R_{TN} and R_{TP}, $R_d = |R_{TN} - R_{TP}|$ can be estimated for arbitrary values of V_D. The value of V_M is given as the $V_{GS} = V_{DS}$ value where R_d reaches a minimum value. If $V_M \neq 0.5V_D$, the range of the V_D can be adjusted numerically until the condition $V_M = 0.5V_D$ is found as described before. Fig. 3d shows the measured bi-stable hysteresis voltage transfer characteristics at a supply voltage of $V_D = 25$ V. The cross-hatched rectangles, defined by the

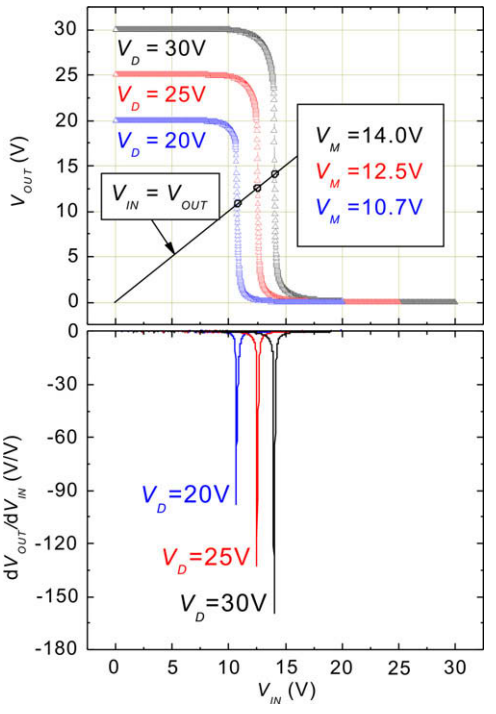

Fig. 4. Voltage transfer characteristics and static gain of the hybrid complementary inverter.

negative slope criteria [13,14], are used to determine a graphical solution of the noise margins for a given inverter characteristic. At $V_D = 25$ V, the inverters show identical noise margin low (NM_L) and noise margin high (NM_H) of 10.5 V (84% of their theoretical maximum). These values are among the highest values obtained in organic, or hybrid inverters. Fig. 4 shows the measured voltage transfer characteristics and static gain values of the inverter for $V_D = 20$, 25, and 30 V. The maximum static gain values for $V_D = 20$ and 30 V are -100 V/V at $V_M = 10.7$ V and -165 V/V at $V_M = 14.5$ V, respectively. The corresponding values of NM_H and NM_L are 7.5 and 9.4 V for $V_D = 20$ V, and 13.9 and 11.4 V for $V_D = 30$ V. As expected from a shift of V_M from its optimum value, unbalanced noise margins are obtained when $V_D \neq 25$ V. While higher gain values are obtained at larger V_D values, from a circuit operation perspective the best compromise is obtained when balanced noise margins are achieved. At the switching threshold voltage values, $R_{TP} = R_{TN}$ are 164, 54.3, and 23.5 MΩ for $V_D = 20$, 25, and 30 V, respectively. From these values we estimated a maximum dissipated power of 1.22, 5.76, and 19.1 μW for $V_D = 20$, 25 and 30 V respectively.

4. Conclusion

In summary, we demonstrated organic–inorganic hybrid complementary inverters fabricated on flexible PES substrates that use *n*- and *p*-channel TFTs with channels having different aspect ratios to achieve high static gains and balanced high noise margins. With a Si_3N_4 gate dielectrics, *p*- and *n*-channel TFTs show saturation mobility values of 0.13 and 3.8 cm^2/Vs. We also proposed a new approach to find the switching threshold voltage and the optimum value of V_D to operate a complementary inverter. Using this method, we demonstrated hybrid inverters that achieve a very high gain of 130 V/V at $V_D = 25$ V with high and balanced noise margin values of 84% of their theoretical maximum. In contrast with previous analytical methods, the proposed method does not requires fitting to any transistor model, can be implemented with a pair of measurements and should also be applicable to any complementary or complementary-like (one that uses ambipolar TFTs) inverter configuration.

Acknowledgement

This material is based upon work supported in part by the STC Program of the National Science Foundation under Agreement No. DMR-0120967 and by the Office of Naval Research (Grant No. N00014-04-1-0120). This work was performed in part at the Microelectronics Research Center at Georgia Institute of Technology, a member of the National Nanotechnology Infrastructure Network, which is supported by NSF (Grant No. ECS-03-35765).

References

[1] H. Klauk, U. Zschieschang, J. Pflaum, M. Halik, Nature 445 (2007) 745.
[2] X.H. Zhang, W.J. Potscavage, S. Choi, B. Kippelen, Appl. Phys. Lett. 94 (2009) 043312.
[3] C.D. Dimitrakopoulos, P.R.L. Malenfant, Adv. Mater. 14 (2002) 99.
[4] E.M.C. Fortunato, P.M.C. Barquinha, A. Pimentel, A.M.F. Goncalves, A.J.S. Marques, L.M.N. Pereira, R.F.P. Martins, Adv. Mater. 17 (2005) 590.
[5] K. Nomura, H. Ohta, A. Takagi, T. Kamiya, M. Hirano, H. Hosono, Nature 432 (2004) 488.
[6] M.S. Oh, W. Choi, K. Lee, D.K. Hwang, S. Im, Appl. Phys. Lett. 93 (2008) 033510.
[7] J.H. Na, M. Kitamura, Y. Arakawa, Appl. Phys. Lett. 93 (2008) 213505.
[8] H. Iechi, Y. Watanabe, H. Yamauchi, K. Kudo, Ieice Trans. Electron. E91-C (2008) 1843.
[9] F.M. Hossain, J. Nishii, S. Takagi, A. Ohtomo, T. Fukumura, H. Fujioka, H. Ohno, H. Koinuma, M. Kawasaki, J. Appl. Phys. 94 (2003) 7768.
[10] C. Baldacchini, C. Mariani, M.G. Betti, L. Gavioli, M. Fanetti, M. Sancrotti, Appl. Phys. Lett. 89 (2006) 152119.
[11] Y. Shimura, K. Nomura, H. Yanagi, T. Kamiya, M. Hirano, H. Hosono, Thin Solid Films 516 (2008) 5899.
[12] M.H. Choo, J.H. Kim, S. Im, Appl. Phys. Lett. 81 (2002) 4640.
[13] S.-M. Kang, Y. Leblebici, CMOS Digital Integrated Circuits Analysis and Design, third ed., McGraw-Hill, New York, 2003.
[14] J.M. Rabaey, Digital Integrated Circuits: A Design Perspective, first ed., Prentice Hall, New Jersey, 1995.

those in LEC devices, which are dynamic structures that form, readjust, and dissipate in response to changes in the applied voltage [20]. Although the dynamic nature of the electrochemical doping of CPs offers many important advantages, it would for several applications be of interest to permanently stabilize a desired doping structure that is formed during the doping process. For instance, a significant time lag between the application of voltage and attainment of a stable response (e.g., current rectification and/or light emission), during which the doping structure is built *via* a redistribution of mobile ions, is an obvious drawback in applications where a fast and consistent behavior is important. Immobilization of ions is the key to the stabilization of an electrochemically induced doping structure in CPs in general and LECs in particular. More specifically, ion mobility is an obvious prerequisite during the doping process, but the subsequent stabilization of a desired doping structure requires that the mobility of the ions is eliminated.

Gao and co-workers were the first to demonstrate LEC devices with stabilized doping structures, when they utilized the temperature dependence of the ion mobility of lithium-salts in a poly(ethylene oxide) (PEO) matrix, thereby establishing the so-called "frozen-junction" concept [23,24]. They formed the p–n junction at room temperature, at which the lithium-salt ions exhibit a reasonable mobility in the PEO matrix. When the device is subsequently cooled to a low temperature with the bias maintained, the ion mobility drops to essentially zero [23,24]. A number of subsequent studies on the topic of frozen-junction operation have appeared in the scientific literature, but the concept currently suffers from an impractical sub-ambient operation temperature and/or limited long-term stability [25–30]. An alternative novel approach for doping structures with room temperature stability, conceptualized by Cheng and Lonergan, includes the employment of a bi-layer structure comprising charge-complementary ionic CPs and a subsequent solvent-induced removal of the mobile ions [31]. However, the plausibly most practical and generic route towards permanently stabilized doping structures, as introduced by Leger et al., involves a "chemical stabilization" route [32–35]. In the pioneering paper [33], it was the dopant counter-ions (being polymerizable ion-pair monomers) that were chemically modified and effectively locked in place *via* a polymerization reaction. In a later study, Yu et al. have demonstrated that it is possible to attain stabilized doping *via* chemical cross-linking of the ion-transport material (in the form of a polymerizable small molecule) [36].

In this article, we report results on an expanded study of the merits of the chemical stabilization concept. We evaluate and compare the performance of LEC devices comprising light-emitting p–n junctions built and stabilized in accordance with the approaches of Leger et al. and Yu et al., as well as by two new approaches. We find that the best performing LEC devices, from the viewpoints of light-emission, current rectification, and long-term stability, are those that utilize a combination of polymerizable ions, a polymerizable ion-transport material, and a radical-initiator compound.

2. Material and methods

2.1. Ion-pair monomer synthesis

The ion-pair monomer (i.e., the polymerizable salt) 2-(methacryloyloxy)ethyl trimethylammonium 2-acrylamido-2-methyl-1-propane sulfonate (METMA/AMPS) was synthesized in accordance with a previously published procedure [37,38]. About 0.250 g (1.47 mmol) silver nitrate and 0.060 g (1.5 mmol) sodium hydroxide were mixed together in 10 ml of water in darkness, and the resulting silver hydroxide precipitate was filtered over a frit. The recovered silver hydroxide was added to 0.20 g (0.95 mmol) AMPS-H (Aldrich), which had been dissolved in 2 ml water and treated twice with activated carbon. The mixture was stirred in an ice bath for 4 h to yield AMPS-Ag. 0.21 g (1.0 mmol) METMA-Cl (Polysciences) dissolved in 5 ml water was added drop wise to the AMPS-Ag mixture, during which precipitation of silver chloride was observed. This mixture was stirred for 3 h in an ice bath, where after the silver chloride was filtered away and the water allowed to evaporate under vacuum at room temperature. A glassy solid material was extracted using acetone, and this material was subsequently recrystallized to yield a white solid METMA/AMPS compound in a yield of 60%. ^{1}H NMR (D_2O): δ 5.60 and 6.06 (m, 5H, vinyl-H), δ 4.53 (s, 2H), δ 3.69 (s, 2H), δ 3.32 (s, 2H), δ 3.13 (s, 9H), δ 1.81 (s, 3H), δ 1.38 (s, 6H).

2.2. Materials

The CP used throughout this study was a decyloxyphenyl substituted poly(1,4-phenylene vinylene) termed superyellow (SY, Merck, Darmstadt, FRG), and it was used as received. The ion-transport materials, poly(ethylene oxide) (PEO; $M_w = 5 \times 10^6$ g/mol), poly(ethylene glycol) diacrylate (poly-PEO; $M_w = 575$ g/mol) and trimethylolpropane trimethacrylate (TMPTMA), were all purchased from Aldrich (Steinheim, FRG) and used as received. The salt lithium trifluoromethanesulfonate ($LiCF_3SO_3$; Alfa Aesar, Karlsruhe, FRG) was dried at $T = 473$ K under vacuum before use. The radical-initiator 2,2′-azobis(2-methylpropionitrile) (AIBN) was purchased from Serva (Heidelberg, FRG) and used as received. Fig. 1 presents the chemical structures of the compounds used for the fabrication of the LEC devices.

2.3. Device preparation and measurements

The solutions for the fabrication of the presented LEC devices (see Table 1) were prepared by mixing the below listed master solutions in appropriate amounts. System (A): 5 mg/ml SY in chlorobenzene (CB), 10 mg/ml PEO in CB, and 5 mg/ml METMA/AMPS in CB. System (B): 5 mg/ml SY in toluene, 10 mg/ml PEO in cyclohexanone (CH), 5 mg/ml METMA/AMPS in CH, and 10 mg/ml AIBN in CH. System (C): 5 mg/ml SY in tetrahydrofuran (THF), 10 mg/ml TMPTMA in THF, and 10 mg/ml $LiCF_3SO_3$ in THF. System (D): 5 mg/ml SY in toluene, 10 mg/ml PEO in CH, 5 mg/ml METMA/AMPS in CH, and 10 mg/ml AIBN

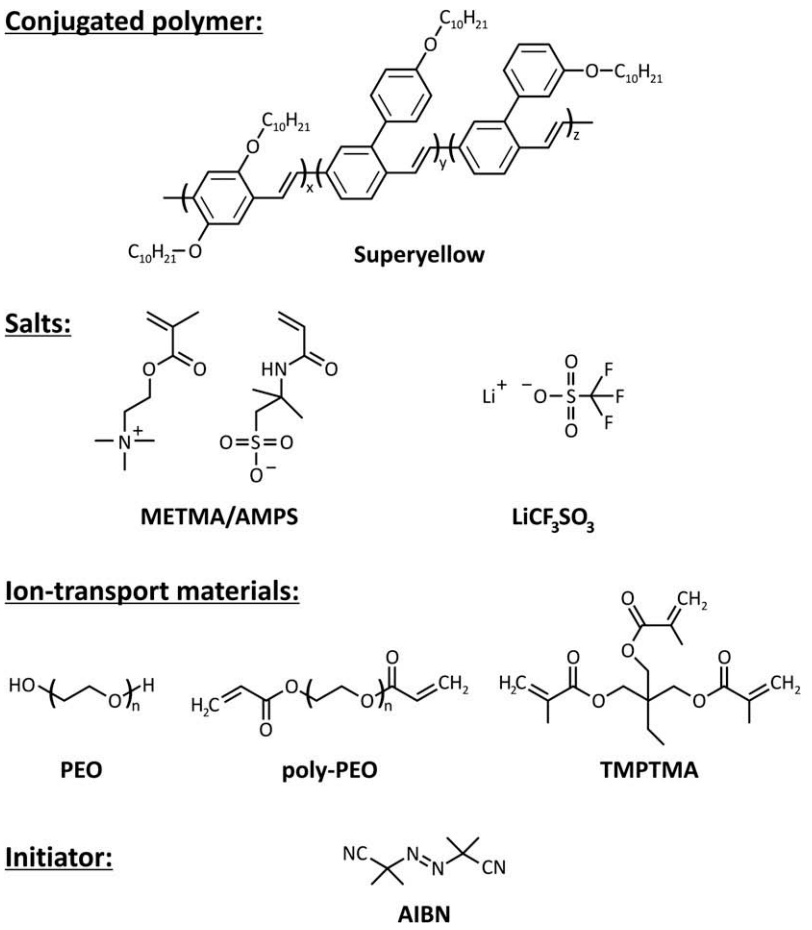

Fig. 1. Chemical structures of the constituent materials in the active layer of the LEC devices.

Table 1
Key devices properties for the four different types of stabilized doping systems.

System group active material constituents (mass ratio)	Current rectification ratio at $V = \pm 10$ V[a]	Initial brightness at $V = +10$ V (cd/m^2)[a]	Retained brightness after 12 h under open-circuit	Current efficacy at $V = +10$ V (cd/A)[a]
(A) SY:PEO:METMA/AMPS (1:0.4:0.1)	NA[b] [22][c]	0 [36][d]	NA (15%)[d]	0 (0.77)[d]
(B) SY:PEO:METMA/AMPS:AIBN (1:0.17:0.06:0.003)	NA[b]	15	2%	1.1
(C) SY:TMPTMA:$LiCF_3SO_3$ (1:0.5:0.1)	700	16	86%	0.06
(D) SY:poly-PEO:METMA/AMPS:AIBN (1:0.17:0.06:0.003)	1900	50	87%	1.1

[a] As measured directly after the removal of the pre-bias.
[b] It was not possible to measure a stable rectification ratio at $V = \pm 10$ V.
[c] The value in parenthesis is the rectification ratio at $V = \pm 15$ V.
[d] The value in parenthesis is measured at $V = +15$ V, as the brightness at $V = +10$ V was <1 cd/m^2.

in CH. The solutions were stirred on a magnetic hot plate at $T = 323$ K for at least 5 h immediately before the deposition.

The indium tin oxide (ITO) coated glass substrates (1.5×1.5 cm^2, 20 Ω/square; Thin Film Devices, Anaheim, CA) were cleaned by sequential ultrasonic treatments at

room temperature in detergent (Extran MA 01, Merck), acetone, and isopropanol. The LEC devices were fabricated in a sandwich cell architecture by spin-coating solution onto an ITO-coated glass substrate for 60 s at 800 rpm (for active materials of systems (A), (B) and (D)) or 2000 rpm (for active materials of system (C)). The resulting active material film was thereafter dried at $T = 333$ K for at least 5 h. The thicknesses of the active material films, as established by atomic force microscopy, were: 200 nm (system (A)), 120 nm (system (B)), 100 nm (system (C)), and 120 nm (system (D)). Aluminium electrodes were deposited on top of the film by thermal evaporation at $p < 2 \times 10^{-4}$ Pa. All of the above device preparation procedures, except the cleaning of the substrates, were carried out in two interconnected N_2-filled glove boxes ($[O_2] < 3$ ppm, $[H_2O] < 0.5$ ppm). Device measurements were performed under

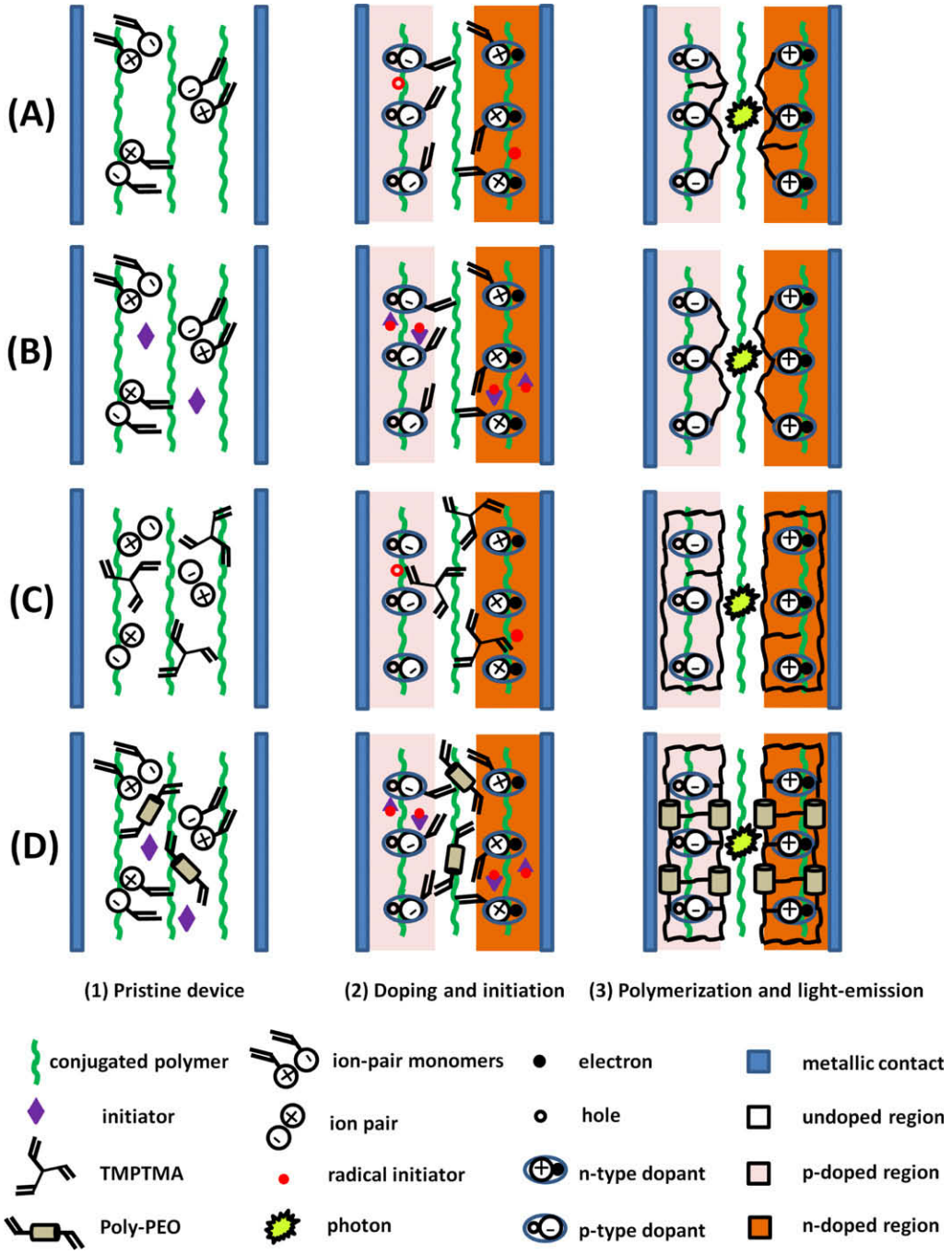

Fig. 2. Schematic illustration of the doping and chemical stabilization processes in the four types of baseline LEC systems (A–D) under study. Note that the dopant radical-initiators depicted in the second column of (A) and (C) correspond to injected holes and electrons, and are as such in reality charge-compensated by counter-ions in close proximity. For clarity, we have chosen to omit these ions from the schematic.

vacuum ($p < 10^{-3}$ Pa) in an optical-access cryostat (Advanced Research Systems). A computer-controlled source-measure unit (Keithley 2400) in combination with a calibrated photo-diode with an eye response filter (Hamamatsu, S9219–01) connected through a current-to-voltage amplifier to a HP 34401A digital multimeter were employed for the optoelectronic characterization of the devices. The scan rate for the *I–V* measurements presented in Figs. 3–6 was 0.5 V/s.

3. Results and discussion

We report results on four different types of baseline systems, for which the permanent stabilization of the doping profile was attempted in accordance with the following basic principles: (A) Chemical cross-linking of ion-pair monomers (i.e., a polymerizable salt); (B) chemical cross-linking of ion-pair monomers utilizing an added radical-initiator compound; (C) chemical cross-linking of the

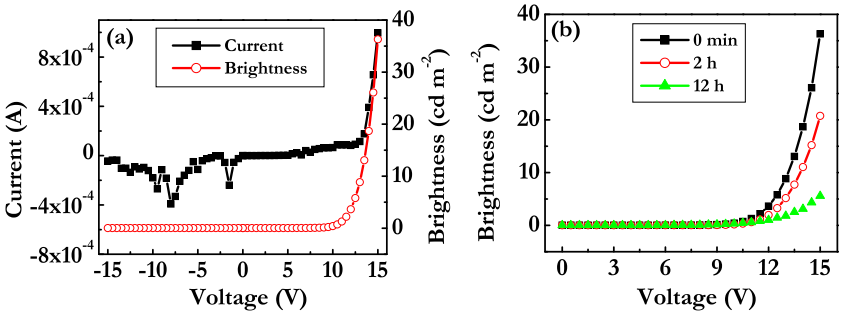

Fig. 3. Optoelectronic data for an LEC device of type (A), which had been pre-biased at $V = +10$ V at room temperature for 1.5 h. (a) The current (black solid squares) and the brightness (red open circles) as a function of voltage, as measured directly following the removal of the pre-bias. (b) The brightness-voltage dependence measured at different times following the removal of the pre-bias, as specified in the inset. The device was left at open-circuit between the measurements. (For interpretation of the references to colour in this figure legend, the reader is referred to the web version of this article.)

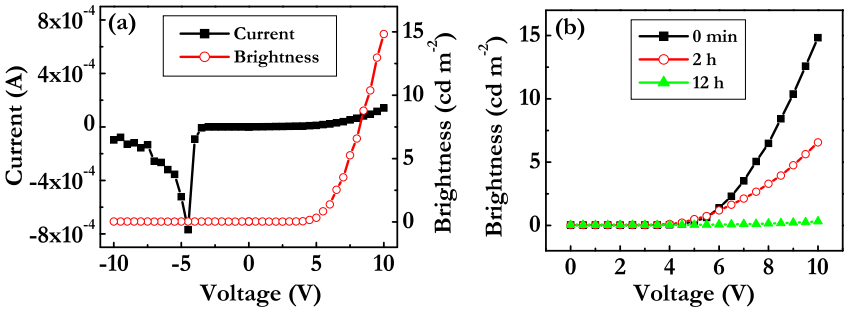

Fig. 4. Optoelectronic data for an LEC device of type (B), which had been pre-biased at $V = +10$ V and $T = 360$ K for 1.5 h. (a) The current (black solid squares) and the brightness (red open circles) as a function of voltage, as measured directly following the removal of the pre-bias. (b) The brightness-voltage dependence measured at different times following the pre-bias, as specified in the inset. The device was left at open-circuit between the measurements. (For interpretation of the references to colour in this figure legend, the reader is referred to the web version of this article.)

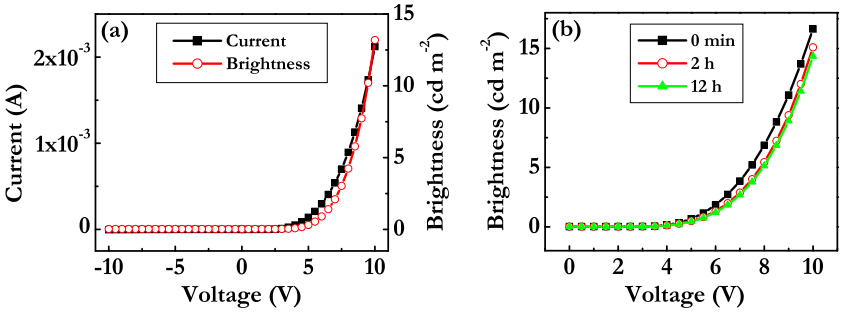

Fig. 5. Optoelectronic data for an LEC device of type (C), which had been pre-biased at $V = +12$ V at room temperature for 3.8 h. (a) The current (black solid squares) and the brightness (red open circles) as a function of voltage, as measured directly following the removal of the pre-bias. (b) The brightness-voltage dependence measured at different times following the pre-bias, as specified in the inset. The device was left at open-circuit between the measurements. (For interpretation of the references to colour in this figure legend, the reader is referred to the web version of this article.)

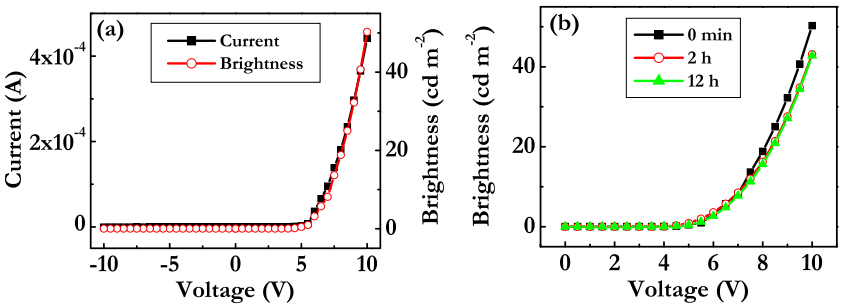

Fig. 6. Optoelectronic data for an LEC device of type (D), which had been pre-biased at $V = +5$ V at room temperature for 2 h. (a) The current (black solid squares) and the brightness (red open circles) as a function of voltage, as measured directly following the removal of the pre-bias. (b) The brightness-voltage dependence measured at different times following the pre-bias, as specified in the inset. The device was left at open-circuit between the measurements. (For interpretation of the references to colour in this figure legend, the reader is referred to the web version of this article.)

ion-transport material; and (D) chemical cross-linking of ion-pair monomers and the ion-transport material utilizing an added radical-initiator compound. Fig. 2 presents a schematic of our view on how the initial doping and the subsequent stabilization of the doping should be attained.

For clarity, we have chosen to present data (and experimental detail) for only one device structure for each system group. However, it is appropriate to point out that we have tested a large number of different device structures under different biasing conditions, and that the presented data represent the "best" performing device in each system group. Moreover, in order to accommodate a straightforward comparison and evaluation of the different system groups from a stabilized doping and functional device perspective, we have chosen to focus on a number of distinct device properties, specifically the current rectification ratio (RR), the initial brightness following the pre-bias step, the retained brightness after a 12 h period of storage under open-circuit condition, and the current efficacy for light-emission. These values for the best performing device structures in each group are summarized in Table 1 above, and the performance of each device structure is discussed in detail in the following four sections.

3.1. System (A): cross-linking of ions

Leger and co-workers [33] introduced an innovative concept for the permanent stabilization of a p–n junction doping profile in LEC devices, when they replaced the conventionally used "inert" salt (typically an alkaline metal salt or an ionic liquid) with an ion-pair monomer that can be polymerized *via* radical initiation. Following a pre-bias period, such LEC devices exhibit uni-polar light-emission and a high current rectification ratio of RR > 100 at high operating voltage, which are both indicators of stabilized doping. The authors proposed that the polymerization of the ion-pair monomers could be initiated at the site of the electrochemical doping of the conjugated polymer, since the hole and electron dopants in effect are highly reactive radicals that presumably can initiate a polymerization reaction of the ion-pair monomers in accordance with the process depicted in Fig. 2A.

We have utilized METMA/AMPS as the ion-pair monomer and fabricated sandwich cells with an active material blend, comprising SY, PEO, and METMA/AMPS in a (1:0.4:0.1) mass ratio, sandwiched between an ITO anode and an Al cathode. The devices were initially "pre-biased" at $V = +10$ V at room temperature for an extended period of 1.5 h (data not shown). During the pre-bias period the current is observed to increase significantly with time in a continuous fashion, and at the end of the pre-bias period the device begins to emit light. These are well-known fingerprints of a functional LEC device, and it is accordingly clear that the employed METMA/AMPS ion-pair monomer: (i) exhibits ionic mobility in the active material, and (ii) can function as counter-ions to accommodate electrochemical doping of SY.

The data displayed in Fig. 3 (and summarized in Table 1) for the device of system (A) were recorded after the pre-bias had been removed. In agreement with the results presented by Leger et al., we found that a pre-biased device exhibited uni-polar light-emission, i.e., it only emitted light when biased with the same voltage polarity as it had been pre-biased. In contrast, conventional LECs comprising mobile ions typically exhibit bi-polar light-emission, as the doping is reversible, and the light-emitting p–n junction accordingly can form in both bias directions [20]. However, a device based on a stabilized p–n junction doping profile is also expected to exhibit a high current rectification, but as we found a large and rather erratic current at reverse voltages up to $V < -15$ V (see Fig. 3a), the current rectification ratio was very low (and also difficult to quantify). Moreover, a practical stabilized doping profile should be stabile over time under open-circuit conditions, but we found that the brightness at $V = +15$ V had dropped to 15% of its initial value after 12 h at open-circuit (see Fig. 3b). A further drawback seen with the pre-biased devices of system (A) was that the brightness was invariably very low. This was also manifested in the turn-on voltage for light-emission (defined to be the voltage at which the device emits 1 cd/m^2), which for the pre-biased device depicted in Fig. 3 was very high at $V_{\text{turn-on}} = 11$ V.

3.2. System (B): cross-linking of ions with added initiator

The poor long-term stability of the pre-biased devices of system (A) under open-circuit conditions (see Fig. 3 and Table 1) implies that a significant fraction of the

ion-pair monomers were not polymerized during the pre-bias step. Moreover, the low brightness indicates that the assumed polymerization mechanism with onset *via* dopant radical initiation might not be preferable, as this process plausibly damages the fluorescent and/or electronic-transport capacity of the conjugated polymer (here, SY). In order to rectify these problems, and to attain a higher degree of polymerization and a more stable doping profile as well as higher brightness, we chose to investigate the effects of adding AIBN as a radical-initiator to the active material blend. The expectation was that the AIBN initiator would assist in the formation of an extended and stabile cross-linked chemical network between the different ion-pair monomers without including – and potentially damaging the electroluminescent properties of – the conjugated polymer, as illustrated in Fig. 2B.

A sandwich cell, comprising an active material blend of SY, PEO, METMA/AMPS, and AIBN in a (1:0.17:0.06:0.003) mass ratio sandwiched between an ITO anode and an Al cathode, was pre-biased at $V = +10$ V for 1.5 h at $T = 360$ K. The employment of the elevated temperature was motivated by that the decomposition of AIBN into two free-radical fragments and the related rate of the subsequent radical-initiated polymerization will both increase with increasing temperature. During the pre-bias period the current and brightness were found to increase with time, in a similar fashion as for the device of system (A). The turn-on time for light-emission was, however, notably faster, which can be attributed to a significantly higher ion mobility of the METMA/AMPS ion-pair monomer in an amorphous PEO matrix (at $T = 360$ K), as compared to a semi-crystalline PEO matrix (at room temperature) [16].

The typical performance of a pre-biased device of system (B) is shown in Fig. 4 and summarized in Table 1. Following the removal of the pre-bias, it exhibited uni-polar light-emission, a relatively high current efficacy for a conjugated-polymer-based LEC of 1.1 cd/A at $V = +10$ V, and a notably increased brightness. (Note the expanded voltage range in Fig. 3.) However, although the overall performance of pre-biased devices of system (B) was improved in comparison to devices of system (A), it was still not satisfying. The latter is exemplified by the large and rather erratic current that was once again observed at reverse voltages, which precluded a meaningful establishment of a current rectification ratio. The long-term stability was furthermore not impressive, as manifested in the brightness that dropped to 2% of its initial value after 12 h storage under open-circuit conditions.

3.3. System (C): cross-linking of the ion-transport material

Yu and co-workers [36] recently demonstrated an alternative approach for the attainment of chemically stabilized doping structures in LEC devices, when they employed a polymerizable "small molecule" ion-transport material in combination with a non-polymerizable alkaline salt as the electrolyte. In the seminal study, the liquid trivinylic monomer TMPTMA was utilized as ion-transport material instead of the commonly employed PEO. The chemical structure of TMPTMA is presented in Fig. 1. Its three methacrylate groups can readily be polymerized into a rigid, covalently cross-linked network that effectively impedes diffusion of other molecules. The authors demonstrated pre-biased LEC devices with rather impressive stability and relatively high light-emission efficiency following this concept, and it was proposed, in analogy with the physical "frozen-junction" approach [13,24,39], that the stability resulted from an effective elimination (freeze-in) of the ion-transport capacity of TMPTMA when it was spatially immobilized *via* polymerization [36].

We have fabricated sandwich cells with an active material blend, comprising SY, TMPTMA and $LiCF_3SO_3$ in a (1:0.5:0.1) mass ratio, sandwiched between an ITO anode and an Al cathode. The devices were pre-biased at $V = +12$ V at room temperature for almost 4 h. At the end of the pre-bias period, the light-emission intensity and the current exhibited a drastic rapid increase to high values, in agreement with the observation for a similar system in Ref. [36], but it is notable that the elapsed time up to this point was markedly longer in our experiments. We attribute this difference to a thicker active material in the herein studied devices, which is concomitant with a lower ionic conductance and a slower turn-on time [40].

The data for a typical pre-biased device of system (C) are displayed in Fig. 5 and summarized in Table 1. The sandwich cell device showed promising uni-polar current and emission characteristics, and the current rectification ratio was rather high (RR = 700 at $V = \pm 10$ V). These data are in good qualitative agreement with those reported by Yu et al. on a similar system, but the quantitative values for the brightness and current efficacy were lower in the experiments reported here. Furthermore, the p–n junction doping profiles in system (C) are considerably more stabile over time in comparison to systems (A) and (B), as evidenced by the brightness drop by only 14% from its initial value after 12 h under open-circuit conditions.

3.4. System (D): cross-linking of ions and ion-transport material with added initiator

Inspired by the promising results for devices of system (C), we attempted to combine the approaches taken in systems (B) and (C). In other words, we simultaneously employed a polymerizable ion-pair monomer (METMA/AMPS), a polymerizable ion-transport compound (poly-PEO), and a radical-initiator compound (AIBN) in addition to the conjugated polymer (SY) as the active material. The goal was to induce a doping profile by the pre-bias, which would at the end of the pre-bias period include both the ions and the ion-transport material as integral parts of a large and interconnected immobile ionic network. We further hoped that the addition of the radical-initiator compound would facilitate an efficient and complete polymerization and eliminate the need for polymerization initiation *via* dopant radicals generated on the conjugated polymer SY, as we suspected that a dopant-initiation could lead to quenching of the electroluminescence and result in low brightness and current efficacy values. An idealized view of the operation and stabilization of such an LEC is illustrated in Fig. 2D.

Sandwich cells, with (SY:poly-PEO:METMA/AMPS:AIBN) in a (1:0.17:0.06:0.003) mass ratio as the active material positioned between an ITO anode an Al cathode,

were pre-biased at $V = +5$ V for 2 h at room temperature. The current and brightness increased in a continuous manner during the initial part of the pre-bias period, but at the end of the period they stabilized at essentially constant values, which were taken as an indicator of stabilized doping.

The data displayed in Fig. 6 and Table 1 were recorded after the pre-bias had been removed. Such pre-biased devices exhibited notably well-behaved uni-polar current and emission characteristics, as for instance quantified by an excellent current rectification of RR = 1900 at $V = \pm 10$ V. Moreover, the brightness and current efficacy for the pre-biased devices of system (D) were clearly higher than in the other investigated systems, and the stability over time was relatively impressive as the drop in brightness after 12 h under open-circuit was a mere 13%, with the major drop taking place during the first 2 h following the removal of the pre-bias. Thus, the overall performance of stabilized devices of system (D) was superior to the other investigated systems (see Table 1), although it is clear that further improvement in the long-term stability of the doping structure is clearly needed for practical applications. It should also be noted that the optoelectronic performance of these stabilized devices are not yet on par with state-of-the-art dynamic LEC devices, as demonstrated by that turn-on voltages of the order of the band-gap potential and current efficacies of the order of 3–9 cd/A have recently been reported for various manifestations of dynamic-junction LECs based on the same conjugated polymer SY [41–43].

4. Conclusions

We have systematically tested, evaluated, and compared a number of different "old" and new approaches for the attainment of a chemically stabilized doping structure in LEC devices. We found that the pioneering concept of chemically connecting the dopant counterions *via* utilization of polymerizable ion-pair monomers alone resulted in light-emitting devices with poor stability and low brightness. The addition of a radical-initiator compound to this type of active material blend improved the brightness, presumably because the emissive conjugated polymer is relieved of the role of acting as radical initiation site for polymerization; however, the stability remained poor. The alternative concept of employing a small molecule ion-transport material that can be cross-linked into large and immobile polymeric structures during the initial pre-bias operation yielded distinctly improved results in the form of a high current rectification ratio and a decent stability under open-circuit conditions. The best performance was, however, attained from a device that combined all of the above concepts, as its active material comprised polymerizable ion-pair monomers, a cross-linkable ion-transport material, and a radical-initiator in addition to the conjugated polymer. Such chemically stabilized devices exhibited a highly respectable current rectification ratio of almost 2000, a good light-emission efficiency, and a decent long-term stability under idle conditions.

Acknowledgments

The authors wish to thank Jeroen Verhage and Ryan Chadwick for valuable preliminary experiments in the synthesis of ion-pair monomers, and Andreas Sandström for assistance with the LEC characterization. The authors are grateful to Kempestiftelserna, Carl Tryggers Stiftelse, and the Swedish Research Council (Vetenskapsrådet) for financial support. L.E. is a "Royal Swedish Academy of Sciences Research Fellow" supported by a grant from the Knut and Alice Wallenberg Foundation.

References

[1] nobelprize.org/nobel_prizes/chemistry/laureates/2000/public.html.
[2] H. Shirakawa, E.J. Louis, A.G. Macdiarmid, C.K. Chiang, A.J. Heeger, J. Chem. Soc.-Chem. Commun. (16) (1977) 578–580.
[3] C.K. Chiang, C.R. Fincher, Y.W. Park, A.J. Heeger, H. Shirakawa, E.J. Louis, S.C. Gau, A.G. Macdiarmid, Phys. Rev. Lett. 39 (17) (1977) 1098–1101.
[4] M. Gross, D.C. Muller, H.G. Nothofer, U. Scherf, D. Neher, C. Brauchle, K. Meerholz, Nature 405 (6787) (2000) 661–665.
[5] M.H. Bolin, K. Svennersten, D. Nilsson, A. Sawatdee, E.W.H. Jager, A. Richter-Dahlfors, M. Berggren, Adv. Mater. 21 (43) (2009) 4379.
[6] J.H. Zhao, R.G. Pillai, M. Pilapi, M.S. Freund, D.J. Thomson, Polypyrrole Nanoionic Composites for Solid State Electronics, CRC Press-Taylor & Francis Group, Boca Raton, 2008.
[7] J.M. Leger, Adv. Mater. 20 (4) (2008) 837–841.
[8] L. Edman, Electrochim. Acta 50 (19) (2005) 3878–3885.
[9] Q.B. Pei, Y. Yang, G. Yu, C. Zhang, A.J. Heeger, J. Am. Chem. Soc. 118 (16) (1996) 3922–3929.
[10] .Q.B. Pei, G. Yu, C. Zhang, Y. Yang, A.J. Heeger, Science 269 (5227) (1995) 1086–1088.
[11] Q.J. Sun, Y.F. Li, Q.B. Pei, J. Dispersion Sci. Technol. 3 (2) (2007) 211–224.
[12] Z.B. Yu, L.B. Hu, Z.T. Liu, M.L. Sun, M.L. Wang, G. Gruner, Q.B. Pei, Appl. Phys. Lett. 95 (20) (2009).
[13] D.H. Lee, J.H. Park, H. Chae, S.M. Cho, Org. Electron. 10 (7) (2009) 1345–1351.
[14] J. Fang, P. Matyba, N.D. Robinson, L. Edman, J. Am. Chem. Soc. 130 (13) (2008) 4562–4568.
[15] J.F. Fang, P. Matyba, L. Edman, Adv. Funct. Mater. 19 (16) (2009) 2671–2676.
[16] J.H. Shin, A. Dzwilewski, A. Iwasiewicz, S. Xiao, A. Fransson, G.N. Ankah, L. Edman, Appl. Phys. Lett. 89 (1) (2006) 013509.
[17] J.H. Shin, L. Edman, J Am. Chem. Soc. 128 (49) (2006) 15568–15569.
[18] J. Gao, J. Dane, Appl. Phys. Lett. 83 (15) (2003) 3027–3029.
[19] J. Gao, J. Dane, J. Appl. Phys. 98 (6) (2005).
[20] P. Matyba, K. Maturova, M. Kemerink, N.D. Robinson, L. Edman, Nat. Mater. 8 (8) (2009) 672–676.
[21] S. Reineke, F. Lindner, G. Schwartz, N. Seidler, K. Walzer, B. Lussem, K. Leo, Nature 459 (7244) (2009) 234. U116.
[22] S.G. Robinson, D.H. Johnston, C.D. Weber, M.C. Lonergan, Chem. Mater. 22 (1) (2009) 241–246.
[23] J. Gao, Y.F. Li, G. Yu, A.J. Heeger, J. Appl. Phys. 86 (8) (1999) 4594–4599.
[24] J. Gao, G. Yu, A.J. Heeger, Appl. Phys. Lett. 71 (10) (1997) 1293–1295.
[25] J.H. Shin, S. Xiao, A. Fransson, L. Edman, Appl. Phys. Lett. 87 (4) (2005) 043506.
[26] L. Edman, M. Pauchard, D. Moses, A.J. Heeger, J. Appl. Phys. 95 (8) (2004) 4357–4361.
[27] Y. Cao, Q.B. Pei, M.R. Andersson, G. Yu, A.J. Heeger, J. Electrochem. Soc. 144 (12) (1997) L317–L320.
[28] J. Dane, C. Tracy, J. Gao, Appl. Phys. Lett. 86 (15) (2005).
[29] C.H. Yang, Q.J. Sun, J. Qiao, Y.F. Li, J. Phys. Chem. B 107 (47) (2003) 12981–12988.
[30] G. Yu, Y. Cao, M. Andersson, J. Gao, A.J. Heeger, Adv. Mater. 10 (5) (1998) 385–388.
[31] C.H.W. Cheng, M.C. Lonergan, J. Am. Chem. Soc. 126 (34) (2004) 10536–10537.
[32] J.M. Leger, D.G. Patel, D.B. Rodovsky, G.P. Bartholomew, Adv. Funct. Mater. 18 (8) (2008) 1212–1219.
[33] J.M. Leger, D.B. Rodovsky, G.R. Bartholomew, Adv. Mater. 18 (23) (2006) 3130.
[34] L.S.C. Pingree, O.G. Reid, D.S. Ginger, Adv. Mater. 21 (1) (2009) 19–28.

[35] L.S.C. Pingree, D.B. Rodovsky, D.C. Coffey, G.P. Bartholomew, D.S. Ginger, J. Am. Chem. Soc. 129 (51) (2007) 15903–15910.
[36] Z.B. Yu, M.L. Sun, Q.B. Pei, J. Phys. Chem. B 113 (25) (2009) 8481–8486.
[37] J.C. Salamone, N.A. Mahmud, M.U. Mahmud, T. Nagabhushanam, A.C. Watterson, Polymer 23 (6) (1982) 843–848.
[38] J.C. Salamone, M.K. Raheja, Q. Anwaruddin, A.C. Watterson, J. Polym. Sci. Part C-Polym. Lett. 23 (12) (1985) 655–659.
[39] Y.G. Zhang, J. Gao, J. Appl. Phys. 100 (8) (2006).
[40] N.D. Robinson, J.H. Shin, M. Berggren, L. Edman, Phys. Rev. B 74 (15) (2006) 155210.
[41] P. Matyba, H. Yamaguchi, G. Eda, M. Chhowalla, L. Edman, N.D. Robinson, ACS Nano 4 (2) (2010) 637–642.
[42] A. Sandstrom, P. Matyba, L. Edman, Appl. Phys. Lett. 96 (5) (2010) 053303.
[43] Y. Shao, G.C. Bazan, A.J. Heeger, Adv. Mater. 19 (3) (2007) 365.

a flexible OLED panel using a gravure printed light emitting polymer [8]. No formulation details or efficiency values were reported, but the device operated at 100 cd/m^2 for 1000 h. Indium-tin oxide (ITO) nanoparticles have been successfully printed on flexible substrates [9]. Tuomikoski et al. reported OLEDs with printed poly (3,4-ethylene dioxythiophene): poly (styrene sulfonate) (PEDOT:PSS) and a polyfluorene light emitting polymer on these substrates [10]. These achieved a maximum electroluminescent quantum efficiency of 0.1% and a luminance of 100 cd/m^2 at a drive bias of 5 V. Recently, OLEDs with printed PEDOT:PSS and an unidentified light emitting polymer have also been fabricated [11]. Although no efficiency values were reported, the devices achieved 100 cd/m^2 at a drive bias of 4.2 V and a maximum luminance of 5000 cd/m^2.

Despite these advances, device performance so far has been relatively poor and no luminosity (lm/W) or luminous efficiency (cd/A) values have been reported. There has also been minimal discussion on the development of ink formulations and what may be occurring during film formation and drying.

Here we report in detail the gravure contact printing of the hole injection layer and the organic emissive layer for high performance, flexible, polymer light-emitting diodes (PLEDs). We develop a wide range of PEDOT:PSS and light emitting polymer printing formulations which, when optimised, achieve highly uniform films of appropriate thickness and very low surface roughness. We explain and discuss these formulations in terms of such factors as substrate wetting and lateral Marangoni forces. Our optimised devices have an identical performance to spin-coated control devices. They also achieve maximum luminosity and luminance values in the range reported for state-of-the-art green-emitting flexible PLEDs.

2. Experimental

2.1. Materials

The PEDOT:PSS (Baytron Clevios™ AI4083) dispersion was purchased from H.C. Starck GmbH. Triton X-100 and other solvents were obtained from Sigma–Aldrich. Substrates were polyethylene terephthalate (PET) coated in sputtered ITO (R_s = 40–60 Ω/sq) OC50 films from CPFilms Inc. The ITO on PET substrates were first etched by hydrochloric (HCl) acid diluted with DI water at a ratio of 2:1 (HCl:DI water) for 80 s to form ITO stripes, defined by acid resistant tape, with a width of 0.8 mm. They were then cleaned with acetone and IPA in an ultrasonic bath and then washed with deionized (DI) water. This was followed by oxygen plasma treatment using an Emitech K 1050X plasma asher.

2.2. LED preparation and characterization

Printing was with a Labratester I from Schläfli Maschinen. Cleaned substrates were printed with PEDOT:PSS formulations using a steel cliché with an engraved pattern of 70 or 90 lines/cm of tetragonal shaped cells with a width of about 140 and 110 μm, respectively, and depth of 35–40 μm. This was at a printing speed of 35 m/min. After baking at 75 °C for 10 min in air, the LEP formulations were printed using a cliché with an engraved pattern of 40 lines/cm of tetragonal shaped cells with a width of 250 μm and depth of 60–70 μm at the same speed. The cliché surface area is about 17 cm × 23 cm. The total engraved area is about 12 cm × 12 cm. Film thicknesses were measured by profilometer-calibrated optical absorption using an ATI Unicam UV–Vis spectrophotometer. For reference devices, 55 ± 5 nm layers of PEDOT:PSS were deposited by spin-coating at 2000 rpm and then baked at 75 °C for 10 min in air. 75 ± 5 nm layers of LG1300 were deposited by spin-coating at 2500 rpm a 1.15 wt% LEP in *p*-xylene solution. Layer thicknesses were measured by a Tencor Instruments Alpha Step 200 surface profilometer (accuracy ±10%).

After deposition of LG1300, all samples were transferred to a nitrogen atmosphere glove box (<2 ppm H_2O, <0.1 ppm O_2) to anneal at 120 °C for 1 h. The cathode of 10 nm Ca followed by 100 nm Al was then thermally evaporated (vacuum pressure 4×10^{-6} mbar) with a shadow mask to define electrodes of 4.2 mm^2 (3 mm × 1.2 mm) area. JVL measurements were performed using a Keithley 2410 Source-Measure Unit and a Topcon BM-9 luminance meter. PLEDs were assumed to be Lambertian sources. No cavity effects were observed. Electroluminescent emission spectra were recorded using a Keithley 2400 SourceMeter an Ocean Optics USB 2000 charge-coupled device spectrophotometer.

Additional demonstration devices were fabricated with a larger light emission area of 0.42 cm^2 (width: 1.4 cm, height: 0.3 cm).

2.3. Contact angle measurement and morphology

Contact angle measurements and wetting envelope calculations were performed with a Krüss DSA 100. The surface energy of the substrates were calculated by measuring the contact angle of the Sessile droplet using threes reference fluids (water, diiodomethane and ethylene glycol). For the surface energy of PEDOT:PSS surface, only diiodomethane and ethylene glycol were used as water is likely to swell the polymer layer. These two fluids were found to have a negligible effect on the polymer surface after the films had been thermally annealed. The surface tension (SFT) of the different formulations were calculated by measurements using the Pendant droplet method. The SFT of the fluid was then analyzed to obtain its polar and dispersive components by measuring the contact angle of the fluid on Teflon substrate using the Sessile droplet method. Wetting envelopes of the substrates were calculated from these measured surface energy components using the Fowkes method. All SFT values are listed in Supplementary Tables S1 and S2. The tapping mode atomic force microscope (AFM) measurements were conducted using a Nano-R™ AFM from Pacific Nanotechnology. A Zeiss Axioplan Microscope with a Nikon Coolpix P5100 digital camera was used to capture micron scale surface images.

3. Results and discussions

3.1. Gravure printing process and printing of PEDOT:PSS

The gravure printing process is illustrated in Fig. 1a. Unlike spin-coating or ink-jet printing it is a contact technique. The printer configuration used in this work (i) consists of a planar cliché (printing plate) and a flexible substrate attached to a freely-rotating cylindrical drum. Upon printing the cliché moves to the left and doctor blade (used to scrape ink into the cliché ink cells (ii)) and substrate drum move to the right. The tetrahedral cells (typical width 50–200 μm) on the cliché surface form the pattern to be printed. The substrate and cliché are then pressed together (iii), the lower surface energy of the substrate relative to the cliché and the shear forces pulling the ink onto the substrate. The ink droplets deposited from the cells then coalesce (iv), form a continuous layer of thickness 5–10 μm (v), the solvents evaporate (vi) depositing a thin film of the solute (vii).

PEDOT:PSS is the standard hole injection layer material used in PLEDs, being deposited between the transparent indium-tin oxide (ITO) anode contact and the light emitting polymer (LEP) (Fig. 1b and c). It planarizes the anode surface, allows better adhesion between anode and LEP, and improves hole injection into the LEP by increasing the anode work function to 5.1–5.2 eV [12,13]. Commercial PEDOT:PSS formulations developed for spin-coating are water based with a high surface tension of 70–80 mN/m. Initial attempts to gravure print the unaltered formulations on untreated ITO gave very poor results.

This can be explained by considering the surface tension (made up of polar σ_p and dispersive σ_d components) of the unaltered PEDOT:PSS formulation (point A) and the surface-energy wetting envelope (calculated using the Fowkes method) of the untreated ITO shown in Fig. 2a. The formulation lies far outside the wetting envelope and as result dewets. To vary the surface energy, the ITO was exposed to an oxygen plasma [2,14]. Fig. 2a shows the resultant wetting envelopes for 30 and 50 W exposure for 1 min. The plasma treatment increases the oxygen content of the ITO, greatly increasing its polar component and decreasing its dispersive component. This increases the surface energy envelope towards the unaltered PEDOT:PSS formulation, but it still lies outside. Gravure printing the unaltered formulation is shown in Fig. 2b(i). The result is still very poor, the film breaking up into large non-uniform streaks in the printing direction. Although not as extreme as the untreated ITO situation, solution surface tension is still too large compared to the substrate surface energy.

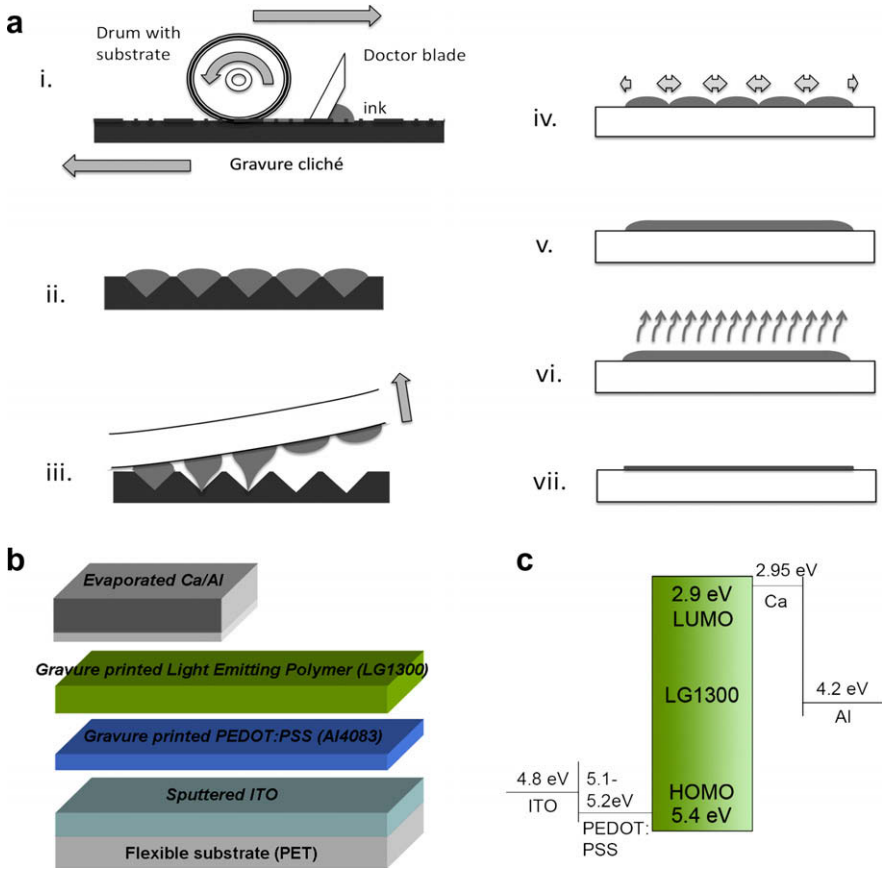

Fig. 1. (a) Gravure printing process. (b) Structure of gravure printed PLEDs. (c) Energy level diagram of the printed PLED consisting of ITO (anode), PEDOT:PSS (hole injection layer), LG1300 (LEP), Ca (cathode) and Al (capping layer).

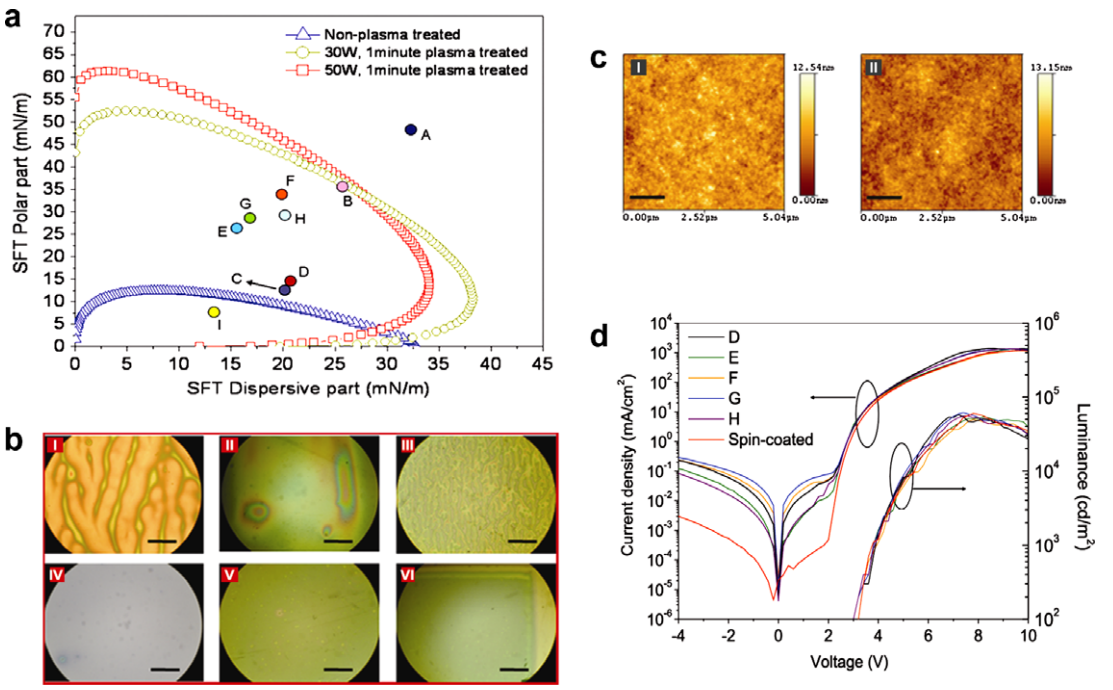

Fig. 2. (a) Wetting envelopes of oxygen plasma treated ITO on PET substrate with various surface tensions of mixtures: Pristine PEDOT:PSS (AI4083), A; This was modified (vol.%) at 5 (PEDOT:PSS): 1 (solvent) ratio with ethylene glycol, B; Triton X-100, C; IPA, D; ethanol, E; methanol, F; acetone, G; acetonitrile, H; vol.% of 10 (PEDOT:PSS): 5 (IPA): 1 (Triton X-100) ratio, I. (b) Optical microscopic images from these printed PEDOT:PSS formulations: i, A; ii, B; iii, C; iv, D; v, I; vi, edge of I; (scale bar indicates 1 mm). (c) AFM images of spin-coated (i) and gravure printed formulation D (ii) (scale bar indicates 1 μm). (d) Performance of PLEDs with spin-coated and printed PEDOT:PSS (formulations as above) and spin-coated LEP.

PLEDs have been fabricated with spin-coated films of PEDOT:PSS formulations blended with ethylene glycol [15,16]. PEDOT:PSS mixed with ethylene glycol (5:1 ratio by volume) lies just inside the wetting envelope (see Fig. 2a, point B). The printed formulation (Fig. 2b(ii)) gives poor coverage and large regions of different thickness. Ethylene glycol has a high boiling point (B_p = 197.3 °C) and will take a long time to evaporate. Mixing a water-based formulation with a higher boiling point, lower surface tension solvent is expected to oppose solution spreading due to the Marangoni effect [17] which, especially when combined with de-pinning of the contact line [18] and a slow evaporation rate [19], will pull the solute inwards during drying [20]. These effects along with the small difference between surface tension and substrate surface energy are likely to result in this unevenness.

Triton X-100 [21] is a viscous non-ionic detergent with a high boiling point ($B_p \geqslant 200$ °C). It has both hydrophilic and hydrophobic endgroups, which should allow a change in the balance between surface tension and surface energy favoring better wetting. A formulation of PEDOT:PSS mixed with Triton X-100 (5:1 by volume) lies deep within the wetting envelope (Fig. 2a, point C). The printed formulation (Fig. 2b(iii)) gives good overall coverage, but the film is non-uniform and has broken up into fine interconnected streaks aligned in the printing direction. This is again a high boiling point, low surface tension solvent, which will take a long time to dry and will have the same spreading issues as ethylene glycol.

However, surfactants can disrupt the surface tension driven Marangoni forces at very low concentrations [22]. Certainly the large scale aggregation and poor coverage found for ethylene glycol is not seen here. The fine streaks in Fig. 2b(iii) are of approximately the same width as the cliché ink cells (200 μm), indicating that it is at the moment of printing (Fig. 1a(iii)–(iv)) where this formulation has failed. We note that at the concentrations here the surfactant should form a close packed monolayer at the air–liquid interface with the hydrophobic head groups on the air side and the hydrophilic tail groups on the water side. During printing it will be torn out of the ink cells onto the substrate, which will involve considerable shear forces. This is likely to disrupt the monolayer, intermixing the surfactant with the liquid. Even if this intermixing does not occur and the monolayer is intact, it then faces the problem that what was the air–liquid interface is now the substrate–liquid interface. The droplet has been inverted. This will not only change the wetting properties at the moment of printing but may disrupt the spreading of the film if the monolayer cannot reorganize itself onto the air–liquid interface sufficiently quickly. We suggest that these type of effects may form a possible explanation as to why this printed formulation, combined with its high boiling point and low surface tension, retains some memory of the cliché ink cells.

To stay deep within the wetting envelope and also avoid high boiling point solvents, the PEDOT:PSS formulation was blended with IPA (B_p = 82.4 °C). Fig. 2b(iv) shows a gravure printed film of PEDOT:PSS mixed with IPA (5:1 ratio by volume). This formulation lies within the wetting

envelope (Fig. 2a, point D). The printed films are highly uniform and show very good coverage. Similar good printing results were obtained using PEDOT:PSS blended at a 5:1 ratio by volume with low boiling point, low surface tension solvents such as ethanol (B_p = 78.5 °C), methanol (64.6 °C), acetone (56.2 °C) and acetonitrile (81.6 °C). These all lie within the wetting envelope (Fig. 2a, points E, F, G and H, respectively). The use of a lower boiling point, lower surface tension solvent will result in Marangoni forces which favor spreading and act against aggregation during drying [17]. The faster evaporation rate, which may also result in evaporative cooling and an increase in formulation viscosity [23], will additionally act against the possibility of formulation flow and aggregation during the later stages of drying (Fig. 1a(vi)). All of these factors should contribute to the observed excellent printing results. All printed PEDOT:PSS films have a thickness of 55 ± 5 nm over an area of order 1 cm^2 (within the accuracy of the profilometer this was identical to that achieved by spincoating).

The coffee-stain effect [24], a major problem found for ink-jet printing [18,20,25], was observed for some of the above films. This can be ascribed to the capillary forces and Marangoni forces acting in the same direction, depositing solute at the film edge [25]. To avoid this, the above formulations were printed with a small amount of the surfactant. PEDOT:PSS: IPA: Triton X-100 blended at a ratio 10:5:1 volume lies very deep within the wetting envelope (Fig. 2a, point I) and gives a highly uniform printed film (Fig. 2b(v)). The edge of the gravure printed film is very well defined, the surfactant disrupting enough of the Marangoni flow and lowering the contact angle at the pinning-line to avoid non-uniform deposition. The corner of the film in Fig. 2b(v) is shown in Fig. 2b(vi). This exactly follows the cell pattern of the particular plate, consisting of a large uniform area with a thin border of width 200 μm. This demonstrates the ability to print PEDOT:PSS to this resolution.

Fig. 2c shows AFM images of spin-coated and gravure printed (5:1 by volume IPA) PEDOT:PSS films. The gravure printed film shows a slightly greater thickness variation over the 5 × 5 μm^2 area, but the overall RMS roughness of about 1.2 nm is the same for both films.

The gravure printed films were tested in PLEDs with spin-coated LEP layers. The current density–voltage–luminance (JVL) characteristics are shown in Fig. 2d. All the gravure printed PEDOT:PSS devices compared very favorably against a spin-coated PEDOT:PSS device. The highest current density and luminance values for a given bias were obtained for the IPA formulation (5:1 by volume), this having the optimum bulk and interfacial morphology.

3.2. Gravure printing of LEP layer

Having successfully printed PEDOT:PSS, we next consider printing the LEP as well. The wetting envelope of the surface of PEDOT:PSS is shown in Fig. 3a. It has a less polar but more dispersive wetting envelope compared to the 50 W oxygen plasma treated ITO. This envelope

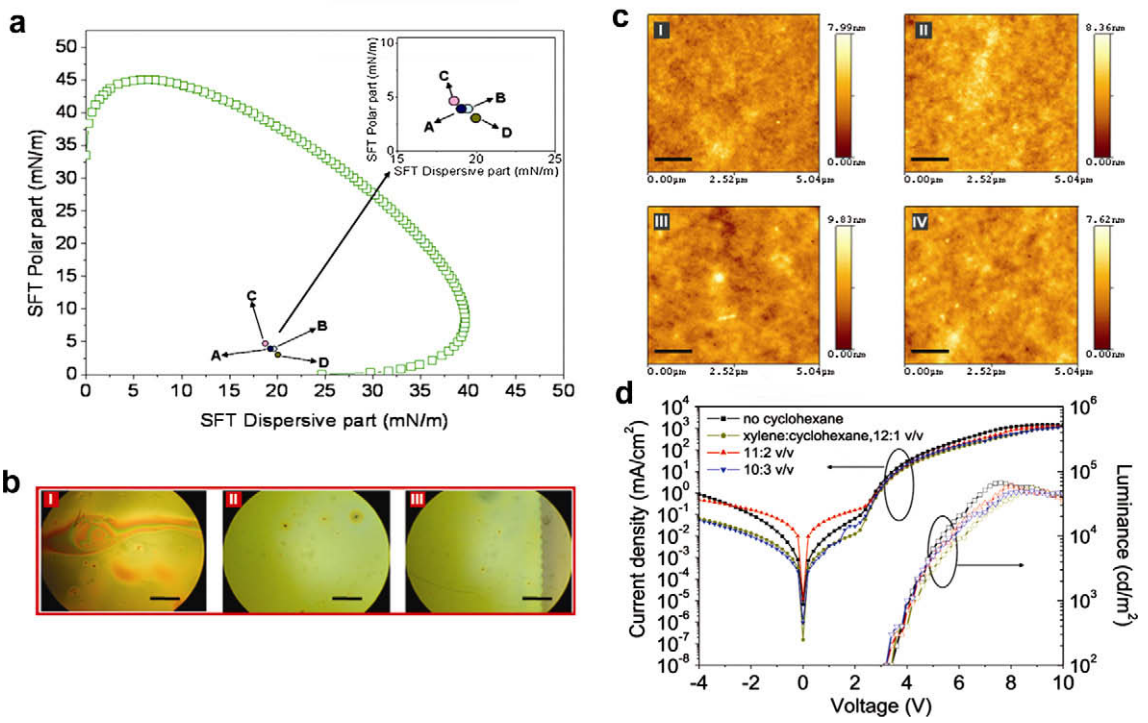

Fig. 3. (a) Wetting envelope of printed PEDOT:PSS surface with surface tensions of formulations of 0.8 wt.% LG1300 in: pure *p*-xylene, A; pure toluene, B; *p*-xylene:indan 5:1 v/v, C; *p*-xylene:cyclohexane 5:1 v/v, D. (b) Optical microscopic images of printed LG1300 formulations: i, C; ii, D; iii, edge of D; (scale bar indicates 1 mm). (c) AFM images of spin-coated (i) and printed LG1300 from pure *p*-xylene (ii) and printed LG1300 *p*-xylene:cyclohexane 12:1 v/v (iii) and 10:3 v/v (iv); (scale bar indicates 1 μm). (d) Performance of PLEDs with gravure printed LG1300 at different *p*-xylene:cyclohexane volume ratios.

encompasses a broad range of dispersive, non-polar organic solvents. The LEP used in this study was LUMATION™ Green 1300 (LG1300), a green emitting polyfluorene copolymer [26–28]. The solvents conventionally used for spin-coating LG1300 are *p*-xylene (B_P = 138.3 °C) and toluene (B_P = 110.6 °C). LG1300 formulations of *p*-xylene and toluene (0.8% by weight) lie close to each other within the PEDOT:PSS wetting envelope (Fig. 3a, points A and B). However, gravure printing of these formulations resulted in non-uniform films.

Given the results for PEDOT:PSS, solvent blends were investigated using indan (B_P = 177 °C) and cyclohexane (B_P = 80.7 °C). Fig. 3a shows the position of LG1300 formulations (0.8% by weight) of *p*-xylene blended with 5:1 ratio by volume of indan and cyclohexane (points C and D, respectively). Both lie very close to each other and the *p*-xylene and toluene points within the PEDOT:PSS wetting envelope. Fig. 3b(i) and (ii) shows gravure printed films of the blended formulations. The indan formulation produces a highly uneven, non-uniform film of poor quality. The cyclohexane formulation, however, printed with excellent homogeneity comparable to that of spin-coated films. These again follow the trend found for PEDOT:PSS: adding the lower boiling point, lower surface tension solvent (cyclohexane) produces homogeneous printing, whereas adding the higher boiling point, lower surface tension solvent (indan) produces relatively poor printing. However, compared to the successful PEDOT:PSS formulations, the difference in solvent surface energy is nearly an order of magnitude smaller so we expect a smaller Marangoni effect [20,23]. Other factors such as more rapid drying and evaporative cooling increasing the polymer solution viscosity [23] may contribute to the cyclohexane formulation being favorable.

During drying polymer solutions form surface gels at the solution–air interface [23,29]. Such surface gel formation has typically been observed to occur at higher polymer concentrations and thicker film thicknesses than used here. However, the evaporation from the surface layer of the lower boiling point, more favourable solvent component combined with the drop in temperature from evaporative cooling may be enough to drive the surface layer into this regime. If it does occur, such surface gel formation would be expected to help stabilize the drying formulation.

Evaporative cooling driven Bénard–Marangoni convection has been observed in evaporating polymer solutions of thickness >500 μm [23], but the solution thickness here of 10 μm would give a vertical Marangoni number far below the instability threshold. Vertical solution density driven Rayleigh–Bénard or Rayleigh–Taylor type instabilities [23,30,31] are also precluded by the film thickness and the continuously changing, multi-directional *g*-forces experienced in this printing method.

We also note that Fig. 3b(iii) shows the complete absence of any coffee-stain effect, consistent with a relatively low outward Marangoni flow. It means that gravure printing can achieve very well defined pixels with uniform emission over the whole device area. An additional advantage of low boiling point solvent formulations is that residual solvent removal can be done quickly at room temperature. This is vital for high-speed, R2R printing on low heat resistance, flexible plastic substrates.

Fig. 3c shows AFM images of the surface of LG1300 spin-coated from *p*-xylene (i), printed from *p*-xylene (ii) and printed from *p*-xylene blended with cyclohexane at ratios of 12:1 (iii) and 10:3 (iv) by volume. The RMS surface roughness is 0.73, 0.92, 0.88 and 0.7 nm, respectively. As the fraction of cyclohexane is increased, the gravure printed films become increasingly smooth on a sub-micron level, eventually reaching the value found for the spin-coated films. This indicates that the film uniformity and smoothness achieved with these formulations occurs on both large (>1 mm) and small scales (<1 μm).

PLEDs were gravure printed using LEP formulations with different fractions of cyclohexane (Fig. 3d). All printed LEP films had a thickness of 75 ± 5 nm over an area of order 1 cm^2 (within the accuracy of the profilometer this was identical to that achieved by spincoating). An increased fraction of cyclohexane generally decreases the current and maximum luminance values but increases device efficiency. This indicates a lower hole and/or electron current but a better charge balance and/or recombination zone position [12]. The maximum device efficiency was found to be at a ratio by volume of 10:3.

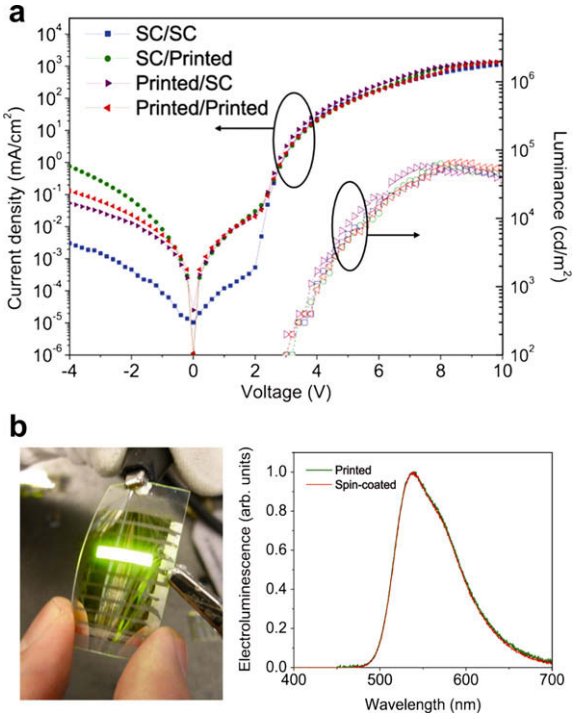

Fig. 4. (a) Performance of spin-coated and gravure printed PLEDs (PEDOT:PSS/LG1300). The formulations used for gravure printing are PEDOT:PSS (AI4083) mixed with IPA in vol.% of 5:1 (AI4083:IPA) and 0.8 wt.% of LG1300 in vol.% of 10:3 (*p*-xylene:cyclohexane). (b) Photograph of light emission from a fully printed flexible PLED (left) and electroluminescence spectrum of fully gravure printed and fully spin-coated PLEDs (right). The size of the light emission area is 0.42 cm^2 (width: 1.4 cm, height: 0.3 cm).

Table 1
Performance parameters of spin-coated and gravure printed PLEDs. The first two columns indicate the deposition methods used for the PEDOT:PSS and LG1300 layers. L_{max} is the maximum luminance achieved. η_L and η_P are the efficiency (cd/A) and luminosity (lm/W) values, respectively (reported at representative luminance of 100 and 1000 cd/m^2; the absolute maxima are also reported). The voltage values (in brackets) indicate the bias voltages applied to the devices for each measurement.

PEDOT:PSS	LG1300	L_{max} (cd/m^2)	~100 cd/m^2		~1000 cd/m^2		η_{max}	
			η_L	η_P	η_L	η_P	η_L	η_P
Spin-coating	Spin-coating	55,700 (8.6 V)	5.4 (3 V)	5.7	4.7 (4 V)	3.7	9 (7 V)	5.7 (3 V)
Spin-coating	Printing	62,800 (8 V)	5.9 (3 V)	6.2	4.9 (4 V)	3.9	8.3 (6.6 V)	6.2 (3 V)
Printing	Spin-coating	58,000 (7.4 V)	6.1 (3 V)	6.4	4.5 (3.8 V)	3.7	9.3 (6.4 V)	6.4 (3 V)
Printing	Printing	65,900 (8.6 V)	5.16 (3 V)	5.4	4.4 (4 V)	3.5	8.8 (7 V)	5.4 (3 V)

3.3. Performance comparison between gravure printed and spin-coated PLEDs

Finally, we compare PLEDs with the PEDOT:PSS and the LEP layers either spin-coated or gravure printed using the optimised formulations. Fig. 4a shows the JVL characteristics. Table 1 lists the PLED performance values. The relatively high drive bias for the maximum luminance of the PLEDs can be attributed to the poor conductivity of the ITO on PET substrates (σ = 1282 S/cm) compared to a reference ITO on glass substrates (σ = 5000–6000 S/cm). There is a higher leakage current when gravure printed layers are present, indicating increased surface roughness at the anode. However, the built-in potential just above 2 V is unchanged. When in the on state, the JV and LV characteristics of all devices are almost identical across all applied bias values. The PLED performance values in Table 1 are also similar. When both layers are spin-coated, at a display brightness of 100 cd/m^2 the devices have luminosity, efficiency and drive bias values of 5.7 lm/W, 5.4 cd/A and 3 V, respectively. When both layers are gravure printed, the values are 5.4 lm/W, 5.2 cd/A and 3 V, respectively. The maximum luminance values for fully spin-coated and gravure printed are 56,000 and 66,000 cd/m^2, respectively. The values for devices with one layer printed and one layer spin-coated cover a similar range.

State-of-the-art polyfluorene copolymer green-emitting flexible PLEDs have been fabricated on transparent barrier-layer substrates with high conductivity anodes [32]. These have achieved a maximum luminosity of 9.9 lm/W, a maximum efficiency of 10 cd/A and a maximum luminance of 20,000 cd/m^2. Our gravure printed devices achieve values of 8.8 lm/W, 5.4 cd/A and 66,000 cd/m^2, respectively. These are very comparable, even though we are using a poorer conductivity anode.

Fig. 4b also shows light emission from a device where both PEDOT:PSS and LEP layers are gravure printed. The flexible PLED has highly uniform emission over all drive voltages. The emission spectrum is also identical to the spin-coated control device.

4. Conclusions

In summary, we have shown that gravure contact printing can be used to deposit the organic layers in high performance, flexible PLEDs. We have designed multi-component formulations to print both the hole injection layer of PEDOT:PSS and the light emitting layer of a polyfluorene copolymer. The optimum formulation for PEDOT:PSS was found to consist of adding a low boiling point organic solvent to the as-purchased water-based formulation with the optional addition of a small amount of surfactant to eliminate any coffee-stain effects which can sometimes occur. The optimum formulation for the light emitting polymer was found to consist of a blend of low and high boiling point organic solvents. We suggest that the success of these formulations is due to optimising both substrate wetting, the lateral Marangoni forces and the stability of the film during drying. We were able to achieve highly uniform films with a very low surface roughness and a thickness optimised for PLED performance. Our final optimised devices have an identical performance to spin-coated control devices and achieve maximum luminosity and luminance values in the range reported for state-of-the-art, green-emitting flexible PLEDs. Recently, we have shown that Ag ink can also be gravure printed to form the gate electrode in multilayer gravure printed polymer field-effect transistors [33]. Development of low work function metal inks or other electron injection materials should allow the PLED cathode to be printed. Suitable flexible barrier-layer substrates can also be used to provide appropriate encapsulation after printing [32]. All the components necessary for the high-speed, mass production of large-area organic electronic displays and lighting are finally coming together.

Acknowledgements

The authors thank the Sumitomo Chemical Company Ltd. for providing the LUMATION™ Green 1300 (LG1300) light emitting polymer and Professor Jenny Nelson for experimental support. We also thank Dr. Monika Voigt, Dr. Jongin Hong and Justin Dane for useful discussions on printing and surface chemistry.

Appendix A. Supplementary data

Supplementary data associated with this article can be found, in the online version, at doi:10.1016/j.orgel.2010.03.010.

References

[1] B.J. de Gans, P.C. Duineveld, U.S. Schubert, Adv. Mater. 16 (2004) 203.
[2] J.Z. Wang, Z.H. Zheng, H.W. Li, W.T.S. Huck, H. Sirringhaus, Nat. Mater. 3 (2004) 171.
[3] Georges Hadziioannou, George G. Malliaras (Eds.), Semiconducting Polymers: Chemistry, Physics and Engineering, Wiley-VCH, 2007.
[4] S.R. Forrest, Nature 428 (2004) 911.
[5] D.J. Gundlach, Nat. Mater. 6 (2007) 173.
[6] M. Berggren, D. Nilsson, N.D. Robinson, Nat. Mater. 6 (2007) 3.
[7] H. Sirringhaus, Nature 457 (2009) 667.
[8] H. Nakjima, S. Morito, H. Nakajima, T. Takeda, M. Kadowaki, K. Kuba, S. Handa, D. Aoki, Society Information Display Symposium Digest of Technical Papers, vol. 36, 2005, p. 1196.
[9] J. Puetz, M.A. Aegerter, Thin Solid Films 516 (2008) 4495.
[10] M. Tuomikoski, R. Suhonen, M. Valimakia, T. Maaninen, A. Maaninen, M. Sauer, P. Rogin, M. Mennig, S. Heusing, J. Puetz, M.A. Aegerter, Org. Optoelectron. Photonics II 6192 (2006) 19204.
[11] P. Kopola, M. Tuomikoski, R. Suhonen, A. Maaninen, Thin Solid Films 517 (2009) 5757.
[12] R.H. Friend, R.W. Gymer, A.B. Holmes, J.H. Burroughes, R.N. Marks, C. Taliani, D.D.C. Bradley, D.A. Dos Santos, J.L. Bredas, M. Logdlund, W.R. Salaneck, Nature 397 (1999) 121.
[13] J.S. Huang, P.F. Miller, J.S. Wilson, A.J. de Mello, J.C. de Mello, D.D.C. Bradley, Adv. Funct. Mater. 15 (2005) 290.
[14] H. Sirringhaus, T. Kawase, R.H. Friend, T. Shimoda, M. Inbasekaran, W. Wu, E.P. Woo, Science 290 (2000) 2123.
[15] T.J. Wang, Y.Q. Qi, J.K. Xu, X.J. Hu, P. Chen, Appl. Surf. Sci. 250 (2005) 188.
[16] P. Levermore, Ph.D. Thesis, Imperial College London, 2008.
[17] D. Pesach, A. Marmur, Langmuir 3 (1987) 519.
[18] T. Kajiya, E. Nishitani, T. Yamaue, M. Doi, Phys. Rev. E 73 (2006) 011601.
[19] M. Kaneda, H. Ishizuka, Y. Sakai, J. Fukai, S. Yasutake, AIChE J. 53 (2007) 1100.
[20] J. Park, J. Moon, Langmuir 22 (2006) 3506.
[21] N.J. Kaihovirta, D. Tobjork, T. Makela, R. Osterbacka, Adv. Eng. Mater. 10 (2008) 640.
[22] H. Hu, R.G. Larson, Langmuir 21 (2005) 3972.
[23] G. Toussaint, H. Bodiguel, F. Doumenc, B. Guerrier, C. Allain, Int. J. Heat Mass Transfer 51 (2008) 4228.
[24] R.D. Deegan, O. Bakajin, T.F. Dupont, G. Huber, S.R. Nagel, T.A. Witten, Nature 389 (1997) 827.
[25] J.A. Lim, W.H. Lee, H.S. Lee, J.H. Lee, Y.D. Park, K. Cho, Adv. Funct. Mater. 18 (2008) 229.
[26] D. Poplavskyy, W.C. Su, F. So, J. Appl. Phys. 98 (2005) 014501.
[27] P.A. Levermore, R. Jin, X.H. Wang, L.C. Chen, D.D.C. Bradley, J.C. de Mello, J. Mater. Chem. 18 (2008) 4414.
[28] M.J. Harding, D. Poplavskyy, V.E. Choong, A.J. Campbell, F. So, Org. Electron. 9 (2008) 183.
[29] T. Okuzono, K. Ozawa, M. Doi, Phys. Rev. Lett. 97 (2006) 136103.
[30] T.E. Faber, Fluid Dynamics for Physicists, Cambridge University Press, Cambridge, 1997.
[31] S. Chandrasekhar, Hydrodynamic and Hydromagnetic Stability, Oxford University Press, Oxford, 1961.
[32] J. Kanicki, S.-J. Lee, Y. Hong, C.-C. Su, J. Soc. Inform. Display 13 (2005) 993.
[33] M.M. Voigt, A. Guite, D.-Y. Chung, R.U.A. Khan, A.J. Campbell, D.D.C. Bradley, F. Meng, J.H.G. Steinke, S. Tierney, I. McCullough, H. Penxten, L. Lutsen, J. Manca, O. Douheret, U. Brokmann, K. Sönnichsen, D. Hülsenberg, W. Bock, C. Barron, N. Blanckaert, S. Springer, J. Grupp, A. Mosley, Adv. Funct. Mater. 20 (2010) 239.

semiconducting properties, oligothiophene-based molecules can also self-assemble into crystalline nanoaggregates under special growth conditions [22], which could further increase their application potential in future, nanoscale optoelectronic devices.

In addition to OFETs and OLEDs, the organic light-emitting field-effect transistor (OLEFET) is an excellent platform to investigate charge transport and light-emitting mechanisms of organic materials. Moreover, the combination of current modulation and light emission in OLEFETs make them interesting for display applications since the number of components could be reduced compared to the traditional design with an LED and a driver transistor. However, unipolar devices with bottom contact configuration operated by direct current (DC) voltages at the gate contact suffer from weak light emission, which in addition is restricted to the vicinity of the contact with the highest energy barrier for charge-carrier injection [3,23]. These drawbacks are mainly due to (a) the necessity to inject holes and electrons simultaneously and (b) to the different mobilities of those species. They can be overcome by a novel operating method, in which an alternating electric field is used to sequentially inject holes and electrons [24]. Here, we report on the electroluminescence properties of two novel naphthyl end-capped (bi)thiophenes (NaT and NaT_2) examined in an AC-biased OLEFET geometry. We observe electroluminescence from both compounds even when only one of the source–drain electrodes is biased relative to the gate electrode; the other electrode floating. The observation of light emission in this configuration, which basically corresponds to a metal–insulator–semiconductor diode, shows that a single injecting electrode is sufficient to produce clear electroluminescence that can be modulated by the applied gate voltage amplitude and/or frequency.

2. Experimental

2.1. Materials synthesis

Scheme 1 depicts the synthesis of the two naphthyl-end-capped (bi)thiophenes, 5,5-bis(naphthyl)-2,2′-bithiophene (NaT_2) and 2,5-bis(naphthyl)-thiophene (NaT). Actually, the synthesis of NaT_2 has been achieved before using a Stille cross-coupling approach [21], while NaT has only been part of some recent patents [25]. Recently, we were able to employ Suzuki cross-coupling protocols for the synthesis of oligophenylenes and oligothiophenephenylenes similar to NaT and NaT_2 thereby avoiding toxic organotin compounds [26]. Thus, we decided to make use of this strategy here, too.

Solvents were dried, distilled and stored under argon according to standard procedures. 2-Bromonaphthylboronic acid, 2,5-dibromothiophene, and 5,5′-dibromo-2,2′-bithiophene were purchased from commercial sources and used as received. Reactions were performed under an argon atmosphere in oven-dried glassware using standard Schlenk techniques. Thin-layer chromatography was performed on aluminum TLC plates (silica gel 60 F254) from Merck and the products were visualized under UV-light

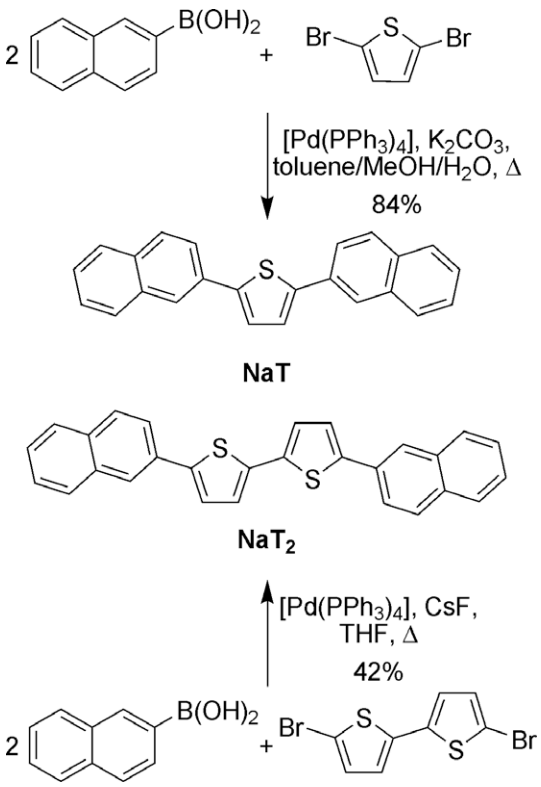

Scheme 1. Synthesis of naphthyl end-capped thiophenes NaT and NaT_2.

(254 or 366 nm). Products were purified by sublimation under ultra-high-vacuum.

Mass spectra were recorded on a Finnigan MAT-95XL. UV/Vis spectra were measured on a Jena Analytic Specord 200 spectrometer in a 1 cm quartz cuvette. Fluorescence spectra were taken on an Aminco Bowman AB2 spectrometer in a 1 cm quartz cuvette. Elemental analyses were carried out with a Heraeus Vario EL.

2.1.1. NaT

A two-neck flask equipped with a condenser was charged with 2,5-dibromothiophene (1.5 g, 6.20 mmol), 2-naphtylboronic acid (2.24 g, 13.02 mmol), K_2CO_3 (2.57 g, 18.6 mmol) and $[Pd(PPh_3]_4$ (358 mg, 0.31 mmol, 5 mol%). A mixture of toluene, MeOH and water (60/30/3 mL) was added and the reaction mixture was refluxed for 50 h. After the mixture was allowed to cool down to room temperature the precipitate was collected and washed with toluene, CH_2Cl_2, and H_2O (2×80 mL each). The crude product was sublimed in ultra-high-vacuum (5.4×10^{-7} mbar, 296 °C (sand bath temperature)) to give 1.75 g (84%) of the desired product.

UV–vis (CH_2Cl_2): $\lambda_{max} = 282$, 352 nm; fluorescence (CH_2Cl_2): $\lambda_{max} = 399$, 420 nm; MS (EI): *m*/*z* (%): 336.1 (100) $[M]^{\cdot+}$, 168.0 (15) $[M]^{2+}$; HRMS (EI, *m*/*z*): $[M]^{\cdot+}$ calcd for $C_{24}H_{16}S$, 336.0969; found: 336.0977. Anal. calcd for $C_{24}H_{16}S{\cdot}1/5H_2O$: C, 84.77; H, 4.86; S, 9.43; found: C, 84.74; H, 4.65; S, 9.51.

2.1.2. NaT_2

A two-neck flask equipped with a condenser was charged with 5,5′-dibromothiophene (794 mg, 2.46 mmol), 2-naphtylboronic acid (888 mg, 5.05 mmol), CsF (1.12 g, 7.38 mmol), and $[Pd(PPh_3]_4$ (123 mg, 0.074 mmol, 3 mol%). THF (50 mL) was added and the reaction mixture was refluxed for 50 h. After allowing to cool to room temperature the precipitate was collected and washed with THF, CH_2Cl_2, and H_2O (2 × 50 ml each). The crude product was sublimed in ultra-high-vacuum (1.4×10^{-7} mbar, sand bath temperature 278–319 °C) to give 433 mg (42%) of the desired compound.

UV/Vis (CH_2Cl_2): λ_{max} = 303 nm; fluorescence (CH_2Cl_2): λ_{max} = 383 nm; EI–MS (*m*/*z* (%)); 418.1 (100) $[M]^{\cdot+}$, 209.0 (18) $[M]^{2+}$; HRMS (EI, *m*/*z*): $[M]^{\cdot+}$ calcd for $C_{28}H_{18}S_2$, 418.0844; found: 418.0858. Anal. calcd for $C_{28}H_{18}S_2$: C, 80.34; H, 4.33; S, 15.32; found: C, 80.34; H, 4.25; S, 15.25.

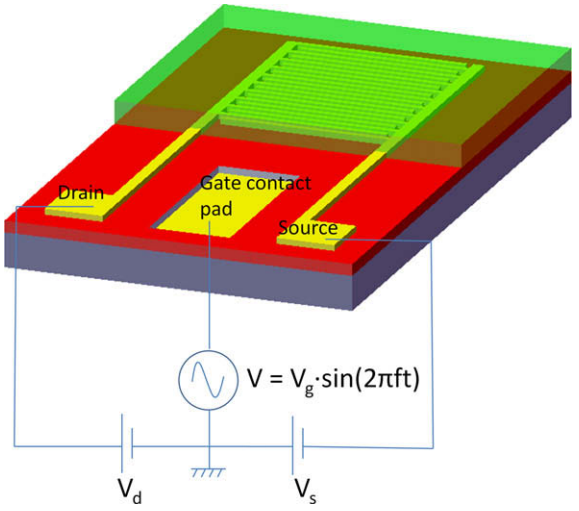

Fig. 1. Schematic diagram of the electrical circuit together with a bottom contact/bottom gate OLEFET configuration.

2.2. Device fabrication and characterization

Both compounds with p-type characteristics are thermally stable solids so that they can be vapor deposited to form high quality polycrystalline films providing high charge-carrier mobility and air stability. Therefore, such organic thin films with a thickness of 52 nm are chosen as active light-emitting layers in a bottom gate/bottom contact (BG/BC) OLEFET configuration with various channel lengths (Fig. 1).

The device architecture is adapted from Yamao et al. who proposed a novel biasing method, in which an alter-

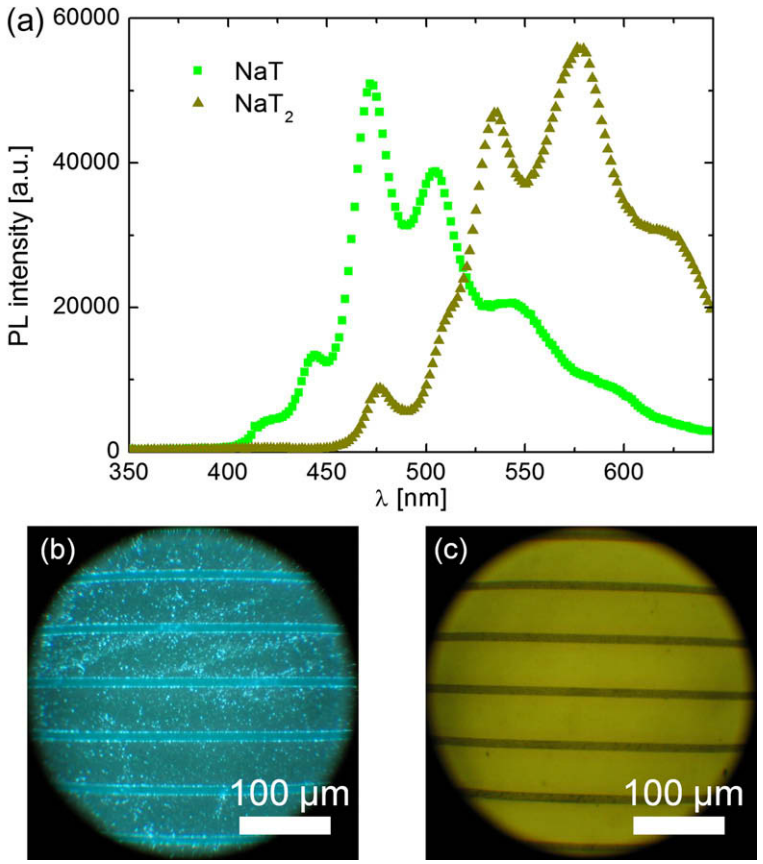

Fig. 2. (a) Photoluminescence spectra of NaT and NaT_2 thin films after excitation with a 325 nm wavelength laser. Fluorescence microscope images of (b) NaT and (c) NaT_2 thin films deposited on the FET device substrate.

nating current (AC) voltage is applied to the gate terminal of a BG/BC OLEFET with a phenylene–thiophene oligomer as the active organic layer [24]. Their study demonstrated that the AC gate voltage allows injection of holes and electrons from source and drain electrodes, respectively, leading to intense light emission within the channel region. Moreover, a noble metal (Au) can be used to inject both holes and electrons and gold is therefore also used in our study.

Highly n-doped silicon (ρ = 0.025 Ω cm) served as back gate electrode, on which 300 nm SiO_2 (C = 11.5 nF cm^{-2}) was thermally grown. An interdigitated array of titanium/gold (2 nm/30 nm) source and drain electrodes was fabricated on SiO_2 by optical lithography, metal evaporation (electron beam heating), and lift-off. The channel width W is summed up to 2.66 cm, and the channel length L varies from 2.5, 5 to 10 μm. The substrate fabrication was completed by etching out a rectangular area (defined by photolithography) in the SiO_2 film using buffered hydrofluoric acid and then depositing titanium/gold (10 nm/50 nm) as the contact pad to the back gate, which is depicted in Fig. 1. The substrates were cleaned by one minute ultrasonic agitation in acetone followed by five minutes DI-water rinse. Organic thin films with a thickness of 52 nm were then deposited onto the substrates at room temperature and under vacuum conditions (2×10^{-6} mbar) at a rate of 0.1–0.4 Å s^{-1}.

The photoluminescence spectra of both materials were collected by exciting the materials with a He–Cd laser (wavelength of 325 nm) and recording the spectra with an ARC SpectraPro-150 spectrometer in ambient air. A Nikon eclipse ME 600 epifluorescence microscope with a mercury UV lamp was used to obtain fluorescence images of the deposited organic materials. The electroluminescence experiments have been carried out under vacuum conditions ($\sim 8 \times 10^{-5}$ mbar). Source and drain were symmetrically biased relative to ground using two Delta Elektronika ES075-2 DC power supplies, while the gate electrode was biased by a Grundig FG100 function generator amplified by a Falco Systems WMA-300 voltage amplifier. A schematic diagram of the electrical circuit along with an OFET structure is illustrated in Fig. 1. Light emission was detected either with a Navitar microscope and a Lumenera Infinity1 camera or an ARC SpectraPro-150 spectrometer.

3. Results and discussion

3.1. Photoluminescence

Fig. 2(a) shows the photoluminescence characteristics of 52 nm thin films obtained upon vapor deposition of NaT and NaT_2, respectively. The spectra indicate green–blue light emission from NaT and yellow light emission from NaT_2. This is consistent with the fluorescence images shown in Fig. 2(b) and (c), respectively. Since naphthyl end-capped (oligo)thiophenes are semiconducting materials, the peaks of the spectra can be attributed to the transition from the vibrational ground state of the electronic excited state to vibrational states of the electronic ground state. The wider HOMO–LUMO gap of NaT compared with NaT_2 suggested by the spectra in Fig. 2(a) is in agreement with the HOMO–LUMO gap decreasing trend with the increasing number of thiophene rings in naphthyl end-capped oligothiophenes reported by Tian et al. [21].

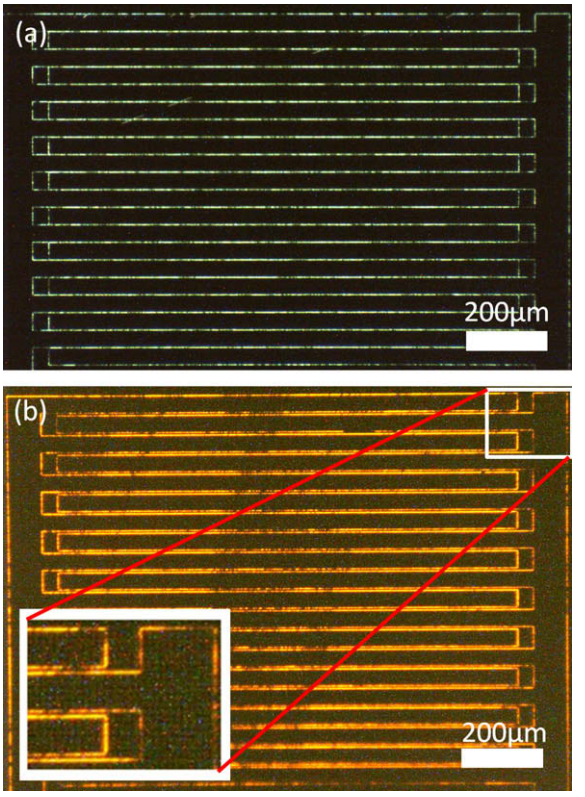

Fig. 3. Optical microscope image of electroluminescence from a 52 nm thin film of NaT (a) and a 52 nm thin film of NaT_2 (b) operated by a sinusoidal AC gate voltage.

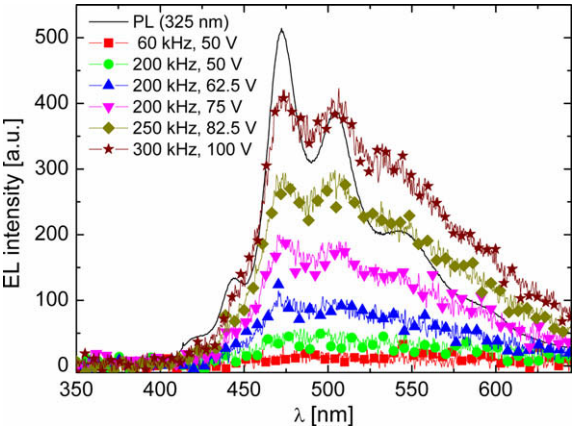

Fig. 4. Electroluminescence spectra of a 52 nm NaT thin film operated under drain and source voltages of $V_d = -V_s = 0$ V and an AC gate voltage with varying frequencies and amplitudes. The photoluminescence spectrum (scaled by a factor of 100) is also shown for comparison.

3.2. Electroluminescence

Both the green–blue electroluminescence from NaT and the yellow electroluminescence from NaT_2 can be observed in an optical microscope. Fig. 3(a) shows a NaT device with 2.5 μm channel length emitting green–blue light generated by drain and source voltages of $V_d = -V_s = 10$ V and an AC gate voltage with a frequency of $f = 200$ kHz and an amplitude of $V_g = 87.5$ V. Electroluminescence of a NaT_2 device with 10 μm channel length is presented in Fig. 3(b) ($V_d = -V_s = 15$ V, $f = 200$ kHz, and $V_g = 62.5$ V). The inset of Fig. 3(b) demonstrates that electroluminescence can be observed from both sides of the channel close to the injecting contacts, and also occurs along the periphery of an individual electrode. This is consistent with previous observations on other organic semiconductors [4]. However, light emission from opposing electrodes cannot be distinguished in devices with short channel lengths such as 2.5 and 5 μm. It is important to note that the electroluminescence from NaT_2 is more intense than that from NaT under the same experimental conditions. This is related to the smaller HOMO–LUMO gap and assumed higher carrier mobility of NaT_2 compared with NaT [21].

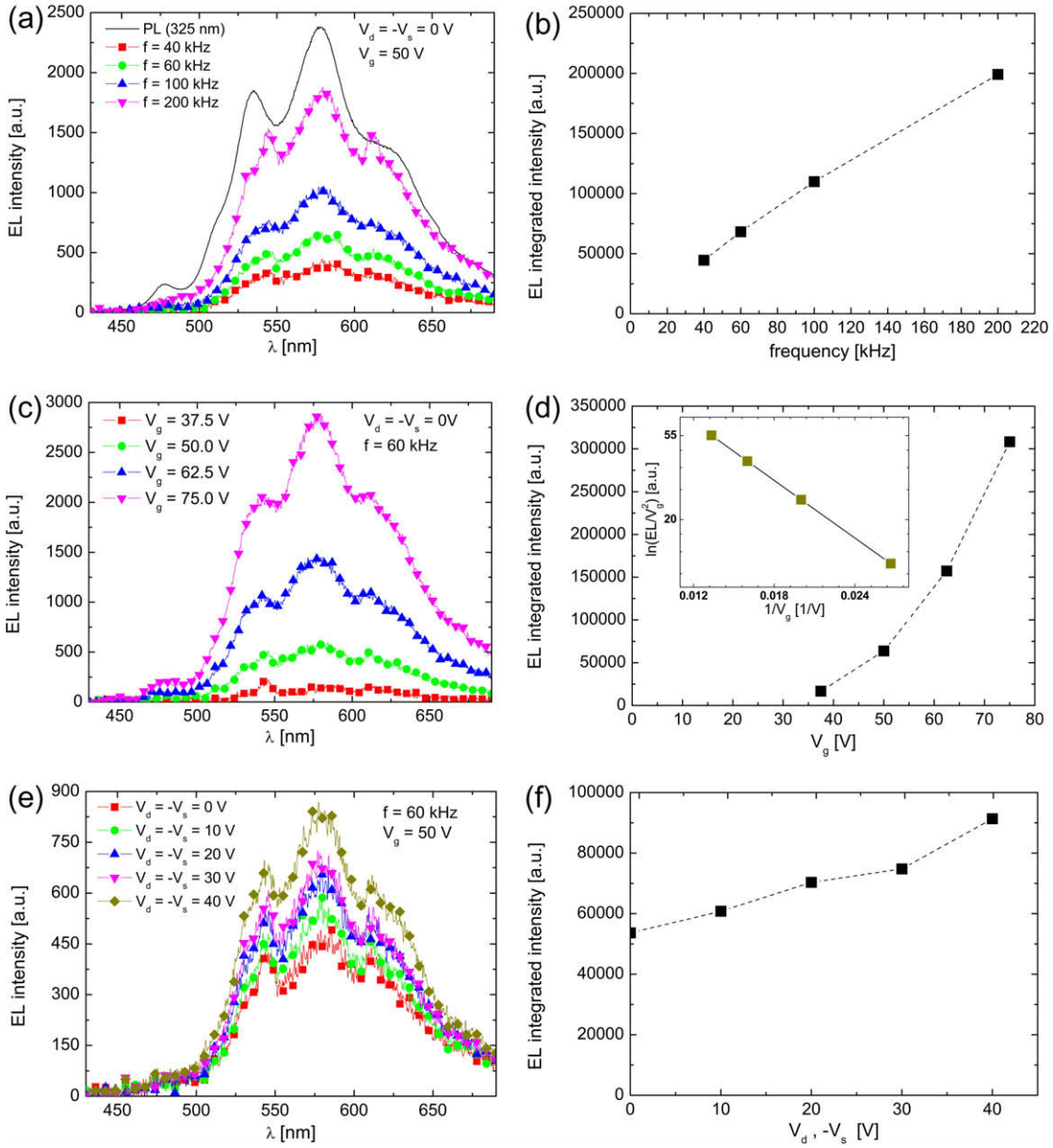

Fig. 5. Electroluminescence spectra of a 52 nm NaT_2 thin film (channel length 5 μm) with variable frequency of AC gate voltage (a), AC gate voltage amplitude (c) and drain and source voltages (e). The graphs on the right hand side show the total intensity (spectra integrated from 431 to 690 nm) as a function of frequency (b), amplitude of AC gate voltage (d), and drain and source voltages (f). The inset in (d) is a Fowler–Nordheim type plot of the intensity vs. gate voltage amplitude.

Since emission takes place from both sides of the channel and along the periphery of an individual electrode, the mechanism of electroluminescence cannot involve charge-carriers drifting across the channel to meet and recombine with their counterparts at the opposite electrode. We elaborate on this aspect in the next section.

Fig. 4 shows the electroluminescence spectra of a NaT device with 2.5 μm channel length. The source and drain voltages are maintained at zero volts for the whole series of experiments while the frequency and the amplitude of the AC gate voltage are varied. A photoluminescence spectrum is also depicted in Fig. 4 in order to compare to the electroluminescence spectra. Obviously, the intensity of the electroluminescence output increases with frequency and with voltage amplitude. The EL spectra show background noise due to their relatively low intensity, however, it is still clear that the peak positions correspond to those observed in the PL spectrum and that the same electronic transitions are therefore responsible for the light emission.

The light emission intensity from NaT_2 is significantly higher than that of NaT, leading to more well-resolved electroluminescence peaks as demonstrated in Fig. 5. Fig. 5(a) shows a clear dependence of the electroluminescence intensity on the AC gate voltage frequency. Fig. 5(c) and (e) illustrate how the EL spectrum depends on the gate voltage amplitude as well as drain and source voltages, respectively. Fig. 5(b), (d), and (f) show the relationships between the total EL intensity and the various operating parameters. The data points have been obtained by integrating the corresponding spectra in Fig. 5(a), (c), and (e), respectively, from 431 to 690 nm. The intensity increases approximately linearly with the frequency of the gate voltage (Fig. 5(b)) whereas it depends non-linearly on the gate voltage amplitude (Fig. 5(d)). The inset in Fig. 5(d) shows a Fowler–Nordheim type plot of the intensity vs. gate voltage amplitude including a fit line.

3.3. Discussion

The initial linear relationship between intensity and the AC gate voltage frequency can be interpreted as a result of more holes and electrons recombining if more AC voltage cycles are accomplished within a fixed time interval. For a further increase in frequency, a deviation from the linear dependence is expected [4,27]. This can also be inferred from Fig. 5(b), which indicates that the EL intensity tends to deviate from a straight line at 200 kHz. This deviation could be caused by the short time period for injection at high frequencies. At the highest frequencies, sample degradation made it impossible to study further the high-frequency behaviours.

To explain the observed EL output occurring both from the periphery of an individual electrode and from two different areas within the channel region, we propose a light generation mechanism composed of two sequential steps as depicted in Fig. 6. During the positive half-period of the gate voltage, electrons are injected from the gold electrode to the organic material, where they are trapped. In the second (negative) half-period, holes are injected and

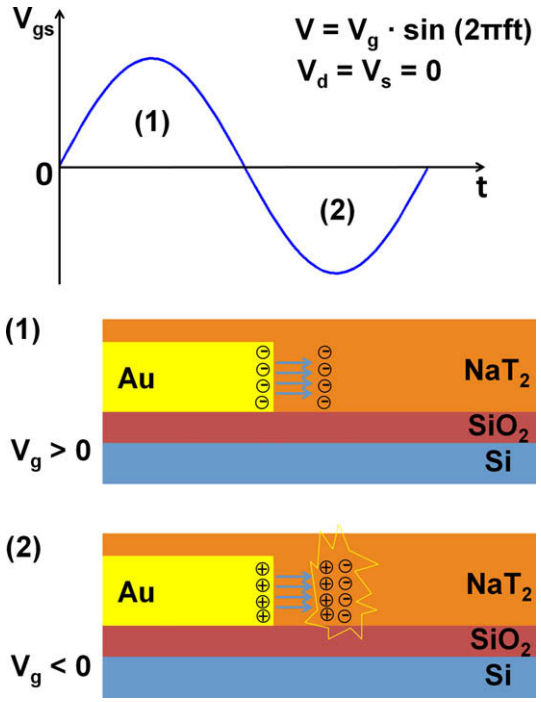

Fig. 6. Schematic diagram of the device operating mechanism. During the positive semi-period of the gate voltage (marked '1'), electrons are injected from the Au electrode into the organic semiconductor. During the subsequent negative semi-period (marked '2'), hole injection causes recombination and photon emission.

can recombine with the trapped electrons. The total intensity output then depends on either the electron or the hole injection process, whichever is less probable. One way to further elaborate on the light generation mechanism in our devices would be to study the time-resolved light output and correlate with the source–drain current as done by Yamao et al. [24].

The inset in Fig. 5(d) shows a Fowler–Nordheim (F–N) type plot using light intensity and gate voltage as parameters [27]. Strictly speaking, the F–N theory describes tunneling through a barrier into a delocalized state, which is not the case here where the charge-carriers form trapped states (polarons) in the organic semiconductor and the charge transport occurs as incoherent hopping [28]. However, the excellent fit of the measured data points to the F–N behaviour does suggest that the device current and thus the light intensity are governed by an injection barrier at the metal–organic interface.

In the data presented in Fig. 5(d), both the source and drain contact were connected to ground. If they are biased symmetrically (i.e. $V_d = -V_s$), the light intensity increases with increasing magnitude of the drain and source voltages as seen in Fig. 5(f). Adding a negative voltage to the source electrode must increase the electron injection during the first (positive) semi-period of the gate voltage compared to the injection occurring with the source electrode connected to ground. In the second (negative) half-period, the subsequent hole injection will likewise be reduced. However, in the symmetri-

cally biased configuration, the hole injection occurring from the drain contact should increase and the electron injection should decrease. Assuming that the limiting factor on the light emission is electron injection, one should therefore anticipate that the light emission occurring at the source (drain) electrode would increase (decrease). Since the data in Fig. 5(f) represent the average over a large area, it therefore suggests that the increase occurring at the source electrodes more than outweighs the intensity decrease at the drain electrodes. However, the detailed mechanism of this effect is still not clearly understood. Yamao et al. also observed an increasing light intensity with increasing magnitude of the drain and source voltages [24], however their model deals with recombination of holes and electrons injected from opposite electrodes as opposed to ours that only includes one injecting electrode, so a direct comparison is not feasible.

4. Conclusions and outlook

Two naphthyl end-capped (oligo)thiophenes are implemented in an easy-fabricated OLEFET structure utilizing an AC gate voltage to obtain intensified electroluminescence. The intensity of the electroluminescence emission is linearly proportional to the frequency of the AC gate voltage amplitude and is non-linearly dependent on the amplitude of the AC voltage. We propose that this non-linearity is caused by the carrier injection process, which, although occurring into localized states in an organic semiconductor nevertheless obeys a simple Fowler–Nordheim relationship. Further experiments are aimed at studying this effect in more detail and at integrating nanostructured organic material [22] on the device substrate to realize nanoscale OLEFETs [4]. In addition, it must be expected that tuning of the injection barrier can lead to more efficient light emission. This could for example be realized by modifying the gold electrodes via, e. g., adsorption of an organic layer prior to deposition of the organic semiconductor [29].

Acknowledgements

I. Wallmann and A. Lützen are grateful to the Deutsche Forschungsgemeinschaft for financial support. The VELUX Foundation and the BHJ-Foundation are acknowledged for financial support. Finally, we thank Henrik H. Henrichsen for assisting with the sample preparation.

References

[1] C.D. Dimitrakopoulos, P.R.L. Malenfant, Adv. Mater. 14 (2002) 99–117.
[2] A.L. Briseno, S.C.B. Mannsfeld, S.A. Jenekhe, Z. Bao, Y. Xia, Mater. Today 11 (2008) 38–47.
[3] A. Hepp, H. Heil, W. Weise, M. Ahles, R. Schmechel, H. von Seggern, Phys. Rev. Lett. 91 (2003) 157406.
[4] J. Kjelstrup-Hansen, X. Liu, H.H. Henrichsen, K. Thilsing-Hansen, H.G. Rubahn, Phys. Status Solidi (c), in press.
[5] H. Yanagi, T. Morikawa, S. Hotta, Appl. Phys. Lett. 81 (2002) 1512–1514.
[6] D.H. Kim, D.Y. Lee, H.S. Lee, W.H. Lee, Y.H. Kim, J.I. Han, K. Cho, Adv. Mater. 19 (2007) 678–682.
[7] J.H. Oh, H.W. Lee, S. Mannsfeld, R.M. Stoltenberg, E. Jung, Y.W. Jin, J.M. Kim, J.-B. Yoo, Z. Bao, Proc. Natl. Acad. Sci. USA 106 (2009) 6065–6070.
[8] C. Rost, S. Karg, W. Riess, M.A. Loi, M. Murgia, M. Muccini, Appl. Phys. Lett. 85 (2004) 1613.
[9] J. Zaumseil, C.L. Donley, J.S. Kim, R.H. Friend, H. Sirringhaus, Adv. Mater. 18 (2006) 2708–2712.
[10] R. Rotzoll, S. Mohapatra, V. Olariu, R. Wenz, M. Grigas, K. Dimmler, Appl. Phys. Lett. 88 (2006) 123502.
[11] S.R. Forrest, Nature 428 (2004) 911–918.
[12] M. Muccini, Nat. Mater. 5 (2006) 605–613.
[13] G. Horowitz, D. Fichou, X. Peng, Z. Xu, F. Garnier, Solid State Commun. 72 (1989) 381–384.
[14] F. Geiger, M. Stoldt, H. Schweizer, P. Bäuerle, E. Umbach, Adv. Mater. 5 (1993) 922–925.
[15] G. Horowitz, Adv. Mater. 10 (1998) 365–377.
[16] Y.-Y. Lin, D.J. Gundlach, S.F. Nelson, T.N. Jackson, IEEE Trans. Electron. Dev. 44 (1997) 1325–1331.
[17] K. Wong, C. Wang, C.H. Chou, Y.O. Su, G. Lee, S. Peng, Org. Lett. 25 (2002) 4439–4442.
[18] T. Noda, H. Ogawa, N. Noma, Y. Shirota, J. Mater. Chem. 9 (1999) 2177–2181.
[19] H. Yanagi, Y. Araki, T. Ohara, S. Hotta, M. Ichikawa, Y. Taniguchi, Adv. Funct. Mater. 13 (2003) 767–773.
[20] J.A. Merlo, C.R. Newman, C.P. Gerlach, T.W. Kelley, D.V. Muyres, S.E. Fritz, M.F. Toney, C.D. Frisbie, J. Am. Chem. Soc. 127 (2005) 3997–4009.
[21] H. Tian, J. Shi, B. He, N. Hu, S. Dong, D. Yan, J. Zhang, Y. Geng, F. Wang, Adv. Funct. Mater. 17 (2007) 1940–1951.
[22] M. Schiek, F. Balzer, K. Al-Shamery, A. Lützen, H.-G. Rubahn, J. Phys. Chem. C 113 (2009) 9601–9608.
[23] T. Sakanoue, M. Yahiro, C. Adachi, J.H. Burroughes, Y. Oku, N. Shimoji, T. Takahashi, A. Toshimitsu, Appl. Phys. Lett. 92 (2008) 053505.
[24] T. Yamao, Y. Shimizu, K. Terasaki, S. Hotta, Adv. Mater. 20 (2008) 4109–4112.
[25] R. Soumya, M. Charette, S.P. Finkelstein, PCT Int. Appl. (2009) WO 2009088975 A2 20090716.;
Y. Geng, H. Tian, J. Shi, Faming Zhuanli Shenqing Gongkai Shuomingshu (2006) CN 1807428 A 20060726.;
O. Hotta, T. Tamaoki, Jpn. Kokai Tokkyo Koho (2000) JP 2000-26451 A 20000125.
[26] M. Schiek, K. Al-Shamery, A. Lützen, Synthesis (2007) 613–621;
I. Wallmann, M. Schiek, R. Koch, A. Lützen, Synthesis (2008) 2446–2450;
I. Wallmann, G. Schnakenburg, A. Lützen, Synthesis (2009) 79–84.
[27] R.J. Walters, G.I. Bourianoff, H.A. Atwater, Nat. Mater. 4 (2005) 143–146.
[28] J. Shinar, R. Shinar, J. Phys. D: Appl. Phys. 41 (2008) 133001.
[29] B.H. Hamadani, D.A. Corley, J.W. Ciszek, J.M. Tour, D. Natelson, Nano Lett. 6 (2006) 1303–1306.

ting, light absorbing, and charge transporting ability in order to be able to perform multiple functions in OSCs, OLEDs, and OTFTs. Thus, it is rare to use the same organic materials as the active layer in individual devices based on different mechanisms. For these reasons, only a few dual functional or tri-functional organic materials have been reported in the literature [6,7]. For dual functional materials, rubrene [6a], triphenylamine–thiophene derivatives [6b], and triarylamine–carbazole based dendrimers [6c] have been investigated as both OLEDs emitting and OSCs donor material and tri-functional materials for the use in OSCs, OLEDs, and OTFTs using triphenylamine–oligothiophene conjugated molecules and fluorene–silole conjugated copolymers have been reported [7]. However, tri-functional materials based on triphenylamine–oligothiophene conjugated molecules showed a power conversion efficiency of 0.32% in OSCs, a poor green light emitting efficiency in OLEDs, and a field-effect mobility of 1.1×10^{-2} $cm^2 V^{-1} s^{-1}$ and on/off current ratio of 200 in OTFTs [7a]. Also, while a tri-functional material based on fluorene–silole conjugated copolymers showed a good power conversion efficiency of 2.01% in OSC devices, it showed a poor red emitting ability of external quantum efficiency of 0.17% in OLEDs, and poor field-effect mobility of 4.5×10^{-5} $cm^2 V^{-1} s^{-1}$ in OTFTs [7b]. The overall efficiency of these tri-functional materials is not high.

On the other hand, acene derivatives [8] have been extensively investigated as organic semiconductors for individual optoelectronic devices [9–11]. In particular, among the acene molecules, tetracene [12,17], pentacene [13,14,18], picene [15], anthanthrene [16], anthradithiophene [19a], and anthracene [19b], derivatives have been widely investigated as useful organic semiconductors for OSCs, OLEDs, and OTFTs [12–16,19]. However, tri-functional acene materials which can be used for emitting material in OLEDs, donor material in OSCs, and active material in OTFTs have not, to our knowledge, been reported so far in the literature.

Herein, we report that naphtho[2,3,*a*]pyrene (**NP**) (Fig. 1), a fused aromatic acene, can be utilized as an efficient multifunctional organic semiconductor material for optoelectronic devices to fabricate OSCs, OLEDs, and OTFTs devices by a vacuum deposition method. **NP** exhibited a maximum power conversion efficiency of 0.48% in OSCs which is considered a good efficiency among the acene molecules [19]. In addition, sky blue OLEDs at 3% **NP** doping exhibited a current efficiency of 4.4 cd A^{-1} and a power efficiency of 3.4 lm W^{-1} which are considered generally good EL efficiencies compared to that of sky blue acene based dopants such as chrysene [10] and anthanthrene derivatives [16a,b]. Also, 5% **NP** doping green OLEDs exhibited a power efficiency of 1.8 lm W^{-1} and a current efficiency of 3.9 cd A^{-1}. In particular, OTFTs using **NP** as an active layer exhibited a field-effect mobility (μ_{FET}) of 0.12 $cm^2 V^{-1} s^{-1}$, a threshold voltage (V_{th}) of −10.8 V, and an on/off current ratio of 6.8×10^6.

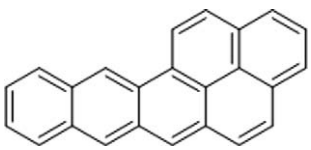

Fig. 1. Molecular structure of **NP**.

2. Experimental

2.1. Materials and instrument

The organic materials such as **NP**, C_{60}, CuPc, NPD, BPhen, and CBP were purchased from Aldrich, Lumtree, and Gracel. Poly(3,4-ethylenedioxythiophene):poly(styrenesulfonate) (PEDOT:PSS) was purchased from H.C. Stark. All the materials were purified by temperature gradient vacuum sublimation prior to use for devices. UV–Vis spectra were recorded on a Beckman DU 650 spectrophotometer. Fluorescence spectra were recorded on a Jasco FP-7500 spectrophotometer. Cyclic voltammetry (CV) was performed using a CH Instruments 660 Electrochemical Analyzer (CH Instruments, Inc., Texas). AFM experiments were performed using an asylum MFP-3D instrument in AC mode with Si_3N_4 cantilevers and XRD analyses were carried out with a Rigaku (λ = 1.5418 Å, 298 K) X-ray instrument. Decomposition temperatures (T_d) were obtained using a Q−5000−IR TGA instrument.

2.2. OSCs fabrication

A 30 nm-thickness of PEDOT:PSS was used as a hole injection layer (HIL). The thin film thickness of **NP** was prepared by an evaporation process from 10 to 100 nm. Then, a 30 nm-thickness of fullerene (C_{60}) as an acceptor was also evaporated. Next, a 8 nm-thickness layer of 4,7-diphenyl-1,10-phenanthroline (Bphen) as a exciton blocking layer (EBL) was evaporated. Finally, 100 nm-thickness of aluminum was evaporated onto the Bphen layer (Fig. S2). The current–voltage measurements of the devices were measured on a Keithley 237 instrument. The device performances were characterized under uniform illumination (AM 1.5G illumination intensity of 100 mW cm^{-2}) using a solar simulator (Newport, 91160A). The light intensity at each wavelength was calibrated using the standard Si solar cell as a reference.

2.3. OLEDs fabrication

A 10 nm-thickness of copper phthalocyanine (CuPc) was used as a hole injection layer (HIL) and a 30 nm-thickness of 4,4′-bis[*N*-(naphthyl-*N*-phenylamino)biphenyl (NPD) was used as a hole transport layer (HTL). A 30 nm-thickness of emitting layer (EML) was prepared by co-evaporating *N*,*N*′-dicarbazolyl-4,4′-biphenyl (CBP) as a host and 1, 3, 5 wt.% of **NP** as a fluorescent dopant. The fluorescent dopant concentration of **NP** was varied from 1 to 5 wt.%. Next, 30 nm-thickness layer of 4-biphenyloxolatoaluminium(III)bis(2-methyl-8-quinolinato)-4-phenylphenolate (Balq), as a hole blocking layer (HBL) and electron transporting layer (ETL) was evaporated. Then, LiF as an electron injection layer (EIL) was also evaporated. Finally, a 100 nm-thickness of aluminum was deposited on the LiF layer (Fig. S3). The emission properties were

determined using PR650 spectra scan spectracolorimeter as a source meter.

2.4. OTFTs fabrication

The transistors based on **NP** were fabricated with the top-contact geometry. We used a heavily doped Si wafer as the gate electrode and non-pretreated or octadecyltrichlorosilane (OTS)-pretreated SiO_2 layer (thickness, ca. 300 nm) as the gate dielectric. Prior to deposition, the **NP** starting material was purified by temperature gradient vacuum sublimation to improve the purity of the active layer. The **NP** films (ca. 500 Å) were then grown by vacuum sublimation, using a home-made apparatus, at a rate range of 0.4–0.8 Å s^{-1} under a working pressure of 2.0–2.5 $\times$ 10^{-6} torr. Gold source/drain electrodes were evaporated on top of the films through a shadow mask with a channel length (L) of 50 μm and a channel width (W) of 1000 μm (Fig. S6). Electrical characterization of the transistors was performed at room temperature in air by using a Keithley 4200-SCS semiconductor analyzer. The field-effect mobility (μ) was calculated in the saturation region (V_{DS} = −100 V) from the plot of the square-root of drain current vs. V_{GS} using the following equation: $I_{DS} = (W\text{-}C_i\mu(V_{GS} - V_T)^2)/2L$, where I_{DS} is the source-drain saturation current; C_i (1.1 $\times$ 10^{-8} F) is the capacitance of the SiO_2 insulator; W/L is the ratio of the width to the channel length; V_{GS} and V_T are the gate-source and threshold voltages, respectively.

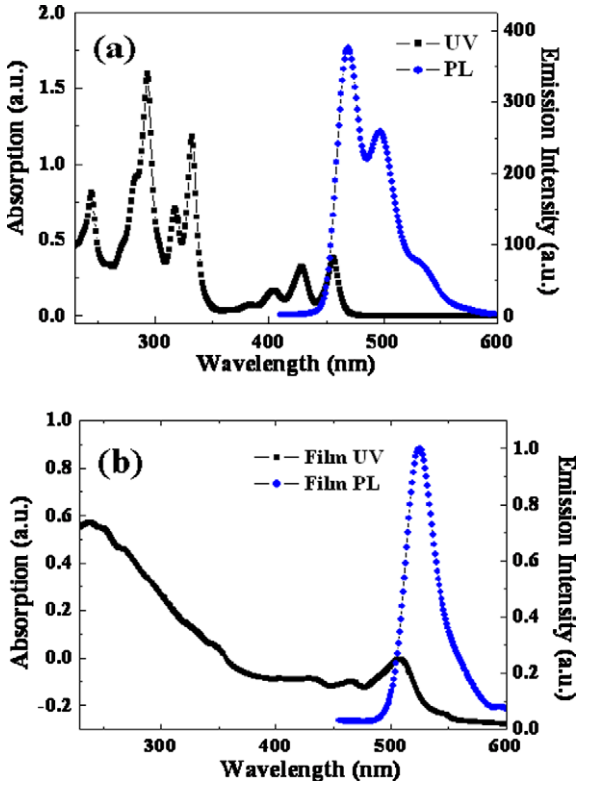

Fig. 2. UV and PL spectra of 0.02 mM **NP** in CH_2Cl_2 (a) and solid film (b).

3. Results and discussion

The UV spectra of **NP** show multiple absorption bands at 292, 332, 428, and 456 nm in CH_2Cl_2 and broad absorption bands at 269, 465, and 507 nm in solid film, respectively. The PL spectra of **NP** show sky blue emission at 468 and 497 nm in CH_2Cl_2 and green emission at 523 nm in solid film, respectively (Fig. 2). Both film UV and PL spectra of **NP** were significantly red-shifted in comparison with those in CH_2Cl_2, which is attributed to the flat structure of the **NP** molecule.

The photoluminescence quantum yield of **NP** was estimated to be 0.61 using anthracene as a standard [20]. Thermal gravimetric analysis (TGA) data reveal that **NP** has high thermal stability (T_d = 271 °C, Fig. S7).

In order to study the electrochemical properties of **NP**, we measured the cyclic voltammetry. **NP** shows a reversible oxidation process associated with stable cation radical generation. On the other hand, the reduction potential of **NP** was not observed in cyclic voltammetry. The half oxidation potential of **NP** was observed at $E_{1/2}$ = 0.50 V after ferrocene/ferrocenium correlation (Fig. S1). From these results, the HOMO energy value of **NP** (−5.30 eV) was calculated. The LUMO energy value of **NP** (−2.80 eV) was calculated from the cross-section wavelength between absorption and emission spectra (Table 1).

To investigate the efficient multifunctional properties of **NP**, we fabricated three representive types of organic electronic devices. First, we fabricated OSCs with the configuration of ITO/PEDOT:PSS (30 nm)/**NP** (x nm)/C_{60} (30 nm)/Bphen (8 nm)/Al (100 nm). The thickness of **NP** was varied from 10 to 100 nm.

Fig. 3 shows the current density vs. voltage (I–V) characteristics of heterojunction solar cells. All the OSCs show the solar cell behavior. Heterojunction solar cell using 10 nm-thick **NP** exhibited a significantly low power conversion efficiency (PCE) of 0.003% and short circuit current (I_{sc}) of 0.056 mA cm^{-2} due to the thin **NP** film, which cannot efficiently absorb the sunlight. On the other hand, an OSC device using 45 nm-thick **NP** exhibited the open circuit voltage (V_{oc}) of 0.37 V, short circuit current of 2.0 mA cm^{-2}, and power conversion efficiency of 0.35%, under simulated AM 1.5 solar irradiation at 100 mW cm^{-2}. In particular, when the thickness of **NP** was optimized at 80 nm, the OSC device exhibited a significantly increased power conversion efficiency of 0.48%, an open circuit voltage of 0.59 V, and a short circuit current of 1.9 mA cm^{-2}, under simulated AM 1.5 solar irradiation at 100 mW cm^{-2}. However, as the thickness of **NP** increased further to 100 nm, the device exhibited a significantly reduced short circuit current of 0.46 mA cm^{-2} and power conversion efficiency of 0.02% due to the thick **NP** film, in which excitons cannot be efficiently separated between hole and electron. We found that the performance of OSC devices using **NP** depends critically on the donor (**NP**) film thickness of the active layer. Typically, varying **NP** film thickness in the active layer resulted in changing the power conversion efficiency from 0.003% to 0.48%. Despite the narrow absorption range of **NP**, the maximum power conversion

Table 1
Photophysical and electrochemical data of **NP**.

	Absorption (λ_{nm}) [$\varepsilon \times 10^4$ M^{-1} cm^{-1}] [a]	Emission (λ_{nm}) [b]	Φ[c]	HOMO (eV)[d]	LUMO (eV)[e]
NP	243(3.90), 292(7.70), 332(5.90), 404 (0.80), 428(1.55), 456(1.90) (solution) 269, 349, 405, 433, 465, 507 (film)	468, 497 (solution) 523 (film)	0.61	5.30	2.80

[a,b] The absorption and emission spectra were measured in 0.02 mM in CH_2Cl_2 solution and quartz solid film.
[c] Photoluminescence quantum yield (Φ_{PL}) was determined by anthracene reference in ethanol solution.
[d] HOMO energy level was determined in CH_2Cl_2 solution (0.1 M $TBAPF_6$).
[e] LUMO energy level was calculated from the cross-section wavelength between absorption and emission spectra.

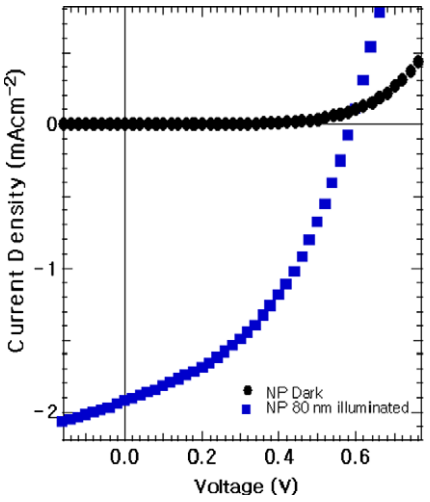

Fig. 3. *I–V* characteristics of ITO/PEDOT (30 nm)/**NP** (80 nm)/C_{60} (30 nm)/BPhen (8 nm)/Al (100 nm) device under simulated AM 1.5 solar irradiation at 100 mW cm^{-2}.

efficiency (0.48%) obtained in this study is considered high among the acene derivatives in OSCs (due to the good hole mobility of **NP**). This is the first report on **NP** based OSC donor materials. Our results indicate that among the acene derivatives, **NP** can be regarded as a good donor material for heterojunction solar cells. The overall device performance data based on **NP** and C_{60} are summarized in Table 2.

Second, OLED devices were fabricated using **NP** as a dopant molecule, with the configuration of ITO/CuPc (10 nm)/NPD (30 nm)/emitting layer (EML 30 nm)/Balq (30 nm)/LiF (1 nm)/Al (100 nm). Emitting layers of 30 nm-thickness were prepared by co-evaporating CBP as

Table 2
OSC data based on various film thickness of **NP** and C_{60} under simulated AM 1.5 solar irradiation at 100 mW cm^{-2}.

Thickness of **NP** (nm)	V_{OC} (V)[a]	I_{SC} (mA cm^{-2})[b]	FF (%)[c]	PCE (%)[d]
10	0.54	0.056	10	0.003
45	0.37	2.0	46	0.35
80	0.59	1.9	42	0.48
100	0.38	0.46	11	0.02

[a] Open circuit voltage.
[b] Short circuit current.
[c] Fill factor.
[d] Power conversion efficiency.

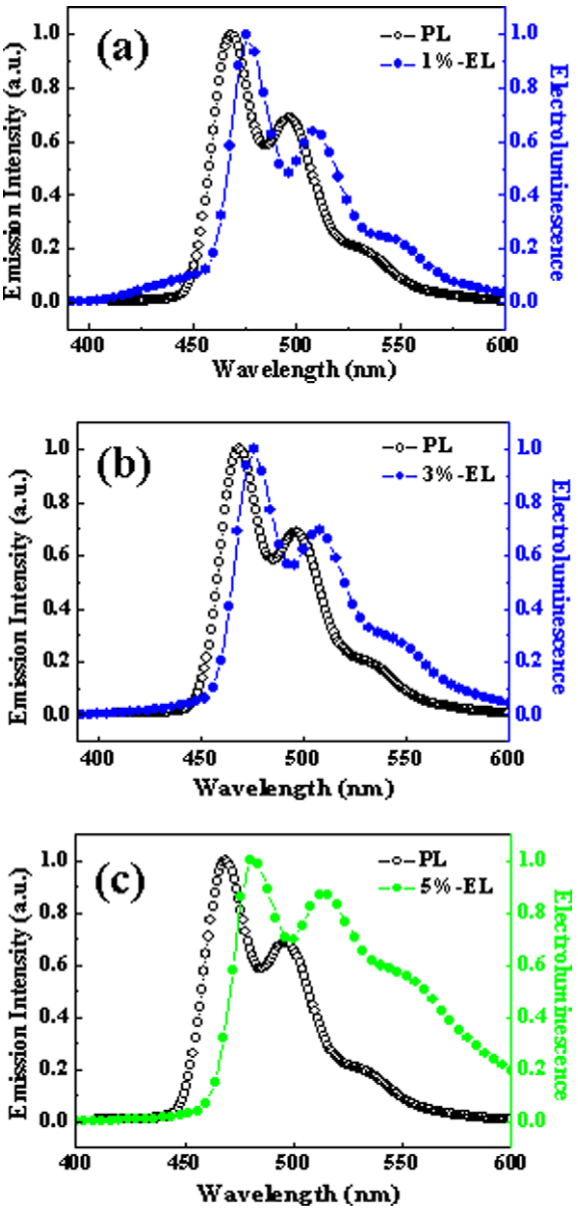

Fig. 4. EL spectra according to different **NP** doping ratios (a) 1%, (b) 3%, and (c) 5% in OLEDs with configuration of ITO/CuPc (10 nm)/NPD (30 nm)/EML (30 nm)/Balq (30 nm)/LiF (1 nm)/Al (100 nm).

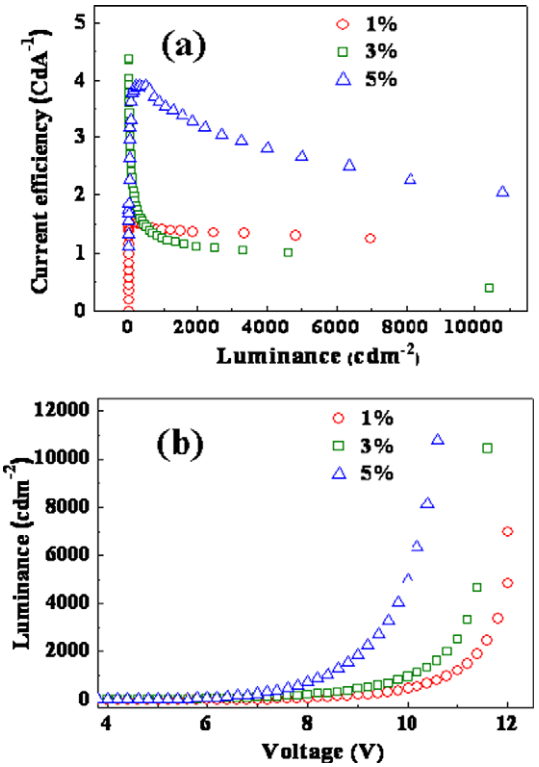

Fig. 5. Characteristics of ITO/CuPc (10 nm)/NPD (30 nm)/EML (30 nm)/Balq (30 nm)/LiF (1 nm)/Al (100 nm) devices. (a) Luminance (cd m^{-2}) vs. current efficiency (cd A^{-1}). (b) voltage (V) vs. luminance (cd m^{-2}).

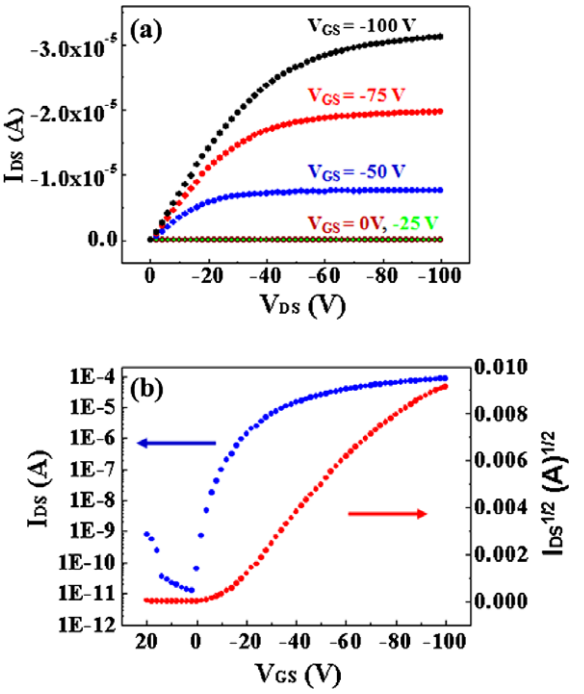

Fig. 6. The output (a) and transfer characteristics (b) of the OTFTs using **NP** deposited at T_{sub} = 75 °C on OTS-treated SiO_2.

Table 4
OTFT data.

T_{sub} (°C)	μ_{FET} (cm^2 V^{-1} s^{-1})[a]	V_{th} (V)[b]	I_{on}/I_{off}[c]
Bare SiO_2			
RT	0.02	−21.3	2.5×10^5
75	0.01	−17.8	4.2×10^5
110	No FET	–	–
OTS-SiO_2			
RT	0.05	−18.4	2.0×10^6
75	0.12	−10.8	6.8×10^6
110	0.005	−19.4	3.1×10^5

[a] Field-effect mobility.
[b] Threshold voltage.
[c] On–off ratio.

a host and *x* wt.% **NP** as a fluorescent dopant. Fig. 4 shows the photoluminescence (PL) in CH_2Cl_2 and electroluminescence (EL) spectra with different doping ratios of **NP**. The PL spectra of **NP** in CH_2Cl_2 show the sky blue emission centered at 468 and 497 nm. At 1% and 3% **NP** doping, the EL spectra show the similar sky blue emission compared to that of PL emission (Fig. 4).

The similar pattern of the PL and EL spectra of 1% and 3% **NP** doped device suggests that EL spectra should be attributed to an emission from a singlet excited state of **NP** in the emitting layer. On the other hand, the 5% **NP** doped device shows green emission centered at about 479, 514, and 550 nm (Fig. 4). This is most likely due to the formation of an excimer resulting from the aggregation of **NP** dopant molecules in the emitting layer. This could be due to the planar molecular structure of **NP**, which cannot prevent aggregation in the emitting layer. We were able to change the emission color from sky blue to green by varying the

Table 3
OLED data.

NP (%)[a]	Max η_p (lm W^{-1})[b]	Max η_c (cd A^{-1})[c]	Max η_{ext} (%)[d]	Max η_l (cd m^{-2})[e]	EL (λ_{nm})[f]	CIE
1	0.7	1.7	0.7	6988 at 12.0 V	476, 509	(0.16, 0.36)
3	3.4	4.4	1.8	10430 at 11.6 V	476, 512	(0.17, 0.39)
5	1.8	3.9	1.4	10780 at 10.6 V	479,514, 550	(0.31, 0.52)

[a] **NP** doping ratio. ITO/CuPc (10 nm)/NPD (30 nm)/EML (30 nm) **NP** *x* wt.% doping/Balq (30 nm)/LiF (1 nm)/Al (100 nm).
[b] Power efficiency.
[c] Current efficiency.
[d] External quantum efficiency.
[e] Luminance.
[f] The EL spectra were obtained from OLEDs.

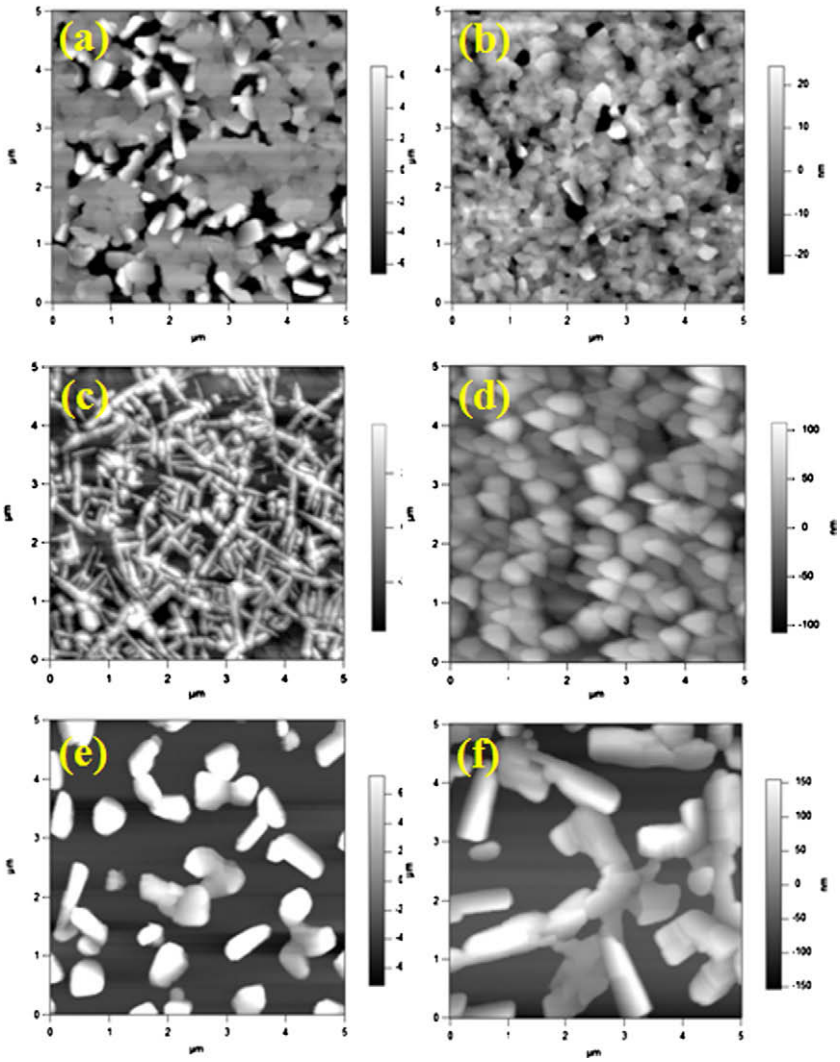

Fig. 7. 5 × 5 μm AFM topography images of 50 nm **NP** thin films (measured by the quartz crystal microbalance) deposited on SiO_2 (left column) and OTS/SiO_2 (right column) at various substrate temperatures: (a, b) RT; (c, d) 75 °C; (e, f) 110 °C.

NP doping ratio. This result indicates that the EL emission depends on the **NP** doping ratio in the emitting layer.

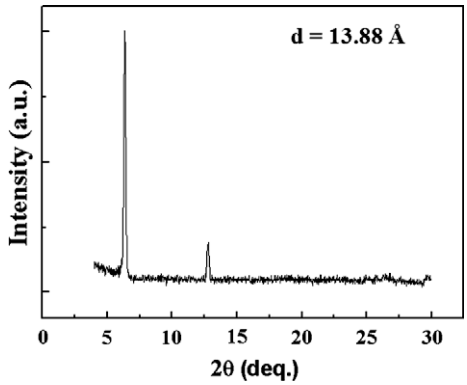

Fig. 8. X-ray diffraction (XRD) pattern of the thin films of **NP** grown on SiO_2 at RT.

Fig. 5 shows the sky blue and green emitting EL device data. The sky blue OLED device at 1% **NP** doping shows a power efficiency of 0.7 lm W^{-1} and current efficiency of 1.7 cd A^{-1}. In particular, the OLED device at 3% **NP** doping shows the maximum power efficiency of 3.4 lm W^{-1} and current efficiency of 4.4 cd A^{-1}, and a Commission Internationale de l'Eclairage (CIE) coordinates of (0.17, 0.39). At 3% **NP** doping, the maximum power efficiency and current efficiency of the EL device are considered generally good. Therefore, the efficiencies of OLEDs using **NP** are higher than those of devices using other acene materials such as chrysene [10] and anthanthrene derivatives [16a,b].

Furthermore, at 5% **NP** doping, the green OLED device shows a power efficiency of 1.8 lm W^{-1} and current efficiency of 3.9 cd A^{-1}, and a CIE coordinates of (0.31, 0.52). As a result, the EL at 5% **NP** doping showed green emission with generally good luminous power efficiency and current efficiency in OLED devices. Also, the turn-on voltage is reduced as the doping concentration of **NP** increases. It

is presumably because **NP** can be used as efficient carrier transport channel at high doping concentration of **NP** (Fig. 5b) [16c]. All EL device data are summarized in Table 3. As a result, **NP** can be used as sky blue dopant material as well as green dopant material in fluorescent OLEDs. Although the operation mechanisms of OLEDs and OSCs are different, **NP** shows good efficiencies for both OLEDs and OSCs due to the good photoluminescence quantum yield and hole mobility.

Third, the possibility of **NP** being used for charge transport channels in OTFTs was investigated by the fabrication of OTFTs using top-contact geometry (Fig. S6).

Fig. 6 shows the output and transfer characteristics of top-contact OTFTs using **NP** deposited at a substrate temperature (T_{sub}) of 75 °C on OTS-treated SiO_2. From the electrical transfer characteristics, we obtained parameters such as the field-effect mobility, on/off current ratio, and threshold voltage for the devices. The OTFTs based on **NP** showed a field-effect mobility of 0.12 $cm^2 V^{-1} s^{-1}$, threshold voltage of −10.8 V, and on/off current ratio of 6.8×10^6 under ambient conditions. The electrical properties of **NP** based OTFT devices fabricated under various conditions are summarized in Table 4. To investigate the cause of the different OTFTs performance under various conditions, we studied the film morphology of thin **NP** active layers using atomic force microscopy (AFM). Fig. 7 shows AFM images of **NP** active layers deposited on SiO_2 (left column) and OTS/SiO_2 (right column) at RT, 75 °C, and 110 °C. The connectivity of **NP** grains deposited on a SiO_2 substrate at RT has poor, low field-effect mobility. However, **NP** films deposited on an OTS/SiO_2 substrate at RT show improved film connectivity and field-effect mobility. In particular, densely packed grains on an OTS/SiO_2 substrate at 75 °C were observed and showed the best field-effect mobility among **NP** based devices under various conditions, due to improved interconnectivity in the channels of the **NP** films. Also, at 110 °C, we observed that sub-micron-sized **NP** grains deposited on SiO_2 were disconnected, and as a result, showed no electrical properties. However, the films deposited on OTS/SiO_2 were connected, and as a result, showed electrical properties.

When the morphological characteristics of thin-film **NP** were investigated by X-ray diffraction (XRD), the patterns displayed 2nd order diffraction peaks and the intense XRD peaks in low angle side indicated a highly ordered lamellar structure within **NP** with a period of 13.88 Å (Fig. 8).

4. Conclusion

We found that **NP** can be commonly used as an effective tri-functional material for three representative kinds of devices in organic electronics. In order to prove the fact, we fabricated the OSCs, OLEDs, and OTFTs using **NP** molecules as active layers. First, an optimized 80 nm-thick **NP** based OSC device exhibited a good power conversion efficiency of 0.48%. Second, an OLED device with 3% **NP** doping showed sky blue emission and a power efficiency of 3.4 lm W^{-1} and a current efficiency of 4.4 cd A^{-1}, and a CIE coordinates of (0.17, 0.39). OLEDs with 5% **NP** doping showed green emission and a power efficiency of 1.8 lm W^{-1} and a current efficiency of 3.9 cd A^{-1}. Third, OTFTs based on **NP** exhibited a field-effect mobility of 0.12 $cm^2 V^{-1} s^{-1}$, a threshold voltage of −10.8 V, and an on/off ratio of 6.8×10^6. Consequently, **NP** turned out to be a promising organic semiconductor material which can be used as an efficient blue or green light emitting material, and efficient solar cell donor, and an organic semiconductor for OTFTs. Further studies on modified **NP** based organic semiconductors for optoelectronic devices are in progress.

Acknowledgements

This work was supported by Basic Science Research Program through the National Research Foundation of Korea (NRF) grant funded from the Ministry of Education, Science and Technology (MEST) of Korea for the Center for Next Generation Dye-sensitized Solar Cells (No. 2010-0001842), the National Research Foundation of Korea Grant funded by the Korean Government (MEST) (NRF-C1AAA001-2009-0093282), KOSEF through CNNC, and the Seoul R&BD Program (10543). We also acknowledge the BK21 program and Nanosystems Institute National Core Research Center for student financial support.

Appendix A. Supplementary material

Supplementary data associated with this article can be found, in the online version, at doi:10.1016/j.orgel.2010.03.017.

References

[1] (a) C.W. Tang, Appl. Phys. Lett. 48 (1986) 183;
(b) C.W. Tang, S.A. VanSlyke, Appl. Phys. Lett. 51 (1987) 913;
(c) A. Tsumura, H. Koezuka, T. Ando, Appl. Phys. Lett. 49 (1986) 1210.
[2] (a) H. Meng, F. Sun, M.B. Goldfinger, G.D. Jaycox, Z. Li, W.J. Marshall, G.S. Blackman, J. Am. Chem. Soc. 127 (2005) 2406;
N.M. Kronenberg, M. Deppisch, F. Würthner, H.W.A. Lademann, K. Deing, K. Meerholz, Chem. Commun. (2008) 6489.
[3] (a) K.L. Mutolo, E.I. Mayo, B.P. Rand, S.R. Forrest, M.E. Thompson, J. Am. Chem. Soc. 128 (2006) 8108;
(b) F. Silvestri, M.D. Irwin, L. Beverina, A. Facchetti, G.A. Pagani, T.J. Marks, J. Am. Chem. Soc. 130 (2008) 17640;
(c) C. He, Q. He, Y. Yi, G. Wu, F. Bai, Z. Shuai, Y. Li, J. Mater. Chem. 18 (2008) 4085.
[4] (a) M.-C. Um, J. Kwak, J.-P. Hong, J. Kang, D.Y. Yoon, S.H. Lee, C. Lee, J.-I. Hong, J. Mater. Chem. 18 (2008) 4698;
(b) M.-C. Um, J. Jang, J.-P. Hong, J. Kang, D.Y. Yoon, S.H. Lee, J.-J. Kim, J.-I. Hong, New J. Chem. 32 (2008) 2006;
(c) J.-P. Hong, A.-Y. Park, S. Lee, J. Kang, N. Shin, D.Y. Yoon, Appl. Phys. Lett. 92 (2008) 143311;
(d) J.A. Letizia, A. Facchetti, C.L. Stern, M.A. Ratner, T.J. Marks, J. Am. Chem. Soc. 127 (2005) 13476;
(e) J.-P. Hong, S. Lee, Angew. Chem., Int. Ed. 48 (2009) 3096;
(f) A. Facchetti, M. Mushrush, M.-H. Yoon, G.R. Hutchison, M.A. Ratner, T.J. Marks, J. Am. Chem. Soc. 126 (2004) 13859;
(g) M. Mushrush, A. Facchetti, M. Lefenfeld, H.E. Katz, T.J. Marks, J. Am. Chem. Soc. 125 (2003) 9414.
[5] M. Berggren, D. Nilsson, N.D. Robinson, Nature Mater. 6 (2007) 3.
[6] (a) A.K. Pandey, J.-M. Nunzi, Adv. Mater. 19 (2007) 3613;
(b) A. Cravino, P. Leriche, O. Alévêque, S. Roquet, J. Roncali, Adv. Mater. 18 (2006) 3033;
(c) J. Lu, P.F. Xia, P.K. Lo, Y. Tao, M.S. Wong, Chem. Mater. 18 (2006) 6194.
[7] (a) A. Cravino, S. Roquet, O. Alévêque, P. Leriche, P. Frère, J. Roncali, Chem. Mater. 18 (2006) 2584;

(b) F. Wang, J. Luo, K. Yang, J. Chen, F. Huang, Y. Cao, Macromolecules 38 (2005) 2253.
[8] (a) J.E. Anthony, Chem. Rev. 106 (2006) 5028;
(b) J.E. Anthony, Angew. Chem., Int. Ed. 47 (2008) 452;
(c) S. Subramanian, S.K. Park, S.R. Parkin, V. Podzorov, T.N. Jackson, J.E. Anthony, J. Am. Chem. Soc. 130 (2008) 2706;
(d) K.C. Dickey, J.E. Anthony, Y.-L. Loo, Adv. Mater. 18 (2006) 1721;
(e) M.-C. Um, J. Jang, J. Kang, J.-P. Hong, D.Y. Yoon, S.H. Lee, J.-J. Kim, J.-I. Hong, J. Mater. Chem. 18 (2008) 2234;
(f) J.-P. Hong, M.-C. Um, S.-R. Nam, J.-I. Hong, S. Lee, Chem. Commun. (2009) 310.
[9] R.J. Tseng, R. Chan, V.C. Tung, Y. Yang, Adv. Mater. 20 (2008) 435.
[10] A.S. Ionkin, W.J. Marshall, B.M. Fish, L.M. Bryman, Y. Wang, Chem. Commun. (2008) 2319.
[11] M.M. Payne, S.R. Parkin, J.E. Anthony, C.-C. Kuo, T.N. Jackson, J. Am. Chem. Soc. 127 (2005) 4986.
[12] S.A. Odom, S.R. Parkin, J.E. Anthony, Org. Lett. 5 (2003) 4245.
[13] M.A. Wolak, J. Delcamp, C.A. Landis, P.A. Lane, J. Anthony, Z. Kafafi, Adv. Funct. Mater. 16 (2006) 1943.
[14] C.D. Sheraw, T.N. Jackson, D.L. Eaton, J.E. Anthony, Adv. Mater. 15 (2003) 2009.
[15] H. Okamoto, N. Kawasaki, Y. Kaji, Y. Kubozono, A. Fujiwara, M. Yamaji, J. Am. Chem. Soc. 130 (2008) 10470.
[16] (a) B.K. Shah, D.C. Neckers, J. Shi, E.W. Forsythe, D. Morton, J. Phys. Chem. A 109 (2005) 7677;
(b) B.K. Shah, D.C. Neckers, J. Shi, E.W. Forsythe, D. Morton, Chem. Mater. 18 (2006) 603;
(c) T. Zheng, W.C.H. Choy, Adv. Funct. Mater. 20 (2010) 651–652.
[17] C.-W. Chu, Y. Shao, V. Shrotriya, Y. Yang, App. Phys. Lett. 86 (2005) 243506.
[18] S. Yoo, B. Domercq, B. Kippelen, App. Phys. Lett. 85 (2004) 5427.
[19] (a) M.T. Lloyd, A.C. Mayer, S. Subramanian, D.A. Mourey, D.J. Herman, A.V. Bapat, J.E. Anthony, G.G. Malliaras, J. Am. Chem. Soc. 129 (2007) 9144;
(b) L. Valentini, D. Bagnis, A. Marrocchi, M. Seri, A. Taticchi, J.M. Kenny, Chem. Mater. 20 (2008) 32.
[20] W.R. Dawson, M.W. Windsor, J. Phys. Chem. 72 (1968) 3255.

conductivity [8–13], roughness, mechanical strength, etc., of the vacuum deposited metal thin film. The first steps of growth of a typical and largely used noble metal like silver have been deeply investigated, showing different growth mode, like Volmer-Weber [14–17] or Stranski-Krastanov [18,19], depending on the substrate type and on the vacuum metal deposition rate.

Moreover the vacuum deposition technique can induce different growth modes, therefore thermal evaporation, RF/DC sputtering, ion-beam assisted deposition and e-beam evaporation have been investigated in the last years by numerous research teams [20–25]. The growth mode can influence the final RMS roughness of the metal thin film, as well as the other physical properties, such as the transparency or the conductivity. In particular, the growth mode associated to e-beam is very similar to that observed in thermal evaporation. In both cases the metal atoms are evaporated heating the bulk material inserted in a crucible obtaining a vapor of atoms that have a low energy and momentum. The big advantage of the e-beam deposition is that it limits the heating of the material to a small area of the bulk material avoiding problems related to the over-heating of the crucible and the possible alloying between the bulk and the crucible material. The thin films obtained with these techniques are not very dense and, in general, show a polycrystalline columnar growth. In contrast, more dense films can be obtained using sputtering or high energy deposition techniques where the ejected atoms have high energy and momentum and tend to form dense amorphous thin films. However, in these last cases small clusters of evaporated material can be projected on the thin film surface decreasing the thin film surface uniformity and increasing its roughness. Considering these aspects, the e-beam evaporation technique has been selected to obtain the thin Silver films to be used as anode in our micro-cavity OLEDs. Moreover, it has been observed by atomic force microscopy (AFM) analysis that rough surface topography of silver thin films grown with different deposition techniques is directly related with the substrate (for example, Si or SiO_2). Preliminary deposition tests of silver thin films directly on our borosilicate glass substrate highlight the high surface roughness of the thin film as well as its poor adhesion to the substrate, incompatible with the fabrication of a working OLED device. To improve this aspect, and also the adhesion properties, nucleation layers have been used on the substrates.

The aim of our investigation was to found the optimized growth condition to obtain a semi-transparent, conductive and adherent silver thin film to be used as anode of a small molecule blue emitting bottom micro-cavity OLED, based on bis-(2-methyl-8-quinolinato)-4-(phenyl-phenolato)aluminum-(III) ($BAlq_3$). By optical simulation and by resistivity and mechanical consideration [8–13], a silver thickness of 25 nm has been selected to obtain the micro-cavity spectral peak at a wavelength of 460 nm and to optimize the OLED efficiency at that wavelength. The silver anode must also present a sufficiently strong adherence on the borosilicate glass to allow the spin-coating deposition of a 40 nm hole injection poly(3,4-ethyl-enedioxythiophene)/polystyrene-sulphonate (PEDOT-PSS) layer avoiding the modification of the anode (roughness, breaks). The PEDOT-PSS layer has been used to improve hole injection by the anode. The molecular architecture of our micro-cavity OLED, implies a 60 nm thick multilayer stack (described in the Chapter 3 of this paper) beside the 40 nm PEDOT-PSS layer that leads to a very high sensitivity to short circuit induced by Ag surface spikes or roughness.

In this paper, we present the optimization of thin film deposition of a 25 nm thick silver film on cleaned borosilicate glass using different nucleation layers (Cr, Ge and a-C:H). The deposition rates of both the nucleation and silver layers can be modified by tuning the process parameters.

To measure the surface roughness of the different thin Ag films with and without PEDOT-PSS layer over large areas, of the order of 1 mm^2, a high resolution white-light interferometer based optical profiler has been used instead of an AFM that only allows the measure of very small surface ($100 \times 100\ \mu m^2$). Surface morphology investigations of the same samples have also been performed using a field emission gun scanning electron microscope (FEG-SEM).

The PEDOT-PSS layer deposition effect on the total surface roughness has been measured for all different bi-layers (Cr/Ag, a-C:H/Ag and Ge/Ag) deposited at different rates. In particular, the deposition conditions of an optimized Ag surface with a 40 nm PEDOT-PSS over-layer presents a very smooth surface and does not exhibit significant spikes (higher than 8.3 nm) over a large measured surface of 1 mm^2, have been identified.

2. Experimental

For this experiment high quality polished borosilicate glass substrates of 1 mm thick have been used. Before coating the samples with the different nucleation layers, an ultrasonic cleaning with organic solvents (acetone, iso-propanol and ethyl alcohol) and de-mineralized water in a class 10 clean-room has been performed on each substrate. All samples have then been dried with nitrogen. After cleaning, the samples have been transferred in different vacuum chambers for the deposition of the nucleation layers of 5 nm thick, the choice of this thickness being driven by adherence improvement requirements, selected during previous tests. Different high vacuum deposition techniques have been used:

- Pure chromium (99.999%) thin film of 5 nm was thermally evaporated in a VEECO evaporator at a pressure of 2×10^{-4} Pa and a deposition rate of 0.04 nm/s.
- Multi-polar microwave plasma excited at distributed electron cyclotron resonance (MMP-DECR) was used in this work for hydrogenated amorphous carbon (a-C:H) deposition. The plasma reactor is described in the literature [26]. Methane gas was injected through a mass flow controller with a rate of 7.4 sccm and the working pressure was set at 0.1 Pa. The microwave power was 400 W. In order to obtain a homogeneous 5 nm thick a-C:H thin film, the deposition time lasted 2 min.
- Pure germanium (99.999%) was deposited by electron beam-technique in a BOC EDWARDS 500 evaporator. Two different evaporation rates of 0.01 nm/s (low rate

deposition) and 0.2 nm/s (high rate deposition) have been used for the germanium thin film evaporation. During both evaporations the pressure was maintained at 5×10^{-4} Pa.

Pure silver (99.999%) was evaporated at 0.05 or 1.1 nm/s on the nucleation layers by electron-beam deposition in a BOC EDWARDS 500 evaporator. A silver film was first evaporated with a deposition rate of 0.05 nm/s on glass substrates previously coated with chromium, hydrogenated amorphous carbon and low rate deposited germanium. A second silver evaporation was realized with a deposition rate of 1.1 nm/s on samples with chromium, hydrogenated carbon and high rate deposited germanium. For all the samples the silver film thickness was 25 nm, as monitored by a calibrated quartz microbalance; during depositions the pressure was maintained at 5×10^{-4} Pa. All evaporations have been performed at ambient temperature and no post-processing have been done on the prepared samples. For each different nucleation layer, two samples were prepared. The first ones were used to analyze the Ag deposition, the second ones were coated with a 40 nm layer of PEDOT-PSS, using a spin-coating process. The PEDOT-PSS was deposited at a speed of 2500 rpm for 30 s in the clean room. After the PEDOT-PSS coating, the samples were annealed at 100 °C in air atmosphere for 5 min.

The surface morphology of the samples has then been investigated with two different techniques. Roughness measurements have been carried out with a noncontact white-light interferometer precision optical profiler WYKO NT3000, using the instrument in Phase Shifting Interferometry (PSI) mode. The PSI measurements mode allows to obtain a vertical resolution as high as 0.3 nm. A 5× objective has been used to measure a 1 mm^2 sample surface. For each sample, mean roughness (R_a), root mean square roughness (R_q) and maximum peak-to-valley height of the surface (R_t) have been determined over probed surface.

A JEOL JSM 6700 F field emission gun scanning electron microscope has also been used to image the samples surface with a resolution of 1 nm at 15 kV and 2.2 nm at 1 kV. The samples coated with PEDOT-PSS were metalized with less than 1 nm of platinum before being observed. All the samples were cleaved and the measures were carried out with a base voltage of 5 kV.

3. Results and discussion

The roughness parameters, measured with the optical profiler, of the thin Ag films (over coated or not by the 40 nm PEDOT-PSS layer) deposited on different nucleation layers are reported in Table 1, as function of the deposition rate of the Ag thin films. R_a is the most common parameter to characterize a surface but R_q provide information about roughness heterogeneity over surface. Therefore, a small difference between the R_a and R_q values indicates a low spike density and, in general, a more uniform surface. R_t represents the distance between higher peak and lower valley and provides information about spikes height, but this value represents a point and not a statistical value, opposite to the first two. Considering the most significant roughness parameters, R_a and R_q, it is evident from the table that the surface roughness depends on the nucleation layer in the following way: Cr > a-C:H > Ge, for both low and high deposition rates.

Moreover in all measured samples the micro-roughness shows a dependence from the deposition rate. In particular, independently of the nucleation layer, the Ag films deposited with a high rate present a smoother surface, as can be seen from Figs. 1 and 2, where the 3D surface profile of the low (0.05 nm/s) and high (1.1 nm/s) deposition rate Ag films on the nucleation layers are reported together with the histograms of their surface height distributions.

The silver thin film growth on different nucleation layers has been ascribed by several authors [11,28–31] to an heterogeneous nucleation process. So, the surface smoothing observed using a high rate deposition can be explained by some consideration on heterogeneous nucleation in the first phases of thin film growth. The heterogeneous nucleation is governed by the following rules:

$$\left[\frac{\partial \Delta G^*}{\partial T}\right]_R > 0 \qquad \left[\frac{\partial r^*}{\partial T}\right]_R > 0 \quad \text{and}$$

$$\left[\frac{\partial \Delta G^*}{\partial R}\right]_T < 0 \qquad \left[\frac{\partial \Delta G^*}{\partial R}\right]_T < 0$$

where ΔG^* is the volume critical free energy, r^* is the critical radius for heterogeneous nucleation, T is the temperature and R is the deposition rate. Typically higher temperatures lead to larger r^* and subsequently larger ΔG^*. Consequently the barrier for nucleation is higher at

Table 1
The roughness measured values of the Ag evaporated surfaces are presented in this table. The measurements have been performed with a WYKO NT 3000 optical profiler; the values of R_a (arithmetic average roughness), R_q (root mean square roughness) and R_t (peak to valley) are listed, expressed in nm. The thickness of the Cr, a-C:H and Ge nucleation layers has been set to 5 nm each. The values obtained both at low (0.05 nm/s) and high (1.1 nm/s) deposition rates are here compared. For both deposition rates, the surfaces have been measured without and with the over-coating of a 40 nm PEDOT-PSS layer.

Low rate (0.05 nm/s)						High rate (1.1 nm/s)					
Without PEDOT			With PEDOT			Without PEDOT			With PEDOT		
R_a	R_q	R_t	R_a	R_q	R_t	R_a	R_q	R_t	R_a	R_q	R_t
Cr/Ag											
0.59	0.74	7.60	0.67	0.95	41.46	0.46	0.58	6.77	0.61	0.77	10.75
a-C:H/Ag											
0.50	0.64	7.68	0.93	1.17	14.26	0.39	0.50	10.88	0.70	0.88	12.82
Ge/Ag											
0.40	0.50	7.85	0.57	0.72	9.02	0.33	0.41	3.78	0.49	0.62	8.34

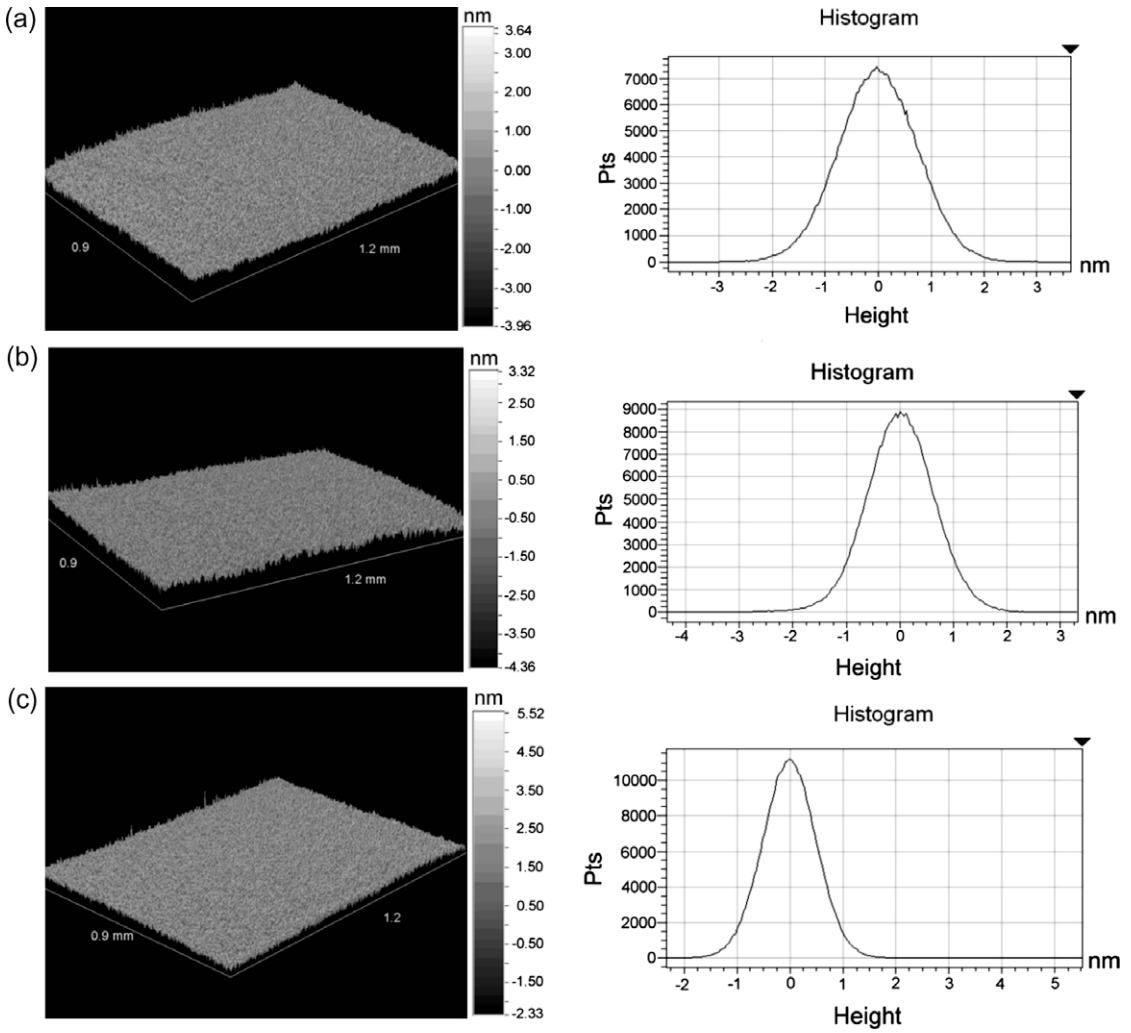

Fig. 1. 3D surface profile of the Ag low rate (0.05 nm/s) evaporated surfaces measured by WYKO NT3000 in PSI mode and histograms of the height distribution, measured in nm, over the measured surface of $1.2 \times 0.9\ mm^2$ (image size: 736×480, step size of 1.65 μm): (a) 5 nm chromium and 25 nm silver, (b) 5 nm hydrogenated amorphous carbon and 25 nm silver, and (c) 5 nm germanium and 25 nm silver.

higher temperature which leads to a decrease in N^* (larger and fewer grains). Once more, higher deposition rates lead to lower r^* and, subsequently, lower ΔG^*. Consequently the barrier for nucleation is reduced at higher evaporation rates which leads to an increase of N^* (i.e. smaller, more numerous grains).

SEM images reported in Figs. 3a and c & 4a and c show that the nucleation of Ag on Cr and a-C:H nucleation layers starts from isolated Ag clusters. The morphology of the Ag surface over Cr and a-C:H nucleation layers presents large voids and isolated islands that are denser for the samples grown at high evaporation rate confirming that high rate imply a larger number of nucleation sites and, consequently, an earlier silver coalescence with a reduced surface roughness. This is also evident considering that the differences between the R_a and R_q values, reported in Table 1, are always smaller in the case of high rate deposition. This implies a higher surface homogeneity over a large area, as measured by the optical profiler.

Silver, and in general the noble metals, has been reported [13,28–30] to grow on oxidized surfaces in 3D island mode. Cr is easily oxidized when extracted from the evaporator and then the successive growth is governed by the accumulation of Ag atoms by surface diffusion and coalescence into large three dimensional clusters (Volmer-Weber growth mode). In contrast, a-C:H layers can not be as oxidized as Cr [32]. It suggests that Ag growth on a-C:H layer is controlled by another process.

The morphology of Ag thin film grown on a Ge nucleation layer, shown in Fig. 5a and c, appears to be different from the first two. In particular, it is possible to note that even if the silver film grows from Volmer-Weber mechanisms, the grain texture is smaller and the grain density is much higher than in the previous cases. No voids can be observed between adjacent grains that form a dense columnar continuous Ag film with high grain density and a smooth surface. Also in this case the high rate deposited film has a lower roughness than the low rate one, as it can

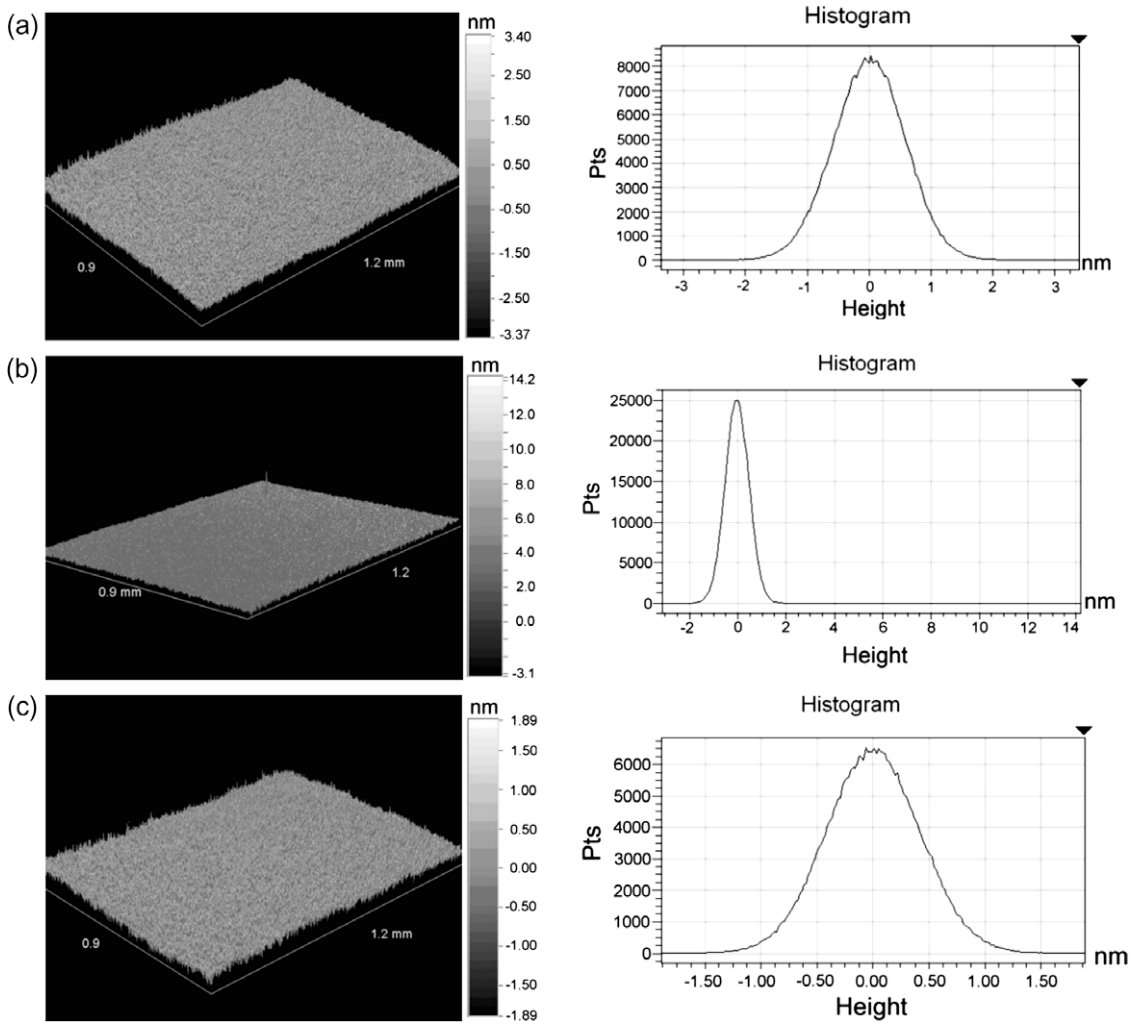

Fig. 2. 3D surface profile of the Ag high rate (1.1 nm/s) evaporated surfaces measured by WYKO NT3000 in PSI mode and histograms of the height distribution, measured in nm, over the measured surface of 1.2×0.9 mm^2 (image size: 736×480, step size of 1.65 μm): (a) 5 nm chromium and 25 nm silver, (b) 5 nm hydrogenated amorphous carbon and 25 nm silver, and (c) 5 nm germanium and 25 nm silver.

be seen from Table 1. In the low rate deposition Ge/Ag film it is possible to observe, from Fig. 5a, the growth of some tenths nanometer large Ag grains over the smooth under layer. These Ag grains induce a slight increase in surface roughness over large area.

A possible explanation to the significantly different surface morphologies observed in the Ge/Ag bi-layer is the strong affinity of Ag and Ge. It is known that, in certain Ag concentration [33,34] and at room temperature, an amorphous alloy of Ag and Ge could be formed in the very first stage of Ag evaporation on Ge. In our experimental condition this effect is possible considering that the eutectic temperature of an Ag/Ge alloy is 924 °C and that the evaporation temperature of the Ag is 958 °C at a pressure of 10^{-4} Pa. However, as reported by Randhawa et al. [35,36], the Silver largest content which could form the homogeneous amorphous phase deposited at room temperature for the Ge/Ag alloy is around 12%. With increasing the silver content, very fine Ag crystalline grains are observed, their density being dependent on the silver content and therefore on the film deposition rate. Therefore, we suppose that in our case the growth of polycrystalline silver thin film is preceded by an initial Ge/Ag alloy homogeneous amorphous layer, the thickness of which amounts only few nm. On the contrary the immiscibility of Cr/Ag in terms of characteristic of electronic structures of constituent metals is well known and a possible metastable Cr/Ag alloy is possible only after a thermal annealing, which was not performed in our case. The same holds also for the a-C:H/Ag bi-layer. In the last two cases the coalescence of the 3D Ag crystalline grains formed at the Ag/nucleation layer interface is retarded (coalescence thickness of 10 nm) as compared to the Ge/Ag case where there is a coalescence evidence at a silver film thickness of 5 nm, as confirmed by mechanical profilometer and ellipsometric measurements that will be discussed elsewhere. Also the morphology of the 40 nm thick PEDOT-PSS film deposited on the different Ag surfaces is strongly dependent on the

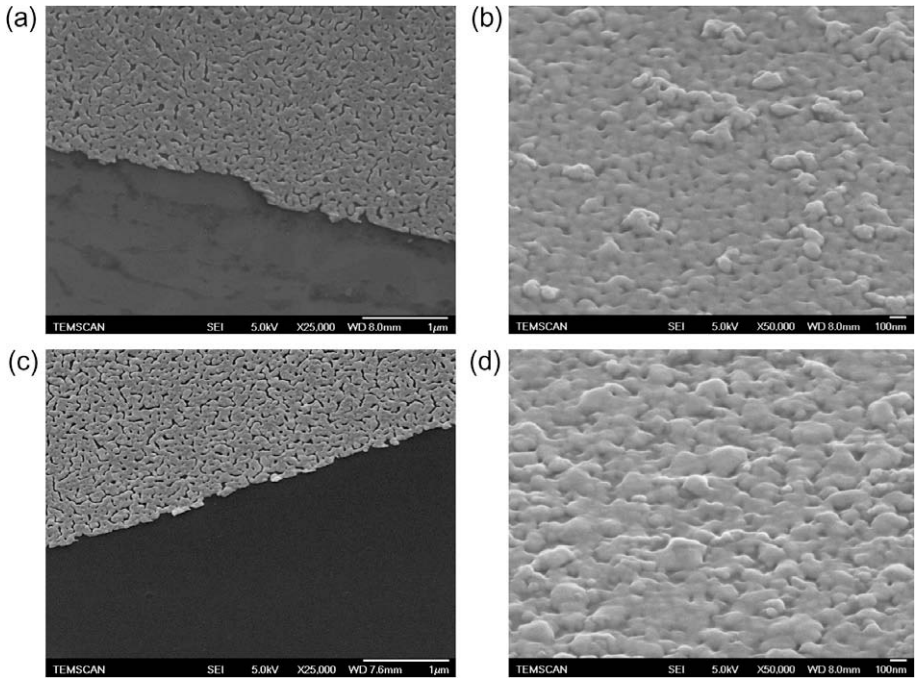

Fig. 3. FEG-SEM images of the surface morphology of the Cr/Ag evaporated bi-layer with and without a 40 nm PEDOT-PSS over-layer: (a) 5 nm Cr and 25 nm Ag evaporated at low rate (0.05 nm/s) without PEDOT-PSS, (b) 5 nm Cr and 25 nm Ag evaporated at low rate (0.05 nm/s) with PEDOT-PSS layer, (c) 5 nm Cr and 25 nm Ag evaporated at high rate (1.1 nm/s) without PEDOT-PSS layer, (d) 5 nm Cr and 25 Ag evaporated at high rate (1.1 nm/s) with PEDOT-PSS layer. ((a) and (c) Magnification 25,000× and (b) and (d) magnification 50,000×, 5 kV acceleration voltage).

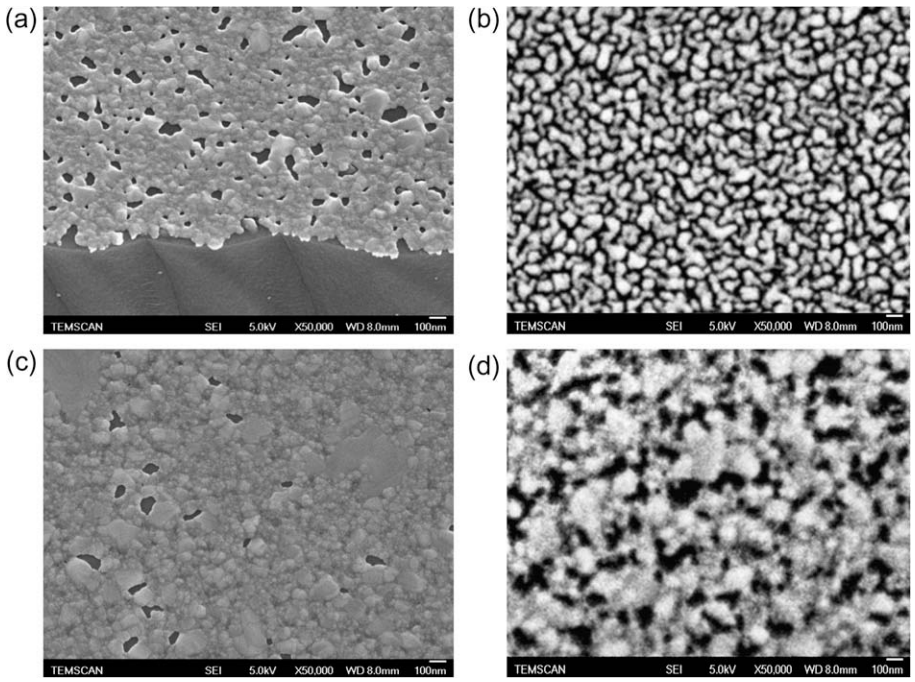

Fig. 4. FEG-SEM images of the surface morphology of the a-C:H/Ag evaporated bi-layer with and without a 40 nm PEDOT-PSS over-layer: (a) 5 nm a-C:H and 25 nm Ag evaporated at low rate (0.05 nm/s) without PEDOT-PSS, (b) 5 nm a-C:H and 25 nm Ag evaporated at low rate (0.05 nm/s) with PEDOT-PSS layer, (c) 5 nm a-C:H and 25 nm Ag evaporated at high rate (1.1 nm/s) without PEDOT-PSS layer, (d) 5 nm a-C:H and 25 Ag evaporated at high rate (1.1 nm/s) with PEDOT-PSS layer. (Magnification 50,000× and 5 kV acceleration voltage).

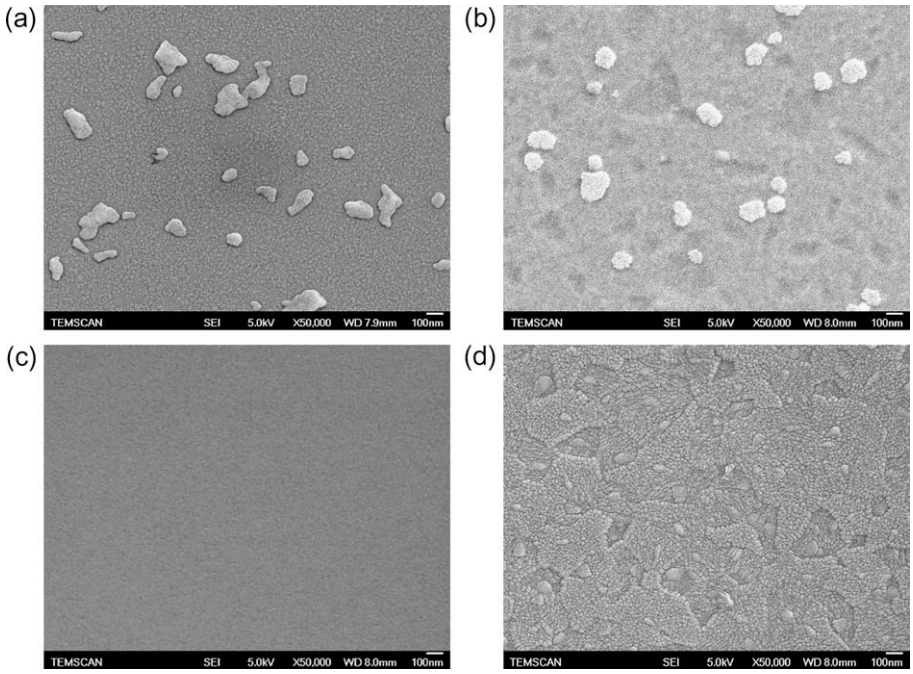

Fig. 5. FEG-SEM images of the surface morphology of the Ge/Ag evaporated bi-layer with and without a 40 nm PEDOT-PSS over-layer: (a) 5 nm Ge and 25 nm Ag evaporated at low rate (0.05 nm/s) without PEDOT-PSS, (b) 5 nm Ge and 25 nm Ag evaporated at low rate (0.05 nm/s) with PEDOT-PSS layer, (c) 5 nm Ge and 25 nm Ag evaporated at high rate (1.1 nm/s) without PEDOT-PSS layer, (d) 5 nm Ge and 25 Ag evaporated at high rate (1.1 nm/s) with PEDOT-PSS layer. (Magnification 50,000× and 5 kV acceleration voltage).

nucleation layer, as it can be seen from the SEM images reported in Figs. 3b and d, 4b and d, & 5b and d. This effect is observable also in the surface roughness values (Table 1): in contrast with what is measured for Ag on nucleation layer, the PEDOT-PSS layer roughness is more important on a-C:H/Ag than in Cr/Ag. As can be seen in Figs. 3b and d & 4b and d, on Cr/Ag and on a-C:H/Ag surfaces the voids are not completely filled by the polymer and some small PEDOT-PSS aggregates appear on the surface. In the case of Ge/Ag films, where the surface previous to the PEDOT-PSS coating is more uniform, a smooth 2D PEDOT-PSS distribution is clearly observable (Fig. 5b and d). Also in this case, it is possible to note the aggregation of smaller PEDOT-PSS grains. The higher planarity of the Ge/Ag surfaces is maintained, also with a slight worsening of the total roughness. It is evident that in all cases the PEDOT-PSS deposition is not smoothing the surfaces but it leads to a slight worsening of the micro-roughness, probably due to the centrifugal force applied during the spin-coating process. The latter may induce accumulation of polymer near the spikes of the Ag surface. This effect could depend on the different PEDOT-PSS surface wettability of the Ag surfaces grown on the different nucleation layers. So, an investigation of surface wettability and surface energy of the different bi-layers has been carried out as well. These measurements, performed with a contact angle DIGI-DROP (GBX-Instrumentation) instrument, will be discussed more extensively elsewhere, but a PEDOT-PSS wettability dependence on the nucleation layer has been found with the following result: Ge > Cr > a-C:H. Moreover, the Ag film grown on Ge nucleation layer at high rate presents the higher water and PEDOT-PSS wettability with a contact angle of 15.6° and 22.8°, respectively.

The Ag thin films, grown on different nucleation layers and coated with the 40 nm PEDOT-PSS layer, were then used as anode for a blue emitting small molecule based bottom micro-cavity OLED fabrication. The following molecular architecture has been used to produce the samples: nucleation layer [5 nm], Ag [25 nm], PEDOT-PSS [40 nm], a-NPB (*N*,*N*′-bis(naphthalene-1y1)-*N*,*N*′-bis(phenyl)benzidine) [20 nm], $BAlq_3$ (bis-(2-methyl-8-quinolinato)-4-(phenyl-phenolato)aluminum-(III)) [40 nm], LiF [0.7 nm] and Al [100 nm]. The total thickness of the organic layers is rather small, so the emitting device is prone to short circuits.

In order to fabricate the OLED samples a mask with four circles of different diameters (1, 2, 4 and 6 mm, respectively) has been used. The OLED have been fabricated by thermal evaporation from Knudsen cells under high vacuum condition ($<10^{-4}$ Pa) in the same evaporation chamber used to prepare the Ag anode (BOC EDWARDS 500). The final samples have then been encapsulated in a pure nitrogen filled glove box directly connected with the evaporation chamber.

The OLED samples prepared with the Cr/Ag and a-C:H/Ag, both at high and low rate, presented short circuits distributed all over the whole surface and it was not possible to switch them on. The use of the bi-layer Ge/Ag anode deposited at low rate allows to obtain only very unstable devices of small dimension (not more than 1 mm diameter) with a very short lifetime and prone to short circuit formation after the voltage application. But the samples

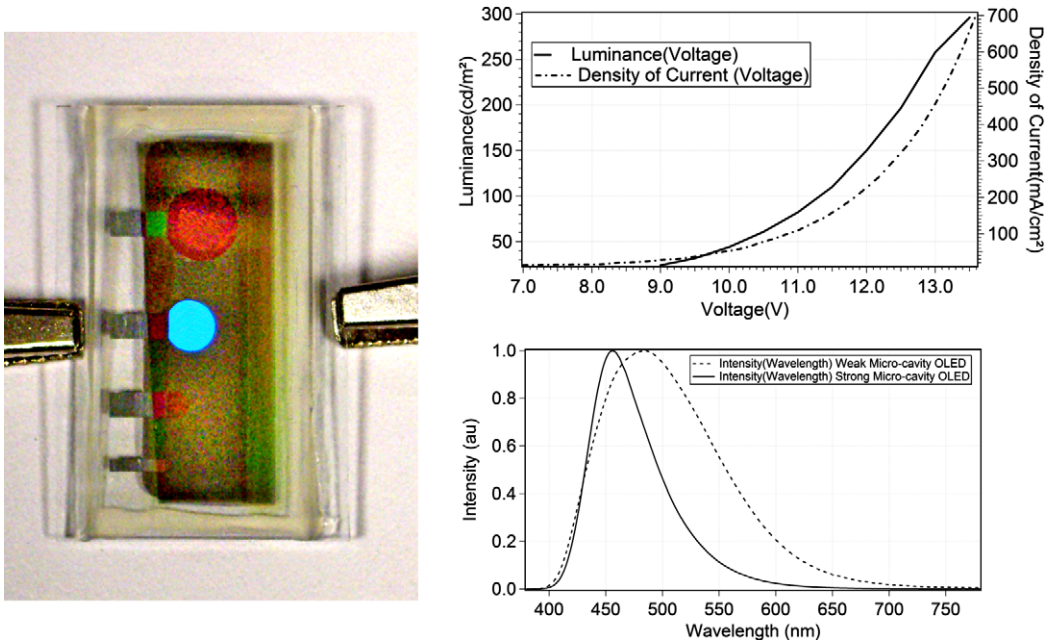

Fig. 6. Left: picture of a bottom blue emitting micro-cavity OLED fabricated over a 5 nm Ge and 25 Ag bi-layer anode evaporated at high rate (1.1 nm/s) on a borosilicate glass substrate. The lighting device is based on fluorescent $BAlq_3$ emitting layer and has a 4 mm diameter. Right: upper graph *L–V* and *J–V* curves of the imaged device, recorded with a source meter specifically developed at LAPLACE laboratory. Bottom graph: comparison of the spectral emissions of the strong micro-cavity (Ag anode – full line) and the weak micro-cavity (ITO anode – dashed line) OLED devices, measured at normal incidence with a Minolta CS-1000 spectrophotometer. For the strong micro-cavity OLED the peak wavelength is at 459 nm with a FWHM of 55 nm, for the weak micro-cavity OLED the peak wavelength is at 485 nm with a FWHM of 123 nm.

fabricated using the Ge/Ag deposited at high rate showed a very interesting behavior. No short circuits were evident in the first three devices (1, 2 and 4 mm diameter), the emitting surfaces were very uniform and the switching voltage at 1 cd/m^2 was at 8.9 V, comparable (V = 8.8 V) with that obtained using the same molecular architecture and a commercial ITO anode (thickness = 120 nm with a sheet resistance of ≈20 Ω/□). A picture of the 4 mm diameter device with the *J–V* and *L–V* curves, measured in air, is shown in Fig. 6. In the same figure, the spectral emission of the Ag based micro-cavity OLED (strong micro-cavity) and that of the device fabricated using an ITO anode (weak micro-cavity) are compared. The strong micro-cavity peak wavelength is at 459 nm and the spectrum is quite narrow (FWHM of 55 nm), confirming the simulated micro-cavity effect, while the weak micro-cavity OLED peak wavelength is at 485 nm with a FWHM of 123 nm. The luminous efficiencies (LE) of both devices are quite low, but comparable with that of literature reported devices fabricated with fluorescent emitters with similar spectral emission [37]. In particular, the weak-micro-cavity device presented a LE = 1 cd/A at a luminance of 100 cd/m^2 while the strong micro-cavity OLED exhibit a LE = 0.35 cd/A, at the same luminance. The difference in LE can be ascribed to the photopic response which is much weaker in the blue region of the spectrum. Our micro-cavity OLEDs are envisaged for a particular application, where only the normal viewing angle is important, so the luminance has been measured only at normal incidence. Several OLED samples using the Ge/Ag with high deposition rate anode have been fabricated with a good repeatability and with a long lifetime (more than 1500 h at a luminance of 100 cd/m^2).

A different method of Silver OLED anode fabrication for both top and bottom emission devices with good injection properties has been reported in literature [38,39]. However, in this latter case a modification of the Ag anode surface with a CF_x plasma treatment is required to improve the hole injection, making the fabrication process quite complicated and expensive. In our case, the very simple fabrication method and the absence of post-processing make the silver based bi-layer anode very interesting for application in bottom micro-cavity OLED devices, also for relatively large area, due to its small roughness and to the very low significant spikes density.

4. Conclusion

A systematic investigation on roughness smoothing of a thin film Ag based OLED micro-cavity anode has been performed using different nucleation layer and deposition rates. A very accurate surface morphology investigation, based on a white-light interferometry optical profiler and on a field emission gun scanning electron microscope, on vacuum deposited bi-layers have indicated that high rate (1.1 nm/s) deposition of silver films allows to obtain smoother surfaces on all the nucleation layers used in this study (Cr, a-C:H and Ge). In particular, an optimized silver anode obtained using a 5 nm Ge nucleation layer and a high Ag (1.1 nm/s) deposition rate has been successfully used to obtain a long lifetime,

large area (12.5 mm^2) and short circuit free blue emitting bottom OLED micro-cavity.

Acknowledgments

The authors would like to thanks for the valuable discussions Prof. Maya Kiskinova of Sincrotrone Trieste, Trieste (Italy). We are also grateful to Mr. Benoit Schlegel of Service Instrumentation-LAPLACE, Univ. Paul Sabatier, Toulouse (France) for the Chromium deposition and to "Lumière et Matière" group of the LAPLACE for the support in the research activities.

References

[1] H. Ishii, T. Minotani, T. Nagatsuma, K. Kudou, M. Yano, K. Machida, Tech. Dig. Sens. Symp. 20 (2003) 259–262.
[2] X. Hong, F.J. Kao, Appl. Opt. 43 (14) (2004) 2868–2873.
[3] C.W. Wong, P.T. Rakich, S.G. Johnson, M. Qi, H.I. Smith, E.P. Ippen, L.C. Kimerling, Y. Jeon, G. Barbastathis, S.G. Kim, Appl. Phys. Lett. 84 (8) (2004) 1242–1244.
[4] S. Juodkazis, A. Yamaguchi, H. Ishii, S. Matsuo, H. Takagi, H. Misawa, Jpn. J. Appl. Phys. 40 (2001) 4246–4251.
[5] M. Rill, C. Plet, M. Thiel, M. Wegener, Quantum Electronics and Laser Science Conference (QELS), May 4, San Jose, California, 2008.
[6] V. Poborchii, T. Tada, T. Kanayama, A. Moroz, Appl. Phys. Lett. 82 (4) (2003) 508–510.
[7] D.M. Koller, A. Hohenau, H. Ditlbacher, N. Galler, F.R. Aussenegg, A. Leitner, J.R. Krenn, S. Eder, S. Sax, E.J.W. List, Appl. Phys. Lett. 92 (2008) 103304.
[8] K. Schröder, J. Hollander, Thin Solid Films 458 (2004) 322–324.
[9] P. Wißmann, H.U. Finzel, Electrical Resistivity of Thin Metal Films, Springer-Verlag, Berlin, Heidelberg, 2007 (Chapter 3).
[10] N. Artunç, M.D. Bilge, G. Utlu, Surf. Coat. Technol. 201 (2007) 8377–8381.
[11] V.J. Logeeswaran, N.P. Kobayashi, M. Saif Islam, W. Wu, P. Chaturvedi, N.X. Fang, S.Y. Wang, R.S. Williams, NanoLetters 9 (1) (2009) 178–182.
[12] V.J. Logeeswaran, M.L. Chan, Y. Bayam, M. Saif Islam, D.A. Horsley, X. Li, W. Wu, S.Y. Wang, R.S. Williams, Appl. Phys. A 87 (2007) 187–192.
[13] A. Anders, E. Byon, D.H. Kim, K. Fukuda, S.H.N. Lim, Solid State Commun. 140 (2006) 225–229.
[14] K. Kushida, K. Hattori, S. Arai, T. Iimori, F. Komori, Surf. Sci. 442 (1999) 300–306.
[15] C.V. Thompson, Stress Evolution During Volmer-Weber Growth of Thin Films. <http://www.icf11.com/proceeding/EXTENDED/5678.pdf>.
[16] E. Placidi, M. Fanfoni, F. Arciprete, F. Patella, N. Motta, A. Balzarotti, Mater. Sci. Eng. B 69–70 (2000) 243–246.
[17] L.H. Chan, E.I. Altman, Surf. Sci. 511 (2002) 229–239.
[18] F. Komori, K. Kushida, K. Hattori, S. Arai, T. Iimori, Surf. Sci. 438 (1999) 123–130.
[19] S.G. Corcoran, G.S. Chakarova, K. Sieradzki, Phys. Rev. Lett. 71 (10) (1993) 1585–1588.
[20] N. Maréchal, E. Quesnel, Y. Pauleau, J. Vac. Sci. Technol. A 12 (3) (1994) 707–713.
[21] D.L. Allara, A.F. Hebard, F.J. Padden, R.G. Nuzzo, D.R. Falcone, J. Vac. Sci. Technol. A. 1 (2) (1983) 376–382.
[22] S. Kundu, S. Hazra, S. Benerjee, M.K. Sanyal, S.K. Mandal, S. Chaudhuri, A.K. Pal, J. Phys. D: Appl. Phys. 31 (1998) L73–L77.
[23] K.L. Jonas, V. Von Oeynhausen, J. Bansmann, K.H. Meiwes-Broer, Appl. Phys. A 82 (2006) 131–137.
[24] S.S. Todorov, H. Bu, K.J. Boyd, J.W. Rabalais, C.M. Gilmore, J.A. Sprague, Surf. Sci. 429 (1) (1999) 63–70.
[25] Jing Lv, Fachun Lai, Limei Lin, Yongzhong Lin, Zhigao Huang, Rong Chen, Appl. Surf. Sci. 253 (2007) 7036–7040.
[26] M. Calafat, D. Escaich, R. Clergereaux, P. Raynaud, Y. Segui, Appl. Phys. Lett. 91 (2007) 81502.
[28] M. Hu, S. Noda, H. Komiyama, Surf. Sci. 513 (2002) 530.
[29] M. Ohring, Materials Science of Thin Films. Deposition and Structure, second ed., Academic Press, San Diego, 2002.
[30] C.T. Campbell, Surf. Sci. Rep. 27 (1997) 1.
[31] G. Rossi, I. Abbati, L. Braicovich, I. Lindau, W.E. Spicer, Phys. Rev. B 25 (1982) 3619–3626.
[32] R. Clergereaux, D. Escaich, S. Martin, F. Gaillard, P. Raynaud, Thin Solid Films 482 (1–2) (2005) 216–220.
[33] Z. Renji, L. Li, W. Ziquin, J. Mater. Sci. 28 (1993) 1705–1724.
[34] H. Oughaddou et al., Phys. Rev. B 62 (24) (2000).
[35] H.S. Randhawa, L.K. Malhatra, K.L. Chopra, J. Appl. Phys. 49 (1978) 4294.
[36] H.S. Randhawa, P. Nath, L.K. Malhatra, K.L. Chopra, Solid State Commun. 21 (1976) 73.
[37] H. Suh, Y. Jin, S. Song, C. Yoo, J. Kim, Proc. SPIE 6655 (2007) 66550A.
[38] H.J. Peng, X.L. Zhu, J.X. Sun, X.M. Yu, M. Wong, H.S. Kwok, SID 05 Digest 22.3 (2005) 1066–1069.
[39] H.J. Peng, J.X. Sun, X.L. Zhu, X.M. Yu, M. Wong, H.S. Kwok, Appl. Phys. Lett. 88 (2006) 073517.

pioneering works [13–17] based on this formalism, which are very interesting from the theoretical as well as experimental point of view.

Several *ab initio* methods [18–21] are there which may be utilized to study electron transport properties through molecular junctions. At the same time, tight-binding model has been extended to density functional theory (DFT) for transport calculations [22]. But in case of molecular systems, the investigations based on this theory (DFT) have some quantitative discrepancies compared to the experimental predictions. Moreover, these *ab initio* theories are computationally very expensive. To avoid this we do model calculations by using a simple tight-binding framework.

In the present article we do a theoretical study of multi-terminal electron transport through a single phenalenyl molecule [23,24] attached to semi-infinite one-dimensional (1D) metallic leads. We do numerical calculations based on single particle Green's function formalism [25,26] to evaluate conductance, reflection probability and current–voltage characteristics. Quite interestingly, we show that the positions where the leads are connected to the molecule as well as the presence of other leads have eloquent effects on these transport properties. Moreover, these characteristics are also influenced significantly by the molecule-to-lead coupling strengths. These aspects can be utilized in designing nanoelectronic devices.

We organize the paper as follows. With a brief introduction (Section 1), in Section 2 we describe our model and the theoretical background. Results are analyzed in Section 3. Finally we conclude our results in Section 4.

2. Model and a view of theoretical formulation

In this section we focus our attention on the systems where a single phenalenyl molecule is attached symmetrically or asymmetrically to semi-infinite 1D metallic leads through thiol (SH bond) groups. The models are shown schematically in Fig. 1(a)–(c) where, the number of leads attached to the molecule is 2–4, respectively. To evaluate the conductance (g) and current (I) through this single molecular system we adopt the Green's function technique. For this, first we define the Green's function for the whole system as,

$$G = (E - H)^{-1} \tag{1}$$

where $E = \epsilon + i\eta$ with η arbitrarily very small number which can be set as zero in the limiting approximation. ϵ is the injecting electron energy. H is the Hamiltonian of the entire system which is of infinite dimension. So, the above equation deals with the inversion of an infinite dimensional matrix corresponding to the system consisting of a finite size molecule and semi-infinite leads. However, the full Hamiltonian can be partitioned into sub-matrices that correspond to the individual sub-systems like,

$$H = H_M + \sum_{p=1}^{N} \left(H_p + H_{pM} + H_{pM}^{\dagger} \right) \tag{2}$$

where H_M and H_p are the Hamiltonians of the molecule and lead-p, respectively. N is the number of leads to which the molecule is attached. H_{pM} represents the coupling matrix that will be non-zero only for the adjacent points in the molecular system (molecule with sulfur atoms) and the lead-p. Here all the leads are treated on an equal footing. Within the non-interacting picture, the tight-binding Hamiltonian of the molecular system can be manifested as,

$$H_M = \sum_i \epsilon_i c_i^{\dagger} c_i + \sum_{\langle ij \rangle} t \left(c_i^{\dagger} c_j + c_j^{\dagger} c_i \right) \tag{3}$$

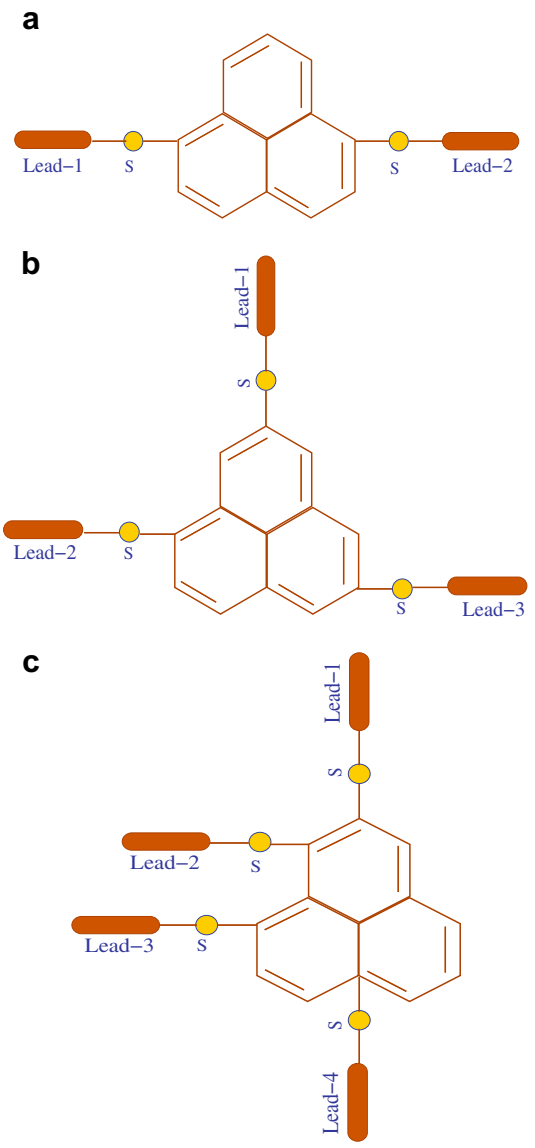

Fig. 1. Multi-terminal quantum system. A phenalenyl molecule is attached symmetrically or asymmetrically to semi-infinite 1D metallic leads through thiol (SH bond) groups in the chemisorption technique where sulfur (S) atoms reside and hydrogen (H) atoms remove. The filled yellow circles correspond to the location of S atoms. The number of leads attached to the molecule is 2, 3 and 4 as shown in (a), (b) and (c), respectively. Leads are denoted by lead-1, lead-2, lead-3 and lead-4. (For interpretation of the references to color in this figure legend, the reader is referred to the web version of this article.)

where ϵ_i is the on-site energy, t is the nearest-neighbor hopping integral and $c_i^\dagger$ (c_i) is the creation (annihilation) operator of an electron at the site i. Each lead can be described by using a similar kind of tight-binding Hamiltonian, as given in Eq. (3), characterized by two parameters ϵ_0, the on-site potential and t_0, the nearest-neighbor hopping integral.

Following the partition of the Hamiltonian, the Green's function can also be partitioned into sub-matrices and the effective Green's function for the molecular system can be indited (using Lowdin's partitioning technique [27,28]) as,

$$G_M = \left(E - H_M - \sum_{p=1}^{N} \Sigma_p\right)^{-1} \tag{4}$$

where Σ_p is the self-energy due to the coupling of the molecular system to the lead-p. It is straightforward to obtain an explicit expression for self-energy corresponding to lead-p,

$$\Sigma_p = H_{pM}^\dagger G_p H_{pM} \tag{5}$$

where $G_p = (E - H_p)^{-1}$ is the Green's function of lead-p. All the coupling informations are inscribed into this self-energy expression. Once the Green's function is established, the coupling function Γ_p can be easily obtained from the equation [29,30],

$$\Gamma_p(E) = i\left[\Sigma_p^r(E) - \Sigma_p^a(E)\right] \tag{6}$$

where the advanced self-energy Σ_p^a is the Hermitian conjugate of the retarded self-energy Σ_p^r. Thus, we can write,

$$\Gamma_p = -2\mathrm{Im}(\Sigma_p^r) \tag{7}$$

In order to evaluate the conductance for the multi-terminal quantum system, we use the Büttiker formalism [29], valid at much low temperature and bias voltage, in the form,

$$g_{pq} = \frac{2e^2}{h} T_{pq} \tag{8}$$

where T_{pq} is the transmission probability of an electron across the molecular system from the lead-p to lead-q and it is related to the reflection probability by the equation,

$$R_{pp} + \sum_{q(\neq p)} T_{qp} = 1 \tag{9}$$

which is obtained from the condition of current conservation [31]. Now, this transmission probability can be expressed in terms of the effective Green's function of the molecular system and molecule-to-lead coupling as,

$$T_{pq} = \mathrm{Tr}\left[\Gamma_p G_M^r \Gamma_q G_M^a\right] \tag{10}$$

where G_M^r and G_M^a are the retarded and advanced Green's functions of the molecular system, respectively. Γ_p and Γ_q represent the couplings of the molecule to the lead-p and lead-q, respectively. Since the coupling matrix H_{pM} is non-zero only for the adjacent points, n and m, the transmission probability becomes [32],

$$T_{pq} = 4\Delta_p(nn)\Delta_q(mm)|G_M(nm)|^2 \tag{11}$$

where $\Delta_p(nn) = \langle n|\Delta_p|n\rangle, \Delta_q(mm) = \langle m|\Delta_q|m\rangle, G_M(nm) = \langle n|G_M|m\rangle$ and Δ_p, Δ_q are the imaginary parts of Σ_p and Σ_q, respectively.

In case of two-terminal system [33], Eq. (8) becomes quite simpler like,

$$g = \frac{2e^2}{h} T \tag{12}$$

and accordingly, the reflection probability becomes $R = 1 - T$. For the two-terminal quantum system the above expression (Eq. (12)) is the so-called Landauer conductance formula.

The current I_p passing through the lead-p can be obtained from the following expression [29],

$$I_p = \frac{2e}{h} \sum_q \int_{-\infty}^{\infty} T_{pq}(E)\left[f_p(E) - f_q(E)\right] dE \tag{13}$$

where $f_{p(q)} = f(E - \mu_{p(q)})$ is the Fermi distribution function with the chemical potential $\mu_{p(q)} = E_F \pm eV_{p(q)}/2$. E_F is the equilibrium Fermi energy. Throughout this calculation, we assume that the entire voltage is dropped across the molecule-lead interfaces as this assumption introduces a minimal effect on the behavior of the I–V characteristics. In this article we set $c = h = e = 1$ for the sake of simplicity.

3. Numerical results and discussion

In order to illustrate the results, let us first mention the values of different parameters used in our numerical calculations. All the on-site energies of molecule, sulfur atom and leads are set to zero, while the nearest-neighbor hopping strengths are fixed at 3 for both the molecule (t) and leads (t_0). But the values of molecule-to-lead coupling strengths (τ_p for lead-p) are different from the value assigned for t and t_0. Based on the molecular coupling strength, we analyze our results in two distinct regimes. One is the weak-coupling regime and the other is the strong-coupling regime. In the first case, $\tau_p \ll t$ and we set $\tau_p = 0.5$. In the second case, $\tau_p \sim t$ and for this regime we fix $\tau_p = 2.5$. Here we consider that τ_p's are identical for all the leads p and set the equilibrium Fermi energy E_F at 0.

3.1. Conductance–energy characteristics

In the forthcoming sub-sections we present the characteristic properties of electron transport for two-, three- and four-terminal molecular systems where the molecules are attached to leads via thiol-linking groups (SH bond). In experiments, leads are generally designed from gold (Au) and the thiol groups are linked by using chemisorption technique [34] where hydrogen (H) atoms remove and sulfur (S) atoms survive.

3.1.1. Two-terminal conductance

In Fig. 2 we present the variation of two-terminal conductance g (red curves) and reflection probability R (green curves) with injecting electron energy E. The results in the weak molecule-to-lead coupling limit are shown in (a) and

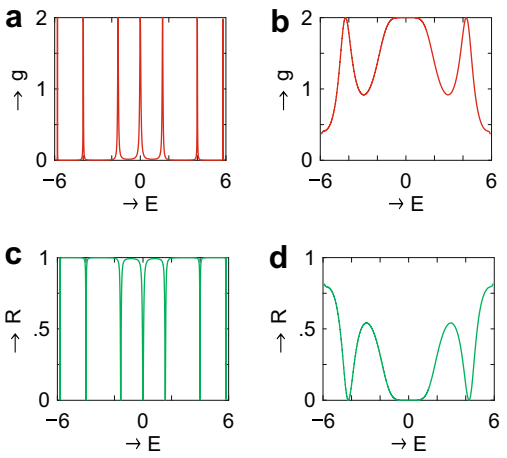

Fig. 2. Conductance g (red lines) and reflection probability R (green lines) as a function of energy E for the two-terminal molecular system. (a) and (c) Represent the results for the weak-coupling limit, while (b) and (d) correspond to the same for the strong-coupling limit. Conductance g is measured in unit of e^2/h, while the energy E is measured in unit of t. (For interpretation of the references to color in this figure legend, the reader is referred to the web version of this article.)

(c), while (b) and (d) represent the same for the strong molecule-to-lead coupling limit. In the weak-coupling regime, the presence of sharp resonant peaks indicates that electron transmission occurs at some typical energy values, while for all other energies conductance vanishes (see Fig. 2(a)). All these resonant peaks are associated with the energy eigenvalues of the molecular system, and therefore, we predict that conductance spectrum is a fingerprint of the electronic structure of the system. Most of the resonant peaks approach the value 2, the maximum value of g following the Landauer conductance formula (see Eq. (12)) and hence T goes to unity at these resonances indicating ballistic transmission through the molecular wire. But the behavior of conductance spectrum changes in case of the strong molecule-to-lead coupling limit. Width of each resonant peak becomes larger and larger as we increase gradually the molecule-to-lead coupling strength and for a large molecular coupling, we have the situation where electron transmission takes place for the entire energy range (for illustration, see Fig. 2(b)). The effect of such broadening comes from the imaginary parts of the self-energies [29]. All these phenomena emphasize that fine tuning in the energy scale is necessary as long as the coupling strength is much weak, while it is not required in case of the strong molecule-to-lead coupling limit.

This scenario is just inverted in case of reflection probability R. In the weak-coupling regime, sharp dips appear (Fig. 2(c)) for some particular energy values where conductance shows resonant peaks, as R follows the simple relation $R = 1 - T$ for the two-terminal molecular system. For all other energy values, $R = 1$ indicating no transmission of electron across the molecule. The effect of molecule-to-lead coupling is exactly similar to that for conductance spectrum. In the strong-coupling regime (see Fig. 2(d)), the reflection probability no longer reach the maximum value (1) for the entire energy range.

3.1.2. Three-terminal conductance

To illustrate the results for the three-terminal quantum system, constructed by attaching three leads to the molecule (see Fig. 1(b)), let us start by referring to Fig. 3 where the first column shows the conductance spectra g_{pq} (from lead-p to lead-q) and the second column presents the nature of reflection probability R_{pp}. Similar to the two-terminal molecular system, some sharp peaks appear in the conductance spectra. But the point is that for the three-terminal system most of the resonant peaks do not reach the value 2. From the conductance spectra it is clear that the heights are much reduced compared to the two-terminal case. This is solely due to the effect of quantum interference of the electronic waves passing through different arms of the molecular rings. In this three-terminal system, three leads are attached asymmetrically to the molecule at three different locations, which provide different path ways for electron transmission between the leads. This introduces anomalous features in the conductance spectra as illustrated in Fig. 3(a)–(c). Moreover, in this three-terminal case, nature of variations of reflection probabilities is not so simple as we get in the case of two-terminal molecular system. Here, it is not necessary that R_{pp} shows dips or peaks where g_{pq} has peaks or dips since it (R_{pp}) depends on the combined effect of T_{pq}'s obeying the expression given in Eq. (9). Another important point we like to mention here is that, one can easily find T_{qp} for any two leads q and p if T_{pq} is known since the relation $T_{pq} = T_{qp}$ holds true following the time-reversal symmetry. The effect of

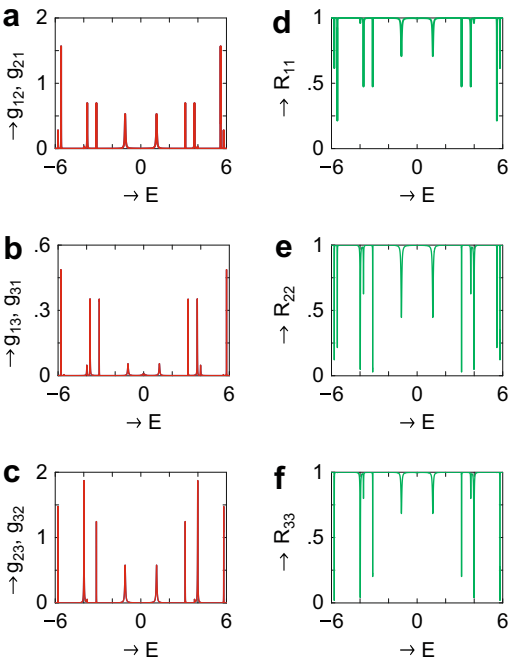

Fig. 3. Conductance g_{pq} (red curves) and reflection probability R_{pp} (green curves) as a function of energy E for the three-terminal molecular system. All the spectra are given only for the weak-coupling regime. Conductance is measured in unit of e^2/h, while the energy is measured in unit of t. (For interpretation of the references to color in this figure legend, the reader is referred to the web version of this article.)

molecule-to-lead coupling strength is identical to the case of two-terminal conductance and therefore, we do not show those results further.

3.1.3. Four-terminal conductance

The transport properties of the four-terminal molecular system are also described by investigating various conductances g_{pq} and reflection probabilities R_{pp} those are obtained from Eqs. (8) and (9), respectively. The results are plotted in Fig. 4 considering the weak molecule-to-lead coupling. In each figure g_{pq} and g_{qp} are plotted and they are superposed to each other due to their symmetry. Sharp resonant peaks of different heights for some particular energies appear in the conductance spectra similar to the two- or three-terminal conductance spectra. From the conductance spectra, the effect of quantum interference associated with the molecule-to-lead interface geometry is well understood. Also the dependence of electron transport on molecular coupling strength is exactly similar to that in Fig. 2 and accordingly, the results are not given further. Comparing the results given in Figs. 3 and 4 we observe that, the conductances for two particular leads located at the same positions of the molecule exhibit completely different features in presence of the other leads. For instance, g_{13} of the four-terminal system and g_{12} of the three-terminal system show different spectra though these two conductances are evaluated for the two leads located at the same positions of the molecule. Similarly, careful observation depicts that pathways between the lead-2 and lead-3 of the three-terminal system are exactly similar to that between lead-2 and lead-4 of the four-terminal system. In spite of this the corresponding spectra, i.e., g_{23} of Fig. 3 and g_{24} of Fig. 4 are different from each other due to the presence of the fourth lead. The effect of the leads are incorporated into the self-energies which lead to the change in conductance spectra. Thus, we can say that the presence of additional leads has a pronounced effect on the electron transport properties. In R–E spectra given in Fig. 5, we get various dips at different energies depending on the combined effect of the transmission probabilities (Eq. (9)), similar to the case of three-terminal system. All the reflection probabilities are calculated only for the limit of weak molecular coupling. Exactly similar feature, except the broadening, will be observed in the case of strong-coupling.

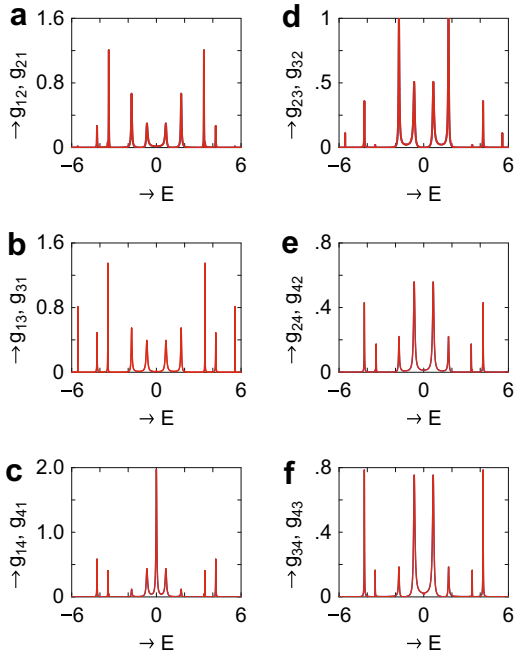

Fig. 4. Four-terminal conductance g_{pq} (in unit of e^2/h) as a function of energy E (in unit of t) in the limit of weak molecular coupling.

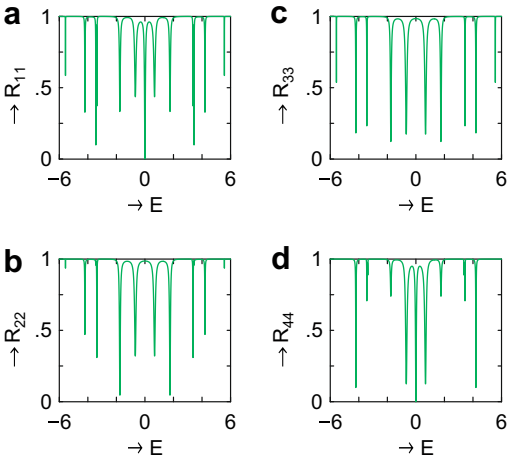

Fig. 5. Reflection probability R_{pp} as a function of energy E (in unit of t) for the four-terminal quantum system. These results correspond to the weak-coupling regime.

3.2. Current–voltage characteristics

The scenario of electron transport through molecular junction becomes much more transparent when we discuss the current–voltage (I–V) characteristics, where the current is evaluated by integrating the transmission probability T using Eq. (13). The nature of the variation of transmission probability is exactly similar to that of conductance spectra except the factor 2 as we have assumed $e = h = 1$ in the Landauer conductance formula (Eq. (12)). Here, we discuss the I–V characteristics for two-, three- and four-terminal molecular systems separately in the following sub-sections.

3.2.1. Two-terminal molecular system

As an illustration, we display the I–V characteristics for the two-terminal system in Fig. 6, where (a) and (b) correspond to the results for the weak and strong molecule-to-lead coupling limits, respectively. For this two-terminal case, current can be expressed mathematically as follows,

$$I = g(V_1 - V_2) = gV_{12} \tag{14}$$

where V_{12} is the voltage difference between the lead-1 and lead-2. In the case of two-terminal molecular system, we have attached two leads to the molecule and their chemi-

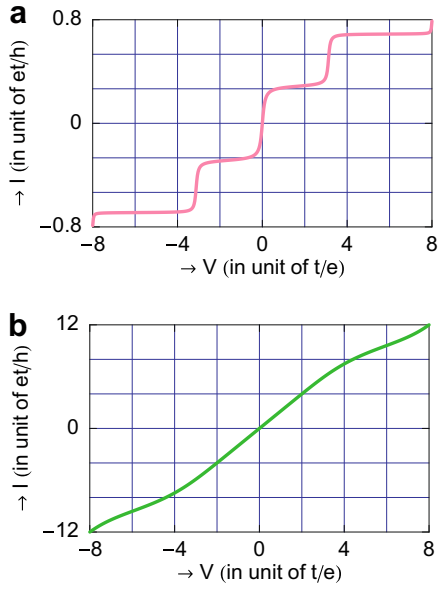

Fig. 6. Current I (in unit of et/h) as a function of applied bias voltage V (in unit of t/e) for the two-terminal molecular system. (a) Weak-coupling limit and (b) strong-coupling limit.

cal potentials are changed as the bias voltage is applied. With the increase of the voltage, the gap increases more and more and eventually crosses molecular energy levels one after another. Accordingly, current channels are opened up and jumps in the I–V curve appear. This provides staircase-like structure in the current–voltage spectrum and only for the case of weak molecular coupling these sharp steps appear. But this feature, i.e., step-like changes gradually towards continuous nature with the increase of molecule-to-lead coupling strength. In addition to that, current amplitude becomes much higher compared to the case of weak-coupling limit. By noting the area under the curve of Fig. 2(b) the reason behind this enhancement of current amplitude is clearly understood. Thus, it can be manifested that molecule-to-lead coupling strength has a significant influence on molecular transport.

3.2.2. Three-terminal molecular system

Now, we describe the current–voltage characteristics for the three-terminal system where we find the current I_p in lead-p by integrating the transmission function T_{pq} considering the effects of other terminals. To be more precise, we write the current expressions for three different leads as follows,

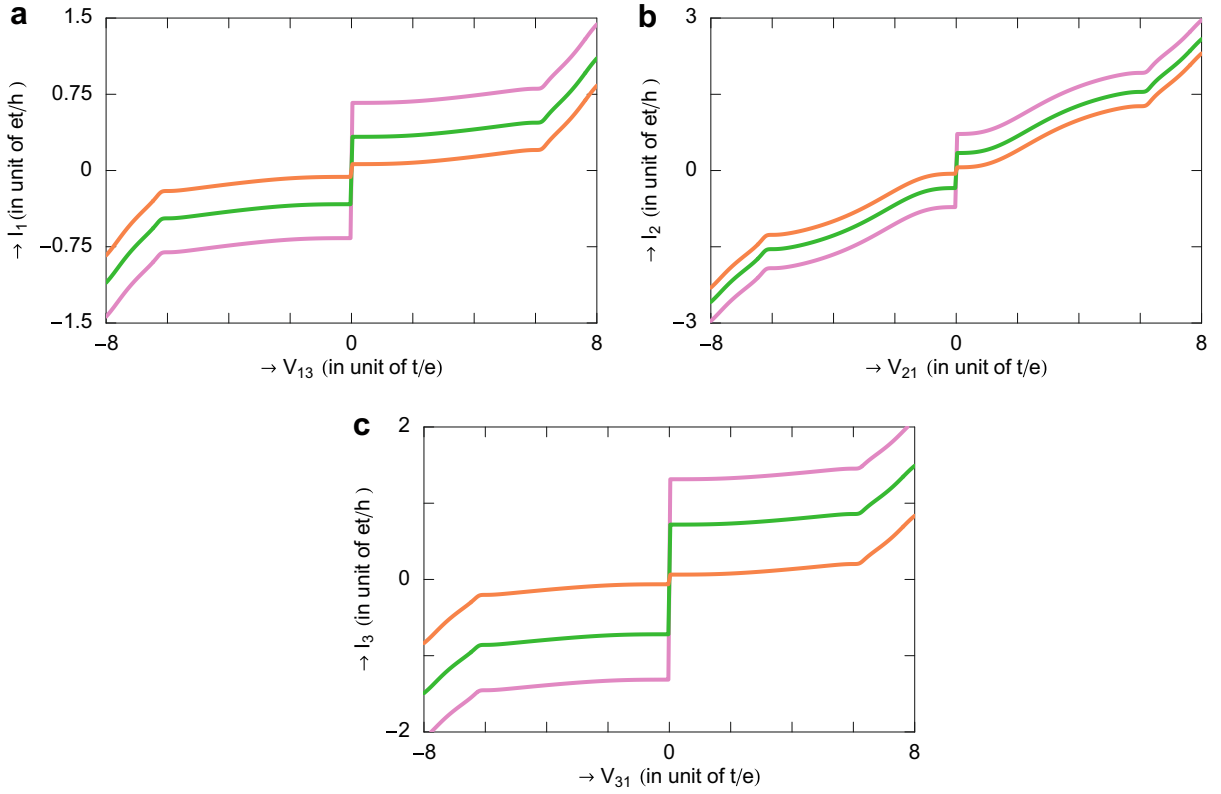

Fig. 7. I–V characteristics for the three-terminal molecular system in the limit of strong-coupling. (a) I_1 as a function of V_{13} $(= V_1 - V_3)$, keeping V_{12} $(= V_1 - V_2)$ as a constant. The orange, green and magenta colors correspond to $V_{12} = 1, 2$ and 3, respectively. (b) I_2 as a function of V_{21} $(= V_2 - V_1)$, considering V_{23} $(= V_2 - V_3)$ as a constant. The orange, green and magenta colors correspond to $V_{23} = 1, 2$ and 3, respectively. (c) I_3 as a function of V_{31} $(= V_3 - V_1)$, keeping V_{32} as a constant. The orange, green and magenta colors correspond to $V_{32} = 1, 3$ and 5, respectively. Current is measured in unit of et/h, and the bias voltage is measured in unit of t/e. (For interpretation of the references to color in this figure legend, the reader is referred to the web version of this article.)

$$I_1 = g_{12}(V_1 - V_2) + g_{13}(V_1 - V_3) = g_{12}V_{12} + g_{13}V_{13} \quad (15)$$
$$I_2 = g_{21}(V_2 - V_1) + g_{23}(V_2 - V_3) = g_{21}V_{21} + g_{23}V_{23} \quad (16)$$
$$I_3 = g_{31}(V_3 - V_1) + g_{32}(V_3 - V_2) = g_{31}V_{31} + g_{32}V_{32} \quad (17)$$

where $V_{pq} = (V_p - V_q)$ is the voltage difference between the two leads named as lead-p and lead-q.

In Fig. 7(a), we plot I_1 for the lead-1 as a function of V_{13} for different fixed values of V_{12} in the strong molecule-to-lead coupling limit. The orange, green and magenta curves represent the currents for $V_{12} = 1, 2$ and 3, respectively. It is clear from the figure that for a constant value of V_{12}, the moment we switch on the bias voltage between lead-1 and lead-3, current rises to a large value. Then, for a wide range of V_{13}, it (I_1) slowly increases with the rise of V_{13} and finally the rate of increment of the current gets enhanced when V_{13} is quite high. This behavior, i.e., the rate of increment of the current with bias voltage solely depends on the positions of resonant peaks in the g–E spectrum. For a particular value of V_{13}, I_1 increases as we increase V_{12} which is clearly visible from three different curves plotted in Fig. 7(a).

The variation of current I_2 through lead-2 as a function of V_{21} is shown in Fig. 7(b), keeping the voltage V_{23} as a constant. The currents are evaluated in the strong-coupling limit, where the orange, green and magenta lines correspond to $V_{23} = 1, 2$ and 3, respectively.

In a similar fashion in Fig. 7(c) we display I_3—V_{31} characteristics for different fixed values of V_{32} considering the case of strong-coupling limit. The orange, green and magenta curves correspond to $V_{32} = 1, 3$ and 5, respectively.

The characteristic features of the currents I_1, I_2 and I_3 passing through three different leads are quite analogous to each other. Depending on the conductance–energy spectra, we get different current amplitudes for three different leads which are clearly observed from the results presented in Fig. 7(a)–(c). All these currents are computed only for the strong-coupling limit. We can also determine the currents for the limit of weak-coupling and in that case we will get sharp step-like features as a function of bias voltage with much reduced amplitude compared to the strong-coupling case. The origin of step-like behavior in current is clearly mentioned in the case of two-terminal molecular system (Section 3.2.1).

From the above current expressions (Eqs. (15)–(17)) we see that the current in anyone lead is related to two potential functions. For instance in Eq. (15), there are two

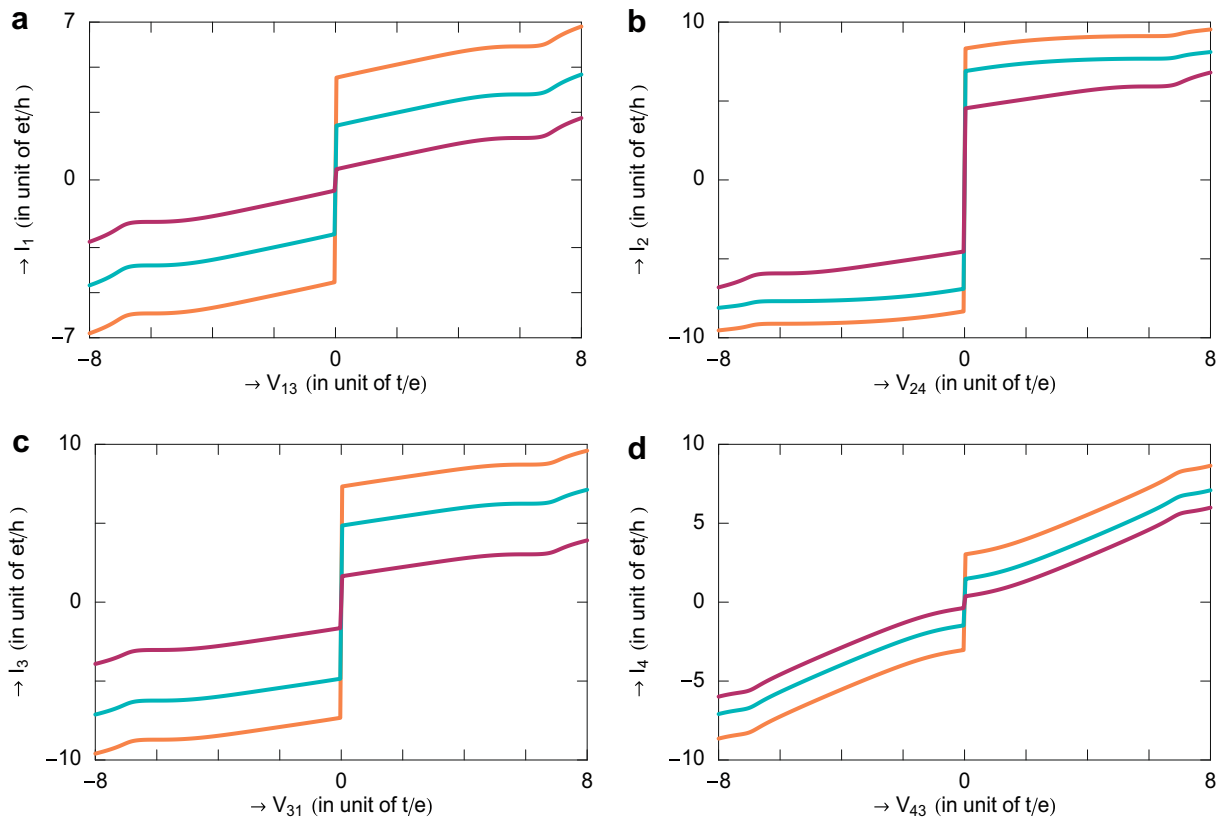

Fig. 8. I–V characteristics for the four-terminal molecular system in the strong-coupling regime. (a) I_1 as a function of V_{13}, keeping V_{12} and V_{14} as constant. The dark-red, blue and orange colors correspond to $V_{12} = V_{14} = 1, 3$ and 5, respectively. (b) I_2 as a function of V_{24} ($= V_2 - V_4$), keeping V_{21} and V_{23} as constant. The dark-red, blue and orange lines correspond to $V_{21} = V_{23} = 2, 4$ and 6, respectively. (c) I_3 as a function of V_{31} considering V_{32} and V_{34} as constant. The dark-red, blue and orange curves correspond to $V_{32} = V_{34} = 1, 3$ and 5, respectively. (d) I_4 as a function of V_{43} ($= V_4 - V_3$) keeping V_{41} and V_{42} as constant, where the dark-red, blue and orange lines correspond to $V_{41} = V_{42} = 1, 5$ and 9, respectively. Current is measured in unit of et/h, and the bias voltage is measured in unit of t/e. (For interpretation of the references to color in this figure legend, the reader is referred to the web version of this article.)

parameters like V_{12} and V_{13}. Keeping V_{12} as a constant we plot the current I_1 in terms of V_{13} (see Fig. 7(a)). At the same time, we can also draw the I_1–V_{12} characteristics, considering V_{13} as a constant. Both for these two cases, the characteristic features are quite similar. This argument is also valid for the other two current expressions (Eqs. (16) and (17)).

All the above features of current–voltage characteristics in this three-terminal molecular system clearly support the basic features of a traditional macroscopic transistor. Thus we can predict that the three-terminal molecular system may be utilized to design a nanoscale molecular transistor.

3.2.3. Four-terminal molecular system

Finally, we focus our attention on the current–voltage characteristics for the four-terminal molecular system. In this molecular system, the current expressions for the four different leads are as follows,

$$I_1 = g_{12}(V_1 - V_2) + g_{13}(V_1 - V_3) + g_{14}(V_1 - V_4) = g_{12}V_{12} + g_{13}V_{13} + g_{14}V_{14} \quad (18)$$

$$I_2 = g_{21}(V_2 - V_1) + g_{23}(V_2 - V_3) + g_{24}(V_2 - V_4) = g_{21}V_{21} + g_{23}V_{23} + g_{24}V_{24} \quad (19)$$

$$I_3 = g_{31}(V_3 - V_1) + g_{32}(V_3 - V_2) + g_{34}(V_3 - V_4) = g_{31}V_{31} + g_{32}V_{32} + g_{34}V_{34} \quad (20)$$

$$I_4 = g_{41}(V_4 - V_1) + g_{42}(V_4 - V_2) + g_{43}(V_4 - V_3) = g_{41}V_{41} + g_{42}V_{42} + g_{43}V_{43} \quad (21)$$

where V_{pq} is the voltage difference between the lead-p and lead-q.

As representative examples, in Fig. 8(a) we plot the current in lead-1 (I_1) as a function of V_{13} keeping V_{12} and V_{14} as constant. The results are computed for the strong-coupling limit, where the dark-red, blue and orange curves correspond to $V_{12} = V_{14} = 1, 3$ and 5, respectively. The variation of current I_1 as a function of V_{13} in this four-terminal molecular system is quite similar to that as presented in the case of three-terminal system (Fig. 7(a)). For a particular value of V_{13}, here also the current amplitude gets increased with the rise of V_{12} and V_{14}. But quite significantly we observe that, for a particular value of V_{13}, the current I_1 passing through the lead-1 of four-terminal system acquires much higher amplitude compared to the three-terminal system (see Figs. 7(a) and 8(a)). The reason behind this enhancement of current amplitude is explained as follows. From Eq. (18) we see that I_1 contains three additive terms where the contributions come from other leads, while in Eq. (15) there are two additive terms. The additional term appears in Eq. (18) is due to the presence of fourth terminal which is responsible for the larger current in four-terminal system compared to the three-terminal one.

In case of the current I_2 through lead-2 we show the variation with respect to V_{24}, keeping V_{21} and V_{23} fixed to a particular value as presented in Fig. 8(b). The currents are determined in the strong-coupling regime, where the dark-red, blue and orange lines correspond to $V_{21} = V_{23} = 2, 4$ and 6, respectively.

Similarly, in Fig. 8(c) we display I_3–V_{31} characteristics considering V_{32} and V_{34} as constants in the limit of strong-coupling. The dark-red, blue and orange lines represent the currents for $V_{32} = V_{34} = 1, 3$ and 5, respectively.

At the end, in Fig. 8(d) we show the variation of current I_4 passing through lead-4 as a function of V_{43} in the limit of strong molecular coupling, when V_{41} and V_{42} are kept as constants. The dark-red, blue and magenta curves correspond to the currents for $V_{41} = V_{42} = 1, 5$ and 9, respectively.

Similar to the case of three-terminal molecular system, for this four-terminal case, we can also plot the current through any lead-p in aspect of the other potential functions as given in Eqs. (18)–(21). For all these cases, the characteristic features are very much similar those are presented in Fig. 8(a)–(d), and hence, we do not re-plot the results further.

4. Closing remarks

In the present paper we have used a parametric approach to study multi-terminal electron transport through a single phenalenyl molecule. Using a simple tight-binding framework we have performed all the numerical calculations through single particle Green's function formalism. The basic features of electron transport in this molecular system are explored by investigating the multi-terminal conductance, reflection probability and current. Following a detailed description of electron transport in two-terminal quantum system, we have revealed the essential features of electron transport in the three- and four-terminal quantum systems separately.

Our clear investigation predicts that the electron transport in multi-terminal molecular system significantly depends on (a) the molecule–lead interface geometry, (b) the presence of other leads and (c) the strength of molecular coupling to the side attached leads. The unique characteristics of this phenalenyl molecule with a very small size has enhanced the importance of the present article. Our parametric study provides several significant features to reveal electron transport through any complicated multi-terminal quantum system.

In the present paper we have done all the calculations by ignoring the effects of temperature, electron–electron correlation, etc. We need further study by incorporating all these effects.

References

[1] N.J. Tao, Nat. Nanotechnol. 1 (2006) 173.
[2] A. Aviram, M. Ratner, Chem. Phys. Lett. 29 (1974) 277.
[3] M.B. Nardelli, Phys. Rev. B 60 (1999) 7828.
[4] T. Dadosh, Y. Gordin, R. Krahne, I. Khivrich, D. Mahalu, V. Frydman, J. Sperling, A. Yacoby, J. Bar-Joseph, Nature 436 (2005) 677.
[5] M.A. Reed, C. Zhou, C.J. Muller, T.P. Burgin, J.M. Tour, Science 278 (1997) 252.
[6] Y. Xue, S. Datta, M.A. Ratner, Chem. Phys. 281 (2002) 151.
[7] R. Baer, D. Neuhauser, Chem. Phys. 281 (2002) 353.
[8] R. Baer, D. Neuhauser, J. Am. Chem. Soc. 124 (2002) 4200.
[9] D. Walter, D. Neuhauser, R. Baer, Chem. Phys. 299 (2004) 139.
[10] K. Walczak, Cent. Eur. J. Chem. 2 (2004) 524.
[11] K. Walczak, Phys. Status Solidi (b) 241 (2004) 2555.
[12] M. Büttiker, Phys. Rev. Lett. 57 (1986) 1761.
[13] H.Q. Xu, Appl. Phys. Lett. 78 (2001).

[14] C.A. Stafford, D.M. Cadamone, S. Mazumdar, Nanotechnology 18 (2007) 424014.
[15] Q. Sun, B. Wang, J. Wang, T. Lin, Phys. Rev. B 61 (2000) 4754.
[16] H.K. Zhao, Phys. Lett. A 226 (1997) 105.
[17] E.G. Emberly, G. Kirczenow, Phys. Rev. B 62 (2000) 10451.
[18] P.S. Damle, A.W. Ghosh, S. Datta, Phys. Rev. B 64 (2001) R201403.
[19] P.A. Derosa, J.M. Seminario, J. Phys. Chem. B 105 (2001) 471.
[20] J. Taylor, H. Guo, J. Wang, Phys. Rev. B 63 (2001) 245407.
[21] Y. Xue, S. Datta, M.A. Ratner, J. Chem. Phys. 115 (2001) 4292.
[22] K. Tagami, M. Tsukada, Y. Wada, T. Iwasaki, H. Nishide, J. Chem. Phys. 119 (2003) 7491.
[23] K. Tagami, L. Wang, M. Tsudaka, NanoLetters 4 (2004) 209.
[24] L. Wang, K. Tagami, M. Tsukada, Jpn. J. Appl. Phys. 43 (2004) 2779.
[25] S.K. Maiti, Phys. Lett. A 373 (2009) 4470.
[26] S.K. Maiti, J. Phys. Soc. Jpn. 78 (2009) 114602.
[27] P.O. Lowdin, J. Mol. Spectrosc. 10 (1963) 12.
[28] P.O. Lowdin, J. Math. Phys. 3 (1962) 969.
[29] S. Datta, Electronic Transport in Mesoscopic Systems, Cambridge University Press, Cambridge, 1997.
[30] S. Datta, Quantum Transport: Atom to Transistor, Cambridge University Press, Cambridge, 2005.
[31] H.Q. Xu, Phys. Rev. B 66 (2002) 165305.
[32] V. Mujica, M. Kemp, M.A. Ratner, J. Chem. Phys. 101 (1994) 6849.
[33] S.K. Maiti, Physica E 40 (2008) 2730.
[34] A.W. Holleitner, R.H. Blick, A.K. Hüttel, K. Eberl, J.P. Kotthaus, Science 297 (2002) 70.

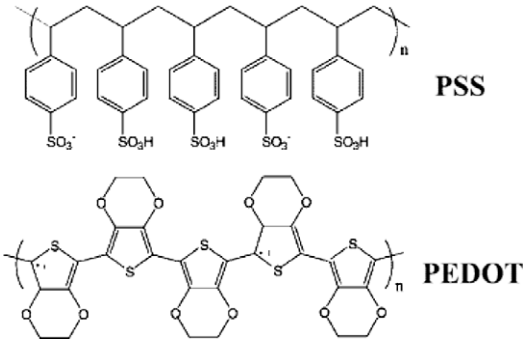

Scheme 1. Chemical structure of PEDOT:PSS.

the conductivity of PEDOT:PSS. Thus, there is still room for the further improvement of the conductivity of the PEDOT:PSS film.

Recently, we reported a new and simple method to significantly enhance the conductivity of PEDOT:PSS by treating the PEDOT:PSS film with aqueous solution of a certain salt, such as $CuCl_2$ or $InCl_3$ [27]. Conductivity enhancement by a factor of 700 was achieved. The conductivity enhancement was related to the softness parameter of the metal ion of the salt. A salt whose metal ion has a positive softness parameter can significantly enhance the conductivity of PEDOT:PSS, while a salt whose metal ion has negative softness parameter has negligible effect. Based on those results, we proposed that the mechanism for the conductivity enhancement of PEDOT:PSS by a salt treatment is related to the ion-induced charge screening between the positively charged PEDOT and negatively charged PSS chains, which results into the replacement of some PSS^- with the small anions from the salt as the counter anions of $PEDOT^+$, the loss of some PSS chains and the conformational change of the PEDOT chains. Though the role of the metal ions on the conductivity enhancement was well studied, it is unknown whether the anion of the salt affects the conductivity enhancement. In this manuscript, we report the anion effect on the salt-induced conductivity enhancement of PEDOT:PSS. The conductivity of the PEDOT:PSS film can be enhanced by a factor of more than 1000 after treated with aqueous solution of $CuBr_2$ or InI_3. In contrast, the conductivity enhancement was less significant and negligible when the PEDOT:PSS film was treated with aqueous solutions of $CuSO_4$ and $Cu(CH_3COO)_2$, respectively. This study on the anion effect helps elucidate the mechanism for the salt-induced conductivity enhancement of PEDOT:PSS.

2. Experimental

PEDOT:PSS aqueous solution (Baytron P, renamed to Clevios™ P, Item No. 1802705, Lot No. HCE07P107) was purchased from H.C. Starck. The concentration of PEDOT:PSS was 1.3% by weight, and the weight ratio of PSS to PEDOT was 2.5. All other chemicals were purchased from Sigma–Aldrich. These materials were used without further purification.

PEDOT:PSS films were prepared by spin-coating the PEDOT:PSS aqueous solution on $1.3 \times 1.3\ cm^2$ glass substrates. The substrates were pre-cleaned by detergent, de-ionized (DI) water, acetone and isopropyl alcohol in sequence. The PEDOT:PSS films were dried at 110 °C on a hot plate for 30 min. The film thickness was *ca.* 130 nm. The salt treatment was similar to that in our early report [27]. The treatment with a salt solution was performed by dropping 150 μL aqueous solution of a salt on a PEDOT:PSS film on a hot plate at 140 °C. The film dried after about 5 min. The salt-treated PEDOT:PSS films were cooled down to room temperature in air and rinsed with de-ionized water triply. Then, they were dried at 140 °C again.

The conductivities of the polymer films were measured by the van der Pauw four-point probe technique with a Keithley 2400 source/meter. The electrical contacts were made by pressing indium on the four corners of each PEDOT:PSS film on glass substrate. The UV–Vis–NIR absorption spectra of the polymer films were taken with a Varian Cary 5000 UV–Vis–NIR spectrometer. The X-ray photoelectron spectra (XPS) were taken with an Axis Ultra DLD X-ray photoelectron spectrometer equipped with an Al Ka X-ray source (1486.6 eV). The samples for FTIR were prepared by dispersing polymers in KBr pellets, and the FTIR spectra were acquired with a Varian 3100 FT-IR spectrometer. The atomic force microscopic (AFM) images of the polymer films were obtained using a Veeco NanoScope IV Multi-Mode AFM with the tapping mode. The thicknesses of the films were determined with an Alpha 500 step profiler. The temperature dependences of the resistivities of the untreated and salt-treated PEDOT:PSS films were measured using a Janis Research VPF-475 dewar with liquid nitrogen as coolant and a Conductus LTC-11 temperature controller.

3. Results and discussion

3.1. Salt-induced conductivity enhancement

The as-prepared PEDOT:PSS films exhibited a conductivity of 0.2 S cm^{-1}. They are treated with solutions of various salts. Table 1 listed the conductivities of the PEDOT:PSS films after treated with 0.1 M and 1 M aqueous

Table 1
Conductivities of PEDOT:PSS films after a treatment with 0.1 M and 1 M aqueous solution of various salts.

Salt	Softness parameter of cation[a]	Softness parameter of anion[a]	Conductivity[b] (S cm^{-1})	Conductivity[c] (S cm^{-1})
$CuSO_4$	+0.38	−0.38	5.1	33.4
$Cu(CH_3COO)_2$	+0.38	−0.22	1.1	1.2
$Cu(ClO_4)_2$	+0.38	−0.3	57.1	127.8
$CuCl_2$	+0.38	−0.09	29.0	168.7
$CuBr_2$	+0.38	+0.17	74.3	187.5
$InCl_3$	+0.48	−0.09	95.5	136.0
$InBr_3$	+0.48	+0.17	145.9	152.0
InI_3	+0.48	+0.5	177.5	191.6

[a] The softness parameter values were obtained from Ref. [28].
[b] Treated with 0.1 M solution.
[c] Treated with 1 M solution.

solutions of cupric (Cu^{2+}) and indium (In^{3+}) salts with various anions. These results indicate that the anions significantly affected the conductivity of PEDOT:PSS. The conductivity of the PEDOT:PSS film increased to 74.3 S cm^{-1} after it was treated with 0.1 M $CuBr_2$ aqueous solution, while it was only 5.1 S cm^{-1} after treated with 0.1 M $CuSO_4$ aqueous solution. In addition, the conductivity just slightly increased to 1.1 S cm^{-1} after it was treated with 0.1 M $Cu(CH_3COO)_2$ aqueous solution. The remarkable difference was observed on the conductivities of the PEDOT:PSS films treated with various 1 M Cu^{2+} aqueous solutions as well. The anion effect on the conductivity enhancement was also observed when the PEDOT:PSS films were treated with solutions of various In^{3+} salts.

The results presented in Table 1 indicate that I_3^- and Br^- salts give rise to the most significant conductivity enhancement. In fact, the conductivity of the PEDOT:PSS film was enhanced from 0.2 S cm^{-1} to 220 S cm^{-1} and 264.8 S cm^{-1} after treatments with 2 M $CuBr_2$ aqueous solution and 2 M InI_3 aqueous solution, respectively. The latter conductivity is higher than that of the as-prepared PEDOT:PSS film by a factor of more than 1300.

The conductivities of the salt-treated PEDOT:PSS films were plotted against the softness parameters of the anions of the salts (Fig. 1a). The conductivities of the PEDOT:PSS films treated with 0.1 M aqueous solutions of various sodium (Na^+) salts were presented as well. Two conclusions were obtained from Fig. 1a. The first conclusion is that the dominant factor for the salt-induced conductivity enhancement is the metal ions of the salts. No remarkable conductivity enhancement was observed for PEDOT:PSS treated with Na^+ salts, whose anions have softness parameters varied from −0.38 to 0.5, while significant conductivity enhancement was observed for that treated with solutions of Cu^{2+} and In^{3+} salts. The second conclusion is that the anion effect on the conductivity enhancement is inconsistent with the softness parameters of the anions. For example, ClO_4^- had a softness parameter lower than Cl^-, while the 0.1 M $Cu(ClO_4)_2$-treated PEDOT:PSS films exhibited a conductivity higher than the 0.1 M $CuCl_2$-treated PEDOT:PSS film. The $CuSO_4$-treated PEDOT:PSS films had a conductivity higher than the $Cu(CH_3COO)_2$-treated PEDOT:PSS films as well, though SO_4^{2-} has a softness parameter lower than CH_3COO^-. This is different from the effect of the metal ions on the conductivity enhancement of PEDOT:PSS, for which the conductivity enhancement is consistent with the softness parameters of the metal ions [27].

Presumably, the inconsistence of the conductivity enhancement with the softness parameter of the anions is because only the enthalpy change is taken into account in the softness parameter [28,29]. Thus, the softness parameters can provide only a rough estimation for the association of an ion with other species. As we proposed, the salt treatment of the PEDOT:PSS films involves three processes: the dissociation of the salt, the association of the metal ions with PSS^-, and the association of the anions with $PEDOT^+$. The reason for the consistence of the softness parameters with the effect of metal ions on the conductivity enhancement of PEDOT:PSS is that the entropy change for the association of the metal ions with PSS^- is close since

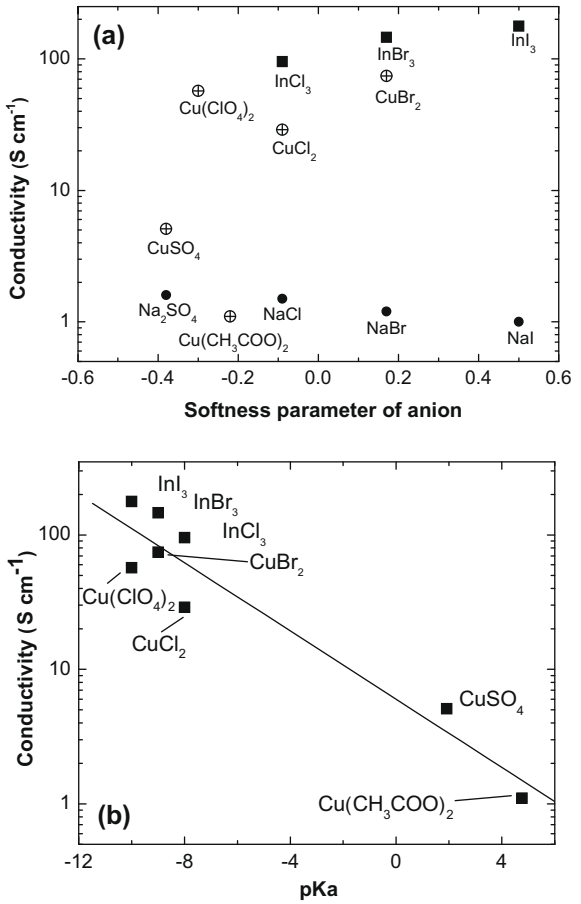

Fig. 1. Conductivities of PEDOT:PSS films treated with 0.1 M solutions of salts. (a) Conductivities versus softness parameters of anions, and (b) conductivities versus pK_a values of acids corresponding to the anions. The softness parameters are obtained from reference 28. The pK_a value for SO_4^{2-} is the pK_{a2} of sulfuric acid. The straight line in (b) is a linear fitting of the data.

all the metal ions have close sizes. This becomes different for the anion effect on the conductivity enhancement of PEDOT:PSS. The entropy changes can be quite different for different anions, particularly multi-atom anions like SO_4^{2-} and CH_3COO^-. Hence, the softness parameters are too rough to estimate the processes involving the anions. We turn to other parameters characteristic of the association of the anion with cation. The dissociation of the salts may be linearly related to the dissociation constants of the acids corresponding to the anions, since the association of metal ions with organic ligands is proportional to the association of metal ions with hydroxide [30]. The value of the acid dissociation K_a for an acid HA, which defined as

$$HA \rightarrow H^+ + A^-,\ K_a = [A^-][H^+]/[HA], \text{and } pK_a = -\log K_a,$$

can provide more accurate information for the dissociation of the anion A^- with other species. We plotted the conductivity enhancement against the pK_a values of the corresponding acids of the anions (Fig. 1b). The conductivities of the salt-treated PEDOT:PSS films are consistent with

the pK_a values of the anions. The conductivity enhancement became more significant for the anions with lower pK_a values. The logarithm of the conductivity almost linearly decreases with the increasing pK_a value. The best fitting of this linear relationship indicates

$$\log\sigma = 0.78 - 0.127pK_a.$$

The relationship between the anion effect on the conductivity enhancement of PEDOT:PSS and the acid association constants of the anions is consistent with the mechanism we proposed. The association of the metal ions with PSS^- can be roughly described in terms of the softness parameters of the metal ions, while the softness parameters of the anions cannot provide accurate information for the dissociation of the salts and association of the anions with $PEDOT^+$. The latter two processes involve the anions from the salt. The metal ions and $PEDOT^+$ compete for the anions during the treatment. A high dissociation constant for a salt, or a low association constant for the metal ions with the anions, benefits the association of the anions with $PEDOT^+$. Consequently, more significant conductivity enhancement can be obtained for the salts with anions of lower pK_a values.

The three processes during the salt treatment of PEDOT:PSS result into the weakening of the Coulombic attraction between $PEDOT^+$ and PSS^-, the replacement of the PSS^- chains with small anions from the salt as the counter anions of $PEDOT^+$, and the loss of PSS chains from the PEDOT:PSS films. Grain structure has been observed for the as-prepared PEDOT:PSS films with a PSS-rich shell and PEDOT-rich core for each grain [31–34]. The removal of some PSS chains, which are insulator, can effectively reduce the shell thickness, which will benefit the charge transport through the PEDOT:PSS film. Moreover, the $PEDOT^+$ chains will experience a conformational change during the salt treatment. All these contribute to the conductivity enhancement of the PEDOT:PSS films. The anion exchange between the salts and PEDOT:PSS is different from the anion exchange observed on conducting polymers doped with small anions, in which no conductivity change was usually observed [35,36].

3.2. PSS loss from PEDOT:PSS and presence of small ions in PEDOT:PSS

As discussed above, the anions from the salts affect the loss of PSS chains from the PEDOT:PSS film. This is evidenced by the absorption spectroscopy and XPS of the PEDOT:PSS treated with Cu^{2+} salts with various anions. Fig. 2 presents the absorption spectra of the treated and untreated PEDOT:PSS films in the UV range. The two bands with the absorption maxima at 193 nm and 225 nm are the absorption due to PSS [8]. The decreasing intensity of the two bands suggests the loss of some PSS chains from the PEDPT:PSS films after the treatment with the Cu^{2+} salts. In terms of these absorption spectra, the PSS loss increases with the treatment salts at this sequence: $CuSO_4$-treated < $CuCl_2$-treated < $CuBr_2$-treated PEDOT:PSS.

The PSS loss from the PEDOT:PSS films during the salt treatment is also confirmed by the S_{2p} XPS of the salt-treated PEDOT:PSS films (Fig. 3). The XPS bands with binding energies below and above 166 eV arise from the sulfur atoms in PEDOT and in PSS, respectively [33,37]. The intensity ratio of these XPS bands are related to the PSS loss from the PEDOT:PSS films. The PSS loss from PEDOT:PSS was observed in the XPS of the PEDOT:PSS films treated with polar solvents as well. The S_{2p} XPS intensity ratio of PEDOT to PSS increases after the salt treatment, and it increases at the sequence: untreated < $CuSO_4$-treated < $CuCl_2$-treated < $CuBr_2$-treated PEDOT:PSS. This is consistent with the absorption spectra of the salt-treated PEDOT:PSS films. These results can be interpreted in terms of the dissociation of the salts. A salt with higher dissociation gives rise to higher ion concentration, which can more effectively screen the Coulombic attraction between PEDOT and PSS chains, so that more PSS chains are removed from the PEDOT:PSS film during the salt treatment.

When salts of Cu^{2+} or In^{3+} that has positive softness parameter are used to treat the PEDOT:PSS, the metal ions can associate with PSS^- in PEDOT:PSS. This can result into the presence of the small anions from the salts into the PEDOT:PSS films. This is supported by the FTIR spectros-

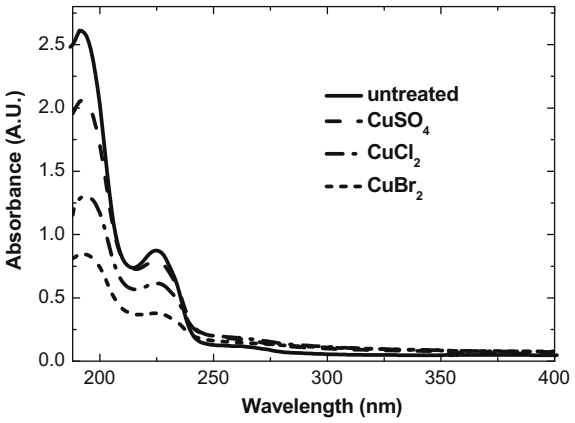

Fig. 2. UV–Visible absorption spectra of PEDOT:PSS films untreated and treated with 1 M $CuSO_4$, $CuCl_2$ and $CuBr_2$.

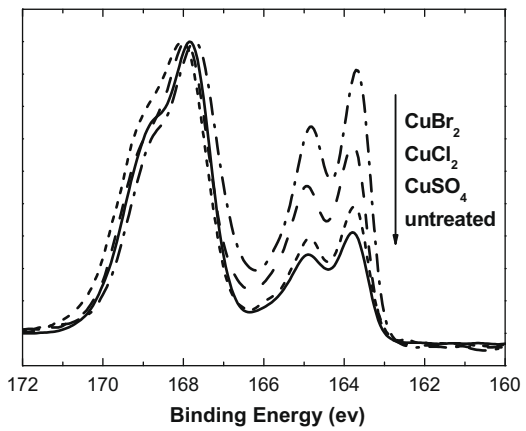

Fig. 3. S_{2p} XPS spectra of PEDOT:PSS films untreated and treated with 1 M $CuSO_4$, $CuCl_2$ and $CuBr_2$.

copy and XPS of the salt-treated PEDOT:PSS films. PEDOT:PSS films treated with salts of multi-atom anions, such as $CuSO_4$ and $Cu(ClO_4)_2$ were studied by the FTIR spectroscopy, since the multi-atom anions have IR-active vibrational bands. Fig. 4 shows the FTIR spectra of the untreated and $CuSO_4$-treated PEDOT:PSS films, $CuSO_4$ and poly(styrenesulfonic acid) (PSSH). Two vibrational bands at 661 and 603 cm^{-1} due to SO_4^{2-} were observed in the FTIR spectrum of the $CuSO_4$-treated PEDOT:PSS film. This suggests the presence of the SO_4^{2-} anions in the PEDOT:PSS films after the treatment with $CuSO_4$ solution.

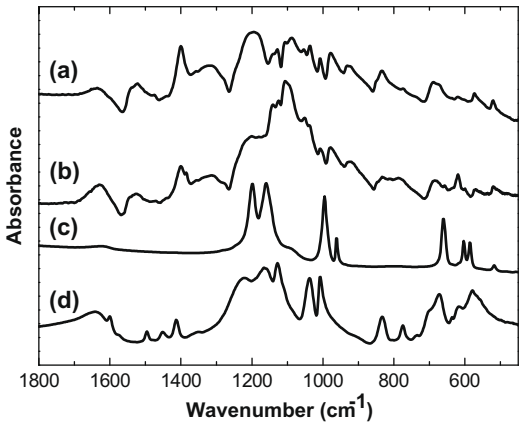

Fig. 4. FTIR spectra of (a) untreated PEDOT:PSS, (b) PEDOT:PSS treated with 0.1 M $CuSO_4$, (c) $CuSO_4$ and (d) PSSH.

The PEDOT:PSS films treated with salts of mono-atom anion, such as $CuCl_2$ and InI_3, were investigated by XPS. XPS signals of Cu^{2+}, Cl^- and In^{3+} were detected in the PEDOT:PSS films treated with these salts. This also indicates the presence of the salts in the PEDOT:PSS films after the salt treatment.

3.3. Morphology and conduction mechanism of PEDOT:PSS films

The loss of some PSS chains and the presence of salt in the PEDOT:PSS film can affect the film morphology. This is revealed by the AFM study of the salt-treated PEDOT:PSS films (Fig. 5). An as-prepared PEDOT:PSS film was quite smooth with a roughness of 1.06 nm. It became rough for the PEDOT:PSS film treated with 0.1 M $CuSO_4$ solution and quite rough for the one treated with 0.1 M $CuBr_2$ or 0.1 M InI_3 solution. The roughnesses were 1.86 nm, 2.59 nm, and 3.00 nm for the PEDOT:PSS films treated with 0.1 M $CuSO_4$, 0.1 M $CuBr_2$ and 0.1 M InI_3 solutions, respectively. The increase in the roughness is due to the increasing grain size after the salt treatment. The grain size increases at the sequence of untreated < $CuSO_4$-treated < $CuBr_2$-treated < InI_3-treated PEDOT:PSS. The increasing gain size can be attributed to the loss of some PSS chains from the PEDOT:PSS films.

The increased grain size can facilitate the charge transport across the grains. Effect of the salt treatment on the conduction mechanism was investigated by characterizing the temperature dependence of resistivities of the PEDOT:PSS films before and after the treatment with various

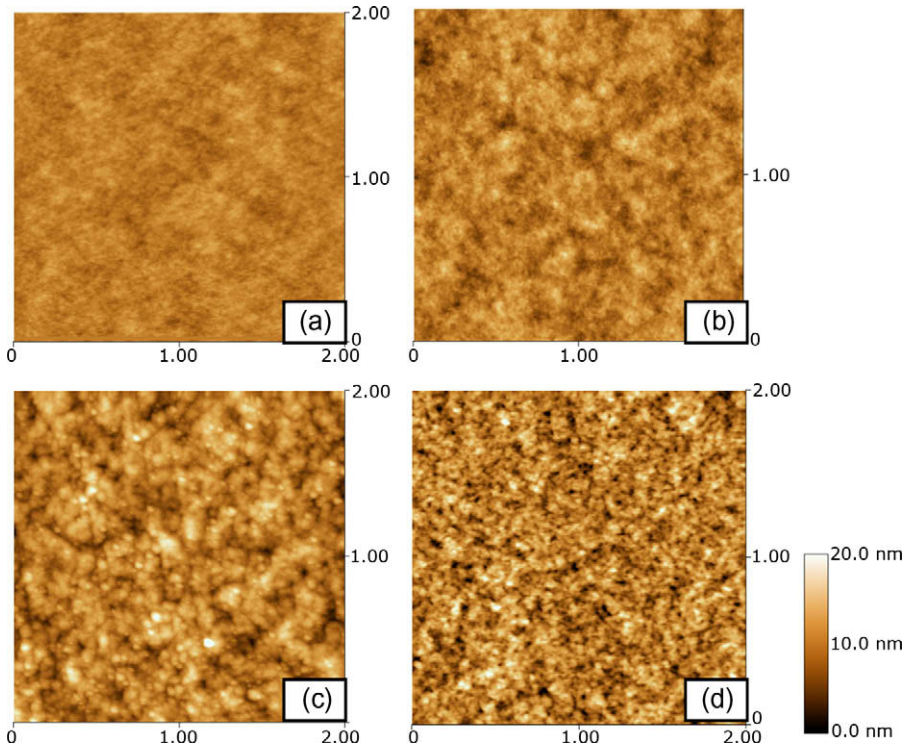

Fig. 5. AFM images of PEDOT:PSS films (a) untreated and treated with 1 M (b) $CuSO_4$, (c) $CuCl_2$ and (d) $CuBr_2$. The unit for the AFM images is μm.

salts. The resistivities of the PEDOT:PSS films treated with various solutions of 1 M Cu^{2+} salts was studied from 300 K down to 110 K (Fig. 6). The temperature dependences of the resistivities can be fitted by the one-dimensional variable range hopping (VRH) mechanism [10,38,16]

$$R(t) = R_0 \exp\left[\left(\frac{T_0}{T}\right)^{1/2}\right],$$

where $T_0 = 16/k_B N(E_F) L_{\parallel} L_{\perp}^2$ is the energy barrier between localized states with $N(E_F)$ being the density of the states at the Fermi level and $L_{\parallel}$ ($L_{\perp}$) being the localization length in the parallel (perpendicular) direction. The T_0 value remarkably changed for the PEDOT:PSS film after the salt treatment. It was 2660 K for the untreated PEDOT:PSS film, and it decreased to 974 K, 407 K and 359 K for the PEDOT:PSS films treated with 1 M $CuSO_4$, $CuCl_2$ and $CuBr_2$, respectively. The T_0 values are consistent with the conductivities of these PEDOT:PSS films at room temperature, which are 0.2, 33, 169 and 188 S cm^{-1} for the untreated, $CuSO_4$-treated, $CuCl_2$-treated and $CuBr_2$-treated PEDOT:PSS films, respectively. Therefore, the conductivity enhancement of the PEDOT:PSS film by the salt treatment can be attributed to the lowering energy barrier. The lowering energy barrier suggests that the salt treatment may increase the localization length.

3.4. Transient resistances of PEDOT:PSS during salt treatment

The anions of the salts can affect the dynamic process of the salt treatment, since they affect the dissociation of the salts and the association of the anions with $PEDOT^+$. This was studied by monitoring the resistance of the PEDOT:PSS films during the treatment with various salts (Fig. 7a). The configuration for the resistance measured is schematically shown in the inset of Fig. 7b. Indium (In) was pressed at the four corners of a PEDOT:PSS film to facilitate the electrical contact. Because the salt treatment was performed with indium at the four corners of each PEDOT:PSS film, the areas of the PEDOT:PSS film under indium were not treated by the salts, that is, the parts of the PEDOT:PSS film under indium kept the high resistance during the salt treatment. This is why the resistance decrease shown in Fig. 7a is less than in Table 1. Though the absolute transient resistances were not very meaningful, their change during the salt treatment provided important information for the dynamic process during the salt treatment.

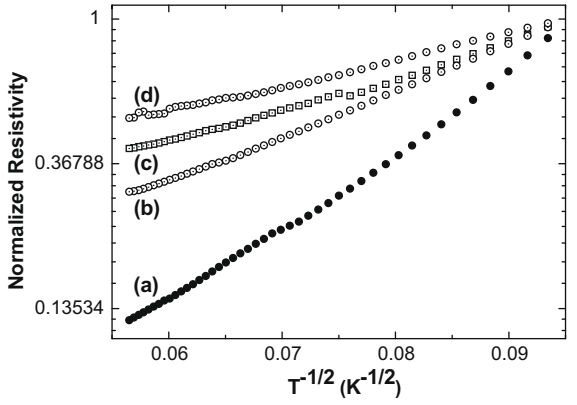

Fig. 6. Temperature dependences of the normalized resistances of PEDOT:PSS films. (a) Untreated and treated with 1 M (b) $CuSO_4$, (c) $CuCl_2$ and (d) $CuBr_2$. The resistances are normalized to that at 110 K.

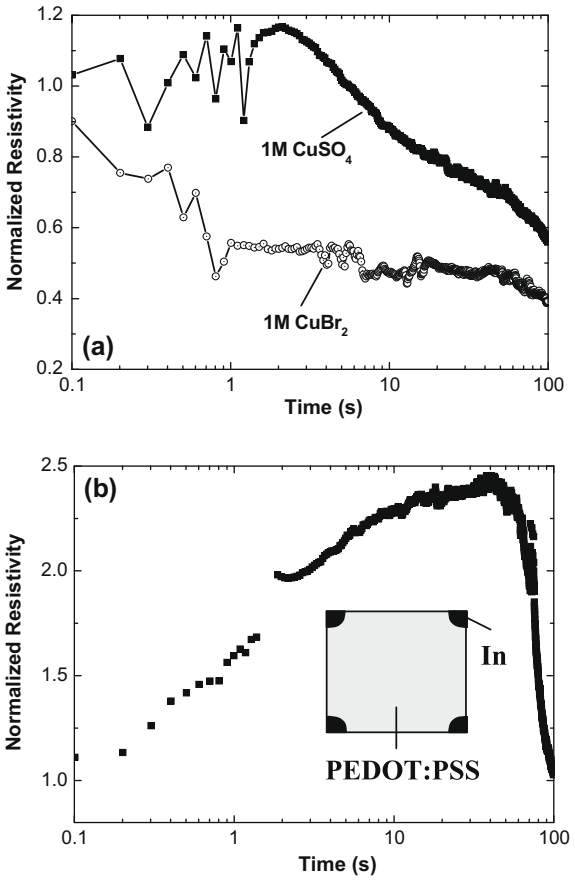

Fig. 7. Transient resistances of PEDOT:PSS films during the treatments. (a) 1 M $CuBr_2$ and 1 M $CuSO_4$ and (b) water. The resistances were normalized to the resistance of the as-prepared PEDOT:PSS film. The inset in (b) shows the configuration for the resistance measurements.

Fig. 7a presents the transient resistances of the PEDOT:PSS films during the treatment with 1 M $CuSO_4$ and 1 M $CuBr_2$ aqueous solutions. The resistance immediately decreased when the PEDOT:PSS film was treated with 1 M $CuBr_2$ solution, while it increased then gradually decreased when treated with 1 M $CuSO_4$ solution. The transient resistances are affected by two processes. One process is the swollen of the polymer chains by water, which gives rise to the decrease in the interchain charge transport and the increase in the resistance, as shown in Fig. 7b. Another process is the salt-induced resistivity decrease. The second process is the dominant process for the treatment with $CuBr_2$ aqueous solution, while the dominant process shifts from the first process to the second process for the treatment with $CuSO_4$ aqueous solution. The different transient resistances of the PEDOT:PSS films treated by the two salts can be attributed to the effect

of the anions on the dissociation of the salts and association with $PEDOT^+$.

4. Conclusions

The conductivity of the PEDOT:PSS film can be significant enhanced through a treatment with solutions of some salts. The anions of the salts can affect the salt-induced conductivity enhancement of the PEDOT:PSS film. Conductivity enhancement by a factor of more than 1000 was observed when the PEDOT:PSS film was treated with $CuBr_2$ or InI_3 aqueous solution, while the conductivity enhancement became less significant and negligible when the PEDOT:PSS film was treated with $CuSO_4$ and $Cu(CH_3COO)_2$ aqueous solutions, respectively. The anion effect on the conductivity enhancement of PEDOT:PSS is related to the competition of two processes, the dissociation of the salts and the association of the anions with $PEDOT^+$. A salt with a higher dissociation benefit the loss of more PSS chains from the PEDOT:PSS film after the salt treatment, so that it results into more significant conductivity enhancement.

Acknowledgement

The research work was financially supported by a grant from the Ministry of Education, Singapore (Project No.: RG-284-001-175).

References

[1] G. Heywang, F. Jonas, Adv. Mater. 4 (1992) 116.
[2] L. Groenendaal, F. Jonas, D. Freitag, H. Peilartzik, J.R. Reynolds, Adv. Mater. 12 (2000) 481.
[3] A. Chipman, Nature 449 (2007) 131.
[4] S. Forrest, P. Burrows, M. Thompson, IEEE Spectr. 37 (2000) 29.
[5] R.H. Friend, R.W. Gymer, A.B. Holmes, J.H. Burroughes, R.N. Marks, C. Taliani, D.D.C. Bradley, D.A. Dos Santos, J.L. Brédas, M. Lögdlund, W.R. Salaneck, Nature 493 (1999) 121.
[6] Y. Cao, G. Yu, R. Menon, A.J. Heeger, Synth. Met. 87 (1997) 171.
[7] Q. Pei, G. Zuccarello, M. Ahlskogt, O. Inganäs, Polymer 35 (1994) 1347.
[8] Y.H. Ha, N. Nikolov, S.K. Pollack, J. Mastrangelo, B.D. Martin, R. Shashidhar, Adv. Funct. Mater. 14 (2004) 615.
[9] G. Zotti, S. Zecchin, G. Schiavon, F. Louwet, L. Groenendaal, X. Crispin, W. Osikowicz, W. Salaneck, M. Fahlman, Macromolecules 36 (2003) 3337.
[10] J.Y. Kim, J.H. Jung, D.E. Lee, J. Joo, Synth. Met. 126 (2002) 311.
[11] L.A.A. Pettersson, S. Ghosh, O. Inganäs, Org. Electron. 3 (2002) 143.
[12] S.K.M. Jönsson, J. Birgerson, X. Crispin, G. Greczynski, W. Osikowicz, A.W. Denier van der Gon, W.R. Salaneck, M. Fahlman, Synth. Met. 139 (2003) 1.
[13] J. Ouyang, Q. Xu, C.W. Chu, Y. Yang, G. Li, J. Shinar, Polymer 85 (2004) 8443.
[14] X. Crispin, F.L.E. Jakobsson, A. Crispin, P.C.M. Grim, P. Andersson, A. Volodin, C. van Haesendonck, M. Van, W.R. der Auweraer, M. Salaneck, Berggren, Chem. Mater. 18 (2006) 4354.
[15] A.M. Nardes, M. Kemerink, M.M. de Kok, E. Vinken, K. Maturova, R.A.J. Janssen, Org. Electron. 9 (2008) 27.
[16] A.M. Nardes, R.A.J. Janssen, M. Kemerink, Adv. Funct. Mater. 18 (2008) 865.
[17] W.H. Kim, A.J. Mäkinen, N. Nikolov, R. Shashidhar, H. Kim, Z.F. Kafafi, Appl. Phys. Lett. 80 (2002) 3844.
[18] F. Zhang, M. Johansson, M.R. Andersson, J.C. Hummelen, O. Inganäs, Adv. Mater. 14 (2002) 662.
[19] C.S. Lee, J.Y. Kim, D.E. Lee, Y.K. Koo, J. Joo, S. Han, Y.W. Beag, S.K. Koh, Synth. Met. 135 (2003) 13.
[20] A.A. Argun, A. Cirpan, J.R. Reynolds, Adv. Mater. 15 (2003) 1338.
[21] J. Ouyang, C.W. Chu, F.C. Chen, Q. Xu, Y. Yang, Adv. Funct. Mater. 15 (2005) 203.
[22] J. Ouyang, Y. Yang, Adv. Mater. 18 (2006) 2141.
[23] S.I. Na, S.S. Kim, J. Jo, D.Y. Kim, Adv. Mater. 20 (2008) 4061.
[24] M. Döbbelin, R. Marcilla, M. Salsamendi, C. Pozo-Gonzalo, P.M. Carrasco, J.A. Pomposo, D. Mecerreyes, Chem. Mater. 19 (2007) 2147.
[25] B.H. Fan, X.G. Mei, J. Ouyang, Macromolecules 41 (2008) 5971.
[26] Y. Xia, J. Ouyang, ACS Appl. Mater. Interf. 2 (2010) 474.
[27] Y. Xia, J. Ouyang, Macromolecules 42 (2009) 4141.
[28] Y. Marcus, Thermochim. Acta 104 (1986) 389.
[29] Y. Marcus, in: A.G. Volkov, D.W. Deamer (Eds.), Liquid–Liquid Interfaces: Theory and Methods, CRC Press, Boca Raton, 1996, p. 39.
[30] R.D. Hancock, A.E. Martell, Chem. Rev. 39 (1989) 1875.
[31] U. Lang, E. Müller, N. Naujoks, J. Dual, Adv. Funct. Mater. 19 (2009) 1215.
[32] G. Greczynski, T. Kugler, M. Keil, W. Osikowicz, M. Fahlman, W.R. Salaneck, J. Electron. Spectrosc. Relat. Phenom. 121 (2001) 1.
[33] X. Crispin, S. Marciniak, W. Osikowicz, G. Zotti, A.W. Denier van der Gon, F. Louwet, M. Fahlman, L. Groenendaal, F. De Schryver, W.R. Salaneck, J. Polym. Sci. Part B-Poly. Phys. 41 (2003) 2561.
[34] A.M. Nardes, M. Kemerink, R.A.J. Janssen, J.A.N. Bastiaansen, M.M.M. Kiggen, B.M.W. Langeveld, A.J.J.M. van Breemen, M.M. de Kok, Adv. Mater. 19 (2007) 1196.
[35] Y. Li, J. Ouyang, J. Yang, Synth. Met. 74 (1995) 49.
[36] Q. Pei, O. Inganäs, J. Phys. Chem. 96 (1992) 10507.
[37] U. Voigt, W. Jaeger, G.H. Findenegg, R. Klitzing, J. Phys. Chem. B 107 (2003) 5273.
[38] J. Joo, S.N. Long, J.P. Pouget, E.J. Oh, A.G. MacDiarmid, A.J. Epstein, Phys. Rev. B 57 (1998) 9567.

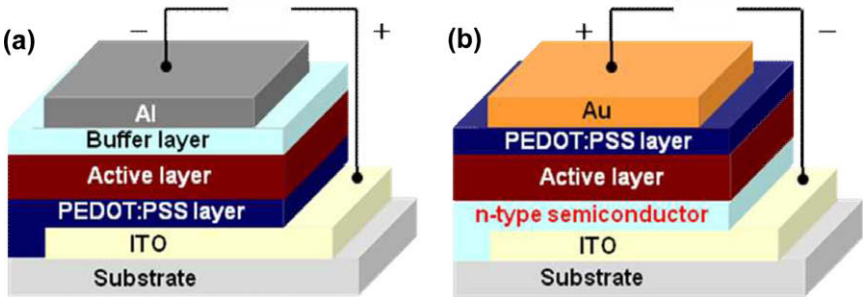

Fig. 1. Schematic structures of normal (a) and inverted-type organic solar cells (b).

continuous illumination for 100 h in pure air [17]. Therefore, its structure is expected as a promising approach from the viewpoints of durability improvement.

Chemical bath deposition (CBD) is one of the simplest methods for preparing semiconductor films as well as electrochemical deposition and sol–gel method, having an advantage such as low cost and easy technique to realize large area devices. TiO_2 or TiO_x may function as both of electron collection layer and hole blocking layer for organic solar cells [18,19]. However, to our knowledge, the CBD method for preparing titanium oxide layer has not yet been used to fabricate the PV device. In this paper, we report a readily-prepared CBD-TiO_x film working as electron collection layer of organic solar cells which exhibited PCE of 3.8% under the AM1.5G simulated sunlight.

2. Experimental

The ITO electrode was ultrasonicated in 2-propanol, and then cleaned in boiling 2-propanol, and subsequently dried in air. The CBD-TiO_x film was prepared according to the following procedure. A titanium(IV) oxysulfate ($TiOSO_4$) solution was added in a diluted hydrogen peroxide (H_2O_2) aqueous solution, and then the mixed solution was diluted just to 50 ml with ultrapure water. The concentrations of H_2O_2 and $TiOSO_4$ were adjusted to 0.03 M, respectively. This solution was transferred to a screw vial to use as the reaction bath for film deposition. The glass side of the ITO substrate was covered with an imide tape to prevent an extra deposition of TiO_x, and then the ITO substrate was immersed in the bath at 80 °C. The solution became cloudy by the application of heat, and after appropriate dipping time starting from this cloudy point, the immersed ITO substrate was pulled out from the bath. The as-deposited TiO_x film on the ITO was ultrasonicated for 10 min in water and heated on a hot plate at 150 °C for 1 h in air. Then, the chlorobenzene (CB) solution or the 2,6-dichlorotoluene: chloroform (1:1 by volume ratio, DCT:CHL) cosolvent solution containing poly(3-hexylthiophene) (P3HT) and [6,6]-phenyl C61 butyric acid methyl ester (PCBM) of 5:4 by weight ratio was spin-coated onto the ITO/TiO_x substrate in a glove box less than 1 ppm of moisture, being subsequently heated at 120 °C for 20 min on the hot plate. Then, a PEDOT:PSS dispersion solution was spin-coated onto the P3HT:PCBM layer in an simple glove box of the relative humidity less than 35%. An Au metal as the back electrode was vacuum-deposited on the PEDOT:PSS layer. Finally, the device was heated at 150 °C for 5 min on the hot plate in air and then at 70 °C for 30 min. The effective area of the solar cell was restricted to 1.0 cm^2 by depositing the Au electrode using a shadow mask. The photocurrent–voltage (*I–V*) curves of the solar cells were measured by linear sweep voltammetry (LSV) at a scan rate of 5 V min^{-1} under an AM 1.5G simulated sunlight with 100 mW cm^{-2} intensity. The light source was from a SAN-EI Electric XES-502S solar simulator calibrated by an EKO MS-601 pyranometer equipped with a silicon diode. All the dc electric measurements were implemented using a Hokuto Denko HZ-5000 electrochemical analyzer. All measurements were carried out for non-sealed devices in an ambient atmosphere, that is, at room temperature of 15–30 °C and under relative humidity of 40–60%.

3. Results and discussion

We assumed the deposition mechanism of a TiO_x film on the ITO electrode as follows:

$$(TiO^{2+} + H_2O_2 \rightarrow Ti(O)_2^{2+} + H_2O) \quad (1)$$

$$(mTi(O)_2^{2+} + nH_2O \rightarrow [TiO_p(OH)_q]_m \cdot rH_2O + 2mH^+) \quad (2)$$

$$([TiO_p(OH)_q]_m \cdot rH_2O \rightarrow mTiO_x + sH_2O), \quad (3)$$

where the italicized characters *m*, *n*, *p*, *q*, *r*, *s*, and *x* in the above equations are unknown numbers, although the *x* value in TiO_x is less than 2. Titanyl ions are oxidized to titanium(IV) peroxide ($Ti(O)_2^{2+}$) ions by H_2O_2 (Eq. (1)) at room temperature, then a titanium(IV) oxyhydroxide ($[TiO_p(OH)_q]_m \cdot rH_2O$) is deposited on the ITO plate by hydrolysis (Eq. (2)) around 80 °C. Finally, the as-deposited $[TiO_p(OH)_q]_m \cdot rH_2O$ is converted to the amorphous-titanium(IV) oxide (TiO_x) by heat treatment at 150 °C for 1 h in air (Eq. (3)). Fig. 2 shows the photographs before and after the hydrolysis in the chemical bath containing $TiOSO_4$ and H_2O_2. As-prepared CBD solution displays red color based on the generation of $Ti(O)_2^{2+}$ ions as shown in Fig. 2a. When heated at 80 °C for about 10 min, the solution got clouded defining as 0 s of deposition initiation, see Fig. 2b. Then, an increase in white turbidity was observed by keeping at 80 °C as shown in Fig. 2c–e.

Surface AFM images of the TiO_x films are shown against the dipping time in the chemical bath at 80 °C, see Fig. 3.

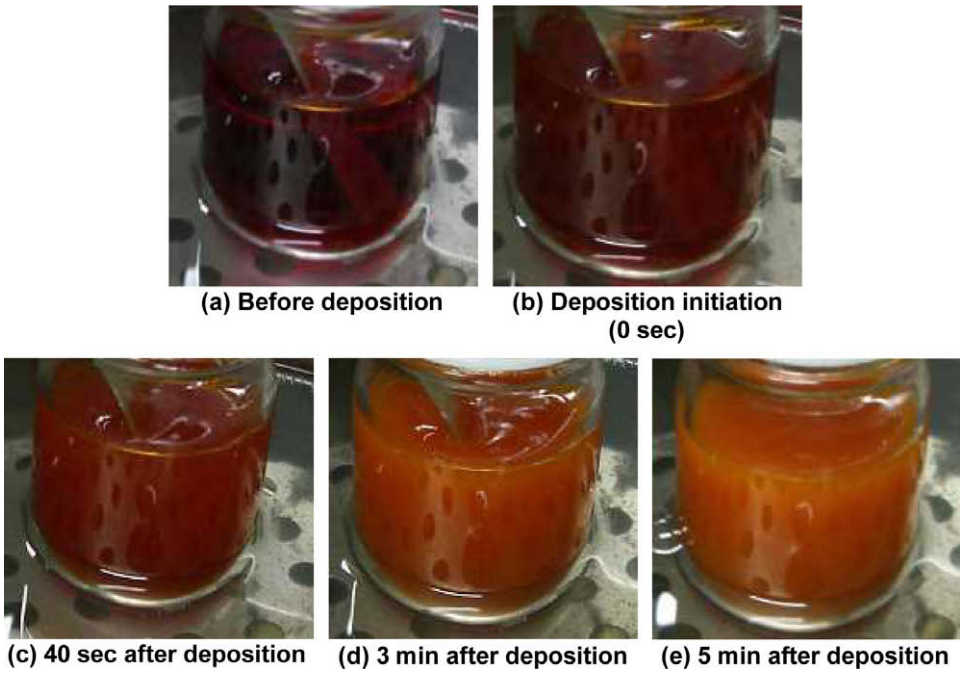

Fig. 2. Photographs before and after the hydrolysis in the chemical bath for depositing TiO_x.

The AFM images showed that the ITO substrates are gradually covered with TiO_x precursor particles. The film thickness of TiO_x film increased about linearly with the dipping time as shown in Fig. 4, but its film was considerably flat in the nano-scale, see the height scale of surface AFM images in Fig. 3.

The photo *I–V* curves of the ITO/CBD-TiO_x/PCBM:P3HT/PEDOT:PSS/Au solar cells with various thicknesses of the CBD-TiO_x layer is shown in Fig. 5, where the PCBM:P3HT (5:4 by weight ratio) blend film was prepared by spin-coating the CB solution. The cell without TiO_x layer showed the PCE of 0.82%, see dash curve in Fig. 5. Whereas the cell with TiO_x layer of 20 nm thickness exhibited a large increase in the short-circuit current (J_{sc}) and the fill factor (FF) due to rectification improvement, after all, we obtained the maximum J_{sc} of 7.22 mA cm^{-2}, the open-circuit voltage (V_{oc}) of 0.57 V, the FF of 0.57, and the PCE of 2.35%, see green solid curve in Fig. 5. This result shows that the CBD-TiO_x film acts effectively as an electron collection layer for the organic solar cell.

Fig. 6 shows the PCE change against irradiation time in air for the TiO_x cell without sealing. The PCE maintained 94% of the maximum value even after continuous light irradiation for 100 h. Further, even when the non-sealing TiO_x cell was put in relative humidity of 85% and at environmental temperature of 85 °C in the dark for 50 h, the PCE surprisingly maintained 54% of the maximum value. Very high stability was demonstrated for the non-sealing CBD-TiO_x inserted cell.

In order to improve the energy conversion efficiency of the solar cells, we have attempted to prepare an organic active layer with better morphology by thermal-annealing and controlling solvent evaporation speed after spin-coating. In a similar manner of previous report for the sol–gel TiO_x inserted solar cells [16], the PCBM:P3HT film prepared by DCT:CHL cosolvent solution showed slightly high PCE compared with that prepared by the CB solution in the CBD-TiO_x inserted solar cells, see Fig. S1. The cosolvent cell showed the J_{sc} of 8.49 mA cm^{-2}, the V_{oc} of 0.61 V, the FF of 0.62, and the PCE of 3.21%, reasonably increasing compared to the CB cell (PCE = 2.35%). The improvement of the device performance may be caused by a morphology change in the blend film suppressing the solvent evaporation rate by the DCT of higher boiling temperature. The PCE of the CBD-TiO_x inserted solar cell is by 30% higher than the PCE (2.47%) of the sol–gel TiO_x inserted solar cells under equal conditions [16]. This may be because the stabilizing agent such as acetylacetone remained in the sol–gel TiO_x film and resulted in higher film resistance. The morphology of the PCBM:P3HT film prepared by DCT:CHL exhibited much smaller nano-scale phase separation than that by CB, see Fig. S2. Therefore, the enhanced J_{sc} and FF as shown in Fig. S1 suggest that more well-connected networks were formed for each micro-separated phase of donor and acceptor in the PCBM:P3HT film prepared by DCT:CHL.

It is known that blending [6.6] diphenyl C62 bis(butyric acid methyl ester) (bis-PCBM) as an acceptor into P3HT as a donor enhances the V_{oc} of normal type solar cells compared to blending PCBM as the acceptor, because bis-PCBM has higher LUMO by ca. 100 meV than PCBM [20]. The performance of the CBD-TiO_x cell with the PCBM:P3HT or the bis-PCBM:P3HT prepared by DCT:CHL cosolvent is summarized in Table 1. The bis-PCBM cell showed the J_{sc} of 7.84 mA cm^{-2}, the V_{oc} of 0.76 V, the FF of 0.63, and the PCE of 3.81%. The photocurrent slightly decreased compared to the PCBM cell and the FF was the same. On the

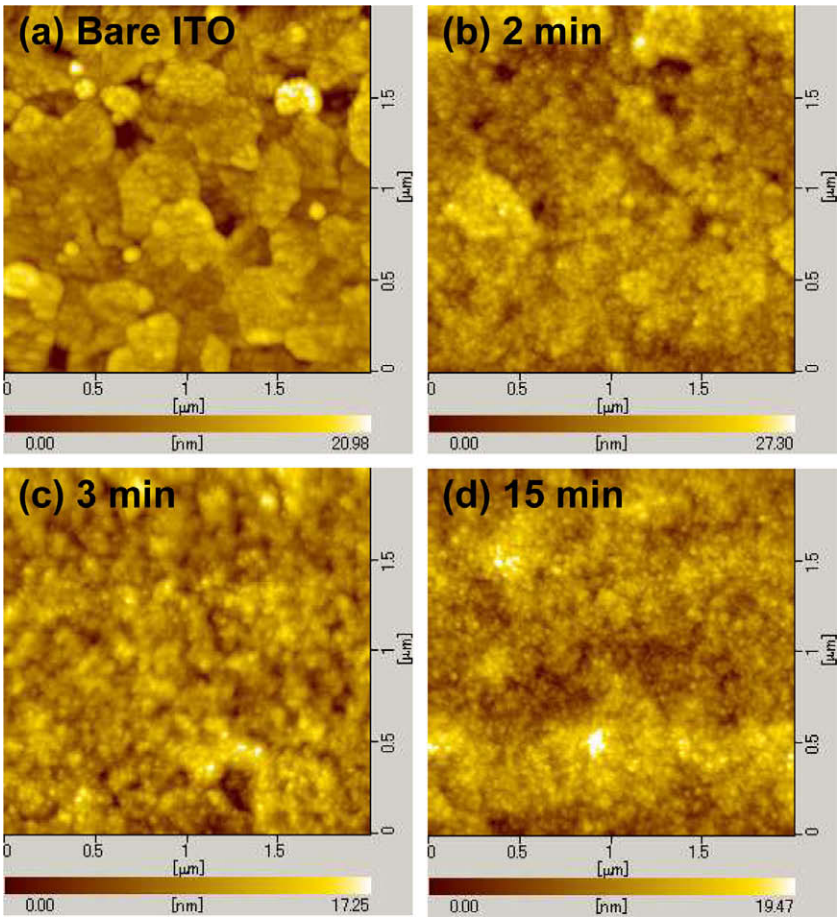

Fig. 3. Dipping time dependence of the surface AFM images of the TiO_x films prepared by CBD method. Dipping time: (a) 0 min (bare ITO), (b) 2 min, (c) 3 min, and (d) 15 min.

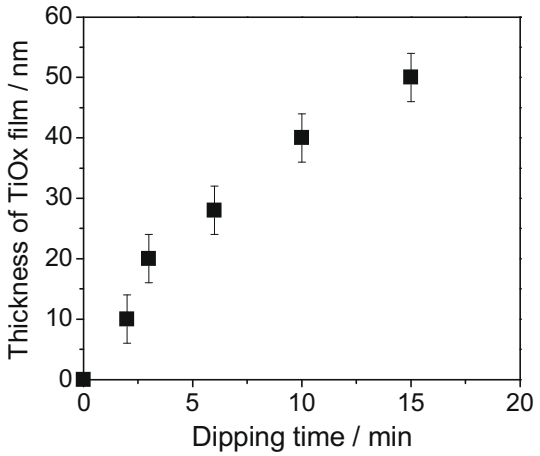

Fig. 4. Plots of the thickness of TiO_x film versus the dipping time.

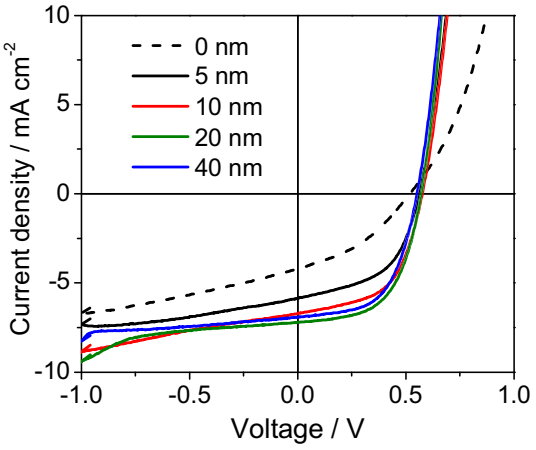

Fig. 5. Photo *I–V* curves of the organic solar cells with various thicknesses of the CBD-TiO_x layer. The PCBM:P3HT blend film was prepared using the CB solution.

other hand, the V_{oc} increased by ca. 0.15 V, leading higher PCE of the bis-PCBM cell. We confirmed that the V_{oc} increment by using bis-PCBM was obtained even for the inverted-type solar cell. The slightly decreased J_{sc} of the bis-PCBM:P3HT cell may be explained by the fact that

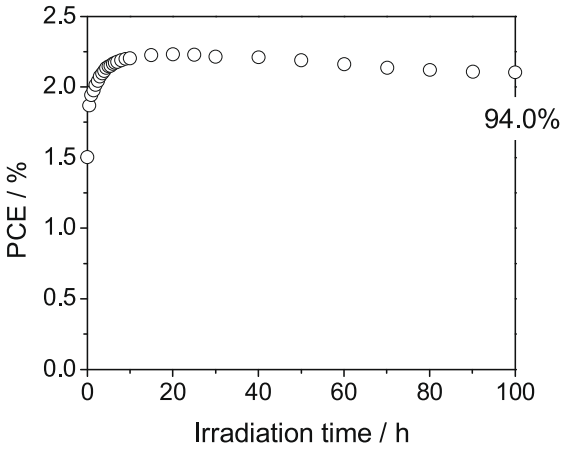

Fig. 6. Irradiation time dependence of the PCE for the non-sealed CBD-TiO_x inserted cell in air. The PCBM:P3HT blend film was prepared using the CB solution. The PCE maintained 94.0% of the maximum value (2.23%) even after continuous light irradiation for 100 h.

Table 1
Photovoltaic parameters of the PCBM:P3HT and bis-PCBM:P3HT solar cells under AM 1.5G light irradiation at 100 mW cm^{-2}.

Active layer	Solvent	J_{sc}/mA cm^{-2}	V_{oc}/V	FF	PCE/%
PCBM:P3HT	CB	7.22	0.57	0.57	2.35
PCBM:P3HT	DCT:CHL	8.49	0.61	0.62	3.21
bis-PCBM:P3HT	DCT:CHL	7.84	0.76	0.63	3.81

the electron transfer from donor P3HT to acceptor bis-PCBM became inconsiderably difficult due to the increase of the acceptor LUMO level.

4. Conclusion

In conclusion, we have proposed very convenient and useful CBD-TiO_x thin film as the electron collection layer of the inverted-type organic solar cell. In the ITO/CBD-TiO_x/bis-PCBM:P3HT/PEDOT:PSS/Au device, we obtained relatively large PCE value of 3.8%. We believe that the chemically stable CBD-TiO_x film works as a promising electron collection layer for developing polymer solar cells with high efficiency and high durability. Since the uniformed and air-stable CBD-TiO_x film can be easily prepared onto large-area ITO substrates in air, the fabrication of large-area inverted-type organic solar cell will be possible, being important to develop low-cost solar cells.

Acknowledgements

This work was supported by a Grant-in-Aid for Young Scientists (A) from the Ministry of Education, Culture, Sports, Science and Technology (21686011). This research was also supported by the Environment Research and Technology Development Fund (B-0807) of the Ministry of the Environment, Japan.

Appendix A. Supplementary data

Supplementary data associated with this article can be found, in the online version, at doi:10.1016/j.orgel.2010.04.008.

References

[1] B. Kippelen, J.-L. Bredas, Energy Environ. Sci. 2 (2009) 251–261.
[2] M. Helgesen, R. Sondergaard, F.C. Krebs, J. Mater. Chem. 20 (2010) 36–60.
[3] S.H. Park, A. Roy, S. Beaupre, S. Cho, N. Coates, J.S. Moon, D. Moses, M. Leclerc, K. Lee, A.J. Heeger, Nat. Photon. 3 (2009) 297–302.
[4] H.-Y. Chen, J. Hou, S. Zhang, Y. Liang, G. Yang, Y. Yang, L. Yu, Y. Wu, G. Li, Nat. Photon. 3 (2009) 649–653.
[5] H.-H. Liao, L.-M. Chen, Z. Xu, G. Li, Y. Yang, Appl. Phys. Lett. 92 (2008) 173303-1-3.
[6] R. Steim, S.A. Choulis, P. Schilinsky, C.J. Brabec, Appl. Phys. Lett. 92 (2008) 093303-1-3.
[7] W. Gaynor, J.-Y. Lee, P. Peumans, ACS Nano. 4 (2009) 30–34.
[8] M. Jorgensen, K. Norrman, F.C. Krebs, Sol. Energy Mater. Sol. Cells 92 (2008) 686–714.
[9] C.-H. Hsieh, Y.-J. Cheng, P.-J. Li, C.-H. Chen, M. Dubosc, R.-M. Liang, C.-S. Hsu, J. Am. Chem. Soc. 132 (2010) 4887–4893.
[10] F.C. Krebs, Org. Electron. 10 (2009) 761–768.
[11] F.C. Krebs, S.A. Gevorgyan, J. Alstrup, J. Mater. Chem. 19 (2009) 5442–5451.
[12] K. Takahashi, T. Nishi, S. Suzaka, Y. Sigeyama, T. Yamaguchi, J.-I. Nakamura, K. Murata, Chem. Lett. 34 (2005) 768–769.
[13] T. Kuwabara, H. Sugiyama, T. Yamaguchi, K. Takahashi, Thin Solid Films 517 (2009) 3766–3769.
[14] T. Kuwabara, M. Nakamoto, Y. Kawahara, T. Yamaguchi, K. Takahashi, J. Appl. Phys. 105 (2009) 124513-1-6.
[15] T. Kuwabara, Y. Kawahara, T. Yamaguchi, K. Takahashi, ACS Appl. Mater. Interfaces 1 (2009) 2107–2110.
[16] T. Kuwabara, T. Nakayama, K. Uozumi, T. Yamaguchi, K. Takahashi, Sol. Energy Mater. Sol. Cells 92 (2008) 1476–1482.
[17] F.C. Krebs, Sol. Energy Mater. Sol. Cells 92 (2008) 715–726.
[18] A. Hayakawa, O. Yoshikawa, T. Fujieda, K. Uehara, S. Yoshikawa, Appl. Phys. Lett. 90 (2007) 163517-1-3.
[19] G.K. Mor, K. Shankar, M. Paulose, O.K. Varghese, C.A. Grimes, Appl. Phys. Lett. 91 (2007) 152111-1-3.
[20] M. Lenes, G.-J.A.H. Wetzelaer, F.B. Kooistra, S.C. Veenstra, J.C. Hummelen, P.W.M. Blom, Adv. Mater. 20 (2008) 2116–2119.

printing. The PEDOT:PSS conducting polymer was Baytron P ink from H.C. Starck. The top electrode was printed using graphite ink or Ag-filled polymer thick film (DuPont).

The device fabrication methods were graphic arts printing methods. The CuPc layer and the PEDOT:PSS layer were deposited via spray coating due to their low viscosity. The thickness of the CuPc layer was between 0.5 and 1 μm, while the thickness of the PEDOT:PSS layer was between 1 and 1.5 μm. The pitch size for each bit was 1 mm for line and space. The Ag or graphite electrodes were then patterned by screen-printing or "doctor blading" to form top electrodes and complete the devices. No barrier layer or other protecting layer was required. In addition to the printed devices, a Cu/CuPc/PEDOT:PSS/Cu laminated structure was investigated. In the laminated structure, the CuPc and PEDOT:PSS were spray coated on two separate pieces of Cu coated PET films, which were then mechanically assembled through lamination.

The electrical behaviour of the devices was characterized using *I–V* and AC impedance methods. *I–V* measurements were performed with an EG&G 263A potentiostat. For each *I–V* test, the voltage was scanned forward and reverse at a rate of 1 V/s from 0 to +5 V. Impedance spectra were obtained on a Solartron 1255 Impedance/Gain Phase Analyzer interfaced with the 263A potentiostat over a frequency range of 100 kHz to 1 Hz with a 50 mV AC voltage. All processes and tests were performed under ambient conditions.

3. Results and discussion

In order to differentiate the contribution of printing-induced interface effects from materials related effects, we have compared the DC and AC characteristics of laminated Cu/CuPc/PEDOT:PSS/Cu with a fully printed Cu/CuPc/PEDOT:PSS/Ag device. Fig. 1 depicts the *I–V* curves from a laminated and a printed crossbar cell for comparison. Both curves clearly demonstrated a bi-stable behaviour with applied voltage bias. When a voltage scan was applied, the cell current was low (10^{-5} to 10^{-7} A) at first with an exponential "diode-like" behaviour until a threshold voltage (E_{th}) was reached. At E_{th}, the current suddenly jumped a few orders of magnitude followed by linear "ohmic" behaviour (see the inset in Fig. 1 for the linear current response). After switching to the ON state, the retention of this state can be observed in the subsequent reverse voltage scan showing that the current remained high with linear *I–V* response. Such *I–V* curves are characteristics of memory devices: the ON/OFF ratios for both laminated and printed devices were greater than 10^5 when reading at 1 V.

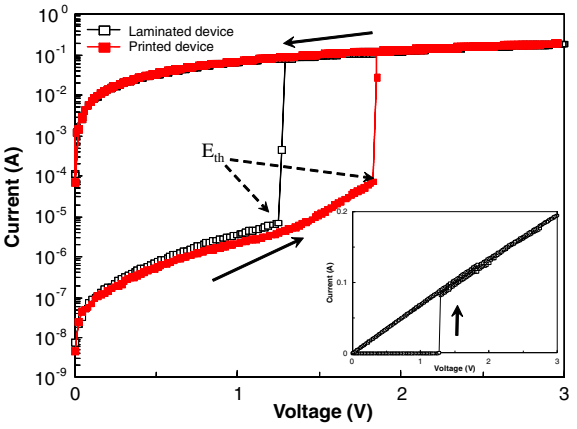

Fig. 1. *I–V* curves of printed and laminated memory device in log scale and linear scale (inset). The threshold voltages are labelled E_{th}.

However, one significant difference in the *I–V* curves for laminated and printed memory devices (Fig. 1) can be observed in the OFF state. While both displayed a similar initial current response in the OFF state, the printed device exhibited a second stage before switching to the ON state. Further analyses of the *I–V* curves for several known charge transfer mechanisms resulted in the best fit for the two stages, shown in Fig. 2. For both laminated and printed devices, it appeared that in the low voltage region Schottky charge injection from the electrode was the dominating factor. The second stage observed on the printed device fits well with Poole–Frenkel emission.

Since the printed cross-bar memory cells contain four material layers with three interfaces, we performed a layer-by-layer analysis to investigate their interfacial interactions. We measured the *I–V* curves of Cu/PEDOT:PSS, PEDOT:PSS/Ag and graphite ink (both serving as top electrodes) in direct contact, over the same voltage range as depicted in Fig. 1. The *I–V* of Cu/PEDOT:PSS, Ag/PEDOT:PSS, and C/PEDOT:PSS all showed linear current responses, suggesting ohmic contacts at these interfaces. Therefore, by elimination, we can infer that CuPc, a known hole-injecting semiconductor [7–12], is solely responsible

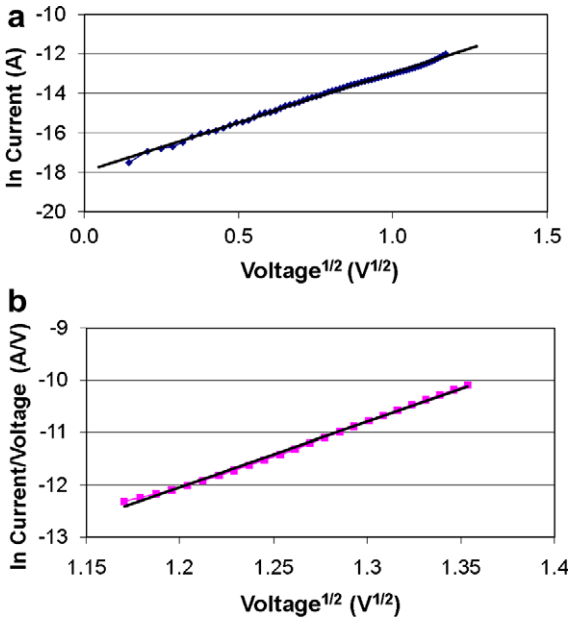

Fig. 2. Fitting of the *I–V* curve for printed Cu/CuPc/PEDOT:PSS/Ag memory in its OFF state against: (a) Schottky thermionic emission at low voltage; (b) Poole–Frenkel emission at medium voltage.

for the bi-stable behaviour observed in Fig. 1. In this case, PEDOT:PSS functioned as a hole-injection promoter as well as a conductive barrier to facilitate the printing process.

Electrochemical impedance spectroscopy (EIS) was further utilized to characterize the laminated and printed cross-bar memory cell before and after switching conditions. Fig. 3 shows the Bode plots of the laminated and printed devices in the ON and OFF states, respectively. Several interesting observations are worth noting in this figure:

1) In the ON state, impedance was under 100 Ω for both laminated and printed devices, while the phase angle was around 0°. This suggests that both devices behaved similar to pure resistors in the ON state and current was conducted through ohmic contact. This corresponds well to the *I*–*V* results in Fig. 1.
2) In the OFF state, the impedance values were in the mega-ohms range for both laminated and printed devices. The difference in the magnitude of the impedance between the ON and OFF states (Fig. 3a) was in the same order as the difference obtained from *I*–*V* measurements (Fig. 1).
3) Also in the OFF state, the phase angles of the laminated and printed devices deviated significantly from 0° (ON state), suggesting that very different current conduction mechanisms take place in the ON and OFF states.
4) Furthermore, the trend in the phase angle differed substantially between the laminated and printed devices. There was only one peak (−80°) at high frequency for the laminated device. In the case of printed device, we see a continuous distribution of phase angles from −75° at the high frequency region to around 30° at low frequencies with no clear peak distinctions.

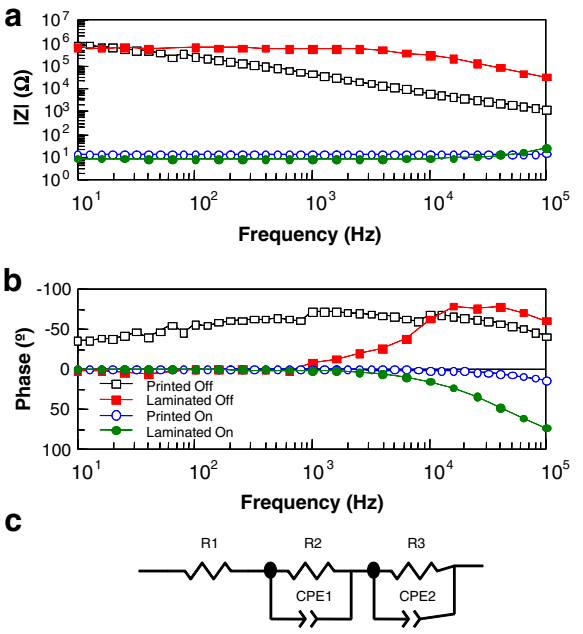

Fig. 3. Impedance spectra of a printed Cu/CuPc/PEDOT:PSS/Ag and a laminated Cu/CuPc/PEDOT:PSS/Cu memory device in OFF and ON states: (a) Bode plot for magnitude; (b) Bode plot for phase angle; (c) equivalent circuit model in OFF state.

Comparing the phase angle of both devices in the OFF state, the laminated structure had a single RC time constant. Based on our earlier work, we infer that CuPc is the sole layer responsible for the switching behaviour [6]. Considering the CuPc layer as the semiconducting layer in the laminated structure, we can see a single time constant derived from the CuPc layer in the Cu/CuPc/PEDOT:PSS/Cu structure. CuPc functioned as an insulator with capacitive Schottky-type current response (Fig. 2a) and high impedance in the OFF state until a voltage pulse switched the device to an ohmic current response and low impedance.

Judging from the phase angle, the printed device also had a near capacitive response at high frequencies which can be attributed to the capacitive behaviour of CuPc. This response was accompanied by a series of distributed elements at low frequencies. These elements and the Poole–Frenkel current conducting mechanism observed in Fig. 2b can be explained as follows: During the printing process, CuPc was sprayed down with a water based solution, and PEDOT:PSS containing water was sprayed on top of the CuPc layer, likely forming an intermediate layer containing a mixture of CuPc and PEDOT:PSS. Since PSS is a film forming polymer, we can consider this intermediate layer as a PEDOT:PSS film fused with the CuPc solid, which could be either continues or nodule-like. In such structure, one would expect to obtain a widely distributed phase angle as shown in Fig. 3b, as phase angles between 40° and 75° are an indication of a distribution of "leaking capacitors" and rough surfaces. This phenomenon is further supported by the curve fitting result in Fig. 2b for a Poole–Frenkel charge transfer. In a Poole–Frenkel mechanism, charge transfer occurs in the bulk of the materials which are filled with electrically charged defects [13,14], PEDOT and CuPc in this case. This intermediate layer does not form in the laminated structure, and therefore, in the laminated device we only see one RC due to the CuPc layer.

The impedance spectra of the printed devices fit well with a two time constant equivalent circuit (Fig. 3c). In this model, at high frequencies the spectra are dominated by a parallel RC component (also true for the laminated device), while at low frequencies a distributed (non-ideal) RC component dominates. In both cases, C is represented by the constant phase element (CPE), although the CPE at low frequencies is more like a "leaky" capacitor compared with the CPE at high frequencies. A similar equivalent circuit model was proposed for a barium/polymer/aluminum bistable system in [15], where the two RC time constants were attributed to capacitive switching followed by resistive switching. In our case, it is likely to be capacitive switching (Schottky) followed by bulk switching (Poole–Frenkel) until E_{th} is reached. When in the ON state, only the resistor is in effect. For writing and reading, having one-stage or two-stage current transmission before the ON state may not affect the overall behaviour. An alternative solvent for CuPc that is immiscible with the PEDOT:PSS solution could be used to remove the second stage if desired.

I–V and impedance measurements provided insights in terms of the current conducting mechanisms and the contributions from the manufacturing processes. Impedance spectroscopy is very sensitive to the surface and interface conditions and can provide additional information on the phase change which could not be detected by DC methods. Therefore, in the applications for cross-bar memories, one can track the variation either in resistance or phase or both, providing a much more flexible means for data storage, tracking, and management.

4. Conclusions

We have demonstrated printed Cu/CuPc/PEDOT:PSS/Ag (or C) WORM devices on a PET substrate and characterized these devices using both DC and AC techniques. The memories exhibited bi-stable behaviour with an ON/OFF ratio greater than 10^5. We examined the printing-induced material interactions in the fabricated device and observed a two-stage transition in the *I–V* curve, related to Schottky and Poole–Frenkel emission, the latter resulting from an interfacial layer formed due to the printing process. Impedance analysis proved to be an excellent tool to study this effect as it is able to deconvolute the two transmission processes.

Acknowledgements

The authors would like to thank the University of Toronto for financial support.

References

[1] R. Reuss, D. Hopper, J. Park, MRS Bull. 31 (2006) 447.
[2] M. Berggren, D. Nilsson, N. Robinson, Nat. Mater. 6 (2007) 3.
[3] D. Gamota, P. Brazis, K. Kalyanasundaram, J. Zhang, Printed Organic and Molecular Electronics, Kluwer Academic Publishers, 2004.
[4] M. Chason, D. Gamota, P. Brazis Jr., K. Kalyanasundaram, J. Zhang, K. Lian, R. Croswell, MRS Bull. 31 (2006) 471.
[5] S. Forrest, Nature 428 (2004) 911.
[6] K. Lian, J. Zhang, R. Li, H. Wang, W. Hsi, ECS Trans. 16 and 20 (2008) 35.
[7] A. Mahapatro, S. Ghosh, Appl. Phys. Lett. 80 (2002) 4840.
[8] W. Yu, J. Pei, Y. Cao, W. Huang, Appl. Phys. Lett. 89 (2003) 2343.
[9] Y. Yuan, S. Han, D. Grozea, Z. Lu, Appl. Phys. Lett. 88 (2006) 093503.
[10] S. Rajaputra, S. Vallurupalli, V. Singh, J. Mater. Sci. Electron. 18 (2007) 1147.
[11] G. Jarosz, J. Non-Cryst. Solids 352 (2006) 4264.
[12] H. Meng, N. Herron, in: Z. Li, H. Meng (Eds.), Organic Light Emitting Materials and Devices, vol. 305, CRC Press, 2006.
[13] R. McCreery, Chem. Mater. 16 (2004) 4477.
[14] Y. Yang, J. Ouyang, L. Ma, R. Tseng, C. Chu, Adv. Funct. Mater. 16 (2006) 1001.
[15] H. Gomes, A. Benvenho, D. de Leeuw, M. Colle, P. Stallinga, F. Verbakel, D. Taylor, Org. Electron. 9 (2008) 119.

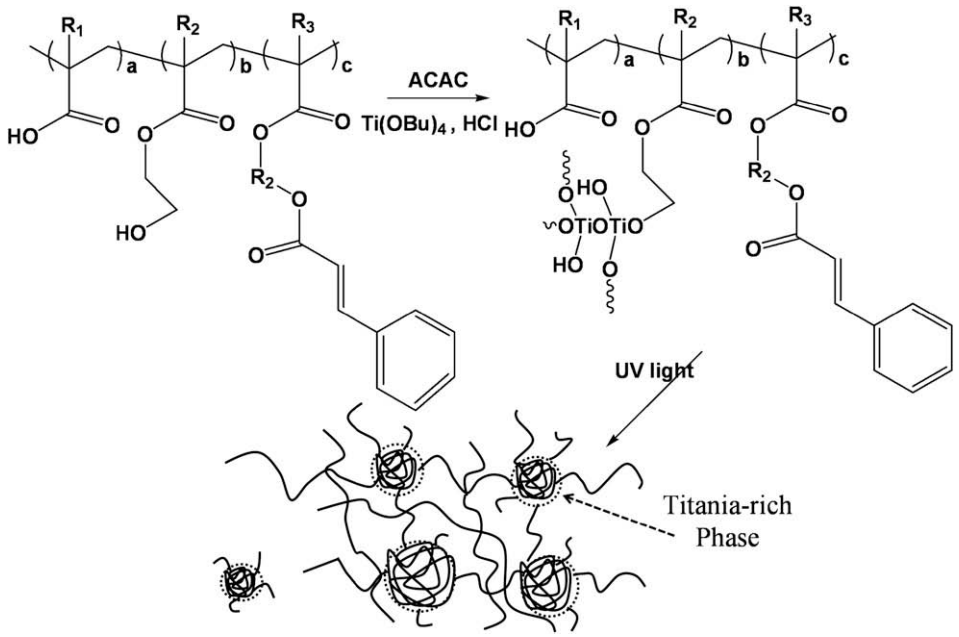

Fig. 1. Flow chart of hybrid fabrication process for sol–gel reaction and UV curing in this study.

Table 1
Compositions of sol–gel mixtures for preparing hybrid thin films as gate dielectrics and electrical parameters of OTFTs fabricated using sol–gel mixtures.

Sample	Composition				Parameter		
	DCS-SP210 (g)	$Ti(O–Bu)_4$ (g)	ACAC (g)	0.1 N HCl (g)	V_{th} (V)	μ_{eff} ($cm^2 V^{-1} s^{-1}$)	I_{on}/I_{off}
DCS-SP210	10	–	–	–	−11.13	0.10	2.5×10^4
SG10	8.454	0.8	0.235	0.082	−12.91	0.14	2.0×10^4
SG20	7.514	1.6	0.470	0.165	−4.12	0.34	1.6×10^4
SG30	6.575	2.4	0.706	0.248	−2.81	0.86	1.0×10^4
SG40	5.625	3.2	0.941	0.330	−1.21	0.54	10^3

at 25 °C under magnetic stirring for 2 h (molar ratio of $Ti(O–Bu)_4$/ACAC = 1/1). ACAC prevented $Ti(O–Bu)_4$ from forming crystalline precipitates by acting as a chelating agent prior to the sol–gel reaction [12,13]. Subsequently, 0.082 g of 0.1 N HCl and 8.454 g of DCS-SP210 were added to the solution at 25 °C and stirred for 10 h (molar ratio of $Ti(O–Bu)_4/H_2O$ (0.1 N HCl) = 1/2). The other samples (Table 1) followed the same procedure. The sol–gel reaction was heated at 80 °C for 30 min after spin-coating in the absence of UV light. The coated hybrid film was patterned through shadow mask (gab 150 μm) by exposure to 365 nm UV irradiation (200 mJ/cm^2), which induced polymerization by free radical initiation, was developed to remove uncured region by KOH developing solution (Dongjin Semichem Co., Ltd.; DCD-260CF), and was subsequently cured at 120 °C for 1 h. The hybrid film prepared in this manner was composed of cross-linked acrylic resin matrix and titania matter.

Organic thin-film transistors were fabricated on glass substrates using bottom-gate/top-contact geometry. Gold was used as the gate metal on a molybdenum buffer layer, and the sol–gel hybrid acrylic resin was used as a gate dielectric. The sol–gel mixtures were spun onto the gate metal at 2000–3000 rpm for 30 s. Hybrid films were fabricated by heating and irradiating with UV light, producing a layer of the thickness 800–1000 nm. The pentacene active layer (pentacene, Aldrich, was used without purification) was fabricated by thermal evaporation deposition, producing a layer of the thickness 80 nm, measured by a surface profiler (Alpha-Step, P-10, Tencor). The top contact OTFT devices were fabricated with variable channel width to length (W/L) and metal–insulator–metal (MIM) structures were also fabricated to analyze the electrical characteristics of organic/inorganic hybrid films on one substrate in this study.

The dielectric constant and frequency characteristics were obtained from signal capacitance measurements (impedance analyzer, SI 1260, Solartron Analytical) on the SG samples and on acryl UV resin. The current–voltage (I–V) characteristics were obtained using a Keithly 236 source-measure unit, operated by a local Igor program with GPIB communication. All the electrical characteristics of OTFTs were carried out using two Keithly 236 source-measure units, in a dark room.

3. Results and discussion

Hybrid thin films were prepared by spin-coating, UV curing, and submitting to the sol–gel reaction using the

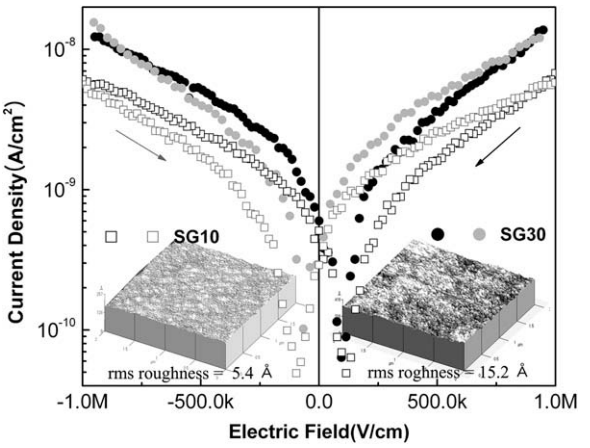

Fig. 2. Leakage current density versus electric field for hybrid dielectric films with different titania (TiO_2) content. Film thicknesses were 890 (SG10) and 995 nm (SG30). Insets show AFM images of hybrid dielectric films.

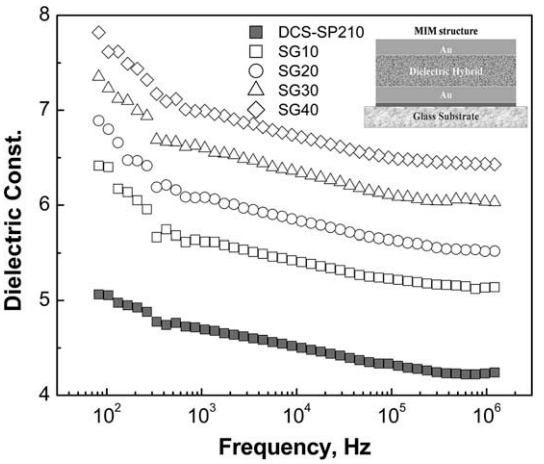

Fig. 3. Dielectric constant versus frequency characteristics with different titania (TiO_2) content. The Inset shows MIM structure employed.

procedure described in Section 2. AFM images of SG samples demonstrated that the surface morphology depended on the theoretical titania (TiO_2) content of the hybrid (Fig. 2). An increase in the theoretical titania (TiO_2) content in the mixture appeared to contribute to an increase in rms roughness. In principle, materials prepared via the sol–gel reaction due to forming crystalline phase are porous, but in this study we observed that the hybrid materials prepared via UV curing and the sol–gel reaction at nearly the same time as described previously were not porous for the reason of controlling nano crystalline phase. Hybrid films were relatively smooth, with a low rms roughness of 5.4–15.2 Å that increased with titania (TiO_2) content, and exhibited no major defects. The rms roughness of SG samples, evaluated via the *I–V* characteristics, also revealed quantitative leakage currents for the gate insulators. Fig. 2 shows typical the current density–electric field (*I–V*, exactly *J–E*) plots for a MIM structure fabricated with SG samples. Leakage current densities of at 1 MV/cm of SG samples are 5.8 nA/cm^2 (SG 10) and 12 nA/cm^2 (SG 30), respectively. Although the leakage current increased with the presence of a titania-rich phase structure in the hybrid dielectrics, SG samples acted as gate insulators in the OTFTs due to the high dielectric constant. Fig. 3 shows the dielectric constant–frequency plot for a MIM structure fabricated with cross-linked acrylic resin and SG samples. Dielectric constants increased with titania (TiO_2) content of the hybrid, but hybrid films with amorphous titania phase have the relatively low value. The dielectric constants were calculated using the equation for MIM structures:

$$C = \kappa\varepsilon_0 A/t \quad \text{(MIM structure)} \tag{1}$$

where C is the measured capacitance, ε_0 is the permittivity of free space, A is the area of the capacitor, and t is the thickness of the dielectric film. The use of high-κ materials could afford greater or comparable surface charge density at the interface with lower leakage currents even if the thicker insulators are applied. From this point of view, the possibility of dielectric constant control is one of the advantages for the hybrid dielectrics. In this study, hybrid films which have been considered both suitable capacitance and leakage currents were fabricated with a layer of the thickness 800–1000 nm.

OTFTs were fabricated using SG samples as gate insulators and pentacene as the active layer, as described in Section 2. Fig. 4(a) shows typical transfer characteristics of OTFTs, I_{ds}, $(I_{ds})^{1/2}$ versus V_g, for the device with an SG sample as the gate insulator. Transfer characteristics were determined by the saturation region, as described by the following equation:

$$I_{ds} = \frac{WC_i}{2L}\mu(V_g - V_{th})^2 = \frac{W}{2L}\frac{\kappa\varepsilon_0}{t}\mu(V_g - V_{th})^2 \quad \text{(at the saturation region)} \tag{2}$$

where C_i is the capacitance per unit area of gate insulator, V_{th} is the threshold voltage, and μ is the effective mobility. In this study, the channel width (W) and the channel length (L) of OTFTs were 2000 and 100 μm, respectively. The OTFT data and parameters calculated from (1) and (2) are summarized in Table 1. In general, the carrier mobility of OTFTs with the conventional hybrid gate insulator is deteriorated because crystalline inorganic nanoparticles blended in polymer matrix act as a charged center and a surface phonon. In addition, the blended nanoparticles increase surface roughness and –OH groups which increase the leakage current [14]. In this study, the measured carrier mobility of SG 30 was higher than that of other samples. The measured mobility was shown to be ~0.86 cm^2/V s. It was thought that the presence of the titania (TiO_2)-rich site as the amorphous phase at the interface had any effect on active sites for pentacene deposition. Furthermore, inorganic/organic hybrid in amorphous phase decreased density of –OH groups thus leakage current was reduced as shown in Fig. 4. In Fig. 4, the hysteresis behavior of SG 30 compared to SG 10 showed negligible

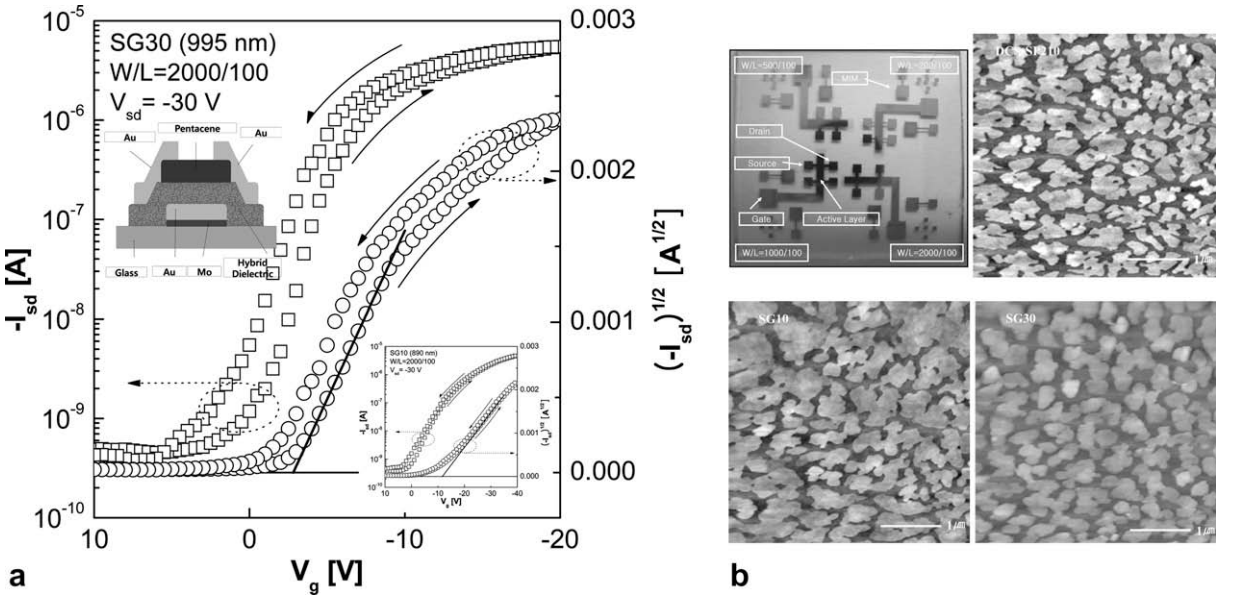

Fig. 4. (a) Transfer characteristics of OTFTs with SG30 (995 nm) and SG10 (890 nm) (the inset graph) as gate insulators. Insets show the cross sectional view of bottom-gate/top-contact OTFT employed. (b) The structure of devices fabricated in this study and atomic force microscopy images of pentacene films (5 nm) deposited on DCS-SP210, SG10, and SG30.

change, this means that the amorphous titania (TiO_2)-rich site inhibits the formation of –OH group.

Pentacene grain size of SG30 was little small, but characteristics of OTFTs were not bad. However, an excess of the titania (TiO_2)-rich sites disturbed pentacene deposition, as observed for SG 30. I_{on}/I_{off} of SG10 samples was shown to be $\sim 10^4$ larger than for other samples. I_{on}/I_{off} was not as high due to leakage current, although the output current could be enhanced by the high-κ gate insulator of the sol–gel hybrid. Threshold voltage decreased with the increase of dielectric constant according to the titania (TiO_2)-content in the sample. One result was reported by Kang et al., where V_{th} of OTFT using amorphous Gd_2O_3 as the gate insulator was smaller than crystalline SiO_2 despite the size of pentacene and the roughness of the gate insulator at the interface [15]. It was thought that amorphous titania site at the interface had any effect pentacene grain. Additional research is necessary to understand this behavior further. It was thought that in light of these results, the characteristics of OTFTs prepared with sol–gel hybrid gate insulators were sensitive to the quantity of the titania (TiO_2)-rich sites. This problem is likely to be resolved by enhancing control of the sol–gel process.

4. Conclusion

In summary, we have shown that a hybrid material formed by the appropriate combination of polymer and amorphous titania (TiO_2)-rich phase produces high capacitance relatively low-leakage gate dielectric materials. These hybrid films are easily deposited, can be patterned, are characterized by controllable dielectric constants, and are suitable for gate insulators in OTFTs. Gate insulators formed from hybrid films constitute alternatives to other candidate materials for flexible OTFTs.

Acknowledgements

This research was supported by a Grant (code #: 2009k000463) from 'Center for Nanostructured Materials Technology' under the '21st Century Frontier R&D Programs' of the Ministry of Science and Technology, Korea.

References

[1] J. Collet, O. Tharaud, A. Chapoton, D. Vuillaume, Appl. Phys. Lett. 76 (2000) 1941.
[2] J.-M. Kim, J.-W. Lee, J.-K. Kim, B.-K. Ju, J.-S. Kim, Y.-H. Lee, M.-H. Oh, Appl. Phys. Lett. 85 (2004) 6368.
[3] T.W. Kelley, L.D. Boardman, T.D. Dunbar, D.V. Muyres, M.J. Pellerite, T.P. Smith, J. Phys. Chem. B 107 (2003) 5877.
[4] M.-H. Yoon, H. Yan, A. Facchetti, T.J. Marks, J. Am. Chem. Soc. 127 (2005) 10388.
[5] H.-W. Zan, K.-H. Yen, Electrochem. Solid-State Lett. 11 (2008) H222.
[6] F.-C. Chen, C.-W. Chu, J. He, Y. Yang, J.-L. Lin, Appl. Phys. Lett. 85 (2004) 3295.
[7] R. Schroeder, L.A. Majewski, M. Grell, Adv. Mater. 17 (2005) 1535.
[8] C.G. Choi, B.-S. Choi, Org. Electron. 8 (2007) 743.
[9] H.Y. Noh, Y.G. Seol, S.I. Kim, N.-E. Lee, Electrochem. Solid-State Lett. 11 (2008) H218.
[10] J.-M. Choi, J.H. Kim, S. Im, Appl. Phys. Lett. 91 (2007) 083504.
[11] O. Acton, G. Ting, H. Ma, A.K.-Y. Jen, Appl. Phys. Lett. 93 (2008) 083302.
[12] U. Schubert, J. Mater. Chem. 15 (2005) 3701.
[13] J.-M. Yeh, C.-J. Weng, K.-Y. Huang, H.-Y. Huang, Y.-H. Yu, C.-H. Yin, J. Appl. Polym. Sci. 94 (2004) 400.
[14] C.S. Kim, S.J. Jo, S.W. Lee, W.J. Kim, H.K. Baik, S.J. Lee, Adv. Funct. Mater. 17 (2007) 958.
[15] S.J. Kang, K.B. Chung, D.S. Park, H.J. Kim, Y.K. Choi, M.H. Jang, M. Noh, C.N. Whang, Synth. Met. 146 (2004) 351.

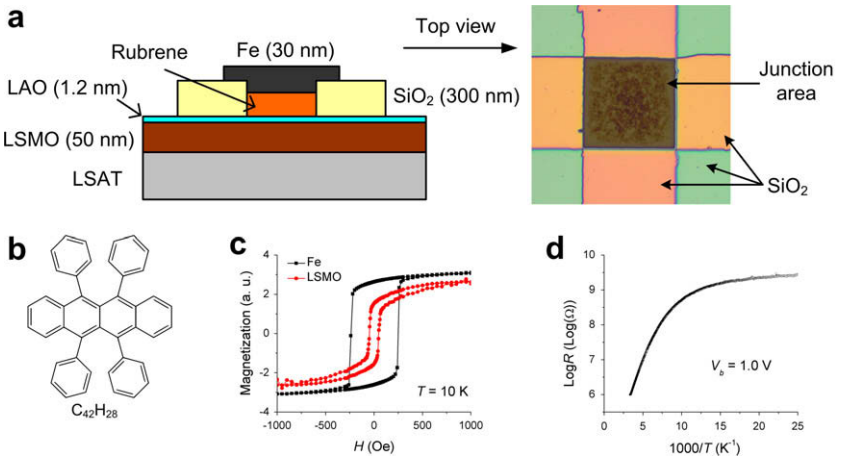

Fig. 1. (a) The schematic device structure. On the right side is the optical image of the cross-section. 50 nm rubrene is deposited in the center area of 0.2 mm by 0.2 mm surrounded by SiO_2. 30 nm Fe film will be deposited on top of rubrene layer. (b) Chemical structure of rubrene ($C_{42}H_{28}$). (c) Magnetic hysteresis loops of LSMO (50 nm) on LSAT (0 0 1) substrate and Fe (30 nm) on glass substrate. (d) Temperature dependent resistance (OFF state) of the LSMO (50 nm)/LAO/rubrene (50 nm)/Fe (30 nm) junction.

by 0.2 mm was enclosed by 300 nm SiO_2 deposited by e-beam. The sublimed rubrene (Aldrich) was used as an organic semiconductor channel and thermally deposited with controlled source temperature (~105 °C). The thickness of the rubrene layer was measured by a quartz crystal monitor and verified with a profilometer. A rigorous inspection of the surface morphology over wide range of area via AFM showed the typical RMS roughness of our thermally deposited rubrene layer was 1 ± 0.3 nm and maximum peak to peak distances were 7 ± 3 nm. On top of the rubrene layer, 30 nm of Fe was used as a second ferromagnetic layer which was deposited by e-beam evaporation. The magnetotransport measurements were performed using a Quantum Design Physical Property Measurement System (PPMS) with an external Keithley 2400 sourcemeter. Fig. 1(c) displays the magnetic hysteresis loops of a 50 nm LSMO film on LSAT (0 0 1) substrate and a 30 nm Fe film, respectively.

3. Results and discussion

The temperature dependence of the resistance of the device LSMO/LAO/rubrene (50 nm)/Fe in the initial OFF state is presented in Fig. 1(d). This temperature dependent resistance reflects the carrier injection at the metal/organic interface, which introduces the strong increase of the device resistance as the temperature is lowered. This effect of carrier injection typically saturates below 100 K [14]. Further increase of the device resistance below 100 K can be attributed to the hopping transport in the bulk of rubrene layer. This temperature dependent resistance indicates the device in the initial OFF state is controlled by carrier transport through the bulk of the organic semiconductor layer and free of pinhole channels and/or filamentary conduction channels of metallic inclusions. The current versus voltage curves were recorded in a series of bias scans at 10 K, using a two-probe configuration. Fig. 2 displays typical *I–V* curves of our device, which show the electrical bistable effect. In the first sweep, the device shows very low current in the high negative bias to low positive bias range, indicating it stays in the OFF state. However, at a threshold bias, about 4.5 V, the current increases sharply, showing the device has undergone a transition from the OFF state to the ON state. This transition can be regarded as the "write" operation in the digital memory. Furthermore, the device is able to remain in the ON state without any supplied power, which is an essential characteristic of the non-volatile memory. In the second bias sweep, started at +5 V, the current remains at the high level. The *I–V* curve is completely different from the first scan, indicating the device remains in the ON state. The device will not recover to the initial OFF state unless a high negative bias (−5 V) is applied, and this process is analogous to the "erase" operation in the digital memory. The third bias scan is identical with the fist one, and the *I–V*

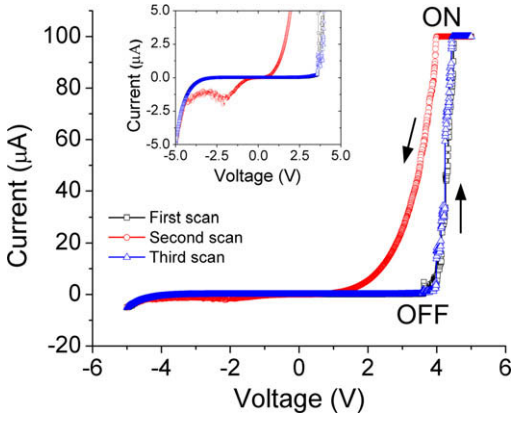

Fig. 2. *I–V* curves of the hybrid organic bistable device of structure LSMO (50 nm)/LAO/rubrene (50 nm)/Fe (30 nm) at 10 K. Initially, the device is in the OFF state. At about 4.5 V, the current increases sharply, indicating the transition of the device from the OFF to the ON state. The device is able to return to the OFF state by applying a high negative voltage. The inset shows the enlarged curves near zero bias.

curve overlaps the first sweep curve. The comparison of the *I–V* curves in the two states at different temperatures is displayed in Fig. 3. The current goes up as the temperature increases, and the two states are distinct at both low temperature and room temperature.

In addition to the electrical bistability, the magnetic field dependence of the device resistance was measured while an in-plane magnetic field was swept from +3000 Oe to −3000 Oe and then back to +3000 Oe. The spin valve magnetoresistance (MR) value is defined as: MR (%) = 100 × ($R_{AP} - R_P$)/R_P, where R_{AP} and R_P refer to the device resistance when the magnetization directions of the two ferromagnetic layers are anti-parallel and parallel, respectively. We obtained a spin valve MR value of up to 3.75% in the ON state, while no spin valve effect was observed in the OFF state. Fig. 4(c)–(e) shows the magnetoresistance curves of a 50 nm rubrene device in the ON state with a bias of 2.0, 2.5 and 3.0 V, respectively. The bias voltage dependence of the spin valve MR value is presented in Fig. 4(f), and the maximum spin valve MR 3.75% was obtained when 3.0 V was applied. We emphasize here that the spin valve effect of our device was controllable via applied bias, and it was observed only when the device was in the ON state. We did not observe this spin valve effect in room temperature, because the polarization of the LSMO decreases as the temperature increases [18]. Another difference of the magnetoresistance curves between the two states is the shape. As shown in Fig. 4(a) and (b), the high field magnetoresistance curve in the OFF state is almost flat, while the high field magnetoresistance curves in the ON state show a "wing" shape that the device resistance decreases as the external magnetic field increases. We define a high field magenetoresistance (HFMR) as HFMR (%) = 100 × ($R(0)_{max} - R(\pm 3000\ Oe)_{min}$)/$R(0)_{max}$.

Several mechanisms have been proposed to explain the electrical bistability of OBDs. Ma et al. developed a model for their three-layer OBDs involving the polarization of the metal-nanoparticle layer and charge storage at the interfaces between the nanoparticle layer and organic semiconductor [5]. Bozano et al. claimed that charge trapping and space-charge field inhibition of injection should be the reason for the resistive switching [6,7]. Cölle et al. suggested that switching was due to the oxide layer at the electrode and transport through filament [19]. Other proposed mechanisms include the bulk phenomena of the organic material [20], and the existence of localized conducting microchannels [21], etc.

Here, we propose an explanation for this combination of the electrical bistability and the bias-controlled spin valve effect. The magnetoresistance curves we obtained from the ON state show additional "wing" shape magnetoresistance. Note this shape of MR effects is similar to the reported results of Sakai et al. in a Co–C_{60} hybrid nanocomposite channel [22] and Kusai et al. in a Co–rubrene hybrid nanocomposite channel between nonmagnetic electrodes [23]. The MR effects in those previous results were attributed to the spin dependent tunneling between the Co nanoparticles through the organic molecules. Another similar MR behavior can be found in the phenomenon that was termed organic magnetoresistance (OMAR) [24–27]. In our de-

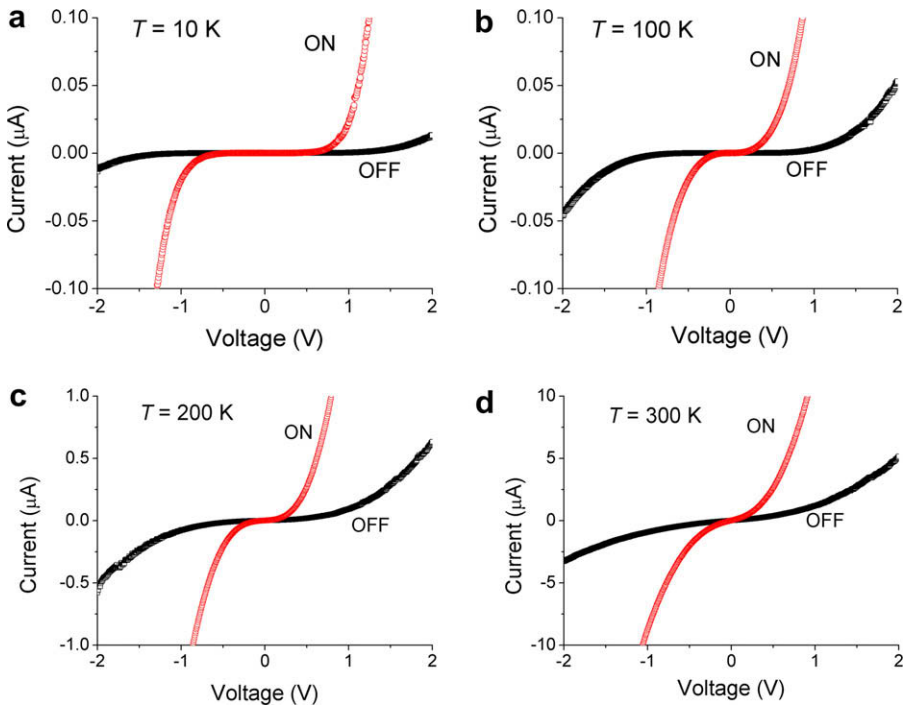

Fig. 3. Temperature dependence of the *I–V* curves. Red circles represent data points in the ON state, and black squares represent data points in the OFF state. (a) *T* = 10 K. (b) *T* = 100 K. (c) *T* = 200 K. (d) *T* = 300 K. (For interpretation of the references to colour in this figure legend, the reader is referred to the web version of this article.)

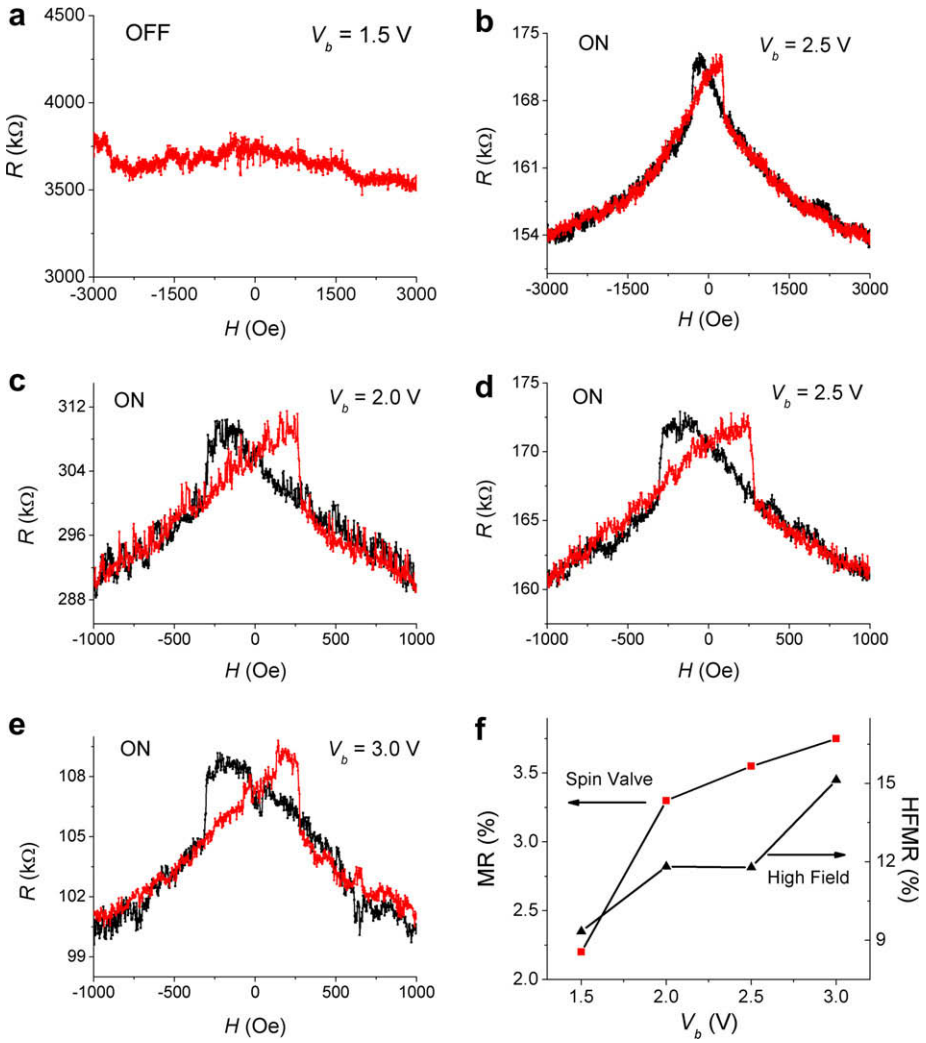

Fig. 4. Magnetoresistance curves of the 50 nm rubrene device at 10 K. (a) In the OFF state under 1.5 V (+3000 Oe to −3000 Oe). (b) In the ON state under 2.5 V (+3000 Oe to −3000 Oe). (c) In the ON state under 2.0 V bias. (d) In the ON state under 2.5 V bias. (e) In the ON state under 3.0 V bias. (f) Bias dependence of the spin valve MR value and high field MR value.

vices, this MR feature appeared only when the device was switched to "ON" states. This indicates that this additional high field MR feature in our devices is not intrinsic as the case in OMAR. We suggest that some Fe atoms migrate into the rubrene layer under high bias, forming conductive channels, although the microscopic mechanism still needs to be investigated. Starting from the OFF state in which the channels were closed, the device showed low current. At a threshold voltage, the conductive channels were turned on and the current jumped to a high level. After the power supply was removed, the channels were still open and the device remained in the ON state. Only if a high negative bias was applied, those channels were disrupted and the device recovered to the OFF state. In the ON state the conductive channels also provided efficient transport paths for the spin-polarized carriers. This high-voltage induced conduction channel introduces high field MR effects similar to the reports of Co–rubrene nanocomposite channel with nonmagnetic electrodes [23]. In addition, the ferromagnetic electrodes in our devices introduce spin valve effects at the same time.

In the OFF state, the bulk resistance of the rubrene layer dominated and it was much larger than the interface resistance. In principle, the spin valve effects rely on the spin dependent scattering at the interface. The device resistance in the OFF state was almost one order of magnitude larger than that in the ON state. Given the fact that even the maximum MR value we obtained in the ON state was relatively small—3.75%, any resistance change at the interface in the OFF state is likely overshadowed by the bulk resistance of rubrene layer. Additionally in the OFF state, the travel distance through the rubrene layer for the spin-polarized carriers could be longer than the spin-diffusion length (λ_S). The carriers would lose their spin information before they reach the other ferromagnetic electrode. Though the spins in carbon based materials are typically perceived to have

long lifetime, the transport in small molecule film heavily rely on the hopping between neighboring molecules leading to long transit time between two ferromagnetic electrodes. However, in the ON state, the presence of the conductive channels made the effective spin travel distance much shorter. The carriers could effectively maintain their initial spin states during the transport, leading to the spin valve effect.

In order to fully understand the mechanism, further detailed studies on bias and temperature dependence as well as careful study on the morphology are in progress with a variation of the device configuration and materials.

4. Conclusion

We report the integration of the electrical bistability and the bias-controlled spin valve effect in an LSMO/rubrene/Fe trilayer device. The spin valve effect can be turned on and off by applying different bias voltages. This finding is attributed to the formation of conductive channels by the migration of Fe atoms under high bias voltage. Further experimental studies are needed to fully understand the microscopic mechanism.

Acknowledgements

The authors wish to thank V.N. Prigodin and N.P. Raju for helpful discussions. This work was supported in part by DOE Grant No. DE-FG02-01ER45931, DE-FG02-86ER45271, DE-FG02-06ER46327, AFOSR Grant No. FA9550-06-1-0175, ONR Grant No. N00014-07-1-0215, the Institute for Materials Research at the Ohio State University, and the Center for Emergent Materials at the Ohio State University (an NSF MRSEC; Grant No. DMR-0820414).

References

[1] Y. Yang, J. Ouyang, L. Ma, R.J.-H. Tseng, C.-W. Chu, Adv. Funct. Mater. 16 (2006) 1001.
[2] J.C. Scott, L.D. Bozano, Adv. Mater. 19 (2007) 1452.
[3] L. Ma, J. Liu, S. Pyo, Y. Yang, Appl. Phys. Lett. 80 (2002) 362.
[4] L.P. Ma, J. Liu, Y. Yang, Appl. Phys. Lett. 80 (2002) 2997.
[5] L. Ma, S. Pyo, J. Ouyang, Q. Xu, Y. Yang, Appl. Phys. Lett. 82 (2003) 1419.
[6] L.D. Bozano, B.W. Kean, M. Beinhoff, K.R. Carter, P.M. Rice, J.C. Scott, Adv. Funct. Mater. 15 (2005) 1933.
[7] L.D. Bozano, B.W. Kean, V.R. Deline, J.R. Salem, J.C. Scott, Appl. Phys. Lett. 84 (2004) 607.
[8] D. Tondelier, K. Lmimouni, D. Vuillaume, C. Fery, G. Haas, Appl. Phys. Lett. 85 (2004) 5763.
[9] V. Dediu, M. Murgia, F.C. Matacotta, C. Taliani, S. Barbanera, Solid State Commun. 122 (2002) 181.
[10] Z.H. Xiong, D. Wu, Z.V. Vardeny, J. Shi, Nature 427 (2004) 821.
[11] T.S. Santos, J.S. Lee, P. Migdal, I.C. Lekshmi, B. Satpati, J.S. Moodera, Phys. Rev. Lett. 98 (2007) 016601.
[12] J.H. Shim, K.V. Raman, Y.J. Park, T.S. Santos, G.X. Miao, B. Satpati, J.S. Moodera, Phys. Rev. Lett. 100 (2008) 226603.
[13] V. Dediu, L.E. Hueso, I. Bergenti, A. Riminucci, F. Borgatti, P. Graziosi, C. Newby, F. Casoli, M.P. De Jong, C. Taliani, Y. Zhan, Phys. Rev. B 78 (2008) 115203.
[14] J.-W. Yoo, H.W. Jang, V.N. Prigodin, C. Kao, C.B. Eom, A.J. Epstein, Phys. Rev. B 80 (2009) 205207.
[15] J.-W. Yoo, H.W. Jang, V.N. Prigodin, C. Kao, C.B. Eom, A.J. Epstein, Synth. Met. 160 (2010) 216.
[16] L.E. Hueso, I. Bergenti, A. Riminucci, Y. Zhan, V. Dediu, Adv. Mater. 19 (2007) 2639.
[17] H. Yamada, Y. Ogawa, Y. Ishii, H. Sato, M. Kawasaki, H. Akoh, Y. Tokura, Science 305 (2004) 646.
[18] J.-H. Park, E. Vescovo, H.-J. Kim, C. Kwon, R. Ramesh, T. Venkatesan, Phys. Rev. Lett. 81 (1998) 1953.
[19] M. Cölle, M. Büchel, D.M. de Leeuw, Org. Electron. 7 (2006) 305.
[20] R.S. Potember, T.O. Poehler, D.O. Cowan, Appl. Phys. Lett. 34 (1979) 405.
[21] M.L. Wang, J. Zhou, X.D. Gao, B.F. Ding, Z. Shi, X.Y. Sun, X.M. Ding, X.Y. Hou, Appl. Phys. Lett. 91 (2007) 143511.
[22] S. Sakai, I. Sugai, S. Mitani, K. Takanashi, Y. Matsumoto, H. Naramoto, P.V. Avramov, S. Okayasu, Y. Maeda, Appl. Phys. Lett. 91 (2007) 242104.
[23] H. Kusai, S. Miwa, M. Mizuguchi, T. Shinjo, Y. Suzuki, M. Shiraishi, Chem. Phys. Lett. 448 (2007) 106.
[24] T.L. Francis, Ö. Mermer, G. Veeraraghavan, M. Wohlgenannt, New J. Phys. 6 (2004) 185.
[25] Ö. Mermer, G. Veeraraghavan, T.L. Francis, Y. Sheng, D.T. Nguyen, M. Wohlgenannt, A. Köhler, M.K. Al-Suti, M.S. Khan, Phys. Rev. B 72 (2005) 205202.
[26] V.N. Prigodin, J.D. Bergeson, D.M. Lincoln, A.J. Epstein, Synth. Met. 156 (2006) 757.
[27] J.D. Bergeson, V.N. Prigodin, D.M. Lincoln, A.J. Epstein, Phys. Rev. Lett. 100 (2008) 067201.

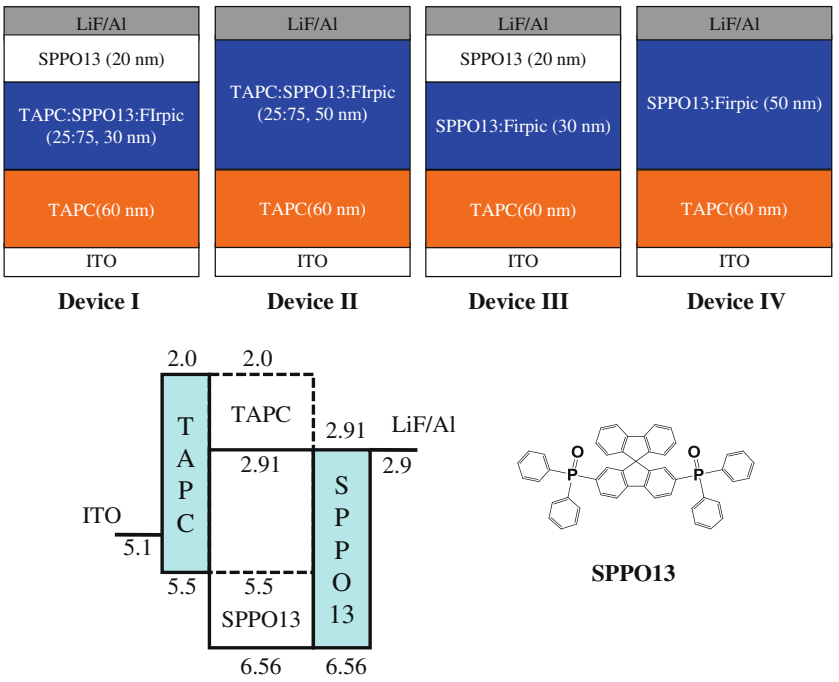

Fig. 1. Device structures of the blue devices, energy level diagram and chemical structure of the SPPO13. (For interpretation of the references in colour in this figure legend, the reader is referred to the web version of this article.)

chemical structure of the SPPO13. All materials were evaporated at a vaccum pressure of 8×10^{-7} torr and all devices were encapsulated with a glass lid and a CaO getter. The device performances of the blue PHOLEDs were measured with Keithley 2400 source measurement unit and CS 1000 spectroradiometer.

3. Results and discussion

The SPPO13 has a high triplet energy of 2.73 eV and it can be used as the host material for the FIrpic blue dopant. In addition, it has the lowest unoccupied molecular orbital (LUMO) level of 2.91 eV and it is suitable as the electron transport layer of the blue PHOLEDs. Therefore, the SPPO13 was used as the host in the emitting layer and the electron transport material. The TAPC has been known to have a high triplet energy of 2.87 eV and it has the highest occupied molecular orbital (HOMO) of 5.5 eV for hole injection [4]. It has been widely used as the hole transport layer in the blue PHOLED because it can confine triplet excitons inside the emitting layer [5]. Therefore, the TAPC was used as the hole transport material and it was also combined with the SPPO13 as the host in the mixed host emitting layer [12]. The energy level diagram of the blue PHOLEDs is shown in Fig. 1.

Four blue PHOLEDs with different host materials and electron transport layer structures were fabricated. Current density–voltage and luminance–voltage curves of the blue PHOLEDs are shown in Fig. 2. The device I with the TAPC:SPPO13 mixed host showed higher current density than the device III and device IV with the SPPO13 host. The high current density of the blue PHOLEDs with the mixed host emitting layer can be explained by efficient hole injection from the TAPC hole transport layer to the emitting layer. There is an energy barrier of 1.06 eV for hole injection between the TAPC and the SPPO13. In the case of the device III and device IV, the hole injection from the TAPC to the SPPO13 emitting layer is difficult due to the HOMO level difference of 1.06 eV between the TAPC hole transport layer and the SPPO13 host. The addition of the TAPC in the SPPO13 emitting layer improves the hole injection because holes can be directly injected from the TAPC hole transport layer to the TAPC in the mixed host. Therefore, the current density of the device I was much higher than that of the device III and device IV.

Comparing the device I and device II, the device I with the SPPO13 as the electron transport layer showed higher current density than the device II without the SPPO13 electron transport layer. The TAPC:SPPO13 mixed host enhanced the hole injection, but reduced the electron injection due to electron blocking properties of the TAPC. Therefore, the current density of the device I was higher than that of the device II. However, the SPPO13 electron transport layer was not effective in the blue PHOLEDs with the SPPO13 host material. The SPPO13 has strong electron transport properties and electrons could be directly injected from the LiF/Al electrode to the SPPO13:FIrpic emitting layer. There was only 0.1 eV difference of the LUMO level between the SPPO13 and FIrpic. The small energy level difference does not induce the electron trapping by the FIrpic and the electron transport is not hindered by the FIrpic. Therefore, the device III and device IV showed similar current density and the SPPO13 electron transport layer

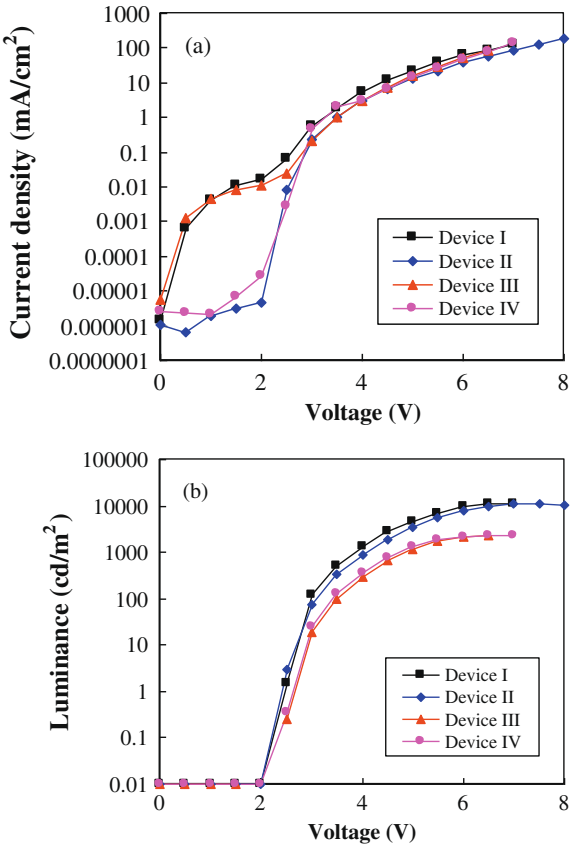

Fig. 2. Current density–voltage (a), and luminance–voltage (b) curves of the simple blue PHOLEDs. (For interpretation of the references in colour in this figure legend, the reader is referred to the web version of this article.)

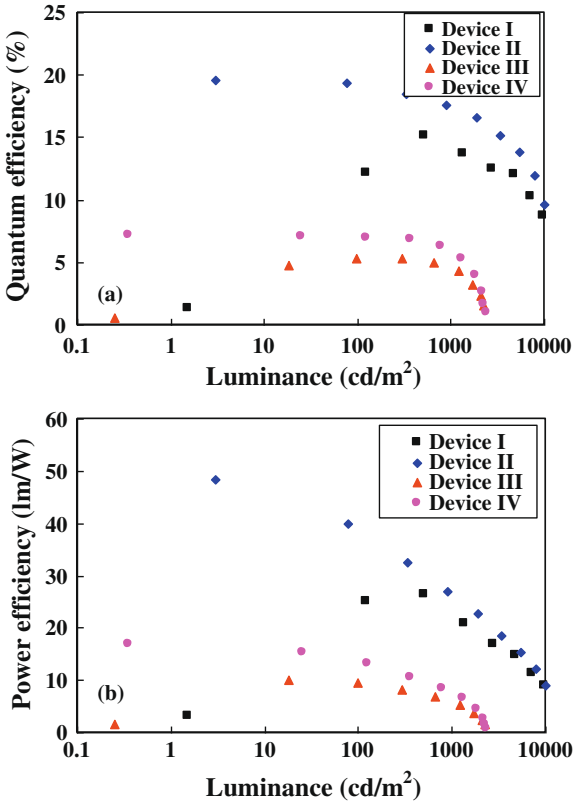

Fig. 3. Quantum efficiency–luminance (a), and power efficiency–luminance (b) curves of the simple blue PHOLEDs. (For interpretation of the references in colour in this figure legend, the reader is referred to the web version of this article.)

could not greatly affect the current density. The difference of the current density below turn-on voltage (2 V) is due to the electron injection from the cathode to the electron transport layer or emitting layer. The efficient electron injection from the LiF/Al to the SPPO13 layer increased the current density at low voltage in the device I and device III, while it was difficult in the device II and device IV.

The luminance of the blue device is also shown in Fig. 2. The luminance followed the same tendency as the current density. The device I showed the highest luminance at the same voltage due to the high current density. The driving voltages of the device I at 100 and 1000 cd/m^2 were only 2.9 and 3.8 V, while those of the device II at 100 and 1000 cd/m^2 were 3.1 and 4.1 V even without the SPPO13 electron transport layer. The good hole injection property of the TAPC and the electron injection property of the SPPO13 significantly lowered the driving voltage of the blue PHOLEDs.

The quantum efficiency and power efficiency of the simple blue PHOLEDs are shown in Fig. 3. The device I and device II showed higher quantum efficiency than the device III and device IV. In particular, the device II exhibited the highest quantum efficiency. The maximum quantum efficiency of the device II was 19.6% and the quantum efficiencies at 100 and 1000 cd/m^2 were 19.2% and 17.5%, respectively. The high quantum efficiency of the device II can be explained the charge balance in the emitting layer. Holes are efficiently injected from the TAPC hole transport layer to the TAPC:SPPO13 mixed host emitting layer and electrons can also be injected from the LiF/Al electrode to the mixed host emitting layer. The efficient hole and electron injection improves the charge balance in the emitting layer, resulting in high quantum efficiency in the device II. The charge balance is degraded in the device I because of too high electron density in the emitting layer. The low quantum efficiency of the device III and device IV is mainly due to the poor hole injection originated from the high energy barrier for hole injection. Efficient electron injection and poor hole injection disrupt the charge balance in the emitting layer, leading to low quantum efficiency. The quantum of the device II was similar to that of other devices with three layer or four layer device structures [4,5,11]. The use of the TAPC:SPPO13 mixed emitting layer enabled the fabrication of simplified high efficiency blue PHOLEDs. The efficiency roll-off of the blue PHOLED was also affected by the device structure and the efficiency roll-off was reduced in the device with a mixed host emitting structure. This results is in agreement with the data reported in the literature [12].

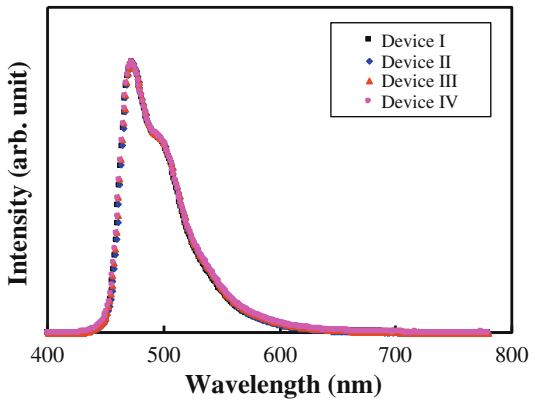

Fig. 4. Electroluminescence spectra of the simple blue PHOLED. (For interpretation of the references in colour in this figure legend, the reader is referred to the web version of this article.)

The power efficiency of the blue PHOLEDs was also high in the device II. The quantum efficiency of the device II was high and the driving voltage of the device II was as low as 3.1 V at 100 cd/m^2 and 4.1 V at 1000 cd/m^2 even without any p or n doped charge transport layer. The low driving voltage and high quantum efficiency of the device II enhanced the power efficiency of the device II. The maximum power efficiency of the device II was 48.5 lm/W and the power efficiencies at 100 and 1000 cd/m^2 were 38.1 and 26.0 lm/W. The good electron injection property of the SPPO13 and hole injection property of the TAPC enabled the fabrication of the simple two layer blue PHOLED with high power efficiency. In the case of the device I, the low quantum efficiency of the device I reduced the power efficiency although the driving voltage of the device I was less than 3 V at 100 cd/m^2. The low power efficiency of the device III and device IV is due to the low quantum efficiency and high driving voltage. The power efficiency level of the device II with only TAPC charge transport layer and mixed emitting layer was comparable to that of the state of the art value reported in the literature using common device structure with two or three charge transport layers for high efficiency and low driving voltage [4,5,11].

Electroluminescence (EL) spectra of the simplified blue PHOLEDs are shown in Fig. 4. All devices showed similar emission spectra with a peak maximum at 474 nm corresponding to the FIrpic emission. The EL spectra was not affected by the device structure. The change of the emission in the blue device induces the change of the EL spectra, but the emission zone of the blue PHOLED fabricated in this work may be close to the electron transport layer side due to strong electron transport properties of the SPPO13. Therefore, there was little change of the vibrational peak in the EL spectra of the simplified blue PHOLEDs.

4. Conclusions

In summary, high power efficiency blue PHOLEDs with simple device structure made up of only two organic layers could be effectively fabricated by combining the hole transport type TAPC and electron transport type SPPO13 host materials. A high power efficiency of 48.5 lm/W and a high quantum efficiency of 19.6% were achieved in the simple blue PHOLEDs. Therefore, this approach can be useful to simplify the device structure and improve the device structure of the blue PHOLEDs.

References

[1] R.J. Holmes, B.W. D'Andrade, S.R. Forrest, X. Ren, J. Li, M.E. Thompson, Appl. Phys. Lett. 83 (2003) 3818.
[2] M.H. Tsai, H.W. Lin, H.C. Su, T.H. Ke, C.C. Wu, F.C. Fang, Y.L. Liao, K.T. Wong, C.I. Wu, Adv. Mater. 18 (2006) 1216.
[3] L. Xiao, S.-J. Su, Y. Agata, H. Lan, J. Kido, Adv. Mater. 10 (2009) 1271.
[4] Y. Zheng, S. Eom, N. Chopra, J. Lee, F. So, J. Xue, Appl. Phys. Lett. 92 (2009) 223301.
[5] N. Chopra, J. Lee, Y. Zheng, S. Eom, J. Xue, F. So, Appl. Phys. Lett. 93 (2008) 143307.
[6] S.O. Jeon, K.S. Yook, C.W. Joo, J.Y. Lee, Adv. Funct. Mater. 19 (2009) 3644.
[7] S.O. Jeon, K.S. Yook, C.W. Joo, J.Y. Lee, Adv. Mater. (2010), doi:10.1002/adma.200903321.
[8] X. Ren, J. Li, R.J. Holmes, P.I. Djurovich, S.R. Forrest, M.E. Thompson, Chem. Mater. 4743 (2003) 2004.
[9] A.B. Padmaperuma, L.S. Sapochak, P.E. Burrows, Chem. Mater. 18 (2006) 2389.
[10] P.E. Burrows, A.B. Padmaperuma, L.S. Sapochak, P. Djurovich, M.E. Thompson, Appl. Phys. Lett. 88 (2006) 183503.
[11] J. Lee, J. Lee, J.Y. Lee, H. Chu, Appl. Phys. Lett. 95 (2009) 253304.
[12] M.E. Kondakova, J.C. Deaton, D.Y. Kondakov, T.D. Pawlik, R.H. Young, C.T. Brown, D.J. Giesen, SID Dig. 38 (2007) 837.

efficiency as well as reduced efficiency roll-off at high current density.

In this work, high efficiency deep blue PHOLEDs with peak external quantum and power efficiencies of 22.9% and 41.2 lm/W were developed with a mixed host structure, which were combination of two hosts with a hole transport-type host and a electron transport-type host both doped with the FIr6. We have demonstrated the device characteristics including the charge carrier balance mechanism for both the single host and the mixed host structure devices. Moreover, we found that the mixed host structure was effective to control the charge carrier injection and transport in EML, thus obtained highly improved efficiency in deep blue PHOLEDs.

2. Experimental

Two hole transport-type host materials, *N*,*N*′-dicarbazolyl-3-3-benzene (mCP) and 4,4′,4″-tris(*N*-carbazolyl)triphenylamine (TcTa), were combined with an electron transport-type host UGH3 because they have high hole mobility as well as high triplet energy of 2.9 and 2.85 eV, respectively [14,21]. A series of organic light-emitting devices in this study were made using the configuration: indium tin oxide (ITO) (70 nm)/1,1-bis[(di-4-tolylamino)phenyl]cyclohexane (TAPC) (50 nm)/EML (30 nm)/1,3,5-tri(m-pyrid-3-yl-phenyl)benzene (Tm3PyPB) (20 nm)/Tm3PyPB:Cs (30 nm)/LiF (1 nm)/Al (120 nm). For deep blue PHOLEDs, six different mixed host devices and standard device with single UGH3 host material as reference were prepared to investigate the effect of host property on device characteristics. Hole transport-type mCP (Device A) or TcTa (Device B) composition in the mixed host device were 50%, 30%, and 10%, respectively. A deep blue light-emitting FIr6 dopant which has high triplet energy of 2.80 eV [17–20], was doped in the EML and the doping concentration of FIr6 was fixed at 10%.

To achieve efficient blue PHOLEDs, effective confinements of both the charge carriers and the triplet excitons are necessary [10,14,17]. Therefore, TAPC and Tm3PyPB with wider triplet energy level (T_1 = 2.9 and 2.78 eV, respectively, which are higher than that of FIr6 (T_1 = 2.72 eV)) and low-lying the highest occupied molecular orbital (HOMO) and high-lying the lowest unoccupied molecular orbital (LUMO) energy levels, respectively, were used as a hole-transporting layer (HTL) and as an electron transporting layer (ETL), respectively. The electron mobility of Tm3PyPB ($\sim 7.0 \times 10^{-4}$ cm^2/V s at 2.5×10^5 V/cm) [21–23] is one to two orders of magnitude lower than the hole mobility of TAPC ($\sim 1.0 \times 10^{-2}$ cm^2/V s at $\sim 10^5$ V/cm) [17]. Accordingly, n-doped ETL (4 mol% cesium doped TmPyPB) was introduced for effective electron injection and charge carrier balance within EML. The chemical structures of materials and energy level diagrams used in this study were shown in Figs. 1 and 2.

ITO was cleaned with the standard oxygen plasma treatment. The OLED grade materials were purchased and used without further purification. All organic layers were deposited in a high vacuum chamber below 5×10^{-7} torr and thin films of LiF and Al were deposited as a cathode electrode. The OLEDs were transferred directly from vacuum into an inert environment glove-box, where they were encapsulated using a UV-curable epoxy, and a glass cap with a moisture getter. The electroluminescence spectrum was measured using a Minolta CS-1000. The current–voltage (*J*–*V*) and luminescence–voltage (*L*–*V*) characteristics were measured with a current/voltage source/measure unit (Keithley 238) and a Minolta CS-100, respectively.

3. Results and discussion

The current density–voltage–luminance curves of the mCP:UGH3 mixed host devices (Device A) are shown in Fig. 3a according to the relative content of two host

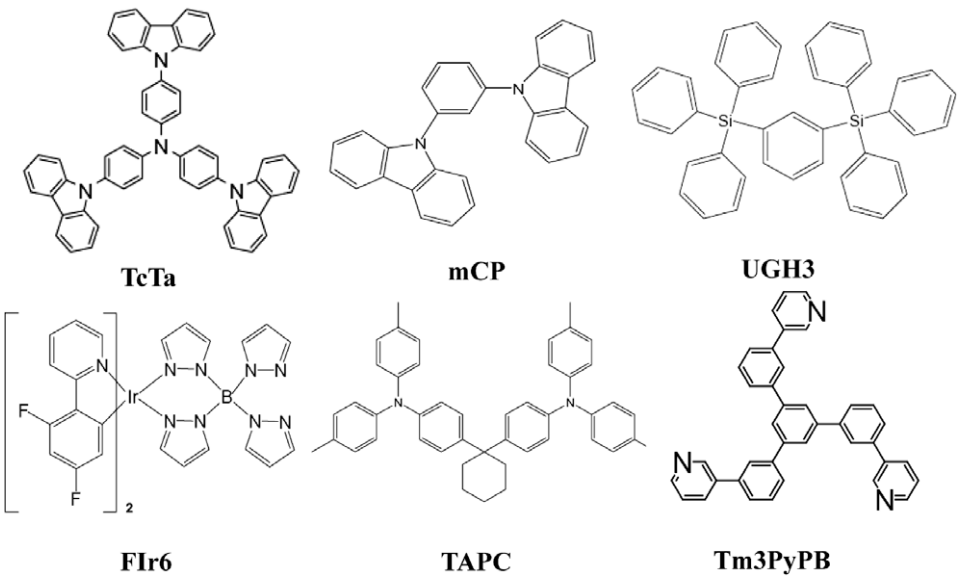

Fig. 1. Chemical structures for the materials tested in this study.

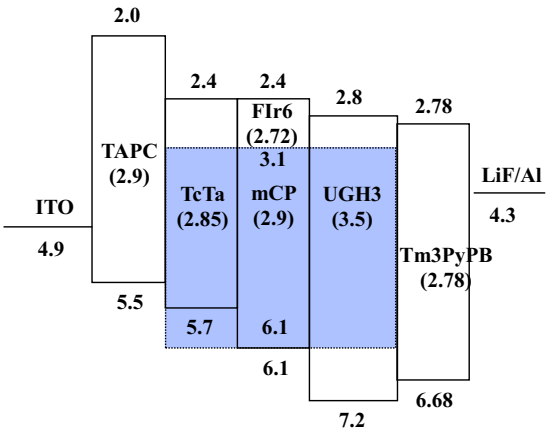

Fig. 2. Energy level diagrams for the materials tested in this study.

materials. The current density of Device A was gradually increased with increasing mCP content in the mixed host devices. Moreover, the driving voltages of Device A at a luminance of 1000 cd/m^2 reduced consequently and were 6.6, 6.3, 5.4, and 5.15 V, respectively. These increased current densities and reduced driving voltages in Device A with the addition of mCP to UGH3 can be explained by facilitated hole injection and transport from TAPC to UGH3 through mCP content. As shown in Fig. 2, the highest occupied molecular orbital (HOMO) level of the TAPC and UGH3 are 5.7 and 7.2 eV, respectively, therefore the hole injection from TAPC to UGH3 was greatly restricted due to the HOMO level difference of 1.5 eV between TAPC and UGH3. However, in case of mCP:UGH3 mixed host Device A, the HOMO level of mCP (6.1 eV) is higher-lying than that of UGH3 (7.2 eV) which led to lower energy barrier for hole injection. Moreover, mCP is also better than UGH3 in terms of hole mobility because mCP is a hole-transport-type host, while the UGH3 is slightly electron-transport-type host. Based on these carrier-transporting ability and the HOMO energy level differences between two hosts, the current density and the luminance at the same voltage in mixed host devices were highly increased.

As shown in Fig. 3b, the current density as well as luminance behavior in case of the combination of TcTa and UGH3 host (Device B) was more definite than those in case of Device A. The driving voltages difference of Device B (TcTa:UGH3 = 5:5, 4.15 V) and Device B (TcTa:UGH3 = 0:10, 6.6 V) at a luminance of 1000 cd/m^2 is 2.45 V which is almost 40% reduction. Therefore, we could also expect huge luminance efficiency improvement in mixed host structure. Both TcTa and mCP have similar LUMO levels (2.4 eV) and hole mobility, thus more dramatic current density enhancement can be understood by speculating HOMO level difference. Compared with mCP, TcTa has only 0.2 eV hole injection barrier from TAPC to TcTa, which leads to much higher current density and lower operating voltage in Device B. By gathering up above results, we found that proper introduction of hole transport-type host (mCP or TcTa) into electron transport-type host (UGH3)

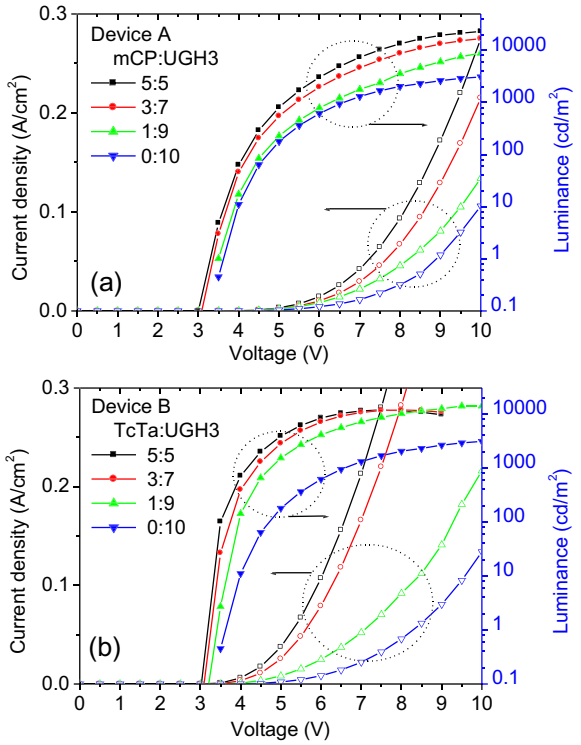

Fig. 3. Current density–voltage–luminescence (*J*–*V*–*L*) characteristics of (a) Device A and (b) Device B.

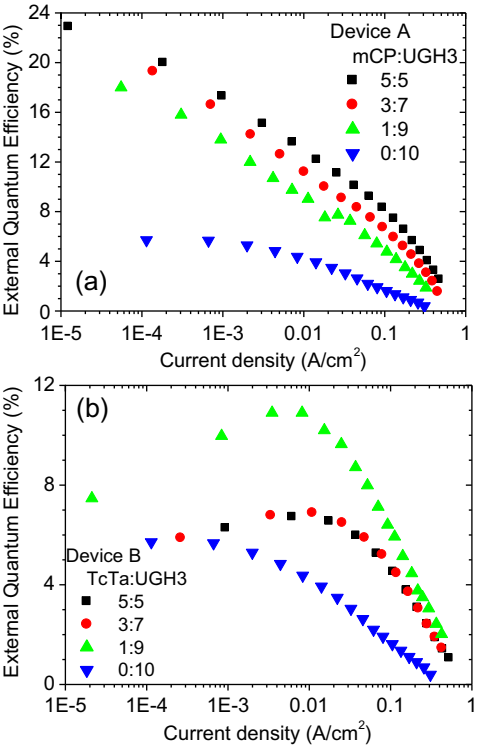

Fig. 4. External quantum efficiency versus current density characteristics of (a) Device A and (b) Device B.

can enhance charge carrier density and reduce driving voltage in the EML.

The external quantum efficiency of the deep blue PHOLEDs with mixed host structure were plotted against current density and luminance in Figs. 4 and 5. Both Device A and B with mixed host structure showed remarkably enhanced performance than UGH3 single host device. In case of Device A, the peak external quantum efficiencies (EQEs) were increased with increasing mCP content in the mixed host devices and the peak EQE of 22.9% at a luminance of 4.9 cd/m^2 were obtained in Device A (mCP:UGH3 = 5:5). This value is better than any other external quantum efficiency values for FIr6 based deep blue PHOLEDs and more than four times higher than that of UGH3 single host device (peak EQE of UGH3 sing host device is 5.71% at 11.0 cd/m^2).

The current efficiency of the deep blue PHOLEDs with mixed host structure were also highly improved as shown in Fig. 6. The peak current efficiency of mixed host Device A are 39.5, 37.7, and 36.7 cd/A, respectively, and those of mixed host Device B are 11.6, 11.8, and 18.7 cd/A, respectively, while that of single UGH3 host device is only 9.68 cd/A.

As we mentioned earlier, the light-emitting efficiency of OLEDs is determined by holes and electrons balance in the EML [20–24]. In case of UGH3 single host device, there is a quite mismatch between holes and electrons because UGH3 was known as slightly electron transport-type host material and its hole carrier mobility is quite low. Moreover, the recombination zone of UGH3 single host device is positioned at shallow region of the TAPC/EML interface due to this hole/electron imbalance which resulted in detrimental triplet quenching process such as the triplet–triplet annihilation (TTA) or triplet-polaron annihilation (TPA) in the EML [25,26]. However, an efficient hole injection through introduction of hole-transport-type host with high hole mobility and adequate HOMO level into the EML resulted in improved charge balance as well as recombination zone distribution overall EML, therefore highly enhanced light-emitting performances in deep blue PHOLEDs were obtained as shown in this study.

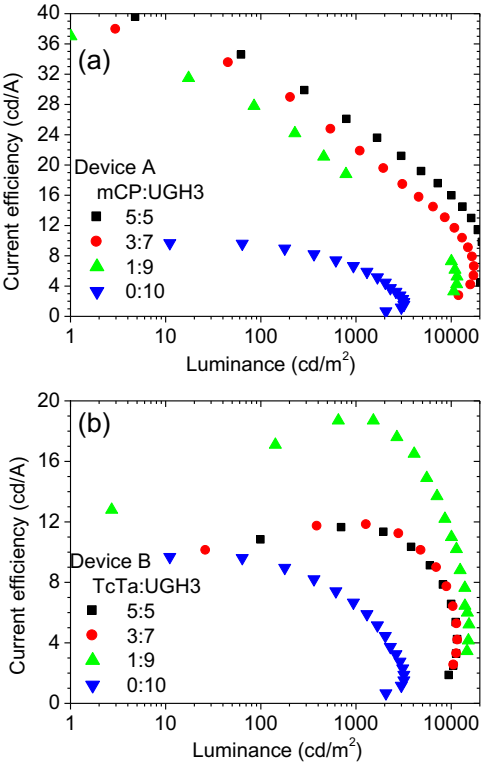

Fig. 6. Current efficiency versus current density characteristics of (a) Device A and (b) Device B.

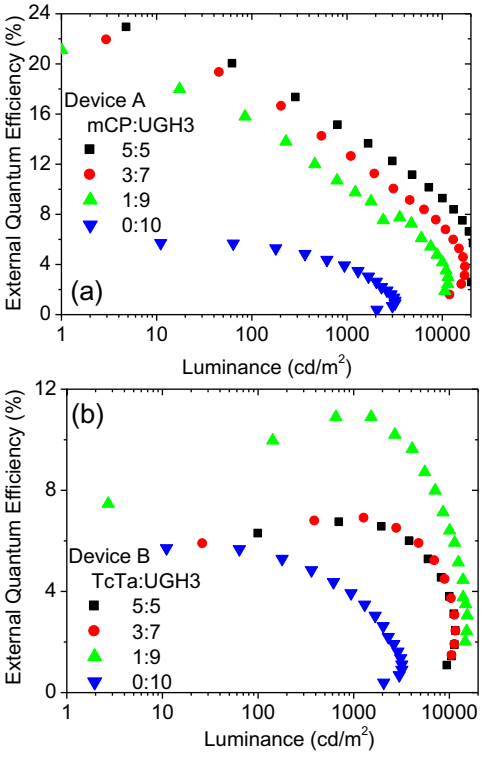

Fig. 5. External quantum efficiency versus luminance characteristics of (a) Device A and (b) Device B.

Note that the performance trends as increasing TcTa content in Device B are slightly different from those in Device A. Even though the EQEs of mixed host Device B are also increased compared to UGH3 single host, the maximum EQE is only 10.9% and obtained in the 1:9 mixed host structure not in the 5:5 mixed ratio. This phenomenon is contrary result to our previous report that the best light-emitting performances of FIrpic based blue PHOLEDs were obtained in the 5:5 mixed TcTa:UGH3 host structure [21].

To examine this discrepancy, we inspected the electroluminescent (EL) spectrum of Device A and B in detail. As shown in Fig. 7, all Device A and B exhibited a similar maximum luminescence wavelength at a driving current of 10 mA/cm^2, near 460 nm, which is originated from the triplet emission of FIr6 dopant and the second vibration peaks with a wavelength of approximately 490 nm. However, we could find some differences between Device A

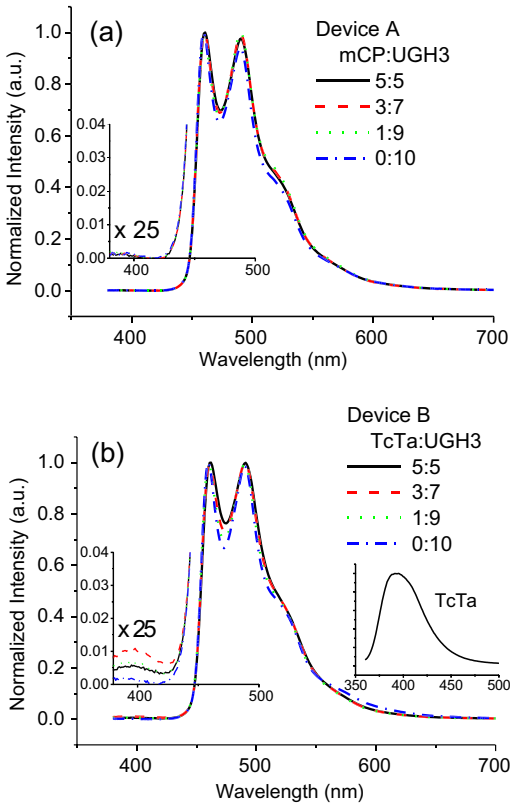

Fig. 7. Normalized electroluminescence spectra of (a) Device A and (b) Device B at a driving current of 10 mA/cm^2 (left inset: magnified EL spectra; right inset: photoluminescence (PL) emission of TcTa 30 nm-thick films on quartz plate).

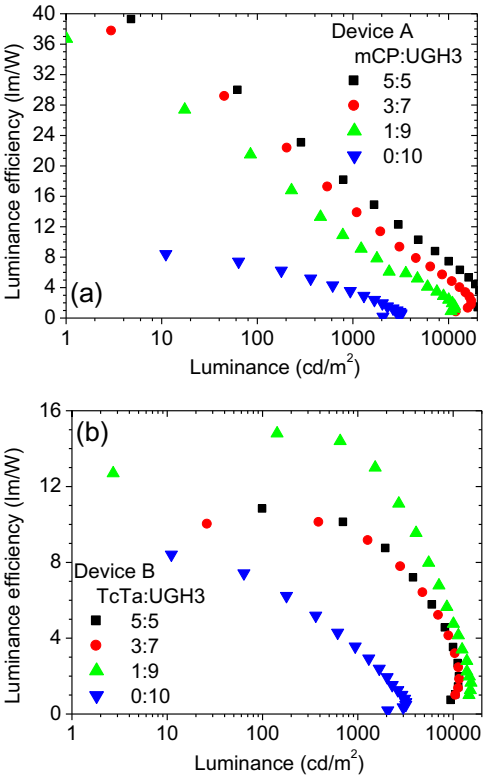

Fig. 8. Luminance efficiency versus brightness characteristics of (a) Device A and (b) Device B.

and B from the provided left inset of Fig. 7a and b, which shows the magnified EL spectra in the range of 380–500 nm. In case of the mCP:UGH3 mixed host Device A, there are little emission appeared even at the magnified EL spectra. On the other hands, new EL spectra appeared near 393 nm in case of the TcTa:UGH3 mixed host Device B. This new EL spectra could be presumed to be TcTa fluorescent emission which is shown in the right inset of Fig. 7b. The more precise cause of this new EL emission is being investigated and will be reported elsewhere.

Relatively lower light-emitting performance of TcTa:UGH3 mixed host Device B compared to mCP:UGH3 mixed host Device A could be understood by ineffective hosting property of TcTa host [27]. As shown in Fig. 2, the HOMO energy level of FIr6 (6.1 eV) is 0.4 eV lower-lying than that of TcTa (5.7), however that of mCP (6.1 eV) is identical. Therefore, this mismatching of HOMO energy level between TcTa and FIr6 would lead to inefficient deep blue electro-phosphorescent emission even though hole injection of TcTa incorporated Device B is highly improved.

The luminance efficiency of the deep blue PHOLEDs with mixed host structure were plotted against luminance in Fig. 8. Increased EQEs along with reduced driving voltages result in a significantly enhanced luminance efficiency of 39.2 lm/W with Device A (mCP:UGH3 = 5:5) without any out-coupling enhancement technique, in which is 4.6 times enhancement comparing with that of UGH3 single host device (peak luminance efficiency of UGH3 sing host device is 8.41 lm/W at 11.0 cd/m^2). The luminance efficiency of Device A (mCP:UGH3 = 5:5) slightly reduced to 27.9 and 17.2 lm/W at a luminance of 100 and 1000 cd/m^2, respectively. With considering the potential of improved out-coupling technique to achieving 2.3 times enhancement, the external luminance efficiency can be expected over 90 lm/W [3,10,28].

4. Conclusion

We have demonstrated that the performances of deep blue PHOLEDs were significantly improved by using mixed host structure and found that device characteristics depend on combination/composition of mixed host material properties. A peak external quantum and luminance efficiencies of 22.9% and 39.2 lm/W were achieved in the mCP:UGH3 mixed host device, which is mainly attributed to the charge carrier injection/transport balance as well as the recombination region distribution within EML by the optimization of mixed host properties.

Acknowledgments

We gratefully acknowledged Prof. Jun Yeob Lee (Department of Polymer Science and Engineering of Dankook University) for fruitful discussion, and Ms. K.-I. Song

and Ms. S.J. Lee (ETRI) for assistance of EL device experiments. This work was supported by IT R&D program of MKE/KEIT (2009-F-016-01, Development of Eco-Emotional OLED Flat-Panel Lighting) and the future technology development program of MKE/KEIT (2006-10028439, OLED Lighting).

References

[1] M.A. Baldo, D.F. O'Brien, Y. You, A. Shoustikov, S. Sibley, M.E. Thompson, S.R. Forrest, Nature (London) 395 (1998) 151.
[2] G. He, M. Pfeiffer, K. Leo, M. Hofmann, J. Birnstock, R. Pudzich, J. Salbeck, Appl. Phys. Lett. 85 (2004) 3911.
[3] S. Reineke, F. Lindner, G. Schwartz, N. Seidler, K. Walzer, B. Lussem, K. Leo, Nature 459 (2009) 234.
[4] J. Lee, J.-I. Lee, H.Y. Chu, ETRI J. 31 (2009) 642.
[5] J. Lee, J.-I. Lee, H.Y. Chu, Synth. Met. 159 (2009) 991.
[6] C. Adachi, M.A. Baldo, M.E. Thomposon, S.R. Forrest, J. Appl. Phys. 90 (2001) 5048.
[7] C. Adachi, R.C. Kwong, P. Djurovich, V. Adamovich, M.A. Baldo, M.E. Thompson, S.R. Forrest, Appl. Phys. Lett. 79 (2001) 2082.
[8] R.J. Homes, S.R. Forrest, Y.-J. Tung, R.C. Kwong, J.J. Brown, S. Garon, M.E. Thompson, Appl. Phys. Lett. 82 (2003) 2422.
[9] S. Tokito, T. Iijima, Y. Suzuri, H. Kira, T. Tsuzuki, F. Sato, Appl. Phys. Lett. 83 (2003) 569.
[10] S.-J. Su, E. Gonmori, H. Sasabe, J. Kido, Adv. Mater. 20 (2008) 4189.
[11] J. Lee, J.-I. Lee, H.Y. Chu, Synth. Met. 159 (2009) 1460.
[12] J. Lee, J.-I. Lee, K.-I. Song, S.J. Lee, H.Y. Chu, Appl. Phys. Lett. 92 (2008) 133304.
[13] R.J. Holmes, B.W. D'Andrade, S.R. Forrest, X. Ren, J. Li, M.E. Thompson, Appl. Phys. Lett. 83 (2003) 3818.
[14] J. Lee, J.-I. Lee, K.-I. Song, S.J. Lee, H.Y. Chu, Appl. Phys. Lett. 92 (2008) 203305.
[15] R.J. Holmes, S.R. Forrest, T. Sajoto, A. Tamayo, P.I. Djurovich, M.E. Thompson, J. Brooks, Y.-J. Tung, D.W. D'Andrade, M.S. Weaver, R.C. Kwong, J.J. Brown, Appl. Phys. Lett. 87 (2005) 243507.
[16] K.S. Yook, S.O. Jeon, C.W. Joo, J.Y. Lee, Org. Electron. 10 (2009) 170.
[17] S.-H. Eom, Y. Zheng, N. Chopro, J. Lee, Franky So, J. Xue, Appl. Phys. Lett. 93 (2008) 133309.
[18] Y. Zheng, S.-H. Eom, N. Chopra, J. Lee, F. So, J. Xue, Appl. Phys. Lett. 92 (2008) 223301.
[19] H. Fukagawa, K. Watanabe, T. Tsuzuki, S. Tokito, Appl. Phys. Lett. 93 (2008) 133312.
[20] J. Lee, J.-I. Lee, J.Y. Lee, H.Y. Chu, Synth. Met. 159 (2009) 19560.
[21] J. Lee, J.-I. Lee, J.Y. Lee, H.Y. Chu, Appl. Phys. Lett. 94 (2009) 193305.
[22] J. Lee, J.-I. Lee, J.Y. Lee, H.Y. Chu, Appl. Phys. Lett. 95 (2009) 253304.
[23] J. Lee, J.-I. Lee, J.Y. Lee, H.Y. Chu, Org. Electron. 10 (2009) 1529.
[24] H. Aziz, Z.D. Popovic, N.-X. Hu, Appl. Phys. Lett. 81 (2002) 370.
[25] M.A. Baldo, C. Adachi, S.R. Forrest, Phys. Rev. B 62 (2000) 10967.
[26] S. Reineke, K. Walzer, Karl Leo, Phys. Rev. B 75 (2007) 125328.
[27] V.I. Adamovich, S.R. Cordero, P.I. Djurovich, A. Tamayo, M.E. Thompson, B.W. D'Andrade, S.R. Forrest, Org. Electron. 4 (2003) 77.
[28] S.-H. Eom, Y. Zheng, E. Wrzesniewski, J. Lee, N. Chopro, Franky So, J. Xue, Org. Electron. 10 (2009) 686.

emitters with simpler device structures, which might eventually replace the existing illumination sources [18,19]. Up to date, almost all phosphor excimer based WOLEDs utilized Pt complexes as dopant emitters [18–22]. In our insight, no Ir complex has been applied in this technique.

Recently, we reported highly efficient orange-red OLEDs based on a new iridium complex $(DMBA)_2Ir(acac)$ (DMBA = 5,6-dihydro-9,10-methylenedioxy-benzo[c]acridine, acac = acetylacetonate) with relatively broad excimer emission [23]. In the present work, we report the first example of WOLEDs incorporating the complex $(DMBA)_2Ir(acac)$ in combination with an efficient blue iridium complex bis(4′,6′-difluorophenylpyridinato) iridium (III) picolinate (FIrpic). Through adjusting the doping concentration, varying the thicknesses and locations of emission layers, pure white emission and high luminescent efficiencies were achieved.

2. Experimental

2.1. Materials

The complex $(DMBA)_2Ir(acac)$ was synthesized as we reported before [23]. Other materials were purchased and all compounds used were subject to temperature-gradient sublimation under high vacuum before fabrication of the devices.

Selected spectroscopic data of $(DMBA)_2Ir(acac)$: ^1H NMR ($CDCl_3$, 400 MHz) δ: 8.08 (s, 2 H), 7.71 (s, 2 H), 7.01 (s, 2 H), 6.64 (d, J = 7.2 Hz, 2 H), 6.56 (t, J = 7.2 Hz, 2 H), 6.33 (d, J = 7.6 Hz, 2 H), 6.04 (s, 2 H), 6.00 (s, 2 H), 4.90 (s, 1 H), 3.26–3.30 (m, 2 H), 3.04–3.15 (m, 6 H), 1.60 (s, 6 H). Anal. Calcd for $C_{41}H_{31}IrN_2O_6$: C, 58.63; H, 3.72; N, 3.34. Found: C, 58.48; H, 3.85; N, 3.48.

2.2. OLED fabrication and measurement

The EL devices were fabricated by vacuum deposition of the materials at 10^{-4} Pa onto a clean glass sheet that was pre-coated with a layer of indium tin oxide with a sheet resistance of 10 Ω square^{-1}. The deposition rate for the organic compounds was 0.1–0.2 nm s^{-1}. The cathode of LiF/Al was deposited by first evaporating LiF (1 nm) at a deposition rate of 0.01 nm s^{-1} and then evaporating aluminum (100 nm) at a rate of 0.1–0.2 nm s^{-1}. The cathode was then capped with silver metal (100 nm) by evaporation silver at a rate of 0.3 nm s^{-1}. Current, voltage, and light-intensity measurements were made simultaneously using a Keithley 2400 source meter and a Newport 1835-C optical meter equipped with a Newport 818-ST silicon photodiode.

3. Results and discussion

As described in our previous report [23], the complex $(DMBA)_2Ir(acac)$ had been used to fabricate highly efficient orange to red phosphorescent OLEDs with an external quantum efficiency of 17.7% and maximum brightness of 66,312 cd m^{-2}. An additional benefit of the complex $(DMBA)_2Ir(acac)$ is its relatively broad emission band with an emission peak at 620 nm and a shoulder at 572 nm covering the spectral range from yellow to saturated red. On the other hand, the well known complex FIrpic have been used widely for the fabrication of WOLEDs due to its very high photoluminescence (PL) quantum efficiency in wide gap host and high EL efficiencies [12,13]. Thus the orange-red phosphorescent iridium complex $(DMBA)_2Ir(acac)$ and the blue phosphorescent iridium complex FIrpic were selected in this work for the fabrication of WOLEDs. The molecular structures of the two Ir complexes and the related materials are shown in Fig. 1.

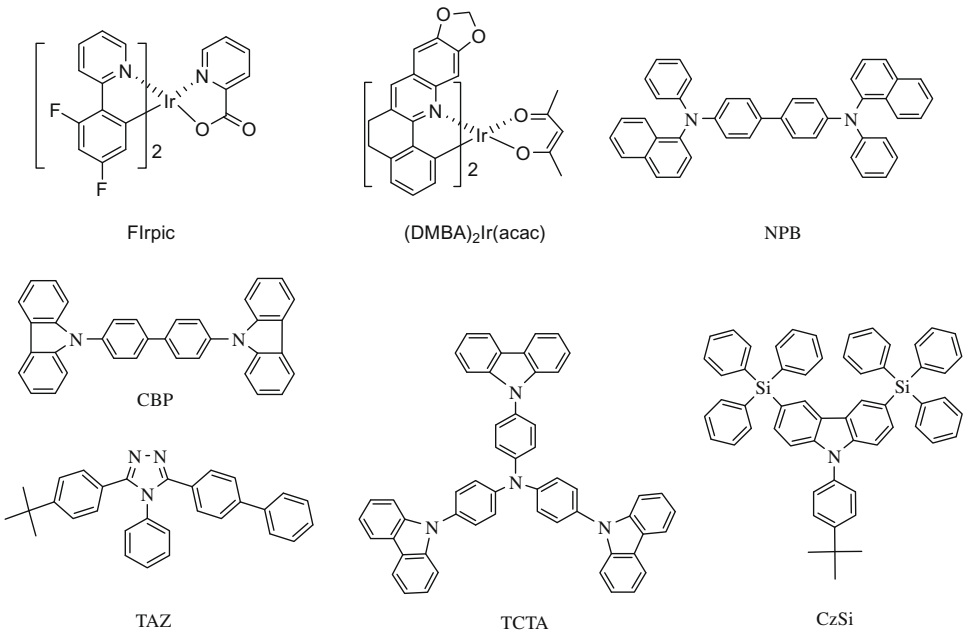

Fig. 1. Molecular structures of compounds used in EL devices.

According to our previous investigations, the highest EL efficiencies and broad emission could be achieved by doping $(DMBA)_2Ir(acac)$ into CBP (4,4′-*N*,*N*′-dicarbozole biphenyl) host at a doping concentration of 5%. So the doping concentration of $(DMBA)_2Ir(acac)$ was kept 5% for the first type of WOLEDs, while the thickness of the orange-red layer varied. Firstly, Device A was fabricated with a structure of ITO/NPB (30 nm)/TCTA (20 nm)/FIrpic:CzSi (7%, 20 nm)/$(DMBA)_2Ir(acac)$:CBP (5%, 200 nm)/TAZ (50 nm)/LiF (1 nm)/Al (100 nm), where 4,4′-bis(1-naphthylphenylamino)-biphenyl (NPB) and 4,4′,4″-tris[*N*-carbazolyl]-yriphenylamine (TCTA) were used together as the hole-transporting layers, 9-(4-*tert*-butylphenyl)-3,6-bis(trisphenylsilyl)-9H-carbazole (CzSi) and CBP as the host of the blue and orange-red emission layers, respectively, 3-(4-biphenylyl)-4-phenyl-5-(tert-butylphenyl)-1,2,4-triazole (TAZ) as the electron transporting layer, and LiF as the electron injection layer (Fig. 2). Device B was fabricated, where the thickness of the orange-red emission layer was reduced to 100 nm.

The maximum brightness of the two devices reached 24,150 cd m^{-2} and 24,012 cd m^{-2}, while the maximum external quantum efficiencies (EQE) were as high as 12.7% and 9.8%, respectively. Unfortunately, as shown in Fig. 3, both of the two devices exhibited bluish-white emission. Compared with the blue emission from FIrpic, the relative intensities of the orange-red emission from $(DMBA)_2Ir(acac)$ were weak for both of the devices. It should be noted that the relative intensity of orange-red emission of device B was greater than that of device A, although the thickness of the orange-red emission layer of device B was only half of device A. It can be presumed that it was the holes combining with electrons in the blue emission layer that gave the intense blue emission band in the EL spectra. This phenomenon also showed that increasing the thickness of the orange-red emission layer may not increase the relative intensity of the orange-red emission for this type of WOLEDs. With the hint of this preliminary result, we designed and fabricated device C, with the doping concentration of FIrpic reduced to 4% to decrease the

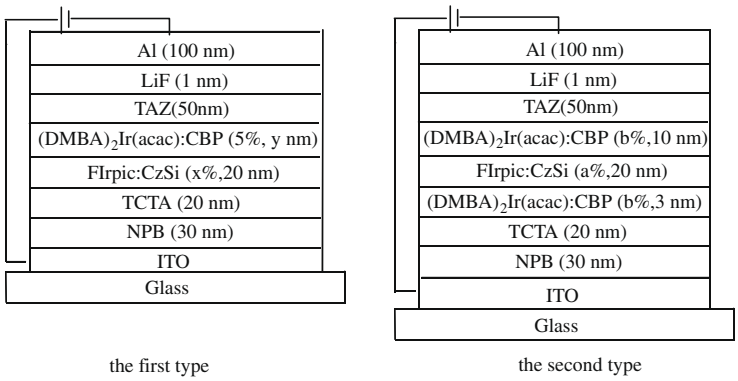

Fig. 2. Structures of the EL devices.

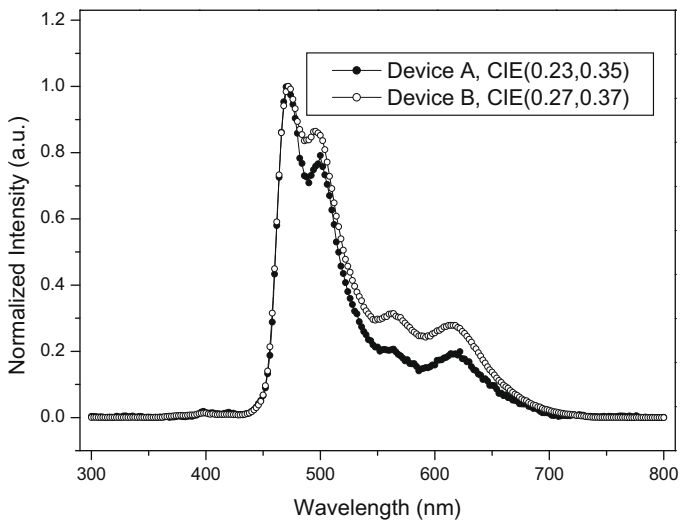

Fig. 3. EL spectra of devices A and B at an applied voltage of 8 V.

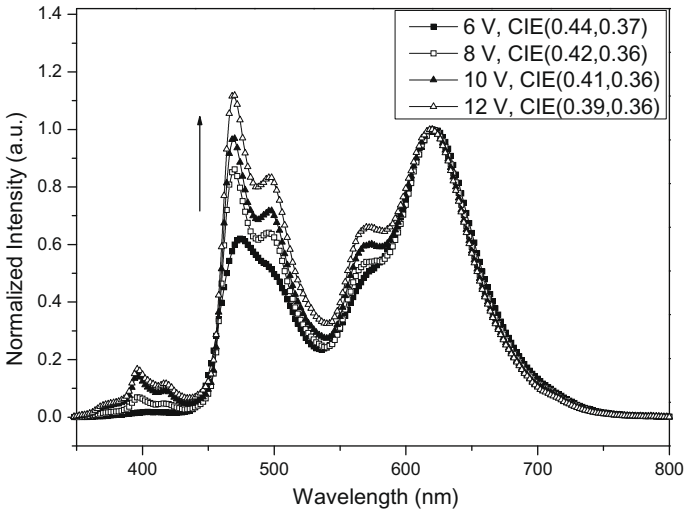

Fig. 4. EL spectra of device C at different applied voltages.

Table 1
Summary of the device characteristics.[a]

Devices	Brightness (V) (max, cd m^{-2})	External quantum efficiency (%)		Current efficiency (cd A^{-1})		Power efficiency (lm W^{-1})		CIE(x,y) at 10 V
		Max	1000 cd m^{-2}	Max	1000 cd m^{-2}	Max	1000 cd m^{-2}	
A	24,150 (16.5)	12.7	8.9	25.6	18.0	20.2	8.1	(0.23, 0.35)
B	24,012 (11.5)	9.8	7.5	20.9	16.1	16.4	8.4	(0.27, 0.38)
C	19,386 (14.0)	10.4	7.3	21.6	15.1	17.0	6.3	(0.41, 0.36)
D	15,648 (11.5)	9.9	8.9	23.6	21.0	14.8	11.0	(0.27, 0.38)
E	18,676 (16.5)	12.2	8.8	27.0	19.2	18.9	6.3	(0.35, 0.37)

[a] Detailed structures of the emitting layers of the devices: A: FIrpic:CzSi (7%, 20)/$(DMBA)_2Ir(acac)$:CBP (5%, 200); B: FIrpic:CzSi (11%, 20)/$(DMBA)_2Ir(acac)$:CBP (5%, 100); C: FIrpic:CzSi (4%, 10)/$(DMBA)_2Ir(acac)$:CBP (5%, 20); D: $(DMBA)_2Ir(acac)$:CBP (1%, 3)/FIrpic:CzSi (11%, 20)/$(DMBA)_2Ir(acac)$:CBP (1%, 10); E: $(DMBA)_2Ir(acac)$:CBP (5%, 3)/FIrpic:CzSi (7%, 20)/$(DMBA)_2Ir(acac)$:CBP (5%, 10).

relative intensity of the blue emission. The thicknesses of the blue and orange-red emission layers were reduced to 10 and 20 nm, respectively.

The EL spectra at different applied voltages (normalized at the emission peak of $(DMBA)_2Ir(acac)$) of device C are shown in Fig. 4. The EL showed balanced contributions from both blue emission of FIrpic and orange–red emission of $(DMBA)_2Ir(acac)$, giving a pure white emission. At the applied voltage of 12 V, the Commission International de l'Eclairage (CIE) coordinates were calculated to be (0.39, 0.36), which was very close to the ideal white point of (0.33, 0.33). A summary of the device characteristics is listed in Table 1. A maximum brightness of 19,386 cd m^{-2} at 14.0 V, an EQE of 10.4%, power efficiency (η_p) of 17.0 lm W^{-1} and current efficiency (η_c) of 21.6 cd A^{-1} at 4.0 V were achieved (Table 1). In the characterization of WOLEDs for lighting applications, the light emitted from all surfaces of the substrates can in principle be directed to the forward viewing direction by some lighting fixture. According to previous report, the total quantum and power efficiencies (η_t) are about 1.7 times of the forward viewing efficiencies [1,13,20]. As such, device C gave a peak total EQE and a total power efficiency of 17.7% and 28.9 lm W^{-1}, respectively. At the brightness of 1000 cd m^{-2}, the forward viewing EQE and current efficiency remained high at around 7.3% and 15.1 cd A^{-1}, respectively.

Color variation with increased bias/brightness was observed for device C, which is commonly seen in previous reported WOLEDs [24–27]. Blue emission grew relatively to the orange-red emission at high applied voltages, causing the CIE coordinates to shift from (0.44, 0.37) at 6 V to (0.39, 0.36) at 12 V. The transportation of holes and electrons in the EL device is related to the highest occupied molecular orbital (HOMO) and lowest unoccupied molecular orbital (LUMO) energy levels of the materials used in EL devices. The LUMO energy level of $(DMBA)_2Ir(acac)$ (2.73 eV) is close to that of FIrpic (2.9 eV), while FIrpic has a much deeper HOMO energy of 5.8 eV than that of $(DMBA)_2Ir(acac)$ (5.07 eV). It can be predicted that $(DMBA)_2Ir(acac)$ may function as effective hole traps. The combinations of holes and electrons may concentrate in the orange-red emitting layer at low applied voltages in device C due to the relatively low mobility of electrons. As the applied voltages increased, the stronger electronic field enhanced the electron mobility, therefore, the blue emission was enhanced due to the shift of combination zone closer to the blue emission layer. According to previous report, the color variation issue may be mitigated by

creating another channel in the device [13]. With the help of such a strategy, the second type of WOLEDs were designed by inserting a thin layer of $(DMBA)_2Ir(acac)$ doped in CBP between the hole-transporting layer and the blue emission layer to balance the blue and orange-red emission at different voltages.

Device D was fabricated using the structure of ITO/NPB (30 nm)/TCTA (20 nm)/$(DMBA)_2Ir(acac)$:CBP (1%, 3 nm)/FIrpic:CzSi (11%, 20 nm)/$(DMBA)_2Ir(acac)$:CBP (1%, 10 nm)/TAZ (50 nm)/LiF (1 nm)/Al (100 nm). The EL spectra at different applied voltages are presented in Fig. 5. The color variation was greatly reduced, giving stable white emission. The CIE coordinates were calculated to be (0.30, 0.38) at an applied voltage of 6 V. At an applied voltage of 10 V, the CIE coordinates were calculated to be (0.27, 0.38), which were very close to that of 6 V, giving a slight CIE shift ($\Delta x = 0.03$, $\Delta y = 0.00$).

It can be predicted that the addition of a layer of $(DMBA)_2Ir(acac)$ in CBP between the hole-transporting layer and the blue emission layer could effectively trap the holes at low voltages. At the same time, the thickness was only 3 nm in device D, so the combination zone might concentrate next to the blue emission layer leading to balanced white emission at low applied voltages. In other words, the hole transportation and recombination with electrons was confined by the addition of a layer of $(DMBA)_2Ir(acac)$. While at high voltages, the combination zone might shift toward the other interface of the blue-emitting layer, but it would be restricted by the other layer of $(DMBA)_2Ir(acac)$ in CBP. Therefore, stable white emission could be obtained at different applied voltages. For device D, a maximum brightness of 15,647 cd m^{-2} at 11.5 V, a maximum EQE of 9.9%, power efficiency of 14.8 lm W^{-1} and current efficiency of 23.6 cd A^{-1} at 5.0 V were achieved

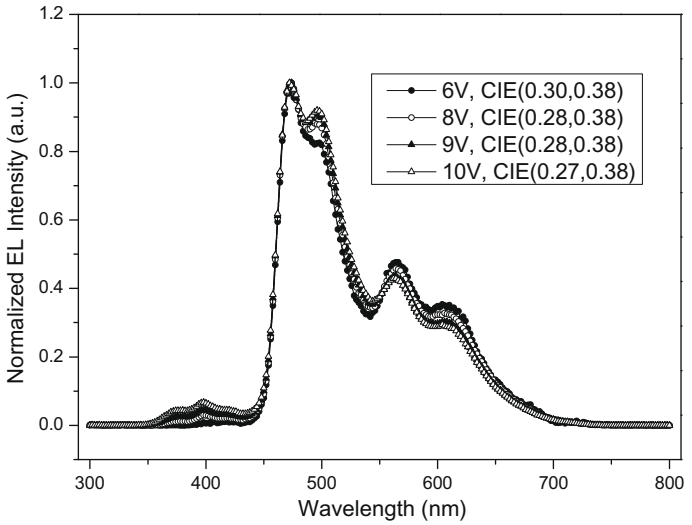

Fig. 5. EL spectra of device D at different applied voltages.

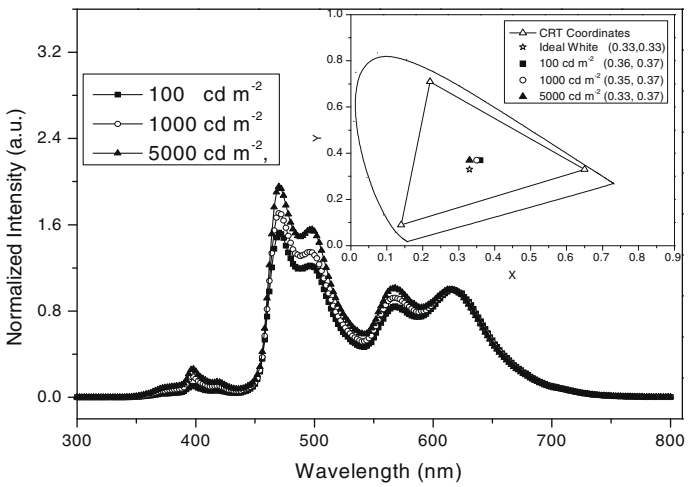

Fig. 6. EL spectra and CIE coordinates of device E at different brightnesses.

(Table 1). At a high brightness of 1000 cd m^{-2}, the forward viewing EQE and current efficiency remained quite high at 8.9% and 21.0 cd A^{-1}, respectively. The maximum brightness of device D was not as high as that of the previous three devices, but the efficiencies at high brightness (1000 cd m^{-2}) were the highest among these four devices.

Encouraged by the results of device D, we conducted further optimization of the doping concentrations of blue and orange-red emitters in order to get white emission with better color purity. In device E, the doping concentration of FIrpic was reduced to 7%, while the doping concentration of $(DMBA)_2Ir(acac)$ was increased to 5%. As shown in Fig. 6, more balanced emission with best CIE coordinates was achieved. No significant color variation at different brightnesses was observed for device E. At a practical brightness of 100 cd m^{-2}, the CIE coordinates were calculated to be (0.36, 0.37), close to (0.33, 0.37) at a high brightness of 5000 cd m^{-2}. A maximum brightness of 18,676 cd m^{-2} at 16.5 V, with a maximum EQE of 12.2%, power efficiency of 18.9 lm W^{-1} and current efficiency of 27.0 cd A^{-1} at 4.5 V was achieved (Fig. 7, Table 1), corresponding to total efficiencies of 19.7%, 45.9 cd A^{-1} and 32.1 lm W^{-1}, respectively. At a high brightness of 1000 cd m^{-2}, the forward viewing EQE and current efficiency remained quite high at 8.8% and 19.2 cd A^{-1}, respectively. Compared with the first type of devices (A, B, and C), devices D and E exhibited higher efficiencies (Fig. 8), especially at higher brightness (Table 1).

As shown in Figs. 5 and 6, the excitons were not firmly confined inside the desired emitting layers as evidenced by the blue emission centered at 400 nm in these devices. It is reported that such high-energy emission might origin from

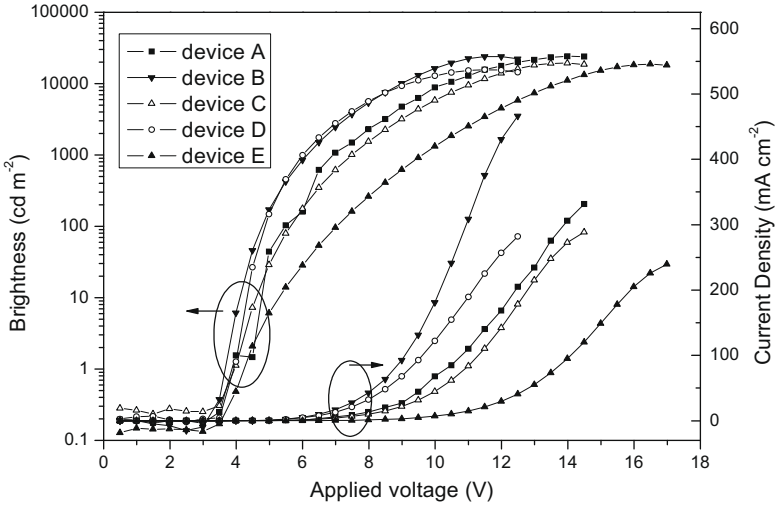

Fig. 7. Brightness–voltage–current density characteristics of the devices.

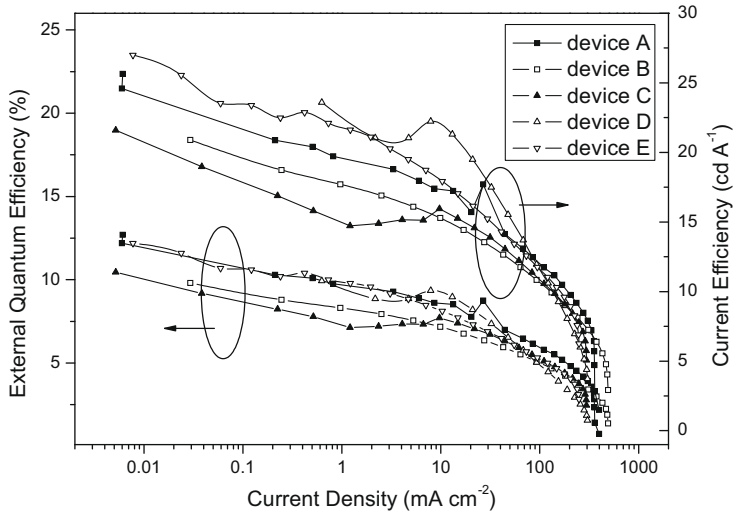

Fig. 8. External quantum efficiency–current density–current efficiency characteristics of the devices.

TCTA or/and TAZ [28]. In the red-emitting devices using $(DMBA)_2Ir(acac)$ as dopant emitter and TCTA as hole-transporting materials, no emission band at 400 nm was observed [23]. So it can be predicted that the high-energy emission comes from TAZ. In order to eliminate such an emission band, BCP was used instead of TAZ in a reference device E1 [NPB (30 nm)/TCTA (20 nm)/$(DMBA)_2Ir(acac)$: CBP (5%, 3 nm)/FIrpic:CzSi (7%, 20 nm)/$(DMBA)_2Ir(acac)$: CBP (5%, 10 nm)/BCP (10 nm)/LiF (1 nm)/Al (100 nm)]. For device E1, no emission at 400 nm was observed. A maximum brightness of 8968 cd m^{-2} and a maximum EQE of 4.3% were achieved, which were much lower than those of device E. These results indicate that the use of TAZ can improve the device efficiencies much more than BCP, although the emission at 400 nm with a relative intensity of below 0.1 was observed.

4. Conclusions

In conclusion, we report the first application of excimer emission of an iridium complex in highly efficient white OLEDs. By utilizing the iridium complex $(DMBA)_2Ir(acac)$ with broad excimer emission and an efficient blue Ir complex FIrpic, highly efficient phosphorescent WOLEDs can be obtained. The two-component phosphorescent WOLEDs exhibited pure white emission with CIE coordinates close to the ideal white emission (0.33, 0.33). By incorporating a blue-emitting layer sandwiched between two red-emitting layers and thereby forming a triple-emitting-layer device structure, WOLEDs exhibit stable white emission at different biases/brightnesses with maximum EL efficiencies of up to 12.2%, and 27.0 cd A^{-1} for the forward viewing direction, corresponding to total efficiencies of 19.7%, 45.9 cd A^{-1} and 32.1 lm W^{-1}. At a high brightness of 1000 cd m^{-2}, the EL efficiencies remained high at 8.8% and 19.2 cd A^{-1}.

Acknowledgements

Financial supports from the National Natural Science Foundation of China (Project Nos. 20772057, 20773066, and 20972068), the Leading Academic Discipline Program, 211 Project for Nanjing Normal University (the 3rd phase), the Graduate Student Innovation Fund of Education Department of Jiangsu Province (Grant No. CX09S_042Z) and Nanjing Normal University are gratefully acknowledged.

References

[1] B.W. D'Andrade, S.R. Forrest, Adv. Mater. 16 (2004) 1585.
[2] D. Gupta, M. Katiyar, Deepak, Opt. Mater. 28 (2006) 295.
[3] A. Misra, P. Kumar, M.N. Kamalasanan, S. Chandra, Semicond. Sci. Technol. 21 (2006) R35.
[4] Z. Zhang, Q. Wang, Y. Dai, Y. Liu, L. Wang, D. Ma, Org. Electron. 10 (2009) 491.
[5] Y.H. Lee, B.K. Ju, W.S. Jeon, J.H. Kwon, O.O. Park, J.W. Yu, B.D. Chin, Synth. Met. 159 (2009) 325.
[6] P. Chen, Q. Xue, W. Xie, Y. Duan, G. Xie, Y. Zhao, J. Hou, S. Liu, L. Zhang, B. Li, Appl. Phys. Lett. 93 (2008) 153508.
[7] C.L. Ho, W.Y. Wong, Q. Wang, D. Ma, L. Wang, Z. Lin, Adv. Funct. Mater. 18 (2008) 928.
[8] C.L. Ho, M.F. Lin, W.Y. Wong, W.K. Wong, C.H. Chen, Appl. Phys. Lett. 92 (2008) 083301.
[9] K.S. Yook, S.O. Jeon, J.Y. Lee, K.H. Lee, Y.S. Kwon, S.S. Yoon, J.H. Yoon, Org. Electron. 10 (2009) 1378.
[10] G. Schwartz, S. Reineke, T.C. Rosenow, K. Walzer, K. Leo, Adv. Funct. Mater. 19 (2009) 1319.
[11] B.W. D'Andrade, R.J. Holmes, S.R. Forrest, Adv. Mater. 16 (2004) 624.
[12] Y.S. Park, J.W. Kang, D.M. Kang, J.W. Park, Y.H. Kim, S.K. Kwon, J.J. Kim, Adv. Mater. 20 (2008) 1957.
[13] C.H. Chang, Y.H. Lin, C.C. Chen, C.K. Chang, C.C. Wu, L.S. Chen, W.W. Wu, Y. Chi, Org. Electron. 10 (2009) 1235.
[14] P. Chen, L. Zhang, Y. Duan, W. Xie, Y. Zhao, J. Hou, S. Liu, B. Li, J. Phys. D: Appl. Phys. 42 (2009) 05515.
[15] S. Reineke, F. Lindner, G. Schwartz, N. Seidler, K. Walzer, B. Lussem, K. Leo, Nature 459 (2009) 234.
[16] Y. Sun, S.R. Forrest, Appl. Phys. Lett. 91 (2007) 263503.
[17] X.M. Yu, G.J. Zhou, C.S. Lam, W.Y. Wong, X.L. Zhu, J.X. Sun, M. Wong, H.S. Kwok, J. Organomet. Chem. 693 (2008) 1518.
[18] V. Adamovich, J. Brooks, A. Tamayo, A.M. Alexander, P.I. Djurovich, B.W. D'Andrade, C. Adachi, S.R. Forrest, M.E. Thompson, New J. Chem. 26 (2002) 1171.
[19] B.W. D'Andrade, J. Brooks, V. Adamovich, M.E. Thompson, S.R. Forrest, Adv. Mater. 14 (2002) 1032.
[20] E.L. Williams, K. Haavisto, J. Li, G.E. Jabbour, Adv. Mater. 19 (2007) 197.
[21] X. Yang, Z. Wang, S. Madakuni, J. Li, G.E. Jabbour, Appl. Phys. Lett. 93 (2008) 193305.
[22] G. Zhou, Q. Wang, C.L. Ho, W.Y. Wong, D. Ma, L. Wang, Chem. Commun. (2009) 3574.
[23] G.H. Zhang, H.H. Chou, X.Q. Jiang, P.P. Sun, C.H. Cheng, Y. Ooyama, Y. Harima, Org. Electron. 11 (2010) 632.
[24] G. Cheng, Y. Zhang, Y. Zhao, Y. Lin, C. Ruan, S. Liu, T. Fei, Y. Ma, Y. Cheng, Appl. Phys. Lett. 89 (2006) 043504.
[25] X.M. Yu, H.S. Kwok, W.Y. Wong, G.J. Zhou, Chem. Mater. 18 (2006) 5097.
[26] G. Schwartz, M. Pfeiffer, S. Reineke, K. Walzer, K. Leo, Adv. Mater. 19 (2007) 3672.
[27] K.S. Yook, J.Y. Lee, Appl. Phys. Lett. 92 (2008) 193308.
[28] C.H. Chang, K.C. Tien, C.C. Chen, M.S. Lin, H.C. Cheng, S.H. Liu, C.C. Wu, J.Y. Hung, Y.C. Chiu, Y. Chi, Org. Electron. 11 (2010) 412.

nanoparticles at the organic–cathode interface and show that this results in a more efficient light emission mainly attributed to an enhanced internal quantum efficiency. We achieved an enhancement of a factor of 4.1 for a current density of 60 mA/cm^2.

2. Experimental

Nanoparticles of different materials and sizes were introduced between the emission layer and the cathode. Our devices were designed as shown in Fig. 1: a 1 mm-thick glass substrate covered with 130 nm of indium tin oxide (ITO), a layer of 20 nm of poly(3,4-ethylenedioxythiophene):poly(styrene sulfonate) (PEDOT:PSS), a layer of 50 nm of phenylene substituted poly(para-phenylenevinylene) (Ph-PPV; better known as Super Yellow from Merck OLED Materials GmbH) followed by nanoparticle clusters and a cathode consisting of 50 nm calcium and 250 nm aluminum. The substrates are 25 mm × 25 mm in size and feature four active areas of 5 mm × 5 mm each.

The PLED fabrication steps were as follows. The ITO-covered glass substrates were cleaned first with acetone and then with isopropanol in an ultrasonic bath for 15 min, respectively. The surface of the ITO was then exposed to an oxygen plasma as a last cleaning procedure and to make the surface hydrophilic. All following fabrication steps were conducted in a glove box under nitrogen atmosphere. The PEDOT:PSS was spin coated onto the ITO surface at a spinning speed of 2000 rpm. Afterwards, the substrates were baked in a vacuum oven at 140 °C for 30 min to eliminate the residues of water in the PEDOT:PSS layer. On top of this film the Super Yellow was applied by spinning the solution (3 mg/ml) at 1000 rpm. The modified PLEDs had an extra spin coating step before they were metalized with calcium and aluminum. Three different dispersions were prepared with SiO_2 and TiO_2 nanoparticles. The nanoparticles both were available as aqueous solutions (Ludox: 34 wt.% SiO_2 in H_2O, 20–30 nm in diameter, and a 10 wt.% suspension of TiO_2 in H_2O, 20–130 nm in diameter; purchased from Sigma–Aldrich). Due to the strong dependance of the physical parameters on the fabrication method, it is difficult to determine the exact values. Typically, the refractive indices of SiO_2- and TiO_2-thin films are in the range of 1.46–1.55 and 2.4–2.6, respectively. Since the surface of Super Yellow is hydrophobic, we mixed the aqueous solutions with diethylene glycol (DEG) to enhance adhesion of the dispersions and thus of the nanoparticles during the spin coating process. The first dispersion was a mixture of SiO_2 and DEG at a ratio of 1:1. The second and third dispersions contained SiO_2 and TiO_2 at ratios of 1:1 and 1:4, respectively, and were then mixed with DEG at a 1:1 ratio. All three dispersions were spin coated at 3000 rpm and 5000 rpm to investigate the effect of different particle concentrations on the performance of the devices. When applying the dispersion via a pipette onto the samples the wettability was not high enough to spread the dispersion over the whole device surface. The dispersion was concentrated around a circle of about 1.5 cm in diameter before starting the spin coating process. From SEM micrographs the nanoparticle concentration could be determined to 1–2 nanoparticle clusters per 4 μm^2. During operation these parts of the active areas on each substrate covered with the nanoparticles reveal an enhanced light output. An additional DEG-reference PLED with DEG but without nanoparticles was fabricated to investigate any effects originating from DEG. The PLEDs were then completed with a cathode of calcium and a cover layer of aluminum. To allow for electrical and optical characterization at normal atmospheric conditions, the samples are encapsulated using epoxy resin adhesive and a glass cover. Measurements of *J–V* curves and electroluminescence (EL) of the devices were made with a source-measure unit (Keithley SMU 238) and an integrating sphere (Gigahertz-Optik, UMBB-210) being connected via a multimode fiber to a spectrometer (Acton Research Corporation SpectraPro-300i) with an intensified charge-coupled device (Princeton Instruments PiMax:512). Angle resolved EL measurements were performed using the same source-measure unit, spectrometer and intensified charge-coupled device. In that case, the device was mounted on a goniometer and was rotated around the vertical axis, while the multimode fiber was kept fixed. For comparison angle resolved photoluminescence (PL) measurements were carried out in a similar way. A UV laser (Newport, Explorer Scientific All Solid State UV Laser, EXPL-349-120-CDRH) was coupled into a UV optical fiber, which was attached to the goniometer to maintain a constant spot size on the PLED while rotating the goniometer.

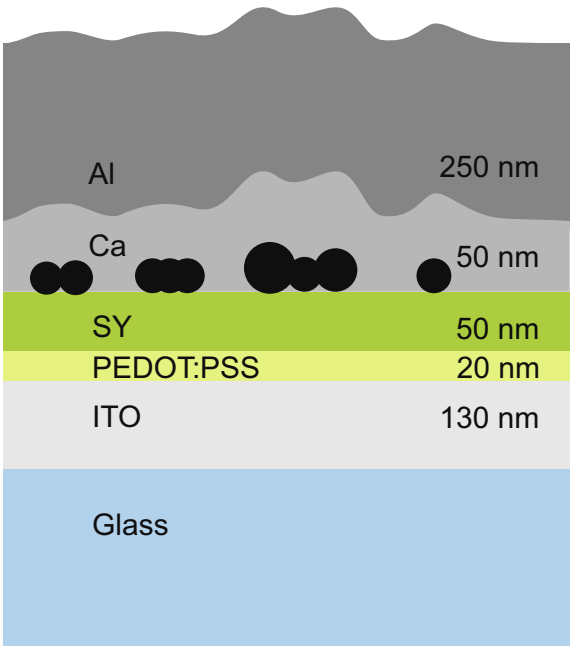

Fig. 1. Schematic diagram of the PLED with nanoparticle clusters.

3. Results and discussion

Fig. 2 shows the current density–voltage (*J–V*) characteristics (a) and the luminous flux versus voltage (b) and current density (c). The DEG-reference shows the lowest

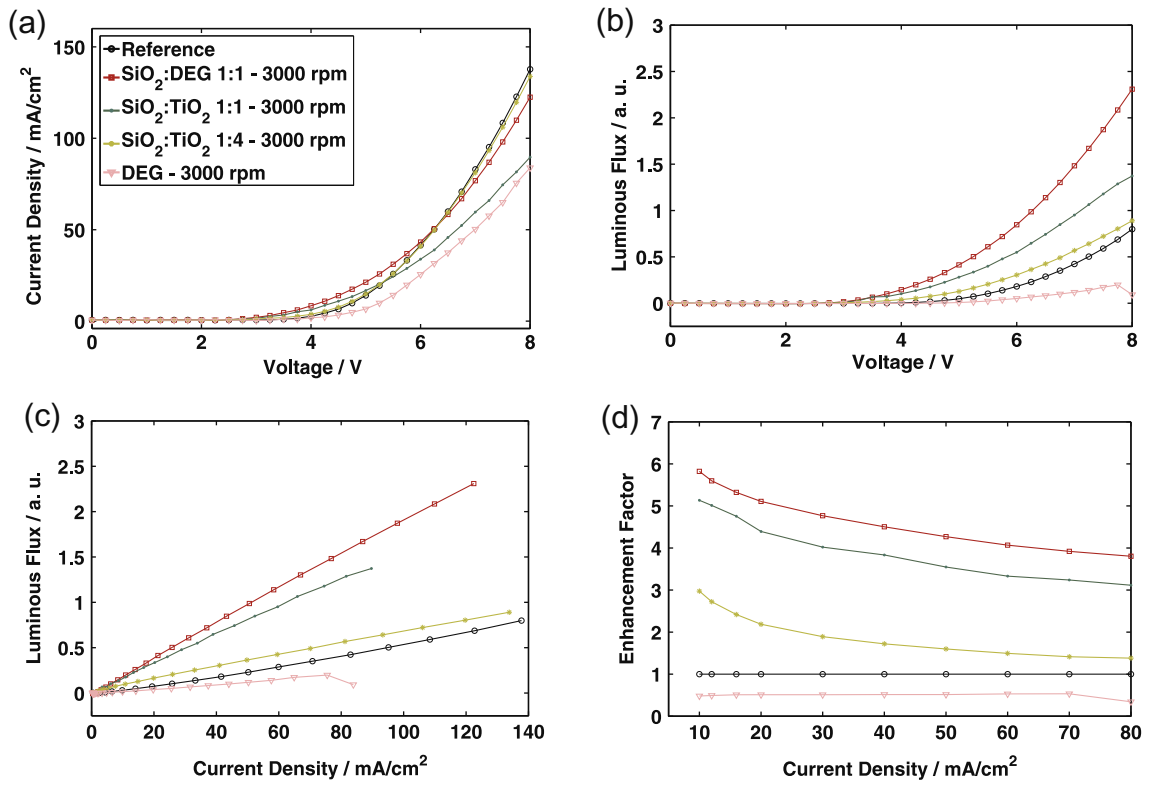

Fig. 2. Electronic and optical measurements of PLEDs with nanoparticle clusters between the emission layer and the cathode for different nanoparticle composites. The *J–V* curve (a) shows an increase in current injection for the modified devices at low current densities. The luminous flux versus the voltage (b) and the current density (c) reveal the increased performance for all devices with embedded nanoparticle clusters. The overall enhancement factor normalized to the reference PLED depending on the current density is shown in (d).

current values. Fig. 2(b) reveals that devices with SiO_2 and a low or zero TiO_2 content start to emit light with an onset voltage reduced by at least 1 V as compared to the other devices (see also Table 1). In addition, these PLEDs perform also much better at higher voltages. The same picture can be drawn from Fig. 2(c), where the light output is shown in dependence of the current density. Devices with only SiO_2 or with SiO_2 and a low TiO_2 content show the best performance with an efficiency enhancement of factor 4.1 and 3.3, respectively (at 60 mA/cm^2 current density). PLEDs with SiO_2 and a higher TiO_2 content achieved a better light output than devices with no nanoparticles at all. The DEG-reference performed very poorly. Different spin coating velocities resulted in no difference in the performance for most devices. Only for the PLEDs with the SiO_2:TiO_2 1:1 dispersion a small difference is obtained. For clarity reasons only the data for the samples spin coated at 3000 rpm is shown. The overall enhancement factor normalized to the reference device depending on the current density is shown in Fig. 2(d). We observe the highest relative enhancement for low current densities. For higher current densities space charge effects might lead to a lower enhancement factor. The angle resolved EL measurements in Fig. 3(a) were performed while supplying a constant current density of 20 mA/cm^2. The PLEDs with only SiO_2 nanoparticles had an over eight times higher light output than the reference device, independent of the spin coating velocity. With increasing TiO_2 content the performance decreased, whereas the DEG-reference again performed poorly. All devices feature a nearly Lambertian emission characteristic. Fig. 3(b) shows the angle resolved PL measurements. In contrast to all EL measurements the reference device reveals the best performance. The light output decreases with increasing TiO_2 content, while the DEG-reference offers the worst light output. Again, a Lambertian profile is observed. The variation in light output is much smaller compared to the EL measurements.

Table 1
Voltages of the different samples at a current density of 5 mA/cm^2.

Sample	Voltage at 5 mA/cm^2 (V)
Reference	4.32
SiO_2:DEG 1:1 – 3000 rpm	3.57
SiO_2:TiO_2 1:1 – 3000 rpm	3.73
SiO_2:TiO_2 1:4 – 3000 rpm	4.19
DEG – 3000 rpm	4.78

There are several aspects to be considered in order to explain the behavior of the nanoparticle-modified devices. The fact that the DEG-reference performs so poorly compared to all other devices proves that DEG as a source of any positive effect in the performance of all modified devices can be excluded. The enhancement cannot be

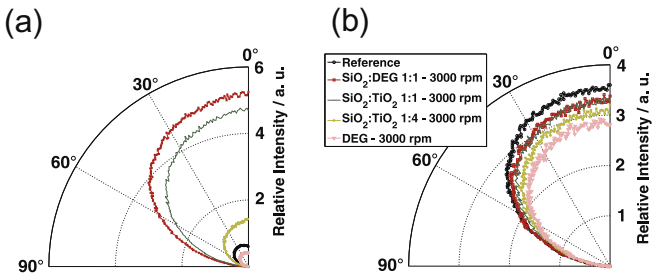

Fig. 3. Angle resolved EL and PL measurements of PLEDs with nanoparticle clusters between the emission layer and the cathode for different nanoparticle composites. EL measurements in (a) were performed at a constant current density of 20 mA/cm^2. PL measurement in (b) were conducted using a UV laser (349 nm) as excitation source.

attributed to an optical scattering effect either, since in this case the PL measurements should reveal a similar enhancement as the EL measurements while the *J–V*-characteristics should remain unchanged. This is not observed. In contrast to Bliznyuk et al. [14] the current density of the modified devices is decreased at higher voltages, which at first sight might indicate a worsened electron injection, due to a blocking effect of the nanoparticle clusters. However, this seems to be very unlikely when considering the lower turn-on voltage for the modified devices. The hole mobility in ordinary PPV is two orders of magnitude higher than the electron mobility [19], resulting in a recombination zone that is very close to the calcium cathode. In addition the barrier for hole injection is lower than the barrier for electron injection. Hence, the *J–V*-characteristics of the devices is mainly determined by the holes [20]. The nanoparticle clusters, arbitrarily distributed between the Super Yellow and the calcium layer, create a randomly nanopatterned cathode interface. This gives rise to locally enhanced fields again resulting in an higher electron injection rate, in turn leading to a better charge balance. The enhanced internal quantum efficiency entails finally an increased luminescence. This interpretation is supported by the lower turn-on voltage and the high enhancement factor at low current densities. The variation in the enhancement for different nanoparticle cluster mixtures is mainly attributed to the size of the nanoparticles itself and to the size of the clusters they form.

4. Conclusion

In conclusion, we have fabricated PLEDs with SiO_2 and TiO_2 nanoparticle clusters between the emission layer and the cathode. We have demonstrated a 300% increase in the EL efficiency of these devices. The nanoparticle clusters increase the electron injection at the nanoparticle cluster–cathode interface therefore enhancing the internal quantum efficiency. This effect is particularly beneficial for solution processed devices, since these nanoparticles are low cost and easy to handle and might be an alternative to additional polymer layers for controlling charge injection and balance.

Acknowledgments

We acknowledge support by the Bundesministerium für Bildung und Forschung (BMBF) within the project NanoFutur Project 03X5514. B.R. and J.H. are pursuing their Ph.D. within in the Karlsruhe School of Optics & Photonics (KSOP).

References

[1] S. Forrest, Org. Electron. 4 (2003) 45.
[2] W. Brütting, Physics of Organic Semiconductors, Vch Verlagsgesellschaft Mbh, 2005.
[3] W.L. Barnes, J. Lightwave Technol. 17 (1999) 2170.
[4] M.-H. Lu, J.C. Sturm, J. Appl. Phys. 91 (2002) 595.
[5] N. Greenham, R. Friend, D. Bradley, AM 6 (1994) 491.
[6] F. Li, X. Li, J. Zhang, B. Yang, Org. Electron. 8 (2007) 635.
[7] T. Yamasaki, K. Sumioka, T. Tsutsui, Appl. Phys. Lett. 76 (2000) 1243.
[8] H.J. Peng, Y.L. Ho, X.J. Yu, H.S. Kwok, J. Appl. Phys. 96 (2004) 1649.
[9] S. Reineke, F. Lindner, G. Schwartz, N. Seidler, K. Walzer, B. Lüssem, K. Leo, Nature 459 (2009) 234.
[10] Y. Sun, S.R. Forrest, Nat. Photon. 2 (2008) 483.
[11] J.M. Lupton, B.J. Matterson, I.D.W. Samuel, M.J. Jory, W.L. Barnes, Appl. Phys. Lett. 77 (2000) 3340.
[12] U. Geyer, J. Hauss, B. Riedel, S. Gleiss, U. Lemmer, M. Gerken, J. Appl. Phys. 104 (2008) 093111.
[13] M. Fujita, K. Ishihara, T. Ueno, T. Asano, S. Noda, H. Ohata, T. Tsuji, H. Nakada, N. Shimoji, Jpn. J. Appl. Phys., Part 1 44 (2005) 3669.
[14] V. Bliznyuk, B. Ruhstaller, P. Brock, U. Scherf, S. Carter, Adv. Mater. 11 (1999) 1257.
[15] C. Oey, A. Djurišić, C. Kwong, C. Cheung, W. Chan, J. Nunzi, P. Chui, Thin Solid Films 492 (2005) 253.
[16] N. Dinh, T. Thuy, T. Trung, J. Appl. Phys. 105 (2009) 093518.
[17] A. Hussain, B. Neppolian, S. Kim, J. Kim, H. Choi, K. Lee, S. Park, A. Heeger, Appl. Phys. Lett. 94 (2009) 073306.
[18] S. Carter, J. Scott, P. Brock, Appl. Phys. Lett. 71 (1997) 1145.
[19] I. Hulea, R. Van Der Scheer, H. Brom, B. Langeveld-Voss, A. Van Dijken, K. Brunner, Appl. Phys. Lett. 83 (2003) 1246.
[20] G. Malliaras, J. Salem, P. Brock, C. Scott, Phys. Rev. B: Condens. Matter 58 (1998) 13411.

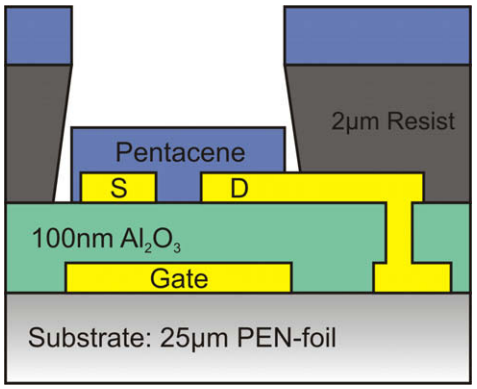

Fig. 1. Cross-section of the organic thin-film transistor process on foil having Al_2O_3, treated with a self-assembled monolayer of trichloro(phenethyl)silane, as gate dielectric.

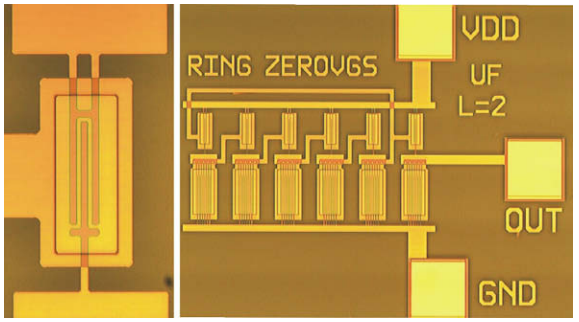

Fig. 2. Micrograph image of (left) a single transistor with channel length $L = 2$ μm and source/drain finger size of 5 μm and (right) a 5-stage ring oscillator with channel length $L = 2$ μm.

capacitance of 70 nF/cm^2, treated by a self-assembled monolayer of trichloro(phenethyl)silane. That, in turn, allows for some downscaling the transistor channel length, in our case to 2 μm, while maintaining a reasonable output resistance in saturation of Ro = 9.75 MΩ at 0 V gate-source voltage. A cross-section of this process flow is depicted in Fig. 1. Fig. 2 shows a micrograph image of a 5-stage ring oscillator realized in this technology.

This organic thin-film circuit technology allows to design with lower overlap capacitance and to downscale the transistor channel length, within the boundaries achievable by existing high-throughput tools (e.g. steppers used in backplane manufacturing). In this work, we varied the channel lengths (L) of the circuits between 20 μm and 2 μm. We also limited the gate-source and gate-drain overlap capacitances by decreasing the width of the finger-shaped source and drain contacts (that overlap the gate) from 5 μm to 2 μm. Fig. 2 shows a micrograph image of one transistor. All devices and circuits are processed on 25 μm thick polyethylene naphthalate (PEN) foil, which was, during processing, laminated on a 150 mm carrier substrate, and delaminated after completion of the process.

3. Results and discussion

Typical transfer and output curves of transistors fabricated in this technology, having $L = 5$ μm and 2 μm, are depicted in Fig. 3. The transistors are normally-on and the charge carrier (hole) mobility exceeds 0.5 cm^2/Vs for both 2 and 5 μm channel length devices. The output resistance in saturation at gate-source voltage of 0 V is 206.6 ± 8.1 MΩ for $L = 5$ μm and 9.75 ± 0.22 MΩ for $L = 2$ μm. Fig. 4 shows a typical transfer curve of a zerovgs-load

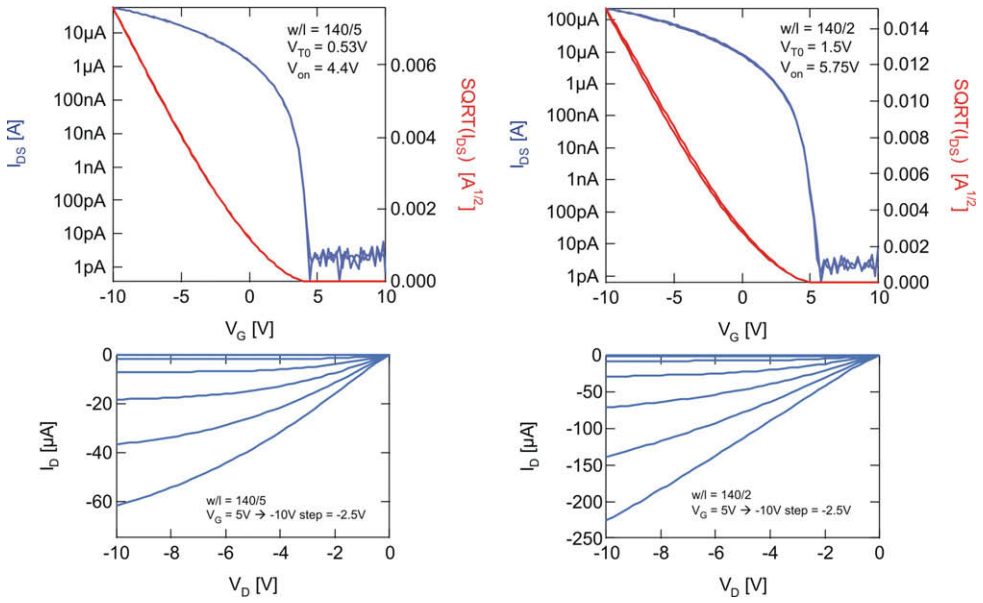

Fig. 3. Typical measured (top) transfer and (bottom) output curves of transistors with (left) $W/L = 140/5$ and (right) $W/L = 140/2$. The mobility exceeds 0.5 cm^2/Vs, off-current is below 10 pA.

inverter [3] with channel lengths of 5 μm and 2 μm, having reduced gate-drain and gate-source overlap while varying the supply voltage between 5 and 20 V. The ratio between drive and load transistor is 1:10. Both inverters show high gains and noise margins.

In Fig. 5, the extracted main parameters of an inverter (noise margin and gain) are plotted as a function of supply voltage for different inverters with varying channel length and overlap capacitance. The gain of these inverters varies from 3.8 to 34.5 for increasing channel length at a supply voltage of 20 V. This is mainly due to a lower output resistance with increasing channel lengths. The noise margin figure indicates that long channel lengths yield more robust inverters with larger noise margins at different supply voltages. As a consequence, the inverters with long channel lengths are more robust at supply voltages below 10 V, at the expense of lower speed. This effect is shown in Fig. 6, where we plot the inverter stage delay as a function of

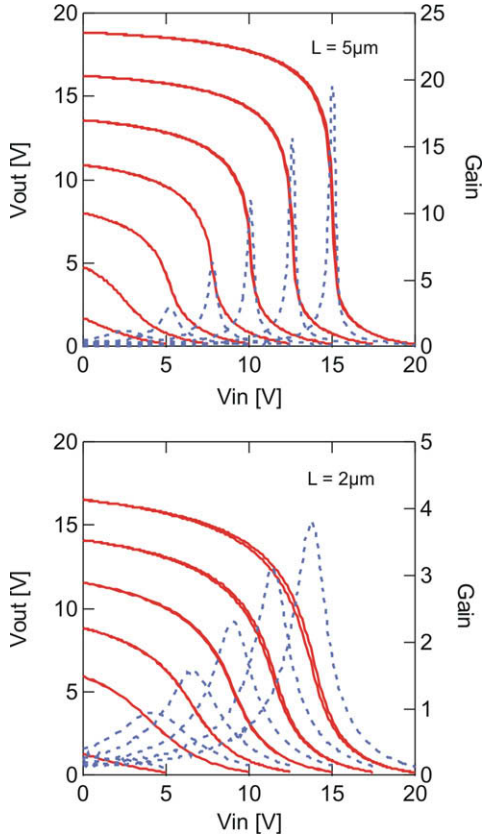

Fig. 4. Series of measured transfer curves of an inverter when varying the supply voltage between 5 and 20 V for transistors having a drive:load transistor ratio of 1:10 (zerovgs-load inverter configuration), source/drain finger sizes of 2 μm and a channel length of (top) 5 μm and (bottom) 2 μm. The solid lines represent the measured transfer curves, whereas the dashed lines represent the calculated gain.

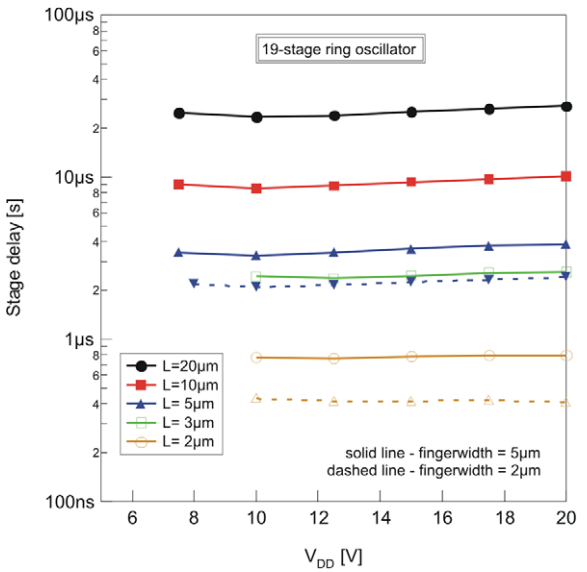

Fig. 6. Overview of stage delays versus supply voltage, measured on 19-stage ring oscillators with varying channel lengths, between 20 μm and 2 μm (color and symbol codes) and source/drain finger sizes of 5 μm (solid lines) and 2 μm (dashed lines).

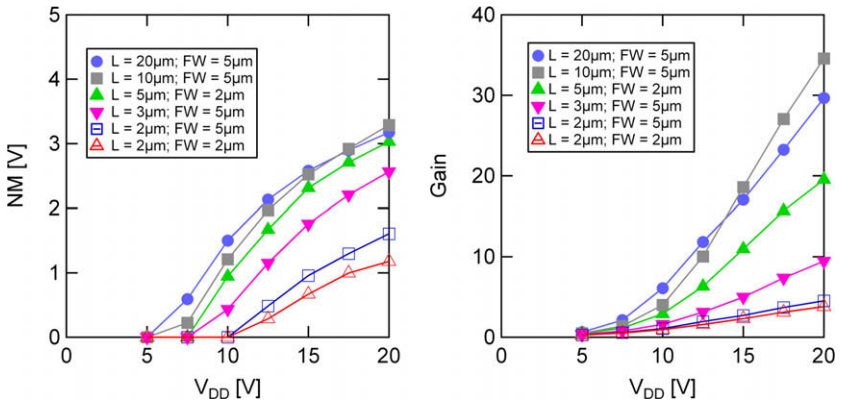

Fig. 5. Noise margin (left) and gain (right) as a function of increasing supply voltage, extracted out of the measured transfer curves of inverters having different channel lengths (20–2 μm) and different overlap capacitance (finger width FW = 5–2 μm).

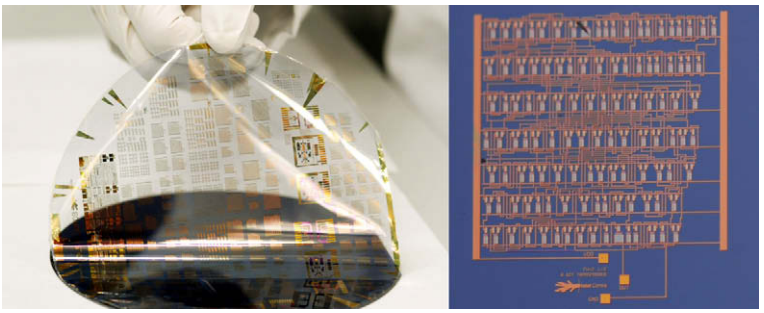

Fig. 7. Photograph of the 150 mm foil being delaminated from the carrier wafer (left) and a detailed die picture of the 8 bit RFID transponder chip on foil (right). The die size is 24.73 mm^2. The design comprises 294 transistors.

supply voltage, as extracted from 19-stage ring oscillators, for transistors with channel lengths varying from 20 μm to 2 μm and with gate-overlap of the transistor-fingers ranging from 5 μm to 2 μm. Stage delays below 1 μs, and as low as 400 ns, are shown at V_{DD} as low as 10 V. The effect of decreasing the overlap capacitance is also shown in Fig. 6 for the circuits having a channel length of 2 μm and 5 μm: shrinking the overlap from 5 μm to 2 μm improves the stage delay by a factor of 1.5–2.

We proceeded with the design and realization of 8 bit RFID transponder chips, having a channel length of 2 μm and either 5 μm or 2 μm finger widths. Fig. 7 shows the photographs of the 150 mm wafer and a zoom of the die. The corresponding schematic is depicted in the inset of Fig. 8. This figure also depicts the output signal of both types of transponders having a channel length of 2 μm. The obtained data rate is 8.69 kb/s for the channel length of 5 μm and finger width of 2 μm. A data rate of 21.68 kb/s has been obtained for a channel length of 2 μm and finger width of 5 μm. In agreement with the two-fold faster inverter stage delay for the 2 μm fingers, the data rate of this transponder is also twice as high as that of the design with 5 μm fingers. The obtained data rate of the 8 bit transponder with channel length and fingers of 2 μm is a record 50 kb/s, which is a 25-fold improvement over the latest published result [4].

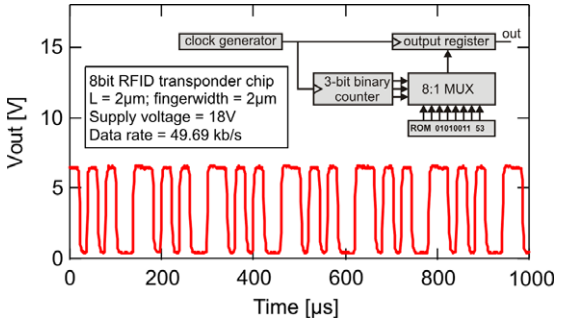

Fig. 8. Measured signal of the 8 bit RFID transponder chip having transistors with channel length of 2 μm. The width of the source-drain fingers is also 2 μm. The supply voltage for the 8 bit transponder chip was 18 V, yielding a data rate of 49.69 kb/s. The inset shows the schematic overview of the digital logic portion of the 8 bit transponder chip.

4. Conclusions and outlook

In summary, this work shows that organic RFID transponder chips with EPC-compatible data rates can be realized with organic semiconductors, mainly thanks to the combination of such semiconductors with high-k dielectrics without penalty in the charge carrier mobility. The high-k dielectrics allow high accumulation charge densities, hence drive current, and open options for shorter channel lengths, down to 2 μm, without loss of saturation in the transistor output characteristics. Specific figures for the speed that we achieved are gate delays in 19-stage ring oscillators down to 400 ns at V_{DD} = 10 V, and bit rates for 8 bit RFID transponders of 50 kb/s at V_{DD} = 18 V.

This work was performed in collaboration between IMEC and TNO in the frame of the HOLST Centre.

References

[1] RFID Handbook, Klaus Finkenzeller, second ed., Wiley, 2003.
[2] EPC Standard, see <http://www.epcglobalinc.org/standards/specs/>.
[3] E. Cantatore, T.C.T. Geuns, G.H. Gelinck, E. van Veenendaal, A.F.A. Gruijthuijsen, L. Schrijnemakers, S. Drews, D.M. de Leeuw, A 13.56-MHz RFID system based on organic transponders, IEEE J. Solid-State Circuits 42 (1) (2007) 84–92.
[4] K. Myny, S. Steudel, P. Vicca, M.J. Beenhakkers, N.A.J.M. van Aerle, G.H. Gelinck, J. Genoe, W. Dehaene, P. Heremans, Plastic circuits and tags for 13.56 MHz radio-frequency communication, Solid State Electron. 53 (12) (2009) 1220–1226.
[5] A. Ullmann, M. Böhm, J. Krumm, W. Fix, Polymer Multi-Bit RFID Transponder, International Conference on Organic Electronics (ICOE), June 4–7, abstract 53, Eindhoven, The Netherlands, 2007.
[6] C. Rolin, S. Steudel, P. Vicca, J. Genoe, P. Heremans, Functional pentacene thin films grown by in-line organic vapor phase speeds above 2 m/min, Appl. Phys. Exp. 2 (2009) 086503.
[7] S. De Vusser, S. Steudel, K. Myny, J. Genoe, P. Heremans, Integrated shadow mask method for patterning small molecule organic semiconductors, Appl. Phys. Lett. 88 (2006) 103501.

2. Experimental

2.1. Materials

C_4-DFQA and C_4-QA (Chart 1) were synthesized according to the reported procedure [6,10], and Alq_3 and NPB were purchased from Aldrich and purified by vacuum sublimation.

C_4-DFQA (75% yield): MS: *m/z* 460.2 $[M]^+$. Anal. Calcd for $C_{28}H_{26}F_2N_2O_2$ (460.51): C, 73.03; H, 5.69; N, 6.08. Found: C, 73.26; H, 5.67; N, 6.05. ^1H NMR ($CDCl_3$): δ 8.75 (s, 2H), 8.18–8.20 (d, 2H), 7.52 (s, 2H), 7.54 (s, 2H), 4.49–4.55 (t, 4H), 1.97–2.02 (m, 4H), 1.56–1.67 (m, 4H), 1.09–1.14 (t, 6H).

C_4-QA (91% yield): MS: *m/z* 424.0 $[M]^+$. Anal. Calcd for $C_{28}H_{28}N_2O_2$ (424.0): C, 79.22; H, 6.65; N, 6.60. Found: C, 79.01; H, 6.90; N, 6.33. ^1H NMR ($CDCl_3$): δ 8.75 (s, 2H), 8.55 (dd, J = 8.0 Hz, J = 1.0 Hz, 2H), 7.74 (td, J = 7.75 Hz, J = 1.50 Hz, 2H), 7.50 (d, J = 9.0 Hz, 2H), 7.25 (t, J = 7.5 Hz, 2H), 4.5 (t, J = 8.0 Hz, 4H), 2.0 (m, 4H), 1.67 (m, 4H), 1.12 (t, 7.5, 6H).

2.2. Instrumentation

^1H NMR spectra were recorded on Bruker AVANVE 500 MHz spectrometer with tetramethylsilane as the internal standard. Mass spectra were recorded on a GC/MS mass spectrometer. Photoluminescence spectra were recorded on a Perkin–Elmer LS 55 spectrophotometer. UV–vis spectra were recorded on a Shimadzu UV-2550 PC spectrometer. Electrochemical measurements were performed in anhydrous CH_2Cl_2 with a BAS 100 W bioanalytical electrochemical work station, using Pt working electrode, platinum wire as auxiliary electrode, and a porous glass wick Ag/Ag^+ as reference electrode, standardized against ferrocene/ferrocenium couple, scan rate 100 mV s^{-1}. Element analyses were performed on a Flash EA 1112 spectrometer. The EL spectrum, brightness, CIE coordinates and the current–luminance–voltage characteristics of the devices were measured with a rapid scan system using a Photo Research PR650 spectrophotometer and a computer-controlled, programmable, direct-current (DC) source (Keithley 2400).

2.3. OLEDs fabrication and characterizations

The devices were grown on a glass, which was precoated with indium tin oxide (ITO) having a sheet resistance equal to 20 $\Omega\,cm^{-2}$. The ITO glass was routinely cleaned by ultrasonic treatment in detergent solutions, followed by rinsed with acetone, boiled in isopropanol, rinsed in methanol, and then in de-ionized water. The glass was dried in vacuum oven between each cleaning step above. The devices were fabricated by successive vacuum deposition of organic materials onto ITO-coated glass substrate. Prior to the deposition, all the organic materials were purified by sublimation method. The deposition sources Alq_3 and the QA derivatives were set in separate quartz crucibles whose temperatures were independently controlled by coil heaters. A very thin layer of LiF could enhance electron injection from aluminum cathode. A shadow mask with 2 × 3 mm^2 openings was used to define the cathodes. EL spectra, brightness, and current–voltage characteristics were measured at room temperature under ambient atmosphere.

3. Results and discussion

3.1. Absorption and photoluminescent (PL) properties

The UV/vis and PL spectra of C_4-DFQA are shown in Figs. 1 and 2, and for comparison, the corresponding spectra of C_4-QA were also measured under the same conditions. Both of QA derivatives in dilute THF solution exhibited intense absorption bands at 490, 520 nm for C_4-DFQA and 500, 535 nm for C_4-QA. The comparison of the absorption spectra of QA derivatives and the PL spectrum of Alq_3 indicates a perfect overlap of them suggesting a possible energy transport from Alq_3 (as a host) to QA derivatives. Fig. 2 showed the comparison of the PL spectra of C_4-DFQA and C_4-QA in THF solution (1.0×10^{-6} M). The emission spectra profiles are approximately similar with a sharp emission peak at 535 and 520 nm, and a shoulder at around 575 and 555 nm, which demonstrate a spectral shift with molecular modification by the influence of the introduction of fluorine atom. In addition, the very high PL quantum yields in solution (97% for C_4-DFQA and 91% for C_4-QA) implied that both of them could be highly valuable fluorophores for OLEDs.

3.2. EL properties

To investigate the EL properties, two devices (I and II) were fabricated with the same configuration of [ITO/NPB (30 nm)/emitter (25 nm)/Alq_3 (35 nm)/LiF (0.5 nm)/Al] (NPB = 4,4-bis(*N*-(1-naphthyl)-*N*-phenylamino)biphenyl).

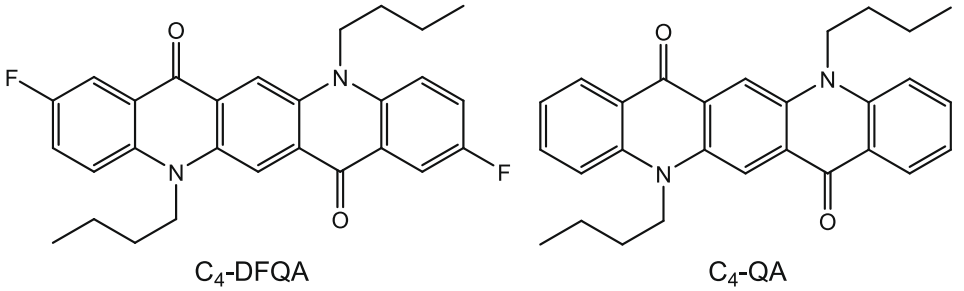

C_4-DFQA C_4-QA

Chart 1. Chemical structures of C_4-DFQA and C_4-QA.

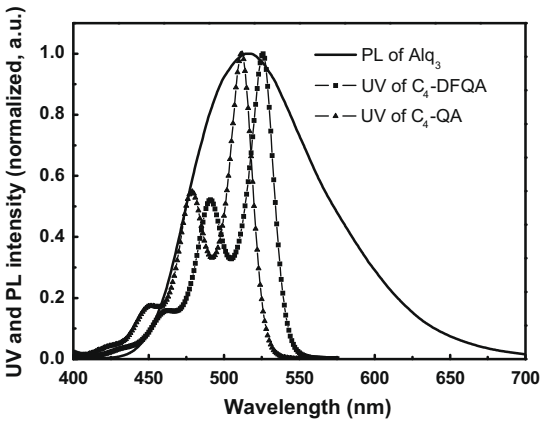

Fig. 1. UV absorption spectra of C_4-DFQA and C_4-QA and PL spectrum of Alq_3 in THF.

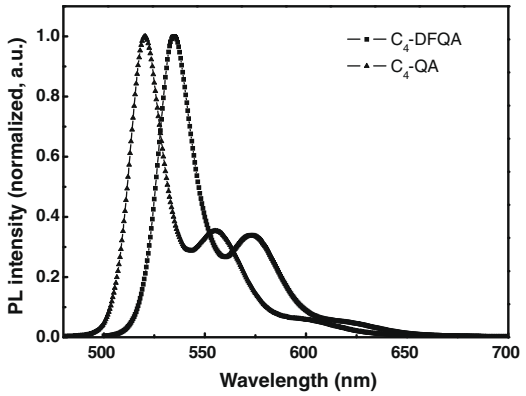

Fig. 2. PL emission spectra of C_4-DFQA and C_4-QA in THF.

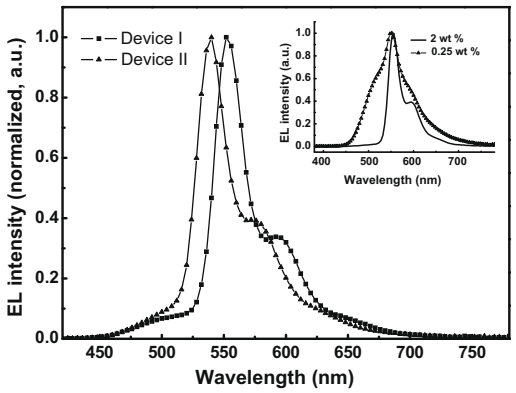

Fig. 3. EL spectra of devices I and II at the brightness of 1000 cd m^{-2}. Inset: EL spectra of the Alq_3: C_4-DFQA-based devices with the doping concentration of 2 and 0.25 wt.% at the brightness of 1000 cd m^{-2}.

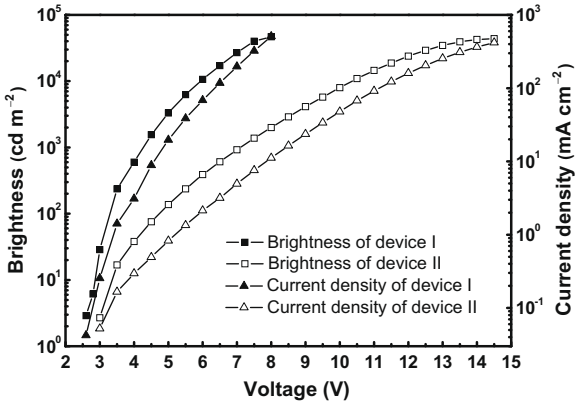

Fig. 4. Brightness vs. current density vs. voltage characteristics of devices I and II.

In the devices, the Alq_3: QA derivatives (Alq_3: C_4-DFQA for device I and Alq_3: C_4-QA for device II) doped films were employed as emitting layer with the doping concentrations of 0.5% (weight concentration). Here, NPB, and Alq_3 were served as hole-transporting and electron-transporting layers, respectively.

The EL spectra (Fig. 3) of devices I and II (at 1000 cd m^{-2}) displayed the expected emission features, and only slight emission in the wavelength of about 500 nm being observed indicating that the energy transfer from Alq_3 to C_4-DFQA and C_4-QA occurred almost completely. Both devices above exhibited bright yellowish-green emission, independent of the applied voltages in the range of 3–16 V, and the Commission Internationale de l'Eclairage (CIE) coordinates are (CIE: 0.42 and 0.56) and (CIE: 0.36 and 0.60) for device I (with C_4-DFQA) and device II (with C_4-QA), respectively.

Device I exhibited a rather low turn-on voltage (1 cd m^{-2} at 2.5 V), which is even lower than that of device II (3.0 V), and the EL intensity of device I showed rapid rise after the onset voltages (Fig. 4). At 8.0 V, devices I reached the peak radiance (46,680 cd m^{-2}), whereas devices II needed higher voltages (14.5 V) to obtain the same brightness levels (43,680 cd m^{-2}). Moreover, device I showed very low driving-voltages at the practical brightness of 100 and 1000 cd m^{-2} as low as 3.2 and 4.2 V, respectively, which are much lower than those of device II (4.7 and 7.1 V, respectively). In addition to its better brightness/driving-voltage performance, devices I also exhibited significantly higher power efficiency than that of device II in the whole brightness range (Fig. 5). For device I, a maximum power efficiency of 15.2 lm W^{-1} was obtained at the voltage of 4 V with a brightness of 598 cd m^{-2}, which is much higher than that of device II (10.7 lm W^{-1} was achieved at the voltage of 4.5 V with a brightness of 75 cd m^{-2}). It is also noteworthy that at the practical brightness of 100 and 1000 cd m^{-2}, the power efficiencies of device I remained as high as 13.6 and 13.5 lm W^{-1}, respectively, which are also higher than those of device II (10.6 and 8.2 lm W^{-1}, respectively). In view of almost same peak current efficiency (19.3 cd A^{-1} for device I at 4 V and 19.2 cd A^{-1} for device II at 6.5 V) and similar current efficiency-brightness curves of devices I and II each other, the pronounced power efficiency enhancement of the C_4-DFQA-based device could partly profit from the very low driving-voltages, which may suggest that an effective charge injection and well balanced charge carrier should

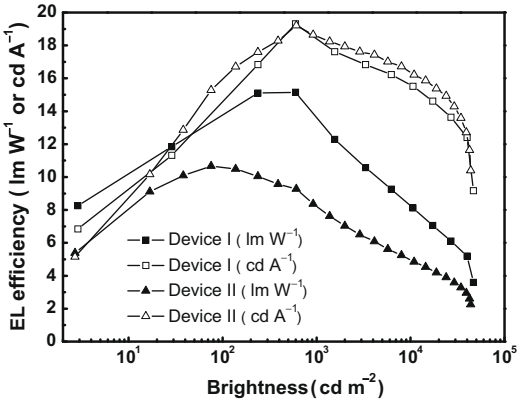

Fig. 5. Current efficiency vs. power efficiency vs. brightness characteristics of devices I and II.

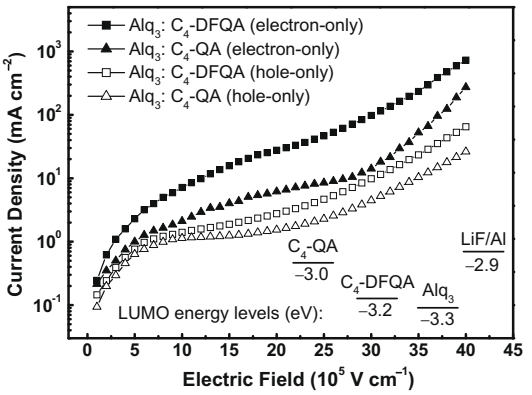

Fig. 6. Current density–electric field characteristics of Alq_3: C_4-DFQA and Alq_3: C_4-QA films in single-carrier devices. The inset shows the LUMO energy levels of the materials.

be achieved in the device I based on C_4-DFQA [8]. In addition, for comparison purpose, Alq_3: C_4-DFQA-based devices with the doping concentration of 2 and 0.25 wt.% were fabricated. The inset of Fig. 3 shows C_4-DFQA concentration dependence of spectra. At the concentration of 0.25 wt.%, one shoulder in the wavelength region of 500 nm due to Alq_3 was observed. More than this, the EL efficiency of C_4-DFQA also displayed obviously concentration-dependent property, which is similar to other QA derivatives [6]. A significant decrease in power efficiency was observed at higher (2 wt.%) and lower (0.25 wt.%) doping concentration due to significant self-quenching of C_4-DFQA and insufficient energy transfer from Alq_3 to C_4-DFQA, respectively.

To further understand both charge injection and carrier transport in the emitting layer, single-carrier devices [12–14] were fabricated using the following configurations: [Al/active molecular layer (60 nm)/Al] (electron-only device) and [ITO/active molecular layer (60 nm)/Au] (hole-only device). A low work function metal (Al) is used as the electrodes in electron-only devices, whereas a metal (Au) or a metal oxide (ITO) with a high work function is used as the electrodes in hole-only devices. For comparison purpose, Alq_3: C_4-DFQA (0.5%) and Alq_3: C_4-QA (0.5%) doped films were used as the active molecular layers for both electron-only and hole-only devices (Fig. 6). Clearly, in the hole-only devices, both current densities are comparable. However, in the electron-only devices, the current density of Alq_3: C_4-DFQA is much higher than that of Alq_3: C_4-QA. The results can be explained by the lower LUMO energy level of C_4-DFQA (−3.2 eV) than that of C_4-QA (−3.0 eV) (Fig. 6 inset) induced by introducing the strong electron-withdrawing fluorine atoms into the QA derivative, which in direct conjunction with the main emissive π-backbone [11]. More importantly, according to the Hammett substituent parameters, meta-substituting to the carbonyl groups in the phenyl ring would enhance the electron-withdrawing ability of fluorine atoms, which is a favorable factor to lower the LUMO level in the C_4-DFQA. Therefore, the electron injection barrier from Alq_3 to C_4-DFQA (0.1 eV) is obviously lower than that from Alq_3 to C_4-QA (0.3 eV), thus in the C_4-DFQA-based device, electron injection from Alq_3 to C_4-DFQA was accelerated. In addition, Fig. 7 shows the cyclic voltammograms for cathodic reductions of C_4-DFQA and C_4-QA, and both compounds exhibited one reversible redox couple. However, the half-wave reduction potential ($E_{1/2}^{red}$) of C_4-DFQA was obviously higher than that of C_4-QA, and it suggests that C_4-DFQA has stronger electron-accepting property, which could lead to its higher electron-transporting ability than C_4-QA [15].

On the other hand, since the charge mobility of NPB is generally 1–2 orders higher than in the other materials used [16–18], this improvement of electron injection and transporting in the Alq_3: C_4-DFQA layer may result in that there are more electrons counterpoise the holes injecting into the emitting layer from NPB in device I than in device II [19,20]. Consequently, it led to a stable charge carrier balance, and efficient recombination within the emitting layer of the C_4-DFQA-based device, which was consistent with the pronounced EL performance enhancement of the C_4-DFQA-based device with lower onset and driving-voltages than that of the C_4-QA based device presented in Fig. 4.

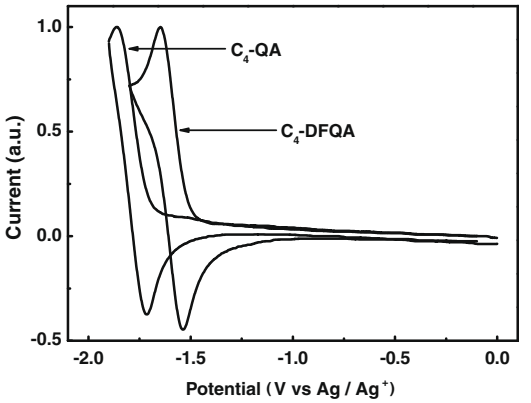

Fig. 7. Cyclic voltammograms of C_4-DFQA and C_4-QA.

4. Conclusions

In summary, we have fabricated the remarkably high-efficient fluorescent OLEDs by using a novel fluorinated QA derivative (C_4-DFQA) doped in Alq_3 as the emitting layer, which showed very low driving-voltage (the turn-on voltage is 2.5 V, the practical brightness of 100 and 1000 cd m^{-2} are realized at 3.2 and 4.2 V, respectively) and high power efficiency with the peak value of 15.2 lm W^{-1} (4 V, 598 cd m^{-2}, and 19.3 cd A^{-1}). These results represent very high EL performance based on the simple HTL–EML–ETL architecture from fluorescent organic emitters. The stability studies of device based on C_4-DFQA and further optimization of molecular structure to enhance the EL performance of QA derivatives are in progress.

Acknowledgements

This work was partly supported by National Basic Research Program of China (973 Program, 2009CB623600), Natural Science Foundation of China (50733002 and 50903036), Jilin Provincial Science and Technology Bureau of Jilin Province (20070107), and Special Project from MOST of China (10409A111463).

References

[1] C.W. Tang, S.A. Vanslyke, Appl. Phys. Lett. 51 (1987) 913.
[2] J. Shi, C.W. Tang, Appl. Phys. Lett. 70 (1997) 1665.
[3] S.E. Shaheen, B. Kippelen, N. Peyghambarian, J.F. Wang, J.D. Anderson, E.A. Mash, P.A. Lee, N.R. Armstrong, J. Appl. Phys. 85 (1999) 9739.
[4] H. Aziz, Z.D. Popovic, N.X. Hu, Appl. Phys. Lett. 81 (2002) 370.
[5] E.M. Gross, J.D. Anderson, A.F. Slaterbeck, S. Thayumanavan, S. Barlow, Y. Zhang, S.R. Marder, H.K. Hall, M.F. Nabor, J.F. Wang, E.A. Mask, N.R. Armstrong, R.M. Wightman, J. Am. Chem. Soc. 122 (2000) 4972.
[6] K.Q. Ye, J. Wang, H. Sun, Y. Liu, Z.C. Mu, F. Li, S.M. Jiang, J.Y. Zhang, H.X. Zhang, Y. Wang, C.M. Che, J. Phys. Chem. B 109 (2005) 8008.
[7] Y. Sakamoto, T. Suzuki, A. Miura, H. Fujikawa, S. Tokito, Y. Taga, J. Am. Chem. Soc. 122 (2000) 1832.
[8] M. Ikai, S. Tokito, Y. Sakamoto, T. Suzuki, Y. Taga, Appl. Phys. Lett. 79 (2001) 156.
[9] Y. Wang, N. Herron, V.V. Grushin, D. LeCloux, V. Petrov, Appl. Phys. Lett. 79 (2001) 449.
[10] Y. Zhao, X.M.C. Bao, Y. Fan, J. Zhang, Y. Wang, Langmuir 25 (2009) 3264.
[11] L. Zhao, J.-H. Zou, J. Huang, C. Li, Y. Zhang, C. Sun, X.-H. Zhu, J. Peng, Y. Cao, J. Roncali, Org. Electron. 9 (2008) 649.
[12] G.G. Malliaras, J.R. Salem, P.J. Brock, C. Scott, Phys. Rev. B 58 (1998) R13411.
[13] S. Tang, M.R. Liu, P. Lu, H. Xia, M. Li, Z.Q. Xie, F.Z. Shen, C. Gu, H.P. Wang, B. Yang, Y.G. Ma, Adv. Funct. Mater. 17 (2007) 2869.
[14] T. Peng, H. Bi, Y. Liu, Y. Fan, H. Gao, Y. Wang, Z. Hou, J. Mater. Chem. 19 (2009) 8072.
[15] T. Noda, Y. Shirota, J. Am. Chem. Soc. 120 (1998) 9714.
[16] H. Antoniadis, M.A. Abkowitz, B.R. Hsieh, Appl. Phys. Lett. 65 (1994) 2030.
[17] Y. Fukuda, T. Watanabe, T. Wakimoto, S. Miyaguchi, M. Tsuchida, Synth. Met. 111 (2000) 1.
[18] H. Kanno, R.J. Holmes, Y. Sun, S. Kena-Cohen, S.R. Forrest, Adv. Mater. 18 (2006) 339.
[19] S.J. Su, E. Gonmori, H. Sasabe, J. Kido, Adv. Mater. 20 (2008) 4189.
[20] Y. Liu, K.Q. Ye, Y. Fan, W.F. Song, Y. Wang, Z.M. Hou, Chem. Commun. (2009) 3699.

iridium complex as the dopant [10]. Recently, we reported blue-green-emitting polymer OLEDs using cationic iridium complexes as dopants [11]. The devices showed a peak current efficiency of 20.2 cd A^{-1} [11]. Nevertheless, a systematic evaluation of the use of cationic iridium complexes in OLEDs has not been reported, and white OLEDs using cationic iridium complexes as emitters have not yet been explored.

In this paper, a systematic investigation on blue-green to red and white OLEDs is carried out using cationic iridium complexes as dopants and poly(*N*-vinylcarbazole) (PVK) as the host. These cationic iridium complexes have been previously developed and used in highly efficient LECs [7,12]. Due to the low sublimability of cationic iridium complexes, light-emitting layers of OLEDs have been deposited from cost-effective solution processes.

2. Experimental

2.1. Materials

The cationic iridium complexes (Scheme 1): Irdf-pyim, Ir-pzpy, Irdf-pybi, Ir-pyim, Ir-pybi, and Ir-qlbi, which are blue-green-emitting (489 nm), blue-green-emitting (475 nm), green-emitting (528 nm), yellow-green-emitting (554 nm), orange-emitting (588 nm), and red-emitting (627 nm) in CH_3CN solutions, were prepared in the laboratory and crystallized from CH_2Cl_2/hexane before use [7,12]. Poly(3,4-ethylenedioxythiophene:poly(styrene sulfonate) (PEDOT:PSS) was purchased from H.C. Starck, Inc. PVK was purchased from TCI, Inc. And 1,3-bis[5-(4-*tert*-butylphenyl)-1,3,4-oxadiazol-2-yl]benzene (OXD-7), 2-(4-biphenylyl)-5-(4-*tert*-butylphenyl)-1,3,4-oxadiazole (PBD), 1,3,5-tris(1-phenyl-1H-benzo[d]imidazol-2-yl)benzene (TPBI), and bis(2-methyl-dibenzo[f,h]quinoxalinato-*N*,C2′)-iridium(III)(acetylacetonate) [Ir(MDQ)$_2$(acac)] were purchased from Nichem Fine Technology Co., Ltd. All materials were used as received without further purification.

2.2. Fabrication and characterizations of OLEDs

Indium–tin-oxide (ITO) substrates with a sheet resistance of 15 Ω/□ were sufficiently cleaned by ultrasonication in detergent and deionized water and then treated with UV-zone before use. The PEDOT:PSS layer was spin-coated in air and baked at 200 °C for 10 min. The light-emitting layer was spin-coated onto the PEDOT:PSS-coated substrates from 1,2-dichloroethane solutions of PVK:OXD-7 or PBD:cationic iridium complexes in a nitrogen-filled glove box. The coated substrates were annealed at 80 °C for 30 min. The substrate was transferred to an evaporation chamber integrated with the glove box. TPBI was evaporated at a rate of 1–2 Å/s under a pressure of 4×10^{-4} Pa. The Cs_2CO_3/Al bilayer cathode was evaporated at rates of 0.2 and 10 Å/s for Cs_2CO_3 and Al, respectively, under a pressure of 1×10^{-3} Pa. The current–voltage–brightness characteristics of the devices were characterized with a Keithley 4200 semiconductor characterization system. The EL spectra were collected with a Photo Research PR705 spectrophotometer. All measurements were performed in an ambient atmosphere without encapsulations.

3. Results and discussion

3.1. Single-layer devices

Cationic iridium complexes, which emit light ranging from blue-green to red, are shown in Scheme 1. The detailed photophysical and electrochemical characteristics of the complexes have been presented in previous studies

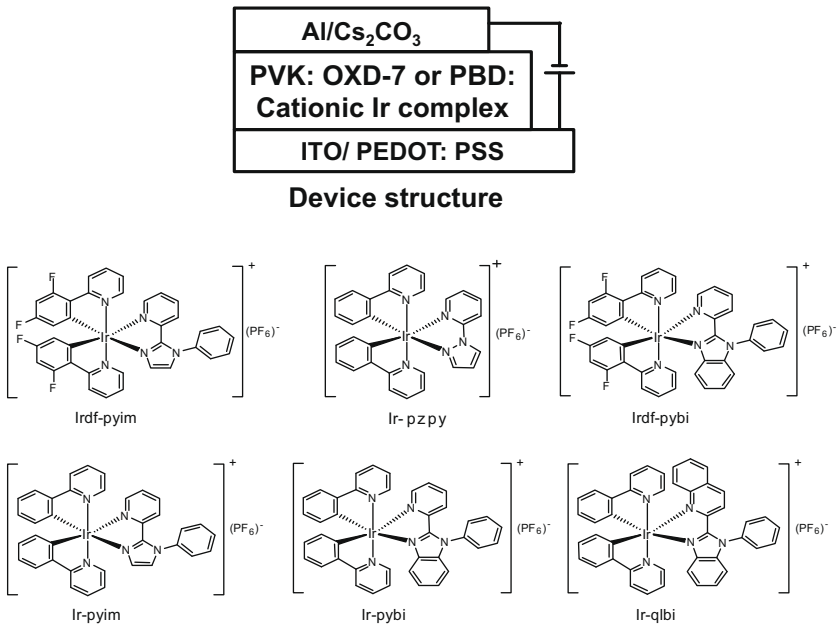

Scheme 1. OLED device structure and the cationic iridium complexes.

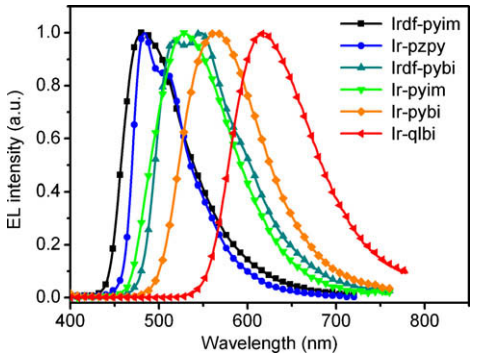

Fig. 1. EL spectra of the single-layer devices doped with different cationic iridium complexes.

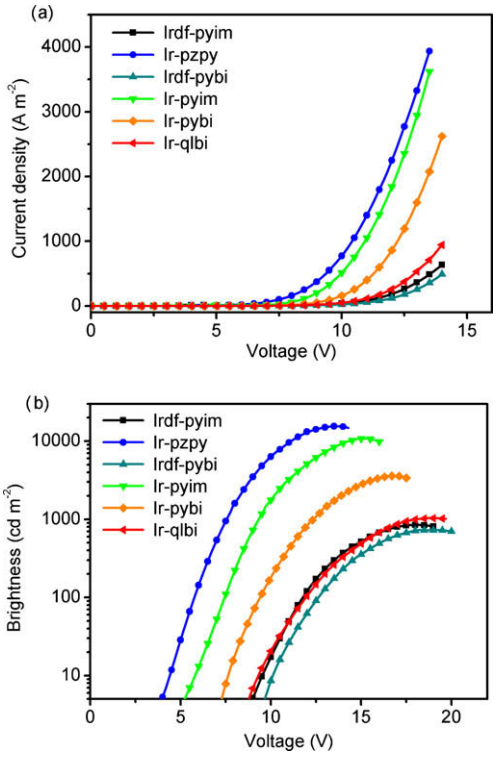

Fig. 2. Current density–voltage (a) and brightness–voltage (b) characteristics of the single-layer devices doped with different cationic iridium complexes.

[7,12]. PVK was used as a host material for the cationic iridium complexes because of its high triplet energy, excellent film-forming properties, and high hole-transport ability [13]. To facilitate electron transport in the light-emitting layers, PBD or OXD-7 was mixed into the PVK host [14–20]. The structure of the single-layer devices (Scheme 1) is ITO/PEDOT:PSS (40 nm)/PVK:30% PBD or OXD-7:10% cationic iridium complexes (80 nm)/Cs_2CO_3 (4 nm)/Al (120 nm). OXD-7 was used for the blue-green-emitting Irdf-pyim and Ir-pzpy because of its high triplet energy, while PBD was used for the other four complexes that have low-energy emissions [17]. Fig. 1 depicts the EL spectra of the devices. The devices showed blue-green to red electroluminescence, with the emission spectra covering nearly the entire visible region. The EL spectra resemble the PL spectra of the cationic iridium complexes in solutions or thin films, indicating that electroluminescence originated from the doped cationic iridium complexes [7,12].

Fig. 2 shows the current density–voltage and brightness–voltage curves of the single-layer devices. The detailed electrical characteristics are summarized in Table 1. In Fig. 2a, the current density–voltage curves shift toward the high voltage region when the doped complexes change from Ir-pyim, Ir-pybi to Ir-qlbi. The complexes Ir-pyim, Ir-pybi, and Ir-qlbi have the same cyclometalated ligands, 2-phenylpyridine (Ppy), on which the highest occupied molecular orbitals (HOMOs) of the complexes are localized. However, the complexes Ir-pyim, Ir-pybi, and Ir-qlbi have different ancillary ligands, on which the lowest unoccupied molecular orbitals (LUMOs) are localized [7,12]. As a result, the HOMO levels of Ir-pyim, Ir-pybi, and Ir-qlbi, ranging from −5.6 to −5.7 eV, are almost the same, while the LUMO levels of Ir-pyim, Ir-pybi, and Ir-qlbi are −2.8, −3.0, and −3.3 eV, respectively, which show a descending order as the conjugation length of the ancillary ligands increases [12]. The energy level diagrams of the single-layer devices are illustrated in Scheme 2. The LUMO levels of the complexes are below those of PVK (−2.2 eV) or PBD (−2.4 eV), leading to deep electron traps in the complexes [8,11,20]. The HOMO levels of the complexes (−5.6 to −5.7 eV) are relatively above that of PVK (−5.8 eV), leading to shallow hole traps in the complexes. Since the LUMO levels descend from Ir-pyim, Ir-pybi to Ir-qlbi, the strength of electron-trapping by the complexes increases, which leads to the shift of the current density–voltage curves toward the high voltage region (Fig. 2a) and the gradual increase in turn-on voltages (Table 1) when the doped complexes change from Ir-pyim, Ir-pybi to Ir-qlbi.

Due to severe electron-trapping by the complexes, recombination zones in OLEDs are expected to be located close to the cathodes, leading to exciton quenching and, thereby, inferior device performance. Nevertheless, the peak current efficiency of the single-layer, blue-green device doped with Ir-pzpy reaches 10.5 cd A^{-1}, which approaches the efficiency of counterpart devices using the conventional blue-green phosphorescent emitter, FIrpic, as the dopant [16]. Better performance of the device doped with Ir-pzpy is related to less severe electron-trapping by Ir-pzpy because the LUMO level of Ir-pzpy (−2.6 eV) is the highest among the six complexes.

At the same biasing voltages, the current density of the device doped with Irdf-pyim is lower than that of the device doped with Ir-pyim (Fig. 2a). Although Irdf-pyim and Ir-pyim have the same ancillary ligands, 2-(1-phenyl-1H-imidazol-2-yl)pyridine (Scheme 1), the LUMO level of Irdf-pyim (−2.9 eV) is lower than that of Ir-pyim (−2.8 eV) because the electron-withdrawing fluorine atoms in Irdf-pyim make the complex more electron deficient. Electrons are expectedly trapped more strongly by Irdf-pyim than by Ir-pyim. In contrast, the HOMO level of Irdf-pyim (−5.9 eV) is much lower than that of Ir-pyim (−5.6 eV) because of the fluorine atoms attached to the

Table 1
Electrical characteristics of the single-layer devices.[a]

Complex	V_{on} (V)[b]	J (A m^{-2})[c]	$\eta_{c,max}$ (cd A^{-1})[d]	B_{max} (cd m^{-2})	EL λ (nm)	CIE (x, y)
Irdf-pyim	6.9	40.4	0.6 (0.3%)	890	484	(0.21, 0.38)
Ir-pzpy	3.6	774.2	10.5 (4.1%)	15,500	482, 508	(0.19, 0.46)
Irdf-pybi	6.5	23.6	0.5 (0.2%)	730	516, 548	(0.37, 0.57)
Ir-pyim	4.0	515.7	4.1 (1.3%)	11,500	528	(0.35, 0.56)
Ir-pybi	5.1	160.1	1.2 (0.4%)	3600	566	(0.47, 0.52)
Ir-qlbi	6.1	49.0	0.4 (0.3%)	1100	618	(0.62, 0.38)

[a] The device structure is ITO/PEDOT:PSS (40 nm)/PVK:30% OXD-7 or PBD:10% complexes (80 nm)/Cs_2CO_3 (4 nm)/Al (120 nm); OXD-7 was used for Irdf-pyim and Ir-pzpy while PBD was used for the other four complexes.
[b] The voltage to reach 1 cd m^{-2}.
[c] The current density at 10 V.
[d] Data in parenthesis denote the external quantum efficiencies.

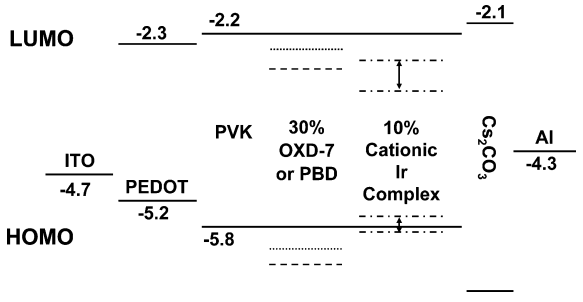

Scheme 2. Energy level (unit: eV) diagrams of the single-layer devices. The HOMO and LUMO levels of the complexes were calculated from their redox potentials [7,12] and the double arrows represent the range of energy levels of the six complexes. The HOMO and LUMO levels of OXD-7 (dashed lines) are −6.5 and −2.8 eV, respectively; those of PBD (dotted lines) are −6.3 and −2.4 eV, respectively [21].

cyclometalated ligands in Irdf-pyim [12]. During the device operation, carriers are expected to hop between the complex molecules, forming another carrier-transportation channel, because the doping concentration (10 wt.%) of the complexes in the light-emitting layers is relatively high [8,11]. For the device doped with Ir-pyim, holes can be directly injected into the HOMOs of Ir-pyim. The holes can then move along the HOMOs and eventually combine with electrons to form excitons. In the device doped with Irdf-pyim that has a stabilized HOMO, holes cannot be easily injected into the HOMOs of Irdf-pyim nor move along them because the HOMO of Irdf-pyim is below that of PVK. Largely due to strengthened electron-trapping and suppressed hole injection and transportation via the complex molecules, the device doped with Irdf-pyim shows lower current density and inferior performance (higher turn-on voltage and lower efficiency) compared with the device doped with Ir-pyim (Fig. 2a and Table 1). Similar to the cases concerning Irdf-pyim and Ir-pyim, the device doped with Irdf-pybi shows lower current density and inferior device performance compared with the device doped with Ir-pybi (Fig. 2a and Table 1).

3.2. Devices with electron-transporting/exciton-blocking layers

To improve device performances, electron-transporting/exciton-blocking TPBI layers were inserted between light-emitting layers and cathodes. The device structure is ITO/PEDOT:PSS (40 nm)/PVK:30% OXD-7 or PBD:10% cationic iridium complexes (80 nm)/TPBI (30 nm)/Cs_2CO_3 (4 nm)/Al (120 nm). The detailed electrical characteristics are summarized in Table 2. Fig. 3 shows the current density–voltage and brightness–voltage curves of the devices. Similar to the case of single-layer devices, current density–voltage curves shift toward the high voltage region when the doped complexes change from Ir-pyim, Ir-pybi to Ir-qlbi (Fig. 3a), due to gradually strengthened electron-trapping by the complexes. The device doped with Irdf-pyim shows lower current density and inferior device performance compared with the device doped with Ir-pyim. Similarly, the device doped with Irdf-pybi shows lower current density and inferior device performance compared with the device doped with Ir-pybi (Fig. 3a and Table 2).

After insertion of the TPBI layers, the device performance largely improves because of suppressed exciton quenching at the cathode interfaces [8,11]. The peak current efficiencies of the blue-green, green, yellow, and red-emitting devices reach 24.3, 25.3, 20.5, and 4.2 cd A^{-1}, which correspond to external quantum efficiencies (EQE) of 9.7%, 8.1%, 7.1%, and 3.2%, respectively. The high efficiencies indicate the great feasibility of using cationic iridium complexes as phosphorescent dopants in OLEDs. Higher device performances are believed to be achievable if the doping concentrations of the complexes and the thickness of the TPBI layers are optimized. The relatively low efficiency of the red-emitting device is largely due to the low luminescent efficiency of Ir-qlbi compared with those of other complexes [7,12].

In phosphorescent OLEDs, efficiency always exhibits a severe roll-off at high brightness mainly because of triplet–triplet annihilation [22–24]. Fig. 4 shows the dependence of the current efficiency–brightness characteristics of devices with TPBI layers. In Fig. 4, devices with cationic iridium complexes used in this study show efficiency roll-offs at high brightness, similar to phosphorescent OLEDs with neutral iridium complexes [22–24]. However, for the blue-green device doped with Ir-pzpy, the maximum efficiency (24.3 cd A^{-1}) is reached at 1020 cd m^{-2}, and at 10,100 cd m^{-2}, the efficiency remains 19.6 cd A^{-1}. For the green device doped with Ir-pyim, the maximum efficiency (25.3 cd A^{-1}) is reached at 600 cd m^{-2}, and at 6200 cd m^{-2}, the efficiency remains 20.0 cd A^{-1}. For the yellow device doped with Ir-pybi, the maximum efficiency (20.5 cd A^{-1})

Table 2
Electrical characteristics of the devices with TPBI blocking layers.[a]

Complex	V_{on} (V)[b]	J (A m^{-2})[c]	$\eta_{c,max}$ (cd A^{-1})[d]	B_{max} (cd m^{-2})	EL λ (nm)	CIE (x, y)
Irdf-pyim	5.2	19.1	6.8 (2.9%)	6100	486	(0.20, 0.40)
Ir-pzpy	4.2	258.8	24.3 (9.7%)	30,300	484, 508	(0.19, 0.47)
Irdf-pybi	6.5	2.4	11.6 (3.7%)	5800	514, 540	(0.35, 0.57)
Ir-pyim	4.4	107.6	25.3 (8.1%)	38,500	526	(0.34, 0.56)
Ir-pybi	5.5	7.8	20.5 (7.1%)	22,100	564	(0.46, 0.52)
Ir-qlbi	6.5	4.4	4.2 (3.2%)	6300	620	(0.61, 0.38)

[a] The device structure is ITO/PEDOT:PSS (40 nm)/PVK:30% OXD-7 or PBD:10% complexes (80 nm)/TPBI (30 nm)/Cs_2CO_3 (4 nm)/Al (120 nm); OXD-7 was used for Irdf-pyim and Ir-pzpy while PBD was used for the other four complexes.
[b] The voltage to reach 1 cd m^{-2}.
[c] The current density at 10 V.
[d] Data in parenthesis denote the external quantum efficiencies.

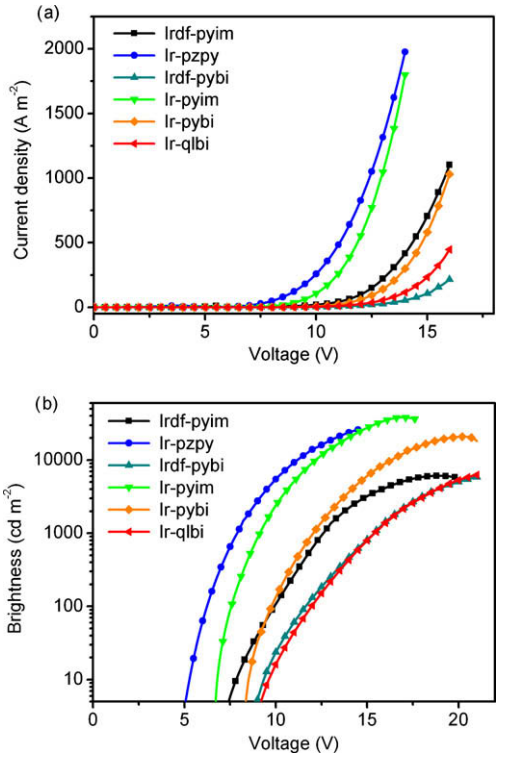

Fig. 3. Current density–voltage (a) and brightness–voltage (b) characteristics of the devices with TPBI layers.

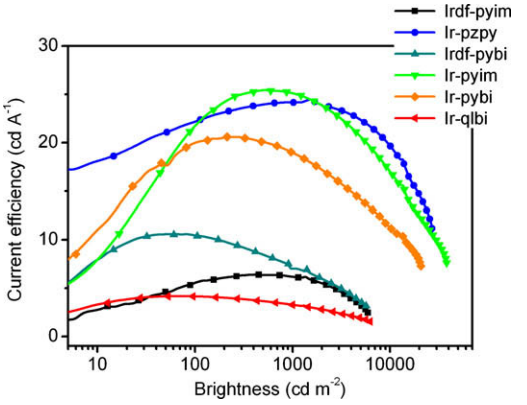

Fig. 4. Current efficiency–brightness characteristics of the devices with TPBI layers.

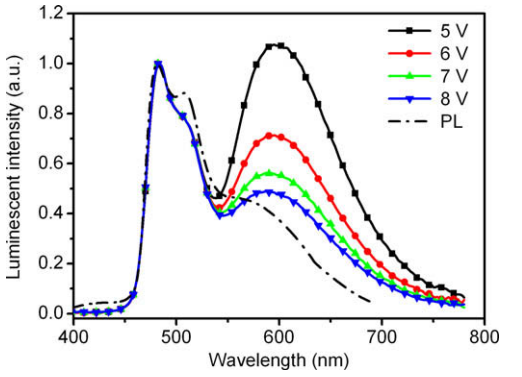

Fig. 5. EL spectra of the white device W1 biased at different voltages. The dashed line represents the PL spectrum of the light-emitting layer.

is reached at 240 cd m^{-2}, and at 2400 cd m^{-2}, the efficiency remains 16.6 cd A^{-1}. The largely retained efficiencies at high brightness suggest that the bipolar transporting host of PVK:PBD or OXD-7 helps to broaden the recombination zone and reduce the concentration of triplet excitons. Moreover, the ionic nature of the chromophores will be beneficial in reducing aggregations of dopants in the polar host and thus producing less severe triplet–triplet annihilations at high current densities.

3.3. White devices

White OLEDs were fabricated by co-doping blue-green and red-emitting complexes. In this study, Ir-pzpy was selected as the blue-green emitter because of its higher device performance compared with Irdf-pyim. The structure of the white OLED is ITO/PEDOT:PSS (40 nm)/PVK:30% OXD-7:10% Ir-pzpy:0.25% Ir-qlbi (80 nm)/TPBI (30 nm)/Cs_2CO_3 (4 nm)/Al (120 nm) (Device W1). Fig. 5 shows the EL spectra of the white-emitting device that were biased at different voltages. The relative intensity of the red to the blue component in the EL spectra is larger than that in the PL spectrum, indicating that charge-trapping by the low-gap Ir-qlbi plays an important role in the operation of the white-emitting device [19]. At low voltages,

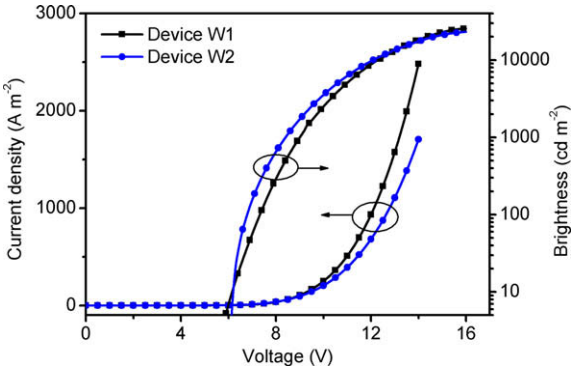

Fig. 6. Current density–brightness–voltage characteristics of the white devices.

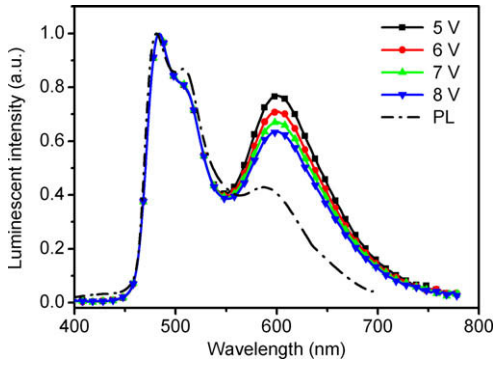

Fig. 7. EL spectra of the white device W2 biased at different voltages. The dashed line represents the PL spectrum of the light-emitting layer.

electrons are more likely injected into Ir-qlbi with a low LUMO level, trapped, and combined with holes. As a result, the relative intensity of the red to the blue emission at low voltages is higher than that at high voltages in white electroluminescence. This leads to a change of CIE coordinates from (0.43, 0.43) to (0.35, 0.44) when the biasing voltage increases from 5.0 to 8.0 V.

The current density brightness–voltage curves of the white-emitting devices are shown in Fig. 6, and the detailed electrical characteristics are summarized in Table 3. For the white-emitting device W1, the peak current efficiency reaches 16.7 cd A^{-1}, corresponding to an EQE of 7.8%, and the peak power efficiency reaches 6.8 lm W^{-1}.

Among the six cationic iridium complexes, the luminescent efficiency of Ir-qlbi (3% in CH_3CN solution) is the lowest [7,12]. To further improve the performance of the white-emitting device, the red-emitting Ir-qlbi was replaced with an efficient red-emitting neutral iridium complex $Ir(MDQ)_2(acac)$, which has a high luminescent efficiency of 48% in CH_2Cl_2 solution [25]. The device structure is ITO/PEDOT:PSS (40 nm)/PVK:30% OXD-7:10% Ir-pzpy:0.25% $Ir(MDQ)_2(acac)$ (80 nm)/TPBI (30 nm)/Cs_2CO_3 (4 nm)/Al (120 nm) (Device W2). Fig. 7 shows the EL spectra of the white-emitting device that were biased at different voltages. By comparing the EL and PL spectra in Fig. 7, the important role of charge-trapping in the operation of the white-emitting device can be observed [19]. The HOMO (−5.4 eV) and LUMO (−2.8 eV) levels of $Ir(MDQ)_2(acac)$ are within the energy gap of the PVK host, indicating that both holes and electrons will be deeply trapped by $Ir(MDQ)_2(acac)$. The CIE coordinates of the white-emitting device W2 change from (0.39, 0.43) to (0.37, 0.44) when the biasing voltages increase from 5.0 to 8.0 V.

Fig. 6 also shows the current density brightness–voltage curve of the white device W2. The detailed electrical characteristics are summarized in Table 3. Due to the high luminescent efficiency of $Ir(MDQ)_2(acac)$, the peak current efficiency of the white device W2 reaches 20.7 cd A^{-1}, corresponding to an EQE of 9.8%, and the peak power efficiency reaches 8.5 lm W^{-1}.

Similar to other phosphorescent OLEDs with unstable PVK hosts, all devices reported in this study show short lifetimes [19]. In OLEDs, the doping concentration (10 wt.%) of the cationic iridium complexes is low, and the PF_6^- anions are hindered from migrating in the dense polymer film of PVK. This is quite different from LECs, where a large quantity (>80 wt.%) of cationic iridium complexes are used in the active layer and abundant PF_6^- anions migrate easily under electrical biases [2–5]. The detailed degradation mechanism for LECs, although unclear, is believed to be associated with migration of ions and accumulation of ions at electrode interfaces [2,4]. Therefore, we believe that degradation processes in LECs are not likely to occur in OLEDs with a small quantity of cationic iridium complexes functioning only as the phosphorescent dopants. Using solution-processable and stable host materials, OLEDs doped with cationic iridium complexes can achieve longer operating lifetimes.

4. Conclusion

Using cationic iridium complexes as dopants, solution-processed OLEDs were fabricated with peak current efficiencies of 24.3, 25.3, 20.5, and 4.2 cd A^{-1} for the blue-green, green, yellow, and red electroluminescence,

Table 3
Electrical characteristics of the white devices.[a]

	Red dopant	V_{on} (V)[b]	$\eta_{c,max}$ (cd A^{-1})[c]	B_{max} (cd m^{-2})	EL λ (nm)	CIE (x, y)	
						5 V	8 V
W1	Ir-qlbi	4.2	16.7 (7.8%)	25,700	484, 594	(0.43, 0.43)	(0.35, 0.44)
W2	$Ir(MDQ)_2$ (acac)	4.0	20.7 (9.6%)	23,300	484, 600	(0.39, 0.43)	(0.37, 0.44)

[a] The device structure is ITO/PEDOT:PSS (40 nm)/PVK:30% OXD-7:10% Ir-pzpy:0.25% red dopant (80 nm)/TPBI (30 nm)/Cs_2CO_3 (4 nm)/Al (120 nm).
[b] The voltage to reach 1 cd m^{-2}.
[c] Data in parenthesis denote the external quantum efficiencies.

respectively. During device operation, electrons were trapped by the complexes, especially by complexes with low-energy emissions; that is, low LUMO levels. Complexes with cyclometalated 2-phenylpyridine ligands were found to show better device performances compared with complexes with cyclometalated 2-(2,4-difluorophenyl)pyridine ligands. White OLEDs were fabricated with a peak current efficiency of 16.7 cd A^{-1}, which was improved to 20.7 cd A^{-1} when the red-emitting ionic complex was replaced with an efficient red-emitting neutral iridium complex. Thus, cationic iridium complexes, in addition to their use in LECs, are promising phosphorescent dopants in solution-processed OLEDs. This material and technique can be used to produce highly efficient blue-green to red and white electroluminescence.

Acknowledgement

This research was supported by the National Key Basic Research and Development Program of China (Grant Nos. 2006CB806203, 2009CB623604 and 2009CB930602).

References

[1] Q.B. Pei, G. Yu, C. Zhang, Y. Yang, A.J. Heeger, Science 269 (1995) 1086.
[2] J.D. Slinker, D. Bernards, P.L. Houston, H.D. Abruña, S. Bernhard, G.G. Malliaras, Chem. Commun. 2392 (2003).
[3] A.B. Tamayo, S. Garon, T. Sajoto, P.I. Djurovich, I.M. Tsyba, R. Bau, M.E. Thompson, Inorg. Chem. 44 (2005) 8723.
[4] J.D. Slinker, J. Rivnay, J.S. Moskowitz, J.B. Parker, S. Bernhard, H.D. Abruña, G.G. Malliaras, J. Mater. Chem. 17 (2007) 2976.
[5] C. Ulbricht, B. Beyer, C. Friebe, A. Winter, U.S. Schubert, Adv. Mater. 21 (2009) 4418.
[6] H.J. Bolink, L. Cappelli, S. Cheylan, E. Coronado, R.D. Costa, N. Lardiés, M.K. Nazeeruddin, E. Ortí, J. Mater. Chem. 17 (2007) 5032.
[7] L. He, L. Duan, J. Qiao, R. Wang, P. Wei, L.D. Wang, Y. Qiu, Adv. Funct. Mater. 18 (2008) 2123.
[8] E.A. Plummer, V.A. Dijken, H.W. Hofstraat, L.D. Cola, K. Brunner, Adv. Funct. Mater. 15 (2005) 281.
[9] W. Wong, G. Zhou, X. Yu, H. Kwok, Z. Lin, Adv. Funct. Mater. 17 (2007) 315.
[10] Y. Byun, Y. Lyu, R.R. Das, O. Kwon, T.W. Lee, Y.J. Park, Appl. Phys. Lett. 91 (2007) 211106.
[11] L. He, L. Duan, J. Qiao, D. Zhang, G. Dong, L. Wang, Y. Qiu, Org. Electron. 10 (2009) 152.
[12] L. He, J. Qiao, L. Duan, G. Dong, D. Zhang, L. Wang, Y. Qiu, Adv. Funct. Mater. 19 (2009) 2950.
[13] K. Kawamura, S. Yanagida, S.R. Forrest, J. Appl. Phys. 92 (2002) 87.
[14] S. Lamansky, P.I. Djurovich, F. Abel-Razzaq, S. Garon, D.L. Murphy, M.E. Thompson, J. Appl. Phys. 92 (2002) 1570.
[15] X. Gong, M.R. Robinson, J.C. Ostrowski, D. Moses, G.C. Bazan, A.J. Heeger, Adv. Mater. 14 (2002) 581.
[16] A. Nakamura, T. Tada, M. Mizukami, S. Yagyua, Appl. Phys. Lett. 84 (2004) 130.
[17] X.H. Yang, F. Jaiser, S. Klinger, D. Neher, Appl. Phys. Lett. 88 (2006) 021107.
[18] M.K. Mathai, V. Choong, S.A. Choulis, B. Krummacher, F. So, Appl. Phys. Lett. 88 (2006) 243512.
[19] H. Wu, J. Zou, F. Liu, L. Wang, A. Mikhailovsky, G.C. Bazan, W. Yang, Y. Cao, Adv. Mater. 20 (2008) 696.
[20] F. Chen, S. Chien, Y. Chen, Appl. Phys. Lett. 94 (2009) 043306.
[21] Y. Shirota, H. Kageyama, Chem. Rev. 107 (2007) 953.
[22] W. Staroske, M. Pfeiffer, K. Leo, M. Hoffmann, Phys. Rev. Lett. 98 (2007) 197402.
[23] S. Reineke, K. Walzer, K. Leo, Phys. Rev. B 75 (2007) 125328.
[24] N.C. Giebink, S.R. Forrest, Phys. Rev. B 77 (2008) 235215.
[25] J. Duan, P. Sun, C. Cheng, Adv. Mater. 15 (2003) 224.

lasing threshold and cavity-size-dependence of the threshold. We believe that observed size-dependence of the lasing threshold indicates the participation of cavity QED.

2. High temperature deposition of BP1T crystals

If organic crystal films without grain boundaries and/or cracks can be formed on Si/SiO_2 substrates over large area, it is ideal situation for fabricating the laser devices. However, it takes rather long time to develop the organic crystals epitaxy technology. Therefore, it is realistic approach to clip microcavities from a part of the organic crystal film without grain boundaries and/or cracks. Actually, TPCO crystals with the size over several hundred micrometer were grown on a substrate in liquid phase [14]. We also tried to grow the one of TPCO co-oligomers, 2,5′-bis(4-biphenylyl)-thiophene (BP1T) onto Si/SiO_2 substrates by using the high temperature deposition method.

Fig. 1 shows micrographs of BP1T co-oligomer films formed on the bare thermally-oxidized silicon films on the Si substrates. The deposition rate of BP1T was fixed around 0.1 nm/s. The substrate temperatures are indicated in the figure. The pressure of the deposition chamber was on the order of 10^{-6} Pa during the deposition. With the increase of the temperature, the re-evaporation effect becomes strongly, and island like single crystals grow and overlap each other. Therefore, we can grow BP1T single crystals over several tens of micrometers by choosing the proper temperature and deposition rate. Fig. 2 shows micrographs of BP1T crystal films fabricated by annealing (left part) and by the high temperature deposition method (right part). In the case of annealing, films are annealed on a hot plate and are crystallized at 220 °C [12,13].

We have been used annealed films to form microcavities. These films had many grain boundaries and cracks, as shown in the left part of Fig. 2. On the other hand, the crystal film fabricated by the high temperature deposition method has cracks, but no grain boundary, as shown in the right part of Fig. 2. Therefore, we can form the microcavity from a BP1T single crystal when we choose a part of the crystal film without grain boundaries and cracks.

In order to obtain crystal films without grain boundaries by using the high temperature deposition method, we need a substrate with a flat and defect-less surface. Actually, single crystal like growth is obtained only on the bare thermally-oxidized silicon films or polymer films, as shown in the bottom part of Fig. 3. We used amorphous fluorocarbon polymer, cytop (CTX804.5A, ASAHI GLASS Co., Ltd., Japan; in the report, we indicate the cytop polymer as CTX), which was spin-coated on a Si/SiO_2 substrate with the thickness of 300 nm. When BP1T films were fabricated on the sputtered SiO_2 film and slightly processed thermally-oxidized silicon films, we could not obtained single crystal like films, as shown in the upper part of Fig. 3. The high temperature deposition method, described here, is only the usual thermal vapor deposition method, but we can fabricate single crystals over several tens of micrometers on the proper substrates. Usual organic films like pentacene fabricated by the thermal vapor deposition frequently have grain boundaries [15]. The reason is not clear now, but it is a very good property of BP1T and suitable for fabricating microcavities.

3. Fabrication processes of microdisk cavities in BP1T crystals

If we fabricate microcavities in the high temperature deposition films, we need to use the clip-out fabrication process [12]. In this process, Cr/Si/Cr layers were formed before resist baking. Metallic layers have much smaller thermal expansion factor than that of organic layers, so that the thin metallic layers frequently wrinkled or at worst were removed from underground organic layers. Therefore, we improved the fabrication method by using a lift-off process of metallic layers. Fig. 4 shows the improved fabrication process. Here, we first fabricated organic layers, by using the high temperature deposition method with thickness of 200–400 nm. We have used electron-beam (EB) lithography

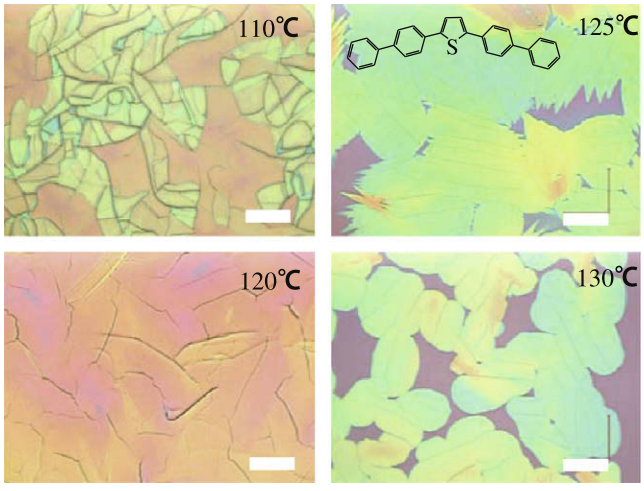

Fig. 1. Microscope images of high temperature deposition films. Substrate temperature is shown in each figure. White lines shown in the bottom right part indicate the scale of 20 μm. The molecular structure of BP1T is also indicated in the inset.

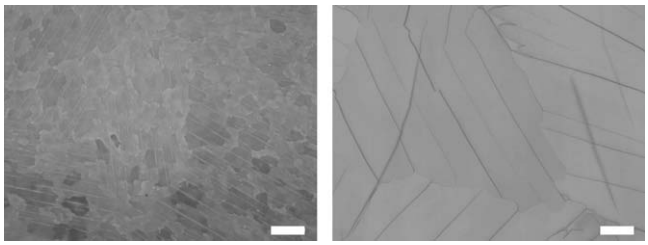

Fig. 2. The left part shows the microscope image of the annealed film and the right part shows that of the high temperature deposition film. White lines shown in the bottom right part indicate the scale of 10 μm.

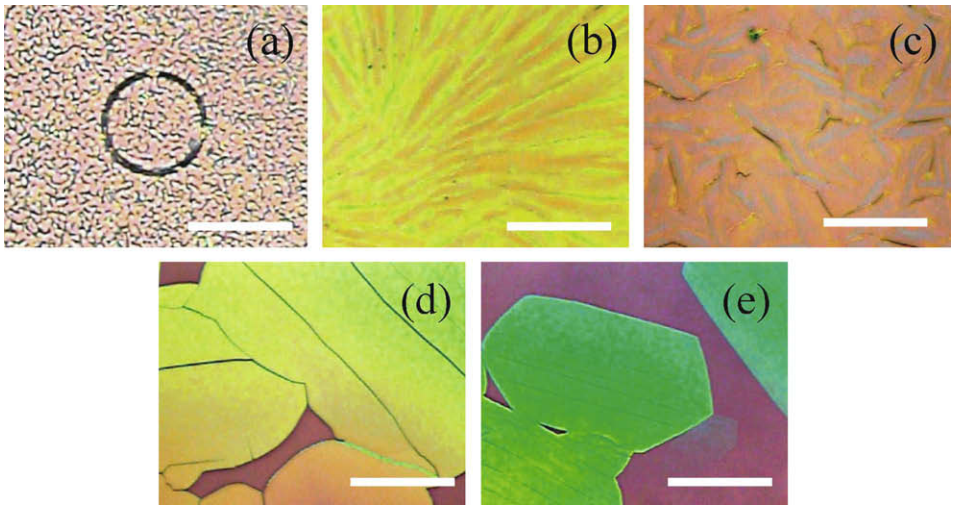

Fig. 3. Microscope images of high temperature deposition films observed on the various substrates; (a) on the sputtered SiO_2 film, (b) on the slightly ashing (by using a O_2-plasma asher, 300 W-10 Pa-300 s) surface of the thermally-oxidized silicon film, (c) on the slightly ashing (in 5% diluted HF solution-30 s) surface of the thermally-oxidized silicon film, (d) on the bare surface of the thermally-oxidized silicon film, and (e) on the bare CTX804.5A film, respectively. White lines shown in the bottom right part indicate the scale of 20 μm.

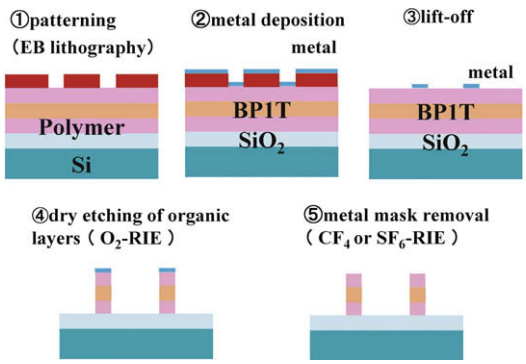

Fig. 4. Schematic drawing of fabrication processes of microcavities; ① EB lithography, ② metal deposition on the patterned substrate, ③ lift-off of the metal on the resist, ④ O_2-RIE of BP1T crystal films and buffered CTX and overcoated CTX layers, and ⑤ CF_4-RIE of the Cr-mask layer or SF_6-RIE of the Ti-mask layer, respectively.

to define microdisk patterns on the resist (OEBR-1000, Tokyo Ohka Kogyo Co., Ltd., Japan). To avoid charging of samples during EB irradiation, Espacer (Showa Denko K.K., Japan) films were formed on the resist films.

After EB lithography, a metallic mask layer was deposited by using thermal vapor deposition. Resist films and metal films onto the resist layer were removed by using the ultrasonic cleaning in acetone solution. After the lift-off process, O_2 reactive ion etching (RIE) was adopted to fabricate organic microdisk cavities. All of the RIE processes were carried out under the condition of 50 sccm-70 W-2.5 Pa by using SAMCO, RIE-200L. Two kinds of metal masks, Cr and Ti were used and removed by using CF_4 and SF_6 gases, respectively. Thickness of both Cr and Ti masks was 25 nm. RIE durations of the O_2, CF_4 and SF_6 were approximately 270, 1200 and 150 s, respectively. The O_2-RIE duration was determined to be nearly complete etching of BP1T crystals without metal masks, and CF_4 and SF_6-RIE durations were determined to remove metal masks completely.

Fig. 5 shows scanning electron micrographs (SEM) images of microdisks fabricated by using Ti masks. Slight surface roughness is observed on the side wall of cavities, but we can obtain quite complete disk shaped cavities by using the Ti-mask process. Microdisks fabricated by using Ti masks showed bright luminescence, almost same with that of unprocessed films.

On the other hand, when Cr masks were used instead of Ti masks, the top part of 1 μm disk was removed.

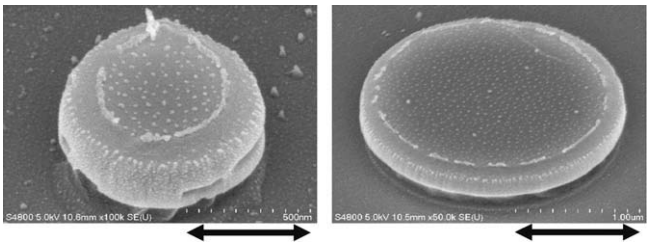

Fig. 5. SEM images of microdisks fabricated by using Ti masks. Black arrows indicate the scale of 1 μm in both images.

Luminescence yield of the microdisks were very low and disks were not lasing under the optical excitation. Therefore, microdisks fabricated by using Cr masks were probably damaged during the long CF_4-RIE duration. The short RIE duration to removing the metal masks are important to obtain good disk cavities.

Slight residuals of films and dotted structures are observed on the disks, as shown in Fig 5. They are probably remained CTX films, which have been almost removed during the SF_6-RIE process. The yield of 2 μm disks was higher than that of others. Disks with small diameter tend to remove from substrate. Disks with large diameter tend to contain cracks of organic crystals and slight residual of metal masks around the edge of disks.

4. Optical excitation experiments

We carried out experiments of pulse excitation at 397 nm with a 10–15 ps width onto BP1T microcavities. The spot size was estimated to be $33 \times 23\ \mu m^2$. We assumed uniform lateral distribution of the excitation beam. Therefore, the excitation density was estimated to be the incident light energy divided by the spot size. The transition dipole moment of each BP1T molecule is aligned to a molecule length axis and is nearly vertical to the substrate. Therefore, *p*-polarized light with the incident angle of 60° was used to excite BP1T microdisks for efficient optical pumping. Luminescence was collected by an 50× objective lens and detected by a liquid N_2 cooled charge-coupled device attached to a monochromator. All experiments were carried out at room temperature.

Fig. 6 shows the laser emission spectra of BP1T microcavities. Amplification and lasing were observed both at inhomogeneously broadened 0–1 and 0–2 vibration lines [2–4]. The lasing threshold of the 0–1 line is usually lower than that of the 0–2 line, and almost all of our samples show lasing peaks around the 0–1 vibration line, as shown at 2.63–2.70 eV. Note that almost all of the modes have doublet structures. It is well known that the high-*Q* WGM show the doublet mode structure reflecting clockwise (CW) and counterclockwise (CCW) propagation [16]. If we adopt this model as an origin of the doublet, we can obtain the estimated values of the cavity lifetime from the width of the mode, and the scattering lifetime from the mode separation of the doublet. The inverse of the lifetime was estimated to be 1.0–1.2 meV for the cavity lifetime and 1.8–4.0 meV for the scattering lifetime. The *Q* value can be estimated from the cavity lifetime as 2400. This *Q*

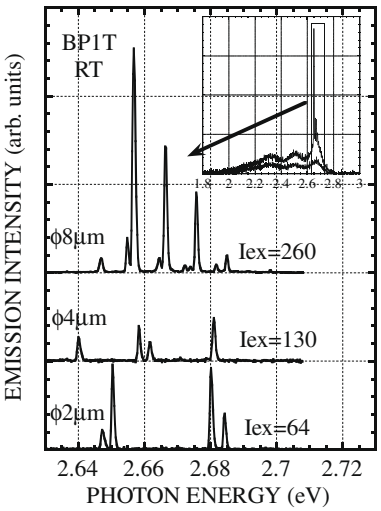

Fig. 6. Lasing spectra of BP1T microdisks. Whole luminescence spectra observed in the 8 μm disk are shown in the inset, before (I_{ex} = 51 μJ/cm^2) and after (I_{ex} = 200 μJ/cm^2) the lasing. The disk diameters and excitation densities in the unit of μJ/cm^2 are shown.

value seems to be too small to observe such large splitting of CW and CCW doublet modes [17].

Another origin of the doublet modes is higher WGM, which has multi peaks of electromagnetic field in the radial direction. Actually, in the finite differential time domain (FDTD) analysis, higher WGMs were sometimes appeared around the main WGM. However, in the 4 μm disk case, only the central mode is doublet. Some additional structures and/or deficits may be the origin of the doublet only in the central mode. Anyway, the actual origin of the doublet mode is not identified now, we ignore the doublet structures. In the 4 μm disk case, we chose the high energy-side peak of the central mode so as to be equal interval of the mode separation. In the 2 μm disk case, the mode interval between two high energy-side peaks are nearly equals to that between two low energy-side peaks, so that the mode interval is determined to be unique.

When we assume the situation mentioned above, the lasing spectra show the regular intervals, indicating the WGMs in microdisks. Mode intervals of all the microcavities are plotted in Fig. 7, as a function of the inverse of the resonator length *L*, which is assumed to be the circumference length. The energy intervals are inversely proportional to the circumference length, so that the lasing mode intervals are ascribed to WGM.

Fig. 8 shows the sum of the lasing mode intensity as a function of the excitation density. The lasing threshold values of microdisks 8, 4, and 2 μm in diameter were estimated to be 99, 57, and 32 μJ/cm^2, respectively, as indicated by arrows in Fig. 8. The threshold for the microdisk 2 μm in diameter is the smallest. The lasing threshold is almost proportional to $1/L$, as is shown in Fig. 7. In the framework of cavity QED, the lasing threshold should decrease with the increase of the cavity-mode separation, leading to the lower lasing threshold of the smaller cavity [18,19]. Such behavior was observed in III–V inorganic microdisk cavities and well described cavity-QED calculations [19]. The observed results of the cavity-size-dependence, including the lowest lasing threshold of the smallest microdisk is well coincide with the previous report.

Note that we did not provide any measurement showing QED effects directly. However, in the early work on the microdroplets showed cavity-QED effects (stimulated emission enhancement) even in the multimode cavity, microspheres with 14 μm in diameter [20]. The stimulated emission enhancement is also reported in the 40 μm cylindrical microcavities made of polymer [21]. Situations of light confinement in the microsphere, microcylinder and microdisk are different, but we believe that our observations in the 2–8 μm microdisks are ascribed to cavity-QED effects (also stimulated emission enhancement). The condition where the stimulated emission enhancement can be observed holds, because the cavity resonance width is much broader than the radiative width of BP1T [22].

The lasing threshold of the thermally annealed crystalline films was reported to be 1400 μJ/cm^2 in the bulk film part [12]. The thickness of the annealed film was fixed at 400 nm and that of films in this report is 200–400 nm. The thicker films tended to be lasing easily in this thickness range, so that the lasing threshold can be compared directly. Lasing threshold of the microdisk 2 μm in diameter is reduced to 2.3% of it. In a previous report, the threshold was 200 μJ/cm^2 in a microring cavity 8 μm in diameter [13]. Comparing the value with lasing threshold for a microdisk 8 μm in diameter in this report, 99 μJ/cm^2, we can reduce the lasing threshold by half. This reduction is achieved by the high temperature vapor deposition method. Additional reduction is considered to be due to the cavity-QED effect which accompanies reduction of number of lasing modes 8 μm to that with 2 μm [22].

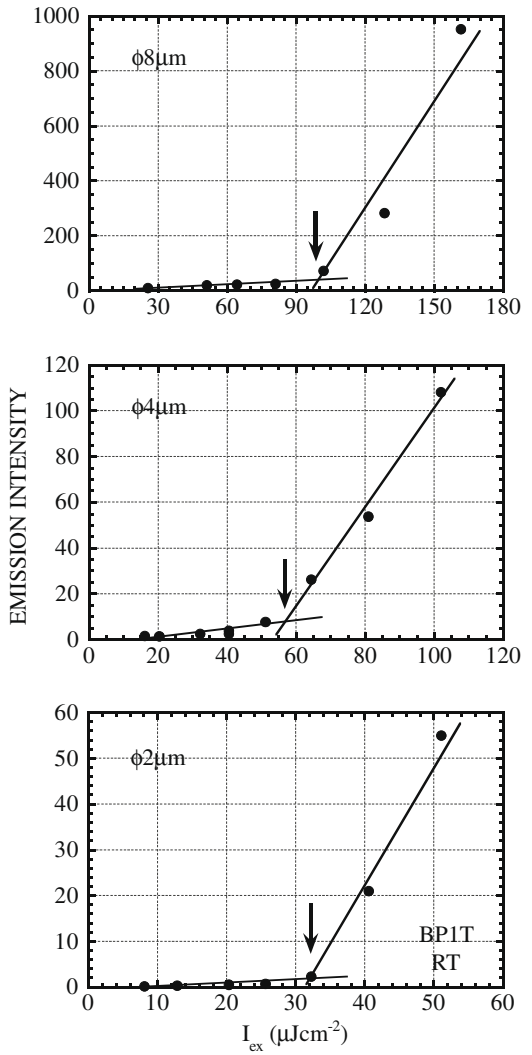

Fig. 8. Excitation density dependence of spectral peaks of the 0–1 line on the microdisks. Results on all microcavities show clear lasing threshold.

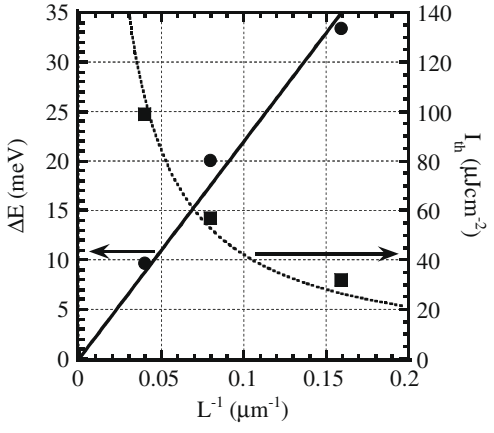

Fig. 7. Mode intervals ΔE observed on microdisks (the left axis) and lasing threshold (the right axis), respectively. Solid and dotted lines indicate liner dependence of L^{-1} and L, respectively.

We could not observe the lasing threshold of the microdisk 1 μm in diameter, because the luminescence intensity of the 1 μm disk below the lasing threshold was lower than the detection limit. When the excitation density was 30 μJ/cm^2, the luminescence spectrum of the 1 μm disk was sharp peak indicating lasing. Therefore, threshold of the 1 μm disk is found to be as low as that of the 2 μm disk. Further study will be needed to observe the threshold of smaller microdisks.

In case of inorganic semiconductor microdisks, smaller microdisks less than 1 μm in diameter were fabricated and single mode lasing was observed [23,24]. In case of organic semiconductors, micropillar cavities with the

diameter of 3 μm were fabricated [25]. From time resolved fluorescence experiments on the pillar cavities with 3–9 μm in diameter, the participation of Purcell Effect was reported. These reports clearly indicate the progress of microdisk cavities of both inorganic and organic semiconductors. However, there is no report where microdisk cavities of organic semiconductor crystals with a few μm in diameter are fabricated. To our knowledge, this is the smallest microdisk cavity made from organic crystals ever reported.

5. Transport experiments

As already mentioned, TPCO materials have good performance of the transport property as well as the optical properties. We also observe the field effect transistor (FET) properties of the BP1T film fabricated by the high temperature deposition method described above. Fig. 9 shows a micrograph of FET structures. A schematic of the FET is also shown in the inset. The deposition condition was similar with that of the microdisks fabrication. Gate dielectric layers were composed from the 500 nm thick SiO_2 layer and the 300 nm cytop layer. Gold source and drain electrodes were deposited on the BP1T crystal film by using a thin stainless mask. After the metal electrodes deposition, FETs were overcoated by cytop layer except for the contact parts.

Fig. 10 shows plots of source drain current–voltage (Isd–Vsd) FET output characteristics with the change of the gate voltage (Vg). The output curves show clear p-channel FET properties. Fig. 11 shows the plot of Isd–Vg transfer characteristics operated at Vsd = 100 V by solid circles. Field effect mobility of holes was found to be 0.034 $cm^2\ V^{-1}\ s^{-1}$ from the fitting. The fitting line is shown by the solid line in the figure. This value is two orders of magnitude smaller than that of 5,5″-bis(biphenyl-4-yl)-2,2′:5′,2″-terthiophene (BP3T) single crystals [26], but comparable to the shorter TPCO crystals such as 5,5′-bis(4-biphenylyl)-2,2′-bithiophene (BP2T) and/or 1,4-bis(5-phenylthiophene-2-yl)benzene (AC5), probably the highest value for BP1T [14,27,28]. This fact indicates the high temperature deposition method described in this report is good fabrication method for optical microcavities and also for electrical pumping devices.

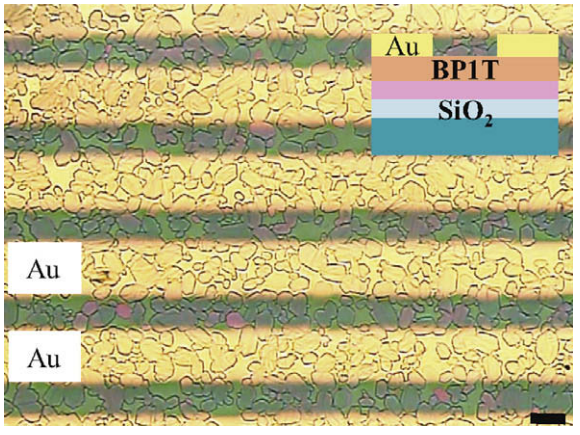

Fig. 9. Microscope images of FET devices fabricated by using high temperature deposition films. A black line shown in the bottom right part indicates the scale of 50 μm.

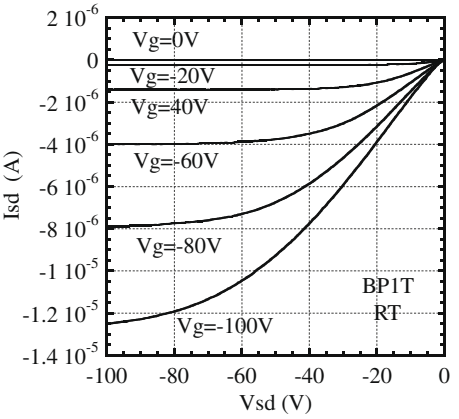

Fig. 10. Source–drain current (Isd) FET output for various gate voltage (Vg) fabricated by using high temperature deposition films.

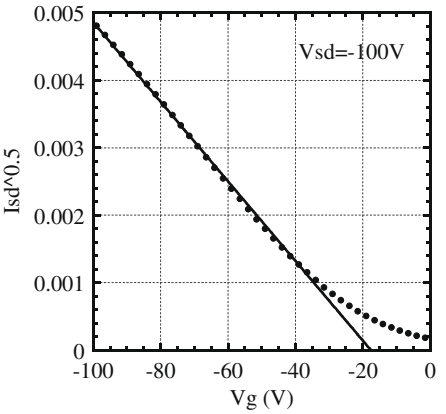

Fig. 11. Solid circles show the observed transfer curve of p-channel FET devices operated at Vsd = −100 V. The solid line shows the fitting line indicating the field effect mobility of 0.034 $cm^2\ V^{-1}\ s^{-1}$.

For the future developments of electrical pumping devices, there are many possible bottleneck processes such as electron and hole injection yields from electrodes [29], the conversion efficiency from electrons and holes to excitons [30], loss mechanisms of electrons, holes and excitons [31], and some kinds of thermal effects. Under the relatively low carrier mobility the bottleneck is considered to be the conversion efficiency from electrons and holes to excitons [30]. On the other hand, under the high mobility over 1 $cm^2\ V^{-1}\ s^{-1}$ the conversion efficiency is over 10% (assuming the same condition of Ref. [30] except for mobility), so that one of other processes may become the main bottleneck for electrical pumping. The FET devices reported here do not reach this region, but BP3T single crystal FET devices reported in Ref. [26] reach the region. Further as already pointed out by the high efficient electroluminescence work, when electrically injected electrons and holes directly form excitons such as direct gap

inorganic III–V semiconductor crystals, the intermediated states are not the bottleneck of exciton formation [32]. There are no reports of these bottleneck processes in TPCO systems, but further studies are needed to clarify the effectiveness of TPCO systems to the application for current injected devices.

6. Summary

We have fabricated BP1T microdisk laser cavities by using the high temperature deposition method and improved fabrication process. As a result, we can obtain microdisk cavities 1 μm in diameter. The cavities have no grain boundaries and cracks, so that each cavity is composed from a single crystal. The lasing spectra show the regular intervals, indicating the WGM in microdisks. The lasing threshold is almost proportional to $1/L$, as indicated by cavity QED. The smallest lasing threshold is reduced to 2% of bulk annealed films on the microdisk 2 μm in diameter. A part of the reduction comes from the improved quality of crystal films and another part of the reduction from the small disk size. The BP1T crystal films fabricated by using the high temperature deposition method also show the good performance of p-channel FET operation.

Acknowledgement

A part of this work was conducted at the AIST Nano-Processing Facility, supported by "Nanotechnology Network Japan" of the Ministry of Education, Culture, Sports, Science and Technology (MEXT), Japan.

References

[1] S. Hotta, M. Goto, Adv. Mater. 14 (2002) 498.
[2] M. Nagawa, R. Hibino, S. Hotta, H. Yanagi, M. Ichikawa, T. Koyama, Y. Taniguchi, Appl. Phys. Lett. 80 (2002) 544.
[3] M. Ichikawa, R. Hibino, M. Inoue, T. Haritani, S. Hotta, K. Araki, T. Koyama, Y. Taniguchi, Adv. Mater. 17 (2005) 2073.
[4] K. Shimizu, Y. Mori, S. Hotta, J. Appl. Phys. 99 (2006) 063505.
[5] M. Ichikawa, H. Yanagi, Y. Shimizu, S. Hotta, N. Suhanuma, T. Koyama, Y. Taniguchi, Adv. Mater. 14 (2002) 1272.
[6] K. Nakamura, M. Ichikawa, R. Fushiki, T. Kamikawa, M. Inoue, T. Koyama, Y. Taniguchi, Jpn. J. Appl. Phys. 44 (2005) L1367.
[7] K. Yamane, H. Yanagi, A. Sawamoto, S. Hotta, Appl. Phys. Lett. 90 (2007) 162108.
[8] H. Yanagi, T. Morikawa, S. Hotta, Appl. Phys. Lett. 81 (2002) 1512.
[9] M. Ichikawa, K. Nakamura, M. Inoue, H. Mishima, T. Haritani, R. Hibino, T. Koyama, Y. Taniguchi, Appl. Phys. Lett. 87 (2005) 221113.
[10] H. Yanagi, A. Yoshiki, S. Hotta, S. Kobayashi, J. Appl. Phys. 96 (2004) 4240.
[11] F. Sasaki, S. Kobayashi, S. Haraichi, H. Yanagi, S. Hotta, M. Ichikawa, Y. Taniguchi, Jpn. J. Appl. Phys. 45 (2006) L1206.
[12] S. Fujiwara, K. Bando, Y. Masumoto, F. Sasaki, S. Kobayashi, S. Haraichi, S. Hotta, Appl. Phys. Lett. 91 (2007) 021104.
[13] F. Sasaki, S. Kobayashi, S. Haraichi, S. Fujiwara, K. Bando, Y. Masumoto, S. Hotta, Adv. Mater. 19 (2007) 3653.
[14] T. Yamao, T. Miki, H. Akagami, Y. Nishimoto, S. Ota, S. Hotta, Chem. Mater. 19 (2007) 3748.
[15] M. Shtein, J. Mapel, J.B. Benziger, S.R. Forrest, Appl. Phys. Lett. 81 (2002) 268.
[16] T.J. Kippenberg, S.M. Spillane, K.J. Vahala, Opt. Lett. 27 (2002) 1669.
[17] M. Borselli, T.J. Johnson, O. Painter, Opt. Express 13 (2005) 1515.
[18] H. Yokoyama, S.D. Brorson, J. Appl. Phys. 66 (1989) 4801.
[19] T. Baba, IEEE J. Sel. Top. Quantum Electron. 3 (1997) 808.
[20] A.J. Campillo, D.J. Eversole, H.-B. Lin, Phys. Rev. Lett. 67 (1991) 437.
[21] M. Djiango, T. Kobayashi, Werner J. Blau, Appl. Phys. Lett. 93 (2008) 143306.
[22] Y. Ido, Y. Masumoto, F. Sasaki, M. Mori, S. Haraichi, S. Hotta, Appl. Phys. Express 3 (2010) 012702.
[23] Z. Zhang, L. Yang, V. Liu, T. Hong, K. Vahala, A. Scherer, Appl. Phys. Lett. 90 (2007) 111119.
[24] Q. Song, H. Cao, S.T. Ho, G.S. Solomon, Appl. Phys. Lett. 94 (2009) 061109.
[25] A.M. Adawi, A. Cadby, L.G. Connolly, Wen-Chang Hung, R. Dean, A. Tahraoui, A.M. Fox, A.G. Cullis, D. Sanvitto, M.S. Skolnick, D.G. Lidzey, Adv. Mater. 18 (2006) 742.
[26] S.Z. Bisri, T. Takenobu, Y. Yomogida, H. Shimotani, T. Yamao, S. Hotta, Y. Iwasa, Adv. Funct. Mater. 19 (2009) 1728.
[27] H. Yanagi, Y. Araki, T. Ohara, S. Hotta, M. Ichikawa, Y. Taniguchi, Adv. Funct. Mater. 13 (2003) 767.
[28] Y. Wang, R. Kumashiro, Z. Li, R. Nouchi, K. Tanigaki, Appl. Phys. Lett. 95 (2009) 103306.
[29] L.S. Hung, C.W. Tang, M.G. Mason, Appl. Phys. Lett. 70 (1997) 152.
[30] N. Tessler, Adv. Mater. 11 (1999) 363.
[31] M.A. Baldo, R.J. Holmes, S.R. Forrest, Phys. Rev. B 66 (2002) 035321.
[32] C. Adachi, M.A. Baldo, M.E. Thompson, S.R. Forrest, J. Appl. Phys. 90 (2001) 5048.

requires the development of top-absorbing devices. Furthermore, metallization in CMOS-technology is generally accomplished with a low work-function material such as aluminum, which can also be used as cathode material in organic devices. But when a low work-function material is used as bottom electrode of an hybrid detector, the layer sequence of the whole device has to be inverted [5–11].

An inverted layout is also appealing for flexible organic solar cells, since the brittle and expensive ITO conventionally used as bottom electrode can be replaced by a metal deposited with a cost-efficient roll-to-roll process [12–14]. Furthermore, as metals can be patterned with soft lithography techniques, periodic structures can be introduced to increase the optical mean free path in the device and therefore the amount of absorbed light [10,13,15–17]. In bottom-absorbing devices various metal grid electrodes with high electrical conductivity and high optical transmittance can replace conventional ITO contacts [18–20].

The challenge in inverting the layer sequence mainly concerns the spin-coating of the water-based poly(3,4-ethylenedioxythiophene):poly(styrenesulfonate) (PEDOT:PSS) solution on top of the hydrophobic photoactive layer. The electron-blocking PEDOT:PSS layer in photodiodes is used for decreasing the dark current and for enhancing charge injection/collecting properties. To attain a sufficient wetting of PEDOT:PSS, the surface of the photoactive layer can be modified [6,11,21]. Alternatively, wetting agents can be added to the PEDOT:PSS [7,8].

We focused on an oxygen plasma process which improves the wettability of the hydrophobic photoactive layer for the following water-based PEDOT:PSS deposition. Plasma treatment is a widespread application in the plastics industry to activate polymeric surfaces for subsequent lacquer coating, but its importance for organic electronics, i.e. sequent deposition of aromatic and water-based solutions, is not yet realized. Recently, we applied this method to overcome biocompatibility problems of solution-processed organic layers, enabling growth of living cells on those modified surfaces [22]. Hsiao et al. [11] first used an oxygen plasma treatment to fabricate an inverted solar cell but without reporting about changes of wettability. In this paper, we present a solution-processed top-absorbing inverted organic photodetector using oxygen plasma treatment and discuss the impact of the plasma on material and device properties.

2. Experimental methodology

2.1. Fabrication

The fabrication of the photodetectors is performed in a glove box under nitrogen atmosphere. For the plasma treatment, the devices were transferred in air from the glove box to a plasma asher (TePla 100-E) within a minute. The layer sequence of an inverted device is shown in Fig. 1.

The bottom electrode, consisting of 100 nm aluminum, was thermally evaporated on a glass substrate in a vacuum chamber situated in the glove box. The photoactive blend material, PCBM:P3HT, was processed with a weight ratio of 1:1 and solved in toluene with a mixing ratio of blend:toluene = 2:100 (wt.), stirred overnight and spin-coated on the bottom electrode, resulting in a layer thickness of about 110 nm, on the subsequent day. P3HT was purchased from Rieke Metals Inc. and PCBM from Solenne BV. The low-pressure oxygen plasma treatment was performed with a magnetron (2.45 GHz) coupling microwaves into an oxygen gas at a pressure of about 0.2 Torr. After plasma treatment, the PEDOT:PSS formulation Clevios P VP CH 8000 by H.C. Starck was spin-coated on the active layer with a thickness of about 170 nm. Semi-transparent gold electrodes (20 nm) with an area of 7 mm^2 were thermally evaporated on top of the device using a shadow mask.

Non-inverted photodiodes without plasma treatment as references for the inverted ones were also fabricated. As

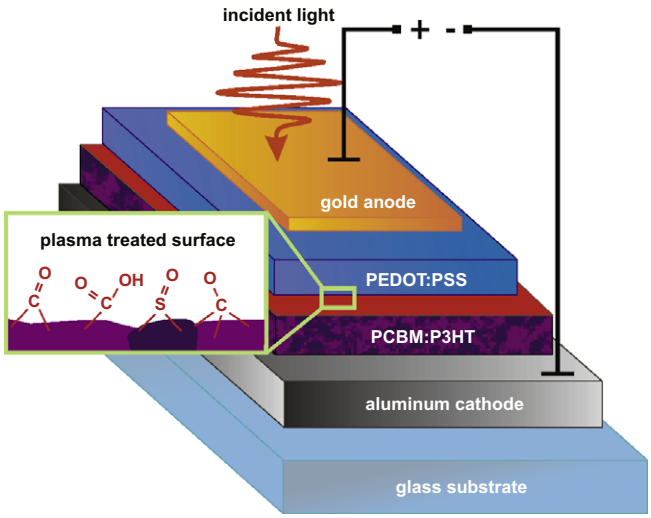

Fig. 1. Layer structure of the inverted design. The incident light is transmitted through a semi-transparent, 20 nm thick gold electrode. The enlargement illustrates the oxidation of the PCBM:P3HT blend surface due to plasma treatment.

anode material gold was replaced with indium-tin-oxide (ITO). Apart from that, processing conditions and layer thicknesses were the same as compared to the inverted devices.

Before characterization outside the nitrogen atmosphere, the devices were lateral encapsulated with a UV-hardened epoxy resin and thin glass sheets.

2.2. Characterization

Morphological characterization was performed with an atomic force microscope (AFM) JEOL 5100, operated in tapping mode. The root-mean-square (RMS) surface roughness was determined evaluating an area size of 4 μm^2.

The adhesion of PEDOT:PSS on top of a plasma-treated PCBM:P3HT blend layer has been evaluated by measuring the contact angle of a PEDOT:PSS drop on top of the blend. We used a setup consisting of a CCD-camera, a backlight and a horizontal leveled stage. A drop of the water-based PEDOT:PSS solution was deposited on a spin-coated blend layer on top of a glass substrate and a picture was taken immediately afterwards. The contact angle between drop and surface is determined assuming that the drop shape is spherical. The accuracy of the measurement is limited by the manual procedure and it is estimated to be <2°.

The blend surface was analyzed per X-ray photoelectron spectroscopy (SPECS MCD5 XPS instrument). The base pressure in the XPS analysis chamber was about 5×10^{-10} mbar. The samples were excited with X-rays with a monochromatic MgKα radiation at 1253.6 eV. The photoelectrons were detected with a hemispherical analyzer positioned normal to the sample surface. The energy resolution was about 0.3 eV. The C(1s) and S(2p) high resolution spectra were taken at a pass energy of 15 eV and with a 0.025 eV energy step.

For voltage-current characterization under illuminated conditions an halogen lamp with a calibrated power density of 100 mW/cm^2 was used. The spectral resolved external quantum efficiency was measured by lock-in-technique (Merlin Digital Lock-in Radiometry system), using a solar simulator with 300 W power and an Oriel Cornerstone 260 monochromator.

For dynamic measurements a green LED, illuminating the organic photodiode with square light pulses, was used. Pulses were generated by a waveform generator Keithley 2602. The photocurrent of the diode was amplified by a FEMTO Current Amplifier DHPCA-100 and the transient voltage measured by a 1.5 GHz digital sampling oscilloscope (LeCroy Wavepro 715zi). The response time of the whole setup (mainly determined by the LED and the current amplification) is <0.5 μs.

3. Impacts of oxygen plasma treatment

3.1. Wettability change of the PCBM:P3HT blend

We investigated the adhesion of the water-based PEDOT:PSS solution on top of spin-coated PCBM:P3HT blend layers which were exposed to an oxygen plasma.

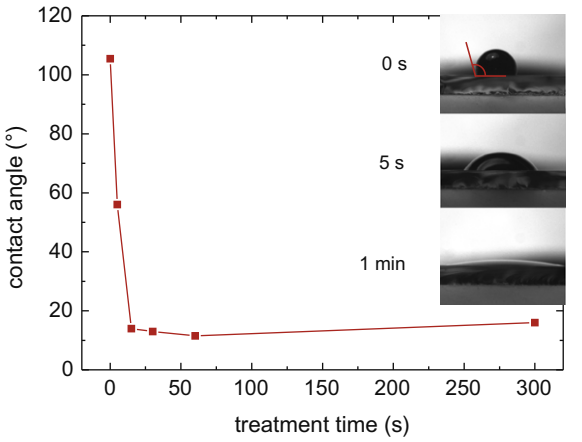

Fig. 2. Decrease of the PEDOT:PSS droplet contact angle on different long treated blend surfaces. The evaluation was performed with photographs as shown as inset.

High contact angles imply that cohesion forces inside the liquid dominate over adhesion to the solid surface. On hydrophobic surfaces the contact angles are larger than 90°, while highly hydrophilic surfaces exhibit contact angles close to zero.

The effect of oxygen plasma can be mainly controlled by varying process parameters such as treatment time and microwave power density. Fig. 2 shows the change of the contact angle of a PEDOT:PSS droplet as a function of the plasma treatment duration. The untreated blend surface has a very hydrophobic contact angle of about 106°. Even very short plasma treatment times result in a strong decrease of the contact angle which is saturating for treatments longer than 15 s. The plasma treatment leads to highly hydrophilic surfaces with contact angles <15° which are suitable for subsequent spin-coating of homogenous PEDOT:PSS layers. The best adhesion shown in Fig. 2 corresponds to a contact angle of 11° for 1 min treatment time.

3.2. Physical impact on the PCBM:P3HT blend

AFM-measurements on the blend surfaces were performed before and after the plasma treatment to find out if the quality of the surface is influenced by the process. Since metals, as the bottom electrode in the inverted device, can heat up in a plasma environment and therefore may enhance the chemical reaction with oxygen on the blend surface, the blend layers were spin-coated on glass substrates which were previously covered with an aluminum layer (100 nm). Several samples with 1 min and 5 min treatment times (with 100 W input power) were investigated. The root-mean-square roughness was determined before the exposure to the plasma and subsequently remeasured after the treatment. The untreated samples as well as the treated ones show the same root-mean-square roughness of about 1.3 ± 0.1 nm. For treatment times longer than 5 min an etching process starts at the edges of the samples while the blend distant from the edges remains unaffected. We conclude that the oxygen plasma treatment with appropriate settings of time and input power leads

primarily to a surface activation and does not act as an etching process.

Unless otherwise noted, a temporal setting of one minute is applied in device fabrication since the wettability of the PCBM:P3HT blend is best (Fig. 2) and etching effects can be excluded.

3.3. Chemical change of the PCBM:P3HT blend surface

Blend layers were investigated using X-ray photoelectron spectroscopy (XPS) in order to extract qualitative and quantitative information about the oxygen species generated on the blend layer surface (within material depths <5 nm) with subject to different long plasma treatments (100 W, 0.2 Torr).

Fig. 3 shows the S(2p) spectra. Without plasma treatment, only a signal at 164 eV is present which is related to the sulfur in the thiophene ring of P3HT. Beside the main peak, a second feature appears after plasma treatment at about 169 eV, which can be assigned to sulfur oxides. The oxidation of the thiophenes is getting more dominant with longer treatment times. After an abrupt rise to an oxide content of about 25% at 15 s, it increases to 60% at 5 min treatment as shown in the inset of Fig. 3. In spite of such high amounts of oxygen on the blend surface, the device performance is not negatively influenced, as it will be discussed later.

The C(1s) spectrum of an untreated and a 1 min long treated blend surface is shown in Fig. 4. Here the chemical change of the main components of the organic blend, the C—C and C—H bonds (P1), is represented. With plasma treatment a higher energy shoulder besides the main peak at 285.0 eV becomes apparent. According to typical chemical species found on plasma treated polymers [23,24], we can qualitatively identify three different components (P2, P3, P4) to the spectrum shoulder on the right side of the main peak (see Fig. 4). The P2 peak at 286.5 eV corresponds to C—O bonds (hydroxyl, ether), P3 at 287.5 eV to carbonyl

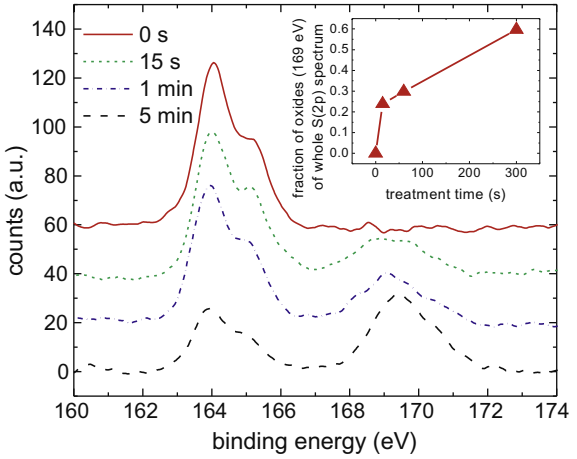

Fig. 3. Decomposition of the S(2p) peak (164 eV) of P3HT due to different long plasma treatments. The inset shows the increase of the integrated area of the sulfur oxides (around 169 eV) with respect to the integrated area of the whole spectrum. At 165 eV the $S(2p\frac{3}{2})$ signal is visible.

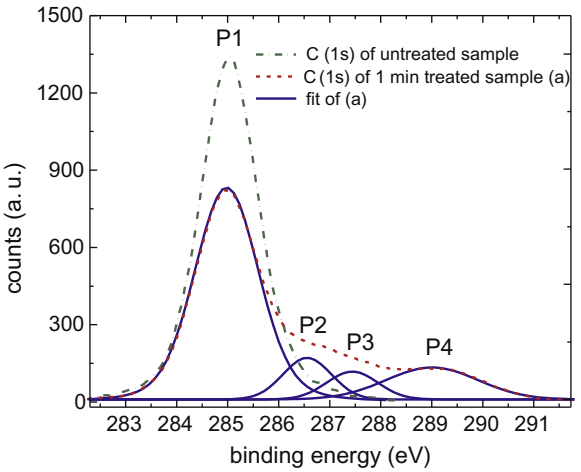

Fig. 4. Decomposition of the C(1s) peak of the PCBM:P3HT blend after a 1 min long plasma treatment. The envelope curve represents the measured spectrum of the 1 min treated sample. Using Lorentz–Gauss shapes, different peaks (P1–P4) were fitted.

(C=O) or double ether (O—C—O) bonds, and P4 at 289.0 eV is due to ester (O=O—OH) and carboxyl (O=C—O) groups. All these species are polar functional groups enhancing the hydrophility of the blend surface.

3.4. Inverted photodetector characteristics

3.4.1. IV-characteristics

IV-curves of an inverted organic photodiode together with those of a non-inverted device are shown in Fig. 5. The plasma treatment was performed with 100 W input power and applied for 1 min.

The non-inverted photodiode exhibits typical light and dark current characteristics [1]. In comparison, the inverted device shows an equally good light-on/light-off ratio for an external bias larger than −1 V indicating an efficient

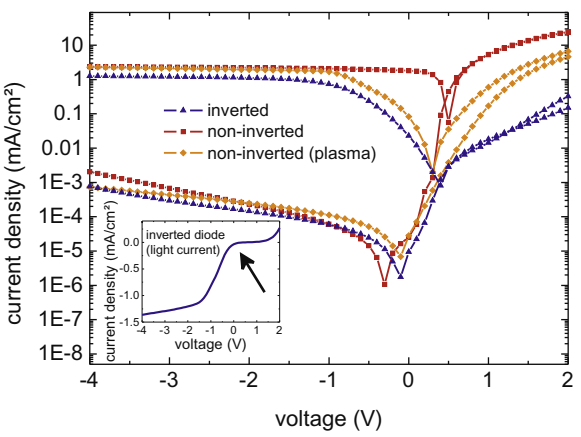

Fig. 5. Typical IV-curves of an inverted diode and a non-inverted reference diode (with an ITO-anode) with and without additional plasma treatment for dark and illuminated conditions. The applied light intensity was 100 mW/cm². The inset shows the light current of the inverted diode in a linear scale, the kink is indicated by the arrow.

current transfer through the plasma treated blend and into the high work-function gold anode. The decreased light-current for the whole reverse bias range is due to reduced light transmission through the semi-transparent gold anode. This point will be discussed further in Section 3.6.

Obvious differences to the non-inverted reference are the decreased forward current of the inverted diode (factor 100 @ +2 V) and an inflection point of the light IV-curve close to the open circuit voltage V_{oc} which is observable as a kink in the linear scale (see inset in Fig. 5).

The forward photocurrent density of an inverted diode measured up to 3 V is shown in Fig. 6. For bias voltage <0.5 V the current can be well fitted with an exponential increase $e^{qV/nkT}$ (with q = elementary charge, n = ideality factor, k = Boltzmann constant, T = temperature) according to the Shockley equation for inorganic diodes. For increasing voltage the current slope begins bending downwards (which might be related to a serial resistance) before it increases stronger again for bias larger than +2.2 V best fitted with a V^4 voltage dependence. The V^m law with $m \geqslant 2$ is valid for space charge limited current (SCLC) [25]. Without traps and without an effect of the electrical field on the mobility $m = 2$ is valid, but if traps or a field dependent mobility are involved $m > 2$ accounts. Since the plasma treatment introduces interface states by generating oxides on the blend, we assume that the current transport across this interface is dominated by trap-assisted hopping processes at sufficient large bias.

In organic electronics, a kink in the IV-curve is often observed during lifetime measurements [26,27] of solar cells and is related with oxygen diffusion into the device forming insulating interfaces, especially between the low work-function electrode and the polymer layers. The formation of the photocurrent kink can be explained by a slow charge transfer at the material interfaces [28]. Considering the decreased forward current, we can assign the kink of the IV-curve of Fig. 5 to space charge limited current due to the oxides introduced by the plasma treatment. This will be further discussed in Section 3.5 where it is shown that the slow charge transport across the plasma treated blend-PEDOT:PSS interface is due to charge accumulation which in turn reduces the internal electric field of the device. To compensate the built-in voltage, which corresponds almost to the open circuit voltage, a smaller external bias voltage has to be applied. Thus, the V_{oc} of the plasma treated device shifts to lower values (Fig. 5) compared to the reference one. Considering the application of the inverted devices as organic solar cells, this effect acts detrimental on the device performance as well as the negative curvature of the photocurrent kink in the fourth quadrant which reduces the short circuit current and the fill factor.

To find out if the impact of the plasma treatment is different strong on the constituents (PCBM, P3HT) of the blend, we fabricated a non-inverted device, as described in Section 2.1, with a blend layer exposed to an oxygen plasma (100 W, 1 min) prior to aluminum evaporation. Since the blend(PCBM)-Al interface of the non-inverted device enables electron transport and the blend(P3HT)-PEDOT:PSS interface of the inverted device enables hole transport, a different device performance would indicate a different impact of the interface states, introduced by the plasma treatment, on the carrier transport through PCBM and P3HT. While the non-inverted photodiode which was not exposed to an oxygen plasma presents no kink (Fig. 5) the plasma-treatment leads to the formation of a kink similar to that of the inverted device. A pronounced difference between the plasma-treated non-inverted (diode (a)) and inverted diodes is the increased forward current density (factor 25 @ +2 V) although both show a SCLC regime with a V^4 behavior, for diode (a) even starting at bias voltage >0.5 V. The increased current of diode (a) has to be related with an increased density of trapping states of the PCBM molecules. This is currently still under investigation.

To determine the influence of an increasing oxidation of the blend layer on the electronic performance, inverted devices were fabricated with different treatment times and different microwave powers. The on/off ratio between light and dark current was similar for different samples, but a change of the forward current density, especially of the photocurrents (Figs. 7, 8), could be observed. For either increasing treatment time or plasma power the current

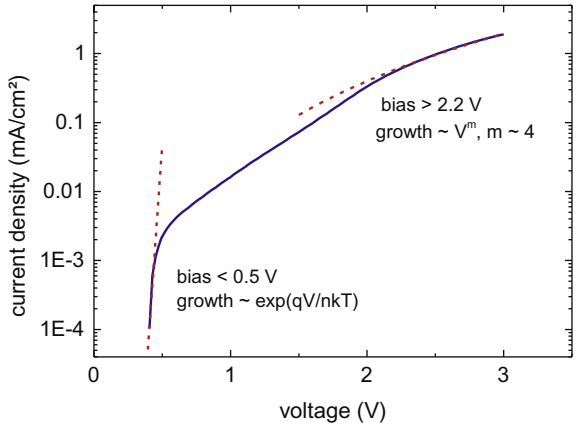

Fig. 6. Semilogarithmic plot of forward current density of an inverted device. The dashed curves represent fitted curves.

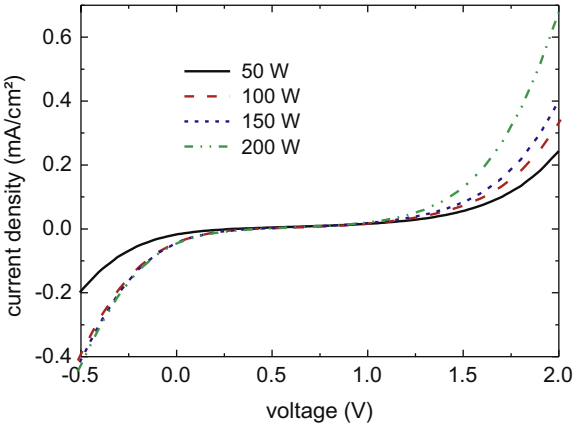

Fig. 7. IV-curves (linear scale) under illuminated conditions (100 mW/cm^2) for plasma treatment performed with different power settings.

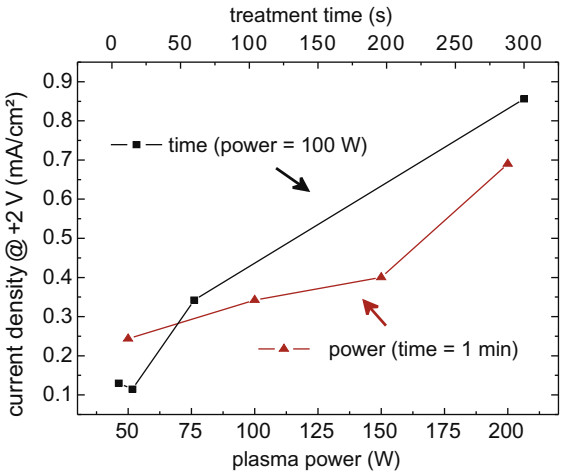

Fig. 8. Increase of the forward photocurrent density @ +2 V with increasing plasma treatment time and microwave power.

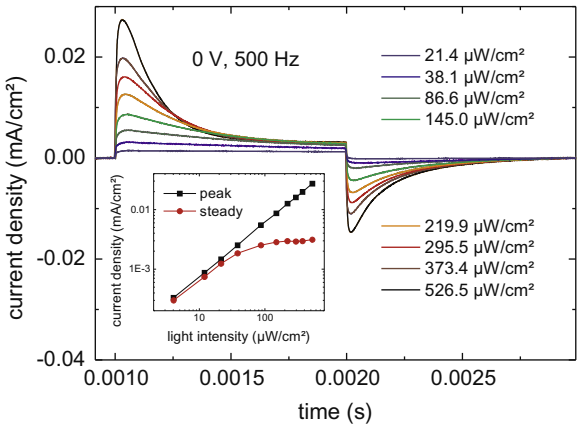

Fig. 9. Photocurrent density shape versus time of various light intensities (1 ms long square pulse) without applied bias voltage. The inset shows the increase of the photocurrent peak and the steady state value as function of the light intensity on a double-logarithmic scale.

density increases too. This is again a consequence of the current transport by trap-assisted hopping. As shown in Fig. 3, the amount of sulfur oxides increases on the blend surface with time and thus consequently also the number of hopping states. An increased oxidation is also expected with rising power. The varying input power has also an effect on the kink shown in Fig. 7. For the smallest applied power (respective times $\leqslant$15 s, not shown here) the kink is more pronounced. Since the kink has a negative impact on the quantum efficiency and the dynamic behavior (see Section 3.6, 3.5) minimum settings for plasma power and time have to be chosen for good device performance.

3.5. Dynamic behavior

The decreased photocurrent at small reverse bias voltages across the plasma treated blend surface, which is shown as kink in the IV-curve, leads to a characteristic shape of the photodiode dynamic response. In Fig. 9 the photocurrent of an inverted device after illumination with a 1 ms long square light pulse with different intensities is shown.

Illumination of the device with the pulse leads to the formation of a peak at the beginning of the light pulse response which starts to decrease within a time range of about 0.5 ms to a steady state value. A similar transient shape was observed before by Zaus et al. [29] when inserting a hole-conductor layer with low hole mobility in a non-inverted PCBM:P3HT photodetector. The effect observed in the inverted diodes can be explained by a hampered charge transport at the blend-PEDOT:PSS interface because of hole trapping at the plasma induced oxides. The consequence is a continuous increase of accumulated positive charge at the interface, associated with a reduction of the electric field inside the active layer and also of the light-current flowing [29]. This effect corresponds to the decrease of the peak value in Fig. 9. While the peak value increases linearly with increasing light intensity (see inset) as for normal organic photodiodes [1], for the steady state value a saturation effect occurs at about 50 µW/cm² indicating a decreasing internal electrical field with an increasing amount of photogenerated carriers.

For external bias voltage larger than −1 V, a value at which the kink of the IV-curves disappears, we observed a behavior typical for organic photodetectors independent of the light intensity. Within typical rise times of about 5 µs @ −1 V the photocurrent reaches a plateau, see Fig. 10. The −3 db-cut-off frequency of an inverted device measured @ −4 V is about 500 kHz (Fig. 11) which is also a typical value for organic photodetectors [30] and high enough for many imaging applications.

3.6. Quantum efficiency

To prove that the plasma treatment does not have a negative impact on the active layer we tried to compare the external quantum efficiency, defined by the ratio of generated electrons to incoming photons, of the inverted device with that of the non-inverted reference as shown

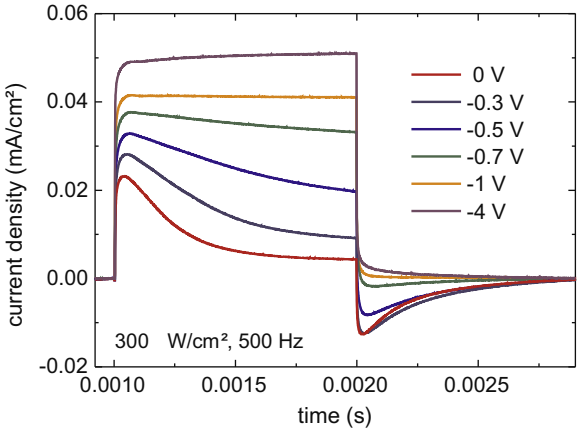

Fig. 10. Dependence of the dynamic photocurrent density shape of various bias voltages. The light intensity is 0.3 mW/cm².

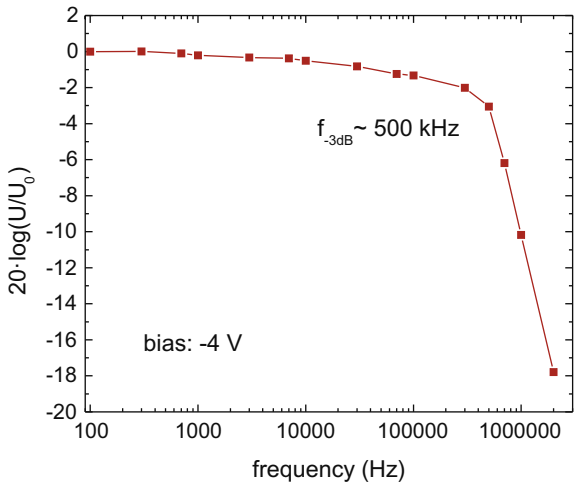

Fig. 11. Frequency response of the inverted diode for an applied voltage of −4 V.

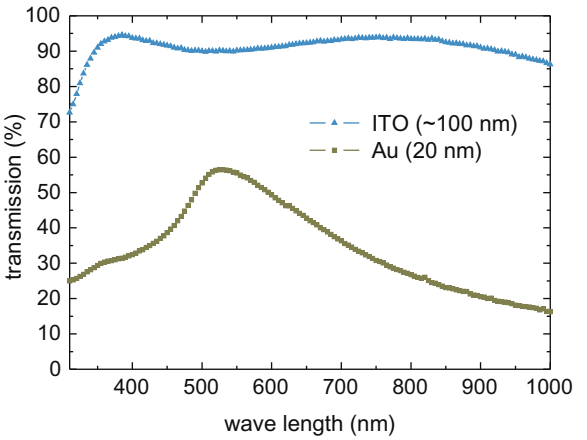

Fig. 13. Transmission of a 20 nm thick gold layer and of an about 100 nm thick ITO-anode.

in Fig. 12. Since the transparent electrodes consist of gold respectively ITO, the different transmittances of the materials have to be taken into account. In Fig. 13 the transmittance of 100 nm ITO and 20 nm gold are shown. Although the transmittance maximum of the semi-transparent gold anode corresponds to the absorption maximum of the PCBM:P3HT layer in the device, the overall transmittance is significantly reduced compared to the anode of the non-inverted device. At 500 nm, for a non-inverted device, about 80% of the incoming light is transmitted to the blend layer (through the glass substrate, the ITO-anode and a 170 nm thick PEDOT:PSS-layer). In an inverted device only about 50% of the photons @ 500 nm reach the blend layer after passing the encapsulation, the gold and the PEDOT:PSS layer. Both values are measured at a complete stack of relevant materials after substracting the absorbance of the glass substrate. The spectral resolved EQE @ −4 V for both devices is shown in Fig. 12. Comparing the EQE @ 500 nm with the amount of light reaching the active layer after transmission, 80% of the photons are converted into current for both the non-inverted and the inverted diode. Thus the reduced EQE of inverted devices can be completely explained by the loss of light due to the reduced transmission of gold. By patterning the gold we are currently trying to improve the light transmission.

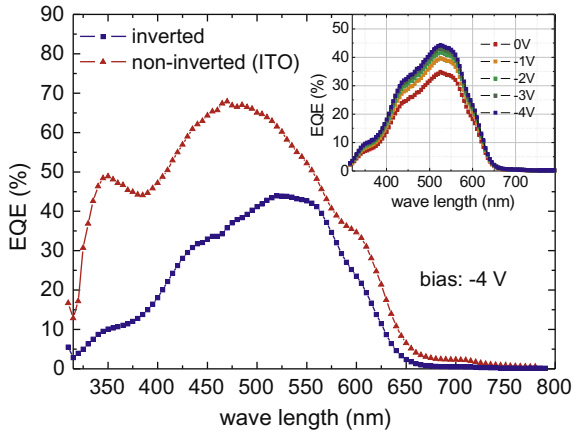

Fig. 12. External quantum efficiency (EQE) of an inverted and a non-inverted diode (gold respective ITO as transparent anode material) for an external bias voltage of −4 V. The inset shows the bias dependence of the EQE of the inverted diode.

The EQE of inverted devices increases strongly non-linear with increasing bias voltage. As can be seen in the inset of Fig. 12, from −1 V to 0 V bias the EQE decreases as much as between −4 V to −1 V. This strong decrease of the EQE for bias voltages close to 0 V can be attributed to accumulated charges at the plasma induced oxide layer and the resulting slow charge transfer which can also be seen in the kink of the IV-curves of Fig. 5 in Section 3.4.1 and discussed in Section 3.5. A saturation of the efficiency is reached for bias voltages larger than −5 V, resulting in a maximum EQE for the inverted device with a 110 nm thick photoactive layer of about 45%.

4. Conclusion

We successfully demonstrated the fabrication of an inverted organic photodiode using an oxygen plasma treatment process in order to spin-coat PEDOT:PSS on top of the photoactive blend layer. The device performance is influenced by the oxides introduced by the plasma treatment. Acting as traps, the oxides shape the IV-curves according to space charge limited current (SCLC), leading also to a kink of the photocurrent for biasing smaller than −1 V. Thus the dynamic photoresponse and the quantum efficiency are strongly influenced in this regime, but since photodetectors are usually driven at higher reverse bias, the effects do not hamper the device performance for usual operating voltages. Inverted devices fabricated with suitable plasma parameters show comparable on/off-ratios between dark and photocurrent for sufficient reverse bias as non-inverted reference diodes. Also the EQE, taking the decreased transmission of the gold anode into account, is not lowered compared with the references. Thus we conclude that the plasma treatment does not introduce severe

damages to the blend layer and these promising results allow the application of the inverted diodes as photodetectors, also in combination with inorganic electronics as CMOS-technology.

Acknowledgements

The authors thank Sebastian Schoell (Walther Schottky Institute, TU München, Germany) for performing the XPS measurements. The financial support by the German Exchange Service through the Vigoni-program is gratefully acknowledged.

References

[1] P. Schilinsky, C. Waldauf, J. Hauch, C.J. Brabec, Thin Solid Films 451–452 (2004) 105–108.
[2] X. Gong, M. Tong, Y. Xia, W. Cai, J. Sun Moon, Y. Cao, G. Yu, C. Shieh, B. Nilsson, A.J. Heeger, Science 325 (5948) (2009) 1665.
[3] T. Rauch, M. Böberl, S. Tedde, J. Fürst, M. Kovalenko, G. Hesser, U. Lemmer, W. Heiss, O. Hayden, Nat. Photonics 3 (2009) 332–336.
[4] S. Tedde, E.S. Zaus, J. Fürst, D. Henseler, P. Lugli, IEEE Electron Device Lett. 11 (2007) 893–895.
[5] S.K. Hau, H.L. Yip, O. Acton, N.S. Baek, H. Ma, A.K.Y. Jen, J. Mater. Chem. 18 (2008) 5113.
[6] T. Nyberg, Synth. Met. 140 (2004) 281.
[7] M. Glatthaar, M. Niggemann, B. Zimmermann, P. Lewer, M. Riede, A. Hinsch, J. Luther, Thin Solid Films 491 (2005) 298.
[8] B. Zimmermann, M. Glatthaar, M. Niggemann, M.K. Riede, A. Hinsch, A. Gombert, Sol. Energy Mater. Sol. Cells 91 (2007) 374.
[9] J. Kim, D.Y. Khang, J.H. Kim, H.H. Lee, Appl. Phys. Lett. 92 (2008) 133307.
[10] K. Tvingstedt, N.K. Persson, O. Inganäs, Appl. Phys. Lett. 91 (2007) 113514.
[11] Y. Hsiao, C. Chen, C. Chao, W. Whang, Org. Electron. 10 (2009) 551–561.
[12] S. Ahn, L. Guo, Adv. Mater. 20 (2008) 2044–2049.
[13] L.S. Roman, O. Inganäs, T. Granlund, T. Nyberg, M. Svensson, M.R. Andersson, J.C. Hummelen, Adv. Mater. 12 (2000) 189.
[14] F. Krebs, Org. Electron. 10 (2009) 761–768.
[15] M. Niggemann, M. Glatthaar, A. Gombert, A. Hinsch, V. Wittwer, Thin Solid Films 451–452 (2004) 619–623.
[16] S.-B. Rim, S. Zhao, S.R. Scully, M.D. McGehee, P. Peumans, Appl. Phys. Lett. 91 (2007) 243501.
[17] C. Cocoyer, L. Rocha, L. Sicot, B. Geffroy, R. de Bettignies, C. Sentein, C. Fiorini-Debuisschert, P. Raimond, Appl. Phys. Lett. 88 (2006) 133108.
[18] K. Tvingstedt, O. Inganäs, Adv. Mater. 19 (2007) 2893–2897.
[19] T. Aernouts, P. Vanlaeke, W. Geens, J. Poortmans, P. Heremans, S. Borghs, R. Mertens, R. Andriessen, L. Leenders, Thin Solid Films 451–452 (2004) 22.
[20] M. Kang, M. Kim, J. Kim, L. Jay Guo, Adv. Mater. 20 (2008) 4408–4413.
[21] M. Roberts, S. Mannsfeld, R. Stoltenberg, Z. Bao, Org. Electron. 10 (2009) 377–383.
[22] G. Scarpa, A. Idzko, S. Götz, S. Thalhammer, Macromol. Biosci. 10 (2010) 378–383.
[23] G.P. Lopez, D.G. Castner, B.D. Ratner, Surf. Interface Anal. 17 (1991) 267–272.
[24] M. Liston, L. Martinu, J. Adhes. Sci. Technol. 7 (1993) 10. pp. 1091–1127.
[25] S.C. Jain, W. Geens, A. Mehra, V. Kumar, T. Aernouts, J. Poortmans, R. Mertens, M. Willander, J. Appl. Phys. 89 (2001) 3804–3810.
[26] F.C. Krebs, K. Norrman, Prog. Photovoltaics Res. Appl. 15 (2007) 697–712.
[27] M. Jørgensen, K. Norrman, F.C. Krebs, Sol. Energy Mater. Sol. Cells 92 (2008) 686–714.
[28] M. Glatthaar, M. Riede, N. Keegan, K. Sylvester-Hvid, B. Zimmermann, M. Niggemann, A. Hinsch, A. Gombert, Sol. Energy Mater. Sol. Cells 91 (2007) 390–393.
[29] E.S. Zaus, S. Tedde, J. Fürst, D. Henseler, G.H. Döhler, J. Appl. Phys. 101 (2007) 044501.
[30] M. Ramuz, L. Bürgi, C. Winnewisser, P. Seitz, Org. Electron. 9 (2008) 369–376.

In this work, we present all-polymer ECTs, where the electrolyte is patterned within a self-supported membrane. The membranes are prepared by the roll-to-roll suitable electron beam irradiation induced grafting (EB) technique (Fig. 1) that was recently used by our group for fabricating low-voltage EDLC gated OFETs [10]. The ion conducting membranes provide a number of benefits: (1) the membrane is thick and robust, but still flexible. (2) The membrane is chemically resistant. (3) By using the EB technique we can tailor-make the membrane to be ion conducting in any desired way and pattern. (4) We may vary the base-material and/or the functional group. The latter is especially attractive for various sensor applications [4]. We use flexography, which is a roll-to-roll manufacturing technique [11], to print the PEDOT/PSS source-, drain- and gate-electrodes onto the patterned membrane. Because of an intrinsic feature of the PEDOT, we also demonstrate a write-once read many times (WORM) memory device that is based upon the printed all-polymer ECT.

2. Materials and methods

The porous poly(vinylidene difluoride) (PVDF) (Millipore GVHP00010, 125 μm of thickness, 0.22 μm of pore size), styrene (Acros), toluene (LabScan) and 1,2-dichloroethane were all of reagent grade and used as received. Irradiation was carried out through a patterned aluminum mask using an ESI Electrocurtain 175 electron accelerator (Energy Sciences Inc.) under ambient air at an acceleration voltage of 175 kV. The irradiated (20 kGy) membranes were immediately immersed in 140 ml of styrene and 60 ml of isopropanol. The monomer solution was purged with nitrogen for 30 min prior to grafting and an inert atmosphere was maintained throughout the reaction. The reaction was carried out in nitrogen atmosphere at 80 °C for 2.5 h. After the reaction the grafted membranes were extracted with chloroform and dried at 40 °C in a vacuum oven. For sulfonation the patterned membranes were immersed in 0.5 M chlorosulfonic acid in 1,2-dichloroethane at 30 °C for 24 h. The sulfonated membranes (PVDF:PSSA) were washed thoroughly with ethanol and water. The overall process is illustrated in Fig. 1.

Before printing of the PEDOT/PSS-structures, the membranes were boiled in water for 30–60 min and, thereafter, dried at room temperature. A tabletop flexographic printing unit (Flexiproof 100 from R K Print Coat Instruments Ltd.) was used to print the structures. The selected anilox-roll had a transfer-volume of 18 cm^3/m^2. A lithographically patterned OHKA-rubber plate (Espoon Painolaatta Oy) was used as the flexible printing plate. The conductive polymer dispersion was a mixture of water based PEDOT/PSS (Baytron P) and ethylene glycol. The latter was used as a conductivity enhancer. Two mixtures of the dispersion were separately used in this work. The first one was Baytron P with added ethylene glycol (60 vol%) (PEDOT content approx. 0.45 wt.%), while in the second mixture the viscosity of Baytron P was adjusted by partially removing water by evaporation. The concentrated "gelled" PEDOT/PSS dispersion had an added ethylene glycol content of 20 vol% (PEDOT content approx. 1.2 wt.%). Seven consecutive layers were printed in order to gain high pristine conductivity. Between each printing step the printed layer was dried with a hot air blower. In the measured ECTs, the distance between the gate and the transistor channel (i.e., the PEDOT/PSS-channel between the source and the drain that covers the PVDF:PSSA-pattern [5]) was varied between 200 and 600 μm. The transistor channel area was varied between 0.9 and 1.7 mm^2, while the gate area was kept at about 50 mm^2.

The ECTs were stored and characterized at room temperature and in controlled humid atmosphere. In this work all devices were tested in relative humidity (RH)-levels of RH = 40–70%. All current–voltage characteristics, except for the current–time measurement, were measured with a Keithley 2636 System SourceMeter (source/drain-probes) and a Keithley 2400 SourceMeter (gate-probe) and further connected to a computer with suitable software. The current–time measurements were done with an Agilent 4142B Parameter Analyzer connected to a computer with suitable software. The voltage step for all current–voltage measurements was 0.1 V and different delay-times were used. For the WORM-experiments the WRITE-voltage (gate-voltage) was $V_G = -25$ V and was applied for 30 s.

3. Results and discussion

A schematic figure of the flexographic printing technique is shown in Fig. 2. By using a porous membrane, the transfer of the water based PEDOT/PSS is improved, including on the ungrafted PVDF-surface. This results in a good print pattern, as shown in Fig. 2c. The ECT is a three-terminal device with the source, the drain and the gate placed laterally to each other on the PVDF:PSSA-pat-

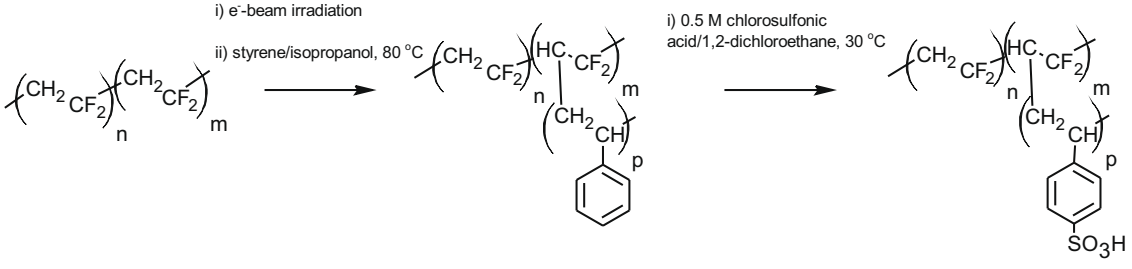

Fig. 1. The preparation procedure of the PVDF:PSSA membrane. The three major steps are (1) electron beam irradiation through a patterned mask, (2) grafting and (3) sulfonation.

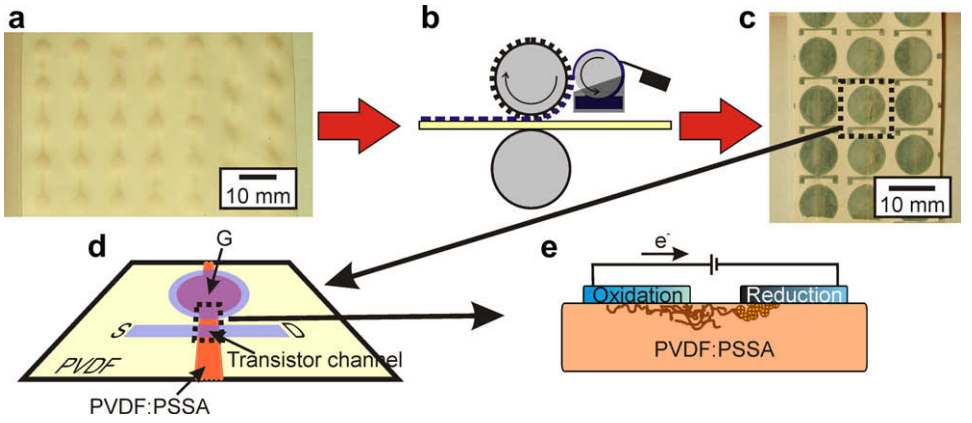

Fig. 2. (a) The patterned porous PVDF:PSSA-membrane. (b) Flexography is a roll-to-roll manufacturing technique. (c) The photograph shows a strip of printed PEDOT/PSS based ECTs. (d) A schematic figure of the PEDOT/PSS based ECT. D, S and G are the drain, the source and the gate respectively. (e) The gate and the transistor channel are connected via the PVDF:PSSA (dotted area in (d)). Thus, as schematically shown, they form an electrochemical cell.

tern (Fig. 2c and d). Thus, the electrodes can be placed on the same printing plate, which means that problems such as aligning of the electrodes may be avoided. Furthermore, the flexographic printing can, in principle, be done in one step. In practice, though, up to seven consecutive PEDOT/PSS layers were printed in order to get a high pristine conductivity. We note, however, that the number of printed layers may be reduced, since PEDOT/PSS and ethylene glycol compositions can provide conductivities of up to 500 S/cm with a dry thickness of only a few tens of nanometers [12]. The calculated dry thickness of the printed structure is 0.6–1.5 μm. The actual dry thickness may slightly vary due to an incomplete transfer of ink from the anilox roll and due to some possible penetration into the pores of the membranes. Local thickness analysis determined by atomic force microscopy on the printed PEDOT/PSS pattern is in agreement with the calculated value. Noteworthy is that the gelled PEDOT/PSS/ethylene glycol dispersion provides a sharper print pattern and, thus, a reduced risk for electronic short-cuts. Moreover, the pristine conductivity of the transistor channel is slightly higher compared to the other PEDOT/PSS dispersion (uppermost by a factor of three).

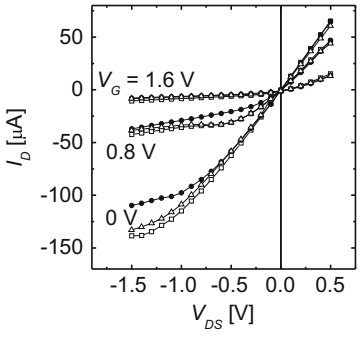

Fig. 3. Output-characteristics of an all-polymer ECT subsequently measured at delay-times 1 s (open square), 5 s (filled circle) and at 1 s again (open triangle).

Three output-characteristics for a printed ECT are shown in Fig. 3. The characteristics are subsequently measured at delay-times 1 s (open square), 5 s (filled circle) and 1 s (open triangle). The ECT was allowed to rest for 3 min between the characteristics. Since the PVDF:PSSA is hygroscopic, the ionic conductivity varies at different RH-levels [13]. The ECTs are therefore better operated in a slightly humid atmosphere. The devices were also tested after 3 months of storing in a controlled humidity and showed similar output-current levels and behavior, as compared to the pristine device. This is anticipated, since PEDOT is known to be a stable conducting polymer [14]. The modulation of the drain-current (I_D) is governed by the well-known redox-reaction for PEDOT/PSS:

$$\mathrm{PEDOT^+PSS^-} + \mathrm{M^+} + e^- \leftrightarrow \mathrm{PEDOT^0} + \mathrm{M^+PSS^-}, \quad (1)$$

where $\mathrm{M^+}$ is a proton in the case of PVDF:PSSA. By operating the ECT in the third quadrant, the transistor channel is reduced and the current is quenched. Therefore, the ECTs are "normally-on" devices and the transistor-operation is reversible in this mode. Based on the calculated thickness values for the PEDOT/PSS layer, the pristine conductivity in the transistor channel range from 5 to 15 S/cm (measured at a delay-time of 1 s, at $V_G = 0$ V and at a drain-voltage of $V_{DS} = -0.5$ V). The on/off ratios for the ECTs are usually 10^2–10^3.

If assuming that the gate, the PVDF:PSSA and the transistor channel forms an ideal electrochemical cell (Fig. 2e), and further neglecting any possible electronic leakage, then the total number of protons ($\mathrm{M^+}$) that participates in the redox-reaction can simply be estimated from:

$$Q = \int_0^{t_f} I_G dt, \quad (2)$$

where Q is the charge, I_G is the gate-current and t is the time. Indeed, the subsequent variation of the delay-time in Fig. 3 corresponds with the time-dependence of Eq. (2). A longer delay-time results in a decline in both the on- and off-currents as well as in a change in the pinch-off. Consequently, a higher number of charges participate

in reducing the transistor channel, as described by (1) and (2). There is a small mismatch between the first and the third output-characteristic (open symbols, delay-time 1 s), which could result from an incomplete re-oxidation of the transistor channel. The pinch-off at $V_G = 0$ V is caused by protons from PVDF:PSSA that attract towards the drain at higher negative V_{DS} and reduces the transistor channel [15]. Consistently, we observed that the same pinch-off disappears within the used measurement range when the transistor channel is thicker. In a thicker PEDOT/PSS layer a part of the transistor channel still remains oxidized (conducting) and, therefore, I_D maintains an ohmic behavior throughout the sweep at $V_G = 0$ V.

Several inherently conductive polymers, e.g., PEDOT, possess a finite potential window of high conductivity [16,17]. At elevated potentials and in the presence of nucleophiles (such as water) the polymer undergoes overoxidation and is, hence, susceptible for structural modifications. The charge percolation in the conjugated polymer is terminated, due to disrupted π-conjugation, and the polymer looses its high electronic conductivity [18,19]. Overoxidation of PEDOT results in a drop of conductivity by orders of magnitude [19], also shown in Fig. 4. On the other hand, an opposite high potential (i.e., a high reduction potential of the transistor channel) does not destroy the percolation path. Instead, though, the PEDOT-gate is subjected to a high oxidation potential. Nevertheless, the PEDOT/PSS based ECT can be operated in the third quadrant (Fig. 3) with a fast recovery of the high conducting state, as demonstrated by Fig. 4.

Overoxidation is acknowledged as a major challenge for conducting polymers in general and ECTs in particular. Overoxidation has, however, also been utilized, e.g., for designing isolated conductive patterns on PEDOT/PSS-sheets [20] and for pumping ions in an ECT-like set-up [21]. We use overoxidation of PEDOT to demonstrate a WORM memory functionality of the ECT. WORM-devices, that employ at least one organic layer, have earlier been motivated and successfully demonstrated by others [22–24]. In the WORM-device, the active material acts like a fuse. The transition from a high-conductivity state (“1”) to a low-conductivity state (“0”) is realized by applying a high, negative WRITE-pulse (V_G). The PEDOT is overoxidized and the conductivity is permanently destroyed by almost three orders of magnitude (Fig. 5). The “0”-state is permanent at controlled RH-levels (±3% in Fig. 5).

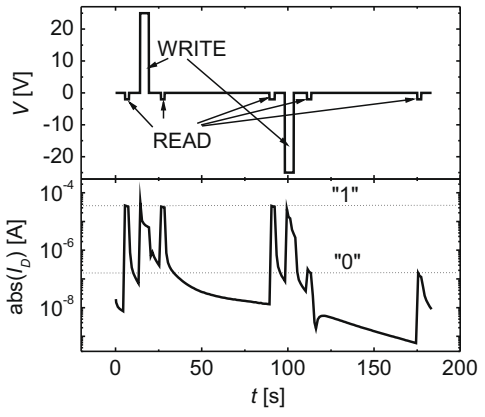

Fig. 4. By applying a positive V_G pulse (WRITE) the transistor channel is reduced. However, the electronic current recovers almost immediately. By applying a negative V_G pulse, the transistor channel is overoxidized and the electronic conductivity is permanently terminated. The WRITE-voltage is $V_G = \pm 25$ V, respectively, and applied for 5 s. The READ-voltage is $V_D = -2$ V and applied for 2 s.

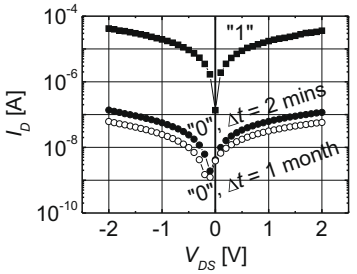

Fig. 5. A WORM-ECT characterized before and after the WRITE-pulse. Δt denotes the time-step between the WRITE-pulse and reading. The deviation in the “0”-currents are mainly due to slightly different RH-levels during the sweeps.

Basically, I_D in Fig. 5 can be expressed as $I_D = I_{SD} + I_{GD}$, where I_{SD} is the current between the source and the drain and I_{GD} between the gate and the drain respectively. $I_D \approx I_{SD}$ at “1”, that is, the electronic current in the transistor channel dominates ($I_{SD} \geqslant 100\, I_{GD}$). At “0”, on the other hand, $I_D = I_{SD} + I_{GD}$ albeit I_{GD} being the dominating term. In the “0”-state, I_D is also highly sensitive to changes in RH, which is due to the hygroscopic nature of the PVDF:PSSA. This results in a reversible increase of I_D at higher RH and vice versa. I_{SD} behaves identically at various RH, which clearly indicates that the conductivity of the PEDOT/PSS is dominated by its ionic contribution [25]. At RH = 100%, though, $I_D \approx I_{GD}$ ($I_{SD} \leqslant 0.1\, I_{GD}$). At this RH-level the increased I_D did still not reach up to the high current level at “1”. Moreover, below RH = 20% there were minimal ionic contribution from both I_{GD} and I_{SD} and the measured I_D was five to six orders of magnitude lower than at “1”. Consequently, the electronic resistance has increased by more than five orders of magnitude after overoxidizing the PEDOT, which corresponds with earlier reported values [19,20]. We note that a fairly long WRITE-pulse (30 s) was intentionally selected in order to ensure terminal reduction of I_D. The WRITE-pulse is therefore not optimized for applications. Several parameters affect the degree of overoxidation, such as the volume (area × thickness) of the transistor channel, the degree of grafting of the PVDF:PSSA (i.e., the ionic conductivity) [13], various contact effects and resistances as well as the ambient RH. Nevertheless, the demonstrated WORM-ECT provides a simple and low-cost possibility for permanent storing of information, such as for intelligent labeling.

4. Summary

Low-voltage and all-polymer ECTs have been fabricated on self-supported and patterned PVDF:PSSA membranes. The fabrication and the characterization of all devices have been carried out in air. The PVDF:PSSA is prepared by the electron beam irradiation induced grafting technique. The

transistor structure is printed with flexography using a PEDOT/PSS/ethylene glycol dispersion as the redox-active material. The ECTs are fabricated in lateral device geometry and display reversible behavior when operated in the third quadrant. However, when applying a sufficiently high negative gate bias, the transistor channel is irreversibly overoxidized. We have utilized overoxidation for demonstrating WORM memory functionality in the ECT. This work provides an example of a simple and low-cost application for all-polymer electronics.

Acknowledgments

N.K. gratefully acknowledges Dr. Kjell-Mikael Källman and Dr. Himadri Majumdar for help with setting up the humidity chamber. Dr. Himadri Majumdar is further acknowledged for fruitful advices regarding the memory functionality. This work was done within the Finnish Funding Agency for Technology and Innovation through the FLEXSENS project. The authors acknowledge partial funding from the Academy of Finland through the National Center of Excellence program.

References

[1] H.S. White, G.P. Kittlesen, M.S. Wrighton, J. Am. Chem. Soc. 106 (1984) 5375–5377.
[2] C.D. Dimitrakopoulos, P.R.L. Malenfant, Adv. Mater. 14 (2002) 99–117.
[3] M.J. Panzer, C.D. Frisbie, Adv. Mater. 20 (2008) 3177–3180.
[4] J.T. Mabeck, G.G. Malliaras, Anal. Bioanal. Chem. 384 (2006) 343–353.
[5] D. Nilsson, N. Robinson, M. Berggren, R. Forchheimer, Adv. Mater. 17 (2005) 353–358.
[6] P. Andersson, R. Forchheimer, P. Tehrani, M. Berggren, Adv. Funct. Mater. 17 (2007) 3074–3082.
[7] M. Hamedi, R. Forchheimer, O. Inganäs, Nat. Mater. 6 (2007) 357–362.
[8] D. Nilsson, M. Chen, T. Kugler, T. Remonen, M. Armgarth, M. Berggren, Adv. Mater. 14 (2002) 51–54.
[9] R. Mannerbro, M. Ranlöf, N. Robinson, R. Forchheimer, Synth. Met. 158 (2008) 556–560.
[10] N.J. Kaihovirta, C.-J. Wikman, T. Mäkelä, C.-E. Wilén, R. Österbacka, Adv. Mater. 21 (2009) 2520–2523.
[11] H. Kipphan, Handbook of Print Media, Springer-Verlag, Berlin, Heidelberg, New York, 2001.
[12] Y. Xia, W. Zhang, M. Ha, J.H. Cho, M.J. Renn, C.H. Kim, C.D. Frisbie, Adv. Funct. Mater. 20 (2010) 587–594.
[13] T. Lehtinen, G. Sundholm, S. Holmberg, F. Sundholm, P. Björnholm, M. Bursell, Electrochim. Acta 43 (1998) 1881–1890.
[14] Q. Pei, G. Zuccarello, M. Ahlskog, O. Inganäs, Polymer 35 (1994) 1347–1351.
[15] N.D. Robinson, P.-O. Svensson, D. Nilsson, M. Berggren, J. Electrochem. Soc. 153 (2006) H39–H44.
[16] D. Ofer, R.M. Crooks, M.S. Wrighton, J. Am. Chem. Soc. 112 (1990) 7869–7879.
[17] M. Lapkowski, A. Pron, Synth. Met. 110 (2000) 79–83.
[18] U. Barsch, F. Beck, Electrochim. Acta 41 (1996) 1761–1771.
[19] P. Tehrani, A. Kanciurzewska, X. Crispin, N.D. Robinson, M. Fahlman, M. Berggren, Solid State Ionics 177 (2007) 3521–3527.
[20] P. Tehrani, N.D. Robinson, T. Kugler, T. Remonen, L.-O. Hennerdal, J. Häll, A. Malmström, L. Leenders, M. Berggren, Smart Mater. Struct. 14 (2005) N21–N25.
[21] J. Isaksson, P. Kjäll, D. Nilsson, N.D. Robinson, M. Berggren, A. Richter-Dahlfors, Nat. Mater. 6 (2007) 673–679.
[22] S. Möller, C. Perlov, W. Jackson, C. Taussig, S.R. Forrest, Nature 426 (2003) 166–169.
[23] E.Y.H. Teo, Q.D. Ling, Y. Song, Y.P. Tan, W. Wang, E.T. Kang, D.S.H. Chan, C. Zhu, Org. Electron. 7 (2006) 173–180.
[24] J. Lin, D. Ma, J. Appl. Phys. 103 (2008) 024507.
[25] A.M. Nardes, M. Kemerink, M.M. de Kok, E. Vinken, K. Maturova, R.A.J. Janssen, Org. Electron. 9 (2008) 727–734.

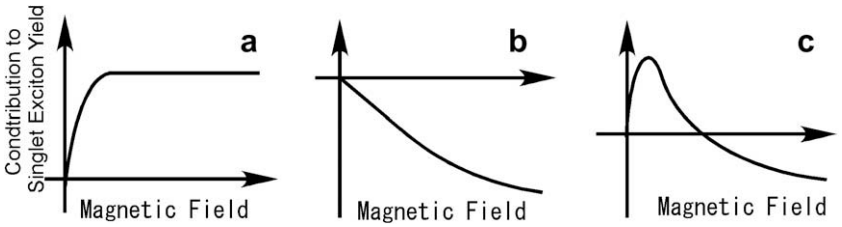

Fig. 1. Schematic drawing of the magnetic field effect on singlet exciton yield. (a) Hyperfine coupling (hfc) (b) difference in the *g*-factor (Δg) (c) triplet–triplet annihilation (TTA).

2. Experiments

2.1. Sample preparation

The structure of fluorescent device is shown in Fig. 2a. An indium tin oxide (ITO) coated glass substrate (purchased from Aldrich) with a sheet resistivity of 8–12 Ω/square was used as the substrate. About 100 nm N′,N′-di(naphthalene-1-yl)-N,N′-dipheyl-benzidine (α-NPD) and 100 nm tris-(8-hydroxyquinolino) aluminum (Alq_3) were deposited successively as the hole transporting layer and emitting/electron transporting layer, respectively. Then a cathode was deposited consisting of a 2 nm Cs layer followed by 150 nm of Al. The ITO substrate was cleaned by ultrasonicating in ethanol and acetone. Following this, the ITO was treated in ozone for 20 min. The α-NPD and Alq_3 were purchased from Luminescence Technology Corporation. The deposition of the organic layers was performed using Knudsen-cells in a vacuum chamber with a base pressure during evaporation of $\sim 10^{-7}$ Torr. Cs was deposited with alkali metal dispenser (purchased from SAES Getters). The deposition rate of organic materials was about 0.1 nm/s. Calibrated quartz crystal microbalances were used to determine the deposition rate. The structure of phosphorescence device is shown in Fig. 2b. Doping of 5% Btp_2Ir(acac) in CBP was performed by controlling the evaporation rate by monitoring the quartz crystal microbalances.

The sample OLEDs and unipolar devices were transferred from the deposition chamber to glove box filled with dry N_2 (concentration of H_2O and oxygen was less than 100 ppm) without exposing them to air. The electrical connection to the OLED was made using 20 μm-diameter Cu wire with In contact. Then the OLED sample was sealed in a glass box using photo-hardening epoxy (Threebond 3124) together with a zeolite desiccant (Shinagawa Kasei Co., Ltd.).

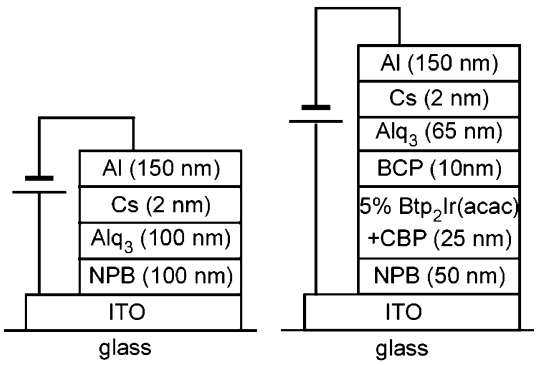

Fig. 2. Device structures (a) fluorescent device (b) phosphorescent device. The abbreviations are as follows. BCP: 2,9-dimethyl-4,7-diphenyl-phenanthroline, Btp2Ir(acac): bis(2-(2′-benzo[4,5-α]thienyl) pyridinato-N,$C^{3\prime}$) iridium (acetyl-acetonate), CBP: 4,4′-N,N′-dicarbazole-diphenyl.

2.2. Measurement

MFE was measured at 300 K in superconducting magnet using Physical Property Measurement System (PPMS; Quantum Design). The magnetic field was perpendicular to the device plane. The magnetic field was increased from 0 to 9 T and then was decreased from 9 to 0 T in order to check the temporal changes. The results are shown after confirming pure MFE is observed, unless stated otherwise. The emission intensity was measured with photon counter H7155-21 (Hamamatsu Photonics) in magnetic shielding made of thick iron plates and cylinders. The shielding of photon counter was tested by introducing light with vari-

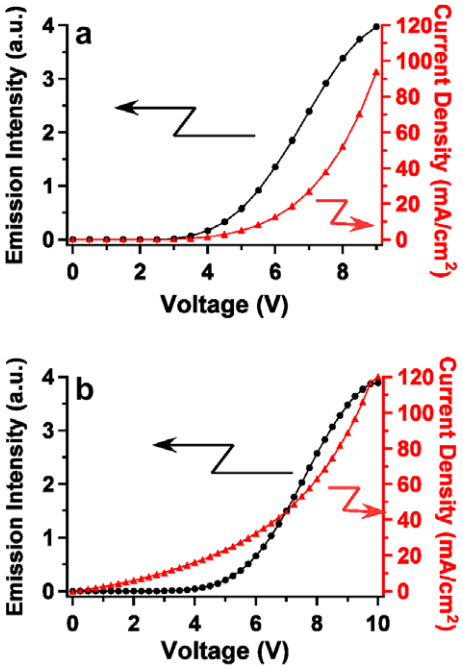

Fig. 3. Normalized emission intensity and current density as a function of the voltage without applying the magnetic field (0 T) (a) fluorescent device (b) phosphorescent device.

ous intensities by optical fiber to make sure there was no magnetic field dependence on its output. The bias was applied by the Keithley 6487 picoammeter/voltage source in constant voltage mode.

3. Results

3.1. Fluorescent OLED

First we show the characteristics of the fluorescent device without applying the magnetic field. Fig. 3 shows the emission intensity and current of the fluorescent and phosphorescent OLED as a function of voltage. It is reported that TTA in Alq_3-based fluorescent OLEDs occurs when the current density is larger than 100 mA/cm^2 [17] and some of our measurement exceeds this limit. However, since the magnetic field dependence of TTA appears only at low temperatures [13,14], we consider we can neglect contribution from TTA in the present measurement at 300 K.

The emission intensity, current, and emission efficiency of the same device under the magnetic field are shown in Fig. 4. The emission intensity and current show different magnetic field dependence on the sweep direction (0 T → 9 T → 0 T) (Fig. 4a and b). However, their ratio, i.e. emission efficiency, does not show the hysteresis as shown in Fig. 4c. It means that the hysteresis comes from the charge injection process from the electrodes to the emission layer. We found that the "hysteresis" is dependent on both of the magnetic field and the time from the start of the current flow. The time dependence is probably due to the bias stress on the device, but the magnetic field dependence might be related with MFE of the trap/detrap processes.

The emission efficiency (and also the emission intensity and the current) increase steeply as a function of B when it was less than 0.02 T as reported in the literature, and gradually decreases as B was further increased. It should be noted that the decrease in the mid–high B region is *convex* function, which cannot be explained by widely accepted behavior of hfc, Δg, and TTA mechanisms which exhibit *concave* behavior against B. We will discuss this point later.

In order to see dependence on B more clearly, we re-plotted Fig. 4c as a function of B^2. Fig. 5a clearly shows the linear decrease of the fluorescent efficiency against B^2 in the range of 0.1–6.5 T. On the other hand, by re-plotting Fig. 4c as a function of $B^{1/2}$ (Fig. 5b), it is noticed that the decrease of the emission efficiency shows $B^{1/2}$ dependence in the range of 6.5–9 T.

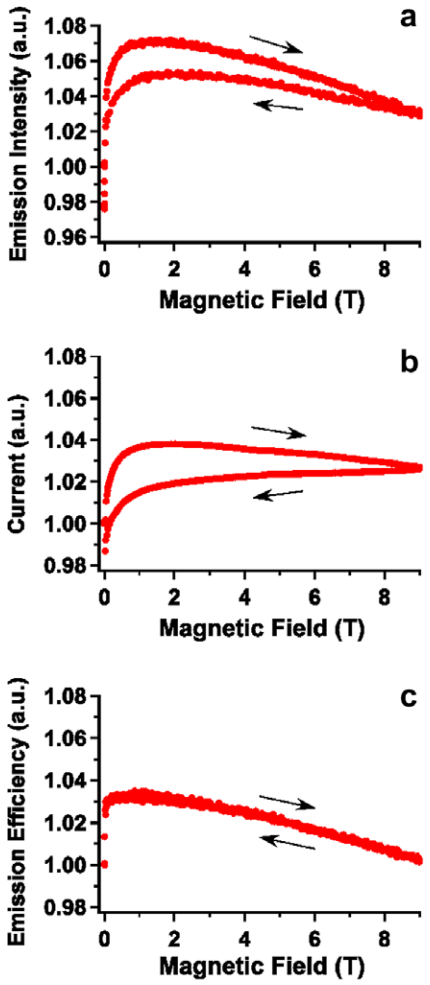

Fig. 4. Magnetic field effect of the fluorescent device (normalized at zero field). (a) Emission intensity, (b) current, (c) emission efficiency at 4 V. The arrows show the sweep direction of the magnetic field (0–9/9–0 T).

3.2. Phosphorescent OLED

Fig. 6 shows the MFE on the emission efficiency of the phosphorescent OLED. In contrast to the results of the fluorescent device, it did not show the magnetic field depen-

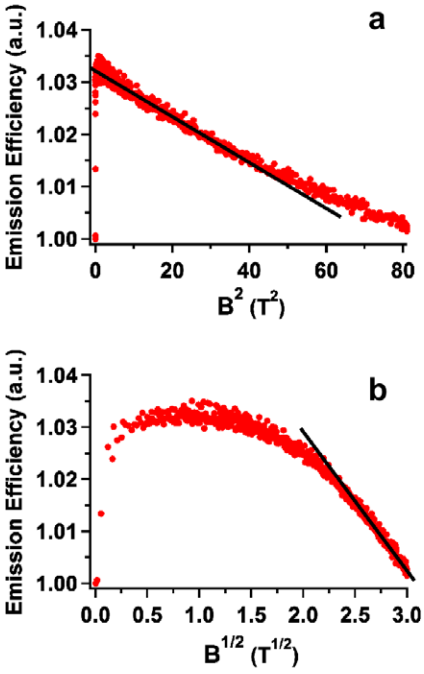

Fig. 5. Normalized emission efficiency of the fluorescent device plotted against (a) B^2 (b) $B^{1/2}$.

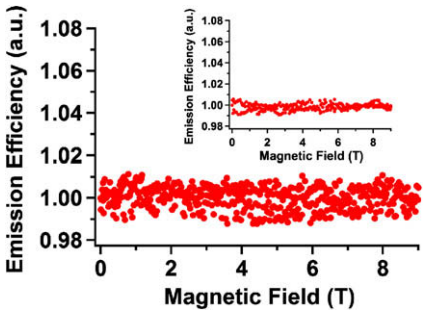

Fig. 6. Magnetic field effect of the phosphorescent device (normalized at zero field). The result at 10 V is shown in the inset.

dence. Although we changed the driving voltage (4, 6, 8, 10 V), the magnetic field dependence did not appear.

3.3. Magnetoresistance measurement of unipolar devices

In order to investigate the charge balance factor which might influence the EL efficiency, we measured the magnetoresistance of the majority and minority carriers in α-NPD and Alq_3 by making the unijunction devices with different work function electrodes (Au and Cs). All of the devices showed Ohmic *I–V* characteristics in the measured range (−10 to 10 V). The results of MFE on the current at constant voltage are shown in Fig. 6a–d. The voltages were chosen to give current in the range of 10–100 μA and the results are shown after normalization at zero field. It is easily noticed that the MFEs on the conductivity of the majority carriers (holes in α-NPD and electrons in Alq_3) are negligible, whereas linear decreases in the conductivity was observed for the minority carriers (electrons in α-NPD and holes in Alq_3). Since the *I–V* characteristics are Ohmic, it shows the mobility values of the minority carriers decrease linearly as a function of the magnetic field.

4. Discussion

We found the decrease in the fluorescent efficiency in organic EL devices proportional to B^2 in the range of 0.1–6.5 T. Such dependence has not been reported to the authors' knowledge.

The EL efficiency (η_{ext}) is given by the following:

$$\eta_{ext} = \alpha \times \Phi_{PL} \times \Phi_{exciton} \times \gamma \quad (1)$$

Here, α, Φ_{PL}, $\Phi_{exciton}$, γ are the light extra efficiency, quantum efficiency of organic material, exciton formation efficiency, and carrier balance factor, respectively.

α is related with the magnetic field via Faraday/Kerr effects with interference. The Faraday rotation of the nonmagnetic and thin organic layers is not significant even at 9 T and interference would not change as a function of magnetic field. Thus we can neglect α. The fluorescent in optically excited organic dyes in the magnetic field has been studied in detail [18], but B^2 dependence in high magnetic field was not reported in the literature. Therefore, our result cannot be explained by Φ_{PL}. Since all known mechanism of MFE on $\Phi_{exciton}$ gives concave dependence on *B* as mentioned earlier, we here tentatively rule out the contribution from $\Phi_{exciton}$ as the main mechanism of the present B^2 dependence.

The remaining factor in Eq. (1) is the charge balance factor. We examined various models to relate the MFE on the charge balance factor, and the following is the only model that can barely explain the B^2 dependence. We observed that the conductance of the minority carrier changes linearly as a function of magnetic field as shown in Fig. 6. We considered various models based on our observation (Fig. 7) that the mobility of the minority carrier (μ) depends upon the magnetic field (B) as

$$\mu = \mu_0(1 - aB) \quad (2)$$

where μ_0 and a are materials dependent constants. Since the EL intensity is determined only by the charge balance if the carrier recombination rate is proportional to the radiation [19], Eq. (2) gives the fluorescent efficiency linearly related with B^1. However, our experiments showed that the current remains almost constant as a function of the magnetic field in the mid–high *B* range. We have found that we can deduce the B^2 dependence from Eq. (2) with additional two assumptions. The assumptions are as follows: (i) the emission region is very narrow and only the recombination at this region contributes to the emission. This is reasonable because Alq_3 layer (200 nm) is much thicker than the thickness of emission region of ordinary devices [20]. The interfacial mixing and the damage caused by the electrode formation might also justify this assumption, (ii) the hole current (J_h) and electron current (J_e) are balanced in the emission region when $B = 0$. Since the mobility of the majority carrier is smaller in Alq_3 than α-

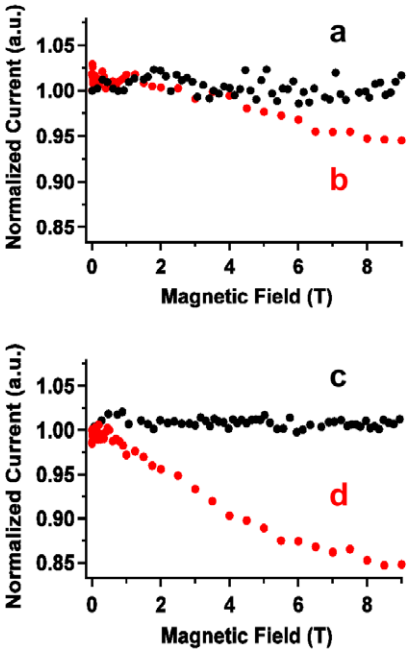

Fig. 7. Magnetic field effect of conductance of unipolar devices (normalized at zero field). (a) Au/α-NPD/Au (holes), (b) Au/Cs/α-NPD/Cs/Au (electrons), (c) Au/Cs/Alq_3/Cs/Au (electrons), and (d) Au/Alq_3/Au (holes).

NPD [21,22], it is believed that the recombination and the emission occurs in Alq_3. This assumption is also reasonable because the device characteristics (Fig. 3), in which turn-on voltage of current is almost the same as that of emission intensity, show that this device has good carrier balance.

Since the current is constant as a function of B, $J_h + J_e$ is constant. From the assumption (ii), $J_h = J_e$ at the emission region when $B = 0$. The emission region is in Alq_3 and Eq. (2) becomes

$$J_h = J_0(1 - aB),$$

where J_0 is a constant.Because $J_h + J_e$ is constant, J_e at the emission region can be written as

$$J_e = J_0(1 + aB).$$

The recombination rate is proportional to $J_h J_e$

$$J_h J_e = J_0^2(1 - aB)(1 + aB) = J_0^2(1 - a^2B^2)$$

and the decrease of the emission proportional to B^2 is explained.

Although this model is based on several assumptions which are not commonly considered so far, we could not think of better ones. We understand that the carrier transport of unipolar devices are not the same as the bipolar devices, for example, charge injection at the electrodes might be strongly involved in the minority carriers. However, our finding of linear MFE on minority carriers has not been reported and no theoretical prediction has been made to the author's knowledge. There might exist other mechanisms which also explain these results, but we hope the present result and discussions may stimulate the study of MFE on organic semiconductors and devices. Although TTA is not likely to work at room temperature and hfc will saturate at relatively low magnetic field, ΔG works at high magnetic field region and might be cooperative with other factors.

There is another mechanism which might explain the B^2 dependence, although it is not consistent with the results on the unipolar devices (Eq. (2)). It is theoretically predicted that the decrease of the conductivity proportional to B^2 is characteristics of magnetoresistance of hopping transport and that it levels off to the B^1 dependence when the magnetic field is high [21]. If it is applicable to the carriers in the emission layer of an OLED, the charge balance of the device will change in the same manner as the conductance and the emission decrease proportional to B^2 will be observed. The difficulty of this model is that we did not see such magnetoconductance in unipolar devices with n-type and p-type organic single layers.

In the range beyond 6.5 T, we observed $B^{1/2}$ dependence (Fig. 5b). In the study of the radical pair in solution, it is known that the density of singlet excitons decreases in proportion to $B^{1/2}$ by Δg mechanism [23]. The magnetoconductance of the minority carriers shown in Fig. 7 start to saturate in the range beyond 6.5 T. Although we do not know the mechanism of this saturation, it might be the reason why $B^{1/2}$ dependence due to Δg mechanism start to appear in this region.

5. Conclusion

We measured EL efficiency of fluorescent and phosphorescent OLEDs in the magnetic field up to 9 T and we found quadratic decrease as a function of the magnetic field between 0.1 and 6.5 T. We also measured magnetoconductance of unipolar devices and observed that only minority carriers show significant magnetoconductance decreasing linearly with the magnetic field (15% at 9 T in Alq_3). $B^{1/2}$ dependence in the range beyond 6.5 T can be explained by MFE on the density of singlet exciton caused by Δg mechanism.

Acknowledgment

This work was supported by GCOE "Chemistry Innovation through Collaboration of Science and Technology" from MEXT, Japan and Shorai Science and Technology Foundation.

References

[1] J. Kalinowski, Organic Electroluminescent Materials and Devices, Gordon Publishers, New York, 1997.
[2] J. Kalinowski, M. Cocchi, D. Virgili, P.D. Marco, V. Fattori, Chem. Phys. Lett. 380 (2003) 710.
[3] J. Kalinowski, M. Cocchi, D. Virgili, V. Fattori, P.D. Marco, Phys. Rev. B 70 (2004) 205303.
[4] Y. Sakaguchi, Y. Iwasaki, T. Osasa, M. Asahi, M. Matsumura, Phys. Rev. B 74 (2006) 195209.
[5] A.H. Davis, K. Bussmann, J. Vac. Sci. Technol. A 22 (2004) 1885.
[6] H. Okada, Y. Okimoto, T. Yamada, H. Okamoto, M. Kawasaki, Y. Tokura, Appl. Phys. Lett. 88 (2006) 123501.
[7] B. Hu, Y. Wu, Nat. Mater. 6 (2007) 985.
[8] P. Desai, P. Shakya, T. Kreouzi, W.P. Gillin, J. Appl. Phys. 102 (2007) 073710.
[9] Y. Shemg, T.D. Nguyen, G. Veeraraghavan, O. Mermer, Phys. Rev. B 75 (2007) 035202.
[10] P. Shakya, P. Desai, M. Somerton, G. Gannaway, T. Kreouzis, W.P. Gillin, J. Appl. Phys. 103 (2008) 103175.
[11] P.A. Bobbert, T.D. Nguyen, F.W.A. van Oost, B. Koopmans, M. Wohlgenannt, Phys. Rev. Lett. 99 (2007) 216801.
[12] P. Desai, P. Shakya, T. Kreouzis, W.P. Gillin, Phys. Rev. B 75 (2007) 094423.
[13] Y.L. Lei, Y. Zhang, R. Lui, P. Chen, Q.L. Song, Z.H. Xiong, Org. Electron. 10 (2009) 889.
[14] R. Liu, Y. Zhang, Y.L. Lei, P. Chen, Z.H. Xiong, J. Appl. Phys. 105 (2009) 093719.
[15] M. Reufer, M.J. Walter, P.G. Lagoudakis, A.B. Hummel, H.S. Kolb, H.G. Roskos, U. Scherf, J.M. Lupton, Nat. Mater. 4 (2005) 340.
[16] H. Hayashi, Y. Sakaguchi, J. Photochem. Photobiol. C: Photochem. Rev. 6 (2005) 25.
[17] D.Y. Kondakov, J. Appl. Phys. 102 (2007) 114504.
[18] R. Katoh, M. Kotani, Chem. Phys. Lett. 196 (1992) 108.
[19] J.C. Scott, S. Karg, S.A. Carter, J. Appl. Phys. 82 (1997) 1454.
[20] C.W. Tang, S.A. Vanslyke, C.H. Chen, J. Appl. Phys. 65 (1989) 3610.
[21] R.G. Kepler, P.M. Beeson, S.J. Jacobs, R.A. Anderson, M.B. Sinclair, V.S. Valencia, P.A. Cahill, Appl. Phys. Lett. 66 (1995) 3618.
[22] N.D. Nguyen, M. Schmeits, H.P. Loebl, Phys. Rev. B 75 (2007) 075307.
[23] Y. Sakaguchi, H. Hayashi, Chem. Phys. Lett. 245 (1995) 591.

spiro-OMeTAD on top of the TiO_2 film. Immediately after solution deposition, the solution fills the pores effectively, and the filling fraction of spiro-OMeTAD inside the pores is the same as the volumetric concentration of the solution. The wet layer on top of the film then acts as a reservoir to increase the filling fraction beyond the macroscopic solubility of spiro-OMeTAD in the solvent. As the solution evaporates, the concentration of spiro-OMeTAD in the reservoir increases, and more spiro-OMeTAD diffuses into the pores. This infiltration process stops when enough solvent has evaporated for the spiro-OMeTAD to become immobile. For thicker films, the maximum filling fraction is further limited kinetically by the quantity of spiro-OMeTAD that can infiltrate into the pores before the critical solution concentration is reached. The filling fraction of thick films may increase if the solution evaporation is slowed down. Doctor-blading allows for slower solvent evaporation than spin coating because it does not introduce rapid air flow during film deposition. The size of the reservoir on top of the dyed TiO_2 film is very important in pore filling. An under-sized reservoir leads to low filling fraction and over-sized reservoir leads to a thick spiro-OMeTAD overlayer. Both scenarios result in suboptimal charge transport. In developing a new deposition technique for HTMs in ss-DSCs, optimizing the reservoir size is required to maximize performance.

2.2. Effect of solution concentration

The first parameter we varied in optimizing the reservoir size is the spiro-OMeTAD solution concentration. We performed pore filling on TiO_2 films with two different thicknesses (2.5 and 5.0 μm) and compared the filling fraction from doctor-blading and spin coating. The parameters for doctor-blading are documented in the experimental section. The detailed procedure for measuring the filling fraction is reported elsewhere [18]. First, the overlayer thickness is measured with SEM cross-section. Then, the sample is immersed in a known volume of chlorobenzene to dissolve the spiro-OMeTAD out from the pores. The spiro-OMeTAD can be quantified by measuring the absorption in the solution phase.

Fig. 1a and b shows the filling fraction and overlayer thickness of 2.5- and 5-μm thick TiO_2 films as a function of spiro-OMeTAD solution concentration. It shows that a solution concentration below 270 mg/mL results in an under-sized reservoir (evident from the absence of overlayer) and low filling fraction. When the solution concentration was raised above 360 mg/mL, there was a spiro-OMeTAD overlayer on top of TiO_2 film. The formation of an overlayer usually indicates that the filling fraction can no longer be increased by increasing solution concentration [18]. Indeed, when the solution concentration was further

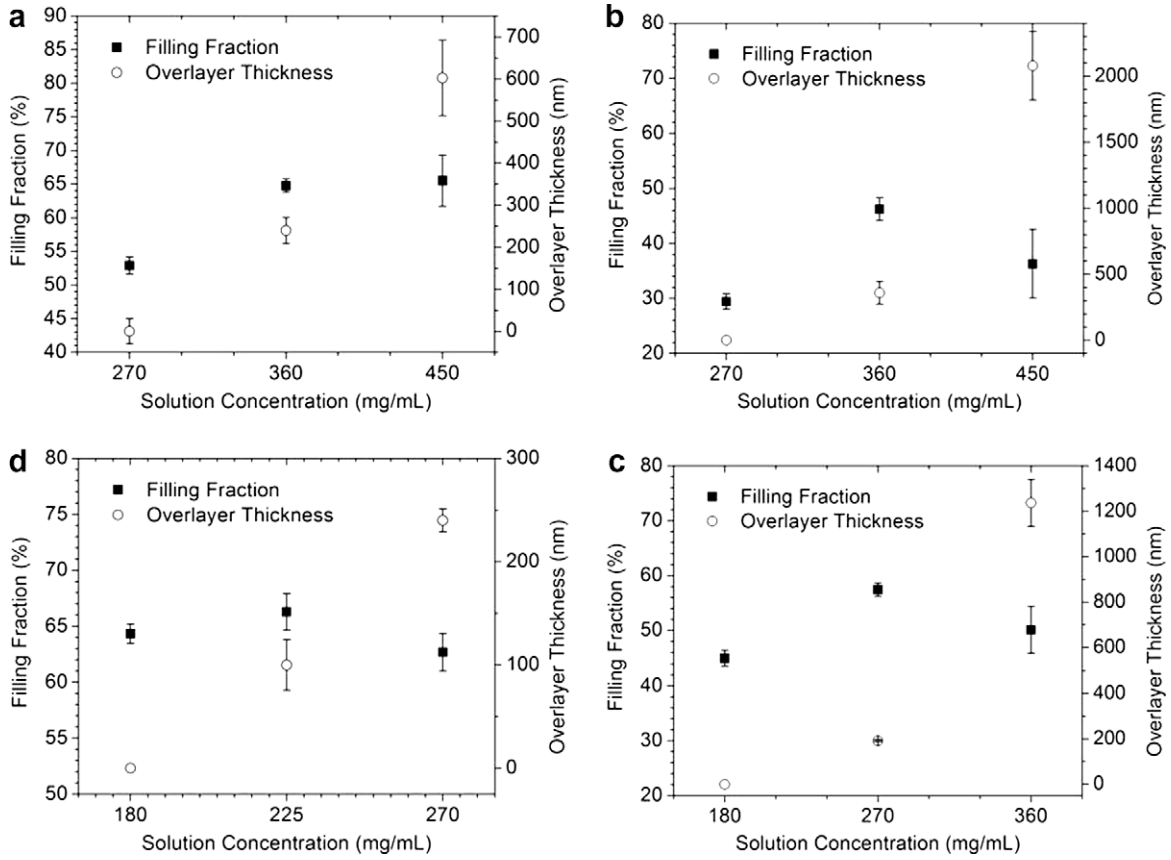

Fig. 1. Filling fractions and overlayer thicknesses of TiO_2 films with two different thicknesses and spiro-OMeTAD deposition techniques. (a) 2.5 μm, doctor-blading; (b) 5.0 μm, doctor-blading; (c) 2.5 μm, spin coating; (d) 5.0 μm, spin coating.

increased to 450 mg/mL, the filling fraction remained relatively constant and the overlayer became much thicker.

The 5-μm thick TiO_2 film infiltrated with 450 mg/mL solution appears to have lower filling fraction than other samples. The reason is as follows: in measuring the filling fraction, the spiro-OMeTAD in the pores is calculated by the total spiro-OMeTAD amount minus the amount presented in the overlayer. When the overlayer thickness becomes comparable with TiO_2 film thickness, any error in overlayer thickness measurement causes large error in the filling fraction.

For comparison purposes, the filling fractions and overlayer thicknesses of samples filled with spin coating are shown in Fig. 1c and d. For spin coating, the optimized solution concentration depends strongly on the TiO_2 film thickness. The optimized solution concentration changed from 180 mg/mL for 2.5-μm thick TiO_2 films to 270 mg/mL for 5-μm thick films. Also, for 2.5-μm thick TiO_2 films, doctor-blading at room temperature can already attain a filling fraction around 65%, which is comparable to the value obtained from spin coating. However, for 5-μm thick TiO_2 films, the filling fraction from doctor-blading at room temperature is lower than that obtained from spin coating. To increase the filling fraction, the spiro-OMeTAD solution is doctor-bladed at elevated temperature.

2.3. Effect of solution temperature

The advantages of doctor-blading at an elevated temperature are twofold: it lowers the solution viscosity and increases the solubility of spiro-OMeTAD in chlorobenzene. Both factors facilitate the infiltration of spiro-OMeTAD and consequently increase the filling fraction.

The effect of increasing the doctor-blading temperature on the filling fraction of 5-μm TiO_2 films is shown in Fig. 2. When the temperature was raised from 20 to 80 °C, the filling fraction increased from 46% to 53%, while the overlayer thicknesses remained relatively unchanged. The filling fraction of 53% at 80 °C is comparable with the value obtained from optimized spin-coating condition as shown in Fig. 1d. We note that increasing the deposition temperature only increased filling fraction for doctor-blading samples and not for spin-coating samples, possibly because spin-coating samples cool much more rapidly. It is conceivable that raising the temperature even higher may further increase filling fraction. However, when the temperature was raised to 100 °C, the rapid evaporation of chlorobenzene made the doctor-blading process hard to control and resulted in non-uniform overlayers. Therefore, we stopped the temperature study at 80 °C and used this temperature in the fabrication of the solar cell.

2.4. Solar cell performance

After deposition of spiro-OMeTAD, the silver electrodes were thermally evaporated onto the sample, and the *J–V* curves of the solar cell were measured under simulated one-sun illumination. Fig. 3 shows the current density–voltage (*J–V*) curves of devices made from doctor-blading and spin coating. The two deposition techniques give approximately equal device efficiencies, which is expected because of the equal filling fractions. Devices from doctor-blading tend to have a slightly higher fill factor and lower open-circuit voltage compared with spin coating. The nature of these differences is outside the scope of this study, but it is possible that these differences resulted from different spiro-OMeTAD overlayer thicknesses of films deposited by doctor-blading and spin coating.

The reproducibility of the device performances from doctor-blading was also tested. For each device thickness, we made at least four identical devices, and the standard deviations of the efficiencies were within 7%. Table 1 compares the average device performances of ss-DSCs made from two spiro-OMeTAD deposition techniques.

In addition to delivering equally efficient devices as spin coating, doctor-blading also uses far less material. The loss of coating solution can be as high as 95% for spin coating [20] and as low as 5% for doctor-blading [21]. The efficient usage of materials by doctor-blading is demonstrated for

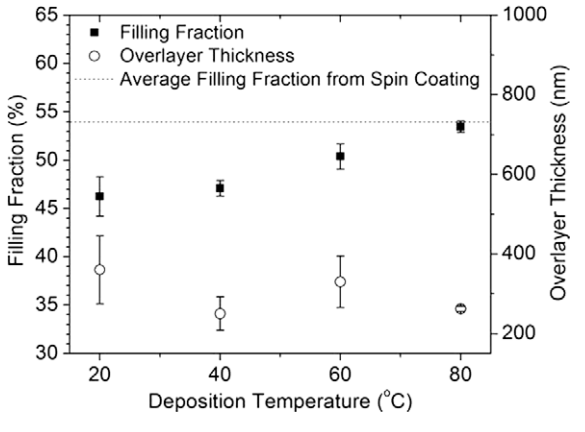

Fig. 2. Filling fractions and overlayer thicknesses of 5-μm thick TiO_2 films doctor-bladed at different temperatures with 360 mg/mL spiro-OMeTAD solution in chlorobenzene. The dotted line indicates the average filling fraction of 5-μm thick TiO_2 films from spin coating.

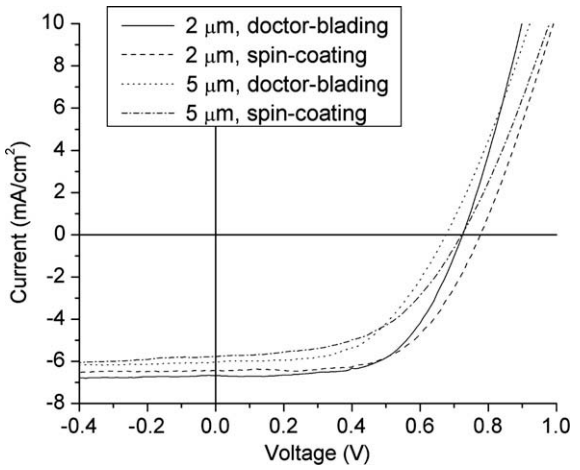

Fig. 3. Current density–voltage (*J–V*) curves of solid-state dye-sensitized solar cells made from doctor-blading and spin-coating spiro-OMeTAD. Two different device thicknesses were tested: 2 and 5 μm.

Table 1
The device performance of ss-DSCs made from spin coating and doctor-blading deposition of spiro-OMeTAD. The values shown above are averaged values and standard deviations of at least four devices made under identical conditions.

	Jsc (mA/cm^2)	Voc (V)	Efficiency (%)	Fill factor
2 μm, doctor-blading	6.86 ± 0.37	0.73 ± 0.01	3.01 ± 0.13	0.61 ± 0.03
2 μm, spin coating	6.80 ± 0.26	0.76 ± 0.03	3.02 ± 0.16	0.58 ± 0.02
5 μm, doctor-blading	5.88 ± 0.45	0.68 ± 0.01	2.13 ± 0.13	0.54 ± 0.02
5 μm, spin coating	5.77 ± 0.90	0.71 ± 0.02	2.00 ± 0.10	0.49 ± 0.04

our relatively small device areas as well. For 5-μm thick TiO_2 films (1.5 cm by 2 cm), we used 35 μL of 270 mg/mL spiro-OMeTAD solution for spin coating, and 10 μL of 360 mg/mL solution for doctor-blading; in this case, doctor-blading uses 60% less spiro-OMeTAD than spin coating. When the device area is further increased, the reduction of material usage by doctor-blading will be much more pronounced.

2.5. Directions to improve filling fraction

The optimized thickness of ss-DSCs is approximately 2 μm due to the compromise between light absorption and charge collection [19]. Devices made with TiO_2 films thicker than 4 μm are usually less than 2% [22]. In contrast, the 5-μm thick ss-DSCs reported here, made from either doctor-blading or spin-coating concentrated spiro-OMeTAD solution, achieved an average efficiency well over 2%. We propose that the improved efficiency results directly from the enhanced filling fraction. When spiro-OMeTAD is deposited on 5-μm thick TiO_2 film by conventional recipe of spin coating a 180 mg/mL solution, the filling fraction is extrapolated to be only 41% [18], much lower than the 53% filling fraction reported in our optimized recipe. This indicates that one of the possible directions of improving the performance of thick ss-DSCs is to increase the filling fraction because higher filling fraction results in better charge collection. However, the fact that 5-μm thick devices still have a lower short-circuit current and open-circuit voltage than 2-μm thick ones means there is room for improvement.

It is instructive to consider what limits the filling fraction at values substantially below unity. For 2-μm films, we found that changing the particle size from 20 to 45 nm does not increase the filling fraction. This indicates the filling fraction for 2 μm films is not limited by the constrictions inside the porous network, but by the viscosity-concentration curve of the spiro-OMeTAD solution. We propose that when the spiro-OMeTAD-chlorobenzene mixture contains 65% spiro-OMeTAD by volume, the viscosity is too high for spiro-OMeTAD to easily diffuse; this is when the infiltration stops. If this hypothesis is right, it has the following implications: (1) solution-based infiltration methods will never be able to achieve 100% filling fraction because there have to be some solvent molecules inside the HTM film to make HTM molecules mobile. Void formation occurs when the solvent molecules evaporates. (2) To get to 100% filling fraction, a solvent-free method such as melt infiltration has to be used [23,24]. Unfortunately spiro-OMeTAD has very high melting temperature (248 °C as determined by differential scanning calorimetry), which makes it impossible to be used for melt infiltration since the sensitizing dye is damaged at this temperature [25]. To get to 100% filling fraction, new HTMs that have lower glass transition temperatures and stay amorphous even when being heated above T_g must be developed [26].

Despite the aforementioned fundamental limitation of spiro-OMeTAD pore filling, the filling fraction for thick films can still be improved by optimizing the solution deposition techniques. It was mentioned previously in Section 2.1 that using doctor-blading to deposit spiro-OMeTAD solution results in a slower evaporation, which gives spiro-OMeTAD more time to infiltrate prior to the drying of solution. In our previous studies, slowing down the evaporation by decreasing the spin-coating speed appears to improve filling fraction [18]. However, in this study, the slightly slower evaporation rate from doctor-blading did not result in substantial increase of filling fraction. A more detailed study on the evaporation rate and its influence on pore filling with doctor-blading deposition will be necessary to further optimize this technique. We have tried treating the deposited spiro-OMeTAD film with solvent vapor to soften the film to enhance diffusion [27], but it led to extensive crystallization of spiro-OMeTAD that can be observed in the optical microscope, which hurts the device performance. Other possible methods to accomplish higher filling fraction include switching to a high boiling point solvents during doctor-blading or spin coating.

3. Conclusions

We have demonstrated the use of doctor-blading to deposit spiro-OMeTAD in solid-state dye-sensitized solar cells. After optimizing the solution concentration and temperature, we achieved an equal pore filling fraction with doctor-blading and spin coating for 2.5 and 5-μm thick films. The efficiencies of devices made with these two deposition techniques are comparable, and the materials utilization of spiro-OMeTAD is significantly better for doctor-blading. This demonstrates the potential for doctor-blading to be used in future commercial production of solid-state dye-sensitized solar cells.

4. Experimental

4.1. Sample preparation

FTO substrates (Hartford Glass TEC 15) were first patterned through etching with Zinc powder and HCl (12%). Then, the substrates were cleaned by sonication sequentially in 10% Extran solution, acetone and isopropanol [28]. Samples used for solar cell measurements were coated with a compact layer of TiO_2 (50 nm) by aerosol spray pyrolysis using air as carrier gas [29]. Mesoporous

TiO_2 films were then deposited from commercially-available paste (Dyesol 18NR-T) using screen-printing. These sheets were slowly heated to 500 °C and baked for 30 min in air. Samples used for solar cell measurements are treated with acidic $TiCl_4$ solution [30] by immersing the samples in 0.02 M $TiCl_4$ aqueous solution overnight at room temperature. The samples were then heated to 450 °C and subsequently cooled to 80 °C before being immersed in Z907 dye solution for 12–18 h. The dye solution comprised of 0.3 mM of Z907 (Solaronix SA) in 1:1 mixture of acetonitrile and tert-butyl alcohol. Prior to making the solution, Z907 dye has been purified by column chromatography following published procedure [31].

4.2. Spiro-OMeTAD infiltration

The formulation of spiro-OMeTAD solution has been published elsewhere [18]. For spin coating, a small quantity (30–50 μL) of the spiro-OMeTAD solution was deposited onto each TiO_2 film (1.5 cm by 2 cm) at room temperature and left for 1 min before spin coating at 2000 rpm for 45 s in air. Doctor-blading was done with a commercially-available machine (CX-4 motorized film applicator, mtv Messtechnik oHG) with blade speed of 15 mm/s. The blade height was controlled by adjusting the screws on the doctor-blade (UA 3000 universal film applicator, mtv Messtechnik oHG). The blade height was 40 μm for TiO_2 films of 2 μm thick, and 80 μm for TiO_2 films of 5-μm thick. The solution (10 μL) was first deposited using a micropipette onto an area of the FTO substrate not covered by TiO_2, then spread onto TiO_2 film with doctor-blade. For the temperature-dependence experiment, we first put the both the spiro-OMeTAD solution and the TiO_2 film on top of a hot plate that has been set to the desired temperature, and let the system equilibrate for 5 min. Then, the TiO_2 film was transferred onto the doctor-blading machine and the solution was immediately deposited. We note that because the doctor-blading machine does not contain a heating element, the true doctor-blading temperature may be slightly lower than the value reported. After spiro-OMeTAD deposition, the film was left to dry overnight in air at room temperature.

4.3. Device fabrication and photovoltaic measurements

For efficiency measurements, silver electrodes (200 nm) were thermally evaporated onto the film under vacuum below 10^{-6} torr.

Current density–voltage (J–V) measurements were carried out with a Keithley 2400 source meter and a 91160 300 W Oriel solar simulator equipped with a 6258 ozone-free Xenon arc lamp and an air mass (AM 1.5 G) filter. The lamp intensity was measured with an NREL calibrated silicon photodiode, with spectral mismatch accounted for.

Acknowledgements

This publication was partially based on work supported the Center for Advanced Molecular Photovoltaics (Award No. KUS-C1-015-21), made by King Abdullah University of Science and Technology (KAUST). It was also partially supported by the Office of Naval Research. We thank Brian E. Hardin for valuable discussions. I.-K. Ding is supported by a Chevron Stanford Graduate Fellowship.

References

[1] C.Y. Chen, M. Wang, J.Y. Li, N. Pootrakulchote, L. Alibabaei, N.-L. Cevey-Ha, J.D. Decoppet, J.H. Tsai, C. Gratzel, C.G. Wu, S.M. Zakeeruddin, M. Grätzel, Highly efficient light-harvesting ruthenium sensitizer for thin-film dye-sensitized solar cells, ACS Nano 3 (2009) 3103–3109.
[2] B.C. O'Regan, M. Grätzel, A low-cost, high-efficiency solar cell based on dye-sensitized colloidal TiO_2 films, Nature 353 (1991) 737–740.
[3] J.R. Durrant, S.A. Haque, E. Palomares, Towards optimisation of electron transfer processes in dye sensitised solar cells, Coord. Chem. Rev. 248 (2004) 1247–1257.
[4] M. Grätzel, Photoelectrochemical cells, Nature 414 (2001) 338–344.
[5] A.F. Nogueira, C. Longo, M.A. De Paoli, Polymers in dye sensitized solar cells: overview and perspectives, Coord. Chem. Rev. 248 (2004) 1455–1468.
[6] U. Bach, D. Lupo, P. Comte, J.E. Moser, F. Weissortel, J. Salbeck, H. Spreitzer, M. Grätzel, Solid-state dye-sensitized mesoporous TiO_2 solar cells with high photon-to-electron conversion efficiencies, Nature 395 (1998) 583–585.
[7] J.-H. Yum, P. Chen, M. Grätzel, M.K. Nazeeruddin, Recent developments in solid-state dye-sensitized solar cells, ChemSusChem 1 (2008) 699–707.
[8] S.-J. Moon, J.-H. Yum, R. Humphry-Baker, K.M. Karlsson, D.P. Hagberg, T. Marinado, A. Hagfeldt, L. Sun, M. Grätzel, M.K. Nazeeruddin, Highly efficient organic sensitizers for solid-state dye-sensitized solar cells, J. Phys. Chem. C 113 (2009) 16816–16820.
[9] H.J. Snaith, L. Schmidt-Mende, Advances in liquid-electrolyte and solid-state dye-sensitized solar cells, Adv. Mater. 19 (2007) 3187–3200.
[10] H.J. Snaith, A.J. Moule, C. Klein, K. Meerholz, R.H. Friend, M. Grätzel, Efficiency enhancements in solid-state hybrid solar cells via reduced charge recombination and increased light capture, Nano Lett. 7 (2007) 3372–3376.
[11] M. Wang, S.-J. Moon, M. Xu, K. Chittibabu, P. Wang, N.-L. Cevey-Ha, R. Humphry-Baker, S.M. Zakeeruddin, M. Grätzel, Efficient and stable solid-state dye-sensitized solar cells based on a high-molar-extinction-coefficient sensitizer, Small 6 (2009) 319–324.
[12] J.-H. Yum, B.E. Hardin, S.-J. Moon, E. Baranoff, F. Nüesch, M.D. McGehee, M. Grätzel, M.K. Nazeeruddin, Panchromatic response in solid-state dye-sensitized solar cells containing phosphorescent energy relay dyes, Angew. Chem. Int. Ed. 48 (2009) 9277–9280.
[13] Y.H. Chang, S.R. Tseng, C.Y. Chen, H.F. Meng, E.C. Chen, S.F. Horng, C.S. Hsu, Polymer solar cell by blade coating, Org. Electron. 10 (2009) 741–746.
[14] P. Schilinsky, C. Waldauf, C.J. Brabec, Performance analysis of printed bulk heterojunction solar cells, Adv. Funct. Mater. 16 (2006) 1669–1672.
[15] M. Kaelin, D. Rudmann, A.N. Tiwari, Low cost processing of CIGS thin film solar cells, Sol. Energy 77 (2004) 749–756.
[16] L. Schmidt-Mende, M. Grätzel, TiO_2 pore-filling and its effect on the efficiency of solid-state dye-sensitized solar cells, Thin Solid Films 500 (2006) 296–301.
[17] D.M. Huang, H.J. Snaith, M. Gratzel, K. Meerholz, A.J. Moule, Optical description of solid-state dye-sensitized solar cells. II. Device optical modeling with implications for improving efficiency, J. Appl. Phys. 106 (2009) 073112.
[18] I.-K. Ding, N. Tetreault, J. Brillet, B.E. Hardin, E.H. Smith, S.J. Rosenthal, F. Sauvage, M. Gratzel, M.D. McGehee, Pore-filling of spiro-OMeTAD in solid-state dye sensitized solar cells: quantification, mechanism, and consequences for device performance, Adv. Funct. Mater. 19 (2009) 2431–2436.
[19] H.J. Snaith, R. Humphry-Baker, P. Chen, I. Cesar, S.M. Zakeeruddin, M. Grätzel, Charge collection and pore filling in solid-state dye-sensitized solar cells, Nanotechnology 19 (2008) 424003.
[20] C.J. Brabec, J.R. Durrant, Solution-processed organic solar cells, MRS Bull. 33 (2008) 670–675.
[21] F.C. Krebs, Fabrication and processing of polymer solar cells: a review of printing and coating techniques, Sol. Energy Mater. Sol. Cells 93 (2009) 394–412.
[22] L. Schmidt-Mende, S.M. Zakeeruddin, M. Grätzel, Efficiency improvement in solid-state-dye-sensitized photovoltaics with an amphiphilic ruthenium-dye, Appl. Phys. Lett. 86 (2005) 013504.

[23] K. Fredin, E.M.J. Johansson, T. Blom, M. Hedlund, S. Plogmaker, H. Siegbahn, K. Leifer, H. Rensmo, Using a molten organic conducting material to infiltrate a nanoporous semiconductor film and its use in solid-state dye-sensitized solar cells, Synth. Met. 159 (2009) 166–170.
[24] K.M. Coakley, Y. Liu, M.D. McGehee, K.L. Frindell, G.D. Stucky, Infiltrating semiconducting polymers into self-assembled mesoporous titania films for photovoltaic applications, Adv. Funct. Mater. 13 (2003) 301–306.
[25] K. Fredin, K.F. Anderson, N.W. Duffy, G.J. Wilson, C.J. Fell, D.P. Hagberg, L. Sun, U. Bach, S.-E. Lindquist, Effect on cell efficiency following thermal degradation of dye-sensitized mesoporous electrodes using N719 and D5 sensitizers, J. Phys. Chem. C 113 (2009) 18902–18906.
[26] M.Y. Lo, C. Zhen, M. Lauters, G.E. Jabbour, A. Sellinger, Organic-inorganic hybrids based on pyrene functionalized octavinylsilsesquioxane cores for application in OLEDs, J. Am. Chem. Soc. 129 (2007) 5808–5809.
[27] F. Pschenitzha, J.C. Sturm, Three-color organic light-emitting diodes patterned by masked dye diffusion, Appl. Phys. Lett. 74 (1999) 1913–1915.
[28] G.F. Burkhard, E.T. Hoke, S.R. Scully, M.D. McGehee, Incomplete exciton harvesting from fullerenes in bulk heterojunction solar cells, Nano Lett. 9 (2009) 4037–4041.
[29] H.J. Snaith, M. Grätzel, The role of a "Schottky Barrier" at an electron-collection electrode in solid-state dye-sensitized solar cells, Adv. Mater. 18 (2006) 1910–1914.
[30] P.M. Sommeling, B.C. O'Regan, R.R. Haswell, H.J.P. Smit, N.J. Bakker, J.J.T. Smits, J.M. Kroon, J.A.M. van Roosmalen, Influence of the $TiCl_4$ treatment on nanocrystalline TiO_2 films in dye-sensitized solar cells, J. Phys. Chem. B 110 (2006) 19191–19197.
[31] P. Wang, B. Wenger, R. Humphry-Baker, J.-E. Moser, J. Teuscher, W. Kantlehner, J. Mezger, E.V. Stoyanov, S.M. Zakeeruddin, M. Grätzel, Charge separation and efficient light energy conversion in sensitized mesoscopic solar cells based on binary ionic liquids, J. Am. Chem. Soc. 127 (2005) 6850–6856.

sensitive to oxidizing species [16,17], even at very low concentrations [18] and insensitive to reducing gases [19]. Among all gases present in atmospheric air, only NO_2 and O_3 induce significant electrical responses [20]. Consequently, these organic materials provide to sensing devices a first level of selectivity.

We have previously demonstrated that the selective and real-time monitoring of O_3 in atmosphere can be achieved using the faster kinetics of reaction between O_3 and copper phthalocyanine (CuPc) thin films as compared to NO_2 [21]. As complementary, the selective measurement of NO_2 could be achieved by means of chemical filters removing O_3 from air sample and being chemically inert toward the target gas. Because of their high reactivity with O_3, organic dyes like indigo and its derivatives are relevant [22–24]. Indeed, the carbon–carbon double bond of indigo molecules strongly reacts with O_3 through an ozonolysis process, leading to the irreversible formation of isatin groups [25]. However, in previous published papers, the use of indigo as filter was limited to cartridges [26] or impregnated membranes placed upstream the sensing device.

This paper is focused on the development of an all-organic gas microsensor dedicated to the selective monitoring of NO_2 at low concentrations. The innovation of this work is based on the realization of indigo thin films by thermal evaporation as integrated O_3 filter onto semiconductor chemical gas sensors. As compared to filtering cartridges, the strong interests of the development of integrated filters are an easiest miniaturization of the device, a higher level of mobility and the possibility to improve filtering efficiency by working at higher temperature not requiring additional heating system.

The filtering yield of indigo powder was firstly established. After filtering film characterization by FT-IR spectroscopy, electrical responses of sensor have been determined toward oxidizing pollutants. The metrological characteristics will be discussed. The influence of indigo film thickness on electrical response was investigated too.

2. Experimental

2.1. Device

The design of the gas sensor is reported in Fig. 1. The sensitive layer is a 300 nm thin film of copper phthalocyanine, CuPc and the filtering membrane consists in a thin film of indigo with thickness in the range 10–100 nm. These two organic layers have been successively realized from commercial powder by thermal sublimations. The deposition processes have been performed by means of a commercial high vacuum thin film evaporator (VE-770, VEECO) into a specific chamber maintained into secondary vacuum (residual pressure close to 2×10^{-6} mbar). Thin film thickness and deposition rate have been measured by in situ quartz crystal microbalance maintained at room temperature and controlled by means of a commercial automatic deposition control system (ADS-220, VEECO). To obtain homogenous thin films, the deposition rate was set to 0.2 nm s^{-1}.

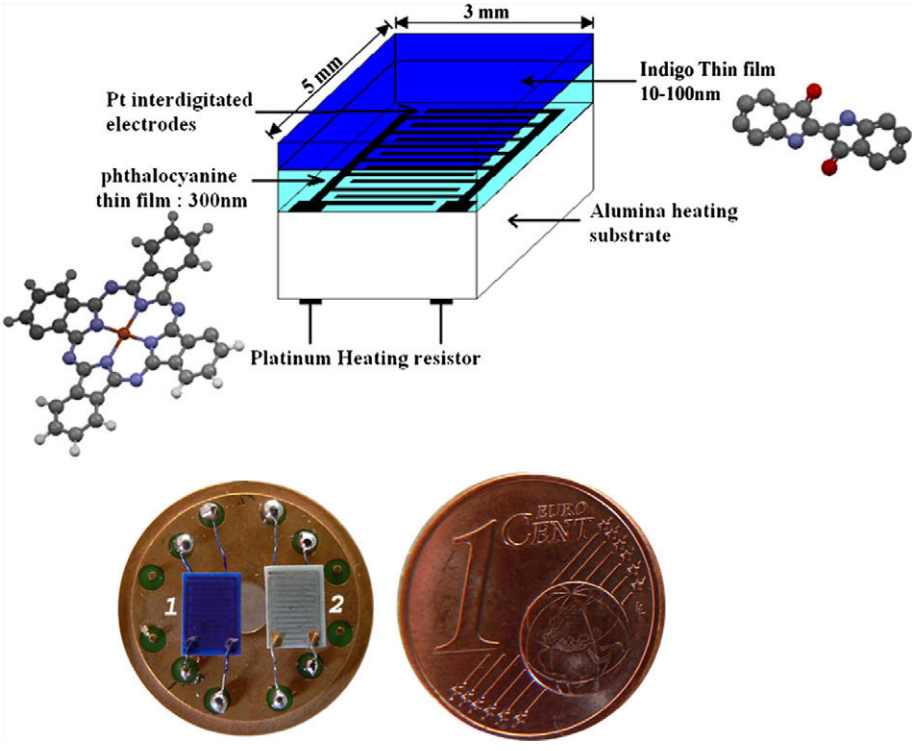

Fig. 1. Scheme of the all-organic sensor structure; (1) CuPc (300 nm)/indigo (50 nm) sensor device; (2) indigo (50 nm) thin film onto alumina substrate with screen-printed interdigitated electrodes.

This organic bi-layer system was realized onto $5 \times 3 \times 0.6\ mm^3$ alumina substrates maintained at room temperature. These substrates included screen-printed platinum interdigitated electrodes on the upper side to measure phthalocyanine electronic conductivity and Pt heating resistor with a predefined thermal coefficient = $2–3 \times 10^{-3}\ °C^{-1}$ on the lower side to control device temperature. No consecutive post-deposition annealing was realized to obtain more sensitive layers [27]. The dimensions of the interdigitated electrodes being perfectly determined (L: length = 25 mm; l_s: inter-electrode space = 0.125 mm), the CuPc electronic conductivity $\boldsymbol{\sigma}$ of thin film with thickness **e** can be determined from electrical current **I** passing through the sensor polarized under bias voltage **U** according to the following equation:

$$\boldsymbol{\sigma} = \frac{\mathbf{I} \cdot l_s}{\mathbf{U} \cdot L \cdot \mathbf{e}} \quad (2)$$

Electrical conductivity being an intrinsic parameter of materials, i.e., both independent from layer thickness, polarization conditions and electrode dimensions, sensor response will be defined as conductivity variations versus time.

2.2. FT-IR characterization

Indigo thin films were investigated and compared to powdered sample by a THERMO NICOLET 5700 FT-IR spectrometer in the range 400–4000 cm^{-1} with 4 cm^{-1} resolution. Thin films were realized by thermal evaporation under secondary vacuum on transparent silicon substrates without any subsequent thermal or gas treatment.

2.3. Gas exposures

For measurements under gas, two experimental test benches have been developed. The first was devoted to the determination of filtering yield of indigo powder towards O_3 and NO_2. Indigo powder was put into a polytetrafluorethylene (PTFE) exposition chamber between two PTFE filter membranes with low porosity (pore size = 5 μm). O_3 was delivered and monitored, respectively, by ozone generator and UV photometric commercial analyzer (ozone analyzer with internal ozone generator Thermo Electron Corporation, model 49i). NO_2 in air was delivered by commercial calibrated cylinders (MESSER France) and monitored by chemiluminescent NO_x analyzer (Thermo Electron Corporation, model 42i). Experiments in a large concentration scale were possible by dilution under pure and dried air by means of mass flow controllers. A three-way solenoid valve driven by an external timer has allowed the cyclic quantification of gas concentrations upstream and downstream the filter and consequently the determination of the filtering yield.

The second experimental bench was devoted to the determination of the sensing performances of all-organic gas sensor prototypes. A schematic representation and a complete description of this apparatus have been already reported [21]. Sensors were put in a PTFE exposure chamber, polarized under 1.5 V d.c. via interdigitated electrodes and regulated at 80 °C. At the chamber output, commercial gas analyzers have monitored in real-time O_3 and NO_x concentrations. Studied concentrations range was 20–200 ppb and all experiments have been realized under dry atmosphere (RH < 2%).

3. Results and discussion

3.1. Filtering efficiency

If the high filtering yield of indigo toward O_3 is well-established, its behaviour toward NO_2 must be determined for such application. Fig. 2 represents the filtering yield of indigo powder at room temperature versus gas concentration for NO_2 and O_3 exposures. The filtering yield $\boldsymbol{\eta}$ and its uncertainty are then defined by the following equations:

$$\boldsymbol{\eta} = (C_{\text{upstream}} - C_{\text{downstream}})/C_{\text{upstream}} \quad (3)$$

$$\Delta\boldsymbol{\eta} = \boldsymbol{\eta} \cdot \frac{C_{\text{upstream}} \cdot \Delta C_{\text{downstream}} + C_{\text{downstream}} \cdot \Delta C_{\text{upstream}}}{C_{\text{upstream}}(C_{\text{upstream}} - C_{\text{downstream}})} \quad (4)$$

with concentration uncertainties (ΔC) determined according to analyzer manufacturer data. Taking into account the determination method of yield uncertainty, this later is obtained in the worst case and obviously overestimated.

The great reactivity of indigo with O_3 molecules is confirmed by the high filtering yields in the overall investigated concentration range. Whatever the concentration, the O_3 filtering yield remains constant at 99%. Taking into consideration the value with their errors, the filtering yield of indigo is close to 100%.

For NO_2, the filtering yield is between (5 ± 5)% and (8 ± 2)%, the highest yields being determined at the highest concentrations. The highest errors are obtained at lowest concentrations and are intrinsic to the commercial analyzers. Thus, between 20 and 200 ppb, a concentration range commonly measured in urban atmosphere, indigo powder exhibits total ozone filtering with a high level of selectivity. After 100 ppm h of gas exposure, this trend remains unaltered.

3.2. IR characterization of indigo thin film

Thermal evaporation is a simple method to realize thin films. Nevertheless, it's necessary to check that no chemical decomposition occurs during the thermal process. Therefore, just after thermal evaporation, the nature of the thin films was characterized by FT-IR spectroscopy. Fig. 3 represents IR spectra of powder and of as-prepared 50- and 100-nm thick films of indigo in the 400–3500 cm^{-1} range. No major difference is noticed between spectra obtained with 50 nm of indigo and with 100 nm. So, the thickness is not influent on the chemical composition of the layer. Moreover, spectra of powder and films are closely similar. Both wavenumbers and relative intensities of the various vibration bands being similar, chemical bonding and molecular interactions are nearly similar in the powdered and layered samples. That justify that the powder and the thin films correspond to the same material. So, indigo molecules are not altered by its thermal sublimation. The most important difference between

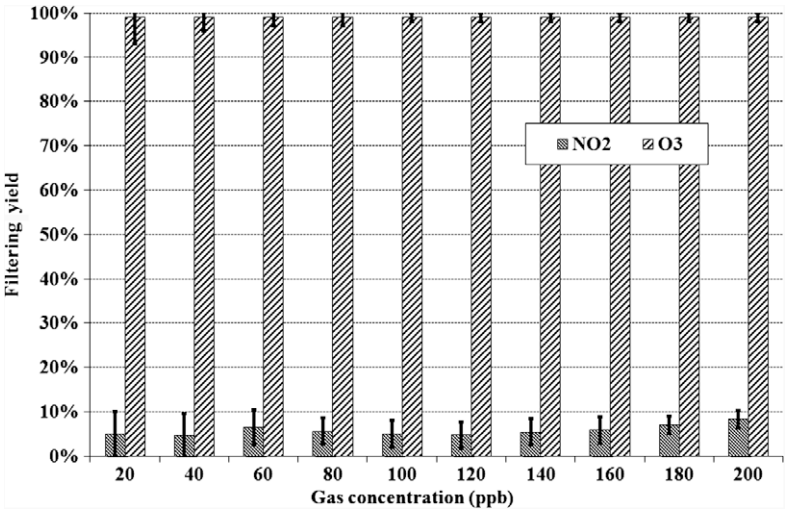

Fig. 2. Filtering power of indigo powder versus nitrogen dioxide (NO_2) and ozone (O_3) concentrations in the 20–200 ppb range, determined at room temperature.

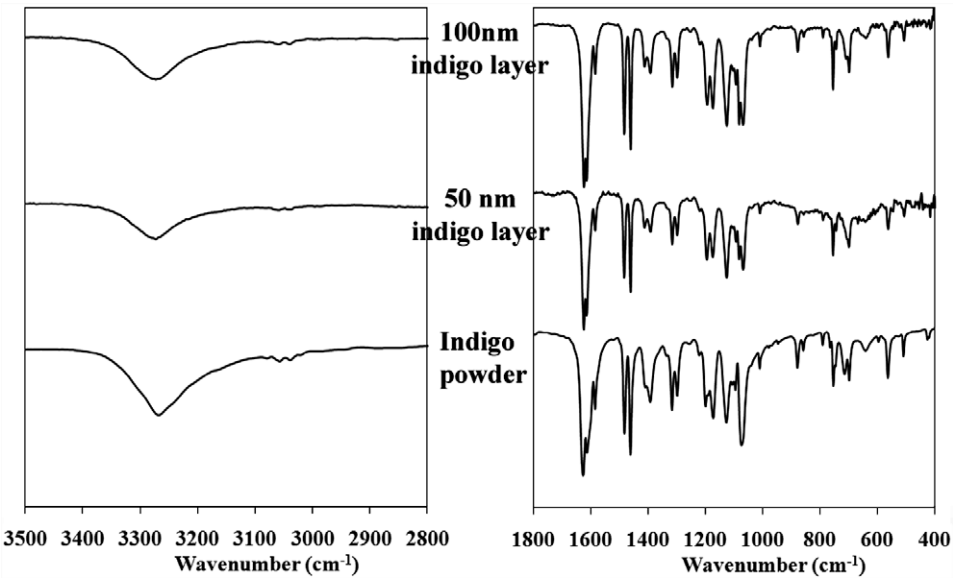

Fig. 3. FT-IR spectra of indigo powder, 50 and 100 nm as-prepared thin films on transparent Si in the 400–3500 cm^{-1} range.

powder and thin films appears on the spectra at 1060–1100 cm^{-1}. Such disparity can be attributed to carbon–oxygen bonds. This is interpreted as a weak unintentional oxidation of indigo layers by atmospheric air before FT-IR analysis. Nevertheless, this phenomenon of weak extend should be mainly localized at the surface [17].

3.3. Gas responses

To reach a NO_2 selective response, it becomes necessary to optimize the indigo layer thickness. Indeed, a too thin filtering film would induce a non-negligible sensor response to O_3 while a too thick film could prevent the diffusion of NO_2 molecules to the sensing element inducing low sensor sensitivity. Fig. 4 represents the conductivity variations versus time of 300 nm CuPc layer with and without additional upper indigo layer, exposed to 75 ppb of ozone during 2 h with consecutive return under purified air. Two thicknesses have been reported, i.e., 10 and 50 nm, and experimental results were obtained for sensors maintained at 80 °C. This figure highlights various phenomena occurring on the devices. During the initialization stage, the initial electrical conductivity of copper phthalocyanine sensitive film determined under purified air decreases with indigo thickness. The authors interpret this behaviour as a protection effect of the sensitive film by the filtering layer. Indeed, the conductivity of metallophthalocyanines is predominantly extrinsic and due to

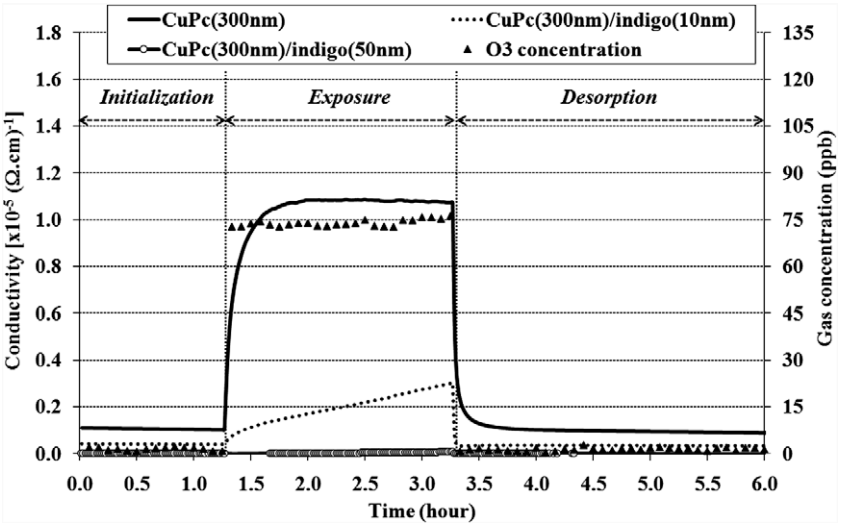

Fig. 4. Electronic conductivity versus time of CuPc (300 nm) thin film with and without upper integrated indigo filtering layer exposed to 75 ppb of ozone in purified air at 80 °C.

doping process by oxidizing species like O_2, NO_2 and O_3. In our case, because the devices were not maintained in confined atmosphere prior to tests under gas, indigo thin film prevents the non-intentional exposure of CuPc to O_3 and therefore, contributes to lower value of initial conductivity. Thicker is the filtering layer, lower is the initial conductivity.

During exposure, whereas for 10 nm indigo film sensor response is strongly reduced, no significant response toward O_3 was measured above 50 nm. This thickness is sufficient to prevent the diffusion of ozone through the filtering layer to the sensitive element and to involve all O_3 molecules in ozonolysis reaction with indigo molecular units. Moreover, during desorption step, the conductivity measured after exposure remains constant and equal to the initial value. So, the reaction products of ozonolysis, i.e., isatin groups, have no influence on the electrical conductivity of the sensitive film. As a consequence, integrated indigo thin film with thickness as high as 50 nm acts as a total O_3 filter and no sensor response is measured when this pollutant is present in air.

To demonstrate the selectivity of our all-organic device, sensor responses for the target and major interfering gases, obtained in the same working conditions, have been compared. Fig. 5 represents conductivity variations versus time of CuPc (300 nm)/indigo (50 nm) bi-layer structure maintained at 80 °C and consecutively exposed to the same NO_2 and O_3 increasing concentrations during

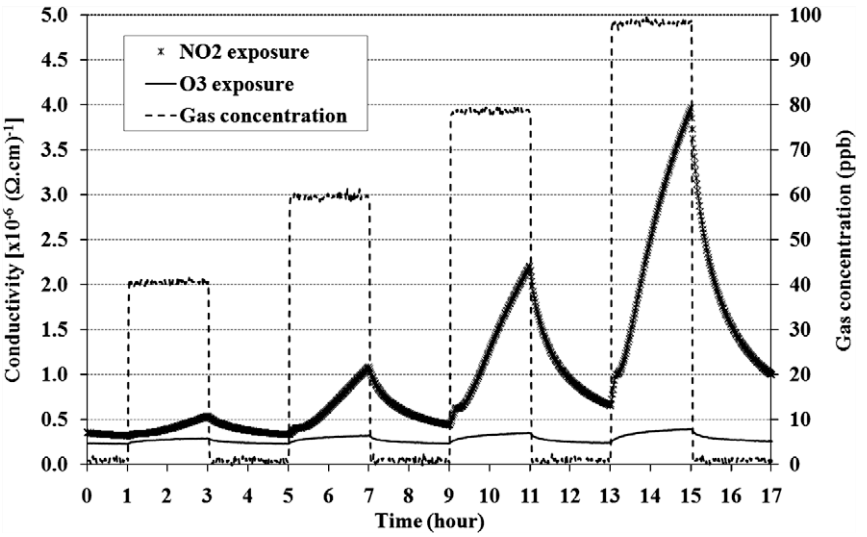

Fig. 5. Time dependence of the electronic conductivity of CuPc (300 nm)/indigo (50 nm) sensor structure exposed to the same NO_2 (⁎) and O_3 (▬) concentrations between 40 and 100 ppb at 80 °C with consecutive return under purified air.

2 h. After each exposure, sensor was maintained at the same temperature under purified air during 2 h too. During experiments, gas concentrations at the output of the exposure chamber were monitored by commercial gas analyzers and are reported on the right scale. Results illustrated by Fig. 5 emphasize the high sensitivity to low NO_2 concentrations. The electrical conductivity increases by 70% for 40 ppb as compared to initial value determined before gas submission and is multiplied by 6 for 100 ppb. Moreover, the signal/noise ratio is high. That implies a threshold of detection lower than 40 ppb and a resolution lower than 20 ppb. But the better improvement remains the selectivity toward NO_2 due to the high O_3 filtering yield of indigo. For comparison, conductivity variation due to 40 ppb of NO_2 is three times greater than this induced by the same concentration of ozone. For 100 ppb, this ratio increases to 23. Nevertheless, the shape of the conductivity versus time curves (Fig. 5) indicates low kinetics of adsorption and desorption. This results in longer response and recovery times and could be an important disadvantage for the NO_2 monitoring application in atmosphere. Such problem can be easily resolved by the implementation of a judicious methodology of measurement already experimented in previous works [28].

4. Conclusion

The efficient measurement of NO_2 in air has been successfully performed by the development of an original all-organic gas sensor. The judicious choice of CuPc as the sensitive material provide to our device a partial selectivity toward oxidizing gases because its electrical conductivity is only influenced by these species. Moreover, a low threshold of detection and a high resolution are obtained due to the high sensitivity of CuPc to NO_2 and O_3. The high level of selectivity to NO_2 is due to the relevant use of indigo and its ability to filter selectively O_3 as experimentally established in this work. Indigo thin layers with controlled thickness can be easily realized by thermal evaporation without chemical alteration as demonstrated by FT-IR analysis. As a result, CuPc-based NO_2 sensors with integrated O_3 filtering thin film exhibit selective responses at low concentrations, a threshold of detection to few ppb and a high resolution lower than 20 ppb. Real-time measurements could be easily obtained by the implementation of a judicious methodology already experimented. The very high resistivity of indigo thin films allows their integration on sensing devices avoiding short-circuits. Thus, it constitutes an universal ozone chemical filter for all types of semiconductor gas sensors and generally, for various electronic devices.

Acknowledgments

This work has been made in the context of POLL-CAP project (06BLAN-0127) and the authors wish to gratefully acknowledge the Agence Nationale de la Recherche (A. N. R., France) for its financial support.

References

[1] J. Wollenstein, H. Bottner, M. Jaegle, W.J. Becker, E. Wagner, Material properties and the influence of metallic catalysts at the surface of highly dense SnO_2 films, Sens. Actuators, B 70 (2000) 196–202.
[2] M. Fleischer, S. Kornely, T. Weh, J. Frank, H. Meixner, Selective gas detection with high-temperature operated metal oxides using catalytic filters, Sens. Actuators, B 69 (2000) 205–210.
[3] A. Ryzhikov, M. Labeau, A. Gaskov, Al_2O_3 (M = Pt, Ru) catalytic membranes for selective semiconductor gas sensors, Sens. Actuators, B 109 (2005) 91–96.
[4] T. Tanaka, T. Ohyama, Y.Y. Maruo, T. Hayashi, Coloration reactions between NO_2 and organic compounds in porous glass for cumulative gas sensor, Sens. Actuators, B 47 (1998) 65–69.
[5] T. Ohyama, Y.Y. Maruo, T. Tanaka, T. Hayashi, A ppb-level NO_2 detection system using coloration reactions in porous glass and its humidity dependence, Sens. Actuators, B 64 (2000) 142–146.
[6] M.I.H. Helaleh, S. Ngudiwaluyo, T. Korenaga, K. Tanaka, Development of passive sampler technique for ozone monitoring. Estimation of indoor and outdoor ozone concentration, Talanta 58 (2002) 649–659.
[7] K. Yoshizako, K. Hosoya, Y. Iwakoshi, K. Kimata, N. Tanaka, Porogen imprinting effects, Anal. Chem. 70 (1998) 386–389.
[8] M. Matsuguchi, T. Uno, Molecular imprinting strategy for solvent molecules and its application for QCM-based VOC vapor sensing, Sens. Actuators, B 113 (2006) 94–99.
[9] M. Avila, M. Zougagh, A. Escarpa, A. Rios, Molecularly imprinted polymers for selective piezoelectric sensing of small molecules, Trends Anal. Chem. 27 (2008) 54–65.
[10] T. Weh, M. Fleischer, H. Meixner, Optimization of physical filtering for selective high temperature H_2 sensors, Sens. Actuators, B 68 (2000) 146–150.
[11] G. Tournier, C. Pijolat, Selective filter for SnO_2-based gas sensor: application to hydrogen traces detection, Sens. Actuators, B 106 (2005) 553–562.
[12] K.M. Adams, S.M. Japar, W.R. Pierson, Development of a MnO_2-coated, cylindrical denuder for removing NO_2 from atmospheric samples, Atmos. Environ. 20 (1986) 1211–1215.
[13] L. Pommer, J. Fick, B. Andersson, C. Nilsson, Development of a NO_2 scrubber for accurate sampling of ambient levels of terpenes, Atmos. Environ. 36 (2002) 1443–1452.
[14] M. Hyttinen, P. Pasanen, P. Kalliokoski, Removal of ozone on clean, dusty and sooty supply air filters, Atmos. Environ. 40 (2006) 315–325.
[15] T.A. Metts, S.A. Batterman, Effect of VOC loading on the ozone removal efficiency of activated carbon filters, Chemosphere 62 (2006) 34–44.
[16] S. Dogo, J.P. Germain, C. Maleysson, A. Pauly, Interaction of NO_2 with copper phthalocyanine thin films II: application to gas sensing, Thin Solid Films 219 (1992) 251–256.
[17] M. Bouvet, A. Leroy, J. Simon, F. Tournilhac, G. Guillaud, P. Lessnick, A. Maillard, S. Spirkovitch, A. De Haan, A. Decroly, Detection and titration of ozone using metallophthalocyanine based field effect transistors, Sens. Actuators, B 72 (2001) 86–93.
[18] J. Brunet, L. Talazac, V. Battut, A. Pauly, J.P. Blanc, J.P. Germain, S. Pellier, C. Soulier, Evaluation of atmospheric pollution by two semiconductor gas sensors, Thin Solid Films 391 (2001) 308–313.
[19] C. Maleysson, M. Passard, J.-P. Blanc, V. Battut, J.-P. Germain, A. Pauly, V. Demarne, A. Grisel, C. Tiret, R. Planade, Elaboration and tests of microelectronically designed gas sensors with phthalocyanine sensitive layers, Sens. Actuators, B 26–27 (1995) 144–149.
[20] J. Brunet, J.P. Germain, A. Pauly, J.P. Blanc, Comparisons between NO_2- and O_3-sensing properties of phthalocyanines and n-InP thin films in controlled and noncontrolled atmospheres, Sens. J., IEEE 4 (2004) 735–742.
[21] J. Brunet, A. Pauly, L. Mazet, J.P. Germain, M. Bouvet, B. Malezieux, Improvement in real time detection and selectivity of phthalocyanine gas sensors dedicated to oxidizing pollutants evaluation, Thin Solid Films 490 (2005) 28–35.
[22] K. Takeuchi, T. Ibusuki, Quantitative determination of aqueous-phase ozone by chemiluminescence using indigo-5, 5′-disulfonate, Anal. Chem. 61 (1989) 619–623.
[23] E.P. Felix, K.A.D. De Souza, C.M. Dias, A.A. Cardoso, Measurements of ambient ozone using indigo blue-coated filters, J. AOAC Int. 89 (2006) 480–485.
[24] Y.Y. Maruo, Measurement of ambient ozone using newly developed porous glass sensor, Sens. Actuators, B 126 (2007) 485–491.

[25] M. Alexy, G. Voss, J. Heinze, Optochemical sensor for determining ozone based on novel soluble indigo dyes immobilised in a highly permeable polymeric film, Anal. Bioanal. Chem. 382 (2005) 1628–1641.
[26] J.P. Viricelle, A. Pauly, L. Mazet, J. Brunet, M. Bouvet, C. Varenne, C. Pijolat, Selectivity improvement of semi-conducting gas sensors by selective filter for atmospheric pollutants detection, Mater. Sci. Eng. C26 (2006) 186–195.
[27] Y.-L. Lee, W.-C. Tsai, C.-H. Chang, Y.-M. Yang, Effects of heat annealing on the film characteristics and gas sensing properties of substituted and un-substituted copper phthalocyanine films, Appl. Surf. Sci. 172 (2001) 191–199.
[28] J. Brunet, V. Parra Garcia, A. Pauly, C. Varenne, B. Lauron, An optimized gas sensor microsystem for accurate and real-time measurement of nitrogen dioxide at ppb level, Sens. Actuators, B 134 (2008) 632–639.

using a combination of p-type and n-type inorganic metal oxides as a middle connection unit in tandem polymer PV cells and investigating the origin of V_{OC} in tandem PV cell. Herein, we fabricate tandem polymer PV cells using a combination of TiO_x and MoO_3 as a middle connection unit to link the two subcells. It is found that inserting a thin Al layer between the TiO_x and MoO_3 layers realizes tandem PV cells and the V_{OC} of the tandem cell is summation of the two subcells. The origin of V_{OC} in tandem PV cells is discussed.

2. Experimental details

Fig. 1 shows the designed device structure of the tandem polymer PV cell and the chemical structures of active materials used in this study. The blends of poly(3-hexylthiophene) (P3HT)/[6,6]-phenyl C61-butyric acid methyl ester (PCBM) and of poly[2,6-(4,4-bis-(2-ethylhexyl)-4H-cyclopenta[2,1-b;3,4-b′]dithiophene)-alt-4,7-(2,1,3-benzothiadiazole)] (PCPDTBT)/[6,6]-phenyl C71-butyric acid methyl ester ($PC_{70}BM$) are used as the active layers in subcells, respectively. PCPDTBT is a kind of low-band-gap conjugated polymer, and its lowest unoccupied molecular orbital (LUMO) and highest occupied molecular orbital (HOMO) levels are −3.6 and −5.3 eV respectively [20]. The dominant absorption of PCPDTBT is located at the region of 600–900 nm. The absorption of P3HT:PCBM (1:0.8 in weight ratio) and PCPDTBT:$PC_{70}BM$ (1:3 in weight ratio) blends are shown in Fig. 2. The absorption of P3HT:PCBM blend film dominates at the range of 500–650 nm, which is complementary to the absorption of PCPDTBT:$PC_{70}BM$ blend film. The indium tin oxide (ITO)-coated glass with a sheet resistance of 10 Ω/square was used as the substrate. A 40-nm-thick PEDOT:PSS (Baytron P AI 4083) layer was spin-coated onto the ITO glass substrate to serve as an anode buffer layer. The sample was then baked at 120 °C for 30 min in an oven. A P3HT:PCBM blend layer (1:0.8 in weight ratio, 100 nm) was spin-coated on PEDOT:PSS layer from chlorobenzene solution in glove box to serve as an active layer in bottom subcell. An electron-transporting layer of TiO_x (9 nm) was deposited on top of the P3HT:PCBM layer by means of sol–gel chemistry from ethanol solution of tetrabutyl titanate ($Ti[OC_4H_9]_4$) precursor. The film is subjected to hydrolysis to form a TiO_x layer (the ratio of Ti to O is 1:1.74). The sample was then annealed at

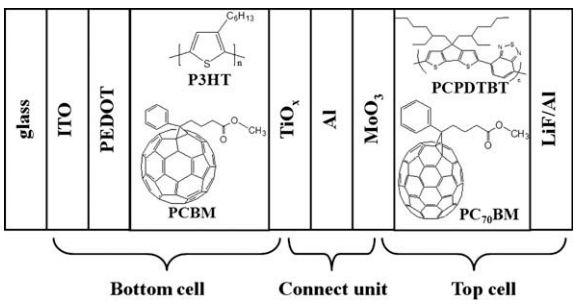

Fig. 1. The tandem PV cell architecture and the active materials used in this study.

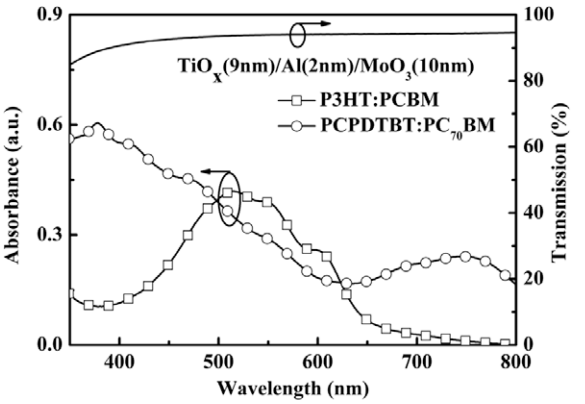

Fig. 2. Transmittance of the middle connection unit with a structure of TiO_x (9 nm)/Al (2 nm)/MoO_3 (10 nm), and absorbance of the P3HT:PCBM (1:0.8, 100 nm) and PCPDTBT:$PC_{70}BM$ (1:3, 100 nm) blend film.

150 °C for 10 min in glove box. The Al (2 nm)/MoO_3 (10 nm) layers were thermally deposited onto the TiO_x layer *in vacuo* at a pressure of about 4×10^{-4} Pa. A PCPDTBT:$PC_{70}BM$ blend (1:3 in weight ratio) layer was spin-coated on the MoO_3 layer from chlorobenzene solution to serve as an active layer in the top subcell. Finally, the LiF (1 nm)/Al (100 nm) electrode was thermally deposited. The devices were annealed at 160 °C for 5 min inside glove box and encapsulated for measurement. The active area of the PV cells was about 0.12 cm^2.

Current density–voltage (*J–V*) characteristics of the PV cells were measured using a computer-controlled Keithley 236 source meter in the dark and under AM1.5G illumination from a calibrated solar simulator with an irradiation intensity of 100 mW/cm^2. Ultraviolet photoelectron spectroscopy (UPS) was carried out using Thermo ESCALAB 250 surface analysis system equipped with a He-discharge lamp providing He–I photons of 21.22 eV. The absorption and transmission measurement was performed using Shimadzu UV-3600 spectrophotometer.

3. Results and discussion

In order to investigate influence of the middle connection unit on the PV performance of tandem polymer PV cell, the tandem cells with P3HT:PCBM blend as the active layers in subcells are fabricated. For tandem polymer PV cells with two subcells being linked in series, the middle connection unit should act as a recombination site for electrons and holes photo-generated in bottom and top subcells. The PV performance of the tandem polymer PV cells with TiO_x/MoO_3 as a middle connection unit is summarized in Table 1. The TiO_x layer in the middle connection unit serves as an electron-collecting layer in bottom cell since its LUMO level is −4.4 eV, providing an Ohmic contact with the LUMO of PCBM (−4.3 eV) for electrons generated in the bottom subcell. The MoO_3 with a HOMO level of −5.4 eV serves as a hole-collecting layer in top subcell. However, the tandem PV cell with TiO_x (18 nm)/MoO_3 (10 nm) as a middle connection unit merely shows a V_{OC} of 0.51 eV, close to its single active layer PV cells. It indi-

Table 1
PV performance of the tandem polymer PV cells based on P3HT:PCBM blend with different middle connection units.

TiO_x/Al/MoO_3 (nm)	V_{OC} (V)	J_{SC} (mA/cm^2)	FF	PCE (%)	R_S (Ω cm^2)
18/0/10	0.51	2.66	0.29	0.40	671
18/2/12	1.04	2.17	0.23	0.52	52
18/2/10	1.02	2.69	0.23	0.63	55
18/2/8	0.84	1.97	0.30	0.49	189
9/2/10	1.03	3.74	0.39	1.50	30
6/2/10	0.86	0.78	0.39	0.26	610

cates that the tandem architecture is not well realized and there exists large V_{OC} loss. While the tandem PV cell with a structure of TiO_x (18 nm)/Al (2 nm)/MoO_3 (10 nm) as the middle connection unit demonstrates well tandem effect as shown in Table 1, which shows a V_{OC} of 1.02 V, much higher than that of the tandem cell with TiO_x (18 nm)/MoO_3 (10 nm) as the middle connection unit. The series resistance (R_S) of the tandem PV cells is decreased from 671 to 55 Ω cm^2 by inserting a thin layer of Al (2 nm) between the TiO_x and MoO_3 layers. It may be attributed that the thin Al layer acts as an efficient recombination site for holes and electrons generated in the two subcells. The tandem PV structure is well established with TiO_x/Al/MoO_3 as the middle connection unit since V_{OC} of the tandem PV cell is double of V_{OC}s in P3HT:PCBM blend PV cells [21]. The thicknesses of TiO_x and MoO_3 layers in the middle connection unit are optimized for achieving best PV performance and the results are also summarized in Table 1. The tandem PV cell with optimized TiO_x (9 nm)/Al (2 nm)/MoO_3 (10 nm) as the middle connection unit shows a V_{OC} of 1.03 V, a short-circuit current (J_{SC}) of 3.74 mA/cm^2, and a fill factor (FF) of 0.39. The values give an overall PCE of 1.5%. The tandem PV cell with TiO_x (9 nm)/Al (2 nm)/MoO_3 (10 nm) structure shows a smallest R_S of 30 Ω cm^2 among these PV cells. Further increasing the thicknesses of TiO_x or MoO_3 would increase R_S of PV cells. However, decreasing their thicknesses also increases R_S of the tandem PV cell, together with decreased V_{OC} and J_{SC}. This may be attributed to that the spin-coated 6-nm-thick TiO_x layer after hydrolysis is not a continuous film, which may result in the active layer of the bottom cell is in contact with the MoO_3 layer or the active layer of the top cell is directly in contact with the TiO_x layer. Hence, the function of the TiO_x/Al/MoO_3 structure is weakened and the formed reverse current would reduce the PV performance of the tandem PV cell. Transmittance of the TiO_x (9 nm)/Al (2 nm)/MoO_3 (10 nm) structure is shown in Fig. 2. It can be seen that the TiO_x (9 nm)/Al (2 nm)/MoO_3 (10 nm) structure shows a transmittance higher than 95% in the range of 400–800 nm due to wide band-gap of TiO_x and MoO_3. The high transmittance of the middle connection unit may favor the incident light passing through it and being absorbed efficiently by the top subcell.

As demonstrated above, the V_{OC} of the tandem PV cells is dramatically increased by replacing the TiO_x/Al/MoO_3 structure for the TiO_x/MoO_3 structure. It is speculated that the energy level alignment at TiO_x/MoO_3 interface may play an important role in determining the final V_{OC} of the tandem PV cell. In order to explore the underlying physical mechanism, UPS measurements were conducted for the TiO_x, TiO_x/MoO_3 and TiO_x/Al/MoO_3 films that were deposited on silicon substrate to determine the electronic structures at the TiO_x/MoO_3 and TiO_x/Al/MoO_3 interfaces. Since the TiO_x layer is prepared via spin-coating and it is difficult to measure *in situ* the electronic structure at the TiO_x/MoO_3 and TiO_x/Al/MoO_3 interfaces via sequential deposition of each layer, individual samples of the TiO_x, TiO_x/MoO_3 and TiO_x/Al/MoO_3 films are prepared and measured under same condition for comparison. The proposed energy level diagrams at the TiO_x/MoO_3 and TiO_x/Al/MoO_3 interfaces are shown in Fig. 3. The values of HOMO for TiO_x and MoO_3, the work function (E_F) for Al, and the vacuum level for each material were extracted from the UPS spectra. The values of LUMO for TiO_x and MoO_3 were determined from UPS spectra together with their absorption spectra. Compared to the vacuum level of TiO_x layer, the vacuum levels of MoO_3 in the TiO_x/MoO_3 and TiO_x/Al/MoO_3 structure shift upwards 0.34 and 0.84 eV, respectively. The vacuum level shift results in the offset changes between the LUMO of TiO_x and HOMO of MoO_3. As shown in Fig. 3(a), there is an offset of 0.66 eV between the LUMO of TiO_x and HOMO of MoO_3 for the TiO_x/MoO_3 structure. Such a large offset would result in a large V_{OC} loss during charge recombination for the tandem polymer PV cells. When a thin layer of Al is inserted between the TiO_x and MoO_3 layers, the electronic levels at the TiO_x/MoO_3 interface are realigned due to negative charge transfer from Al to MoO_3 as shown in Fig. 2(b), and the offset between the LUMO of TiO_x and HOMO of MoO_3 is reduced to 0.16 eV. The small offset between the LUMO of TiO_x and HOMO of MoO_3 reduces energy loss when the photo-generated electrons and holes in the subcells recombine in the middle connection unit, and hence the V_{OC} of the resulted tandem polymer PV cells is enhanced.

The tandem polymer PV cells with the blends of P3HT:PCBM and PCPDTBT:PC_{70}BM as the active layer in the two subcells are fabricated by using the TiO_x (9 nm)/Al (2 nm)/MoO_3 (10 nm) structure as a middle connection unit. The complementary absorption of the P3HT:PCBM

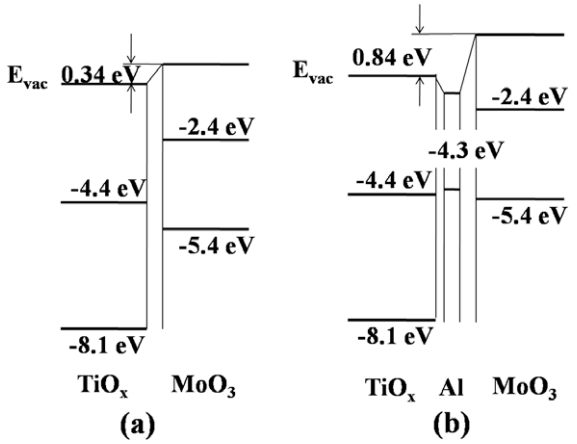

Fig. 3. Proposed energy level diagrams at the TiO_x/MoO_3 (a) and TiO_x/Al/MoO_3 (b) interfaces.

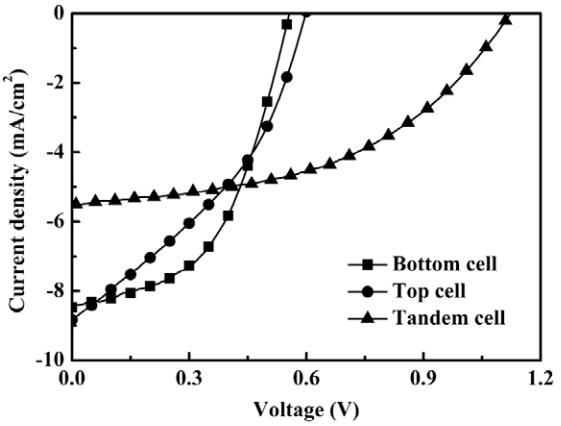

Fig. 4. *J–V* characteristics of the bottom and top PV cells, and tandem PV cell under 100 mW/cm^2 AM 1.5G illumination.

Table 2
PV performance of the bottom and top PV cells, and the tandem PV cell.

Device	V_{OC} (V)	J_{SC} (mA/cm^2)	FF	PCE (%)
Bottom cell	0.56	8.48	0.50	2.37
Top cell	0.60	8.83	0.37	1.97
Tandem cell	1.12	5.51	0.47	2.92

and PCPDTBT:PC_{70}BM blends covers the whole visible region. The single active layer PV cells with structures of ITO/PEDOT (40 nm)/P3HT:PCBM (100 nm)/TiO_x (9 nm)/Al (100 nm) and ITO/MoO_3 (10 nm)/PCPDTBT:PC_{70}BM (100 nm)/LiF (1 nm)/Al (100 nm) were also fabricated for comparison studies. The illuminated *J–V* characteristics of the tandem PV cell and the two single active layer PV cells under 100 mW/cm^2 AM 1.5G illumination are shown in Fig. 4, and their PV parameters are summarized in Table 2. It can be seen that the V_{OC} of the tandem PV cell is 1.12 V, which is nearly the sum of the V_{OC}s of the two subcells (0.56 and 0.60 V), indicating that the TiO_x (9 nm)/Al (2 nm)/MoO_3 (10 nm) structure is a kind of good candidate for the middle connection unit in tandem polymer PV cells. The J_{SC} of the tandem PV cell is about 5.51 mA/cm^2, lower than each single PV cell based on different active layers. This may be attributed to that the partial overlapped absorption of the P3HT:PCBM and PCPDTBT:PC_{70}BM films at the visible region and the optical field redistribution in the tandem structure when the two cells are stacked. The overall PCE of the tandem PV cell is 2.92%, higher than those of the single active layer PV cells (2.37% and 1.97%). The PCE of the tandem PV cell is expected to be further enhanced if the morphology of the P3HT:PCBM and PCPDTBT:PC_{70}BM blends is well optimized and the photocurrent of the two subcells is well matched.

4. Conclusion

In summary, we developed a kind of highly transparent middle connection unit for tandem polymer PV cells, which consists of an electron-transporting TiO_x, a thin Al layer and a hole-transporting MoO_3 layer. The open-circuit voltage origin of the resulted tandem PV cells is demonstrated. It is found that the thin Al layer inserted between the TiO_x and MoO_3 layers not only provides an efficient recombination site for electrons and holes photogenerated in the two subcells, but also realigns the electronic energy levels at the TiO_x/MoO_3 interface to increase the open-circuit voltage of the tandem PV cell.

Acknowledgments

The authors acknowledge the financial support from the National Natural Science Foundation of China (Nos. 50873100, 20834005 and 20921061), 973 project (2009CB623602 and 2009CB930603) and the Chinese Academy of Sciences (KJCX2-YW-M11).

References

[1] G. Yu, J. Gao, J.C. Hummelen, F. Wudl, A.J. Heeger, Science 270 (1995) 1789.
[2] C.J. Brabec, N.S. Sariciftci, J.C. Hummelen, Adv. Funct. Mater. 11 (2001) 15.
[3] J. Peet, J.Y. Kim, N.E. Coates, W.L. Ma, D. Moses, A.J. Heeger, G.C. Bazan, Nat. Mater. 6 (2007) 497.
[4] H.-Y. Chen, J. Hou, S. Zhang, Y. Liang, G. Yang, Y. Yang, L. Yu, Y. Wu, G. Li, Nat. Photon. 3 (2009) 649.
[5] J.Y. Kim, K. Lee, N.E. Coates, D. Moses, T.-Q. Nguyen, M. Dante, A.J. Heeger, Science 317 (2007) 222.
[6] G. Dennler, H.-J. Prall, R. Koeppe, M. Egginger, R. Autengruber, N.S. Sariciftci, Appl. Phys. Lett. 89 (2006) 073502.
[7] A. Hadipour, B. de Boer, J. Wildeman, F.B. Kooistra, J.C. Hummelen, M.G.R. Turbiez, M.M. Wienk, R.A.J. Janssen, P.W.M. Blom, Adv. Funct. Mater. 16 (2006) 1897.
[8] V. Shrotriya, E.H. Wu, G. Li, Y. Yao, Y. Yang, Appl. Phys. Lett. 88 (2006) 064104.
[9] X. Guo, F. Liu, W. Yue, Z. Xie, Y. Geng, L. Wang, Org. Electron. 10 (2009) 1174.
[10] Y. Zhao, Z. Xie, Y. Qu, Y. Geng, L. Wang, Appl. Phys. Lett. 90 (2007) 043504.
[11] J. Gilot, M.M. Wienk, R.A.J. Janssen, Appl. Phys. Lett. 90 (2007) 143512.
[12] T. Ameri, G. Dennler, C. Waldauf, P. Denk, K. Forberich, M.C. Scharber, C.J. Brabec, K. Hingerl, J. Appl. Phys. 103 (2008) 084506.
[13] A.G.F. Janssen, T. Riedl, S. Hamwi, H.-H. Johannes, W. Kowalsky, Appl. Phys. Lett. 91 (2007) 073519.
[14] J.Y. Kim, S.H. Kim, H.-H. Lee, K. Lee, W. Ma, X. Gong, A.J. Heeger, Adv. Mater. 18 (2006) 572.
[15] C. Waldauf, M. Morana, P. Denk, P. Schilinsky, K. Coakley, S.A. Choulis, C.J. Brabec, Appl. Phys. Lett. 89 (2006) 233517.
[16] A. Hayakawa, O. Yoshikawa, T. Fujieda, K. Uehara, S. Yoshikawa, Appl. Phys. Lett. 90 (2007) 163517.
[17] S. Tokito, K. Noda, Y. Taga, J. Phys. D Appl. Phys. 29 (1996) 2750.
[18] H. You, Y. Dai, Z. Zhang, D. Ma, J. Appl. Phys. 101 (2007) 026105.
[19] V. Shrotriya, G. Li, Y. Yao, C.-W. Chu, Y. Yang, Appl. Phys. Lett. 88 (2006) 073508.
[20] D. Mühlbacher, M. Scharber, M. Morana, Z. Zhu, D. Waller, R. Gaudiana, C. Brabec, Adv. Mater. 18 (2006) 2884.
[21] F. Padinger, R.S. Rittverger, N.S. Sariciftci, Adv. Funct. Mater. 13 (2003) 85.

future application as the active semiconductor in circuits fabricated on flexible substrates. It is not surprising therefore that increasing interest has been shown in films composed of blends of small molecules in a host polymer matrix. Of particular interest are blends in which the small molecule undergoes phase-segregation after deposition, yielding a stratified layer of the semiconductor at the surfaces of the binder. Madec et al. [8,9] have shown that such behaviour occurs in blends of TIPS-pentacene in semicrystalline, side-chain aromatic insulating binders such as isotactic polystyrene (iPS) and isotactic poly(α-vinyl naphthalene) (iPVN). Significantly, TFTs fabricated from such blends retained high saturation hole mobility down to 10 wt.% of the active material [8,9]. In the case of TMTES, we believe that the naphthalene pendant core of iPVN enhances π–π stacking. Furthermore, the tacticity of the binder has an influence on phase segregation in favour of stratification, thus enriching the active interface with the organic semiconductor species [8]. An atactic binder on the other hand, due to strong interaction between the components rather than weaker Van der Waals interaction associated with iPVN, results ultimately in an amorphous glass that does not exhibit transistor action.

While the primary focus of the investigation reported here was to establish the performance of organic TFTs formed from a blend of TMTES-pentacene in the binder iPVN over a wide temperature range, the study provided evidence for the robustness of devices formed from such blends when subjected to thermal stress, which could prove beneficial for integration in the R2R process.

2. Experimental

The synthesis of TMTES-pentacene has been fully described elsewhere [7]. A blend composed of 50 wt.% of TMTES-pentacene in iPVN was made by mixing equal volumes of freshly prepared stock solutions (1% w/w in tetralin) of TMTES-pentacene and iPVN. TFTs were fabricated as discrete, bottom-gate, top contact transistors on silicon dioxide thermally grown on heavily doped, silicon wafers (see inset of Fig. 4). The oxide was 300 nm thick and after cleaning for 15 min each in de-ionised water, methanol and acetone was immersed in a 10 mM solution of octadecyl trichlorosilane in anhydrous toluene for 20 min at 60 °C. After drying the substrates on a hot-plate for 2 h in air at 120 °C, aliquots of the pure TMTES-pentacene or the blend were drop-cast onto the pre-treated oxide, and dried at room temperature under normal atmosphere. Then the substrates were left under vacuum overnight to remove any entrapped solvent. Film quality for the blend-based devices was good with no sign of de-wetting from the surface. Gold source and drain electrodes, 50 nm thick, were thermally evaporated at a pressure of 10^{-6} mbar through a shadow mask defining 9 transistors per substrate each with a channel 60 μm long and 2 mm wide.

Device characteristics were measured several days after fabrication, initially in air in the dark, using a Keithley Model 4200 Semiconductor Characterisation System. Subsequently, the devices were placed in an Oxford Instruments Cryostat and their characteristics measured over the temperature range 353 K to 153 K under a vacuum of $\sim 10^{-5}$ mbar. Voltages V_G and V_D were applied to the gate and drain electrodes, respectively with the source grounded. Device current, I_D, was measured at the drain. Output characteristics were obtained first, followed by the transfer characteristics. Except for a few cases, the voltage sweeps were started from zero.

Atomic force microscope (AFM) images were obtained using a XE100 AFM (PSIA Inc, Seoul, Korea) in the non-contact mode at a scan rate of 0.3 Hz. The silicon cantilever had a nominal spring constant of 40 N/m, a resonant frequency of 325 kHz and an aluminium coating on the back to increase signal feedback. Topography and phase images were recorded simultaneously.

3. Results and discussion

Typical output characteristics of pure TMTES-pentacene and iPVN–TMTES-pentacene transistors, measured at room temperature in air, are given by the continuous curves in Fig. 1a and b, respectively. Both device types exhibit behaviour consistent with the standard equations for TFTs in the linear and saturation regimes, namely,

$$I_D = \frac{W}{L}\mu C_{OX}\left[(V_G - V_T)V_D - \frac{1}{2}V_D^2\right] \quad (1)$$

and

$$I_{Dsat} = \frac{W}{2L}\mu_{sat} C_{OX}(V_G - V_T)^2 \quad (2)$$

respectively, where W and L are the width and length of the channel region, μ and μ_{sat} the mobilities in the linear and saturation regimes, respectively, C_{OX} the oxide capacitance per unit area, and V_T the threshold voltage. The performance of the pure material was clearly superior to that of the blend, showing a saturation mobility, μ_{sat}, $\sim$0.3 $cm^2/V\,s$ for (V_G = 30 V) compared with $\sim$0.07 $cm^2/V\,s$ in the blend for the same applied voltage. This is not surprising given the structural differences in the deposited films highlighted by the AFM phase images in Fig. 2. Here are shown films of (a) the pure TMTES-pentacene and (b) the iPVN–TMTES-pentacene blend prepared utilising the same drop-casting technique used for TFT fabrication. The pure material crystallised into flat, interconnected platelets while the blend phase-separated into TMTES-pentacene-rich regions characterised by a feathery morphology separated by narrow, electrically more insulating iPVN-rich regions. Although device currents were generally lower in the blend, the presence of iPVN did confer some compensating benefits. For example, it improved the temperature stability of devices (demonstrated below) and increased the apparent ON–OFF ratio of devices. Lateral conduction through the unpatterned, more conductive pure TMTES-pentacene film led to high gate leakage through regions of gate oxide remote from the TFT under test. As a result, OFF currents were several orders of magnitude greater than for an iPVN–TMTES-pentacene TFT measured under the same conditions.

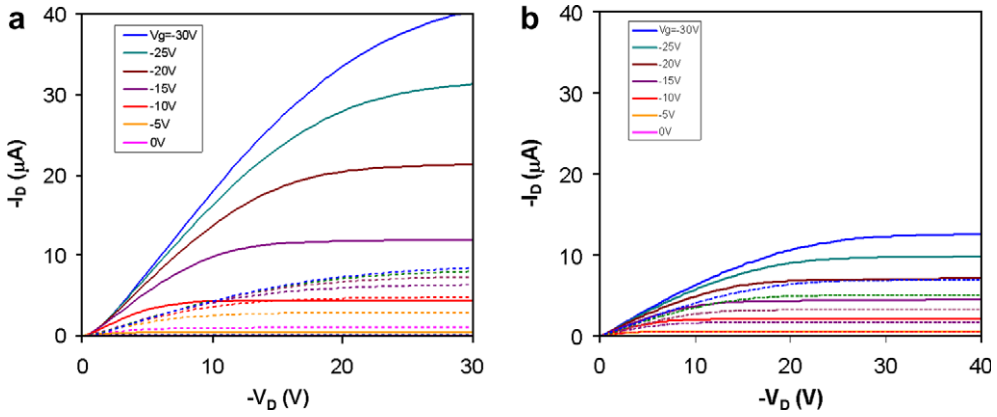

Fig. 1. Output characteristics of a TFT fabricated from (a) pure TMTES-pentacene and (b) TMTES-pentacene: iPVN blend, measured at 293 K in air (continuous curves) and in vacuum (dashed curves).

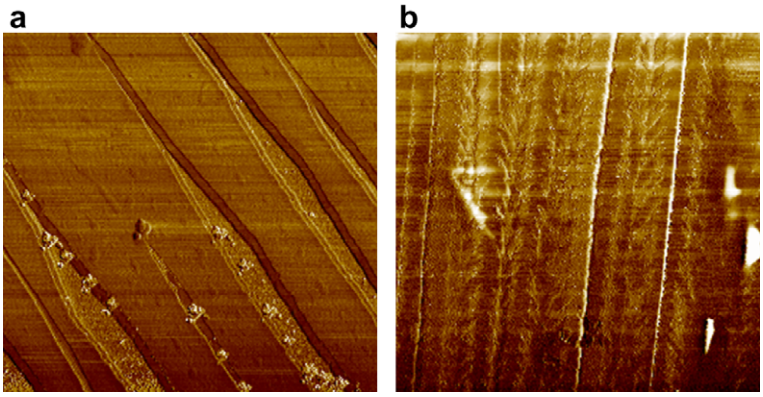

Fig. 2. AFM phase images of (a) a pure TMTES-pentacene and (b) iPVN–TMTES-pentacene films prepared following the same drop-casting and spreading procedures used for fabricating OFETs. The feathery regions in the blend are TMTES-pentacene-rich regions separated by narrow, bright iPVN-rich regions. The images are both 20 μm × 20 μm.

Interestingly, after several hours under vacuum, I_D decreased for both device types although the effect was greater for the pure semiconductor. Consequently, there was little difference in the output characteristics of the two device types measured under vacuum (Fig. 1 dashed curves), with $\mu_{sat} \sim 0.06$ cm^2/V s for pure TMTES-pentacene and $\sim$0.04 cm^2/V s in the blend. It seems, therefore, that exposure to atmosphere is important for achieving the highest performance in TMTES-pentacene devices. That both device types perform better in air than in vacuum points to oxygen doping of the semiconductor as reported for other organic semi-conductors [10]. The blend appears to be less sensitive, presumably owing to the encapsulation of the TMTES-pentacene by the iPVN.

A set of measurements was then taken starting at 353 K and ranging down to 153 K before warming the devices slowly to room temperature overnight for further characterisation (Fig. 3). A significant difference in behaviour was then observed. The iPVN–TMTES-pentacene device recovered its previous performance, albeit with a small shift in threshold voltage. The pure TMTES-pentacene device suffered permanent degradation (dashed curves in Fig. 3c) with μ_{sat} now reduced by more than an order of magnitude to $\sim$0.003 cm^2/V s. Indeed several such devices failed completely, particularly at low temperatures. In this context, differential scanning calorimetry measurements in the range from room temperature down to −100 °C proved interesting. Samples of pure TMTES showed a reversible phase transition near −80 °C which was absent in the blend. Anthony and co-workers [11] in their study of the phase change in TIPS pentacene at $\sim$124 °C observed that even though the change of polymorph was reversible upon thermal cycling, crystals still showed signs of thermal stress as evidenced by the presence of long fracture lines along the slip axis of the crystal. When these macro defects are present the mobility of the devices can drop by several orders of magnitude because of disrupted charge flow. We suggest that iPVN has a protective effect by preventing the low temperature phase change and the associated physical modification in the TMTES.

Owing to the unreliability of pure TMTES-pentacene devices, the remainder of this study focused only on TFTs fabricated from the blend. These devices retained excellent device characteristics with good saturation over a wide

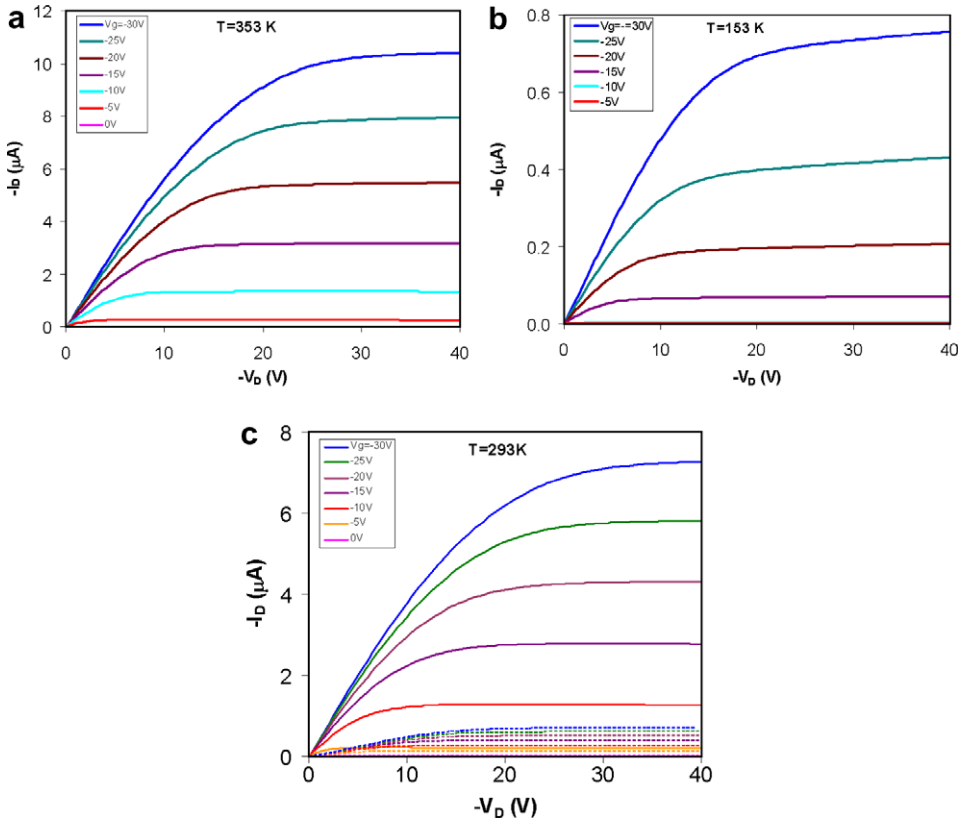

Fig. 3. Output characteristics of TFTs fabricated from the iPVN–TMTES-pentacene blend and pure TMTES-pentacene, measured at (a) 353 K, (b) 153 K and then back at (c) 293 K after warming up of the measurement cell. For comparison in (c) are also shown (dashed curves) the characteristics of one of the few pure TMTES-pentacene devices that survived temperature cycling.

temperature range and, as demonstrated in Fig. 3, room temperature performance was recovered following the temperature cycle.

Transfer characteristics obtained at several different temperatures for the blend are plotted in semi-logarithmic form in Fig. 4. In all cases, the threshold for the onset of channel conductance is clearly visible. Taking the current flow at threshold to be the OFF current and the maximum current observed to be the ON current, the ON–OFF ratio is seen to decrease from just under $\sim 10^6$ at 353 K to $\sim 10^4$ at 153 K.

The iPVN appears to confer a beneficial thermo-mechanical property on films formed from the resulting blend which enables the TFTs to withstand cooling from 353 K to 153 K with little loss of performance upon returning back to room temperature. However, the presence of the insulating iPVN component of the blend leads to a general decrease in the effective mobility which may be attributed partly to the reduced TMTES-pentacene concentration at the oxide/blend interface and partly due to the presence of a parasitic resistance associated with the source and drain contacts.

The presence of contact resistances in organic TFTs has been widely reported [12–18] and methods described for extracting resistance values from device currents using, for example, the transfer line method (TLM) and also by combining device currents with measurement of the contact potential drop using Scanning Kelvin Probe Microscopy (SKPM) [19].

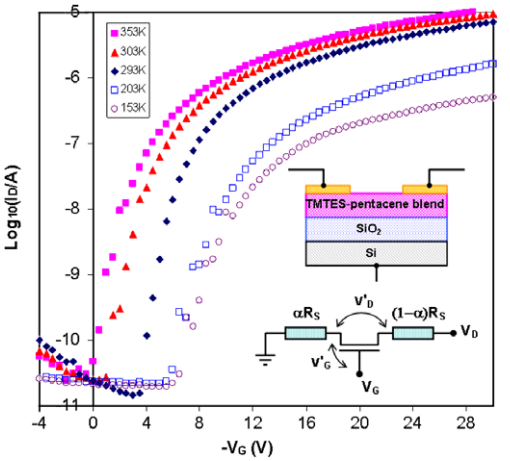

Fig. 4. Transfer characteristics of a TFT fabricated using the iPVN–TMTES-pentacene blend measured at different temperatures in the order 293 K, 353 K, 303 K, 203 K and 153 K. The inset shows a diagram of the device cross-section and a circuit description with parasitic resistances αR_S and $(1-\alpha)R_S$ associated with the source and drain contacts, respectively.

In the present bottom gate, top contact devices the semiconductor layer is relatively thick ($\sim$100 nm) as a

result of the drop-casting technique used in the fabrication. Consequently, the parasitic resistances of the bulk semiconductor layer between the source/drain contacts and the respective ends of the induced channel could be significant and will add to any resistance associated with the contacts themselves. In Fig. 4 we represent such resistances by αR_S and $(1-\alpha)\,R_S$ in series with the source and drain, respectively with $0 \leqslant \alpha \leqslant 1$. The gate and drain voltages sensed by the channel now differ from the applied voltages in which case Eq. (1) for the linear regime becomes

$$I_D = \frac{W}{L}\mu C_{OX}\left[(V'_G - V_T)V'_D - \frac{1}{2}V'^2_D\right] \tag{3}$$

where $V'_G = (V_G - \alpha I_D R_S)$ and $V_D' = (V_D - I_D R_S)$. For very low device currents, when both $I_D R_S$ and V_D are very much smaller than $(V_G - V_T)$ then Eq. (3) reduces to the form used by Horowitz et al. [14] i.e.

$$I_D = \frac{W}{L}\mu C_{OX}(V_G - V_T)(V_D - I_D R_S). \tag{4}$$

The total series resistance, R_S, may then be calculated from the channel conductance, $g_d = \partial I_D/\partial V_D$, measured at low voltages: in the present case for $0 \leqslant V_D \leqslant 0.5$ V. Since the dependence of μ on V_G is not known *a priori*, following Horowitz et al. [14], we first assume the empirical form

$$\mu = a(V_G - V_T)^b \tag{5}$$

where a and b are arbitrary constants. Substituting for μ in Eq. (4) then yields

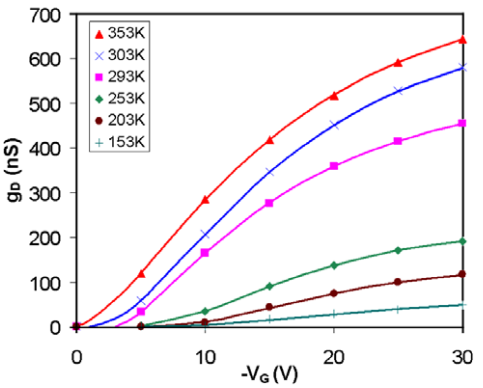

Fig. 5. Channel conductance extracted from the linear regime of the output characteristics ($0 \leqslant V_D \leqslant 0.5$ V) plotted as a function of the gate voltage, V_G. The marked points are from experiment, while the curves show the fits based on Eq. (6). The measurements were carried out in the sequence 293 K, 353 K, 303 K, 253 K, 203 K and 153 K.

$$g_D = \frac{Ka(V_G - V_T)^{1+b}}{1 + KR_S a(V_G - V_T)^{1+b}} \tag{6}$$

where $K = (W/L)C_{OX}$. In principle, a 4-parameter, least squares fit can now be performed to experimental g_D vs. V_G data to obtain values for a, b, R_S and V_T.

However, given the limited data available for each curve (Fig. 5), V_T was assumed to be the turn-on voltage observed in the transfer characteristics [12]. This is justified since V_T can be estimated to a reasonable degree of precision from this data and, in all but one case, was consistent with the onset of conduction in the output characteristics.

The fits obtained following this procedure (full curves in Fig. 5) are excellent when using the V_T and R_S values listed in Table 1. Values for a and b are not included since they have little significance. As explained by Horowitz et al. [14] they are simply dummy variables used to provide a crude, initial approximation to the voltage dependence of μ.

The width-normalised value of R_S at room temperature are at the upper end of the range (2–200 kΩ cm) reported by Gundlach et al. [13] for top-contact pentacene TFTs. Interestingly, the results show a gradual progression of V_T from positive to increasingly negative values as the temperature decreases, suggesting a gradually increasing positive trapped charge at the insulator-semiconductor interface or in the insulator itself, as observed for pentacene TFTs [20]. Over the same temperature range, R_S increased from 234 kΩ cm to 2.64 MΩ cm.

For the second run at 293 K, i.e. the measurements made after warming up the device from 153 K, the approach described above was not possible. Seemingly, the thermal cycle made the device prone to voltage stressing; the turn-on voltage shifted from ~0 V in the output characteristics to ~3.5 V in the subsequently measured transfer characteristics. Such behaviour is indicative either of deeply trapped electrons at the interface [21] or polarisation within the insulator. When fitting the curve for this case, therefore, V_T was constrained to a value in the range ±1 V and gave a good fit with $V_T = +0.7$ V i.e. similar to the value estimated from the output plots. It is worth noting that after the thermal cycle, R_S measured at room temperature had increased from 1.6 MΩ to 2.1 MΩ. This suggests that the morphological changes we believe to be responsible for the failure of the pure TMTES devices also occur in the iPVN-TMTES devices but are limited in the blend by the beneficial action of the binder.

The resistances, R_S, listed in Table 1 are plotted in Arrhenius format in Fig. 6 and are seen to lie moderately well on a straight line corresponding to an activation

Table 1
Values of V_T and R_S giving the best fit to the conductance plots in Fig. 5. For comparison with the literature, R_S is also quoted as the channel-width-normalised value. Values for the parameters a and b are not listed since these were dummy variables used to give an initial approximation to the voltage dependence of V_G [14]. For comparison, the corresponding values extracted from the initial measurements made in air for the same device were $V_T = 0$ V and $R_S = 1.13$ MΩ.

	353 K	303 K	293 K	252 K	203 K	153 K	292 K (2)
V_T (V)	0.50	−1.0	−3.0	−3.5	−5.5	−5.5	0.70
R_S (MΩ)	1.17	1.30	1.60	4.10	6.28	13.2	2.10
Normalised R_S (MΩ cm)	0.234	0.260	0.320	0.820	1.26	2.64	0.420

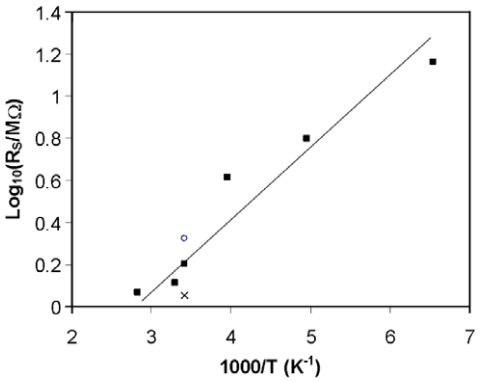

Fig. 6. Arrhenius plot of the series resistance R_S extracted by fitting Eq. (6) to the conductance data in Fig. 5. The 3 data points shown for 293 K correspond to the initial measurements in air (×) and in vacuum (■), and the subsequent measurement under vacuum after the low temperature measurements (○).

energy of ~0.07 eV, giving confidence that the adopted approach is reasonable. Interestingly, the highest occupied molecular orbital (HOMO) of TMTES-pentacene has been estimated to lie at −5.19 eV below the vacuum level [7]. A gold electrode with workfunction ~5.1 eV would, therefore, create a barrier of ~0.09 eV for hole injection into the semiconductor – a similar value to the activation energy estimated above, which suggests that R_S may be associated with the source contact.

The values of R_S and V_T estimated above may now be combined in an attempt to determine the true dependence of μ on V_G. In the presence of parasitic series resistances, pinch-off i.e. the onset of saturation occurs when

$$V'_D = V'_G - V_T \tag{7}$$

i.e. when

$$V_D = (V_G - V_T) + (1-\alpha) I_{Dsat} R_S \tag{8}$$

It is readily shown that, so long as the device is in saturation ($I_D = I_{Dsat}$), the true mobility may be determined from the transfer characteristic using the equation

$$\mu = \frac{2L}{WC_{OX}} \cdot \frac{I_{Dsat}}{(V_G - V_T)^2 - 2\alpha R_S I_{Dsat}(V_G - V_T) + \alpha^2 R_S^2 I_{Dsat}^2}. \tag{9}$$

Since the parameter α is not known, we consider three possible cases that set bounds on the true mobility. Examples of the gate-voltage dependence of the effective mobility, calculated from the Eq. (2) (solid diamonds) are compared in Fig. 7 to the results calculated from Eq. (9). (i) $\alpha = 0$: In this case, R_S is associated entirely with the drain

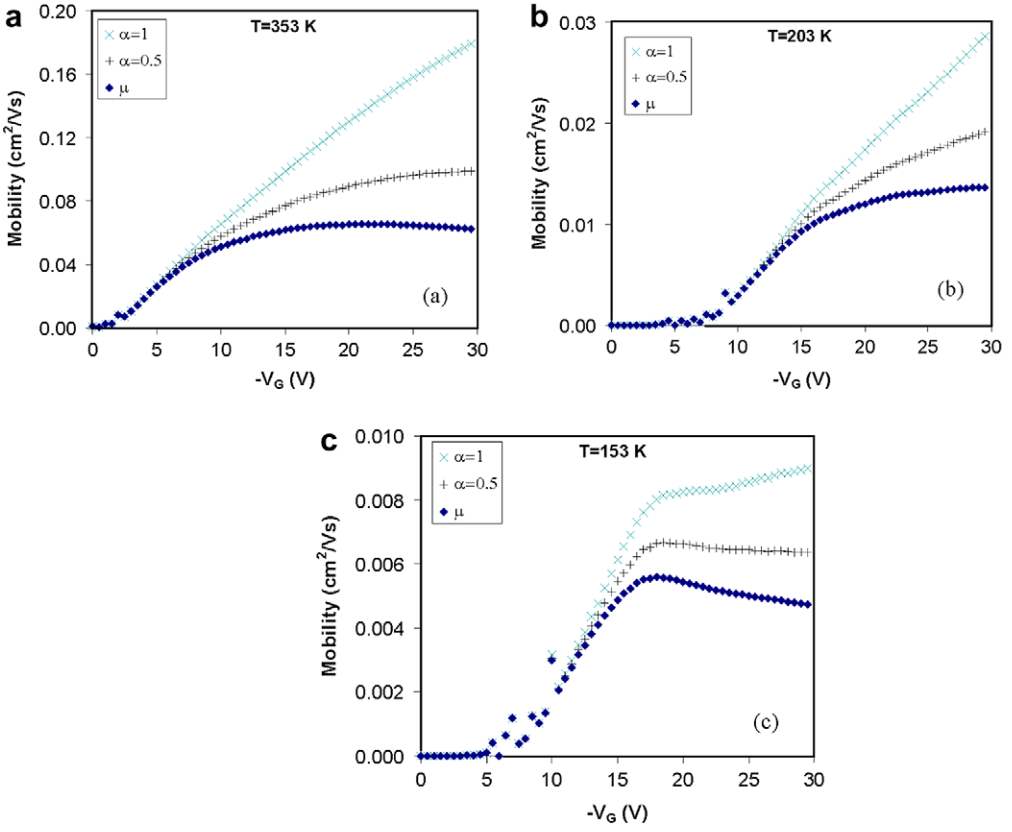

Fig. 7. Effective mobility (filled diamonds) at (a) 353 K, (b) 203 K and (c) 153 K calculated directly from the transfer data using Eq. (2). Also shown are the corrected mobilities calculated using Eq. (9) and assuming the presence of a series resistance associated entirely with the source ($\alpha = 1$) and divided equally between source and drain ($\alpha = 0.5$).

contact so that Eq. (9) reduces to that for an ideal device and the effective mobility (filled diamonds in Fig. 7) will be the true mobility. We may discount this case because (a) μ is unlikely to decrease at higher values of V_G and (b) there will inevitably be limits on the ability of the source to supply carriers to the channel.

(ii) $\alpha = 1$: Now R_S is associated entirely with the source electrode so that applying Eq. (9) to the transfer data in Fig. 4 now produces the almost linear dependence on V_G reported by others for organic TFTs [14,20]. That the activation energy deduced for R_S is close to that expected for the hole injection barrier from gold into TMTES-pentacene supports the notion that R_S could be associated mainly with the source. However, the monotonic increase with V_G appears to break down at 153 K pointing to limitations of the model at this low temperature. Further work will be necessary to check this point.

(iii) $\alpha = 0.5$: In this scenario, R_S is shared equally between source and drain contacts. This is a feasible proposition given the thickness of the semiconductor lying between the contacts and the extremities of the channel. Application of Eq. (9) to the transfer data now produces plots intermediate between the other two but which tend to saturation.

Supplementary Scanning Kelvin Probe Microscopy showed a linear change in potential between the electrodes, even with the device in saturation. Furthermore, no discontinuity in potential, a characteristic feature associated with a contact resistance, was observed at the electrode edges. We believe, therefore, that contact resistance at the electrodes is small and that the measured potential was that developed by the parasitic source-drain leakage current which masked the underlying potentials associated solely with the accumulation channel. Measurements conducted on a series of devices with different channel lengths, the so-called transmission line (TLM) method, were similarly inconclusive owing to significant scatter in the data obtained from devices with different channel lengths. We believe that such variability arose from randomness in the phase separation of the blend and that the series resistance in the device is most likely to be associated with the bulk material interposed between the contacts and the channel i.e. the case corresponding to $\alpha = 0.5$. A reduction in the semiconductor film thickness coupled with better control of phase separation should then lead to significant improvement in device performance.

4. Conclusions

A detailed study has been undertaken into the electrical behaviour of TMTES-pentacene and iPVN–TMTES-pentacene bottom gate top contact TFTs over the temperature range 153–353 K.

Uncorrected estimates of the saturation mobility in the iPVN–TMTES-pentacene devices displayed the commonly observed gate voltage-dependence i.e. increase to a maximum followed by a slight decrease in response to increasing gate voltage [14,22]. In keeping with other reports, we associate such behaviour with the presence of parasitic series resistance, R_S, in the device. Not surprisingly, R_S extracted from conductance measurements in the linear regime, is related to an activated process with activation energy ~0.07 eV which we conclude is associated with bulk semiconductor material lying between the source/drain electrodes and the accumulation channel.

When corrected for series resistance effects, the true mobility in the blend-based devices is likely to be a continually increasing function of V_G, depending on the extent to which the source resistance dominates device behaviour. Significantly increased mobilities should be achievable at room temperature by reducing the series resistance e.g. by reducing the thickness of the semiconductor layer.

It has also been shown that atmospheric oxygen improves device performance presumably through a slight reduction in bulk series resistance by its doping effect on the semiconductor. Furthermore, incorporating TMTES-pentacene in a binder appears to confer the advantage of reducing lateral transport, an important property for reducing cross-talk between devices in printed circuits.

Finally, devices based on the iPVN–TMTES-pentacene blend show good transistor behaviour over the whole temperature range from 353 K down to 153 K. In contrast, the pure TMTES-pentacene devices were unreliable, frequently failed and showed diode-like characteristics at the lowest temperature. Furthermore, devices formed from the blend were more robust, recovering their initial room temperature behaviour after the thermal cycle, albeit at the cost of changes in turn-on voltage and parasitic series resistance. We believe that this is the first reported observation of the thermo-mechanical stabilisation of semi-crystalline organic semiconductor behaviour through blending with an insulating polymer. From a materials science perspective, such a finding offers the opportunity for rapid transfer of this technology to the R2R process since it allows more flexibility in the temperature range permitted in subsequent processing steps.

Acknowledgements

The authors wish to thank the following organisations for their financial support: Egyptian Ministry of Higher Education (MMI), FAPESP, Brazil (ACM), Engineering and Physical Sciences Research Council (CPW), Higher Education Funding Council for Wales (DMT) and the Technology Strategy Board (M-BM, SGY).

References

[1] O.D. Jurchescu, J. Baas, T.M. Palstra, Appl. Phys. Lett. 84 (2004) 3061.
[2] H. Klauk, M. Halik, U. Zschiesschang, G. Schmid, W. Radlik, W. Weber, J. Appl. Phys. 92 (2002) 5259.
[3] W.L. Kalb, K. Mattenberger, B. Batlogg, Phys. Rev. B 78 (2008) 035334.
[4] F. de Angelis, M. Gaspari, A. Procopio, G. Cuda, E. Di Fabrizio, Chem. Phys. Lett. 468 (2009) 193.
[5] J.E. Anthony, D.L. Eaton, S.R. Parkin, Org. Lett. 4 (2002) 15.
[6] S.K. Park, T.N. Jackson, J.E. Anthony, D.A. Mourey, Appl. Phys. Lett. 91 (2007) 063514.
[7] G.R. Llorente, M.-B. DuFourg-Madec, D.J. Crouch, R.G. Pritchard, S. Ogier, S.G. Yeates, Chem. Commun. (2009) 3059.
[8] M.-B. Madec, D. Crouch, G.R. Llorente, T.J. Whittle, M. Geoghegan, S.G. Yeates, J. Mater. Chem. 18 (2008) 3230.
[9] G. Rincon-Llorente, M.-B. Madec, D.J. Crouch, S.G. Yeates, in: Proc. MRS Fall Meeting, Boston 2008, Paper 1114-G06-05.

[10] D.M. Taylor, H. Gomes, A.E. Underhill, S. Edge, P.I. Clemenson, J. Phys. D: Appl. Phys. 24 (1991) 2032.
[11] J. Chen, J. Anthony, D.C. Martin, J. Phys. Chem. B 110 (2006) 16397.
[12] C. Reese, Z. Bao, Adv. Funct. Mater. 19 (2009) 763.
[13] D.J. Gundlach, L. Zhou, J.A. Nichols, T.N. Jackson, P.V. Necliudov, M.S. Shur, J. Appl. Phys. 100 (2009) 024509.
[14] G. Horowitz, M.E. Hajlaoui, R. Hajlaoui, J. Appl. Phys. 87 (2000) 4456.
[15] R.A. Street, A. Salleo, Appl. Phys. Letts. 81 (2002) 2887.
[16] P.V. Necliudov, M.S. Shur, D.J. Gundlach, T.N. Jackson, Solid State Electr. 47 (2003) 259.
[17] H. Klauk, G. Schmid, W. Radlik, W. Weber, L. Zhou, C.D. Sheraw, J.A. Nichols, T.N. Jackson, Solid State Electr. 47 (2003) 297.
[18] B.H. Hamadani, D. Natelson, Appl. Phys. Letts. 84 (2004) 443.
[19] L. Burgi, T. Richards, M. Chiesa, R.H. Friend, H. Sirringhaus, Synth. Met. 146 (2004) 297.
[20] S.-J. Kim, M.-S. So, M.C. Suh, H.-K. Chung, Jpn. J. Appl. Phys. 44 (2005) L1414.
[21] P. Stallinga, H.L. Gomes, Synth. Met. 156 (2006) 1316.
[22] M. Ullah, D.M. Taylor, R. Schwödiauer, H. Sitter, S. Bauer, N.S. Sariciftci, Th.B. Singh, J. Appl. Phys. 106 (2009) 114505.

hole transporter [5]. Among them, the dye is essential in DSSC since it is the origin of the photocurrent generation. In most cases, Ru-based organometallic compounds such as N719 (red dye) [6] and N749 (green dye) [7] as well as other black dyes have been used as sensitizers for the DSSCs with PCE of more than 11%. However, due to the high price of $RuCl_3$ and the difficulties of synthesizing Ru (II)–polypyridine complexes, metal-free organic dyes have recently attracted a lot of attention because of higher molar extinction coefficient [8–17] and impressive efficiencies in the range 8–9.7% have been achieved. Moreover, the highest occupied molecular orbital (HOMO) and the lowest unoccupied molecular orbital (LUMO) energy levels can be rather easily tuned by controlling their molecular structures, which leads to various colors. Certain metal-free photosensitizers have been very recently synthesized and used for DSSCs [18].

Overall power conversion efficiency (PCE) of a DSSC is basically decided by the short circuit current density (J_{sc}), open circuit voltage (V_{oc}) and fill factor (FF). There are reports about a number of organic dyes giving very high J_{sc} but the overall PCE of the cell was mainly attributed to small observed V_{oc} [19,20]. V_{oc} plays an important role in controlling the PCE and is basically decided by the difference in the conduction band level of TiO_2 and potential of I_3^-/I^- redox couple in DSSCs. In an interesting report O'Regan and Grätzel [21] advocated the role of electron recombination in governing the V_{oc} based on their transient photovoltage and photocurrent measurements in the DSSCs.

A series of low band gap small molecules and polymers bearing 4-nitro-α-cyanostilbene moieties were synthesized in our laboratory and used for bulk heterojunction solar cells [22] and DSSCs [23] very recently. In continuation of this research line, herein we successfully synthesized two simple photosensitizers **D1** and **D2** based on 4-nitro-α-cyanostilbene which contain carboxy or hydroxy anchoring group, respectively. These dyes were synthesized from a one-step reaction in high yields utilizing widely available and inexpensive starting materials. A literature survey revealed that dye **D1** has not been previously synthesized. Dye **D2** has been synthesized by condensing equimolar quantities of 4-nitrobenzylcyanide with 4-hydroxybenzaldehyde [24]. A photoresponsive effect has been observed with polyamide/cyanostilbene systems [25]. Upon comparing the present dyes **D1** and **D2** to those of reference 23 the following differences are observed. (i) The dyes **D1** and **D2** are very simple, while the previous dyes are complex. **D1** and **D2** are among the simplest photosensitizers which have been reported in the literature. (ii) The most remarkable difference is that **D1** and **D2** are prepared from one step reaction only, while the previous from multiple step reactions. (iii) **D1** and **D2** are unsymmetrical molecules while the previous are symmetrical. The dyes **D1** and **D2** were characterized in DSSCs using quasi-solid-state polymer electrolyte, FTO/TiO_2 photoanode and Pt/FTO counter electrode. The DSSC based on **D1** showed higher PCE than that for **D2**, which is attributed to the higher dye loading and electron lifetime for the **D1** based cell.

2. Experimental

2.1. Reagents and solvents

4-Nitrobenzyl cyanide was synthesized from the nitration of benzyl cyanide with concentrated nitric and sulfuric acid [26]. 4-Carboxybenzaldehyde and 4-hydroxybenzaldehyde were recrystallized from ethanol and water, respectively. Tetrahydrofuran (THF) was dried by distillation over CaH_2. All other reagents and solvents were commercially purchased and were used as supplied.

2.2. Synthesis of dyes

2.2.1. 4-Nitro-4′-carboxy-α-cyanostilbene (*D1*)

A flask was charged with a solution of 4-carboxybenzaldehyde (0.5102 g, 3.33 mmol) and 4-nitrobenzyl cyanide (0.5400 g, 3.33 mmol) in ethanol (30 mL). Sodium hydroxide (0.60 g, 15.00 mmol) dissolved in ethanol (10 mL) was added portionwise to the stirred solution. The mixture was stirred for 1 h at room temperature under N_2 and then it was concentrated under reduced pressure to remove ethanol. Water was added to the concentrate and then dilute hydrochloric acid was added to this solution to precipitate **D1** as a dark-green solid. It was filtered and washed thoroughly with water (0.70 g, 72%).

FT-IR (KBr, cm^{-1}): 3408 (O–H deformation of carboxyl); 2170 (cyano); 1684 (carboxylic C=O); 1592 (aromatic); 1534, 1384 (nitro).

^1H NMR ($CDCl_3$, ppm): 12.09 (broad, 1H, carboxyl); 8.19–8.12 (m, 4H, aromatic ortho to nitro and carboxyl); 7.70 (s, 1H, olefinic); 7.51–7.45 (m, 4H, aromatic meta to nitro and carboxyl).

Anal. Calc. for $C_{16}H_{10}N_2O_4$: C, 65.31; H, 3.43; N, 9.52. Found: C, 64.94; H, 3.40; N, 9.58%.

2.2.2. 4-Nitro-4′-hydroxy-α-cyanostilbene (*D2*)

This dye was similarly prepared in 60% yield from the reaction of 4-hydroxybenzaldehyde with 4-nitrobenzyl cyanide (mol ratio 1:1) in ethanol in the presence of sodium hydroxide. The reaction mixture was stirred for 1 h at room temperature under N_2 and then it was concentrated under reduced pressure to remove ethanol. Water was added to the concentrate and **D2** precipitated as a dark-green solid.

FT-IR (KBr, cm^{-1}): 3422 (O–H stretching of hydroxyl); 2168 (cyano); 1592 (aromatic); 1530, 1342 (nitro).

^1H NMR ($CDCl_3$, ppm): 8.18 (m, 2H, aromatic ortho to nitro); 7.71 (s, 1H, olefinic); 7.48 (m, 2H, aromatic meta to nitro); 7.24 (m, 2H, aromatic meta to hydroxyl); 6.84 (m, 2H, aromatic ortho to hydroxyl); 5.34 (s, 1H, hydroxyl).

Anal. Calc. for $C_{15}H_{10}N_2O_3$: C, 67.67; H, 3.79; N, 10.52. Found: C, 67.26; H, 3.85; N, 10.63%.

2.3. Fabrication of dye-sensitized TiO_2 electrode and DSSC assembly

TiO_2 paste was prepared by mixing 1 g of TiO_2 powder (P25, Degussa), 0.2 mL of acetic acid, 1 mL of water. Then 60 mL of ethanol was slowly added while sonicating the

mixture for 3 h. Finally, Triton X-100 was added and a well dispersed colloidal paste was obtained (TiO_2). The whole procedure is slow under vigorous stirring. The mixture was stirred vigorously for 2–4 h at room temperature and then stirred for 4 h at 80 °C to form a transparent colloidal paste. The TiO_2 paste was deposited on the F-doped tin oxide (FTO) coated glass substrates by the doctor blade technique. The TiO_2 coated FTO films were sintered at 450 °C for 30 min. Before immersing into the dye solution, these films were soaked in a 0.2 M aqueous $TiCl_4$ solution overnight in a closed chamber. After being washed with deionized water and fully rinsed with ethanol, the films were heated again at 450 °C for 30 min, followed by cooling to 60 °C.

The nitrogen doped TiO_2 paste was synthesized via sol gel method using urea as nitrogen source. A solution of urea was prepared by dissolving an appropriate amount of urea in 90 mL of deionised water and it was added to the paste of TiO_2 under vigorous stirring at 80 °C. The deposition of the nitrogen doped TiO_2 film is the same as described earlier. The crystallite size of nitrogen doped TiO_2 was determined using X-ray diffraction analysis with Cu Kα as radiant source and wavelength ($\lambda = 0.1541$ nm). The crystallite size D was calculated by the Sherrer equation.

The dyes were dissolved in THF solution (0.5 mM) and the TiO_2 electrode was immersed in the dye solution for 10 h and after sensitization the dye electrode was washed.

For the composite electrolytes preparation, 0.0383 g of TiO_2 powder (P25, Degussa) was dried for about 24 h at 250 °C. After drying a quasi-solid-state polymer electrolyte containing 0.0383 g of P25 TiO_2 powder, 0.1 g of LiI, 0.019 g of I_2, 0.264 g of PEO, and 44 μL of 4-*tert*-butylpyridine in 1:1 acetone/propylene carbonate was prepared. The mixture was continuously stirred at 80 °C in water bath for about 4–5 h. The polymer electrolyte was spread on the sensitized TiO_2 film by spin coating to form a hole-conducting layer. The counter electrode was platinized by spin coating H_2PtCl_6 solution (2 mg in 1 mL isopropanol) onto the FTO coated glass substrate and then heated at 450 °C for 30 min in air. The dye-sensitized photoelectrode containing the quasi-solid-state polymer electrolyte and the counter electrode were clamped together and separated by 20 μm spacer.

2.4. Characterization methods

IR spectra were recorded on a Perkin–Elmer 16PC FT-IR spectrometer with KBr pellets. ^{1}H NMR (400 MHz) spectra were obtained using a Brucker spectrometer. Chemical shifts (δ values) are given in parts per million with tetramethylsilane as an internal standard. UV–vis spectra were recorded on a Beckman DU-640 spectrometer with spectrograde THF. Elemental analyses were carried out with a Carlo Erba model EA1108 analyzer.

The electrochemical properties of both dyes were studied by using cyclic voltammetry (CV) (HCH instrument). The dyes were coated on platinum disk and immersed in 0.1 M Bu_4NPF_6 acetonitrile solution. CV was recorded using Platinum disk as working electrode and Ag/Ag^+ as the reference electrode at a scan rate of 20 mV s^{-1}.

The current–voltage (*J–V*) characteristics of the devices in dark and under illumination were measured by semiconductor parameter analyzer (Keithley 4200-SCS). A xenon light source (Oriel, USA) was used to give an irradiance of 100 mW/cm^2 (the equivalent of one sun at AM 1.5) at the surface of the device. The photoaction spectrum of the devices was measured using a monochromator (Spex 500 M, USA) and the resulted photocurrent was measured with Keithley electrometer (model 6514), which is interfaced to the computer by LABVIEW software. The electrochemical impedance spectra (EIS) measurements were carried out by applying bias of the open circuit voltage (V_{oc}) and recorded over a frequency range of 1 mHz to 10^5 Hz with ac amplitude of 10 mV. The above measurements were recorded with an electrochemical impedance analyzer equipped with FRA.

3. Results and discussion

3.1. Synthesis and characterization

Dyes **D1** and **D2** were conveniently synthesized by the one-step reaction outlined in Scheme 1. In particular, 4-carboxybenzaldehyde or 4-hydroxybenzaldehyde reacted with an equivalent amount of 4-nitrobenzyl cyanide in ethanol in the presence of sodium hydroxide to afford **D1** and **D2**, respectively. **D1** was obtained as sodium salt and the acidification of the latter by hydrochloric acid yielded the free dye. *tert*-Butoxide could be used instead of sodium hydroxide for the condensation reaction. Both compounds were obtained as dark-green solids which were soluble in common organic solvents like THF, chloroform and dichloromethane. Moreover, they were soluble in ethanol due to the presence of the carboxy or hydroxy group. Even though these dyes are small molecules, films of them could be obtained from their solutions by spin-casting.

Structural characterization of dyes was accomplished by FT-IR and ^{1}H NMR spectroscopy. Since these dyes are differentiated only from their anchoring groups, their spectra were similar. They showed common absorption bands around 1530, 1380 (NO_2), 2170 (cyano) and 1592 cm^{-1} (aromatic). Besides, **D1** displayed absorptions at 3408 and 1684 cm^{-1} (carboxyl), while **D2** at 3422 cm^{-1} (hydroxyl). The ^{1}H NMR spectra showed common peaks approximately at 8.18 (aromatic ortho to nitro) and 7.70 ppm (olefinic). Finally, **D1** and **D2** displayed characteristics signals at 12.09 and 5.34 ppm assigned to the carboxyl and hydroxyl, respectively.

3.2. Photophysical properties

The photophysical properties of the dyes were investigated in both dilute (10^{-5} M) THF solution and thin film.

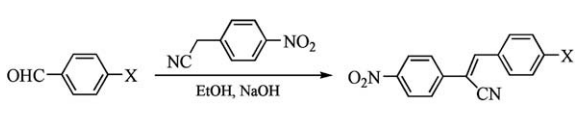

Scheme 1. Synthesis of dyes **D1** and **D2**.

Fig. 1 depicts the UV–vis absorption spectra of the dyes which have been normalized with respect the long-wavelength absorption. The photophysical characteristics of the dyes are summarized in Table 1.

Generally, the absorption curves of the dyes were broad and covered a wide range of the spectrum from 300 to ~750 nm. This attractive feature was attributed to the 4-nitro-α-cyanostilbene segment as it has been well established in our previous publications [22,23]. The long-wavelength absorption maximum ($\lambda_{a,max}$) was located at 617–655 nm. The thin film absorption curves of the dyes absolutely coincided above 550 nm and exhibited absorption onset at 761 nm corresponding to an optical band gap (E_g^{opt}) of 1.63 eV. This value of E_g^{opt} conforms to those of other related materials which contain 4-nitro-α-cyanostilbene moieties [22,23].

The UV–vis spectra of the sensitizers absorbed on TiO_2 film are shown in Fig. 2. The absorption spectrum of the blank TiO_2 film was subtracted from the curve. It can be seen in this figure that the absorption spectra were broadened, when anchored at the TiO_2 surface, as compared to pure dye spectra. Such broadening has been observed in other organic sensitizers on TiO_2 electrodes [27]. Strong interaction between the adsorbed dye molecules and oxide molecules in the TiO_2 surface leads to aggregate formation and consequently broadening the absorption spectrum. This might be correlated with the dye–TiO_2 and dye–dye interactions. The broadened absorption of dyes loaded on the TiO_2 film is advantageous for light harvesting of the solar spectrum. The concentration of the **D2** dye adsorbed on the film is lower than that of **D1**. This is attributable to impaired surface packing due to OH anchoring group of **D2**.The energetic alignment of the HOMO and LUMO energy levels is crucial for an efficient operation of the sensitizer in a DSSC. To ensure efficient electron injection from the excited dye into the conduction band of the TiO_2 films, the LUMO level must be higher in energy than the TiO_2 conduction band edge. The HOMO level of the sensitizer must be lower in energy than the redox potential of the I^-/I_3^- redox couple for efficient regeneration of the sensitizer cation after photoinduced electron injection into the TiO_2 film. The electrochemical behaviour of the sensitizers was investigated by CV [28] and the data are listed in Table 1. The HOMO and LUMO levels of both sensitizers are suitable for DSSCs. The difference between the LUMO of dye and the conduction band of TiO_2 should be higher than 0.2 eV for efficient electron injection. The LUMO energy levels (**D1**: −3.5 eV and **D2**: −3.7 eV) are sufficiently higher than the conduction band of TiO_2 (−4.0 eV). Hence, an efficient electron transfer from the excited dye to the TiO_2 is

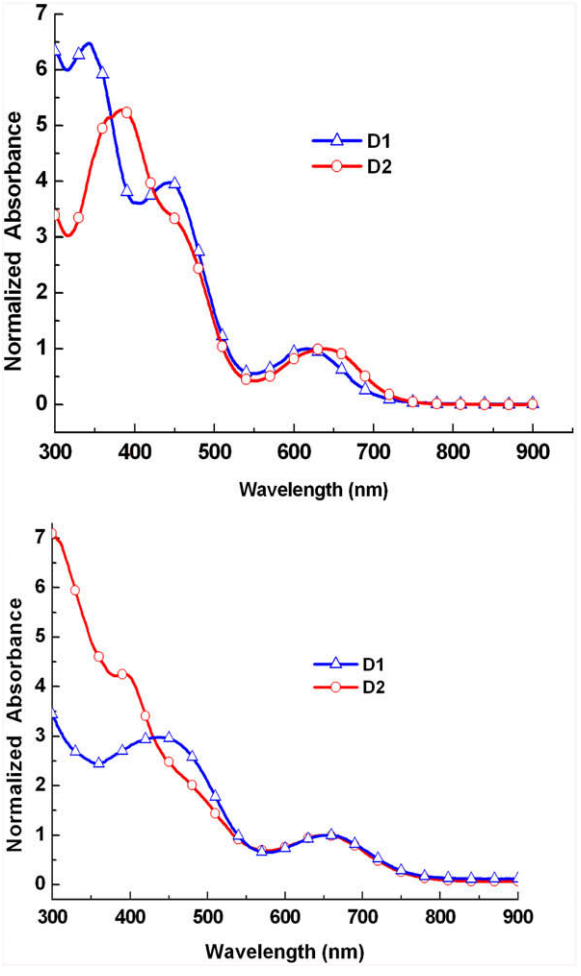

Fig. 1. Normalized absorption spectra of dyes in THF solution (top) and thin film (bottom).

Table 1
Optical and electrochemical properties of **D1** and **D2**.

Dye	D1	D2
$\lambda_{a,max}$[a] in solution (nm)	617	639
$\lambda_{a,max}$[a] in thin film (nm)	652	655
Thin film absorption onset (nm)	761	761
E_g^{opt}[b] (eV)	1.63	1.63
HOMO (eV)	−5.2	−5.4
LUMO (eV)	−3.5	−3.7
E_g^{el}[c] (eV)	1.7	1.7

[a] $\lambda_{a,max}$: the long-wavelength absorption maxima from the UV–vis spectra in THF solution or in thin film.
[b] E_g^{opt}: optical band gap determined from the absorption onset in thin film.
[c] E_g^{el}: electrochemical band gap determined from cyclic voltammetry.

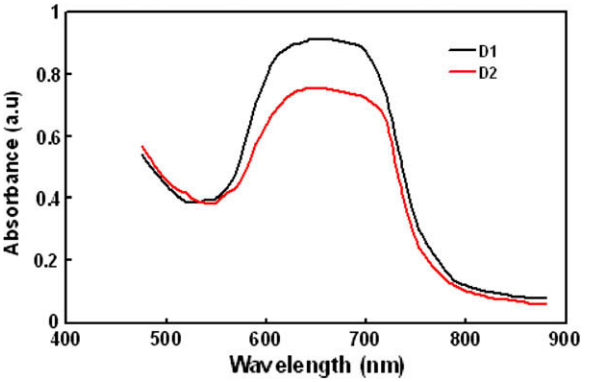

Fig. 2. UV–vis absorption spectra of the dyes adsorbed on TiO_2 films.

ensured. The HOMO energy levels of the dyes (**D1**: −5.2 eV and **D2**: −5.4 eV) are lower than the standard potential of the I^-/I_3^- redox couple (−4.83 eV vs. vacuum) [29]. Thus sufficient driving force for the regeneration of the oxidized sensitizer is available in DSSCs using these materials.

3.3. Photovoltaic performance

Fig. 3 shows the incident photon to current efficiency (IPCE) spectra for the DSSCs based on **D1** and **D2**. The IPCE data of **D1** sensitizer exhibit efficiency higher than 55% in the range 550–750 nm with a maximum value about 70% at 650 nm. On the other hand, the IPCE value for the DSSC based on **D2** dye is lower than that for **D1** in the same wavelength region. The IPCE for a DSSC can be expressed as

$$\mathrm{IPCE}(\lambda) = \mathrm{LHE}(\lambda)\phi_{\mathrm{inj}}\eta_{\mathrm{c}}$$

where LHE(λ) is the light harvesting efficiency of the photoelectrode, ϕ_{inj} is the charge injection efficiency from the excited state of dye into conduction band of the nano-crystalline semiconductor, and η_{c} is the collection efficiency of the injected electron by the electrode. The parameter LHE(λ) is related to the dye loading on the surface of the TiO_2 photoanode. We have estimated the amount of dye loading for both devices and found that it is slightly higher for **D1** than **D2**. In particular, the amount of the adsorbed dyes (dye loading) on the TiO_2 films were estimated by desorbing the dyes with basic solution, and the surface concentrations were determined to be 3.21×10^{-8} and 3.14×10^{-8} mol cm^{-2} for **D1** and **D2**, respectively. Therefore, the LHE(λ) does not much affect the IPCE. The improvement in the IPCE for DSSCs based on the **D1** may be mainly due to the other parameters, such as ϕ_{inj} and η_{c}. The parameter ϕ_{inj} depends on the energy difference between the LUMO of the dye and conduction band of TiO_2. This energy difference is higher for the DSSCs based on **D1** than **D2**. Therefore, the electron injection efficiency is higher for solar cells based on **D1** than **D2** leading to improved IPCE. The loss in the IPCE is probably caused by the reduced charge collection efficiency. The slightly lower dye loading favors the increased charge recombination between free electrons in the TiO_2 conduction band and oxidized species (tri-iodide) in the electrolyte at the uncovered TiO_2 surface.

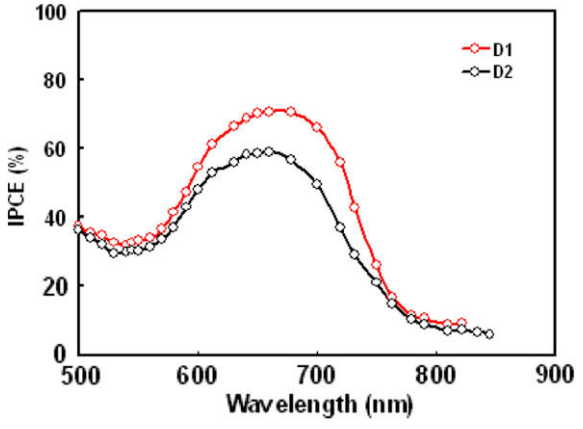

Fig. 3. The IPCE spectra of DSSCs fabricated with **D1** and **D2**.

The *J–V* characteristics of the DSSCs based on **D1** and **D2** are shown in Fig. 4. The photovoltaic parameters i.e. short circuit photocurrent (J_{sc}), open circuit voltage (V_{oc}), fill factor (FF) and power conversion efficiency (η) are summarized in Table 2. Depending on different anchoring groups, these dyes show different PCE in spite of the same band gap. The lower J_{sc} for DSSC based on **D2** is consistent with the lower IPCE, because the adsorbed amount of **D2** on the surface of TiO_2 is lower than **D1**. The lower value of V_{oc} can be explained by the increased charge recombination with the redox species which are present in the electrolyte.In DSSCs, the charge separation occurs in the adsorbed dyes by the injection of excited electrons into the conduction band of TiO_2 and reduction of the resulting dye cations by I^- in the electrolyte. Then, at short circuit conditions, the electrons and I_3^- diffuse towards the photoanode and Pt counter electrodes, respectively. Consequently, the charge collection efficiency is related to electron diffusion coefficient (D) and electron lifetime (τ) in TiO_2. The electron lifetime is defined as the average time spent in the TiO_2 electrode. If the electron diffusion length, which is $(D\tau)^{0.5}$, is shorter than the thickness of the TiO_2 electrode, the electrons in TiO_2 are recombined with the dye cations and/or I_3^- during the diffusion. The high IPCE of the present DSSCs indicates that the recombination at short circuit conditions is negligible. At open circuit conditions, the injected electrons in TiO_2 are accumulated until the charge injection rate is balanced with the recombination rate. The recombination rate depends upon the electron lifetime in the TiO_2 electrode. The electron lifetime of the electron also depends on the reorganization energy of dye used in the DSSC [30].

The electrochemical impedance spectra of the DSSCs based on **D1** and **D2** were measured to investigate the kinetic process about the back reaction. The electrochemical

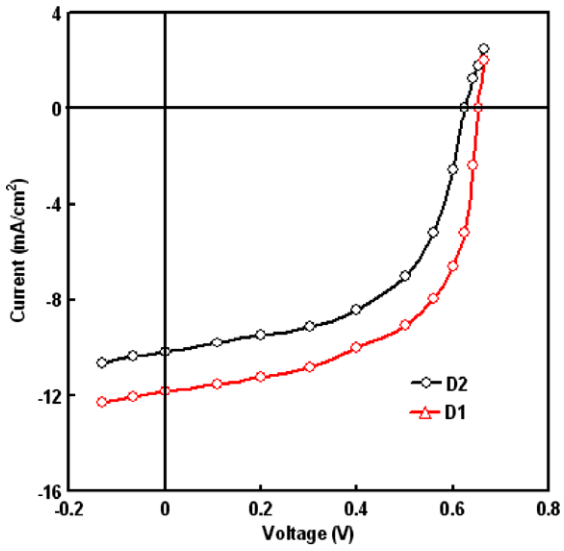

Fig. 4. *J–V* characteristics under illumination of DSSCs based on **D1** and **D2** dye.

Table 2
Photovoltaic performance of the quasi solid state DSSCs for the two dyes on different measured conditions.

Dye	Short-circuit current (J_{sc}) (mA/cm^2)	Open circuit voltage (V_{oc}) (V)	Fill factor (FF)	Power conversion efficiency (η) (%)
D1[a]	11.8	0.65	0.63	4.80
D2[a]	10.2	0.61	0.56	3.50
D1[b]	11.9	0.69	0.66	5.42
D2[b]	10.4	0.65	0.60	4.00

[a] With undoped TiO_2 photoanode.
[b] With nitrogen doped TiO_2 photoanode.

impedance spectra of the DSSCs based on **D1** and **D2** in the form of Bode plots in dark at forward bias of 0.65 V are presented in Fig. 5. The peak at intermediate frequencies (~100–1 Hz) is mainly attributed to the charge transfer at the TiO_2/electrolyte interface [31]. The electron lifetime (τ) can be calculated by the reciprocal of peak frequency (f_p) [31]

$$\tau = 1/\omega_p = 1/2\pi f_p$$

The electron lifetime for the DSSC based on **D1** is 25 ms which is about 1.6 times longer than the DSSC based on **D2** with electron lifetime of 15 ms. The open circuit voltage decay analysis also shows that DSSC based on **D1** has a longer electron lifetime than that of DSSC with **D2**. The longer electron lifetime of the DSSC with **D1** contributes to its superior photovoltaic performance.

We measured photovoltage decay of the devices at various white light intensities in order to study the charge recombination rates between electrons in TiO_2 conduction band and tri-iodide ions in the electrolyte [32]. The recombination rates are plotted in Fig. 6 versus the open circuit voltage of the DSSC, adjusted by varying the white light intensities. The V_{oc} in the cell is given by the difference between the redox level of the electrolyte and the quasi Fermi level of TiO_2. It can be determined by the concentration of free charge carriers. This plot allows us to compare the recombination rate at equal charge density concentration in the TiO_2 films. The recombination rate is known to increase exponentially with increasing light intensity due to a filling of intra-band trap states in the TiO_2. This allows a faster de-trapping of electrons to the conduction band

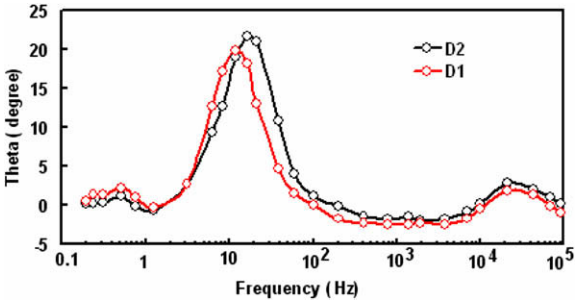

Fig. 5. The electrochemical impedance spectra of the DSSCs based on **D1** and **D2** in the form of Bode plots in dark at forward bias of 0.65 V.

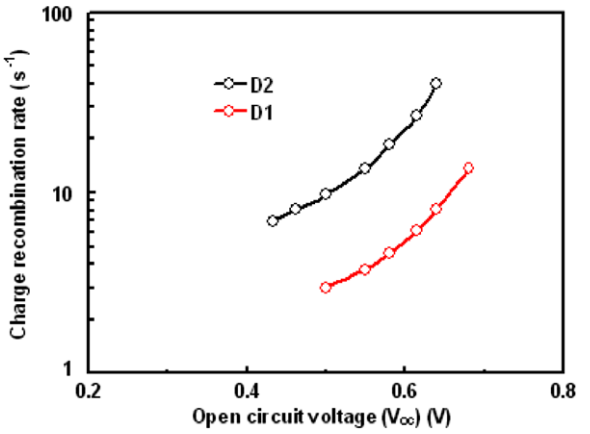

Fig. 6. Comparison of charge recombination rate in DSSCs based on the **D1** and **D2**.

and subsequent recombination with tri-iodide [33]. The recombination rate for DSSC based on **D2** is about two times higher than that for DSSC with **D1**, which can be attributed to an increased current (dark current) due to the recombination of electrons in conduction band of TiO_2 with the tri-iodide ions in the electrolyte. The higher recombination rate also leads to a decrease in the free charge carriers in the conduction band of TiO_2, which induces a downward shift of conduction band of TiO_2 towards the iodide /tri-iodide potential. Both the higher recombination rate and the downward shifted conduction band in the DSSC based on **D2** explain the lower V_{oc} measured in the *J–V* characteristics. Additionally, the higher charge recombination rate reduces the charge collection efficiency and consequently the J_{sc} and PCE.

It has been reported that the addition of nanoparticles such as TiO_2 and SiO_2 in the electrolyte can increase the ionic conductivity [34]. In these nanocomposite electrolytes, the anion species are aligned around the nanoparticles, facilitating the electron exchange reaction [33]. It is noted that the TiO_2 nanoparticles with particle size of 5–10 nm are selected because they are sufficiently smaller that the pore diameter of the typical nanoporous TiO_2 layer (15–25 nm). In our case the ionic conductivity of electrolyte with and without TiO_2 nanoparticle is 0.11 and 0.18 mS cm^{-1}, respectively. For comparison, we have also measured the *J–V* characteristics of the DSSC of **D1** dye based on the quasi solid state electrolyte without TiO_2 nanoparticles, under illumination intensity of 100 mW/cm^2 and found that the J_{sc} and V_{oc} are about 9.6 mA/cm^2 and 0.72 V, respectively. This is attributed to the lower concentration of free tri-iodide ions near the dye attached to TiO_2 surface, because the surfaces of the nanoparticles can immobilize the ions. This also results in slightly smaller V_{oc} owing to the high electron concentration at TiO_2 surface of electrolyte. The charge transport in electrolyte medium may be effectively facilitated by adding nanoparticles to the polymer electrolyte. The enhancement in the solar cell performance upon the introduction of the TiO_2 nanoparticles in the polymer electrolyte is due to the improved ion conductivity.

3.4. Effect of nitrogen doped TiO_2 photoanode

One crucial component in DSSCs is that the nanostructure TiO_2 electrode has some oxygen deficiency in the crystal structure [35]. The oxygen deficiency could create electron–hole pairs. The oxidizing holes can react with dye or be scavenged by iodide ions [36]. These processes result in shortening the electron life time. Consequently doping with nitrogen into the TiO_2 crystal structure can improve the oxygen deficiency and decrease the back reaction. Asahi et al. reported at 2001 that photocatalytic activity can be achieved by nitrogen doping. Considerable research on nitrogen doping in TiO_2 film has been extensively conducted [37]. Recently, doping of nitrogen into TiO_2 for the improvement of DSSCs performance has been reported [38]. We have attempted to improve the photovoltaic performance of the DSSCs using nitrogen doped TiO_2 photoelectrode.

The nitrogen doped TiO_2 materials prepared by modified sol gel method using urea as nitrogen carrier display a yellow color and are characterized by X-ray diffraction (XRD) analysis. XRD spectrum of the nitrogen doped TiO_2 powder shows anatase phase. The average crystallite size calculated from the broadening of the (1 0 1) XRD peak of the anatase phase was 20.3 and 17.5 nm for doped and undoped TiO_2, respectively. We have observed a little shift in the (1 0 1) peak position for nitrogen doped TiO_2 which is consistent with the work reported earlier [39].

Fig. 7a shows the *J–V* characteristics of the DSSCs based on the nitrogen doped photoelectrode using **D1** and **D2**. The photovoltaic performance of the DSSCs is shown in Table 2. It is apparent from this table that V_{oc} and FF shift to higher values with the nitrogen doped TiO_2 electrode, whereas J_{sc} remains almost unchanged. The increase of V_{oc} in the presence of nitrogen compared with that in the absence of nitrogen may be explained by the change in the quasi Fermi level (E_f) of TiO_2 photoelectrode. Using Fermi level pinning, these two parameters are described by the relationship [40]:

$$V_{oc} = |E_f - E_{red}|$$

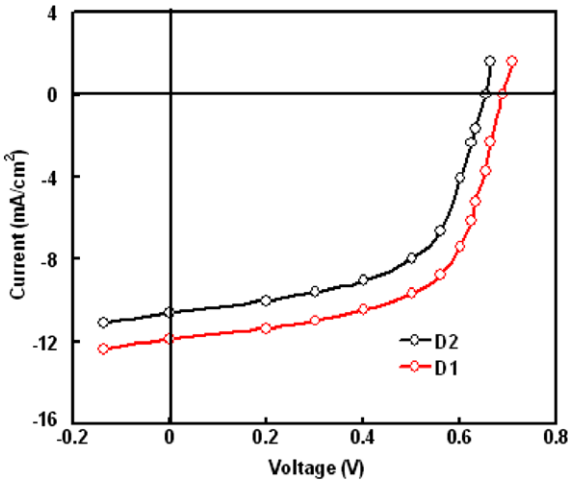

Fig. 7a. *J–V* characteristics under illumination of DSSCs based on **D1** and **D2** dye using nitrogen doped TiO_2 photoelectrode.

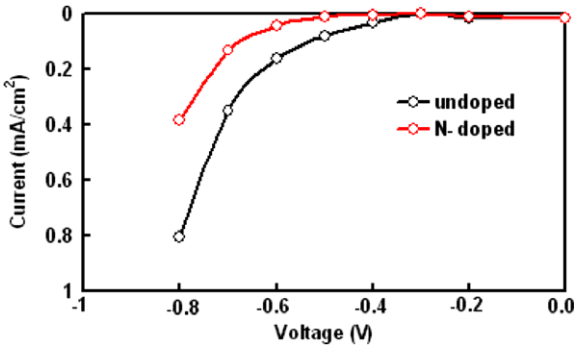

Fig. 7b. Dark *J–V* characteristics under illumination of DSSCs based on **D1** and **D2** using nitrogen doped and undoped TiO_2 photoelectrode.

where E_{red} is the standard reduction potential of redox couple, assuming that the E_{red} does not vary with the addition of nitrogen. Therefore, the increase in V_{oc} of the DSSCs with the addition of nitrogen in the TiO_2 photoelectrode, may be attributed to the retarding of the dark current, as shown in Fig. 7b, or to the decrease of the charge recombination. The addition of nitrogen in the TiO_2 can suppress the production of the dark current. By comparing the dark current of DSSCs based on nitrogen doped TiO_2 and bare TiO_2 photoanode, it is observed that the nitrogen doped DSSC exhibit smaller dark current. This indicates that the nitrogen doping could successfully retard the charge recombination at the TiO_2/dye/electrolyte interface. Thus, the nitrogen doped TiO_2 introduced formation of O–Ti–N structure which can suppress the reduction of I_3^- on the TiO_2 electrode. The onset voltage in the dark current for DSSC also shifts to higher voltage with nitrogen doped TiO_2 electrode as compared to undoped TiO_2 electrode. This means that E_{fb} of TiO_2 shifts towards the vacuum level with doping, leading to higher value of V_{oc}.

In the Bode plots of electrochemical impedance spectral data, it can be seen that adding nitrogen into TiO_2 shifts the middle frequency peak to lower frequency, as shown in Fig. 8. This corresponds to an increase in the electron lifetime and suppressing the back transfer of photoexcited electron from nitrogen doped TiO_2 nanoparticles to the electrolyte at TiO_2/dye/electrolyte interface. This confirms that the nitrogen doping into TiO_2 photoanode can improve the performance of the DSSC.

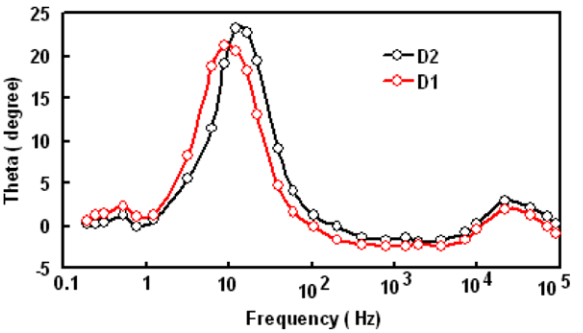

Fig. 8. The electrochemical impedance spectra of the DSSCs based on **D1** and **D2** using nitrogen doped TiO_2 electrode in the form of Bode plots in dark at forward bias of 0.65 V.

4. Conclusions

Two new photosensitizers **D1** and **D2** based on 4-nitro-α-cyanostilbene with carboxy or hydroxyl anchoring group were synthesized in high yields from a one-step reaction only. The long-wavelength absorption maximum was located at 617–655 nm with thin film absorption onset at 761 nm which corresponds to an optical band gap of 1.63 eV. Quasi solid state dye-sensitized solar cells were fabricated using polymer gel electrolyte and dyes **D1** and **D2**. In DSSC based on **D1**, IPCE about 70% at the absorption maxima was observed with overall PCE of 4.8%. The lower PCE in the case of **D2** is ascribed to the reduction in the photocurrent due to less dye loading on the TiO_2 surface, since **D2** has the OH anchoring group. The lower PCE of the DSSC based on the **D2** has also been ascribed in terms of increased recombination rate and lower electron lifetime. It was found that the PCE of the DSSCs has been enhanced when a nitrogen doped TiO_2 photoanode is used. The increase in PCE is attributed to the retardation of charge recombination and the introduction of nitrogen, which replaced the oxygen deficiency in the titania crystal lattice. The enhanced electron lifetime for doped TiO_2 DSSCs could be attributed to the formation of O–Ti–N in the TiO_2 electrode to retard the recombination reaction at the TiO_2/electrolyte interface, as compared to DSSC based on undoped TiO_2 electrode. Additionally, the E_{fb} of TiO_2 is also affected slightly by the presence of nitrogen which is responsible for the improvement in V_{oc} and PCE.

References

[1] B. O'Regan, M. Grätzel, Nature 353 (1991) 737.
[2] A. Hagfeldt, M. Grätzel, Acc. Chem. Res. 33 (2000) 269.
[3] M.K. Nazeeruddin, P. Pechy, M. Grätzel, Chem. Commun. (1997) 1705.
[4] A. Hagfeldt, M. Grätzel, Chem. Rev. 95 (1995) 49.
[5] H.J. Snaith, L. Schmidt-Mende, Adv. Mater. 19 (2007) 3187.
[6] (a) Md.K. Nazeeruddin, S.M. Zakeeruddin, R. Humphry-Baker, M. Jirousek, P. Liska, N. Vlachopoulos, V. Shklover, C.-H. Fischer, M. Grätzel, Inorg. Chem. 38 (1999) 6298;
(b) P. Wang, B. Wenger, R. Humphry-Baker, J.E. Moser, J. Teuscher, W. Kantlehner, J. Mezger, E.V. Stoyanov, S.M. Zakeeruddin, M. Grätzel, J. Am. Chem. Soc. 127 (2005) 6850;
(c) P. Wang, C. Klein, R. Humphry-Baker, S.M. Zakeeruddin, M. Grätzel, J. Am. Chem. Soc. 127 (2005) 808;
(d) L. Schmidt-Mende, J.E. Kroeze, J.R. Durrant, M.K. Nazeeruddin, M. Grätzel, Nano Lett. 5 (2005) 1315;
(e) C.S. Karthikeyan, H. Wietasch, M. Thelakkat, Adv. Mater. 19 (2007) 1091;
(f) A. Staniszewski, S. Ardo, Y. Sun, F.N. Castellano, G.J. Meyer, J. Am. Chem. Soc. 130 (2008) 11586;
(g) Y. Cao, Y. Bai, Q. Yu, Y. Cheng, S. Liu, D. Shi, F. Gao, P. Wang, J. Phys. Chem. C 113 (2009) 6290.
[7] M.K. Nazeeruddin, P. Péchy, T. Renouard, S.M. Zakeeruddin, R. Humphry- Baker, P. Comte, P. Liska, Le Cevey, E. Costa, V. Shklover, L. Spiccia, G.B. Deacon, C.A. Bignozzi, M. Grätzel, J. Am. Chem. Soc. 123 (2001) 1613.
[8] S. Ito, S.M. Zakeeruddin, R. Humphry-Baker, P. Liska, R. Charvet, P. Comte, Md.K. Nazeeruddin, P. Péchy, M. Takata, H. Miura, S. Uchida, M. Grätzel, Adv. Mater. 18 (2006) 1202.
[9] K. Hara, Z.-S. Wang, T. Sato, A. Furube, R. Katoh, H. Sugihara, Y. Danoh, C. Kasada, A. Shinpo, S. Suga, J. Phys. Chem. B 109 (2005) 15476.
[10] Z.-S. Wang, N. Koumura, Y. Cui, M. Takahashi, H. Sekiguchi, A. Mori, T. Kubo, A. Furube, K. Hara, Chem. Mater. 20 (2008) 3993.
[11] S. Kim, J.K. Lee, S.O. Kang, J. Ko, J.H. Yum, S. Fantacci, F. De Angelis, D. Di Censo, Md.K. Nazeeruddin, M. Grätzel, J. Am. Chem. Soc. 128 (2006) 16701.
[12] R. Chen, X. Yang, H. Tian, X. Wang, A. Hagfeldt, L. Sun, Chem. Mater. 19 (2007) 4007.
[13] S. Hwang, J.H. Lee, C. Park, H. Lee, C. Kim, C. Park, M.-H. Lee, W. Lee, J. Park, K. Kim, N.-G. Park, C. Kim, Chem. Commun. 46 (2007) 4887.
[14] K. Hara, T. Sato, R. Katoh, A. Furube, Y. Ohga, A. Shinpo, S. Suga, K. Sayama, H. Sugihara, H. Arakawa, J. Phys. Chem. B 107 (2003) 597.
[15] H. Choi, C. Baik, S.O. Kang, J. Ko, M.S. Kang, Md.K. Nazeeruddin, M. Grätzel, Angew. Chem., Int. Ed. 47 (2008) 327.
[16] S. Kim, H. Choi, D. Kim, K. Song, S.O. Kang, J. Ko, Tetrahedron 63 (2007) 9206.
[17] W.-H. Liu, I.-C. Wu, C.-H. Lai, C.-H. Lai, P.-T. Chou, Y.-T. Li, C.-L. Chen, Y.-Y. Hsub, Y. Chi, Chem. Commun. 41 (2008) 5152.
[18] (a) C.P. Hsieh, H.P. Lu, C.L. Chiu, C.W. Lee, S.H. Chuang, C.L. Mai, W.N. Yen, S.J. Hsu, E.W.G. Diau, C.Y. Yeh, J. Mater. Chem. 20 (2010) 1134;
(b) J.A. Mikroyannidis, M.M. Stylianakis, P. Suresh, M.S. Roy, G.D. Sharma, Energy Environ. Sci. 2 (2009) 1301;
(c) J.A. Mikroyannidis, M.M. Stylianakis, M.S. Roy, P. Suresh, G.D. Sharma, J. Power Sources 194 (2009) 1179;
(d) W. Zhang, Z. Fang, M.J. Su, M. Saeys, B. Liu, Macromol. Rapid Commun. 30 (2009) 1537;
(e) C.W. Lee, H.P. Lu, C.M. Lan, Y.L. Huang, Y.R. Liang, W.N. Yen, Y.C. Liu, Y.S. Lin, E.W.G. Diau, C.Y. Yeh, Chem. Eur. J. 15 (2009) 1412;
(f) N. Koumura, Z.-S. Wang, M. Miyashita, Y. Uemura, H. Sekiguchi, Y. Cui, A. Mori, S. Mori, K. Hara, J. Mater. Chem. 19 (2009) 4829.
[19] (a) Q.H. Yao, F.S. Meng, F.Y. Li, H. Tian, C.H. Huang, J. Mater. Chem. 13 (2003) 048;
(b) M. Xu, S. Wenger, H. Bala, D. Shi, R. Li, T. Zhou, S.M. Zakeeruddin, M. Grätzel, P. Wang, J. Phys. Chem. C 113 (2009) 2966.
[20] Z.S. Wang, F.Y. Li, C.H. Huang, Chem. Commun. (2000) 2063.
[21] B.C. O'Regan, S. Scully, A.C. Mayer, E. Palomares, J. Durrant, J. Phys. Chem. B 109 (2005) 4616.
[22] (a) J.A. Mikroyannidis, M.M. Stylianakis, P. Balraju, P. Suresh, G.D. Sharma, ACS Appl. Mater. Interfaces 1 (8) (2009) 1711;
(b) J.A. Mikroyannidis, M.M. Stylianakis, P. Suresh, P. Balraju, G.D. Sharma, Org. Electron. 10 (7) (2009) 1320;
(c) J.A. Mikroyannidis, S.S. Sharma, Y.K. Vijay, G.D. Sharma, ACS Appl. Mater. Interfaces 2 (1) (2010) 270.
[23] J.A. Mikroyannidis, A. Kabanakis, P. Balraju, G.D. Sharma, J. Phys. Chem. C, submitted for publication.
[24] R. Merck, Bull. Soc. Chim. Belg. 58 (1949) 460.
[25] H.S. Blair, T.-K. Law, Polymer 21 (1980) 1475.
[26] G.R. Robertson, Org. Synth. Coll. 1 (1941) 396, 2 (1922) 57.
[27] (a) N. Cho, H. Choi, D. Kim, K. Song, M.S. Kang, S.O. Kang, J. Ko, Tetrahedron 65 (2009) 6236;
(b) K. Sayama, K. Hara, N. Mori, M. Satsuki, S. Suga, S. Tsukagoshi, Y. Abe, H. Sugihara, H. Arakawa, Chem. Commun. (2000) 1173.
[28] H. Tian, X. Yang, J. Cong, R. Chen, C. Teng, J. Liu, Y. Hao, L. Wang, L. Sun, Dyes Pigm. 84 (2010) 62.
[29] G. Zhang, H. Bala, Y. Cheng, D. Shi, X. Lv, Q. Yu, P. Wang, Chem. Commun. (2009) 2198.
[30] (a) N. Koumura, Z.S. Wang, S. Mori, M. Miyashita, E. Suzuki, K. Hara, J. Am. Chem. Soc. 128 (2006) 14256;
(b) M. Miyashita, K. Sunahara, T. Nishikawa, Y. Uemura, N. Koumura, K. Hara, A. Mori, T. Abe, E. Suzuki, S. Mori, J. Am. Chem. Soc. 130 (2008) 17874.
[31] M. Adachi, M. Sakamoto, J. Jin, Y. Ogata, S. Isoda, J. Phys. Chem. B 110 (2006) 13872.
[32] N.W. Duffy, L.M. Peter, K.G.U. Wijayantha, Electrochem. Commun. 2 (2000) 262.
[33] J. Bisquert, V.S. Vikhrenko, J. Phys. Chem. B 108 (2004) 2313.
[34] (a) M. Berginc, M. Hocevar, U.O. Krasovec, A. Hinsch, R. Santrawan, M. Topic, Thin Solid Films 516 (2008) 4645;
(b) M.S. Kang, K.S. Ahn, J.W. Lee, J. Power Sources 180 (2008) 896.
[35] (a) I. Inakamura, N. Negishi, S. Kutsuma, T. Ihara, S. Sugihara, K. Takeuchi, J. Mol. Catal. A: Chem. 161 (2000) 205;
(b) H. Irie, Y. Watanabe, K. Hashimoto, J. Phys. Chem. B 107 (2003) 5483.
[36] M. Mrowetz, W. Balcerski, A.J. Colussi, M.R. Hoffmann, J. Phys. Chem. B 108 (2004) 17269.
[37] (a) R. Asahi, T. Morkawa, T. Ohwaki, K. Aoki, Y. Taga, Science 293 (2001) 269;
(b) T. Lindgren, J.M. Mwabora, E.D. Avendano Soto, J. Jonsson, A. Hoel, C.G. Granqvist, S.E. Lindquist, J. Phys. Chem. B 107 (2003) 5709;
(c) S. Sakthivel, H. Kisch, Chem. Phys. Chem. 4 (2003) 487.
[38] T. Ma, M. Akiyama, E. Abe, I. Imai, Nano Lett. 5 (2005) 2543.
[39] T.C. Jagadake, S.P. Takale, R.S. Sonawane, H.M. Joshi, S.I. Patil, B.B. Kale, S.B. Ogale, J. Phys. Chem. C 112 (2008) 14595.
[40] T.S. Kang, K.H. Chun, J.S. Hong, S.H. Moon, K. Kim, J. Electrochem. Soc. 147 (2000) 3049.

Despite these unique advantages, however, the vast majority of organic phototransistors demonstrated to date operate at high voltages that typically exceed |20| V [9–12]. This represents a major technology bottleneck since most targeted device applications – e.g. portable and battery-powered optical sensors etc. – require significantly lower voltages (i.e. <|10| V). Therefore, successful implementation of the phototransistor technology in future generations of optical sensors would not only require the development of high performance device architectures but also the demonstration of low operating voltage organic phototransistors.

Here we demonstrate the first low-voltage and low-power ambipolar organic transistors based on self-assembled monolayer (SAM) gate dielectrics and suitably designed p/n-heterostructure semiconducting layers. The incorporation of SAM gate dielectrics has proven effective at reducing the dielectric thickness and thereby reducing the operating voltage of organic field-effect transistors to <3 V [15–18]. Interestingly, these low-voltage ambipolar transistors are found to respond to visible light. For instance, by illuminating the device with blue light, the source–drain current can be modulated by a few orders of magnitude. This effect is attributed to electron transfer from the donor material – i.e. the pentacene layer in this case – to the acceptor material, namely [6,6]-phenyl-C_{61}-butyric acid methyl ester [$PC_{61}BM$], occurring at the pentacene/$PC_{61}BM$ interface (see Fig. 1a). Simultaneous measurement of incident light intensity and photoinduced channel current allows the response speed and external quantum efficiency (EQE) of these phototransistors to be estimated. By integrating two phototransistors we are also able to demonstrate low-voltage complementary-like inverters with high signal gain and interesting light-sensing properties.

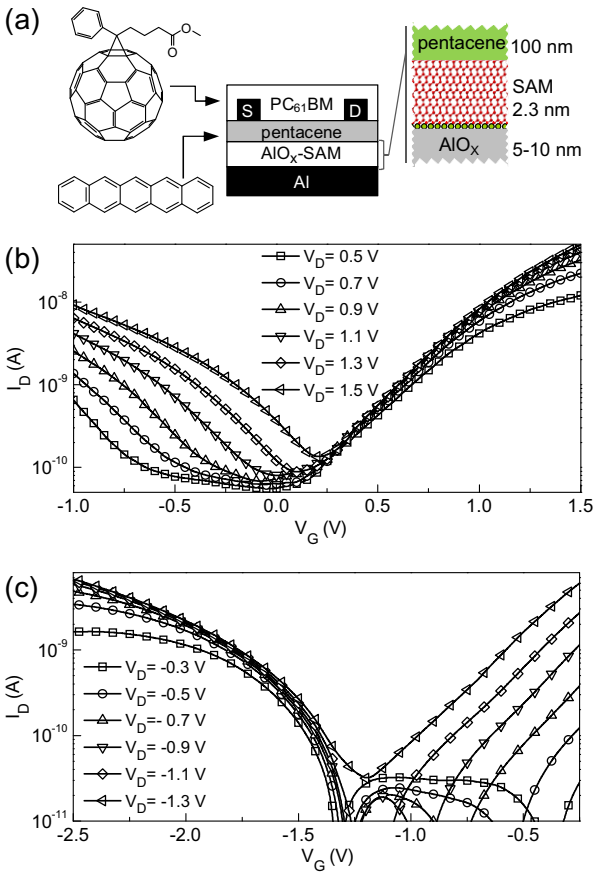

Fig. 1. (a) Molecular structures of $PC_{61}BM$ and pentacene and a schematic representation of the bottom-gate, middle-contact p–n heterostructure transistor used in this study. (b) Transfer characteristics of the low-voltage heterostructure ambipolar OFET (L = 50 μm, W = 1 mm) measured in the dark with positive V_D. (c) Transfer characteristics of the same OFET measured in the dark with negative V_D.

2. Experimental

Aluminium gate electrodes were thermally deposited onto glass substrates under high vacuum. The surfaces of the gate electrodes were oxidized in oxygen plasma leading to the formation of native alumina a few nanometres thick [16]. A 1.7 mg/ml solution of octadecylphosphonic acid (ODPA) in isopropanol was drop-cast onto the electrodes followed by rinsing with pure isopropanol. The substrates were then thermally annealed for 20 h at 140 °C under ambient-pressure in N_2. Following this a pentacene layer (100 nm) was deposited by thermal sublimation under high vacuum (10^{-9} bar) at a rate of 1 Å s^{-1}. Gold source (S) and drain (D) electrodes (45 nm) were then thermally deposited onto the pentacene layer. Finally, a 20 mg/ml solution of $PC_{61}BM$ in chlorobenzene was spin-cast onto the devices at 1000 rpm for 60 s. Commercially available 99.9% pure sublimed grade pentacene and 99.5% pure $PC_{61}BM$ were used in this study. A schematic of the device architecture and the molecular structures of the materials used are shown in Fig. 1a. Electrical characterisation was carried out in N_2 at atmospheric pressure using a Keithley 4200 semiconductor parameter analyser. An indium gallium nitride (InGaN) light emitting diode (LED) with a peak emission at 469 nm (blue light) was used for optical illumination.

3. Results and discussion

Fig. 1b shows the ambipolar transfer characteristics of a low-voltage OFET with a channel length (L) and width (W) of 50 μm and 1 mm, respectively, measured in the dark with drain voltages between V_D = 0.5 V and V_D = 1.5 V. Fig. 1c shows the ambipolar transfer characteristics of the same low-voltage OFET measured in the dark with drain voltages between V_D = −0.3 V and V_D = −1.3 V. The transistor can be considered to consist of a separate bottom-gate, top-contact pentacene p-channel (formed at the SAM/pentacene interface) and a bottom-gate, bottom-contact $PC_{61}BM$ n-channel (formed at the pentacene/$PC_{61}BM$ interface). Depending on the applied voltage at the gate and drain electrodes, charge injection will take place into the different semiconducting channels. The ODPA SAM dielectric implemented in this device has been thoroughly characterised in our previous work [17,18]. Geometrical capacitances in the range of 600–800 nF cm^{-2} [17] and

leakage current densities of metal–insulator–metal structures on the order of 10^{-9} A cm^{-2} [18] were observed.

The specific device structure of Fig. 1a can be referred to as bottom-gate, middle-contact (BG-MC). Middle-contact heterostructure OFETs based on pentacene and C_{60} have previously been shown to exhibit good ambipolar transistor behaviour [19]. Using standard OFET models [1], the electron and hole mobilities were calculated from the transfer characteristics to be $\mu_e = 0.2$ cm^2/Vs and $\mu_h = 7 \times 10^{-4}$ cm^2/Vs, respectively. The asymmetry of the two channels is attributed to a disruption of the pentacene layer morphology upon deposition of the $PC_{61}BM$ solution. Prior to deposition of the $PC_{61}BM$ layer, the hole mobility was measured to be $\mu_h \sim 10^{-1}$ cm^2/Vs (data not shown), possibly suggesting that the $PC_{61}BM$ solution affects the integrity of the pentacene film slightly. This is incidentally believed to also lead to a very smooth pentacene/$PC_{61}BM$ interface, facilitating good electron transport. The threshold voltages calculated from plots of $I_D^{1/2}$ versus V_G in the saturation regime (not shown) were found to be 0.7 V and −1.4 V for the n- and p-channels, respectively. Using impedance measurements performed on the OFETs, the geometrical capacitances of the gate dielectrics for the $PC_{61}BM$ and pentacene channels were calculated yielding ~70 nF cm^{-2} and ~800 nF cm^{-2}, respectively. These measurements were carried out at a frequency of 400 Hz. Above 200 Hz the dependence of the measured capacitance on signal frequency was found to be negligible (data not shown).

To examine the suitability of these low-voltage ambipolar OFETs as light-sensors, we have studied their operating characteristics under illumination. When illuminated with blue light (λ_{peak} = 469 nm) the drain current (I_D) of the transistors was found to increase (Fig. 2a). The n-channel threshold voltage (V_T) also changed by −0.2 V under illumination at 3.2 mW cm^{-2} whilst the p-channel V_T remained constant. The threshold voltage shift is attributed to changes in the density of trapped charges at the interface between the two semiconductors [20], whilst the increase in off-current is attributed to the creation and dissociation of photo-generated excitons near the $PC_{61}BM$/pentacene interface, a process similar to that observed in pentacene/fullerene heterojunction solar cells [21]. These two effects have previously been referred to as photoconductive and photovoltaic effects, respectively [9]. The inset in Fig. 2a shows the energy levels of the two semiconductor materials and the suitability of this energetic interface for effective charge transfer from the lowest unoccupied molecular orbital (LUMO) level of pentacene to the LUMO of $PC_{61}BM$. The fact that the p-channel threshold voltage remains unchanged under illumination suggests the majority of dissociated charges do not reach the rather distant pentacene:SAM interface – approximately 100 nm away, i.e. the thickness of the pentacene layer – where hole transport across the channel is taking place. By analysing the evolution of either V_T or I_D, under p-channel operation as a function of illumination intensity, one could in principle calculate the density of photo-generated charges, i.e. the number of electrons transferred from pentacene to $PC_{61}BM$. Although these measurements are beyond the scope of this work, they clearly demonstrate the potential of bi-layer phototransistors for use not only as photosensors but also as a test-bed for fundamental studies.

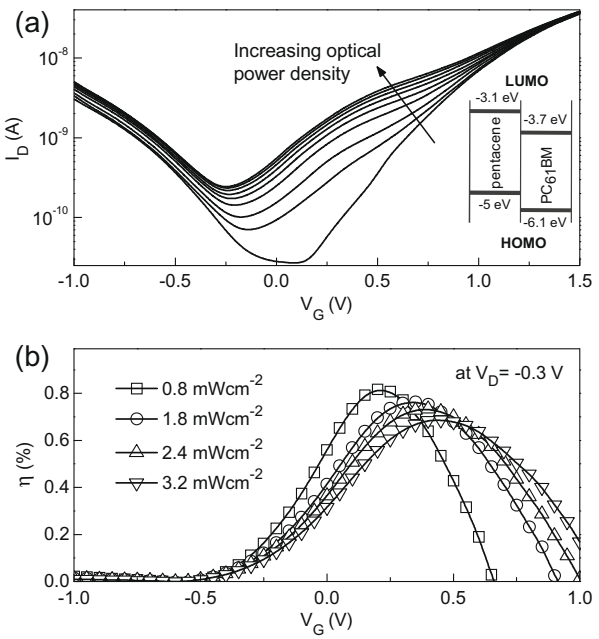

Fig. 2. (a) Transfer characteristics of heterostructure ambipolar OFET (L = 50 μm, W = 1 mm) measured at V_D = −1 V, under blue light illumination (using a λ_{peak} = 469 nm LED) with incident optical power densities between 0 and 3.2 mW cm^{-2}. Inset: simplified energy diagram of the pentacene/$PC_{61}BM$ interface. (b) External quantum efficiency of the same OFET, measured at V_D = −0.3 V, as a function of V_G for different incident optical power densities.

From Fig. 2a it can clearly be seen that the magnitude of photo-generated current in the off-state is modulated by the power density of incident light. By defining the external quantum efficiency (EQE) η, as the ratio of the number of photo-generated carriers that contribute to the drain current to the number of photons incident on the transistor channel area, the EQE of the phototransistors can be defined as:

$$\eta = \frac{(I_{light} - I_{dark})hc}{ePA\lambda_{peak}}$$

Here I_{light} and I_{dark} are the transistor drain currents under illumination and in the dark, respectively, h is the Plank constant, c is the speed of light in *vacuo*, e is the magnitude of the fundamental unit of charge, P is the incident optical power density, A is the area of the transistor channel and λ_{peak} is the peak wavelength of the incident light. For these measurements the LED source is approximated to be monochromatic.

A plot of η versus V_G for a range of optical power densities is shown in Fig. 2b.The observed reduction in the peak EQE with increasing optical power density is most likely attributed in the saturation of photo-generated carriers. Further details on this mechanism can be found elsewhere [22]. The peak EQE of these phototransistors was found to be approximately 0.8%. From Fig. 2b it can also be seen that the transistor photoresponsivity can be tuned by the V_G potential. By biasing the transistor at V_G = 0.5 V and V_D = 1 V and pulsing the LED, the dynamic response of the

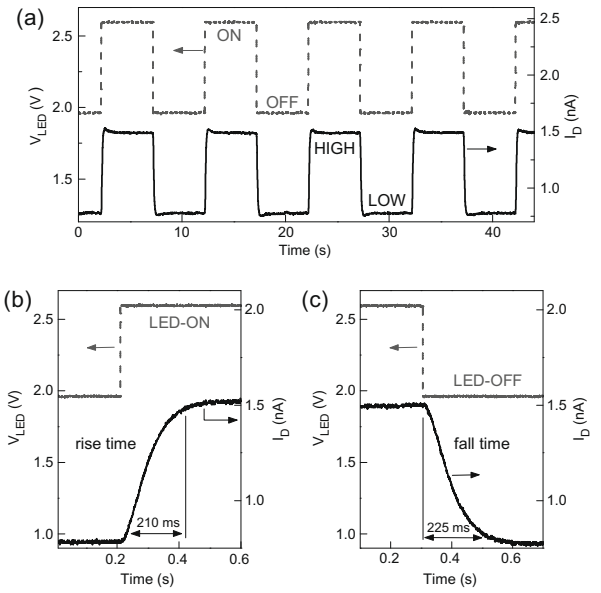

Fig. 3. (a) Evolution of channel current in an OFET (L = 50 μm, W = 1 mm), measured at V_D = 1 V and V_G = 0.5 V, as a function of time under pulsed light (λ_{peak} = 469 nm) illumination. The upper (dashed) trace shows the voltage applied to the LED (V_{LED}) while the lower (solid) trace shows the evolution of the channel current versus time. (b) Switch-on and (c) switch-off optical response of OFET as a function of time.

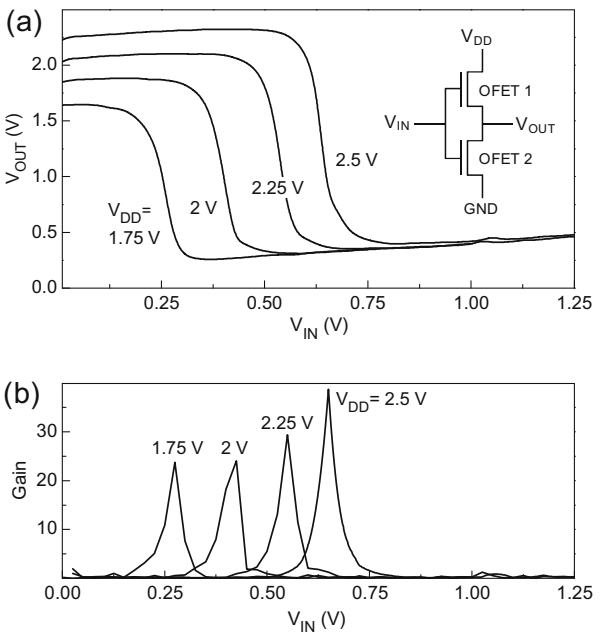

Fig. 4. (a) Transfer characteristics (V_{OUT} versus V_{IN}) of a low-voltage complementary-like inverter consisting of two SAM-based heterostructure OFETs measured at different supply voltages (V_{DD}). Inset: circuit diagram of complementary-like inverter. (b) Small-signal gain versus V_{IN} at different V_{DD}.

phototransistor was also measured (Fig. 3). The switch-on and switch-off times for this device were approximated from the dynamic measurements shown in Fig 3b and c, respectively, yielding values in the range 210–225 ms. The relatively low switching speed is attributed to the large overlap between the source/drain and gate electrodes and the large channel length, resulting in: (i) high RC constants and (ii) long carrier transit times. Significant improvement is anticipated through device design optimisation such as development of phototransistors with aligned gate electrodes and shorter channel lengths. The response time, whilst long for most photodetector applications, is significantly shorter than observed lifetimes of trapped charges (minutes to days) [20]. This supports our interpretation that the changes in I_D observed in the off-state are mainly due to photo-generated charges and not changes in trap-state occupation densities. Hence, there is a clear benefit in using a heterojunction ambipolar phototransistor as opposed to a unipolar phototransistors for optical sensing [9].

By using two low-voltage ambipolar transistors with similar channel dimensions we have also been able to fabricate low-voltage complementary-like voltage inverters. The inverter circuit employed together with a representative set of operating characteristics are shown in Fig. 4a. The gain characteristics as a function of V_{IN}, at different supply voltages, are also shown in Fig. 4b. The circuit exhibits sharp voltage swings indicating good inverter operation. The peak small-signal gain for this particular circuit is on the order of 35 and is obtained at maximum supply voltage. The signal gain together with the asymmetry of the trip point could in principal be further improved by circuit design optimisation but is beyond the scope of this work.

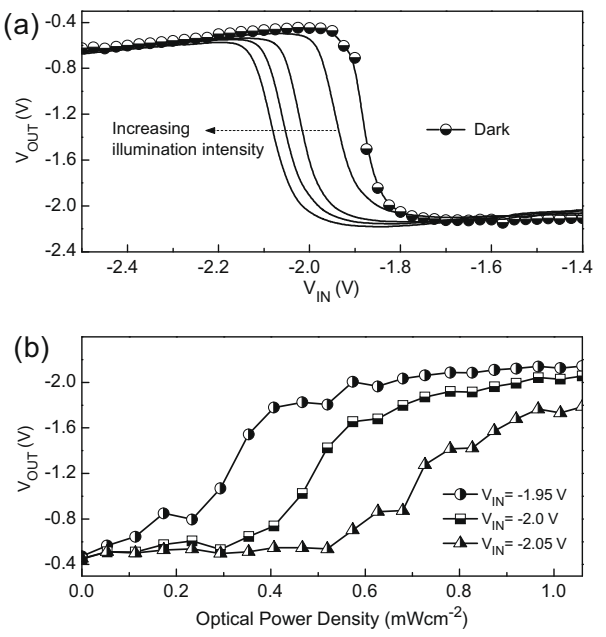

Fig. 5. (a) Transfer characteristics of a low-voltage inverter measured in the dark and under blue light (λ_{peak} = 469 nm) illumination with incident optical power densities between 0–1.2 mW cm^{-2}. (b) Effect of incident optical power density on V_{OUT} measured at a fixed V_{DD} (−2.5 V) and different V_{IN} biases.

One very interesting property of these low-voltage complementary-like circuits is the strong dependence of their operating characteristics on incident light. This effect is demonstrated in Fig. 5a where the transfer characteristics measured in dark are plotted together with those measured under blue light illumination with different intensities. This effect is believed to be due to changes in the n-channel threshold voltage under illumination. By biasing the inverter at an appropriate V_{DD} and V_{IN}, the device can hence be used as an optical switch, switching from a low $|V_{OUT}|$ to a high $|V_{OUT}|$ once light above a threshold power density is detected. The threshold optical power density can be tuned through a choice of V_{DD} and V_{IN}, as shown in Fig. 5b.

4. Conclusions

Low-voltage ambipolar organic field-effect transistors have been fabricated from bi-layer semiconductor structures and self-assembled monolayer gate dielectrics. Under optical illumination the source–drain current was found to increase, allowing the devices to be used as low-voltage phototransistors. The peak external quantum efficiency of the devices was found to be approximately 0.8%, while the response time was in the range 210–225 ms. Using two transistors with similar dimensions, low-voltage complementary-like inverters were demonstrated. The operating characteristics of these circuits were shown to be light-intensity dependent, allowing the inverters to be used as optical sensors with tuneable responsivity. This work is a significant step towards the fabrication of low-power phototransistor-based imaging arrays.

Acknowledgements

This work was funded by the Engineering and Physical Sciences Research Council (EPSRC) Grant Number EP/F023200 and Research Councils UK (RCUK). T.D.A. is an EPSRC Advanced Fellow and a RCUK Fellow/Lecturer. D.D.C.B. is the Lee-Lucas professor of Experimental Physics.

References

[1] J. Zaumseil, H. Sirringhaus, Chem. Rev. 107 (2007) 1296–1323.
[2] C.J. Drury, C.M. Mutsaers, C.M. Hart, D.M. de Leeuw, Appl. Phys. Lett. 73 (1998) 108–110.
[3] E.C.P. Smits, S.G.J. Mathijssen, P.A. van Hal, S. Setayesh, T.C.T. Geuns, K.A.H.A. Mutsaers, E. Cantatore5, H.J. Wondergem, O. Werzer, R. Resel, M. Kemerink, S. Kirchmeyer, A.M. Muzafarov, S.A. Ponomarenko, B. de Boer, P.W.M. Blom, D.M. de Leeuw, Nature 455 (2008) 956–959.
[4] G.H. Gelinck, H.E.A. Huitema, E. van Veenendaal, E. Cantatore, L. Schrijnemakers, J.B.P.H. van der Putten, T.C.T. Geuns, M. Beenhakkers, J.B. Giesbers, B.H. Huisman, E.J. Meijer, E.M. Benito, F.J. Touwslager, A.W. Marsman, B.J.E. van Rens, D.M. de Leeuw, Nat. Mater. 3 (2004) 106–110.
[5] E.J. Meijer, D.M. de Leeuw, S. Setayesh, E. van Veenendaal, B.H. Huisman, P.W.M. Blom, J.C. Hummelen, U. Scherf, T.M. Klapwijk, Nat. Mater. 2 (2003) 678–682.
[6] T.D. Anthopoulos, S. Setayesh, E. Smits, M. Cölle, E. Cantatore, B. de Boer, P.W.M. Blom, D.M. de Leeuw, Adv. Mater. 18 (2006) 1900–1904.
[7] J. Zaumseil, R.H. Friend, H. Sirringhaus, Nat. Mater. 5 (2006) 69–74.
[8] E.C.P. Smits, S. Setayesh, T.D. Anthopoulos, M. Buechel, W. Nijssen, R. Coehoorn, P.W.M. Blom, B. de Boer, D.M. de Leeuw, Adv. Mater. 19 (2007) 734–738.
[9] N. Marjanović, Th.B. Singh, G. Dennler, S. Günes, H. Neugebauer, N.S. Sariciftci, R. Schwödiauer, S. Bauer, Org. Electr. 7 (2006) 188–194.
[10] T.D. Anthopoulos, Appl. Phys. Lett. 91 (2007) 113513.
[11] M.C. Hamilton, S. Martin, J. Kanicki, IEEE Trans. Electron Dev. 51 (2004) 877.
[12] T.B. Singh, R. Koeppe, N.S. Sariciftci, M. Morana, C.J. Brabec, Adv. Funct. Mater. 19 (2008) 789–795.
[13] T.N. Ng, W.S. Wong, M.L. Chabinyc, S. Sambandan, R.A. Street, Appl. Phys. Lett. 92 (2008) 213303.
[14] T. Rauch, M. Böberl, S.F. Tedde, J. Fürst, M.V. Kovalenko, G. Hesser, U. Lemmer, W. Heiss, O. Hayden, Nat. Photon. 3 (2009) 332–336.
[15] M. Halik, H. Klauk, U. Zschieschang, G. Schmid, C. Dehm, M. Schütz, S. Maisch, F. Effenberger, M. Brunnbauer, F. Stellacci, Nature 431 (2004) 963–966.
[16] H. Klauk, U. Zschieschang, J. Pflaum, M. Halik, Nature 445 (2007) 745–748.
[17] P.H. Wöbkenberg, J. Ball, F.B. Kooistra, J.C. Hummelen, D.M. de Leeuw, D.D.C. Bradley, T.D. Anthopoulos, Appl. Phys. Lett. 93 (2008) 013303.
[18] J.M. Ball, P.H. Wöbkenberg, F. Colléaux, M. Heeney, J.E. Anthony, I. McCulloch, D.D.C. Bradley, T.D. Anthopoulos, Appl. Phys. Lett. 95 (2009) 103310.
[19] E. Kuwahara, Y. Kubozono, T. Hosokawa, T. Nagano, K. Masunari, A. Fujiwara, Appl. Phys. Lett. 85 (2004) 4765–4767.
[20] A. Salleo, R.A. Street, J. Appl. Phys. 94 (2003) 471–479.
[21] S. Yoo, B. Domercq, B. Kippelen, Appl. Phys. Lett. 85 (2004) 5427–5429.
[22] K. Wasapinyokul, W.I. Milne, D.P. Chua, J. Appl. Phys. 105 (2009) 024509.

elusive due to the complexity of designing such material: broadband absorption covering the whole visible spectrum (400–800 nm) in the neutral state, extra requirement of distinct and low oxidation potentials for electropolymerization, simultaneous depletion of absorption bands upon doping and so forth. Indeed, to date, only one example of black PEC has emerged from Reynolds' laboratory [30] by using chemical co-polymerization of an increasingly substituted donor–acceptor (D–A) system [31]. Therefore, it is a challenging task to access electrochemically to a neutral state black polymer in view of optoelectronic devices, displays (road signs, clocks and shop displays), windows shades along with many flexible and portable art and design applications [32,33]. Furthermore, black polymers would also be highly valuable for solar cell applications [34].

Recently, our endeavors directed to the design and synthesis of novel organic π-conjugated polymers [29,35] prompted us to investigate the fate of two D–A systems, **1** and **2**. We found that D–A systems **1** and **2** were able to produce saturated blue and green colors after electropolymerization (**P1** and **P2**), respectively (Fig. 1) [36]. Since the oxidation potential values of both monomers are very close to each other (1.01 V for **1** and 0.98 V for **2** vs. Ag/AgCl), oxidation of **1** and **2** in the same medium can form random copolymers due to competing reactions between them during the electrolysis.

Since the sum of the electronic absorption spectra of **P1** and **P2** covered the whole range of visible spectrum (400–800 nm) (see Fig. 1), it was envisaged that electrochemical co-polymerization via repetitive cycling or constant potential electrolysis of **1** and **2** with a certain monomer feed-ratio might provide an entry into neutral state black polymers. In this paper, we wish to report the electrochemical polymerization of a discreet combination of two D–A systems which provided a soluble neutral state black polymeric electrochromic (**P(1-co-2)**). To the best of our knowledge, (**P(1-co-2)**) is the first electropolymerized polymer absorbing virtually the whole visible spectrum (400–800 nm) in the neutral state with a low bandgap (1.45 eV). Furthermore, it exhibits excellent operational and/or environmental stability.

2. Results and discussion

2.1. Electropolymerization

Initially, the redox behavior of a mixture of **1** and **2** was investigated by cyclic voltammetry (CV). Although both monomers were highly soluble in dichloromethane (DCM), the cyclic voltammograms of **1**, **2** and their mixture were recorded in a mixture of DCM and acetonitrile (ACN, as a non-solvent) in order to hinder the solubility of the polymer film, which was formed on the electrode surface, by cosolvent effects. The cyclic voltammogram of a mixture of **1** and **2** with 1:4 monomer feed ratio in 0.1 M tetrabutylammonium hexafluorophosphate (TBAH)/DCM–ACN (3/2, v/v) exhibits two consecutive oxidation peaks at 0.93 V and 1.01 V indicating that the electrochemical co-polymerization of **1** and **2** was feasible. Upon successive scans a new reversible redox couple was also noted, which indicates the formation of corresponding copolymer (**P(1-co-2)**) film on the electrode surface (Fig. 2).

The as-prepared polymer film had black color in the neutral state and it was soluble in common organic solvents (DCM, $CHCl_3$, etc.) and slightly soluble in toluene and diethylether, which clearly suggested that it could easily be processed over surfaces via spin coating, spraying and printing techniques (Fig. 3).

However, it was noteworthy that the peak current versus scan rate curve of the copolymer during p-type doping was linear which brought convincing evidence that the redox process is not diffusion-limited. Interestingly, it was also found that the polymer film has shown almost the same charge/discharge behavior between the scan rates of 50 mV/s and 200 mV/s. The data suggests that the charge transport takes place rapidly through the coated polymer film and the electroactive sites remain unaltered

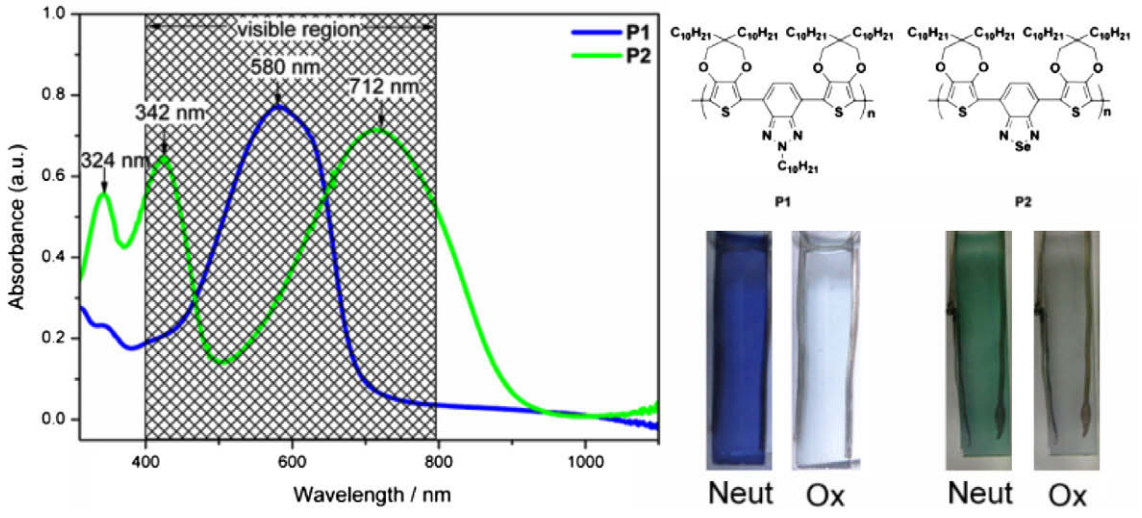

Fig. 1. Electronic absorption spectra of **P1** and **P2** in their neutral states in 0.1 M TBAH dissolved in ACN and the colors of the polymers in different redox states.

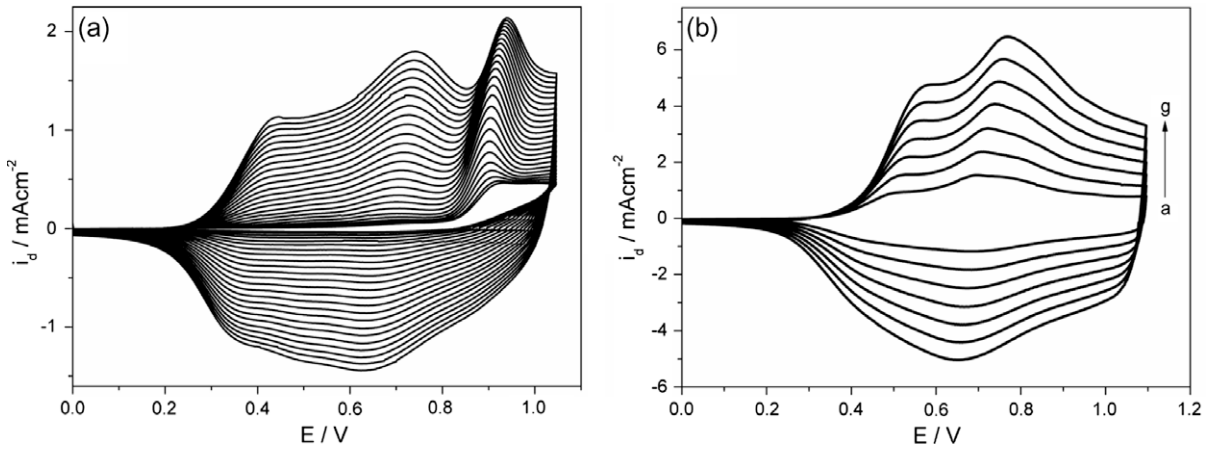

Fig. 2. (a) Cyclic voltammogram during the repeated scan electropolymerization of a mixture of **1** and **2** with 1:4 monomer feed ratio to give **P(1-co-2)** in 0.1 M TBAH/DCM–ACN (3/2, v/v) at a scan rate of 100 mV/s, Pt disk working electrode, and (b) scan rate dependence of the **P(1-co-2)** film in 0.1 M TBAH/ACN at different scan rates (mV/s); (a) 50; (b) 75; (c) 100; (d) 125; (e) 150; (f) 175; and (g) 200.

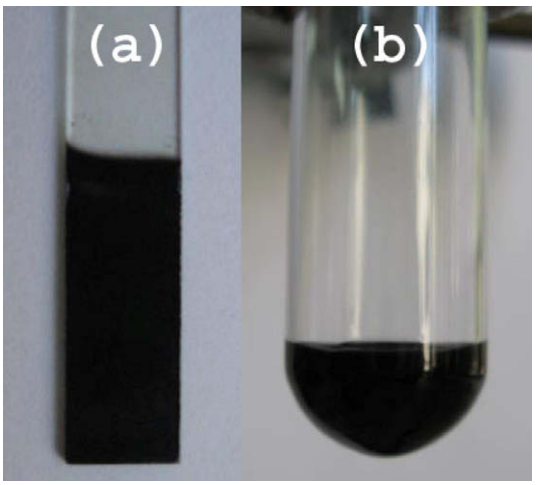

Fig. 3. **P(1-co-2)** film on ITO glass slide and **P(1-co-2)** in DCM.

independent of the externally induced potential. This intriguing feature paves the way for utilizing **P(1-co-2)** as p-type material in supercapacitors and/or transistors [37].

The long-term stability upon switching and/or cycling plays a key role on the electrochromic performance of the devices and smart windows. Therefore, the electrochemical stability of **P(1-co-2)** was tested by cycling the polymer film between its neutral and oxidized states at a scan rate of 200 mV/s. As shown in Fig. 4, no appreciable change in the electrochemical response of **P(1-co-2)** was observed and 90% of the electroactivity was still kept even after four thousands of cycles. Note that the stability tests were carried out under air atmosphere and the system was not sealed (sealing would further increase the long-term stability of the material upon switching and/or cycling). It can be safely concluded that **P(1-co-2)** exhibits both operational stability and environmental robustness under ambient conditions.

2.2. Spectroelectrochemistry

The changes in the optical absorption spectrum of **P(1-co-2)** film coated on ITO glass slide were recorded in situ to elucidate the electro-optical properties. In the neutral state, **P(1-co-2)** exhibited a broad absorption band with three shoulders at 422 nm, 522 nm and 660 nm extending virtually over the full visible spectrum (Fig. 5). When compared to the absorption bands of **P1** (580 nm) and **P2** (342 nm, 712 nm) in Fig. 1, the spectrum of the product confirms the formation of a copolymer since the absorption bands of the claimed copolymer do not exactly match the corresponding homopolymers. **P(1-co-2)** had a lower band gap of 1.45 eV, which was calculated from the commencement of the low energy end of the π–π^* transition at 660 nm, than chemically obtained black random copolymer of Reynolds and coworkers [30] (E_g = 1.64 eV). The intensities of the π–π^* transition bands decreased simultaneously upon p-type doping, which unambigiously indicated the presence of a homogeneous polymer film rather than bilayer. Furthermore, a new absorption band beyond 900 nm started to intensify due to the formation of charge carriers during doping process (Fig. 5). These absorbance variations occurred around an isosbestic point which appeared at 796 nm (1.56 eV), suggesting that only two phases coexisted. Upon further oxidation, the polaron band reached a maxima while the π–π^* transition band diminished completely.

Finally, these changes in the electronic absorption spectra of **P(1-co-2)** film upon doping nicely reflected by a color change from black (L = 14.3, a = 0.29, b = 0.35) in the neutral state to transmissive grey (L = 39.2, a = 0.29, b = 0.33) in the oxidized state (Fig. 5). The percentage transmittance change ($\Delta\%T$) between the redox states was found to be 15.3% for 522 nm. The optical stability is an important feature for such materials to be amenable for use in electrochromic and optical devices. It was noted that the copolymer film did not loose its electroactive property completely when switched between its neutral and oxidized states. For example, the copolymer film re-

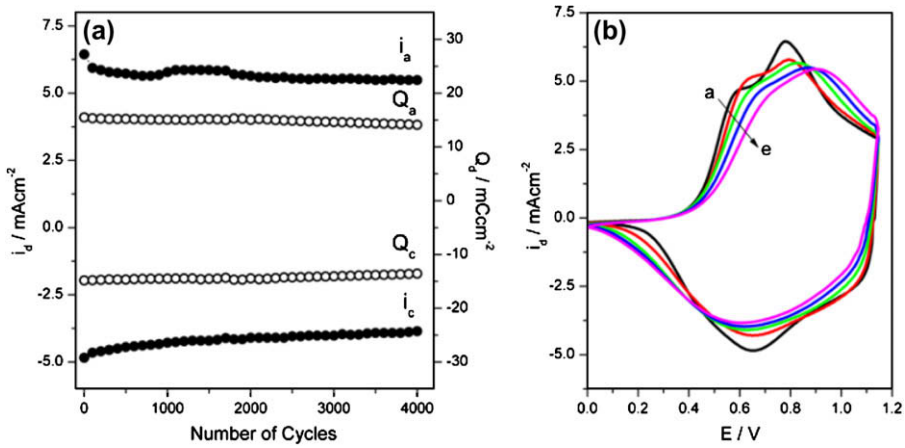

Fig. 4. (a) Relationship of anodic (i_a), cathodic (i_c) peak currents and the charge (Q_a)/discharge (Q_c) variations of **P(1-co-2)** as a function of number of cycles and (b) cyclic voltammetry stability of **P(1-co-2)** film at a scan rates of 200 mV/s between 0.0 V and 1.1 V in 0.1 M TBAH/ACN. Number of cycle: (a) 1; (b) 1000; (c) 2000; (d) 3000; and (e) 4000.

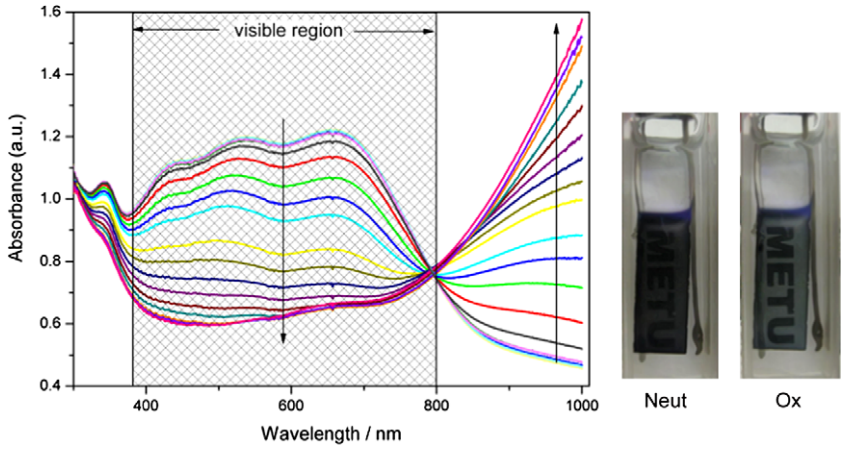

Fig. 5. Electronic absorption spectra of the **P(1-co-2)** film coated on ITO electrode at various applied potentials between 0.0 V and +1.2 V in 0.1 TBAH/ACN, and the colors of the **P(1-co-2)** in different redox states.

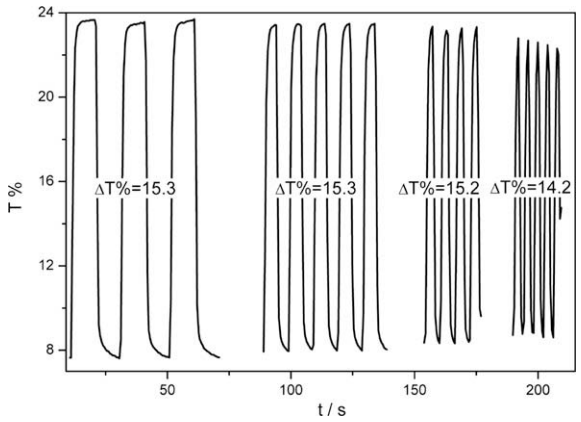

Fig. 6. Chronoabsorptometry experiment at 522 nm for **P(1-co-2)** film on ITO electrode in 0.1 M TBAH/ACN while the polymer was switched between −0.1 V and 1.0 V (vs. Ag wire) with a switching time of 10 s, 5 s, 3 s and 2 s.

tains 72.3% of its electroactivity for the first 2000 cycles. Switching time between the redox states or different colors is also a crucial parameter to realize the versatility of the electrochrome. Hence, the transmittance changes (optical contrast) was recorded via square-wave potential methods between 0.0 V and 1.2 V with switching times of 10 s, 5 s, 3 s and 2 s. As shown in Fig. 6, **P(1-co-2)** film preserved its electro-optical properties with no appreciable changes and the polymer film gave response in a very short time. For example, only 1.1% optical contrast change was observed when the switching time was decreased to 2 s. These features show the versatility of the polymer film for the construction of high performance displays and electrochromic devices.

3. Conclusion

In conclusion, a new soluble neutral state black PEC, (**P(1-co-2)**), which was obtained by electrochemical means

was disclosed. To the best of our knowledge, this is the first example of electropolymerized materials absorbing nearly the whole visible spectrum (400–800 nm) in the neutral state. Furthermore, (**P(1-co-2)**) has a low bandgap (1.45 eV) and it exhibits excellent operational and environmental stability. Considering the fact that low bandgap black polymers hold promise for both solar cells and electronic ink-based applications, we hope that **P(1-co-2)** would give us ample opportunity for innovative technological applications. Work along these lines is currently underway in our laboratories.

4. Experimental

4.1. Materials and methods

All chemicals were purchased from Aldrich Chemical and used as received unless otherwise noted. 0.1 M tetrabutylammonium hexafluorophosphate (TBAH) dissolved in dichloromethane (DCM) and acetonitrile (ACN) was used as electrolyte solution. A platinum disk (0.02 cm^2) and a platinum wire were used as working and counter electrodes, respectively, as well as a Ag/AgCl in 1.0 M NaCl reference electrode or a silver wire as a pseudo-reference electrode (calibrated externally using 5 mM solution of ferrocene/ferrocenium couple). Repetitive cycling or constant potential electrolysis was used to obtain the polymer films. Electro-optical properties were investigated by using an indium tin oxide (ITO, Delta Tech. 8–12 Ω, 0.7 cm × 5 cm) electrode as well as a platinum wire as counter electrode and a Ag wire as a pseudo-reference electrode. In order to equilibrate the redox behavior of the polymer film and to obtain repeated results, the coated polymer films were switched between their neutral and oxidized states several times before electroanalytical and optical studies. Electroanalytical measurements were performed using a Gamry PCI4/300 potentiostat–galvanostat. The electro-optical spectra were monitored on a Hewlett–Packard 8453A diode array spectrometer. FT-IR spectra were recorded on Nicolet 510 FT-IR with attenuated total reflectance. Photographs of the polymer films were taken by using a Canon (PowerShot A75) digital camera. The details of synthesis, characterization and properties for **1**, **2**, **P1** and **P2** will be reported elsewhere. 4,7-Dibromobenzo[c][1,2,5]selenadiazole [38] was prepared according to literature procedures.

4.1.1. Representative procedure for the synthesis of *1* and *2*

To an argon degassed solution of tributyl(3,3-didecyl-3,4-dihydro-2H-thieno[3,4-b][1,4]dioxepin-8-yl)stannane (243 mg, 0.334 mmol) and 4,7-dibromo-2-decyl-2H-benzo[d][1,2,3]triazole or 4,7-dibromobenzo[c][1,2,5]selenadiazole (0.134 mmol) in dry toluene (15 ml) was added $Pd(PPh_3)_2Cl_2$ (18.8 mg, 0.0268 mmol) and the mixture was heated under reflux overnight. After cooling to room temperature, the solvent was removed under reduced pressure. The crude mixture was chromatographed on silica gel by eluting with methanol:chloroform (4:1, v/v) to give **1** or **2**.

4.1.2. 2-Decyl-4,7-bis(3,3-didecyl-3,4-dihydro-2H-thieno[3,4-b][1,4]dioxepin-6-yl)-2H-benzo[d][1,2,3]triazole (*1*)

40% yield; ^{1}H NMR (400 MHz, $CDCl_3$, δ): 7.94 (s, 2H), 6.49 (s, 2H), 4.69 (t, J = 7.2 Hz, 2H), 3.95 (s, 4H), 3.86 (s, 4H), 2.09 (t, J = 7.2 Hz, 2H), 1.43–1.37 (m, 8H), 1.31–1.22 (m, 62H), 0.85–0.82 (m, 12H); ^{13}C NMR (100 MHz,$CDCl_3$, δ): 150.3, 147.5, 142.4, 124.7, 122.0, 118.3, 105.1, 78.05, 77.97, 44.1, 44.0, 32.3, 30.8, 30.2, 29.8, 29.6, 29.5, 29.3, 23.2, 23.1, 14.3; FT-IR (ATR, cm^{-1}): 2917, 2851, 1516, 1480, 1451, 1407, 1378, 1255, 1164, 1029, 833, 797, 727, 647, 611. Anal. Calc. for $C_{70}H_{117}N_3O_4S_2$: C, 74.48; H, 10.45; N, 3.72; S, 5.68. Found: C, 74.44; H, 10.47; N, 3.69; S 5.66.

4.1.3. 4,7-Bis(3,3-didecyl-3,4-dihydro-2H-thieno[3,4-b][1,4]dioxepin-6-yl)-2,1,3-benzoselenadiazole (*2*)

35% yield; ^{1}H NMR (400 MHz, $CDCl_3$, δ): 8.11 (s, 2H, Ar H), 6.57 (s, 2H, Ar), 3.96 (s, 4H), 3.87 (s, 4H), 1.40–1.35 (m, 8H), 1.30–1.20 (m, 64H), 0.83–0.77 (m, 12H); ^{13}C NMR (100 MHz,$CDCl_3$, δ): 157.08, 148.45, 146.68, 127.01, 124.44, 116.50, 105.20, 78.08, 77.92, 42.48, 30.73, 30.60, 29.20, 28.34, 28.24, 28.03, 25.62, 21.57, 12.79; FT-IR (ATR, cm^{-1}): 3115, 2920, 2853, 1478, 1377, 1259, 1168, 1028, 798; Anal. Calc. for $C_{60}H_{96}N_2O_4S_2Se$: C, 68.47; H, 9.19; N, 2.66; S, 6.09. Found: C, 68.45; H, 9.21; N, 2.58; S, 6.01.

Acknowledgements

We gratefully acknowledge the financial support from the Scientific and Technical Research Council of Turkey (TUBITAK) and European Cooperation in Science and Technology (COST D36-108T959). M.P. is indebted to TUBITAK for a fellowship.

References

[1] N.C. Greenham, S. Moratti, D.D.C. Bradley, R.H. Friend, A.B. Holmes, Nature 365 (1993) 628.
[2] R.H. Friend, R.W. Gymer, A.B. Holmes, J.H. Burroughes, R.N. Marks, C. Taliani, D.D.C. Bradley, D.A. Dos Santos, J.L. Bredas, M. Logdlund, W.R. Salaneck, Nature 397 (1999) 121.
[3] E.J.W. List, R. Guentner, P.S. De Freitas, U. Scherf, Adv. Mater. 14 (2002) 374.
[4] A. Goel, M. Dixit, S. Chaurasia, A. Kumar, R. Raghunandan, P.R. Maulik, R.S. Anand, Org. Lett. 10 (2008) 2553.
[5] L. Schmidt-Mende, A. Fechtenkotter, K. Mullen, E. Moons, R.H. Friend, J.D. Mackenzie, Science 293 (2001) 1119.
[6] A. Liscio, G. De Luca, F. Nolde, V. Palermo, K. Müllen, P. Samori, J. Am. Chem. Soc. 130 (2008) 780.
[7] J.M.J. Fréchet, B.C. Thompson, Angew. Chem. Int. Ed. 47 (2008) 58.
[8] M. Muccini, Nat. Mater. 5 (2006) 605.
[9] P. Gao, D. Beckmann, H.N. Tsao, X. Feng, V. Enkelmann, W. Pisula, K. Müllen, Chem. Commun. 13 (2008) 1548.
[10] H. Usta, A. Facchetti, T.J. Marks, J. Am. Chem. Soc. 130 (2008) 8580.
[11] C. Yang, J.Y. Kim, S. Cho, J.K. Lee, A.J. Heeger, F. Wudl, J. Am. Chem. Soc. 130 (2008) 6444.
[12] M. Palma, J. Levin, V. Lemaur, A. Liscio, V. Palermo, J. Cornil, Y. Geerts, M. Lehmann, P. Samori, Adv. Mater. 18 (2006) 3313.
[13] I. Schwendeman, R. Hickman, G. Sonmez, P. Schottland, K. Zong, D. Welsh, J.R. Reynolds, Chem. Mater. 14 (2002) 3118.
[14] H. Meng, D. Tucker, S. Chaffins, Y. Chen, R. Helgeson, B. Dunn, F. Wudl, Adv. Mater. 15 (2003) 146.
[15] G. Sonmez, Chem. Commun. (2005) 5251.
[16] G. Sonmez, H.B. Sonmez, J. Mater. Chem. 16 (2006) 2473.
[17] K. Bange, T. Gambke, Adv. Mater. 2 (1990) 10.

[18] A.A. Argun, P.H. Aubert, B.C. Thompson, I. Schwendeman, C.L. Gaupp, J. Hwang, N.J. Pinto, D.B. Tanner, A.G. MacDiarmid, J.R. Reynolds, Chem. Mater. 16 (2004) 4401.
[19] A.A. Argun, A. Cirpan, J.R. Reynolds, Adv. Mater. 15 (2003) 1338.
[20] R.G. Mortimer, Chem. Soc. Rev. 26 (1997) 147.
[21] D.R. Rosseinsky, R.J. Mortimer, Adv. Mater. 13 (2001) 783.
[22] P. Chandrasekhar, B.J. Zay, G.C. Birur, S. Rawal, E.A. Pierson, L. Kauder, T. Swanson, Adv. Funct. Mater. 12 (2002) 95.
[23] S. Beaupré, A.-C. Breton, J. Dumas, M. Leclerc, Chem. Mater. 21 (2009) 1504.
[24] T.A. Skotheim, J.R. Reynolds, Handbook of Conducting Polymers, CRC Press, Boca Raton, 2007.
[25] A. Balan, G. Gunbas, A. Durmus, L. Toppare, Chem. Mater. 20 (2008) 7510.
[26] G. Sonmez, C.K.F. Shen, Y. Rubin, F. Wudl, Angew. Chem. Int. Ed. Engl. 43 (2004) 1498.
[27] P.M. Beaujuge, S. Ellinger, J.R. Reynolds, Adv. Mater. 20 (2008) 2772.
[28] A. Durmus, G. Gunbas, P. Camurlu, L. Toppare, Chem. Commun. 31 (2007) 3246.
[29] A. Cihaner, F. Algı, Adv. Funct. Mater. 18 (2008) 3583.
[30] P.M. Beaujuge, S. Ellinger, J.R. Reynolds, Nat. Mater. 7 (2008) 795.
[31] E.E. Havinga, W. Hoeve, H. Wynberg, Synth. Met. 55 (1993) 299.
[32] F.C. Krebs, Nat. Mater. 7 (2008) 766.
[33] P.M. Beaujuge, J.R. Reynolds, Chem. Rev. 110 (2010) 268.
[34] G. Dennler, M.C. Scharber, C. Brabec, J. Adv. Mater. 21 (2009) 1323.
[35] F. Algı, A. Cihaner, Org. Electron. 10 (2009) 453.
[36] A detailed report concerning the synthesis and properties of **1**, **2**, **P1** and **P2** is forthcoming.
[37] Y. Sakamoto, T. Suzuki, M. Kobayashi, Y. Gao, Y. Fukai, Y. Inoue, F. Sato, S. Tokito, J. Am. Chem. Soc. 126 (2004) 8138.
[38] R. Yang, R. Tian, J. Yan, Y. Zhang, J. Yang, Q. Hou, W. Yang, C. Zhang, Y. Cao, Macromolecules 38 (2005) 244.

density dependence of the hole mobility into account. Neglecting the charge–carrier density dependent effect would lead to an overestimation of p_0 by an order of magnitude for the 1:600 doping ratio. Further understanding of the charge transport in doped conjugated polymers is required to advance the performance of polymeric optoelectronic devices. In this study we investigate the field (E) and temperature (T) dependence of the charge transport of p-type doped MEH-PPV. We demonstrate that in order to describe the hole transport at low temperatures and high electric fields a field-assisted ionization of the F4-TCNQ dopants has to be taken into account.

Upon addition of p-type doping free holes are introduced into the organic semiconductor. At low voltages these free holes, or background density p_0, will largely outnumber the charges that are injected from the contacts. As a result an Ohmic-like current will flow, given by

$$J_\Omega(V,T) = qp_0(T)\mu_p(T,p_0(T),E)\frac{V}{d} \tag{1}$$

with q the magnitude of electron charge, p_0 the free hole density, μ_p the hole mobility, d the thickness of the polymer layer, and $E = V/d$. At higher voltages space–charge due to holes injected from the contacts will start building up and a transition to the space–charge limited current (SCLC) will occur. From Eq. (1) it is already obvious that the analysis of the temperature dependence of the J–V characteristics is not straightforward: the amount of free holes p_0 might be temperature-dependent due to a thermally activated ionization process of the dopant. Furthermore, the mobility will not only depend on temperature due to the hopping of holes in a disorder broadened Gaussian DOS, but also on the free hole density p_0 (that in itself also might be temperature-dependent) due to the filling of states in the tail of the Gaussian DOS [19,20]. All these possible temperature-dependent contributions from the density and mobility have to be disentangled in order to understand the charge transport. To measure the T-dependence of the transport in conducting polymers upon doping, MEH-PPV hole-only devices were made by sandwiching the matrix in between two metal contacts. As a bottom electrode indium–tin-oxide (ITO) covered with PEDOT:PSS was used, and a Pd top electrode of 20 nm was thermally evaporated on top of the MEH-PPV layer under a chamber pressure of 8×10^{-7} mbar and then capped with 100 nm of Au. The MEH-PPV was dissolved in toluene, whereas for F4-TCNQ tetrahydrofuran (THF) was used as the solvent. Further details of the processing are given in Ref. [18]. A Keithley 2400 SourceMeter and a Solartron SI 1260 Impedance/Gain-Phase analyzer were used for the I–V and C–V measurements, respectively. All electrical measurements were performed in a nitrogen-purged glove box and the temperature was controlled by a cyrosystem with liquid nitrogen.

As a first step we investigate the temperature- and density dependence of the hole mobility in MEH-PPV by measuring the SCLC in *undoped* MEH-PPV. Fig. 1(a) shows the current density versus voltage (J–V) characteristics of a PEDOT:PSS/ undoped MEH-PPV /Pd/Au hole-only device at various temperatures. The J–V characteristics are numerically modeled by using a recently developed transport model, that takes into account both the field E and density p dependence of the hole mobility μ_p [19]. The mobility is given by

$$\mu_p(T,p,E) \approx \mu_p(T,p)f(T,E), \tag{2}$$

with

$$\mu_p(T,p) = \mu_0(T)\exp\left[\frac{1}{2}\hat{\sigma}^2 - \hat{\sigma})(2pa^3)^\delta\right], \tag{3}$$

$$\mu_0(T) = \mu_0 c_1 \exp(-c_2\hat{\sigma}^2), \tag{4}$$

$$\delta = 2\frac{In(\hat{\sigma}^2 - \hat{\sigma}) - In(In4)}{\hat{\sigma}^2}, \tag{5}$$

$$\mu_0 = \frac{a^2\upsilon_0 e}{\sigma}, \tag{6}$$

and

$$f(T,E) = \exp\left\{0.44(\hat{\sigma}^{3/2} - 0.22)\left[\sqrt{1 + 0.8\left(\frac{Eea}{\sigma}\right)^2} - 1\right]\right\} \tag{7}$$

where, $\hat{\sigma} \equiv \sigma/K_bT$ with σ the width of the Gaussian DOS, and a is the lattice constant. The lines in Fig. 1(a) are the numerically calculated J–V characteristics using a μ_{p0} of 6.4×10^3 m^2/Vs, an a_{p0} of 1.55 nm, and a σ_{p0} of 0.143 eV. These parameters are similar to the ones reported for another PPV derivative with a similar mobility [19], and the temperature dependence of the J–V characteristics is well described, both at low and high voltages. The activation energy of the mobility Δ_{mobility} at low fields and densities, defined as $\mu_p\ (T,\ 0) = \mu_0\ \exp(-\Delta_{\text{mobility}}/kT)$, typically amounts to 0.42 eV.

With $\mu_p(T,p,E)$ known we can analyze the J–V characteristics of the p-type doped MEH-PPV. Fig. 1(b) shows the J–V characteristics of p-type doped MEH-PPV with a molar doping ratio of 1:150. The linear part of the J–V characteristic (Eq. (1)) is governed by the product of the hole density p_0 and the hole mobility μ_p. With $\mu_p(T,p,E)$ known (Eqs. (2)–(7)) we can determine them individually, leading to $p_0 = 2.2 \times 10^{23}$ m^{-3} and $\mu_p = 1.2 \times 10^{-9}$ m^2/V s at room temperature. The enhanced mobility upon doping is a direct result from the filling of the tail states of the Gaussian DOS by holes. The resulting rise of the Fermi-level decreases the energy step required for hopping towards the transport states, which enhances the mobility.

Under the assumption that the temperature dependence $p_0(T)$ is very small and can be neglected the full temperature- and voltage dependence of the transport in the doped MEH-PPV can be numerically calculated. The calculations using $\mu_p(T,p,E)$ in combination with a constant p_0 of 2.2×10^{23} m^{-3} are shown in Fig. 1b by the solid lines. However, we observe that the model calculations become inconsistent with the experiments at high electric fields (E) and low T (<270 K). At low voltages the experimental hole currents exhibit a weaker temperature dependence as expected from the model. Furthermore, at high voltages the experimental J–V curves show a stronger dependence

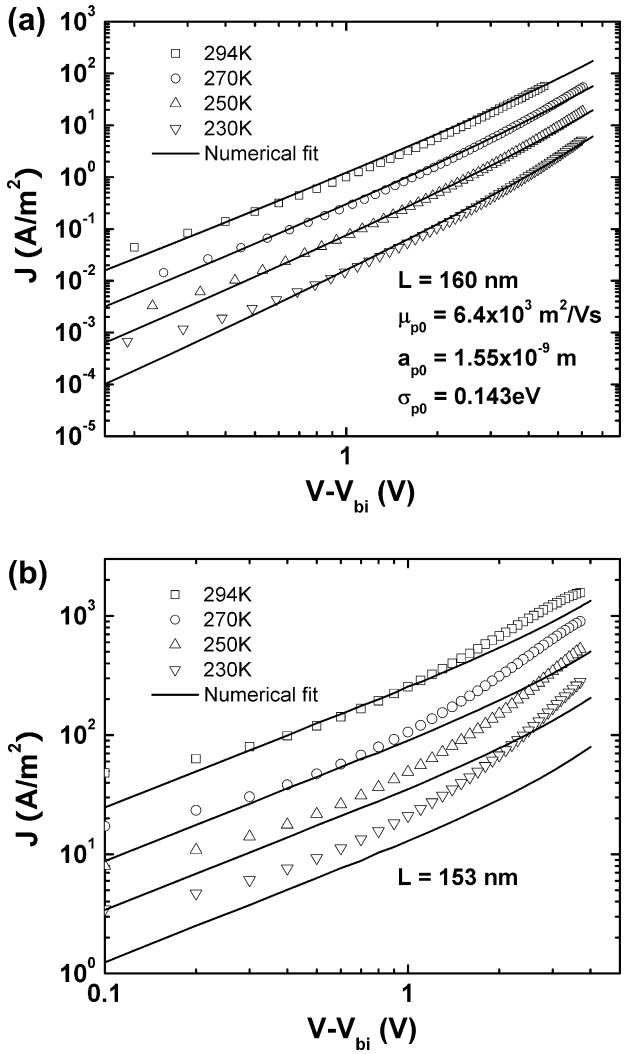

Fig. 1. Current density versus voltage characteristics of (a) an undoped and (b) a doped MEH-PPV hole-only device with a molar doping ratio of 1:150. Shown by the solid lines are the numerically calculated currents using a constant free hole density (p_0).

on voltage. As a result the inclusion of only a constant background density p_0 in the existing charge transport model characterized by $\mu_p(T,p,E)$ is not sufficient to explain the *J–V* characteristics of *p*-type doped MEH-PPV.

One could argue that the mobility as measured in the undoped sample is not only changed by the density p_0, but also by the presence of the F4-TCNQ$^-$ counter ions. The hole transport in undoped conjugated polymers is dominated by energetic and positional disorder [21,22]. Upon doping the energetic disorder and corresponding width of the Gaussian density of states (DOS) is expected to increase due to potential fluctuations caused by the Coulomb field of randomly distributed dopant ions [23,24]. Such a modification of the DOS upon doping would lead to a reduction of the mobility as well as to an increased temperature dependence of the mobility. This enhanced temperature dependence would even further increase the discrepancy between calculations and experiments at low fields. Furthermore, in a previous study [18] we verified by *C–V* measurements that the p_0 as extracted from the *J–V* measurements, thereby making use of the intrinsic density dependence of the mobility as obtained in the undoped sample, is indeed correct. If the mobility would have been strongly modified upon doping other than due to the increase of the carrier density our extracted densities from the *J–V* measurements would deviate from the densities as obtained from the *C–V* measurements. Theoretically, the modification of the Gaussian DOS upon doping is also expected to set in at higher densities, typically when $N_A^- > 10^{23}$ m^{-3} [24,25]. As a result in our experimental regime with the amount of ionized acceptors N_A^- low in the $\sim 10^{23}$ m^{-3} no significant change of the mobility is expected other than due to the increased free carrier concentration.

By comparing the amount of doping with the free hole density we find that only ~1% of the F4-TCNQ molecules in the MEH-PPV are ionized. A possible explanation for this low doping efficiency may be phase separation between the

host and the dopant, in which case only dopant molecule at the interface between the two phases will ionize. Our modeling results shown in Fig. 1(b) demonstrate that the field- and temperature dependence of the doped sample can not be described assuming a constant p_0. We postulate that the strong increase of the J–V characteristics at high voltages and the reduced temperature dependence is a result of a *field-assisted* release of holes from the dopants. We therefore introduce a field-dependent p_0 with a Poole–Frenkel like dependence on the applied electric field,

$$p_0(E) = p_0 \exp(\gamma\sqrt{E}) \tag{8}$$

where, p_0 is now the zero-field free hole density, and γ the field-enhancement factor. In Fig. 2 the J–V characteristics are shown at various temperatures for doped MEH-PPV hole-only devices with varying molar doping ratios of 1:600, 1:350, 1:250 and 1:150. The corresponding free hole density p_0 is ranging from 5×10^{22} to $2.0 \times 10^{23}\ m^{-3}$, respectively. Since for every molar doping ratio a new solution is made the thickness after spin coating is slightly varying. The lines are the numerical simulations by combining the mobility from Eqs. (2)–(7) and the field-enhanced free carrier density given by Eq. (8). We assume that p_0 is temperature independent. Taking the field-assisted ionization of the dopants into account a good description of the J–V characteristics can be made, as shown by the solid lines in Fig. 2. The variation of γ with temperature and doping concentration is shown in Fig. 3a. We find that similar to the prefactor that is responsible for the field-dependent mobility in disordered materials [26], γ follows the empirical relation

$$\gamma = B\left(\frac{1}{k_B T} - \frac{1}{k_B T_0}\right) \tag{9}$$

with $T_0 = 400$ K and the prefactor B ranging from 1.3×10^{-5} to 6.4×10^{-6} eV(m/V)$^{1/2}$ for the range of $p_0 = 5 \times 10^{22}\ m^{-3}$ to $p_0 = 2 \times 10^{23}\ m^{-3}$, respectively. These values for B are considerably smaller than the values reported for the field-dependent mobilities [26]. The increase of p_0 as a function of the electric field is plotted in Fig. 3(b) to illustrate the impact of the electric field on the background hole density from doping. We find that a p_0 of $\sim 10^{22}\ m^{-3}$ is enlarged by $\sim$5 times at high E and 2–3 times for a p_0 of $\sim 10^{23}\ m^{-3}$. In the field-enhanced charge transport the factor γ is usually related to a hopping distance [27]. For higher doping concentrations it is expected that the average distance that holes will have to hop from a dopant molecule to a site of the matrix will decrease. This would result

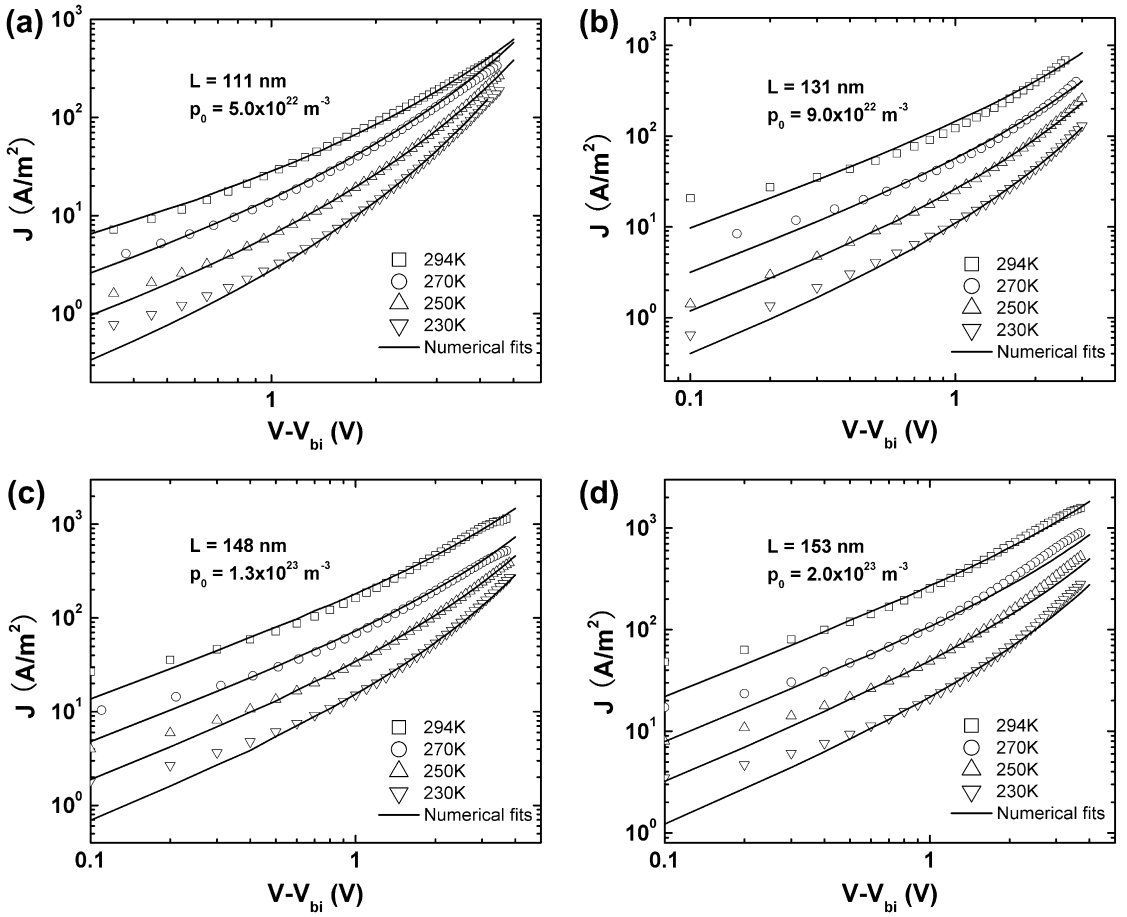

Fig. 2. Current density versus voltage characteristics of MEH-PPV hole-only devices with various doping concentrations. Also represented (solid lines) are the calculated current densities taking a field-dependent background hole density into account.

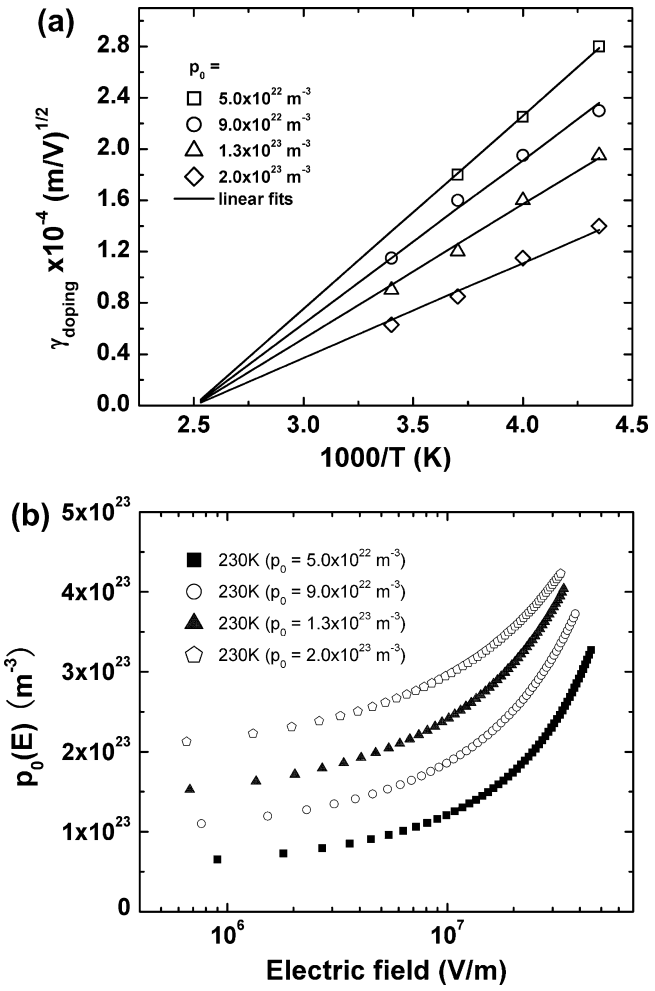

Fig. 3. (a) Field-enhancement factor γ versus temperature for different doping concentrations. (b) Free hole density calculated as a function of electric field at T = 230 K.

in a weakening of the field-enhanced ionization factor, but at present a microscopic theory or explanation is still lacking.

As a last step we investigate the temperature dependence of the low-field background density p_0 using impedance spectroscopy. For this we fabricate Ag/MEH-PPV Schottky diodes with an Ohmic PEDOT:PSS back contact. The molar doping ratio amounts to 1:500. Fig. 4(a) shows the capacitance of the depletion region versus voltage at room temperature. The capacitance at zero-voltage slightly reduces upon cooling down, indicating that the density of free holes is slightly reduced at low temperatures. A reduced density will lead to an enlargement of the depletion region with a resulting smaller capacitance. The capacitance of the depletion region C is given by

$$\frac{1}{C^2} = \frac{2\left(V - V_{bi} - \frac{kT}{q}\right)}{q\varepsilon_s p_0}, \tag{10}$$

with V_{bi} the built-in voltage and ε_s the permittivity of the semiconductor. As a result, from the slopes of the lines in Fig. 4(a) p_0 can be determined at various temperatures. The temperature dependence of p_0 is plotted in Fig. 4(b). At a doping level of 3.4×10^{22} m^{-3} we obtain that the activation energy for the ionization of free holes from the F4-TCNQ acceptor in MEH-PPV only amounts to 46 meV. This means that in the entire temperature interval of 230–300 K the p_0 only changes by a factor 1.5. For higher doping levels the change of p_0 with temperature is within experimental error. The observed activation energy of p_0 is so small that its weak temperature dependence does not affect the modeling results shown in Fig. 2b. Therefore, the C–V measurements confirm that a temperature independent p_0 is a valid assumption in the modeling.

It might seem counterintuitive that the strongest γ occurs at the lowest doping densities, whereas in a previous study [18] we showed that at low background densities the room temperature J–V characteristics could be reasonably well described by a constant background density p_0. At low voltages the J–V characteristics of doped semiconductors exhibit an Ohmic behavior, as given by Eq. (1). At a certain voltage V_t the charges injected from the contact overwhelm the charges from the doping and the current becomes space–charge limited. This transition voltage V_t

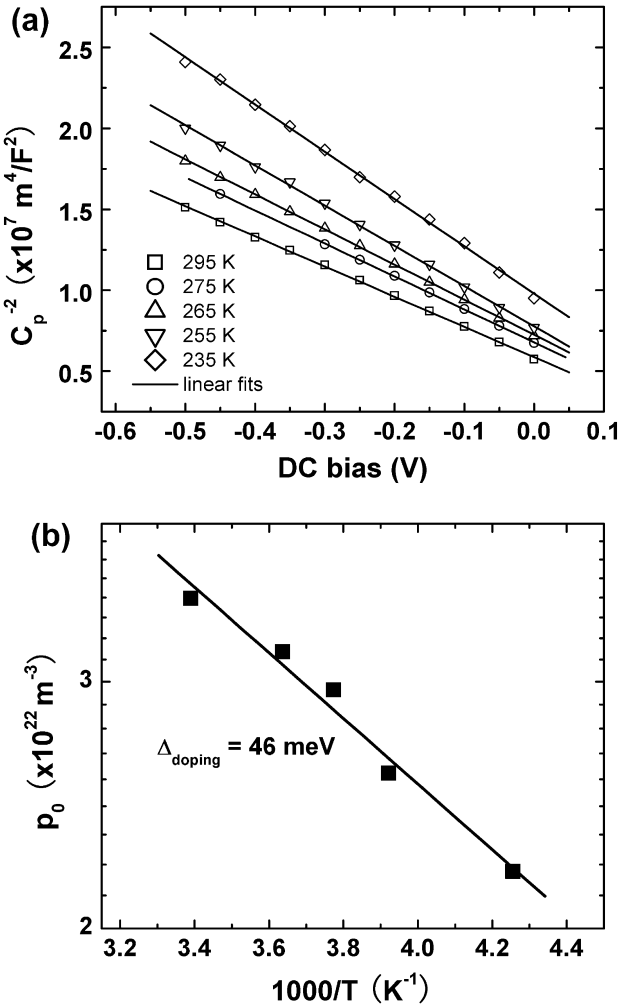

Fig. 4. (a) Depletion capacitance as a function of negative bias for a MEH-PPV Schottky diode at various temperatures. (b) Extracted background hole density as a function of temperature. The activation energy amounts to $\Delta_{doping} = 46$ meV for $p_0 = 3.4 \times 10^{22}$ m^{-3}.

depends on the amount of doping; for low doping densities V_t is also low, meaning that the Ohmic regime is only observable in a small voltage range. The enhancement of p_0 at higher voltages ($>V_t$) and fields is then not really visible in the J–V characteristic. For high doping densities the resulting Ohmic behavior due to the large p_0 dominates the J–V characteristics over a much larger voltage range, and then the increase of p_0 with field, together with the enhancement of the mobility by the increased p_0, make this effect strongly visible.

In conclusion, the transport in MEH-PPV doped with F4-TCNQ can be explained by taking into account a field-assisted ionization of the dopant, leading to a field-dependent background carrier density. The ionization of the dopants becomes more pronounced at low temperatures and high electric field.

References

[1] C.K. Chiang, C.R. Fincher Jr., Y.W. Park, A.J. Heeger, H. Shirakawa, E.J. Louis, S.C. Gau, A.G. MacDiarmid, Phys. Rev. Lett. 39 (1977) 1098.
[2] M. Pfeiffer, A. Beyer, T. Fritz, K. Leo, Appl. Phys. Lett. 73 (1998) 3202.
[3] W. Gao, A. Kahn, Appl. Phys. Lett. 79 (2001) 4040.
[4] W. Gao, A. Kahn, J. Appl. Phys. 94 (2003) 359.
[5] J. Blochwitz, T. Fritz, M. Pfeiffer, K. Leo, D.M. Alloway, P.A. Lee, N.R. Armstrong, Org. Electron. 2 (2001) 97.
[6] W. Gao, A. Kahn, J. Phys.: Condens. Matter 15 (2003) S2757.
[7] X. Zhou, J. Blochwitz, M. Pfeiffer, A. Nollau, T. Fritz, K. Leo, Adv. Funct. Mater. 11 (2001) 310.
[8] Y. Cao, G. Yu, A.J. Heeger, Adv. Mater. 10 (1998) 917.
[9] Y. Kishigami, K. Tsubaki, Y. Kondo, J. Kido, Synth. Met. 153 (2005) 241.
[10] M.F. Craciun, S. Rogge, M.J.L. den Boer, S. Margadonna, K. Prassides, Y. Iwasa, A.F. Morpurgo, Adv. Mater. 18 (2006) 320.
[11] C.K. Chan, F. Amy, Q. Zhang, S. Barlow, S. Marder, A. Kahn, Chem. Phys. Lett. 431 (2006) 67.
[12] C.K. Chan, S. Barlow, Q. Zhang, S.R. Marder, A. Kahn, J. Appl. Phys. 102 (2007) 014906.
[13] C.K. Chan, W. Zhao, Stephen Barlow, S.R. Marder, A. Kahn, Org. Electron. 9 (2008) 575.
[14] C.K. Chan, A. Kahn, Appl. Phys. A 95 (2009) 7.
[15] K. Walzer, B. Maennig, M. Pfeiffer, K. Leo, Chem. Rev. 107 (2007) 1233.
[16] K. Fehse, G. Schwartz, K. Walzer, K. Leo, J. Appl. Phys. 101 (2007) 124509.
[17] K.-H. Yim, G.L. Whiting, C.E. Murphy, J.J.M. Halls, J.H. Burroughes, R.H. Friend, J.-S. Kim, Adv. Mater. 20 (2008) 3319.

[18] Y. Zhang, B. de Boer, P.W.M. Blom, Adv. Funct. Mater. 19 (2009) 1901.
[19] W.F. Pasveer, J. Cottaar, C. Tanase, R. Coehoorn, P.A. Bobbert, P.W.M. Blom, D.M. de Leeuw, M.A.J. Michels, Phys. Rev. Lett. 94 (2005) 206601.
[20] R. Coehoorn, W.F. Pasveer, P.A. Bobbert, M.A.J. Michels, Phys. Rev. B 72 (2005) 155206.
[21] I.I. Fishchuk, A. Kadashchuk, H. Bässler, M. Abkowitz, Phys. Rev. B 70 (2004) 245212.
[22] I.I. Fishchuk, A. Kadashchuk, H. Bässler, Phys. Stat. Sol. Cells 2 (2006) 271.
[23] V.I. Arkhipov, E.V. Emelianova, P. Heremans, H. Bässler, Phys. Rev. B 72 (2005) 235202.
[24] V.I. Arkhipov, E.V. Emelianova, P. Heremans, H. Bässler, Phys. Rev. B 71 (2005) 045214.
[25] V.I. Arkhipov, P. Heremans, E.V. Emelianova, G.J. Adriaenssens, H. Bässler, Appl. Phys. Lett. 82 (2003) 3245.
[26] P.W.M. Blom, M.J.M. de Jong, M.G. van Munster, Phys. Rev. B 55 (1997) R656.
[27] S.V. Novikov, D.H. Dunlap, V.M. Kenkre, P.E. Parris, A.V. Vannikov, Phys. Rev. Lett. 81 (1998) 4472.

we compared the performances of PPE pentacene TFTs with and without SAM layer using pentafluorobenzenthiol (PFBT) on Au. The SAM can enhance the hole injection to p-type semiconductor [12].

An inverter circuit composed of two enhancement mode PPE pentacene TFTs, was demonstrated in this work. The channel widths of driver and load transistors of a inverter were 500 μm and 100 μm, respectively, with channel length of 6 μm.

A PPE pentacene was synthesized according to the method described in the literature [13]. PPE pentacene has photo-oxidation stability through delocalized π-electrons from the pentacene at C_6, C_{13} positions. Fig. 1(a) shows the chemical structures of PPE pentacene and PFBT. A PPE pentacene is soluble in various solvents such as toluene, chlorobenzene and 1,2-dichlorobenzene. The PPE pentacene solution was prepared by dissolving it in 1,2-dichlorobenzene (10 mg/mL) and filtered through 0.45 μm poly(tetrafluoroethylene) membrane filter.

The PPE pentacene TFT reported here has an inverted coplanar structure. The 100 nm thick AlNd layer was deposited by sputtering and then patterned for use as gate electrodes. Poly(4-vinylphenol) (PVP) layer was used for organic gate dielectric that was coated by spin-casting onto the patterned gate electrodes. Organic gate dielectric precursor was prepared from a solution of PVP and poly(melamine-co-formaldehyde) as a cross-linking agent, in propylene glycol mono-methyl ether acetate (PGMEA). This gate dielectric was cured at 180 °C in a vacuum oven [14]. The Cr/Au (5 nm/50 nm) source/drain electrode deposited by sputtering was made on the cross-linked PVP. To have selective coating on the TFT region, a bank of 450 nm thick poly(vinylalcohol) (PVA) layer was formed by photolithography.

Then, O_2 plasma was treated on the gate dielectric to make it clean. And the substrate was immersed in PFBT (10 mL in ethanol) solution for 2 h and rinsed using ethanol several times for SAM treated Au surface. The electrode modification was performed in a dry nitrogen glove box to avoid the influence of air. Finally, PPE pentacene was coated by spin-casting at 2000 rpm for 10 s and then the TFT was annealed at 80 °C for 30 min in N_2 environment to eliminate the solvent residue. The ratio of channel width to length for the OTFT studied in this work was 200 μm/6 μm.

Fig. 1(b) shows the selective growth process on the TFT region. The PVA bank acts an organic semiconductor (OS) solution reservoir and the wettability of OS on the PVP gate dielectric affects the selective growth. Upon spin-coating using PPE pentacene solution, the OS solution covers whole region of substrate at first and then de-wetting process starts in a few minutes from the PVA surface and it is accelerated by the difference in thickness between PVA and PVP layer which has better wettability compared to PVA surface. As a result, OS solution gathered inside of a PVA bank. PPE pentacene grain grows during the solvent evaporation so that OS island pattern inside of banks could be achieved. The film thickness depends on the amount of OS solvent inside of a bank. To improve the performance of the PPE pentacene TFT, Au surface was modified with PFBT to increase its work function, which decreases the injection barrier between Au and PPE pentacene [15].

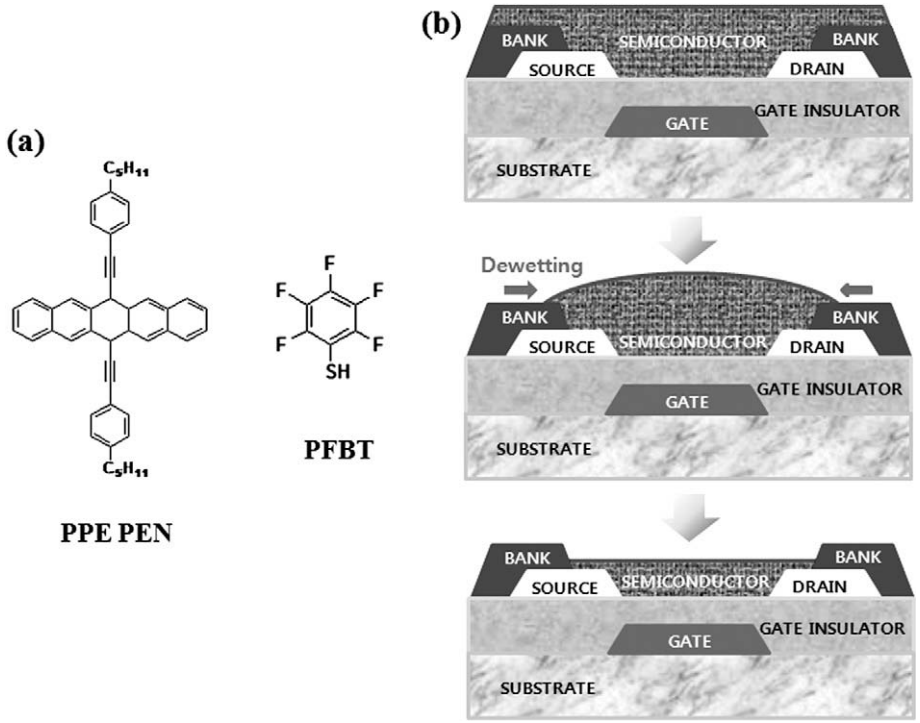

Fig. 1. Chemical structures of PPE pentacene and PFBT (a) and selective coating process of PPE pentacene on the channel region (b).

Fig. 2 shows the polarized optical microscope image of the TFTs with and without PFBT treatment on Au (a) and the transfer characteristics of the OTFTs (b). The semiconductor solution gathered together, resulting in selective crystallization of the PPE pentacene inside of banks. Regardless of PFBT treatment, the selective coating of PPE pentacene could be possible. The device having PFBT layer on the Au exhibited higher on-current compared to that of the OTFT with bare Au.

Fig. 2(c) shows the output characteristics of PPE PEN TFT with PFBT modified Au. A HOMO energy level of PPE pentacene is ~5.28 eV and the work function of bare Au is 5.1 eV, so there is a 0.18 eV injection barrier between PPE pentacene and Au. However, after modification of Au with PFBT, the work function of Au increases to 5.3 eV so that injection barrier decreases and thus TFT performance is improved.

The drain current I_D in the saturation region was achieved from

$$I_D = \frac{C_{PVP}\mu_{FE}W}{2L}(V_G - V_T)^2, \quad (1)$$

where, C_{PVP} is the capacitance of a cross-linked PVP gate insulator, μ_{FE} is the field-effect mobility, W/L is the ratio of channel width to channel length, and V_T is the threshold voltage. The thickness of the cross-linked PVP used as the gate dielectric was 550 nm and its permittivity was 3.6 [14].

The PPE pentacene OTFT with bare Au electrode exhibited the field-effect mobility (μ_{FE}) of 0.005 $cm^2/V\,s$ in the saturation region, an on/off current ratio (I_{on}/I_{off}) of 10^6, a V_T of 4.0 V and a gate voltage swing (S) of 1.2 V/dec. On the other hand, the PPE pentacene TFT with PFBT modified Au exhibited the μ_{FE} of 0.02 $cm^2/V\,s$ in the saturation region, an I_{on}/I_{off} of 10^7, and V_T of −0.4 V and S of 0.8 V/dec.

Fig. 3 shows the polarized microscope optical images of array pattern before (a) and after (b) selective coating. There is clearly selective coating on the TFT region, not on the pixel region. This demonstrates the growth of organic semiconductor only on the TFT region, not on the ITO pixel region for display and sensor applications.

Fig. 4(a) shows the polarized microscope optical image of inverter circuit by selective coating process and voltage transfer characteristics (b) and signal gain of the inverter (c). The inverter composes of two enhancement mode p-channel transistors, the channel widths of driver and load transistors are 500 μm and 100 μm, respectively with channel length of 6 μm.

In order to make organic inverter using p-type transistors, depletion and enhancement mode characteristics are needed for zero drive inverter which has some advantages such as wider swing range, higher gain, lower power dissipation compared to that of diode-connected inverter [15,16]. Although we used two enhancement mode p-channel transistors for inverter, good transfer characteristics with a signal gain ($\partial V_{OUT}/\partial V_{IN}$) of >1.5 were achieved.

In conclusion, we have developed the selective coating process using spin-casting of PPE pentacene solution inside of banks. PFBT modification on Au electrode improves the TFT performance. A bottom contact TFT with the PPE pentacene, using self-organize process, exhibited the μ_{FE} of 0.02 $cm^2/V\,s$, I_{on}/I_{off} of 10^7 and S of 0.8 V/dec. An inverter

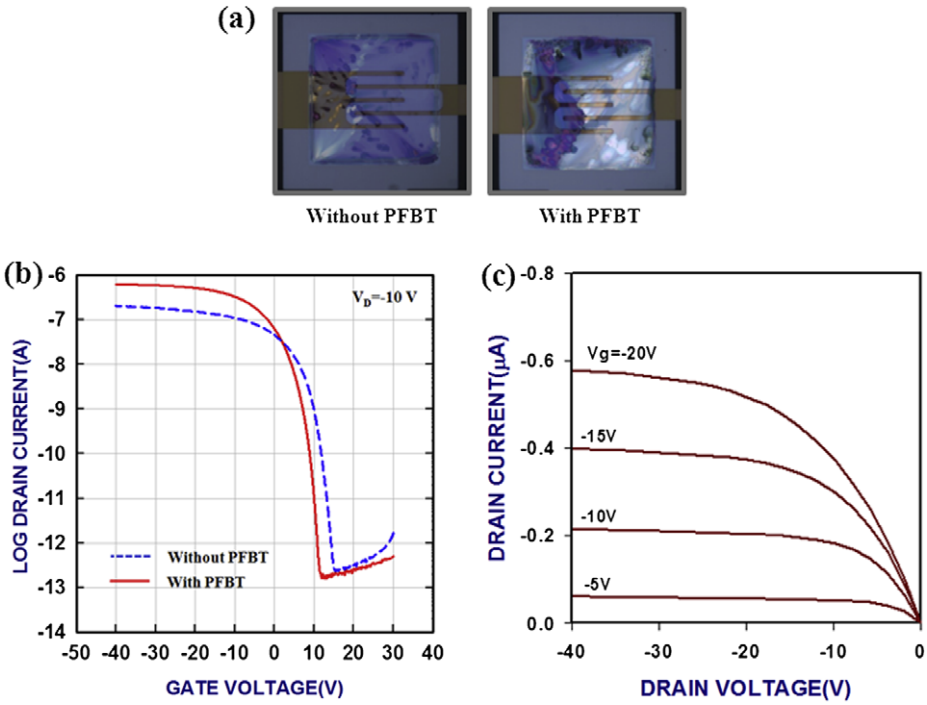

Fig. 2. Polarized optical microscope images of the channel region after selective coating with and without PFBT treatment (a), transfer characteristics with and without PFBT (b), and output characteristics of a TFT with PFBT (c).

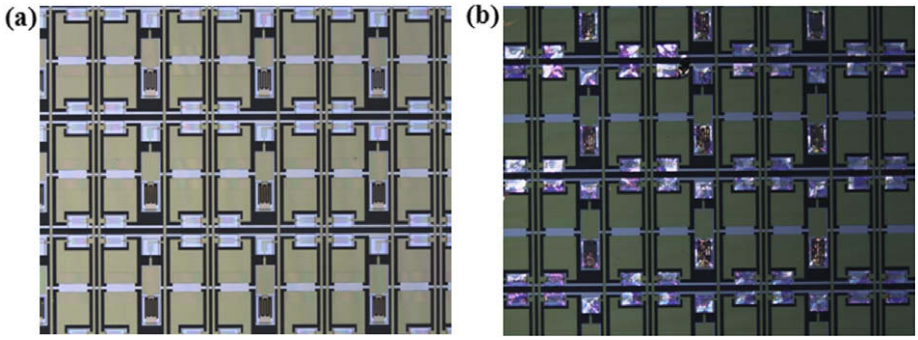

Fig. 3. Optical images of array pattern before (a) and after (b) selective coating.

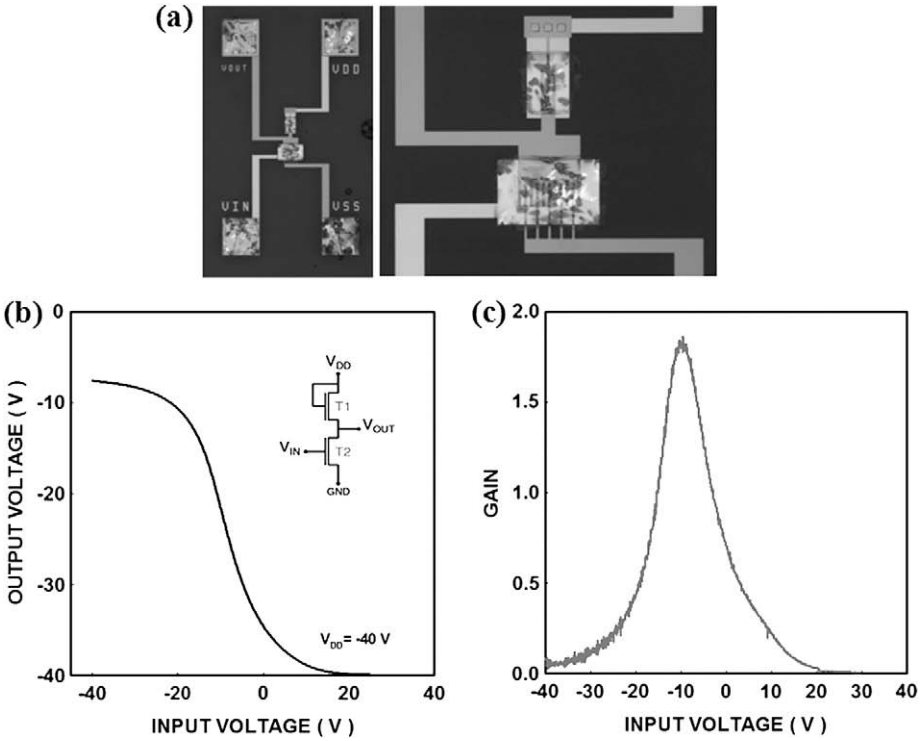

Fig. 4. Polarized optical microscope image of an inverter by selective coating (a), output voltage characteristics of an inverter as a function of input voltage (b) and signal gain of an inverter (V_{DD} = −40 V) (c).

circuit made of PPE pentacene TFTs was demonstrated using the selective coating. This result indicates that self-organized process can be applied to make low-cost flexible organic electronics.

Acknowledgement

This research was supported by the Ministry of Commerce, Industry and Energy of Korean government.

References

[1] K. Nomoto, N. Hirai, N. Yoneya, N. Kawashima, M. Noda, M. Wada, J. Kasahara, IEEE Trans. Electron. Devices 52 (2005) 1519.
[2] C.D. Dimitrakopoulos, D.J. Mascaro, IBM J. Res. Dev. 45 (2001) 11.
[3] B.J. de Gans, P.C. Duineveld, U.S. Schubert, Adv. Mater. 16 (2004) 203.
[4] D.J. Gundlach, J.E. Royer, S.K. Park, S. Subramanian, O.D. Jurchescu, B.H. Hamadani, A.J. Moad, R.J. Kline, L.C. Teague, O. Kirillov, C.A. Richter, J.G. Kushmerick, L.J. Richter, S.R. Parkin, T.N. Jackson, J.E. Anthony, Nat. Mater. 7 (2008) 216.
[5] M. Ando, M. Kawasaki, S. Imaseki, H. Sasaki, T. Kamata, Appl. Phys. Lett. 85 (2004) 1849.
[6] H.Y. Choi, S.H. Kim, J. Jang, Adv. Mater. 16 (2004) 732.
[7] S. Liu, W.M. Wang, S.C. Mannsfeld, J. Locklin, P. Erk, M. Gomez, F. Richter, Z. Bao, Langmuir 23 (2007) 7824.
[8] T. Minari, M. Kano, T. Miyadera, S.D. Wang, Y. Aoyagi, M. Seto, T. Nemoto, S. Isoda, K. Tsukagoshi, Appl. Phys. Lett. 92 (2008) 173301.
[9] B.S. Liu, A.L. Briseno, C.B. Mannsfeld, W. You, J. Locklin, H.W. Lee, Y. Xia, Zhenan Bao, Adv. Funct. Mater. 17 (2007) 2891.
[10] T. Minari, M. Kano, T. Miyadera, S. Wang, Y. Aoyagi, K. Tsukagoshi, Appl. Phys. Lett. 94 (2009) 093307.

[11] K. Suemori, S. Uemura, M. Yoshida, S. Hoshino, N. Takada, T. Kodzasa, T. Kamata, Appl. Phys. Lett. 91 (2007) 192112.
[12] J.P. Hong, A.Y. Park, S.H. Lee, J.H. Kang, N.Y. Shin, D.Y. Yoon, Appl. Phys. Lett. 94 (2009) 093307.
[13] Y. Li, Y. Wu, P. Liu, Z. Prostran, S. Gardner, B.S. Ong, Chem. Mater. 19 (2007) 418.
[14] H. Klauk, M. Halik, U. Zschieschang, G. Schmid, W. Radlik, W. Weber, J. Appl. Phys. 92 (2002) 5259.
[15] C.A. Lee, S.H. Jin, K.D. Jung, J.D. Lee, B.G. Park, Solid State Electron. 50 (2006) 1216.
[16] C.H. Baek, S.M. Seo, Appl. Phys. Lett. 94 (2009) 153305.

processing. The CIE coordinates of the white light are improved from (0.45, 0.46) to (0.39, 0.39). Most importantly, the hole and electron fluxes are balanced after solvent processing, which favors improving the luminous efficiency. A light-emitting efficiency of 12 cd/A is achieved, about 50% increase compared to the as-spincoated device.

2. Experimental methods

The white light polymer material used in this study is poly(9,9-di-*n*-octylfluorene)-co-4,7-bis(4-(N-phenyl-N-(4-methylphenyl)amino)pheny-2,1,3-benzothiadiazole) (PF-BT05) and its chemical structure is shown in Fig. 1. PF-BT05 is a white emissive polymer by controlling the content of benzothiadiazole (0.05 mol%) for realizing incomplete energy transfer from fluorescent PFO backbone to orange fluorescent benzothiadiazole moieties. The white PLEDs have a structure of indium tin oxide (ITO)/60 nm poly(ethylenedioxythiophene):poly(styrene sulfonic acid) (PEDOT:PSS)/130 nm PF-BT05/10 nm Ca/Al (100 nm). The PEDOT:PSS was first spincoated onto the ITO-coated glass substrate from water solution and then annealed at 110 °C in air for 30 min. The PF-BT05 white emissive layer was deposited on the PEDOT:PSS layer via spincoating from toluene solution and exposed to toluene vapor for 24 h at room temperature and then annealed for 30 min at 20 °C in a vacuum oven. The solvent processing procedure: PF-BT05 films spincoated on ITO glass substrates were hung above the toluene liquid in the airtight container at room temperature for 12, 24 h to obtain different contents of crystalline phase. The Ca/Al cathode was thermally evaporated under vacuum at a base pressure of 3×10^{-4} Pa. The EL characteristics of the WPLEDs were measured using Keithley 2400 source meter and PR650 Spectroscan photometer. All the measurements were carried out at room temperature under ambient conditions.

3. Results and discussion

Fig. 2 shows the absorption and photoluminescence (PL) spectra of PF-BT05 thin films without and with solvent processing for 12, 24 h. The absorption of PF-BT05 films is similar to that of pure PFO because of the low contents of benzothiadiazole moieties in PF-BT05. The main absorption peak of the as-spincoated and solvent processing PF-BT05 films is located at about 380 nm, which is attributed to the π–π^* absorption of PFO backbone. However, the absorption spectra of PF-BT05 film shows an additional peak at 432 nm after being exposed to toluene vapor for

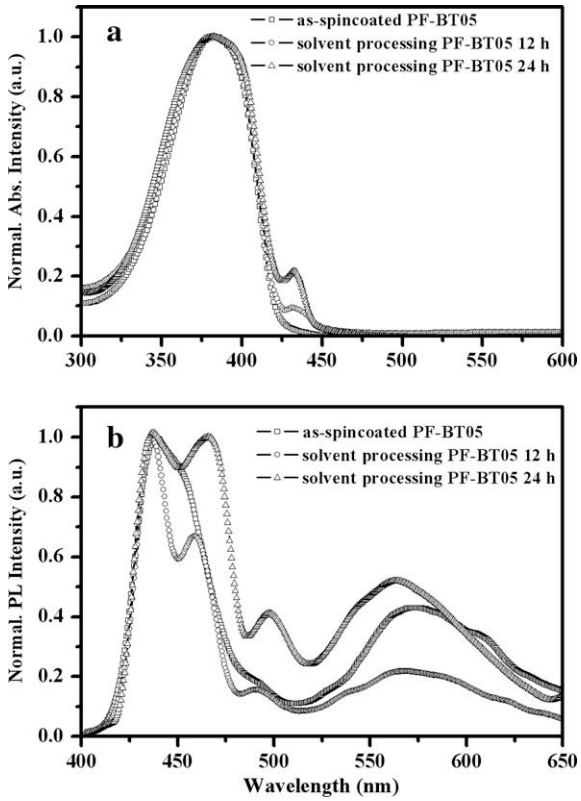

Fig. 2. UV–visible absorption (a) and PL spectra (b) of the as-spincoated and solvent processing PF-BT05 films.

12, 24 h and the intensity of the peak at 432 nm increases with increasing the treatment time, which indicates that the content of crystalline PFO increases with the increasing the treatment time. Considering the results, we note that the presence of small contents of crystalline PFO phase that has an extended conjugation length in amorphous PFO matrix leads to the formation of the additional absorption peak [18]. This is in accordance with the previously reported by Lu et al. [19]. The corresponding PL spectra of the PF-BT05 film exposed to toluene vapor exhibits a crystalline PFO phase emission shape with the three characteristic peaks at 439, 467, 496 nm, as shown in Fig. 2(b) [19].

Moreover, the EL intensity of blue emission increases compared to that of the orange emission from benzothiadiazole moieties after solvent processing, as shown in Fig. 3(a). Although a white emission consisting of blue and orange component is observed for the device based

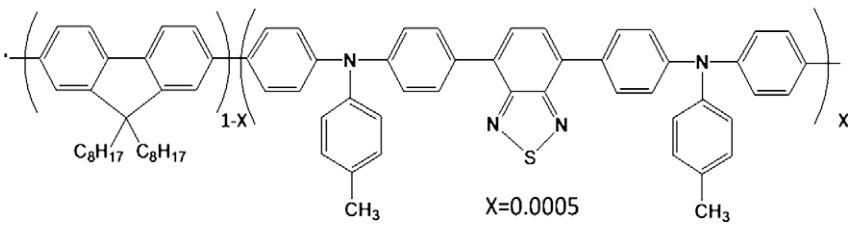

Fig. 1. The chemical structure of single white emissive polymer PF-BT05.

on as-spincoated PF-BT05 film, the CIE coordinates of (0.45, 0.46) are not pure white emission because of the weak blue emission from the PFO backbone. However, the EL spectra of the device is greatly enhanced while exposing the PF-BT05 film to toluene vapor for 24 h at 20 °C and the CIE coordinates are improved to (0.39, 0.39). This indicates that there exits efficient energy transfer from amorphous PFO to the crystalline phase of PFO and the presented crystalline phase acts as efficient blue dopants [19]. Thus, the crystalline phase of PFO and the benzothiadiazole moieties serve as blue and orange fluorescent dopants in the amorphous PFO matrix, respectively, and the white emission of PF-BT05 is enhanced. Fig. 3(b) shows EL spectra of the device based on the solvent processing PF-BT05 film under driving voltages of 8, 10, 12 V, respectively and no obvious variation in the EL spectra or the CIE coordinates was observed as the bias was varied, which indicates that the recombination zone is confined in the emissive layer.

We also carried out the experiment of Grazing-incident X-ray diffraction for the as-spincoated and solvent processing PF-BT05 films, as shown in Fig. 4. The as-spincoated PF-BT05 film is almost amorphous phase while the solvent processing PF-BT05 film shows three diffraction peaks at 7.15°, 14.65°, and 20.3°, corresponding to (2 0 0), (1 4 0), and (2 5 0) + (5 3 0) reflections of crystalline PFO backbone, respectively [16,18].

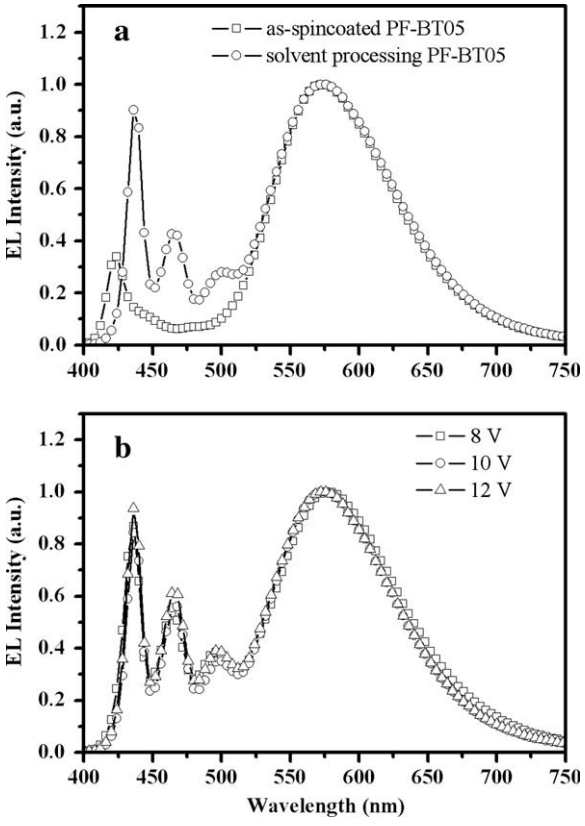

Fig. 3. EL spectra (a) of the WPLEDs based on the as-spincoated or solvent processing PF-BT05 films and EL spectra (b) of the WPLED based on the solvent processing PF-BT05 film under different voltages.

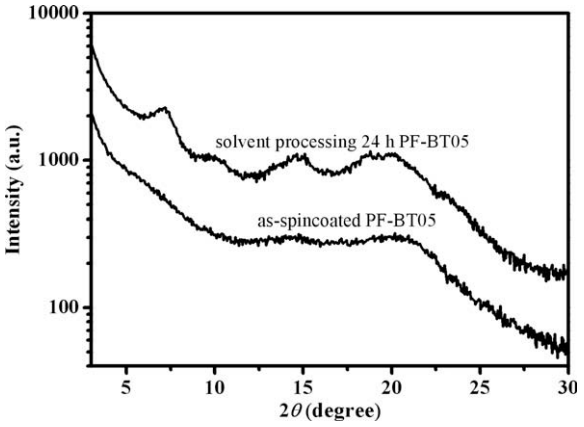

Fig. 4. Grazing-incident X-ray diffraction for the as-spincoated and solvent processing PF-BT05 films.

Fig. 5 plots the EL characteristics of the WPLEDs with and without solvent processing. For as-spincoated device, maximum brightness and current efficiency are 24,840 cd/m^2, and 8.2 cd/A, respectively. For solvent processing device, the corresponding results are 37,820 cd/m^2, and 12.1 cd/A, respectively. The performance of the latter device is better than that of as-spincoated device. It is noted that the current of the solvent processing device decreases compared to that of the as-spincoated device.

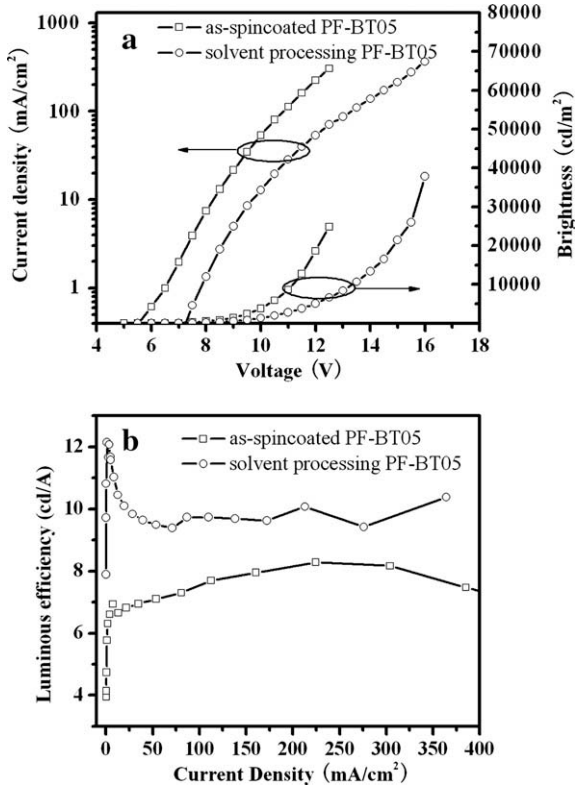

Fig. 5. The V–J–B characteristics (a) and luminous efficiencies (b) of the WPLEDs based on the as-spincoated or solvent processing PF-BT05 films.

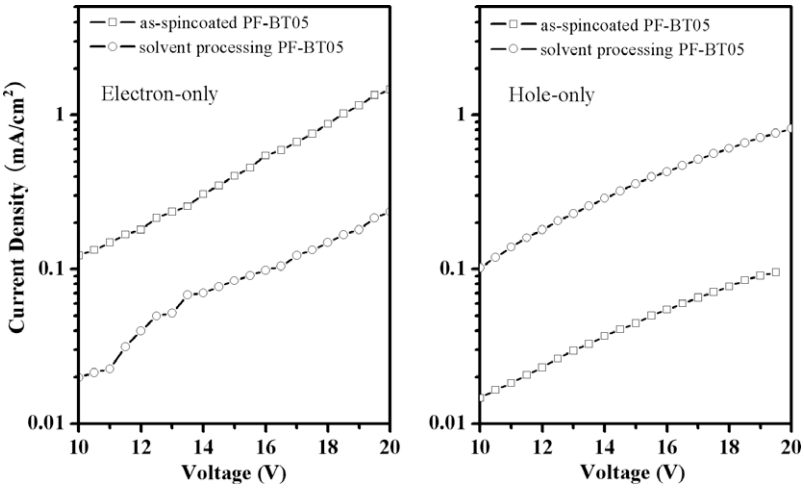

Fig. 6. V–J characteristics of the electron-only and hole-only devices based on the as-spincoated or solvent processing PF-BT05 films.

The physics behind the high performance due to the presence of crystalline PFO is described below. Single-carrier devices of electrons and holes reveal that the hole flux increases and the electron flux decreases with the solvent processing, as shown in Fig. 6. Hole-only and electron-only devices have structures of ITO/PEDOT:PSS (60 nm)/PF-BT05 (200 nm)/MoO_3 (5 nm)/Al (80 nm) and Al (80 nm)/PF-BT05 (200 nm)/Ca (10 nm)/Al (80 nm), respectively. It is found that the ratio of electron flux to hole flux decreases from 7.8 to 1.2 at a voltage of 12 V and from 9.9 to 1.5 at a voltage 16 V after solvent processing, indicating that the hole and electron fluxes are well balanced. The enhanced hole transport after solvent processing may be attributed to more compact stack of PFO backbone and longer conjugated length of crystalline PFO chains [20], while the decreased electron current is due to the presence of crystalline phase of PFO acting as electron traps [19]. The balanced hole and electron fluxes in PF-BT05 film after solvent processing enhance the luminous efficiency of the device.

The above findings show that the overall performance of the device based on the solvent processing PF-BT05 film was improved. On the other hand, the use of thermal annealing could also enhance the EL intensity and luminous efficiency of WPLEDs, which was presented in our earlier publication [21].

4. Conclusions

In summary, both luminous efficiency and color purity of the WPLED based on single white emissive polymer PF-BT05 are enhanced in virtue of solvent processing. Solvent processing not only induces presence of crystalline phase of PFO backbone that acts as blue dopants for enhancing color purity, but also favors balancing the hole and electron transport to improve the light-emitting efficiency, about 50% increase compared to the as-spincoated device. It may provide a new way to improve the device performance of PFO-based WPLEDs.

Acknowledgements

The authors acknowledge the financial support by the research startup fund of Jilin University (Nos. 4305050102H8; 4305050102B5) and the basic research and operational costs of Jilin University (No. 421031196604).

References

[1] J. Kido, M. Kimura, K. Nagai, Science 267 (1995) 1332.
[2] B.W. D'Andrade, S.R. Forrest, Adv. Mater. 16 (2004) 1585.
[3] Q.F. Xu, H.M. Duong, F. Wudl, Y. Yang, Appl. Phys. Lett. 85 (2004) 3357.
[4] Y. Kawamura, S. Yanagida, S.R. Forrest, J. Appl. Phys. 92 (2002) 87.
[5] X. Gong, S. Wang, D. Moses, G.C. Bazan, A.J. Heeger, Adv. Mater. 17 (2005) 2053.
[6] H.A. Al Atter, A.P. Monkman, M. Tavasli, S. Bettington, M.R. Bryce, Appl. Phys. Lett. 86 (2005) 121101.
[7] Y.H. Xu, J.B. Peng, J.X. Jiang, W. Xu, W. Yang, Y. Cao, Appl. Phys. Lett. 87 (2005) 193502.
[8] Y. Zhang, F. Huang, Y. Chi, A.K.-Y. Jen, Adv. Mater. 20 (2008) 1565.
[9] F.C. Chen, S.C. Chien, Y.S. Chen, Appl. Phys. Lett. 94 (2009) 043306.
[10] G.K. Ho, H.F. Meng, S.C. Lin, S.F. Horng, C.S. Hsu, L.C. Chen, S.M. Chang, Appl. Phys. Lett. 85 (2004) 4076.
[11] J.S. Huang, G. Li, E. Wu, Q.F. Xu, Y. Yang, Adv. Mater. 18 (2006) 114.
[12] M. Berggren, O. Inganäs, G. Gustasson, J. Rasmusson, M.R. Andersson, T. Hjerberg, O. Wennerström, Nature 372 (1994) 444.
[13] Y.H. Xu, J.B. Peng, Y.Q. Mo, Q. Hou, Y. Cao, Appl. Phys. Lett. 86 (2005) 163502.
[14] J. Liu, L. Chen, S.Y. Shao, Z.Y. Xie, Y.X. Cheng, Y.H. Geng, L.X. Wang, X.B. Jing, F.S. Wang, Adv. Mater. 19 (2007) 4224.
[15] X. Guo, C.J. Qin, Y.X. Cheng, Z.Y. Xie, Y.H. Geng, X.B. Jing, F.S. Wang, L.X. Wang, Adv. Mater. 21 (2009) 3682.
[16] S.H. Chen, A.C. Su, C.H. Su, Macromolecules 38 (2005) 379.
[17] A.J. Cadby, P.A. Lane, H. Mellor, S.J. Martin, M. Grell, C. Giebeler, D.D.C. Bradley, Phys. Rev. B 62 (2000) 15604.
[18] M. Grell, D.D.C. Bradley, G. Ungar, J. Hill, K.S. Whitehead, Macromolecules 32 (1999) 5810.
[19] H.H. Lu, C.Y. Liu, C.H. Chang, S.A. Chen, Adv. Mater. 19 (2007) 2574.
[20] W. Chunwaschirasiri, B. Tanto, D.L. Huber, M.J. Winokur, Phys. Rev. Lett. 94 (2005) 107402.
[21] Xiaodi Niu, Baohua Zhang, Zhiyuan Xie, Yanxiang Cheng, Lixiang Wang, Appl. Phys. Lett. 96 (2010) 073303.

Sato et al. have shown that VCC can be expressed as a space integration of the vibronic coupling density (VCD) η, which gives a local picture of vibronic coupling in a molecule [14–18]. VCD is the product of the electron-density difference $\Delta\rho$ and the derivative of the nuclear–electronic potential v. $\Delta\rho$ is the electron-density difference between the ionic and neutral states. The magnitude of η depends on the degree of overlap between $\Delta\rho$ and v. A molecule with small overlap has small VCCs and is expected to be good for charge-transporting material. We have calculated the VCDs of N,N′-bis(3-methylphenyl)-N,N′-diphenyl-[1,1′-biphenyl]-4,4′-diamine (TPD) cation and reported that localization of $\Delta\rho$ on N atoms makes η small, which results in small VCCs for the cation [19]. The good transport property of TPD originates from the small VCCs. The importance of N atom in a mechanism of hole-transporting process has been discussed elsewhere [20,21]. The VCD analysis further suggests that conformational change in tolyl and phenyl groups as well as central biphenyl unit contributes to the reorganization energy [21]. This result is consistent with that obtained by Wang and co-workers using a different method [22].

Various carbazole derivatives having good thermal stability have been synthesized and used as hole-transporting materials [23–25]. Carbazole N atom is expected to localize $\Delta\rho$, reduce VCCs, and enhance the hole mobility. In this study, we calculate VCDs for biphenyl, fluorene, and carbazole (Fig. 1) cations and investigate the reason for the VCC ordering by analyzing VCDs. Because methylene- and imino-bridging of biphenyl yields fluorene and carbazole, respectively, we investigate the effect of the methylene and imino on the VCDs and VCCs.

2. Theory

The Hamiltonian of a molecule is expressed as

$$\mathscr{H}(\mathbf{r},\mathbf{R}) = \mathscr{H}_{\mathrm{e}}(\mathbf{r},\mathbf{R}) + \mathscr{T}_{\mathrm{n}}(\mathbf{R}), \tag{1}$$

where $\mathscr{H}_{\mathrm{e}}(\mathbf{r},\mathbf{R})$ is an electronic Hamiltonian, $\mathscr{T}_{\mathrm{n}}(\mathbf{R})$ is the nuclear kinetic energy, and $\mathbf{r}$ and $\mathbf{R}$ denote sets of electronic and nuclear coordinates, respectively. Herzberg–Teller expansion of the electronic Hamiltonian yields

$$\mathscr{H}_{\mathrm{e}}(\mathbf{r},\mathbf{R}) = \mathscr{H}_{\mathrm{e}}(\mathbf{r},\mathbf{R_0}) + \sum_i \left(\frac{\partial \mathscr{H}_{\mathrm{e}}(\mathbf{r},\mathbf{R})}{\partial Q_i}\right)_{\mathbf{R_0}} Q_i + \cdots, \tag{2}$$

where $\{Q_i\}$ is a set of mass-weighted normal coordinates for the ith vibrational mode and $\mathbf{R_0}$ is the nuclear configuration of the equilibrium geometry in the neutral state. The VCC for the ith mode is defined by

$$V_i = \left\langle \Psi^+(\mathbf{r},\mathbf{R_0}) \middle| \left(\frac{\partial \mathscr{H}_{\mathrm{e}}(\mathbf{r},\mathbf{R})}{\partial Q_i}\right)_{\mathbf{R_0}} \middle| \Psi^+(\mathbf{r},\mathbf{R_0}) \right\rangle, \tag{3}$$

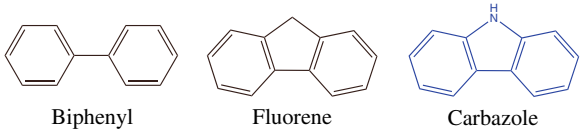

Fig. 1. Structural formulas for biphenyl, fluorene, and carbazole.

where $\Psi^+(\mathbf{r},\mathbf{R_0})$ is the electronic wave function of the cation state at the equilibrium geometry in the neutral state. Eq. (3) can be written as

$$V_i = \sum_A \frac{1}{\sqrt{M_A}} \mathbf{e}_A^{(i)} \cdot \left\langle \Psi^+(\mathbf{r},\mathbf{R_0}) \middle| \left(\frac{\partial \mathscr{H}_{\mathrm{e}}(\mathbf{r},\mathbf{R})}{\partial \mathbf{R}}\right)_{\mathbf{R_0}} \middle| \Psi^+(\mathbf{r},\mathbf{R_0}) \right\rangle = \sum_A V_{i,A}, \tag{4}$$

where M_A is the mass of nucleus A. $\mathbf{e}_A^{(i)}$ is the mass-weighted 3D component of atom A of the ith vibrational mode $\mathbf{e}^{(i)}$, and denotes the relative magnitude of displacement of nucleus A. The direction of $\mathbf{e}^{(i)}$ is defined such that V_i becomes negative; that is, structural deformation toward $\mathbf{e}^{(i)}$ lowers the energy of the cationic state. $V_{i,A}$ is called the atomic vibronic coupling constant (AVCC) of the Ath atom and represents the contribution from the Ath atom to VCC V_i.

When the Hellmann–Feynman theorem [26] holds, V_i can be expressed in terms of the electron-density difference $\Delta\rho$ and the derivative of the nuclear–electronic potential v_i [14–18]:

$$V_i = \int \Delta\rho(\mathbf{x}) \times v_i(\mathbf{x}) d\mathbf{x}, \tag{5}$$

where

$$\Delta\rho(\mathbf{x}) = \rho^+(\mathbf{x}) - \rho(\mathbf{x}), \tag{6}$$

$$v_i(\mathbf{x}) = \sum_A v_{i,A}(\mathbf{x}) = \sum_A -\frac{Z_A}{\sqrt{M_A}} \mathbf{e}_A^{(i)} \cdot \frac{\mathbf{x}-\mathbf{R}_A}{|\mathbf{x}-\mathbf{R}_A|^3}, \tag{7}$$

where Z_A is atomic number, $\rho^+(\mathbf{x})$ and $\rho(\mathbf{x})$ are electron densities for the cationic and neutral states, respectively, and $\mathbf{x}$ denotes a position in 3D space. The product $\Delta\rho(\mathbf{x}) \times v_i(\mathbf{x})$ is called the VCD [14–18] and is denoted by $\eta_i(\mathbf{x})$,

$$\eta_i(\mathbf{x}) = \Delta\rho(\mathbf{x}) \times v_i(\mathbf{x}), \tag{8}$$

which gives a local picture of the vibronic couplings in the molecule.

Atomic vibronic coupling density (AVCD) $\eta_{i,A}$ is defined by

$$\eta_{i,A}(\mathbf{x}) = \Delta\rho(\mathbf{x}) \times v_{i,A}(\mathbf{x}) = \Delta\rho(\mathbf{x}) \times \left(-\frac{Z_A}{\sqrt{M_A}} \mathbf{e}_A^{(i)} \cdot \frac{\mathbf{x}-\mathbf{R}_A}{|\mathbf{x}-\mathbf{R}_A|^3}\right). \tag{9}$$

AVCD represents the contribution from the Ath atom to η_i. Space integration gives the AVCC $V_{i,A}$:

$$V_{i,A} = \int \eta_{i,A}(\mathbf{x}) d\mathbf{x}. \tag{10}$$

The sum of the AVCDs is equal to the VCD η_i,

$$\eta_i(\mathbf{x}) = \sum_A \eta_{i,A}(\mathbf{x}). \tag{11}$$

3. Method of calculation

We used the 6-31G basis set with their first derivatives [27] (denoted as 6-31G+der) so as to satisfy the Hellmann–

Feynman theorem [26], and confirmed that the theorem was satisfied for all systems. We optimized the structures of neutral biphenyl, fluorene, and carbazole at the B3LYP/6-31G+der level of theory. We assumed D_2 symmetry for biphenyl and C_{2v} symmetry for fluorene and carbazole, and confirmed by vibrational analysis that they are stationary minima. A scaling factor of 0.963 [28] was used for B3LYP/6-31G+der theoretical frequencies. We calculated electronic structures of the cationic states at the UB3LYP/6-31G+der level using the optimized geometries of the neutral states. All the DFT calculations were done using Gaussian 03 software [29]. Current and power loss calculations were performed based on Datta [13]. Neighboring molecules are considered as electrodes with the Fermi levels which are set to the HOMO levels shown in Fig. 3. We employed the electronic coupling $\tau = 0.5$ eV and temperature $T = 298$ K.

4. Results and discussion

4.1. Equilibrium geometries

Fig. 2 shows B3LYP/6-31G+der optimized geometries for neutral biphenyl, fluorene, and carbazole with an atomic numbering scheme. Biphenyl has a twisted structure (Fig. 2a). Deviation from planarity is due to steric repulsion between H1–H1′ atoms and H5–H5′ atoms. In a planar structure, the calculated distance between H1 and H1′ atoms is 1.949 Å; in the twisted conformation, the estimated distance is 2.403 Å. The calculated torsion angle between the two benzene rings of biphenyl is 40.3°, being small compared with experimental values of 44.4° [30] and $45 \pm 10°$ [31] determined by gas-phase electron diffraction. In solutions, the estimated twisted angles are 19–26° [32]; in a solid crystalline form at room temperature, the two benzene rings are coplanar [33–36]. These facts suggest that intermolecular interaction overcomes steric repulsion between H atoms. Our calculated geometrical parameters are listed in Table 1, along with experimental results obtained by X-ray analysis for crystalline biphenyl at 110K [37]. Although calculated and experimental results are not in agreement, especially for the dihedral angle between the two benzene rings, nonplanarity does not affect VCC ordering for the biphenyl cation, as discussed in Section 4.2.

The carbon skeleton of fluorene is calculated to be coplanar (Fig. 2b). Whether it is coplanar or bent has been controversial in experiments. By X-ray analysis of crystalline fluorene, Brown et al. [38] and Belsky et al. [39] determined that it is coplanar, while Gerkin et al. determined that it is bent[40]. Although lack of planarity can arise from intermolecular interaction between the H6 atom of one molecule and the C1 and C1′ atoms of a neighboring molecule, our calculation does not consider such interactions. Our calculated geometrical parameters, listed in Table 1, are in good agreement with experimental results [40]. The molecular structure of carbazole resembles that of fluorene, with the methylene group replaced by an imino group. In their solid crystalline forms, intermolecular interactions cause both fluorene and carbazole to be

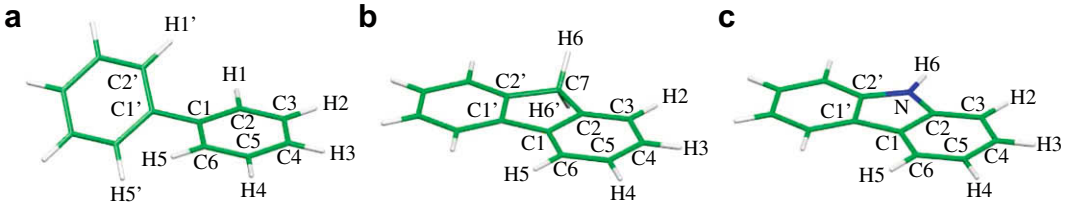

Fig. 2. Geometries optimized at the B3LYP/6-31G+der level of theory with the atomic numbering scheme for various neutral moieties: (a) biphenyl; (b) fluorene; and (c) carbazole.

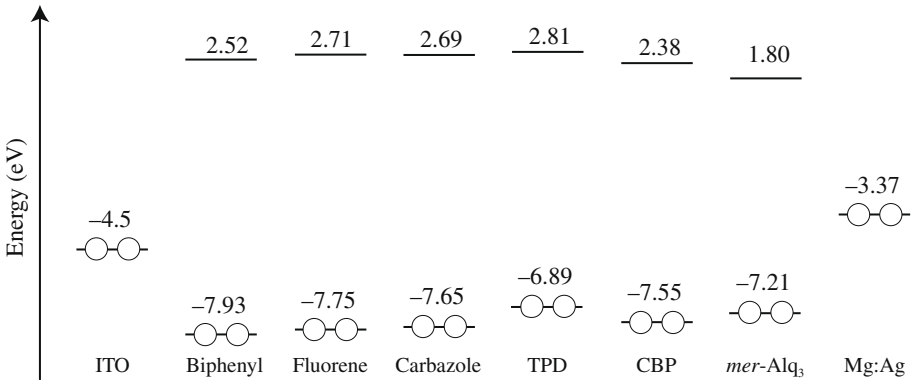

Fig. 3. HOMO/LUMO energy-level diagrams for neutral biphenyl, fluorene, carbazole, TPD, CBP, and *mer*-Alq_3 calculated at the RHF/6-31G+der level of theory. Experimental work functions with opposite signs of an ITO thin film [44] and Mg:Ag alloy [45] are also shown as the Fermi energies of ITO and Mg:Ag electrode surfaces.

Table 1
Geometrical parameters of optimized structures of neutral biphenyl, fluorene, and carbazole calculated at the B3LYP/6-31G+der level. Numbers in parentheses are experimental values [37,40,41]. Bond lengths are in Å; bond angles and dihedral angles are in degrees.

	Biphenyl	Fluorene	Carbazole
Bond lengths			
C1–C2	1.403 (1.394)	1.409 (1.397)	1.419 (1.401)
C2–C3	1.392 (1.391)	1.389 (1.386)	1.395 (1.393)
C3–C4	1.394 (1.379)	1.397 (1.385)	1.391 (1.373)
C4–C5	1.394 (1.390)	1.397 (1.385)	1.404 (1.394)
C5–C6	1.392 (1.385)	1.394 (1.390)	1.390 (1.379)
C6–C1	1.403 (1.399)	1.395 (1.387)	1.399 (1.388)
C1–C1′	1.484 (1.496)	1.469 (1.472)	1.450 (1.4151)
C2–C7(N)		1.515 (1.504)	1.388 (1.387)
C2–H1	1.084 (1.04)		
C3–H2	1.084 (1.08)	1.085 (1.00)	1.084 (1.00)
C4–H3	1.084 (1.05)	1.084 (1.00)	1.084 (0.96)
C5–H4	1.084 (1.04)	1.084 (0.99)	1.083 (1.02)
C6–H5	1.084 (0.96)	1.084 (0.97)	1.084 (1.01)
C7(N)–H6		1.096 (1.01)	1.004 (0.98)
Bond angles			
C1–C2–C3	120.9 (120.57)	120.5 (120.5)	121.6 (122.3)
C2–C3–C4	120.2 (120.98)	119.1 (118.7)	117.7 (116.7)
C3–C4–C5	119.5 (118.91)	120.5 (120.9)	121.3 (122.0)
C4–C5–C6	120.2 (120.43)	120.7 (120.7)	120.8 (121.0)
C5–C6–C1	120.9 (121.25)	118.9 (118.5)	119.2 (118.4)
C6–C1–C2	118.2 (117.86)	120.4 (120.7)	119.2 (119.7)
C2–C1–C1′	120.9 (120.63)	108.6 (108.3)	106.7 (106.6)
C1–C2–C7(N)		110.0 (110.4)	108.5 (109.0)
C2–C7(N)–C2′		102.8 (102.7)	109.6 (108.7)
C7(N)–C2–C3		129.5 (129.1)	129.7 (128.7)
H1–C2–C1	119.4 (122.0)		
H1–C2–C3	119.7 (117.3)		
H2–C3–C2	119.7 (118.9)	120.8 (119.5)	121.3 (121)
H2–C3–C4	120.0 (120.1)	120.1 (121.8)	121.0 (122)
H3–C4–C3	120.3 (120.6)	119.8 (119.2)	119.3 (119)
H3–C4–C5	120.3 (120.5)	119.7 (119.8)	119.4 (119)
H4–C5–C4	120.0 (117.3)	119.6 (119.3)	119.4 (118)
H4–C5–C6	119.7 (122.3)	119.7 (119.9)	119.8 (121)
H5–C6–C5	119.7 (115.6)	120.2 (121.2)	120.3 (124)
H5–C6–C1	119.4 (122.9)	120.8 (120.3)	120.5 (118)
C1′–C1–C6	120.9 (121.5)	131.0 (131.0)	134.1 (133.7)
H6–C7(N)–C2		111.9 (111.9)	125.2
H6–C7–H6′		106.5 (105)	
Dihedral angles			
C1–C2–C3–C4	−0.1	0.0	0.0
C2–C3–C4–C5	0.0	0.0	0.0
C3–C4–C5–C6	0.0	0.0	0.0
C4–C5–C6–C1	−0.1	0.0	0.0
C5–C6–C1–C2	0.0	0.0	0.0
C6–C1–C2–C3	0.0	0.0	0.0
C2′–C1′–C1–C6	139.7	180.0	180.0
C1′–C1–C2–C7(N)		0.0	0.0
C1–C2–C7(N)–H6		120.3	180.0
C2′–C7(N)–H6–C2		114.7	180.0
C6–C1–C2–H1	178.3		
C1–C2–C3–H2	179.4	180.0	180.0
C2–C3–C4–H3	180.0	180.0	180.0
C3–C4–C5–H4	−179.4	180.0	180.0
C4–C5–C6–H5	−178.3	180.0	180.0

slightly bent [41,42], whereas the optimized geometry of carbazole is planar (Fig. 2c). Differences in the geometrical parameters of carbazole and fluorene are observed in five-membered rings; the C2–N bond is much shorter than the C2–C7 bond because of π delocalization in the pyrrole ring. Our calculated bond lengths and angles, listed in Table 1, are in satisfactory agreement with experimental results [41].

Fig. 3 shows orbital energy levels of HOMOs and lowest unoccupied molecular orbitals (LUMOs) for biphenyl, fluorene, and carbazole together with those for TPD, CBP, and meridional tris(8-quinolinolato)aluminum (*mer*-Alq_3). TPD and CBP are widely used as hole-transporting materials, and Alq_3 as an emitting material and electron-transporting material [1]. HOMOs and LUMOs were calculated at the RHF/6-31G+der level using General Atomic and

Molecular Electronic Structure System (GAMESS) general *ab initio* quantum chemistry package program [43]. Experimental work functions with opposite signs to those for ITO thin film [44] and Mg:Ag alloy [45] are also shown in the figure as Fermi energies of ITO and Mg:Ag electrode surfaces. ITO and Mg:Ag electrodes are widely used as anodes and cathodes, respectively, in multilayer OLEDs. Carbazole has a higher HOMO energy level than do biphenyl and fluorene, suggesting that it exhibits higher hole-injection efficiency.

4.2. Vibronic coupling density analysis

Fig. 4 shows calculated VCCs for biphenyl, fluorene, and carbazole cations. VCCs are smaller for carbazole than for the others. The trend in VCC ordering for fluorene is similar to that for biphenyl. For both biphenyl and fluorene, the largest VCC corresponds to a C–C stretching mode (1589.13 and 1594.25 cm^{-1}, respectively). The experimental frequencies are 1610 [46] and 1612 [47] cm^{-1}, respectively, which are in satisfactory agreement with our theoretical results; for carbazole, the largest two VCCs correspond to a C–C stretching mode (1608.91 cm^{-1}) and a N–H stretching mode (3529.22 cm^{-1}). The calculated frequencies are in agreement with the experimental frequencies of 1625 and 3421 cm^{-1} [48]. These various C–C stretching modes are clearly different; the associated VCCs are -4.192×10^{-4} au for biphenyl, -3.440×10^{-4} au for fluorene, and -2.390×10^{-4} au for carbazole. In spite of their similarities in molecular structure, the largest VCC for carbazole is small compared with those for biphenyl and fluorene, suggesting that carbazole is the superior transporting material. The reorganization energy for biphenyl is calculated to be 0.387 eV, which is close to the value calculated using the different basis set (0.36 eV) [49].

Fig. 5a1–c1 shows the (largest VCC) C–C stretching modes for biphenyl, fluorene, and carbazole cations. Note that these modes involve inter-ring C–C (C1–C1′) stretching and intra-ring C–C (C2–C3 and C5–C6) stretching vibrations. For biphenyl and fluorene, the mode directions correspond to a quinoid deformation, which converts the molecular geometry from benzenoid to quinoid. The C1–C1′, C2–C3, and C5–C6 bonds shorten, while the C1–C2, C3–C4, C4–C5, and C6–C1 bonds lengthen. Since we have defined the mode directions such that their VCCs become negative, quinoid deformations stabilize the cationic states. For carbazole, the vibration phase is the opposite: the C1–C1′, C2–C3, and C5–C6 bonds lengthen, while the C1–C2, C3–C4, C4–C5, and C6–C1 bonds shorten. Quinoid deformation does not occur, and the optimized structure of carbazole cation is not quinoid-like. The AVCCs of the three C–C stretching modes in the figure are listed in Table 2. Values for the C1 and C3 atoms are much smaller for carbazole than for biphenyl and fluorene. A value for the carbazole C5 atom is much smaller for the biphenyl C5 atom. Values for the carbazole C4 and C6 atoms are comparable to those for the fluorene C4 and biphenyl C6 atoms. Contributions to the VCCs from H and C7 (N) atoms are small. Hence, the smaller VCC of the carbazole C–C stretching mode is due to the C1, C3, and C5 atoms. We can understand the reason for this result by considering VCD distributions.

Fig. 5a2–c2 shows derivatives of nuclear–electronic potential v for C–C stretching modes with the same isosurface value. The distribution of v_i reflects the vibrational mode; v_i around atom A is distributed along a component of vibrational vector $\mathbf{e}_A^{(i)}$, and is large around an atom for which $|\mathbf{e}_A^{(i)}|$ is large (Eq. 7). $|\mathbf{e}_A^{(i)}|$ is the relative magnitude of displacement of nucleus A toward a negative (blue) region around it. For in-plane modes, v_i has a large negative value at which interatomic distance is small. Values of $|\mathbf{e}_A^{(i)}|$ for the three C–C stretching modes in Fig. 5a1–c1 are listed in Table 3. For biphenyl and fluorene, v_i distributions of the C–C stretching modes are similar because the associated $|\mathbf{e}_A^{(i)}|$ values are close. Large negative v_i values (blue regions in Fig. 5a2 and b2) are observed for the C1–C1′, C2–C3, and C5–C6 bonds (that is, the bond lengths are shorter), and large positive values are observed for the C1–C2, C3–C4, C4–C5, and C6–C1 bonds. For carbazole, the phase of v_i is opposite to that for biphenyl and fluorene, but the magnitudes of $\mathbf{e}_A^{(i)}$ is comparable to that for fluorene. Thus, the $|v_i|$ distribution for carbazole is almost identical to that for fluorene, suggesting that differences in VCC magnitude among the three molecules is due to the differences in the distribution patterns of the electron-density difference $\Delta\rho$.

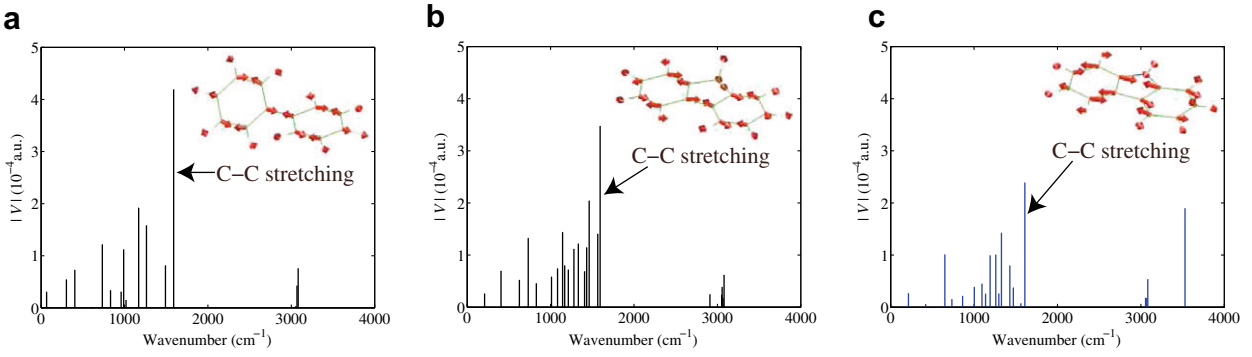

Fig. 4. Absolute values of vibronic coupling constants $|V|$ for various cations calculated at the UB3LYP/6-31G+der level of theory: (a) biphenyl; (b) fluorene; and (c) carbazole.

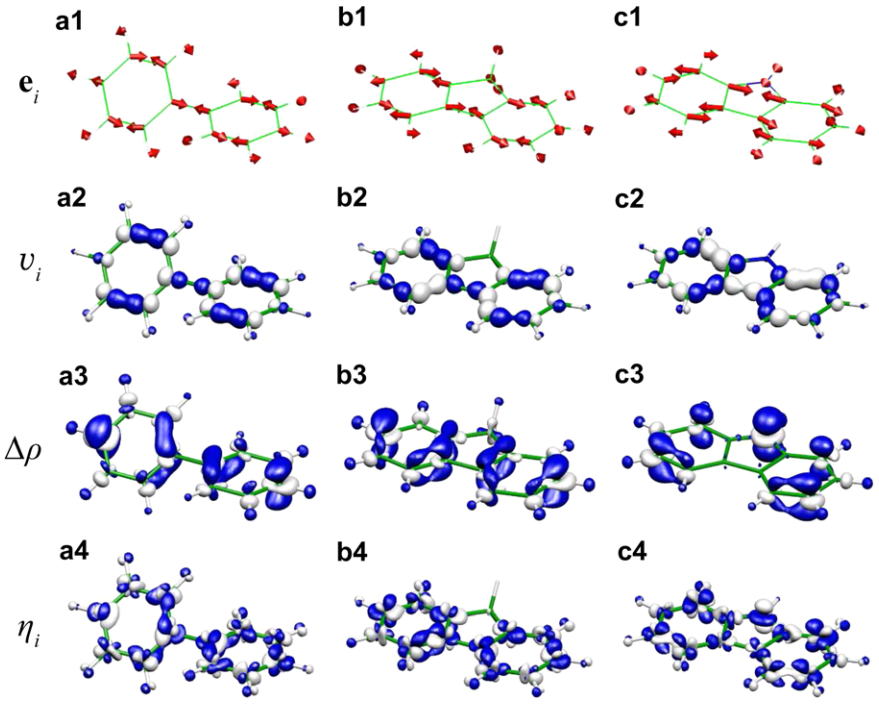

Fig. 5. (a1)–(c1) C–C stretching modes for biphenyl, fluorene, and carbazole. (a2)–(c2) Corresponding nuclear–electronic potential derivatives at an isosurface value of 0.01 au. (a3)–(c3) Electron-density differences due to ionization at an isosurface value of 0.04 au. (a4)–(c4) Vibronic coupling densities of the C–C stretching modes at an isosurface value of 2.0×10^{-5} au. Blue shows where values are negative; white shows where values are positive. (For interpretation of the references to colour in this figure legend, the reader is referred to the web version of this article.)

Table 2
Atomic vibronic coupling constants for C–C stretching modes shown in Fig. 5a1–c1. Atomic vibronic coupling constants are in 10^{-4} au.

	Biphenyl	Fluorene	Carbazole
C1	−0.582	−0.628	−0.335
C2	−0.425	−0.127	−0.140
C3	−0.334	−0.269	−0.105
C4	−0.051	0.030	0.042
C5	−0.334	−0.206	−0.153
C6	−0.425	−0.535	−0.505
C7(N)		−0.003	−0.027
H1	0.023		
H2	0.004	0.001	0.014
H3	0.001	0.000	−0.007
H4	0.004	−0.002	0.003
H5	0.023	0.009	−0.003
H6		0.000	0.015
Total	−4.192	−3.440	−2.390

Table 3
Values of $|\mathbf{e}_A^{(i)}|$ for the three C–C stretching modes in Fig. 5a1–c1.

	Biphenyl	Fluorene	Carbazole
C1	0.296	0.309	0.316
C2	0.311	0.279	0.315
C3	0.268	0.320	0.317
C4	0.133	0.169	0.170
C5	0.268	0.190	0.174
C6	0.311	0.337	0.317
C7(N)		0.012	0.011
H1	0.133		
H2	0.099	0.126	0.117
H3	0.045	0.060	0.059
H4	0.099	0.069	0.063
H5	0.133	0.146	0.137
H6		0.010	0.006

Fig. 5a3–c3 shows electron-density difference $\Delta\rho$. For biphenyl, $\Delta\rho$ is large across the C1–C2 and C6–C1 bonds and C4 atom (Fig. 5a3). For fluorene, $\Delta\rho$ is similarly distributed (Fig. 5b3) and, on the C1–C2 and C6–C1 bonds, greatly overlaps with v_i. $\Delta\rho$ is small on fluorene's methylene group. In contrast, for carbazole, $\Delta\rho$ distribution changes as a result of imino-group substitution. $\Delta\rho$ is large on the N atom; it is also large on the benzene ring C3 and C5 atoms (where, for biphenyl and fluorene, it is small) and relatively small on the benzene ring C1 and C2 atoms. For carbazole, $\Delta\rho$ is limited around the N, C3, and C5 atoms, whereas for biphenyl and fluorene, it extends over the C1–C2 and C6–C1 bonds. This difference affects the degree of overlap between $\Delta\rho$ and v_i.

Fig. 5a4–c4 shows vibronic coupling densities η_i. For biphenyl and fluorene, since v_i and $\Delta\rho$ overlap significantly on the C1–C2 and C6–C1 bonds, the AVCDs of the C1, C2, and C6 atoms are large. The sums of the AVCCs of the C1, C1′, C2, C2′, C6 and C6′ atoms are -2.864×10^{-4} au for biphenyl and -2.580×10^{-4} au for fluorene, corresponding to 68.3% and 75.0% of their respective VCCs. This result suggests that vibronic coupling in biphenyl and fluorene occurs mainly on the C1–C2 and C6–C1 bonds, where η_i is large. However, around the C4

atom, although $\Delta\rho$ is large, since v_i is small, η_i is small, which explains why the associated AVCCs are small. For fluorene, since the methylene group's $\Delta\rho$ and v_i are small, its η_i is also small.

Fig. 6 shows HOMO electron densities for neutral biphenyl, fluorene, and carbazole. The HOMO electron densities have a π-orbital character. By comparing Fig. 6a–c with Fig. 5a3–c3, we find that regions where $\Delta\rho$ is negative also have a π-orbital character, with similar distribution patterns, suggesting that electron difference comes mainly from the HOMOs. In addition, regions where $\Delta\rho$ is positive have a σ-orbital character, due to relaxation of the occupied molecular orbitals other than the HOMOs. The positive $\Delta\rho$ reduces Coulomb repulsion from the negative $\Delta\rho$ of the π-orbitals.

Figs. 7 and 8 show the AVCDs and reduced AVCDs (RAVCDs), respectively, of the C and N atoms for the C–C stretching mode for carbazole. The AVCD $\eta_{i,A}$ contains contributions for which the space integrals vanish because of symmetries of basis functions and $v_{i,A}$. The RAVCD $\bar{\eta}_{i,A}$ is calculated by subtracting such contributions from the AVCD $\eta_{i,A}$ [50]. Hence, the space integrals of the AVCDs and RAVCDs give the corresponding AVCCs:

$$\int \eta_{i,A}(\mathbf{x})d\mathbf{x} = \int \bar{\eta}_{i,A}(\mathbf{x})d\mathbf{x} = V_{i,A}. \tag{12}$$

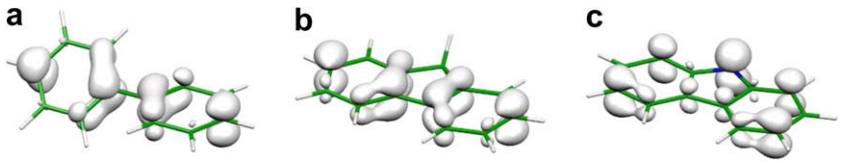

Fig. 6. HOMO electron-density distributions for various neutral moieties at an isosurface value of 0.04 au: (a) biphenyl; (b) fluorene; and (c) carbazole.

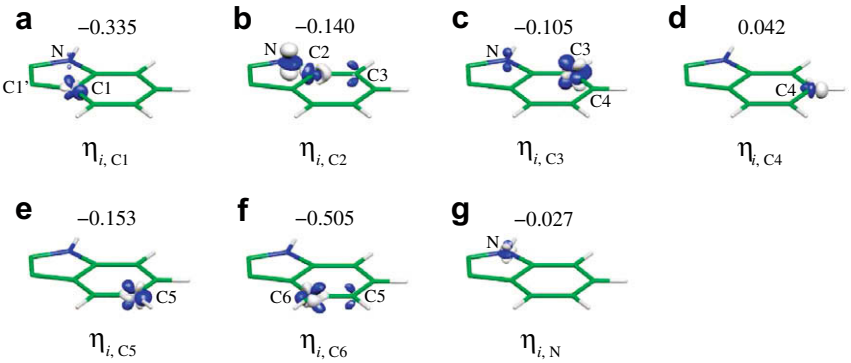

Fig. 7. Atomic vibronic coupling densities $\eta_{i,A}$ of the C and N atoms for the C–C stretching mode of carbazole at an isosurface value of 2.0×10^{-5} au. Blue shows where values are negative; white shows where values are positive. The number above each figure is the corresponding atomic vibronic coupling constant. (For interpretation of the references to colour in this figure legend, the reader is referred to the web version of this article.)

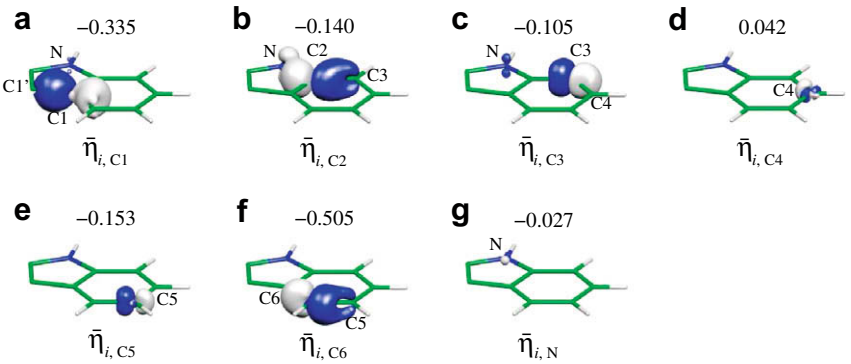

Fig. 8. Reduced atomic vibronic coupling densities $\bar{\eta}_{i,A}$ of the C and N atoms for the C–C stretching mode of carbazole at an isosurface value of 2.0×10^{-5} au. Blue shows where values are negative; white shows where values are positive. The number above each figure is the corresponding atomic vibronic coupling constant. (For interpretation of the references to colour in this figure legend, the reader is referred to the web version of this article.)

The distribution pattern for $\bar{\eta}_{i,A}$ is simpler than that for $\eta_{i,A}$. For carbazole, the C1 and C6 atoms contribute significantly to the VCCs (Table 2). On the C1 atom, although $\Delta\rho$ is relatively small, since v_i is large, the AVCD $\eta_{i,C1}$ gives a large positive or negative value around the C1 atom (Fig. 7a). The region where values are negative is larger than the region where they are positive. This feature is also observed for $\bar{\eta}_{i,C1}$ (Fig. 8a). On the C1 atom, the region where $\bar{\eta}_{i,C1}$ is negative is large, so the AVCC is large and negative (-0.335×10^{-4} au). Similarly, on the C6 atom above and below the benzene ring, overlap between v_i and $\Delta\rho$ gives a negative distribution, so the C6 atom has a large negative AVCC (-0.505×10^{-4} au), whose contribution is clearly seen for $\bar{\eta}_{i,C6}$ (Fig. 8f).

On the C5 atom, since $\Delta\rho$ is large, $\bar{\eta}_{i,\,C5}$ is also large (Fig. 8e). The region where values are negative is larger than the region where they are positive, so the AVCC is negative (-0.153×10^{-4} au). However, since the difference between the negative and positive regions is small, the AVCC is smaller for the C5 atom than for the C1 and C6 atoms.

The AVCC of the C3 atom (-0.105×10^{-4} au) is close to that of the C5 atom. This is because the distribution pattern for $\eta_{i,C3}$ (Fig. 7c) is similar to that for $\eta_{i,C5}$ (Fig. 7e). $\eta_{i,C3}$ and $\bar{\eta}_{i,C3}$ are negative for the N atom because the C3 atom is located nearby. The region where values are negative is slightly larger than the region where they are positive, which explains why the C3 atom has a small negative AVCC (Fig. 8c).

$\Delta\rho$ has a small positive value on the C4-H3 bond. Hence, around the C4 atom, $\eta_{i,C4}$ and $\bar{\eta}_{i,\,C4}$ are small (Figs. 7d and 8d). Because the positive region of $\eta_{i,C4}$ is larger than the negative region, the C4 atom has a small positive AVCC(0.042×10^{-4} au).

For the C2 atom, both negative and positive $\bar{\eta}_{i,\,C2}$ (Fig. 8b) regions are largely distributed on the C2–N and C2–C3 bonds. The small AVCC for the C2 atom results from cancellation of these positive and negative regions on the C2–N and C2–C3 bonds.

By comparing $\eta_{i,C2}$ (Fig. 7b) with η_i (Fig. 5c4), we find that for the N atom, the η_i distribution comes from $\eta_{i,C2}$ and not $\eta_{i,N}$ (Fig. 7g). The latter is considerably small because v_i is negligibly small. The small overlap between $\Delta\rho$ and v_i is responsible for the small AVCC of the N atom. v_i for the N–H stretching mode (Fig. 4c) is distributed on the N–H6 bond and can overlap with $\Delta\rho$ around the N atom. However, since the overlap region is limited on the N–H6 bond, the VCC of the N–H stretching mode is not large (1.894×10^{-4} au). Thus, imino-bridging changes the $\Delta\rho$ distribution pattern and weakens vibronic coupling in the benzene rings.

We calculated current through a single fluorene and carbazole molecule employing the NEGF theory including inelastic scattering [13]. Here, we consider a suppression effect originating from the intramolecular vibronic coupling on the current. Actually, in the bulk systems, intermolecular vibronic coupling can be a dominant factor governing the suppression effect. However, the small intramolecular vibronic coupling is a necessary condition for design of transporting materials and first, we should consider the suppression effect due to the intramolecular vibronic coupling.

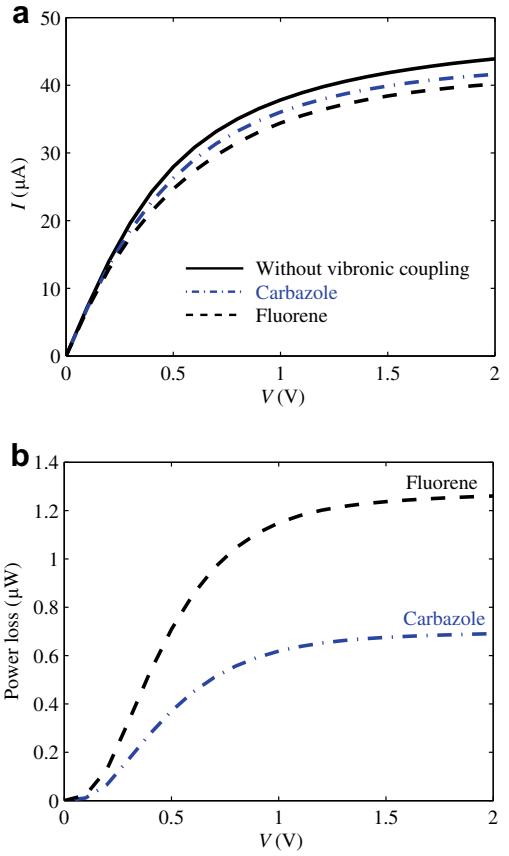

Fig. 9. (a) Current–voltage characteristics and (b) power loss.

Fig. 9a shows I–V characteristics. The solid line shows the I–V characteristics in the absence of vibronic coupling; the dot-dashed and dashed lines show the I–V characteristics for carbazole and fluorene, respectively, in the presence of the vibronic coupling. Fig. 9a shows that the vibronic coupling reduces the current and the suppression effect is larger for fluorene (having the large VCCs) than for carbazole (having the small VCCs). Fig. 9b shows power loss due to the vibronic coupling. Note that, without vibronic coupling, the power loss dose not occur. At $V = 2$ V, the power loss in carbazole is about half that in fluorene. Fig. 9 suggests that a molecule with small VCCs is good charge-transporting and low power-loss material. The carbazole N atom can weaken the vibronic coupling and enhance hole-transporting property.

Fig. 10a1–c1 shows Hartree–Fock (HF) VCCs for biphenyl, fluorene, and carbazole cations. Geometry optimization and vibrational analysis for neutral biphenyl, fluorene, and carbazole were done at the RHF/6-31G+der level of theory. Cationic states of the molecules were calculated at the UHF/6-31G+der level of theory. A scaling factor of 0.8929 [51] was used for RHF/6-31G+der theoretical frequencies. All the HF calculations were done using GAMESS package program. The trend in VCC ordering in

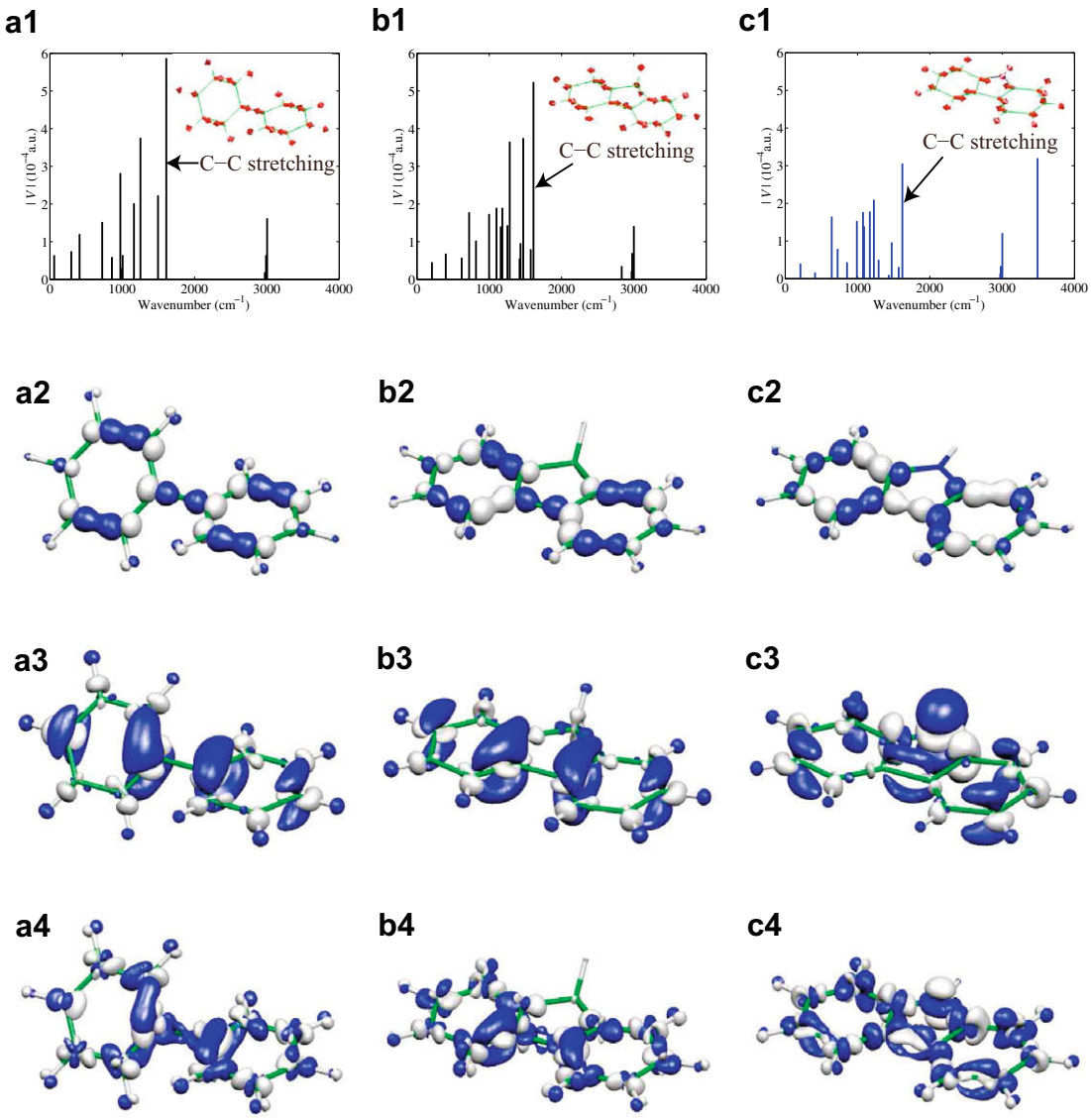

Fig. 10. Absolute values of vibronic coupling constants $|V|$ for various cations calculated at the UHF/6-31G+der level of theory: (a1) biphenyl; (b1) fluorene; and (c1) carbazole. (a2)–(c2) Nuclear–electronic potential derivatives of the modes shown in (a1)–(c1) at an isosurface value of 0.01 au. (a3)–(c3) Electron-density differences due to ionization at an isosurface value of 0.04 au. (a4)–(c4) Vibronic coupling densities at an isosurface value of 2.0×10^{-5} au. Blue shows where values are negative; white shows where values are positive. (For interpretation of the references to colour in this figure legend, the reader is referred to the web version of this article.)

Fig. 10a1–c1 is similar to that in Fig. 4a–c; for biphenyl and fluorene, the largest VCC corresponds to a C–C stretching mode (1608.87 and 1610.88 cm^{-1}, respectively); for carbazole, the largest two VCCs correspond to a C–C stretching mode (1620.01 cm^{-1}) and a N–H stretching mode (3490.04 cm^{-1}). The C–C stretching modes having the large VCCs are shown in Fig. 10a1–c1. Comparing Fig. 10a1–c1 with Fig. 4a–c, the VCCs calculated at the UHF/6-31G+der level are large compared with those calculated at the UB3LYP/6-31G+der level. We can understand the reason for the difference in VCC size using the VCD analysis.

Fig. 10a2–c2 shows ν_i for the modes shown in Fig. 10a1–c1. Comparing Fig. 10a2–c2 with Fig. 5a2–c2, ν_i calculated using the HF method is as large as that calculated using the B3LYP method, suggesting that electron correlation does not influence ν_i distribution significantly.

Fig. 10a3–c3 shows $\Delta\rho$ for biphenyl, fluorene, and carbazole. The isosurface value in Fig. 10a3–c3 is the same in Fig. 5a3–c3. $\Delta\rho$ calculated using the HF method has a large value. This is because without electron correlation, electron delocalization is underestimated. $\Delta\rho$ across the C1–C2 and C6–C1 bonds is larger in Fig. 10a3 than in Fig. 5a3; $\Delta\rho$ across the C1–C2 and C6–C1 bonds is larger

in Fig. 10b3 than in Fig. 5b3; $\Delta\rho$ on the N atom is larger in Fig. 10c3 than in Fig. 5c3.

Fig. 10a4–c4 shows η_i calculated at the UHF/6-31G+der level of theory. Large $\Delta\rho$ leads to large η_i and consequently large VCCs. Since $\Delta\rho$ is less delocalized for carbazole than for biphenyl and fluorene, electron correlation effects on $\Delta\rho$ is smaller. Hence, for carbazole, the differences between η_i calculated using the UB3LYP and UHF methods are small compared with those for biphenyl and fluorene. For biphenyl and fluorene, the HF method significantly overestimates the VCCs because $\Delta\rho$ is highly delocalized. The AVCC of the C1 atom of biphenyl and fluorene calculated using the HF method are -1.263×10^{-4} and -1.346×10^{-4} au, respectively, which are more than twice those calculated using the B3LYP method (-0.582×10^{-4} and -0.628×10^{-4} au, respectively). The VCCs are closely related to the reorganization energy. Large/Small VCCs give a large/small reorganization energy. The overestimation of the reorganization energy with the HF method has been reported by Sancho-García et al. [52] For vibronic coupling calculations, the UHF/6-31G+der level of theory gives qualitatively good results, and sometimes quantitative results.

5. Conclusions

We calculated the VCDs of biphenyl, fluorene, and carbazole cations. VCD analysis reveals that strong localization of the electron-density difference on the N atom leads to the small VCCs of carbazole. In general, localized electron-density differences on an atom decreases the vibronic coupling and enhance hole mobility. Replacing the biphenyl or fluorenyl moieties in the molecule with the carbazolyl moiety can weaken vibronic coupling in the molecule and improve hole mobility. This guiding principle opens a new way for molecular design of carrier-transporting materials based on VCD analysis. Though the HF method gives qualitatively good results, it sometimes yields overestimated VCC. This is because the electron-density difference calculated by the HF method is highly delocalized over the bonds, compared with the DFT method. Therefore, for carbazole, the HF method yield quantitatively good result, since the electron-density difference in carbazole does not largely delocalized over the bonds.

Acknowledgements

Numerical calculations were performed partly in the Supercomputer Laboratory of Kyoto University and Research Center for Computational Science, Okazaki, Japan. This work was supported by a Grant-in-Aid for Scientific Research (C) (20550163), Priority Areas "Molecular theory for real systems" (20038028) from the Japan Society for the Promotion of Science (JSPS). This work was also supported in part by the Global COE Program "International Center for Integrated Research and Advanced Education in Materials Science" (No. B-09) of the Ministry of Education, Culture, Sports, Science and Technology (MEXT) of Japan, administrated by the Japan Society for the Promotion of Science.

References

[1] C.W. Tang, S.A. VanSlyke, C.H. Chen, J. Appl. Phys. 65 (1989) 3610–3616.
[2] C.W. Tang, S.A. VanSlyke, Appl. Phys. Lett. 51 (1987) 913–915.
[3] Y. Shirota, Y. Kuwabara, D. Okuda, R. Okuda, H. Ogawa, H. Inada, T. Wakimoto, H. Nakada, Y. Yonemoto, S. Kawami, K. Imai, J. Lumin. 72–74 (1997) 985–991.
[4] Y. Hamada, T. Sano, K. Shibata, K. Kuroki, Jpn. J. Appl. Phys. 34 (1995) L824–L826.
[5] Y. Shirota, Y. Kuwabara, H. Inada, T. Wakimoto, H. Nakada, Y. Yonemoto, S. Kawami, K. Imai, Appl. Phys. Lett. 65 (1994) 807–809.
[6] R.A. Marcus, J. Electroanal. Chem. 483 (2000) 2–6.
[7] R.A. Marcus, Electron transfer reactions in chemistry theory and experiment, J. Electroanal. Chem. 438 (1997) 251–259.
[8] R.A. Marcus, N. Sutin, Biochim. Biophys. Acta 811 (1985) 265–322.
[9] R.A. Marcus, J. Chem. Phys. 43 (1965) 679–701.
[10] R.A. Marcus, J. Chem. Phys. 24 (1956) 966–978.
[11] P.F. Barbara, T.J. Meyer, M.A. Ratner, J. Phys. Chem. 100 (1996) 13148.
[12] V. Coropceanu, N. Gruhn, S. Barlow, C. Lambert, J. Durivage, T. Bill, G. Nöll, S. Marder, J.-L. Brédas, J. Am. Chem. Soc. 126 (2004) 2727–2731.
[13] S. Datta, Quantum Transport: Atom to Transistor, Cambridge University Press, Cambridge, 2005.
[14] T. Sato, K. Tokunaga, K. Tanaka, J. Phys. Chem. A 112 (2008) 758–767.
[15] K. Tokunaga, T. Sato, K. Tanaka, J. Mol. Struct. 838 (2007) 116–123.
[16] K. Tokunaga, T. Sato, K. Tanaka, J. Chem. Phys. 124 (2006) 154303.
[17] T. Sato, K. Tokunaga, K. Tanaka, J. Chem. Phys. 124 (2006) 024314.
[18] T. Sato, K. Tokunaga, N. Iwahara, K. Shizu, K. Tanaka, Vibronic coupling constant and vibronic coupling density, in: H. Köppel, H. Barentzen, D.R. Yarkony (Eds.), The Jahn–Teller-Effect – Fundamentals and Implications for Physics and Chemistry, Springer-Verlag, Berlin and Heidelberg, 2009.
[19] T. Sato, K. Shizu, T. Kuga, K. Tanaka, H. Kaji, Chem. Phys. Lett. 458 (2008) 152–156.
[20] B.-C. Wang, H.-R. Liao, J.-C. Chang, L. Chen, J.-T. Yeh, J. Lumin. 124 (2007) 333–342.
[21] K. Shizu, T. Sato, K. Tanaka, H. Kaji, Chem. Phys. Lett. 486 (2010) 130–136.
[22] J.-H. Pan, Y.-M. Chou, H.-L. Chiu, B.-C. Wang, J. Phys. Org. Chem. 20 (2007) 743–753.
[23] Q. Zhang, J. Chen, Y. Cheng, L. Wang, D. Ma, X. Jing, F. Wang, J. Mater. Chem. 14 (2004) 895–900.
[24] B.E. Koene, D.E. Loy, M.E. Thompson, Chem. Mater. 10 (1998) 2235–2250.
[25] V. Rani, K. Santhanam, J. Solid State Electrochem. 2 (1998) 99–101.
[26] R.P. Feynman, Phys. Rev. 56 (1939) 340–343.
[27] H. Nakatsuji, K. Kanda, T. Yonezawa, Chem. Phys. Lett. 75 (1980) 340–346.
[28] G. Rauhut, P. Pulay, J. Phys. Chem. 99 (1995) 3093–3100.
[29] M.J. Frisch, G.W. Trucks, H.B. Schlegel, G.E. Scuseria, M.A. Robb, J.R. Cheeseman, J.A. Montgomery, Jr., T. Vreven, K.N. Kudin, J.C. Burant, J.M. Millam, S.S. Iyengar, J. Tomasi, V. Barone, B. Mennucci, M. Cossi, G. Scalmani, N. Rega, G.A. Petersson, H. Nakatsuji, M. Hada, M. Ehara, K. Toyota, R. Fukuda, J. Hasegawa, M. Ishida, T. Nakajima, Y. Honda, O. Kitao, H. Nakai, M. Klene, X. Li, J.E. Knox, H.P. Hratchian, J.B. Cross, V. Bakken, C. Adamo, J. Jaramillo, R. Gomperts, R.E. Stratmann, O. Yazyev, A.J. Austin, R. Cammi, C. Pomelli, J.W. Ochterski, P.Y. Ayala, K. Morokuma, G.A. Voth, P. Salvador, J.J. Dannenberg, V.G. Zakrzewski, S. Dapprich, A.D. Daniels, M.C. Strain, O. Farkas, D.K. Malick, A.D. Rabuck, K. Raghavachari, J.B. Foresman, J.V. Ortiz, Q. Cui, A.G. Baboul, S. Clifford, J. Cioslowski, B.B. Stefanov, G. Liu, A. Liashenko, P. Piskorz, I. Komaromi, R.L. Martin, D.J. Fox, T. Keith, M.A. Al-Laham, C.Y. Peng, A. Nanayakkara, M. Challacombe, P.M.W. Gill, B. Johnson, W. Chen, M.W. Wong, C. Gonzalez, J.A. Pople, GAUSSIAN 03, Revision D. 02, Gaussian Inc., Wallingford, CT, 2004.
[30] A. Almenningen, O. Bastiansen, L. Fernholt, B.N. Cyvin, S.J. Cyvin, S. Samdal, J. Mol. Struct. 128 (1985) 59–76.
[31] O. Bastiansen, Acta Chem. Scand. 3 (1949) 408–414.
[32] H. Suzuki, Bull. Chem. Soc. Jpn. 32 (1959) 1340–1350.
[33] G.P. Charbonneau, Y. Delugeard, Acta Crystallogr. Sect. B 33 (1977) 1586–1588.
[34] A. Hargreaves, S.H. Rizvi, Acta Crystallogr. 15 (1962) 365–373.
[35] J. Trotter, Acta Crystallogr. 14 (1961) 1135–1140.
[36] G. Robertson, Nature 191 (1961) 593–594.
[37] G.P. Charbonneau, Y. Delugeard, Acta Crystallogr. Sect. B 32 (1976) 1420–1423.
[38] G.M. Brown, M.H. Bortner, Acta Crystallogr. 7 (1954) 139.

[39] V.K. Belsky, V.E. Zavodnik, V.M. Vozzhennikov, Acta Crystallogr. Sect. C 40 (1984) 1210–1211.
[40] R.E. Gerkin, A.P. Lundstedt, W.J. Reppart, Acta Crystallogr. Sect. C 40 (1984) 1892–1894.
[41] R.E. Gerkin, W.J. Reppart, Acta Crystallogr. Sect. C 42 (1986) 480–482.
[42] M. Kurahashi, M. Fukuyo, A. Shimada, A. Furusaki, I. Nitta, Bull. Chem. Soc. Jpn. 42 (1969) 2174–2179.
[43] M.W. Schmidt, K.K. Baldridge, J.A. Boatz, S.T. Elbert, M.S. Gordon, J.H. Jensen, S. Koseki, N. Matsunaga, K.A. Nguyen, S.J. Su, T.L. Windus, M. Dupins, J.A. Montgomery, J. Comput. Chem. 14 (1993) 1347–1363.
[44] Y. Park, V. Choong, Y. Gao, B.R. Hsieh, C.W. Tang, Appl. Phys. Lett. 68 (1996) 2699–2701.
[45] P.A. Lane, G.P. Kushto, Z.H. Kafafi, Appl. Phys. Lett. 90 (2007) 023511.
[46] A. Bree, C.Y. Pang, L. Rabeneck, Spectrochim. Acta A 27 (1971) 1293–1298.
[47] A. Bree, R. Zwarich, J. Chem. Phys. 51 (1969) 912–920.
[48] A. Bree, R. Zwarich, J. Chem. Phys. 49 (1968) 3344–3355.
[49] M. Malagoli, J.-L. Brédas, Chem. Phys. Lett. 327 (2000) 13–17.
[50] K. Shizu, T. Sato, K. Tanaka, Chem. Phys. Lett. 491 (2010) 65–71.
[51] J.A. Pople, M. Head-Gordon, D.J. Fox, K. Raghavachari, L.A. Curtiss, J. Chem. Phys. 90 (1989) 5622–5629.
[52] J.C. Sancho-García, A.J. Pérez-Jiménez, J. Chem. Phys. 129 (2008) 024103.

materials as active layers in several different devices. Therefore, only a few bi-functional or tri-functional organic materials have been developed thus far [11,2b,12]. To the best of our knowledge, triarylamine derivatives have not been used as multifunctional materials such as light-emitting and hole-transporting materials in OLEDs, donor materials in OSCs, and organic semiconductors in OTFTs.

Here, we report the first example of a multifunctional material that can be used as a deep blue emitting and hole-transporting material in OLEDs, a donor material in OSCs, and an active material in OTFTs. In particular, an OLED device derived from 4,4′,4″-tris(4-naphthalen-1-yl-phenyl)amine (**1-TNPA**) emitted blue light similar to the National Television Standard Committee (NTSC) standard blue and exhibited good electroluminescence (EL) efficiency compared to known blue fluorescent dopants [13–15]. Furthermore, in the case of **1-TNPA**, more efficient hole transport, compared to 4,4′-bis[*N*-(naphthyl-*N*-phenyl amino)]biphenyl (NPD), was observed [5,6,16]. Further, **1-TNPA** can be used as a donor in OSCs and as an organic semiconductor in OTFTs.

2. Experimental section

2.1. Materials and instruments

Organic compounds such as C_{60}, CuPc, NPD, BCP, Alq_3, and ADN were purchased from Aldrich, Lumtree, and Gracel Display. Absorption (UV) spectra were recorded on a Beckman DU 650 spectrophotometer. PL spectra were recorded on a Jasco FP-7500 spectrophotometer. CV spectra were obtained using a CH Instruments 660 electrochemical analyzer. AFM experiments were performed using an Asylum MFP-3D instrument in AC mode and XRD analyses were carried out using a Rigaku (λ = 1.5418 Å; 298 K) X-ray instrument. Decomposition temperatures (T_d) and glass transition temperatures (T_g) were obtained using Q-5000-IR thermal gravimetric analysis (TGA) and DSC-Q-1000 differential scanning calorimetry (DSC), respectively. These TGA and DSC analyses were performed at 5 °C min^{-1} under a N_2 atmosphere.

2.2. Synthesis

4,4′,4″-Tris(4-naphthalen-1-yl-phenyl)amine (**1-TNPA**): a mixture of tris(4-bromophenyl)amine (2.00 g, 4.14 mmol), 1-naphthaleneboronic acid (2.50 g, 14.5 mmol), potassium carbonate (2 M, 20 mL), and tetrakis(triphenylphosphine) palladium (238 mg, 0.206 mmol) in THF/H_2O was heated at 80 °C for 24 h. After cooling to room temperature, all the volatiles were evaporated in vacuum and the reaction mixture was extracted with dichloromethane. The organic phase was washed with H_2O and dried over $MgSO_4$. The solvent was evaporated to give the product, which was purified by silica gel column chromatography using a mixture of ethyl acetate and hexane as the eluent (1:20) and then recrystallized from dichloromethane and hexane to give a solid product (yield: 680 mg, 34%). ^{1}H NMR (300 MHz, $CDCl_3$): δ (ppm) 8.17 (d, 9 Hz, 3H), 8.01 (d, 6 Hz, 3H), 7.94 (d, 18 Hz, 3H), 7.61 (d, 9 Hz, 6H), 7.58 (d, 6 Hz, 6H), 7.54 (d, 6 Hz, 6H), 7.51 (d, 12 Hz, 6H). ^{13}C NMR (125 MHz, $CDCl_3$): δ (ppm) 147.0, 140.0, 135.4, 134.1, 131.8, 131.2, 128.5, 127.6, 127.1, 126.2, 126.1, 125.9, 125.6, 124.2. Mass: Calcd. for $C_{48}H_{33}N$ $[M]^+$ 623.2613, HR-Mass: 623.2613.

2.3. Cyclic voltammetry

The electrochemical properties of **1-TNPA** were studied using cyclic voltammetry (CV) in CH_2Cl_2 solutions (1.00 mM) with 0.1 M tetra-*n*-butylammoniumhexafluorophosphate ($TBAPF_6$) as the supporting electrolyte. A glassy carbon electrode was employed as the working electrode and referenced to an Ag reference electrode. All potential values were calibrated against the ferrocene/ferrocenium (Fc/Fc^+) redox couple.

2.4. Blue OLED device fabrication

A 10-nm-thick layer of copper phthalocyanine (CuPc) was used as a hole injection layer (HIL), and a 60-nm-thick layer of NPD was used as a hole-transporting layer (HTL). A 50-nm-thick emitting layer (EML) was prepared by using 9,10-di(2-naphthyl)anthracene (ADN) as a host and 5–12 wt% **1-TNPA** as a fluorescent blue dopant. The fluorescent dopant concentration of **1-TNPA** was varied from 5 wt% to 12 wt%. Next, a 20-nm-thick tris(8-hydroxyquinolinato)aluminum (Alq_3) layer, which served as an electron transporting layer (ETL), was evaporated. Then, a LiF layer, which served as an electron injection layer (EIL), was also evaporated. Finally, a 100-nm-thick Al layer was deposited onto the LiF layer (Fig. S1). The emission properties were determined using a PR-650 spectrascan spectracolorimeter as a source meter.

2.5. Green OLED device fabrication

A 70-nm-thick NPD layer and a 70-nm-thick **1-TNPA** layer were used as a reference HTL and as a new HTL, respectively. Next, a 60-nm-thick Alq_3 layer was evaporated as an electron transporting layer and a green emitting layer. Then, LiF as an electron injection layer was also evaporated. Finally, a 100-nm-thick Al layer was deposited onto the LiF layer (Fig. S2).

2.6. OSC device fabrication

A 30-nm-thick poly(3,4-ethylenedioxythiophene) poly(styrenesulfonate) (PEDOT:PSS) layer was used as a hole injection layer (HIL). Various **1-TNPA** layers with thicknesses from 10 nm to 20 nm were prepared by evaporation. Then, a 40-nm-thick fullerene (C_{60}) layer, which served as an acceptor, was also evaporated. Next, a 5-nm-thick 2,9-dimethyl-4,7-diphenyl-1,10-phenanthroline (BCP) layer, which served as an exciton blocking layer (EBL), was evaporated. Finally, a 100-nm-thick Al layer was evaporated onto the BCP layer (Fig. S3). The current–voltage measurements for the devices were performed on a Keithley 237 instrument. The device performances were characterized under uniform illumination (AM 1.5G illumination intensity of 100 mW cm^{-2}) using a solar simulator

(Newport, 91160A). The light intensity at each wavelength was calibrated using the standard Si solar cell as a reference.

2.7. OTFT device fabrication

We used a heavily doped Si wafer as a gate electrode and a SiO_2 or an octadecyltrichlorosilane (OTS)-pretreated SiO_2 layer (thickness: ca. 300 nm) as the gate dielectric. The **1-TNPA** films (thickness: ca. 500 Å) were grown by vacuum sublimation at rates of 0.4–0.8 Å s^{-1} under a working pressure of 2.0–2.5 $\times$ 10^{-6} torr using an apparatus devised in our laboratory. Au source/drain electrodes with a channel length (L) of 50 μm and a channel width (W) of 1000 μm were evaporated on top of the films through a shadow mask. The electrical characterization of the transistors was performed in air at room temperature using a Keithley 4200-SCS semiconductor analyzer. The field-effect mobility (μ) was calculated in the saturation region (V_{DS} = −100 V) from a plot of the square-root of drain current *vs.* V_{GS} by using the following equation: $I_{DS} = (WC_i\mu(V_{GS} - V_T)^2)/2L$, where I_{DS} is the source–drain saturation current; C_i (1.1 $\times$ 10^{-8} F) is the capacitance of the SiO_2 insulator; W/L is the ratio of the channel width to the channel length; and V_{GS} and V_T are the gate–source and threshold voltages, respectively.

3. Results and discussion

3.1. Synthesis and photophysical properties

Scheme 1 shows the synthesis of **1-TNPA** examined in this study. A mixture of tris(4-bromophenyl)amine, 1-naphthaleneboronic acid, potassium carbonate, and tetrakis(triphenylphosphine)palladium was refluxed in a N_2 atmosphere in tetrahydrofuran/water solution to afford **1-TNPA** in 34% yield. The photophysical properties of **1-TNPA** are shown in Fig. 1. The absorption spectrum of **1-TNPA** in dichloromethane shows intense bands at 279 nm and 340 nm. The photoluminescence (PL) spectrum of **1-TNPA** in dichloromethane shows a deep blue emission at 436 nm. The full width at half maximum (FWHM) of **1-TNPA** in dichloromethane solution is 63 nm. The PL quantum yield of **1-TNPA** in ethanol solution was estimated to be 0.22 using anthracene as a standard [17].

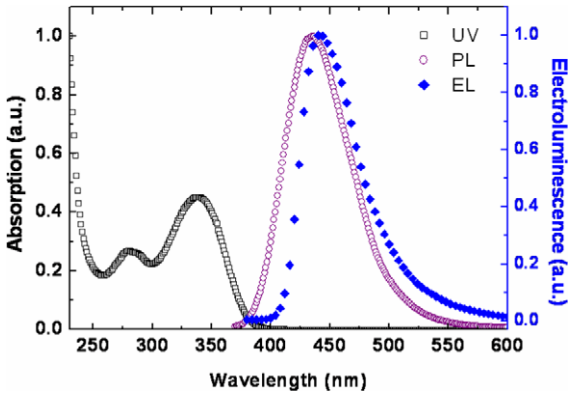

Fig. 1. UV and PL spectra of **1-TNPA** (0.02 mM) in dichloromethane and EL spectra of 3% **1-TNPA**-doped device.

3.2. Thermal and electrochemical properties

The thermal stability of **1-TNPA** was investigated by TGA and DSC. **1-TNPA** shows a thermal stability of T_d = 470 °C, as revealed by the TGA thermogram (Fig. S10), which suggests that **1-TNPA** is stable during the vacuum thermal sublimation process used in organic semiconductor fabrication. When the sample of **1-TNPA** was heated, an endothermic peak was observed at around 176 °C. However, no crystallization and glass transition were observed in the DSC analysis. When the heated sample of **1-TNPA** was cooled to room temperature, it formed an amorphous glass. When the glass sample of **1-TNPA** was heated again, glass transition took place at around 109 °C (Fig. S11). DSC experiments revealed that **1-TNPA** has the property of an amorphous glass with a glass transition temperature (T_g) of 109 °C and therefore no crystallinity.

Fig. 2 shows the cyclic voltammogram of **1-TNPA** in dichloromethane. **1-TNPA** undergoes a reversible oxidation process associated with stable cation radical generation. The half oxidation potentials ($E_{1/2,ox}$) of **1-TNPA**, NPD, and ferrocene were observed to be 0.76 V, 0.59 V, and 0.31 V, respectively (Figs. 2 and S12). Therefore, the highest occupied molecular orbital (HOMO) energy values of **1-TNPA** and NPD were calculated to be $E_{HOMO} = -[(1.4 \pm 0.1) \times (0.45) - (4.6 \pm 0.08)\,eV] = -5.23$ and $E_{HOMO} = -[(1.4 \pm 0.1) \times (0.28) - (4.6 \pm 0.08)\,eV] = -5.00$ eV, respectively [18]. However, the half reduction potential was not determined from CV measurements. The lowest

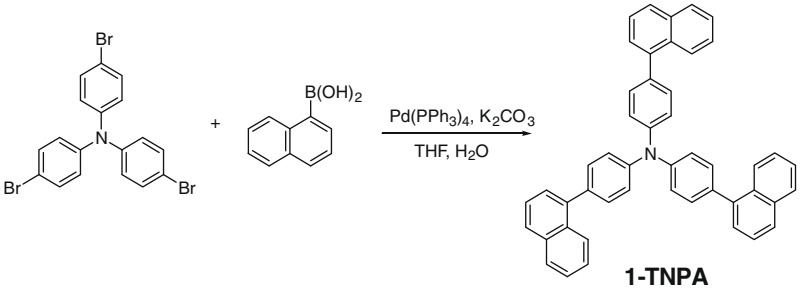

Scheme 1. Synthesis of **1-TNPA**.

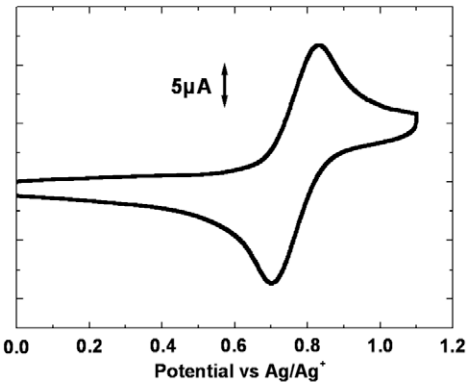

Fig. 2. Cyclic voltammogram of 1.00 mM **1-TNPA** in dichloromethane.

unoccupied molecular orbital (LUMO) energy value of **1-TNPA** (−3.27 eV) was determined from the cross-sectional wavelength between the absorption and emission spectra.

3.3. Blue emitting material in OLEDs

To investigate the versatility of **1-TNPA** as an organic semiconductor, we fabricated four types of organic electronic devices using **1-TNPA**: blue and green emitting OLEDs, an OSC, and an OTFT. To investigate the blue emitting property of **1-TNPA**, we fabricated blue fluorescent OLEDs with the configuration of ITO/CuPc (10 nm)/NPD (60 nm)/emitting layer (50 nm)/Alq_3 (20 nm)/LiF (1 nm)/Al (100 nm). Emitting layers were prepared by co-evaporating ADN as a host and *x* wt% **1-TNPA** as a fluorescent dopant.

Fig. S5 shows the PL in dichloromethane and EL spectra for different doping ratios of **1-TNPA**. All the EL spectra show a deep blue emission. These results indicate that hole–electron recombination takes place at the **1-TNPA** layer. The FWHM of the EL spectrum for 3% **1-TNPA** doping is 61 nm. Since the FWHMs of PL and EL spectra are similar, we attribute the blue EL to the intrinsic emission of **1-TNPA** with no emission interference from Alq_3 [13b]. In particular, the 3% **1-TNPA**-doped EL device showed a pure blue emission with Commission Internationale de l'Eclairage (CIE) coordinates of (0.15, 0.12) at a current density of 6.3 mA cm^{-2}, which is similar to the NTSC standard blue CIE coordinates (0.15, 0.09). Similarly, for a device with 5−8% **1-TNPA** doping, the EL spectra also show the deep blue emission. Since the EL spectra of **1-TNPA** devices with different doping levels have similar patterns, it is suggested that the EL spectra should be attributed to emission from an excited state of **1-TNPA** in the emitting layer. On the other hand, the EL device showed blue emission centered at around 460 nm (Fig. S5) for 10−12% **1-TNPA** doping. As the doping ratio of **1-TNPA** was increased from 3% to 12%, the λ_{max} of the EL spectra was slightly red-shifted because of the aggregation of **1-TNPA** dopant molecules in the emitting layer. This could be due to the molecular structure of **1-TNPA**, which cannot prevent the aggregation in the emitting layer.

Fig. 3 shows plots of the current density (mA cm^{-2}) *vs.* current efficiency (cd A^{-1}) and current density (mA cm^{-2}) *vs.* external quantum efficiency (%) characteristics of ITO/CuPc (10 nm)/NPD (60 nm)/EML (ADN + **1-TNPA** = 50 nm)/Alq_3 (20 nm)/LiF (1 nm)/Al (100 nm) devices. The EL performances depend on the doping ratio of **1-TNPA** in the emitting layer. The optimized 3% **1-TNPA**-doped device had a maximum current efficiency of 3.1 cd A^{-1} and an external quantum efficiency of 3.0% at a current density of 3.4 mA cm^{-2}. At this doping ratio, maximum EL efficiency and a blue emission similar to NTSC blue were observed. We attribute the improved EL performance to the greater charge balance and better exciton confinement within the emission layer. A comparison of the EL device, involving the use of **1-TNPA** as a fluorescent dopant, with the known NTSC standard deep blue fluorescent dopant materials reveals that the current efficiency of 3.1 cd A^{-1} and the external quantum efficiency of 3.0% are generally satisfactory [13–15]. The 8% **1-TNPA**-doped EL device had a slightly reduced current efficiency of 2.5 cd A^{-1} and an external quantum efficiency of 2.3% at a current density of 4.3 mA cm^{-2}. The 12% **1-TNPA**-doped EL device had a current efficiency of 2.1 cd A^{-1} and an external quantum efficiency of 1.7% at 4.7 mA cm^{-2}. When the doping ratio of **1-TNPA** changed from 3% to 12%, the current efficiency and external quantum efficiency slightly decreased from 3.1 cd A^{-1} to 2.1 cd A^{-1} and from 3% to 1.7%, respectively. The relatively reduced EL efficiency can be attributed to a

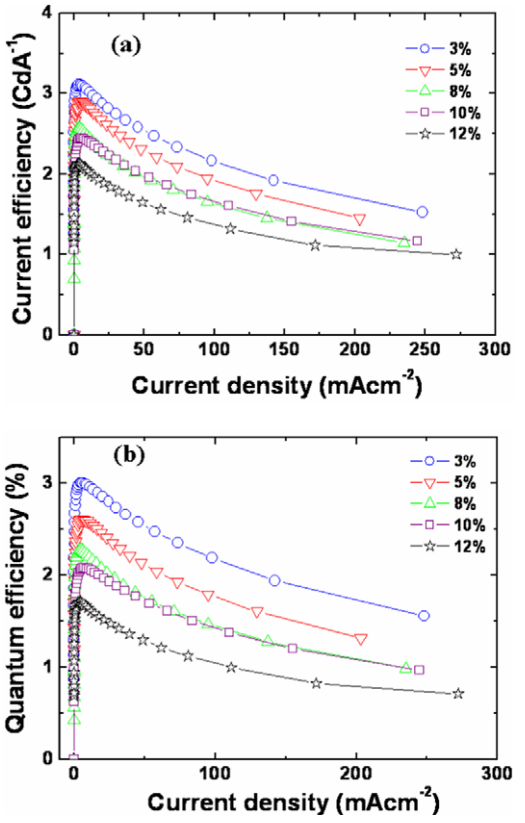

Fig. 3. A blue emitting EL device with configuration ITO/CuPc (10 nm)/NPD (60 nm)/EML (ADN:**1-TNPA** = 50 nm)/Alq_3 (20 nm)/LiF (1 nm)/Al (100 nm). (a) Current density (mA cm^{-2}) *vs.* current efficiency (cd A^{-1}) characteristics and (b) current density (mA cm^{-2}) *vs.* external quantum efficiency (%) characteristics.

Table 1
Blue emitting OLED data.

	η_p (lm W^{-1})[a]	η_c (cd A^{-1})[b]	η_{ext} (%)[c]	η_L (cd m^{-2})[d]	EL (λ_{nm})	CIE
3%	1.0	3.1	3.0	3784	440	(0.15, 0.12)
5%	0.9	2.7	2.5	2945	456	(0.16, 0.13)
8%	0.8	2.5	2.3	2694	456	(0.16, 0.14)
10%	0.7	2.4	2.0	2849	460	(0.16, 0.15)
12%	0.6	2.1	1.7	2717	460	(0.16, 0.17)

Device structure: ITO/CuPc (10 nm)/NPD (60 nm)/EML (50 nm)/Alq_3 (20 nm)/LiF (1 nm)/Al (100 nm).
[a] Power efficiency at 100 cd m^{-2}.
[b] Current efficiency at 100 cd m^{-2}.
[c] External quantum efficiency at 100 cd m^{-2}.
[d] Maximum luminance.

less balanced hole and electron recombination at the emitting layer caused by the aggregation of **1-TNPA** dopant molecules. The entire EL device data are summarized in Table 1; the data indicate that **1-TNPA** can be used as an efficient deep blue emitting material.

3.4. Hole-transporting material in green emitting OLEDs

Recently, NPD has been widely used as a standard hole-transporting material in OLEDs [5,6,16]. In this study, in order to compare the hole-transporting properties of **1-TNPA** with those of NPD, we fabricated two types of fluorescent OLEDs with the configuration of ITO/**1-TNPA** or NPD (70 nm)/Alq_3 (60 nm)/LiF (1 nm)/Al (100 nm). Figs. 4(a) and S8 show the EL spectra and CIE coordinates of the NPD- and **1-TNPA**-based OLED devices. The EL spectra of both the **1-TNPA**- and NPD-based devices showed identical green emissions centered at 528 nm, and the CIE coordinates of both **1-TNPA**- and NPD-based devices were almost equal. The similar EL spectra and CIE coordinates of NPD- and **1-TNPA**-based devices suggest that the EL spectra and CIE coordinates should be attributed to an emission from an excited state of Alq_3 in the emitting layer. This indicates that **1-TNPA** can also be used as a hole-transporting material in green emitting OLEDs.

Fig. 4(b) shows that the maximum current efficiency of the **1-TNPA**-based device is 4.4 cd A^{-1}, which is 45% higher than that of the NPD-based reference device (3.0 cd A^{-1} at 25 mA cm^{-2}). Fig. S7(e) shows that the maximum power efficiency of the **1-TNPA**-based device is 2.0 lm W^{-1}, which is 33% higher than that of the NPD-based reference device (1.5 lm W^{-1} at 25 mA cm^{-2}, Table 2). The enhancement of both current efficiency and power efficiency when using **1-TNPA** as the hole-transporting material can be attributed to a more balanced recombination of holes and electrons at the emitting layer because of the formation of a hole blocking barrier which results from the low HOMO energy level of **1-TNPA**. This finding is supported by the current density *vs.* voltage data (Fig. S7(g)); at all voltages, the **1-TNPA**-based device shows a lower current density than the NPD-based reference device [5a]. Also, the turn-on voltage of the **1-TNPA**-based device (2.6 V) was slightly lower than that of the NPD-based reference device (2.8 V) because of a more balanced hole and electron recombination in the emitting layer. The **1-TNPA** device needs a higher voltage than the

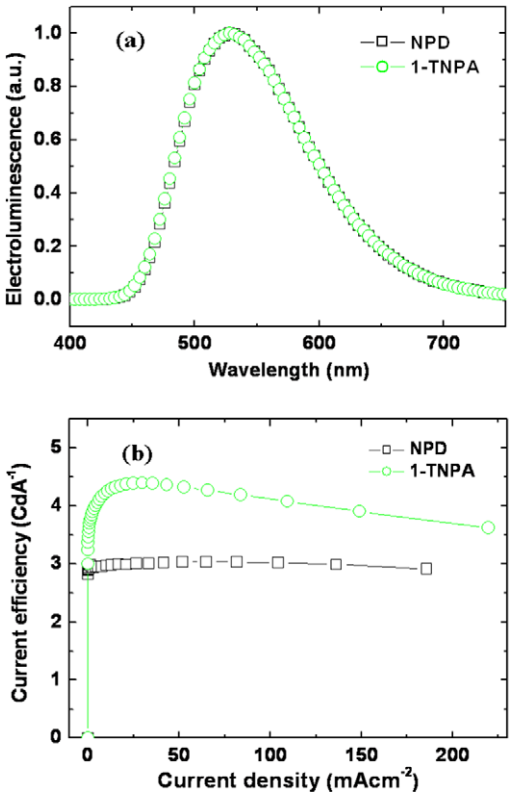

Fig. 4. A green emitting EL device with configuration ITO/NPD or **1-TNPA** (70 nm)/Alq_3 (60 nm)/LiF (1 nm)/Al (100 nm). (a) EL spectra and (b) current density (mA cm^{-2}) *vs.* current efficiency (cd A^{-1}) characteristics.

NPD-based reference device for these two devices to have the same current density or luminance. It is because the HOMO (−5.23 eV) energy level of **1-TNPA** is lower than that of NPD (−5.00 eV) and results in a higher hole blocking barrier which consequently retards the hole-transporting in the **1-TNPA**-based device. Therefore, **1-TNPA** can be used in green emitting OLEDs as a better hole-transporting material when compared to NPD.

3.5. Donor material in OSCs

To investigate the photovoltaic effect of **1-TNPA**, we fabricated OSCs with the configuration of ITO/PEDOT:PSS (30 nm)/**1-TNPA** (*x* nm)/C_{60} (40 nm)/BCP (5 nm)/Al (100 nm).

Table 2
Green emitting OLED data.

	η_p (lm W^{-1})[c]	η_c (cd A^{-1})[d]	η_{ext} (%)[e]	η_L (cd m^{-2})[f]	EL (λ_{nm})	CIE
NPD[a]	1.5	3.0	1.1	5409	528	(0.34, 0.53)
1-TNPA[b]	2.0	4.4	1.7	7956	528	(0.35, 0.53)

[a] ITO/NPD (70 nm)/Alq_3 (60 nm)/LiF (1 nm)/Al (100 nm).
[b] ITO/**1-TNPA** (70 nm)/Alq_3 (60 nm)/LiF (1 nm)/Al (100 nm).
[c] Power efficiency at 100 cd m^{-2}.
[d] Current efficiency at 100 cd m^{-2}.
[e] External quantum efficiency at 100 cd m^{-2}.
[f] Maximum luminance.

Fig. 5 shows the current–voltage characteristics of **1-TNPA**- and C_{60}-based heterojunction solar cells under AM 1.5 simulated solar illumination (intensity: 100 mW cm^{-2}). All the devices show photovoltaic behavior. In general, increasing the active-layer thickness increases the absorption ability; however, the absorption will be limited by the slow charge transport and separation in the active layer of the heterojunction device. Thus, it is important to optimize the active-layer thickness to improve the power conversion efficiency of the heterojunction devices. The 10-nm **1-TNPA**-based device had a short circuit current (I_{sc}) of 1.02 mA cm^{-2}, an open circuit voltage (V_{oc}) of 0.72 V, and a fill factor (FF) of 28%; from these data, the power conversion efficiency (PCE) was determined to be 0.21%, and this was attributed to the thin **1-TNPA** film. In the case of the thin **1-TNPA** active layer (10 nm), the absorption of the sunlight is reduced. The optimized **1-TNPA**-based device (film thickness: 15 nm) had an increased short circuit current of 1.35 mA cm^{-2} and an open-circuit voltage of 0.87 V; the FF was 38%. From these data, an increased maximum power conversion efficiency of 0.45% was calculated. By contrast, the device with a 20-nm **1-TNPA** active layer had a slightly reduced short circuit current of 1.3 mA cm^{-2}, an open-circuit voltage of 0.70 V, and an FF of 39%; from these data, a slightly reduced power conversion efficiency of 0.36%, which is attributed to the thicker thin film, was calculated. In the case of the thick **1-TNPA** active layer, effective charge transport and separation were affected, and they were limited by the low charge carrier mobility and diffusion length. In this study, the optimal thickness of the **1-TNPA** layer (15 nm) results in a maximum power conversion efficiency of 0.45%. Therefore, the change in the thickness of the **1-TNPA** film in the active layer changed the power conversion efficiency from 0.21% to 0.45%. Overall, the power conversion efficiency of **1-TNPA**-based OSCs was not high compared with other small-molecule-based OSCs because of the short absorption range (250–370 nm) and poor crystalline property of **1-TNPA**. Nevertheless, to the best of our knowledge, there are no reports of organic electronic materials that act as blue emitting materials as well as hole-transporting materials in OLEDs and donor materials in

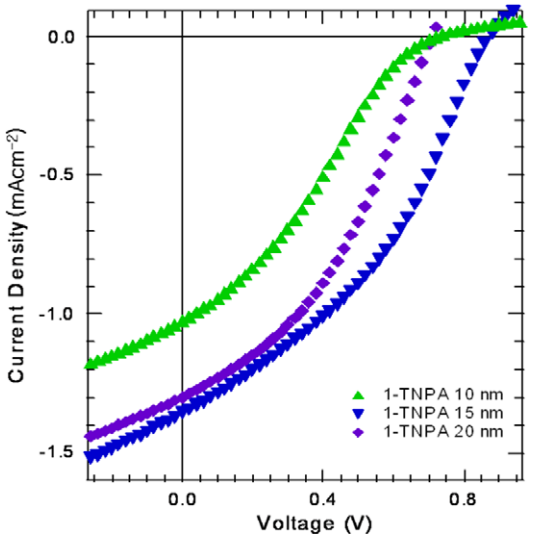

Fig. 5. Current–voltage characteristics of ITO/PEDOT (30 nm)/**1-TNPA** (x nm)/C_{60} (40 nm)/BCP (5 nm)/Al (100 nm) devices under simulated AM 1.5 solar irradiation at 100 mW cm^{-2}.

Table 3
OSC data.

1-TNPA (nm)	V_{oc} (V)[a]	I_{sc} (mA cm^{-2})[b]	FF (%)[c]	PCE (%)[d]
10	0.72	1.02	28	0.21
15	0.87	1.35	38	0.45
20	0.70	1.3	39	0.36

Device structure: ITO/PEDOT (30 nm)/**1-TNPA** (x nm)/C_{60} (40 nm)/BCP (5 nm)/Al (100 nm).
[a] Open circuit voltage.
[b] Short circuit current.
[c] Fill factor.
[d] Power conversion efficiency.

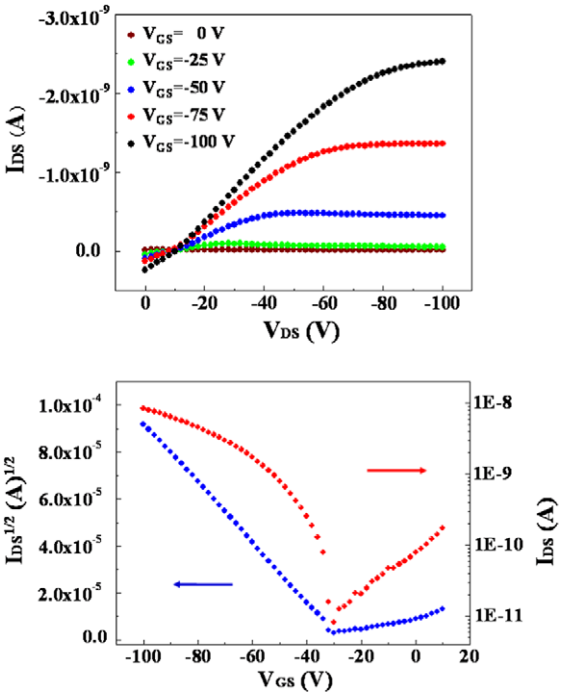

Fig. 6. The output and transfer characteristics of the OTFTs involving the use of **1-TNPA** deposited at T_{sub} = 75 °C on OTS treated SiO_2.

Table 4
Data on OTFTs.

1-TNPA	T_{sub} (°C)	μ (cm^2 V^{-1} s^{-1})[a]	V_{th} (V)[b]	I_{on}/I_{off}[c]
Bare SiO_2	RT	4.2×10^{-6}	−28.3	1.1×10^3
Bare SiO_2	75	3.2×10^{-6}	−27.1	1.3×10^3
OTS/SiO_2	RT	4.7×10^{-6}	−45.4	6.9×10^2
OTS/SiO_2	75	1.5×10^{-5}	−27.6	1.0×10^3

[a] Field-effect mobility.
[b] Threshold voltage.
[c] On/off ratio.

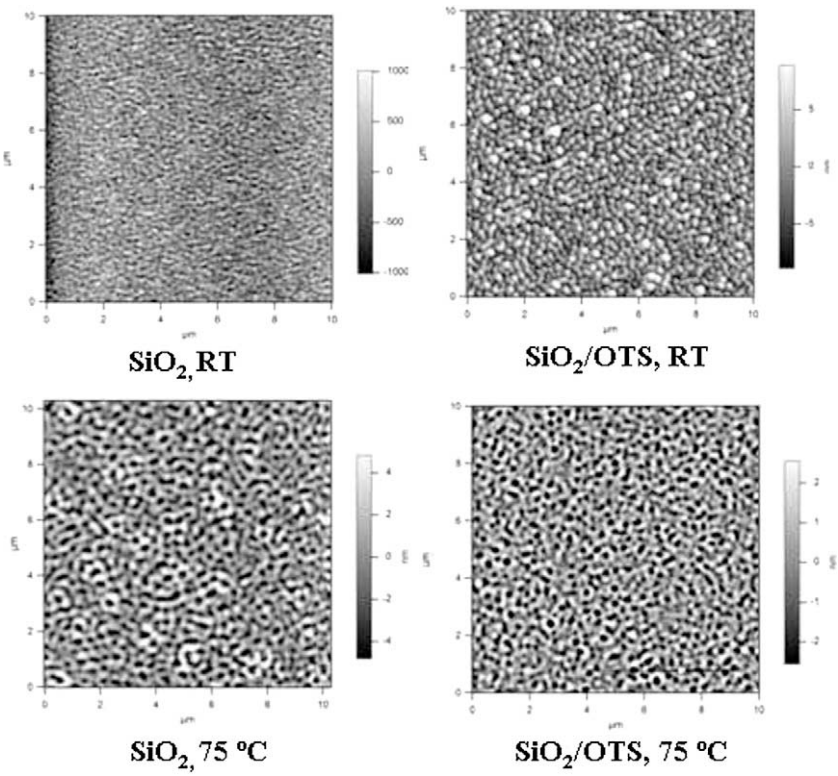

Fig. 7. $10 \times 10\ \mu m^2$ AFM topography images of **1-TNPA** films deposited on SiO_2 (left column) and OTS/SiO_2 (right column) at substrate temperatures equal to RT and 75 °C.

OSCs. The data on the overall performance of **1-TNPA**- and C_{60}-based devices are summarized in Table 3.

3.6. Active material in OTFTs

To investigate the field-effect mobility of **1-TNPA**, we fabricated an OTFT involving the use of **1-TNPA** as an active material with top-contact geometry (Fig. S4). Fig. 6 shows the output and transfer characteristics of top-contact OTFTs involving the use of **1-TNPA** deposited on OTS/SiO_2 at a substrate temperature (T_{sub}) of 75 °C. From the electrical transfer characteristics, we obtained device parameters such as the field-effect mobility, on/off current ratio, and threshold voltage. The **1-TNPA**-based OTFT device showed a field-effect mobility (μ) of $1.5 \times 10^{-5}\ cm^2\ V^{-2}\ s^{-1}$, a threshold voltage ($V_{th}$) of −27.6 V, and an on/off current ratio (I_{on}/I_{off}) of 1.0×10^3 at 75 °C. The moderate field-effect mobilities of the OTFT devices derived from **1-TNPA** and triphenylamine derivatives [7b] can be attributed to the fact that it is difficult to maintain these derivatives perpendicular to the substrate. **1-TNPA**-based OTFTs exhibited similar field-effect mobilities of $1.5 \times 10^{-5}\ cm^2\ V^{-2}\ s^{-1}$, which were moderate compared to those of other triphenylamine derivatives [7b]. The morphological characteristics of **1-TNPA** were investigated by X-ray diffraction (XRD) and atomic force microscope (AFM). The thin-film XRD patterns indicated a poorly ordered structure of **1-TNPA** on the substrate (Fig. S9). Fig. 7 shows AFM images of **1-TNPA** active layers deposited on SiO_2 (left column) and OTS/SiO_2 (right column) at RT and 75 °C. The connectivity of **1-TNPA** grains deposited on a SiO_2 and OTS/SiO_2 substrate at RT and 75 °C is poor, which leads to low field-effect mobility. The data on the **1-TNPA**-based OTFT device for various conditions are summarized in Table 4.

4. Conclusion

We have developed the first multifunctional organic material (**1-TNPA**), which can be used as a deep blue emitting and hole-transporting material in OLEDs, as a donor material in OSCs, and as an active material in OTFTs. In particular, in the case of **1-TNPA**-based devices, efficient, deep blue emission similar to the NTSC standard blue was observed. **1-TNPA** can be used as a hole-transporting material which is more efficient and thermally stable than NPD. **1-TNPA** can be also used as a donor in OSCs and as an organic semiconductor in OTFTs.

Acknowledgements

This work was supported by Basic Science Research Program through the National Research Foundation of Korea (NRF) grant funded from the Ministry of Education, Science and Technology (MEST) of Korea for the Center for Next Generation Dye-sensitized Solar Cells (No. 2010-0001842), the Seoul R&BD Program (10543), the National Research Foundation of Korea Grant funded by the Korean

Government (MEST) (NRF-C1AAA001-2009-0093282). We also acknowledge the BK21 fellowship grants to J.K. and W.L.

Appendix A. Supplementary material

Supplementary data associated with this article can be found, in the online version, at doi:10.1016/j.orgel.2010.04.005.

References

[1] (a) Y. Shirota, J. Mater. Chem. 10 (2000) 1;
(b) Y. Shirota, J. Mater. Chem. 15 (2005) 75.
[2] (a) S. Roquet, A. Cravino, P. Leriche, O. Alévêque, P. Frère, J. Roncali, J. Am. Chem. Soc. 128 (2006) 3459;
(b) A. Cravino, S. Roquet, O. Alévêque, P. Leriche, P. Frère, J. Roncali, Chem. Mater. 18 (2006) 2584;
(c) H. Kageyama, H. Ohishi, M. Tanaka, Y. Ohmori, Y. Shirota, Appl. Phys. Lett. 94 (2009) 063304.
[3] (a) A. Cravino, S. Roquet, P. Leriche, O. Alévêque, P. Frère, J. Roncali, Chem. Commun. (2006) 1416;
(b) C. He, Q. He, X. Yang, G. Wu, C. Yang, F. Bai, Z. Shuai, L. Wang, Y. Li, J. Phys. Chem. C 111 (2007) 8661.
[4] (a) S. Tao, Y. Zhou, C.-S. Lee, S.-T. Lee, D. Huang, X. Zhang, J. Phys. Chem. C 112 (2008) 14603;
(b) J.M. Hancock, A.P. Gifford, Y. Zhu, Y. Lou, S.A. Jenekhe, Chem. Mater. 18 (2006) 4924.
[5] (a) Q.-X. Tong, S.-L. Lai, M.-Y. Chan, K.-H. Lai, J.-X. Tang, H.-L. Kwong, C.-S. Lee, S.-T. Lee, Chem. Mater. 19 (2007) 5851;
(b) J. Li, D. Liu, Y. Li, C.-S. Lee, H.-L. Kwong, S. Lee, Chem. Mater. 17 (2005) 1208;
(c) J. Li, C. Ma, J. Tang, C.-S. Lee, S. Lee, Chem. Mater. 17 (2005) 615.
[6] H. Tsuji, C. Mitsui, L. Ilies, Y. Sato, E. Nakamura, J. Am. Chem. Soc. 129 (2007) 11902.
[7] (a) Y. Song, C. Di, X. Yang, S. Li, W. Xu, Y. Liu, L. Yang, Z. Shuai, D. Zhang, D. Zhu, J. Am. Chem. Soc. 128 (2006) 15940;
(b) M. Sonntag, K. Kreger, D. Hanft, P. Strohriegl, S. Setayesh, D.D. Leeuw, Chem. Mater. 17 (2005) 3031.
[8] A. Cravino, P. Leriche, O. Alévêque, S. Roquet, J. Roncali, Adv. Mater. 18 (2006) 3033.
[9] J.N. Moorthy, P. Venkatakrishnan, D.-F. Huang, T.J. Chow, Chem. Commun. (2008) 2146;
(a) S. Tao, L. Li, J. Yu, Y. Jiang, Y. Zhou, C.-S. Lee, S.-T. Lee, X. Zhang, O. Kwon, Chem. Mater. 21 (2009) 1284.
[10] M. Berggren, D. Nilsson, N.D. Robinson, Nat. Mater. 6 (2007) 4.
[11] (a) A.K. Pandey, J.-M. Nunzi, Adv. Mater. 19 (2007) 3613;
(b) J. Lu, P.F. Xia, P.K. Lo, Y. Tao, M.S. Wong, Chem. Mater. 18 (2006) 6194.
[12] F. Wang, J. Luo, K. Yang, J. Chen, F. Huang, Y. Cao, Macromolecules 38 (2005) 2253.
[13] (a) M.-T. Lee, C.-H. Liao, C.-H. Tsai, C.H. Chen, Adv. Mater. 17 (2005) 2493;
(b) Y.-H. Kim, H.-C. Jeong, S.-H. Kim, K. Yang, S.-K. Kwon, Adv. Funct. Mater. 15 (2005) 1799.
[14] (a) Y.-I. Park, J.-H. Son, J.-S. Kang, S.-K. Kim, J.-H. Lee, J.-W. Park, Chem. Commun. (2008) 2143;
(b) J.N. Moorthy, P. Venkatakrishnan, P. Natarajan, D.-F. Huang, T.J. Chow, J. Am. Chem. Soc. 130 (2008) 17320.
[15] C.-H. Chien, C.-K. Chen, F.-M. Hsu, C.-F. Shu, P.-T. Chou, C.-H. Lai, Adv. Funct. Mater. 19 (2009) 560.
[16] S.A. Van Slyke, C.H. Chen, C.W. Tang, Appl. Phys. Lett. 69 (1996) 2160.
[17] W.R. Dawson, M.W. Windsor, J. Phys. Chem. 72 (1968) 3255.
[18] B.W. D'Andrade, S. Datta, S.R. Forrest, P. Djurovich, E. Polikaropov, M.E. Thompson, Org. Electron. 6 (2005) 11.

material content in discrete field-effect transistors (FETs) can indeed be reduced by addition of a suitable second component. In fact, when using *semicrystalline:semicrystalline* macromolecular binaries, most prominently of P3HT and high-density polyethylene (HDPE), this concept lead to ultra-low threshold systems, in which only a few weight percent of the semiconducting species was required for providing a percolating network. A percolation threshold of as little as 3 wt.% was indeed demonstrated in these systems, which yielded devices with an electronic performance equal to devices comprising neat P3HT. Moreover, blending resulted in additional benefits, including mechanical toughness and improved air stability [9].

However, the crystalline nature of the two components in P3HT:HDPE binaries reduced the flexibility in selecting certain processing parameters, most importantly with regard to the solution deposition temperature, as the crystallization sequence needed to be strictly controlled in order to realize a low-percolation threshold structure [9]. In fact, it was shown that the semiconductor had to solidify prior to the electronically inactive material. In the case of P3HT:HDPE blends, this implied that deposition from solution had to be performed above the crystallization temperature T_c of the added insulator; i.e. at temperatures > 115 °C (depending on molecular weight, chain linearity, etc., of the HDPE utilized). Yet, a process requiring such elevated deposition temperatures can be technologically impractical and may increase production cost beyond the scope of the envisioned market for most plastic electronics products as, among other things, thermally robust substrates such as polyethylene naphthalate (PEN) would be required rather than the much cheaper polyethylene terephthalate (PET). Furthermore, control of film uniformity and the printing procedure in general could be problematical at application temperatures above 120 °C, especially when employing fabrication methods such as flexure/gravure technologies [15] or ink-jet processing [16].

One way to decrease the processing temperature of such crystalline:crystalline semiconductor:insulator blends would be to use an inactive component that has a lower melting temperature [17]. This option may, however, compromise the temperature range that final products can be utilized in, limiting their application to relative low-temperature environments only. We, therefore, set out to find a semicrystalline bulk polymer permitting the realization of low-percolation blends via low-temperature processes without, however, sacrificing the temperature window that the final device can be used in. As a consequence, we attempted to find a low-cost commodity polymer with (i) a better solubility than P3HT in a given solvent with $T_c^{\text{insulator}} < T_c^{\text{P3HT}}$ when processing the blend from solution and (ii) a high melting temperature (T_m > 150 °C) to allow for an application temperature (i.e. the maximum temperature the final product can be used at) of >80 °C.

We selected poly(vinylidene fluoride) (PVDF) as the inactive second component as this relatively low-cost, semicrystalline polymer is readily available, soluble in a variety of commercially available solvents and melts at 165 °C [18]. Additional functionalities may also be introduced in blends with PVDF, due to the different crystalline

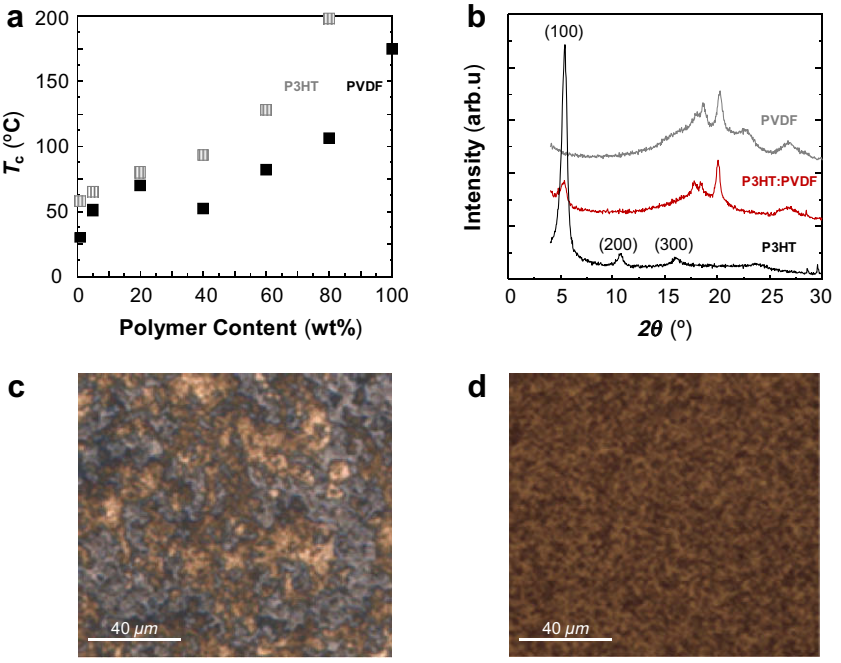

Fig. 1. (a) Superimposed phase diagram showing the crystallization temperature of P3HT (open symbols) and PVDF (black symbols) in cyclohexanone as measured in the respective binary system in differential scanning calorimetry. P3HT crystallizes prior to PVDF at all concentrations. (b) Wide-angle X-ray 2θ-diffractograms of cast P3HT:PVDF blend structures. Data of reference films of the neat components are also shown for comparison. (c, d) Polarized optical micrographs of blend films formed by spin-coating a formulation comprising 4 wt.% P3HT from (c) xylene, and (d) a xylene:cyclohexanone mixture.

phases that this polymer can form, some of which feature ferroelectric properties [18].

For realizing low-percolation blends, we were required to find a solvent for the P3HT:PVDF blends systems that favours PVDF dissolution over P3HT. One such solvent is cyclohexanone, in which, conveniently, P3HT was found based on differential scanning calorimetry data to solidify prior to PVDF at all temperatures and compositions (cf. Fig. 1a). This solution phase behavior in principal should allow for the casting or printing of the active layer and subsequent solvent extraction within a relatively broad processing window, provided that the deposition temperature is kept above T_c^{P3HT}. However, unfortunately, the relatively large difference between the solidification temperatures of the two components resulted in rather inhomogeneous thin-film architectures when cast from cyclohexanone, with large domains of 10–20 μm-size being visible (cf. optical micrograph presented in Fig. 1c); and as a consequence, variable, often very poor transistor device performances were obtained.

Clearly, use of just one solvent does not afford itself to gain sufficient control over the final microstructure of P3HT:PVDF blends. This limitation can, however, be readily overcome by the use of solvent mixtures. For instance, when adding xylene to the P3HT:PVDF:cyclohexanone solutions, which is known to be a good solvent for P3HT even at room temperature, the difference between the two polymers' solidification temperatures could be significantly reduced; i.e. the solubility of P3HT was slightly increased (and thus T_c^{P3HT} was lowered), whilst the solubility of PVDF was not significantly affected by the addition of xylene (i.e. T_c^{PVDF} essentially remained unaltered). Therefore, introduction of xylene lead to a minor increase in solidification rate of PVDF, whilst the one of P3HT was decreased. Thereby a solvent mixture of a cyclohexanone:xylene ratio of 3:1 (by weight) seemed to provide the best compromise between solubility and solidification rate of the two components, allowing blends to be spin-coated at substrate temperatures as low as 40 °C. Indeed, homogenous thin-film architectures were obtained with such solvent mixtures (Fig. 1d), with domains of the size of 5 μm and less being visible in optical microscopy, which we attribute to the fact that P3HT and PVDF solidified at very similar temperatures (P3HT prior to PVDF) and rates. However, we like to note that due to the *semi*crystalline nature of both P3HT and PVDF the full extent of the phase separation is difficult to estimate, especially within their amorphous regions. Some information was, nonetheless, obtained from wide-angle X-ray scattering (WAXS), in which reflections characteristic for both P3HT as well as the common, paraelectric α-phase of PVDF [18] was found (Fig. 1b).

Encouraged by the fact that homogenous films could be produced directly from solution using deposition temperatures as low as 40 °C, we fabricated field-effect transistor devices by spin-coating PVDF-rich blends from such 3:1 cyclohexnanone:xylene solutions (kept at 80 °C) onto pre-patterned (lift-off) transistor structures with a 230 nm-thick, thermally grown silicon dioxide as gate dielectric. The latter had been treated with octyltricholorosilane (OTS). Several semiconductor:insulator ratios were investigated.

The transistor performance was found to be almost independent of composition of the P3HT:PVDF blends used in the formulation. Devices of good transistor performance were reliably obtained at a P3HT content of as little as 4 wt.%. Only at less than 3 wt.% P3HT the device uniformity started to be adversely affected, resulting in a lower yield of working FETs (<20%) compared to the high reproducibility in device fabrication we obtained at higher P3HT contents (Fig. 2a). The FETs featured very low gate leakage currents and high field-effect mobilities of up to 0.04 cm^2/Vs, which is comparable to neat P3HT devices. Some minor hysteresis between forward and backwards scans and relatively large turn-on voltages were observed (Fig. 2). These characteristics are, however, not uncommon features for P3HT devices. In fact, such properties are more

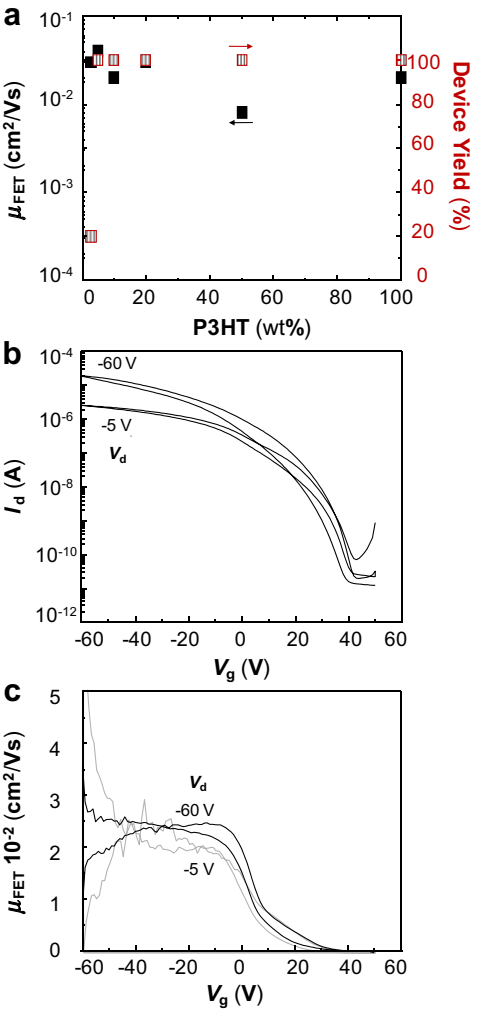

Fig. 2. (a) Field-effect mobility (black symbols) and device fabrication yield (open symbols) of P3HT:PVDF blends, plotted as function of P3HT content. The mobility was unaffected by the addition of the insulating PVDF, and the yield of working devices was only drastically reduced at a P3HT content of less than 3 wt.%. (b, c) FET device performance of a typical FET fabricated from a P3HT:PVDF binary comprising 4 wt.% semiconductor: (b) transfer characteristic and (c) corresponding field-effect mobilities.

likely to be related to the OTS layer quality and the SiO_2 dielectric that was used [19]. For instance, reference devices made from neat P3HT showed very similar transfer plots to the blend devices. Furthermore relatively large variations were found between devices fabricated on the same substrate type, but with different OTS treatments.

In order to illustrate that our P3HT:PVDF formulations are transferable to roll-to-roll processing and have the potential to be used on flexible substrates, we fabricated transistors using an organic gate dielectric. For this purpose, devices were fabricated by depositing the organic insulator D206 (supplied by Merck) onto the gate via spin-coating. To provide a passive, orthogonal surface, the dielectric was then crosslinked by UV irradiation before gold source-drain electrodes were deposited. In the final fabrication step, the semiconducting blend formulation (4.4% wt.% P3HT; 95.6 wt.% PVDF) was spin-coated in inert atmosphere on top of these multilayer architectures.

The resultant devices were measured in inert conditions (to minimize affects from ambient air). Good device performance was achieved with high charge-carrier mobilities (Fig. 3a and b), however, unfortunately, high OFF-currents were observed. This is, though, not uncommon for P3HT devices, especially when they were exposed to, e.g., oxygen from ambient conditions [20,21]. We therefore attributed these undesirable device characteristics not to the presence of the PVDF in the active layer, but rather to doping of the P3HT component. Indeed, the D206 dielectric layer (deposited in ambient conditions) may be susceptible to absorption of O_2 originating in such doped P3HT structures at the active layer/dielectric interface [*NB:* Note that we attempted to increase the ON–OFF current ratio by annealing blend transistors in vacuum at elevated temperatures in the range of 80–100 °C, however, no improvement was, unfortunately, observed in field-effect transistor characterization after this treatment].

We continued exploring P3HT:PVDF formulations comprising 4 wt.% P3HT and more, and scrutinized if these formulations can be deposited in a scaleable manner. For this purpose devices were flexographically [22] printed in air onto bottom-gate devices comprising of the organic Merck D206 gate dielectric, emulating printing speeds of up to 90 m/min. Good device performance was obtained also for such printed FETs, however, as already observed for the spin-coated devices, relatively large OFF-currents were again recorded due to the strong tendency of P3HT for doping. In addition, a rather pronounced hysteresis was observed in these printed devices, which we attribute to the fact that printing of the P3HT:PVDF blend was conducted in air, in contrast to the above described spin-coated FETs, in which the active layer was deposited in an inert atmosphere and thus featured essentially identical forward and backwards scans. Nonetheless, our results illustrate that roll-to-roll techniques for the manufacture of low-cost organic electronics products can be used for the fabrication of organic FETs.

In summary, we have addressed one key bottleneck of crystalline:crystalline semiconductor:insulator blends,

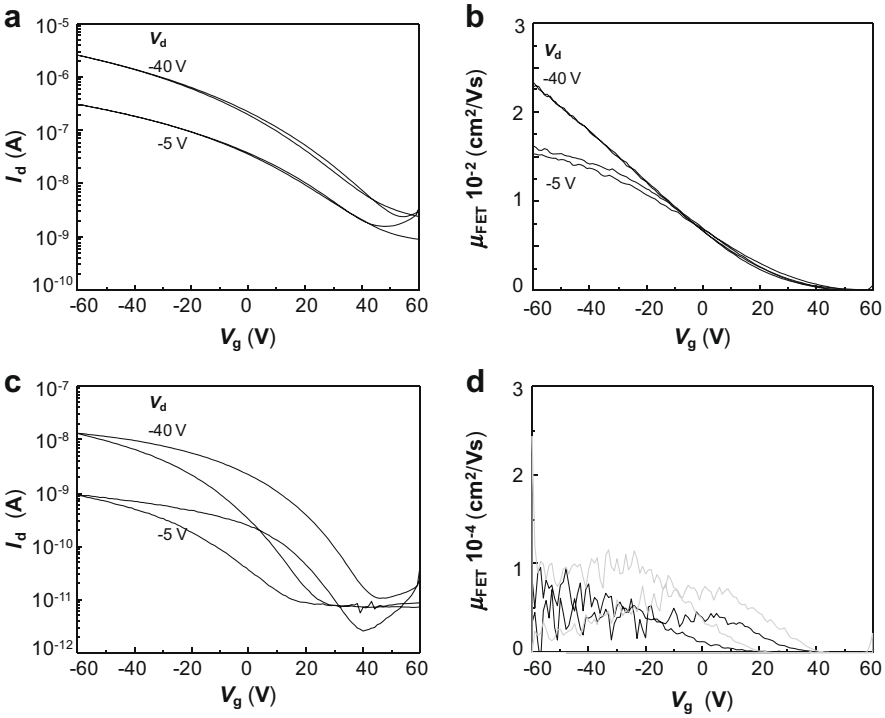

Fig. 3. (a, b) Typical FET performance of a P3HT:PVDF blend device (4 wt.% P3HT content) spin-coated in inert atmosphere, comprising the Merck organic dielectric D206, fabricated onto a flexible PEN substrate: (a) transfer characteristics and (b) corresponding FET charge-carrier mobility. (c, d) Device performance of a FET structure (with the an D206 gate dielectric) manufactured *in air* by flexo-printing using a 4 wt.% P3HT formulation.

such as P3HT:HDPE binaries, i.e. that fact that they require relatively high deposition temperatures, thus, are not compatible with certain flexible substrates and/or deposition methodologies, such as ink-jet printing, gravure printing and the like. We demonstrated here that systems based on P3HT:PVDF seem to provide interesting alternatives as they allow deposition from solution at temperatures well below 50 °C permitting fabrication of organic field-effect structures using flexographic processes. Obviously, our formulations may be adjusted for use in even less demanding methodologies, for instance, gravure techniques, which do not need an intermediate rubber transfer as patterning is achieved by a structured analox. In addition, further work is ongoing to substitute P3HT with a more environmentally stable semiconductor, such as poly(2,5-bis(3-alkylthiophene)thieno(2,3-*b*)thiophenes) [23]. This may assist in avoiding the high OFF-currents due to the doping of the semiconductor. Moreover, materials could be investigated which have been demonstrated to have higher charge-carrier mobilities than P3HT [24,25].

Acknowledgements

We would like to thank Dr. Thomas Anthopoulos and Dr. P. Wobkenberg (Department of Physics, Imperial College London) for highly useful discussions and air stability measurements. NS acknowledges support from the EC through the EC FP7 ONE-P large-scale project No. 212311, as well from UK's Engineering and Physical Sciences Research Council (EPSRC) and Technology Strategy Board (TSB) (DT/F006144/1).

References

[1] M. Grell, W. Knoll, D. Lupo, A. Meisel, T. Miteva, D. Neher, H.-G. Nothofer, U. Scherf, A. Yasuda, Adv. Mater. 11 (1999) 671–675.
[2] R.J. Kline, M.F. Toney, M.D. McGehee, Nat. Mater. 5 (2006) 222–228.
[3] G.H. Gelinck, H.E.A. Huitema, E. van Veenendaal, E. Cantatore, L. Schrijnemakers, J.B.P.H. van der Putten, T.C.T. Geuns, M. Beenhakkers, J.B. Giesbers, B. Huisman, E.J. Meijer, E.M. Benito, F.J. Touwslager, A.W. Marsman, B.J.E. van Rens, D.M. de Leeuw, Nat. Mater. 3 (2004) 106–110.
[4] M.R. Lee, R.D. Eckert, K. Forberich, G. Dennler, C.J. Brabec, R.A. Gaudiana, Science 324 (2009) 232–235.
[5] J.H. Burroughes, D.D.C. Bradley, A.R. Brown, R.N. Marks, K. Mackay, R.H. Friend, P.L. Burns, A.B. Holmes, Nature 347 (1990) 539–541.
[6] H. Sirringhaus, P. Brown, R.H. Friend, M.M. Nielsen, K. Bechgaard, B.M.W. Langeveld-Voss, A.J.H. Spiering, R.A.J. Janssen, E.W. Meijer, P. Herwig, D.M. de Leeuw, Nature 401 (1999) 685–688.
[7] R.D. McCullough, R.D. Lowe, M. Jayaraman, D.L. Anderson, J. Org. Chem. 58 (1993) 904–912.
[8] Z. Bao, A. Dodabalapur, A.J. Lovinger, Appl. Phys. Lett. 69 (1996) 4108–4110.
[9] S. Goffri, C. Muller, N. Stingelin-Stutzmann, D.W. Breiby, C.P. Radano, J. Andreasen, R. Thompson, R.A.J. Janssen, M.M. Nielsen, P. Smith, H. Sirringhaus, Nat. Mater. 5 (2006) 950–956.
[10] A.C. Arias, F. Endicott, R.A. Street, Adv. Mater. 18 (2006) 2900–2904.
[11] J.A. Babel, S.A. Jenekhe, Macromolecules 37 (2004) 9835–9840.
[12] B.A. Brown, D. Cupertino, J. Veres, J.D. Schofield, S.W. Leeming, S.G. Yeates, US2004/0038459 A1, 2004.
[13] C. Müller, P. Wolfer, P. Smith, M.A. Baklar, N. Stingelin-Stutzmann, Synth. Met. 157 (2007) 827–833.
[14] N. Stingelin-Stutzmann, E. Smits, H. Wondergem, C. Tanase, P. Blom, P. Smith, D. de Leeuw, Nat. Mater. 4 (2005) 601–606.
[15] M.M. Voigt, A. Guite, D.-Y. Chung, R.U.A. Khan, A.J. Campbell, D.D.C. Bradley, F. Meng, J.H.G. Steinke, S. Tierney, I. McCulloch, H. Penxten, L. Lutsen, O. Douheret, J. Manca, U. Brokmann, K. Sönnichsen, D. Hülsenberg, W. Bock, C. Barron, N. Blanckaert, S. Springer, J. Grupp, A. Mosley, Adv. Func. Mater. 20 (2010) 239–246.
[16] D. Kim, S. Jeong, S.H. Lee, J. Moon, J.K. Song, Synth. Met. 159 (2009) 1381–1385.
[17] P. Flory, J. Chem. Phys. 10 (1941) 51–61.
[18] R.G. Kepler, R.A. Anderson, Adv. Phys. 41 (1992) 1–57.
[19] Y. Wang, M. Lieberman, Langmuir 19 (2003) 1159–1167.
[20] D.M. de Leeuw, M.M.J. Simenon, A.R. Brown, R.E.F. Einerhand, Synth. Met. 87 (1997) 53–59.
[21] D.B.A. Rep, A.F. Morpurgo, T.M. Klapwijk, Org. Electron. 4 (2003) 201–207.
[22] T. Mäkelä, S. Jussila, H. Kosonen, T.G. Bäcklund, H.G.O. Sandberg, H.T. Stubb, Synth. Met. 153 (2005) 285–288.
[23] M. Heeney, C. Bailey, K. Genevicius, M. Shkunov, D. Sparrowe, S. Tierney, I. McCulloch, J. Am. Chem. Soc. 127 (2005) 1078–1079.
[24] I. McCulloch, M. Heeney, C. Bailey, K. Genevicius, I. MacDonald, M. Shkunov, D. Sparrowe, S. Tierney, R. Wagner, W. Zhang, M.L. Chabinyc, R.J. Kline, M.D. McGehee, M.F. Toney, Nat. Mater. 5 (2006) 328–333.
[25] T.N. Ng, S. Sambandan, R. Lujan, A.C. Arias, C.R. Newman, H. Yan, A. Facchetti, Appl. Phys. Lett. 94 (2009) 233307.

the UV-PDs has been focused on inorganic counterparts with wide-band gap semiconductor such as GaN (150 mA/W) [10] and SiC (150 mA/W) [11], but these inorganic partners require complicated fabrication technique with high expenses. Since organic UV-PDs have the strongpoint of simple fabrication process, recently organic UV-PDs based on blend of N,N-diphenyl-N,N-bis(3-methylphenyl)-(1,1-biphenyl)-4,4-diamine (TPD) and tris(8-hydroxy-quinoline) aluminum (Alq) was reported, but its UV responsivity is distinctively lower than the inorganic partners [12].

It is recognized that the dissociation of photo-generated exciton must occur at DA interface that needs the D and A species to have low ionization potential (IP) and high electron affinity (EA), respectively, to have as large carrier motilities as possible for both materials. 1,3,5-Tris(3-methylphenyl-phenylamino) triphenyamine (m-MTDATA) presents high hole mobility of 3×10^{-5} cm^2/V s [13] and a low IP of 5.1 eV [14], moreover, it was used as D-material in UV sensitive PV devices [15–17]. Our group has fabricated m-MTDATA/tris(8-hydroxy-quinoline) gallium (Gaq) based UV PD diode by using m-MTDATA as the donor and Gaq as the acceptor [18], but its photo-response spectrum evidently covers visible waveband, i.e., it is not visible-blind, which was attributed to its stronger absorption at visible region of 400–450 nm [18]. Therefore, a new A-material with weaker light absorption at visible spectral region must be selected. Zhang et al. have observed that the absorption peak of the metal-8-hydroxy-quinoline (Mq) complexes is dependent on the metal ion radii, that is, larger ion radii based Mq complex must lead to blue-shift of the absorption peak due to the stronger polarization [19]. We have noted that trivalent Gd (Gd^{3+}) with larger ion radii of 0.11 nm should exhibit weaker absorption at visible spectral region in comparison with Gaq complex due to smaller ion radii of Ga^{3+} (0.047 nm). In addition, Gdq should have larger electron-transporting (ET) property because erbium-q complex (Erq) has higher ET and electrical properties. Moreover, Erq also belongs to one of RE elements and has almost identical ion radii; hence Gdq also seems to exhibit larger ET ability [20,21]. Basing on the argument, it is expected that the PD diode with m-MTDATA/Gdq blend could offer high photo-response and it could be sensitive to the pure UV waveband.

In this letter, we will demonstrate PD diodes using Gdq as the A-material. For comparison, photo-sensitivities of other REq-PD diodes (RE = Y, La, Lu or Eu) were also studied. For the reason that the trivalent RE ions (RE^{3+}) in REq complexes behave inert electric configuration and do not contribute to light radiation from the RE^{3+} ions at UV excitation except for Eu^{3+} ion that emits red luminescence under UV illumination or electrical excitation. It is observed that 1:1 ratio m-MTDATA:Gdq-PD (Gdq-PD) diode exhibits a maximum photo-responsivity of 230 mA/W with VB among the REq-PDs at −7.5 V bias. We have noted that the responsivity considerably related to the exciplex formation of D:A blends and the optical properties of the REq complexes.

2. Experimental

All the REq complexes were synthesized according to methods reported in Refs. [20,21] and function as the A-materials in the PD diode system. Their blend films were thermally deposited on the quartz substrates in a vacuum chamber at the pressure of 5×10^{-4} Pa for the absorption and photoluminescence (PL) measurements. The PD diodes were fabricated on cleaned indium tin oxide (ITO) coated glass substrates with a sheet resistance of 25 Ω/sq in vacuum chamber. The organic layers were deposited at a rate of 2 Å/s; the evaporating rate of LiF and Al cathode were controlled to be 0.5 and 10 nm/s with the thickness of 1 and 200 nm, respectively. All the vacuum chambers were controlled at pressure of 5×10^{-4} Pa; the deposition rates and thickness of the layers were monitored using oscillating quartz monitors. Absorptions and PL spectra of the neat D- and A-material films and their blend films were determined with a Shimadzu UV-3101 PC spectrophotometer and a Hitachi F-4500, respectively. The PD diodes with structures of ITO/m-MTDATA:REq (1:1, 60 nm)/LiF (1 nm)/Al were fabricated, but the m-MTDATA-to-Gdq ratio for Gdq-PD diodes was 1:3, 1:1 and 3:1, respectively. Photocurrent spectral responses of all the PD diodes were measured under illumination of a 40 μW/cm^2 Xe lamp. Current–voltage (I–V) characteristics of the devices were recorded in dark and under illumination of 365 nm UV light with different intensities through the ITO side. The excited state lifetime of the exciplex emission of (m-MTDATA:Gdq) 1:1 blend film was measured by an F-900 Fluorescence and Phosphorescence lifetime spectrophotometer. All the measurements were carried out at room temperature under ambient condition. Besides, the operational lifetime of the UV PD is about 440 min under a constant illumination of 365 nm UV light with an intensity of a 8 μW/cm^2 Xe lamp and an illumination of a fluorescent lamp with an illumination power of 20 mW/cm^2 for observing its durability.

3. Results and discussion

The absorption spectra of the blend films of m-MTDATA:REq and the neat films of m-MTDATA and Gdq are indicated in Fig. 1(a), respectively. For comparison, the inset indicates relative absorption spectra of 1:1 blend film of m-MTDATA:REq, here RE are Y, La, Gd, Lu and Eu, respectively. We have noted that blue-shifting absorption peak of the Gdq film occurs comparing to Gaq [18], which describes that the photocurrent response of Gdq-PD diode could focus on the pure UV spectrum region. This is attributed to markedly lower absorption intensity of Gdq complex at 400–475 nm comparing with that of Gaq [18]. From the inset it can be seen that the figure of the absorption band of m-MTDATA:Gdq blend film is semblable with the other REq but the absorption intensity of m-MTDATA:Gdq and m-MTDATA:Euq blend films are maximum and minimum, respectively, which will be discussed later. Fig. 1(b) describes the photocurrent spectral responses of REq-PD diodes with 1:1 ratio of m-MTDATA:REq at zero bias, note that the photocurrent response locates almost at 300–400 nm UV spectrum region and Gdq-PD diode offers a maximum photocurrent density.

Fig. 2(a) depicts I–V characteristics of the five REq diodes at reverse biases under illumination of 365 nm UV

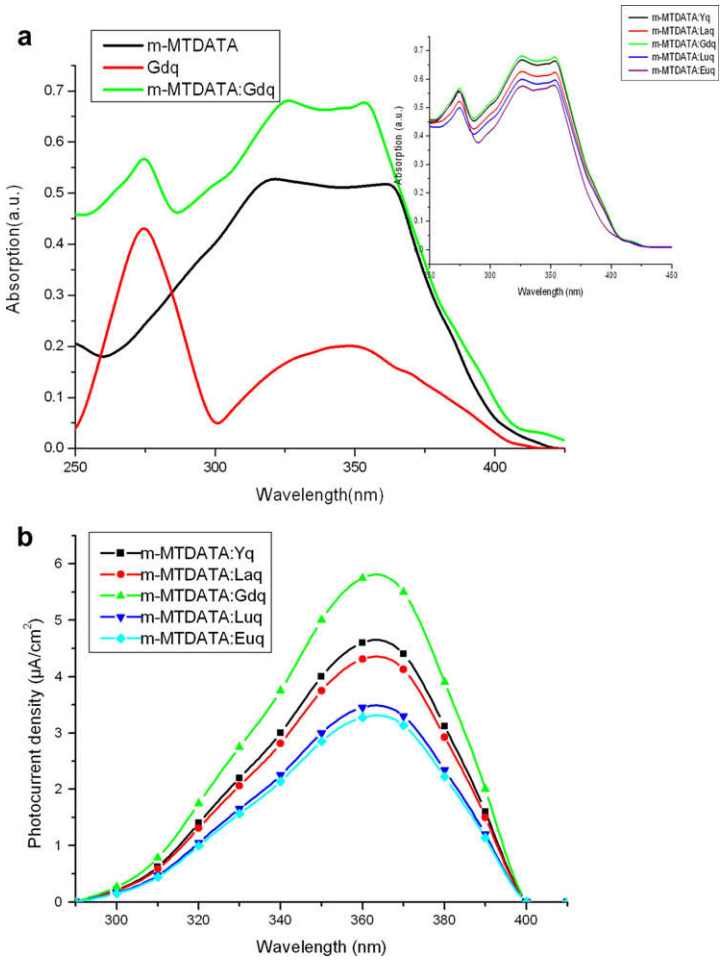

Fig. 1. (a) The absorption spectra of the blend films of m-MTDATA:Gdq and neat films of m-MTDATA and Gdq, the inset: relative absorption spectra of 1:1 blend films of m-MTDATA:REq (RE is Y, La, Gd, Lu and Eu). (b) The photocurrent spectral response of PD diode with m-MTDATA:REq blend with 1:1 ratio at zero bias.

light with a 1.2 mW/cm^2 and *I–V* characteristic of the Gdq-PD at dark, respectively, as well the inset indicates the photo-responses of the five REq-PD diodes as a function of UV light intensity at −7.5 V. It can be seen that current density of the REq-PD diodes significantly increases with the reverse voltage. The dark currents of the Gdq and other REq-PD devices are extremely low, the photocurrent-to darkcurrent ratio is about 260. Fig. 2(b) depicts the photo-responses of Gdq-PD device at −2, −6 and −7.5 V as a function of UV light intensity. It can observe that Gdq-PD diode exhibits a maximum photocurrent density of 276 μA/cm^2 and a peak photo-response of 230 mA/W among the five PD diodes. From Fig. 2(b) we obtained that the photo-sensitivities of Gdq-PD diodes are 64, 169, and 230 mA/W at −2, −6 and −7.5 V under illumination of 365 nm UV light, respectively. We can see that Gdq-PD presents a peak photosensitivity at any irradiation intensity comparing with other REq-PD diodes. Moreover, the photocurrent response of the PD device at a given voltage is almost unchanged with the increase in irradiation intensity from 0.4 to 7.0 mW/cm^2. This suggests that there is no obvious buildup of space charge, which can cause derivation from linear dependence of irradiation. Therefore, achievement of so high photosensitivity for Gdq-PD diode could be explained as below. It is noticed that the photocurrent densities of a PD diode at zero bias is actually short circuit current density (*Isc*) of a PV diode [1,22]. From Fig. 2(a) we also obtained that the photocurrent densities of Gdq, Laq, Yq, Luq and Euq-PD diodes at zero bias are 52.3, 33.1, 32.7, 27.8 and 25.7 μA/cm^2, respectively, and Gdq-PD diode offers a maximum high photocurrent response. That is, if a PV diode could offer higher *Isc*, a higher PD response could be obtained for the same structure PV diode because the PV and photodetection performances of the organic devices are likely to approach at zero bias [1,22]. Note that the five REq-PD diodes have the same structure so the fact that the PV performance increases with the increase in *Isc* would also lead to the same increasing trend of their PD photo-responses at reserve biases.

Fig. 3(a) and (b) depicts the PL spectra of above five blends, neat m-MTDATA and the neat REq films, respec-

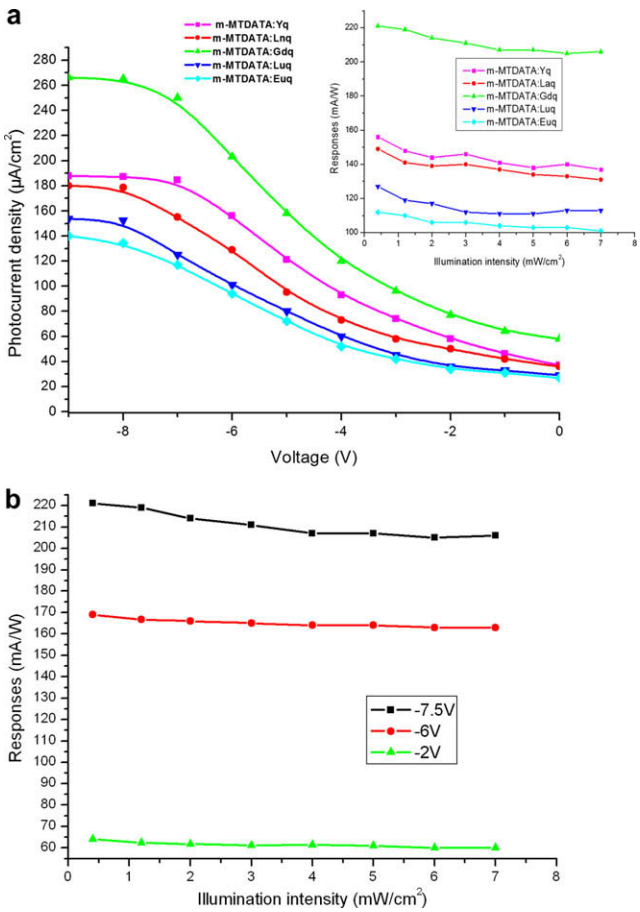

Fig. 2. (a) *I–V* characteristics of PD devices with various REq complexes at changing reverse bias under illumination of a 365 nm UV light with an intensity of 1.2 mW/cm^2. Inset: the photo-responses of the five REq-PD diodes at −7.5 V. (b) The photo-responses of the Gdq-PD device at −2, −6 and −7.5 V, respectively.

tively, as well (c) indicates PL spectra of 3:1, 1:1 and 1:3 blend films of m-MTDATA:Gdq under excitation of an 365 nm UV light, respectively. Comparing Fig. 3(a) and (b) we can seen that the PL spectral peaks are longer for the five blend films than for the five neat REq films, which were ascribed to overlapping of the D:A interfacial exciplex emission bands with the bulk PL. We also observe that PL intensities of the either blend or neat films of Gdq and Euq are, respectively, weakest and strongest among the five REq systems, which are corresponding to their photosensitivity (see Fig. 2(a) and the inset). From Fig. 3(c) we also see that the 1:1 ratio film behaves most low PL intensity among the PL spectra of 3:1, 1:1 and 1:3 blend films of m-MTDATA:Gdq, While both PL spectra of 3:1 and 1:3 blend films composed of not only the intermolecular exciplex emission, but also of the m-MTDATA and Gdq-bulks, the PL emissions of the two blends provide highly stronger than the 1:1 blend film. We note that 1:1 m-MTDATA:Gdq blend based PD diode offers the highest PD response over other two PD diodes based on 3:1 (162.8 μA/cm^2) and 1:3 (193.7 μA/cm^2) blend ratio of m-MTDATA:Gdq. So we can conclude that the photosensitivity is related closely to PL emission of the blend, i.e., the stronger the PL intensity the blend and/or bulk films are, the photosensitivity is the lower.

The findings can also be understood as follows. The geminate electron–hole pairs could be resulted from the intermolecular interface in the m-MTDATA:REq blend film under UV illumination, and thus there would be competition processes between the dissociation and collapse of the geminate carrier pairs [23,24]. We observed that the relative intensity of the exciplex emission of 1:1 ratio m-MTDATA:Gdq blend is the lowest among the three ratio based Gdq diode, and no bulk emissions were almost determined comparing with other REq-PD diodes, as shown in Fig. 3(a) and (b) although neat Gdq film also provides PL (Fig. 3(b)). For m-MTDATA:Euq blend film, both PL emissions of Eu^{3+} center and 8-hydroxyquinoline ligand of the complex occurred, leading to the lowest PD response due to the competition of the PL emission coming from exciplex, Euq and Eu^{3+} centers with the exciton dissociation. Thus the dissociation of the geminate carrier pairs should be less so that Euq-PD diode offers the lowest photocurrent response. The responses of Yq, Laq and Luq-PD diodes are lower than that of Gdq-PD diode due to their stronger bulk PL emissions as well. The competition be-

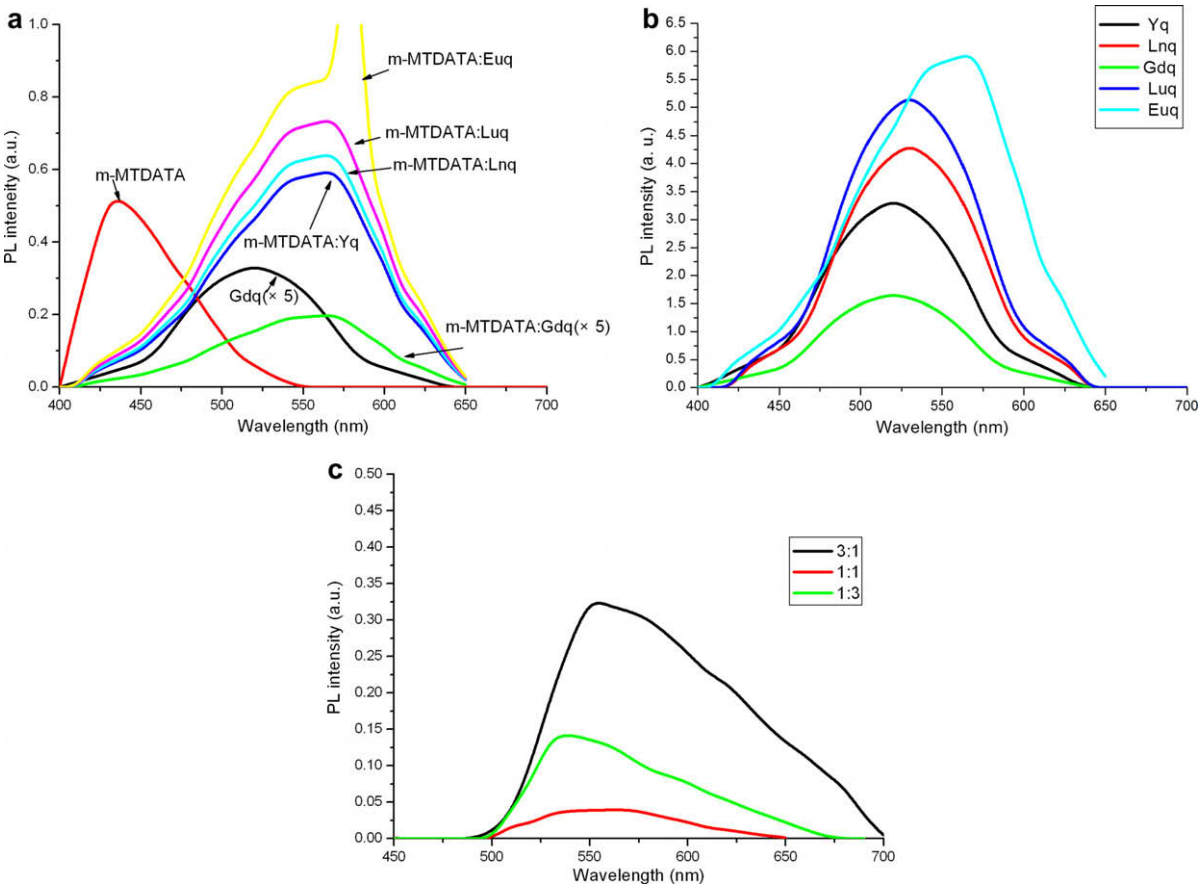

Fig. 3. (a) The PL spectra of above five blends and neat m-MTDATA and Gdq films, (b) the PL spectra of above five RE complexes at excitation by 365 nm UV light and (c) the PL spectra of 3:1, 1:1 and 1:3 blend films of m-MTDATA:Gdq under excitation 365 nm, respectively.

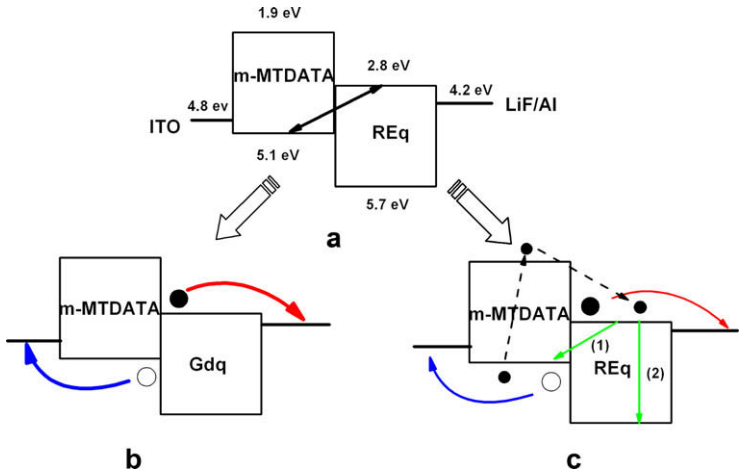

Fig. 4. (a) The geminate charge pair formation at the intermolecular interface of m-MTDATA/REq, (b) the dominant PV (PD) process of m-MTDATA/REq devices at very weak emissions of bulk and/or exciplex, and (c) weaken PV work at intensive emissions of exciplex (1) and/or bulk (2). Double direction arrow: Generated electron–hole pair; ● and ○: electron and hole that are resulted from exciton decomposing at the interface. Red and blue arrows denote the electron and hole transports into the respective electrodes, respectively. Dash arrow: electron transfer processes from HOMO of m-MTDATA to LUMO of REq, green arrow (1) and (2) represent emissions from exciplex and/or bulk of another REq-PD diodes except for Gdq at zero bias. The lowest unoccupied molecular orbital (LUMO) and the highest occupied molecular orbital (HOMO) levels of REq were cited from Ref. [24] and the LUMO and HOMO of m-MTDATA cited from Ref. [25]. (For interpretation of the references to colour in this figure legend, the reader is referred to the web version of this article.)

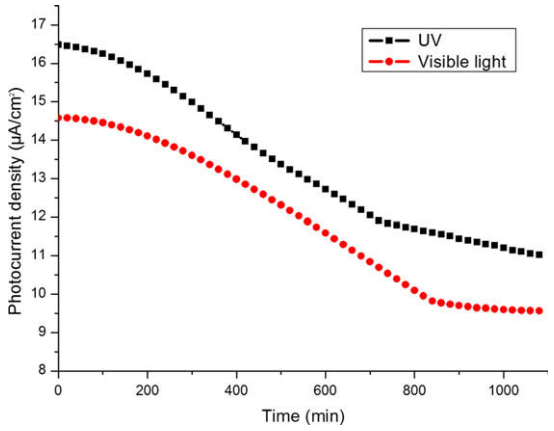

Fig. 5. The dependence of the photosensitivity on the illumination time by 365 nm UV light illumination with a 8 μW/cm^2 Xe lamp and an illumination of a fluorescent lamp with a power of 20 mW/cm^2.

tween dissociation and collapse of the geminate carrier pairs is depicted in Fig. 4. Fig. 4(a) depicts the schematic level diagram of the geminate charge pair formation. It also describes the dominant dissociation process of the geminate carrier pairs forwards into free electrons and holes (Fig. 4(b)) as well as provides the dominant exciplex and/or bulk emission processes which produced from collapse of the geminate carrier pairs (Fig. 4(c)). But the fact that the difference in photocurrent responses among Yq, Laq and Luq-PD diodes is not clearly understood now.

The reason that the photosensitivity is markedly high for Gdq-PD diode than for other REq-PD diodes may be also attributed to the paramagnetic property of Gd^{3+} ion and a very long exited state lifetime (1.3 μs) of PL emission of the exciplex between m-MTDATA:Gdq blend film is different from that of exciplex fluorescence [23], while it is more like to triplet, i.e., phosphorescence exciplex [25], and the more details are under studying. It is well known that organic materials generally are not so much stable under UV illumination, thus we measured the dependence of the photosensitivity on the illumination time by 365 nm UV light illumination and fluorescent lamp, respectively, as described in Fig. 5. We note that the degradation of the photo sensitivity not so much serious, which will be further studied.

4. Conclusion

In conclusion, visible-blind UV photo-detectors (PDs) were fabricated by using series of complexes of RE (RE = Y, La, Gd, Lu or Eu) with 8-hydroxyquinoline (REq) as the A component and m-MTDATA as the D components, respectively. It is discovered that Euq diode offers a maximum bulk PL emission that leads to a small photo-response. The fact is that the peak photosensitivity of Gdq-PD among the REq-PD diodes is attributed to its dominant exciton dissociation process resulted from extreme weak exciplex and bulk emissions and the strongest UV absorption. On the other hand, the realization of visible-blind UV Gdq-PD diode should be resulted from the blue-shift of the absorption band. These findings inspired us to realize that Gdq is an intriguing complex because of its excellent PD performance, and it can be expected that Gdq complex may also be used to design other organic electronic device with high performance. Beside it is believed that the photo-degradation of the Gdq-PD diode is not so much severe the working lifetime of the PD diode will be considerably improved if the PD device will be enveloped to obstruct from atmosphere.

Acknowledgements

This work was supported by the National Natural Science Foundation of China (Grant No. 60877027) and Knowledge Innovation Project of Chinese Academy of Sciences (No. KJCX2-YW-M11).

References

[1] P. Peumans, A. Yakimov, S.R. Forrest, J. Appl. Phys. 93 (2003) 3693.
[2] G. Yu, J. Gao, J.C. Hummelen, F. Wudl, J. Heeger, Science 270 (1995) 1789.
[3] M. Granstrom, K. Petritsch, A.C. Arias, A. Lux, M.R. Andersson, R.H. Friend, Nature (London) 395 (1998) 257.
[4] P. Peumans, S. Uchida, S.R. Forrest, Nature (London) 425 (2003) 158.
[5] J.G. Xue, B.P. Rand, S. Uchida, S.R. Forrest, Adv. Mater. 17 (2005) 66.
[6] G. Yu, K. Pakbaz, A.J. Heeger, Appl. Phys. Lett. 64 (1994) 3422.
[7] L. Ouali, V.V. Krasnikov, U. Stalmach, G. Hadziioannou, Adv. Mater. 11 (1999) 1515.
[8] H.-W. Lin, S.-Y. Ku, H.-C. Su, C.-W. Huang, Y.-T. Lin, K.-T. Wong, C.-C. Wu, Adv. Mater. 17 (2005) 2489.
[9] Y. Kim, M. Ballarotto, D. Park, M. Du, W. Cao, C.H. Lee, W.N. Herman, D.B. Romero, Appl. Phys. Lett. 91 (2007) 193510.
[10] J.C. Carrano, P.A. Grudowski, C.J. Eiting, R.D. Dupuis, J.C. Campbell, Electron. Lett. 33 (1997) 1980.
[11] P. Sandvik, D. Brown, J. Fedison, K. Matocha, J. Kretchmer, J. Electrochem. Soc. 152 (2005) G 199.
[12] D. Ray, K.L. Narasimhan, Appl. Phys. Lett. 91 (2007) 093516.
[13] C. Giebeler, H. Antoniadis, D.D.C. Bradley, Y. Shirota, Appl. Phys. Lett. 72 (1998) 2448.
[14] Y. Shirota, Y. Kuwabara, H. Inada, T. Wakimota, H. Nakada, Y. Yonemoto, S. Kawai, K. Imai, Appl. Phys. Lett. 65 (1994) 807.
[15] L.L. Chen, W.L. Li, M.T. Li, B. Chu, J. Lumin. 122–123 (2007) 667.
[16] H.Z. Wei, W.L. Li, M.T. Li, W.M. Su, Q. Xin, J.H. Niu, Z.Q. Zhang, Z.Z. Hu, Appl. Surf. Sci. 252 (2006) 220.
[17] G. Zhang, W.L. Li, B. Chu, S.Z. Sheng, D.F. Yang, F. Yan, Z.J. Zhuo, Org. Electron. 10 (2009) 352.
[18] Z.S. Su, W.L. Li, B. Chu, T.L. Li, J.Z. Zhu, G. Zhang, F. Yan, X. Li, Y.R. Chen, C.S. Lee, Appl. Phys. Lett. 93 (2008) 103309.
[19] L.G. Zhang, X.G. Ren, D.P. Jiang, A.D. Lu, J.S. Yuan, Spectrosc. Spect. Anal. 17 (1997) 12 (in Chinese).
[20] R.J. Curry, W.P. Gillin, Curr. Opin. Solid State Mater. Sci. 5 (2001) 481.
[21] R.J. Curry, W.P. Gillin, Synth. Met. 111–112 (2000) 35.
[22] P. Peumans, V. Bulović, S.R. Forrest, Appl. Phys. Lett. 76 (2000) 3856.
[23] A.C. Morteani, P. Sreearunothai, L.M. Herz, R.H. Friend, Phys. Rev. Lett. 92 (2004) 247402.
[24] A.C. Morteani, A.S. Anoop, R.H. Friend, Carlos Silva, Adv. Mater. 15 (2003) 1708.
[25] M. Cocchi, D. Virgili, C. Sabatini, J. Kalinowski, Chem. Phys. Lett. 421 (2006) 351.

developed a range of orthogonal solvents for the non-damaging patterning of organic materials [12], whilst some of the present authors have reported a simplified lithographic method, known as interlayer lithography, in which the resist layer is placed between the substrate and the material to be patterned [11]. Both methods allow for the fabrication of high quality electronic devices utilizing conventional photolithographic equipment, indicating that photolithography has considerable potential as a versatile patterning method for plastic electronics.

In previous work, we used interlayer lithography in combination with an intermediate conductivity formulation of PEDOT:PSS (Clevios P) to fabricate efficient organic light-emitting diodes and photodetectors with feature sizes at the millimetre scale [11]. In this paper, using a recently released high conductivity formulation of PEDOT:PSS (Clevios PH500), we extend the interlayer technique to organic field-effect transistors (OFETs) with source–drain electrode spacings in the micron range.

2. Results and discussion

Fig. 1 shows a schematic illustration of the interlayer method as applied here. First, a conventional negative photoresist (SU 8-2) is spin-coated on the substrate (Fig. 1a). Second, the resist is exposed through a mask by a UV source, initiating a cross-linking reaction that renders the exposed regions insoluble (Fig. 1b). Third, the target material (PEDOT:PSS) is spin-coated on top of the resist (Fig. 1c). Finally, the coated substrate is immersed in a developer, which dissolves the unexposed resist and simultaneously removes the target material above, leaving a patterned layer of PEDOT:PSS on top of an identically patterned layer

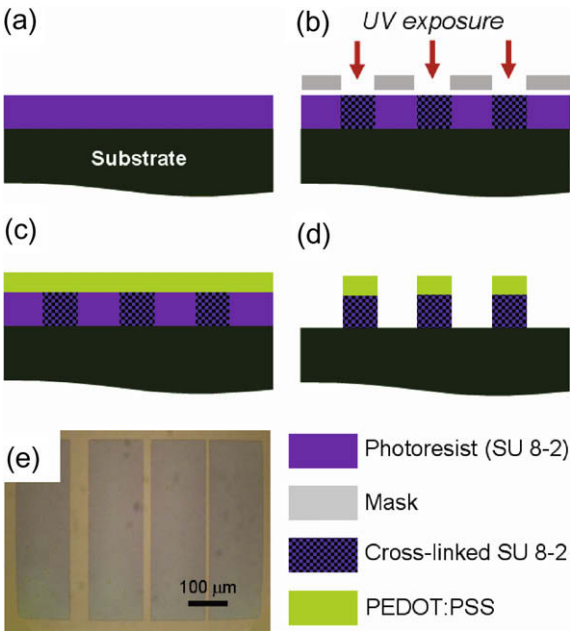

Fig. 1. (a–d) Schematic of the interlayer patterning method. (e) Micrograph of patterned PEDOT:PSS (150 μm width and 500 μm length) stripes on glass with inter-stripe spacings of 50, 20, and 10 μm from left to right.

of the cross-linked resist (Fig. 1d). In conventional photolithography the cross-linked resist is physically or chemically stripped away after patterning. In the interlayer approach, by contrast, it is retained between the target material and the substrate, meaning fewer (less damaging) process steps are required to complete the patterning procedure. The interlayer lithography process can also be configured in other ways – e.g. one can use a positive resist or carry out the exposure step after deposition of the target material [11].

SU 8-2 was selected as the resist material due to its high transparency and its good thermal, chemical and mechanical properties [24]. To minimize the obtrusiveness of the interlayer on the subsequent device architecture, the as-received SU 8-2 precursor was diluted with an SU 8 thinner prior to use, thereby reducing the thickness of the final film from ~1.4 μm to 230 ± 20 nm under standard spin-coating conditions (see Section 4). The combined height of the patterned [SU 8-2]/PEDOT:PSS bilayer was 350 ± 20 nm, implying a PEDOT:PSS thickness of ~120 nm for the chosen spin conditions. Fig. 1e shows an optical micrograph of four adjacent 500 × 150 μm rectangles of PEDOT:PSS, separated by distances of 50, 20, and 10 μm from left to right. The procedure can easily replicate features on the near micron-scale, yielding highly transparent patterned films of PEDOT:PSS with transmission $T > 90\%$ at 550 nm. The spacings shown do not reflect the ultimate feature sizes achievable with the interlayer method and in recent work we have achieved electrode separations down to 4 μm (see Fig. S1), close to the ~1 μm resolution limit of the equipment employed. Under specific circumstances, it is even possible to pattern at sub-micron length scales (700 nm) [25].

The patterning procedure was found to cause a ~15% drop in conductivity compared to unpatterned Clevios PH500 on glass (see Fig. S2), but the patterned films still exhibited conductivities >360 S/cm – a value that is higher than has been recently reported by others for the same PH500 formulation [8,26–28] and which is significantly above the baseline value of 300 S/cm specified by the supplier H.C. Starck GmbH.

To evaluate the utility of the interlayer method, arrays of closely spaced source and drain electrodes were patterned in PEDOT:PSS using glass and polyethylene terephthalate (PET) substrates (Fig. 2a and b). The electrodes were prepared with different channel lengths (L) in the range of 20–100 μm and channel widths (W) of 500, 1000 and 2000 μm. The enlarged image in Fig. 2c shows typical source and drain electrodes with $L = 20$ μm and $W = 1000$ μm.

Top-gate/bottom-contact p-type OFETs were fabricated using either 2,8-difluoro-5,11-bis(triethylsilylethynyl)-anthradithiophene (diF-TESADT) or a blend of diF-TESADT and poly(tri-arylamine) (PTAA) [29] as the semiconductor, CYTOP as the dielectric and Al as the gate electrode (Fig. 2d). Both pristine and blended forms of diF-TESADT have been used effectively in OFETs, the latter exhibiting superior stability at the expense of lower mobility. Ambipolar transistors were fabricated in the same way, except a spin-coated layer of [6,6]-phenyl-C_{61}-butyric acid methyl-ester (PCBM) [30] was used as the semiconductor.

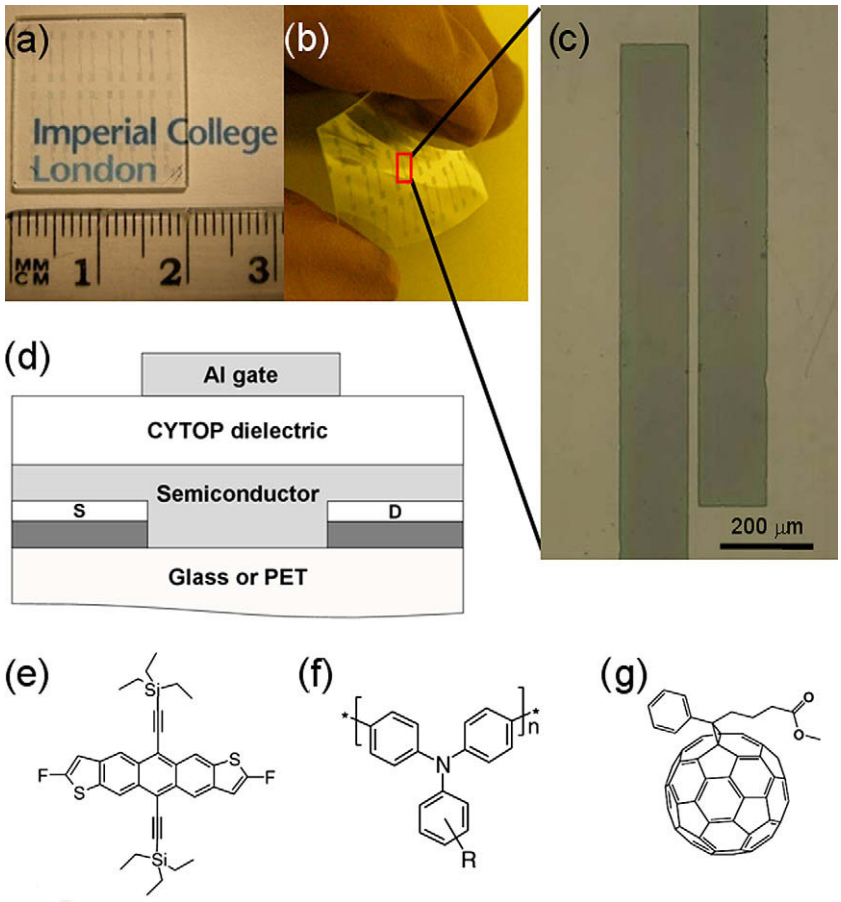

Fig. 2. (a and b) PEDOT:PSS array patterns fabricated on glass and PET, respectively. (c) Individual PEDOT:PSS source and drain electrodes patterned with 20 μm spacing on PET. (d) A schematic diagram of the *top-gate/bottom-contact* OFET configuration. (e–g) Chemical structures of diF-TESADT, PTAA, and PCBM, respectively.

Using the interlayer method with a metal shadow mask to control exposure of the photoresist, we were able to fabricate functioning transistors with channel lengths down to 20 μm. Excessively short values of L resulted in heavily injection limited device characteristics, and the best results were obtained using source–drain separations of 60, 30 and 50 μm for the diF-TESADT, diF-TESADT/PTAA and PCBM devices, respectively.

Fig. 3a and b shows transfer and output characteristics of a typical pristine diF-TESADT transistor with $L = 60$ μm. The device had an on/off ratio of $\sim 10^4$ and a hole mobility of 1 $cm^2/V\,s$, determined from plots of $I_D^{1/2}$ versus V_G in the saturation regime using the gradual channel approximation [31]:

$$I_{D,Sat} = \frac{WC_i}{2L}\mu(V_G - V_T)^2 \quad (1)$$

where W and L are the width and length of the transistor channel, C_i is the geometrical capacitance of the gate dielectric, V_G is the gate voltage, V_T is the threshold voltage, and I_D is the measured drain current. Fig. 3c and d shows the transfer and output characteristics of a typical diF-TESADT/PTAA transistor with $L = 30$ μm. The device had a moderate on/off ratio of $\sim 10^3$ and a lower mobility of 0.25 $cm^2/V\,s$. For both devices, I_D was observed to increase non-linearly with drain voltage (V_D) in the low V_D regime (Fig. 3b and d), which is attributable to a combination of contact resistance effects arising from the ~0.35 eV barrier[1] to hole injection at the PEDOT:PSS/diF-TESADT interface and possible access resistance effects associated with the transport of charge from the contact to the conducting channel [14].

The mobilities reported here compare favourably with values obtained from diF-TESADT based OFETs utilizing untreated gold electrodes (0.1–1 $cm^2/V\,s$). In the case of diF-TESADT/PTAA OFETs, improvements in hole mobility up to 2.4 $cm^2/V\,s$ have been reported when the source and drain electrodes are treated with a self-assembling monolayer of pentafluorobenzenethiol due to enhanced film crystallinity and an increase in the effective work function of gold [32,33]. Since no treatment of the PEDOT:PSS layer was carried out here, it is likely that similar enhancements in OFET mobility could be achieved through

[1] Note: the Fermi level of the PEDOT:PSS electrode is ~5.0 eV [7,8] while the highest occupied molecular orbital of diF-TESADT is ~5.35 eV [29].

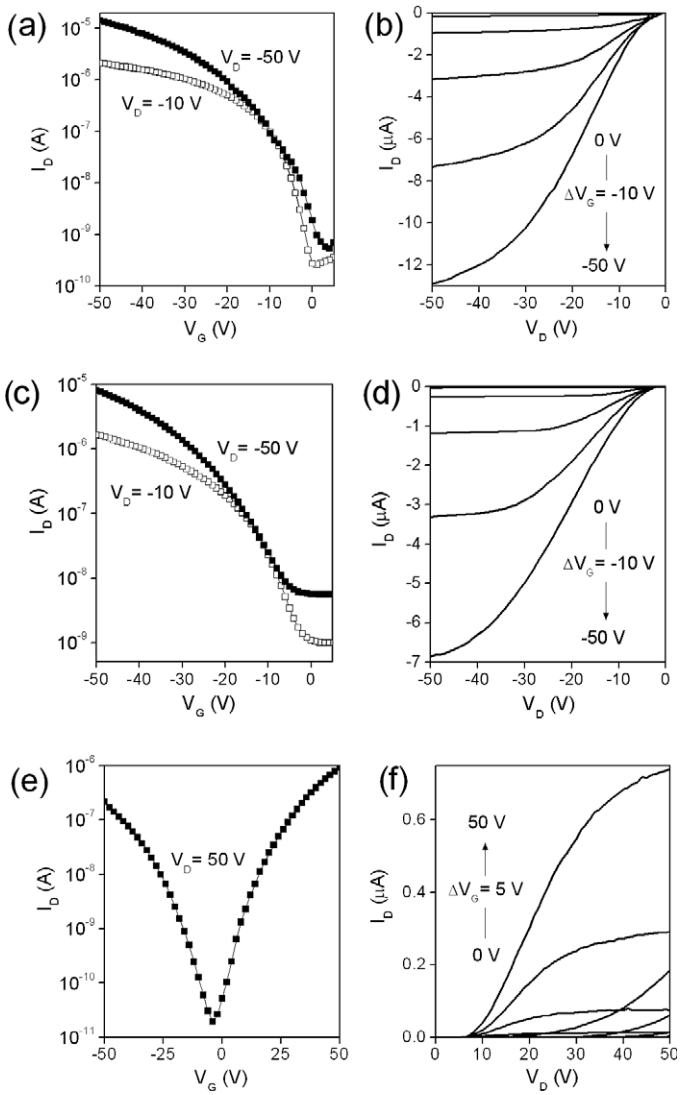

Fig. 3. Transfer and output curves for typical transistors with PEDOT:PSS source and drain electrodes patterned on glass by interlayer lithography, using: (a and b) pristine diF-TESADT (L = 60 μm, W = 1 mm, and C_i = 2 nF/cm^2), (c and d) diF-TESADT/PTAA blend (L = 30 μm, W = 1 mm, and C_i = 2 nF/cm^2), and (e and f) ambipolar PCBM (L = 50 μm, W = 1 mm, and C_i = 2 nF/cm^2).

appropriate surface modification (there are several reports of improved carrier injection from surface-modified PEDOT electrodes, e.g. treatment with octadecyltrichlorosilane has been shown to aid hole injection in OLED devices [34], while treatment with tetrakis-(dimethylamino)ethylene was reported to assist electron injection by inducing a ~0.5 eV reduction in the effective work function [35]).

To determine whether the interlayer method could be applied to the fabrication of transistors on flexible substrates, a diF-TESADT/PTAA based device with L = 30 μm was fabricated on PET as previously described. The hole mobility was lower than the equivalent device on glass at ~0.015 cm^2/V s (see Fig. S3), which we attribute to the poor surface adhesion of the organic layer to PET and changes in crystallization arising from the different surface energy of the PET substrate. This agrees with previous reports where it has been found that carefully controlled treatment with oxygen plasma (which was not employed here) is needed to achieve high mobilities [33]. (Note, treatment by oxygen plasma has previously been reported also to have a beneficial effect on the surface properties of PEDOT:PSS, leading to improved hole injection and transport when applied to OLEDs and OPVs [36]).

Fig. 3e and f show typical transfer and output characteristics for a PCBM transistor on glass with L = 50 μm. The frontier orbital energies of PCBM are 6.1 and 3.7 eV, resulting in energy barriers to hole and electron injection of 1.1 and 1.3 eV, respectively. The transistors accordingly exhibit ambipolar characteristics and can operate in both hole ($V_G << 0$ V) and electron ($V_G >> 0$ V) accumulation modes (Fig. 3e). On/off ratios of >10^4 were observed in both modes with the hole mobility (0.005 cm^2/V s) being an order of

magnitude lower than the electron mobility (0.05 $cm^2/V\,s$) in agreement with previous reports [30]. To our knowledge, this is the first demonstration of ambipolar charge transport in PCBM based transistors employing PEDOT:PSS source/drain electrodes. The performance parameters of the p-type and ambipolar OFETs are summarized in Table 1.

To verify whether the interlayer method could be applied to simple electronic circuits, we fabricated complementary voltage inverters comprising a diF-TESADT/PTAA p-type transistor and a PCBM n-type transistor (inset of Fig. 4) on separate substrates connected by metal wires. The lower hole mobility obtained with diF-TESADT/PTAA is beneficial here as it results in a better match to the low electron mobilities obtained with PCBM. The transfer characteristics of the inverter measured in a quasi-static mode at various supply voltages (V_{DD}) are shown in Fig. 4. The inverter executed the expected logic function with a maximum signal gain ($|dV_{OUT}/dV_{IN}|$) of ~16 at V_{DD} = |70| V and a noise margin equal to half the maximum theoretical value (i.e. $NM_{max} = V_{DD}/2$), similar to previously reported solution-processed complementary inverters [37]. The slight hysteresis in the operating characteristics of the inverter is a direct consequence of the hysteresis in the transfer curves of the PCBM transistor.

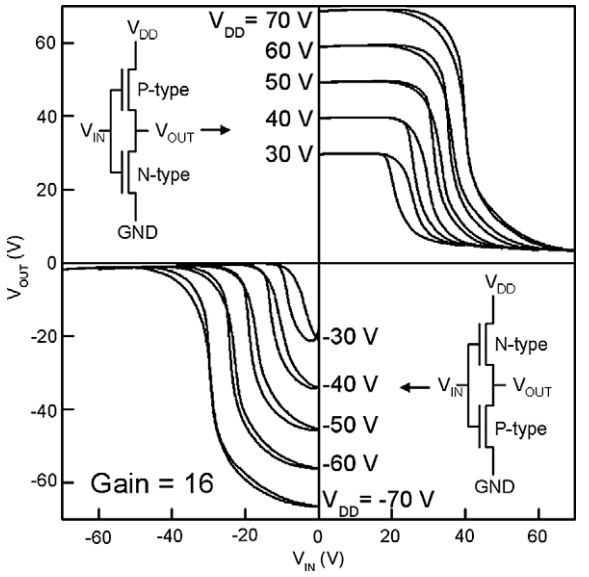

Fig. 4. Transfer characteristics of a complementary voltage inverter consisting of a p-type transistor with diF-TESADT/PTAA and an n-type transistor with PCBM, both fabricated using interlayer lithography (L = 50 μm and W = 1 mm). Inset: circuit diagram of complementary inverter.

3. Conclusions

We have used interlayer lithography to pattern high conductivity PEDOT:PSS electrodes for OFET applications, with conductivities >360 S/cm and pattern gaps $\geqslant$4 μm. Despite the 350 nm thickness of the [SU 8-2]/PEDOT:PSS electrodes, the resultant transistors exhibited similar performance characteristics to conventional Au-based transistors, whilst offering high transparency in the visible spectrum (>90% at 550 nm), sufficient for many screen- and window-integrated applications. Hole transporting OFETs based on diF-TESADT and diF-TESADT/PTAA exhibited high mobilities of up to 1 and 0.25 $cm^2/V\,s$, respectively, while ambipolar OFETs based on PCBM exhibited electron and hole mobilities of 0.05 and 0.005 $cm^2/V\,s$, respectively. Complementary voltage inverters based on diF-TESADT/PTAA and PCBM OFETs fabricated by the interlayer technique exhibited excellent operating characteristics with wide noise margin and high signal gain. Hence, it is evident that interlayer lithography offers a viable route to cost efficient, solution-processed, and flexible organic electronics. Finally, we note that although we have focused here on top-gate/bottom-contact OFETs with PEDOT:PSS source and drain electrodes, the interlayer method can also be applied to metals, including Ag and Al, and to other device configurations such as bottom-gate transistors as will be described in a future manuscript.

Table 1
Summary of device characteristics obtained for p-type and ambipolar transistors using PEDOT:PSS source–drain electrodes patterned on different substrates.

	p-Type diF-TESADT Glass	diF-TESADT/PTAA Glass	diF-TESADT/PTAA PET	Ambipolar PCBM Glass
μ_h ($cm^2/V\,s$)	~1	0.1–0.25	0.015	0.005
μ_e ($cm^2/V\,s$)	–	–	–	0.05
I_{on}/I_{off}	$\sim10^4$	$\sim10^3$	$\sim10^2$	$>10^4$

4. Experimental

SU 8-2 photoresist was diluted with SU 8 thinner in a 1:3 weight ratio and spin-coated onto clean glass or PET at 5000 rpm for 40 s. The resist was soft-baked on a hot plate at 65 °C for 1 min and at 95 °C for 1 min, before being exposed to 250 mJ cm^{-2} of 365 nm radiation using a Karl Suss MJB 3 mask aligner. After exposure, the resist was baked on a hot plate at 65 °C for 1 min and at 95 °C for 2 min. Clevios PH500 (H.C. Starck GmbH) doped with 5% dimethylsulphoxide was spin-coated onto the SU 8-2 at 1000 rpm for 20 s, and then annealed at 120 °C for 10 min (PET) or 130 °C for 10 min (glass). The unexposed SU 8-2, together with the overlying PEDOT:PSS, was removed by sonicating the sample in the developer (propylene glycol monomethyl ether acetate) for 3–5 min, leaving behind a patterned layer of PEDOT:PSS on top of an identically patterned resist layer. The conductivity of the PEDOT:PSS films was measured using the standard four-point probe technique. *Top-gate/bottom-contact* OFETs were fabricated on glass and PET using patterned PEDOT:PSS as the source and drain electrodes, prepared as above. For the p-type transistors, either a pristine film of 2,8-difluoro-5,11-bis(triethylsilylethynyl)-anthradithiophene (diF-TESADT) in toluene (15 mg/ml) or a 2:1 by weight composite film of diF-TESADT and poly(triaryl-amine) (PTAA) in anhydrous tetralin (40 mg/ml) was used as the organic semiconductor, and spin-coated onto the PEDOT:PSS layer at 1500 rpm before baking at 95 °C for 5 min in nitrogen.

Ambipolar OFETs were fabricated using methanofullerene [6,6]-phenyl-C_{61}-butyric acid methyl-ester (PCBM) in chlorobenzene (10 mg/ml) as the semiconductor, which was deposited by spin-coating at 1000 rpm in nitrogen. In both cases a dielectric layer of CYTOP was spin-coated on top of the semiconductor layer at 1700 rpm and dried at 95 °C for 15 min in nitrogen. Finally, a top-gate aluminum electrode was deposited by thermal evaporation under high vacuum (10^{-6} mbar) through a shadow mask. Electrical characterization of the samples was performed in air (diF-TESADT) or in an inert nitrogen atmosphere using a Keithley SCS 4200 parameter analyzer. To fabricate the inverters, separate n- and p-type transistors were connected via metal wires as shown in the inset to Fig. 4.

Acknowledgements

We thank the EPSRC for financial support under Grant EP/C539516, and the Royal Society for supporting this work via the 2007 Brian Mercer Award for Innovation in Nanotechnology. JdM is a Royal Society Industry Fellow and DDCB is Lee-Lucas Professor of Experimental Physics.

Appendix A. Supplementary data

Supplementary data associated with this article can be found, in the online version, at doi:10.1016/j.orgel.2010.04.002.

References

[1] P.A. Levermore, L. Chen, X. Wang, R. Das, D.D.C. Bradley, Adv. Mater. 19 (2007) 2379.
[2] L. Groenendaal, F. Jonas, D. Freitag, H. Pielartzik, J.R. Reynolds, Adv. Mater. 12 (2000) 481.
[3] Q. Cao, J.A. Rogers, Adv. Mater. 21 (2009) 29.
[4] K.S. Kim, Y. Zhao, H. Jang, S.Y. Lee, J.M. Kim, K.S. Kim, J.-H. Ahn, P. Kim, J.Y. Choi, B.H. Hong, Nature 457 (2009) 706.
[5] K. Nomura, H. Ohta, A. Takagi, T. Kamiya, M. Hirano, H. Hosono, Nature 432 (2004) 488.
[6] J. Huang, X. Wang, A.J. de Mello, J.C. de Mello, D.D.C. Bradley, J. Mater. Chem. 17 (2007) 3551.
[7] S.-I. Na, S.-S. Kim, J. Jo, D.-Y. Kim, Adv. Mater. 20 (2008) 4061.
[8] Y. Zhou, F. Zhang, K. Tvingstedt, S. Barrau, F. Li, W. Tian, O. Inganäs, Appl. Phys. Lett. 92 (2008) 233308.
[9] D. Hohnholz, H. Okuzaki, A.G. MacDiarmid, Adv. Funct. Mater. 15 (2005) 51.
[10] H. Kang, T. Kim, H.H. Lee, Appl. Phys. Lett. 93 (2008) 203308.
[11] (a) J. Huang, R. Xia, Y. Kim, X. Wang, J. Dane, O. Hofmann, A. Mosley, A.J. de Mello, J.C. de Mello, D.D.C. Bradley, J. Mater. Chem. 17 (2007) 1043;
(b) D.D.C. Bradley, J.C. de Mello, J. Huang, PCT/GB06/004261.
[12] P.G. Taylor, J.-K. Lee, A.A. Zakhidov, M. Chatzichristidi, H.H. Fong, J.A. DeFranco, G.G. Malliaras, C.K. Ober, Adv. Mater. 21 (2009) 2314.
[13] Y. Jang, Y.D. Park, J.A. Lim, H.S. Lee, W.H. Lee, K. Cho, Appl. Phys. Lett. 89 (2006) 183501.
[14] H. Sirringhaus, T. Kawase, R.H. Friend, T. Shimoda, M. Inbasekaran, W. Wu, E.P. Woo, Science 290 (2000) 2123.
[15] B.-J. de Gans, P.C. Duineveld, U.S. Schubert, Adv. Mater. 16 (2004) 203.
[16] D. Zielke, A.C. Hubler, U. Hahn, N. Brandt, M. Bartzsch, U. Fugmann, T. Fischer, J. Veres, S. Ogier, Appl. Phys. Lett. 87 (2005) 123508.
[17] R. Parashkov, E. Becker, T. Riedl, H.-H. Johannes, W. Kowalsky, Adv. Mater. 17 (2005) 1523.
[18] P. Cosseddu, A. Bonfiglio, Appl. Phys. Lett. 88 (2006) 023506.
[19] A. Takakuwa, M. Ikawa, M. Fujita, K. Yase, Jpn. J. Appl. Phys. 46 (2007) 5960.
[20] D. Li, L.J. Guo, J. Phys. D: Appl. Phys. 41 (2008) 105115.
[21] M. Halik, H. Klauk, U. Zschieschang, G. Schmid, W. Radilik, W. Weber, Adv. Mater. 14 (2002) 1717.
[22] J.R. Chan, X.Q. Huang, A.M. Song, J. Appl. Phys. 99 (2006) 023710.
[23] J.A. DeFranco, B.S. Schmidt, M. Lipson, G.G. Malliaras, Org. Electron. 7 (2006) 22.
[24] M. Agirregabiria, F.J. Blanco, J. Berganzo, M.T. Arroyo, A. Fullaondo, K. Mayora, J.M. Ruano-Lopez, Lab Chip 5 (2005) 545.
[25] D.-S. Leem, D.D.C. Bradley, J.C. de Mello, unpublished.
[26] A. Colsmann, F. Stenzel, G. Balthasar, H. Do, U. Lemmer, Thin Solid Films 517 (2009) 1750.
[27] E. Ahlswede, W. Muhleisen, M.W.M. Wahi, J. Hanisch, M. Powalla, Appl. Phys. Lett. 92 (2008) 143307.
[28] C. Piliego, M. Mazzeo, B. Cortese, R. Cingolani, G. Gigli, Org. Electron. 9 (2008) 401.
[29] J. Smith, R. Hamilton, M. Heeney, D.M. de Leeuw, E. Cantatore, J.E. Anthony, I. McCulloch, D.D.C. Bradley, T.D. Anthopoulos, Appl. Phys. Lett. 93 (2008) 253301.
[30] T.D. Anthopoulos, C. Tanase, S. Setayesh, E.J. Meijer, J.C. Hummelen, P.W.M. Blom, D.M. de Leeuw, Adv. Mater. 16 (2004) 2174.
[31] S.F. Nelson, Y.Y. Lin, D.J. Gundlach, T.N. Jackson, Appl. Phys. Lett. 72 (1998) 1854.
[32] S.K. Park, D.A. Mourey, S. Subramanian, J.E. Anthony, T.N. Jackson, Appl. Phys. Lett. 93 (2008) 043301.
[33] R. Hamilton, J. Smith, S. Ogier, M. Heeney, J.E. Anthony, I. McCulloch, J. Veres, D.D.C. Bradley, T.D. Anthopoulos, Adv. Mater. 21 (2009) 1166.
[34] Y.K. Lee, S.K. Kwon, T.J. Park, D.J. Choi, J.H. Kwon, J. Jang, J.K. Jin, H. You, Electrochem. Solid-State Lett. 10 (2007) J55.
[35] L. Lindell, A. Burquel, F.L.E. Jakobsson, V. Lemaur, M. Berggren, R. Lazzaroni, J. Cornil, W.R. Salaneck, X. Crispin, Chem. Mater. 18 (2006) 4246.
[36] (a) Y. Zhou, Y. Yuan, J. Lian, J. Zhang, H. Pang, L. Cao, X. Zhou, Chem. Phys. Lett. 427 (2006) 394;
(b) Y. Zhou, Y. Yuan, L. Cao, J. Zhang, H. Pang, J. Lian, X. Zhou, J. Lumin. 122–123 (2007) 602;
(c) P. Peumans, S.R. Forrest, Appl. Phys. Lett. 79 (2001) 126.
[37] P.H. Wöbkenberg, D.D.C. Bradley, D. Kronholm, J.C. Hummelen, D.M. de Leeuw, M. Cölle, T.D. Anthopoulos, Synth. Met. 158 (2008) 468.

polymer-ZnO QDs and the graphene layer. Current–voltage (*I–V*) measurements on the UV photodetectors under an illumination of a 365-nm-UV light at 300 K were performed to characterize device performance. The carrier transport mechanisms at work in the UV photodetectors are described on the basis of the *I–V* results.

The hybrid poly-*N*-vinylcarbazole (PVK)–ZnO QD composites, the graphene layer, and the PEDOT:PSS layer used in this study were prepared on indium–tin–oxide (ITO)-coated glass substrates by using spin-coating and attachment methods. The ITO-coated glass substrates were alternately cleaned ultrasonically in acetone and methanol at 27 °C for 10 min and were rinsed in de-ionized water. The chemically-cleaned ITO-coated glass substrates were then dried by using N_2 gas with a purity of 99.9999%. The PEDOT:PSS (Sigma–Aldrich) was spin coated on the pre-cleaned ITO glass substrates and then annealed at 150 °C for 10 min. ZnO QDs were synthesized by modifying a simple method with the use of a dimethylformamide (DMF) reduction. Solutions were formed by dissolving zinc acetate dehydrate [$Zn(CH_3COO)_2{\cdot}H_2O$] (1 wt%) in DMF in the proper proportion, after which the zinc-acetate-dehydrate/DMF solution was stirred for 10 min at room temperature. The mixture was then heated to 105 °C at a heating rate of 2 °C/min and was maintained at the that temperature for 5 h, resulting in the formation of colloidal ZnO QDs. After the ZnO QDs had been synthesized at 105 °C for 5 h, they were cooled to room temperature. The colloidal ZnO QDs were mixed with the PVK. Subsequently, the ZnO QDs and PVK dispersed in the DMF solution were deposited onto a PEDOT:PSS film by using a spin-coating method at 2000 rpm for 25 s, and the solvents existing on the samples were removed by putting the samples onto a hotplate at 90 °C for 30 min.

The graphene films were synthesized by modifying the SiO_2-coated Si substrates. The SiO_2-coated Si substrates for growing the graphene films were cleaned ultrasonically by using acetone and ethanol, and then rinsed in de-ionized water. After a chemically-cleaned SiO_2-coated Si substrate had been dried by using N_2 gas with a purity of 99.9999%, a Ni thin film with a thickness of 200 nm was grown on the SiO_2-coated Si substrate by using thermal evaporation. Graphene films were synthesized by using a chemical vapor deposition (CVD) method. A 200-nm polycrystalline Ni film was deposited onto a pre-cleaned SiO_2-coated Si substrate by using a thermal evaporator. Subsequently, the Ni thin film on the SiO_2-coated Si substrate was annealed at 1000 °C for 20 min. The graphene layer was formed with gas mixtures of CH_4, Ar, and H_2. After the graphene films had been grown by using the CVD reaction, the substrates were immersed in a HF solution to remove the SiO_2 layer, were etched in a TFG solution to remove the Ni film, and were then rinsed with de-ionized water. Because graphene floats on water due to the hydrophobic nature of graphene, the formed graphene layer was attached to the hybrid PVK–ZnO QD composites layer. Finally, an Al top electrode with a thickness of 150 nm was thermally deposited through a metal mask at a system pressure of 1×10^{-6} Torr. A schematic diagram of the UV photodetectors fabricated in this work is shown in Fig. 1.

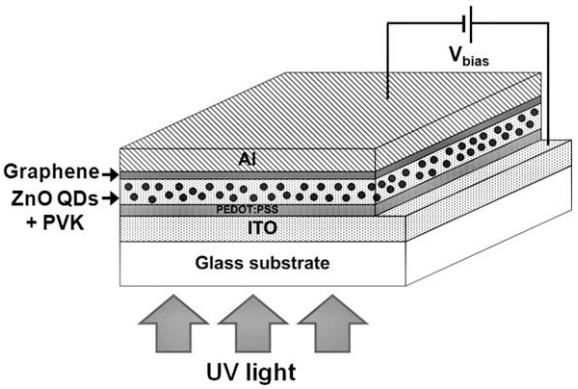

Fig. 1. Schematic diagram of the structure of the UV photodetector studied in this work.

I–V measurements were performed by using a HP 4140B *I–V* meter at room temperature. The TEM measurements were performed in a JEM 2100F transmission electron microscope operating at 200 kV.

Fig. 2 shows a cross-sectional SEM image of the UV photodetectors consisting of hybrid PVK–ZnO QD composites incorporating graphene and PEDOT:PSS layers. The top layer is graphene, and the thicknesses of the PEDOT:PSS layer and of the hybrid ZnO QDs + PVK layer were both about 80 nm.

Fig. 3(a) shows a plane-view TEM image of the hybrid ZnO QDs + PVK layer. The ZnO QDs are randomly distributed in the PVK matrix. A particle-like structure with a diameter of 110 nm was formed in the PVK layer, as shown in Fig. 3(a). The ZnO QDs, indicated by arrows, were attached to the surface of the particle-like PVK, and graphene sheets with a thickness of about 2 nm were formed on the PVK layer, as shown in Fig. 3(b).

Fig. 4 shows an absorbance spectrum for the hybrid ZnO QD and PVK/PEDOT:PSS layers grown on the ITO substrate. The optical absorbance spectrum of the ITO-coated glass substrate is chosen as a reference background. The absorbance of the ITO-coated glass substrate has been subtracted from the spectrum to remove the effects of the substrate. The dominant absorbance peak at 360 nm is attributed to the hybrid ZnO QDs and PVK layer. The broad absorbance peak around 550 nm is related to the PEDOT:PSS layer [21].

Fig. 5 shows the *I–V* curves for the UV photodetectors under illumination with a 365-nm UV light at a power of 6 W and in the dark. When the UV light was used to irradiate the fabricated photodetectors, the difference between the dark current and the photocurrent increased linearly at lower bias voltages and then increased exponential at higher bias voltages, as shown in Fig. 5(a). The plots shown in Fig. 5(b) indicate that the photocurrent of the UV photodetector devices with a graphene under illumination with 365-nm light at 0.4 V was 7.15×10^{-3} A and that the dark current at 0.4 V was 7.98×10^{-11} A. The ratio of the photocurrent to the dark current was about 10^8.

Fig. 6 shows the *I–V* characteristics for the UV photodetectors with and without a graphene layer. The

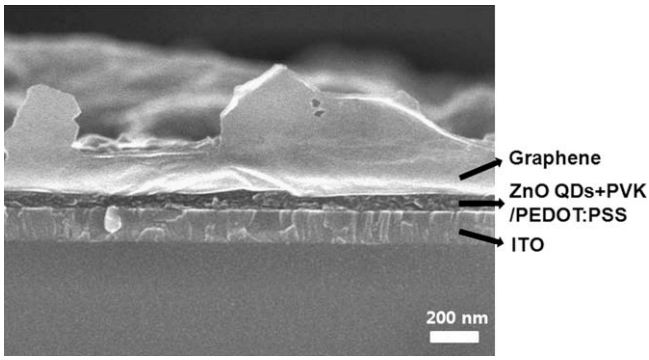

Fig. 2. Cross-sectional SEM image of the UV photodetector.

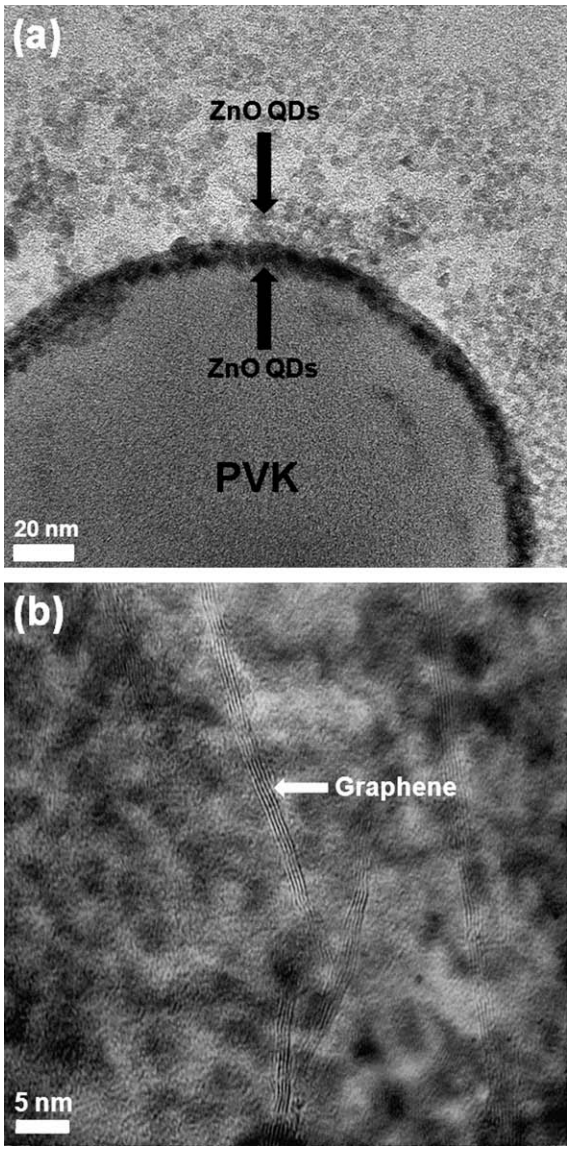

Fig. 3. TEM images of (a) ZnO QDs attached to the surface of PVK and of (b) graphene sheets.

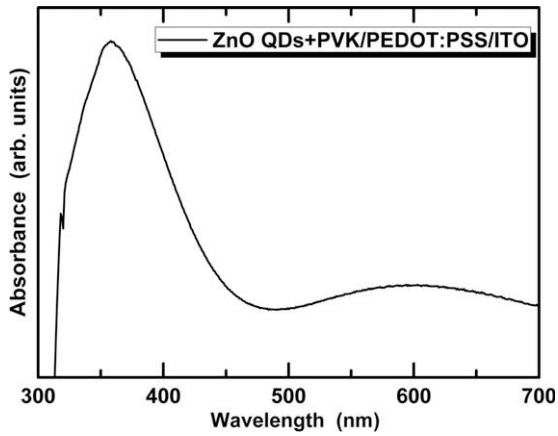

Fig. 4. Absorbance spectrum for the hybrid ZnO QDs and PVK/PEDOT:PSS grown on the ITO substrate.

photocurrents of the UV photodetectors at 0.4 V with and without a graphene layer were 7.15×10^{-3} and 3.36×10^{-5} A, respectively. ZnO QDs under illumination with UV light generated electron–hole pairs. Because the holes move through the PEDOT:PSS layer, the holes located at the ground state of ZnO QDs are transferred to the ITO electrode. A PVK hole transport layer is utilized to reduce the energy barrier between the ZnO QDs and the PEDOT:PSS layer. The introduction of the PVK layer facilitates the transport of the separated holes, resulting in an enhancement of the photodetectors performance [8]. The graphene layer with a high electrical conductivity provides an efficient pathway for the conduction-band electrons to move to the Al electrode. The attachment of the graphene layer to the hybrid ZnO QDs and the PVK layer might facilitate the transport of separated electrons, thus enhancing the photoresponse of the photodetectors, as shown in Fig. 6. Furthermore, the large area of the graphene layer allows large-area photodetectors to be fabricated. When the photodetectors were left in the ambient air conditions during 1 month, the same photocurrents of the UV photodetectors were obtained. No significant degradation of the photodetectors under illumination of the UV light after several hours of continuous

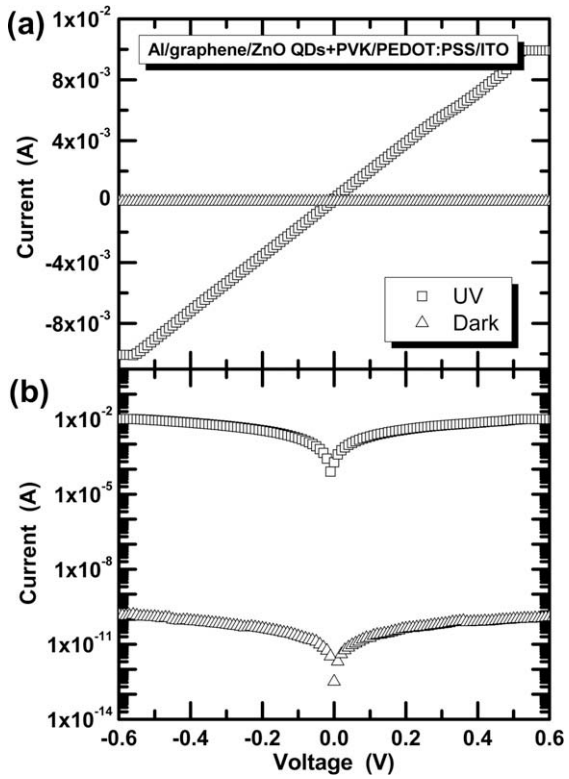

Fig. 5. (a) Currents as functions of the applied voltage for the UV photodetector in the dark (rectangles) and under illumination by a 365-nm UV light at a power of 6 W (triangles). (b) Plot of log currents of Fig. 4(a) as functions of the voltage.

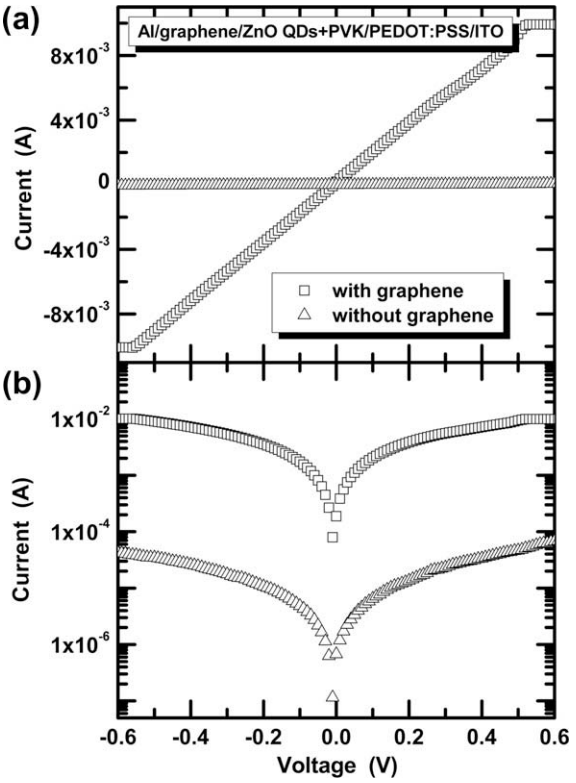

Fig. 6. (a) Photocurrents as functions of the applied voltage for the UV photodetector with (rectangles) and without (triangles) a graphene. (b) Plot of log photocurrents of Fig. 5(a) as functions of the voltage.

stress was observed, indicative of the photoresponse stability of the photodetectors.

Fig. 7 shows a schematic diagram of the energy bands corresponding to the carrier transport mechanisms of the holes and electrons during UV illumination for the device. When a 365-nm UV light illuminates the photodetectors through the ITO electrode, the photons penetrate into the hybrid ZnO QDs and PVK layer, resulting in the creation of the excitons. When the photogenerated excitons diffuse into both the PEDOT:PSS and the graphene layers, while the electrons move to the Al electrode through the graphene layer, the holes transfer to the ITO layer through the PVK and the PEDOT:PSS layers. Therefore, the electrons and holes are accumulated at the ITO and the Al layers, respectively, resulting in the generation of the photocurrent of the UV photodetectors.

In summary, UV photodetectors were fabricated utilizing hybrid ZnO QDs and PVK layer incorporating graphene and PEDOT:PSS layers. TEM images showed that the ZnO QDs were distributed on the surface of the PVK layer and that the graphene layers were deposited on the PVK layer containing the ZnO QDs. The graphene layer served as an electron transport layer. The UV photodetectors under illumination with 365-nm light at 0.4 V showed a ratio of the photocurrent to the dark current of approximately 10^8. The photocurrent of the UV photodetectors containing the graphene layer was much higher than that of the detectors

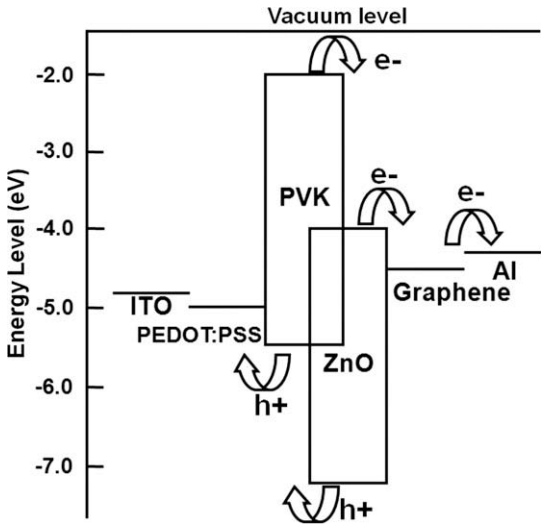

Fig. 7. Schematic diagram of the energy bands corresponding to the carrier transport mechanisms of the holes and electrons during UV illumination for the device.

without the graphene layer. These results indicate that a hybrid ZnO QDs–PVK layer incorporating graphene and PEDOT:PSS layers hold promise for potential applications in next-generation large-area UV photodetectors.

Acknowledgements

This work was supported by the Korea Science and Engineering Foundation (KOSEF) grant funded by the Korea Government (MEST) (No. R0A-2007-000-20044-0).

References

[1] M.H. Huang, S. Mao, H. Feick, H.Q. Yan, Y.Y. Wu, H. Kind, E. Weber, R. Russo, P.D. Yang, Science 292 (2001) 1897.
[2] T. Makino, Y. Segawa, A. Tsukazaki, A. Ohtomo, M. Kawasaki, Appl. Phys. Lett. 87 (2005) 022101.
[3] U. Ozgur, Ya.I. Alivov, C. Liu, A. Teke, M.A. Reshchikov, S. Dogan, V. Avrutin, S.-J. Cho, H. Morkoc, J. Appl. Phys. 98 (2005) 041301.
[4] Y.H. Tong, Y.C. Liu, C.L. Shao, R.X. Mu, Appl. Phys. Lett. 88 (2006) 123111.
[5] C. Soci, A. Zhang, B. Xiang, S.A. Dayeh, D.P.R. Aplin, J. Park, X.Y. Bao, Y.H. Lo, D. Wang, Nano Lett. 7 (2007) 1003.
[6] L.W. Ji, S.M. Peng, Y.K. Su, S.J. Young, C.Z. Wu, W.B. Cheng, Appl. Phys. Lett. 94 (2009) 203106.
[7] W.J.E. Beek, M.M. Wienk, R.A.J. Janssen, Adv. Mater. 16 (2004) 2009.
[8] F. Li, S.H. Cho, D.I. Son, T.W. Kim, S.-K. Lee, Y.-H. Cho, S. Jin, Appl. Phys. Lett. 94 (2009) 111906.
[9] A. Tsukazaki, A. Ohtomo, T. Onuma, M. Ohtani, T. Makino, M. Sumiya, K. Ohtani, S.F. Chichibu, S. Fuke, Y. Segawa, H. Ohno, H. Koinuma, M. Kawasaki, Nat. Mater. 4 (2005) 42.
[10] D.I. Son, C.H. You, W.T. Kim, T.W. Kim, Nanotechnology 20 (2009) 345204.
[11] H. Kim, C.M. Gilmore, J.S. Jorwitz, A. Pigue, H. Murafa, G.P. Kushto, R. Schlaf, Z.H. Kafafi, D.B. Chrisey, Appl. Phys. Lett. 76 (2000) 259.
[12] Z.L. Wang, Mater. Sci. Eng., R 64 (2009) 33.
[13] H.M.P. Wong, P. Wang, A. Abrusci, M. Svensson, M.R. Andersson, N.C. Greenham, J. Phys. Chem. C 111 (2007) 5244.
[14] Y. Zin, J. Wang, B. Sun, J.C. Blakesley, N.C. Greenham, Nano Lett. 8 (2008) 1649.
[15] C. Berger, Z. Song, X. Li, X. Wu, N. Brown, C. Naud, D. Mayou, T.L. Joanna, Science 312 (2006) 1191.
[16] J.C. Meyer, A.K. Geim, M.I. Katsnelson, K.S. Novoselov, T.J. Booth, S. Roth, Nature 446 (2007) 60.
[17] T. Cohen-Karni, Q. Qing, Q. Li, Y. Fang, C.M. Lieber, Nano Lett. 10 (2010) 1098.
[18] Q. Liu, Z. Liu, X. Zhang, N. Zhang, L. Yang, S. Yin, Y. Chen, Appl. Phys. Lett. 92 (2008) 223303.
[19] Z. Liu, Q. Liu, Y. Huang, Y. Ma, S. Yin, X. Zhang, W. Sun, Y. Chen, Adv. Mater. 20 (2008) 3924.
[20] X. Wang, L. Zhi, K. Müllen, Nano Lett. 8 (2008) 323.
[21] L.A.A. Pettersson, S. Ghosh, O. Inganäs, Org. Electron. 3 (2002) 143.

2. Experimental

Among the various techniques to grow 1D ZnO nanostructures, the cost-effective electrodeposition method was used in this work for the preparation of large area of nanorods because of the low-temperature processing, arbitrary substrate shapes, and precise control of the size of nanorods. ZnO nanorods were electrodeposited in 0.005 M $Zn(NO_3)_2$ and 0.005 M hexamethylenetramine aqueous solutions. Devices were fabricated on cleaned indium tin oxide (ITO) coated glass substrates with a sheet resistance of 25 Ω/□. All depositions were carried out in a configured glass cell at 90 °C, in which an ITO substrate, a platinum plate, and a Ag/AgCl electrode in saturated KCl served as the working electrode, the counter electrode and the reference electrode, respectively. All electrodepositions were done at a potential of −0.9 V vs. the reference electrode. The durations of the deposition were 20 min. PVK (10 mg/ml) was spin-coated onto ZnO nanorods at 800 r/min. Then films were baked in a vacuum oven for 30 min at 100 °C. A thin layer of poly(3,4-ethylenedioxythiophene)-poly(styrenesulfonate) (PEDOT:PSS) was spin-coated on the PVK film at 2000 r/min. After this step the films were baked in a vacuum oven for 1 h at 120 °C. Finally, Au was evaporated onto the device as the top electrode. The field emission scanning electron microscopy (FESEM) measurements were performed on the Hitachi FESEM S-4800. The optical transmission spectra and the absorption spectra were recorded using a Shimadzu UV-3101PC spectrophotometer. The photoluminescence (PL) measurement was carried out in a JY-630 micro-Raman spectrometer employing the 325 nm line of a He–Cd laser as the excitation source. The photoresponse of the ZnO nanorods/PVK hybrid photodetector was studied using a 150 W Xe lamp, a monochromator, a chopper (EG&G 192), and a lock-in amplifier (EG&G 124A). Current–voltage (*I*–*V*) characteristics of the devices were measured using a Keithley 2400 source meter connected with a GPIB controller to a computer under dark or illumination at 365 nm. PL decay time was measured using an Edinburgh FL 920 Spectrometer, in which the exciting wavelength was 325 nm by using a hydrogen lamp and the PL emission wavelength was probed at 380 nm. All the measurements were carried out at room temperature under ambient conditions.

3. Results and discussion

Fig. 1(a) shows the typical FESEM image of ZnO nanorods almost aligned vertically on the ITO substrate. The diameter and the length of the nanorods are in the ranges of 20–40 and 800–1000 nm, respectively. Fig. 1(b) shows the PL spectra of the ZnO nanorods excited by the 325 nm line of a He–Cd laser. In the PL spectrum, a strong and sharp UV near-band-emission is observed with a peak centered at 378 nm, which is explained by the recombination of free excitons [13,14]. Meanwhile, a weak deep level green emission is found. The origin of the deep level emission in ZnO is not yet clearly understood but is generally

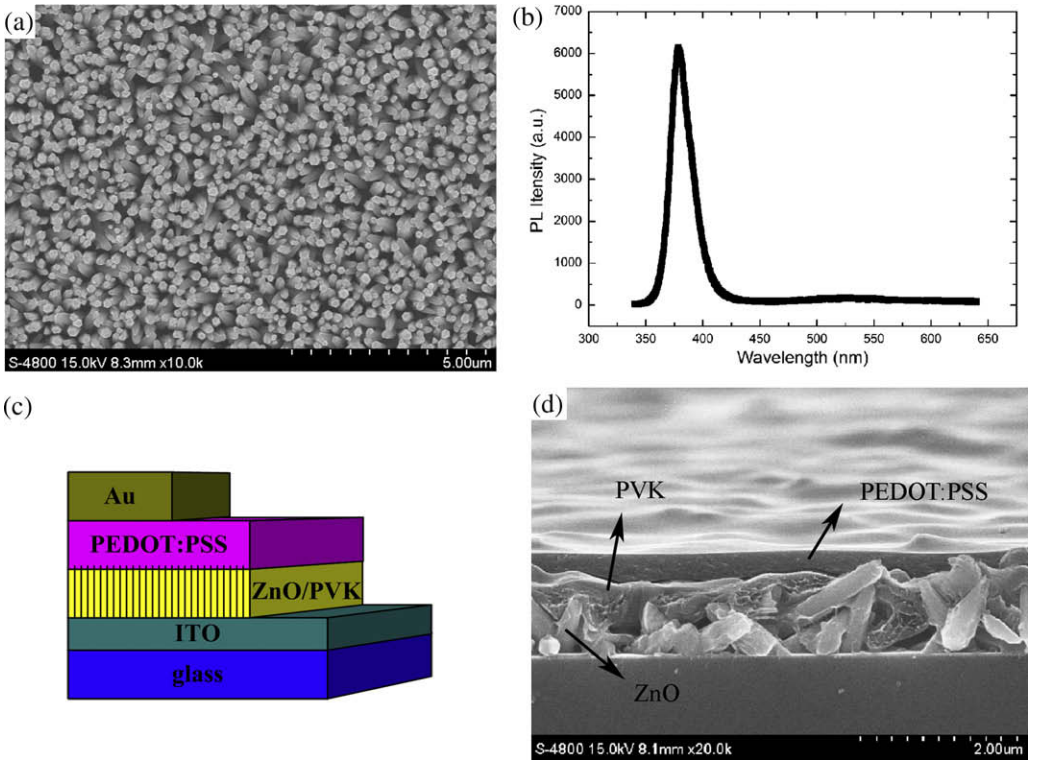

Fig. 1. (a) The FESEM image of ZnO nanorods. The scale bar is 5 μm. (b) The PL spectra of the ZnO nanorods. (c) The schematic diagram of the ZnO/PVK hybrid device. (d) The cross-section field emission SEM images of ZnO nanorods after covered with PVK and PEDOT:PSS by spin-coating. The scale bar is 2 μm.

attributed to structural defects, single ionized vacancies, and impurities [15]. The excellent optical properties of ZnO nanorods, deduced from the strong and sharp excitonic emission and the low deep level emission, indicate that the ZnO nanorods are of high optical quality, making them more suitable for fabricating UV-PDs. Fig. 1(c) shows the schematic diagram of the ZnO/PVK hybrid device. From the cross-section FESEM image shown in Fig. 1(d), different layers could be observed clearly. ZnO nanorods are completely covered with PVK and PEDOT:PSS. And the Au electrode does not directly connected with nanorods, which ensures a junction could be formed between ZnO nanorods and PVK.

The *I–V* characteristics of the ZnO/PVK heterojunction device measured in the dark is shown in Fig. 2. The current density of the device increases gradually with the bias voltage, and a typical *p–n* junction behavior with the clearly rectifying *I–V* characteristics was found, indicating the formation of a *p–n* junction interfaces between the PVK and ZnO nanorods. The *I–V* characteristics of the PD under illumination of a 1.2 mW/cm^2 365 nm UV lamp was also shown in Fig. 2. A maximum current density of 132 μA/cm^2 is obtained at −5 V bias, corresponding to a response of 110 mA/W.

Fig. 3(a) shows the absorption spectra of ZnO nanorods and PVK and the transmission spectrum of the ITO glass. It could be observed that the transmission of ITO glass is as high as 80%, when the wavelength is longer than 350 nm. And there is a sharp absorption edge for the wavelength shorter than 350 nm. For PVK a strong absorption band presents between 320 and 350 nm, and there is no absorption for the light wavelength longer than 360 nm. The absorption spectrum of ZnO nanorods shows a typical semiconductor property. A sharp absorption edge located at 380 nm could be clearly detected. Fig. 3(b) shows the photoresponse spectra of the device illuminated from both the ITO glass and Au electrode sides. As shown in the figure, the photoresponse of the PD illuminated from ITO glass presents a peak at 364 nm with a weak shoulder at around 335 nm. It is interesting to found that the photoresponse is a narrow band with a full width at half maximum (FWHM) of only 26 nm, indicating a high spectrum selectivity property of the PD. At the same time a very sharp cutting-off at about 400 nm is observed in the photoresponse spectrum. The ultraviolet–visible rejection ratio (R364/R400 nm) for the devices is as high as 10^3. While the PD illuminated from Au electrode the photoresponse shows the same shape (shown in the insert of Fig. 3), but a little broader in the short-wavelength region than the one illuminated from ITO glass side. And the intensity of the photoresponse peak is lowered one order of magnitude because of the high reflection for the Au electrode.

Due to the absorption peak of PVK is predominantly located in the range of 320–350 nm, the photoresponse of the PD at 335 nm could be deduced originated from PVK. Based on the absorption and transmission spectra shown in the Fig. 3(a), there are no absorptions for PVK and ITO for the light wavelength longer than 360 nm. Only ZnO has the absorption edge of 380 nm, which is in agreement with other reports [11,16]. Thus, the photoresponse peak located at 364 nm could be attributed to the absorption of the ZnO nanorods. When illuminated from the ITO side the light would meet ZnO at first and most UV light could be absorbed by ZnO nanorods, which induces the photoresponse for the wavelength smaller than 400 nm. A part of UV light with the wavelength shorter than 360 nm could reach the PVK layer to form another photoresponse peak

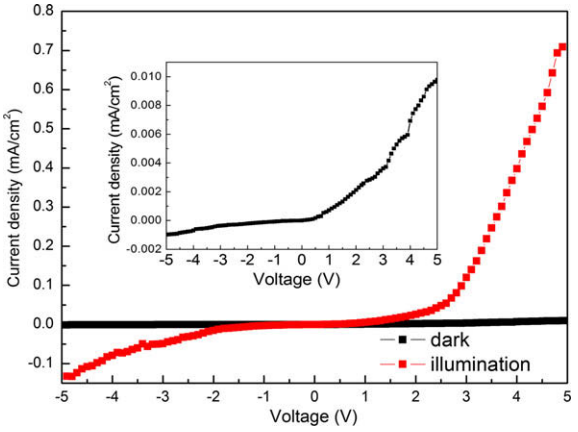

Fig. 2. The current–voltage characteristics of the ZnO/PVK heterojunction diode measured in the dark and under illumination at 365 nm, respectively. The inset shows the current–voltage characteristics of the ZnO/PVK heterojunction diode individually measured in the dark.

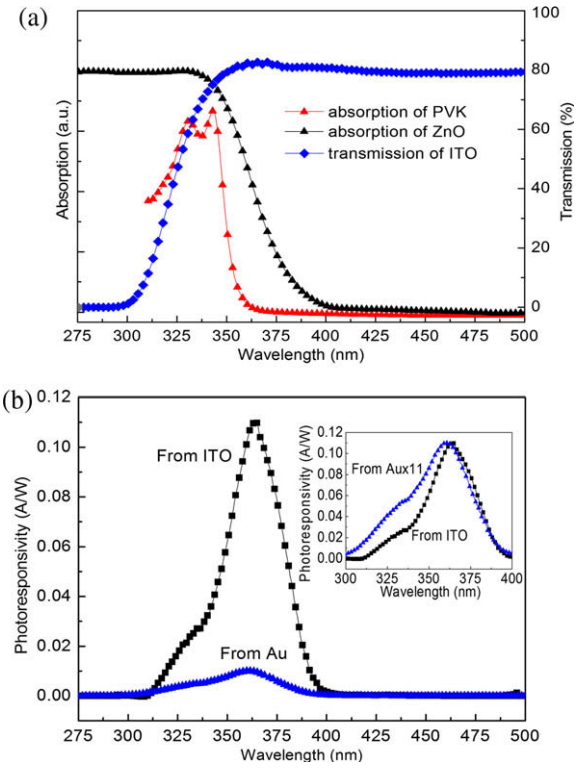

Fig. 3. (a) The absorption spectra of ZnO nanorods and PVK and the transmission spectrum of the ITO glass. (b) The photoresponse spectra of the device illuminated from both the ITO glass and Au electrode. The inset shows the shape comparison of the photoresponse spectra of the device illuminated from the ITO glass and Au electrode.

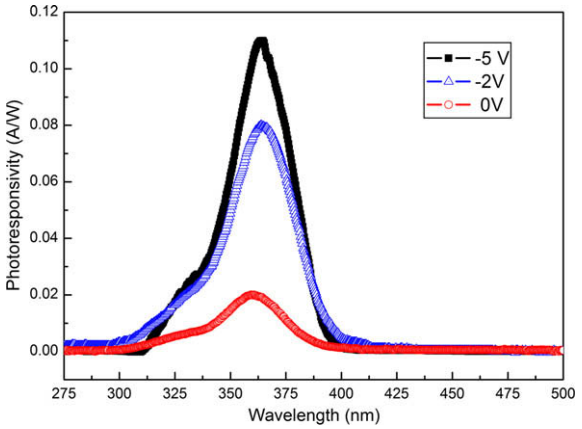

Fig. 4. The photoresponse spectra of the device illuminated from the ITO glass at different biases.

at 335 nm. But when illustrated from the Au side, the light would meet the PVK layer at first, which induced the intensity ratio of the photoresponse peaks located at 335 and 364 nm became increased a little. And in both cases, the ITO glass and the PVK layer serve as filters when the wavelength of the incident light shorter than 350 nm, which induced the weak photoresponse for the device in the short-wavelength region. Fig. 4 shows the photoresponse spectra of the device at different biases, in which the position of the photoresponse band keeps almost unchanged. This result conforms the active region of PDs is ZnO nanorods.

To further understand the charge transfer processes in the ZnO/PVK hybrid system, the PL spectra of the ZnO nanorods, PVK pristine film, and the ZnO nanorods/PVK hybrid film and the PL decay spectra of the PVK pristine film, and the ZnO nanorods/PVK hybrid film were investigated, as shown in Fig. 5. The PL spectra of ZnO nanorods and PVK pristine film showed emission peaks located at 380 and 410 nm, respectively. The PL intensity of the ZnO nanorods/PVK hybrid film is dramatically reduced compared with both the ZnO nanorods and the PVK pristine film, which indicates an efficient charge transfer process from ZnO to PVK and PVK to ZnO. (In order to make the PL spectra comparable, all the condition, such as the sample position, the wide of slid, the power of incident light, et al., were kept the same.)

The transient PL decay measurements were carried out for the PVK pristine film, and the ZnO nanorods/PVK hybrid film. The decay curves were shown in Fig. 5(b). The exciting light was illuminated from the PVK side for the ZnO/PVK hybrid sample. Although from the PL spectra shown in Fig. 5(a), both ZnO and PVK have the PL emission at 380 nm, the signals of the PL decay time measurement were mainly from the PVK layer. By fitting these curves, decay times can be obtained, PVK shows an exponential decay with a decay time of 27.95 ± 0.92 ns. In the ZnO nanorods/PVK hybrid film, a shorter decay time of 21.74 ± 0.76 ns ascribe to PVK were obtained. The shortened lifetimes indicate a new deactivation pathway for the excited state. The ZnO emission decay reflects the charge recombination via radiative and nonradiative processes. With constructing the ZnO/PVK hybrid system an additional pathway is introduced through the electronic coupling in the interface of ZnO and PVK.

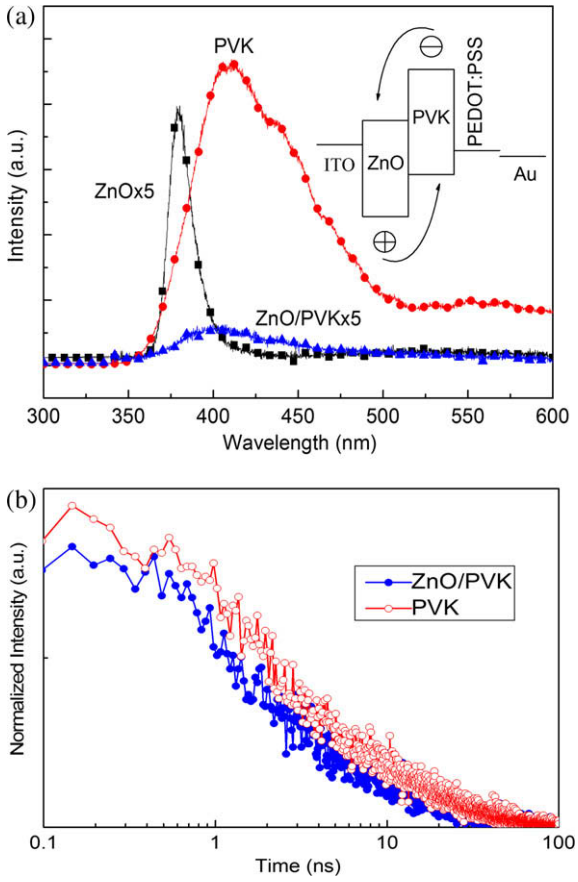

Fig. 5. (a) The PL spectra of ZnO nanorods, PVK layer and ZnO/PVK. The inset shows the corresponding energy levels for the materials used in the hybrid device. (b) The decay curve of PVK and ZnO/PVK hybrid film. The exciting wavelength was chosen at 325 nm, and the PL emission wavelength was probed at 380 nm.

The inset of Fig. 5(a) shows the charge carriers generation processes in the UV-PDs. Under the illumination of UV lamp, photogenerated electron–hole pairs are produced in both ZnO nanorods and PVK. The holes in ZnO nanorods will migrate from the valance band to the highest occupied molecular orbital (HOMO) of PVK due to the higher HOMO of PVK (5.8 eV) than the valance band of ZnO (7.2 eV), while the electrons in PVK will migrate from the LUMO to the conduction band of ZnO due to the lower conduction band of ZnO (4.0 eV) than the LUMO of PVK (2.3 eV) [17]. Then the holes and electrons in the PVK HOMO and ZnO conduction band will transport to the Au and ITO electrodes, respectively. The energy level matching between ZnO and PVK facilitates the fast interfacial charge transfer and increases the separation efficiency of electron–hole pairs and the carrier generation efficiency. Such an interfacial charge transfer between ZnO nanorods and PVK reduces the probability of the recombination of electron and hole. Due to the above charge transfer and separation processes the PL intensity is decreased and the photoresponse is promoted.

4. Conclusions

In summary, high spectrum selectivity visible-blind UV-PD based on ZnO nanorods was demonstrated. The photo-response showed a narrow band centered at 364 nm with a FWHM of only 26 nm. This finding has potential values for further study of high spectrum selectivity and low-cost PD since the complete processes are compatible for large area and flexible substrate fabrications.

Acknowledgments

This work is supported by the Key Project of National Natural Science Foundation of China under Grant No. 50532050, the "973" program under Grant No. 2006CB604906, the CAS Innovation Program, the National Natural Science Foundation of China under Grant No. 60506014.

Reference

[1] M.H. Huang, S. Mao, H. Feick, H. Yan, Y. Wu, H. Kind, E. Weber, R. Russo, P. Yang, Science 292 (2001) 1897.
[2] C.S. Lao, M.C. Park, Q. Kuang, Y. Deng, A.K. Sood, D.L. Polla, Z.L. Wang, J. Am. Chem. Soc. 129 (2007) 12096.
[3] L.E. Greene, M. Law, J. Goldberger, F. Kim, J.C. Johnson, Y. Zhang, R.J. Saykally, P. Yang, Angew. Chem., Int. Ed. 42 (2003) 3031.
[4] A. Tsukazaki, A. Ohtomo, T. Onuma, M. Ohtani, T. Makino, M. Sumiya, K. Ohtani, S.F. Chichibu, S. Fuke, Y. Segawa, H. Ohno, H. Koinuma, M. Kawasaki, Nat. Mater. 4 (2005) 42.
[5] M. Law, L.E. Greene, J.C. Johnson, R. Saykally, P. Yang, Nat. Mater. 4 (2005) 455.
[6] N. Sekine, C.H. Chou, W.L. Kwan, Y. Yang, Org. Electron. 10 (2009) 1473.
[7] S.J. Pearton, D.P. Norton, K. Ip, Y.M. Heo, T. Steiner, Prog. Mater. Sci. 50 (2005) 293.
[8] W.I. Park, J.S. Kim, G.C. Yi, M.H. Bae, H.J. Lee, Appl. Phys. Lett. 85 (2003) 5052.
[9] S.H. Cha, A. Park, K.H. Lee, S. Im, B.H. Lee, M.M. Sung, Org. Electron. 11 (2010) 159.
[10] W.J. Beek, M.M. Wienk, R.A. Janssen, Adv. Funct. Mater. 16 (2006) 1112.
[11] Y.Y. Lin, C.W. Chen, W.C. Yen, W.F. Su, C.H. Ku, J.J. Wu, Appl. Phys. Lett. 92 (2008) 233301.
[12] H.G. Li, G. Wu, M.M. Shi, L.G. Yang, H.Z. Chen, M. Wang, Appl. Phys. Lett. 93 (2008) 153309.
[13] D.M. Baganall, Y.F. Chen, Z. Zhu, T. Yao, M.Y. Shen, T. Goto, Appl. Phys. Lett. 73 (1998) 1038.
[14] S.W. Jung, W.I. Park, H.D. Cheong, G.C. Yi, H.M. Jang, Appl. Phys. Lett. 80 (2002) 1924.
[15] G.C. Yi, W.I. Park, Adv. Mater. 14 (2002) 1841.
[16] D. Zhu, Q. He, H. Cao, J. Cheng, S. Feng, Y. Xu, T. Lin, Appl. Phys. Lett. 93 (2008) 261909.
[17] F. Li, S.W. Cho, D.I. Son, T.W. Kim, S. Lee, Y. Cho, S. Jin, Appl. Phys. Lett. 94 (2009) 111906.

on μCP-OTS is less ordered and exhibits a lower crystallinity compared with P3HT deposited on conventional LPD-OTS. In spite of the lower degree of crystallinity, P3HT FETs fabricated on μCP-OTS exhibit a high field-effect mobility that is comparable to the mobility for LPD-OTS. Furthermore, P3HT FETs on μCP-OTS exhibit even better subthreshold characteristics.

2. Experimental section

A highly doped Si wafer with a 300-nm surface layer of thermally grown SiO_2 was used as a substrate. The substrate was immersed in hot, concentrated H_2SO_4 for 30 min and then repeatedly washed with deionized water, acetone, and hexane in an ultrasonic bath, followed by UV/O_3 cleaning. For the μCP, a poly(dimethylsiloxane) (PDMS) sheet was used as a stamp. The PDMS stamp was immersed in a solution of 50 mM OTS in hexane for 1 h. After removing it from the solution, the PDMS stamp was dried for 10 min and put in contact with the SiO_2 substrate surface for 2 h to fabricate the OTS SAM. The OTS-modified substrate was then rinsed with hexane and ultrasonically cleaned in ethanol for 1 min to remove any excess layers. Finally, the substrate was dried at 100 °C for 5 min. For the LPD, the cleaned Si/SiO_2 substrate was directly immersed in a solution of 10 mM OTS in anhydrous toluene for 7 days, and then rinsed with toluene and ultrasonically cleaned in ethanol for 1 min. Other treatments were the same as those for the μCP-SAMs. All SAM depositions were performed under an N_2 atmosphere with a humidity of approximately 3%. The formation of SAMs on the substrate was confirmed by ellipsometry and water-contact angle measurements. Plexcore OS 1100 P3HT (regioregularity > 95%, average molecular weight = 25,000–35,000, Plextronics, Inc.) was used. P3HT thin films were fabricated onto the OTS-treated substrates by spin coating from 1 wt.% solution in toluene under ambient conditions. The thicknesses of P3HT films were approximately 100 nm on both μCP and LPD SAMs. GIXD measurements were performed at the beam line BL46XU of the SPring-8 synchrotron at the energy of 10 keV. Rocking curves were measured in the secular setup looking at the (1 0 0) peak by Cu Kα X-rays (~8.0 keV) with a rotating target energy of 15 kW.

For FET measurements, gold source and drain electrodes were evaporated onto the P3HT films through a shadow mask. The channel length and width were 50 μm and 1.5 mm, respectively. The FET characteristics of the fabricated devices were measured in ambient conditions after annealing at 150 °C under vacuum for 1 h.

3. Results and discussion

We carefully deposited the SAMs under controlled water conditions to obtain good SAMs with smoother surfaces [15]. Table 1 shows the characteristics of OTS SAMs prepared by the μCP and LPD methods on SiO_2 surfaces. Ellipsometry measurements indicate that both OTS SAMs are slightly thicker than reported values of about 28 Å [16,17]. However, the thicknesses are constant for prolonged deposition of OTS, indicating the formation of well-defined monolayers. Both OTS-treated surfaces have a high water-contact angle and a small root mean square (R_{MS}) roughness, which are comparable to published values [16,17]. No clear differences between both SAMs were observed by these measurements.

Table 1
Ellipsometric thickness, water-contact angle, and RMS roughness of OTS SAMs prepared by μCP and LPD methods.

	Thickness (Å)	Contact angle (°)	R_{MS} (Å)
μCP	30.8	108	4.7
LPD	29.3	108	5.7

Fig. 1(a) and (b) shows the typical transfer characteristics of P3HT FETs on OTS SAMs fabricated by the μCP and LPD methods, respectively. Both devices exhibit good FET characteristics with on/off ratios of over 10^3, but the device with μCP-OTS exhibits a lower subthreshold swing than that with LPD-OTS. The electrical performance of P3HT FETs is summarized in Table 2. We characterized more than 40 devices for each OTS SAM. The field-effect mobilities of the devices on each OTS SAM are almost the same, and are typical of P3HT with similar molecular weight [9,10]. However, the device on μCP-OTS has a smaller negative threshold voltage V_{th} compared with LPD-OTS. Similar negative V_{th} has generally been observed in P3HT FETs with OTS-treated substrates [5,9]. The smaller V_{th} in the device on μCP-OTS indicates a lower density of charge traps at the P3HT/SiO_2 interface [18], which leads to good subthreshold characteristics, as shown in Fig. 1(a).

Fig. 2(a) and (b) shows the out-of-plane and in-plane GIXD patterns of P3HT films spin-coated onto LPD-OTS and μCP-OTS SAMs, respectively. For the P3HT film on LPD-OTS, three orders of intense peaks are observed in the out-of-plane pattern, and the in-plane diffraction displays a distinct (0 1 0) peak. The (h 0 0) and (0 k 0) diffraction peaks of P3HT films are attributed respectively to a lamellar structure caused by interdigitating alkyl side chains and π-stacked polymer backbones that result from the self-organization of P3HT molecules [5].

The results for the P3HT film on LPD-OTS indicate that highly ordered lamellae are preferentially oriented parallel to the substrate (edge-on orientation). Such self-orientation behavior on SAM-treated substrates is consistent with previous reports [5,9,10] and provides efficient π-stacking of P3HT molecules along the substrate surface and enhanced field-effect mobility. In contrast, P3HT orientation on the μCP-OTS is quite different. The out-of-plane diffraction of the P3HT film on the μCP-OTS shows relatively intense (1 0 0), (2 0 0), and (3 0 0) peaks and, in addition, exhibits a clear (0 1 0) peak. For in-plane diffraction, the (0 1 0) peak disappears. This result indicates that μCP-OTS induces face-on orientation of P3HT molecules and decreases π–π stacking along the in-plane direction.

The rocking-curve measurement also reveals the decrease in edge-on oriented structure for P3HT film on the μCP-OTS surface (Fig. 3). The intensity of the (1 0 0) lamella peak for P3HT film on μCP-OTS is weaker than that for P3HT film on LPD-OTS. However, the peak width for P3HT film on μCP-OTS is almost the same as that for

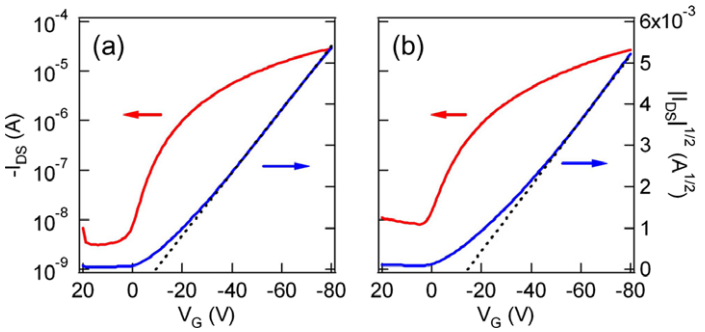

Fig. 1. Transfer characteristics measured in P3HT FETs on (a) μCP-OTS and (b) LPD-OTS SiO_2 dielectrics at a drain voltage of −80 V.

Table 2
Electrical performances of P3HT FETs deposited on OTS SAMs fabricated with the μCP and LPD methods.

	Field-effect mobility (cm^2/Vs)	V_{th} (V)
μCP-OTS	$(3.0 \pm 1.1) \times 10^{-2}$	-4.7 ± 3.4
LPD-OTS	$(3.1 \pm 0.4) \times 10^{-2}$	-12.6 ± 3.5

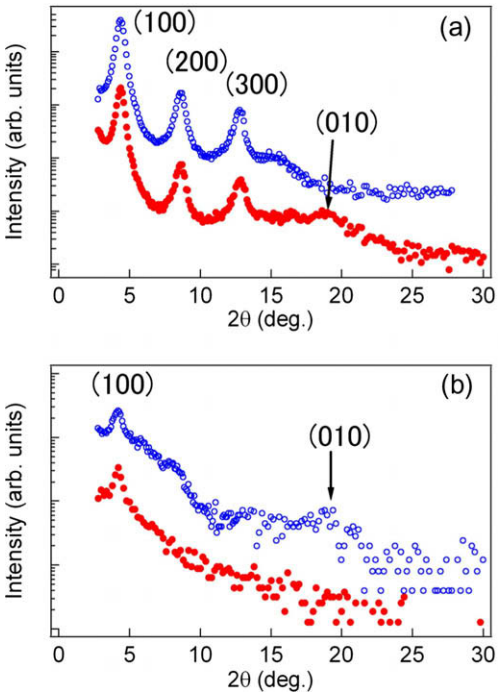

Fig. 2. (a) Out-of-plane and (b) in-plane GIXD profiles for P3HT films on LPD-OTS (upper line) and on μCP-OTS (lower line) SiO_2 dielectrics.

P3HT film on LPD-OTS, indicating that the edge-on structure in P3HT films on μCP-OTS is also less disordered. The results displayed in Figs. 2 and 3 indicate that P3HT film on μCP-OTS exhibits lower crystallinity than P3HT film on LPD-OTS and that P3HT film on μCP-OTS contains crystalline grains oriented face-on as well as edge-on.

It has been widely accepted that the low crystallinity and face-on orientation of P3HT molecules prevent efficient charge transport in the π-stacking direction and significantly decrease field-effect mobility [5,9]. However, our results indicate otherwise. P3HT FETs on μCP-OTS exhibit high mobility comparable to the device on LPD-OTS and exhibit better subthreshold characteristics. The improved subthreshold characteristics observed in the device on μCP-OTS clearly indicate a decrease in the density charge traps, suggesting that the disordered region between crystalline regions strongly affects charge transport in P3HT films with OTS-treated substrates. The influence of grain boundaries has been extensively studied in polycrystalline thin films such as pentacene, and the field-effect mobility in these systems is significantly limited by charge trapping in grain boundaries [19,20].

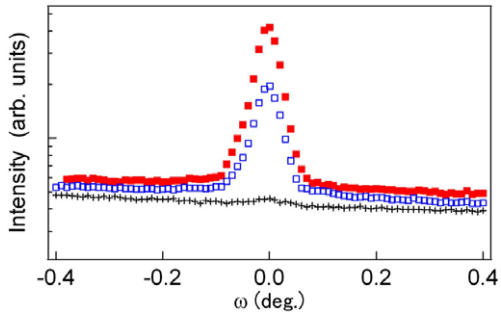

Fig. 3. Rocking curve on the (1 0 0) peaks of P3HT films on LPD-OTS (solid squares), μCP-OTS (open squares), and untreated SiO_2 dielectrics (crosses).

Conversely, the influence of grain boundaries on mobility has been less studied for polycrystalline polymer semiconductors. However, the influence of grain boundaries on charge-carrier transport (similar to that observed in pentacene) has been reported for poly(2,5-bis(3-alkylthiophene-2-yl)thieno[3,2-*b*]thiophene) (pBTTT) [21,22]. The lower subthreshold swing observed in P3HT FETs on μCP-OTS is attributed to charge trapping in a lower density of energetically distributed trapping centers at the grain boundaries [23]. P3HT on μCP-OTS exhibits a lower crystallinity and is less edge-on oriented than P3HT on LPD-OTS, but the field-effect mobility of P3HT FETs on μCP-OTS is almost the same as that of P3HT FETs on LPD-OTS. The results obtained here suggest that the

charge-carrier transport in highly ordered P3HT films is significantly limited by carrier trapping at the grain boundaries, similar to polycrystalline pentacene. In the highly ordered P3HT films on LPD-OTS, the formation of well-ordered P3HT grains can induce a higher degree of disorder at the grain boundaries to relax the strains caused by the adjacent grains with different orientations. The disorder at the grain boundaries causes frequent carrier trapping and hence reduces field-effect mobility. By contrast, the degree of disorder at the grain boundaries is expected to be lower in the less ordered P3HT film on μCP-OTS, which is evident from the improved subthreshold characteristics in P3HT FET on μCP-OTS. Less frequent carrier trapping in case of the lower degree of disorder improves the field-effect mobility in the less ordered P3HT film on μCP-OTS. As a result, the field-effect mobility in the less ordered P3HT film on μCP-OTS is comparable to that in the highly ordered P3HT film on LPD-OTS.

4. Conclusions

We have demonstrated the high performance of P3HT FETs on μCP-OTS. The electrical characteristics are comparable to those of P3HT FETs on LPD-OTS. Surface treatment of the SiO_2 dielectrics with OTS SAMs prepared by the μCP method influences the molecular orientation in the P3HT films, which is quite different from the orientation obtained with the conventional LPD method. The P3HT molecules on μCP-OTS exhibit a lower crystallinity and are less edge-on oriented than those on LPD-OTS, but both P3HT films exhibit almost the same field-effect mobility. The comparable field-effect mobility in P3HT thin films on μCP-OTS originates in the lower density of trapping centers located at the grain boundaries.

Acknowledgement

The synchrotron radiation experiments were performed at the beam line BL46XU at the SPring-8 synchrotron with the approval of the Japan Synchrotron Radiation Research Institute (JASRI) (No. 2009A1773).

References

[1] G. Horowitz, J. Mater. Res. 19 (2004) 1946.
[2] M.L. Chabinyc, A. Salleo, Chem. Mater. 16 (2004) 4509.
[3] H. Katz, Z. Bao, J. Phys. Chem. B 104 (2000) 671.
[4] C. Dimitrakopoulos, P. Malenfant, Adv. Mater. 14 (2002) 99.
[5] H. Sirringhaus, P.J. Brown, R.H. Friend, M.M. Nielsen, K. Bechgaard, B.M. Langeveld-Voss, A.J.H. Spiering, R.A.J. Janssen, E.W. Meijer, P. Herwig, D.M. de Leeuw, Nature 401 (1999) 685.
[6] R.J. Kline, M.D. McGehee, E.N. Kadnikova, J. Liu, J.M. Frechet, Adv. Mater. 15 (2003) 1519.
[7] J.-F. Chang, B. Sun, D.W. Breiby, M.M. Nielson, T.I. Solling, M. Giles, I. McCulloch, H. Sirringhaus, Chem. Mater. 16 (2004) 4772.
[8] H. Yang, T.J. Shin, L. Yang, K. Cho, C.Y. Ryu, Z. Bao, Adv. Func. Mater. 15 (2005) 671.
[9] R.J. Kline, M.D. McGehee, M.F. Toney, Nat. Mater. 5 (2006) 222.
[10] S. Grecu, M. Roggenbuck, A. Opitz, W. Brütting, Org. Electron. 7 (2006) 276.
[11] A. Kumar, G.M. Whitesides, Appl. Phys. Lett. 63 (1993) 2002.
[12] Y. Xia, M. Mrksich, E. Kim, G.M. Whitesides, J. Am. Chem. Soc. 117 (1995) 4576.
[13] C.R. Kagan, T.L. Breen, L.L. Kosbar, Appl. Phys. Lett. 79 (2001) 3536.
[14] M.L. Chabinyc, W.S. Wong, A. Salleo, K.E. Paul, R.A. Street, Appl. Phys. Lett. 81 (2002) 4260.
[15] Y. Wang, M. Lieberman, Langmuir 19 (2003) 1159.
[16] S.R. Wasserman, Y.T. Tao, G.M. Whitesides, Langmuir 5 (1989) 1074.
[17] A.Y. Fadeev, T.J. McCarthy, Langmuir 16 (2000) 7268.
[18] A. Ralland, J. Richard, J.P. Kleider, D. Mencaraglia, J. Electrochem. Soc. 140 (1993) 3679.
[19] A.B. Chwang, C.D. Frisbie, J. Appl. Phys. 90 (2001) 1342.
[20] T.W. Kelley, C.D. Frisbie, J. Phys. Chem. B 105 (2001) 4538.
[21] M.L. Chabinyc, M.F. Toney, R.J. Kline, I. McCulloch, M. Heeney, J. Am. Chem. Soc. 129 (2007) 3226.
[22] B.H. Hamadani, C.A. Richter, D.J. Gundlach, R.J. Kline, I. McCulloch, M. Heeney, J. Appl. Phys. 102 (2007) 044503.
[23] M. Shur, M. Hack, J. Appl. Phys. 55 (1984) 3831.

vacuum-free PSCs [8–10]. The high transmittance of PH500 film also makes it a good electrode for semi-transparent solar cells [11–14]. However, the wettability of the solution on the present layer is a crucial problem in all-solution-processed fabrication of PSCs. For example, the surface of the active layer poly(3-hexylthiophene) (P3HT):[6,6]-phenyl C61-butyric acid methyl ester (PCBM) is really hydrophobic, so that the deposition of the aqueous PEDOT:PSS solution on the surface of P3HT:PCBM by spin-coating becomes difficult. Many methods have been developed recently to solve this problem, including the modification of the wettability of PEDOT:PSS by doping surfactants, such as Zonyl [2], D-sorbital [15] or isopropanol [16]. However, it is known that doping surfactants could possibly decrease the conductivity and the work function of PEDOT:PSS at the same time [2,8,15,16]. Hau et al. reported that they got a PEDOT:PSS (Baytron 4083) film on P3HT:PCBM by spin-coating where the PEDOT:PSS (Baytron 4083) was diluted with isopropyl alcohol and n-butyl alcohol. However, the process needs repetitious thermal treatments, and thus becomes complicated and time-consuming [9,17]. The plasma treatment on P3HT:PCBM was also proposed to make its surface more hydrophilic [7], but this could damage the surface of P3HT:PCBM film. Several novel techniques were also developed to deposit the aqueous PEDOT:PSS onto hydrophobic surface of the active layer of PSCs such as spray-coating process [10], However, the thick films formed from spray-coating lead to non-transparent electrodes and high vacuum process must be used to remove the excess moisture.

In this work, we fabricated semi-transparent inverted PSCs by all-spin-coating vacuum-free process. ITO modified by ZnO NPs was used as cathode and PAH-D [18] was introduced as an interfacial layer on the surface of P3HT:PCBM. The aqueous PAH-D microgels can be directly spin-coated onto the hydrophobic active layer without any pre-treatment or post-treatment. At the same time, the PAH-D interfacial layer can effectively transfer the surface of P3HT:PCBM from hydrophobic to hydrophilic as well as increase the adhesion and bonding strength between the active layer and the PH500 anode. The photovoltaic performance of the semi-transparent PSCs under top and bottom illumination was investigated and the highest PCE of about 1.86% was achieved under simulated AM 1.5 illumination (100 mW/cm^2) from bottom side with a reflective white paper on the back side. The semi-transparency of Cell A have the potential for use as the subcell of tandem solar cells and power-generating tinted thin-film coatings on windows and other architectural surfaces [11,15]. The all-spin-coating vacuum-free processing provides a possibility for the high-throughput all-solution-processed fabrication of PSCs by roll-to-roll processing [9].

We fabricated two types of PSCs in current work. For all-spin-coating processed PSC (Cell A), patterned ITO (20 Ω) was cleaned by sequential ultrasonic treatment in detergent deionized water, acetone, and isopropyl alcohol for 10 min, respectively, then treated by O_2 plasma for 5 min. A thin layer of ZnO NPs (~50 nm), synthesized using the method described by Beek et al. [19], was spin-coated onto ITO-coated glass. Afterward, a chlorobenzene (CB) solution of P3HT:PCBM (Lumin Tech Inc.) (50 mg/ml) with a weight ratio of 1:0.8 was spin-coated onto the ZnO NPs modified layer to achieve a thickness of 250 nm. Then the film was annealing at 150 °C for 15 min in glove box [4]. Subsequently the aqueous PAH-D (1 mg/ml), synthesized according to the literature [18], was dipped on the surface of the P3HT:PCBM film and spin-coating at 3000 rpm for 30 s. At last a PH500 layer of about 200 nm was spin-coated on the PAH-D film (~10 nm). The active area of Cell A was defined by the overlapped area of PH500 and ITO. For conventional PSC (Cell B), PEDOT:PSS (Baytron P VP A1 4083) was spin-coated onto cleaned patterned ITO glass to form a film of 40 nm and dried at 120 °C for 10 min. Later, a P3HT:PCBM film (~250 nm) was spin-coated onto the top of PEDOT/PSS (Baytron P VP A1 4083) layer and treated by the same methods as Cell A. At last, a patterned LiF (0.6 nm)/Al (100 nm) electrode was deposited by thermal evaporation in vacuum through a shadow mask. Both of Cell A and Cell B have an identical active area of 10 mm^2 which was defined by the overlapped area between the anode and cathode. The current density–voltage (J–V) characteristics were recorded using Keithley 2400 Source Meter in the dark and under simulated AM 1.5 illumination (100 mW/cm^2) by Solar Simulators (SCIENCETECH SS-0.5 K). The transmittance data were measured by UV–Vis–NIR Spectrophotometer (Shimadzu UV 3600). Film thicknesses were measured by Veeco DEKTAK 150 surface profilometer. Atomic force microscopy (AFM) images and root mean square (RMS) roughness were measured by atomic force microscopy (S II Nanonavi probe station 300hv). All fabrication and characterizations were performed in an ambient environment.

The device structure of Cell A is ITO/ZnO NPs/P3HT:PCBM/PAH-D/PH500, which is shown in Fig. 1a. The structure of Cell B is ITO/PEDOT:PSS/P3HT:PCBM/LiF/Al. In the inverted Cell A, ZnO NPs was used as a hole blocking and electron collecting layer which can be more easily processed into thin layer via spin-coating at room temperature compared to the high temperature sol–gel processed ZnO layer [20]. The AFM image of ZnO NPs film on ITO is shown in Fig. 1b. The RMS roughness of ITO coated by ZnO NPs is 2.02 nm which is slightly rougher than that of ITO (1.78 nm).

To investigate the function of the PAH-D layer, the contact angles of P3HT:PCBM surfaces before and after deposing PAH-D were measured by dipping a drop of water on the surface. As shown in Fig. 2a, the contact angles are

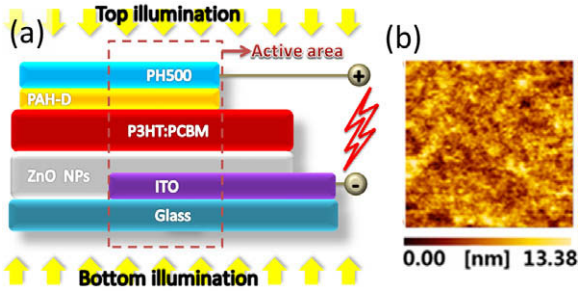

Fig. 1. (a) The schematic structure of Cell A. (b) AFM image of ZnO NPs film, the scan size was 2 × 2 μm^2.

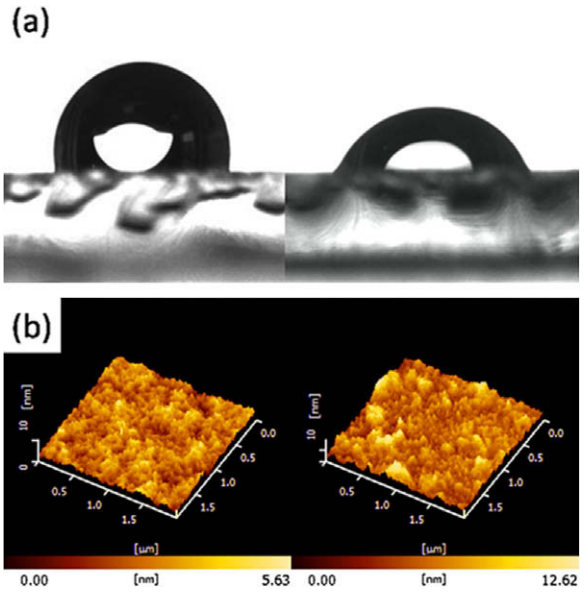

Fig. 2. (a) Pictures of a drop of water on the surface of P3HT:PCBM and P3HT:PCBM/PAH-D. (b) AFM images of the surfaces of P3HT:PCBM and P3HT:PCBM/PAH-D, the scan size was $2 \times 2\ \mu m^2$ and the increment of Z range was 10 nm.

about 101 ± 2° and 62 ± 3° for the surfaces of P3HT:PCBM without and with PAH-D, which means the surface is changed from hydrophobic to hydrophilic after depositing a PAH-D layer. Fig. 2b shows the AFM images of the surface morphologies of P3HT:PCBM without and with PAH-D. The RMS roughness of P3HT:PCBM with PAH-D is 1.99 nm which is slightly rougher than that of P3HT:PCBM without PAH-D (0.86 nm). The deposition of PAH-D on P3HT:PCBM is mainly based on the hydrophobic/hydrophobic interaction between the hydrophobic surface of P3HT:PCBM and the hydrophobic backbone of PAH and dextran in PAH-D microgel where the van der Waals interactions and other multiple weak interactions might contribute to the deposition of PAH-D at the same time [18,21]. The PAH-D microgel is positively charged in aqueous solution due to the amine groups. Therefore, during the spin-coating process of PH500 which contains polyanion PSS, there will be electrostatic interaction between the PSS and PAH-D. This interaction enhances the adhesion and bonding strength between the top PH500 electrode and PAH-D interfacial layer as well as improves the wettability of PH500 on the active layer [18].

The transmittance curves of ITO substrate, PH500 (200 nm) and Cell A with a structure of Glass/ITO/ZnO NPs (50 nm)/P3HT:PCBM (250 nm)/PAH-D (10 nm)/PH500 (200 nm) were shown in Fig. 3. Both of the electrodes ITO and PH500 have a high transmittance over the visible spectral range. While in the spectral region of 400–650 nm, where the main absorption of P3HT:PCBM locates, the transmittance of the ITO-coated glass substrates is 81–87%, about 10% higher than that of PH500 (200 nm) (70–80%). For Cell A, in the spectral region between 300 and 350 nm, the transmittance of Cell A is less than 10% due to the low transmittance of ITO-coated glass substrate. In

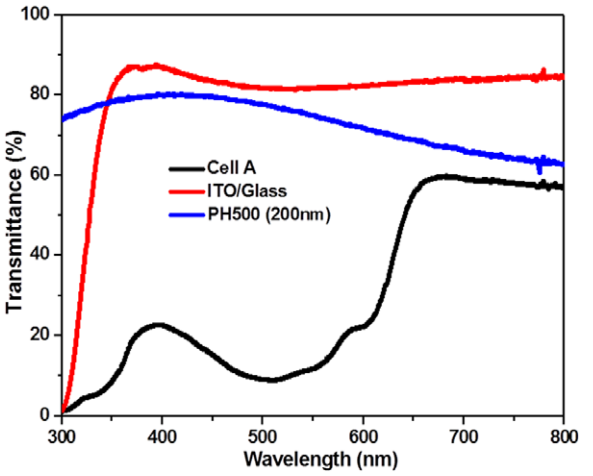

Fig. 3. Transmission spectra of ITO-coated glass substrate (20 Ω), PH500 (200 nm) and Cell A with a structure of Glass/ITO/ZnO NPs (50 nm)/P3HT:PCBM (250 nm)/PAH-D (10 nm)/PH500 (200 nm).

the region between 350 and 600 nm, where the P3HT:PCBM active layer has efficient absorption, the transmittance is mainly in the range of 10–20%. And the transmittance increased from 20% to 60% in the region between 600 and 650 nm. Transmittance of around 60% is found in the region from 650 to 800 nm.

Table 1 presents the overall photovoltaic performance of Cell A and Cell B, while Fig. 4 shows the J–V characteristics of Cell A and Cell B under 100 mW/cm^2 AM 1.5 simulated solar light and in dark. Cell A shows a V_{oc} of 0.58 V, a J_{sc} of 5.18 mA/cm^2, an FF of 42.8% and a PCE of 1.29% under top illumination from PH500 side. The J_{sc}, FF and PCE are 6.10 mA/cm^2, 46.7% and 1.68% when illuminated through glass/ITO side. The increase of PCE of Cell A under bottom illumination is mainly due to the higher J_{sc} caused by the higher transparency of ITO than that of PH500 (200 nm). Because both PH500 anode and ITO cathode are transparent, the J_{sc} of Cell A is sensitive to the light reflection which could be enhanced effectively by simply adding a reflective Al foil or white paper on the back side of the solar cells [8]. As shown in Fig. 4, when a reflector of Al foil or white paper is added on the back side of Cell A and light illuminated from ITO side, the J_{sc} is enhanced from 6.10 to 6.68 mA/cm^2 because of the reflection of the unabsorbed light back into the active layer and the PCE is enhanced from 1.68% to 1.86%.

In order to confirm the performance of Cell A, we measured 30 cells under simulated AM 1.5 illumination

Table 1
Photovoltaic performance of Cell A and Cell B.

Device	Illumination	V_{oc} (V)	J_{sc} (mA/cm^2)	FF (%)	PCE (%)
Cell A	Bottom	0.59	6.10	46.7	1.68
Cell A	Top	0.58	5.18	42.8	1.29
Cell A (paper)	Bottom	0.59	6.68	47.3	1.86
Cell B	Bottom	0.59	7.16	62.1	2.62

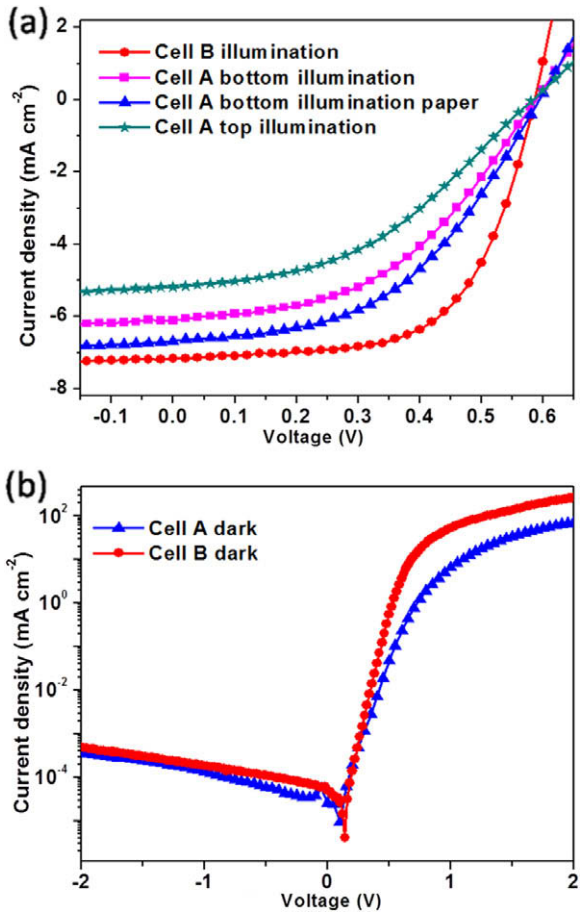

Fig. 4. (a) *J–V* characteristics of Cell B (circle) and Cell A under bottom illumination (square), bottom illumination with a white paper backside (triangle) and top illumination (star) by simulated AM 1.5 solar light (100 mW/cm^2). (b) *J–V* characteristics of Cell A (triangle) and Cell B (circle) in dark.

(100 mW/cm^2) (with a white paper on the back side). According to the statistical results, the J_{sc}, V_{oc}, FF and PCE are mainly in the range of 7.14 ± 0.75 mA/cm^2, 0.58 ± 0.02 V, 45 ± 3% and 1.85 ± 0.15%, respectively.

Cell B exhibited a V_{oc} of 0.59 V, a J_{sc} of 7.16 mA/cm^2, an FF of 62.1% and a PCE of 2.62%. Comparing the performances of Cell A and Cell B, they have the same V_{oc} of about 0.59 V which indicates the introduction of PAH-D layer has little influence on the V_{oc}. The J_{sc} of Cell A (6.68 mA/cm^2) which illuminated from bottom side with a reflector is 6.7% lower than Cell B (7.16 mA/cm^2). The lower J_{sc} is due to the transparency electrode which cannot reflect the unabsorbed light back into the active layer for further efficient absorbance. The FF of Cell A (47.3%) was about 24% lower than Cell B (62.1%) under bottom illumination with a reflective layer. The decrease in FF is mainly due to the higher sheet resistance of the PH500 electrode than the Al electrode [2,9]. We fitted the series resistance of Cell A and Cell B through the forward portion of dark current to be 14.1 and 6.1 Ω cm^2. The higher resistance of Cell A leads to a reduced FF. The lower J_{sc} and FF limited the PCE of Cell A which is about 70 percent that of Cell B.

In conclusion, semi-transparent inverted PSCs were fabricated by all-spin-coating vacuum-free process. A PAH-D layer was introduced to modify the surface wettability of P3HT:PCBM film for depositing the aqueous-solution-processed PH500 anode as well as enhancing the adhesion and bonding strength between the active layer (P3HT:PCBM) and conducting polymer electrode (PH500). The photovoltaic performance of the semi-transparent PSCs under top and bottom illumination was investigated and the highest PCE of about 1.86% was achieved under simulated AM 1.5 illumination (100 mW/cm^2) from bottom side with a reflective layer on the back side which is about 70% that of conventional PSCs. The semi-transparency of Cell A have the potential for use as the subcell of tandem solar cells and power-generating tinted thin-film coatings on windows and other architectural surfaces. The all-spin-coating vacuum-free processing provides a viability of high-throughput all-solution-processed fabrication of PSCs by roll-to-roll processing.

Acknowledgements

This work was supported by the State Key Development Program for Basic Research of China (973 program, 2009CB623605), National Natural Science Foundation of China (50673035), the 111 Project (B06009), Key Project of Science and Technology of Jilin Province (20080305) and Project 20091008 Supported by Graduated Innovation Fund of Jilin University. Prof. Junqi Sun and Dongdong Chen are greatly acknowledged for the supply of PAH-D and helpful discussion.

References

[1] B.C. Thompson, J.M.J. Frechet, Angew. Chem. Int. Ed. 47 (2008) 58–77.
[2] Y.H. Zhou, F.L. Zhang, K. Tvingstedt, S. Barrau, F.H. Li, W.J. Tian, O. Inganas, Appl. Phys. Lett. 92 (2008) 233308.
[3] S.H. Park, A. Roy, S. Beaupre, S. Cho, N. Coates, J.S. Moon, D. Moses, M. Leclerc, K. Lee, A.J. Heeger, Nat. Photonics 3 (2009) 297–303.
[4] G. Li, V. Shrotriya, J.S. Huang, Y. Yao, T. Moriarty, K. Emery, Y. Yang, Nat. Mater. 4 (2005) 864–868.
[5] K. Tvingstedt, S. Dal Zilio, O. Inganas, M. Tormen, Opt. Express 16 (2008) 21608–21615.
[6] S.K. Hau, H.L. Yip, K. Leong, A.K.Y. Jen, Org. Electron. 10 (2009) 719–723.
[7] C. Girotto, B.P. Rand, S. Steudel, J. Genoe, P. Heremans, Org. Electron. 10 (2009) 735–740.
[8] Y.H. Zhou, F.H. Li, S. Barrau, W.J. Tian, O. Inganas, F.L. Zhang, Sol. Energy Mater. Sol. Cells 93 (2009) 497–500.
[9] S.K. Hau, H.L. Yip, J. Zou, A.K.Y. Jen, Org. Electron. 10 (2009) 1401–1407.
[10] Y.F. Lim, S. Lee, D.J. Herman, M.T. Lloyd, J.E. Anthony, G.G. Malliaras, Appl. Phys. Lett. 93 (2008) 193301.
[11] R.F. Bailey-Salzman, B.P. Rand, S.R. Forrest, Appl. Phys. Lett. 88 (2006) 233502.
[12] H. Schmidt, H. Flügge, T. Winkler, T. Bülow, T. Riedl, W. Kowalsky, Appl. Phys. Lett. 94 (2009) 243302.
[13] J. Meiss, M.K. Riede, K. Leo, Appl. Phys. Lett. 94 (2009) 013303.
[14] G.M. Ng, E.L. Kietzke, T. Kietzke, L.W. Tan, P.K. Liew, F.R. Zhu, Appl. Phys. Lett. 90 (2007) 103505.
[15] J.S. Huang, G. Li, Y. Yang, Adv. Mater. 20 (2008) 415–419.
[16] C. Waldauf, M. Morana, P. Denk, P. Schilinsky, K. Coakley, S.A. Choulis, C.J. Brabec, Appl. Phys. Lett. 89 (2006) 233517.
[17] S.K. Hau, H.L. Yip, O. Acton, N.S. Baek, H. Ma, A.K.Y. Jen, J. Mater. Chem. 18 (2008) 5113–5119.

[18] L. Wang, X. Wang, M.F. Xu, D.D. Chen, J.Q. Sun, Langmuir 24 (2008) 1902–1909.
[19] W.J.E. Beek, M.M. Wienk, M. Kemerink, X.N. Yang, R.A.J. Janssen, J. Phys. Chem. B 109 (2005) 9505–9516.
[20] S.K. Hau, H.L. Yip, N.S. Baek, J.Y. Zou, K. O'Malley, A.K.Y. Jen, Appl. Phys. Lett. 92 (2008) 253301.
[21] K. Sato, I. Suzuki, J. Anzai, Langmuir 19 (2003) 7406–7412.

a-Si:H thin-film transistors from the transfer electrical characteristics of these devices measured at different temperatures [10]. The method is based on the analysis of the thermal activation energy of the channel conductance. In particular, the activation energy reduces when increasing the gate voltage as the Fermi level moves towards the band edge. The rate at which the Fermi level shifts when increasing the gate voltage is influenced by the density of localised states in the gap. Then, assuming that charge density within the channel is dominated by trapped carriers, the DOS can be related to the derivative of the activation energy with respect to gate bias. Lang et al. followed the same method to calculate the DOS of single-crystal pentacene field-effect transistors [11]. Research on single-crystal organic semiconductors is interesting because it contributes to establish limits to the device performance based on intrinsic transport properties [12]. Single-crystal devices are also helpful to detect electronic levels in the gap related to contaminants unintentionally incorporated during the growth of the crystal or due to ambient operation [13]. However, real applications are still based on thin-film devices with much higher densities of localised states. Hence, the study of the DOS in OTFTs will give a more accurate description of the trap-limited transport in this kind of devices. In a previous work, our group reported the DOS in the gap of PTCDI-C_{13} active layers used in *n*-channel OTFTs [14]. In this work, we have characterized pentacene OTFTs to study the variation in the DOS of the active layer after a thermal annealing in vacuum. These results are compared to those reported in the literature by different methods for single-crystal and thin-film pentacene devices.

2. Experimental – Fabrication and characterization

The OTFTs studied in this work were fabricated using the inverted-staggered (top contact) structure shown schematically in the inset of Fig. 1. The substrate consisted in a thermally oxidized silicon wafer that provided the gate dielectric (SiO_2) of thickness (t_{ox}) 150 nm. Pentacene was used as purchased from Aldrich Chemical (99.9% purity) and neither self-assembled monolayers were used to improve the device performance. The pentacene active layer (50 nm) was deposited in a vacuum system with base pressure below 10^{-6} mbar that is only used to evaporate organic molecules. The sublimation temperature for pentacene was regulated near to 160 °C to maintain a stable deposition rate around 0.5 Å/s. After pentacene deposition, the samples were exposed to air for a few minutes while they were transferred to a different vacuum chamber used to evaporate the metallic contacts. The drain and source gold electrodes were obtained using a shadow mask that defines a channel length (L) and width (W) of 50 and 600 μm, respectively. The fabricated OTFTs were electrically characterized in dark and under vacuum conditions (10^{-1} mbar) to reduce oxidation effects during the electrical characterization process. The electrical characteristics were measured using an Agilent 4156C parameter analyzer. The device temperature was varied from 300 to 390 K by means of a MMR Technologies controller (model K-20).

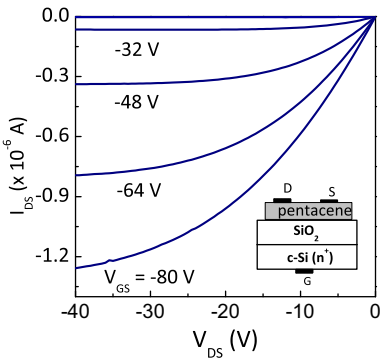

Fig. 1. Output characteristic of one of the fabricated pentacene OTFTs. The inset shows the inverted-staggered (top contact) structure of the studied devices.

The electrical characteristics of organic devices can be strongly influenced by the history of the sample (bias stress, thermal treatments) and by measuring conditions. Factors such as temperature and ambient exposure can lead to significant differences in the measured characteristics, especially concerning subthreshold and leakage currents [15]. Therefore, strict control was taken in order to obtain confident electrical measurements for the OTFTs under study. First, initial tests were performed at room temperature in order to check the correct functioning of the fabricated devices. Afterwards, the samples were heated to 110 °C and annealed for 1 h in vacuum to eliminate any rest of moisture. During the initial temperature rise, the OTFTs were electrically characterized between 30 and 90 °C in 10 °C steps by measuring the output, transfer and saturation characteristics. In order to ensure thermal stabilization, the samples were kept around 20 min at each temperature before doing electrical measurements. Besides, several voltage sweeps were done to check the reproducibility of the electrical characteristics before taking definitive data. These measurements were repeated while the samples slowly cooled down to room temperature. Finally, a second temperature rise and its corresponding electrical characterization were done to observe the effect of the previous annealing on the device performance. Either for temperature rise or fall, each set of complete measurements lasted for approximately 2 h including stabilization times.

3. Results and discussion

Fig. 1 shows the output characteristic of one of the fabricated pentacene OTFTs. The expected electrical characteristics for *p*-channel field-effect transistors were obtained. The field-effect mobility was calculated from a linear fit to the saturation characteristic (not shown) obtaining a relatively high value of 0.41 cm^2/Vs. In a previous work we observed dendritic microstructures for similar pentacene samples, which is a typical feature of device quality films. In particular, X-ray diffraction spectra and atomic force microscopy images revealed a polycrystalline structure with domains of diameter in the range of 100–200 nm [16].

The transfer characteristics were measured at different temperatures during heating and cooling cycles (see

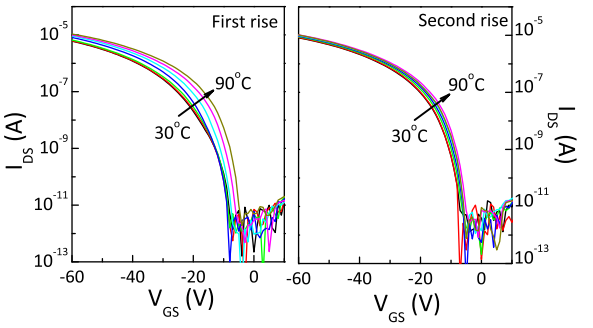

Fig. 2. Transfer characteristics of the pentacene OTFTs measured at different temperatures (from 30 to 90 °C) in vacuum while cooling down the device after an annealing (left) and in a final temperature rise (right). The V_{DS} voltage was −10 V for all these measurements.

Fig. 2) following the procedure described in the previous section. The main differences with temperature were observed for weak accumulation in the above threshold regime. As it can be clearly observed in Fig. 2, the transfer curves spread more during the first temperature rise (left) than in the second one. These differences would indicate that thermal treatments have induced a variation in the DOS of the pentacene active layer. In order to better understand this effect, the drain current has been plotted as a function of the reciprocal temperature (Arrhenius plot) for different gate voltages (inset of Fig. 3). Since the transfer characteristics were measured at a fixed V_{DS} voltage, the drain current is proportional to the conductivity σ of the accumulation channel:

$$I_D = V_{DS} t \frac{W}{L} \sigma \tag{1}$$

where t is the thickness of the channel (typically a few nanometers) [3]. The inset of Fig. 3 evidences that σ presents a thermally activated behaviour $\sigma = \sigma_0 \exp(-E_a/kT)$ with E_a decreasing with the gate voltage in the whole measured range. The activation energy E_a in the MTR model is

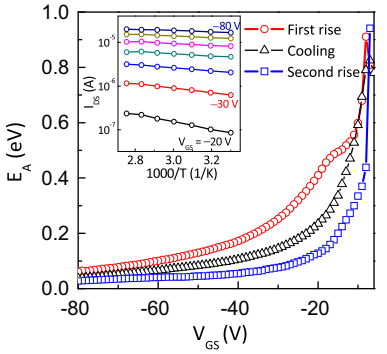

Fig. 3. Activation energy of the channel conductivity as a function of V_{GS} for the transfer characteristics measured during an initial temperature rise, while cooling down the device after a thermal annealing (110 °C for 1 h) and in a last temperature rise. The inset shows the Arrhenius plot of the drain current for different gate voltages corresponding to the first temperature rise cycle shown in Fig. 2. The lines are exponential fits to calculate the activation energy of the channel conductivity.

interpreted as the energy barrier for thermal release of trapped carriers, which can be considered the distance from the Fermi level position to the transport band edge (in this case the valence band). The dependence of E_a with the gate voltage is shown in Fig. 3 for the three measured cycles: during the first temperature rise, while cooling down the samples and in a final temperature rise. The overall behaviour of the activation energy with the gate voltage is similar in all cases. The E_a value is relatively high (0.6 eV) for low gate voltages (just above threshold), but it steadily decreases with V_{GS} until it saturates in a value below 50 meV (strong accumulation). However, the rate at which E_a varies with the gate voltage is clearly different for each curve. A fast variation of E_a with V_{GS} indicates that the Fermi level easily shifts towards the band edge. This behaviour would indicate a low density of localised states that have to be filled by trapped carriers. On the contrary, a high DOS in the gap would result in slower variations of E_a with V_{GS}. Actually, the DOS can be estimated from the derivative of E_a with respect to V_{GS} [10,11]:

$$N(E) = \frac{C_i}{q} \frac{1}{t \frac{dE_a}{dV_{GS}}} \tag{2}$$

where E is the energy measured from the valence band edge, C_i the capacity of the insulator per unit area and q the elementary charge. Eq. (2) has been applied to the data shown in Fig. 3 in order to calculate the DOS in the region from the valence band edge to approximately the middle of the gap (see Fig. 4). A channel thickness (t) of 5 nm has been considered for the calculation according to previous works [3,11]. In all three cases the DOS exponentially increases up to 10^{19} cm^{-3} close to the valence band edge ($E < 0.2$ eV). In analogy to inorganic amorphous semiconductors, this exponential region of the DOS can be assumed as a band tail of localised states induced by structural disorder [3]:

$$N_t(E) = N_0 \exp\left(-\frac{E - E_v}{kT_0}\right) \tag{3}$$

where the slope of the exponential distribution kT_0 is an indirect measure of disorder. A clear difference observed

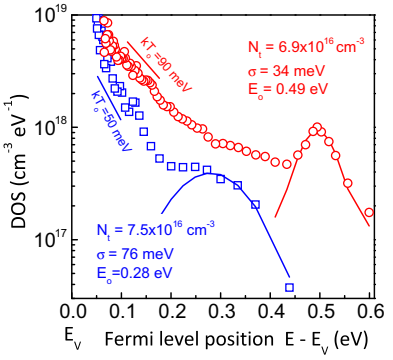

Fig. 4. Density-of-states in the gap of pentacene calculated from the derivative of the activation energy of the channel conductivity in the heating and cooling cycles shown in Fig. 3. The slopes of the exponential band tails (Eq. (3)) and Gaussian fits (Eq. (4)) to the resolved deep level distributions are also indicated.

in Fig. 4 is the broader band tail (kT_0 = 90 meV) for the first temperature rise compared to the second one (kT_0 = 50 meV). Such thinning of the band tail seems to indicate that the thermal annealing done between both measurements has effectively reduced some structural disorder in the pentacene layer. Moreover, the field-effect mobility calculated from the saturation characteristic increased from an initial value of 0.41–0.55 cm^2/Vs. The curve for the cooling cycle is probably affected by thermal quenching effects because release times from deep localised states can be relatively long. Therefore, electrical measurements taken during the cooling cycle were rather likely obtained out of thermal equilibrium and will not be discussed.

Apart from band tails attributed to the intrinsic disorder of pentacene molecules, other features most probably due to extrinsic contaminants can be resolved in Fig. 4. The initial DOS shows a deep level in the gap that can be fitted considering a Gaussian distribution of states:

$$N(E) = \frac{N_d}{\sqrt{2\pi\sigma^2}} \exp\left(-\frac{(E-E_0)^2}{2\sigma^2}\right) \quad (4)$$

where N_d is the total density-of-states related to this defect, E_0 its position in the band gap and σ the standard deviation of the distribution. According to the fit shown in Fig. 4 the defect density is 6.9×10^{16} cm^{-3} and it is located at E_v + 0.49 eV with a standard deviation of 34 meV. This level could not be detected in the final temperature rise for the annealed device. In a previous work [17], charge DLTS measurements on pentacene Schottky diodes also evidenced a deep level after bias stress. As in the present case, a thermal annealing in vacuum was able to heal the defect and prevent its regeneration. Such similar metastable behaviour suggests that both defect levels could be related to a same contaminant. Goldmann et al. [18] have also proposed a deep level in pentacene to interpret the electrical characteristics of single-crystal field-effect transistors after bias stress. They related this defect to water molecules adsorbed to the SiO_2 dielectric, since it could not be detected when a self-assembled monolayer was used to provide a hydrophobic surface. Pernstich et al. [19] determined that a discrete trap at E_v + 0.43 eV was necessary to fit the experimental data reported by Goldmann. Considering experimental uncertainties and that these results were obtained for single-crystal devices, the metastable defect that we observe in Fig. 4 could also correspond to adsorbed water molecules. Then, one might expect that a thermal annealing at 110 °C for 1 h in vacuum would be enough to remove most water content in the OTFT.

On the other hand, a Gaussian distribution of localised states centered at E_v + 0.28 eV can be resolved in the second temperature rise. According to the fit shown in Fig. 4 the density-of-states related to this level is 7.5×10^{16} cm^{-3} with a broader energy distribution of standard deviation 76 meV. Surely, this last distribution was already present in the first rise but hidden by the much wider band tail. Recently, Knipp and Northrup [20] comprehensively studied the electrical characteristics of pentacene OTFTs exposed to oxygen under different bias conditions. They concluded that a Gaussian distribution of acceptor states at E_v + 0.29 eV should be included to fit experimental data. These states were attributed to the dissociation of oxygen and its bonding to carbon atoms of adjacent pentacene molecules. The persistence of this level after a thermal annealing would be in accordance with a strong chemical bond of the contaminant. Actually, a number of studies can be found in the literature reporting levels around E_v + 0.3 eV in pentacene. These works include the electrical characterization of single-crystal pentacene devices [11,21], capacitance DLTS measurements on OTFTs [22] and even theoretical first-principles pseudopotential density functional calculations [23].

4. Conclusions

This study contributes to a more complete understanding of trap-limited transport in OTFTs. The activation energy of the channel conductance as a function of the gate voltage collects valuable information about the DOS in the active layer. Particularly, the DOS from approximately mid gap to the band edge can be calculated in the accumulation channel close to the interface with the dielectric. This approach can be a good complement to more elaborated characterization techniques as DLTS. The method can be applied to thin-film transistors based on any other organic semiconductor offering valuable information about the density of localised states in the gap, either due to structural disorder or related to extrinsic contaminants. In this work, we have studied the effect of a thermal annealing (110 °C for 1 h) in the DOS of pentacene thin-films under vacuum conditions. A deep level in as deposited pentacene was completely healed by the thermal annealing. Desorption of water molecules is a plausible explanation of this metastability. We also observed a reduction in the width of the band tail, which could be interpreted as an enhanced ordering of pentacene molecules due to the annealing process. This effect could be also promoted by the desorption of water molecules that would be disarranging the pentacene structure. Finally, a persistent broad band of localised states around 0.3 eV has been attributed to oxygen atoms strongly bond to pentacene molecules.

Acknowledgements

We acknowledge financial support from the Consolider HOPE project CSD2007-07 of the Spanish government. Work has been partially supported from the European Community's 7th Framework Programme (FP7/2007–2013) under grant agreement no. 227127. We also thank the financial collaboration from XaRMAE of the Generalitat of Catalunya.

References

[1] S.R. Forrest, M.E. Thompson, Chem. Rev. 107 (4) (2007) 923.
[2] C.D. Dimitrakopoulos, P.R.L. Malenfant, Adv. Mater. 14 (2) (2002) 99.
[3] A.R. Völkel, R.A. Street, D. Knipp, Phys. Rev. B 66 (2002) 195336.
[4] N.I. Craciun, J. Wildeman, P.W.M. Blom, Phys. Rev. Lett. 100 (2008) 056601.
[5] G. Horowitz, M.E. Hajlaoui, Adv. Mater. 12 (14) (2000) 1046.

[6] A. Fleissner, H. Schmid, C. Melzer, H. von Seggern, Appl. Phys. Lett. 91 (2007) 242103.
[7] T.P. Nguyen, Mater. Sci. Sem. Proc. 9 (2006) 198.
[8] M.C.J.M. Vissenberg, M. Matters, Phys. Rev. B 57 (20) (1998) 12964.
[9] G. Horowitz, M.E. Hajlaoui, R. Hajlaoui, J. Appl. Phys. 87 (9) (2000) 4456.
[10] T. Globus, H.C. Slade, M.S. Shur, M. Hack, Mat. Res. Soc. Proc. 336 (1994) 883.
[11] D.V. Lang, X. Chi, T. Siegrist, A.M. Sergent, A.P. Ramirez, Phys. Rev. Lett. 93 (8) (2004) 086802.
[12] C. Goldmann, C. Krellner, K.P. Pernstich, S. Haas, D.J. Gundlach, B. Batlogg, J. Appl. Phys. 99 (2006) 034507.
[13] O.D. Jurchescu, J. Baas, T.T.M. Palstra, Appl. Phys. Lett. 84 (16) (2004) 3061.
[14] J. Puigdollers, M. Della Pirriera, A. Marsal, A. Orpella, S. Cheylan, C. Voz, R. Alcubilla, Thin Solid Films 517 (23) (2009) 6271.
[15] Z.T. Zhu, J.T. Mason, R. Dieckmann, G.G. Malliaras, Appl. Phys. Lett. 81 (24) (2002) 4643.
[16] J. Puigdollers, C. Voz, I. Martin, A. Orpella, M. Vetter, R. Alcubilla, J. Non-Cryst. Solids 338–340 (2004) 617.
[17] V. Nádaždy, R. Durný, J. Puigdollers, C. Voz, S. Cheylan, K. Gmucová, Appl. Phys. Lett. 90 (2007) 092112.
[18] C. Goldmann, D.J. Gundlach, B. Batlogg, Appl. Phys. Lett. 88 (2006) 063501.
[19] K.P. Pernstich, D. Oberhoff, C. Goldmann, B. Batlogg, Appl. Phys. Lett. 89 (2006) 213509.
[20] D. Knipp, J.E. Northrup, Adv. Mat. 21 (2009) 1.
[21] D.V. Lang, X. Chi, T. Siegrist, A.M. Sergent, A.P. Ramirez, Phys. Rev. Lett. 93 (7) (2004) 076601.
[22] Y.S. Yang, S.H. Kim, J.I. Lee, H.Y. Chu, L.M. Do, H. Lee, J. Oh, T. Zyung, M.K. Ryu, M.S. Jang, Appl. Phys. Lett. 80 (9) (2002) 1595.
[23] J.E. Northrup, M.L. Chabinyc, Phys. Rev. B (68) (2003) 041202.

zone, whereas has reduced quenching effects in the green emission region.

2. Experimental

The OLEDs consisted of organic multilayers sandwiched between indium tin oxide (ITO) and Al electrodes. The pre-patterned ITO glass substrates (sheet resistance ~15 Ω/□) were sequentially cleaned in acetone, ethanol, and de-ionized water, and then exposed to oxygen plasma for 5 min. The organic films were deposited by high-vacuum thermal evaporation at rates of about 0.1 nm/s. The structure consisted of a 45 nm *N*,*N*′-di(naphth-2-yl)-*N*,*N*′-diphenylbenzidine (NPB) hole transporting layer (HTL), an $Ir(ppy)_3$ EML sandwiched between two 20 nm 4,4′-*N*,*N*′-dicarbazole-biphenyl (CBP) layers, a 15 nm 2,9-dimethyl-4,7-diphenyl-phenanthroline (BCP) hole blocking layer (HBL), and a 15 nm tris-(8-hydroxyquinoline) aluminum (Alq_3) electron transporting layer. Finally, a 0.5 nm LiF and 120 nm Al cathode were deposited on the organic film through a shadow mask. A set of samples was prepared, which differed only in the thickness of the neat $Ir(ppy)_3$ layer from 1 to 26 nm. For comparison, green OLEDs doped with 7 wt.% $Ir(ppy)_3$ as well as OLEDs with a 3 nm neat $Ir(ppy)_3$ EML and a 15 nm 4,4′,4″,-tris(*N*-carbazolyl) triphenylamine (TCTA) EBL were also fabricated. All the devices have an emitting area of 3 mm × 3 mm. The energy level diagram of the OLED structure is schematically shown in Fig. 1. The OLEDs were encapsulated with glass lids in N_2 and characterized at room temperature. The electrical characteristics were measured using an Agilent 4156C semiconductor analyzer. The emission spectra were recorded as a function of injection current in the range of 10^{-5}–10^{-1} A/cm^2 using a silicon photodiode-array fiber-optic spectrometer. To calculate EQE, the OLEDs were placed directly onto the surface of a calibrated silicon photodetector and all emitted photons from the glass side were captured.

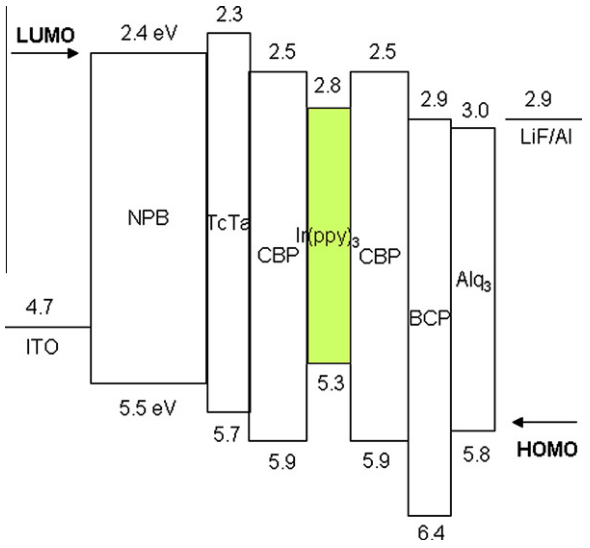

Fig. 1. Energy level diagram of OLEDs with a neat $Ir(ppy)_3$ EML.

3. Results and discussion

Fig. 2 compares the EL spectra of the OLEDs having 4 nm $Ir(ppy)_3$ with and without a TCTA EBL at increasing injection currents. The OLED with TCTA has a recombination zone limited to the $Ir(ppy)_3$ layer, emitting green light with a main peak at 523 nm and a shoulder at ~546 nm. The spectrum exhibits a red shift of ~9 nm with respect to the emission of OLEDs doped with 7 wt.% $Ir(ppy)_3$ as well as an increased tail band at red wavelengths. These are characteristic features of an aggregate state of $Ir(ppy)_3$ molecules [4,7]. At low injection currents (<50 μA), the OLED without TCTA has similar green EL spectra. However, above 50 μA, a broad band emerges at the high-energy side

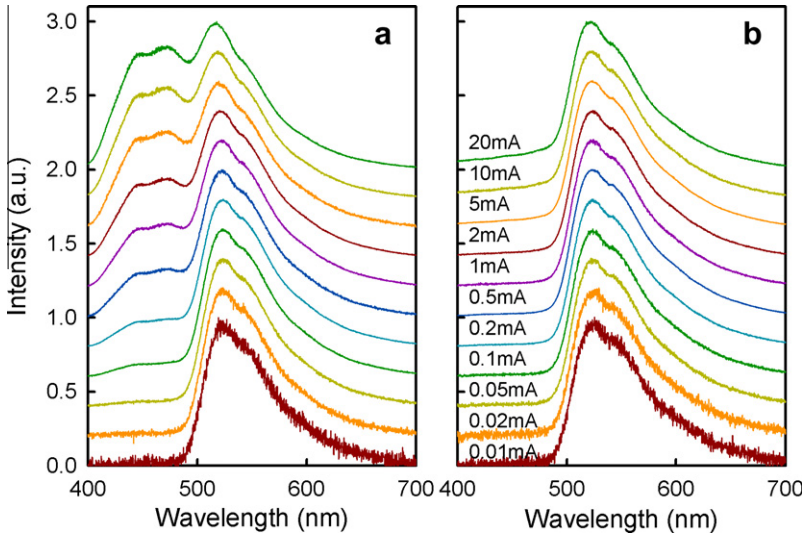

Fig. 2. Normalized EL spectra of OLEDs with and without a TCTA EBL at increasing injection currents. Both OLEDs have a 4 nm neat $Ir(ppy)_3$ EML.

of the main peak, which is attributed to blue fluorescent emission from NPB. The blue band increases rapidly with increasing current, and its intensity is comparable with that of the green emission at 20 mA. It is evident that at elevated injection levels, a significant amount of electrons can surmount the barrier at the NPB/CBP interface and recombine with injected holes in the NPB HTL. In other words, the exciton formation and recombination zone is partially shifted and broadened as the current is increased.

The light output power–current–voltage (*L–I–V*) characteristics of the two OLEDs are displayed in Fig. 3a. As seen, the TCTA EBL causes an additional 1.2 V voltage drop at 20 mA. Interestingly, the OLED without TCTA is roughly twice as bright as its counterpart with TCTA over the tested current range. The current-dependent EQE of the OLEDs is shown in Fig. 3b. At low currents, both OLEDs emit green light and have comparable efficiencies. The EQE of the OLED with TCTA decreases steadily as the current is increased due to increasing quenching effects such as TTA and triplet-polaron quenching (TPQ) [5]. In contrast, the EQE of the OLED without TCTA starts to increase at 50 μA, which marks the onset of electron leakage from the EML to HTL and shift of the recombination zone. It reaches the maximum value at 0.2 mA and then drops significantly at higher currents due to current-induced quenching. It is thus clear that the zone shift caused by electron overflow doubles the chance for excitons to recombine radiatively. The overall emission of both OLEDs is remarkably reduced, as compared to OLEDs doped with $Ir(ppy)_3$, due to strong concentration quenching in neat $Ir(ppy)_3$. The EQE of the OLED with TCTA is found to be one order of magnitude lower than that of OLEDs doped with 7 wt.% $Ir(ppy)_3$ at 10 mA/cm^2.

In order to gain further insight of the underlying luminescence mechanism, we decompose the spectra of the OLED without TCTA into two components: green and blue. An example is shown in Fig. 4. The blue band, which is the subtraction of the scaled spectrum of the OLED with TCTA at 10 mA from the overall spectrum, matches well with the EL of a device which has a simple structure of ITO/NPB/BCP/Al (also shown in Fig. 4). The latter is believed to be dominated by the fluorescence from NPB. The intensity ratio of the green peak and the overall emission is plotted as a function of current in Fig. 5. As seen, the ratio is equal to 1 at low currents and starts to drop at 50 μA. At 20 mA, the green peak accounts for only 53% of the overall emission. Fig. 5 also shows the intensity ratios of green emission of the OLEDs with and without TCTA. The ratios are close to unity at low currents (<0.02 mA), where the current-induced quenching is minimal, as well as high currents (>5 mA), when both OLEDs suffer severely from TTA and TPQ. In the intermediate injection regime, stronger quenching effects can be expected in the OLED with TCTA due to carrier confinement by the electron and hole blockers. Indeed, the green intensity of the OLED without TCTA is considerably higher at moderate currents (by 48% at 0.2 mA), suggesting reduced quenching in the EML as a result of electron overflow. We have found that the efficiencies of the OLEDs with and without TCTA at 20 mA are 12% and 23%, respectively, assuming a unity efficiency for OLEDs with 7 wt.% $Ir(ppy)_3$ randomly doped in CBP. Therefore, in the former, 88% excitons suffer nonradiative decay in the $Ir(ppy)_3$ layer due to quenching. However, we estimate that less than 45% of excitons are quenched in the latter, considering that NPB singlet emission account for 47% of the overall emission as well as only 25% of the excitons (singlets) in NPB can be harvested due to spin statistics.

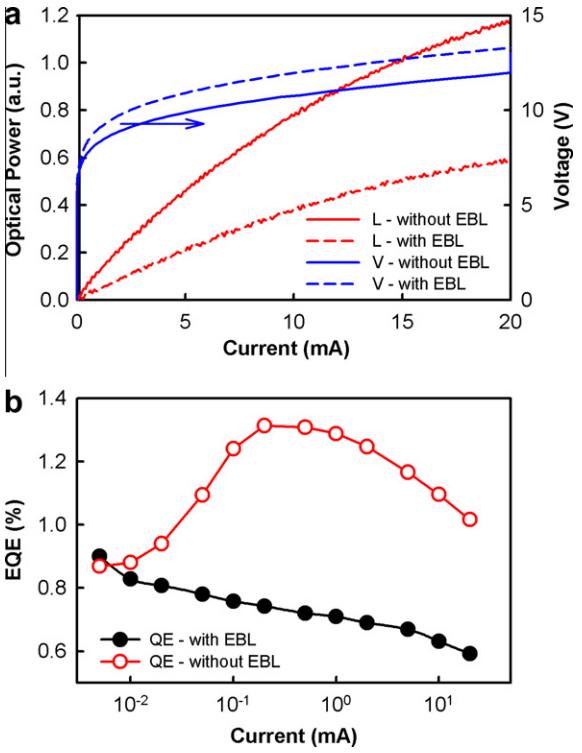

Fig. 3. (a) *L–I–V* characteristics and (b) current-dependent EQE of OLEDs with and without a TCTA EBL. Both OLEDs have a 4 nm neat $Ir(ppy)_3$ EML.

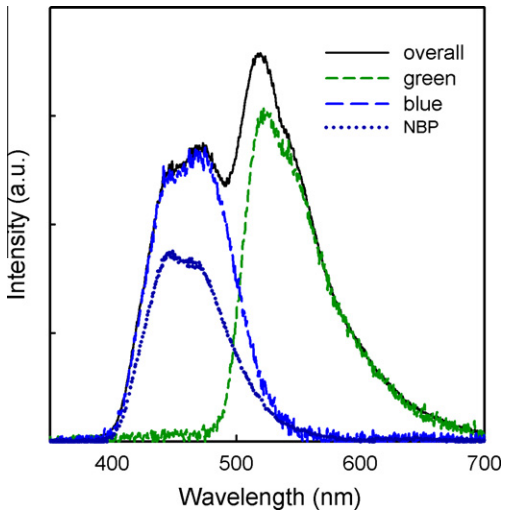

Fig. 4. EL spectrum of $Ir(ppy)_3$-OLEDs without a TCTA EBL at 10 mA, decomposed into blue and green emission components. The fluorescence of NPB is also shown for comparison.

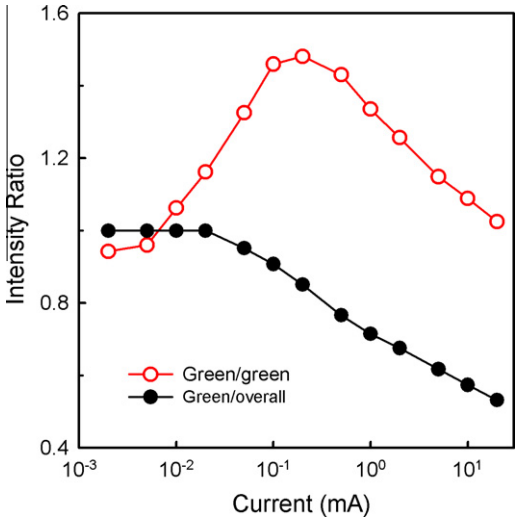

Fig. 5. Intensity ratio of green emission and overall EL of an OLED without a TCTA EBL, along with the intensity ratio of green emission from OLEDs with and without an EBL, as a function of injection current.

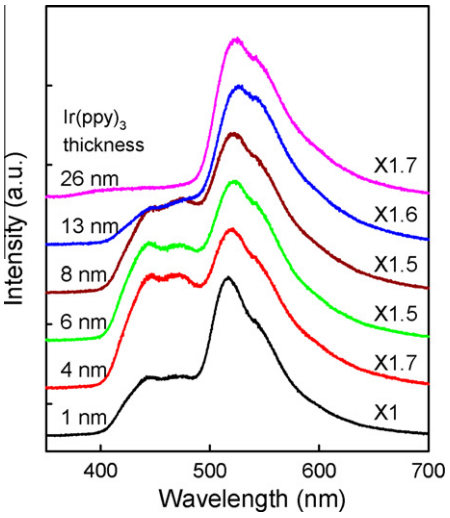

Fig. 7. Normalized EL spectra of OLEDs with a neat $Ir(ppy)_3$ EML of 1–26 nm measured at 10 mA.

To investigate the possible impact of quenching on the distribution of injected carriers and their recombination zone, we characterized OLEDs with the $Ir(ppy)_3$ EML thickness varying from 1 to 26 nm. It was found that the forward voltage increases gradually with increasing $Ir(ppy)_3$ thickness (Fig. 6), suggesting that a small extra bias must be applied to maintain the current transport across the neat $Ir(ppy)_3$ layer. The normalized EL spectra of these OLEDs at 10 mA are depicted in Fig. 7. The OLED with 1 nm $Ir(ppy)_3$ has the highest light output. This is because the EML is less than one monolayer thick, so the $Ir(ppy)_3$ likely forms a partial layer with a relatively small degree of aggregation and concentration quenching. Significant blue emission is seen for OLEDs with $Ir(ppy)_3$ up to 13 nm. With increasing thickness, its relative intensity increases, peaks at 4 nm, and then decreases. Despite a lower overall emission power, the OLED with 4 nm $Ir(ppy)_3$ has an integrated blue intensity ~16% higher than that of the OLED with 1 nm $Ir(ppy)_3$. This unusual behavior suggests that the bands in the 4 nm EML are more easily filled up due to stronger concentration quenching. It appears that, like phosphorescence itself, quenching of phosphorescence in $Ir(ppy)_3$ is also a slow process which increases the dwell time of electrons in the EML, allowing electrons to escape. In other words, electron overflow and the shift of the recombination zone are enhanced by quenching in the $Ir(ppy)_3$ EML.

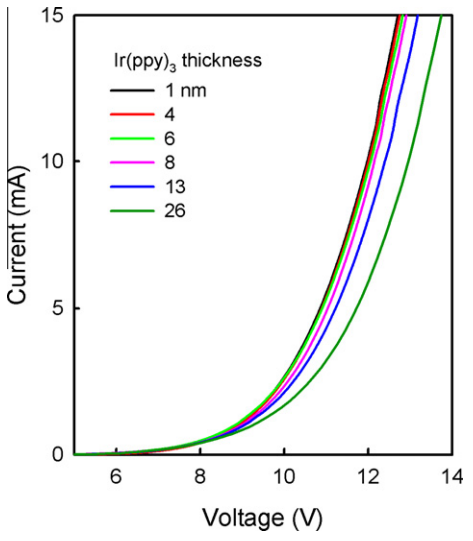

Fig. 6. Forward *I–V* characteristics of OLEDs with a neat $Ir(ppy)_3$ EML of 1–26 nm.

As the $Ir(ppy)_3$ layer grows thicker, the blue emission decreases because the EML functions as a more effective carrier blocking layer due to its low mobilities [12]. As seen, an $Ir(ppy)_3$ layer of 26 nm is able to prevent electrons from overinjection and limit the recombination zone in the $Ir(ppy)_3$ layer. However, the green light emission does not increase with increasing $Ir(ppy)_3$ thickness as expected from the suppressed blue emission. As seen in Fig. 8a, which shows the green emission intensity of the OLEDs at three different currents, plotted as a function of the $Ir(ppy)_3$ thickness. The OLEDs with $Ir(ppy)_3$ >6 nm have nearly constant output power of green light. This may suggest that the effective green emission zone is limited to ~6 nm wide. Since no singlet emission from CBP was observed, singlet and triplet excitons formed on the CBP molecules close to the interface are quickly transferred to $Ir(ppy)_3$ molecules through Förster and Dexter energy transfer, respectively [11]. The latter is a short-range process, whereas the former features long-range energy transfer with the transfer rate k_{Fnr} proportional to $(R_0/R)^6$, where R_0 is the Förster radius and R is the CBP–$Ir(ppy)_3$ spacing. The majority of the excitons are therefore generated on $Ir(ppy)_3$ molecules located near the CBP/$Ir(ppy)_3$ interfaces [13]. The Förster radius between CBP and $Ir(ppy)_3$ has been found to ~3 nm [8]. Assuming that excitons form at both interfaces, the effective $Ir(ppy)_3$ emission zone width should be on the order of 6 nm, which is consistent with

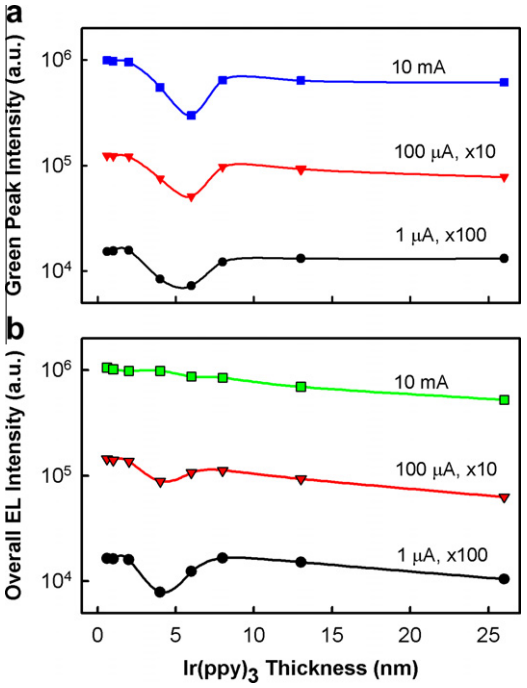

Fig. 8. (a) Green light intensity of OLEDs with a neat $Ir(ppy)_3$ EML of 1–26 nm measured at 1 μA, 100 μA and 10 mA. (b) Overall emission power of the OLEDs as a function of the $Ir(ppy)_3$ thickness at various current densities.

above finding. For OLEDs with thin $Ir(ppy)_3$, both the green light and overall emission (see Fig. 8b) decrease initially and reach the minimum value at 4 nm. In another study, we found that the EL intensity of OLEDs with neat $Ir(ppy)_3$ sandwiched between EBL and HBL also reached the minimum at 4 nm, which marked the saturation of the tail band emission centered at 580 nm as well. Both are indicative of the maximum concentration quenching in the $Ir(ppy)_3$ EML [4]. The correlation between the maximum quenching in the 4 nm EML and the strongest blue emission from the HTL (as seen in Fig. 7) supports our conclusion that electron overflow and zone shifting are enhanced by the quenching effects in the EML. The slight decrease in the overall emission power above 6 nm can be attributed to stronger photon reabsorption and carrier trapping by thicker films.

The fact that the minimum light emission occurs at 4 nm may suggest that the concentration quenching in $Ir(ppy)_3$ mainly arises from a long-range energy transfer from excited molecules to unexcited molecules with a Förster radius $R_0 \approx 4$ nm [4]. One possible mechanism is that dipole–dipole interactions and energy exchange between excited molecules and adjacent unexcited molecules readily occur and repeat for multiple times [3]. The resonant energy transfer may facilitate deactivation processes which account for the loss of most excited state energy to thermal vibrations in neat $Ir(ppy)_3$. Such a quenching process would be even slower than phosphorescence, supporting our earlier hypothesis. When $Ir(ppy)_3$ grows thicker than R_0, the distant molecules will have a minimal quenching impact on the excitons generated mainly near

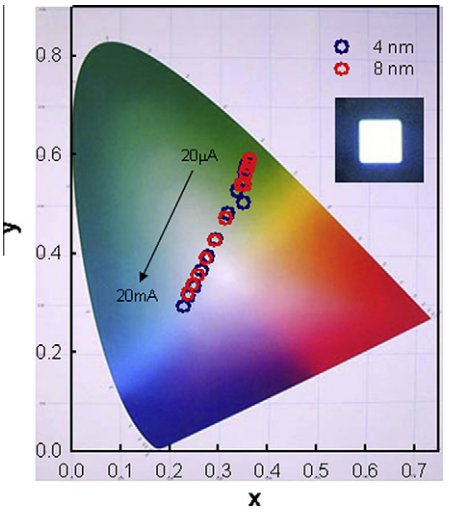

Fig. 9. CIE coordinates of OLEDs with 4 and 8 nm $Ir(ppy)_3$ at various currents. The inset shows a photograph of the OLED with 4 nm $Ir(ppy)_3$ recorded at 5 mA.

the CBP/$Ir(ppy)_3$ interfaces, but still contribute to EL emission if they are still located in the effective green emission zone. Our results also suggest that TTA and TPQ may play a minor role in concentration quenching processes. As the $Ir(ppy)_3$ grows thicker, excitons spread out and are further separated, the rates of TTA and TPQ at the same injection current are expected to decrease. However, this is different from the trend we observed above. This conclusion is also supported by the finding that the quenching magnitude exhibits a very weak dependence on the injection current.

The OLEDs with an $Ir(ppy)_3$ EML of 4–10 nm take advantage of the increased band tail emission at red wavelengths from aggregate $Ir(ppy)_3$ molecules and emit white light. Fig. 9 illustrates the *Commission internationale de l'Eclairage* (CIE) diagram with CIE coordinates of the OLEDs with 4 and 8 nm $Ir(ppy)_3$ at various currents. The coordinates are strongly dependent on current. From 50 μA to 20 mA, the emission color shifts from greenish white to bluish white. At 1 mA, the CIE coordinates of the OLED with 4 nm $Ir(ppy)_3$ are (0.28 and 0.39), corresponding to a cold white light. The efficiency is 6.5 cd/A, which is comparable with the performance of typical white florescent OLEDs [1,14]. A photograph of such a white OLED is shown in the inset. It is known that the color stability of state-of-the-art phosphorescent white OLEDs is limited by the short lifetimes of phosphorescent blue emitters [1]. Based on the results obtained herein, we may envision an alternative cost-effective white OLED concept which combines a stable fluorescent blue emitter and an efficient phosphorescent yellow–green emitter, given that the brightness of different colors can be balanced through good spatial control of the recombination zone.

4. Conclusion

In summary, we studied the influence of concentration quenching on the carrier dynamics in OLEDs with a neat $Ir(ppy)_3$ EML. It has been found that electron overflow from

the EML at elevated currents was enhanced by the quenching effects, leading to a broadened recombination zone and blue emission from the NPB HTL. Combining the blue florescence of NPB and less-quenched yellowish green phosphorescence of $Ir(ppy)_3$, the OLEDs emitted white light with an overall efficiency twice as high as compared to similar OLEDs with an additional TCTA EBL. These findings suggest that concentration quenching in $Ir(ppy)_3$ is probably a slow process involving multistep dipole–dipole energy exchange interactions, allowing for carrier escape from the EML.

References

[1] H. Meng, N. Herron, in: Z. Li, H. Meng (Eds.), Organic Light-emitting Materials and Devices, Taylor & Francis, Boca Raton, FL, 2007, pp. 295–413.
[2] M. Ikai, S. Tokito, Y. Sakamoto, T. Suzuki, Y. Taga, Appl. Phys. Lett. 79 (2001) 156.
[3] Y. Kawamura, K. Goushi, J. Brooks, J.J. Brown, H. Sasabe, C. Adachi, Appl. Phys. Lett. 86 (2005) 071104.
[4] Y.Q. Zhang, G.Y. Zhong, X.A. Cao, J. Appl. Phys., submitted for publication.
[5] M.A. Baldo, S. Lamansky, P.E. Burrows, M.E. Thompson, S.R. Forrest, Appl. Phys. Lett. 75 (1999) 4.
[6] Y. Divayana, X.W. Sun, Phys. Rev. Lett. 99 (2007) 143003.
[7] T. Tsuboi, N. Aljaroudia, Opt. Mater. 30 (2008) 1375.
[8] J. Kalinowski, W. Stampor, M. Cocchi, D. Virgili, V. Fattori, P. Di Marco, Chem. Phys. 297 (2004) 39.
[9] S. Reineke, G. Schwartz, K. Walzer, M. Falke, K. Leo, Appl. Phys. Lett. 94 (2009) 163305.
[10] W. Staroske, M. Pfeiffer, K. Leo, M. Hoffmann, Phys. Rev. Lett. 98 (2007) 197402.
[11] S. Reineke, K. Walzer, K. Leo, Phys. Rev. B 75 (2007) 125328.
[12] N. Matsusue, Y. Suzuki, H. Naito, Jpn. J. Appl. Phys. 44 (2005) 3691.
[13] Y. Sun, N.C. Giebink, H. Kanno, B. Ma, M.E. Thompson, S.R. Forrest, Nature 440 (2006) 908.
[14] J.H. Jou, Y.S. Chiu, R.Y. Wang, H.C. Hu, C.P. Wang, H.W. Lin, Organ. Electron. 7 (2006) 8–15.

excellent film-forming properties upon solution process. Highly efficient white emission (22.3 cd A^{-1}, 11.6%) was obtained from a single emitting layer formed after spin-coating a solution of blue- and red-phosphor co-doped tBu-OXDTFA [10]. However, in these reports, an additional hole-blocking/electron-transporting layer which was made by thermal vapor deposition was introduced into the device structure in order to achieve high efficiency, thus leading to increased fabrication complexity.

In this paper, we demonstrate high performance, single emitting layer small-molecule WOLEDs via solution process. A home-made host material with good solubility in common organic solvents, excellent film-forming ability and high triplet energy (2.88 eV), namely 9,9-bis[4-(3,6-di-tert-butylcarbazol-9-yl)phenyl]fluorene (TBCPF) [19,20], was used as the host material in this study. 1, 3-Bis[(4-tert-butylphenyl)-1,3,4-oxadiazolyl]phenylene (OXD-7) was included in the host to facilitate electron transport [21]. Two or three phosphorescent iridium complexes were doped into the host matrix to enable white light emission. An optimized single active layer device having a pure-white emission shows a maximum luminance efficiency of 20.8 cd A^{-1} (7.2 lm W^{-1}), and a maximum luminance of 26,600 cd m^{-2}. While by adding a hole-blocking/electron-transporting layer, a maximum luminance efficiency of 29.6 cd A^{-1} (15.6 lm W^{-1}), and a maximum luminance of 22,300 cd m^{-2} were obtained. The origin of the efficient white emission and energy transfer in this white-emitting system are also discussed by using photophysical measurements and transient techniques.

2. Experimental

For the device fabrication, a sufficiently cleaned indium-tin-oxide (ITO)-coated glass substrate was treated with O_2-plasma. An approximate 40 nm of poly(ethylendioxythiophene):poly(styrene sulfonic acid) (PEDOT:PSS) was first spun-cast onto the substrate as the hole-injecting layer. The substrates were then taken into a nitrogen glove-box, where phosphorescent dyes doped TBCPF:OXD-7 layer was spin coated onto PEDOT:PSS layer from chlorobenzene solution, and annealed at 100 °C for 30 min, yielding a smooth film with a thickness of approximate 100 nm. For instance, a root mean square (RMS) surface roughness value is 0.86 nm and peak-valley (P-V) value is 7.34 nm (an area of 5 × 5 μm^2) for the triply-phosphorescence-doped light-emitting layer. We used bis(2-(4,6-difluorophenyl)-pyridinato-*N*,$C^{2'}$) picolinate (FIrpic) for blue dye, iridium tris(2-(4-tolyl)pyridinato-*N*,$C^{2'}$) ($Ir(mppy)_3$) for green dye, and iridium bis(1-phenylisoquinoline) (acetylacetonate) ($Ir(piq)_2acac$) for red dye. The substrate was then transferred into an evaporation chamber, where the 2,2′,2″-(1,3,5-phenylene)-tris(1-phenyl-1H-benzimidazole) (TPBI, if needed) was evaporated at an evaporation rate of 1–2 Å/s under a pressure of 8×10^{-4} Pa. The Cs_2CO_3/Al bilayer cathode of the device was formed by the thermal evaporation of Cs_2CO_3 and Al under a pressure of around 1×10^{-3} Pa. The diode area is 9 mm^2.

TBCPF was synthesized in our laboratory [19]. The device architectures and the molecular structures used for fabrication of the devices are shown in Fig. 1.

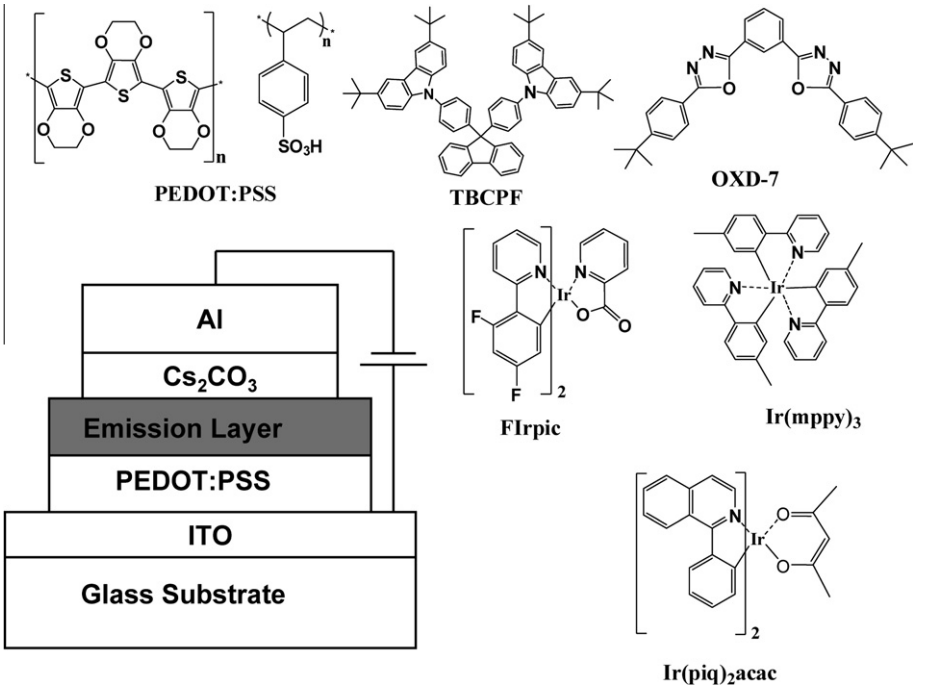

Fig. 1. The device architecture used in this study and the molecular structures of the used materials.

Thin films for photophysical characterization were formed onto quartz substrates by spin-coating chlorobenzene solutions. Absorption spectra were recorded with a UV–vis spectrophotometer (Agilent 8453) and PL spectra were recorded with a fluorospectrophotometer (Jobin Yvon, FluoroMax-3). The transient PL measurements were carried out using steady state and time-resolved fluorescence/phosphorescence spectrometer (FLSP920, Edinburgh Instruments Ltd.). Nanosecond Flashlamp nF900, which operates with a hydrogen gas fill to provide sub-nanosecond optical pulses in 110–850 nm depending on optics and gas fill at repetition rates to 100 kHz, was used as the photoexcitation source. The thickness and surface morphology of the films were measured by using an Atomic Force Microscopy (AFM, Seiko, SPA-400). The *J–L–V* characteristics were performed with a Keithley 4200 semiconductor characterization system. The EL spectra and the CIE coordinators were collected on a spectrophotometer (Photo Research PR705). All the measurements were carried out in air at room temperature without further encapsulation.

3. Results and discussion

3.1. Solution-processed small-molecule WOLEDs characterization

The composition and performance of the all phosphorescent WOLEDs are summarized in Table 1. The blue phosphor FIrpic concentration was maintained at 10 wt.% of the total blend while the weight ratio of TBCPF:OXD-7 was fixed at 2:1. White emission could be realized through carefully adjusting the concentrations of the green and red dyes so as to balance the contributions from different emitters.

For the doubly-doped devices with FIrpic and red dye $Ir(piq)_2acac$, according to the weight ratio of FIrpic:$Ir(piq)_2acac$, devices are designated as Device I (50:1), II (40:1), III (30:1), and IV (20:1). Fig. 2a shows the electroluminescence (EL) spectra at 9.0 V of these devices. Two major peaks at 476 nm, from FIrpic, and 622 nm, from $Ir(piq)_2acac$, and a small shoulder peak at 500 nm, from FIrpic, are observed. There is a monotonous increase in the red emission as the doping concentration of $Ir(piq)_2acac$ relative to that of FIrpic increases from 1:50 to 1:20. As shown in Table 1, the CIE coordinates of devices at 9.0 V fluctuate from (0.332, 0.392) to (0.453, 0.355). Of which, the EL colors of Devices I (0.332, 0.392), II (0.342, 0.366) are close to the ideal CIE coordinates of pure white color.

For the triply-doped structure with different weight ratios of FIrpic:$Ir(mppy)_3$:$Ir(piq)_2(acac)$ (50:1:1, 40:1:1, 30:1:1, 20:1:1, 30:0.5:1, 20:0.5:1), the performances of the corresponding Devices V–X are also summarized in Table 1, the EL spectra of the devices are shown in Fig. 2b. The light emissions are all dominated by the contribution from green emitter $Ir(mppy)_3$ despite its low concentration. The CIE coordinates of all devices, together with the pure white light CIE coordinates of (0.333, 0.333), are shown in Fig. 2c for comparison. Significantly, the emission color remains stable upon the variation of the applied voltage. For instance, Fig. 2d shows the EL spectra and the CIE coordinates of Device II at varied current density. When the current density changes from 15 A m^{-2} to 1650 A m^{-2}, the CIE coordinates of Device II change from (0.352, 0.366) to (0.368, 0.371), all around the white light equi-energy point (0.333, 0.333). From the EL spectra, it can be observed that the relative intensity of the blue component of the emission increases initially with the applied voltage, and then the red emission starts to increase slightly at high applied voltage. We attribute the high color stability of these devices, which is important for illumination, to the simple structure with a single emission layer and the minimized shift of excitons in the recombination zone [22,23].

Table 1
The performance of all-phosphorescent dyes doped white-emitting devices.

Device	Ratio	V_{on} [V][c]	L_{max} [cd m^{-2}][d]	$\eta_{L,\,max}$ [cd A^{-1}][e]	η_L at 2000 cd m^{-2} [cd A^{-1}]	$\eta_{p,\,max}$ [lm W^{-1}][f]	$\eta_{ext,\,max}$ [%][g]	CIE [x,y][h]	CT [K][i]	CRI[j]
I	50:1[a]	4.2	26,000	15.6	15.0	6.3	9.7	0.332, 0.392	5540	62
II	40:1[a]	4.5	27,200	16.0	15.2	5.9	10.5	0.343, 0.366	5145	50
III	30:1[a]	4.6	22,200	10.6	9.7	4.0	7.6	0.392, 0.369	3728	41
IV	20:1[a]	4.9	15,600	7.1	6.3	2.6	5.9	0.453, 0.355	2342	34
V	50:1:1[b]	4.4	26,800	17.1	16.2	6.5	8.1	0.338, 0.475	5405	70
VI	40:1:1[b]	4.8	25,800	18.2	17.4	6.2	8.8	0.351, 0.475	5134	72
VII	30:1:1[b]	4.5	26,600	20.8	19.6	7.2	10.7	0.344, 0.442	5161	75
VIII	20:1:1[b]	4.5	27,300	19.1	18.7	6.9	10.0	0.353, 0.447	5020	74
IX	30:0.5:1[b]	4.7	27,000	16.9	16.4	5.6	8.3	0.387, 0.489	4370	74
X	20:0.5:1[b]	4.6	26,300	17.6	16.1	6.7	9.9	0.424, 0.474	3575	71
XI[k]	30:1:1	4.7	22,300	29.6	28.2	15.6	15.7	0.350, 0.454	5098	76

[a] The doubly-doped devices; the weight ratio of FIrpic:$Ir(piq)_2(acac)$.
[b] The triply-doped devices; the weight ratio of FIrpic:$Ir(mppy)_3$:$Ir(piq)_2(acac)$. FIrpic is fixed at 10 wt.% of the emission layer blend.
[c] Turn-on voltage.
[d] Maximum luminance.
[e] Maximum luminance efficiency.
[f] Maximum power efficiency.
[g] Maximum extern quantum efficiency.
[h] Commission Internationale de l'Eclairage (CIE) coordinates at 9.0 V; observer: 2 degrees.
[i] Color temperature (CT).
[j] Color rendering index (CRI).
[k] For this device with a 20 nm thick TPBI layer inserted between the light-emitting layer (80 nm) and the Cs_2CO_3/Al layer.

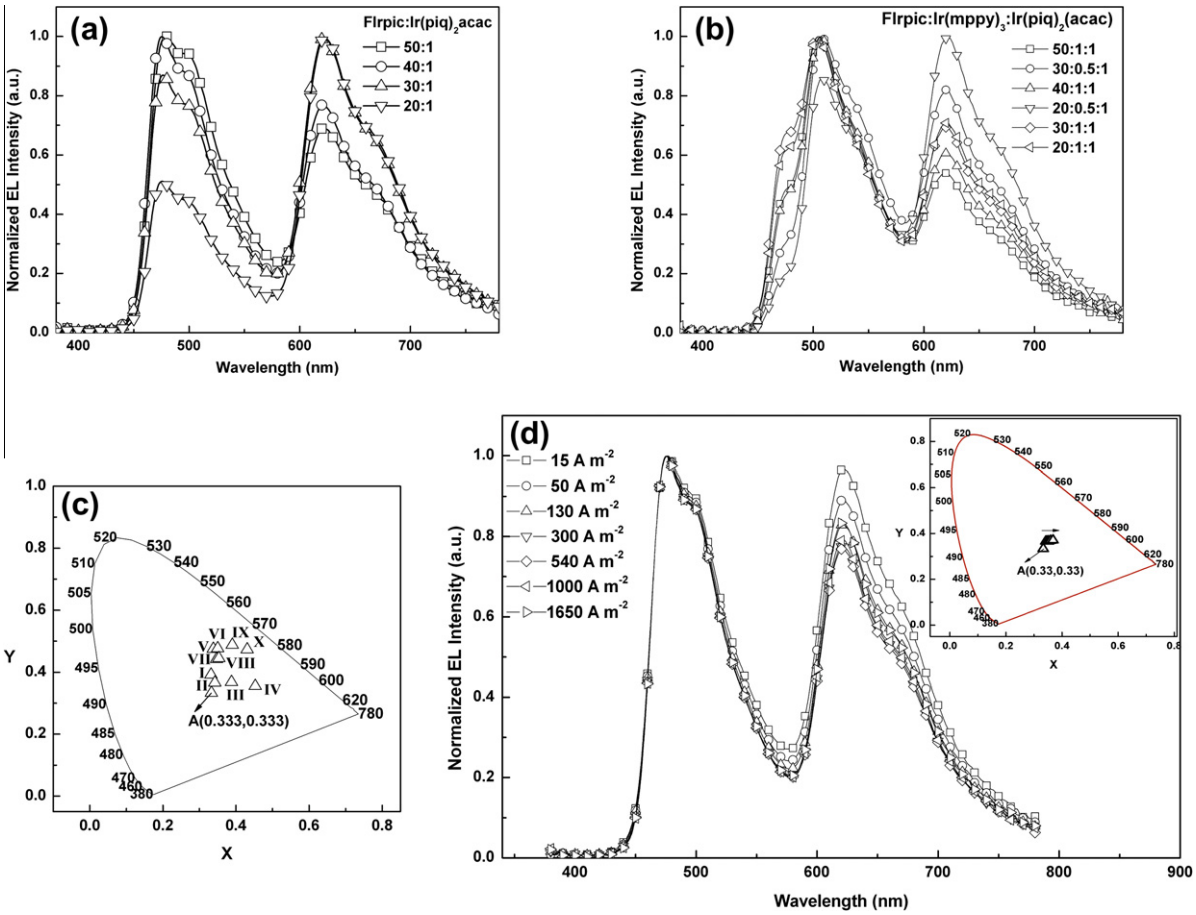

Fig. 2. (a) The EL spectra of the doubly-devices with different ratio of FIrpic to $Ir(piq)_2acac$ at 9.0 V. (b) The EL spectra of the triply-devices with different ratios of FIrpic:$Ir(mppy)_3$:$Ir(piq)_2(acac)$ at 9.0 V. (c) The CIE coordinates of all the WOLEDs at 9.0 V, together with equi-energy white point (0.333, 0.333). (d) The EL spectra and the CIE coordinates (inset) of Device II with different current density.

Current density-luminance-voltage (*J–L–V*) characteristics and luminous efficiency-power efficiency-current density characteristics of Devices I–IV are presented in Fig. 3. Device II is closest to pure-white emission color and is characterized by a maximum forward viewing luminous efficiency of 16.0 cd A^{-1} at 70 A m^{-2} and 8.3 V. Furthermore, the maximum power efficiency of Device II is 5.9 lm W^{-1} at 28 A m^{-2} and 7.4 V. Device II reaches a maximum luminance of 27,200 cd m^{-2} at 15.8 V and 4490 A m^{-2}.

The triply-doped devices with the green emitter $Ir(mppy)_3$ in the emission layer have higher efficiencies than those of doubly-doped devices. This can be explained by the fact that $Ir(mppy)_3$ is a very efficient green emitter. Besides, the photonic response of human eyes to green light is much stronger than those to blue and red lights. Device VII with the CIE coordinates of (0.347, 0.442) at 9.0 V has the best performance with the corresponding efficiencies of 20.8 cd A^{-1} at 65 A m^{-2} and 8.8 V, and 7.2 lm W^{-1} at 34 A m^{-2} and 7.7 V, respectively. Device VII reaches a maximum luminance of 26,600 cd m^{-2} at 14.2 V and 2237 A m^{-2} (Table 1). The high performance could be attributed to the excellent film-forming ability and the high triplet energy of TBCPF as well as charge balance in the emitting layer. It is worth pointing out that these single-active-layer WOLEDs achieved high efficiencies comparable to previously reported solution-processed WOLEDs with an additional thermally deposited hole-blocking/electron-transporting layer [7,10].

To further improve the device performance, a 20-nm-thick hole-blocking/electron-transporting TPBI layer was inserted between the 80-nm-thick light-emitting layer and the cathode with the active layer kept at 100 nm. As shown in Table 1, after the insertion of the TPBI layer, in spite of slightly degraded white color purity, a substantially enhanced luminance efficiency of 29.6 cd A^{-1} with the external quantum efficiency of 15.6% at 22 A m^{-2} and 6.8 V, and 15.6 lm W^{-1} at 6.3 A m^{-2} and 5.3 V, respectively (Device XI). The enhanced performance of double-layer Device XI with a thin TPBI layer are mainly due to the thin TPBI layer as a hole-blocking/electron-transporting layer, and confining the exciton in the emitting layer.

In addition, color quality must be considered if the devices are used for illuminance. As shown in Table 1, the triply-doped Devices V–XI all have appropriate color

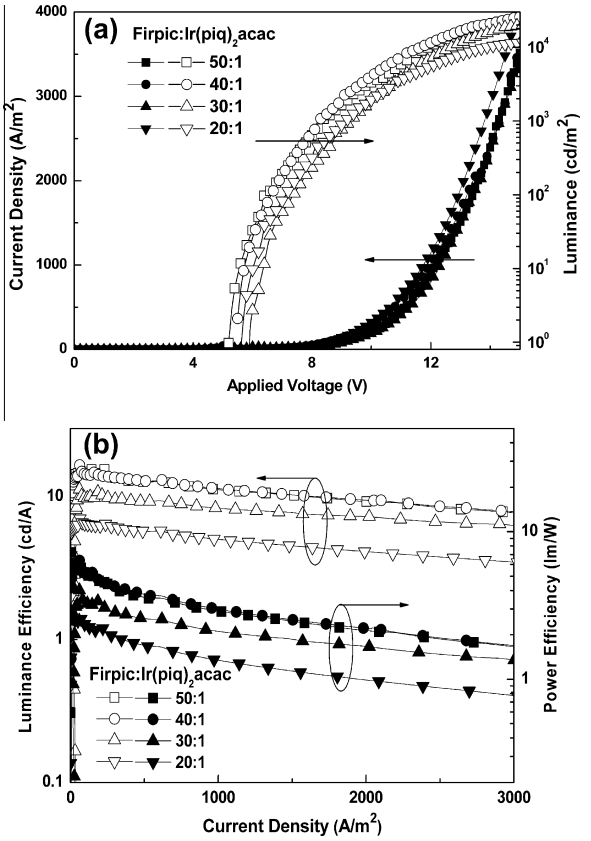

Fig. 3. Current density–luminance–voltage (*J–L–V*) characteristics (a) and luminous efficiency-power efficiency-current density (b) characteristics of the doubly-devices with different ratio of FIrpic to $Ir(piq)_2acac$.

temperature (CT) within 3600–5500 K and relative higher Color Rendering Index (CRI > 70). It is worth noting that single-layer Device VII has a CT value of ~5160 K (which is close to the CT of standard daylight 5500 K) and a relatively higher CRI value of 75.

3.2. Energy transfer mechanism in the single emission layer

Since TBCPF and OXD-7 in the host matrix both have relatively high triplet energy levels, when charge carriers are injected into the single emission layer, two independent processes which are related to the emission of the dopants may occur: energy transfer from the host to the phosphorescent guests via Förster or Dexter process, and charge trapping at the narrow band gap dyes. To understand the energy transfer mechanism in the single white emission layer, photoluminescence (PL) and transient PL decay analyses were employed.

Fig. 4 shows the PL spectrum of TBCPF:OXD-7 in chlorobenzene, absorption spectra of FIrpic, $Ir(mppy)_3$ and $Ir(piq)_2acac$ in chlorobenzene. All complexes exhibit an intense ligand $^1\pi$–π^* absorption band centered around 280–350 nm with a weak absorption band extending from 350 nm to the visible region, which is originated from the metal–ligand charge-transfer (MLCT). The PL spectrum of TBCPF:OXD-7 overlaps well with the MLCT absorption

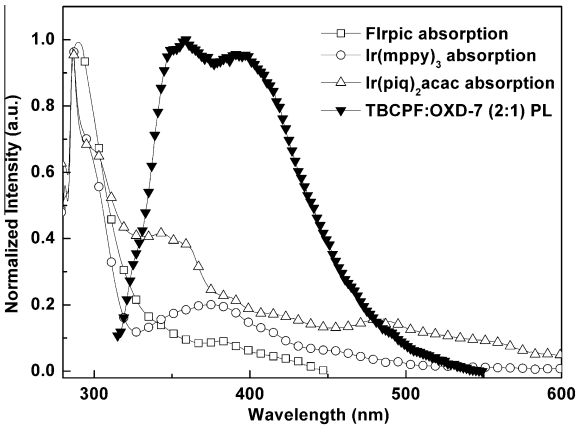

Fig. 4. The PL spectrum of TBCPF:OXD-7 film spun cast from chlorobenzene solution, absorption spectra of FIrpic, $Ir(mppy)_3$ and $Ir(piq)_2acac$ in chlorobenzene solution.

bands of FIrpic and $Ir(mppy)_3$, implying an efficient Förster energy transfer from host to FIrpic and $Ir(mppy)_3$. However, the MLCT absorption of $Ir(piq)_2acac$ is centered around 420–480 nm, which has almost no overlap with the emission spectrum of TBCPF:OXD-7, indicating the Förster energy transfer unlikely occur from the host to $Ir(piq)_2acac$. Moreover, comparing the PL spectra (Fig. 5) from the emission layers with the EL spectra (Fig. 2) of the corresponding devices, the relative intensities of the narrow band gap green and red dyes in EL spectra are both higher than those in PL spectra of films with the same concentration. It indicates that both energy transfer from host matrix to $Ir(mppy)_3$ and charge trapping in $Ir(mppy)_3$ may occur, just as the case of FIrpic in the same host matrix [20]. Charge trapping is regarded to be the dominant process for the formation of $Ir(piq)_2acac$ excitons because of inefficient Förster energy transfer between host and $Ir(piq)_2acac$. In addition, the fact that the host emission peaked at 380 nm was observed in PL but not in EL also supports the presence of charge trapping process in the dye-doped systems.

Fig. 6 gives room temperature time-resolved transient PL decays of the doubly-doped films. For the doubly-doped

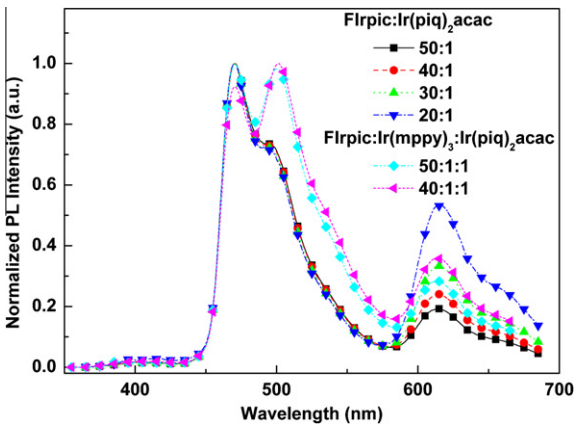

Fig. 5. PL spectra of the films with various ratios of dyes.

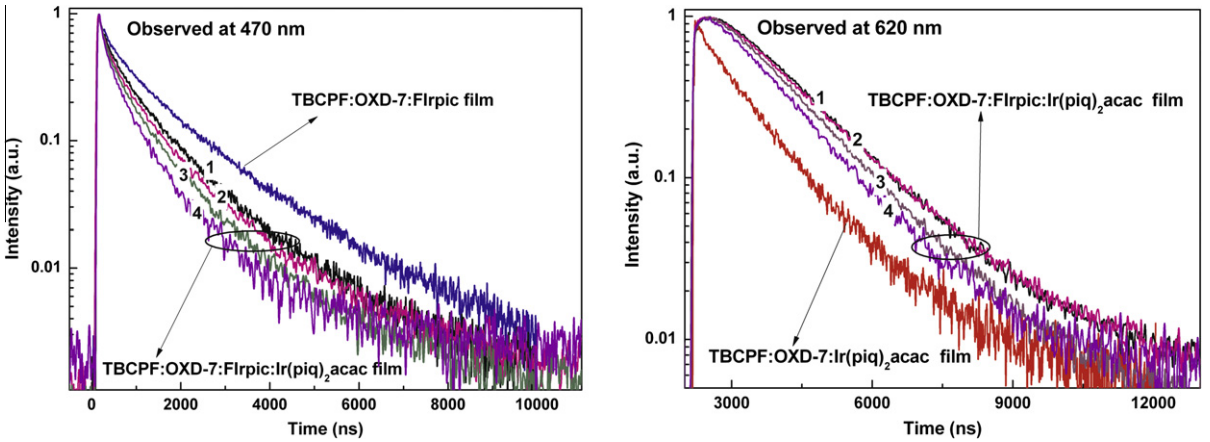

Fig. 6. Room temperature time-resolved transient PL decays for the doubly-doped films with various weight ratios. FIrpic: observed at 470 nm; $Ir(piq)_2acac$: observed at 620 nm. The weight ratios of FIrpic:$Ir(piq)_2acac$ are 50:1(1), 40:1(2), 30:1(3) and 20:1(4), respectively.

system (Fig. 6), the response of FIrpic in the film doped with FIrpic:$Ir(piq)_2acac$ is obviously shorter than that of the only FIrpic-doped film. Moreover, it becomes shorter with the relative weight ratio of $Ir(piq)_2acac$ increases. While the decay of $Ir(piq)_2acac$ in the film doped with FIrpic:$Ir(piq)_2acac$ is much slower than that of the only $Ir(piq)_2acac$-doped film. It means that energy transfer from the triplet of FIrpic to that of $Ir(piq)_2acac$ via Dexter energy transfer process occurs in the co-doped system. By comparing transient PL decays of the films with or without $Ir(mppy)_3$ (Fig. 7), it is noted that the decay of FIrpic in the triply-doped film is faster than that in the doubly-doped film, indicating the presence of Dexter energy transfer process from the triplet of FIrpic to that of $Ir(mppy)_3$. However, the response of $Ir(mppy)_3$ in the triply-doped film is shorter than that of the only $Ir(mppy)_3$-doped film, implying Dexter energy transfer also arises from $Ir(mppy)_3$ to $Ir(piq)_2acac$. Additionally, the decay of $Ir(piq)_2acac$ in the triply-doped film is faster than that in doubly-doped film, because the total Dexter energy transfer to $Ir(piq)_2acac$ decreases in the presence of $Ir(mppy)_3$. The efficient white emission could be attributed to the high triplet energy level of TBCPF and the full utilization of both singlet and triplet excitons.

4. Conclusions

In summary, highly efficient solution-processed single layer white-emitting OLEDs based on small molecules have been realized. For the devices with all-phosphorescent dopants, a maximum luminance efficiency of 20.8 cd A^{-1} and a maximum luminance of 26,600 cd m^{-2} were achieved. After a thin TPBI layer was inserted between the light-emitting layer and the cathode, the maximum efficiency of white emission was further improved to 29.6 cd A^{-1} (15.6 lm W^{-1}). The CIE coordinates of all white-emitting devices, which are all within or close to the white emission region, shift slightly with the variation of the bias voltage. The study on the origin of the white emission demonstrated that energy transfer from the host to the dyes via Förster or Dexter process, the energy transfer from the wide-gap dyes to the narrow-gap dyes via Dexter process, and charge trapping at the phosphorescent dyes all exist in the dye-doped systems. The simplicity of the device structure and the fabrication method, together with the high efficiencies observed, suggests that these white-emitting single layer WOLEDs fabricated by wet process based on small molecules are a promising candidate for low cost and high performance WOLEDs.

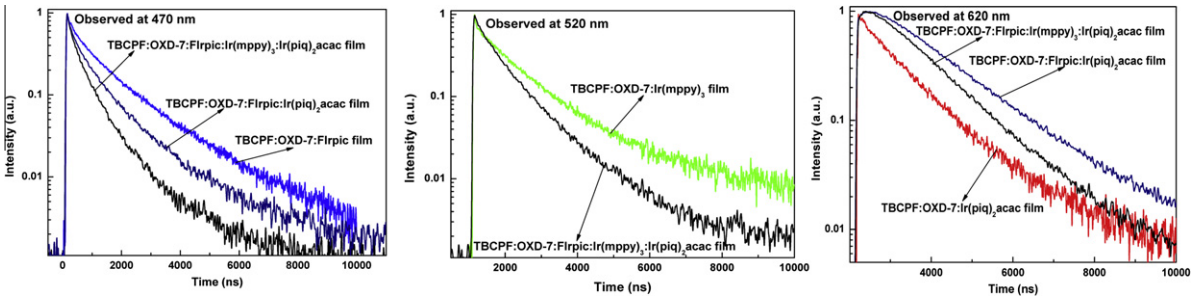

Fig. 7. Room temperature time-resolved transient PL decays for the various dyes doped films with or without $Ir(mppy)_3$. The FIrpic: observed at 470 nm; $Ir(mppy)_3$: observed at 520 nm; $Ir(piq)_2acac$: observed at 620 nm.

Acknowledgements

This work was supported by the National Key Basic Research and Development Program of China (Nos. 2006CB806203, 2009CB930602 and 509,90,060).

References

[1] C.W. Tang, S.A. VanSlyke, Appl. Phys. Lett. 51 (1987) 913.
[2] J. Kido, M. Kimura, K. Nagai, Science 267 (1995) 1332.
[3] B.W. D'Andrade, S.R. Forrest, Adv. Mater. 16 (2004) 1585.
[4] Y.R. Sun, N.C. Giebink, H. Kanno, B.W. Ma, M.E. Thompson, S.R. Forrest, Nature 440 (2006) 908.
[5] M.A. Baldo, D.F. O'Brien, Y. You, A. Shoustikov, S. Sibley, M.E. Thompson, S.R. Forrest, Nature 395 (1998) 151.
[6] J.H. Burroughes, D.D.C. Bradley, A.R. Brown, R.N. Marks, K. Mackay, R.H. Friend, P.L. Burns, A.B. Holmes, Nature 347 (1990) 539.
[7] J.H. Jou, M.C. Sun, H.H. Chou, C.H. Li, Appl. Phys. Lett. 87 (2005) 043508.
[8] D. Pisignano, M. Mazzeo, G. Gigli, G. Barbarella, L. Favaretto, R. Cingolani, J. Phys. D 36 (2003) 2483.
[9] C.L. Ho, W.Y. Wong, G.H. Zhou, B. Yao, Z.Y. Xie, L.X. Wang, Adv. Funct. Mater. 17 (2007) 2925.
[10] C.H. Chien, L.R. Kung, C.H. Wu, C.F. Shu, S.Y. Chang, Y. Chi, J. Mater. Chem. 18 (2008) 3461.
[11] A. Elschner, H.W. Heuer, F. Jonas, S. Kirchmeyer, R. Wehrmann, K. Wussow, Adv. Mater. 13 (2001) 1811.
[12] J.A. Cheng, C.H. Chen, C.H. Liao, Chem. Mater. 16 (2004) 2862.
[13] Y. Hino, H. Kajii, Y. Ohmori, Org. Electron. 5 (2004) 265.
[14] X. Gong, H. Benmansour, G.C. Bazan, A.J. Heeger, J. Phys. Chem. B 110 (2006) 7344.
[15] Z. Ge, T. Hayakawa, S. Ando, M. Ueda, T. Akiike, H. Miyamoto, T. Kajita, M.-a. Kakimoto, Adv. Funct. Mater. 18 (2008) 584.
[16] C.L. Ho, W.Y. Wong, Z.Q. Gao, C.H. Chen, K.W. Cheah, B. Yao, Z.Y. Xie, Q. Wang, D.G. Ma, L.A. Wang, X.M. Yu, H.S. Kwok, Z.Y. Lin, Adv. Funct. Mater. 18 (2008) 319.
[17] S.J. Su, H. Sasabe, T. Takeda, J. Kido, Chem. Mater. 20 (2008) 1691.
[18] S.J. Su, D. Tanaka, Y.J. Li, H. Sasabe, T. Takeda, J. Kido, Org. Lett. 10 (2008) 941.
[19] W. Li, J. Qiao, L. Duan, L. Wang, Y. Qiu, Tetrahedron 63 (2007) 10161.
[20] L.D. Hou, L. Duan, J. Qiao, W. Li, D.Q. Zhang, Y. Qiu, Appl. Phys. Lett. 92 (2008) 263301.
[21] X.H. Yang, F. Jaiser, S. Klinger, D. Neher, Appl. Phys. Lett. 88 (2006) 021107.
[22] Y. Shao, Y. Yang, Appl. Phys. Lett. 86 (2005) 073510.
[23] Y.S. Park, J.W. Kang, D.M. Kang, J.W. Park, Y.H. Kim, S.K. Kwon, J.J. Kim, Adv. Mater. 20 (2008) 1957.

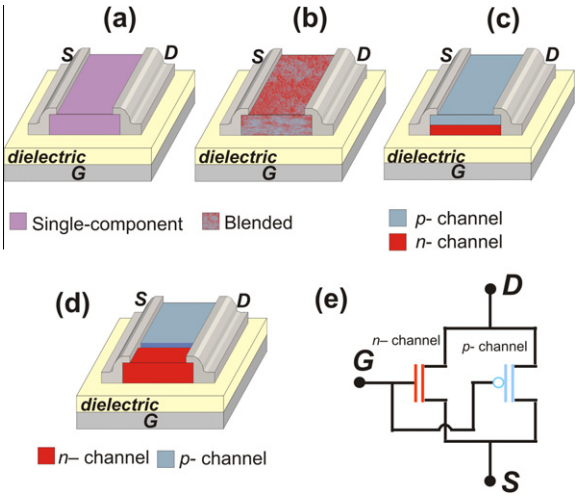

Fig. 1. (a) Ambipolar TFTs geometries: (a) single-component; (b) blended; (c) vertical bilayer; (d) co-planar. (e) Equivalent circuit of an ambipolar TFT with geometry (d) or in the limit of infinite recombination.

In previous ATFT geometries, with a shared channel aspect ratio, this requirement led to the stringent condition of finding a material or material combination with matched electron and hole mobilities. This condition constitutes a major barrier for the realization of ATFTs with balanced operation, particularly when following a hybrid organic–inorganic material approach.

Transparent transition metal-oxide semiconductors, such as ZnO and amorphous-IGZO (a-IGZO), are attractive because they can be processed at low temperatures on flexible substrates and have better electron mobility values and ambient shelf stability than their organic counterparts [9,10]. Amorphous-IGZO is a particularly attractive alternative to *n*-channel organic materials because despite its amorphous morphology, the isotropic nature of the metal *s* orbitals constituting the bottom of its conduction band leads to high electron mobility (10 cm^2/Vs) [9]. Oxide semiconductor-based ATFTs so far rely on the use of hybrid organic–inorganic structures with semiconductor channels vertically distributed (Fig. 1c) because *p*-channel oxide semiconductors that match the electrical performance and low processing temperatures of their *n*-channel counterparts are proving difficult to realize [11]. Such hybrid ATFTs, using pentacene and various metal-oxide semiconductors with vertically distributed channels, have recently been demonstrated [12,13]. However, they either show balanced mobilities during *n*- and *p*- mode operation, $\mu_{n\text{-}op}$, $\mu_{p\text{-}op}$ respectively, with low values in the range of 10^{-2} cm^2/Vs [12,13], or when higher mobility values have been reported ($\mu_{n\text{-}op}$ = 13.6 cm^2/Vs and $\mu_{p\text{-}op}$ = 0.16 cm^2/Vs), the difference in material properties has led to unbalanced ATFT operation [14]. Note that we refer to *p*- and *n*-mode operation to emphasize the fact that this refers to the way an ATFT is biased and not to transport characteristics of its channels.

In this work, we introduce co-planar channel geometry for the realization of ATFTs. Fig. 1d illustrates this geometry, wherein *n*- and *p*-channels, with different aspect ratio, are distributed horizontally without overlapping with each other. In the limit of an infinite recombination rate in the channel, ATFTs operate equivalently to *n*- and *p*-channel TFTs connected in parallel [15]. Fig. 1e shows the equivalent circuit in such a limit. The proposed ATFTs physically realize this geometry. Furthermore, in this geometry, the differences in electron (μ_e) and hole (μ_h) mobility, and threshold voltages are compensated by resizing the aspect ratio of the *n*- and *p*-channels. The absence of a *pn*-heterojunction removes potential problems associated with charge recombination, trapping, and control of the semiconductor morphology at this interface. We show that in this configuration, the number of regimes of operation of an ATFT are increasing from six [15] to eleven, and lead to ATFTs that achieve a high performance because the onset of operation for ambipolar behavior can be controlled. While a similar geometry has been reported in the past [16], a key difference of our approach is that channel resizing allows the implementation of ATFTs with a variety of materials regardless of their relative mobility. This removes a key barrier for the realization of high performance ATFTs since the high charge mobility and optimized performance of unipolar TFTs can be preserved. We demonstrate that the proposed approach leads to hybrid organic–inorganic ATFTs with a performance similar to that of unipolar TFTs, preserving high charge mobility and threshold voltages. Furthermore, despite the large difference in mobility between materials, these ATFTs achieve balanced *n*- and *p*-type operation.

2. Device fabrication and electrical characterization

We fabricated thin-film transistors with a bottom gate top electrode geometry on heavily *n*-doped silicon substrates (*n* + -Si) with a Ti/Au (20/200 nm) layer, deposited with a Kurt J. Lesker electron-beam (AXXIS e-beam) deposition system on the backside, to act as the gate electrode. A 200 nm-thick Al_2O_3 (Al_2O_3, ε_r = 9) layer grown by atomic layer deposition (ALD) (Savannah100, Cambridge Nanotech Inc.) served as the gate dielectric. The Al_2O_3 films were deposited at 110 °C using alternating exposures of tri-methyl-aluminum ($Al(CH_3)_3$) and H_2O vapor at a deposition rate of approximately 0.1 nm per cycle. Each deposition cycle (one monolayer) lasted 24 s, yielding a total deposition time of around 13 h for 2000 cycles [17]. Measurements of the capacitance of metal–insulator-metal (MIM) structures with geometry Au/Al_2O_3/Si/Ti/Au and with areas ranging from 1 to 5 mm^2 yielded a capacitance density of 40 nF/cm^2.

Non-overlapping pentacene (hole transport) and amorphous-InGaZnO (*a*-IGZO) (electron transport) channels horizontally distributed with different aspect ratios were fabricated on top of the Al_2O_3 gate dielectric as shown in the insets of Fig. 3. We deposited a 30 nm-thick *n*-channel *a*-IGZO (Ga_2O_3:In_2O_3:ZnO = 1:1:2 mol%) active layer by rf-sputtering through a shadow mask at room temperature using a power of 125 W, at a working pressure of 5 mTorr, in an O_2/Ar (1/10) atmosphere, and we annealed the devices at 275 °C for 25 min in air. Then, we deposited 50 nm of pentacene as a *p*-channel active layer using thermal evaporation at a deposition rate of 0.3 Å/s, with a

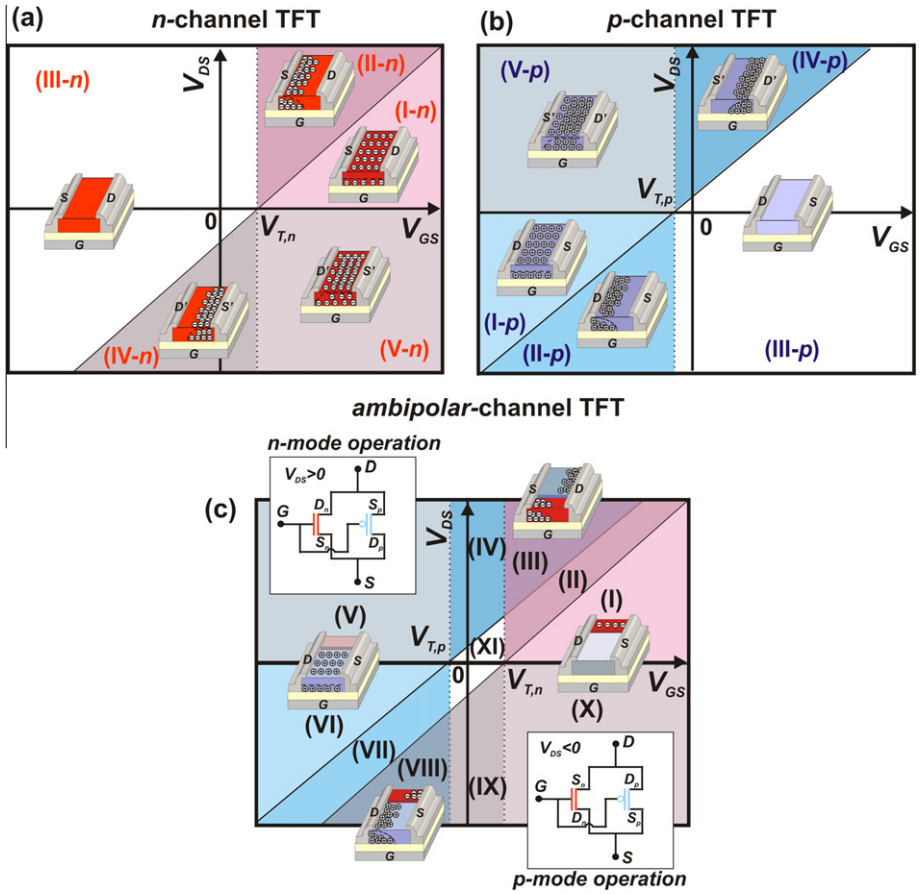

Fig. 2. Charge distributions and energy diagrams under five different regimes found during *n*-channel (a) and *p*-channel (b) operation of TFTs, respectively. (c) Equivalent circuit, 11 different operation regimes, and schematics of charge distributions found during ambipolar TFT operations.

substrate temperature of 25 °C, and at an initial pressure of 2×10^{-8} Torr. Prior to thermal evaporation, we purified pentacene using gradient zone sublimation. The horizontal channels had a channel length of $L = 180$ μm and channel widths of $W^p = 4000$ μm and $W^n = 400$ μm for the *p*- and *n*-channel, respectively. We fabricated independent unipolar pentacene and *a*-IGZO TFTs with the same geometry as reference. The channel width ratio of $W^n/W^p = 10$, was selected to compensate for: 1) differences in μ_e and μ_h; and 2) differences in the threshold voltage observed in unipolar devices.

Finally, we deposited a 50 nm-thick Au film through a metal shadow mask to define the top source/drain electrodes. Gold was used because it provides a similar charge injection energy barrier of $\sim$ 0.6 eV for the injection of holes into pentacene and electrons into *a*-IGZO [18,19]. In ATFTs with a co-planar geometry, further optimization of the injection characteristics can easily be achieved by selecting suitable metals for the source and drain electrodes of each channel. The samples were transferred in a vacuum-tight vessel, to avoid air exposure, into a nitrogen glove box (O_2, $H_2O < 0.1$ ppm) for electrical testing. The output characteristics (drain current I_{DS} vs. drain-source voltage V_{DS} at multiple constant gate-source voltages V_{GS}) and transfer characteristics (I_{DS} vs. V_{GS} at fixed V_{DS}) of the TFTs were measured using an Agilent E5272A medium-power source/monitor unit connected to a probe station.

3. Operation of ambipolar thin-film transistors

Holes, electrons or both can dominate the current flowing through an ATFT depending on the electrical bias across the channel. In the literature, six different regimes have been identified in the operation of an ATFTs by assuming a single threshold voltage for *n*- and *p*-type operation [15]. However, assuming a single V_T is in general not a good approximation for two unipolar TFTs operating in parallel.

In the most general case, the threshold voltage of the *n*-channel ($V_{T,n}$) and *p*-channel ($V_{T,p}$) can be expected to be different. The implications of such a change are better understood by reviewing the operation of unipolar TFTs. Fig. 2a shows the five regimes of operation of an unipolar *n*-channel TFT. For positive V_{DS} values the current varies linearly with V_{DS} if $0 < V_{DS} < V_{GS} - V_{T,n}$ (regime I-*n*), and saturates if $0 < V_{GS} - V_{T,n} < V_{DS}$ (regime II-*n*). These regions are divided by the pinch-off condition defined as $V_{DS} = V_{GS} - V_T$ and represented by the diagonal line in Fig. 2a. If $V_{GS} - V_T < 0$ (regime III-*n*), the TFT is off because the barrier for

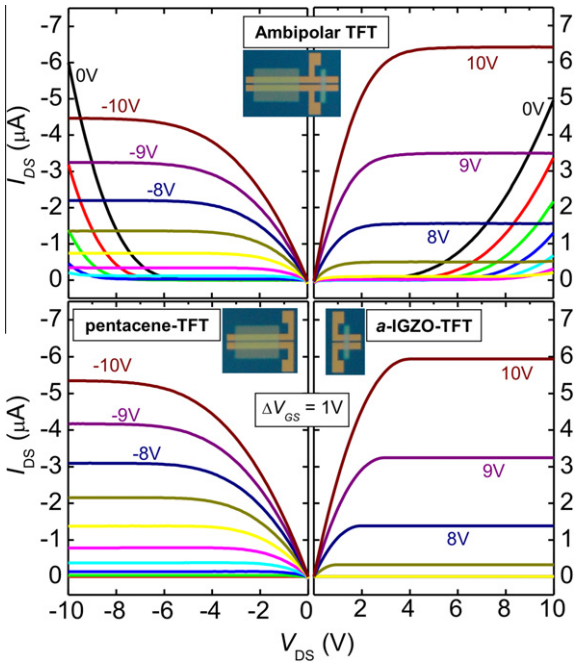

Fig. 3. Comparison of output characteristics of ambipolar TFTs during *p*-mode and *n*-mode operation with corresponding unipolar *p*-channel (pentacene) TFT and *n*-channel (*a*-IGZO) TFT output characteristics. Insets show pictures of the devices.

electron injection from either electrode increases as $V_{GS} - V_T$ becomes increasingly negative. If now we apply a negative V_{DS}, the driving force for electron injection at the drain is larger than at the source electrode. Under this condition, electron currents can flow from the drain to the source. Since the terms drain and source are relative to the direction of current flow, the roles of source and drain are reversed. Therefore, an *n*-channel TFT biased at $V_{DS} < 0$ is being referred to as operating in reverse mode. In reverse mode operation, $S = D'$, and $D = S'$, where the primes denote the effective role played by that electrode. Considering that the source electrode remains grounded, $V_S = 0$ V, the main consequence of this change is that a change in $V_{DS} = V_D - V_S = V_D = V_{S'}$ leads to a simultaneous change of $V_{GS'}$ and $V_{D'S'}$. This implies that for an *n*-channel TFT that follows the square-law model, the current–voltage equations in reverse mode are given by:

$$I(V_{DS} < V_{GS} - V_{Tn} < 0) \propto -(V_{GS'} - V_{Tn})^2 = -(V_{GD} - V_{Tn})^2, \quad (1)$$

$$I(V_{DS} < 0 < V_{GS} - V_{Tn}) \propto -(V_{GS'} - V_{Tn})V_{D'S'} + V_{D'S'}^2 = (V_{GD} - V_{Tn})V_{DS} + V_{DS}^2. \quad (2)$$

These equations describe the current–voltage characteristics of regimes IV-*n* and V-*n*, respectively. If $V_{GS} - V_{T,n} < V_{DS} < 0$, the TFTs remains off (regime III-*n*) due to the large barrier for electron injection at the drain and source electrodes. Fig. 2b shows the analogous five regimes of operation for a *p*-channel TFT.

In the most general case, the current–voltage characteristics of an ATFT arise from the linear superposition of the five operating regimes of its unipolar channels due to its parallel circuit configuration. Fig. 2c shows the eleven operating regimes that result from such a superposition. The key difference provided in this configuration with respect to the previous descriptions of ambipolar TFT behavior, is that two additional regimes exist, regime II (intersection of II-*n* and III-*p*) and VII (intersection of II-*p* and III-*n*), where unipolar currents can reach saturation in one channel without experiencing significant "leakage" currents from the other channel. By displacing the onset of ambipolar operation, regime III (intersection of II-*n* and IV-*p*) and VII (intersection of II-*p* and IV-*n*), a co-planar channel geometry leads to the possibility of controlling the "leakage" currents in ATFTs if the threshold voltages are tailored independently. Note that if $V_{T,n} = V_{T,p}$, the six regimes of operation for an ATFT commonly described in the literature are recovered.

4. Co-planar channel ATFTs

Fig. 3 shows the output characteristics of hybrid ATFTs and of unipolar pentacene and *a*-IGZO TFTs. The relatively high gate-dielectric capacitance density allows all TFTs to reach saturation at low V_{DS}. The drain-source currents (I_{DS}) measured in ATFTs yield values similar to those measured in unipolar TFTs. In contrast with unipolar TFTs, for $V_{GS} < V_{T,n(p)}$ and at large V_{DS}, I_{DS} increases due to "opposite" carrier electron ($-3\text{ V} < V_{GS} < 0$) and hole currents ($0 < V_{GS} < 5$ V) that arise in reverse mode operation. As previously mentioned, the appearance of these "leakage" currents is directly related with the values of the threshold voltages for the *n*- and *p*-channels $V_{T,n(p)}$. As V_{GS} is increased above threshold, I_{DS} monotonically increases due to unipolar operation (regimes I and VI) until it reaches saturation (regimes II and VII) when $|V_{GS} - V_{T,n(p)}| < |V_{DS}|$. Due to channel resizing, the on-currents for the *p*- and *n*-mode operation are well-balanced. Furthermore, since in the saturation regimes II and VII, only one channel remains active in the ATFT, the current–voltage characteristics are nearly identical to those of unipolar TFTs, with no "opposite" carrier contributions even at large $|V_{DS}|$ values.

Fig. 4a shows the overlapping hysteresis transfer characteristics for ATFTs at different values of V_{DS} below saturation. At $|V_{DS}| = 0.5$ V, the transfer characteristics of ATFTs are due to single carrier charge transport in the operating regimes I and II for *n*-mode operation, VI and VII for *p*-mode operation and the regime XI where both channels remain off. This allows the on–off current ratio (I_{on-off}) to approach 10^5 at $|V_{DS}| = 0.5$ V as shown in Fig. 4a. In these regimes the field-effect mobility (μ_{FE}) can be determined through the transconductance, g_m, using the following equation:

$$g_m = (\partial I_{DS}/\partial V_{GS})|_{V_{DS}=\text{small}} = (\mu_{FE}\,\varepsilon_0\,\varepsilon_r\,WV_{DS})/(Ld) \quad (3)$$

where W is the channel width, L is the channel length, ε_0 is the free-space permittivity, ε_r is the dielectric constant of the gate insulator, and d is the thickness of the gate insulator. Fig. 4b shows a direct comparison of the field-effect

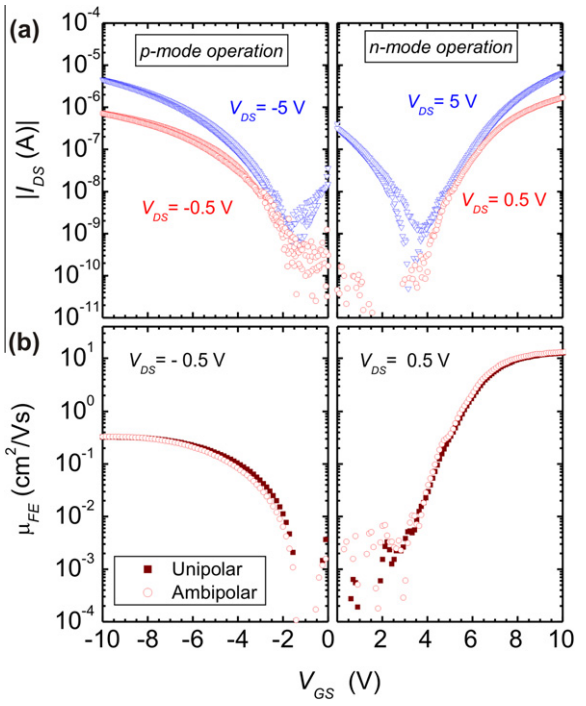

Fig. 4. (a) Hysteresis transfer characteristics at low V_{DS} measured in ambipolar TFT during *p*-mode and *n*-mode operation. (b) Comparison of the field-effect mobility measured in an ambipolar TFT during *p*-mode and *n*-mode operation with that measured on *p*-channel (pentacene) TFT and *n*-channel (*a*-IGZO) TFT in the linear regime.

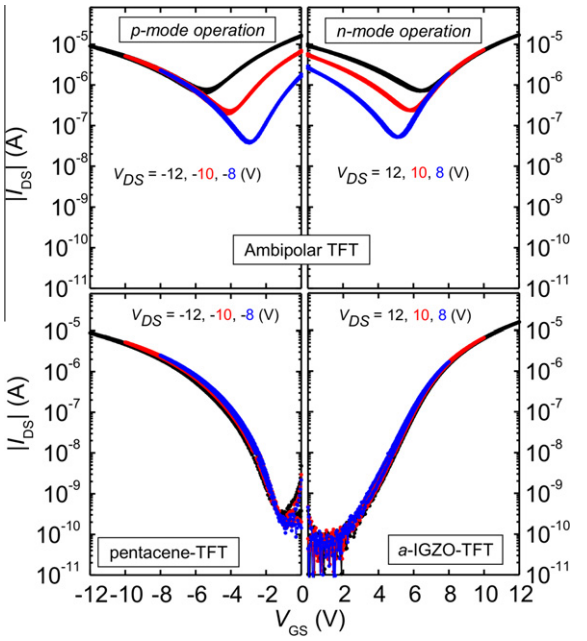

Fig. 5. Hysteresis transfer characteristics in saturation measured in ambipolar TFT during *p*-mode and *n*-mode operation and the corresponding transfer characteristics measured on *p*-channel (pentacene) TFT and *n*-channel (*a*-IGZO) TFTs.

mobility values (μ_{FE}) in ATFTs and unipolar TFTs. Unlike previous approaches, the values of μ_{FE} found in ATFTs equal those in their unipolar counterparts with values approaching $\mu_{p\text{-}op} = \mu_h = 0.3$ cm^2/Vs and $\mu_{n\text{-}op} = \mu_e = 10.5$ cm^2/Vs. Within the resolution of our setup, all parameters between ATFTs and unipolar TFTs are identical in this regime. Close to saturation, at 5 V, I_{on-off} approaches 10^4 despite the increase of the off-currents due to ambipolar operation in regimes III and VIII. Fig. 5 shows that at larger values of $|V_{DS}|$, the I_{on-off} in ATFTs is further reduced due to "opposite carrier" contributions in the ambipolar regimes. This is a typical signature of ATFTs and is expected even if, as in this case, the individual channels of the ATFT show a performance similar to that of unipolar TFTs. However, Fig. 5 also shows that for large enough values of V_{GS}, the values of I_{DS} in these ATFTs rapidly converge to the values found in unipolar TFTs. Since around pinch-off ($|V_{DS}| = |V_{GS} - V_{T,n(p)}|$) the ATFT is expected to operate like a unipolar TFT, the source-to-drain current for both unipolar and ambipolar TFTs can be approximated by:

$$I_{DS} = \frac{\mu \varepsilon_0 \varepsilon_r W}{2Ld}(V_{GS} - V_{T,n(p)})^2, \quad (4)$$

where μ is the effective saturation mobility, and $V_{T,n(p)}$ is the effective threshold voltage. A summary of the parameters extracted through a fitting procedure using Eq. (4) is found in Table 1. Although in the linear regime the output and transfer characteristics of these ATFTs show nearly identical performance with respect to unipolar TFTs, in saturation, I_{on-off} values are reduced due to ambipolar operation. However, the effective mobility, threshold voltages and values of I_{DS} are similar to the ones measured in unipolar TFTs.

Table 1
Summary of parameters extracted, using Eq. (4), on ambipolar TFTs and on *p*-channel (pentacene) TFT and *n*-channel (*a*-IGZO) TFTs.

	V_{DS} [V]	V_{GS} [V]	μ_{SAT} [cm^2/Vs]	V_T [V]	I_{Max} [A]
Ambipolar TFTs					
p-mode operation	−8	[0, −8]	0.27	−3.4	-2.3×10^{-6}
	−10	[0, −10]	0.32	−3.7	-5.1×10^{-6}
	−12	[0, −12]	0.33	−3.7	-9.0×10^{-6}
n-mode operation	8	[0, 8]	8.09	5.6	1.9×10^{-6}
	10	[0, 10]	11.10	6.0	7.3×10^{-6}
	12	[0, 12]	13.00	6.3	1.7×10^{-6}
Unipolar TFTs					
p-channel pentacene	−8	[0, −8]	0.29	−3.3	-2.5×10^{-6}
	−10	[0, −10]	0.34	−3.7	-5.3×10^{-6}
	−12	[0, −12]	0.35	−4.0	-8.9×10^{-6}
n-channel a-IGZO	8	[0, 8]	7.28	5.6	1.7×10^{-6}
	10	[0, 10]	10.20	6.0	6.6×10^{-6}
	12	[0, 12]	12.30	6.6	1.6×10^{-6}

5. Conclusion

In conclusion, we proposed a co-planar channel geometry for the realization of high performance ambipolar TFTs. Using non-overlapping horizontal channels of pentacene and *a*-IGZO we demonstrated hybrid organic–inorganic ambipolar TFTs with channels that show electrical

properties comparable to those found in unipolar TFTs with the same channel aspect ratios. By retaining key parameters of the electrical performance of unipolar TFTs, this geometry can easily be implemented with other material platforms, and may be particularly useful for printable materials. From a materials perspective, this work shows that future breakthroughs in performance of unipolar *n*-channel and *p*-channel semiconductors could directly transposed into ambipolar transistors and circuits. We expect that this geometry will provide new strategies for the realization of high performance ambipolar TFTs and novel ambipolar microelectronic circuits.

Acknowledgements

This material is based upon work supported in part by the STC Program of the National Science Foundation under Agreement No. DMR-0120967 and by the Office of Naval Research (Grant No. N00014-04-1-0120). This work was performed in part at the Microelectronics Research Center at Georgia Institute of Technology, a member of the National Nanotechnology Infrastructure Network, which is supported by NSF (Grant No. ECS-03-35765).

References

[1] E.J. Meijer, D.M. De Leeuw, S. Setayesh, E. Van Veenendaal, B.H. Huisman, P.W.M. Blom, J.C. Hummelen, U. Scherf, T.M. Klapwijk, Nat. Mater. 2 (2003) 678.
[2] T.D. Anthopoulos, D.M. de Leeuw, E. Cantatore, S. Setayesh, E.J. Meijer, C. Tanase, J.C. Hummelen, P.W.M. Blom, Appl. Phys. Lett. 85 (2004) 4205.
[3] W.J. Yu, U.J. Kim, B.R. Kang, I.H. Lee, E.H. Lee, Y.H. Lee, Nano. Lett. 9 (2009) 1401.
[4] J. Zaumseil, H. Sirringhaus, Chem. Rev. 107 (2007) 1296.
[5] A. Dodabalapur, H.E. Katz, L. Torsi, R.C. Haddon, Appl. Phys. Lett. 68 (1996) 1108.
[6] J. Cornil, J.-L. Brédas, J. Zaumseil, H. Sirringhaus, Adv. Mater. 19 (2007) 1791.
[7] J. Wang, H.B. Wang, X.J. Yan, H.C. Huang, D.H. Yan, Appl. Phys. Lett. 87 (2005) 093507.
[8] S.D. Wang, K. Kanai, Y. Ouchi, K. Seki, Org. Electron. 7 (2006) 457.
[9] K. Nomura, H. Ohta, A. Takagi, T. Kamiya, M. Hirano, H. Hosono, Nature 432 (2004) 488.
[10] W.T. Lim, J.H. Jang, S.H. Kim, D.P. Norton, V. Craciun, S.J. Pearton, F. Ren, H. Shen, Appl. Phys. Lett. 93 (2008) 082102.
[11] Y. Ogo, H. Hiramatsu, K. Nomura, H. Yanagi, T. Kamiya, M. Hirano, H. Hosono, Appl. Phys. Lett. 93 (2008) 032113.
[12] Dhananjay, C.W. Ou, C.Y. Yang, M.C. Wu, C.W. Chu, Appl. Phys. Lett. 93 (2008) 033306.
[13] B.N. Pal, P. Trottman, J. Sun, H.E. Katz, Adv. Funct. Mater. 18 (2008) 1832.
[14] H. Nakanotani, M. Yahiro, C. Adachi, K. Yano, Appl. Phys. Lett. 90 (2007) 262104.
[15] E.C.P. Smits, T.D. Anthopoulos, S. Setayesh, E. van Veenendaal, R. Coehoorn, P.W.M. Blom, B. de Boer, D.M. de Leeuw, Phys. Rev. B 73 (2006) 205316.
[16] Z.M. Wei, W. Xu, W.P. Hu, D.B. Zhu, J. Mater. Chem. 18 (2008) 2420.
[17] J.B. Kim, C. Fuentes-Hernandez, W.J. Potscavage, X.H. Zhang, B. Kippelen, Appl. Phys. Lett. 94 (2009) 142107.
[18] C. Baldacchini, C. Mariani, M.G. Betti, L. Gavioli, M. Fanetti, M. Sancrotti, Appl. Phys. Lett. 89 (2006) 152119.
[19] Y. Shimura, K. Nomura, H. Yanagi, T. Kamiya, M. Hirano, H. Hosono, Thin Solid Films 516 (2008) 5899.

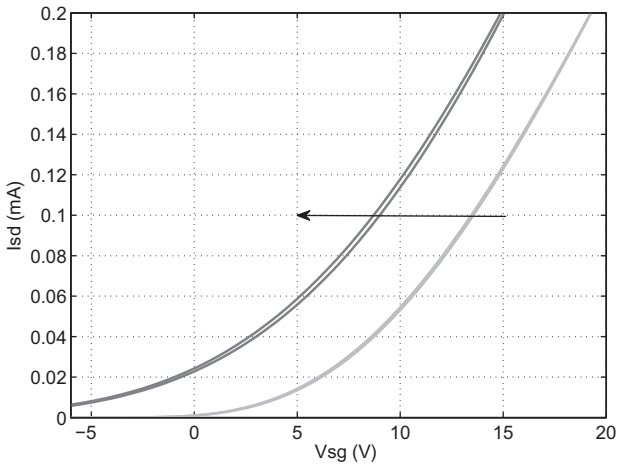

Fig. 1. Effect of bias stress on the transfer curve. The stress conditions are $V_{SG} = V_{SD} = 15$ V, for 24 h under ambient conditions, i.e., with exposure to O_2, H_2O, light and temperature fluctuations. The effect is mainly a V_t shift.

design strategy for technologies with p-OTFTs only is presented.

The second most important technological issue for analog circuit design is the shift of the mean threshold voltage (V_t) value. This V_t shift can have different causes. Run-to-run variations at production-time can result in a shift of the mean V_t value. Moreover, bias stress as well as trapping caused by water and oxygen occur at run-time and cause V_t shift over time. Bias stress in organic semiconductors follows from carrier trap states at the dielectric–semiconductor interface or in the dielectric that compensate for the applied electric field [10,11]. Bias stress can be exacerbated by the presence of water and oxygen molecules at the semiconductor, as well as by light [12–14]. The effect of oxygen is explained by chemical reaction with the pentacene molecule, according to Refs. [15,16]. Other Refs. [17,18] explain the behavior by diffusion of O_2 in the pentacene. Bias stress at negative V_{SG} (with the pentacene transistor in the off-state or mild electron accumulation) is faster and more degrading than bias stress at positive V_{SG} (transistor in on-state with hole accumulation) [11]. As can be seen in Fig. 1, our measurements confirm that V_t shifts over several volts when the transistor is biased in the O_2- and H_2O-containing ambient environment, where also light and temperature changes are present. From this figure it can be concluded that V_t shift is a very important and hardly predictable effect to deal with when designing analog circuits.

A third technological effect that needs to be considered for circuit design is mobility (μ) variation. A certain variation of mobility is present on wafer as well as from run-to-run. Moreover, mobility degradation occurs when transistors are biased or exposed to ambient environment, containing O_2 and H_2O, for long time [19]. Mobility variation influences the current through a transistor. In a main amplifier and assuming that all transistors undergo the same mobility change, this effect results in a bandwidth variation only. As the current through each transistor varies linearly with the mobility, the DC behavior of the circuit is not affected. Mobility variation becomes an issue when transistors are biased in the linear region as resistors, i.e. as a resistor in an RC integrator. Then the exact value of R is important for the RC product. In general, μ variation is to first instance of less importance for basic analog design than V_t shift.

A fourth important drawback of the technology is the mismatch between V_t of different transistors, resulting from on-wafer variations. Despite certain variability over

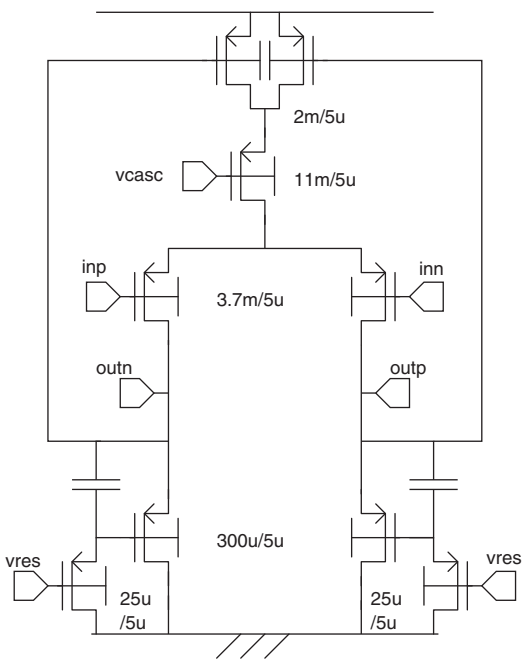

Fig. 2. Proposed schematic of the single-stage differential amplifier with p-type load, bootstrapped gain enhancement, CMFB, cascoding and backgate steering.

the full wafer, adjacent transistors show a satisfying likeliness [1]. Therefore special attention is required for the placement and lay-outing of transistors. Furthermore it is also very important to reduce mismatch sensitivity during the circuit design.

The applied pentacene-based technology [1,2] with three metal layers provides p-type organic bottom-gate thin-film transistors (p-OTFT) with typical length of 5 μm and metal–organic insulator–metal capacitors. The substrate for this technology is a plastic foil.

3. Design strategy and simulation

The presented design strategy is adapted to the limitations of the technology, starting with the unavailability of n-OTFTs. Therefore solutions must be found for replacing n-type load transistors. Moreover, as discussed above, V_t shift over time as well as μ shift and mismatch have to be considered in the design strategy. This work focuses on the design of a single-stage differential amplifier and improves a basic differential pair with four techniques, applying bootstrapped gain enhancement, linear common-mode feedback, backgate steering and cascoding. Fig. 2 gives the schematic of the presented single-stage amplifier.

As no n-OTFTs are available, p-OTFTs are applied as load transistors. Two straightforward options are shown in Fig. 3a and b. The gate of the load p-OTFT can be connected to the drain, resulting in a diode load with the load transistor biased in saturation region, or to the source, hence be biased in cut-off region. The diode-connected load scores better for higher BW and is less sensitive to V_t shift over time whereas the cut-off load implies higher input–output gain but is sensitive to leakage current variations. A bootstrapped gain enhancement technique, shown in Fig. 3c, adds a high-pass filter with very low 3 dB frequency from source to gate. This technique combines the advantages,

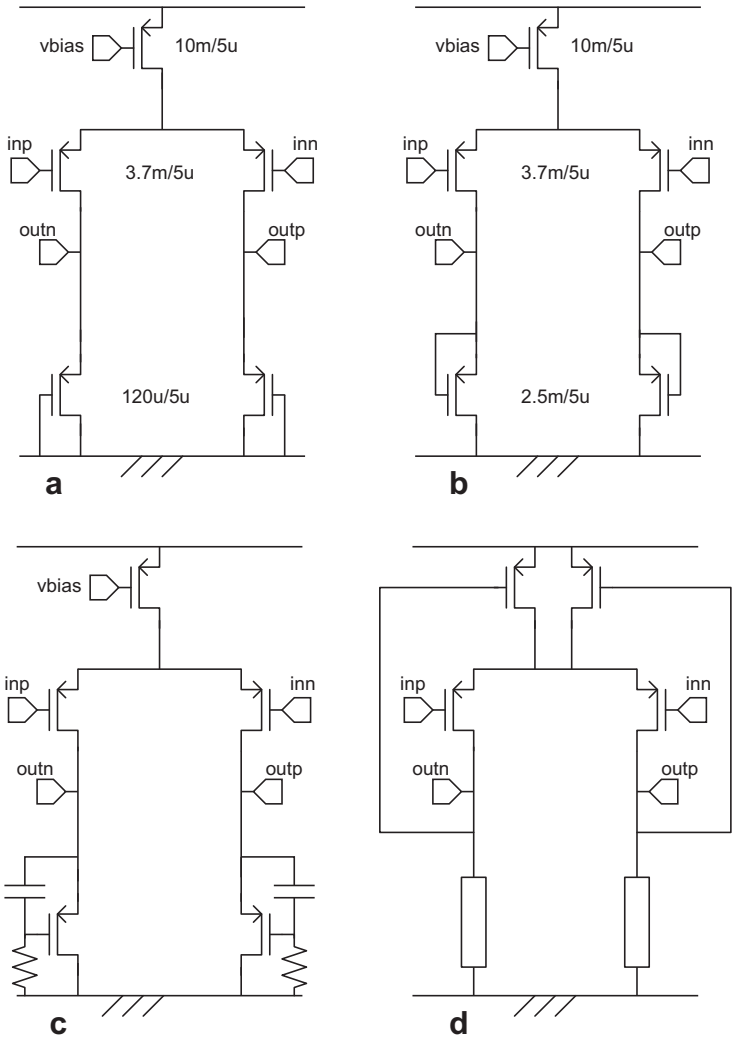

Fig. 3. Differential pairs with (a) a diode-configuration load, with device dimensions as in simulation, (b) a cut-off configuration load, with device dimensions as in simulation, (c) bootstrapped gain enhancement and (d) linear common-mode feedback.

low V_t-sensitivity and high gain, in one load topology. Compared to diode loads the gain is now increased, due to bootstrapping of the transimpedance. Compared to cut-off loads, the sensitivity to V_t and leakage current is reduced due to higher overdrive biasing. However, V_t mismatch still causes current difference in the branches, degrading offset, CMRR, and gain. Also, higher gain of 'bootstrapped' loads compared to diode loads causes worse offset and linearity from input pair V_t mismatch. Nevertheless this topology is an expedient trade-off between the diode and cut-off loads. The price paid for this trade-off is the low-frequent pole of the high-pass filter. By pushing it to very low frequencies, its influence is neutralized. In this work the high-pass filter is implemented with a metal–insulator–metal capacitor and a transistor in (deep) cut-off region with the gate off-chip tunable as the resistor.

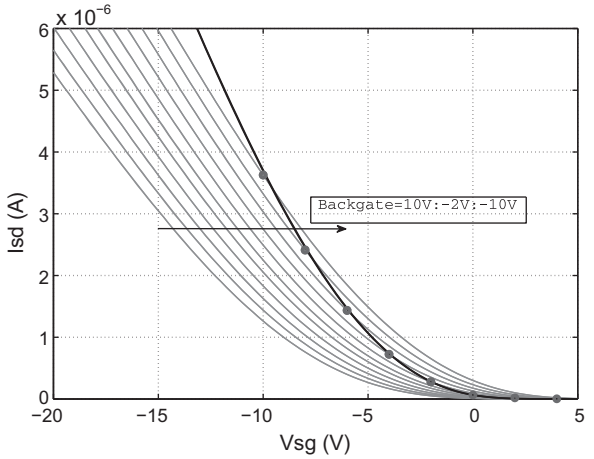

Fig. 4. Measured V_G–I_D-curves for a varying voltage applied to the backgate of the transistor. The black curve shows the measured behavior when gate and backgate are connected.

Therefore a 3 dB-point lower than 50 mHz is obtained by tuning this cut-off resistor.

The input differential pair is biased with small $V_{SG} - V_t$. To reduce their mismatch sensitivity a linear common-mode feedback (CMFB) circuit is applied. This circuit technique is shown in Fig. 3d. It applies a feedback loop and therefore overcomes common-mode input signals and stabilizes the DC output voltage. V_t shift in the presented differential amplifier influences mostly the differential pair. V_t shift over time can thus be modeled as a common-mode input effect. Therefore this technique reduces again V_t-sensitivity of the circuit. Measurements show that the CMRR for the presented topology is 12 dB.

The cascode transistor influences the CMFB loop gain slightly positively. Its effect is limited since the lowest resistance at the virtual ground node is seen through the sources of the differential input pair.

In our technology, the transistors can be designed to have two gates, i.e., the thin-film semiconductor is located between two dielectrics, and metal layers can be defined on each side to operate as gates [20]. The bottom-gate is the nominal gate. The top-gate is a backgate. We can use steering of the backgate to our advantage, to shift the threshold voltage of the transistor V_G–I_D transfer characteristics of the nominal gate. V_t shifts almost linearly by 350 mV/V applied to the backgate, as can be seen in Fig. 4. When this backgate is now connected to the gate of the transistor, the V_G–I_D behavior becomes steeper and therefore results in a higher g_m. An additional advantage of the backgate, physically located on top of the pentacene thin-film, is that it acts as encapsulation that shields the semiconductor from air, providing better air-stability of V_t and μ.

Simulations are performed to compare the behavior of the topology, proposed in this work, against the initial topologies in Fig. 3a and b, for two separate cases: The effect of an overall V_t shift for all the transistors and the effect of V_t mismatch in one load transistor. The

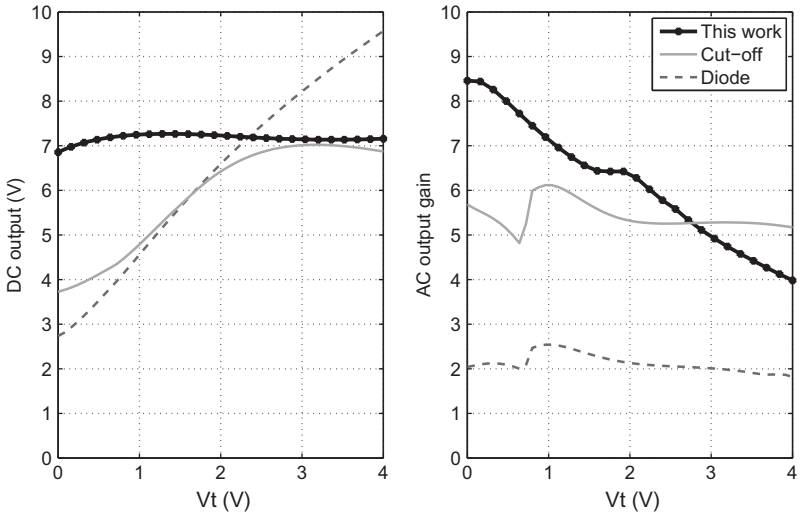

Fig. 5. Simulated effect of an equal V_t shift in all transistors for the cut-off load topology, diode load topology and for the topology described in this work. The DC common-mode output voltage (left) and the AC differential-mode output gain (right).

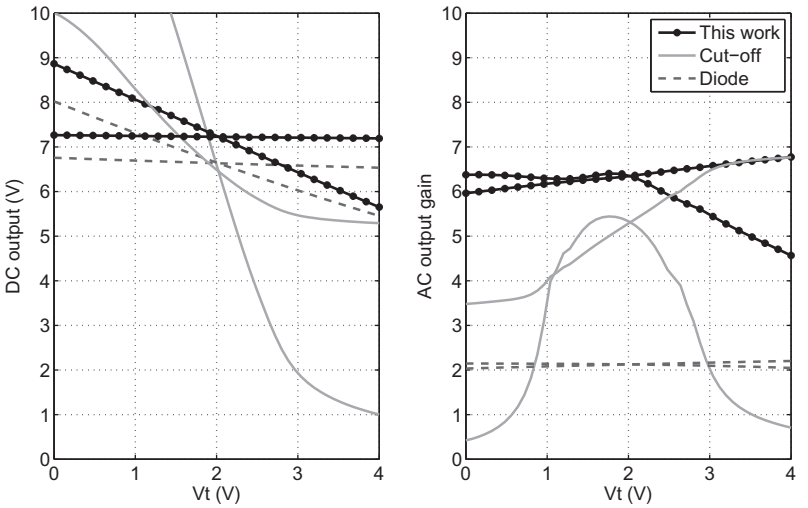

Fig. 6. Simulated effect of a V_t shift of one load transistor for the cut-off load topology, diode load topology and for the topology described in this work. The DC output node voltages (two per topology) (left) and the differential-mode output node AC gains (right).

simulations are carried out for a 15 V supply voltage and with the transistor sizes given in the figures. All three topologies were simulated with the backgate steering technique. Fig. 5 shows the effect of an overall V_t shift for all transistors. The figure shows that the DC output of the diode-connected load is very sensitive to this type of variations. This is due to the unbalanced effects of V_t on the input pair (low $V_{GS} - V_t$) and on the load transistors (high $V_{GS} - V_t$). The cut-off load topology is flat in a small region but becomes, for the same reason, equally sensitive as the diode load when V_t goes below 2 V. For large shifts of V_t the presented topology performs the best due to the bootstrapping technique and CMFB. The AC plot on the right panel shows that the AC behavior of the presented topology is higher but varies the most. This is explained by the varying current when CMFB loop resettles the output voltage. Fig. 6 shows the effect on the (differential) output node voltages of mismatch on the load transistors. The cut-off load is very sensitive to V_t mismatch, both in DC and AC behavior, since the currents in the branches are very sensitive to V_t mismatch. Therefore different currents will flow in the branches and cut-off load is therefore unwanted. Both other topologies perform well, as their currents are less sensitive to V_t mismatch, yet the CMFB topology reaches much higher gain. Globally, we prefer the CMFB topology, as we favor a circuit with a known and reliable DC behavior with as much as possible gain.

4. Measurement results

The measurement results of the single-stage amplifier are presented in Fig. 7. It shows the AC behavior of the pristine single-stage amplifier and after 4 months shelving and then DC biasing it for 10 days at a 15 V supply voltage, both in ambient environment. We can distinguish two different effects on the AC gain curve. The band pass gain decreases as a result of the V_t shift that was discussed above. This decrease amounts only to 4 dB, which is quite moderate.

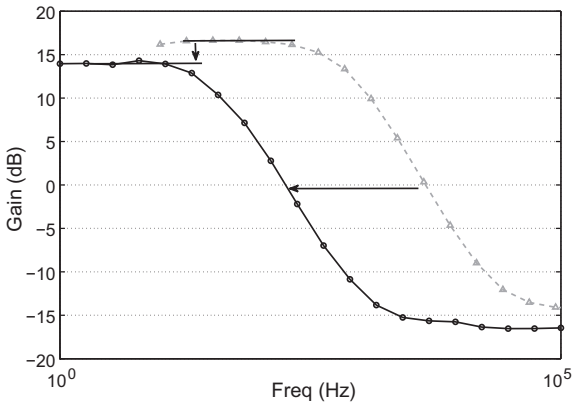

Fig. 7. Gain curve for pristine amplifier (gray) and after 4 months shelved in air followed by continuous biasing for 10 days at 15 V supply voltage in ambient (black). The gain and the bandwidth decrease as a result of V_t shift and μ degradation. By applying analog techniques the gain decrease is limited to only 4 dB.

Furthermore, the bandwidth is reduced owing to the mobility degradation while being shelved and biased in the presence of O_2 and H_2O mentioned in Section 2. Finally, as a measure for the distortion the IP3 interception point in this differential amplifier after degradation is measured to be 18 dB V.

5. Conclusion

We discuss the challenges for analog design in pentacene technology and present a strategy for V_t-insensitive design. The strategy was applied to a single-stage differential amplifier. It applies CMFB, bootstrapped gain enhancement, cascoding and backgate steering and reduces the V_t-sensitivity of the circuit. The circuit performs with 18 dB gain. After 4 months of storing and 10 days of

stressing at a 15 V supply voltage, both in ambient environment, the DC output does not change significantly and AC gain degrades only by 4 dB. We conclude that such robust design of analog circuits will enable the design of organic AD converters that are applicable for organic smart-sensor systems.

References

[1] G.H. Gelinck et al., Flexible active-matrix displays and shift registers based on solution-processed organic transistors, Nature Materials 3 (2004) 106–110.

[2] H.E.A. Huitema et al., Rollable displays: the start of a new mobile device generation, in: Seventh Annual Flexible Electronics and Displays Conference USDC, Phoenix, Arizona, USA, January 2008.

[3] K. Myny et al., A 128b organic RFID transponder chip, including Manchester encoding and ALOHA anti-collision protocol, operating with a data rate of 1529b/s, in: ISSCC Digest of Technical Papers, February 2009, pp. 206–207.

[4] H. Marien et al., A mixed-signal organic 1 kHz comparator with low VT sensitivity on flexible plastic substrate, in: ESSCIRC, 2009, ESSCIRC '09 Proceedings, September 2009, pp. 120–123, 14–18.

[5] W. Xiong et al., A 3V 6b successive-approximation ADC using complementary organic thin-film transistors on glass, in: ISSCC Digest of Technical Papers, February 2010, pp. 134–135.

[6] F. Ante et al., Low-voltage metal-gate top-contact organic thin-film transistors and complementary inverters with submicron channel length, in: Device Research Conference 2009, 2009, pp. 179–180.

[7] E. Namdas et al., Organic light emitting complementary inverters, Applied Physics Letters 96 (2010).

[8] U. Zschieschang et al., Deterministic and continuous control of the threshold voltage and noise margin of organic thin-film transistors and organic complementary circuits using mixed phosphonic acid self-assembled monolayer gate dielectrics, in: Device Research Conference 2009, 2009, pp. 181–182.

[9] D. Bode et al., Noise-margin analysis for organic thin-film complementary technology, Electron Devices, IEEE Transactions 57 (2010) 201–208.

[10] Tse Nga Ng et al., Bias stress effects in organic thin film transistors, in: Reliability Physics Symposium, 2007, Proceedings of 45th Annual IEEE International, 2007, pp. 243–247.

[11] J. Genoe et al., Bias stress in pentacene transistors measured by four probe transistor structures, in: ESSDERC, 2004, Proceeding of the 34th European, 2004, pp. 413–416.

[12] K.P. Pernstich et al., Modeling the water related trap state created in pentacene transistors, Applied Physics Letters 89 (2006).

[13] K. Diallo et al., Stability of pentacene top gated thin film transistors, Applied Physics Letters 91 (2007).

[14] M. Debucquoy et al., Correlation between bias stress instability and phototransistor operation of pentacene thin-film transistors, Applied Physics Letters 91 (2007).

[15] C. Pannemann et al., On the degradation of organic field-effect transistors, in: Microelectronics, 2004, ICM 2004 Proceedings, The 16th International Conference, 2004, pp. 76–79.

[16] C. Pannemann et al., Encapsulating the active layer of organic thin-film transistors, in: Polytronic 2005, Fifth International Conference, October 2005.

[17] A. Vollmer et al., The interaction of oxygen and ozone with pentacene, Surface Science 600 (2006) 4004–4007.

[18] O.D. Jurchescu et al., Electronic transport properties of pentacene single crystals upon exposure to air, Applied Physics Letters 87 (2005).

[19] R.A. Street et al., Extended time bias stress effects in polymer transistors, Journal of Applied Physics 100 (2006).

[20] G.H. Gelinck et al., Dual-gate organic thin-film transistors, Applied Physics Letters 87 (2005).

cessable p-channel triethylsilylethynyl **ADT** derivative (**TES–ADT; E**) with a mobility as high as 1.0 $cm^2/V\,s$ was reported by Jackson and co-workers [9]. Meanwhile, trimethoxyphenylethynyl-substituted **PEN** and **ADT** (**D**) derivatives have also been reported with relatively low carrier mobility from solution-processed films [10]. All of these studies demonstrated that ethynyl/phenyl substituents on the **PEN**/**ADT** cores significantly influence the solid state electrical performance [11]. Presumably, more conjugated phenyl groups connected to the ethynyl group might be expected to further enhance self-assembly of the aromatic moieties into closely π-stacked arrays, therefore improving intermolecular orbital overlap and the resulting device performance. To prove this postulation, four solution-processable **PEN** and **ADT** derivatives (**1**–**4**) bearing phenylethynyl and triethylsilylphenylethynyl substituents were synthesized, characterized, and incorporated in OTFTs. From the single-crystal X-ray diffractions and film morphologies of these four compounds, it has been clearly seen that both substituents did strongly affect the intermolecular stacking of these new derivatives. With the bulky triethylsilyl (TES) moiety appended to the phenylethynyl group, the molecular packings of compounds **2** and **4** via X-ray analysis were peculiarly engaged in 2-D "slipped-crossed" stacking to accommodate the bulky TES groups, which were very different from those of compounds **1** and **3**, and therefore, substantially directed their electronic performance fabricated via drop-casting (*vide infra*).

2. Experimental section

2.1. Materials and methods

All chemicals and solvents used in this work were of reagent grade and were obtained from Aldrich, Arco, or TCI Chemical Co. Reaction solvents (toluene, benzene, ether, and THF) were distilled under nitrogen from sodium/benzophenone ketyl, and halogenated solvents were distilled from CaH_2. ^1H and ^{13}C NMR spectra were recorded on a Bruker 500 or a Bruker DRX-200 instrument. Differential scanning calorimetry (DSC) was carried out on a Mettler DSC 822 instrument at a scan rate of 10 K/min. Thermogravimetric analysis (TGA) was performed on a Perkin–Elmer TGA-7 thermal analysis system using dry nitrogen as a carrier gas at a flow rate of 40 mL/min. The optical absorption and fluorescence spectra were obtained using JASCO V-530 and Hitachi F-4500 spectrometers, respectively, and all spectra were measured in a specified solvent at room temperature. The IR spectra were obtained using a JASCO FT/IR-4100 spectrometer. Differential pulse voltammetry experiments were performed using a CH Instruments/CHI621C Electrochemical Analyzer. All measurements were carried out at the temperatures indicated with a conventional three-electrode configuration consisting of a platinum disk working electrode, an auxiliary platinum wire electrode, and a non-aqueous Ag reference electrode. The supporting electrolyte was 0.1 M tetrabutylammonium hexafluorophosphate ($TBAPF_6$) in a specified dry solvent. All potentials reported were referenced to an Fc^+/Fc internal

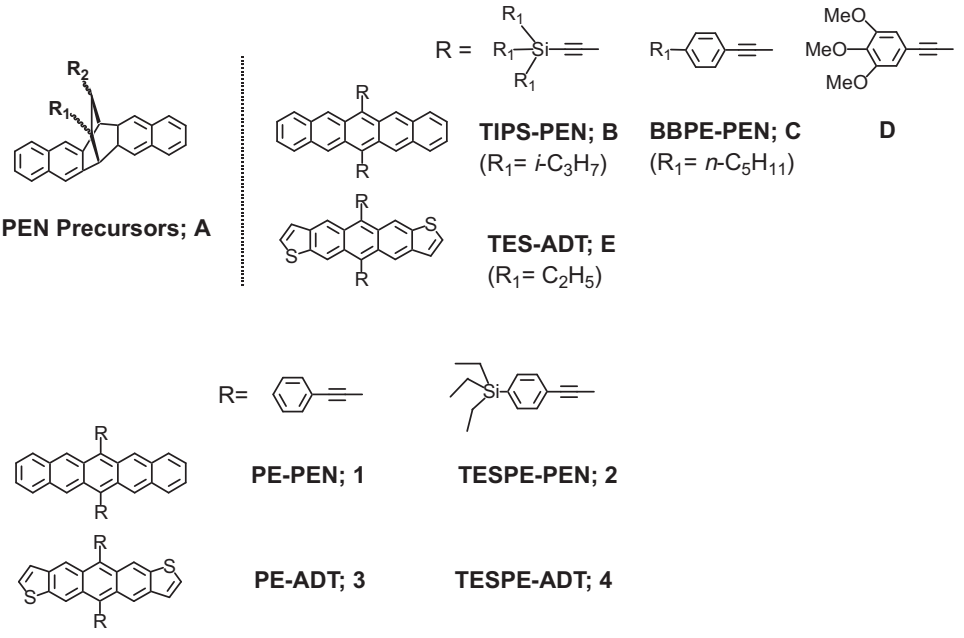

standard (at +0.6 V). Elemental analyses were performed on a Heraeus CHN-O-Rapid elemental analyzer. Mass spectrometric data were obtained with a JMS-700 HRMS instrument. Prime grade silicon wafers (p^+-Si) with ~300 nm (±5%) of thermally grown oxide (from Montco Silicon) were used as device substrates.

2.2. Synthesis

2.2.1. Synthesis of 6,13-bis(phenylethynyl)pentacene (*PE-PEN*; *1*)

The procedure was reported in the literature [12]. ^{1}H NMR (200 MHz, $CDCl_3$): δ 9.32(s, 4H), 8.08(dd, J = 6 Hz, 3 Hz, 4H), 7.93(dd, J = 8 Hz, 1 Hz, 4H), 7.55–7.41(m, 10H). Deep blue crystals suitable for X-ray diffraction were crystallized by slow diffusion of hexane into a xylene solution of compound **1**. The molecular structure of **1** was confirmed by X-ray diffraction and is shown in Fig. 4 below (cif file of 1 is in SI).

2.2.2. Synthesis of 4-triethylsilylphenyl acetylene (*5*) [13]

As shown in Scheme 1, under nitrogen, 35.6 mL of 2.5 M *n*-BuLi (in hexane, 0.089 mol) was slowly added to a 100 mL dry ether solution of 1,4-dibromobenzene (20 g, 0.085 mol) at −50 to −30 °C, and the mixture was then stirred at 0 °C for 1 h. Next, 15.1 mL of chlorotriethylsilane (0.085 mol) was slowly added to the above mixture and stirring was continued for 8 h. Water was then added to the reaction mixture, and the organic layer was collected. After solvent evaporation, the desired oily 1-bromo-4-triethylsilylbenzene was purified by distillation at 110 °C/0.02 Torr giving 21.7 g of product (94% yield). ^{1}H NMR ($CDCl_3$): δ 7.47(d, J = 8 Hz, 2H), 7.33(d, J = 8 Hz, 2H), 0.96(t, J = 8 Hz, 9H), 0.78(q, J = 8 Hz, 6H).

Under nitrogen, a mixture of dry 1-bromo-4-triethylsilylbenzene (2.0 g, 7.4 mmol), $Pd(PPh_3)_2Cl_2$ (0.103 g, 0.15 mmol), CuI (56 mg, 0.3 mmol), and 15 mL of dry piperidine was stirred at 0 °C for 10 min, and then trimethylsilylacetylene (1.58 mL, 11 mmol) was added to the mixture. The mixture was then stirred at 80 °C for 18 h. After cooling to room temperature, the solvent was removed under vacuum, and a methanol (20 mL) solution of K_2CO_3 (3.07 g, 22.2 mmol) was added to the mixture and stirring was continued at room temperature for 2 h. The methanol was then removed under vacuum, and the organic product was extracted with hexane and then filtered through a Celite flash column. The concentrated crude product was finally purified via chromatography (silica gel; hexane as the eluent) giving 1.36 g of desired oily product (85% yield). ^{1}H NMR($CDCl_3$): δ 7.46–7.45(m, 4H), 3.09(s, 1H, C–H), 0.95(t, J = 8 Hz, 9H), 0.79(q, J = 8 Hz, 6H).

2.2.3. Synthesis of 6,13-(4-triethylsilylphenylethynyl)-pentacene (*TESPE–PEN*; *2*)

Under nitrogen, 2.5 mL of 2.5 M *n*-BuLi (in hexane, 6.25 mmol) was slowly added to a 20 mL THF solution of 4-triethylsilylphenylacetylene (1.24 g, 5.7 mmol) at 0 °C, and the mixture was stirred at 60 °C for 3 h. The resulting black-brown lithium phenyl acetylide solution was then transferred to a dry THF (50 mL) solution of pentacen-6,13-dione (0.3 g, 1.0 mmol) at 0 °C, and the mixture was refluxed for 12 h. After cooling to room temperature, 5 mL of water was added into the reaction mixture and a deoxygenated $SnCl_2$ (3 g, 15.7 mmol)/HCl (5 mL, 10%) solution was added to the reaction and stirring was continued at room temperature for 3 h. Water was added to the reaction mixture and the organic layer was collected and purified by chromatography (silica gel; hexanes as the eluent) and recrystallization from hexane, giving 39 mg of blue solid (5.6% yield). ^{1}H NMR (200 MHz, $CDCl_3$): δ 9.29(s, 4H), 8.04(m, 4H), 7.87(d, J = 8 Hz, 4H), 7.65(d, J = 8 Hz, 4H), 7.41(m, 4H), 0.91(t, J = 8.0 Hz, 18H), 0.85(q, J = 8.0 Hz, 12H). Deep green crystals suitable for X-ray diffraction were crystallized by slow evaporation of an ether solution of compound **2**. The molecular structure of **2** was confirmed by X-ray diffraction and is shown in Fig. 6 below (cif file of 2 is in SI).

2.2.4. Synthesis of 5,11-bis(phenylethynyl)anthradithiophene (*PE-ADT*; *3*)

Under nitrogen, 7.6 mL of 2.5 M *n*-BuLi (in hexane, 0.019 mol) was slowly added to a 20 mL dioxane solution of phenylacetylene (1.95 g, 0.019 mol) at 0 °C, and the mixture was stirred at room temperature for 1 h. The resulting black-brown solution was transferred to a dry dioxane solution (30 mL) of anthradithiophene-5,11-dione [4a] (0.306 g, 0.96 mmol) at 0 °C, and then the mixture was refluxed for 4 h. After cooling to room temperature, 0.5 M NH_4Cl solution (50 mL, 0.25 mol) was added to the reaction mixture, and the organic layer was collected. Hexane was then added to the collected solution to precipitate green-brown 5,11-dihydroxy-5,11-bis(phenylethynyl) anthradithiophene (0.28 g, 54% yield). ^{1}H NMR (200 MHz, $CDCl_3$):

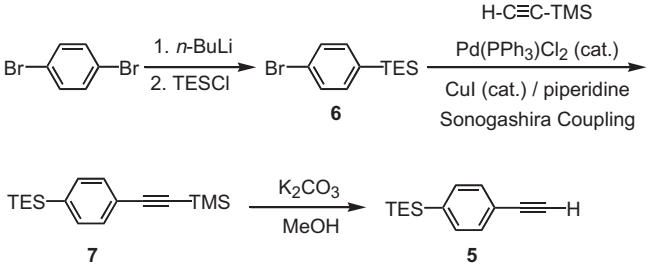

Scheme 1. Synthesis of 4-triethylsilylphenyl acetylene 5.

δ 8.79(s, 2H), 8.73(s, 2H), 7.76–7.72(m, 4H), 7.56(d, J = 5 Hz, 2H), 7.47–7.35(m, 8H), 4.33(t, J = 5 Hz, 2H, OH).

Under nitrogen, a deoxygenated acetic acid (7.5 mL, 50%) solution of $SnCl_2$ (8.4 g, 0.044 mol) was added to the above dioxane solution (45 mL) of 5,11-dihydroxyl-5,11-bis(phenylethynyl)anthradithiophene (0.28 g, 0.53 mmol), and the mixture was stirred at room temperature for 2 h. Next, water was added to the resulting pink-red solution and the resulting purple precipitate was collected by filtration and washed with ether and hexane. The product was further purified via recrystallization from *p*-xylene giving 0.12 g of the product (46% yield). ^{1}H NMR (200 MHz, $CDCl_3$): δ 9.23(s, 2H), 9.17(s, 2H), 7.87–7.84(m, 4H), 7.57–7.47(m, 10H). MS (FAB) (*m*/z) calcd. for $C_{34}H_{18}S_2$: 490 (M^+), Found: 490. Purple-red crystals suitable for X-ray diffraction were crystallized by slow diffusion of hexane into a xylene solution of compound **3**. The molecular structure of **3** was confirmed by X-ray diffraction and is shown in Fig. 5 below (cif file of 3 is in SI).

2.2.5. Synthesis of 5,11-Bis(4-triethylsiliylphenylethynyl)-anthradithiophene (*TESPE–ADT*; *4*)

Under nitrogen, 2.0 mL of 2.0 M isopropyl magnesium chloride (4.0 mmol) in THF was slowly added to a 20 mL THF solution of 4-triethylsilylphenylacetylene (0.86 g, 3.95 mmol) at 0 °C, and the mixture was stirred at 60 °C for 2 h. The resulting black-brown solution was then transferred to a dry THF solution (50 mL) of an anthradithiophene-5,11-dione (200 mg, 0.624 mmol) at room temperature, and then the mixture was refluxed at 60 °C overnight. After cooling to room temperature, 1.5 mL of water and a deoxygenated $SnCl_2$ (3.0 g, 15.7 mmol)/HCl (5 mL, 10%) solution was added to the reaction mixture, and stirring was continued at 60 °C for 3 h. Water was next added to the reaction mixture, and the organic layer was collected and purified by chromatography (silica gel; hexane as the eluent) and recrystallization from ether, giving 160 mg of purple-red precipitate (36% yield). ^{1}H NMR (300 MHz, $CDCl_3$): δ 9.22(s, 2H), 9.16(s, 2H), 7.83(d, J = 7.5 Hz, 4H), 7.63(d, J = 7.5 Hz, 4H), 7.56(d, J = 6 Hz, 2H), 7.48(d, J = 6 Hz, 2H), 1.02(t, J = 7.5 Hz, 18H), 0.88(t, J = 7.5 Hz, 12H). Purple-red crystals suitable for X-ray diffraction were crystallized by slow evaporation of an ether solution of compound **4**. The molecular structure of **4** was confirmed by X-ray diffraction and is shown in Fig. 7 below (cif file of 4 is in SI).

2.3. X-ray crystal structure determinations of compounds *1–4*

The selected crystals were mounted on a glass fiber. Data collection on compounds **1**–**3** and **4** were carried out on a BRUKER SMART APEX CCD and a NONIUS Kappa CCD diffractometer, respectively, with Mo radiation (λ = 0.71073 Å) at 150(2) K. After data collection, the frames were integrated and absorption corrections were applied. The initial crystal structure was solved by a direct method, the structure solution was expanded through successive least-squares cycles, and the final solution was determined. All non-hydrogen atoms were refined anisotropically. Hydrogen atoms attached to the carbons were fixed at calculated positions and were refined using a riding mode. Crystal data, data collection, and refinement parameters are summarized in Table 1.

Table 1
Summary of crystal structure data for compounds **1**–**4**.[a]

Compound	**1**	**2**	**3**	**4**
Empirical formula	$C_{38}H_{22}$	$C_{50}H_{50}Si_2$	$C_{34}H_{18}S_2$	$C_{46}H_{46}S_2Si_2$
Formula weight	478.56	707.08	490.60	719.13
Temperature (K)[b]	150(2)	150(2)	150(2)	150(2)
Crystal system	Triclinic	Orthorhombic	Monoclinic	Triclinic
Space group	$P\bar{1}$	$Pca2(1)$	$P2(1)/n$	$P\bar{1}$
Unit cell dimensions (Å)	a = 10.1371(6)	a = 23.6356(11)	a = 12.019(3)	a = 7.4170(3)
	α = 72.515(1)°	α = 90°	α = 90°	α = 81.015(2)°
	b = 12.9940(7)	b = 47.245(2)	b = 5.3975(11)	b = 12.5298(6)
	β = 82.654(1)°	β = 90°	β = 100.571(5)°	β = 85.000(2)°
	c = 19.8189(11)	c = 7.3483(3)	c = 18.780(4)	c = 22.1051(10)
	γ = 78.759(1)°	γ = 90°	γ = 90°	γ = 85.107(2)°
V (Å^3)	2435.5(2)	8205.5(6)	1197.6(4)	2016.01(16)
Z	4	8	2	2
d (calc) (g/cm^3)	1.305	1.145	1.361	1.185
Absorption coefficient (mm^{-1})	0.074	0.120	0.245	0.222
F(0 0 0)	1000	3024	508	764
Crystal size (mm)	0.70 × 0.10 × 0.07	0.70 × 0.10 × 0.10	0.70 × 0.07 × 0.01	0.60 × 0.10 × 0.10
Reflections collected	26,841	70,259	5790	17,924
Independent reflections	8571	14,375	2113	7008
R_{int}	0.0536	0.0940	0.1229	0.0544
Final R indices [$I > 2\sigma(I)$][c]	R_1 = 0.0961	R_1 = 0.0809	R_1 = 0.1674	R_1 = 0.0636
	wR_2 = 0.2501	wR_2 = 0.1580	wR_2 = 0.3203	wR_2 = 0.1727
R indices (all data)	R_1 = 0.1489	R_1 = 0.1019	R_1 = 0.2107	R_1 = 0.1014
	wR_2 = 0.2883	wR_2 = 0.1694	wR_2 = 0.3432	wR_2 = 0.1949

[a] CCD area detector diffractometer; Mo Kα radiation; λ = 0.71073 Å.
[b] Temperature for data collection.
[c] Refinement method: full-matrix least-squares on F^2.

2.4. Semiconductor film deposition and characterization

All p^+-Si/SiO_2 substrates were cleaned via sonication in absolute ethanol for 3 min and then by oxygen plasma treatment for 5 min (20 W, 0.5 Torr). For an SiO_2 coating layer, –$SiMe_3$ groups were introduced using hexamethyldisilazane (HMDS) and were deposited by placing the clean SiO_2 substrates in a N_2-filled chamber saturated with HMDS vapor for 48–72 h. For vacuum deposition, semiconducting materials were thermally deposited at $\sim 6 \times 10^{-6}$ Torr (~500 Å, 0.2–0.3 Å/s) at 20 or 50 °C. For drop-casting, a 0.1–0.2 wt.% solution (in toluene, tetrachloromethane, chlorobenzene, or dichlorobenzene) of each compound was placed on a clean substrate (1 cm × 1 cm) on a hot plate at a preset temperature. The temperature setting was ~50 °C lower than the boiling point of the corresponding solvent. The substrates were kept under a saturated vapor of solvent (the same solvent used to dissolve the compound) until the solvent evaporated completely. Films were then annealed in a vacuum oven to remove the residual solvent. Thin films of the organic semiconductors were analyzed by optical microscopy and wide angle $\theta - 2\theta$ X-ray diffraction (XRD) (Rigaku ATXG) using monochromated Cu Kα radiation. For TFT device fabrication, top-contact electrodes (~70 nm) were deposited by evaporating gold ($\sim 1 \times 10^{-6}$ Torr) through a shadow mask with a channel length (L) of 100 μm and a channel width (W) of 500–5000 μm.

2.5. Electrical Measurements

All OTFT measurements were carried out in ambient conditions using a Keithly 6430 subfemtoammeter and a Keithly 2400 source meter, operated by a local Labview program and GPIB communication. The mobilities (μ) were calculated in the saturation regime using the relationship [14]: $\mu_{sat} = (2I_{DS}L)/[WC_i(V_G - V_T)^2]$, where I_{DS} is the source–drain saturation current, C_i is the gate dielectric capacitance (per area), V_G is the gate voltage, and V_T is the threshold voltage. The latter can be estimated as the x intercept of the linear section of the plot of V_G vs. $(I_{DS})^{1/2}$.

3. Results and discussion

3.1. Synthesis

The synthesis of four soluble **PEN**- (**1** and **2**) and **ADT**- (**3** and **4**) based compounds was achieved according to Scheme 2 following known synthetic approaches for other soluble **PEN** or **ADT** derivatives [9]. Starting from pentacene or ADT quinone, phenylethynyl-substituted **1** and **2** as well as triethylsilylphenylethynyl-substituted **3** and **4** were obtained via phenylethynyl anion alkylation and $SnCl_2$/HCl reduction, with overall yields of 50%, 6%, 46%, and 36%, respectively. Compared to **PEN** or **ADT**, compounds **1**–**4** exhibited significantly enhanced solubility in common organic solvents. Noteworthy is that triethylsilylphenylethynyl (**TESPE**-) substituted compounds **2** and **4** were very soluble in common organic solvents such as hexanes, ether, and benzene.

3.2. Thermal and optical properties

As summarized in Table 2, **ADT** derivatives exhibited greater thermal stability than do the analogous **PEN** derivatives. Thus, compounds **3** and **4** exhibited higher thermal decomposition temperatures (339 and 168 °C, respectively) than compounds **1** and **2** (255 and 86 °C, respectively). Note that **ADT** derivative **3**, the most thermally stable compound prepared in this study, did not exhibit a melting endotherm up to 339 °C in differential scanning calorimetry (DSC) measurements and exhibited weight loss only on heating above 320 °C, as demonstrated by thermogravimetric analysis. Compared to the phenylethynyl groups, triethylsilylphenylethyl substituents significantly decreased the thermal stability of the corresponding arenes. In particular, pentacene derivative **2** decomposed at 86 °C, which might explain the low synthetic yield of the corresponding compound. **Pen** and **ADT** derivatives with the present core substituents exhibited significantly red-shifted optical absorption spectra. Pentacene derivatives **1** and **2** in C_6H_5Cl exhibited λ_{max} values of ~664 nm (vs. ~579 nm for pentacene), while ADT

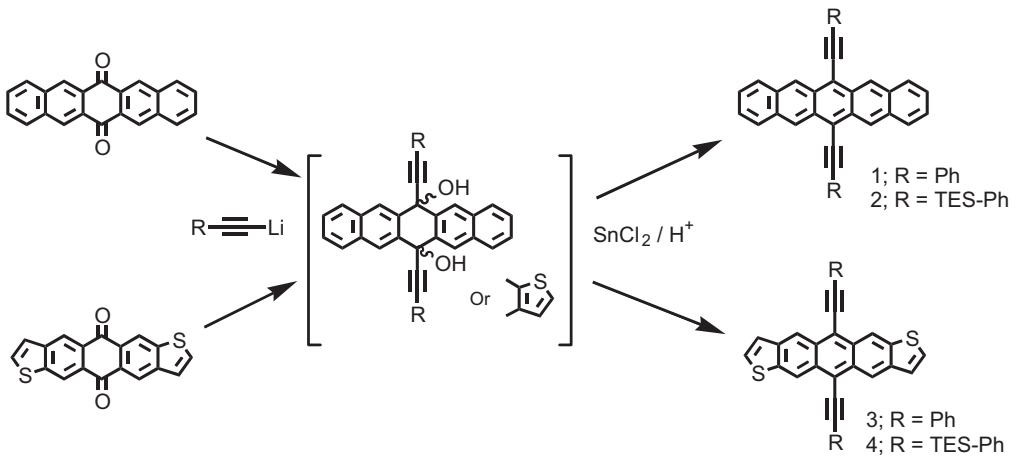

Scheme 2. Synthesis of soluble **PEN** and **ADT** derivatives **1**–**4**.

Table 2
Thermal, optical absorption/emission, and electrochemical data for compounds **1–4**.

Comp.	Decomp. T_d (°C)	TGA (°C; 5%)	Optical[b] λ_{max} (nm)	Reductive potential (V)[c]	Oxidative potential (V)[c]	ΔE_{gap} (eV)	
						(UV)[b]	(DPV)[c]
1	255	423	662	−0.924	0.876	1.76	1.80
2	86	382	666	−0.864	0.836	1.73	1.70
PEN	373[a]	297	579	−1.27	0.820	2.07	2.09
3	339	320	571	−1.14	0.948	2.06	2.09
4	168	239	576	−1.14	0.956	2.05	2.10
ADT	450[a]	306	490	−1.63	0.940	2.47	2.57

[a] Melting temperature.
[b] In C_6H_5Cl.
[c] In *o*-$C_6H_4Cl_2$ at 100 °C (Fc/Fc^+ as an internal standard at +0.6 V).

derivatives **3** and **4** exhibited λ_{max} values of ~574 nm (vs. ~490 nm for ADT; Fig. 1), demonstrating extended π-electron delocalization from the molecular core to the phenylethenyl substituents. Calculated from the onset of the optical absorption, pentacene derivatives **1** and **2** exhibited smaller HOMO−LUMO energy gaps than do ADTs **3** and **4**, which was consistent with the energy gap values derived electrochemically (*vide infra*).

The photooxidative stability of derivatives **1–4** was investigated by monitoring the absorbance decay at λ_{max} in aerated C_6H_5Cl solutions while exposing to white light (fluorescent lamp) at room temperature (Fig. 2) [15].

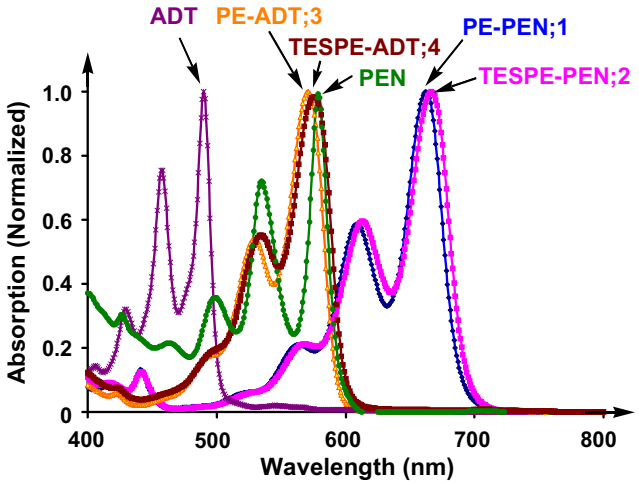

Fig. 1. Optical absorption spectra of compounds **1–4** in C_6H_5Cl solution.

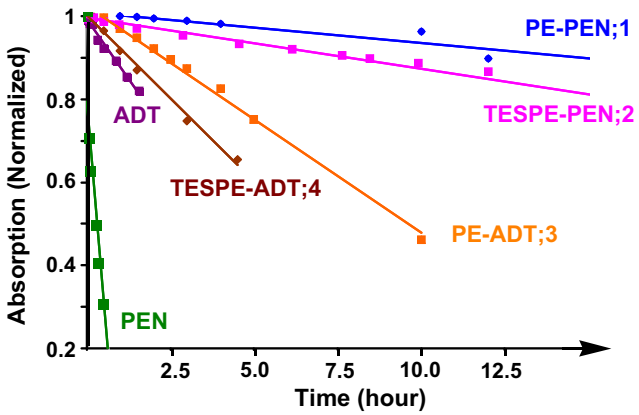

Fig. 2. Photostability of compounds **1–4** in a C_6H_5Cl solution, as monitored by optical spectroscopy under white light at room temperature.

Decomposition was observed for all compounds under these conditions over 24 h. Nevertheless, the core-substituted compounds in this study exhibited longer half-lives than non-substituted **PEN** and **ADT**, demonstrating enhanced stability via core substitution, as observed for other pentacene derivatives [16]. The phenylethynyl-substituted compounds (**1** and **3**) exhibited enhanced photostability compared to triethylsilylphenylethynyl-substituted derivative **2** and **4**. Note that under ambient conditions (O_2 and H_2O present) without white light, no decomposition was observed for these soluble **ADT**s and **PEN**s, demonstrating their potential as solution-processable organic semiconductors.

3.3. Electrochemical characterization

Differential pulse voltammograms (DPVs; using ferrocene/ferrocenium as internal standard at +0.6 V) of compounds **1–4** were recorded in dichlorobenzene at 100 °C [17], and the resulting oxidation and reduction potentials are summarized in Table 2 [18]. For the **PEN** series, the DPV spectra of compounds **1** and **2** exhibited oxidative peaks at +0.84 V and +0.88 V as well as reductive peaks at −0.86 V and −0.92 V, respectively (using ferrocene/ferrocenium as the internal standard at +0.6 V); both oxidative and reductive peaks were shifted to more positive values than those of **PEN** (+0.82 V and −1.27 V, respectively). Similar shifts of both oxidative and reductive peaks were observed for the **ADT** series. The HOMO levels of the ADT derivatives were therefore slightly lower than those of the pentacene derivatives (Fig. 3; assuming ferrocene/ferrocenium oxidation at 4.8 eV). In contrast, the LUMO levels of these soluble compounds were significantly lower in both series compared to unsubstituted **PEN** and **ADT**, which can be attributed to more extensive π-electron delocalization [19]. Overall, the electrochemically-derived HOMO−LUMO energy gaps were ranked in the order of **1** ≈ **2** < **PEN** ≈ **3** ≈ **4** < **ADT** (Fig. 3), in agreement with the values obtained from optical spectroscopy (Table 2).

3.4. Single-crystal structure analysis

The diffraction-derived crystal structures of compounds **1–4** are shown in Figs. 4–7, respectively, and the corresponding data are summarized in Table 1. The molecular packings of phenylethynyl-substituted compounds **1** and **3** were similar to that reported for **BBPE–PEN** [3g]. As shown in Figs. 4–7, the phenyl moieties attached to the ethynyl group were not coplanar with the central **PEN** or **ADT** cores, but had torsional angles of 11.8° and 22.5° (**1**; Fig. 4D), 10.1° (**3**; Fig. 5D), 16.6° (**2**; Fig. 6D), and 18.1° and 28.2° (**4**; Fig. 7D), respectively [20]. The molecular pac-

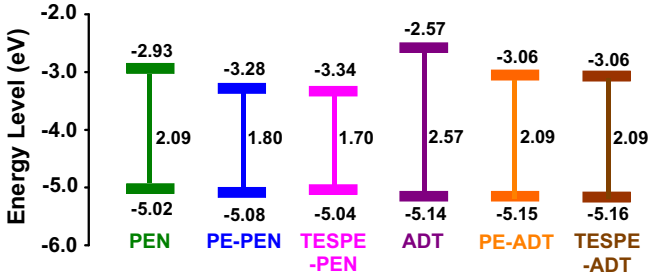

Fig. 3. Electrochemically-derived HOMO and LUMO energies of compounds **1–4**, **PEN**, and **ADT**.

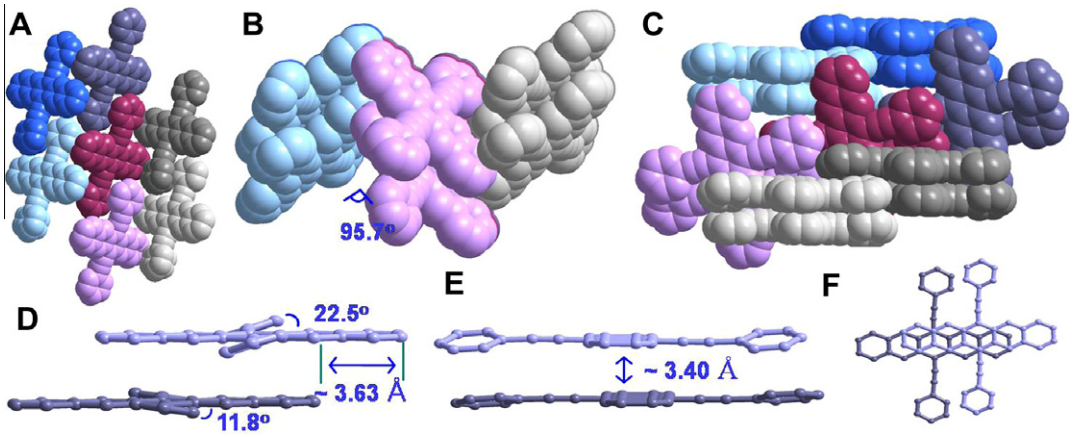

Fig. 4. Crystal structure of compound **1**. (A) Top view (space filling model). (B) Front view. Each of the π-stacks interweave with each another in a herringbone packing at an angle of 95.7°. (C) Side view. (D) Front view. The core interlayer spacing (~3.40 Å) and C_6H_5 groups have torsional angles of about 11.8° and 22.5° with respect to the **PEN** plane. (E) Side view. (F) Top view. The **PEN** cores form 2-D slipped stacks.

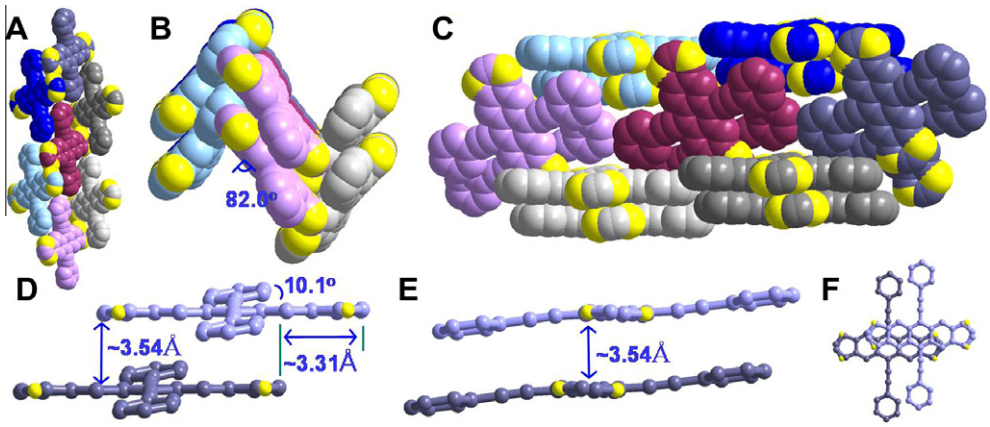

Fig. 5. Crystal structure of compound **3**. (A) Top view (space filling model). (B) Front view. Each of the **ADT** π-stacks interweave with each another in a herringbone motif at an angle of 82°. (C) Side view. (D) Front view. The core interlayer spacing (~3.54 Å) and C_6H_5 groups have torsional angles of about 10.1° with respect to the **ADT** plane. (E) Side view. (F) Top view. The **ADT** cores form 2-D slipped stacks.

kings of **1** and **3** were similar, exhibiting a herringbone-type packing with tilt angles of 95.7° and 82.0° (Figs. 4B and 5B), respectively [20]. In each packing column, the **PEN** or **ADT** cores formed 2-D slipped stacks and adopted a nearly face-to-face packing motif (Figs. 4 and 5), with an interplanar angle of ~0° and interplanar distances of

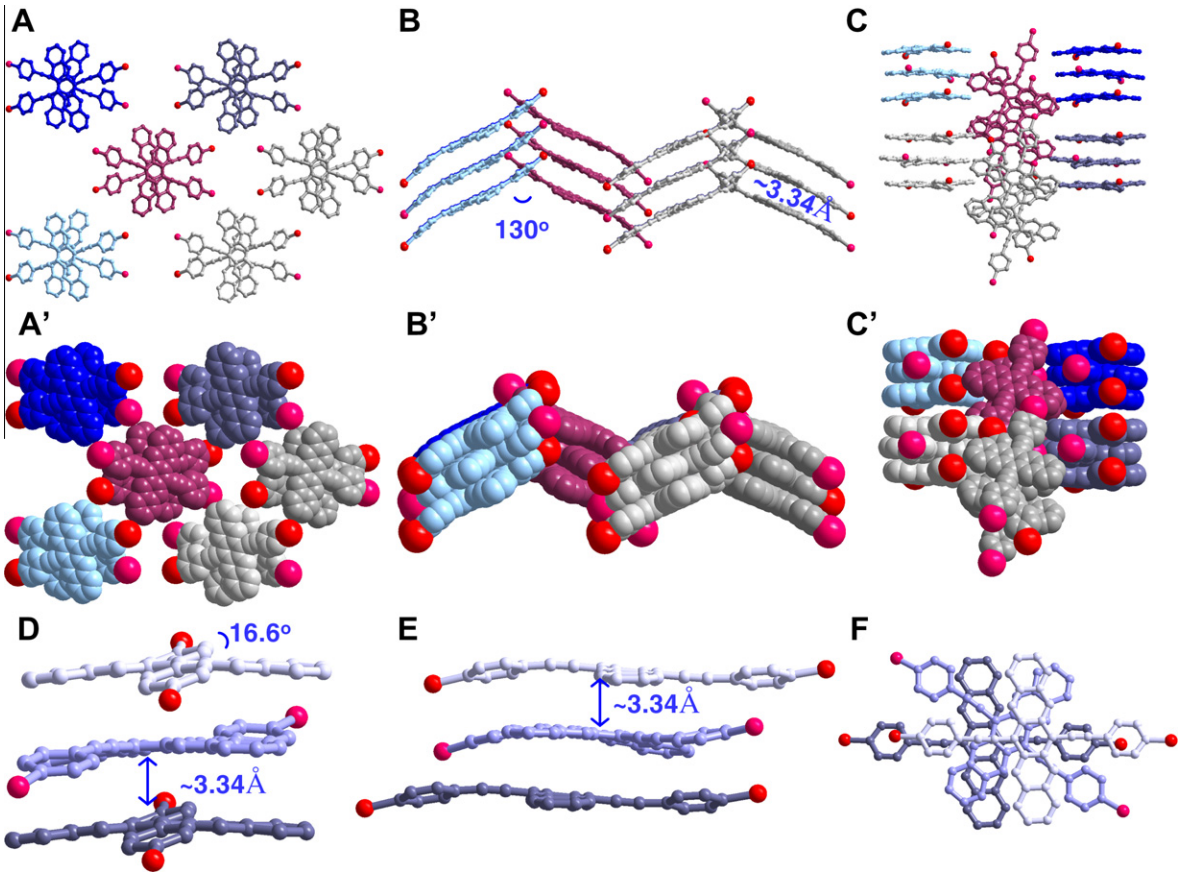

Fig. 6. Crystal structure of compound **2**. (A) Top view. The **PEN** cores form 2-D "slipped-crossed" stacks. (B) Front view. Each of the **PEN** π-stacks interweave with one another in a herringbone motif at an angle of 130°. (C) Side view. (D) Front view. The core interlayer separation (~3.34 Å) and the C_6H_5 groups have torsional angles of ~16.6° with respect to the **PEN** plane. (E) Side view. (F) Top view. The "slipped-crossed" π-stacks of **PEN**s (A′, B′, and C′ are space filling models of A, B, and C, respectively).

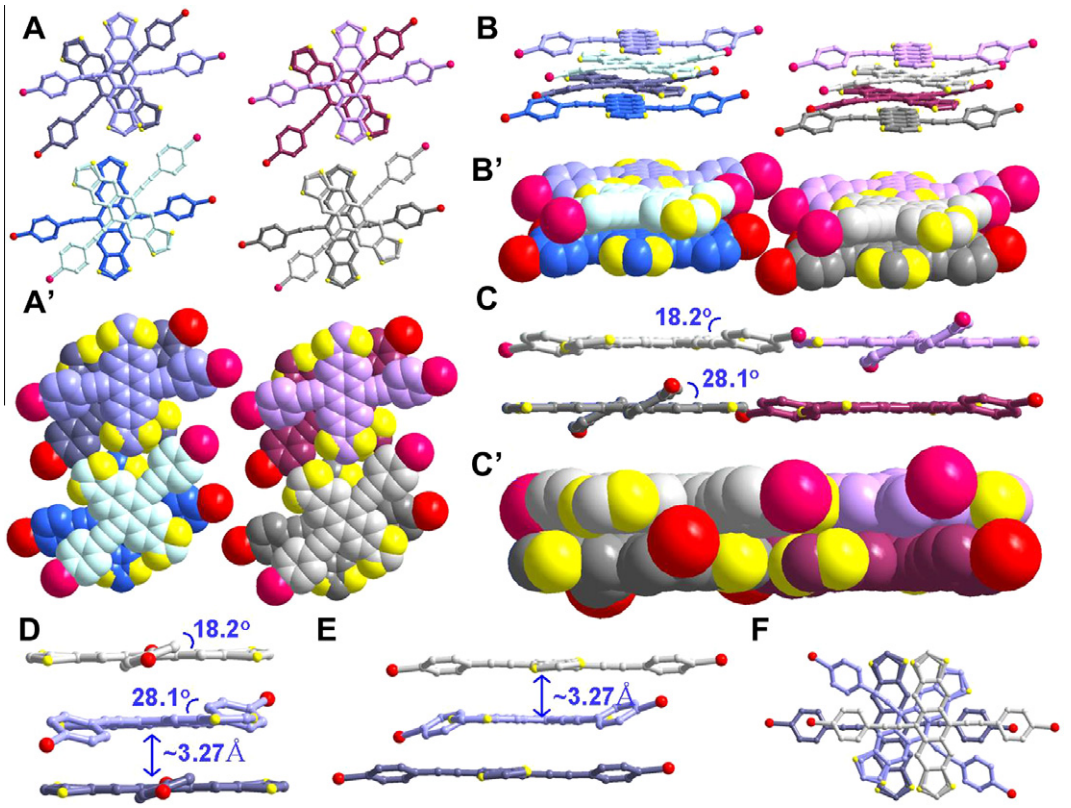

Fig. 7. Crystal structure packing of compound **4**. (A) Top view. The **ADT** cores form 2-D "slipped-crossed" stacks. (B) Front view. Each of the **ADT** π-stacks interweave with each another. (C) Side view. (D) Front view. The core interlayer separation (~3.27 Å) and C_6H_5 groups have torsional angles of ~18° and 28° with respect to the **ADT** core. (E) Side view. (F) Top view. The "slipped-crossed" π-stacks of **ADT**s (A′, B′, and C′ are space filling models of A, B, and C, respectively).

~3.40 Å and ~3.54 Å (Figs. 4D and 5D), respectively [20]. Note that the **PEN** or **ADT** cores were not perfectly aligned with each other but were slipped ~3.63 Å (**1**) and ~3.31 Å (**3**) along the long axis as well as half a unit cell length along the short axis (Figs. 4E and 5F), revealing a close-packed layered structure with intimate π–π overlap.

With the bulky triethylsilyl (TES) moiety appended to the phenylethynyl group, the molecular packings of compounds **2** and **4** were very different from compounds **1** and **3,** as shown in Figs. 6 and 7, respectively. The substitutions of relatively bulky TESPE groups into peripositions of polyacenes did disrupt the herringbone structure of the main Pen and ADT core [21]. Compounds **2** and **4** engaged in 2-D "slipped-crossed" stacking to accommodate the bulky TES groups. For compound **2**, each of the **PEN** π-stacks interweaved with one another in a herringbone motif at an angle of 130° (Fig. 6B), while this interweaving angle is nearly 180° for compound **4** (Fig. 7B and C). The **PEN** or **ADT** cores stacked with interplanar separations of ~3.34 Å and ~3.27 Å (Figs. 6E and 7E), respectively. Note that this bulky TES substituent induced significant deviations from planarity in the **PEN** core of compound **2**, in contrast to the other three compounds of this study (Fig. 6D and E). For compound **4**, the interplanar distance is very comparable to those in TES–ADT (3.25 Å) [3a]. The shortest interplanar distance and planarity (with core interweaving angle of ~180°) of compound **4** may explain the highest electronic performance among all compounds employed in this study (*vide infra*; [22]).

3.5. Thin-film transistor characterization

Top-contact/bottom-gate OTFTs were fabricated by drop-casting [23] films of compounds **1**–**4** onto bare and HMDS-treated p^+-Si/SiO_2 substrates (compound **3** was also fabricated via vacuum deposition on both substrates) [24], followed by Au deposition through a shadow mask to define the source and drain electrodes. OTFT characterization

Table 3
Charge carrier mobility (μ, $cm^2/V\,s$)[a], current on/off ratio (I_{on}:I_{off}), and threshold voltage (V_T, V) data for OTFTs fabricated with compounds **1**–**4** on bare Si/SiO_2 substrates.

Compound	Solvent	μ	I_{on}:I_{off}	V_T
1	C_6H_5Cl	0.001	10^4	−1.0
2	C_6H_5Cl	0.0004	10^4	−7.3
3	C_6H_5Cl	0.005	10^4	−10.0
3[b]		0.015	10^{3-4}	−1.2
4	Toluene	0.013	10^4	−15.0

[a] Calculated in the saturation regime.
[b] This device was fabricated on an HMDS-treated SiO_2 substrate by vacuum deposition.

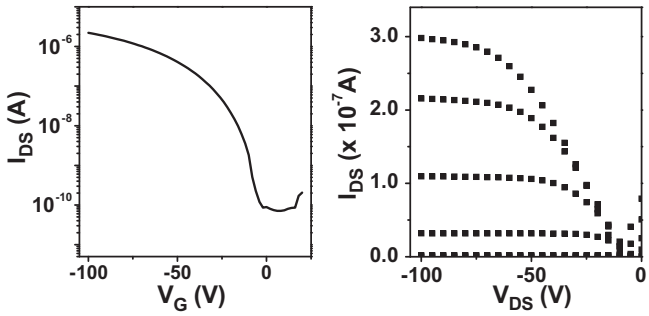

Fig. 8. Transfer and output characteristics of a representative OTFT fabricated with compound **4**. The films were drop-cast from toluene.

was performed in ambient conditions, and the corresponding device characteristics are summarized in Table 3 and Fig. 8 [25].

The devices fabricated with compounds **1**–**4** all exhibited TFT activity as p-channel semiconductors. In general, enhanced performance was observed: (a) in the **ADT** families versus the **PEN**s, and (b) when chlorobenzene was used as the drop-casting solvent. All the compounds employed in this study were sufficiently soluble in common solvents (e.g., toluene, chlorobenzene, and dichlorobenzene) at room temperature. As a preliminary fabrication of the device via solution-process, we prepared for thin films of each compound via drop-casting from the solution. For **PEN** derivatives, the highest carrier mobility values of 0.001 and 0.0004 cm^2/V s were observed for films of compounds **1** and **2,** respectively, drop-cast from chlorobenzene. The corresponding I_{on}:I_{off} and V_T values were 10^4 and −1 to −7 V for these **PEN**-based materials. In contrast, **ADT**-based devices fabricated by drop-casting exhibited relatively high mobilities of 0.005 cm^2/V s for compound **3** (from chlorobenzene), and 0.013 cm^2/V s for compound **4** (from toluene). Similarly to the **PEN** series, I_{on}:I_{off} and V_T values of 10^4 and −10 to −15 V were observed for the **ADT** derivatives. All of the devices were characterized after two months of storing under nitrogen (without being exposed to light) and did not show any degradation in performance (both mobility and current on/off ratios).

3.6. Thin-film microstructure

Film crystallinity and morphology are frequently strongly correlated with OTFT performance. Film morphologies and microstructures for the present new class of materials were studied by optical microscopy and X-ray diffraction for drop-cast thin films. Optical microscopic examination of the drop-cast films revealed pronounced differences in morphology between the **PEN** and **ADT** derivatives (Fig. 9). Polycrystalline platelet-like features were observed for the **ADT**-based films, while relatively fewer crystalline features were observed for drop-cast films of the **PEN** derivatives, which is in accord with the performance of the corresponding TFTs (*vide supra*).

With crystal structure in hand, we could simulate the XRD powder pattern and assign the reflections observed in the film XRD data (Fig. 10). Comparing these data can be useful to analyze the molecular ordering of the compounds. Fig. 10 shows a graphical comparison of experimental and simulated data, with a $\theta - 2\theta$ scan for a drop-casted film of

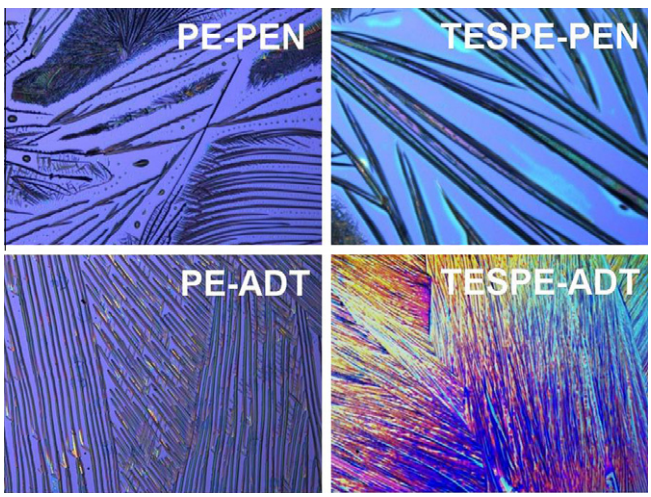

Fig. 9. Optical micrographs of drop-cast films of compounds **1**–**4**. All images were taken at 50× magnification.

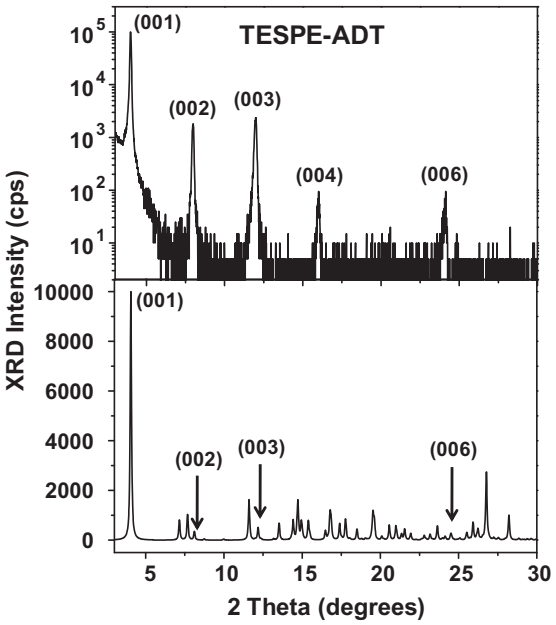

Fig. 10. Comparison of the $\theta - 2\theta$ XRD scans of drop-cast films of **TESPE–ADT** on bare Si/SiO_2 substrates (top) with the simulated powder pattern (bottom).

compound **4** on bare Si/SiO_2 substrate, and a powder pattern generated from the single-crystal data. As shown, (0 0 1) reflection family from (0 0 1) to (0 0 6) was pronounced, indicating predominant ordering of the molecules in c direction. For other compounds, the (0 1 1) reflections for compound **1** and (1 2 0) reflections for compound **2** could be assigned, indicating no predominant ordering in the direction of the unit cell axis for both compounds (Fig. S5). For compound **3**, powder pattern did not show (1 0 0) reflections which were present in the film XRD [26].

Overall, the thin film XRD microstructural analysis showed features in agreement with the optical microscopic analysis. Fig. 11 shows representative $\theta/2\theta$ out-of-plane XRD scans for drop-cast films on bare Si/SiO_2 substrates. As shown, the **ADT** derivatives exhibited more highly textured films having large peak intensities with multiple Bragg reflections. Notably, compound **4** exhibited the highest film texturing with multiple Bragg reflections up to (0 0 6), indicating high film crystallinity and in agreement with the TFT performance (*vide supra*). The estimated *d*-spacing value from the (1 0 0) reflection for compound **4** was 22.2 Å (which corresponds to the length of the *c* axis of the unit cell in the crystal structure), indicating a crystalline polymorph where the majority of the molecules have edge-on orientation on the substrate surface and with the π–π stacking direction parallel to the substrate, thereby facilitating in-plane charge transport from source to drain. The diffraction patterns of compounds **1** and **3** showing relatively low carrier mobilities (0.001–0.005 $cm^2/V\,s$) exhibited multiple Bragg reflections (up to three peaks) but with modest peak intensities, and with the latter material evidencing two different phases or growth orientations. Estimated *d*-spacings for these compounds were in the narrow range of 11.6–12.0 Å, probably

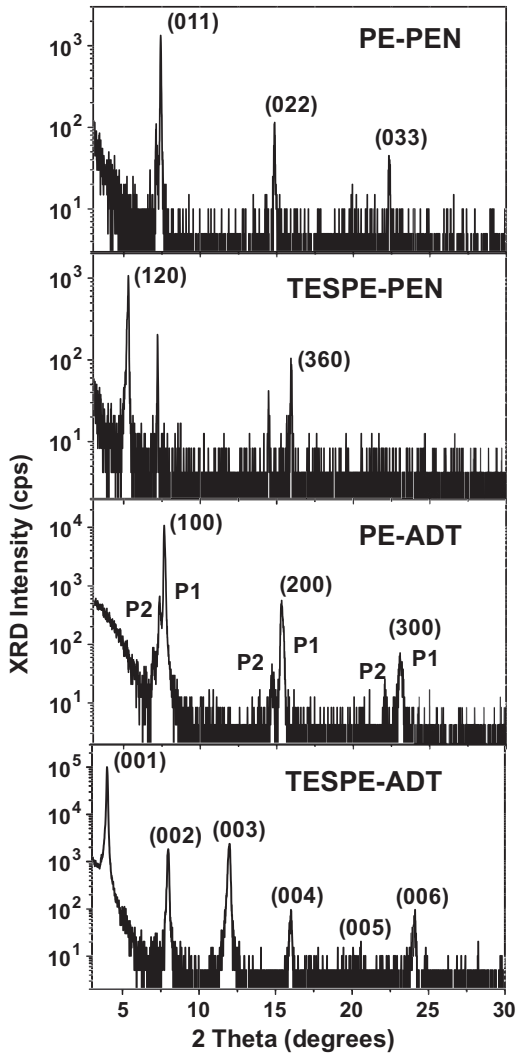

Fig. 11. Representative $\theta - 2\theta$ XRD scans (in logarithmic scale) of drop-cast films of the indicated materials on bare Si/SiO_2 substrates (P1 and P2 indicate two different phases). Peaks are assigned in comparison with the powder pattern generated from the single crystal structures.

indicating similar molecular organization in the films. Compound **2**, with the lowest OTFT performance, exhibited two Bragg reflections having modest peak intensities.

4. Conclusions

In summary, four solution-processable pentacene (**PEN**) and anthradithiophene (**ADT**) derivatives have been synthesized and found to exhibit OTFT p-channel transport. The phenylethynyl substituents were found to be effective in increasing the solubility and environmental stability of the corresponding semiconductors. From the preliminary fabrication of the device via drop-casting, compared to the **PEN** derivatives, the **ADT**-based compounds exhibited higher device performance with respectable carrier mobilities of 0.005–0.013 $cm^2/V\,s$. The magnitudes of the mobilities were strongly correlated with the film

morphology and microstructure. These results provide new information about the structural characteristics of **PEN** and **ADT**-based semiconductors and the attractions of using these cores and substitutents for designing more solution-processable OTFT materials. A further complete and detailed device fabrication via other solution-processing methods is underway [22].

Acknowledgements

We thank the National Science Council, Taiwan, Republic of China (Grant Numbers NSC98-2628-M-008-003, NSC97-2113-M-008-003, and NSC98-2627-E-006-003) and Industrial Technology Research Institute of Taiwan for support. Research at Northwestern was supported by AFOSR (FA9550-08-1-0331) and by the NSF-MRSEC program through the Northwestern Materials Research Center (DMR-0520513).

Appendix A. Supplementary material

Supplementary data associated with this article can be found, in the online version, at doi:10.1016/j.orgel.2010.04.029.

References

[1] (a) For recent reviews on this topic, see: A.C. Arias, J.D. MacKenzie, I. McCulloch, J. Rivnay, A. Salleo, Chem. Rev. 110 (2010) 3;
(b) C.-A. Di, Y. Liu, Y. Yungi, Z. Gui, D. Zhu, Acc. Chem. Res. 42 (2009) 1573;
(c) M. Chabinyc, Y.-L. Loo, J. Macrom. Sci. Polym. Rev. 46 (2006) 1;
(d) A. Dodabalapur, Nature 434 (2005) 151;
(e) H. Sirringhaus, Adv. Mater. 17 (2005) 2411;
(f) A. Facchetti, M.-H. Yoon, T.J. Marks, Adv. Mater. 17 (2005) 1705.

[2] (a) For recent studies, see: X. Gao, C. Di, Y. Hu, X. Yang, H. Fan, F. Zhang, Y. Liu, H. Li, D. Zhu, J. Am. Chem. Soc. 132 (2010). ASAP;
(b) C. Kim, J.R. Quinn, A. Facchetti, T.J. Marks, Adv. Mater. 22 (2010) 342;
(c) C. Kim, M.-C. Chen, Y.-J. Chiang, Y.-J. Guo, J. Youn, H. Huang, Y.-J. Liang, Y.-J. Lin, Y.-W. Huang, T.-S. Hu, G.-H. Lee, A. Facchetti, T.J. Marks, Org. Electron. (2010) 801;
(d) R. Hamilton, M. Heeney, T. Anthopoulos, I. McCulloch, Org. Electron. (2010) 393;
(e) H. Yan, Z. Chen, Y. Zheng, C.E. Newman, J.R. Quinn, F. Dolz, M. Kastler, A. Facchetti, Nature 457 (2009) 679;
(f) X. Cheng, Y.-Y. Noh, J. Wang, M. Tello, J. Frisch, R.-P. Blum, A. Vollmer, J.P. Rabe, N. Koch, H. Sirringhaus, Adv. Funct. Mater. 19 (2009) 2407;
(g) C. Reese, M.E. Roberts, S.R. Parkin, Z. Bao, Adv. Mater. 21 (2009) 3678;
(h) G.R. Llorente, M.-B. Dufourg-Madec, D.J. Crouch, R.G. Pritchard, S. Ogier, S.G. Yeates, Chem. Commun. (2009) 3059;
(i) M.-C. Chen, Y.-J. Chiang, C. Kim, Y.-J. Guo, S.-Y. Chen, Y.-J. Liang, Y.-W. Huang, T.-S. Hu, G.-H. Lee, A. Facchetti, T.J. Marks, Chem. Commun. (2009) 1846.

[3] (a) S.K. Park, D.A. Mourey, J.-I. Han, J.E. Anthony, T.N. Jackson, Org. Electron. 10 (2009) 486;
(b) T.W. Kelly, P.F. Baude, C. Gerlach, D.E. Ender, D. Muyres, M.A. Hasse, D.E. Vogel, S.D. Theiss, Chem. Mater. 16 (2004) 4413;
(c) M.M. Payne, S.R. Parkin, J.E. Anthony, J. Am. Chem. Soc. 127 (2005) 4986;
(d) C.R. Swartz, S.R. Parkin, J.E. Bullock, J.E. Anthony, A.C. Mayer, G.G. Malliaras, Org. Lett. 7 (2005) 3163;
(e) D.J. Gundlach, Y.Y. Lin, T.N. Jackson, S.F. Nelson, Appl. Phys. Lett. 80 (2002) 2925;
(f) H. Meng, M. Bendikov, G. Mitchell, R. Helgeson, F. Wudl, Z. Bao, T. Siegrist, C. Kloc, C.H. Chen, Adv. Mater. 15 (2003) 1090;
(g) Y. Li, Y. Wu, P. Liu, Z. Prostran, S. Gardner, B.S. Ong, Chem. Mater. 19 (2007) 418.

[4] (a) J.G. Laquindanum, H.E. Katz, A.J. Lovinger, J. Am. Chem. Soc. 120 (1998) 664;
(b) M.M. Payne, S.A. Odom, S.R. Parkin, J.E. Anthony, Org. Lett. 6 (2004) 3325;
(c) O.D. Jurchescu, S. Subramanian, R.J. Kline, S.D. Hudson, J.E. Anthony, T.N. Jackson, D.J. Gundlach, Chem. Mater. 20 (2008) 6733;
(d) M.-C. Chen, C. Kim, S.-Y. Chen, Y.-J. Chiang, M.-C. Chung, A. Facchetti, T.J. Marks, J. Mater. Chem. 18 (2008) 1029.

[5] (a) C.E. Mauldin, K. Puntambekar, A.R. Murphy, F. Liao, V. Subramanian, J.M.J. Frechet, D.M. Delongchamp, D.A. Fischer, M.F. Toney, Chem. Mater. 21 (2009) 1927;
(b) K. Takimiya, Y. Kunugi, Y. Konda, H. Ebata, Y. Toyoshima, T. Otsubo, J. Am. Chem. Soc. 128 (2006) 3044;
(c) Y.M. Sun, Y.Q. Ma, Y.Q. Liu, Y.Y. Lin, Z.Y. Wang, Y. Wang, C.A. Di, K. Xiao, X.M. Chen, W.F. Qiu, B. Zhang, G. Yu, W.P. Hu, D. Zhu, Adv. Funct. Mater. 16 (2006) 426;
(d) K. Xiao, Y. Liu, T. Qi, W. Zhang, F. Wang, J. Gao, W. Qiu, Y. Ma, G. Cui, S. Chen, X. Zhan, G. Yu, J. Qin, W. Hu, D. Zhu, J. Am. Chem. Soc. 127 (2005) 13281;
(e) X. Zhang, A.P. Cote, A.J. Matzger, J. Am. Chem. Soc. 127 (2005) 10502;
(f) S. Ando, J. Nishida, H. Tada, Y. Inoue, S. Tokito, Y. Yamashita, J. Am. Chem. Soc. 127 (2005) 5336.

[6] (a) G.S. Tulevski, Q. Miao, A. Afzali, T.O. Graham, C.R. Kagan, C. Nuckolls, J. Am. Chem. Soc. 128 (2006) 1788;
(b) K.P. Weidkamp, A. Afzali, R.M. Tromp, R.J. Hamers, J. Am. Chem. Soc. 126 (2004) 12740.

[7] (a) J.E. Anthony, J.S. Brooks, D.L. Eaton, S.R. Parkin, J. Am. Chem. Soc. 123 (2001) 9482;
(b) C.D. Sheraw, T.N. Jackson, D.L. Eaton, J.E. Anthony, Adv. Mater. 15 (2003) 2009;
(c) C.P. Benard, Z. Geng, M.A. Heuft, K. VanCrey, A.G. Fallis, J. Org. Chem. 72 (2007) 7229;
(d) D. Lehnherr, R. McDonald, R.R. Tykwinski, Org. Lett. 10 (2008) 4163.

[8] (a) Pentacene precursors are soluble derivatives, however, the intrinsic unstability of pentacene remains. M.A. Wolak, B.B. Jang, L.C. Palilis, Z.H. Kafafi, J. Phys. Chem. B 108 (2004) 5492;
(b) A. Maliakal, K. Raghavachari, H. Katz, E. Chandross, T. Siegrist, Chem. Mater. 16 (2004) 4980;
(c) H. Yamada, Y. Yamashita, M. Kikuchi, H. Watanabe, T. Okujima, H. Uno, T. Ogawa, K. Ohara, N. Ono, Chem. Eur. J. 11 (2005) 6212;
(d) P. Coppo, S.G. Yeates, Adv. Mater. 17 (2005) 3001;
(e) A.R. Reddy, M. Bendikov, Chem. Commun. (2006) 1179.

[9] (a) M.M. Payne, S.R. Parkin, J.E. Anthony, C.-C. Kuo, T.N. Jackson, J. Am. Chem. Soc. 127 (2005) 4986;
(b) S. Subramanian, S.K. Park, S.R. Parkin, V. Podzorov, T.N. Jackson, J.E. Anthony, J. Am. Chem. Soc. 130 (2008) 2706.

[10] R. Schmidt, S. Göttling, D. Leusser, D. Stalke, A. Krause, F. Würthner, J. Mater. Chem. 16 (2006) 3708.

[11] J.E. Anthony, Chem. Rev. 106 (2006) 5028.

[12] D.R. Maulding, B.G. Roberts, J. Org. Chem. 34 (1969) 1734.

[13] Although this 4-triethylsilylphenyl acetylene has been reported in the literature (see ref below) this ligand can be obtained via the Sonogashira coupling in a simple procedure with good yield. C. Eaborn, A.R. Thompson, D.R.M. Walton, J. Chem. Soc. C. Org. 15 (1967) 1364.

[14] S.M. Sze, Physics of Semiconductor Devices, second ed., John Wiley & Sons, USA, 1981.

[15] Since the concentration of the solution has a strong influence on the rate of decomposition, a very dilute solution ($\sim 4.0 \times 10^{-5}$ M) was used.

[16] Alkynyl substitution lowers the LUMO energy for pentacene derivatives as compared to that of pentacene, which has been known to hinder photooxidation. M. Akhtaruzzaman, N. Kamata, J. Nishida, S. Ando, H. Tada, M. Tomura, Y. Yamashita, Chem. Commun. (2005) 3183. and Ref. [3a].

[17] Because Pen is not sufficiently soluble, the DPV was performed at high temperature. There was no indication of thermal decomposition under this condition (under N_2).

[18] Measured with a Pt working electrode in an *o*-dichlorobenzene solution using 0.1 mol dm^{-3} Bu_4NPF_6 as the supporting electrolyte. N. Jun-ichi Nishida, D. Kumaki, S. Tokito, Y. Yamashita, J. Am. Chem. Soc. 128 (2006) 9598.

[19] Similar trends were reported in: J. Wang, K. Liu, Y.-Y. Liu, C.-L. Song, Z.-F. Shi, J.-B. Peng, H.-L. Zhang, X.-P. Cao, Org. Lett. 11 (2009) 2563.

[20] The planar angle ($\sim 8.1°$) and interweaving angle (82°) were smaller for BBPE-Pen with an interplanar core distance of 3.44 Å. In

comparison, both the interplanar distances of compound **1** (3.40 Å) and 3 (3.34 Å) were shorter than BBPE-Pen.
[21] J.E. Anthony, D.L. Eaton, S.R. Parkin, Org. Lett. 4 (2002) 15.
[22] Improved TFT performance for compound 4 was achieved by device fabrication via spin-coating.
[23] Standard deviations for 5 devices are typically <20%.
[24] All the compounds were fabricated via vacuum deposition on bare Si/SiO_2 and HMDS-treated substrates at various temperatures. But only one compound (compound 3) exhibited good device performance. The other compounds are inactive or exhibit very low performance (mobility $<10^{-6}$ cm^2/V s).
[25] All the available data for all compounds are in the Supporting Information (Tables S1–S2 and Figs. S1–S4).
[26] Except compound **4**, the X-ray diffraction pattern of the semiconductor films did not match the simulated powder pattern. This is likely due to polymorph formation (which is clearly shown in compound **3**).

The transferred bilayer active layer pure poly(3-hexylthiophene)/pure [6,6]-phenyl C61-butyric acidmethyl ester (pure P3HT/pure PCBM) should have discrete composition profile at the P3HT/PCBM interface. This study demonstrates, that a bilayer of P3HT and PCBM prepared by means of a stamping transfer method has an unexpected film composition that is, similar to the composition gradient of BHJ film generated from a P3HT/PCBM blended solution. In this study, we also discuss how a intermixing of P3HT/PCBM bilayer is occurred and affects the performance of the device.

2. Experimental details

First, a ITO glass was cleaned by chloroform, acetone and isopropanol to remove residual organic materials on the ITO surface which was then treated by oxygen plasma for 10 min in order to enhancing hydrophilic property. A sample of poly(3,4-ethylene dioxythiophene: poly(styrene sulfonate) (PEDOT:PSS, Baytron P), which is conducting polymer of hole transporting material was diluted to methanol and spin-coated to a thickness of approximately 35 nm. Using a digital-controlled hotplate, we pre-baked the devices in PEDOT:PSS at 200 °C for 5 min to evaporate the water contents. The stamping-transferred bilayer device, which composed of P3HT (approximately 150 nm) and PCBM (approximately 85 nm) from chlorobenzene, was well coated on the UV-PC film (as shown in inset of Fig. 1 and Fig. S1). Each P3HT and PCBM layer was then individually transferred from the UV-PC film to the PEDOT:PSS-coated ITO substrate, which was heated on a hotplate at 90 °C. The UV-PC film with the P3HT or PCBM layer was attached to the heated substrate and rubbed with cotton swabs with uniform force of 18.8 kg/cm^2 until the P3HT or PCBM layer coated on the PC film totally adhered to the heated substrate. When the stamping transfer process was conducted with simple physical force at a suitable temperature, the coated layer from the UV-PC film was perfectly transferred to the PEDOT:PSS-coated ITO with a reproducibility. A TiO_x interlayer with a thickness of approximately 3 nm was inserted between the bilayer and the Al cathode to enhance the device performance [3]. Subsequently, an Al metal electrode with a thickness of 150 nm was thermally deposited under a pressure of 1.7×10^{-6} Torr. To improve the interfacial contact between the active layer and the Al cathode, we used a thermal annealing process that involved the use of a digitally controlled hotplate at 150 °C for 30 min in a glove box. The active area of the printed bilayer with the thermally deposited Al electrode was correctly confirmed in the range of 3–6 mm^2 with a video microscope (SV-35). The *J–V* curves were measured at an illumination rating of AM 1.5 by using a Keithley 2400 source measure unit. A 1000 W xenon lamp of Oriel 91193 which is intensity was calibrated using a silicon reference cell (Fraunhofer ISE, Certificate No. C-ISE269) served as the light source to the devices. The surface morphology and the roughness of the transferred bilayer were analyzed with an atomic

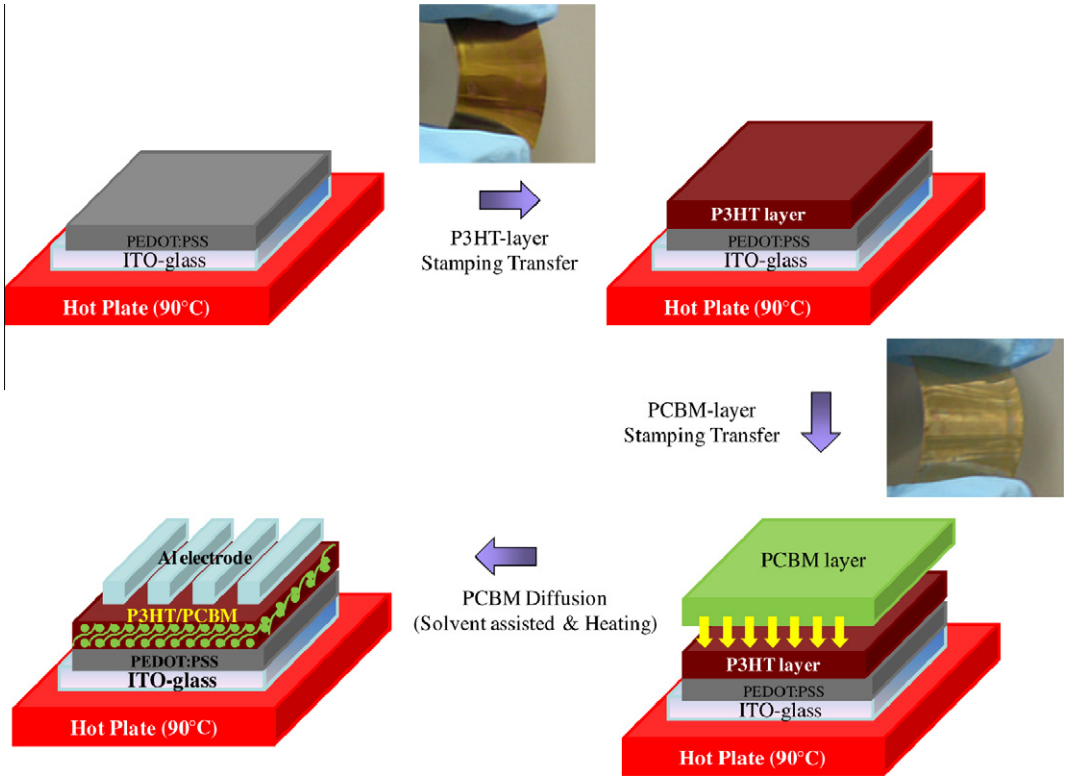

Fig. 1. Schematic diagram of the proposed device structure produced by using a stamping transfer technique of the P3HT/PCBM bilayer with a UV-curable resin-coated polycarbonate film.

force microscope (Veeco, USA; noncontact tapping mode, D3100).

3. Results and discussion

As shown in Fig. 1, for the device fabrication of P3HT/PCBM bilayer we used stamping transfer technique. The preparation involved a method of making UV-curable resin-coated polycarbonate (UV-PC) film as reported in our previous results [12]. A silicon wafer was cleaned by organic solvent, and treated by Trichloro-(1H, 1H, 2H, 2H – perfluorooctyl) silane (FOTS) to reduce the surface energy of the wafer, then the self-assembled monolayers (SAMs) were generated in the film to get the imprinting property [23]. The UV-curable resin was uniformly dropped between the flexible PC film and silicon wafer and flattened with a roller to well adhesion. The PC film was cured by UV for 3 min at the wavelength of 365 nm and wafer was detached. The size of UV-PC film is dependent on the area of used silicon wafer therefore it is easy to maximize the film areas.

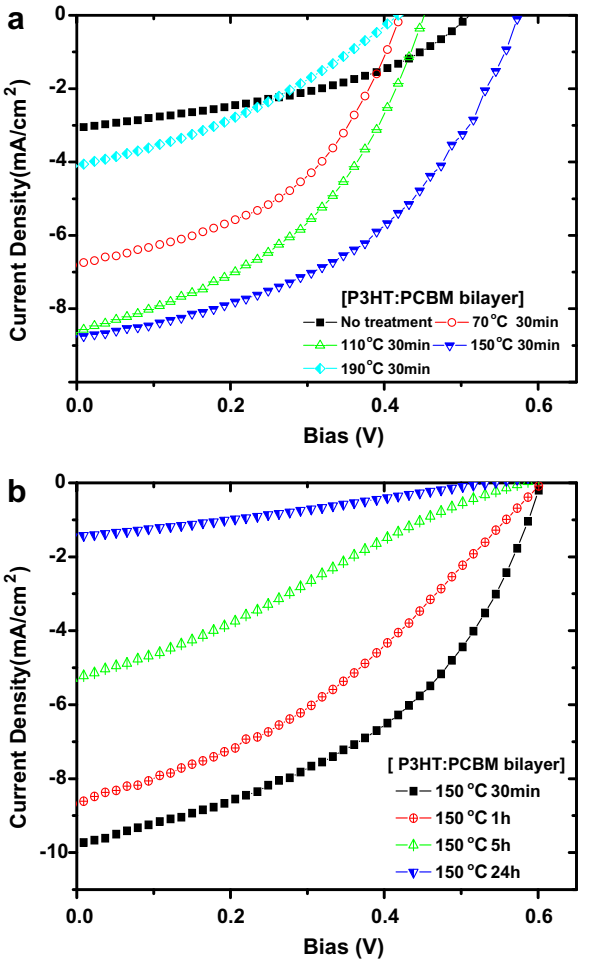

Fig. 2. (a) photocurrent–potential (*J–V*) curves of the stamping-transferred P3HT/PCBM bilayer devices in relation to various kinds of annealing temperatures; (b) *J–V* curves of P3HT/PCBM transferred bilayer devices that use a TiO_x interlayer as an effective electron transporting layer in relation to the annealing time.

Fig. 2a illustrates the photocurrent–potential (*J–V*) curves of the stamping-transferred P3HT/PCBM bilayer devices in relation to various kinds of annealing temperatures. For a device without the thermal annealing process, the power conversion efficiency (PCE) shows only 0.64% with the rms (root mean square surface roughness) value of 13 nm from AFM images of Fig. 3a and b. This result can be explained by low photocurrent density value due to decreased charge carrier mobility of no annealing [24]. However, when the annealing temperature is increased from 70 °C to 150 °C over the glass temperature of P3HT, all the device values, namely V_{oc}, J_{sc}, FF, and η (%), are enhanced because the closed packing structures of the reorganized P3HT polymer chain provide an efficient exciton dissociation [25]. Additionally, thermal annealing process plays an important role to produce an effective nanoscale interpenetrating network with crystalline order for P3HT/PCBM components in the bilayer structure [26]. This result confirms that the PCE value is increased from 0.64% to 2.34% in stamping-transferred bilayer devices after the devices annealed at an optimum temperature with the rms value of 8 nm from AFM images of Fig. 3c and d. Generally, p-type and n-type double-layer solar cells have low conversion efficiency. However, the devices prepared by means of the transfer stamping method with pure P3HT and pure PCBM have high level of efficiencies without destroy of previous printed bottom layer, as shown in Fig. 2. Moreover, Fig. 2b shows *J–V* curves of P3HT/PCBM transferred bilayer devices that use a TiO_x interlayer as an effective electron transporting layer in relation to the annealing time. Annealing of the device at 150 °C for 30 min enhances the PCE (%) to 2.63% with the increased photocurrent density value of 9.76 mA/cm^2. Also, the stamping-transferred bilayer device with a TiO_x interlayer showed improved fill factor value of 0.45 [27,28]. However, the efficiency of the device rapidly decreases if the device is heated continually for 24 h.

Fig. 4 shows the SEM images of P3HT/PCBM bilayer with post-annealing of 150 °C for 30 min or with post-annealing after continuous heating of 100 °C for 24 h. From these results, it can be demonstrated that the morphologies of bilayer active film were closely related to the annealing condition. This outcome suggests that prolonged annealing induces thermal degradation as well as the possibility of negative changes in the active layer at the inner region of the P3HT/PCBM interface with unwanted morphological changes, thus resulted in deterioration of the active polymer in the device due to the irregular aggregated domains as shown in the SEM images of Fig. 4b. Therefore, the rms values of the bilayer with P3HT/PCBM active film were gradually changed depending on annealing time from Fig. 3.

Fig. 5 shows the peak-to-peak Auger signal of the P3HT/PCBM bilayer as a function of the depth (nm) from the top to bottom layer. The sulfur element was only detected in the P3HT composition; therefore the degree of interpenetration in the P3HT/PCBM layer can be confirmed by Auger electron spectroscopy depending on the distribution and concentration gradient of the sulfur contents. Interestingly,

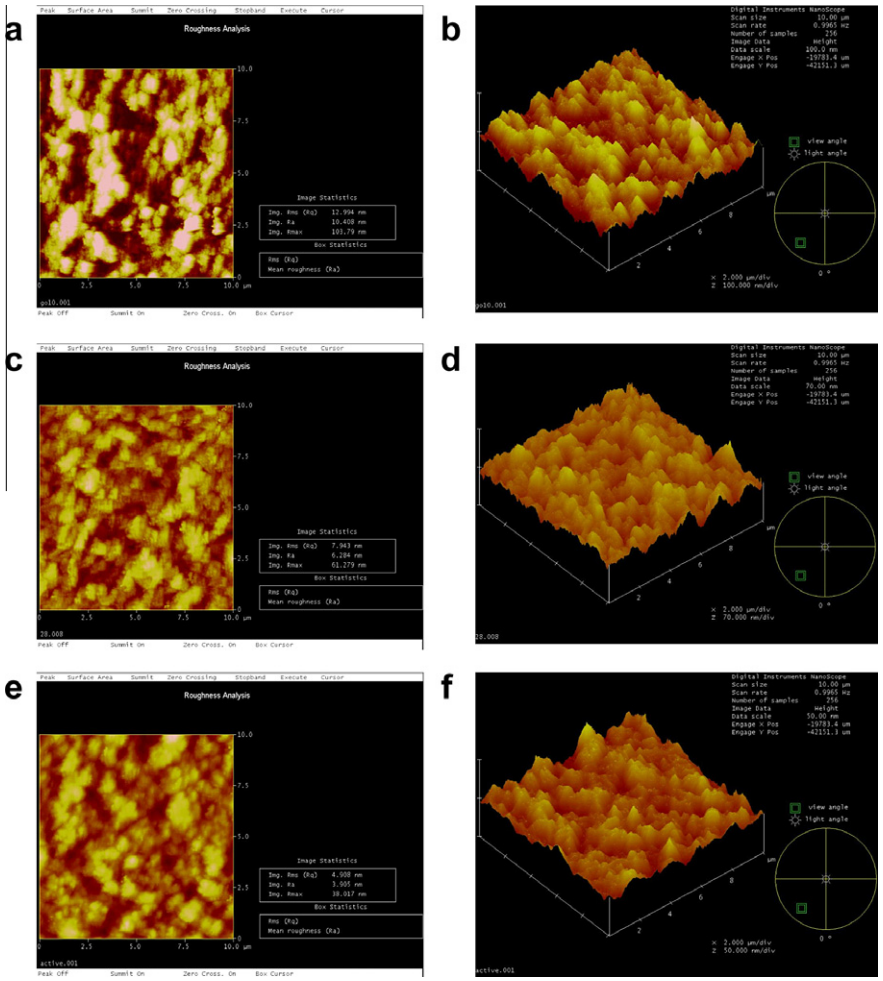

Fig. 3. AFM 2D or 3D images of stamping-transferred P3HT/PCBM bilayer depending on annealing time; (a and b) no annealing, (c and d) annealing with 150 °C for 30 min, and (e and f) annealing with 150 °C for 24 h.

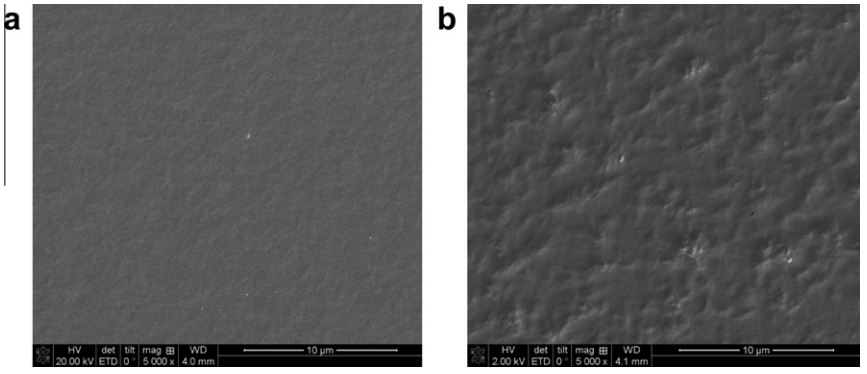

Fig. 4. SEM images of stamping-transferred P3HT/PCBM (a) bilayer with post-annealing of 150 °C for 30 min (b) bilayer with post-annealing and continuous heating of 100 °C for 24 h.

the transferred bilayer film (100% P3HT/100% PCBM) with an annealing time of 30 min does not show a sharp increase in the sulfur signal throughout the entire active region of the P3HT/PCBM bilayer. In our previous paper, a sharply increased gradient slope at the interface between the P3HT-rich region and the PCBM-rich region during the stamping process were observed, as shown in Fig. S2. As a results, when the Auger spectroscopy of the P3HT/PCBM bilayer is compared with that of the P3HT/PCBM BHJ film as shown in Fig. 5, the concentration profile of the bilayer looks like that of the BHJ film, suggesting the solid–solid intermixing behavior during the stamping

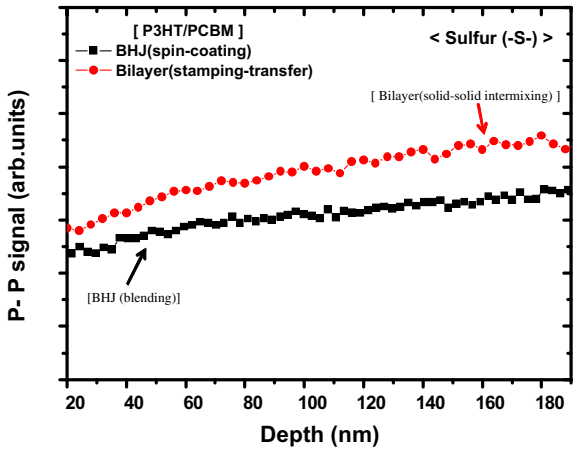

Fig. 5. Depth profile of P3HT/PCBM BHJ or bilayer with stamping transfer technique after the post-annealing of 150 °C for 30 min (Auger electron spectroscope).

transfer process. It seems that the residual chlorobenzene solvent in PCBM films on the UV-PC film after the spin-coating process can help swelling of P3HT bottom layer during rubbing process with cotton swabs (fully dried PCBM film do not have such a smooth profile). Then PCBM molecules might be able to penetrate into the P3HT molecules in the bottom layer because of the small molecular size of PCBM. However, when P3HT/PCBM blended film was transferred on the bottom layer by stamping method, this solid–solid intermixing behavior was not observed because of the large molecular size of P3HT. Polymeric P3HT molecules might induce steric-hindrance for the PCBM molecules to migrate into the P3HT bottom layer.

4. Conclusions

In conclusion, solid–solid intermixing was firstly observed in a stamping-transferred P3HT/PCBM bilayer film, firstly. Owing to the residual solvent, the stamping-transferred P3HT/PCBM bilayer film have BHJ like concentration profile; it does so by means of solid–solid intermixing. This unique discovery can be applied in preparing concentration-graded BHJ film from controlling solid–solid intermixing behavior for more in-depth understanding of the correlation between cell performances and P3HT/PCBM bilayer concentration profile.

Acknowledgement

This work was partially supported by a grant from the Fundamental R&D Program for Core Technology of Materials funded by the Ministry of Knowledge Economy, Republic of Korea. This work was also supported by a grant from the ERC program of the National Research Foundation (NRF), which is funded by the Korean Ministry of Education, Science and Technology (MEST) [No.R11-2007-045-01002-0(2009)]. The authors Choi and Lee of the Korea Institute of Machinery and Materials acknowledge the support of a grant (M102KN010001-08K1401-00210) from the CNMM.

Appendix A. Supplementary data

Supplementary data associated with this article can be found, in the online version, at doi:10.1016/j.orgel.2010.05.018.

References

[1] G. Dennler, M.C. Scharber, C.J. Brabec, Adv. Mater. 21 (2009) 1323.
[2] G. Yu, J. Gao, J.C. Hummelen, F. Wudl, A.J. Heeger, Science 270 (1995) 1789.
[3] D.H. Wang, S.H. Im, H.K. Lee, J.H. Park, O.O. Park, J. Phys. Chem. C 113 (2009) 17286.
[4] F.C. Krebs, M. Jørgensen, K. Norrman, O. Hagemann, J. Alstrup, T.D. Nielsen, J. Fyenbo, K. Larsen, J. Kristensen, Sol. Energy Mater. Sol. Cells 93 (2009) 422.
[5] M. Jørgensen, K. Norrmana, F.C. Krebs, Sol. Energy Mater. Sol. Cells 92 (2008) 686.
[6] I. Gonzalez-Valls, M. Lira-Cantu, Energy Environ. Sci. 2 (2009) 19.
[7] T. Ameri, G. Dennler, C. Lungenschmied, C.J. Brabec, Energy Environ. Sci. 2 (2009) 347.
[8] F.C. Krebs, Sol. Energy Mater. Sol. Cells 93 (2009) 394.
[9] M. Helgesen, R. Sondergaard, F.C. Krebs, J. Mater. Chem. 20 (2010) 36.
[10] D.E. Markov, E. Amsterdam, P.W.M. Blom, A.B. Sieval, J.C. Hummelen, J. Phys. Chem. A 109 (2005) 5266.
[11] J.B. Emah, R.J. Curry, S.R.P. Silva, Appl. Phys. Lett. 93 (2008) 103301.
[12] M.S. Kim, J.S. Kim, J.C. Cho, M. Shtein, L.J. Guo, J. Kim, Appl. Phys. Lett. 90 (2007) 123113.
[13] A. Baumann, J. Lorrmann, C. Deibel, V. Dyakonov, Appl. Phys. Lett. 93 (2008) 252104.
[14] D. Chirvase, J. Parisi, J.C. Hummelen, V. Dyakonov, Nanotechnology 15 (2004) 1317.
[15] D.H. Wang, H.K. Lee, D.G. Choi, J.H. Park, O.O. Park, Appl. Phys. Lett. 95 (2009) 043505.
[16] D.H. Wang, D.G. Choi, K.J. Lee, J.H. Jeong, S.H. Jeon, O.O. Park, J.H. Park, Org. Electron. 11 (2010) 285.
[17] D.H. Wang, D.G. Choi, K.J. Lee, O.O. Park, J.H. Park, Langmuir, 2010, doi: 10.1021/la100164k.
[18] F.C. Krebs, S.A. Gevorgyan, J. Alstrup, J. Mater. Chem. 19 (2009) 5442.
[19] F.C. Krebs, Sol. Energy Mater. Sol. Cells 93 (2009) 1636.
[20] F.C. Krebs, K. Norrman, ACS Appl. Mater. Interface 2 (2010) 877.
[21] J.H. Huang, Z.Y. Ho, T.H. Kuo, D. Kekuda, C.W. Chu, K.C. Ho, J. Mater. Chem. 19 (2009) 4077.
[22] K.H. Yim, Z. Zheng, Z. Liang, R.H. Friend, W.T.S. Huck, J.S. Kim, Adv. Funct. Mater. 18 (2008) 1012.
[23] D.G. Choi, J.H. Jeong, Y.S. Shim, E.S. Lee, W.S. Kim, B.S. Bea, Langmuir 21 (2005) 9390.
[24] F. Padinger, R.S. Rittberger, N.S. Sariciftci, Adv. Funct. Mater. 13 (2003) 85.
[25] K. Youngkyoo, S.A. Choulis, J. Nelson, D.D.C. Bradley, Appl. Phys. Lett. 86 (2005) 063502.
[26] X. Yang, J. Loos, S.C. Veenstra, W.J.H. Verhees, M.M. Wienk, J.M. Kroon, M.A.J. Michels, R.A.J. Janssen, Nano Lett. 5 (2005) 583.
[27] S.J. Yoon, J.H. Park, H.K. Lee, O.O. Park, Appl. Phys. Lett. 92 (2008) 143504.
[28] A. Hayakawa, O. Yoshikawa, T. Fujieda, K. Uehara, S. Yoshikawa, Appl. Phys. Lett. 90 (2007) 163517.

and explicit hypothesis and approximations, based on specific organic materials physics.

Charge transport efficiency in organic semiconductors has been constantly improved during the past two decades, probably due to improved material elaboration and better control of the device process. The transport efficiency is commonly quantified through the carrier mobility, characteristic of an average carrier speed versus electric field, whatever the transport physics at the molecular scale. Best reported values at room temperature are in the order of 1–10 $cm^2 V^{-1} s^{-1}$ [12].

The second most limiting factor of OFET performances is the poor injection efficiency from source to drain electrodes through the transistor channel [11,13]. This behavior is closely linked to the device process and should find solutions in near future using appropriate electrode material and surface treatment [14]. However, this nonlinear injection problem must be accurately described and taken into account in an OFET model, as it strongly influences the extraction of important parameters such as mobility or threshold voltage.

This work focuses on the influence of nonlinear injection on the device performances. A self-consistent model is developed and described in detail, implementing the nonlinear injection at the source contact in an original manner, with explicit assumptions whenever needed in order to allow deeper discussion of the organic physics involved.

In Section 2, highlighting the differences between the conventional silicon metal-oxide-semiconductor field effect transistor (MOSFET) model and its organic counterpart, we describe the transistor structure and the model basics, including leakage resistance, ohmic drain and source series resistances, and a mobility dependence on the local gate voltage. In Section 3, the method for implementing nonlinear injection at the source contact is described, allowing a self-consistent calculation of the drain/source current/voltage characteristics. In Section 4 the impact of nonlinear injection is illustrated through simulations with typical OFET parameters, and comparison with experimental data is given. Following, impact of nonlinear injection on mobility and threshold voltage is described in-depth. Finally, a study of the internal injecting field allows to predict instabilities and even breakdown in organic FETs.

2. OFET model: basics

2.1. OFET assumptions and structure

The OFET schematic structure considered in this paper is a bottom-contact structure as depicted in Fig. 1.

The organic semiconductor (OSC) is considered intrinsic, with no doping and no traps, and with a uniform spatial concentration of sites N_0, available to carriers accumulated by the gate bias and injected by the source contact. Any generation, either optical or thermal for example, is neglected in the semiconductor material. Consequently, carriers are always brought from source and/or drain electrodes [15,16]. The isolating material is assumed to be ideal, with no leakage current, no charge and no traps. Source and drain electrodes always behave ohmic (i.e. linear).

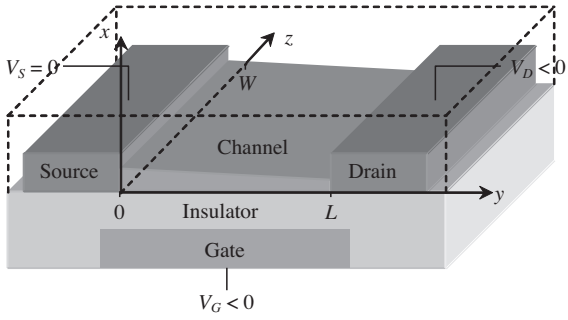

Fig. 1. Schematic drawing of a bottom-contact OFET structure, where the conductive channel is in linear regime.

In an ideal situation, the OSC can transport either electrons or holes, as demonstrated in several publications [17,18], and the transistors should be ambipolar. This happens if both types of charges are injected in the channel and are mobile. In the usual case, only one carrier type contributes to the OFET drain/source current characteristic (I_{DS}). This can be understood considering that either only one carrier type can be injected, due to a high electrode/channel energy barrier [18], or that one carrier type is not mobile, for example if it is trapped at the insulator/OSC interface as stated in [17]. Most published OFET current-voltage characteristics are dominated by only one carrier type, and the devices are usually called p-type transistor or n-type transistors if the carriers are respectively holes or electrons.

In this work, single carrier OFETs are considered, in particular p-type OFETs, as they are widely studied. However, the model can be easily transposed to n-type OFET with minor sign changes.

The OFET structure considered in this paper takes the ohmic source and drain series resistances R_S and R_D into account. Also, an intrinsic conductivity in the OSC bulk (independent of the gate bias) is modeled by an ohmic resistance R_B set between the source and drain electrodes, as depicted in Fig. 2. This conductivity may result from residual doping of the OSC (see for example [19]), and is responsible for poor saturation of the drain current characteristic.

When carrier injection from the source electrode into the transistor channel is linear (i.e. ohmic behavior), the channel is formed near the source contact edge and the intrinsic source potential is $V_{Si0} = V(y = 0)$ (Fig. 2). Thus for a given bias point (U_{DS},U_{GS}), the intrinsic voltage drops U_{GSi0} and U_{DSi0} are given by:

$$U_{GSi0} = V_G - V_{Si0} = U_{GS} - R_S I_{DSi}, \quad (1)$$

$$U_{DSi0} = V_{Di} - V_{Si0} = U_{DS} - (R_S + R_D) I_{DSi}, \quad (2)$$

where I_{DSi} is the intrinsic drain current. Note that we will use the following notations: V stands for potentials, whereas U is used for voltage drops. The external drain to source current I_{DS} is expressed by:

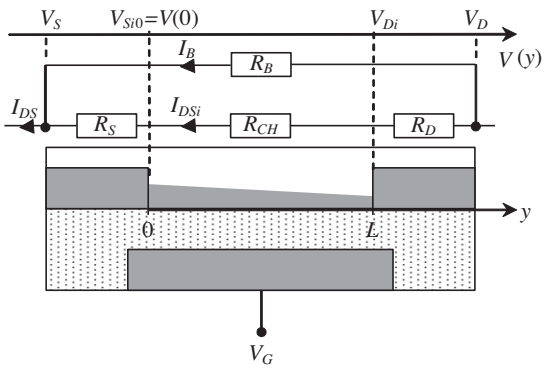

Fig. 2. OFET schematic and associated electrical model, with intrinsic and extrinsic potentials, parasitic resistances, and leakage currents.

$$I_{DS} = I_{DSi} + I_B, \tag{3}$$

where $I_B = U_{DS}/R_B$ is the leakage current due to R_B (Fig. 2).

In practical transistor characterization, the source potential is usually grounded and is the reference potential (Fig. 1). We will now focus on the computation of the intrinsic drain current $I_{DSi}(U_{DSi},U_{GSi})$ in presence of injection phenomena, as equation (Eq. 3) easily allows to determine the extrinsic drain current I_{DS}.

2.2. Source/drain intrinsic current model

The model basics are derived from the silicon MOS transistor model [20]. Within the gradual channel approximation, given the intrinsic drain current follows:

$$I_{DSi}dy = -W\mu(y)C_i[V_G - V(y) - U_T]dV(y) \tag{4}$$

where U_T is the threshold voltage, $C_i = \varepsilon_i/d_i$ is the insulator capacitance per unit area, and ε_i and d_i are respectively the insulator permittivity and thickness. Considering a mobility dependence on the local gate bias $\mu(y) = \beta[-(V_G - V(y) - U_T)]^\gamma$ (see [13,21,22]), where β and γ are fitting parameters, integration of (Eq. 4) gives the intrinsic drain current in the linear (Eq. 5) and saturated (Eq. 6) regime:

$$I_{DSi} = \frac{W}{L(\gamma+2)}\beta C_i[(U_{DSi0} - U_{GSi0} + U_T)^{\gamma+2} - (U_T - U_{GSi0})^{\gamma+2}] \tag{5}$$

$$I_{DSi} = I_{DSi\,sat} = -\frac{W}{L(\gamma+2)}\beta C_i(U_T - U_{GSi0})^{\gamma+2} \tag{6}$$

2.3. Potential and longitudinal electric field along the channel

The potential profile $V(y)$ and the longitudinal electric field $E_y(y)$ are required to implement nonlinear injection at the source contact, since injection phenomena are highly sensitive to the electric field. For a given intrinsic current I_{DSi}, integrating (Eq. 4) from (y) to the intrinsic drain $(y = L)$ gives the voltage drop in the channel referenced to the extrinsic source $U_{yS}(y) = V(y) - V_S$:

$$U_{yS}(y) = U_{GS} - U_T + \left[(U_{DSi} - U_{GSi} + U_T)^{\gamma+2} - \frac{I_{DSi}(\gamma+2)(L-y)}{WC_i\beta}\right]^{\frac{1}{\gamma+2}} \tag{7}$$

The electric field along the channel is obtained by derivating $U_{yS}(y)$:

$$E_y(y) = \frac{-I_{DSi}}{WC_i\beta}\left[(U_{DSi} - U_{GSi} + U_T)^{\gamma+2} - \frac{I_{DSi}(\gamma+2)(L-y)}{WC_i\beta}\right]^{-\left(\frac{\gamma+1}{\gamma+2}\right)} \tag{8}$$

3. OFET model with nonlinear injection

Nonlinear injection at the conductor/OSC interface may occur due to combined effects: the barrier height Φ_B at the conductor/OSC interface, the tunneling distance for injected carriers [23], the concentration of accessible sites in the OSC (N_0) [24], the carrier mobility, or the presence of molecular dipoles [25]. These injection phenomena limit the drain current and are partially controlled by the temperature in organic devices. The effects of nonlinear injection at the source and drain electrodes have been quantitatively measured by different near-field techniques: the near-field microwave microprobe (NFMM) [26] or the scanning-probe potentiometry using the atomic force microscopy principles, called Kelvin Probe Force Microscopy (KPFM) [27]. The KPFM measurements provide the electrostatic potential profile along the channel of a biased OFET [21,27–31]. Fig. 4 in Bürgi et al. [28] shows an example of such a potential profile, where most of the potential drop occurs at the injecting electrode (the source), as stated in [28,29]. In the following, as a first approximation, we will only consider the potential drop near the source, U_{inj}, neglecting the potential drop near the drain contact as in [28,31] and [32].

3.1. Nonlinear injection model and OFET specific assumptions

Nonlinear injection has been widely studied in OLEDs [33] and several models have been proposed to explain the current/voltage characteristic: thermoionic and/or tunnel injection [34], Space Charge Limited Current [35], injection in amorphous systems [22,24,25,36,37]. They all aim at a current density expression (J_{inj}) as a function of the electric field (E_{inj}) at the injecting interface. The corresponding injecting current I_{inj} can be expressed as:

$$I_{inj} = S_{inj} \times J_{inj}(E_{inj}), \tag{9}$$

where S_{inj} is the injecting surface.

The injection model used in this paper was proposed by Campbell Scott [24,37]. It describes carrier injection from a conductive electrode into an amorphous OSC, and has been successfully compared to experimentally results [38]. As stated in [24], the injecting current density can be expressed by:

$$J_{inj}(E_{inj}) = -4\Psi^2(f)N_0e\mu(0)E_{inj}\exp(f^{1/2})\exp\left(-\frac{e\Phi_B}{kT}\right) \tag{10}$$

where $f = e^3E_{inj}/4\pi\varepsilon_S k^2T^2$, k is the Boltzmann constant and $\psi(f) = f^{-1} + f^{-1/2} - f^{-1}(1 + 2f^{1/2})^{1/2}$.

Note that when the carrier mobility depends on the local gate voltage, the expression of $\mu(y)$ (Section 2.B) is used and the mobility in (Eq. 10) is evaluated at $y = 0$.

In OLED, the injecting surface S_{inj} simply corresponds to the surface of the injecting electrode, and E_{inj} can be approximated by the ratio of the applied bias to the electrode separation. This relation suggests that the electric field lines are perpendicular to the injecting electrode and that the region between the electrodes is fully depleted. Implementing the injection model becomes straightforward, allowing comparison of the simulated $I_{inj}(E_{inj})$ with the $I-V$ measurements.

In OFETs, the situation is different. First, the depleted area doesn't extend on the entire channel length but on a distance called Y_{inj} from the intrinsic source ($y = 0$). The associated voltage drop U_{inj} is defined by $U_{inj} = V(Y_{inj}) - V(0) = V_{Si} - V_{Si0}$ where V_{Si} is the new intrinsic source potential in presence of nonlinear injection (Fig. 3). Also, the longitudinal injecting electric field is no more uniform over the entire injecting surface, located at the source contact edge. The intrinsic drain current I_{DSi} being equal to I_{inj}, and considering the transistor geometry, (Eq. 9) rewrites for bottom contact OFET as:

$$I_{DSi} = W\int_0^{X_m} J_{inj}(E_{inj}(x))dx \tag{11}$$

where X_m is the thickness of the source electrode (Fig. 3).

Some approximations are necessary to evaluate (Eq. 11). The total injecting thickness X_m is divided in two intervals: $[0;X_C]$ and $[X_C;X_m]$ where X_C is the channel thickness at $y = 0$ (i.e. the thickness of the conductive part of the OSC where most of the accumulated charges are located). The injection region near the source contact edge is divided in two regions I and II (Fig. 3) with corresponding longitudinal electric fields E_{inj_I} and E_{inj_II} evaluated at $y = 0$. The drain current is then:

$$I_{DSi} = WX_C J_{inj}(E_{inj_I}) + W(X_m - X_C)J_{inj}(E_{inj_II}) \tag{12}$$

Finally, taking nonlinear injection into account, the computation of the intrinsic drain current $I_{DSi}(U_{DSi},U_{GSi})$ requires the evaluation of six variables (J_{inj}, E_{inj_I}, E_{inj_II}, U_{inj}, Y_{inj} and X_C) from six independent equations. The following paragraph describes our approach to obtain these equations and the method to solve them in a self-consistent approach.

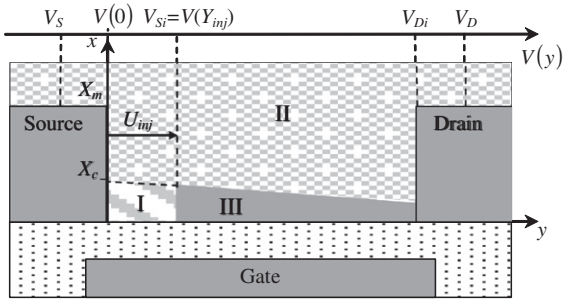

Fig. 3. Schematic bottom contact OFET channel cross-section figuring three regions used in the nonlinear injection model. Region I: depleted zone where the gradual channel approximation fails. Region II: intrinsic OSC. Region III: accumulated charge forming the channel in which the gradual channel approximation is valid.

3.2. Method to implement injection self-consistently

OFETs $I_{DS}(U_{DS},U_{GS})$ characteristics have already been simulated with nonlinear injection, in Refs. [32,39,40] and [41]. However, all of these implementations show limitations. In [39] if the injecting current model does not require the knowledge of S_{inj} and Y_{inj}, two fitting parameters are used instead. In Ref. [40], two head to tail diodes are used to account for $I-V$ nonlinearities. If suitable for circuit design, this approach does not help to understand the device physics. Finally, in Ref. [32] and [41], the depleted length Y_{inj} is a parameter adjusted at each bias to fit experimental results.

The present approach computes simultaneously the I_{DS} drain current and all internal injecting variables in a self-consistent way, without the help of any fitting parameter, in particular without any dependence of internal parameters on gate or drain bias (threshold voltage, concentration of accessible sites...). The hypothesis and approximations used in our approach are described in the following.

1. Channel thickness at the source contact
   Considering a uniform carrier distribution over the available site concentration N_0 (see discussion in section D), the accumulated charge density per unit channel area at the source contact $Q_S(y = 0) = C_i(U_{GSi0} - U_T)$ is equal to eN_0X_C, giving:
   $$X_C = -\frac{C_i}{eN_0}(U_{GSi0} - U_T) \tag{13}$$
2. Poisson's equation in the injecting region
   The abrupt change in the potential slope near the source contact, experimentally observed [28], results from a strong longitudinal electric field gradient: the usual gradual channel approximation may fail near the source electrode. Consequently, according to the 2D Poisson equation, the longitudinal electric field gradient will induce a modification of the channel charge density, compared to the usual accumulated charge due to the gate bias when no nonlinear injection occurs: a depleted region is created at the source contact edge, due to the presence of a high injecting electric field and its gradient.
   Fig. 3 shows a schematic drawing of the source/drain area, divided into three regions. Region I is the depleted zone in front of the channel where the accumulated charge is pushed away by the injecting electric field. Region II and III are respectively the intrinsic OSC and the channel where the usual gradual channel approximation is still valid. To allow an analytic resolution, abrupt transitions have been considered between the different regions.
   In presence of nonlinear injection, the 2D Poisson's equation in depleted region I becomes:
   $$\frac{\partial E_{x_I}(x,y)}{\partial x} + \frac{\partial E_{y_I}(x,y)}{\partial y} = 0 \tag{14}$$
   The main assumption at this step is that the gradient of the transverse electric field $\frac{\partial E_{x_I}(x,y)}{\partial x}$ due to the applied gate bias is not modified compared to the usual gradual channel approximation: i.e. there should be an accumulated

charges ρ_{ch} due to the still present gate bias, but these charges are pushed away from the contact edge by the high longitudinal field. The longitudinal field gradient in region I is then given by:

$$\frac{\partial E_{y_I}(y)}{\partial y} = -\frac{\rho_{ch}(y)}{\varepsilon_S} \tag{15}$$

3. Electric field at the injecting contact and potential drop due to nonlinear injection
Integrating (Eq. 15) using the uniform charge density eN_0 gives the expression of the injecting longitudinal electric field in region I:

$$E_{y_I}(y) = \frac{eN_0}{\varepsilon_S}(Y_{inj} - y) + E_y(Y_{inj}) \tag{16}$$

where $E_y(Y_{inj})$ is the electric field at the depleted zone edge given by (Eq. 8). The injecting electric field $E_{y_I}(0)$ at the source contact edge in region I is given by:

$$E_{y_I}(0) = E_{inj} = \frac{eN_0}{\varepsilon_S} Y_{inj} + E_y(Y_{inj}) \tag{17}$$

This longitudinal field at the electrode edge E_{inj} determines the current density in the case of nonlinear injection (Eq. 10). The potential profile in region I can be obtained integrating (Eq. 16):

$$V_{y_I}(y) = \frac{eN_0}{2\varepsilon_S} y^2 - \left(\frac{eN_0}{\varepsilon_S} Y_{inj} + E_y(Y_{inj})\right) y \tag{18}$$

Finally, the potential drop due to nonlinear injection $U_{inj} = V_{y_I}(y = Y_{inj}) - V_{y_I}(y = 0)$, according to (Eq. 18), is expressed as:

$$U_{inj} = -Y_{inj}\left(\frac{eN_0}{2\varepsilon_S} Y_{inj} + E_y(Y_{inj})\right) \tag{19}$$

The injecting electric field E_{inj_II} at the source contact in region II is obtained from (Eq. 8) at $y = 0$:

$$E_{inj_II} = \frac{-I_{DSi}}{WC_i\beta}\left[(U_{DSi} - U_{GSi} + U_T)^{\gamma+2} - \frac{I_{DSi}(\gamma+2)L}{WC_i\beta}\right]^{-\left(\frac{\gamma+1}{\gamma+2}\right)} \tag{20}$$

4. Intrinsic drain current expressions including nonlinear injection
In presence of nonlinear injection, the intrinsic gate and drain voltages are respectively given by:

$$U_{GSi} = U_{GSi0} - U_{inj} = U_{GS} - R_S I_{DSi} - U_{inj} \tag{21}$$

$$U_{DSi} = U_{DSi0} - U_{inj} = U_{DS} - (R_S + R_D) I_{DSi} - U_{inj} \tag{22}$$

These equations show that nonlinear injection will be observed on the transistor characteristics only if the voltage drop U_{inj} is significant compared to the applied biases U_{GS} and U_{DS}.
The channel being formed from $y = Y_{inj}$ to $y = L$, integration of (Eq. 4) along the channel gives the drain current in linear regime (Eq. 23) and in saturated regime (Eq. 24):

$$I_{DSi} = \frac{W}{(L - Y_{inj})(\gamma+2)}\beta C_i[(U_{DSi} - U_{GSi} + U_T)^{\gamma+2} - (U_T - U_{GSi})^{\gamma+2}] \tag{23}$$

$$I_{DSi} = I_{DSi\,sat} = -\frac{W}{(L - Y_{inj})(\gamma+2)}\beta C_i (U_T - U_{GSi})^{\gamma+2} \tag{24}$$

Note that equations Eqs. 12,23,24 are implicit and use the previous expressions of E_{inj_I}, E_{inj_II}, U_{inj}, Y_{inj} and X_C.

5. Algorithm
At a given bias point (U_{DS},U_{GS}), the drain current I_{DS} must be computed using an iterative process. The calculation requires a set of parameters: the temperature (T), some technological parameters (W, L, and γ, U_T, ε_S, C_i, R_S, R_D, R_B, N_0 and X_m), and parameters linked to the injection model (in our case the barrier height Φ_B Eq. 10). From a given drain current at step n, the next step current is evaluated using successively Eqs. (13), (20), (12), (17), (19), (21)–(23) or Eq. 24, and finally Eq. 3. A Newton–Raphson convergence method [42] is used to minimize the relative error on the drain current.

4. Results and discussion

4.1. characteristics and internal injection variables

In this section, the model outputs are illustrated. All simulations are performed at room temperature for $W/L = 50$, a 100 nm insulator thickness, and a threshold voltage of −5 V (Table 1). To emphasize nonlinear injection effects, and unless otherwise stated, the mobility will be considered constant for all simulations ($\beta \equiv \mu = 10^{-2}$ cm^2 V^{-1}s^{-1} and $\gamma = 0$ in the expression of the mobility given in paragraph II.B). Other parameters are specified for each simulation: resistances R_S, R_D, and R_B, barrier height Φ_B and concentration of accessible sites N_0.

Typical values have been chosen for both the concentration of accessible sites, ($N_0 = 5 \times 10^{18}$ cm^{-3}, lower than the molecular concentration [43,44]), and for the barrier height ($\Phi_B = 0.55$ eV [32,45,46]). These values are representative of a number of organic semiconductor materials. For example, a barrier height in the range 0.2–0.6 eV is often observed between Au or Cr and organic semiconductor such as P3HT or pentacene [32,45,46], and even higher barriers can be expected from ionization energy and electron affinity measurements [47]. Φ_B and N_0 will be varied in section C to account for various situations. Fig. 4 compares the simulated OFET $I - V$ characteristics with or without ($\Phi_B = 0$) nonlinear injection phenomena. As expected, in the case of nonlinear injection, a diode like characteristic is observed at low drain bias (as often reported [29,31,32,48–51]), as well as a decrease of the drain current for all regimes.

Table 1
OFET parameters used for all simulations.

$W = 1000$ μm	$L = 20$ μm	$\mu = 10^{-2}$ cm^2 V^{-1} s^{-1} $T = 300$ K	$C_i = 3.45 \times 10^{-4}$ Fm^{-2} $\varepsilon_S = 2.65 \times 10^{-11}$ Fm^{-1}	$U_T = -5$ V	$X_m = 300$ nm

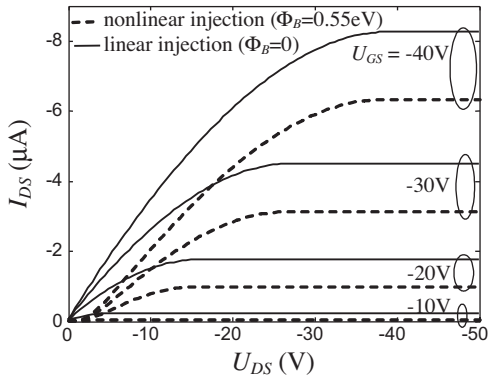

Fig. 4. Simulated $I_{DS}(U_{DS})$ at different U_{GS} with or without nonlinear injection ($R_S = R_D = 500k\Omega$, $R_B = \infty$ and $N_0 = 5 \times 10^{18}$ cm^{-3}).

The internal nonlinear injection parameters, E_{inj} and U_{inj}, calculated self consistently and corresponding to the simulation given Fig. 4, have been plotted in Fig. 5. Both E_{inj} and U_{inj} follow the $I_{DS}(U_{DS},U_{GS})$ characteristic shape: they increase with the drain bias, saturate with the drain current and increase with the gate bias. The injecting electric field (0–5 MV cm^{-1}) is found within the range usually measured in OLEDs [23,25]. The injecting potential drop (0–3 V) is also in agreement with KPFM measurements [28].

The depleted length Y_{inj} and the channel thickness X_C (Eq. 13) are reported in Table 2 for each gate bias, in saturation. The depleted length, never exceeding 20nm in this case, is always very small compared to the channel length ($L = 20$ μm for this simulation). This is a major difference with injection models developed in OLEDs. An experimental verification using the KPFM technique will be challenging since the spatial resolution is about 50nm [27], however improving in high vacuum conditions.

4.2. Comparison with experimental results

$I_{DS}(U_{DS},U_{GS})$ characteristics from Hamadani and Natelson [32] and from our measurements with strong nonlinear behavior have been fitted using the OFET model.

Table 2
Simulated depleted length and channel thickness in saturation for nonlinear injection. The gate bias conditions are those of Fig. 4. ($R_S = R_D = 500$ kΩ, $R_B = \infty$, $\Phi_B = 0.55$ eV and $N_0 = 5 \times 10^{18}$ cm^{-3}).

U_{GS} (V)	−10	−20	−30	−40
Y_{inj} (nm)	12.9	15.9	17.1	17.8
X_C (nm)	2.1	6.3	10.1	13.7

First, experimental data from Ref. [32] were used. These measurements were performed on P3HT bottom-contact organic transistor on degenerated P$^+$ silicon substrate used as gate. The insulator was a thermal SiO_2, with evaporated Chrome electrodes. The Cr/P3HT barrier height is about 0.4–0.5 eV [28,52], inducing nonlinear effects on the $I_{DS}(U_{DS},U_{GS})$ characteristics. The technological parameters given in Ref. [32] are listed in Table 3. The $I_{DS}(U_{DS},U_{GS})$ measurements at low drain bias and the corresponding simulations are depicted in Fig. 6. The fitting parameter values used for these simulations are given in Table 4.

A good agreement is observed all over the characteristics, with a unique parameter set, constant for all bias points. The mobility value is that of usual P3HT devices. The barrier height is in the order of the theoretical value, considering a reasonable concentration of accessible sites, which allows reproducing the shape of the current curves. The series resistances were found negligible compared to the minimum channel resistance (about 3MΩ). In addition, the potential drop at the source contact was found in the range [0; −4V], and the injecting electric field does not exceed 5 MV cm^{-1}, below the breakdown limit (see paragraph yD). Finally, the depletion length varies from 3nm to 15nm (not accessible to present KPFM resolution), and the channel thickness lies within [4; 13nm], corresponding to a few monolayers.

In order to validate the model up to saturation, P3HT bottom-contact OFET were fabricated, on degenerated P$^+$ silicon substrate used as gate. The gate insulator is 116nm of thermal SiO_2. Ti (10nm) / Au (300nm) circular source and drain electrodes are patterned by lithography. The P3HT was drop casted from a chloroform solution, and measured under vacuum conditions. The Au/P3HT barrier height is about 0.5 eV [28], inducing nonlinear effects

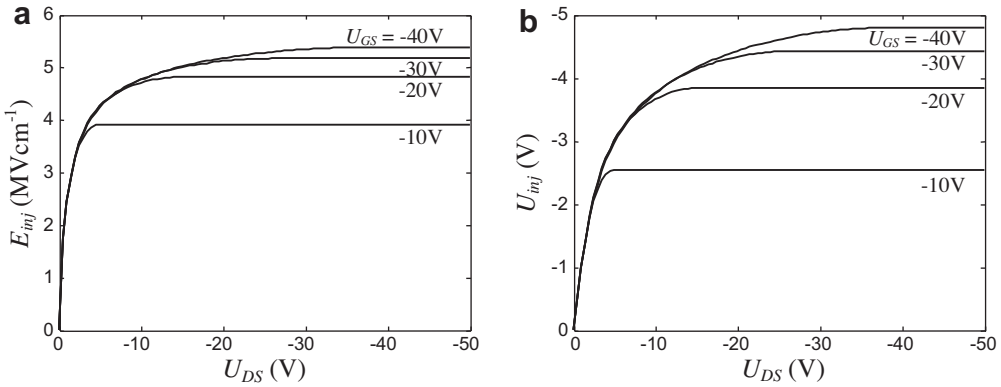

Fig. 5. Simulated injecting electric field (a) and injecting potential drop (b). The bias conditions are those of Fig. 4. ($R_S = R_D = 500$ kΩ, $R_B = \infty$, $\Phi_B = 0.55$ eV and $N_0 = 5 \times 10^{18}$ cm^{-3}).

Table 3
Physical OFET parameters used in Hamadani and Natelson [32].

$W = 200\ \mu m$	$L = 25\ \mu m$	$C_i = 1.73 \times 10^{-4}\ F m^{-2}$	$\varepsilon_S = 2.65 \times 10^{-11}\ F m^{-1}$	$X_m = 30\ nm$	$T = 300\ K$

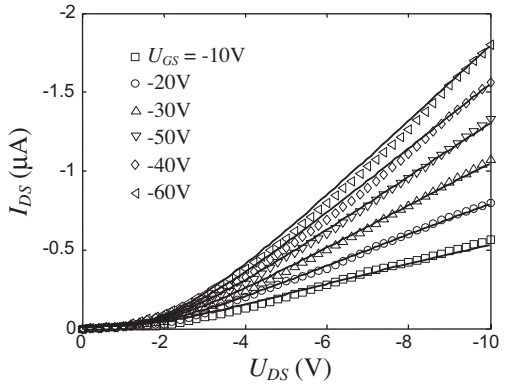

Fig. 6. $I_{DS}(U_{DS})$ characteristics in linear regime (symbols: measurements [32]/full lines: simulations).

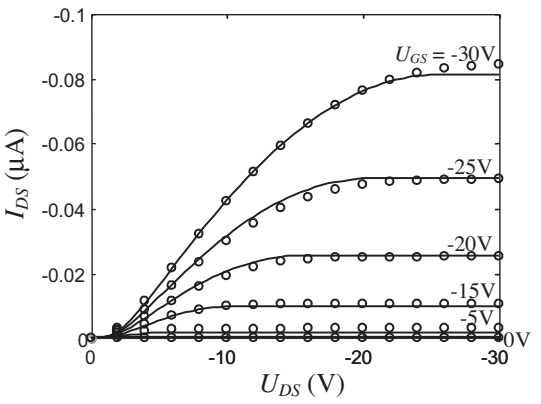

Fig. 7. Measured and fitted non-linear $I_{DS}(U_{DS})$ characteristic, in both linear and saturated regimes (open symbols: measurement/full lines: simulation).

on the $I_{DS}(U_{DS},U_{GS})$ characteristics. The technological parameters of the device are given in Table 5. The transistor $I_{DS}(U_{DS},U_{GS})$ characteristic in both linear and saturated regimes, and the corresponding simulations, are depicted in Fig. 7. The resulting parameter values are listed in Table 6.

Again, agreement is observed all over the characteristic, both in linear and saturated regimes, with a unique parameter set for all bias points. The series resistances were found negligible and set to zero, with no bulk leakage. The barrier height is in the order of the theoretical value. The mobility is found constant, close to $10^{-3}\ cm^2\ V^{-1}s^{-1}$. In addition, the potential drop at the source contact was found in the range [0; −4V], and the injecting electric field is lower than 5 MV cm^{-1}. Finally, the depletion length varies from 5nm to 17nm, and the channel thickness lies within [2; 10nm], corresponding to a few monolayers.

These comparisons demonstrate the model ability to simulate non-linear OFET characteristic in a self-consistent approach, with a single and constant parameter set. In the latter case, only four parameters were used to fit the entire characteristic with good agreement: μ, U_T, Φ_B and N_0. Note that the apparent mobilities found with the usual method (see section C.1 bellow) differ from those used to fit the measurements. This extraction error is illustrated in the next paragraph.

4.3. Mobility and threshold voltage extraction

1. Usual extraction procedure
   The usual mobility and threshold voltage extraction procedure uses the $\sqrt{I_{DS}}$ versus U_{GS} plot in saturation regime [20], based on the first order equation $I_{DS} = \frac{W\mu C_i}{2L}(U_{GS} - U_T)^2$ (see Fig. 8). From this equation in the ideal case, the plot is linear with. In practical case, the abscise intercept is the apparent threshold voltage $U_{T_{app}}$, and the apparent mobility is obtained from the slope following $\mu_{app} = \frac{2L}{WC_i}\frac{\partial\sqrt{I_{DS}}}{\partial U_{GS}}$.
   However, the presence of parasitic effects (series resistances and nonlinear injection in particular) will strongly affect this plot, as will be illustrated below. The extracted threshold voltage and mobility behavior with gate bias for example may be misleading, and the extracted apparent mobility μ_{app} and threshold voltage $U_{T_{app}}$ may be far from their intrinsic values.
   Fig. 8 highlights this issue: a plot of $\sqrt{I_{DS}}$ versus U_{GS} is shown, calculated (i) without any uneven contact contribution, (ii) with series resistances, or (iii) with series resistances and injection barrier. Compared to the ideal situation (i), the plot is no more linear and the slope of the characteristic decreases with either series resis-

Table 4
OFET parameters used to fit measurements from Ref. [32].

$\mu = 3.2 \times 10^{-2}\ cm^2\ V^{-1}\ s^{-1}$	$U_T = 12\ V$	$\Phi_B = 0.57\ eV$	$N_0 = 6 \times 10^{18}\ cm^{-3}$	$R_S = R_D = 100\ k\Omega$	$R_B = 100\ M\Omega$

Table 5
Technological OFET parameters.

$W = 1289\ \mu m$	$L = 100\ \mu m$	$C_i = 2.98 \times 10^{-4}\ F m^{-2}$	$\varepsilon_S = 2.65 \times 10^{-11}\ F m^{-1}$	$X_m = 300\ nm$	$T = 293\ K$

Table 6
Optimized OFET parameter set used to fit measurements of Fig. 7.

$\mu = 0.92 \times 10^{-3}$ cm^2 V^{-1} s^{-1}	$U_T = -4.4$ V	$\Phi_B = 0.58$ eV	$N_0 = 5 \times 10^{18}$ cm^{-3}	$R_S = R_D = 0$	$R_B = \infty$

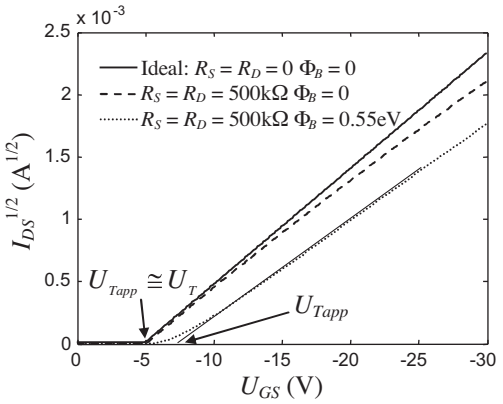

Fig. 8. Usual $\sqrt{I_{DS}}$ versus U_{GS} plot in saturation regime ($U_{DS} = -50$ V), used for the mobility and threshold voltage extraction ($U_T = -5$ V, and $N_0 = 5 \times 10^{18}$ cm^{-3}).

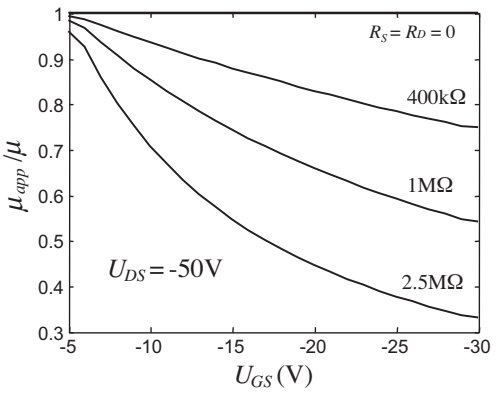

Fig. 9. Extracted apparent mobility on bulk mobility ratio versus gate bias for different series resistances.

tances or injection barrier. The extracted mobility μ_{app} is reduced, and may even show an apparent dependence on the gate voltage. Also, the apparent threshold voltage $U_{T_{app}}$ is clearly over estimated in presence of an injection barrier whereas it is not modified ($U_{T_{app}} \cong U_T$) when only ohmic series resistances are considered. A quantitative analysis of the extracted values is given below.

2. Series resistances and effective mobility
The detrimental influence of the series resistances on the effective mobility is well known [20,51]: the mobility decreases with the gate bias in presence of series resistances, as illustrated in Fig. 9, where the ratio of the extracted apparent mobility μ_{app} to the bulk mobility μ (the model parameter) is plotted against gate bias. The series resistance values (here $R_S = R_D$) are swept from 0Ω up to the channel resistance calculated at $U_{GS} = -30$ V and $U_{DS} = -2$ V. The extracted apparent mobility decreases to a third of its bulk value when the series resistances equal the channel resistance. Series resistances should be estimated prior to the mobility extraction for a better understanding of the transistor physics. For example, the Transfer Line Method (TLM) may be used [40,51,53–55].
3. Nonlinear injection effects on extracted mobility
Figs. 10 and 11 illustrate the influence of an injection barrier on the extracted apparent mobility in saturation regime ($U_{DS} = -50$ V), varying the injection model parameters Φ_B and N_0. Both figures show a decrease of the apparent mobility when the injection efficiency decreases (i.e. when Φ_B increases or when N_0 decreases). An increase of the apparent mobility with gate bias is also observed. Figs. 10b and 11b show the corresponding evolution of μ_{app}/μ in saturated regime ($U_{GS} = -30$ V and $U_{DS} = -50$ V) respectively versus the barrier height Φ_B or versus the concentration of accessible sites N_0. These results show that the knowledge of the injecting parameters is mandatory for an accurate extraction of the mobility.
It is now obvious that the apparent mobility is highly sensitive to uneven source/channel contacts. The apparent mobility decreases with gate bias when series resistances are high (Fig. 9), whereas when nonlinear injection occurs, it increases with gate bias (Figs. 10a and 11a). Unfortunately, these two parasitic source/channel phenomena (and possibly others) are likely to be simultaneously present in organic transistors, leading to various dependences of the apparent mobility on gate bias [43,51,54–58]. By combining series resistances and nonlinear injection effects, exotic behaviors can be simulated for $\mu_{app}(U_{GS})$ (linear increase or decrease, with or without saturation...) for a given intrinsic mobility. Despite that the mobility dependence on gate bias is supported by serious arguments [22,56,59,60], the above discussion demonstrates that such analysis from experimental results should be undertaken very carefully, particularly when both series resistances and nonlinear injection are present on the device. Although some correction procedures are possible for series resistances alone [56,57], an analytical correction is no more possible when both effects are present.
4. Nonlinear injection effects on extracted threshold voltage
In the literature, high threshold voltages are often reported when OFETs present nonlinearities (see for example Fig. 6 in Ref [54]). In this section, we will establish that nonlinear injection shifts the extracted apparent threshold voltage $U_{T_{app}}$ from the intrinsic value U_T, when using the usual extraction method. Such plots have been simulated in Fig. 12a for various injection efficiencies, through different barrier heights. These simulations show an increase of the apparent threshold voltage when increasing barrier heights.

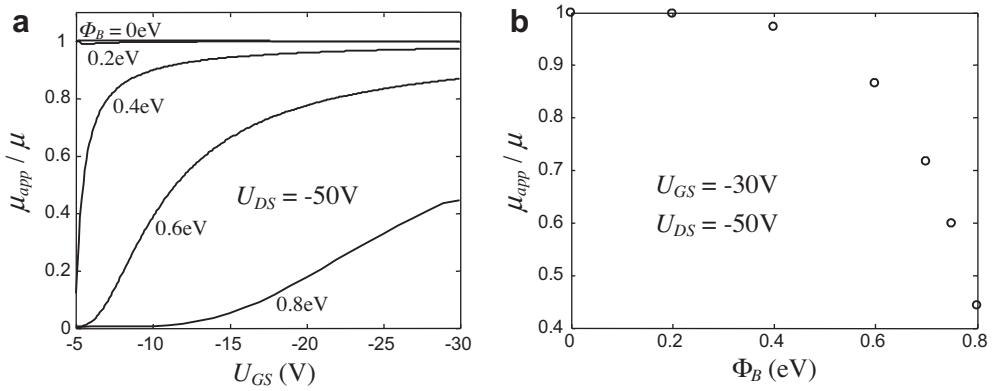

Fig. 10. (a) Extracted apparent mobility versus gate bias for different barrier height values ($R_S = R_D = 0$, $R_B = \infty$ and $N_0 = 5 \times 10^{18}$ cm^{-3}). (b) Corresponding μ_{app}/μ ratio versus Φ_B for an operating point in saturation.

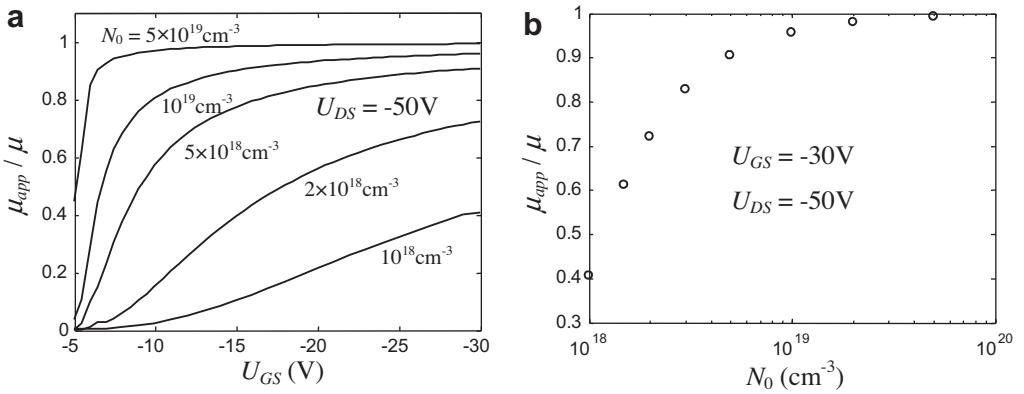

Fig. 11. (a) Extracted apparent mobility versus gate bias for different concentration of accessible sites ($R_S = R_D = 0$, $R_B = \infty$ and $\Phi_B = 0.55$ eV). (b) Corresponding μ_{eff}/μ ratio versus N_0 for an operating point in saturation.

When extracted at very high gate bias, we found that the threshold voltage shift equals the injection voltage drop U_{inj}, as shown Fig. 12b (full line). This can be understood considering that $U_{GS} = U_{GSi} + U_{inj}$ (Eq. (21) for $R_S = 0$). At threshold, $U_{GS} = U_{T_{app}}$ and $U_{GSi} = U_T$ which gives $U_{T_{app}} = U_T + U_{inj}$. However, for real devices, the measurements are usually performed at limited gate bias to prevent gate breakdown, which lowers the extracted threshold values, between the intrinsic value U_T and the maximum shifted value $U_T + U_{inj}$.

To illustrate these trends, simulations have been performed at three operating points in saturation regime ($U_{GS} = U_{DS} = -20, -50, -100$ V) and for various barrier heights. For a given operating point, $U_{T_{app}}$ varies linearly with U_{inj} for the different barrier heights (the different symbols on dashed lines). The asymptote $U_{T_{app}} = U_T + U_{inj}$ (full line in Fig. 12b) is reached when the bias point is taken extremely high, where the $\sqrt{I_{DS}} = f(U_{GS})$ characteristic becomes linear whatever the barrier height.

As for the apparent mobility, it is now clear that the apparent threshold voltage is highly sensitive to any injection barrier at the source/channel contact. The usual extraction method will fail in presence of both contact resistances and nonlinear injection. The simulations have shown that the extracted values can be far from the threshold voltage U_T. Even if nonlinear injection is not the only reason for high extracted threshold voltages, it must be taken into account to interpret experimental results. In this respect, studies of threshold voltage under different physical conditions (temperature change, voltages stress...) must be undertaken with care each time nonlinear effects are suspected on the device. The log(I_{DS}) versus U_{GS} plot should be preferred to study the gate behavior near threshold since in this case, the extraction is much less sensitive to parasitic effects: it is performed at lower current, where the injecting voltage drop is negligible.

Mobility and the threshold voltage are both highly process-dependent, and are first order parameters to evaluate an OFET technology. The previous section emphasized the difficulties encountered to obtain these parameters accurately from measured current characteristics. Injection barriers may ruin usual correction procedures. The self-consistent OFET model developed here is a useful tool for OFET technology evaluation, providing better understanding of nonlinear injection effects, and even allowing intrinsic parameter extraction. Due to the numerous

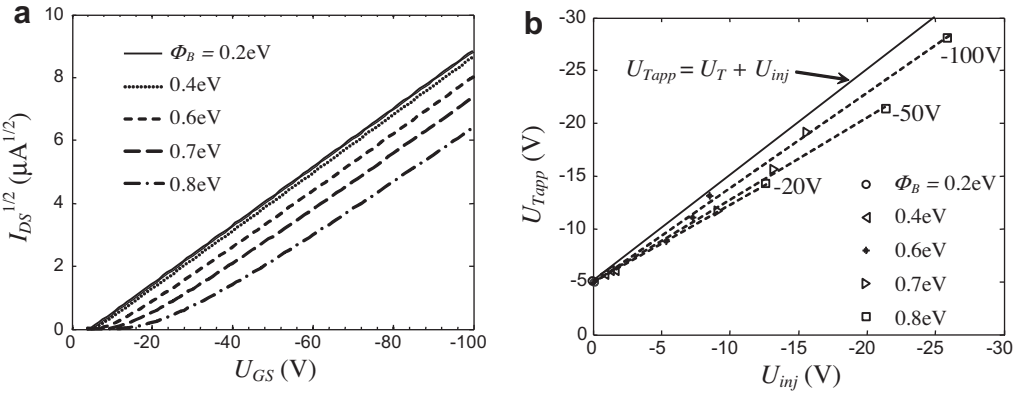

Fig. 12. (a) $\sqrt{I_{DS}}$ versus U_{GS} characteristics in saturation regime ($U_{DS} = -100$ V) for various barrier heights. (b) Corresponding apparent threshold voltage $U_{T_{app}}$ as a function of the calculated injection voltage drop U_{inj}. Extractions are performed at three operating points: $U_{GS} = U_{DS} = -20, -50, -100$ V(dotted lines), and at extremely high gate bias (full line). ($U_T = -5$ V, $R_S = R_D = 0$, $R_B = \infty$ and $N_0 = 5 \times 10^{18}$ cm^{-3}).

physical effects at work in an OFET, various characterization tools should also be used to improve the overall OFET understanding. In particular, Φ_B and N_0 contribution to current-voltage nonlinear characteristics appear to be strongly correlated, and complementary experiments should be used to clarify their respective contribution.

4.4. Prediction of instabilities and breakdown in OFET

OFET electrical characteristics sometimes present unexpected behaviors like noise, instabilities, or even breakdown. This could be due to high internal electric fields in the device. The critical electric field (at breakdown) depends on the nature of the organic materials, but may also be highly sensitive to the technological process. This limit can be estimated to 5–6 MV cm^{-1} [32]. The following study focuses on the electric field intensity at the source electrode (where the electric field is maximum) in presence of nonlinear injection. Note that the injection model used in this work was not developed to describe carrier injection under very high electric fields, where other contributions to the current density could take place. The present work intends to highlight possible high fields in the transistor channel rather than to describe the breakdown physics itself.

As it could be anticipated, simulation shows that low injection efficiency causes high injecting fields. Nonlinear injection can also produce a diode like behavior at low drain biases, as already mentioned (Fig. 4). However, in some cases, the effect of an injection barrier is not directly visible on the measured characteristics, as shown in the inset of Fig. 13, and it is then sometimes difficult to associate the observed instabilities with a poor contact. This section discusses these issues.

The inset in Fig. 13 shows an example of simulated $I_{DS}(U_{DS},U_{GS})$ characteristics where nonlinear injection effects are hardly visible. This occurs when both the barrier height and the concentration of accessible sites are high. The corresponding injecting electric fields at the source are plotted in Fig. 13. For a large range of operating points,

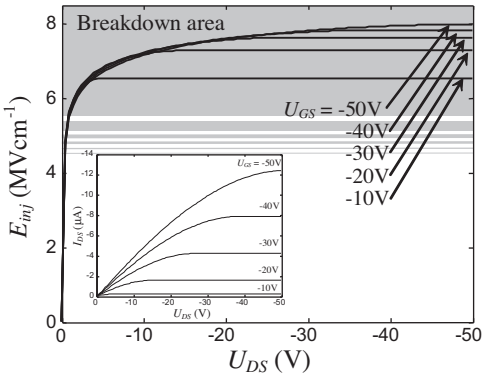

Fig. 13. Injecting electric field versus U_{DS} corresponding to the simulated $I_{DS}(U_{DS},U_{GS})$ characteristics in presence of (invisible) nonlinear injection (inset) ($R_S = R_D = 500$ kΩ, $R_B = \infty$ and $\Phi_B = 0.65$ eV and $N_0 = 5 \times 10^{19}$ cm^{-3}).

the electric field exceeds the 5–6 MV cm^{-1} breakdown limit. Moreover, the breakdown field is reached at very low drain bias, just above a few volts. In such situations, unexpected breakdown can occur even at low drain bias.

Fig. 14a and b shows the electric field behavior versus the barrier height for different concentrations of accessible sites, respectively in linear regime ($U_{GS} = -50$ V and $U_{DS} = -5$ V) and in saturation regime ($U_{GS} = -30$ V and $U_{DS} = -50$ V). The electric field values are found to increase with increasing Φ_B: the higher the barrier height, the higher the electric field required to inject charges from the source contact into the channel. In linear regime (Fig. 14a), a barrier height higher than 0.6 eV causes the electric field to exceed the breakdown limit over a wide range of available site concentrations, except for low N_0 values (<5 × 10^{18} cm^{-3}). This trend is even more pronounced in saturated regime (Fig. 14b). The injecting field values are also found to increase with increasing N_0, which goes against the intuitive idea that a high concentration of available sites should promote the injection efficiency, as in OLEDs. However it can be easily understood. For a given gate bias, the conductive channel thickness X_C varies as $1/N_0$ (Eq. 13). A high concentration of available sites

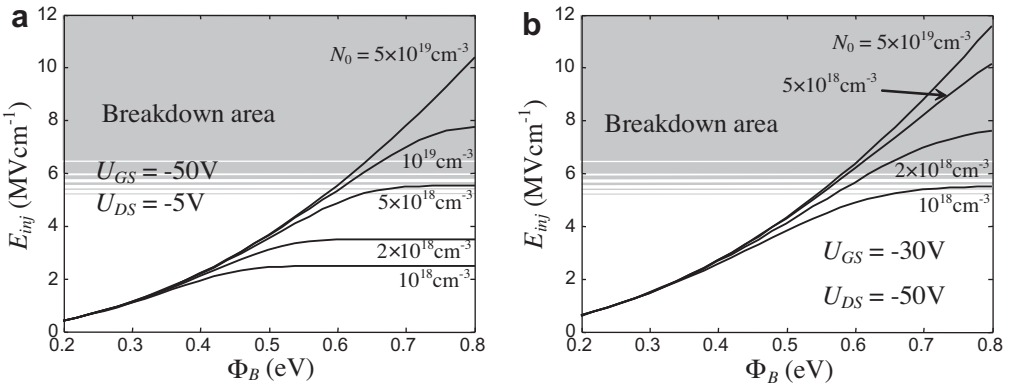

Fig. 14. Simulated injecting electric field versus barrier height for different concentrations of accessible sites (a) in linear regime and (b) in saturated regime ($R_S = R_D$ = 500 kΩ and $R_B = \infty$). The breakdown is estimated to 5–6 MV cm^{-1}.

reduces the channel thickness, which in turn reduces the injecting surface. A higher injecting field is then necessary to achieve a given drain current.

Nonlinear injection is found to cause very high electric fields at the source contact, in particular when a high concentration of accessible sites is available. It is believed that these high fields are responsible for instabilities, noise, and even breakdown in organic FETs suffering from poor contacts.

Also, importantly, simulations show that a nonlinear diode-like characteristic is only observed for low concentrations of accessible sites. At high concentrations, results indicate that injection effects should not be observed on the current characteristic (see Fig. 13). However, many nonlinear characteristics are observed in the literature (and in the labs), suggesting that the concentration of available sites is much lower than the molecular concentration, and that the injecting surface extends far from the insulator interface. This is the main reason why the spatial concentration of accumulated carriers was considered constant in this work, rather than governed by a Boltzmann or Fermi Dirac statistic over a given density of states. Indeed, simulations have been performed using a conventional 3D DOS and the Boltzmann approximation, with an effective density of states N_V taken close to the molecular concentration. Main results were: (i) the resulting carrier concentration is located very close to the insulator/OSC interface, approaching the molecular concentration at high gate bias, (ii) the channel thickness is limited to a few monolayers and the injecting surface is reduced consequently (iii) the resulting $I_{DS}(U_{DS},U_{GS})$ characteristic never exhibits a nonlinear diode-like behavior, even for high barrier heights. This does not agree with widely reported experimental results. Consequently, the only strategy would have been to reduce the effective density of states to very small values, which does not make much sense. In order to provide a clear and simple view of the problem, highlighting the issue of the low density of accumulated carriers and its large extension far from the interface, it was preferred to use a simple low density repartition, uniform in space, even though when the origins of this low density will be clarified, a statistical energetic approach will be required for precise quantitative modeling.

5. Summary and perspectives

OFET performances are mainly limited by the transport efficiency in the channel and by the quality of the source and drain ohmic contacts, often suffering from high series resistances and nonlinear injection. These parasitic effects often occur simultaneously in OFETs. To study the influence of uneven contacts, we developed a one-dimensional self-consistent bottom-contact OFET electrical model.

The model is based on the usual silicon MOS field-effect transistor model, and the different assumptions relative to the organic based FET have been detailed and discussed. To take some of the organic FET specific parasitic effects into account, the model includes source and drain series resistances, a bulk leakage resistance, and nonlinear injection effects at the source electrode, that constitute the main and most original contribution of this paper. The calculation of the drain current uses a specific current density versus injecting electric field model developed for OLED, adapted to the bottom-contact organic transistor. All of the physical variables associated to the nonlinear injection (injecting electric field, potential drop near the source, corresponding depleted length) are calculated at the same time, in a self-consistent approach. This has the advantage of avoiding the use of any fitting parameters (bias dependent or arbitrary fixed) in place of internal variables. An overall coherence is obtained, and the calculated internal variables can be used to analyze and understand some of the OFET misbehaviors.

The model capabilities were first illustrated through various current/voltage and internal variables simulation results with a set of typical parameters. In presence of an injection barrier, the nonlinear diode-like behavior of the drain current at low drain bias has been evidenced, as well as an overall decrease of the drain current characteristic. All internal injecting variables were found to be coherent with measurements, as demonstrated for different P3HT based OFETs. The self-consistent model proved to be an efficient characterization tool, providing intrinsic internal

parameters such as mobility and threshold voltage, as well as internal potential profiles and electric fields.

The model was used to illustrate the influence of the parasitic effects on the extracted mobility and threshold voltage. The square root of the drain current versus gate voltage curve in saturation regime is commonly used to extract an effective mobility and an effective threshold voltage. Whereas all simulations have been performed with a unique mobility and threshold voltage, we have shown that the combined effects of series resistances and nonlinear injection could lead to various types of extracted apparent mobility variation with gate bias. We have also shown that the shift of the extracted threshold voltage in presence of nonlinear effects can reach the injecting voltage drop at the source contact. This section shows that the apparent mobility behavior with gate bias obtained from such measurements should be considered with precautions since it is most of the time unreliable. The self-consistent OFET model is believed to improve the extraction results since the main source/channel contact parasitic effects are taken into account.

A study of possible instabilities and breakdown due to nonlinear injection in OFETs was undertaken, based on the calculation of the internal injecting electric field. For a source/channel barrier higher than 0.5–0.6 eV, a 5–6 MV cm^{-1} breakdown limit is reached over a wide range of concentrations of accessible sites, above $3–5 \times 10^{18}$ cm^{-3}. At high concentrations, breakdown conditions can appear even at low drain bias, with hardly visible effect on the transistor current/voltage characteristics. Finally, from an experimental point of view, this study suggests that very high electric fields, responsible for instabilities, electric stress, or even breakdown, can be present in devices suffering from contact injection barrier. Improvements of the source and drain contacts appear as a key priority.

The self-consistent OFET model developed in this paper is a powerful tool for electrical characterization. Its capabilities have been demonstrated through simulations and comparison with experimental data, providing a coherent set of internal parameters. It should help to improve and to gain confidence in the knowledge of organic field effect transistor physics.

Acknowledgement

This work was financially supported by Région Champagne-Ardenne, the French Ministère de l'Enseignement supérieur et de la Recherche, and the European Community through the CPER project 'PEPITA'.

References

[1] F. Carpi, D. De Rossi, Opt. Laser Technol. 38 (2006) 292–305.
[2] K. Myny, S. Steudel, P. Vicca, M.J. Beenhakkers, N.A.J.M. van Aerle, G.H. Gelinck, J. Genoe, W. Dehaene, P. Heremans, Solid-State Electron. 53 (2009) 1220–1226.
[3] W. Clemens, W. Fix, J. Ficker, A. Knobloch, A. Ullmann, J. Mater. Res. 19 (2004) 1963–1973.
[4] A. Das, R. Dost, T.H. Richardson, M. Grell, D.C. Wedge, D.B. Kell, J.J. Morrison, M.L. Turner, Sens. Actuators B 137 (2009) 586–591.
[5] L. Torsi, N. Cioffi, C. Di Franco, L. Sabbatini, P.G. Zambonin, T. Bleve-Zacheo, Solid-State Electron. 45 (2001) 1479–1485.
[6] R. Parashkov, E. Becker, T. Riedl, H.-H. Johannes, W. Kowalsky, Proc. IEEE 93 (2005) 1321–1329.
[7] Z. Bao, J. Locklin (Eds.), Organic Field-effect Transistors, CRC Press Taylor & Francis Group, NY, 2007.
[8] F. Ebisawa, T. Kurokawa, S. Nara, J. Appl. Phys. 54 (1983) 3255–3259.
[9] J.H. Burroughes, C.A. Jones, R.H. Friend, Nature 335 (1988) 37.
[10] G. Horowitz, D. Fichou, X. Peng, Z. Xu, F. Garnier, Solid State Commun. 72 (1989) 381.
[11] O. Marinov, M.J. Deen, B. Iniguez, IEE Proc. Circ. Dev. Syst. 152 (2005) 189–209.
[12] V. Podzorov, S.E. Sysoev, E. Loginova, V.M. Pudalov, M.E. Gershenson, Appl. Phys. Lett. 83 (2003) 3504–3506.
[13] G. Horowitz, J. Mater. Res. 19 (2004) 1946–1962.
[14] K. Tsukagoshi, I. Yagi, Y. Aoyagi, Sci. Technol. Adv. Mater. 7 (2006) 231–236.
[15] S. Ogawa, T. Naijo, Y. Kimura, H. Ishii, M. Niwano, Synth. Met. 153 (2005) 253–256.
[16] E. Lim, T. Manaka, R. Tamura, M. Iwamoto, Jpn. J. Appl. Phys. 45 (2006) 3712–3716.
[17] L.-L. Chua, J. Zaumseil, J.-F. Chang, E.C.-W. Ou, P.K.-H. Ho, H. Sirringhaus, R.H. Friend, Nature 434 (2005) 194–199.
[18] T. Kaji, S. Entani, S. Ikeda, K. Saiki, Adv. Mater. 20 (2008) 2084–2089.
[19] M. Koehler, I. Biaggio, Phys. Rev. B 70 (2004) 045314.
[20] S.M. Sze, Physics of Semiconductor Devices, Wiley, New York, 1981.
[21] E.C.P. Smits, S.G.J. Mathijssen, M. Cölle, A.J.G. Mank, P.A. Bobbert, P.W.M. Blom, B. De Boer, D.M. De Leeuw, Phys. Rev. B 76 (2007) 125202.
[22] M.C.J.M. Vissenberg, M. Matters, Phys. Rev. B 57 (1998) 12964–12967.
[23] V.I. Arkhipov, U. Wolf, H. Bässler, Phys. Rev. B 59 (1999) 7514–7520.
[24] J.C. Scott, J. Vac. Sci. Technol. A 21 (2003) 521–531.
[25] M.A. Baldo, S.R. Forrest, Phys. Rev. B 64 (2001) 085201.
[26] E. Lim, T. Manaka, M. Iwamoto, B. Friedman, A. Babajanyan, S. Kim, Y. Yoon, S. Kim, K. Lee, Thin Solid Films 516 (2008) 2573–2576.
[27] V. Palermo, M. Palma, P. Samori, Adv. Mater. 18 (2006) 145–164.
[28] L. Bürgi, T.J. Richards, R.H. Friend, H. Sirringhaus, J. Appl. Phys. 94 (2003) 6129–6137.
[29] J.A. Nichols, D.J. Gundlach, T.N. Jackson, Appl. Phys. Lett. 83 (2003) 2366–2368.
[30] K.P. Puntambekar, P.V. Pesavento, C.D. Frisbie, Appl. Phys. Lett. 83 (2003) 5539–5541.
[31] A. Petrovic, E. Pavlica, G. Bratina, A. Carpentiero, M. Tormen, Synth. Met. 159 (2009) 1210–1214.
[32] B.H. Hamadani, D. Natelson, J. Appl. Phys. 97 (2005) 064508.
[33] D. Braun, J. Polym. Sci. Part B: Polym. Phys. 41 (2003) 2622–2629.
[34] I.H. Campbell, P.S. Davids, D.L. Smith, N.N. Barashkov, J.P. Ferraris, Appl. Phys. Lett. 72 (1998) 1863–1865.
[35] Y. Preezant, Y. Roichman, N. Tessler, J. Phys.: Condens. Matter 14 (2002) 9913–9924.
[36] V.I. Arkhipov, E.V. Emelianova, Y.H. Tak, H. Bässler, J. Appl. Phys. 84 (1998) 848–856.
[37] J.C. Scott, G.G. Malliaras, Chem. Phys. Lett. 299 (1999) 115–119.
[38] Y. Shen, M.W. Klein, D.B. Jacobs, J.C. Scott, G.G. Malliaras, Phys. Rev. Lett. 86 (2001) 3867–3870.
[39] R.A. Street, A. Salleo, Appl. Phys. Lett. 81 (2002) 2887–2889.
[40] P.V. Necliudov, M.S. Shur, D.J. Gundlach, T.N. Jackson, Solid-State Electron. 47 (2003) 259–262.
[41] M. Koehler, I. Biaggio, M.G.E. da Luz, Phys. Rev. B 78 (2008) 153312.
[42] Endre Süli, David Mayers, An Introduction to Numerical Analysis, Cambridge University Press, 2003.
[43] G. Wang, J. Swensen, D. Moses, A.J. Heeger, J. Appl. Phys. 93 (2003) 6137–6141.
[44] M.J. Panzer, C.D. Frisbie, Adv. Funct. Mater. 16 (2006) 1051–1056.
[45] H. Ishii, K. Sugiyama, E. Ito, K. Seki, Adv. Mater. 11 (1999) 605–625.
[46] K. Hong, J.W. Lee, S.Y. Yang, K. Shin, H. Jeon, S.H. Kim, C. Yang, C.E. Park, Org. Electron. 9 (2008) 21–29.
[47] J. Hwang, A. Wan, A. Kahn, Mater. Sci. Eng. R 64 (2009) 1–31.
[48] W. Geens, S.E. Shaheen, B. Wessling, C.J. Brabec, J. Poortmans, N.S. Sariciftci, Org. Electron. 3 (2002) 105–110.
[49] J.G. Lee, Y.G. Seol, N.-E. Lee, Thin Solid Films 515 (2006) 805–809.
[50] W. Porzio, S. Destri, U. Giovanella, M. Pasini, T. Motta, D. Natali, M. Sampietro, M. Campione, Thin Solid Films 492 (2005) 212–220.
[51] D.J. Gundlach, L. Zhou, J.A. Nichols, T.N. Jackson, P.V. Necliudov, M.S. Shur, J. Appl. Phys. 100 (2006) 024509.
[52] Z. Chiguvare, J. Parisi, V. Dyakonov, J. Appl. Phys. 94 (2003) 2240–2248.
[53] L. Giraudet, S. Fauveaux, O. Simonetti, C. Petit, K. Blary, T. Maurel, A. Belkhir, Synth. Met. 156 (2006) 838–842.

[54] H. Klauk, G. Schmid, W. Radlik, W. Weber, L. Zhou, C.D. Sheraw, J.A. Nichols, T.N. Jackson, Solid-State Electron. 47 (2003) 297–301.
[55] T. Richards, H. Sirringhaus, Appl. Phys. Lett. 92 (2008) 023512.
[56] G. Horowitz, R. Hajilaoui, D. Fichou, A. El Kassmi, J. Appl. Phys. 85 (1999) 3202–3206.
[57] G. Horowitz, P. Lang, M. Mottaghi, H. Aubin, Adv. Funct. Mater. 14 (2004) 1069–1074.
[58] D. Gupta, Y. Hong, Org. Electron. 11 (2010) 127–136.
[59] W.F. Pasveer, J. Cottaar, C. Tanase, R. Coehoorn, P.A. Bobbert, P.W.M. Blom, D.M. de Leeuw, M.A.J. Michels, Phys. Rev. Lett. 94 (2005) 206601.
[60] S. Baranovski, O. Rubel, Description of charge transport in disordered organic materials, in: S. Baranovski (Ed.), Charge Transport in Disordered Solids with Applications in Electronics, John Wiley & Sons, Ltd., Chichester, 2006, p. 221.

the use of SiO_2/Si substrates coated with hydrophobic polymer drastically reduced the hysteresis (increasing $|V_G|$ is called the forward measurement mode, and decreasing $|V_G|$ the reverse measurement mode). Furthermore, we have quantitatively analyzed the suppression of drain current in a plot of $|I_D|^{1/2}$ vs. $|V_G|$ for high $|V_G|$ by the introduction of a mobility reduction factor θ.

2. Experimental

The structure of the picene thin film FET is shown in Fig. 1a. The surface of the 400 nm thick SiO_2 gate dielectric was coated with either Cytop™ or polystyrene after cleaning the SiO_2 surface as described elsewhere [6]. M-type Cytop™ was purchased from Asahi Glass Co., and polystyrene from Aldrich Co. Coating solutions were 8.6 wt% Cytop™ in CT-solv 180 (Asahi Glass Co.), and 1.8 wt% polystyrene in toluene. The Cytop™ films were formed by spin coating at 500 rpm for 5 s and 4000 rpm for 40 s; polystyrene films were formed by spin-coating at 1000 rpm for 5 s and 4000 rpm for 40 s. Picene films 17 and 20 nm thick were deposited on the Cytop™ and polystyrene-coated SiO_2/Si substrates, respectively. Source/drain Au electrodes 40 nm thick were formed on the picene thin films. Channel length L and channel width W were 30 μm and 2.9 mm, respectively, for the picene FET with a Cytop™-coated SiO_2 gate dielectric, while L and W were 30 μm and 2.2 mm, respectively, for the picene FET with a polystyrene-coated SiO_2 gate dielectric. O_2 gas with 0.014 ppm of water was used to measure the effect of O_2 exposure on the picene FETs. The O_2 gas was introduced into the measurement cell to investigate the FET characteristics and the amount of O_2 was precisely regulated by monitoring the vacuum gauge. Experimental details (O_2 concentration, exposure time, pumping time, etc.) of O_2 gas exposure and pumping are described in the text.

3. Results and discussion

Fig. 1b shows the transfer curve for the picene thin film FET with a hexamethyldisilazane (HMDS)-coated SiO_2/Si gate dielectric (picene/HMDS/SiO_2 FET), measured after dynamic pumping at 10^{-6} Torr for 1 h. The transfer curves show a large hysteresis between forward and reverse measurements, as reported previously [7,8]. The μ values were determined to be 0.019 and 0.13 $cm^2\,V^{-1}\,s^{-1}$, respectively, from the forward and reverse transfer curves, consistent with earlier reports [7,8]. Fig. 1b includes a photo of water on the HMDS-coated SiO_2/Si surface, with a contact angle of 84°. Fig. 1c shows the transfer curves for the picene/Cytop™/SiO_2 FET, measured after dynamic pumping at 10^{-6} Torr for 1 h. The hysteresis is drastically reduced. Fig. 1c includes a photo of water on a Cytop™-coated SiO_2/Si surface, with a contact angle of 90°, suggesting a more hydrophobic surface. The μ values determined from the forward and reverse transfer curves were 0.051 and 0.17 $cm^2\,V^{-1}\,s^{-1}$, respectively. These μ values show that the operational speed of a picene FET is not reduced by the use of a Cytop™-coated SiO_2/Si gate dielectric.

Fig. 1d shows the transfer curves for a picene/polystyrene/SiO_2 FET, measured after dynamic pumping at 10^{-6} Torr for 1 h; the μ values were determined to be 0.08 and 0.16 $cm^2\,V^{-1}\,s^{-1}$ from the forward and reverse transfer curves, respectively. The transfer curves show less

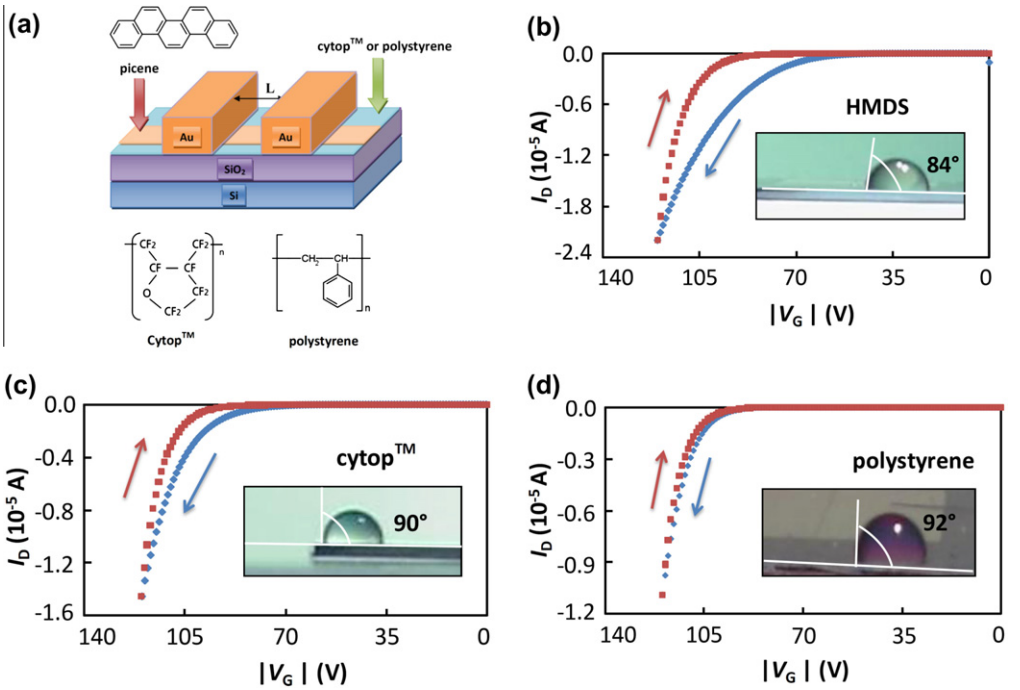

Fig. 1. (a) Structure of the picene thin film FET. Molecular structures of picene, Cytop™ and polystyrene are shown. Transfer curves for (b) picene/HMDS/SiO_2, (c) picene/Cytop™/SiO_2 and (d) picene/polystyrene/SiO_2 FETs. Inset photos show water on the surfaces.

hysteresis than those for the picene/Cytop™/SiO_2 FET. Fig. 1d includes a photo of water on a polystyrene-coated SiO_2/Si substrate. The contact angle of 92° was almost the same as that of water on Cytop™ (Fig. 1c). As seen from Fig. 1b and d, the pronounced hysteresis found in the transfer curves of the picene/HMDS/SiO_2 FET substantially disappeared in the picene/polystyrene/SiO_2 FET. This result strongly supports the hypothesis that water is responsible for the hysteresis in the transfer curves. Here it should be noted that despite displaying the same water contact angle, the picene/polystyrene/SiO_2 FET hysteresis is much smaller than that of the picene/Cytop™/SiO_2 FET. In order to identify the origin of the lower hysteresis with the polystyrene-coated SiO_2/Si substrate, we examined the surfaces of Cytop™ and polystyrene-coated SiO_2/Si substrates with atomic force microscopy (AFM) (not shown). The surface roughness of Cytop™-coated SiO_2/Si is much larger than that of polystyrene-coated SiO_2/Si. Actually, the root mean square roughness, R_{rms}, of the Cytop™-coated SiO_2/Si surface was 1.5 nm, which is larger by a factor of 5 than the 0.34 nm roughness of the polystyrene-coated SiO_2/Si surface. This large roughness difference may explain the hysteresis difference between the FETs, *i.e.*, the H_2O molecules involved in the nanoscale concavity in the Cytop™-coated SiO_2/Si surface may produce the bias-stressed hysteresis in transfer curves, and the contact angle should not be affected by H_2O molecules in the nanoscale concavity, because contact angle is a macroscopic phenomenon.

Fig. 2a shows the O_2-exposure response of $|I_D|$ ($|I_D|^{max}$) for picene/Cytop™/SiO_2 FET, measured at $V_G = -120$ V and $V_{DS} = -120$ V. The period of O_2 exposure and dynamic pumping was set at 24 h in the investigation of O_2 exposure effects on the picene FETs. The $|I_D|^{max}$ value increased within a few minutes of O_2 exposure, and after 5 h $|I_D|^{max}$ had increased to 70% of its value after a 24 h exposure for a wide range of O_2 concentrations from 0.1 to 8 Torr. After 24 h of O_2 exposure, $|I_D|^{max}$ increased to a value 1.4 times higher than that measured just before O_2 exposure. When the O_2 gas exposure was greater than 100 Torr, after 24 h $|I_D|^{max}$ increased to a value 1.8 times higher than that measured just before O_2 exposure (not shown).

As can be seen from Fig. 2a, $|I_D|^{max}$ decreases rapidly with dynamic pumping at 10^{-6} Torr, reaching the minimum value within 5 h. We previously observed an increase in $|I_D|^{max}$ for the picene/HMDS/SiO_2 FET with increasing O_2 exposure from 16 to 500 Torr, which could be directly related to the increase in μ caused by shallow trap reduction [8]. Our scenario for the O_2 gas sensing effect of a picene thin film FET is that the shallow traps which consist of positively charged defects and impurities are screened by polarized O_2, $O_2^{\delta-}$ when the picene FET is exposed to O_2, so the effective trap abundance decreases, thus increasing μ and the absolute value of the switch-on drain current [8]. On the other hand, when the O_2 gas contained in the picene thin film is dynamically exhausted, the effective trap abundance increases owing to the removal of $O_2^{\delta-}$ around trap centers, thus decreasing μ and the absolute switch-on drain current [8].

In this study, we reduced the O_2 concentration down to 0.01 Torr and investigated the $|I_D|^{max}$ response to O_2 exposure. In practice, the difference, $\Delta|I_D|^{max}$, between the minimum and the maximum $|I_D|^{max}$ values slowly decreases down to that at 0.01 Torr of O_2, as is shown in Fig. 2b (0.01 Torr of O_2 corresponds to ~10 ppm of O_2). The ratio of $\Delta|I_D|^{max}$ at specified O_2 concentrations to that at 7.5 Torr of O_2 is shown together with the estimated standard deviation (error bar) in the inset of Fig. 2b. Here, the plot shows the average value of three picene FET devices, and the clear dependence of O_2 sensing properties on the O_2 concentration is apparent. Actually, even in 10^{-2} Torr of O_2, a non-vanishing $\Delta|I_D|^{max}$ is observed. Thus, the reproducibility of O_2 sensing properties is confirmed in a picene thin film FET.

The minimum value of $|I_D|^{max}$ (Fig. 2a) corresponds to the $|I_D|^{max}$ at 10^{-6} Torr. The minimum value (baseline shown by dashed line in Fig. 2a) decreases monotonically

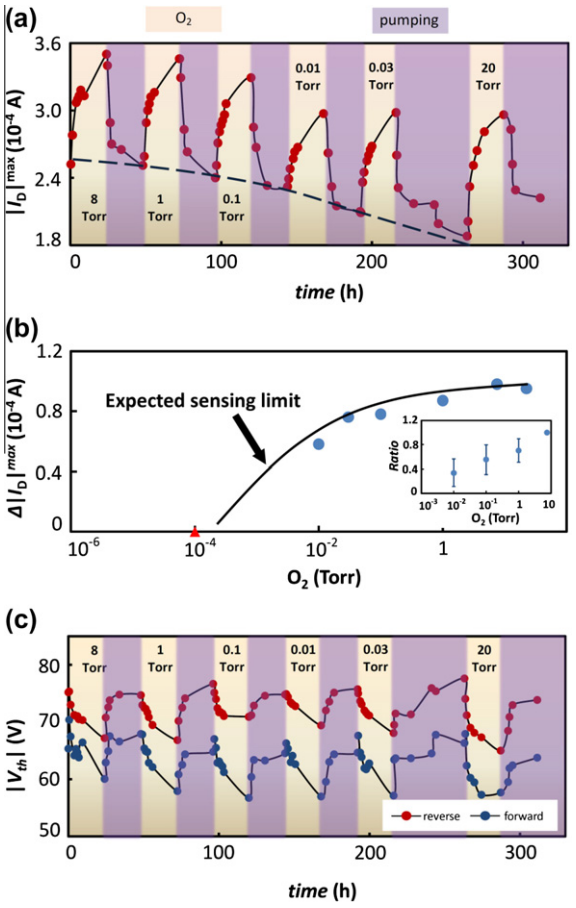

Fig. 2. (a) Plots of $|I_D|^{max}$ vs. O_2-exposure/exhaust time and (b) $\Delta|I_D|^{max}$ vs. O_2 concentration in the picene/Cytop™/SiO_2 FET. The dashed line in (a) refers to the baseline, *i.e.*, the minimum $|I_D|^{max}$ values after dynamic pumping at 10^{-6} Torr. In (b), the expected sensing curve is drawn as a function of O_2 concentration, and the expected minimum sensing limit is shown in the graph. Inset in (b), the average value at certain times of the ratio of $\Delta|I_D|^{max}$ to that at 7.5 Torr (estimated with three picene thin film FETs). (c) Plots of $|V_{TH}|$ vs. O_2-exposure/exhaust time in the picene/Cytop™/SiO_2 FET. In (c) the red and blue circles refer to the $|V_{TH}|$ determined from the reverse and forward transfer curves, respectively. (For interpretation of the references to colour in this figure legend, the reader is referred to the web version of this article.)

with repeated pumping, suggesting that repeated O_2-exposure causes no accumulation of O_2 at interface between the Cytop™-coated SiO_2 and the picene layer.

The $\Delta|I_D|^{max}$ at 0.01 Torr of O_2 went down to 80% of the $\Delta|I_D|^{max}$ at 0.1 Torr of O_2, as can be seen from Fig. 2a and b, suggesting that even an O_2 exposure of less than 0.01 Torr can cause a significant increase in $|I_D|^{max}$. As we obtained no FET response to an O_2 exposure of 10^{-4} Torr in the preliminary experiment on the O_2-exposure effect on a picene FET, the $\Delta|I_D|^{max}$ vs. O_2 concentration curve can be represented as in Fig. 2b. This curve refers to the expected detection curve of this picene field-effect sensor for O_2 gas. When the picene/Cytop™/SiO_2 FET was exposed to 0.03 Torr of O_2 after a 0.01 Torr O_2 exposure and subsequent dynamic pumping, the $\Delta|I_D|^{max}$ recovered to the value expected for 0.03 Torr on the detection curve drawn in Fig. 2b. The picene thin film FET can detect a level as low as 0.001 Torr (~1 ppm) of O_2, as indicated by the curve (Fig. 2b); the preliminary experiment on the O_2-sensing properties of a picene thin film FET confirms a non-vanishing $\Delta|I_D|^{max}$ after exposure to 1 ppm of O_2. These results clearly indicate the potential usefulness of a picene thin film FET as an O_2-gas sensor.

The response of the μ value of the picene/Cytop™/SiO_2 FET to O_2 exposure is clear, and in particular the μ value determined from the forward transfer curve shows a large response to O_2 exposure (not shown). O_2 exposure enhanced the μ values determined from both the forward and reverse transfer curves, and the response was exactly consistent with that of $|I_D|^{max}$ (Fig. 2a), supporting our previous model in which the increase in $|I_D|^{max}$ due to O_2 exposure originates substantially from the response of μ as produced by the shallow trap reduction [8]. As can be seen from Fig. 2c, exposing the picene/Cytop™/SiO_2 FET to O_2 lowered $|V_{TH}|$, and removing the O_2 enhanced $|V_{TH}|$. These results clearly show that the O_2 exposure influences the traps formed in the band gap, because the variation of $|V_{TH}|$ is closely associated with the quantities of shallow and middle traps. Thus we can conclude from these investigations that the trap reduction caused by O_2 exposure produces the observed increase in $|I_D|^{max}$ and μ, as well as the decrease in $|V_{TH}|$.

Plots of $|I_D|^{\frac{1}{2}}$ vs. $|V_G|$ for the picene/Cytop™/SiO_2 and picene/polystyrene/SiO_2 FETs stored for 0, 6 and 24 h under an O_2 atmosphere are shown in Fig. 3a and b. Before O_2 exposure these FETs were dynamically pumped for 24 h under 10^{-6} Torr, and then exposed to 8 and 10 Torr of O_2 gas. The V_{DS} was −120 V, *i.e.*, a saturation regime. Here, it should be noted that the $|I_D|^{\frac{1}{2}}$ vs. $|V_G|$ plots of the picene/Cytop™/SiO_2 FET (Fig. 3a) and the picene/polystyrene/SiO_2 FET (Fig. 3b) stored for 6 and 24 h under an O_2 atmosphere deviate from the expected straight line and the plots are suppressed in the high $|V_G|$ region, showing that the μ values are not constant but decrease with an increase in $|V_G|$. The $|I_D|^{\frac{1}{2}}$ vs. $|V_G|$ plots show more suppression of the drain current with extended O_2 exposure. This suppression of drain current in the $|I_D|^{\frac{1}{2}}$ vs. $|V_G|$ plot in the high $|V_G|$ region can be attributed to the reduction of mobility caused by the scattering of carriers.

Since the carriers are often pushed against the gate dielectric in a vertical electric field, the spatially averaged

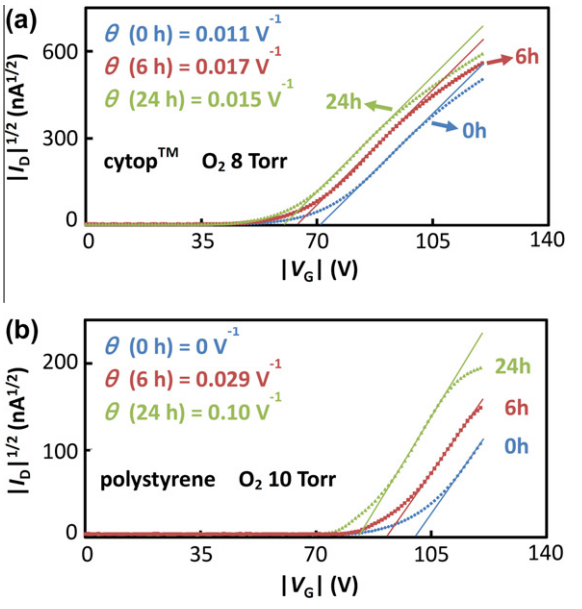

Fig. 3. (a) $|I_D|^{\frac{1}{2}}$ vs. $|V_G|$ plots for the picene/Cytop™/SiO_2 FET and (b) the picene/polystyrene/SiO_2 FET. The O_2 exposure time is given in the graphs. Straight lines indicate the lines without the suppression effect expected from the general MOS formula in the saturation regime. The θ values estimated are given in the graphs.

surface mobility, μ_{eff}, estimated under the applied V_G, known as the gate-dependent effective surface mobility, is reduced in comparison with the surface mobility, μ_0, in the absence of V_G. The relation between μ_{eff} and μ_0 is expressed by [9],

$$\mu_{eff} = \frac{\mu_0}{1 + \theta(|V_G| - |V_{TH}|)} \quad (1)$$

As seen from Eq. (1), μ_0 is affected by two variables, θ and effective gate voltage $|V_G| - |V_{TH}|$. Therefore, μ_0 can be reduced by increasing $|V_G| - |V_{TH}|$ if θ does not vanish. As the $|V_{TH}|$ of the picene FET is reduced under O_2-exposure, the decrease in μ at high $|V_G|$ (Fig. 3a and b) may be explained by the increase in $|V_G| - |V_{TH}|$. In order to investigate whether θ remains constant with O_2-exposure, the θ values for the picene/Cytop™/SiO_2 and picene/polystyrene/SiO_2 FETs were estimated at $V_G = -120$ V; μ_{eff} $(= \frac{L}{WC_0(|V_G|-|V_{TH}|)} \frac{d|I_D|}{d|V_G|})$ was estimated from the numerical derivative, $\frac{d|I_D|}{d|V_G|}$, of the $|I_D|$ vs. $|V_G|$ curve at 120 V, while μ_0 was estimated from the $|I_D|^{\frac{1}{2}}$ vs. $|V_G|$ plots in the linear region with the general MOS FET formula [10], *i.e.*, μ_0 refers to the general μ in the saturation regime. The θ value estimated from each plot is described in Fig. 3a and b. These results show an enhancement of θ with an increase in O_2 exposure time. Actually, the θ value saturates in picene/Cytop™/SiO_2 FET for O_2 exposures longer than 6 h, although it increases monotonously in picene/polystyrene/SiO_2 FET with an increase in O_2 exposure time. Furthermore, θ was vanishing in the $|I_D|^{\frac{1}{2}}$ vs. $|V_G|$ plot (0 h) measured just after the O_2-exposure of picene/polystyrene/SiO_2 FET (Fig. 3b), while a non-zero θ value (0.011 V^{-1}) is obtained even immediately after O_2 exposure of the picene/Cytop™/SiO_2

FET (Fig. 3a). These may directly reflect the difference in the surface roughness/morphology between Cytop™-coated and polystyrene-coated SiO_2 surfaces. As a consequence, the suppression in $|I_D|^{\frac{1}{2}}$ vs. $|V_G|$ plots observed in the high $|V_G|$ region is produced both by an increase in θ and a reduction in $|V_{TH}|$. Although it is difficult to precisely identify the physical origin of θ, this value is closely associated with the scattering effects that prevent carrier migration from source to drain electrodes. As is described above, the θ value may be enhanced by an increase in surface roughness as well as the existence of scattering centers. This means that θ may provide a new measure to evaluate surface morphology.

4. Conclusion

We have fabricated a selective and efficient O_2 gas sensing system using picene thin film FETs. The large hysteresis in the transfer curves that was observed in an earlier picene thin film FET [7,8] was substantially eliminated by the use of SiO_2 coated with strongly hydrophobic polymers. A picene thin film FET will sense O_2 usefully at concentrations as low as 1 ppm. Furthermore, we found a suppression of drain current in $|I_D|^{\frac{1}{2}}$ vs. $|V_G|$ plots in the high $|V_G|$ region and analyzed it quantitatively by introducing a mobility reduction factor. The suppression effect increases with increasing O_2 exposure time, and the mobility reduction factor is enhanced, indicating the enhancement of hole scattering by O_2 adsorption on the surface, which is the opposite effect to the enhancement of $|I_D|$ produced by the shallow trap reduction.

Acknowledgements

This work was partly supported by a Grant-in-Aid (18340104 and 20045012) from MEXT, Japan, by the Japan Science and Technology Agency, and by the Support Unit for Strategic Programs of Okayama University.

References

[1] A. Ho, A. Rose, T. Swager, V. Bulovic, in: D.A. Bernard, R.M. Owens, G.G. Malliaras (Eds.), Organic Semiconductors in Sensor Applications, Springer, New York, 2007.
[2] A. Bonfiglio, I. Manunza, P. Cosseddue, E. Orgiu, in: D.A. Bernard, R.M. Owens, G.G. Malliaras (Eds.), Organic Semiconductors in Sensor Applications, Springer, New York, 2007.
[3] J.B. Chang, V. Liu, V. Subramanian, K. Sivula, C. Luscombe, A. Murphy, J.S. Liu, J.M.J. Frechet, J. Appl. Phys. 100 (2006) 7.
[4] M. Bouvet, Anal. Bioanal. Chem. 384 (2006) 366.
[5] C.S. Haung, B.R. Huang, Y.H. Jang, M.S. Tsui, C.Y. Yeh, Diam. Relat. Mater. 14 (2005) 1872.
[6] T. Kanbara, K. Shibata, S. Fujiki, Y. Kubozono, S. Kashino, T. Urisu, M. Sakai, A. Fujiwara, R. Kumashiro, K. Tanigaki, Chem. Phys. Lett. 379 (2003) 223.
[7] H. Okamoto, N. Kawasaki, Y. Kaji, Y. Kubozono, A. Fujiwara, M. Yamaji, J. Am. Chem. Soc. 130 (2008) 10470 (2008).
[8] N. Kawasaki, Y. Kubozono, H. Okamoto, A. Fujiwara, M. Yamaji, Appl. Phys. Lett. 94 (2009) 043310.
[9] J.P. Colinge, C.A. Colinge, Physics of Semiconductor Devices, Kluwer Academic, Boston, 2002.
[10] S.M. Sze, Semiconductor Devices: Physics and Technology, second ed., Springer, New York, 2007.

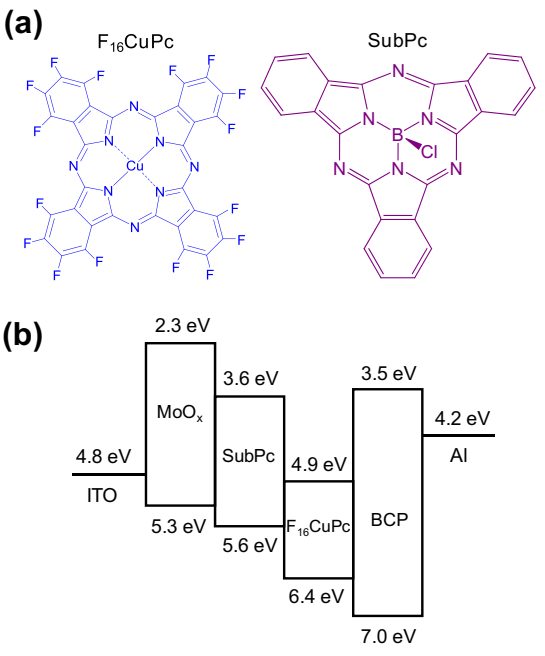

Fig. 1. (a) Molecular structures of $F_{16}CuPc$ and SubPc and (b) electronic energy level diagram for the OPV cell ITO/MoO_x/SubPc/$F_{16}CuPc$/BCP/Al.

increased V_{oc}. In this study, we show how boron subphthalocyanine chloride (SubPc, Fig. 1a) is a suitable donor material for use in conjunction with $F_{16}CuPc$ and bilayer OPV cells are demonstrated with significantly improved PCE values of 0.56%.

2. Experimental details

The OPV cells were fabricated on commercially available indium-tin-oxide (ITO) coated glass substrates (Psiotec, 100 nm thick ITO, $R_s < 15\ \Omega\ sq^{-1}$) after initial solvent cleaning. The substrates were then exposed to an atmosphere of UV/ozone to remove any remaining carbon residues. The materials used in the cells were molybdenum oxide (MoO_x, Aldrich, 99.99%), SubPc (Aldrich), $F_{16}CuPc$ (Aldrich) and bathocuproine (BCP, Aldrich). The organic materials were purified twice by thermal gradient sublimation prior to deposition. All layers were grown by vacuum deposition in an organic molecular beam deposition system (Kurt J. Lesker Spectros) with a base pressure of about 5×10^{-8} mbar and the deposition rates were monitored using a series of quartz–crystal microbalances, where $\sim$0.4 Å s^{-1} was used for MoO_x, $F_{16}CuPc$ and BCP, while $\sim$1.5 Å s^{-1} was used for SubPc. Al cathodes were deposited *in situ* by evaporation through a shadow mask to a thickness of 100 nm, giving an active area of 0.16 cm^2.

Current–voltage (J–V) curves for the cells were measured with a Keithley 2400 sourcemeter in air under AM1.5 solar illumination at $\sim$100 mW cm^{-2} using a Newport Oriel solar simulator, where the intensity was calibrated using a monocrystalline silicon solar cell (PV Measurements, Inc.). Electronic absorption spectra were recorded using a Perkin–Elmer Lambda 2 spectrometer. External quantum efficiency (EQE) measurements were obtained using the Newport Solar Simulator and a PTI Monochromator. The monochromatic light intensity was calibrated with a Si photodiode (Thorlabs) and chopped at 500 Hz. Signal detection was performed with a current–voltage amplifier (Laser Component UK Ltd., DHPCA-100) and a lock-in amplifier (Stanford Research SR 830 DSP).

3. Results and discussion

Three basic SubPc/$F_{16}CuPc$ OPV cells were fabricated: (A) ITO/SubPc(14 nm)/$F_{16}CuPc$(35 nm)/Al; (B) ITO/SubPc(14 nm)/$F_{16}CuPc$(35 nm)/BCP(8 nm)/Al; and (C) ITO/MoO_x(5 nm)/SubPc(14 nm)/$F_{16}CuPc$(35 nm)/BCP(8 nm)/Al. Given the known low exciton diffusion length of SubPc films, the thickness of the donor layer in each cell was fixed at 14 nm [16,17]. The optimum thickness of the $F_{16}CuPc$ layer for the cells was determined to be 35 nm. The experimental results for the different cells are summarised in Table 1. Cell A demonstrates a very low PCE of 0.02%, with the V_{oc}, short-circuit current density (J_{sc}) and fill factor (FF) being 0.22 V, 0.46 mA cm^{-2} and 0.21, respectively. After inserting the BCP and MoO_x layers all cell parameters increase very significantly. BCP is a wide-band-gap organic material and plays an important role in the SubPc/$F_{16}CuPc$ cell. Firstly, it can act as an exciton-blocking barrier and stops excitons diffusing towards the Al electrode [18]. It also acts as a diffusion barrier for the top Al contact, helping to eliminate the creation of Al-induced charge-transfer states in the $F_{16}CuPc$ layer [18]. Perhaps most importantly, BCP also behaves as a buffer layer and prevents direct contact between the $F_{16}CuPc$ and Al, which otherwise can lead to a low conductivity phase region comprising three-dimensional $(F_{16}CuPc)_3Al$ species [19]. Hence in cell B, in which a BCP layer is incorporated into the cell, J_{sc} increases from 0.46–1.90 mA cm^{-2}, and the FF increases accordingly from 0.21 to 0.31. The MoO_x acts as a more efficient hole-extracting layer than the bare ITO substrate. The ITO Fermi level can be pinned to the valance band of the MoO_x interlayer [20], where the latter is closely aligned with the HOMO of the SubPc donor, as shown in Fig. 1b. Inclusion in cell C results in an improvement of the V_{oc} from 0.2 to 0.4 V. Additionally, the insertion of the MoO_x layer also minimises variations in cell performance by decoupling the photoactive layer from the electrically inhomogeneous ITO electrode [20]. The combined effect of adding the BCP and MoO_x layers leads to a dramatic increase in PCE from 0.02% to 0.56%, with V_{oc} = 0.40 V, J_{sc} = 2.54 mA cm^{-2} and the FF = 0.55. Corresponding J–V curves of the three cells

Table 1
Key cell performance parameters obtained under 1 sun illumination from SubPc/$F_{16}CuPc$ OPV cells fabricated on ITO: (A) ITO/SubPc(14 nm)/$F_{16}CuPc$(35 nm)/Al; (B) ITO/SubPc(14 nm)/$F_{16}CuPc$(35 nm)/BCP(8 nm)/Al; (C) ITO/MoO_x(5 nm)/SubPc(14 nm)/$F_{16}CuPc$(35 nm)/BCP(8 nm)/Al.

Cells	V_{oc}/V	J_{sc}/mA cm^{-2}	FF	PCE/%
A	0.22	0.46	0.21	0.02
B	0.21	1.90	0.31	0.13
C	0.40	2.54	0.55	0.56

recorded under 1 sun illumination are shown in Fig. 2. In these cells, although the energy gap between the Al cathode and the F_{16}CuPc LUMO is large (0.70 eV), Fermi level pinning can occur and spontaneous charge transfer between the Al and the LUMO of the F_{16}CuPc becomes possible [21].

Electronic absorption spectra of single layer F_{16}CuPc and SubPc thin films as well as a F_{16}CuPc/SubPc bilayer film are shown in Fig. 3. The EQE obtained for cell C is also shown. For F_{16}CuPc, absorption occurs between 550 and 850 nm with three peaks at about 640, 704 and 788 nm. For SubPc, absorption occurs between 450 and 650 nm with two main peaks at about 540 and 588 nm. The bilayer structure therefore demonstrates good absorption in the visible range of the spectrum from 450 to 850 nm, although the absorption intensity of the F_{16}CuPc layer is only about half that of the SubPc layer. Consequently, the EQE of the corresponding OPV cell suggests that the major contribution to the photocurrent in the wavelength range 450–650 nm comes from the SubPc donor layer, while the F_{16}CuPc acceptor layer provides a small contribution from 550 to 850 nm where the EQE is about 5%.

Fig. 4 shows the device parameters obtained for cell C as a function of the thickness of the F_{16}CuPc acceptor layer (in the range 15–45 nm). The V_{oc} and FF change marginally with typical values of 0.40 V and 0.55, respectively. By contrast, the J_{sc} changes considerably increasing from about 1.7 mA cm^{-2} at 15 nm to the peak value of 2.54 mA cm^{-2} at 35 nm which results in the optimised PCE of 0.56%. The exciton diffusion length in phthalocyanine materials such as CuPc is reported to be about 10 nm [22,23]. Consequently, in the case of F_{16}CuPc, it is almost certainly less than the 35 nm layer thickness required for optimisation of the OPV cells. This optimum thickness represents a balance between optical interference effects and the built-in electron field strength within the device [24,25].

The stability of cell C was measured under constant illumination for 60 min under ambient conditions. Fig. 5 shows the percentage degradation of each key device parameter from the value at 0–60 min. The percentage degradation of the V_{oc}, J_{sc}, and FF are about 2.5%, 5%, and 4%, respectively, resulting in an approximately 10% degradation in the overall PCE. This stability is much better than that typically observed for equivalent bilayer heterojunction cells

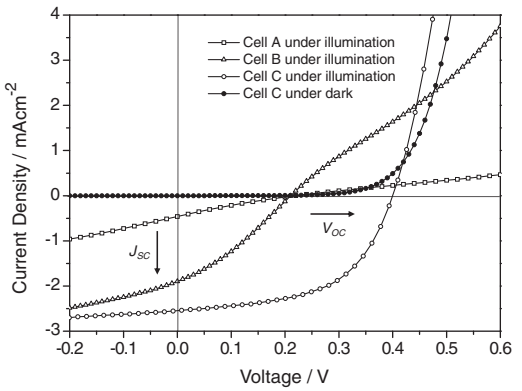

Fig. 2. *J–V* curves recorded under 1 sun illumination for cell A: ITO/SubPc(14 nm)/F_{16}CuPc(35 nm)/Al; cell B: ITO/SubPc(14 nm)/F_{16}CuPc-(35 nm)/BCP(8 nm)/Al; and cell C: ITO/MO_x(5 nm)/SubPc(14 nm)/F_{16}CuPc-(35 nm)/BCP(8 nm)/Al. The corresponding *J–V* curve for cell C recorded in the dark is also shown.

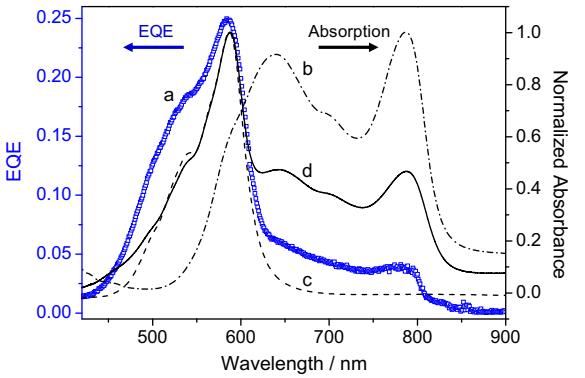

Fig. 3. (a) EQE of the device with the structure ITO/MoO_x(5 nm)/SubPc(14 nm)/F_{16}CuPc(35 nm)/BCP(8 nm)/Al. (b)–(d) are the normalized electronic absorption spectra of a F_{16}CuPc single layer (35 nm), a SubPc single layer (14 nm) and a SubPc (14 nm)/F_{16}CuPc (35 nm) double layer.

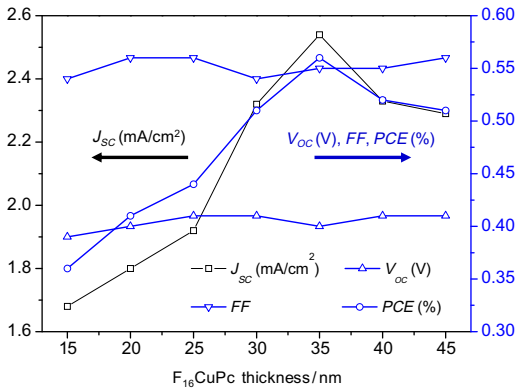

Fig. 4. Effect of F_{16}CuPc thickness on the V_{oc}, J_{sc}, FF and PCE for the cell structure ITO/MoO_x(5 nm)/SubPc(14 nm)/F_{16}CuPc(15–45 nm)/BCP-(8 nm)/Al.

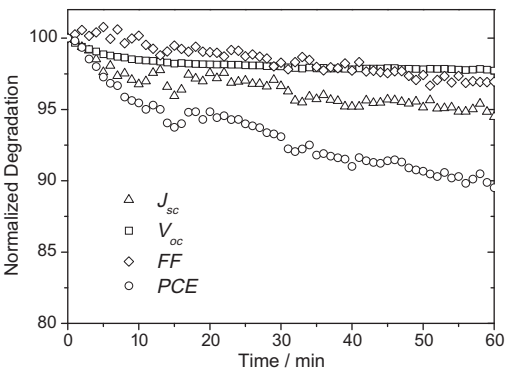

Fig. 5. Normalised degradation of the V_{oc}, J_{sc}, FF and PCE values obtained for cell C under constant illumination for 60 min under ambient conditions.

fabricated with the more commonly used C_{60} acceptor for nominally identical conditions (ca. 50% degradation) [26]. This improvement results from the improved stability of the acceptor materials as well as the use of the MoO_x interlayer which blocks adverse interfacial effects at the ITO/SubPc interface.

4. Conclusion

In summary, we have shown that F_{16}CuPc can be used as an electron accepting layer in bilayer heterojunction OPV cells using a SubPc donor. The F_{16}CuPc/SubPc heterojunction cells show good performance and stability, with a PCE of 0.56% obtained for optimum layer thickness and only 10% degradation in cell performance after constant illumination for 60 min under ambient conditions. The EQE demonstrates that the photocurrent comes from excitons created in both the SubPc and F_{16}CuPc layers although the latter shows a small contribution. The results suggest that F_{16}CuPc has the potential to be a promising electron acceptor material in small molecule OPV cells.

Acknowledgements

This work was funded by Engineering and Physical Sciences Research Council (EPSRC), UK, through the Basic Technology Project "Molecular Spintronics". R.A. Hatton is grateful to the Royal Academy of Engineering/EPSRC for the award of a Fellowship. The authors thank Prof. D.H. Yan and Dr. H.B. Wang (Changchun Institute of Applied Chemistry, Chinese Academy of Sciences) for their discussions in this work.

References

[1] B. Kippelen, J.L. Brédas, Energy Environ. Sci. 2 (2009) 251.
[2] L.M. Chen, Z. Hong, G. Li, Y. Yang, Adv. Mater. 21 (2009) 1434.
[3] M. Riede, T. Mueller, W. Tress, R. Schueppel, K. Leo, Nanotechnology 19 (2008) 424001.
[4] C.W. Tang, Appl. Phys. Lett. 48 (1986) 183.
[5] H.Y. Chen, J.H. Hou, S.Q. Zhang, Y.Y. Liang, G.W. Yang, Y. Yang, L.P. Yu, Y. Wu, G. Li, Nat. Photonics 3 (2009) 649.
[6] N. Beaumont, A. Duraud, L.J. Pegg, R. da Campo, R.A. Hatton, M. Shipman, T.S. Jones, J. Mater. Chem., submitted for publication.
[7] X. Jiang, J. Dai, H. Wang, Y. Geng, D. Yan, Chem. Phys. Lett. 446 (2007) 329.
[8] A. Opitz, B. Ecker, J. Wagner, A. Hinderhofer, F. Schreiber, Jo Manara, J. Pflaum, W. Brütting, Org. Electron. 10 (2009) 1259.
[9] A. Opitz, J. Wagner, W. Brütting, A. Hinderhofer, F. Schreiber, Phys. Status Solidi A 206 (2009) 2683.
[10] Z. Bao, A.J. Lovinger, J. Brown, J. Am. Chem. Soc. 120 (1998) 207.
[11] Q. Tang, H. Li, Y. Liu, W. Hu, J. Am. Chem. Soc. 128 (2006) 14634.
[12] H.B. Wang, F. Zhu, J.L. Yang, Y.H. Geng, D.H. Yan, Adv. Mater. 19 (2007) 2168.
[13] Y.L. Gao, H.J. Ding, H.B. Wang, D.H. Yan, Appl. Phys. Lett. 91 (2007) 142112.
[14] H.B. Wang, J. Wang, H.C. Huang, X.J. Yan, D.H. Yan, Org. Electron. 7 (2006) 369.
[15] K.M. Lau, J.X. Tang, H.Y. Sun, C.S. Lee, S.T. Lee, D.H. Yan, Appl. Phys. Lett. 88 (2006) 173513.
[16] R.R. Lunt, N.C. Giebink, A.A. Belak, J.B. Benziger, S.R. Forrest, J. Appl. Phys. 105 (2009) 053711.
[17] K.L. Mutolo, E.I. Mayo, B.P. Rand, S.R. Forrest, M.E. Thompson, J. Am. Chem. Soc. 128 (2006) 8108.
[18] P. Peumans, V. Bulović, S.R. Forrest, Appl. Phys. Lett. 76 (2000) 2650.
[19] C. Shen, A. Kahn, J. Schwartz, J. Appl. Phys. 90 (2001) 6236.
[20] I. Hancox, K.V. Chauhan, P. Sullivan, R.A. Hatton, A. Moshar, C.P.A. Mulcahy, T.S. Jones, Energy Environ. Sci. 3 (2010) 107.
[21] S. Braun, W.R. Salaneck, M. Fahlman, Adv. Mater. 21 (2009) 1450.
[22] P. Peumans, A. Yakimov, S.R. Forrest, J. Appl. Phys. 93 (2003) 3693.
[23] S. Banerjee, A.P. Parhi, S.S. Kumar Iyer, S. Kumar, Appl. Phys. Lett. 94 (2009) 223303.
[24] Q.L. Song, H. Yang, H.R. Wu, F.Y. Li, J. Lumin. 119–120 (2006) 142.
[25] T. Stübinger, W. Brütting, J. Appl. Phys. 90 (2001) 3632.
[26] S. Heutz, P. Sullivan, B.M. Sanderson, S.M. Schultes, T.S. Jones, Sol. Energy Mater. Sol. Cells 83 (2004) 229.

dihydroxide). Thus, a layered-structure of the nanocomposite PEI/TiO_x gate dielectric layer is easily prepared using conventional LBL deposition techniques, as PEI in water has a positive electric charge and TALH has a negative charge in water.

2. Experiment

Fig. 1a–c show schematic illustrations of the SWCNT–TFT structure and the LBL self-assembly process utilized for preparing the PEI/TALH gate dielectric layer. The octahedral coordination structure of TALH is shown in Fig. 1d. The experimental process involved alternating adsorption of 0.1 wt.% PEI and 5 wt.% TALH via a dipping method, onto the oppositely charged substrate, followed by rinsing with deionized (DI) water and drying. More specifically, cleaned Si-wafer substrates were first exposed to a 0.1 wt.% PEI solution for 15 min and then thoroughly rinsed with excess DI water for 5 min. Subsequently, the PEI coated substrates were dipped into a 5 wt.% TALH solution for 15 min, washed with DI water, and then dried with N_2 gas. The above deposition procedure was repeated 15 times to obtain the multi-layered structure $(PEI/TALH)_{15}$. The resulting substrate was then heated to 95 °C for 24 h in order to convert the precursor into a TiO_x nanostructure [11]. The specific details of the LBL deposition and annealing conditions to form the PEI/TALH composite have been reported previously. Unlike the water-sensitive alkoxide precursor, the deposited TiO_x precursor TALH on PEI is slowly converted into a TiO_x nanostructure, then into a densely structured titania-polymer network by heating at 95 °C [11–13].

The thickness and nanostructure of $(PEI/TALH)_{15}$ nanocomposite films was characterized via high-resolution transmission electron microscopy (HRTEM), as shown in Fig. 2. The film used for analysis consisted of three layers with a $(PEI/TALH)_{15}/SiO_x/Si$ structure (Si is the substrate and SiO_x is a naturally oxidized layer formed during cleaning of the Si). The presence of a thin SiO_x inter-layer would significantly reduce the total gate capacitance due to its low-k properties. The thickness of the $(PEI\text{-}TiO_x)_{15}$ nanocomposite film, as measured by HRTEM imaging, was about 70 nm, and the average deposition thickness was calculated to be 4.7 nm/bilayer. Notably, the latter value is similar to that previously reported by Gentle, 4.9 ± 0.5 nm/bilayer [11].

The surface morphology of the gate dielectric layer produced by the LBL deposition process was characterized using atomic force microscopy (AFM), as shown in Fig. 3a. We found that the surface roughness of the titania nanocomposite films $(PEI\text{-}TiO_x)_{15}$ was R_q = 5.07 nm (R_a = 3.66) and suggest that incomplete cleaning and the bulky structure of TALH may contribute to the creation of such a rough surface. In the application of SWCNT–TFTs, the dielectric surface roughness would not be a significant factor in the device performance, as well-crystallized SWCNT strands are randomly deposited on the dielectric surface and make a network structure of active layers. On the other hand, active layers of most other organic/inorganic semiconducting materials are disturbed by a rough dielectric surface, because they are crystallized on the surface of the gate dielectric layer after deposition [14–16].

The SWCNT coating solution was produced by the dispersion of thermally and chemically purified SWCNTs (ASP-100F, Hanwha Nanotech) in 1-methyl-2-pyrrolidone

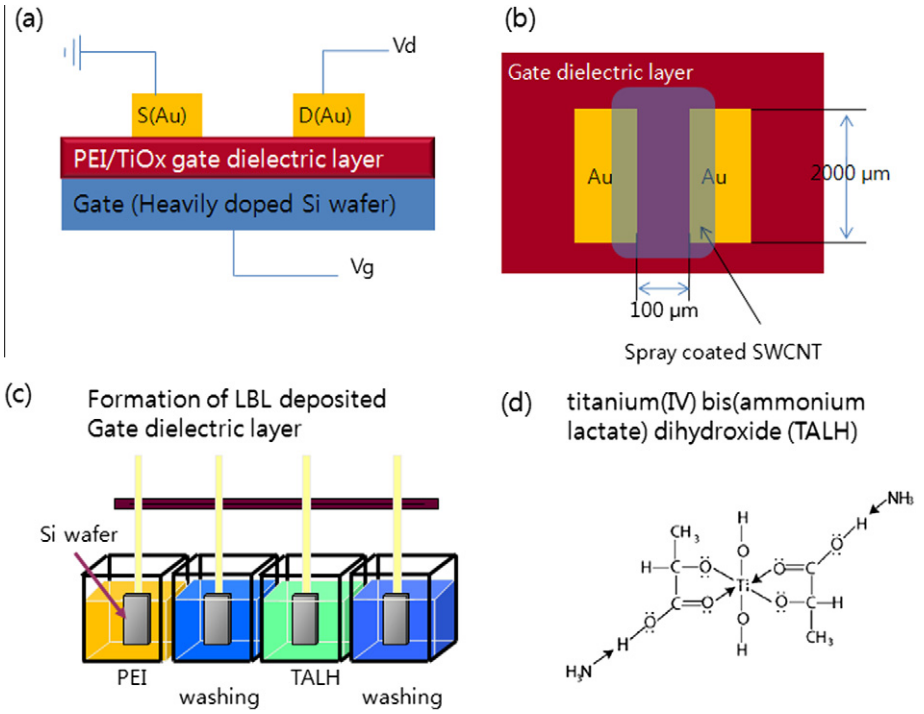

Fig. 1. (a–b) Schematic illustrations of SWCNT–TFT structure (c) preparation of a PEI/TiO_x nanocomposite gate dielectric layer through layer-by-layer deposition methods, and (d) the octahedral structure of the titanium oxide precursor, TALH.

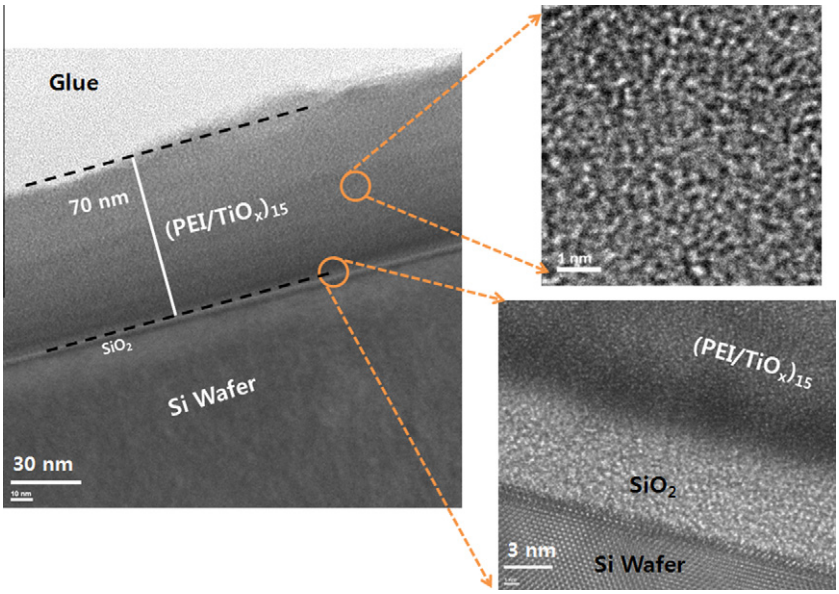

Fig. 2. High resolution TEM images of the PEI/TALH nanocomposite gate dielectric layer. A cross-section of the gate dielectric layer shows that the $(PEI/TiO_x)_{15}$ gate dielectric layer has a thickness of about 70 nm and a calculated average deposition thickness of 4.7 nm/bilayer.

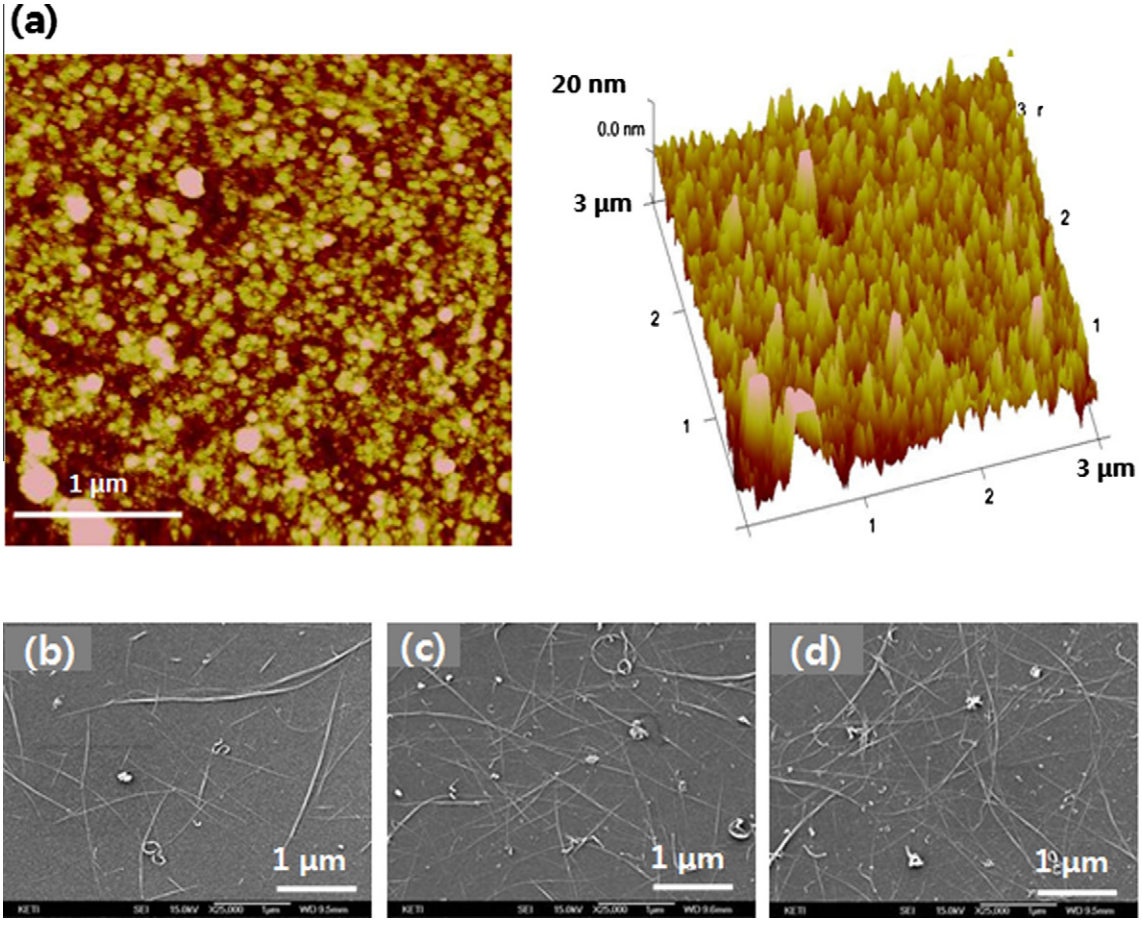

Fig. 3. (a) AFM images of the surface morphology of the PEI/TALH deposited gate dielectric layer. The surface roughness of the nanocomposite films formed by LBL assembly was found to be R_q = 5.07 nm (R_a = 3.66). (b–d) The morphology of the sprayed SWCNTs on the gate dielectrics, for spray times of 60, 120, and 150 s, respectively.

(NMP; Sigma–Aldrich). SWCNTs (ASP-100F) synthesized by the arc-discharge method are usually 15 μm in length and 1.2 ± 0.2 nm in diameter. The SWCNT concentration used was 0.01 mg/ml, and the polystyrene was added to prevent SWCNT aggregation in the dispersion. In previous experiments, we found that the amount of polystyrene used significantly affected the current density of the TFT channel. With increasing polymer binder content, the on/off ratio increased while the mobility declined due to improved insulation characteristics. According to previous results, an SWCNT/polymer mass ratio of 1/45 was suitable for spray-coating methods; hence we prepared our SWCNT solutions following the same methodology.

3. Result and discussion

The capacitance of the gate dielectric, determined through measurements in which the PEI/TALH dielectric layer was sandwiched between Au dots and heavily-doped Si substrates, was found to be 118 nF/cm^2 when measured at 100 kHz. The calculated dielectric constant from the measured capacitance and dielectric thickness is 13.3, which is much lower than literature values for amorphous titanium oxide (40–50) [17]. This discrepancy is likely due to the PEI inter-layer and SiO_2 layer in the dielectric composite, and presence of residual precursor decreasing the capacitance.

The SWCNT–TFT active layers were deposited by spray coating method and directly patterned using a metal shadow mask. Fig. 3b–d show FE-SEM images of the SWCNT networks in the channel after spray coating for 60, 120, and 150 s, respectively. As the spray coating time increased, SWCNTs within the channel became layered and more numerous, thus increasing the number of electric current paths in the channel. In our coating system, spray coating for over 150 s deposits an excessive amount of SWCNTs on the active layer, thereby generating a conductive film and decreasing the on/off ratio. In our system, a spray time of 120 s was suitable for active layer deposition.

The transfer and output characteristics of the fabricated top-contact geometry of SWCNT–TFT are shown in Fig. 4a and b, respectively. The transfer curves show that our PEI/TiO_x layered dielectric-based devices could be operated at gate voltages below −2 V and that they exhibit good linear/saturation behavior in their output characteristics. The field-effect mobility measured in the linear regime was as high as 6.7 cm^2/V s (V_D = −0.1 V), and the threshold voltage was −0.88 V. The sub-threshold swing was as low as 260 mV/decade, and the on/off current ratio was 500. Without any separation process of SWCNTs, both metallic and semiconducting SWCNTs were present in the active

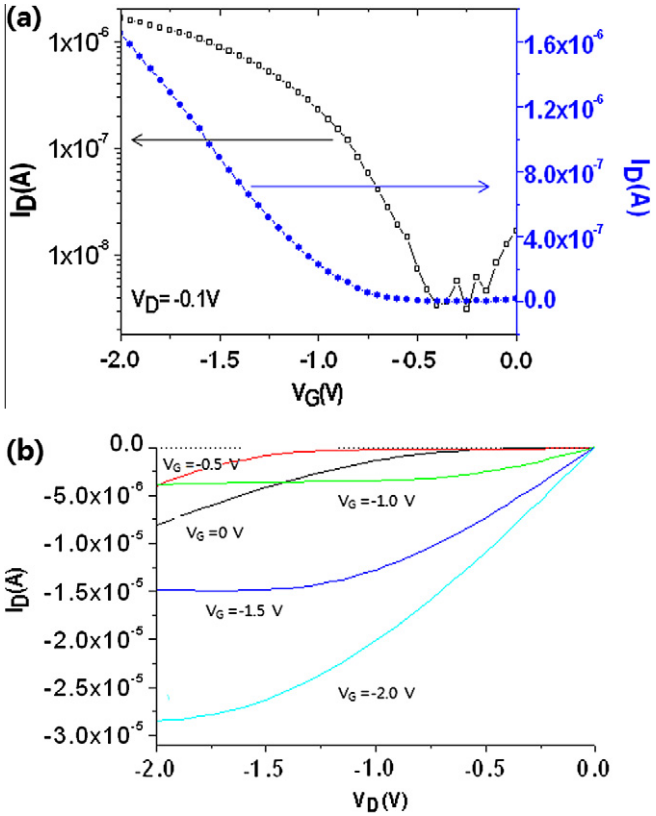

Fig. 4. Electric characteristics of the SWCNT–TFT. (a) The transfer curve of the TFT, measured at V_D = −0.1 V. The leakage current is less than 0.01 μA and the on/off ratio is about 500. (b) The output curve, exhibiting good linear/saturation behavior. The leakage current shown at low V_D originated from the high-k material with a narrow band gap.

layer, resulting in a relatively low on/off ratio compared to other semiconducting materials. However, the high mobility (>6.7 $cm^2/V\,s$) and low operating voltage (<2 V) of the TFTs reported here make them well suited to switch device applications that do not require a high on/off ratio, such as RF-IF tags.

Our TFT shows outstanding operational characteristics with drain current (I_D) saturation in the elevated drain voltage (V_D) region and good linear behavior near $V_D = 0$. It is likely that this high dielectric capacitance produces charge carriers at a low operation voltage, thereby reducing the effective driving force for leakage. However, at gate voltage (V_G) = −0 V, or −0.5 V, a relatively large leakage current is shown in the output curve in the region of elevated V_d. This likely arises due to the electric field through the gate dielectric layer being maximized under these conditions, thus inducing leakage current through the high-*k* dielectric material with a narrow band gap.

4. Conclusion

We have developed a simple and promising LBL self-assembly method for a high-*k* titania nanocomposite gate dielectric layer, and fabricated a TFT with an SWCNT active layer. The high capacitance of the dielectric layer results in a high mobility at a low operating voltage and a relatively low leakage current without separation of the metallic and semiconducting SWCNTs. We envisage that this simple solution deposition process will find applications in the fabrication of switch devices for low-end market products.

Acknowledgements

This work was partially supported by the Ministry of Knowledge Economy (MKE) through the project of Research Consortium for R2R printed RFID Tags.

References

[1] M.F. Yu, B.S. Files, S. Arepalli, R.S. Ruoff, Phys. Rev. Lett. 84 (2000) 5552.
[2] S.G. Rao, L. Huang, W. Setyawan, S. Hong, Nature 425 (2003) 36.
[3] W.B. Choi, D.S. Chung, J.H. Kang, H.Y. Kim, Y.W. Jin, Appl. Phys. Lett. 75 (1999) 3129.
[4] H. Murakami, M. Hirakawa, C. Tanaka, H. Yamakawa, Appl. Phys. Lett. 76 (2000) 1776.
[5] S.J. Tans, A.R.M. Verschueren, C. Dekker, Nature 393 (1998) 49.
[6] V. Derycke, R. Martel, J. Appenzeller, P. Avouris, Nano Lett. 1 (2001) 453.
[7] S.J. Wind, J. Appenzeller, R. Martel, V. Derycke, P. Avouris, Appl. Phys. Lett. 80 (2002) 3817.
[8] Y. Zhou, A. Gaur, S.H. Hur, C. Kocabas, M.A. Meitl, M. Shim, J.A. Rogers, Nano Lett. 4 (2004) 2031.
[9] E.S. Snow, P.M. Campbell, M.G. Ancona, J.P. Novak, Appl. Phys. Lett. 86 (2005) 03310.
[10] Y. Lu, W.H. Lee, H.S. Lee, Y. Jang, K. Cho, Appl. Phys. Lett. 94 (2009) 113303.
[11] A. Yu, G.Q.M. Lu, J. Drennan, I.R. Gentle, Adv. Funct. Mater. 17 (2007) 2600.
[12] A. Hanprasopwattana, T. Rieker, A.G. Sault, A.K. Dayte, Catal. Lett. 45 (1997) 165.
[13] X. Shi, T. Cassagneau, Frank Caruso, Langmuir 18 (2002) 904.
[14] D. Knipp, R.A. Street, A.R. Völkel, Appl. Phys. Lett. 82 (2003) 3907.
[15] S. Steudel, S.D. Vusser, S.D. Jonge, D. Janssen, S. Verlaak, J. Genoe, P. Heremans, Appl. Phys. Lett. 85 (2004) 4400.
[16] S.E. Fritz, T.W. Kelley, C.D. Frisbie, J. Phys. Chem. B 109 (2005) 10574.
[17] http://www.clippercontrols.com/info/dielectric_constants.html.

in a blue-emitting polyfluorene-triaryamine (PF-TAA) based copolymer [13,14] and in the archetypical small-molecule material α-NPD [15], which is frequently used in OLEDs. Both studies revealed that equally good descriptions of the steady-state current density *versus* voltage ($J(V)$) curves could be obtained from both models, but that a distinction could be made on the basis of the effective hopping site densities obtained. For PF-TAA only the GDM led to a hopping site density close the actual molecular site density, whereas for the same reason the CDM was found to be most appropriate for α-NPD. Using the alternative model led for both cases to a discrepancy of almost one order of magnitude or more in the site density.

The question now arises whether it would also be possible to describe the $J(V)$ curves of single-carrier devices based on *electron* transporting materials using the GDM or the CDM, and whether it would again be possible to make a distinction between both models on the basis of the site density obtained. Making such a comparison is expected to be more difficult than for hole-transporting materials, as in polymers [16–18] as well as in small-molecule materials [19,20] the electron mobility is often affected by trap states. So far, no comparison was given of analyzes of the electron mobility in disordered organic semiconductors using the GDM and the CDM, including the possible effect of the presence of trap states and including the effects of the charge carrier density dependence of the mobility.

In this paper, we investigate whether such an extensive analysis can be given for the electron transport in sandwich-type devices based on the small-molecule material bis(2-methyl-8-quinolinolato)(4-phenylphenolato)aluminum (BAlq). This material is used in OLEDs as a (sky-blue) emitting layer [21–23], as a host material in dye-doped emitting layers [22,24], as a hole-blocking layer [21,25–28], and as a "barrier-softening" interfacial layer in between the electron transporting and emissive layers [29]. As a hole-blocking material it is known to allow for high lifetimes, up to 160,000 hours at a luminance level of 100 cd/m^2 [25]. BAlq is photochemically stable [30], and has a glass transition temperature of 92 °C [31]. The structure of BAlq (see Fig. 1(a)) is similar to that of the frequently used material tris(8-quinolinolato)aluminum (Alq_3). We study devices operating in the space-charge-limited current regime, so that the current density is to a large extent determined by the bulk transport rather than by the injection process. The temperature and layer-thickness dependence of the $J(V)$ curves is found to be well described by assuming that the DOS is a superposition of a Gaussian "host" DOS and an exponential "trap" DOS. A similar shape of the DOS was found recently to provide a good description of the electron transport in poly-phenylene-vinylene (PPV) derivatives [17] and in a polyfluorene-based copolymer [32]. Good descriptions can be obtained within the GDM as well as the CDM. However, as for α-NPD, the analysis within the CDM provides a hopping site density which is by far closest to the experimental value, which provides a strong indication that also for BAlq the site energies are spatially correlated.

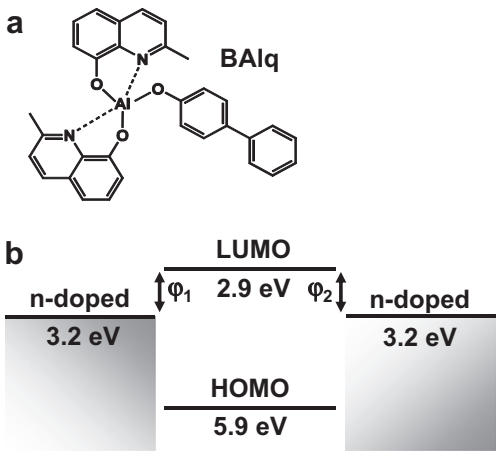

Fig. 1. Chemical structure of the BAlq molecule (a) and schematic energy diagram of the device structures used in this study, indicating the electron injection barriers at the anode (ϕ_1) and at the cathode (ϕ_2), and the HOMO and LUMO energies of BAlq (b).

2. Device structure and experimental results

For investigating the electron mobility in BAlq, devices with the following layer structure were fabricated:

Glass|**ITO**|**NDL**|**BAlq**|**NDL**|**Al**,

with NDL a ~50 nm n-doped small-molecule layer. After a UV/ozone treatment of the indium tin oxide (ITO, ~100 nm) patterned glass substrates, NDL and BAlq layers were evaporated in a high-vacuum system, with a substrate temperature of ~295 K, followed by evaporation of an aluminum cathode layer. The devices were encapsulated with a glass lid enclosing a desiccant getter to prevent water and oxygen contamination. Four series of four nominally identical devices with an active area of 20 mm^2 were fabricated on a single substrate. Combining the total thicknesses of the NDL|BAlq|NDL stacks, obtained from Transmission Electron Microscopy (TEM), with the relative thicknesses of the separate layers as deduced from Ion-Beam Etching X-ray Photoelectron Spectroscopy (IBE-XPS) measurements, the BAlq layer thicknesses of the four series were determined to be 70, 106, 158 and 258 nm, with an uncertainty of ~7%. The separate organic layers were not easily resolved from TEM. The aluminum and oxygen in the BAlq layers yielded good contrast using IBE-XPS.

The highest occupied molecular orbital (HOMO) and lowest unoccupied molecular orbital (LUMO) energies of BAlq are located at ~5.9 eV and ~2.9 eV below the vacuum level, respectively [25]. Fig. 1(b) gives a schematic energy diagram of the device structure, indicating the energy-level alignment at the interface between BAlq and the NDLs. The NDL used is molecularly doped using an organic material with a high-lying HOMO level, as described for various host–guest combinations by Waltzer et al. [33]. The NDL is known to give rise to good electron injection into BAlq, judged from the observation of efficient light emission from multilayer OLEDs using BAlq together with the NDL

at the electron injecting side. From low-frequency capacitance–voltage ($C(V)$) measurements a symmetrical peak in the capacitance is observed at $V = 0$ V with a height ~8% larger than the geometrical capacitance, C_{geom}, measured at high frequencies. We view this as an indication that the built-in voltage (V_{bi}) is close to 0 V, as expected from the use of the symmetric NDL sandwich structure. Furthermore, the relatively small peak height (which would be $\sim 1.29 \times C_{geom}$ in the absence of an injection barrier and disorder [34]) indicates that the electron injection barrier at the interface between the NDL and BAlq is expected not to be larger than a few tenths of an eV. From the analysis presented below we find $\phi = 0.3$ eV for both interfaces, leading to an effective Fermi energy of the NDLs of 3.2 eV. The relative permittivity (ε_r) of BAlq obtained from the analysis of C_{geom} at frequencies in the range 10^2–10^5 Hz is 3.8 ± 1.0. For a variation of ε_r within these uncertainty margins there is no significant change in the quality of the description provided by the models for the experimental data, nor in the optimal parameters found, except for a change in the mobility values obtained. A change of ε_r from 3.8 to 2.8 (4.8) was found to lead to an increase (decrease) of the mobility values obtained of less than 25%.

The BAlq volume density, taken equal to the density of Al atoms in a series of BAlq thin films deposited on silicon substrates as obtained from Inductively Coupled Plasma Atomic Emission Spectrometry (ICP-AES) measurements, is $(1.5 \pm 0.1) \times 10^{27}$ molecules per m^3. It is essentially identical to the volume density in the crystalline bulk material, 1.507×10^{27} m^{-3} [35].

Fig. 2 shows measured $J(V)$ curves for the four thicknesses at room temperature, both on a linear voltage and current density scale (inset), and on a log–log scale (main panel). A maximum electrical power density $\sim 1 \times 10^3$ W/m^2 was allowed, in order to prevent substantial heating of the devices. The curves are highly symmetric around $V = 0$ V, consistent with the complementary evidence from the $C(V)$ measurements that $V_{bi} \cong 0$ V. The observation of a $J(V)$ curve with a slope of 2 on log–log scale (dotted line) would indicate space-charge-limited current

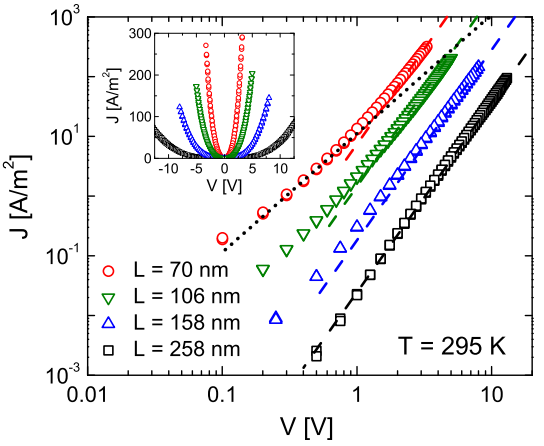

Fig. 2. Experimental $J(V)$ curves for four thicknesses of the BAlq layer, at 295 K. The dotted line has a slope of 2. The dashed lines are fits to the data at high voltages with a slope of 3.2. The inset shows the same data on a linear scale.

with a constant mobility. However, the experimental curves are much steeper, in particular above 1 V. The dashed lines are linear fits to the data at high voltages, and have a slope of ~3.2. Within a drift-only transport model, the observation of a linear log(J)–log(V) curve with a slope much larger than 2 is an indication of trap-limited charge transport in an exponential trap density of states [20,36,37,16,38].

3. Analysis of $J(V)$ curves

The temperature-dependent $J(V)$ curves for the four thicknesses of the BAlq layer are shown in Fig. 3 (symbols). They are analyzed using a drift-diffusion device model as presented in Ref. [39], assuming carrier density and electric field dependent mobility functions as described by the GDM and the CDM, and including the possible presence of injection barriers (see Ref. [15]) and of an additional exponential trap DOS. The total DOS is for energies $E < 0$ described as

$$\rho(E) = \frac{N_t}{\sqrt{2\pi\sigma^2}} \exp\left(-\frac{E^2}{2\sigma^2}\right) + \frac{N_{trap}}{k_B T_0} \exp\left(\frac{E}{k_B T_0}\right), \qquad (1)$$

with σ and N_t the width and the density of hopping sites for the Gaussian DOS, k_B the Boltzmann constant and T_0 and N_{trap} the parameters determining the characteristic depth and density of trap sites (if defined as the integral of the exponential trap DOS up to the top of the Gaussian DOS), respectively. The DOS is shown schematically in Fig. 4. For $E > 0$ the exponential contribution is assumed to vanish. The experiments are only sensitive to those trap states which are actually occupied, in the tail of the DOS. Therefore, the precise energy at which the formal (rather artificial) cutoff of the exponential trap DOS is taken, in this work at $E = 0$, is of no significance to the current density as long as it is sufficiently high. Furthermore, the actual total density of trap states can therefore be much smaller than N_{trap}, which is only meant to provide (in combination with the Gaussian "host" DOS) the most proper description of DOS in the tail region. We also note that in the model no distinction is made concerning the physical nature of the states forming the "host" and the "guest" DOS. The local occupancies of host and trap sites at any position in the device are calculated by assuming local thermal equilibrium, i.e. assuming thermally induced detrapping as described within the multiple-trap-and-release model. The current density is calculated using the local free carrier densities and the mobility and diffusion coefficient enhancements corresponding to these densities, whereas the field across the device is calculated by solving Poisson's equation using the total carrier density distribution.

The optimal parameter set for each mobility model is obtained as follows. For a given $\{N_t, \sigma, N_{trap}, T_0\}$ combination, we determine the fitting error between the experimental and calculated $J(V)$ curves for each individual layer thickness and temperature. For each calculated curve, the (temperature dependent) mobility in the zero electric field and carrier density limit, $\mu_0(T)$, is treated as a free parameter. It only shifts the log(J)–V curves vertically. The built-in voltage, $V_{bi} \equiv (\phi_1 - \phi_2)/e$, with e the elementary charge, is set to 0 V. For each $\{N_t, \sigma, N_{trap}, T_0\}$ combination

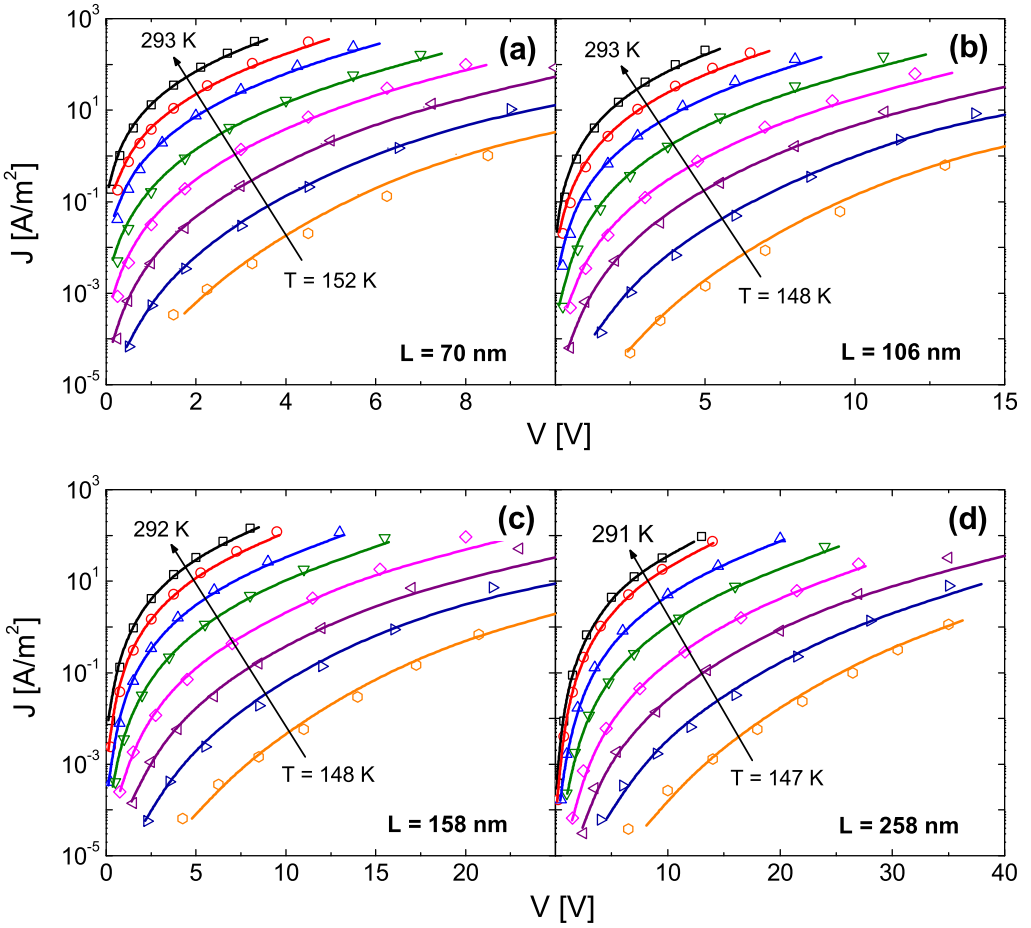

Fig. 3. Measured (symbols) and calculated (solid curves) $J(V)$ for devices with a BAlq layer thickness of 70 nm (a), 106 nm (b), 158 nm (c), and 258 nm (d), as a function of temperature. The temperature was varied in steps of ~20 K. The calculations were performed using a drift-diffusion device model assuming correlated Gaussian disorder (CDM) and a superimposed exponential density of trap states, using the parameters given in Table 1.

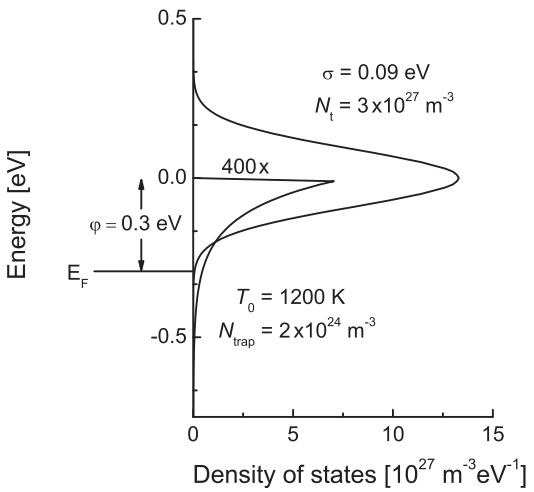

Fig. 4. Schematic of the energy-level alignment in the devices studied, indicating the Gaussian DOS and the exponential trap DOS (enhanced by a factor 400), and the injection barrier at the electrodes. The parameter values indicated are the result of this study, and have been obtained using the CDM.

the total error is calculated as a sum of mean square errors of the fits for all thicknesses and temperatures. By minimizing this total error, we obtain the optimal parameter set. The procedure is repeated for several values of the injection barriers with the constraint $\phi = \phi_1 = \phi_2$, leading to $\phi = 0.3 \pm 0.1$ eV. This value is within the range expected from the $C(V)$ measurements.

The best simultaneous description of all thickness-dependent and temperature-dependent $J(V)$ data using the GDM and using the CDM were obtained for the set of parameters given in Table 1. The parameters μ_0^* and C mentioned in the table describe the temperature dependence of μ_0 and are discussed below. Fig. 3 shows the results for the CDM (solid curves). The results for the GDM led to an equally good fit. For both models, a description of the full set of $J(V)$ curves without traps led to very high error values and to unphysically high thickness and temperature dependent values of V_{bi}. To our point of view, the assumption that the material is free of traps can therefore be discarded. We consider the parameter values obtained from the analysis using the GDM including traps as physically realistic, except for the site density, which is ~7 times *smaller* than the volume density of BAlq

Table 1
Overview of the GDM and CDM parameter values that optimally describe the experimental $J(V)$ curves.

Parameter	GDM	CDM
N_t (10^{27} m^{-3})	0.20 ± 0.04	3 ± 1
σ (eV)	0.08 ± 0.01	0.09 ± 0.01
N_{trap} (10^{24} m^{-3})	1.0 ± 0.5	2.0 ±Ł0.5
T_0 (K)	1200 ± 100	1200 ± 100
μ_0^* (10^{-8} m^2/(V s))	4 ± 1	1.7 ± 0.5
C	0.59 ± 0.16	0.46 ± 0.11
$\phi_{1,2}$ (eV)	0.3 ± 0.1	0.3 ± 0.1
ε_r	3.8 ± 1.0	3.8 ± 1.0

molecules. For the CDM, which leads to otherwise similar parameter values, the site density is ~2 times *larger* than the density of molecules. We view this much better correspondence as an indication that for BAlq the LUMO site energies are spatially correlated. The finding that N_t is a factor ~2 larger than the molecular density could be rationalized by assuming that each BAlq molecule contributes two LUMO states, localized on the two identical ligands. This picture is supported by the results of electronic structure calculations [26]. Both ligands may be viewed as a hopping site for electrons if the electronic coupling between these two ligands is small, so that these states are almost degenerate. A similar situation was encountered in Ref. [15] for the case of α-NPD.

Within the GDM and the CDM, the temperature dependence of μ_0 is given by $\mu_0(T) = \mu_0^* \exp\{-C[\sigma/(k_B T)]^2\}$ [8,5]. Fig. 5 shows that both $\log(\mu_{0,CDM}(T))$ and $\log(\mu_{0,\ GDM}(T))$ vary linearly with $1/T^2$, in a manner which is essentially the same for the four BAlq layer thicknesses. Both results are thus consistent with the assumption of hopping in a Gaussian DOS. The uncertainty attributed to the C-values is almost completely due to the uncertainty in the σ-values, which in part determine the slope of the fit lines. The C-values depend weakly on the decay length α^{-1} of the wavefunctions in between which the hopping takes place, at least for the case of the GDM [5,40], and increase slightly with a decreasing decay length. It is assumed that α^{-1} is typically equal to a tenth of the intersite distance [3]. Within the GDM the C-value is then expected ~0.42 (see Ref. [4]), and for the CDM Monte Carlo modeling [7] and 3D-ME modeling [8] have then yielded $C \sim 0.36$ and $C \sim 0.29$, respectively. The values obtained from the fits, $C = 0.59 \pm 0.16$ and 0.46 ± 0.11 for the GDM and the CDM, respectively, are both relatively high but (given the error margins) not inconsistent with the typical values mentioned above. The (at present preliminary) indication that the C-values are relatively large would indicate that the wavefunction decay length in BAlq is relatively small. A small value of the wavefunction decay length would be expected to lead to a small value of μ_0^*, the mobility in the zero-density, zero-field and high temperature limit. Indeed, μ_0^* is a factor of ~30 smaller than for α-NPD, for which the site density is essentially the same as for BAlq (if evaluated within the CDM) but for which the experimental value of $C = 0.34 \pm 0.07$ [15] is more close to the typical values of C mentioned above.

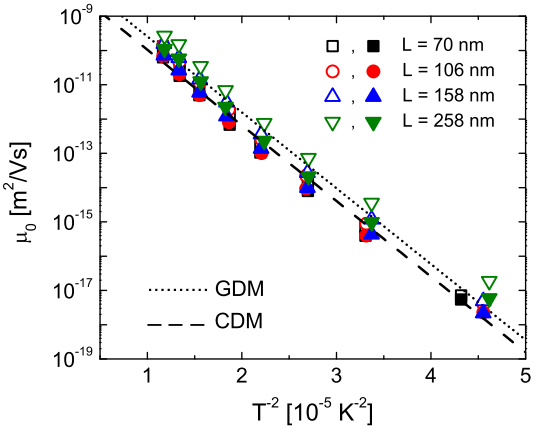

Fig. 5. Temperature dependence of the mobility in the zero field and carrier density limit for the CDM (closed symbols) and the GDM (open symbols). The results are shown for a thickness of the BAlq layer of 70 nm (squares), 106 nm (circles), 158 nm (triangles pointing up), and 258 nm (triangles pointing down). The dashed (CDM) and dotted (GDM) lines are linear fits to all data.

4. Conclusions

In conclusion, we have shown that a consistent description of the layer-thickness and temperature dependence of the current density in BAlq-based devices may be obtained by assuming a DOS that is a superposition of a Gaussian DOS and an exponential trap DOS. Accurate descriptions can be obtained assuming random disorder (Gaussian Disorder Model) as well as correlated disorder (Correlated Disorder Model), in the latter case making use of a recent description of the field and charge carrier density dependence of the mobility in systems with correlated Gaussian disorder resulting from charge–dipole interactions [8]. Based on a comparison of the hopping site densities with the experimental molecular site density, we argue that in BAlq the LUMO site energies are spatially correlated. We emphasize that, although the specific form of the CDM used in this work is based on the assumption of dipolar disorder, any microscopic model giving rise to a similar distance dependence of the energy correlation function [8] would give rise to a similar mobility function. Our findings thus support the point of view that upon modeling the electron transport in small-molecule OLEDs, the roles of energetic disorder, spatial correlation and the presence of trap states cannot be disregarded.

Acknowledgements

The authors would like to thank A.C.A. Jonkers for carrying out the ICP-AES measurements, and M.A. Verheijen and R.G.R. Weemaes for carrying out the TEM measurements. This research has received funding from the Dutch nanotechnology program NanoNed (contribution S.L.M.v.M.), and from the European Community's Program No. FP7-213708 (AEVIOM, contribution R.C.).

References

[1] S. Reineke, F. Lindner, G. Schwartz, N. Seidler, K. Walzer, B. Lüssem, K. Leo, Nature 459 (2009) 234.

[2] B.W. D'Andrade, S.R. Forrest, Adv. Mater. 16 (2004) 1585.
[3] H. Bässler, Phys. Status Solidi B 175 (1993) 15.
[4] W.F. Pasveer, J. Cottaar, C. Tanase, R. Coehoorn, P.A. Bobbert, P.W.M. Blom, D.M. de Leeuw, M.A.J. Michels, Phys. Rev. Lett. 94 (2005) 206601.
[5] R. Coehoorn, W.F. Pasveer, P.A. Bobbert, M.A.J. Michels, Phys. Rev. B 72 (2005) 155206. and references therein on earlier semi-analytical expressions for the mobility within the GD.
[6] Y.N. Gartstein, E.M. Conwell, Chem. Phys. Lett. 245 (1995) 351.
[7] S.V. Novikov, D.H. Dunlap, V.M. Kenkre, P.E. Parris, A.V. Vannikov, Phys. Rev. Lett. 81 (1998) 4472.
[8] M. Bouhassoune, S.L.M. van Mensfoort, P.A. Bobbert, R. Coehoorn, Org. Electron. 10 (2009) 437.
[9] Y. Nagata, C. Lennartz, J. Chem. Phys. 129 (2008) 034709.
[10] S.V. Rakmanova, E. Conwell, Appl. Phys. Lett. 76 (2000) 2388.
[11] Z.G. Yu, D.L. Smith, A. Saxena, R.L. Martin, A.R. Bishop, Phys. Rev. Lett. 84 (2000) 721.
[12] In various previous publications, we labeled the model descriptions obtained from the numerical calculations carried out in Refs.[4] and [8] as ''EGDM" and ''ECDM", respectively, in order to emphasize the extension of the model description of the mobility to include the charge carrier density dependence. However, as the underlying model assumptions are not changed, we avoid here any possible confusion by referring to this work also as ''GDM" and ''CDM", respectively.
[13] S.L.M. van Mensfoort, S.I.E. Vulto, R.A.J. Janssen, R. Coehoorn, Phys. Rev. B 78 (2008) 085208.
[14] R.J. de Vries, S.L.M. van Mensfoort, V. Shabro, R.A.J. Janssen, R. Coehoorn, Appl. Phys. Lett. 94 (2009) 163307.
[15] S.L.M. van Mensfoort, V. Shabro, R.A.J. Janssen, R. Coehoorn, J. Appl. Phys. 107 (2010) 113710.
[16] P.W.M. Blom, M.J.M. de Jong, J.J.M. Vleggaar, Appl. Phys. Lett. 68 (1996) 3308.
[17] M.M. Mandoc, B. de Boer, G. Paasch, P.W.M. Blom, Phys. Rev. B 75 (2007) 193202.
[18] S.L.M. van Mensfoort, J. Billen, S.I.E. Vulto, R.A.J. Janssen, R. Coehoorn, Phys. Rev. B 80 (2009) 033202.
[19] P.M. Borsenberger, D.S. Weiss, Organic Photoreceptors for Xerography, Marcel Dekker, New York, 1998.
[20] W. Brütting, S. Berleb, A.G. Mückl, Org. Electron. 2 (2001) 1.
[21] W. Li, J. Yu, L. Li, Y. Jiang, J. Lumin. 126 (2007) 487.
[22] Y. Iwama, T. Itoh, T. Mori, T. Mizutani, Thin Solid Films 499 (2006) 364.
[23] T. Itoh, T. Mizutani, T. Mori, Colloid Surf. A 284 (2006) 594.
[24] J. Niu, W. Li, H. Wei, M. Li, W. Su, Q. Xin, Z. Zhang, Z. Hu, J. Phys. D: Appl. Phys. 38 (2005) 1136.
[25] J.-W. Kang, D.-S. Lee, H.-D. Park, J.W. Kim, W.-I. Jeong, Y.-S. Park, S.-H. Lee, K. Gob, J.-S. Lee, J.-J. Kim, Org. Electr. 9 (2008) 452.
[26] T.-Y. Chu, Y.-S. Wu, J.-F. Chen, C.H. Chen, Chem. Phys. Lett. 404 (2005) 121.
[27] R. Meerheim, K. Walzer, M. Pfeiffer, K. Leo, Appl. Phys. Lett. 89 (2006) 061111.
[28] R. Meerheim, S. Scholz, S. Olthof, G. Schwartz, S. Reineke, K. Walzer, K. Leo, J. Appl. Phys. 104 (2008) 014510.
[29] K.S. Son, M. Yahiro, T. Imai, H. Yoshizaki, C. Adachi, Chem. Mater. 20 (2008) 4439.
[30] S. Scholz, C. Corten, K. Walzer, D. Kuckling, K. Leo, Org. Electr. 8 (2007) 709.
[31] H.-H. Huang, S.-Y. Chu, P.-C. Kao, C.-H. Yang, I.-W. Sun, Thin Solid Films 517 (2009) 3788.
[32] S.L.M. van Mensfoort, J. Billen, S.I.E. Vulto, R.A.J. Janssen, R. Coehoorn, Phys. Rev. B 80 (2009) 033202.
[33] K. Walzer, B. Maennig, M. Pfeiffer, K. Leo, Chem. Rev. 107 (2007) 1233.
[34] S.L.M. van Mensfoort, R. Coehoorn, Phys. Rev. Lett. 100 (2008) 086802.
[35] J.C. Deaton, D.W. Place, C.T. Brown, M. Rajeswaran, M.E. Kondakova, Inorg. Chim. Acta 361 (2008) 1020.
[36] P. Mark, W. Helfrich, J. Appl. Phys. 33 (1962) 205.
[37] K.C. Kao, W. Hwang, Electrical Transport in Solids, Pergamon Press, Oxford, 1981.
[38] M.M. Mandoc, B. de Boer, P.W.M. Blom, Phys. Rev. B 73 (2006) 155205.
[39] S.L.M. van Mensfoort, R. Coehoorn, Phys. Rev. B 78 (2008) 085207.
[40] S.D. Baranovski̇, I.P. Zvyagin, H. Cordes, S. Yamasaki, P. Thomas, Phys. Status Solidi (b) 230 (2002) 281.

PEDOT:PSS can serve as both an HTL and as an EBL in normal and inverted device architectures due to its band structure, which has a lower electron affinity (or higher lowest unoccupied molecular orbital (LUMO)) than P3HT, providing an energy barrier for electron transfer to the anode. The band offset of the HTL in a BHJ is critical to establish the device polarity [7]. However, PEDOT:PSS has been shown to degrade or limit device performance in multiple ways. Although the reported energy levels for PEDOT:PSS and P3HT vary dependent upon material preparation and measurement technique, the LUMO of PEDOT:PSS is essentially fixed at about 0.6 eV above the LUMO of P3HT [9], which may be insufficient as an electron barrier. The aqueous PEDOT:PSS suspension is also highly acidic, with a measured pH of 1.2 [10]. This prohibits use of PEDOT:PSS as an HTL on a number of high performance and low cost transparent conductors that are easily etched in acidic solutions. In addition, due to the hygroscopic nature of PEDOT:PSS films, water may be absorbed resulting in proton release and corrosion of the ITO anode subsequently allowing indium diffusion throughout the device [11]. This, combined with the possible release of water from PEDOT:PSS into the active layer or the cathode can substantially degrade devices [12], lowering lifetimes and overall performance. These limitations have led to investigations of other materials to effectively replace PEDOT:PSS as the HTL in OPV devices [7,13].

An ideal candidate to replace PEDOT:PSS as the HTL would be a wide band-gap ($E_g > 3$ eV) *p*-type material transparent to most of the solar spectrum. It should minimize TCO/donor contact resistance and the dark current by providing a large energy barrier to electron transfer while maximizing charge transfer between the TCO and the highest occupied molecular orbital (HOMO) of the donor material. We note that HTL performance also depends upon conductivity but varies with the junction type and loss mechanisms. Intrinsic stability and chemical compatibility with the active layer and the ITO or other ZnO-based TCO materials are also necessary for long device lifetimes [7].

As shown in the band diagram below, a p-type metal oxide, such as NiO, has a wide band-gap and valence band energy close to the HOMO of P3HT. The high conduction band energy of NiO inhibits electron recombination with the anode while the valence band allows for efficient conduction of holes to the anode. Favorable vacuum energy level alignment and material stability indicate that NiO has many of the required characteristics of an efficient HTL material in OPV devices.

Recently, NiO deposited via pulsed laser deposition (PLD) has been shown to work well as a HTL for polymer solar cells, with devices exhibiting improved open-circuit voltage (V_{OC}), short-circuit current density (J_{SC}), and fill factor (*FF*) relative to a PEDOT:PSS control [7,14]. The NiO was shown to be chemically stable and inert in relation to ITO and P3HT:PCBM [7]. We have previously demonstrated that the work function of the NiO film can be tailored by controlling the oxygen partial pressure during the deposition [14]. Additionally, we have also been able to induce large increases in the NiO work function by O_2-plasma treatment of the NiO prior to deposition of the active layer [14].

However, the NiO layers in these studies were deposited via PLD, which is neither scalable nor a cost effective deposition method. Previous efforts to deposit NiO from solution have been attempted but require very high annealing temperatures to make NiO [15]. In this article we explore using solution deposited NiO (sNiO) followed by a lower temperature anneal as an HTL to improve device efficiency and stability while maintaining low-cost methods of production.

In this work, we demonstrate that sNiO films from a nickel metal organic ink precursor achieve similar OPV device performance to results seen with NiO films from PLD. The device structure, ITO/NiO/P3HT:PCBM/Ca/Al, is shown schematically in Fig. 1. Our results show sNiO thin-films to be an effective replacement for PEDOT:PSS in OPV devices. We achieve a tunable φ_w in the sNiO films by post-processing with an O_2-plasma of varied power and time. The change in φ_w with plasma treatment is found to be greater in magnitude and have a faster decay time than PLD based materials [14]. While the plasma treatment is necessary for proper device function, the φ_w of the sNiO layer was shown to be higher than necessary to match to the HOMO of P3HT without negatively affecting the device performance. To elucidate the nature of the change in the φ_w and determine if it results from a change in effective band-gap or enhanced electric field at the interface resulting from changes in the local carrier concentration we employ a simple 1-D Poisson solver to model the NiO/Active Layer interface.

The precursor solution used to synthesize the sNiO films was based on a patented nickel ink developed in our lab for the deposition of Ni using direct write solution processing contacts via ink-jet or continuous flow printing, resulting in material with conductivities rivaling that produced by vacuum deposition [16]. The ink is a complex in which the Ni coordinates to two diamine groups, $[Ni(en)_2](HCO_2)_2$; en = $H_2N(CH_2)_2NH_2$, and is suspended in the solvent. At increased temperatures the solvent and the metal organic decomposes leaving behind a high quality metal contact [16]. The complex was hydrated by mixing 50% by volume DI water and had a final Ni ink concentration of 0.34 M as measured by ICP.

All films were deposited onto commercially patterned ITO (~10 Ω/sq, thin-film devices) substrates after 5 min of ultrasonic cleaning in acetone followed by isopropyl alcohol. Substrates were plasma-cleaned immediately prior to HTL deposition in 0.8 Torr of O_2 at 155 W. The sNiO films were synthesized by spin-coating the diluted nickel ink at 4000 rpm for 60 s followed by annealing on a hot plate in air at 250 °C for 1 h, resulting in approximately 10 nm thick films. Film thickness was determined using a Dektak 8 Profilometer after masking a section of the substrate with Kapton tape prior to the spinning process.

sNiO films were characterized to examine their structural, optical, and electrical properties. The grain-size and surface morphology were also examined via an Asylum Research MFP-3D AFM. Reflectance and transmittance spectra were collected for the sNiO and PEDOT:PSS films on ITO over the UV, visible, and Near-Infrared (NIR) regions using a Shimadzu UV-3600 UV–Vis–NIR Spectrophotometer. Surface potential measurements were conducted using

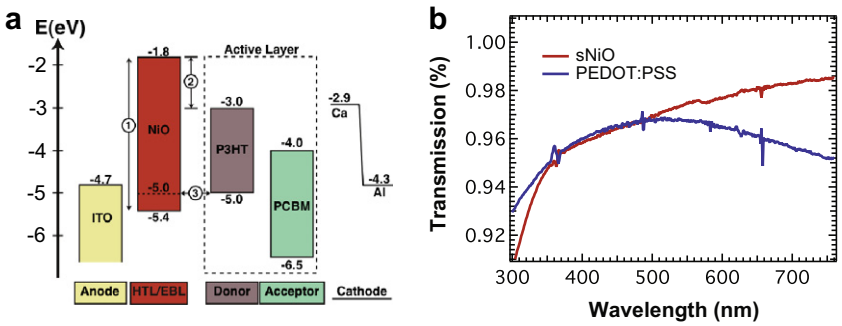

Fig. 1. (a) Energy diagram of the NiO BHJ cells fabricated in this work. NiO provides favorable HTL properties: (1) a wide band-gap for transparency, (2) sufficient electron blocking energy and (3) Fermi-level lineup with the HOMO of the donor for hole collection. (b) Graph of transmission versus wavelength for sNiO and PEDOT:PSS on quartz substrates.

an Electrostatic Voltmeter (Monroe Electronics ISOPROBE 244A) in an inert atmosphere of N_2. The work function (φ_w) of a material is often assumed to approximate the Fermi energy but may include effects from both surface dipoles and changes in carrier concentration via doping or changes in defect densities. All φ_w measurements were taken relative to the Inconel™ stainless steel reference, which was measured to have a φ_w of −4.33 eV as determined from ultraviolet photoelectron spectroscopy (UPS). To examine the effect of surface treatments and processing procedures on the φ_w of NiO films, they were plasma treated using an RF O_2-plasma at various powers and treatment times with no bias applied to the substrate.

PEDOT:PSS films were used as the control HTL, two coats of PEDOT:PSS (Baytron P VP AI 4083 filtered to 0.45 μm using a nylon filter) were spin cast at 6000 rpm for 50 s followed by a 1 h anneal at 130 °C in air. For the O_2-plasma treated sNiO films the active layer was immediately spun on in an inert atmosphere. A solution of 1:1 P3HT:PCBM (used as received from Rieke Metals and Nano-C, respectively) in 1,2-dichlorobenzene (50 mg/mL total) was stirred at 60 °C and 600 rpm for several hours prior to deposition at room temperature. The active layer was spun at 600 rpm for one minute then allowed to slow dry in a covered petri dish for approximately 1 h [4]. After drying, the active layer was annealed at 110 °C for 10 min in N_2. Top electrodes were then deposited with 20 nm of Ca followed by 100 nm of Al via thermal evaporation through a shadow mask to form six 0.11 cm^2 devices or one 1.0 cm^2 device on each substrate at a pressure of less than 7×10^{-8} Torr [7].

Devices were characterized using a solar simulator housed in an inert atmosphere. Contact was made to both the ITO and Al electrodes, from which voltage was sourced and the resulting current was measured. The short-circuit current (J_{SC}) was calculated based on measured device areas of 0.11 cm^2 or 1.0 cm^2. Shunt resistance and series resistance (R_s) were calculated at 0 V and 0 mA/cm^2, respectively. External quantum efficiency (EQE) was measured without white light biasing the device on a system calibrated with a Si photo-diode illuminated with a Xe 300 W lamp chopped to create an excitation signal detected by lock-in amplification. Integrated EQE spectra were used to verify J_{SC} values.

The sNiO films were characterized by AFM to evaluate the surface morphology and roughness. The root-mean square surface roughness of the films synthesized from the hydrated ink was 2.47 nm as determined by AFM, which is similar to roughness values typically obtained for commercially available ITO [17,18].

The optical transmittance and reflectance over the UV and visible spectrum of the sNiO films are comparable to PEDOT:PSS. The transmittance of the two films shown in Fig. 1 indicates that PEDOT:PSS is more transparent in the UV and at lower wavelengths, while sNiO is more transparent approaching the NIR wavelengths. The reflectance, however, indicates that PEDOT:PSS is slightly less reflective over most of the UV and visible compared to the sNiO film. Overall, the transmitted light that reaches the active layer is similar for both HTLs.

To better determine the dependence of φ_w with plasma treatment, the φ_w of sNiO films was measured in N_2immediately after O_2-plasma treatment at 155 W. The O_2-plasma treatment power and exposure time were varied for sNiO films revealing significant differences in the measured φ_w. The main reactive components of the plasma, O^- and O^{2+} were assumed to drive oxidation of the Ni films. The results, shown in Fig. 2, demonstrate that sNiO films respond to plasma treatment by increasing the φ_w. The sNiO films display a saturation behavior at longer treatment times (~5 min), after which the φ_w no longer increased with further plasma treatment.

We stored all solar cells in a dark inert environment and retested solar cells with sNiO and PEDOT:PSS over two weeks after fabrication. All OPV devices showed similar V_{OC} degradation. This is due to the sensitive Ca electrode dominating the degradation of the devices. Thus the in device HTL stability is at a minimum comparable to PEDOT:PSS.

In order to investigate the effect of the plasma treatment on sNiO, a time dependent φ_w study was conducted by measuring the φ_w every 20 s over a time-span of 2 h in an inert atmosphere. It was observed that the φ_w of films degraded quickly as shown in Fig. 2. This would indicate a change in the surface chemistry of the plasma treated sNiO. Because of the magnitude of the transient behavior in the φ_w, the experimental technique used to evaluate φ_w, and the lack of measurable conductivity in the sNiO, this effect may be associated with a change in either the

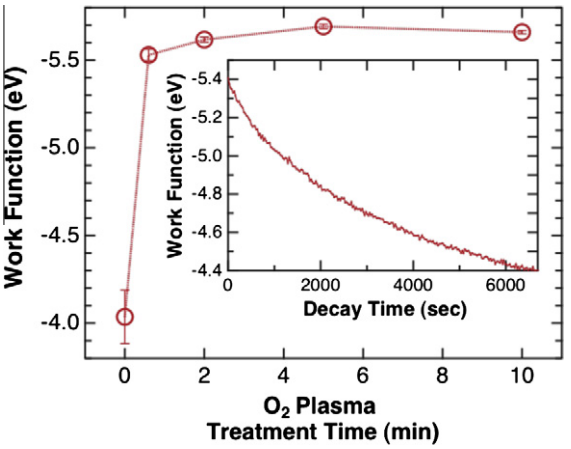

Fig. 2. φ_w response of sNiO films synthesized from Ni ink to O_2-plasma treatment time at 155 W at 0.8 Torr O_2. Inset: φ_w transient of sNiO films after O_2-plasma treatment as measured in N_2.

density of oxygen vacancies or the oxidation state of the Ni in the sNiO [19]. Further studies are underway to evaluate the exact affect of the O_2-plasma treatment on the sNiO films.

In order to compare the performance of solution deposited sNiO in OPV devices, BHJ solar cells were fabricated and tested under simulated one-sun conditions. The best sNiO-based devices were those O_2-plasma treated so that the observed φ_w immediately before deposition of the active layer was in the range of −5.0 eV up to −5.6 eV. The optimized sNiO devices, resulted in PCE that are equivalent to PEDOT:PSS control devices. These devices utilized a sNiO HTL that had a φ_w of −5.6 eV before deposition of the active layer. Table 1 summarizes the results obtained via current–voltage characteristics of the solar cells with a spectral mismatch of 1.0.

The thickness of the sNiO films also has important effects. Thicker films produced devices with lower V_{OC}, lower J_{SC} and higher R_s. Thinner films failed to produce uniform devices on a substrate causing inconsistent performance, perhaps due to incomplete surface coverage. In addition, previous studies have shown that 10 nm was the optimal thickness in PLD deposited NiO films with an active layer thickness of about 220 nm [7]. This optimal thickness of the active layer blend, however, could be different for devices with sNiO as opposed to PEDOT:PSS, though this was not considered in this study.

With the optimal sNiO devices, higher *FF*, slightly lower J_{SC} and similar V_{OC} were obtained, in relation to the PEDOT:PSS control device. This leads to similar PCE of 3.6% for both sNiO and PEDOT:PSS HTLs. Reported series and shunt resistances were calculated by taking the inverse slopes at V_{OC} and J_{SC}, respectively. The series resistance is lower in the sNiO devices as compared to PEDOT:PSS. The lateral conductivity of the sNiO cannot be measured using our 4-point probe setup, unlike PEDOT:PSS, indicating that the bulk conductivity of the sNiO is lower than that of PEDOT:PSS. Therefore, the decrease in series resistance in the OPV devices is likely due to reduced contact resistance at the ITO/sNiO and sNiO/active layer interfaces. Fig. 3 displays the current–voltage characteristics of PEDOT:PSS and sNiO-based devices. Device yield was above 90%, similar for all tested HTLs.

An unexpected aspect of the device performance was the sNiO films with much deeper observed φ_w than the assumed optimal −5.0 eV worked best. It should be noted that the plasma treatment of these films is the key to producing the best-functioning devices with non-treated films exhibiting poor *FF* and low V_{OC}. It is possible that it is simply cleaning off any organic contaminants or remaining solvent at the surface, revealing the higher φ_w sNiO beneath. Or it may be that the surface oxidation state is shifted during O_2-plasma treatment either reducing a tunneling barrier or pinning the P3HT HOMO level closer to the NiO valence band. However, higher than expected φ_w indicates that there may be charging of the surface from the plasma, and it is subsequently degrading quickly over time. It is most likely that there is surface oxidation, which would change the φ_w and the doping of the p-type NiO thin-film, modestly increasing conductivity while facilitating good ohmic contact, hole collection, and electron blocking characteristics. We can also not yet rule out other mechanisms, which may result in effective charge transport at this interface such as Fermi-level pinning. However, these types of interfacial mechanisms demand that more importance be placed on the electric field, and therefore surface doping in the sNiO layer than the measured φ_w of the layer. Before recombination can occur, a high electric field would accelerate the already dissociated charge

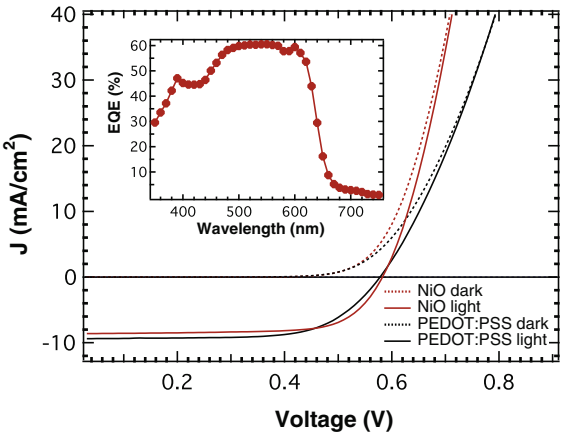

Fig. 3. Current–voltage characteristics of the best OPV devices based on sNiO and PEDOT:PSS HTLs. Inset: IPCE of sNiO device.

Table 1
Solution NiO and PEDOT:PSS control device summaries.

HTL	V_{OC} (mV)	J_{SC} (mA/cm^2)	*FF*	PCE (%)	R_{shunt} (Ω cm^2)	R_{series} (Ω cm^2)
sNiO	583 ± 5	−8.6 ± 0.1	0.71 ± 0.004	3.6 ± 0.1	1600 ± 400	6.0 ± 0.2
PEDOT:PSS	578 ± 3	−9.4 ± 0.3	0.66 ± 0.02	3.6 ± 0.1	2200 ± 300	8.1 ± 0.2

carrier toward the proper electrode. Higher electric fields would therefore correspond to enhanced current collection. This hypothesis is consistent with a simple 1-D Poisson model that was compiled in an earlier study to evaluate both the electric field and band-bending due to such doping effects at the interface [14]. This simple model does show very high fields across the NiO for the case of a reasonable enhancement of the carrier concentration at the NiO surface and will be the subject of future studies.

The results of this study indicate that solution processed NiO may be used in lieu of PLD NiO thin-films in standard BHJ OPV devices. Furthermore, sNiO is an effective replacement for PEDOT:PSS as an HTL. Results showed similar efficiency for solar cells with sNiO compared to PEDOT:PSS controls. Both the precursor ink formulation and the processing conditions were optimized to produce 10 nm sNiO HTL films that enabled both electron blocking and hole collection indicative of high quality selective contacts essential for BHJ devices. Further studies will evaluate the effect of the sNiO films on the device lifetime and the specific mechanisms present enabling high performance.

Acknowledgements

We received support for this work from: (1) Center for Energy Efficient Materials, an Energy Frontier Research Center funded by the U.S. Department of Energy, Office of Science, Office of Basic Energy Sciences under Award No. DE-SC0001009, (2) the U.S. Department of Energy, Office of Science's Science Undergraduate Laboratory Internship Program, (3) U.S. Department of Energy under Contract No. DOE-AC36-08GO28308 with the National Renewable Energy Laboratory DOE SETP program through the National Center for Photovoltaics and (4) the Center for Interface Science: Solar-Electric Materials (CIS:SEM), an Energy Frontier Research Center Funded by the U.S. Department of Energy, Office of Basic Sciences, under Award No. DE-SC0001084. K.X. Steirer is supported by (1), Jordan P. Chesin was supported by (2) N. Edwin Widjonarko is supported by (3) and (4), Alex Miedaner is supported by (3) and Joseph J. Berry, David S. Ginley, and Dana C. Olson are supported by (1), (3), and (4).

References

[1] N. Lewis, D.G. Nocera, Powering the planet: chemical challenges in solar energy utilization, in: Proc. Natl. Acad. Sci. USA, vol. 103, 2006, pp. 15729–15735.
[2] S.E. Shaheen, R. Radspinner, N. Peyghambarian, G.E. Jabbour, Fabrication of bulk heterojunction plastic solar cells by screen printing, Applied Physics Letters 79 (18) (2001) 2996–2998.
[3] C.J. Brabec, J.R. Durrant, Solution-processed organic solar cells, MRS Bulletin 33 (July) (2008) 670–675.
[4] G. Li, V. Shrotriya, J. Huang, Y. Yao, T. Moriarty, K. Emery, Y. Yang, High-efficiency solution processable polymer photovoltaic cells by self-organization of polymer blends, Nature Materials 4 (11) (2005) 864–868.
[5] H. Chen, J. Hou, S. Zhang, Y. Liang, G. Yang, Y. Yang, L. Yu, Y. Wu, G. Li, Polymer solar cells with enhanced open-circuit voltage and efficiency, Nature Photonics 3 (11) (2009) 649–653.
[6] M.C. Scharber, D. Mühlbacher, M. Koppe, P. Denk, C. Waldauf, A.J. Heeger, C.J. Brabec, Design rules for donors in bulk-heterojunction solar cells – towards 10% energy-conversion efficiency, Advanced Materials 18 (6) (2006) 789–794.
[7] M.D. Irwin, D.B. Buchholz, A.W. Hains, R.P.H. Chang, T.J. Marks, p-Type semiconducting nickel oxide as an efficiency-enhancing anode interfacial layer in polymer bulk-heterojunction solar cells, Proceedings of the National Academy of Sciences 105 (8) (2008) 2783–2787.
[8] S.E. Shaheen, D.S. Ginley, G.E. Jabbour, Organic-based photovoltaics: toward low-cost power generation, MRS Bulletin 30 (January) (2005) 10–15.
[9] W.-C. Lin, Y.-C. Lin, W.-B. Wang, B.-Y. Yu, S.-I. Iida, M. Tozu, M.-F. Hsu, J.-H. Jou, J.-J. Shyue, Effect of fabrication process on the microstructure and the efficiency of organic light-emitting diode, Organic Electronics 10 (3) (2009) 459–464.
[10] S.H. Choi, S.M. Jeong, W.H. Koo, S.J. Jo, H.K. Baik, S.-J. Lee, K.M. Song, D.W. Han, Diamond-like carbon as a buffer layer in polymeric electroluminescent device, Thin Solid Films 483 (1–2) (2005) 351–357.
[11] M.P. de Jong, L.J. van Ijzendoorn, M.J.A. de Voigt, Stability of the interface between indium-tin-oxide and poly(3,4-ethylenedioxythiophene)/poly(styrenesulfonate) in polymer light-emitting diodes, Applied Physics Letters 77 (14) (2000) 2255–2257.
[12] M. Jörgensen, K. Norrman, F.C. Krebs, Stability/degradation of polymer solar cells, Solar Energy Materials and Solar Cells 92 (7) (2008) 686–714.
[13] A.W. Hains, T.J. Marks, High-efficiency hole extraction/electron-blocking layer to replace poly(3,4-ethylenedioxythiophene): poly(styrenesulfonate) in bulk-heterojunction polymer solar cells, Applied Physics Letters 92 (2) (2008) 023504.
[14] J.J. Berry, N.E. Widjonarko, B.A. Bailey, A.K. Sigdel, D.S. Ginley, D.C. Olson, Surface modification of NiO hole transport layers for organic solar cells, IEEE Journal of Selected Topics in Quantum Electronics, accepted for publication.
[15] B. Mashford, T. Nguyen, G. Wilson, P. Mulvaney, All-inorganic quantum-dot light-emitting devices formed via low-cost, wet-chemical processing, Journal of Materials Chemistry 20 (1) (2010) 167–172.
[16] D.S. Ginley, C.J. Curtis, A. Miedaner, M.F.A.M. van Hest, T. Kaydanova, Metal Inks, 2008, US Patent 0003364 A1.
[17] K. Steirer, J. Berry, M. Reese, M. Van Hest, A. Miedaner, M. Liberatore, R. Collins, D. Ginley, Ultrasonically sprayed and inkjet printed thin film electrodes for organic solar cells, Thin Solid Films 517 (8) (2009) 2781–2786.
[18] N. Armstrong, Interface modification of ITO thin films: organic photovoltaic cells, Thin Solid Films 445 (2) (2003) 342–352.
[19] D.J. Yun, S.W. Rhee, Pentacene thin-film transistor with NiO_x as a source/drain electrode deposited with sputtering, Journal of the Electrochemical Society 155 (11) (2008) H899–H902.

large amount of organic materials and devices. We demonstrate inverted solar cells with precursor ZnO electron transport layers for three well-studied polymer:fullerene systems, i.e. based on poly(3-hexylthiophene) (P3HT), poly[9,9-didecanefluorene-*alt*-(bis-thienylene) benzothiadiazole] (PF10TBT) and poly[2,6-(4,4-bis-(2-ethylhexyl)-4H-cyclopenta[2,1-*b*;3,4-*b*′]dithiophene)-*alt*-4,7-(2,1,3-benzothiadiazole)] (PCPDTBT). As an acceptor the standard [6,6]-phenyl-C_{61}-butyric acid methyl ester (PCBM) has been used. All three blends can provide power conversion efficiencies in excess of 4% in combination with a fullerene acceptor [23–25]. Our inverted solar cell structures using precursor ZnO exhibit a performance that is identical to conventional bottom-anode–top-cathode geometry solar cells.

2. Experimental

Zinc oxide layers were prepared by dissolving 20 mg/mL of $Zn(acac)_2$ hydrate (obtained from Sigma–Aldrich) in absolute ethanol under ambient conditions, stirring for several hours at 50 °C and subsequently filtering with a 0.2 μm pore size PTFE filter. ITO covered glass substrates were cleaned with soap and deionised water, followed by ultrasonic treatment in acetone and 2-isopropanol. Afterwards they were dried in an oven at 140 °C for 10 min in ambient conditions, followed by UV-ozone treatment for 20 min. $Zn(acac)_2$ was spin cast in air at 1000 rpm, while both solution and substrates were held at 50 °C. Hydrolysis of the precursor was carried out in air during 30 s on a hotplate at 120 °C. This generally resulted in a 20 nm thick layer of ZnO. ZnO typically requires UV illumination to transform from an intrinsic semiconductor into an n-type material by desorption of O_2^- radicals from the surface [26,27]. After illumination with a Steuernagel SolarConstant 1200 metal halide lamp, a reduction of the work function from 4.2 to 3.7 eV was measured with a Kelvin probe calibrated to a gold reference. This is in line with the assumption of injection of electrons into the conduction band by UV illumination and a corresponding raise of the Fermi level. P3HT:PCBM (1:0.8 by weight, 15 mg/mL of polymer) was dissolved in chloroform. PCPDTBT:PCBM (1:2.5 by weight, 7 mg/mL of polymer) was dissolved in a chlorobenzene solution containing 1.5 wt.% 1,8-octanedithiol, which was added to increase the photovoltaic performance of the resulting devices as described in literature [23,28]. PF10TBT:PCBM (1:4 by weight, 3 mg/mL of polymer) was dissolved in pristine chlorobenzene. ITO substrates were cleaned as described before. PEDOT:PSS (Clevios P VP AI 4083) was spin cast in air to yield a 50 nm layer on the substrate. Spin casting of the P3HT:PCBM and PCPDTBT:PCBM blends was done in a nitrogen atmosphere, while PF10TBT:PCBM was spin cast in air. Thermal evaporation was performed at a pressure of 10^{-6} mbar for all materials (LiF, Al and MoO_3). MoO_3 powder was obtained from Sigma–Aldrich and was used as received. The evaporation rate was held constant at 0.05 nm/s to produce a smooth film of 10 nm and 1 nm for MoO_3 and LiF, respectively. Finished cells were illuminated through illumination masks with a Steuernagel SolarConstant 1200 metal halide lamp, calibrated to 1 sun intensity and corrected for spectral mismatch with the AM1.5G spectrum using a Si reference cell. The calculated mismatch factors for P3HT:PCBM, PF10TBT:PCBM and PCPDTBT:PCBM in this setup amounted to 1.40, 1.40 and 1.03, respectively [29]. Electrical characterization was done with a Keithley 2400 SourceMeter.

3. Results and discussion

The optical absorbance of a 20 nm layer of ZnO was measured with respect to a glass reference with a Perkin-Elmer Lambda 900 spectrophotometer and is shown in Fig. 1. Note the excellent optical transparency in the visible range of wavelengths of the precursor made ZnO film. The optical absorbance of the precursor layer before conversion is shown for reference. The inset provides a determination of the optical band gap of the ZnO films through extrapolation of the linear regime in the quadratic absorption to 3.53 eV. Furthermore, the structure of $Zn(acac)_2$ is shown for clarity. Fig. 2 shows the structure of the completed cells, along with the materials used for the active layers. The current density–voltage characteristics of the P3HT:PCBM, PF10TBT:PCBM and the PCPDTBT:PCBM cells under illumination are shown in Fig. 3. All photoactive layers were approximately 80 nm thick. Table 1 shows the performance parameters for all solar cells presented in this study. We observe that the performance parameters and thus the cell efficiencies are very close for cells with the conventional and inverted geometry. The reported efficiencies are in good agreement with previously published values for optimized PF10TBT:PCBM cells [24]. The efficiency of the PCPDTBT:PCBM cells has been increased in comparison to a previous publication, which is due to decreased recombination by addition of 1,8-octanedithiol in these devices [28,30]. Furthermore, optical absorption simulations based on the transfer matrix formalism have been performed on the two structures for the PF10TBT:PCBM blend [31–34]. The optical constants needed for this simulation

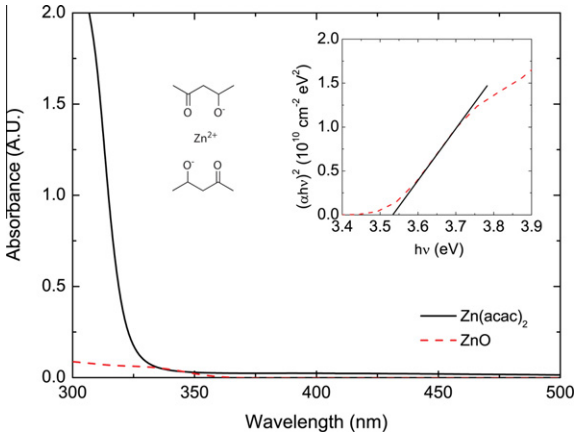

Fig. 1. Optical absorbance of a 20 nm layer of ZnO. The absorbance of the $Zn(acac)_2$ precursor layer is shown for reference. The inset shows the determination of the optical band gap for the ZnO layer. The chemical structure of $Zn(acac)_2$ is shown for clarity.

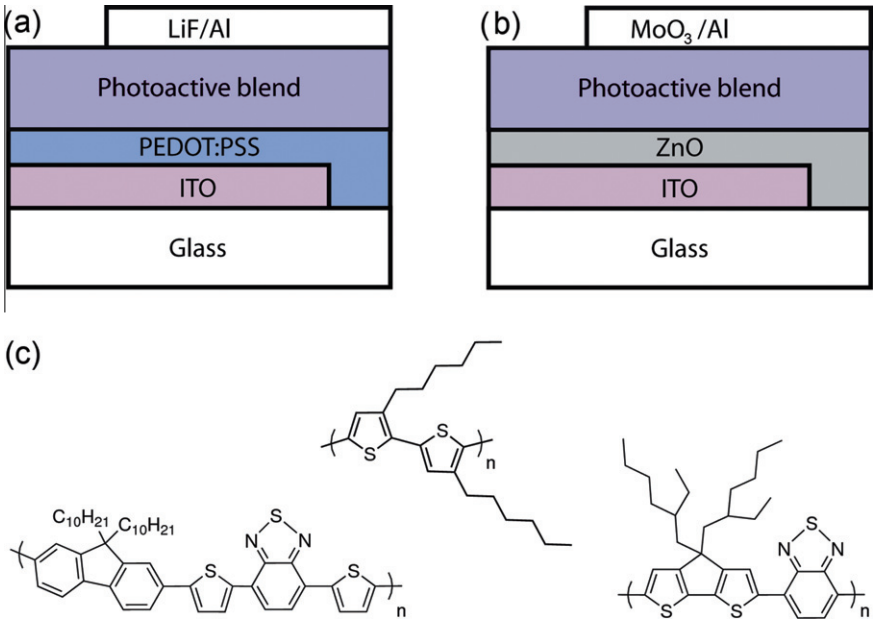

Fig. 2. Solar cell geometries and polymers used in this study. (a) Conventional bottom-anode–top-cathode structure. (b) Inverted bottom-cathode–top-anode structure. (c) Chemical structures of PF10TBT (left), P3HT (middle) and PCPDTBT (right).

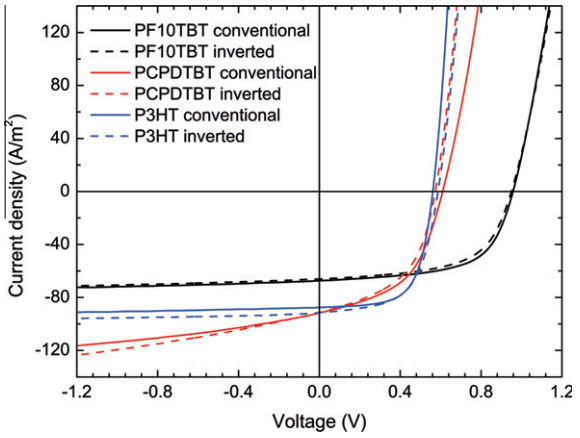

Fig. 3. *J–V* characteristics of solar cells employing both contact geometries for the two material blends. 'Inverted' denotes the bottom-cathode–top-anode structure.

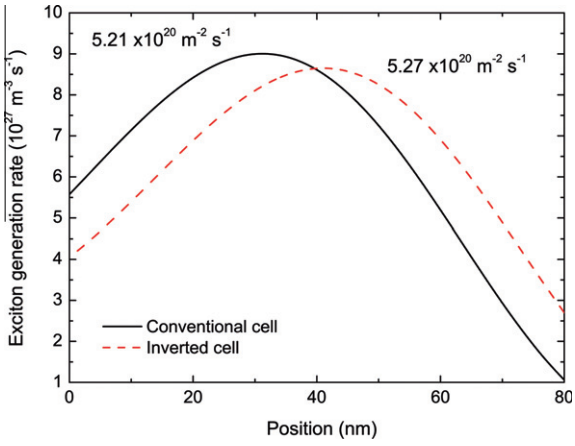

Fig. 4. Simulated exciton generation rates in conventional and inverted geometry cells. The origin is defined as the substrate side of the device. The integrated generation rates are shown for the two geometries.

Table 1
Photovoltaic properties of conventional and inverted PF10TBT:PCBM, P3HT:PCBM and PCPDTBT:PCBM solar cells under 1 sun white light illumination.

Photoactive layer	Type	J_{sc} (A m^{-2})	V_{oc} (V)	FF (%)	MPP (mW cm^{-2})
PF10TBT:PCBM	Conventional	67.3	0.96	61	4.0
	Inverted	66.1	0.95	59	3.7
P3HT:PCBM	Conventional	87.6	0.57	66	3.2
	Inverted	91.5	0.59	60	3.2
PCPDTBT:PCBM	Conventional	91.8	0.61	50	2.8
	Inverted	91.4	0.58	50	2.6

were obtained with variable angle spectroscopic ellipsometry [24,35]. The layer thicknesses of the ZnO and MoO_3 layers for this simulation have been defined as 20 and 10 nm, respectively. This was done to mimic the actual devices as closely as possible, and as such these thicknesses are not necessarily optimized for the optical field. As can be seen in Fig. 4, the calculated integrated exciton generation rates for both the conventional and inverted cells are equal to within 1% for the two structures. This validates the experimentally observed equal short-circuit currents under the assumption of equal internal quantum efficiencies. In this figure the origin is defined as the point in the photoactive layer where the light first enters the device,

i.e. the substrate side. For the conventional device the light is directly reflected at the aluminium top electrode, whereas for the inverted device the 10 nm of MoO_3 acts as an optical spacer, thereby changing the shape of the absorption envelope.

4. Conclusions

In summary, we have shown the electrical operation of inverted solar cells with an ITO/ZnO cathode, fabricated through the low temperature decomposition of $Zn(acac)_2$. The performance of these cells is shown to be equivalent to cells made in the conventional bottom-anode–top-cathode geometry. The simplicity of fabrication of these inverted solar cells without loss of performance will stimulate a further systematic investigation on their enhanced stability.

Acknowledgements

The authors thank J. Harkema and F. van der Horst for technical assistance. The work of P. de Bruyn was supported by the Dutch Polymer Institute (DPI), project DPI No. 660. The work of D.J.D. Moet was funded by SenterNovem via the EOS Long Term program ZOMER (EOS LT 03026).

References

[1] M.A. Green, K. Emery, Y. Hishikawa, W. Warta, Prog. Photovoltaics 17 (2009) 320.
[2] Y. Liang, Z. Xu, J. Xia, S. Tsai, Y. Wu, G. Li, C. Ray, L. Yu, Adv. Mater. 22 (2010) 1.
[3] M.P. de Jong, L.J. van IJzendoorn, M.J.A. de Voigt, Appl. Phys. Lett. 77 (2000) 2255.
[4] K.W. Wong, H.L. Yip, Y. Luo, K.Y. Wong, W.M. Lau, K.H. Low, H.F. Chow, Z.Q. Gao, W.L. Yeung, C.C. Chang, Appl. Phys. Lett. 80 (2002) 2788.
[5] C. Tao, S. Ruan, X. Zhang, G. Xie, L. Shen, X. Kong, W. Dong, C. Liu, W. Chen, Appl. Phys. Lett. 93 (2008) 193307.
[6] G. Li, C. Chu, V. Shrotriya, J. Huang, Y. Yang, Appl. Phys. Lett. 88 (2006) 253503.
[7] H. Liao, L. Chen, Z. Xu, G. Li, Y. Yang, Appl. Phys. Lett. 92 (2008) 173303.
[8] F.C. Krebs, Org. Electron. 10 (2009) 761.
[9] S.K. Hau, H.L. Yip, H. Ma, A.K.Y. Jen, Appl. Phys. Lett. 93 (2008) 233304.
[10] F.C. Krebs, Sol. Energy Mater. Sol. Cells 92 (2008) 715.
[11] A.K.K. Kyaw, X.W. Sun, C.Y. Jiang, G.Q. Lo, D.W. Zhao, D.L. Kwong, Appl. Phys. Lett. 93 (2008) 221107.
[12] J. Gilot, M.M. Wienk, R.A.J. Janssen, Appl. Phys. Lett. 90 (2007) 143512.
[13] D.J.D. Moet, L.J.A. Koster, B. de Boer, P.W.M. Blom, Chem. Mater. 19 (2007) 5856.
[14] W. Beek, M. Wienk, R. Janssen, Adv. Mater. 16 (2004) 1009.
[15] S.D. Oosterhout, M.M. Wienk, S.S. van Bavel, R. Thiedmann, L. Jan Anton Koster, J. Gilot, J. Loos, V. Schmidt, R.A.J. Janssen, Nat. Mater. 8 (2009) 818.
[16] C. Pacholski, A. Kornowski, H. Weller, Angew. Chem., Int. Ed. 41 (2002) 1188.
[17] T. Matsushima, Y. Kinoshita, H. Murata, Appl. Phys. Lett. 91 (2007) 253504.
[18] X. Jiang, Z. Zhang, J. Cao, W. Zhu, Solid-State Electron. 52 (2008) 952.
[19] H. You, Y. Dai, Z. Zhang, D. Ma, J. Appl. Phys. 101 (2007) 026105.
[20] H. Lee, S.W. Cho, K. Han, P.E. Jeon, C. Whang, K. Jeong, K. Cho, Y. Yi, Appl. Phys. Lett. 93 (2008) 043308.
[21] D.Y. Kim, J. Subbiah, G. Sarasqueta, F. So, H. Ding, Irfan, Y. Gao, Appl. Phys. Lett. 95 (2009) 093304.
[22] T. Arii, A. Kishi, J. Therm. Anal. Calorim. 83 (2006) 253.
[23] M. Morana, M. Wegscheider, A. Bonanni, N. Kopidakis, S. Shaheen, M. Scharber, Z. Zhu, D. Waller, R. Gaudiana, C. Brabec, Adv. Funct. Mater. 18 (2008) 1757.
[24] L.H. Slooff, S.C. Veenstra, J.M. Kroon, D.J.D. Moet, J. Sweelssen, M.M. Koetse, Appl. Phys. Lett. 90 (2007) 143506.
[25] M. Lenes, G.A.H. Wetzelaer, F.B. Kooistra, S.C. Veenstra, J.C. Hummelen, P.W.M. Blom, Adv. Mater. 20 (2008) 2116.
[26] F. Verbakel, S.C.J. Meskers, R.A.J. Janssen, Appl. Phys. Lett. 89 (2006) 102103.
[27] W.J.E. Beek, M.M. Wienk, M. Kemerink, X. Yang, R.A.J. Janssen, J. Phys. Chem. B 109 (2005) 9505.
[28] J. Peet, J.Y. Kim, N.E. Coates, W.L. Ma, D. Moses, A.J. Heeger, G.C. Bazan, Nat. Mater. 6 (2007) 497.
[29] J.M. Kroon, M.M. Wienk, W.J.H. Verhees, J.C. Hummelen, Thin Solid Films 403–404 (2002) 223.
[30] M. Lenes, M. Morana, C.J. Brabec, P.W.M. Blom, Adv. Funct. Mater. 19 (2009) 1106.
[31] J.D. Kotlarski, P.W.M. Blom, L.J.A. Koster, M. Lenes, L.H. Slooff, J. Appl. Phys. 103 (2008) 084502.
[32] L.A.A. Pettersson, L.S. Roman, O. Inganas, J. Appl. Phys. 86 (1999) 487.
[33] H. Hoppe, N. Arnold, D. Meissner, N.S. Sariciftci, Thin Solid Films 451–452 (2004) 589.
[34] N. Persson, H. Arwin, O. Inganas, J. Appl. Phys. 97 (2005) 034503.
[35] D.J.D. Moet, M. Lenes, J. Kotlarski, S. Veenstra, J. Sweelssen, M.M. Koetse, B. de Boer, P.W.M. Blom, Org. Electron. 10 (2009) 1275.

the moment, according to Starck's Clevios company, the product TM PH 510 has conductivity of 300 S cm^{-1}. For organic LED applications the electrical conductivity must be as high as possible and independent of moisture. However, the electrical conductivity of PEDOT:PSS layers depends on the level of humidity. From 20% RH up to 57% RH the conductivity increases to the value higher than 13% and from 57% RH to 90% RH it decreases to 70% of the original value (see Fig. 1). With the number of recurrent cycles the change is a little bit smaller but still exists.

The aim of the present work was to prepare a polymer on the basis of PEDOT with conductivity independent of humidity (further mentioned as PEDOT:PTSA) and to characterize its surface properties with photoemission spectroscopies and SEM, as well as to investigate the interface properties with nickel phthalocyanine (NiPc) thin films. Increasing research efforts were devoted to metal phthalocyanines [(MePcs) M-C32H16N8] which are planar molecules formed by stable π-conjugated macrocycles coordinating a central metal atom. Due to their unique optical and electronic properties, the high temperature chemical and photochemical stabilities, the low-cost of preparation processes and their tendency to self-assemble on metal surfaces forming ordering aggregates, make MePcs suitable to easily control the properties at the organic/metal or/and inorganic interfaces and therefore they are considered to be promising materials for many electronic applications such as gas sensors, field-effect transistors, and solar cells [10,11]. In this study, we compare the electronic structure of the NiPc/PEDOT:PTSA interface investigated by core level X-ray and valence band ultra-violet photoemission spectroscopies (XPS and UPS, respectively), with the energy level alignment for NiPc thin films on other technically relevant substrates such as PEDOT:PSS, ITO and Au which have been studied previously [12–14]. PEDOT:PSS has quite similar chemical structure to PEDOT:PTSA, ITO has similar work function to PEDOT:PTSA and, Au is a metal electrode which forms ohmic contacts and can be used as reference for the determination of the position of the energy levels in respect to the Fermi level. All interfaces are formed and investigated in ultra high vacuum (UHV) to eliminate all possibilities of ambient contamination.

2. Experimental

PEDOT:PTSA (the chemical structure is given in Fig. 2a) was prepared by the polymerization of the 3,4-(ethylenedioxy)thiophene (EDOT) monomer in the presence of a

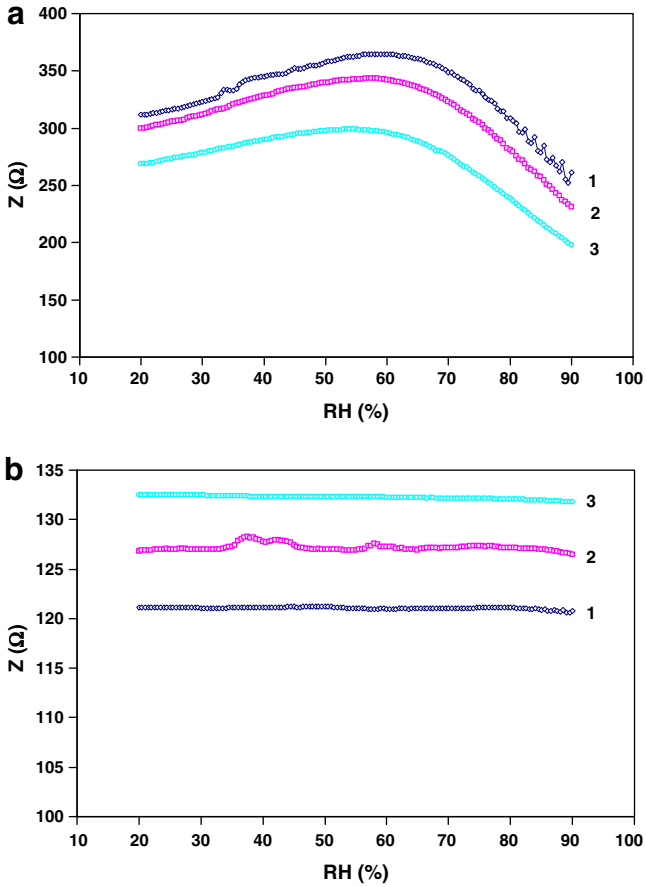

Fig. 1. Humidity dependences of the impedance at different temperatures for: (a) PEDOT:PSS, (b) PEDOT:PTSA (before ethanol washing). Curve 1 – 20 °C, curve 2 – 30 °C, and curve 3 – 50 °C.

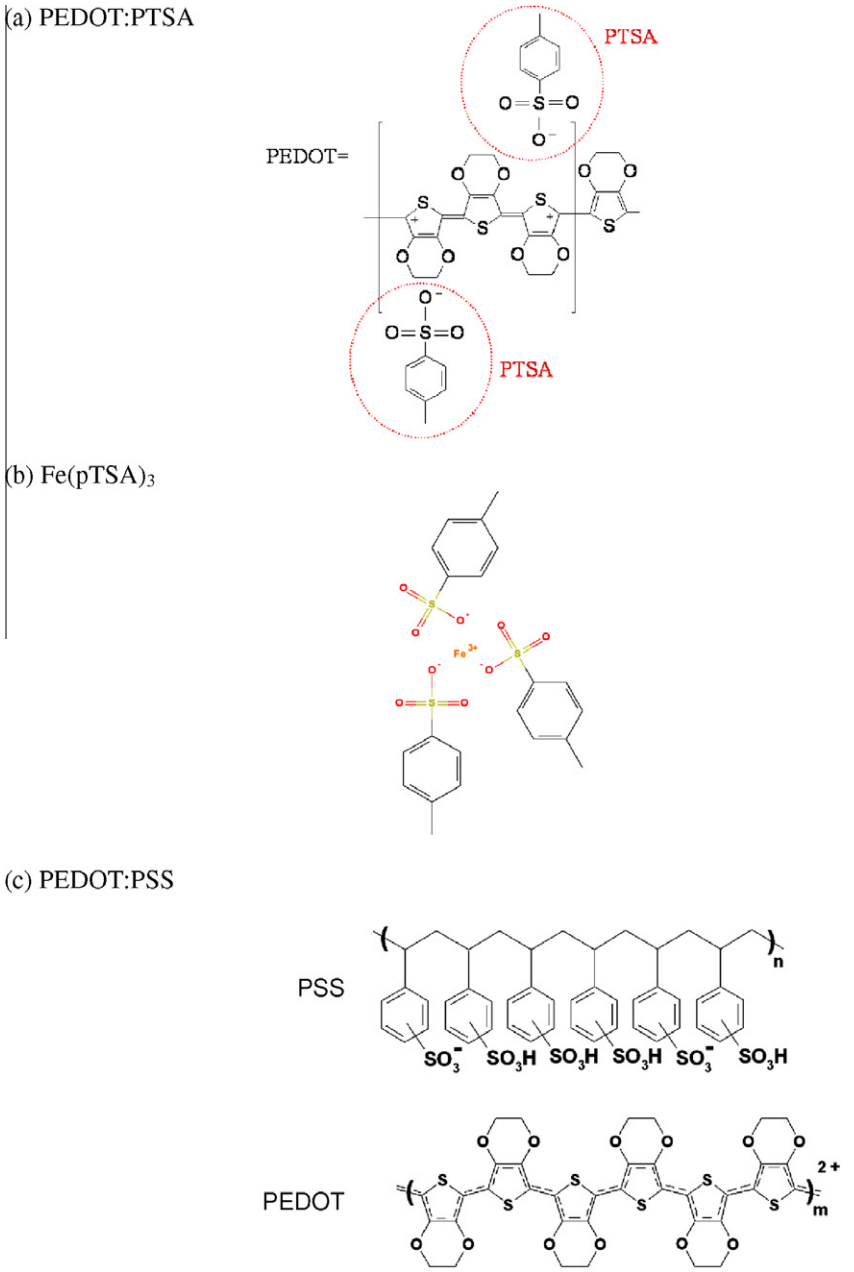

Fig. 2. Chemical structure of (a) PEDOT:PTSA, (b) iron(III) toluensulfonate $Fe(pTSA)_3$ and (c) PEDOT:PSS.

stoichiometric or less than stoichiometric amount of the catalyst, iron(III) toluensulfonate $Fe(pTSA)_3$ (see Fig. 2b), which is an organic acid ligand combined with iron III and butan-1-ol. When the components are mixed in solution, a small portion of the monomer tends to polymerize even at room temperature. The polymerization solution may also contain a dopant. However, iron(III)toluenesulfonate supplies both the dopant (anion toluenesulfonate) and the oxidative polymerization catalyst (iron(III) cation). In particular, the PEDOT:PTSA films were prepared by dipping in the polymerization solution consisting of the mixture of solutions: iron(III) toluensulfonate (10 parts, Clevios™ CB) in butan-1-ol, *N*-methylpyrrolidone (0.1 part, Sigma–Aldrich) and ethyl alcohol (12 parts), 1 part of EDOT (Clevios™ M) in isopropyl alcohol and butyl alcohol (all parts are by weight). All chemicals of reagent grade were used without purification. PEDOT:PSS films were prepared by dipping in an aqueous dispersion (Clevios™ P – chemical structure displayed in Fig. 2c). The PEDOT:PTSA thin films were prepared by spin coating (2100 rpm) on the surface of a fluorinated tin oxide (FTO) coated-glass. After the deposition, the PEDOT:PTSA samples were kept 24 h on air to finish the polymerization and finally, the samples were washed in ethanol.

The surface of the samples was studied right after their introduction in UHV, after thermal treatment at 110 °C for 1 h and after in situ mild argon sputtering for 5 min (4×10^{-6} mbar of argon pressure, accelerating voltage of 0.2 keV and incidence angle of 45°), by XPS (non-monochromatic Al Kα) and UPS (HeI excitation line). The measurements were performed in a multi-chamber ultra high vacuum system described previously [12]. The characterization of the surface was followed by thermal evaporation of commercial NiPc powder (Alfa Aesar) in a step-wise manner from a home-made Knudsen cell kept at 425 °C in a vacuum of about 5×10^{-8} mbar. The temperature of the substrate (PEDOT:PTSA) was 20 °C and the total thickness of the NiPc film was about 7.0 nm. After every deposition step the analysis of the surface was carried out with XPS (Al Kα, analyser pass energy of 97 eV) and UPS (HeI). The calibration of the spectrometer is described elsewhere [12]. The work function was measured biasing the specimen at −12.30 V to separate sample and analyser high binding energy cut-offs.

Humidity dependence of impedance was measured by Hewlet–Packard AC Bridge (type HP4274A). Thin films were deposited by spin coating on the system of interdigital gold electrodes, gap 20 μm.

3. Results and discussion

3.1. PEDOT:PTSA

3.1.1. Surface characterization

Fig. 3 shows the SEM pattern of the film prepared by dipping in pre-polymerized solution consisting of the monomer and oxidizer (catalyst) in the ratio of 2:1 and then washed in ethanol. The film was quite homogeneous while its thickness was about three times lower than before the washing process. Note, that PEDOT:PSS films forms very homogeneous films with much smaller grains in comparison with PEDOT:PTSA.

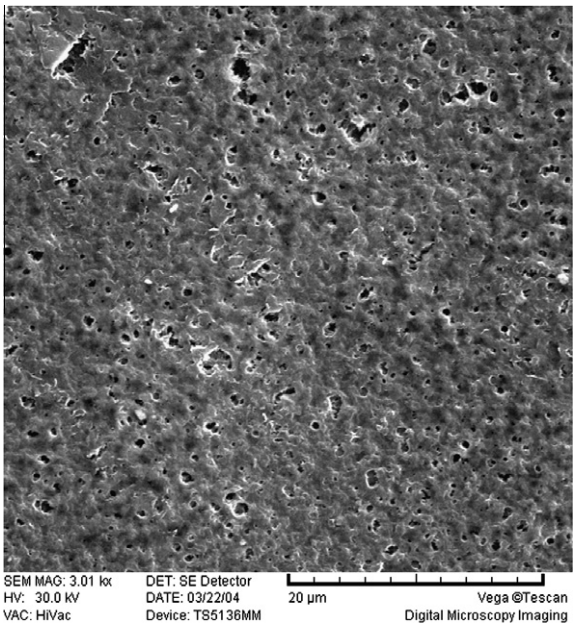

Fig. 3. PEDOT film prepared by the polymerization of EDOT in the presence of less than the stoichiometric amount of the oxidative polymerization catalyst (PTSA), after the ethanol washing.

Analysis of the XPS (Al Kα) plots shows that the overview spectra of the PEDOT:PTSA surface is dominated by the expected elements (C, O and S) in agreement with the chemical structure of the polymer. The S2p band consists of two components with binding energies 164.2 ± 0.1 and 167.7 ± 0.1 eV. The peak at lower binding energy is due to the sulphur atoms linked to carbon in the chemical structure of PEDOT, while the peak at higher binding energy is attributed to the sulphur atoms in PTSA (Fig. 4a). Both contributions are splitted in two spin orbit doublets at the binding energies 164.0 ± 0.1 and 165.3 ± 0.1 eV for PEDOT and 167.4 ± 0.1 and 168.6 ± 0.1 eV for PTSA, respectively, with the ratio of $2p_{3/2}$ to $2p_{1/2}$ peaks equal to 2:1 [15,16]. During the annealing and argon sputtering procedures no significant change in the position of the overall S2p peak was observed (not shown). However, the PEDOT-to-PTSA ratio calculated from the areas under the S2p core level spectra seems to change from 1:0.4 for the as received surface to 1:0.25 upon annealing, without any further change after sputtering (1:0.24). It should be noted here that the nominal ratio of PEDOT-to-PTSA is 1:0.5 (1:1.2 by weight). From the spectrum it is also possible to estimate the thickness of the surface PTSA component [15]. The thickness equivalent of PTSA amount at the surface is 3.80 nm for the as-loaded polymer and 3.30 nm for the annealed one revealing a partial removal of the blend from the surface during the annealing procedure. During the sputtering no significant (thickness) reduction was observed.

The binding energy of the XPS O1s peak from the as-loaded PEDOT:PTSA surface is 533.00 ± 0.05 eV and can be splitted into three components according to the different chemical bonds of the oxygen atoms (Fig. 4b). The component at 533.4 eV of binding energy is attributed to the C–O–C bonds from PEDOT [15], the component at 533.0 eV is due to –OH groups and the component at 531.9 eV can be attributed to O═S bonds in PTSA. Upon heat treatment and sputtering procedure the contribution of PTSA to the overall O1s signal significantly decreases, confirming the possible partly removal of PTSA.

The XPS C1s peak was found at 285.20 ± 0.05 eV and can be analysed in two components attributed to C–C bonds (285.2 eV) and to C–O and C–S bonds (286.7 eV) (Fig. 4c). In the case of C1s peak it is not possible to distinguish the contributions of PEDOT and PTSA to the overall signal. Upon annealing and sputtering no significant change in the shape and energetic position of C1s peak was observed.

The valence band structure of the as-loaded PEDOT:PTSA surface as obtained by UPS is shown in Fig. 5. The $HOMO_{cut\text{-}off}$ was determined at about 2.5 eV, while two broad peaks in the energy range of 6–7 eV and 9–10 eV are clearly visible. The work function was found equal to $e\Phi = 4.2 \pm 0.1$ eV for the as-loaded surface, similar to that measured for a sputtered clean ITO surface [17]. After

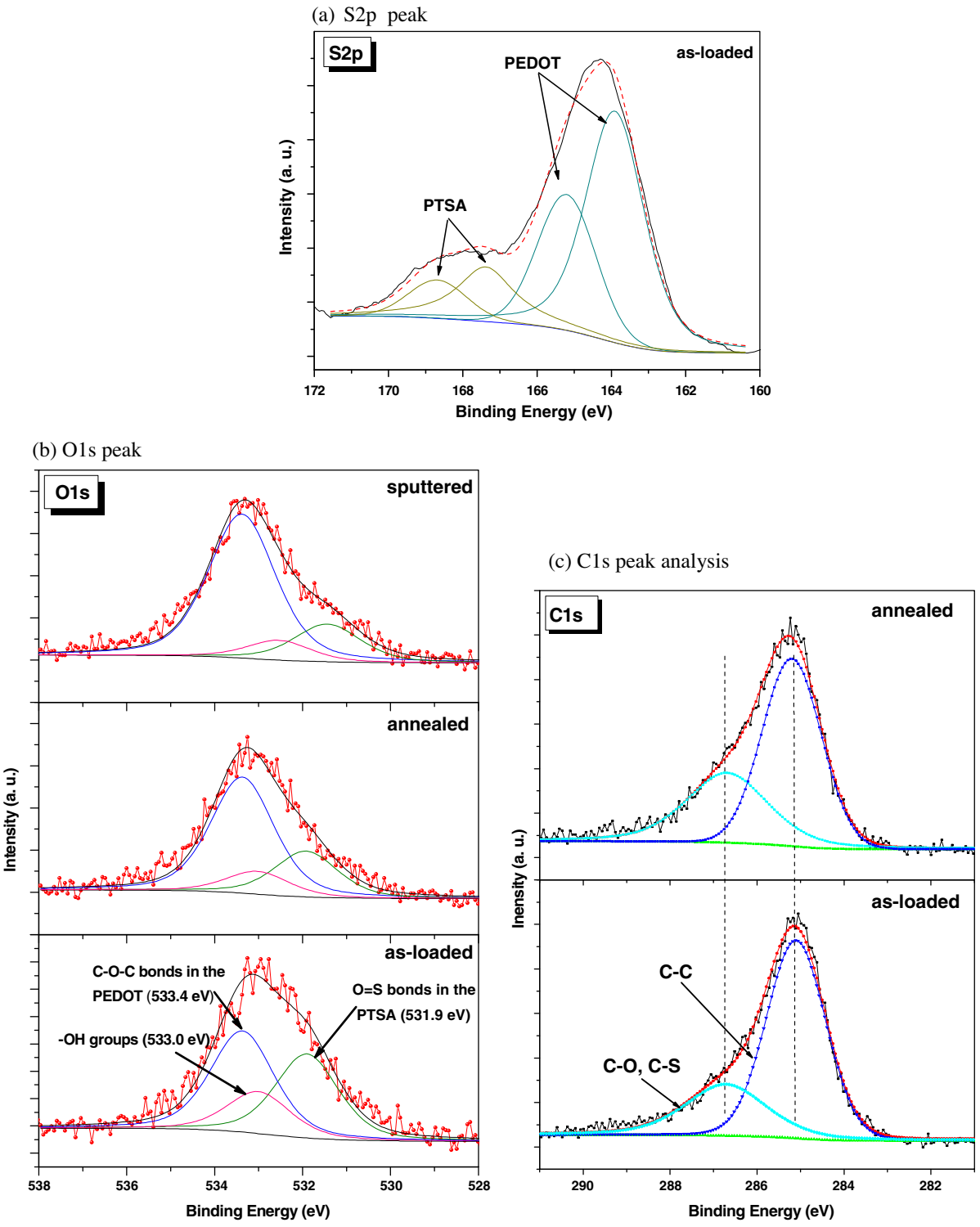

Fig. 4. Analysis of the XPS (Al Kα) data for the (a) S2p (smoothed) for the as-loaded PEDOT:PTSA surface, (b) O1s peak for the as-loaded, thermal treated and sputtered surface, and the (c) C1s peak for the as-loaded and annealed surface.

sputtering the work function decreases to 3.9 ± 0.1 eV, while we observe a slight increase of the density of states close to the Fermi level, indicating a more conductive surface.

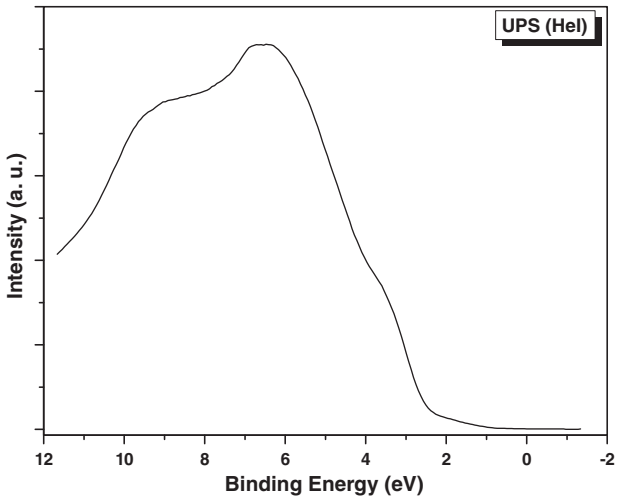

Fig. 5. Valence band structure for the as-loaded PEDOT:PTSA surface.

3.1.2. Dependence of impedance on humidity

As already mentioned in the introduction, PEDOT layers can be used for the construction of gas sensors. The accurate determination of the gas concentration assumes that the measured signal is independent on humidity of an environs or it is compensated by electrical element which uses the data from a humidity sensor. The first way is more simple, but it requires a sensing element which is not humidity dependent. The PEDOT:PTSA polymer seems to fulfill this condition. In Fig. 1 the humidity dependences for PEDOT:PSS (Fig. 1a) and PEDOT:PTSA (Fig. 1b) films for different temperatures are displayed. The humidity independency of PEDOT:PTSA film is clearly seen therefore, the result suggests that PEDOT:PTSA is suitable material for sensing applications. However, two facts must be mentioned: (i) the impedance of PEDOT:PSS is higher and for the used electrode configuration, it is nearly independent on the film thickness in comparison to PEDOT:PTSA. For the later, the impedance is lower and further decreases with the increasing of the film thickness. (ii) From the temperature dependences of the humidity derives that the PEDOT:PSS films behave as semiconductors whereas those of PEDOT:PTSA behaves as metals (electrical conductivity decreases with increasing temperature).

3.2. NiPc/PEDOT:PTSA interface

The characterization of the PEDOT:PTSA surface was followed by successive depositions of NiPc thin films on the as-loaded surface of the polymeric surface (substrate in the following). The binding energy of the XPS peaks related to the substrate does not change upon the deposition procedure, indicating the absence of chemical reaction with the NiPc molecules. The N1s peak will be used to obtain useful information for the formed interface, as the C1s peak is not suitable for the analysis due to the contribution from the carbon of the substrate. Fig. 6, exhibits the change of the energetic position of the XPS N1s peak with increasing NiPc film thickness. There is no band bending at the organic NiPc energy levels, while at the thick film the N1s peak reaches a plateau at about 399.30 ± 0.05 eV, in agreement with the recently investigated inert interfaces (NiPc/Au, NiPc/Ag and NiPc/ITO) [13,14]. The main contribution to the N1s peak is due to the two chemically non-equivalent N-atoms of the organic molecule, separated by about 0.3 eV and a weaker shake-up feature at higher binding energy (not shown). For better comparison, the change of the energetic position of the XPS N1s peak at the NiPc/ITO, NiPc/PEDOT:PSS and NiPc/Au interfaces are also given in the same figure (Fig. 6). Similar to the NiPc/PEDOT:PTSA interface, at the NiPc/ITO interface the final position of the N1s peak is also found at 399.30 ± 0.05 eV. There is a slight upward shift of the binding energy at low coverage, while for thicker films the energetic position of the N1s core level peak remains almost stable indicating the absence of band bending at the NiPc energy levels [14]. At the NiPc/PEDOT:PSS interface, the N1s peak remains almost stable up to ~3.0 nm of organic film thickness indicating a Fermi level pinning in the gap of NiPc, while for thicker films it exhibits an upward shift of ~0.3 eV and reaches the final position at 399.00 ± 0.05 eV of binding energy [12]. In the case of the metallic substrate, the final state effects and the pillow effect contribute strongly to the shifts of the core levels up to 1.0 nm of organic film thickness, while for thicker films the organic energy levels bend, leading to the alignment of the NiPc and Au foil Fermi levels [13]. The XPS Ni2$p_{3/2}$ peak exhibits similar behavior to the N1s peak and it is centered at 855.90 ± 0.05 eV of binding energy for a 5.0 nm thick film.

The question now arises whether or not the UPS characteristics of the substrate are affected by the presence of the organic molecules. The UP spectra gradually changes upon the deposition process, as shown in the left part of Fig. 7. The valence band of NiPc is fully developed at ~2.0 nm of film thickness and is composed of four peaks in agreement with previous spectroscopic studies [13]. The highest occupied molecular orbital (HOMO) cut-off position is located at 0.80 ± 0.05 eV for a 2.0 nm thick NiPc film and remains constant upon further depositions (right part of Fig. 7). The expected position for the bulk is near the midgap as

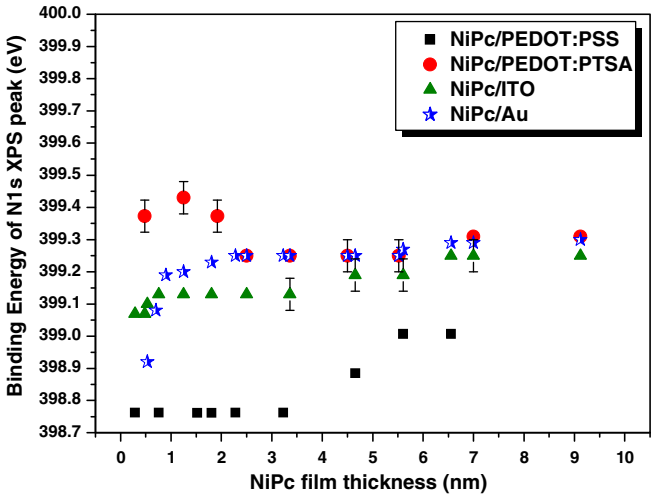

Fig. 6. Binding energy shift of the XPS N1s peak during the formation of the NiPc/ PEDOT:PTSA interface. For comparison, the corresponding shifts of the N1s peak for the NiPc/PEDOT:PSS, NiPc/ITO and NiPc/Au interfaces are also shown.

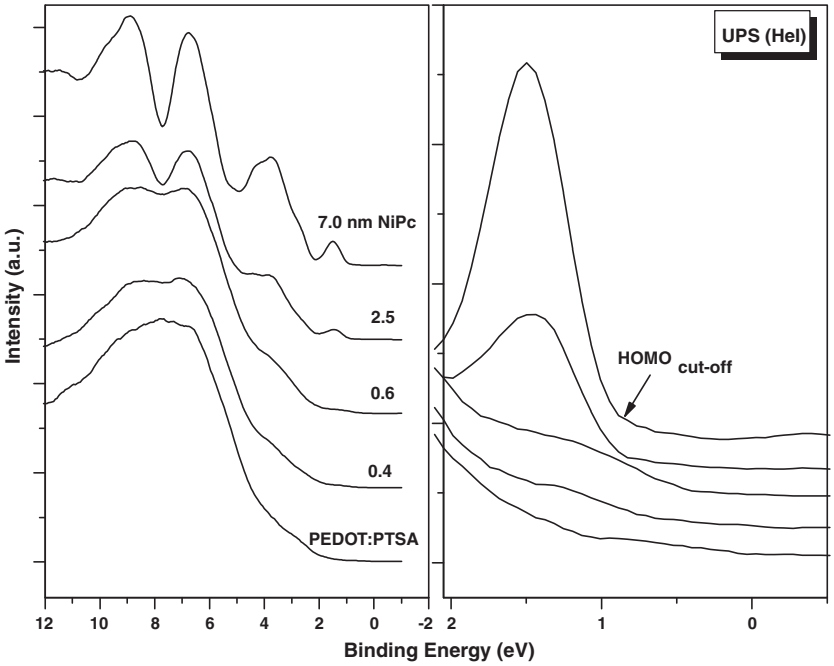

Fig. 7. Evolution of the UPS spectra (HeI) for the NiPc/PEDOT:PTSA interface with increasing NiPc film thickness. On the right part, the low binding energy region is shown magnified (3×) for the determination of the $HOMO_{cut\text{-}off}$ position.

for the NiPc/metals interfaces [13], which is not the case in the present study, revealing that NiPc is more p-doped as at the NiPc/PEDOT:PTSA interface. This behavior will be discussed later on in the context of the chemical type of each substrate.

Upon the successive depositions of NiPc films on the as-loaded polymeric substrate, the cut-off in the spectrum which defines the vacuum level, is shifted to higher binding energy. Thus, the work function of the surface is shifted towards lower binding energies. This is displayed in Fig. 8, where the change of the vacuum level position as a function of the NiPc thickness is shown. At the first steps of deposition and for coverage up to ~1.5 nm, the vacuum level is shifted towards lower energies. For thicker NiPc films it reaches a plateau at about 3.9 ± 0.1 eV, which corresponds to the work function of the NiPc considering Fermi level alignment between the two materials in contact. This value is in agreement with the reported value for the NiPc overlayer in the case of the NiPc/metal interface [13]. For comparison, the vacuum level shift at the

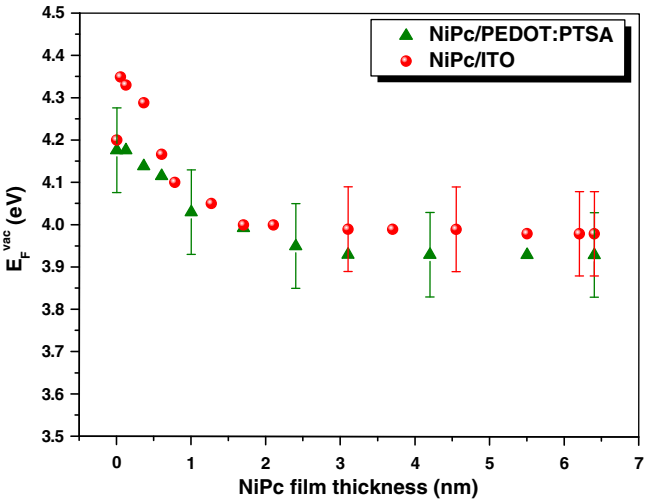

Fig. 8. Vacuum level shifts (E_F^{vac}) as a function of the organic (NiPc) film thickness deposited on the as-loaded PEDOT:PTSA surface and on sputter-cleaned ITO.

NiPc/ITO interface is also shown at the same figure, as the two substrates, ITO and PEDOT:PTSA, have similar work function values.

During the deposition of NiPc on the PEDOT:PTSA and on ITO surface the drop of the vacuum level can be understood on the basis of an interface dipole formed between the substrate and the organic layer as no chemical interaction is observed. The total decrease of the work function at NiPc/PEDOT:PTSA and NiPc/ITO interfaces is 0.3 eV and 0.2 eV, respectively, resulting in an interfacial dipole layer of the same magnitude. In both interfaces, in the absence of a strong chemical interaction, the equilibration of the chemical potentials across the full layer stack leads to the formation of an outward pointing electric dipole at the interface. As a result the lowering of the vacuum level is observed which influences the energy level alignment. The difference between the Fermi level and the $HOMO_{cut\text{-}off}$ position represents the hole injection barrier (Φ_{bh}) at the interface which was found to be 0.8 ± 0.1 eV, similar to that found in the case of the NiPc/metals interfaces, lower than the corresponding barrier at the NiPc/ITO interface (1.0 eV) and significantly higher than the Φ_{bh} in the case of NiPc/PEDOT:PSS interface (0.5 eV). The $HOMO_{cut\text{-}off}$ energy is related to the ionization potential (E_{ion}) of the NiPc overlayer according to the equation

$$HOMO_{cut\text{-}off} = E_{ion} - e\Phi_{(NiPc)}$$

where $e\Phi_{(NiPc)}$ is the work function of phthalocyanine. The barrier for the injection of electrons Φ_{be} can be expressed as

$$\Phi_{be} = \Phi_{bh} - E_g$$

where the energy gap E_g (the energy difference between HOMO and LUMO) is taken from electronic structure calculations and it is equal to E_g = 2.4 eV for the NiPc layer [18]. Fig. 9 summarizes the energy level line-up at the NiPc/PEDOT:PTSA interface as derived by the photoemission results. In Table 1 the properties of the interfaces between

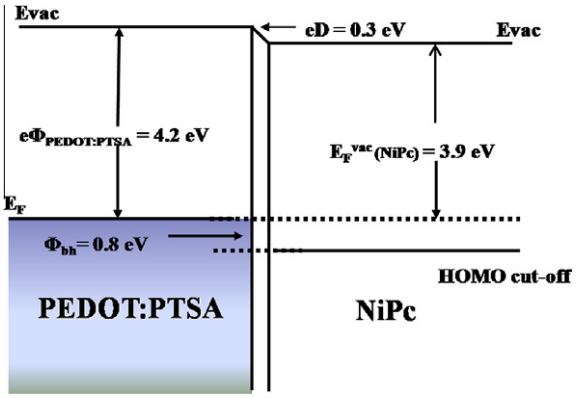

Fig. 9. Schematic energy level diagram for the NiPc/PEDOT:PTSA interface.

NiPc and other substrates (Au, ITO and PEDOT:PSS) are displayed for comparison. According to this table, NiPc forms abrupt interfaces with Au, ITO, PEDOT:PSS and PEDOT:PTSA. In all cases, the direction of the dipole points outwards, with '+' away from the surface. The large interface dipole observed at the NiPc/Au interface is related to the significant electron density at the metal surface, which is rearranged by the presence of the organic NiPc molecules. In the case of metals, when an atom or molecule is deposited on a metallic surface, Coulomb repulsions between the atom and the surface metal electrons locally suppresses the tail of the metal electron cloud that spills into vacuum. This phenomenon leads to the reduction of the metal work function and it is known as "pillow effect" [19,20]. In contrary, in the case of ITO and PEDOT:PTSA, the absence of surface electron tail in addition with the low density of states of the NiPc molecules leads to the formation of small interface dipoles. However, although both substrates have similar work functions, in the case of PEDOT:PTSA the hole injection process is more efficient. The Φ_{bh} at the NiPc/PEDOT:PTSA interface is similar to that found in the case

Table 1
The properties of the interfaces between NiPc and Au, ITO, PEDOT:PTSA and PEDOT:PSS substrates. eD represents the interface dipole, $e\Phi$ is the work function, E_F is the Fermi level position, Φ_{bh} is the hole injection barrier and V_b is the band bending at the organic NiPc energy levels.

	$eD \pm 0.10$ (eV)	$HOMO_{cut\text{-}off} \pm 0.05$ (eV)	$e\Phi_{sub} \pm 0.10$ (eV)	E_F^{vac} (NiPc) ± 0.10 (eV)	$\Phi_{bh} \pm 0.10$ (eV)	$V_b \pm 0.05$ (eV)
Au	1.05	1.00	5.2	4.0	0.85	0.15
ITO	0.20	1.00	4.2	4.0	1.00	–
PEDOT:PTSA	0.30	0.80	4.2	3.9	0.80	–
PEDOT:PSS	0.70	0.50	4.9	3.9	0.50	0.30

of NiPc/Au, revealing the possibility of this material to be used in the development of electronic devices with increased efficiency. Furthermore, it is also possible to prepare PEDOT:PTSA films on flexible substrates and fabricate devices which would attribute mechanical flexibility. Comparing now PEDOT:PTSA with PEDOT:PSS, we would expect similar results, as both substrates have about the same chemical structure. However, this is not the case, as in the NiPc/PEDOT:PSS interface the pinning of the Fermi level in the gap of the NiPc in addition with the presence of band bending at the NiPc energy levels, results in a more efficient electron transfer from the substrate to the organic NiPc film than in the case of the PEDOT:PTSA substrate.

4. Summary

The surface electronic structure of a new synthesized polymer film (PEDOT:PTSA) with higher conductivity than PEDOT:PSS was characterized upon annealing and sputtering procedures. PEDOT:PTSA acts as an ordinary conducting substrate for which the initial work function is lowered upon adsorbing the NiPc molecules. AC electrical conductivity is independent of humidity in the range of 20–90% RH which makes the PEDOT:PTSA polymer suitable for sensor applications. From the temperature dependence of the conductivity one can expect metallic behavior. This is also confirmed by the photoemission results where the properties of the NiPc/PEDOT:PTSA interface resemble those of the NiPc/metals.

Acknowledgements

The work was supported by the by grant of the Ministry of Education, Youth and Sport of the Czech Republic (Grant No. 1041/2006-32) and by Grant Agency of the Academy of Sciences of the Czech Republic (Grant No. KAN401770651). Authors thank Dr. A. Hamáček and Dr. J. Řeboun for the electrical measurements.

References

[1] S. Nespurek, V. Cimrova, J. Pfleger, I. Kminek, Polym. Adv. Technol. 7 (1996) 457.
[2] N. Karl, A. Bauer, J. Holzäpfel, J. Marktanner, M. Möbus, F. Stölzle, Mol. Cryst. Liq. Cryst. 252 (1994) 243.
[3] M. Granstrom, M. Berggren, O. Inganas, Science 267 (1995) 1479.
[4] S.V. Frolov, A. Fujii, D. Chinn, Z.V. Vardeny, K. Yoshino, R.V. Gregory, Appl. Phys. Lett. 72 (1998) 2811.
[5] D.J. Gundlach, Y.Y. Lin, T.N. Jackson, D.G. Schlom, Appl. Phys. Lett. 71 (1997) 3853.
[6] H. Kuhn, W.C. Kimbrell, J.E. Fowler, C.N. Barry, Synth. Met. 55–57 (1993) 3707.
[7] T. Taka, Synth. Met. 41–43 (1991) 1177.
[8] L.B. Groenendaal, F. Jonas, D. Freitag, H. Pielartzik, J.L. Reynolds, Adv. Mater. 12 (2000) 481.
[9] G. Heywang, F. Jonas, Adv. Mater. 4 (1992) 116.
[10] S. Günes, H. Neugebauer, N.S. Sariciftci, Chem. Rev. 107 (2007) 1324.
[11] R.D. Gould, Coord. Chem. Rev. 156 (1996) 237.
[12] F. Petraki, S. Kennou, S. Nespurek, J. Appl. Phys. 103 (2008) 033710.
[13] F. Petraki, V. Papaefthimiou, S. Kennou, Org. Electron. 8 (2007) 522.
[14] F. Petraki, S. Kennou, Org. Electron. 10 (2009) 1382 (and references therein).
[15] G. Greczynski, Th. Kugler, M. Keil, W. Osikowicz, M. Fahlman, W.R. Salaneck, J. Electron. Spectrosc. Relat. Phenom. 121 (2001) 1.
[16] J. Hwang, F. Amy, A. Kahn, Org. Electron. 7 (2006) 387.
[17] D.J. Milliron, I.G. Hill, C. Shen, A. Kahn, J. Schwartz, J. Appl. Phys. 87 (2000) 572.
[18] B. Bialek, I.G. Kim, J.I. Lee, Synth. Met. 129 (2002) 151.
[19] J. Hwang, A. Wan, A. Kahn, Mater. Sci. Eng. R 64 (2009) 1.
[20] I. Hill, A. Rajagopal, A. Kahn, Y. Hu, Appl. Phys. Lett. 73 (1998) 662.

most recent observation of the effect of Madelung potential on work function [16] indicates the complicated interface electronic configuration of the PEDT:PSS system with both electronic and ionic conducting components.

In the context of the complex electric and electronic behaviors introduced above, this work reports some new phenomena associated with the charge conduction of PEDT:PSS films. We present the negative differential resistance (NDR) observed for a metal/PEDT:PSS/metal sandwich configuration. The NDR peaks exhibit different manifestations as a function of the films thickness and the PEDT:PSS/electrode interface. We propose that hole injection and resonance tunneling, hole trapping and extraction, and ionic motion are responsible for the NDR behaviors and remnant voltage observed in this work. Our results emphasize the effect of film/electrode interface and film thickness on the formation of distinctive *IV* characteristics, and is useful for a complete understanding on the charge conduction mechanism of PEDT:PSS.

2. Results and discussion

PEDT:PSS aqueous solution (Baytron 4083, H.C. Stark GmbH, Germany) was drop-cast onto an Al foil substrate to form thin films (see Supporting Information SI-i for experimental). The typical thickness of the films is ~100 nm and ~1.0 μm, respectively. Fig. 1(a) exhibits the optical photos of the 100-nm-thick and 1.0-μm-thick films respectively collected using the CCD camera of our atomic force microscope (AFM) [17,18] system. Under identical photo-taking conditions, the thicker film exhibits a darker contrast relative to the Al substrate. The specific value of the thickness was obtained by using AFM to measure the Al-PEDT:PSS cross section height (i.e., the boundary of the bright and dark regions in Fig. 1(a)). Fig. 1(b) shows a typical AFM morphology image of the 1.0-μm-thick film, and Fig. 1(c) is the representative current map of the same film collected using conductive AFM (cAFM) [19]. Due to the conducting property of PEDT:PSS, many microscopic conductive sites are observed on the current map. Fig. 1(d) displays the optical absorption spectrum of the 1.0-μm-thick film, and the spectrum is in agreement with the oxidation state or doping level (0.3 hole/ring) of the Baytron 4083 PEDT:PSS used in this work [1,2,20]. Similar AFM morphology and current images, and absorption spectrum were also observed for 100-nm-thick films (data not shown).

Fig. 2(a) shows the typical *JE* (current density~field) curves collected for the 100-nm-thick PEDT:PSS film in the ITO/PEDT:PSS/Al sandwich configuration (see SI-ii for experimental). The *JE* curves were obtained by scanning the ITO electrode voltage from −10 to 10 V at different rate of 0.2, 1.0 and 4.0 V/s, respectively. It can be seen that, instead of the most common monotonous *JE* dependence, the *JE* curves are characterized by large current peaks in both negative and positive voltage regions. Such current peaks are referred to as negative differential resistance (NDR) in the literature, and are often reported for self-assembled monolayers, organic films, and polymer/nanoparticles (NPs) composites [21–25]. In self-assembled monolayers, the NDR behavior arises from the redox centers of the molecules [21], while it is induced by NPs-based trap states in the case of polymer/NPs composites [22,23]. To the best of our knowledge, Fig. 2(a) represents the first observation of NDR for a 100-nm-thick PEDT:PSS film. In Fig. 2(b), we show the energy diagram of the ITO/PEDT:PSS/Al device and propose an interface-states-facilitated hole resonant tunneling mechanism for the observed NDR characteristic. Since PEDT:PSS is a well-known hole-transporting polymer, charge conduction in the sandwich device should be dominated by hole injection from the electrode to PEDT:PSS and subsequent hole hopping/tunneling

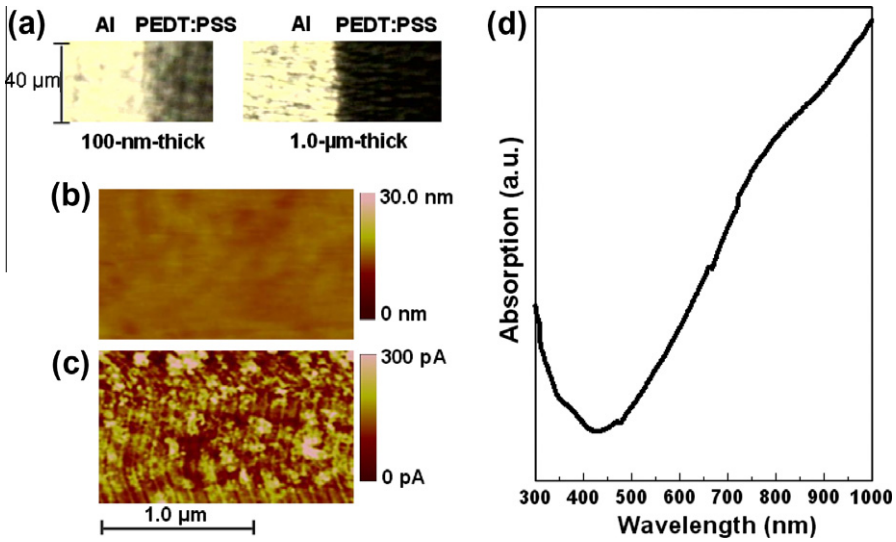

Fig. 1. (a) Optical micrographs showing the formation of the 100-nm-thick and 1.0-μm-thick PEDT:PSS films drop-cast on Al foil substrate, respectively. AFM morphology image (b) and cAFM current map (c) of the 1.0-μm-thick PEDT:PSS film, respectively. A tip bias of −2 V was used for current mapping. (d) Optical absorption spectrum of a 1.0-μm-thick PEDT:PSS film drop-cast on a transparent glass slide.

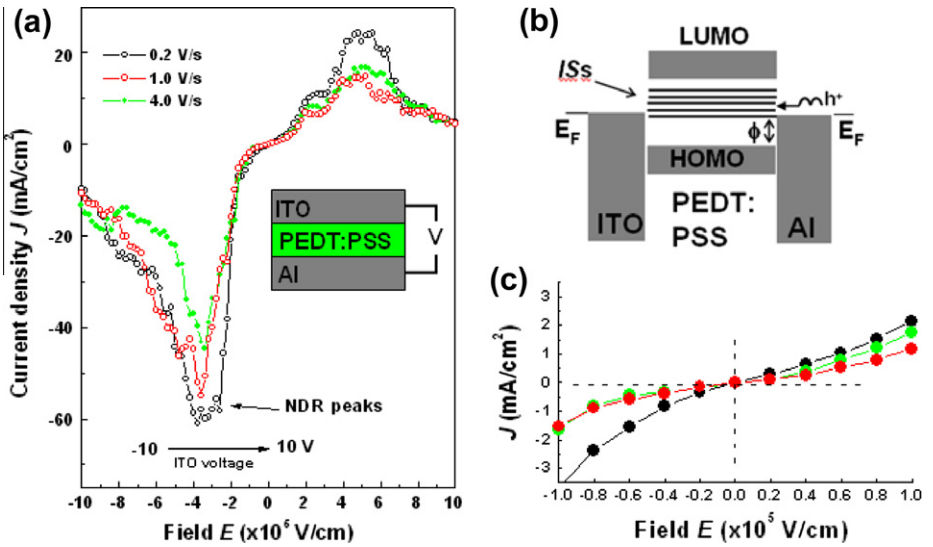

Fig. 2. Typical *JE* curves observed for the ITO/100 nm PEDT:PSS/Al sandwich device (see the inset). The *JE* curves were collected by scanning the ITO electrode voltage from −10 to 10 V at different rate of 0.2, 1.0 and 4.0 V/s, respectively. (b) Proposed NDR mechanism involving interface states (*ISs*) formation at the metal/PEDT:PSS interfaces and subsequent hole resonant tunneling through the *ISs*. (c) Fine features of the same *JE* curves in (a) near the zero-field region showing no remnant field, that is, the *JE* curves all pass through the origin of the coordinates.

throughout the film. Without interface states (*ISs*) formation at the Al/PEDT:PSS contact, there is an energy barrier ϕ for hole injection from the Fermi level E_F of Al to the HOMO (highest occupied molecular orbital) of PEDT:PSS. This often leads to nonlinear monotonous *JE* dependence as a function of the reduction of ϕ by electrode voltage. However, the NDR peaks observed in Fig. 2(a) indicate that charge conduction in the present case is not governed by the energy barrier ϕ. Therefore we propose there are *ISs* formed at the PEDT:PSS/electrode interfaces (see Fig. 2(b)), and these *ISs* provide the resonant states for holes to tunnel through the PEDT:PSS film. In Fig. 2(a), in the $-10 \rightarrow 0$ V voltage range, holes are injected from Al to PEDT:PSS, and the resonant tunneling is peaked at -3.4 V (or -3.4×10^5 V/cm). In the $0 \rightarrow 10$ V range, holes are injected from ITO, and the resonant tunneling peak appears at ~5.0 V (or 5.0×10^5 V/cm). The different NDR peak locations reflect the different E_F alignment of ITO and Al respectively relative to the *ISs*. In addition, the NDR peak intensity in the negative voltage region is systematically higher than that in the positive voltage region. Again, this is an outcome of the different density of *ISs* formed at the two metal/PEDT:PSS interfaces. The correlation of NDR to interface states will be further discussed in Fig. 4 which shows the quenching of NDR by using photoexcitation to saturate the *ISs*. The *JE* curves in Fig. 2(a) are reversible: in our experiments, when the ITO electrode voltage was scanned forward from −10 to 10 V (trace) and backward from 10 to −10 V (retrace) in one go, NDR peaks similar to those in Fig. 2(a) were observed in both the trace and retrace *JE* curves (see Fig. S1 in SI-iii). We also fabricated Au/100-nm thick PEDT:PSS/Au symmetrical devices for *JE* curve measurements. In this case, NDR peaks almost symmetrically located in the negative and positive voltage regions were observed (see Fig. S2 in SI-iv). In addition, we also compared the *JE* curves obtained at 25 and 100 °C respectively (see Fig. S2), and essentially no difference was observed in the NDR behavior between the two temperatures.

All the above results indicate that charge conduction in the 100-nm-thick PEDT:PSS films is electronic in nature. Firstly, the NDR peak intensity and position observed in Fig. 2(a) do not show a systematic dependence on the voltage scan rate *r*. In our experiments, the voltage scan was conducted at different rate of $r = 0.2$–4.0 V/s, and similar NDR peaks were observed regardless of *r*. The alteration (<20%) of the NDR peak intensity observed in Fig. 2(a) for $r = 0.2$, 1.0 and 4.0 V/s, respectively, is within our experimental error caused by sample-to-sample and measurement-to-measurement variations. Based on the resistivity (500–5000 Ωcm) of the PEDT:PSS polymer used in this work, hole resonant tunneling is a fast process in the sub-μs time scale, [26] so the change of scan rate in the ms-s scale should not affect the tunneling process. This is why no rate-dependence is observed for the NDR peaks shown in Fig. 2(a). Secondly, the fine features (see Fig. 2(c)) of the same *JE* curves shown in Fig. 2(a) near the zero-field (or zero-voltage) region clearly show that all the *JE* curves pass through the origin of the coordinates. This observation rules out the formation of remnant field/voltage during the *JE* curve measurements. If ionic process is involved, it will cause a large remnant field E_r (or remnant voltage V_r) and a strong rate-dependence as demonstrated below in Fig. 3 for 1.0-μm-thick PEDT:PSS films.

Fig. 3(a) displays the typical *JE* curves obtained for the 1.0-μm-thick PEDT:PSS film sandwiched between ITO and Al electrodes. Although the *JE* curves were collected under identical conditions used in Fig. 2(a), they are distinctly different from those displayed in Fig. 2(a). It can be seen in Fig. 3(a) that the *JE* curves are highly asymmetric: the current in the negative voltage region is monotonous, and is two orders higher than that in the positive

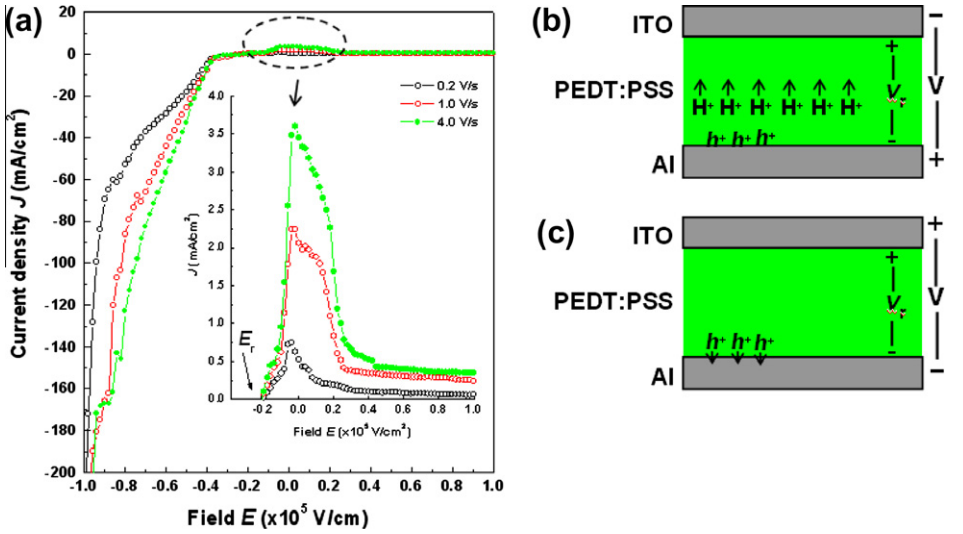

Fig. 3. Typical *JE* curves of the ITO/1.0 μm PEDT:PSS/Al device collected by scanning the ITO electrode voltage from −10 to 10 V at different rate of 0.2, 1.0 and 4.0 V/s, respectively. The inset displays the fine features of the *JE*s in the −2 to 10 V region. (b) Hole injection and trapping, H^+ ionic motion and remnant voltage V_r formation in the −10 → 0 V ITO electrode voltage scan. (c) Hole extraction by the Al electrode in the 0 → 10 V ITO electrode voltage scan.

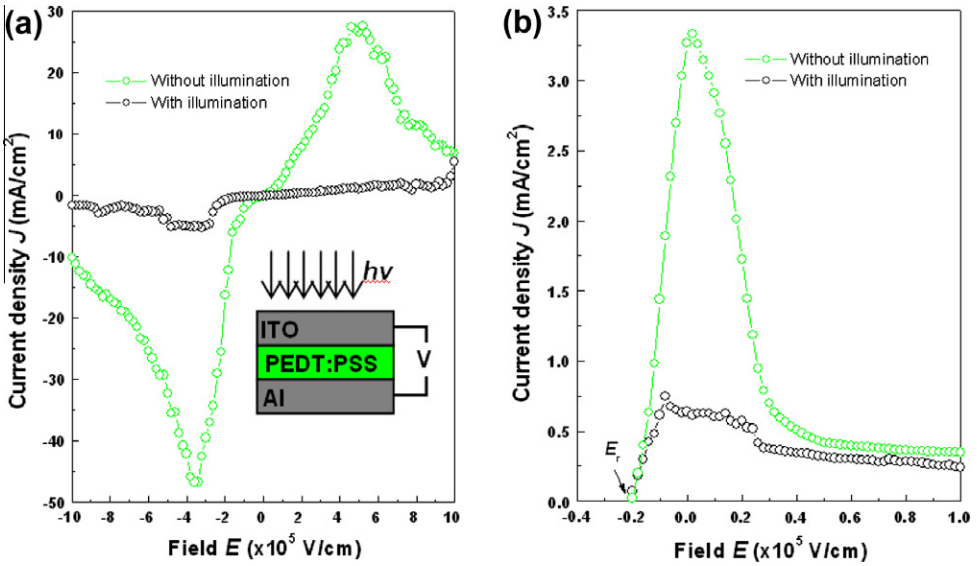

Fig. 4. *JE* curves of the ITO/PEDT:PSS/Al device collected with and without 405 nm light illumination, respectively. The *JE* curves were obtained by scanning the ITO voltage from −10 to 10 V at a rate of 4.0 V/s. The thickness of the PEDT:PSS film is (a) 100 nm and (b) 1.0 μm, respectively.

voltage region. The fine features in the inset of Fig. 3(a) reveal the formation of NDR peaks only in the positive voltage region. Moreover, the NDR peak height and peak area increase monotonously with the increase of voltage scan rate, and a large remnant field of $E_r = 0.2 \times 10^5$ V/cm (or remnant voltage of $V_r = 2.0$ V) is observed for all the *JE* curves in the inset of Fig. 3(a). This observation is in sharp contrast to the nearly symmetrical, rate-independent, and E_r-free *JE* curves observed in Fig. 2(a) for the 100-nm-thick PEDT:PSS films. We suggest that not only electronic but also ionic processes are involved in charge conduction in Fig. 3(a). As proposed in Fig. 3(b), in the −10 → 0 V ITO voltage scan, holes are injected from Al to PEDT:PSS, but due to the large thickness (~1.0 μm) of the film, they are not able to tunnel through the film. So the injected holes are trapped at the interface, thus leading to the absence of NDR peaks in the voltage scan. At the same time, H^+ ionic motion is switched on in the thicker PEDT:PSS film (see Fig. 3(b)), and the cationic motion contributes large ionic current to the total current. This is why the current density is very large (e.g., −200 mA/cm² at $E = -1.0 \times 10^5$ V/cm) in the −10 → 0 V voltage scan shown in Fig. 3(a). In PEDT:PSS, only the small H^+ is highly mobile, while the large polyanion PSS^- chain is essentially immobile. This causes a dipole-like remnant field $E_r = 0.2 \times 10^5$ V/cm or remnant voltage $V_r = 2.0$ V (see the inset of Fig. 3(a)) whose polarity is

opposite to that of the electrode voltage V (see Fig. 3(b)). Similar ionic motion in solid-state PEDT:PSS films has also been observed in previous works,[8,9] and in those early cases, the ionic motion were observed to cause hysterestic *JE* characteristics.

When the ITO voltage enters the $0 \rightarrow 10$ V positive region, the electrode voltage V is in the same polarity as V_r. Both V and V_r facilitate the extraction of trapped holes by the Al electrode (see Fig. 3(c)). It is the extraction of trapped holes at the PEDT:PSS/Al interface that leads to the NDR peaks observed in the inset of Fig. 3(b). Due to the large V_r of 2.0 V, the NDR peak is located near $V = 0$ V, and the NDR behavior dominates the *JE* characteristic in the entire $0 \rightarrow 10$ V voltage region as displayed in the inset of Fig. 3(a). It is clear that in the negative voltage region, charge conduction is governed by hole injection/trapping and cationic motion, while it is characterized by hole extraction and ionic relaxation in the positive voltage region. This is the origin for the drastically different current level and *JE* characteristic between negative and positive voltage regions observed in Fig. 3(a). Compared to hole hopping, ionic motion in polymer is in general a slow process, [27] and recent scanning Kelvin probe measurements [26] revealed that the time constant for ion motion in PEDT:PSS films is in the order of second. Since the *JE* curves in Fig. 3(a) have a strong ionic component, the *JE* dependence should be sensitive to the voltage scan rate used in this work. This is reflected by the monotonous increase of the NDR peak intensity and peak area when the scan rate r is increased from 0.2 to 4.0 V/s shown in the inset of Fig. 3(a).

It is instructive to discuss why the current density J of the 1.0-μm-thick film (Fig. 3a) at a lower field of -1.0×10^5 V/cm is ~20 times that of the 100-nm-thick film at a higher field of -10×10^5 V/cm (Fig. 2a). Intuitively, one would expect a larger current density for a higher field. However, it should be noted that this expectation is mainly valid for steady-state charge transport in which the injected charges are immediately conducted and collected without being trapped in the conducting medium. Typical examples include space-charge limited transport and thermionic emission limited transport, in both of which, the current density increases as a monotonous function of increasing field [28]. In the case of Fig. 2a, however, the *JE* curves are dominated by dynamic and non-steady charge transport due to the formation of interface states (*IS*s) in the HOMO–LUMO gap. Here, the *IS*s can trap the injected holes, and the trapped charges are conductable only under certain resonant fields or voltages. The observation that the current density at -4.0×10^5 V/cm is 5 times that at -10×10^5 V/cm (Fig. 2a) is an indication that a higher field does not necessarily yield a larger current density when *IS*s-induced transient switching behavior is at work in carrier conduction. In Fig. 3a, the *JE* curves also contain the element of transient conduction as signified by the NDR peaks, and are further complicated by the involvement of H^+ ionic transport. Therefore, in the case of non-steady transport and charge trapping/releasing, the *JE* characteristic can significantly deviate from that predicated by rules based on steady-state transport. So it is possible that, under identical voltage, the 1.0-μm-thick film has a higher current density than that of the 100-nm-thick film. Moreover, the current of the 1.0-μm-thick film comprises significant amount of ionic component as evidenced by the -0.2×10^5 V/cm remnant field caused by ionic motion, while the one of the 100-nm-thick film only contains electronic current without the ionic component. This provides another source for the higher current density of the 1.0-μm-thick film shown in Fig. 3a.

It is important to clarify why H^+ ionic motion is present in the thick film, while it is absent in the thin film. In the case of the thick film shown in Fig. 3b, holes are injected from the Al electrode and are then trapped at the Al/film interface because they cannot tunnel throughout the large thickness of the film. The trapping of holes would raise the positive potential of the film in contact with the Al electrode. We believe that the hole-induced positive potential generates the driving force for the motion of positive H^+ ions to the other side of the film. In the thin film shown in Fig. 2, however, holes can conduct through the thin film by resonant tunneling during the voltage scan. So the hole-trapping-induced positive potential present in the thick film is absent in the thin film. Therefore, H^+ motion is not activated in the thin film due to the lack of the positive potential associated with the trapped holes.

It is observed that the NDR behavior is sensitive to photoexcitation, while the ionic motion is inert to it. As demonstrated in Fig. 4(a), without photon illumination, the *JE* curve collected for the 100-nm-thick PEDT:PSS film is characterized by NDR peaks in negative and positive voltage regions. When 405 nm photons was used to illuminate the PEDT:PSS film (see the inset of Fig. 4(a)), the NDR peaks were observed to disappear from the *JE* curves. In the case of 1.0-μm-thick films, the NDR peak is also significant quenched by photon illumination as shown in Fig. 4(b). We propose that the quenching of NDR in Fig. 4(a) is due to photoexcitation in PEDT:PSS, such that the *IS*s shown in Fig. 2(b) are occupied by excitons, and are therefore not available for hole injection and subsequent resonant tunneling. The energy of the 405 nm photon is $h\nu = 3.1$ eV, which is high enough to create excitons in PEDT:PSS whose band gap is $E_g = 1.5$ eV [1–3]. Similarly in Fig. 4(b), photon illumination saturates the *IS*s for hole injection and extraction, again causing the quenching of the NDR peak. The above observation provides a support to the interface states-facilitated resonant tunneling model proposed in Fig. 2(b), because such states are located in the band gap, and are usually very sensitive to photoexcitations. Note that in Fig. 4(b), light illumination does not affect the remnant field E_r: both of the *JE* curves exhibit the same E_r of 0.2×10^5 V/cm regardless of photon illumination. Therefore, it is clear that photoexcitation quenches the NDR behavior by saturating the interface states, while it does not affect the ionic motion which is a bulk property and is independent of interface electronic configurations.

The above thickness-dependent *JE* behavior is a common phenomenon generally observed for the metal/PEDT:PSS/metal sandwich configurations. In our experiments, we used other metals including Ag, Au, and graphite as electrodes for *IV* measurements, and obtained results

qualitatively similar to those shown in Figs. 2–4. In a control experiment, when one metal electrode is replaced by Si semiconductor (lightly B-doped, 0.1–0.3 S/cm) to form the metal/PEDT:PSS/Si device configuration, the NDR behavior disappears, and the *JE* curve follow the common monotonous dependence. Fig. 5(a) displays the typical *JE* curves collected for an ITO/100 nm PEDT:PSS/Si device. It can be seen that the *JE* curve exhibits rectification behavior that is characteristic of p-n junction formation in the device. When the device was illuminated by 405 nm light, photocurrent is generated especially in the negative ITO voltage region. Similar results were also obtained for 1.0-μm-thick PEDT:PSS films, and the *JE* curves obtained in this case showed no rate-dependence. The observation in Fig. 5(a) is in sharp contrast to that of Figs. 2–4, and indicates that the manifestation of the NDR peak is only associated with PEDT:PSS/metal interfaces. In Fig. 5(b–c), we compare the difference between PEDT:PSS/metal and PEDT:PSS/semiconductor (Si) interfaces. Since both PEDT:PSS and Si have band gaps, their interface is governed by the formation of a depletion layer with a height V_d and a width W_d. For such a p-n junction configuration, charge conduction is usually dominated by thermionic emission [28] over the depletion layer, and the corresponding *JE* curve is rectifying as shown in Fig. 5(a). In addition, the built-in voltage V_d is essential for the transfer for photoexcited carriers from PEDT:PSS to Si, thus leading to the formation of photocurrent under conditions of light illumination (see Fig. 5(a)). In the case of PEDT:PSS/metal interfaces, there is no depletion layer and thus no V_d to help draw photocarriers across the junction, therefore no photocurrent is observed in Fig. 4. Consequently, the photoexcited carriers stay in the interface states of PEDT:PSS, thus causing the quenching of NDR observed in Fig. 4. In Fig. 5(c), the continuous band structure of metal makes the metal → PEDT:PSS charge injection the dominant transport mechanism in the metal/PEDT:PSS/metal device. So the difference in electron and hole injection dynamics, and the presence of interface states which accommodate the injected charges, often work jointly to cause novel *JE* characteristics. Indeed, numerous previous results on the electric peculiarity of PEDT:PSS were also observed in metal/PEDT:PSS/metal device configurations [4,10,11,16]. For example, current peaks were observed for an ITO/40 nm PEDT:PSS/Au sandwich device, and the origin was attributed to the sequential oxidation and reduction (doping and de-doping) of PEDT in the voltage scan [4]. In other works, the faster electron injection rate relative to that of hole injection in a Au/PEDT:PSS/Au device leads to the formation of insulating states, which provides a basis for the operation of erasable read-only memory devices [10,11]. The novel observation of the Madelung potential effect [16] is the latest example of the complex electronic properties of the PEDT:PSS/metal interfaces. In our case, we interpret the NDR behaviors observed in Figs. 2–4 as a consequence of hole injection and resonance tunneling through interface states, and this phenomenon is again mainly associated with the PEDT:PSS/metal charge-injection interface.

It is instructive to discuss the drastic difference in *JE* characteristics between the 100-nm-thick (see Fig. 2) and 1.0-μm-thick (see Fig. 3) PEDT:PSS films. Here, hole resonant tunneling and NDR behavior dominate the charge conduction in the 100-nm-thick film, while ionic motion, remnant voltage formation, and hole extraction are the key features of the *JE* curves observed for the 1.0-μm-thick film. One tentative mechanism for the thickness dependence is related to the phase segregation of PEDT and PSS layers in PEDT:PSS films. There are reports [12–15] showing that hole-conducting PEDT

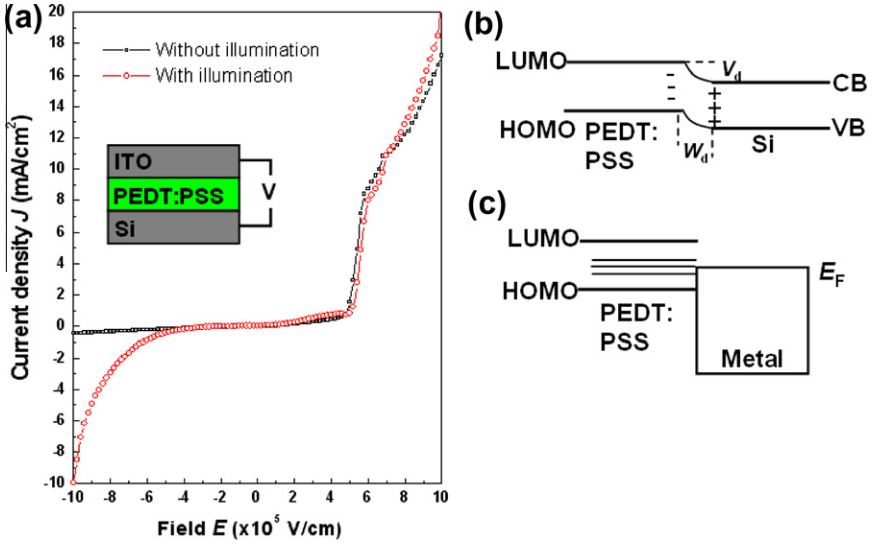

Fig. 5. (a) *JE* curves of an ITO/PEDT:PSS/Si device collected with and without 405 nm light illumination, respectively. The thickness of the PEDT:PSS films is ~100 nm, and the voltage scan rate is 1.0 V/s. Comparison of the different electronic configuration between the PEDT:PSS/Si (b) and PEDT:PSS/metal (c) interfaces.

segments are separated by hole-insulting PSS segments in a layer-by-layer fashion in the PEDT:PSS film. So hole hopping in the vertical direction is hindered by the alternative conducting/insulating layer arrangement, while it is not affected in the lateral direction because the in-plane hole transport can proceed through any of the conducting PEDT layers. On the basis of this, we propose that in the 100-nm-thick film, the degree of phase segregation is low, or the number of segregated layers is small, such that hole transport in the vertical direction is not affected. Therefore, when holes are injected into the interface resonant states, they can tunnel throughout the thickness of the film, thus leading to the observation of NDR peaks shown in Fig. 2(a). When the film thickness increases to 1.0 μm, the phase segregation would also increase, causing the formation of more alternating PEDT and PSS layers in the film. Consequently, holes cannot tunnel throughout the film due to the blockage by the insulting layers. Instead, the injected holes are trapped at the PEDT:PSS/metal interface, and are then extracted from the interface only when the polarity of the electrode voltage changes. At the same time, H^+ cationic motion is not influenced by such phase segregation because ions can move in both PEDT and PSS phases with a high mobility.[8,9] So in the 1.0-μm-thick film, when hole transport is blocked, hole are then trapped at the interface, and the trapping generates a positive potential. This positive potential in turn provides a driving force to facilitate H^+ ionic motion as discussed in Fig. 3b. Therefore, the thickness dependence is associated with the switching from hole-dominated conduction to cation-dominated conduction when the thickness of the PEDT:PSS film is increased.

In conclusion, we have presented some new charge conduction mechanisms based on hole resonant tunneling and ionic motion in PEDT:PSS films. Negative differential resistance peaks, asymmetrical ionic current, and remnant voltage are observed for PEDT:PSS films with different thickness. These distinct *JE* characteristics are an outcome of hole injection/tunneling, hole blockage by phase segregation, and cationic motion and relaxation. Our results highlight the decisive role of PEDT:PSS/metal interface and film thickness in the determination of charge transport mode, and is helpful in clarifying the diverse *JE* characteristics reported in the literature.

Acknowledgment

This work is supported by NUS Nanoscience and Nanotechnology Initiative (NUSNNI), National University of Singapore.

Appendix A. Supplementary data

Supplementary data associated with this article can be found, in the online version, at doi:10.1016/j.orgel.2010.05.013.

References

[1] L.B. Groenendaal, F. Jonas, D. Freitag, H. Pielartzik, J.R. Reynolds, Adv. Mater. 12 (2002) 481.
[2] H.W. Heuer, R. Wehrmann, S. Kirchmeyer, Adv. Funct. Mater. 12 (2002) 89.
[3] X. Crispin, S. Marciniak, W. Osikowicz, G. Zotti, A.W. Denier Van Der Gon, F. Louwet, M. Fahlman, L. Groenendaal, F. De Schryver, W.R. Salaneck, J. Polym. Sci Part B 2561 (2003) 41.
[4] S. Moller, C. Perlov, W. Jackson, C. Taussig, S.R. Forrest, Nature 426 (2003) 166.
[5] S. Ghosh, O. Inganas, Adv. Mater. 11 (1999) 1214.
[6] J. Joo, S.-K. Park, D.-S. Seo, S.-J. Lee, H.-S. Kim, K.-S. Ryu, T.-J. Lee, S.-H. Seo, C.-J. Lee, Adv. Funct. Mater. 15 (2005) 1465.
[7] A.V. Murugan, A.K. Viswanath, G. Campet, C.S. Gopinath, K. Vijayamohanan, Appl. Phys. Lett. 87 (2005) 243511.
[8] F.-C. Hsu, V.N. Prigodin, A.J. Epstein, Phys. Rev. B 74 (2006) 235219.
[9] A.J. Epstein, F.-C. Hsu, N.R. Chiou, V.N. Prigodin, Curr. Appl. Phys. 2 (2002) 339.
[10] P.-J. Chia, L.-L. Chua, S. Sivaramakrishnan, J.-M. Zhou, L.-H. Zhao, W.-S. Sim, Y.-C. Yeo, P.K.-H. Ho, Adv. Mater. 19 (2007) 4202.
[11] P.-J. Chia, Y.-C. Yeo, J.H. Burroughes, R.H. Friend, P.K.-H. Ho, Appl. Phys. Lett. 93 (2008) 033314.
[12] A.M. Nardes, M. Kemerink, R.A.J. Janssen, Phys. Rev. B 76 (2007) 085208.
[13] A.M. Nardes, M. Kemerink, R.A.J. Janssen, J.A.M. Bastiaansen, N.M.M. Kiggen, B.M.W. Langeveld, A.J.J.M. van Breemen, M.M. de Kok, Adv. Mater. 19 (2007) 1196.
[14] L.S.C. Pingree, B.A. Macleod, D.S. Ginger, J. Phys. Chem. C 112 (2008) 7922.
[15] C. Ionescu-Zanetti, A. Mechler, S.A. Carter, R. Lal, Adv. Mater. 16 (2004) 385.
[16] P.-J. Chia, S. Sivaramakrishnan, M. Zhou, R.-Q. Png, L.-L. Chua, R.H. Friend, P.K.H. Ho, Phys. Rev. Lett. 102 (2009) 096602.
[17] X.N. Xie, H.J. Chung, Z.J. Liu, S.W. Yang, C.H. Sow, A.T.S. Wee, Adv. Mater. 19 (2007) 2618.
[18] X.N. Xie, H.J. Chung, C.H. Sow, A.A. Bettiol, A.T.S. Wee, Adv. Mater. 17 (2005) 1386.
[19] X.N. Xie, H.J. Chung, C.H. Sow, A.T.S. Wee, Appl. Phys. Lett. 86 (2005) 023112.
[20] D.M. DeLongchamp, B.D. Vogt, C.M. Brooks, K. Kano, J. Obrzut, C.A. Richter, O.A. Kirillov, E.K. Lin, Langmuir 21 (2005) 11480.
[21] J. Chen, M.A. Reed, A.M. Rawlett, J.M. Tour, Science 286 (1999) 1550.
[22] L.P. Ma, S.M. Pyo, J.Y. Ouyang, Q.F. Yu, Y. Yang, Appl. Phys. Lett. 82 (2003) 1419.
[23] L.D. Bozano, B.W. Kean, M. Beinhoff, K.R. Carter, P.M. Rice, J.C. Scott, Adv. Funct. Mater. 15 (2005) 1993.
[24] X.N. Xie, J. Wang, K.P. Loh, A.T.S. Wee, Appl. Phys. Lett. 95 (2009) 203302.
[25] X.N. Xie, X. Gao, D. Qi, Y. Wang, J. Wang, K.P. Loh, A.T.S. Wee, Appl. Phys. Lett. 95 (2009) 063301.
[26] D.M. Talor, D. Morris, J.A. Cambridge, Appl. Phys. Lett. 85 (2004) 5266.
[27] X.N. Xie, S. Sivaramakrishnan, Q. Song, X. Gao, P.K.H. Ho, C.K. Ong, A.T.S. Wee, J. Phys. Chem. 113 (2009) 3683.
[28] S.M. Sze, Physics of Semiconductor Devices, John Wiley and Sons Inc., 1969 (Chapter 8).

$$k(E) = \beta_L \frac{3}{4\pi a^3} e^{-\frac{\Delta E}{kT}} \left(1 + b + \frac{b^2}{3} + \frac{b^3}{18} + \cdots\right) \quad (2)$$

where; $\beta_L = e(\mu_h + \mu_e)/\varepsilon_0\varepsilon$ is the Langevin recombination coefficient, μ_h, μ_e are hole and electron mobilities, respectively, ε is the dielectric constant, ΔE is the coulumbic binding energy of the geminate e–h pair, a is the initial e–h pair separation, $b = \frac{e^3 E}{8\pi\varepsilon_0\varepsilon(kT)^2}$.

Consequently, the photocurrent can be written as:

$$J_{ph}(E) = eG(E)L \quad (3)$$

where $G(E) = G_{\max}P(E)$ is the generation rate of free carriers.

2. Experiment

Sexithiophene photovoltaic cells used here are of the sandwich type in which an organic material is deposited between two metallic contacts with different work functions. Samples were made by evaporating a 150 nm thick -6T onto ITO coated glass followed by vacuum deposition of the top semi-transparent aluminum contact which determines the dimensions and the shape of our pixels (Fig. 1). *I–V* characterization of sandwich cells both in the dark and under illumination were performed using a HP 4140 pico-Amperemeter/DC voltage source. Samples were illuminated by a halogen–tungsten lamp.

In transient measurements we used a N_2 laser pulse of short duration (0.4 ns) at 337 nm delivering an energy of 10 μJ which corresponds to 2×10^{13} incident photons per incident pulse. The sample was illuminated through the Al side as shown in Fig. 1. The photocurrent was measured with a Tektronik TDS 620 Fast Oscilloscope.

3. Results and discussion

3.1. I–V characterization

Electric characterization of ITO/6T/Al samples showed a diode-like behavior with an on/off ratio of 10^3. Current versus voltage bias results in an asymmetric curve as shown in Fig. 2.

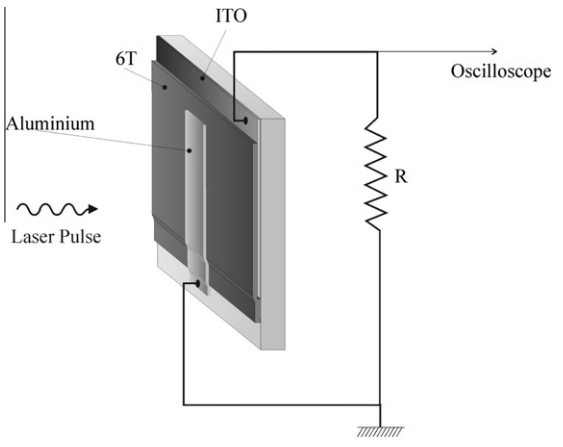

Fig. 1. Experimental setup for transient measurements.

This behavior is usually accounted for either by a classical Schottky-type contact between organic layer and the top aluminum electrode or by a Metal–Insulator–Metal (MIM) structure with the metal electrodes are of different work functions. The latter type is the most probable in organic materials because both low thickness (typically few hundreds of nanometers) and carrier density (in the range of 10^{-17} cm^{-3}) contribute to the so-called rigid band diagram which best describes the optoelectronic properties of sandwich-type organic diodes. In this approximation we assume that the intrinsic electric field is uniform over the organic active layer and its magnitude is proportional to work function difference of the two electrodes. Photovoltaic behavior of ITO/6T/Al is perceptible by comparison of both *I–V* curves in dark and under white light illumination. In the first case short circuit current is nearly 10^3 times lower than in the latter case. However in the region between 0 and V_{OC} the curve is far from the ideal case as can be seen in Fig. 2. Originally this behavior used to be accounted for by strong contact resistance which is known to be responsible for poor photovoltaic conversion efficiency, but this does not account for the inversed curvature of the *I–V* characteristic in the region 0–V_{OC}. To account for this behavior we plotted the effective photocurrent versus effective potential lying in the layer.

The effective electric field in the bulk results from the algebraic sum of the built-in field E_{bi} and the applied field E_a, hence the effective potential lying in the bulk is the difference between the applied voltage (V) and the built-in potential (V_{bi}). Fig. 3 shows effective photocurrent density ($J_{ph} = J_d - J_l$) obtained by subtracting the dark current (J_d) from recorded current under illumination (J_l) versus effective potential. In the case of pristine crystalline materials, which is our case, we assume that initial separation of the e–h pair a is constant, in contrast with polymers where one should consider a spatial distribution of separation distances [9].

Experimental data is fitted according to Eq. (3) for an initial electron–hole pair separation $a = 0.5$ nm and $\beta_L = 1.35 \times 10^{-5}$ cm^3 s^{-1} assuming an average mobility of 1.5×10^{-6} cm^2 V^{-1} s^{-1} and a dielectric constant $\varepsilon = 2$.

In sexithiophene the distance between two nearest neighbor molecules is 0.5 nm which is equal to the initial e–h pair separation. This would suggest that the CT exciton which is the precursor of the free carriers [7], lies between two neighboring molecules.

3.2. Transient measurements

Time-resolved response of ITO/6T/Al cell is shown in Fig. 4. The inset shows that photocurrent can not be fitted by a simple exponential decay, which indicates that the photocurrent is neither a trap controlled process nor a phonon-assisted one as is the case in Schottky-type porous silicon cells [10]. In turn this would suggest a different kinetic flow of free carriers.

Fig. 5 shows the absorption spectrum of the 150 nm thick film deposited on quartz. The absorption coefficient

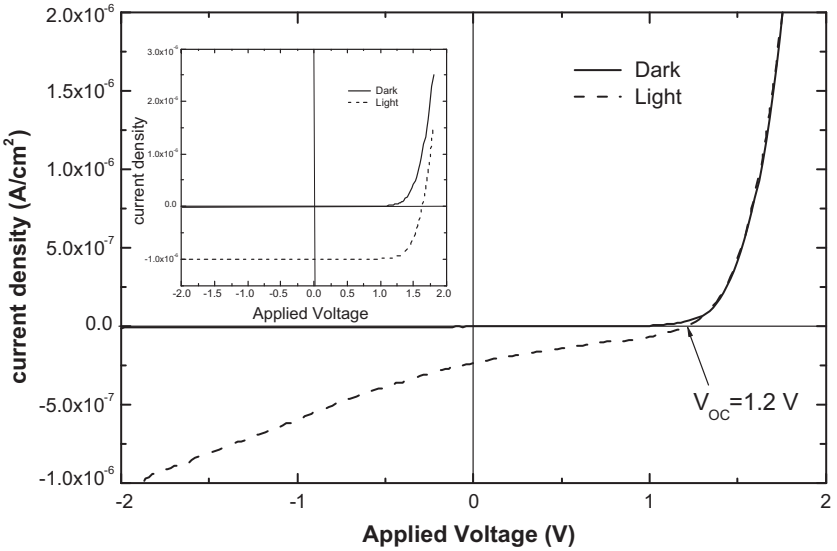

Fig. 2. Current versus applied voltage of ITO/6T/Al in dark and under illumination. The inset shows an ideal case according to which photocurrent is field independent.

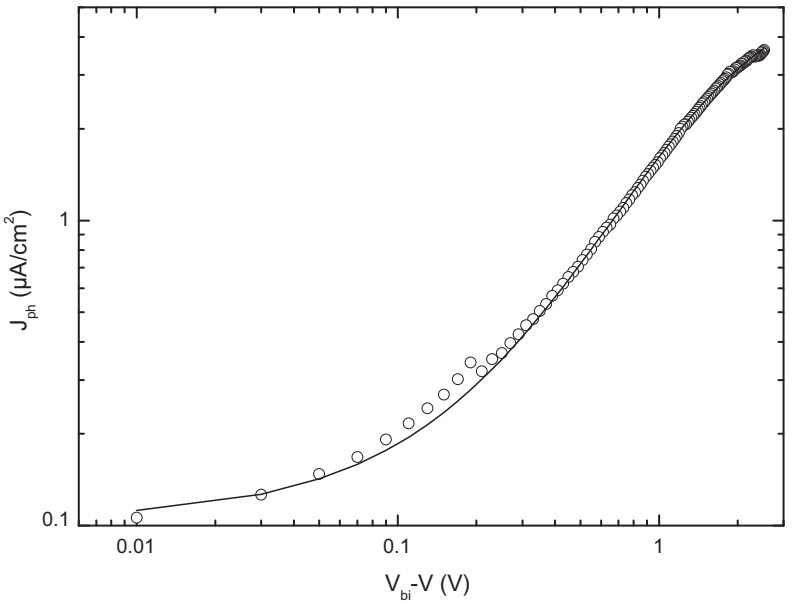

Fig. 3. Effective photocurrent versus effective potential. Experimental data (○) is well fitted (–) according to Eq. (3).

corresponding to the laser excitation wavelength is 10,421 cm^{-1}. Consequently, the penetration depth being assumed to the distance at which the incident light intensity is divided by e is about 900 nm which is by far greater than the thickness of the sample. Therefore one can assume to a very good approximation that the exciting laser pulse is absorbed within the whole sample thickness. This would suggest that photogenerated charge carriers arise from the bulk.

Transient photoconductivity in 6T single crystals revealed a bimolecular recombination process [11,12] which is described by the following equation.

$$\frac{\partial n_{ph}}{\partial t} = G - \beta n_{ph}^2 - \frac{n_{ph}}{\tau} \quad (4)$$

where β is the bimolecular recombination rate and τ is the charge carrier's lifetime. Comparing the scale over which we observe photocurrent decay (tens of microseconds) to pulse width (0.4 ns) one can reasonably make the assumption that carrier flow starts after the generation process is over. Consequently within this approximation we may consider $G = 0$ in Eq. (4)

$$\frac{\partial n_{ph}}{\partial t} = -\beta n_{ph}^2 - \frac{n_{ph}}{\tau} \quad (5)$$

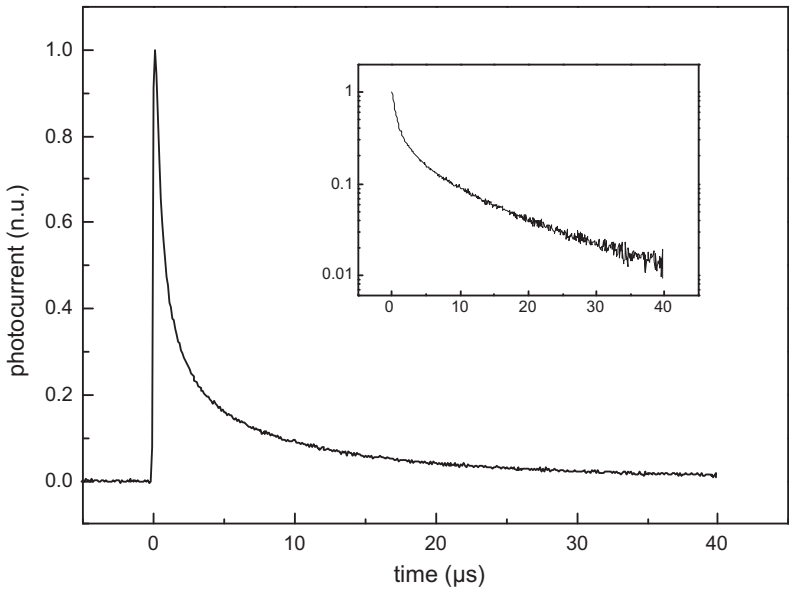

Fig. 4. Transient response of ITO/6T/Al cell illuminated by a 0.4 ns–370 nm laser pulse. The inset shows *y*-log scale of photocurrent decay.

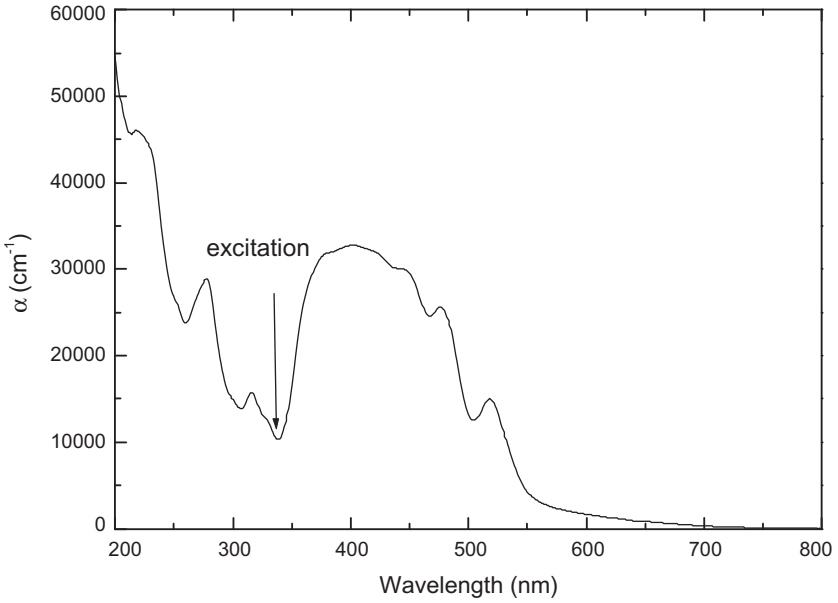

Fig. 5. Absorption spectrum of 6T(150 nm) deposited on quartz. The arow shows the excitation wavelength.

Eq. (5) is a Bernoulli-type differential equation the solution of which can be written as follows:

$$n_{\mathrm{ph}}(\mathrm{t}) = \frac{1}{\mathrm{A}\ \exp(\frac{\mathrm{t}}{\tau}) - B} \tag{6}$$

where: $A = \frac{1}{n_0} + \beta\tau$ and $B = -\beta\tau$, n_0 is the carrier density generated at $t = 0$. The transient photocurrent is directly proportional to carrier density $n(t)$ and may be fitted by this equation assuming that intrinsic electric field and mobility do not vary in time. Assuming that the built-in electric field E_{bi} is constant during carriers transit, transient photocurrent and photogenerated carrier density can be related by the following equation:

$$j_{ph}(t) = n_{ph}(t)\, e\, \mu_T\, E_{bi} \tag{7}$$

And rearranging gives:

$$n_{ph}(t) = \frac{j_{ph}(t)}{e\, \mu_T\, E_{bi}} \tag{8}$$

Fig. 6 shows a *y*-log-scale fit of transient photocurrent with a carrier lifetime $\tau = 30$ μs and a bimolecular rate constant β of 8.7×10^{-7} cm^3 s^{-1}. Assuming mobility of carriers

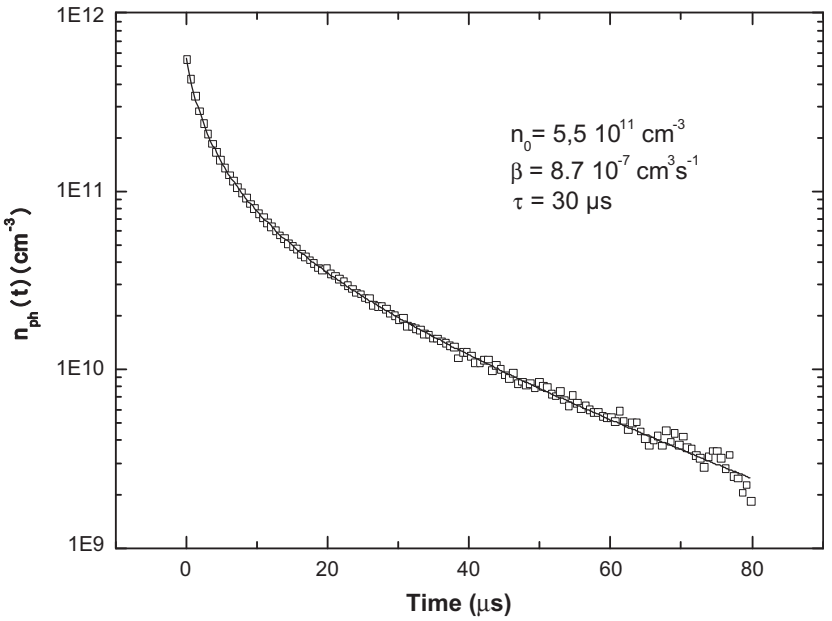

Fig. 6. *y*-Log scale fit of the density of photogenerated carriers decay using Eq. (6). The bimolecular model fits perfectly experimental results.

in polycrystalline sexithiophene thin films of 1.5×10^{-6} $cm^2\,V^{-1}\,s^{-1}$ [13] and static dielectric constant of 2 one can estimate the Langevin recombination coefficient $\beta_L = 1.35 \times 10^{-5}\ cm^3\,s^{-1}$.

According to Pivrikas et al. [14] the necessary condition to achieve conversion efficiency worthy of a solar cell is the inequality: $\mu\frac{\beta_L}{\beta} > 5 \times 10^{-3}\ cm^2\,V^{-1}\,s^{-1}$ where μ is the mobility of free carriers. In our case this condition is not fulfilled since: $\mu\frac{\beta_L}{\beta} \approx 2.25 \times 10^{-9} \ll 5 \times 10^{-3}\ cm^2\,V^{-1}\,s^{-1}$

The charge carrier transit time t_{tr} is related to the mobility by the following equation

$$t_{tr} = \frac{d}{\mu E}$$

The built-in electric field is related to the sample thickness by $E = \frac{\Delta\varphi}{d}$ where $\Delta\varphi = \varphi_{Al} - \varphi_{ITO} \approx 0.6$ eV φ_{Al} and φ_{ITO} being respectively the Aluminum and ITO work functions; $d = 1.5 \times 10^{-5}$ cm is the sample thickness and $\mu = 1.5 \times 10^{-6}\ cm^2\,V^{-1}\,s^{-1}$ is the charge carrier mobility, that is:

$$t_{tr} = \frac{d^2}{\mu\Delta\varphi} \approx 2.5 \times 10^{-4}\ s.$$

It turns out that only a small fraction of photogenerated carriers that can reach the electrodes contribute to the photocurrent so those carriers should not be located far from the electrodes than a distance d_0 which is deduced by equating the transit time t_{tr} to the lifetime τ that is

$$d_0 = \sqrt{\mu\tau\Delta\varphi} = 5\ nm.$$

4. Conclusions

The unsatisfactory performance of organic photovoltaic cells can be accounted for by two main factors. The first is attributed to the nature of photogenerated excitons that is the strong biding energy which prevents an efficient creation of free carriers in the bulk. This behavior is interpreted in terms of Braun–Onsager theory according to which the dissociation of geminate photocreated tightly bound pairs occurs with a quasi-vanishing probability. In the case of polycrystalline sexithiophene thin films the initial separation of geminate pairs is in the order of the nearest neighbor separation distance which is about 0.5 nm. The second is due to the conjunction between the low mobility of free carriers in organic materials and their short lifetime. Indeed the free photogenerated carriers in the bulk i.e. far from electrodes do not have enough time to reach the contacts and contribute to photocurrent.

Acknowledgment

This work was supported by DGRST/CNRS.

References

[1] G. Horowitz, F. Garnier, A. Yassar, R. Hajlaoui, F. Kouki, Adv. Mater. 8 (1996) 52–56.
[2] Soichi Uchida, Jiangeng Xue, Barry P. Rand, Stephen R. Forrest, Appl. Phys. Lett. 84 (2004) 4218–4220.
[3] Jiangeng Xue, Soichi Uchida, Barry P. Rand, Stephen R. Forrest, Appl. Phys. Lett. 84 (2004) 3013–3015.
[4] Marisol Reyes-Reyes, Kyungkon Kim, David L. Carroll, Appl. Phys. Lett. 87 (2005) 083506.
[5] L. Onsager, J. Chem Phys. 2 (1934) 599.
[6] Charles L. Braun, J. Chem. Phys. 80 (9) (1984) 4157.
[7] S. Barth, H. Bässler, H. Rost, H.H. Hörhold, Phys. Rev. B 56 (7) (1997) 3844.
[8] V.I. Arkhipov, H. Bässler, Phys. Stat. Sol. (a) 201 (6) (2004) 1152–1187.
[9] V.D. Mihailetchi, L.J.A. Koster, J.C. Hummelen, P.W.M. Blom, Phys. Rev. Lett. 93 (2004) 21–216601.

[10] Shiyou Zhao, Xingze Lu, Fulong Zhang, Hongbing Jiang, Wencheng Wang, Xiaoyuan Ou, Xun Wang, J. Phys. D: Appl. Phys. 29 (1996) 1326.
[11] Gilles Horowitz, Fayçal Kouki, Pierre Valat, Philippe Delannoy, Joseph Roussel, Phys. Rev. B 59 (16) (1999) 10651.
[12] Y.Q. Shen, H. Lindenberger, H. Bleier, S. Roth, Springer Series in Solid-State Science, vol. 91, Springer-Verlag Berlin, Heidelberg, 1989.
[13] H. Bedis Ouerghemmi, F. Kouki, P. Lang, H. Ben Ouada, H. Bouchriha, Synt. Met. 159 (2009) 551–555.
[14] A. Pivrikas, J. Juska, A.J. Mozer, M. Scharber, K. Arlauskas, N.S. Sariciftci, H. Stubb, R. Österbacka, Phys. Rev. Lett. 94 (2005) 176806.

synthesized in 1996 have remained unchanged over time [12,13]. PDPV, whose chemical structure is reported in Fig. 1, consists of a poly(para-biphenylene vinylene) chain where the hydrogen atoms on the vinylene double-bond are substituted with phenyl rings. This chemical modification has been shown to increase the photostability of this polymer, slowing down the photo-oxidative degradation processes [14]. Other interesting chemical and photophysical properties result from the replacement of the vinylene hydrogens by phenyls, such as solubility in a range of common organic solvents, relatively high solid-state PL quantum efficiency (~60%) due to increased conformational entropy in the solid state that reduces π–π interactions and consequent detrimental aggregation [15,16]. Importantly, a large Stokes' shift (~1.14 eV) between the absorption and the emission band is observed in this compound, due to conformational relaxation in the excited state of the substituted vinylene unit allowed in this glassy polymer [15,17]. This particular feature has been recently applied for the production of white-emitting LEDs based on non-resonant polymer blends [18].

In the following, we report the optical properties of solid films and LEDs incorporating an active layer of PDPV, fabricated with a similar batch of PDPV to the one that was used in similar studies published immediately following the synthesis in 1996 [12]. The synthesis of PVPD was reported in 1983 [19]. Subsequently it was shown that this sample has a 50:50 distribution of *cis* and *trans* vinylenes and can be regarded as a polymeric derivative of tetraphenylethene, it has a disordered structure and the phenyl units are twisted with respect to the planes of the vinylenes [15]. The use of this sample allows a direct comparison of the photophysical and EL properties of PDPV. We present CW and time-resolved PL along with EL and current–voltage–luminance (IVL) response of LEDs whose characteristics are comparable to those reported for a similar batch of PDPV 13 years ago.

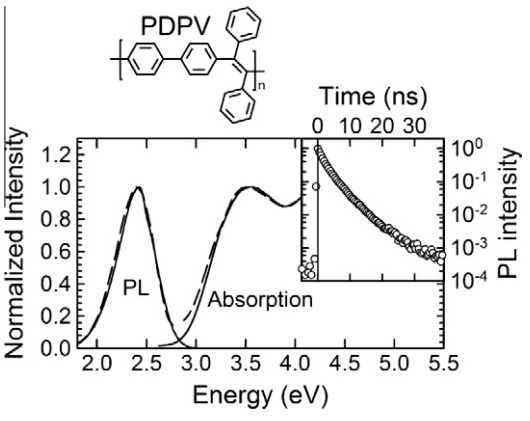

Fig. 1. Top: Chemical structure of poly(4,4'-diphenylene diphenylvinylene); Bottom panel: optical absorption and PL spectrum of a spin cast film of PDPV on fused silica (solid line). The absorption and PL spectra for solid films of a similar batch of PDPV from Cacialli et al. are reported as dashed lines [12]; Inset: PL decay profile at 2.39 eV for a spin cast film of PDPV excited at 3.30 eV.

2. Experimental details

The synthesis of the materials is described in Ref. [19]. The material was stored in powder form, in the dark (inside a glass transparent vial which was in turn kept inside a cardboard container that prevented light from reaching the material), in air, and at room temperature. Optical absorption spectra were obtained using an Agilent 8453 spectrophotometer. CW and time-resolved PL measurements were carried out using a ps-pulsed diode laser (pulse duration = 40 ps, 371 nm) as excitation source and detecting the PL with a photomultiplier coupled to a monochromator and a time-correlated single-photon counting unit (time resolution ~150 ps). The PL efficiency of solid films was measured in a N_2-saturated integrating sphere using the same excitation source. LEDs were fabricated by cleaning ITO covered soda-lime glass in acetone, isopropanol and sequentially in O_2-plasma [20,21], followed by spin coating of the hole-injecting layer poly(3,4-ethylenedioxythiophene):poly(styrenesulfonic acid) (PEDOT:PSS) and PDPV. The cathode consisted of 50 nm Ca capped with 150 nm of Al. A Keithley 2400 sourcemeter was used to apply the voltage and measure the current, while a calibrated Si photodiode, coupled to a Keithley 2000 multimeter through a preamplifier, measured the light output. The electroluminescence (EL) spectra were obtained by an Andor Shamrock spectrograph coupled with an Andor Newton CCD unit cooled to −50 °C.

3. Results and discussion

In Fig. 1, we present the optical absorption and PL spectrum for solid films of PDPV on spectrosil (solid curves). The characteristic Stokes' shift of about 1.15 eV can be observed between the first absorption band (3.44 eV) and the PL spectrum (centred at 2.39 eV). Our data coincide with the results reported in 1996 (dashed lines) [12]. In both cases, the PL spectrum is featureless and shows a full width at half-maximum of about 0.5 eV due to structural disorder in solid PDPV films [13]. The shape of the room temperature PL spectrum does not show vibronic structure, and appears to be essentially featureless, suggesting that decay is not mono-molecular in nature. In fact, we find that the PL decay (excited at 3.30 eV, and collected at 2.39 eV) of PDPV films follows a multi-exponential kinetics, with an effective lifetime of 2.2 ns (as defined from the time at which the PL intensity decays by a factor $1/e$) [22]. The PL efficiency is measured to be 60 ± 6% [23], which is in essential agreement, or even slightly better than previously reported [12].

Fig. 2a shows the current–voltage–luminance (IVL) characteristics of PEDOT:PSS/PDPV/Ca LEDs. Luminous turn-on (defined at 0.01 cd/m^2) occurs at 5.1 V (although the characteristics only deviate from zero at ~6 V on a linear-scale plot) and a luminance above 800 cd/m^2 is achieved at 10 V. This is a significant improvement compared to the operating voltage of 30 V or so that was required to obtain a similar luminance for the multilayer devices reported in 1996 [12]. We relate this increase in light output to improved LED design, in particular to better

hole-injection by the PEDOT:PSS hole-injection layer, and to the absence of an intermediate polyvinylcarbazole (PVK) film, as already noted in reference [24].

The inset of Fig. 2a shows the EL spectrum of our LEDs and that of the ITO/PPV/PVK/PDPV/Ca LED from Ref. [12]. We find that the shape of the EL does not change over the range of voltage investigated, i.e. 5–15 V. In addition, there is again a lack of vibronic structure that is entirely analogous to what observed for the PL. A similar shape is observed for the low energy portion of the emission between the two spectra, with only a very minor blue shift, which we consider is due to differences in the device architecture and the expected influence of interference effects. Note, in fact, that the present structures do not include the PPV and PVK layers (and related refractive indices mismatch), as in the "1996 LEDs". This has implications for both the partial reflections and subsequent constructive/destructive interference of the light generated within the active layer, as well as for the location of the recombination region as a function of the distance from the electrodes, and again on the particular nature of the ensuing interference effects [25].

The more significant difference in the blue tail of the spectra in the "1996 LEDs" is due to re-absorption of the emitted photons by the PPV hole-injection layer in those devices [12].

The external quantum efficiency (EQE) as a function of the current density is reported in Fig. 2b for our devices.

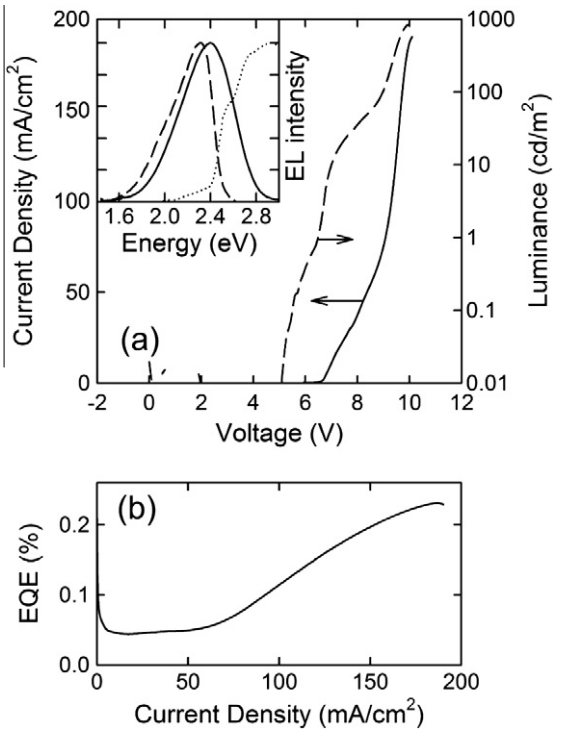

Fig. 2. (a) Current density (solid line) and luminance (dashed line) as a function of voltage for a PEDOT:PSS/PDPV/Ca LED. Inset: EL spectrum for the same device (solid line), and the extracted EL spectrum for the ITO/PPV/PVK/PDPV/Ca LED (dashed line) reported by Cacialli et al. [12]; (b) External quantum efficiency (EQE) as a function of current density corresponding to the electrical response in (a).

A maximum EQE of 0.23% is obtained for the PEDOT:PSS/PDPV/Ca. This agrees remarkably well with the maximum internal quantum efficiency (IQE) of 1.2% reported in 1996 [12], which had been calculated according to the formula IQE = $2 \times n^2 \times$ EQE, with $n = 1.5$ [26–28].

4. Conclusions

In summary, we have shown that the optical and electroluminescence properties of a polyphenylene vinylene derivative (PDPV) are stable over a period of time of at least one decade. As a result, we are able to produce LEDs with similar efficiencies to those reported soon after the synthesis of the polymer, but with higher light output and lowered turn-on voltage due to improved LED design. We conclude that lack of saturated aliphatic C–H bonds adjacent to either an aromatic ring or an ether oxygen, that are notoriously susceptible to oxidation, in addition to storage in dark, to avoid both photo-doping and photo-oxidation effects [29], offer effective protection against degradation.

Acknowledgements

We thank the EC (EU-contract: MRTN-CT-2006-036040: THREADMILL), the EPSRC and the ESF EUROCORES Programme SONS with supplementary funds from EPSRC, the EC Sixth Framework Programme, under contract N. ERAS-CT-2003-980409 and the EC Seventh Framework Programme (FP7/2007-2013) under grant agreement N. 212311 (ONE-P).

References

[1] R.H. Friend, R.W. Gymer, A.B. Holmes, J.H. Burroughes, R.N. Marks, C. Taliani, D.D.C. Bradley, D.A. dos Santos, J.L. Brédas, M. Logdlund, W.R. Salaneck, Nature 397 (1999) 121–128.
[2] L. Bürgi, T.J. Richards, R.H. Friend, H. Sirringhaus, J. Appl. Phys. 94 (2003) 6129–6137.
[3] H. Hoppe, N.S. Sariciftci, J. Mater. Res. 19 (2004) 1924–1945.
[4] G. Heliotis, D.D.C. Bradley, G.A. Turnbull, I.D.W. Samuel, Appl. Phys. Lett. 81 (2002) 415–417.
[5] D.T. McQuade, A.E. Pullen, T.M. Swager, Chem. Rev. 100 (2000) 2537–2574.
[6] F.E. Oddy, S. Brovelli, M.T. Stone, E.J.F. Klotz, F. Cacialli, H.L. Anderson, J. Mater. Chem. 19 (2009) 2846–2852.
[7] N. Dam, R.D. Scurlock, B.J. Wang, L.C. Ma, M. Sundahl, P.R. Ogilby, Chem. Mater. 11 (1999) 1302–1305.
[8] G.D. Hale, S.J. Oldenburg, N.J. Halas, Appl. Phys. Lett. 71 (1997) 1483–1485.
[9] A.P. Kulkarni, Y. Zhu, S.A. Jenekhe, Macromolecules 41 (2008) 339–345.
[10] M. Schaer, F. Nuesch, D. Berner, W. Leo, L. Zuppiroli, Adv. Funct. Mater. 11 (2001) 116–121.
[11] R.Q. Png, P.J. Chia, S. Sivaramakrishnan, L.Y. Wong, M. Zhou, L.L. Chua, P.K.H. Ho, Appl. Phys. Lett. 91 (2007) 3.
[12] F. Cacialli, R.H. Friend, N. Haylett, R. Daik, W.J. Feast, D.A.D. Santos, J.L. Brédas, Appl. Phys. Lett. 69 (1996) 3794–3796.
[13] W.J. Feast, I.S. Millichamp, R.H. Friend, M.E. Horton, D. Phillips, S.D.D.V. Rughooputh, G. Rumbles, Synth. Met. 10 (1985) 181–191.
[14] A.T.H. Koch, N.T. Harrison, N. Haylett, R. Daik, W.J. Feast, R.H. Friend, Synth. Met. 100 (1999) 113–122.
[15] W.J. Feast, F. Cacialli, A.T.H. Koch, R. Daik, C. Lartigau, R.H. Friend, D. Beljonne, J.L. Brédas, J. Mater. Chem. 17 (2007) 907–912.
[16] A. Petrozza, S. Brovelli, J.J. Michels, H.L. Anderson, R.H. Friend, C. Silva, F. Cacialli, Adv. Mater. 20 (2008) 3218.
[17] F. Cacialli, R. Daik, W.J. Feast, R.H. Friend, C. Lartigau, Opt. Mater. 12 (1999) 315–319.

[18] S. Brovelli, H. Guan, G. Winroth, O. Fenwick, F. Di Stasio, R. Daik, W.J. Feast, F. Meinardi, F. Cacialli, Appl. Phys. Lett. 96 (2010) 213301–213303.
[19] W.J. Feast, I.S. Millichamp, Polym. Commun. 24 (1983) 102.
[20] J.S. Kim, R.H. Friend, F. Cacialli, J. Appl. Phys. 86 (1999) 2774–2778.
[21] J.-S. Kim, F. Cacialli, R. Friend, Thin Solid Films 445 (2003) 358–366.
[22] M.H. Chang, M.J. Frampton, H.L. Anderson, L.M. Herz, Appl. Phys. Lett. 89 (2006) 232110.
[23] This value of PL efficiency is higher than previously reported (45 ± 5%). However, the discrepancy is only 4%, once the error bars are considered, and is well within the scatter that is generally observed between different batches of the same material. This may depend, for example on a different cis–trans ratio (not precisely controlled in this material), which has a significant influence, as demonstrated for a similar, although different material [15]. We also note that the results are not entirely comparable since a different laser source was used here.
[24] T.M. Brown, J.S. Kim, R.H. Friend, F. Cacialli, R. Daik, W.J. Feast, Appl. Phys. Lett. 75 (1999) 1679–1681.
[25] F. Cacialli, S.E. Burns, H. Becker, Opt. Mater. 9 (1998) 168–172.
[26] N.C. Greenham, R.H. Friend, D.D.C. Bradley, Adv. Mater. 6 (1994) 491–494.
[27] J.S. Kim, P.K.H. Ho, N.C. Greenham, R.H. Friend, J. Appl. Phys. 88 (2000) 1073–1081.
[28] Please note that although a more refined model for calculation of the outcoupling has been proposed in 2000 by Kim [21], reference to the older work has been necessary to establish a meaningful comparison.
[29] J.-M. Zhuo, L.-H. Zhao, R.Q. Png, L.-Y. Wong, P.J. Chia, J.-C. Tang, S. Sivaramakrishnan, M. Zhou, E.C.-W. Ou, S.-J. Chua, W.-S. Sim, L.L. Chua, P.K.H. Ho, Adv. Mater. 21 (2009) 4747–4752.

improving the power conversion efficiency for small laboratory cells [19–21] through optimization of materials and the protocol used for preparation.

Titanium dioxide has been extensively employed as photoresponse material [22]. Particularly, TiO_2 in the form of nanotube is expected to have some improved properties for photoresponse applications compared with colloidal or other forms of titania [23,24]. Titania nanotubes (TiO_2NTs) have been extensively investigated due to their distinguishing feature of one-dimension nanostructure nature for applications in the areas of photocatalysis and solar cells [25]. Some efforts have been paid to modify TiO_2 nanotubes or explore new TiO_2 nanotubes-based systems [26–29]. One of the promising approaches is based on the association of TiO_2 nanotubes with other semiconductors. These nanocomposites can provide strong coupling effects, which are distinctive from the primary nanomaterials [30]. The obtained materials with heterostructure exhibit improved physical and chemical properties over their single-component counterparts [31].

There were many literature about solar cells based on hybrid of polymers and inorganic [32–37]. However, there is little report about nanocomposites based on polythiophene and TiO_2 nanotubes.

In this paper, amorphous titania nanotubes with diameters between 20 and 30 nm were successfully synthesized by hydrothermal method. Poly(3-octylthiophene) and titania nanotubes were combined to form a new organic/inorganic material by situ-chemical method. Chemical interaction in the material was found by X-ray photoelectron spectroscopy, infrared spectrum and X-ray diffraction. Results from UV–vis spectra, fluorescence spectra and cyclic voltammetry curves indicate that P3OT/TiO_2NTs nanocomposite is a new kind of p-n type promising material with excellent performance in photoelectric applications. Solar cell was sensitized by P3OT/TiO_2NTs. A solar-to-electric energy conversion efficiency of 0.593% was attained with the system.

2. Experiments details

2.1. Synthesis of poly(3-octylthiophene)/titania nanotubes composite

2.1.1. Preparation of titania nanotubes by hydrothermal method

TiO_2 nanotubes were prepared by hydrothermal method. 6 g TiO_2 as precursor was added to 10 M NaOH, stirring vigorously at ambient temperature for 24 h. The suspension liquid was further transferred into the stainless steel reactor with Teflon substrate. The reactor was placed in the oven at 120 °C. After maintaining for 72 h, the solution was filtered by centrifugation and washed to neutral. The alcogel was added to 0.1 M hydrochloric acid, stirring vigorously at ambient temperature for 5 h. The solution was filtered by centrifugation and washed to neutral. The water in the sol was replaced by absolute ethanol. The alcogel obtained was transferred into a crucible and dried at room temperature. The powders of TiO_2 nanotubes were finally prepared.

2.1.2. Synthesis of poly(3-octylthiophene)

The conducting poly(3-octylthiophene) was synthesized with Fe(III) as catalyst according to Ref. [38].

2.1.3. Synthesis of poly(3-octylthiophene)/titania nanotubes composite

8 ml chloroform, 0.2 g 3-octylthiophene, 0.2 g TiO_2NTs prepared above were added into 100 ml flask, ultrasonic dispersing for about 15 min. Some amount of $FeCl_3$ was dissolved in chloroform, and then gradually dropped into the system. After above dropping, the system reacted stirring with the protection of high-purity nitrogen for 3 h at 0 °C. Product was slowly added into methanol followed by a settlement and filtration. Then they were washed by methanol in a soxhlet extraction for 20 h. P3OT/TiO_2NTs nanocomposite powder was finally prepared by vacuum drying at room temperature.

Dissolve 0.01 g P3OT/TiO_2NTs in 2 ml isopropyl alcohol, drop the liquid obtained above evenly on a clean quartz glass and ITO conductive glass. Then red-brown P3OT/TiO_2NTs nanocomposite films were prepared by vacuum drying method.

2.1.4. Solar cell sensitized by P3OT/TiO_2NTs

The solar cell was prepared according to Ref. [39]. Dissolve 0.01 g TiO_2NTs in 2 ml ethanol, drop the liquid obtained above evenly on a clean FTO substrate, meanwhile suffered spinning by a uniform plastic machine at the rate of 3000 r/min for 20 s. After drying at room temperature, the anode was sensitized by P3OT P3OT/Precursor and P3OT/TiO_2NTs isopropyl alcohol solution, respectively. H_2PtCl_6 was evenly dropped on another FTO substrate, calcining at 380 °C for 30 min to prepare Pt electrode, which packaged with the sensitized anode. And then inject electrolyte and seal. The sensitized solar cells were finally prepared.

2.2. Measurements

Transmission electron microscope (TEM) and scanning electron microscope (SEM) measurements were performed on a HITACHI-800. X-ray diffraction (XRD) measurements were performed using a Shimadzu HR6000X (Cu target X tube, voltage 40.0 kV, current 30.0 mA). Infrared spectra (IR) were recorded by a prestige-21IR spectrophotometer with KBr pellet. X-ray photoelectron spectroscopy (XPS) analyses were conducted by ESCALAB 250, testing the electronic binding energy of the samples. UV–vis spectra were measured using Hitachi U-3010 spectrophotometer. The Fluorescence spectra were measured by Hitachi F-7000 spectroluorophotometer at room temperature. Cyclic voltammetry measurements were carried out with the Potentiostiostat/Galvanostat (EG&G PAR Model 283). The counter electrode was platinum and the reference electrode was non-aqueous Ag/Ag^+. The CV curves were record in acetonitrile with 0.1 M $LiClO_4$ at a scan rate of 50 mV/s. Before using, the solution was insufflated with N_2 for 30 min. Current–voltage (I–V) measurements were taken in air at room temperature (298 K) using a Keithley 236 high current source power meter under white-light illumination from a 500 W xenon lamp. The light intensity was

about 100 mW/cm^2 on the sample surfaces measured by a photodetector. To measure the decay, the short-circuit current (J_{SC}) and open-circuit voltage (V_{OC}) as a function of the illumination time were recorded.

3. Results and discussion

3.1. TEM and SEM measurements of TiO_2NTs

Fig. 1(a) and (b) demonstrated TEM and SEM results of TiO_2NTs separately. The capillary tubes can be seen from the Fig. 1(a) clearly. It proved that both open ends titania nanotubes with internal diameters between 25 and 30 nm and tube wall thickness of 5–8 nm were successfully synthesized. The straight tubes with complete morphology and external diameter 30–40 nm can be seen from the Fig. 1(b) clearly. In addition, the titania nanotubes have excellent crystal form and a high conversion rate. Layered structure can be seen clearly from the end of the nanotubes by zooming in multiples of electron microscopy. The results suggested that the synthesis of titania nanotubes was controlled by "curl" reaction mechanism [40], that is, the precursor curl for multi-walled nanotubes under high-temperature and alkaline hydrothermal conditions.

3.2. XRD Characterization of TiO_2NTs

The XRD patterns for the precursor TiO_2 and TiO_2NTs are shown in Fig. 2. In XRD patterns of precursor TiO_2 particles, the peaks at 25.40°, 37.92°, 48.12°, 53.96°, 55.16°, 62.72°, 68.80°, 70.36° and 75.08° are assigned to the (101), (004), (200), (105), (106), (213), (116), (107) and (215) lattice planes, which are attributed to the signals of the anatase phase. It can be calculated that the average TiO_2 particle is 41 nm by Scherrer formula. After concentrated alkali treatment, the lower diffraction peak intensities of product indicated that the crystallinity decreased. X-ray diffraction patterns of TiO_2NTs have also changed. There are no obvious diffraction peaks of TiO_2 except for Ti-based diffraction peaks (24.32° and 48.44°). This indicated that the TiO_2NTs are amorphous TiO_2. The strong diffraction peak in the 9.6° (<10°) is characteristic peaks of pore structure. (200) lattice plane indicated that the layer spacing of TiO_2NTs is 4.19 nm. TiO_2NTs are multi-layer tube, each single-layer equivalent to the "one-TiO_2 molecular layer" thickness, a lattice structure of the three-dimensional extension cannot form between layers, so TiO_2NTs are amorphous. In the hydrothermal process and under the high-temperature, high pressure and alkalic condition, TiO_2 particles were peeled off into thin slices along the (010) crystal face. TiO_2 particles of the smaller size are greatly influenced by environmental. The original surface of anatase crystal structure subject to relatively large extent of the damage. The ordered state between crystal particles suffer from damage, the amorphous structure of TiO_2NTs is formed.

3.3. IR results of TiO_2NTs

The IR spectra for the precursor TiO_2 and TiO_2NTs are shown in Fig. 3. The peak at about 3410 cm^{-1} belongs to the stretching vibration of –OH groups in water, which is physically adsorbed on the surface of TiO_2. The bending vibration occurs at 1636 cm^{-1}. The weak peak at about 1500 cm^{-1}corresponds to Ti–OH characteristic absorption. In the IR spectra for the precursor TiO_2, there is the characteristic absorption band of Ti–O–Ti in the 440–780 cm^{-1} region [41]. It is wide and flat. But for TiO_2NTs, the vibration band at about 666.2 cm^{-1} becomes acromion and the vibration band at about 496.5 cm^{-1} becomes sharp visibly. This implies that the Ti–O vibrational frequencies become smaller after the formation of tube and Ti–O bond length changes in a certain extent. In addition, the fine structure disappears and the band becomes broad after the formation of tube. This is due to quantum size effect and surface effect of nano-particles. This shows that the shape size of TiO_2NTs is smaller.

3.4. XPS Characterization of TiO_2NTs

Fig. 4a–e is the high-resolution XPS of the precursor TiO_2 and TiO_2NTs.

In the TiO_2NTs sample (Fig. 4a), the XPS shows Ti, C and O. The impurities, Na and Cl were not evident in the sample. The electronic binding energy of the Ti2p in the

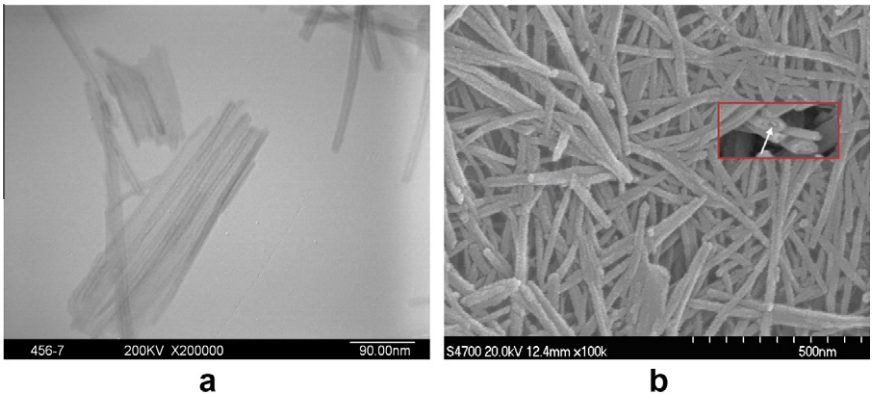

Fig. 1. (a) TEM patterns of TiO_2NTs. (b) SEM patterns of TiO_2NTs.

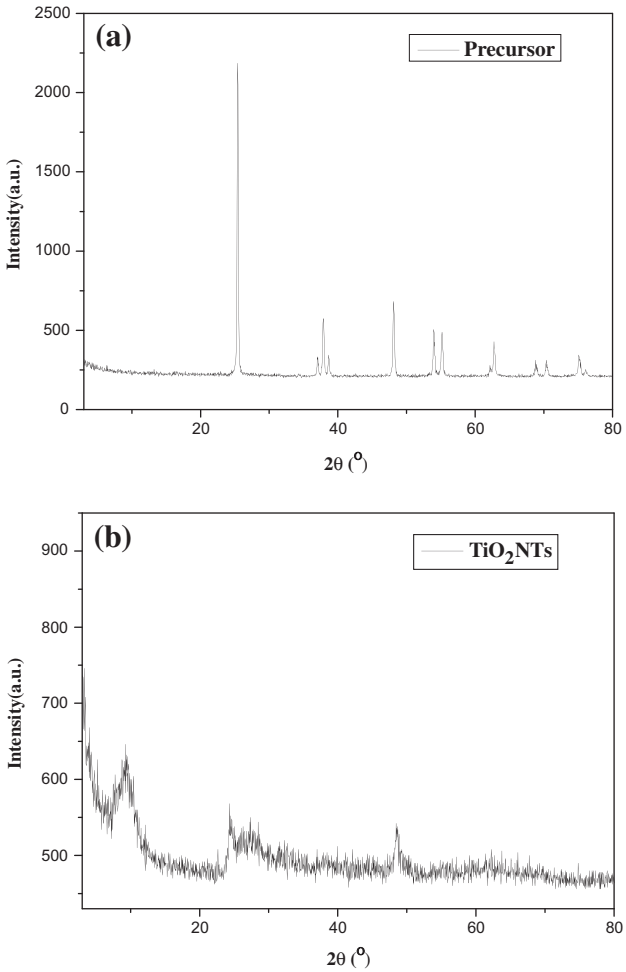

Fig. 2. XRD patterns of Precursor and TiO_2NTs.

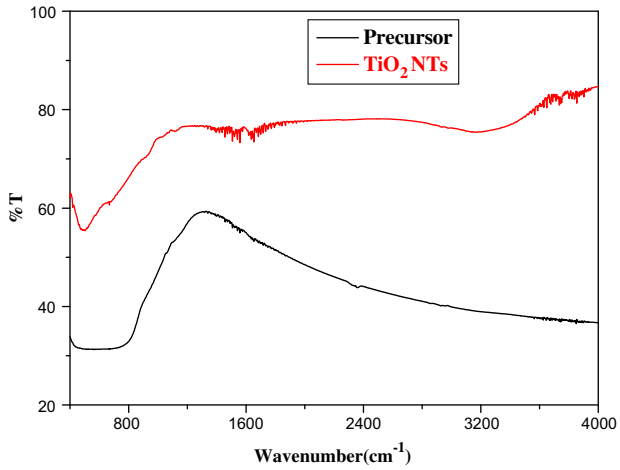

Fig. 3. FT-IR spectra of Precursor and TiO_2NTs.

precursor TiO_2 is consistent with the data found in Ref. [42]. It is seen that Ti in TiO_2 is mainly tetravalent in Ti–O. Fig. 4b shows the narrow scans for Ti2p peaks located at 464.45 eV (Ti $2p_{1/2}$) and 458.71 eV (Ti $2p_{3/2}$) of the TiO_2NTs. Compared to precursor TiO_2, a low binding energy-shift has taken place. This indicates that the

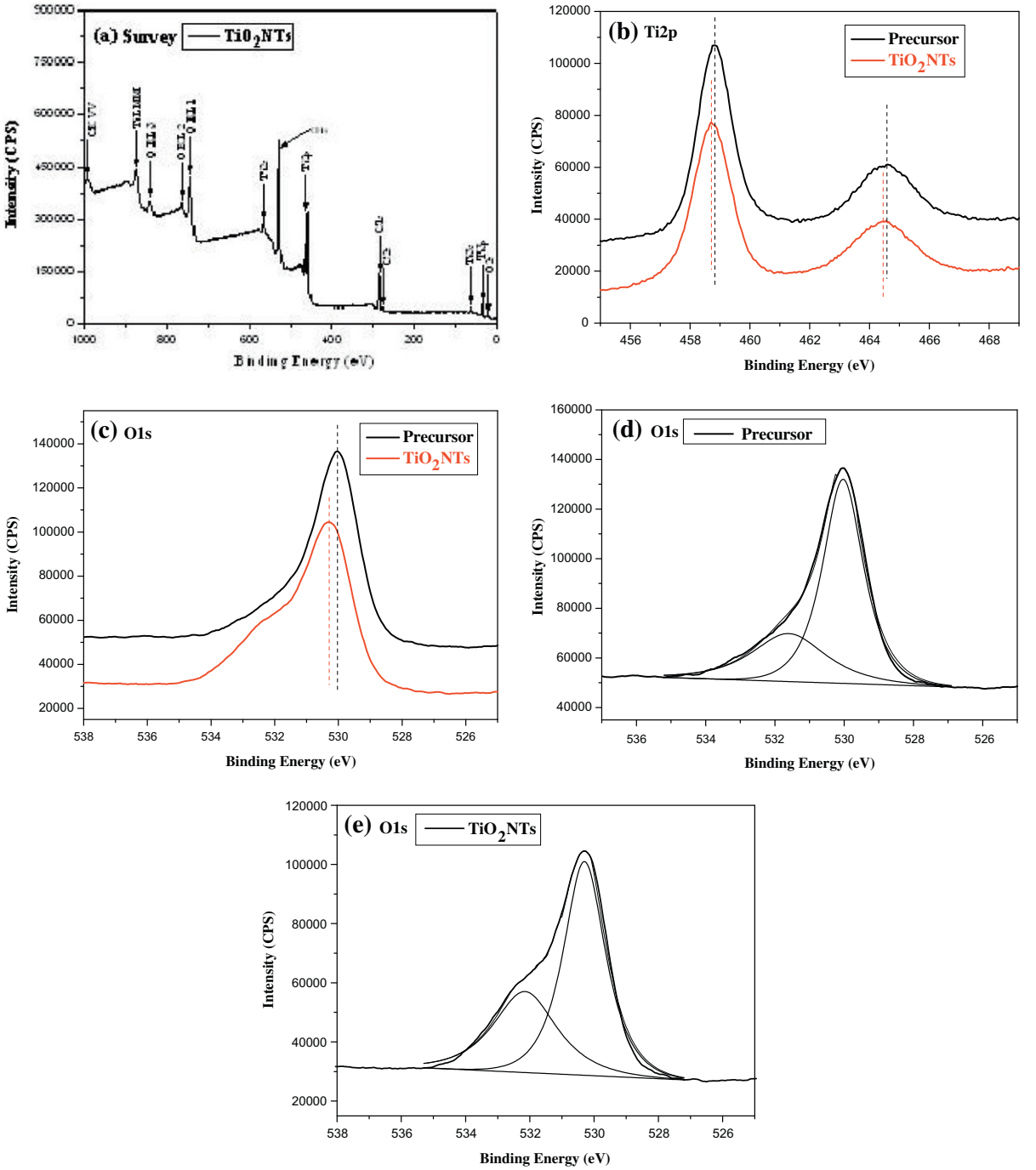

Fig. 4. XPS spectra of Precursor and TiO_2NTs.

chemical environment around Ti atom changes after formation of the tube. The electronic binding energy of the O1s in the precursor TiO_2 is consistent with the data found in Ref. [42]. It is seen that O in TiO_2 is mainly negative bivalent in Ti–O. Fig. 4c shows the narrow scans for O1s peaks located at 530.30 eV of the TiO_2NTs. Compared to precursor TiO_2, a high binding energy-shift has taken place. This indicates that the chemical environment around O atom changes after formation of the tube.

Two oxygen peaks at 531.60 eV and 530.03 eV were found in the spectra of precursor TiO_2 after curve fitting (see Fig. 4d). The former is attributed to anatase Ti–O of common vertex O, and the latter is attributed to anatase Ti–O of common side O.

Two oxygen peaks at 532.17 eV and 530.30 eV were found in the spectra of TiO_2NTs after curve fitting (see Fig. 4e). The former is attributed to anatase aberrance Ti–O of common vertex O, and the latter is attributed to anatase aberrance Ti–O of common side O. The precursor curls for multi-walled nanotubes under hydrothermal conditions, resulting in the original Ti–O bond distortion and rigider. Therefore, the vibrational frequencies become smaller. The results are basically the same with the IR measurements.

3.5. SEM measurements of P3OT and P3OT/TiO_2NTs

The P3OT and P3OT/TiO_2NTs samples were studied by SEM. The results are summarized in Fig. 5. In Fig. 5, the morphology of (Fig. 5a) P3OT is compared at a magnification of 5000× and the morphology of (Fig. 5b) P3OT/TiO_2NTs is compared at a magnification of 100,000×. As it is clearly visible, the layered structure of the P3OT is well distinguishable from the P3OT/TiO_2NTs where surface inhomogeneity is much more expressed. In Fig. 5b, it can be seen clearly that a majority of TiO_2NTs were linked and coated by the P3OT film compared with scanning electron microscope of TiO_2NTs in Fig. 1b. Due to the extreme thinness of the P3OT shell (approximately 1–2 nm), it is not possible to make it visible in the SEM micrograph. The incomplete covering of the nanotubes could be explained by the fact, that these nanotubes were always agglomerated. Some nanotubes were shielded and could not be covered with P3OT. For the following investigations this small amount of uncovered or partially covered nanotubes had no significant influence on the results.

3.6. XRD characterization of P3OT/TiO_2NTs

The XRD patterns for the P3OT, TiO_2NTs and P3OT/TiO_2NTs nanocomposite are shown in Fig. 6. For the P3OT, the broad peak at 15–28° indicates the presence of an amorphous phase, while the peaks at 5.52°, 5.52°, 9.56°, 13.96° and 24.76° reflect the crystalline structure. The peak at 24.76° is attributed to the interchain distance between the π-stacking oxidized chains. The Bragg equation gives 1.31 nm for this value. Peaks at 5.52°, 9.56° and 13.96° are consistent with the layered structure of POT, which has a dominant first-order reflection at 5.52°. The angle indicates that the lamellar interlayer spacing is

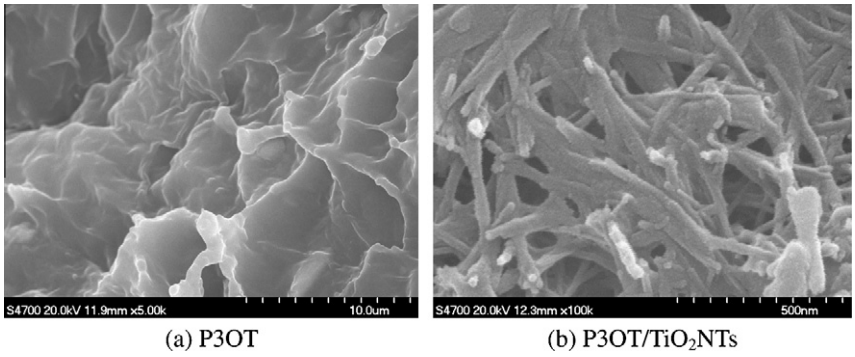

Fig. 5. SEM patterns of P3OT and P3OT/TiO_2NTs nanocomposite.

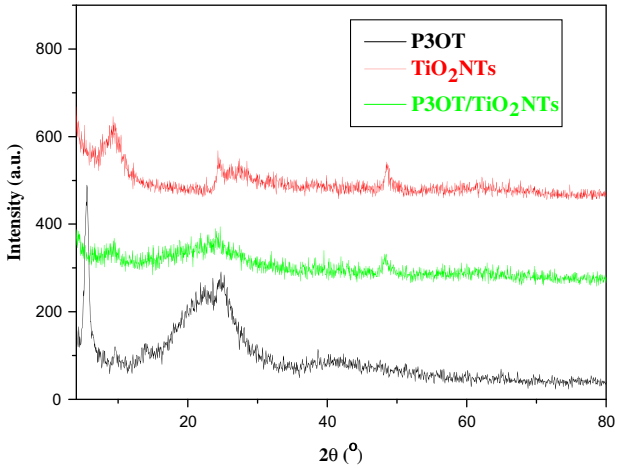

Fig. 6. XRD patterns of P3OT, TiO_2NTs and P3OT/TiO_2NTs nanocomposite.

1.60 nm [43]. The diffraction peak of polythiophene is quite narrow, showing a high degree of crystallization, plane structure and high regularity and orderly manner.

The XRD patterns of TiO_2NTs were discussed in Section 3.2 in detail.

For the P3OT/TiO_2NTs composite, the XRD data mainly show strong peaks of TiO_2NTs. The characteristic P3OT broad peak cannot be seen easily on the XRD patterns of P3OT/TiO_2NTs composite. The XRD patterns of the nanocomposite have higher background intensity, lower diffraction peak intensities, smaller interplaner spacing and reduced sharpness of the peak profiles than TiO_2NTs, which confirm the chemical interaction between P3OT and TiO_2NTs.

3.7. XPS Characterization of P3OT/TiO_2NTs

Fig. 7a–f is the high-resolution XPS spectra of P3OT, TiO_2NTs and P3OT/TiO_2NTs.

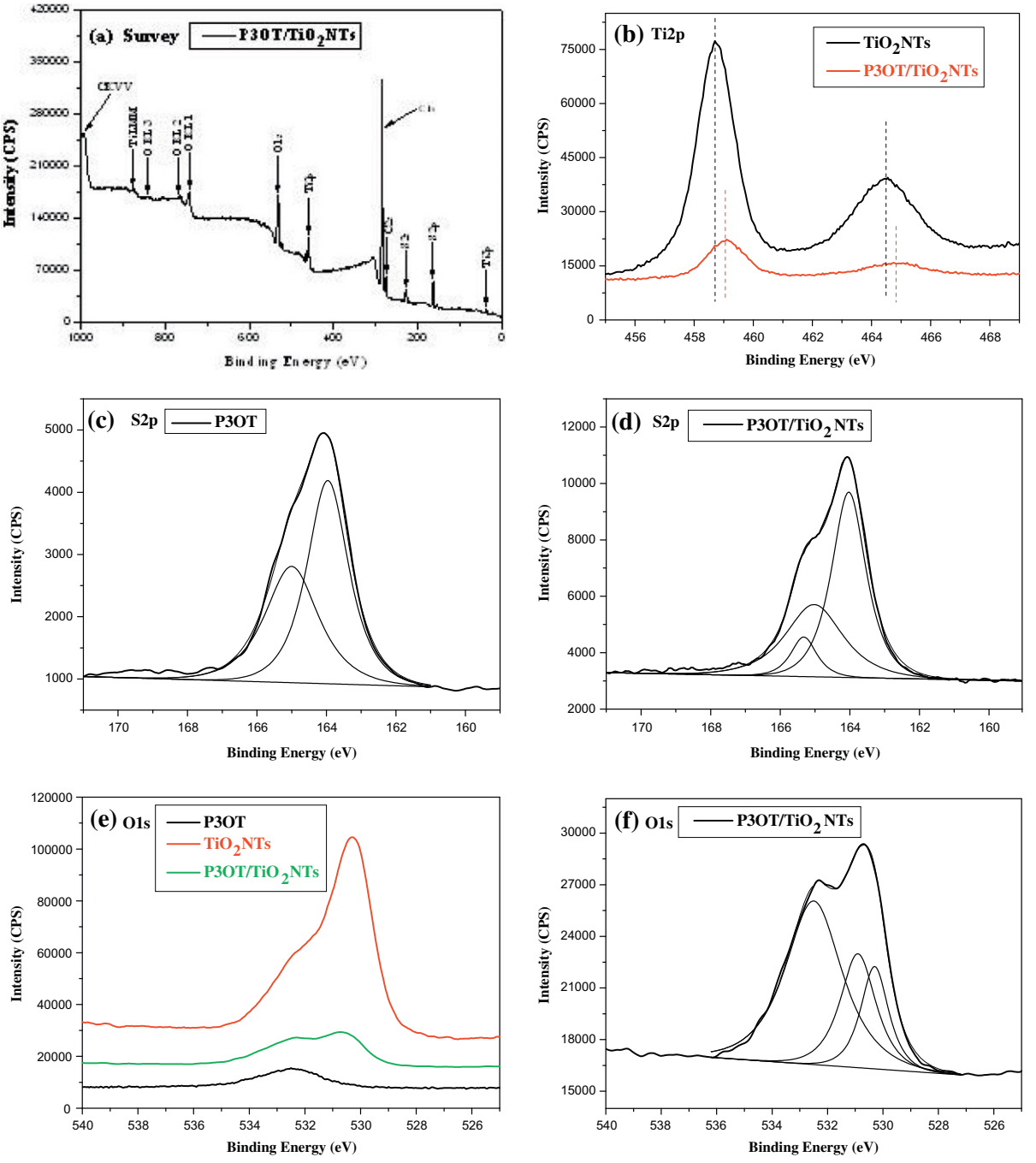

Fig. 7. XPS spectra of P3OT, TiO_2NTs and POT/TiO_2NTs nanocomposite.

In the P3OT/TiO_2NTs sample (Fig. 7a), the XPS shows Ti, O, C and S. The oxidation medium, $FeCl_3$, and the reduced form, $FeCl_2$, were not evident in the composite.

The electronic binding energy of the Ti 2p in TiO_2NTs was discussed in Section 3.4 in details. Fig. 7b shows the narrow scans for Ti2p peaks located at 464.82 eV ($Ti2p_{1/2}$) and 459.06 eV ($Ti2p_{3/2}$) of the P3OT/TiO_2NTs. Compared to TiO_2NTs, high binding energy-shift took place obviously. This indicates that the Ti atom interacted with some other atoms except O after composite reaction.

In Fig. 7c, two sulfur peaks (S2p3/2) were found, one with the binding energy 164 eV for neutral thiophene units in the polymer chain and the other with the binding energy 165 eV for oxidized thiophene units, enlarged binding energy scale between 160 and 170 eV [44,45]. In Fig. 7d, there are there sulfur peaks 164,165 and 165.3 eV in the XPS spectra of P3OT/TiO_2NTs. The peak at 165.3 eV indicates that the S atom interacted with some other atoms except C after composite reaction. In the investigated examples, there are 8.80% of the peak area at 165.3 eV in P3OT/TiO_2NTs, 35.65% of the peak area at 165 eV in P3OT/TiO_2NTs and 34.12% of the peak area in P3OT. This indicates that the S atoms lose their valence electron due to the interaction with some other atom than C on formation of the composite.

Two oxygen peaks at 532.5 eV and 530.3 eV were found in the spectra of P3OT/TiO_2NTs (see Fig. 7e and f). The former is attributed to P3OT, and the latter to TiO_2NTs. A strong peak at 530.9 eV is obtained after curve fitting. The result indicates that O atom will interact with atom(s) other than C and Ti after reaction. It is inferred that there are two chemical interactions in the complex, one between the π-stacking chains of P3OT and the O on the surface of TiO_2NTs and the other between the S of P3OT and the Ti at the surface of TiO_2NTs.

3.8. IR results of P3OT/TiO_2NTs

Fig 8 shows the FT-IR spectra of P3OT, TiO_2NTs and P3OT/TiO_2NTs nanocomposite. Peaks from both TiO_2NTs and P3OT are observed in the spectra of the nanocomposite, but the band originating from P3OT shifts to a lower wave number. For the nanocomposite, a broad band at about 3360 cm^{-1} indicates the presence of –OH groups on the surface of the complex. There is a low-intensity peak at about 2953 cm^{-1}, which may be attributed to the thiophene ring C_β–H stretching vibration. Peaks at 2920 cm^{-1} and 2842 cm^{-1} belong to the C–H of CH_2 or CH_3 symmetric and asymmetric stretching modes. The asymmetric and symmetric deformation vibrations occur at 1311 cm^{-1} and 1453 cm^{-1}. The peak at about 1640 cm^{-1} corresponds to thiophene ring C–S stretching vibration and the peak at about 1505 cm^{-1} corresponds to thiophene ring C = C stretching vibration. The 1135 cm^{-1} band corresponds to the C_α–C_α single resonance absorption. These are the characteristic peaks of P3OT [46]. In addition, there is the characteristic absorption band of Ti–O–Ti at about 470 cm^{-1} in TiO_2NTs, which was discussed in Section 3.3 in detail. It is noteworthy that this broad peak becomes sharper and narrower as the introduction of TiO_2NTs, which correspond to the chemical interaction between P3OT and TiO_2NTs.

3.9. UV–vis spectra of P3OT/TiO_2NTs nanocomposite film

The UV–Vis spectra of P3OT solid film, TiO_2NTs and P3OT/TiO_2NTs nanocomposite films are presented in Fig. 9. It shows the characteristic spectrum of TiO_2NTs ranges from 220 to 360 nm, which is its fundamental absorption of Ti–O bond in TiO_2NTs. The UV–Vis spectrum of P3OT indicates a λ_{max} at 489 nm and corresponds to a π–π* transition, and displays a weak absorption near TiO_2NTs. From the spectrum of P3OT/TiO_2NTs nanocomposite film, it can be seen that there were two absorption bands with maximum wavelength of 271 and 518 nm in ultraviolet region and visible light region, respectively. The band from 220 to 300 nm is assigned to the characteristic absorption of TiO_2NTs and the P3OT adsorption band in the UV light region. The other band is attributed to the electron transition from the valence bond to the antibonding polaron state (π–π* type) of P3OT [47,48]. Compared with the spectrums of TiO_2NTs and P3OT, the P3OT/

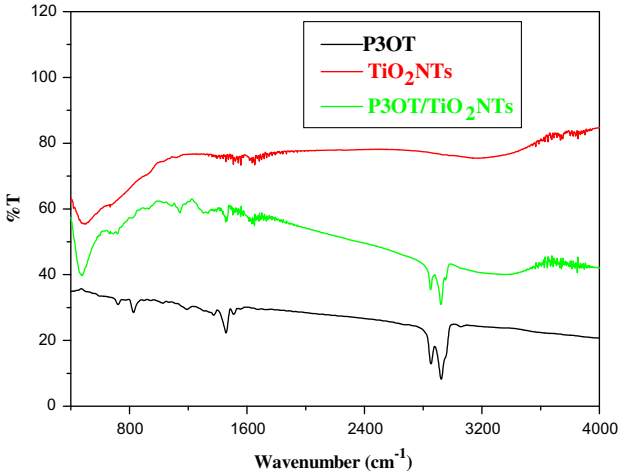

Fig. 8. FT-IR spectra of P3OT, TiO_2NTs and P3OT/TiO_2NTs nanocomposite.

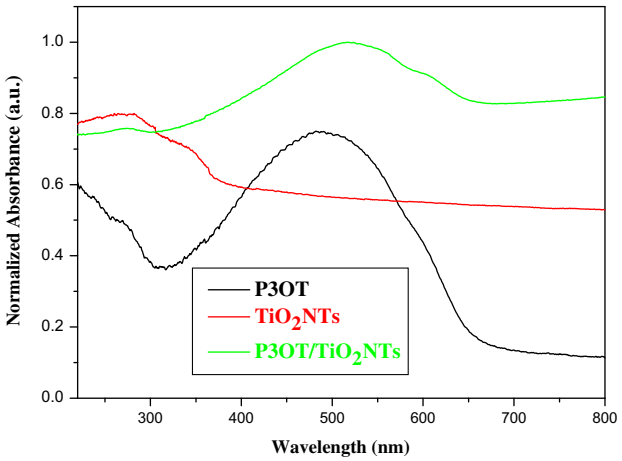

Fig. 9. UV–Vis absorption spectra of P3OT, TiO_2NTs and P3OT/TiO_2NTs nanocomposite.

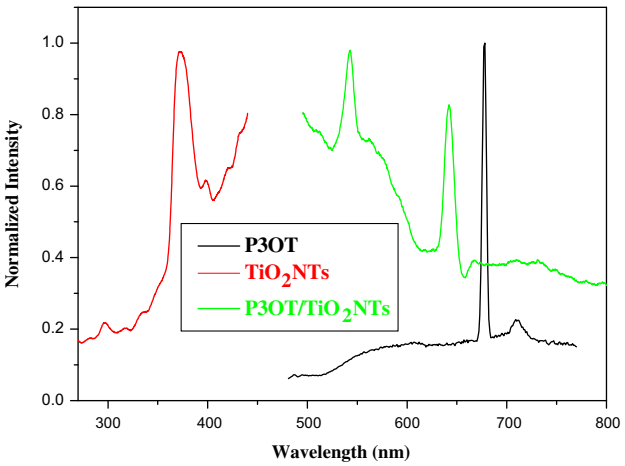

Fig. 10. Luminescence emission spectra of P3OT, TiO_2NTs and P3OT/TiO_2NTs nanocomposite.

TiO_2NTs nanocomposite film absorbs much more UV–Vis light, obviously. The red-shift in visible region and much more absorption of visible light may result from the chemical interaction between P3OT and TiO_2NTs in the composite, which refer in the discussion of XRD, XPS and IR above.

3.10. Fluorescence spectra of P3OT/TiO_2NTs nanocomposite film

The emission spectra of P3OT solid film, TiO_2NTs and P3OT/TiO_2NTs nanocomposite films are shown in Fig. 10. The emission peak of P3OT ranges from 650 to 750 nm with the maximum emission in 677 nm. The emission peaks of TiO_2NTs mainly range from 300 to 400 nm with the maximum emission in 373 nm. The blue-shift appears compared with TiO_2 film [49], which results from quantum size effect of nanotube. The luminescence spectrum of the P3OT/TiO2NTs nanocomposite film is totally different; for example, there are two main emission peaks in visible light region with λ_{em} of 542 nm and 642 nm, respectively. This represents a novel optical property for a new chemical interaction between P3OT and TiO_2NTs. The similar discussion was present in Ref. [39]. The experiment results prove that the P3OT/TiO_2NTs is a new material.

3.11. Cyclic voltammetry

From the CV curves in Fig. 11, the samples' potential can be gained [7]. The frontier orbital and energy gap of P3OT, TiO_2NTs and P3OT/TiO_2NTs nanocomposite are listed in Table 1. The values are in accordance with the literature for P3OT [50] and TiO_2NTs [51]. From the CV curves of P3OT, it is found that its oxidation area (where the potential is higher than zero) is larger than the reduction area (where the potential is lower than zero), and the initial oxidation potential is fairly low compared to TiO_2NTs. The initial oxidation potentials of the P3OT/TiO_2NTs nanocomposite film are lower than each of the components, while the initial reduction potentials of the P3OT/TiO_2NTs nanocomposite film are higher than each of the components. The energy gap of P3OT/TiO_2NTs nanocomposite is only 0.672 eV. The results indicated that P3OT/TiO_2NTs

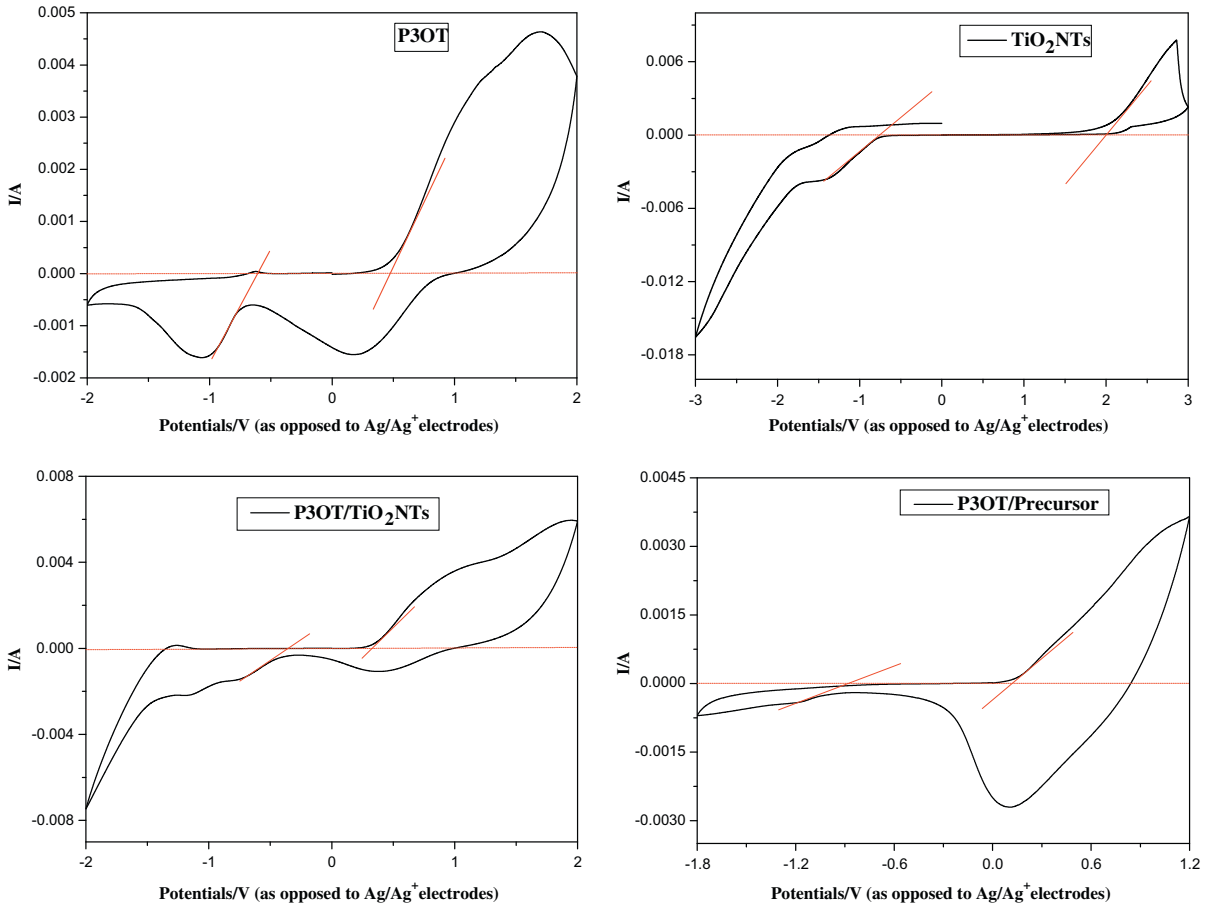

Fig. 11. Cyclic voltammetry waves of P3OT, TiO_2NTs and P3OT/TiO_2NTs nanocomposite.

Table 1
The frontline molecular orbital and energy gap of P3OT, TiO_2NTs, P3OT/Precursor and P3OT/TiO_2NTs.

Sample	Φ_{ox} (eV)	Φ_{red} (eV)	EHOMO (eV)	ELUMO (eV)	Eg (eV)
P3OT	0.470	−0.610	−4.910	−3.830	1.080
TiO_2NTs	2.019	−0.759	−6.459	−3.681	2.778
P3OT/TiO_2NTs	0.355	−0.317	−4.795	−4.123	0.672
P3OT/Precursor	0.117	−0.916	−4.557	−3.524	1.033

Φ_{ox} and Φ_{red} potentials (vs 0.01 Ag^+/Ag in CH_3CN) determined by cyclic voltammetry. Calculated according to $Eg = \Phi_{ox} - \Phi_{red}$. *E*HOMO and *E*LUMO from *E*HOMO = $-(\Phi_{ox} + 4.44)$ eV, and *E*LUMO = $-(\Phi_{red} + 4.44)$ eV [52,53].

composite is a new promising p–n type composite material.

3.12. Performance parameters of dye-Sensitized Solar Cells

The photovoltaic performance of the device is shown in Fig 12 and all the parameters of P3OT and P3OT/TiO_2NTs sensitized solar cell are listed in Table 2. Under standard global AM 1.5 G (100 mW/cm^2) solar condition, the P3OT sensitized solar cell gave a short-circuit current (J_{SC}) of 0.350 mA, open-circuit voltage (V_{OC}) of 0.350 V, effective area (Sea) of 0.482 cm^2 and fill factor (FF) of 0.338, corresponding to an overall conversion efficiency (η) of 0.086%; the P3OT/Precursor sensitized solar cell gave a short-circuit current (J_{SC}) of 0.406 mA, open-circuit voltage (V_{OC}) of 0.510 V, effective area (Sea) of 0.375 cm^2 and fill factor (FF) of 0.688, corresponding to an overall conversion efficiency (η) of 0.380%. the P3OT/TiO_2NTs sensitized solar cell gave a short-circuit current (J_{SC}) of 0.543 mA, open-circuit voltage (Voc) of 0.566 V, effective area (Sea) of 0.250 cm^2 and fill factor (FF) of 0.483, corresponding to an overall conversion efficiency (η) of 0.593%. The overall conversion efficiency enhancement of P3OT/TiO_2NTs can be related to the chemistry interaction between P3OT and TiO_2NTs in the composite, which refer to the XPS discussion. In the UV–vis spectra, the P3OT/TiO_2NTs nanocomposite film ab-

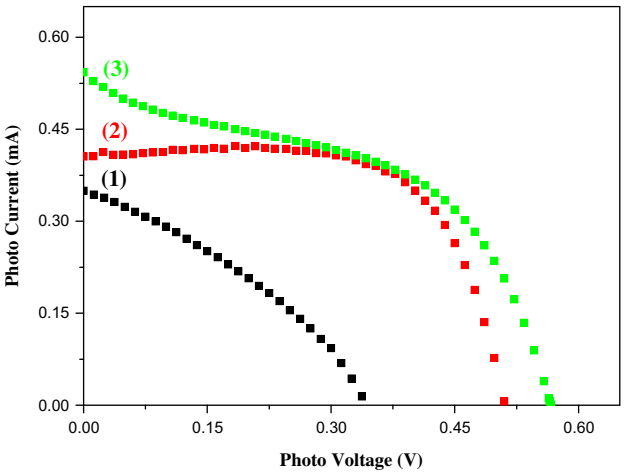

Fig. 12. Photochemical study of P3OT, P3OT/Precursor and P3OT/TiO_2NTs.

Table 2
Performance parameters of dye-sensitized solar cells.

Dye	J_{SC}(mA)	V_{OC}(V)	P_{max}(mW)	FF	Sea(cm^2)	η (%)
P3OT	0.350	0.350	0.0414	0.338	0.482	0.086
P3OT/Precursor	0.406	0.510	0.1425	0.688	0.375	0.380
P3OT/TiO_2NTs	0.543	0.566	0.1483	0.483	0.250	0.593

FF = $P_{max}/(J_{SC} * Voc)$. $\eta(\%) = P_{max} * 100\%/(P * Sea)$. AM 1.5: P = 100 mW/$cm^2$.

sorbs much more visible light, so the incident photon-to-current conversion efficiency was high.

4. Conclusion

Amorphous titania nanotubes with diameters between 20 and 30 nm were successfully synthesized by hydrothermal method using anatase TiO_2 as the precursor and 10 M NaOH as the mine to the agent. A conducting polymer composite, poly(3-octylthiophene)/titania nanotubes (P3OT/TiO_2NTs) was synthesized by chemical method. Transmission electron microscope (TEM) and scanning electron microscope (SEM) depict the morphology of the samples, defining that TiO_2NTs were successfully coated by poly(3-octylthiophene) molecules. X-ray diffraction (XRD), X-ray photoelectron spectroscopy (XPS) and infrared spectroscopy (IR) showed the chemical interaction of poly(3-octylthiophene) and titania nanotubes in the composite. Cyclic voltammetry (CV) curves showed that the forbidden band gap of the P3OT/TiO2NTs composite is 0.672 eV, realizing the complementary advantages of n and p semiconductor. Ultraviolet–visible spectra (UV–vis) and fluorescence spectra (PL) show that its optical performance is far superior to poly(3-octylthiophene) and titania nanotubes separately. Solar cell was sensitized by P3OT/TiO_2NTs. A solar-to-electric energy conversion efficiency of 0.593% was attained with the system. The results show that P3OT/TiO_2NTs nanocomposite is a promising material with excellent performance in photoelectric applications.

Acknowledgments

This work was supported by the National High Technology Research and Development Program of China (863 Program) under Grant No. 2006AA03z412, the Department of Education Research Project of Hainan under Grant No. Hj2010-52, the Scientific Research Foundation of Graduate School of Beijing University of Chemical and Technology No. 09Si005 and the National High Technology Research and Development Program of Hainan under Grant No. 509013.

References

[1] R.D. McCullough, The chemistry of conducting polythiophenes, Adv. Mater. 10 (1998) 93–116.
[2] R. Gangopadhyay, A. De, Conducting polymer nanocomposites: a brief overview, Chem. Mater. 12 (2000) 608–622.
[3] P. Gomez-Romero, Hybrid organic–inorganic materials – in search of synergic activity, Adv. Mater. 13 (2001) 163–174.
[4] A. Malinauskas, Chemical deposition of conducting polymers, Polymer 42 (2001) 3957–3972.
[5] F. Caruso, Nanoengineering of particle surface, Adv. Mater. 13 (2001) 11–22.
[6] P.G. Hill, P.J.S. Foot, R. Davis, Novel inorganic conjugated polymer nano-composites, Synth. Met. 76 (1996) 289–292.
[7] N. Hebestreit, J. Hofmann, U. Rammelt, W. Plieth, Physical, electrochemical characterization of nanocomposites formed from polythiophene, titanium dioxide, Electrochimica Acta 48 (2003) 1779–1788.
[8] G.D. Sharma, P. Suresh, Shailendra Kumar Sharma, M.S. Roy, Optical electrical properties of hybrid photovoltaic devices from poly(3-phenyl hydrazone thiophene) (PPHT) TiO_2 blend films, Sol. Energy Mater. Sol. Cells 92 (2008) 61–70.

[9] C.L. Huisman, A. Goossens, J. Schoonman, Preparation of a nanostructured composite of titanium dioxide and polythiophene: a new route towards 3D heterojunction solar cells, Synth. Met. 138 (2003) 237–241.
[10] H. Spanggaard, F.C. Krebs, A brief history of the development of organic and polymeric photovoltaics, Sol. Energy Mater. Sol. Cells 83 (2004) 125–146.
[11] S. Günes, H. Neugebauer, N.S. Sariciftci, Conjugated polymer-based organic solar cells, Chem. Rev. 107 (2007) 1324–1338.
[12] M. Jorgensen, K. Norrman, F.C. Krebs, Stability/degradation of polymer solar cells, Sol. Energy Mater. Sol. Cells 92 (2008) 686–714.
[13] Woon-Hyuk Baek, I.l. Seo, Tae-Sik Yoon, Hyun Ho Lee, Chong Man Yun, Yong-Sang Kim, Hybrid inverted bulk heterojunction solar cells with nanoimprinted TiO_2 nanopores, Sol. Energy Mater. Sol. Cells 93 (2009) 1587–1591.
[14] F.C. Krebs, Air stable polymer photovoltaics based on a process free from vacuum steps and fullerenes, Sol. Energy Mater. Sol. Cells 92 (2008) 715–726.
[15] Byeong-Kwan An, Rhiannon Mulherin, Benjamin Langley, Paul Burn, Paul Meredith, Ruthenium complex-cored dendrimers: shedding light on efficiency trade-offs in dye-sensitised solar cells, Org. Electron. 10 (2009) 1356–1363.
[16] Frederik C. Krebs, Suren A. Gevorgyan, Jan Alstrup, A roll-to-roll process to flexible polymer solar cells: model studies, manufacture and operational stability studies, J. Mater. Chem. 19 (2009) 5442–5451.
[17] Frederik C. Krebs, Suren A. Gevorgyan, Bobak Gholamkhass, Steven Holdcroft, Cody Schlenker, Mark E. Thompson, Barry C. Thompson, Dana Olson, David S. Ginley, Sean E. Shaheen, Husam N. Alshareef, John W. Murphy, W. Justin Youngblood, Nathan C. Heston, John R. Reynolds, Shijun Jia, Darin Laird, Sachetan M. Tuladhar, Justin G.A. Dane, Pedro Atienzar, et al., A round robin study of flexible large-area roll-to-roll processed polymer solar cell modules, Sol. Energy Mater. Sol. Cells 93 (2009) 1968–1977.
[18] Frederik C. Krebs, Torben D. Nielsen, Jan Fyenbo, Mads Wadstrøm, Marie S. Pedersen, Manufacture, integration, demonstration of polymer solar cells in a lamp for the "Lighting Africa" initiative, Energy Environ. Sci. 3 (2010) 512–525.
[19] G. Li, V. Shrotriya, J. Huang, Y. Yao, T. Moriarty, K. Emery, Y. Yang, High-efficiency solution processable polymer photovoltaic cells by self-organization of polymer blends, Nat. Mater. 4 (2005) 864–868.
[20] W. Ma, C. Yang, X. Gong, K. Lee, A.J. Heeger, Thermally stable, efficient polymer solar cells with nanoscale control of the interpenetrating network morphology, Adv. Funct. Mater. 15 (2005) 1617–1622.
[21] J.Y. Kim, K. Lee, N.E. Coates, D. Moses, T.Q. Nguyen, M. Dante, A.J. Heeger, Efficient tandem polymer solar cells fabricated by all-solution processing, Science 317 (2007) 222–225.
[22] S.Z. Chu, S. Inoue, K. Wada, D. Li, H. Haneda, S. Awatsu, J. Phys. Chem. B 107 (2003) 6586–6589.
[23] J.M. Macak, M. Zlamal, J. Krysa, P. Schmuki, Small 3 (2007) 300–304.
[24] A. Ghicov, J.M. Macak, H. Tsuchiya, J. Kunze, V. Haeublein, L. Frey, P. Schmuki, Nano. Lett. 6 (2006) 1080–1082.
[25] H. Ou, S. Lo, Sep. Purif. Technol. 58 (2007) 179–191.
[26] T. Kasuga, M. Hiramatsu, A. Hoson, T. Sekino, K. Niihara, Adv. Mater. 11 (1999) 1307–1311.
[27] G.H. Du, Q. Chen, R.C. Che, Z.Y. Yuan, L.M. Peng, Appl. Phys. Lett. 79 (2001) 3702–3704.
[28] Q. Chen, W.Z. Zhou, G.H. Du, L.M. Peng, Adv. Mater. 14 (2002) 1208–1211.
[29] C.C. Tsai, J.N. Nian, H. Teng, Appl. Surf. Sci. 253 (2006) 1898–1902.
[30] Q. Shen, T. Sato, M. Hashimoto, C.C. Chen, T. Toyoda, Thin Solid Films 499 (2006) 299–305.
[31] J. Du, J.L. Zhang, Z.M. Liu, B.X. Han, T. Jiang, Y. Huang, Langmuir 22 (2006) 1307–1312.
[32] J. Bouclé, S. Chyla, Hybrid bulk heterojunction solar cells based on blends of TiO_2 nanorods and P3HT, C. R. Phys. 9 (2008) 110–118.
[33] D.C. Olson, J. Piris, R.T. Collins, S.E. Shaheen, D.S. Ginley, Hybrid photovoltaic devices of polymer and ZnO nanofiber composites, Thin Solid Films 496 (2006) 26–29.
[34] S. Park, S.J. Tark, J.S. Lee, H. Lim, D. Kim, Effects of intrinsic ZnO buffer layer based on P3HT/PCBM organic solar cells with Al-doped ZnO electrode, Sol. Energy Mater. Sol. Cells 93 (2009) 1020–1023.
[35] D.E. Motaung, G.F. Malgas, C.J. Arendse, S.E. Mavundla, C.J. Oliphant, D. Knoesen, Thermal-induced changes on the properties of spin-coated P3HT:C60 thin films for solar cell applications, Sol. Energy Mater. Sol. Cells 93 (2009) 1674–1680.
[36] F.C. Krebs, M. Jørgensen, K. Norrman, O. Hagemann, J. Alstrup, T.D. Nielsen, J. Fyenbo, K. Larsen, J. Kristensen, A complete process for production of flexible large area polymer solar cells entirely using screen printing—first public demonstration, Sol. Energy Mater. Sol. Cells 93 (2009) 422–441.
[37] F.C. Krebs, Polymer solar cell modules prepared using roll-to-roll methods: knife-over-edge coating slot-die coating and screen printing, Sol. Energy Mater. Sol. Cells 93 (2009) 465–475.
[38] R. Sugimoto, Preparation of soluble polythiophene derivatives utilizing transition metal halides as catalysts and their property, Chem. Expr. 1 (1986) 635–638.
[39] Z. Han, J. Zhang, X. Yang, H. Zhu, W. Cao, Synthesis and photoelectric property of poly(3-octylthiophene)/zinc oxide complexes, Sol. Energy Mater. Sol. Cells 94 (2010) 194–200.
[40] Jia Wei, Jingchang Zhang, Hydrothermal synthesis and characterization of vanadium oxide nanotubes, Adv. Mater. Res. 11–12 (2006) 535–538.
[41] J.C. Xu, W.M. Liu, H.L. Li, Mater. Sci. Eng. Biomimetic Supramolecular Syst. C. 25 (2005) 444.
[42] J.F. Moulder, W.F. Stickle, P.E. Sobol, K.D. Bomben, Handbook of X-ray Photoelectron Spectroscopy, Physical Electronics, Inc, 1995.
[43] Csaba Visy, Electrochimica Acta. 53 (2008) 3942–3947.
[44] E.T. Kang, Surface modifications of poly(3-alkylthiophene) films by graft copolymerization, Macromolecules 25 (1992) 6842–6848.
[45] E.T. Kang, X-ray photoelectron spectroscopic studies of poly(2,2′-bithiophene) and its complexes, Phys. Rev. B. 44 (1991) 10461–10469.
[46] Z. Han, J. Zhang, X. Yang, H. Zhu, W. Cao, Synthesis and photoelectric property of poly(3-octylthiophene)/titanium dioxide nano-composite material, J. Mater. Sci.: Mater. Electron. 21 (2010) 554–561.
[47] J.E. Mark, Polymer Data Handbook, Oxford University Press, Oxford, 1999.
[48] A.O. Patil, A.J. Heeger, F. Wudl, Chem. Rev. 88 (1988) 183.
[49] Z. Han, J. Zhang, X. Yang, H. Zhu, W. Cao, Synthesis and photoelectric property of poly(3-octylthiophene)/titanium dioxide hybrid. J. Inorg. Organometall. Polym. Mater., in press, doi: 10.1007/s10904-009-9317-1.
[50] T. Ahn, B. Choi, S.H. Ahn, S.H. Han, H. Lee, Synth. Met. 117 (2001) 219.
[51] A. Fujishima, T.N. Rao, D.A. Tryk, J. Photochem Photobiol. C: Photochem. Rev. 1 (2000) 1–21.
[52] Y. Liu, M.S. Liu, A.K.-Y. Jen, Acta Polymer. 50 (1999)105.
[53] S.-W. Hwang, Y. Chen, Macromolecules 3 (2001) 2981.

doping by potassium. The molecular structure of FePc ($C_{32}H_{16}N_8Fe$) is schematically shown in Fig. 1.

It has a planar structure with D_{4h} point symmetry. The molecule consists of the central Fe atom surrounded by four nitrogen atoms (pyrrole, N_1); four other nitrogen atoms – (bridging aza, N_2); 32 carbon atoms – the pyrrole (C_1) and the benzenes (C_{BZ}: C_2, C_3 and C_4). Our measurements were performed by photoemission spectroscopy (PES) and near-edge X-ray absorption fine structure (NEXAFS) using synchrotron radiation, and the experimental results are completed by DFT calculations.

2. Experimental details

The PES experiments were performed using the soft-X-ray synchrotron light emitted by the high-energy resolution I511 beamline at MAX-Lab (Lund, Sweden). The beam line is designed for surface science experiments and is equipped with a SCIENTA electron analyzer for PES.

The NEXAFS measurements were done using the soft-X-ray light provided by the Russian-German high-energy resolution dipole beam line (RGBL) at the Berliner Speicherring für Synchrotronstrahlung (BESSY, Berlin, Germany). This line delivers moderate-intensity radiation with a continuous distribution over a wide photon energy range and therefore is well suited for the NEXAFS measurements of organic materials which are relatively fragile and potentially could be damaged under intense irradiation. In a previous investigation [11] it was shown that the FePc films are very resistant for 3–4 h to typical X-ray fluxes at a bending magnet beamline. Nevertheless, during the measurements we regularly changed the spot position of the radiation beam on the sample surface to avoid possible damage of the organic film. The spectra were recorded in total electron yield mode and normalized to the incident photon flux. The resolution for the NEXAFS measurements is determined exclusively by the performance of the beam line and varied from 80 meV to 90 meV FWHM when going from the C 1*s* (~283 eV) to the N 1*s* (~400 eV) thresholds, and was approximately 100 meV for the Fe absorption thresholds. The acquired spectra were energy calibrated using the C $1s \rightarrow \pi^*$ and N $1s \rightarrow \pi^*$ photoionization spectra of CO_2 and N_2 gases. In NEXAFS experiments the photon incidence angle was selected to be 35° relative to the normal to the sample surface. We have chosen this angle to explore simultaneously both: the $1s \rightarrow \pi^*$ and $1s \rightarrow \sigma^*$ transitions. The pressure in the experimental systems during data acquisition was always better than 5×10^{-10} Torr. All measurements were carried out at room temperature.

As the substrate for FePc film formation, we used the (001) surface of a gold single crystal. The surface was prepared by repeated sputtering and annealing cycles after which a 5×20 surface reconstruction was observed using low energy electron diffraction, while no remaining contamination was detected in core level photoemission spectra. The FePc film was deposited from a Knudsen-type evaporator in sample preparation chambers (base pressure of 2.5×10^{-10} Torr) directly linked to the analyzer chambers. The deposition rate, monitored by a quartz microbalance, was 1–2 Å/min. The core level photoemission spectra indicated clean FePc films without detectable traces of contamination including oxygen. The FePc films used for our studies were about 70 Å thick, which is large enough to minimize signals from the gold substrate in the photoemission spectra, and small enough to avoid charging effects.

Pure potassium was evaporated onto the FePc film at rates ranging from 1 to 50 Å/min from a properly outgassed SAES alkali-metal dispenser, without detectable pressure enhance during deposition. This resulted in a uniform distribution of the potassium in the organic film as proved upon varying the emission angle of the photoelectrons. The K concentration in the FePc films was evaluated from a comparison of the relative intensities of the K 2*p* and C 1*s* core-level signals. The sensitivity factors of the core-levels for the respective photon energies were taken from the tabulated cross-sections, and we also took into account the throughput of the analyzer [12]. After each FePc or potassium deposition step, the PE measurements in the normal emission geometry were carried out with photon energies of 110 eV for the valence band (VB), 400 eV for K 2*p* and C 1*s*, 500 eV for N 1*s* core levels (CL). The overall energy resolution [full width at half maximum (FWHM)] also accounting for the thermal broadening was 130 meV for photon energies of 110 eV (valence band), 240 meV for photon energies of 400–500 eV. The E_F position in the spectra was determined after each move of the monochromator by measuring the Fermi edge and/or the Au $4f_{7/2}$ electron emission from a gold foil cleaned by ion bombardment in electrical contact with the FePc film.

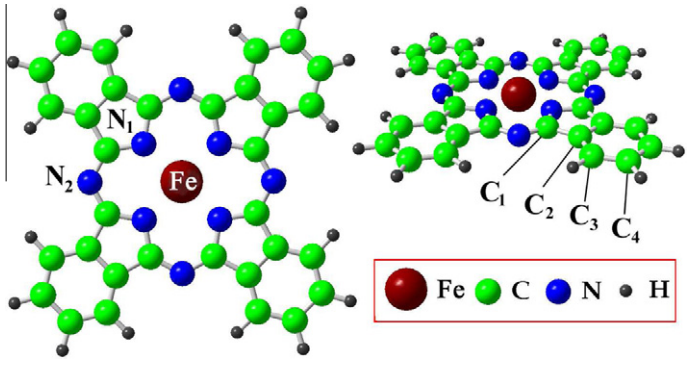

Fig. 1. Schematic demonstration of the molecular structure of the FePc molecule, where the central iron atom is surrounded by four nitrogen atoms.

The core-level C 1*s* and N 1*s* PE spectra were decomposed by a least-squares-fitting procedure in order to differentiate contributions from C and N atoms in different chemical environments. The fit was performed with Lorentzian line shapes convoluted with a Gaussian function to take into account the finite experimental resolution. Other experimental details can be found elsewhere [13,14].

3. Results and discussion

Fig. 2(a–b) shows the C 1*s* and N 1*s* core levels recorded from a FePc film as a function of potassium doping. X indicates the amount of potassium atoms per FePc molecule. The top spectra in both Figs. (for $X = 0$) represent the photoelectron emission from core levels of pristine FePc just after of organic film formation. The decomposition of the C 1*s* spectrum of pristine FePc is presented in Fig. 2(c) ($X = 0$). It appears to be very similar to decompositions, performed earlier for pristine CuPc [14–17] and CoPc [18] films just confirming previous conclusions that the C 1*s* core level is comprised of two main components: B which corresponds to the aromatic carbon of the benzene rings of Metal–Pc (C_2, C_3, and C_4) and P shifted by 1.4 eV toward higher binding energy and attributed to the carbon C_1 linked to nitrogen atoms N_1 and N_2 (pyrrole carbon). The energy shift between C 1*s* (B) and C 1*s* (P) is due to a transfer of valence charge from pyrrole carbon to the more electronegative nitrogen in the –N–C=N– bonds. The shoulder SB and the feature SP are the satellites of the B and P components, respectively [13,15,16,19–22]. The fact that we have managed to perform C 1*s* decomposition using the same parameters as in Refs. [14,17,18], could mean that the replacement of the central atom leaves the organic ligand rather unchanged.

The N 1*s* core-level spectrum of pristine FePc is shown in the Fig. 2(b). The spectrum consists of the strong peak centered at 398.62 eV and weaker peaks at 400.4 eV and 402.5 eV. Taking into account the fact that we have the same resolution as in Refs. [14,17,18] and taking the similar fitting parameters, which were used for CuPc [14,17] and CoPc [18], we have managed to decomposed the peak of 398.62 eV by two components: C centered at 398.38 eV and P centered at 398.86 eV (Fig. 2(d), $X = 0$).

The energy difference between the peaks corresponds to 0.36 eV. Component **C** at lower BE can be assigned to the four nitrogen atoms connected to the central Fe atom (N_1 in Fig. 1), while the P component can be assigned as originating from the four nitrogen atoms linked to the pyr-

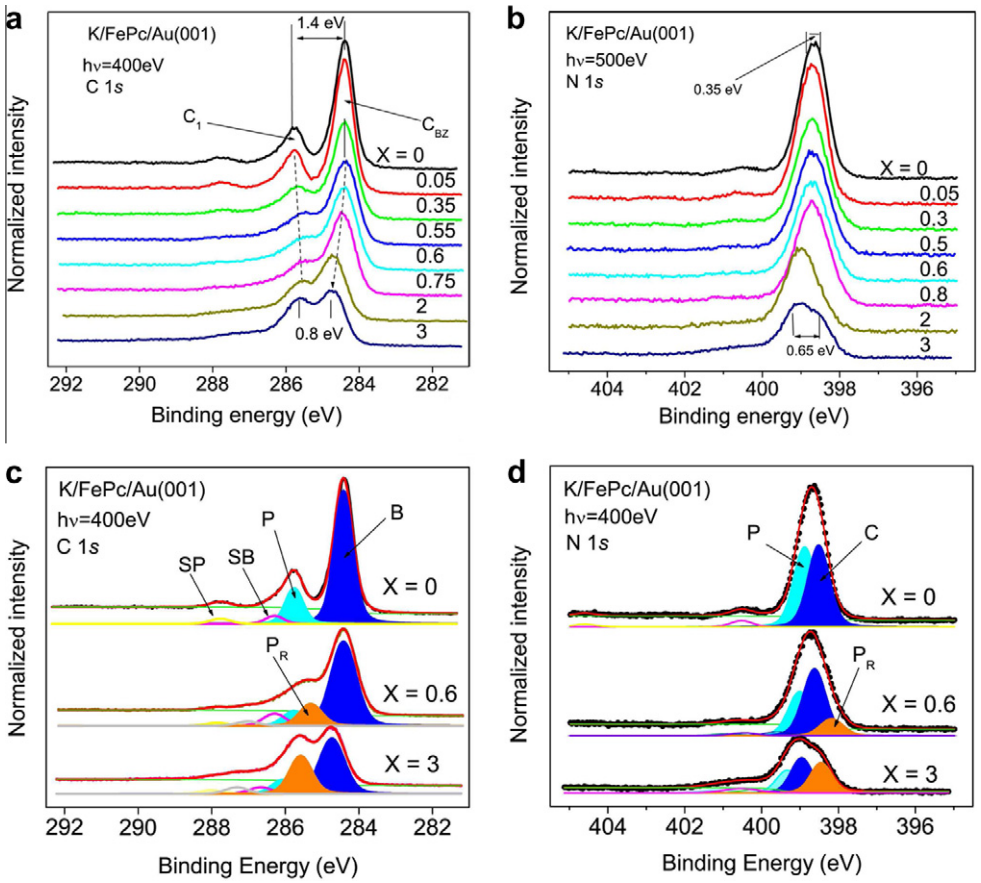

Fig. 2. C 1*s* core level (a) and N 1*s* core level (b) measured using photoemission spectroscopy of FePc thin film at RT as a function of *X* which characterize the amount of potassium atoms per FePc molecule. Decomposition of the C 1*s* (c) and N 1*s* (d) spectra of pristine ($X = 0$) and dopped ($X = 0.6$ and $X = 3$) FePc. See details in the text.

olle carbons. Probably unlike to the case of CuPc, where both nitrogen sites N_1 and N_2 are characterized by the same or a very similar binding energy (BE) and the main N 1*s* peak was fitted by only one component [14,17], the central Fe atom differently interacts with these N_1 nitrogen atoms which is associated with a stronger charge transfer. The latter provokes the N_1 chemical shift to lower BE by 0.36 eV. A similar shift of about 0.3 eV for FePc [23] was found from DFT calculations. Our discussion above is consistent with metal–Pc binding energy calculations [24], while the calculated BE were found to be 9.81 eV for FePc and 6.96 eV for CuPc.

With potassium doping the K 2*p* spin-orbit doublet is observed at binding energies of 294 eV and 296.7 eV and increases in intensity with increasing potassium content (Fig. 3). The energy positions of the doublet indicates that the outer *s* electrons of potassium are transferred to the FePc molecules upon intercalation [5,25]. The shape of the K 2*p* doublet basically does not change with doping till a concentration of about four potassium atoms per FePc molecule which is an indication of the existence mostly of only one inequivalent potassium site in this doping range. At a higher potassium concentration ($X = 7.5$) considered in the present investigation the spectrum shows one more feature shifted by about 2.4 eV to lower BE relative to K $2p_{3/2}$ component of main doublet. From such K 2*p* core level behavior we can conclude that at doping range $0 < X \leqslant 4$ most probably potassium ions occupy one type of equivalent positions in FePc molecule. As we will see below the first type of sites, corresponding to higher BE, is located near the asa-bridging nitrogens N_2 of the FePc molecules (see Fig. 4(b)) and is fully saturated at potassium concentration $X \simeq 4$, while another site type, corresponding to lower BE is located probable near the benzene carbons and is occupied by K ions at concentration $X \geqslant 4$. This behavior of the K 2*p* core-levels with potassium doping would parallel the effects of Rb intercalation into C_{60}, where it was concluded, that three clear features in Rb 3*d* core-level result from overlapping contributions from

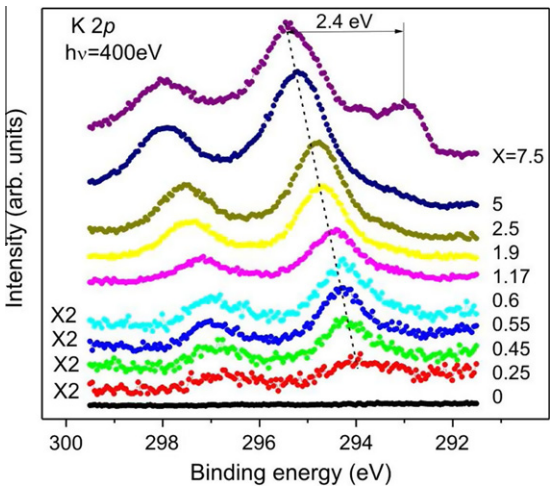

Fig. 3. K 2*p* core level measured using photoemission spectroscopy as a function of K intercalation of FePc thin film at RT.

Rb ions in tetrahedral and octahedral sites [25]. In general starting from the first deposition up to $X \simeq 7$ the total K 2*p* core-level shift of about 1 eV to higher BE was observed.

Fig. 2(a) also depicts the evolution of the C 1*s* spectra with increasing potassium doping. Upon initial potassium intercalation till about $X = 0.2$–0.3 there is a small the spectral shape change. With increasing potassium doping both C 1*s* core-level features (C_1 and C_{BZ}) show broadening, but C_1 spreads much more drastically and is shifted to lower BE. And finally C_1 becomes separated from C_{BZ} component by 0.8 eV, which is contrasted by the 1.4 eV distance in pristine FePc (see above). Note, that this feature is attributed to the carbon atoms linked to nitrogens N_1 and N_2 (pyrrole carbon). On the other hand, the line shape of the C_{BZ} feature, which corresponds to the aromatic carbon of the benzene rings C_2–C_4 almost does not change. The decomposition of the C 1*s* core level at selected potassium concentrations which is presented in Fig. 2(c) shows the appearance and growth of a new C 1*s* component P_R presented in Fig. 2(c), which is at energies in between those (C 1*s* (P) and C 1*s* (B)) related to undoped FePc, while intensity of P component reduces essentially. Such a behavior indicates, that the potassium atoms impact the pyrolle carbon atoms which results in splitting P (pyrolle component of C 1*s* CL spectrum) to two ones: (i) P (pyrolle) which originates from pyrolle C_1 atoms not influenced yet by potassium and (ii) P_R component, which originates from the same pyrolle C_1 atoms, but with different chemical environment. This component is shifted to lower BE and growths in intensity with potassium addition.

This conclusion is corroborated by the evolution of the N 1*s* core-level peak centered at 398.62 eV upon doping as shown in Fig. 2(b). With increasing potassium intercalation the spectrum shows an increase of peak width. In order to obtain a deeper insight into the chemical interaction between potassium and FePc film, we have performed a numerical peak decomposition, the results of which for selected potassium intercalations are shown in Fig. 2(d). The width of each component was taken from the N 1*s* core-level spectrum of pristine FePc (top spectrum in Fig. 2(d)) and was kept unchanged at all potassium doping. From Fig. 2(d) it is evident that components P and C which were found above as a result of decomposition of peak centered at 398.62 eV for undoped FePc show a shift to higher binding energy with doping and as a result of K addition the component P_R appears at lower binding energy, which leads to the overall N 1*s* peak broadening observed. With increasing doping one sees a rapid attenuation of left component P of the N 1*s* core level, which was attributed to the N_2 atoms linked to pyrrole carbon atoms and simultaneously a growth of component P_R which leads to an asymmetric line-shape. Thus, our data demonstrate a scenario, where upon potassium doping the K atoms ($X \leqslant 3$) occupy one type of equivalent positions in FePc molecule, namely – close to asa-bridging nitrogens N_2 as schematically drawn in Fig. 4. This decreases the relative amplitude of this P component and gives rise to the new reactive one P_R, appearing at lower binding energy as a consequence of strong charge transfer from K to N. Thus we conclude that K stronger impacts the asa nitrogen and pyrrole carbon atoms (N_2 and C_1 in Fig. 1). Moreover, there is a nega-

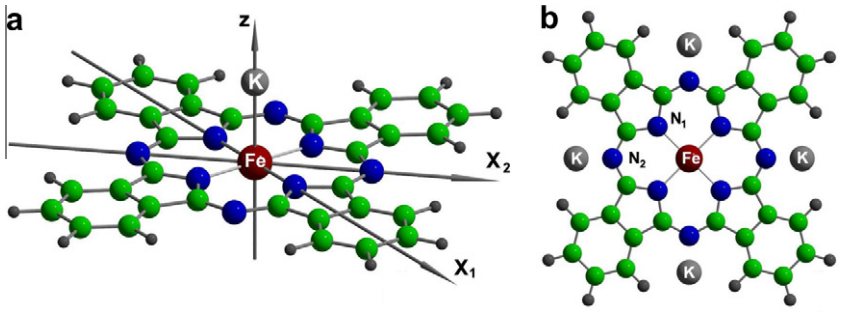

Fig. 4. (a) Schematic presentation of FePc molecule, potassium atom above of iron atom and two high symmetry axes X_1 and X_2 along which the K atom was moved being 2.0 Å above the molecular plane. (b) Schematic diagram of the possible positions of the K atoms or ions intercalated in FePc molecule for the doping concentration of four ions for one FePc molecule.

tive charge transfers to the Pc molecule. The latter is evident because one observes a strong total shift of PE spectra to higher BE, which indicates a Fermi level shift to the lowest unoccupied molecular orbital (LUMO)of FePc. Furthermore, at higher doping levels (in our measurements – at X = 7.5), different lattice sites have to be occupied. Indeed, it was shown earlier, that probably after saturation of sites closed to asa-bridging nitrogens corresponding to four potassium atoms per one FePc molecule, K atoms occupy sites close to the aromatic carbon of the benzene rings and interacts to some degree with them.

We present here also a single molecule density functional theory (DFT) study, which allows us to determine the most favorable sites, which potassium ions occupy close to FePc molecules. The calculations were performed using the linear combination of atomic orbital (LCAO) formalism based on density functional theory and realized in the CRYSTAL code [26]. We use the three parametric Becke + Lee–Yang–Parr (B3LYP) exchange-correlation functional [27] which correct self-interaction error inherent in local density and generalized gradient approximations. The electron subsystem was described by the all electron basis sets in Gaussian form, namely, we use 6-311+G** basis set for C, N and H atoms [28] and TZVP [29] basis for Fe and K. The structure of the FePc molecule was optimized. We found that the FePc molecule has a planar structure and a total magnetic moment of 2 μ_B in the ground state. The next excited magnetic configuration is a quintet ($\mu_{total} = 4\ \mu_B$) with planar atomic structure. The excited magnetic state is only 0.62 eV higher in energy then the ground state.

Taking into account our previous conclusion, that potassium strongly reacts with the asa nitrogen atoms and pyrrole carbon, we move K across the FePc molecule along two high symmetry axes X_1 and X_2 as is shown in Fig. 4(a). For detailed investigations, we assume that the potassium atom can be neutral and ionized (K^1+) and the FePc molecule can be in two magnetic states.

The results of our calculations are shown in Fig. 5. The curve with square symbols in two Fig. 5(a and b) corresponds to binding energy calculations between a FePc molecule in the excited magnetic state and neutral K. The circles show the binding energy data between a FePc molecule in the ground state and neutral potassium. Here, we have to note that we present the energetically preferable configuration where the magnetic moment of the molecule and the neutral K atom are antiparallel for both magnetic states of FePc. Thus, the curves with squares correspond to the FePc + K system with a total magnetic moment of 3 μ_B and the circles are related to the system with the total magnetic moment of 1 μ_B. The triangles describe the interaction between ionized K^+ and FePc molecule in the ground state (total magnetic moment is 2 μ_B).

For the X_1 direction (Fig. 5(a)) the interaction energy between K atom or ion and the FePc molecule is positive for any distance up to 7.5 Å, which means a repulsion between potassium and molecule. The displacement of the K atom along X_2 axis shows that the potassium atom and ion can create a stable bond with FePc molecule in both magnetic states. In this case, the potassium is situated close to the asa-bridging nitrogen N_2. The energetically preferable configuration corresponds to the system with the smallest total magnetic moment $\mu(\mathrm{FePc} + \mathrm{K}^0) = 1\ \mu_B$. We also found the charge transfer from originally neutral K atom in amount of $1e^-$ to FePc molecule. Now, taking into account that the binding energy between FePc molecule and ionized K^{1+} atom is quite large (see Fig. 5(b)) we can assume that only ionized K atoms can migrate into the FePc slab. The further relaxation of the FePc molecule with the K atom or ion shows that the potassium is still situating close to N_2 atom but out of the molecular plane. Therefore, for the comparison of the theoretical and experimental spectra one needs to analyze the interaction of the potassium with two or more FePc molecules. Finally, our theoretical data confirm conclusions above, that K atoms (ions) intercalated into FePc film occupy one type of equivalent positions in FePc molecule along X_2 axis, namely – close to of asa-bridging nitrogens N_2 as schematically shown in Fig. 4(b).

We now discuss the experimental valence-band photoemission spectra shown in Fig. 6(a and b). Here we should remark that the molecular planes of FePc deposited onto the Au(001) substrate lie parallel to substrate surface and the FePc layer is highly ordered with a square unit cell of approximately $14.2 \times 14.2\ \text{Å}^2$ aligned along the (110) and $(1\bar{1}0)$ axes of the gold surface [11]. Therefore we have recorded the VB spectra from the FePc film as a function of potassium doping at two different experimental geometries: with the **E** vector of the incoming photons near normal to the surface (P-p, Fig. 6(a)) and almost parallel to the

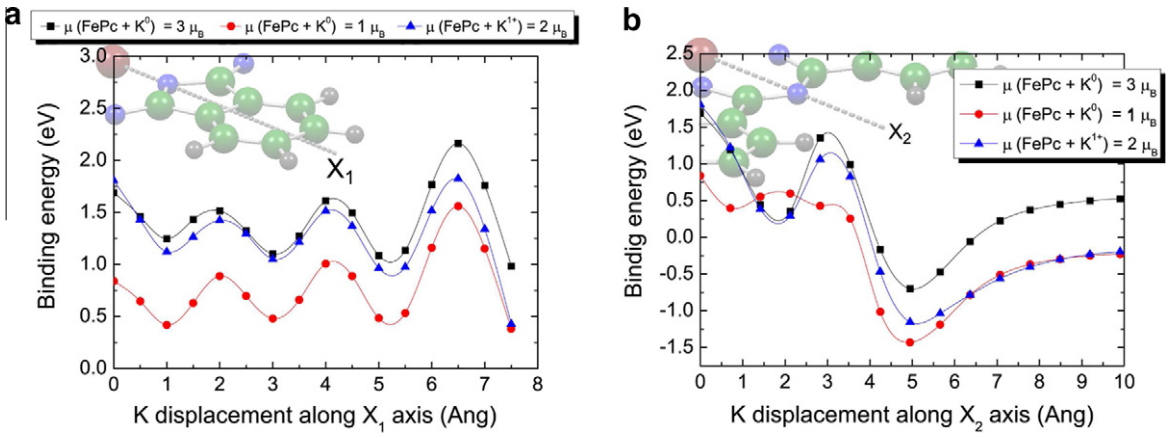

Fig. 5. The binding energy between FePc molecule in different magnetic states and potassium atom and ion as a function of K displacement along X_1 (a) and X_2 (b) axes. The details of the figure see in the text.

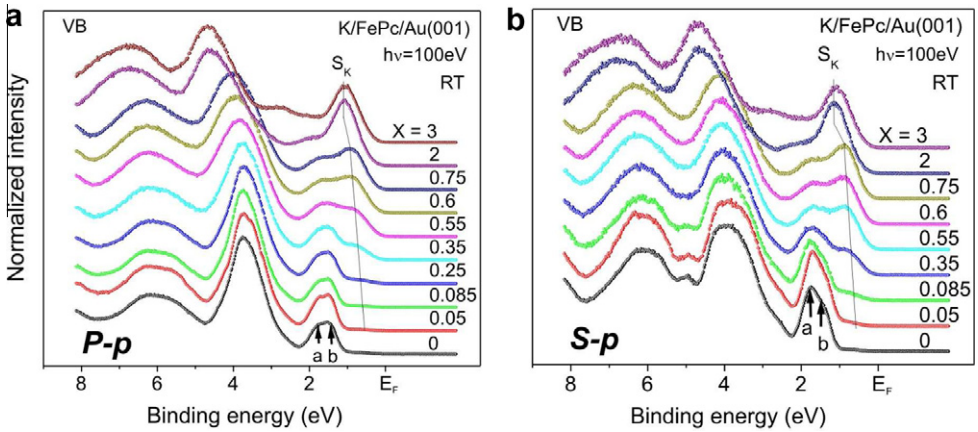

Fig. 6. VB spectra recorded from a FePc film as a function of potassium doping. (a) For the polarization vector **E** perpendicular (P-p) to the sample surface and (b) parallel (S-p) to the one.

surface (S-p, Fig. 6(b)), while the emission direction was always parallel to the **E** vector. The lowest spectra in both Fig. 6(a and b) represent the VB photoelectron emission from pristine FePc just after organic film formation. A comparison of the spectra recorded from the Au(001) substrate just before FePc film deposition (not shown here) to the spectra from the pristine organic film shows that no valence-band features of the gold substrate are visible in the VB spectra of the pristine FePc film thus confirming that the organic film spectra are representative of FePc. The polarization dependence of VB spectra can help to identify different features of the spectra [23,30]. Our calculations indicate, that the top of the VB of pristine FePc with a spectral weight maximum located around 1.7 eV below E_F has two, (a and b) components, where the first one originates from Fe 3*d* electrons, while second one is mostly due to emission from carbon of benzene rings [31]. Some earlier investigation also point out that the highest occupied molecular orbital for FePc has strong metal 3*d* character [24,32]. The onset of the FePc valence band is found at about 1.25 eV below E_F. The valence-band onset for the pristine FePc film indicates that the initial E_F position is located near the middle of the transport gap which has been reported to be 2.6 eV [33]. The midgap position of the E_F is consistent with the intrinsic nature of the FePc films as prepared in this study.

As a result of K deposition one new peak appears in the VB spectra at about 0.7 eV below E_F which is marked "S_K" (see Fig. 6). The spectral weight of this feature rises with increasing doping and can be assigned to the electron emission from the past LUMO of FePc which now becomes filled as a result of the transferred electrons from potassium, or to emission from Fe 3d states that become occupied upon charge transfer. The appearance of such a doping-induced feature in the energy gap of the organic semiconductor corresponds to what has been found for another doped organic semiconductors [10,17,34,35]. In addition, as a result of potassium doping we have found a shift of the spectra to higher binding energy, which corresponds to the E_F motion towards the conduction-band minimum.

Few years ago by means of electron-transport measurement techniques and scanning tunneling spectroscopy

(STS) the insulator-metal transitions have been observed for alkali-metal-doped Pc's and perylene tetracarboxylic dianhydride (PTCDA) [3,4]. Taking into account the fact that the PES is a direct method to prove metallicity, we recorded a series of photoemission spectra from the FePc films in the vicinity of E_F as a function of potassium doping. We did not detect any corroboration for emission from E_F in the whole doping range studied here. Therefore, we conclude that none of the K_x FePc films studied here was metallic. This is in agreement to previous PE studies [13,17], performed for K_x CuPc systems. The possible reasons for the discrepancy of the PE results and those from transport and STS measurements remains unclear (see also discussion in Ref. [17]). Finally we would like to draw attention to the fact, that upon potassium doping the polarization dependence of the photoemission data is lost. This might be due to the fact that potassium addition induces disorder or the formation of small grains of a doped phase.

In order to obtain deeper insight into the FePc electronic structure evolution upon potassium doping, we have also performed NEXAFS N 1*s* and C 1*s* measurements, which are discussed in the following.

Figs. 7 and 8 show the NEXAFS spectra of FePc at the N 1*s* and C 1*s* absorption edges as a function of K doping. The lowest absorption spectra ($X = 0$) are recorded from a pristine FePc film. The rather sharp features A, B, and C in Figs. 7 and 8 can be attributed to N 1*s* → π^* and C 1*s* → π^* excitations [36–40]. Moreover, we can suggest in analogy with [39] that the A, B, and C empty states revealed in the N 1*s* absorption spectra (Fig. 7) and the A, B, and C empty states probed in the C 1*s* absorption spectra [see Fig. 8] correspond to essentially the same π^* states, which have finite probability located at the pyrrole carbon and the nitrogen atoms linked to each other. This does not exclude contributions from excitations into C–C – π^* orbitals to these peaks.

Note that the N 1*s* core level consists of two components originating from both N_1 and N_2 nitrogen atoms (see Fig. 1) and the two core level binding energies differ by about 0.38 eV (see Fig. 2(d), top spectrum). Therefore the feature A in the N 1*s* absorption edge represents transitions from 1*s* core levels of both N_1 and N_2 nitrogen

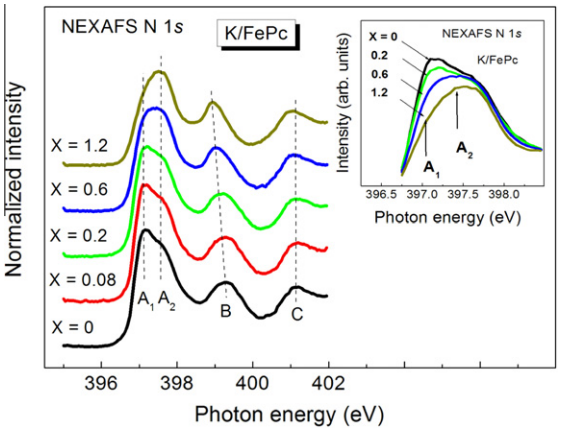

Fig. 7. NEXAFS spectra of FePc taken at the N 1*s* absorption edge as a function of potassium atoms concentration (X) per FePc molecule. The spectra were recorded at room temperature.

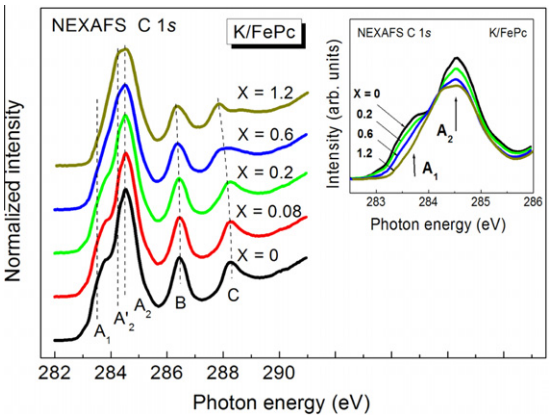

Fig. 8. NEXAFS spectra of FePc taken at the C 1*s* absorption edge as a function of potassium atoms concentration (X) per FePc molecule. The spectra were recorded at room temperature.

atoms into energetically low lying π^* states and consists also of two components: A_1 and A_2 separated by 0.38 eV, while A_1 and A_2 represent transition from N 1*s* core levels of N_1 and N_2 sites correspondently.

Now we will talk about the evolution of the NEXAFS absorption spectra at the N 1s absorption edge with potassium doping. The profile of feature *A* changes upon doping mostly by an decrease of spectral weight at the low energy side (feature A_1 in Fig. 7). This is especially evident by a direct comparison of the N 1*s* absorption spectra with different K doping in inset of Fig. 7. The intensity of the A_1 feature in Figure substantially reduces upon doping. This is a direct result of the filling of LUMO by charge transfer from the potassium ions. The intensity reduction as seen in Figs. 7 and 8 is in good correlation with the doping level. The spectral features B and C at higher photon energies show a shift to lower energies as a function of doping (see Fig. 6(a)), which parallels the situation in potassium-doped C_{60} (Ref. [41]) and can be associated with the relaxation of the molecular structure and bond lengths of the FePc molecules upon adding charge to the LUMO, which is of antibonding π^* character.

The evolution of the C 1*s* NEXAFS spectrum for FePc films as a function of potassium doping is presented in Fig. 8. With increasing potassium quantity the intensity of spectral feature A_1, which can be attributed to transitions from C 1*s* core levels of the benzene carbon atoms (C_2, C_3, C_4) into the LUMO, decreases. This behavior becomes more evident in inset of Fig. 8, where the C 1*s* absorption spectra for selected potassium content are superimposed. We can conclude that the density of states of the LUMO decreases with K doping as a consequence of filling this molecular orbital. Assuming that the LUMO wave function has a finite probability at both carbon and nitrogen sites in FePc, it is obvious that the filling of this molecular orbital becomes observable at both the N 1*s* and C 1*s* absorption edges. The second finding in the C 1*s* NEXAFS spectra is emergence and development of a new peak at the lower photon energy of about 0.3 eV relative to the A_2 absorption peak as a result of increasing K concentration (see Fig. 8, A_2). This observation becomes more

clear in inset of Fig. 8. We can attribute this appearance to a chemical shift to lower BE of the C 1*s* level of a number of pyrrole carbon atoms C_1 (see Fig. 1) due to the existence of potassium ions close to the FePc molecules, which leads to a downshift of the absorption edge. Indeed, the fit analysis of the C 1*s* core level photoemission data for selected doping levels proves the appearance and growth of a new C 1*s* component shown in Fig. 2(c), which is at energies in between those (C 1*s* (P) and C 1*s* (B)) related to undoped FePc. This explanation is in full agreement with the chemical shift observed for the pyrrole nitrogen atoms as a function of doping (see Fig. 2(d) and the discussion above). Besides, the absorption peaks B and C at higher photon energies as presented in Fig. 8 move to lower energies with increasing potassium content, similar to what is seen for the nitrogen absorption data.

4. Summary

This contribution presents the photoemission and photoabsorption studies of K doped FePc using synchrotron radiation. Our findings indicate that with potassium doping the density of states in the energy region of the LUMO is reduced. In addition, the spectral alteration as established for both C 1s and N 1s absorption edges can be explained in consideration of the charge transfer and the related changes (chemical shifts) of the corresponding core levels. Moreover, our observations indicate the filling of the LUMO of FePc with electrons that stem from potassium, and it is established that the potassium ions are located closely to pyrolle nitrogen atoms of the FePc molecule.

Acknowledgement

This work was supported by the DFG under Grants Nos. KN393/9 and KN393/14, by the RFBR under Grant Nos. 08-02-01170 and 10-02-00269. We are grateful to R. Hubel, R. Schonfelder, and S. Leger for technical assistance.

References

[1] M. Pfeiffer, A. Beyer, T. Fritz, K. Leo, Appl. Phys. Lett. 73 (1998) 3202.
[2] A. Nollau, M. Pfeiffer, T. Fritz, K. Leo, J. Appl. Phys. 87 (2000) 4340.
[3] V. Shklover, S. Schmitt, E. Umbach, F.S. Tautz, M. Eremtchenko, Y. Shostak, J.A. Schaefer, M. Sokolowski, Surf. Sci. 482 (2001) 1241.
[4] M.F. Craciun, S. Rogge, M.J.L. den Boer, T.M. Klapwijk, A.F. Morpurgo, J. Phys. IV 114 (2004) 607.
[5] M. Knupfer, Surf. Sci. Rep. 42 (2001) 1.
[6] O. Gunnarsson, Rev. Mod. Phys. 69 (1997) 575. and references therein.
[7] G. Brocks, J. van den Brink, A.F. Morpurgo, Phys. Rev. Lett. 93 (2004) 146405.
[8] E. Tosatti, M. Fabrizio, J. Tobik, G.E. Santoro, Phys. Rev. Lett. 93 (2004) 117002.
[9] R.W. Lof, M.A. van Veenendaal, B. Koopmans, H.T. Jonkman, G.A. Sawatzky, Phys. Rev. Lett. 68 (1992) 3924.
[10] M. Knupfer, H. Peisert, T. Schwieger, Phys. Rev. B 65 (2002) 033204.
[11] O.V. Molodtsova, M. Knupfer, Yu.A. Ossipyan, V.Yu. Aristov, J. Appl. Phys. 104 (2008) 083704.
[12] X-ray Photoelectron Spectroscopy (XPS) Database, Version 3.4 (<http://srdata.nist.gov/xps/>).
[13] T. Schwieger, H. Peisert, M.S. Golden, M. Knupfer, J. Fink, Phys. Rev. B 66 (2002) 155207.
[14] V. Yu. Aristov, O.V. Molodtsova, V.M. Zhilin, D.V. Vyalikh, M. Knupfer, Phys. Rev. B 72 (2005) 165318.
[15] L. Ottaviano, S. Di Nardo, L. Lozzi, M. Passacantando, P. Picozzi, S. Santucci, Surf. Sci. 373 (1997) 318.
[16] G. Dufour, C. Poncey, F. Rochet, H. Roulet, M. Sacci, M. De Santis, M. De Crescenzi, Surf. Sci. 319 (1994) 251.
[17] O.V. Molodtsova, V.M. Zhilin, D.V. Vyalikh, V.Yu. Aristov, M. Knupfer, J. Appl. Phys. 98 (2005) 093702.
[18] V.V. Maslyuk, V.Y. Aristov, O.V. Molodtsova, D.V. Vyalikh, V.M. Zhilin, Y.A. Ossipyan, T. Bredow, I. Mertig, M. Knupfer, Appl. Phys. A 94 (2009) 485.
[19] H. Peisert, M. Knupfer, J. Fink, Surf. Sci. 515 (2002) 491.
[20] N. Papageorgiu, Y. Ferro, E. Salomon, A. Allouche, J.M. Layet, L. Giovanelli, G. Le Lay, Phys. Rev. B 68 (2003) 235105.
[21] B. Brena, Y. Luo, M. Nyberg, S. Carniato, K. Nilson, Y. Alfredsson, J. Ahlund, N. Martensson, H. Siegbahn, C. Puglia, Phys. Rev. B 70 (2004) 195214.
[22] B. Bialek, I.G. Kim, J.I. Lee, Thin Solid Films 51 (2006) 110.
[23] J. Ahlund, K. Nilson, J. Schiessling, L. Kjeldgaard, S. Berner, N. Martensson, C. Puglia, B. Brena, M. Nyberg, Y. Luo, J. Chem. Phys. 125 (2006) 034709.
[24] M.-S. Liao, S. Scheiner, J. Chem. Phys. 114 (2001) 9780.
[25] D.M. Poirier, D.W. Owens, J.H. Weaver, Phys. Rev. B 51 (1995) 1830.
[26] V.R. Saunders, R. Dovesi, C. Roetti, R. Orlando, C.M. Zicovich-Wilson, N.M. Harrison, K. Doll, B. Civalleri, I. Bush, Ph. D'Arco, M. Llunell CRYSTAL2003 User's Manual, University of Turin, Turin, 2003.
[27] A.D. Becke, J. Chem. Phys. 98 (1993) 5648.
[28] R. Krishnan, J.S. Binkley, R. Seeger, J.A. Pople, J. Chem. Phys. 72 (1980) 650.
[29] Turbomole Database (<ftp://ftp.chemie.uni-karlsruhe.de/pub/basen/fe> and <ftp://ftp.chemie.uni-karlsruhe.de/pub/basen/k>).
[30] B. Kessler, Appl. Phys. A: Mater. Sci. Process. 67 (1998) 125.
[31] M. Grobosch, V.Yu. Aristov, O.V. Molodtsova, C. Schmidt, B.P. Doyle, S. Nannarone, M. Knupfer, J. Phys. Chem. C 113 (2009) 13219.
[32] X. Lu, K.W. Hipps, J. Phys. Chem. B 101 (1997) 5391.
[33] G.D. Sharma, R. Kumar, M.S. Roy, Sol. Energy Mater. Sol. Cells 90 (2006) 32.
[34] N. Johansson, T. Osada, S. Stafstrom, W.R. Salaneck, V. Parente, D.A. dos Santos, X. Crispin, J.L. Bredas, J. Chem. Phys. 111 (1999) 2157.
[35] L. Yan, N.J. Watkins, S. Zorba, Y. Gao, C.W. Tang, Appl. Phys. Lett. 79 (2001) 4148.
[36] H. Peisert, T. Schwieger, J.M. Auerhammer, M. Knupfer, M.S. Golden, J. Fink, J. Appl. Phys. 90 (2001) 466.
[37] T. Okajima, H. Fujimoto, M. Sumitomo, T. Araki, E. Ito, H. Ishiil, Y. Ouchi, K. Seki, Surf. Rev. Lett. 9 (2002) 441.
[38] G. Cabailh, J.W. Wells, I.T. McGovern, A.R. Vearey-Roberts, A. Bushell, D.A. Evans, Appl. Surf. Sci. 234 (2004) 144.
[39] O.V. Molodtsova, M. Knupfer, V.V. Maslyuk, D.V. Vyalikh, V.M. Zhilin, Yu. A. Ossipyan, T. Bredow, I. Mertig, V. Yu. Aristov, J. Chem. Phys. 129 (2008) 154705.
[40] O.V. Molodtsova, M. Knupfer, V.Yu. Aristov, D.V. Vyalikh, V.M. Zhilin, Yu.A. Ossipyan, J. Appl. Phys. 103 (2008) 053711.
[41] M. Knupfer, J.F. Armbruster, H.A. Romberg, J. Fink, Synth. Met. 70 (1995) 1321.

molecular orbital (LUMO) levels were obtained in thin films made from the solution-processible quinoidal oligothiophene [QQT(CN)4] by laser irradiation treatment using a near infrared scanning laser system. The excitation wavelength was carefully chosen to match the absorption band of this material in thin film in order to be able to heat locally the devices in micro-sized regions delimited by the laser spot size. The majority carrier type conversion was attributed to the effects of a thermal treatment on QQT(CN)4 film morphology, resulting in dramatic changes in both charge injection processes and charge carrier hopping distances [23,27]. The proposed new patterning method was then used to realize complementary organic inverters, NAND and NOR logic circuits in QQT(CN)4 thin films spin-coated on top of a polyimide gate dielectric [23].

In this manuscript, we report a comparative experimental study of the electrical performance of solution-processed organic inverters based on the combination of ambipolar as-prepared and n-type top-contact QQT(CN)4 OFETs patterned by direct laser writing. These logic circuits were fabricated using SiO_2 and polyimide as gate insulating materials. The results show the effects of the laser irradiation on the characteristics of the inverters including a significant increase of the gain and a notable improvement of the on-state. We also found that the insertion of a thin polyimide film between the QQT(CN)4 and the SiO_2 layers could reduce selectively the electron field-effect mobility and improve the off-state of the inverters. Spatial and selective control of the ambipolar characteristics in QQT(CN)4 thin films by combining the direct laser writing technique and the patterning of the polyimide film enables the fabrication of purely CMOS organic inverters based on a solution-processed organic thin film made from a single organic semiconductor. The high performance of these devices, together with their good stability in air and their ease of fabrication via solution-processing methods show the high potential of QQT(CN)4 and quinoidal oligothiophenes for future organic electronic applications.

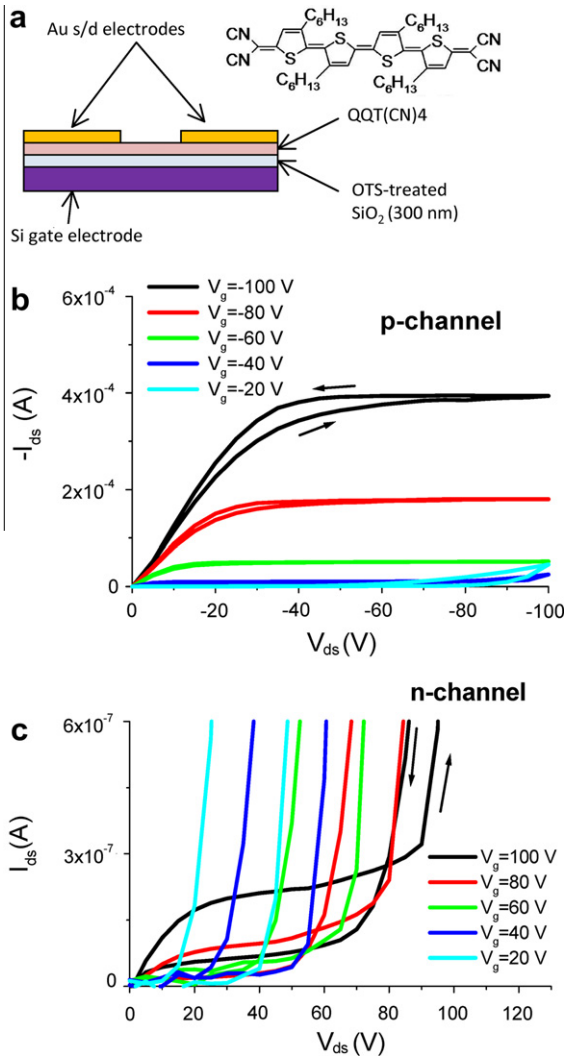

Fig. 1. (a) Schematic representation of an ambipolar Au top-contact QQT(CN)4 OFET with an OTS-treated 300 nm thick SiO_2 dielectric layer. Output characteristics of this device in (b) hole enhancement and (c) electron enhancement modes. The QQT(CN)4 thin film was used as-prepared and had a thickness of about 90 nm. Channel length and width are 45 μm and 4 mm, respectively.

2. Experimental

QQT(CN)4 was synthesized according to an improved procedure that has been described in the literature [28]. Its chemical structure is shown in Fig. 1a. OFETs and complementary inverters were fabricated on top of heavily doped n-type silicon wafer substrates with thermally grown SiO_2 layers. Three different gate dielectrics were used in this work: (i) an octadecyltrichlorosilane (OTS)-treated 300 nm thick SiO_2 layer, (ii) a 1 μm thick polyimide film and (iii) a 300 nm thick SiO_2 layer onto which a 150 nm thick polyimide film was formed by spin-coating. The OTS treatment of the precleaned SiO_2 surface was achieved by a soak in 5 mM solution in hexane for nearly 10 h. The samples were then rinsed in hexane solution and heated at 120 °C for 2 min. The 1 μm thick polyimide films were spin-coated from a solution of precursor (Kyocera CT4112) in *N*-methyl-2-pyrrolidinone onto 25 nm thick Al gate electrodes thermally evaporated through a shadow mask on the substrates (silicon wafers with 1 μm thick SiO_2 layer). To form 150 nm thick polyimide films, the solution of polyimide precursor was diluted appropriately prior to the deposition by spin-coating. QQT(CN)4 thin films were then spin-coated onto the dielectric layers from a 10 mg/ml chloroform solution at 3000 rpm. Top contact Cr drain/source electrodes were thermally evaporated on top of the devices (ii). The two other types of OFETs [(i) and (iii)] used gold as top-contact metal electrodes. Channel length (L) and channel width (W) were 45 μm and 4 mm. Laser-conversion of the QQT(CN)4 films by direct laser writing was performed before the evaporation of the source/drain electrodes using the laser patterning system and the experimental conditions previously described [23]. The laser irradiation of the samples at a wavelength of 1060 nm and a power of 6.7 W was carried out in air. The laser spot size illuminating the organic thin

films corresponding to the full-width at half maximum was measured by a beam profiler to be around 300 μm. The distance between two consecutive lines during the sample scanning was chosen to be half of the spot size. The speed of the laser irradiation scanning was 0.1 mm/s for the OFETs using the 1 μm thick polyimide film and 0.04 mm/s for the two other device structures. The electrical measurements were performed in ambient atmosphere using a couple of picoammeter/voltage source units (Keithley, model 6487) and a source meter unit (Keithley, model 2400).

3. Results and discussion

The ambipolar nature of charge transport in QQT(CN)4 OFETs using OTS-treated SiO_2 as gate dielectric and Au top contact source/drain electrodes (schematic device structure shown in Fig. 1a) can be seen in the output characteristics displayed in Fig. 1b and c. At both high positive and negative bias V_g and low source–drain voltage V_d, saturation of the drain current I_d is clearly observed, indicating that the device operates in electron and hole accumulation modes, respectively. On the other hand, at low V_g and high V_d, the device shows diode-like curves with a rapid increase of I_d with V_d, this effect being much more pronounced in the n-channel. Such a behavior is typical for ambipolar OFETs and is due to the presence of both charge carriers in the channel. In contrast, the output characteristics measured in the device based on laser-converted QQT(CN)4 thin film (Fig. 2) indicate that this device works well in the electron accumulation mode with saturation of I_d observed at positive V_g. These results are in good consistency with previous reports displaying the output and transfer characteristics of similar OFETs based on ambipolar as-prepared and n-type thermally-converted QQT(CN)4 thin films using either OTS-treated SiO_2 or polyimide as gate dielectric [23,27]. The leakage current in these devices was typically much lower than 5×10^{-7} A/cm^2 at 2 MV/cm. While electron field-effect mobility extracted from the transfer characteristics in the saturation regime is not significantly affected by laser irradiation and is about 0.004 cm^2/V s, hole field-effect mobility is measured to be around 0.07 cm^2/V s in as-prepared QQT(CN)4 film and can be decreased by the direct laser writing technique. It is important to note that the laser irradiation conditions chosen in this work (wavelength of 1060 nm, power of 6.7 W, spot size of 300 μm and scanning speeds lower than 0.1 mm/s) are sufficiently strong to completely suppress hole conduction in the devices without causing any degradation of the samples [23].

As displayed in Fig. 3a, two identical ambipolar p-type dominant as-prepared QQT(CN)4 OFETs were fabricated on the same OTS-treated 300 nm thick SiO_2 gate dielectric layer. These transistors were connected to form an inverter circuit. Fig. 3b shows the transfer characteristics of the inverter for various supply voltages (V_{DD}) ranging from 20 to 50 V. The complementary-like logic circuit operates reliably within this range of V_{DD}, as revealed by the switching behavior at an input voltage (V_{IN}) lower than V_{DD}. As shown in Fig. 3c, the highest gain for this inverter is about

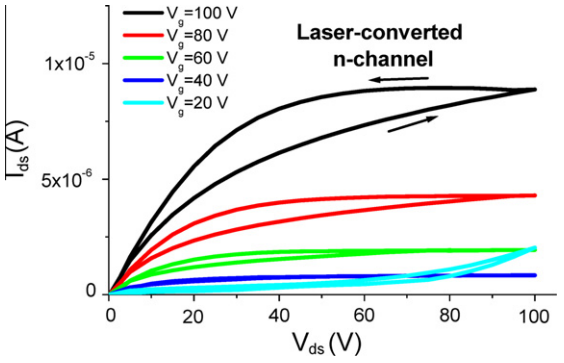

Fig. 2. Output characteristics of the laser-converted n-type Au top-contact QQT(CN4) OFET with an OTS-treated 300 nm thick SiO_2 dielectric layer in electron enhancement mode. Laser-irradiation of the sample was carried out using a fiber laser emitting at 1060 nm with a power of 6.7 W. The scanning speed was 0.04 mm/s and the spot size was measured to be around 300 μm. Channel length and width are 45 μm and 4 mm, respectively.

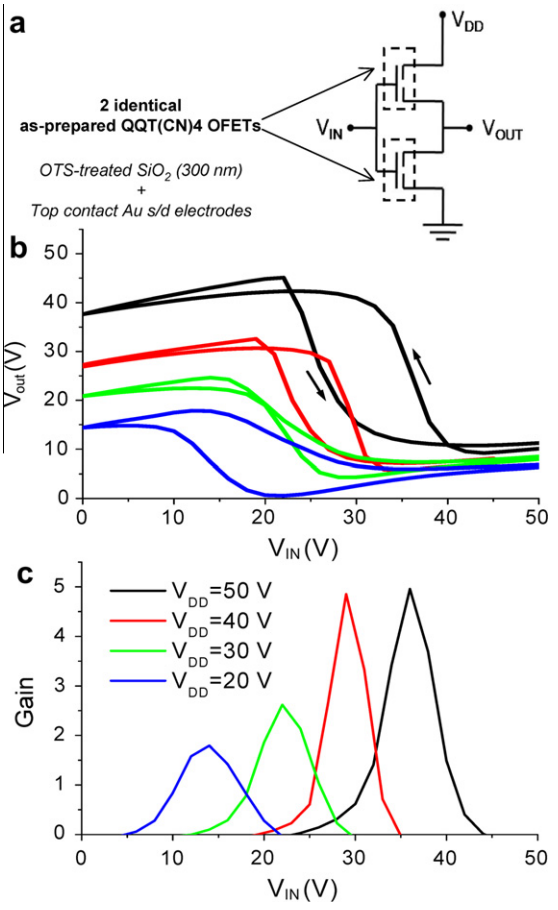

Fig. 3. (a) Schematic of the complementary inverter employing two identical ambipolar as-prepared QQT(CN)4 OFETs with an OTS-treated 300 nm thick SiO_2 gate dielectric layer and Au source drain electrodes. (b) Transfer characteristics and (c) gain of the inverter. The supply voltage (V_{DD}) was varied from 20 to 50 V.

5 for V_{DD} = 50 V and decreases up to 1.8 for V_{DD} = 20 V. These moderate values are on the same order of magnitude as those typically reported in organic inverters based on two identical ambipolar OFETs [29,30]. Because the two as-prepared QQT(CN)4 OFETs can never be completely switched off during the inverter operation, the output voltage (V_{OUT}) does not reach V_{DD} and zero, at small and large V_{IN}, respectively. The output voltage swing that we define as the difference between the minimum and maximum values of V_{OUT} is found to be 33 V for V_{DD} = 50 V. As a specific feature of ambipolar inverters [8], one must note that this circuit presents similar switching characteristics in the first and third quadrant (V_{IN} < 0 and V_{OUT} < 0) of the V_{IN} versus V_{OUT} plot (data not shown). It is also essential to mention that these inverters operate well and are stable in ambient conditions.

Similar measurements were performed in an organic inverter based on two identical ambipolar as-prepared QQT(CN)4 OFETs using 1 μm polyimide layer as gate dielectric and Cr as source/drain metal electrodes. The schematic structure of these OFETs and a picture of the inverter are shown in Fig. 4a. The transfer characteristics and the gain measured in this inverter for several V_{DD} ranging from 20 to 50 V are reported in Fig. 4b and c. We found that, for V_{DD} = 50 V, the highest gain and the output voltage swing of this circuit are about 6.1 and 35 V, respectively. These results show that the ambipolar as-prepared QQT(CN)4 inverters fabricated on OTS-treated SiO_2 and polyimide present very similar performance. The large hysteresis observed in the transfer characteristics of these logic circuits might be a real problem for practical applications and further studies are still needed to identify the causes of this effect.

As displayed in Fig. 5a, ambipolar as-prepared and laser-converted n-type QQT(CN)4 OFETs were then fabri-

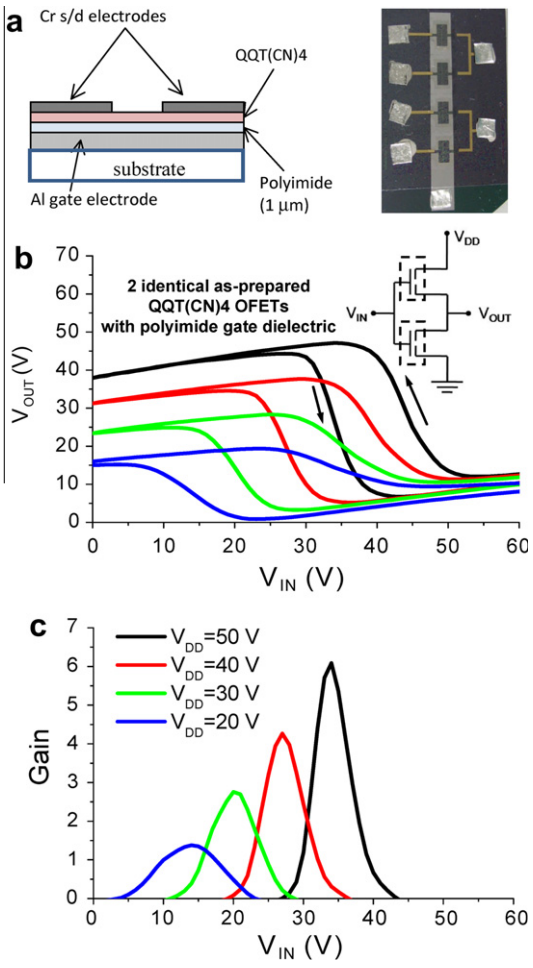

Fig. 4. (a) Schematic structure of an inverter employing two identical ambipolar as-prepared QQT(CN)4 OFETs with a 1 μm thick polyimide gate dielectric layer and Cr source drain electrodes. A top view picture of two inverter circuits fabricated on a same substrate is also shown. (b) Transfer characteristics and (c) gain of the inverter V_{DD} was varied from 20 to 50 V.

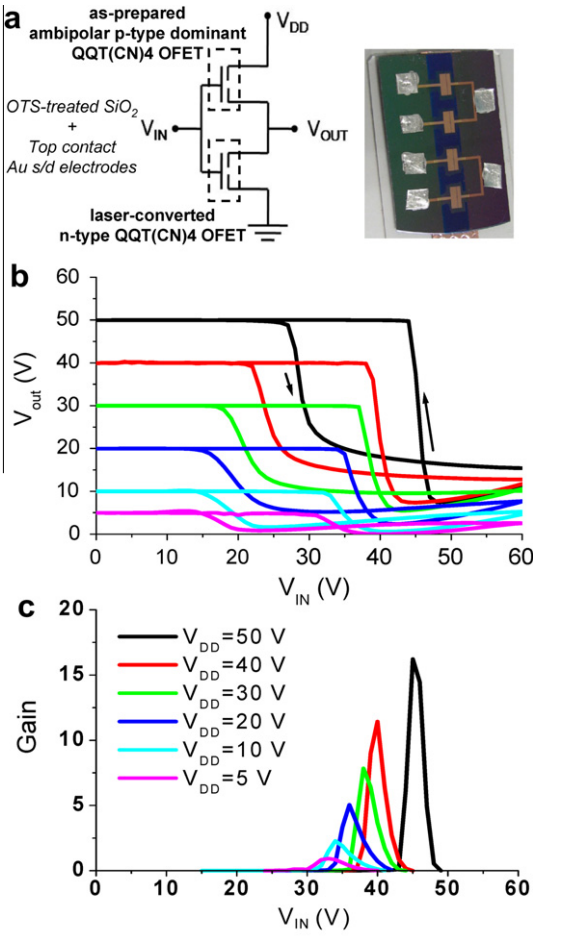

Fig. 5. (a) Schematic structure of a complementary inverter employing one ambipolar as-prepared and one laser-converted n-type QQT(CN)4 OFETs. Both transistors used an OTS-treated 300 nm thick SiO_2 gate dielectric layer and Au source drain electrodes. Laser-conversion was achieved by direct laser writing using a fiber laser emitting at 1060 nm with a power of 6.7 W. The scanning speed was 0.04 mm/s and the spot size was 300 μm. A top view picture of two inverters based on such a structure and prepared on a same substrate is also shown. (b) Transfer characteristics and (c) gain of the complementary inverter with V_{DD} varying from 5 to 50 V.

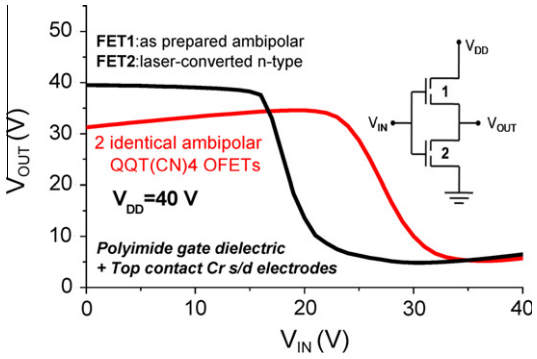

Fig. 6. (a) Transfer characteristics of the inverters employing (a) two identical ambipolar as-prepared QQT(CN)4 OFETs (red line) and (b) one ambipolar as-prepared and one laser-converted n-type QQT(CN)4 OFETs (black line). Both logic circuits used 1 μm thick polyimide film as gate dielectric layer and Cr source drain electrodes. V_{DD} was equal to 40 V. Laser-conversion was performed by direct laser writing using a fiber laser emitting at 1060 nm with a power of 6.7 W. The scanning speed was 0.1 mm/s and the spot size was 300 μm. (For interpretation of the references to colour in this figure legend, the reader is referred to the web version of this article.)

cated on a single silicon substrate with OTS-treated 300 nm thick SiO_2 gate dielectric layer and were connected together to form an inverter stage. Fig. 5b shows the transfer characteristics of this logic circuit for V_{DD} ranging from 5 to 50 V. At small V_{IN} values, the ambipolar as-prepared QQT(CN)4 OFET which shows high hole field-effect mobility is on while the laser-converted OFET is off. As a result, the output voltage V_{OUT} is equal to V_{DD}. As V_{IN} is increased, the n-channel OFET is turned on and switching of V_{OUT} to low values occurs. However, because the ambipolar as-prepared QQT(CN)4 OFET is not turned off at high V_{IN} values, both devices are on and V_{OUT} cannot reach zero in the off-state of the inverter. For V_{DD} = 50 V, the output voltage swing characterizing the inversion of this circuit dramatically depends on the sweeping direction of V_{IN} and is measured to be either 42.6 V or 34.6 V. As shown in Fig. 5c, highest gain extracted from the transfer characteristics of the inverter is found to be as high as 16.2 at V_{DD} = 50 V and is still equal to nearly 1 at V_{DD} = 5 V. Overall, these results show that the laser-conversion of one QQT(CN)4 OFET from ambipolar to n-type by the direct laser writing technique can significantly improve the on-state of the inverter

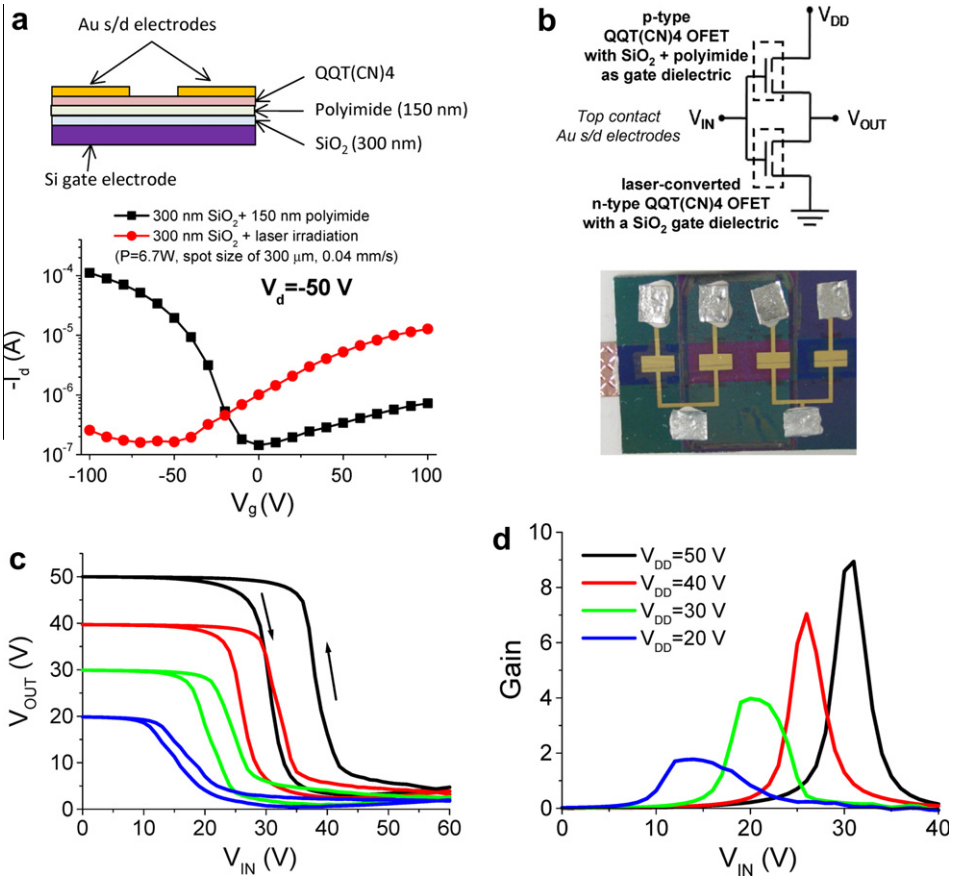

Fig. 7. (a) Transfer characteristics of p-type and n-type QQT(CN)4 OFETs at $V_d = -50$ V. The n-type device was obtained by direct laser writing and used an OTS-treated 300 nm thick SiO_2 gate dielectric layer. The structure of the p-type device is displayed. This OFET was based on an as-prepared QQT(CN)4 thin film and used a 150 nm thick polyimide layer spin-coated on top of a 300 nm thick SiO_2 layer as gate dielectric. Both transistors used top-contact Au source/drain electrodes with channel length of 45 μm and width of 4 mm. (b) Schematic representation of a purely CMOS inverter based on a single QQT(CN)4 thin film. The picture shows two inverters fabricated on the same substrate. (c) Transfer characteristics of the CMOS inverter with V_{DD} ranging from 20 to 50 V. (d) Corresponding gain measured at different V_{DD}.

and its gain. However, this approach does not lead to any improvement in the off-state and does not reduce the large hysteresis observed in ambipolar QQT(CN)4 inverters.

Fig. 6 compares, for V_{DD} = 40 V, the transfer characteristics of an ambipolar inverter and an inverter based on the combination of one ambipolar as-prepared and one photoconverted n-type QQT(CN)4 OFETs. Both logic circuits were fabricated onto a single 1 μm thick polyimide gate dielectric layer. The inversion properties of these logic circuits present similar trends as those obtained in the inverters using OTS-treated SiO_2 as gate dielectric, with the on-state improved by direct laser writing. For V_{DD} = 40 V, the output voltage swing of the photoirradiated logic circuit is measured to be around 35.2 V and is higher than the value of 29.4 V found in the ambipolar inverter. In addition, the highest gain at V_{DD} = 40 V is increased from 4.3 to 7.3 by our direct laser writing technique. Note that this behavior has been previously reported in similar QQT(CN)4 inverters fabricated onto flexible plastic substrates and patterned by thermal lithography [23].

Fig. 7a shows the schematic structure and the transfer characteristics of an ambipolar as-prepared QQT(CN)4 OFET using a 150 nm thick polyimide film on top of a 300 nm thick SiO_2 layer as gate dielectric. The device was fabricated in a top-contact configuration with gold electrodes and was characterized at $V_d = -50$ V. The result clearly shows ambipolar operation and allows us to estimate in the saturation regime hole and electron field-effect mobilities of 0.05 $cm^2/V\,s$ and 7×10^{-5} $cm^2/V\,s$, respectively. Whereas hole field-effect mobility is not notably affected by the introduction of this thin polyimide gate dielectric layer, electron transport is strongly reduced with a decrease of about one order of magnitude in mobility. This finding suggests a simple way to improve the off-state of the QQT(CN)4 inverters, the electron current in the OFET using the thin polyimide film being significantly lower than that observed in the laser-converted n-type OFET with an OTS-treated 300 nm thick SiO_2 gate dielectric. The new inverter structure is schematically represented in Fig. 7b and necessitates the patterning of the 150 nm thick polyimide film onto the substrate which can be done via the simple use of protecting tapes. Fig. 7c shows the transfer characteristics of this inverter for various supply voltages V_{DD} ranging from 20 to 50 V. This logic circuit almost shows an ideal CMOS response with V_{OUT} approaching V_{DD} and zero at low and high V_{IN}, respectively. For V_{DD} = 50 V, the output voltage swing of the CMOS inverter is equal to 46.9 V and the highest gain value is about 8.9 (Fig. 7d). It is also important to mention the notable reduction of the hysteresis in these transfer curves. Overall, these results demonstrate the possibility to fabricate a purely CMOS QQT(CN)4 inverter with enhanced performance by combining the direct laser writing technique and the patterning of a thin polyimide film onto the SiO_2 gate dielectric layer. The gain of this inverter is lower than that measured in the laser-converted QQT(CN)4 logic circuit using OTS-treated SiO_2 as gate dielectric. However, this lower gain issue is largely compensated by both the smaller hysteresis and the strong improvement of the off-state which should lead to a significant reduction of the power consumption.

4. Conclusion

In summary, we have fabricated and characterized in details the electrical properties of a series of solution-processed organic inverters based on single QQT(CN)4 thin films. Laser patterning from ambipolar to n-type QQT(CN)4 OFETs by the direct laser writing technique leads to a clear improvement of the performance in organic inverters using either OTS-treated SiO_2 or polyimide as gate dielectric layer. The laser-structured logic circuits show improved on-state at low input voltage and enhanced gain. However, they also display large hysteresis and non zero output voltage values in the off-state. To overcome these issues, we found that the introduction of a thin polyimide film spin-coated on top of a SiO_2 gate dielectric layer enables to selectively decrease the electron field-effect mobility. One laser-converted n-type OFET prepared onto OTS-treated SiO_2 and one p-type OFET fabricated onto a SiO_2/polyimide gate dielectric were successfully combined to realize a purely CMOS inverter based on a single solution-processed QQT(CN)4 thin film. This inverter presents enhanced on- and off-states as well as reduced hysteresis and gain as high as 8.9. Such a good performance qualifies this device structure as a promising candidate for applications in organic CMOS technology.

References

[1] B. Crone, A. Dodabalapur, Y.Y. Lin, R.W. Filas, Z. Bao, A. LaDuca, R. Sarpeshkar, H.E. Katz, W. Li, Nature 403 (2000) 521.
[2] H. Klauk, U. Zschieschang, J. Pflaum, M. Halik, Nature 445 (2007) 745.
[3] S. De Vusser, S. Steudel, K. Myny, J. Genoe, P. Heremans, Appl. Phys. Lett. 88 (2006) 162116.
[4] J.H. Na, M. Kitamura, Y. Arakawa, Appl. Phys. Exp. 1 (2008) 021803.
[5] X.H. Zhang, W.J. Potscavage, S. Choi, B. Kippelen, Appl. Phys. Lett. 94 (2009) 043312.
[6] J. Zaumseil, H. Sirringhaus, Chem. Rev. 107 (2007) 1296.
[7] J. Cornil, J.L. Brédas, J. Zaumseil, H. Sirringhaus, Adv. Mater. 19 (2007) 1791.
[8] E.J. Meijer, D.M. de Leeuw, S. Setayesh, E. Van Veenendaal, B.H. Huisman, P.W.M. Blom, J.C. Hummelen, U. Scherf, T.M. Klapwijk, Nat. Mater. 2 (2003) 678.
[9] M. Shkunov, R. Simms, M. Heeney, S. Tierney, I. MacCulloch, Adv. Mater. 17 (2005) 2608.
[10] K. Tada, H. Harada, K. Yoshino, Jpn. J. Appl. Phys. 35 (Part 2) (1996) L944.
[11] A. Babel, J.D. Wind, S.A. Jenekhe, Adv. Mater. 14 (2004) 891.
[12] S. Cho, J. Yuen, Y. Kim, K. Lee, A.J. Heeger, Appl. Phys. Lett. 89 (2006) 153505.
[13] H. Wang, J. Wang, X. Yan, J. Shi, H. Tian, Y. Geng, D. Yan, Appl. Phys. Lett. 88 (2006) 133508.
[14] A. Dodabalapur, H.E. Katz, L. Torsi, R.C. Haddon, Science 269 (1995) 1560.
[15] E. Kuwahara, Y. Kubozono, T. Hosakawa, T. Nagano, K. Masunari, A. Fujiwara, Appl. Phys. Lett. 85 (2004) 2098.
[16] S.J. Kang, Y. Yi, C.Y. Kim, J.H. Seo, M. Noh, K. Jeong, K.H. Yoo, C.N. Whang, Appl. Phys. Lett. 87 (2005) 233502.
[17] R. Ye, M. Baba, Y. Oishi, K. Mori, K. Suzuki, Appl. Phys. Lett. 86 (2005) 253505.
[18] T.D. Anthopoulos, D.M. de Leeuw, E. Cantatore, S. Setayesh, E.J. Meijer, C. Tanase, J.C. Hummelen, P.W.M. Blom, Appl. Phys. Lett. 85 (2004) 4205.
[19] T.D. Anthopoulos, S. Setayesh, E. Smits, M. Cölle, E. Cantatore, B. de Boer, P.W.M. Blom, D.M. de Leeuw, Adv. Mater. 18 (2006) 1900.
[20] L. Bürgi, M. Turbiez, R. Pfeiffer, F. Bienewald, H.J. Kirner, C. Winnewisser, Adv. Mater. 20 (2008) 2217.
[21] T. Yasuda, T. Goto, K. Fujita, T. Tsutsui, Appl. Phys. Lett. 85 (2004) 2098.
[22] M. Chikamatsu, T. Mikami, J. Chisaka, Y. Yoshida, A. Shimizu, T. Kubo, Y. Morita, K. Nakasuji, Appl. Phys. 91 (2007) 043506.

[23] J.C. Ribierre, T. Fujihara, S. Watanabe, M. Matsumoto, T. Muto, A. Nakao, T. Aoyama, Adv. Mater. 22 (2010) 1722.
[24] N. Benson, M. Schidleja, C. Melzer, R. Schmechel, H. von Seggern, Appl. Phys. Lett. 89 (2006) 182105.
[25] M. Ahles, R. Schmechel, H. von Seggern, Appl. Phys. Lett. 87 (2005) 113505.
[26] W. Takashima, T. Murasaki, S. Nagamatsu, T. Morita, K. Kaneto, Appl. Phys. Lett. 91 (2007) 071905.
[27] J.C. Ribierre, S. Watanabe, M. Matsumoto, T. Muto, T. Aoyama, Appl. Phys. Lett. 96 (2010) 083303.
[28] H. Higuchi, T. Nakayama, H. Koyama, J. Ojima, T. Wada, H. Sasabe, Bull. Chem. Soc. Jpn. 68 (1995) 2363.
[29] M.M. Ling, Z. Bao, P. Erk, M. Koenemann, M. Gomez, Appl. Phys. Lett. 90 (2007) 093508.
[30] T.B. Singh, P. Senkarabacak, N.S. Sariciftci, A. Tanda, C. Lackner, R. Hagelauer, G. Horowitz, Appl. Phys. Lett. 89 (2006) 033512.

interface [7]. For example, Kobayashi et al. have described the modification and control of the electrical performance in *p*-type pentacene thin film transistors by varying the head groups of the SAM molecules, and have characterized the impact of different dipole moments of the SAM molecules at the interface [8]. Full control on the threshold voltage (V_{TH}) and the impact of the thin film morphology of the organic semiconductor has been demonstrated by using an extended series of self-assembled molecules with different functional groups (chain and head groups) [9].

Apart from the changes in properties that have been observed by using different combinations of surfaces and anchor groups (e.g., thiols, carboxylic acids, silanes, and phosphonic acids), homologous series of molecules with the same anchor group and chemically comparable molecular structure in the chain and head groups (e.g., *n*-alkanes) behave differently depending on their chain length. Although a temperature-independent exponential decrease of the tunneling current with increasing molecular chain length of *n*-alkanes is expected, several groups have observed anomalous behavior with increasing molecule length. It has been proposed that irregularities or defects in the SAM composition (loops or collapsed sites) lead to a decreased tunneling distance between the electrodes [10–12]. However, even SAMs that have been shown to form highly reliable systems, show remarkably reproducible changes in device characteristics that cannot be explained by defects, formed during SAM deposition, but rather must be due to morphological changes caused by characteristic intermolecular interactions. Recently, it was shown that the properties of organic field-effect transistors vary when the chain length of self-assembled *n*-alkyl phosphonic acids is modified. The charge carrier mobility and the morphology of a subsequent pentacene layer are affected [13–15]. Approximately, monotonic scaling is expected with increasing chain length. However, the leakage current (current density through the monolayer) saturates at long chain lengths using different *n*-alkyl phosphonic acids in molecular scale hybrid dielectrics. This effect is inconsistent with current theoretical pictures of electron tunneling through saturated *n*-alkanes. Intermolecular interactions are thus clearly of great importance for the assembly process and are instrumental in determining the SAM characteristics. A deeper understanding of these correlations is necessary in order to be able to construct molecular scale electronics rationally and to design suitable component molecules.

We now report a combined experimental and computational study of the morphology of SAMs based on *n*-alkyl phosphonic acids. The insulating nature of the SAMs, in particular those with longer chain lengths, on insulating Al_2O_3, means that direct access at atomic scale resolution (e.g., scanning tunneling microscopy – STM) is not possible. Other techniques require extremely flat surfaces (small angle X-ray scattering – SAX) and/or provide average data on thin films, lacking in local or 3D-resolution important for understanding the intermolecular effects of assembly (XPS, AFM). However, as the conduction mechanism in self-assembled monolayers of saturated alkyl chains has been clearly identified as non-resonant tunneling, electrical data can give information about the structural properties and the nature of the molecular ordering [16–19]. We report divergence of the dependence of the electrical properties of SAM-based capacitors and pentacene transistors from that expected on the basis of extrapolations of the chain length. These observations are consistent with a change in the self-assembled monolayer morphology from an amorphous state for short alkyl chains (C_6) to a quasi-crystalline state for alkyl chains from C_{10} to C_{18}. The data from electrical measurements of the thin film devices were interpreted using the Simmons model to account for the observed properties of these layers in terms of their structural organization [19]. We have also used molecular dynamics (MD) simulations as tool to provide deeper insight into the nature of the intermolecular interactions and to identify the most probable molecular assembly of the different monolayers. The proposed change in SAM morphology is consistent with the measurements of the current densities and supported by vibrational sum frequency generation (VSFG) spectroscopy results.

2. Experimental details

2.1. Device fabrication

For the fabrication of the organic/inorganic dielectrics, heavily *p*-doped silicon wafers act as substrate and serve as bottom (gate-) electrode. The inorganic part of the hybrid dielectric is grown via atomic layer deposition, yielding uniform aluminum oxide films of 2 nm thickness. The deposition was realized in a commercial Cambridge Inc. ALD reactor at 250 °C with a constant deposition rate of 1 Å per cycle. The layer thickness and composition was validated by ellipsometry and XPS measurements. The RMS roughness of the almost stoichiometric Al_2O_3 layer (relative precursor concentration <5%) was determined by AFM (contact mode) to be in the range of 0.2 nm for 1 μm^2 (Veeco Digital Instruments Dimension 3100). The organic part of the dielectric is generated by a self-assembling monolayer of *n*-alkyl phosphonic acids from solution, according to literature [2,14]. The thickness of the self-assembled monolayer correlates to the length of the stretched molecule which was calculated with ChemBioOffice 2008 (tilt angles were not considered). The capacitor stacks, containing hybrid dielectric were completed by 50 nm gold evaporated through a stencil mask (deposition rate: 0.1 nm s^{-1}), yielding single devices with an electrode area of 150 × 150 μm^2. In the case of organic transistors, preliminary to the deposition of the gold source/drain contacts, defining a channel length of 20 μm and a channel width of 150 μm, 30 nm pentacene was thermally evaporated (rate of 0.01 nm) through another stencil mask.

2.2. Electrical characterization

The electrical characterization of the capacitors and transistors was performed in ambient conditions by manually probing single devices (yield of ~90%). The transistors and the capacitor stack were contacted from the back via the low noise chuck of the probe station. To guarantee the intactness of the SAM, the top electrode was probed accurately by special probe tips for small targets

(Micromanipulator Probe Tips 7F10). Capacitance measurements with a LCZ meter (HP4277) are proceeded in the voltage range between −2 V and 2 V (double sweep, in steps of 100 mV) at a frequency of 100 kHz. Reference measurements to obtain the dielectric constant of the Al_2O_3 were performed previously (Supplementary data). Each measurement was repeated on at least five devices, yielding identical results. Electrical data of capacitor and transistor devices were recorded with a semiconductor parameter analyzer (Agilent 4156C). A minimum of 20 capacitors of each species, 10 in positive (0 to +2 V) and 10 in negative (0 to −2 V) bias polarity were investigated in single sweep mode, in steps of 40 mV. The thermal stability of the tunneling current through the hybrid dielectric was preliminary verified over a temperature range of ~80 K. The conduction mechanism in the observed voltage range was identified as direct tunneling, which is generally accepted for SAMs of saturated alkyl chains [16,17]. Transfer characteristics of at least 10 pentacene transistors for each SAM are recorded for source–gate voltage V_{GS} between 0 and −2 V in double sweep mode at a source–drain voltage of $V_{DS} = -1$ V. For each TFT the charge carrier mobility was calculated in the saturation regime using the standard formalism for field-effect transistors: $\mu = 2 \times L/(W \times C_{diel}) \times (\delta\sqrt{I_D}/\delta V_{GS})^2$, where C_{diel} is the measured dielectric capacitance, I_D is the drain current, and V_{GS} is the gate-source voltage [14,20]. Benefiting from the smooth substrate the deviations are negligible.

2.3. Simulation

All molecular dynamics simulations were carried out, using the program NAMD [21]. For the initial setup and for parts of the analysis the programs *antechamber*, *leap*, and *ptraj* from the Amber package were used [22]. The parameters are based on the general Amber force field (GAFF) [23]. The Al_2O_3 surface represents a regular 1 0 0 surface with 850 atoms in total (52 × 38 nm) and was build with Materials Studio [24]. The surface atoms were constrained in their position during the simulations. For each simulation 80 phosphonic acids were placed on the surface. The phosphonic acids were treated singly deprotonated (most reasonable approach, due to DFT calculations) and the atomic AM1-VESPA point charges were derived from semiempirical calculations with VAMP 10.0 [25,26]. Each system was minimized, equilibrated, and simulated in vacuo with periodic boundary conditions. The electrostatics were treated with particle-mesh Ewald (PME) long range electrostatics and a 10 Å cutoff for non-bonded interactions [27]. The width of the non-bonded skin was 2.0 Å. Langevin molecular dynamics with a target temperature of 350 K were performed. The complete simulation time for each system was 10 ns with an integration time step of 1 fs.

3. Results and discussion

The morphology and device characteristics of SAMs of *n*-alkyl phosphonic acids (C_6-, C_{10}-, C_{14}- and C_{18}-PA) were investigated on 2 nm thick atomic layer deposited (ALD) Al_2O_3 deposited on *p*-doped single crystalline silicon as back electrode. This stack was chosen to achieve full control of the Al_2O_3 thickness and to provide a smooth surface to ensure that the self-assembly is not significantly affected by surface roughness (typical ALD-Al_2O_3 surface roughness RMS of a 1 μm² is 0.2 nm). In Fig. 1a the drain

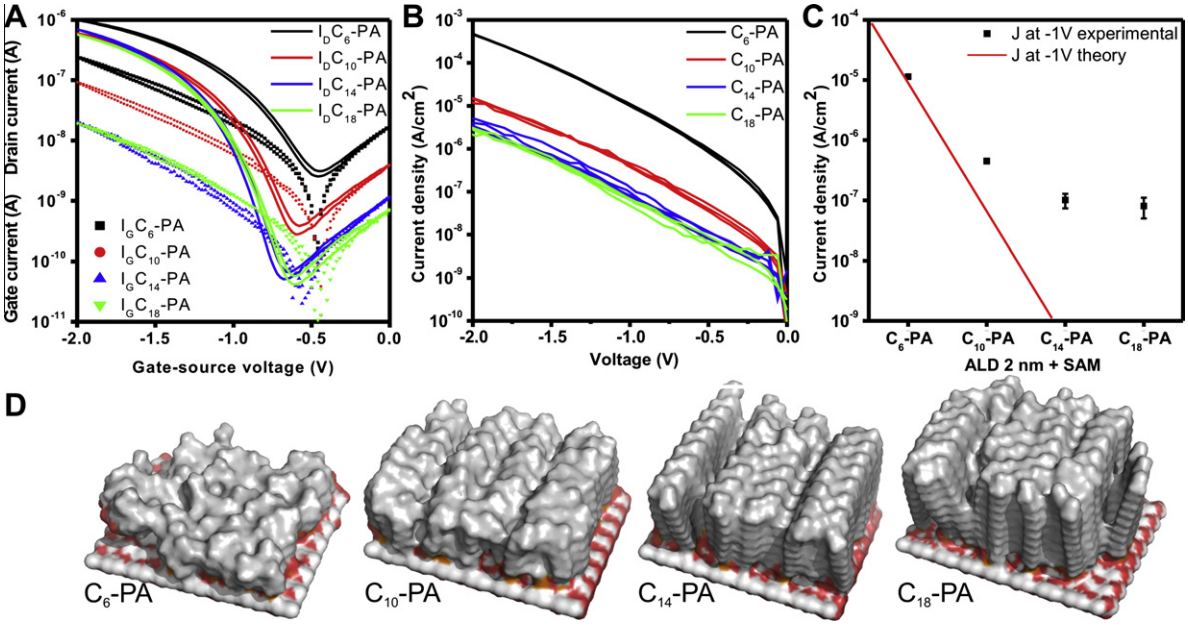

Fig. 1. The impact of sub-nanometer changes of the molecule length on device characteristics. (a) Transfer characteristics of pentacene transistors at V_{DS}: −1 V (channel dimension 150 × 20 μm²) with different monolayers. (b) Current density of capacitor devices (150 × 150 μm²). (c) Current density versus molecule length plot at a voltage of −1 V, extracted from (b). (d) Van der Waals surface representation of time-averaged structures extracted from molecular dynamics simulations of several *n*-alkyl phosphonic acids.

currents (I_D) and gate currents (I_G) of the pentacene transistor devices with different SAMs are presented. As the electrical characteristics (I_D/I_G, ON/OFF ratio, and V_{TH} – Table 1) scale with the chain length as expected for C_6-PA, C_{10}-PA and C_{14}-PA, the devices with C_{18}-PA behave very similarly to those with C_{14}-PA. The most remarkable feature is the resemblance in the progress of I_G, despite the fact that the C_{18}-PA is approximately 0.5 nm longer than the C_{14}-PA. This anomaly is even more pronounced in capacitor devices (Si/ALD-Al_2O_3/SAM/Au – Fig. 1b) and is consistent with results found for integrated devices (Al/Al_2O_3/SAM/Au) with the same molecules [14]. While the values of capacitance (measured and calculated) fit the theoretical monolayer thickness well, the current densities (J) do not follow the theoretical exponential decrease (for a constant SAM morphology) with molecule length for longer chains (Fig. 1c). Although the capacitance as an average area depending parameter is only sensitive to the mean thickness in an alternating electrical field, the current density (J) is very sensitive to weakest point in the layer. The results of MD simulations of the corresponding SAMs on Al_2O_3 surfaces are shown in Fig. 1d. The MD simulations were performed for a time scale of 10 ns, which should be long enough to provide insight into the molecular structure of the SAMs. The calculated SAM morphology changes with increasing chain length from an amorphous state for C_6-PA to a more ordered state for C_{10}-PA to highly ordered (crystalline) domains separated by gaps for C_{14}-PA and C_{18}-PA.

Considering that these morphologies, and in particular the gaps, can be penetrated by the subsequently evaporated layer (e.g., Au in a capacitor device), a reduced distance between the bottom (Si) and top electrode (Au) is expected. Schematic sketches of the corresponding device cross sections are shown in Fig. 2a. Using these assumptions, the experimental results of the capacitor devices were correlated to the Simmons model for tunneling through a thin isolating film to calculate the effective monolayer thickness [28]. No gaps are expected for amorphous SAMs with short chains (C_6-PA). The distance between the electrodes is shorter at a gap in the SAM for longer chains (C_{18}-PA) because the thermally deposited gold can penetrate into the gap to reduce the effective thickness of the layer. This increases the tunneling current through the monolayer significantly [19,28]. The Simmons model for direct tunneling through large area molecular junctions was used to fit the experimental data. The tunneling current density J is given by:

$$J = J_0\left(\phi \cdot \exp\left(-A\sqrt{\phi}\right) - (\phi + eV) \cdot \exp\left(-A\sqrt{\phi + eV}\right)\right) \quad (1)$$

where

Table 1
Device parameters of capacitors and pentacene transistors.

SAM	Elongated molecule length d[a] (nm)	Capacitance calculated[b] ($\mu F\,cm^{-2}$)	Capacitance measured[b] ($\mu F\,cm^{-2}$)	Mobility[c] ($cm^2\,V^{-1}\,s^{-1}$)	I_D/I_G[c]	ON/OFF ratio[c]	Threshold voltage V_{Th}[c] (V)
C_6-PA	0.91	0.51	0.59	0.20	<10	10^2	−0.51
C_{10}-PA	1.43	0.46	0.55	0.21	10	10^3	−0.76
C_{14}-PA	1.95	0.41	0.43	0.35	10^2	10^4	−0.89
C_{18}-PA	2.44	0.38	0.37	0.33	10^2	10^4	−0.87

[a] Calculated using ChemBioOffice 2008.
[b] Capacitor devices.
[c] Transistor devices, parameters calculated using the measured capacitances of [b].

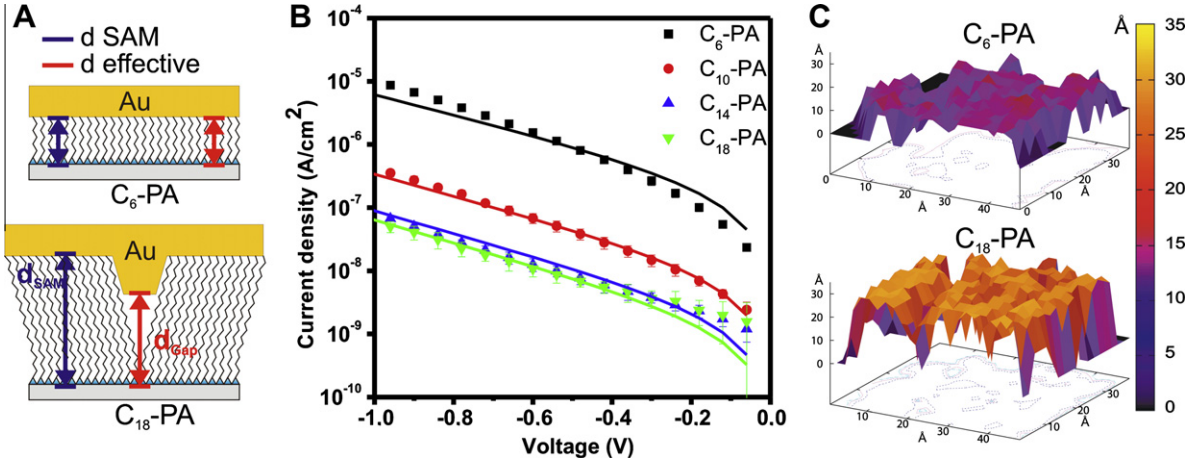

Fig. 2. (a) Scheme of the proposed mechanism for C_6-PA and C_{18}-PA exemplarily. (b) Results of Simmons modeling and MD calculations. Fit of the current density data of capacitor devices (area: 150 × 150 μm^2) for n-alkyl phosphonic acids. (c) Surface topography extracted from MD calculations for C_6-PA and C_{18}-PA.

$$J_0 = \frac{e}{2\pi h(\beta d)^2} \quad (2)$$

and

$$A = \frac{4\pi\beta d\sqrt{2m_e^*}}{h} \quad (3)$$

with h being the Planck constant, e the electron charge, β a correction parameter (0.96) and V the applied voltage (intermediate voltage range $V < \Phi/e$). According to literature a fixed effective electron mass of $m_e^* = 0.28$ me, common for saturated n-alkanes and an arbitrary mean barrier height of 5.1 eV, only one fit parameter remains for modeling the experimental tunneling current, the width d of the potential barrier [19,29]. Fig. 2b, shows the fitting results for the chosen parameters and varying barrier widths. The total length of the tunneling path between the two electrodes correlates to the different SAM thickness. The experimental values for J are described well in the intermediate voltage range (-0.3 to -1 V) by the parameter set used. Details are provided in Table S1 of the Supplementary data. While the effective monolayer thickness of 0.9 nm for C_6-PA and 1.2 nm for C_{10}-PA agree well with the calculated molecule length, there is a clear mismatch with respect to the real layer thickness for C_{14}-PA and C_{18}-PA. For extended molecular lengths of approximately 1.9 nm for C_{14}-PA and 2.4 nm for C_{18}-PA, the fitted barrier width corresponds to an effective monolayer thickness of only 1.3 nm for C_{14}-PA and 1.4 nm for C_{18}-PA.

These reduced thicknesses can be attributed to the formation of leakage paths such as gaps in the monolayers and result in the observed increase of current density. Fig. 2c shows a quantitative evaluation of the MD data. By imposing an XYZ matrix grid of 2 Å, the cell occupancy and accessibility from the top can be obtained as functions of the surface distance and topography. Exemplarily, the data for C_6-PA and C_{18}-PA demonstrate the length-dependent trend to form gaps and crystalline domains. Longer molecules are more likely to organize into crystalline domains than shorter ones because of the increased van der Waals interactions between the longer chains, that also cause the semi crystalline behavior of polyethylene (PE), which consists of the same building blocks than our SAM chains [30]. Further investigations of the SAMs by VSFG lead to the same conclusion. By comparing the intensity ratio of the CH_3 and CH_2 symmetric stretch modes in the sum frequency spectra, the ordering of a SAM can be qualitatively determined. This ratio is a measure of molecular order since conformational disorder decreases the CH_3 symmetric stretch intensity and increases the CH_2 intensity because they lose their locally centrosymmetric structure [31,32]. Our measurements reveal a clear tendency to a more ordered morphology for longer molecules indicated by an increasing CH_3 to CH_2 intensity ratio (Supporting information).

We propose that the self-assembling of molecules with shorter alkyl chain is dominated by the footprint of the phosphonic acid and yields electrically dense and amorphous monolayers. Molecules with longer alkyl chains organize into highly ordered quasi-crystalline domains separated by gaps, due to competition between the space requirements of the phosphonic acid and the van der Waals interactions of the alkyl chain [15]. Fig. 3 shows snapshots from the MD simulations that illustrate the change in morphology for increased chain lengths.

The surface distance for each of the four phosphonic acid molecules investigated is plotted against the occupancy. The first few nanometers of each monolayer are closely packed (occupancy of one) and impenetrable for arriving atoms and molecules of the subsequent layer. As the distance to the surface increases the occupancy value drops to zero at the stretched length of the molecule. For densely packed monolayers this decrease occurs abruptly, as shown for C_6-PA at a surface distance of about 1 nm. For longer molecules (C_{10}-PA to C_{18}-PA) a more gradual decrease is observed, indicating a closer stacking of the molecules to form crystalline domains and free space. This gradual decrease is most pronounced for C_{18}-PA and reflects the anomalistic feature of long chain SAMs. As the occupancy can be expressed as the geometrical dimension of the gaps at a certain distance to the surface, a critical value can be defined where gold atoms or semiconductor molecules are able to penetrate into the surface and consequently reduce the tunneling distance for the charge carriers. Setting the critical surface occupancy to an arbitrary value of about 0.90, the corresponding layer thickness can be determined from the plot. The monolayer thicknesses thus obtained (C_6-PA = 0.85 nm, C_{10}-PA = 1.13 nm,

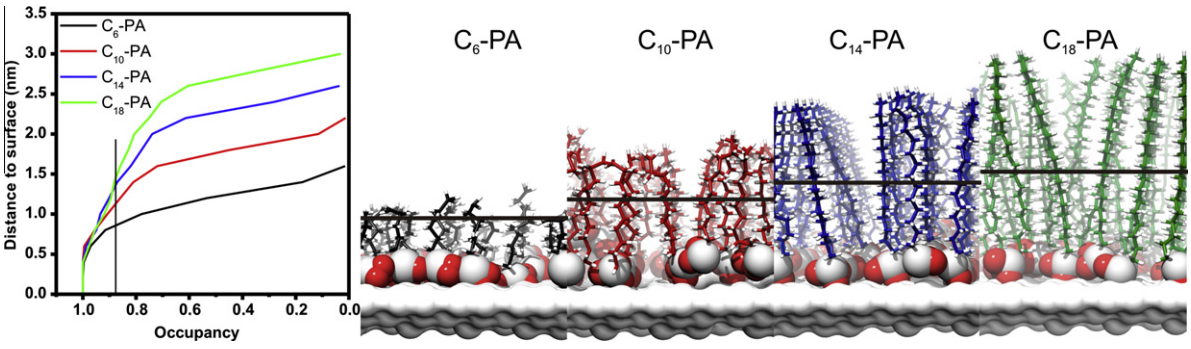

Fig. 3. Distance to surface versus occupancy plot correlated to snapshots of the MD calculations for n-alkyl phosphonic acids. The black lines indicate an occupancy of about 90% and the corresponding effective monolayer thickness.

C_{14}-PA = 1.39 nm, and C_{18}-PA = 1.46 nm) agree well with the calculated effective monolayer thickness obtained by the Simmons model described above.

However, the influence of the top layer of the devices on the ordering of the molecules and the effective monolayer thickness is not yet clear. In fact, both device setups, transistors and capacitors, show the observed feature, independent of the subsequent layer. As the MD simulations do not include the top conductor layer, it is conceivable that the penetrating molecules and atoms may expand the gaps or even cause additional gaps to form, thus increasing the number of short tunneling pathways. The presence of gaps and crystalline domains can have a strong impact on the morphology (grain size) of the subsequent pentacene layer, as observed by Hill [13]. An increased number of nucleation centers (edges of the crystalline domains) translate directly to smaller grain sizes in pentacene layers on C_{18}-SAMs (Supplementary data – Fig. S2), which affects the transistor parameters as observed [33]. As the reported feature is attributed to the different space requirements of anchor groups and alkyl chains, in other systems like thiols or silanes, similar effects are not observed so far. However, a possible way to benefit from the stability of the phosphonic acids and to overcome the structural mismatch is to synthesize molecules containing head groups or substituents that may compensate the different space requirements [1].

4. Conclusion

In conclusion, we have investigated the molecular ordering of self-assembled monolayers, both experimentally and using simulations. Combining the Simmons model with the results of the molecular dynamics simulations allows us to reproduce the observed anomalistic dependence of the electronic properties on the molecular chain length in SAMs based on *n*-alkyl phosphonic acids. The combination of the two approaches results in a reduced effective monolayer thickness compared to those expected for extended chains. This trend is more pronounced for longer alkyl chains as the molecular interaction of the carbon backbone facilitates the formation of highly ordered domains with gaps between them. Simultaneously, a change in SAM morphology from amorphous to quasi-crystalline from shorter to longer alkyl chains was observed by VSFG measurements. In general, our study shows that even small changes in the chain length can change the molecular interactions and monolayer assembly significantly. This is of enormous importance in molecular scale electronics as the device parameters are actively tunable by the molecular design (anchor group, chain, or possible "active" head group).

Acknowledgments

The authors gratefully acknowledge the funding of the German Research Council (DFG), which, within the framework of its 'Excellence Initiative' supports the Cluster of Excellence 'Engineering of Advanced Materials' (www.eam.uni-erlangen.de), the Erlangen Graduate School of Molecular Science (GSMS), the Erlangen Graduate School in Advanced Optical Technologies (SAOT) at the University of Erlangen-Nuremberg and F. Ante and H. Klauk from MPI Stuttgart.

Appendix A. Supplementary data

Supplementary data associated with this article can be found, in the online version, at doi:10.1016/j.orgel.2010.05.009.

References

[1] M. Halik, H. Klauk, U. Zschieschang, G. Schmid, C. Dehm, M. Schutz, S. Malsch, F. Effenberger, M. Brunnbauer, F. Stellacci, Low-voltage organic transistors with an amorphous molecular gate dielectric, Nature 431 (2004) 963–966.
[2] H. Klauk, U. Zschieschang, J. Pflaum, M. Halik, Ultralow-power organic complementary circuits, Nature 445 (2007) 745–748.
[3] S.G.J. Mathijssen, E.C.P. Smits, P.A. van Hal, H.J. Wondergem, S.A. Ponomarenko, A. Moser, R. Resel, P.A. Bobbert, M. Kemerink, R.A.J. Janssen, et al., Nature Nanotechnologie 4 (2009) 674–680.
[4] E.C.P. Smits, S.G.J. Mathijssen, P.A. van Hal, S. Setayesh, T.C.T. Geuns, K.A.H.A. Mutsaers, E. Cantatore, H.J. Wondergem, O. Werzer, R. Resel, et al., Nature 455 (2008) 956–959.
[5] R.L. McCreery, A.J. Bergren, Progress with molecular electronic junctions: meeting experimental challenges in design and fabrication, Advanced Materials 21 (2009) 4303–4322.
[6] D.J. Gundlach, J.E. Royer, S.K. Park, S. Subramanian, O.D. Jurchescu, B.H. Hamadani, A.J. Moad, R.J. Kline, L.C. Teague, O. Kirillov, et al., Nature Materials 7 (2008) 216–221.
[7] M. Mottaghi, G. Horowitz, Field-induced mobility degradation in pentacene thin-film transistors, Organic Electronics 7 (2006) 528–536.
[8] S. Kobayashi, T. Nishikawa, T. Takenobu, S. Mori, T. Shimoda, T. Mitani, H. Shimotani, N. Yoshimoto, S. Ogawa, Y. Iwasa, Control of carrier density by self-assembled monolayers in organic field-effect transistors, Nature Materials 3 (2004) 317–322.
[9] K.P. Pernstich, S. Haas, D. Oberhoff, C. Goldmann, D.J. Gundlach, B. Batlogg, Threshold voltage shift in organic field effect transistors by dipole monolayers on the gate insulator, Journal of Applied Physics 96 (2004) 6431.
[10] H.B. Akkerman, A.J. Kronemeijer, P.A. van Hal, D.M. de Leeuw, P.W.M. Blom, B. de Boer, Self-assembled-monolayer formation of long alkanedithiols in molecular junctions, Small 4 (2008) 100–104.
[11] H.O. Finklea, S. Avery, M. Lynch, T. Furtsch, Blocking oriented monolayers of alkyl mercaptans on gold electrodes, Langmuir 3 (1987) 409–413.
[12] P. Diao, D. Jiang, X. Cui, D. Gu, R. Tong, B. Zhong, Studies of structural disorder of self-assembled thiol monolayers on gold by cyclic voltammetry and ac impedance, Journal of Electroanalytical Chemistry 464 (1999) 61–67.
[13] I.G. Hill, C.M. Weinert, L. Kreplak, B.P. van Zyl, Influence of self-assembled monolayer chain length on modified gate dielectric pentacene thin-film transistors, Applied Physics A 95 (2008) 81–87.
[14] A. Jedaa, M. Burkhardt, U. Zschieschang, H. Klauk, D. Habich, G. Schmid, M. Halik, The impact of self-assembled monolayer thickness in hybrid gate dielectrics for organic thin-film transistors, Organic Electronics 10 (2009) 1442–1447.
[15] K. Fukuda, T. Hamamoto, T. Yokota, T. Sekitani, U. Zschieschang, H. Klauk, T. Someya, Effects of the alkyl chain length in phosphonic acid self-assembled monolayer gate dielectrics on the performance and stability of low-voltage organic thin-film transistors, Applied Physics Letters 95 (2009) 203301/1–3.
[16] D.K. Aswal, S. Lenfant, D. Guerin, J.V. Yakhmi, D. Vuillaume, Self assembled monolayers on silicon for molecular electronics, Analytica Chimica Acta 568 (2006) 84–108.
[17] S.A. DiBenedetto, A. Facchetti, M.A. Ratner, T.J. Marks, Charge conduction and breakdown mechanisms in self-assembled nanodielectrics, Journal of the American Chemical Society 131 (2009) 7158–7168.
[18] K. Seo, H. Lee, Molecular electron transport changes upon structural phase transitions in alkanethiol molecular junctions, ACS Nano 3 (2009) 2469–2476.

[19] H.B. Akkerman, R.C.G. Naber, B. Jongbloed, P.A. van Hal, P.W.M. Blom, D.M. de Leeuw, B. de Boer, Electron tunneling through alkanedithiol self-assembled monolayers in large-area molecular junctions, PNAS 104 (2007) 11161–11166.
[20] G. Horowitz, P. Lang, M. Mottaghi, H. Aubin, Extracting parameters from the current–voltage characteristics of organic field-effect transistors, Advanced Functional Materials 14 (2004) 1069–1074.
[21] J.C. Phillips, R. Braun, W. Wang, J. Gumbart, E. Tajkhorshid, E. Villa, C. Chipot, R.D. Skeel, L. Kale, K. Schulten, Scalable molecular dynamics with NAMD, Journal of Computational Chemistry 26 (2005) 1781–1802.
[22] D.A. Case, T.A. Darden, T.E. Cheatham III, C.L. Simmerling, J. Wang, R.E. Duke, R. Luo, M. Crowley, R.C. Walker, et al., AMBER 10, University of California, San Francisco, 2008.
[23] J. Wang, R.M. Wolf, J.W. Caldwell, P.A. Kollman, D.A. Case, Development and Testing of a General Amber Force Field, Journal of Computational Chemistry 25 (2004) 1157–1174.
[24] Materials Studio 4.4, Accelrys Inc., San Diego (2008).
[25] B. Beck, T. Clark, R.C. Glen, VESPA: A new, fast approach to electrostatic potential-derived atomic charges from semiempirical methods, Journal of Computational Chemistry 18 (1997) 744–756.
[26] T. Clark, A. Alex, B. Beck, F. Burkhardt, J. Chandrasekhar, P. Gedeck, A. Horn, M. Hutter, B. Martin, G. Rauhut, et al., VAMP 10.0, Accelrys Inc., San Diego, 2008.
[27] T. Darden, D. York, L. Pedersen, Particle mesh Ewald: an N log (N) method for Ewald sums in large systems, Journal of Chemical Physics 98 (1993) 10089–10092.
[28] J.G. Simmons, Generalized formula for the electric tunnel effect between similar electrodes separated by a thin insulating film, Journal of Applied Physics 34 (1963) 2581–2590.
[29] J.K. Tomfohr, O.F. Sankey, Complex band structure, decay lengths, and Fermi level alignment in simple molecular electronic systems, Physical Review B 65 (2002) 245105.
[30] D.M. Spori, V.N. Venkataraman, S.G.P. Tosatti, F. Durmaz, N.D. Spencer, S. Zürcher, Influence of alkyl chain length on phosphate self-assembled monolayers, Langmuir 23 (2007) 8053.
[31] A.G. Lambert, P.B. Davies, D.J. Nievandt, Implementing the theory of sum frequency generation vibrational spectroscopy: a tutorial review, Applied Spectroscopy Reviews 40 (2005) 103–145.
[32] R.N. Ward, D.C. Duffy, P.B. Davies, C.D. Bain, Sum frequency spectroscopy of surfactants adsorbed at a flat hydrophobic surface, Journal of Physical and Chemical 98 (1994) 8536–8542.
[33] G. Horowitz, M.E. Hajlaoui, Grain size dependent mobility in polycrystalline organic field-effect transistors, Synthetic Metals 122 (2001) 185–189.

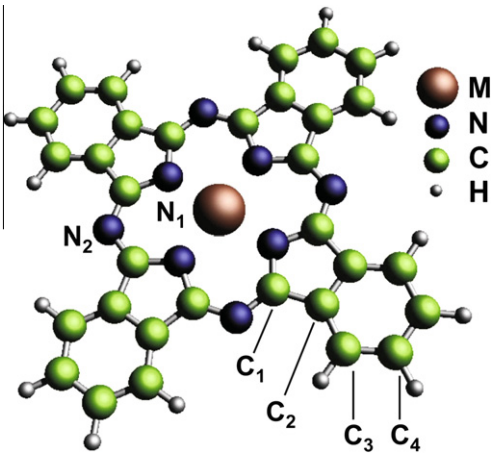

Fig. 1. Schematic illustration of the chemical structure of a transition metal phthalocyanine molecule. With M the central transition metal ion is denoted, which is surrounded by four pyrrole nitrogen (N1) and four bridging aza nitrogen (N2) atoms. The 24 carbon atoms in the outer benzene rings are labeled with C-2, C-3, and C-4, respectively. With the label C-1 the 8 pyrrole carbon atoms are denoted.

TMPc's remained unknown, which is contrasted by the profound importance of the electronic properties for the physical behavior of these materials.

Transition metal phthalocyanines as carbon-based molecules are build by a well defined and very stable π-conjugated macrocycle ring (abbreviated Pc for the phthalocyanato ion $C_{32}H_{16}N_8^{2-}$). The structure of a TMPc is shown in Fig. 1. They are characterized by the presence of a transition metal (M) ion (e.g. Mn, Fe, Co, Ni, Cu or Zn) in the formal oxidation state 2+ in their central cavity, which is surrounded by four pyrrole nitrogen (N_1), four bridging aza nitrogen (N_2), eight pyrrole carbon (C_1) as well as 24 benzene ring carbon (C_2, C_3, and C_4) atoms. Thereby, the Pc ring acts as ligand to the central transition metal ion, and the Pc^{2-} ligand forms a neutral complex with the divalent transition metal ions, whereas the bonding between the ligand and the central transition metal ion is also significantly covalent [29]. TMPc's have a planar structure with a D_{4h} point symmetry, which has been well established by experiments and calculations [30,31]. The crystal structure of the TMPc's is practically identical [32], and thin semiconducting films of TMPc's can be grown of equivalent quality independent of the transition metal [33–36]. Under the consideration that the molecules are placed in the *xy*-plane, the five metal 3*d* orbitals transform as a_{1g} (d_{z^2}), b_{1g} ($d_{x^2-y^2}$), e_g (d_π, i.e., d_{xz} and d_{yz}), and b_{2g} (d_{xy}). Thereby, the energetic order of the orbitals depends on the strength and the type of the distortion, and on hybridization effects of the metal 3*d* orbitals with the ligand orbitals. An *a-priori* determination of the energetic orbital order is not easily possible, but has to be verified by experimental investigations. For many transition metal phthalocyanines there is no complete microscopic understanding of the electronic and spin ground state. In particular, there are contradicting predictions and experiments in regard of the orbital ground state of the transition metal center [37–44].

In this contribution, we investigate experimentally the impact of the transition metal center on the electronic properties of TMPc's using electron energy-loss (EELS) and photoemission (PES) spectroscopy. By our combined spectroscopic approach we demonstrate that for the d^{10}–d^8 case (ZnPc, CuPc, and NiPc) low energy electronic properties are exclusively determined by the ligand π states. For CoPc, FePc, and MnPc the metal 3*d* states however have increased impact as they come very close in energy to the lowest unoccupied ligand orbital.

2. Experimental details

For our investigations using electron energy-loss spectroscopy (EELS) in transmission we have prepared TMPc films with a thickness of about 100 nm by thermal evaporation of the organic material onto single crystalline KBr substrates. The KBr crystals were kept at room temperature during the deposition process. Subsequently, the TMPc films were floated off in distilled water and mounted onto standard electron microscopy grids. By using this procedure we could prepare free-standing films for the EELS investigations. Prior to the EELS measurements the films were characterized in-situ using electron diffraction. This revealed that the films were essentially polycrystalline.

The electron energy-loss spectroscopy measurements in transmission were carried out at room temperature using a 170 keV spectrometer described elsewhere [45], and we note that at this high primary beam energy only singlet excitations are possible. The energy and momentum resolution were chosen to be 85 meV and 0.03 $Å^{-1}$, respectively. We have measured the loss function $\Im(-1/\epsilon(\vec{q},\omega))$ ($\epsilon(\vec{q},\omega)$ is the dielectric function) for a small momentum transfer $\vec{q}$, parallel to the film surface [45]. Further details of the sample preparation procedure and the experimental technique can be found in previous publications [45,46].

The X-ray (XPS) and ultra-violet (UPS) photoelectron spectroscopy experiments have been carried out using a commercial PHI 5600 spectrometer, which is equipped with two light sources. A monochromatized Al K_α source provides photons with an energy of 1486.6 eV for XPS. Photons with an energy of 21.21 eV from a He discharge lamp can be used to perform valence band measurements. All ultra-violet photoemission spectroscopy measurements were done by applying a sample bias of −5 V to obtain the correct, sample determined, secondary electron cutoff. The recorded spectra were corrected for the contributions of He satellite radiation. The total energy resolution of the spectrometer was determined by analyzing the width of the Au Fermi edge to be about 350 meV (XPS) and 100 meV (UPS), respectively. The binding energy (BE) scale was aligned by measuring the Fermi edge (0 eV) and the Au4$f_{7/2}$ emission feature (84.0 eV) of a polycrystalline gold substrate. Applying several cycles of Ar^+ sputtering (3 keV, 10^{-8} mbar), the polycrystalline gold foils were cleaned. Additionally, we have checked the surface composition of the sputter cleaned substrates by using X-ray photoelectron spectroscopy and did not monitor any sign of contaminations.

In a preparation chamber (base pressure 3×10^{-10} mbar), which is directly attached to the spectrometer system, TMPc films with a film thickness of about 50–60 Å have been prepared by in situ thermal evaporation with a typical evaporation rate between 1 Å/min. and 2.5 Å/min. on the gold substrates. Subsequently, the films were transferred to the analyzer chamber (base pressure 1×10^{-10} mbar) without breaking the vacuum and characterized taking a full range XPS spectrum. The number of impurities in the films was very small and below the detection limit of XPS due to the ultra-high vacuum conditions during the preparation process of the organic films. To estimate the thickness of the individual TMPc films we have monitored the attenuation of the intensity of the Au4$f_{7/2}$ substrate peak due to the organic film. Considering the procedure of Seah and Dench [47] we have calculated the mean free path of the electrons in the TMPc films to be about 2.54 nm for the kinetic energy of 1402.6 eV of the Au4$f_{7/2}$ signal from the substrate and a density of 1.62 g/cm^3 for the transition metal phthalocyanines [48,49]. We point out that this procedure to determine the thickness of the organic layers is only correct for a layer-by-layer growth. If the organic films does not grow uniformly this methods underestimates the film thickness, which is not important for our results discussed below.

3. Results and discussion

3.1. Electron energy-loss spectroscopy

As mentioned above TMPc's exhibit remarkable optical properties with an intense absorption in the visible energy region due to the conjugated π-system of the molecules. In the past decades the interpretation of this behavior has been the subject of a large number of theoretical studies [1,32,50–57]. The excitation spectra in the visible are characterized by two major excitation features. First, the Q-band located at about 2 eV is generally interpreted in terms of $\pi - \pi^*$ transitions between bonding and antibonding molecular orbitals [54]. In the UV region at higher energies the Q-band is followed by the so-called Soret (B)-band arising also from $\pi - \pi^*$ transitions.

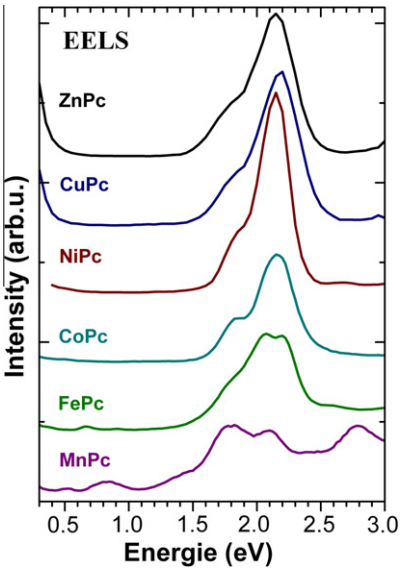

Fig. 2. Electronic excitation spectrum for TMPc films as measured using electron energy-loss spectroscopy at a momentum transfer q of 0.1 Å^{-1} representing the optical limit.

Fig. 2 displays the electronic excitation spectra of TMPc's as measured by electron energy-loss spectroscopy at a momentum transfer q of 0.1 Å^{-1} up to 3 eV. At such a small momentum transfer the data obtained by EELS can be directly compared with the optical once, since the momentum transfer q of 0.1 Å^{-1} represents the optical limit [45]. Inspection of Fig. 2 allows the identification of a number of excitation maxima and shoulders for the different TMPc's summarized in Table 1. We note that all excitation features >0.6 eV are also observed for the TMPc's disolved in dimethylsulfoxide (DMSO) as well as α-chlornapthalene (data not shown). This is also well documented in the literature [58]. On going from solution, i.e., individual molecules, to thin films a drastic broadening of the excitations occurs, also in correspondence to previous studies [59,60]. In the past this broadening has been discussed in terms of a Davydov splitting and/or the consequence of intermolecular interaction that give rise to charge transfer excitations [61,62]. The first, prominent excitation feature is clearly visible for all TMPc's at about 1.7–2 eV and is due to excitations from the ligand a_{1u} orbital into the ligand e_g orbital.

Only for FePc and MnPc there are further excitations visible at energies below the Q-band region. In detail, the excitation spectrum of FePc is characterized by low energy excitations at 0.65, 0.9, and 1.1 eV, while in the case of MnPc we observe low energy features at about 0.5, 0.75–0.9, and 1.34–1.4 eV. We emphasize that especially the excitations below 1 eV are scarcely addressed in the literature so far despite the fact that they are most likely related to the interaction between the central ion and the phthalocyanine macrocycle, and thus can give valuable insight into the orbital ground state of the central metal ion [50,63]. Various theoretical works addressed the ground state and the orbital ordering in FePc [64,41,39,37] and MnPc [65,25,53,37], respectively. We emphasize that there is no agreement between published calculations, instead three different types of ordering have been proposed for FePc [64,41,39,37] and MnPc [65,25,53,37]. In the vicinity of the chemical potential, the relevant orbitals are the ligand orbitals with a_{1u} and e_g symmetry, but also the metal 3d orbitals with e_g ($d_{xz,yz}$), a_{1g} ($d_{z^2-r^2}$), b_{2g}($d_{xz,yz}$) symmetry become very close in energy [1,38,66]. The presence of low energy excitations for FePc and MnPc clearly depicts partially filled metal 3d states slightly above the ligand (a_{1u}) orbital [50,63]. In such a case, excitations from the ligand a_{1u} state into these metal 3d states would appear at low energies as observed in Fig. 2. Moreover, in consideration of selection rules for such excitations, the only metal 3d states that can give rise to visible electronic excitation in the optical limit are those with e_g symmetry.[1] Thus, from

[1] Considering the direct products of the irreducible representations of the highest occupied ligand orbital (a_{1u}) and the metal 3d levels (b_{1g}, b_{2g}, a_{1g}, e_g) in point group D_{4h}, only $a_{1u} \times e_g = e_u$ is optically allowed.

Table 1
Absorption energies of transition metal phthalocyanines measured by electron energy-loss spectroscopy (all values given in eV).

MnPc	2.07	1.7–1.8	1.35–1.4	0.75–0.9	0.5
FePc	2.0	1.8	1.1	0.9	0.65
CoPc	2.2	1.8			
NiPc	2.15	1.7–1.9			
CuPc	2.18	1.7–1.9			
ZnPc	2.15	1.7–1.9			

our EELS studies we can already conclude the presence of only partially filled metal e_g states somewhat above the ligand a_{1u} orbital. Since these 3d states with e_g symmetry hybridize with the (lowest unoccupied) ligand e_g states, other properties of the phthalocyanine molecules must also be affected by the close vicinity of further (partially) empty states to the chemical potential.

3.2. Photoemission spectroscopy

Fig. 3 displays the measured C1s core level photoemission spectra of the transition metal phthalocyanines for a film thickness of 50–60 Å. These data slightly differ in the binding energy of the C1s emission features of the different TMPc's, which we attribute to slightly different positions of the chemical potentials in the films. The decomposition of the spectra confirms previously reported conclusions [67–72] that the C1s excitation consists of two different main features (labeled C–C and C–N in Fig. 3b) accompanied by two satellite features (labeled S_{C-C} and S_{C-N}) at higher binding energies (BE). Previously, the two main features C–C and C–N have been attributed to photoelectrons from the 24 carbon atoms in the outer benzene rings (see labels C-2, C-3, and C-4 in Fig. 1) and to the 8 pyrrole carbon atoms (label C-1 in Fig. 1), respectively. In addition, each component is accompanied by an additional less intense satellite contribution (S_{C-C} and S_{C-N}) at higher BEs. These are due to shake-up structures ($\pi \rightarrow \pi^*$ satellites) related to final state screening [67–72]. Note that the S_{C-C} satellite overlaps with the C–N main feature, i.e., a detailed analysis can only be achieved by a fit as presented in Fig. 3b. Prior to the fitting procedure, a Shirley background was subtracted from the experimental data. The results from this fitting procedure give a relative intensity ratio of the emission from the two sets of carbon atoms of about 3, which is exactly what is expected.

While the overall shape of the spectra as shown in Fig. 3a hardly changes between the different TMPc's, the fit analysis reveals that the relative binding energies of the two main components do change, which is depicted in Fig. 3c. While this energy difference is virtually constant going from ZnPc to CoPc, it substantially decreases for FePc

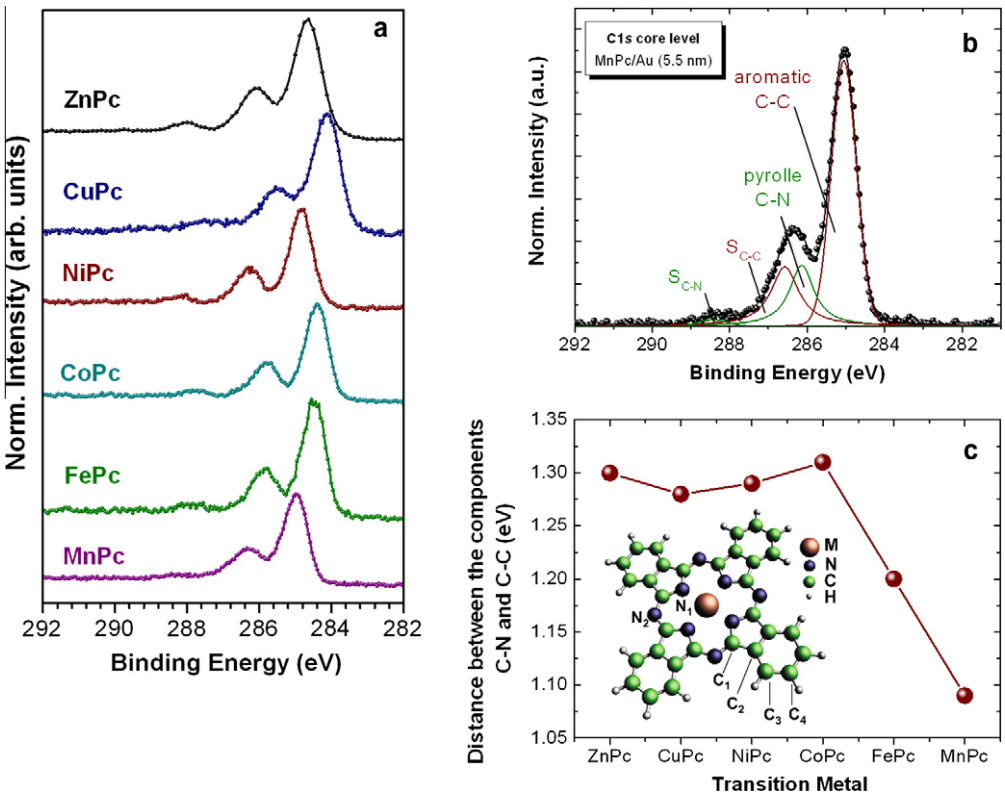

Fig. 3. C1s XPS excitation spectra as a function of the transition metal center ion (CuPc, NiPc, CoPc, FePc, and MnPc).The film thickness of the TMPc films was about 50–60 Å (a). In (b) the C1s core level spectrum for MnPc is shown. One can distinguish the aromatic carbon (C–C) and its satellite (S_{C-C}). and the carbon atoms which are linked to nitrogen atoms (C–N) and its satellite (S_{C-N}). (c) Depicts the change of the binding energy of the C–C as well as C–N components of the C1s excitation feature for the different transition metal phthalocyanines films with a thickness of 50–60 Å. As reference point we have used the values for ZnPc. The inset in Fig. 3c depicts the molecular structure of TMPc's as also depicted in Fig. 1.

and MnPc. This signals that the two sets of carbon atoms become less inequivalent for the latter two molecules. In connection to the EELS data discussed in the previous section, we ascribe this change to the increasing mixing of the metal and ligand wave functions, in particular to the hybridization of the metal 3*d* and ligand e_g states. This hybridization causes an internal charge transfer with the ligand e_g state now being slightly occupied. In view of the distribution of the ligand e_g wave function over the molecule, which has a stronger pyrrole character [42,73], it is no surprise that the additional charge on the ligand due to hybridization of the metal and ligand e_g states also affects the C1*s* core level data differently. Thus, the behavior of the binding energies as expressed in Fig. 3c confirms our picture that for FePc and MnPc the metal e_g states are energetically close to the ligand states with the same symmetry and that these two then significantly mix.

Finally, we present the valence band spectra of the transition metal phthalocyanines in Fig. 4. In general, the data in Fig. 4 confirm what has been published previously for some of the materials [74–77]. All spectra show a structure around 1.5 eV which is due to the emission from the highest occupied a_{1u} ligand state. At higher energies, further features from deeper lying orbitals are seen. Close inspection of the series as shown in Fig. 4 reveals additional information. There is a valence band feature, highlighted by the arrow, which is moving towards the chemical potential on going from top to bottom. We assign this feature to an electronic state that has significant metal 3*d* character. This first assignment is in agreement with the expectation that going down the transition metal series, the metal 3*d* levels move upwards in energy, mainly due to the smaller effective nuclear charge [38]. The consideration of photoemission cross sections can give more information on this state. At the photon energy of 21.21 eV as used in this study, the probability for emission from a carbon or nitrogen 2*p* orbital, which form the π system of the ligand, is larger than that from a transition metal 3*d* state [35,74,78,79]. This has already been demonstrated previously by other photoemission studies [80]. Therefore, the photoemission feature moving to lower binding energy in Fig. 4 most likely represents an electronic state that has a mixed wave function, which consists of metal 3*d* and ligand states. Then, this state becomes visible owing to the ligand contribution, while its energy shift reflects the energy variation of the metal 3*d* states relative to those of the ligand. Thus, the photoemission data exactly reflect what has been concluded above, i.e., the close vicinity of 3*d* and ligand states in particular for FePc and MnPc. Moreover, the most likely candidate of a metal 3*d* level that can hybridize with ligand orbitals close to the chemical potential is that with e_g symmetry, also in good correspondence to the discussion above.

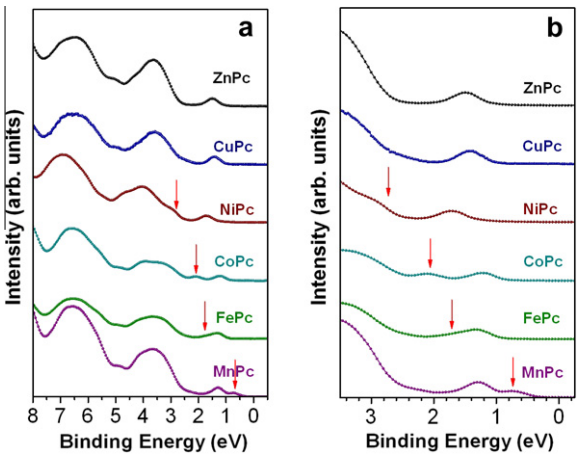

Fig. 4. The comparison of the valance band photoemission spectra of CuPc, NiPc, CoPc, FePc, and MnPc taken with a photon energy of 21.21 eV up to 8 eV is depicted in (a). On the right hand side in (b) for a better distinction of the differences in the spectra the valence band spectra are shown up to 3.5 eV. The film thickness of the TMPc films was about 50–60 Å.

Finally, we note that recent photoemission studies of CoPc with photon energies larger than 21.21 eV revealed the presence of an additional valence band feature at smaller binding energies than the ligand a_{1u} state [79]. This additional state has also been observed in scanning tunneling spectroscopy studies [81], and it has been attributed to the Co 3*d* a_{1g} orbital, which does not mix with the ligand π system. This demonstrates that further studies of other TMPc's are necessary in order to unravel all relevant electronic states near the chemical potential and their consequences, and to achieve a complete microscopic picture of the electronic degrees of freedom.

4. Summary

To summarize, our systematic spectroscopic study of transition metal phthalocyanines using electron energy-loss and photoemission spectroscopy has shown that the electronic states near the chemical potential become substantially influenced by metal 3*d* states in the case of FePc and MnPc. This has direct consequences on physical properties such as electronic excitation spectra or ionization potentials. CoPc represents an intermediate case where metal 3*d* states already are present but with lesser impact, and the low energy electronic behavior of NiPc, CuPc and ZnPc is determined by ligand orbitals only.

Acknowledgments

We thank R. Hübel, R. Schönfelder, and S. Leger for technical assistance. The project was funded by the DFG, Project Nos. KN 393/5 and KN 393/9.

References

[1] C.C. Leznoff, A.B.P. Lever, Phthalocyanines: Properties and Applications, VCH, 1993.
[2] K.M. Kadish, The Porphyrin Handbook, vol. 19, Academic Press, San Diego, 2003.
[3] P. Gregory, J. Porphyrins Phthalocyanines 4 (2000) 432.
[4] R.D. Yang, J. Park, C.N. Colesniuc, I.K. Schuller, J.E. Royer, W.C. Trogler, A.C. Kummel, J. Chem. Phys. 130 (2009) 164703.
[5] C.C. Koch, Nanostructured Materials – Processing Properties and Potential Applications, Noyes Publications, New York, 2002.
[6] J. Ma, Y. Liu, P. Zhang, J. Wang, Electrochem. Commun. 10 (2008) 100.
[7] W. Chan, J.F. Marshall, G.Y.F. Lam, I.R. Hart, Cancer Res. 48 (1988) 3040.

[8] L.M. Moreira, F. Vieira dos Santos, J.P. Lyon, M. Maftoum-Costa, C. Pacheco-Soares, N. Soares da Silva, Aust. J. Chem. 61 (2008) 741.
[9] S. Saini, A. Jena, J. Dey, A.K. Sharma, R. Singh, Magn. Reson. Imaging 13 (1995) 985.
[10] K. Walzer, B. Maennig, M. Pfeiffer, K. Leo, Chem. Rev. 107 (2007) 1233.
[11] S.A. Van Slyke, C.H. Chen, C.W. Tang, Appl. Phys. Lett. 69 (1996) 2160.
[12] N.R. Armstrong, D.M. Wang, W. Alloway, D. Placencia, E. Ratcliff, M. Brumbach, Macromol. Rapid Commun. 30 (2009) 717.
[13] Z. Bao, A.J. Lovinger, A. Dodabalapur, Appl. Phys. Lett. 69 (1996) 3066.
[14] M.-M. Ling, Z. Bao, Org. Electron. 7 (2006) 568.
[15] P. Peumans, S.R. Forrest, Appl. Phys. Lett. 79 (2001) 126.
[16] B.P. Rand, J. Genoe, P. Heremans, J. Poortmans, Prog. Photovolt. 15 (2007) 659.
[17] L. Chen, Z.P. Hu, A.D. Zhao, B. Wang, Y. Luo, J.L. Yang, J.G. Hou, Phys. Rev. Lett. 99 (2007) 146803.
[18] V. Dediu, M. Murgia, F.C. Matacotta, C. Taliani, S. Barbanera, Solid State Commun. 122 (2002) 181.
[19] W.J.M. Naber, S. Faez, W.G.v.d. Wiel, J. Phys. D Appl. Phys. 40 (R205) (2007) 0022–3727.
[20] S. Heutz, C. Mitra, W. Wu, A.J. Fisher, A. Kerridge, M. Stoneham, T.H. Harker, J. Gardener, H.-H. Tseng, T.S. Jones, et al., Adv. Mater. 19 (2007) 3618.
[21] C. Hamann (Ed.), Organische Festkörper und organische dünne Schichten, Akademische Verlagsgesellschaft Geest & Portig K.G., 1978.
[22] N.B. McKeown, Phthalocyanine Materials, Cambridge University Press, 1998.
[23] F.H. Moser, A.L. Thomas, Phthalocyanines: Properties, CRC Press, 1983.
[24] F.H. Moser, A.L. Thomas, Phthalocyanines: Manufacture and Application, CRC Press, 1983.
[25] M.-S. Liao, J.D. Watts, M.-J. Huang, Inorg. Chem. 44 (2005) 1941.
[26] P.A. Reynolds, B.N. Figgis, Inorg. Chem. 30 (1991) 2294.
[27] J.M. Assour, W.K. Kahn, J. Am. Chem. Soc. 87 (1965) 207.
[28] O. Kahn, Molecular Magnets, VCH Publishers, 1993.
[29] A.B.P. Lever, Adv. Org. Chem. Radiochem. 7 (1965) 27.
[30] K.A. Nguyen, R. Pachter, J. Chem. Phys. 114 (2001) 10757.
[31] A. Rosa, G. Ricciardi, E.J. Baerends, S.J.A. van Gisbergen, J. Phys. Chem. A 105 (2001) 3311.
[32] D. Dini, M.J. Hanack, J. Porphyrins Phthalocyanines 8 (2004) 915.
[33] T.S. Ellis, K.T. Park, S.L. Hulbert, M.D. Ulrich, J.E. Rowe, J. Appl. Phys. 95 (2004) 982.
[34] S. Kera, M. Casu, K. Bauchspieß, D. Batchelor, T. Schmidt, E. Umbach, Surf. Sci. 600 (2006) 1077.
[35] T.S. Ellis, K.T. Park, M.D. Ulrich, S.L. Hulbert, J.E. Rowe, J. Appl. Phys. 100 (2006) 093515.
[36] J. Ahlund, K. Nilson, P. Palmgren, E. Gothelid, J. Schiessling, M. Gothelid, N. Martensson, C. Puglia, J. Phys. Chem. C 112 (2008) 6887.
[37] C.G. Barraclough, R.L. Martin, S. Mitra, R.C. Sherwood, J. Chem. Phys. 53 (1970) 1643.
[38] M.-S. Liao, S. Scheiner, J. Chem. Phys. 114 (2001) 9780.
[39] M.-S. Liao, S. Scheiner, J. Comp. Chem. 23 (2002) 1391.
[40] M.-S. Liao, J.D. Watts, M.-J. Huang, J. Phys. Chem. A 109 (2005).
[41] M. Sumimoto, Y. Kawashima, K. Hori, H. Fujimoto, Spectrochim. Acta A 71 (2008) 286.
[42] N. Marom, O. Hod, G.E. Scuseria, L. Kronik, J. Chem. Phys. 128 (2008) 164107.
[43] N. Marom, L. Kronik, Appl. Phys. A 95 (2009) 165.
[44] N. Marom, L. Kronik, Appl. Phys. A 95 (2009) 159.
[45] J. Fink, Adv. Electron. Electron. Phys. 75 (1989) 121.
[46] M. Knupfer, Surf. Sci. Rep. 42 (2001) 1.
[47] M.P. Seah, W.A. Dench, Surf. Interface Anal. 1 (1979) 2.
[48] T. Schwieger, Thesis, Technische Universität Dresden, 2002.
[49] C. Hamann, Thesis, Technical University Dresden, 1966.
[50] R. Kraus, M. Grobosch, M. Knupfer, Chem. Phys. Lett. 469 (2009) 121.
[51] R. Seoudi, G. El-Bahy, Z.E. Sayed, Opt. Mater. 29 (2006) 304.
[52] A. Ruocco, M.P. Donzello, F. Evangelista, G. Stefani, Phys. Rev. B 67 (2003) 155408.
[53] B.E. Williamson, T.C. VanCott, M.E. Boyle, G.C. Misener, M.J. Stillman, P.N. Schatz, J. Am. Chem. Soc. 114 (1992) 2412.
[54] A.T. Davidson, J. Chem. Phys. 77 (1982) 168.
[55] L. Edwards, M. Gouterman, J. Mol. Spectrosc. 33 (1970) 291.
[56] E.A. Lucia, F.D. Verderame, J. Chem. Phys. 48 (1968) 2674.
[57] M. Schott, J. Chem. Phys. 429 (1966) 1966.
[58] P.E. Fielding, A.G. MacKay, Aust. J. Chem. 17 (1964) 750.
[59] H. Peisert, M. Knupfer, T. Schwieger, J. Fink, Appl. Phys. Lett. 80 (2002) 2916.
[60] J.H. Sharp, M. Abkowitz, J. Phys. Chem. 77 (1973) 477.
[61] M. Knupfer, T. Schwieger, H. Peisert, J. Fink, Phys. Rev. B 69 (2004) 165210.
[62] B.R. Hollebone, M.J. Stillman, Chem. Phys. Lett. 29 (1974) 284.
[63] A. König, F. Roth, R. Kraus, M. Knupfer, J. Chem. Phys. 130 (2009) 214503.
[64] M.D. Kuz'min, R. Hayn, V. Oison, Phys. Rev. B 79 (2009) 024413.
[65] W. Wu, A. Kerridge, A.H. Harker, A.J. Fisher, Phys. Rev. B 77 (2008) 184403.
[66] A. Calzolari, A. Ferretti, M.B. Nardelli, Nanotechnology 18 (2007) 424013.
[67] Y. Niwa, H. Kobayashi, T. Tsuchiya, J. Chem. Phys. 60 (1974) 799.
[68] G. Dufour, C. Poncey, F. Rochet, H. Roulet, M. Sacchi, M.D. Santis, M.D. Crescenzi, Surf. Sci. 319 (1994) 251.
[69] H. Peisert, M. Knupfer, J. Fink, Surf. Sci. 515 (2002) 491.
[70] T. Schwieger, H. Peisert, M.S. Golden, M. Knupfer, J. Fink, Phys. Rev. B 66 (2002) 155207.
[71] N. Papageorgiou, Y. Ferro, E. Salomon, A. Allouche, J.M. Layet, L. Giovanelli, G. Le Lay, Phys. Rev. B 68 (235) (2003) 105.
[72] B. Brena, Y. Luo, M. Nyberg, S. Carniato, K. Nilson, Y. Alfredsson, J. Åhlund, N. Mårtensson, H. Siegbahn, C. Puglia, Phys. Rev. B 70 (2004) 195214.
[73] J. Bruder, I. an Schöneboom, R. Dinnebier, A. Ojala, S. Schäfer, R. Sens, P. Erk, J. Weis, Org. Electron. 11 (2010) 377.
[74] P. Gargiani, M. Angelucci, C. Mariani, M.G. Betti, Phys. Rev. B 81 (2010) 085412.
[75] A. Kahn, W. Zhao, W. Gao, H. Vazquez, F. Flores, Chem. Phys. 325 (2006) 129.
[76] L. Lozzi, S. Santucci, S. La Rosa, J. Vac. Sci. Technol. A 22 (2004) 1477.
[77] H. Peisert, M. Knupfer, T. Schwieger, J.M. Auerhammer, M.S. Golden, J. Fink, J. Appl. Phys. 91 (2002) 4872.
[78] J.J. Yeh, I. Lindau, Atom. Data Nucl. Data Tables 32 (1985) 1.
[79] V. Maslyuk, V. Aristov, O. Molodtsova, D. Vyalikh, V. Zhilin, Y. Ossipyan, T. Bredow, I. Mertig, M. Knupfer, Appl. Phys. A 94 (2009) 485.
[80] M. Grobosch, V.Y. Aristov, O.V. Molodtsova, C. Schmidt, B.P. Doyle, S. Nannarone, M. Knupfer, J. Phys. Chem. C 113 (2009) 13219.
[81] D.E. Barlow, L. Scudiero, K.W. Hipps, Langmuir 20 (2004) 4413.

UV laser. It was found that the highly absorbed wavelength produces a good film and poorly absorbed will result in a powdery film. It was also found that, even though molecular weight is reduced there is no change in chemical composition of the molecules during ablation [13]. Satoru Nishio et al. studied the structural difference in the polyacrylonitrile (PAN) films with various laser wavelengths. Films of PAN were deposited for wavelengths 308 nm (XeCl), 248 nm (KrF) and 193 nm (ArF). It was found that the original structure of PAN is retained for the films deposited by ablation at 308 nm and deformation and elimination of nitrile groups occur for the films prepared by ablation at 248 nm and 193 nm, respectively. Furthermore, power dependent structural change at 248 nm was found [14]. Recently a new method of ablation has been developed called matrix assisted pulsed laser ablation (MAPLE) [15]. Sellinger et al. produced PMMA films with up to 2 wt.% carbon nanotube (CNT) in MAPLE technique using KrF laser [9]. Vrnata et al. deposited thin layers polypyrole (PPy) by MAPLE technology. Deposition was carried out by KrF excimer laser with PPy in water and dimethylsulfoxide matrix [10]. In this paper, we will discuss about fabrication of device quality films from polypyrrole-multiwalled carbon nanotube (PPy–MWCNT) nanocomposites with high loadings by pulsed laser ablation. Nanotube loadings up to 80 wt.% were used to evaluate appropriateness of employing laser ablation technique for fabrication of device quality films of nanocomposites.

2. Experimental section

2.1. Materials

MWCNT's (diameter 10–20 nm, length 10–50 μm) produced by catalytic vapor decomposition technique and with a purity of >95% were purchased from Iljin Nanotech Co. Ltd., South Korea. Pyrrole monomer (99% purity, Aldrich) was distilled under reduced pressure and stored at low temperature prior to use. Benzoyl peroxide (BPO), sodium dodecyl-sulfate (SDS), nitric acid (60% purity), hydrochloric acid (37% purity) and all other organic solvents used in this study were of analytical grade and used without further purification.

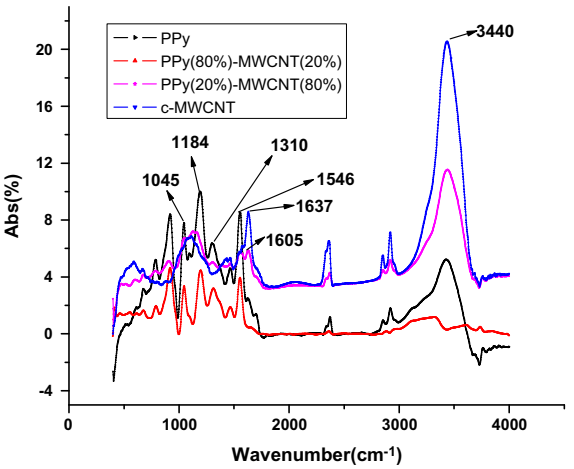

Fig. 1. FTIR of PPy, PPy–MWCNT nanocomposites and c-MWCNT.

2.2. Equipment details

Deposition of PPy and PPy–MWCNT nanocomposites were carried out by Q-switched Nydonium-doped Yttrium Aluminium Garnet (Nd-YAG) laser source (Quanta ray INDI-Newport Corporation). Operating wavelength used during deposition was 1064 nm. Analysis of nanocomposites and deposited films were carried out by X-ray photoelectron spectroscopy (XPS, ThermoFisher Scientifitic Multilab 2000), Fourier transform infrared spectroscopy (FTIR) was used to characterize the integrity of chemical composition of the polymer and nanocomposites before and after ablation. FTIR spectra were recorded on a JASCO FTIR-300E spectrometer in the wave number range of 4000–400 cm^{-1} with a resolution of 4 cm^{-1}. Samples were dispersed in KBr powder and compressed into pellets for analysis. Thickness and RMS roughness of the films were measured by optical profilometer (WYKO NT1100), X-ray powder diffraction patterns were recorded on a Panalytical Debye–Scherrer powder diffraction camera to study the bulk and film crystallinity. Scanning electron microscopy (SEM-Sirion field emission) and transmission electron microscopy (TEM-Tecnai F-30) were used for morphological studies, electrical conductivity was measured by Keithley 2182A (nanovoltmeter), 6221 (current source).

Table 1
Conductivity, thickness and roughness data of PPy, PPy–MWCNT nanocomposites.

Sample no.		Conductivity (S/cm)		Thickness (μm)	RMS roughness (nm)
Bulk	Film	Bulk	Film		
P1	P1–2	0.11 ± 0.02	1.80 ± 0.26	0.05 ± 0.0056	26
	P1–5		61.35 ± 8	0.23 ± 0.0098	22
	P1–10		26.50 ± 3.5	0.52 ± 0.0066	128
P2	P2–2	231.68 ± 15	93.25 ± 10.2	0.23 ± 0.0158	152
	P2–5		56.50 ± 11.9	0.66 ± 0.0186	357
	P2–10		23.09 ± 0.63	0.85 ± 0.0220	385
P3	P3–2	105.80 ± 2.1	102.07 ± 2.68	0.19 ± 0.0068	115
	P3–5		41.07 ± 0.89	0.49 ± 0.0162	334
	P3–10		21.11 ± 0.28	0.89 ± 0.0224	325
P4	P4–2	243.90 ± 10.74	256.04 ± 66.45	0.17 ± 0.0114	64
	P4–5		64.78 ± 3.79	0.30 ± 0.0200	93
	P4–10		30.56 ± 0.74	0.63 ± 0.0104	186

Table 2
XPS data of nanocomposites.

Sample	Binding energy (eV)									
	Bulk					Film				O1s
	C1s (Gaussian fitting)		N1s (Gaussian fitting)		O1s	C1s (Gaussian fitting)		N1s (Gaussian fitting)		
	Before	After	Before	After		Before	After	Before	After	
P1	284.7	284.9	399.9	399.8	532	285	284.7	399.9	399.9	531.8
		286.4		403.5			286.5		400.9	
P2	284.7	284.8	400	400	532.2	285	285	400	399.7	532.5
		287.4		402			287.1		404.4	
P3	285	284.8	399.6	399.7	532.5	284.9	284.9	399.8	399.6	532.5
		286.4		403.5			286.5		400.8	
P4	284.8	284.6	399.6	399.4	532.4	284.7	284.8	399.5	399.6	532.6
		286.3		402.4			286.4		400.6	

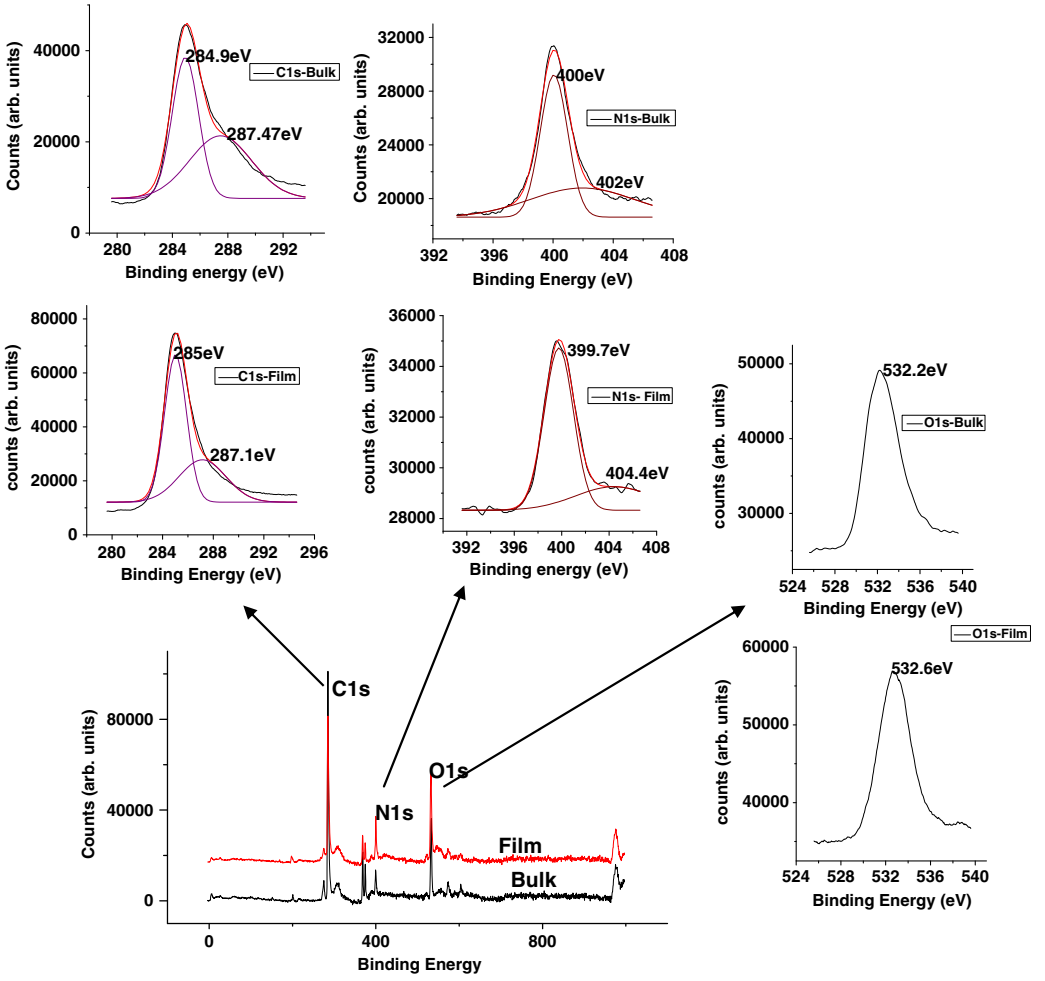

Fig. 2. X-ray Photoelectron Spectra of P2.

2.3. Oxidation of MWCNT's

In the oxidation process, 0.5 g of untreated MWCNT's were suspended in 10 ml of concentrated nitric acid and refluxed for 30 min in an ultrasonic bath. Subsequently, oxidation was carried out in a two necked, round-bottomed flask, equipped with a reflux condenser, mechanical stirrer and thermometer, which was mounted in a preheated oil bath. Reaction was carried out at 100 °C for 1 h. Obtained carboxy functionalized MWCNT's (c-MWCNT) were filtered using a 0.1 μm Teflon filter paper, washed with copious amount of de-ionized water until the pH value was about 7 and dried at 80 °C for 24 h [16].

2.4. Synthesis of PPy/c-MWCNT nanocomposites

Nanocomposites of PPy/c-MWCNT's were synthesized by inverted emulsion polymerization technique [17,18]. Emulsion was formed using SDS (0.2 M) in 1 M HCl solution with vigorous stirring. Various weight percentages of c-MWCNT's (20, 40, and 80 wt.%) were then dispersed in an emulsion under sonication for 1 h. For convenience, following nomenclature has been adopted in this paper: P-1 for 100% PPy, P-2 for 80% PPy and 20% MWCNT, P-3 for 60% PPy and 40% MWCNT, P-4 for 20% PPy and 80% MWCNT. Precooled solution of pyrrole monomer (0.25 M) was added to the above dispersion with constant stirring. Finally, BPO solution (0.25 M) in chloroform was added drop wise over a period of 30 min with constant stirring to initiate the polymerization. Pyrrole adsorbed on the surface of c-MWCNT's (core layer) was polymerized to form outer shell of the nanotubes. Within 30 min of the addition of BPO suspension turned black, indicating formation of polypyrrole. Reaction was continued for 5 h at room temperature. Polymerization was quenched by pouring the reaction mixture into acetone where, PPy/c-MWCNT composites precipitated out and excess BPO was dissolved in acetone. Precipitated product was then filtered and washed with copious amount of de-ionized water to remove unreacted monomer and excess SDS. Finally resulting mixture was washed with acetone and was dried under vacuum at 60 °C for 24 h.

Most of the electroactive polymers are difficult to dissolve, even if it is dissolved, presence of residual solvent in the film affects the device performance [19,20]. Furthermore, addition of nanoparticles to the polymer matrix would decrease the processability. Hence alternate methods of fabricating device quality films were evaluated. Laser ablation is an interesting technique where polymer films can be fabricated.

Pellets of nanocomposite were fabricated and used as target material for laser ablation. Pellets with 15 mm diameter and 3 mm thickness were fabricated using a desk top press, with applied pressure of 10 ton. Care was taken to keep the pellet thickness above 3 mm to safeguard the integrity of the target during ablation. Films were deposited for laser energy of 100 mJ and 50 mJ. Target and substrate are rotated at a constant speed of 60 rpm to achieve uniform ablation. Films of nanocomposites on all three different substrates i.e. silicon, glass and ITO were deposited in a single deposition to minimize batch to batch process variations that might occur. For convenience, samples were named according to deposition time, for example films of P1 is labeled as P1–2, P1–5 and P1–10 deposited for 2 min, 5 min and 10 min, respectively (Table 1).

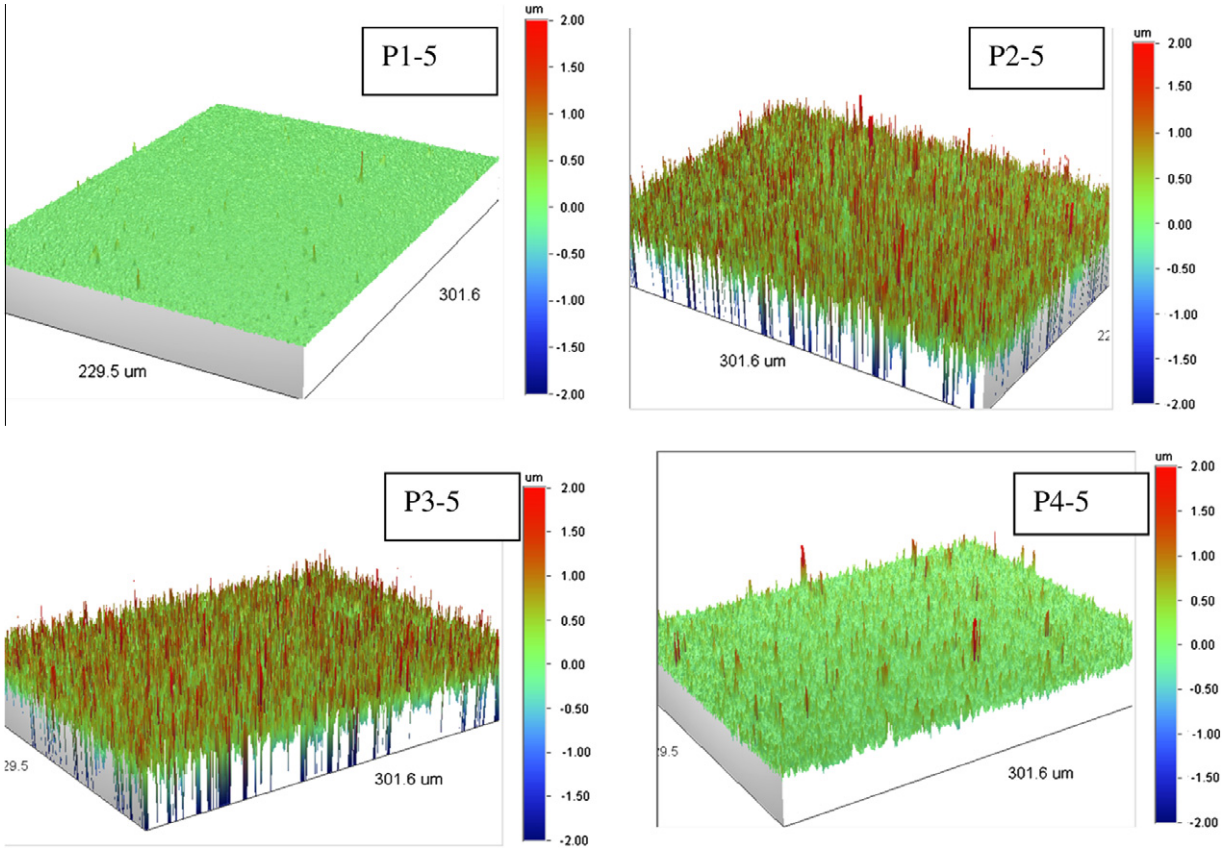

Fig. 3. Optical Profilometer of P1–5, P2–5, P3–5 and P4–5.

3. Result and discussion

FTIR spectra of chemically modified MWCNT's, PPy and PPy-coated MWCNT's are shown in Fig. 1. Characteristic bands due to newly formed polar functional groups were observed in the FTIR spectra of the MWCNT's after acid treatment in HNO_3. IR bands at 3440, 1637, and 1182 cm^{-1} were consistent with the OH stretching, C = O stretching and C–C–O stretching in modified MWCNT's, respectively [21]. In case of PPy, characteristic fundamental ring vibration appeared at 1546 cm^{-1}, and C–H in-plane vibration and C–N stretching vibration appeared at 1310 and 1045 cm^{-1}, and at 1184 cm^{-1}, respectively [22]. PPy–MWCNT's nanocomposites showed characteristics peaks for both PPy and MWCNT's. From the spectra it is evident that there is a shift in C–O peak from 1637 cm^{-1} in neat PPy to 1605 cm^{-1} in the case of PPy–MWCNT nanocomposites. Presence of carboxylic groups on the nanotube surface will increase the interaction between NH groups of the PPy and COOH groups of chemically modified MWCNT's. This indicates that PPy has modified the MWCNT surface.

Furthermore, according to Tian and Zerbi, the intensity ratios of the 1560 and 1480 cm^{-1} bands (I_{1560}/I_{1480}) is inversely proportional to the extent of delocalization [23]. Thus, polymer molecules with high concentrations of defect sites (short conjugation lengths) showed high values of I_{1560}/I_{1480}, whereas, polymer molecules with low concentrations of defect sites (long conjugation lengths) showed low values of I_{1560}/I_{1480}. It was observed that the I_{1560}/I_{1480} increases with increasing MWCNT content (i.e., with decreasing thickness of the PPy layer). This indicates that the layer of PPy that is deposited directly on the surfaces of MWCNT's has a shorter conjugation length than subsequently deposited layers, probably due to the π–π interaction between MWCNT's and pyrrole monomers. With increase in MWCNT concentration, the defect on PPy increases because nanotubes act as dopant and also due to the fact that network structure of

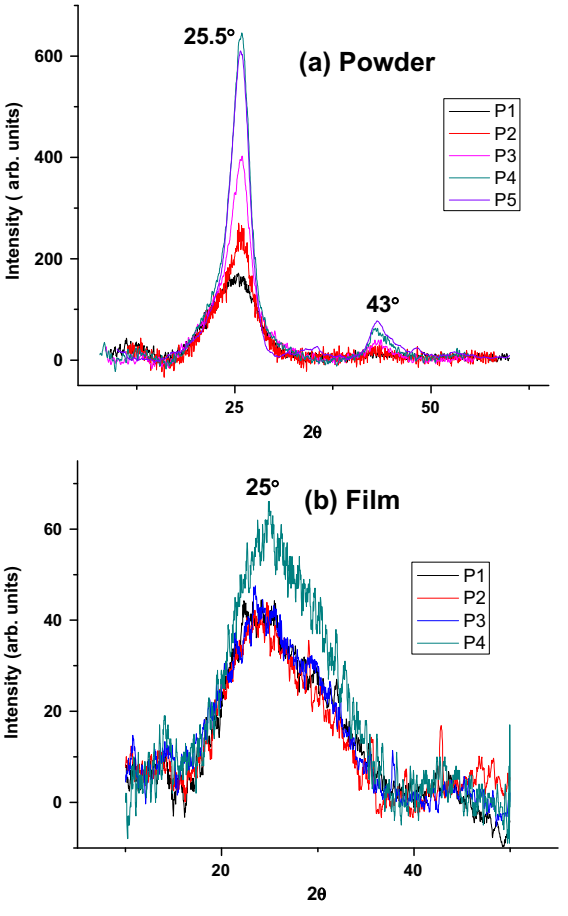

Fig. 4. XRD of PPy-MWCNT nanocomposite (a) powders, (b) films.

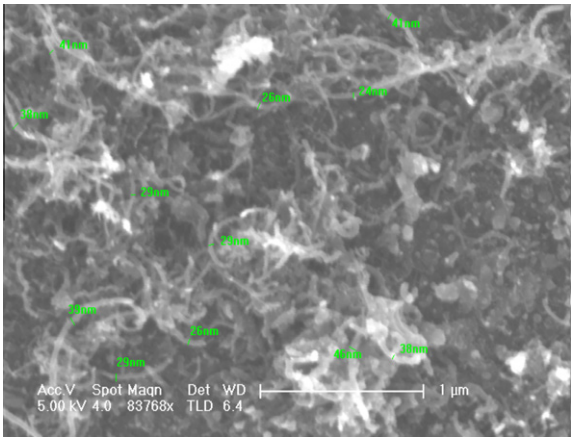

Fig. 5. Scanning electron microscopy image of P4-film.

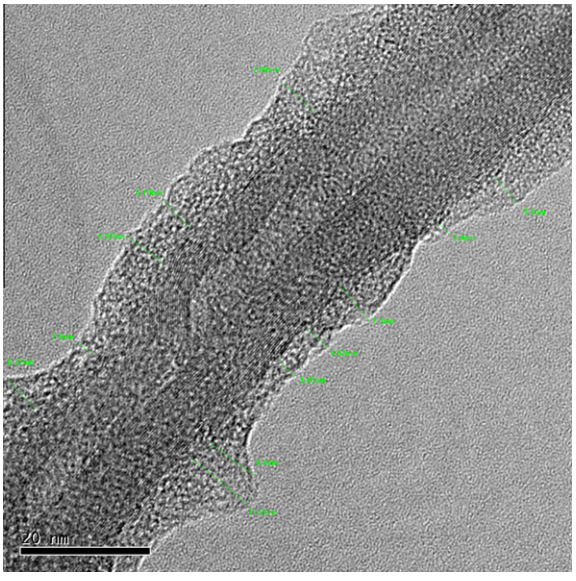

Fig. 6. Transmission electron microscopic image of P2.

MWCNT's. On the other hand, with decrease in PPy thickness some parts of MWCNT will not interact fully with PPy molecules. This results in shorter conjugation length of PPy [24].

XPS was employed to determine chemical composition of nanocomposite before and after ablation and results are tabulated in Table 2. XPS spectrum of the target material P2 is as shown in the Fig. 2. C1s peak was observed at 284.7 eV. Gaussian fitting resolves this into two peaks at 284.8 eV and 287.4 eV indicating the presence of C–C bonding and C–N, C–H bonding, respectively. N1s peak was observed at 400 eV. Gaussian fitting resolves this into two peaks at 400 eV and 402 eV indicating the presence of N–H bonding and N–C bonding, respectively. O1s peaks are observed in the spectra at 532.2 eV was believed to be due to adsorbed oxygen, on exposure to environment. Absence of peaks at 390 eV and 406 eV indicate that there is no bonding with C or N, which indicates that the films are not oxidized [25–27]. XPS of ablated film is shown in Fig. 2. C1s peak was observed at 285 eV. Gaussian fitting resolves this into two peaks at 285 eV and 287.1 eV indicating the presence of C–C bonding and C–N, C–H bonding, respectively. N1s peak was observed at 400 eV. Gaussian fitting resolves this into two peaks at 399.7 eV and 404.4 eV indicating the presence of N–H bonding and N–C bonding, respectively. O1s peaks are observed at 532.5 eV. These results are in good agreement with that of the target material. These results indicate nanocomposite does not get degraded during ablation process. XPS studies for P1 (Fig. 7 supporting information) film which is pure PPy also shows a good agreement with bulk indicating even though PLD process may change the molecular weight it does not change the chemical composition of polymer [13].

Surface roughness is very important parameter in polymer thin film devices. Higher the roughness, chances of electrically shorting the electrodes due to pin holes increases. Hence low roughness is desirable. Surface roughness and thickness of the films were measured by 3D optical surface profilometer (Fig. 3 and Table 1). It was observed that surface roughness increases initially with addition of MWCNT's however on further addition, surface roughness decreases. P1 films were found to be

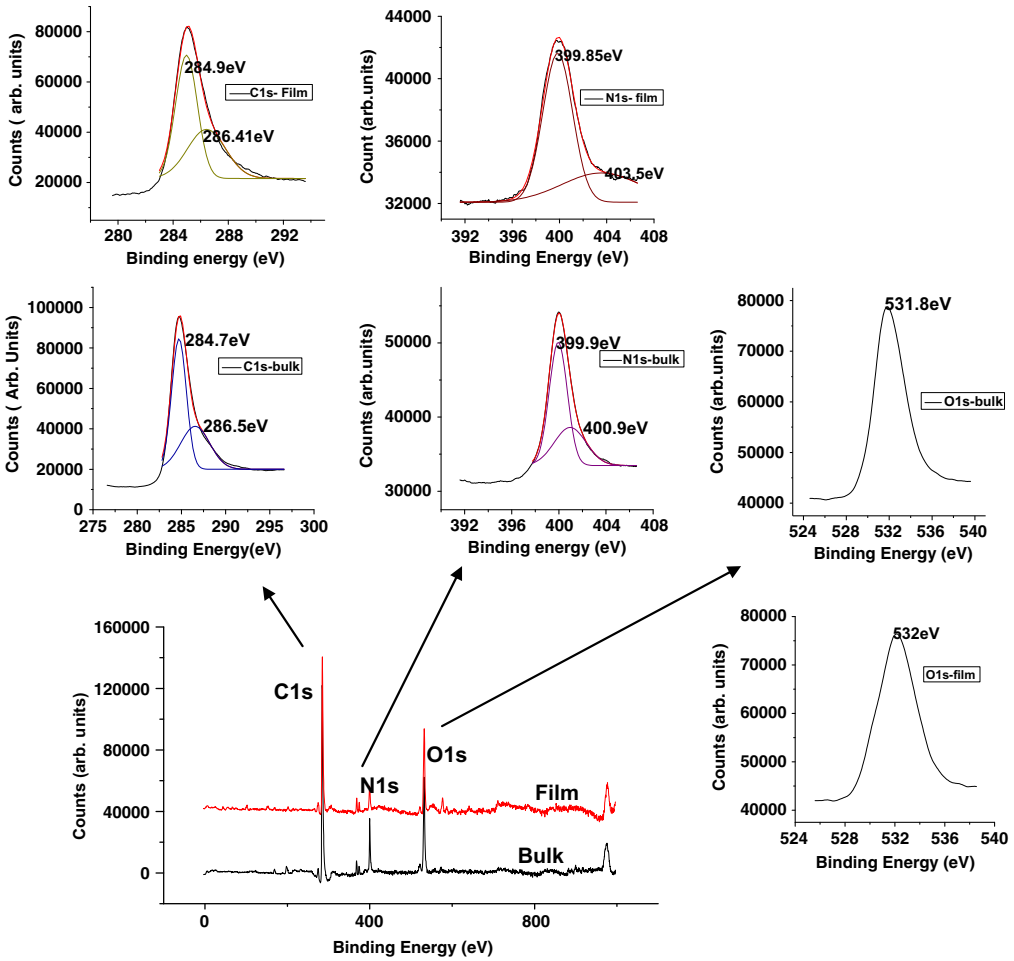

Fig. 7. (a) X-ray photoelectron spectra of P1. (b) X-ray photoelectron spectra of P3. (c) X-ray photoelectron spectra of P4.

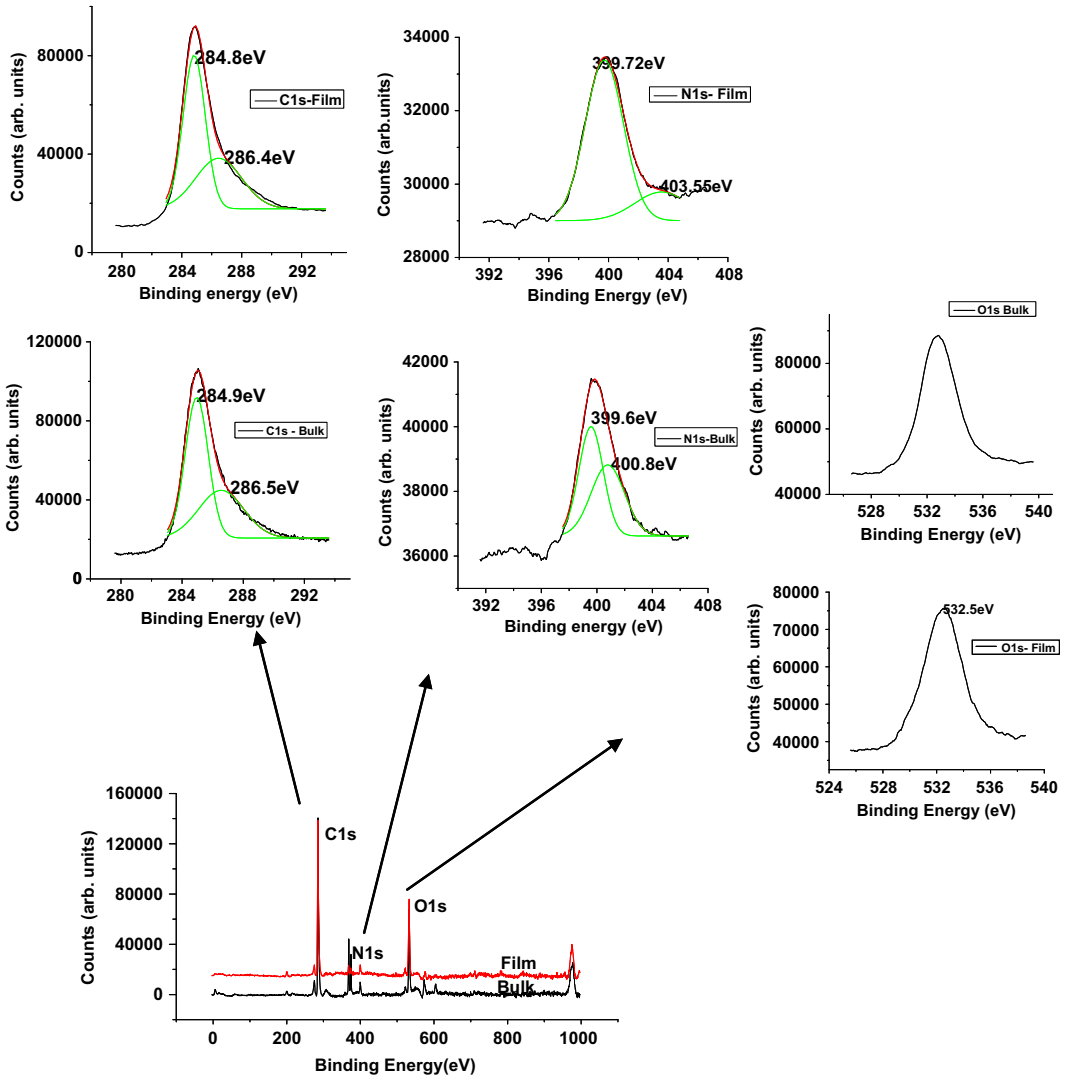

Fig. 7 (*continued*)

smoother than P2, P3 and P4 because it is not a mixture, but single homogeneous material system. On the contrary, P4, mixture of different materials viz, nanotubes and polymer, was found to be smoother than P2 and P3. Because at such high loadings, major component in the composite will be nanotubes and polymer would get filled in intricacy of MWCNT's mat structure upon film fabrication. Consequently, roughness decreases by filling up of crests and troughs formed by the nanotube matrix. In case of P2 and P3 MWCNT mat will have bigger voids because of lesser nanotube wt.% than P4. Hence, films of P2 and P3 show higher values of roughness indicating insufficient filling of voids in the matrix by the polymer. Hence intermixing of PPy-MWCNT at such loadings will result in rough surface. Films deposited for 100 mJ were rougher (RMS 320 nm) than the films deposited for 50 mJ (RMS 152 nm) moreover at 100 mJ deposition rate is too high to control the thickness. Hence, all the films fabricated in this study are at 50 mJ.

XRD analysis of pure PPy and nanocomposite powders are as shown in Fig. 4a. A broad peak at 25.5° was observed for pure PP, indicating amorphous nature of PPy. In case of nanocomposite powders, in addition to peak at 25.5° another peak at 43°, which is attributed to (1 0 0) reflection from MWCNT, was observed [28]. It was also observed that as MWCNT loading increases in nanocomposite, intensity of the peak at 43° increases and peaks become sharper. Since XRD of MWCNT show peaks at same 2θ values, increase in intensity can be attributed to increase of MWCNT loading in nanocomposites. XRD patterns of the films also show that the films are amorphous (Fig. 4b).

Distribution of MWCNT in the matrix is analyzed by scanning electron microscopy of both film and the powder (Fig. 5). Film morphology of P1 which is pure PPy, is smooth with a RMS roughness of 22 nm. Film images of P2, P3and P4 which are MWCNT loaded in various wt.% shows presence of MWCNT's and also images, which has MWCNT wt.% of 20, 40 and 80, respectively, shows that

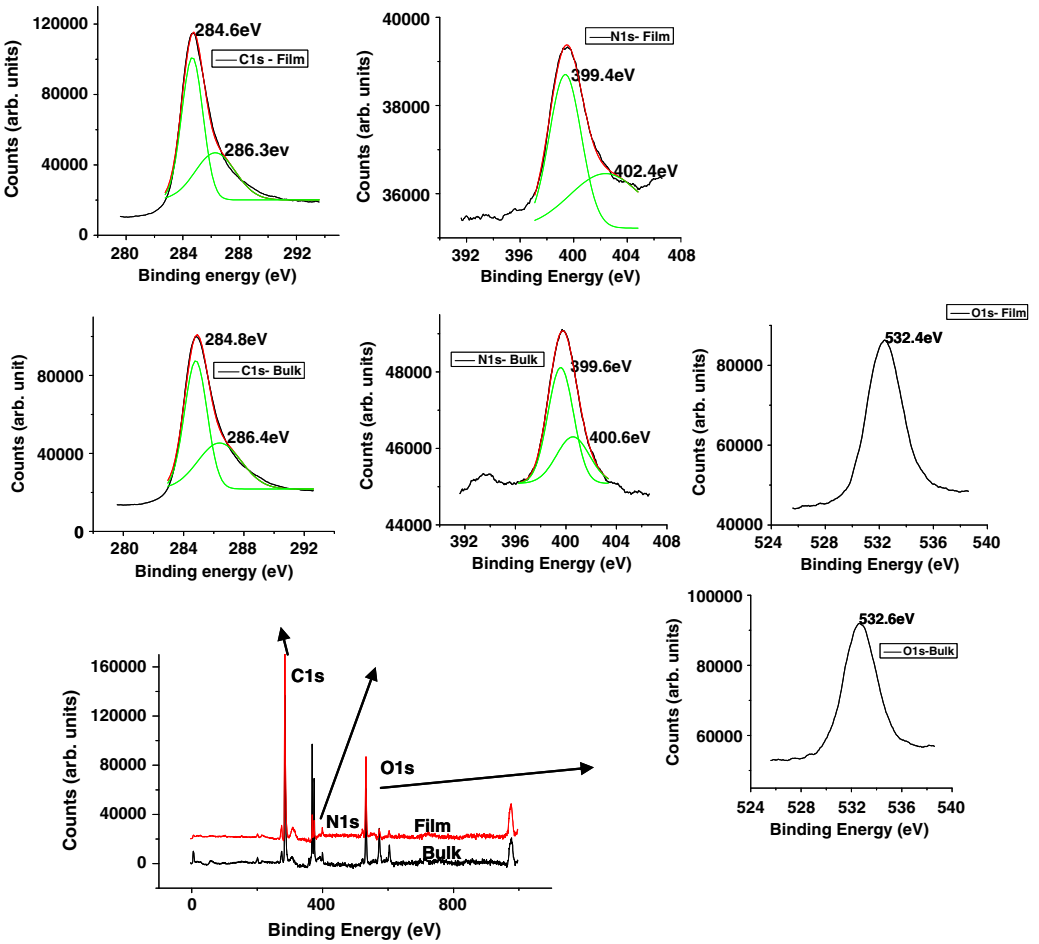

Fig. 7 (*continued*)

along with polymer MWCNT's are also ablated. Moreover, MWCNT's are distributed through out the matrix. Diameter of the MWCNT's for both film and the bulk were measured and indicated on the images. For both bulk and film, diameter of MWCNT coated with PPy varies from 24 nm to 66 nm. This indicates that polymer layer wrapped on nanotube remains intact during ablation. Many drop like features were observed in the nanocomposite films, which are attributed to the pure PPy molecular cluster (Fig. 8 supporting information).

High resolution TEM image of the MWCNT in nanocomposite (Fig. 6) shows presence of PPy coating on MWCNT wall. It was observed that polymer layer thickness is not uniform throughout the film. In this particular example we found it varies from 2 to 8 nm. This supports FTIR analysis that reason for short conjugation length as the nonuniform thickness of PPy on MWCNT walls. Polymer layer thickness was measured for all the three nanocomposites using TEM and thickness values are indicated on Fig. 9 (supporting information). Even though coating is not uniform it was observed that polymer layer thickness does not vary much from bulk to film indicating during ablation nanocomposite remains intact further supporting the evidence of the integrity of the polymer coating that was observed in SEM analysis. Measured polymer thickness of P2, P3 and P4 varies from 3–15 nm, 5–12 nm and 2–3 nm, respectively. Polymer layer thickness decreases with decrease in PPy wt.% as indicated by SEM analysis. It is evident from TEM micrographs that MWCNT web is held together by the polymer matrix indicating better intermixing of PPy and MWCNT (Fig. 9 supporting information). Even though PPy coating on MWCNT is not uniform low magnification TEM image of both bulk and film shows polymer wrapping on MWCNT's.

Conductivity of both bulk and films were measured and compared using four point probe setup. Conductivity of both bulk and films are shown in Table 1. Ablation targets were used for bulk conductivity measurement. It was observed that conductivity increases by addition of (20 wt.%) MWCNT from 0.11 S/cm to 231 S/cm. Electrical percolation threshold for carbon nanotubes in a polymer matrix are about 5–8% [29]. Increase in MWCNT loading here does not further enhance the conductivity indicating percolation threshold has already been reached. Furthermore these results also indicate that

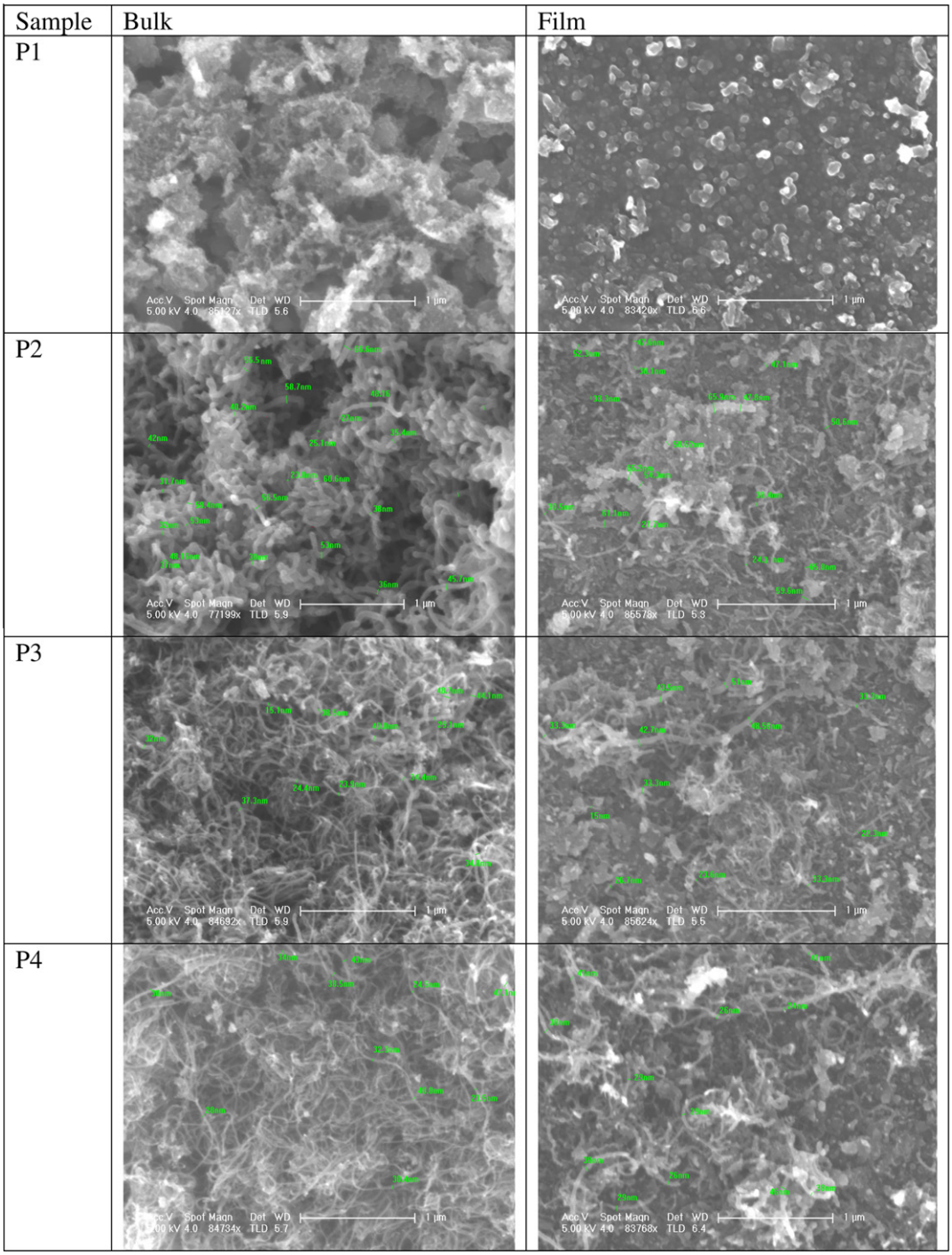

Fig. 8. Scanning electron microscopy images of P1, P2, P3 and P4.

conductivity measurements on a bulk material in pellet form is not appropriate method as conductivity varies with packing density of the pellet, pressure applied by the four point probe etc. Even slight variation of these parameters will change the conductivity values. Hence conductivity measurements of a polymer material in a thin film are appropriate compared to bulk measurements. Increase in conductivity with increase in MWCNT loading was observed in films. It was also observed that in films, conductivity decreases with increase in film thickness for all compositions except in the case of P1–2 made from neat PPy. This is because P1–2 is not continuous film (at 50 nm thickness) as indicated by SEM (Fig. 10 supporting information). Optical profilometer

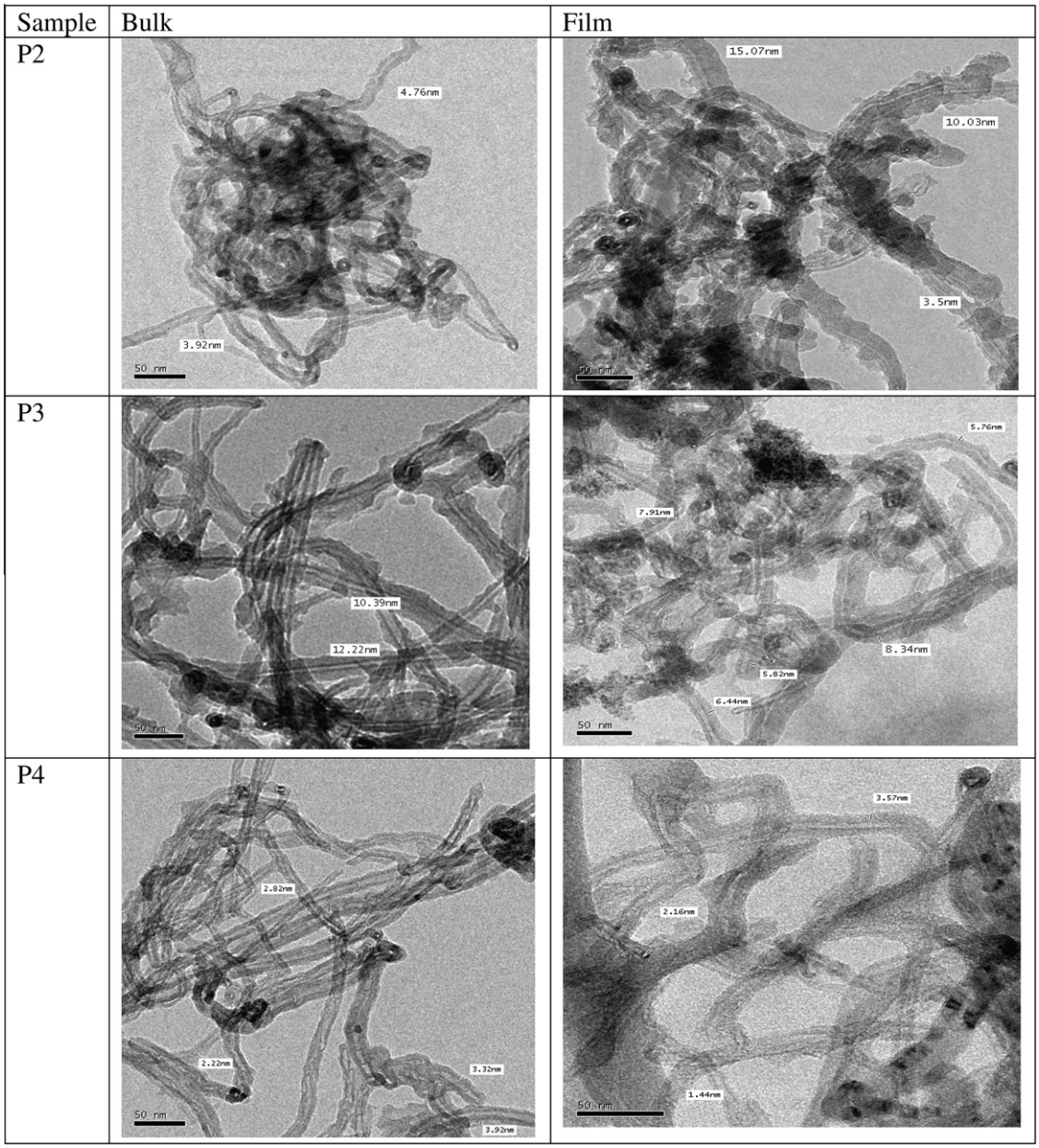

Fig. 9. Transmission electron microscopic image of nanocomposites.

indicates that the film roughness increases with increase in film thickness (Table 1). Furthermore, with increase in film thickness, impurities, structural defect density will increase, hence conductivity decreases with increasing film thickness [30]. Comparison of film conductivity with film thickness indicates that maximum conductivity was observed about 0.2 μm.

4. Conclusions

Device quality films of highly loaded nanocomposites were fabricated by pulsed laser deposition. Comparative study of X-ray photoelectron spectroscopy (XPS) of bulk and film show that polymer does not degrade during ablation. Both SEM and TEM micrographs indicate that the MWCNT's are distributed in the ablated films. Further more, MWCNT diameter does not change from bulk to film indicating that the polymer layer wrapped on MWCNT remains intact during ablation. Conductivity of both bulk and film were measured using collinear four point probe setup. It was found that conductivity of films increases with addition of MWCNT and decrease with increasing thickness. Comparative study of thickness with conductivity indicates that maximum conductivity was observed around 0.2 μm. Even for very high loading (80 wt.%) device

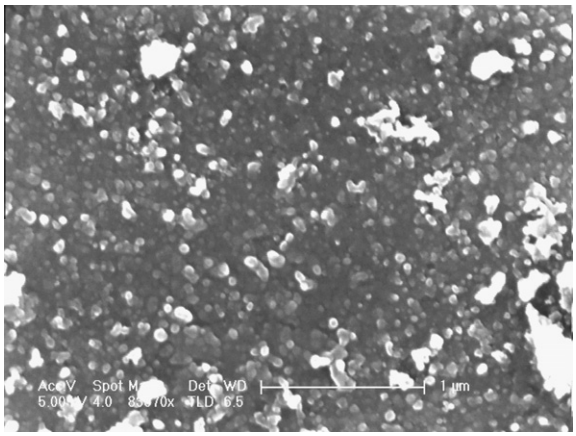

Fig. 10. SEM image of P1–2.

quality films were able to fabricate using PLD technique, indicating laser ablation is an appropriate technique for fabrication of device quality films for organic electronic applications.

Acknowledgements

This work is partially supported by Korea Research Council of Fundamental Science and Technology (KRCF) and Korea Institute of Science and Technology (KIST) for National Agenda Project (NAP) program. In addition authors gratefully acknowledge the financial support from DST No. SR/S3/ME/025/2008 and Technical Support from IISc advanced characterization center. One of the authors (Dr. T. Jeevananda) would like to thank management of RNSIT for their support.

References

[1] Cossement, F. Plumier, J. Delhalle, L. Hevesi, Z. Mekhalif, Synth. Met. 138 (2003) 529–536.
[2] D.E. Tallman, C. Vang, G.G. Wallace, G.P. Bierwagen, J. Electrochem. Soc. 149 (2002) C173–C179.
[3] G. Han, J. Yuan, G. Shi, F. Wei, Thin Solid Films 474 (2005) 64–69.
[4] X. Lin, Y. XuFacile, Electrochim. Acta 53 (2008) 4990–4997.
[5] V.M. Kopecky, F. Vyslouzil1, O. Ekrt, V. Myslík, P. Fitl, M. Jelinek, T. Kocourek, J. Phys.: Conf. Ser. 76 (2007) 012044.
[6] M. Kuhnke, L. Cramer, P.E. Dyer, J.T. Dickinson, T. Lippert, H. Niino, M. Pervolaraki, C.D. Walton, A. Wokaun, J. Phys. Conf. Ser. 59 (2007) 625–631.
[7] F. Kannari, CLEO/Pacific Rim '99 I ThL1 (Invited), IEEE (1999) 686–687.
[8] Y.F. Lu, Z.M. Ren, Z.H. Mai, T.C. Chong, S.C. Ng, P. Miao, B.A. Cheong, S.K. Chow, T.Y.F. Liew, J. Mater. Res. 15 (2000) 536–540.
[9] A.T. Sellinger, E.M. Leveugle, K. Gogick, L.V. Zhigilei, J.M. Fitz-Gerald, J. Vac. Sci. Technol. A 24 (2006) 1618–1622.
[10] M. Yudasaka, Y. Tasaka, M. Tanaka, H. Kamo, Y. Ohki, S. Usami, S. Yoshimura, Appl. Phys. Lett. 64 (1994) 3237–3239.
[11] Y. Tsuboi, M. Goto, A. Itaya, J. Appl. Phys. 85 (1999) 4189–4195.
[12] W.O. Siew, T.Y. Tou, K.H. Wong, Appl. Surf. Sci. 248 (2005) 281–285.
[13] S.G. Hanson, T.E. Robitaille, Appl. Phys. Lett. 52 (1988) 81–83.
[14] S. Nishio, T. Chiba, A. Matsuzaki, J. Appl. Phys. 79 (1996) 7198–7200.
[15] R.A. McGill, D.B. Chrisey, United States Patent 6025036 (2000).
[16] I.D. Rosca, F. Watari, M. Uo, T. Akasaka, Carbon 43 (2005) 3124–3131.
[17] H. Guo, H. Zhu, H. Lin, J. Zhang, Colloid. Polym. Sci. 284 (2008) 587–591.
[18] C. Saravanan, R.C. Shekhar, S. Palaniappan, Macromol. Chem. Phys. 207 (2006) 342–348.
[19] G.J. Lee, S.H. Lee, K.S. Ahn, K.H. Kim, J. Appl. Polym. Sci. 84 (2002) 2583–2590.
[20] P.C. Ramamurthy, W.R. Harrell, R.V. Gregory, Electrochem. Solid-State Lett. 6 (2003) G113–G116.
[21] J.W. Cho, J.W. Kim, Y.C. Jung, N.S. Goo, Macromol. Rapid. Commun. 26 (2005) 212–216.
[22] C. He, C. Yang, Y. Li, Synth. Met. 139 (2003) 539–545.
[23] B. Tian, G. Zerbi, J. Chem. Phys. 92 (1990) 3892–3898.
[24] T.M. Wu, S.H. Lin, J. Polym. Sci. Part B Polym. Phys. 44 (2006) 1413–1418.
[25] S. Suzer, O. Birer, Tr. J. Chem. 22 (1998) 59–65.
[26] S. Hino, K. Iwasaki, H. Tatematsu, K. Matsumoto, Bull. Chem. Soc. Jpn. 63 (1990) 2199–2205.
[27] C. Malitesta, I. Losito, L. Sabbatini, P.G. Zambonin, J. Electron Spectrosc. Relat. Phenom. 76 (1995) 629–634.
[28] W.J. Xu, H.Z. Chen, M.M. Shi, Y.G. Huang, M. Wang, Nanotechnology 17 (2006) 728–733.
[29] P.C. Ramamurthy, W.R. Harrell, R.V. Gregory, A.M. Rao, J. Electrochem. Soc. 154 (2007) H495–H499.
[30] R. Schmechel, H. Seggern, Phys. Stat. Sol. (a) 201 (2004) 1215–1235.

determined by at least two different emitting materials, high color stability can theoretically be accomplished as long as the exciton competition among the emitting sites is delicately managed [7,11–16]. For instance, a dichromatic or trichromatic OLED with a stack of different emitting layers (EML) generally suffers from lower color stability due to the variations in exciton distribution at different driving voltages [17–19]. In this case, a spacer inserted in between the different EMLs can greatly alleviate color variation by stabilizing the exciton distribution [7,9,14,20]. Instead of using spacers, adopting phosphorescent sensitization as the main emission mechanism or fabricating independent emitting units in a pixel open up another possibility for stabilizing the color emission [14,21]. In this paper, we investigated the dependence of the color stability of green–blue OLED on the thickness of the EML and measured the carrier mobilities of *N,N′*-dicarbazolyl-3, 5-benzene (mCP) and 4,7-diphenyl-1,10-phenanthroline (BPhen). On account of the stronger electric field dependence of the carrier mobility of mCP than that of BPhen, and the larger voltage drop across the blue-EML (B-EML) than across the green-EML (G-EML) within the devices, the higher sensitivity of the EL spectrum to the applied driving voltage in the device with a thinner EML was attributed to the sharply increasing electric field. For an optimal device, the CIE coordinates were slightly shifted from (0.256, 0.465) to (0.259, 0.467) with increased luminance from 48.7 to 12,700 cd/m^2. Based on the backbone of this green–blue OLED, a highly efficient WOLED with maximum efficiencies of 26.4 cd/A and 19.8 lm/W was fabricated. It also exhibited high color stability, that is, the CIE coordinates shifted from (0.310, 0.441) to (0.318, 0.446) in the practical luminance range from 1050 to 9120 cd/m^2.

2. Experiments

Indium-tin-oxide (ITO) glass with sheet resistance of 30 Ohm/sqr and thickness of 100 nm was used as the substrate. The active region size of a test pixel was 2×2 mm^2 and the fabrication process consisted of pre-cleaning of the ITO, thermal deposition of the materials, and finally encapsulation with a glass cap [22]. The pre-cleaning process of the ITO-coated glass adhered to a standard solvent cleaning procedure, followed by an oxygen plasma treatment. The thermal deposition was performed in a high vacuum chamber ($\sim 3 \times 10^{-6}$ torr) for growing the organic and cathode materials. Finally, the as-fabricated device was hermetically sealed in a nitrogen glove box with water and oxygen at less than 0.1 ppm [23].

A hole-transporting *N,N′*-diphenyl-*N,N′*-bis(1-napthyl)-1,1′-biphenyl-4,4′-diamine (NPB) was used as the hole-transporting layer (HTL) on the ITO side and an electron-transporting BPhen the electron-transporting layer (ETL) on the complex LiF/Al side. An EML in between the HTL and ETL was created by a combination of two phosphorescent dopants of green-emitting tris(phenylpyridine)iridium (Ir(ppy)$_3$) and blue-emitting [(4,6-difluorophenyl)-pyridinato-N,C$^{2'}$]picolinate (FIrpic) and one host of mCP. For implementing a white OLED, tris(2-phenyl-1-quinoline)iridium(III), Ir(phq)$_3$ was used as a red emitting phosphorescent dopant [24]. For future discussion of the OLED, the main structure was ITO/NPB (50 nm)/EML/BPhen (30 nm)/LiF (1.2 nm)/Al (120 nm). The various EML structures under investigation will be mentioned in the corresponding discussion sections. The electrical and optical performances of the OLED were measured by a test system comprising of a Keithley 2400 source-meter and a Minolta CS-1000 spectrometer.

For the time-of-flight (TOF) measurements, the test material was deposited at a constant rate of 0.3 nm/s on the ITO substrate to form a nearly 1.5 μm thick film, which was subsequently covered by 15 nm of Al, which functioned as an electrode. The actual thickness of the organic layer was measured by a surface profiler (Dektak 150; Veeco). The frequency-doubled output of a 5-ns pulsed dye laser at 295 nm was chosen to match the peak optical absorption of the organic layer and aimed at the samples from the semitransparent Al electrode to generate carriers. The transient photocurrent created by the drift of the photoexcited carriers was monitored by a 1 GHz digital oscilloscope (LC574 AM, LeCroy). The carrier mobility μ was determined by $\mu = D/t_T E$, where D is the thickness of the organic layer, t_T is the transit time, and E is the applied electric field [25].

3. Results and discussion

3.1. Electrical properties of dichromatic (B + G) OLEDs with different B-EML thicknesses

In a blue–green dichromatic OLED, excitons would naturally be formed in or diffuse toward the G-EML due to its lower exciton energy. This EML structure often exhibited higher green emission at lower carrier injection conditions due to the abovementioned nature of the excitons, but lower green emission at higher carrier injection conditions due to the saturation of the emitting sites in the G-EML or the shift of the carrier recombination zone toward the B-EML [14]. These carrier injection related phenomena resulted in color variations at different injection conditions. As such, it was necessary to introduce a spacer to separate the two EMLs and thus improve the color stability (by resolving the color variation). The function of the spacer was to deter diffusion of the higher energy excitons in the B-EML to the G-EML [7,14]. In accordance with the necessity of a spacer for high color stability, our OLED under investigation had an EML configuration of 9%Ir(ppy)$_3$:mCP (G-EML)/mCP (spacer)/9%FIrpic:mCP (B-EML). The thicknesses of the G-EML and spacer were fixed at 30 and 4.5 nm, respectively, and that of B-EML was left as a variable. The constant G-EML thickness was decided based on efficiency optimization considerations while the constant spacer thickness was chosen to play a pivotal role in the confinement of the exciton formation zone. These two constant parameters thereby narrowed down the possible causes of color stability within the scope we will discuss later on.

Fig. 1 illustrates the device configuration and highest occupied molecular orbital (HOMO) and lowest

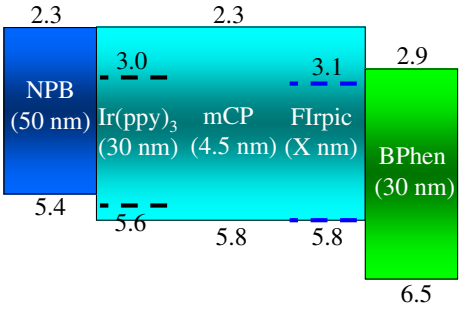

Fig. 1. HOMO and LUMO values of the organic materials.

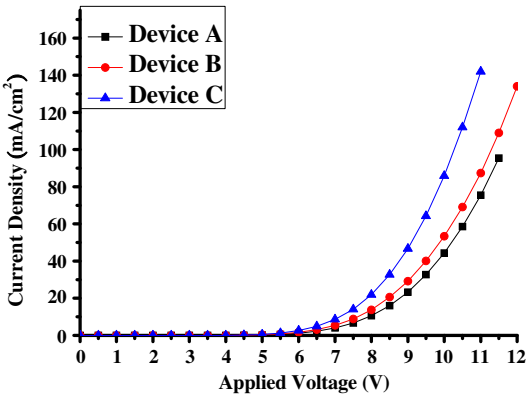

Fig. 2. J–V characteristics of devices A, B, and C with B-EML thicknesses of 18, 15, and 9 nm, respectively.

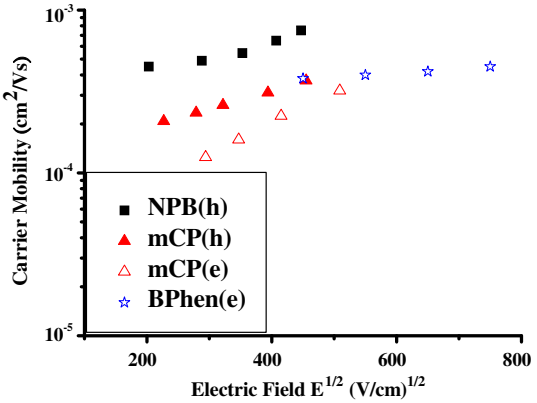

Fig. 3. Hole (h) and electron (e) mobility of NPB, mCP, and BPhen at various electric fields, as measured by the TOF technique. The closed symbol represents the hole mobility while the open symbol represents the electron mobility.

unoccupied molecular orbital (LUMO) of the organic materials, along with the corresponding thicknesses of the different components. The variable *X*, i.e. B-EML thickness, was set to be 18, 15, and 9 nm for Devices A, B and C, respectively. The performances of Devices A, B, C were summarized in Table 1. As shown in Fig. 2, Device A exhibited the highest driving voltage of 11.6 V at 100 mA/cm^2. As *X* was further decreased from 15 nm (Device B) to 9 nm (Device C), the driving voltage at 100 mA/cm^2 decreased from 11.3 to 10.3 V. It was observed that a 9 nm reduction in the B-EML thickness led to a reduction in driving voltage of 1.3 V.

To study the carrier transport characteristics, TOF measurements were performed to obtain the carrier mobilities of NPB, mCP, and BPhen. As shown in Fig. 3, the highest hole mobility of NPB directly indicated that the EML and ETL, either individually or in conjunction, accounted for most of the voltage drop. Since the primary drawback of TOF measurements is that they only provide information on the carrier transport properties, we sought the missing information on carrier injection properties through investigating the electrical characteristics of the OLED. For the purpose of understanding the integrated effects of carrier injection and transport in a guest:host film, devices with single G-EML, B-EML, and pure mCP EML as listed in Table 2 were examined. As shown in Fig. 4, Device S1 with a 9%FIrpic:mCP layer (B-EML) exhibited a higher driving voltage than Device S2 with a 9%Ir(ppy)$_3$:mCP (G-EML) and Device S3 with a pure mCP layer, respectively. Comparing S2 and S3, one can see that doping Ir(ppy)$_3$ into mCP reduced the driving voltage, because the Ir(ppy)$_3$ facilitated hole injection from the HTL into the EML and its hole-transport characteristics contributed to the carrier transport [26]. Therefore, as compared to the case of the B-EML, the vastly superior carrier transport properties of NPB, G-EML, mCP and BPhen therefore led to the reasonable conjecture that the a relatively large voltage drop occurred across the B-EML, as suggested by the electrical properties of Devices A, B and C.

We next considered the mCP spacer/B-EML interface, where electrons were blocked by an energy barrier established by the large LUMO difference between the FIrpic

Table 1
EML structures of Devices A, B, C, and their corresponding current efficiencies (cd/A), driving voltages, and CIE coordinates.

Device	EML (nm)						
	G-EML	Spacer	B-EML	[a]cd/A	[b]Driving voltage (V)	CIE coordinate	
A			18	22.1	11.6	[c](0.256, 0.465)	[d](0.259, 0.467)
B	30	4.5	15	21.3	11.3	[c](0.259, 0.471)	[d](0.270, 0.480)
C			9	19.9	10.3	[c](0.261, 0.466)	[d](0.289, 0.500)

[a] Measured at injection current density of 10 mA/cm^2.
[b] Measured at injection current density of 100 mA/cm^2.
[c] Measured at driving voltage of 5 V.
[d] Measured at driving voltage of 11 V.

Table 2
Device structures of S1, S2, S3, and their driving voltages.

Devices	NPB	EML (30 nm)	BPhen	Driving voltage (V) at 100 mA/cm^2
S1		9%FIrpic:mCP		9.1
S2	30 nm	9%Ir(ppy)$_3$:mCP	30 nm	8.2
S3		mCP		8.7

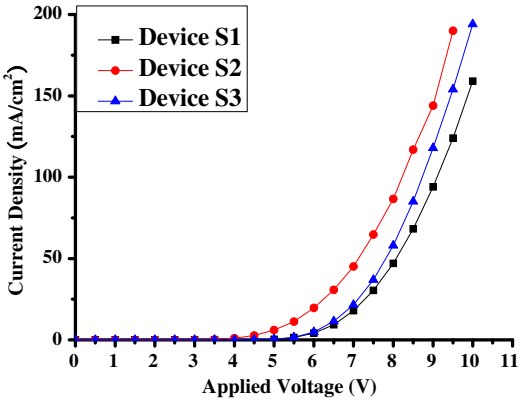

Fig. 4. J–V characteristics of Devices S1, S2, and S3 with single EML of 9%FIrpic:mCP, 9%Ir(ppy)$_3$:mCP, and mCP, respectively.

and mCP, and accumulated on the FIrpic molecules due to their relatively lower LUMO than that of the mCP molecules. At the B-EML/BPhen interface, even though the electron injection barrier created by the LUMO of the mCP host and BPhen reduced the possibility of electron injection from the BPhen to mCP, the LUMO matching between the FIrpic and BPhen allowed a portion of the electrons to be injected into the B-EML through this interface. Based on the discussion above, the electron injection and transport mechanism in the device structure shown in Fig. 1 are likely to be as illustrated in Fig. 5.

The hole-transport mechanism in an identical device to that in Fig. 1 could also be understood by examining Device S2. The lower driving voltage of Device S2 than that of Device S3 with pure mCP accounted for a better hole carrier injection and transport due to the existence of Ir(ppy)$_3$. At the NPB/G-EML interface, the similar HOMO of Ir(ppy)$_3$ to NPB provided an additional injection channel. Within the G-EML, both the similar HOMO between the Ir(ppy)$_3$ and mCP and the outstanding hole-transport properties

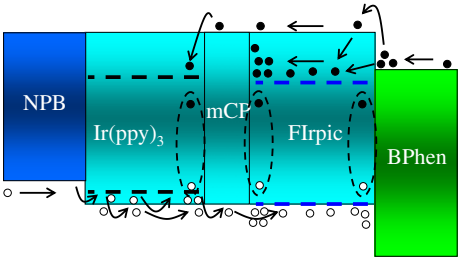

Fig. 5. Illustration of carrier injection and transport behavior in the device with structure as shown in Fig. 1. (closed circle: electron; open circle: hole). A pair of electron and hole indicates an exciton.

of Ir(ppy)$_3$ were likely to play a significant role in the transport of most of the holes through the dopants and host channels or in between [26]. At the G-EML/mCP spacer interface, the holes could easily traverse the spacer over to the B-EML due to the small HOMO difference between the Ir(ppy)$_3$ and mCP. So far, the overall picture of the carrier transport mechanism was obtained entirely as illustrated in Fig. 5, where the main recombination zone was straightforwardly found to lie within the B-EML. From the analysis of blue (FIrpic) and green (Ir(ppy)$_3$) composition in the EL spectrum of Device A, we could also recognize the location of main recombination zone. Fig. 7(a) shows that the EL spectrum of Device A comprised of 61.6% FIrpic emission along with 38.4%Ir(ppy)$_3$ emission. Furthermore, due to the lower quantum efficiency of the FIrpic [27] and the existence of exciton diffusion from the B-EML to G-EML, we could deduce that most of excitons (>61.6%) were formed in the B-EML, thus verifying the location of the main recombination zone within B-EML.

3.2. Exciton dynamics and emission properties of B + G OLED with different B-EML thicknesses

In addition to the driving voltage, different B-EML thicknesses also resulted in significant variations in the efficiency and EL spectrum. Fig. 6 shows a sharper current efficiency and external quantum efficiency (EQE) roll-off for Device C, which was mainly attributed to triplet–triplet annihilation (TTA) [28]. At low injection current densities less than 0.1 mA/cm^2, the current efficiencies of Devices A and C were similar. In this case, the TTA was not significant due to the low exciton concentration for both devices. However, as the injection current density rose to a higher level, the current efficiency of Device C dropped more

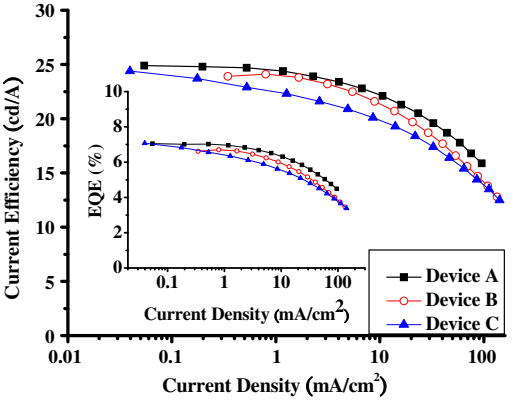

Fig. 6. Current efficiencies (cd/A) and EQE (Inset) of Devices A, B, C under different current densities.

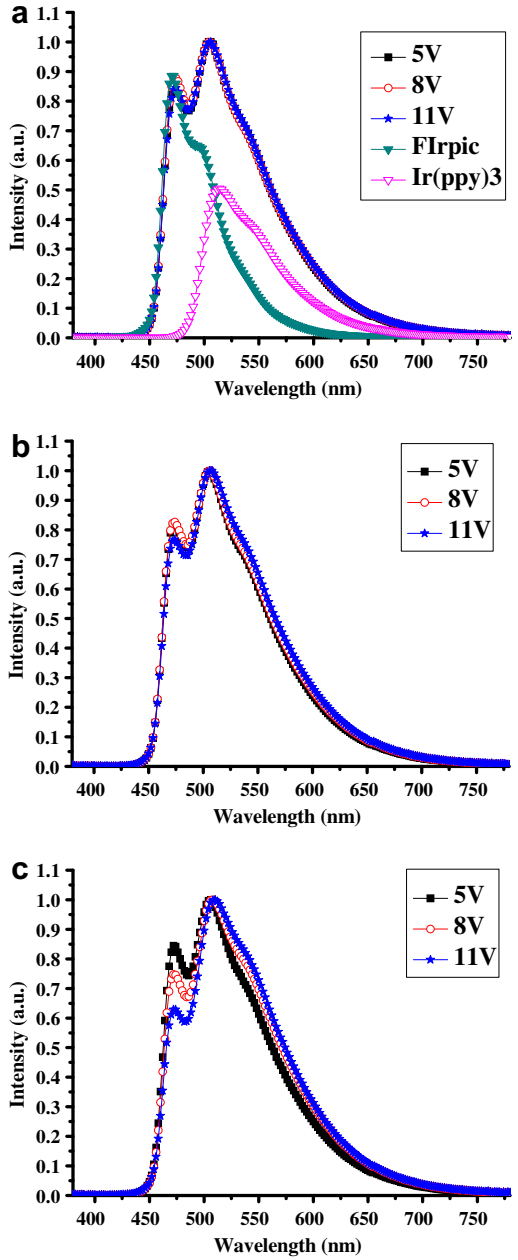

Fig. 7. Normalized EL spectra of Devices A (a), B (b), and C (c) at 5, 8, 11 V. The EL spectra consisted of FIrpic emission with peak at 470 nm and $Ir(ppy)_3$ emission with peak at 520 nm shown in (a). The fitting procedure for decomposition was: (1) transforming EL spectra from energy to photon number distribution; (2) normalizing their respective total number based on an assumption of the same EQE values in blue and green OLED; (3) finding a combination of 61.6% normalized FIrpic and 38.4% normalized $Ir(ppy)_3$ contributed to the EL spectrum of Device A.

sharply than that of Device A since the more rapid growth of the exciton concentration for the thinner B-EML resulted in more significant TTA.

As can be seen in Fig. 7, Device A (with a thicker B-EML) exhibited a constant EL spectrum, while Device C (with a thinner B-EML) exhibited notable variations in the EL spectrum as the applied voltage was increased. Naturally, the performance of Device B lied somewhere between those of Devices A and C due to its intermediate B-EML thickness. In Table 1, the CIE coordinate variation for Device A was (0.003, 0.002) from 5 to 11 V, while that for Device C was (0.028, 0.034). In other words, Device C possessed poorer color stability. Since both Devices A and C experienced TTA as the applied voltage was increased, the disparity between their color stability must be attributed to their different sensitivities to the electric field during carrier injection and transport. As discussed previously, a relatively large voltage drop occurred across the B-EML, indicating sharp changes in the electrical field on both boundaries of the B-EML. The variations in the electric field resulted in a voltage across the spacer/B-EML and B-EML/ETL interfaces. Therefore, under the same external applied voltage, the thinner B-EML in Device C would be subject to a larger electric field and a larger voltage drop would occur across the two boundaries, thereby lowering the effective injection barrier height [29]. Therefore, more electrons were accumulated on these two interfaces, with a higher possibility for injection as the driving voltage became higher.The carrier mobilities for both the mCP and BPhen were electric field dependent, as indicated by our TOF measurements as shown in Fig. 3. The parameters for the Poole–Frankel mobility of $\mu = \mu_0 \exp(\beta\sqrt{E})$ were extracted from our experimental results, and listed in Table 3. The parameter $_0$ represents the zero-field carrier mobility, β describes the electric field dependence of the mobility, and E is the applied electrical field [29–31]. As can be seen in Table 3, the β value of the electron mobility of mCP was 0.00426, which implied the highest sensitivity to the electric field. Therefore, the increase in electron mobility with the electric field could enable the electron to penetrate deeper from the B-EML/ETL interface and accumulate at the spacer/B-EML interface. Coupled with the increasing penetration probability at the spacer/B-EML interface due to the barrier lowering, the number of electrons leaking out of the B-EML to G-EML would increase, thereby intensifying the green emission with increasing driving voltage, as observed in Device C. In contrast, Device A did not encounter a significant increase in the electric field and barrier lowering due to the thicker B-EML, and therefore exhibited high color stability. At a low driving voltage (5 V), Devices A, B, C exhibited similar EL spectra. This indicated that the recombination zone distribution was similar for these three devices since no electron leakage out of the B-EML occurred at a low electric field.

The poor color stability of Device C, due to the extension of the recombination zone, was further exacerbated by TTA. In Device C, as the voltage increased, the green

Table 3
Carrier mobility μ (h for hole; e for electron), zero-field mobility μ_0 and Poole–Frankel slope β of mCP and BPhen.

Mobility μ(cm^2/V^{-s})	μ_0 (cm^2/V^{-s})	β ($(V/cm)^{-1/2}$)
mCP(h)	1.20E-04	0.00254
mCP(e)	4.00E-05	0.00426
BPhen(h)	7.34E-06	0.00174
BPhen(e)	2.90E-04	0.00056

emission grew due to the increase in excitons in the G-EML. On the other hand, the blue emission decreased due to the severe TTA in the B-EML. As a result, the percentage of blue emission was reduced, as observed in Fig. 7(c). On the contrary, Device A, which experienced the same difficulties with TTA as Device C, exhibited no deterioration in its color stability. This disparity offered a glimpse into the energy transfer paths in Device A. It pointed to the fact that excitons in the G-EML were derived mainly from the B-EML. In this case, the percentages of blue and green emission in EL spectrum would not be changed since the increase in applied voltage could only affect the exciton number in the B-EML, and not the exciton diffusion and energy transfer from the B-EML to G-EML.

Based on the knowledge of the model shown in Fig. 5 and location of the main recombination zone, we could deduce the energy transfer paths and exciton diffusion in Device A. As shown in Fig. 8, most excitons were formed in the FIrpic and mCP molecules. Subsequently, the FIrpic excitons were radiatively released to their ground states without energy being transferred to the $Ir(ppy)_3$ molecules since this energy transfer was prohibited by spin conservation. On the other hand, the mCP excitons were allowed to impart their energies to excite the FIrpic molecules or diffuse out to the $Ir(ppy)_3$ in the G-EML to generate green emission. The energy transfer paths would not be altered at different current densities since the energy transfer was independent of the number of charge carriers. For the case of Device A in which the recombination zone was entirely located within the B-EML, the color stability would not be deteriorated by TTA since the green excitons came from the energy transfer from excitons in the B-EML. The TTA only diminished the source of excitons, but was unable to alter the green and blue composition in the EL spectrum and thus the CIE coordinate. Device A exhibited high color stability with a nearly fixed CIE coordinate around (0.25, 0.46) from 5 V ((0.256, 0.465), 48.7 cd/m^2) to 11 V ((0.259, 0.467), 12,700 cd/m^2). In contrast, in Device C, the extension of the recombination zone into the G-EML due to the electron leakage out of the B-EML led to a gradually increasing percentage of green emission in the EL spectrum as the applied voltage was increased. In conjunction with a gradually decreasing percentage of blue emission due to more significant TTA in the B-EML with the increasing injection current, Device C equivalently experienced a great reduction in the blue emission in the EL spectrum and exhibited a rather low color stability, with the CIE coordinates shifting from (0.261, 0.466) at 5 V (121 cd/m^2) to (0.289, 0.500) at 11 V (17,700 cd/m^2).

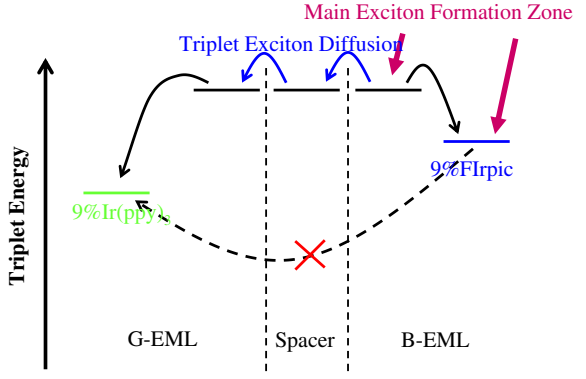

Fig. 8. Energy transfer paths in the EML of G-EML/spacer/B-EML. The dashed line indicates a prohibited energy transfer path.

3.3. White OLED with high color stability and high efficiency

Based on the EML structure of the G-EML (30 nm)/spacer (4.5 nm)/B-EML (18 nm), we further fabricated a WOLED, labeled as Device D, by doping 0.5%$Ir(phq)_3$ into the G-EML. Due to the rather low $Ir(phq)_3$ concentration, the J–V characteristics of Device D were almost the same as those of the corresponding Device A. In the inset of Fig 9(a), Device D inherited high color stability of Device A, on which it was based. Although the direct exciton formation on red dopants was inevitable, much lower red dopant concentration than green one would reduce the possibility of catching excitons by $Ir(phq)_3$ prior to $Ir(ppy)_3$

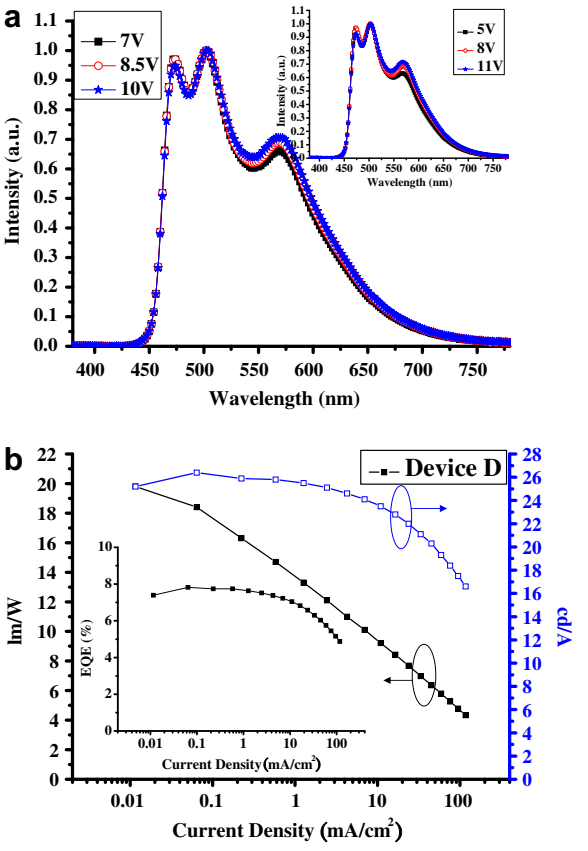

Fig. 9. (a) EL spectra of Device D at 7 V (1050 cd/m^2), 8.5 V (3740 cd/m^2), and 10 V (9120 cd/m^2). The emission with a peak around 570 nm was contributed by $Ir(phq)_3$. Inset: EL spectra of Device D at 5, 8, and 11 V. (b) Current and power efficiency of Device D with respect to current density. Device D exhibited maximum efficiencies of 26.4 cd/A and 19.8 lm/W. Inset: EQE of Device D at different current density.

[15,16], and therefore red excitons would be mainly generated by green excitons via energy transfer. The energy transfer from green to red dopants was almost independent of carrier and exciton concentration since carrier and exciton concentration was absent in the process of Förster or Dexter energy transfer [32].

As can be seen from Fig. 9(a), over the practical luminance range from 1050 (7 V) to 9120 cd/m^2 (10 V), the EL spectra were almost identical, and, thus, the CIE coordinates of Device D varied slightly from (0.310, 0.441) to (0.318, 0.446). Inset of Fig. 9(a) showed the EL spectrum of Device D when voltage changed from 5 to 11 V for a better comparison with blue–green devices (A, B, and C in Fig. 7). In addition to the outstanding color performance, Device D attained a maximum current and power efficiency, and EQE of 26.4 cd/A, 19.8 lm/W, and 7.82%, respectively, as shown in Fig. 9(b). A WOLED with high efficiency and stable color emission can be also obtained by using a thin EML (e.g. 15 nm) and suitable HTL/ETL design for confining carriers in a narrow recombination zone [16]. However, in such a device, efficiency decreased sharply with increasing current density due to serious triplet–triplet annihilation [33]. In this regard, for lower luminance applications (e.g. displays), one could design a thinner EML as proposed in Ref. [16]. For higher luminance application such as lighting, a thicker EML as revealed in this study could be needed instead.

4. Conclusion

Due to the relatively larger voltage drop across a thinner B-EML, stronger electric field dependence of the electron mobility of mCP, and energy barrier lowering at the B-EML/ETL and spacer/B-EML interfaces, it was suggested that the recombination zone extended into the G-EML for devices with a thinner B-EML as the applied voltage was increased. The extension of the recombination zone in conjunction with more significant TTA in the thinner B-EML resulted in a rather low color stability. Therefore, in addition to using a spacer to stabilize the color variation with the applied voltage, the thicknesses of individual EML should also be taken into consideration. In accordance with these two points, a blue–green OLED possessed an ultrahigh color stability, that is, its CIE coordinates were almost pinned across a wide luminance range from 48.7 to 12,700 cd/m^2. A WOLED utilizing the high color stability green–blue EML as the backbone inherited the latter's high color stability, with a nearly fixed CIE coordinate across the practical luminance range from 1050 to 9120 cd/m^2, and attained maximum efficiency of 26.4 cd/A and 19.8 lm/W.

Acknowledgements

This work was supported by the National Science Council of Taiwan, under Grant No. NSC 98-2221-E-002-038-MY3. We also acknowledge the financial support by Chung-Shan Institute of Science and Technology of the Republic of China.

References

[1] C.W. Tang, S.A. VanSlyke, Appl. Phys. Lett. 51 (1987) 913.
[2] M.A. Baldo, D.F. O'Brien, Y. You, A. Shoustikov, S. Sibley, M.E. Thompson, S.R. Forrest, Nature 395 (1998) 151.
[3] L.S. Hung, C.H. Chen, Mater. Sci. Eng. R 39 (2002) 143.
[4] Y. Luo, H. Aziz, G. Xu, Z.D. Popovic, Chem. Mater. 19 (2007) 2288.
[5] T. Zheng, C. Wallace, H. Choy, Adv. Funct. Mater. 20 (2009) 648.
[6] B.W. D'Andrade, S.R. Forrest, Adv. Mater. 16 (2004) 1585.
[7] Y. Sun, N.C. Giebink, H. Kanno, B. Ma, M.E. Thompson, S.R. Forrest, Nature 440 (2006) 908.
[8] S.-J. Su, E. Gonmori, H. Sasabe, J. Kido, Adv. Mater. 20 (2008) 4189.
[9] C.-L. Ho, M.-F. Lin, W.-Y. Wong, W.-K. Wong, C.H. Chen, Appl. Phys. Lett. 92 (2008) 083301.
[10] S. Reineke, F. Lindner, G. Schwartz, N. Seidler, K. Walzer, B. Lüssem, K. Leo, Nature 459 (2009) 234.
[11] K.S. Yook, S.O. Jeo, J.Y. Lee, K.H. Lee, Y.S. Kwon, S.S. Yoon, J.H. Yoon, Org. Electron. 10 (2009) 1378.
[12] S.H. Kim, J. Jang, J.Y. Lee, Appl. Phys. Lett. 91 (2007) 123509.
[13] C.-L. Ho, M.-F. Lin, W.-Y. Wong, W.-K. Wong, C.H. Chen, Appl. Phys. Lett. 92 (2007) 083301.
[14] C.H. Hsiao, J.H. Lee, J. Appl. Phys. 106 (2009) 024503.
[15] K.S. Yook, S.O. Jeon, C.W. Joo, J.Y. Lee, M.S. Kim, H.S. Choi, S.J. Lee, C.-W. Han, Y.H. Tak, Org. Electron. 10 (2009) 681.
[16] Q. Wang, J. Ding, D. Ma, Y. Cheng, L. Wang, F. Wang, Adv. Mater. 21 (2009) 2397.
[17] B.W. D'Andrade, R.J. Holmes, S.R. Forrest, Adv. Mater. 16 (2004) 624.
[18] X.-M. Yu, H.-S. Kwok, W.-Y. Wong, G.-J. Zhou, Chem. Mater. 18 (2006) 5097.
[19] Y. Sun, S.R. Forrest, Appl. Phys. Lett. 91 (2007) 263503.
[20] P. Chen, W. Xie, J. Li, T. Guan, Y. Duan, Y. Zhao, S. Liu, C. Ma, L. Zhang, B. Li, Appl. Phys. Lett. 91 (2007) 023505.
[21] K.S. Yook, S.O. Jeon, C.W. Joo, J.Y. Lee, Org. Electron. 10 (2009) 384.
[22] J.H. Lee, Y.H. Ho, T.C. Lin, C.F. Wu, J. Electrochem. Soc. 154 (2007) J226.
[23] C.H. Hsiao, C.F. Lin, J.H. Lee, J. Appl. Phys. 102 (2007) 094508.
[24] K. Saito, N. Matsusue, H. Kanno, Y. Hamada, H. Takahashi, T. Matsumura, Jpn. J. Appl. Phys. 43 (2004) 2733.
[25] S.W. Liu, J.H. Lee, C.C. Lee, C.T. Chen, J.K. Wang, Appl. Phys. Lett. 91 (2007) 142106.
[26] B.D. Chin, M.C. Suh, M.-H. Kim, S.T. Lee, H.D. Kim, H.K. Chung, Appl. Phys. Lett. 86 (2005) 133505.
[27] Y. Kawamura, K. Goushi, J. Brooks, J.J. Brown, H. Sasabe, C. Adachi, Appl. Phys. Lett. 86 (2005) 071104.
[28] C. Adachi, M.E. Thompson, S.R. Forrest, IEEE J. Sel. Top. Quan. Electron. 8 (2002) 372.
[29] W. Brütting, S. Berleb, A.G. Mückl, Org. Electron. 2 (2001) 1.
[30] C.H. Hsiao, Y.H. Chen, T.C. Lin, C.C. Hsiao, J.H. Lee, Appl. Phys. Lett. 89 (2006) 163511.
[31] C.H. Hsiao, J.H. Lee, C.A. Tseng, Chem. Phys. Lett. 427 (2006) 305.
[32] J. Kalinowski, Orgainc Light-Emitting Diodes: Principles Characteristics and Processes, Marcel Dekker, New York, 2005.
[33] Q. Wang, C.L. Ho, Y. Zhao, D. Ma, W.Y. Wong, L. Wang, Org. Electron. 11 (2010) 238.

limitation of the fabrication process. ALD-grown Al_2O_3 dielectric has several desired characteristics such as a high breakdown field (>1 V/nm), a high dielectric constant (7.8 as measured in metal/oxide/metal structure), and a low roughness (<1 nm). However, since the surface of Al_2O_3 is hydrophilic and attracts water, it is difficult to fabricate OTFTs in ambient conditions since the presence of water molecules often cause hole trapping in organic semiconductors. In order to eliminate this factor we used the well-known hydrophobic self-assembled monolayer (SAM) (1H,1H,2H,2H-perfluorooctyl) trichlorosilane (FOTS) [16] to modify the Al_2O_3 surface and make it hydrophobic. The modification of oxide gate dielectrics with hydrophobic surface modifiers is known to increase the mobility of OTFTs (see for instance [9]). The removal of residual water on the surface of the dielectric is often invoked as the origin of this increase. In our case, however, we show that it is a combination of hydrophobicity of the surface with the partial doping of the polythiophene semiconductor that drastically improves transport in the channel and leads to improved OFTF performance at comparatively low operation voltages.

2. Experimental

Heavily-doped silicon wafers were used as gate electrodes. The Al_2O_3 gate dielectric (50 nm) was deposited using a FlexAL® Atomic Layer Deposition Tool (Oxford Instruments) at 300 °C, after the native SiO_2 oxide was wet etched in buffered hydrofluoric acid. Subsequently, a 3-mercaptopropyltrimethoxysilane (MPTMS) self-assembled monolayer [17] was deposited in molecular vapor deposition tool MVD100 (Applied Microstructures, Inc.) to improve gold adhesion. Source and Drain electrodes were formed by depositing 50 nm of gold and were patterned using standard photolithography. The substrate was then cleaned in organic solvents and exposed to O_2 RF plasma (150 W) for 10 min. The FOTS layer was formed using the MVD100 tool. A 2 mg/ml solution of P3HT (Mn 25 000–35 000 Plexcore® OS 1100) in chloroform was prepared. It was spin-coated onto the substrate at 4000 rpm to give a 20 nm thick film. Electrical characterization was performed in air using a probe station equipped with two Keithley source-measure units. Structural analysis was performed using Grazing Incidence Wide Angle X-ray Scattering (GIWAXS) at the D1 station of the Cornell High Energy Synchrotron Source (CHESS). A wide bandpass (1.5%) double-bounce multilayer monochromator defined a 10.0 keV photon beam. Samples were studied under various incident angles ranging from above the critical angle of the organic thin film to slightly above the critical angle of the underlying oxide. Scattering intensities were recorded using a 2-D area detector (MedOptics).

4. Results and discussion

Typical output characteristics from the transistors are shown in Fig. 1. The $I_{DS} - V_{DS}$ curves show linear behavior in low V_{DS} regime indicating good electrical contact between the gold electrodes and the P3HT. The field-effect hole mobility was calculated in the saturation region using [18]:

$$I_{sd,sat} = \frac{W}{2L}\mu_{sat}C_i(V_g - V_{Th})^2,$$

where W (L) is the channel width (length), C_i is the capacitance per unit area of the gate dielectric and V_{th} the threshold voltage. Good device-to-device uniformity was observed with typical mobilities ranging between 0.1 and 0.2 $cm^2 V^{-1} s^{-1}$ and with no apparent dependence on L (from 2 to 100 μm) and/or W/L ratio.

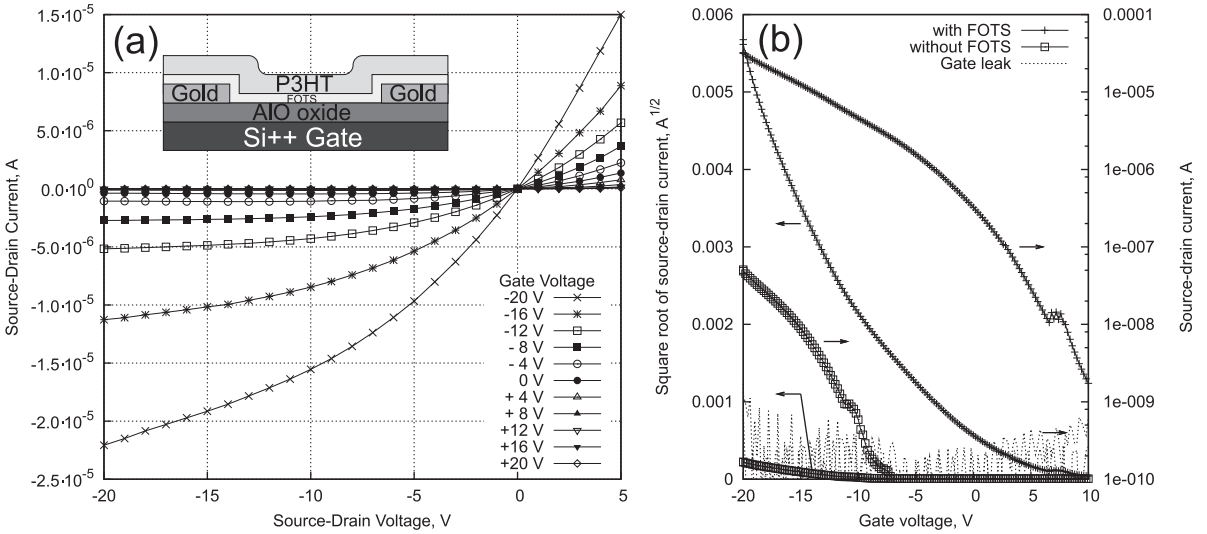

Fig. 1. (a) Output characteristic of a P3HT OTFT fabricated at ambient conditions. The channel length is 100 μm and the width is 1000 μm. Inset: schematic drawing of device structure. (b) Transfer characteristics, measured at source-drain bias of −20 V. Transfer characteristics of an OTFT without FOTS treatment also shown for comparison. The field-effect hole mobility (at $V_G = -15$ V) is 0.29 cm^2/vs. and the on/off ratio is 1.8×10^4.

Table 1
Summary of the electrical properties of P3HT OTFTs with modified Al_2O_3 surface dielectrics.

SAM treatment	Best mobility ($cm^2 V^{-1} s^{-1}$)	On/off	V_{on} (V)	References
Bare Al_2O_3	4.1×10^{-4}	$7{\cdot}10^4$	-3.6	[19]
Bare Al_2O_3	1×10^{-3}	$1{\cdot}10^3$	-10	This study
OTS	9.2×10^{-2}	54	5.6	[19]
FOTS	2.9×10^{-1}	$1.8{\cdot}10^4$	10	This study

In order to understand the influence of FOTS we fabricated a set of reference devices with a bare Al_2O_3 surface. Typical device parameters are summarized in Table 1. It is clear that the FOTS treatment significantly improves field-effect mobility and also causes a significant shift of the turn-on voltage V_{on}. The latter was determined from the transfer characteristics as the V_G that corresponds to I_{DS} = 1 nA. Data from literature on bare and *n*-octadecyltrichlorosilane (OTS)-functionalized Al_2O_3 [19] (Table 1) show a similar trend: Namely the SAM improves mobility and changes V_{on} from negative to positive values. The FOTS treatment, however, is shown to yield the highest field-effect mobility and also the largest turn-on voltage V_{on}. In addition, it causes the drain current that flows through the P3HT film at $V_G = 0$ to increase by more than three orders of magnitude (Fig. 1b).

The significant shift of V_{on} observed between the devices utilizing bare and FOTS-functionalized Al_2O_3 and the increase in the channel conductance at $V_G = 0$ constitute strong indications of doping of the P3HT from FOTS. This effect has been observed in different organic semiconductors [20,21] and was attributed to electrostatic doping due to the high dipole moment of the FOTS molecule. Another proposed mechanism of doping involves ground-state charge transfer at the interface between the organic semiconductor and FOTS [22,23]. A similar shift of V_{on} was also observed when P3HT transistors were exposed to ambient conditions presumably due to doping by oxygen [24]. Since our fabrication and testing were done in air we cannot exclude this effect, yet based on our bare Al_2O_3 device data we believe that this effect is much less pronounced than the doping caused by the FOTS. Moderate doping of polymer semiconductors is known to improve OTFT performance, an effect attributed to the formation of mobile carriers which reduce the resistance at the metal/organic interface and in the channel [25,26]. However, excessive doping leads to low on/off ratios which makes the OTFTs practically insensitive to external electrical field modulation. In contrast, the FOTS treatment of Al_2O_3 described here provides a good tradeoff between improving mobility and maintaining a high on/off ratio.

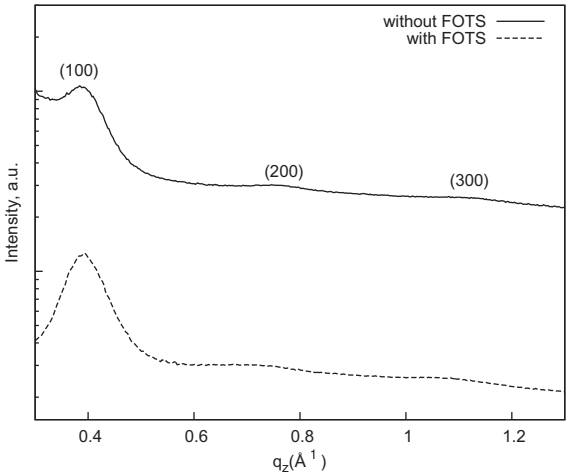

Fig. 3. Scattering intensity along the q_z from P3HT films on bare and on FOTS-functionalized Al_2O_3. The lamellar spacing was found to be 16.0 Å in both films.

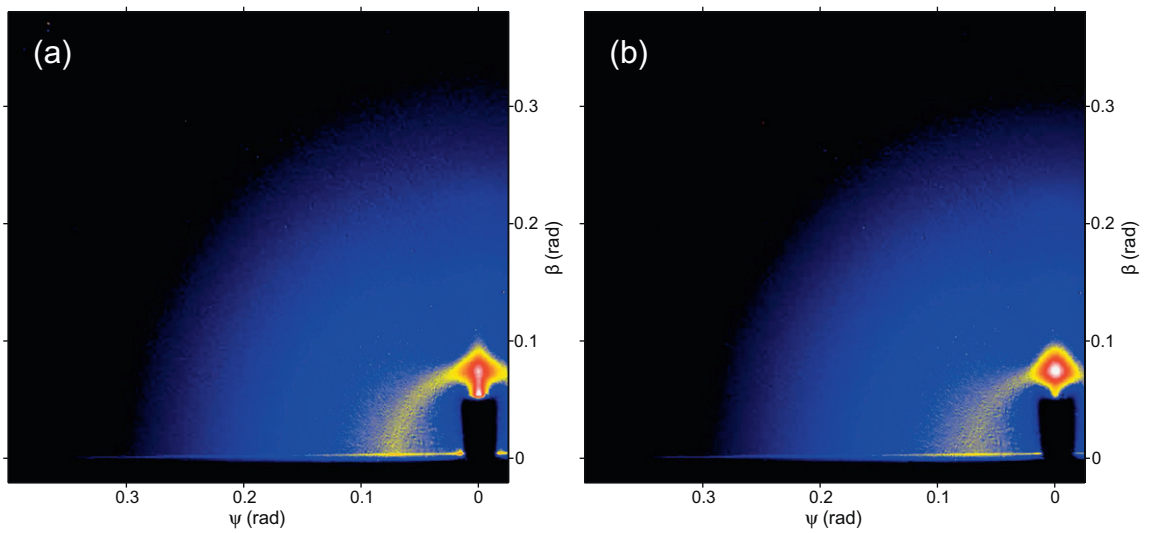

Fig. 2. 2-D GIWAXS patterns from P3HT films on bare (a), and on FOTS-functionalized Al_2O_3 (b).

2-D GIWAXS patterns from P3HT films deposited on bare and FOTS-functionalized Al_2O_3 are shown in Fig. 2, while the extracted scattering intensities along the q_z direction are shown in Fig. 3. The GIWAXS patterns are consistent with previously reported diffraction patterns [27] of P3HT with lamella forming parallel to the substrate. The lamellar spacing is 16.0 Å regardless of FOTS treatment of the dielectric. Additionally there is no difference in grain size, as is evident from the FWHM of the (1 0 0) diffraction peaks, or from the π–π stacking distance which is found to be 3.80 Å in both cases. The mosaicity of the film on FOTS shows a marginally more defect-free planar arrangement as compared to the film on bare oxide. Since bare oxide is hydrophilic and FOTS-treated oxide is fluorinated, both surfaces have oleophobic behavior, which allows P3HT film to self-organize with little or no effect of the substrate on its structure. The lack of a significant structural difference of P3HT on bare and on FOTS-treated oxide supports the conclusion that doping at the FOTS/P3HT interface is responsible for improvement of the transport properties of the film.

5. Conclusion

We showed that high-mobility polymer OTFTs can be fabricated at ambient conditions and with a process that does not require annealing of the polymer. Treatment of the Al_2O_3 gate dielectric with a FOTS self-assembled monolayer makes it possible to reach a field-effect hole mobility of 0.29 $cm^2\ V^{-1}s^{-1}$. Synchrotron X-ray scattering reveals no major influence of FOTS on film structure (as compared to bare oxide), which implies that the enhancement of device performance is caused by an interaction at the FOTS/P3HT interface rather than a structural modification of the P3HT film itself.

Acknowledgements

This work was supported by the Academy of Finland (Grant # 126200) and the US Air Force Office for Scientific Research. This work was performed in part at the Cornell NanoScale Facility, a member of the National Nanotechnology Infrastructure Network, which is supported by the National Science Foundation (Grant ECS 03-35765). Part of this work was also performed at the Cornell High Energy Synchrotron Source, supported by the National Science Foundation and NIH-NIGMS (NSF DMR-0225180).

References

[1] G. Malliaras, R. Friend, Phys. Today 58 (2005) 53.
[2] H. Sirringhaus, N. Tessler, R.H. Friend, Science 280 (1998) 1741.
[3] J.A. Rogers, Z. Bao, K. Baldwin, A. Dodabalapur, B. Crone, V.R. Raju, V. Kuck, H. Katz, K. Amundson, J. Ewing, P. Drzaic, PNAS 98 (2001) 4835–4840.
[4] R. Rotzoll, S. Mohapatra, V.Olariu.R. Wenz, M. Grigas, K. Dimmler, O. Shchekin, A. Dodabalapur, Appl. Phys. Lett. 88 (2006) 123502.
[5] B. Crone, A. Dodabalapur, A. Gelperin, L. Torsi, H.E. Katz, A.J. Lovinger, Z. Bao, Appl. Phys. Lett. 78 (2001) 2229.
[6] A. Dodabalapur, Mater. Today 9 (2006) 24.
[7] H. Kanga, K. Hana, J. Parka, H.H. Lee, Org. Electron. 8 (2007) 460–464.
[8] T. Kawase, T. Shimoda, C. Newsome, H. Sirringhaus, R.H. Friend, Thin Solid Films 438 (2003) 279–287.
[9] H. Sirringhaus, T. Kawase, R.H. Friend, T. Shimoda, M. Inbasekaran, W. Wu, E.P. Woo, Science 290 (2000) 2123–2126.
[10] Z. Bao, A. Dodabalapur, A.J. Lovinger, Appl. Phys. Lett. 69 (1996) 4108–4110.
[11] R.D. McCullough, S. Tristram-Nagle, S.P. Williams, R.D. Lowe, M.J. Jayaraman, Am. Chem. Soc. 115 (1993) 4910–4911.
[12] H. Sirringhaus, P.J. Brown, R.H. Friend, M.M. Nielsen, K. Bechgaard, B.M.W. Langeveld-Voss, A.J.H. Spiering, R.A.J. Janssen, E.W. Meijer, Synth. Metals 111–112 (2000) 129–132.
[13] Y.G. Seol, J.G. Lee, N.-E. Lee, S.S. Lee, J. Ahn, Thin Solid Films 515 (2007) 5065–5069.
[14] G. Wang, T. Hirasa, D. Moses, A.J. Heeger, Synth. Metals 146 (2004) 127–132.
[15] Y. Fua, C. Lina, F.-Y. Tsai, Org. Electron. 10 (2009) 883–888.
[16] B. Bhushan, D. Hansford, K.K. Lee, J. Vac. Sci. Technol. A24 (2006) 1197.
[17] A.K. Mahapatro, A. Scott, A. Manning, D.B. Janes, Appl. Phys. Lett. 88 (2006) 151917.
[18] J. Zaumseil, H. Sirringhaus, Chem. Rev. 107 (2007) 1296–1323.
[19] L. Fumagalli, D. Natali, M. Sampietro, E. Peron, F. Perissinotti, G. Tallarida, S. Ferrari, Org. Electron. 9 (2008) 198–208.
[20] S. Kobayashi, T. Nishikawa, T. Takenobu, S. Mori, T. Shimoda, T. Mitani, H. Shimotani, N. Yoshimoto, S. Ogawa, Y. Iwasa, Nat. Mater. 3 (2004) 317–322.
[21] K.P. Pernstich, S. Haas, D. Oberhoff, C. Goldmann, D.J. Gundlach, B. Batlogg, A.N. Rashid, G. Schitter, J. Appl. Phys. 96 (2004) 6431.
[22] M.F. Calhoun, J. Sanchez, D. Olaya, M.E. Gershenson, V. Podzorov, Nat. Mater. 7 (2008) 84–89.
[23] C.Y. Kao, B. Lee, L.S. Wielunski, M. Heeney, I. McCulloch, E. Garfunkel, L.C. Feldman, V. Podzorov, Adv. Funct. Mater. 19 (2009) 1906–1911.
[24] E.J. Meijer, C. Detcheverry, P.J. Baesjou, E. van Veenendaal, D.M. de Leeuw, T.M. Klapwijk, J. Appl. Phys. 93 (2003) 4831.
[25] E. Lim, B.J. Jung, M. Chikamatsu, R. Azumi, Y. Yoshida, K. Yase, L. M. Do, H.K. Shim, J. Mater. Chem. 17, 1416 (2007],
[26] L. Ma, W.H. Lee, Y.D. Park, J.S. Kim, H.S. Lee, K. Cho, Appl. Phys. Lett. 92 (2008) 063310.
[27] H. Sirringhaus, P.J. Brown, R.H. Friend, M.M. Nielsen, K. Bechgaard, B.M.W. Langeveld-Voss, A.J.H. Spiering, R.A.J. Janssen, E.W. Meijer, P. Herwig, D.M. de Leeuw, Nature 401 (1999) 685–688.

was measured in an integrating sphere (the total η_p measured in an integrating sphere roughly equals to the forward viewing η_p multiplied by 1.7) [12].

Another common approach for making WOLEDs involves the mixing of blue and yellow (B/Y) emissions. The main advantages of such devices are their much simpler structures and more stable colors. However, unlike fluorescent materials, the development for yellow phosphorescent materials still lags behind the materials emitting with monochromatic primary colors RGB. For example, maximal η_p for each monochromatic device has been demonstrated to be 42.7 lm/W for red (iridium(III) bis-(2-phenylquinolyl-N,$C^{2'}$)acetylacetonate, PQIr), 68.3 lm/W for green (tris-(phenylpyridine)iridium, Ir(ppy)$_3$), and 22.5 lm/W for blue (iridium(III) bis-(4′,6′-difluorophenylpyridinato)tetrakis(1-pyrazolyl)borate, FIr6) [8], respectively. On the contrary, there are only few yellow phosphorescent materials reported for achieving WOLEDs, in which the maximal η_p for monochromatic device is only 12 lm/W (bis(2-(9,9-diethyl-9H-fluoren-2-yl)-1-phenyl-1H-benzoimidazol-N,C^3) iridium(acetylacetonate), (fbi)$_2$-Ir(acac)) [9,13], whereas the chemical structures and device performance [10,11,14,15] have not been fully disclosed in other yellow-emitting OLEDs. In order to achieve white light with better color balance, the relatively low η_p for yellow phosphorescent materials unavoidably sacrifices the excessive blue emission, resulting in poor efficiency for WOLEDs. Recently, the highly efficient (η_p = 29 lm/W) yellow OLED based on yellow phosphor dopant p-PF-py has been reported by Tsuzuki et al. [16]. Nevertheless, it is desirable to develop more high performance yellow emitters and explore their applications for white OLED.

In this work, we report phosphorescent WOLEDs using a commercially available blue, iridium-bis-(4,6,-difluorophenyl-pyridinato-N,C^2)-picolinate (FIrpic) and a self-designed and synthesized yellow bis[2-(2-naphthyl)-pyridine] (acetylacetonate) iridium(III) (Ir(npy)$_2$acac) phosphors. Without using light out-coupling or p–i–n confinement structure, the WOLEDs attain a maximal forward viewing η_p of 29.2 lm/W, and a balanced white light with CIE coordinates of (0.32, 0.45).

2. Experimental

All glass substrates were coated with patterned anode indium tin oxide (sheet resistance 30 Ω/square), cleaned with Decon 90, rinsed in de-ionized water, dried in an oven, and finally treated in an ultraviolet–ozone cleaner prior to film deposition. The organic materials used have acronyms as follows: NPB: N, N′-diphenyl-1,1′-biphenyl-4,4′-diamine; mCP: N,N′-dicarbazolyl-3,5-benzene; UGH2: *p*-bis-(triphenylsilyly)benzene; and BAlq: aluminum(III) bis(2-methyl-8-quinolinato)4-phenylphenolate. WOLEDs with a structure of ITO/NPB (40 nm)/*x*%Ir(npy)$_2$acac:mCP (10 nm)/8%FIrpic:UGH2 (20 nm)/BAlq (40 nm)/LiF (0.5 nm)/Al (80 nm) were fabricated by thermal evaporation in high vacuum chamber (base pressure $\sim 10^{-6}$ Torr). The devices have a cascade-type energy band structure with a NPB hole-transporting layer, yellow- and blue-emitting hosts of mCP and UGH2, respectively, followed by a BAlq electron-transporting layer, and a LiF/Al cathode. Ir(npy)$_2$acac and FIrpic are respectively used as yellow and blue phosphorescent dopant emitters. All films were sequentially deposited at a rate of 0.1–0.2 nm/s without vacuum break. A shadow mask was used to define the cathode and to make four 0.1 cm^2 devices on each substrate. Current density–voltage–luminance (J–V–L) characteristics and electroluminescence (EL) spectra were measured simultaneously with a programmable Keithley model 237 power source and a Photoresearch PR650 spectrometer. All measurements were carried out without using light out-coupling enhancement or integrating sphere. Energies of highest occupied molecular orbital (HOMO) values of the materials were measured by using ultraviolet photoelectron spectroscopy, while energies of lowest unoccupied molecular orbital (LUMO) values were estimated by subtracting optical band gaps from the HOMO energies.

3. Results and discussion

The inset of Fig. 1 depicts the molecular structure of the iridium complex Ir(npy)$_2$acac. Identity of Ir(npy)$_2$acac was confirmed by ^{1}H-nuclear magnetic resonance, elemental analysis and mass spectrometry. Details of the molecular design and synthetic route for Ir(npy)$_2$acac will be published elsewhere. Fig. 1 shows absorption and PL spectra of Ir(npy)$_2$acac in a dilute dichloromethane solution. The EL spectra obtained from the monochromatic devices with structures of ITO/NPB (40 nm)/6%Ir(npy)$_2$acac:mCP (30 nm)/BAlq (40 nm)/LiF (0.5 nm)/Al (80 nm) for yellow and ITO/NPB (40 nm)/mCP (10 nm)/8%FIrpic:UGH2 (20 nm)/BAlq (40 nm)/LiF (0.5 nm)/Al (80 nm) for blue, denoted as Ir(npy)$_2$acac and FIrpic, respectively, are also shown in Fig. 1. It can be seen that the PL and EL peak positions of Ir(npy)$_2$acac show negligible difference (about 1 nm), while FIrpic has an EL peak at 472 nm with a shoulder at 494 nm. In addition, both FIrpic and Ir(npy)$_2$acac devices demonstrate similar maximal forward viewing η_p of 25.6 and 21.8 lm/W (device characteristics for Ir(npy)$_2$acac are shown in Fig. 2), respectively. It is worth noting that Ir(npy)$_2$acac exhibits a slightly broader emission spectrum (with a full width at half maximum (FWHM) of 87 nm) than those of (fbi)$_2$Ir(acac) (FWHM = 70 nm) [9,13] and (R-C^N^N)PtCl (FWHM = 80 nm) [10,14]. This would be beneficial for obtaining a better white color. Fig. 3 gives a schematic energy level diagram for the WOLEDs. It can be observed that the WOLED has a cascade-type energy band structure (stepped progression of HOMO or LUMO levels) for both the holes from the anode and the electrons from the cathode to the EML. This would clearly favor efficient carriers transport to the emission regions.

Fig. 4 shows normalized EL spectra of the WOLEDs with different concentrations (*x*%) of Ir(npy)$_2$acac viewed in the normal direction at a luminance of 100 cd/m^2. The EL of the WOLEDs is basically the sum of the emissions of FIrpic and Ir(npy)$_2$acac. With increasing Ir(npy)$_2$acac concentration, the relative intensity of the yellow emission (551 nm) increases and the CIE coordinates of WOLEDs shift from

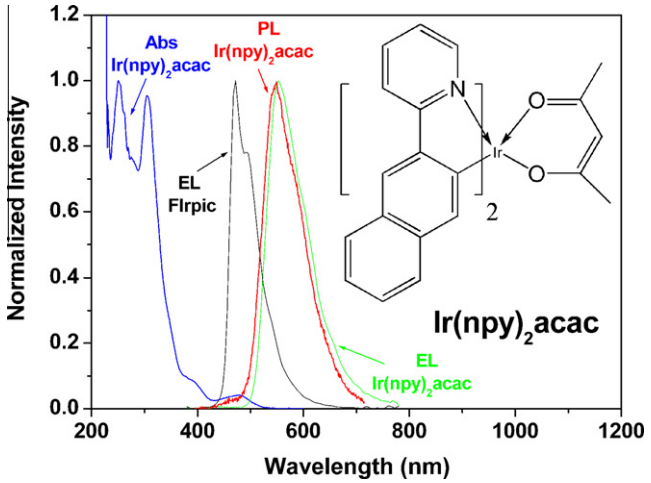

Fig. 1. Absorption and PL spectra of $Ir(npy)_2acac$ in a dilute dichloromethane solution. EL spectra from the yellow-emitting device: ITO/NPB (40 nm)/6%$Ir(npy)_2acac$:mCP (30 nm)/BAlq (40 nm)/LiF (0.5 nm)/Al (80 nm) and the blue-emitting device: ITO/NPB (40 nm)/mCP (10 nm)/8%FIrpic:UGH2 (20 nm)/BAlq (40 nm)/LiF (0.5 nm)/Al (80 nm) are also shown. Inset shows the molecular structure of $Ir(npy)_2acac$.

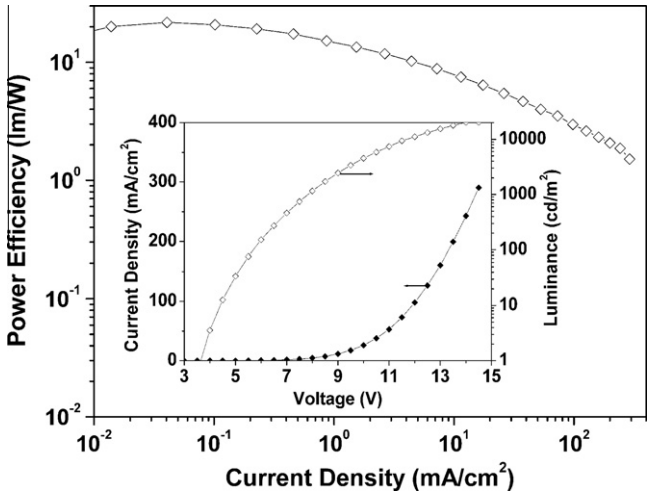

Fig. 2. Power efficiency as a function of current density of the yellow OLED. Inset shows J–V–L characteristics of the yellow OLED. Yellow OLED: ITO/NPB (40 nm)/6%$Ir(npy)_2acac$:mCP (30 nm)/BAlq (40 nm)/LiF (0.5 nm)/Al (80 nm).

(0.24, 0.39) to (0.44, 0.53). This phenomenon may be attributed to the increase in hole trapping sites formed by $Ir(npy)_2acac$ inside mCP, which is typically observed in the other yellow iridium phosphors [9]. With an optimum $Ir(npy)_2acac$ dopant concentration of 1%, the device shows balanced white emission with CIE coordinates of (0.32, 0.45). The inset of Fig. 4 shows a photograph of the WOLED with 1% $Ir(npy)_2acac$ operated at 9 V. Table 1 summarizes key operation parameters of the WOLEDs including external quantum efficiencies (η_{EQE}), η_P, and current efficiencies (η_C) etc. Upon increasing the concentration of $Ir(npy)_2acac$, η_C increases from 34.7 to 39.6 lm/W and then falls off to 36.8 lm/W. Similar trend can be observed for η_P. However, η_{EQE} shows a monotonic decrease with increasing dopant concentration. It is mainly due to the fact that η_{EQE} is independent of emission wavelength whereas η_C is sensitive to the photopic response, $g(\lambda)$, of human eye (the dotted line as shown in Fig. 4) [17]. In particular, η_{EQE} and η_C can be described by the following equation:

$$\eta_{EQE} = \frac{C\eta_c \int \lambda I(\lambda) d\lambda}{\int I(\lambda) g(\lambda) d\lambda} \quad (1)$$

where λ is the wavelength, $I(\lambda)$ is the EL intensity measured, $g(\lambda)$ is the photopic response of human eye at a particular wavelength, and C is a constant that depends on the Plank's constant, the velocity of light, and the electronic charge. Eq. (1) reveals that η_{EQE} is directly proportional to η_C and inversely proportional to $\int I(\lambda)g(\lambda)d\lambda$. In other words, the η_{EQE} increases with increasing η_C or decreasing $g(\lambda)$. $g(\lambda)$ is described by a spectral shape with a peak value

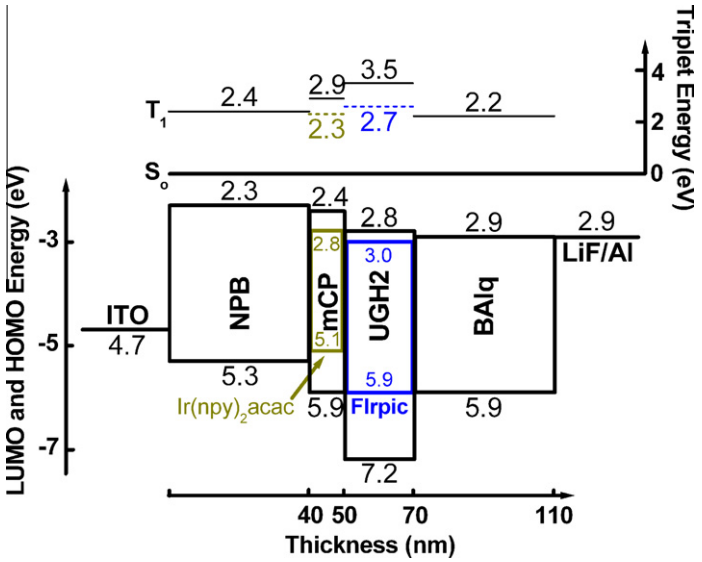

Fig. 3. A schematic energy level diagram of the WOLED.

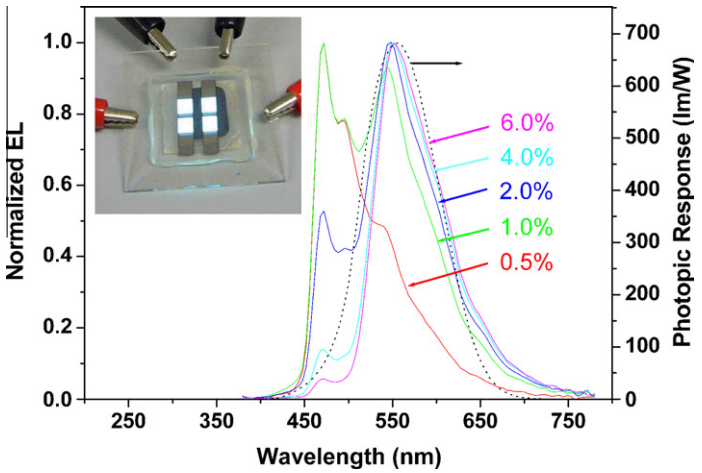

Fig. 4. Normalized EL spectra of various WOLEDs with different concentrations of $Ir(npy)_2acac$ viewed in the normal direction at a luminance of 100 cd/m^2. Inset shows a photograph of the WOLED with the optimal concentration of 1% $Ir(npy)_2acac$ at 9 V.

Table 1
Characteristics of WOLEDs with the structure: ITO/NPB (40 nm)/*x*%$Ir(npy)_2acac$:mCP (10 nm)/8%FIrpic:UGH2 (20 nm)/BAlq (40 nm)/LiF (0.5 nm)/Al (80 nm). η_{EQE}, η_P, η_C are the maximum external quantum, power, and current efficiencies.

Device (*x*)	η_P [lm/W]	η_C [cd/A]	η_{EQE} [%]	*V* at *J* = 10 mA/cm^2 (at *L* = 1 cd/m^2) [*V*]	CIE coordinates [*x*, *y*][a]
0.5	27.9	34.7	13.5	9.2 (3.9)	0.24, 0.39
1.0	29.2	37.2	12.6	9.3 (3.8)	0.32, 0.45
2.0	34.4	38.3	12.1	9.3 (3.7)	0.38, 0.50
4.0	30.4	39.6	12.3	9.5 (3.6)	0.43, 0.53
6.0	26.9	36.8	11.5	9.5 (3.6)	0.44, 0.53

[a] The value taken at *L* = 100 cd/m^2.

of 683 lm/W at λ = 555 nm and falls off rapidly towards either the red or blue. Taking the eye's spectral sensitivity into account, the η_{EQE} of yellow-emitting OLED is usually smaller than those of red- or blue-emitting devices when all devices have the same η_C, and it is also the reason why η_{EQE} decreases when the concentration of yellow

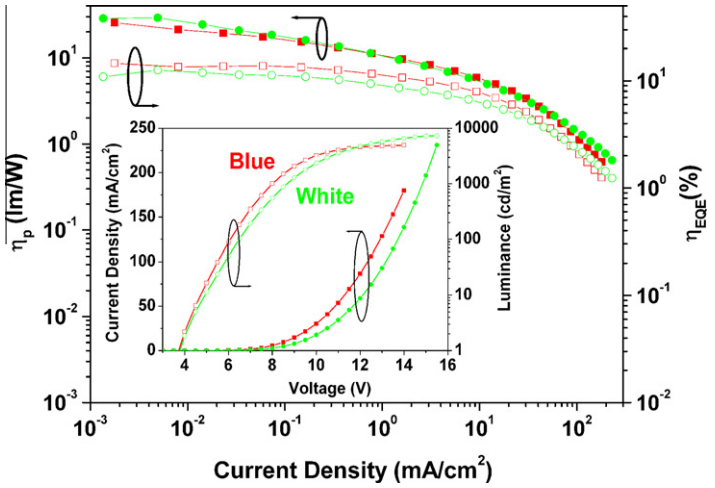

Fig. 5. Power and external quantum efficiencies as a function of current densities of the blue and the white OLEDs. Inset shows J–V–L characteristics of the blue and the white OLEDs. Blue OLED: ITO/NPB (40 nm)/mCP (10 nm)/8%FIrpic:UGH2 (20 nm)/BAlq (40 nm)/LiF (0.5 nm)/Al (80 nm). White OLED: ITO/NPB (40 nm)/1%Ir(npy)$_2$acac:mCP (10 nm)/8%FIrpic:UGH2 (20 nm)/BAlq (40 nm)/LiF (0.5 nm)/Al (80 nm).

Ir(npy)$_2$acac increases as the η_C increases. It is one of the reasons responsible for the intrinsically higher η_{EQE} of three emitters RGB WOLEDs as compared to B/Y emission WOLEDs.

Fig. 5 shows η_p, η_{EQE} and J–V–L characteristics of the white and the blue OLEDs. The turn-on (defined as the voltage required to obtain $L = 1$ cd/m^2) and operating voltages at 10 mA/cm^2 for white OLED are respectively 3.8 and 9.3 V, which are slightly larger than those (3.7 and 8.6 V) of the blue OLED. The higher driving voltage of the WOLED may be due to the charge trapping effect of the Ir(npy)$_2$acac dopants. At a luminance of 1000 cd/m^2 (a typical brightness required for lighting source purpose), the CIE coordinates and the η_p are (0.27, 0.33) and 6.5 lm/W for the white OLED and (0.16, 0.33) and 7.0 lm/W for the blue OLED, respectively. In addition, it can be seen that the maximal forward viewing η_p, η_C, and η_{EQE} are 29.2 lm/W (roughly equivalent to a total η_p of 50 lm/W) [12], 37.2 cd/A, and 12.6% for the WOLEDs and 25.6 lm/W, 28.5 cd/A, and 14.6% for the blue OLEDs, respectively. The differences in η_C and η_{EQE} of the two devices suggest that the yellow Ir(npy)$_2$acac dopant has negative effect on the η_{EQE} while the η_C is increased by 30%. Significantly, the forward viewing efficiencies of the present WOLEDs are among the highest values reported for B/Y emission WOLEDs without optical out-coupling [1,8,11] or a p–i–n confinement structure [1].

4. Conclusion

In conclusion, we report phosphorescent WOLEDs based on the combination of our self-designed and synthesized yellow Ir(npy)$_2$acac phosphor and the commercial blue FIrpic. Such WOLEDs show a maximal forward viewing η_p of 29.2 lm/W and balanced white light with CIE coordinates of (0.32, 0.45) with superior efficiencies.

Acknowledgment

This work was supported by the Innovation and Technology Commission (Grant No. ITP/011/08NP) of Hong Kong SAR. The author S.L. Tao thanks for the financial supports from the Fundamental Research Funds for the Central University and Dongguan LITEWELL (OLED) Technology Incorporation.

References

[1] S. Reineke, F. Lindner, G. Schwartz, N. Seidler, K. Walzer, B. Lüssem, K. Leo, Nature (London) 459 (2009) 234.
[2] S.J. Su, E. Gonmori, H. Sasabe, J. Kido, Adv. Mater. (Weinheim, Ger.) 20 (2008) 4189.
[3] C.H. Chang, Y.H. Lin, C.C. Chen, C.K. Chang, C.C. Wu, L.S. Chen, W.W. Wu, Y. Chi, Org. Electron. 10 (2009) 1235.
[4] Y.J. Lu, C.H. Chang, C.L. Lin, C.C. Wu, H.L. Hsu, L.Y. Chen, Y.T. Lin, R. Nishikawa, Appl. Phys. Lett. 92 (2008) 123303.
[5] Q.X. Tong, S.L. Lai, M.Y. Chan, J.X. Tang, H.L. Kwong, C.S. Lee, S.T. Lee, Appl. Phys. Lett. 91 (2007) 023503.
[6] S.L. Tao, Y.C. Zhou, C.S. Lee, D. Huang, X.H. Zhang, S.T. Lee, J. Mater. Chem. 18 (2008) 3981.
[7] J.H. Jou, C.C. Chen, Y.C. Chung, M.F. Hsu, C.H. Wu, S.M. Shen, M.H. Wu, W.B. Wang, Y.C. Tsai, C.P. Wang, J.J. Shyue, Adv. Funct. Mater. 18 (2008) 121.
[8] X. Qi, M. Slootsky, S. Forrest, Appl. Phys. Lett. 93 (2008) 193306.
[9] Q. Wang, J. Ding, D. Ma, Y. Cheng, L. Wang, Appl. Phys. Lett. 94 (2009) 103503.
[10] B.P. Yan, C.C.C. Cheung, S.C.F. Kui, H.F. Xiang, V.A.L. Roy, S.J. Xu, C.M. Che, Adv. Mater. (Weinheim, Ger.) 19 (2007) 3599.
[11] M.T. Lee, J.S. Lin, M.T. Chu, M.R. Tseng, Appl. Phys. Lett. 93 (2008) 133306.
[12] B.W. D'Andrade, R.J. Holmes, S.R. Forrest, Adv. Mater. (Weinheim, Ger.) 16 (2004) 624.
[13] W.S. Huang, J.T. Lin, C.H. Chien, Y.T. Tao, S.S. Sun, Y.S. Wen, Chem. Mater. 16 (2004) 2480.
[14] S.C.F. Kui, I.H.T. Sham, C.C.C. Cheung, C.W. Ma, B. Yan, N. Zhu, C.M. Che, W.F. Fu, Chem. Eur. J. 13 (2007) 417.
[15] H. Zhen, C. Luo, W. Yang, W. Song, B. Du, J. Jiang, C. Jiang, Y. Zhang, Y. Cao, Macromolecules 39 (2006) 1693.
[16] T. Tsuzuki, N. Shirasawa, T. Suzuki, S. Tokito, Adv. Mater. (Weinheim, Ger.) 15 (2003) 1455.
[17] S.R. Forrest, D.D.C. Bradley, M.E. Thompson, Adv. Mater. (Weinheim, Ger.) 15 (2003) 1043.

element in the development of inkjet-printing-based solar cells. In an earlier report, we have demonstrated the use of ZnO as a buffer layer for the inkjet-printing of a silver cathode in a polymer solar cell [9]. We have also reported on the performance of bulk heterojunction polymer solar cells fabricated with an inkjet-printed poly(3,4-ethylenedioxythiophene):poly(styrenesulfonate) (PEDOT:PSS) layer. The morphology and electrical properties of the inkjet-printed PEDOT:PSS layer, as well as the overall device performance, were dramatically affected by the ink formulations containing additives, such as glycerol and a surfactant [10].

Employing a spin-coated P3HT:PCBM active layer, several research groups have reported on the formation of a phase separated morphology with crystalline P3HT and PCBM domains inside the active layer of bulk-heterojunction solar cells. Such a morphology has been achieved by use of an appropriate solvent with a specific boiling point for precise control over the evaporation rate [11,3,12], reducing the drying speed of the spin-coated films [13–15], melting of the bilayers [16], thermal annealing of the fabricated films with or without an applied external voltage [17–19], and using chemical additives [20–22]. Few efforts have been made to fabricate inkjet-printed bulk-heterojunction solar cells. Brabec et al. recently reported the solar cell devices fabricated by inkjet-printing P3HT:PCBM inks formulated with various solvent mixtures on doctor-bladed PEDOT:PSS layer [23–25]. Aernouts et al. also reported the device performance of P3HT:PCBM active layer with high boiling point (b.p.) solvent mixtures for reducing coffee-ring effect [26]. However, to the best of our knowledge, no researchers have reported on efficient polymer solar cells fabricated by inkjet-printing both the PEDOT:PSS layer and the P3HT:PCBM active layer.

In this work, we report on highly efficient and cost-effective inkjet-printed PSCs based on P3HT and PCBM inks containing various additives. All solution-processed solar cell layers—a hole transporting layer of PEDOT:PSS and a photoactive layer based on P3HT and PCBM with various additives—were inkjet-printed. The conditions of the inkjet-printed PEDOT:PSS layers were optimized based on the results of our previous study [10]. Changes in the morphology, optoelectronic properties, and overall device performance that resulted from the addition of various high b.p. additives, such as 1,8 octanedithiol (ODT), o-dichlorobenzence (ODCB), and 1-chloronaphthalene (Cl-naph), to chlorobenzene (CB) solvents were investigated.

Regioregular poly(3-hexylthiophene) (P3HT) as an electron donor and [6,6]-phenyl-C61 butyric acid methylester (PCBM) as an electron acceptor were purchased from Rieke metals and Nano-C, respectively. Poly(3,4-ethylenedioxythiophene):poly-(styrene sulfonic acid) (PEDOT:PSS) was purchased from Bayer (Baytron P AI 4083). Several high b.p. additives, such as ODT, ODCB, and Cl-naph, were obtained from Sigma-Aldrich and used as-received. In the present study, the configuration of the polymer solar cell devices was indium tin oxide (ITO)/PEDOT:PSS/active layer of P3HT:PCBM/LiF-Al. Patterned ITO glass was cleaned with chloroform, acetone, and isopropyl alcohol using an ultrasonication method. The ITO was then subject to an O2-plasma treatment. To PEDOT:PSS inks for inkjet-printing, PEDOT:PSS was mixed with additives of glycerol (0.431) and ethylene glycol butyl ether (EGBE, 0.014). Details regarding the optimization of the additive concentrations to obtain the best PEDOT:PSS layer can be found in our previous report [10]. After a solvent cleaning, the PEDOT:PSS inks were deposited on the ITO substrates using an inkjet-printing (UJ2100, Unijet, Korea) technique. The films were then dried for 20 min at 140 °C.

To optimize the parameters for the inkjet-printing of an active layer, blends (inks) of P3HT:PCBM (1:0.7, 2 wt%) in CB with different high b.p. additives of ODT, ODCB, and Cl-naph were prepared (details are given in Table 1). These inks were printed on top of the PEDOT:PSS layers by the same printer used for the PEDOT:PSS deposition. Temperatures of inkjet-printer head and substrate were kept as 26C. The printed films were then dried for 1 h at room temperature in a nitrogen atmosphere. By varying the ink concentrations and the printing speed, the optimum thickness of the P3HT:PCBM layers was found to be 150 nm. Thermal evaporation was used to deposit a LiF layer (0.5 nm thickness) on the active layer. To complete the device, an Al layer (150 nm thickness) was evaporated on top of the LiF layer. All evaporations were performed under vacuum (10-6 torr). Each completed device was encapsulated so as to measure the solar cell performance.

The current density–voltage (J–V) characteristics of the solar cell devices in the dark and under white light illumination were measured with an AM 1.5G solar simulator (300 W, Newport, USA) calibrated to 100 mW/cm2 with a standard PV reference cell (a 2 × 2 cm monocrystalline silicon solar cell, calibrated at NREL, Colorado, USA) using a Keithley 2400 source-measure unit. The open circuit voltage (Voc), short circuit current density (Jsc), fill factor (FF), and power conversion efficiency (PCE) were calculated from the J-V curves. The incident photon to collected electron efficiency (IPCE) of the devices was measured with a commercial photomodulation spectroscopic setup that included a xenon lamp (Oriel), iris diaphragms, and an AM 1.5 filter. In order to avoid an underestimation of the area of the devices due to cross-conduction through

Table 1
Formulation details of the P3HT:PCBM inks containing different high b.p. additives.

Inks	P3HT:PCBM (1:0.7)	CB (b.p = 132 °C)	ODT (b.p = 269 °C)		ODCB (b.p = 179 °C)		Cl-naph (b.p = 259 °C)	
	g	ml	ml	vol.%	ml	vol.%	ml	vol.%
1	0.2	10	-	-	-	-	-	-
2	0.2	10	0.5	5	-	-	-	-
3	0.2	10	-	-	0.5	5	-	-
4	0.2	10	-	-	-	-	0.5	5

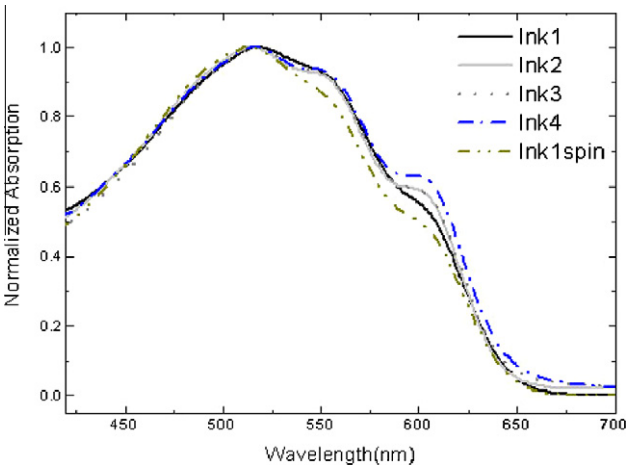

Fig. 1. UV–Vis absorption spectra of the inkjet-printed active layers fabricated from different inks.

the highly conducting PEDOT:PSS used in this study, a black mask fitted to the active area (3×3 mm) of the devices was employed [27–29]. The surface morphology and absorption spectra of the inkjet-printed active layers were analyzed using atomic force microscopy (AFM, Nanoscope IV, Multimode) and UV–Vis spectroscopy (JASCO, V-670), respectively. The crystallinity of the P3HT was examined with X-ray diffractometry (XRD, Rigaku, with a Cu Kα source). All characterizations were performed at room temperature.

Shown in Fig. 1 are the optical absorption spectra as a function of wavelength for the inkjet-printed active layers containing different additives; the reference film was fabricated by spin-coating. The film spin-coated with ink1, formulated with CB and no additives, exhibits an absorption spectrum with a maximum centered at 509 nm with two indistinct shoulders at 544 and 595 nm. For the inkjet-printed films from ink2 contained 5 vol% ODT, ink3 contained 5 vol% ODCB, and ink4 contained 5 vol% Cl-naph, a red shift with relatively wide absorption in the longer wavelength region was clearly observed; maxima were located at 513 nm, and two pronounced vibronic peaks emerged at 552 and 602 nm [30,31]. As the film thickness is identical for all four films, the observed red shift is evidence of improved π–π^* transition absorption due to the increased conjugation length of polymer chains. The increased conjugation length of the polymer chains was caused by a reduction in the density of conformational defects. The addition of a moderate amount of high b.p. additives to the CB allows for the slow evaporation of the solvent and hence, leads to enhanced P3HT crystallinity. The improvement in the crystallinity is generally observed in the case of post-annealed P3HT-based polymer solar cells [4,19]. As such, the inkjet-printing method with modified inks containing high b.p. additives can act as a substitute for crucial post-annealing treatments. When compared to spin-coated devices, inkjet-printed solar cells fabricated with inks containing additives have improved crystallinity and better light harvesting properties over a wider spectral region. Consequently, the inkjet-printed solar cells are expected to exhibit improved photovoltaic performance.

The XRD results for the inkjet-printed active layer films fabricated with different inks are shown in Fig. 2. The peak intensity at $2\theta \approx 5.3$, which corresponds to the interchain spacing associated with the interdigitated alkyl chain in P3HT [4,32], was more enhanced in the films fabricated with high b.p. additives (inks 2–4). The maximum peak intensity was observed in the film fabricated with ink4, which contained the Cl-naph additive. These results are in agreement with the trends observed for the vibronic peak in the UV absorption spectra shown in Fig. 1. In addition, when high b.p. additives are added to the inks (inks 2–4), the 2θ angle of (100) of films is moved to higher angle: 5.24 for ink 1, 5.30 for ink 2 and 3, and 5.42 for ink 4. According to the Bragg's equation ($n\lambda = 2d \sin\theta$, where n, λ, d, and θ denote the order of diffraction, wavelength of an X-ray beam, interlayer spacing, and Bragg peak position, respectively) [33,34], a interlayer spacing of films fabricated with high b.p. additives (inks 2–4) is less than that of film prepared from pure P3HT:PCBM ink (ink1). It indicates that modification of inks with high b.p. additives induces closer P3HT chains, resulting in the lower resistance to the hopping of charge carriers.

Morphology is one of the key factors that affect the performance of bulk-heterojunction solar cells. To investigate the effects of additives and inkjet-printing on the morphology, the surface of the active layer films was imaged using an atomic force microscope (AFM). Shown in Fig. 3 are the AFM images of the inkjet-printed active layers fabricated with different inks; the reference cell fabricated from spin-coating is shown for comparison. From the AFM images ($100 \times 100\mu$m), it is clear that the morphology is greatly influenced by the addition of different high b.p. additives to the CB solvent. The film prepared with ink1 (CB with no additives) possesses an rms roughness of 64 nm, which is very high when compared to the films fabricated from inks 2–4. Such a high rms roughness may be due to the high evaporation rate of the CB. If the rate of evaporation of the solvent is high, then there may not be

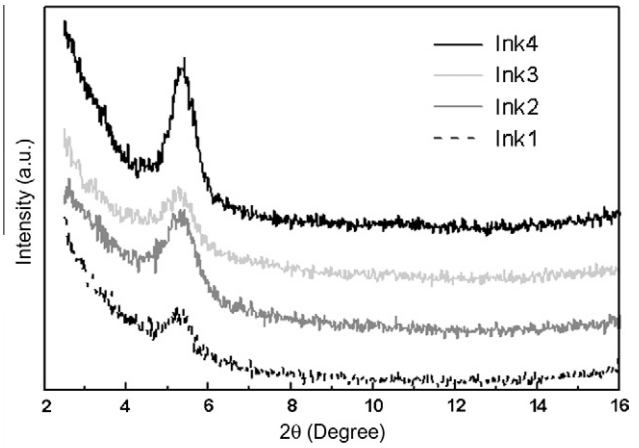

Fig. 2. XRD spectra of the inkjet-printed active layers fabricated from different inks.

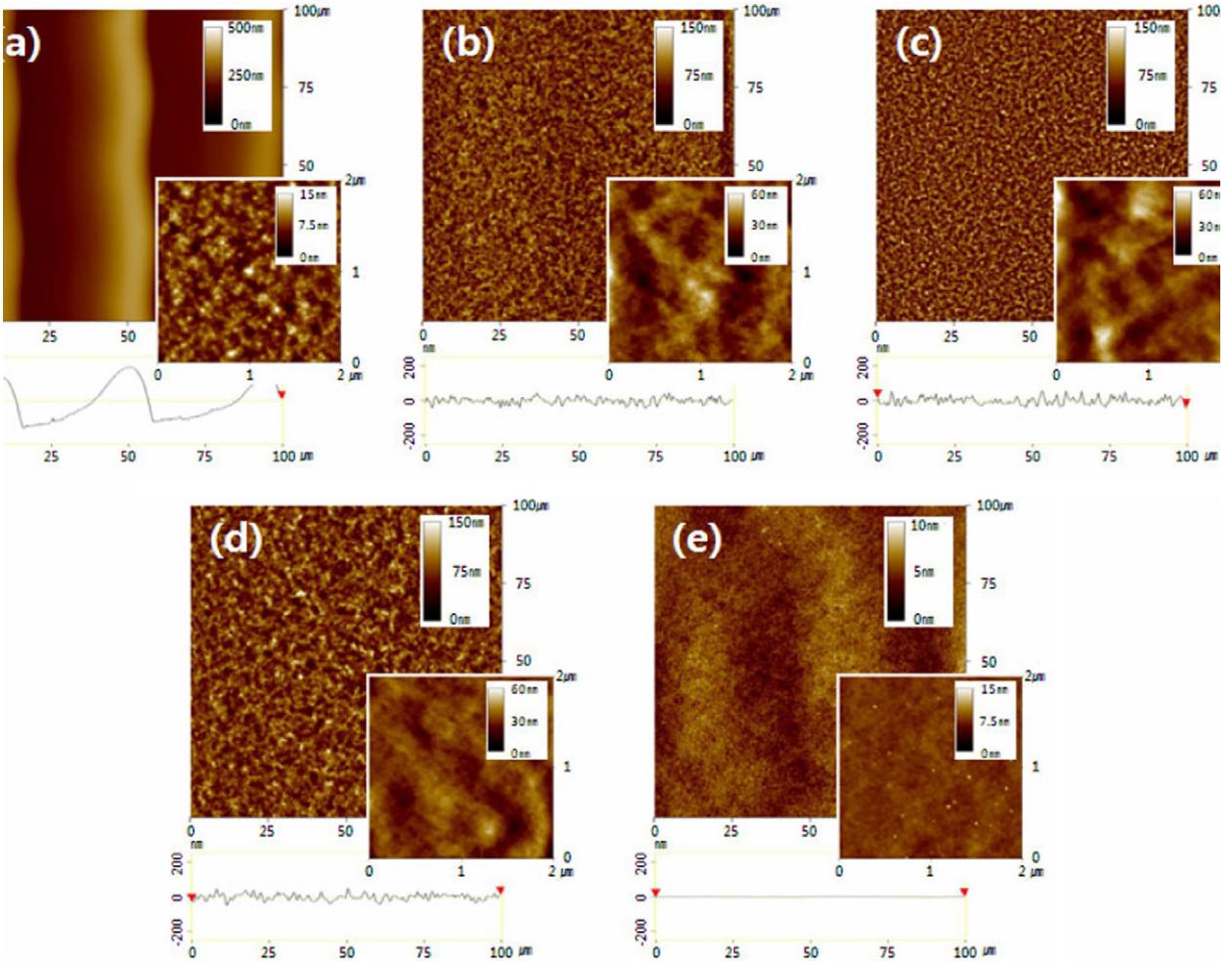

Fig. 3. AFM images of the P3HT:PCBM active layers fabricated from different inks: inkjet-printed (a) ink1 (b) ink2 (c) ink 3 (d) ink 4 and (e) spin-coated ink1.

sufficient time for self organization of the blended P3HT polymer molecules. This would result in a coating with a rough and uneven surface. On the other hand, the films from ink2, ink3, and ink4 possess moderate rms roughnesses on the order of 17.7, 20.9, and 17.9 nm, respectively. As stated above, ink2, ink3, and ink4 contain high b.p.

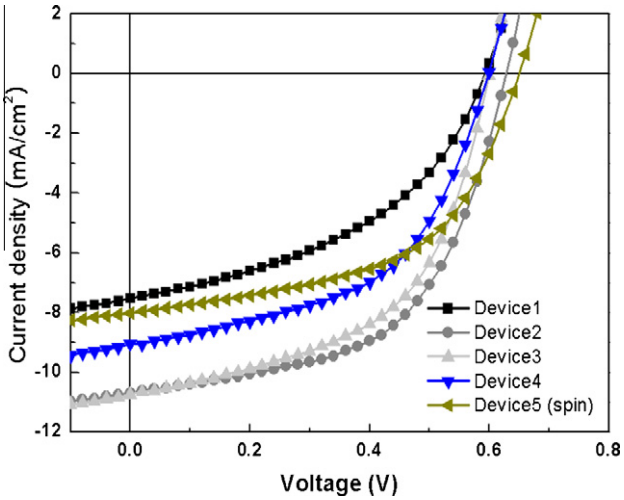

Fig. 4. J–V characteristics of the solar cell devices with P3HT:PCBM active layers fabricated from different inks.

additives of 5 vol% ODT, 5 vol% ODCB, and 5 vol% Cl-naph, respectively. The observed decrease in the rms roughness values can be attributed to the low evaporation rates of the high b.p. additives. These high b.p. additives allow for a controlled evaporation and sufficient time for self organization to occur. The additives may also provide enhanced wettability of the P3HT:PCBM inks on the PEDOT:PSS layer, leading to an active layer with a uniform film morphology and reducing the coffee-ring effect [35]. In general, it can be concluded that the addition of high b.p. additives offers control over the morphology of the P3HT and PCBM domains in the inkjet-printed active layer. The reference device (ink1) fabricated by spin-coating possessed a very low rms roughness of 1 nm, which may be due to the high spinning rate used in this study. However, when compared to the inkjet-printed films, the film spin-coated from ink1 exhibited a homogeneous morphology with no significant phase separation. The AFM images in the inset of Fig. 3 ($2 \times 2\mu m$ scan size) more clearly reveal that the films inkjet-printed from inks 2–4 show more distinct nanoscale phase separation than in the spin-coated film. The increased phase separation is a result of polymer self organization and leads to an increase in device efficiency. However, it should be noted that the film inkjet-printed from ink4 exhibits an undesirably large degree of phase separation between the P3HT and PCBM (the average size of the domains is greater than 100 nm), which may result in the restriction of charge transport.

To directly evaluate the effect of high b.p. additives on the overall device performance, the J–V characteristics of all the solar cells were measured under illumination with a solar simulator. Shown in Fig. 4 are the J–V plots for all devices; the calculated values of the solar cell parameters are summarized in Table 2. As clearly evident in Fig. 4, the device fabricated with ink1 (device 1) without any additives exhibits very poor performance with a PCE ~1.9% resulting relatively lower Voc, Jsc and FF than other devices. The observed low device performance may be due to poor P3HT crystallinity, relatively weak absorption in the longer wavelength region and undesirable film morphology (see Figs. 1–3) that serve to restrict the transport of the photo-generated charges towards the electrodes. In contrast, the device fabricated with ink2 (device 2) exhibited the best performance with a PCE of ~3.7% and an FF that increased up to ~56%. Such a result was believed to arise from a higher level of P3HT crystallinity and distinct nanoscaled phase separation morphology. These factors, in turn, led to a lower serial resistance and defect-free contact with the metal cathode. The device prepared with ink3 (device 3) had a Jsc of ~10.7 mA/cm2, which was similar to the Jsc from device 2. However, a slight reduction in the Voc to ~0.6 V was observed in device3, which led to a decrease in the PCE to ~3.4%. The device prepared with ink4 (device 4) yielded a PCE of 2.83% and lower Jsc and Voc values than those found for devices 2–3. This may due to a low photo current, which is in turn attributed to limitations in the charge transport and collection by the large phase separated morphology (see the AFM images in Fig. 3). The exact reasons of lower Voc are not clearly reported yet even though several efforts have been made to fabricate inkjet-printed bulk-heterojunction solar cells with active layer of P3HT:PCBM [24,25]. In organic solar cells, the Voc is generally governed by the energy difference between the highest occupied molecular orbital (HOMO) of the donor and the lowest unoccupied molecular orbital (LUMO) of acceptor [36]. An increase in the conjugation length due to strong chain interactions improves the crystallinity with long wavelength absorption. Such a scenario leads to an improved Jsc, but may cause a reduction in the Voc in the devices 1–4 fabricated by

Table 2
Summary of the solar cell device performance for the different P3HT:PCBM active layers containing different additives.

Devices with inks	V_{oc} (V)	J_{sc} (mA/cm^2)	FF (%)	PCE (%)
Device 1 (ink 1)	0.593	7.53	44.25	1.97
Device 2 (ink 2)	0.628	10.68	55.27	3.71
Device 3 (ink 3)	0.600	10.73	53.28	3.43
Device 4 (ink 4)	0.599	9.49	52.23	2.83
Device 5 (ink 1, spin)	0.650	8.02	53.58	2.79

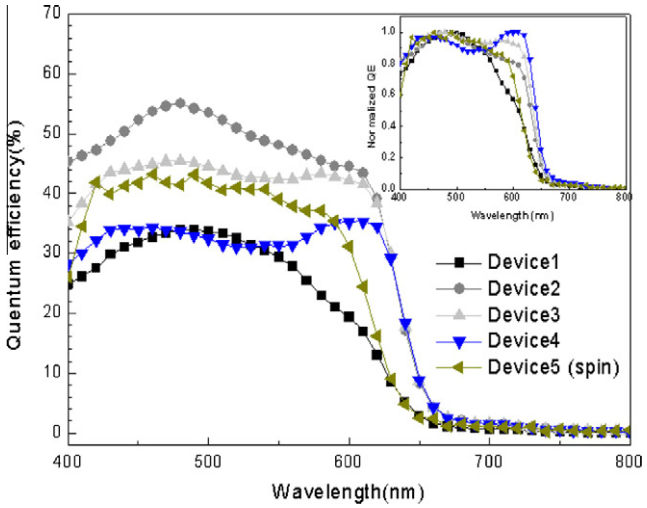

Fig. 5. The IPCE spectra of solar cell devices with P3HT:PCBM active layers fabricated from different inks.

inkjet-printing, especially in device 4 showing a high crystallinity (see Fig. 2). Device5, fabricated by spin-coating with ink1, exhibited a PCE of 2.79%, which was lower than that found in the inkjet-printed devices (devices 2–4) even though it shows a higher Voc and comparable FF than inkjet-printed devices (devices 2–4). Such a low PCE may due to poor P3HT crystallinity and weak absorption in the longer wavelength region, resulting a lower Jsc, for the active layer fabricated by the spin-coating method (see Figs. 1 and 2).

Shown in Fig. 5 are the plots of the IPCE measured for all of the devices. The dependence of the IPCE on the post-production treatment has been reported by several groups; IPCE values of up to 70–80% have been achieved [19,37–40]. Devices 2–4, which were inkjet-printed from inks 2–4 with additives, showed significant IPCE improvement in the longer wavelength region, when compared to device 1 (no additives) and device 5 (spin-coated from ink1) (see the inset of Fig. 5). While device 5 possessed a low rms roughness, it exhibited a low IPCE of 50%, when compared to devices 2–3 due to its low optical absorption in the longer wavelength region. A maximum IPCE of up to 55% was measured with device 2. Device 1, fabricated from ink1, containing no high b.p. additive, exhibited the lowest IPCE of about 30%. This may due to its low crystallinity and relatively weak absorption in the longer wavelength region. Device 4, made with ink4, exhibited a relatively low IPCE value even though it displayed good absorption at longer wavelengths. Such a scenario may be due to the limited charge transport that is related to the large degree of phase separation. The attained IPCE results are in good agreement with the trends observed in the optical absorption spectra and the device performance data shown in Figs. 1 and 4. The profound improvement in the IPCE with the addition of different additives is believed to increase both the optical absorption and the charge transport, as well as reduce recombination losses due to improvements in crystallinity and surface morphology. Therefore, it can be concluded that inkjet-printing provides a two-fold improvement in the overall solar cell performance, i.e. efficient light harvesting by improved P3HT crystallinity and enhanced charge transport and offering a better surface morphology for the top metal contact.

Bulk heterojunction polymer solar cells have been prepared with an inkjet-printed active layer of P3HT:PCBM and a PEDOT:PSS layer. For an optimum ink formulation, different high b.p. additives, such as ODT, ODCB, and Cl-naph were added to CB. The addition of high b.p. additives has greatly influenced the morphology, the optical and electrical properties, and the solar cell performance of the devices. The devices fabricated from inks formulated with high b.p. additives have exhibited improved device performance, when compared to the devices prepared without additives. Such behavior was due to optimum film morphology, improved light absorption properties, and reduced recombination losses due to an improved crystallinity and charge transport. The inkjet-printed device with an active layer of P3HT:PCBM containing the high b.p. additive ODT and a modified PEDOT:PSS layer has demonstrated the best solar cell performance with a PCE of ~3.7% and an IPCE of ~55%.

Acknowledgments

This work was supported by Ministry of Commerce, Industry and Energy (MOCIE) under Grant No. 200701-0041. This research was also financially supported by the Ministry of Education, Science Technology (MEST) and Korea Industrial Technology Foundation (KOTEF) through the Human Resource Training Project for Regional Innovation.

References

[1] N.S. Sariciftci, L. Smilowitz, A.J. Heeger, F. Wudl, Science 258 (1992) 1474.
[2] J.J.M. Halls, C.A. Walsh, N.C. Greenham, E.A. Marseglia, R.H. Friend, S.C. Moratti, A.B. Holmes, Nature 376 (1995) 498.

[3] G. Yu, J. Gao, J.C. Hummelen, F. Wudl, A.J. Heeger, Science 270 (1995) 1789.
[4] W. Ma, C. Yang, X. Gong, K. Lee, A.J. Heeger, Adv. Funct. Mater. 15 (2005) 1617.
[5] Y. Kim, S. Cook, S.M. Tuladhar, S.A. Choulis, J. Nelson, J.R. Durrant, D.D.C. Bradley, M. Giles, I. Mcculloch, C.-S. Ha, M. Ree, Nat. Mater. 5 (2006) 197.
[6] M. Svensson, F. Zhang, S.C. Veenstra, W.J.H. Verhees, J.C. Hummelen, J.M. Kroon, O. Inganãs, M.R. Andersson, Adv. Mater. (Weinheim, Ger.) 15 (2003) 988.
[7] M. Granström, K. Petritsch, A.C. Arias, A. Lux, M.R. Andersson, R.H. Friend, Nature (London) 395 (1998) 257.
[8] R.W. Vest, K.F. Teng, Metallization of solar cells with ink jet printing and silver metallo-organic inks, IEEE transactions on components, hybrids and manufacturing technology 11 (3) (1988) 291–297.
[9] S.H. Eom, S. Senthilarasua, P. Uthirakumar, C.H. Hong, Y.S. Lee, J. Lim, S.C. Yoon, C. Lee, S.H. Lee, Solar Energy Materials and Solar Cells 92 (2008) 564.
[10] S.H. Eom, S. Senthilarasua, P. Uthirakumar, S.C. Yoon, J. Lim, C. Lee, H.S. Lim, J. Lee, S.H. Lee, Organic Electronics 10 (2009) 536.
[11] S.E. Shaheen, C.J. Brabec, N.S. Sariciftci, Appl. Phys. Lett. 78 (2001) 841.
[12] Y. Kim, S.A. Choulis, J. Nelson, D.D.C. Bradley, S. Cook, R. Durrant, Appl. Phys. Lett. 86 (2005) 063502.
[13] G. Li, V. Shrotriya, J. Huang, Y. Yao, T. Moriarty, K. Emery, Y. Yang, Nat. Mater. 4 (2005) 864.
[14] P. Vanlaeke, G. Vanhoyland, T. Aernouts, D. Cheyns, C. Deibel, J. Manca, P. Heremans, J. Poortmans, Thin Solid Films 511 (2006) 358.
[15] V.D. Mihailetchi, H. Xie, B. de Boer, L.M. Popescu, J.C. Hummelen, P.W.M. Blom, L.J.A. Koster, Appl. Phys. Lett. 89 (2006) 012107.
[16] K. Kim, J. Liu, D.L. Carroll, Appl. Phys. Lett. 88 (2006) 181911.
[17] H. Hoppe, N.S. Sariciftci, J. Mater. Chem. 16 (2006) 45.
[18] H. Hoppe, N.S. Sariciftci, J. Mater. Res. 19 (7) (2004) 1924.
[19] F. Padinger, R.S. Rittberger, N.S. Sariciftci, Adv. Funct. Mater. 13 (2003) 85.
[20] J. Peet, J.Y. Kim, N.E. Coates, W.L. Ma, D. Moses, A.J. Heeger, G.C. Bazan, Nat. Mater. 6 (2007) 497.
[21] K.J. Lee, W.L. Ma, C.J. Brabec, J. Yuen, J.S. Moon, J.Y. Kim, K. Lee, Guillermo C. Bazan, A.J. Heeger, J. Am. Chem. Soc. 130 (2008) 3619.
[22] F.-C. Chen, H.-C. Tseng, C.-J. Ko, Appl. Phys. Lett. 92 (2008) 103316.
[23] C.N. Hoth, S.A. Choulis, P. Schilinsky, C.J. Brabec, Adv. Mater. 19 (2007) 3973.
[24] C.N. Hoth, P. Schilinsky, S.A. Choulis, C.J. Brabec, Nano Lett. 8 (2008) 2806.
[25] C.N. Hoth, S.A. Choulis, P. Schilinsky, C.J. Brabec, J. Mater. Chem. 19 (2009) 5398.
[26] T. Aernouts, T. Aleksandrov, C. Girotto, J. Genoe, J. Poortmans, Appl. Phys. Lett. 92 (2008) 033306.
[27] J. Park, H.-J. Koo, B. Yoo, K. Yoo, K. Kim, W. Choi, N.-G. Park, Sol. Energy Mater. Sol. Cells 91 (2007) 1749.
[28] A. Cravino, P. Schilinsky, C.J. Brabec, Adv. Funct. Mater. 17 (2007) 3906.
[29] M.-S. Kim, M.-G. Kang, L.J. Guo, J.S. Kim, Appl. Phys. Lett. 92 (2008) 133301.
[30] G. Li, Y. Yao, H. Yang, V. Shrotriya, G. Yang, Y. Yang, Adv. Func. Mater. 17 (2007) 1636.
[31] T.-F. Guo, T.-C. Wen, G.L. Pakhomov, X.-G. Chin, S.-H. Liou, P.-H. Yeh, C.-H. Yang, Thin solid film 516 (2008) 3138.
[32] S. Kim, S. Na, S. Kang, D. Kim, Sol. Energy Mater. Sol. Cells 94 (2010) 171.
[33] A. Zen, J. Pflaum, S. Hirschmann, W. Zhuang, F. Jaiser, U. Asawapirom, J.P. Rabe, U. Scherf, D. Neher, Adv. Func. Mater. 14 (2004) 757.
[34] T. Erb, U. Zhokhavets, G. Gobsch, S. Raleva, B. Stühn, P. Schilinsky, C. Waldauf, C.J. Brabec, Adv. Funct. Mater. 15 (2005) 1193.
[35] M. Singh, H.M. Haverinen, P. Dhagat, C.E. Jabbour, Adv. Mater. 22 (2010) 673.
[36] M.C. Scharber, D. Mühlbacher, M. Koppe, Patrick Denk, C. Waldauf, A.J. Heeger, C.J. Brabec, Adv. Mater. 18 (2006) 789.
[37] D. Chirvase, J. Parisi, J.C. Hummelen, V. Dyakonov, Nanotechnology 15 (2004) 1317.
[38] G. Li, V. Shrotriya, Y. Yao, Y. Yang, J. Appl. Phys. 98 (2005) 043704.
[39] I. Riedel, V. Dyakonov, Phys. Status Solidi (A), Phys. Appl. Res. 201 (6) (2004) 1332.
[40] M.R. Reyes, K. Kim, D.L. Carroll, Appl. Phys. Lett. 87 (2005) 083506.

characteristics measurement of a transistor. In order to handle this problem, Petit et al. utilized pulsed gate voltage instead of constant bias to minimize the bias stress effects in OTFTs [8]. Although, this measurement method enables device characterization, which is free of hysteresis effects, it cannot be used to investigate the hysteresis itself. Therefore, in reports focusing on hysteresis characteristics, standard sweep measurements, where the bias voltages (e.g., gate voltage) are not pulsed but swept, are primarily utilized.

In this report we show the impact of electrical measurement parameters on hysteresis in standard *I–V* characteristics of OTFT. We first introduce the hole trap related hysteresis mechanism and describe how the measurement parameters can influence the hysteresis in transfer and output characteristics. In the experimental section, we explain the fabrication and characterization of our devices and show the results of the measurements performed on these devices. The results of the simulations, performed with the device simulator ATLAS, are given in Section 4, which give an insight to the trapping/detrapping process in the active layer of a pentacene TFT at different bias conditions.

2. Theory

Electronic trap states in the active layer of pentacene-based OTFTs cause a hysteresis in the *I–V* characteristics by affecting the number of available charge carriers. As explained in detail in Ref. [4], during a gate bias sweep, at negative gate biases, positive charge carriers (holes) in the accumulation layer of the pentacene film are trapped. This reduces the number of effective charge carriers and thus the drain-source current I_{DS}. When the negative gate bias is removed, the trapped carriers are slowly released and the number of available charge carriers increases. Due to this bias dependent trapping/detrapping dynamics all device characteristics including transfer and output characteristics exhibit hysteresis. The mechanism of this phenomenon is discussed in the following two subsections.

2.1. Hysteresis in transfer characteristics

In order to explain the hysteresis in the transfer characteristics of a p-type OTFT, the transient behavior of I_{DS} at different gate-source biases and the resulting *I–V* characteristics are illustrated in Fig. 1. In this example, the drain-source voltage (V_{DS}) is assumed to be set to a certain negative value and kept constant through the entire measurement, while the gate-source voltage (V_{GS}) is swept from 0 V to a negative voltage (OFF-to-ON) and then back to 0 V (ON-to-OFF). For the sake of simplicity, only one intermediate V_{GS} step is considered for each sweep direction (Fig. 1(a)). It can be seen in Fig. 1(b) that during OFF-to-ON sweep, in both steps at $t = t_1$ and $t = t_2$, I_{DS} increases stepwise as the gate voltage V_{GS} becomes more negative, but then decreases again as the number of available charge carriers decreases in time due to trapping ($t_1 < t < t_2$ and $t_2 < t < t_3$). On the contrary, during ON-to-OFF sweep, I_{DS} decreases stepwise as V_{GS} becomes less negative ($t = t_3$), but then increases transiently as the

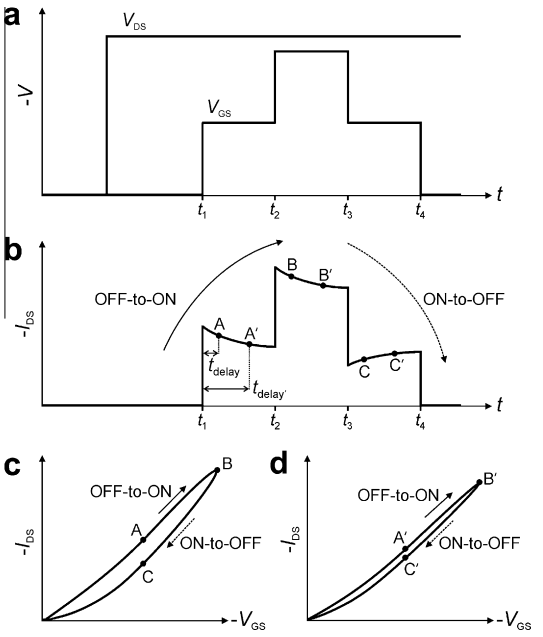

Fig. 1. Illustration of the transient response of the channel current I_{DS} during the transfer characteristics measurement of an OTFT. (a) Successive steps of drain and gate biases. (b) Transient response of I_{DS}. (c) Transfer characteristics measured with shorter delay time t_{delay}. (d) Transfer characteristics measured with longer delay time $t_{delay'}$. Hysteresis width decreases with increasing delay time.

detrapping increases the number of available charge carriers ($t_3 < t < t_4$). Due to the long time constants of the trapping/detrapping process, I_{DS} does not reach a steady state even a long time after a change in V_{GS}.

In *I–V* characteristics measurements, it is a good practice to introduce a time delay, which ensures that the DUT settles after stepping the bias. Since the time constants of hysteresis dynamics exceed the duration of a typical electrical measurement, the delay time plays a crucial role on the resulting *I–V* characteristics. To illustrate this, two different sets of measurement points with different delay times, i.e., t_{delay} and $t_{delay'}$, are depicted in Fig. 1(b), which are marked with letters A, B, C and A′, B′, C′, respectively. The resulting *I–V* characteristic from the first set of measurement points (A, B, C) with the shorter delay time t_{delay} is given in Fig. 1(c), which indicates different I_{DS} values at points A and C, although the bias voltages (V_{DS}, V_{GS}) are exactly the same at these measurement points. This leads to the hysteresis in the transfer characteristics with higher currents during OFF-to-ON sweep. If the second set of measurement points (A′, B′, C′) with the longer delay time $t_{delay'}$ is used, a different *I–V* characteristic is obtained due to the transient characteristics of I_{DS} (Fig. 1(d)). A hysteresis with the same rotational direction is still present in the characteristics; however, the width of the hysteresis becomes smaller with increasing delay time.

2.2. Hysteresis in output characteristics

The electric field in the channel of an OTFT is responsible for the accumulation of charge carriers in the active

layer and, thus, for the trapping/detrapping process. If the source electrode is grounded and kept at this potential, the electric field in the channel is determined primarily by the gate bias. The drain bias has a contribution to the field, particularly in the vicinity of the drain electrode. Regarding the electric field in this region, an increase in drain bias has the same effect, i.e., a decrease in electric field strength, as a decreasing gate bias and vice versa. This means, in case of a constant negative gate bias, a change in drain bias toward more negative voltages reduces the electric field strength near the drain electrode and trapped charges in this region are released resulting in an increase in I_{DS} [4]. If the negative drain bias is removed, the electric field strength increases, charge carriers are trapped and I_{DS} decreases. Hence, analogous to the case in transfer characteristics, a hysteresis exists in output characteristics, which will be explained using the illustration in Fig. 2. In this example, V_{GS} is assumed to be set to a certain negative value and kept constant throughout the measurement, while V_{DS} is swept from 0 V to a negative voltage and then back to 0 V to extract the output characteristics. First, we investigate the case when the hold time t_{hold}, which is the time between setting V_{GS} to a constant value and the first step of V_{DS} sweep (see Fig. 2(a)), is long such that gate bias related effects can be neglected and only the change in V_{DS} influences the current I_{DS}. Under this assumption, the transient behavior of I_{DS}, which is depicted with a solid line on the right hand side of Fig. 2(b), can be explained as follows. As V_{DS} is swept to negative voltages, in both steps, I_{DS} increases stepwise as V_{DS} becomes more negative and it increases further as the number of available charge carriers increases in time due to detrapping at the drain end of the channel. In contrary, during the other sweep direction, I_{DS} decreases stepwise as V_{DS} becomes less negative and it decreases further as the trapping reduces the number of available charge carriers. The output characteristics, extracted from the measurement points marked with letters A, B, C in Fig. 2(b), show a clear hysteresis behavior (Fig. 2(d)). At this point, it should be noted that the rotational direction of hysteresis in the output characteristics is the opposite of the case for the transfer characteristics given in Fig. 1.

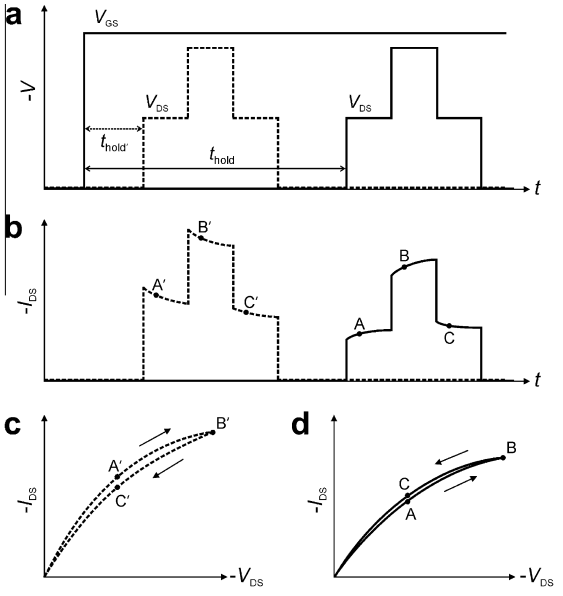

Fig. 2. Illustration of the transient response of the channel current I_{DS} during output characteristics measurement of an OTFT for two different hold times t_{hold} and $t_{hold'}$. (a) Time sequences of gate and drain biases. Wave form of V_{DS} for t_{hold} is shown with solid line and for $t_{hold'}$ with dashed line. (b) Transient responses of I_{DS}. Solid line for t_{hold}, dashed line for $t_{hold'}$. (c) Output characteristics extracted from measurement points A′, B′, C′. (d) Output characteristics extracted from measurement points A, B, C. The rotational direction of the hysteresis switches depending on the hold time.

The above explanation of hysteresis in output characteristics is only valid in case of a long hold time (t_{hold}). If the same V_{DS} sweep is applied with a shorter hold time ($t_{hold'}$), as depicted with dashes in Fig. 2(a), the effects of the V_{GS} step at the beginning of the measurement overlap with those of the consequent V_{DS} sweep. The transient effects of drain and gate bias sweeps are contradictory. Yet, regarding the effect on the strength of the electric field in the channel, hence, the trapping dynamics, gate bias predominates since it affects the field strength in the whole channel area while the drain has an influence limited to its vicinity. Consequently, in case of a short hold time ($t_{hold'}$), the transient characteristics of I_{DS} – shown with dashes on the left hand side of Fig. 2(b) – are similar to the case for the transfer characteristics given in Fig. 1(b). Consistently, the rotational direction of hysteresis in the output characteristics extracted from the measurement points A′, B′, C′ is opposite to that of the characteristics extracted from the points A, B, C (Fig. 2(c, d)).

3. Experimental

Our transistors are built in bottom gate configuration on heavily arsenic-doped Si wafer (resistivity $\leqslant 0.005\ \Omega$ cm) which serves as the gate electrode (Fig. 3). 300 nm thick, thermally grown SiO_2 forms the gate dielectric. Drain/source electrodes are deposited on the polished side of the wafer (roughness $\leqslant 2$ nm) from Cr (5 nm) and Au (40 nm) through electron beam evaporation, where Cr acts as an adhesion layer. Prior to semiconductor film deposition, the wafer is wet cleaned with acetone, isopropanol and deionized water in ultrasonic bath. Pentacene is purchased from Sigma–Aldrich and a 50 nm layer is thermally evaporated as-is at 1 Å/s through another shadow

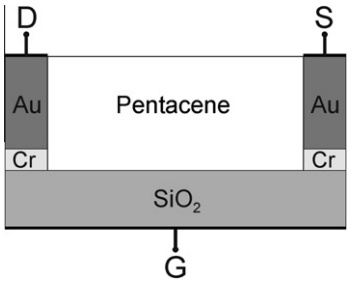

Fig. 3. Schematic cross section of a pentacene OTFT.

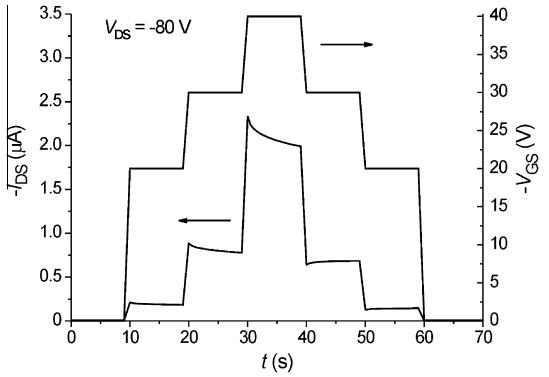

Fig. 4. Measured I_{DS} characteristics of an OTFT in response to a V_{GS} sweep.

mask. Electrical characterization is performed under dry N_2 atmosphere with $O_2 < 0.1$ ppm with an Agilent 4156C semiconductor parameter analyzer.

The transient response of I_{DS} is shown in Fig. 4 at various gate biases. At each V_{GS} step the bias is kept constant for 9 s and switched to next step with 10 V/s sweep rate. V_{DS} is set to −80 V at $t = 0$ and kept constant through the entire measurement. As explained in the previous section, in case of a constant V_{DS}, I_{DS} increases or decreases transiently depending on the change in V_{GS}. A change in V_{GS} toward more negative voltages causes a transient decrease in I_{DS} due to the decreasing number of free charge carriers through trapping. As V_{GS} is swept to less negative voltages, the charge carriers are released from the traps and I_{DS} shows a transient increase. The result is in accordance with the theory which is explained in the previous section and depicted in Fig. 1.

In order to figure out the impact of the hold time (t_{hold}) on device characteristics, output characteristics measured with different t_{hold} are also investigated. For the sake of simplicity, the output characteristic is measured at a single gate bias, i.e., $V_{GS} = -80$ V. V_{DS} is swept from 0 to −80 V and then back to 0 V with 5 V/s sweep rate. A delay time of 1 s is introduced to achieve stable measurements. An initialization step, which is suggested in Ref. [4], is utilized between subsequent measurements. Yet, the measurements are repeated with different sequences to verify that the results are free of long term degradation.

The output characteristic measured with $t_{hold} = 30$ s exhibits a hysteresis with higher currents during the backward sweep (Fig. 5(a)). This is the case where the effects of the V_{GS} change at the beginning of the measurement can be neglected since t_{hold} is long enough to ensure that V_{GS} dependent effects settle during t_{hold}. However, with decreasing t_{hold}, the rotational direction of hysteresis in the output characteristic tends to change such that the forward and backward characteristics intersect (Fig. 5(b)). This is due to the fact that the gate and drain bias related hysteresis effects are contradictory and gate bias dependent hysteresis appears in the output characteristic as t_{hold} becomes shorter. The shorter the hold time, the more dominant is the gate bias dependent hysteresis and the intersection point in the characteristic moves toward more negative V_{DS} values (Fig. 5(c)). Thus, it is possible to have contradicting rotational directions of hysteresis in the output characteristics. This result is in accordance with the theory which is depicted in Fig. 2 in the previous section. It can also be seen in Fig. 5 that the maximum value of I_{DS} decays with increasing t_{hold}.

4. Simulation

In order to get a deeper insight into the physical behavior of OTFTs during the above mentioned measurements, we performed numerical simulations with the two-dimensional device simulator ATLAS (Silvaco). The simulations are based on the solution of drift–diffusion equations coupled with the Poisson equation [9]. The device structure shown in Fig. 3 with a channel length of 25 μm has been used for simulations. The 5 nm chromium layer, which has barely effect on the electrical behavior but which is necessary as an adhesive medium for the gold electrodes in the fabricated devices, has also been considered in the simulations. For the pentacene layer, typical values have been chosen for the band gap (2.0 eV), the electron affinity (3.0 eV) and the relative permittivity (4.0). The effective density of states has been set equal to the density of molecules, i.e., 1×10^{21} cm^{-3} in accordance with Refs. [10,11]. The pentacene is assumed to be nominally undoped.

The hole mobility of 5×10^{-3} $cm^2V^{-1}s^{-1}$ has been extracted from OFF-to-ON transfer characteristic of the fabricated devices for the voltage range relevant for the simulations. A Poole–Frenkel mobility model has been

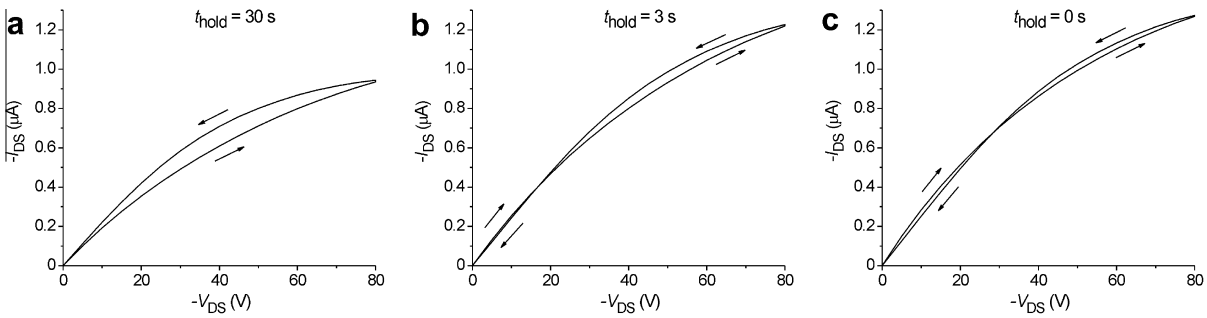

Fig. 5. Output characteristics from an OTFT measured with different hold times (t_{hold}). Gate bias dependent effects dominate in measurements with shorter hold times causing a change in the rotational direction of the hysteresis.

utilized in order to account for the electric field dependence of the charge carrier mobility. The hole Poole–Frenkel factor, β_p, has been calculated from the permittivity of pentacene [9]. Donor-type bulk traps are assumed to concentrate at a discrete energy level of 0.1 eV above the HOMO band of pentacene. A trap density of 2×10^{19} cm^{-3} is calculated from the energetic distribution of bulk traps in accordance with the literature [12]. Trap lifetimes of 5 s and 140 s have been extracted from the transient behavior of the fabricated transistors according to Ref. [6].

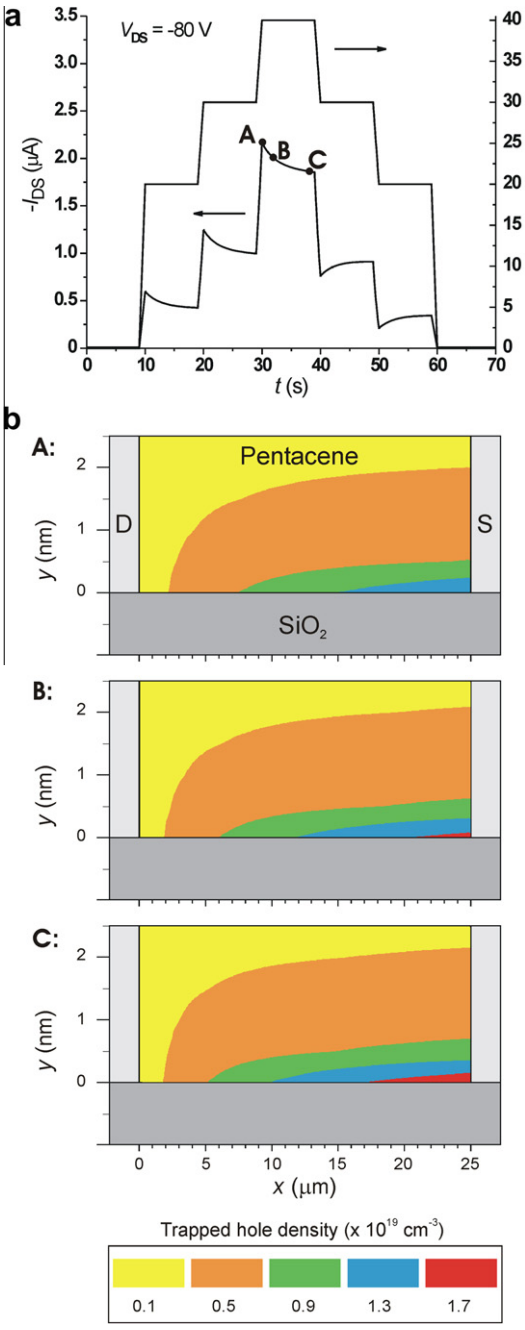

Fig. 6. Simulations performed with ATLAS. (a) Simulation of the transient response of I_{DS} of a pentacene OFET at different gate biases. (b) The density of trapped charge carriers (holes) in the channel at time points t = 30 s (A), t = 32 s (B), and t = 38 s (C). The increase in the number of trapped holes in the channel is in accordance with the transient decay in I_{DS} for 30 s < t < 38 s shown in (a).

Since the traps in the active layer of a pentacene FET are primarily responsible for the hysteresis in the device characteristics, we have performed simulations to investigate the transient response of the transistor following a change in gate bias. For this purpose, we have simulated the measurement which is given in Fig. 4, where the transient response of I_{DS} has been investigated. Parameters such as bias voltage, voltage sweep rate, and duration of the measurement are set exactly the same as in the measurement. The simulation result given in Fig. 6(a) is in good accordance with the measurement. In order to clarify the physical background of the transient change in I_{DS} during the measurement, we have investigated the change in the trapped hole density in the active layer of the transistor. For this purpose, three consecutive time points are chosen in a time span in which the bias is kept constant. These are marked with letters A, B, C, which refer to t = 30 s, t = 32 s, t = 38 s, respectively (Fig. 6(a)). At these time points, the simulated trapped hole densities are shown on the cross section of a pentacene transistor in Fig. 6(b). In order to make the change at higher concentrations more remarkable, only the first couple of nanometers of the pentacene layer are shown and a linear scale is chosen between 1×10^{18} and 1.7×10^{19} cm^{-3} for the trapped charge carrier density. As the simulation advances, an increase in the trapped charge carrier density in the channel is observed (Fig. 6(b)). This increase in the number of trapped charge carriers reduces the number of effective charge carriers in the accumulation layer causing the transient decrease in I_{DS} for 30 s < t < 38 s in Fig. 6(a). These results prove that the measurements shown in the previous section can be explained by the theory presented in this study.

5. Conclusion

The slow trapping/detrapping of bulk traps plays an important role in the transient behavior of organic semiconductor-based thin-film transistors (OTFTs) causing a hysteresis in the I–V characteristics. In this report we have presented a theory which explains how the electrical measurement parameters affect the measured hysteresis in pentacene thin-film transistors. The theory is verified through experiments and simulations where we have demonstrated that solely by changing the hold time and/or the delay time in the measurements, it is possible to change the width and even the rotational direction of the hysteresis. Therefore, it is crucial to consider the measurement parameters thoroughly prior to any comparison or conclusion on the hysteresis behavior of different OTFT samples. Yet, in many reports in literature these parameters are not given completely, which makes the reproduction of measurements and the comparison between particular results impossible. Therefore, the authors propose that it shall be a routine to comment on the electrical measurement parameters such as hold time, delay time, voltage sweep rate in all reports on OTFTs since the

influence of electrical measurement parameters on the measured device characteristics is intense.

References

[1] G.H. Gelinck, H.E.A. Huitema, E. van Veenendaal, E. Cantatore, L. Schrijnemakers, J.B.P.H. van der Putten, T.C.T. Geuns, M. Beenhakkers, J.B. Giesbers, B.-H. Huisman, E.J. Meijer, E.M. Benito, F.J. Touwslager, A.W. Marsman, B.J.E. van Rens, D.M. de Leeuw, Flexible active-matrix displays and shift registers based on solution-processed organic transistors, Nat. Mater. 3 (2004) 106–110.

[2] A. Knobloch, A. Manuelli, A. Bernds, W. Clemens, Fully printed integrated circuits from solution processable polymers, J. Appl. Phys. 96 (4) (2004) 2286–2291.

[3] V. Subramanian, P.C. Chang, J.B. Lee, S.E. Molesa, S.K. Volkman, Printed organic transistors for ultra-low-cost RFID applications, IEEE Trans. Compon. Packag. Technol. 28 (4) (2005).

[4] C. Ucurum, H. Goebel, F.A. Yildirim, W. Bauhofer, W. Krautschneider, Hole trap related hysteresis in pentacene field-effect transistors, J. Appl. Phys. 104 (2008) 084501.

[5] M. Egginger, S. Bauer, R. Schwödiauer, H. Neugebauer, N.S. Sariciftci, Current versus gate voltage hysteresis in organic field effect transistors, Monatsh. Chem./Chemical Monthly 140 (7) (2009) 735–750.

[6] G. Gu, M.G. Kane, J.E. Doty, A.H. Firester, Electron traps and hysteresis in pentacene-based organic thin-film transistors, Appl. Phys. Lett. 87 (2005) 243512.

[7] IEEE Standard 1620TM, in: IEEE Standard Test Methods for the Characterization of Organic Transistors and Materials, IEEE, New York, USA, 2004.

[8] C. Petit, D. Zander, K. Lmimouni, M. Ternisien, D. Tondelier, S. Lenfant, D. Vuillaume, Gate pulse electrical method to characterize hysteresis phenomena in organic field effect transistor, Org. Electron. 9 (2008) 979–984.

[9] ATLAS User's Manual, SILVACO, Santa Clara, USA (2009).

[10] C. Erlen, F. Brunetti, M. Fiebig, G. Scarpa, B. Nickel, A.D. Carlo, P. Lugli, Role of charge interaction in the behavior of organic thin film transistors, Mater. Res. Soc. Symp. Proc. 1003E (2007). 1003-O11-10.

[11] D. Gupta, M. Katiyar, Deepak, Effect of pentacene thickness on organic thin film transistors: role of pentacene/insulator interface, International Workshop on Physics of Semiconductor Devices, 2007. IWPSD 2007, (2007) 594-596.

[12] The energetic distribution of bulk traps can be described by the general form of the density of states given by $N(E) = N_0 \exp(-|E-E_0|/E_S)$ [13,14]. For the sake of simplicity, we assumed the trap distribution to be concentrated at a discrete energy level of 0.1 eV above the HOMO band of pentacene, i.e. $E_0 = 0.1$ eV. Then the volume density of traps at this energy level can be calculated by integrating the above-mentioned energetic distribution function over the band gap of pentacene. Consequently, a trap density of 2×10^{19} cm^{-3} is calculated by using the typical values from the literature, i.e. the maximum of distribution function $N_0 = 10^{20}$ cm^{-3} eV^{-1}, the characteristic width of the distribution $E_s = 0.1$ eV [13].

[13] S. Scheinert, K.P. Pernstich, B. Batlogg, G. Paasch, Determination of trap distributions from current characteristics of pentacene field-effect transistors with surface modified gate oxide, J. Appl. Phys. 102 (2007) 104503.

[14] W.L. Kalb, B. Batlogg, Calculating the trap density of states in organic field-effect transistors from experiment: a comparison of different methods, Phys. Rev. B 81 (2010) 035327.

of light response and current modulation of the ink-jet printed low-molecular ordered TIPS-pentacene transistors, a suspended top-contact (STC) structure was employed [14].

2. Experimental

The ink-jet printed STC–TIPS-pentacene phototransistors were fabricated by the following sequence. On Corning 1737 glass substrates, 100-nm-thick indium–tin-oxide (ITO) gate electrode was deposited by sputtering and then patterned. On the top of the gate electrode, an organic gate insulator, poly-4-vinylphenol (PVP) was spin-coated and thermally cured. The PVP solution was prepared with 10 wt.% of PVP powder mixed with 5 wt.% of poly (melamine-co-formaldehyde) methylated as a cross-linking agent in propylene glycol monomethyl ether acetate. The curing temperature and time were 200 °C and 30 min, respectively. For source/drain electrode, a STC electrode structure has been built. The STC electrode structure was fabricated with 50 nm-thick Cr and 50 nm-thick Au bi-layers. With over-etching of the Cr adhesion layer, suspended Au source/drain electrodes can be formed, resulting in somewhat similar to Au top-contact structure on TIPS-pentacene films. The channel width and length of were 125 μm and 10 μm, respectively. The organic semiconductor ink, TIPS-pentacene was prepared from 1 wt.% anisole solution. The deposition of TIPS-pentacene was then performed using a piezoelectric ink-jet printing system (UniJet UJ2100) on the STC electrodes. The piezoelectric ink-jet nozzle had a diameter of 50 μm (orifice size of 50 μm). The frequency of the jetting was 150 Hz and the diameter of the ink drop was approximately 30–50 μm.

The electrical measurements were performed using a Keithley 4200-SCS in a dark and air ambient at room temperature. The steady-state white light response characteristics were carried out using a halogen lamp as a light source. For UV irradiation tests, low-pressure mercury lamp (Hamamatsu Photonics, L937-02) was used as a light source. All the light sources were placed on the top of the sample. The X-ray diffraction patterns of TIPS-pentacene films were obtained by using X-ray diffractometer (Philips, X'pert MPD, λ = 1.5406 Å).

3. Results and discussion

The STC-structured device has suspended source/drain electrode over the gate insulator. There is a very narrow gap in between (typically 50 nm), and TIPS-pentacene solution fills this gap forming a channel layer. Therefore, the device is more likely to behave as a top-contact device (Fig. 1). Typical transfer characteristics of the ink-jet printed STC–TIPS-pentacene and conventional bottom-contact TIPS-pentacene phototransistors measured in the dark are shown in Fig. 2. As shown in this figure, the STC–TIPS-pentacene phototransistors typically show much improved mobility, on-current, subthreshold slope, and reduced off-current, possibly resulting from contact improvement [14]. Such a low off-current and subthreshold slope may enable the high photosensitivity and high dynamic range of the phototransistor. For the application of the STC–TIPS-pentacene transistors as photosensitive

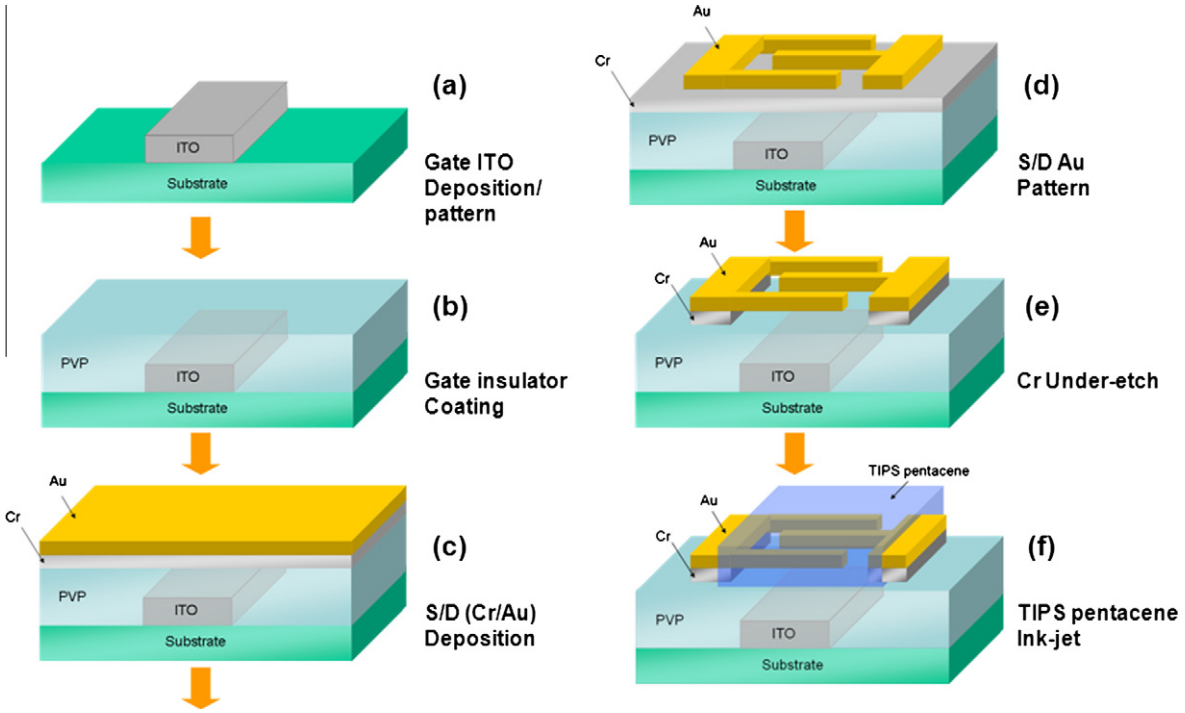

Fig. 1. Fabrication procedure of ink-jet printed TIPS-pentacene phototransistor with suspended top-contact (STC) structure.

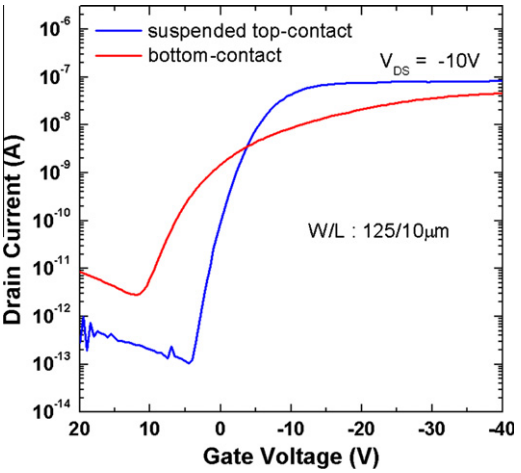

Fig. 2. The comparison of transfer characteristics of ink-jet printed conventional and STC–TIPS-pentacene phototransistor measured under dark. The channel width and length of the phototransistor were 125 μm and 10 μm, respectively.

devices, we characterized the devices in the linear regime. The linear field-effect mobility was 0.02 cm^2/V-s and the on/off ratio was 10^6–10^7. The threshold voltage (V_{th}) and subthreshold slope were determined as −4 V and 2.5 V/decade, respectively. The STC–TIPS-pentacene phototransistor showed extremely low off-current level (10^{-14}–10^{-15} A) at a low source-to-drain bias (V_{ds} = −1 V) (Fig. 3).

The gate bias dependent current modulation (I_{light}/I_{dark}) and dynamic range (20 log (I_{light}/I_{dark})) of a phototransistor are shown in Fig. 4. The illuminated light power density was controlled as 9, 11 and 13 mW/cm^2. When the light is illuminated on the phototransistor, the drain current of the phototransistor is increased due to the photogenerated excitons and localized heating by absorption and rapid thermalization of light [15]. With the light illumination the drain current (I_{light}) increased up to 10^{-8} A in the off-state showing a current modulation of 10^6–10^7. In strong accumulation regime (V_{gs} < −10 V), the current modulation is nearly unity since the number of the photogenerated charge carriers is comparable to the number of carriers accumulated by the field-effect. On the other hand, as the gate bias moves toward positive, the current modulation increases and reaches a maximum point. Further increase of the gate bias towards positive direction decreases the current modulation due to increased I_{dark}.

In a-Si:H TFTs, the dependence of photocurrent (I_{ph}; $I_{ph} = I_{light} - I_{dark}$) on illumination flux and gate bias can be explained by using the photofield effect model [16]. According to this model, the photocurrent shows a power law dependency on the illumination flux, as in Eq. (1),

$$I_{ph} \propto F^{\gamma(V_{gs})} \quad (1)$$

where, F is the illumination flux and γ is power law exponent which is a gate bias dependent factor and describes the dependency of photocurrent on light intensity. When a gate bias is applied, conduction and valence bands are bent and electrons or holes are accumulated near the insulator/semiconductor interface depending on the polarity of

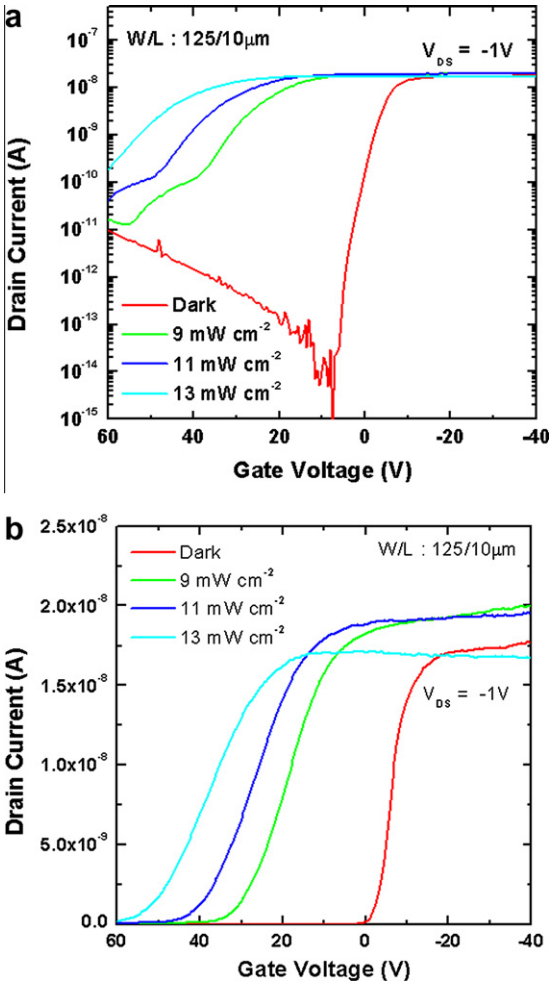

Fig. 3. The transfer characteristics of TIPS-pentacene phototransistors with a steady-state light illumination (at V_{ds} = −1 V). The light power density was varied as 9, 11 and 13 mW/cm^2; (a) in logarithm scale, and (b) in linear scale of the drain current.

the gate bias. However, when light is illuminated on the semiconductor, a redistribution of space charge in localized donor- and acceptor-like states takes place and band bending is relaxed [16]. Also, under illumination the semiconductor is at a non-equilibrium steady-state and quasi-Fermi levels (QFLs) for trapped electrons and holes are created [17]. The QFLs are separated from the equilibrium Fermi level (Fermi level under dark condition) by the factor ΔE_f, which depends on the intensity of the illumination. That is, ΔE_f increases as the illumination intensity increases and for a very high illumination level the QFLs can reach their respective band edges [17]. In the case of a-Si:H TFTs, the γ exponent gradually decreases as the gate bias is swept from negative to positive. Similar behavior of gate bias dependent γ is observed in the case of STC–TIPS-pentacene phototransistors, although the polarity of the gate bias is opposite. However, these models may not be directly applicable to organic semiconductor based TFTs since the charge transport mechanism is different and also the conventional band theory may be not appropriate to

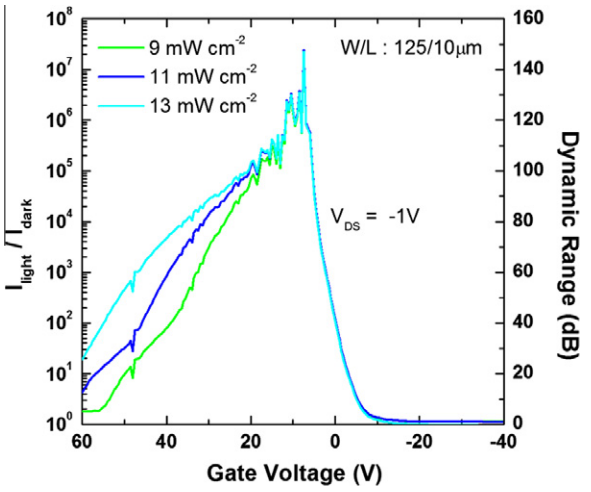

Fig. 4. The dependence of current modulation (I_{light}/I_{dark}) and dynamic range on the illuminated light power density and the gate bias. The dynamic range was calculated from the following equation. (*dynamic range* = 20 log (I_{light}/I_{dark})).

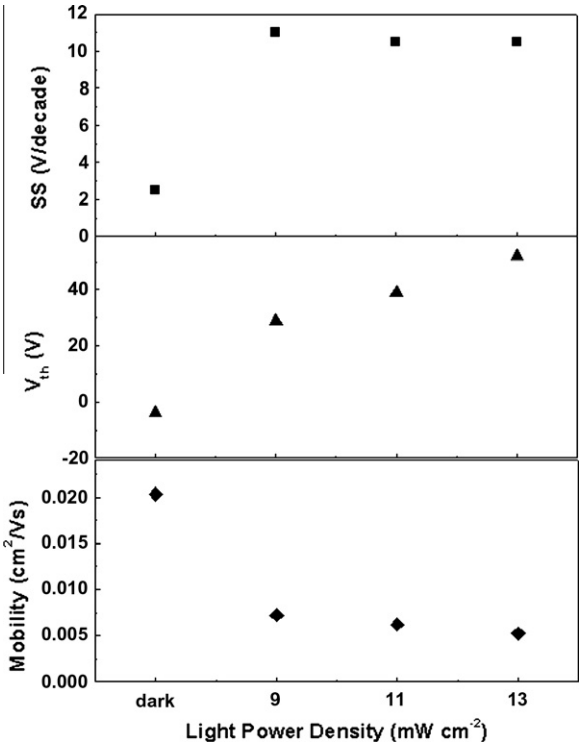

Fig. 5. The variation of field-effect mobility, threshold voltage and subthreshold slope of STC–TIPS-pentacene phototransistor as a function of incident light power density.

explain the conducting behavior of organic semiconductors.

In Fig. 5, the field-effect mobility, V_{th} and subthreshold slope of the phototransistors are shown, as a function of illuminated light power density. The field-effect mobility decreases from 0.021 cm^2/V-s to ~0.005 cm^2/V-s when the device was illuminated and the V_{th} shifts to positive as the power density increases. Also, the subthreshold slope degrades from 2.5 V/decade to ~11 V/decade. It is likely that the dependency of V_{th} on light power density is due to increasing photogenerated excitons and dissociated charged carriers. When the light is illuminated, the photogenerated carriers are formed in the bulk region of the STC–TIPS-pentacene and increase the off-current of the phototransistor resulting in the V_{th} shift. Concerning the continuous decrease of mobility, we notice from Fig. 3b that the on-state drain current decreases as the illuminated light power density increases. Especially at a light power density of 13 mW/cm^2, the drain current is even lower than that measured under dark conditions. From this observation, it is clearly understood that the white-light illumination may be one of the reasons for decreased drain current and mobility. Previously it has been reported that UV irradiation of vacuum deposited pentacene TFTs destroys the crystalline structure of pentacene film by dissociation of pentacene molecules [18]. Since most of the light sources emit at least partly into the UV spectrum, the TIPS-pentacene active layer may be damaged by irradiation by the white-light source.

To clarify the effect of UV irradiation on the electrical and physical characteristics of STC–TIPS-pentacene phototransistor, UV light was irradiated on the device and the results are shown in Fig. 6a. The intensity of irradiated UV light at a distance of 2 cm was ~12.5 mW/cm^2. During the UV exposure, photogenerated excitons are formed as in the case of light illumination and increase the drain current in the off-state. However, dissimilar to white-light illumination, the on-current level is reduced by 2–3 orders of magnitude compared to a fresh device and no gate field modulation is observed. After turning off the UV source the gate field modulation is again observed. However, the on-current level is much lower than for the fresh sample.

As suggested in the literature [18], the TIPS-pentacene film can be damaged seriously by the UV exposure losing its molecular structure, its unique crystal packing structure and its ordering. Fig. 6b shows the X-ray diffraction patterns of spin-coated TIPS-pentacene films before and after UV irradiation. Single crystal TIPS-pentacene has a triclinic structure with unit cell parameters a = 7.5650 Å, b = 7.7500 Å, c = 16.835 Å, α = 89.15°, β = 92.713° and γ = 83.63° [19]. Therefore, the peaks observed at 5.4° correspond to intermolecular spacing of 16.8 Å indicating preferential orientation of the (0 0 1)-axis normal to the surface. While the as-coated TIPS-pentacene film has a polycrystalline structure, the UV-irradiated film typically exhibits amorphous features with no diffraction peaks, which may show that the intense UV irradiation disrupts the molecular order in the film, likely by decomposition of the TIPS-pentacene molecules. Since the carrier mobility in organic semiconductors is closely related to the molecular ordering of the semiconductors [20], the degradation of field-effect mobility and reduced drain current are possibly due to the decomposition of TIPS-pentacene molecules caused by UV irradiation. These results suggest that in order to employ TIPS-pentacene phototransistors as photo-sensing elements, a proper UV-protective

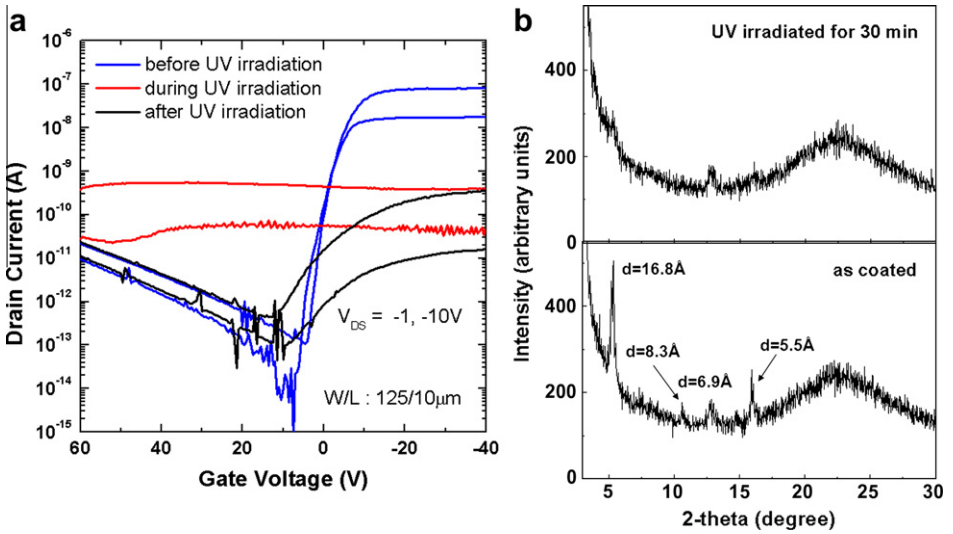

Fig. 6. (a) Effect of UV irradiation on the transfer characteristics of TIPS-pentacene phototransistors. The transfer characteristics were measured before, after and during the UV irradiation. (b) X-ray diffraction patterns ($\theta/2\theta$ mode) of TIPS-pentacene films before and after UV irradiation.

passivation layer should be integrated into the phototransistor to enhance their reliability.

4. Conclusion

We demonstrated highly light-responsive organic phototransistors employing STC electrode structure and ink-jet printed TIPS-pentacene as a photo-sensing active layer. Under a steady-state illumination, the STC–TIPS-pentacene phototransistor showed high current modulation and dynamic range which suggests that the organic phototransistors based on ink-jet printed TIPS-pentacene can be a new promising candidate for the low-cost and high-performance photosensors for digital imaging applications.

References

[1] S.E. Burns, W. Reeves, B.H. Pui, K. Jacobs, S. Siddique, K. Reynolds, M. Banach, D. Barclay, K. Chalmers, N. Cousins, P. Cain, L. Dassas, M. Etchells, C. Hayton, S. Markham, A. Menon, P. Too, C. Ramsdale, J. Herod, K. Saynor, J. Watts, T. von Werne, J. Mills, C.J. Curling, H. Sirringhaus, M.D. McCreary, SID Int. Symp. Digest Tech. Papers 37 (2006) 74.
[2] S.K. Park, J.E. Anthony, D.A. Mourey, T.N. Jackson, Appl. Phys. Lett. 91 (2007) 0563514.
[3] J.B. Chang, V. Liu, V. Subramanian, K. Sivula, C. Luscombe, A. Murphy, J. Liu, J.M.J. Fréchet, J. Appl. Phys. 100 (2006) 014506.
[4] T. Someya, T. Sekitani, S. Iba, Y. Kato, H. Kawaguchi, T. Sakurai, Proc. Natl. Acad. Sci. U.S.A. 101 (2004) 9966.
[5] V. Subramanian, J.M.J. Fréchet, P.C. Chang, D.C. Huang, J.B. Lee, S.E. Molesa, A.R. Murphy, D.R. Redinger, S.K. Volkman, Proc. IEEE 93 (2005) 1330.
[6] M. Mizukami, N. Hirohata, T. Iseki, K. Ohtawara, T. Tada, S. Yagyu, T. Abe, T. Suzuki, Y. Fujisaki, Y. Inoue, S. Tokito, T. Kurita, IEEE Elec. Dev. Lett. 27 (2006) 249.
[7] L. Zhou, S. Park, B. Bai, J. Sun, S.-C. Wu, T.N. Jackson, S. Nelson, D. Freeman, Y. Hong, IEEE Elec. Dev. Lett. 26 (2005) 640.
[8] J.A. Rogers, Z. Bao, K. Baldwin, A. Dodabalapur, B. Crone, V.R. Raju, V. Kuck, H. Katz, K. Amundson, J. Ewing, P. Drzaic, Proc. Natl. Acad. Sci. USA 98 (2001) 4835.
[9] K.S. Narayana, N. Kumar, Appl. Phys. Lett. 79 (2001) 1891.
[10] G. Yu, G. Srdanov, J. Wang, H. Wang, Y. Cao, A.J. Heeger, Synth. Met. 111–112 (2000) 133.
[11] G. Yu, Y. Cao, J. Wang, J. McElvain, A.J. Heeger, Synth. Met. 102 (1999) 904.
[12] S.R. Forrest, IEEE J. Sel. Top. Quant. 6 (2000) 1072.
[13] M.C. Hamilton, J. Kanicki, IEEE J. Sel. Top. Quant. 10 (2004) 840.
[14] Y.H. Kim, S.M. Han, W. Lee, M.K. Han, Y.U. Lee, J.I. Han, Appl. Phys. Lett. 91 (2007) 042113.
[15] T. Tokumoto, J.S. Brooks, R. Clinite, X. Wei, J.E. Anthony, D.L. Eaton, S.R. Parkin, J. Appl. Phys. 92 (2002) 5208.
[16] R.E.I. Schropp, T. Franke, J.F. Verwey, J. Non-Cryst. Solids 90 (1987) 199.
[17] J.G. Simmons, G.W. Taylor, Phys. Rev. B 4 (1971) 502.
[18] W.J. Kim, W.H. Koo, S.J. Jo, C.S. Kim, H.K. Baik, D.K. Hwang, K. Lee, J.H. Kim, S. Im, Electrochem. Solid-State Lett. 9 (2006) G251.
[19] J.E. Anthony, J.S. Brooks, D.L. Eaton, S.R. Parkin, J. Am. Chem. Soc. 123 (2001) 9482.
[20] C.R. Newman, R.J. Chesterfield, M.J. Panzer, C.D. Frisbie, J. Appl. Phys. 98 (2005) 084506.

Here, we report a bias-assisted natural-drying method in film drop-casting for the formation of organic interfaces with unusual photocurrent NDR behaviors. We use PEDT:PSSH (poly(3,4-ethelynedioxythiophene:poly(styrene sulfonic acid)) as a model organic. PEDT:PSSH is a typical p-type conducting polymer blend widely used as a hole-injection layer in organic photovoltaics [6–12]. It is a phase-segregated blend due to the different water-solubility of the PEDT and PSSH phases [18–21]. As illustrated in Scheme 1, an aqueous drop of PEDT:PSSH blend is cast onto a p-type Si substrate, and the drop is then left in the ambient to dry naturally (~3 h) for the formation of the PEDT:PSSH bulk film. In a preceding work [22], we have reported that such slow natural-drying allows for phase segregation and self-organization of the blend, such that a water-insoluble interfacial layer is formed between the bulk film and substrate after the drying of the drop (Scheme 1b). In this work, we further apply a negative bias to the Si substrate simultaneously during the natural-drying of the drop. It is observed that the substrate bias can significantly modify the electronic configuration of the resultant interfacial layer, and consequently, an organic hetero-junction is formed between the bulk film and interfacial layer. The embedded hetero-junction not only enhances the $e_p - h_p$ pair separation, but also enables the storage and extraction of photocarriers. Therefore, photocurrent with strong NDR behavior is achieved for an organic optoelectronic device.

The experimental details for film preparation and photocurrent measurements are provided in Supporting information (SI). Fig. 1a displays a typical photo of the PEDT:PSSH bulk film (~1.0 μm thick) drop-cast on Si using a substrate bias (SB) of −20 V (SI-i). The bulk film is then dissolved by water rinsing to expose the interfacial layer, and when examined by the naked eyes, no feature could be observed in the interfacial area in Fig. 1b. However, our AFM [23] (atomic force microscope, SI-ii) measurements revealed the formation of nanosegregants in the interfacial area. As shown in Fig. 1c, the bare Si surface is very flat with a RMS roughness of <0.15 nm, while the interfacial area is composed of nanosegregants with an average height of ~2.5 nm (Fig. 1d). The nanosegregants are water-insoluble and superhydrophilic, similar to those prepared without SB in our preceding work [22]. Fig. 1e compares the S2p core-level spectra collected using PES [24] (photoelectron spectroscopy, SI-ii) for the bulk film and interfacial layer, respectively. The S2p spectrum of the bulk film consists of two peaks at 163.5 and 167.8 eV, which correspond to the PEDT and PSSH phases, respectively [18,20,21]. The S2p spectrum of the interfacial layer also consists of the PEDT and PSSH phases, but the peak intensity is relatively weak, and the peaks are shifted towards higher binding energy by ~1.6 eV. We attribute the shift to the charging of the interfacial layer, as similar shifts were also systematically observed for other core levels such as C1s and O1s. The above AFM and PES results are almost identical to those of the interfacial layer prepared earlier [22] without SB. Indeed, the AFM images and PES spectra of interfacial layers prepared using SB = −5, −10, and −15 V, respectively, are all similar to that shown in Fig. 1c–e. This indicates that SB does not affect the morphology and chemical composition of the interfacial layer. However, the secondary electron (SE) emission results in Fig. 1f–h reveal the effect of SB on the electronic structure of the interfacial layer. Fig. 1f displays the SE peak of the bulk film. A work function of W_F = 5.1 eV is obtained, and it is in good agreement with that reported for p-type PEDT:PSSH films [25]. The SE emission of the bulk film does not depend on the SB, because films cast using different SBs all exhibit the same SE spectrum as that shown in Fig. 1f. Fig. 1g compares the SE peaks of interfacial layers formed under SB = 0, −10, −15, and −20 V, respectively. It can be seen these interfacial layers show a lower W_F of 4.5 eV. Since charging has been observed in Fig. 1e for the interfacial layer, and the charging can result in a lower W_F by shifting the SE peak to low kinetic energy, so the value of W_F = 4.5 eV cannot be unambiguously used for the interfacial layers. However, the shape and width of the SE peaks are usually not affected by sample charging, and a clear dependence of peak width on SB can be identified in Fig. 1g. For example, the FWHM (full width at half maximum) of the sample formed without bias is only 0.5 eV, while the FWHM increases significantly when the SB is increased. The FWHM is measured to be 0.8, 1.3, and 1.8 eV for interfacial layers cast with a bias of −10, −15, and −20 V, respectively (Fig. 1g). Since SEs are located at the conduction band edge, the width of the SE peak often reflects the energy dispersion of the unoccupied states: the narrower the peak, the more discrete the electronic states; the wider the peak, the more dispersive the energy levels [24]. The increase of FWHM from 0.5 to 1.8 eV indicates that the SB can induce significant amount of electronic states in the interfacial layer. As discussed below in Figs. 2 and 3, these bias-induced empty states provide the necessary host states for the accommodation of photocarriers, and are thus responsible for the photocurrent NDR reported in this work. The dependence of FWHM on SB is

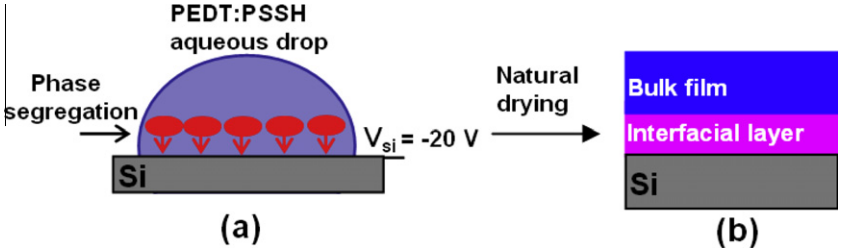

Scheme 1. (a) A PEDT:PSSH aqueous drop is cast onto a Si substrate to which a negative bias of V_{Si} = −20 V is applied. (b) Interfacial layer formation between the Si substrate and PEDT:PSSH bulk film after the natural-drying of the aqueous drop.

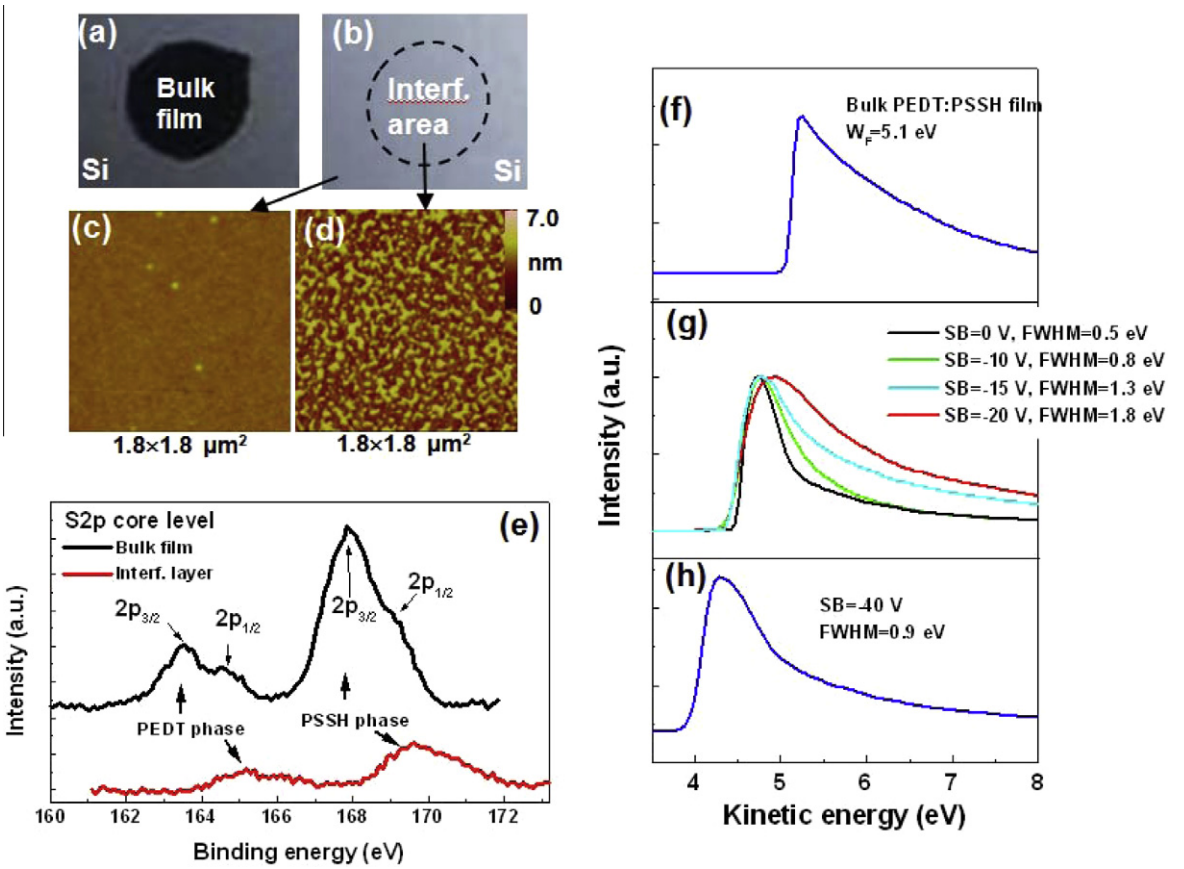

Fig. 1. Optical photos of the bulk film (a) and interfacial layer (b), respectively. AFM morphology images of the bare surface (c) and interfacial area (d) shown in (b). (e) S2p spectra of the bulk film and interfacial layer, respectively. SE spectrum of the bulk film (f) interfacial layers (g–h) prepared using different substrate bias.

not monotonous: when a larger bias of −40 V is used, the FWHM of the SE peak is reduced to 0.9 eV, and the low energy cut-off is shifted to 4.1 eV (Fig. 1h).

Fig. 2a compares the photocurrent I_{ph} and dark-current I_d collected for an ITO/PEDT:PSSH/Si sample device (see the inset of Fig. 2a) by scanning the Si electrode voltage from −25 to 25 V at a scan rate of 1.0 V/s (see SI-iii and Ref. [26] for experimental). The PEDT:PSSH film in the sample device was drop-cast with a SB of −20 V, and therefore there are bias-induced host states in the interfacial layer. It can be seen the I_d is rectifying, with a much higher current in the positive voltage region. In Fig. 2a, the photocurrent is also observed in the positive voltage region, and the I_{ph} exhibits a pronounced peak, in sharp contrast to the monotonous I_d. The current peak is the so-called NDR peak previously observed only for intrinsic or dark-current [13–17]. This NDR characteristic is better viewed by subtracting I_d from I_{ph} to obtain the net photocurrent $(I_{ph} - I_d)$. As displayed in Fig. 2b, the $(I_{ph} - I_d)$ difference current is dominated by the sharp NDR peak with a peak-to-valley ratio (PVR) of ~700. Fig. 2c displays the I_{ph} and I_d collected for a control device in which the PEDT:PSSH film was drop-cast without SB. It is seen from I_d that the control device is not as rectifying as the sample device. In addition, photocurrent is observed in both the positive and negative voltage region, and most importantly, the I_{ph} does not show any NDR behavior. Since there is no bias-induced host states (Fig. 1g) in the interfacial layer of the control device, the I_{ph} NDR observed in Fig. 2a and b can be attributed to the dispersive host states induced by the SB during film drop-casting. Fig. 2d displays the I_{ph} of the sample device in Fig. 2a using different voltage scan rate of 0.17–4.0 V/s, respectively. The corresponding $(I_{ph} - I_d)$ net current in the positive voltage region is plotted in Fig. 2e. It is seen that the NDR peak shifts to higher voltage positions with increasing scan rate.

In Fig. 3, we propose a mechanism, involving the separation, storage and extraction of photocarriers, to explain the NDR behavior observed in Fig. 2. As shown in Fig. 1e, the interfacial layer causes charging in PES measurements, and is therefore more insulating compared to the bulk film. So there is a hetero-junction formed between the insulating interfacial layer and conducting bulk film. Since the bulk film is a typical p-type semiconductor, and the interfacial layer is "de-doped" as judged by its insulating nature, the hetero-junction can thus be treated as an organic p–n junction for the convenience of discussion (Fig. 3a). It is known in photovoltaics that the build-in field E_{in} of the p–n junction can attract photoelectrons from the p-side to the n-side, thus achieving the separation of

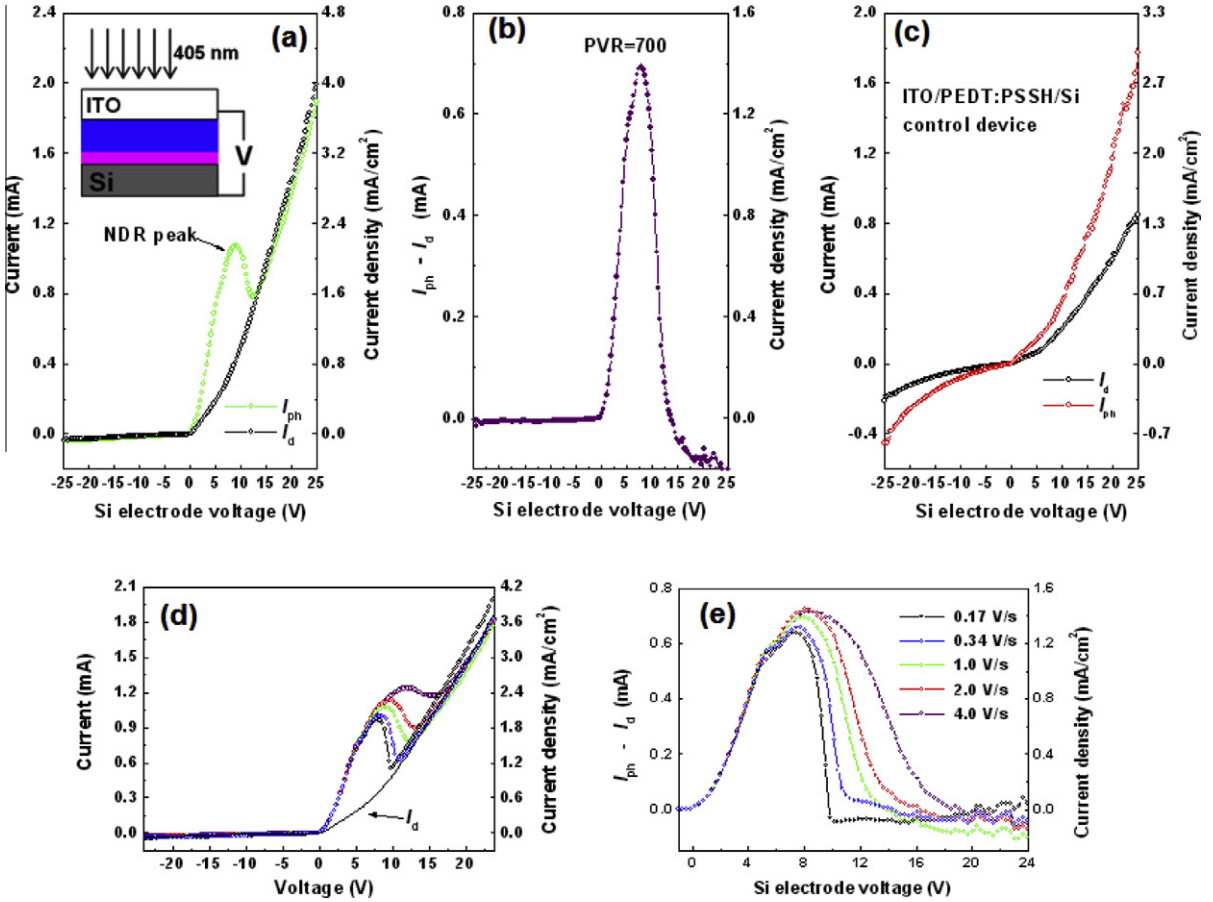

Fig. 2. (a) I_{ph} and I_d of the sample device shown in the inset. (b) The corresponding ($I_{ph} - I_d$) difference current of (a). (c) I_{ph} and I_d of the control device. (d) I_{ph} of the sample device in (a) collected using different voltage scan rates. (e) The corresponding ($I_{ph} - I_d$) difference current of (d).

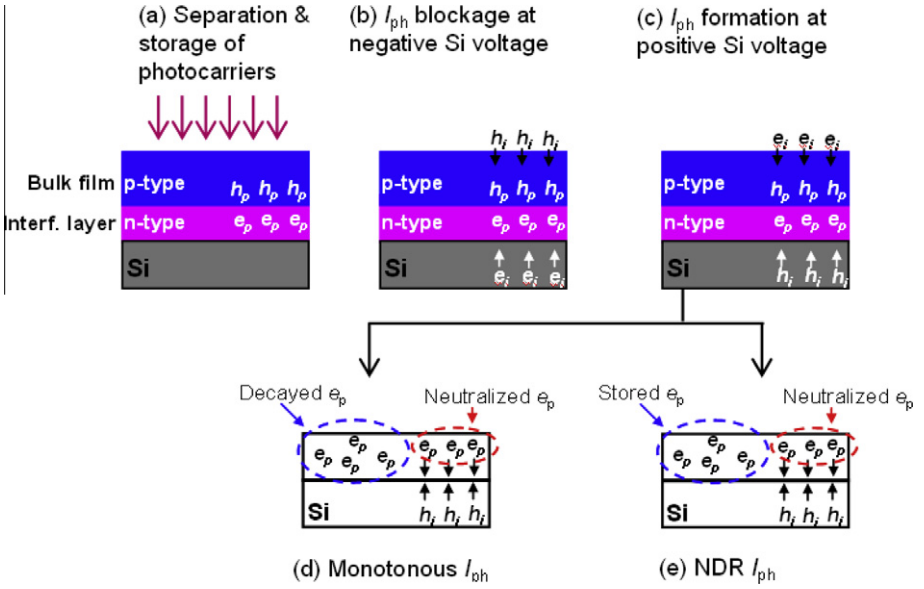

Fig. 3. Proposed I_{ph} NDR mechanism: (a) $e_p - h_p$ pair separation by the p–n junction; (b) blockage of photocurrent at negative Si electrode voltage; (c) neutralization of photocarriers at positive Si electrode voltage; (d) formation of monotonous photocurrent due to the fast decay of excess photocarriers; (e) formation of NDR due to the storage of unneutralized photocarriers.

$e_p - h_p$ pairs [5]. When the sample device is photo-illuminated, $e_p - h_p$ pairs are generated in the top bulk film. Due to the E_{in} of the p–n junction, the e_p is attracted to the n-type interfacial layer, while the h_p is kept in the p-type bulk film (Fig. 3a). Moreover, the bias-induced dispersive empty states at the junction can act as host states to accommodate and store the photoelectrons. When the Si electrode voltage is negative, intrinsic electrons e_i are injected from Si to the interfacial layer, while intrinsic holes h_i are injected from the top ITO electrode to the bulk film (Fig. 3b). Due to the Coulomb repulsion between e_i and e_p (h_i and h_p), photocurrent conduction is hindered. This is why no I_{ph} is observed in the negative voltage region in Fig. 2a. When the voltage is positive, h_i and e_i are injected into the interfacial layer and bulk film, respectively (Fig. 3c). The neutralization of h_i with e_p (and e_i with h_p) contributes additional current, thus leading to the large photocurrent in the positive voltage region in Fig. 2a. Note that in Fig. 2a the I_{ph} does not increase as a monotonous function of voltage, but instead shows a NDR peak. This unusual characteristic reflects the photocarrier-storage function of the host states. Under our experimental condition of steady photo-illumination, there is a fixed number of mobile photocarriers due to the dynamic balance between the generation and decay of photocarriers. At a low voltage, only a limited number of h_i are injected from Si (Fig. 3d), and they neutralize with the same number of e_p. The excess e_p are decayed due to their short lifetime, and thus have no contribution to I_{ph}. When the voltage is increased, more h_i are injected, and more e_p are neutralized. So the I_{ph} increases stepwise as a function of the injection voltage, as observed for the control device in Fig. 2c. In the case of the sample device with host electronic states, the excess e_p are stored in the host states, and they have a long lifetime (Fig. 3d). At a low voltage, they are not immediately neutralized because there is not enough h_i injected from Si. But these excess e_p remain mobile, and can be neutralized by h_i injected later at a higher voltage. When the voltage is increased sufficiently high, all the stored e_p are neutralized, and accordingly, the I_{ph} exhibits a peak. From this point onwards, the high external voltage overcomes the E_{in} of the organic p–n junction, such that the junction ceases its function of $e_p - h_p$ pair separation, and therefore no photocurrent can be further generated. This is why in Fig. 2a the I_{ph} drops to the level of I_d after the NDR peak. We also observed an open circuit voltage of 312 mV, and a short circuit current (flowing from ITO to Si) of 11.0 μA for the sample device. The direction of the voltage and current confirms the polarity of the embedded p–n junction proposed in Fig. 3. In Fig. 2a, the NDR is observed only for I_{ph}, but not for I_d. This is because the I_d is governed by the thermoionic emission of intrinsic carriers with a monotonous dependence on the electrode voltage. While for I_{ph}, it is based on the organic p–n junction and host states for photocarrier separation and storage.

It is possible to derive the density of the host states using the results shown in Fig. 2d and e. In Fig. 2e, when the scan rate is slow, sufficient time is allowed at each voltage step for the extraction of stored photocarriers, so more photocarriers are extracted, and the extraction completes at a lower voltage. A fast scan rate, on the other hand, leads to incomplete photocarrier collection, and consequently the NDR peak appearances at a higher voltage. At a slow rate of 0.17 V/s, the NDR peak completes in a duration of $t \approx 60$ s (Fig. 2e), and the corresponding number of extracted photocarriers is estimated to be 1.4×10^{14} by integrating the $(I_{ph} - I_d) \sim t$ plot (data not shown). This represents the maximum number of extractable photocarriers, because the NDR peak obtained using even slower rates (e.g., $\leqslant$0.02 V/s) is almost identical to that observed using 0.17 V/s rate. In the case of fast scan rate of 4.0 V/s, the completion of the NDR peak only takes 5 s, and the number of extracted photocarriers is 1.1×10^{13}, which is only 1/10 of that extracted at 0.17 V/s scan rate. The maximum number of 1.4×10^{14} photocarriers corresponds to an effective density of $7.0 \times 10^{14}\,\mathrm{cm}^{-2}$ estimated for the bias-induced host states. The formation of NDR is dependent on the polarity and magnitude of the SB during drop-casting, and can only be achieved under suitable biases which facilitate the formation of host electronic states (Fig. 4). Fig. 4 displays the evolution of I_{ph} collected for PEDT:PSSH films prepared using different substrate biases. Here, an identical bias duration of 3 h was kept while biases different in magnitude and polarity were used, respectively, to cast the PEDT:PSSH films. When the bias is zero (Fig. 4a), the I_{ph} is monotonous, and no NDR peak is observable. At a bias of −10 V (see Fig. 4b), the I_{ph} exhibits a turning point T which divides the I_{ph} into a high-slope region (0–3.3 V) and a low-slope region (3.3–15 V), but no clear NDR peak is formed. When the bias is increased to −15 V (see Fig. 4c), the NDR peak is weak but identifiable, and the NDR peak is fully developed when the bias is further increased to −20 V (see Fig. 4d). The above observation arises from the bias-induced host states discussed in Fig. 1g: when the bias is zero, the interfacial host states necessary for NDR are not formed, so the I_{ph} is monotonous. Increasing the substrate bias leads to the formation of more host states, and thus the photocurrent NDR develops accordingly. However, if the bias is too high (e.g., −40 V, see Fig. 4e), the NDR would disappear, and the I_{ph} becomes monotonous again. This observation coincides with the SE peak in Fig. 1h which shows a decrease in the dispersion of the empty states at a substrate bias of −40 V. For comparison, positive substrate biases in the range of 0–40 V were also used for film casting, but no NDR was observed for films thus prepared. Therefore, the NDR is dependent on the polarity and magnitude of the substrate bias, and can only be achieved under suitable biases which facilitate the formation of host electronic states. The NDR behavior is very stable and reproducible as demonstrated in SI-iv, and is a permanent feature inherent to the interfacial layer formed by the bias-assisted natural-drying of films. In this method, the PEDT:PSSH drop is allowed to dry naturally, such that the phase segregation and reorganization can proceed under electrostatic and thermodynamic equilibrium conditions. Such a process facilitates the formation of interfaces with the most stable configuration, as sufficient relaxation time is available during the interface formation. While in the conventional fast spin-coating method, the organic is almost "quenched" from its solution configuration onto the substrate without a chance of rearrangement. Indeed, some recent works

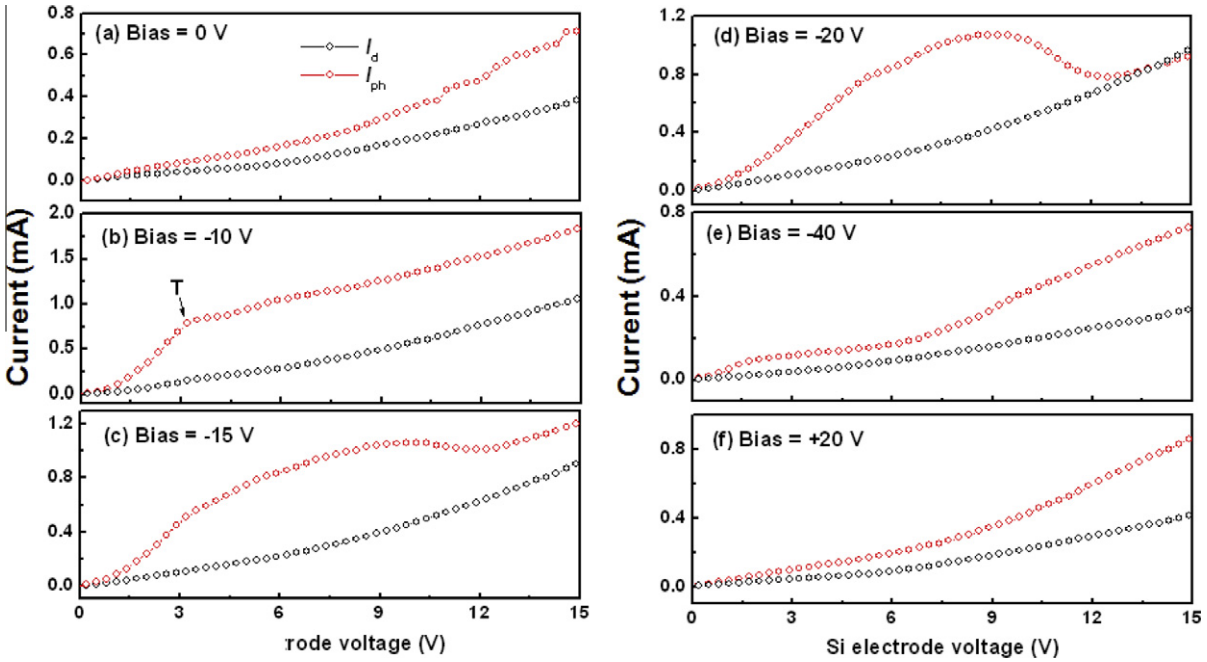

Fig. 4. Evolution of I_{ph} collected for PEDT:PSSH films drop-cast with a substrate bias of 0, −10, −15, −20, −40, and +20 V, respectively. An identical bias duration of 3 h was used for the drop-casting of the above samples. The I_{ph} and I_d were obtained by scanning the Si electrode voltage from −25 to 25 V with at a rate of 1.0 V/s. Only the 0–15 V region with the NDR peak is shown.

have pointed out that slow-drying is advantageous over fast-drying in facilitating the desired phase segregation and self-organization of photovoltaic organic blends [9,10].

In conclusion, we have demonstrated a bias-assisted natural-drying method for the formation of embedded organic hetero-junction and host electronic states. This wet method is simple, economical, and extendable to other organic systems. The hetero-junction and host states allow for the separation and storage of photocarriers, and thus photocurrent with NDR characteristic is achieved. The mechanism of the NDR and its dependence on the drop-casting substrate bias is discussed. Both the method for organic interface formation and the resulting photocurrent NDR behavior could open up new applications in organic optoelectronics.

Acknowledgement

This work is supported by NUS Nanoscience and Nanotechnology Initiative (NUSNNI), National University of Singapore.

Appendix A. Supplementary material

Supplementary data associated with this article can be found, in the online version, at doi:10.1016/j.orgel.2010.06.014.

References

[1] N. Koch, ChemPhysChem 8 (2007) 1438.
[2] C.J. Brabec, N.S. Sariciftci, J.C. Hummelen, Adv. Funct. Mater. 11 (2001) 15.
[3] J. Peet, M.L. Senatore, A.J. Heeger, G.C. Bazan, Adv. Mater. 21 (2009) 1521.
[4] M.C. Scharber, D. Wuhlbacher, M. Koppe, P. Denk, C. Waldauf, A.J. Heeger, C.L. Brabec, Adv. Mater. 18 (2006) 789.
[5] J.F. Rabek, Photochemistry and Photophysics V. II, CRC Press Inc., 1990.
[6] P. Peumans, S. Uchida, S.R. Forrest, Nature 425 (2003) 158.
[7] F. Yang, M. Shtein, S.R. Forrest, Nat. Mater. 4 (2005) 37.
[8] G. Li, V. Shrotriya, J.S. Huang, Y. Yao, T. Moriarty, K. Emery, Y. Yang, Nat. Mater. 4 (2005) 864.
[9] M. Campoy-Quiles, T. Ferenczi, T. Agostinelli, et al., Nat. Mater. 7 (2008) 158.
[10] C.S. Kim, L.L. Tinker, B.F. DiSalle, E.D. Gomez, S. Lee, S. Bernhard, Y.-L. Loo, Adv. Mater. 21 (2009) 3110.
[11] S. Sista, M.-H. Park, Z. Hong, Y. Wu, J. Hou, W.L. Kwan, G. Li, Y. Yang, Adv. Mater. 21 (2009) 1.
[12] J.Y. Kim, K. Lee, N.E. Coates, D. Moses, T.Q. Nguyen, M. Dante, A.J. Heeger, Science 317 (2007) 222.
[13] L.P. Ma, S.M. Pyo, J.Y. Ouyang, Q.F. Yu, Y. Yang, Appl. Phys. Lett. 82 (2003) 1419.
[14] R.J. Tseng, J. Ouyang, C.-W. Chu, J. Huang, Y. Yang, Appl. Phys. Lett. 88 (2006) 123506.
[15] J.C. Scott, L.D. Bozano, Adv. Mater. 19 (2007) 1452.
[16] X.N. Xie, X. Gao, Y. Wang, J. Wang, K.P. Loh, A.T.S. Wee, Appl. Phys. Lett. 95 (2009) 063301.
[17] X.N. Xie, J. Wang, K.P. Loh, A.T.S. Wee, Appl. Phys. Lett. 95 (2009) 203302.
[18] G. Greczynski, Th. Kugler, W.R. Salaneck, Thin Solid Films 354 (1999) 129.
[19] A.M. Nardes, M. Kemerink, R.A.J. Janssen, et al., Adv. Mater. 19 (2007) 1196.
[20] X. Crispin, S. Marciniak, W. Osikowicz, et al., J. Polym. Sci. Part B: Polym. Phys. 41 (2003) 2561.
[21] G. Greczynski, Th. Kugler, M. Keil, et al., J. Electron Spectrosc. Relat. Phenom. 121 (2001) 1.
[22] X.N. Xie, X. Lim, Y. Wang, X. Gao, K.K. Lee, C.H. Sow, X. Chen, K.P. Loh, A.T.S. Wee, Macromol. Chem. Phys. (2010), in press.
[23] X.N. Xie, H.J. Chung, A.A. Bettiol, C.H. Sow, A.T.S. Wee, Adv. Mater. 17 (2005) 1386.
[24] X.N. Xie, X.Y. Gao, D.C. Qi, Y.L. Xie, L. Shen, S.-W. Yang, C.H. Sow, A.T.S. Wee, ACS Nano 3 (2009) 2722.
[25] M.P. de Jong, A.W.D. van der Gon, X. Crispin, W. Osikowicz, W.R. Salaneck, J. Chem. Phys. 118 (2003) 6495.
[26] X.N. Xie, Y.L. Xie, X. Gao, C.H. Sow, A.T.S. Wee, Adv. Mater. 21 (2009) 3016.

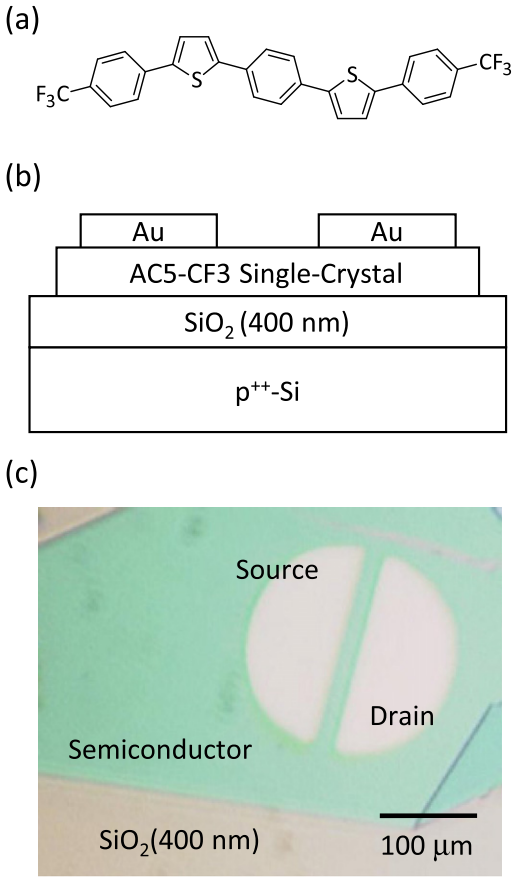

Fig. 1. (a) Chemical structure of AC5-CF3, (b) schematic cross-sectional structure and (c) example top-view photograph of FET with an AC5-CF3 single-crystal.

[22], and synthesized AC5-CF3 as shown in the Fig. 1a based on a report by Katz et al. [23]. In that article, the authors reported that a material similar to AC5-CF3 but without a CF_3 group worked as a p-type FET material with a field-effect hole mobility of 0.04 $cm^2\,V^{-1}\,s^{-1}$ at best. Here, we demonstrate that AC5-CF3 could be a potential candidate for organic n-type semiconductors that have high electron mobility. Note that Hotta et al. recently reported the synthesis of the same material [24], formation of its crystal [25], the crystal structure and its field-effect transistors (FETs) [26]. However, Hotta et al. reported that AC-CF3 single-crystal FETs showed n-type behavior and that the electron mobility of the FETs ranged from 1.6 to 3.9×10^{-2} $cm^2\,V^{-1}\,s^{-1}$. Here, we report the performance of optimally fabricated AC5-CF3 TFTs and single-crystal FETs, and demonstrate that AC-CF3 will be able to be utilised as an n-type organic transistor material with high mobility.

2. Material and methods

2.1. Material synthesis and characterisation

AC5-CF3 was synthesized by the Stille coupling reaction of 4-trifluoromethyl benzene with the corresponding stannyl reagent in the presence of Pd_2(*trans*, *trans*-dibenzylidene acetone)$_3$ and (*tert*-butyl)$_3$P in dimethylformamide with microwave heating. The synthetic root was slightly different as per a report by Katagiri et al. [24]. We confirmed its structure by matrix-assisted laser desorption/ionization (MALDI) time-of-flight (TOF) mass spectroscopy (Perspective Biosystems, Voyager-DE PRO) and ^{1}H NMR (Bruker AVANCE 400)). We used the material after sublimating it in a pure argon gas flow, and prepared AC5-CF3 single-crystals from its vapour in a chamber filled with nitrogen adding 10 vol.% hydrogen. Details of this method have been described elsewhere [27].

The ionization potential (I_p) of AC5-CF3 was determined by photoelectron emission yield spectroscopy with Riken–Keiki AC-2 at an irradiation light power of 10 nW cm^{-2}. The sample films of the organic materials were prepared by vacuum evaporation in the same conditions as can be used to fabricate TFTs on glass substrates whose surface was covered with indium thin oxide to prevent charging. We determined the lowest unoccupied molecular orbital (LUMO) level of AC5-CF3 from the difference between I_p and the band gap that was estimated from the absorption edge of 100-nm-thick AC5-CF3 thin film deposited on a quartz substrate.

X-ray diffraction (XRD) patterns were measured with a Rigaku Rotaflex using Cu Kα radiation at $\theta/2\theta$ geometry. The sample films, all with thicknesses 100 nm, were evaporated onto silicon wafers with SiO_2 in the same conditions as can be used for TFT fabrication. The X-ray was generated from a 150-mA electron beam accelerated at 40 kV. The crystal structure of AC5-CF3 was analyzed with a Bruker-AXS APEX II. We prepared the crystal for analysis from the vapour phase.

2.2. Device fabrications and measurements

AC5-CF3 FETs with a single-crystal of AC5-CF3 were fabricated as follows. A crystal was placed on a silicon wafer that had a 400-nm-thick thermally grown silicon dioxide layer as a gate insulator. Without treating the surface of the gate insulator, we simply washed the substrates with 2-propanol. After placing the crystal, we deposited gold electrodes on the source and drain electrodes on the crystal through a shadow mask. Channel length and width of the transistors were 25 and 200 μm, respectively.

We also prepared thin-film transistors using AC5-CF3 by depositing AC5-CF3 on a silicon wafer with a 200-nm-thick SiO_2 layer through thermal evaporation. We kept temperature of the substrates at a temperature in a range from room temperature to 120 °C during the deposition. The thickness of AC5-CF3 thin film was 60 nm. Finally, we prepared source and drain electrodes on the thin film by thermal evaporation of gold. Channels of the thin-film transistors were made with another shadow mask. We varied the channel length of the thin-film transistors from 30 to 100 μm, and kept the width of all the TFTs constant at 2000 μm. An Agilent semiconductor parameter analyzer (B1500A) or a pair of two Keithley source meters (2410) recorded characteristics of the transistors in a probe station (Measure Jig, MJ-10) under vacuum at room temperature.

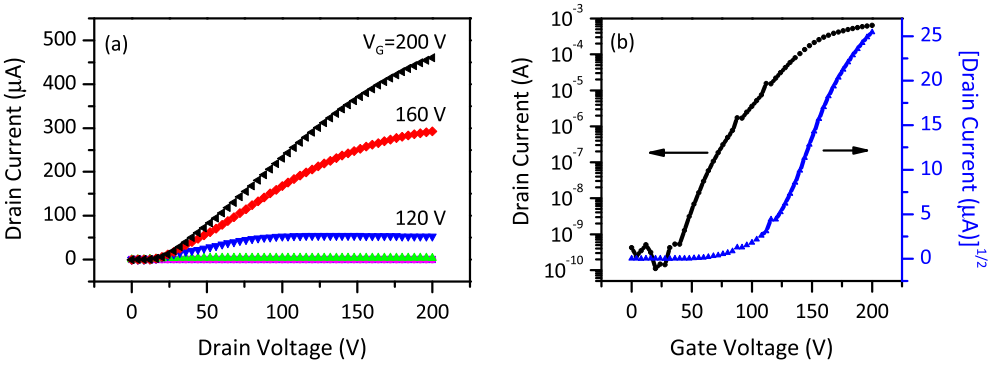

Fig. 2. (a) $I_D - V_D$ and (b) $I_D - V_G$ characteristics of AC5-CF3 single-crystal FET. We measured the $I_D - V_G$ curves at V_D of 200 V.

3. Results and discussion

Fig. 1c shows a photograph of AC5-CF3 single-crystal FET prepared by fixing a single-crystal of AC5-CF3 on silicon wafer, which has a thermally grown 400-nm-thick silicon dioxide layer, as a gate insulator. Fig. 1b shows the schematic cross-sectional structure of the FET; the configuration of the electrodes is the so-called top contact and bottom gate configuration. The crystal seems to uniformly contact the insulator as there were no obvious voids or defects in the area of the crystal seen in the photograph, and hence, the FET device should work well.

Fig. 2a shows drain current versus drain voltage ($I_D - V_D$) characteristics of AC5-CF3 single-crystal FET at several different gate voltages (V_G). As clearly shown in the figure, the device works as an n-type FET, and this means that AC5-CF3 single-crystal is an n-type semiconducting material in which electrons behave as charge carriers. The drain current at a low V_D region (below 20 V) was limited, and thus we could not observe the linear behavior. The current limitation at the low V_D region probably resulted from the configuration of the source and drain electrodes for the device. In short, similar current limitations are frequently observed in the case of the so-called top contact FETs in general, and/or the LUMO level of AC5-CF3 at 3.1 eV [28] results in a slightly large electron injection barrier from the gold source electrode to the semiconductor. However, the $I_D - V_D$ characteristics exhibited well-defined saturation behavior. Fig. 2b shows $I_D - V_G$ and the square root of $I_D - V_G$ characteristic of the FET at a drain voltage of 200 V. We obtained the field-effect mobility (μ_{FE}) of an electron in AC5-CF3 single-crystal FET from saturated drain currents ($I_{D,sat}$) based on Fig. 2b using the following equation [29]:

$$I_{D,sat} = W/2LC_i\mu_{FE}(V_G - V_T)^2 \quad (1)$$

where W and L are width and length of the channel, respectively, and C_i and V_T are specific capacitance of the gate dielectric and the threshold voltage, respectively. The obtained mobility was as high as 3.1 $cm^2\,V^{-1}\,s^{-1}$. The field-effect mobility of electrons of 3.1 $cm^2\,V^{-1}\,s^{-1}$ is higher compared to other highly mobile electrons in organic semiconductors that have been already reported [17,18,30]. This means that AC5-CF3 should be a potential candidate for n-type organic transistors. Note that the high operation voltage of 200 V probably is a result of the rather thick (400 nm) SiO_2 layer as gate insulator.

Fig. 3a shows XRD pattern of the FET with mobility of 3.1 $cm^2\,V^{-1}\,s^{-1}$. We can observe several peaks whose width is very narrow; the full width at half maximum (FWHM) of a peak at 2θ of 10.76° is only 0.09°. All the peaks result from a reflection by the *c*-axis; they are first-order and other higher-order diffractions as assigned in the figure. This indicates that the crystal is of high quality and on the substrate in which the normal direction corresponds with the direction of the *c*-axis. As shown in Fig. 4, the molecular interactions due to π-electrons appear to be stronger in the *ab* plane than in other planes, and consequently, charge carriers move smoothly in the *ab* plane. The high quality of the crystal also enhances the carrier transport in the crystal. As a result, the FET device showed a high electron mobility, which was larger than twice of a mobility in a very recent report on AC5-CF3 single-crystal FETs [31].

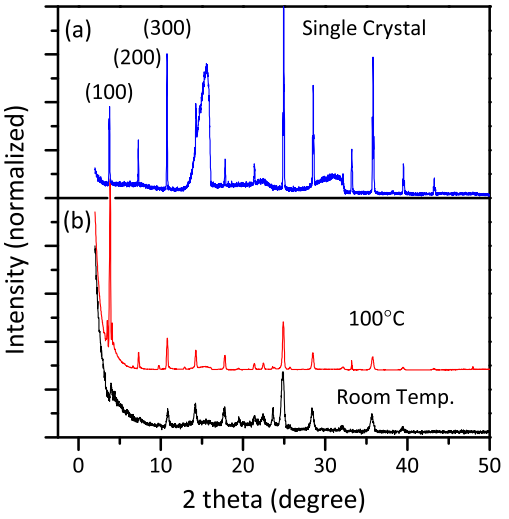

Fig. 3. (a) X-ray diffraction pattern of AC5-CF3 single-crystal that was used for the FET with electron mobility of 3.1 $cm^2\,V^{-1}\,s^{-1}$. (b) X-ray diffraction patterns of AC5-CF3 thin films deposited at different substrate temperatures.

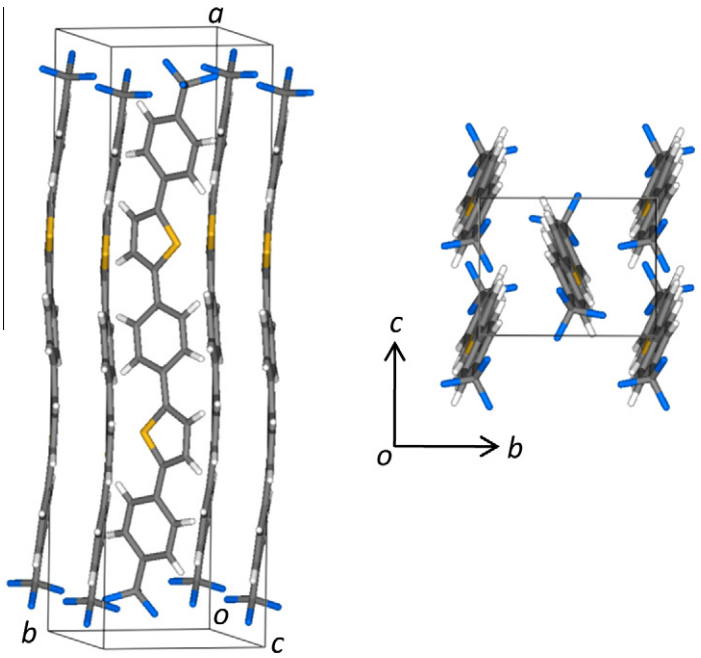

Fig. 4. Crystal structure of AC5-CF3. Images on the left and right are side and top-views, respectively. Crystal structure is as follows: crystal system: monoclinic; space group: $P2_1/c$; number of molecules in cell = 2; cell parameters: $a = 25.070(9)$ Å, $b = 7.354(3)$ Å, $c = 5.742(2)$ Å, $\alpha = \gamma = 90°$ and $\beta = 94.327(5)°$. CCDC 780290 contains the supplementary crystallographic data for this paper. These data can be obtained free of charge from The Cambridge Crystallographic Data Centre via www.ccdc.cam.ac.uk/data_request/cif.

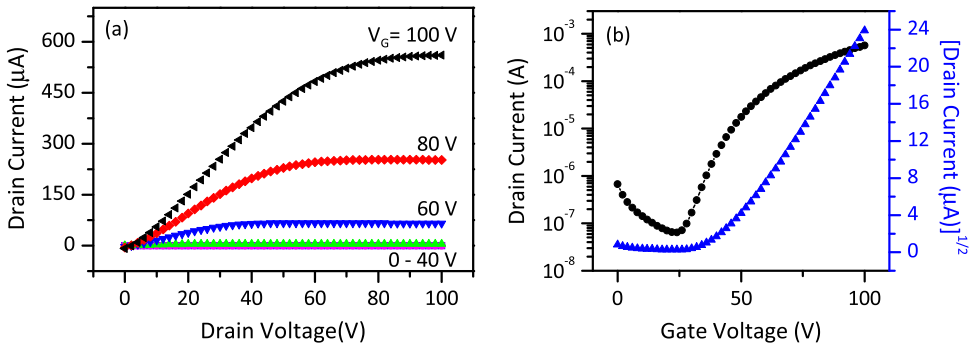

Fig. 5. (a) $I_D - V_D$ and (b) $I_D - V_G$ characteristics of AC5-CF3 thin-film transistor whose channel length is 50 μm, where AC5-CF3 thin film was deposited at a substrate temperature of 100 °C.

We demonstrated above that AC5-CF3 is a potential candidate for high mobility n-type organic semiconductors for transistors from the results of the AC5-CF3 single-crystal FET. However, mobility in thin-film states not a single-crystalline state should be more important from the viewpoint of practical use because organic transistors have received a lot of interests in the field of large-area and/or flexible electronic devices. Consequently, we describe the characteristics of thin-film transistors based on AC5-CF3 in the following paragraphs. Fig. 5a shows an example curve set of the output characteristic of AC5-CF3 thin-film transistor, where we deposited AC5-CF3 on the substrate at a temperature of 100 °C. Here, we employed Si wafers with a thin (200 nm) SiO_2 layer to reduce the operation voltage. The figure clearly shows that the device worked as an n-type TFT. Fig. 5b shows the transfer curve of TFT and also shows the square root of I_D versus V_G plot at a drain voltage of 100 V. We determined the field-effect mobility of the device from the slope of the root I_D versus V_G curve using Eq. (1); the mobility was 0.60 $cm^2\ V^{-1}\ s^{-1}$. We fabricated six TFTs under the same condition, and the average mobility was $0.55 \pm 0.05\ cm^2\ V^{-1}\ s^{-1}$. While this mobility is obviously lower than that of the FET based on a single-crystal, the mobility is sufficiently large, as large as n-type organic TFT materials [15,17].

Fig. 6 shows field-effect electron mobility, threshold voltages and sub-threshold slopes (SS) of TFTs with AC5-CF3 thin films deposited at different substrate tempera-

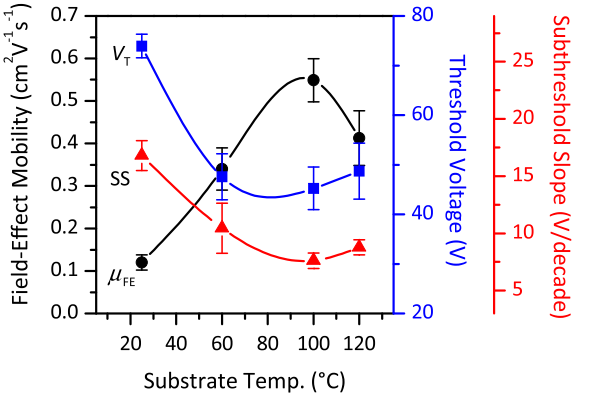

Fig. 6. Field-effect electron mobility (●), threshold voltage (■) and subthreshold slope (▲) of AC5-CF3 thin-film transistors (channel length of 50 μm) as a function of substrate temperature during the deposition of AC5-CF3.

tures. The figure clearly indicates certain tendencies: mobility increased and threshold voltage and SS decreased with increasing substrate temperature, while all the parameters became worse at a temperature of 120 °C. Fig. 7 shows the set of surface morphologies of AC-CF3 thin films prepared at different substrate temperatures. The morphological change shown in the figure is sufficiently consistent with the temperature dependences of mobility and threshold voltage. In short, the grain sizes of AC5-CF3 thin films became large with increasing substrate temperature. We believe that increasing the grain sizes directly and beneficially influences mobility. As shown in Fig. 7c, however, some deep valleys that seemed to segment adjacent grains were observed. Although we are unsure about the appearance of the valleys on the film, we speculate that the valleys appear because of a difference in the coefficients of thermal expansion (CTE) of AC5-CF3 thin films and silicon wafers because CTEs of organic materials are generally much larger than Si whose linear CTE is only $4 \times 10^{-6}\,K^{-1}$. The valleys probably interfered with electron transport of inter-grains, resulting in reduced mobility at 120 °C. Note that clear step-terrace structures appeared on all the images and the height of the steps corresponded to the length of the *a*-axis of the unit cell of AC5-CF3.

Furthermore, the threshold voltage decreased from the improved quality of AC5-CF3 thin film induced by temperature-controlled deposition. Enlarging grains at higher temperature depositions may be accompanied by qualitative improvement of thin films such as fewer defects that work as charge carrier traps. XRD patterns from AC5-CF3 thin films prepared at different temperatures shown in Fig. 3 support the qualitative improvement of the thin films. In short, the change of threshold voltage shown in Fig. 6 can be consistent with this improvement. Fig. 8 shows the channel length dependence of the field-effect mobility of AC5-CF3 TFTs prepared at different deposition temperatures. In case of the room temperature deposition of AC5-CF3, the field-effect mobility of TFTs slightly decreased with increasing channel lengths. In contrast, the mobility showed no dependence on the channel length in the case of 100 °C deposition of AC5-CF3. According to the atomic force microscope (AFM) observation shown in Fig. 7, the size of the grains is much smaller than the channel length of 30 μm even in the case of 100 °C deposition of AC5-CF3. Consequently, the independence of the mobility from the channel length observed in the case of the 100 °C deposition indicates that the deposition at higher temperature probably improves the quality of not only

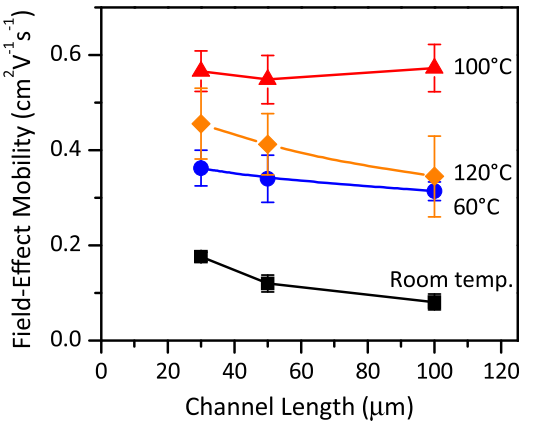

Fig. 8. Channel length dependence of field-effect mobility of AC5-CF3 thin-film transistors prepared at different substrate temperatures for AC5-CF3 depositions.

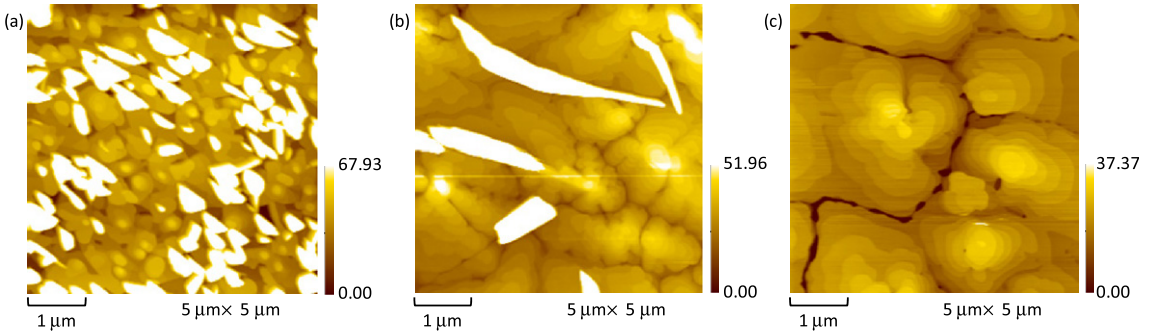

Fig. 7. Surface morphologies of AC5-CF3 thin films deposited at different substrate temperatures: (a) room temperature, (b) 100 °C and (c) 120 °C. The vertically long, color bars on the right of each image mean height scale in nanometres. (For interpretation of the references to colour in this figure legend, the reader is referred to the web version of this article.)

grains but also boundaries of grains. We can see from the AFM image shown in Fig. 7b that the grains with the size of about 1–3 μm tightly pack. However, the mobility of the TFTs with 120 °C depositions also decreased with increasing channel length. This phenomenon occurs because of the presence of the valleys observed in the film (see Fig. 7a).

4. Summary

We demonstrated the performance of optimally fabricated AC5-CF3 TFTs and its single-crystal FET. AC5-CF3 single-crystal FET showed field-effect mobility as high as 3.1 $cm^2 V^{-1} s^{-1}$. This value implies that AC5-CF3 must be a useful n-type organic semiconducting material. We also prepared AC5-CF3 TFTs, and the performance of the TFTs depended on the substrate temperatures during AC5-CF3 deposition. We obtained the highest performance from the viewpoint of mobility, threshold voltage and subthreshold slope when AC5-CF3 thin films were deposited at the substrate temperature of 100 °C. This was because a higher substrate temperature for the deposition enlarged the size of grains of AC-CF3 and improved the characteristics of grain boundaries. However, the 120 °C deposition induced deep valleys such as cracks and worsening mobility. AC5-CF3 TFTs prepared at 100 °C depositions showed no channel length dependence of the field-effect mobility. This is a very useful property for practical applications.

Acknowledgements

This work was supported by Regional Innovation Cluster Program of Nagano, granted by MEXT, Japan. This article is dedicated to the first principal of the Faculty of Textile Science and Technology, Shinshu University, Chotaro Harizuka, on the occasion of the 100th anniversary of the faculty.

References

[1] C.D. Dimitrakopoulos, P.R.L. Malenfant, Adv. Mater. 14 (2002) 99.
[2] S.R. Forrest, Nature 428 (2004) 911.
[3] S.F. Nelson, Y.Y. Lin, D.J. Gundlach, T.N. Jackson, Appl. Phys. Lett. 72 (1998) 1854.
[4] H. Klauk, M. Halik, U. Zschieschang, G. Schmid, W. Radlik, W. Weber, J. Appl. Phys. 92 (2002) 5259.
[5] T.W. Kelley, L.D. Boardman, T.D. Dunbar, D.V. Muyres, M.J. Pellerite, T.P. Smith, J. Phys. Chem. B 107 (2003) 5877.
[6] M. Ichikawa, H. Yanagi, Y. Shimizu, S. Hotta, N. Suganuma, T. Koyama, Y. Taniguchi, Adv. Mater. 14 (2002) 1272.
[7] H. Meng, J. Zheng, A.J. Lovinger, B.-C. Wang, P.G.V. Patten, Z. Bao, Chem. Mater. 15 (2003) 1778.
[8] M. Halik, H. Klauk, U. Zschieschang, G. Schmid, W. Radlik, S. Ponomarenko, S. Kirchmeyer, W. Weber, J. Appl. Phys. 93 (2003) 2977.
[9] T. Yamamoto, K. Takimiya, J. Am. Chem. Soc. 129 (2007) 2224.
[10] C.R. Newman, C.D. Frisbie, D.A.d.S. Filho, J.-L. Bredas, P.C. Ewbank, K.R. Mann, Chem. Mater. 16 (2004) 4436.
[11] Z. Bao, A.J. Lovinger, J. Brown, J. Am. Chem. Soc. 120 (1998) 207.
[12] H.E. Katz, A.J. Lovinger, J. Johnson, C. Kloc, T. Siegrist, W. Li, Y.-Y. Lin, A. Dodabalapur, Nature 404 (2000) 478.
[13] P.R.L. Malenfant, C.D. Dimitrakopoulos, J.D. Gelorme, L.L. Kosbar, T.O. Graham, Appl. Phys. Lett. 80 (2002) 2517.
[14] A. Facchetti, M.-H. Yoon, C.L. Stern, H.E. Katz, T.J. Marks, Angew. Chem. Int. Ed. 42 (2003) 3900.
[15] S. Ando, R. Murakami, J.-I. Nishida, H. Tada, Y. Inoue, S. Tokito, Y. Yamashita, J. Am. Chem. Soc. 127 (2005) 14996.
[16] N.J. Haddock, B. Domercq, B. Kippelen, Electron. Lett. 41 (2005) 444.
[17] S. Tatemichi, M. Ichikawa, T. Koyama, Y. Taniguchi, Appl. Phys. Lett. 89 (2006) 112108.
[18] D. Shukla, S.F. Nelson, D.C. Freeman, M. Rajeswaran, W.G. Ahearn, D.M. Meyer, J.T. Carey, Chem. Mater. 20 (2008) 7486.
[19] M. Chikamatsu, A. Itakura, Y. Yoshida, R. Azumi, K. Yase, Chem. Mater. 20 (2008) 7365.
[20] M. Mamada, J.-I. Nishida, D. Kumaki, S. Tokito, Y. Yamashita, Chem. Mater. 19 (2007) 5404.
[21] C.-A. Di, J. Li, G. Yu, Y. Xiao, Y. Guo, Y. Liu, X. Qian, D. Zhu, Org. Lett. 10 (2008) 3025.
[22] S. Ando, J.-I. Nishida, H. Tada, Y. Inoue, S. Tokito, Y. Yamashita, J. Am. Chem. Soc. 127 (2005) 5336.
[23] X.M. Hong, H.E. Katz, A.J. Lovinger, B.-C. Wang, K. Raghavachari, Chem. Mater. 13 (2001) 4686.
[24] T. Katagiri, S. Ota, T. Ohira, T. Yamao, S. Hotta, J. Heterocyclic Chem. 44 (2007) 853.
[25] T. Yamao, T. Miki, H. Akagami, Y. Nishimoto, S. Ota, S. Hotta, Chem. Mater. 19 (2007) 3748.
[26] S. Hotta, Y. Shimizu, T. Yamao, M. Goto, R. Azumi, Chem. Lett. 38 (2009) 294.
[27] M. Ichikawa, R. Hibino, M. Inoue, T. Haritani, S. Hotta, T. Koyama, Y. Taniguchi, Adv. Mater. 15 (2003) 213.
[28] I_p and bandgap of AC5-CF3 were 5.8 and 2.7 eV, respectively.
[29] S.M. Sze, Physics of Semiconductor Devices, second ed., John Wiley & Sons, New York, 1981.
[30] X.H. Zhang, B. Kippelen, Appl. Phys. Lett. 93 (2008) 133305.
[31] T. Yamao, Y. Shimizu, H. Kuriki, T. Katagiri, S. Hotta, Jpn. J. Appl. Phys. 49 (2010) 01AB01.

application of flexible low-cost, large-area solid-state lighting. However, to the best of our knowledge, there have been no published demonstrations of a high-efficiency blue phosphorescent OLED (the most challenging component for white OLED lighting applications) using an alternative anode material on a flexible substrate.

In this letter, we report the use of a scalable coating technique to deposit high-quality Ga-doped ZnO (GZO) films on flexible substrates at near room temperature. While we recognize that gallium is also a scarce, relatively expensive material, the total amount of gallium used in the GZO films is very small (5 at.%), whereas ITO contains >90 at.% indium. Hence, these GZO anodes may be a cost effective replacement for ITO. Using these GZO/PET substrates, we demonstrate blue phosphorescent OLEDs with high quantum and power efficiencies at a practical brightness level suitable for general lighting.

Radio frequency (RF) magnetron sputtering of GZO films was performed on glass and flexible PET substrates simultaneously in a 0.9 m box vacuum chamber having a base pressure of 4×10^{-7} Torr. A 15 cm diameter sputtering target containing 97.5% ZnO/2.5% Ga_2O_3 (at.%) with 99.99% purity (Cerac Inc., Milwaukee, WI) was used as the source. Substrates were mounted on one of three 30.5 cm diameter stainless steel pallets suspended from the chamber ceiling which allows double planetary rotation to improve coating uniformity. The plane of rotation of the substrate holders was 16.5 cm above the sputtering cathode. Prior to coating, the substrates were cleaned *in situ* with an ion beam generated by a source mounted on the chamber floor. Sputtering parameters including gas pressure and gas composition were evaluated for the production of high quality GZO films. 4% hydrogen in Ar sputtering gas at a pressure of 1 to 3 mTorr was found to be optimal for this system in this geometry. With the application of the double planetary rotation during deposition, the average variation of film thickness over the 30.5 cm pallet area was ~4%. The glass transition temperature of PET (150 °C) limits the maximum processing temperature for PET substrates [3]. During deposition, no supplementary heating was applied to the substrates and their temperature was up to 60 °C due to the energetic sputtering conditions. No damage was observed on PET substrates after deposition. Selected samples of GZO/PET films were annealed after deposition to investigate its effect on GZO film roughness, conductivity, and transparency as compared to the as-deposited films. Specifically (Table 1), annealing was performed at 110 °C under two different conditions: (a) 10 h in an air ambient at reduced pressure (253 Torr) and (b) 150 min in the atmosphere of 4% H_2/Ar (4% H_2/Ar flux at 25 standard cm^3/minute (sccm) to maintain the system pressure at 1.3 mTorr on top of the high vacuum background of 4×10^{-7} Torr). After these annealing processes no damage was noticeable on PET substrates. As seen in Table 1, annealing improves the conductivity of the GZO film on PET mainly by enhancement of mobility. However, this improvement did not lead to an observable difference between the performances of OLEDs built on the annealed GZO/PET and those built on the as-deposited GZO/PET.

GZO and ITO substrates not subject to UV ozone treatment were characterized using a series of methods. The commercial ITO/glass substrates were purchased from Colorado Concept Coatings LLC, having a 1400 Å thickness and nominal sheet resistance of 15 Ω/□ for the ITO layer. The morphology of the as-deposited GZO films on PET substrates was characterized by atomic force microscope (See supporting information in the supplemental), with a statistical grain height of 7.4 nm and a Z_{max} of 18.5 nm, comparable to commercial ITO on glass (grain height of 4.5 nm and a Z_{max} of 13.8 nm). The electrical properties of these materials without UV ozone treatment were determined using conductive atomic force microscope (c-AFM), Hall measurement and four-point probe measurements. The overall scale of c-AFM images in Fig. 1 shows that the as-deposited GZO film on PET conducts less current under the same bias (500 mV) compared to the commercial ITO on glass used as a control sample. This is explained by the difference in texture seen in Fig. 1, which suggests that compared to the control sample, the GZO film on PET has more uniformly distributed conductive domains, but those domains are much smaller in size. Carrier mobilities were measured with Hall measurement at room temperature using the Van der Pauw technique on a commercial Hall system from MMR Technologies. The thickness of the films was measured separately with a step profilometer (Tencor Instruments, Alpha Step 200 model). It was found that the carrier mobilities in the GZO films were one order of magnitude lower than that in commercial ITOs (see Table 1). The higher grain boundary density in the GZO films, and thus lower mobility due to increased disorder at grain boundaries, translates into higher resis-

Table 1
Comparison of commercial ITO/glass to GZO films fabricated on glass and flexible PET substrates with different post-deposition processing environments. The annealing temperature was 110 °C for both annealing environments. Key OLED performance metrics are also reported at a current density of 1 mA/cm^2 for OLEDs built on these anode materials.

Fabrication condition	Resistivity (ohm cm)	Carrier concentration (cm^{-3})	Mobility (cm^2/Vs)	Thickness (Å)	Optical transmittance at 475 nm	OLED operating voltage (V)	EQE (%)	η_p (lm W^{-1})	CIE coordinates
ITO/glass	1.42×10^{-4}	5.47×10^{21}	8.05	1400	89.2%	4.35 ± 0.03	16.7 ± 0.5	32.1 ± 0.9	(0.15, 0.38)
GZO/glass (as deposited)	1.66×10^{-3}	3.62×10^{21}	1.04	1550	88.0%	4.05 ± 0.02	15.2 ± 0.1	31.6 ± 0.3	(0.14, 0.39)
GZO/PET (as deposited)	3.03×10^{-3}	5.88×10^{21}	0.351	1550	85.2%	4.21 ± 0.02	16.6 ± 0.2	33.1 ± 0.3	(0.14, 0.38)
GZO/PET (annealed in 4% H_2/Ar)	2.20×10^{-3}	5.59×10^{21}	0.508	1550	86.5%	4.06 ± 0.02	16.3 ± 0.3	33.7 ± 0.4	(0.13, 0.35)
GZO/PET (annealed in low vacuum)	2.19×10^{-3}	5.73×10^{21}	0.498	1550	86.3%	3.99 ± 0.01	16.0 ± 0.6	33.7 ± 1.2	(0.14, 0.37)

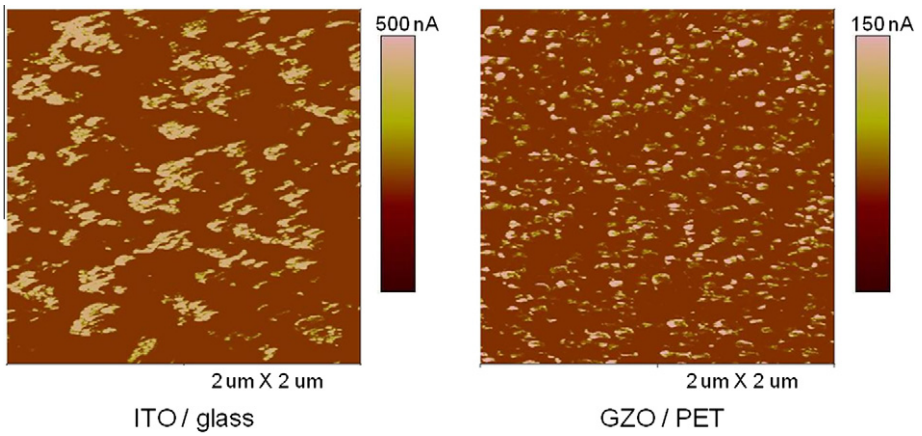

Fig. 1. Conductive AFM (c-AFM) images of films of ITO on glass (left) and GZO on PET (right), where the ITO/glass was obtained commercially and the GZO film was sputtered onto PET in 4% H_2/Ar at low temperature without annealing. Images were taken under a DC bias of 500 mV. No UV ozone treatment was performed prior to the c-AFM experiment.

tivity. This was confirmed by four-point probe measurements showing an order of magnitude higher resistivity for the GZO films than that of the ITO deposited on glass (Table 1).

The optical properties of the GZO films on PET were examined using UV–vis-NIR spectrometry and compared to the corresponding properties of ITO and GZO on glass. As seen in Fig. 2, the GZO films deposited on PET and glass, including the samples annealed under different conditions, all exhibited transmittance spectra close to that of the commercial ITO on glass. The transmittance curves for GZO on PET mainly reflect the optical properties of the deposited GZO film as is evident when comparing the GZO/PET transmittance spectra to the GZO/glass transmittance spectrum. However, the transmittance curves of all the GZO films on PET featured small oscillations as a function of wavelength showing larger periods of oscillation at longer wavelengths. This behavior can be attributed to the hard coating on the other side (opposite to the side with GZO film) of the GZO/PET substrates (PET with hard coating on one side were purchased from Tekra Inc.) which caused a noticeable interference effect. A detailed discussion of this phenomenon can be found in the supplemental information.

We utilized GZO films deposited on both glass and PET substrates to fabricate phosphorescent blue OLEDs with the device architecture: TCO/350 Å TAPC/150 Å HM-A1:5% FIrpic/500 Å PO15/10 Å LiF/1000 Å Al. Here the 1,1-bis [(di-4-tolylamino)phenyl]cyclohexane (TAPC) serves as the hole-transport layer (HTL) [12]. The emissive layer

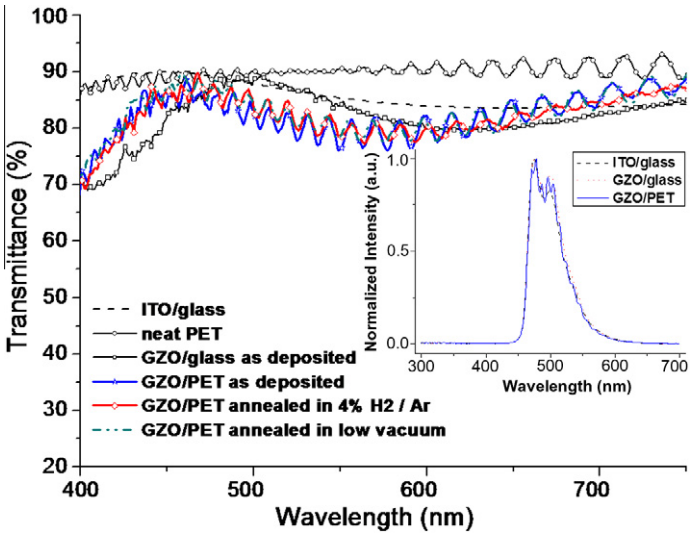

Fig. 2. Optical transmittance spectra for commercial ITO/glass, neat PET, GZO/glass, GZO/PET as deposited, GZO/PET annealed under 4%H_2/Ar, and GZO/PET annealed under low vacuum (253 Torr). The inset – electroluminescent spectra for OLEDs with the structure of TCO anode/350 Å TAPC/150 Å HM-A1:5% FIrpic/500 Å PO15/10 Å LiF/1000 Å Al. The oscillations in the spectra of GZO/PET films are due to an interference effect involving the PET substrate (see the supplementary information).

(EML) is composed of the host material 4-(diphenylphosphoryl)-N,N-diphenylaniline (HM-A1) [13] doped with phosphorescent emitter iridium (III) bis[(4,6-difluorophenyl)-pyridinato-$N,C^{2'}$]picolinate (FIrpic). The hole-blocking/electron-transporting layer (ETL) is 2, 8-bis(diphenylphosphoryl)dibenzothiophene (PO15) [14]. A thin lithium fluoride (LiF) layer facilitates electron injection from the aluminum (Al) cathode. GZO/PET substrates were cleaned in three steps: in a dilute Tergitol solution, deionized water, and 2-propanol with sonication. As controls, TCO films (GZO and ITO) on glass substrates were cleaned by sonication in a sequential series of solvents: a dilute Tergitol solution, deionized water, trichloroethylene, acetone, and 2-propanol. These substrates were then dried with flowing nitrogen. As a final step before device fabrication, all the glass and PET substrates were treated with UV ozone (UVO-Cleaner, Jelight Company, Inc.) at 15 mW/cm^2 for 15 min. Organic layers were sequentially deposited onto the substrates by thermal sublimation from tantalum boats in a high vacuum chamber with base pressure below 3×10^{-7} Torr. LiF/Al cathodes were defined by thermal deposition through a shadow mask with 1 mm diameter circular openings. Quartz crystal oscillators were used to monitor the thicknesses of the films, which were calibrated *ex situ* using ellipsometry or profilometry.

Key OLED performance metrics at a current density of 1 mA/cm^2 are summarized in Table 1. All the OLEDs employing a GZO anode, whether on a rigid or flexible substrate, manifested performance comparable to OLEDs produced using an ITO anode. OLEDs built on PET substrates exhibit a low operating voltage ($\sim$4 V), high external quantum efficiency (EQE) (16%), and high power efficiency (η_p) (33 lm/W). Fig. 3a is a typical plot of EQE and η_p as a function of luminance. It can be seen throughout the practical brightness range for general lighting (1000–4000 cd/m^2) that the OLEDs fabricated using GZO anode on PET performed nearly the same as the OLEDs fabricated using commercial ITO anode on glass. The voltage dependence of current density and luminescence of these devices are shown in Fig. 3b. The OLED devices built on GZO/PET and GZO/glass show charge transport behavior similar to ITO/glass devices, clearly demonstrating a transition from the intrinsic bulk transport regime (at low voltages, free charges are thermally generated in organic layers) to the trap filling transport regime (at high voltages, free charges injected from electrodes are filling traps in organic layers) [15]. Ohmic type *J–V* curve is observed in the intrinsic bulk transport regime for all three types of devices, indicating that none of the three TCO anodes is limiting charge transport by hole injection. GZO/glass devices exhibit a higher leakage current at low voltages as opposed to GZO/PET and ITO/glass devices, which is possibly attributable to a greater asperity on the surface of GZO/glass substrates. All three types of devices show similar turn-on voltage around 3 V. This low turn-on voltage contributes to the achieved high power efficiency as shown in Table 1. It is noteworthy that in yielding high-performance devices, the GZO/PET anode material fully processed at near room temperature performs as well as those films with post-deposition annealing (Table 1), thus indicating that the annealing step may be eliminated. This would allow a reduction in processing cost and time, and accommodate the low temperature requirements for certain devices such as top-emitting OLEDs. Additionally, as shown in the inset of Fig. 2, the electroluminescence (EL) spectra for all of the devices produced on various substrates appear very similar. Small oscillations can be observed in the EL spectra for OLEDs fabricated on GZO/PET substrates due to the interference effect previously mentioned. Consistently with the comparable EL spectra, similar Commission internationale de l'éclairage (CIE) coordinates were obtained (shown in Table 1) from operating OLEDs on the various TCO substrates. All these facts demonstrate that GZO/PET is a potential substitute for ITO/glass.

Based on the transmittance curves (Fig. 2), we calculated the average refractive index (n) and extinction coefficient (k) over visible spectrum for the materials used in this work: n(ITO) = 1.683, k(ITO) = 0.033; n(GZO) = 1.834, k(GZO) = 0.064. Since the refractive index of GZO is higher than ITO, more light will be trapped in the GZO layer of the OLED device and thus potentially reduce outcoupling efficiency so that the GZO/glass devices exhibit a slightly lower EQE than ITO/glass devices (Table 1). We also note that in spite of similar transmittance around the FIrpic emission peaks, GZO/PET substrates give slightly higher EQE than GZO/glass substrates for the same OLED device stack. We attribute this increase of EQE to the enhanced light outcoupling through a combination of two factors. First, more light escapes the GZO layer into the PET due to its higher refractive index (1.58) compared to glass (1.50) [16]. Second, due to total internal reflection above the critical angle at the air-substrate interface, only a fraction of the light can escape the substrate [17] and get collected by the photo detector. Given the certain experimental setting of finite distance from a sample's bottom to the surface of photo detector, the smaller thickness of the PET substrate (0.19 mm) compared to the glass substrate (1 mm) translates into shorter distance from light emission to the photodetector and thereby allows for less loss in the light collection. A detailed optical model is needed to quantitatively analyze the outcoupling factors in comparing devices built on GZO/PET and GZO/glass substrates. Together, these two effects are responsible for the slightly higher EQE of OLEDs based on GZO/PET versus GZO/glass. Interestingly, the higher resistivity of the GZO versus ITO and the as-deposited versus annealed GZO as the anode does not affect the OLED performance for these small pixel devices (diameter = 1 mm, 7.854×10^{-3} cm^2). For the OLEDs tested in this work, the lateral conductance (GZO film sheet resistance $\sim$100 $\Omega/\square$) across the anode is far higher than that of vertical transport through the device stack which thereby dominates the overall conductance of an OLED. The same organic layers deposited on different TCO anode materials (GZO or ITO) exhibited similar charge transport behavior (as seen from *J–V* characteristics in Fig. 3b) and operating voltage (shown in Table 1), indicating that hole injection from different TCO anodes into the same HTL is not a limiting factor for charge transport in these devices. We attribute the similar injection properties for the different TCO anodes (GZO or ITO) to the modification of anode surface work function through UV ozone treatment [18]. When the pixel size is small, the higher

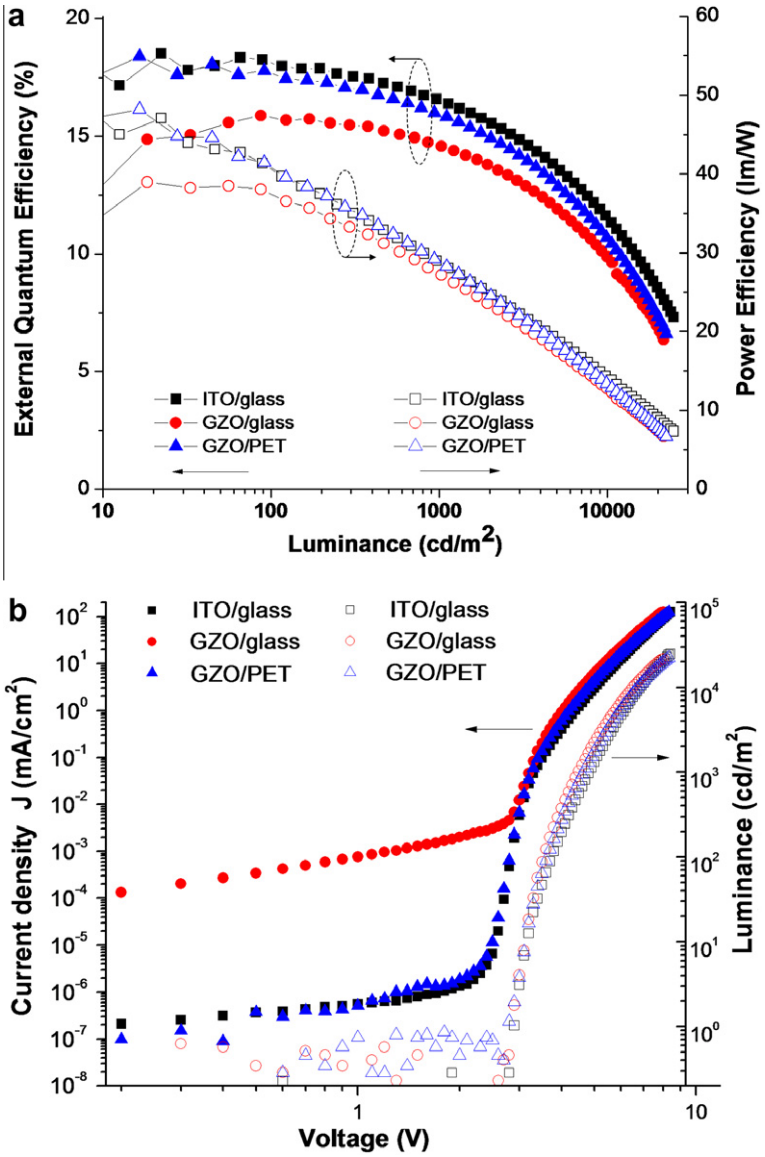

Fig. 3. (a) The luminescence dependence of EQE and power efficiency and (b) the voltage dependence of current density and luminescence for OLEDs with the structure: TCO anode/350 Å TAPC/150 Å HM-A1:5% FIrpic/500 Å PO15/10 Å LiF/1000 Å Al. Here ITO/glass was commercially purchased and GZO/glass and GZO/PET were as deposited with no post annealing. All the TCO anode substrates were treated with UV ozone before organic deposition.

resistivity of the GZO films will not significantly influence device performance. For applications where larger pixel sizes are involved (>1 cm^2) such as lighting panels for solid-state lighting purposes, the resistivity of the GZO films needs to be decreased by at least an order of magnitude to be at levels near that of commercial ITO in order to operate the large-area devices at low and uniform voltages and avoid Joule heating. As is seen in Table 1, the annealing process for GZO/PET substrates served to decrease the resistivity of the GZO films by 28%. Unfortunately, this is still an order of magnitude higher than the resistivity of commercial ITOs. Hence different strategies need to be applied such as inserting a thin, nearly transparent silver layer into the GZO film [19] or placing metal grids on the GZO surface to help distribute electrical current better [20].

In summary, indium-free GZO films have been uniformly deposited on flexible substrates over a large area using a low temperature sputtering process. Highly efficient phosphorescent blue OLED devices were built on the GZO films, which functioned as the anode. The performance of these devices compared favorably with that of the same device stack built on rigid (glass) substrates using a commercial ITO anode. This result demonstrates that indium-free TCOs on flexible substrates can serve as a low-cost and flexible substitute for OLED device manufacturing. Another interesting application of sputtered TCO films is the top contact electrode in a top-emitting, inverted OLED.

Based on our results, the as-deposited GZO, even without a post-deposition anneal, should be able to function as a top electrode in a top emitting inverted OLED for small area pixels. The greater challenge in using the GZO deposition process to form a top electrode in this device architecture would be to modify the process in order to reduce and/or eliminate damage to the underlying organic layer during the GZO deposition [21].

Acknowledgements

The authors thank Mark Gross for helpful discussions on the optical measurement of substrates. This project was funded by the Solid-State Lighting Program within the Building Technologies Program (BT; managed by the National Energy Technology Laboratory/NETL) of the Energy Efficiency and Renewable Energy Division of the US Department of Energy, award No. M6642866. A portion of the research described in this paper was performed in the Environmental Molecular Sciences Laboratory, a national scientific user facility sponsored by the Department of Energy's Office of Biological and Environmental Research and located at Pacific Northwest National Laboratory. Pacific Northwest National Laboratory (PNNL) is operated by Battelle Memorial Institute for the US Department of Energy (DOE) under Contract DE-AC06-76RLO 1830.

Appendix A. Supplementary material

Supplementary data associated with this article can be found, in the online version, at doi:10.1016/j.orgel.2010.06.018.

References

[1] T.Y. Tsai, C.Y. Lee, N.H. Tai, W.H. Tuan, Appl. Phys. Lett. 95 (2009) 013107.
[2] Wantae Lim, Jung Hun Jang, S.-H. Kim, D.P. Norton, V. Craciun, S.J. Pearton, F. Ren, H. Shen, Appl. Phys. Lett. 93 (2008) 082102.
[3] Myeon-Cheon Choi, Youngkyoo Kim, Chang-Sik Ha, Prog. Polym. Sci. 33 (2008) 581–630.
[4] Tadatsugu Minami, Toshihiro Miyata, Thin Solid Films 517 (2008) 1474–1477.
[5] T. Minami, Semicond. Sci. Technol. 20 (2005) S35;
T. Minami, Thin Solid Films 516 (2008) 5822.
[6] J. Cui, A. Wang, N.L. Edleman, J. Ni, P. Lee, N.R. Armstrong, T.J. Marks, Adv. Mater. 13 (19) (2001) 1476;
X. Jiang, F.L. Wong, M.K. Fung, S.T. Lee, Appl. Phys. Lett. 83 (2003) 1875;
Y. Tomita, C. May, M. Toerker, J. Amelung, M. Eritt, F. Loeffler, C. Luber, K. Leo, K. Walzer, K. Fehse, Q. Huang, Appl. Phys. Lett. 91 (2007) 063510;
J.J. Berry, D.S. Ginley, P.E. Burrows, Appl. Phys. Lett. 92 (2008) 193304;
M. Nakano, T. Fukumura, H. Toyosaki, K. Ueno, M. Kawasaki, Jpn. J. Appl. Phys. 47 (2008) 1276.
[7] Jyh-Jier Ho, Chin-Ying Chen, J. Electrochem. Soc. 152 (1) (2005) G57–G61.
[8] Jeung Hun Park, Yong Chan Cho, Jong Moon Shin, Su-Young Cha, Chae Ryong Cho, Hye Sung Kim, Su Jong Yoon, Se-Young Jeong, Sang Eon Park, Ae-Ran Lim, J. Korean Phys. Soc. 51 (6) (2007) 1968–1972.
[9] Jung-Hyeok Bae, Jong-Min Moon, Soon Wook Jeong, Jang-Joo Kim, Jae-Wook Kang, Do-Geun Kim, Jong-Kuk Kim, Jeong-Woo Park, Han-Ki Kima, J. Electrochem. Soc. 155 (1) (2008) J1–J6.
[10] Jae-Wook Kang, Won-Ik Jeong, Jang-Joo Kim, Han-Ki Kim, Do-Geun Kim, Gun-Hwan Lee, Electrochem. Solid-State Lett. 10 (6) (2007) J75–J78.
[11] Sung-Woo Cho, Jin-A Jeong, Jung-Hyeok Bae, Jong-Min Moon, Kwang-Hyuk Choi, Soon Wook Jeong, No-Jin Park, Jang-Joo Kim, Se Hyung Lee, Jae-Wook Kang, Min-Su Yi, Han-Ki Kim, Thin Solid Films 516 (2008) 7881–7885.
[12] P.M. Borsenberger, L. Pautmeier, R. Richert, H. Bassler, J. Chem. Phys. 94 (1991) 8276.
[13] E. Polikarpov, J.S. Swensen, N. Chopra, F. So, A.B. Padmaperuma, Appl. Phys. Lett. 94 (2009) 223304.
[14] L.S. Sapochak, A.B. Padmaperuma, P.A. Vecchi, X. Cai, P.E. Burrows, Proc. SPIE-Org. Light-Emit. Dev. Mater. XI 6655 (2007) 665506.
[15] P.E. Burrows, Z. Shen, V. Bulovic, D.M. McCarty, S.R. Forrest, J.A. Cronin, M.E. Thompson, J. Appl. Phys. 79 (10) (1996) 7991.
[16] M.-H. Lu, J.C. Sturm, Appl. Phys. Lett. 78 (13) (2001) 1927.
[17] G. Gu, D.Z. Garbuzov, P.E. Burrows, S. Venkatesh, S.R. Forrest, M.E. Thompson, Opt. Lett. 22 (6) (1997) 396.
[18] Kiyoshi Sugiyama, Hisao Ishii, Yukio Ouchi, J. Appl. Phys. 87 (1) (2000) 295;
H. Kim, J.S. Horwitz, W.H. Kim, A.J. Makinen, Z.H. Kafafi, D.B. Chrisey, Thin Solid Films 420–421 (2002) 539.
[19] Jin-A Jeong, Jae-Young Lee, Han-Ki Kim, Electrochem. Solid-State Lett. 12 (11) (2009) J105.
[20] C. May, Y. Tomita, M. Toerker, M. Eritt, F. Loeffler, J. Amelung, K. Leo, Thin Solid Films 516 (14) (2008) 4609.
[21] L.S. Liao, L.S. Hung, W.C. Chan, X.M. Ding, T.K. Sham, I. Bello, C.S. Lee, S.T. Lee, Appl. Phys. Lett. 75 (1999) 1619;
Hui Lin, Junsheng Yu, Shuangling Lou, Jun Wang, Yadong Jiang, J. Mater. Sci. Technol. 24 (2) (2008) 179;
Han-Ki Kim, D.-G. Kim, K.-S. Lee, M.-S. Huh, S.H. Jeong, K.I. Kim, Tae-Yeon Seong, Appl. Phys. Lett. 86 (2005) 183503.

leading to back transfer [15–17]. As a result we have decided to follow the approach of using a non-conjugated polymer backbone [10,11,13,18–22]. However, non-conjugated homopolymers with small iridium(III) complexes can have poor solubility. For example, a homopolymer comprised of a norbornenyl derived backbone and *fac*-tris(2-phenylpyridyl)iridium(III) side chains attached to every unit was reported to be insoluble [23] and more recently a polystyrene backboned homopolymer with bis(2-phenylpyridyl)iridium(III) acetylacetonate complex side chains had only limited solubility in solvents normally used for processing [11].

Phosphorescent polymers also have difficulties with concentration quenching due to the proximity of the iridium(III) complex cores, particularly in the solid-state [11]. While most others have used co-polymers to reduce the effect of intra- and inter-polymer chromophore interactions [15,17–22,24,25], here we explore an alternative approach of a polymer composed of dendrimer side chains with the aims of controlling interactions between chromophores, enhancing the viscosity of dendrimers towards a level suitable for ink-jet printing and ensuring solubility. We have also compared the polymer to model monomers in order to determine the effects of polymerisation on the interactions between chromophores.

2. Synthesis

Poly(dendrimer) **7** has several important design features: first, it is a homopolymer; second, the core emissive unit is a heteroleptic iridium(III) complex comprising two 2-phenylpyridyl ligands and a pyridyltriazolyl co-ligand with the former responsible for the green emission; third, first generation biphenyl-based dendrons with 2-ethylhexyloxy surface groups are attached to each of the 2-phenylpyridyl ligands to control the inter-chromophore interactions and provide solubility; finally, the norbornenyl derived polymer backbone was chosen as it can be easily formed by Ring Opening Metathesis Polymerisation. The pyridyltriazolyl co-ligand was chosen as the attachment point to the polymer backbone, as it can be added to the iridium(III) without scrambling of the other ligands. The synthetic strategy for forming the poly(dendrimer) **7** is shown in Scheme 1. In principle, aldehyde **1** could be used to cleave the tetra[2-(5-{3,5-bis[4-(2-ethylhexyloxy)phenyl]phenyl}phenyl)pyridyl]diiridium(III) dichloride **4** [26] to form a complex that with subsequent reduction and ester formation with *exo*-bicyclo[2.2.1]hept-5-ene-2-carboxylic acid [27] could lead to monomer **5**. However, this route requires an increased number of steps using the advanced dimer intermediate **4**, and hence the alternative route illustrated in Scheme 1 was used. The ^{1}H NMR spectra of the very polar pyridyltriazolyl and its derivatives often showed a minor component in addition to the desired compound. However, the elemental analyses were within the accepted limits, and it may be that the other components were regioisomers. Nevertheless, we have reported the yields for the early transformations as approximate. Aldehyde **1** was formed in ≈68% yield by metalation of 2-(5-trifluoromethyl-2-H-1,2,4-triazol-yl)-5-bromopyridine with *t*-butyllithium followed by reaction with *N*,*N*-dimethylformamide and subsequent hydrolysis with dilute hydrochloric acid. Reduction of the aldehyde **1** to alcohol **2** utilised lithium aluminium hydride, and **2** was isolated in ≈92% yield. Alcohol **2** was then coupled with the pre-formed acid chloride of *exo*-bicyclo[2.2.1]hept-5-ene-2-carboxylic acid to give ester **3** in ≈85% yield. We chose pure *exo*-norbornene isomers for the polymerisation as they have been shown to exhibit significantly higher rates of propagation under milder conditions, with higher conversions and more control than the 80:20 *endo*/*exo* isomeric mixtures that can be formed during the Diels–Alder reaction to prepare the norbornene [28]. The higher rate of propagation is primarily due to reduced steric interactions between the growing polymer chains and the incoming monomer [29]. As expected, the cleaving of dimer **4** proceeded smoothly at room temperature, and the monomer **5** was formed in ≈43% yield. In previous work on polymers bearing small molecule iridium(III) complexes on a poly(styrene) backbone it was found that the presence of double bonds caused quenching of the luminescence. Therefore, we hydrogenated the double bond of the norbornenyl unit with hydrogen and a palladium on carbon catalyst to give compound **6** in quantitative yield as a model compound to study the effect of the double bond on the luminescent properties. Finally, polymer **7** was formed in 72% yield from monomer **5** using Grubbs III catalyst [30].

Infrared spectroscopy showed that the ester functionality of ligand **3** survived the subsequent synthetic steps with **5**, **6**, and **7** all having carbonyl stretches at 1735 cm^{-1}. The polymer was found to be thermally stable, with thermogravimetric analysis showing just a 5% weight loss at 410 °C. Differential scanning calorimetry showed that there were no thermal transitions between −20 °C and 250 °C. Gel permeation chromatography (GPC) against poly(styrene) narrow standards showed that polymer **7** had an $\overline{M}_w$ and $\overline{M}_n$ of 5.5×10^4 and 2.2×10^4, respectively, and hence a polydispersity of 2.2. Living polymerisations normally give a polydispersity close to unity, and the higher value for polymer **7** may be due to the large size of the monomer that needs to be added to the chain end where steric factors may play a much more important role in chain growth. It was possible to analyse the molecular weight of the polymer using MALDI-TOF mass spectrometry, which showed that the polymer had a peak molecular weight of 171 kDa. It is interesting to note that the GPC analysis underestimates the true molecular weight of the polymer and this arises from a different conformation of the poly(dendrimer) in solution when compared with the poly(styrene) standards.

3. Photophysical properties

Fig. 1a shows the absorption spectra of the materials. The absorption peak at less than 350 nm is attributed to π–π^* transitions in the 2-phenylpyridyl, the pyridyltriazolyl ligands, and the biphenyl chromophores in the dendrons. The weaker absorptions from 350 to 460 nm are normally reported as being due to the metal-to-ligand

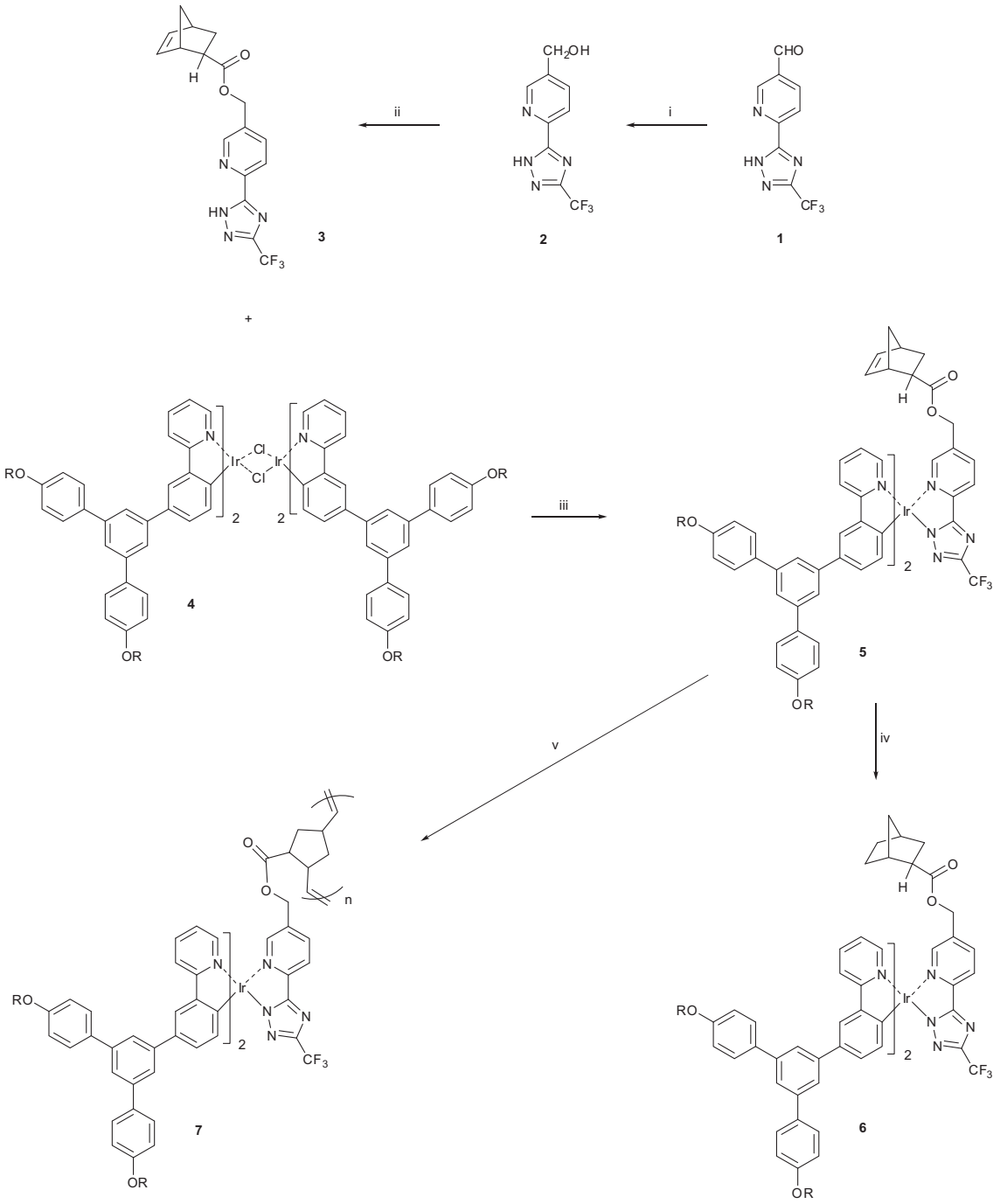

Scheme 1. R = 2-ethylhexyl. *Reagents* and *conditions*: (i) $LiAlH_4$, diethylether, 0 °C to r.t., N_2; (ii) *exo*-bicyclo[2.2.1]hept-5-ene-2-carboxylic acid chloride, py, CH_2Cl_2, 0 °C to r.t., 16 h, N_2; (iii) CH_2Cl_2, r.t., 18 h; (iv) Pd/C, H_2; (v) Grubbs III catalyst, CH_2Cl_2, 16 h then $EtOCH{=}CH_2$.

charge-transfer states of the iridium(III) complex. The spectra do not change on polymerisation or when the materials are spin cast into thin films indicating that strong aggregation phenomena are not occurring in either case.

Fig. 1b shows the photoluminescence spectra of the materials. All three materials have strong green luminescence in solution, with a peak at 497 nm and a shoulder at 525 nm. The similarities in the solution spectra show that, to a first approximation, the emissive properties of the iridium(III) complexes are not significantly affected either by the presence of a double bond in the norbornenyl unit in monomer **5** or by being incorporated into a polymer. Monomers **5** and **6** gave very similar solution photoluminescence quantum yields (PLQYs) of 53% and 56%. The

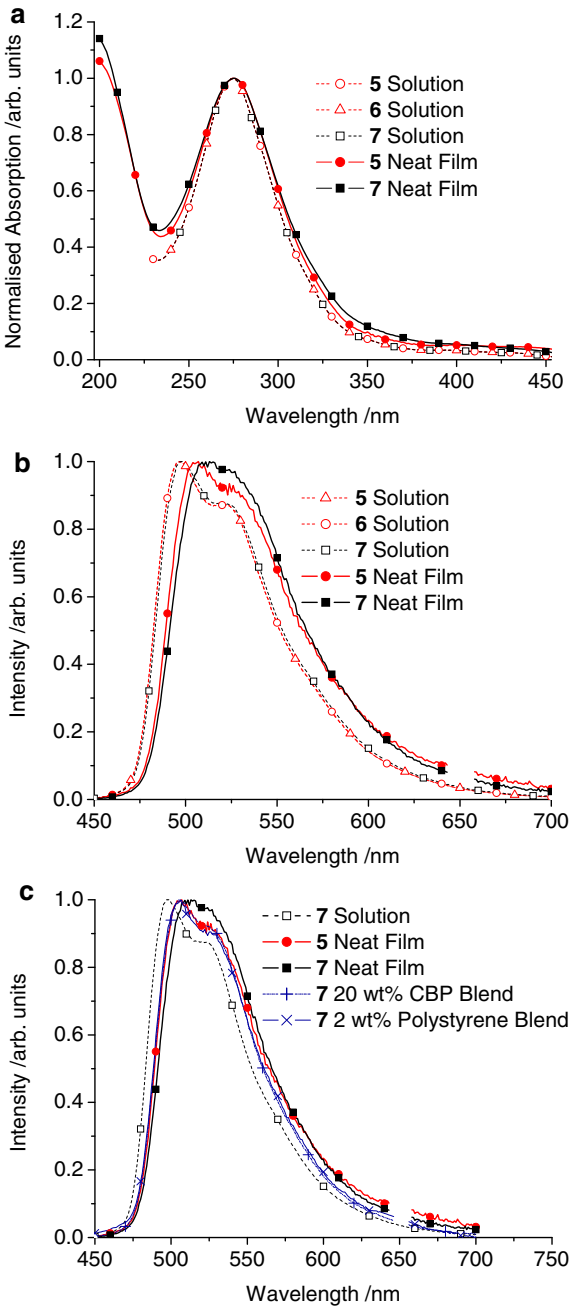

Fig. 1. Normalised spectra showing (a) the absorption of monomers **5** and **6** and polymer **7** in dilute dichloromethane solutions and monomer **5** and polymer **7** in thin films, (b) emission spectra of monomers **5** and **6** and polymer **7** in dilute degassed dichloromethane solutions and monomer **5** and polymer **7** in thin films, and (c) a comparison of the emission spectra of polymer **7** in dilute degassed dichloromethane solution, monomer **5** and polymer **7** in neat thin films, and blended films consisting of 20 wt.% of polymer **7** in a CBP host and 2 wt.% of polymer **7** in a polystyrene host.

transient luminescence lifetimes shown in Fig. 2 were also comparable at 3.07 and 3.03 μs. This indicates that the structure of the ester-linked group on the pyridyltriazolyl ligand does not significantly affect the photophysics in solution.

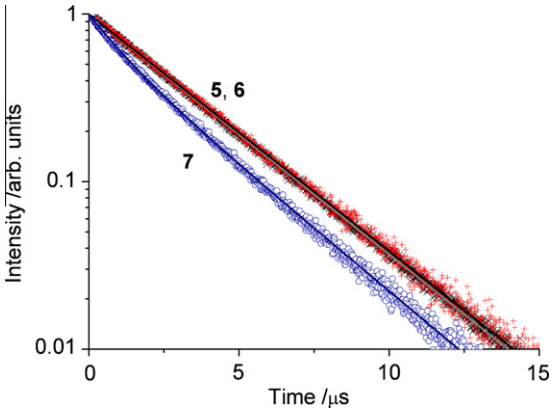

Fig. 2. Time resolved luminescence data for dilute solutions of monomers **5** (red vertical crosses) and **6** (black diagonal crosses) and polymer **7** (blue circles) in degassed dichloromethane. Fits are shown as solid lines. (For interpretation of the references to colour in this figure legend, the reader is referred to the web version of this article.)

Polymer **7** had a solution PLQY of 37%. The transient luminescence was best fitted by a bi-exponential decay with lifetimes (pre-exponential factors) of 1.08 μs (0.30) and 2.90 μs (0.70). The 2.9 μs component is similar to the lifetime of the monomers. However, the reduced PLQY and the shorter 1.08 μs component compared to the monomer indicate that even in the dilute solution there is some quenching of the luminescence by intra-polymer chromophore interactions due to the proximity of the iridium(III) complexes along the polymer backbone. These results compare favourably to the luminescent efficiencies reported for other norbornenyl polymers with small molecule iridium(III) complex side chains which only had a 2% PLQY in solution and a *fac*-tris(2-phenylpyridyl)iridium(III) copolymer (the homopolymer was completely insoluble) which had a PLQY of 24% [23].

The effects of inter-chromophore interactions become more pronounced in neat films of monomer **5** and poly(dendrimer) **7**. The emission peaks in Fig. 1b were both red-shifted by 10–15 nm in the film relative to the solution measurements, and the PLQY was reduced to 13% and 15%, respectively. The red-shift in the emission of the poly(dendrimer) in the solid-state is more significant than in the monomer, suggesting that it is more susceptible to aggregation effects. Nevertheless, these results are far superior to neat films of homopolymers containing small molecule iridium(III) complex side chains without dendrons [11] where the PLQY was reduced to less than 1% in the solid-state. This confirms that the addition of dendrons is an effective strategy for controlling intermolecular chromophore interactions and producing neat films with good phosphorescence [31–33].

In order to reduce intermolecular interactions and improve charge transport, 20 wt.% of poly(dendrimer) **7** was blended with the commonly-used charge transport host 4,4′-bis(*N*-carbazolyl)-2,2′-biphenyl (CBP) for the production of OLEDs. The PLQY of these blended films improved significantly to 52% and a typical photoluminescence spectrum of the blended film is shown in Fig. 1c. The

photoluminescence spectrum of the CBP blend is blue-shifted compared to the neat film, and closely resembles that of the film of neat monomer **5**. These results both suggest that inter-chromophore interactions were successfully reduced by the blend.

By contrast monomer **5** only gave a CBP blended film PLQY of 29%. This is attributed to the fact that the monomer only has dendrons attached to two ligands to protect it from aggregating and it lacks the polymer's backbone which controls the orientation of the neighbouring units. Both these effects may allow more interaction of the chromophores than in the polymer blend.

Fig. 3 shows a comparison of the phosphorescence lifetime of **7** in solution, in a 20 wt.% of **7** in a CBP blend film, 2 wt.% of **7** in a polystyrene blend film and in neat films. In all the films the phosphorescent decay is faster than in solution. It is interesting that the CBP blend film has a faster decay of 0.81 μs (0.39) and 2.02 μs (0.61) components than the solution despite the blend having a higher PLQY. The increased PLQY of the blend combined with an increased proportion of the decay in the fast component and a decrease in the lifetime of both components strongly implies an increase in the radiative rate in the CBP blended film compared to the solution.

In order to understand more fully this effect, PL lifetime studies of neat films and poly(styrene) blends with 2 wt.% of poly(dendrimer) **7** were conducted. These results are also shown in Fig. 3. The neat films gave a relatively fast three-component decay of 0.35 μs (0.26), 1.04 μs (0.72), and 2.9 μs (0.02), which indicates that there are strong chromophore–chromophore interactions quenching emission. This corresponds well to the lower PLQY of 15% for the neat film. The poly(styrene) blended films gave a slower two-component decay of 0.74 μs (0.73) and 2.16 μs (0.27), with a PLQY of 13%. From Fig. 3 it can be seen that the luminescence decay of the poly(styrene) film is slower than that of the neat film, and despite this the PLQY appears comparable. In addition, the PLQY of the 2 wt.% blend in polystyrene is much less than the 20 wt.% blend with CBP.

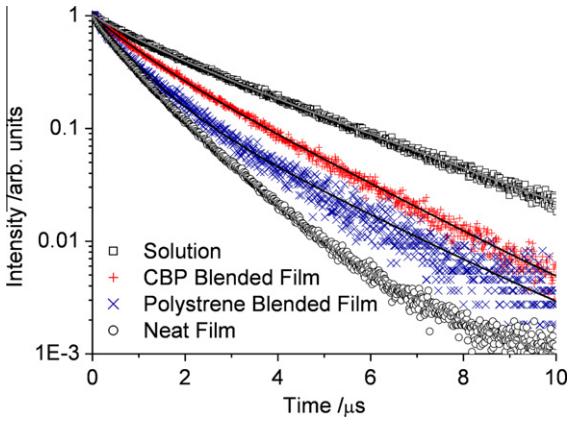

Fig. 3. Time resolved luminescence data and fits for polymer **7** in degassed dichloromethane solution and films in vacuum. The films are composed of neat polymer, 20 wt.% of the polymer dispersed in CBP and 2 wt.% of the polymer in polystyrene. Fits are shown as solid lines.

The low PLQY in the polystyrene could indicate that **7** is not well dispersed in the film however the luminescence decay in the poly(styrene) film is slower than that of the neat film. This suggests the chromophores in the poly(styrene) film do not share the same environment as in the neat film implying that phase separation alone cannot explain the low PLQY. These results, together with the apparent increase in the radiative rate of the polymer going from solution phase to the CBP blend, suggest that the emissive properties of the iridium polymer in film are dependent on other components in the blend and may be a function of differences in the chains' conformation or phase separation in the blends. These observations are consistent with the report on norbornenyl homopolymers with small molecule iridium(III) complex side chains where mixing the polymer with solutions of a 'non-polar' copolymer would lead to turbidity or even complete precipitation from solution [23].

4. Viscosity and electrical properties

The viscosity of the polymer at different concentrations in chlorobenzene was measured. Chlorobenzene was found to have a viscosity of 0.75 mPa s, and a 5 mg/ml solution of polymer **7** had a viscosity of 0.83 mPa s, which increased to 1.1 mPa s at a concentration of 25 mg/ml. This viscosity is 36% higher than simple first generation dendrimers at

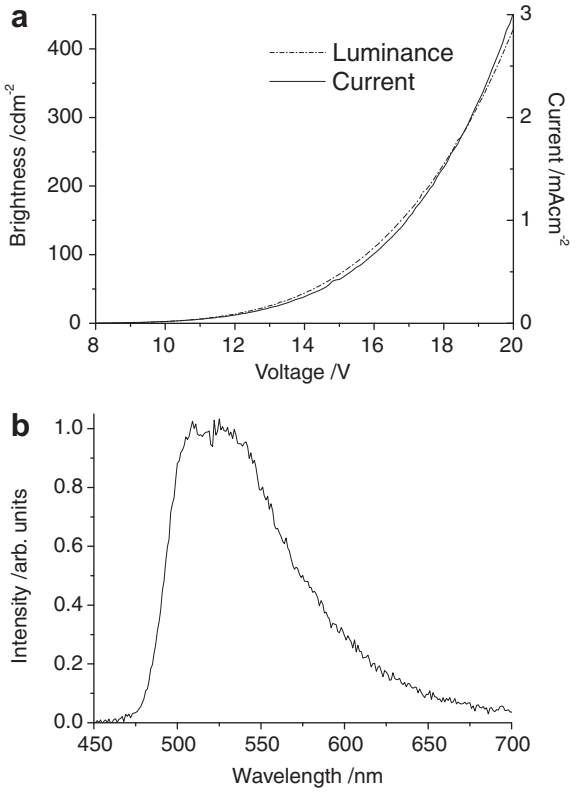

Fig. 4. Characteristics of bi-layer OLEDs using 20 wt.% polymer **7** blended into a CBP host as the emissive layer. The figures show (a) luminance and current curves and (b) the electroluminescence at 15 V.

the same concentration and is approaching the viscosity required for ink-jet printing.

The most promising blend of 20 wt.% poly(dendrimer) **7** in CBP was studied as the emissive layer in an OLED device. The devices used an aluminium/LiF cathode and a 2,2′,2″-(1,3,5-benzenetriyl)tris-[1-phenyl-1*H*-benzimidazole] (TPBI) electron transporting layer on top of the blended emissive layer on a transparent ITO anode. The devices achieved an external quantum efficiency of 5.1% and luminous efficiency of 16.4 cd/A at a brightness of 100 cd/m^2 at 15.8 V. By contrast similar devices made with blends of monomer **5** only achieved 1% EQE. The current and luminance characteristics for the polydendrimer are shown in Fig. 4a. The CIE co-ordinates of the electroluminescence were measured to be $X = 0.32$, $Y = 0.60$ at a driving voltage of 15 V. The electroluminescence spectrum is shown in Fig. 4b. A high drive voltage and the modest quantum efficiency suggest that charge transport and balance in the blend need further improvement.

5. Conclusion

The phosphorescent poly(dendrimer) reported here had excellent solubility and successfully achieved our aim of enhancing the viscosity of solutions towards the level required for ink-jet printing. The poly(dendrimer) was also moderately successful in achieving our aim of controlling chromophore–chromophore interactions in the neat film, achieving much better results than previous non-dendronised polymers. This, together with the relatively high PLQY in the film blended with CBP and the demonstration of an OLED, suggests that poly(dendrimer)s are a promising approach to ink-jet printable materials for phosphorescent LEDs.

6. Experimental methods

Commercial reagents were used as received unless otherwise noted. Use of inert atmosphere, dry glassware, and dry solvents is assumed where appropriate; the inert atmosphere used was nitrogen unless otherwise stated. Solvents were dried by passage through activated alumina in a Grubbs' column unless otherwise noted. Use of Schlenk line techniques implies the use of an argon atmosphere; dichloromethane and ethylvinyl ether were distilled from calcium hydride and deoxygenated before use. ^{1}H NMR spectra were recorded using a Bruker AV500 spectrometer, in deuterated chloroform or dichloromethane solution. For the ^{1}H NMR spectra 7.27 p.p.m. and 5.32 p.p.m. were used as the residual peaks for deuterated chloroform and dichloromethane, respectively. Abbreviations used in the assignment of the spectra are: G1-bpH = first generation branching phenyl H, spH = surface phenyl H, LH = ligand H, and NbH = norbornenyl, norbornyl or polymer backbone H. Coupling constants are quoted to the nearest 0.5 Hz. Peaks corresponding to the main component are reported. Gel permeation chromatography was carried out using PLgel Mixed-A columns (600 mm + 300 mm lengths, 7.5 mm diameter) from Polymer Laboratories calibrated with poly(styrene) narrow standards (Mp = 580–3.2 × 10^6) in tetrahydrofuran. The tetrahydrofuran was deoxygenated with helium and pumped at a rate of 1 cm^3/min at 30.0 °C. Microanalyses were carried out at London Metropolitan University, UK. UV–visible absorption spectra were recorded as solutions in HPLC grade dichloromethane or as films with a Perkin–Elmer UV–vis Lambda 25 spectrometer or a Varian Cary 300 spectrophotometer and absorption maxima are reported. Infrared spectra were recorded on a Bruker Tensor 27 FT-IR spectrometer. Thermogravimetric analysis (TGA) was carried out on a Perkin–Elmer STA6000 and differential scanning calorimetry was performed using a Perkin–Elmer Diamond DSC by ANFF-Q (the Australian National Fabrication Facility – Queensland Node, University of Queensland, QLD, Australia). Mass spectra were recorded on an Applied Biosystems Voyager DE-STR MALDI-TOF instrument, using 2-[(2*E*)-3-(4-*tert*-butylphenyl)-2-methylprop-2-enylidene]malononitrile (DCTB) matrix in positive reflection or linear mode, at the EPSRC National Mass Spectrometry Service Centre (NMSSC), Swansea, UK.

Solution samples were dissolved in dichloromethane and freeze–thaw degassed. Solution photoluminescence quantum yields were measured following the method described in [34]. Samples were excited at 360 nm. Their fluorescence was compared to a quinine sulphate in 0.05 M sulphuric acid standard, taken to have a solution quantum yield of 0.55. The optical densities of the standard and sample were similar and small (∼0.1). The accuracy of these measurements is estimated to be ±10% of the stated value.

All film samples were spin coated on fused silica substrates from dichloromethane solutions. Film photoluminescence was measured in an integrating sphere under nitrogen purge using the method described in [35]. The samples were excited by the 325 nm line of a He–Cd laser with a power of 0.1–0.2 mW.

All photoluminescence spectra were recorded in a JY Horiba Fluoromax 2 fluorimeter. Solution samples were excited at 360 nm and all film samples were excited at 325 nm.

The time-resolved luminescence measurements were performed using the time-correlated single photon counting technique making use of a cooled Hamamatsu R3809U-64 microchannel plate detector. The detection monochromator was centred at 520 nm wavelength. The samples were excited by a pulsed 393 nm Picoquant GaN laser diode. The system had a measured instrument response function with a FWHM of 200 ps. Solution samples were freeze–thaw degassed and film samples were measured in vacuum.

OLEDs were prepared on ITO substrates that had been etched with 37% hydrochloric acid and zinc powder. The ITO was then cleaned by sonication in acetone and *iso*-propyl alcohol followed by oxygen plasma ashing. The organic layer was spin cast from a dichloromethane solution containing a blend of the phosphorescent material with 80% 4,4′-*N*,*N*′-dicarbazolyl-biphenyl (CBP) by weight. The solution concentration was 10 mg/ml and spin coating at 2000 rpm resulted in ∼100 nm films. The samples were then placed in an evaporator operating at a pressure of 2 × 10^{-6} mb. A 60 nm electron transport and hole-blocking

layer of 2,2′,2″-(1,3,5-benzenetriyl)tris-[1-phenyl-1*H*-benzimidazole] (TPBI), a 0.7 nm layer of LiF and ~100 nm aluminium cathode were then sequentially deposited by thermal evaporation. A shadow mask was used to give a final active area of 6 mm^2.

The electroluminescence spectrum was recorded using a cooled Andor DV420-BV CCD spectrometer. The current and voltage characteristics were recorded using a Keithley source-measure unit and the light emission was measured using a calibrated photodiode assuming lambertian emission.

6.1. 2-(3-Trifluoromethyl-1H-1,2,4-triazol-5-yl)-5-formylpyridine **1**

t-Butyl lithium (1.7 M in hexane, 3.93 mL, 6.69 mmol) was added to a solution of 2-(5-trifluoromethyl-2-*H*-1,2,4-triazolyl)-5-bromopyridine [9] (490 mg, 1.67 mmol) in tetrahydrofuran (20 mL) at −78 °C. After 1 h *N*,*N*-dimethylformamide (565 μL, 7.36 mmol) was added and the solution was allowed to warm to room temperature over 16 h. The solution was cooled to 0 °C and aqueous hydrochloric acid (1 M, 8 mL) added. The solution was then neutralised with saturated aqueous sodium hydrogen carbonate before being extracted with dichloromethane (100 mL, 2 × 50 mL). The combined organic extracts were dried over magnesium sulfate and filtered, and the solvents were removed. The residue was purified by column chromatography over silica using diethyl ether:ethyl acetate mixture (9:1) as eluent to give **1** as a white solid (274 mg, ≈68%). (Found: C, 44.6; H, 1.9; N, 23.1. $C_9H_5F_6N_4O$ requires C, 44.6; H, 2.1; N, 23.1%); λ_{max} (DCM)/nm 215, 248; ν_{max} (KBr)/cm^{-1} 1687 (C═O); δ_H (500 MHz; $CDCl_3$) 7.65 (1H, dd, J = 7.5, J = 4.5, LH), 8.47 (1H, dd, J = 7.5, J = 1.5, LH), 8.90 (1H, dd, J = 4.7, J = 1.6, LH), 11.39 (1H, s, HCO) and 12.70 (1H, br. s, NH); δ_F (470 MHz; $CDCl_3$) −65.4; *m*/*z* (ESI) 241.0340 ($M-H^+$, 100%). $C_9H_3F_3N_4O$ requires 241.0343.

6.2. 2-(3-Trifluoromethyl-1H-1,2,4-triazol-5-yl)-5-hydroxymethylpyridine **2**

A solution of **1** (215 mg, 0.890 mmol) in diethyl ether (5 mL) was added to a stirred suspension of lithium aluminium hydride (135 mg, 3.56 mmol) in diethyl ether (5 mL) at 0 °C. The reaction mixture was allowed to warm to room temperature over 40 min. It was then cooled to 0 °C and quenched by careful addition of water (30 mL). The pH was adjusted to 5 with aqueous hydrochloric acid (3 M), and the resultant solution was extracted with diethyl ether (3 × 50 mL). The combined organic extracts were dried over magnesium sulfate and filtered, and the solvents were removed to give **2** as an off-white solid (201 mg, ≈92%). (Found: C, 44.4; H, 3.05; N, 22.85. $C_9H_5F_6N_4O$ requires C, 44.3; H, 2.9; N, 22.95%); λ_{max} (DCM)/nm 242, 280; ν_{max} (KBr)/cm^{-1} 3250 (OH); δ_H (500 MHz; CD_2Cl_2) 1.62 (1H, br. s, OH), 4.91 (2H, s, CH_2O), 7.59 (1H, dd, J = 7.5, 4.5, LH), 7.90 (1H, dd, J = 7.5, 1.5, LH), 8.63 (1H, dd, J = 4.5, 1.5, LH) and 12.53 (1H, br. s, NH); δ_F (377 MHz; CD_2Cl_2) −65.7; *m*/*z* (ESI) 267.0466 ($M+Na^+$, 100%). $C_9H_7F_3N_4NaO$ requires 267.0464.

6.3. [2-({3-Trifluoromethyl}-1H-1,2,4-triazol-5-yl)-5-hydroxymethylpyridine]-exo-bicyclo[2.2.1]hept-5-ene-2-carboxylate **3**

Oxalyl chloride (286 μL, 3.28 mmol) and *N*,*N*-dimethylformamide (one drop, cat.) were added to a solution of *exo*-bicyclo[2.2.1]hept-5-ene-2-carboxylic acid (226 mg, 1.64 mmol) in dichloromethane (2 mL) at 0 °C. After 2.5 h the volatiles were removed *in vacuo* and the resultant crude acid chloride was dissolved in pyridine (250 μL, 3.09 mmol) and dichloromethane (250 μL) at 0 °C. A solution of **2** (100 mg, 0.410 mmol) in pyridine (250 μL, 30.9 mmol) and dichloromethane (250 μL) was added and the reaction mixture was allowed to warm to room temperature over 16 h. The mixture was diluted with diethyl ether (20 mL) and water (20 mL) and then neutralised with aqueous hydrochloric acid (3 M, ≈1 mL). The layers were separated and then the organic phase was washed with water (3 × 20 mL) and brine (50 mL), dried over magnesium sulfate and filtered, and the solvents were removed. The residue was purified by chromatography over silica using ethyl acetate:diethyl ether mixtures (0:1 to 1:9) as eluent to give **3** as a light brown oil (127 mg, ≈85%). (Found: C, 56.1; H, 4.1; N, 15.3. $C_{17}H_{15}F_3N_4O_2$ requires C, 56.0; H, 4.15; N, 15.4%); λ_{max} (DCM)/nm 242, 280; ν_{max} (KBr)/cm^{-1} 1742 (C═O); δ_H (500 MHz; CD_2Cl_2) 1.36–1.44 (2H, m, NbH), 1.53 (1H, dd, J = 8.5, J = 1.5, NbH), 1.93–1.98 (1H, m, NbH), 2.27–2.35 (1H, m, NbH), 2.93 (1H, br. s, NbH), 3.09 (1H, bd, J = 9.5, NbH), 5.76 (1H, m, CH_2O), 6.11–6.18 (2H, m, NbH), 7.54 (1H, dd, J = 8, 4.5, LH), 8.01 (1H, dd, J = 8, 1.5, LH), 8.63 (1H, dd, J = 4.5, 1.5, LH) and 12.31 (1H, s, NH); δ_F (377 MHz; CD_2Cl_2) −65.6; *m*/*z* (ESI) 387.1034 ($M+Na^+$, 100%). $C_{17}H_{15}F_3N_4NaO_2$ requires 387.1039.

6.4. [Bis(2-{5-[3,5-bis(4-{2-ethylhexyloxy}phenyl)-phenyl]phenyl}pyridyl)-(2-{[3-trifluoromethyl]-1H-1,2,4-triazol-5-yl}-5-hydroxymethylpyridyl-exo-bicyclo[2.2.1]hept-5-ene-2-carboxylic acid ester)]iridium(III) **5**

Tetra[2-(5-{3,5-bis[4-(2-ethylhexyloxy)phenyl]phenyl}phenyl)pyridyl]diiridium(III) dichloride **4** [22] (100 mg, 33.2 μmol) and **3** (42.2 mg, 116 μmol) were dissolved in dichloromethane (5 mL) and stirred for 18 h in the dark. The solvents were removed, and the residue was purified by column chromatography over Sephadex™ LH-20 with methanol:dichloromethane 1:3 as eluent and then iterative preparative thin layer chromatography over silica using dichloromethane as eluent to give **5** as a green luminescent solid (51.9 mg, ≈43%). (Found: C, 70.2; H, 6.5; N, 4.5. $C_{107}H_{118}F_3IrN_6O_6$ requires C, 70.1; H, 6.5; N, 4.6%); ν_{max} (KBr)/cm^{-1} 1735 (C═O); δ_H (500 MHz; CD_2Cl_2) 0.91–0.97 (24H, m, CH_3), 1.34–1.58 (35H, m, CH_2, NbH), 1.72–1.79 (4H, m, CH), 1.97–2.01 (1H, m, Nb), 2.37–2.40 (1H, m, NbH), 2.95 (1H, br. s, NbH), 3.12 (1H, br. s, NbH), 3.91 (8H, m, OCH_2), 6.00 (2H, m, CH_2O), 6.13–6.19 (2H, m, NbH), 6.50 (1H, d, J = 8, LH), 6.54 (1H, d, J = 8 LH), 6.98–7.03 (9H, m, spH and LH), 7.06 (1H, dd, J = 7, J = 7, LH), 7.22–7.27 (2H, m, LH), 7.32 (1H, dd, J = 8, J = 2, LH), 7.60 (1H, d, J = 5.5, LH), 7.62–7.66 (8H, m, spH), 7.67 (1H, dd, J = 1.5, J = 1.5, G1-bpH), 7.71 (1H, dd, J = 1.5, J = 1.5, G1-

bpH), 7.74 (4H, d, J = 1.5, G1-bpH), 7.76–7.79 (3H, m, LH), 7.95–7.97 (2H, m, LH), 8.03–8.06 (3H, m, LH) and 8.09 (1H, d, J = 8.5, LH); δ_F (377 MHz; CD_2Cl_2) −63.6; m/z (MALDI-TOF) 1830.9 (39%), 1831.9 (55%), 1832.9 (100%), 1833.9 (95%), 1834.9 (54%), 1835.9 (20%) and 1836.9 (8%) ($M^{+\cdot}$). $C_{107}H_{118}F_3IrN_6O_6$ requires 1830.9 (42%), 1831.9 (50%), 1832.9 (100%), 1833.9 (96%), 1834.9 (54%), 1835.9 (21%) and 1836.9 (6%).

6.5. [Bis(2-{5-[3,5-bis(4-{2-ethylhexyloxy}phenyl)-phenyl]phenyl}pyridyl)-(2-{[3-trifluoromethyl]-1H-1,2,4-triazol-5-yl}-5-hydroxymethylpyridyl-exo-bicyclo[2.2.1]heptane-2-carboxylic acid ester)]iridium(III) **6**

Palladium on carbon (10%, 1 mg) was added to a solution of **5** (10 mg, 5.5 μmol) in ethyl acetate (1.0 mL). The reaction mixture was deoxygenated with three pump/fill (argon) cycles, and placed under an atmosphere of hydrogen with three pump/fill (hydrogen) cycles before being stirred for 3.5 h. The suspension was then filtered through Celite® and the solvents were removed to give **6** as a green luminescent yellow solid (10.6 mg, 100%). (Found: C, 69.9; H, 6.5; N, 4.4. $C_{107}H_{120}F_3IrN_6O_6$ requires C, 70.0; H, 6.6; N, 4.6%); ν_{max} (KBr)/cm^{-1} 1735 (C=O); δ_H (500 MHz; CD_2Cl_2) 0.90–0.97 (24H, m, CH_3), 1.18–1.60 (39H, m, CH_2, NbH), 1.72–1.79 (4H, m, CH), 1.86–1.92 (1H, m, NbH), 2.35 (1H, br. m, NbH), 2.47–2.50 (1H, m, NbH), 2.57 (1H, br. m, NbH), 3.91 (8H, m, OCH_2), 5.96 (2H, m, CH_2O), 6.50 (1H, d, J = 8, LH), 6.54 (1H, d, J = 7.5 LH), 6.98–7.02 (9H, m, spH and LH), 7.06 (1H, m, LH), 7.22–7.26 (2H, m, LH), 7.31 (1H, dd, J = 8, J = 2, LH), 7.60 (1H, br. d, J = 5.5, LH), 7.62–7.66 (8H, m, spH), 7.69 (1H, dd, J = 1.5, J = 1.5, G1-bpH), 7.70 (1H, dd, J = 1.5, J = 1.5, G1-bpH), 7.73 (4H, d, J = 1.5, G1-bpH), 7.75–7.80 (3H, m, LH), 7.93–7.96 (2H, m, LH), 8.03–8.06 (3H, m, LH) and 8.09 (1H, d, J = 8, LH); δ_F (377 MHz; CD_2Cl_2) −63.6; m/z (MALDI-TOF) 1832.8 (52%), 1833.8 (55%), 1834.8 (100%), 1835.8 (98%), 1836.8 (53%), 1837.8 (25%) and 1838 (5%) ($M^{+\cdot}$). $C_{107}H_{120}F_3IrN_6O_6$ requires 1832.9 (42%), 1833.9 (50%), 1834.9 (100%), 1835.9 (96%), 1836.9 (54%), 1837.9 (21%) and 1838.9 (6%).

6.6. Poly[(bis{2-[5-(3,5-bis{4-[2-ethylhexyloxy]phenyl}phenyl) phenyl]pyridyl}-(2-{3-trifluoromethyl-1H-1,2,4-triazol-5-yl}-5-hydroxymethylpyridyl]iridium(III))-1,4-vinylcyclopentane-2-carboxylic acid ester] **7**

Using standard Schlenk techniques, a solution of Grubbs (III) catalyst [26] in dichloromethane (1.0 mg/ml, 800 μL, 0.90 μmol) was added to a vigorously stirred solution of **6** (81 mg, 44 μmol) in dichloromethane (3.2 mL). Ethyl vinyl ether (three drops, excess) was added after 16 h. After a further 5 min the solvents were removed. The resultant crude material was then purified by iterative column chromatography over Sephadex™ LH-20 (four iterations) with methanol:dichloromethane 1:3 as eluent to remove remaining initiator and monomer, giving **7** as a green luminescent solid (58.5 mg, 72%). ν_{max} (KBr)/cm^{-1} 1735 (C=O); δ_H (400 MHz; CD_2Cl_2) 0.80–1.00 (24H, br. m, CH_3), 1.20–1.80 (35H, br. m, CH_2, CH, NbH), 1.82–2.32 (1H, br. m, NbH), 2.56–2.77 (1H, br. m, NbH), 2.91–3.47 (1H, br. m, NbH), 3.68–3.95 (8H, br. m, OCH_2), 5.10–5.46 (2H, br. m, alkene-H), 5.72–6.20 (2H, br. m, CH_2O), 6.37–6.54 (2H, br. s, LH), 6.72–7.29 (13H, br. m, spH and LH), 7.03–7.77 (18H, br. d, G1-bpH, spH, LH) and 7.79–8.07 (6H, br. s, LH); δ_F (377 MHz; CD_2Cl_2) −63.4; m/z (MALDI-TOF; DCTB) M_p = 171 kDa; GPC $\overline{M}_w = 5.5 \times 10^4$, $\overline{M}_n = 2.5 \times 10^4$, PDI = 2.2.

References

[1] M.A. Baldo, D.F. O'Brien, Y. You, A. Shoustikov, S. Sibley, M.E. Thompson, S.R. Forrest, Nature 395 (1998) 151.
[2] C. Adachi, M.A. Baldo, M.E. Thompson, S.R. Forrest, J. Appl. Phys. 90 (2001) 5048.
[3] Q. Wang, J.Q. Ding, D.G. Ma, Y.X. Cheng, L.X. Wang, X.B. Jing, F.S. Wang, Adv. Funct. Mater. 19 (2009) 84.
[4] S.C. Lo, N.A.H. Male, J.P.J. Markham, S.W. Magennis, P.L. Burn, O.V. Salata, I.D.W. Samuel, Adv. Mater. 14 (2002) 975.
[5] S.R. Forrest, Nature 428 (2004) 911.
[6] J.P.J. Markham, S.C. Lo, S.W. Magennis, P.L. Burn, I.D.W. Samuel, Appl. Phys. Lett. 80 (2002) 2645.
[7] J.P.J. Markham, I.D.W. Samuel, S.C. Lo, P.L. Burn, M. Weiter, H. Bassler, J. Appl. Phys. 95 (2004) 438.
[8] P.L. Burn, S.C. Lo, I.D.W. Samuel, Adv. Mater. 19 (2007) 1675.
[9] E. Tekin, P.J. Smith, U.S. Schubert, Soft Matter 4 (2008) 703.
[10] J.P. Gunning, K.A. Knights, J.C. Ribierre, R.E. Harding, J.W. Levell, P.L. Burn, I.D.W. Samuel, Proc. IEEE 7051 (2008) X511.
[11] W.Y. Lai, J.W. Levell, P.L. Burn, S.C. Lo, I.D.W. Samuel, J. Mater. Chem. 19 (2009) 4952.
[12] E. Tekin, E. Holder, V. Marin, B.J. de Gans, U.S. Schubert, Macromol. Rapid Commun. 26 (2005) 293.
[13] J.P. Gunning, J.W. Levell, M.F. Wyatt, P.L. Burn, J. Robertson, I.D.W. Samuel, Polym. Chem. (2010) doi: 10.1039/c0py00039f.
[14] J.X. Jiang, Y.H. Xu, W. Yang, R. Guan, Z.Q. Liu, H.Y. Zhen, Y. Cao, Adv. Mater. 18 (2006) 1769.
[15] X.W. Chen, J.L. Liao, Y.M. Liang, M.O. Ahmed, H.E. Tseng, S.A. Chen, J. Am. Chem. Soc. 125 (2003) 636.
[16] M. Sudhakar, P.I. Djurovich, T.E. Hogen-Esch, M.E. Thompson, J. Am. Chem. Soc. 125 (2003) 7796.
[17] A.J. Sandee, C.K. Williams, N.R. Evans, J.E. Davies, C.E. Boothby, A. Kohler, R.H. Friend, A.B. Holmes, J. Am. Chem. Soc. 126 (2004) 7041.
[18] S. Tokito, M. Suzuki, F. Sato, M. Kamachi, K. Shirane, Org. Electron. 4 (2003) 105.
[19] S. Tokito, M. Suzuki, F. Sato, Thin Solid Films 445 (2003) 353.
[20] P.T. Furuta, L. Deng, S. Garon, M.E. Thompson, J.M.J. Frechet, J. Am. Chem. Soc. 126 (2004) 15388.
[21] M. Suzuki, S. Tokito, F. Sato, T. Igarashi, K. Kondo, T. Koyama, T. Yamaguchi, Appl. Phys. Lett. 86 (2005) 3.
[22] L. Deng, P.T. Furuta, S. Garon, J. Li, D. Kavulak, M.E. Thompson, J.M.J. Frechet, Chem. Mater. 18 (2006) 386.
[23] J.R. Carlise, X.Y. Wang, M. Weck, Macromolecules 38 (2005) 9000.
[24] J.X. Jiang, C.Y. Jiang, W. Yang, H.G. Zhen, F. Huang, Y. Cao, Macromolecules 38 (2005) 4072.
[25] H.Y. Zhen, C. Luo, W. Yang, W.Y. Song, B. Du, J.X. Jiang, C.Y. Jiang, Y. Zhang, Y. Cao, Macromolecules 39 (2006) 1693.
[26] M.J. Frampton, E.B. Namdas, S.C. Lo, P.L. Burn, I.D.W. Samuel, J. Mater. Chem. 14 (2004) 2881.
[27] D.D. Manning, L.E. Strong, X. Hu, P.J. Beck, L.L. Kiessling, Tetrahedron 53 (1997) 11937.
[28] J.M. Pollino, L.P. Stubbs, M. Weck, Macromolecules 36 (2003) 2230.
[29] J.D. Rule, J.S. Moore, Macromolecules 35 (2002) 7878.
[30] J.A. Love, J.P. Morgan, T.M. Trnka, R.H. Grubbs, Angew. Chem.-Int. Edit. 41 (2002) 4035.
[31] T.S. Qin, J.Q. Ding, L.X. Wang, M. Baumgarten, G. Zhou, K. Mullen, J. Am. Chem. Soc. 131 (2009) 14329.
[32] S.C. Lo, E.B. Namdas, P.L. Burn, I.D.W. Samuel, Macromolecules 36 (2003) 9721.
[33] T.D. Anthopoulos, M.J. Frampton, E.B. Namdas, P.L. Burn, I.D.W. Samuel, Adv. Mater. 16 (2004) 557.
[34] J.N. Demas, G.A. Crosby, J. Phys. Chem. 75 (1971) 991.
[35] N.C. Greenham, I.D.W. Samuel, G.R. Hayes, R.T. Phillips, Y. Kessener, S.C. Moratti, A.B. Holmes, R.H. Friend, Chem. Phys. Lett. 241 (1995) 89.

zinc oxide has been successfully used in hybrid solar cells [3] and bilayers of the thermally evaporated pentacene on ZnO have been investigated [4], the advantages of ZnO-polymer hybrids for ambipolar field effect transistors have not been explored yet.

In this work we used sol–gel processed ZnO nanoparticles with various Al doping levels, as the n-type semiconductor, and regioregular poly(3-hexylthiophene) (P3HT), as the p-type component, to fabricate field effect transistors (FETs) with gold source and drain contacts on a SiO_2 dielectric. Our previous work [5] evinced, *interalia*, that doping has a strong effect on the structural and electrical properties of sol–gel processed sintered ZnO:Al. The electron mobility is slightly decreasing due to structural, morphological, and ionic defects.

For the fabrication of the hybrid system presented in this paper, it was necessary to omit the sintering step for the Al doped ZnO in order to allow intrusion of P3HT into the ZnO-matrix. We show that by doping the zinc oxide nanoparticles as well as by morphological changes in the blend it is possible to adjust a balanced electron and hole mobility in the hybrid material, which is indispensable for a good performance of an ambipolar transistor. The presented data will be discussed in terms of the charge transport mechanisms in field effect transistors together with their morphology of the thin films which was monitored via X-ray reflectivity (XRR) measurements.

2. Experimental

2.1. Materials and synthesis

The synthesis of Al doped ZnO was performed according to the route introduced by Xue et al. [6]. 2-methoxyethanole (MTE), monoethanolamine (MEA), zincacetate dihydrate (ZAD) and aluminiumnitrate nonahydrate (ANN) were purchased from Sigma–Aldrich. The stabilizer MEA (2.1 ml) were dissolved in 100 ml of the solvent MTE to lead to a 0.35 M solution. The starting material ZAD (35 mmol) was added. Depending on the designated doping level ANN was admixed to the solution to achieve up to 10 at.% Al doping. The solution was stirred for 2 h. at 60 °C and subsequently aged for at least one day.

Regioregular poly(3-hexylthiophene) (P3HT) was purchased from Rieke Metals and used without further purification. P3HT was dissolved in chlorobenzene at 0.1 wt%.

2.2. Sample preparation and measurement

The field effect transistor structures were prepared on Sb-doped silicon wafers purchased at Si–Mat. The highly *n*-doped Si(001) with a nominal resistivity of about 0.02 Ωm serves as the gate electrode. The top layer of the wafer consists of 200 nm thermally grown SiO_2 which forms the dielectric. Photolithography was used to get well defined source–drain structures. Ti (1 nm) as an adhesion layer and subsequently 19 nm thick Au contacts were thermally evaporated on top of the dielectric. After cleaning the substrate with acetone and isopropanol, the ZnO solution with various Al doping level was spin coated for one minute at 3000 rpm. Thereafter, the substrate was heated to 300 °C in an oven in ambient atmosphere for 100 min in order to remove MEA. Then the samples were transferred to a glovebox where the P3HT solution was spin coated. Finally, the samples were slowly dried for 15 h. The electronic reproducibility of FETs was confirmed for several samples. The relative error was smaller than 5% and 10%, for the bare ZnO:Al and ZnO:Al/P3HT-transistors, respectively. The estimates for the conductivity and the charge carrier density show relative errors of about 20%.

The current–voltage measurements were carried-out using an Agilent Parameter Analyzer 4155C. The room temperature measurements were performed in nitrogen atmosphere before and after the infiltration of P3HT. In either transistor measurement we chose channel lengths of 160 μm, so that the channel resistance dominates the contact resistance and, hence, minimizes the influence of the contact on the measured transport parameters [7].

The X-ray reflectivity measurements were carried-out using a Diffractometer General Electrics 3003 T–T in Bragg–Brentano geometry. The X-ray measurement provides a non-destructive way of probing the layer thickness, interface roughness and the electron density of single and multi layers. For XRR, the sample is being illuminated with Cu Kα radiation at the characteristic wavelength of $\lambda = 1.5406$ Å. Typically, the reflected intensity is being plotted vs. the wave vector transfer q_z perpendicular to the surface. q_z and θ are related via $q_z = 4\pi/\lambda \sin\theta$. From $\theta = 0^\circ$ up to a critical angle θ_c, total reflection dominates, as radiation can penetrate the layer only evanescently. By the relation $\theta \sim \sqrt{\rho}$, θ_c is a measure for the electron density ρ and hence, a measure for the effective material density. The intermixing of the two phases can be determined from the attenuation of the corresponding Kiessig fringes.

3. Results

3.1. Field effect transistor measurements

The hybrid FETs were built upon a device structure using a SiO_2 dielectric and Au source and drain bottom contacts in two steps, first spin coating and heating the inorganic component, subsequently deposition of the organic component. This approach resulted in Ohmic–like contacts for electron and hole injection. The electrical parameters of the devices were investigated before and after the deposition of P3HT.

In a field effect transistor charge carriers are accumulated via a source–gate voltage V_g where the hole or electron accumulation are determined by the sign of V_g, corrected for the threshold voltage V_{th}. This provides a way to selectively determine the electron and hole mobility at various carrier densities from the transfer characteristics in the linear and saturation regime, μ_{lin} and μ_{sat}, respectively, via

$$\mu_{lin} = \frac{L}{wC_iV_d}\frac{\partial I_d}{\partial V_g} \quad \text{and} \quad \mu_{sat} = \frac{2L}{wC_i}\left(\frac{\partial\sqrt{I_d}}{\partial V_g}\right)^2, \tag{1}$$

where L and w are the channel length and width, C_i is the dielectric capacitance per unit area, I_d is the current between source and drain and V_d is the source–drain field.

An output characteristic of a transistor with unsintered 2 at.% Al doped ZnO as an active layer is shown in Fig. 1. The gate and the drain voltage, respectively, have been switched between 0 and 70 V. The output characteristic exhibits Ohmic behaviour in the linear regime, indicating efficient injection from the gold contact into the conduction band of ZnO:Al and saturation at high drain voltages. The pinch-off voltage increases quadratically with the applied gate voltage. The threshold voltage V_{th} (see Fig. 2) has been extracted from the transfer characteristic in the saturation regime. V_{th} is a measure for trapped charges in the material and at the ZnO:Al/dielectric interface and also for free charge carriers intrinsically present in the channel. It has to be noted that additional charge carriers introduced via Al doping will compensate these electron traps. The threshold voltage of ZnO:Al transistors varies between 5.5 V for the 0.8 at.% Al doped transistor and 25 V for the 5 at.% doping (see Fig. 2a).

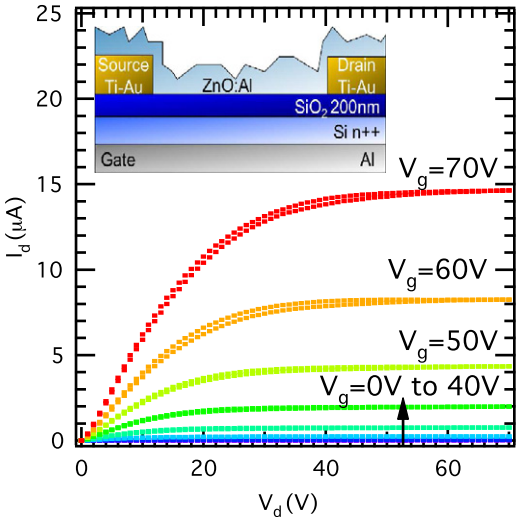

Fig. 1. ZnO:Al (2 at.%) output characteristic. Transistor details: Au bottom contacts $L = 160$ μm, $w = 62.4$ mm, SiO_2 thickness $d = 200$ nm. The inset shows a schematic drawing of the device.

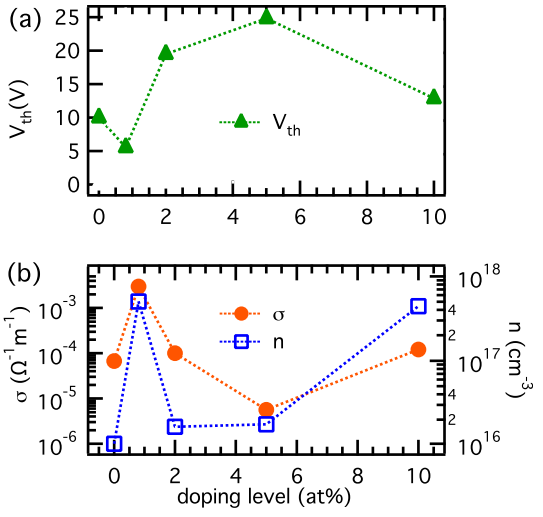

Fig. 2. Bare ZnO:Al: (a) Threshold voltage for electron transport in the saturation regime. (b) Estimated conductivity and free charge carrier density. As indicated, there is a defined correlation between V_{th} and n.

In order to investigate the electrical properties of ZnO:Al, we estimated the conductivity σ in ZnO:Al from the linear regime (low V_d) at $V_g = 0$ V using $I_d = jwd_{Au} = \sigma V_d / L \cdot wd_{Au}$, where d_{Au} is the thickness of the gold contact, $w \cdot d_{Au}$ is the area of the injecting contact (see Fig. 2b). We observe a maximum in the estimated effective conductivity of $3 \cdot 10^{-3} \Omega^{-1}$ m^{-1} for the 0.8 at.% Al doped ZnO layer, as expected for ZnO:Al [5]: Doping presumably leads to higher charge carrier densities but also leads to additional scattering centers. With $\sigma = \mu ne$, where μ is the mobility at low gate and drain voltages and e is the elementary charge, we are able to provide a rough estimate of the charge carrier density n. The charge carrier density varies

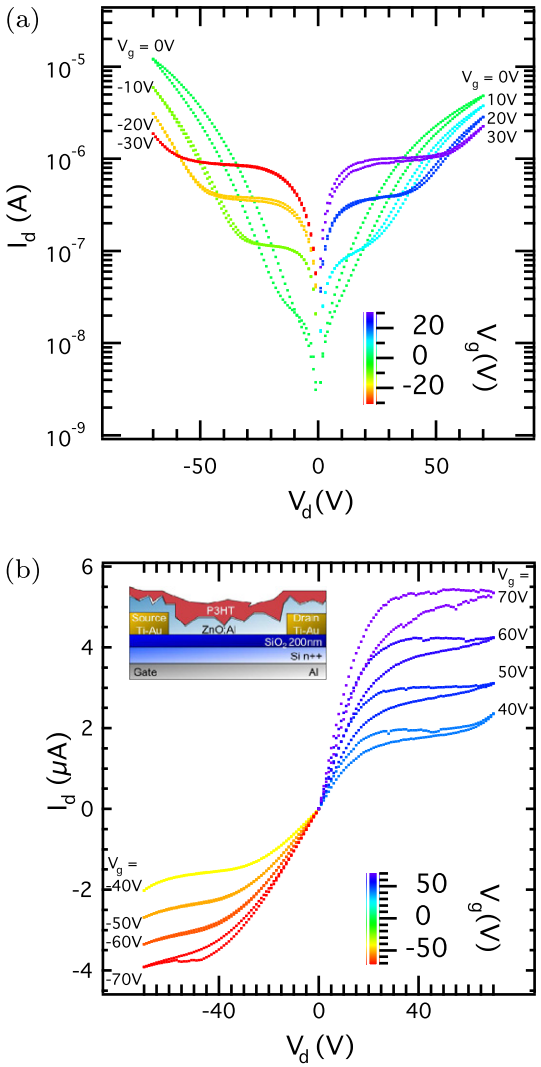

Fig. 3. ZnO:Al (2 at.%)/P3HT-transistor: output characteristic; V_g is indicated by the color scale and by the legend. Shown is the same device as in Fig 1 but with additional P3HT hole transport layer: (a) from $V_g = -30$ to 30 V, (b) from $V_g = -70$ to -40 V and from 40 to 70 V. The inset shows a schematic drawing of the device.

between $1 \cdot 10^{16}$ cm^{-3} in the nominally undoped case and $5 \cdot 10^{17}$ cm^{-3} for the 0.8 at.% Al doped layer. Additionally, we observe a relatively high charge carrier density for the highest doping level of 10 at.%. The threshold voltage V_{th} reflects the density of free charge carriers, i.e. the high n value for 0.8 at.% Al doping corresponds to a low V_{th} of 5.5 V.

3.1.1. Hybrid ZnO:Al/P3HT-transistor

After the characterization of the field effect transistors with bare ZnO:Al at several doping levels, the electronic behaviour of transistors with ZnO:Al/P3HT layers were analyzed. An output characteristic of the 2 at.% Al doped ZnO/P3HT-transistor is shown in Fig. 3. At high V_d and low V_g both, electrons and holes can be injected into the channel and form a pn-junction which leads to a diode-like behaviour. Applying high negative (positive) V_g and low V_d depletes the electrons (holes) from the channel and the device behaves as an unipolar hole (electron) accumulating transistor. Furthermore, the unipolar regime in both, hole and electron accumulation regions, shows Ohmic behaviour at low V_d. It has to be noted that we reached this Ohmic behaviour using gold for electron and hole injection and no additional modification of the dielectric was applied, making the device architecture straightforward and simple to prepare. Comparing the output characteristic of the bare ZnO:Al (2 at.%) FET (see Fig. 1) to the device, where P3HT had been coated, we observe only a slight decrease in the maximum drain current. Also, in the electron accumulation regime, an enhanced hystereses can be observed, which indicates additional trap states. We note that with Au contacts no hole accumulation could be observed in bare ZnO:Al.

The transfer characteristics of the P3HT/ZnO:Al transistors at various doping level in saturation at $|V_d| = 40$ V are shown in Fig. 4a–e. The undoped system exhibits unipolar behaviour for electrons. Similar values for the current at high positive V_g can be observed at negative V_d and low gate voltages although hole accumulation occurs only below $V_g = -50$ V. We attribute the high current at $V_g = 0$ V and $V_d = -40$ V to an enhanced efficiency of electron *and* hole injection upon applying a negative bias. The

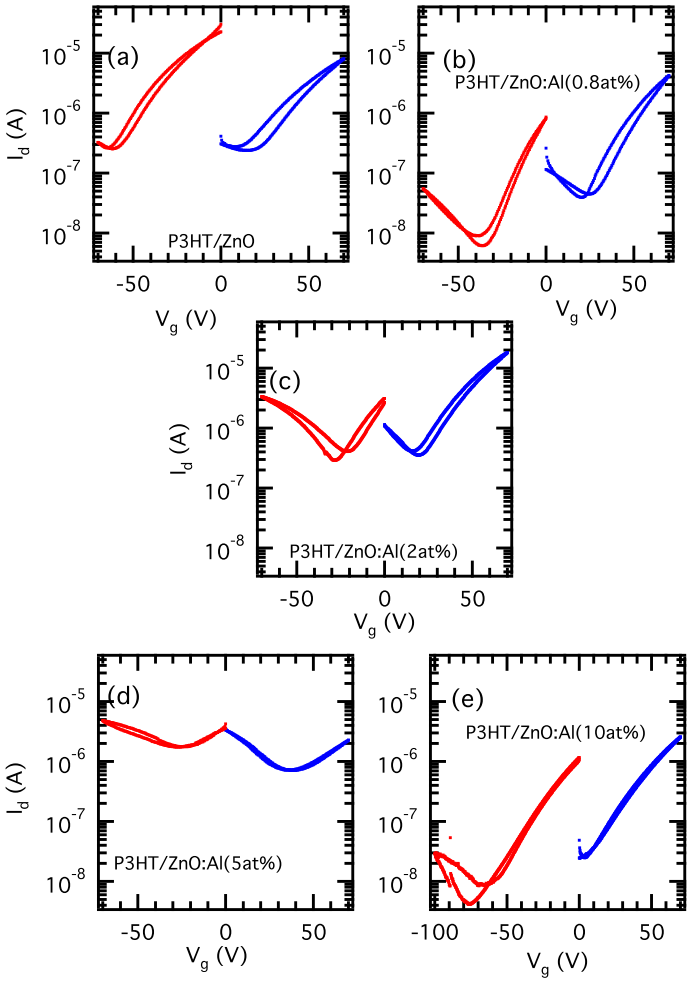

Fig. 4. ZnO:Al/P3HT-transistor: (a)–(e) transfer characteristics in saturation regime at $|V_d| = 40$ V for hole (red line) and electron (blue line) accumulation. Forward and backward direction show little charging effects. V_g ranges from −70 to +70 V, except for the 10 at% system (e). (For interpretation of the references to colour in this figure legend, the reader is referred to the web version of this article.)

difference between the drain current at $V_g = 0$ V at positive and negative V_d is directly correlated to the difference in the hole and electron mobility, which will be discussed in the following. Almost symmetric behaviour can be observed for the 2 at.% doped system. The transfer characteristics of the 5 at.% doped ZnO/P3HT has the drawback of a small on/off ratio. For 10 at.% doping, the onset of hole accumulation occurs at negative voltages higher than $|V_g| = 70$ V.

Fig. 5a shows the threshold voltage V_{th} *vs.* doping level for electrons ($V_{th,n}$, closed symbols) and holes ($V_{th,p}$, open symbols) for the saturation regime. Whereas V_{th} for the electron operating mode increases from around 0 V in the undoped case to 17.5 V and stays nearly constant for higher doping levels, we observe large fluctuations of values for the threshold voltage of holes between +23.6 and −50.9 V.

The electron mobility, μ_e, at $|V_g - V_{th}| = 40$ V and $|V_d| = 40$ V is shown in Fig. 5b. μ_e decreases over one order of magnitude from $3.2 \cdot 10^{-3}$ cm^2 V^{-1} s^{-1} for the undoped system to $6.5 \cdot 10^{-5}$ cm^2 V^{-1} s^{-1} at an Al concentration of 10 at.%. This behaviour is attributed to additional defects of structural, ionic and/or electronic origin introduced via doping [5]. Obviously, the infiltration of P3HT does not significantly affect the electron mobility, μ_e in the hybrid system decreases from $2 \cdot 10^{-3}$ cm^2 V^{-1} s^{-1} to $2 \cdot 10^{-4}$ cm^2 V^{-1} s^{-1}.

The hole mobility (see Fig. 5b) in the hybrid system, without Al doping and at a doping level of 0.8 at.%, is about two orders of magnitude lower than the hole mobility observed in bare P3HT transistors (not shown). Al (2 at.%) doping of ZnO induces an increase of the hole mobility of more than one order of magnitude to $5 \cdot 10^{-4}$ cm^2 V^{-1} s^{-1}.

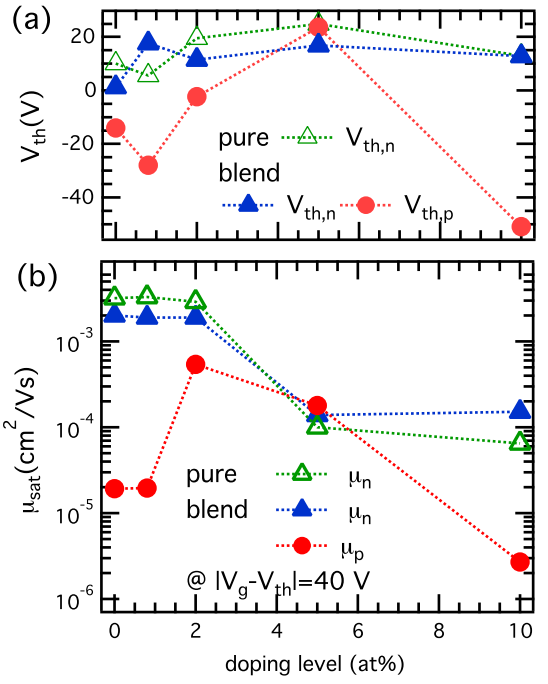

Fig. 5. ZnO:Al/P3HT-transistor: (a) threshold voltage $V_{th,n}$ for electrons and $V_{th,p}$ for holes at various doping levels. $V_{th,n}$ for bare ZnO:Al has been included for comparability, same as in Fig. 2. (b) Saturation mobility derived from the transfer characteristics; green triangles: electron mobility in bare ZnO:Al as reference, blue full triangles and red circles: electron and hole mobility in ZnO:Al/P3HT, respectively. (For interpretation of the references to colour in this figure legend, the reader is referred to the web version of this article.)

In the case of hole accumulation, ZnO:Al can be assumed to be an additional dielectric. The accumulated charge per unit area Q depends on the thickness of the dielectric

$$Q = \epsilon\epsilon_0/d \cdot (V_g - V_{th}), \tag{2}$$

where ϵ and ϵ_0 are the relative and absolute permittivity of the dielectric and d is the thickness of the dielectric. Note that the calculated hole mobilities refer to a 200 nm SiO_2 dielectric solely. The assumption of a constant capacitance was verified experimentally. Capacitance measurements on Si n^{++}/SiO_2(200 nm)/ZnO:Al/Au, i.e. treating SiO_2 and ZnO:Al as two series capacitors did not reveal significant changes with respect to the bare SiO_2 dielectric. This result is plausible since the smallest capacitance, here that of SiO_2, determines the total serial capacitance.

Evidently, the undoped and the 0.8 at.% Al doped ZnO/P3HT hybrid transistors do not exhibit balanced electron and hole mobilities. μ_e and μ_p differ by two orders of magnitude. In the case of 2 at.% Al doping we observe a hole mobility of $5 \cdot 10^{-4}$ cm^2 V^{-1} s^{-1} and the value differs by only a factor of five from μ_e at the same doping level. For a doping levels of 5 at.% we indeed obtain balanced mobilities and aside from that, a decrease of the electron mobility. The highest Al doping level of 10 at.% leads to a strong decrease in μ_p and a large difference between μ_p and μ_e.

3.2. Interface morphology

The dependence of the P3HT hole mobility on the Al doping level of ZnO cannot be understood merely from the data of the electrical measurements. The relation between μ_p and doping level could have several reasons:

(i) the crystallinity of P3HT,
(ii) the interface condition of ZnO and the related ability to infiltrate P3HT,
(iii) the dielectric properties at the interface
(iv) defects or charged traps at the organic/inorganic interfaces generated by doping.

Obviously, in any of the four cases the interface morphology is of essential relevance for the density of free holes in the FET channel.

3.2.1. X-ray reflectivity

The intermixing of both semiconductor phases at the interface can be quantified via X-ray reflectivity measurements: XRR is sensitive to the electron density of the materials which differs by one order of magnitude for P3HT and undoped/Al doped ZnO. XRR has the unique advantage over, e.g. AFM, that buried interfaces can be probed on the complete sample.

The XRR measurements of ZnO/P3HT for different Al doping levels are shown in Fig. 6. The XRR measurements were carried-out on SiO_2 and additionally on sapphire

substrates. The qualitative intensity behaviour was highly reproducible. All data are from one series on SiO_2.

Four of the five hybrid structures clearly indicate Kiessig fringes. The most pronounced fringes can be detected for the 5 and 10 at.% Al doped compounds: one can distinguish between two different oscillations hinting at the two layers, P3HT and nc-ZnO:Al, respectively, and a surprisingly small roughness at their interface. The spectra of the undoped and 0.8 at.% Al doped samples comprise fringes, as well. The spectrum of the 2 at.% Al doped ZnO/P3HT does not show pronounced interference features indicating a high level of interpenetration of the organic and the inorganic component accompanied by a high effective interface roughness.

To obtain quantitative information about the thickness of P3HT and ZnO and about the interface roughness it is essential to perform simulations and fitting of the experimental data. This allows a direct determination of the interface roughness related to the infiltration of P3HT. The theoretical reflectivity was calculated by an optical matrix method, with a refinement procedure minimizing the difference between the calculated and the measured XRR curve: the program MOTOFIT [8] based on the Paratt formalism[9]. The optimization of the parameters was done by minimizing the chi square in logarithmic form. Here, χ^2 values around 5% could be obtained The real part of the scattering length density (SLD) which is directly related to the mass density and the atomic number ranges between $30.0 \cdot 10^{-5}$ and $35.5 \cdot 10^{-5}$ Å^{-2} for ZnO and between $3.0 \cdot 10^{-5}$ and $9.3 \cdot 10^{-5}$ Å^{-2} for P3HT. The layer thickness of ZnO:Al ranges between 12 and 23 nm, for P3HT between 19 and 26 nm. The extracted data including the electron density, derived from $\rho = \mathrm{SLD}/r_e$, with r_e the classical electron radius, are shown in Table 1.

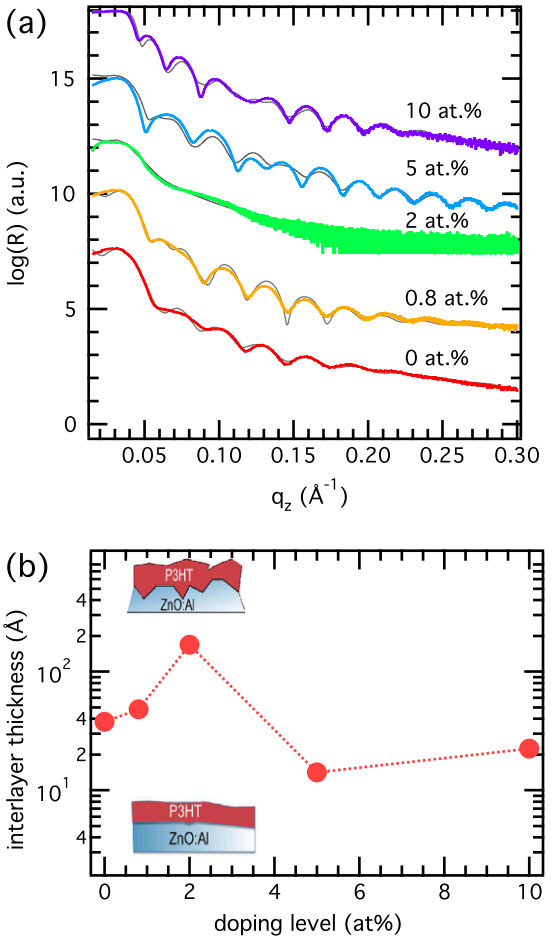

Fig. 6. (a) X-ray reflectivity curve of nc-ZnO:Al/P3HT at various Al doping levels as indicated by the legend. Grey lines are corresponding to fits based on the Paratt formalism. The profiles have been offset for clarity. (b) ZnO:Al/P3HT effective layer thickness of intermixing as derived from XRR spectra. A schematical drawing of intermixing is provided by the insets: upper drawing, high level of intermixing; lower drawing, low level of intermixing.

Table 1
Electron density ρ, thickness d and *rms* roughness r of the ZnO:Al layer resulting from fits of the XRR spectra shown in Fig. 6.

	0 (at.%)	0.8 (at.%)	2 (at.%)	5 (at.%)	10 (at.%)
$\rho_{\mathrm{ZnO:Al}}$ (e$^-$ Å^{-3})	1.1	1.1	1.3	1.1	1.2
ρ_{P3HT} (e$^-$ Å^{-3})	0.1	0.2	0.1	0.2	0.3
$\rho_{\mathrm{interlayer}}$ (e$^-$ Å^{-3})	0.1	0.4	0.2	0.9	1.0
$d_{\mathrm{ZnO:Al}}$ (nm)	15	16	12	17	23
d_{P3HT} (nm)	20	19	23	26	25
$d_{\mathrm{interlayer}}$ (nm)	4	5	19	1	2
$r_{\mathrm{ZnO:Al}}$ (nm)	2	1	1	0	1

The fits based on the Paratt formalism are shown in Fig 6a. In order to obtain appropriate fits, it was necessary to assume intermixing of the P3HT and the ZnO:Al phases. A thin intermixing layer between 1 and 5 nm is estimated for 0, 0.8, 5 and 10 at.% Al doping and a very high value of 18.6 nm for 2 at.% as shown in Fig. 6b.

4. Discussion

Al doping of ZnO results in modifications of the electron transport, which will be discussed first. Remarkably it also influences the hole mobility of the subsequently applied P3HT. The reasons for the latter will be discussed in the second part of this section.

The mobility of the inorganic ZnO decreases over an order of magnitude with increasing Al doping and it remains nearly unaffected by the infiltration of P3HT. Unlike in the sintered system [5], we observe two mobility plateaus (see Fig. 5). The mobility stays at a nearly constant level at $2\text{–}3 \cdot 10^{-3}$ cm^2 V^{-1} s^{-1} for the undoped, the 0.8 and the 2 at.% Al doped ZnO. Also no significant change could be observed for 5–10 at.% Al doping. We attribute this effect mainly to scattering of electrons: we assume, the transport in unsintered ZnO:Al is preferentially limited by charge carrier scattering effects due to the low level of crystallinity in the material, additional defects due to doping do not have a drastic effect on the mobility. It is worth mentioning, that the investigated layers are X-ray amorphous. The values for σ and the corresponding charge carrier density n of around 10^{-4} Ω^{-1} m^{-1} and 10^{17} cm^{-3} are rather low for ZnO:Al due to the omitted sintering step and, therefore, the low level of crystallinity. Also, errors due to the contact resistance can not be neglected. However, we expect this

effect to be small due to the long channel length, i.e. the transport within the semiconductor limits the current between source and drain.

The hole mobility was found to depend on the Al doping level of ZnO. The origin of this behaviour will be discussed in the following:

(i) We assume the hole transport to occur solely in P3HT, e.g. we modify the surface conditions of the undoped and doped zinc oxide layer and observe the influence on the morphology of the polymer. The hole mobility, again, is influenced by the morphology of P3HT, i.e. determined by the order of π–π-stacking and also by the orientation to the substrate because of the anisotropy of charge transport [10], and by the nanostructure of infiltration. Absorption spectra (not shown, refer to appendix) revealed interchain absorption and a similar vibronic structure and therefor a similar degree of short range order of the polymer chains on top of the variously Al doped ZnO. We note that optical absorption is a bulk sensitive technique, while the FET mobility is an interface property. However, in case of very thin layers and of layers with crystalline fraction induced by the underlying surface, the optical absorption spectra yields to (indirect) information on the interface topography.

(ii) The porosity of ZnO determines the ability to infiltrate P3HT. The hole mobility sensitively depends on the roughness of the Al doped ZnO layer. XRR spectra exhibit a strong interconnection of the organic/inorganic interface layer and the doping level. The sample with 2 at.% Al doping shows a high level of intermixing, i.e. a value of around 18.6 nm (see Fig. 6) and also the highest hole mobility (see Fig. 5) in the set of doping levels. The effective thickness of the dielectric alone can not explain the origin of the hole mobility dependence on the doping level of ZnO. Nevertheless, the highest roughness value coincides with the highest hole mobility value.

(iii) The polarizability of the dielectric, i.e. ZnO:Al in the case of hole accumulation, influences the mobility of holes accumulated at the organic/inorganic interface. Fröhlich polarons, reported for organic single crystals with different dielectrics by Hulea et al. [11], where the mobility depends on the value of the dielectric constant of the oxide, cannot describe μ_p vs. doping level, due to the necessity of a largely varying dielectric constant with doping level. A $\mu \sim 1/\epsilon$ behaviour was found. A change in ϵ of almost two orders of magnitude would be mandatory in our case, e.g. from 8 to 0.08. In the case of ZnO, we can estimate a change in ϵ from $\sim$8 to $\sim$11 [12], if Al_2O_3 is present in a high percentage at the interface at high Al doping levels. Hence, Fröhlich polarons can be excluded from having a significant influence on the dependence of the hole mobility on the Al doping level. On the other hand, the mobility in disordered organic FETs was found to be diminished due to the systematic broadening of the Gaussian density of states with dipolar disorder at the semiconductor/dielectric interface due to the value of ϵ [13]. This scenario can also be excluded from having a drastic influence.

(iv) Defects or charged traps at the organic/inorganic interfaces generated by doping can positively or negatively influence the accumulated density of free holes. In order to reach ambipolar behaviour, a balanced intrinsic carrier density of both types of charge carriers is mandatory [4]. If, e.g. the density of free electrons outbalances that of the holes, a higher negative gate voltage is needed in order achieve hole accumulation. The threshold voltage for electron transport in bare ZnO:Al transistors has been investigated (Fig. 2a). It ranges between 15.5 and 33.4 V for the undoped and the 0.8 at.% Al doped ZnO and for the 5 at.% doped system, respectively, and reflects the doping dependence of n. The threshold voltage for holes (Fig. 5), which qualitatively indicates the density of trap states, nearly parallels the hole mobility. The trap scenario is affirmed by the fact that a low threshold voltage for electrons results in a high V_{th} for holes after application of P3HT. The free electron density n reaches a maximum in the 0.8 at.% and also in the 10 at.% Al doped samples. In both cases we observe low hole mobilities, namely $2.0 \cdot 10^{-5}$ cm^2 Vs^{-1} and $2.7 \cdot 10^{-6}$ cm^2 Vs^{-1}. A lower mobility value for the highest doping level is attributed to additional traps. The lowest charge carrier density was estimated to be $1.0 \cdot 10^{16}$ cm^{-3} and was observed for undoped ZnO, although 2 at.% Al doping with $1.6 \cdot 10^{16}$ cm^{-3} and 5 at.% with $1.8 \cdot 10^{16}$ cm^{-3} do not show a significant difference. If only the free electron density was responsible for the hole mobility dependence on the doping level of ZnO, the highest hole mobility should be observed in three cases: the undoped, the 2 and 5 at.% Al doped system. This is clearly not the case.

Here, an interplay of different parameters, mainly the P3HT/ZnO:Al intermixing (ii) and the free electron density in ZnO:Al (iv), causes the maximum hole mobility at 2 at.% Al doping. Interestingly, a minimum in σ, i.e., minimum in $\mu \cdot n$ can be found for the 5 at.% Al doped sample, where we indeed observe balanced electron and hole mobilities after application of P3HT. Nevertheless, the highest hole mobility was observed for 2 at.% Al doping. The Debye screening length in ZnO:Al at 0, 2, and 5 at .% Al doping, i.e. at the moderate electron densities of about 10^{16} cm^{-3}, amounts to $\sim$20 nm. This extends over the ZnO:Al thickness and hence, the free electrons will be depleted to the P3HT/ZnO:Al interface. In the case of the 2 at.% Al doped sample, where we observe the highest degree of intermixing, we expect local field enhancement at the P3HT/oxide interface and therefore better injection and accumulation of holes.

5. Conclusion

We were able to demonstrate ambipolar charge transport in a hybrid organic/inorganic transistor consisting of the polymer P3HT and the sol–gel synthesized undoped

and Al doped ZnO. We observe the influence of doping of ZnO on its electron mobility and also on the hole mobility in P3HT. The maximum for the conductivity in unsintered ZnO has been reached for 0.8 at.% Al doping and also various Al doping levels strongly affect the density of free electrons. The electron mobility decreases with increasing doping level and stays nearly unaffected by the infiltration of the organic component. Remarkably, the hole mobility has been found to be dependent on the Al doping level of ZnO. The hole mobility reaches its maximum at the doping level of 2 at.%. By discussing several possibilities, we attribute this effect to an enhanced intermixing of ZnO:Al and P3HT, derived via X-ray reflectivity data, which is necessary for the infiltration of P3HT and to the charge carrier density variation with Al contents. To summarize, the intrinsically free electrons and the morphology, i.e. intermixing, can be controlled via Al doping of ZnO and, hence, a balanced electron and hole mobility can be adjusted in P3HT/ZnO:Al hybrids. This is the fundamental precondition for the implementation of hybrid field effect transistors in organic electronics.

Acknowledgements

We acknowledge the BMBF (project GREKOS, 03SF0356A and 03SF0356B) and the EU (project Dephotex, NMP-SE-214458 and -214459) for financial support. C.D. gratefully acknowledges the support of the Bavarian Academy of Sciences and Humanities. V.D.s work at the ZAE Bayern is financed by the Bavarian Ministry of Economic Affairs, Infrastructure, Transport and Technology.

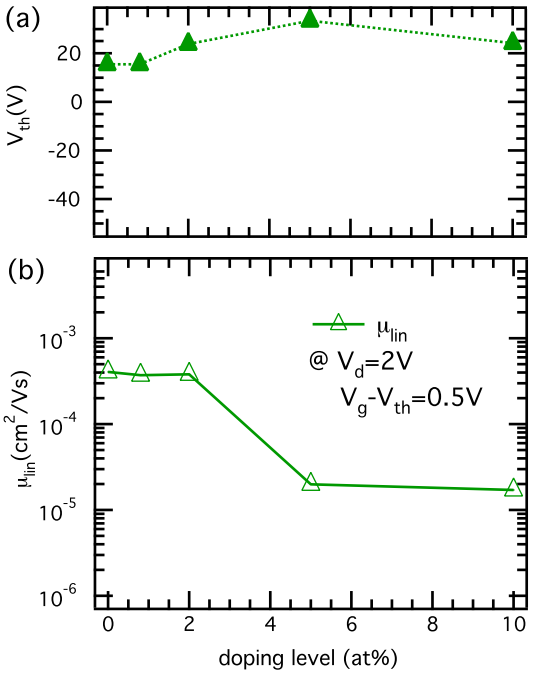

Fig. A.7. ZnO:Al characteristics, used for the evaluation of the free charge carrier density $n = \sigma/\mu_e$ in bare ZnO:Al layers.

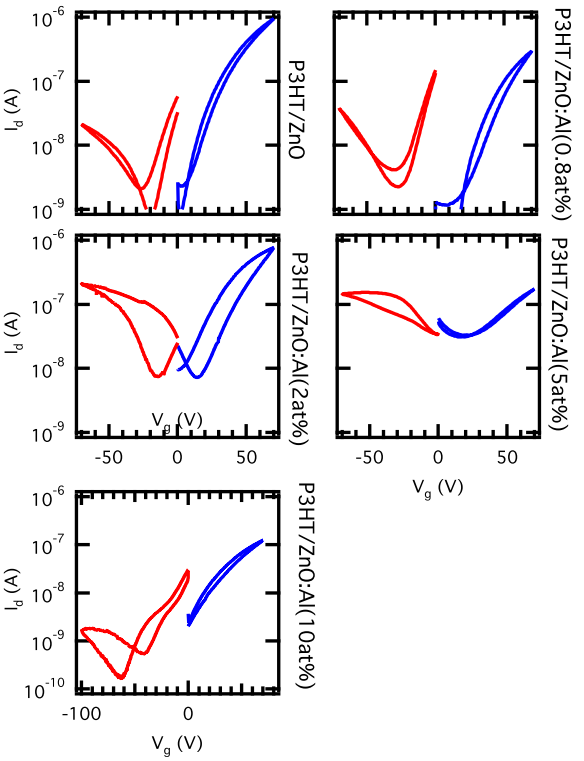

Fig. A.8. ZnO:Al/P3HT-transistor: linear transfer characteristics.

Appendix A. Electrical characteristics of ZnO:Al and ZnO:Al/P3HT hybrids in the linear regime

Additionally to the data presented in Figs. 2 and 4 we present here the data in the linear regime for clarity. See Figs. A.7 and A.8.

Appendix B. Absorption

The absorption spectra of the material system on sapphire were recorded using a PerkinElmer Lambda950. We investigated absorption spectra in order to monitor the interchain orientation relative to the next neighbors of the infiltrated P3HT and to clarify the effect of doping on the absorption edge of ZnO:Al. The absorption spectra are shown in Fig. B.9. We observe absorption by ZnO in the UV region at wavelength lower than 380 nm, in good agreement with literature [14]. Using $(\alpha h\nu)^2 = A(h\nu - E_g)$ [15], where A is a function of the refractive index of the material, the reduced mass and the speed of light in vacuum, h is the Plancks constant, ν is the frequency of the radiation and E_g is the energy band gap. From a plot of $(\alpha h\nu)^2$ versus the photon energy an optical band gap was obtained by applying a linear fit and an extrapolation of E_g to $(\alpha h\nu)^2 = 0\ \mathrm{eVm}^{-1}$. The undoped material exhibits an optical band gap of 3.26 eV (ca. 381 nm) and a shift of 100 meV to higher energies for the highest Al doping level was observed.

The polymer P3HT absorbs in the visible between ~1.9 and ~3 eV. It has been reported that enhanced ordering of

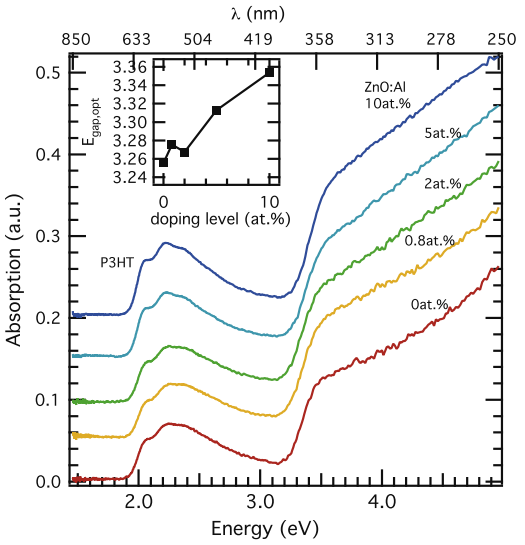

Fig. B.9. nc-ZnO:Al/P3HT absorption.

this polymer gives rise to an increased absorption at ~2.09 eV [16,17]. The absorption spectra in Fig. B.9 indicate high ordering of P3HT for all doping levels.

References

[1] R. Schmechel, R. Ahles, H. von Seggern, A pentacene ambipolar transistor: experiment and theory, J. Appl. Phys. 98 (2005) 084511.
[2] E.J. Meijer, D.M. de Leeuw, S. Setayesh, E. van Veenendaal, B.-H. Huisman, P.W.M. Blom, J.C. Hummelen, U. Scherf, T.M. Klapwijk, Solution-processed ambipolar organic field-effect transistors and inverters, Nat. Mater. 2 (2003) 678.
[3] J.E. Beek, L.H. Slooff, M.M. Wienk, J.M. Kroon, R.A.J. Janssen, Hybrid solar cells using a zinc oxide precursor and a conjugated polymer, Adv. Funct. Mater. 15 (2005) 1703.
[4] B.N. Pal, P. Trottman, J. Sun, H.E. Katz, Solution-deposited zinc oxide and zinc oxide/pentacene bilayer transistors: high mobility n-channel, ambipolar, and nonvolatile devices, Adv. Funct. Mater. 18 (2008) 1832.
[5] M.S. Hammer, D. Rauh, V. Lorrmann, C. Deibel, V. Dyakonov, Effect of doping- and field-induced charge carrier density on the electron transport in nanocrystalline ZnO, Nanotechnology 19 (2008) 485701.
[6] S.W. Xue, X.T. Zu, W.G. Zheng, H.X. Deng, X. Xiang, Effects of al doping concentration on optical parameters of ZnO:Al thin films by sol–gel technique, Physica B: Condens. Matter 381 (2006) 209.
[7] I.G. Hill, Numerical simulations of contact resistance in organic thin-film transistors, Appl. Phys. Lett. 87 (2005) 163505.
[8] A. Nelson, Co-refinement of multiple-contrast neutron/X-ray reflectivity data using MOTOFIT, J. Appl. Cryst. 39 (2006) 273.
[9] L. Paratt, Phys. Rev. 95 (1954) 359.
[10] R.J. Kline, M.D. McGehee, Morphology and charge transport in conjugated polymers, Polym. Rev. 46 (2006) 27.
[11] I.N. Hulea, S. Fratini, H. Xie, C.L. Mulder, N.N. Iossad, G. Rastelli, S. Ciuchi, A.F. Morpurgo, Tunable Fröhlich polarons in organic single-crystal transistors, Nat. Mater. 5 (2006) 982.
[12] K.F. Young, H.P. Frederikse, Compilation of the static dielectric constant of inorganic solids, J. Phys. Chem. Ref. Data 2 (1973) 313.
[13] J. Veres, S.D. Ogier, S.W. Leeming, D.C. Cupertino, S.M. Khaffaf, Low-k insulators as the choice of dielectrics in organic field-effect transistors, Adv. Funct. Mater. 13 (3) (2003) 199.
[14] J.-P. Lin, J.-M. Wu, The effect of annealing processes on electronic properties of sol–gel derived Al-doped ZnO films, Appl. Phys. Lett. 92 (2008) 134103.
[15] E.A. Davis, N.F. Mott, Conduction in non-crystalline systems v. conductivity, optical absorption and photoconductivity in amorphous semiconductors, Philos. Mag. 22 (1970) 903.
[16] P.J. Brown, D.S. Thomas, A. Köhler, J.S. Wilson, J.-S. Kim, C.M. Ramsdale, H. Sirringhaus, R.H. Friend, Effect of interchain interactions on the absorption and emission of poly(3-hexylthiophene), Phys. Rev. B 67 (2003) 064203.
[17] D. Chirvase, J. Parisi, J.C. Hummelen, V. Dyakonov, Influence of nanomorphology on the photovoltaic action of polymer–fullerene composites, Nanotechnology 15 (2004) 1317.

are bilayers of metal–metal oxide, organic–metal oxide, or organic–organic heterojunctions [1–17]. Among them, WO_3 has drawn much attention in the intermediate connectors because of its high work function (>6.0 eV) and optical transparency [19,20]. For example, tandem structures with a WO_3-based intermediate connector have been used to achieve high-efficiency OLEDs, [21,22] or organic photovoltaic cells [23]. Another advantage for using WO_3 in an intermediate connector is its operational stability compared to the p-type doped organic HTL, because the latter might cause a significant increase in the driving voltage during long-time operation [6].

Despite the extensive use of WO_3 in intermediate connectors of tandem OLEDs, its working mechanism for charge carrier generation and injection process is not yet clearly understood at the film interface level. In particular, the elucidation of the interfacial electronic structures of WO_3-based intermediate connectors is highly desirable and advantageous for interface engineering and optimization of tandem organic devices. In this work, we study the electronic structures and energy level alignment of WO_3-based intermediate connectors, consisting of an n-type organic layer, a WO_3 interlayer, and an organic HTL, by using ultraviolet and X-ray photoemission spectroscopies (UPS and XPS). Here, the n-type layer is formed by using Mg (10 vol.%) doped tris-(8-hydroxyquinoline) aluminum (Mg:Alq_3), and *N*,*N*′-bis(1-naphthyl)-*N*,*N*′-diphenyl-1,1′-biphenyl-4,4′-diamine (NPB) is used as the HTL of the adjacent EL unit. Furthermore, we investigate the impacts of the constituent materials on the functional effectiveness of a WO_3-based intermediate connector with the aim of providing insight on the design of effective connectors in tandem organic devices. For comparison, four systems, including (1) NPB/WO_3/Mg:Alq_3, (2) NPB/WO_3/Alq_3, (3) NPB/Mg:Alq_3, and (4) NPB/Alq_3, were studied.

2. Experimental

Experiments were carried out in a Kratos AXIS Ultra^{DLD} ultrahigh vacuum (UHV) surface analysis system, consisting of a multiport carousel chamber, a deposition chamber, and an analysis chamber. Base pressures in the three chambers are better than 5×10^{-10}, 5×10^{-10}, and 3×10^{-10} Torr, respectively. All organic materials were carefully sublimed twice and entirely out-gassed to ensure material purity and the study of intrinsic behavior. Film thickness was monitored by a quartz crystal microbalance. Prior to film deposition, ITO (30 Ω/□)-coated glass substrates were subjected to a routine cleaning process and *ex situ* treated by UV-ozone exposure. WO_3 and organic materials, including Alq_3 and NPB, were *in situ* evaporated in steps onto the ITO substrate from resistively heated tantalum boats in the deposition chamber at a rate of 1–2 Å/s. Samples were transferred to the analysis chamber without breaking vacuum for UPS and XPS measurements after each deposition step. UPS measurement was carried out with an unfiltered He I (21.2 eV) gas discharge lamp to characterize the valence states and the vacuum level (VL). There was no sign of sample charging in all measurements, even when the thickness of organic films reached several hundreds of Angstroms. A monochromatic aluminum Kα source (1486.6 eV) was used in the XPS measurements to study the interfacial chemical reactions and the development of possible molecular level bending across the interface. For the collection of secondary electrons, samples were negatively biased at 4 V. All measurements were performed at room temperature. The photoelectrons were collected by a hemispherical analyzer with a total instrumental energy resolution of 0.1 eV for the UPS measurements and 0.5 eV for the XPS measurements. In all the UPS and XPS spectra, the Fermi level (E_F) is referred as the zero binding energy (BE).

3. Results and discussion

3.1. Comparison of electronic structures

To understand the working mechanism of the WO_3-based intermediate connectors, electronic structure evolutions at the aforementioned four heterostructure systems were measured with UPS. Fig. 1a shows HeI UPS spectra of the WO_3/Mg:Alq_3 interface with increasing WO_3 overlayer thicknesses. The bottom spectrum was recorded from a 100 Å thick Mg:Alq_3 layer deposited on ITO substrate. Consistent with the reports in the literature [24], Alq_3 radical anion is formed upon reaction with Mg, leading to the appearance of a gap state (E_{gs}) in the forbidden energy gap as marked in Fig. 1a. The edge of the highest occupied molecular orbital (HOMO) of Mg:Alq_3 (denoted as E_H) is estimated by linear extrapolation at low BE side of the HOMO peak maximum, which locates at 3.0 eV below E_F.

As shown in Fig. 1a, deposition of the WO_3 overlayer at increasing thickness results in a progressive shift of the characteristic emission features of Mg:Alq_3 and WO_3 towards the lower BE region. This is accompanied by a 3.3 eV rising of VL. The top spectrum corresponds to the photoemission from a 50 Å thick WO_3 layer, from which the valence band edge is estimated to be at 3.3 eV below E_F. Taking into account the transport gap of 3.3 eV, the conduction band edge of the WO_3 layer seems to be pinned at the Fermi level, consistent with the previous report that WO_3 is an n-type semiconductor material [25]. In addition, it is noted that a new state can be observed in the forbidden band gap upon a 10 Å thick WO_3 deposition. It has been demonstrated that the imperfect stoichiometry of WO_3 can induce a state below Fermi level, originating from W 5*d* band [26]. As a result, the formation of the new state as observed in UPS spectra may be attributed to partial reduction of W^{6+} cation as discussed later by XPS measurement.

For comparison, Fig. 1b shows the HeI UPS spectra of the WO_3/Alq_3 interface as a function of the overlayer thickness. Spectral evolution at the WO_3/Alq_3 interface is consistent with its chemically inert nature, showing no additional spectral structures upon WO_3 deposition on Alq_3, and is different from the case of WO_3 on Mg:Alq_3 as shown in Fig. 1a.

The HeI UPS spectra of NPB deposited onto WO_3 layer on Mg:Alq_3/ITO substrate are shown in Fig. 2, where NPB

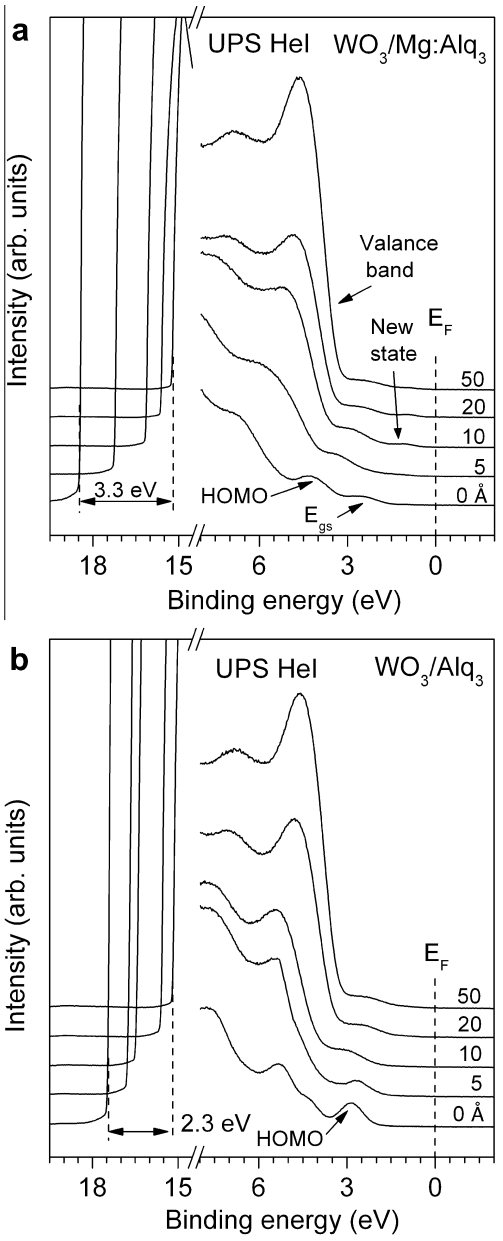

Fig. 1. HeI UPS spectra of (a) WO_3/Mg:Alq_3 and (b) WO_3/Alq_3 interfaces on ITO substrates for increasing thicknesses of the deposited layer.

thickness ranges from sub-monolayer (~2 Å) to 120 Å. The bottom spectrum is the same as that of 50 Å thick WO_3 layer in Fig. 1a. The evolution of the NPB/WO_3 interface as observed here is identical to those previously reported organic/transition metal–oxide interfaces [20,27–29]. Upon deposition of NPB, the frontier molecular orbitals of NPB gradually shift towards higher BE side, accompanied by a VL downward shift of 1.6 eV. Additionally, there is no observable feature in the organic energy gap region at the NPB/WO_3 interface, suggesting the absence of chemical interaction at the interface. Moreover, the UPS spectra evolution of NPB/WO_3 interface on Alq_3/ITO substrate (not

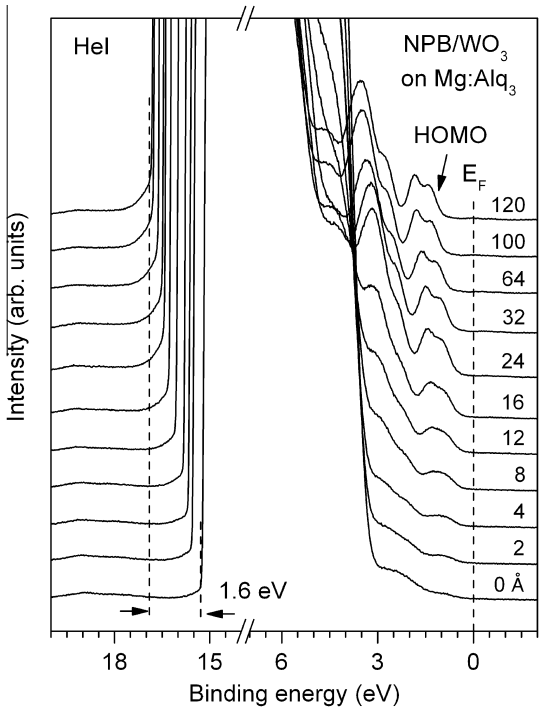

Fig. 2. HeI UPS spectra as a function of incremental NPB deposition on the WO_3/Mg:Alq_3 substrate.

shown here) is almost identical to that on Mg:Alq_3/ITO, implying the independence of its electronic structures on the underlying substrate.

In addition, UPS spectra of the NPB/Mg:Alq_3 and the NPB/Alq_3 interfaces on ITO substrate (not shown here) demonstrated that except for the intensity attenuation of the features of the Alq_3 underlayer, all the molecular level positions remain constant with a negligible vacuum level shift at the interface, indicating the absence of interface dipole and band bending in either layer.

3.2. Chemical structures and XPS spectra

To accurately separate the contributions of interface dipole and energy level bending to the interfacial energy level alignment and to determine the origin of the new state formation in the forbidden gap at the WO_3/Mg:Alq_3 interface, XPS measurements were also taken after each deposition step. Evolution of selected W 4*f* core level spectra for the NPB/WO_3/Mg:Alq_3 and NPB/WO_3/Alq_3 systems are shown in Fig. 3a and b, respectively. It is obvious that the W 4*f* spectra of a 50 Å thick WO_3 overlayer on Mg:Alq_3 and Alq_3 are virtually identical, showing sharp doublet peaks at 35.7 (W $4f_{7/2}$) and 37.9 (W $4f_{5/2}$) eV, respectively. In accordance with previous reports [26], these peak positions can be assigned to the chemical state of W^{6+}. As evident in Fig. 3a, however, an additional feature at the low BE side can be observed in W 4*f* spectra at low WO_3 coverage (i.e., <20 Å) on Mg:Alq_3, which obviously differ from those of WO_3 deposited on Alq_3. The W 4*f* spectra of a 10 Å thick WO_3 overlayer can be nicely least-square fitted by means

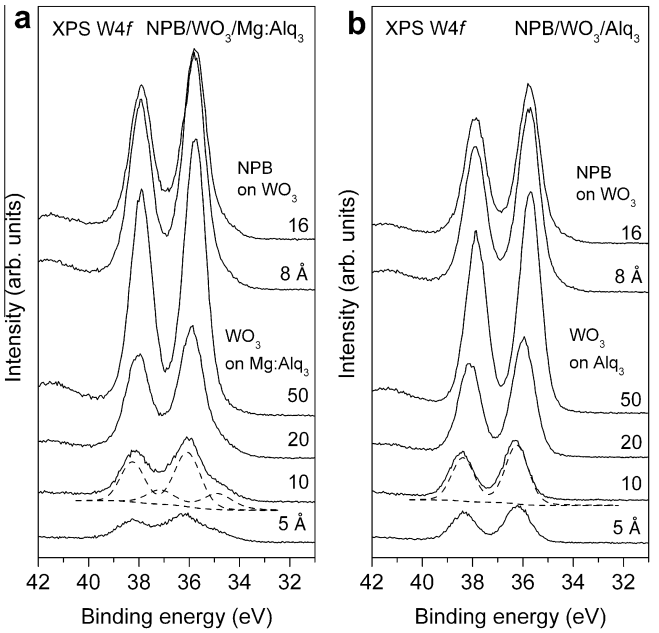

Fig. 3. XPS W 4*f* core level spectra obtained upon formation of (a) NPB/WO_3/Mg:Alq_3 and (b) NPB/WO_3/Alq_3 interfaces. The results of the least-square peak fitting of a 10 Å thick WO_3 on Mg:Alq_3 and Alq_3 substrates are represented by dashed lines.

of two main doublets to analyze the contributions of the individual components. The fitting was performed, within the experimental error, by keeping constant the energy intervals (2.2 eV) and relative intensity ratios (4:3) between W $4f_{7/2}$ and W $4f_{5/2}$ signals at the level obtained from the 50 Å thick WO_3 overlayer. Absolute energy position and width of individual sub-spectra were free fitting variables. The spectra were simulated with a fixed mixture of Lorentzian and Gaussian line shapes, and the Shirley integral background was applied to remove contributions of the inelastically scattered electrons. Consequently, the energy positions for W $4f_{7/2}$ are located at 36.1 and 34.9 eV, respectively for WO_3 overlayer on Mg:Alq_3, while W $4f_{7/2}$ is located at 36.2 (thin solid line) for WO_3 on Alq_3. The new feature (thin dashed line in Fig. 3a) in the 10 Å thick WO_3 overlayer has a chemical shift of about 1.2 eV relative to the bulk one of WO_3 (thin solid line in Fig. 3a), indicating the reduced W atoms in WO_{3-x}. This can be attributed to the reduction of W^{6+} cations by charge transfer from Mg, consistent with the appearance of a new state in the forbidden band gap as shown in Fig. 1a. These results were further confirmed by directly depositing Mg onto WO_3 layer (not shown here). Upon NPB deposition on WO_3 films, the W 4*f* doublet peak shows only changes in peak height with neither additional component nor peak broadening (Fig. 3a and b). These further confirm the absence of chemical reaction between NPB and WO_3 as observed in the UPS measurements.

3.3. Energy shifts and energy level alignment

Relative energy shifts of the valence band features and core levels extracted from UPS and XPS measurements

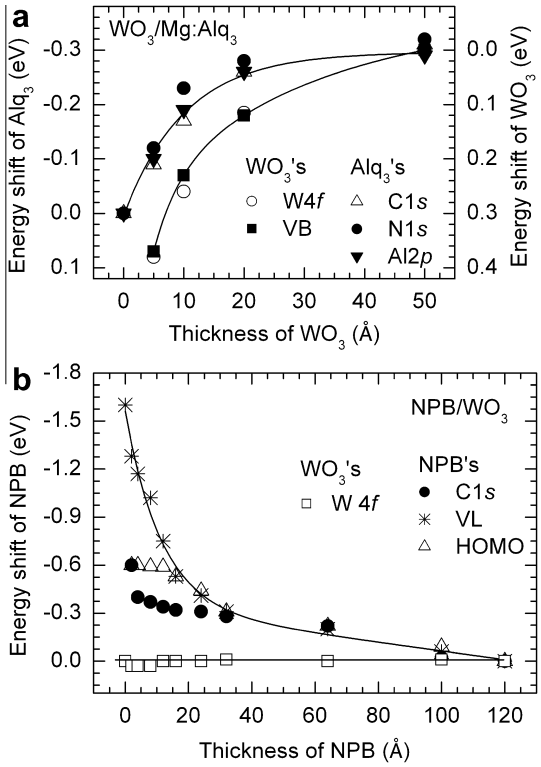

Fig. 4. Energy level shifts for HOMO, VL, and core levels of (a) WO_3 and Alq_3 in WO_3/Mg:Alq_3 and (b) NPB in NPB/WO_3 on Mg:Alq_3 substrate deduced from UPS and XPS measurements. The zero of the energy scale refers to the bulk value. The solid lines mark the energy shift.

for the NPB/WO_3/Mg:Alq_3 interface are shown in Fig. 4. It can be seen that all the core levels follow the trends of the valence band at the WO_3/Mg:Alq_3 interface. The spectral features of WO_3 at the interface show a similar upward shift of ~0.4 eV with increasing WO_3 coverage; whereas those of Alq_3 display a ~0.3 eV rigid upward shift toward the interface as shown in Fig. 4a. These results rule out the contribution from charging in Alq_3 and accurately reflect the energy level bending in organic materials at the interface. Similar phenomena can be found at the NPB/WO_3 interface, where the spectral features of NPB show a rigid downward shift with increasing NPB thickness while those of WO_3 remain almost negligible change (Fig. 4b). By comparing the amplitudes of energy shift of the core levels and the valence band features obtained by XPS and UPS measurements, respectively, the contributions of interface dipole and energy level bending to the abrupt VL shift at the two interfaces can be accurately separated [30].

Based on the UPS and XPS measurements, energy level diagrams are depicted in Fig. 5 for NPB/WO_3/Mg:Alq_3, NPB/WO_3/Alq_3, NPB/Mg:Alq_3, and NPB/Alq_3 systems on ITO substrate, respectively. Here, the E_H for organic and WO_3 layers in the intermediate connectors is extracted from the UPS spectra. Charge-transport gaps are used for more accurate estimation of the lowest unoccupied molecular orbital (LUMO) or conduction band position, E_L, for organic and WO_3 layers, which were determined by combined UPS and inverse photoemission spectroscopy (IPES) measurements (3.7 eV for Alq_3, 4.0 eV for NPB, and 3.3 eV for WO_3, respectively) [25,31]. Also, the Mg:Alq_3 films are assumed to have the same energy gap as the pristine Alq_3 films. Fermi levels are aligned across the interface in a thermodynamic equilibrium state.

It can be seen from Fig. 5a and c that upon Mg doping, LUMO of Alq_3 is closer to the Fermi level. This shows that Mg functions as an n-type dopant in Alq_3. Meanwhile, energy level bending appears at the interfaces of WO_3/Mg:Alq_3, WO_3/Alq_3, and NPB/WO_3 as shown in Fig. 5a and b. Interface dipole formation can be distinguished by subtracting the contribution of energy level bending from the VL shift for these interfaces. The interface dipoles, Δ, formed between WO_3 and organic layer suggest that WO_3 draws charges from the neighboring organic layers.

It has been demonstrated that tandem OLEDs with NPB/WO_3/Mg:Alq_3 as the intermediate connector offer good electrical behavior and luminance output, while devices without the WO_3 interlayer in the intermediate connector require high driving voltage [6]. According to the energy level diagram as depicted in Fig. 5a, the functional effectiveness of the NPB/WO_3/Mg:Alq_3 intermediate connector and thus the enhanced performance in the corresponding tandem OLED can be understood. For the NPB/WO_3/Mg:Alq_3 system, Mg:Alq_3 and WO_3 layers exhibit the n-type semiconductor property, while the NPB film is a p-type layer. As a result, upon the operation of a tandem OLED, the NPB/WO_3/Mg:Alq_3 system is actually a p/n/n junction under the reverse-bias condition. Under an applied bias, electrons can be effectively transferred from the HOMO level of NPB to the conduction band of WO_3 due to the small energy level offset. Moreover, the WO_3 interlayer between Mg:Alq_3 and NPB provides a better energy level matching in the intermediate connector. Accordingly, electrons can easily inject into the LUMO of Mg:Alq_3 due to small injection barrier at the WO_3/Mg:Alq_3 interface. In addition, Mg:Alq_3 can help to block the holes flowing from the ITO side directly into the second EL unit

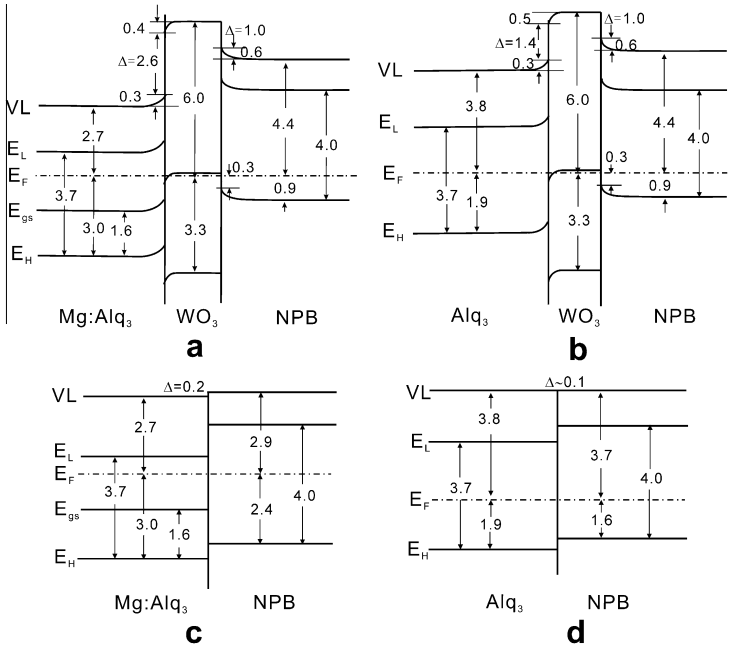

Fig. 5. Schematic energy level diagrams of (a) NPB/WO_3/Mg:Alq_3, (b) NPB/WO_3/Alq_3, (c) NPB/Mg:Alq_3, and (d) NPB/Alq_3 interfaces on ITO substrate, respectively. All the values shown are in the units of eV. The energetic positions of VL, E_F, E_{gs}, and E_H are obtained from UPS, and E_L is derived from charge-transport gaps plus E_H.

and hence reduce the leakage hole-current. As a result, such an intermediate connector facilitates efficient carrier injection from the intermediate connector into the appropriate carrier-transporting layers [6].

In the case of NPB/WO_3/Alq_3 system, the corresponding energy level diagram in Fig. 5b shows that the incorporation of a doped n-type organic layer in the intermediate connectors is critical for tandem OLEDs to function efficiently with enhanced EL efficiency. The energy offset at the NPB/WO_3 interface is identical to that of the NPB/WO_3/Mg:Alq_3 system, indicating the similar efficiency of the charge generation process. However, due to the energy level mismatch at the WO_3/Alq_3 interface, the electrons generated in WO_3 layer cannot effectively inject into Alq_3 layer, leading to the elimination of the emission in the first EL unit [17]. This is the reason why a tandem device with a NPB/WO_3/Alq_3 intermediate connector performs the *I–V* characteristics similar to that with a NPB/WO_3/Mg:Alq_3 connector, but a much lower current efficiency [6].

In contrast, the absence of WO_3 interlayer results in typical flat vacuum level alignment with neither interface dipole nor energy level bending at the NPB/Mg:Alq_3 and NPB/Alq_3 interfaces (as shown in Fig. 5c and d). The energy offset at NPB/Mg:Alq_3 (or NPB/Alq_3) interface is as large as 3.1 (or 3.4) eV. It indicates that charge transport channel between NPB's HOMO and Mg:Alq_3's (or Alq_3's) LUMO is blocked unless a higher driving voltage is applied. This is the reason why tandem devices without WO_3 interlayer exhibited poor electrical properties with current density two order of magnitude lower than that with WO_3 [6]. These findings suggest that an accurate picture of the energy level alignment at the interfaces is essential for the understanding and optimization of intermediate connectors, and the significance of a WO_3 interlayer on the intermediate connector is associated with favorable energy level matching between adjacent EL units via reducing the energy offset to a minimum.

4. Conclusions

In summary, we have obtained a comprehensive picture of electronic structures of WO_3-based intermediate connectors used in tandem OLEDs via photoemission spectroscopy. We showed that energy level offset between adjacent EL units induced by an intermediate connector is an important factor for efficient operation of tandem OLEDs. The significance of the WO_3 interlayer lies in its capability in pronouncedly modifying the energy level alignment, leading to interface dipole and energy level bending, which favor carrier injections into suitable molecular energy levels of the adjacent EL units. These results provide insight on the working mechanisms of the Mg:Alq_3/WO_3 intermediate connector and are useful references for designing new high-performance intermediate connectors in tandem organic electronic devices.

Acknowledgements

We are grateful to the financial support by National Natural Science Foundation of China (No. 60937001), National High-Tech R&D Program of China (863 Program) (No. 2008AA03A327), and City University of Hong Kong, SRG Grant (No. 7002434).

References

[1] T. Matsumoto, T. Nakada, J. Endo, K. Mori, N. Kavamura, A. Yokoi, J. Kido, SID Int. Symp. Digest Tech. Papers 34 (2003) 979.
[2] C.W. Chen, Y.J. Lu, C.C. Wu, E.H.E. Wu, C.W. Chu, Y. Yang, Appl. Phys. Lett. 87 (2005) 241121.
[3] L.S. Liao, K.P. Klubek, C.W. Tang, Appl. Phys. Lett. 84 (2004) 167.
[4] J. Drechsel, M. Pfeiffer, X. Zhou, A. Nollau, K. Leo, Synth. Met. 127 (2002) 201.
[5] X.D. Gao, J. Zhou, Z.T. Xie, B.F. Ding, Y.C. Qian, X.M. Ding, X.Y. Hou, Appl. Phys. Lett. 93 (2008) 083304.
[6] C.C. Chang, S.W. Hwang, C.H. Chen, J.F. Chen, Jpn. J. Appl. Phys., Part 1 43 (2004) 6418.
[7] C.C. Chang, J.F. Chen, S.W. Hwang, C.H. Chen, Appl. Phys. Lett. 87 (2005) 253501.
[8] H. Kanno, R.J. Holmes, Y. Sun, S.K. Cohen, S.R. Forrest, Adv. Mater. 18 (2006) 339.
[9] L.S. Liao, X.F. Ren, W.J. Begley, Y.S. Tyan, C.A. Pellow, SID 08 DIGEST, 2008, p. 818.
[10] F. Guo, D. Ma, Appl. Phys. Lett. 87 (2005) 173510.
[11] T. Tsutsui, M. Terai, Appl. Phys. Lett. 84 (2004) 440.
[12] T.Y. Cho, C.L. Lin, C.C. Wu, Appl. Phys. Lett. 88 (2006) 111106.
[13] M.K. Fung, K.M. Lau, S.L. Lai, C.W. Law, M.Y. Chan, C.S. Lee, S.T. Lee, J. Appl. Phys. 104 (2008) 034509.
[14] M.Y. Chan, S.L. Lai, K.M. Lau, M.K. Fung, C.S. Lee, S.T. Lee, Adv. Funct. Mater. 17 (2007) 2509.
[15] S.L. Lai, M.Y. Chan, M.K. Fung, C.S. Lee, S.T. Lee, J. Appl. Phys. 101 (2007) 014509.
[16] L.S. Liao, W.K. Slusarek, T.K. Hatwar, M.L. Ricks, D.L. Comfort, Adv. Mater. 20 (2008) 324.
[17] J.X. Tang, M.K. Fung, C.S. Lee, S.T. Lee, J. Mater. Chem. 20 (2010) 2539.
[18] B.W. D'Andrade, S.R. Forrest, Adv. Mater. 16 (2004) 1585.
[19] M.J. Son, S. Kim, S. Kwon, J.W. Kim, Org. Electron. 10 (2009) 637.
[20] J. Meyer, M. Kröger, S. Hamwi, F. Gnam, T. Riedl, W. Kowalsky, A. Kahn, Appl. Phys. Lett. 96 (2010) 193302.
[21] H.M. Zhang, Y.F. Dai, D.G. Ma, J. Phys. D Appl. Phys. 41 (2008) 102006.
[22] F.X. Wei, L. Fang, J. Mater. Sci: Mater. Electron. 19 (2008) 1202.
[23] A.G.F. Janssen, T. Riedl, S. Hamwi, H.H. Johannes, W. Kowalsky, Appl. Phys. Lett. 91 (2007) 073519.
[24] M.G. Mason, C.W. Tang, L.S. Hung, P. Raychaudhuri, J. Madathil, D.J. Giesen, L. Yan, Q.T. Le, Y. Gao, S.T. Lee, L.S. Liao, L.F. Cheng, W.R. Salaneck, D.A. dos Santos, J.L. Brédas, J. Appl. Phys. 89 (2001) 2756.
[25] L. Weinhardt, M. Blum, M. Bär, C. Heske, B. Cole, B. Marsen, E.L. Miller, J. Phys. Chem. C 112 (2008) 3078.
[26] F. Bussolotti, L. Lozzi, M. Passacantando, S. La Rosa, S. Santucci, L. Ottaviano, Surf. Sci. 538 (2003) 113.
[27] K. Kanai, K. Koizumi, S. Ouchi, Y. Tsukamoto, K. Sakanoue, Y. Ouchi, K. Seki, Org. Electron. 11 (2010) 188.
[28] D.Y. Kim, J. Subbiah, G. Sarasqueta, F. So, Irfan, Y. Gao, Appl. Phys. Lett. 95 (2009) 093304.
[29] M. Kröger, S. Hamwi, J. Meyer, T. Riedl, W. Kowalsky, A. Kahn, Appl. Phys. Lett. 95 (2009) 123301.
[30] J.X. Tang, C.S. Lee, S.T. Lee, J. Appl. Phys. 101 (2007) 064504.
[31] A. Kahn, N. Koch, W. Gao, J. Polym. Sci., Part B: Polym. Phys. 41 (2003) 2529.

for fabricating practical large-scale devices. We are interested in BTBT moieties that contain large number of heteroatomic groups and superior molecular order. Molecules with high formula weights have been designed to realize liquid crystalline behavior at moderately high temperatures.

In this paper, we present two LC semiconducting molecules bearing thienylethenyl [1] BTBT with two different alkyl end groups. We investigated the optical, thermal, electrochemical, and photophysical properties of the new conjugated molecules. We used these solution-processable LC molecules to fabricate OTFTs and investigate their device performance. The two molecules incorporating a BTBT moiety not only offer high carrier mobility of the order of 10^{-2} $cm^2/(Vs)$ but also a high current on/off ratio, which we attributed to the annealing effect due to liquid crystalline behavior.

2. Experiment

2.1. Synthesis

All commercially available starting materials and solvents were purchased from Aldrich, TCI, and Acros Co. Compounds **1**, **2**, and **3** were synthesized following the method in the literature and a slightly modified method. [18–21]

2.1.1. 2,7-Bis((E)-2-(5-hexylthiophen-2-yl)vinyl)[1]benzothieno[3,2-b]benzothiophene (**4**)

100 mL of oven-dried, magnetically stirred RBF was charged with a solution of **1** (0.7 g, 1.29 mmol) and 5-hexylthiophene-2-carbaldehyde, with **2** (0.63 g, 3.24 mmol) in 20 mL of freshly distilled tetrahydrofuran (THF). The reaction was allowed to stand for 0.5 h, and then, potassium *tert*-butoxide (0.36 g, 3.24 mmol) was added to it. After the reaction was complete, the solution was poured into ethanol to collect the precipitates. The product was obtained after column chromatography using toluene as an eluent. Yield: 84%, 0.68 g of yellow powder. ^{1}H NMR (300 MHz, CDCl3): δ (ppm) 7.95 (s, 2H), 7.83 (d, J = 8.2 Hz, 2H), 7.58 (d, J = 8.5 Hz, 2H), 7.30 (d, J = 3.8 Hz, 2H), 6.93 (d, J = 3.8 Hz, 2H), 6.88 (d, J = 3.6 Hz, 2H), 6.71 (d, J = 3.6 Hz, 2H), 2.83 (t, 4H), 1.71∼1.55 (m, 4H), 1.44∼1.28 (m, 12H), 0.92 (t, 6H).

Anal. calcd. for $C_{38}H_{40}S_4$: C, 73.03; H, 6.45; S, 20.52. Found: C, 73.02; H, 6.43; S, 20.55.

2.1.2. 2,7-Bis((E)-2-(5-octylthiophen-2-yl)vinyl)[1]benzothieno[3,2-b]benzothiophene (**5**)

The preparation method was identical to that for **4**. Instead of 5-hexylthiophene-2-carbaldehyde, 5-octylthiophene-2-carbaldehyde was employed. After completing the reaction, the solution was poured into methanol to collect the precipitates. The product was obtained after column chromatography using toluene as an eluent. Yield: 74%, 0.65 g of yellow powder. ^{1}H NMR (300 MHz, CDCl3): δ (ppm) 7.95 (s, 2H), 7.83 (d, J = 8.2 Hz, 2H), 7.59 (d, J = 8.5 Hz, 2H), 7.31 (d, J = 3.8 Hz, 2H), 6.93 (d, J = 3.8 Hz, 2H), 6.88 (d, J = 3.6 Hz, 2H), 6.71 (d, J = 3.6 Hz, 2H), 2.83 (t, 4H), 1.71∼1.54 (m, 4H), 1.33∼1.28 (m, 20H), 0.90 (t, 6H).

Anal. calcd. for $C_{42}H_{48}S_4$: C, 74.06; H, 7.10; S, 18.83. Found: C, 74.04; H, 7.09; S, 18.78.

2.2. Instrumental analysis

^{1}H NMR spectra were recorded on a Varian Mercury NMR 400-Hz spectrometer using deuterated chloroform (Cambridge Isotope Laboratories, Inc.). Elemental analyses were performed using an EA1112 elemental analyzer (Thermo Electron Corp.). The optimized molecular geometry was calculated employing the density functional theory (DFT) using Spartan'06.

Thermal properties were studied under a nitrogen atmosphere by differential scanning calorimetry (DSC) using a Mettler DSC 821e instrument. Thermogravimetric analysis (TGA) was conducted on a Mettler TGA50 (temperature rate of 10 °C/min under N_2). Phase transition behaviors of the liquid crystals were observed in micrographic optical textures under a polarized light microscope (Olympus BH-2) with a hot stage (Mettler Toledo 90/F82HT hot stage).

The redox properties of the two molecules were examined by using cyclic voltammetry (Model: EA161 eDAQ). The electrolyte solution employed was 0.10 M tetrabutylammonium hexafluorophosphate (Bu_4NPF_6) in freshly dried methylenechloride (MC). Ag/AgCl and Pt wire (diameter: 0.5 mm) electrodes were utilized as reference and counter electrodes, respectively. The scan rate was 50 mV/s.

X-ray diffraction (XRD) experiment was performed at varying temperatures using the synchrotron radiation (wavelength: ∼1.54 Å) of the 3C2 beam line at the Pohang Synchrotron Laboratory, Pohang, Korea. Grazing incidence XRD (GI-XRD) measurements were performed at the 10C1 beamline (wavelength: ∼1.54 Å) at the same laboratory. The measurements were obtained using scanning intervals of 2θ between 2.5° and 32°. The film samples were fabricated by drop-casting on a silicon wafer followed by drying at 70 °C under vacuum (solvent: chloroform, conc. of the solution: 10 mg/mL).

Atomic force microscopy (Digital Instruments Multimode equipped with a Nanoscope IIIa controller) operating in tapping mode with a silicon cantilever was used to characterize the surface morphologies of the samples. The film samples were fabricated by spin coating (1500 rpm) on a silicon wafer followed by drying at 70 °C under vacuum (solvent: chloroform, conc. of the solution: 10 mg/mL).

2.3. UV–Vis absorption and photoluminescence (PL) spectroscopy

Absorption spectra of samples in a solution state (chloroform, conc.: 1×10^{-6} mol/L) were obtained using a UV–VIS spectrometer (HP 8453, photodiode array type) in the wavelength range of 190–1100 nm. PL spectra of the solutions at room temperature were acquired using a Hitachi F-7000 FL spectrophotometer.

2.4. OTFT fabrication

To characterize the TFT performance, a bottom-gate top-contact device geometry was employed. Spin-coated

films (thickness: ~40–50 nm) of **4** and **5** were prepared on the heavily n-doped Si/SiO_2 substrate with monochlorobenzene as a solvent. Surface modification was carried out with octyltrichlorosilane (OTS) to produce a hydrophobic dielectric surface for more edge-on over-coated molecules. Source and drain electrodes were then thermally evaporated (100 nm) through a shadow mask with a channel width and length of 1500 and 150 μm, respectively. All field effect mobilities were extracted in the saturation regime using the relationship $\mu_{sat} = (2I_{DS}L)/(WC(V_g - V_{th})^2)$, where I_{DS} is the saturation drain current, C is the capacitance of the oxide dielectric, V_g is the gate bias, and V_{th} is the threshold voltage. The device performance was evaluated in air using a high-voltage Keithley 237 sourcemeter under ambient conditions.

3. Results and discussion

3.1. Synthesis

We report here the facile and high-yield synthesis of the new p-type BTBT-based semiconducting molecules. Scheme 1 illustrates the synthetic route for preparing the two molecules **4** and **5**. The Horner–Emmons reaction with potassium *tert*-butoxide proved beneficial as it had a high reaction yield and did not produce a catalytic residue after purification of the molecules. Two alkyl chains were added at the ends of both thienyl groups to serve as solubilizing groups and crystallization promoting moieties.

The resulting material was then purified by silica-gel column chromatography or by reprecipitation into ethanol. The identity and purity of the synthetic materials were confirmed by ^1H NMR and elemental analysis. They were found to process superior self-film forming properties and high solubility in various organic solvents such as chloroform, xylene, MC, chlorobenzene, and THF. In particular, more than 5 mg of both materials can be dissolved in 1 mL chloroform at room temperature.

3.2. UV–Vis absorption spectroscopy

The absorption spectra of the molecules in chloroform (conc.: 1×10^{-5} mol/L) are illustrated in Fig. 1. Identical absorption maxima for **4** and **5** in solution states are located at 403 (425) nm. The absorption bands of the spectrum resolved the $\pi-\pi^*$ transitions originating from the planar conjugated molecular structure. The length of alkyl chain did not affect the conjugative effect, although two thienylethenyl groups were tethered into rigid BTBT moiety. The optical band gap energies of the two molecules were determined to be around 2.75 eV. In addition, the identical PL spectra of the two molecules were observed to be mirror images of the absorption spectra and results from the same species when excited.

3.3. Thermal characterization of liquid crystalline molecules

The thermal properties of the two materials were investigated by means of thermogravimetric analysis (TGA), differential scanning calorimetry (DSC), and hot-stage polarized optical microscopy (POM).

The TGA of these molecules at a heating rate of 10 °C/min under nitrogen indicated that they have good thermal stability. Compared to the onset decomposition temperature of linear α,ω-dihexylsexithiophene (DH6T), which is at around 309 °C, these molecules have high onset decomposition temperatures (~425–433 °C) (see Table 1).

The DSC thermograms of **4** and **5** displayed phase transition behaviors (see Fig. 2). Both molecules exhibit liquid crystalline behaviors owing to the presence of a rigid BTBT central unit in combination with the heteroaromatic moieties and aliphatic parts of the molecules.

As shown in Fig. 2A, small enthalpy changes of mesophase with some extent of molecular thermal movement were observed at around 37 °C and 90 °C during the second heating cycle. Molecule **4** starts melting at 230 °C, and a liquid crystalline (LC) phase clearly appears at 260 °C. The undefined smectic LC phase exists up to 367 °C and transforms into a completely isotropic phase at around 373 °C (see Fig. 2A).

Molecule **5**, which contains longer alkyl chain tails, starts melting at 247 °C during the second heating cycle and forms a smectic phase that exists up to 356 °C. At around 360 °C, this phase becomes completely isotropic, as shown in Fig. 2B. Some transition peaks with relatively small enthalpy changes appeared during a heating cycle,

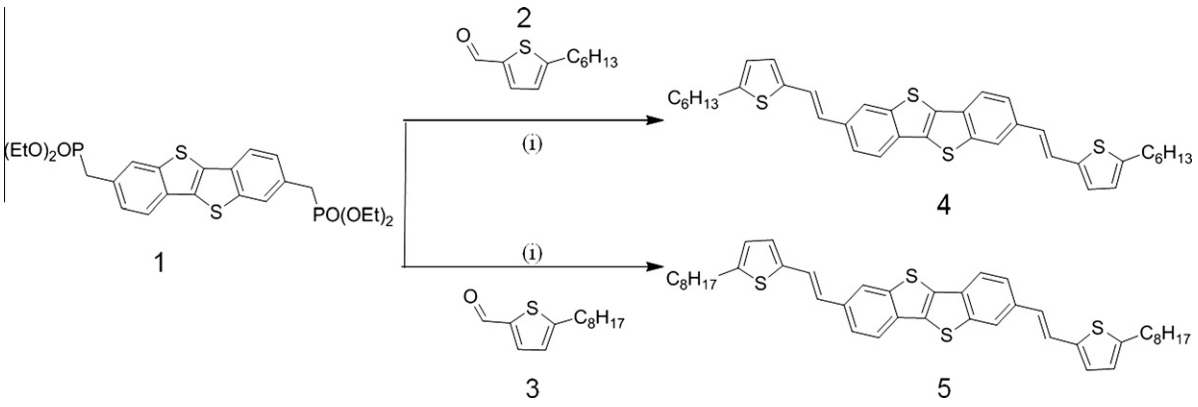

Scheme 1. Synthesis of BTBT-based conjugated molecules. (i) Potassium *t*-butoxide, THF, rt.

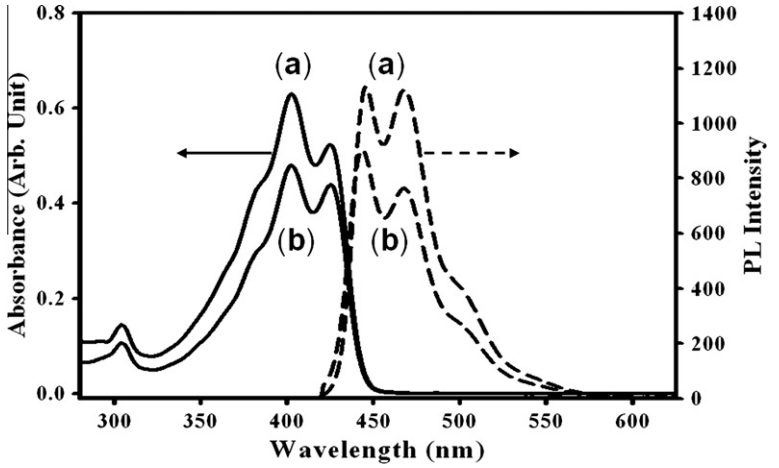

Fig. 1. UV/Vis absorption and PL spectra of (a) **4** and (b) **5**. *Solid line: absorption, Dotted line: PL spectra.

Table 1
Measured and calculated parameters of two molecules.

	T_d (°C)	Transition temperature (°C)				λ_{max}[a] (nm)	λ_{em}[a] (nm)	$\lambda_{cut\ off}$[a] (nm)	E_g^{opt} (eV)[a]	Energy level	
		Heating[b]		Cooling[b]						HOMO (eV)	LUMO(eV)[c]
		T_1	T_2	T_3	T_4						
4	425	253	367	346	228	403, 425	446, 468	449	2.76	−5.5	−2.74
5	433	236	342	337	231	403, 425	444, 468	449	2.76	−5.5	−2.74

[a] Solution state.
[b] T_1, T_2: transition temperatures during heating cycle. T_3, T_4: transition temperatures during cooling cycle.

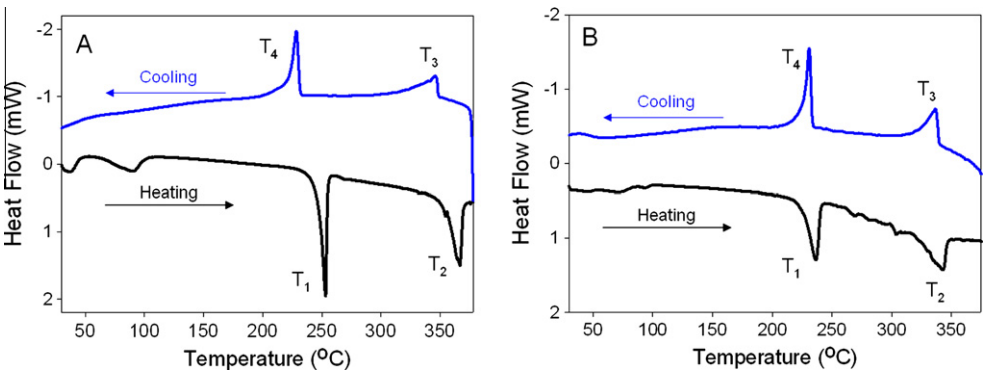

Fig. 2. DSC thermograms of molecules **4** (A) and **5** (B). (Scan rate is 10 °C/min under N_2). Enthalpy change (ΔH, Jg^{-1}): (A) T_1 (16.49), T_2 (15.89), T_3 (12.19), T_4 (14.10); (B) T_1 (14.39), T_2 (9.30), T_3 (14.23), T_4 (17.71).

which indicates the occurrence of either solid–solid transitions with some thermal motion or ordered-to-disordered crystalline transitions. When the sample is cooled, these peaks almost disappeared owing to the stabilization of the molecules.

In order to study the crystallinity of the molecules more precisely, X-ray diffraction (XRD) studies were performed on drop-cast films at varying temperatures using synchrotron radiation of a 3C2 beamline. The two molecules were confirmed to be highly crystalline, as evidenced by sharp diffraction peaks with high intensity at 25 °C.Figs. 3 and 4 show the XRD profiles of the two molecules at two different temperatures. A high temperature of 260 °C was selected between the T_1 (T_3) and T_2 (T_4) temperatures obtained in the DSC thermograms. The frozen phase of molecule **4** at 25 °C displays distinct diffraction peaks at $2\theta = 4.42°$ and 6.66° with *d*-spacings of 20.0 Å and 13.3 Å, which correspond to the intermolecular spacings of two different types of crystalline molecules (see Fig. 3). We assumed that the length of molecule **4** in a fully extended conformation (calculated by Spartan'06, DFT mode) is approximately 36.2 Å and suggested that at 13.3 °C, the

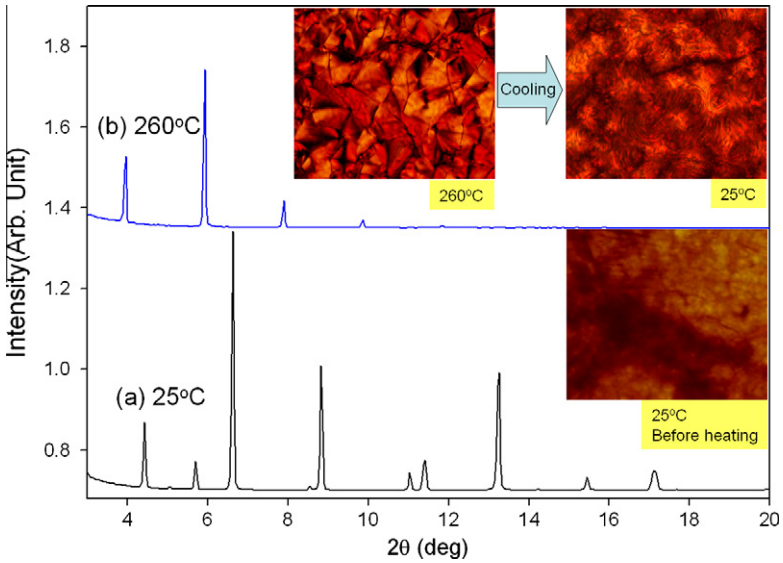

Fig. 3. X-ray diffraction patterns of molecule **4** for comparing the liquid crystalline phase recorded at 260 °C with the crystalline phase obtained at 25 °C before heating. The POM images of the phases at 25 °C and 260 °C during heating and the image obtained by cooling from 260 to 25 °C are also shown.

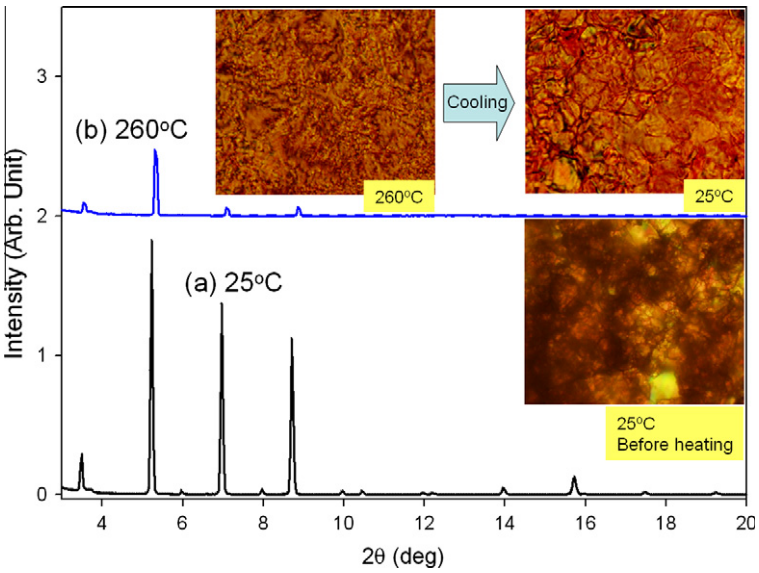

Fig. 4. X-ray diffraction patterns of molecule **5** for comparing the liquid crystalline phase recorded at 260 °C with the crystalline phase obtained at 25 °C before heating. The POM images of the phases at 25 °C and 260 °C during heating and the image obtained by cooling from 260 to 25 °C are also shown.

molecules are probably arranged vertically to the substrate with an inclination of 44.1°, owing to the interdigitation of hexyl chains. The wide angle diffraction of these molecules shows several diffraction patterns that are mostly multiple orders of the same *d*-spacing, which indicates the presence of a long-range positional order that is typical of a crystalline structure. The small angle X-ray profile at 260 °C showed layer spacings of 22.5 Å ($2\theta = 3.93°$) and 15.0 Å ($2\theta = 5.9°$); these spacings are larger than those at 25 °C, owing to the transition from the liquid crystalline state to the glassy crystal state. Concomitantly, at 260 °C, the small multiple diffraction peaks completely disappeared and the overall degree of crystallinity decreased. In order to investigate the LC properties of the molecules, POM analysis was conducted; this analysis showed a clear phase change of molecule **4** (Insets of Fig. 3). At 25 °C, an unidentified crystalline texture of the frozen glassy state was observed as a relatively dark image. When molecule **4** was further heated above 260 °C, a clear fan-like texture image of smectic C phases was observed. This texture was almost retained when the molecule was cooled to 25 °C, although some defect lines were observed in the mosaic image; this image is indicative of the crystal smectic phases.

However, the diffractogram of molecule **5** shows more than two different types of crystalline phases at 25 °C

(see Fig. 4). Although DSC thermograms showed clear phase transition peaks with a reasonable value of enthalpy change, the optical microscope did not show clear LC textures. When the sample temperature was increased up to 260 °C, a diffraction peak with the highest intensity appeared at 5.3° (*d*-spacing = 16.6 Å). When the sample temperature was increased, the intensity and position of the diffraction peak varied owing to the decrease in crystallinity. Although any specific textures were not clearly observed in the optical micrographs of molecule **5,** liquid crystallinity was verified by repeated observation. One promising property of this molecule is that the texture of the glassy solid state is quite similar to the LC texture at 260 °C as it retains the LC orderness.

3.4. Electrochemical analysis

Electrochemical characterization of the two molecules as solutions evidenced that their oxidation is reversible, which is a necessary condition for a TFT active material. The values of the ionization potential matched well with the work-function of a gold electrode. Cyclic voltammograms were recorded on a film sample, and the potentials were obtained relative to an internal ferrocene reference (Fc/Fc^+). These CV scans in the range of −2.0 V to +2.0 V (vs. Ag/Ag^+) showed quasi-reversible oxidation peaks. Unfortunately, the reduction behaviors were irreversible; therefore, we were unable to accurately estimate their HOMO and LUMO energies. To determine the LUMO levels, we combined the oxidation potential in CV with the optical energy bandgap (E_g^{opt}) resulting from the absorption edge in the absorption spectrum. Voltammograms of 4 and 5 in the film state showed that their lowest common oxidative waves are at +1.1 V. As shown in Table 1, molecules **4** and **5** have identical HOMO levels of −5.5 eV, indicating no effect of the length of alkyl chain on the electronic properties. In addition, the annealed films of **4** and **5** have identical LUMO energy levels of −2.74. The relatively higher HOMO levels may endow the material with better environmental stability.

3.5. GI-XRD

To determine the chain orientation and crystallinity of thin films for the two molecules, synchrotron grazing incidence X-ray diffraction (GI-XRD) measurements were carried out on the drop-cast films. By using a fixed grazing incidence angle (0.18°) that was above the critical angle for total internal reflection from the thin films but below the critical angle of the insulator surface, the scattering from the substrate was reduced relative to the scattering from the films [22–27].

Significantly, two different chain orientations, such as edge-on orientation of the nanocrystalline molecular domains with respect to the insulator substrates, when treated with SAMs were clearly observed in annealed films. They were evident from the different intensity distributions of the (1 0 0) reflections due to the lamellar layer structure (*d*-spacing: 29.17 Å for **4** and 32.38 Å for **5**) and the (0 1 0) reflections due to π−π interchain stacking (4.65 Å for **5**; for **4**, the diffraction peak could not be resolved clearly) through out-of-plane and in-plane geometric modes.

The highly packed crystalline molecules on the substrate may help induce carrier transport with good connection behavior. More specifically, the out-of-plane XRD pattern of as-spun **4** films on the Si/SiO_2 substrate shows seventh-order (1 0 0) reflections at 3.19°, 6.38°, 9.57°, 12.75°, 15.95°, 19.15°, and 22.40°, indicating that the film has a highly crystalline order along the out-of-plane direction. (see Fig. 5) After thermal annealing, other periodic diffraction peaks (1' 0 0) at a slightly lower angles were observed, indicating an elongated spacing between the molecules. The (1' 0 0) diffractions peaks may be due to the distortion and rearrangement of the molecules. As shown in Fig. 6, out-of plane diffraction modes were also observed; after annealing, the diffraction peak at 19.1° was observed to correlate to the distance between molecular planes. A clear diffraction was observed in the in-plane XRD measurement, also indicating high crystalline order. Analysis of the diffractograms shown in Figs. 5 and 6 leads us to conclude that both molecules are oriented perpendicular to the substrate in an edge-on manner.

3.6. Atomic force microscope (AFM) images of films

The GI-XRD measurements revealed the type of nanocrystalline structural order that prevails throughout the molecular films, while AFM observations provided images of the top surface. The morphologies of the thin films for

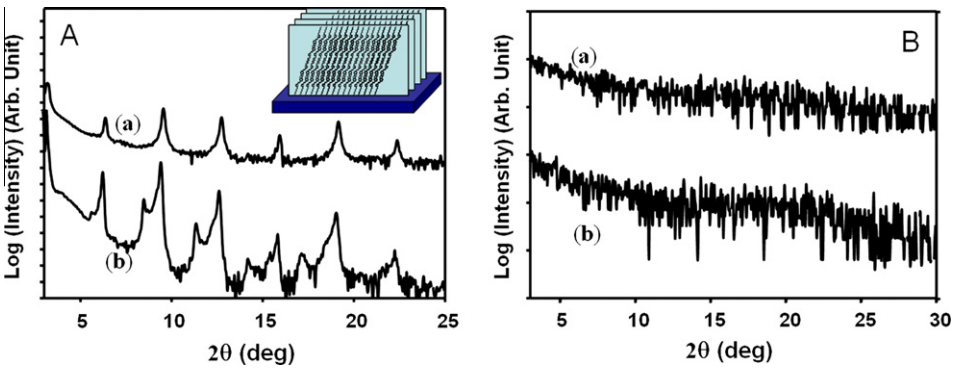

Fig. 5. (A) Out-of-plane and (B) in-plane GI-XRD intensities as a function of scattering angle 2θ for films of molecule **4** deposited on insulator surface modified with OTS. (a) Before and (b) after annealing at 180 °C.

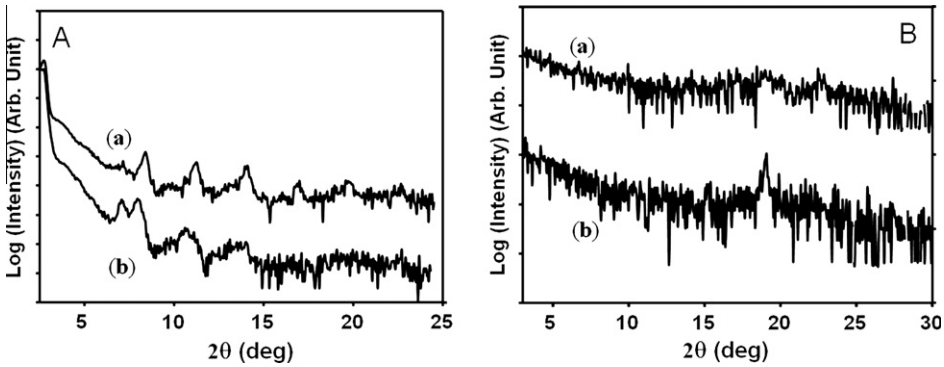

Fig. 6. (A) Out-of-plane and (B) in-plane GI-XRD intensities as a function of scattering angle 2θ for films of molecule **5** deposited on insulator surface modified with OTS.* (a) Before and (b) after annealing at 180 °C.

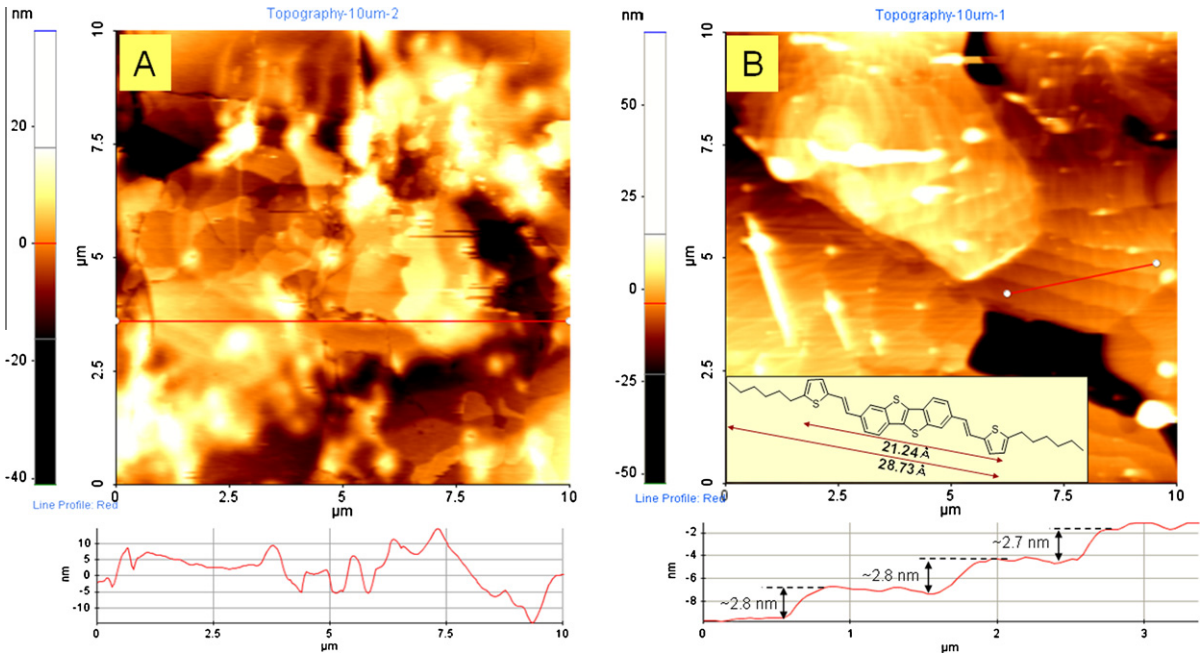

Fig. 7. AFM height images (10 × 10 μm) of molecule **4**: (A) before and (B) after annealing at 180 °C.

4 and **5** on OTS-treated Si/SiO_2 were visualized with AFM before and after thermal annealing. We prepared solutions of the two molecules and then performed spin coating to cover the dielectric surface with each solution. After completely drying the thin films, we took two micrographs before and after thermal annealing at the temperature of the liquid crystalline region, as shown in Figs. 7 and 8. In the topographic images of molecule **4**, the initial unannealed film is microcrystalline and exhibits localized large-size aggregations in a random manner. However, after thermal annealing at 180 °C for 30 min, the films reorganize into large crystalline terraces with layers lying parallel to the OTS-treated SiO_2 surface; the step height was found to be 2.6–2.7 nm, which is consistent with the length of the molecule excluding the hexyl chain on one side and the interlayer distance extracted from XRD data (Figs. 5 and 6). The terrace and step-wise structure is typical of representative organic single crystals such as rubrene and pentacene. The excellent flatness and well-defined molecular steps indicate that highly oriented crystalline films are grown on the dielectric surface. Fig. 8 shows the same phenomenon. After annealing the sample, although the domain size became larger, the step lines were nearly straight and parallel to each other in a localized crystalline domain. The average width of the molecularly flat terraces was about 3.0–3.1 nm, which is almost consistent with the molecular dimension shown in the inset. Before annealing the image of molecule **5** showed relatively smaller continuous polycrystalline grains with better network interconnection between them. However, the difference of surface topography between **4** and **5** was not so significant in this study.

3.7. Properties of OTFT made of molecules *4* and *5*

Bottom-gate top-contact OTFT devices were fabricated using gold source and drain electrodes that were thermally

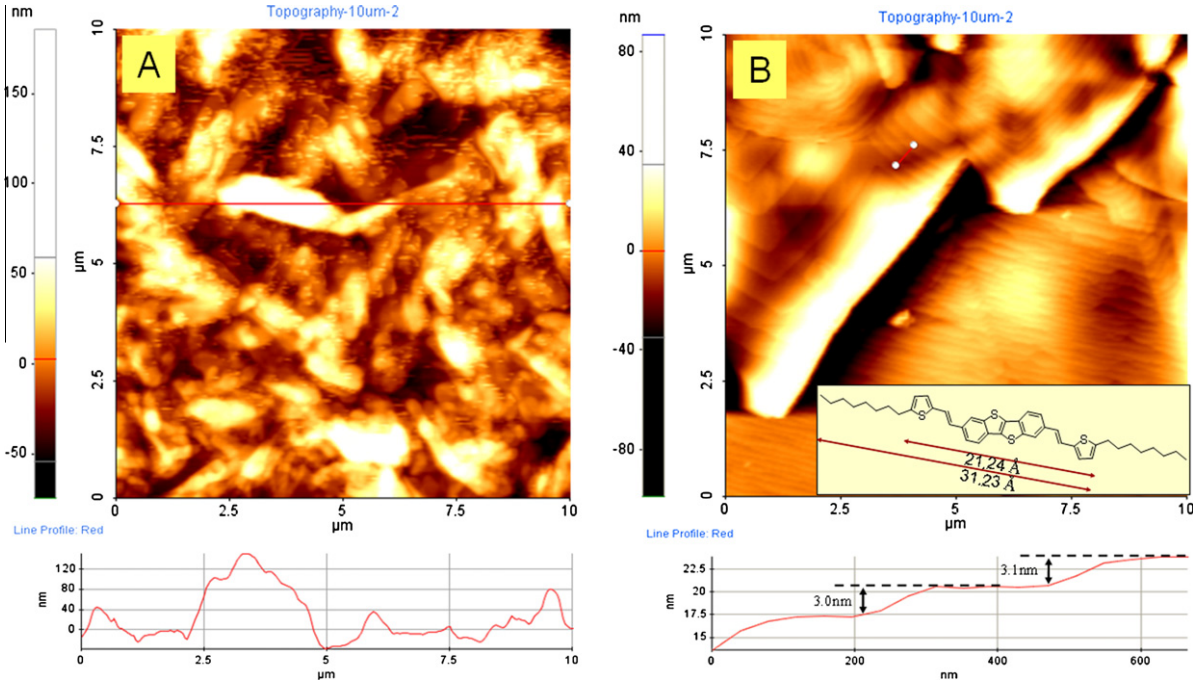

Fig. 8. AFM height images (10 × 10 μm) of molecule **5**: (A) before and (B) after annealing at 180 °C.

evaporated using the conventional method. P-doped polycrystalline silicon was used as the gate electrode, with the OTS-treated SiO_2 surface layer used as the gate dielectric insulator. A 300-nm thin film of the semiconductor was

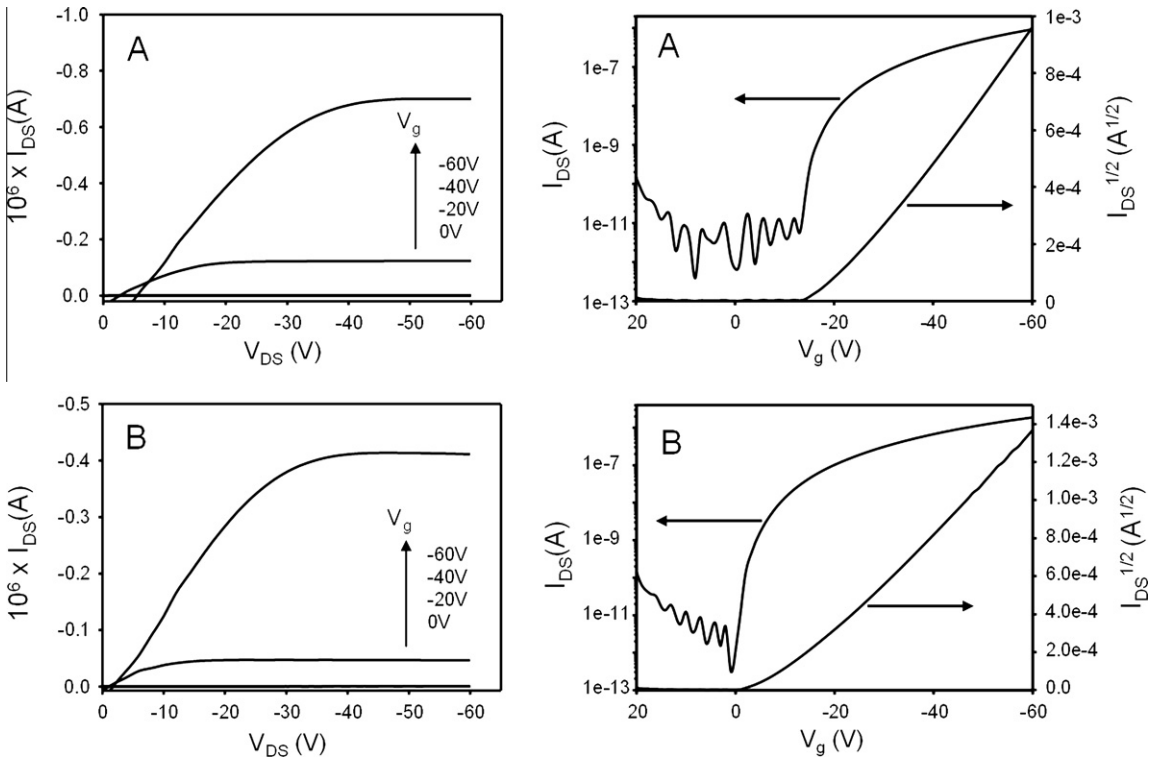

Fig. 9. Output (left) and transfer (right) characteristics of OTFT made by spin coating (A) **4** and (B) **5** from chloroform solution and annealing at 180 °C for 30 min. Insulator: OTS-treated SiO_2.

deposited by spin coating a 0.5 wt.% solution of the molecules in monochlorobenzene. After spin coating the solution on the insulator surface, the gold was deposited via thermal evaporation. To achieve optimal device performance, the OTFT devices made of **4** and **5** were each further annealed at 180 °C for 30 min.

The output characteristics showed very good saturation behavior and clear saturation currents that were quadratic to the gate bias (see Fig. 9). The saturated field-effect mobility μ_{FET} can be calculated from the amplification characteristics by using the classical equations describing field-effect transistors. [28] The mobility values obtained by measuring five different devices are listed in Table 2.Fig. 9 shows the typical drain current (I_{DC}) versus source-drain voltage (V_{DS}) plots at various gate voltages in accumulation mode for **4**- and **5**-based TFTs, respectively. When using OTS-treated SiO_2 insulators and annealing the OSC layer, the transistor devices made from **4** and **5** provided field effect mobilities of 0.020 and 0.023 cm^2/(Vs), respectively, as well as a high current on/off ratio (>10^5) and low threshold voltage ($V_{th} < -15$ V).

The molecules include alkyl chains in addition to the BTBT main structure; these chains enhance solubility and grasp adjacent neighboring molecules through molecular attractive interactions. Therefore, studies have shown that molecular distances are shorter for molecules with longer alkyl chains, resulting in the tendency of larger mobility in the TFTs. [29] The stronger attractive interaction also facilitates rapid crystal growth, so multi-domain thin films are easily fabricated on the substrates. [30] Our results are also consistent with the results in these studies.

Optical spectroscopy and GI-XRD results provided direct evidence of the strong intermolecular interaction and preferred molecular orientation of **4** and **5** in the thermally annealed crystalline film. Therefore, the predominant edge-on orientation of **4** and **5** can explain the higher values of the field effect mobilities as compared to that of as-spun molecular films, which exhibit random or less-ordered orientations of the chain molecules. For example, the unannealed film of **4** shows a mobility of the order of 10^{-3} cm^2/(Vs), which is one order of magnitude lower than that of a device with an annealed film; this can be attributed to liquid crystalline ordering under the annealing temperature. However, in this study, the mobility of the two molecules did not show significant differences, although they showed good film formation and liquid crystalline properties.

Table 2
TFT characteristics: μ_{FET} (cm^2/(Vs)) is the carrier mobility, $I_{on/off}$ is the on/off current ratio, V_{TH} (V) is the threshold voltage. *Samples: unannealed OSC layer and device with annealed OSC layer.

Molecule	Solvent	SAM	μ (cm^2/Vs)	V_{th} (V)	I_{on}/I_{off}
4[a]	MCB	OTS	0.002	−13.2	2.26×10^5
4[b]	MCB	OTS	0.020	−14.5	1.42×10^5
5[a]	MCB	OTS	0.001	−3.3	1.30×10^5
5[b]	MCB	OTS	0.023	−2.0	1.20×10^6

[a] Unannealed film.
[b] Annealed film.
* MCB, monochlorobenzene; OTS, octyltrichlorosilane.

4. Conclusions

We successfully synthesized and characterized new liquid crystalline molecules that are solution-processable. The molecules showed good film formation properties and a high degree of crystallinity in the solid states after thermal annealing. In addition to the molecular arrangement on the substrate in a predominant edge-on manner, the small crystallites of **4** and **5** covered the substrate uniformly and with good network interconnection between them; this is probably responsible for the moderately high carrier mobility in the solution-processed organic semiconductors for FETs. The field effect mobilities of TFT devices were measured to be around 0.02 cm^2/Vs, which indicates no effect of alkyl substituent in two molecules. The improved solution processability and high field-effect mobility make liquid crystalline **4** and **5** promising candidates for a new class of semiconducting materials meant for future flexible electronic devices.

Acknowledgments

This research work was supported by 21st century Frontier Research Program (F0004091-0000-00). Particularly, D.H. Choi acknowledges the financial support by the Seoul R&BD Program (10543; 2009-2010). X-ray experiments at PLS were supported by the Ministry of Science and Technology and Pohang Steel Company. This research was supported by Korea Science and Engineering, (KOSEF R0120070001128402008).

References

[1] H. Klauk, M. Halik, U. Zschieschang, G. Schmid, W. Radlik, J. Appl. Phys. 92 (2002) 5259.
[2] S.F. Nelson, Y.-Y. Lin, D.J. Gundlach, T.N. Jackson, Appl. Phys. Lett. 72 (1998) 1854.
[3] G.R. Llorente, M.-B.D. Madec, D.J. Crouch, R.G. Pritchard, S. Ogier, S.G. Yeates, Chem. Commun. (2009) 3059.
[4] A.L. Briseno, R.J. Tseng, M.M. Ling, E.H.L. Falcao, Y. Yang, F. Wudl, Z. Bao, Adv. Mater. 18 (2006) 2320.
[5] H. Meng, F. Sun, M.B. Goldfinger, F. Gao, D.J. Londono, W.J. Marshal, G.S. Blackman, K.D. Dobbs, D.E. Keys, J. Am. Chem. Soc. 128 (2006) 9304.
[6] M. Halik, H. Klauk, U. Zschieschang, G. Schmid, W. Radlik, J. Appl. Phys. 93 (2003) 2977.
[7] I. McCulloch, M. Heeney, C. Bailey, K. Genevicius, I. Macdonald, M. Shkunov, D. Sparrowe, S. Tierney, R. Wagner, W. Zhang, M.L. Chabinyc, R.J. Kline, M.D. McGehee, M.F. Toney, Nature Mater 5 (2006) 328.
[8] T. Umeda, D. Kumaki, S. Tokito, J. Appl. Phys. 105 (2009) 024516.
[9] F. Cicoira, C. Santato, A. Dadvand, C. Harnagea, A. Pignolet, P. Bellutti, Z. Xiang, F. Rosei, H. Meng, D.F. Perepichka, J. Mater. Chem. 18 (2008) 158.
[10] S.K. Park, T.N. Jackson, J.E. Anthony, D.A. Mourey, Appl. Phys. Lett. 91 (2007) 063514.
[11] M.M. Payne, S.R. Parkin, J.E. Anthony, C.C. Kuo, T.N. Jackson, J. Am. Chem. Soc. 127 (2005) 4986.
[12] D.J. Gundlach, J.E. Royer, S.K. Park, S. Subramanian, O.D. Jurchescu, B.H. Hamadani, A.J. Moad, R.J. Kline, L.C. Teague, O. Kirillov, C.A. Richter, J.G. Kushmerick, L.J. Richter, S.R. Parkin, T.N. Jackson, J.E. Anthony, Nature Mater 7 (2008) 216.
[13] J.H. Park, D.S. Chung, J.W. Park, T. Ahn, H. Kong, Y.K. Jung, J. Lee, M.H. Yi, C.E. Park, S.K. Kwon, H.K. Shim, Org. Lett. 9 (2007) 2573.
[14] R. Schmidt, S. Göttling, D. Leusser, D. Stalke, A.M. Krause, F. Würthner, J. Mater. Chem. 16 (2006) 3708.
[15] H. Ebata, T. Izawa, E. Miyazaki, K. Takimiya, M. Ikeda, H. Kuwabara, T. Yui, J. Am. Chem. Soc. 129 (2007) 15732.

[16] T. Izawa, E. Miyazaki, K. Takimiya, Chem. Mater. 21 (2009) 903.
[17] T. Izawa, E. Miyazaki, K. Takimiya, Adv. Mater. 20 (2008) 3388.
[18] M.-C. Um, J.H. Kwak, J.-P. Hong, J.H. Kang, D.Y. Yoon, S.H. Lee, C.H. Lee, J.-I. Hong, J. Mater. Chem. 18 (2008) 4698.
[19] M.J. Mio, L.C. Kopel, J.B. Braun, T.L. Gadzikwa, K.L. Hull, R.G. Brisbois, C.J. Markworth, P.A. Grieco, Org. Lett. 19 (2002) 3199.
[20] K. Takimiya, H. Ebata, K. Sakamoto, T. Izawa, T. Otsubo, Y. Kunug, J. Am. Chem. Soc. 128 (2006) 12604.
[21] B. Košata, V. Kozmik, J. Svoboda, V. Novotná, P. Vank, M. Glogarová, Liquid Crystals 30 (2003) 603.
[22] H.-S. Kim, Y.-H. Kim, T.-H. Kim, Y.-Y. Noh, S.M. Pyo, M.H. Yi, D.-Y. Kim, S.-K. Kwon, J. Mater. Chem. 19 (2007) 3561.
[23] L. Zhang, L. Tan, Z. Wang, W. Hu, D. Zhu, Chem. Mater. 21 (2009) 1993.
[24] S.-J. Kang, Y.-Y. Noh, K.-J. Baeg, J.E. Ghim, J.-H. Park, D.-Y. Kim, J.S. Kim, J.H. Park, K.W. Cho, Appl. Phys. Lett. 92 (2008) 052107.
[25] M.-C. Chen, C. Kim, S.-Y. Chen, Y, -Ju Chiang, M. -C. Chung, A. Facchetti, T. J. Marks, J. Mater. Chem. 18 (2008) 1029.
[26] M.O. Ahmed, C. Wang, P. Keg, W. Pisula, Y.-M. Lam, B.S. Ong, S.-C. Ng, Z.-K. Chen, S.G. Mhaisalkar, J. Mater. Chem. 19 (2009) 3449.
[27] C.V. Ackermann, H. Brisset, J. Zhang, J. Ackermann, S. Nénon, F. Fages, P. Marsal, T. Tanisawa, N. Yoshimoto, J. Phys. Chem. C. 113 (2009) 1567.
[28] K.H. Kim, Z. Chi, M.J. Cho, J.-I. Jin, M.Y. Cho, S.J. Kim, J.-S. Joo, D.H. Choi, Chem. Mater. 19 (2007) 4925.
[29] T. Izawa, E. Miyazaki, K. Takimiya, Adv. Mater. 20 (2008) 3388.
[30] T. Minari, M. Kano, T. Miyadera, S.-D. Wang, Y. Aoyagi, K. Tsukagoshi, Appl. Phys. Lett. 94 (2009) 093307.

Here, we synthesize a perfluoro-alkyl functionalized fullerene compound, *N*-methyl-2-(4-perfluorooctylphenyl)-fulleropyrrolidine (C60-F), and demonstrate that it is possible to pattern solution-processed C60-F films by a notably benign and scalable method. The patterning method encompasses an initial *direct* exposure of the semiconducting film to green laser light and a subsequent development by immersion into a heptane developer solution. By introducing a shadow mask between the laser and the C60-F film during the exposure step, we realize complex patterns with well-defined features. The patterned C60-F films have been utilized as the active material in field-effect transistors, and both the electron mobility ($>4 \times 10^{-2}$ cm^2/Vs) and the ambient stability are markedly improved in comparison to other more commonly employed fullerene materials, such as [6,6]-phenyl-C_{61}-butyric acid methyl ester (PCBM). We further demonstrate that the crystallinity of the solution-deposited C60-F film increases during the exposure, presumably via thermal heating induced by the absorbed laser light, while its chemical properties remain unaffected. We propose that this ordering and related densification rationalizes the decreased solubility in the developer solution, the high electron mobility, and the improved ambient stability.

2. Experimental

2.1. Synthesis of N-methyl-2-(4-perfluorooctylphenyl)-fulleropyrrolidine

The fullerene *N*-methyl-2-(4-perfluorooctylphenyl)-fulleropyrrolidine (C60-F) was synthesized in accordance with a method reported in refs [27,28], and the synthesis can be divided into two major steps, as described below and depicted schematically in Scheme 1. ^{1}H NMR spectra were recorded on a Bruker DRX 400 or Bruker DRX 360 at 298 K. The MS analysis was performed with a triple quadrupole mass spectrometer (MS/MS) (API 2000 PE Bio system, Foster City, CA, USA) equipped with a Heated Nebulizer Ion Source (APCI) and a syringe pump. The quadrupole operated in a negative mode and the ion spray voltage was set to −4.2 kV.

2.1.1. Synthesis of 4-(perfluorooctyl)benzaldehyde

A mixture of 4-iodobenzaldehyde (800 mg, 3.45 mmol), $C_8F_{17}I$ (2 mL, 7.50 mmol) and copper bronze (2.60 g, 14.3 mmol) was dissolved in dimethylformamide (DMF) (20 mL) and stirred for 22 h at 120 °C. The mixture was subsequently filtered with Celite® and washed with Et_2O and H_2O. The aqueous layer was extracted with Et_2O (15 mL × 2). The organic layer was washed with H_2O and dried over $MgSO_4$. The evaporation of the organic phase gave the crude product, which was purified by silica gel column chromatography with n-hexane to afford 900 mg (50% yield) of 4-(perfluorooctyl)benzaldehyde. ^{1}H NMR (400 MHz, $CDCl_3$): δ 7.80 (d, J = 8 Hz, 2H), 8.04 (d, J = 8.0 Hz, 2H), 10.12 (s, 1H).

2.1.2. Synthesis of N-methyl-2-(4-perfluorooctylphenyl)-fulleropyrrolidine (C60-F)

4-perfluorooctylbenzaldehyde (1.0 mmol, 524 mg) and *N*-methylglycine (2.5 mmol, 223 mg) were added to C_{60} (0.5 mmol, 360 mg) in 200 mL of chlorobenzene. The solution was heated to reflux for 20 h. The solvent was then condensed and the crude product was purified by long-path chromatography eluted by toluene/hexane (1:4). After evaporation of the solvent, 210 mg (33% yield) of the product C60-F (brown powder) was obtained. ^{1}H NMR (400 MHz, $CDCl_3$): δ 2.82 (s, 3H), 4.31 (d, J = 9.7 Hz, 1H), 5.02 (d, J = 9.7 Hz, 1H), 5.02 (s, 1H), 7.66 (d, J = 7.8 Hz, 2H), 7.97 (d, J = 7.8 Hz, 2H). LC–MS (m/z): calcd. $C_{77}H_{10}F_{17}N$ 1271.05; found 1271.0 (M^-).

2.2. Fabrication and patterning of fullerene films

The herein studied fullerene materials are the in-house synthesized C60-F, PCBM (≥99.5%, Solenne) and C_{60} (≥99.5%, SES research). The latter two were used as received. C60-F and PCBM were separately dissolved in chlorobenzene (99.8%, anhydrous, Sigma–Aldrich) in a

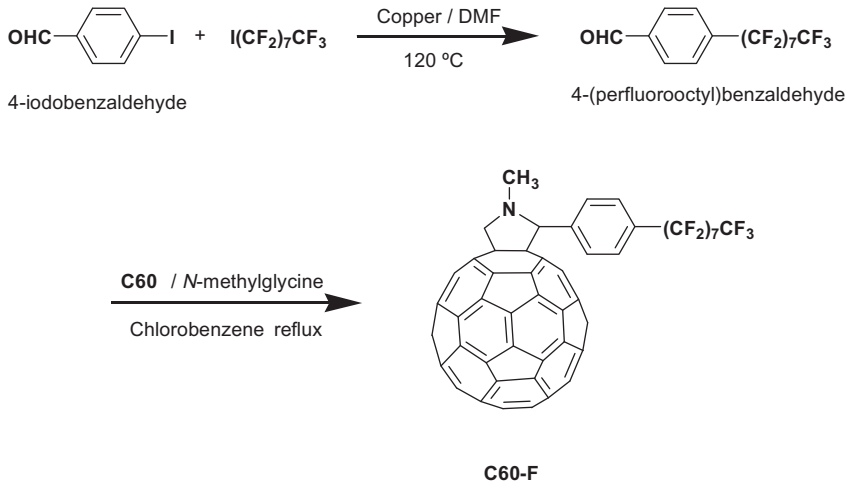

Scheme 1. Synthesis route and chemical structure of C60-F.

concentration of 20 g/l. The solutions were stirred at 333 K for 5 h on a magnetic hot plate, and filtered through a poly(tetrafluoroethylene) (PTFE) filter with a 0.45 μm pore size. The fullerene solution was thereafter spin-coated on top of a substrate (spin speed = 1400 rpm, spin acceleration = 1400 rpm/s, time = 60 s), and the resulting thin film, with a typical thickness of 100 nm, was annealed at 313 K for 5 h.

A green laser (λ = 532 nm) was utilized for the exposure of the C60-F films. The laser power intensity incident on the film was controlled by placing a negative lens at different positions in the optical path between the laser and the film. The emerging beam from the laser had a diameter of 0.8 mm, and the diameter of the incident beam on the C60-F film ranged between 2 and 10 mm in different experiments depending on the positioning of the lens. The exposure of the C60-F films was typically executed with an incident laser power intensity of p = 2.0 mW/mm^2 (corresponding to an incident laser beam diameter on the fullerene film of 5 mm) for 1 h, although other incident laser power intensities and exposure times (*e.g.,* p = 0.6 mW/mm^2 for 4 h) were also employed with a satisfying outcome. It is notable that other laser wavelengths are expected to be functional as well, but that we choose a green laser since C60-F exhibits an absorption peak at 520 nm in the visible range. The development was executed by immersing the C60-F film into a heptane developer solution for ~10 s. The resulting patterned film was dried at 333 K for 3 min before characterization. The patterning process of PCBM films in our lab has been described in detail in previous publications [29–31].

2.3. Transistor fabrication and measurements

Highly p-doped Si wafers (Cemat Silicon SA) were utilized as a combined substrate and gate electrode in transistor experiments. The wafers were coated on one side with a 200 nm thick layer of SiO_2, which functioned as the gate dielectric. The fullerene solution was spin-coated on top of the gate dielectric (as detailed in the previous section), and the resulting active material was annealed at T = 313 K for 5 h. Au source and drain electrodes (thickness = 40 nm) were deposited on top of the active material by thermal evaporation at $p = 10^{-6}$ mBar, using a shadow mask to define the electrode structure and the channel size (W = 1300 μm, L = 50 μm). The transistor characterization was performed using a Keithley 4200 semiconductor characterization system, with the source electrode grounded. All device fabrication and characterization were carried out under inert atmosphere in two interconnected N_2-filled glove boxes ([O_2], [H_2O] < 1 ppm) with an integrated thermal evaporation unit.

2.4. Characterization of the fullerene films during the patterning process

The IR vibrational spectra were recorded in attenuated total reflection Fourier transform IR (ATR-FTIR) mode. A horizontal single-reflection ATR accessory in the form of a ZnSe crystal was used as the internal reflection element (Harrick Scientific), and the spectra were collected with a Bruker IFS 66v/S spectrometer equipped with a deuterated triglycine sulfate (DTGS) detector and a water-cooled Globar source. The angle of incidence with respect to the ATR cell is ~45°, which is far above the critical angle of ~30°. The presented spectra are averages from 4096 scans, and the resulting resolution is ~2 cm^{-1}. All measurements were performed under vacuum (3 mbar) to eliminate undesired interfering contributions from H_2O(g) and CO_2(g). The samples for IR spectroscopy measurements were prepared by drop-casting a 10 g/l C60-F solution in chloroform onto the ZnSe crystal, and allowing the film to dry at room temperature in consideration of the heat-sensitive crystal substrate. A "patterned" C60-F film was prepared by first exposing a pristine film to the green laser (p = 0.6 mW/mm^2 for 4 h), and thereafter dropping heptane onto the exposed film from a pipette. A peak fit program (Seasolve, PeakFit v4.12) was used to deconvolute the IR absorption bands by symmetric Voigt type peaks for the analysis of sample crystallinity, as presented in Section 3.3.

The tapping mode AFM images were obtained on a MultiMode SPM microscope with a Nanoscope IV Controller (Veeco Metrology) operating under ambient conditions. LTESP Specialty Etched Silicon Probes with a nominal tip radius <10 nm, mounted on a 225 μm long, single-beam rectangular cantilever, were used. The probes were operated at driving frequencies in the range of 176.8–179.1 kHz, which is slightly below the resonance frequency of the cantilever.

The XRD data were recorded with a Siemens/Bruker D5000 diffractometer, using Cu Kα radiation (λ = 1.54 Å) as the probing beam. The probing beam was generated by an X-ray tube, with a typical applied voltage between the cathode and the Cu anode of 40 kV and with the current set to 30 mA. The XRD results were analyzed using the PeakFit v 4.12 software.

The absorption spectra were recorded using a high speed spectrometer (Ocean Optics, HR4000, entrance aperture = 5 μm, grating range = 200–1100 nm) and a tungsten halogen lamp (Ocean Optics, HL-2000-HP-232), both computer controlled with the Spectral Suite software via the RS232 port. The spectra were recorded with an integration time of 190 ms, and background effects (stemming, *e.g.,* from the influence of the substrate and stray light) were corrected for via the parallel acquisition of background spectra. A thicker drop-cast C60-F film deposited on a glass slide was utilized for the attainment of a stronger signal. The C60-F film did, however, not adhere as strongly on the glass (as on, *e.g.,* a SiO_2 layer), which resulted in that both the exposed and non-exposed film areas were removed during the development stage. We have therefore recorded absorption data for the exposed, and not the patterned, C60-F film.

The cyclic voltammetry (CV) measurements were carried out with a computer-controlled potentiostat/galvanostat (Autolab, PGSTAT302/FRA2, Eco Chemie) using the general Purpose Electrochemical Software (GPES, Eco Chemie). All of the measurements were performed in a N_2-filled glove box ([O_2] < 3 ppm, [H_2O] < 1 ppm). The solution for CV experiments comprised the "electrochemically active" fullerene (C60-F, PCBM or C_{60}) dissolved in a

concentration of 0.02 g/l in a mixture of anhydrous toluene and acetonitrile (v:v = 3:1) and with 0.1 M tetrabutylammonium hexafluorophosphate (TBAPF6, ≥99.0%, Fluka) as the inert supporting electrolyte. Two carefully cleaned platinum rods were utilized as the working and counter electrodes, and an Ag wire was used as the pseudo-reference electrode. The Ag wire was calibrated *vs.* the bis-(η-cyclopentadienyl)-iron (II)/bis-(η-cyclopentadienyl)iron(II)$^+$ ion (ferrocene/ferrocenium ion, Fc/Fc$^+$) reference redox couple (ferrocene, ≥98%; Fluka) at the end of each measurement by adding $\sim 10^{-5}$ mol of ferrocene into the solution and performing a sweep. The reduction onset potentials were defined to correspond to the crossing point between the baseline and the half-peak-height tangent line.

3. Result and discussion

3.1. Patterning of C60-F films

We have recently introduced a technique for the straightforward patterning of fullerene thin films, which comprises two main steps: A direct laser-light exposure of selected regions of the fullerene film, followed by development via immersion into a tuned development solution that solely removes (dissolves) the non-exposed regions of the film. The mechanism that allows the patterning has been established to be of a *chemical* origin for the up-to-now investigated fullerene materials, C_{60} [29] and PCBM [30], as photo-exposed C_{60} monomers transform into a low-solubility polymeric state via intermolecular bond formation, and exposed PCBM monomers connect chemically to form low-solubility dimers.

The patterning method has obvious similarities to the well-known and ubiquitous photo-lithography (in negative mode) in that the non-exposed areas of the film are selectively removed by the developer solution, but it is both notable and highly convenient that the sacrificial photo-resist material, which is a critical – and costly – component in photo-lithography, is completely absent in the herein presented patterning process. The fullerene material can accordingly be considered to have two parallel functions: (negative) photo-resist and semiconductor. This attractive opportunity is effectuated by that the semiconducting properties (notably the electron mobility) of the fullerene film are left essentially unaffected by the laser-light exposure, while its solubility in a tuned developer solution is drastically lowered in comparison to the non-exposed material. The merit of the technique has been demonstrated by the successful patterning of vacuum-deposited C_{60} films [29] as well as solution-processed PCBM films [30], and the subsequent realization of well-functioning arrays of n-type field-effect transistors and CMOS inverters based on such patterned fullerene films [31].

A drawback with the two up-to-now investigated fullerene materials is a very limited ambient stability. In order to address the stability problem, and to investigate whether the patterning opportunity for fullerene films is a generic feature, we have in this study synthesized and attempted to pattern thin films of a perfluoro-alkyl functionalized C_{60}-derivative, C60-F (see bottom part of Scheme 1 for chemical structure). C60-F is particularly interesting in this context as the pristine material is reported to exhibit a significantly improved ambient stability over other fullerenes, such as PCBM, presumably due to the existence of a crystalline C60-F structure comprising a dense packing of the perfluoro-alkyl side chains that functions as an effective gas barrier against an undesired and detrimental influx of oxygen and/or water molecules [32].

Fig. 1 presents optical micrographs of a spin-cast C60-F film before (a) and after (b and c) the patterning process. The resulting pattern demonstrates that it is indeed possible to pattern the C60-F film with the resist-free laser-patterning process. The Umeå University logo was defined during the exposure step by allowing the green laser light to pass through a shadow mask, while the subsequent development step was executed by dipping the entire film into a heptane developer solution for ~10 s.

Here, we want to call attention to two points: First, it was relatively difficult to find an appropriate developer solution that was capable of discriminating between the exposed and the non-exposed C60-F material, and that, *e.g.,* toluene (as used for C_{60} patterning) and mixtures of chloroform and acetone (as used for PCBM patterning) removed both the exposed and non-exposed C60-F film areas. Second, we anticipated problems with the patterning of C60-F films via the formation of intermolecular chemical bonds (*i.e.,* the mechanism in effect in the previously studied fullerene materials), as C60-F molecules within a crystalline matrix comprising aligned perfluoro-alkyl chains can be expected to be rotationally frozen-in-place, and since a free rotation has been considered to be a general prerequisite for the formation of intermolecular chemical bonds between adjacent fullerene molecules [33,34]. In contrast, films of C_{60} (crystalline but freely rotating molecules at room temperature, RT) [35] and PCBM (typically amorphous) comprise molecules that exhibit vibrant rotational motion at RT and, consequently, fulfill the prerequisites for intermolecular chemical bond formation.

3.2. Transistor performance and air stability of pristine and patterned C60-F

In order to establish the semiconducting performance and ambient stability of the C60-F fullerene during the patterning process, we have fabricated field-effect transistors (FETs) comprising a thin film of spin-cast C60-F as the active material. The performance of an FET can be quantified by establishing the electron mobility (μ_n) and the threshold voltage (V_T) in the saturation regime with the following equation:

$$I_D^{0.5} = \left(\frac{WC\mu_n}{2L}\right)^{0.5} \times (V_G - V_T) \quad (1)$$

where I_D is the drain current, W and L represent the transistor channel width and length, respectively, C is the capacitance per unit area of the gate dielectric, and V_G is the gate voltage [36]. We have further defined the on/off ratio ($I_{on/off}$) of the FET as the drain current at $V_D = 60$ V

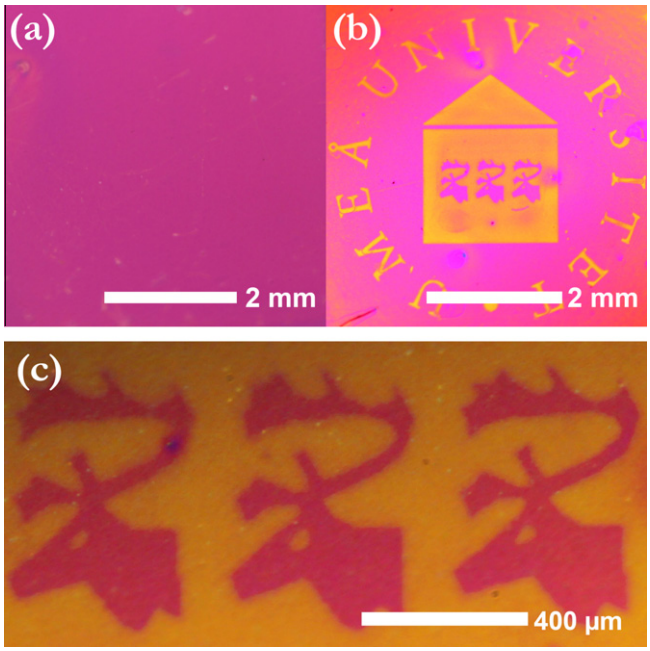

Fig. 1. Optical micrographs of a pristine spin-cast C60-F film (a) and the same C60-F film following patterning with the direct exposure-development technique (b and c). The pattern features were defined by positioning a shadow mask (with the shape of the logo of Umeå University) in conformal contact with the C60-F film during the laser exposure step.

and V_G = 60 V divided by the drain current at V_D = 60 V and V_G = 0 V.

We have fabricated and characterized >40 C60-F transistors in total, and the average performance values for FETs comprising pristine C60-F as the active material are: $\mu_n = 6.0(\pm 2.4) \times 10^{-2}$ cm^2/Vs, V_T = 15 V, and $I_{on/off} = 3 \times 10^3$. The highest mobility value within the group is: $\mu_n = 1.1 \times 10^{-1}$ cm^2/Vs. We note that our results are similar to those reported in a recent study on a pristine C60-F transistor ($\mu_n = 6.7 \times 10^{-2}$ cm^2/Vs) [32]. We have also tested >20 transistors with PCBM as the active material, and we find that such pristine PCBM-FETs exhibit average performance values of: $\mu_n = 2.0(\pm 1.0) \times 10^{-2}$ cm^2/Vs, V_T = 7 V and $I_{on/off} = 1 \times 10^3$. These results are also in reasonable agreement with previous literature reports (although the performance of the latter varies depending on the details of the preparation procedure) [16,17,30,31,37–41]. We call attention to that in our study the electron mobility of C60-F is distinctly higher by a factor of three over that of PCBM.

Fig. 2 illustrates the effects of the patterning of C60-F on the transistor performance. The transfer characteristics (left column) and the output characteristics (right column) of two representative C60-F transistors ("A" and "B") on the same substrate were recorded following the various stages of the patterning process, and the performance is quantified by calculating the electron mobility using Eq. (1). The mobility of the pristine C60-F material in transistor "A" is $\mu_n = 6.9 \times 10^{-2}$ cm^2/Vs (see Fig. 2a and b), but after the laser-light exposure the mobility has dropped to $\mu_n = 3.6 \times 10^{-2}$ cm^2/Vs (see Fig. 2c and d). Following the final development step, *i.e.*, at the end of the patterning cycle, the mobility of the patterned C60-F material in transistor "A" recovers somewhat to $\mu_n = 4.2 \times 10^{-2}$ cm^2/Vs (see Fig. 2e and f). A transistor "B" on the same substrate was also characterized during the patterning procedure, but with the notable difference that the exposure step for the C60-F material in the transistor channel was cancelled. The development step visually removed the non-exposed C60-F from the channel of transistor "B", and as expected the mobility for such a solely developed C60-F transistor is effectively zero (see Fig. 2g and h).

The air stability of pristine and patterned C60-F and PCBM films was estimated by exposing (a total of 80) transistors based on such films to ambient air for 24 h, and then returning them into a glove box for FET characterization after 5 min. For the pristine fullerene films, we find that the "ambient stability" of C60-F is better than that of PCBM, as quantified by that the former exhibits an average electron mobility of $\mu_n = 4.0 \times 10^{-3}$ cm^2/Vs and the latter exhibits $\mu_n = 2.0 \times 10^{-4}$ cm^2/Vs, following one day of air exposure. In relative terms, the average retained mobility is ~7% for the pristine C60-F film and ~1% for the pristine PCBM film. These results are in good agreement with a previous study performed by Chikamatsu et al. [32], which in combination with a small sample-to-sample variation yield support for that the employed measurement protocol is an appropriate indicator on the ambient stability.

For the patterned fullerene films, we find a markedly improved ambient stability, as the average retained mobility is ~24% for patterned C60-F films and ~16% for patterned PCBM films. In absolute terms, this corresponds to an average mobility of $\mu_n = 1.0 \times 10^{-2}$ cm^2/Vs for patterned C60-F and $\mu_n = 8.0 \times 10^{-4}$ cm^2/Vs for patterned PCBM following one day of air exposure. The results for

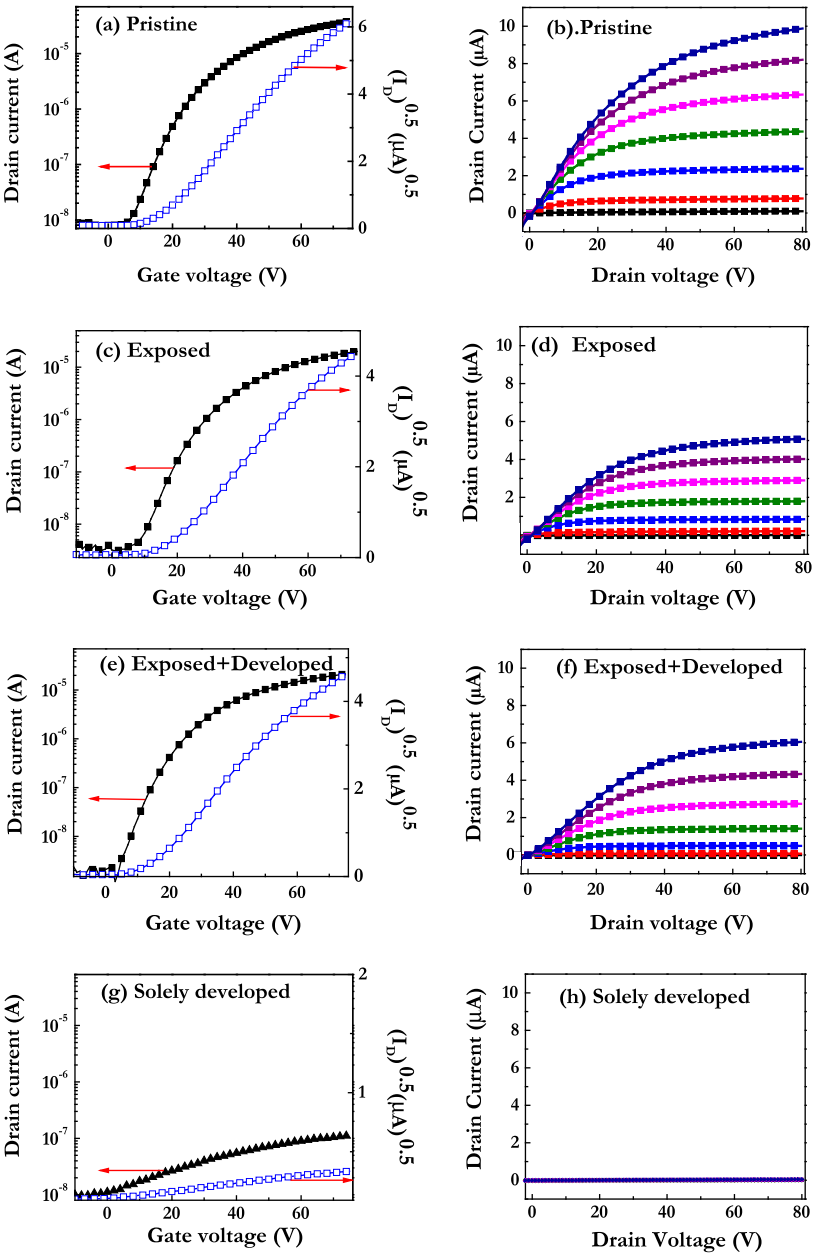

Fig. 2. Transfer (left column) and output (right column) characteristics of two representative C60-F transistors, as measured following the different stages of the patterning process. The data presented in (a–f) were recorded on the same transistor "A", while the data in (g and h) were recorded on a second transistor "B" on the same substrate. The transfer characteristics were measured at V_D = 60 V, and the output characteristics were measured at V_G ranging from 0 V (bottom trace) to 60 V (top trace), with a ΔV_G step of 10 V.

C60-F are promising in that they, for instance, suggest that it should be possible to perform processing and patterning of thin C60-F films for electronic applications in the ambient before a final encapsulation step.

3.3. Mechanism allowing for patterning and improved device performance

We now shift our attention to a material characterization of the C60-F material, with the goal of unraveling the mechanisms that allow the patterning as well as the improvement in electron mobility and air stability over PCBM. We start with an IR absorption spectroscopy study, and Fig. 3 presents data over various wave-number regions for a pristine C60-F film (bottom black trace i) and a patterned C60-F film (top red trace ii).

In our previous investigations on patterning of C_{60} and PCBM fullerene films, the fullerene breathing mode – the so-called $A_g(2)$-mode – was exploited as a qualitative indicator on the formation of new chemical bonds during the

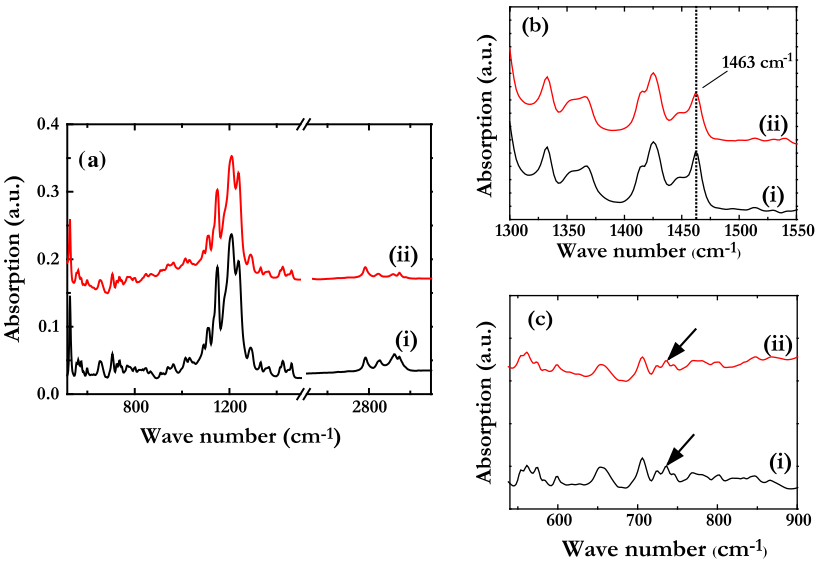

Fig. 3. IR absorption spectra for a pristine C60-F film (bottom black trace i) and a patterned C60-F film (top red trace ii) over an expanded wave-number range (a), over the $A_g(2)$-mode region (b), and over the "crystalline-indicator"-mode region (c).

patterning process, as it is well-established that this mode down-shifts in a regular fashion when new intermolecular chemical bonds are formed between the fullerene molecules. More specifically, it has been demonstrated that the $A_g(2)$-mode down-shifts with ~5 cm^{-1}/intermolecular bond/fullerene molecule [42–44]. Accordingly in PCBM, where dimers are formed during the laser-light exposure step, the $A_g(2)$-mode is down-shifted with 5 cm^{-1} following patterning [30], and in C_{60}, where preferentially linear polymers are created during the exposure, the $A_g(2)$-mode is found to down-shift by 9 cm^{-1} [29]. In the pristine C60-F film we find that the $A_g(2)$-mode, as expected, is positioned at 1463 cm^{-1}, but it is notable that the position of the $A_g(2)$-mode is unaffected by the patterning (see dotted line in Fig. 3b). This observation demonstrates that no intermolecular chemical bonds form during the laser-light exposure of the C60-F film, and also suggests that the *chemical* structure of C60-F – in contrast to its C_{60} and PCBM counterparts – remains intact during the patterning process.

Previous studies on polytetraflouroethylene materials (similar in structure to the perfluoro-alkyl side chain of C60-F) have shown that the IR absorption band at ~740 cm^{-1} is a useful probe of perfluoro-alkyl crystallinity, since this mode is completely absent in "perfectly" crystalline polytetraflouroethylene materials and since it increases in amplitude with increasing amorphicity [45,46]. Fig. 3(c) presents an enlarged view of this "crystallinity-indicator" region, where the data have been normalized by the strong IR absorption band at 1242 cm^{-1} (following the procedure outlined by Starkweahter et al. in Ref. 38). We find that the magnitude of the normalized 740 cm^{-1} peak decreases in magnitude by approximately 10% following patterning, and interpret this as an indication of increased C60-F side-chain crystallinity in the patterned film in comparison to the pristine film. We also note that the characteristic CH vibrations between 2850–3000 cm^{-1} decrease quite drastically in the patterned sample (see Fig. 3a), and that a similar observed decrease has been reported for a PMMA polymer gel during an amorphous–crystalline transition [47]. These observations indicate that the crystallinity of the C60-F film increases during the patterning process.

The notion that the spin-coated C60-F films are partially crystalline (or semi-crystalline) is supported by AFM and XRD studies. Fig. 4 presents AFM topographic images of a pristine C60-F film (a), a patterned C60-F film (b), and a pristine PCBM film (c). Both C60-F films exhibit a distinct surface morphology comprising a small number of micrometer-sized aligned rod-like grains as base units. In contrast, the PCBM film exhibits a completely flat surface morphology without any distinguishable features, which is a characteristic feature of an all-amorphous material and in agreement with previously published data [48]. A closer inspection of the AFM data for the pristine and patterned C60-F films reveals that the average grain size and the root-mean-square surface roughness are persistently larger in the patterned material over the pristine material; specifically, we find that the average grain size increases from 1.1 ± 0.16 to 1.9 ± 0.17 μm and that the surface roughness increases from 24.2 to 33.2 nm following patterning.

The conclusive evidence for that the spin-coated C60-F films indeed are crystalline and that the degree of crystallinity increases following patterning is provided by the XRD data presented in Fig. 5. Both the pristine C60-F film (Fig. 5a) and the patterned C60-F film (Fig. 5b) exhibit four distinct XRD peaks positioned at 6.4°, 9.6°, 12.8°, and 16.0°, corresponding to (0 0 2), (0 0 3), (0 0 4) and (0 0 5) reflections, respectively [32,49]. Moreover, the peak height increases and the full width at half maximum (FWHM) decreases following the patterning, as exemplified by that

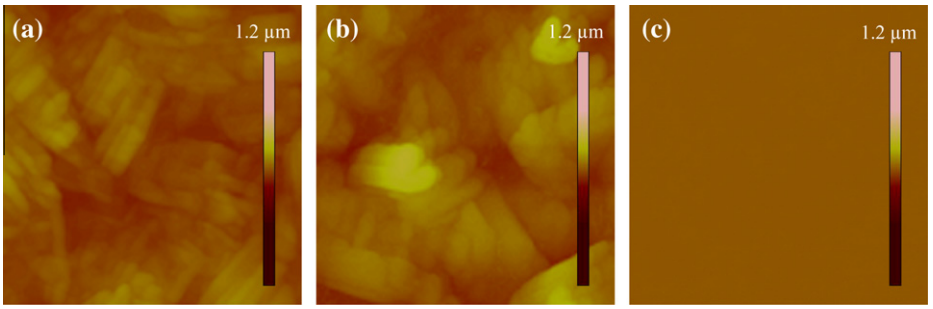

Fig. 4. Topographic AFM images recorded on a pristine C60-F film (a), a patterned C60-F film (b) and a pristine PCBM film (c). The scanning area is $4.4 \times 4.4\ \mu m^2$.

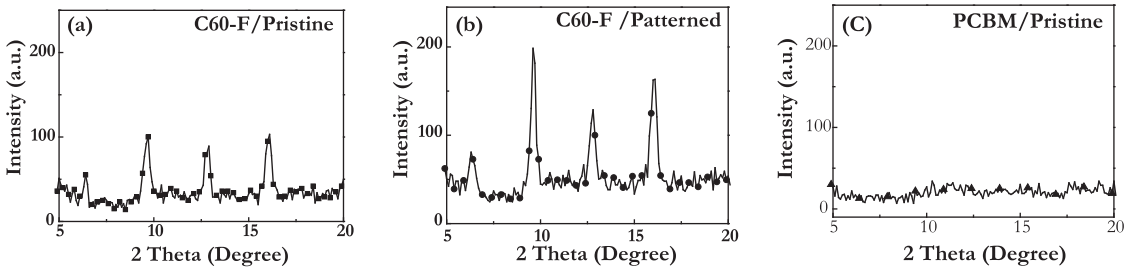

Fig. 5. XRD data recorded on a pristine C60-F film (a), a patterned C60-F film (b), and a pristine PCBM film (c).

the FWHM for the largest (0 0 3) peak at 9.6° is found to decrease from 0.43° to 0.28°. Both these trends are expected for a sample that increases its order and crystallinity. We also note that the PCBM film (Fig. 5c) exhibits no distinguishable XRD peaks, as should be the case for an all-amorphous material.

We have in addition performed complementary UV–vis absorption and CV measurements (data not shown), which verify that the patterning process indeed is effectuated by a physical ordering transition within the C60-F film and not by chemical changes. The UV–vis absorption spectra were recorded on pristine and exposed C60-F, either as dissolved in a toluene solvent or deposited as a spin-coated film. We find that the absorption spectra for the "free" C60-F molecules in solution are identical, regardless of whether the material had been exposed to laser-light or not before dissolution, which supports the notion that the pristine and exposed C60-F molecules have an identical chemical structure. In contrast, the absorption data for the spin-coated films differ in that the exposed film exhibits a more narrow and well-defined absorption profile over the pristine film, which is an expected signature change within a film that has increased its degree of crystallinity. The CV data demonstrates that the LUMO level of both pristine and exposed C60-F films is essentially identical and positioned outside the so-called "thermodynamic stability window" [22], which in turn implies that the observed improvement in air stability for the patterned C60-F film (see final paragraph in Section 3.2.) also can be traced to an increase in crystallinity. More specifically, and as discussed in Ref. [28], ordered and dense perfluoroalkyl layers within a crystalline C60-F matrix can be expected to function as an effective barrier towards an undesired influx of water and/or oxygen molecules.

At this point, it is relevant to include a brief discussion on the mechanism that provokes the observed increase in crystallinity of the C60-F film during the patterning process. First of all, as the pattern is defined during the exposure step, it is clear that it is the laser-light exposure that induces the order. A typical laser-light power intensity incident on the C60-F film surface is $\sim$2 mW/mm^2, and with a typical film thickness of 100 nm, this corresponds to approximately 20 W of irradiation that hits one cubic-millimeter of C60-F material for an extended time period of approximately 1 h during the exposure step. Moreover, as the wavelength of the incident laser light (λ_{laser} = 532 nm) is very close to the absorption peak (in the visible range) for the C60-F film ($\lambda_{abs\ peak}$ $\sim$520 nm), it is clear that a significant fraction of the incident photon flux is absorbed by the exposed areas of the thin C60-F film. With this information at hand, it is not difficult to realize that the exposed film areas become very hot, and we propose that such localized heating within the exposed regions is the cause for the increase in C60-F crystallinity via a thermal annealing process. In this context, we also note recent reports that show that perfluoro-alkyl-based materials are prone to the attainment of highly ordered structures [25,50,51].

Finally, as alluded to at the end of Section 3.1, it did not come as a complete surprise that the origin to the patterning of C60-F did not have a chemical origin, as the baseline criteria for the formation of chemical bonds between different fullerene molecules is that the individual molecules are rotating freely [33–35], which is a requirement that is

fulfilled for a crystalline C60 film [29] and an amorphous PCBM film [30], but not for a crystalline C60-F film.

4. Conclusions

We demonstrate that it is possible to pattern a solution-cast thin film of a perfluoro-alkyl functionalized fullerene compound using a resist-free laser-patterning technique. The patterning is done without use of a sacrificial photoresist material and comprises solely two steps: laser-light exposure and solution development. The exposure step selectively increases the crystallinity within the exposed fullerene regions, while the subsequent development removes the non-exposed fullerene material, so that a well-defined fullerene film structure emerges in reflection of the selected exposure pattern. We show that the patterned and crystalline fullerene film exhibits notably high electron mobility in transistor applications and a strongly improved ambient stability.

Acknowledgements

The authors are grateful to Kempestiftelserna, Carl Tryggers Stiftelse, and the Swedish Research Council (Vetenskapsrådet) for financial support. L.E. is a "Royal Swedish Academy of Sciences Research Fellow" supported by a grant from the Knut and Alice Wallenberg Foundation. The authors also wish to thank Christian Larsen and Tomas Kindahl at Umeå University for valuable assistance during measurements and chemical synthesis, respectively.

Reference

[1] D. Voss, Cheap and cheerful circuits, Nature 407 (2000) 442–444.
[2] J.-H. Shin, L. Edman, Light-emitting electrochemical cells with millimeter-sized interelectrode gap: low-voltage operation at room temperature, J. Am. Chem. Soc. 128 (2006) 15568–15569.
[3] A.P. Kulkarni, C.J. Tonzola, A. Babel, S.A. Jenekhe, Electron transport materials for organic light-emitting diodes, Chem. Mater. 16 (2004) 4556–4573.
[4] C.R. Newman, C.D. Frisbie, D.A. Da Silva Filho, J.-L. Bredas, P.C. Ewbank, K.R. Mann, Introduction to organic thin film transistors and design of n-channel organic semiconductors, Chem. Mater. 16 (2004) 4436–4451.
[5] J. Zaumseil, H. Sirringhaus, Electron and ambipolar transport in organic field-effect transistors, Chem. Rev. 107 (2007) 1296–1323.
[6] P. Matyba, K. Maturova, M. Kemerink, N.D. Robinson, L. Edman, The dynamic organic p–n junction, Nat. Mater. 8 (2009) 672–676.
[7] J. Xue, S. Uchida, B.P. Rand, S.R. Forrest, 4.2% Efficient organic photovoltaic cells with low series resistances, App. Phys. Lett. 84 (2004) 3013–3015.
[8] S. Kim, J.K. Lee, S.O. Kang, J. Ko, J.-H. Yum, S. Fantacci, F. De Angelis, D. Di Censo, M.K. Nazeeruddin, M. Grätzel, Molecular engineering of organic sensitizers for solar cell applications, J. Am. Chem. Soc. 128 (2006) 16701–16707.
[9] S. Bertho, W.D. Oosterbaan, V. Vrindts, J. D'Haen, T.J. Cleij, L. Lutsen, J. Manca, D. Vanderzande, Controlling the morphology of nanofiber-P3HT:PCBM blends for organic bulk heterojunction solar cells, Org. Electron. 10 (2009) 1248–1251.
[10] M. Vehse, B. Liu, L. Edman, G.C. Bazan, A.J. Heeger, Light amplification by optical excitation of a chemical defect in a conjugated polymer, Adv. Mater. 16 (2004) 1001–1004.
[11] E.J. Meijer, D.M. de Leeuw, S. Setayesh, E. van Veenendaal, B.-H. Huisman, P.W.M. Blom, J.C. Hummelen, U. Scherf, T.M. Klapwijk, Solution-processed ambipolar organic field-effect transistors and inverters, Nat. Mater. 2 (2003) 678–682.
[12] F. Silvestri, M.D. Irwin, L. Beverina, A. Facchetti, G.A. Pagani, T.J. Marks, Efficient squaraine-based solution processable bulk-heterojunction solar cells, J. Am. Chem. Soc. 130 (2008) 17640–17641.
[13] P. Matyba, H. Yamaguchi, G. Eda, M. Chhowalla, L. Edman, N.D. Robinson, Graphene and mobile ions: the key to all-plastic, solution-processed light-emitting devices, ACS Nano 4 (2010) 637–642.
[14] M.M. Ling, Z. Bao, Thin film deposition, patterning, and printing in organic thin film transistors, Chem. Mater. 16 (2004) 4824–4840.
[15] G. Yu, J. Gao, J.C. Hummelen, F. Wudl, A.J. Heeger, Polymer photovoltaic cells: enhanced efficiencies via a network of internal donor-acceptor heterojunctions, Science 270 (1995) 1789–1791.
[16] Y. Shirota, H. Kageyama, Charge carrier transporting molecular materials and their applications in devices, Chem. Rev. 107 (2007) 953–1010.
[17] C. Yang, J.Y. Kim, S. Cho, J.K. Lee, A.J. Heeger, F. Wudl, Functionalized methanofullerenes used as n-type materials in bulk-heterojunction polymer solar cells and in field-effect transistors, J. Am. Chem. Soc. 130 (2008) 6444–6450.
[18] L. Edman, A. Ferry, P. Jacobsson, Effect of C-60 as a filler on the morphology of polymer-salt complexes based on poly(ethylene oxide) and $LiCF_3SO_3$, Macromolecules 32 (1999) 4130–4133.
[19] P. Strobel, J. Ristein, L. Ley, Ozone-mediated polymerization of fullerene and fluorofullerene thin films, J. Phys. Chem. C 114 (2010) 4317–4323.
[20] T.D. Anthopoulos, G.C. Anyfantis, G.C. Papavassiliou, D.M.D. Leeuw, Air-stable ambipolar organic transistors, App. Phys. Lett. 90 (2007) 122105.
[21] X. Wang, Y. Guo, Y. Xiao, L. Zhang, G. Yu, Y. Liu, Synthesis and characterization of fullerene derivatives with perfluoroalkyl groups, J. Mater. Chem. 19 (2009) 3258–3262.
[22] D.M. de Leeuw, M.M.J. Simenon, A.R. Brown, R.E.F. Einerhand, Stability of n-type doped conducting polymers and consequences for polymeric microelectronic devices, Syn. Met. 87 (1997) 53–59.
[23] Z. Bao, A.J. Lovinger, J. Brown, New air-stable n-channel organic thin film transistors, J. Am. Chem. Soc. 120 (1998) 207–208.
[24] H.E. Katz, A.J. Lovinger, J. Johnson, C. Kloc, T. Siegrist, W. Li, Y.-Y. Lin, A. Dodabalapur, A soluble and air-stable organic semiconductor with high electron mobility, Nature 404 (2000) 478–481.
[25] B.A. Jones, M.J. Ahrens, M.-H. Yoon, A. Facchetti, T.J. Marks, M.R. Wasielewski, High-mobility air-stable n-type semiconductors with processing versatility: dicyanoperylene-3, 4:9, 10-bis(dicarboximides)13, Angew. Chem. Int. Ed. 43 (2004) 6363–6366.
[26] B.A. Jones, A. Facchetti, M.R. Wasielewski, T.J. Marks, Tuning orbital energetics in arylene diimide semiconductors. Materials design for ambient stability of n-type charge transport, J. Am. Chem. Soc. 129 (2007) 15259–15278.
[27] M. Maggini, G. Scorrano, M. Prato, Addition of azomethine ylides to C60: synthesis, characterization, and functionalization of fullerene pyrrolidines, J. Am. Chem. Soc. 115 (1993) 9798–9799.
[28] K.J.L. Paciorek, S.R. Masuda, J.G. Shih, J.H. Nakahara, The synthesis of perfluoroalkyl and perfluoroalkylether substituted benzyls, J. Fluorine Chem. 53 (1991) 233–248.
[29] A. Dzwilewski, T. Wågberg, L. Edman, C60 field-effect transistors: effects of polymerization on electronic properties and device performance, Phys. Rev. B 75 (2007) 075203.
[30] A. Dzwilewski, T. Wågberg, L. Edman, Photo-induced and resist-free imprint patterning of fullerene materials for use in functional electronics, J. Am. Chem. Soc. 131 (2009) 4006–4011.
[31] A. Dzwilewski, P. Matyba, L. Edman, Facile fabrication of efficient organic CMOS circuits, J. Phys. Chem. B 114 (2010) 135–140.
[32] M. Chikamatsu, A. Itakura, Y. Yoshida, R. Azumi, K. Yase, High-performance n-type organic thin-film transistors based on solution-processable perfluoroalkyl-substituted c60 derivatives, Chem. Mater. 20 (2008) 7365–7367.
[33] T. Wågberg, P.-A. Persson, B. Sundqvist, Structural evolution of low-pressure polymerised C60 with polymerisation conditions, J. Phys. Chem. Solids 60 (1999) 1989–1994.
[34] R. Moret, T. Wågberg, B. Sundqvist, Influence of the pressure-temperature treatment on the polymerization of C60 single crystals at 2 GPa-700 K, Carbon 43 (2005) 709–716.
[35] R. Moret, Structures, phase transitions and orientational properties of the C-60 monomer and polymers, Acta Crystallogr. Sec. A 61 (2005) 62–76.
[36] S.M. Sze, K.K. Ng, Physics of Semiconductor Devices, Wiley-Interscience, 2006.
[37] Q. Wei, K. Tajima, K. Hashimoto, Bilayer ambipolar organic thin-film transistors and inverters prepared by the contact-film-transfer method, ACS App. Mater. Interfaces 1 (2009) 1865–1868.

[38] J.H. Seo, A. Gutacker, B. Walker, S. Cho, A. Garcia, R. Yang, T.-Q. Nguyen, A.J. Heeger, G.C. Bazan, Improved injection in n-type organic transistors with conjugated polyelectrolytes, J. Am. Chem. Soc. 131 (2009) 18220–18221.
[39] C. Waldauf, P. Schilinsky, M. Perisutti, J. Hauch, C.J. Brabec, Solution-processed organic n-type thin-film transistors, Adv. Mater. 15 (2003) 2084–2088.
[40] S. Chao-Feng, K. Dhananjay, C. Li Fen, L. Yuh-Zheng, C. Fang-Chung, W. Meng-Chyi, C. Chih-Wei, Flexible fullerene field-effect transistors fabricated through solution processing, Adv. Mater. 21 (2009) 4845–4849.
[41] C.-W. Chu, C.-F. Sung, Y.-Z. Lee, K. Cheng, Improved performance in n-channel organic thin film transistors by nanoscale interface modification, Org. Electron. 9 (2008) 262–266.
[42] V.A. Davydov, L.S. Kashevarova, A.V. Rakhmanina, V.M. Senyavin, R. Céolin, H. Szwarc, H. Allouchi, V. Agafonov, Spectroscopic study of pressure-polymerized phases of C60, Phys. Rev. B 61 (2000) 11936–11945.
[43] P.C. Eklund, Z. Ping, W. Kai-An, G. Dresselhaus, M.S. Dresselhaus, Optical phonon modes in solid and doped C60, J. Phys. Chem. Solids 53 (1992) 1391–1413.
[44] T. Wågberg, P. Jacobsson, B. Sundqvist, Comparative Raman study of photopolymerized and pressure-polymerized C60 films, Phys. Rev. B 60 (1999) 4535–4538.
[45] H.W. Starkweather, R.C. Ferguson, D.B. Chase, J.M. Minor, Infrared spectra of amorphous and crystalline poly(tetrafluoroethylene), Macromolecules 18 (1985) 1684–1686.
[46] N. Cioffi, L. Torsi, I. Farella, D. Altamura, A. Valentini, N. Ditaranto, L. Sabbatini, P.G. Zambonin, T. Bleve-Zacheo, Deposition and analytical characterization of fluoropolymer thin films modified by palladium nanoparticles, Thin Solid Films 449 (2004) 25–33.
[47] O. Andersson, T. Wågberg, In situ, high-pressure differential thermal analysis and ionic conductance of PMMA-based gels with and without TiO_2 nano-particle filler, Electrochim. Acta 51 (2006) 4537–4543.
[48] M. Chikamatsu, S. Nagamatsu, Y. Yoshida, K. Saito, K. Yase, K. Kikuchi, Solution-processed n-type organic thin-film transistors with high field-effect mobility, App. Phys. Lett. 87 (2005) 203504.
[49] M. Chikamatsu, A. Itakura, Y. Yoshida, R. Azumi, K. Kikuchi, K. Yase, Correlation of molecular structure, packing motif and thin-film transistor characteristics of solution-processed n-type organic semiconductors based on dodecyl-substituted C60 derivatives, J. Photochem. Photobiol. A 182 (2006) 245–249.
[50] J.H. Oh, S. Liu, Z. Bao, R. Schmidt, F. Wurthner, Air-stable n-channel organic thin-film transistors with high field-effect mobility based on N,N′-bis(heptafluorobutyl)-3, 4:9, 10-perylene diimide, App. Phys. Lett. 91 (2007) 212107.
[51] R. Schmidt, J.H. Oh, Y.-S. Sun, M. Deppisch, A.-M. Krause, K. Radacki, H. Braunschweig, M. Könemann, P. Erk, Z. Bao, F. Würthner, High-performance air-stable n-channel organic thin film transistors based on halogenated perylene bisimide semiconductors, J. Am. Chem. Soc. 131 (2009) 6215–6228.

blue color of CIE_y = 0.09 than those of control devices (CIE_y = 0.13). These results show that the D-EML system containing 2-methyl-9,10-di(2-naphthyl)anthracene (MADN) and 4′-(dinaphthalen-2-yl)-1,1′-binaphthyl (DNBN) as hosts and 9-N-phenylcarbazole-3-vinyl-*p*-terphnyl (PCVtPh) as a dopant was employed to broaden the recombination zone and confine holes and electrons to that zone.

2. Experimental

2.1. Emitting material synthesis

All reactions were performed under nitrogen. Solvents were carefully dried and distilled from appropriate drying agents prior to use. Commercially available reagents were used without further purification unless otherwise stated. 4,4′-Dibromo-1,1′-binaphthyl [20], *p*-terphenylphosphonate [21], and 9-(4-*tert*-butylphenyl)-9H-carbazole [22] were prepared according to literature methods. ^1H and ^{13}C NMR were recorded on a Varian Unity Inova 300Nb spectrometer. FT-IR spectra were recorded using a Bruker VERTEX70 FT-IR spectrometer. EA was measured using an EA 1108 spectrometer. Low-resolution mass spectra were measured using a Jeol JMS-600 spectrometer in the EI mode. The UV–Vis absorption and PL spectra of DNBN were measured in CH_2Cl_2 (10^{-5} M) using a Shimadzu UV-1650PC and an Amincobrowman series 2 luminescence spectrometer. The fluorescent quantum yields were determined in CH_2Cl_2 solution at 293 K and compared with the host (Φ_{DPA} = 0.90) as a Ref. [23]. The energy level was measured with a low-energy photo-electron spectrometer (Riken-Keiki, AC-2). Thermal property was measured using thermogravimetric analysis (TGA) (DTA-TGA, TA-4000) under nitrogen at a heating rate of 10 °C/min.

A mixture of 4,4′-dibromo-1,1′-binaphthyl (1 g, 2.42 mmol), 2-naphthalene boronic acid (1.25 g, 7.28 mmol), tetrakis(triphenylphosphine)palladium(0) (0.112 g, 0.1 mmol), 2 M Na_2CO_3 (2.58 g, 24.2 mmol), toluene (24 mL) and EtOH (12 mL) were refluxed at 120 °C for 4 h. The crude solid product was filtered and then washed with water. The filtered solid was dissolved with CH_2Cl_2, dried over $MgSO_4$, filtered with silica-gel, and then the solvent was removed under reduced pressure to afford a crude product. The crude product was recrystallized from CH_2Cl_2/EtOH, affording 1.11 g (90.6% yield) of the white solid. ^1H NMR (300 MHz, $CDCl_3$, δ): 8.07 (d, J = 9.6 Hz, 4H), 8.01 (d, J = 8.4 Hz, 2H), 7.98–7.93 (m, 4H), 7.76 (dd, J = 1.5, 8.4 Hz, 2H), 7.68–7.55 (m, 10H), 7.40 (td, J = 1.5, 7.7 Hz, 2H), 7.34 (td, J = 1.2, 7.5 Hz, 2H); ^{13}C NMR (75 MHz, $CDCl_3$, δ): 140.4, 138.6, 138.5, 133.7, 133.5, 132.9, 132.1, 129.2, 128.9, 128.4, 128.1, 128.0, 127.8, 127.4, 127.1, 126.7, 126.6, 126.4, 126.3, 126.2; FT-IR [ATR]: ν = 3050, 1598, 1502, 843, 822, 769, 745 cm^{-1}; MS (m/z, EI^+) 506 (M^+); anal. for $C_{40}H_{26}$: C 93.30, H 5.15; found: C 94.83, H 5.17.

PCVtPh: To a mixture of 9-phenyl-9H-carbazole-3-carbaldehyde (170 mg, 0.627 mmol) and *p*-terphenylphosphonate (238 mg, 0.627 mmol) in 8.0 mL of anhydrous THF at 0 °C was added dropwise 0.70 mL of 1.0 M KO(*t*-Bu) (0.70 mmol) in THF under N_2. The reaction mixture was stirred for 10 min at 0 °C, followed by 1 h at room temperature and quenched with water. The solution mixture was filtered with water. The filtered solid was dissolved in CH_2Cl_2, dried over Na_2SO_4, filtered with silica-gel, and the solvent removed under reduced pressure to afford a crude product recrystallized from $CHCl_3$/EtOH, affording 290 mg (93.2%) of a yellow solid. ^1H NMR (300 MHz, $CDCl_3$, δ): 8.31 (s, 1H), 8.20 (d, J = 7.6 Hz, 1H), 7.43 (d, J = 4.7 Hz, 3H), 7.68–7.62 (m, 8H), 7.61 (d, J = 4.1 Hz, 3H), 7.51–7.31 (m, 10H), 7.26 (s, 1H); ^{13}C NMR (75 MHz, $CDCl_3$, δ): 141.6, 141.0, 140.3, 140.0, 139.5, 137.8, 137.3, 130.2, 129.9, 129.8, 129.0, 128.4, 127.8, 127.7, 127.6, 127.5, 127.3, 127.2, 127.0, 126.4, 126.2, 125.1, 125.0, 124.1, 123.6, 120.6, 120.4, 118.8, 110.3, 110.2, 29.9, 1.2, 0.2; MS (FAB^+) m/z 497 (M^+); HRMS (FAB^+) calcd. for $C_{38}H_{29}N$: 497.6415 (M^+); found: 497.2139.

2.2. OLEDs fabrication

For the fabrication of OLEDs, indium tin oxide (ITO)-coated glass substrates were used, which have a sheet resistivity of 10 Ω per square and a thickness of 1500 Å. The ITO-coated glass substrates were cleaned in an ultrasonic bath in the following sequence: with acetone, methyl alcohol, distilled water, and isopropyl alcohol. The substrates were treated by O_2 plasma under conditions of 2×10^{-2} Torr at 125 W for 2 min. All organic materials and metals were deposited under high vacuum (5×10^{-7} Torr). The deposition rates were 0.1 nm/s for all organic materials and 0.01 nm/s for lithium quinolate (Liq). Without breaking the vacuum after the deposition of the organic layers, the Al cathode was deposited at a rate of 10 nm/s. The doping concentration of the emitters was optimized. Using DC voltage bias, the optical and electrical properties of OLEDs, such as the current density, luminance, current efficiency, external quantum efficiency (EQE), $CIE_{x,y}$ coordinates, and electroluminescence (EL) spectra of the emission, were measured with Keithley 2400 and Chroma Meter CS-1000A instruments. All measurements were carried out under ambient conditions at room temperature.

3. Results and discussion

Scheme 1 shows the synthetic route for DNBN and PCVtPh as the fluorescent emitter material and molecular structures of MADN as the fluorescent host materials used in this study. Horner–Emmons reaction between the *p*-terphenylphosphonate and the 9-phenyl-9H-carbazole-3-carbaldehyde afforded the PCVtPh as dopant material in moderate yields. DNBN host material was synthesized via the Suzuki Cross-Coupling reaction with moderate yields and was characterized by ^1H and ^{13}C NMR, FT-IR, elemental analysis (EA) and low-resolution mass spectroscopy. The various optical properties of the host materials, MADN and DNBN, are presented in Table 1. The decomposition temperature (T_d; corresponding to 5% weight loss) of DNBN (398 °C) was as high as that of MADN (397 °C). The HOMO energy level of DNBN was −6.0 eV as measured by a low-energy photo-electron spectrometer (Riken-Keiki AC-

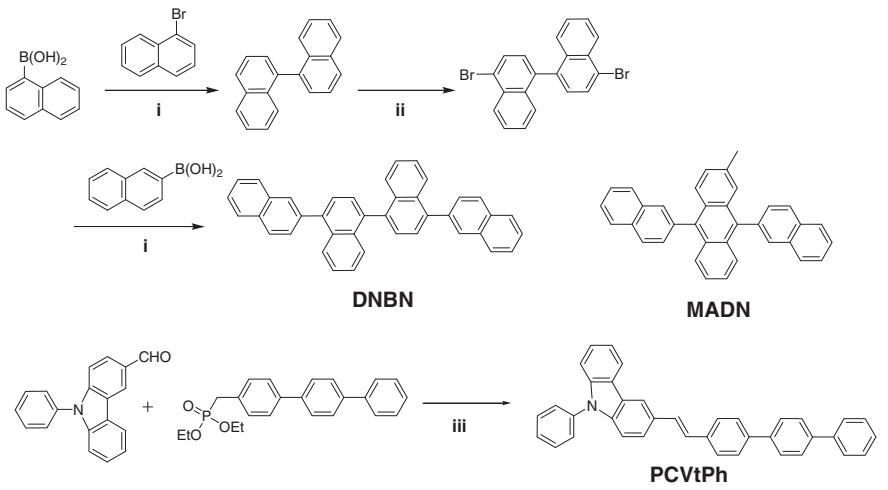

Scheme 1. Synthetic route for DNBN and PCVtPh and molecular structures of MADN used in this study. Reagents; (i) $Pd(PPh_3)_4$/2 M Na_2CO_3/toluene/EtOH; (ii) Br_2/CH_2Cl_2; (iii) KO(*t*-Bu)/THF.

Table 1
Various optical properties of MADN and DNBN.

Compound	T_g[a] (°C)	UV λ_{max}[b] (nm)	PL λ_{max}[b/c] (nm)	FWHM[b] (nm)	HOMO/LUMO[d] (eV)	E_g	Φ[e]
MADN	397[f]	377	425/447[f]	54	−5.5/−2.5	3.0	0.54
DNBN	398	305	412/403	62	−6.0/−2.6	3.4	0.45
PCVtPh		353	436/450	69	−5.6/−2.5	3.1	0.41

[a] Onset decomposition temperature, as measured with 5% mass loss by TGA with a heating rate of 10 °C/min under N_2.
[b] Measured in CH_2Cl_2 solution (1×10^{-5} M).
[c] In film state.
[d] Obtained from AC-2 and UV–Vis absorption measurements.
[e] Using DPA as a standard; λ_{ex} = 360 nm (Φ = 0.90 in CH_2Cl_2).
[f] Ref. [24].

2). The optical energy bandgap (E_g) of DNBN is 3.4 eV, as determined from the absorption spectrum. The lowest unoccupied molecular orbital (LUMO) energy level of DNBN, calculated as the difference between the HOMO levels and E_g, was −2.6 eV.

Fig. 1 shows PL emission spectra of the host materials, MADN and DNBN, and UV–Vis absorption spectra of dopant material, PCVtPh, where the main emission peaks of MADN and DNBN in the PL spectra are 425 and 412 nm, respectively. It was found that the introduction of the

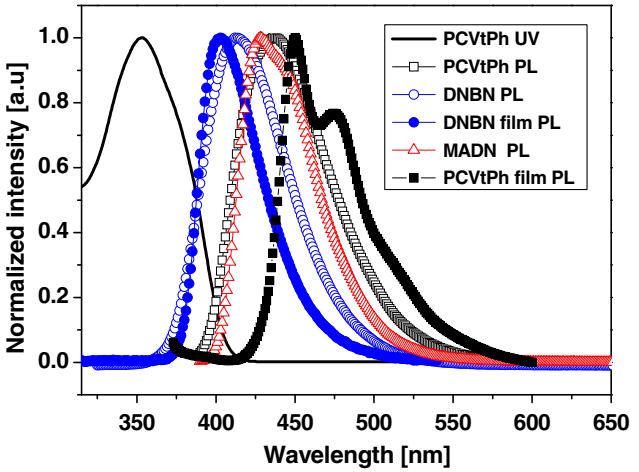

Fig. 1. PL emission spectra of the host materials, MADN and DNBN, and UV–Vis absorption spectra of dopant material, PCVtPh.

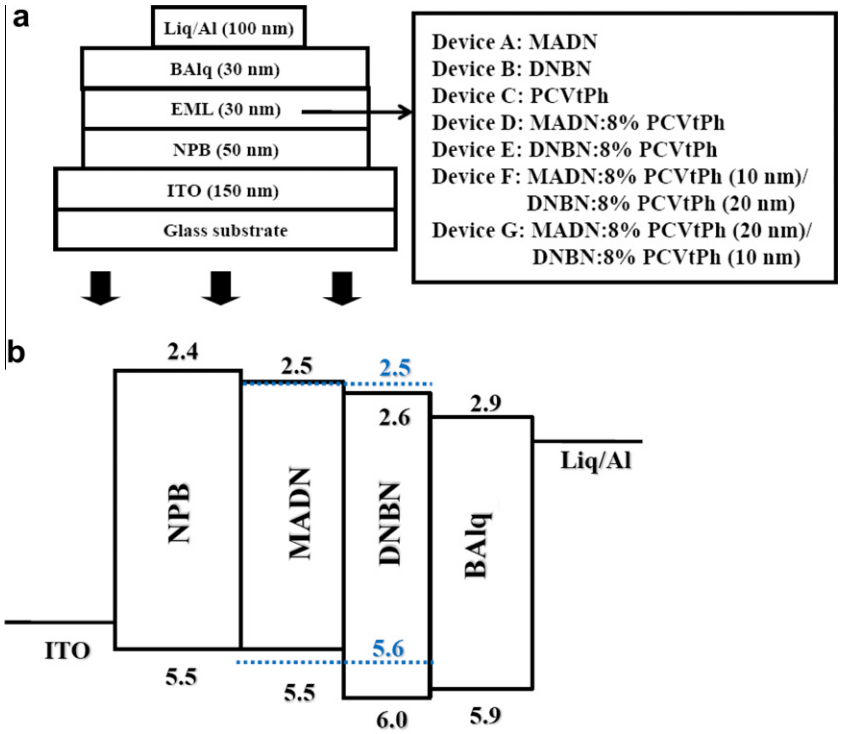

Fig. 2. (a) The structures of all devices fabricated in this study. (b) Energy level diagrams for devices F and G. Numbers denote the energy level for the HOMO and LUMO of various materials used in this study, where the HOMO and LUMO of PCVtPh represented by blue dotted line, respectively. (For interpretation of the references to color in this figure legend, the reader is referred to the web version of this article.)

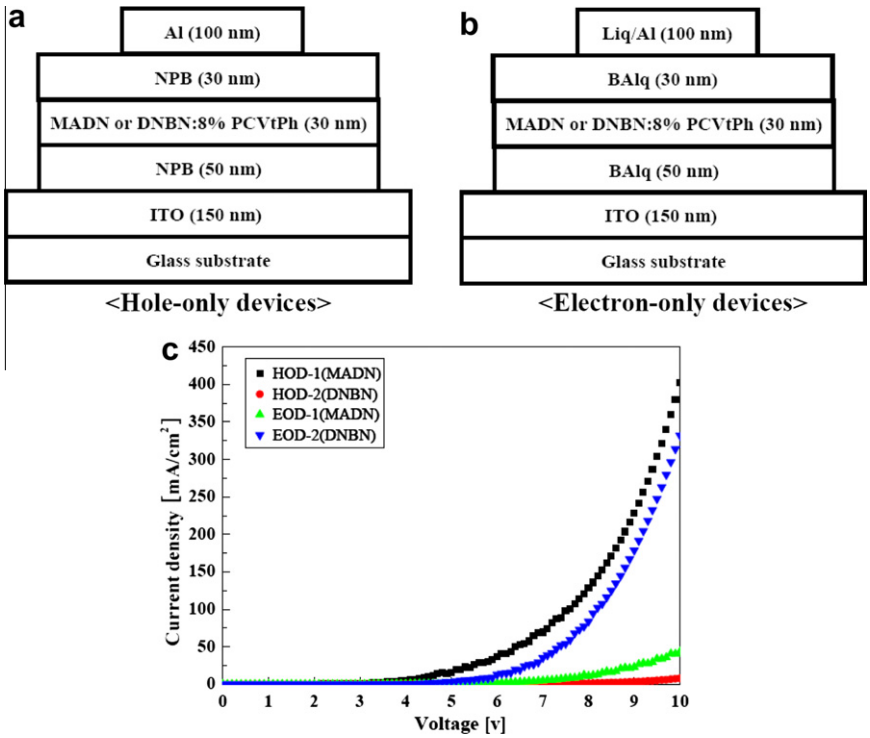

Fig. 3. (a) and (b) HODs and EODs structures of ITO (150 nm)/NPB (50 nm)/MADN:8% PCVtPh (HOD-1) or DNBN:8% PCVtPh (HOD-2) (8%, 30 nm)/NPB (30 nm)/Al (100 nm) and ITO (150 nm)/BAlq (50 nm)/MADN:8% PCVtPh (EOD-1) or DNBN:8% PCVtPh (EOD-2) (8%, 30 nm)/BAlq (30 nm)/Al (100 nm), respectively. (c) Current density versus voltage characteristics of HODs and EODs.

binaphthyl core between the terminal naphthalene as in DNBN results in a notable blue-shift in PL spectrum. Intriguingly, DNBN with 1,1′-binaphthyl core group showed a maximum emission wavelength that was blue-shifted (9 nm) in thin film compared to the solution. Therefore, it is shown in Fig. 1 that the PL emission peak of the DNBN overlapped more with the absorption peak of the PCVtPh than that of the host MADN. Moreover, DNBN has a higher energy bandgap (3.4 eV) than that of PCVtPh (3.1 eV), while the energy bandgap of MADN (3.0 eV) is smaller than that of PCVtPh (3.1 eV). These results indicate that the Förster-type energy transfer from the host to the emitter of PCVtPh may be more efficient in the DNBN host rather than the MADN host.

Fig. 2(a) shows seven device structures fabricated in this study, and the detailed structures are as follows: ITO/N,N′-bis-(1-naphthyl)-N,N′-diphenyl-1,1′-biphenyl-4,4′-diamine (NPB) (50 nm)/MADN (30 nm) (device A) or DNBN (30 nm) (device B) or PCVtPh (30 nm) (device C) or MADN:8% PCVtPh (30 nm) (device D) or DNBN:8% PCVtPh (30 nm) (device E) or MADN:8% PCVtPh (10 nm)/DNBN:8% PCVtPh (20 nm) (device F) or MADN:8% PCVtPh (20 nm)/DNBN:8% PCVtPh (10 nm) (device G)/bis-(2-methyl-8-quinolinolate)-4-(phenylphenolato)aluminum (BAlq) (30 nm)/Liq (2 nm)/Al (100 nm). Here, NPB, BAlq, and Liq were used as hole-transporting, hole-blocking and electron-transporting, and electron injection layers, respectively. The doping concentrations of PCVtPh in MADN or DNBN were optimized to 8%. Proposed energy level diagrams of devices F and G with D-EML are shown in Fig. 2(b). Devices A and D used MADN as an emitter and host, having the recombination zone (RZ) at the interface of EML and BAlq layer because there is no hole injection barrier between the highest occupied molecular orbital (HOMO) level of NPB and that of MADN, but there is an electron injection barrier of 0.4 eV between the LUMO level of BAlq and that of MADN. Moreover, NPB has a considerably higher hole mobility of 10^{-4} $cm^2/V\,s$ compared to BAlq, which has an electron mobility of 10^{-5} $cm^2/V\,s$ [25,26]. On the other hand, devices B and E used DNBN as an emitter and host, respectively, having RZ at the interface of the hole-transporting layer (HTL) and the EML because of the deep HOMO level (6.0 eV) of DNBN. Therefore, devices F and G with the D-EML system are expected to have an RZ at the interface of MADN and DNBN. When an RZ is generated at the interface of the HTL/EML or EML/electron-transporting

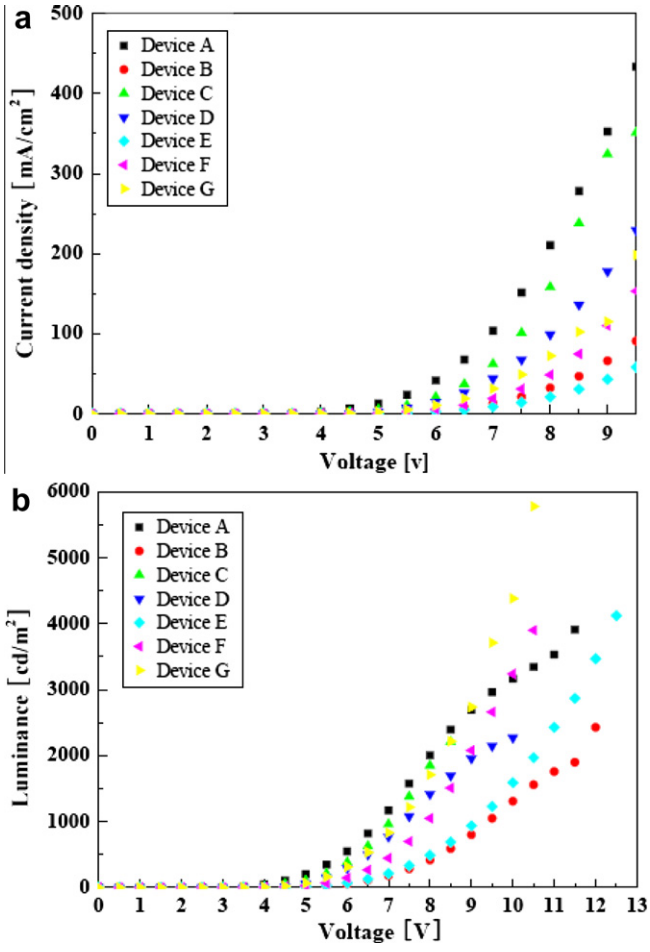

Fig. 4. (a) Current density versus voltage characteristics of all devices. (b) Luminance versus voltage characteristics of all devices.

layer (ETL), an emission zone is narrow and this produces a negative effect on the efficiency. On the other hand, the excitons of devices F and G with D-EML are generated from the interface of MADN/DNBN, i.e., in the middle of the EML, and are diffused in the direction of both anode and cathode sides, generating a wide RZ. Therefore, the D-EML system improves device efficiency effectively.

Hole-only devices (HOD) and electron-only devices (EOD) were fabricated to prove the previous assumption in Fig. 3(a) and (b) whose structures are as follows: ITO (150 nm)/NPB (50 nm)/MADN:8% PCVtPh (HOD-1) or DNBN:8% PCVtPh (HOD-2) (30 nm)/NPB (30 nm)/Al (100 nm) as HODs and ITO (150 nm)/BAlq (50 nm)/MADN:8% PCVtPh (EOD-1) or DNBN:8% PCVtPh (EOD-2) (30 nm)/BAlq (30 nm)/Al (100 nm) as EODs, respectively. It was found in Fig. 3(c) that HODs show current densities of 401.77 and 7.95 mA/cm^2 at 10 V and EODs also show current densities of 43.28 and 331.92 mA/cm^2 at 10 V. HOD-1 using MADN and EOD-2 using DNBN shows higher current density at the whole voltage than HOD-2 using DNBN and EOD-1 using MADN, respectively. This indicates that MADN and DNBN have excellent holes and electrons unipolar characteristics, respectively. Therefore, in order to maximize the efficiency by balancing charge carriers from both the anode and cathode, MADN and DNBN layers must be located near the anode and cathode sides, respectively, in the D-EML system.

Fig. 4(a) and (b) shows current density versus voltage characteristics and luminance versus voltage characteristics of all devices. It was found in Fig. 4(a) that the current densities for all seven devices were 433, 91, 351, 229, 58, 153, and 198 mA/cm^2 at 9.5 V. Devices A and C had the highest current densities due to the most efficient hole- and electron-pathways without trapping carriers in the EML. Device E, using the host of DNBN, showed lower current density at the operating voltage than device D, using the host of MADN. This indicated that DNBN has lower mobility than that of MADN. DNBN also has unipolar characteristics with excellent electron-transporting ability compared with MADN, which has good hole-transporting ability in our devices as shown in Fig. 3(c). Device G with MADN (20 nm)/DNBN (10 nm) showed a higher current density than device F with MADN (10 nm)/DNBN (20 nm), which also seems to be due to the MADN having

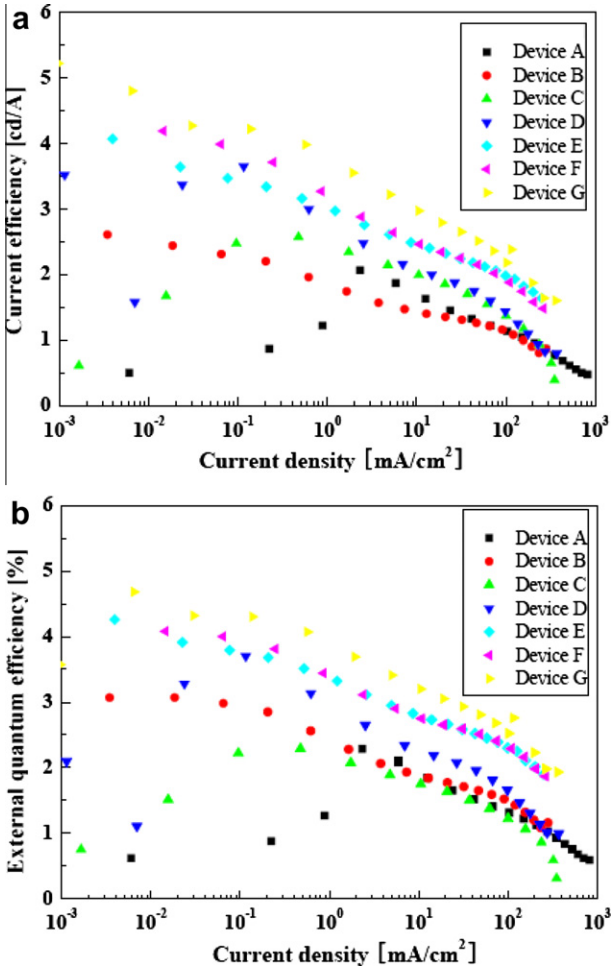

Fig. 5. (a) Current efficiency versus current density of all devices. (b) External quantum efficiency versus current density characteristics of all devices.

higher mobility than of DNBN. It is also found in Fig. 3(b) that the maximum luminances for all seven devices were 3910, 2430, 2210, 2270, 4120, 3900, and 5780 cd/m^2 at 11.5, 12.0, 8.5, 10.0, 12.5, 10.5, and 10.5 V, respectively, where device G showed the highest luminance among them. Devices E, F, and G, with the host of DNBN, tend to show higher luminance characteristics at operating voltages than devices C and D without the host of DNBN. Consequently, the large enhancement of luminance in devices containing DNBN seems to be due to the slowing down of hole mobility by the deep HOMO level of DNBN.

Fig. 5(a) and (b) shows current efficiency and EQE versus current density characteristics of all devices, where the maximum current efficiency values for all devices were 2.06, 2.61, 2.57, 3.65, 4.07, 4.19, and 5.22 cd/A at 2.336, 0.003, 0.476, 0.116, 0.004, 0.015, and 0.001 mA/cm^2, and

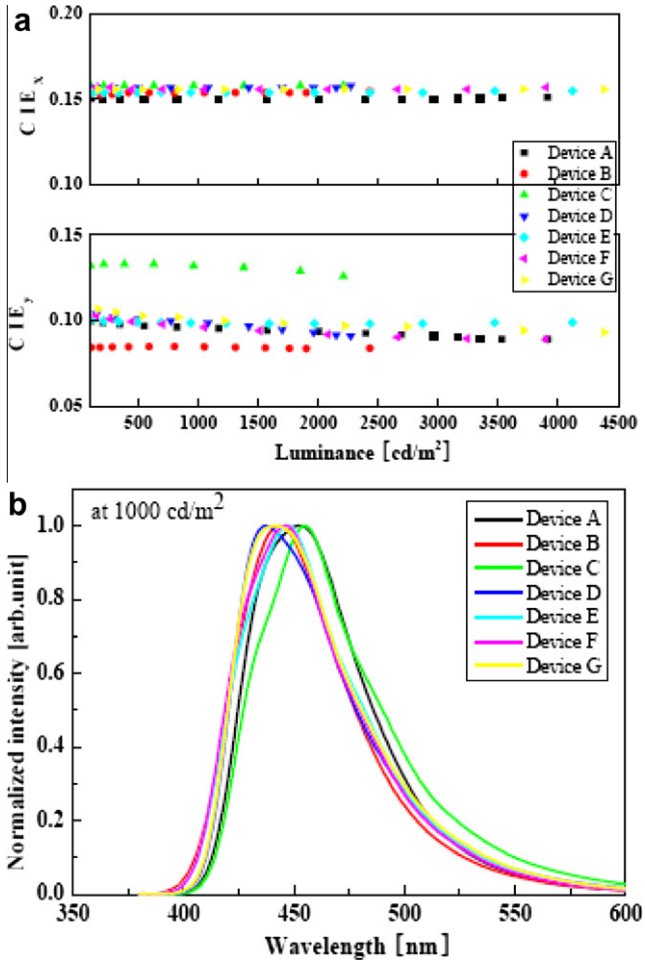

Fig. 6. (a) Commission Internationale d'Eclairage coordinates of all devices for luminance from 100 to 4500 cd/m^2. (b) Electroluminescence spectra of all devices from 350 to 700 nm at 1000 cd/m^2.

Table 2
Various characteristics of all devices, including a maximum luminance, current efficiency, power efficiency, EQE, and CIE$_{x,y}$ coordinates at 1 mA/cm^2, respectively.

Devices	Max. luminance (cd/m^2)	Current efficiency[a] (cd/A)	Power efficiency[a] (lm/W)	EQE[a] (%)	CIE$_{x,y}$[a]
A	3910	1.35	1.20	1.46	(0.15, 0.10)
B	2430	1.84	1.13	2.42	(0.15, 0.08)
C	2210	2.43	1.77	2.17	(0.15, 0.13)
D	2270	2.81	1.90	2.97	(0.15, 0.09)
E	4120	3.02	1.74	3.36	(0.15, 0.09)
F	3900	3.23	2.02	3.40	(0.15, 0.09)
G	5780	3.81	2.58	3.91	(0.15, 0.09)

[a] At a current density of 1 mA/cm^2.

the maximum EQE values for all devices were 2.28%, 3.07%, 2.29%, 3.70%, 4.26%, 4.08%, and 4.68% at 2.336, 0.003, 0.476, 0.116, 0.004, 0.015, and 0.006 mA/cm^2, respectively. The current efficiency values for all devices were also shown to be 1.35, 1.84, 2.43, 2.81, 3.02, 3.23, and 3.81 cd/A and 1.46%, 2.42%, 2.17%, 2.97%, 3.36%, 3.40%, and 3.91% at 1 mA/cm^2. Device G, with the D-EML system with MADN (20 nm)/DNBN (10 nm), exhibits EQE close to almost 5%, which is one of the highest EQEs previously reported on deep-blue OLEDs with CIE$_y$ < 0.10 to the best of our knowledge. This indicates that device G showed better carrier recombination zone in the D-EML system compared to other devices having a single-emitting layer (S-EML), where the RZ in the D-EML, when located far away from the interface of HTL/EML or EML/ETL, prevents excitons from approaching any quenching sites at these interfaces. Device G, with MADN (20 nm)/DNBN (10 nm), had higher efficiency than device F with MADN (10 nm)/DNBN (20 nm) since excitons are generated farther from the NPB layer in device G than in device F, where the NPB was known to have many quenching sites. Moreover, the devices in this study have hole-dominant characteristics due to higher hole mobility of the HTL than electron mobility of the ETL. In order to enhance the recombination of holes and electrons by charge balance, the MADN layer used as a hole-dominant EML should be thicker than the DNBN layer used as an electron-dominant EML. Therefore, although device F with MADN (10 nm)/DNBN (20 nm) had D-EML, it did not show higher performance compared to S-EML.

Fig. 6(a) shows CIE$_{x,y}$ coordinates versus luminance characteristics from 100 to 4500 cd/m^2 of all devices. They had emission characteristics of CIE$_{x,y}$ coordinates from (0.15, 0.10), (0.15, 0.08), (0.15, 0.13), (0.15, 0.10), (0.15, 0.10), (0.15, 0.10), and (0.15, 0.10) at 100 cd/m^2 to (0.15, 0.09), (0.15, 0.08), (0.15, 0.12), (0.15, 0.09), (0.15, 0.09), and (0.15, 0.09) at the maximum luminances (device A = 3910, device B = 2430, device C = 2210, device D = 2270, device E = 4120, device F = 3900, and device G = 5780 cd/m^2). Fig. 6(b) also shows the EL spectra of all devices from the wavelength of 350–600 nm at 1000 cd/m^2. All devices showed maximum peaks at 452, 444, 455, 437, 448, 446, and 440 nm. Various characteristics of all devices are summarized in Table 2, such as maximum luminance, current efficiency, EQE, and CIE$_{x,y}$ coordinates at 1 mA/cm^2.

4. Conclusions

In conclusion, a deep-blue OLED has been successfully demonstrated by introducing a novel emitter of PCVtPh, and the D-EML system consisted of MADN and DNBN. The D-EML system, with MADN (10 nm)/DNBN (20 nm), had good confinement of holes and electrons within the EML and good charge balance for carrier recombination. This optimized deep-blue OLED showed a maximum luminance of 5780 cd/m^2 at 10.5 V, a maximum EQE of 4.68%, a maximum current efficiency of 5.22 cd/A, and CIE$_{x,y}$ coordinates of (0.15, 0.09). This deep-blue OLED also showed higher efficiency by a factor of two and more deep-blue emission than the control device.

Acknowledgements

This work was supported by the ERC program of the Korea Science and Engineering Foundation (KOSEF) grant funded by the Korea Ministry of Education, Science and Technology (MEST) (No. R11-2007-045-03001-0) and Basic Science Research Program through the NRF funded by the Ministry of Education, Science and Technology (20100007370).

References

[1] C.W. Tang, S.A. Van Slyke, Appl. Phys. Lett. 51 (1987) 913.
[2] J. Kido, M. Kimura, K. Nagai, Science 267 (1995) 1332.
[3] B.W. D'Andrade, S.R. Forrest, Adv. Mater. 16 (2004) 1585.
[4] J.H. Seo, J.H. Kim, J.H. Seo, G.W. Hyung, J.H. Park, K.H. Lee, S.S. Yoon, Y.K. Kim, Appl. Phys. Lett. 90 (2007) 203507.
[5] S. Reineke, F. Lindner, G. Schwartz, N. Seidler, K. Walzer, B. Lüssem, K. Leo, Nature 459 (2009) 234.
[6] C. Adachi, M.A. Baldo, M.E. Thompson, S.R. Forrest, Appl. Phys. Lett. 90 (2001) 5048.
[7] D.W. Kang, J.W. Kang, J.W. Park, S.O. Jung, S.H. Lee, H.D. Park, Y.H. Kim, S.C. Shin, J.J. Kim, S.K. Kwon, Adv. Mater. 20 (2008) 2003.
[8] D.K. Rayabarapu, B.M.J.S. Paulose, J.P. Duan, C.H. Cheng, Adv. Mater. 17 (2005) 349.
[9] T.J. Park, W.S. Jeon, J.J. Park, S.Y. Kim, Y.K. Lee, J. Jang, J.H. Kwon, R. Pode, Appl. Phys. Lett. 92 (2008) 113308.
[10] M.T. Lee, C.H. Liao, C.H. Tsai, C.H. Chen, Adv. Mater. 17 (2005) 2493.
[11] C.C. Wu, Y.T. Lin, K.T. Wong, R.T. Chen, Y.Y. Chien, Adv. Mater. 16 (2004) 61.
[12] M.H. Ho, Y.S. Wu, S.W. Wen, M.T. Lee, T.M. Chen, C.H. Chin, K.C. Kwok, S.K. So, K.T. Yeung, Y.K. Cheng, Z.Q. Gao, Appl. Phys. Lett. 89 (2006) 252903.
[13] C.J. Tonzola, A.P. Kulkarni, A.P. Gifford, W. Kaminsky, S.A. Jenekhe, Adv. Funct. Mater. 17 (2007) 863.
[14] S.J. Lee, J.S. Park, K.J. Yoon, Y.I. Kim, S.H. Jin, S.K. Kang, Y.S. Gal, S.W. Kang, J.Y. Lee, J.W. Kang, S.H. Lee, H.D. Park, J.J. Kim, Adv. Mater. 18 (2008) 3922.
[15] C.H. Chien, C.K. Chen, F.M. Hsu, C.F. Shu, P.T. Chou, C.H. Lai, Adv. Funct. Mater. 19 (2009) 560.
[16] Z.Q. Gao, Z.H. Li, P.F. Xia, M.S. Wong, K.W. Cheah, C.H. Chen, Adv. Funct. Mater. 17 (2007) 3194.
[17] J.H. Lee, C.L. Huang, C.H. Hsiao, M.K. Leung, C.C. Yang, C.C. Chao, Appl. Phys. Lett. 94 (2009) 223301.
[18] J.W. Kang, S.H. Lee, H.D. Park, W.I. Jeong, K.M. Yoo, Y.S. Park, J.J. Kim, Appl. Phys. Lett. 90 (2007) 223508.
[19] W.S. Jeon, T.J. Park, S.Y. Kim, R. Pode, J. Jang, J.H. Kwon, Appl. Phys. Lett. 93 (2008) 063303.
[20] J.Y. Lee, J.-Y. Park, S.-H. Min, K.-W. Lee, Y.G. Baek, Thin Solid Films 515 (2007) 7726.
[21] M.-T. Lee, C.-H. Liao, C.-H. Tasi, C.H. Chen, Adv. Mater. 17 (2005) 2493.
[22] J.F. Ambrose, L.L. Carpenter, R.F. Nelson, J. Electrochem. Soc. 122 (1975) 876.
[23] D.F. Eaton, in: J.C. Scaiano (Ed.), Handbook of Organic Photochemistry, vol. 1, CRC Press, Boca Raton, FL, 1989.
[24] J. Luo, Y. Zhou, Z.-Q. Niu, Q.-F. Zhou, Y. Ma, J. Pei, J. Am. Chem. Soc. 129 (2007) 11314.
[25] S. Naka, H. Okada, H. Onnagawa, Y. Yamaguchi, T. Tsutsui, Synth. Met. 111 (2000) 331.
[26] G. Schwartz, Doctor Rerum Naturalium, Novel Concepts for High-Efficiency White Organic Light-Emitting Diodes, 2007, p. 75.

deposited on the surface of SiO_2 gate dielectric to isolate the electron traps. However, not all hydroxyl groups on polymeric dielectrics would trap electrons when OFETs were operated in the n-type regime. For example, by using polyvinyl alcohol (PVA) as gate dielectrics [14–16], ambipolar pentacene devices or the n-type only pentacene-based OFETs were demonstrated. Accordingly, correlations of the electron traps with the hydroxyl groups of the dielectric layer should be further studied.

In this study, pentacene-based OFETs were made with three kinds of polymer gate dielectrics, such as PVA, PVP, or PS, and with Ca, aluminum (Al), or gold (Au) metals as source-drain electrodes to investigate the mechanism of the n-type conduction in pentacene-based OFETs. The results show that the hydroxyl groups of PVP gate dielectric, trapping electrons as those of SiO_2 gate dielectrics, restrict n-channel formation in pentacene-based OFETs, but the hydroxyl groups of PVA don't. It could be clearly explained by the difference of the dissociation constant of protons on PVP and PVA. Additionally, while PS was used as the gate dielectric, the types of OFET conductive channels mainly depend on the charge injection conditions as determined by the work function of the source-drain electrodes. Finally, a pentacene-based OFET device using Ca as source-drain electrodes with PS as gate dielectric was fabricated, and its electron mobility could be up to 0.077 $cm^2s^{-1}V^{-1}$.

2. Experiments

The basic device in top contact bottom gate configuration herein, presented in Fig. 1a, comprises a pre-patterned indium–tin–oxide (ITO) on glass (RITEK Corp.) as the gate electrode that was sequentially coated with a thin layer of poly(3,4-ethylenedioxythiophene):polystyrenesulfonate (PEDOT:PSS Bayer Corp. VP-CH 8000), a double-layer gate dielectric (PS, PVA, or PVP on cross-linked PVP), a pentacene active layer, and metal source-drain electrodes. PEDOT:PSS layer was cast on a pre-patterned ITO glass substrate at 4000 rpm. The low conductivity PEDOT:PSS layer is used to smoothen the relatively rough ITO surface, which reduces the gate leakage current, improves the stabilities of devices during the long-term operation, and also increases the adhesion of PVP layer on the gate electrode. The bottom layer of gate dielectric was prepared by spin-coating (at 6000 rpm) the PVP (110 mg)/poly(melamine-*co*-formaldehyde) methylated (40 mg) in propylene glycol monomethyl ether acetate (PGMEA) solution (1 ml) on

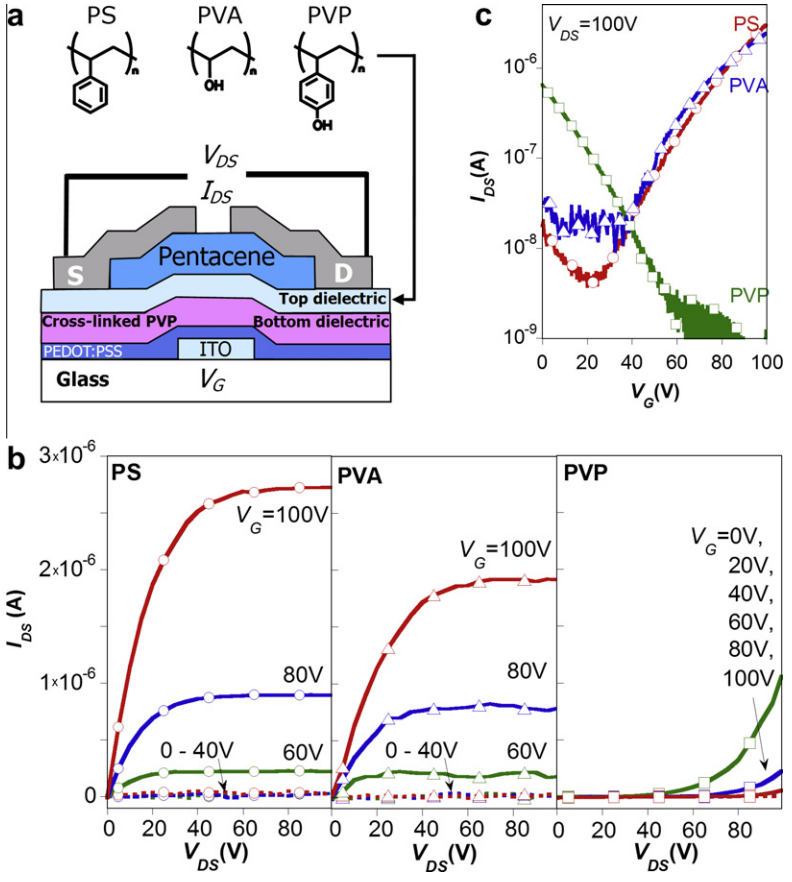

Fig. 1. (a) The structure of a pentacene-based OFET with metal electrodes, and PS, PVA, or PVP polymeric dielectrics spin-cast on cross-linked PVP as double-layer gate dielectrics. The chemical structures of PS, PVA, and PVP polymer are illustrated. (b)The output characteristics of I_{DS} vs. V_{DS} plot of pentacene-based OFETs with Ca source-drain electrodes, and three polymers as top gate dielectrics at V_G of 0 V to +100 V. (c) The transfer characteristics of I_{DS} vs. V_G plot of pentacene-based OFETs at a constant V_{DS} of +100 V with PS (○), PVA (△), and PVP (□) as the top gate dielectrics.

the PEDOT:PSS/ITO glass substrate. The substrate was baked at 120 °C for 5 min and then at 200 °C for 20 min to enable the formation of a cross-linked PVP dielectric [17]. The bottom dielectric provides good insulation and smooth surfaces which effectively reduced gate leakage currents. Next, the top dielectric made from one of three polymer solutions, PVA, PS, or PVP, was cast on the surface of the cross-linked PVP layer at 6000 rpm. PVA solution was made from 50 mg/1 ml de-ioned water solution, PS solution was made from 50 mg/1 ml toluene solution, and PVP was made from 50 mg/1 ml PGMEA solution. The substrate was heated to eliminate the residual solvent after spin-coating the second polymeric layer. The chemical structures of the three top dielectric polymers are shown in Fig. 1a. The pentacene (800 Å) active layer was deposited through a shadow mask on double-layer dielectric/PEDOT:PSS/ITO glass substrate inside the vacuum thermal evaporator (10^{-6} Torr). Through a shadow mask, a chosen metal material was thermally deposited on the surface of pentacene layer. The channel length (L) and width (W) of deposited electrodes in this work are 140 and 1000 μm, respectively. All of these steps were implemented inside a nitrogen-filled glove box, except for the preparation of the two layers of polymeric gate dielectrics and PEDOT:PSS/ITO glass substrate.

For studying the correlation of the different injection barriers of electrons or holes with device performance, Ca, Al, and Au, with work functions of 2.9, 4.2, and 5.1 eV, respectively, were selected as source-drain electrodes, respectively [11]. The electrodes of Ca are suitable for injection of electron carriers, for the smallest barrier height to the LUMO of pentacene molecules. For injection of hole carriers, the Au electrodes are suitable because of the matching of the work function of Au and the highest occupied molecular orbital (HOMO) of pentacene molecules (5.0). Then, the barrier heights from work function of Al to LUMO and to HOMO of pentacene are comparable, so ambipolar behaviors of OFETs with Al as source-drain electrodes are expectably observed.

Polymeric dielectrics, PS (M_w = 20,000), PVP (M_w = 20,000), PVA (M_w = 30,000–70,000, P8136), and cross-link agent, poly(melamine-*co*-formaldehyde) methylated, were purchased from Aldrich and used directly. Pentacene was also purchased from Aldrich without further purification.

The output and transfer characteristics of pentacene-based field-effect transistors were measured by HP 4145B semiconductor analyzer under N_2 environment. A pentacene-based field effect mobility with hole and electron mobility were extracted from the measured transfer curves according to the standard transistor's current–voltage equation in the saturation regime as follows: [18].

$$I_{DSsat} = (WC_i/2L)\mu(V_G - V_t)^2 \quad (1)$$

where W and L are the width and length of the channel, respectively, Ci is the gate dielectric capacitance, V_G is the gate voltage, and V_T is the threshold voltage. The μ value is field effect mobility for hole and electron conduction.

The capacitance–voltage (C–V) measurements were conducted with an HP 4284A Precision LCR meter. C–V measurements were carried out under biased voltage (−40–40 V) plus modulated voltage (100 mV) conditions. The alternate current responses versus bias voltages were measured to estimate the capacitance at the frequency modulated from 500 to 1 MHz. The device of metal–insulator-semiconductor (MIS) configuration as shown in the inset of Fig. 2 is composed of the ITO glass substrate, a PEDOT:PSS layer, a double-layer dielectric of cross-linked PVP with PVA, PVP, or PS, a pentacene active layer, and a metal (Ca) top electrode for the C–V measurements. The device area of MIS devices for the measurement of capacitance is of 2.0 mm^2. All MIS devices were measured inside a nitrogen glove box.

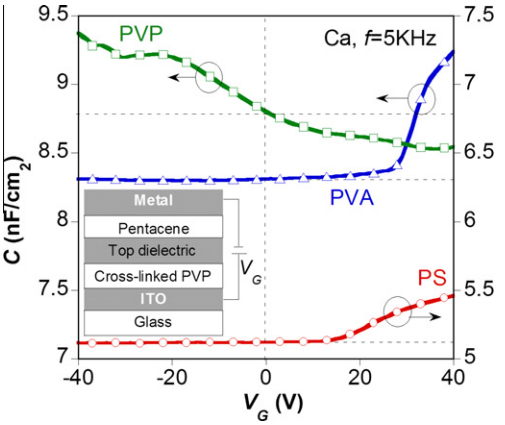

Fig. 2. Capacitance–voltage plots of the three devices with MIS configuration with PS (○), PVA(△), and PVP(□) as top dielectrics, respectively, and Ca metal as gate electrodes measured at the frequency of 5 KHz. The insert illustrates the device of MIS configuration.

3. Results and discussion

3.1. The influence of polymeric gate dielectrics on n-channel formation

In order to observe n-type conduction of pentacene-based OFETs, Ca was used as the source-drain metal electrodes of low work function (2.9 eV) for the injection of electrons to the LUMO level of pentacene molecules. Fig. 1b plots the output characteristics, drain current (I_{DS}) versus source-drain voltage (V_{DS}) of pentacene-based OFETs, which were operated at positive gate voltage from 0 to +100 V, n-channel accumulation regime. Three sets of curves represent three OFETs with PS, PVA, and PVP, as top gate dielectrics. OFETs with PS and PVA as top gate dielectrics performed the clear n-type channels with saturated and apparent pinch-off drain output currents. However, the OFET with PVP as top gate dielectric outputted diode-like currents. The currents are decreased as the gate voltage increased, which can be attributed to the hole flows. There was no n-channel formation in the OFET with PVP, although Ca electrodes were used for the efficient injection of electrons.

Fig. 1c plots the transfer characteristics of OFETs in Fig. 1b at V_{DS} of +100 V. The I_{DS} currents of OFETs with PS

or PVA are increased as the gate voltage increased, but the I_{DS} current of the OFET with PVP was declined as the gate voltage increased. It indicates that OFETs with PS or PVA are able to induce negative charges to form n-type channels, but the OFET with PVP is not. These results suggest that n-type channels of pentacene-based OFETs are correlated with both the effective injection of electrons from source-drain electrodes and the interfacial properties of gate dielectrics.

The *C–V* measurement was applied to investigate the types of accumulated charges between an organic semiconductor layer and a gate dielectric. The quasi-static capacitance per area versus bias voltage of devices of MIS structure is presented in Fig. 2. The pentacene was deposited on PS, PVA, and PVP top gate dielectric correspondingly with Ca as top electrodes. The baselines of capacitance curves of devices with PVP gate dielectric and PVA gate dielectric are higher than that of PS gate dielectric due to higher dielectric constants by the hydroxyl groups. Two of capacitance curves start to rise up when biased voltages are larger than +15 V for PS and +30 V for PVA, but the capacitance of devices with PVP gate dielectric drops as voltage bias increasing positively. The result of *C–V* measurements indicates that charge accumulation depends on the bias voltage applying to the interfaces of pentacene and polymer gate dielectrics, such as PS or PVA, when the n-type channel is formed. However, there is no n-type channel formation existing on the interface of pentacene and PVP gate dielectrics.

Accordingly, the functional groups on polymeric gate dielectrics should be the important parameters to determine the type of accumulated charge carriers, n-type or p-type accumulation. Comparing the chemical structures of the polymer gate dielectrics used in this study, firstly, both PVP and PS contain benzene rings attached on the side chain of polymers, but PVP has an additional hydroxyl group on the benzene ring. Secondly, both PVA and PVP are with hydroxyl groups. The chemical schematics of three polymers are shown in Fig. 1a. It is assumed that the hydroxyl groups on PVP interfere with the formation of n-type channel. The functionality of hydroxyl groups on PVA is different from that of PVP, because OFETs of PVA gate dielectrics present the decent n-type output characteristics.

3.2. The hydroxyl groups on PVP for n-channel formation

Fig. 3 demonstrates a transfer curve comparison of pentacene-based OFETs with different blend ratios of PVP and PS mixture as top layer of the double-layer gate dielectric at a constant V_{DS} of +100 V. The OFET structure with Ca electrodes was the same in Fig. 1a, and PVP:PS mixture was made from total 50 mg of PVP and PS in 1 ml PGMEA solution. When the ratio of PVP is 100%, a transfer characteristics curve is pure p-type. As decreased to 75% and to 50%, hole currents of devices are obviously decreased. Curves begin to appear ambipolar at 25% and to become n-type completely at 0%. Obviously, the transfer characteristics shifted from p-type to n-type depend strongly on the composition of PVP in the top gate dielectric. The ratio of PVP presents the percentage of hydroxyl groups on the interface of pentacene and the mixed PVP:PS gate dielectrics relatively. To further investigate the correlation between mixture ratio and surface hydroxyl groups, the result of contact angle measurements are presented in Fig. 3. As expected, an increase in contact angle of water from about 67° to about 94° when the portion of PVP decreases from 100% to 0%. The change of conductive channels from p-type to n-type suggests that hydroxyl groups on PVP dielectric cause the suppression of n-channel formation in pentacene-based OFETs. It agrees with the research reported by Chua et al. that the hydroxyl groups on the surface of silicon dioxide gate dielectric trap electrons and limit n-channel formation of OFETs [10]. However, PVA with hydroxyl groups had been reported as gate dielectrics for n-type or ambipolar pentacene-based OFETs [14–16]. The different functionalities of hydroxyl groups on PVP and PVA should be discussed.

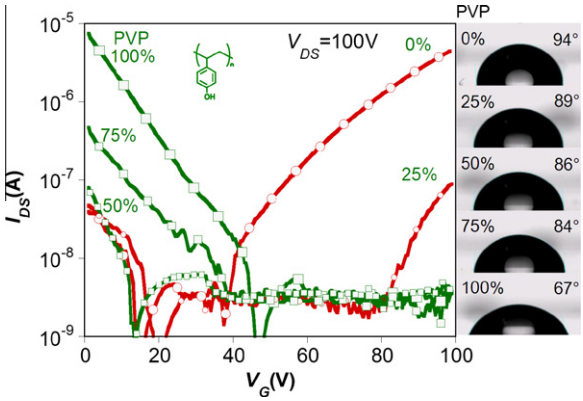

Fig. 3. The transfer characteristics of I_{DS} vs. V_G plot of pentacene-based OFETs with PVP and PS mixture as top gate dielectrics. PVP:PS mixture ratio is made from 100% of PVP to 0%. Currents of hole carriers are decreased gradually, and currents of electron carriers appear when PVP portion is less than 50%. The measurements of contact angles of water on the surfaces of PVP:PS mixture are presented.

3.3. The difference of hydroxyl groups on PVP and on PVA

The dissociation constants of protons for aliphatic alcohols are different from those of aromatic alcohols. The *pKa* value of methanol, ethanol, and 1-propanol are 15.5, 15.9, and 16.1, respectively. However, *pKa* value of phenol is about 9.5–10 [19,20]. Aromatic alcohols are mostly like a very weak acid because the negative charge after the dissociation of protons on the hydroxyl group can be stabilized by the conjugated molecule. Although both PVP and PVA have hydroxyl groups, the polymer of phenol, PVP, trends to lose its proton on the hydroxyl group as compared to PVA. Protons dissociated from PVP gate dielectrics result in the traps of electrons on the channels of OFETs. However, the hydroxyl groups in PVA have the minor effect on the generation of electron traps, because of the lower dissociation constant of protons. Fig. 4 illustrates a schematic drawing for the influence of dissociated protons on the electron channel in the pentacene active layer. When positive bias is applied on the gate electrode, an external electric field probably accelerate the dissociation of pro-

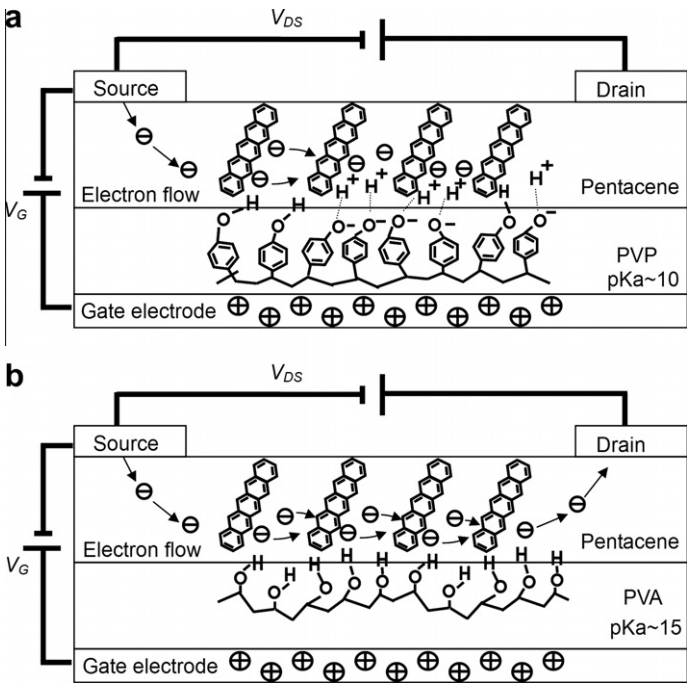

Fig. 4. A schematic demonstrates that electrons flow near the interface of pentacene and top gate dielectric. (a) Electrons are trapped by dissociated protons from PVP dielectric whose *pKa* is estimated around 9–10. (b) For PVA ($pKa \sim 15$) dielectric case, protons are not dissociated from hydroxyl groups, and electrons are not trapped.

tons on the hydroxyl groups of PVP gate dielectrics. Numerous traps of electrons are created to capture the injected electrons and block the electron flow. For OFETs of PVA ($pKa \sim 15$) as gate dielectrics, the influence of dissociated protons on the formation of the electron channel is minor, and characteristics of the n-type conduction can be observed as shown in Fig. 1b.

Dissociation of protons from PVP gate dielectrics was proposed to explain the output characteristics of OFETs. It was reported that PVP gate dielectrics output mobile ions, protons, in P3HT based OFETs when PVP gate dielectrics were exposed to moisture [21]. Additionally, the *pKa* value of hydroxyl groups on the surface of silicon dioxide was approximately 9–10 [22,23], which is similar to that of PVP. It might explain electron traps which are the dissociated protons on the surface of SiO_2 gate dielectrics. Without a modification layer on the SiO_2 gate dielectric, there is no n-type output characteristics in pentacene-based OFETs [10].

The different functionality of hydroxyl groups on PVP and PVA gate dielectrics can be detected by *C–V* measurements of devices with MIS configuration as shown in the insert of Fig. 2. For the MIS device made of PVP as the top layer of the double-layer dielectric, the magnitude of capacitance is decreased as the bias voltage operates from −40 to +40 V. This result interprets the accumulation of holes in the MIS device (probably at interface between pentacene and PVP) is favorable while the device is operated at negative gate voltage, p-type conduction regime. However, the accumulation of electrons is unfavorable while the MIS device is operated at positive gate voltage, n-type conduction regime. The magnitude of capacitance is decreased as the bias voltage increased. It is suggested that the n-type channel is inhibited by the dissociated protons from PVP gate dielectrics. We note that the magnitude of capacitance at $V_G = 0$ is higher than it at 20 V, which probably suggests the dissociation of protons in PVP gate dielectric, causing the interfacial doping effect. For MIS devices of PVA and PS as the gate dielectrics, the magnitudes of capacitance are increased while the devices are operated at the positive gate voltage, n-type conduction regime. The accumulation of electrons at the interface between pentacene and PVA or PS accounts for the n-type output characteristics of OFETs as shown in the Fig. 1b and c.

3.4. Influence of source-drain electrodes on the output characteristics of pentacene-based OFETs

The output performance of pentacene-based OFETs made of three metals (Au, Al, and Ca) of different work functions and three polymers (PVP, PS, and PVA) as the source-drain electrodes and top gate dielectrics, respectively, are summarized in Table 1. A comparison of OFETs of different source-drain metal electrodes provides the information regarding the correlations of the charge injection ability with n-type or p-type channel in OFETs. Additionally, OFETs of three different top gate dielectrics (PVP, PS, and PVA) are fabricated to investigate the influence of the top gate dielectrics on the formation of n-type or p-type channel.

In the case of OFETs with PVP as top gate dielectrics, there was no I_{DS} of n-type measured because the interface

Table 1
Electrical parameters of pentacene-based OFETs in both n-type and p-type operations with three different work function metals as source-drain electrodes and three polymers as top gate dielectrics.

Top dielectric	S-D metal*	C_i (nF/cm^2)**		I_{DS} (A) ***		μ (cm^2/V^{-s})	
		N	P	N	P	N	P
PVP	Ca	8.55	9.38	–	-2.89×10^{-6}	–	0.041
	Al	10.55	11.87	–	-3.93×10^{-5}	–	0.122
	Au	10.03	11.42	–	-7.19×10^{-5}	–	0.364
PS	Ca	6.61	5.96	2.90×10^{-6}	–	0.077	–
	Al	6.29	6.67	3.79×10^{-7}	-4.49×10^{-6}	0.019	0.118
	Au	6.82	7.45	–	-2.83×10^{-5}	–	0.425
PVA	Ca	10.99	9.78	2.45×10^{-6}	–	0.018	–
	Al	11.21	11.55	6.42×10^{-6}	–	0.031	–
	Au	10.35	11.11	1.20×10^{-6}	1.55×10^{-5}	0.014	0.089

* The channel length (L) and width (W) of source-drain electrodes are L = 140 μm and W = 1 mm.
** Capacitance values are obtained from capacitance–voltage measurement at +40 V for n-type and −40 V for p-type capacitance in driving frequency of 5 kHz.
*** I_{DS} (A) are measured in the saturation region at V_G of +100 V for n-type and at V_G of −100 V for p-type characteristics.

of pentacene and PVP interferes with the formation of n-type channel. However, the current I_{DS} of p-type is relatively higher than those with PS or PVA as top gate dielectrics which could be probably contributed to the larger size of pentacene grains on PVP [24,25]. Nevertheless, the intensity of the current I_{DS} went larger when the injection barrier from the work function of electrode metals to the HOMO level of pentacene molecules became smaller.

When top gate dielectrics of OFETs were replaced by PS, the type of conduction channel was highly correlated with the work function of source-drain electrodes. The operations of OFETs with PS are able to be the type of n-, ambipolar, or p-, while electrode metals of Ca, Al, or Au are adopted, respectively. In this case, the work function of metals simply determines the type of charge carriers in pentacene-based OFETs. It also indicates that the interface of pentacene and PS is likely trap-free for both hole and electron transport.

For the case of OFETs with PVA as top gate dielectrics, the output characteristics seem to prefer n-type operation. Using Ca as electrodes, the I_{DS} is about one third of that of the OFET using Al as electrodes. The cause of degradation could be the oxidization of Ca electrodes by water molecules attached on PVA. When adopting Al as source-drain electrodes, the OFETs only perform n-type behaviors which were also reported in our previous study [16]. When the OFETs use Au as electrodes, the output characteristic is ambipolar. The same ambipolar behaviors of pentacene-based OFETs with PVA as gate dielectrics and Au as source-drain electrodes agreed well with in the studies by Singh et al. [14,15]. These results could not explain by the barrier height of charge injection from the metal to the pentacene layer. So far, these extraordinary phenomena of OFETs with PVA are still under investigation.

In spite of the influence of gate dielectrics, the work function of source-drain electrode metals majorly determines the type of, negative, ambipolar, or positive, of output characteristics of pentacene-based OFETs. Further, the interface of pentacene and top gate dielectrics influences the conduction channels of OFETs which are related to charge transport through organic semiconductors. PVP gate dielectrics limit the formation of n-type channels regardless of metals of source-drain electrodes. PS gate dielectrics provide trap-free interfaces for both hole and electron carriers. For the case of PVA top gate dielectrics, the OFETs tend to operate rather in n-type channels than in p-type channels. To fabricate better n-type pentacene-based OFETs, it is suggested to adopt Ca as source-drain electrodes and PS as top gate dielectrics, and the n-type performance has achieved the electron mobility of 0.077 cm^{2}s^{-1}V^{-1}, which is a decent magnitude for pentacene-based n-type OFETs without further optimization.

4. Conclusions

In summary, this study presents the influence of polymer gate dielectrics and S-D electrodes on the formation of n-type channel in pentacene-based OFETs. For fabricating n-type pentacene-based OFETs, these gate dielectrics with hydroxyl groups and higher dissociation constant of protons, such as PVP or the surface of SiO_2, should not be considered because dissociated protons from dielectrics will trap electrons. It is recommended to employ Ca as source-drain electrodes and PS as top gate dielectrics, and its electron mobility could reach up to 0.077 cm^{2}s^{-1}V^{-1}. For further enhancing the n-type performance of pentacene-based devices, better charge transport quality will be required by improving crystallization of organic semiconductor material, such as optimizing deposition and post anneal treatments. In addition, favorable charge injection from metal electrodes to semiconductor material is also significant by minimizing injection barrier height. However, to balance low work function for n-type injection and air-stability of electrodes will be a challenge for n-type pentacene-based devices.

Acknowledgements

The authors would like to thank the National Science Council (NSC) of Taiwan (NSC96-2113-M-006-009-MY3) and the Asian Office of Aerospace Research and Development (AOARD-09-4055) for financially supporting this research.

References

[1] A. Dodabalapur, H.E. Katz, L. Torsi, R.C. Haddon, Science 269 (1995) 1560.
[2] Z. Bao, A. Dodabalapur, A.J. Lovinger, Appl. Phys. Lett. 69 (1996) 4108.
[3] Y.Y. Lin, D.J. Gundlach, S.F. Nelson, T.N. Jackson, IEEE Trans. Electron Devices 44 (1997) 1325.
[4] H. Sirringhaus, T. Kawasem, R.H. Friend, T. Shimoda, M. Inbasekaran, W. Wu, E.P. Woo, Science 290 (2000) 2123.
[5] M. Stein, J. Mapel, J.B. Benziger, S.R. Forrest, Appl. Phys. Lett. 81 (2002) 268.
[6] J.G. Laquindanum, H.E. Katz, A. Dodabalapur, A.J. Lovinger, J. Am. Chem. Soc. 118 (1996) 11331.
[7] H.E. Katz, A.J. Lovinger, J. Johnson, C. Kloc, T. Siegrist, W. Li, Y.-Y. Lin, A. Dodabalapur, Nature 404 (2000) 478.
[8] T. Yasuda, T. Goto, K. Fujita, T. Tsutsui, Appl. Phys. Lett. 85 (2004) 2098.
[9] M. Ahles, R. Schmechel, H. von Seggern, Appl. Phys. Lett. 85 (2004) 4499.
[10] L.-L. Chua, J. Zaumseil, J.-F. Chang, E.C.-W. Ou, P.K.-H. Ho, H. Sirringhaus, R.H. Friend, Nature 434 (2005) 194.
[11] C.-Y. Yang, S.-S. Cheng, C.-W. Ou, Y.-C. Chuang, M.-C. Wu, Dhananjay, C.-W. Chu, J. Appl. Phys. 103 (2008) 094519.
[12] M. Ahles, R. Schmechel, H.V. Seggem, Appl. Phys. Lett. 87 (2005) 113505.
[13] A. Facchetti, M.H. Yoon, T.J. Marks, Adv. Mater. 17 (2005) 1705.
[14] Th B. Singh, F. Meghdadi, S. Günes, N. Marjanović, G. Horowitz, P. Lang, S. Bauer, N.S. Sariciftci, Adv. Mater. 17 (2005) 2315.
[15] Th B. Singh, P. Senkarabacak, N.S. Sariciftci, A. Tanda, C. Lackner, R. Hagelauer, G. Horowitz, Appl. Phys. Lett. 89 (2006) 033512.
[16] T.-F. Guo, Z.-J. Tsai, S.-Y. Chen, T.-C. Wen, C.-T. Chung, J. Appl. Phys. 101 (2007) 124505.
[17] M. Halik, H. Klauk, U. Zshieschang, G. Schmid, W. Radlik, W. Weber, Adv. Mater. 14 (2002) 1717.
[18] S.M. Sze, Physics of Semiconductor Devices, Wiley, New York, 1981.
[19] O. Mitsunobu, M. Yamada, Bull. Chem. Soc. Jpn. 40 (1967) 2380.
[20] E.V. Anslyn, D.A. Dougherty, Modern Physical Organic Chemistry, University Science, California, 2006.
[21] T.G. Bäcklund, R. Österbacka, H. Stubb, J. Bobacka, A. Ivaska, J. Appl. Phys. 98 (2005) 074504.
[22] C. Eaborn, W. Stanczyk, J. Chem. SOC. Perkin Trans. 11 (1984) 2099.
[23] A. Gunzbourg, J.-C. Favier, P. Hemery, Polym. Int. 35 (1994) 179.
[24] C. Kim, A. Facchetti, T.J. Marks, Adv. Mater. 19 (2007) 2561.
[25] C.S. Kim, S.J. Jo, S.W. Lee, W.J. Kim, H.K. Baik, S.J. Lee, Adv. Funct. Mater. 17 (2007) 958.

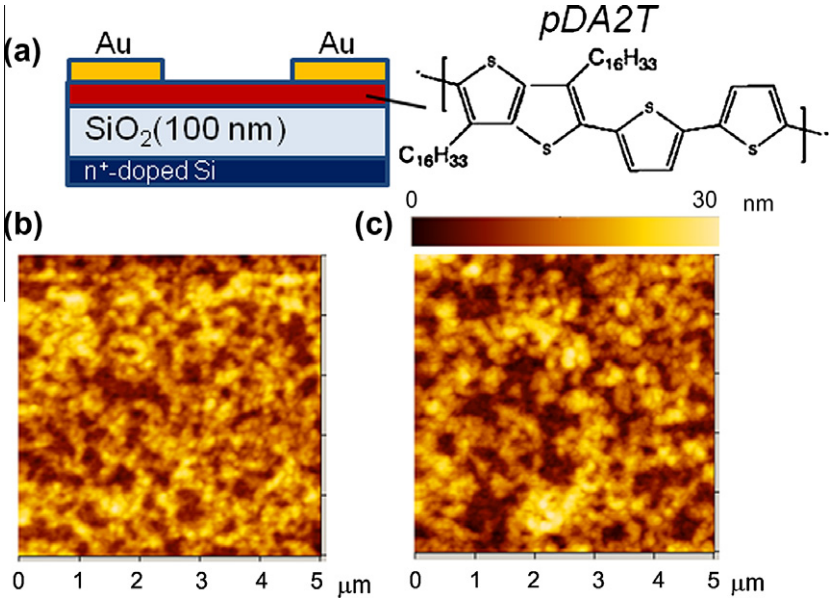

Fig. 1. (a) Schematic illustration of the present pDA2T TFTs (b) and (c) atomic-force microscope views of (b) a pDA2T TFT with DTS SAMs and (c) a pDA2T TFT with FDTS SAMs.

to be $\sim 0.2\ cm^2/V\,s$ at the highest [1]. The order of the air-stability in the family is naturally explained by difference in ionization potentials (IPs) of these compounds, where IP for pDA2T is reported to be 0.05–0.1 eV deeper than for pBTTT [1]. In this work, we employ surface modification with vapor-grown self-assembled monolayers (SAMs) of decyltriethoxysilane (DTS) and (heptadecafluoro-1,1,2,2-tetrahydrodecyl)triethoxysilane (FTS), with which we previously reported their effect of reducing the number of surface-trap levels and very high performance for organic single-crystal transistors [6,7]. In addition, the effect of prolonged annealing is investigated to maximize performance of the pDA2T TFTs, expecting improved ordering during the treatment above the glass-transition temperature. Moreover, lower surface energy on the SAMs-coated Si/SiO_2 substrates favors "edge-on" orientation of the thiophene chains, so that larger probability of the π-stacks orientated parallel to the channel can increase the mobility, as is argued in pBTTT devices [3].

Before depositing the SAMs, highly doped silicon substrates with thermally grown SiO_2 insulating layer (with the thickness of 100 nm) were carefully cleaned with acetone and isopropyl alcohol. The surface is ozone-treated for 2 min. We deposit hydrophobic organosilane SAMs of DTS or FTS by a vapor deposition process [8]. A *o*-dichlorobenzene solution of 10 mg/mL is prepared with pDA2T polymers. The polymer pDA2T was spun from the solution at a rate of 4000 rpm on the substrates in a relatively dry circumstances at less than 1%-humidity in a glove box at around 20 °C. The atmosphere is substituted to nitrogen gas with its content of more than 99%. The samples were dried and annealed at 100 °C, which is well above the glass-transition temperature of ~50 °C [9] in the glove box. In order to investigate the effect of the annealing time, we prepared samples annealed for 10 min, 120 min and

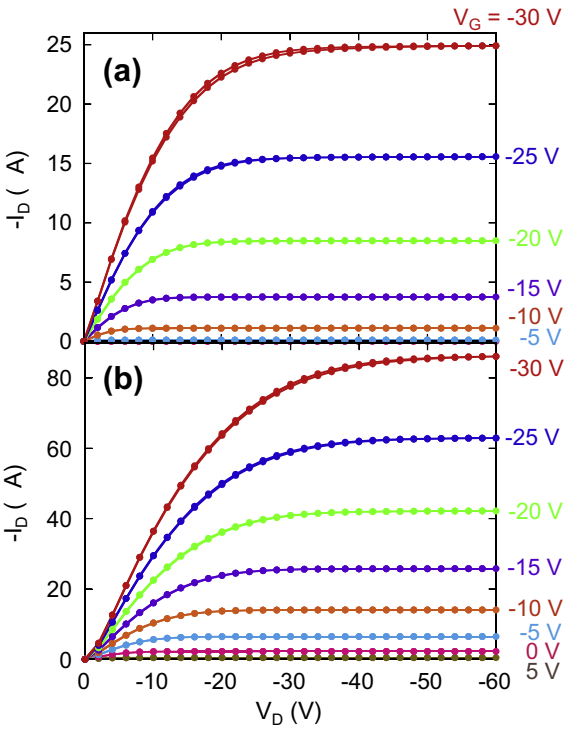

Fig. 2. Output characteristics of the pDA2T TFT annealed for 120 min. (a) For the sample with DTS SAMs. (b) For the sample with FTS SAMs.

16 h. The samples are slowly cooled to room temperature in the dry nitrogen atmosphere. Fifty-nanometer-thick gold contacts were deposited on the samples through shadow masks to form the source and drain electrodes. The

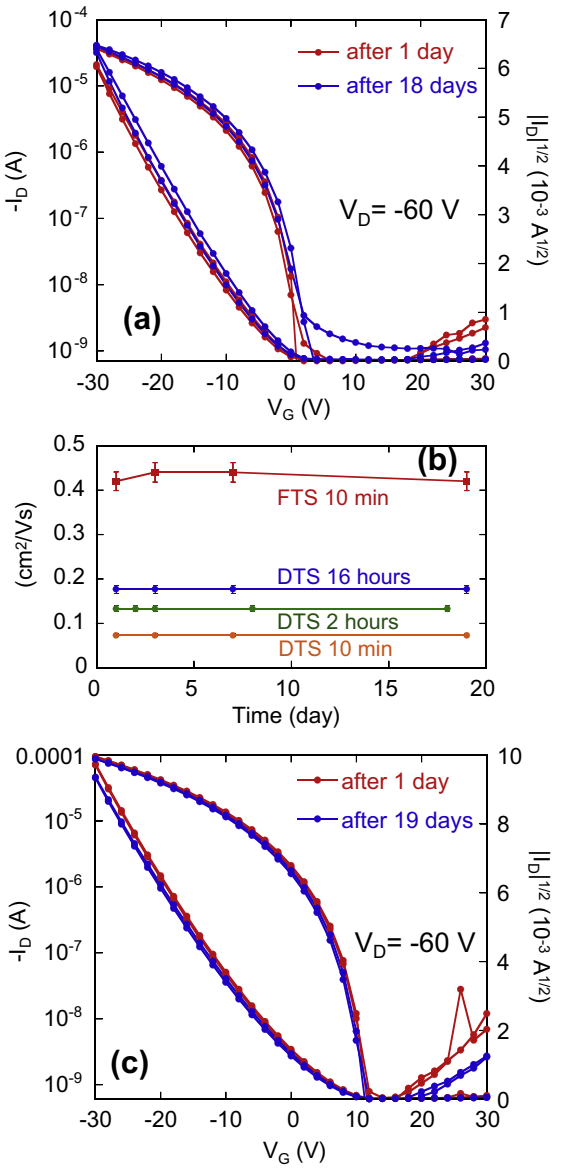

Fig. 3. (a) Transfer characteristics of the pDA2T TFT with DTS SAMs annealed for 120 min. The four curves with different colors are for the results measured after keeping the device in the air with 60% humidity. Red and blue filled circles represent the data taken 1 day and 18 days after the preparation, respectively. (b) Time evolution of mobility in the pDA2T TFTs with DTS SAMs annealed for 10 min, 120 min, and 16 h. The result for the pDA2T TFTs with FTS SAMs annealed for 10 min is plotted together. (c) Transfer characteristics of the pDA2T TFT with FTS SAMs annealed for 120 min. The four curves with different colors are for the results measured after keeping the device in the air with 60% humidity. Red and blue filled circles represent the data taken 1 day and 19 days after the preparation, respectively. (For interpretation of the references to colour in this figure legend, the reader is referred to the web version of this article.)

channel lengths L and the channel width W are 50–100 μm and 1500 μm, respectively. Electrical measurements of the transistors were carried out in ambient condition with a Keithley 4200 semiconductor parameter analyzer. To examine the air-stability, samples were stored in the conditions of 60%RH and the measurements were performed from time to time for over several weeks after the sample preparation. Fig. 1(a) shows schematic illustration of the devices.

Surface morphology is characterized by atomic-force microscopy. The samples with DTS and FTS with the annealing time of 120 min are shown in Fig. 1(b) and (c), respectively. As both surfaces are hydrophobic, the grain grew rather large. The grain size is typically ~100 nm, reproducing the morphology reported in [1]. We note that the morphology appears to be similar among samples with different annealing times.

Fig. 2(a) and (b) shows output characteristics of the samples with DTS and FTS, respectively. The results of the well-saturated characteristics indicate that both TFTs are typical field-effect transistors well approximated by the gradual-channel model with sufficiently long L (= 100 μm). Therefore, the use of the equation

$$I_D^{sat} = \frac{L}{2W}\mu C(V_G - V_{th})^2 \quad (1)$$

is fully guaranteed, where C is capacitance of the gate dielectric insulator (100-nm thick SiO_2). Therefore, mobility μ is evaluated from the plot of the saturation current $\sqrt{I_D^{sat}}$ *vs.* gate voltage V_G with the intercept of the threshold voltage V_{th}.

Such plots are given in Fig. 3(a) for the pDA2T sample with DTS SAMs annealed for 120 min. We keep the sample in a container with the humidity of ~60% and measured the characteristics after 1 day, 3 days, 8 days and 18 days. The nearly merged curves demonstrate that good stability in the humid air is indeed realized. Mobility is estimated to be ~ 0.13 $cm^2/V\,s$ using Eq. (1) from the slope of the linearly regressing part. The estimated μ is plotted as a function of time in Fig. 3(b) together with the results for similarly prepared samples with different annealing times. For all the samples, μ is essentially unchanged for more than 2 weeks, demonstrating significant improvement in the air-stability as compared to previous report [1]. We note that our present DTS SAMs are deposited from vapor, while mostly solution-processed SAMs are used in literatures [1–3], which could be related to the improvement in the stability. It is to be further investigated experimentally to elucidate the detailed mechanisms of the device instability in air.

The values of mobility are in the range of 0.08—0.17 $cm^2/V\,s$, which essentially reproduced the reported result for the same compound [1]. The tendency of higher μ with longer annealing time in the glass state suggests that the extent of ordering of the polymer chains can be improved slowly with time. A primitive X-ray diffraction scan did not show difference in the profiles, indicating that the difference is not due to obvious variation in their structures. It is to be further studied by low-angle X-ray diffraction using high-power light sources for more detailed structural change, for example.

Fig. 3(c) shows transfer characteristics of the sample with FTS annealed for 10 min, plotted similarly to Fig. 3(a). The mobility estimated by Eq. (1) is ~ 0.4 $cm^2/V\,s$. The air-stability for this sample is equally good as plotted together in Fig. 3(b). We have prepared other samples with different

annealing times, so that μ ranged in 0.4—0.8 $cm^2/V\,s$, though the variation is not correlated with the annealing times but film wettability. The larger mobility itself can be attributed to lower surface energy on the FTS substrate than on the DTS substrate, favoring better edge-on π stacks, as is argued formerly [3]. We note that the presence of larger dipole in the FTS layer accumulate carriers at the surface of the polymer semiconductor, which is responsible for the shift in V_{th} [6,10].

In conclusion, air-stability and high field-effect mobility comparable to amorphous silicon TFTs are simultaneously realized using high-IP compound pDA2T and employing fabrication processes of surface modification with SAMs and prolonged annealing. Since the polymer TFTs are of significant advantage in solution-based low-cost production for large-area electronics devices, the achievement of the high performance in practically applicable air-stable transistors further strengthens their material advantage and drives their future commercialization.

Acknowledgments

This work was financially supported by Industrial Technology Research Grant Program in 2006 and 2009 from NEDO, Japan, and by a Grant-in-Aid for Scientific Research (Nos. 17069003, 19360009, and 21108514) from MEXT, Japan.

References

[1] I. McCulloch, M. Heeney, M.L. Chabinyc, D. DeLongchamp, R.J. Kline, M. Cölle, W. Duffy, D. Fischer, D. Gundlach, B. Hamadani, R. Hamilton, L. Richter, A. Salleo, M. Shkunov, D. Sparrowe, S. Tierney, Weimin Zhang Adv. Mater. 21 (2009) 1091.
[2] T. Umeda, S. Tokito, D. Kumaki, J. Appl. Phys. 101 (2007) 054517.
[3] T. Umeda, D. Kumaki, S. Tokito, J. Appl. Phys. 105 (2009) 024516.
[4] I. McCulloch, M. Heeney, C. Bailey, K. Genevicius, I. MacDonald, M. Shkunov, D. Sparrowe, S. Tierney, R. Wagner, W. Zhang, M.L. Chabinyc, R.J. Kline, M.D. McGehee, M.F. Toney, Nat. Mater. 5 (2006) 328.
[5] K.-J. Baeg, D. Khim, D.-Y. Kim, J.B. Koo, I.-K. You, W.S. Choi, Y.-Y. Noh, Thin Solid Films 518 (2010) 4024.
[6] J. Takeya, T. Nishikawa, T. Takenobu, S. Kobayashi, Y. Iwasa, T. Mitani, C. Goldmann, C. Krellner, B. Batlogg, Appl. Phys. Lett. 85 (2004) 5078.
[7] J. Takeya, M. Yamagishi, Y. Tominari, R. Hirahara, Y. Nakazawa, T. Nishikawa, T. Kawase, T. Shimoda, Appl. Phys. Lett. 90 (2007) 102120.
[8] T. Nishikawa, S. Kobayashi, T. Nakanowatari, T. Mitani, T. Shimoda, Y. Kubozono, G. Yamamoto, H. Ishii, M. Niwano, Y. Iwasa, J. Appl. Phys. 97 (2005) 104509.
[9] Y. Li, Y. Wu, P. Liu, M. Birau, H. Pan, B.S. Ong, Adv. Mater. 18 (2006) 3029.
[10] S. Kobayashi, T. Nishikawa, T. Takenobu, S. Mori, T. Shimoda, T. Mitani, H. Shimotani, N. Yoshimoto, S. Ogawa, Y. Iwasa, Nat. Mater. 3 (2004) 317.

were considered ideal for host–guest relationship but their crystallization issues and non-uniform film thickness have aggravated as additional problems.

Generally, most of the host materials either transport holes or electrons in a device but unbalanced hole and electron currents makes the recombination zone narrower, thereby shifting it either close to hole transport layer (HTL) or electron transport layer (ETL). Thus narrower charge recombination zone in PHOLEDs are prone to triplet–triplet exciton quenching due to local high density of triplet excitons and also long diffusion of the triplet excitons [12,13]. Therefore, bipolar small molecule hosts can meet the requirements of balancing the charge density for making high performance simple device structure. For improving the charge-transferring capability of bipolar molecules, it is desirable to localize the highest occupied molecular orbital (HOMO) and lowest occupied molecular orbital (LUMO) level at their respective hole and electron transporting moieties. To the best of our knowledge very few devices based on solution process bipolar small molecules have been reported so far [14–16].

Typically, *N*,*N*′-diphenyl-*N*,*N*′-bis(1-naphthyl)(1,1′-biphenyl)-4,4′diamine (NPB) has bipolar characteristics in OLEDs with both hole and electron transporting property. It has 5.4 eV HOMO and 2.3 eV LUMO values and a low triplet energy (2.3 eV) [17]. For practical use of the host in PHOLEDs, its LUMO energy is too high compared with general host materials even though its electron mobility is good as 9×10^{-4} cm^2/vs [18]. In solution process devices, it forms non-uniform surface with high roughness due to crystallization of its molecules upon thermal treatment [19]. Therefore, NPB was reported as a hole-type host in the mixed host system [10]. In order to reduce the electron-injection barrier and enhancing the electron mobility of NPB molecule, we report, NPB modified two novel bipolar molecules, 4,4′-bis[*N*-(1-naphthyl)-*N*-(3-pyridinylamino]biphenyl (NPyB) and 4,4′-bis [*N*-(3-quinolinyl)-*N*-phenylamino]biphenyl (QuPB) with their synthetic method and material characteristics. We also employed NPyB and QuPB host materials for fabricating high-efficiency electrophosphorescent solution processed red OLEDs. The multilayered electrophosphorescent OLEDs fabricated from 1,2-dichlorobenzene solution containing spin-coated NPyB and QuPB hosts blended with a dopant, bis(2-phenylquinoline(acetylacetonate)iridium (Ir(phq)$_2$acac) emitted red phosphorescent light. The bipolar NPyB and QuBP hosts show good solubility and stability in 1,2-dicholobenzene solvent, uniform film growth characteristics without any crystallization issues, and good electron and hole-transporting properties. A luminance of 14,440 cd/m^2 at 8.4 V and luminous efficiency of 21.0 cd/A and 11.3 lm/W at 5.9 V are demonstrated in the NPyB host device.

2. Experimental details

2.1. Material synthesis

The compounds NPyB and QuPB were synthesized according to the procedure shown in Fig. 1. All reagents and solvents were purchased from Aldrich chemical Co. and Fluka. Other reagents in the scheme were used as from commercial sources.

2.1.1. 4,4′-Bis[N-(1-naphthyl)-N-(3-pyridinylamino]biphenyl (NPyB)

To a solid mixture of 1-naphthyl-3-pyridinylamine (3.0 g, 13.6 mmol) and 4,4′-dibromobiphenyl (2.0 g, 6.5 mmol), a solution of 50 ml toluene was added. It was degassed by bubbling nitrogen for 30 min. Additionally, 0.2 mmol of tris(dibenzylideneacetone)dipalladium(0) [$Pd_2(dba)_3$], 0.4 mmol of tri-*tert*-butylphosphine, and 20 mmol of sodium-*tert*-butoxide was added to the mixture. The mixture was vigorously refluxed under nitrogen for 24 h. When the reaction mixture was cooled down to room temperature, 30 ml of water was added to remove some salts. After separating the water, the solution was dried by $MgSO_4$, and then concentrated under reduced pressure. The mixture was purified by column chromatography on silica gel eluting with a 1:2 mixture of ethylacetate and hexane. By removing the eluting solvent, light yellow powder was obtained (2.5 g, 65%).

T_m 241 °C, T_g 93 °C, δ_H (500 MHz; $CDCl_3$; Me_4Si) 8.38 (2H, d, *J* 2.6), 8.16 (2H, d, *J* 4.5), 7.90 (4H, *J* 8.5), 7.49 (4H, m), 7.37 (8H, m), 7.28 (2H, d, *J* 8.7), 7.11 (6H, m). Elemental Analysis Calc. for $C_{42}H_{30}N_4$: C, 85.40; H, 5.12; N, 9.48%. Found: C, 85.54; H, 5.04; N, 9.47%. M/S (*m*/*z*, M$^+$). Found: 591.2543, Calc.: 591.2549.

2.1.2. 4,4′-Bis [N-(3-quinolinyl)-N-phenylamino]biphenyl (QuPB)

The synthetic procedure of QuPB is same except using 3-quinolinyl-phenylamine (3.0 g, 13.6 mmol) instead of 1-naphthyl-3-pyridinylamine. Yellow powder was obtained (2.3 g, 60%).

T_m 186 °C, T_g 94 °C. δ_H (500 MHz; $CDCl_3$; Me_4Si) 8.79 (2H, d, *J* 2.5), 8.03 (2H, d, *J* 8.3), 7.70 (2H, d, *J* 2.2), 7.59 (4H, m), 7.52 (4H, d, *J* 8.6), 7.46 (2H, t, *J* 7.7), 7.32 (4H, t, *J* 7.9), 7.20 (8H, d, *J* 8.4), 7.13 (2H, t, *J* 7.3). Elemental Analysis Calc. for $C_{42}H_{30}N_4$: C, 85.40; H, 5.12; N, 9.48%. Found: C, 85.49; H, 5.11; N, 9.45%. M/S: (*m*/*z*, M$^+$). Found: 591.2551, Calc.: 591.2549.

2.2. OLED fabrication and measurements

OLED devices were fabricated on the indium–tinoxide (ITO) glass having an emission area of 2 mm × 2 mm with a sheet resistance of 12 Ω/square. A line pattern of ITO was formed by the photolithography process. Before coating organic layers, the patterned ITO glasses were cleaned by sonification in isopropyl alcohol (IPA) and acetone, and then rinsed in deionized water; finally it was irradiated in a UV-ozone chamber. A 45 nm poly(ethylenedioxythiophene):poly(styrenesulfonate) (PEDOT:PSS) was spin-coated on the ITO substrates and then dried using a hot plate at 120 °C for 10 min to remove the solvent. A 40 nm thick emissive host system i.e. NPyB and QuPB doped with Ir(phq)$_2$acac in 1,2-dichlorobenzene was later spin-coated on the PEDOT:PSS layer. The spin-coated emissive layer was then baked on a hot plate at 120 °C for 10 min. The spin coating and baking process were carried out in a glove box with nitrogen ambient. Subsequently, 30 nm TPBI was

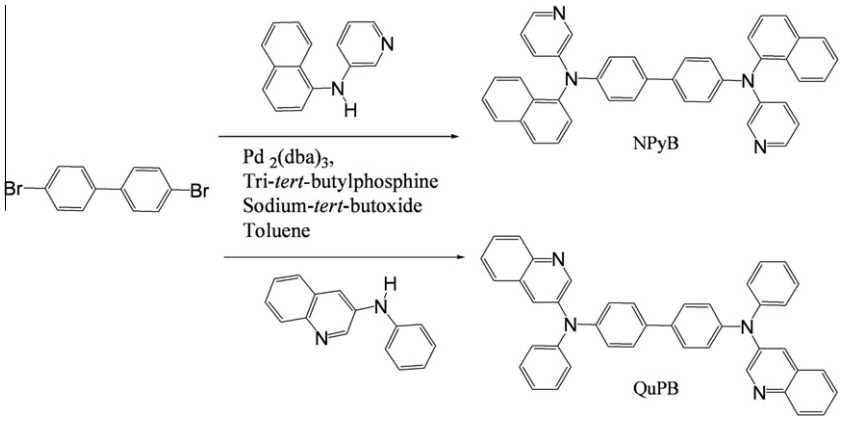

Fig. 1. Synthesis procedure of NPyB and QuPB.

deposited in an organic chamber using vacuum thermal evaporation at a base pressure of 10^{-7} Torr, while LiF (1 nm) and Al (100 nm) were deposited in an adjacent metal chamber without breaking the system vacuum.

Current density–voltage (*J*–*V*) and luminance–voltage (*L*–*V*) characteristics of the fabricated OLEDs were measured using a Keithley SMU 2635 and Konika Minolta CS-100A. Also, the electroluminescence (EL) spectra and CIE color coordinates were obtained using a Konika Minolta CS-1000A spectroradiometer. For optical measurements, UV–Visible absorption spectra of NPyB in dichloromethane solution were recorded with a Shimadzu 3100 UV–VIS–NIR spectrophotometer. In case of photoluminescence (PL) measurement, emission spectrum of NPyB and QuPB in dichloromethane solution, and deposited thin films on glass substrate were measured with a Jasco FP-6500 spectroflurometer. Low temperature emission spectra of NPyB and QuPB solutions were also recorded using liquid nitrogen at 77 K with Jasco FP-6500 spectroflurometer. For investigation of smoothness and homogenous surface of emissive layer, atomic force microscopy (AFM) was done.

Cyclic voltammetry (CV) was performed using EC epsilon electrochemical analysis equipment. Platinum wire and ITO film on glass were used as counter and working electrodes, respectively. Tetrabutylammonium perchlorate (Bu_4NClO_4) is used as a supporting electrolyte. Ag wire in 0.1 M $AgNO_3$ was used as a reference electrode. By means of internal ferrocenium/ferrocene (Fe^+/Fe) standard, the potential values were converted to the saturated calomel electrode (SCE) scale. The position of LUMO of each material is estimated from the optical band gap determined from the absorption onset of the spectra. The films that had been coated with the material were made on ITO glass through the solution drop coating and then dried in a vacuum oven at 80 °C. Solid-state electrochemistry was performed at a scan rate of 150 mV/s and start potential voltage have supplied from 0.5 eV for reducing potential damage.

3. Results and discussion

The chemical structure and synthetic route of 4,4′-bis[*N*-(1-naphthyl)-*N*-(3-pyridinylamino]biphenyl (NPyB) and 4,4′-bis [*N*-(3-quinolinyl)-*N*-phenylamino]biphenyl (QuPB) are shown in Fig. 1. The molecular structures of NPyB and QuPB were confirmed by ^{1}H NMR, mass spectrometry, and elemental analysis. Thermal properties of NPyB and QuPB were investigated by means of differential scanning calorimetry (DSC). A glass-transition temperature (T_g) was obtained from the second heating scan of the glassy samples cooled after the first heating up to melting temperature (T_m). The heating rate was 10 °C/min. The T_m's of NPyB and QuPB appeared at 241 and 186 °C, respectively. The crystallization temperature (T_c) of NPyB was observed about 180 °C by the second heating but no T_c of QuPB was found, which indicates that QuPB has more glass-like property. Considering the melting point of NPB about 280 °C, intermolecular dipole interaction is reduced in the order of NPB, NPyB, and QuPB. However, the glass-transition temperatures of both the molecules are around 93–95 °C which is about same as that of commercialized NPB (95 °C) [20]. NPyB and QuPB can readily dissolve in common organic solvents, such as 1,2-dichloromethane, 1,2-dichlorobenzene, toluene which enables the preparation of uniform thin film by solution processing such as spin coating.

AFM studies of NPyB and QuPB host materials with spin coating in 1,2-dichlorobenzene solution were carried out to investigate the surface morphology of thin films. As shown in Fig. 2, root-mean-square-roughness (rms) values are 1.90 Å and 1.89 Å for NPyB and QuPB. These results shows that both the host films were smooth and homogeneous without any crystallization issues by implementing the host compatibility with dopant material used in fabricating solution-processible devices.

The bipolar host materials, NPyB and QuPB having pyridine and quinoline units as electron transport moieties lead to bipolar charge transport property for both holes and electrons. The photophysical properties of NPyB and QuPB host materials were measured using UV–visible absorption and photoluminescence spectra as depicted in Fig. 3 and Table 1. The absorption and emission spectra of both the host materials were carried out in dilute dichloromethane solution. The absorption spectrum of NPyB has one absorption band from 305 to 360 nm which could be from π–π^* transitions of the conjugated π-electron system.

	NPyB	QuPB
Film	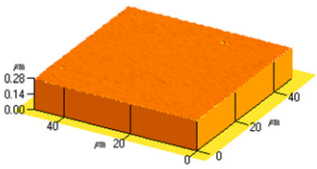	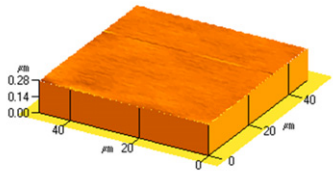
Rms roughness	1.90 Å	1.89 Å

Fig. 2. AFM image of host (a) NPyB and (b) QuPB.

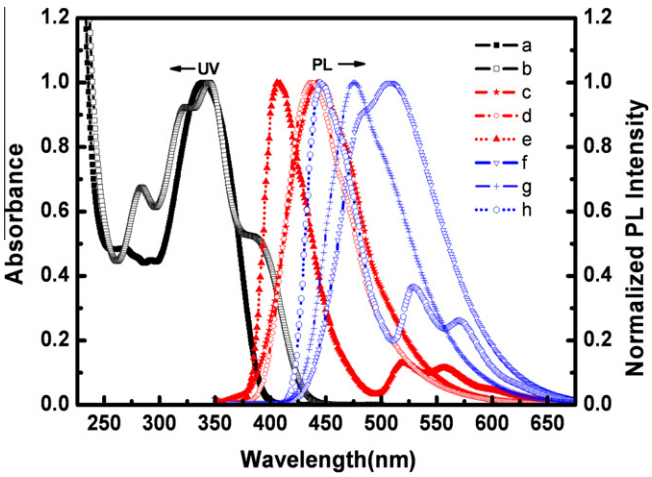

Fig. 3. UV spectra in dichloromethane (a) NPyB, (b) QuPB, and PL spectra in dichloromethane, (c) NPyB solution, (d) NPyB thin film, (e) NPyB low temperature (77 K), (f) QuPB solution, (g) QuPB thin film and (h) QuPB low temperature (77 K).

QuPB exhibits four vibronic absorption bands centered at 284, 320, 345 and 390 nm, respectively. The PL emission maximas of NPyB and QuPB in solution were observed around 442 and 510 nm, respectively. The PL emission spectra of NPyB and QuPB thin films were slightly blue shifted by 6 and 36 nm, respectively. The low temperature phosphorescent spectrum of the NPyB host, measured in 2-methyltetrahydrofuran (THF) solution at 77 K, revealed the shifting of main peak at 405 nm while a phosphorescent sub-band of two peaks with peak positions, 520 and 558 nm could also be noticed. Similarly, QuPB at 77 K shows the main peak at 446 nm and phosphorescent sub-bands with peak positions at 527 and 572 nm. From the phosphorescent spectra, triplet energies of 2.4 and 2.3 eV were calculated from 520 and 527 nm first peaks of NPyB and QuPB materials. It confirms that their triplet energies are in good agreement in transferring excitons from the bipolar hosts to $Ir(phq)_2acac$ dopant. In order to make appropriate comparisons of triplet energies, energy transfer experiments from the red dopant to NPyB and QuPB hosts were carried out in 1,2-dichlorobenzene solution. When NPyB was added to $Ir(phq)_2acac$ solution at different concentrations, the quantum efficiency did not change. However, addition of QuPB has decreased the quantum efficiency, significantly. These results indicate that NPyB triplet energy is higher than the red dopant while QuPB has a triplet energy similar to $Ir(phq)_2acac$ dopant. In order to obtain more accurate results, energy transfer rate of QuPB was calculated using Stern–Volmer plots and it came out $3 \times 10^9\ s^{-1}M^{-1}$, which is similar to diffusion rate of

Table 1
Physical properties of NPyB and QuPB.

Compounds	λ_{abs}[a] (nm)	λ_{PL}[b] (nm) sol./film/77 K	*T*m, *T*g (°C)	HOMO/LUMO$_{calc}$ $\Delta\varepsilon$ (eV)	HOMO/LUMO$_{exp}$ $\Delta\varepsilon$ (eV)	T_1calc/exp (eV)
NPyB	340	442/436/405,520	241, 93	4.4, 2.2, 2.0	5.5, 2.4, 3.1	2.0/2.4
QuPB	284, 320, 345, 390	510/476/445,527	186, 94	4.4, 2.3, 2.3	5.5, 2.7, 2.8	1.8/2.3
NPB	350	467/438/418,528	277, 95	4.2, 2.0, 2.2	5.4, 2.3, 3.1	2.1/2.3

[a] Absorption maximum.
[b] PL maxima, T_m – melting temperature, T_g – glass-transition temperature.

Table 2
A summary of device performance as a function of doping concentration in NPyB and QuPB hosts.

Doping ratios of $Ir(phq)_2acac$	NPyB (1%)	NPyB (2%)	NPyB (3%)	QuPB (3%)	QuPB (5%)	QuPB (7%)	NPB:TPBI (7%)
Turn-on voltage (at 1 cd/m^2)	5.1	5.3	4.3	5.1	4.9	4.5	5.4
Operating voltage (at 1000 cd/m^2)	5.9	5.9	6.1	6.3	5.5	5.3	6.3
Luminance (max.) at voltage	12,820 (8.4 V)	14,400 (8.8 V)	14,190 (9.2 V)	7888 (8.2 V)	7714 (8.0 V)	8751 (8.6 V)	19,250 (9.2 V)
Maximum efficiency (cd/A , lm/W)	17.9, 9.21	21.0, 11.3	12.8, 5.8	6.9, 3.3	7.8, 4.5	7.2, 4.5	11.9, 5.8
Efficiency (cd/A, lm/W at 1000 cd/m^2)	17.6, 9.1	20.6, 10.8	11.6, 5.9	6.7, 3.3	7.6, 3.3	7.2, 4.2	11.9, 5.8
CIE (x, y) at 1000 cd/m^2)	0.57, 0.39	0.59, 0.39	0.59, 0.39	0.60, 0.38	0.60, 0.38	0.60, 0.38	0.61, 0.38
Emission peak (nm)	593	595	596	598	598	598	600

organic solvents. However, NPyB does not reach to such value. This proves that NPyB has higher triplet energy than $Ir(phq)_2acac$ and can be used with red dopant effectively.

In order to investigate the electrochemical properties of NPyB and QuPB, cyclic voltammetry experiments were performed to know HOMO levels. Table 1 summarizes the calculated and experimentally obtained energy levels values. The host materials showed reversible oxidation and reduction waves, indicating that these materials are quite relevant for bipolar transport in OLEDs. The HOMO energy levels for NPyB and QuPB were estimated to be 5.5 eV by cyclic voltammogram, which is considerably close to 5.4 eV HOMO of hole-transporting material, NPB [21]. The LUMO energy levels of both the hosts are at 2.4 and 2.7 eV which can be deduced from calculation of band gaps. The triplet energy values of host materials and NPB were estimated by molecular modeling with density functional theory (DFT) using DMOL3 program (version 4.2) [22–24]. The energy levels of phosphorescent dopant $Ir(phq)_2acac$ were reported to have approximately 2.2 eV triplet energy, 5.3 eV HOMO, and 3.1 eV LUMO energies [25], which allow to receive triplet energy from both the hosts. Our host materials are expected to be good agreement in confining triplet excitons on the guest molecule effectively.

A series of solution processed devices were fabricated by using a host/guest blend system and evaluated in terms of their J–V and L–V output characteristics. Devices A and B were fabricated using NPyB:$Ir(phq)_2acac$ (2 wt.%), and QuPB:$Ir(phq)_2acac$ (5 wt.%), respectively. These devices were fabricated on ITO with a multilayered structure of ITO/PEDOT:PSS (45 nm)/host:dopant (35 nm)/TPBI (30 nm)/LiF(1 nm)/Al(100 nm). For comparison, NPB:TPBI (1:1) type of mixed host device with 7 wt.% of $Ir(phq)_2acac$ concentration in similar experimental conditions was also fabricated [10] and its data is outlined in Table 2. Here PEDOT:PSS improves the hole injection as its HOMO level is 5.2 eV which is close to HOMO of NPyB and QuPB hosts. The operating conditions and characteristics of these devices with varying concentration ranges are compared and summarized in Table 2. Among all the prepared devices, devices A and B demonstrate their best performances with a dopant concentration of 2 and 5 wt.%.

Fig. 4 shows the current density–voltage (J–V) and luminance–voltage (L–V) characteristics of all three devices. Device A exhibited turn-on voltage of 5.3 V which is similar to hole transport NPB:TPBI mixed host doped device while lower turn-on voltage of 4.9 V was obtained in device B. It is interesting to note that NPyB type of device has similar current density compared to NPB:TPBI mixed host system. This clearly indicates that NPyB host has very good hole and electron transporting ability. Devices A and B have lower driving voltages compared to NPB:TPBI based device. It was observed that driving voltages to reach 1000 cd/m^2 were found to be 5.9 and 5.5 V for devices A and B, lower than 6.3 V for NPB:TPBI based device. Fig. 4 also shows L–V characteristics, exhibiting maximum brightness 14,440 cd/m^2 at 8.8 V for device A, and 7714 cd/m^2 at 8.0 V for device B, respectively. However, NPB:TPBI type of device exhibited slightly better maximum brightness compared to device A but overall performance of device A

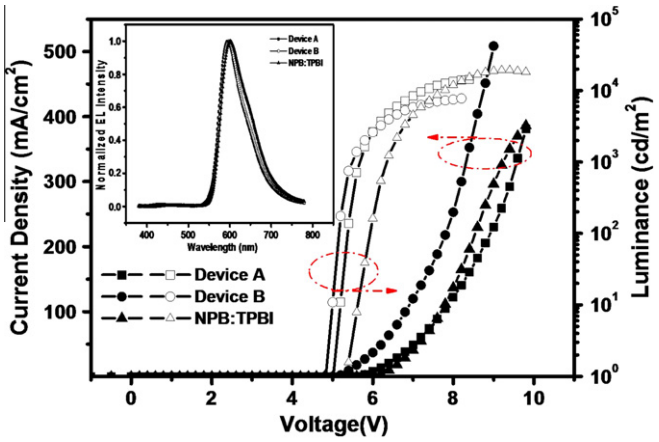

Fig. 4. Current–voltage and luminance–voltage of devices A, B and NPB:TPBI. Inset figure shows EL spectra of devices A, B and NPB:TPBI.

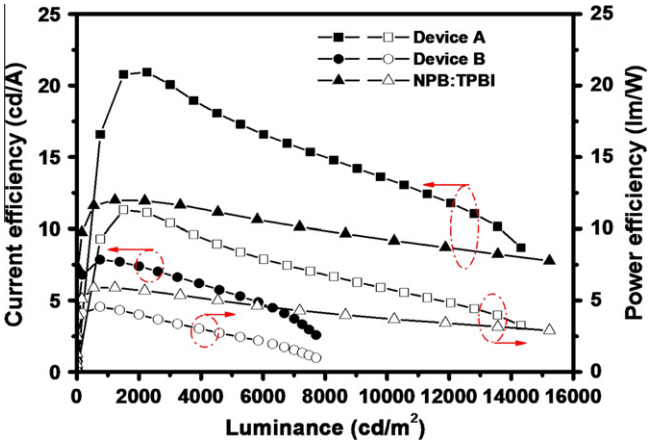

Fig. 5. Current and power efficiency characteristics of devices A, B and NPB:TPBI.

was found to be promising and convincing. This also signifies that NPyB host has better hole and electron transporting properties than NPB:TPBI type devices. Inset of Fig. 4 also shows the EL spectra of devices A and B exhibiting emissions in the red regions. It indicates complete energy transfer from the host materials to the guest due to confinement of triplet excitons at $Ir(phq)_2acac$ dopant molecule. The EL spectral peaks and CIE_{xy} coordinates of all devices are summarized in Table 2. At 1000 cd/m^2, the EL spectral peaks and CIE_{xy} coordinates of devices A and B were 595 nm/(0.59, 0.39) and 598 nm/(0.60, 0.38). The EL spectrum of each device does not change significantly with the applied voltage. It is manifested that phosphorescence photoluminescence quantum efficiency at high doping concentration tends to reduced inevitably due to self quenching or triplet–triplet annihilation by dopant molecules. In both the devices, efficiency decreases at high concentration of the dopant molecules.

The current and power efficiencies of devices A and B are depicted in Fig. 5 and Table 2. At a given constant lumi-

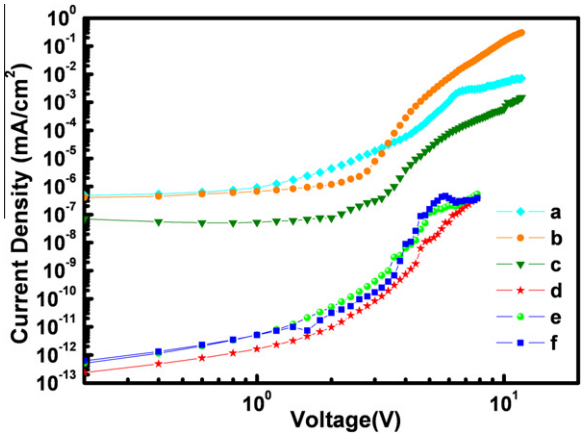

Fig. 6. *I–V* characteristics of the hole-only devices (a) NPB:TPBI, (b) NPyB, (c) QuPB, and electron-only devices (d) NPB:TPBI, (e) NPyB and (f) QuPB.

nance of 1000 cd/m^2, the current and power efficiencies of these devices were 20.6 cd/A and 10.8 lm/W for device A, and 7.6 cd/A and 3.3 lm/W for device B. Furthermore, the maximum current and power efficiencies obtained were 21.0 cd/A and 11.3 lm/W for device A, and 7.8 cd/A and 4.5 lm/W for device B. It clearly reveals that external quantum efficiency (EQE) of device A was 14.2%, which is nearly 40% higher than NPB:TPBI based device exhibiting EQE of about 8.6%. In case of device B, 5.2% of external quantum efficiency was achieved.

To examine the bipolar charge transport ability of NPyB and QuPB host materials, hole-only and electron-only devices were fabricated. For comparison, NPB:TPBI mixed host device as a reference was also fabricated. Fig. 6 shows the *J–V* characteristics of hole-only and electron-only devices. In case of hole-only device, the structure of ITO/PEDOT:PSS(45 nm)/host(35 nm)/sublimated NPB(60 nm)/Al(100 nm) was adopted in which a large barrier of NPB was used to block the electron-injection from Al [26]. The results clearly demonstrate that NPyB host has better hole conduction than NPB:TPBI type of hole-only device while QuPB shows the lowest hole current than that of NPB:TPBI reference. To evaluate the electron transporting performance of host materials, we adopted the device structure of glass/Al(100 nm)/PEDOT:PSS(45 nm)/host(50 nm)/LiF(1 nm)/Al(100 nm). It can be seen that electron transport property of NPyB and QuPB hosts are better than that of NPB:TPBI host system. This suggests that both NpyB and QuPB act as efficient bipolar materials because of comparable hole and electron mobility than that of reference. The above results confirm that NPyB and QuPB hosts have good bipolar charge transport properties.

4. Conclusions

We have synthesized and characterized two new bipolar host materials, NPyB and QuPB, containing both electron and hole-type of moieties. Their phosphorescence and electrochemical studies confirmed that both the hosts are capable of electron and hole-transport, suitable for harvesting red electrophosphorescence. The bipolar transport properties of NPyB and QuPB hosts were investigated by hole-only and electron-only devices. The multilayered solution-processed phosphorescent devices utilizing NPyB host was found superior in red electroluminescence performance. In particularly, this device exhibited a maximum brightness of 14,440 cd/m^2, with promising current and power efficiencies of 21.0 cd/A and 11.3 lm/W, and is considered an efficient bipolar host material for applications in low-cost electroluminescence devices. Consequently, this highly efficient promising red-emitting PHOLED have a possible space for improving its performance for further development of new generation OLEDs. Thus, the present investigation determined that new NPyB host material yielded a promising performance in terms of efficiency and color chromaticity for practical applications.

Acknowledgments

This work was supported by a grant from the Human Resources Development of the Korea Institute of Energy Technology Evaluation and Planning (KETEP) funded by the Korea government Ministry of Knowledge Economy (No. 2009-0074667). This work was also financially supported by the Grant (C1AAA001-2009-0093282) of MEST and the Seoul R&BD Program (10543).

References

[1] N. Koch, Chem. Phys. Chem. 8 (2007) 1438.
[2] M.A. Wolak, J. Delacamp, C.A. Landis, P.A. Lane, J. Anthony, Z. Kafafi, Adv. Funct. Mater. 16 (2006) 1943.
[3] D.H. Kim, D.H. Choi, J.J. Park, S.T. Lee, J.H. Kwon, Chem. Lett. 37 (2005) 1150.
[4] M. Ooe, S. Naka, H. Okada, H. Onnagawa, Jpn. Appl. Phys. Part 1 91 (2007) 093512.
[5] H. Kim, Y. Byun, R.R. Das, B.-K. Choi, P.-S. Ahn, Appl. Phys. Lett. 91 (2007) 093512.
[6] J.H. Kwon, T.J. Park, W.S. Jeon, J.J. Park, Proc. SPIE 6828 (2007) 682802.
[7] C. Adachi, M.A. Baldo, M.E. Thompson, S.R. Forrest, J. Appl. Phys. 90 (2001) 5048.
[8] M. Ikai, S. Tokito, Y. Sakamoto, T. Suzuki, Y. Taga, Appl. Phys. Lett. 79 (2001) 156.
[9] S. Lamansky, P. Djurovich, D. Murphy, F. Abdel-Razzaq, H.-E. Lee, C. Adach, P.E. Burrows, S.R. Forrest, M.E. Thompson, J. Am. Chem. Soc. 123 (2001) 4304.
[10] K.H. Kim, J.Y. Lee, T.J. Park, W.S. Jeon, G.P. Kennedy, J.H. Kwon, Synthetic Met. 160 (2010) 631.
[11] A.P. Monkman, H.D. Burrows, L.J. Hartwell, L.E. Horsburgh, I. Hamblett, S. Navaratnam, Phys. Rev. Lett. 86 (2001) 1358.
[12] S. Reineke, K. Walzer, K. Leo, Phys. Rev. B 75 (2007) 125328.
[13] M.A. Baldo, D.F. O'Brien, M.E. Thompson, S.R. Forrest, Phys. Rev. B 60 (1999) 14422.
[14] S. Tao, L. Lu, J. Yu, Y. Zhou, C.-S. Lee, S.-T. Lee, X. Zhang, O. Kwon, Chem. Mater. 21 (2009) 1284.
[15] T. Youtian, Q. Wang, C. Yang, K. Zhang, Q. Wang, T. Zou, J. Qin, M. Dongge, J. Mater. Chem. 18 (2008) 4091.
[16] Z. Ge, T. Hayakawa, S. Ando, M. Ueda, T. Akike, H. Miyamoto, T. Kajita, M. Kakimoto, Chem. Mater. 20 (2008) 2532.
[17] W.S. Jeon, T.J. Park, Y.S. Kim, R. Pode, J. Jang, J.H. Kwon, Appl. Phys. Lett. 93 (2008) 063303.
[18] S.C. Tse, K.C. Kwok, S.K. So, Appl. Phys. Lett. 89 (2006) 262102.
[19] J.P. Park, T.J. Park, W.S. Jeon, R. Pode, J. Jang, J.H. Kwon, E.-S. Yu, M.-Y. Chae, Org. Elect. 10 (2009) 189.
[20] S.A. VanSlyke, C.H. Chen, C.W. Tang, Appl. Phys. Lett. 69 (1996) 2160.
[21] T.J. Park, W.S. Jeon, J.J. Park, Y.S. Kim, K.Y. Lee, J. Jang, J.H. Kwon, R. Pode, Appl. Phys. Lett. 92 (2008) 113308.
[22] B. Delley, J. Chem. Phys. 92 (1990) 508.
[23] B. Delley, J. Phys. Chem. 100 (1996) 6107.
[24] B. Delley, J. Chem. Phys. 113 (2000) 7756.
[25] M.C. Suh, M.-H. Kim, S.T. Lee, H.D. Kim, H.K. Chung, Appl. Phys. Lett. 86 (2005) 133505.
[26] C.-H. Kuo, K.-C. Peng, L.-C. Kuo, K.-H. Yang, J.H. Lee, M.K. Leung, K.H. Hsieh, Chem. Mater. 18 (2006) 4121.

common approach has been to blend the polymer with [6,6]-phenyl-C61-butyric methyl ester (PCBM), a soluble C60 derivative [1,6].

The overall power conversion efficiency (PCE) has been steadily improving from an initial 1% via a blend of poly[2-methoxy-5-(30,70-dimethyloctyloxy)-1,4-phenylenevinylene] (MDMO-PPV) with PCBM [7] to an impressive ~5% achieved by poly(3-hexylthiophene) (P3HT):PCBM via extensive morphology optimization [8–10]. In order to further improve the efficiency of BHJ polymer solar cells, the research community is searching for new polymers. From the materials perspective, these donor polymers should not only have a low band gap, in order to increase the short circuit current (J_{sc}), but also bear a low energy level of the highest occupied molecular orbital (HOMO) to improve the open circuit voltage (V_{oc}) [11]. Typically, a low band gap polymer is designed via a "donor–acceptor" (D–A) approach, which is to incorporate electron-rich and electron-deficient moieties in the polymer backbone. The low band gap is mainly caused by the intramolecular charge transfer between donor and acceptor units [12]. Currently, state of the art polymer based BHJ solar cells have reached PCEs of more than 6% [13] and 6.7% [14] have been reported for single and tandem solar cells, respectively. However, these numbers are still significantly lower than the critical efficiencies of 10–15% [15].

In parallel efforts, organic solar cells (OSCs) based on small-molecules with vacuum evaporating interpenetrating multilayer structures have also reached PCEs as high as 5–6% [16]. Small-molecule donor materials can also form useable BHJ solar cells by solution processing, although it is more challenging to obtain high-quality films. The highest reported efficiencies for such devices have remained low (PCEs range from 0.3% to ~3.0%) relative to solution-processed solar cells using polymeric donor materials (~5%). Small-molecule materials, however, offer advantages over polymeric materials in terms of ease of synthesis and purification, which greatly improve fabrication reproducibility, as well as possessing a greater tendency to self assemble into ordered domains, which leads to high charge carrier mobilities [17]. Small-molecules do not suffer from batch to batch variations, broad molecular-weight distributions, end-group contamination, or difficult purification methods, which can be significant problems for polymeric materials. These considerations make small-molecules a promising class of donor material for BHJ solar cell applications [18–26]. Solution-processed small-molecules, which have been used for PV cells, have recently been reviewed [27]. Efficient BHJ PV solar cells based on symmetrical *D*–π–A–π–D organic dye molecules [28], squaraine [29,24], phthalocyanines [30,31], oligothiophene with dialkylated diketopyrrolopyrrole [32,33], 2-vinyl-4,5-dicyanoimidazole (vinazene) [34,35] and star-shaped molecules have very recently been reported [36–40]. The highest PCE reported to date for solar cells using solution-processable small-molecules is 3.0% [32].

On the other hand, cyano-poly(*p*-phenylenevinylene) (CN-PPV) and its derivatives with cyanovinylene moieties are one of the most important conjugated polymers with high electron affinity and promising materials used in polymeric light emitting diodes and polymeric PV devices [41–46]. Various low band gap small-molecules and polymers carrying 4-nitro-α-cyanostilbene units have been synthesized in our laboratory and used for BHJ solar cells [47] and dye-sensitized solar cells [48] with enhanced efficiency. In continuation of this research line, herein we describe the synthesis and characterization of two new symmetrical molecules **M1** and **M2** of low band gap with common structural segments. Both molecules contained a central spacer which was connected at both sides via ether bond with terminal 4-nitro-α-cyanostilbene units. The two ether bonds are expected to increase the flexibility of the molecules. Moreover, their aliphatic moieties render these molecules very soluble in common organic solvents thus allowing the facile preparation of thin films by spin casting. The molecules were successfully synthesized by a reaction sequence the last step of which included the condensation of a kye-dialdehyde with 4-nitrobenzylcyanide. We have used **M1** and **M2** as electron donor along with PCBM as electron acceptor for BHJ active layer for the fabrication of organic PV devices. The PCE for the devices based on pristine **M1**:PCBM and **M2**:PCBM blends, is 1.67% and 1.05%, respectively. We have investigated the effect of solvent vapor treatment of blend on the PV response of the BHJ devices and found that the PCE has been increased up to 3.05% and 1.90% for **M1**:PCBM and **M2**:PCBM blends, respectively. This improvement of PCE has been attributed to the increase in hole mobility and surface roughness, leading to better charge separation and collection efficiency. The PCE has been further increased up to 3.57% and 2.42% after thermal annealing of the solvent vapor treated **M1**:PCBM and **M2**:PCBM blends, respectively.

2. Experimental

2.1. Reagents and solvents

4-Nitrobenzylcyanide was synthesized from the nitration of benzyl cyanide with concentrated nitric and sulfuric acid [49]. It was recrystallized from ethanol. 4-Hydroxybenzaldehyde was recrystallized from distilled water. *N*,*N*-dimethylformamide (DMF) and tetrahydrofuran (THF) were dried by distillation over CaH_2. All other reagents and solvents were commercially purchased and were used as supplied.

2.2. Preparation of compounds

2.2.1. 1,4-Bis(p-formylphenoxymethyl)-2,5-bis(hexyloxy) benzene (3)

A flask was charged with a mixture of **2** (0.1650 g, 0.355 mmol), 4-hydroxybenzaldehyde (0.1042 g, 0.853 mmol), K_2CO_3 (0.15 g, 1.08 mmol) and acetonitrile (25 mL). The mixture was stirred and refluxed for 12 h under N_2. It was subsequently concentrated under reduced pressure. Water was added to the concentrate and then it was extracted with dichloromethane. The organic layer was dried (Na_2SO_4) and concentrated to afford **3** (0.1478 g, yield 76%).

FT-IR (KBr, cm^{-1}): 2930, 2870, 2854 (C–H stretching); 1684 (carbonyl of formyl); 3050, 1602, 1506, 1466 (aromatic); 1246, 1210, 1162 (ether bond).

^1H NMR ($CDCl_3$) ppm: 9.90 (s, 2H, formyl); 7.79 (m, 4H, aromatic ortho to formyl); 6.96–6.85 (m, 6H, aromatic

ortho to oxygen); 5.14 (s, 4H, OCH_2Ph); 3.96 (m, 4H, $OCH_2(CH_2)_4CH_3$); 1.81 (m, 4H, $OCH_2CH_2(CH_2)_3CH_3$); 1.37 (m, 12H, $O(CH_2)_2(CH_2)_3CH_3$); 0.91 (t, 6H, $O(CH_2)_5CH_3$).

Anal. Calcd. for $C_{34}H_{42}O_6$: C, 74.70; H, 7.74. Found: C, 74.32; H, 7.40%.

*2.2.2. Molecule **M1***

A flask was charged with a solution of **3** (0.1478 g, 0.270 mmol) and 4-nitrobenzylcyanide (0.0876 g, 0.540 mmol) in ethanol (20 mL). Sodium hydroxide (0.20 g, 5.00 mmol) was added to this solution. The reaction mixture was stirred for 1 h at room temperature under N_2 and then it was concentrated under reduced pressure. Water was added to the concentrate and **M1** precipitated as a dark green solid. It was recrystallized from ethanol/water (0.15 g, yield 66%).

FT-IR (KBr, cm^{-1}): 2922, 2852 (C–H stretching); 2170 (cyano); 1510, 1346 (nitro); 3075, 1600, 1454 (aromatic); 1258, 1162, 1106 (ether bond); 1016 (*trans*-vinylene bond).

^1H NMR ($CDCl_3$) ppm: 8.11 (m, 4H, aromatic ortho to nitro); 7.72 (s, 2H, cyanovinylene); 7.65 (m, 4H, aromatic meta to nitro); 7.26 (m, 4H, aromatic meta to oxygen); 6.88–6.85 (m, 6H, aromatic ortho to oxygen); 5.15 (s, 4H, OCH_2Ph); 3.97 (m, 4H, $OCH_2(CH_2)_4CH_3$); 1.80 (m, 4H, $OCH_2CH_2(CH_2)_3CH_3$); 1.38 (m, 12H, $O(CH_2)_2(CH_2)_3CH_3$); 0.90 (t, 6H, $O(CH_2)_5CH_3$).

Anal. Calcd. for $C_{50}H_{50}N_4O_8$: C, 71.92; H, 6.04; N, 6.71. Found: C, 71.53; H, 6.17; N, 6.90%.

*2.2.3. Molecule **M2***

This molecule was synthesized in 70% yield from the reaction of dialdehyde **4** with a double molar amount of 4-nitrobenzylcyanide in ethanol in the presence of NaOH according to the procedure described for **M1**.

FT-IR (KBr, cm^{-1}): 2936, 2860 (C–H stretching); 2160 (cyano); 1510, 1346 (nitro); 3073, 1600 (aromatic); 1250, 1174, 1106 (ether bond); 1010 (*trans*-vinylene bond).

^1H NMR ($CDCl_3$) ppm: 8.12 (m, 4H, aromatic ortho to nitro); 7.74 (s, 2H, cyanovinylene); 7.66 (m, 4H, aromatic meta to nitro); 7.32 (m, 4H, aromatic meta to oxygen); 6.80 (m, 4H, aromatic ortho to oxygen); 3.92 (m, 4H, OCH_2); 1.68 (m, 4H, OCH_2 CH_2); 1.27 (m, 4H, $O(CH_2)_2$ CH_2).

Anal. Calcd. for $C_{36}H_{30}N_4O_6$: C, 70.35; H, 4.92; N, 9.12. Found: C, 69.94; H, 4.80; N, 9.28%.

2.3. Characterization methods

IR spectra were recorded on a Perkin–Elmer 16PC FT-IR spectrometer with KBr pellets. ^1H NMR (400 MHz) spectra were obtained using a Brucker spectrometer. Chemical shifts (δ values) are given in parts per million with tetramethylsilane as an internal standard. UV–vis spectra were recorded on a Beckman DU-640 spectrometer with spectrograde THF. Elemental analyses were carried out with a Carlo Erba model EA1108 analyzer.

The electrochemical cyclic voltammetry was conducted with Pt disk, Pt wire and Ag/Ag^+ electrode as working electrode, counter electrode, and reference electrode, respectively, in a 0.1 mol/L tetrabutylammonium hexafluorophosphate (Bu_4NPF_6) acetonitrile solution. The **M1** or **M2** films for the electrochemical measurements were coated from THF solution containing **M1** or **M2**.

2.4. Device fabrication and characterization

Organic solar cell devices with the structure ITO/PEDOT:PSS/**M1** or **M2**:PCBM (1:1)/Al were fabricated as follows: After spin-coating of 40 nm layer of poly (3,4-ethylenedioxythiophene):poly(styrenesulfonate) (PEDOT:PSS) onto a pre-cleaned ITO coated glass substrates and baking at 80 °C for 30 min, a 80 nm **M1**:PCBM or **M2**:PCBM blend layer in THF solution was deposited on the top of the PEDOT:PSS layer by controlled spin-coating rate. Finally, an Al electrode (50 nm) was deposited on the top of the active BHJ layer through the thermal evaporation method. The effective area of the each device is 0.08 cm^2. For the solvent treatment, the spin coated blends were transferred into a jar filled with THF. Pre-thermal annealing of the solvent treated active layers was carried out at 120 °C for 2 min on the hot plate before the deposition of the Al electrode. The devices based on pure **M1** or **M2** were also fabricated having structure ITO/PEDOT:PSS/**M1** or **M2**/Al.

Current–voltage (J–V) characteristics of the PV devices were measured using a computer controlled Keithley 238 source meter in dark as well as under illumination intensity of 100 mW/cm^2. A xenon light source (Oriel, USA) was used to give a simulated irradiance of 100 mW/cm^2 (equivalent to AM1.5 irradiation) at the surface of the device. The hole only device having ITO/PEDOT:PSS/**M1** or **M2**:PCBM/Au configuration using as cast the thermally annealed active layers, were fabricated and J–V characteristics in dark at room temperature, were recorded to estimate the hole mobility.

The incident photon to current efficiency (IPCE) of the devices was measured by illuminating the device with a xenon light source using monochromator and measuring the resulting photocurrent with a Keithley electrometer under short circuit conditions according to the following expression:

$$\mathrm{IPCE}(\%) = 1240 J_{sc}/\lambda P_{in}$$

where J_{sc} is the short circuit photocurrent and λ and P_{in} are the wavelength and illumination intensity of the incident light, respectively.

3. Results and discussion

3.1. Synthesis and characterization

Scheme 1 outlines the four-step reaction sequence applied for the synthesis of the target molecule **M1**. In particular, **1** [50] and **2** [50] were synthesized by reported procedures. The reaction of **2** with 4-hydroxybenzaldehyde in a mol ratio 1:2 afforded dialdehyde **3**. This reaction took place in acetonitrile in the presence of K_2CO_3. Finally, the Knoevenagel condensation [51] of **3** with a double molar amount of 4-nitrobenzylcyanide in ethanol in the presence of NaOH yielded **M1**. It is well known that this type of condensation forms double bonds which possess mainly *trans*-conformation [52]. The facile synthesis of the other target molecule **M2** was achieved in only two steps according to Scheme 2. Specifically, 4-hydroxybenzaldehyde reacted

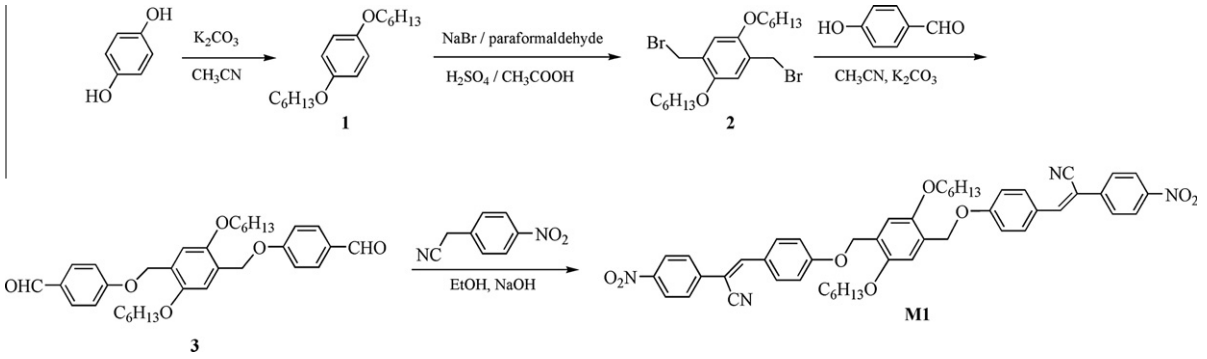

Scheme 1. Synthesis of molecule **M1**.

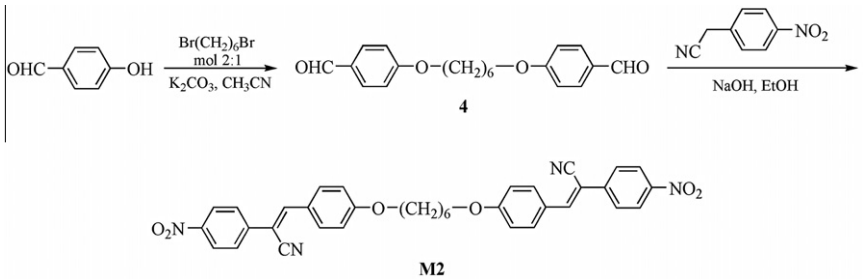

Scheme 2. Synthesis of molecule **M2**.

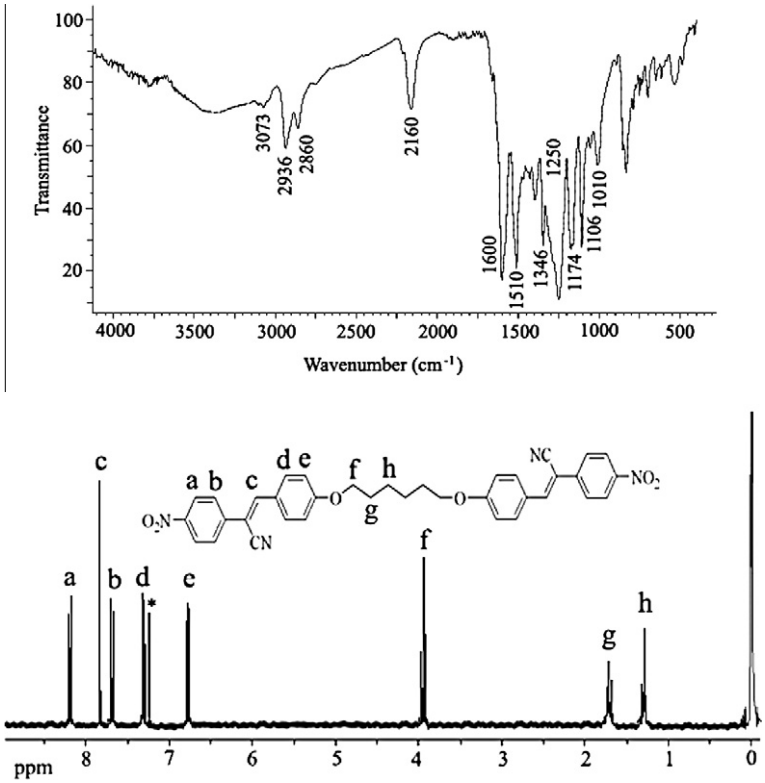

Fig. 1. FT-IR (top) and ^{1}H NMR in $CDCl_3$ solution (bottom) spectra of molecule **M1**.

with 1,6-dibromohexane to afford dialdehyde **4** [53]. The latter was subsequently condensed with 4-nitrobenzylcyanide to give **M2**. Both molecules were obtained in relatively high yields (66–70%) as dark green solids which were purified by recrystallization from ethanol/water. The two hexyloxy side chains of **M1** and the hexylene spacer of **M2** enhanced the solubility of these molecules. Particularly, both molecules were readily soluble in common organic solvents such as THF, dichloromethane, chloroform, acetone and toluene. Thin films of these molecules could be obtained by spin casting from the solutions despite their monomer nature.

Since the molecules have comparable chemical structures, their spectra showed certain common features. Fig. 1 presents the FT-IR and ^{1}H NMR spectra of **M2** as an example. The IR spectrum displayed characteristic absorption bands at 2936, 2860 (C–H stretching of hexylene); 2160 (cyano); 1510, 1346 (nitro); 3073, 1600 (aromatic); 1250, 1174, 1106 (ether bond) and 1010 cm^{-1} (*trans*-vinylene bond). The latter appeared at longer wavelength than usual *trans*-vinylene bonds (970–960 cm^{-1}) owing to the substitution by the electron-withdrawing cyano group. On the other hand, the ^{1}H NMR spectrum of **M2** showed upfield signals at 8.12 and 7.74 ppm assigned to the aromatic ortho to nitro and the cyanovinylene respectively. The other aromatic resonated at 7.66–6.80 ppm, while the aliphatic at 3.92–1.27 ppm.

3.2. Photophysical and electrochemical properties

Fig. 2 depicts the UV–vis absorption spectra of molecules in dilute (10^{-5} M) THF solution and thin film, which were normalized with respect to the long-wavelength absorption. Table 1 summarizes the photophysical and electrochemical characteristics of both molecules. Their absorption curves were broad and extended approximately up to 750 nm. This behavior is attributable to the terminal 4-nitro-α-cyanostilbene units as it has been well established in our previous publications [47,48]. The long-wavelength absorption maximum ($\lambda_{a,max}$) was located at 590–640 nm. The $\lambda_{a,max}$ of **M2** was red-shifted relative to that of **M1** in both solution and thin film. However, both molecules displayed the same thin film absorption onset at 742 nm which corresponds to an optical band gap (E_g^{opt}) of 1.67 eV. This value of E_g^{opt} conforms to those of other related materials [47,48].

Electrochemical cyclic voltammetry has been widely employed to investigate the redox behavior of organic materials and to estimate their HOMO and LUMO energy levels [54]. Fig. 3 shows the cyclic voltammograms of **M1** and **M2** films on Pt electrode in a 0.1 mol/L Bu_4NPF_6–acetonitrile solution. The results of the electrochemical measurements are listed in Table 1. It can be seen from Fig. 3 that there are reversible *n*-doping/depoping (reduction/reoxidation) and *p*-doping/depoping processes in both negative and positive potential range, respectively. The onset oxidation potential (E_{ox}) for **M1** and **M2** is 0.5 V and 0.7 V vs. Ag/Ag$^+$, respectively. The lower value of the oxidation potential for **M1** indicates higher electron donating ability of **M1** as compared to **M2**. In the reduction potential region, the onset reduction potential (E_{red}) is −1.21 V and −1.0 V vs. Ag/Ag$^+$ for **M1** and **M2**, respectively. From the E_{ox} and E_{red} of molecules **M1** and **M2**, their HOMO and

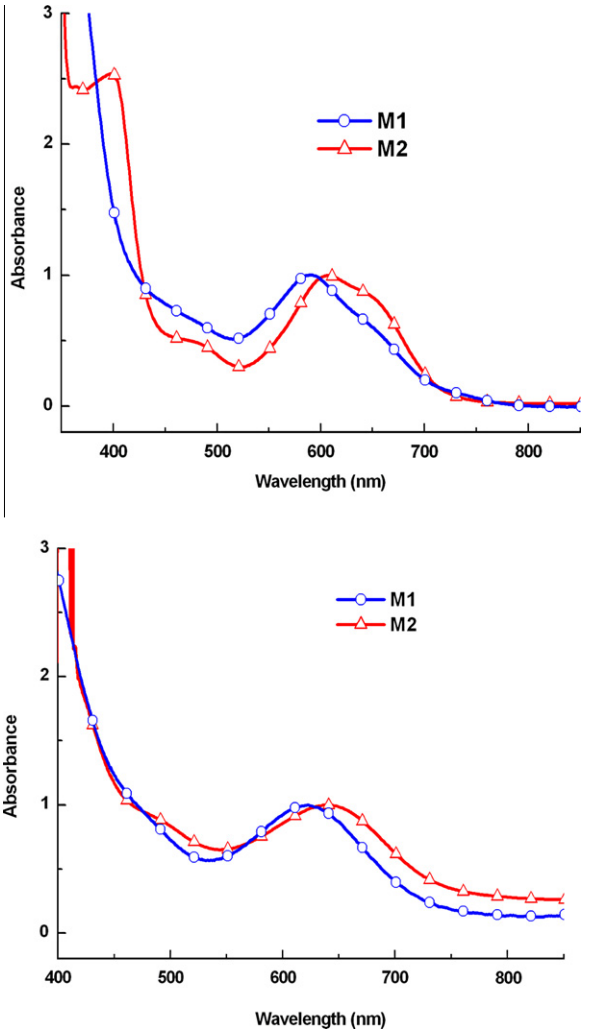

Fig. 2. Normalized absorption spectra of molecules in THF solution (top) and thin film (bottom).

Table 1
Optical and electrochemical properties of molecules.

Molecule	M1	M2
$\lambda_{a,max}$[a] in solution (nm)	590	607
$\lambda_{a,max}$[a] in thin film (nm)	622	640
Thin film absorption onset (nm)	742	742
E_g^{optb} (eV)	1.67	1.67
E_{onset}^{ox} (V)	0.5	0.7
E_{onset}^{red} (V)	−1.2	−1.0
HOMO (eV)	−5.2	−5.4
LUMO (eV)	−3.5	−3.7
E_g^{elc} (eV)	1.7	1.7

[a] $\lambda_{a,max}$: the long-wavelength absorption maxima from the UV–vis spectra in THF solution or in thin film.
[b] E_g^{opt}: optical band gap determined from the absorption onset in thin film.
[c] E_g^{el}: electrochemical band gap determined from cyclic voltammetry.

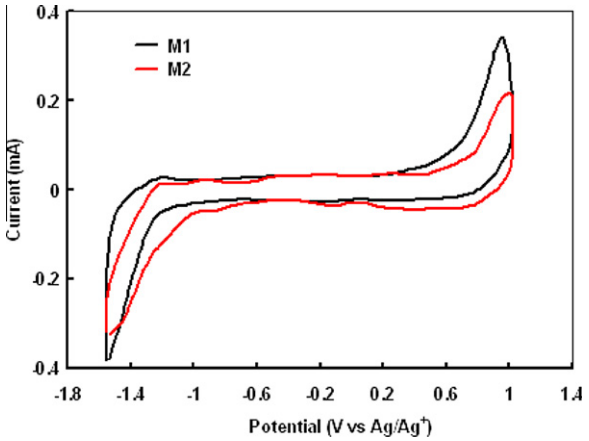

Fig. 3. Cyclic voltammetry data of **M1** and **M2**.

LUMO energy levels as well as their energy gaps were calculated according to equations:

$$\text{LUMO} = -q(E_{\text{red}} + 4.7)\ (\text{eV})$$
$$\text{HOMO} = -q(E_{\text{ox}} + 4.7)\ (\text{eV})$$

where the units of E_{ox} and E_{red} are V vs. Ag/Ag^{+}. The HOMO and LUMO values of these molecules are included in Table 1. It can be seen that the HOMO energy level of **M2** (−5.4 eV) is lower than that of **M1** (−5.2 eV). The LUMO level of **M2** (−3.7 eV) is higher than that of **M1** (−3.5 eV). However, the electrochemical band gap (E_g^{el}) (1.7 eV) is almost the same for both molecules. The E_g^{el} estimated from the electrochemical data is in good agreement with the E_g^{opt} estimated from the thin film absorption onset. The HOMO and LUMO levels of the PCBM were also estimated from the electrochemical data and were found to be −6.5 eV and −4.1 eV, respectively. The difference between the LUMO level of **M1** or **M2** and PCBM is about 0.6 eV and 0.4 eV, respectively, which indicates that the combination of **M1** or **M2** as donor with PCBM as an acceptor can be used for efficient BHJ organic PV devices.

3.3. Electrical and photoelectrical properties of *M1* and *M2*

The *J–V* characteristics of the ITO/PEDOT:PSS/**M1** or **M2**/Al devices in dark and under illumination are shown in Fig. 4. In these curves, the forward bias corresponds to the positive and negative voltage applied to PEDOT:PSS/ITO and Al electrode, respectively. It can be seen from these figures that the *J–V* characteristics show a rectification effect. The HOMO level of PEDOT:PSS (−5.2 eV) is very close to the HOMO level of both **M1** and **M2**. Therefore, this electrode behaves almost as an Ohmic contact for hole injection from the PEDOT:PSS into the HOMO of **M1** and **M2** in their respective devices. However, the LUMO level of both **M1** and **M2** is very far from the work function of the Al (−4.3 eV) and forms the Schottky barrier for the electron injection from the Al into the LUMO level of molecules. Hence, the rectification effect observed in the dark *J–V* characteristics is due to the formation of Schottky barrier at the Al–**M1** or Al–**M2** interfaces.

The charge carrier mobility of the PV materials is also an important factor which influences the performance of organic solar cells. We have measured the hole mobilities of these molecules using the hole only devices with ITO/PEDOT:PSS/**M1** or **M2**/Au structure using the SCLC model [55]. The *J–V* characteristics of the devices were plotted as $\ln[Jd^3/(V_{\text{app}} - V_{\text{bi}})]$ vs. $[(V_{\text{app}} - V_{\text{bi}})/d]^{0.5}$, and the hole mobilities of **M1** and **M2** calculated from the intercept of the corresponding lines are 2.3×10^{-6} and 5.1×10^{-6} cm^2/Vs for **M2** and **M1**, respectively.

The PV parameters, i.e. short circuit current (J_{sc}), open circuit voltage (V_{oc}), fill factor (FF) and PCE are summarized in Table 2. It can be seen from this table that the values of J_{sc} and PCE are higher for the device based on **M1** as compared to **M2**. This is attributed to the higher hole mobility of **M1** as compared to **M2**, since the E_g^{opt} and the absorption spectra

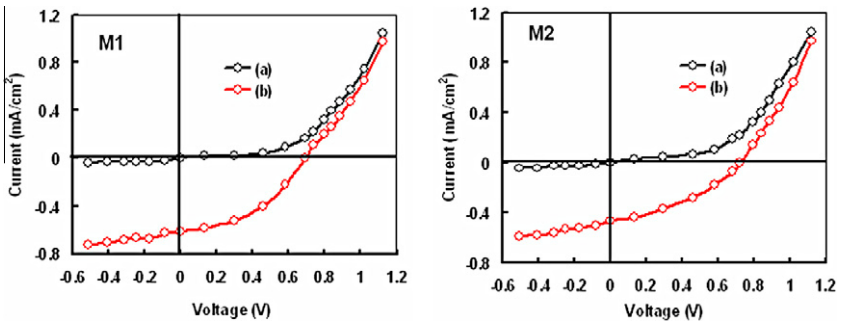

Fig. 4. Current–voltage characteristics of the devices based on pure **M1** and **M2** in dark (a) and under illumination (b).

Table 2
Summary of photovoltaic parameters of the ITO/PEDOT:PSS/**M1** or M2/Al devices.

Active material	Short circuit current (J_{sc}) (mA/cm^2)	Open circuit voltage (V_{oc}) (V)	Fill factor (FF)	Power conversion efficiency (PCE) (%)
M1	0.62	0.69	0.41	0.17
M2	0.47	0.72	0.40	0.13

of both molecules are identical. As the HOMO level of **M1** is very close to the HOMO level of PEDOT:PSS, the better hole collection in the device based on **M1** as compared to **M2**, may also be the reason for the higher PCE.

3.4. Photovoltaic properties of BHJ devices

The BHJ OSCs were fabricated with a structure of ITO/PEDOT:PSS/**M1** or **M2**:PCBM (1:1)/Al, where **M1** or **M2** were used as electron donor and PCBM was used as electron acceptor. Fig. 5 shows the *J*–*V* characteristics of the devices and Table 3 lists the corresponding PV parameters (J_{sc}, V_{oc}, FF and PCE) of the devices under illumination intensity of 100 mW/cm^2. It can be seen from Table 3 that the device based on the as cast **M1**:PCBM blend shows better PV response, having PCE of 1.67% as compared to 1.05% for the device based on the as cast **M2**:PCBM blend. The IPCE spectra of the devices (Fig. 6) show similar shape to the absorption spectra of the respective blends employed in the devices. This indicates that the visible light absorbed by the **M1**:PCBM or **M2**:PCBM photoactive layer in respective devices contributes to the J_{sc}. The maximum of IPCE for the as cast **M1**:PCBM and **M2**:PCBM based devices are about 55% and 42%, respectively at their absorption peak. The IPCE values are consistent with the higher values of J_{sc} and PCE of the **M1**:PCBM blend based organic solar cell.

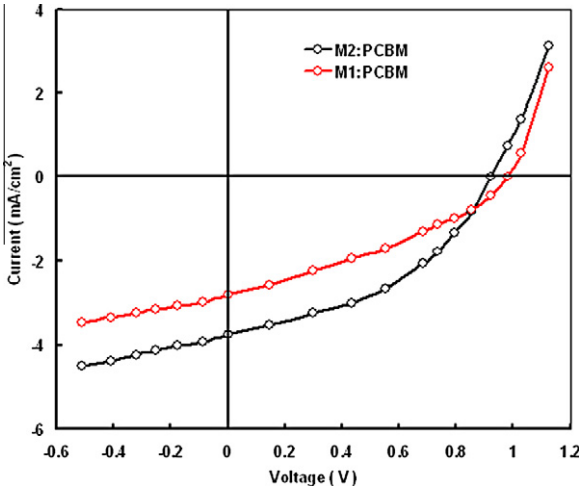

Fig. 5. Current–voltage characteristics of the devices based on pristine **M1**:PCBM and **M2**:PCBM blend under illumination intensity of 100 mW/cm^2.

Table 3
Summary of photovoltaic parameters of BHJ devices, using layer with different processing conditions.

Active material	Short circuit current (J_{sc}) (mA/cm^2)	Open circuit voltage (V_{oc}) (V)	Fill factor (FF)	Power conversion efficiency (PCE) (%)
M1:PCBM[a]	3.76	0.93	0.48	1.67
M1:PCBM[b]	6.4	0.90	0.53	3.05
M1:PCBM[c]	7.12	0.93	0.54	3.57
M2:PCBM[a]	2.38	0.98	0.45	1.05
M2:PCBM[b]	4.15	0.95	0.48	1.90
M2:PCBM[c]	5.16	0.98	0.48	2.42

[a] Pristine blend.
[b] Solvent vapor treated blend.
[c] Thermally annealed solvent treated blend.

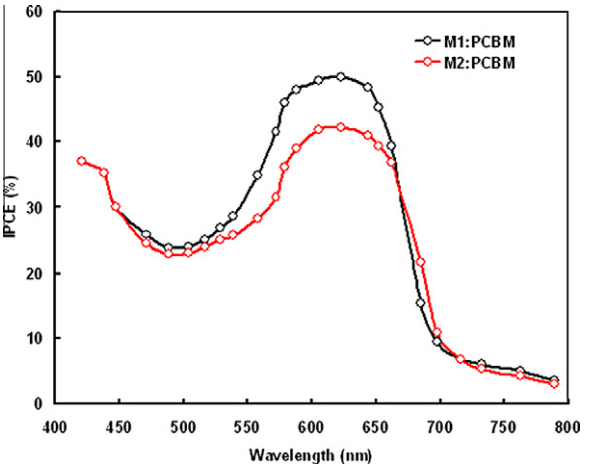

Fig. 6. IPCE spectra of BHJ devices based on pristine **M1**:PCBM and **M2**:PCBM blends.

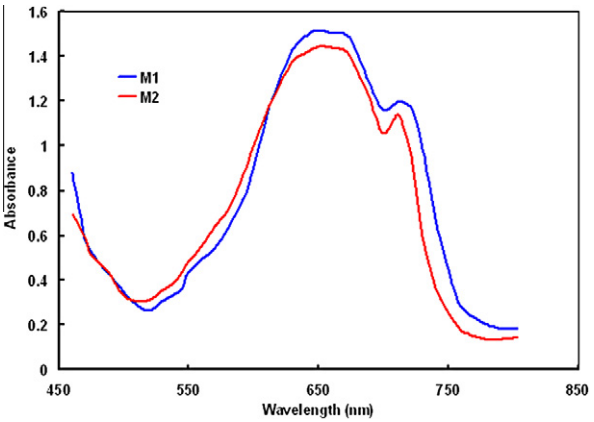

Fig. 7. Absorption spectra of solvent vapor treated **M1**:PCBM and **M2**:PCBM blends.

The J_{sc} is directly related to the product of absorbed photons and external quantum efficiency (EQE) [27]. Since the optical absorption of both **M1**:PCBM and **M2**:PCBM is almost the same, light absorption cannot be the factor for increased J_{sc} and PCE of the device based on **M1**:PCBM as compared to **M2**:PCBM. We assume that the difference in EQE of the devices is responsible for the higher photocurrent of the **M1**:PCBM blend. The EQE is determined by three processes: (i) migration/diffusion of photogenerated excitons towards the *D*/*A* interface, (ii) excitons dissociation and charge separation at the *D*/*A* interfaces, and (iii) collection of charge carrier at the electrodes. The process (i) depends on the nanoscale phase separation between the donor and acceptor components used in the BHJ active layer. It can be seen from the AFM images (Figs. 9 and 10)

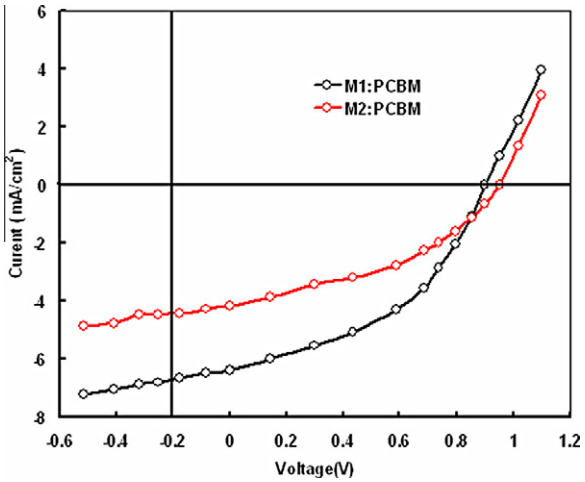

Fig. 8. Current–voltage characteristics of the devices based on THF treated **M1**:PCBM and **M2**:PCBM blend under illumination intensity of 100 mW/cm^2.

that the surface roughness is higher for **M1**:PCBM as compared to **M2**:PCBM, which indicates better nanoscale phase separation in **M1**:PCBM blend. Therefore, we assume that the contribution of EQE from the process (i) is higher for **M1**:PCBM. For process (ii) a sufficient large energy difference between the LUMO of the donor and acceptor material is required for ultra-fast photoinduced charge transfer. This difference is higher for **M1**:PCBM as compared to **M2**:PCBM blend. Photoinduced charge transfer is comparatively faster in the former blend, resulting in higher EQE for the device based **M1**:PCBM blend. Process (iii) depends on the percolated path for electrons and holes in BHJ active layer, mobility of electron and hole, and on the position of HOMO and LUMO level of the donor and acceptor materials, respectively, relative to the work function of anode and cathode. The HOMO level of **M1** is closer to the HOMO level of PEDOT:PSS indicating higher hole mobility for **M1**, which results in more efficient hole collection. Therefore, processes (i–iii) are responsible for the improved J_{sc} and PCE of the device based on **M1**:PCBM as compared to **M2**:PCBM.

Generally, the performance of the organic BHJ PV devices can be improved by controlling the morphology of the BHJ active layer, because efficient photoinduced charge generation, transport and collection of charge carriers at each collecting electrode crucially depend on the nanometer scale morphology of the films [56]. The crystallization of the organic materials improves the light harvesting property by extending the conjugation length and increases the charge carrier mobility, which is the limiting factor for the balance transport of the electrons and holes dissociated from the bound excitons. The increase in the PCE via thermal annealing is attributed to modified nanoscale morphology, enhanced crystallization of blend and improved transport of charges. It has also been reported that self-organization of organic material occurs not only under thermal annealing but also in proper ambience. Li et al. [9] and Zhao et al. [57] reported efficient PV cells based on P3HT/PCBM blend by controlling the growth rate of the active layer from solution to solid state. We have investigated the effect of thermal annealing, and combining solvent vapor treatment and thermal annealing on the PCE of PV devices based on **M1**:PCBM and **M2**:PCBM blends.

Fig. 7 shows the UV–vis absorption spectra of the solvent vapor treated **M1**:PCBM and **M2**:PCBM blends. For the untreated **M1**:PCBM blend film, the **M1** absorption peak is located at 620 nm with an absorption onset at 742 nm. Compared to the pristine **M1**:PCBM blend film, the absorption peak of the solvent treated **M1**:PCBM blend film shifted towards longer wavelength region and became much stronger in this region. In addition, the absorption spectra of the solvent treated **M1**:PCBM blend shows one vibronic absorption shoulder at 680 nm, which is attributed to an enhanced conjugation length and more ordered structure of **M1**. As the solvent molecules can penetrate into the film and increase the space between the molecular chains, the chains become mobile and self-organization can occur to form the ordering.

Fig. 8 shows the *J–V* characteristics of the devices under 100 mW/cm^2 white light illumination with THF treatment. The PV parameters for these PV devices are summarized in Table 3. It can be seen that the J_{sc} of the PV devices with THF vapor treatment increases to 6.4 mA/cm^2 and

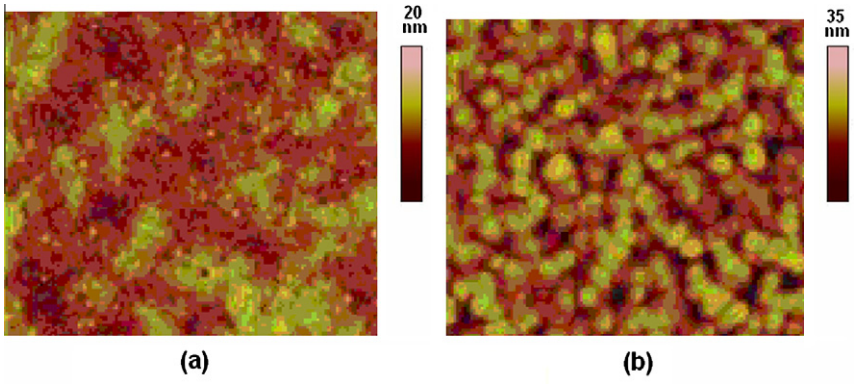

Fig. 9. AFM images of **M1**:PCBM as cast (a) and solvent treated (b) films.

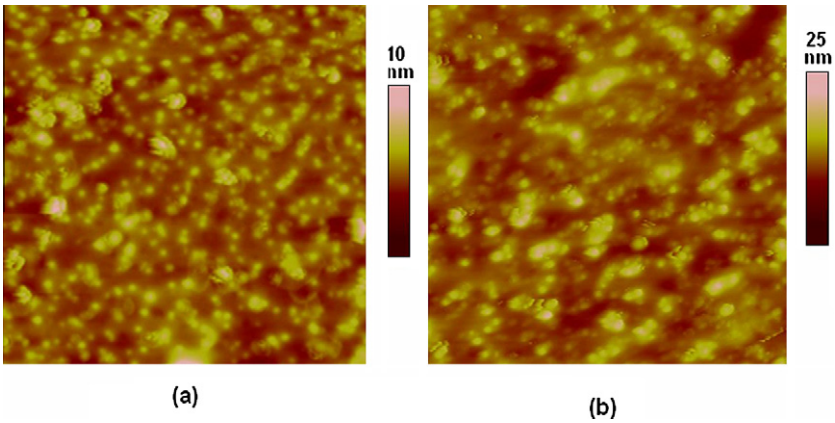

Fig. 10. AFM images of **M2**:PCBM as cast (a) and thermally annealed (b) films.

4.15 mA/cm^2 for **M1**:PCBM and **M2**:PCBM based devices respectively, which is a twofold increase compared to the as produced PV device. The overall PCE of the devices based on the solvent treated **M1**:PCBM and **M2**:PCBM has been increased up to 3.05% and 1.90%, respectively. This improvement is attributed to the self-organization of **M1** or **M2** induced by solvent vapor treatment which enhances the optical absorption and the hole transport. The PCE of the BHJ devices with THF treatment blends are higher than that of pristine blends. The J_{sc} of the organic BHJ PV devices is directly related to the product of light absorption by the photoactive blend used in the device, exciton diffusion, charge separation and charge collection efficiency. As it can be seen from the absorption spectra of the solvent vapor treated blends, the absorption coefficient has been increased as compared to the as cast blend films and also red-shifted. This indicates that more light is absorbed by the solvent vapor treated blends which generated more excitons in the photoactive blend. It is also observed that the IPCE spectra of the devices resemble the absorption spectra of the corresponding blend used in the device. This indicates that the J_{sc} is mainly attributed to the excitons generated because of the absorption of photons in **M1** or **M2**. The value of the IPCE is consistent with the values of J_{sc}. The IPCE is higher for the devices based on the solvent vapor treated blends as compared to the pristine blends, which is consistent with the increased values of J_{sc}.

The nanoscale morphology of the blend films has been investigated by the atomic force (AFM) experiment. Figs. 9 and 10 show the AFM images of the as cast and solvent vapor treated blend films. For the as cast films, an rms surface roughness of 4.2 nm and 3.2 nm, for **M1**:PCBM and **M2**:PCBM, respectively is observed. The solvent vapor treated films are much rougher that the as cast films. The solvent vapor treated **M1**:PCBM and **M2**:PCBM films show rms roughness of 7.6 nm and 5.6 nm, respectively at 5 μm × 5 μm scan sizes. The roughness is considered to be a signal of **M1** or **M2** chains self–organization and phase separation [57]. The increase of the roughness of the blend films after solvent vapor treatment is because of the **M1** or **M2** chains, self organize into ordered structure after solvent vapor treatment. The higher surface roughness of the blends support the increase in the phase separation of **M1**:PCBM or **M2**:PCBM after solvent vapor treatment. The increased phase separation leads to an increase in the *D*/*A* interfacial area for efficient charge separation, resulting in higher J_{sc} and PCE for BHJ PV devices based on the solvent vapor treated blend films.

The V_{oc} values of the devices based on the solvent vapor treated blend films is lower that that of the devices based on the as cast films. It is widely accepted that the energy difference between the HOMO and LUMO of the acceptor determines the V_{oc} value of the organic BHJ PV devices. We have already shown that the overall optical absorption spectrum of the solvent vapor treated blend films is red-shifted. This result can be interpreted assuming that the red-shifted spectrum results from a lower energy state of delocalized exciton in donor materials (**M1** or **M2**), as reported for conjugated polymers [58]. Therefore, the lowering of V_{oc} for devices based on the solvent vapor treated blends can be explained by reduced optical band gap of **M1** or **M2**.

We have investigated the charge collection efficiency by means of the space charge limited current (SCLC) measurements in dark. In the case of the devices based on the as cast blend films, the space charge limits the charge collection efficiency, because the hole mobility is lower than the electron mobility. According to the SCLC criteria, when there is a large difference between the hole and electron mobilities, the half power dependence of the photocurrent on the applied voltage takes place, and the FF can not exceed more than 0.40. Thus, in order to obtain high charge collection efficiency, it is necessary to balance the carrier mobility by enhancing the hole mobility in the blend. To investigate the space charge effects, we extract the hole and electron mobilities from the SCLC *J*–*V* characteristics obtained in the dark for hole and electron only devices [55a,57]. We have fabricated the hole- and electron-only devices having structure ITO/PEDOT:PSS/**M1** or **M2**:PCBM/Au and ITO/PEDOT:PSS/**M1**or **M2**:PCBM/Al, respectively. The hole and electron mobilities have been extracted from the *J*–*V* characteristics using the SCLC model [57] and they are listed in Table 4. It can be seen from this table that the hole mobility has been increased about 7–8 times for the devices based on

Table 4
Hole and electron mobility of **M1**:PCBM and **M2**:PCBM blends films evaluated using the SCLC model.

Film	Hole mobility (μ_h) (cm^2/Vs)	Electron mobility (μ_e) (cm^2/Vs)	μ_e/μ_h
M1:PCBM (as cast)	1.2×10^{-6}	6.4×10^{-5}	53
M1:PCBM (solvent vapor treated)	9.7×10^{-6}	6.5×10^{-5}	6.9
M1:PCBM (thermally annealed solvent vapor treated)	1.5×10^{-5}	6.9×10^{-5}	4.6
M2:PCBM (as cast)	0.96×10^{-6}	6.8×10^{-5}	71
M2:PCBM (solvent vapor treated)	6.8×10^{-6}	7.0×10^{-5}	10.3
M2:PCBM (thermally annealed solvent vapor treated)	9.6×10^{-6}	7.0×10^{-5}	7.3

the solvent vapor treated blend. Moreover, the electron mobilities with and without solvent annealing are almost the same. The increase in hole mobility after solvent vapor treatment is attributed to the enhance in the crystallinity and surface roughness of the **M1** or **M2** as indicated from the absorption spectra and AFM images. The mobility difference between the holes and electrons decreases remarkably and reduces the effect of space charge for the devices based on solvent vapor treated blends. Therefore, we assume that the charge collection efficiency has been increased for these devices resulting in improvement in the overall PCE of the devices.

Finally, we have investigated the PV response of the devices based on thermally annealed on the solvent vapor treated blends. The *J–V* characteristics of these devices are shown in Fig. 11. The PV parameters are summarized in Table 3. Both V_{oc} and J_{sc} have been increased for these devices as compared to devices based on solvent vapor treated blends. The PCE has been further increased up to 3.57% and 2.42% with the thermally annealed solvent treated **M1**:PCBM and **M2**:PCBM blend, respectively. This increase in PCE may be attributed to a further increase in the crystallinity of the blend upon the thermal treatment. We have also measured the hole and electron mobility for the devices based on the thermally annealed solvent vapor treated blends and found that the hole mobility has been further increased (as shown in Table 4). Moreover, the electron mobility has also been increased by 20 times as compared to the solvent treated blend, indicating that thermal annealing can effectively activate PCBM molecules to diffuse and aggregate into clusters for better charge transport. The increase in both electron and hole mobilities for the device based on the thermally annealed solvent vapor treated blends, further reduces the space charge effect, improves the charge transport and charge collection leading to the overall PCE of the device.

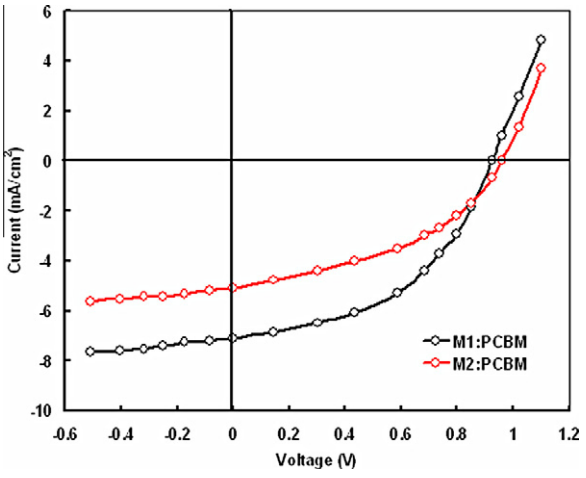

Fig. 11. Current–voltage characteristics of the devices based on THF treated and thermally annealed **M1**:PCBM and **M2**:PCBM blend under illumination intensity of 100 mW/cm^2.

4. Conclusions

Two new molecules **M1** and **M2** of low band gap which contained a central spacer and 4-nitro-α-cyanostilbene terminal units were synthesized. They were soluble in common organic solvents. Their long-wavelength absorption maximum was at 590–640 mm with thin film absorption onset at 742 nm corresponding to an optical band gap of 1.67 eV. The electrochemical band gap estimated from the cyclic voltammetery data is 1.70 eV, which is very close to the optical band gap. However, the HOMO and LUMO of **M1** and **M2** are at different energy levels. We have used both **M1** and **M2** as electron donor for BHJ PV devices along with PCBM as electron acceptor. The hole mobility of **M1** is higher than that of **M2**. The PCE for pristine **M1**:PCBM and **M2**:PCBM is 1.67% and 1.05%, respectively. The higher value of PCE for **M1**:PCBM is due to the higher hole mobility of this molecule. The devices with solvent vapor treated shows PCE 3.05% and 1.90% for **M1**:PCBM and **M2**:PCBM, respectively. The improved PCE has been interpreted in terms of more balanced charge transport due to the modified nanoscale morphology and increased crystallization of the blend. The PCE has been further increased up to 3.57% and 2.42% for the devices based on thermally annealed solvent vapor treated blend **M1**:PCBM and **M2**:PCBM, respectively. This has been attributed to the higher balance charge transport due to both increases in electron and hole mobilities in the blend. Our studies indicate that a combination of thermal annealing and solvent vapor treatment is an effective approach to improve the PCE of organic BHJ PV device.

Acknowledgement

We are thankful to Prof. Y.K. Vijay, for allowing us to undertake the device fabrication and characterization in his laboratory. We are also grateful to the Scientists in IUAC, New Delhi for recording the AFM images of the blend samples.

References

[1] C.J. Brabec, Solar Energy Mater. Solar Cells 83 (2004) 273.
[2] (a) F.C. Krebs, T.D. Nielsen, J. Fyenbo, M. Wadstrom, M.S. Pedersen, Energy Environ. Sci. 3 (2010) 512;
(b) B. Kippelen, J.-L. Bredas, Energy Environ. Sci. 2 (2009) 251;
(c) M. Helgesen, R. Sondergaard, F.C. Krebs, J. Mater. Chem. 20 (2010) 36;
(d) F.C. Krebs, T. Tromholt, M. Jørgensen, Nanoscale 2 (2010) 873.
[3] J.J.M. Halls, C.A. Walsh, N.C. Greenham, E.A. Marseglia, R.H. Friend, S.C. Morrati, A.B. Holmes, Nature 376 (1995) 498.
[4] S.C. Veenstra, W.J.H. Verhees, J.M. Kroon, M.M. Koetse, J. Sweelsen, J.J.A.M. Bastiaansen, H.F.M. Schoo, X. Yang, A. Alexeev, J. Loos, U.S. Schubert, M.M. Wienk, Chem. Mater. 16 (2004) 2503.
[5] T. Kietzke, H.-H. Hörhold, D. Neher, Chem. Mater. 17 (2005) 6532.
[6] F. Padinger, R.S. Rittberger, N.S. Sariciftci, Adv. Funct. Mater. 13 (2003) 85.
[7] S.E. Shaheen, C.J. Brabec, N.S. Sariciftci, F. Padinger, T. Fromherz, J.C. Hummelen, Appl. Phys. Lett. 78 (2001) 841.
[8] W.L. Ma, C.Y. Yang, X. Gong, K. Lee, A.J. Heeger, Adv. Funct. Mater. 15 (2005) 1617.
[9] G. Li, V. Shrotriya, J.S. Huang, Y. Yao, T. Moriarty, K. Emery, Y. Yang, Nat. Mater. 4 (2005) 864.
[10] Y. Kim, S. Cook, S.M. Tuladhar, S.A. Choulis, J. Nelson, J.R. Durrant, D.D.C. Bradley, M. Giles, I. McCulloch, C.S. Ha, M. Ree, Nat. Mater. 5 (2006) 197.
[11] M.C. Scharber, D. Wuhlbacher, M. Koppe, P. Denk, C. Waldauf, A.J. Heeger, C.L. Brabec, Adv. Mater. 18 (2006) 789.
[12] H.A.M. van Mullekom, J.A.J.M. Vekemans, E.E. Havinga, E.W. Meijer, Mater. Sci. Eng. R: Rep. R32 (2001) 1.
[13] S.H. Park, A. Roy, S. Beaupre, S. Cho, N. Coates, J.S. Moon, D. Moses, M. Leclerc, K. Lee, A.J. Heeger, Nat. Photon. 3 (2009) 297.
[14] J.Y. Kim, K. Lee, N.E. Coates, D. Moses, T.Q. Nguyen, M. Dante, A.J. Heeger, Science 317 (2007) 222.
[15] (a) M.C. Scharber, D. Wuhlbacher, M. Koppe, P. Denk, C. Waldauf, A.J. Heeger, C.J. Brabec, Adv. Mater. 18 (2006) 789;
(b) G. Dennler, M.C. Scharber, T. Ameri, P. Denk, K. Forberich, C. Waldauf, C.J. Brabec, Adv. Mater. 20 (2008) 579.
[16] (a) J.G. Xue, B.P. Rand, S. Uchida, S.R. Forrest, Adv. Mater. 17 (2005) 66;
(b) M.Y. Chen, S.L. Lai, M.K. Fung, C.S. Lee, S.T. Lee, Appl. Phys. Lett. 90 (2007) 023504;
(c) J.G. Xue, S. Uchida, B.P. Rand, S.R. Forrest, Appl. Phys. Lett. 85 (2004) 5757.
[17] B.P. Rand, J. Genoe, P. Heremans, J. Poortmans, Prog. Photovoltaics: Res. Appl. 15 (2007) 659.
[18] J. Roncali, P. Frere, P. Blanchard, R. de Bettignies, M. Turbiez, S. Roquet, P. Leriche, Y. Nicolas, Thin Solid Films 567 (2006) 511.
[19] X.B. Sun, Y. Zhou, W. Wu, Y. Liu, W. Tian, G. Yu, W. Qiu, S. Chen, D.J. Zhu, J. Phys. Chem. B 110 (2006) 7702.
[20] N. Kopidakis, W.J. Mitchell, J. van de Lagemaat, D.S. Ginley, G. Rumbles, S.E. Shaheen, Appl. Phys. Lett. 89 (2008) 103524.
[21] M.T. Lloyd, A.C. Mayer, S. Subramanian, D.A. Mourey, D.J. Herman, A. Bapat, V.J.E. Anthony, G.G. Malliaras, J. Am. Chem. Soc. 129 (2007) 9144.
[22] P.F. Xia, X.J. Feng, J. Lu, S.W. Tsang, R. Movileanu, Y. Tao, M.S. Wong, Adv. Mater. 20 (2008) 4810.
[23] S. Roquet, A. Cravino, P. Leriche, O. Alévêque, P. Frère, J. Roncali, J. Am. Chem. Soc. 128 (2006) 3459.
[24] F. Silvestri, M.D. Irwin, L. Beverina, A. Facchetti, G.A. Pagani, T.J. Marks, J. Am. Chem. Soc. 130 (2008) 17640.
[25] N.M. Kronenberg, M. Deppisch, F. Wurthner, H.W.A. Lademann, K. Deing, K. Meerholz, Chem. Commun. (2008) 6489.
[26] T. Rousseau, A. Cravino, T. Bura, G. Ulrich, R. Ziessel, J. Roncali, Chem. Commun. (2009) 1673.
[27] M.T. Lloyd, J.E. Anthony, G.G. Malliaras, Mater. Today 10 (2007) 34.
[28] L. Xue, J. He, X. Gu, Z. Yang, B. Xu, W. Tian, J. Phys. Chem. C 113 (2009) 12911.
[29] S. Wang, E.I. Mayo, M.D. Perez, L. Griffe, G. Wei, P.I. Djurovich, S.R. Forrest, M.E. Thompson, Appl. Phys. Lett. 94 (2009) 233304/1.
[30] T. Taima, J. Sakai, T. Yamanari, K. Saito, Sol. Energy Mater. Sol. Cells 93 (2009) 742.
[31] R. Aich, B. Ratier, F. Tran-van, F. Goubard, C. Chevrot, Thin Solid Films 516 (2008) 7171.
[32] A.B. Tamayo, X.-D. Dang, B. Walker, J. Seo, T. Kent, T.-Q. Nguyen, Appl. Phys. Lett. 94 (2009) 103301/1.
[33] J. Peet, A.B. Tamayo, X.-D. Dang, J.H. Seo, T.-Q. Nguyen, Appl. Phys. Lett. 93 (2008) 163306/1.
[34] M. Schubert, C. Yin, M. Castellani, S. Bange, T.L. Tam, A. Sellinger, H.H. Hörhold, T. Kietzke, D. Neher, J. Chem. Phys. 130 (2009) 094703/1.
[35] Z.E. Ooi, T.L. Tam, R.Y.C. Shin, Z.K. Chen, T. Kietzke, A. Sellinger, M. Baumgarten, K. Mullen, J.C. deMello, J. Mater. Chem. 18 (2008) 4619.
[36] C. He, Q. He, Y. Yi, G. Wu, F. Bai, Z. Shuai, Y. Li, J. Mater. Chem. 18 (2008) 4085.
[37] G. Wu, G. Zhao, C. He, J. Zhang, Q. He, X. Chen, Y. Li, Sol. Energy Mater. Sol. Cells 93 (2009) 108.
[38] G. Zhao, G. Wu, C. He, F.Q. Bai, H. Xi, H.-X. Zhang, Y. Li, J. Phys. Chem. C 113 (2009) 2636.
[39] C. He, Q. He, X. Yang, G. Wu, C. Yang, F. Bai, Z. Shuai, L. Wang, Y. Li, J. Phys. Chem. C 111 (2007) 8661.
[40] C. He, Q. He, Y. He, Y. Li, F. Bai, C. Yang, Y. Ding, L. Wang, J. Ye, Sol. Energy Mater. Sol. Cells 90 (2006) 1815.
[41] R.H. Friend, R.W. Gymer, A.B. Holmes, J.H. Burroughes, R.N. Marks, C. Taliani, D.D.C. Bradley, D.A. Dos Santos, J.L. Brédas, M. Lögdlund, W.R. Salaneck, Nature 397 (1999) 121.
[42] A. Kraft, A.C. Grimsdale, A.B. Holmes, Angew. Chem. Int. Ed. 37 (1998) 402.
[43] U. Mitschke, P. Bäuerle, J. Mater. Chem. 10 (2000) 1471.
[44] N.C. Greenham, S.C. Moratti, D.D.C. Bradley, R.H. Friend, A.B. Holmes, Nature 365 (1993) 628.
[45] M. Granstrom, K. Petritsch, A.C. Arias, A. Lux, M.R. Andersson, R.H. Friend, Nature 395 (1998) 257.
[46] B.C. Thompson, Y.G. Kim, T.D. McCarley, J.R. Reynolds, J. Am. Chem. Soc. 128 (2006) 12714.
[47] (a) J.A. Mikroyannidis, M.M. Stylianakis, P. Balraju, P. Suresh, G.D. Sharma, ACS Appl. Mater. Interfaces 1 (2009) 1711;
(b) J.A. Mikroyannidis, M.M. Stylianakis, P. Suresh, P. Balraju, G.D. Sharma, Org. Electron. 10 (2009) 1320;
(c) J.A. Mikroyannidis, S.S. Sharma, Y.K. Vijay, G.D. Sharma, ACS Appl. Mater. Interfaces 2 (2010) 270;
(d) J.A. Mikroyannidis, A.N. Kabanakis, A. Kumar, S.S. Sharma, Y.K. Vijay, G.D. Sharma, Langmuir 26 (2010) 12909;
(e) J.A. Mikroyannidis, A.N. Kabanakis, P. Balraju, G.D. Sharma, Macromolecules 43 (2010) 5544.
[48] (a) J.A. Mikroyannidis, A.N. Kabanakis, P. Balraju, G.D. Sharma, J. Phys. Chem. C 114 (2010) 12355;
(b) J.A. Mikroyannidis, D.V. Tsagkournos, P. Balraju, G.D. Sharma, J. Power Sources, submitted for publication.
[49] G.R. Robertson, Org. Synth. Coll. 1 (1941) 396;
G.R. Robertson, Org. Synth. Coll. 2 (1922) 57.
[50] T.Y. Wu, Y. Chen, J. Polym. Sci., Part A: Polym. Chem. 40 (2002) 4452.
[51] S.C. Moratti, R. Cervini, A.B. Holmes, D.R. Baigent, R.H. Friend, N.C. Greenham, J. Grüner, P. Hamer, J. Synth. Met. 71 (1995) 2117.
[52] Y. Li, H. Xu, L. Wu, F. He, F. Shen, L. Liu, B. Yang, Y. Ma, J. Polym. Sci., Part B: Polym. Phys. 46 (2008) 1105.
[53] J.A. Mikroyannidis, G.M. Tsivgoulis, J. Polym. Sci., Part A: Polym. Chem. 37 (1999) 3646.
[54] Y.F. Li, Y. Cao, J. Gao, D.L. Wang, G. Yu, A.J. Heeger, Synth. Met. 99 (1999) 243.
[55] (a) V.D. Mihailetchi, H.X. Xie, B. de Boer, L.J.A. Koster, P.W.M. Blom, Adv. Funct. Mater. 16 (2006) 699;
(b) Y.Y. Liang, D.Q. Feng, Y. Wu, S.T. Tsai, G. Li, C. Ray, L.P. Yu, J. Am. Chem. Soc. 131 (2009) 7792.
[56] (a) B.C. Thompson, J.M.J. Frechet, Angew. Chem. Int. Ed. 47 (2006) 58;
(b) J. Jo, S.S. Kim, S.I. Na, B.K. Yu, D.Y. Kim, Adv. Funct. Mater. 19 (2009) 866;
(c) D. Venkataraman, S. Yurt, B.H. Venkataraman, N. Gavvalapalli, J. Phys. Chem. Lett. 1 (2010) 947;
(d) W. Ma, C. Yang, X. Gong, K. Lee, A.J. Heeger, Adv. Funct. Mater. 15 (2005) 1617.
[57] Y. Zhao, Z. Xie, Y. Qu, Y. Geng, L. Wang, Appl. Phys. Lett. 90 (2007) 043504.
[58] (a) P.J. Brown, D.S. Thomas, A. Kohler, J.S. Wilson, J.S. Kim, C.M. Ramsdale, H. Sirringhaus, R.H. Friend, Phys. Rev. B 67 (2003) 064203;
(b) J.H. Park, J.S. Kim, J.H. Lee, W.H. Lee, K. Cho, J. Phys. Chem. C, doi: 10.1021/jp9029562.;
(c) G.D. Sharma, P. Suresh, S.S. Sharma, Y.K. Vijay, J.A. Mikroyannidis, ACS Appl. Mater. Interfaces 2 (2010) 504.

transport occurs far away from the quasi-equilibrium state. In such a case, analyzing the behavior of the device with the assumption that charge carriers have attained the quasi-equilibrium state may result in misleading conclusions. The uncertainty about the state of carriers in these organic photonic devices also raises doubt over the assumptions made in the analysis of the experiments like transient electroluminescence that the charge carriers are in true quasi-equilibrium [11]. Even in the case of well established time of flight mobility measurement technique, the deviation of the carriers from the true quasi-equilibrium is of great concern as far as the analysis of the transients and the extraction of the mobility value is concerned [3,12–14]. Thus, it is highly important to understand the characteristics of non-equilibrium transport and the influence of the same on device characteristics.

In this article we investigate the field dependence of mobility for different values of the sample thickness. By varying the thickness of the sample one can capture the different stages of carriers that approach towards the true quasi-equilibrium and the corresponding evolution of various characteristics such as field and temperature dependence of mobility. Our simulation studies, with zero positional disorder, show a negative field dependence of mobility (NFDM) at low field regime ($\sim < 3.6 \times 10^5$ V/cm) in samples of smaller thickness (of the order of few hundred nanometers). The observed NFDM at low field regime gradually vanishes with the increase of sample thickness. A clear saturation of mobility at low field regime is observed at large sample thicknesses (few microns), which is same as reported earlier [3]. In the present study the observed NFDM is explained on the basis of gradual reduction of carrier's ability to wander in the lattice to find out the least resistance paths when the carrier relaxes toward the bottom of the DOS so as to achieve the true quasi-equilibrium [3]. The dependence of observed results on sample thickness, energetic disorder and temperature is also explained.

Earlier studies [3,4] have reported NFDM at low field regime in thicker samples where carrier is believed to have attained a true quasi-equilibrium condition. It has been explained by GDM on the basis of high positional disorder [3,4] present in the sample. High positional disorder opens up numerous least resistant paths/faster routes to the carriers which enhance the mobility [3,4]. These paths may involve carrier jumps against the field direction that can help the carrier reach transport sites in the direction of the applied field faster than in the absence of positional disorder. The availability of these least resistant paths diminishes with increase of electric field strengths and gets totally eliminated at high field strengths. At higher fields, the field assisted barrier lowering becomes dominant and results in the increase of mobility in Poole–Frenkel fashion [3,4]. Thus, initially mobility decreases with increase of field strength and reaches a minimum before it starts increasing with increase of field in a $\log\mu$ Vs $E^{1/2}$ fashion. In addition, our earlier report has shown that a very low value of energetic disorder, which leads to saturation of drift velocity even at lower electric field strengths, can results in a total NFDM over the entire regime of electric field strength [15]. In this context, our present simulation study, with zero positional disorder, highlights another important fact that an NFDM at low field regime can also be observed if the carriers involved in the charge transport have not attained true quasi-equilibrium condition.

2. Details of simulation

The Monte Carlo simulation is based on the commonly used algorithm reported by Schönherr et al. [16]. A 3D array is considered as the lattice with size 70×70 along x and y direction. Along z direction, the direction of the applied field, various sizes are used for attaining the required sample thickness along this direction. The lattice constant a = 6 Å is used for the whole set of simulation. The site energies of lattice are taken randomly from a Gaussian distribution with a known standard deviation (σ). Throughout the simulation the positional disorder is neglected ($\sum = 0$). Simulation is always performed on this energetically disordered lattice with the assumption that the carrier hops among the lattice sites following Miller–Abrahams equation [17] in which the jump rate v_{ij} of the charge carrier from the site i to site j is given by,

$$v_{ij} = v_0 \exp\left(-2\gamma a \frac{\Delta R_{ij}}{a}\right) \begin{pmatrix} exp\left(-\frac{\varepsilon_j - \varepsilon_i}{kT}\right) & , \quad \varepsilon_j > \varepsilon_i \\ 1 & , \quad \varepsilon_j < \varepsilon_i \end{pmatrix} \tag{1}$$

where $\Delta R_{ij} = | R_i - R_j |$ is the distance between sites i and j, ε_j and ε_i represent the effective energy for the sites i and j, which includes the electrostatic energy due to the applied electric field, a is the inter-site distance, k is the Boltzmann constant, T is the temperature in Kelvin, v_0 is the jump frequency in a lattice without any disorder and $2\gamma a$ is the wave function overlap parameter which controls the electronic exchange interaction between sites. Throughout the simulation we have taken $2\gamma a = 10$ [3,16]. Transit time of a carrier is calculated by adding all the hopping times and averaging over few hundred carriers which are injected one at a time. The mobility is calculated using drift mobility equation. The electric field strengths ($>10^4$ V/cm) over which the simulations are performed is well above the field range ($\sim 10^1 - 10^2$ V/cm) for which the pure diffusion dominates the charge transport [18]. The lowest electric field used in this study ($\sim 4 \times 10^4$ V/cm) is well above the critical field required for the drift mechanism to dominate the charge transport even for the smallest thickness under study [18]. Hence the use of drift mobility equation over the field range of this study is appropriate. The position of the carrier as a function of time is recorded and is used to calculate diffusion co-efficient (D) by using the following formula [3],

$$D = \frac{\left\langle (x - \langle x \rangle)^2 \right\rangle}{2t} \tag{2}$$

Simulation is preformed for various values of energetic disorder (σ), electric field strengths and temperature. All the data presented in this article is simulated with uncorrelated site energies.

Simulations are also carried out using small polaron jump rates [19]. The main observations of this article, presence of NFDM at low field regime ($\sim < 3.6 \times 10^5$ V/cm) in samples of very small thickness and gradual reduction

with increase of thickness, are found to be independent of the choice of jump rate (Miller–Abrahams/small polaron) used for simulation. Even though the main findings of this article are independent of the choice of jump rate, jump rate based on Miller–Abrahams equation is considered to be more appropriate for the present study because the use of small polaron model requires unacceptable values of polaron binding energies or transfer integrals when site energies are uncorrelated [20]. Hence in this report we show the simulation results only for Miller–Abrahams jump rate equation, which is sufficient for demonstrating and explaining the main findings reported in this article.

3. Results and discussion

Fig 1(a-d) shows the field dependence of mobility parametric with thickness for various values of energetic disorder. When the sample thickness is small, for all values of energetic disorder under study, mobility first decreases with increase of electric field strength and reaches a minimum before it starts increasing with increase of electric field strength in a $\mathrm{Log}\mu \propto E^{1/2}$ fashion [3]. Thus, we observed a NFDM at low field regime ($\sim < 3.6 \times 10^5$ V/cm) for all values of the energetic disorder under study when the sample thickness is small. In order to quantify NFDM we define the strength of NFDM ($\Delta\mu_{\mathbf{NFDM}}$) as the difference between the mobility values for the lowest electric field strength under study and the observed minimum of the mobility at low field regime. As we increase the thickness of the sample, the strength of the observed NFDM gradually decreases and finally at large values of sample thickness mobility is nearly a constant at low field regime. For all values of energetic disorder under study, the value of mobility becomes independent of thickness (i.e. attaining true quasi-equilibrium value) in samples of large thickness ($\sim >$ few microns). The thickness of the sample at which the NFDM vanishes depends on the value of the energetic disorder. In case of $\sigma = 40$ meV, NFDM is observed even in micron thick samples while for the higher values of the energetic disorder ($\sigma = 75$ meV, 85 meV) the NFDM vanishes totally when the thickness of samples is increased to few hundreds of nanometers. In addition, for high values of the energetic disorder ($\sigma = 75$ meV, 85 meV), the observed NFDM vanishes before the mobility attaining the true quasi-equilibrium value (i.e. thickness independent mobility). On the other hand, for low values of energetic disorder ($\sigma = 40$ meV, 60 meV) the observed NFDM vanishes approximately at time of mobility reaching its true quasi-equilibrium value. Moreover, the strength of NFDM

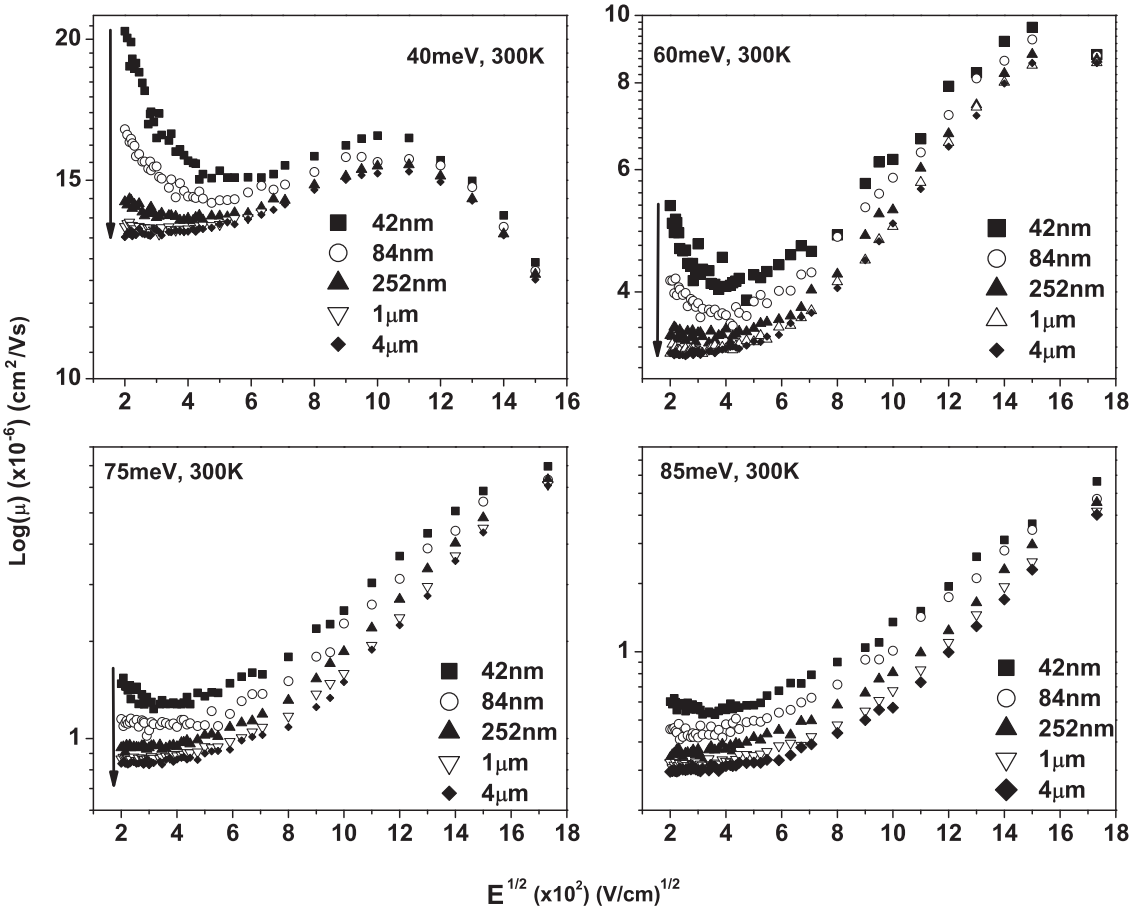

Fig. 1. Simulated field dependence of mobility, at $T = 300$ K, parametric with sample thickness for various values of energetic disorder. Value of energetic disorder is given in the respective figures.

is smaller for higher values of the energetic disorder and vice versa. The strength of the electric field at which the minimum of the mobility at the low field regime occurs also decreases with the increase in the sample thickness and the energetic disorder. In the intermediate field regime, magnitude of mobility decreases with the increase in the sample thickness but the nature of the field dependence of mobility remains same. Increase of mobility with the electric field strength in the Log$\mu \propto E^{1/2}$ fashion, observed in the intermediate field regime, is due to the tilting of density of states by the applied field that leads to the decrease of the energetic barrier seen by the charge carriers [3]. In the high field regime ($E > \sim 1 \times 10^6$ V/cm), we observed a NFDM for the low values of the energetic disorder (σ = 40 meV, 60 meV) under study. This is due to the saturation of drift velocity at high electric field strengths which results in the decrease of mobility with the further increase of electric field [3,21]. For higher values of the energetic disorder (σ = 75 meV, 85 meV), the saturation of drift velocity is not attained even for the highest value of the electric field strength in this study ($E = \sim 8 \times 10^6$ V/cm).

Our main findings which we try to explain here are the origin of the observed NFDM at low field regime in very thin samples and the dependence of the same on sample thickness, energetic disorder, temperature and strength of electric field. An NFDM at low field regime was earlier observed in samples with thickness of the order of few microns [3,4]. The reported data [3,4] establishes that a high value of positional disorder and a reasonable value of energetic disorder is indispensible for observing NFDM at low field regime. However, in our simulation we have considered *only* the energetic disorder ($\sum = 0$). The NFDM at low field regime observed in our simulation studies, even in the absence of any positional disorder, may be associated with non-equilibrium charge transport which need not be the case in the earlier reported data [3,4] where NFDM was observed in samples with thickness of the order of few microns. The similarity between the simulated data for micron thick samples and reported data in Refs. [3,4] supports this conjecture.

In order to understand the origin of the observed NFDM at low field regime, simulation is carried out to figure out as to when the carriers attain the quasi-equilibrium [3]. Coefficient of diffusion along the field direction is calculated as function of time [6,9]. Fig. 2 (a-d) shows variation of the coefficient of diffusion with time (*normalized with the dwell time of carrier in a lattice without disorder,* t_0 [2]), for various values of the energetic disorder and for

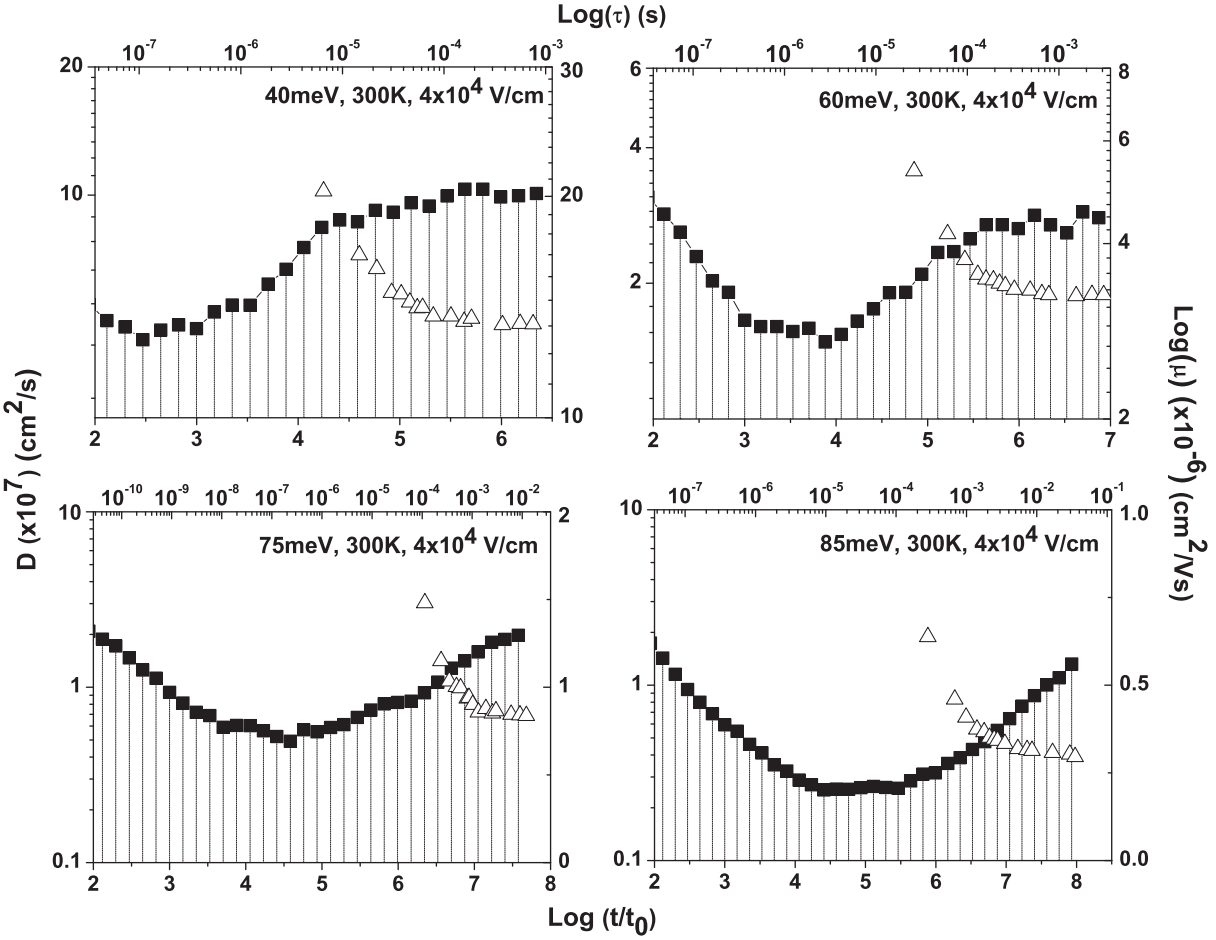

Fig. 2. Calculated coefficient of diffusion (D) of carriers while hopping in a Gaussian DOS, at T = 300 K and $E = 4 \times 10^4$ V/cm. Δ represents the variation of mobility with transit time (τ). t_0 is the dwell time of carrier in a lattice without disorder.

the lowest electric field strength under the study. Variation of mobility with transit time for the lowest electric field strength under study, effectively the variation of mobility with sample thickness, is also shown. For all value of energetic disorder, the coefficient of diffusion initially decreases with time and reaches a minimum before it starts increasing with time. The calculated value of diffusion coefficient contains the usual thermal energy contribution as well as the field and disorder dependent contribution. The field and disorder dependent part of the diffusion produces an additional non-thermal field assisted spreading of the carrier packet [6,22]. This is due to the wide difference in the distribution of jump rates of carriers that are temporally localized at the bottom and top of the DOS [6,22]. The increase in coefficient of diffusion with time is attributed to the non-thermal field assisted spreading of carrier packet. At long time the coefficient of diffusion is expected to attain a time independent value which is considered as the signature of the carriers attaining true quasi-equilibrium state. For low values of the energetic disorder (σ = 40 meV, 60 meV), diffusion coefficient has attained a time independent value in samples of large thicknesses. While for high value of disorder (σ = 75 meV, 85 meV), the diffusion coefficient has not attained a time independent value even for a thicker sample ($\sim$6 μm). For low value of energetic disorder (σ = 40 meV, 60 meV) mobility becomes independent of thickness only when the diffusion coefficient has attained a time independent value. For high value of energetic disorder (σ = 75 meV, 85 meV), mobility becomes independent of thickness even though the diffusion coefficient is not time independent.

So from Fig. 2 it is concluded that the carriers have not attained the true quasi-equilibrium when the thickness of the sample is very small. The decrease in mobility with increase in sample thickness even in the intermediate field regimes also suggests the same. Quasi-equilibrium condition is normally attained only in samples of very large thickness. The observed NFDM at low field regime that decreases with increase of sample thickness can be explained as follows. In case of samples with smaller thickness, at low electric field strengths, a carrier with the help of thermal energy finds numerous least resistance paths by which it can drift faster along the field direction, i.e. the carrier attains high mobility. These least resistance paths may involve carrier jumping against the field direction. Upon increasing the electric field strength these paths are gradually eliminated. Thus the carrier is forced to drift through the higher resistance paths with increase of electric field strength which in turn leads to the decrease of the carrier mobility. This results in an NFDM in low electric field regime in samples of smaller thickness. Similar explanation has been proposed earlier for explaining the observed negative differential hopping conductivity in doped inorganic semiconductors [23,24] and also for explaining NFDM observed at low field regime in thicker samples [3,4]. In the low field regime, in one way the increase of electric field strength decreases the carrier mobility while at the same time the tilting of DOS by the applied field, which reduces the effective barrier seen by the carrier, tends to increase the carrier mobility. Thus, in the low field regime, there exists a competition between the decrease and increase of the carrier mobility with increase of the electric field due to the respective mechanisms explained above. When the field is sufficiently strong the increase in the carrier mobility due to tilting of DOS by the applied field dominates and leads to the increase of the carrier mobility in a $\mathrm{Log}\mu \propto E^{1/2}$ fashion. This results in minimum of mobility in the low electric field regime. The dependence of the strength of electric field at which this minimum of mobility occurs on thickness, energetic disorder and temperature will be explained later. When we increase the thickness of samples, carriers tend towards attaining the quasi equilibrium. In this process they relax more towards the bottom of DOS [1,2,7]. More the carriers relax to the bottom of DOS higher is the required excitation energy to move around the lattice as before. Thus while covering more and more sample length the ability of the carrier to move around the lattice to find numerous least resistance paths diminishes. Thus, at short times carrier move through small resistance paths that results in high carrier mobility. However, as time advances these paths are not readily accessible to the carriers. So the average mobility of the carrier decreases with increase of sample thickness. This explains why the strength of the observed NFDM decreases with increase of thickness. Decrease of mobility with time has been shown analytically and experimentally in the recent reports as well [11,25–27].

In the present study, for small values of the energetic disorder (σ = 40 meV, 60 meV) the observed NFDM vanishes and the mobility attains the true quasi-equilibrium value almost simultaneously when the diffusion becomes time independent, i.e. only when the carriers have attained the true quasi-equilibrium. This suggests that at very large thickness the carrier attains the true quasi equilibrium and thus the positive influence of thermal energy on mobility at short times disappears resulting in the saturation of mobility at low electric field regime. However, for high values of the energetic disorder (σ = 75 meV, 85 meV) NFDM vanishes well before the carrier attaining the true quasi-equilibrium. From Fig. 1, it is clear that for high value of energetic disorder (σ = 75 meV, 85 meV) the mobility continue to decrease with increase of thickness even after the observed NFDM has totally vanished. This suggests that for the observed decrease in strength of NFDM and the subsequent vanishing of NFDM require only the reduction in the ability of the carrier to find the least resistance paths as the carrier relaxes towards the bottom of the DOS. When the value of the energetic disorder is very high, to effectively move around the lattice in search of least resistance paths the carrier requires high excitation energy even after a short relaxation. Once the carrier is not able to find the sufficient number of least resistance paths to keep the mobility high, the NFDM vanishes and a clear saturation of mobility can be observed. This explains why at high value of energetic disorder the observed NFDM vanishes in samples with thickness of few hundreds of nanometers while for low values of energetic disorder it persists even in micron thick samples (for example σ = 40 meV). In addition to this, for high value of energetic disorder the mobility nearly attains a thickness independent value (for example σ = 75 meV) while the calculated diffusion coefficient continues to increase with time. Thus, we have got a situation

where the mobility has nearly attained a quasi-equilibrium value while the diffusion coefficient continues to increase with time. This is termed as quasi-dispersive regime [9]. Our results suggest that quasi-dispersive regime may be observed only at very high value of energetic disorder.

In light of the above discussion it is also easy to understand why the strength of NFDM decreases with increase in energetic disorder. For high energetic disorder, the energetic barrier seen by the carrier is also high. Therefore carriers require high excitation energy to move around in the lattice. Thus at high value of energetic disorder the carrier will find less number of least resistance paths. This results in low carrier mobility which explains why, for a fixed and small enough value of sample thickness, the strength of observed NFDM in the low field regime decreases with increase of energetic disorder (shown in Fig. 1). Hence for any value of energetic disorder under study, if some extra energy is provided to the carrier a stronger NFDM can be expected. Fig. 3(a-c) shows the field dependence of mobility parametric with temperature for the smallest value of sample thickness under study. At high temperature the carrier gains more thermal energy which helps the carrier to find more number of least resistance paths. Thus the mobility of carrier will be high which in turn leads to the increase in strength of NFDM. Fig. 3(d) shows variation of the strength of NFDM ($\Delta\mu$) with temperature. The strength of NFDM is shown to vary linearly with temperature. The rate of increase of strength of NFDM with temperature decreases with increase in the energetic disorder. These observations assert the strong role of energetic disorder in the observed NFDM at low electric field regime in samples of smaller thickness. The decrease in the strength of NFDM with increase in energetic disorder and decrease of temperature supports our conjecture that decrease in strength of NFDM with increase of sample thickness is due to the relaxation of carriers towards the bottom of DOS.

The strength of electric field at which the minimum of the mobility occurs also depends on how far the carrier has approached towards attaining the true quasi-equilibrium or how close is the carrier from its quasi-equilibrium state. As explained above, in samples of smaller thickness carriers find a large number of least resistance paths and hence, these least resistance paths accessed by the carriers get eliminated only at higher electric field strengths. As we increase the sample thickness the effective number of least resistance paths accessed by the carrier reduces and thus the elimination of the least resistance paths occurs at

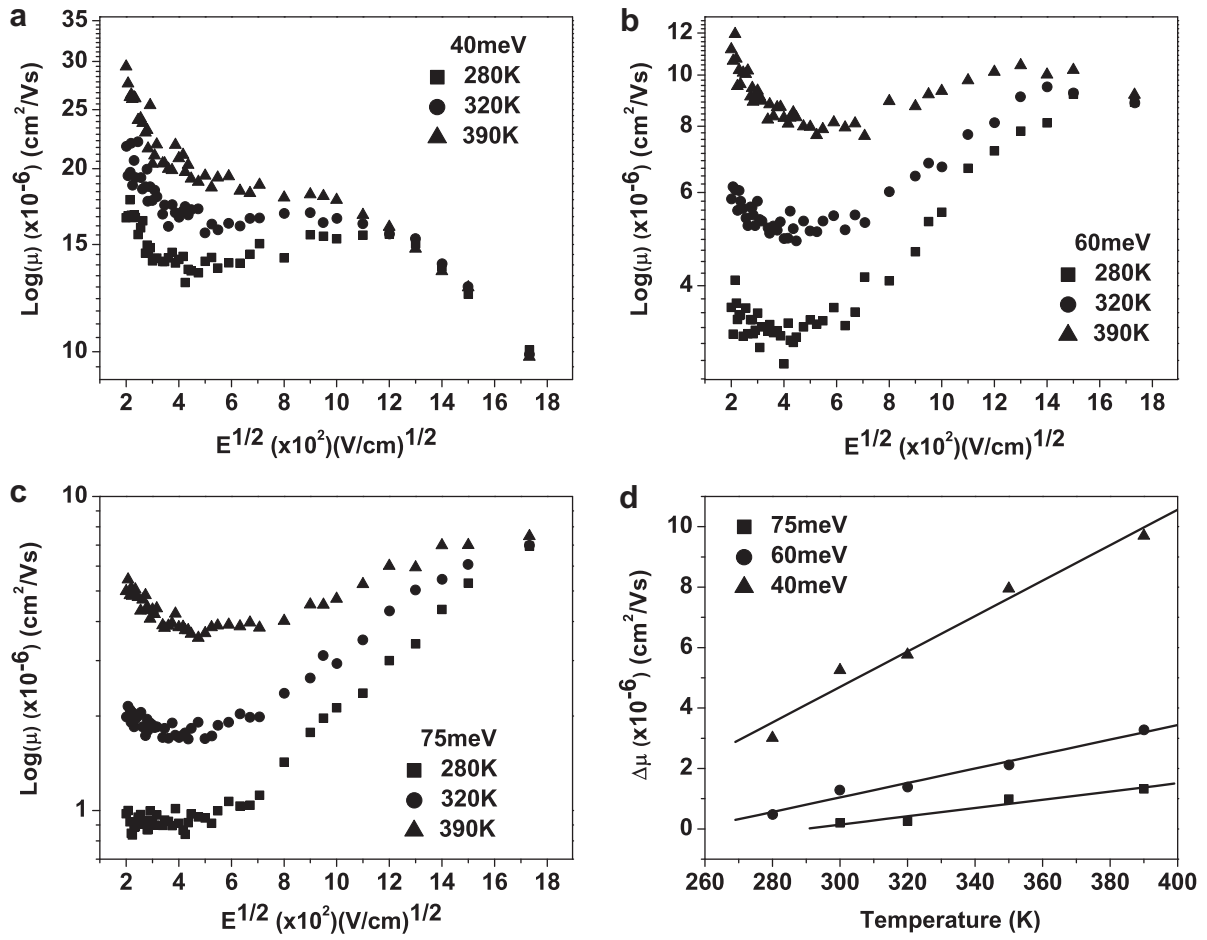

Fig. 3. (a-c) Simulated field dependence of mobility parametric with temperature for various values of energetic disorder. Value of energetic disorder is given in the respective figures. Simulations were carried out in sample of thickness ~ 42 nm. (d) Variation of strength of NFDM with temperature.

lower electric field strengths. Due to the elimination of the least resistance paths at low electric field strengths, the mechanism that leads to the increase of the carrier mobility in a $\mathrm{Log}\mu \propto E^{1/2}$ fashion could dominate at low electric field strengths. Hence, with increase of sample thickness the minima of the mobility at low field regime occur at lower electric field strengths. The occurrence of minimum of mobility at higher electric field strength upon decreasing the value of energetic disorder or increasing the temperature can also be explained in the similar manner.

4. Conclusion

Our simulation study clearly shows the influence of non-equilibrium charge transport on the nature of field dependence of mobility. Even in the absence of positional disorder an NFDM at low field regime is observed in samples of smaller thickness for all values of energetic disorder and temperature. The observed NFDM at low field vanishes with increase of sample thickness. The strength of the observed NFDM is found to be highly dependent on the value of energetic disorder and temperature. The observed NFDM is explained on the basis of carriers relaxing towards the bottom of the DOS in the process of attaining the true quasi-equilibrium. In brief, this study asserts that if the charge transport in the sample under study is not occurring under true quasi-equilibrium condition then an NFDM at low field regime can be observed where the role of the positional disorder as reported in Refs. [3,4] is not very crucial. The results may be relevant for organic photonic devices with active layer thickness in the order of few hundreds of nanometers where one expect non-equilibrium charge transport to take place.

Acknowledgments

Authors are grateful to S.C. Mehendale for his support, encouragement and the critical reading of the manuscript.

References

[1] M. Pope, C.E. Swenberg, Electronic Processes in Organic Crystals and polymers, Oxford University Press, NewYork, 1999.
[2] G. Hadziioannou, Paul F. Van Hutten, Semiconducting Polymers: Chemistry Physics and Engineering, Wiley-VCH, Weinhelm, 2000.
[3] H. Bässler, Phys. Status Solidi (b) 175 (1993) 15.
[4] P.M. Borsenberger, L. Pautmeier, H. Bässler, J. Chem. Phys. 94 (1991) 5447.
[5] Y.N. Gartsetin, E.M. Conwell, Chem. Phys. Lett. 245 (1995) 351.
[6] L. Pautmeier, R. Richert, H. Bässler, Philos. Mag. B 63 (1991) 587.
[7] P.M. Borsenberger, D.S. Weiss, Organic Photoreceptors for Xerography, of Optical Engineering Series, Vol. 59, Marcel Dekker, New York, 1998.
[8] L.M. Andersson, O. Inganäs, Org. Electron. 8 (2007) 423.
[9] V.R. Nikitenko, H. von Seggern, H. Bässler, J. Phys. Condens. Matter. 19 (2007) 136210.
[10] V.R. Nikitenko, A.P. Tyutnev, N.A. Korolev, Semiconductors 43 (2009) 1466.
[11] V.R. Nikitenko, H. von Seggern, J. Appl. Phys. 102 (2007) 103708.
[12] A.P. Tyutnev, V.S. Saenko, E.D. Pozhidaev, R.S. Ikhsanov, J. Phys. Cond. Matt. 20 (2008) 215219.
[13] A.P. Tyutnev, V.S. Saenko, E.D. Pozhidaev, J. Phys. Cond. Matt. 18 (2006) 6365.
[14] A.P. Tyutnev, V.S. Saenko, E.D. Pozhidaev, J. Phys. Cond. Matt. 21 (2009) 115107.
[15] S. Raj Mohan, M.P. Joshi, M.P. Singh, Chem. Phys. Lett. 470 (2009) 279.
[16] G. Schönherr, H. Bässler, M. Silver, Philos. Magz. 44 (1981) 47.
[17] A. Miller, E. Abrahams, Phys. Rev. B 120 (1960) 745.
[18] I.I. Fishchuk, A. Kadashchuk, H. Bässler, M. Abkowitz, Phys. Rev. B 70 (2004) 245212.
[19] N. Tessler, Y. Preezant, N. Rappapot, Y. Roichman, Phys. Rev. B 21 (2009) 1.
[20] L.B. Schein, Philos. Mag. B 65 (1992) 765.
[21] S. Raj Mohan, M.P. Joshi, M.P. Singh, Org. Electron. 9 (2008) 355.
[22] A.I. Rudenko, V.I. Arkhipov, Philos. Mag. B 45 (1982) 177.
[23] E.I. Levin, B.I. Shklovskii, Solid. Stat. Commun. 67 (1988) 233.
[24] N.V. Lein, B.I. Shklovskii, Solid. Stat. Commun. 38 (1981) 99.
[25] A.J. Mozer, S. Sariciftci, L. Lutsen, D. Vanderzande, R. Österbacka, M. Westerling, G. Juška, Appl. Phys. Lett. 86 (2005) 112104.
[26] R. Österbacka, A. Pivrikas, G. Juska, K. Vanderzande, R. Juska, K. Genevicius, K. Arlauskas, H. Stubb, Appl. Phys. Lett. 86 (2005) 112104.
[27] A. Devizis, A. Serbenta, K. Meerholz, D. Hertel, Phys. Rev. Lett. 103 (2009) 027404.

promising properties with field-effect mobilities up to 1.0 $cm^2 V^{-1} s^{-1}$ from drop-cast films [18–20]. However, these molecules still exhibit stability issues. Some thiophene derivatives have also shown promising performances (up to 0.3 $cm^2 V^{-1} s^{-1}$) using alternative solution processing techniques [21,22]. Müllen and co-workers have developed new molecules based on dithieno[2,3-*d*;2′,3′-*d*′]benzo[1,2-*b*;4,5-*b*′]dithiophene that resulted in very good performances in solution processed devices (up to 1.7 $cm^2 V^{-1} s^{-1}$) [23,24]. Such wet processing is amenable to cheap high throughput fabrication using roll-to-roll or inkjet printing technologies. Thus, the overall goal remains the fabrication of stable, solution processable and high performance transistors.

In parallel, carbazole and indolo[3,2-*b*]carbazole derivatives represent a very promising class of materials for OFETs [25–27]. These compounds are good *p*-channel semiconductors, they are stable under ambient conditions and the addition of side chains on the nitrogen atoms results in highly soluble polymers and oligomers [25,28]. Relatively high performances have already been obtained with different carbazole derivatives [29,30]. For instance, hole mobilities as high as 0.3 $cm^2 V^{-1} s^{-1}$ have been obtained with evaporated thin films of 1,4-bis(vinylene-(*N*-hexyl-2-carbazole))phenylene (**CPC**). With indolo[3,2-*b*]carbazoles, the best performance was obtained from vapour deposited thin films of 3,9-diphenyl-5,11-dioctylindolo[3,2-*b*]carbazole [31] and 3,9-di(p-octylbenzene)-5,11-dihydroxyindolo[3,2-b]carbazole with a maximum field-effect mobility of 0.22 $cm^2 V^{-1} s^{-1}$ [32]. Other interesting small molecules have been developed based on the IC framework [33–35]. The only solution processed materials based on carbazole and indolo[3,2-*b*]carbazole are polymers and have shown field-effect mobility up to 0.02 $cm^2 V^{-1} s^{-1}$ [36–40].

New solution processable IC derivatives (Fig. 1) will be presented in this article. These compounds were synthesized based on the CPC class that has been developed by Morin et al. [29]. The synthesis of these new oligomers will be presented as well as their detailed characterization. We will show the influence of substituting the IC unit at the 2- or 3-position and the effect of adding vinylene moieties between the aromatic groups. Due to its high solubility in common organic solvents, 3POIND, whose synthesis and full characterization have been published elsewhere [31], will also be studied. The solution-processed thin films have been obtained by two different deposition techniques: drop-casting and shearing. By using polarized optical microscopy (POM) and XRD techniques, a better understanding of the relationship between the morphology and the performances of each material should be achieved.

2. Results and discussion

2.1. Synthesis of indolo[3,2-b]carbazole derivatives

As mentioned earlier, the synthesis of 3,9-diphenyl-5,11-dioctylindolo[3,2-*b*]carbazole has already been reported in the literature [31]. In order to obtain the four new indolo[3,2-*b*]carbazole derivatives shown in Fig. 1, 2-bromoindolo[3,2-*b*]carbazole and 3-bromoindolo[3,2-*b*]carbazole had to be synthesized. The synthetic pathway of these two unsymmetrical compounds was more complex than expected and is presented in Scheme 1. The first step involved the synthesis of the indole-2-carbonyl chloride (**2**) starting from the indole-2-carboxylic acid by treating it with thionyl chloride. This acid chloride was immediately used to perform an acylation reaction with either 5- or 4-bromoindole as described by Okauchi et al. and also by Wahlström et al. [41,42]. This led to compound (**5**) which was obtained with a 72% yield and compound (**6**) in a 67% yield. The ketone was then reduced into the corresponding alkyl group by simply

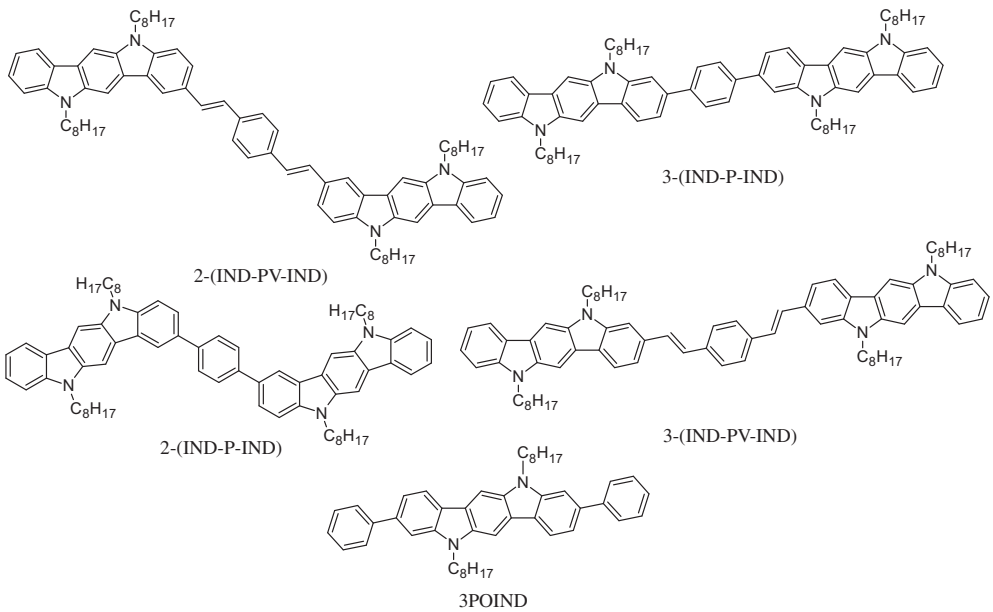

Fig. 1. Chemical structure of indolo[3,2-*b*]carbazole-based oligomers.

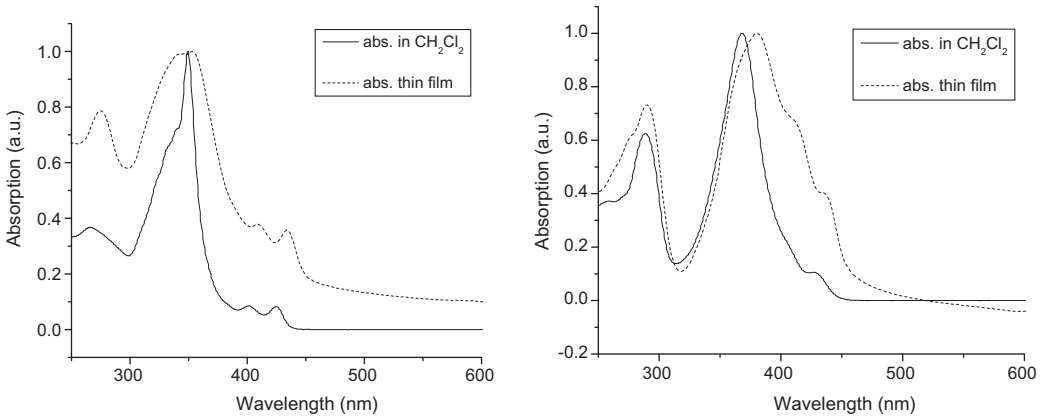

Fig. 2. UV–vis absorption spectra of (a) 2-(IND-P-IND), (b) 3-(IND-P-IND) in solution and vacuum-deposited thin films.

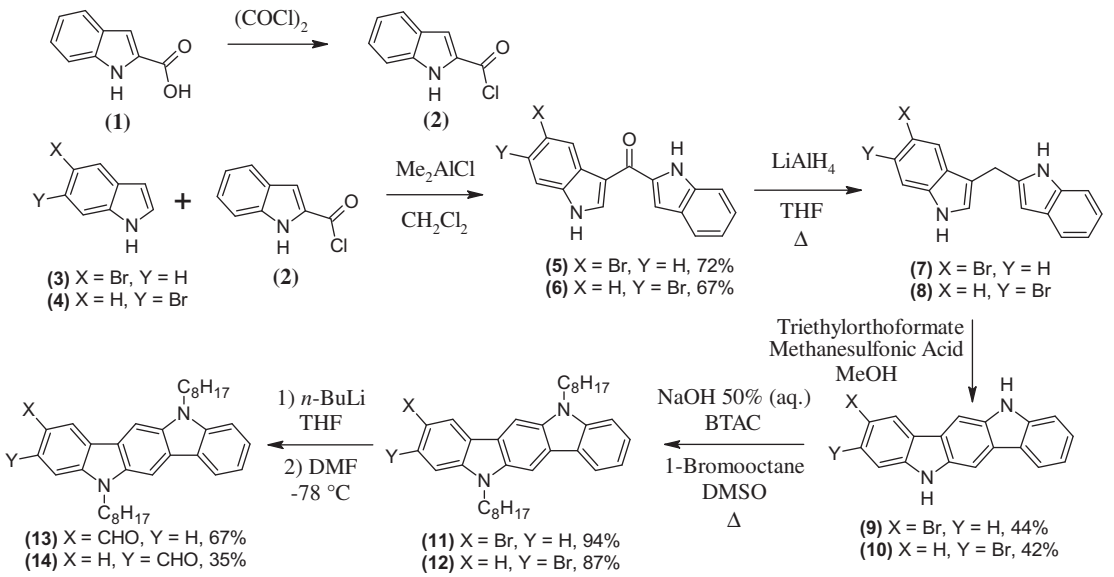

Scheme 1. Synthesis of the unsymmetrical indolo[3,2-b]carbazole. BTAC: benzyltriethylammonium chloride.

treating with lithium aluminum hydride in anhydrous THF. Compounds (**7**) and (**8**) were used without further purification with the following step being the formation of the IC framework. The cyclisation is performed by treatment with triethylorthoformate and catalytic amount of methanesulfonic acid in methanol [43]. Compounds (**9**) and (**10**) were obtained in 44% and 42% yields. Afterward, the 5,11-dihydroindolo[3,2-*b*]carbazole can be alkylated or arylated with different side chains.

Linear octyl side chains were added on both nitrogen atoms through a regular phase transfer condensation [31,34,35]. The starting compounds (**9**) and (**10**) are treated with aqueous sodium hydroxide, 1-bromooctane, and benzyltriethylammonium chloride as the phase transfer agent in DMSO. After heating at 65 °C for 4 h, compounds (**11**) and (**12**) were obtained in high yields (94% and 87%, respectively). These two compounds can be coupled via Suzuki cross-coupling with benzene-1,4-diboronic acid to obtain two new IC derivatives which should be highly soluble in organic solvents. The yields for the two reactions are 33% for 2-IND-P-IND (**15**) and 39% for 3-IND-P-IND (**16**). To achieve the syntheses of compounds (**17**) and (**18**), aldehyde functional groups had to be added instead of the bromine. This substitution is first performed by lithiation of compounds (**11**) and (**12**) and further treatment with N,N-dimethylformamide at −78 °C. Compounds (**13**) and (**14**) were successfully synthesized with 67% and 35% yields. Finally, those two compounds were mixed with 1,4-bis(methylphosphonate)benzene in anhydrous THF to perform Horner–Emmons reactions to obtain compounds (**17**) and (**18**) in 93% and 75% isolated yields. The final step of the synthesis of the materials is presented in Scheme 2.

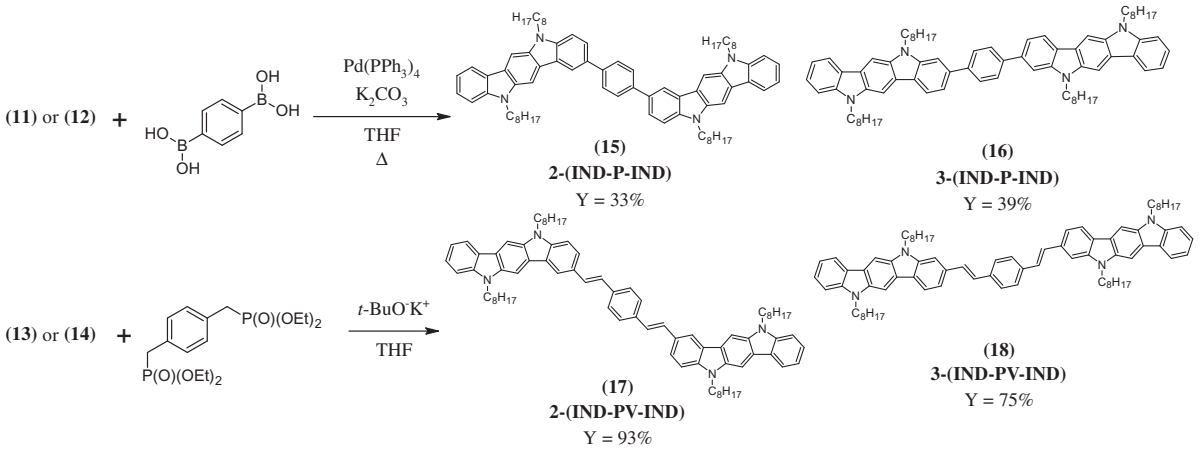

Scheme 2. Synthesis of the four new indolo[3,2-*b*]carbazole derivatives.

2.2. Thermal properties

The thermal properties of the new derivatives were studied using thermogravimetric (TGA) and differential scanning calorimetry (DSC) analyses (Table 1). The full characterization of 3POIND has already been published elsewhere [31]. There were no degradation processes observed for all these indolo[3,2-*b*]carbazole derivatives below 440 °C under a flow of nitrogen. Moreover, the DSC curves do not show any particular thermal phenomenon, meaning that no glass transition temperatures were observed for any of these materials. Small peaks were obtained about 50 °C before the melting peak but those exothermic peaks are probably due to crystallization of the molecules during the heating process.

Table 1
Thermal properties of the oligomers.

Oligomer	T_d (°C)[a]	T_m (°C)[b]	T_c (°C)[b]
2-(IND-P-IND)	–	201	–
3-(IND-P-IND)	470	153	–
2-(IND-PV-IND)	440	212	193
3-(IND-PV-IND)	–	230	170
3POIND	410	237	196

[a] Degradation temperature (T_d) observed from TGA corresponding to 5% weight loss at 10 °C min^{-1} under nitrogen flow.
[b] Melting temperature (T_m) and crystallization temperature (T_c) observed from DSC at 10 °C min^{-1} under nitrogen flow.

2.3. Optical and electrochemical properties

The optical properties were characterized by UV–vis absorption spectroscopy and are summarized in Table 2. The solution and thin-film spectra of 2-(IND-P-IND) and 3-(IND-P-IND) are shown in Fig. 2. The data extracted from these spectra reveals a longer conjugation length for IC derivatives substituted at the 3-positions. It also shows that the addition of a second indolocarbazole into the material does not greatly affect the conjugation length of the molecule. The absorption maximum of the 3POIND is 366 nm compared to 368 nm for the 3-(IND-P-IND). This indicates that the phenyl group in the latter hinders the conjugation due to the phenyl-substituent bond which usually shows torsion angle of about 40° [44].

The UV–vis absorption spectra in the solid state were taken for 2-(IND-P-IND) and 3-(IND-P-IND) and not for the two other derivatives because it was very difficult to cast the films on quartz plates. The spectra exhibit a red shift compared to the solution spectra in CH_2Cl_2. This red shift is typically indicative of favourable interactions and stacking between the molecules in the solid state which leads to greater electron delocalization. A blue shift was observed in the case of 3POIND and it was attributed to

Table 2
Optical absorption maxima (λ_{max}) and electrochemical properties of the new materials.

Oligomer	λ_{abs} (nm) Solution[a]	λ_{abs} (nm) Thin film[b]	E_g (eV) Thin film [b]	$E_{peak\ ox}$ (V versus SCE)[c]	E_{HOMO} (eV)[d]
2-(IND-P-IND)	266, **349**, 401, 425	275, **353**, 409, 434	2.74	0.76 (0.69)	5.40
3-(IND-P-IND)	288, **368**, 427	290, **380**	2.68	0.76 (0.69)	5.40
2-(IND-PV-IND)	282, 338, 355, **405**	–	–	0.72 (0.64)	5.65
3-(IND-PV-IND)	286, **415**	–	–	0.75 (0.70)	5.41
3POIND	**366**, 408, 433	**356**, 420, 450	2.65	0.82 (0.73)	5.44

[a] Measurements performed in CH_2Cl_2.
[b] Measurements performed on 300 Å thin films vacuum-deposited on quartz.
[c] SCE: saturated calomel electrode. The values in parentheses correspond to the oxidation peak onset.
[d] Ionization potential (E_{HOMO}; HOMO: highest occupied molecular orbital) measured from the cathodic onset.

the formation of H-aggregates in the solid state is which often observed in closely packed structures [30,45]. The optical band gaps (E_g) were estimated from the onset of the absorption spectra in the solid state and the E_g for 2-(IND-P-IND) and 3-(IND-P-IND) are 2.74 and 2.68 eV, respectively. These values are very similar to the one obtained for 3POIND (2.65 eV).

Cyclic voltammetry experiments were also performed on the four new derivatives. They all showed one quasi-reversible oxidation process above 0.64 V versus SCE. 3-(IND-PV-IND) showed a second oxidation process at 1.00 V that was also quasi-reversible. The HOMO energy levels were calculated from the oxidation onset and varies from 5.40 to 5.65 eV [46]. The absolute values of these energy levels are higher than those observed for pentacene [47] and several thiophene derivatives [48] and should be high enough to avoid irreversible oxidation by the oxygen in air. Furthermore, the HOMO of the oligomers matches quite well the work function of a gold electrode (5.1 eV) [49].

2.4. Structural and morphological characteristics of Indolo[3,2-b]carbazoles

Because of the relatively large thickness of the solution-processed films for OFET applications, characterization techniques such as atomic force microscopy (AFM) and XRD do not provide any relevant information regarding the organization of the material in the first few layers on top of the substrate. These are the most significant layers since they are directly involved in the charge transport. The most interesting results were obtained by polarized optical microscopy (POM). This simple technique allows us to observe whether a crystalline or an amorphous film is present. One can also qualitatively measure the size of the crystallites. The first studied processing technique was the drop-casting of the films. Thin films were processed with different solvents and concentrations. As shown in Fig. 3, the main problem with this processing technique is the formation of a homogenous surface with large crystallites. In this case, a 2.0 mg/mL concentration in xylene was used. In order to evaporate the solvent left and trapped within the film, the device was heated at 100 °C for 30 min before the measurements. One of the main drawback of heating these type of film is that they tend to crack, resulting in smaller grain size and consequently, lower field-effect mobilities.

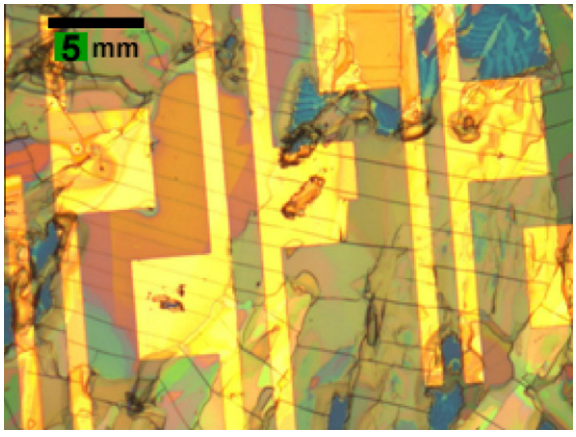

Fig. 3. Bright field micrograph of drop-cast 3POIND film. The gold channels are in yellow and under the organic material film (bottom-contact architecture).

From these observations on 3POIND, films processed by the shearing technique provide much larger crystalline grains than other technique such as drop-casting or spin-coating. As one can see in Fig. 4, by dragging a second substrate on top of the one containing the material in solution, it is fairly easy to obtain highly oriented films. Top-contact architecture was used for these devices since the shearing process could damage the quality of the gold channels. Because of the film orientation, it is very important to evaporate gold in a way that the device will be built along the crystalline grains and not perpendicular to them. With these two figures, it is obvious that the solution sheared will bring a higher crystallinity and therefore probably better performances.

The other four indolocarbazole derivatives led to amorphous-like films. Only small crystalline area could be found on the whole surface of the films. The low level of crystallinity observed by POM may be due to the length of these molecules along with the number of alkyl chains branched on the backbone. This molecular structure may not be adequate for efficient organization and packing. Furthermore, the presence of two IC moieties within each material produces disorder and consequently amorphous films. The addition of vinyl group between the ICs and the phenyl unit does not allow a better organization. Many conformations for this type of molecule create significant disorder which alters the efficient packing of the material. Therefore, it is believed that 3POIND has a great potential compared to the four other synthesized materials.

To prove that point furthermore, XRD experiments were performed to have a better idea of the organization within the films. However, no significant data could be extracted from the drop-cast films, most probably due to their thickness and heterogeneity. XRD experiments still showed out of plane ordering on the sheared films. Comparison with previous XRD experiments with vacuum evaporated thin film were performed [31]. As shown in Fig. 5, the sheared film adopts a very similar organization. The primary diffraction peak was observed at 5.52° which corresponds to a *d*-spacing of 16.0 Å. The second and third-order peaks are less intense than the primary peak but can still be found at 11.1° and 16.7°. The presence of these peaks indicates that the shearing technique gives rise to highly ordered films. This certainly means that the organization in three dimensions is very similar to what was observed for the sublimated thin film. Then, indolo[3,2-*b*]carbazole molecules should lay almost parallel to the substrate. The edge-on configuration have resulted in very promising performances in several studies [50].

2.5. Field-effect transistors

The field-effect transistors were fabricated from these drop-cast and sheared films. First, the drop-cast devices

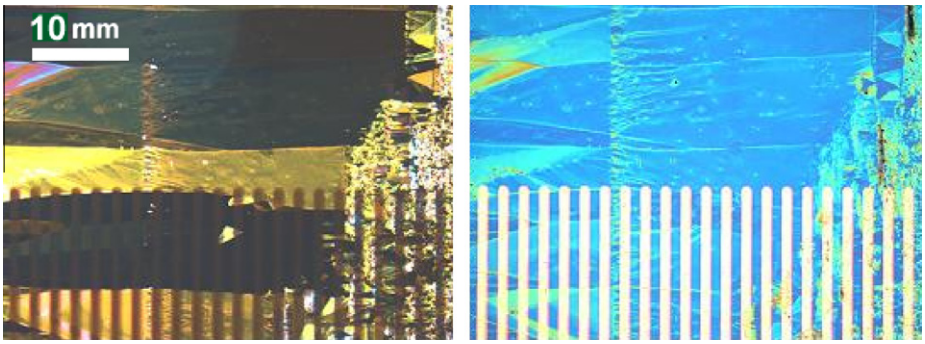

Fig. 4. (Left) Optical micrograph under cross-polarized optical microscopy of 3POIND using the shearing technique for film processing. (Right) The same film under bright-field.

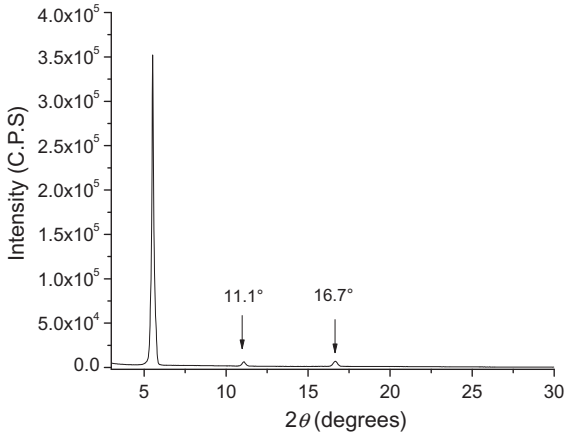

Fig. 5. XRD experiment on a sheared film of 3POIND.

were made in the bottom-contact architecture by vacuum evaporation of gold channels on OTS-treated Si/SiO_2 substrates. In order to obtain good quality films, the solution was deposited on the heated substrate which was covered with a funnel to decrease the evaporation rate of the solvent and promote larger crystal growth. Second, as described by Becerril et al. [21], the shearing technique leads to well-oriented crystals on the substrates. Higher field-effect mobilities can be obtained because the films have a much better uniformity. The sheared films were processed on phenyltrimethoxysilane (PTS)-treated substrates.

For vapour deposited thin films, plain and OTS-treated Si/SiO_2 substrates were used. It has been demonstrated that the treatment of bare Si/SiO_2 wafers has a great impact on the devices performances [51,52]. The addition of a hydrophobic layer on top of the silicon oxide decreases the number of surface hydroxyl groups which can either act as dopant (which increases off current) or act as trap sites [53]. As shown before, carbazole and indolo[3,2-*b*]carbazole derivatives typically behave as *p*-channel semiconductors when the electrode is gold. An example of the electrical measurements performed on the deposited thin films is shown in Fig. 6. A curve of the source–drain current (I_{DS}) versus source–drain voltage (V_{DS}) at various gate voltage is represented as well as I_{DS} versus the gate voltage (V_G) at a fixed V_{DS} (−100 V) both for a sheared film of 3POIND.

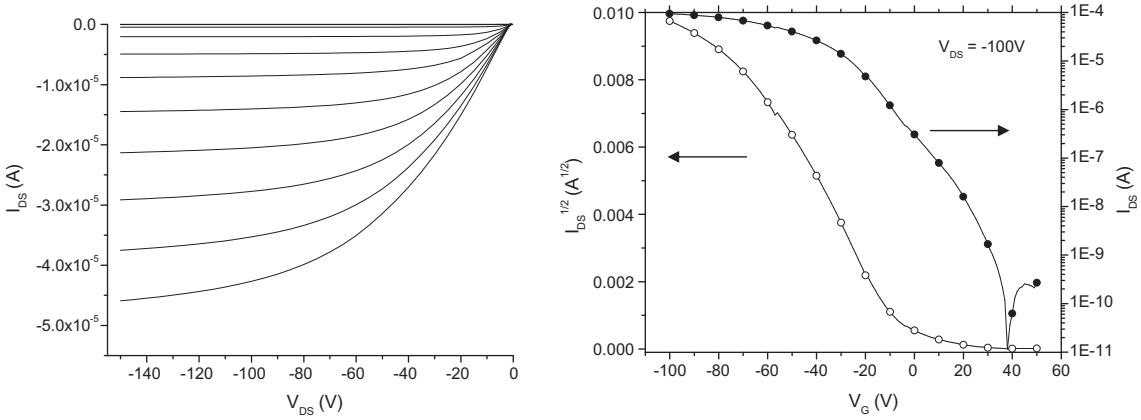

Fig. 6. Source–drain current (I_{DS}) versus source–drain voltage (V_{DS}) at various gate voltages (V_G) for top-contact field-effect transistors using solution processed 3POIND on PTS-treated SiO_2. The transfer characteristics in the saturation regime at a constant source–drain voltage (V_{DS}) −100 V) are also included.

Table 3
Field-effect mobilities, on/off ratios, and threshold voltages of solution processed indolo[3,2-*b*]carbazoles transistors prepared on SiO_2.

Compound	Solvent	[ ] (mg/mL)	T (°C)	μ ($cm^2\,V^{-1}\,s^{-1}$)	On/off	V_T (V)
3POIND	Toluene	1.5	80	0.06	2.2×10^5	−22
[a]	Toluene	6.0	70	0.12	5.6×10^6	−31
2-IND-PV-IND	CB	2.0	70	7.6×10^{-4}	1.0×10^4	−24
3-IND-PV-IND	CB	2.0	75	4.7×10^{-4}	2.3×10^2	−32
2-IND-P-IND	CB	2.0	90	6.3×10^{-4}	1.4×10^4	−29
[a]	CB	6.0	85	7.0×10^{-4}	3.7×10^3	−21
3-IND-P-IND	CB	5.0	80	4.1×10^{-4}	1.0×10^2	−19
[a]	CB	5.0	75	5.9×10^{-4}	6.2×10^3	−32

[a] Obtained by the shearing technique on PTS functionalized substrates.

The promising performances previously obtained with 3POIND [31] were confirmed with the first performances obtained from a drop-cast film with field-effect mobility as high as 0.06 $cm^2\,V^{-1}\,s^{-1}$. The on/off ratio and the threshold voltage (V_T) were also good at 2.2×10^5 and −22 V, respectively. As described in Table 3, the parameters that allow the best performances for this compound are a concentration of 1.5 mg/mL in toluene with a thermal treatment at 80 °C in order to evaporate the solvent. Unfortunately, the new synthesized IC derivatives did not show great mobilities with a maximum of 7.6×10^{-4} $cm^2\,V^{-1}\,s^{-1}$ which is probably due to the very poor film-forming ability of these new materials. The on/off ratio was 1.0×10^4 and V_T was −24 V for that particular device. The maxima obtained with such technique are quite misleading, since it is difficult to repeat those performances with other devices and even within the same film because of their poor uniformity.

To solve this problem, the shearing deposition technique could to be useful. It will help to create a uniform film, with highly and oriented crystalline films. Consequently, the mobility observed for drop-cast films have been increased by a factor of 2 by using this new technique. The maximum observed goes from 0.06 to 0.12 $cm^2\,V^{-1}\,s^{-1}$ with an on/off ratio of 5.6×10^6 and a V_T of −31 V. The most efficient films were formed by solubilizing 6.0 mg/mL of material in toluene and heating the substrates at 70 °C. The main difference between the two techniques is that drop-cast films form randomly and discrete highly crystalline zones while sheared films are almost completely covered with oriented highly crystalline areas. For the newly synthesized oligomers, this technique is not so efficient. The highest mobilities observed are increased but not significantly. Furthermore, the problems observed in drop-cast films are recurrent meaning that the derivatives having vinyl link between the IC and the phenyl units hardly form any quality films.

In order to compare the performances of those newly synthesized materials, vacuum-deposited thin films have been tested at different substrate temperature (T_D). Although 3-IND-PV-IND and 2-IND-PV-IND could not be evaporated due to their low vapour pressure, the two molecules without vinyl links have been fully studied and the highest field-effect mobility was obtained with 2-IND-P-IND with $\mu = 7.4 \times 10^{-3}$ $cm^2\,V^{-1}\,s^{-1}$, on/off ratio = 6.4×10^3 and $V_T = -22$ V. For both compounds, the substrate temperature enabling the highest mobilities is 75 °C. The complete results of this study are detailed in Table 4.

Table 4
Field-effect mobility (μ), on/off current ratios, and threshold voltage (V_T) of indolocarbazole derivatives vacuum-deposited on OTS treated SiO_2 surfaces and at different substrate temperatures (T_D).

Compound	T_D (°C)	μ ($cm^2\,V^{-1}\,s^{-1}$)	On/off	V_T (V)
3-IND-P-IND	25	7.2×10^{-4}	2.5×10^4	−15
	60	5.9×10^{-3}	1.4×10^3	−51
	75	7.0×10^{-3}	2.4×10^3	−33
	90	3.7×10^{-3}	1.8×10^6	−4
	125	1.4×10^{-4}	3.0×10^1	−16
2-IND-P-IND	25	1.3×10^{-3}	2.9×10^2	−31
	50	5.3×10^{-3}	1.3×10^4	−31
	75	7.4×10^{-3}	6.4×10^3	−22
	100	No mobility	–	–

The performances of compound 2-IND-P-IND and 3-IND-P-IND are approximately one order of magnitude lower for solution-processed thin films. This is typically observed for organic semiconductors. As shown with 3POIND, the performances are much closer between vacuum-deposited and solution-processed thin films. The main reason could be this semiconductor has the ability to form highly crystalline thin films quite easily. By using sheared films, it was also possible to control the orientation of the crystallite which leads to higher hole mobility.

3. Conclusion

In this study, small molecules based on indolo[3,2-*b*]carbazole derivatives were used for solution processed field-effect transistors. Despite its rigid rod-like structure, it is possible to fine tune the structure to obtain materials with a high solubility. Using different synthetic strategies, 2- and 3-bromoindolo[3,2-*b*]carbazole were successfully obtained for the first time. Five materials were studied extensively through different solution processing techniques, namely drop-casting, shearing, and spin-coating. This last technique leads to the formation of completely amorphous thin films. Highly crystalline films were obtained using the other techniques. Finally, 3POIND shows great promises with a hole mobility of 0.12 $cm^2\,V^{-1}\,s^{-1}$ which is very close to the performances observed for the evaporated thin film (0.20 $cm^2\,V^{-1}\,s^{-1}$) [31]. For the four new materials, the performances were much lower even with evaporated thin films where the field-effect mobility only reached 10^{-3} $cm^2\,V^{-1}\,s^{-1}$. This is most probably due to the numerous conformations that can adopt the four

new derivatives which creates great disorder. Nevertheless, 3POIND has once again shown its great potential for OFET applications and further work on this particular molecule should be done to investigate further.

4. Experimental details

4.1. Characterization

^{1}H and ^{13}C NMR spectra were recorded on a Varian AS400 apparatus in appropriate deuterated solvent solution at 298 K. Chemical shifts were reported as δ values (ppm) relative to internal tetramethylsilane. Differential scanning calorimetry (DSC) analyses were performed on a Mettler Toledo DSC823^e instrument, calibrated with ultrapure indium. UV–vis absorption spectra were taken using a Varian Cary 500 UV–vis-NIR spectrophotometer. Cyclic voltammetry (CV) measurements were recorded on a Solartron 1287 potentiostat and C3 Cell Stand using platinum electrodes at a scan rate of 50 mV s^{-1} against Ag/Ag$^+$ (0.10 M of $AgNO_3$ in acetonitrile) reference electrode in an anhydrous and argon saturated solution of 0.1 M tetrabutylammonium perchlorate (TBAP) (10^{-1} M) in CH_2Cl_2. In these conditions, the oxidation potential (E_{Ox}) of ferrocene was 0.053 V versus Ag/Ag$^+$, whereas the E_{Ox} of ferrocene was 0.343 V versus saturated calomel electrode (SCE). Top contact devices were made according to a literature procedure [54,55]. Highly doped n-type (1 0 0) Si wafers (<0.004 Ω cm) were used as substrates for the devices. SiO_2 layers (unit area capacitance, C = 10 nF cm^{-2}), as gate dielectric, were thermally grown to 3000 Å thickness onto the Si substrates. The SiO_2/Si substrates were then cleaned with acetone and isopropyl alcohol. The wafers were then treated with octadecyl trimethoxysilane ($C_{18}H_{37}Si(OCH_3)_3$, OTS) in solution in dichloroethylene, which was spin-coated onto the substrates before treating with a saturated atmosphere of NH_4OH overnight. Organic films (40 nm) were vacuum-deposited on the treated SiO_2/Si substrates at room temperature and elevated temperatures, as denoted in the text, at a deposition rate of 0.4–0.5 Å s^{-1} and 10^{-6} Torr. The thin-film thickness of each derivative was determined in situ using a quartz-crystal microbalance (QCM). A top-contact thin-film transistor was used for measuring the charge mobility of the indolo[3,2-*b*]carbazole derivatives: gold source and drain electrodes (channel length (L) and width/length (W/L) of 200 lm and ca. 20, respectively) were vacuum-deposited through a shadow mask. The electrical characteristics of the organic field-effect transistors (OFET) devices were measured under accumulation mode using a Keithley 4200-SCS semiconductor parameter analyzer.

4.2. Materials

1,4-Bis(methylphosphonate)benzene was synthesized according to already published procedures [56]. All starting organic compounds were purchased from Aldrich, Alfa Aesar and TCI America and used without further purification. All reactions were carried out under argon at 1 atm unless mentioned otherwise. Some reaction solvents were distilled before use (THF from potassium/benzophenone; acetonitrile from CaH_2). Column chromatography was carried out on silica gel (Size 40–63 μm, pore size 60 Å, Silicycle). All other compounds have been synthesized following procedures described here.

4.2.1. (6-Bromoindol-3-yl)(indol-2-yl) (**5**)

In a flame-dried flask, 5-bromoindole (6.56 g, 33.4 mmol) was solubilized in dichloromethane (84 mL). Dimethylaluminum chloride (45 mL, 1 M in hexanes) was added at −10 °C and the mixture was stirred at 0 °C for 1 h. Afterward, freshly prepared indole-2-carbonyl chloride (33.4 mmol) was added to the mixture, it was allowed to warm up to room temperature and stirred for 12 h at this temperature. Crushed ice in water was then added to the resulting mixture before treating with ammonium chloride (50 mL). The precipitate was filtered and washed with water to afford 8.17 g of the title compound as a green powder. M.P.: 321 °C. (Yield: 72%).

^{1}H NMR (400 MHz, DMSO-d_6): 12.30 (s, 1H); 11.80 (s,1H); 8.54 (s, 2H); 8.09 (m, 1H); 8.43 (d, J = 1.6 Hz, 1H); 7.71 (d, J = 7.9 Hz, 1H); 7.51 (m, 2H); 7.40 (m, 2H); 7.27 (t, J = 7.4 Hz, 1H); 7.09 (t, J = 7.4 Hz, 1H).

^{13}C NMR (100 MHz, DMSO-d_6): 180.20; 137.18; 135.84; 135.28; 134.91; 128.23; 127.31; 125.62; 124.52; 123.58; 122.32; 120.02; 114.49; 114.46; 114.34; 112.54; 107.57.

HRMS: Calculated for $C_{17}H_{11}N_2OBr$: 338.0055. Found: 338.0063 ± 0.0010.

4.2.2. (5-Bromoindol-3-yl)(indol-2-yl)methanone (**6**)

This product was obtained (via 4-bromoindole) following the same procedure used for the synthesis of compound **5** to provide 8.75 g of the title product as a yellow solid. M.P.: 290 °C. (Yield = 67%).

^{1}H NMR (400 MHz, Acetone-d_6): 11.78 (s, 1H); 11.35 (s, 1H); 8.05 (m, 1H); 7.77 (m, 1H); 7.27 (m, 2H); 7.04 (m, 1H); 6.93 (m, 2H); 6.81 (m, 1H); 6.64 (m, 1H).

^{13}C NMR (100 MHz, DMSO-d_6): 180.35; 137.49; 137.25; 135.99; 134.55; 127.36; 125.53; 124.66; 124.59; 123.23; 122.40; 120.09; 115.62; 115.04; 114.96; 112.60; 107.67.

HRMS: Calculated for $C_{17}H_{11}N_2OBr$: 338.0055. Found: 338.0046 ± 0.0010.

4.2.3. (6-Bromoindol-3-yl)(indol-2-yl)methane (**7**)

To a solution of compound **5** (0.500 g, 1.47 mmol) in anhydrous THF (4 mL) was added $LiAlH_4$ in THF (1.0 mol/L, 8.9 mL, 8.84 mmol). The reaction was refluxed for 1 h and then was allowed to cool down to room temperature before the addition of sodium potassium tartrate until no gas is generated from the reaction. The mixture was then filtered through Celite and washed with ether. This ethereal fraction was washed with water. The organic layer was dried over $MgSO_4$ and the solvent was removed under reduced pressure. The crude compound was used for the next step without any further purification.

4.2.4. (5-Bromoindol-3-yl)(indol-2-yl)methane (**8**)

This product was obtained (via compound **6**) following the same procedure used for the synthesis of compound **7** to afford the desired crude compound which was also used without any further purification.

*4.2.5. 2-Bromo-5,11-dihydroindolo[3,2-b]carbazole (**9**)*

To a solution of compound **7** (1.47 mmol) in methanol (3 mL) was added triethylorthoformate (0.109 g, 0.735 mmol) and methanesulfonic acid (0.014 g, 0.147 mmol). After 12 h of stirring at room temperature, the precipitate was filtered and washed with methanol to afford 0.213 g of the title compound as a brown powder. M.P.: >300 °C. (Yield = 44%).

^{1}H NMR (400 MHz, DMSO-d_6): 11.22 (s, 1H); 11.11 (s, 1H); 8.45 (d, J = 2.0 Hz, 1H); 8.21 (d, J = 7.9 Hz, 1H); 8.18 (s, 1H); 8.14 (s, 1H); 7.46 (m, 3H); 7.38 (m, 1H); 7.13 (m, 1H).

^{13}C NMR (100 MHz, DMSO-d_6): 141.29; 139.69; 135.39; 135.21; 127.66; 125.78; 124.64; 123.40; 122.76; 122.40; 121.52; 120.40; 117.74; 112.34; 110.54; 109.55; 101.02; 100.74.

HRMS: Calculated for $C_{18}H_{11}N_2Br$: 334.0106. Found: 334.0100 ± 0.0010.

*4.2.6. 3-Bromo-5,11-dihydroindolo[3,2-b]carbazole (**10**)*

This product was obtained (via compound **8**) following the same procedure used for the synthesis of compound **9** to afford 0.207 g of the title product as a beige solid. M.P.: 275 °C (degradation). (Yield = 42%).

^{1}H NMR (400 MHz, DMSO-d_6): 11.20 (s, 1H); 11.09 (s, 1H); 8.21 (d, J = 7.9 Hz, 1H); 8.17 (d, J = 8.3 Hz, 1H); 8.14 (d, J = 2.9 Hz, 2H); 7.62 (dd, J = 0.4 et 1.8 Hz, 1H); 7.46 (m, 1H); 7.38 (m, 1H); 7.26 (m, 1H); 7.13 (m, 1H).

^{13}C NMR (100 MHz, DMSO-d_6): 141.94; 141.19; 135.33; 135.10; 125.70; 123.09; 122.45; 121.92; 121.88; 121.82; 120.35; 118.07; 117.76; 112.97; 110.55; 100.84; 100.73.

HRMS: Calculated for $C_{18}H_{11}N_2Br$: 334.0106. Found: 334.0100 ± 0.0010.

*4.2.7. 2-Bromo-5,11-dioctylindolo[3,2-b]carbazole (**11**)*

A freshly prepared 50% aq. NaOH solution (2.6 mL) was added to a well-stirred mixture of compound **9** (0.850 g, 2.54 mmol), benzyltriethylammonium chloride (0.120 g, 0.51 mmol), 1-bromooctane (1.97 g, 10.20 mmol), and DMSO (26 mL) in a 100-mL flask under an argon atmosphere. The mixture was stirred at room temperature for 1 h and then heated at 65 °C and maintained at this temperature for 4 h. Subsequently the reaction mixture was cooled down to room temperature and poured into 100 mL methanol with stirring. The precipitated yellow solid was filtered off and washed with water, and three times each with *N,N*-dimethylformamide and methanol to afford the desired compound. M.P.: 120–121 °C. (Yield = 94%).

^{1}H NMR (400 MHz, Acetone-d_6): 8.43 (s, 1H); 8.39 (s, 1H); 8.34 (s, 1H); 8.26 (d, J = 7.7 Hz, 1H); 7.52 (m, 4H); 7.19 (t, J = 7.3 Hz, 1H); 4.54 (t, J = 7.2 Hz, 4H), 1.98 (m, 4H); 1.33 (m, 20H); 0.83 (m, 6H).

^{13}C NMR (100 MHz, CD_2Cl_2): 142.36; 140.78; 136.70; 136.64; 128.50; 126.50; 12,506; 123.92; 123.24; 123.07; 121.98; 120.74; 118.53; 110.80; 110.47; 109.04; 99.56; 99.41; 43.95; 43.82; 32.39; 32.37; 29.99; 29.96; 29.80; 29.78; 29.29; 29.28; 27.91; 27.86; 23.19; 23.18; 14.41; 14.40.

HRMS: Calculated for $C_{34}H_{43}N_2Br$: 558.2609. Found: 558.2596 ± 0.0017.

*4.2.8. 3-Bromo-5,11-dioctylindolo[3,2-b]carbazole (**12**)*

This product was obtained (via compound **10**) following the same procedure used for the synthesis of compound **11** to afford 0.724 g of the title product as a yellow solid. M.P.: 128 °C. (Yield = 87%).

^{1}H NMR (400 MHz, CD_2Cl_2): 8.20 (m, 1H); 8.06 (m, 2H); 8.02 (d, J = 0.8 Hz, 1H); 7.59 (d, J = 1.7 Hz, 1H); 7.49 (m, 1H); 7.44 (m, 1H); 7.32 (dd, J = 1.7 et 8.2 Hz, 1H); 7.22 (m, 1H); 4.39 (m, 4H); 1.94 (m, 4H); 1.34 (m, 20H); 0.85 (m, 6H).

^{13}C NMR (100 MHz, CD_2Cl_2): 142.97; 142.33; 136.79; 136.58; 126.42; 123.63; 123.16; 122.56; 122.38; 121.77; 121.39; 120.70; 119.65; 118.56; 111.98; 109.07; 99.59; 99.33; 43.98; 43.84; 32.40; 30.00; 29.97; 29.80; 29.33; 29.24; 27.91; 27.85; 23.20; 14.41.

HRMS: Calculated for $C_{34}H_{43}N_2Br$: 558.2609. Found: 558.2602 ± 0.0017.

*4.2.9. 2-Formyl-5,11-dioctylindolo[3,2-b]carbazole (**13**)*

In a flame-dried flask, compound **11** (0.550 g, 0.983 mmol) was solubilized in anhydrous THF (25 mL) before cooling down to −78 °C. *n*-Butyllithium (2.5 M, 0.8 mL, 1.97 mmol) was then added dropwise and kept at this temperature for 2 more hours. After the treatment with dimethylformamide (0.11 mL, 1.47 mmol) the reaction was stirred at −78 °C for 1 h. The mixture was allowed to warm up to room temperature and was stirred overnight. The resulting mixture was extracted with dichloromethane and washed three times with water. The combined organic layers were dried over $MgSO_4$ and the solvent was removed under reduced pressure. The crude compound was purified by column chromatography with dichloromethane/hexanes (80/20) as the eluent. 0.424 g of the title compound is obtained as a yellow powder. M.P.: 132 °C. (Yield = 67%).

^{1}H NMR (400 MHz, Acetone-d_6): 10.10 (s, 1H); 8.83 (s, 1H); 8.52 (s, 1H); 8.43 (s, 1H); 8.29 (d, J = 7.7 Hz, 1H); 8.03 (dd, J = 1.2 et 8.4 Hz, 1H); 7.72 (d, J = 8.5 Hz, 1H); 7.60 (d, J = 8.3 Hz, 1H); 7.50 (t, J = 7.8 Hz, 1H); 7.21 (t, J = 7.4 Hz, 1H); 4.62 (t, J = 7.1 Hz, 2H), 4.58 (t, J = 7.1 Hz, 2H), 2.00 (m, 4H); 1.32 (m, 20H); 0.83 (t, J = 6.8 Hz, 6H).

^{13}C NMR (100 MHz, CD_2Cl_2): 191.81; 145.65; 142.31; 137.10; 136.81; 128.30; 127.85; 126.61; 123.89; 123.60; 123.06; 123.02; 120.77; 118.71; 109.16; 109.03; 100.15; 99.83; 44.08; 43.86; 32.38; 32.36; 30.00; 29.92; 29.80; 29.76; 29.34; 29.28; 27.92; 27.83; 23.19; 23.18; 14.41.

HRMS: Calculated for $C_{35}H_{44}N_2O$: 508.3453. Found: 508.3459 ± 0.0015.

*4.2.10. 3-Formyl-5,11-dioctylindolo[3,2-b]carbazole (**14**)*

This product was obtained (via compound **12**) following the same procedure used for the synthesis of compound **13** to afford 0.240 g of the title product as a yellow solid. M.P.: 119 °C. (Yield = 35%).

^{1}H NMR (400 MHz, CD_2Cl_2): 10.16 (s, 1H); 8.35 (d, J = 7.9 Hz, 1H); 8.23 (d, J = 7.6 Hz, 1H); 8.12 (s, 1H); 8.11 (s, 1H); 7.98 (s, 1H); 7.75 (d, J = 8.2, 1H); 7.49 (m, 2H); 7.24 (m, 1H); 4.50 (t, J = 7.3 Hz, 2H); 4.42 (t, J = 7.4 Hz, 2H); 1.97 (m, 4H); 1.32 (m, 20H); 0.85 (m, 6H).

^{13}C NMR (100 MHz, CD_2Cl_2): 192.96; 142.69; 141.69; 138.12; 136.89; 134.42; 128.50; 126.95; 125.15; 122.98;

122.09; 121.00; 120.74; 120.37; 118.69; 110.08; 109.15; 100.10; 99.70; 44.03; 43.84; 32.40; 32.39; 30.00; 29.98; 29.80; 29.41; 29.30; 27.91; 27.88; 23.20; 14.41.

HRMS: Calculated for $C_{35}H_{44}N_2O$: 508.3453. Found: 508.3444 ± 0.0015.

4.2.11. 1,4-Bis(N-dioctyl-2-indolo[3,2-b]carbazole)benzene (2-IND-P-IND) (**15**)

Compound **11** (0.575 g, 1.03 mmol) and benzene-1,4-diboronic acid (0.080 g, 0.48 mmol) were solubilized in degassed THF (5 mL) and K_2CO_3 2 M (2 mL). $Pd(PPh_3)_4$ (0.023 g, 0.02 mmol) was added before refluxing the reaction for 10 h. The mixture was extracted with dichloromethane and wash with BRINE and water. The combined organic layers were dried over $MgSO_4$ and the solvent was removed under reduced pressure. The crude product was purified by column chromatography with hexanes/dichloromethane (75/25) as the eluent to afford 0.166 g of the desired compound. M.P.: 204 °C. (Yield = 33%).

^{1}H NMR (400 MHz, CD_2Cl_2): 8.56 (s, 1H); 8.23 (d, J = 7.6 Hz, 1H); 8.16 (s, 1H); 8.10 (s, 1H); 7.93 (s, 2H); 7.87 (d, J = 8.1 Hz, 1H); 7.50 (m, 3H); 7.23 (t, J = 7.1 Hz, 1H); 4.46 (m, 4H); 1.99 (m, 4H); 1.35 (m, 20H); 0.86 (m, 6H).

^{13}C NMR (100 MHz, Benzene-d_6): 142.74; 142.20; 141.34; 137.51; 137.17; 132.43; 126.51; 124.64; 124.11; 124.00; 121.10; 119.67; 109.60; 109.29; 99.88; 43.67; 32.57; 32.55; 30.12; 30.10; 29.92; 29.89; 29.47; 29.43; 38.00; 27.97; 23.37; 23.35; 14.67.

HRMS: Calculated for $C_{74}H_{90}N_4$: 1034.7165. Found: 1035.7183 ± 0.0030.

4.2.12. 1,4-Bis(N-dioctyl-3-indolo[3,2-b]carbazole)benzene (3-IND-P-IND) (**16**)

This product was obtained (via compound **12**) following the same procedure used for the synthesis of compound **15** to afford 0.290 g of the title product as a yellow solid. M.P.: 161 °C. (Yield = 39%).

^{1}H NMR (400 MHz, CD_2Cl_2): 8.30 (d, J = 8.1 Hz, 1H); 8.22 (d, J = 7.7 Hz, 1H); 809 (s, 1H); 7.94 (s,1H); 7.74 (s, 1H); 7.59 (d, J = 8.1 Hz, 1H); 7.48 (m, 2H); 7.23 (t, J = 6.9 Hz, 1H); 4.51 (d, J = 7.2 Hz, 2H); 4.44 (d, J = 7.1 Hz, 2H); 2.00 (m, 4H); 1.36 (m, 20H); 0.86 (m, 6H).

^{13}C NMR (100 MHz, CD_2Cl_2): 143.38; 142.74; 142.23; 139.81; 137.66; 137.25; 128.93; 124.05; 124.02; 123.75; 123.42; 121.49; 121.10; 118.92; 118.91; 118.70; 109.28; 109.27; 107.76; 99.78; 99.72; 43.66; 43.62; 43.61; 32.59; 32.56; 30.09; 30.07; 29.92; 29.91; 29.42; 28.00; 27.97; 23.37; 14.69.

HRMS: Calculated for $C_{74}H_{90}N_4$: 1034.7165. Found: 1035.7183 ± 0.0030.

4.2.13. 1,4-Bis(N,N′-dioctyl-2-indolocarbazolene)phenylene (2-IND-PV-IND) (**17**)

To a solution of compound **13** (0.345 g, 0.678 mmol) and 1,4-bis(methylphosphonate)benzene (0.117 g, 0.308 mmol) in anhydrous THF (7 mL) was added potassium *t*-butoxide (0.294 g, 2.62 mmol). The mixture was stirred at room temperature for 12 h and was then dropped in water. The precipitate was washed with methanol and water. Afterward the product was washed by Soxhlet with methanol in order to obtain 0.313 g of the pure yellow compound. M.P.: 217 °C. (Yield = 93%).

^{1}H NMR (400 MHz, CD_2Cl_2): 8.40 (d, J = 1.7 Hz, 2H); 8.21 (d, J = 7.7 Hz, 2H); 8.12 (d, J = 0.6 Hz, 2H); 8.07 (d, J = 0.6 Hz, 2H); 7.73 (dd, J = 1.6 et 8.4 Hz, 2H); 7.63 (s, 4H); 7.45 (m, 8H); 7.23 (m, 4H); 4.44 (m, 4H); 1.98 (m, 4H); 1.36 (m, 20H); 0.87 (m, 6H).

^{13}C NMR (100 MHz, Benzene-d_6): 142.75; 142.46; 17.86; 137.45; 137.22; 130.35; 129.02; 127.48; 127.44; 126.58; 126.44; 125.76; 124.42; 124.13; 123.97; 121.12; 121.11; 119.51; 119.50; 109.40; 109.30; 99.94; 99.88; 43.76; 43.73; 43.72; 43.70; 32.56; 30.12; 30.08; 29.91; 29.46; 28.03; 27.98; 27.96; 23.36; 14.68.

HRMS: Calculated for $C_{78}H_{94}N_4$: 1086.7478. Found: 1086.7452 ± 0.0032.

4.2.14. 1,4-Bis(N-dioctyl-3-indolocarbazolene)phenylene (3-IND-PV-IND) (**18**)

This product was obtained (via compound **14**) following the same procedure used for the synthesis of compound **16** to afford 0.120 g of the title product as a yellow solid. M.P.: 230 °C. (Yield = 75%).

^{1}H NMR (400 MHz, CD_2Cl_2): 8.20 (t, J = 8.1 Hz, 4H); 8.05 (d, J = 7.0 Hz, 4H); 7.65 (s, 4H); 7.59 (s, 2H); 7.45 (m, 8H); 7.32 (d, J = 16.3 Hz, 2H); 7.22 (t, J = 7.8 Hz, 2H); 4.44 (m, 4H); 1.97 (m, 4H); 1.35 (m, 20H); 0.87 (m, 6H).

^{13}C NMR (100 MHz, CD_2Cl_2): 142.64; 142.29; 137.43; 137.22; 136.69; 135.67; 130.23; 127.92; 127.34; 126.24; 123.34; 123.23; 123.14; 123.12; 120.82; 120.62; 118.45; 117.41; 108.99; 107.05; 99.32; 99.21; 43.84; 32.44; 32.39; 30.03; 30.01; 29.84; 29.80; 29.37; 29.33; 27.92; 23.21; 23.19; 14.42; 14.40.

HRMS: Calculated for $C_{78}H_{94}N_4$: 1086.7478. Found: 1086.7494 ± 0.0032.

Acknowledgements

This work was supported by discovery and strategic grants from the Natural Sciences and Engineering Research Council (NSERC) of Canada. P.L.T. Boudreault thanks the NSERC for a Ph.D. scholarship (BESC – S). The authors gratefully acknowledge Gaurav Giri and Dr. Joon Hak Oh for shearing and XRD experiments. We acknowledge the use of shared facilities supported by the National Science Foundation Center for Polymer and Macromolecular Assemblies (CPIMA).

References

[1] T.A. Skotheim, J.R. Reynolds, Handbook of Conducting Polymers, Taylor and Francis Group, Boca Raton, 2007.
[2] H. Klauk, Organic Electronics, Wiley-VCH, Weinheim, 2006.
[3] G. Hadziioannou, G.G. Malliaras, Semiconducting Polymers, Wiley-VCH, Weinheim, 2007.
[4] Z. Bao, J. Locklin, Organic Field-Effect Transistors, CRC Press, Boca Raton, 2007.
[5] C. Reese, M. Roberts, M.-M. Ling, Z. Bao, Mater. Today 7 (2004) 20–27.
[6] I. McCulloch, M. Heeney, C. Bailey, K. Genevicius, I. Macdonald, M. Shkunov, D. Sparrowe, S. Tierney, R. Wagner, S.W. Zhang, M.L. Chabinyc, R.J. Kline, M.D. McGehee, M.F. Toney, Nat. Mater. 5 (2006) 328–333.
[7] K. Takimiya, H. Ebata, K. Sakamoto, T. Izawa, T. Otsubo, Y. Kunugi, J. Am. Chem. Soc. 128 (2006) 12604–12605.

[8] O.D. Jurchescu, J. Baas, T.T.M. Palstra, Appl. Phys. Lett. 84 (2004) 3061–3063.
[9] V. Sundar, J. Zaumseil, V. Podzorov, E. Menard, R. Willett, T. Someya, M. Gershenson, J.A. Rogers, Science 303 (2004) 1644–1646.
[10] H. Klauk, M. Halik, U. Zschieschang, G. Schmid, W. Radlik, J. Appl. Phys. 92 (2002) 5259–5263.
[11] H. Sirringhaus, N. Tessler, R.H. Friend, Science 280 (1998) 1741–1744.
[12] H. Pan, Y. Li, Y. Wu, P. Liu, B.S. Ong, S. Zhu, G. Xu, J. Am. Chem. Soc. 129 (2007) 4112–4113.
[13] M. Zhang, H.N. Tsao, W. Pisula, C. Yang, A.K. Mishra, K. Mullen, J. Am. Chem. Soc. 129 (2007) 3472–3473.
[14] H.N. Tsao, D. Cho, J.W. Andreasen, A. Rouhanipour, D.W. Breiby, W. Pisula, K. Müllen, Adv. Mater. 21 (2009) 209–212.
[15] P.T. Herwig, K. Müllen, Adv. Mater. 11 (1999) 480–483.
[16] A. Afzali, C.D. Dimitrakopoulos, T.L. Breen, J. Am. Chem. Soc. 124 (2002) 8812–8813.
[17] A.R. Murphy, J.M.J. Frechet, P. Chang, J. Lee, V. Subramanian, J. Am. Chem. Soc. 126 (2004) 1596–1597.
[18] J.E. Anthony, J.S. Brooks, D.L. Eaton, S.R. Parkin, J. Am. Chem. Soc. 123 (2001) 9482–9483.
[19] M.M. Payne, S.A. Odom, S.R. Parkin, J.E. Anthony, Org. Lett. 6 (2004) 3325–3328.
[20] M.M. Payne, S.R. Parkin, J.E. Anthony, C.C. Kuo, T.N. Jackson, J. Am. Chem. Soc. 127 (2005) 4986–4987.
[21] H.A. Becerril, M.E. Roberts, Z. Liu, J. Locklin, Z. Bao, Adv. Mater. 20 (2008) 2588–2594.
[22] Z. Liu, H.A. Becerril, M.E. Roberts, Y. Nishi, Z. Bao, IEEE Trans. Electron Devices 56 (2009) 176–185.
[23] P. Gao, D. Beckmann, H.N. Tsao, X. Feng, V. Enkelmann, W. Pisula, K. Mullen, Chem. Commun. (2008) 1548–1550.
[24] P. Gao, D. Beckmann, H.N. Tsao, X. Feng, V. Enkelmann, M. Baumgarten, W. Pisula, K. Müllen, Adv. Mater. 21 (2009) 213–216.
[25] P.-L.T. Boudreault, N. Blouin, M. Leclerc, Adv. Polym. Sci. 212 (2008) 99–124.
[26] N. Blouin, M. Leclerc, Acc. Chem. Res. 41 (2008) 1110–1119.
[27] P.-L.T. Boudreault, S. Beaupré, M. Leclerc, Polym. Chem. 1 (2010) 127–136.
[28] J.-F. Morin, M. Leclerc, D. Adès, A. Siove, Macromol. Rapid Commun. 26 (2005) 761–778.
[29] J.F. Morin, N. Drolet, Y. Tao, M. Leclerc, Chem. Mater. 16 (2004) 4619–4626.
[30] N. Drolet, J.F. Morin, N. Leclerc, S. Wakim, Y. Tao, M. Leclerc, Adv. Funct. Mater. 15 (2005) 1671–1682.
[31] P.-L.T. Boudreault, S. Wakim, N. Blouin, M. Simard, C. Tessier, Y. Tao, M. Leclerc, J. Am. Chem. Soc. 129 (2007) 9125–9136.
[32] P.-L.T. Boudreault, S. Wakim, M.L. Tang, Y. Tao, Z. Bao, M. Leclerc, J. Mater. Chem. 19 (2009) 2921–2928.
[33] S. Wakim, J. Bouchard, M. Simard, N. Drolet, Y. Tao, M. Leclerc, Chem. Mater. 16 (2004) 4386–4388.
[34] Y. Wu, Y. Li, S. Gardner, B.S. Ong, J. Am. Chem. Soc. 127 (2005) 614–618.
[35] Y. Li, Y. Wu, S. Gardner, B.S. Ong, Adv. Mater. 17 (2005) 849–853.
[36] S. Wakim, N. Blouin, E. Gingras, Y. Tao, M. Leclerc, Macromol. Rapid Commun. 28 (2007) 1798–1803.
[37] Y. Li, Y. Wu, B.S. Ong, Macromolecules 39 (2006) 6521–6527.
[38] N. Blouin, A. Michaud, S. Wakim, P.-L.T. Boudreault, M. Leclerc, B. Vercelli, S. Zecchin, G. Zotti, Macromol. Chem. Phys. 207 (2006) 166–174.
[39] N. Blouin, M. Leclerc, B. Vercelli, S. Zecchin, G. Zotti, Macromol. Chem. Phys. 207 (2006) 175–182.
[40] Y. Zou, D. Gendron, R. Badrou-Aïch, A. Najari, Y. Tao, M. Leclerc, Macromolecules 42 (2009) 2891–2894.
[41] T. Okauchi, M. Itonaga, T. Minami, T. Owa, K. Kitoh, H. Yoshino, Org. Lett. 2 (2000) 1485–1487.
[42] N. Wahlström, B. Stensland, J. Bergman, Synthesis (2004) 1187–1194.
[43] R. Gu, A. Hameurlaine, W. Dehaen, Synlett 10 (2006) 1535–1538.
[44] M. Belletete, P.-L.T. Boudreault, G. Durocher, M. Leclerc, THEOCHEM 824 (2007) 15–22.
[45] Y. Sun, Y. Ma, Y. Liu, Y. Lin, Z. Wang, Y. Wang, C. Di, K. Xiao, X. Chen, W. Qiu, B. Zhang, G. Yu, W. Hu, D. Zhu, Adv. Funct. Mater. 16 (2006) 426–432.
[46] B.C. Thompson, Y.G. Kim, J.R. Reynolds, Macromolecules 38 (2005) 5359–5362.
[47] H. Meng, M. Bendikov, G. Mitchell, R. Helgeson, F. Wudl, Z. Bao, T. Siegrist, C. Kloc, C.H. Chen, Adv. Mater. 15 (2003) 1090–1093.
[48] M. Heeney, C. Bailey, K. Genevicius, M. Shkunov, D. Sparrowe, S. Tierney, I. McCulloch, J. Am. Chem. Soc. 127 (2005) 1078–1079.
[49] H.E. Katz, Z. Bao, J. Phys. Chem. B 104 (2000) 671–678.
[50] H. Sirringhaus, P.J. Brown, R.H. Friend, M.M. Nielsen, K. Bechgaard, B.M.W. Langeveld-Voss, A.J.H. Spiering, R.A.J. Janssen, E.W. Meijer, P. Herwig, D.M.D. Leeuw, Nature 401 (1999) 685–688.
[51] A. Salleo, M.L. Chabinyc, M.S. Yang, R.A. Street, Appl. Phys. Lett. 81 (2002) 4383–4385.
[52] M. Shtein, J. Mapel, J.B. Benziger, S.R. Forrest, Appl. Phys. Lett. 81 (2002) 268–270.
[53] J.A. Voorthuyzen, K. Keskin, P. Bergveld, Surf. Sci. 187 (1987) 201–211.
[54] M.M. Ling, Z. Bao, Chem. Mater. 16 (2004) 4824–4840.
[55] J. Locklin, M.E. Roberts, S.C.B. Mannsfeld, Z. Bao, Polym. Rev. 46 (2006) 79–101.
[56] J. Shi, S. Zheng, Macromolecules 34 (2001) 6571–6576.

(PMMA), polystyrene (PS) and poly-4-vinylphenol (PVP) [24,25] and solid state polyelectrolytes which induce high charge carrier density due to the large electric fields created by ionic charge buildup in the electrolyte [26,27].

Barium titanate ($BaTiO_3$) is widely employed in various electronic and electro-optic applications due to its high dielectric constant [28–31]. Previously, $BaTiO_3$ nanoparticles have been synthesized hydrothermally at moderate temperatures and pressures. A method that has received much less attention is the glycothermal synthesis of $BaTiO_3$. Reports [32,33] have shown that glycothermal processing method provides a simple low temperature route for producing tetragonal $BaTiO_3$ nanoparticles. In addition to easy control over the size and shape of the nanoparticles, the glycothermal process significantly reduces the reaction pressure, which is a critical issue for large-scale production. The purpose of this study is firstly to investigate the optimum condition for preparation of uniform nano-size barium titanate particles by the glycothermal method and to employ these solution processable high-k $BaTiO_3$ nanoparticles as the dielectric layer in an organic field effect transistor to reduce the working voltages.

2. Experimental

2.1. Preparation of barium titanate nanocrystals

$BaTiO_3$ nanocrystals were synthesized from barium hydroxide ($Ba(OH)_2{\cdot}8H_2O$, 99.3%, Fisher chemical) and amorphous titanium hydrous gel precursors. The titanium hydrous gel was prepared by diluting the stoichiometric amount of titanium (IV) isopropoxide (Fluka) in 12.5 mL of 2-propanol (Pr^iOH, 99%, Sigma–Aldrich). A mixture solution of 2-propanol and deionized water (1:2, 1:1, 2:1 M ratios of H_2O:Pr^iOH) was added into the above solution to form a titania gel. The gel was washed with CO_2-free deionized water for three times and added into barium hydroxide solution (0.197 g of $Ba(OH)_2$ and 12.5 mL of 1,4-butanediol). The suspension was aged under vigorous stirring for 10 min before transferred to a Teflon-lined stainless steel autoclave. The sealed vessel was placed into the oven and heated at various reaction temperatures (180, 200, 220, 240 °C at fixed ramping rate of 3 °C/min) and times (5, 10, 16, and 20 h). After reaction, the product was cooled to room temperature and washed with pH-adjusted H_2O (CO_2-free deionized water with pH ~10, adjusted by concentrated ammonia solution) for three times to remove the unreacted barium precursor. $BaTiO_3$ powder was separated from the solution part by ultracentrifugation (9000 rpm for 5 min) and dried at 100 °C for 24 h.

2.2. Sol–gel silica synthesis

Sol–gel (SG) silica solution was prepared by a two-step acid–base catalyst procedure by mixing tetraethylorthosilicate (TEOS, 99.9% purity), ethanol, water and HCl in various molar ratios: 1:10:3.5:0.003. After stirring at room temperature for 90 min, 150 μl of the base catalyst (0.1 M NH_4OH) was then added into the solution. The solution was aged for three days under constant stirring at room temperature and was filtered through a 0.2 μm PTFE membrane filter before spincoating.

2.3. Structural characterization

The phase content of the $BaTiO_3$ nanocrystals was extracted from powder X-ray diffraction (XRD) patterns obtained with a Shimadzu diffractometer operating at 4 kW and using Cu Kα radiation. Materials were prepared for diffraction by packing the $BaTiO_3$ powder on a glass slide (2×2 cm) with diffracted intensity collected by step scanning over the 2θ range 10–140° in increments of 0.02° and a dwell time of 0.20 s per step. Rietveld refinement as implemented in TOPAS 3.0 was used for quantitative phase analysis with the starting model being $BaTiO_3$ [34], $BaCO_3$ [35], Ba_2TiO_4 [36] and $BaTi_4O_9$ [37]. For each analysis, a background polynomial, scale factor, cell parameters and zero point correction were refined, to determine phase content, check for mass balance, identify phase transformations and estimate crystal size. Transmission electron microscopy (TEM) was conducted in high resolution mode with a large objective aperture using a JEOL 2100F instrument operating at 200 kV. The TEM samples were prepared by immersion of a holey carbon coated copper grid in an ultrasonically treated $BaTiO_3$ suspension followed by dried at room temperature.

2.4. Device fabrication and electrical characterization

Organic transistors and capacitors were fabricated on highly doped silicon substrates which functioned as the gate electrode. The dielectric layer was prepared using $BaTiO_3$ nanoparticles dispersed in ethanol (99%, Fluka) at 5, 10 and 20 wt.% of $BaTiO_3$, spun coated on the substrate at a coating speed of 2000 rpm for 120 s. The specimens were calcined at 220 °C for 1 h before applying the surface modification layer of sol–gel silica. The original sol–gel silica solution was diluted (50%) and spun coated to form a layer ~150 nm thick. The samples were then dried at ambient conditions at 60 °C with slow heating rate. Gold electrodes (500 μm squares) were evaporated to form capacitor structures. A 45 nm pentacene (Sigma Aldrich) layer was evaporated on the dielectric as the organic semiconductor followed by gold source-drain electrodes to form organic field effect transistors. Capacitors and OFETs were also prepared without the sol–gel capping layer for comparison. I–V and C–V characteristics were measured using a Keithley 4200-SCS semiconductor parametric analyzer and a HP4284 LCR meter, respectively in a TTP-6 probe station at low vacuum.

3. Results and discussion

3.1. Synthesis of $BaTiO_3$ nanocrystals

3.1.1. Effect of reaction time

The influence of reaction time to the crystal structure and size of $BaTiO_3$ was studied at 5, 10, 16 and 20 h (reaction temperature 220 °C, 1:1 M ratio of H_2O:Pr^iOH). The

crystal structures of products were analyzed from their XRD patterns using the Rietveld refinement. The mixture phases of barium compounds ($BaTiO_3$, $BaCO_3$ and Ba_2TiO_4) were obtained from materials synthesized at 5–20 h, where cubic phase $BaTiO_3$ (Eq. (1)) is a major component (Table 1). The crystal size of products (10–13 nm) was not influenced by the variation of reaction time (Table 1 and Fig. 1).

Although CO_2-free DI-H_2O was introduced into the system to prevent the formation of $BaCO_3$, the reaction between $Ba(OH)_2$ and trace amount of CO_2 molecules from the air occurred during the transfer of suspension into the autoclave vessel (Eq. (2)). The formation of $BaCO_3$ can partially be prevented by performing the reaction at longer periods (reduced from 13% to 8% at 5 and 16 h, respectively) due to the reaction between $BaCO_3$ and some titania hydrous gel or synthesized $BaTiO_3$ product, forming the $BaTiO_3$ and Ba_2TiO_4 structures [38–40] (Table 1, Eqs. (3) and (4)). However, the amount of $BaCO_3$ phase became larger at reaction time 20 h (11%) through the reaction between Ba_2TiO_4 and free CO_2 molecules those were subsequently produced at long period (Eq. (5)). Thus, the reaction time 16 h was selected for further studies.

$$Ba(OH)_2 + TiO_2 \rightarrow BaTiO_3 + H_2O \quad (1)$$

$$Ba(OH)_2 + CO_2 \rightarrow BaCO_3 + H_2O \quad (2)$$

$$BaCO_3 + TiO_2 \rightarrow BaTiO_3 + CO_2 \quad (3)$$

$$BaCO_3 + BaTiO_3 \rightarrow Ba_2TiO_4 + CO_2 \quad (4)$$

$$Ba_2TiO_4 + CO_2 \rightarrow BaCO_3 + BaTiO_3 \quad (5)$$

3.1.2. Effect of reaction temperature

The reaction time which resulted in the highest percentage of $BaTiO_3$ (16 h) was selected for the variation of reaction temperature (180, 200, 220 and 240 °C) at fixed molar ratio of H_2O:Pr^iOH (1:1).

At low temperature (180 °C) where the energy is moderate for the reaction between $Ba(OH)_2$ and titania hydrous gel precursors, product with lowest percentage of $BaTiO_3$ (76%) and large amount of $BaCO_3$ (15%) was formed because of the reaction between $Ba(OH)_2$ and CO_2 molecules (Eq. (2)). When reaction temperature was increased to 220 °C, the improvement of $BaTiO_3$ phase (85%) was obtained with lower amount of $BaCO_3$ (8%). However, the development of $BaCO_3$ structure became higher with trace amount of Ba_2TiO_4 at 240 °C. This might occur due to the higher stability of $BaCO_3$ phase at high reaction temperature which reduces the number of $BaCO_3$ molecules reacting with $BaTiO_3$ (Eq. (3)).

3.1.3. Effect of H_2O:Pr^iOH molar ratio

The influence of H_2O:Pr^iOH molar ratio on the formation of titanium hydrous gel and $BaTiO_3$ nanocrystals was studied at 2:1, 1:1 and 1:2 M ratios (reaction temperature

Table 1
The influence of synthesis conditions on the crystal size and crystal structure of $BaTiO_3$ nanocrystals.

Sample	H_2O:Pr^iOH (molar ratio)	Reaction temperature (°C)	Reaction time (h)	% by weight of barium compound			Average crystal size[a] (nm)
				$BaTiO_3$	Ba_2TiO_4 (%)	$BaCO_3$ (%)	
BT1	1:2	220	16	78	11	11	12
BT2	1:1	220	16	85	8	8	10
BT3	2:1	220	16	84	7	9	15
BT4	1:1	220	5	81	5	13	10
BT5	1:1	220	10	81	6	12	13
BT6	1:1	220	20	83	6	11	12
BT7	1:1	180	16	76	8	15	10
BT8	1:1	240	16	83	5	12	15

[a] Determined from TEM micrographs.

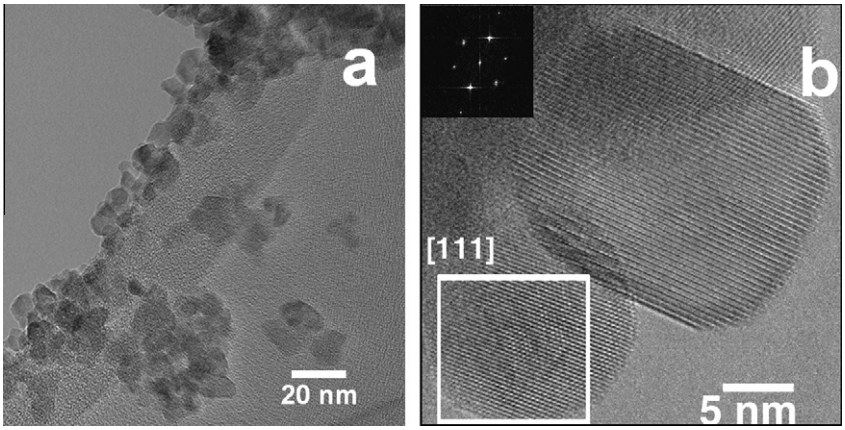

Fig. 1. (a) TEM images of $BaTiO_3$ nanocrystals synthesized at 220 °C, 16 h and 1:1 M ratio of H_2O:Pr^iOH. (b) High resolution TEM image of $BaTiO_3$ nanocrystals with [1 1 1] preferred orientation at, insert is diffraction pattern of the selected area, the position of the reflections show cubic $BaTiO_3$.

220 °C and time 16 h). The optimal H_2O:Pr^{i}OH molar ratio for complete sol–gel process of titania hydrous gel was reported at 1:1 M ratio, in which the highest percentage of $BaTiO_3$ (85%) was obtained (Fig. 2). The incomplete formation of titania gel at less H_2O content causes the lower amount of Ti source for the synthesis of $BaTiO_3$, thus, reduces the amount of final product and increases the extra phases of barium compounds (78% $BaTiO_3$).

3.2. Application of $BaTiO_3$ nanoparticles in OFETs

3.2.1. Dielectric properties of $BaTiO_3$ nanoparticles

The dielectric properties of the as-synthesized nanoparticles (BT2, particle size ~10 nm) were measured by fabricating pellets of the material through compacting. The pellets were calcined at 220 °C for firming of the films before testing at room temperature. It has been shown previously that there is a relationship between the particle size and dielectric constant of $BaTiO_3$ [41–43]. It is generally recognized that the permittivity of $BaTiO_3$ ceramics increases with decreasing grain size at the micron level while it decreases with particle size in submicron ranges. Previous reports have indicated a dielectric constant of 15,000 at 68 nm and 5000 at 140 nm for impurity free $BaTiO_3$ synthesized by thermal decomposition method [41]. Fig. 3 illustrates the dielectric constant of the Barium titanate nanoparticle pellets measured at frequencies from 1 kHz to 1 MHz. The effective dielectric constant reduces from 3500 to 150 in this frequency range. The rather large frequency dispersion in the measured nanoparticles may be caused due to adsorbed molecules as well as the large number of interfaces in the pellet. The temperatures applied during the pellet fabrication (220 °C) is insufficient

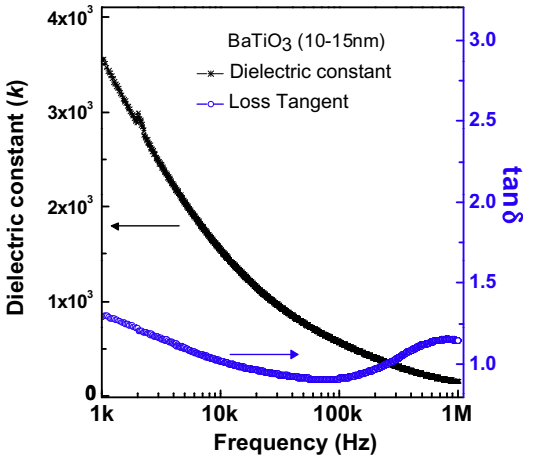

Fig. 3. The dielectric constant and loss tangent of barium titanate pellets measured from 1 kHz to 1 MHz.

to remove adsorbents [44] and maintains the nanocrystalline morphology. Adsorbed water molecules at the nanoparticles' surface can contribute to the total polarizability of the film through Maxwell–Wagner type interfacial polarization mechanism [45]. A k value of 150 for the 10–15 nm sized nanoparticles measured in this experiment is consistent with previous published reports [46] and is indicative of the size effect in barium titanate nanoparticles.

3.2.2. $BaTiO_3$ nanoparticle film as dielectric layer in OFETs

The dielectric layer was prepared using $BaTiO_3$ nanoparticles diluted in ethanol at three different concentrations,

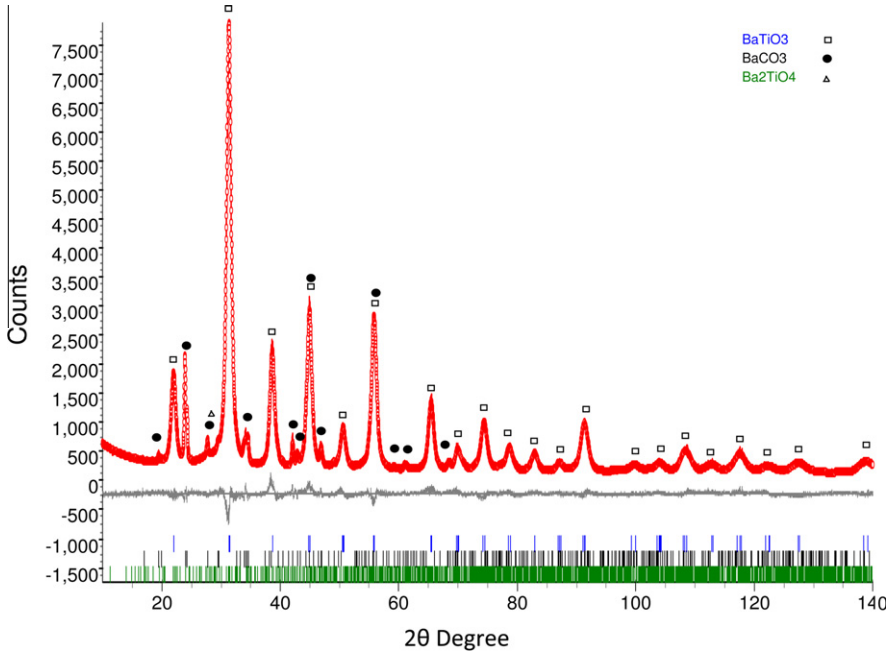

Fig. 2. X-ray diffraction profile of $BaTiO_3$ nanocrystals synthesized at 220 °C, 16 h and 1:1 M ratio of H_2O:Pr^{i}OH. The lower trace is the difference between the calculated and experimental intensities. The Bragg markers from upper to lower are cubic $BaTiO_3$, $BaCO_3$ and Ba_2TiO_4. The phase proportions are summarized in Table 1.

5 wt.% (*T*1), 10 wt.% (*T*2) and 20 wt.% (*T*3). The dielectric film thicknesses of *T*1, *T*2 and *T*3 are 1.2, 2 and 3 μm, respectively. As the concentration of $BaTiO_3$ increases, the surface becomes rougher due to agglomeration effects in the ethanol suspension. The calculated *k* value of the dielectric layer for each sample is shown in Table 2. The relatively lower dielectric constants of the spun coated films (in contrast to pellet measurements) may be attributed to poor film quality that can incorporate voids. Functional devices were obtained for samples fabricated from spin coating 5 wt.% solution and 10 wt.% solution of the $BaTiO_3$ nanoparticles as the dielectric layer (*T*1, *T*2, Table 2). However, devices fabricated from 20 wt.% solutions (*T*3) were not functional, which may be traced to the high surface roughness of the device. The thickness of the pentacene layer (45 nm) evaporated on the dielectric is not enough to form a continuous layer across the active area of the transistor.

From Table 2, we can distinguish that the capacitance per unit area of the device tends to increase with increasing amount of $BaTiO_3$ nanoparticles. Even though the *k* value increases substantially for the barium titanate nanoparticle dielectric, the mobility of the device is far lesser than that of pentacene devices fabricated on silicon dioxide substrates. In addition the on/off ratio decreases, while there is a slight improvement in the threshold voltage. The reduction in the mobility of the device with increasing $BaTiO_3$ concentration, illustrates the critical role played by the semiconductor–dielectric interface. The rough surface of the $BaTiO_3$ does not allow the pentacene molecules to form large grains, resulting in a large grain boundary density and charge traps. $BaTiO_3$ with high dielectric constant is a highly polar compound and is considered as a source of trap at the semiconductor/dielectric interface, which further affects charge carrier mobility adversely [17,47]. In order to improve the active layer morphology and to reduce the number of electrical traps, an insulating overlayer needs to be pursued.

We have previously studied sol–gel silica made from tetraethylorthosilicate precursor as an OFET gate dielectric and interfacial modification layer [8,48,49]. The low surface energy of the sol–gel silica induces crystalline growth of the organic semiconductor which results in enhancement of charge carrier mobilities. Thus the $BaTiO_3$ nanoparticle layer was covered by a second layer consisting of sol–gel silica, which also acts as the planarization layer (Fig. 4(a)). SEM was used to measure the cross sectional thickness of the devices. The dielectric layer thicknesses of *D*1, *D*2 and *D*3 were 1.3, 2.1 and 3.1 μm, respectively. It has already been shown that as the concentration of $BaTiO_3$ increases, the surface become rougher. Table 2 and Fig. 4(b)–(g) shows the improved electrical characteristics of transistors with the sol–gel silica layer. In contrast to the previous samples without the sol–gel layer, the devices possess higher mobility proving that the sol–gel silica can effectively act as planarization layer by reducing the surface roughness of the device. The higher mobility values can also be induced by the favourable low surface energy of the sol–gel silica. The output characteristics in Fig. 4(b)–(d) indicate that the devices have good saturation behaviour. Fig. 4(e) illustrates that there is a hysteresis in the transfer characteristics of the transistor, although no particular trend with the concentration of the nanoparticles is observed. The origin of the hysteresis is most likely from the localization of the charge carriers at the semiconductor–dielectric interface. As Fig. 4(g) illustrates, there is little hysteresis in the *C*–*V* characteristics of the dielectric, ruling out remnant polarization as a reason for the hysteresis.

Please note that the dielectric constant of the top sol–gel silica layer was measured by spin coating the layer on top of a silicon dioxide substrate to calculate the *k*. From Table 2, we find that the capacitance per unit area of the device does not vary much with the changing concentration of the $BaTiO_3$ nanoparticles However if we compare these devices to the *k* value of the samples without sol–gel planarization layer, it is considerably lower. This is caused by the lower capacitance of the device, which is affected by the lower dielectric constant of the additional sol–gel layer as well as the increased thickness. This leads to a reduction in the effective dielectric constants (k_{eff}). Despite this, the bilayer of the two solution processable dielectrics display dielectric constants of up to 44, indicating the advantages of this material combination. The mobility of these devices are much higher than the one without sol–gel planarization layer. Charge carrier mobilities in devices which incorporated 10 wt.% of $BaTiO_3$ in the dielectric layer increased by two orders of magnitude with the deposition of the sol–gel layer. The on/off ratio of the devices, which is critical for their application in logical circuitry, is also improved by the inclusion of the sol–gel layer. Another phenomenon observed is the decrease of the charge carrier mobility with increasing dielectric constant. This can be explained by the nature of polarons at the semiconductor/dielectric interface. Interface dipoles on the insulator surface distorts (polarize) individual electronic states of the HOMO of pentacene. At the interface, polar compounds cause dipolar disorder in the density of states (DOS) of the semiconductor leading to the broadening of the DOS. As a result, the temperature activation of carrier hopping is increased and the mobility is reduced

Table 2
Performance of transistors fabricated on single layer $BaTiO_3$ (*T*1–*T*3) and dual layer (*D*1–*D*3).

Sample	C (nF/cm^2)	k_{eff}	μ_{sat} (cm^2/Vs)	V_T (V)	I_{on}/I_{off}	Subthreshold swing (V/dec)
*T*1	14.7	19.93	0.0086 ± 0.0003	−3.40 ± 0.90	1.41×10^3	2.26
*T*2	15.7	35.48	0.0017 ± 0.00039	−1.06 ± 0.60	7.62×10^3	2.11
*T*3	17.4	58.98	–	–	–	–
*D*1	12.2	17.92	0.370 ± 0.010	−4.94 ± 0.32	1.02×10^4	1.52
*D*2	12.1	29.40	0.311 ± 0.014	−2.99 ± 0.18	2.46×10^5	1.22
*D*3	12.4	43.44	0.022 ± 0.003	−3.24 ± 0.34	6.44×10^4	1.29

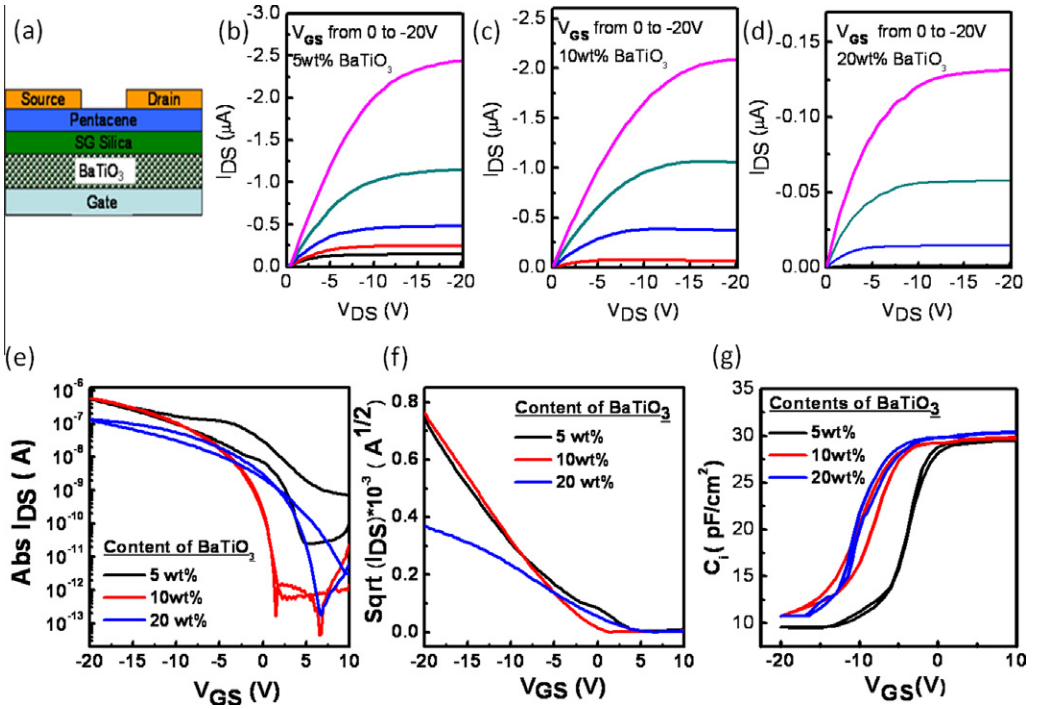

Fig. 4. (a) OFET device structure with $BaTiO_3$ dielectric and with sol–gel overlayer. I_D–V_D characteristics of OFETs with dielectric formed by spin coating (b) 5 wt.% $BaTiO_3$, (c) 10 wt.% $BaTiO_3$, and (d) 20 wt.% $BaTiO_3$ nanoparticles with sol–gel overlayer. (e) I_D–V_G characteristics of OFETs with sol–gel overlayer deposited on $BaTiO_3$ dielectric (double sweep). (f) Square root of ID vs VGS used to extract charge carrier mobilities (g) *C*–*V* characteristics of the dielectric stack.

[17,47]. The electrostatic potential created by the induced polarization exerts an attractive force on the charge carrier itself that increases the tendency toward carrier self-trapping. This self-trapping tendency increases with increasing dielectric constant and leads to the reduction of mobility [6,50].

Despite the use of a high-*k* dielectric layer, the transistors described in this study require working voltages of about 20 V to obtain good drain currents. This is indicative of the important role played by the charge carrier mobility and the number of charge carrier traps at the semiconductor–dielectric interface. The use of a high dielectric constant layer has to be coupled with good surface properties to form favourable semiconductor morphologies that result in good mobilities. Another factor to consider here is the thickness of the dielectrics (ranging from 1 to 3 μm) used in this study. A reduction in the thicknesses of these dielectrics down to 300–400 nm range, while maintaining good dielectric integrity is necessary to realize low voltage operation. Efforts in this direction are underway.

4. Conclusions

In this research, $BaTiO_3$ single crystal nanoparticles were successfully synthesized using the glycothermal process. The experiments showed that the synthesized $BaTiO_3$ nanoparticles have the average particle size of 5–15 nm. It is exhibited that the size and purity of $BaTiO_3$ nanoparticles can be controlled by reaction condition, such as reaction temperature, reaction time and the ratio of hydrolysis agent. An optimum reaction temperature exists in producing nano-size particles, which is 220 °C based on this experimental conditions. However, for both reaction time and temperature, a compromise between the particle size and phase-purity should be considered when deciding the two parameters in order to produce the most desired properties of the nanoparticles.

The direct utilization of barium titanate particles as the dielectric was also partially successful. Too high a concentration of the nanoparticles, results in a rough surface that decreases mobility and has poor characteristics. The use of a sol–gel silica overlayer results in improvement of the device behaviour due to the planarization effects and better semiconductor dielectric morphology. Previous reports have shown that the application of a thin polymer layer planarizes the rough surface of nanocomposite layers and can improve the interfacial properties, including reducing the trap density and changing the relative surface energies between the layers [51–53]. However, the additional layer increases the thickness of the device, which then lowers the capacitance. In addition, these polymers have low dielectric constant thus reducing the effective capacitance. The final result is a high threshold voltage which is unfavorable to the device performance. The combination of the materials described in this manuscript, barium titanate nanoparticle layer with a sol–gel silica overlayer has many advantages. It helps to reduce the surface roughness, which then improves the mobility and on/off ratio of the

devices, while maintaining the high dielectric constant of the dielectric layer. It has already been shown that sol–gel silica has favourable surface properties that promote crystalline pentacene growth. Thus this combination of low temperature solution processable dielectrics is of potential for implementation in low voltage organic electronics.

References

[1] C.D. Dimitrakopoulos, P.R.L. Malenfant, Organic thin film transistors for large area electronics, Advanced Materials 14 (2002) 99.

[2] G.H. Gelinck, H.E.A. Huitema, E.V. Veenendaal, E. Cantatore, L. Schrijnemakers, J.B.P.H. Van Der Putten, T.C.T. Geuns, M. Beenhakkers, J.B. Giesbers, B.H. Huisman, E.J. Meijer, E.M. Benito, F.J. Touwslager, A.W. Marsman, B.J.E. Van Rens, D.M. De Leeuw, Flexible active-matrix displays and shift registers based on solution-processed organic transistors, Nature Materials 3 (2004) 106.

[3] Y.H. Kim, S.K. Park, D.G. Moon, W.K. Kim, J.I. Han, Organic thin film transistor-driven liquid crystal displays on flexible polymer substrate, Japanese Journal of Applied Physics, Part 1: Regular Papers and Short Notes and Review Papers 43 (2004) 3605.

[4] Y. Noguchi, T. Sekitani, T. Someya, Organic-transistor-based flexible pressure sensors using ink-jet-printed electrodes and gate dielectric layers, Applied Physics Letters 89 (2006).

[5] T. Someya, T. Sekitani, S. Iba, Y. Kato, H. Kawaguchi, T. Sakurai, A large-area, flexible pressure sensor matrix with organic field-effect transistors for artificial skin applications, Proceedings of the National Academy of Sciences of the United States of America 101 (2004) 9966.

[6] H.S. Tan, N. Mathews, T. Cahyadi, F.R. Zhu, S.G. Mhaisalkar, The effect of dielectric constant on device mobilities of high-performance, flexible organic field effect transistors, Applied Physics Letters 94 (2009).

[7] A. Facchetti, M.-H. Yoon, T.J. Marks, Gate dielectrics for organic field-effect transistors: new opportunities for organic electronics, Advanced Materials 17 (2005) 1705.

[8] T. Cahyadi, J. Kasim, H.S. Tan, S.R. Kulkarni, B.S. Ong, Y. Wu, Z.K. Chen, C.M. Ng, Z.X. Shen, S.G. Mhaisalkar, Enhancement of carrier mobilities of organic semiconductors on sol–gel dielectrics: investigations of molecular organization and interfacial chemistry effects, Advanced Functional Materials 19 (2009) 378.

[9] M. Shtein, J. Mapel, J.B. Benziger, S.R. Forrest, Effects of film morphology and gate dielectric surface preparation on the electrical characteristics of organic-vapor-phase-deposited pentacene thin-film transistors, Applied Physics Letters 81 (2002) 268.

[10] L.L. Chua, J. Zaumseil, J.F. Chang, E.C.W. Ou, P.K.H. Ho, H. Sirringhaus, R.H. Friend, General observation of n-type field-effect behaviour in organic semiconductors, Nature 434 (2005) 194.

[11] M.H. Yoon, C. Kim, A. Facchetti, T.J. Marks, Gate dielectric chemical structure-organic field-effect transistor performance correlations for electron, hole, and ambipolar organic semiconductors, Journal of the American Chemical Society 128 (2006) 12851.

[12] T.B. Singh, F. Meghdadi, S. Günes, N. Marjanovic, G. Horowitz, P. Lang, S. Bauer, N.S. Sariciftci, High-performance ambipolar pentacene organic field-effect transistors on poly(vinyl alcohol) organic gate dielectric, Advanced Materials 17 (2005) 2315.

[13] W.L. Leong, N. Mathews, S. Mhaisalkar, Y.M. Lam, T. Chen, P.S. Lee, Micellar poly(styrene-b-4-vinylpyridine)-nanoparticle hybrid system for non-volatile organic transistor memory, Journal of Materials Chemistry 19 (2009) 7354.

[14] G. Gu, M.G. Kane, J.E. Doty, A.H. Firester, Electron traps and hysteresis in pentacene-based organic thin-film transistors, Applied Physics Letters 87 (2005) 1.

[15] S. Lee, B. Koo, J. Shin, E. Lee, H. Park, H. Kim, Effects of hydroxyl groups in polymeric dielectrics on organic transistor performance, Applied Physics Letters 88 (2006).

[16] L. Fumagalli, D. Natali, M. Sampietro, E. Peron, F. Perissinotti, G. Tallarida, S. Ferrari, Al_2O_3 as gate dielectric for organic transistors: charge transport phenomena in poly-(3-hexylthiophene) based devices, Organic Electronics 9 (2008) 198.

[17] J. Veres, S.D. Ogier, S.W. Leeming, D.C. Cupertino, S.M. Khaffaf, Low-k insulators as the choice of dielectrics in organic field-effect transistors, Advanced Functional Materials 13 (2003) 199.

[18] I.N. Hulea, S. Fratini, H. Xie, C.L. Mulder, N.N. Iossad, G. Rastelli, S. Ciuchi, A.F. Morpurgo, Tunable Frohlich polarons in organic single-crystal transistors, Nature Materials 5 (2006) 982.

[19] C.S. Kim, S.J. Jo, S.W. Lee, W.J. Kim, H.K. Baik, S.J. Lee, Surface-modified high-k oxide gate dielectrics for low-voltage high-performance pentacene thin-film transistors, Advanced Functional Materials 17 (2007) 958.

[20] J. Collet, O. Tharaud, A. Chapoton, D. Vuillaume, Low-voltage, 30 nm channel length, organic transistors with a self-assembled monolayer as gate insulating films, Applied Physics Letters 76 (2000) 1941.

[21] M. Halik, H. Klauk, U. Zschieschang, G. Schmid, C. Dehm, M. Schutz, S. Maisch, F. Effenberger, M. Brunnbauer, F. Stellacci, Low-voltage organic transistors with an amorphous molecular gate dielectric, Nature 431 (2004) 963.

[22] M.-H. Yoon, A. Facchetti, T.J. Marks, σ–π Molecular dielectric multilayers for low-voltage organic thin-film transistors, Proceedings of the National Academy of Sciences of the United States of America 102 (2005) 4678.

[23] S.A. DiBenedetto, A. Facchetti, M.A. Ratner, T.J. Marks, Charge conduction and breakdown mechanisms in self-assembled nanodielectrics, Journal of the American Chemical Society 131 (2009) 7158.

[24] M.H. Yoon, H. Yan, A. Facchetti, T.J. Marks, Low-voltage organic field-effect transistors and inverters enabled by ultrathin cross-linked polymers as gate dielectrics, Journal of the American Chemical Society 127 (2005) 10388.

[25] Y.-Y. Noh, H. Sirringhaus, Ultra-thin polymer gate dielectrics for top-gate polymer field-effect transistors, Organic Electronics 10 (2009) 174.

[26] M.J. Panzer, C.D. Frisbie, High carrier density and metallic conductivity in poly(3-hexylthiophene) achieved by electrostatic charge injection, Advanced Functional Materials 16 (2006) 1051.

[27] L. Herlogsson, Y.Y. Noh, N. Zhao, X. Crispin, H. Sirringhaus, M. Berggren, Downscaling of organic field-effect transistors with a polyelectrolyte gate insulator, Advanced Materials 20 (2008) 4708.

[28] H. Mostaghaci, R.J. Brook, Microstructure development and dielectric properties of fast-fired $BaTiO_3$ ceramics, Journal of Materials Science 21 (1986) 3575.

[29] S.K. Dey, J.-J. Lee, Cubic paraelectric (nonferroelectric) perovskite PLT thin films with high permittivity for ULSI DRAM's and decoupling capacitors, IEEE Transactions on Electron Devices 39 (1992) 1607.

[30] B. Huybrechts, K. Ishizaki, M. Takata, The positive temperature coefficient of resistivity in barium titanate, Journal of Materials Science 30 (1995) 2463.

[31] Y. Ohara, K. Koumoto, H. Yanagida, Barium titanate ceramics with high piezoelectricity fabricated from fibrous particles, Journal of the American Ceramic Society 68 (1985) c. 108.

[32] B.K. Kim, D.Y. Lim, R.E. Riman, J.S. Nho, S.B. Cho, A new glycothermal process for barium titanate nanoparticle synthesis, Journal of the American Ceramic Society 86 (2003) 1793.

[33] Y.J. Jung, D.Y. Lim, J.S. Nho, S.B. Cho, R.E. Riman, B. Woo Lee, Glycothermal synthesis and characterization of tetragonal barium titanate, Journal of Crystal Growth 274 (2005) 638.

[34] R.H. Buttner, E.N. Maslen, Structural parameters and electron difference density in $BaTiO_3$, Acta Crystallographica Section B 48 (1992) 764.

[35] M.Y. Colby, L.J.B. LaCoste, The crystal structure of witherite, Zeitschrift fuer Kristallographie 90 (1935) 1.

[36] J.R. Gunter, G.B. Jameson, Orthorhombic barium orthotitanate, [alpha]'-Ba_2TiO_4, Acta Crystallographica Section C 40 (1984) 207.

[37] W. Hofmeister, E. Tillmanns, W.H. Baur, Refinement of barium tetratitanate, $BaTi_4O_9$, and hexabarium 17-titanate, $Ba_6Ti_{17}O_{40}$, Acta Crystallographica Section C 40 (1984) 1510.

[38] M. Murata, M. Omatsu, Differential reaction rate determination of barium orthotitanate in barium titanate powder, Analytical Chemistry 47 (1975) 1467.

[39] U. Manzoor, D.K. Kim, Synthesis of nano-sized barium titanate powder by solid-state reaction between barium carbonate and titania, Journal of Materials Science and Technology 23 (2007) 655.

[40] K.H. Felgner, T. Müller, H.T. Langhammer, H.P. Abicht, On the formation of $BaTiO_3$ from $BaCO_3$ and TiO_2 by microwave and conventional heating, Materials Letters 58 (2004) 1943.

[41] S. Wada, H. Yasuno, T. Hoshina, S.M. Nam, H. Kakemoto, T. Tsurumi, Preparation of nm-sized barium titanate fine particles and their powder dielectric properties, Japanese Journal of Applied Physics, Part 1: Regular Papers and Short Notes and Review Papers 42 (2003) 6188.

[42] T. Hoshina, H. Yasuno, S.M. Nam, H. Kakemoto, T. Tsurumi, S. Wada, Size effect on dielectric properties of barium titanate fine particles, Transactions of the Materials Research Society of Japan 29 (2004) 1207.

[43] S. Wada, H. Yasuno, T. Hoshina, S.M. Nam, H. Kakemoto, T. Tsurumi, Dielectric properties of nm-sized barium titanate crystallites with various particle sizes, Ceramic Transactions 150 (2004) 205.
[44] C.K. Tan, G.K.L. Goh, G.K. Lau, Growth and dielectric properties of $BaTiO_3$ thin films prepared by the microwave-hydrothermal method, Thin Solid Films 516 (2008) 5545.
[45] A.R. Von Hippel, Dielectrics and Waves, Wiley, New York, 2006.
[46] T. Hoshina, H. Kakemoto, T. Tsurumi, S. Wada, M. Yashima, Size and temperature induced phase transition behaviors of barium titanate nanoparticles, Journal of Applied Physics 99 (2006).
[47] J. Veres, S. Ogier, G. Lloyd, D. De Leeuw, Gate insulators in organic field-effect transistors, Chemistry of Materials 16 (2004) 4543.
[48] T. Cahyadi, H.S. Tan, E.B. Namdas, S.G. Mhaisalkar, P.S. Lee, Z.K. Chen, C.M. Ng, F.Y.C. Boey, Improved pentacene device characteristics with sol–gel SiO_2 dielectric films, Organic Electronics: Physics, Materials, Applications 8 (2007) 455.
[49] H.S. Tan, T. Cahyadi, Z.B. Wang, A. Lohani, Z. Tsakadze, S. Zhang, F.R. Zhu, S.G. Mhaisalkar, Low-temperature-processed inorganic gate dielectrics for plastic-substrate-based organic field-effect transistors, IEEE Electron Device Letters 29 (2008) 698.
[50] A.F. Stassen, R.W.I. De Boer, N.N. Losad, A.F. Morpurgo, Influence of the gate dielectric on the mobility of rubrene single-crystal field-effect transistors, Applied Physics Letters 85 (2004) 3899.
[51] C. Jung, A. Maliakal, A. Sidorenko, T. Siegrist, Pentacene-based thin film transistors with titanium oxide–polystyrene/polystyrene insulator blends: high mobility on high *K* dielectric films, Applied Physics Letters 90 (2007).
[52] B. Stadlober, M. Zirkl, M. Beutl, G. Leising, S. Bauer-Gogonea, S. Bauer, High-mobility pentacene organic field-effect transistors with a high-dielectric-constant fluorinated polymer film gate dielectric, Applied Physics Letters 86 (2005) 1.
[53] F.C. Chen, C.S. Chuang, Y.S. Lin, L.J. Kung, T.H. Chen, H.P.D. Shieh, Low-voltage organic thin-film transistors with polymeric nanocomposite dielectrics, Organic Electronics: Physics, Materials, Applications 7 (2006) 435.

processing is used most commonly in synthesizing PEDOT in the form of spin-coating, solvent-casting or ink-jet printing. However, these PEDOT systems are relatively insoluble in most solvents, making it necessary to attach soluble functional groups to the polymer or dope it with stabilizing polyelectrolytes [18]. An aqueous dispersion of poly(3,4-ethylenedioxythiophene)-poly(styrenesulfonate) (PEDOT-PSS), commercially available as Baytron P, is a stable polymer system with a high transparency up to 80% [7]. However, the PEDOT-PSS film exhibits relatively low electrical conductivity, 10–500 S/cm [7], which does not often meet the high conductivity required for most applications. In addition, scanning-tunneling microscopy, neutron reflectivity measurements, and X-ray photoelectron spectroscopy have revealed a PSS rich layer on the top of the spin-coated PEDOT-PSS films due to the phase separation [13,19,20]. Since PSS is an electrical insulator, excessive PSS can limit the film conductivity [19], and an acidic PEDOT-PSS dispersion can etch indium tin oxide (ITO) during the polymer spin-coating process. Moreover, the hydrolysis of the deposited PEDOT-PSS by moisture absorption can also etch ITO to cause indium and tin incorporation into the polymer [14].

For the PEDOT systems without using polyelectrolytes, PEDOT can be deposited directly on the substrate surface by several in situ polymerization techniques. One of the options is electrochemical polymerization, which has been reported to have higher electrical conductivity [21]. However, electrochemical polymerization results in a poor transparency and requires conducting substrates, which limits its practical applications. As an alternative, oxidative chemical polymerization either in the liquid or vapor phase is more versatile because it is not restricted by the substrates. In particular, one way of achieving a clear thin film with a smooth surface is to apply the oxidant using solvent coating processes and expose the coated surface to a reactive monomer vapor. This process is often referred to as vapor-phase polymerization (referred to herein as VPP) [4,5,22–26]. The PEDOT films by VPP have been reported to have conductivities of approximately 15 S/cm at a thickness of 300 nm without any additives [22]. Recently, a PEDOT film with high conductivity, exceeding 1000 S/cm, was reported using a base-inhibited VPP [3,4]. However, it should be noted that VPP PEDOT has a high bandgap and relatively low transmittance [23,24].

As another thiophene-based conducting polymer, poly(3-hexylthiophene) (P3HT) is also one of the most indispensable materials in OLEDs, OPVs, field effect transistors (FETs) and thin film transistors (TFTs) [12,17,27,28]. Over the last decade, blending or copolymerization techniques of conducting polymers have been investigated not only to overcome the drawbacks of a pristine conductive polymer, such as inadequate bandgap, rough surface, low conductivity and poor transmittance, but also to tailor the properties for various applications [29–31]. Recently, P3HT has been successfully fabricated by VPP [32] using a similar route to VPP of PEDOT choosing appropriate catalyst and solvent systems. Using the VPP technique, therefore, PEDOT and P3HT may be copolymerized in the state of vaporized monomers and subsequently polymerized to form, most probably, a PEDOT/P3HT copolymer structure. However, it should be mentioned that the traditional VPP route, where the monomer is maintained in the state of thermodynamic equilibrium, may not simply be applied because the vapor pressure and polymerization rate of the EDOT and 3HT are different and, thus, the relative composition of the VPP copolymer is not controllable.

Therefore, the PEDOT to P3HT ratio was kinetically controlled in this study by adjusting the relative feed amount of the evaporating monomers to the reaction chamber to fabricate the PEDOT/P3HT films containing different ratios of PEDOT to P3HT. The developed synchronous VPP technique successfully provided PEDOT/P3HT copolymer thin coatings with tunable bandgap and optoelectronic properties.

2. Experimental method

The main chemicals used in this study were 3HT (99%, Aldrich, St. Louis, MI USA), EDOT (99%, Aldrich, St. Louis, MI USA), iron (III) chloride hexahydrate ($Fe(III)Cl_3{\cdot}6H_2O$, 97%, Aldrich, St. Louis MI USA), MeOH (methyl alcohol anhydrous, 99.9%, Carlo erba reagenti) and EtOH (ethyl alcohol anhydrous, 99.9%, Carlo erba reagent). The substrate materials used in this study were plane glass (1.1 mm, Paul Marienfeld GmbH & Co. KG., Germany), ITO glass (indium–tin-oxide glass, 10 Ω, 185 ± 20 nm ITO thickness, 1.1 mm ITO glass thickness, U. I. D., Korea), PET (polyethylene terephthalate, 100 μm, Hwasung Co. Ltd., Korea) and a Si wafer (Thickness: 525 ± 25 μm, SEMI-MATERIAS Co. Ltd., Korea).

The substrates were washed and rinsed with DI-water and acetone and sonicated for 10 min to remove any organic contaminants. The glass substrates were plasma-treated (PLAMAX, SPS Co. Ltd., Korea) for 30 s, and the ITO glass substrates were UV-treated for 20 min. The oxidant was a mixture of MeOH and EtOH at a 1:1 ratio with iron (III) chloride hexahydrate. The wt.% ratio between the alcohol mixture and $FeCl_3 \cdot 6H_2O$ was 10:1, 5:1, and 3:1. A ratio of 10:1 was chosen to fabricate most thin films in this study. After sonicating the oxidant solution for 2 min at 40 °C, it was spin-coated onto the substrates at a speed of 500 rpm for 5 s and then at 1400 rpm for 5 s. The oxidized substrates were placed in the vapor-phase-polymerization (VPP) chamber, where the containers of 3HT and EDOT were also placed. The vaporized monomers were supplied into the chamber through the feed inlets, which were made at the center of the container ceiling with different inlet diameters of D_{3HT} and D_{EDOT} (Scheme 1). The flow rate of flowing nitrogen was kept constant during polymerization, and the feed ratio of 3HT and EDOT monomer vapors was adjusted by the inlet diameters of D_{3HT} (0, 2, 4, 6, and 8 mm) and D_{EDOT} (fixed at 20 mm). The EDOT and 3HT monomers in the VPP chamber were polymerized for 20 min, 30 min, or 1 h at 60 °C. After polymerization, the sample was soaked and washed sequentially with MeOH to eliminate the monomers and Fe(III) solution remaining on the substrate. The washed PEDOT/P3HT copolymer film was dried further using a hot-air gun for 1 min in an ambient atmosphere to remove the residual MeOH.

The thickness of the VPP PEDOT/P3HT was measured using an alpha step IQ (KLA Tencor corporate, the Yield Management company, San Jose CA, U. S. A.) and FE-SEM (Field emission scanning electron microscope, 1.0 nm guaranteed at 15 kV, JSM6700F, JEOL, Japan). The bandgap was determined by UV–vis-spectrophotometry (UV-3600, SHIMADZU, Japan). AFM (SPA-300HV, SII Nano Technology Inc., Tokyo Japan) was used to examine the surface morphology of the VPP-PEDOT/P3HT coating, where a 5×5 μm area was analyzed to determine the surface roughness. The AFM 3D images revealed the surface roughness of the copolymer films with a *z*-axis of 100 nm. X-ray photoelectron spectroscopy (XPS, ESCA2000, VG MICROTECH) equipped with an Al Kα radiation source ($h\nu = 1486.6$ eV) was used to analyze the components. Attenuated total reflection-Fourier transform infrared (ATR-FTIR) spectroscopy (Bruker IFS-66/S, Bruker, Massachusetts U.S.A.) was also used for component analysis of the VPP-PEDOT/P3HT copolymers. Contact angle measurements were performed using a Digi-drop contact angle goniometer (JinTech, Korea). A water droplet was dropped onto the surface of a small sample. The droplet shape was recorded by a camera and analyzed to determine the contact angle. The electrical conductivity of the synthesized films was measured using a four-point probe method (Keithley 236 current source and Keithley 617 electrometer). The film thickness for the measurement of electrical conductivities ranged 100–500 nm coated on a glass substrate in the area of 25×25 mm^2. The type of the four-probe point was a linear type with 1 mm tip spacing.

3. Results and discussion

The thin copolymers were fabricated by adding a small amount of EDOT monomer in the VPP chamber with excessive 3HT monomers because the polymerization rate of the EDOT monomers was faster than that of the 3HT monomers. More specifically, the composition was controlled by adjusting the feed amount of EDOT to the catalyst-coated layer placed in the reaction chamber, which complies with the typical steady-state plug-flow reactor system [33]. In this case, the feed ratio of EDOT to 3HT may be controlled by the inlet size of the vaporized monomers in the stream of purging nitrogen. Simply quantifying the feed composition, the feed ratio (r) may be defined by the feed inlet sizes of EDOT and 3HT, viz: $r = D_{EDOT}/D_{3HT}$, where D_{EDOT} and D_{3HT} are the cross-sectional diameters of the feeding hole on the ceiling of the EDOT and 3HT containers, respectively.

The ATR-FTIR spectroscopy results of the pristine PEDOT, pristine P3HT and PEDOT/P3HT copolymer films are compared in Fig. 1 at different feed ratios. As the characteristic peaks of each pristine polymer, the peak intensity of the aliphatic C–H bond stretching vibration corresponds to the 3-hexyl group in P3HT, and the C–O–C bond stretching vibration corresponds to the ethylenedioxy group in PEDOT. As seen in Fig. 1B, the aliphatic C–H bond stretching in the 3-hexyl group in P3HT appears at 2854, 2924, and 2954 cm^{-1}, and its peak intensity decreases with the feed ratio of r [34,35]. Assigning the bands at approximately 1058 and 1141 cm^{-1} to the stretching modes of the ethylenedioxy group [36,37], the intensity of these peaks increases with the increasing supply of the EDOT monomer. Consequently, the vapor-phase polymerization ratio of PEDOT appears to reflect the controlled supply of the EDOT monomer via the feed ratio of r. Fig. 1C compares the bands of the pristine PEDOT (doped with $FeCl_3 \cdot 6H_2O$) with the copolymers at different feed ratios of r, seemingly exhibiting a redshift due to copolymerization of 3HT and EDOT. The inset in Fig. 1A shows the camera images of pristine PEDOT, P3HT, and PEDOT/P3HT at different compositions coated on the ITO substrates. Since the colors of the pristine PEDOT and P3HT are blue and orange, respectively, the color of the PEDOT/P3HT copolymers changes gradually from orange to dark blue with the increasing EDOT feed ratio of r demonstrating that the ratio was successfully controlled by the feed ratio in our experiments.

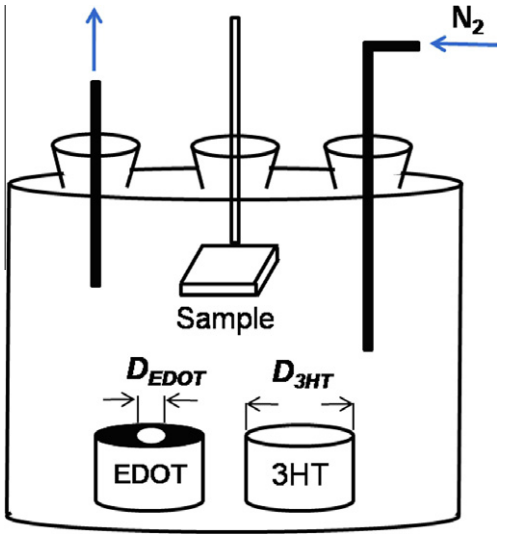

Scheme 1. Schematic of experimental setup for synchronous polymerization of EDOT and 3HT monomers, where the monomer concentrations are controlled by the inlet sizes of monomers (D_{EDOT} and D_{3HT}) to the reaction chamber under the flowing inert gas.

For copolymers, the surface composition may be quantified using several surface-sensitive techniques, such as XPS and time-of-flight secondary ion mass spectrometry (ToF-SIMS) [38], XPS exhibiting somewhat better agreement with the theoretical compositions than ToF-SIMS [39]. Therefore, in this study, XPS was used to quantify the surface concentrations. The formation of PEDOT/P3HT copolymer films can be demonstrated by deconvoluting the XPS peaks at 285.0, 286.5, and 533.0 eV, as shown in Fig. 2. The XPS peaks at 285.0 and 286.5 eV in Fig. 2A can be assigned to C–C/C =C and C–O–C, respectively, corresponding to the spectra of the C(1s) core level [40,41]. Fig. 2A and Table 1 indicate that the intensity of the peak at 285.0 eV decreases with increasing r, whereas that at 286.5 eV increases, which agrees well with the chemical structures of PEDOT and P3HT, as shown in the inset in Fig. 2A. The O photoelectron spectrum in Fig. 2B and Table 1 shows that the O concentration increases with increasing r, as represented by the intensities of the XPS peak at

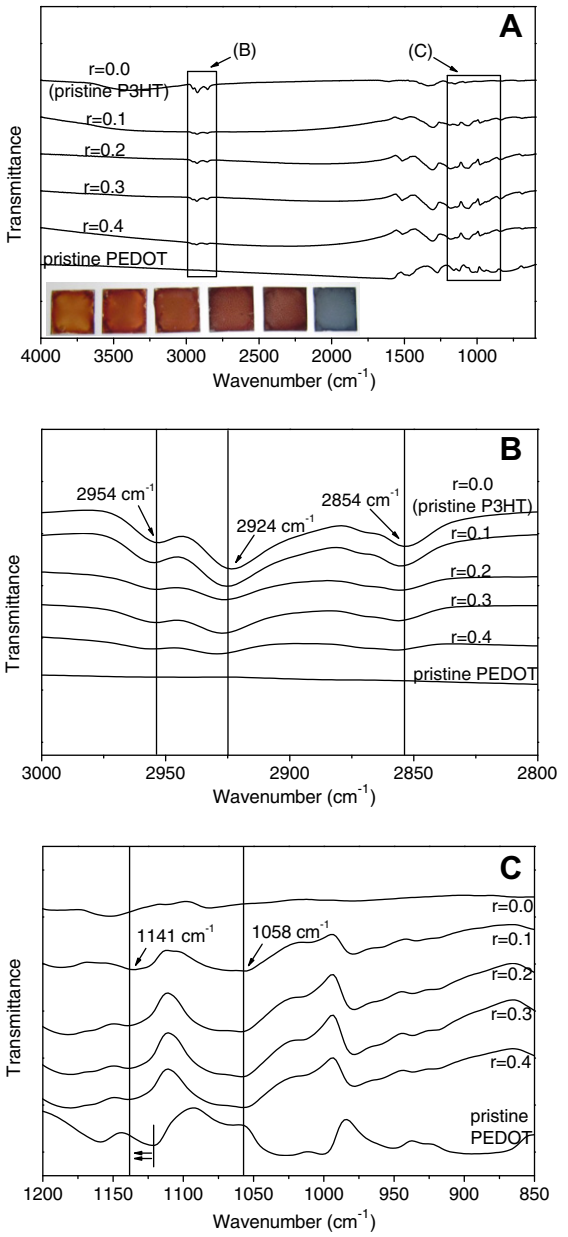

Fig. 1. Comparison of ATR-FTIR spectra of the PEDOT/P3HT copolymers at different feed ratio of *r*. (A) full spectral region: 4000–600 cm^{-1}, (B) enlargement of the region of 3000–2800 cm^{-1}, (C) enlargement of the region of 1200–850 cm^{-1}. The inset in (A) shows pictures of the PEDOT/P3HT copolymer films coated on ITO-coated glass using an oxidant at a 5:1 ratio of the alcohol mixture to ferric chloride hexahydrate, representing $r = 0$, 0.1, 0.2, 0.3, 0.4, and the pristine PEDOT film from left to right, respectively, with a thickness of 500 nm.

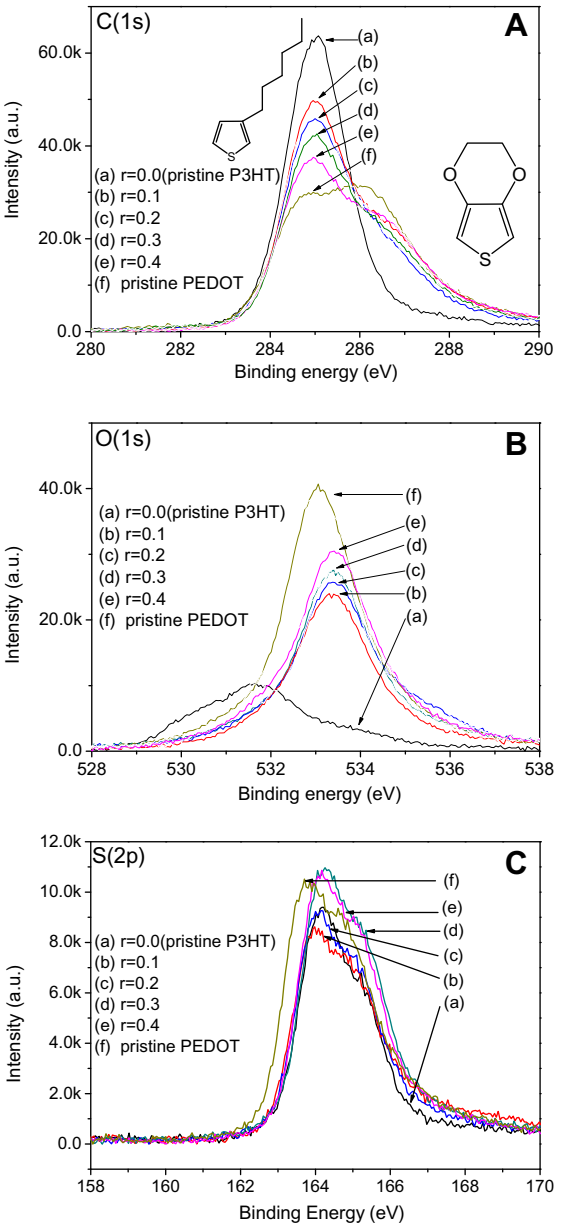

Fig. 2. Deconvolution of XPS spectra of (A) $C_{(1s)}$, (B) $O_{(1s)}$ core-level, and (C) $S_{(2p)}$ for PEDOT/P3HT copolymers at various feed ratio of *r*. The inset in (A) is chemical structures of PEDOT and P3HT, respectively.

533 eV, which can be assigned to the oxygen–ether group (C–O–C) [40,42]. The S photoelectron spectrum is shown in Fig. 2C and analyzed in Table 2. The S(2p) peak positions of pristine P3HT and PEDOT appear at 164.1 and 163.8 eV, respectively, and the peaks of their blend systems at different *r* values seem to appear between the two pristine polymers. Table 2 shows the elemental composition of the fabricated thin films demonstrating that the PEDOT to P3HT ratio increases with the EDOT feed ratio of *r*. As seen in Table 2, the concentration of S and the PEDOT to P3HT elemental ratio apparently increase with increasing *r*. Comparing the experimental and theoretical ratios of C/S, which may represent the ratios of P3HT to PEDOT, there are good agreements between the theoretical and experimental values. The slight discrepancy might be due to adventitious hydrocarbon contamination coming from the contact of the samples with the ambient atmosphere [39].

Table 1
XPS atomic concentrations (%) of C and O for PEDOT/P3HT copolymers with (a) $r = 0.0$, (b) 0.1, (c) 0.2, (d) 0.3, (e) 0.4, and (f) pristine PEDOT.

Samples	C(1s) C atom% at (g) 285.0 eV (C–C/C=C)	(h) 286.5 eV (C–O–C)	h/g	O(1s) O atom% at 533.0 eV (C–O–C)
a	78.4	0	0	0
b	50.0	24.6	0.49	8.6
c	48.1	25.9	0.54	9.1
d	42.4	28.4	0.67	10.4
e	35.1	28.9	0.82	11.6
f	29.2	32.1	1.10	13.8

Table 2
XPS atomic concentrations (%) of C and S comparing C/S ratios between theoretical and experimental results for (a) $r = 0.0$, (b) 0.1, (c) 0.2, (d) 0.3, (e) 0.4, and (f) pristine PEDOT.

Samples	C(1s) atom%	S(2p) atom%	C/S theoretical	C/S experimental	PEDOT:P3HT experimental ratio(mol%)
a	84.1	8.2	10.0	10.3	0:100
b	80.4	8.7	–	9.2	31:69
c	78.4	8.8	–	8.9	39:61
d	75.4	9.7	–	7.8	69:31
e	74.8	9.9	–	7.5	78:22
f	69.5	10.4	6.0	6.7	100:0

Fig. 3 presents the UV–vis absorbance spectra of VPP-PEDOT/P3HT films on glass substrates leading to changes of the bandgap of the VPP-PEDOT/P3HT copolymer at different feed ratio of r values. The bandgap was estimated to be 1.91, 1.98, 2.02, 2.07, and 2.16 eV for the specimens prepared with 0, 2, 4, 6 mm of feed diameters and the pristine VPP-PEDOT film, respectively, by taking the isobestic points at 650, 625, 615, 600, and 575 nm, respectively. The bandgap decreases gradually with decreasing EDOT monomer supply. Accordingly, the bandgap of the VPP-PEDOT/P3HT copolymer film can be desirably adjusted by changing the relative composition of PEDOT and P3HT, especially when a low bandgap is required in such applications as OLEDs and OPVs [16]. The inset in Fig. 3 shows the pristine PEDOT, P3HT and PEDOT/P3HT copolymers at different compositions coated on glass substrates. Similarly to Fig. 1, the color of the specimens clearly indicates that the compositions of PEDOT and P3HT vary with the fabrication conditions to give tunable bandgap.

Fig. 4 shows cross-sectional SEM images of pristine PEDOT, P3HT, and copolymerized PEDOT/P3HT films produced by the developed synchronous technique. In this experiment, the coating thickness of the oxidant was precisely controlled to be constant during the spin-coating process and the same VPP conditions were used. However, as can be seen, the final film thickness varies with the compositions because of the difference in polymerization rates of EDOT and 3HT. Fig. 4A, B, C, D, E and F show cross section images of pristine P3HT, copolymer films and pristine PEDOT, giving the final thicknesses of 52, 71, 87, 110, 131 and 153 nm at $r = 0$, 0.1, 0.2, 0.3, 0.4 and the pristine PEDOT film, respectively. The film thickness increases with increasing r due to the faster polymerization rates of EDOT than 3HT. It should be mentioned that the film thickness can also be controlled at a fixed r by changing the polymerization temperature [32].

Fig. 5 shows the electrical conductivity of the copolymers plotted as a function of r. The electrical conductivity increases from 3.0×10^{-2} S/cm for the pristine P3HT up to 6.28 S/cm for the copolymer with r at 0.4. The conductivity of PEDOT/P3HT copolymer can be increased up to 200 times higher than that of the pristine P3HT, which can be achieved by adjusting the EDOT feed ratio of r. In this study, the conductivity of the pristine VPP-PEDOT was similar to that reported elsewhere [22], where a $FeCl_3$-based oxidant solution was used without any additives. However, the addition of basic inhibitors, such as pyridine [4] and imidazole [25], has been reported to reduce the polymerization reaction kinetics and enhance the conductivity and transparency of the PEDOT film. Therefore, a weak base can be used to the PEDOT/P3HT copolymer systems to

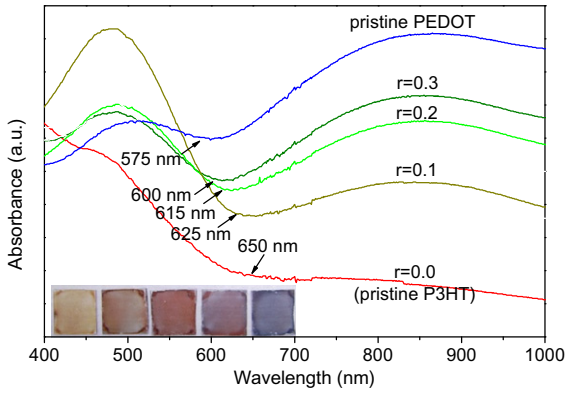

Fig. 3. UV–vis. absorbance spectra of the various PEDOT/P3HT copolymer films. The inset shows pictures of the PEDOT/P3HT copolymer films coated on ITO-coated glass using an oxidant at a 10:1 ratio of mixture to ferric chloride hexahydrate, representing $r = 0$, 0.1, 0.2, 0.3, 0.4, and the pristine PEDOT film from left to right, respectively, with a thickness of 300 nm.

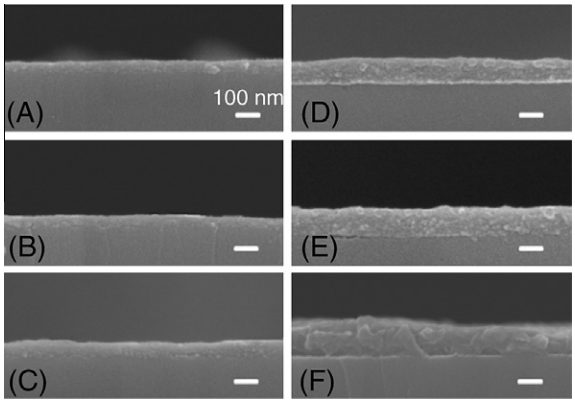

Fig. 4. Cross section of the PEDOT/P3HT copolymer films for (A) $r = 0.0$ (pristine P3HT), (B) $r = 0.1$, (C) $r = 0.2$, (D) $r = 0.3$, (E) $r = 0.4$ and (F) pristine PEDOT synthesized at 60 °C for 20 min. The scale bar is 100 nm in each.

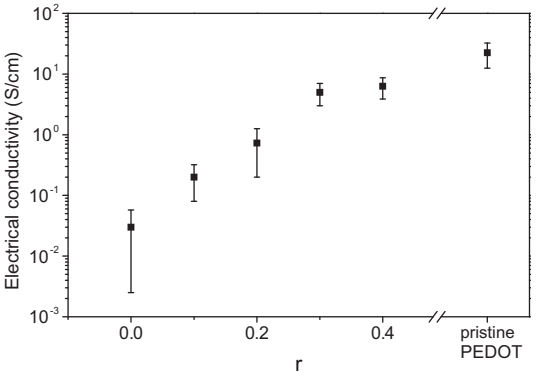

Fig. 5. Electrical conductivities of the pristine PEDOT, P3HT, and PEDOT/P3HT copolymer films.

achieve high conductivities, which is desirable for electrode systems in various electronic devices.

The polymerization rate of conjugated polymers, surface treatment and catalyst removal conditions were reported to affect the surface morphology of thin films substantially [5]. For example, the residual catalyst and monomers were removed successfully in order to synthesize smoother thin conducting polymer films [26]. Fig. 6 shows the surface morphology of the VPP-PEDOT/P3HT thin films in different polymerization conditions at different EDOT feed ratios of *r*. The surface roughness of the film increases with increasing *r*, as shown in Fig. 6A, B, C, D, and E, giving a RMS roughness of 4.88, 3.83, 8.66, 9.31, and 9.54 nm for $r = 0$, 0.1, 0.2, 0.3, and 0.4, respectively. This demonstrates that the surface roughness is affected by the incorporated EDOT monomers. The copolymerized film with $r = 0.1$ shows a lower RMS roughness than the pristine P3HT film (4.88 nm). However, the RMS roughness of the copolymer films increases gradually up to 18.3 nm with increasing *r*. The surface roughness of the pristine PEDOT is relatively high (ca. 18.3 nm) in Fig. 6F because no additional dopant was used in this study. Various additives are normally used to improve both conductivity and surface morphology of PEDOT, for example, such as glycerol, sorbitol and pyridine [5,43]. It should also be mentioned that $FeCl_3$ readily forms crystal-like structures as the

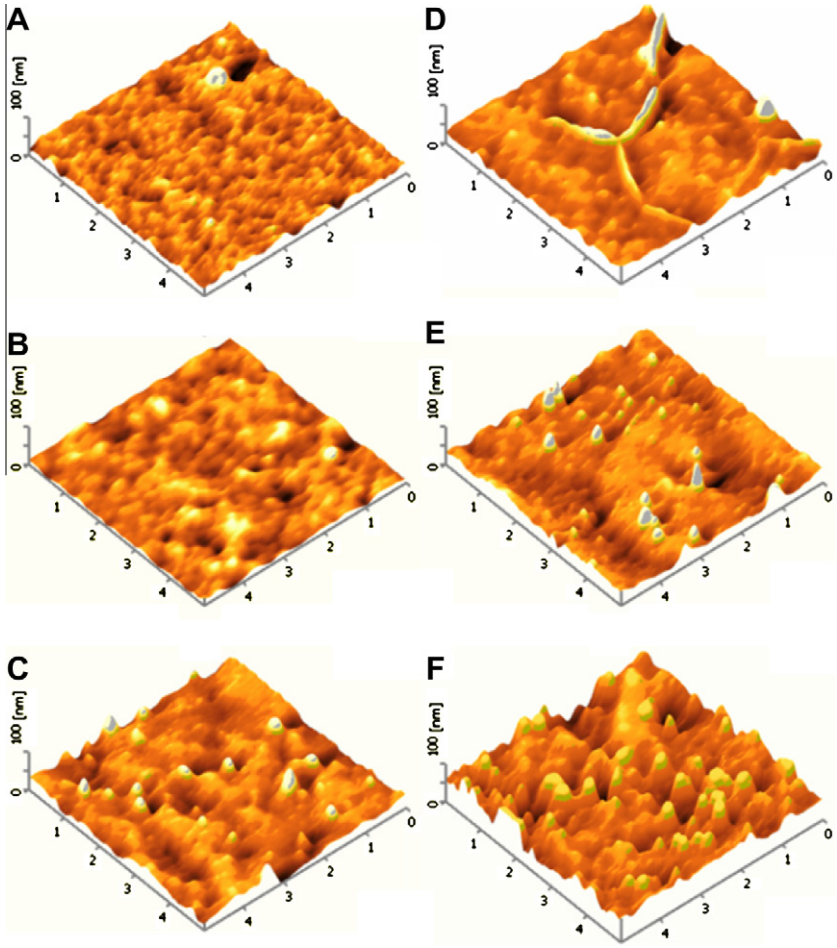

Fig. 6. AFM images of PEDOT/P3HT copolymers for (A) $r = 0.0$ corresponding to pristine P3HT, (B) $r = 0.1$, (C) $r = 0.2$, (D) $r = 0.3$, (E) $r = 0.4$ and (F) pristine PEDOT.

solvent evaporates to give grainy structures, which may act as a seeding template to cause discontinuous film formation [26]. Further work by Winther-Jensen et al. [4,26] shows that Fe(III) tosylate gives relatively smooth and homogeneous film surfaces, however, which often results in an undesirable polymerization route to give partially conjugated polymer chains. Therefore, further study of different additives and catalysts should be performed to enhance the surface morphology of VPP-PEDOT/P3HT.

Fig. 7 shows the water contact angle and RMS surface roughness of the copolymerized films coated on the glass substrates. Since a liquid makes contact with the outermost molecular layer of a surface, the contact angles represent the chemical and structural differences at the coating surface. Furthermore, the wettability of the thin coating is important in the fabrication of many optoelectronic devices, where multilayers should be fabricated in contact with heterogeneous layers. Since the contact angle of the pristine PEDOT at 36° is lower than that of the pristine P3HT at 54°, the PEDOT/P3HT copolymer films show a decreasing feature of the contact angle with a higher *r*, which is likely affected by the roughness of the coating since the water contact angle usually decreases with increasing RMS roughness. At a feed ratio of $r = 0.4$, however, the contact angle is slightly lower than the pristine PEDOT. Exhibited by the camera images of coating in the insets of Fig. 7, the color changes gradually from yellow to blue with the increasing EDOT feed ratio of *r*.

Overall, the developed VPP copolymerizing technique clearly demonstrates that the physicochemical properties of PEDOT/P3HT copolymers were successfully adjusted. Since the vapor pressure and polymerization rates of EDOT and 3HT monomers are different, the variation of the copolymer composition was ensured by adjusting the feed ratio of the monomers to the reaction chamber, which resulted in different reactant concentrations of EDOT and 3HT monomers. Different concentrations of reactants may well give different kinetic polymerization rates of EDOT and 3HT to provide a controllable synthesis route of PEDOT/P3HT copolymer coatings. Further study should be performed to identify the detailed copolymerization reaction and chemical structures of the VPP PEDOT/P3HT copolymer system.

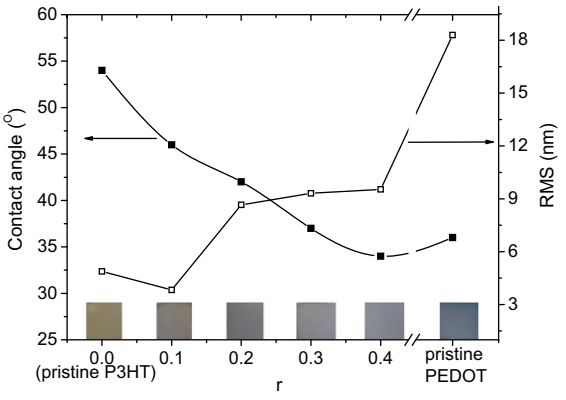

Fig. 7. Water contact angles and RMS surface roughness for different PEDOT/P3HT films. The inset shows the camera images of PEDOT/P3HT copolymer films with thickness of ca. 100 nm.

4. Conclusions

PEDOT/P3HT copolymer films were successfully fabricated as thin films on the glass, Si wafer, ITO-covered glass and PET film substrates using a vapor-phase polymerization technique. The ratios were kinetically controlled to ensure the tunable properties of bandgap, electrical conductivity, surface morphology and water contact angle of the thin copolymer films. The P3HT thin film incorporated with PEDOT may improve the mobility in OTFTs and charge extraction efficiency in OPVs. In addition to being used as a semiconductor with higher mobility, adding dopants to increase the electrical conductivity, P3HT/PEDOT copolymer films can also be used as a HIL in OLEDs with modified energy levels and properties.

Acknowledgments

This research was supported by WCU (World Class University) program through the Korea Science and Engineering Foundation funded by the Ministry of Education, Science and Technology (R31-2008-000-10029-0). The authors wish to express their gratitude for the project and equipment support from Gyeonggi Province and Samsung Electro-mechanics Co. through the GRRC program in Sungkyunkwan University.

References

[1] H. Shirakawa, E. Louis, A. MacDiarmid, C. Chiang, A. Heeger, J.S.C. Chem. Commun. 1977 (1977) 578–580.
[2] C.K. Chiang, C.R. Fincher, Y.W. Park, A.J. Heeger, H. Shirakawa, E.J. Louis, S.C. Gau, A.G. MacDiarmid, Phys. Rev. Lett. 39 (1977) 1098.
[3] B. Winther-Jensen, M. Forsyth, K. West, J. Andreasen, G. Wallace, D. MacFarlane, Org. Electron. 8 (2007) 796–800.
[4] B. Winther-Jensen, K. West, Macromolecules 37 (2004) 4538–4543.
[5] T. Truong, D. Kim, Y. Lee, T. Lee, J. Park, L. Pu, J. Nam, Thin Solid Films (2007).
[6] F. Jonas, L. Schrader, Synth. Met. 41 (1991) 831–836.
[7] L. Groenendaal, F. Jonas, D. Freitag, H. Pielartzik, J. Reynolds, Adv. Mater. 12 (2000).
[8] D. Welsh, A. Kumar, E. Meijer, J. Reynolds, Adv. Mater. 11 (1999).
[9] S. Admassie, F. Zhang, A. Manoj, M. Svensson, M. Andersson, O. Inganas, Sol. Energ. Mat. Sol. C. 90 (2006) 133–141.
[10] A. Gadisa, K. Tvingstedt, S. Admassie, L. Lindell, X. Crispin, M. Andersson, W. Salaneck, O. Inganas, Synthetic Met. 156 (2006) 1102–1107.
[11] D. Wakizaka, T. Fushimi, H. Ohkita, S. Ito, Polymer 45 (2004) 8561–8565.
[12] R. Hatton, N. Blanchard, L. Tan, G. Latini, F. Cacialli, S. Silva, Org. Electron. (2009).
[13] T. Lee, Y. Chung, Adv. Funct. Mater. 18 (2008) 2246–2252.
[14] T. Lee, Y. Chung, O. Kwon, J. Park, Adv. Funct. Mater. 17 (2007) 390–396.
[15] Y. Saito, T. Kitamura, Y. Wada, S. Yanagida, Synthetic Met. 131 (2002) 185–187.
[16] K. Colladet, S. Fourier, T. Cleij, L. Lutsen, J. Gelan, D. Vanderzande, H. Neugebauer, S. Sariciftci, A. Aguirre, G. Janssen, Macromolecules 40 (2007) 65–72.
[17] Y. Kim, S. Choulis, J. Nelson, D. Bradley, S. Cook, J. Durrant, Appl. Phys. Lett. 86 (2005) 063502.
[18] Terje.A. Skotheim, Handbook of Conducting Polymer, Marcel Dekker, New york, 1998.
[19] M. Kemerink, S. Timpanaro, M. De Kok, E. Meulenkamp, F. Touwslager, J. Phys. Chem. B 108 (2004) (1882) 18820–18825.

[20] A. Higgins, S. Martin, P. Jukes, M. Geoghegan, R. Jones, S. Langridge, R. Cubitt, S. Kirchmeyer, A. Wehrum, I. Grizzi, J. Mater. Chem. 13 (2003) 2814–2818.
[21] L. Groenendaal, G. Zotti, F. Jonas, Synthetic Met. 118 (2001) 105–109.
[22] J. Kim, E. Kim, Y. Won, H. Lee, K. Suh, Synthetic Met. 139 (2003) 485–489.
[23] M. Fabretto, K. Zuber, C. Hall, P. Murphy, Macromol. Rapid Comm. 29 (2008).
[24] M. Cho, S. Kim, J. Nam, Y. Lee, Synthetic Met. 158 (2008) 865–869.
[25] Y. Ha, N. Nikolov, S. Pollack, J. Mastrangelo, B. Martin, R. Shashidhar, Adv. Funct. Mater. 14 (2004) 615–622.
[26] B. Winther-Jensen, J. Chen, K. West, G. Wallaces, Macromolecules 37 (2004) 5930–5935.
[27] S. Grecu, M. Roggenbuck, A. Opitz, W. Brutting, Org. Electron. 7 (2006) 276–286.
[28] C. Bartic, H. Jansen, A. Campitelli, S. Borghs, Org. Electron. 3 (2002) 65–72.
[29] D. Kim, P. Lee, S. Kang, K. Jang, J. Lee, M. Cho, J. Nam, Thin Solid Films (2009).
[30] Y. Xu, J. Wang, W. Sun, S. Wang, J. Power. Sources 159 (2006) 370–373.
[31] A. Sarac, G. Sonmez, F. Cebeci, J. Appl. Electrochem. 33 (2003) 295–301.
[32] K. Jang, Y. Eom, T. Lee, D. Kim, Y. Oh, H. Jung, J. Nam, A.C.S. Appl. Mater. Interfaces 1 (2009) 1567–1571.
[33] O. Levenspiel, Chemical reaction engineering, John Wiley and Sons, New York, 1962.
[34] T. Chen, X. Wu, R. Rieke, J. Am. Chem. Soc. 117 (1995) 233–244.
[35] R. Singh, J. Kumar, R. Singh, R. Kant, S. Chand, V. Kumar, Mater. Chem. Phys. 104 (2007) 390–396.
[36] L. Zhan, Z. Song, J. Zhang, J. Tang, H. Zhan, Y. Zhou, C. Zhan, Electrochim. Acta 53 (2008) 8319–8323.
[37] L. Li, Y. Huang, G. Yan, F. Liu, Z. Huang, Z. Ma, Mater. Lett. 63 (2009) 8–10.
[38] X. Vanden Eynde, P. Bertrand, Surf. Interface Anal. 27 (1999).
[39] D. Cossement, R. Gouttebaron, V. Cornet, P. Viville, M. Hecq, R. Lazzaroni, Appl. Surf. Sci. 252 (2006) 6636–6639.
[40] S. Marciniak, X. Crispin, K. Uvdal, M. Trzcinski, J. Birgerson, L. Groenendaal, F. Louwet, W. Salaneck, Synthetic Met. 141 (2004) 67–73.
[41] Y. Hsiao, W. Whang, C. Chen, Y. Chen, J. Mater. Chem. 18 (2008) 5948–5955.
[42] S. Jonsson, J. Birgerson, X. Crispin, G. Greczynski, W. Osikowicz, A. Denier van der Gon, W. Salaneck, M. Fahlman, Synthetic Met. 139 (2003) 1–10.
[43] J. Huang, P. Miller, J. Wilson, A. de Mello, J. de Mello, D. Bradley, Adv. Funct. Mater. 15 (2005) 290–296.

However, these drawbacks can be overcome by applying an additional dielectric organic layer on top of the OLED stack [5–8]. This increases the transmittance through the top electrode, reduces microcavity effects, and alleviates the viewing angle dependence.

In this work, we demonstrate top-emitting white OLEDs based on a multilayer hybrid structure [11], simultaneously exhibiting high efficiencies and very good color coordinates. Furthermore, our devices show enhanced forward directed radiation, which is highly preferred for lighting applications such as ceiling mounted lighting panels. To clarify the mechanisms behind the electrical characteristics in our devices, we further performed UV photoelectron spectroscopy (UPS) and hole-only experiments. Finally, an efficiency analysis and comparison to a comparable bottom-emitting white OLED [11,12] is performed.

2. Material and measurements

2.1. Organic layer stack

The organic light-emitting devices are prepared by evaporating a 60 nm aluminum anode (Al) (device 1 and 2) on precleaned glass substrates (Princeoptics). Overall reflectivity can be enhanced by adding a 15 nm silver layer (Ag) (device 3 and 4). The organic layers are arranged in a p–i–n [13] architecture, starting with 20 nm *N*,*N*,*N*′,*N*′-tetrakis(4-methoxyphenyl)-benzidine (MeO-TPD) doped with 4 wt.% NDP2 provided by Novaled AG as hole transport layer. The following electron blocking layers (EBL) (10 nm), either *N*,*N*′-di(naphthalen-1-yl)-N,N′-diphenyl-benzidine (NPB) (device 1 and 3) or 2,2′,7,7′-tetrakis-(*N*,*N*-diphenylamino)-9,9′-spirobifluoren (S-TAD) (device 2 and 4) are tested with respect to the best device performance. The emission layers are formed by a 5 wt.% iridium(III)bis(2-methyldibenzo-[f,h]chinoxalin)(acetylacetonate) ($Ir(MDQ)_2(acac)$) doped NPB layer (10 nm), 4,4′,4″-tris(carbazol-9-yl)-triphenylamine (TCTA) (3 nm) doped with 5 wt.% tris(2-phenylpyridin)iridium(III) ($Ir(ppy)_3$) and 2-methyl-9,10-bis(naphthalen-2-yl)anthracene (MADN) (10 nm) doped with 1.5 wt.% 2,5,8,11-tetra-tert-butylperylene (TBPe) for orange-red, green and blue emission, respectively. The latter fluorescent emitter is chosen due to its better long-term stability compared to phosphorescent blue systems, which usually exhibit rather high efficiencies but very poor lifetime. Between the phosphorescent emitters and the fluorescent emitter, a 1.5 nm thin exciton blocking layer of TCTA and 2,2′,2″-(1,3,5-phenylen)tris(1-phenyl-1H-benzimidazol) (TPBi) (1:2) is added to avoid mutual exciton quenching of both systems [11]. Intrinsic and cesium (Cs) doped 4,7-diphenyl-1,10-phenanthroline (BPhen) is used as hole blocking (10 nm) and electron transporting layer (35 nm), respectively. Top electrical contacts are realized with a 1 nm thin Al layer for increasing stability reasons, followed by a semitransparent Ag layer (15 nm) to provide adequate conductivity and high transmittance. Finally, a dielectric capping layer of 50 nm NPB is added. The whole schematic layer structure is given in Fig. 1.

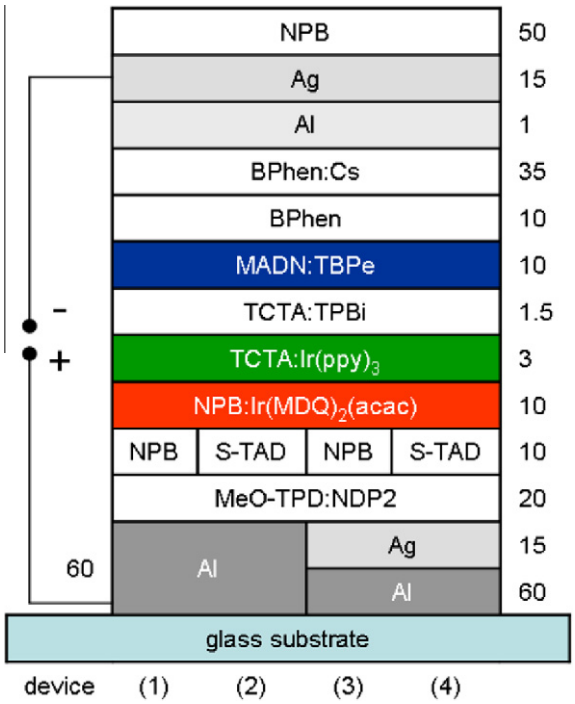

Fig. 1. Schematic layer structure of processed organic LEDs. Layer thicknesses are given in nm.

2.2. Preparation

Thin film evaporation of metals and organic semiconductor materials for the OLED devices is carried out under UHV conditions in a single chamber evaporation tool (K.J. Lesker) with a base pressure of 1×10^{-8} mbar. For the production of the hole-only devices as well as the single organic layers for UPS measurements, a multi chamber deposition tool (Bestec) ($p < 1 \times 10^{-8}$ mbar) is used. After processing, the devices are immediately encapsulated under nitrogen atmosphere.

2.3. Electrical and optical measurements

The current–voltage–luminance (*I*–*V*–*L*) and electroluminescent (EL) characteristics are determined at 0° viewing angle using an automated measuring setup consisting of an array-spectrometer (CAS 140CT-153) in combination with a Keithley 2400 SourceMeter. Since one generally cannot presume Lambertian emission characteristics for top-emitting devices, both luminous efficacy and external quantum efficiency are calculated considering the measured spectral emission at varied viewing angle. The emission characteristics of each device are determined employing a carefully adjusted goniometer setup. Light emitted from the active OLED area in the center of a rotary table is detected for angles θ from 0° to 90° with a spectrometer (USB4000). To avoid unwanted edge contributions, the substrates are covered with masks. Based on the angle dependent spectral radiation, luminous efficacies and external quantum efficiencies are calculated following the procedure given in [14].

2.4. UPS measurements

UPS measurements are carried out under ultrahigh vacuum ($p < 1 \times 10^{-9}$ mbar) with a Phoibos100 system from Specs (Berlin, Germany) using the He I line with an energy of 21.22 eV from a discharge lamp. The experimental error is below 50 meV and can be estimated from the reproducibility achieved in separate measurements. The organic layers for UPS measurements are grown in an UHV cluster tool, which is directly connected to the UPS chamber.

3. Results and discussion

3.1. Influence of different anode materials on the spectral emission

The reflectivity of the electrode mirrors plays an important role in cavity devices since it determines the cavity strength as well as the outcoupled spectra. To evaluate this effect, different metal electrodes have been chosen as described above. The emission spectra of the devices at a luminance of approximately 1000 cd/m^2 are shown in Fig. 2a and b. To verify the effect of different anodes and electron blocking layers, the forward directed cavity emission (Fig. 2c) of all four OLED systems as well as the reflectance of both highly reflecting anode mirrors (Fig. 2d) are additionally illustrated. The cavity emission was obtained by performing optical simulations based on thin film optics [8,15]. This quantity describes the ideal emission spectrum of an optical cavity as obtained by considering wavelength-independent intrinsic luminescence spectra of the emitters, thus providing information on the resonance behavior of the device under examination.

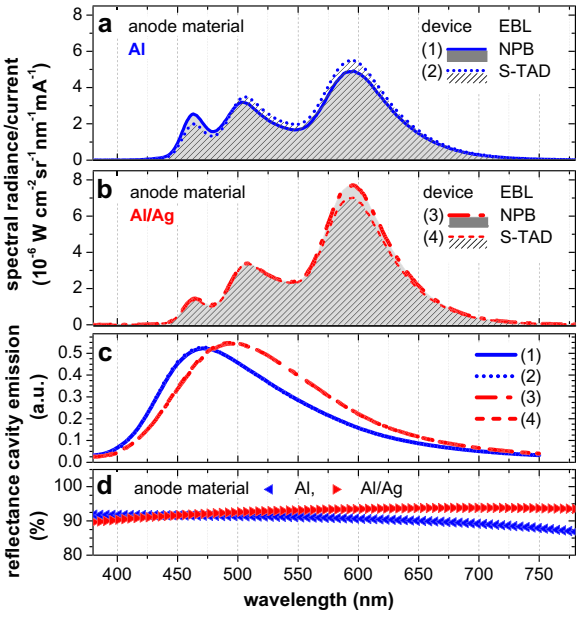

Fig. 2. (a and b) EL spectra of top-emitting white OLEDs containing different anodes (Al, Al/Ag) and different electron blocking layers (NPB, S-TAD). Spectra are measured in forward direction at approximately 1000 cd/m^2 and scaled to their driving current for better comparison. (c) Cavity emission of devices (1–4). The data for NPB and S-TAD fully coincide. (d) Reflectance of anode materials. Cavity emission and reflectance were determined via optical simulation.

The measured spectra of Al (device 1) and Al/Ag (device 3) based OLEDs reveal a dependence of the spectral emission shape on the anode reflectivity. This effect can be explained by a closer look on the cavity emission for Al and Al/Ag based devices and the associated reflectivity of their anode mirrors. The resonance wavelength of Al based devices (1 and 2) is calculated to be 470 nm, which is lower than for Al/Ag devices (495 nm). Accordingly, the cavity emission of Al based devices is enhanced for short wavelengths compared to Al/Ag devices. Therefore, the emission in the high energy region is enhanced, leading to larger contributions in the blue and decreased red emission. By using an Al/Ag anode (devices 3 and 4), the resonant wavelength of the cavity is red-shifted by 25 nm, leading to enhanced light emission in the low energy region. This is related to the larger reflectivity for composite Al/Ag anodes for wavelengths larger than 450 nm when compared to Al systems. Hence, devices with composite anodes present strongly enhanced red emission and suppressed blue contribution.

Due to the larger spectral contribution from the highly efficient phosphorescent orange-red emitting material Ir(MDQ)$_2$(acac), devices with the hybrid anode yield a higher luminous efficacy than OLEDs containing a pure Al anode (cf. Table 1). With the electron blocker NPB, 12.4 lm/W are achieved for device 3 compared to 8.0 lm/W (device 1), having a large spectral blue contribution from the fluorescent emitter TBPe with much lower efficiency. This corresponds to external quantum efficiencies of 5.3% and 3.8%, respectively.

3.2. Investigation of different electron blocking materials

To examine the influence of the electron blocking material on the device performance, we tested the materials NPB and S-TAD. Fig. 3 shows the current–voltage as well as the luminance–voltage characteristics for all processed devices. Devices using S-TAD as electron blocking layer material show steeper *I–V*-curves compared to NPB. Therefore, an approximately 0.5 V lower operating voltage is needed for S-TAD compared to NPB to reach a luminance of 1000 cd/m^2. Thus, the luminous efficacies can be enhanced to 10.4 lm/W (device 2) and 13.3 lm/W (device 4) employing S-TAD. However, the external quantum efficiency remains almost unchanged, as the spectra of the compared blocking materials – shown in Fig. 2a and b – do not show large variations for both cases of anodes.

The slight spectral changes cannot be attributed to a different optical behavior for different blocking materials, since for both anodes the cavity emission of the organic layers is practically independent from the EBL material (Fig. 2c), due to very similar optical constants. Therefore, the differences have to be attributed to the different electrical behavior, which slightly changes the electron–hole balance and therefore alters the emission spectra. A possible explanation for the altered *I–V*-characteristics might be found in different energy barriers from p-doped MeO-TPD to the applied electron blocking layer, S-TAD or NPB, respectively.

Table 1
Driving voltage V, luminance L, current efficiency η_c, luminous efficacy η_l and external quantum efficiency η_q as well as forward CIE coordinates and CRI values.

Device	Anode	EBL	V (V)	L (cd/m^2)	η_c (cd/A)	η_l (lm/W)	η_q (%)	CIE (x, y)	CRI
1	Al	NPB	3.5	1151	14.0	8.0	3.8	0.420, 0.407	75.6
2	Al	S-TAD	3.0	902	15.7	10.4	4.0	0.435, 0.429	74.8
3	Al + Ag	NPB	3.4	1037	20.0	12.4	5.3	0.472, 0.441	69.5
4	Al + Ag	S-TAD	3.0	1220	18.7	13.3	4.9	0.466, 0.444	70.4

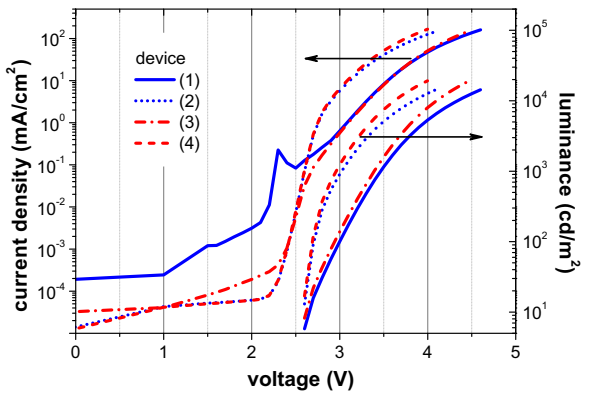

Fig. 3. Current–voltage and luminance–voltage characteristics of the produced devices. Using S-TAD as electron blocking layer leads to steeper curves and reduced driving voltage compared to NPB.

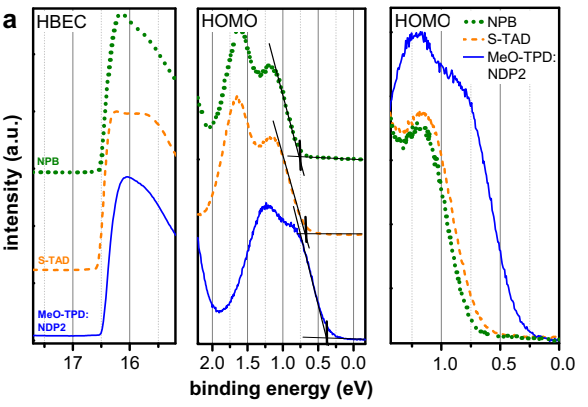

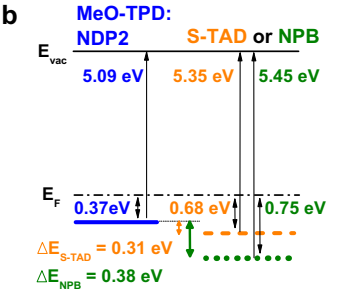

Fig. 4. Interface between NDP2 doped MeO-TPD (solid line) and the blocker materials S-TAD (dashed line) and NPB (dotted line), respectively. (a) High binding energy cutoff (HBEC) and HOMO region of the UPS He I spectra. The thick lines mark the HOMO cutoff positions. (b) Resulting schematic energy level diagram.

Therefore, we perform UPS measurements [16] at the interface of MeO-TPD:NDP2 to each blocker material to determine the hole injection barrier. The measurements and interface alignment between MeO-TPD:NDP2 and the applied electron blocking materials (NPB and S-TAD) are shown in Fig. 4. On top of two 10 nm thick 4 wt.% NDP2 doped MeO-TPD layers, either 5 nm S-TAD or 5 nm NPB are evaporated, respectively. Fig. 4a displays only one curve of MeO-TPD:NDP2, as both measurements show the same curve progression. Hence, for MeO-TPD:NDP2 a hole injection barrier from the Fermi level of 0.37 eV as well as a high binding energy cut-off of 16.50 eV is obtained, leading to an ionization potential (IP) of 5.09 eV. The following electron blocking layers show vacuum level alignment with the doped layer and the injection barriers to MeO-TPD are measured to be 0.31 eV for S-TAD and 0.38 eV for NPB with ionization potentials of 5.35 eV for S-TAD and 5.45 eV for NPB. Thus, the energy barrier for holes is 70 meV higher for NPB compared to S-TAD and is therefore just slightly larger than the experimental error of 50 meV.

Consequently, these small differences in the energy barrier for both electron blocking materials are unlikely to have such a strong influence on the electrical characteristics alone. Thus, it is more likely that the differences in the electrical characteristics are also influenced by an altered hole mobility within the blocking material.

To further investigate the origin of the deviating I–V-characteristics for both electron blocking materials, we additionally fabricate hole-only devices (p–i–p and p–i–i–i–p). In between two 50 nm thick hole transport layers of MeO-TPD:NDP2 (approximately 4 wt.%), the intrinsic material is inserted. For p–i–p devices either 100 nm NPB or 100 nm S-TAD are used as intrinsic layer. The p–i–i–i–p devices contain a layer sequence of 20 nm EBL and 30 nm NPB:Ir(MDQ)$_2$(acac), again followed by the electron blocking material (50 nm), which was used before. The organic p–i–p as well as the p–i–i–i–p stack is evaporated on top of an indium tin oxide (ITO) coated glass substrate and covered with 100 nm aluminum.

In Fig. 5, the forward and backward measured current density for both p–i–p and both p–i–i–i–p devices is shown. All four devices exhibit relatively symmetric I–V-characteristic, whereas the devices containing NPB as electron blocking material show lower current flow compared to the devices with S-TAD. As the current density for NPB at a fixed applied voltage is much lower than for S-TAD, the flow of holes is hindered.

Due to these different electrical characteristics of the device structure using either NPB or S-TAD as blocking

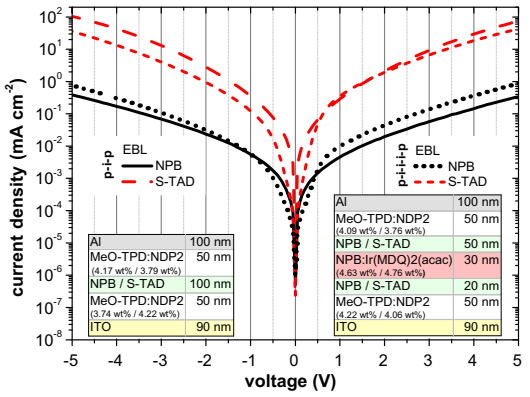

Fig. 5. Current density measured in backward and forward direction for the p–i–p as well as p–i–i–i–p devices. Layer structure for both hole-only devices (inset). The Ir(MDQ)$_2$(acac) doping concentrations for the central intrinsic layer of the p–i–i–i–p devices are 4.63 and 4.76 wt.%, using NPB or S-TAD, respectively, and are therefore almost identical. The slight differences in the p-doping concentration are due to processing.

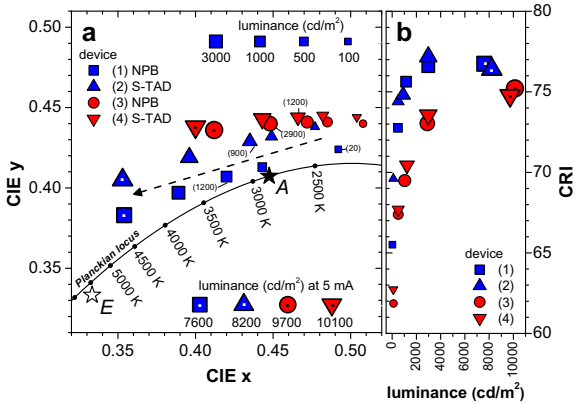

Fig. 6. (a) Color coordinates (CIE) and (b) color rendering indices (CRI) describing emission spectra at 0°. Values are calculated adapted from spectra measured at 100, 500, 1000, 3000 cd/m^2 and a driving current of 5 mA. Variant values are stated in brackets.

material, the electron–hole balance within the device is modified. Consequently, this has an influence on the emission spectra as well as on the OLED efficiency, as the distribution of exciton generation is also changed.

3.3. Chromaticity and color rendering

Based on the OLED spectra at angle of 0°, the chromaticity coordinates (CIE 1931) (Fig. 6a) and color rendering indices (CRI) (Fig. 6b) are calculated. As the organic stack comprises three separate emission layers, the charge carrier balance is modified due to a change in driving current. Hence, CIE and CRI change as a function of the device brightness. For all OLEDs, a shift towards the blue edge of the CIE coordinate diagram can be detected with increasing luminance. Aluminum based devices (1, 2) show a stronger change in both coordinates compared to devices 3 and 4. Furthermore, the CIE coordinates – especially for device 1 – are very close to the black body curve defining ideal white. The choice of the EBL modifies the distance to the Planckian locus, which is closest for device 1 at 500 cd/m^2 featuring a CRI of 73 and color coordinates of (0.44, 0.41) almost exactly matching the warm white standard illuminant A (0.45, 0.41). The color quality of the OLED emission steadily rises with brightness, possessing a stronger increase and higher CRI values for Al based devices, even reaching the highest CRI of 77 for device 2 at 3000 cd/m^2.

3.4. Emission characteristics

The angular emission characteristics of all four devices are comparable and only exhibit slight differences when different anode mirrors as well as electron blocking materials are applied. For the discussion, we take device 1 as representative, whose angular emission characteristics are shown in Fig. 7. Fig. 7a and c additionally provide data obtained via optical simulation based on thin film optics [8,15], which very well coincide with experimental measured data. In Fig. 7a the spectral radiance at different viewing angles is illustrated. The emission peak wavelength of spectral radiation is kept stable with increasing angle. However, the peak emission intensity of all three emission colors decreases with increasing viewing angle differentially for the three emitters, leading to a small blue shift of color (Fig. 7b). However, CIE coordinates exactly move along the Planckian locus.

The device radiance was calculated from the angular-dependent electroluminescence spectra (Fig. 7c). Usually, organic light-emitting diodes are presumed to show Lambertian emission with a cosine shaped decrease of intensity from 0° to 90°. Our devices, however, indicate considerably enhanced emission for small viewing angles. Compared to an ideal Lambertian emitter, featuring the same radiant power density per unit area (6.78 W/m^2 at 3.5 V forward bias), the device reveals larger radiance for viewing angles θ in the range of 0–50°.

In order to explain the observed small angular dependence and the enhanced emission in the forward direction, we evaluated the cavity resonance wavelength λ_R as a function of the viewing angle (Fig. 6d).

For device 1, the resonance wavelength λ_R equals 471 nm in forward direction ($\theta = 0°$). With increasing viewing angle θ, a blue shift in λ_R of 56 nm from 0° to 80° can be observed for TE-polarized radiation, whereas TM-polarized light does not show any change in the complete forward hemisphere. In comparison, the same device without a capping layer shows considerable shifts in both the TE- and TM-components (59 nm and 68 nm, respectively), featuring a resonance wavelength of 510 nm at an angle of 0°.

It can be concluded that the capping layer is very effective in suppressing the blue-shift of the TM-component, whereas the shift of the TE-component is left almost unchanged. Since the resonance conditions of the microcavity exhibit a rather small overall angular dependence, the corresponding color coordinates of the emitted radiations are stable with increasing viewing angle.

The observed forward directed emission feature of the device is as well related to the resonance wavelengths of

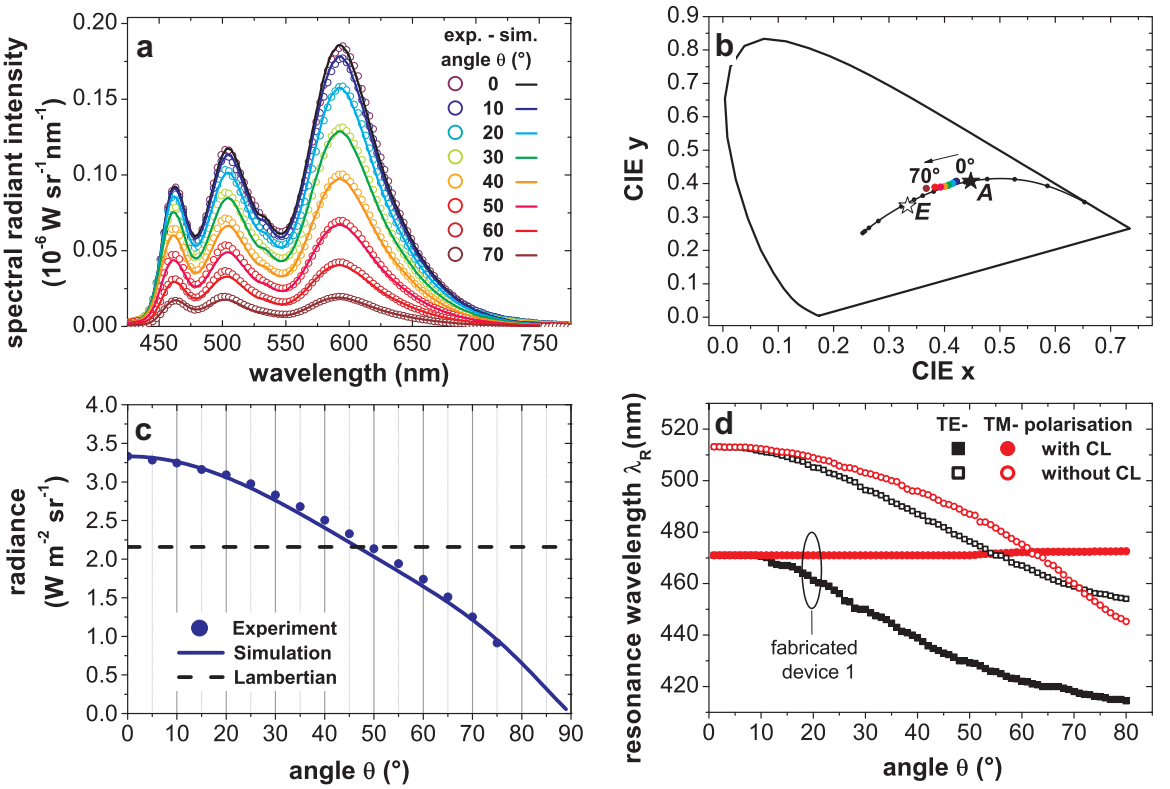

Fig. 7. Emission characteristics of device (1), driven at 3.5 V at a 0°-luminance of 1151 cd/m^2. (a) Experimental measured and simulated spectral emission and (b) measured color coordinate shift at different viewing angle. (c) Determined angular dependent radiance with an absolute radiated power of 6.78 W/m^2 compared to ideal Lambertian emission with the same total power. (d) Simulation of cavity resonance wavelength λ_R at different angles θ for the fabricated device with capping layer compared to a device without capping layer comprising the same layer stack.

the OLED microcavity. It can be observed that λ_R in the forward direction is smaller than the central emission wavelengths of both the green and orange-red emitters (525 nm and 610 nm, respectively) and slightly larger than the emission wavelength of the blue emitter TBPe (460 nm). With increasing viewing angle, the OLED cavity resonates at shorter wavelengths due to the blue shift in λ_R for TE polarized light (see Fig. 6d). Therefore the overlap between the intrinsic cavity emission and the luminescence spectra of the emitters is reduced, especially when considering TBPe. This leads to a consistent and fast reduction in radiated power when considering off-normal directions and, consequently, light emission from the device exhibits a rather strong directionality, rather than a Lambertian behavior [17].

3.5. Analysis of the device efficiency

An optical OLED model [18] is employed in this section to analyze the efficiencies of the OLEDs under examination. Similar calculations are performed for equivalent devices in bottom-emission configuration [11,12] in order to provide meaningful comparisons to existing literature data.

The first step of the modeling approach is the calculation of the outcoupling efficiency η_{out} [15] for each of the emitting layers in the OLED stack. An overall outcoupling efficiency for the white OLED is then derived as an averaged sum of the contribution of the three emitting units, the weights w being determined from the fitting of the electroluminescence spectrum of the device in the forward direction. As last step, an overall internal quantum efficiency η_{IQE} is obtained as the ratio $\eta_{IQE} = \eta_{EQE}/\eta_{out}$, where η_{EQE} denotes the measured external quantum efficiency of the device. This approach allows to obtain an approximate estimate of the internal efficiency of the device and therefore allows to quantify the optical and electrical/excitonic efficiencies of the OLED stack under study.

We consider in the remainder of this section device no. 3, exhibiting the maximum external quantum efficiency (5.3% at 1000 cd/m^2). The η_{out} values obtained for the red, green, and blue emitting layers are 6.9%, 19.9%, and 19.3%, respectively. The low value obtained for the red emitter is related to the fact the OLED cavity is strongly off-resonance for radiation at wavelengths in the range 600–700 nm, the resonance wavelength of the cavity being close to 490 nm. On the other hand, the OLED cavity resonates at wavelengths in the blue-green region of the visible spectrum and thus outcoupling of the green and blue components of the white OLED emission spectrum is favorable. The weights w of the three emitters in the OLED stack extracted from the forward emission spectrum of the device are equal to 0.72, 0.09, and 0.19 for the red, green, and blue emitter, respectively. From the analysis of the values quoted above, it is clear that most of the recombination

events are occurring within the red emitting layer, whereas only recombination within the green and blue emitting layers is comparably lower.

The overall outcoupling efficiency – defined as the total number of outcoupled photons to the total number of photons emitted inside the cavity – is finally evaluated as $\eta_{out} = w_{red} \times \eta_{out,red} + w_{green} \times \eta_{out,green} + w_{blue} \times \eta_{out,blue} =$ 10.4%. It is clear that such a relatively low value is related, on the one hand, to the low outcoupling efficiency of the microcavity for red light and, on the other hand, to the low number of recombination events occurring in the green and blue emitters. From the comparison of the measured η_{EQE} and the calculated η_{out}, the overall internal quantum efficiency equals to 50.8%.

For comparison purposes, we calculate the efficiencies of the white bottom-emitting OLEDs in Refs. [11,12]. These devices feature a very similar structure of the emission units, the main differences between the two stacks is the blue fluorescent emitter (Spiro-DPVBi instead of TPBe) and some of the organic functional layers. The best external quantum efficiency for these devices at 1000 cd/m^2 is $\eta_{EQE} = 7.4\%$ [12]. We calculate for these device an overall outcoupling efficiency $\eta_{out} = 19.6\%$. From the comparison of calculation and experiments, the internal quantum efficiency at 1000 cd/m^2 is estimated to be 37.8%, i.e. considerably lower than the η_{IQE} obtained for the devices presented in this work.

From the comparison of the estimated internal quantum efficiency values for the two device architectures, it can be concluded that the top-emission OLED presented here exhibits a performance superior to similar devices in bottom-emission configuration. The reasons for this can be ascribed to (i) a changed charge carrier balance and (ii) an improved efficiency for the blue fluorescent emitter used in this study.

4. Conclusions

In summary, we demonstrated white-emitting OLEDs with top-emission structure, showing enhanced forward emission up to angles of 50°. The emission maxima can be kept stable with a carefully adjusted optical design of the device. Different anode materials were tested revealing a considerable influence on the spectral emission shape of the devices, due to an altered cavity emission. By changing electron blocking materials the device performance could be enhanced due to a lowered driving voltage for S-TAD. The devices exhibit high efficiencies of 13.3 lm/W luminous efficacy (device 4) and 5.3% external quantum efficiency (device 3). In comparison to comparable bottom-emitting devices the presented top-emission devices feature superior internal quantum efficiency. Besides high efficiencies excellent color coordinates (e.g. (0.44, 0.41), device 1) near the warm white point A were achieved. The emission can be tuned along the Planckian locus via brightness and shows color rendering indices up to 77 (device 2).

Acknowledgements

We thank NOVALED AG, Dresden for providing the p-dopant. This work was funded by the BMBF project FKZ 13N8855 (acronym "R2flex").

References

[1] J. Kido, K. Hogawa, K. Okuyama, K. Nagai, White light-emitting organic electroluminescent devices using the poly(N-vinylcarbazole) emitter layer doped with three fluorescent dyes, Appl. Phys. Lett. 64 (1994) 815.
[2] B.W. D'Andrade, S.R. Forrest, White organic light-emitting devices for solid state lighting, Adv. Mater. 18 (2004) 1585.
[3] S. Reineke, F. Lindner, G. Schwartz, N. Seidler, K. Walzer, B. Lüssem, K. Leo, White organic light-emitting diodes with fluorescent tube efficiency, Nature 459 (2009) 234.
[4] H. Kanno, Y. Sun, S.R. Forrest, Highly-efficiency top-emissive white-light-emitting organic electrophosphorescent devices, Appl. Phys. Lett. 86 (2005) 263502.
[5] S.-F. Hsu, C.-C. Lee, S.-W. Hwang, C.H. Chen, Highly efficient top-emitting white organic electroluminescent devices, Appl. Phys. Lett. 86 (2005) 253508.
[6] X. Zhu, J. Sun, X. Yu, M. Wong, H.-S. Kwok, High-performance top-emitting white organic light-emitting devices, Jpn. J. Appl. Phys. 46 (2007) 4054.
[7] M.-T. Lee, M.-R. Tseng, Efficient, long-life and Lambertian source of top-emitting white OLEDs using low-reflectivity molybdenum anode and co-doping technology, Curr. Appl. Phys. 8 (2008) 616.
[8] M. Thomschke, R. Nitsche, M. Furno, K. Leo, Optimized efficiency and angular emission characteristics of white top-emitting organic electroluminescent diodes, Appl. Phys. Lett. 94 (2009) 083303.
[9] Q. Huang, K. Walzer, M. Pfeiffer, K. Leo, Performance improvement of top-emitting organic light-emitting diodes by an organic capping layer: an experimental study, J. Appl. Phys. 100 (2006) 064507.
[10] H. Riel, S. Karg, T. Beierlein, W. Rieß, K. Neyts, Tuning the emission characteristics of top-emitting organic light-emitting devices by means of a dielectric capping layer: an experimental and theoretical study, J. Appl. Phys. 94 (2003) 5290.
[11] G. Schwartz, K. Fehse, M. Pfeiffer, K. Walzer, K. Leo, Highly efficient white organic light emitting diodes comprising an interlayer to separate fluorescent and phosphorescent regions, Appl. Phys. Lett. 89 (2006) 083509.
[12] G. Schwartz, K. Walzer, M. Pfeiffer, K. Leo, High efficiency white organic light emitting diodes combining fluorescent and phosphorescent emitter systems, Proc. SPIE 6192 (2006) 61920Q.
[13] K. Walzer, B. Maennig, M. Pfeiffer, K. Leo, Highly efficient organic devices based on electrically doped transport layers, Chem. Rev. 107 (2007) 1233.
[14] R. Meerheim, R. Nitsche, K. Leo, High-efficiency monochrome organic light emitting diodes employing enhanced microcavities, Appl. Phys. Lett. 93 (2008) 043310.
[15] M. Furno, R. Meerheim, M. Thomschke, S. Hofmann, B. Lüssem, K. Leo, Outcoupling efficiency in small-molecule OLEDs: from theory to experiment, Proc. SPIE 7617 (2010) 761716.
[16] S. Olthof, R. Meerheim, M. Schober, K. Leo, Energy level alignment at the interfaces in a multilayer organic light-emitting diode structure, Phys. Rev. B 79 (2009) 245308.
[17] C.-L. Lin, H.-C. Chang, K.-C. Tien, C.H. Wu, Influences of resonant wavelengths on performances of microcavity organic light-emitting devices, Appl. Phys. Lett. 90 (2007) 071111.
[18] M. Furno et al., in preparation.

Organic Electronics 11 (2010) 1683–1687

Contents lists available at ScienceDirect

Organic Electronics

journal homepage: www.elsevier.com/locate/orgel

Modified mass printing technique for the realization of source/drain electrodes with high resolution

G.C. Schmidt *, M. Bellmann, B. Meier, M. Hambsch, K. Reuter, H. Kempa, A.C. Hübler

Institute for Print and Media Technology, Chemnitz University of Technology, 09126 Chemnitz, Germany

ARTICLE INFO

Article history:
Received 30 April 2010
Received in revised form 16 July 2010
Accepted 23 July 2010
Available online 4 August 2010

Keywords:
Printed electronics
Mass printing
Flexography
Gravure printing
Surface wetting

ABSTRACT

We report on the development of a technique for the realization of source/drain electrodes of organic field-effect transistors (OFETs) with small channel length down to 10 μm. The process uses a combination of two different mass printing technologies (flexographic and gravure printing), which are both highly productive. In a first step a negative image of the electrode pattern was printed from an amorphous perfluorinated poly(alkenyl vinyl ether) (CYTOP™ CTL-809M), a material forming a surface of very low surface energy, followed by a full-tone-print of a conductive material, e.g. poly(3,4-ethylenedioxythiophene) doped with poly(styrenesulfonate) (PEDOT:PSS). Despite the full-tone-print the conductive ink was transferred in a patterned fashion due to the heterogeneous surface properties and formed very homogenous and smooth source/drain structures. On the basis of these source/drain electrodes OFETs, inverters and ring oscillators were realized by means of mass printing methods only.

© 2010 Elsevier B.V. All rights reserved.

1. Introduction

In the field of printed electronics, mass printing methods like offset, gravure or flexographic printing can play an important role because of their feasibility to produce electronic structures and films with extremely high throughput. Besides the significance of productivity, especially for low-cost products, it is essential to create structures with high resolution and homogeneity, even for simple integrated circuits. To find a solution for the combination of both demands new approaches have to be created.

Standard mass printing technologies have the potential to realize structures in the range of 20–50 μm in the field of graphic arts [1]. A better resolution is not necessary because of the limited ability of the human eye to differentiate between two points printed close to each other. One big challenge is to transfer these dimensions to printed electronics because of the different materials properties and higher quality requirements. However, substantial progress has been made in the last years. Offset printing was used to realize source/drain electrodes for OFETs with a channel length of 100 μm [2] and 50 μm [3], respectively. Flexography was used for this purpose as well, resulting in a channel length of 50–200 μm [4]. Finally, gravure printed source/drain electrodes with a channel length of 100 μm were used in order to set up a ring oscillator circuit with all other layers (semiconductor, insulator and gate) gravure printed too [5]. The usage of gravure printing to apply the active semiconductor was also reported for other electronic devices like rectifier diodes [6], OLEDs [7,8] and organic solar cells [9]. In spite of these promising results there are still no reports on successfully downsizing the channel length to and below values achievable with conventional printing of color inks.

In this paper we present a method to combine flexographic and gravure printing in order to achieve structural dimensions of 10 μm, which was derived from the process introduced in [10]. The technique uses the effect of wetting and dewetting of fluids on heterogeneous surfaces with different surface energy levels. Similar principles were

* Corresponding author. Tel.: +49 371 531 35175; fax: +49 371 531 835175.
E-mail address: georg.schmidt@mb.tu-chemnitz.de (G.C. Schmidt).

1566-1199/$ - see front matter © 2010 Elsevier B.V. All rights reserved.
doi:10.1016/j.orgel.2010.07.018

implemented by different research groups, either for the realization of source/drain electrodes [11–13] or for patterning of semiconductors [14,15]. However, in all of these cases a complicate and time-consuming pre-structuring of the substrate was necessary. Furthermore the application of the functional material was made by inkjet printing, which is a process of much lower productivity in comparison to mass printing, or by dip coating and spray coating [10], which tend to leave residuals on hydrophobic areas.

2. Experimental

The full roll-to-roll process for the realization of source/drain structures, called "Cyflex", is outlined in Fig. 1.

As substrate we used a commercially available smooth polyester foil (PET, DuPont Teijin Films) with a thickness of 100 μm and a surface roughness of 8 nm. After an inline corona pretreatment in order to enhance the surface energy from ~43 to ~60 mN/m, the pre-structuring of the substrate was performed by means of flexographic printing. In contrast to [10], an amorphous perfluorinated poly(alkenyl vinyl ether) (CYTOP™ CTL-809M, Asahi Glass) was transferred from an inked printing plate (Flint Group, FAH nyloflex). The most important reason for choosing this perfluorinated polymer was the ability of this material to generate a very smooth printed film ($R_a \approx 10$ nm, $R_z \approx 45$ nm) with an extremely low surface energy, measured to be $\sigma = 17.2$ mN/m ($\sigma_{pol} = 0.1$ mN/m). This results in a large contrast in terms of surface energy between covered and uncovered, areas of the substrate. Furthermore it was possible to print very thin (thickness $d_{CYTOP} = 10...60$ nm, depending on the polymer concentration) and small structures with a width between 100 and 10 μm. It should be noted that for the pre-structuring step a negative image of the source/drain electrodes had to be printed.

In order to form the electrodes themselves, a non-patterned full-tone gravure print of an in-house reformulated water-based dispersion of poly(3,4-ethylene dioxythiophene) doped with poly(styrene sulfonate) (PEDOT:PSS) formulation was applied. With this system smooth and homogenous layers could be printed on bare substrate areas, while no ink from the cells of the gravure cylinder was transferred to the areas with low surface energy. At least no residuals of the conductive ink could be detected on the CYTOP-structures. For a precise control of this separation process it is essential to optimize the interplay between the properties of the conductive ink (e.g. surface tension, viscosity) and the parameters of the printing process (e.g. cell volume and raster of the printing cylinder) together with the geometrical dimensions of the source/drain electrodes (finger width, channel length). In order to demonstrate the functionality of the printed source/drain structures top-gate OFETs, inverters and ring oscillators were built up using two different processes as depicted in Table 1. A spin-coating process was compared with a purely mass printing process using a roll-to-roll laboratory printing press. Details of the process steps and particularly the printing layout consisting of an endless repetition of source/drain fingers and self-aligned gates have been published elsewhere [5].

The surface tension of the PEDOT:PSS-formulations and the surface energy of the substrates were measured at room temperature on a OCA-20 contact angle meter from DataPhysics Instruments GmbH with the pendant and the sessile drop method, respectively. All geometrical values were determined using a profilometer Dektak 8 from Veeco. The transistors were electrically characterized by sweeping the gate voltage V_{GS} from +60 to −60 V with a constant source/drain-voltage of $V_{SD} = -60$ V under ambient conditions. The mobility was determined from the slope of the transfer curve by means of a standard procedure [16].

3. Results and discussion

As can be seen in Fig. 2, very smooth ($R_a \approx 10$ nm) and homogenous PEDOT:PSS–source/drain electrodes with a channel length of only 10 μm and a finger width of 90 μm were created by means of the "Cyflex" mass printing process. In order to achieve such small structures, all parameters involved were investigated carefully. Fig. 3 shows the relation between contact angle on CYTOP-layers and surface tension of different PEDOT:PSS-formulations, which were used to determine the optimum between good dewetting properties on CYTOP and good wetting behavior on uncovered foil. Micrographic images of examples for

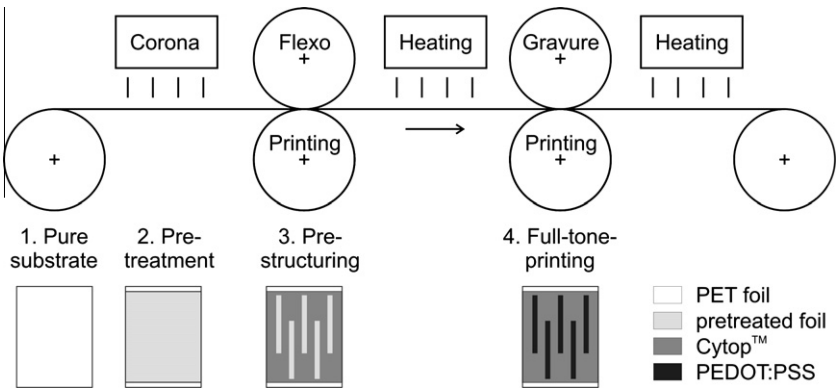

Fig. 1. "Cyflex"-process for the realization of source/drain electrodes.

Table 1
Used materials and technologies for the realization of OFETs.

Layer	Material	Process 1	Process 2	Thickness*
Substrate	PET	/	/	125 μm
Source/drain	PEDOT:PSS	Cyflex (Flexography + gravure)	Cyflex	130–150 nm
Semiconductor	F8T2 (ADS)	Gravure printing	Spin coating	55 ± 10 nm
Insulator (low-k)	P105 (Butylene copolymer, Merck)	Gravure printing	Spin coating	95 ± 15 nm
Insulator (high-k)	PMMA (Sigma–Aldrich)	Gravure printing	Spin coating	1700 ± 100 nm
Gate	Copper particle ink (Eckart)	Flexography	Painting	4800 ± 200 nm

* For printed devices.

different wetting behavior of the formulations are inserted into Fig. 3. The conductivity of the electrodes was measured to be ~30 S/cm, which represents an improvement of more than one order of magnitude in comparison to offset and inkjet printed PEDOT:PSS structures published in [3] and [17], respectively.

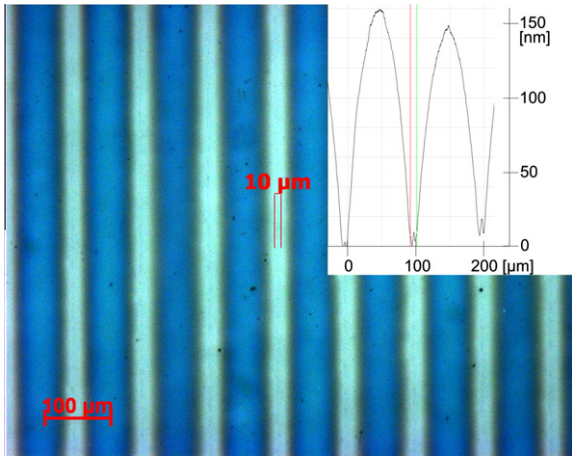

Fig. 2. Microscope image of source/drain electrodes with a channel length of 10 μm and a finger width of 90 μm; inset: profile of the structures.

The transfer characteristics of representative transistors based on "Cyflex"-printed source/drain electrodes with spincoated semiconductor and insulator and with different channel lengths are plotted in Fig. 4. For comparison the characteristics of fully mass-printed OFETs with the same channel length are shown as well. All transistors show good performance with an ON/OFF-ratio between 10^3 and 10^4, a threshold voltage of $-12\ldots-17$ V and a field-effect mobility in the range of $1\ldots3 \times 10^{-3}$ cm^2/Vs, respectively. These values are typical for fully mass-printed devices and the achieved mobility of the used semiconductor F8T2 is in the range of the results of other publications [2,20]. Higher mobility can be obtained using another semiconductor (e.g. TIPS-pentacene), but this would require significant effort in terms of optimization of the printing process. Hence, the more easily printable material was used here in order to demonstrate the structuring approach and leaving the introduction of a more advanced semiconductor for future work. There is, however, no significant difference between all-printed and spin-coated devices, demonstrating the compatibility of the "Cyflex"-process with subsequent printing steps. While the ON-current of the transistors increases nearly linear with decreasing channel length, the OFF-current for small channels of 10 μm is slightly

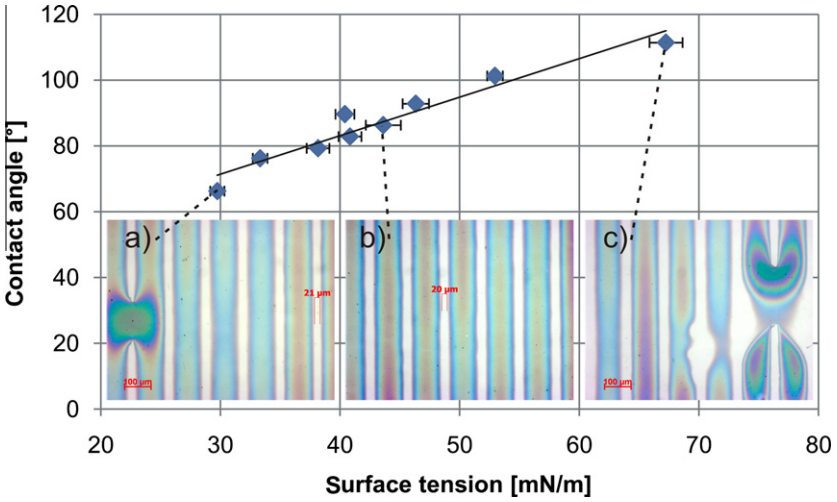

Fig. 3. Contact angle on CYTOP-layers vs. surface tension of different PEDOT:PSS-formulations. Inset: Optimization of the separation process by modification of the surface tension of the PEDOT:PSS formulation: (a) surface tension too low (shorts by bulges); (b) optimum formulation; (c) surface tension too high (dewetting of finger structures and shorts by bulges).

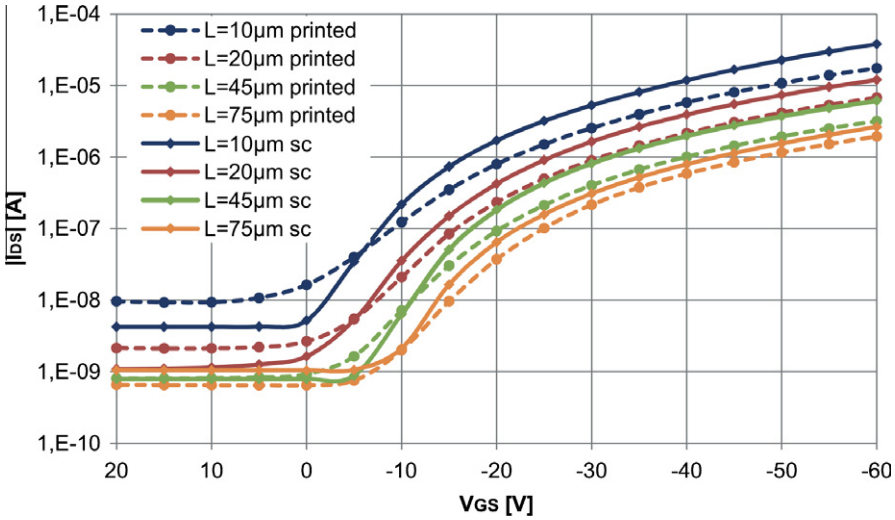

Fig. 4. Transfer characteristic of representative OFETs based "Cyflex"-printed source–drain electrodes with different channel lengths at $V_{DS} = -60$ V. OFETs were built up either by spin-coating (solid lines) or solely by means of mass printing techniques (dashed lines).

higher than the expected value. One reason for this result could be the increasing influence of the so-called short-channel effect [18]. It should be noted, that the thickness of the insulator remains constant while downsizing the channel length in our tests.

The broad range of channel lengths that can be created enables an interesting investigation concerning printed circuits. Ring oscillator circuits with five and seven inverter stages, respectively, were built up on source/drain electrodes with different channel lengths. The channel width

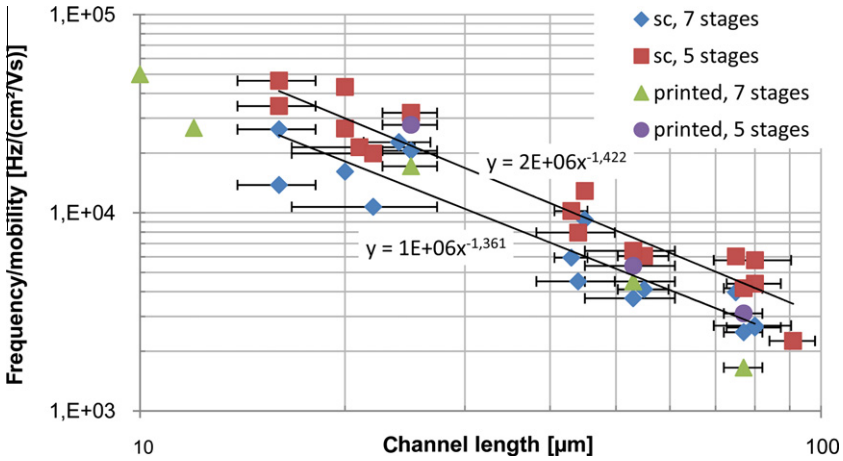

Fig. 5. Frequency–mobility-ratio of 5- and 7-stage ring oscillators made by spin-coating and mass printing techniques, respectively, as a function of the channel length at a supply voltage of $V_{DD} = -80$ V. The lines are power-law fits for the spin-coated devices.

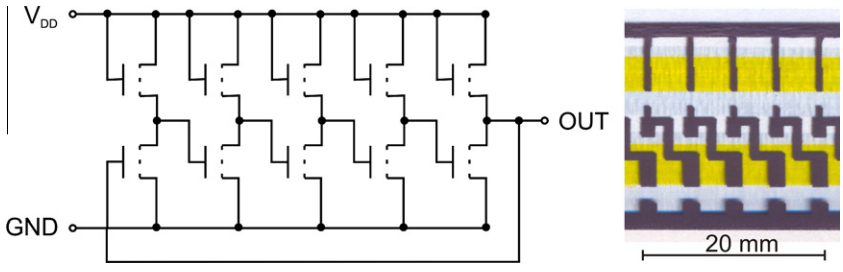

Fig. 6. Schematic circuit and photograph of the printed ring oscillator with five inverter stages.

of the drive and the load transistors was 30 and 6 mm, respectively. A printed circuit with five stages had a lateral size of 20 × 20 mm (Fig. 6). In the case of an ideal behavior of all components (i.e. no parasitic capacitances, no contact resistances, etc.) a quadratic increase of the frequency with decreasing channel length is expected according to

$$f = \frac{1}{2\pi} * \frac{\mu V_{DD}}{L^2} \quad (1)$$

where μ is the charge carrier mobility, V_{DD} is the supply voltage and L is the channel length. Experimental results obtained from spin-coated and all-printed ring oscillators are plotted in Fig. 5. In order to minimize the influence of mobility variations among the circuits, f/μ is plotted as a function of L. Here, μ is the mean mobility determined from the transistors of the respective circuit.

Fitting the data using a power-law dependence reveals that the behavior of all types of circuits is consistent with this kind of dependence. The exponent, however, is close to 1.4 in all cases. We ascribe the deviation from the expected quadratic behavior to parasitic (overlap capacitances, contact resistance, see [19]) and short-channel effects. Finally, we would like to point out that having created all-printed circuits with the up to now smallest channel length, we can extrapolate our data in order to estimate the oscillation frequency potentially achievable with all-printed organic materials. Based on our channel length of 10 μm and assuming a mobility of 1 cm^2/Vs – which can be reached with organic materials, but has not yet been demonstrated for printed devices – the estimation results in 80 kHz. It should be noted that this value can be improved by eliminating parasitic and short-channel effects.

4. Conclusions

The combination of the mass printing techniques flexography and gravure printing for the realization of source/drain electrodes by employing effects of surface wetting and dewetting on heterogeneous substrates turns out to be a promising solution. OFETs with channel length of 10 μm were produced solely by means of highly productive methods. The functionality of these structures was demonstrated with the help of spin-coated and mass-printed transistors and ring oscillators, which confirm a significant improvement of the geometrical and electrical properties in comparison to previous results of mass-printed devices. Fair values of switching frequencies can be expected provided that high-mobility semiconductors will be utilized for printed devices. Apart from further reducing the channel length, improvements are possible by reducing parasitic effects (e.g. by reducing overlap capacitances) and short-channel effects (by reducing the insulator layer thickness).

Acknowledgements

We acknowledge financial support from SMWK/ESF by the project No. 9212-231631-74. We sincerely thank M. Bartzsch, M. Stanel, B. Trnovec and N. Wetzold for technical support and inspiring discussions. Furthermore we wish to thank Esko Artwork for structuring the flexo plates and to Eckart GmbH for supplying us with copper ink.

References

[1] H. Kipphan (Ed.), Handbook of Print Media, Springer, Berlin, 2001.
[2] A.C. Hübler, F. Dötz, H. Kempa, H.E. Katz, M. Bartzsch, N. Brandt, I. Hennig, U. Fügmann, S. Vaidyanathan, J. Granstrom, S. Liu, A. Sydorenko, T. Zillger, G. Schmidt, K. Preissler, E. Reichmanis, P. Eckerle, F. Richter, T. Fischer, U. Hahn, Ring oscillator fabricated completely by means of mass-printing technologies, Org. Electr. 8 (2007) 480–486.
[3] D. Zielke, A.C. Hübler, U. Hahn, N. Brandt, M. Bartzsch, U. Fügmann, T. Fischer, J. Veres, S. Ogier, Polymer-based organic field-effect transistor using offset printed source/drain structures, Appl. Phys. Lett. 87 (12, S) (2005) 123508–123510.
[4] T. Mäkelä, S. Jussila, H. Kosonen, T.G. Bäcklund, H.G.O. Sandberg, H. Stubb, Utilizing roll-to-roll techniques for manufacturing source/drain electrodes for all-polymer transistors, Synth. Met. 153 (2005) 285–288.
[5] M. Hambsch, K. Reuter, M. Stanel, G. Schmidt, H. Kempa, U. Fügmann, U. Hahn, A.C. Hübler, Uniformity of fully gravure printed organic field-effect transistors, Mater. Sci. Eng. B 170 (2010) 93–98.
[6] K.E. Lilja, T.G. Bäcklund, D. Lupo, T. Hassinen, T. Joutsenoja, Gravure printed organic rectifying diodes operating at high frequencies, Org. Electr. 10 (2009) 1011–1014.
[7] J.J. Michels, S. de Winter, L. Symonds, Process optimization of gravure printed light-emitting polymer layers by a neural network approach, Org. Electr. 10 (2009) 1495–1504.
[8] P. Kopola, M. Tuomikoski, R. Suhonen, A. Maaninen, Gravure printed organic light emitting diodes for lighting applications, Thin Solid Films 517 (2009) 5757–5762.
[9] M. Tuomikoski, P. Kopola, H. Jin, M. Ylikunnari, J. Hiitola-Keinänen, M. Välimäki, M. Aikio, J. Hast, Roll-to-Roll Manufacturing of Organic Photovoltaic Modules, IEEE, European Microelectronics and Packaging Conference (EMPC). Rimini, Italy, 15–18 June 2009.
[10] T. Fischer, U. Hahn, M. Dinter, M. Bartzsch, G. Schmidt, H. Kempa, A.C. Hübler, Novel in-line method for patterned deposition of conductive structures, Org. Electr. 10 (2009) 547–550.
[11] H. Sirringhaus, T. Kawase, R.H. Friend, T. Shimoda, M. Inbasekaran, W. Wu, E.P. Woo, High-resolution inkjet printing of all-polymer transistor circuits, Science 290 (2000) 15.
[12] C.W. Sele, T. von Werne, R.H. Friend, H. Sirringhaus, Lithography-free, self-aligned inkjet printing with sub-hundred-nanometer resolution, Adv. Mater. 17 (2005) 997–1001.
[13] J.Z. Wang, Z.H. Zheng, H.W. Li, W.T.S. Huck, H. Sirringhaus, Polymer field effect transistors fabricated by dewetting, Synth. Met. 146 (2004) 287–290.
[14] M.L. Chabinyc, W.S. Wong, A. Salleo, K.E. Paul, R.A. Street, Organic polymeric thin-film transistors fabricated by selective dewetting, Appl. Phys. Lett. 81 (2002) 22.
[15] A.L. Briseno, M. Roberts, M. Ling, H. Moon, E.J. Nemanick, Z. Bao, Patterning organic semiconductors using "dry" poly(dimethylsiloxane) elastomeric stamps for thin film transistors, J. Am. Chem. Soc. 128 (2006) 3880–3881.
[16] A.R. Brown, C.P. Jarret, D.M. Leeuw, M. Matters, Field-effect transistors made from solution-processed organic semiconductors, Synth. Met. 88 (1997) 37–55.
[17] J.A. Lim, J.H. Cho, Y.D. Park, D.H. Kim, M. Hwang, K. Cho, Solvent effect of inkjet printed source/drain electrodes on electrical properties of polymer thin-film transistors, Appl. Phys. Lett. 88 (2006) 082102.
[18] M. Leufgen, U. Bass, T. Muck, T. Borzenko, G. Schmidt, J. Geurts, V. Wagner, L.W. Molenkamp, Optimized sub-micron organic thin-film transistors: the influence of contacts and oxide thickness, Synth. Met. 146 (2004) 341–345.
[19] A. Hoppe, D. Knipp, B. Gburek, A. Benor, M. Marinkovic, V. Wagner, Scaling limits of organic thin film transistors, Org. Electr. 11 (2010) 626–631.
[20] A. Facchetti, Semiconductors for organic transistors, Materialstoday 10 (3) (2007).

Organic Electronics 11 (2010) 1688–1692

Contents lists available at ScienceDirect

Organic Electronics

journal homepage: www.elsevier.com/locate/orgel

Letter

Self-assembly of organic channel/polymer dielectric layer in solution process for low-voltage thin-film transistors

Ji Hoon Park [a], Kwang H. Lee [a], Sung-jin Mun [a], Gunwoo Ko [a], Seung Jin Heo [a], Jae Hoon Kim [a], Eugene Kim [b], Seongil Im [a,*]

[a] Institute of Physics and Applied Physics, Yonsei University, Seoul 120-749, South Korea
[b] Department of Information Display Engineering, Hongik University, Seoul 121-791, South Korea

ARTICLE INFO

Article history:
Received 15 March 2010
Received in revised form 9 July 2010
Accepted 23 July 2010
Available online 4 August 2010

Keywords:
Solution process
Low-voltage
Polymer blend
Organic thin-film transistor

ABSTRACT

We report on the solution-processed thin-film transistors (TFTs) fabricated by the vertical flowing of the viscous 6,13-bis(triisopropylsilylethynyl) pentacene (TIPS-pentacene) and isotatic (*i*-) poly-(methyl methacrylate) (PMMA) blend. According to the optical-absorption and X-ray diffraction spectra, the solution-processed film appeared self-assembled with TIPS-pentacene (up) and *i*-PMMA dielectric (down) layers on substrates. As fabricated on a highly capacitive 100 nm-thick AlO_x dielectric, our device displayed a high mobility of 0.34 cm^2/V s, a low operation voltage of −15 V, and little hysteresis.

© 2010 Elsevier B.V. All rights reserved.

1. Introduction

Organic thin-film transistors (TFTs) have attracted a great deal of attention over last decades, due to their advantage of low cost fabrication, which brings their research scope to solution processes, such as gravure printing, ink jet printing, and spin coating [1–4]. In order to meet the requirements for industrialization of organic TFTs, they should have performance uniformity over batch, a decent mobility at a low operational voltage, and electrical stability without gate hysteresis. A small-molecule semiconducting material, 6,13-bis(triisopropylsilylethynyl) pentacene (TIPS-pentacene) has been demonstrated as one of the potential active materials for solution-based process, due to its good performance and solubility [4–10]. However, its device performance over batch is not uniform in general solution processes such as drop casting, ink jetting, and spin-casting [4–7]. Among above processes, spin-casting is more or less recommendable in terms of one batch uniformity but it usually brings a small grain size of TIPS-pentacene leading to poor device mobilities [4]. Furthermore, gate-bias hysteresis of TFTs with sole-TIPS-pentacene channel has rarely been reported but in fact a large hysteresis is often suspected [5,7]. In the present study, a possible solution for TIPS-pentacene based TFTs to be highly-performing hysteresis-free devices with batch-by-batch uniformity is suggested and was implemented by blending TIPS-pentacene and insulating isotatic (*i*-) poly-(methyl methacrylate) (PMMA), since the *i*-PMMA is reported to have good leakage-protecting and hysteresis-minimizing properties [11,12]. This type of blending has been recently implemented by other groups aiming at the self-assembly of the semiconductor/dielectric layers but is still worthy of re-evaluating. Our work uses "vertical flowing" technique of blend solution and is thus distinguished from the previously-reported works [4–9]. Our study scientifically reveals the layered channel/insulator structure in the organic thin-film, which was not clearly proved but only conjectured [6,8,9]. As a final result of our blending method, we demonstrate a hysteresis-free low-voltage-driven TIPS-pentacene TFT with a high mobility of 0.34 cm^2/V s operating at −15 V on glass substrate.

* Corresponding author. Tel.: +82 2 2123 2842; fax: +82 2 392 1592.
E-mail address: semicon@yonsei.ac.kr (S. Im).

1566-1199/$ - see front matter © 2010 Elsevier B.V. All rights reserved.
doi:10.1016/j.orgel.2010.07.020

2. Experimental section

With purchased TIPS-pentacene (Polysis Pure Products Co.) and *i*-PMMA (Aldrich) 3–3.4 wt.% TIPS-pentacene/*i*-PMMA blend (1:1 weight ratio) was dissolved in cyclohexanone and toluene (Aldrich) co-solvent (weight ratio = 1.3:1), which makes a viscous solution to control the total thickness of TIPS-pentacene/*i*-PMMA blend on a substrate. The two mixed solvents were expected to properly increase the viscosity, simultaneously well dissolving the both of *i*-PMMA and TIPS-pentacene. A cleaned 200 nm-thick SiO_2 on p^+-Si was used as a substrate and common gate dielectric for a high voltage organic TFT, and hexamethyldisilazane (HMDS) was coated by spin-casting and annealed at 110 °C, to make the SiO_2 surface as hydrophobic as *i*-PMMA. TIPS-pentacene/*i*-PMMA blend solution was flowed through pipette on the upstanding SiO_2/p^+-Si substrate as shown in Fig. 1a. (Sole TIPS-pentacene solution without *i*-PMMA was not viscous enough to form a thin-film organic semiconductor on the substrates.) During the drying process, the substrate was kept in upstanding position and we could expect a directional crystallization of solid TIPS-pentacene (Fig. 1b), which was really observed by optical microscopy (Fig. 1c). Boiling point of a solvent cyclohexanone is known as 151 °C which is quite high. In general the high boiling point property of a solvent makes its evaporation slow, so helping solution-based TIPS-pentacene to be highly crystalline during the drying. [3–5,7] After drying the solution, the solution-deposited sample was placed in vacuum desiccators overnight for removal of solvents. The final thickness of our organic film was ~330 nm as its cross section was measured by scanning electron microscopy. The 200 nm-thick source/drain (S/D) Au electrodes were finally deposited on the processed TIPS-pentacene/*i*-PMMA blend by thermal evaporation (Fig. 1d); this TIPS-pentacene TFT has the nominal channel length (L) and width (W) of 90 and 1000 μm, respectively. For low-voltage TFTs on glass, a bottom gate electrode of 50 nm-thick Al was thermally evaporated to be patterned on the glass through a shadow mask. After that, 100 nm-thick AlO_x film was deposited by rf magnetron sputtering at room temperature (RT) [13]. HMDS coating on the oxide, the vertical flowing of TIPS-pentacene/*i*-PMMA blend layer, and S/D Au patterning were conducted on the AlO_x film with the same manner as implemented on the SiO_2/p^+-Si substrate. All electrical characterizations on devices were carried out in the dark at RT. Ultraviolet (UV)-absorption and X-ray diffraction (XRD) measurements were performed on TIPS-pentacene/*i*-PMMA films that was prepared on HMDS-coated glass.

3. Results and discussion

As observed in Fig. 1b and c, the viscous TIPS-pentacene/*i*-PMMA blend showed directional crystallization after vertically flowed on the HMDS-modified substrate. The nucleation and unidirectional growth of pentacene crystalline solid evidently began from the edge of the blend-strip. (In contrast to our vertical flow technique, a conventional drop casting method, where the dropped solution dries in a manner of more-or-less horizontal spreading, can hardly guarantee any uniform performance of OTFT devices, since in that case the crystallization direction of pentacene is not unidirectional but radial from the solution drop edge toward its center) [14]. Moreover, since the TIPS-pentacene/*i*-PMMA blend separated into two

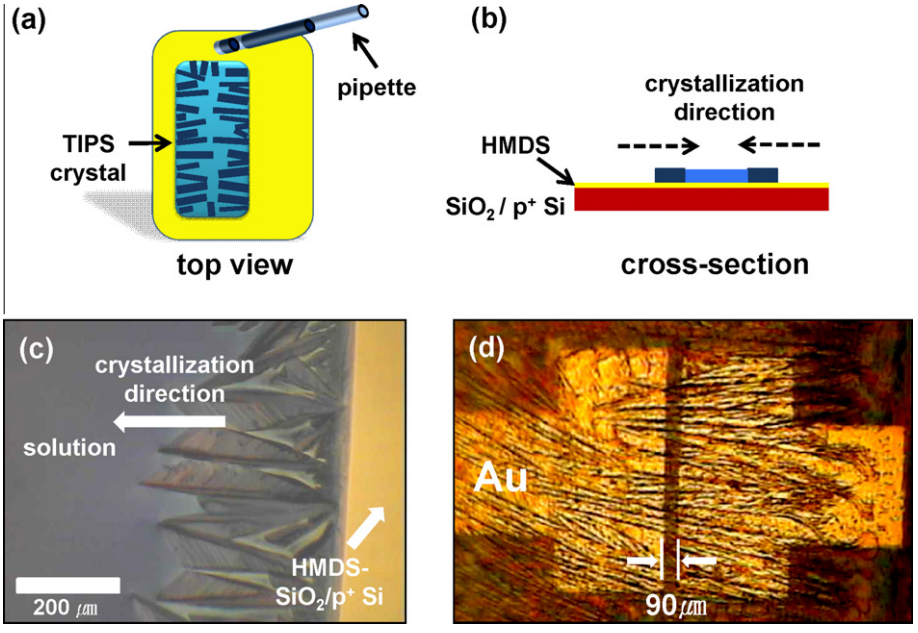

Fig. 1. (a) A schematic top-view of our "vertical flow" method for fabrication of TIPS-pentacene/*i*-PMMA blend layer. (b) Cross-section view of the process. Dotted arrow indicates the direction of crystallization. (c) Optical microscope image obtained from top-view location. (d) Photographic plan view of our TFT fabricated by "vertical flow" method.

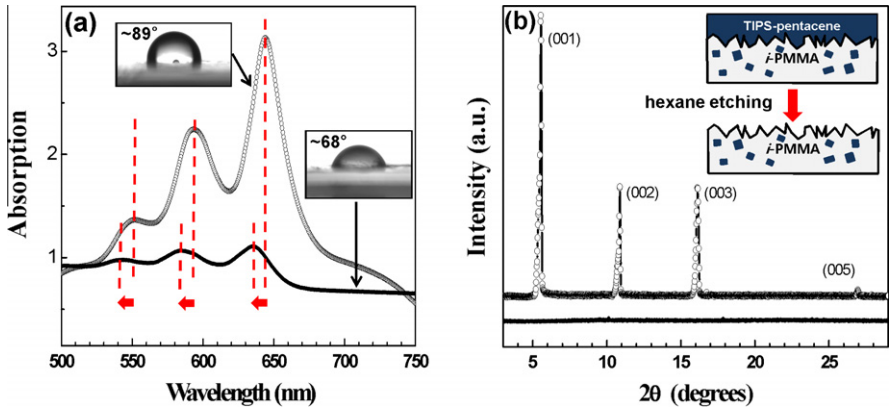

Fig. 2. (a) UV-absorption spectra of TIPS-pentacene/*i*-PMMA self-assembled layer (dotted line) and hexane-etched layer (solid line) on HMDS-treated glass. Inset shows contact angle images of DI water on each film. (b) XRD spectra obtained from identical samples. Inset displays schematic structure of blend film before and after etching.

chemically different solid phases after solidification, it is likely that self-assembly (or segregation) of *i*-PMMA and TIPS-pentacene might take place on the HMDS-functionalized oxide substrate forming two separated layers, prior to the directional crystalline growth. Fig. 2a and b display UV-absorption and XRD spectra, respectively as obtained from our solution-processed TIPS-pentacene/*i*-PMMA film on HMDS-functionalized glass. According to UV-absorption

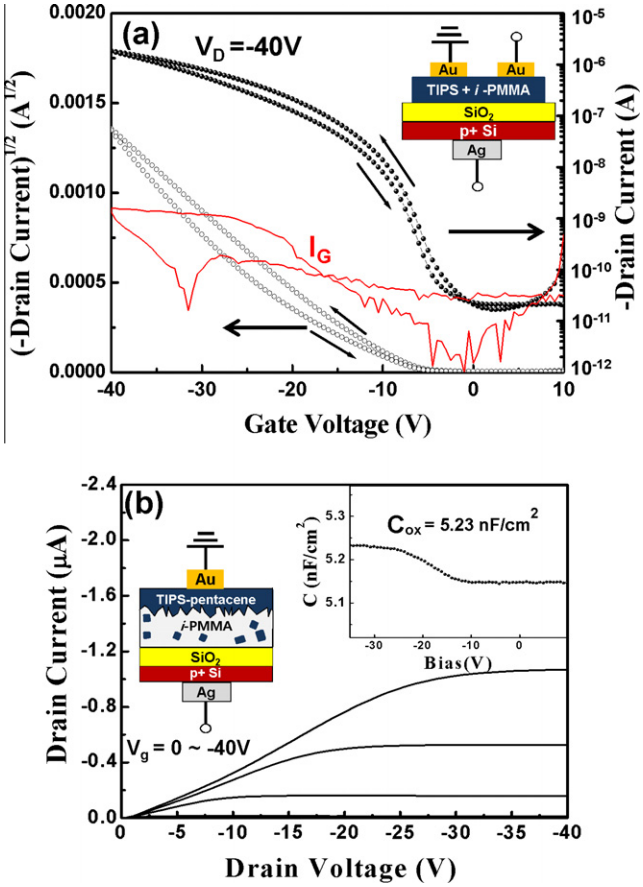

Fig. 3. $\sqrt{-I_D} - V_G$ and $\log_{10}(-I_D) - V_G$ plots obtained from our TFT based on TIPS-blend on SiO_2 (200 nm) gate dielectric. Inset shows schematic cross-section of our device. (b) $I_D - V_D$ curve obtained from the same device. Inset plot shows $C - V$ characteristic directly measured from MIS part of our TFT device. I_G means gate leakage current (<1 nA).

spectra, pristine thin-film exhibits strong absorption peaks at 644, 593.5, and 552 nm which are corresponding to those of reported TIPS-pentacene crystal [10]. However, after hexane-etching was carried out with the same sample, the peak intensities were considerably reduced and some amount of peak shift is also shown (see the arrows). This means that the hexane-etching very much removed the TIPS-pentacene layer [6], and the inset contact angles on the sample surfaces also proves this etching effect as measured before and after hexane-etching, because the surface of *i*-PMMA is less hydrophobic than that of TIPS-pentacene crystal. (It is also important to know that the hydrophobicity or surface energy of *i*-PMMA is somewhat similar to that of the HMDS-functionalized surface in view of contact angle, ~68° and that is why the *i*-PMMA moves down to be segregated on the HMDS-functionalized substrate surface.) The XRD spectra in Fig. 2b further support this hexane-etching effect. Pristine thin-film shows strong diffraction peaks that indicate a well-ordered pentacene crystalline structure with the interlayer spacing of 15.88, 8.11, 5.49, and 3.30 Å [4–8], while the same sample displays no peaks after hexane-etching. So, UV-absorption and XRD results may lead to the following scheme of solid TIPS-pentacene/*i*-PMMA structure; our TIPS-pentacene/*i*-PMMA film consists of two up/down-separated layers but a little amount of pentacene molecules are spatially embedded inside the *i*-PMMA film. The scheme is reasonable because the absorption peaks of hexane-etched film are closer to those of TIPS-pentacene molecules than to those of crystalline TIPS-pentacene.

Based on above understandings, we fabricated two types of TIPS-pentacene TFTs: TFTs on HMDS-functionalized 200 nm-thick SiO_2/p^+-Si and 100 nm-thick sputter-deposited-AlO_x/patterned Al (on glass). We surely expected the formation of bilayer dielectric (namely, *i*-PMMA/oxide bilayer) for the TFTs. Fig. 3a and b shows the transfer curves ($\log_{10}(-I_D) - V_G$) and output curves ($I_D - V_D$) of our devices fabricated on SiO_2/p^+-Si, respectively. Operation voltage was −40 V and the device hysteresis was not as large as ~1.5 V. Interesting to note is the inset *C*–*V* result from Au/TIPS-pentacene/*i*-PMMA-SiO_2 metal–insulator-semiconductor (MIS) sample. For the accumulation state, the *C* value turned out to be only 5.23 nF/cm^2, which is much lower than that of 200 nm-thick SiO_2 (~17 nF/cm^2), and this again proves that the insulator dielectric for the TFT is not just the SiO_2 but also contains thick *i*-PMMA. Adopting the total serial capacitance (5.23 nF/cm^2), the field effect mobility of our TFTs is estimated to be ~0.0324 ± 0.007 cm^2/V s with a high on/off ratio of ~10^5. (In order to confirm batch-to-batch uniformity, we fabricated the TIPS-pentacene devices based on SiO_2/p^+-Si taking three different batches under similar ambient conditions (temperature, humidity). Not quite a different mobility was obtained from all the

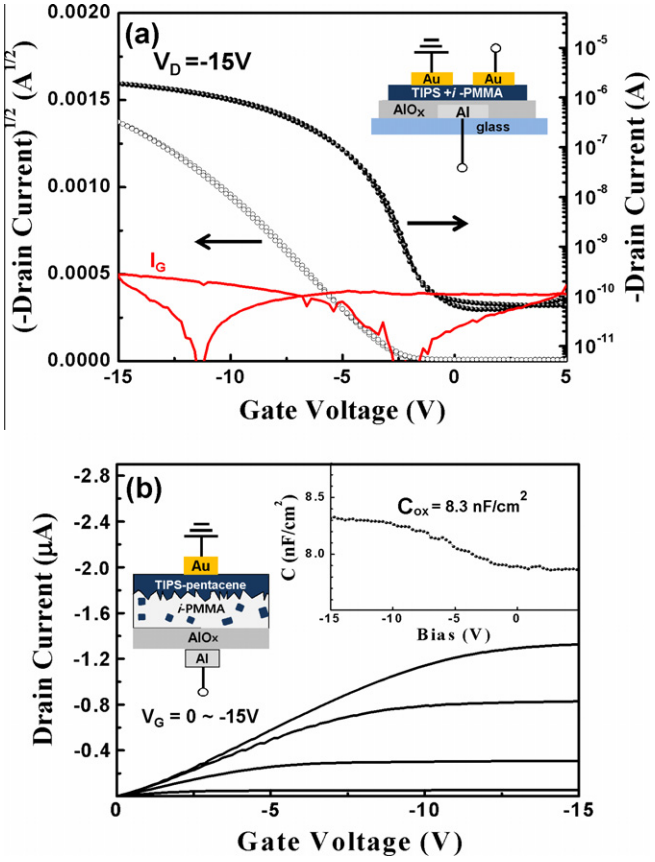

Fig. 4. (a) $\sqrt{-I_D} - V_G$ and $\log_{10}(-I_D) - V_G$ plots obtained from our TFT based on TIPS-blend on AlO_x (100 nm) gate dielectric. Inset shows the device schematic. (b) $I_D - V_D$ curve obtained from the same device. Inset plot shows *C*–*V* characteristic directly measured from MIS part of our TFT device.

batches (6 devices per batch) while the other performance parameters were very similar one another. Saturation mobility was estimated from each batch, to be 0.0319 ± 0.011, 0.0324 ± 0.007, and 0.0432 ± 0.009 cm^2/V s, respectively.

In the same manner of observation, Fig. 4a and b) display the transfer curves ($\log_{10}(-I_D)-V_G$) and output curves ($I_D - V_D$) of our devices fabricated on 100 nm-thick sputter-deposited-AlO_x/patterned Al, respectively. In this case, low-voltage device operation was possible at −15 V, which might be attributed to the dielectric capacitance (∼62 nF/cm^2) of 100 nm-thick AlO_x [13]. However, the total capacitance of Au/TIPS-pentacene/*i*-PMMA-AlO_x MIS capacitor was measured to be only ∼8.30 nF/cm^2 (Fig. 4b inset) due to the low capacitance value of thick *i*-PMMA (the value is 60% increased, compared to that of SiO_2/p^+-Si case). Nevertheless our device on AlO_x operates very well at −15 V without even hysteresis. We think that the 60%-improved dielectric capacitance was still effective to lower the operation gate voltage (from 40 to 15 V). The field effect mobility of this low-voltage TFT was estimated to be as high as ∼0.34 ± 0.03 cm^2/V s with an on/off current ratio over $\sim 10^4$, subthreshold swing of 0.8 V/dec and threshold voltage of −2.7 V. As a final analysis, we also calculated the capacitance of *i*-PMMA layer itself by considering serially connected capacitors (*i*-PMMA-oxide), and obtained the values of 7.6 and 9.5 nF/cm^2 for SiO_2 and AlO_x cases, respectively. Those two were not exactly identical but reasonably similar.

4. Conclusion

In summary, we have fabricated the solution-processed organic TFTs by the vertical flowing of the viscous TIPS-pentacene and *i*-PMMA blend. It was observed through the optical-absorption and X-ray diffraction that the solution-processed film consists of two separated layers of TIPS-pentacene and *i*-PMMA dielectric. When we fabricated the organic TFTs on HMDS-functionalized dielectric oxides, a high saturation mobility of ∼0.34 $cm^2/V{\cdot}s$ was achieved at only −15 V with little hysteresis. We thus conclude that our work and understanding are promising for the realization of stable solution-based low-voltage organic TFTs.

Acknowledgements

The authors acknowledge the financial support from KOSEF (NRL program, No. 2009-8-0403), the 21st Century Frontier R&D Program funded by the MKE (Information Display R&D center, F0004022-2009), and Brain Korea 21 Project. J.H. Park acknowledges the Seoul Science Fellowship.

References

[1] C.C. Dimitrakopoulos, P.R.L. Malenfant, Adv. Mater. 14 (2002) 99.
[2] H. Yan, Z. Chen, Y. Zheng, C. Newman, J.R. Quinn, F. Dötz, M. Kastler, A. Facchetti, Nature 457 (2009) 679.
[3] M.H. Choi, S.H. Lee, S.H. Han, Y.H. Kim, D.J. Choo, Jin Jang, S.K. Kwon, SID '08 Digest (2008) 440.
[4] Y.-H. Kim, Y.U. Lee, J.-I. Han, S.-M. Han, M.-K. Han, J. Electrochem. Soc. 154 (2007) H995.
[5] S.K. Park, T.N. Jackson, J.E. Anthony, D.A. Mourey, Appl. Phys. Lett. 91 (2007) 063514.
[6] M. Madec, D. Crouch, G.R. Llorente, T.J. Whittle, M. Geoghegan, S.G. Yeates, J. Mater. Chem. 18 (2008) 3230.
[7] C.S. Kim, S. Lee, E. Gomez, J.E. Anthony, Y.-L. Loo, Appl. Phys. Lett. 93 (2008) 103302.
[8] J. Kang, N. Shin, D.Y. Jang, V.M. Prabhu, D.Y. Yoon, J. Am. Chem. Soc 130 (2008) 12273.
[9] R. Hamilton, J. Smith, S. Ogier, M. Heeney, J.E. Anthony, I. McCulloch, J. Veres, D.D.C. Bradley, T.D. Anthopoulos, Adv. Mater. 21 (2009) 2106.
[10] Y. Li, Y. Wu, P. Liu, Z. Prostran, S. Gardner, B.S. Ong, Chem. Mater. 19 (2007) 418.
[11] S.H. Kim, J. Jang, H. Jeon, W.M. Yun, S. Nam, C.E. Park, Appl. Phys. Lett. 92 (2008) 183306.
[12] J.H. Park, D.K. Hwang, J. Lee, S. Im, E. Kim, Thin Solid Films 515 (2007) 4041.
[13] J. Lee, S.S. Kim, S. Im, J. Vac, Sci. Technol. B 21 (2003) 953.
[14] J.A. Lim, W.H. Lee, H.S. Lee, J.H. Lee, Y.D. Park, K. Cho, Adv. Funct. Mater. 18 (2008) 229.

Organic Electronics 11 (2010) 1693–1700

Contents lists available at ScienceDirect

Organic Electronics

journal homepage: www.elsevier.com/locate/orgel

Oxygen doping of P3HT:PCBM blends: Influence on trap states, charge carrier mobility and solar cell performance

Julia Schafferhans [a,*], Andreas Baumann [a], Alexander Wagenpfahl [a], Carsten Deibel [a], Vladimir Dyakonov [a,b]

[a] Experimental Physics VI, Faculty of Physics and Astronomy, Julius-Maximilians-University of Würzburg, Am Hubland, 97074 Würzburg, Germany
[b] Bavarian Center of Applied Energy Research e.V. (ZAE Bayern), Am Hubland, 97074 Würzburg, Germany

ARTICLE INFO

Article history:
Received 4 March 2010
Received in revised form 22 June 2010
Accepted 20 July 2010
Available online 3 August 2010

Keywords:
Organic solar cells
Oxygen
Degradation
TSC
CELIV
Macroscopic simulation

ABSTRACT

We investigated the influence of oxygen on the performance of P3HT:PCBM (poly(3-hexylthiophene):[6,6]-phenyl C61 butyric acid methyl ester) solar cells by current–voltage, thermally stimulated current (TSC) and charge extraction by linearly increasing voltage (CELIV) measurement techniques. The exposure to oxygen leads to an enhanced charge carrier concentration and a decreased charge carrier mobility. Further, an enhanced formation of deeper traps was observed, although the overall density of traps was found to be unaffected upon oxygen exposure. With the aid of macroscopic simulations, based on solving the differential equation system of Poisson, continuity and drift-diffusion equations in one dimension, we demonstrate the influence of a reduced charge carrier mobility and an increased charge carrier density on the main solar cell parameters, consistent with experimental findings.

© 2010 Elsevier B.V. All rights reserved.

1. Introduction

Power conversion efficiencies of almost 8% for organic solar cells have already been achieved, with growing tendency [1]. A critical issue yet to be addressed are the factors influencing the device lifetime. To gain a detailed understanding of the device stability, as well as the underlying degradation mechanisms and their impact on the solar cell performance is an important prerequisite for lifetime enhancements.

Organic solar cells undergo many degradation pathways during their lifetime. Efficiency losses due to light [2], oxygen [3,4] and water [5] are reported. The details of the degradation processes, however, are still not completely understood. Other studies, on the contrary, are only focused on the degradation of a single active material instead of the blend. For example for P3HT oxygen is known to form a charge transfer complex [6] resulting in *p*-doping of P3HT [7,8], which is also investigated theoretically by band-structure calculations [9]. Furthermore, oxygen induced degradation of P3HT is reported to result in decreased mobilities [6,10] and increased trap densities [10]. In the case of C60, oxygen also causes decreased electron mobilities [11,12] and increased trap densities [13], as demonstrated by investigations of C60 based field effect transistors.

This paper addresses the oxygen induced degradation of poly(3-hexylthiophene):[6,6]-phenyl C61 butyric acid methyl ester solar cells in the dark, as well as under simultaneous illumination. Detailed investigations including charge carrier mobility, charge carrier density and defect spectroscopic measurements are performed to get an insight of the degradation mechanism due to oxygen in P3HT:PCBM solar cells.

2. Experimental

The investigated bulk heterojunction solar cells were prepared by spin coating P3HT:PCBM (ratio 1:0.8) blends

* Corresponding author. Tel.: +49 931 3180003.
E-mail addresses: julia.schafferhans@physik.uni-wuerzburg.de (J. Schafferhans), dyakonov@physik.uni-wuerzburg.de (V. Dyakonov).

1566-1199/$ - see front matter © 2010 Elsevier B.V. All rights reserved.
doi:10.1016/j.orgel.2010.07.016

made from solutions of 30 mg/ml in chlorobenzene on poly(3,4-ethylenedioxythiophene) poly(styrenesulfonate) (Pedot:PSS) covered indium tin oxide/glass substrates. The active layer was about 240 nm thick. After an annealing step of 10 min at 130 °C, Ca (1.5 nm)/Al (60 nm) contacts were evaporated thermally (base pressure during evaporation $< 7 \cdot 10^{-7}$ mbar). The effective areas of the solar cells were 3 mm^2 and 9 mm^2.

PEDOT:PSS was purchased by H.C. Starck (CLEVIOS P VP Al 4083). P3HT was delivered by BASF (Sepiolid P200), PCBM (purity 99.5%) by Solenne. All materials were used without further purification. All preparation steps were performed in a nitrogen glovebox and an attached thermal vacuum evaporation chamber.

Initial current–voltage (IV) characteristics of the solar cells were measured in the nitrogen glovebox. For the illumination of the cells we used an Oriel 81160 AM1.5G solar simulator. The power conversion efficiencies of the investigated samples were 3–3.5%.

Degradation studies of the unprotected solar cells were performed in a closed cycle cryostat. During the thermally stimulated current (TSC), charge carrier extraction by linearly increasing voltage (CELIV) [14,15] and IV–measurements the cryostat was filled with helium as contact gas. To investigate the influence of oxygen on the solar cells, the helium was replaced with synthetic air ($80\%N_2, 20\%O_2, < 1$ ppm H_2O) for different degradation times. Thus, the effect of humidity was excluded. This exposure was always done at a constant temperature of 300 K. Two different degradation conditions were investigated: in synthetic air either in the dark or under illumination. For the latter we used a 10 W high power white light emitting diode (Seoul). The light intensity was adjusted to match the short circuit current of the non degraded cells obtained under the solar simulator. The LED was also used for the illuminated IV-curves in the cryostat.

For TSC measurements the trap filling was achieved by illumination of the samples at 18 K for 5 min using the 10 W LED. After a dwell time of five minutes the temperature was increased with a constant heating rate of 7 K/min up to 300 K. The TSC signals were detected by a Sub-Femtoamp Remote Source Meter (Keithley 6430) without applying an external field, implying that the detrapped charge carriers were extracted from the samples only due to the built-in voltage. Further details of the TSC measurements are described elsewhere [10].

CELIV measurements were performed at 300 K. The peak voltage of the triangular bias pulse in reverse direction was $V_a = 2$ V applied on the Ca/Al electrode. A voltage pulse width of 50 μs was chosen.

3. Results and discussion

3.1. Experimental results

The IV-curves for different degradation times between 0 and 120 h in synthetic air in the dark are shown in Fig. 1a. The obtained values for the power conversion efficiency (PCE), fill factor (FF), open circuit voltage (V_{oc}) and short circuit current (J_{sc}), normalized to the initial values are presented in Fig. 1b. The observed efficiency loss with dark degradation time is only due to J_{sc}, which decreases about 60% within 120 h, whereas V_{oc} and FF remain almost constant. Since the exposure of the samples to synthetic air in the dark results only in a loss in J_{sc}, a degradation of the electrodes being the origin of these findings can be excluded. Degradation (oxidation) of the Ca/Al electrode would result in the occurrence of an s-shaped IV-curve [16], at least in a strong loss in FF or V_{oc}. Neither of these effects was observed within the timescale of degradation considered here.

In contrast to degradation in synthetic air in the dark, the efficiency loss due to degradation in synthetic air and simultaneous illumination (Fig. 2a and b) occurs on a faster time scale – about 30% efficiency loss within 180 min – and is caused by a decrease of J_{sc}, as well as FF and V_{oc}, which all decrease about 10% within this time scale. Since, in the case of dark degradation, FF and V_{oc} are unaffected, the decrease of both during photodegradation is due to light in

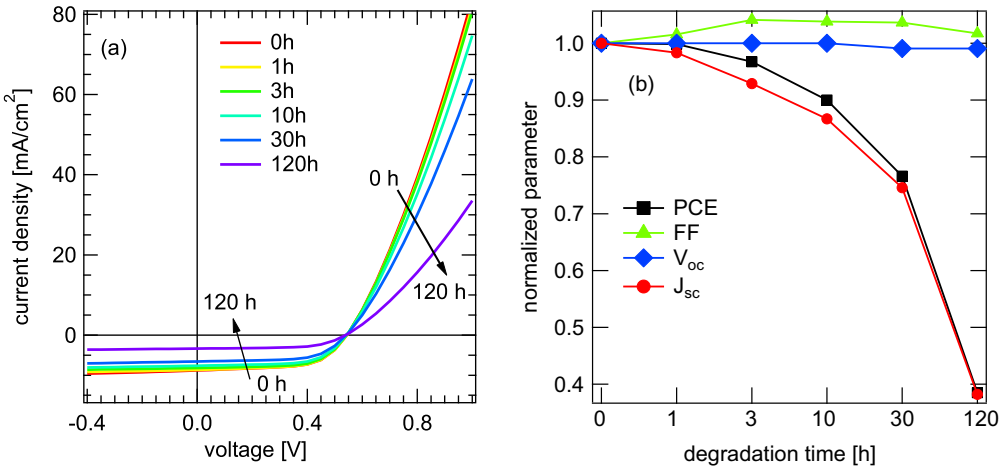

Fig. 1. Illuminated IV-curves of P3HT:PCBM solar cells for different dark degradation times in synthetic air (a) and the normalized values of the PCE, fill factor, open circuit voltage and short circuit current (b). The efficiency loss is due to the decrease of the short circuit current.

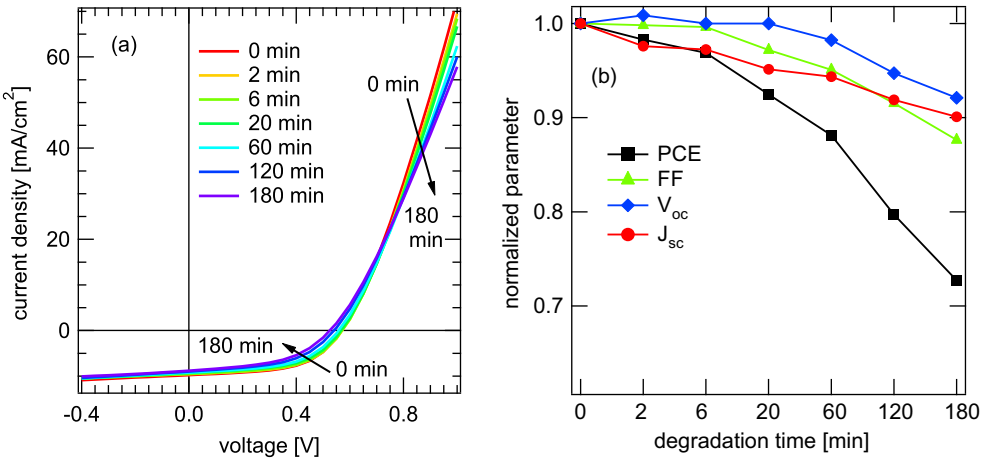

Fig. 2. Illuminated IV-curves of P3HT:PCBM solar cells for different degradation times in synthetic air under simultaneous illumination (a) and the normalized values of the PCE, fill factor, open circuit voltage and short circuit current (b). In contrast to dark degradation in synthetic air all parameters decrease.

the presence of oxygen, indicating an additional degradation path due to photooxidation in addition to doping as found under oxygenation in the dark.

To gain a deeper understanding of the underlying degradation mechanisms, we performed TSC measurements to obtain information about the electronic trap states of P3HT:PCBM solar cells for dark as well as photodegradation. First of all, the trap distribution of non degraded P3HT:PCBM solar cells was investigated by applying a fractional TSC measurement – the so-called $T_{start} - T_{stop}$ technique [10,17] – with T_{stop} varied between 25 and 150 K in steps of 5 K. The resulting density of occupied states (DOOS) distribution is shown in Fig. 3. The continuous activation energies of the traps range from 20 to 400 meV with the center of distribution at about 105 meV. For further

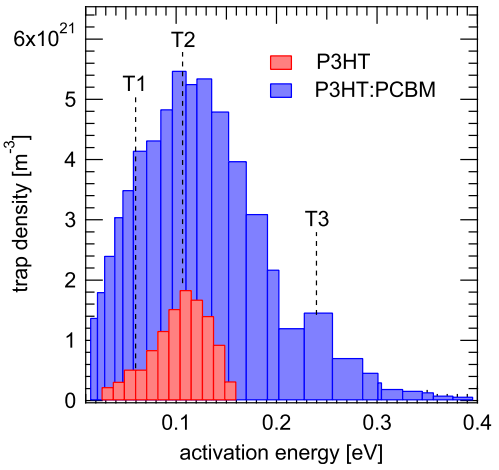

Fig. 3. Comparison of the DOOS distribution of P3HT and P3HT:PCBM blends, as obtained by TSC – $T_{start} - T_{stop}$ measurements. The DOOS of P3HT consists of two different traps (T1, T2), which both also contribute to the DOOS of the blend. Additionally to these two traps the DOOS of the blend features a third trap distribution (T3) with higher activation energy.

interpretation of the DOOS distribution of the blend, we consider the results for pure P3HT. For P3HT, the DOOS was related to two different overlapping traps with approximately Gaussian energy distributions [10], with the center of distribution of the dominant trap at about 105 meV (T2) and the other at about 50 meV (T1) (shoulder at the low energy side of the DOOS distribution) (Fig. 3). Since the centers of distribution for the blend as well as the pure P3HT are at 105 meV, we attribute the dominant trap to P3HT, although the distribution of the main trap in the blend is broadened as compared to the pure P3HT, indicating a higher disorder in the blend. Furthermore, the T1 can also be seen in the DOOS distribution of the blend in the steep onset of the distribution on the low energy side, but is less pronounced due to the higher concentration of the main trap T2, overlapping T1. Additionally to these two traps, the DOOS distribution of the blend features further trap states with activation energies of 200 to 400 meV which are not seen in pure P3HT, with the center at about 250 meV. We refer to the latter trap distribution as T3. Therefore we conclude that the DOOS of the blend consists of three different traps, with the dominant trap T2 at 105 meV. This interpretation is also supported by the TSC spectrum of pristine P3HT:PCBM solar cells, where T2 has a lower concentration compared to T1 and T3, so that T1, T2, and T3 can be clearly distinguished (data not shown). The trap density obtained from the TSC measurements of the investigated P3HT:PCBM solar cells is in the range of $6 - 8 \cdot 10^{22}$ m^{-3} which is considerably higher than the value obtained for P3HT ($1 \cdot 10^{22}$ m^{-3}) [10].

The TSC spectra of P3HT:PCBM solar cells for different dark degradation times in synthetic air are shown in Fig. 4a. Thermally stimulated current is observed between 18 and 160 K. At higher temperatures no additional TSC peaks can be observed up to 300 K. With exposure to synthetic air, a shoulder at about 100 K appears, which increases with longer degradation times within the investigated time scale up to 100 h. The appearance of a shoulder indicates an increase in density of the deeper

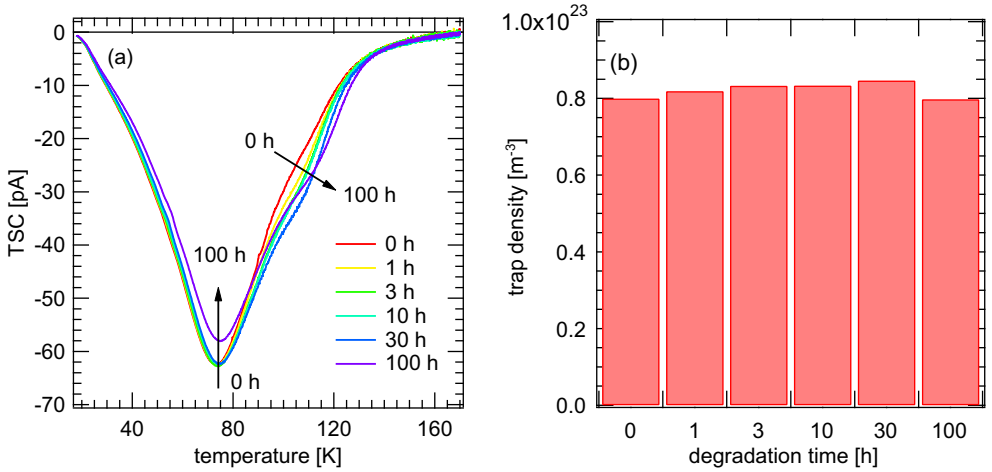

Fig. 4. TSC spectra of P3HT:PCBM solar cells for different dark degradation times in synthetic air (a) and the obtained trap densities (b). The trap density remains almost constant. The slight decrease of the trap density for 100 h degradation time is possibly due to recombination of the detrapped charge carriers.

traps or even the formation of additional traps. The main peak however decreases slightly. As a result the overall trap density of the blend obtained by the TSC measurements remains almost constant for the different degradation times (Fig. 4b). In this context it has to be mentioned that the determined trap density from the TSC spectra is only a lower limit of the actual trap density [18]. One reason is a possible recombination between electrons and holes after one of them got detrapped due to thermal activation. For degradation on synthetic air and simultaneous illumination we monitored almost the same behavior of TSC spectra, but on a faster timescale than during dark degradation.

To get further information about the influence of oxygen on the mobility and also the charge carrier concentration of the blend, we used the CELIV technique, which enables the simultaneous investigation of equilibrium charge carrier density and mobility by recording transient currents . The CELIV measurements for different degradation times in synthetic air in the dark are shown in Fig. 5a. The CELIV curves exhibit a high asymmetry, especially for longer degradation times, which might result from trapped charge carriers being extracted as the higher voltages at longer times promote emission from traps. This is in accordance with the increase of the deeper traps density as revealed by the TSC measurements. The mobility for different degradation times was calculated from the position of the current peak maximum according to Ref. [15]. Only a slight decrease of the mobility with degradation time can be observed (Fig. 5b), resulting in a decrease of about 50% after 120 h in synthetic air. The equilibrium charge carrier density, extracted by the CELIV measurements, however, increases about a factor of two within a degradation time of 120 h in the dark (Fig. 5c). We assign these additional charge carriers to oxygen doping of P3HT, which was also reported for P3HT diodes [10] and P3HT field effect transistors [8,7]. We note that the concentration of charges measured by CELIV provides only a lower limit of the actual charge carrier density, since only charge carriers extracted within the time scale of the experiment (voltage pulse width typically 50 μs) are observed. Thus, the experimental number includes charges from comparably shallow traps which can be emitted from them and then be extracted; charges in deeper traps as well as the ones lost within the sample (by recombination) are disregarded. The degradation on synthetic air and simultaneous illumination shows similar results for the changes in mobility and charge carrier concentration, but again the degradation is accelerated to a timescale of minutes instead of hours.

3.2. Simulation

In order to understand the influence of a decreased mobility as well as charge carrier doping on the solar cell parameters, we performed macroscopic simulations based on solving the differential equation system of the Poisson, the continuity and the drift–diffusion equations in one dimension [19,20]. In the simulation we accounted a bimolecular non-geminate recombination rate according to Langevin [21]. The charge carrier generation by light was assumed to create free polarons, neglecting any influence of electric field driven polaron pair dissociation. Furthermore the charge carrier mobilities of electrons and holes were set equal in the simulations. The used parameters are listed in Table 1. Using this approach we investigated the effect of charge carrier doping by oxygen on the solar cell parameters.

The simulated IV-curves for different hole doping levels are shown in Fig. 6a and the corresponding normalized solar cell parameters in Fig. 6b. For the given parameter set, doping concentration up to 10^{22} m^{-3} does not change the PCE, whereas for higher concentrations the PCE strongly decreases due to a decrease of J_{sc}. FF and V_{oc}, however, remain almost unaffected. This behavior is almost independent of the mobility (within changes of one order of magnitude) used for the simulations. The decreased J_{sc} due to doping can be explained by an increased

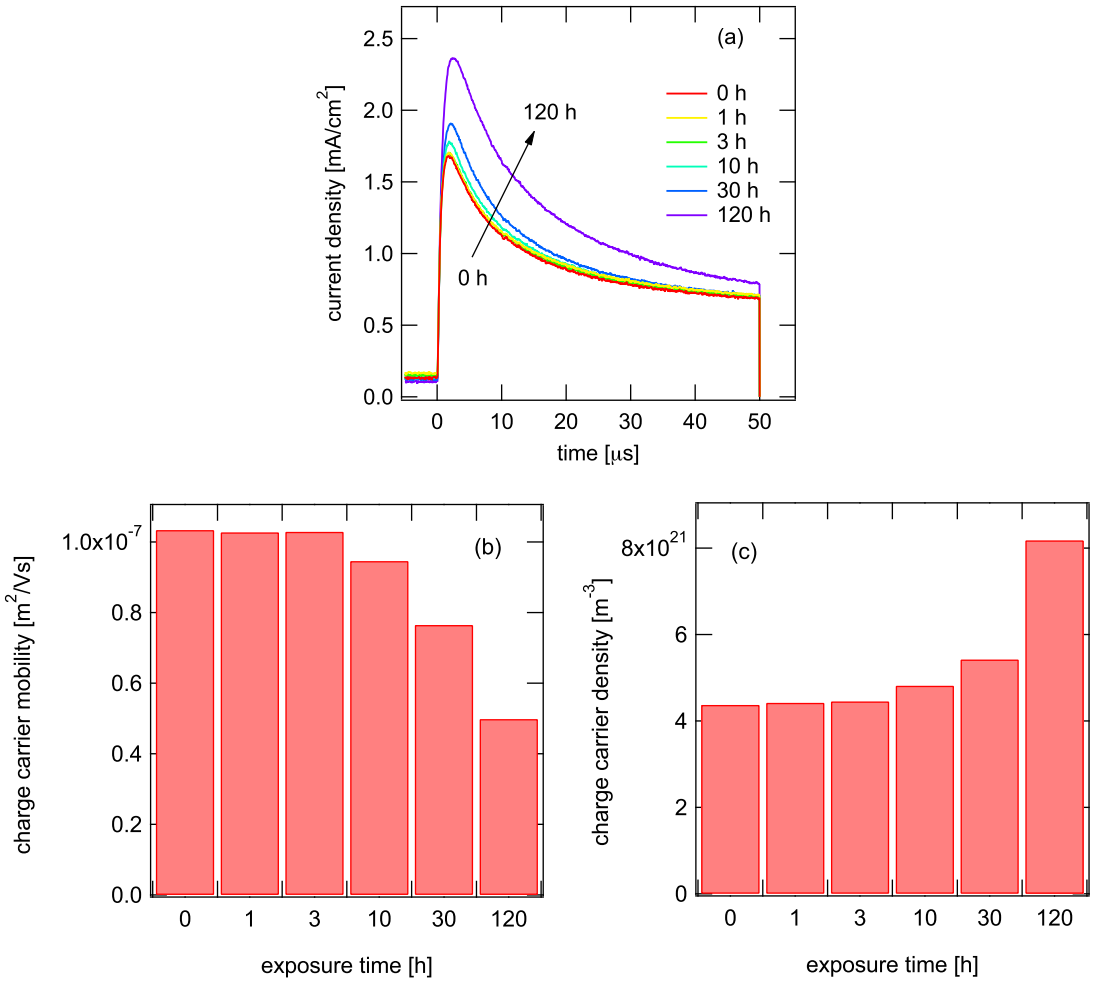

Fig. 5. CELIV measurements of P3HT:PCBM solar cells for different dark degradation times in synthetic air for offset bias of −0.3 V applied at the Ca/Al electrode (a) and the obtained mobilities (b) as well as the charge carrier densities (c). The charge carrier mobility slightly decreases with degradation time, whereas the charge carrier density shows an increase due to oxygen doping.

Table 1
Parameters used for simulation.

Parameter	Symbol	Value	Unit
Temperature	T	300	K
Effective band gap	E_g	1.30	eV
Relative dielectric constant	ϵ_r	3.6	
Active layer thickness	L	100	nm
Effective density of states	N_c, N_v	8×10^{25}	$1/m^3$
Generation rate	G	6.0×10^{27}	$1/m^3$ s
Injection barriers	Φ_a, Φ_c	0.1	eV

bimolecular recombination probability. Since doping implies additional charges within the device, it leads to less band bending and therefore a reduced electrical field within the solar cell. As a consequence the extraction time for the charge carriers increases leading to a higher recombination probability and thus to a lower short circuit current.

The influence of the mobility on the solar cell performance is shown in Fig. 6c and d, revealing a loss of J_{sc} and FF and a small increase of V_{oc} for decreased mobilities. A lower mobility leads to a higher extraction time for the charge carriers and therefore to an enhanced bimolecular recombination probability, which results in the decreased FF. At the same time, the charge extraction becomes less efficient. The slightly increasing open circuit voltage is due to a lower Langevin recombination rate due to decreased mobilities. The higher charge carrier densities and their more balanced distribution reduce the internal electric field and therefore increase the open circuit voltage [22,23]. If the field dependent polaron pair dissociation was also taken into account, it would mostly influence the FF and J_{sc} resulting in an even stronger decrease with lower mobilities.

3.3. Discussion

The influence of oxygen on P3HT:PCBM solar cells results in the case of dark degradation in a loss of J_{sc}, whereas photodegradation results in a decrease of all solar cell parameters. Further, the degradation due to oxygen is

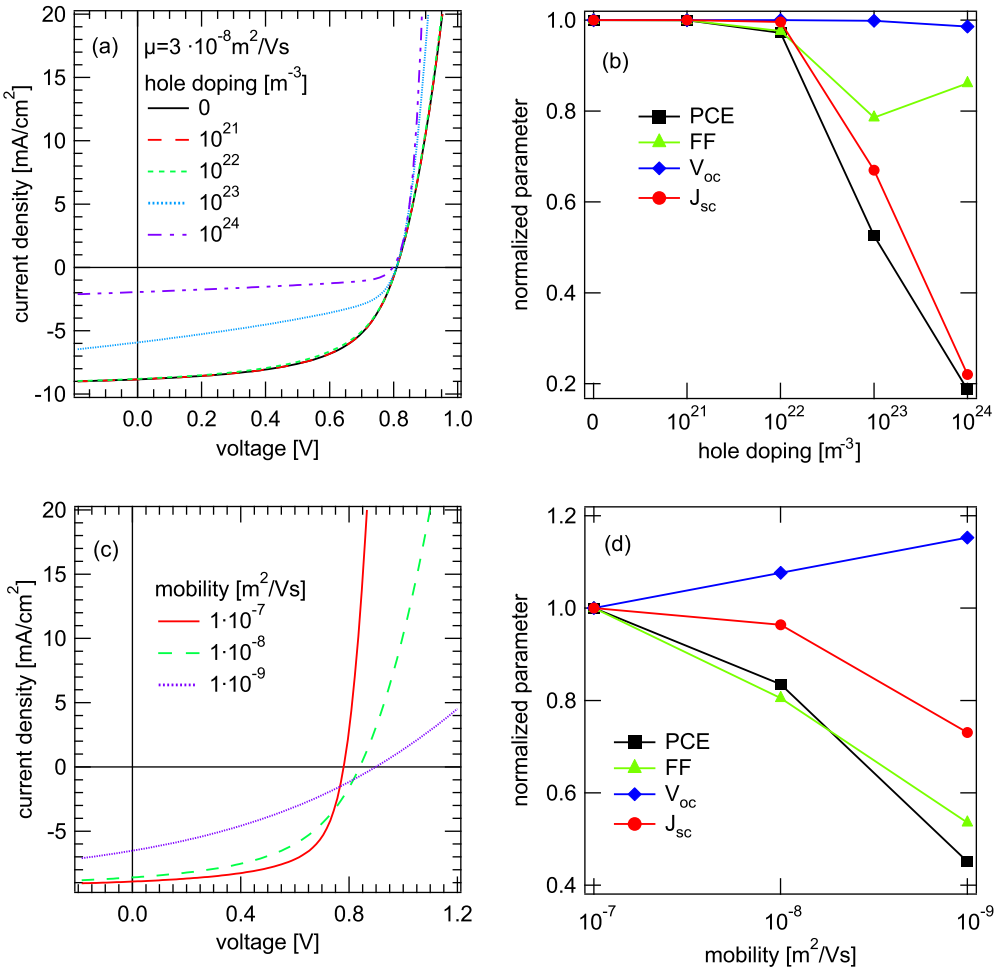

Fig. 6. Simulated IV-curves for different levels of hole doping (a) and the normalized values of the PCE, fill factor, open circuit voltage and short circuit current (b). An increased doping level results in a decrease of J_{sc}. A lowered charge carrier mobility (c) instead leads to a decrease of J_{sc} and FF (d).

accelerated by light. A similar behavior was recently reported for inverted P3HT:PCBM solar cells [3], where the efficiency yields almost no change for dark degradation within the investigated timescale of 1h, whereas a strong loss for photodegradation within 120 min is observed. The loss in J_{sc} can be explained by charge carrier doping, as we demonstrated by using macroscopic simulations. This interpretation is in accordance with the CELIV measurements, which show an increasing charge carrier concentration with degradation time. We attribute the increased charge carrier concentration to oxygen doping of P3HT [10,8,7]. The difference between the doping levels in the simulations and these determined by CELIV can be explained by the fact that the extracted charge carrier density by CELIV is only a lower limit of the actual charge carrier concentration, as mentioned before. The actual charge carrier density can be significantly higher. Furthermore, the accelerated increase of the charge carrier density in the case of photodegradation compared to the dark degradation is in good agreement with results of P3HT transistors, which also showed an expedited oxygen doping with light [7].

In addition to an increased charge carrier concentration, CELIV measurements reveal a decrease of the charge carrier mobility for the P3HT:PCBM blends due to oxygen. A decreasing mobility with degradation time is also reported for pure P3HT [10], but in contrast to pure P3HT, where the mobility decreases about two orders of magnitude within 100 h [10], only a slight decrease in the blend – by about 50% – can be observed. This difference could be due to a stabilization effect of PCBM for P3HT in analogy to findings for MDMO-PPV (poly(2-methoxy-5-(3′,7′- dimethyloctyloxy)-1,4-phenylene-vinylene)):PCBM solar cells [4]. The decreased mobility could also result from a degradation of PCBM due to oxygen. Decreased electron mobilities for C60 based field effect transistors after oxygen exposure have already been reported [11,12]. Since electron and hole mobilities can not be discriminated by CELIV, it is not possible to resolve which carrier mobility decreases.

A lower mobility leads to a decrease of FF and J_{sc}, as revealed by macroscopic simulations. Although our CELIV measurements show a slight decrease in mobility with degradation time, there are some facts indicating that the decreased mobility is not the origin of the FF loss in the

case of photodegradation. First of all the experimentally observed mobility reduction is too limited to have a strong impact on the FF. Furthermore, the mobility decreases in the same range for both dark and illuminated degradation, although the degradation in the illuminated case occurs on a faster timescale. In contrast, the loss in FF is only observed for photodegradation. Additionally, we experimentally observed also a decrease of V_{oc} for photodegradation, whereas a decrease in mobility should result in an increase of V_{oc} as exhibited by the simulation (Fig. 6d). Therefore, the decreased mobility is not the reason for the FF loss.

Another important factor which can negatively influence the solar cell performance are electronic trap states, since they lower the mobility, disturb the internal field distribution and can act as recombination centers. Exposure of P3HT:PCBM solar cells to oxygen results in a rise of the density of deeper traps for both dark and illuminated degradation. On the other hand, the main peak of the TSC slightly decreases due to oxygen exposure, which is in contrast to the observed increase of the main TSC peak of pure P3HT [10]. For comparison, the trap density in pure P3HT increases almost by a factor of three within 100 h under oxygen exposure [10]. In this context we want to mention again that the determined trap density from the TSC spectra is only a lower limit of the actual trap density [18].

The appearance of deeper traps due to oxygen exposure could also be the reason for the observed loss in fill factor, since they can disturb the internal field distribution and act as recombination centers, as mentioned before. Further investigations concerning the influence of deep traps on the solar cell performance have to be done, like the implementation of deep traps within the macroscopic simulation. Other crucial factors concerning FF and V_{oc} we want to address, are imbalanced electron – hole mobilities (resulting in the formation of space charges) and a field dependent photogeneration. These two factors have not been accounted so far and will be addressed in the future to completely clarify the origin of the loss of FF and V_{oc} in the case of oxygen induced degradation under simultaneous illumination.

4. Conclusions

We investigated the influence of oxygen on unprotected P3HT:PCBM solar cells by controlled exposure to synthetic air. Two different degradation conditions were used: in the dark and under simultaneous illumination. Exposure of the solar cells to synthetic air in the dark results in a loss of J_{sc} of about 60% within 120 h. In contrast, simultaneous illumination during oxygen degradation results in a loss of all solar cell parameters, yielding an efficiency loss of about 30% within only 3 h. Thus, the degradation of the P3HT:PCBM solar cells is strongly accelerated by light.

CELIV measurements revealed an increased charge carrier concentration after oxygen exposure for dark, as well as photodegradation. We attributed these additional charge carriers to oxygen doping, which is also known for pure P3HT. With the aid of macroscopic simulations we have shown that doping of the solar cells is the origin of the loss in J_{sc} for both degradation conditions.

Another impact of oxygen exposure on P3HT:PCBM solar cells is a slight decrease of the charge carrier mobility, as also revealed by CELIV measurements. Although a decreased mobility may result in a loss of the fill factor, as shown by macroscopic simulations, the experimentally observed mobility decrease is too small to be the origin of the FF drop in the case of photodegradation.

In addition to an enhanced charge carrier concentration, oxygen induced degradation results in an increase of the density of deeper traps, as was revealed by TSC measurements. These deep traps could be the origin of the decreased FF and V_{oc}, although further investigations to correlate the trap density to the solar cell performance are required for a verification.

Acknowledgements

The current work is supported by the Bundesministerium für Bildung und Forschung in the framework of the OPV Stability Project (Contract No. 03SF0334F). J.S. thanks the Elitenetzwerk Bayern for funding. A.B. thanks the Deutsche Bundesstiftung Umwelt for funding. C.D. gratefully acknowledges the support of the Bavarian Academy of Sciences and Humanities. V.D.'s work at the ZAE Bayern is financed by the Bavarian Ministry of Economic Affairs, Infrastructure, Transport and Technology. The authors thank Jens Lorrmann for fruitful discussion.

References

[1] M.A. Green, K. Emery, Y. Hishikawa, W. Warta, Solar cell efficiency tables (version 35), Prog. Photovolt.: Res. Appl. 18 (2010) 144.
[2] M.O. Reese, A.J. Morfa, M.S. White, N. Kopidakis, S.E. Shaheen, G. Rumbles, D.S. Ginley, Pathways for the degradation of organic photovoltaic P3HT:PCBM based devices, Sol. Energy Mater. Sol. Cells 92 (2008) 746.
[3] A. Seemann, H.-J. Egelhaaf, C.J. Brabec, J.A. Hauch, Influence of oxygen on semi-transparent organic solar cells with gas permeable electrodes, Org. Electron. 10 (2009) 1424.
[4] H. Neugebauer, C. Brabec, J.C. Hummelen, N.S. Sariciftci, Stability and photodegradation mechanisms of conjugated polymer/fullerene plastic solar cells, Sol. Energy Mater. Sol. Cells 61 (2000) 35.
[5] K. Norrman, S.A. Gevorgyan, F.C. Krebs, Water-induced degradation of polymer solar cells studied by H218O labeling, Appl. Mater. Interface 1 (2009) 102.
[6] M.S.A. Abdou, F.P. Orfino, Y. Son, S. Holdcroft, Interaction of oxygen with conjugated polymers: charge transfer complex formation with poly(3-alkythiophene), J. Am. Chem. Soc. 119 (1997) 4518.
[7] H.-H. Liao, C.-M. Yang, C.-C. Liu, S.-F. Horng, H.-F. Meng, J.-T. Shy, Dynamics and reversibility of oxygen doping and de-doping for conjugated polymer, J. Appl. Phys. 103 (2008) 104506.
[8] E.J. Meijer, C. Detcheverry, P.J. Baesjou, E. van Veenendaal, D.M. de Leeuw, T.M. Klapwijk, Dopant density determination in disordered organic field-effect transistors, J. Appl. Phys. 93 (2003) 4831.
[9] C.-K. Lu, H.-F. Meng, Hole doping by molecular oxygen in organic semiconductors: band-structure calculations, Phys. Rev. B 75 (2007) 235206.
[10] J. Schafferhans, A. Baumann, C. Deibel, V. Dyakonov, Trap distribution and the impact of oxygen-induced traps on the charge transport in poly(3-hexylthiophene), Appl. Phys. Lett. 93 (2008) 093303.
[11] A. Tapponnier, I. Biaggio, P. Günter, Ultrapure C60 field-effect transistors and the effects of oxygen exposure, Appl. Phys. Lett. 86 (2005) 112114.
[12] R. Könenkamp, G. Priebe, B. Pietzak, Carrier mobilities and influence of oxygen in C60 films, Phys. Rev. B 60 (1999) 11804.

[13] T. Matsushima, M. Yahiro, C. Adachi, Estimation of electron traps in carbon-60-field-effect transistors by a thermally stimulated current technique, Appl. Phys. Lett. 91 (2007) 103505.
[14] G. Juška, K. Arlauskas, M. Viliûnas, J. Kočka, Extraction current transients: new method of study of charge transport in microcrystalline silicon, Phys. Rev. Lett. 84 (2000) 4946.
[15] C. Deibel, Charge carrier dissociation and recombination in polymer solar cells, Phys. Stat. Sol. A 206 (2009) 2731.
[16] A. Wagenpfahl, D. Rauh, M. Binder, C. Deibel, V. Dyakonov, On the s-shape current–voltage characteristics of organic solar devices, 2010. arXiv: 1005.5669v1.
[17] R. Schmechel, H. von Seggern, Electronic traps in organic transport layers, Phys. Stat. Sol. A 201 (2004) 1215.
[18] A. Kadashchuk, R. Schmechel, H. von Seggern, U. Scherf, A. Vakhnin, Charge-carrier trapping in polyfluorene-type conjugated polymers, J. Appl. Phys. 98 (2005) 024101.
[19] C. Deibel, A. Wagenpfahl, V. Dyakonov, Influence of charge carrier mobility on the performance of organic solar cells, Phys. Stat. Sol. (RRL) 2 (2008) 175.
[20] C. Deibel, A. Wagenpfahl, V. Dyakonov, Origin of reduced polaron recombination in organic semiconductor devices, Phys. Rev. B 80 (2009) 075203.
[21] P. Langevin, Recombinaison et mobilites des ions dans les gaz, Ann. Chim. Phys. 28 (1903) 433.
[22] L.J.A. Koster, V.D. Mihailetchi, R. Ramaker, P.W.M. Blom, Light intensity dependence of open-circuit voltage of polymer:fullerene solar cells, Appl. Phys. Lett. 86 (2005) 123509.
[23] D. Cheyns, J. Poortmans, P. Heremans, C. Deibel, S. Verlaak, B.P. Rand, J. Genoe, Analytical model for the open-circuit voltage and its associated resistance in organic planar heterojunction solar cells, Phys. Rev. B 77 (2008) 165332.

for organic electronic applications, only a few studies up to date have investigated the electronic and optical properties and electron transfer characteristics of silyl-functionalized π-conjugated oligomers [9–11]. On the other hand, even though qualitative interpretations of the well-resolved absorption and emission spectra of oligoacenes can be found in the literature [12,13], to the best of our knowledge, a detailed analysis of the vibronic features in silyl end-capped oligothienoacenes has not yet been conducted.

In our previous studies, we analyzed the structural, electrochemical, and optical properties of a series of triisopropylsilyl end-capped oligothienoacenes to gain insight into the fundamental structure–property relationships with the addition of each fused-thiophene ring. We found that the selective enhancement of a very limited number of Raman scatterings is related to strong vibronic coupling between selected skeletal ν(C=C) stretching modes in the 1600–1300 cm^{-1} range and their respective frontier molecular orbitals [11]. Amplified spontaneous emission was observed in the pentathienoacene derivative doped into polystyrene films indicating that this material is a good candidate for active laser materials [14]. Cyclic voltammetry also reveals the formation of stable radical cations for all these oligothienoacenes, and the formation of dications only for the heptamer and the octamer [15]. The absorption and fluorescence spectra show partially resolved vibronic structures even at room temperature due to the absence of conformational disorder, at low temperature, the absorption spectra of all the series and the emission spectra recorded only for selected systems (i.e., for the pentamer and octamer) show two different vibrational progressions with an energy splitting, corresponding to vibrational modes with energies of $\nu_1 \sim 1530\ cm^{-1}$ and $\nu_2 \sim 490\ cm^{-1}$ [15]. In this contribution, we focus on the analysis of the vibronic structure and optical properties of a series of silyl end-capped oligothienoacenes (TIPS-T*n*-TIPS, where *n* indicates the number of fused-thiophene rings) ranging in length from the tetramer to octamer by using experimental spectroscopic data and quantum-chemical calculations (see Fig. 1). UV–vis absorption and fluorescence emission spectroscopy measurements are used to investigate the spectral profiles of all the series in the ground and first singlet excited-state at low (78 K) and room temperature.

We also employed density functional theory (DFT) and time-dependent DFT (TD-DFT) quantum–mechanical calculations to provide a detailed understanding of the electronic and vibrational interactions and their impact on the characteristics of the absorption and emission profiles of silyl end-capped oligothienoacenes. When compared against the non-silyl-functionalized oligothienoacenes, the DFT-calculated energies of the frontier molecular orbitals of the silyl-functionalized oligothienoacenes point to an effective silicon-induced hyperconjugation effect. Our calculations also reveal that the end-capping silyl groups have an almost negligible contribution to the total structural (intramolecular) reorganization energy upon electronic excitation. This finding suggests that although functionalization with TMS or TIPS groups may affect the overall charge carrier characteristics (mainly due to significant changes in the solid state packing induced by the presence of bulky end-capping silyl groups), to a large extent the vibronic coupling properties in silyl end-capped oligothienoacenes are mainly determined by their oligothienyl molecular backbone. Finally, the theoretically estimated vibrational frequencies and vibronic coupling constants of the silyl end-capped molecules are used to simulate their experimental absorption and emission spectral profiles.

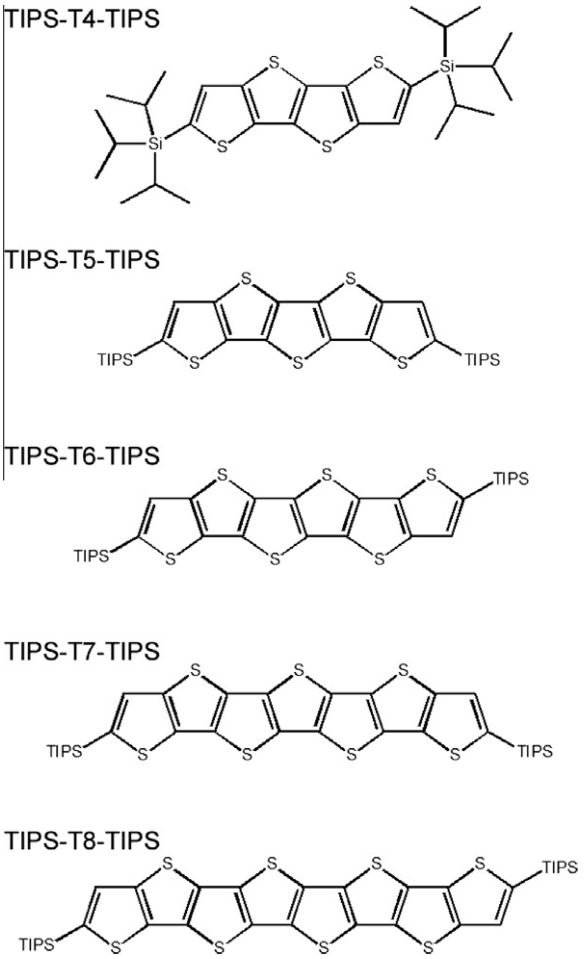

Fig. 1. Chemical structures of the series of end-capped oligothienoacenes investigated in this study (TIPS-T*n*-TIPS; where TIPS stands for triisopropylsilyl and *n* indicates the number of fused-thiophene rings).

2. Methodology

2.1. Experimental

UV–vis–NIR absorption spectra were recorded with a diode array Agilent 8453 instrument allowing for fast recording of all electromagnetic absorptions in the 190–1100 nm spectral region. Fluorescence emission spectra were measured using a FL920P spectrometer from Edinburgh Instruments. No fluorescent contaminants were detected upon excitation in the wavelength region of experimental interest. Solutions for emission measurements

were prepared with an absorbance in the visible spectral region between 0.1 and 0.2. 2-Methyltetrahydrofuran (MeTHF) was pre-dried over KOH for 3 days, filtered, distilled from CaH_2, and stored under inert atmosphere. Low-temperature spectra were recorded using an OptistatDN liquid nitrogen optical spectoscopy cryostat from Oxford Instruments.

2.2. Computational and theoretical methodology

Fig. 2 represents the potential energy surfaces (PES) for the electronic states S_0 and S_1 corresponding to the ground- and excited-state of the molecule, respectively. The intramolecular reorganization energy λ_{reorg} during an electronic transition consists of two terms related to the geometry relaxation energies upon going from the ground-state geometry to the excited-state geometry and vice versa,

$$\lambda_{reorg} = \lambda_{rel}^{(1)} + \lambda_{rel}^{(2)} \quad (1)$$

Here $\lambda_{rel}^{(1)}$ and $\lambda_{rel}^{(2)}$ represent the relaxation of a given molecule as it undergoes $S_0 \rightarrow S_1$ and $S_1 \rightarrow S_0$ electronic transitions; $\lambda_{rel}^{(1)}$ is related to the relaxation of a molecular excited-state to its excited-state potential energy minimum while $\lambda_{rel}^{(2)}$ is related to the relaxation of the molecule to its ground-state potential energy minimum after emission. These two energy terms can be computed directly from the adiabatic potential energy surfaces, as schematically indicated in Fig. 2 and described in detail, e.g., in Refs. [16,17].

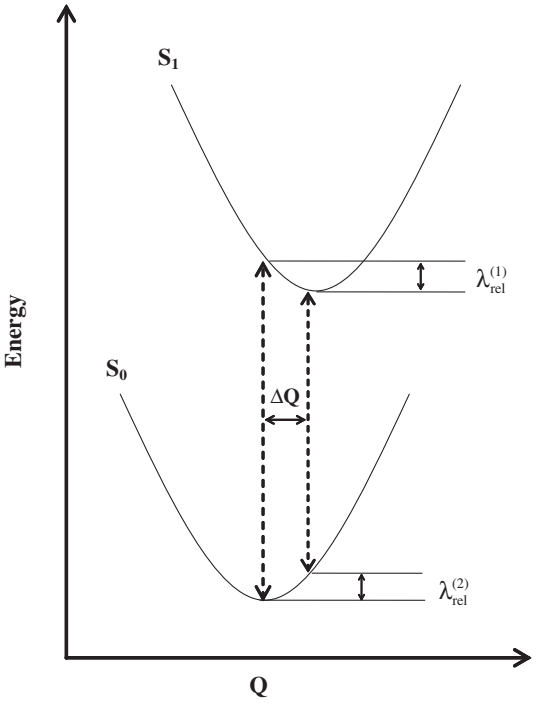

Fig. 2. Sketch of the potential energy surfaces for the molecular ground-state S_0 and excited-state S_1, showing the vertical transitions (dashed lines), the normal mode displacement ΔQ, and the relaxation energies $\lambda_{rel}^{(1)}$ and $\lambda_{rel}^{(2)}$.

The contribution of each vibrational mode to λ_{rel} was obtained by expanding the respective potential energy surfaces into a power series of the normal coordinates. In the harmonic approximation, the relaxation energy λ_{rel} is defined as [18,19]:

$$\lambda_{rel} = \sum \lambda_i = \sum \hbar\omega_i S_i \quad (2)$$

$$\lambda_i = \frac{k_i}{2}\Delta Q_i^2, \quad S_i = \frac{\lambda_i}{\hbar\omega_i} \quad (3)$$

Here, the summations run over the vibrational modes; ΔQ_i represents the displacement along the normal mode (NM) i between the equilibrium positions of the two electronic states of interest; k_i and ω_i are the corresponding force constants and vibrational frequencies; S_i denotes the Huang–Rhys factor (dimensionless electron–vibration coupling constant).

The Huang–Rhys factors S_i related to the S_0–S_1 transitions (and vice versa) were computed using a modified version of the DUSHIN program developed by Reimers [19]. The shapes of the emission and absorption spectra were simulated in the framework of the Born–Oppenheimer and Franck–Condon approximations according to the procedure described in detail elsewhere [17]. In these calculations, the B3LYP frequencies of both the ground- and excited-state have been scaled, according to the literature, with the same empirical factor of 0.9613 [20]. Note that for the simulation of the emission spectra the cubic frequency dependence was not taken into account; for specific details of this effect on π-conjugated molecular systems, see Ref. [21]. The convolution of the resulting spectra was carried out with Gaussian functions of uniform width (σ_{FWHM} = 0.03 eV). The onset of the simulated spectra was chosen to match the maximum of the first peak of the simulated spectrum with the maximum of the (0–0) absorption (emission) line found experimentally.

For the sake of computational convenience and efficiency, in all the quantum-chemical calculations the bulky triisopropylsilyl substituents shown in Fig. 1 were replaced by trimethylsilyl groups. First, the optimized equilibrium structure and vibrational normal modes of the S_0 state were obtained using DFT; for the S_1 state both the geometry optimization and vibrational normal modes calculations were obtained from TD-DFT [22,23]. Geometry determination at the TD-DFT level was recently shown to reproduce very well the vibronic structures in the absorption spectra of many large organic molecules [24,25]. In all cases, we employed the B3LYP exchange–correlation functional [26,27] and the 6-31G(d,p) [28–30] basis set, as implemented in the TURBOMOLE package [31].

3. Results and discussion

3.1. Experimental spectra

Fig. 3 displays the normalized UV–vis absorption and fluorescence spectra of TIPS-T*n*-TIPS recorded at low (78 K) and room temperature. Table 1 shows the wavelengths of the absorption and fluorescence emission maxima recorded at both temperatures.

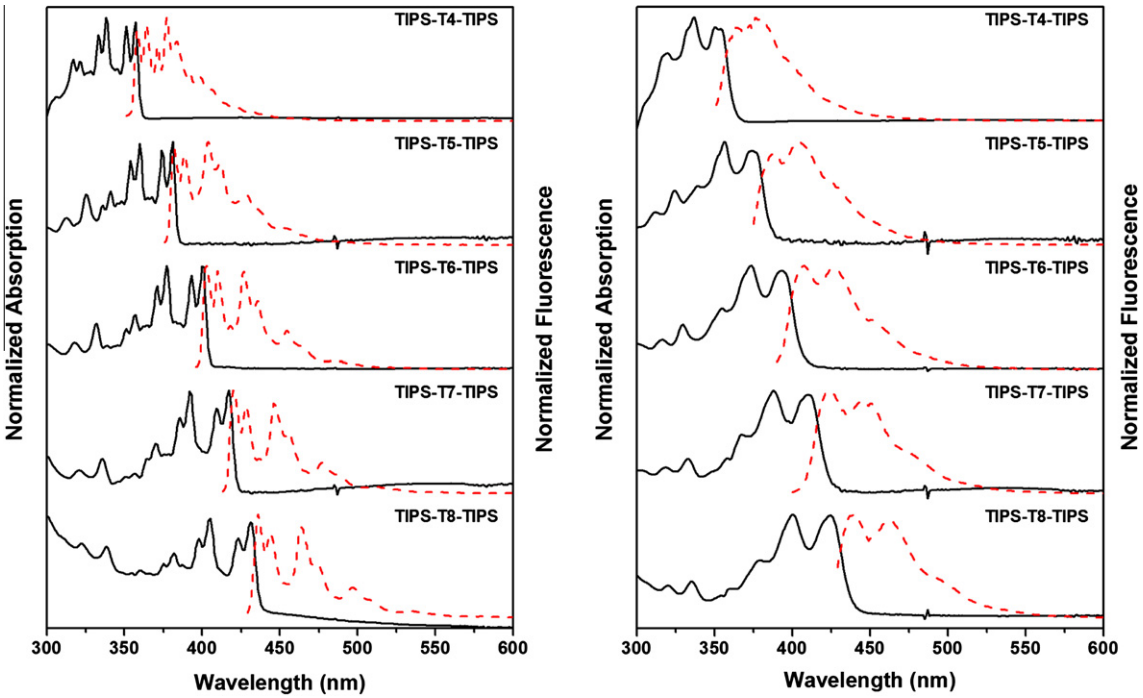

Fig. 3. Normalized UV–vis absorption (solid lines) and fluorescence emission (dashed lines) spectra of TIPS-T*n*-TIPS oligothienoacenes in MeTHF recorded at 78 K (left) and at room temperature (right).

At room temperature, the normalized absorption and fluorescence emission spectra of all the TIPS-T*n*-TIPS oligomers show a broad spectrum with partially resolved vibronic structures in good agreement with our previous data [14,15]. The appearance of vibrational fine structure in the absorption spectra in solution is a fairly unique property of oligothienoacenes, which is generally not observed in non-fused α-oligothiophenes [33]. This, in principle, is attributed to the rigidity of the fully-fused thiophene backbone, which drastically reduces the conformational disorder. In our previous work [15], the single excited electronic states of all these oligomers were calculated at the TD-DFT level. In good agreement with the experimental data, the existence of one strong electronic transition in the near-UV–vis range which undergoes a large bathochromic shift as the oligomer lengthens is predicted. This transition implies the excitation to the first excited-state S_1, which is shown to increase in intensity with the oligomer length. This agrees with the slight increase in the molar absorption coefficient. The fluorescence spectrum recorded at room temperature is also structured; a quite small shift is observed between the corresponding first peaks in UV–vis absorption and photoluminescence spectrum, which becomes smaller as the number of thiophene rings increases. As the π-conjugation is extended, the fluorescence quantum yield increases and the emission maximum shifts to longer wavelengths (i.e., from 363 nm and $\varphi_F = 0.08$ in TIPS-T4-TIPS to 440 nm and $\varphi_F = 0.39$ in TIPS- T8-TIPS, see Table 1).

In agreement with our previous data [15], the vibronic peaks in the UV–vis and fluorescence spectra of TIPS-T*n*-TIPS sharpen and become stronger upon cooling (see Fig. 3). The lowest-energy optical absorption clearly shows two different vibronic progressions with different energy splitting, for which up to three replicas are seen. The vibronic progression corresponds to the vibrational modes having frequencies of $\nu_1 \sim 1530\ cm^{-1}$ and $\nu_2 \sim 490\ cm^{-1}$. Two well-resolved vibronic progressions are also observed in the fluorescence spectrum at low temperature ($\nu_1 \sim 1400\ cm^{-1}$ and $\nu_2 \sim 450\ cm^{-1}$); while, a moderate energy-splitting is observed. In comparison to the UV–vis absorption spectrum, the energy-splitting is smaller. The changes accompanying cooling can be interpreted as a

Table 1
UV–vis absorption and fluorescence emission maxima (λ_{max} in nm) observed for TIPS-T*n*-TIPS at room temperature and low temperature (values given between parentheses), molar absorption coefficient (log ε) and fluorescence quantum yield (φ_F).

Compound	Absorption		Emission	
	λ_{max}[a]	log ε	λ_{max}[a]	φ_F
TIPS-T4-TIPS	350[b] (357–351)[b]	4.52[d]	363[b] (358–364)[c]	0.08[d]
TIPS-T5-TIPS	375[b] (381–374)[b]	4.56[e]	387[b] (382–389)[c]	0.14[c]
TIPS-T6-TIPS	393[b] (400–393)[b]	4.68[d]	408[b] (403–410)[c]	0.32[d]
TIPS-T7-TIPS	409[b] (417–409)[b]	4.86[f]	424[b] (420–428)[c]	0.41[c]
TIPS-T8-TIPS	425[b] (431–423)[b]	4.76[d]	440[b] (436–444)[c]	0.39[d]

[a] In THF.
[b] From Ref. [15].
[c] From this work; φ_F in *o*-dichlorobenzene.
[d] In *o*-dichlorobenzene, from Ref. [5].
[e] In THF, from Ref. [32].
[f] In CH_2Cl_2, from Ref. [6].

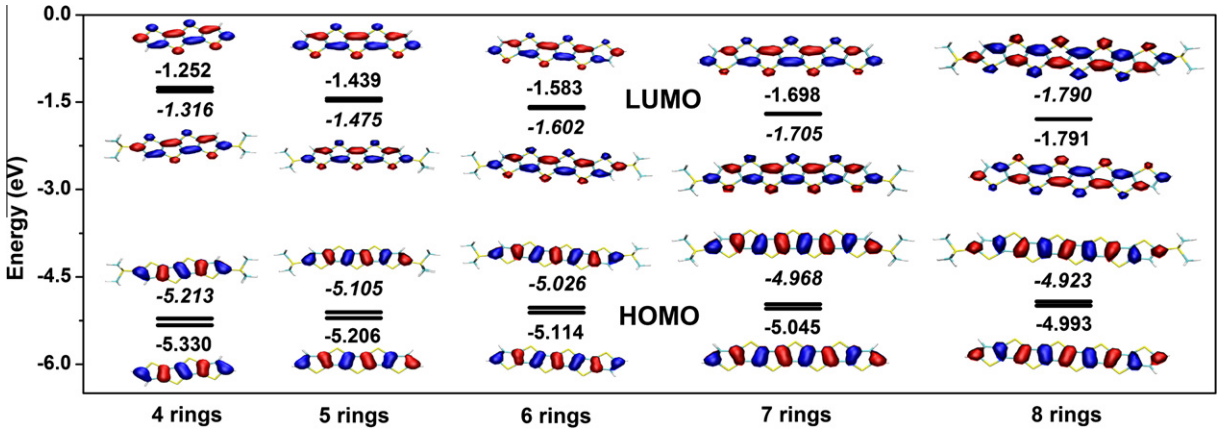

Fig. 4. DFT/B3LYP/6-31G(d,p) energy levels around the HOMO–LUMO gap region and molecular orbital topologies of the HOMO and LUMO of tetra(penta, hexa, hepta, and octa)thienoacene and TMS-T4(5, 6, 7, and 8)-TMS. The italicized energy values correspond to those of the TMS-T*n*-TMS oligomers.

consequence of a reduction in the inhomogeneous broadening induced by the considerable variation of local environments (i.e., the spectra of the individual molecules at low-temperature solids are much similar than in solution because of the loss of some conformational disorder) [34–36]. The resolution of the vibrational structure at low temperature is less pronounced for the longer oligomers (i.e., hexamer, heptamer and octamer) due to the fact that the coupling with low-frequency vibrations ca. 100 cm^{-1} becomes more significant, as discussed in more detail in Section 3.4.

Finally, we discuss the experimentally observed red-shift signatures of the UV–vis absorption peaks of the silyl end-capped oligothienoacenes as compared against their non-silyl-functionalized counterparts. This analysis was carried out by looking at the DFT-calculated energies (and topologies) of the molecular orbitals involved in the $S_0 \rightarrow S_1$ electronic transition of both sets of molecules. For a complete list of the UV–vis absorption peaks in unsubstituted oligothienoacenes see Table S1.

Silicon substituents are known to induce an effective hyperconjugation when coupled with carbon atoms [37]. In the case of organic semiconductors, this effect has been demonstrated both experimentally and theoretically for various silicon-containing π-conjugated organic systems [38,39], for which, the π^*-orbital of the aromatic system mixes effectively with the exocyclic Si–C σ^*-orbital to afford a low-lying lowest unoccupied molecular orbital (LUMO) and a relatively small band gap. In principle, a similar stabilizing effect is also expected for the case of the highest occupied molecular orbital (HOMO) in π-conjugated systems [40,41]. However, as recently observed by Lu et al. [40], the introduction of thiophene rings into the molecular core of silicon-containing organic semiconducting materials leads to an energetic destabilization of the HOMOs and stabilization of the LUMOs.

When compared against their non-silyl-functionalized counterparts, the silyl end-capped oligothienoacenes (except for the LUMO of TMS-T8-TMS) show the above-mentioned stabilization [destabilization] of the LUMO [HOMO] energy levels, as a result of an effective silicon-induced hyperconjugation effect (see Fig. 4). The energy difference between the LUMOs in the 8-ring systems is approximately 1 meV, which is too small to change the overall (observed) LUMO-stabilization trend of the TMS-T*n*-TMS oligomers. This effective silicon-induced hyperconjugation contributes then to the systematic reduction of the calculated HOMO–LUMO gaps and to the observed red-shift of the UV–vis absorption peaks in silicon-contain-

Table 2
Selected bond lengths (Å) in the ground-state and excited-state of TMS-T*n*-TMS molecules ($n = 4$ and 8) as determined by DFT/TD-DFT calculations.

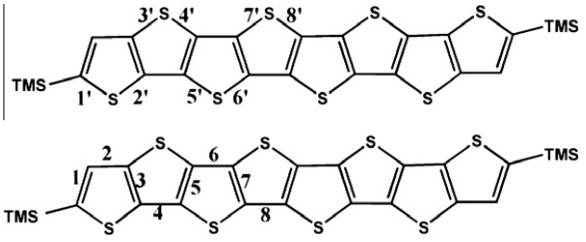

Bonds	TMS-T4-TMS			TMS-T8-TMS		
	S_0	S_1	$\Delta(S_1-S_0)$	S_0	S_1	$\Delta(S_1-S_0)$
C–C						
1	1.379	1.405	0.026	1.379	1.390	0.011
2	1.421	1.394	−0.027	1.421	1.408	−0.013
3	1.394	1.430	0.036	1.395	1.411	0.016
4	1.421	1.382	−0.039	1.419	1.398	−0.021
5	1.396	1.444	0.048	1.397	1.422	0.025
6	1.421	1.382	−0.039	1.418	1.391	−0.027
7	1.394	1.430	0.036	1.397	1.428	0.031
8	1.421	1.394	−0.027	1.417	1.387	−0.030
C–S						
1′	1.770	1.778	0.008	1.770	1.773	0.003
2′	1.738	1.758	0.020	1.738	1.746	0.008
3′	1.761	1.779	0.018	1.762	1.768	0.006
4′	1.756	1.771	0.015	1.755	1.764	0.009
5′	1.756	1.771	0.015	1.756	1.764	0.008
6′	1.761	1.779	0.018	1.755	1.766	0.011
7′	1.738	1.758	0.020	1.756	1.767	0.011
8′	1.770	1.778	0.008	1.756	1.768	0.012

Table 3
BLA values (in Å) calculated for thiophene rings of TMS-T*n*-TMS molecules in their ground-state (S_0) and excited-state (S_1).

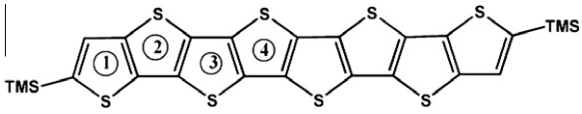

Ring	TMS-T4-TMS		TMS-T5-TMS		TMS-T6-TMS		TMS-T7-TMS		TMS-T8-TMS	
	S_0	S_1	S_0	S_1	S_0	S_1	S_0	S_1	S_0	S_1
1	0.035	−0.024	0.035	−0.012	0.034	−0.004	0.035	0.003	0.034	0.008
2	0.026	−0.053	0.025	−0.043	0.025	−0.033	0.023	−0.025	0.023	−0.019
3	0.026	−0.053	0.023	−0.055	0.023	−0.049	0.021	−0.041	0.021	−0.034
4	0.035	−0.024	0.025	−0.043	0.023	−0.049	0.021	−0.046	0.020	−0.042

ing oligothienoacenes versus those measured in their unsubstituted counterparts. As an example of the silicon-induced effect, in Fig. S1, we report the UV–vis absorption and emission profiles of the pentathienoacene and TMS-T5-TMS molecules.

3.2. Ground- and excited-state structures

We investigate here the ground-state (S_0) and first excited-state (S_1) geometries obtained from DFT and TD-DFT calculations. The calculated bond lengths changes observed upon excitation for TMS-T4-TMS and TMS-T8-TMS are summarized in Table 2 (see Table S2 in Supporting information for the data of the rest of the compounds). The degree of aromatization/quinoidization of the conjugated backbone can be easily quantified by using the C–C bond-length alternation (BLA) parameter. The BLA parameter is computed for each thiophene ring as the difference between the length of the C_β–C_β and the average of the two C_α=C_β bonds. An aromatic ring is thus characterized by a positive BLA value, while a quinoid-like ring shows a negative BLA value. Table 3 collects the BLA values obtained for TMS-T*n*-TMS oligomers. In the ground-state, the thiophene rings display positive BLA values indicating that their molecular structure is of aromatic-type, in agreement with previous findings [7,15]. The geometry changes upon excitation from the S_0 state into the optimized S_1 geometry correspond to an elongation of the C_α=C_β double bonds and a shortening of the C_β–C_β single bonds, i.e., a switch in bond-length alternation. These C–C bond length changes are found to be more pronounced toward the molecular center (i.e., the BLA values computed for TMS-T8-TMS change from 0.034/0.023/0.021/0.020 Å in the S_0 state to 0.008/−0.019/−0.034/−0.042 Å in the S_1 state, going from the outer to the center rings). The change in sign in the BLA values clearly illustrates the quinoidization of the conjugated carbon skeleton. On the other hand, the C–S bond lengths are found to increase on going from S_0 to S_1, with a larger impact on the inner than on the outer rings. It is interesting to note that the geometrical changes upon electronic excitation are less pronounced in the longer oligomers in comparison with the shorter ones; for instance, the C–C bond length changes upon excitation are in the range of −0.039/0.048 Å in TMS-T4-TMS while they are in the range of −0.030/0.031 Å in TMS-T8-TMS (see Table 2 for TMS-T4-TMS and TMS-T8-TMS values and Table S2 for the rest of the compounds).

3.3. Reorganization energy

The intramolecular relaxation energies λ_{rel} related to the $S_0 \rightarrow S_1$ and $S_1 \rightarrow S_0$ transitions for the series of silyl end-capped oligothienoacenes were obtained from potential energy surfaces calculations and by partitioning the intramolecular relaxation energy into the contribution of each normal mode according to Eqs. (2) and (3). The calculated values related to the $S_0 \rightarrow S_1$ and $S_1 \rightarrow S_0$ transitions are listed in Table 4. Overall, we found a good agreement between the potential energy surface calculations and the normal mode approach. The results also show a monotonical reduction of the relaxation energies with the increase of the number of thiophene units in the oligomeric chain of the TMS-T*n*-TMS compounds. This observation is in good agreement with previous quantum-chemical studies of various aromatic-based chemical structures [7,16,42,43].

Also, we observed that along the series of end-capped oligothienoacenes there are only a couple of normal modes that mainly determine the vibronic progressions in spectra of these molecules (vibrational modes with energies of $\nu_1 \sim 1500\ cm^{-1}$ and $\nu_2 \sim 500\ cm^{-1}$). The qualitative characteristics of these vibrations are very similar in both electronic transitions. Thus, one could expect the UV–vis

Table 4
Total relaxation energy λ_{rel} of the $S_0 \rightarrow S_1$ and $S_1 \rightarrow S_0$ transitions of TMS-T*n*-TMS obtained from potential energy surfaces (PES) and normal mode (NM) calculations.

Compound	$S_0 \rightarrow S_1$ transition		$S_1 \rightarrow S_0$ transition	
	λ_{rel} (PES)/meV	λ_{rel} (NM)/meV	λ_{rel} (PES)/meV	λ_{rel} (NM)/meV
TMS-T4-TMS	207	215	226	220
TMS-T5-TMS	192	198	210	206
TMS-T6-TMS	180	185	198	195
TMS-T7-TMS	171	175	189	186
TMS-T8-TMS	164	168	181	179

Table 5
DFT/TD-DFT/B3LYP/6-31G(d,p) estimates of frequencies ω, Huang–Rhys factors S, and relaxation energies λ_{rel} related to $S_0 \rightarrow S_1$ and $S_1 \rightarrow S_0$ transitions of TMS-T5-TMS (only the most-strongly coupled vibrations are shown).

$S_0 \rightarrow S_1$ transition			$S_1 \rightarrow S_0$ transition		
ω (cm^{-1})	S	λ_{rel} (eV)	ω (cm^{-1})	S	λ_{rel} (eV)
41	0.037	0.000	41	0.037	0.000
117	0.039	0.001	116	0.041	0.001
138	0.122	0.002	137	0.124	0.002
240	0.138	0.004	240	0.142	0.004
264	0.030	0.001	264	0.026	0.001
478	0.142	0.008	470	0.433	0.025
499	0.608	0.038	485	0.279	0.017
1290	0.146	0.023	606	0.020	0.002
1482	0.567	0.104	1229	0.145	0.022
1520	0.048	0.009	1578	0.628	0.123

absorption and fluorescence spectra to be near-perfect mirror images; which, indeed, is the case for the series of TMS-T*n*-TMS oligothienoacenes considered in this study. However, we note that the spacing of the vibrational features is slightly larger in absorption than in emission; this agrees with the slightly larger Huang–Rhys factors (see Tables 5 and S3) found for the low-frequency modes (below 600 cm^{-1}) in the $S_0 \rightarrow S_1$ transition versus those observed for the $S_1 \rightarrow S_0$ transition. Additionally, the difference in spacing of the vibronic progression peaks in the spectroscopic profiles of these molecular structures is consistent with the widely accepted view that aromatic-like compounds assume a quinoidal form in the electronic excited-state. For example, we note that the excited-state properties of the silyl end-capped oligothienoacenes show the typical alternation of single and double carbon–carbon bonds and

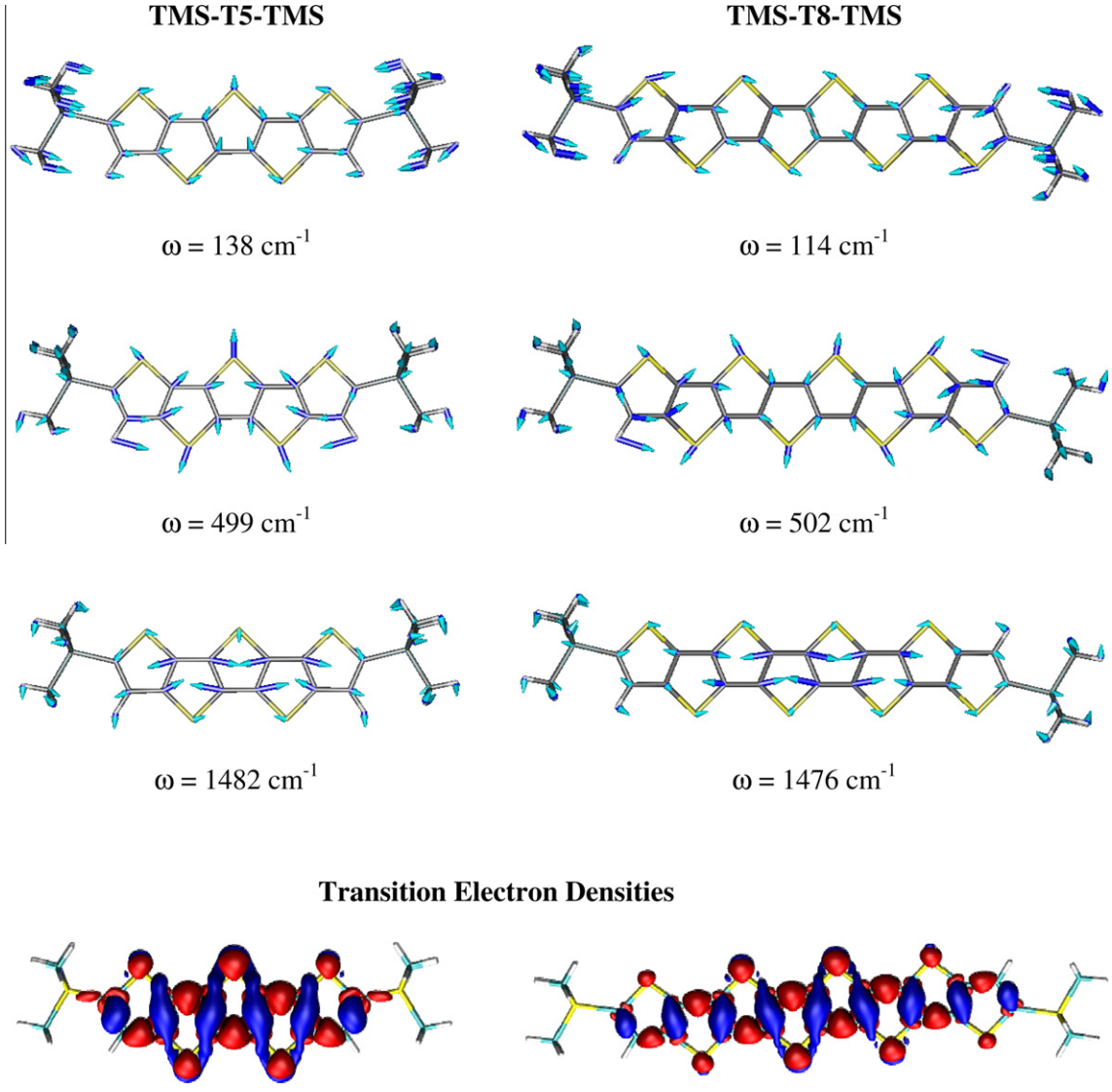

Fig. 5. (top) Illustrations of the normal modes yielding the largest Huang–Rhys factors and (bottom) electron density change in the S_0–S_1 electronic transition of TMS-T5-TMS and TMS-T8-TMS (left and right, respectively). The low-frequency modes involve mostly the sulfur atoms, whereas the high-frequency modes involve the carbon atoms.

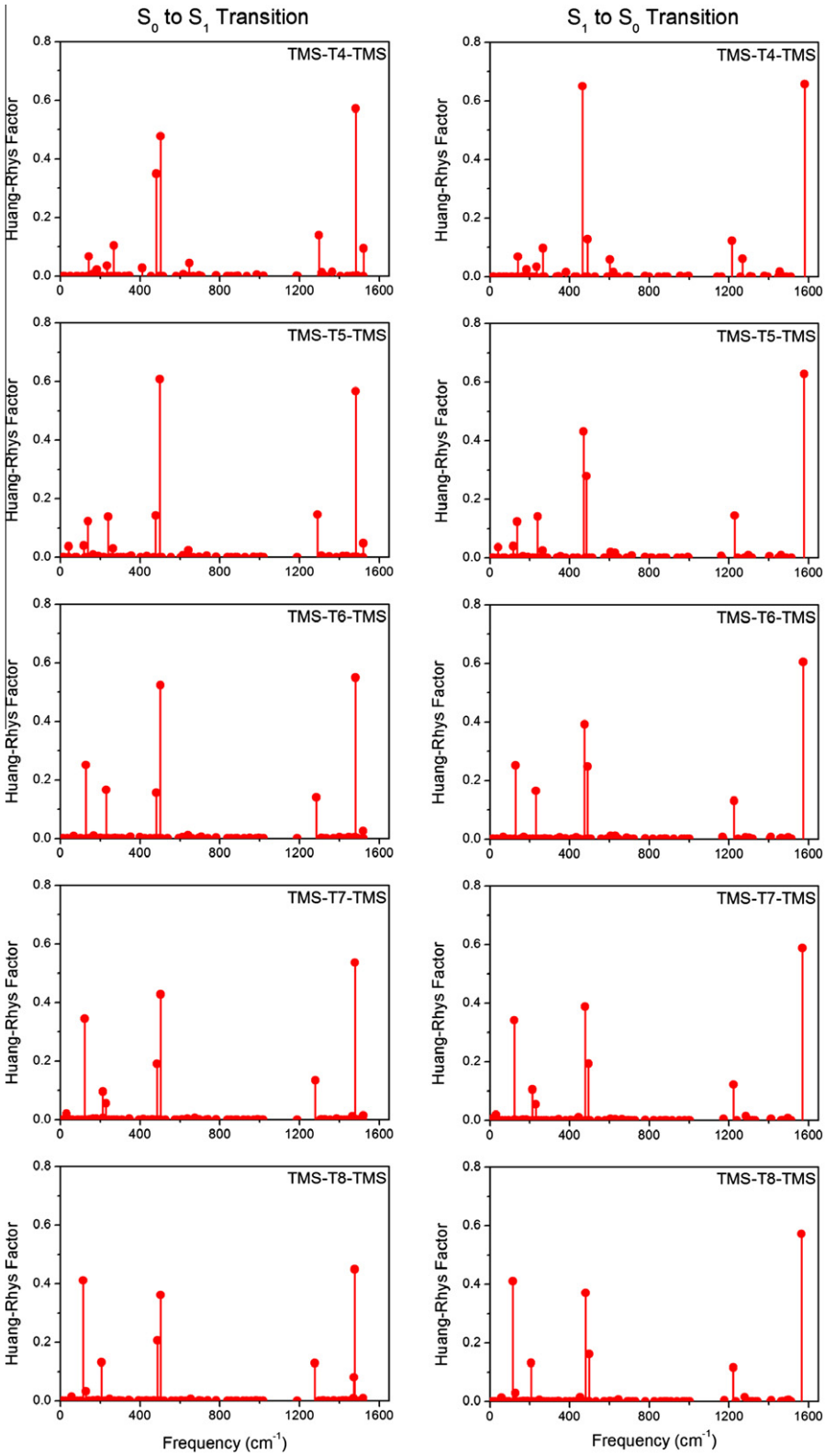

Fig. 6. DFT/TD-DFT/B3LYP/6-31G(d,p) Huang–Rhys factors related to the $S_0 \rightarrow S_1$ and $S_1 \rightarrow S_0$ transitions of TMS-T*n*-TMS as a function of the normal mode frequency.

the characteristic shift of the ring C–C stretching mode toward the high-frequency region of the vibronic spectrum [44,45]. The change in sign of the BLA values reported in Table 3 (from positive to negative) is also in good agreement with the above arguments.

The decomposition of the value of the λ_{rel} into contributions of each normal mode for the TMS-T*n*-TMS oligothienoacenes permits an assignment of the contributions of the low- and high-frequency vibrations to the total value of the calculated relaxation energies. We found that for both electronic transitions approximately 70–75% of the relaxation energy comes from high-frequency vibrations in the range of 1200–1600 cm^{-1}; which include a particularly dominant vibration characterized by a C–C stretching of the inner-most rings (see Fig. 5). On the other hand, the contributions of low-frequency vibrations (below 600 cm^{-1}) account for only 25–30% of the total value of λ_{rel} and include vibrations that are near 500 cm^{-1} and characterized by stretches along the short molecular axis (i.e., via the C–S–C atoms of the thiophene rings). As an illustrative example of decomposition of the λ_{rel} into the normal mode contributions, the DFT/TD-DFT-derived (Huang–Rhys factors, S) related to the $S_0 \rightarrow S_1$ and $S_1 \rightarrow S_0$ transitions in TMS-T5-TMS are shown in Table 5 (see Supporting information for the corresponding data of the other molecular structures investigated in this study).

In Fig. 6, we present the calculated vibrational coupling (Huang–Rhys factors, S) as obtained from DFT/TD-DFT for the complete series of TMS-T*n*-TMS compounds. The different plots of Fig. 6 show consistent vibronic–coupling interactions with both low- and high-frequency vibrations. Further inspection of the most-strongly coupled vibrations shows that the main distortions occur within the molecular backbone (i.e., the fused-thiophene rings) of the TMS-capped compounds. However, we also note that the vibronic–coupling interactions of the larger end-capped oligothienoacenes (TMS-T6-TMS, TMS-T7-TMS, and TMS-T8-TMS) involve a low-frequency vibration at around 100 cm^{-1}. This vibration (shown in Fig. 5) involves, for the case of TMS-T8-TMS, distortions of the silyl-based groups accompanied by lateral distortions of the outer-most thiophene rings; whereas for TMS-T5-TMS, this vibration mainly distorts the atomic positions of the silyl groups. This normal mode posses a large Huang–Rhys factor (i.e., 0.411 for the 114 cm^{-1} mode of TMS-T8-TMS, see Table S3 in Supporting information) and therefore has an effect in the absorption and emission spectra. As discussed in Section 3.4, this low-frequency vibration leads to an effective peak broadening of the absorption and emission profiles of the larger end-capped oligothienoacenes; in which, the extended motions of the outer-most rings distort significantly their respective transition electron densities (see Fig. 5 and Fig. S2).

Lastly, to investigate the effective contributions of the silyl groups to the overall intramolecular reorganization energy λ_{reorg}, we fixed the motions of the oligothienoacene molecular core in the series of TMS-T*n*-TMS oligomers, and computed again their respective λ_{reorg} values. We found that the contributions of TMS groups to the total value of λ_{reorg} upon an electronic excitation from the $S_0 \rightarrow S_1$ state and vice versa, is on the order of 1% (Table 6).

Table 6
Individual contributions of the oligothienoacene core and of the TMS substituents to the total intramolecular reorganization energy (λ_{reorg}) in the TMS-T*n*-TMS oligomers. Energy values are given in meV.

Molecule	TMS[a], λ_{reorg}	Oligothienoacene core[b], λ_{reorg}	Total, λ_{reorg}
TMS-T4-TMS	5	427	432
TMS-T5-TMS	3	395	398
TMS-T6-TMS	1	370	371
TMS-T7-TMS	1	352	353
TMS-T8-TMS	1	337	338

[a] The atomic coordinates of the oligothienoacene core were maintained fixed at the S_0 geometry positions during the optimization of the S_1 state.
[b] The atomic coordinates of the TMS substituents were constrained at the S_0 geometry positions during the optimization of the S_1 state.

3.4. Simulation of the UV–vis absorption and fluorescence

We employed the results of the normal mode analysis to simulate the shape of the absorption and emission profiles of the TMS-T*n*-TMS molecular compounds. Only vibrational modes with Huang–Rhys factors larger than 0.05 were used in these simulations since modes with smaller Huang–Rhys factors essentially do not contribute to the description of the electronic transitions of these almost-rigid molecular structures. The results of the simulation are presented in Fig. 7. The vibronic features of the experimental and theoretical profiles are in good agreement; highlighting the reliability of the DFT/TD-DFT-derived vibronic coupling constants and relaxation energies. However, the experimental intensity distributions cannot be perfectly reproduced by the simulated spectra; the calculated intensities of the (0–1) and (0–2) transitions are smaller with respect to the (0–0) peak than those observed experimentally. This underestimation is likely related to the amount of exact Hartree–Fock exchange in the B3LYP functional, as shown in previous studies [24,43,46].

Although, our quantum–mechanical calculations provide access to all of the predicted vibrational modes involved in the absorption and emission processes of the TMS-capped molecular structures, we have determined that at least for TMS-T4-TMS and TMS-T5-TMS, there are two vibrations that are the most relevant; the first one around 500 cm^{-1} and the second one in the region of 1450 cm^{-1} to 1600 cm^{-1}. However, the situation is different for TMS-T6-TMS, TMS-T7-TMS, and TMS-T8-TMS because, in these molecules, a low-frequency vibration at around 100 cm^{-1} also becomes important to the absorption and emission processes. This particular vibration, which shows a relatively large Huang–Rhys factor (see Table S3), introduces an effective spectral broadening of the absorption/emission features of these three compounds, which is in good agreement with previous reports (see for example, Ref. [44]). In order to account for the broadening effect of this low-frequency vibration, we have also simulated the absorption/emission spectroscopic profiles of the TMS-T*n*-TMS oligomers by introducing a frequency cut-off that only considers strongly coupled normal modes with frequencies larger than 400 cm^{-1}. The simulated spectral profiles are reported in Fig. S3. A simple comparison between the theoretically simulated

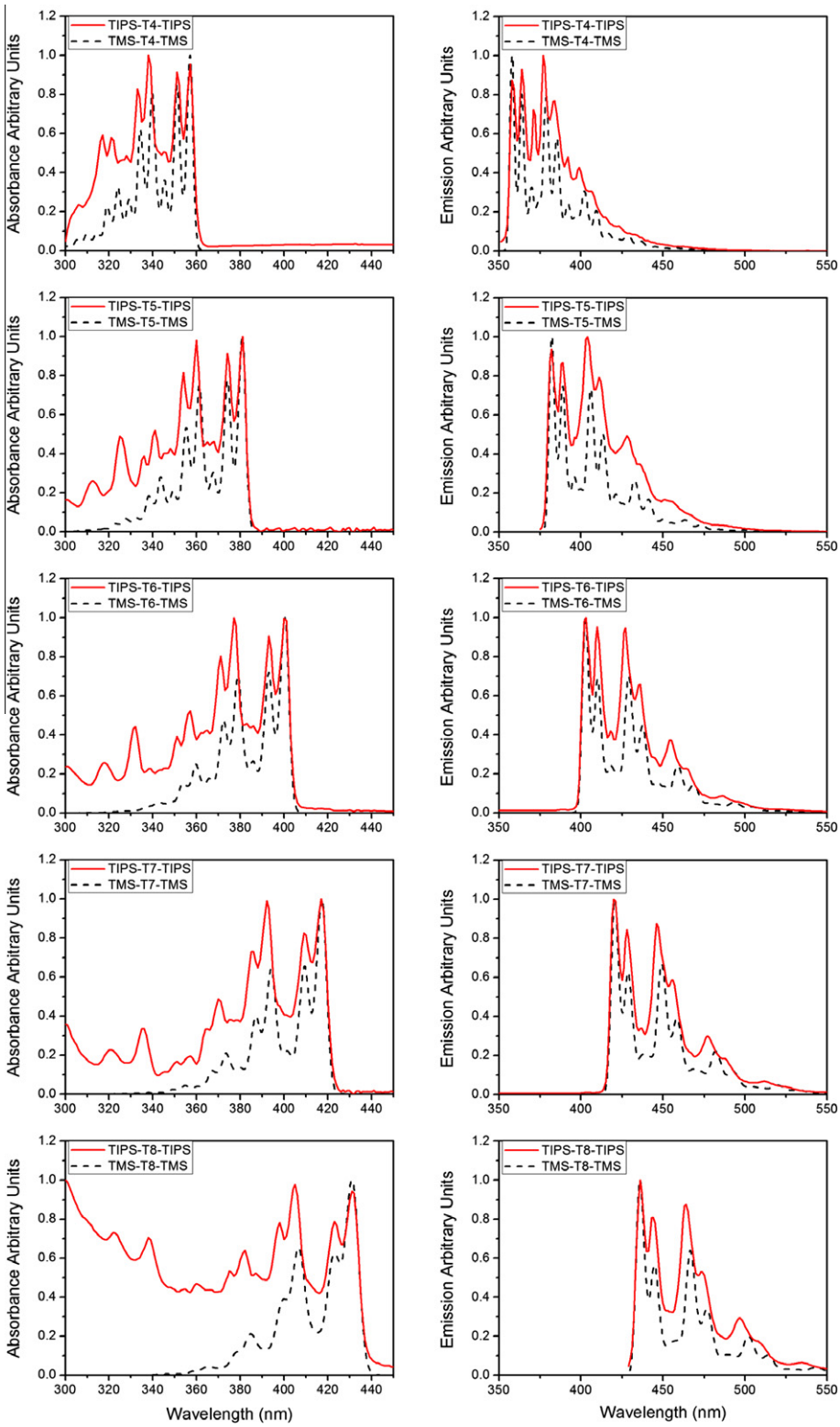

Fig. 7. Normalized UV–vis absorption and fluorescence experimental-spectra of TIPS-T*n*-TIPS (solid lines). The dashed lines represent the simulated (theoretical) spectra convoluted with Gaussian functions. Note that for computational efficiency, in all theoretical simulations we used TMS substituents instead of TIPS substituents. The onset of the simulated spectra is chosen to correspond to the experimental onset.

spectra that used both low- and high-frequency normal modes versus those that only incorporated normal modes with frequencies larger than 400 cm^{-1} reveals that for the shorter TMS-T*n*-TMS ($n = 4$ and 5) oligomers, their spectroscopic characteristics are mainly governed by the high-frequency normal modes (no significant differences between the two simulations, see Fig. S3). However, the simulation and comparison of their respective spectra suggest that, the larger TMS-T*n*-TMS ($n = 6$–8) oligomers require the inclusion of the low-frequency normal modes to account for the observed differences (see Fig. S3).

It is also important to note that the $S_0 \rightarrow S_1$ and $S_1 \rightarrow S_0$ Huang–Rhys factors of ~100 cm^{-1} normal mode become larger as the number of thiophene rings increases. For example, the Huang–Rhys factors related to the absorption transition of this low-frequency vibration along the series of TMS-T*n*-TMS oligothienoacenes are: 0.067 (142 cm^{-1}), 0.122 (138 cm^{-1}), 0.251 (128 cm^{-1}), 0.345 (122 cm^{-1}), and 0.411 (114 cm^{-1}), ongoing from TMS-T4-TMS to TMS-T8-TMS, respectively. This low-frequency mode stretches the thiophene molecular backbone as a whole along the long molecular axis. However, these longitudinal stretches are only more pronounced in the larger end-capped oligothienoacenes ($n = 6$–8), in which the many more internal degrees of freedom, especially those of the outer-most thiophene rings, still distort their respective core-extended transition electron densities, as shown in Figs. 5 and S2.

4. Conclusions

This work presents a detailed joint experimental and theoretical analysis of the optical and electronic properties of a family of silyl end-capped oligothienoacenes, which have emerged as a novel class of solution-processable π-conjugated compounds for organic electronic applications. The experimental absorption and emission profiles showed well-resolved vibronic progressions at both low and room temperature, which is indicative of a minimal conformational disorder of the TIPS-T*n*-TIPS oligomers upon electronic transitions. Also, the systematic red-shift of the absorption maxima of the silyl end-capped oligothienoacenes with the extension of the π-conjugation is in good agreement with the systematic reduction of the calculated HOMO–LUMO gap along the series. When compared to the unsubstituted oligothienoacenes, the insertion of the silyl groups is found to destabilize/stabilize the HOMO/LUMO energies as a consequence of the silicon-induced hyperconjugation effect.

First-principles quantum–mechanical calculations have been used to characterize the experimental absorption and emission profiles of these novel molecular structures. For the smaller molecules (tetramer and pentamer), we found that the vibronic progression of their optical spectra are mainly determined by the presence of two normal modes with frequencies of ~1500 cm^{-1} and 500 cm^{-1}. However, the larger molecules (hexamer, heptamer, and octamer) are not only characterized by those frequencies but also by the presence of a low-frequency normal mode at around 100 cm^{-1}. We note that this particular vibration is responsible for the experimentally observed peak broadening of the vibrational absorption and emission features of these compounds. Also, our theoretical estimates of the intramolecular reorganization energies upon electronic transition reveal that the vibronic–coupling interactions in silyl end-capped oligothienoacenes are only associated with their respective oligothienyl molecular backbone.

Finally, our results suggest that a possible route to explore new soluble organic semiconducting materials should, in principle, include functionalization/modification of their respective molecular backbones. We hope that our results will trigger further experimental investigations for the design of new solution-processable organic semiconducting materials.

Acknowledgements

We thank D. Rappoport and J. Yuen-Zhou for stimulating discussions. We are very grateful to Prof. Adam J. Matzger and Prof. Shigehiro Yamaguchi for kindly providing us the samples. R.S.S.-C. thanks the Mary-Fieser Postdoctoral Fellowship at Harvard University. Financial support by the Ministerio de Ciencia e Innovación (MICINN) of Spain (Project CTQ2009-10098) and the Junta de Andalucia (Grant FQM-0159 and Project P06-FQM-1678) are greatly acknowledged. R.M.O. and C.C.F. are also grateful to the UMA and MICINN, respectively, for personal doctoral grants. We are grateful to Dr. Massimo Malagoli (Georgia Institute of Technology, USA) for making available a copy of the program used to simulate the optical spectra. We also thank Dr. Karin Zojer (Graz University of Technology) for adapting TURBOMOLE output files to the DUSHIN input. This work was also supported through a National Science Foundation grant via Harvard MRSEC, Grant No. DMR-08-20484. We thank the High Performance Technical Computing Center at the Faculty of Arts and Sciences of Harvard University for invaluable support.

Appendix A. Supplementary material

Figure for the normalized (low-temperature) UV–vis absorption and fluorescence emission spectra of TMS-T5-TMS and pentathienoacene in MeTHF. Supporting information also includes a table with selected bond lengths in the ground-state and excited-state of TMS-T*n*-TMS molecules with $n = 5$–7 as determined by DFT/TD-DFT/B3LYP calculations; DFT/TD-DFT/B3LYP estimates of frequencies, Huang–Rhys factors, and relaxation energies related to $S_0 \rightarrow S_1$ and $S_1 \rightarrow S_0$ transitions of TMS-T*n*-TMS ($n = 4$, 6, 7, and 8); and an illustration of the transition electron densities of TMS-T*n*-TMS ($n = 4$, 6, and 7). Finally, we have also included a figure that compares the effect of low- and high-frequency normal modes versus only high-frequency normal modes in the simulated absorption and fluorescence spectral profiles of the TMS-T*n*-TMS ($n = 4$–8) oligomers.

Supplementary data associated with this article can be found, in the online version, at doi:10.1016/j.orgel.2010.07.001.

References

[1] J.E. Anthony, Angew. Chem., Int. Ed. 47 (2008) 452–483.
[2] S. Henning, Adv. Mater. 21 (2009) 3859–3873.
[3] A.R. Murphy, J.M.J. Frechet, Chem. Rev. 107 (2007) 1066–1096.
[4] J. Roncali, Acc. Chem. Res. 42 (2009) 1719–1730.
[5] T. Okamoto, K. Kudoh, A. Wakamiya, S. Yamaguchi, Chem. Eur. J 13 (2007) 548–556.
[6] X.N. Zhang, A.P. Cote, A.J. Matzger, J. Am. Chem. Soc. 127 (2005) 10502–10503.
[7] E.-G. Kim, V. Coropceanu, N.E. Gruhn, R.S. Sánchez-Carrera, R. Snoeberger, A.J. Matzger, J.-L. Brédas, J. Am. Chem. Soc. 129 (2007) 13072–13081.
[8] X.N. Zhang, J.P. Johnson, J.W. Kampf, A.J. Matzger, Chem. Mater. 18 (2006) 3470–3476.
[9] O.L. Griffith, N.E. Gruhn, J.E. Anthony, B. Purushothaman, D.L. Lichtenberger, J. Phys. Chem. C 112 (2008) 20518–20524.
[10] R.M. Osuna, M.C.R. Delgado, V. Hernandez, J.T.L. Navarrete, B. Vercelli, G. Zotti, J.J. Novoa, Y. Suzuki, S. Yamaguchi, J.T. Henssler, A.J. Matzger, Chem. Eur. J 15 (2009) 12346–12361.
[11] R.M. Osuna, V. Hernandez, J.T.L. Navarrete, J. Arago, P.M. Viruela, E. Orti, Y. Suzuki, S. Yamaguchi, J.T. Henssler, A.J. Matzger, ChemPhysChem 10 (2009) 3069–3076.
[12] M. Klessinger, J. Michl, Excited States and Photochemistry of Organic Molecules, VCH, New York, 1995.
[13] J.R. Lakowicz, Principles of Fluorescence Spectroscopy, second ed., Kluwer Academic/Plenum, New York, 1999.
[14] V. Navarro-Fuster, E.M. Calzado, M.G. Ramirez, P.G. Boj, J.T. Henssler, A.J. Matzger, V. Hernandez, J.T.L. Navarrete, M.A. Diaz-Garcia, J. Mater. Chem. 19 (2009) 6556–6567.
[15] J. Aragó, P.M. Viruela, E. Ortí, R.M. Osuna, B. Vercelli, G. Zotti, V. Hernández, J.T. López Navarrate, J.T. Henssler, A.J. Matzger, Y. Suzuki, S. Yamaguchi, Chem. Eur. J 16 (2010) 5481–5491.
[16] J.L. Brédas, D. Beljonne, V. Coropceanu, J. Cornil, Chem. Rev. 104 (2004) 4971–5003.
[17] M. Malagoli, V. Coropceanu, D.A. da Silva Filho, J.L. Brédas, J. Chem. Phys. 120 (2004) 7490–7496.
[18] P.F. Barbara, T.J. Meyer, M.A. Ratner, J. Phys. Chem. 100 (1996) 13148–13168.
[19] J.R. Reimers, J. Chem. Phys. 115 (2001) 9103–9109.
[20] M.W. Wong, Chem. Phys. Lett. 256 (1996) 391–399.
[21] Z. Zhao, F.C. Spano, J. Phys. Chem. C 111 (2007) 6113–6123.
[22] F. Furche, R. Ahlrichs, J. Chem. Phys. 117 (2002) 7433–7447.
[23] D. Rapport, F. Furche, Time-Dependent Density Functional Theory, Springer, Berlin, 2006. pp. 337-357.
[24] M. Dierksen, S. Grimme, J. Phys. Chem. A 108 (2004) 10225–10237.
[25] M. Dierksen, S. Grimme, J. Chem. Phys. 120 (2004) 3544–3554.
[26] A.D. Becke, J. Chem. Phys. 98 (1993) 5648–5652.
[27] C.T. Lee, W.T. Yang, R.G. Parr, Phys. Rev. B 37 (1988) 785–789.
[28] M.M. Francl, W.J. Pietro, W.J. Hehre, J.S. Binkley, M.S. Gordon, D.J. Defrees, J.A. Pople, J. Chem. Phys. 77 (1982) 3654–3665.
[29] P.C. Harihara, J.A. Pople, Theor. Chim. Acta 28 (1973) 213–222.
[30] W.J. Hehre, R. Ditchfie, J.A. Pople, J. Chem. Phys. 56 (1972) 2257–2261.
[31] TURBOMOLE V6.1 2009 a development of University of Karlsruhe and Forschungszentrum Karlsruhe GmbH, 1989–2007, TURBOMOLE GmbH, since 2007. <http://www.turbomole.com>.
[32] Y. Suzuki, T. Okamoto, A. Wakamiya, S. Yamaguchi, Org. Lett. 10 (2008) 3393–3396.
[33] G. Macchi, B. Milian Medina, M. Zambianchi, R. Tubino, J. Cornil, G. Barbarella, J. Gierschner, F. Meinardi, Phys. Chem. Chem. Phys. 11 (2009) 984–990.
[34] E. Leontidis, U.W. Suter, M. Schuetz, H.-P. Luethi, A. Renn, U.P. Wild, J. Am. Chem. Soc. 117 (1995) 7493–7507.
[35] A.M. Stoneham, Rev. Mod. Phys. 41 (1969) 82–108.
[36] D. Wasserberg, S.C.J. Meskers, R.A.J. Janssen, E. Mena-Osteritz, P. Bauerle, J. Am. Chem. Soc. 128 (2006) 17007–17017.
[37] D.M. Wetzel, J.I. Brauman, J. Am. Chem. Soc. 110 (1988) 8333–8336.
[38] C. Risko, G.P. Kushto, Z.H. Kafati, J.L. Brédas, J. Chem. Phys. 121 (2004) 9031–9038.
[39] X. Zhan, C. Risko, F. Amy, C. Chan, W. Zhao, S. Barlow, A. Kahn, J.L. Brédas, S.R. Marder, J. Am. Chem. Soc. 127 (2005) 9021–9029.
[40] G. Lu, H. Usta, C. Risko, L. Wang, A. Facchetti, M.A. Ratner, T.J. Marks, J. Am. Chem. Soc. 130 (2008) 7670–7685.
[41] S. Yamaguchi, Y. Itami, K. Tamao, Organometallics 17 (1998) 4910–4916.
[42] G.R. Hutchison, M.A. Ratner, T.J. Marks, J. Am. Chem. Soc. 127 (2005) 2339–2350.
[43] R.S. Sánchez-Carrera, V. Coropceanu, D.A. da Silva Filho, R. Friedlein, W. Osikowicz, R. Murdey, C. Suess, W.R. Salaneck, J.L. Brédas, J. Phys. Chem. B 110 (2006) 18904–18911.
[44] S. Karabunarliev, M. Baumgarten, E.R. Bittner, K. Mullen, J. Chem. Phys. 113 (2000) 11372–11381.
[45] G. Orlandi, F. Zerbetto, M.Z. Zgierski, Chem. Rev. 91 (1991) 867–891.
[46] K. Schmidt, S. Brovelli, V. Coropceanu, J.L. Brédas, C. Bazzini, T. Caronna, R. Tubino, F. Meinardi, J. Phys. Chem. A 110 (2006) 11018–11024.

Organic Electronics 11 (2010) 1713–1718

Contents lists available at ScienceDirect

Organic Electronics

journal homepage: www.elsevier.com/locate/orgel

A pentacene field-effect transistor with light-programmable threshold voltage

Chengang Feng [a], Ting Mei [b,*], Xiao Hu [c], Neuzil Pavel [d]

[a] School of Electrical and Electronic Engineering, Nanyang Technological University, 50 Nanyang Avenue, Singapore 639798, Singapore
[b] Institute of Optoelectronic Materials and Technology, South China Normal University, Guangzhou 510631, China
[c] School of Materials Science and Engineering, Nanyang Technological University, 50 Nanyang Avenue, Singapore 639798, Singapore
[d] Institute of Microelectronics, 11 Science Park Road, Singapore 117685, Singapore

ARTICLE INFO

Article history:
Received 8 April 2010
Received in revised form 26 June 2010
Accepted 26 July 2010
Available online 6 August 2010

Keywords:
Field-effect transistor
Pentacene
Threshold voltage

ABSTRACT

We report the effect of light illumination on the electrical characteristics of pentacene field-effect transistors with a large-bandgap conjugated polymer PFO as the interfacial layer. The nanostructured PFO servers as charge-trapping centers that capture charges injected from the pentacene active layer. When the device is under light illumination, the threshold voltage (V_{th}) can be modulated by varying positive gate biases such that the operation mode can be switched from the enhancement mode to the depletion mode. This light-programmable feature may motivate the development of this new type of organic memory devices.

© 2010 Elsevier B.V. All rights reserved.

1. Introduction

The organic field-effect transistor (OFET) has been envisioned as a promising candidate for commercial applications due to its demonstrated performance comparable to that of the amorphous silicon (*a*-Si) transistor, together with its potential low-cost fabrication [1–3]. To design and manufacture the integrated circuits (ICs) with organic transistors, a high mobility is required to increase the operation speed. Besides, the threshold voltage is another important parameter that needs to be controlled for the reliability of enhanced integrated circuits (ICs). In the case of silicon metal–oxide-semiconductor field-effect transistors (FETs), the threshold voltage, V_{th}, can be adjusted by doping the channel region and/or a second gate bias to tune the electrostatic potential and the carrier density in the channel [4,5]. The same techniques have not yet been well developed for OFETs, whereas great efforts have been made to develop a few methods to achieve the control of threshold voltage [6–11]. Nevertheless, little research has been done on employing light irradiation as a control apparatus to V_{th}, which will bring about light-controlled OFETs. Although a shift in V_{th} upon light illumination was observed, it was very difficult to strictly control V_{th} in a wide range for a single OFET device.

Previously, chargeable gate dielectrics (sometimes referred as "electrets") were employed to study the effect of photo-induced charge transfer on the shift of the field-effect onset [12,13]. The memory effect in the FET structure due to the photo-induced charge transfer was firstly studied by Dutta and Narayan [12]. It was found that the negative charges are severely trapped and lie in the deep-energy states in the depletion mode after being generated under illumination. Later, the rate of the charge transfer (both holes and electrons) was investigated in detail by Podzorov and Gershenson [13] which was determined by (i) the flux of photons with energies greater than the LUMO–HOMO gap of an organic semiconductor and (ii) the magnitude of the transverse electrical field applied at the semiconductor–dielectric interface. However, both works focuses on the charge transfer from an active layer to a gate dielectric. In this work, a conjugated polymer, poly(9,9-dioctylfluorene) (PFO), was selected to form type

* Corresponding author.
E-mail address: ting.mei@ieee.org (T. Mei).

1566-1199/$ - see front matter © 2010 Elsevier B.V. All rights reserved.
doi:10.1016/j.orgel.2010.07.024

I heterojunction (straddling gap) with pentacene to study the charge transfer effect, where the diagram of energy levels of PFO/pentacene was similar to that of PVA/P3AT or Parylene/rubrene, because of the presence of deep electron trapping states in PFO and the high room-temperature hole mobility with weak field dependence, which have been widely investigated as a hole-transport material in the fabrication of blue LEDs [14,15]. Besides, PFO will emit polarized light if they can be oriented, as it is an emissive liquid–crystal polymer [16]. Such a polarized emitter is of great interest for use as a backlight in a liquid–crystal display since it provides the replacement for the normal backlight and polarizer combination. For these reasons, high performance OFET devices with a pentacene active layer and nanostructured PFO dispersed in PMMA (or an ultrathin PFO film) were fabricated to study the effect of PFO. Under negative gate bias ($|V_g| > |V_{th}|$) in the dark condition, these FETs presented conventional p-channel behavior and operate in the enhancement mode, as the field-induced carriers are expected to be confined in the pentacene layer due to the HOMO offset between PFO (LUMO = −2.3 eV and HOMO = −5.8 eV) [14] and pentacene (LUMO = −3.2 eV and HOMO = −5.1 eV) [17,18]. On the other hand, when it is under illumination, non-equilibrium charge carriers (holes and electrons) are generated and separated under the influence of the electric field. By applying proper positive gate bias, i.e. operating in the depletion mode, electron carriers can be trapped by the nanostructured PFO and the interface, causing a shift in the threshold voltage. As we will show hereinafter, by varying the starting source–gate voltage V_{g_start} in the off-to-on transfer characteristics, V_{th} can be tuned through the effect of photo-induced charge transfer.

2. Experimental

A heavily doped n-type silicon wafer and a 500 nm-thick thermal oxide layer on the surface were used as the gate electrode and the gate dielectric layer, respectively. The interfacial layer, PFO, was deposited on the wafer after a wafer-cleaning process. It consisted of 10–15 nm nanostructured PFO dispersed in PMMA, referred as PFO&PMMA, or 10 nm PFO film in device 1, while another 10 nm-thick PMMA film was used to planarize the surface of PFO&PMMA (or PFO) film in device 2. PFO&PMMA (or PFO) film was spin-coated from toluene solution and the nanostructured PFO was formed during the annealing process at 105 °C for 10 min on a hotplate under the air ambient. PMMA planarizing layer was spin-coated from chlorobenzene solution and annealed at 105 °C for 10 min on the hotplate to remove the residual solvent. Subsequently, a 50–60 nm-thick layer of pentacene (used as received from Sigma–Aldrich) was deposited in a vacuum system by thermal evaporation at a background pressure of 10^{-5} Pa. The deposition rate was controlled at 0.2 Å/s and the substrates were maintained at room temperature. The transistors were completed by the deposition of a 30 nm-thick gold film as the source–drain contacts through a shadow mask. The channel length (L) and the width (W) of the devices are 100 μm and of 2 mm, respectively. To characterize absorption spectra, PFO&PMMA (or

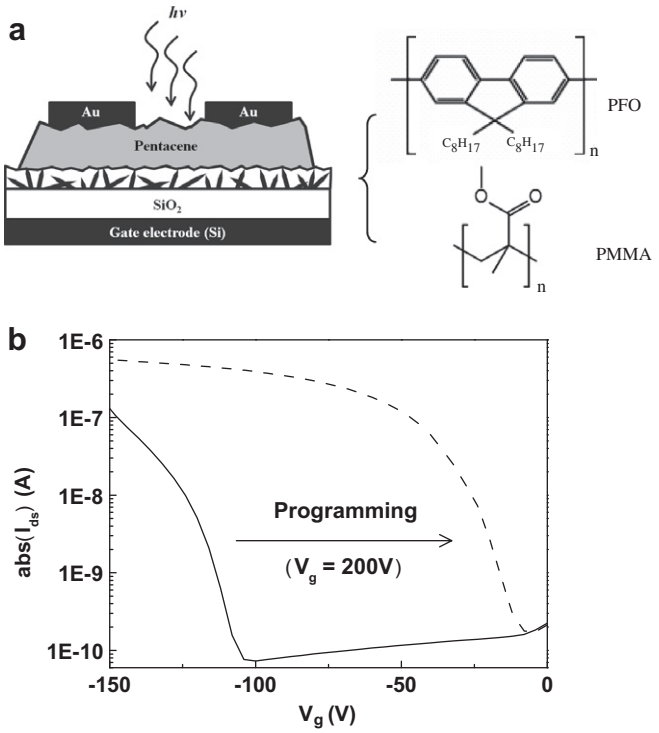

Fig. 1. (a) Molecular structure of poly(methyl methacrylate) (PMMA) and poly(9,9-dioctylfluorene) (PFO), and a schematic of the OFET device, (b) transfer characteristics of device 1 at V_{ds} = −100 V, where V_g = 200 V for 30 s was applied at V_{ds} = 0 V under white light illumination for inducing the shift in V_{th}.

PFO) film with the same thickness was prepared on the quartz substrate.

To investigate the effect of light illumination on the electrical performance of our devices, the devices were illuminated from the top from a halogen lamp, as shown in Fig. 1a. The characterization of the devices was carried out on a standard probe station with or without light illumination. The light intensity was preset using a neutral density filter. To clarify the charge transfer and trapping mechanism in these devices, a Dongwoo Optron TH3 arc lamp together with a Dongwoo Optron DM150i monochromator was used to conduct red light irradiation at a wavelength of 628 nm. The light was focused to a spot size approximately equal to the area of the device to cover the entire channel with an estimated light intensity of 1 mW/cm^2. Electrical characteristics were measured using a Keithley 4200 SCS semiconductor parameter analyzer under ambient condition at room temperature. AFM images were obtained using a Nanoscope IIIa AFM (Digital instrument) in trapping mode. Absorption spectrum was measured at room temperature using a Shimadzu UV–VIS spectrometer.

3. Results and discussion

Fig. 1b shows the device characteristics of p-type pentacene FETs, where the source–drain currents $|I_{ds}|$ are plotted in a logarithmic scale against the gate voltage, V_g, at a constant source–drain voltage of $V_{ds} = -100$ V for device 1. The source–drain current in the saturation region is described by

$$I_{ds} = \frac{W}{2L}\mu C_i (V_g - V_{th})^2, \quad (1)$$

where W and L are the channel width and length, μ is the field-effect mobility, and C is the capacitance per unit area of the gate dielectric layer. Thus, from linear curve fitting to the data of $\sqrt{I_{ds}}$ versus V_g in the saturation region (not shown here), V_{th} is obtained as the intercept to the X-axis of the linear fitting curve, whereas μ is derived from the slope. The evaluated values of the mobility μ, V_{th} and on/off current ratio are 0.028 cm^2/V s, –110 V and 10^3, respectively. By applying light illumination on the device at $V_g = 200$ V for 30 s, the entire curve was shifted to the positive side. The shift of the threshold voltage can be attributed to the trapping of photo-generated electrons and neutralize the positively charged states that contribute to the large initial negative threshold voltage. Therefore, the transferred carrier density Δn can be estimated by the follows:

$$\Delta n = \frac{Q_{\text{trap}}}{q} = \frac{C_i \Delta V_{th}}{q}, \quad (2)$$

where Q_{trap} is the amount of trapped charge and q is the charge of electron. The calculated Δn was around 3.75×10^{12} cm^{-2}. It is to say that the nanostructured PFO played as charge-trapping centers like silicon nanoparticles (NPs) distributed in the gate oxide [19]. In our case, the effect of field-induced electrons on inducing the shift of V_{th} under positive gate bias was suppressed because of (i) the low electron carrier density in the p-type pentacene layer and the large electron injection barriers (ii) between pentacene and Au and (iii) between pentacene and PFO. However, by applying light irradiation, the photo-generation process produced excess high-energy electron carriers, which was an important mechanism of boosting the amount of trapped electrons in nanostructured PFO and the interface, resulting in a significant shift of V_{th}. The calculated mobility was 0.026 cm^2/V s, which was in good consistence with that obtained in the dark condition.

Obviously, the obtained performance of device 1 was not satisfying, e.g. low mobility and terribly large threshold voltage. This might be due to the rough interface between the pentacene and the PFO&PMMA (or PFO) film, as shown in Fig. 2a, since PFO tends to crystallize to form nanostructures during annealing process. This rough interface brings a large amount of interfacial states that trap charge carriers, contributing to the large negative threshold voltage. Besides, the charge transport in the accumulation region became worse due to the charge scattering effect, thereby deteriorating the field-effect mobility. In order to improve the surface condition, a 10 nm-thick thin PMMA layer was employed for planarization, shown in Fig. 2b. The electrical characteristics of device 2 in the dark condition were presented in Fig. 3a. The device performance was greatly improved by the introduction of a 10 nm PMMA buffer layer, giving rise to a mobility of 0.35 cm^2/V s, V_{th} of -15 V and an on/off ratio of >10^5. On the other hand, when varying the starting gate voltage V_{g_start} from 0 to 200 V in the off-to-on transfer curve to induce the shift in threshold voltage in the dark condition, a shift in V_{th} (ΔV_{th}) of 6 V was obtained, namely, V_{th} varied from -15 to -9 V. It indicated that a small amount of field-induced electrons can be injected from pentacene active layer and trapped in nanostructured PFO and the interface, although the thin PMMA planarizing layer provided an additional tunneling barrier for electrons. It is thus expected that when the device is under illumination, the shift in transfer curves would become much more clear due to the participation of photo-excited high-energy electrons. As expected, the transfer curves systematically shifted toward the positive direction with increasing V_{g_start}, by applying light illumination on the channel region, as shown in Fig. 3b. It was observed that V_{th} remarkably shifted from -14.6 to 122.5 V when V_{g_start} changed from 60 to 200 V. It should be noted that the photo-induced threshold voltage shift was so significant that the operation mode can be changed from the enhancement mode to the depletion mode.

The photo-induced shift in V_{th} can be explained through the efficiency of the exciton separation in organic semiconductors and the electron trapping in nanostructured PFO and the interface. When light is absorbed, transitions between two molecular orbitals result in excitonic states with weak or strong Coulomb interaction binding electron and hole depending on photon energy. These paired electrons and holes are separated under proper gate bias. Detailed discussion of charge separation can also be found in studies of organic solar cells [20–22]. As shown in Fig. 4, V_{th} was almost unaffected till $V_{g_start} = 60$ V under light illumination. However, by applying $V_{g_start} = 200$ V, a conducting channel between the source and the drain

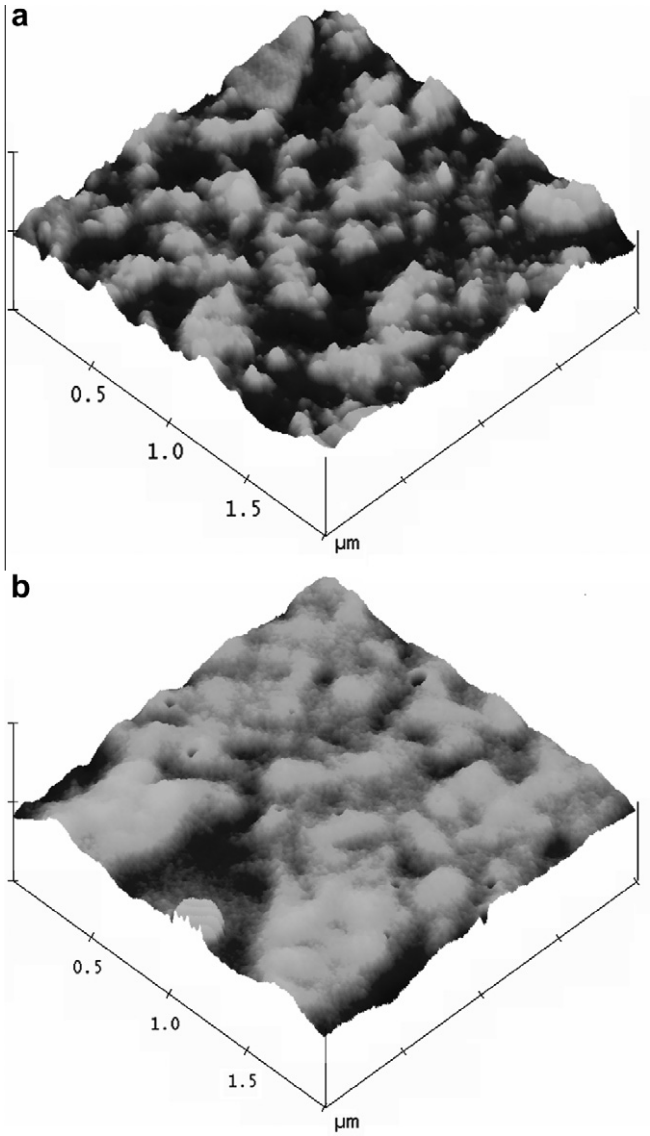

Fig. 2. Atomic force microscope images of surfaces of polymer: (a) PFO&PMMA spin-coated on SiO_2 surface (R_q = 4 nm), (b) PMMA film planarizing PFO&PMMA (R_q = 1.5 nm). Data scale is 50 nm and R_q represents RMS roughness.

began to form even at V_g = 150 V, indicating that a large amount of electrons were injected and trapped. Based on Eq. (2), the estimated density of transferred charges was around $5.14 \times 10^{12}\,cm^{-2}$. These trapped electrons were contributed from the excitonic states dissociated under the transverse electrical field determined by the applied gate bias. The efficiency of exciton dissociation and charge injection from the channel layer depends on the strength of the transverse electrical field and thus the threshold voltage can be set by V_{g_start}, whereas light illumination can be a control parameter for the modulation of the threshold voltage, as seen in response curves in Fig. 4.

In order to investigate the stability of a shifted V_{th}, we did the experiment on the lifetime of trapped charges in the dark. The device was programmed with red light (λ = 628 nm) under a gate bias of 200 V with respect to the short-circuited source and drain electrodes for a duration of 60 s. The considerably enhanced drain current was obtained at zero gate bias at $V_{ds} = -100$ V after programming, showing the "ON" state of the device. On the other hand, by applying an erasing voltage at $V_g = -200$ V at V_{ds} = 0 V in the dark to sweep away the trapped electrons, the transistor can be restored to the "OFF" state. The experiment result indicated that the trapped electrons were injected from the pentacene active layer, as the absorption spectrum of PFO mainly occurred in the blue light region (see the inset of Fig. 5) due to the large HOMO–LUMO bandgap while pentacene film was reported to be sensitive to red light [23]. A decay process in I_{ds} exhibited non-exponential characteristics with two distinguishable decay rates: (i) an initial rapid relaxation due to the recombination of closely packed holes and electrons and (ii) a subse-

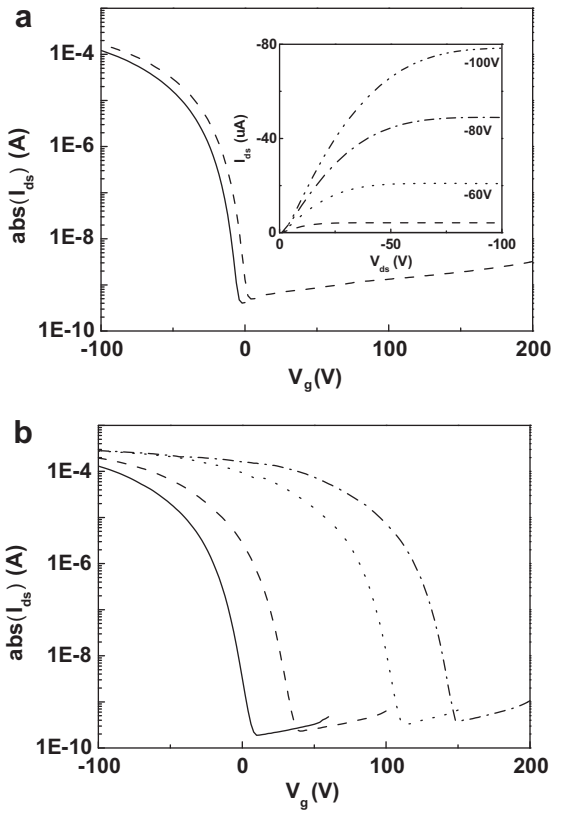

Fig. 3. Transfer characteristics of device 2 measured (a) in the dark condition with different V_{g_start}: 0 V (solid line) and 200 V (dash line), (b) under white light illumination with different V_{g_start}: 60 V (solid line), 100 V (dash line), 150 V (dot line), 200 V (dash dot line). The inset shows the sweeping characteristics with V_g starting from 0 V to −100 V in a step of −20 V in the dark condition.

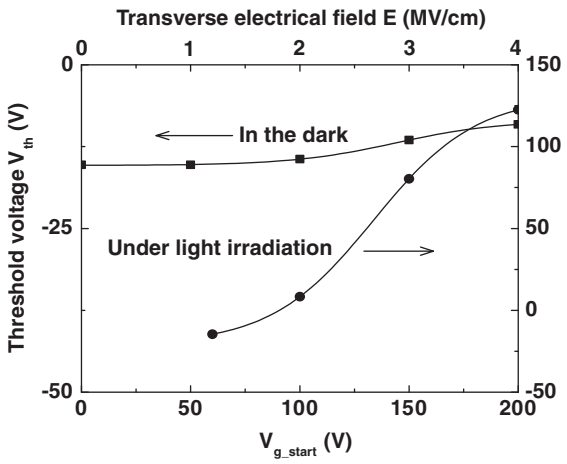

Fig. 4. V_{th} as a function of V_{g_start} with (circle)/without (square) white light illumination.

quent slower relaxation originated from deeply trapped carriers, depending on the quality of the PFO&PMMA (or PFO) film as well as the PMMA buffer layer. A charge storage lifetime of 60 min was obtained in this experiment. Due to the small, but non-zero leakage currents, these device in its current state needs to be refreshed every few hours, which might not reach the requirement for data storage application in organic electronics, but really motivating for the development of OFETs with tunable V_{th} through the photo-induced charge transfer.

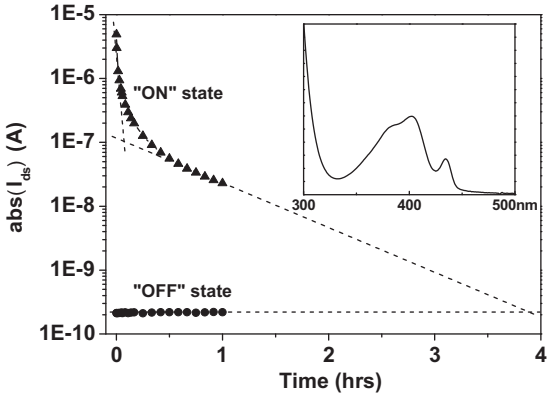

Fig. 5. Time evolution of I_{ds} measured at $V_{ds} = -100$ V and $V_g = 0$ V in the dark. The programming bias ($V_g = 200$ V and $V_{ds} = 0$ V) and erasing bias ($V_g = -200$ V and $V_{ds} = 0$ V) was applied to obtain the "ON"- and "OFF"-current states.

4. Conclusions

In conclusion, the charge transfer effect between pentacene and PFO in the FETs structure was studied and these devices presented a light-programmable electrical feature. The shift of the threshold voltage can be controlled in a wide range by varying V_{g_start} under light illumination, while the field-effect mobility and ON/OFF ratio were well maintained when the surface condition was optimized. It was ascribed to the charge-trapping ability of nanostructured PFO, whereas, to achieve a useful memory device, the improved performance is expected, in terms of charge retention and the operating voltage by introducing new combinations of various materials, smoother interface, along with optimization of geometrical parameters.

Acknowledgment

This work was financially supported by the Ministry of Education, Singapore (Research Grant No. RG 13/06).

References

[1] Y.-Y. Lin, D.J. Gundlach, S.F. Nelson, T.N. Jackson, IEEE Electron Dev. Lett. 18 (1997) 606.
[2] D. Voss, Nature 407 (2000) 442.
[3] S.K. Moore, IEEE Spectrum 39 (2002) 55.
[4] S.M. Sze, Semiconductor Devices, Physics and Technology, Wiley, New York, 1985.
[5] L.C. Parrillo, in: S.M. Sze (Ed.), VLSI Technology, McGraw-Hill, New York, 1983.
[6] S. Kobayashi, T. Nishikawa, T. Takenobu, S. Mori, T. Shimoda, T. Mitani, H. Shimotani, N. Yoshimoto, S. Ogawa, Y. Iwasa, Nat. Mater. 3 (2004) 317.

[7] K.P. Pernstich, S. Haas, D. Oberhoff, C. Goldmann, D.J. Gundlach, B. Batlogg, A.N. Rashid, G. Schitter, J. Appl. Phys. 96 (2004) 6431.
[8] Y. Abe, T. Hasegawa, Y. Takahashi, T. Yamada, Y. Tokura, Appl. Phys. Lett. 87 (2005) 153506.
[9] M. Scharnberg, V. Zaporojtchenko, R. Adelung, F. Faupel, C. Pannemann, T. Diekmann, U. Hilleringmann, Appl. Phys. Lett. 90 (2007) 013501.
[10] Y.L. Guo, Y.Q. Liu, C.A. Di, G. Yu, W.P. Wu, S.H. Ye, Y. Wang, X.J. Xu, Y.M. Sun, Appl. Phys. Lett. 91 (2007) 263502.
[11] Y. Wang, Y.Q. Liu, Y.B. Song, S.H. Ye, W.P. Wu, Y.L. Guo, C.A. Di, Y.M. Sun, G. Yu, W.P. Hu, Adv. Mater. 20 (2008) 611.
[12] S. Dutta, K.S. Narayan, Adv. Mater. 16 (2004) 2151.
[13] V. Podzorov, M.E. Gershenson, Phys. Rev. Lett. 95 (2005) 106602.
[14] M. Redecker, D.D.C. Bradley, M. Inbasekaran, E.P. Woo, Appl. Phys. Lett. 73 (1998) 1565.
[15] A.W. Grice, D.D.C. Bradley, M.T. Bernius, M. Inbasekaran, W.W. Wu, E.P. Woo, Appl. Phys. Lett. 73 (1998) 629.
[16] G. Martin, D.D.C. Bradley, M. Inbasekaran, E.P. Woo, Adv. Mater. 9 (1997) 798.
[17] T. Yasuda, T. Goto, K. Fujita, T. Tsutsui, Appl. Phys. Lett. 85 (2004) 2098.
[18] A. Dodabalapur, H.E. Katz, L. Torsi, Adv. Mater. 8 (1996) 853.
[19] J.I. Wong, T.P. Chen, M. Yang, Y. Liu, C.Y. Ng, L. Ding, C.F. Chong, A.A. Tseng, Appl. Phys. A 91 (2008) 411.
[20] G. Yu, A.J. Heeger, J. Appl. Phys. 78 (1995) 4510.
[21] M. Knupfer, Appl. Phys. A 77 (2004) 623.
[22] H. Hoppe, N.S. Sariciftci, J. Mater. Res. 19 (2004) 1924.
[23] Y.-Y. Noh, D.-Y. Kim, Solid-State Electron. 51 (2007) 1052.

Organic Electronics 11 (2010) 1719–1722

Contents lists available at ScienceDirect

Organic Electronics

journal homepage: www.elsevier.com/locate/orgel

Atomic layer deposited HfO_2 gate dielectrics for low-voltage operating, high-performance poly-(3-hexythiophene) organic thin-film transistors

Woo-Jun Yoon [a], Paul R. Berger [a,b,*]

[a] Department of Electrical and Computer Engineering, The Ohio State University, Columbus, OH 43210, USA
[b] Department of Physics, The Ohio State University, Columbus, OH 43210, USA

ARTICLE INFO

Article history:
Received 11 April 2010
Received in revised form 23 July 2010
Accepted 26 July 2010
Available online 6 August 2010

Keywords:
High-*k* gate dielectric
Atomic layer deposition
Organic thin-film transistor
Field-effect mobility
Poly-(3-hexythiophene)

ABSTRACT

Here we report on low-supply voltage and high-performance regioregular poly-(3-hexythiophene) (P3HT) organic thin-film transistors (OTFT) using a thin atomic layer deposited (ALD) HfO_2 gate dielectric. For the capacitance–voltage characteristics, the measured gate capacitance was ~392 nF/cm^2 at 1 kHz and the dielectric constant was estimated ~18.5 for a 40 nm thick ALD HfO_2 gate dielectric. The gate dielectric showed breakdown fields >5 MV/cm with the leakage current density less than 10^{-7} A/cm^2 at 2 MV/cm. With octadecyltrichlorosilane-treated ALD HfO_2 gate dielectrics, P3HT OTFTs demonstrated high field-effect mobilities up to ~0.01 ± 0.002 cm^2/V s in the saturation region with the drain voltage of −5 V, which is at least one order of magnitude higher than typically reported mobilities particularly for low-voltage regioregular P3HT OTFTs using high-*k* inorganic gate dielectrics. The threshold voltage in the saturation region and on–off current ratio were measured to be −1.2 ± 0.2 V and ~1.1(±0.1) × 10^4, respectively.

© 2010 Elsevier B.V. All rights reserved.

1. Introduction

The performance of organic thin-film transistors (OTFT) have, in general, made tremendous progress in the last decade [1–3]. Using sublimed low molecular weight organic and solution-processed polymeric materials, excellent OTFT results have been reported paving the way for niche applications, such as radio-frequency technologies [4], and pixel drivers and switching elements for active-matrix displays [5,6].

Among the various conjugated polymers for the active channel layer in OTFTs, regioregular poly-(3-hexythiophene) (P3HT) has been one of the most popular channel materials in organic electronics due to its simple solution processibility and relatively high device performance. Stemming from its lamellar structure [7], P3HT films have reported relatively high carrier mobility (μ) in the range of ~0.1 cm^2/V s to ~0.3 cm^2/V s [8–11]. However, extremely high operating voltages persisting up to 60 V are often required to obtain saturation in OTFTs with low-dielectric constant (k) materials for the gate dielectric layer. Alternatively a variety of high-*k* gate dielectrics using inorganic, polymeric, and self-assembled monolayer or multilayer gate dielectrics, has been successfully implemented in OTFTs, greatly reducing OTFTs operating voltages and exhibiting excellent device performance [12,13].

For P3HT OTFTs particularly with metal oxide high-*k* dielectrics, high OTFT performance with low-supply operating voltages have been reported, as summarized in the Table 1 [14–17]. While hafnium-based oxide gate dielectrics were frequently employed in pentacene OTFTs [18,19], it has not yet been reported for regioregular P3HT OTFTs. In this article, we report low-voltage operation (sub −5 V) and high-performance P3HT OTFTs with an atomic layer deposited (ALD) HfO_2 gate dielectric.

* Corresponding author at: Department of Electrical and Computer Engineering, The Ohio State University, Columbus, OH 43210, USA. Tel.: +1 614 247 6235; fax: +1 614 292 7596.
E-mail address: pberger@ieee.org (P.R. Berger).

1566-1199/$ - see front matter © 2010 Elsevier B.V. All rights reserved.
doi:10.1016/j.orgel.2010.07.026

Table 1
Summary of the performance of P3HT OTFTs using metal oxide high-k gate dielectrics; thickness (t_{ox}), accumulation capacitance of metal oxide gate dielectric (C_{ox}), drain voltage (V_D), dielectric constant (k), saturation mobility (μ_{sat}), and threshold voltage (V_T); e-beam – electron-beam evaporation, ALD – atomic layer deposition.

Refs.	Dielectric material	Deposition method	t_{ox} (nm)	C_{ox} (nF/cm^2)	V_D (V)	k	μ_{sat} (cm^2/V s)	I_{on}/I_{off}	V_T (V)
[14]	Ta_2O_5	e-Beam	100	89	0 to −3.0	20.2	2.0×10^{-2}	2.0×10^3	+0.26
[15]	Al_2O_3	ALD	50	–	–	–	4.1×10^{-4}	7.0×10^4	−3.6
[15]	Al_2O_3[a]	ALD	50	–	–	–	9.2×10^{-3}	∼54	+5.6
[16]	Al_2O_3[a]	Anodization	6	625	0 to −2.5	4.2	5.0×10^{-3}	n/a	−1.2
[17]	TiO_2	Sputtering	51	750	0 to −5.0	43.2	1.5×10^{-2}	1.0×10^3	−1.0
This work	HfO_2[a]	ALD	40	392	0 to −5.0	18.6	1.1×10^{-2}	1.2×10^4	−1.4

[a] A self-assembled monolayer of octadecyltrichlorosilane (OTS) treatment applied to the oxide surface.

2. Experimental

The HfO_2 films were deposited on silicon substrates with a commercial ALD reactor. During deposition, the ALD chamber temperature was set at 250 °C. All silicon substrates used in this study were processed through standard degreasing and RCA cleaning procedures prior to the deposition. The thicknesses (t) and the refractive index of the deposited films were estimated to be ∼40 nm and ∼2.07, respectively, as measured by single wavelength ellipsometry.

For capacitance–voltage (C–V) characteristics with an LCR meter (Agilent 4284A), the HfO_2 was deposited on p-type silicon wafers with a resistivity of ∼4.4 Ω cm for metal–oxide-semiconductor (MOS) capacitors. All HfO_2 gate dielectrics were used without any annealing. After deposition, MOS capacitors were completed by standard photolithography and lift-off of the Au (100 nm) gate, defining a square area of 80 μm by 80 μm. A Ti adhesive layer with a 15 nm thickness is used to increase the adhesion between the Au electrode and the ALD films. The final MOS structure fabricated was a p-Si/HfO_2/Ti/Au. The leakage current density through the MOS capacitors was measured with a semiconductor parameter analyzer (Agilent 4156) at room temperature and in darkness.

For the bottom contacted OTFTs, a heavily doped n-type silicon substrate with a resistivity of ∼0.003 Ω cm was used as the gate. The source and drain contacts are formed by standard photolithography and lift-off of the Au (100 nm) with a 15 nm Ti adhesive layer, defining a channel length of 7 μm and width of 115 μm atop the ALD HfO_2 layer. It should be noted that a Ti adhesion layer could affect the charge carrier transport between the source and the drain, requiring an optimized thickness [23]. In this work, the thickness of a Ti adhesive layer was not optimized. After photolithography and metal lift-off, the surface of the HfO_2 was plasma cleaned using an inductively coupled plasma reactive ion etching system with oxygen at an RF power of 20 W for 1 min. To modify the gate dielectric surface, a self-assembled monolayer (SAM) of octadecyltrichlorosilane (OTS; Aldrich, assay >90%) was then formed by immersing the ALD HfO_2 films in a 25 g/L solution of OTS dissolved in cyclohexane at ∼5 °C for 20 min, as described by Majewski et al. [20]. Thin films of the P3HT were then deposited by spin coating from a concentration of 8 mg/ml in chloroform in an inert glove box environment with ⩽1 ppm level of oxygen and moisture. The regioregular P3HT (Merck Chemicals, Ltd.) with 94.5% regioregularity was used without further purification. The P3HT used here has a weight-average molecular weight (M_w) of 26,200 g/mol, corresponding to a number-average molecular weight (M_n) of 13,000 g/mol, and with a polydispersity (M_w/M_n) of ∼2. The P3HT OTFTs were kept in a vacuum at pressures below 10^{-6} Torr for 10 h to remove any unintended doping. Prior to the measurement, the completed P3HT OTFTs were briefly annealed at 110 °C for 10 min in N_2 atmosphere. Small trenches in the P3HT film around the source and drain electrodes were created with a needle in order to minimize leakage currents [20]. Electrical characterizations of the P3HT OTFTs were performed with a semiconductor parameter analyzer (Agilent 4156) at room temperature under darkness in ambient air.

3. Results and discussion

In addition to the OTFTs, MOS capacitors were also studied as a control. Fig. 1 shows a typical C–V response of the ALD HfO_2 MOS capacitors at a frequency range from 1 kHz to 1 MHz at room temperature under darkness. The varying frequency response clearly shows accumulation at negative

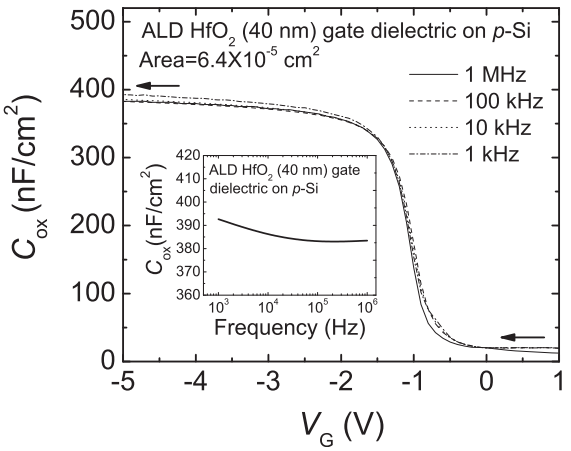

Fig. 1. Capacitance–voltage (C–V) characteristics of MOS capacitors at various frequencies for an atomic layer deposited HfO_2 (∼40 nm) gate dielectric (p-Si/HfO_2/Ti/Au). The inset shows frequency dependency of the gate capacitance per area (C_{ox}) in accumulation and the dielectric constant. The extracted k value at 1 kHz is ∼18.5.

gate bias voltages and depletion at positive gate bias voltages. The hysteresis behavior of the capacitor was observed, exhibiting ~0.5 V hysteresis at 1 MHz (not shown here). The trap charge density (N_t) in the gate dielectric layer is estimated to be $\sim 1.1 \times 10^{11}$ cm^{-2} using the relation $N_t = C_{ox} \cdot \Delta/q$, where C_{ox} is the measured gate capacitance per unit area (F/cm^2), Δ is a voltage shift (V), and q is the magnitude of electronic charge (C). The C_{ox} tends to shift to slightly higher values when decreasing the frequency for all capacitors, as shown in the inset of Fig. 1. No postdeposition heat treatment was used to densify, or passivate, the HfO_2 prior to OTFT fabrication. An observed frequency dependent dispersion in the accumulation region can be attributed to the slow polarization of the gate dielectric at higher frequencies and this polarization can lead to an increase in the induced charge at lower frequencies. The dielectric constant (k) of the ALD HfO_2 gate dielectric was calculated at four different frequencies using $k = C_{ox} \cdot t/\varepsilon_0$, where ε_0 is the permittivity in vacuum, and t is the thickness. The calculated dielectric constants varied from 18.1 at 1 MHz to 18.5 at 1 kHz. For the extraction of carrier mobility values of P3HT OTFTs, the C_{ox} equal to 392 nF/cm^2 at 1 kHz was considered. Upon the addition of the OTS SAM (k = ~2.4 and t = ~2.8 nm) [16], the total capacitance (C_{total}) is considered to be ~262 nF/cm^2 using $1/C_{total} = 1/C_{ox} + 1/C_{OTS}$.

Fig. 2 illustrates the leakage current density versus electric field for the ALD HfO_2 gate dielectric studied here. The dielectric layer shows breakdown fields >5 MV/cm with a leakage current density less than 10^{-7} A/cm^2 at 2 MV/cm for a ~40 nm thick film. The inset of Fig. 2 is the leakage current density versus the gate voltage characteristics for the MIS capacitors.

Fig. 3a shows the output characteristics for P3HT OTFTs with an applied drain voltage (V_D) ranging from 0 to −5 V with a gate bias (V_G) varying from 1 to −5 V in steps of −1 V. The output curves are typical for p-type OTFTs operating in an accumulation region. The OTFTs function well at low-supply voltages due to the high gate capacitance of HfO_2. The inset of the Fig. 3a is a photomicrograph of the Au source–drain contacts atop the ALD HfO_2 gate dielectric.

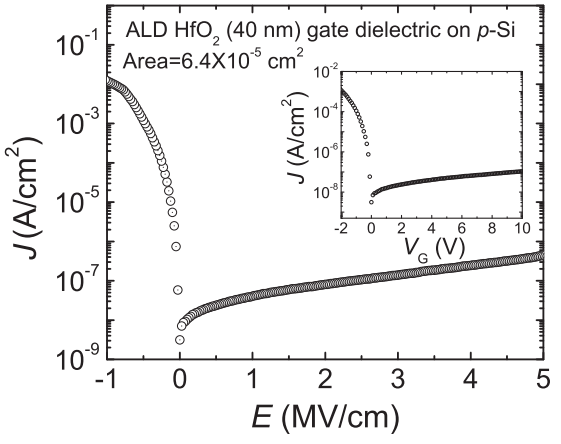

Fig. 2. The leakage current density (J) as a function of electric field (E) of MOS capacitors (p-Si/HfO_2/Ti/Au). The breakdown field is estimated >5 MV/cm. The inset shows current density–voltage characteristics of the devices.

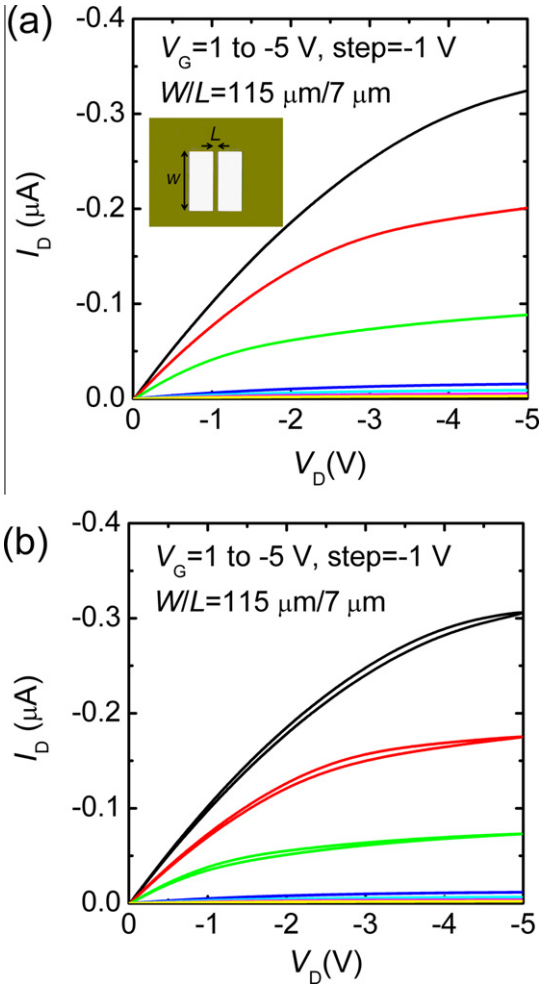

Fig. 3. (a) The output characteristics for P3HT OTFTs with the applied drain voltage (V_D) ranging from 0 to −5 V with gate biases (V_G) varying from 0 to −5 V in steps of −1 V. The inset is the image of the Au source–drain contacts atop the ALD HfO_2 gate dielectric using standard photolithography and lift-off process. (b) The hysteresis behavior of the output characteristic of P3HT OTFTs for an applied voltage V_D (0 → −5 V → 0 V).

At V_G = −2 V and V_D = 0 V, a very small positive I_D of $\sim 2.5 \times 10^{-11}$ A is observed, which increased with higher V_G due to a small drain-gate leakage current. For an applied voltage V_D (0 → −5 V → 0 V), a small hysteresis was observed at V_G > −3 V, and no significant hysteresis behavior was shown for gate voltages less than −3 V (Fig. 3b).

During the electrical measurements in ambient air, a variation of off-state I_D at V_G = 0 V and V_D = −5 V was carefully monitored. For fresh devices, a small off-state I_D (>$\sim 1 \times 10^{-11}$ A) was observed. However, an off-state I_D (>$\sim 1 \times 10^{-9}$ A) was increased by two orders of magnitude over the extended exposure (about 60 min) in ambient air due to the high bulk conductivity of P3HT attributed from unreduced P3HT and oxygen doping [21,22]. The devices exhibiting a high off-state I_D (>$\sim 1 \times 10^{-9}$ A) typically show significant hysteresis behavior at V_G > −3 V due to large excess drain current. Those devices are excluded from extraction of the performance of the OTFTs in this work.

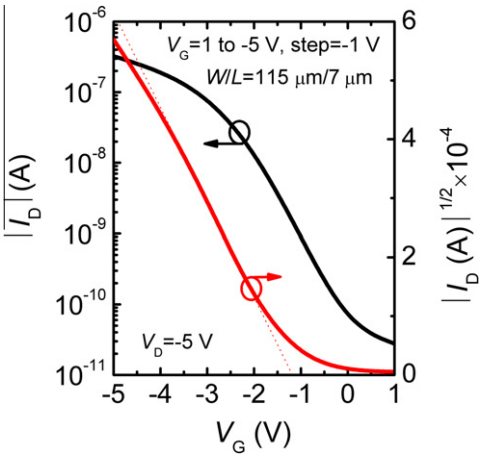

Fig. 4. The saturation region transfer characteristic for P3HT OTFTs with ALD HfO_2 gate dielectrics (~40 nm) with the applied gate voltage (V_G) ranging from 1 V to −5 V with the drain voltage (V_D) of −5 V.

For the transfer characteristics in the saturation region, the saturation mobility (μ_{sat}), the threshold voltage (V_T), and an on/off current ratio (I_{on}/I_{off}) are characterized. Fig. 4 shows the semilog plot of I_D–V_G and the square root of I_D–V_G at $V_D = -5$ V. The μ_{sat}, and the V_T are calculated from

$$I_D = \frac{W}{2L} C_{total} \mu (V_G - V_r)^2 \quad (1)$$

From the square root of I_D as a function of V_G, the maximum μ_{sat} was estimated to be $\sim 0.01 \pm 0.002$ cm^2/V s and the V_T was -1.2 ± 0.2 V. No significant variation of estimated μ_{sat} and V_T was recorded over more than 10 devices. The mobility obtained in this work is one to two orders of magnitude higher than the reported mobilities in low-voltage operating regioregular P3HT OTFTs specifically with metal oxide high-k gate dielectrics, such as ALD Al_2O_3 [15] and anodized Al_2O_3, but was the same order of magnitude mobility using electron-beam evaporated Ta_2O_5 [14], and TiO_2 [17]. Table 1 shows a summary of these gate dielectrics exclusively employed for P3HT OTFTs and their corresponding device performances. For the semilog plot of I_D–V_G at a fixed $V_D = -5$ V, an I_{on}/I_{off} as large as $\sim 1.1(\pm 0.1) \times 10^4$ was measured here, which is similar with previous values reported for P3HT OTFTs using high-k dielectric gate dielectrics (Table 1). From the subthreshold regime in the plot of log I_D as a function of V_G, the subthreshold swing (S) was calculated using $S = dV_G/d(\log I_D)$ and yielded a value of 0.803 ± 0.243 V/decade.

4. Conclusions

In conclusion, we have shown low-voltage operation and high-performance regioregular P3HT OTFTs using ALD HfO_2 gate dielectrics. For the C–V characteristics, the measured C_{ox} was ~392 nF/cm^2 at 1 kHz and the dielectric constant was estimated to be ~18.5 for a 40 nm thick ALD HfO_2 gate dielectric. The HfO_2 gate dielectric showed a breakdown field >5 MV/cm with a leakage current density less than 10^{-7} A/cm^2 at 2 MV/cm. With OTS-treated ALD HfO_2 gate dielectrics, P3HT OTFTs show high mobility up to $\sim 0.01 \pm 0.002$ cm^2/V s in the saturation region, which is at least one order of magnitude higher than typically reported mobilities for low-voltage operating regioregular P3HT OTFTs particularly with metal oxide high-k gate dielectrics. The V_T and I_{on}/I_{off} ratio are -1.2 ± 0.2 V and $\sim 1.1(\pm 0.1) \times 10^4$, respectively.

Acknowledgements

The authors would like to thank Dr. Jill S. Becker and Ray Ritter at Cambridge NanoTech (Cambridge, MA) for ALD deposition. This work was supported by the Center for Photovoltaics Innovation and Commercialization (PVIC) and the Institute for Materials Research (IMR).

References

[1] C.D. Dimitrakopoulos, P.R.L. Malenfant, Adv. Mater. 14 (2002) 99–117.
[2] H.E. Katz, Chem. Mater. 16 (2004) 4748–4756.
[3] H. Sirringhaus, Adv. Mater. 17 (2005) 2411–2425.
[4] V. Subramanian, P.C. Chang, J.B. Lee, S.E. Molesa, S.K. Volkman, IEEE Trans. Compon. Pack. T 28 (2005) 742–747.
[5] H.E.A. Huitema, G.H. Gelinck, J.B.P.H. van der Putten, K.E. Kuijk, C.M. Hart, E. Cantatore, D.M. de Leeuw, Adv. Mater. 14 (2002) 1201–1204.
[6] M. Kitamura, T. Imada, Y. Arakawa, Jpn. J. Appl. Phys. 42 (2003) 2483.
[7] D.M. Richard, Adv. Mater. 10 (1998) 93–116.
[8] B.H. Hamadani, D. Natelson, Appl. Phys. Lett. 84 (2004) 443–445.
[9] J. Park, S. Lee, H.H. Lee, Org. Electron. 7 (2006) 256–260.
[10] C. Shinuk, L. Kwanghee, Y. Jonathan, W. Guangming, M. Daniel, J.H. Alan, S. Mathieu, L. Roberto, J. Appl. Phys. 100 (2006) 114503.
[11] M. Surin, L. Ph, R. Lazzaroni, J.D. Yuen, G. Wang, D. Moses, A.J. Heeger, S. Cho, K. Lee, J. Appl. Phys. 100 (2006) 033712.
[12] A. Facchetti, M.H. Yoon, T.J. Marks, Adv. Mater. 17 (2005) 1705–1725.
[13] J. Veres, S. Ogier, G. Lloyd, D.M. de Leeuw, Chem. Mater. 16 (2004) 4543–4555.
[14] C. Bartic, H. Jansen, A. Campitelli, S. Borghs, Org. Electron. 3 (2002) 65–72.
[15] L. Fumagalli, D. Natali, M. Sampietro, E. Peron, F. Perissinotti, G. Tallarida, S. Ferrari, Org. Electron. 9 (2008) 198–208.
[16] L.A. Majewski, R. Schroeder, M. Grell, P.A. Glarvey, M.L. Turner, J. Appl. Phys. 96 (2004) 5781–5787.
[17] G. Wang, D. Moses, A.J. Heeger, H.-M. Zhang, M. Narasimhan, R.E. Demaray, J. Appl. Phys. 95 (2004) 316–322.
[18] S.W. Cho, J.G. Jeong, S.H. Park, M.H. Cho, K. Jeong, C.N. Whang, Y. Yi, Appl. Phys. Lett. 92 (2008) 213302.
[19] J. Tardy, M. Erouel, A.L. Deman, A. Gagnaire, V. Teodorescu, M.G. Blanchin, B. Canut, A. Barau, M. Zaharescu, Microelectron. Reliab. 47 (2007) 372–377.
[20] L.A. Majewski, R. Schroeder, M. Voigt, M. Grell, J. Phys. D Appl. Phys. (2004) 3367.
[21] M.S.A. Abdou, F.P. Orfino, Y. Son, S. Holdcroft, J. Am. Chem. Soc. 119 (1997) 4518–4524.
[22] D.B.A. Rep, A.F. Morpurgo, T.M. Klapwijk, Org. Electron. 4 (2003) 201–207.
[23] A. Petrovic, G. Bratina, Eur. Phys. J. B 73 (2010) 341–346.

Organic Electronics 11 (2010) 1723–1728

Contents lists available at ScienceDirect

Organic Electronics

journal homepage: www.elsevier.com/locate/orgel

Magnetic field induced grain growth of perylene polycrystalline films

Hyeon-Gu Jeon [a,1], Jang-Joo Kim [b,*]

[a] Department of Materials Science and Engineering, Gwangju Institute of Science and Technology, 1 Oryong-Dong, Buk-Gu, Gwangju 500-712, Republic of Korea
[b] Department of Materials Science and Engineering, Seoul National University, San 56-1, Shillim-dong, Gwanak-gu, Seoul 151-744, Republic of Korea

ARTICLE INFO

Article history:
Received 15 June 2010
Received in revised form 23 July 2010
Accepted 6 August 2010
Available online 19 August 2010

Keywords:
Enlargement of grain size
Organic thin films
Magnetic field
Organic thin-film transistor

ABSTRACT

The authors report magnetic field (MF) induced grain growth of perylene polycrystalline films during vacuum deposition. It is clearly demonstrated that the grain size of perylene polycrystalline film was increased by 2.6 times with a 3.8 kG perpendicular MF to the substrate at the deposition temperature of 30 °C. In contrast, the grain size was decreased by applying a parallel MF to the substrate. This MF effect on the grain growth becomes stronger at higher deposition temperature. The mechanism of this MF effect is discussed through the diamagnetic property and the intralayer interaction of the perylene molecules during the nucleation process.

© 2010 Elsevier B.V. All rights reserved.

1. Introduction

Significant developments in organic thin-film transistors (OTFTs) have been made during the last two decades, and plenty of papers and books have been published [1–7]. Although there are still some debates on the detailed mechanism of charge transport in OTFTs, it is very clear that larger grain size in a deposited organic film leads to a higher charge carrier mobility of the device because the grain boundaries usually act as charge carrier traps [8–15]. In addition, the grain boundary is known to be deeply related to device degradation during operation by the bias stress or environmentally induced chemical reaction of materials [16–19]. Therefore, it is very important to make the grain size as large as possible in order not only to enhance the charge carrier mobility of OTFTs, but also to increase the reliability of the devices. To date, some approaches have been successfully applied to enlarge the grain size. For example, heating the substrate during film formation is very effective to increase the grain size, and is used as a popular method to enhance the charge carrier mobility of the devices [15,20–25]. Annealing after film deposition is also known as an effective method for some materials [26–28]. Surface modification of dielectrics and/or electrodes before film deposition, and solvent vapor treatment after film formation are also reported as effective methods [12,22,29,30]. Those reported methods, however, also have some drawbacks or distinct limits to their ability to enhance the charge carrier mobility of the devices. For example, thermal treatment at a somewhat high temperature usually results in the formation of cracks and/or gaps between the grains, which leads to a deterioration of the device performance even with a very large grain size [22,26,31].

Here we report a novel and very effective method to increase the grain size of organic films: applying a magnetic field (MF) during film deposition. The grain size of perylene polycrystalline film was increased by 2.6 times (from 1.59 to 4.14 μm in diameter) by applying 3.8 kG MF perpendicular to the substrate during vacuum deposition of perylene molecules at the deposition temperature of 30 °C. In contrast, the grain size was reduced by applying a MF parallel to the substrate. This is the first demonstration of the MF effect on the grain growth during vacuum deposition of purely hydrocarbon molecular materials without any metal atoms to the best of our knowledge.

* Corresponding author. Tel./fax: +82 2 880 7893.
E-mail address: jjkim@snu.ac.kr (J.-J. Kim).
[1] Present address: Functional Polymer Science Course, Chemistry and Material Division, Faculty of Textile Science and Technology, Shinshu University, 3-15-1, Tokida, Ueda, Nagano 386-8567, Japan.

1566-1199/$ - see front matter © 2010 Elsevier B.V. All rights reserved.
doi:10.1016/j.orgel.2010.08.005

2. Experimental

2.1. Material and film formation

Perylene of 99% purity was purchased from Aldrich, and purified once using the thermal gradient sublimation method before use. Perylene films were formed by thermal evaporation in vacuum with a base pressure of lower than 5.0×10^{-7} Torr. The perylene was sublimed from a cylindrical quartz crucible whose temperature was carefully controlled to get the deposition rate of 0.5 Å/s. The substrates of the O_2-plasma treated Si wafers with a 300 nm thick oxide layer were ca. 20 cm apart from the crucible. The substrate temperature was controlled from 20 to 40 °C by heating or cooling the substrate holder, and was detected from the surface and the inside of the substrate holder with two thermocouples. At the 40 °C deposition temperature, however, we could not get a homogeneous film but could only achieve discontinuous perylene domains with very large gaps between the domains, probably due to the low wettability onto the substrate and the resublimation of perylene molecules.

2.2. Application of magnetic fields

To apply MFs during deposition, we have used permanent NdFeB magnets whose coercivity of one piece is 11.9 kOe. For a uniform perpendicular MF to the substrate, we installed several magnets just above (top sets) and far below (bottom sets) the substrate for the formation of the sink and the source of MF, respectively, as shown schematically in Fig. 2a. The two magnet sets were separated by about 10 cm, and the size of the magnet sets was large enough to provide a uniform MF for all areas of the substrate. The MF strength was varied by changing the number of magnets of the top sets. For a parallel MF to the substrate, we installed magnets perpendicularly to the substrate on both sides of the substrate, as shown schematically in Fig. 2b. An inevitable problem of this configuration is that the MF strength is strongly dependent on the distance from magnets, and hence on the position of substrate. In our case, the MF strength was about 3.8 kG at the center of the substrate, and about 5.4 kG at the both sides of the substrate.

2.3. Film characterization

The surface morphology of the deposited films was examined with an Atomic Force Microscope (AFM, Digital Instruments Dimension 3100). We have used the contact mode AFM and acquired height images together with friction images for clearer observation of the grain boundaries. The domain size of the films is measured by counting the intercepts of the grain boundaries with 12 arbitrary straight (6 vertical and 6 perpendicular) lines in the AFM friction images of $20 \times 20\ \mu m^2$ size, from which we can calculate the average number of domains in those images. The crystal structure of the perylene films was determined with XRD (Rigaku Co., RU-300) with a Cu K_α (λ = 1.5418 Å) radiation.

3. Results and discussion

3.1. MF induced grain growth

Perylene (Fig. 1) was selected as the target material mainly because perylene and its derivatives have shown very high electron mobility [18,22–24,26,32–36], and partly because it is a simple and representative polycyclic aromatic hydrocarbon molecule. Fig. 1 shows the X-ray diffraction (XRD) pattern of a 100 nm thick perylene film deposited without MF. Four clear diffraction peaks can be assigned to different planes, which range from the (0 0 1) to (0 0 4) planes of the perylene film, respectively. The calculated d spacing of this perylene film is 10.13 Å, which is well matched with the spacing of the ab plane of the well known α-phase perylene crystal [37–39], indicating that the perylene molecules are almost upright standing and adopt a face-on-edge herringbone arrangement along the ab plane, and expected to show a high electron mobility along the parallel direction to the substrate [32–34,37–39].

For the application of MFs during perylene deposition, we have installed magnets around the substrate, as described in Section 2, which are shown schematically in Fig. 2. There was no difference in the MF strength in the temperature range from 20 to 30 °C used in this study. Fig. 3 shows the AFM topography (left column) and friction (right column) images of the perylene films deposited at 25 °C (a) without applying a MF, (b) with the application of a MF of 1.7 kG, and (c) with a 3.8 kG MF applied perpendicular to the substrate, respectively. It is very clear that the grain size increased with the increasing magnitude of the perpendicular MF. The grain size increased from 0.83 to 1.54 μm in diameter by applying a perpendicular MF of 1.7 kG, and even more, up to 1.68 μm by increasing the MF to 3.8 kG.

This MF effect on the grain growth of the perylene film becomes even more obvious when deposited at higher substrate temperatures, as can be seen in Fig. 4. At the deposition temperature of 20 °C, the grain size increased by only 23% by applying the MF of 3.8 kG. The grain size, however, doubled at 25 °C, and increased by 2.6 times at 30 °C. This result indicates that the MF effect on the grain

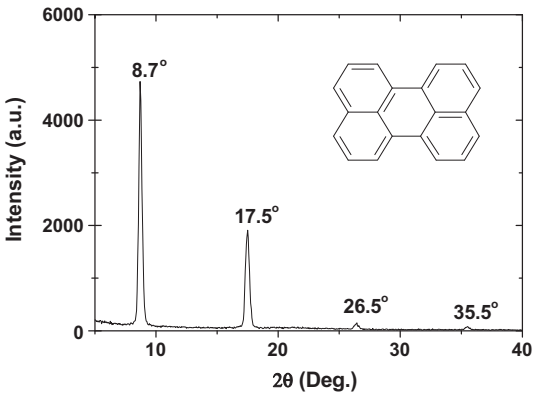

Fig. 1. XRD pattern of the perylene film deposited on an O_2-plasma treated Si wafer with a 300 nm thick oxide layer, and the molecular structure of perylene.

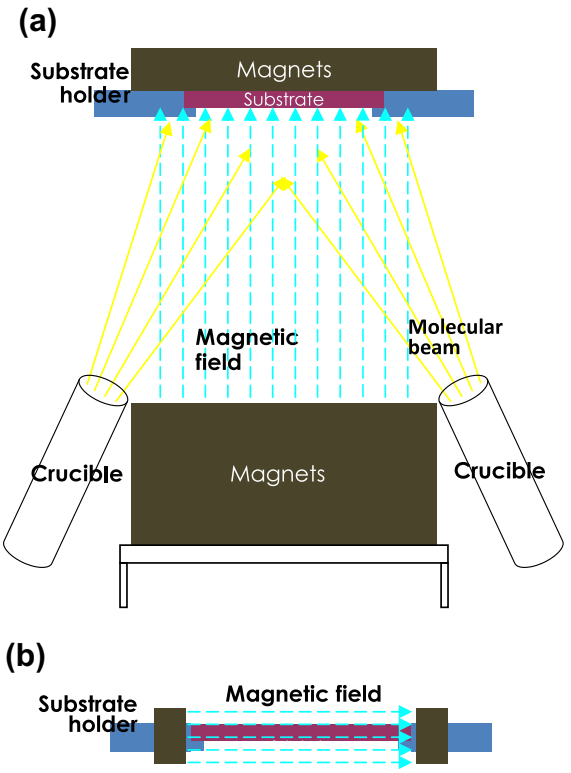

Fig. 2. Schematic illustrations of the deposition set-up with (a) a perpendicular MF and (b) a parallel MF. Note that these illustrations are not to scale.

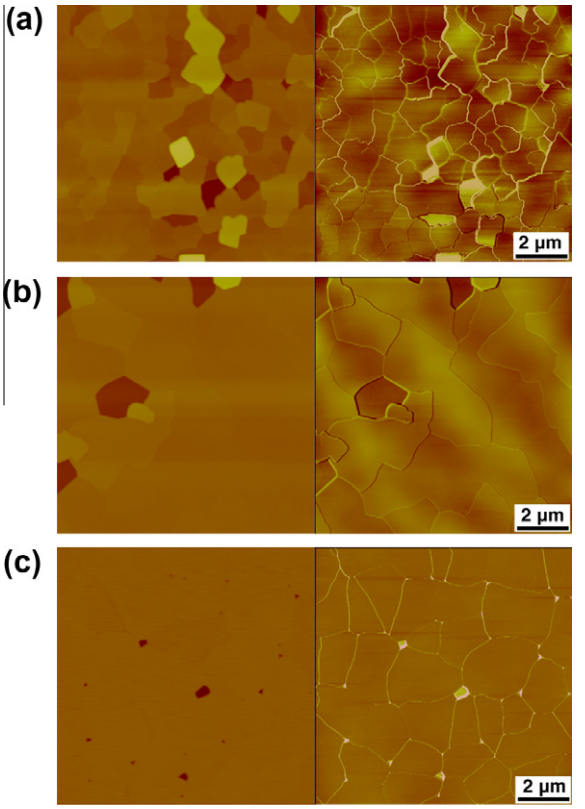

Fig. 3. AFM height (left column) and friction (right column) images of the perylene films deposited at 25 °C (a) without applying a MF, (b) with the application of a perpendicular MF of 1.7 kG, and (c) with the application of a perpendicular MF of 3.8 kG. The grains sizes measure 0.83, 1.54, and 1.68 μm in diameter, respectively.

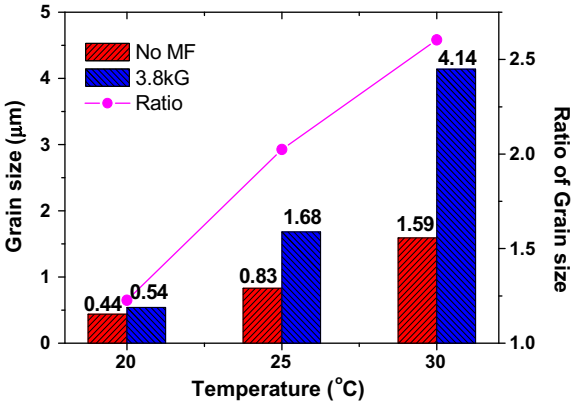

Fig. 4. Graphical comparison of the grain size of the perylene films deposited at various temperatures, and the ratio of the grain sizes. The numbers inserted above the graphic bars indicate the grain size in diameter, and the ratio of the grain sizes was calculated by simply dividing the grain size with the applying MF by the counterpart without the MF at each deposition temperature.

growth of the perylene polycrystalline film becomes stronger at higher deposition temperatures.

It seems that the perpendicular MF not only enlarges the grain size but also improves the crystal quality of the films. Fig. 5 shows the XRD patterns of the films deposited without applying an MF (black line) and with the application of a 1.7 kG perpendicular MF (red line) at 25 °C with the same film thickness. The peak positions are the same between the films, indicating that the lattice spacing is the same in both films grown with and without the MF. The peak intensities remarkably increased by 2.7 times by applying a 1.7 kG perpendicular MF even though the full-width-at-half maximum (FWHM) of the two peaks are almost the same with (FWHM = 0.37) and without (FWHM = 0.36) a magnetic field. This increase cannot be explained simply by the increase in the grain size but indicates an improved crystal quality, such as an increase in the crystal volume fraction of the grains or a more uniform perpendicular orientation of the grains. This proposed improvement of the crystal quality can be observed in the AFM friction images in Fig. 3, where a featureless frictional image, except for the grain boundaries, is obtained in the films grown under the perpendicular MF of 3.8 kG shown in Fig. 3c. In contrast, fluctuations in the friction image were observed not only between the grains but also within the grains, as shown in Fig. 3a when grown without MFs, indicating an inhomogeneity in the grains. This MF effect on the crystal quality of deposited film may be observed more clearly with further examination.

Application of a MF parallel to the substrate resulted in the reduction in the grain sizes, especially at high temperature as shown in Fig. 6. The average grain size in the film

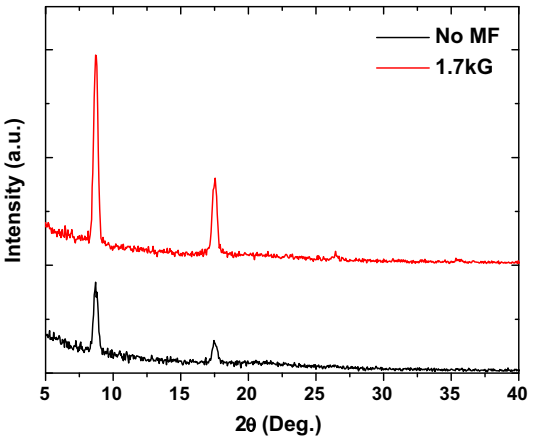

Fig. 5. XRD patterns of perylene films deposited at 25 °C without applying an MF (black) and with the application of a 1.7 kG perpendicular MF (red). (For interpretation of the references to colour in this figure legend, the reader is referred to the web version of this article.)

was reduced from 1.59 to 0.98 μm at 30 °C when a parallel MF of 3.8 kG was applied during the growth. The grains have almost the same size of 0.85 μm if grown at 25 °C with and without the parallel MF. It suggests that a parallel MF to the substrate suppresses the grain growth, in contrast to a perpendicular MF.

From the results described so far, we can conclude that a perpendicular MF to the substrate has an effect of increasing the grain size and improving the crystal quality, but a parallel MF has an opposite effect. These MF effects become stronger at higher deposition temperatures.

3.2. Discussion

As a fundamental cause of this MF effect, we give consideration to the diamagnetic anisotropy of perylene molecules [40–43]. It is well known that liquid crystals (LCs) can be aligned by applying a MF due to the diamagnetic anisotropy of LC materials [44–47]. Similarly, the alignment of nanosized protein crystals in a strong MF was interpreted as being due to the diamagnetic anisotropy of the peptide groups in the amino acid sequence, and of aromatic residues in the protein molecules [48–50]. In those cases, the alignment of LCs and protein crystals was estimated to occur only in crystals or in domains larger than a critical size where the MF effect (or magnetic stabilization energy) can exceed the thermal fluctuation [45,48,49]. The MF effect is known to be negligibly small at the level of individual molecules, and cannot orient the individual molecules. The collective behavior of the molecules in a crystal or in a domain causes the molecular contribution to add up constructively, and the crystal or the molecular domain larger than a critical size can be

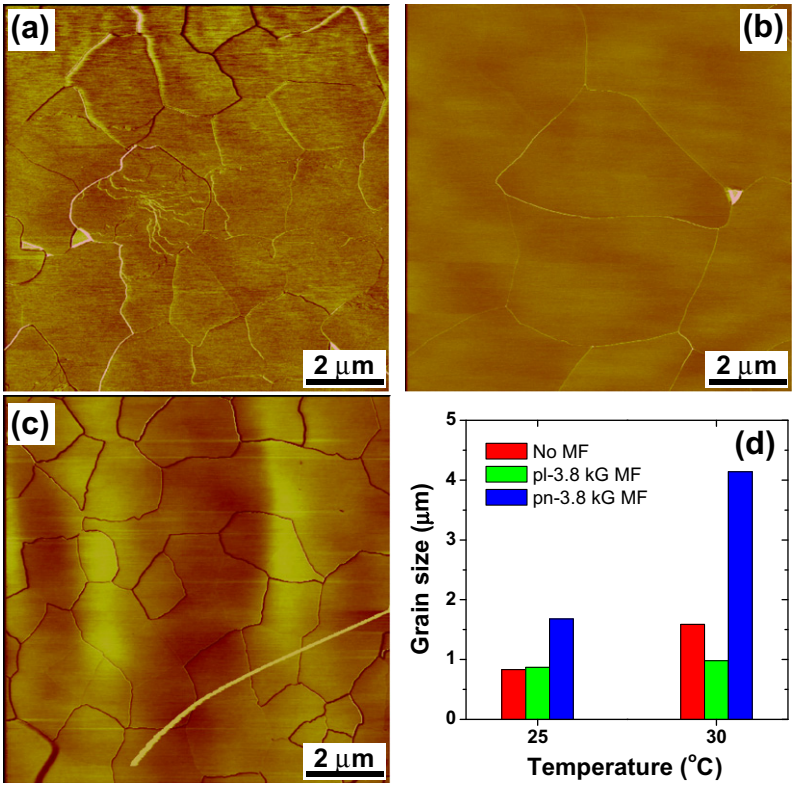

Fig. 6. AFM friction mode images of perylene films deposited at 30 °C (a) without applying MF, (b) with a perpendicular MF of 3.8 kG (pn-3.8 kG MF), (c) with a parallel MF of 3.8 kG (pl-3.8 kG MF), and (d) a graphical representation of the grain sizes of the perylene films deposited at 25 and 30 °C with the indicated deposition condition.

oriented as a whole. For example, it is calculated and proven experimentally that lysozyme crystals larger than 1.3 μm can be magnetically oriented when the magnitude of the MF exceeds 1 T, and most crystals larger than 0.3 μm are oriented when the magnitude of the MF is 10 T [48,49]. In recent years, it was also reported that perylene nanocrystals of 160 nm size can be oriented in a static MF of 2 T, which is interpreted with the same mechanism mentioned above [51].

In our case, however, there are some crucial differences in the detailed situation of the MF effect, although the fundamental cause lies with the diamagnetic anisotropy of the molecules in common. First, the MF effect was stronger at higher temperature in our case, which is completely opposite to the mechanism mentioned above. Second, almost all of molecules in a film align in the same direction, almost perpendicular to the substrate, regardless of the grain size in our case. Third, the subject of the MF effect is the "growth" of crystal domains in our case, which is totally different to the "alignment" of crystals or molecular domains. Therefore, it is not suitable to explain the MF effect of our case by adopting the mechanism mentioned above. It is necessary to consider the grain growth mechanism of perylene molecules in a vacuum deposition.

Perylene molecules are known to show a Stranski–Krastanov growth mode on various metals and on Si substrate during vacuum deposition [37,52–54]. In this growth mode, the perylene molecules usually form a few homogeneous monolayers in the first stage which is followed by the dewetting of multilayer films, which results in a formation of separated crystalline islands. The morphology and the size of the islands, hence the domain size, will be determined from a balance between the diffusion and nucleation of molecules if we rule out the effect of the surface free energy of the substrate, which is usually very important to explain the grain growth, but not in our case because we used the same substrate [25,37,55,56]. In our case, it is very difficult to consider the applied MF to have affected the molecular diffusion. Therefore, it is reasonable to think that the applied MF has affected the nucleation process of the perylene molecules. If the applied MF can reduce the nucleation rate, the grain size will be increased, and vice versa. For the nucleation of some organic semiconductors including perylene during vacuum deposition, Verlaak et al. have reported that the higher intralayer interaction leads to a higher energy of the nuclei which will result in a higher barrier against nucleation and thus contributes to a lower nucleation rate [55]. If we assume that the applied perpendicular MF increases the intralayer interaction of the perylene molecules, the resultant increased grain size obtained by applying a perpendicular MF can be accepted as a reasonable result. For the parallel MF effect, it is just the opposite situation: a decreased intralayer interaction and hence a reduced grain size. The problem is that the magnitude of the MFs in this study is not so large such that we can expect to have a strong effect on the intralayer interaction from the view point of the erstwhile mechanism of the diamagnetic anisotropy of perylene molecules. For the present, the detailed mechanism and the strength of this MF effect on the grain growth is now under further research.

4. Summary

It was clearly demonstrated that a perpendicular MF to the substrate increases the grain size of perylene polycrystalline film. The grain size was increased by 2.6 times (from 1.59 to 4.14 μm in diameter) with applying a 3.8 kG perpendicular MF to the substrate during vacuum deposition of perylene molecules at 30 °C deposition temperature. On the contrary, the grain size was reduced with applying a parallel MF to the substrate. This MF effect becomes stronger at higher deposition temperature in both of directions. We explained this MF effect with a diamagnetic property and the intralayer interaction of the perylene molecules during the nucleation process. This MF effect can be used widely in almost all OTFT materials because they usually have almost the same order of diamagnetic susceptibility with perylene due to benzene rings and/or thiophene rings for large conjugation length.

References

[1] H. Klauk (Ed.), Organic Electronics: Materials, Manufacturing and Applications, Wiley-VCH, Weinheim, Germany, 2006.
[2] C. Wöll (Ed.), Physical and Chemical Aspects of Organic Electronics: From Fundamentals to Functional Devices, Wiley-VCH, Weinheim, Germany, 2009.
[3] D. Braga, G. Horowitz, Adv. Mater. 21 (2009) 1473.
[4] M. Mas-Torrent, C. Rovira, Chem. Soc. Rev. 37 (2008) 827.
[5] A.R. Murphy, J.M.J. Fréchet, Chem. Rev. 107 (2007) 1066.
[6] J. Zanmseil, H. Sirringhaus, Chem. Rev. 107 (2007) 1296.
[7] C.-A. Di, Y. Liu, G. Yu, D. Zhu, Acc. Chem. Res. 42 (2009) 1573.
[8] F.C. Grozema, L.D.A. Siebbeles, Int. Rev. Phys. Chem. 27 (2008) 87.
[9] V. Coropceanu, J. Cornil, D.A. da Silva Filho, Y. Olivier, R. Silbey, J.-L. Brédas, Chem. Rev. 107 (2007) 926.
[10] S. Verlaak, V. Arlchipov, P. Heremans, Appl. Phys. Lett. 82 (2003) 745.
[11] A. Di Carlo, F. Piacenza, A. Bolognesi, B. Stadlober, H. Maresch, Appl. Phys. Lett. 86 (2005) 263501.
[12] T. Yamada, T. Hasegawa, M. Hiraoka, H. Matsui, Y. Tokura, G. Saito, Appl. Phys. Lett. 92 (2008) 233306.
[13] S.S. Lee, C.S. Kim, E.D. Gomez, B. Purushothaman, M.F. Toney, C. Wang, A. Hexemer, J.E. Anthony, Y.-L. Loo, Adv. Mater. 21 (2009) 3605.
[14] S. Verlaak, P. Heremans, Phys. Rev. B 75 (2007) 115127.
[15] R. Schmidt, J.H. Oh, Y.-S. Sun, M. Deppisch, A.-M. Krause, K. Radacki, H. Braunschweig, M. Könemann, P. Erk, Z. Bao, F. Würthner, J. Am. Chem. Soc. 131 (2009) 6215.
[16] C.R. Kagan, A. Afzali, T.O. Graham, Appl. Phys. Lett. 86 (2005) 193505.
[17] D. Li, E.-J. Borkent, R. Nortrup, H. Moon, H. Katz, Z. Bao, Appl. Phys. Lett. 86 (2005) 042105.
[18] Y. Wen, Y. Liu, C. Di, Y. Wang, X. Sun, Y. Guo, J. Zheng, W. Wu, S. Ye, G. Yu, Adv. Mater. 21 (2009) 1631.
[19] R.T. Weitz, K. Amsharov, V. Zschieschang, M. Burghard, M. Jansen, M. Kelsch, B. Rhamati, P.A. van Aken, K. Kern, H. Klauk, Chem. Mater. 21 (2009) 4949.
[20] J. Lee, J.H. Kim, S. Im, J. Appl. Phys. 95 (2004) 3733.
[21] K. Xiao, Y. Liu, G. Yu, D. Zhu, Appl. Phys. A 77 (2003) 367.
[22] B.A. Jones, A. Facchetti, M.R. Wasielewski, T.J. Marks, Adv. Funct. Mater. 18 (2008) 1329.
[23] J.H. Oh, S. Liu, Z. Bao, Appl. Phys. Lett. 91 (2007) 212107.
[24] Y. Hosoi, D. Tsunami, H. Ishii, Y. Furukawa, Chem. Phys. Lett. 436 (2007) 139.
[25] A. Facchetti, Y. Deng, A. Wang, Y. Koide, H. Sirringhaus, T.J. Marks, R.H. Friend, Angew. Chem. Int. Ed. 39 (2000) 4547.
[26] S. Tatemichi, M. Ichikawa, T. Koyama, Y. Taniguchi, Appl. Phys. Lett. 89 (2006) 112108.
[27] P.C. Cheng, J. Lee, D. Huang, V. Subramanian, A.R. Murphy, J.M.J. Fréchet, Chem. Mater. 16 (2004) 4783.
[28] C. Piliego, D. Jarzab, G. Gigli, Z. Chen, A. Facchetti, M.A. Loi, Adv. Mater. 21 (2009) 1573.
[29] K.C. Dickey, J.E. Anthony, Y.-L. Loo, Adv. Mater. 18 (2006) 1721.
[30] S.K. Park, D.A. Mourey, S. Subramanian, J.E. Anthony, T.N. Jackson, Adv. Mater. 20 (2008) 4145.

[31] K. Xiao, Y. Liu, T. Qi, W. Zhang, F. Wang, J. Gao, W. Qiu, Y. Ma, G. Cui, S. Chen, X. Zhan, G. Yu, J. Qin, W. Hu, D. Zhu, J. Am. Chem. Soc. 127 (2005) 13281.
[32] M. Pope, C.E. Swenberg, Electronic Processes in Organic Crystals and Polymers, second ed., Oxford University Press, New York, 1999.
[33] W. Warta, R. Stehle, N. Karl, Appl. Phys. A 36 (1985) 163.
[34] J.L. Brédas, J.P. Calbert, D.A. Da Silva Filho, J. Cornil, PNAS 99 (2002) 5804.
[35] R.J. Chesterfield, J.C. McKeen, C.R. Newman, P.C. Ewbank, D.A. da Silva Filho, J.-L. Brédas, L.L. Miller, K.R. Mann, C.D. Frisbie, J. Phys. Chem. B 108 (2004) 19281.
[36] D.J. Gundlach, K.P. Pernstich, G. Wilckens, M. Grüter, S. Haas, B. Batlogg, J. Appl. Phys. 98 (2005) 064502.
[37] G. Witte, K. Hänel, S. Söhnchen, Ch. Wöll, Appl. Phys. A 82 (2006) 447.
[38] Ch. Näther, H. Bock, Z. Havlas, T. Hauck, Organometallics 17 (1998) 4707.
[39] J. Tanaka, Bull. Chem. Soc. Jpn. 36 (1963) 1237.
[40] H. Shiba, G. Hazato, Bull. Chem. Soc. Jpn. 22 (1949) 92.
[41] G. Hazato, Bull. Chem. Soc. Jpn. 22 (1949) 151.
[42] H. Akamatu, Y. Matsunaga, Bull. Chem. Soc. Jpn. 26 (1953) 364.
[43] H. Akamatu, Y. Matsunaga, Bull. Chem. Soc. Jpn. 29 (1956) 800.
[44] V.G. Chigrinov, Liquid Crystal Devices: Physics and Application, Artech House, Boston London, 1999.
[45] M.I. Boamfa, M.W. Kim, J.C. Maan, Th. Rasing, Nature 421 (2003) 149.
[46] R. Guo, Y. Reznikov, K. Slyusarenko, S. Kumar, Liq. Cryst. 34 (2007) 955.
[47] M.I. Boamfa, S.V. Lazarenko, E.C.M. Vermolen, Th. Rasing, Adv. Mater. 17 (2005) 610.
[48] N.I. Wakayama, Cryst. Growth Des. 3 (2003) 17.
[49] M. Ataka, E. Katoh, N.I. Wakayama, J. Cryst. Growth 173 (1997) 592.
[50] P.L. Worcester, PNAS 75 (1978) 5475.
[51] Y. Kaneko, T. Onodera, H. Kasai, S. Okada, H. Oikawa, H. Nakanish, T. Fukuda, H. Matsuda, J. Mater. Chem. 15 (2005) 253.
[52] S.R. Forrest, Chem. Rev. 97 (1997) 1793.
[53] S. Söhnchen, K. Hänel, A. Birkner, G. Witte, C. Wöll, Chem. Mater. 17 (2005) 5297.
[54] Y. Toda, H. Yanagi, Appl. Phys. Lett. 69 (1996) 2315.
[55] S. Verlaak, S. Steudel, P. Heremans, Phys. Rev. B 68 (2003) 195409.
[56] A.L. Briseno, S.C.B. Mannsfeld, M.M. Ling, S. Liu, R.J. Tseng, C. Reese, M.E. Roberts, Y. Yang, F. Wudl, Z. Bao, Nature 444 (2006) 913.

Organic Electronics 11 (2010) 1729–1735

Contents lists available at ScienceDirect

Organic Electronics

journal homepage: www.elsevier.com/locate/orgel

Local charge accumulation and trapping in grain boundaries of pentacene thin film transistors

S. Yogev [a], R. Matsubara [b], M. Nakamura [b], Y. Rosenwaks [a,*]

[a] School of Electrical Engineering, Tel-Aviv University, Tel-Aviv 69978, Israel
[b] Department of Electrical and Electronic Engineering, Chiba University, Chiba 263-8522, Japan

ARTICLE INFO

Article history:
Received 27 May 2010
Received in revised form 21 July 2010
Accepted 24 July 2010
Available online 6 August 2010

Keywords:
Pentacene
Grain boundaries
Organic thin film transistors
Hole accumulation

ABSTRACT

We present a comprehensive Kelvin probe force microscopy study of grain boundaries in pentacene transistors with different film thicknesses in combination with current–voltage measurements and 3D electrostatics simulations. It is found that in pentacene films thinner than approximately 30 nm, holes are accumulated in the grain boundaries due to negative trapped charge at the SiO_2–pentacene interface. On the other hand, in thicker films we observe hole depletion near the boundaries mainly due to positive charge trapping in the grain boundaries. The results are discussed in view of their effect on pentacene thin film transistors performance.

© 2010 Elsevier B.V. All rights reserved.

1. Introduction

The nature of grain boundaries (GBs) and their role in the charge transport in organic materials in general, and in pentacene in particular is of large interest in recent years. Horowitz and Hajlaoui [1] have shown that the carrier mobility increases with grain size in oligothiophene thin film transistors. Their model suggested that the charge transport is limited by trapping and thermal release at localized states located at the GBs. Other works also suggested that the main bottleneck for the charge transport in organic devices is due to potential barriers both in the GBs, and inside the grains [2–7]. The above works have used macroscopic measurements combined with simulations to study the GBs influence on the device characteristics. It is well known that in organic thin film transistors the current flows very close (few nm) to the gate dielectric interface, which makes the correlation between this accumulation current and the GBs properties extremely difficult.

Puntambekar et al. [8] have used Kelvin probe force microscopy (KPFM) to measure the GBs potential barriers in pentacene thin films (3–5 nm). They have found that the potential drop in the GBs is around 5–10 mV which is an indication of negative trapped charge at the GBs. They also observed that the surface-potential variations within the grains are comparable to the drops at the GBs making it ambiguous whether the GBs poses bottlenecks to hole transport. Wang et al. [9] also argued that the channel mobility and threshold voltage are limited by charged traps in the channel, most of which are not located in the grain boundaries but at the organic/insulating layer interface. Nakamura et al. [10] have shown that the GBs are not always a limiting factor for the carrier mobility, although the mobility had a correlation with the average grain size. Tello et al. [11] have also used KPFM to measure the surface potential in pentacene transistors under bias, and its correlation with the film morphology. They have found that most of the applied drain–source bias drops across a single well-defined grain boundary, which consequently acts as the bottleneck for charge transport. However, these features were scarce, indicating that there is generally sufficient connectivity through the GBs to transport the current.

The above studies indicate that the GBs role in pentacene charge carrier transport and their effect on the device

* Corresponding author.
E-mail address: yossiR@tauex.tau.ac.il (Y. Rosenwaks).

1566-1199/$ - see front matter © 2010 Elsevier B.V. All rights reserved.
doi:10.1016/j.orgel.2010.07.021

performance is not well understood. This is partially due to the lack of simulations combined with local GBs electronic measurements that can quantitatively reveal the effect of the GBs. We present here a comprehensive KPFM study of pentacene thin film organic field effect transistors (OFETs) with different film thicknesses combined with *i–V* measurements and 3D electrostatic simulations in order to reveal and quantify the GBs role on the device characteristics. We distinguish between two different charge trapping regions: the first is the SiO_2–pentacene interface where electrons are trapped, and the second is in the GBs that trap holes (the majority carriers). It is found that the bottom interface charge determines the GBs surface potential in thin layers, while the GBs trapped charge does it in thick layers. The results are discussed in view of their effect on pentacene thin film transistors performance.

2. Experimental

A heavily doped *n*-Si (1 0 0) wafer was used as the substrate and the gate electrode, and thermally oxidized SiO_2 (300 nm) served as the gate dielectric. The pentacene layer was deposited by using the molecular-beam deposition method [12] at a base pressure of 4×10^{-10} Torr and at a growth rate of 0.2 nm min^{-1} with a substrate temperature of 60 °C. The channel width and length of the pentacene transistor were 5 mm and 20 μm, respectively. The source and drain gold electrodes of pentacene TFT were deposited on the pentacene film in vacuum. Four transistors with pentacene layers in thickness of 100, 30, 10 and 5 nm were prepared and transferred to glove box where both the KPFM and electrical measurements were carried out. The KPFM measurements were conducted using a *Dimension 3100* atomic force microscopy (AFM) system in a controlled nitrogen environment glove box (less than ~5 ppm H_2O), in the lift mode where the first scan is a tapping mode topography measurement and in the second scan the tip is raised above the topography trajectory ~5 nm and measures the CPD.

3. Results and discussion

3.1. Thin pentacene layers

Fig. 1 shows topography (top row (a, d and g) and CPD images (second row (b, e and h) for 30, 10 and 5 nm thick pentacene transistors biased above the threshold voltage ($V_g = 0$), respectively. The measured CPD represents the difference between the tip work function (Φ_t) and sample work function (Φ_s) defined as:

$$\mathrm{CPD} = -\frac{1}{q}(\Phi_t - \Phi_s) \quad (1)$$

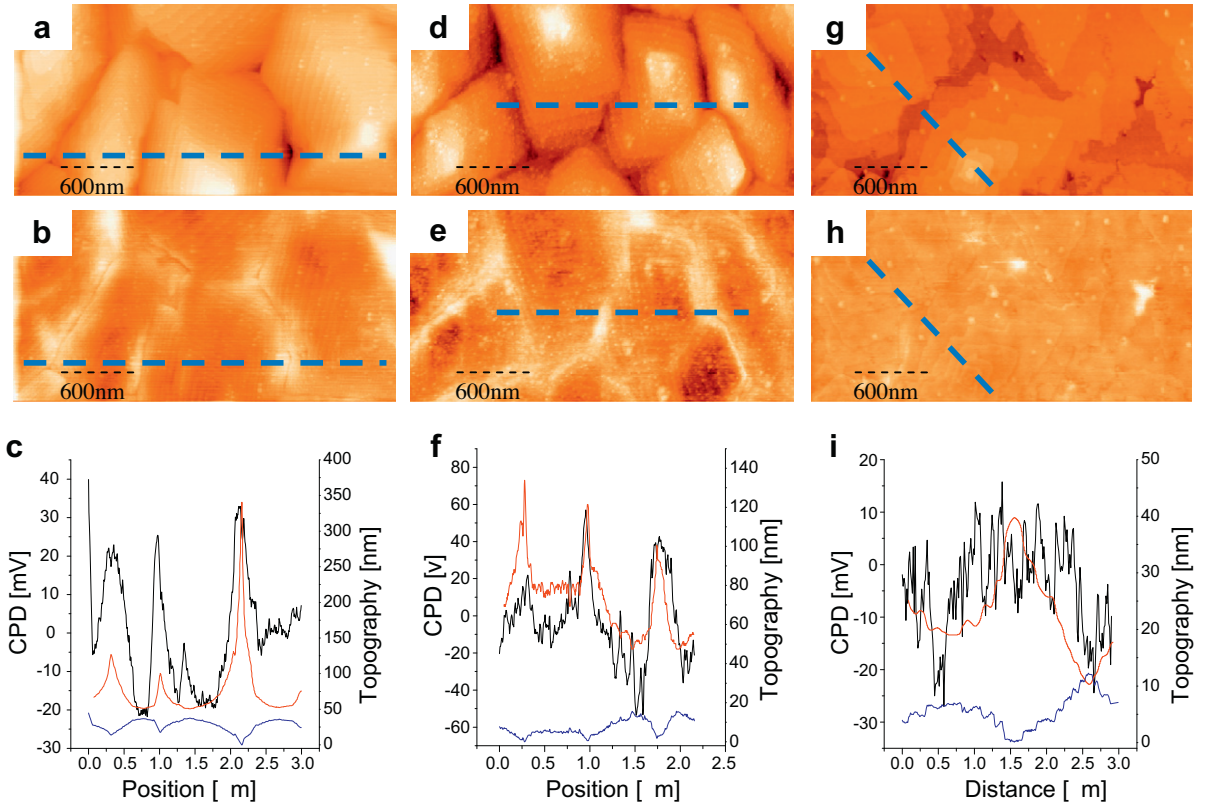

Fig. 1. (a, d and g) Topography of 30, 10 and 5 nm thick pentacene films, respectively. (b, e and h) CPD measurement of 30, 10 and 5 nm thick pentacene film respectively. (c, f and i) lines scans of the calculated and measured CPD of 30, 10 and 5 nm thick pentacene films, respectively. Black line represents the measured CPD, red line the calculated CPD and the blue line represents the measured topography. All the images were measured at $V_g = 0$. (For interpretation of the references in colour in this figure legend, the reader is referred to the web version of this article.)

This means that larger CPD represents increase in the material work function. In the 30 and 10 nm thick samples the CPD is larger at the GBs (Fig. 1b and e) in comparison with the grain interior, which means that the Fermi-level at the GBs is closer to the highest occupied molecular orbital (HOMO) level. In the 5 nm thick sample (Fig. 1h) a minor CPD variation was observed between the GI and the GBs. The CPD is actually increased in the locations where the SiO_2 is exposed. The simulations represented by the solid red lines will be discussed later in this section.

It has been proposed that oxygen may induce new chemical species in pentacene films, shifting the Fermi-level (E_F) towards to the HOMO level, causing *p*-type behavior of the organic semiconductor [13,14]. In our samples the pentacene is assumed *p*-type due to unintentional doping by chemical impurities [15] or by reaction with ambient oxygen and/or H_2O [16]; therefore an upward band bending as shown in Fig. 1c and f represents hole accumulation.

In order to analyze the holes accumulation (CPD increase) in the GBs, we have to consider the charge distribution for the case where the pentacene film thickness (t) is much smaller than the space charge region (SCR) width (w); in such a case an "incomplete" SCR is formed [17]. The surface space charge is "incomplete" in the sense that there is deficiency of charges (dopants) in the film to balance the negative interface charge sheet. Fig. 2a shows schematics of the polycrystalline pentacene where the GBs thickness is smaller than the grains interior (GI) and only unintentional doping is assumed. Fig. 2b shows the corresponding band diagrams in the vicinity of a GB (red lines) and a GI (black lines), respectively. In the absence

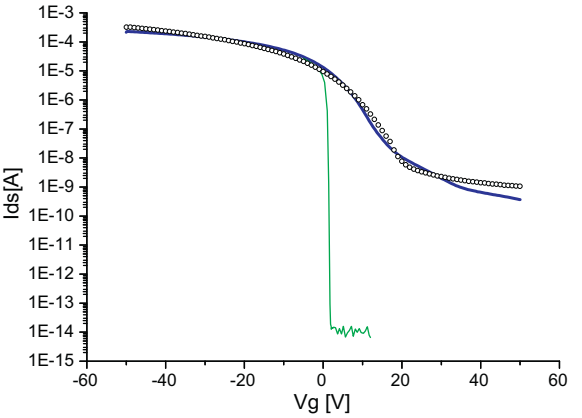

Fig. 3. Measurement (black dots) and simulations of source–drain current as a function of gate voltage of pentacene 30 nm thick film transistor. The simulation including interface traps (blue) is compared to the simulation without interface traps (green). The interface trap distribution responsible for the observed large V_t shift was calculated using: $N_0 = 5e12\ cm^{-2}$, $E_S = 0.22$, $E_0 = 0.55$ and the GBs trapped charge concentration was $N_{GB} = 3e11\ cm^{-2}$. It was assumed that the pentacene layer is compose of eight grains and their morphology was based on the AFM topography map.

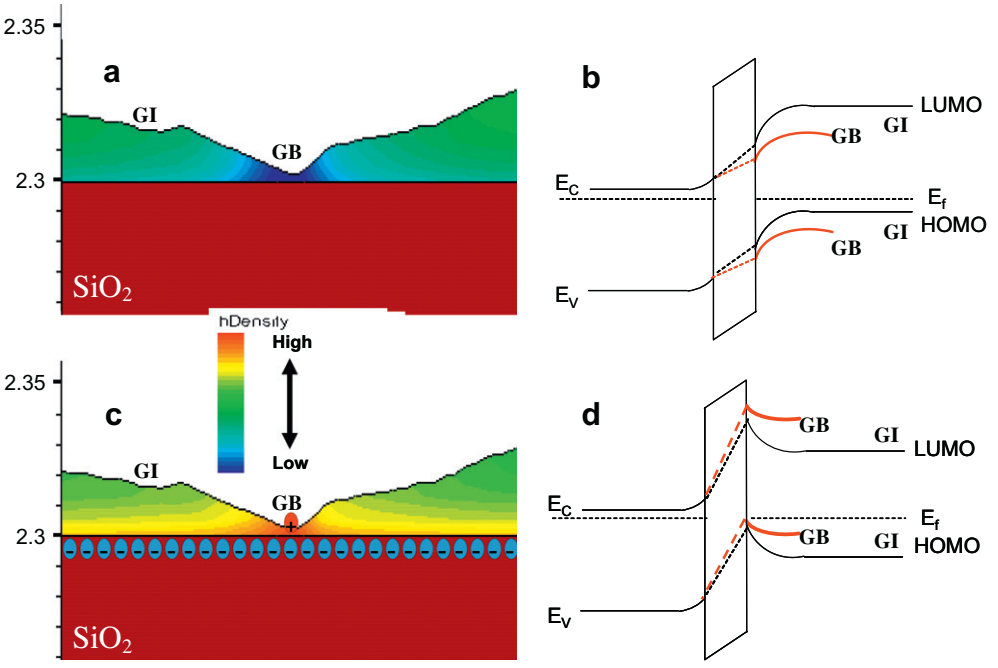

Fig. 2. Schematic charge distribution (a) and band diagram (b) for a pentacene transistor with no interface states and no trapped charge at the GBs. Schematic charge distribution (c) and band diagram (d) in the presence of interface states and trapped charge in the GB. The colour scale represents the mobile hole density in the pentacene film; the positive charge (red) represents trapped holes at the GB, and the negative charge (blue) represents trapped electrons. The grain boundary location is marked by (GB), and the grain interior location is marked by (GI). (a) and (c) clearly show that the space charge region at the vicinity of the GB is incomplete relative to the GI. (For interpretation of the references in colour in this figure legend, the reader is referred to the web version of this article.)

of interface charge, there is a downward band bending in the pentacene layer due to the *n*-type Si substrate. This band bending is larger at the grain interiors *only because there are more acceptors there* (*due* to the pentacene thickness) *to accommodate a larger SCR*. This is clearly demonstrated by the different colours around the GBs in comparison with the GIs in Fig. 2a. Consequently, the SCR is smaller at the GBs leading to a local decrease in the work function and the measured CPD.

Based on these arguments a question arises why an upward band bending at the GBs (hole accumulation) is measured in the 10 and 30 nm thick pentacene films?

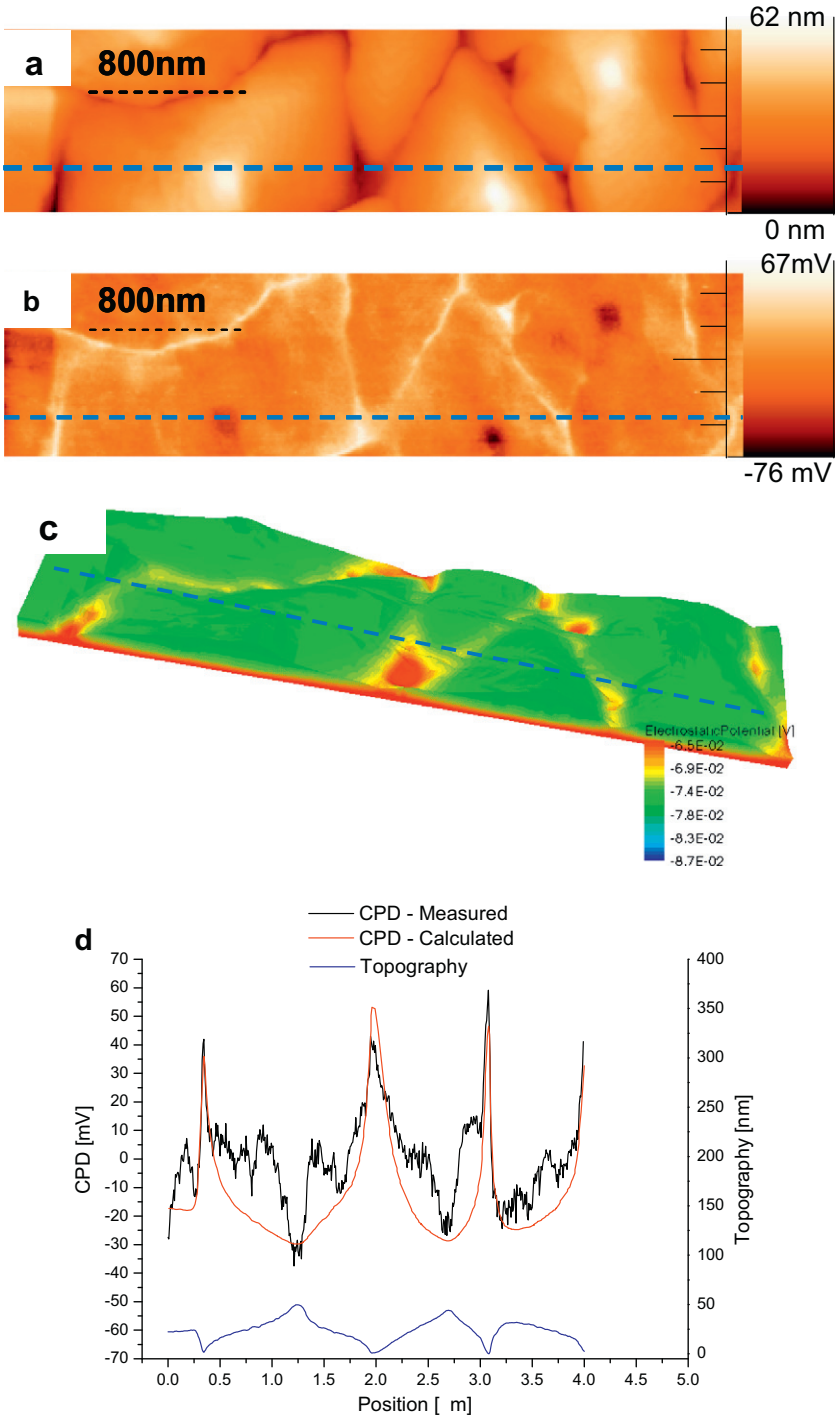

Fig. 4. (a) Topography, (b) measured CPD, (c) calculated CPD in 3D and (d) lines scans of the calculated and measured CPD of 30 nm thick pentacene film. The black line is the measured CPD, the red line is the calculated CPD and the blue line is the topography. The images were measured at $V_g = 0$. (For interpretation of the references in colour in this figure legend, the reader is referred to the web version of this article.)

Below we show that this is due to the interface states present at the pentacene–SiO_2 interface. This interface state density is reported to be relatively high ($\sim 1 \times 10^{12}$ cm^{-2}) due to electron trapping by hydroxyl groups, present in the form of silanols at the SiO_2 pentacene interface [18]. The charge distribution is depicted in Fig. 2c where acceptor-like traps are present at the SiO_2–pentacene interface; the figure also shows the positive trapped charge in the GBs. The corresponding band diagram is shown in Fig. 2d. The negative interface charge induces accumulation of holes in the pentacene layer close to the interface, and consequently an upward band bending as shown in Fig. 2d. It should be noted that the effect of the GBs positive trapped charge is negligible in this case due to the short length of the boundaries, as will be discussed in more details later. In this case of upward band bending, the "incomplete" accumulation layer at the GBs leads to a larger work function and CPD at the GBs as shown schematically in Fig. 2d and by the KPFM measurement in Fig. 1. It should be mentioned that preferential oxidation at the GBs will increase the negative charge concentration there (ionized acceptors) [18] which will consequently reduce the CPD accordingly. However, this is in contrast to what is measured for thin films were the CPD is larger at the GBs. Moreover, this assumption alone cannot explain the CPD differences in the GBs between thin and thick samples demonstrated later on.

3.2. Electrostatic simulations

The simulations were calculated using a 3D device simulator TCAD Sentaurus (*Synopsys* Inc.) that solves the coupled Poisson and continuity equations for holes and electrons. We have assumed an exponential gap state distribution in the pentacene layer which was reported by several groups for thin amorphous organic films [19,20]. Our group have also measured such exponential density of state (DOS) by KPFM for an OFET structure [21]. Following Lang et al. [22] we have used an exponential trap distribution of the form:

$$g(E) = N_0 \exp\left(-\frac{|E - E_0|}{E_S}\right) \quad (2)$$

where E is the energy relative to the valence band edge, and N_0 and E_S are the coefficient and the characteristic energy width of the exponential trap distribution, respectively, and E_0 represents the energy of the conduction band minimum.

A unintentional dopant concentration of 5×10^{16} cm^{-3} was assumed in our simulations, although bulk traps may be present [19]. We have assumed that well-defined grain boundaries are present in the first few mono-layers of pentacene [23], although the evolution of GBs may be different compared with the upper part of the layer [24]. A positive trapped charge density at the GBs with constant energy distribution and with a concentration of $N_{GB} = 3 \times 10^{11}$ cm^{-2} was assumed. The physical parameters of the pentacene were taken from Ref. [25]. The pentacene layer morphology used in the simulations were based on the AFM measured topography.

The interface state density was obtained by comparing the transistor i–V curves to simulations conducted for the 30 nm thick transistor. The dotted line in Fig. 3a shows measured source–drain curve (I_{ds}) of a pentacene OTFT with a channel width of 5 mm and length L of 20 μm in the forward sweep (on to off) at an incremental gate voltage (V_{GS}) from −5 to 30 V in 1 V steps. The solid lines represent i–V simulations with (blue) and without (green) interface states, respectively. The observed large positive threshold voltage, V_{th}, shift is in agreement with previous studies [19,26] which showed that negatively charge interface traps are responsible for the large positive V_{th} shifts. The agreement between the simulation and the measured curve was obtained for an interface acceptor traps with $N_0 = 5 \times 10^{12}$ cm^{-2} eV^{-1}, $E_S = 0.22$ and $E_0 = 0.55$; the trap lateral distribution was assumed homogenous across the interface. We attribute the relatively high off current to the unintentional doping which takes place during the device preparation. Minor deviations in the i–V curves (not

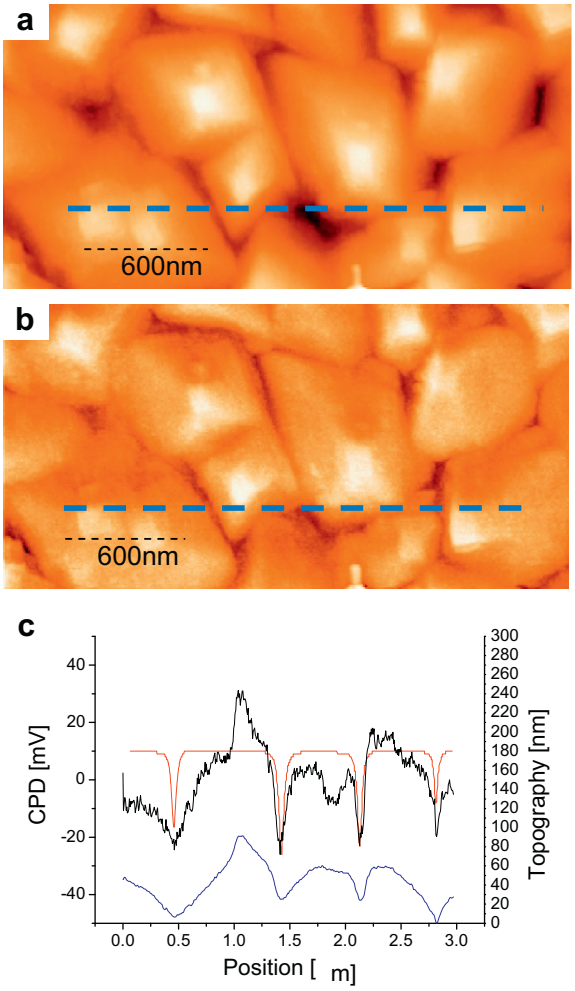

Fig. 5. (a) Topography, (b) measured CPD and (c) line scans of the calculated and measured CPD of 100 nm thick pentacene film. The black line is the measured CPD, the red line is the calculated CPD and the blue line is the topography. The images were measured at $V_g = 0$. (For interpretation of the references in colour in this figure legend, the reader is referred to the web version of this article.)

shown) were observed as a function of trapped charge concentration in the GBs.

Fig. 1c, f and i summarizes the comparison between the simulated and the measured CPD for the 30, 10 and 5 nm thick samples, respectively. Some of the GBs at the 30 and 10 nm thick samples show larger CPD compared with the grain interior in qualitative agreement with the "incomplete" SCR phenomena described in details above. Fig. 1i shows that there are very small differences in the measured CPD between the GBs and grain interiors in the case of the 5 nm thick pentacene layer; this may be due to small variations in the film thickness between the GBs and the grain interior. The effect of trapping and accumulation of holes in the GBs was also reported recently by Hallam et al. [27] for conjugated polymers.

We may note that some GBs potential drops do not show good correlation with the simulated KPFM profile. This can be explained by differences in the local interface state density, different charge density in the GBs, variation in the GBs length and because the simulation are 2D. Since the CPD measurements at around the GBs are affected by the actual 3D electrostatic interactions, we have conducted 3D simulations on the 30 nm thick pentacene film as shown in Fig. 4. The figure shows the layer topography (a), measured CPD (b), calculated CPD (c) and line scan of the calculated and measured CPD (d). The calculations presented in (c) and (d) show that the CPD is larger at the GBs compared to the grain interior in a good agreement with the experimental results.

3.3. Thick pentacene layers

Fig. 5 shows topography (a) and KPFM (b) measurements conducted on a thicker (100 nm) pentacene layer. In such thick layers the interface charge is fully screened by the doped pentacene ($t \gg w$), and consequently the trapped holes in the GBs govern the surface potential rather than the interface states. This is demonstrated in Fig. 5b and c which shows that the CPD at the GBs is smaller than the GI; in the simulations shown in Fig 5c we have assumed that the GBs length is 30 nm. The CPD decrease in the GBs causes downward band bending and consequently hole depletion in the neighboring GIs. We argue that this is due to trapped holes in the GBs which are not screened as in the case of the thinner layers. Fig. 6 shows CPD calculation as a function of the GBs length for $V_g = 0$ V. The GBs length is define here as the distance between the GB surface and the pentacene–SiO_2 interface. The GBs length was varied from 2 to 30 nm while all the other parameters such as the GBs trapped charge, interface trap density and doping concentration were kept constant. The figure clearly demonstrates that for GBs length of less than 10 nm an upward band bending is predicted, while for thicker pentacene layers and longer GBs thickness a downward band bending is expected. This is in agreement with our assumption that for thin layers the GBs charge does not govern the measured CPD.

We have also simulated the effect of donor and acceptor type surface states. It was found that acceptor-like surface states decrease the potential drops in the GBs, while donor-like states increase it. Since the potential measured by the KPFM is affected by the overall charge distribution we cannot confirm or reject the presence of surface states at this stage. We emphasize that the density of surface states in organic materials is quite small because the molecules are typically closed-shell units with negligible concentration of dangling bonds. Based on all the above, we have not included surface states effects in the present study.

4. Summary and conclusions

We have presented a detailed experimental and numerical study of potential distribution at the GBs in pentacene thin film transistors. It was found that for thin film pentacene the CPD is larger at the GBs compare to the grain

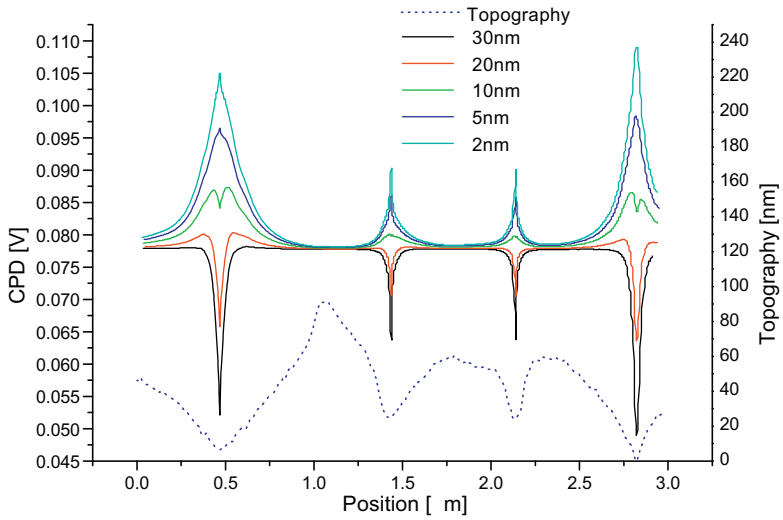

Fig. 6. Calculated potential profiles of different pentacene layers where the GBs length changes from 2 to 30 nm. The figure clearly shows that at a GB of around 10 nm the surface-potential change from accumulation to depletion.

interior. This phenomenon was attributed to interface trapped charge and to the "incomplete" accumulation in the GBs which consequently increases the local work function. On the other hand, in thick pentacene films we observed lower CPD at the GBs compared to grain interiors. In this case the trapped charge in the GBs governs the surface potential. The interface and the GBs trapped charge concentrations were evaluated by comparing the device transfer characteristics to the simulation and by solving the 3D electrostatic potential of pentacene GBs for different film thicknesses.

The effect of holes accumulation at the GBs in thin films may have a large effect on the carrier transport in such devices since it implies that the current density at the GBs may be larger compared to the grain interiors. This phenomenon is currently analyzed and will be the subject of future work.

References

[1] G. Horowitz, M.E. Hajlaoui, Synth. Met. 122 (2001) 185.
[2] Y.W. Wang, H.L. Cheng, Y.K. Wang, T.H. Hu, J.C. Ho, C.C. Lee, T.F. Lei, C.F. Yeh, Thin Solid Films 467 (2004) 215.
[3] L.W. Shang, C.S. Wang, M. Liu, Appl. Phys. Lett. 88 (2006) 202111.
[4] D. Knipp, R.A. Street, A.R. Volkel, Appl. Phys. Lett. 82 (2003) 3907.
[5] C.S. Kim, S.J. Jo, S.W. Lee, W.J. Kim, H.K. Baik, S.J. Lee, J. Electrochem. Soc. 154 (2007) H102.
[6] N. Ohashi, H. Tomii, R. Matsubara, M. Sakai, K. Kudo, M. Nakamura, Appl. Phys. Lett. 91 (2007) 162105.
[7] R. Matsubara, N. Ohashi, M. Sakai, K. Kudo, M. Nakamura, Appl. Phys. Lett. 92 (2008) 242108.
[8] K. Puntambekar, J.P. Dong, G. Haugstad, C.D. Frisbie, Adv. Funct. Mater. 16 (2006) 879.
[9] S.D. Wang, T. Miyadera, T. Minari, Y. Aoyagi, K. Tsukagoshi, Appl. Phys. Lett. 93 (2008) 043311.
[10] M. Nakamura, H. Ohguri, N. Goto, H. Tomii, M.S. Xu, T. Miyamoto, R. Matsubara, N. Ohashi, M. Sakai, K. Kudo, Appl. Phys. A – Mater. Sci. Process. 95 (2009) 73.
[11] M. Tello, M. Chiesa, C.M. Duffy, H. Sirringhaus, Adv. Funct. Mater. 18 (2008) 3907.
[12] H. Yanagisawa, T. Tamaki, M. Nakamura, K. Kudo, Thin Solid Films 464–465 (2004) 398.
[13] A.R. Brown, C.P. Jarrett, D.M. deLeeuw, M. Matters, Synth. Met. 88 (1997) 37.
[14] J. Jo, J.J. Heremans, F. Bradbury, H. Chen, V. Soghomonian, Nanotechnology 15 (2004) 1023.
[15] P. Bauerle, Adv. Mater. 4 (1992) 102.
[16] C. Vaterlein, B. Ziegler, W. Gebauer, H. Neureiter, M. Stoldt, M.S. Weaver, P. Bauerle, M. Sokolowski, D.D.C. Bradley, E. Umbach, Synth. Met. 76 (1996) 133.
[17] D. Redfield, J. Appl. Phys. 54 (1983) 2860.
[18] L.L. Chua, J. Zaumseil, J.F. Chang, E.C.W. Ou, P.K.H. Ho, H. Sirringhaus, R.H. Friend, Nature 434 (2005) 194.
[19] S. Scheinert, K.P. Pernstich, B. Batlogg, G. Paasch, J. Appl. Phys. (2007) 102.
[20] A.R. Volkel, R.A. Street, D. Knipp, Phys. Rev. B (2002) 66.
[21] O. Tal, Y. Rosenwaks, Y. Preezant, N. Tessler, C.K. Chan, A. Kahn, Phys. Rev. Lett. (2005) 95.
[22] D.V. Lang, X. Chi, T. Siegrist, A.M. Sergent, A.P. Ramirez, Phys. Rev. Lett. (2004) 93.
[23] J. Zhang, J.P. Rabe, N. Koch, Adv. Mater. 20 (2008) 3254.
[24] T.W. Kelley, L.D. Boardman, T.D. Dunbar, D.V. Muyres, M.J. Pellerite, T.Y.P. Smith, J. Phys. Chem. B 107 (2003) 5877.
[25] M. Nakamura, N. Goto, N. Ohashi, M. Sakai, K. Kudo, Appl. Phys. Lett. 86 (2005) 122112.
[26] S. Scheinert, G. Paasch, M. Schrodner, H.K. Roth, S. Sensfuss, T. Doll, J. Appl. Phys. 92 (2002) 330.
[27] T. Hallam, M.J. Lee, N. Zhao, I. Nandhakumar, M. Kemerink, M. Heeney, I. McCulloch, H. Sirringhaus, Phys. Rev. Lett. 103 (2009) 4.

Organic Electronics 11 (2010) 1736–1739

Contents lists available at ScienceDirect

Organic Electronics

journal homepage: www.elsevier.com/locate/orgel

Hydrostatic pressure sensor based on carbon sphere – polyvinyl alcohol composites

Wagner S. Machado [a], Patrick L. Athayde [a], Messai A. Mamo [b,c], Willem A.L. van Otterlo [c], Neil J. Coville [b,c], Ivo A. Hümmelgen [a,*]

[a] Departamento de Física, Universidade Federal do Paraná, Caixa Postal 19044, 81531-990 Curitiba, Brazil
[b] DST/NRF Centre of Excellence in Strong Materials, University of the Witwatersrand, PO Wits, 2050 Johannesburg, South Africa
[c] Molecular Sciences Institute, School of Chemistry, University of the Witwatersrand, PO Wits, 2050 Johannesburg, South Africa

ARTICLE INFO

Article history:
Received 27 May 2010
Received in revised form 21 July 2010
Accepted 24 July 2010
Available online 15 August 2010

Keywords:
Carbon spheres
Pressure sensor
Hydrostatic pressure sensor

ABSTRACT

We report on the preparation of hydrostatic pressure sensors, based on carbon sphere–polyvinyl alcohol composites deposited onto interdigitated electrodes, determining the pressure dependence of the conductance and capacitance of the devices. For these devices, we used carbon spheres with average diameter of 124 ± 13 nm at concentrations of 20%, 30% and 40%. The highest relative variation of conductance (0.69% kPa^{-1}) and capacitance (0.24% kPa^{-1}) was obtained using the composite with 30% carbon spheres.

© 2010 Elsevier B.V. All rights reserved.

1. Introduction

Pressure sensors are widely used in several different applications, like airflow measurement and in pressure control in confined vessels (for example tires, pipelines and microphones). Among the various existing pressure sensors [1–3], carbon black dispersed in a hosting polymer matrix has been demonstrated to constitute an interesting system due to the simple low-cost processes involved in their production, as well as their large and fast electrical response. Due to these advantages these systems have been applied to a number of pressure sensor systems, in most cases for uniaxial pressure measurement [4–7].

In conducting particles-host insulating polymer matrix composites, the pressure imposes changes on the average distance between the conducting particles mainly due to volume modification of the matrix, which changes the tunneling probability between conducting particles. By this mechanism, the conductance of the existing percolation paths is modified and new percolation paths may be created or suppressed, directly affecting the conductance of the medium. The capacitance of the system is also modified due to the variation of the separation distance of conducting particles by the insulating material.

In the past two decades a wide range of shaped carbon materials have been produced, including horns, onions, tubes, coils, etc. and many new methodologies to prepare the new and known shaped carbons have been extensively reported. This includes studies on spherical carbons (hollow, core/shell and fullerenes) [8] that are similar to the carbon blacks [9,10].

Herein we report on the use of carbon spheres (CSs) produced in a non-oxidizing environment, with a narrow size distribution, mixed with polyvinyl alcohol (PVA) as a hydrostatic pressure sensor. These CSs, with a narrow diameter range (124 ± 13 nm), are solid carbon balls made up of nanometric sized flakes, have a low surface area and are generally found accreted (Fig. 1). This means that clusters of the CSs are in contact with each other, similar to that found for carbon blacks. This accretion phenomenon should aid CSs in their ability to act in sensing devices.

* Corresponding author.
E-mail address: iah@fisica.ufpr.br (I.A. Hümmelgen).

1566-1199/$ - see front matter © 2010 Elsevier B.V. All rights reserved.
doi:10.1016/j.orgel.2010.07.028

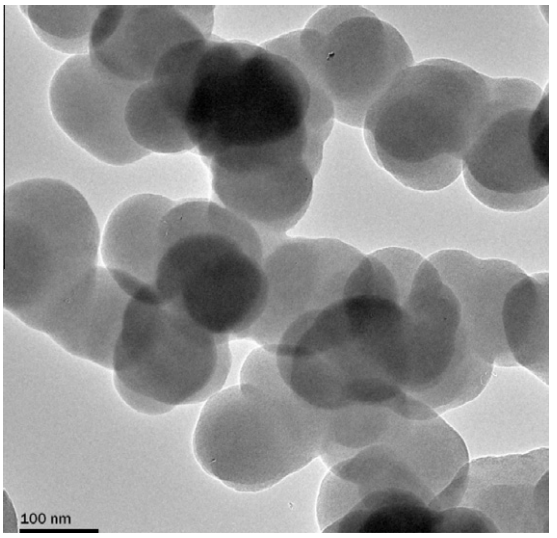

Fig. 1. Transmission electron micrograph of the carbon spheres.

2. Experimental

Polyvinyl alcohol was supplied by Sigma–Aldrich (average molecular weight 130,000) and used without further purification. The synthesis of the CSs was performed by passing a continuous flow of acetylene gas for 10 min at 900 °C, under an argon atmosphere through a quartz tube placed vertically inside a furnace. The acetylene and the argon gases were allowed to flow (100 mL/min each) from top to bottom through the quartz tube and the carbonaceous materials collected in a 500 mL round bottom flask, similar to that reported by Jin et al. [11]. The CSs were characterized by transmission electron microscopy (TEM) using a FEI Tecnai G2 Spirit electron microscope at 120 kV.

The devices were prepared as follows: PVA was added to 1,2-dichlorobenzene and the solution was heated to 80 °C and stirred for 30 min. This gave a homogeneous solution of PVA in the solvent (115 mg/mL). CSs were added to another sample of 1,2-dichlorobenzene, stirred for 30 min and ultrasonicated for 30 min at room temperature, using a 45 W ultrasonic bath, to obtain a uniform dispersion of CSs (2.2 mg/mL). Both solutions were then mixed at room temperature in a proportion chosen to give final solution compositions containing 20%, 30% and 40% CSs (w/w) concentration in the composite.

The pressure sensors used in this work were prepared by depositing the CS–PVA dispersion onto a $8 \times 9\ mm^2$ phenolite printed circuit board with nine pairs of 7.5 mm long tin-coated cooper interdigitated electrodes having a gap of 0.3 mm between them, in a rectangular geometry, as reported elsewhere [12,13]. A μL-pipette was used to deposit a CS–PVA dispersion by sequentially dropping 20, 30 and 35 μL (time interval of 60 min) onto the phenolite substrates.

The devices were then electrically characterized using a programmable Agilent 4284A LCR meter. An AC-signal amplitude of 500 mV was used as the operating voltage under environmental conditions. The pressure dependence measurements were made by placing the sensor in a cylindrical tube with a diameter of 44.5 mm in which the pressure was controlled manually with the aid of a piston (Fig. 2) following the relationship $h_i p_i = h_f p_f$, *i.e.*, the pressure in the cylindrical tube was varied by displacing the piston (h is the height, p is the pressure, i denotes initial and f denotes final) and neglecting the volume of the sensor.

3. Results and discussion

The transmission electron microscope (TEM) image of the CSs produced is shown in Fig. 1. From these TEM images it is evident that the solid CSs are accreted and have a narrow size distribution (diameter: 124 ± 13 nm). The synthesis of the spheres right from the beginning leads to accretion. Clustering of the spheres occurs either due to chemical interaction (accretion) or due to van der Waals interactions. The carbon chains involve from 2 to ~10

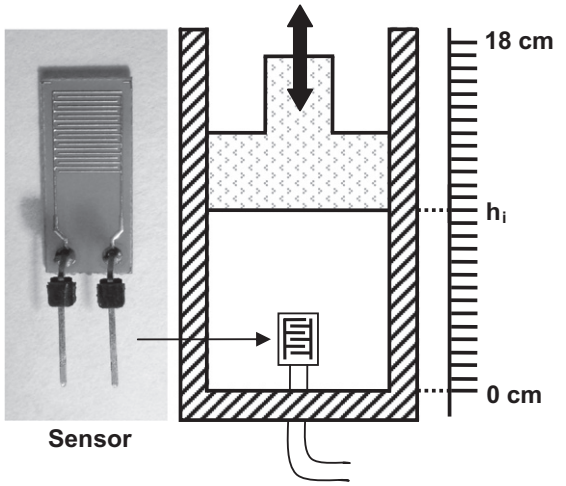

Fig. 2. Scheme of the experimental setup used for the pressure variation.

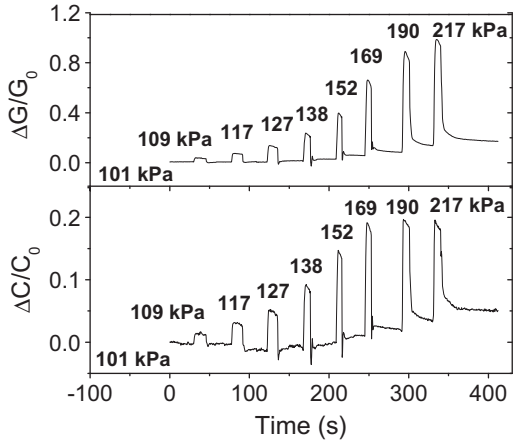

Fig. 3. Illustration of the electrical response of the device to pressure pulses of different magnitude.

spheres. The good yield and the simple production procedure constitute an advantage in using this material, when compared to other carbon materials that have been used in pressure sensors [2,14–16]. In addition, CSs are less expensive to synthesize than fullerenes and carbon nanotubes, and the synthesis constitutes a facile controllable synthetic methodology.

The current conductance G and capacitance C of the sensors were then measured as a function of applied hydrostatic pressure p at 27 kHz. This frequency was

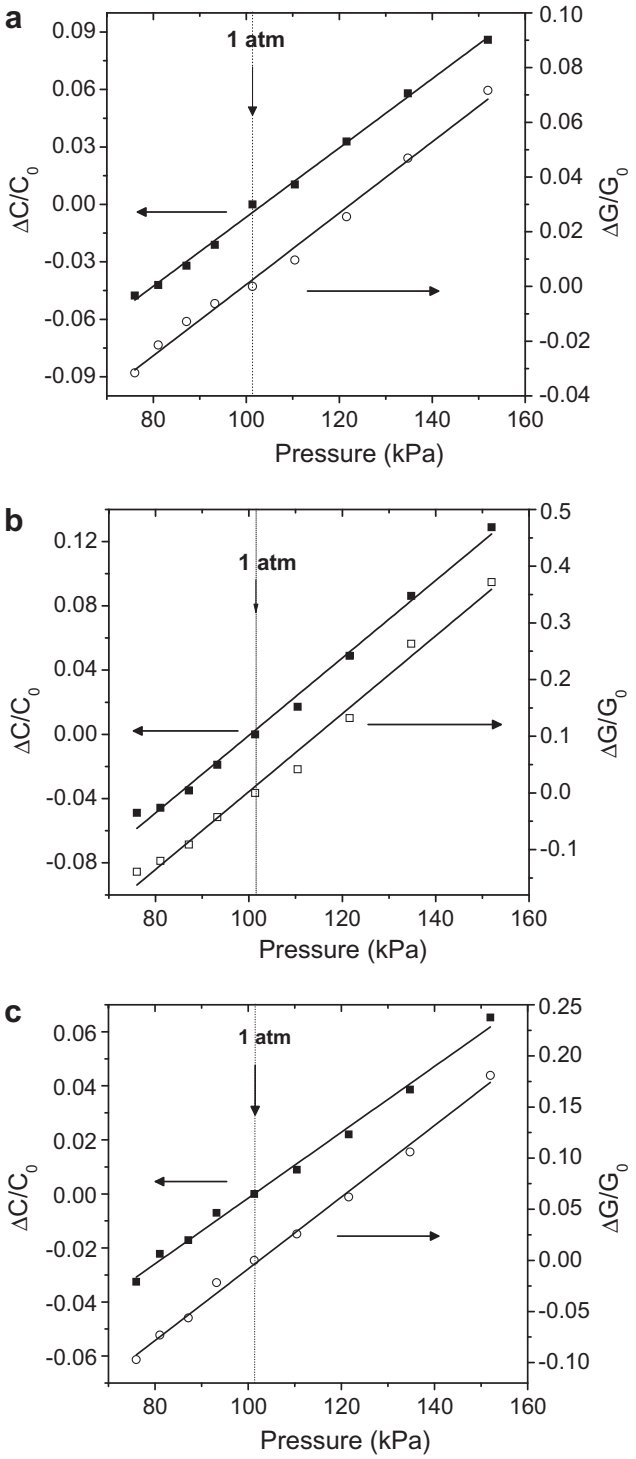

Fig. 4. Relative variation of the capacitance and conductance of devices prepared with different CS concentrations: (a) 20%; (b) 30%; and (c) 40%.

Table 1
Coefficients α_G and α_C as a function of the CS concentration in the device.

	CS concentration (w/w)		
	20%	30%	40%
α_G (kPa^{-1})	0.0013	0.0069	0.0035
α_C (kPa^{-1})	0.0018	0.0024	0.0012

chosen due to the low observed signal to noise ratio at this frequency. The data showing $\Delta G = G(p) - G_0$ and $\Delta C = C(p) - C_0$ (where the subscript 0 indicates initial value) were measured at $p_0 = 101.3$ kPa and are presented in Fig. 3.

It can be seen in Fig. 3 that the sensor responds to pressure variation in the range of atmospheric pressure to 217 kPa. In this experiment the pressure was periodically increased and then decreased back to atmospheric pressure, for different pressure pulse amplitudes. As can be observed, for pressure larger than *ca.* 150 kPa, the base line of the conductance was not recovered and for this reason the measurements were limited up to a maximum of 150 kPa. In the case of the capacitance measurements, the baseline problem was more pronounced and the relative capacitance variation due to pressure variation is small. As a consequence, the conductance was deemed to be more appropriate for measurements aimed at practical applications.

Figs. 4a–c shows the relative conductance variation and relative capacitance variation as a function of pressure, for CS concentrations of 20%, 30% and 40% (w/w). From this data, assuming a linearity of $\Delta G/G_0(p)$ and $\Delta C/C_0(p)$, the coefficients were calculated as follows:

$$\alpha_G \equiv \frac{\partial(\Delta G/G_0)}{\partial p} \tag{1}$$

$$\alpha_C \equiv \frac{\partial(\Delta C/C_0)}{\partial p} \tag{2}$$

The obtained coefficients are summarized in Table 1. It can be seen that both α_G and α_C showed higher values at a CS concentration of 30% and for this reason this is the most appropriate concentration to use for practical pressure sensors.

It is interesting to mention that these values are higher that those reported for carbon black or other polymer based sensors in the range of $p_0 \approx 100$ kPa. The estimate of α_C from the data reported by Arshak et al. for uniaxial stress gives $\sim 10^{-4}$ kPa^{-1} [6]. Wang et al. report $\alpha_G \approx 0.0012$ kPa^{-1} also for compressive stress [17]. From the data reported by Arshak et al. for polyvinylidene fluoride based sensors (in this case without carbon black) we also estimate $\alpha_C \approx 2 \times 10^{-3}$ kPa at $p_0 \approx 100$ kPa.

4. Conclusion

We have demonstrated that narrow size distribution CS–PVA composites at CS concentrations ranging from 20% to 40% are suitable for use as hydrostatic pressure sensors. In this particular work CSs with an average diameter of 124 ± 13 nm show promising results. Larger relative variation of the conductance was observed in devices with 30% CS concentration in both conductance and capacitance measurements.

Acknowledgements

The authors would like to thank CNPq and Renami (Brazil) and DST/NRF (South Africa) for research grants, Prof. J. Gruber for supplying interdigitated electrodes and M. Greenshields for helpful information. M.A.M. gratefully acknowledges funding from Pró-África-CNPq for financial travel support.

References

[1] I. Manunzaa, A. Bonfiglio, Biosens. Bioelectron. 22 (2007) 2775.
[2] Y.C. Chao, W.J. Lai, C.Y. Chen, H.F. Meng, H.W. Zan, S.F. Horng, Appl. Phys. Lett. 95 (2009) 253306.
[3] J.H. Kim, Q. Suna, S. Seo, Org. Electron. 11 (2010) 964.
[4] M. Knite, V. Teteris, A. Kiploka, J. Kaupuzs, Sens. Actuators A 110 (2004) 142.
[5] K. Arshak, D. Morris, A. Arshak, O. Korostynska, E. Moore, Sens. Actuators A 132 (2006) 199.
[6] K. Arshak, D. Morris, A. Arshak, O. Korostynska, Thin Solids Film 516 (2008) 3298.
[7] L. Wang, T. Ding, P. Wang, IEEE Sens. J. 9 (2009) 1130.
[8] A. Deshmulk, S. Mhlanga, N.J. Coville, Mater. Sci. Eng. – R, in press, doi:10.1016/j.mser.2010.06.017.
[9] W.M. Qiao, Y. Song, S.Y. Lim, S.H. Hong, S.H. Yoon, I. Mochida, T. Imaoka, Carbon 44 (2006) 187.
[10] Z.L. Wang, Z.C. Wang, J. Phys. Chem. 100 (1996) 17725.
[11] Y.Z. Jin, C. Gao, W.H. Hsu, Y. Zhu, A. Huczko, M. Bystrzejewski, M. Roe, C.Y. Lee, S. Acquah, H. Kroto, D.R.M. Walton, Carbon 43 (2005) 1944.
[12] M.S. Meruvia, I.A. Hümmelgen, C.S. Gonçalves, A.R.V. Benvenho, J. Gruber, Sensor Lett. 5 (2007) 625.
[13] M.W.C.C. Greenshields, M.S. Meruvia, I.A. Hümmelgen, N.J. Coville, S.D. Mhlanga, H.J. Ceragioli, J.C. Rojas Quispe, V. Baranauskas, J. Nanosci. Nanotechnol., 2010, doi:10.1166/jnn.2010.3518.
[14] M. Knite, V. Teteris, B. Polyakov, D. Erts, Mater. Sci. Eng. C 19 (2002) 15.
[15] M. Knite, V. Tupureina, A. Fuith, J. Zavickis, V. Teteris, Mater. Sci. Eng. C 27 (2007) 1125.
[16] M. Knite, K. Ozols, J. Zavickis, V. Tupureina, I. Klemenoks, R. Orlovs, J. Nanosci. Nanotechnol. 9 (2009) 3587.
[17] S.L. Wang, P. Wang, T.H. Ding, Sens. Actuators A 157 (2010) 36.

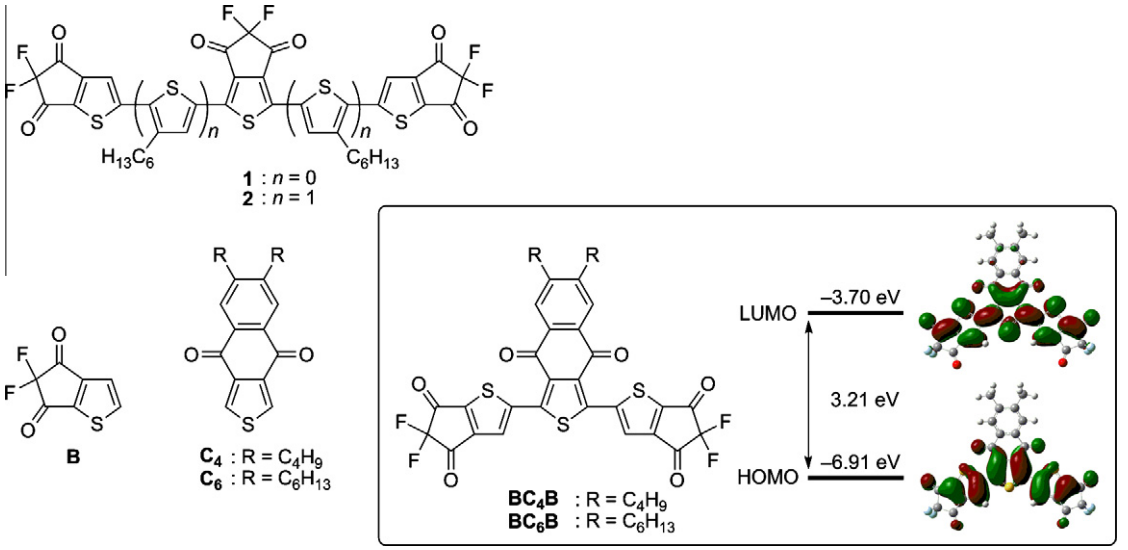

Fig. 1. Chemical structures of **1**, **2**, **B**, $\mathbf{C_4}$, $\mathbf{C_6}$, $\mathbf{BC_4B}$, and $\mathbf{BC_6B}$, and HOMO and LUMO energies of model compound (R=CH_3).

3-hexylthiophene [23]. It should be noted that the presence of electron-donating 3-hexylthiophene causes **2** to exhibit a relatively high LUMO energy level (−3.54 eV). In spite of this fact, OFETs fabricated using **2** by spin coating exhibited a field-effect electron mobility of $1.9 \times 10^{-4}\ cm^2\ V^{-1}\ s^{-1}$. Furthermore, X-ray diffraction (XRD) measurements indicated that the films fabricated using **2** were amorphous or less ordered. For further improving the electron mobility, it is important to both decrease the LUMO energy level and increase the efficiency of self-assembly in the solid state. Therefore, keeping this in mind, we have designed a dialkyl-substituted naphtho[2,3-*c*]thiophene-4,9-dione ($\mathbf{C_4}$ and $\mathbf{C_6}$) unit to be introduced into electronegative oligothiophenes. Herein, we describe the synthesis and properties of newly developed $\mathbf{BC_4B}$ and $\mathbf{BC_6B}$; we also report a substantial improvement in the performance of n-type OFETs, which is in the order of two orders of magnitude.

2. Material and methods

2.1. General Information

Preparative gel-permeation chromatography (GPC) was carried out with Japan Analytical Industry LC-908 equipped with JAI-GEL 1H/2H columns. ^{1}H NMR spectra were recorded on JEOL LA-400 in $CDCl_3$ with tetramethylsilane as an internal standard. Mass spectra were obtained on Shimadzu GCMS-QP-5050. UV–vis spectra were recorded on Shimadzu UV-3100PC. CVs were carried out on a BAS CV-620C voltammetric analyzer. Elemental analyses were performed on PerkinElmer LS-50B. The surface morphology of organic films was observed using an atomic force microscopy (Shimadzu, SPM-9600), and the film crystallinity was evaluated using an X-ray diffractometer (Rigaku, UltimaIV). X-ray diffraction patterns were obtained using Bragg–Brentano geometry with Cu Kα radiation as an X-ray source with an acceleration voltage of 40 kV and a beam current of 40 mA. $\theta - 2\theta$ scans were obtained between 2.5° and −30° a scanning step of 0.01°. The thickness of active-layer organic films was determined using a spectroscopic ellipsometer (HORIBA.UVISEL LT NIR-NNG).

2.2. Synthesis

4a: Compound **3** [24] (366 mg, 1.00 mmol) was placed in a two-necked round-bottomed flask, dissolved in CH_2Cl_2 (10 mL), and degassed with nitrogen. Next, anhydrous aluminum trichloride ($AlCl_3$) (533 mg, 4.00 mmol) was added to it at 0 °C. A solution of 1,2-dibutylbenzene (228 mg, 1.20 mmol) in CH_2Cl_2 (2 mL) was then added dropwise to the stirred mixture at 0 °C. After stirring the reaction mixture at 0 °C for 3 h, it was poured over ice and extracted with $CHCl_3$. The resulting organic layer was washed with water and dried over Na_2SO_4. After removal of the solvent under reduced pressure, the residue was purified by column chromatography on silica gel (hexane/ethyl acetate = 10/1) to yield **4a** (240 mg, 50%).

Yellow solid; Mp 133.5–134.5 °C; ^{1}H NMR ($CDCl_3$) δ 8.07 (s, 2H), 2.76 (t, 4H, J = 7.9 Hz), 1.62 (m, 4H), 1.45 (m, 4H), 0.97 (t, 6H, J = 7.3 Hz); MS (EI) *m/z* 484 (M^+); Anal. Calcd. for $C_{20}H_{20}Br_2O_2S_1$: C, 49.61; H, 4.16. Found: C, 49.89; H, 4.21.

4b: Compound **4b** was synthesized by following the procedure used for the preparation of **4a**, as a yellow solid with a yield of 74%. Mp 89–90 °C; ^{1}H NMR ($CDCl_3$) δ 8.06 (s, 2H), 2.74 (t, 4H, J = 7.9 Hz), 1.66 (m, 4H), 1.33 (m, 12H), 0.90 (t, 6H, J = 7.3 Hz); MS (EI) *m/z* 540 (M^+); Anal. Calcd. for $C_{24}H_{28}Br_2O_2S_1$: C, 53.35; H, 5.22. Found: C, 53.14; H, 5.08.

BC_4B: Compounds **4a** (58 mg, 0.12 mmol), **5** [22] (150 mg, 0.27 mmol), and tetrakis(triphenylphosphine)palladium(0) (25 mg, 0.02 mmol) were placed in a test tube; they were then dissolved in toluene (1 mL) and degassed with nitrogen. The resulting mixture was refluxed

for 15 h. After the removal of the solvent under reduced pressure, the residue was isolated by column chromatography on alumina ($CHCl_3$) to yield ketal-protected **BC_4B** (104 mg, 99%).

Yellow solid; Mp > 300 °C; ^1H NMR ($CDCl_3$) δ 8.06 (s, 2H), 7.66 (s, 2H), 4.30 (s, 16H), 2.75 (t, 4H, J = 7.9 Hz), 1.62 (m, 4H), 1.45 (m, 4H), 0.97 (t, 6H, J = 7.7 Hz); MS (EI) m/z 874 (M^+).

Ketal-protected **BC_4B** (104 mg, 0.12 mmol) was placed in a 50 mL round-bottomed flask and dissolved in THF (2 mL). Conc. H_2SO_4 (5 mL) was added to it, and the mixture was stirred at 60 °C for 12 h. The reaction mixture was poured over ice and extracted with ethyl acetate. The organic layer was washed with sat. $NaHCO_3$ aqueous solution and water and dried over Na_2SO_4. After the removal of the solvent under reduced pressure, the residue was first isolated by column chromatography on silica gel ($CHCl_3$), and then, the fraction containing **BC_4B** was further purified by GPC ($CHCl_3$) to obtain pure **BC_4B** (71 mg, 86%).

Yellow solid; Mp > 300 °C; ^1H NMR ($CDCl_3$) δ 8.08 (s, 2H), 8.05 (s, 2H), 2.80 (t, 4H, J = 7.9 Hz), 1.67 (m, 4H), 1.47 (m, 4H), 0.99 (t, 6H, J = 7.3 Hz); MS (EI) m/z 698 (M^+); Anal. Calcd. for $C_{34}H_{22}F_4O_6S_3$: C, 58.44; H, 3.17. Found: C, 58.72; H, 3.46.

BC_6B: Compound **BC_6B** was synthesized by following the procedure used for the preparation of **BC_4B**, as a yellow solid. Mp > 300 °C; ^1H NMR ($CDCl_3$) δ 8.08 (s, 2H), 8.05 (s, 2H), 2.79 (t, 4H, J = 7.9 Hz), 1.66 (m, 4H), 1.34 (m, 12H), 0.91 (t, 6H, J = 7.3 Hz); MS (EI) m/z 754 (M^+); Anal. Calcd. for $C_{38}H_{30}F_4O_6S_3$: C, 60.46; H, 4.01. Found: C, 60.42; H, 4.14.

2.3. Detailed device fabrication information

The field-effect mobility was measured using a thin-film field-effect transistor (FET) with bottom-contact geometry. A thermally grown silicon oxide (SiO_2) dielectric layer was formed on a gate substrate; this layer had a thickness of 300 nm and a capacitance of 10.0 nF cm^{-2}. An interdigital source and drain electrodes were constructed with gold (30 nm) that were formed on this SiO_2 layer. The channel width (W) and channel length (L) were 38 mm and 5 μm, respectively. The SiO_2 surface was washed with acetone and 2-propanol. It was then activated by ozone treatment and pretreated with octadecyltrichlorosilane (ODTS). The active layers were prepared by spin coating from 1.0 wt% chloroform solution at 1500 rpm for 1 min onto the substrate. Subsequently, the fabricated OFET devices were annealed at 200 °C for 30 min under a pressure of 10^{-3} Pa. Their current–voltage (I–V) characteristics were measured at room temperature under a pressure of 10^{-3} Pa or in air by using a KEITHLEY 4200 semiconductor parameter analyzer.

3. Calculation

All calculations were carried out using the Gaussian 03 program. The geometry of a model compound in which alkyl groups were replaced with methyl groups was optimized by the density functional theory (DFT) at the B3LYP/6-31G (d, p) level. As illustrated in Fig. 1, the highest occupied molecular orbital (HOMO) and LUMO are delocalized over the terthiophene-conjugated backbone. In addition, carbonyl groups are present in both the HOMO and LUMO, because of which these orbitals possess low-lying energy levels.

4. Results and discussion

The synthetic approach to our target compounds **BC_4B**, and **BC_6B** is depicted in Scheme 1. Friedel-Craft acylation of the corresponding 1,2-dialkylbenzene with 2,5-dibromo-3,4-thiophenedicarbonyl dichloride (**3**) in the presence of $AlCl_3$ yielded dioxo-substituted diboromothiophene **4a** or **4b** [24]. The ketal-protected counterpart **5** was synthesized by following the previously reported procedure [22]. The Stille coupling reaction of **4a** and **4b** with **5** and successive deprotection under acidic conditions afforded **BC_4B** and **BC_6B**, respectively, in moderate yields. The chemical structures of **BC_4B** and **BC_6B** were fully characterized by ^1H NMR, mass spectroscopy, and elemental analysis. As expected, these compounds were highly soluble in common organic solvents; therefore, they can be used to fabricate films by solution processing.

The data obtained from electronic absorption and electrochemical measurements provide important insights to ascertain the applicability of materials to organic electronic devices. As shown in Fig. 2a, the UV–vis absorption spectra of the oligomers in THF showed an absorption peak corresponding to the π–π^* transition band at 400–405 nm. Fig. 2b shows the results of CV carried out in fluorobenzene containing 0.1 M tetrabutylammonium hexafluorophosphate ($TBAPF_6$). **BC_4B** and **BC_6B** show three reversible reduction waves with first half-wave potentials of −0.98 and −0.99 V, respectively; they do not show any oxidation wave within the potential window (+1.50 V). These measurements clearly indicate that the difference between the alkyl groups has little influence on the photophysical and electrochemical properties of **BC_4B** and **BC_6B**. Thus, the LUMO energy level of −3.8 eV for our π-conjugated system was calculated from the half-wave reduction potential of ca. −1.0 V, assuming that the energy level of ferrocene/ferrocenium (Fc/Fc^+) was −4.8 eV below the vacuum level [25]. This experimental estimate is in good agreement with the calculated values.

The electron mobilities of **BC_4B** and **BC_6B** were investigated by fabricating OFETs with a bottom-contact configuration. These OFETs were fabricated on the gate electrode of a p-doped silicon substrate. Source and drain gold electrodes with a channel width/channel length (W/L) of 38 mm/5 μm were prepatterned on a layer of SiO_2 dielectric. A thin film (650 nm thick) of **BC_4B** or **BC_6B** as an active layer was spin-coated from chloroform solution (1.0 wt%) on ODTS- treated SiO_2 dielectric. The electrical characteristics of the OFETs were measured under a vacuum condition (10^{-3} Pa). The field-effect mobility (μ) was calculated in the saturation regime at V_{DS} of 80 V using the equation $I_{DS}^{sat} = W/(2L) \cdot C_i \mu^{sat} (V_{GS} - V_{th})^2$, where C_i denotes the capacitance of SiO_2, and V_{th} the threshold gate voltage. Optimization experiments exploring annealing temperatures

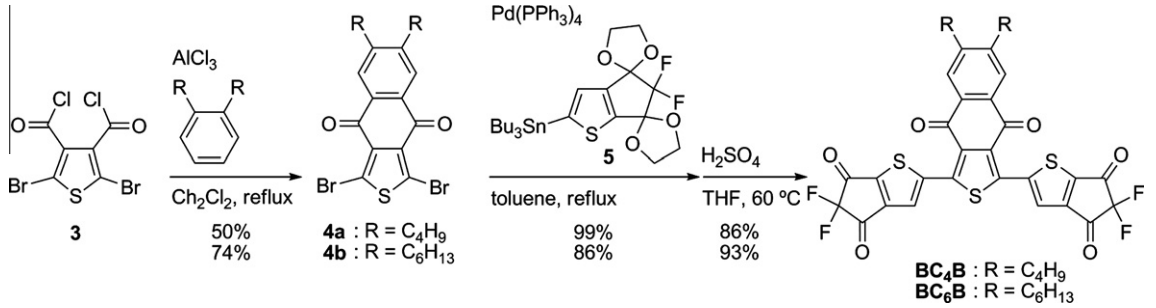

Scheme 1. Synthetic route of **BC_4B** and **BC_6B**.

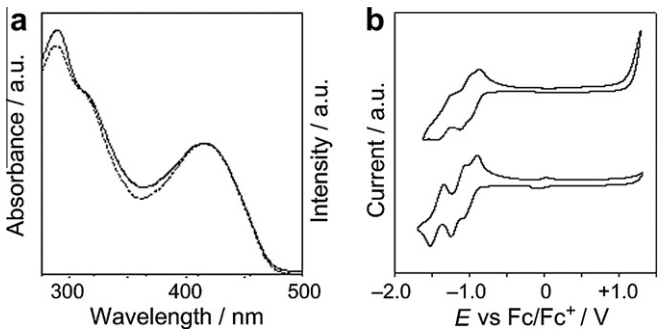

Fig. 2. (a) UV–vis spectra of **BC_4B** (dotted line) and **BC_6B** (solid line) in THF and (b) results of CVs of **BC_4B** (top) and **BC_6B** (bottom) in fluorobenzene containing 0.1 M $TBAPF_6$.

and surface treatments achieved a good electron mobility of 0.016 $cm^2 V^{-1} s^{-1}$. The extracted OFET parameters of the devices fabricated with **BC_4B** and **BC_6B** are summarized in Table 1, and the transfer and output characteristics of **BC_6B**-based device are shown in Fig. 3a and b, respectively. In order to investigate the stability of a **BC_6B** film under bias-stress conditions, we have also measured its source–drain current (I_{DS}) under continuous biases of gate voltage (V_{GS}) between −10 and 50 V with the source–drain voltage (V_{DS}) maintained constant at 50 V. As shown in Fig. 3c, the transfer characteristics exhibited a small degree of hysteresis even after 10 cycles under dual-sweep conditions, indi-

Table 1
n-Channel field-effect characteristics of **BC_4B** and **BC_6B** in vacuum and air.

Compound	Measurement conditions	μ ($cm^2 V^{-1} s^{-1}$)	I_{on}/I_{off}	V_{th} (V)
BC_4B	Under vacuum	0.016	10^7	15
BC_4B	In air	5.3×10^{-4}	10^5	19
BC_6B	Under vacuum	0.014	10^6	10
BC_6B	In air	1.4×10^{-4}	10^5	18

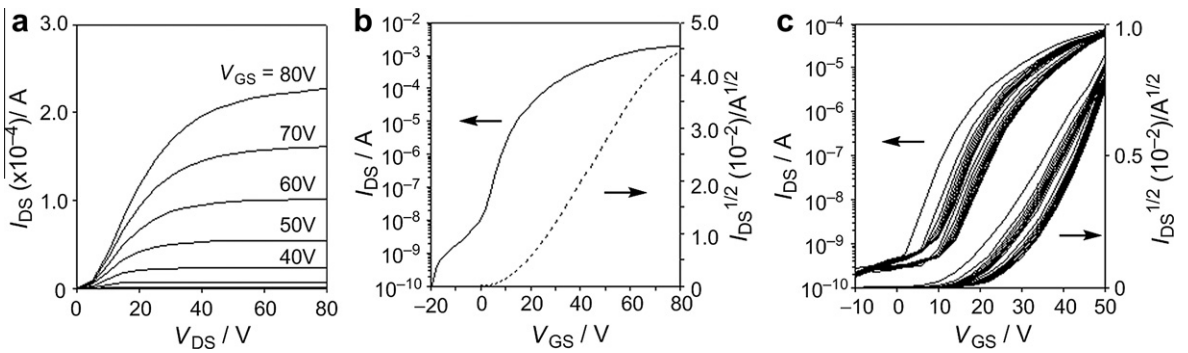

Fig. 3. (a) Output and (b) transfer characteristics of **BC_4B**-based OFET. (c) Transfer characteristics of **BC_4B**-based OFET with repeated biases for up to 10 cycles.

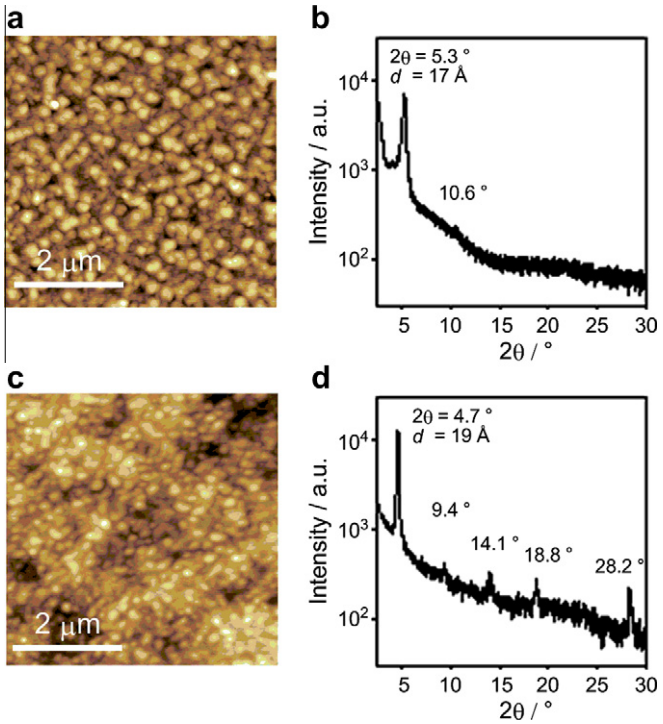

Fig. 4. (a) AFM images, (b) XRD data of a **BC_4B** film deposited on ODTS-modified SiO_2, (c) AFM images and (d) XRD data of a **BC_6B** film deposited on ODTS - modified SiO_2.

cating that this OFET possesses fair stability under switching operation. It is also important to note that **BC_4B-** and **BC_6B**-based OFETs can operate even after they are exposed to air for 1 h (Table 1). However, their performance was inferior to that obtained under vacuum conditions. This performance dependence on the operating conditions can be understood from the higher LUMO energy level (−3.8 eV) exceeding −4.0 eV, whose value is known to be on the borderline of gaining operational air stability [21,26,27].

In order to clarify the surface morphology and the alignment of molecules, AFM and XRD measurements have been performed on the **BC_4B** and **BC_6B** thin-films deposited on SiO_2 substrates. As shown in Fig. 4a and c, both the AFM images showed uniform deposition of the compounds over the SiO_2 surface with the formation of grains; segregation of the grains was not observed. XRD experiments revealed clear diffraction peaks (Fig. 4b and d), indicating that these molecules exhibited an ordered orientation in the solid state. These results clearly explain the formation of efficient electron-transporting pathways, which are responsible for improving the performance of the OFET.

5. Conclusion

In summary, n-type organic semiconductor materials comprising electronegative oligothiophenes have been successfully synthesized, and their electronic properties have been characterized. A combination of difluorodioxocyclopentene-annelated thiophene (**B**) and dialkyl-substituted naphtho[2,3-*c*]thiophene-4,9-dione (**C_4** and **C_6**) units ensured that an n-type OFET fabricated using the resulting terthiophene derivatives (**BC_4B** and **BC_6B**) not only exhibited solution processability but also good performance. An improvement in the performance of **BC_4B**- and **BC_6B**-based OFETs relative to that of the OFET fabricated using **2** can be rationalized on the basis of the low LUMO energy level and molecular ordering of these derivatives in the solid state. These results suggest that a sophisticated molecular design can pave a way for an improvement in the performance of OFETs.

Acknowledgements

This study was supported by the Industrial Technology Research Grant Program in 2008 from the New Energy and Industrial Technology Development Organization (NEDO) of Japan and a Grant-in-Aid for Scientific Research from the Ministry of Education, Culture, Sports, Science and Technology, Japan, and by cooperative research with Sumitomo Chemical Co., Ltd. We acknowledge Mr. Kazufumi Nishida for his assistance in the synthesis of **4**. Thanks are extended to the Elemental Analysis Section of Comprehensive Analysis Center (CAC) of the Institute of Scientific and Industrial Research (ISIR), Osaka University, for assistance in obtaining elemental analyses.

References

[1] J.E. Anthony, Chem. Rev. 106 (2006) 5028.
[2] A.R. Murphy, J.M.J. Fréchet, Chem. Rev. 107 (2007) 1066.
[3] K. Takimiya, Y. Kunugi, T. Otsubo, Chem. Lett. 36 (2007) 578.
[4] J.E. Anthony, Angew. Chem. Int. Ed. 47 (2008) 452.
[5] A. Mishra, C.-Q. Ma, P. Bäuerle, Chem. Rev. 109 (2009) 1141.

[6] V.C. Sunder, J. Zaumseil, V. Podzorov, E. Menard, R.L. Willett, T. Someya, M.E. Gershenson, J.A. Rogers, Science 303 (2004) 1644.
[7] A. Facchetti, Y. Deng, A. Wang, Y. Koide, H. Sirringhaus, T.J. Marks, R.H. Friend, Angew. Chem. Int. Ed. 39 (2000) 4547.
[8] A. Facchetti, M.-H. Yoon, C.L. Stern, G.R. Hutchison, M.A. Ratner, T.J. Marks, J. Am. Chem. Soc. 126 (2004) 13480.
[9] M.-H. Yoon, S.A. DiBenedetto, A. Facchetti, T.J. Marks, J. Am. Chem. Soc. 127 (2005) 1348.
[10] S. Ando, J.-I. Nishida, H. Tada, Y. Inoue, S. Tokito, Y. Yamashita, J. Am. Chem. Soc. 127 (2005) 5336.
[11] Y. Ie, M. Nitani, M. Karakawa, H. Tada, Y. Aso, Adv. Funct. Mater. 20 (2010) 907.
[12] H.E. Katz, A.J. Lovinger, J. Johnson, C. Kloc, T. Siegrist, W. Li, Y.-Y. Lin, A. Dodabalapur, Nature 404 (2000) 478.
[13] B.A. Jones, M.J. Ahrens, M.-H. Yoon, A. Facchetti, T.J. Marks, M.R. Wasielewski, Angew. Chem. Int. Ed. 43 (2004) 6363.
[14] B. Yoo, B.A. Jones, D. Basu, D. Fine, T. Jung, S. Mohapatra, A. Facchetti, K. Dimmler, M.R. Wasielewski, T.J. Marks, A. Dodabalapur, Adv. Mater. 19 (2007) 4028.
[15] X. Zhan, Z. Tan, B. Domercq, Z. An, X. Zhang, S. Barlow, Y. Li, D. Zhu, B. Kippelen, S.R. Marder, J. Am. Chem. Soc. 129 (2007) 7246.
[16] H. Yan, Y. Zheng, R. Blache, C. Newman, S. Lu, J. Woerle, A. Facchetti, Adv. Mater. 20 (2008) 3393.
[17] H. Yan, Z. Chen, Y. Zheng, C. Newman, J.R. Quinn, F. Dötz, M. Kastler, A. Facchetti, Nature 457 (2009) 679.
[18] Z. Chen, Y. Zheng, H. Yan, A. Facchetti, J. Am. Chem. Soc. 131 (2009) 8.
[19] S. Handa, E. Miyazaki, K. Takimiya, Y. Kunugi, J. Am. Chem. Soc. 129 (2007) 11684.
[20] H. Usta, A. Facchetti, T.J. Marks, J. Am. Chem. Soc. 130 (2008) 8580.
[21] H. Usta, C. Risko, Z. Wang, H. Huang, M.K. Deliomeroglu, A. Zhukhovitskiy, A. Facchetti, T.J. Marks, J. Am. Chem. Soc. 131 (2009) 5586.
[22] Y. Ie, Y. Umemoto, M. Okabe, T. Kusunoki, K.-I. Nakayama, Y.-J. Pu, J. Kido, H. Tada, Y. Aso, Org. Lett. 10 (2008) 833.
[23] Y. Ie, M. Okabe, Y. Umemoto, H. Tada, Y. Aso, Chem. Lett. 38 (2009) 460.
[24] Q.T. Zhang, J.M. Tour, J. Am. Chem. Soc. 120 (1998) 5355.
[25] A.J. Bard, L.R. Faulkner, Electrochemical Methods – Fundamentals and Applications, Wiley, New York, 1984.
[26] D.M. de Leeuw, M.M.J. Simenon, A.R. Brown, R.E.F. Einerhand, Synth. Met. 87 (1997) 53.
[27] T.D. Anthopoulos, G.C. Anyfantis, G.C. Papavassiliou, D.M. de Leeuw, Appl. Phys. Lett. 90 (2007) 122105.

Organic Electronics 11 (2010) 1746–1752

Contents lists available at ScienceDirect

Organic Electronics

journal homepage: www.elsevier.com/locate/orgel

Nonvolatile memory transistors using solution-processed zinc–tin oxide and ferroelectric poly(vinylidene fluoride-trifluoroethylene)

Sung-Min Yoon [a,b,*], Soon-Won Jung [a], Shin-Hyuk Yang [a], Chun-Won Byun [a], Chi-Sun Hwang [a], Sang-Hee Ko Park [a], Hiroshi Ishiwara [b,c]

[a] Convergence Components & Material Research Laboratory, Electronics and Telecommunications Research Institute, 138 Gajeong-no, Yuseong-gu, Daejeon 305-700, Republic of Korea
[b] Tokyo Institute of Technology, 4259, Nagatsuta, Midori-ku, Yokohama 226-8502, Japan
[c] Department of Physics, Konkuk University, 1 Hwayang-dong, Gwangin-gu, Seoul 143-701, Republic of Korea

ARTICLE INFO

Article history:
Received 24 April 2010
Received in revised form 1 June 2010
Accepted 6 August 2010
Available online 20 August 2010

Keywords:
Nonvolatile memory transistor
Oxide semiconductor
P(VDF-TrFE)
Solution process
Zn–Sn-O

ABSTRACT

The nonvolatile memory thin-film transistor (MTFT) using a solution-processed zinc–tin oxide (ZTO) semiconducting channel and a poly(vinylidene fluoride-trifluoroethylene) ferroelectric gate insulator was proposed. The crystalline phases of spin-coated ZTO films were essentially amorphous even when the films were annealed at 500 °C and the surface morphology was very smooth and uniform. Although the memory behaviors based on the ferroelectric field-effect were confirmed for all the fabricated MTFTs, the field-effect mobility, memory window, and the *on*/*off* ratio were markedly varied with the changes in annealing temperature and film composition of the ZTO channel. The origins for these differences were examined from the changes in electrical conductivities during the thermal process. The best device performances could be obtained for the MTFT using the 50/50 mol% ZTO channel annealed at 500 °C. The memory window at V_G sweep of ±15 V, field-effect mobility, subthreshold swing, and *on*/*off* ratio were obtained to be approximately 8.1 V, 15.8 $cm^2 V^{-1} s^{-1}$, 1.1 V/dec, and 6.4×10^7, respectively.

© 2010 Elsevier B.V. All rights reserved.

1. Introduction

Thin-film transistors (TFTs) using oxide semiconductors as active channel layers have attracted huge interest for use in the active matrix (AM) backplane of liquid–crystal display (LCD) [1] or organic light-emitting diode (OLED) display [2]. These technology trends are closely related to the fact that the oxide semiconductors with specified electronic configuration offer such features as high mobility, excellent uniformity, and robust stability, compared with the conventional TFTs using polycrystalline and amorphous Si. Requirements for flat-panel display with a larger size and a higher quality would accelerate the demand for the oxide TFTs. Although so many researches have not yet been reported [3–5], nonvolatile memory device application is also one of the most promising novel approaches employing the oxide TFT. The embeddable nonvolatile memory device having characteristics of mechanical flexibility and/or transparency to the visible light can provide us very interesting applications such as a lower-power display panel [6] and memory-embedded sensor sheet [7]. In enhancing the practical functionality of the next generation large-area electronics, this type of memory TFT (MTFT) can be an essential component, which can be realized by using the oxide TFT. Fully transparent nonvolatile memory transistors [8] and two-transistor-type memory cell composed of one access oxide TFT and one memory TFT [9] are good examples. In these approaches, the use of a ferroelectric copolymer as a gate insulator is desirable in the viewpoint of low-temperature process,

* Corresponding author at: Convergence Components & Material Research Laboratory, Electronics and Telecommunications Research Institute, 138 Gajeong-no, Yuseong-gu, Daejeon 305-700, Republic of Korea. Tel.: +82 42 860 6293; fax: +82 42 860 5202.
E-mail address: sungmin@etri.re.kr (S.-M. Yoon).

1566-1199/$ - see front matter © 2010 Elsevier B.V. All rights reserved.
doi:10.1016/j.orgel.2010.08.002

because typical oxide ferroelectric material such as $Pb(Zr,Ti)O_3$ and $SrBi_2Ta_2O_7$ need a high temperature of more than 600 °C for their crystallization.

Solution-based process is an alternative powerful process for the large-area electronics, because it provides simpler process, lower cost, and higher throughput, compared with the vacuum-deposition-based process. A ferroelectric copolymer of poly(vinylidene fluoride-trifluoroethylene) [P(VDF-TrFE)], which has been typically employed for the memory application [10–12], can be simply formed by spin-coating method using precursor solution. As for the solution-processed oxide semiconductors, successful demonstrations were also reported for various materials of ZnO [13,14], indium–gallium–zinc oxide (IGZO) [15,16], indium–zinc oxide (IZO) [17,18], and aluminum–indium oxide (AIO) [19]. We have presented the device characteristics of the top-gate MTFT with P(VDF-TrFE)/IZO structure prepared by using the solution process [20]. Although the role of In is very important in order to achieve high field-effect mobility of the TFT, the use of In-free zinc–tin oxide (ZTO) is more preferable in viewpoints of resource shortage and eco-friendliness. ZTO has also been employed for the oxide TFT using vacuum-deposition [21–25] or solution-based processes [26–29] so far.

In this work, for the organic–inorganic hybrid-type MTFT application, solution-processed ZTO was chosen as a semiconducting active channel for the first time. The effects of the channel composition and process temperature on the memory and transistor behaviors were investigated for the fabricated MTFTs.

2. Experimental details

ZTO precursor solution was prepared by diluting and blending the commercial metal–organic solutions of 2.0 M ZnO and 0.5 M SnO_2 (SYM-ZN20 and SYM-SN05, Kojundo Chemical Lab. Co.). Firstly, each solution was diluted with n-butyl acetate [$CH_3COO(CH_2)_3CH_3$, CAS No. 123-86-4] to be 0.2 M, which was adjusted by considering the solution viscosity and the wettability on the substrate. Two final solutions with different molar ratios (Zn/Sn) of 83/17 and 50/50 were prepared by blending the previous diluted solutions. Dilution and blending processes were performed at 60 °C with stirring for more than 1 h. The solutions were filtered through a 0.45 μm syringe filter (cellulose) and then spin-coated on the substrates at 2500 rpm for 20 s. The thicknesses for the blended solutions with 83/17 and 50/50 molar ratios were obtained to be approximately 10 and 22 nm by one coating process, respectively. The thickness variation with the solution composition resulted from the viscosity difference between the initial solutions. The crystal structures of prepared films were investigated by using X-ray diffraction (XRD, Rigaku RU-200BH). The diffraction patterns were measured with Cu Kα radiation (40 kV/60 mA) at a scan rate of 2°/min. The surface morphology and roughness were examined by scanning electron microscopy (SEM) and atomic force microscopy (AFM), respectively. The sheet resistances of the prepared films were evaluated by the four-point probe method, which were measured with the temperature change in the range from room temperature (RT) to 400 °C.

The solution-processed MTFTs were fabricated using following procedures. Indium–tin oxide (ITO, 150 nm)-coated glass was prepared as a substrate. The ITO layer was patterned into the source/drain (S/D) electrodes using wet etchant. ZTO active layers with two molar ratios (83/17 and 50/50) were deposited by spin-coating method using the previously prepared precursor solutions onto the S/D patterned substrates. The coating processes were repeated twice with the interval of drying process at 250 °C for 10 m. After the ZTO channel regions were defined, thermal treatments were carried out in an oxygen ambient for 1 h, in which the annealing temperatures were varied to 400 and 500 °C in order to examine the temperature dependence for the solution-processed ZTO channels. P(VDF-TrFE) ferroelectric gate insulator was also deposited by spin-coating method using a 3 wt% diluted solution of P(VDF-TrFE) (70/30 mol%, Solvay Solexis) in methyl-ethyl-ketone (MEK). The coated film was crystallized at 140 °C for 1 h in an air ambient. The film thickness of P(DVF-TrFE) was approximately 200 nm. Then, the S/D contacts were opened by removing the given areas of P(VDF-TrFE) layer by using O_2 plasma with a reactive ion etching system (Samco RIE-10NL). The gate electrodes and S/D pads were finally formed by the deposition and patterning of Al film. The metal–ferroelectric–metal capacitors with the structures of Al/P(VDF-TrFE)/ITO were also fabricated through this series of fabrication process. The device properties of all fabricated MTFTs were characterized by using a semiconductor parameter analyzer (Agilent 4156 C). The ferroelectric behaviors of the P(VDF-TrFE) capacitor were examined by a ferroelectric capacitor evaluation system (FCE, Toyo Technica). All measurements were carried at RT in a dark box.

3. Results and discussions

3.1. Properties of solution-processed ZTO thin films

Fig. 1 shows the crystal structures of the prepared ZTO films and their variations with the changes in film composition and annealing temperature. In these evaluations, the film thickness of each film was intentionally increased to more than 100 nm to clearly compare the crystallinity and difference between the samples treated at different annealing temperatures. Feasible peaks for the ZTO can be referred from Joint Committee for Powder Diffraction Standards (JCPDS) File No. 24-1470, such as Zn_2SnO_4 (311) at $2\theta = 34.3°$, (400) at $2\theta = 41.7°$, (222) at $2\theta = 35.9°$, and (220) at $2\theta = 29.1°$. Any distinct peak was not detected over the range of annealing temperature from 250 to 500 °C for the ZTO films with 83/17 (Fig. 1(a)) and 50/50 mol% (Fig. 1(b)). Other phases corresponding to the $ZnSnO_3$ (JCPDS File No. 11-0274), ZnO (JCPDS File No. 36-1451), and SnO_2 (JCPDS File No. 41-1445) were also not detected. Although a tiny and broad peak of approximately 34°, which was observed for the 50/50 mol% film annealed at 400 or 500 °C, appeared, the obtained XRD patterns indicate that the solution-processed ZTO films are basically

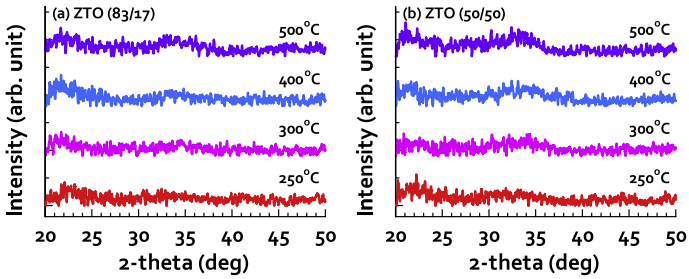

Fig. 1. X-ray diffraction patterns for the ZTO films with different molar ratios (Zn/Sn) of (a) 83/17 and (b) 50/50 at different annealing temperatures of 250, 300, 400, and 500 °C.

amorphous phases, which is consistent with the previous reports [21,27,28].

Fig. 2(a) and (b) shows top-view SEM images of the spin-coated 400 °C-annealed ZTO films with two compositions. The root-mean-square (rms) roughness was also evaluated by AFM, as shown in Fig. 2(c) and (d). The rms roughnesses were estimated to be approximately 0.39 and 0.44 nm for the ZTO films with 83/17 and 50/50 mol%, respectively. It was also found that the surface roughness was not degraded even after the 400 °C-annealing process. These results reveal that the ZTO films have very smooth and homogenous surface and shows no crystalline grains, which is in agreement with XRD results.

3.2. Device characterizations of memory TFT

Prior to the characterization of the fabricated MTFTs, the basic ferroelectric properties of the Al/P(VDF-TrFE)/ITO capacitors were confirmed, as shown in Fig. 3. Top electrode size was defined to be $50 \times 50\ \mu m^2$, which was comparable to the gate area of the memory transistors, by conventional patterning process performed on the P(VDF-TrFE) films. The remnant polarization (P_r) and coercive field (E_c) were typically measured to be approximately 9.6 $\mu C/cm^2$ and 930 kV/cm, respectively, at the frequency of 1 kHz. This result suggest that the prepared P(VDF-TrFE) thin film showed sufficiently good ferroelectric natures even when the ITO bottom electrode was employed and

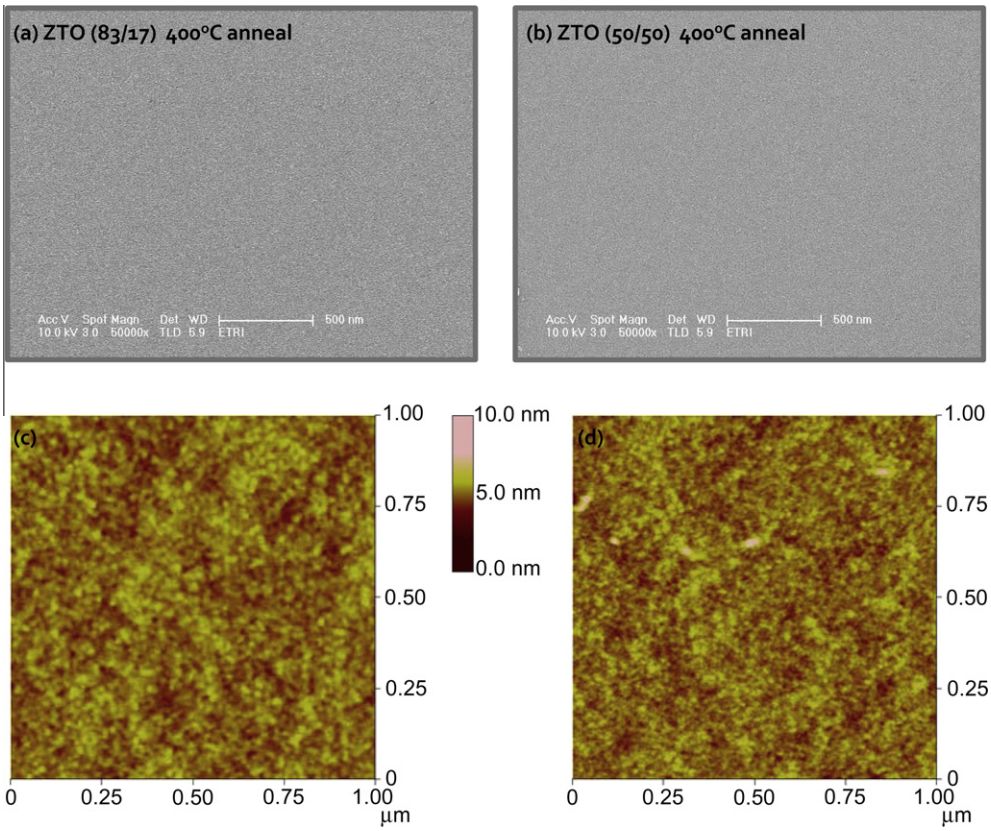

Fig. 2. SEM and AFM images of surface morphologies for the 400 °C-annealed (a), (c) 83/17 mol% and (b), (d) 50/50 mol% ZTO films, respectively. The rms values were evaluated by AFM images.

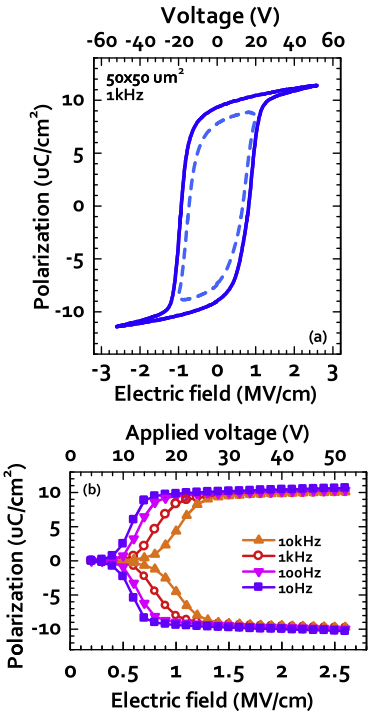

Fig. 3. (a) *P*—*E* characteristics of the Al/P(VDF-TrFE)/ITO capacitor with size of 50×50 μm^2, which was fabricated with the MTFTs on the same substrate. The measurement frequency was set to be 1 kHz. The solid and dotted curves correspond to the *P*—*E* hysteresis obtained at the electric field of 2.6 and 1.0 MV/cm, respectively. (b) Polarization saturation behavior with the increase of applied electric field at various measurement frequencies from 10 Hz to 10 kHz.

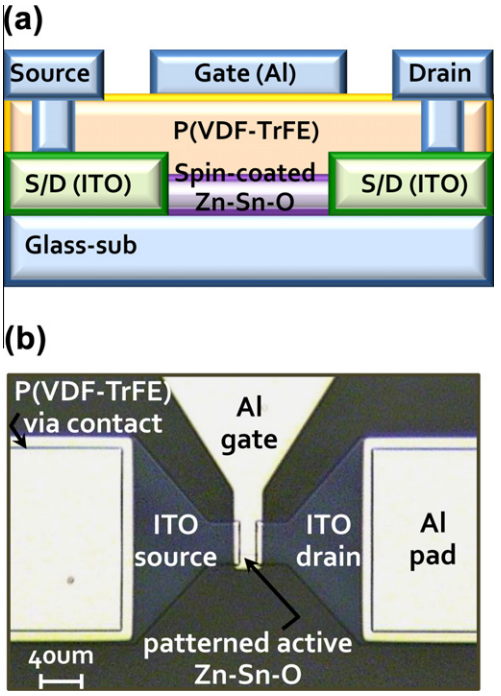

Fig. 4. (a) Schematic cross-sectional diagram and (b) photograph of the top-gate MTFT composed of the solution-processed ZTO active channel and the P(VDF-TrFE) gate insulator, respectively.

patterning process was conducted. It is also interesting to investigate the polarization saturation behavior with the increase of the electric field applied across the ferroelectric film, which provides useful criteria for determining the operation conditions of the MTFT. The electric field required to obtain the full saturation in the ferroelectric polarization decreased with the decrease in signal frequency. It means that the memory behaviors of the proposed MTFT may be sensitively influenced by the duration of programming voltage signals as well as the voltage amplitude [30–34]. The detailed discussions were described in another publication [35].

A cross-sectional schematic diagram and an optical microscope image of the fabricated solution-processed MTFTs using the ZTO channels were shown in Fig. 4(a) and (b), respectively. Fig. 5(a) and (b) shows the drain current (I_D)-gate voltage (V_G) characteristics of the MTFT employing the ZTO channel with 83/17 and 50/50 molar ratios, respectively, when the annealing temperature for the ZTO film was varied to 400 and 500 °C. Each transfer curve was measured in a double sweep mode of V_G (−15 to 15 V) at the drain voltage (V_D) of 5.0 V. The gate width (W) and length (L) of measured devices were 40 and 20 μm, respectively. Although the ferroelectric field-effect-driven counterclockwise hystereses in forward and reverse sweep of V_G were obtained for all devices, there are remarkable differences in device behaviors with the variations in channel composition and annealing temperature. The typical device characteristics such as threshold voltage (V_T), channel field-effect mobility (μ_{FE}), subthreshold swing (SS), and *on*/*off* ratio were summarized in Table 1. For the case of the MTFT using 83/17 mol% ZTO channel, the current drivability was absolutely insufficient. As results, the μ_{FE} and *on*/*off* ratio were no more than 0.02 $cm^2\ V^{-1}\ s^{-1}$ and 1.4×10^5, respectively, even when the annealing temperature increased to 500 °C. The Sn composition was increased to 50 mol% with all, the μ_{FE}, SS, and *on*/*off* ratio were at a standstill for the 400 °C-annealed ZTO channel. Dramatic improvement in TFT performances could be obtained for the 50/50 mol% ZTO channel annealed at 500 °C, that is, the μ_{FE} and *on*/*off* ratio were markedly enhanced to be 15.8 $cm^2\ V^{-1}\ s^{-1}$ and 6.4×10^7, respectively. It was also very inspiring that the *off* current was remained to be as low as 10^{-12} A.

Besides the TFT performances, there was an impressive variation in memory window (MW), which is defined as voltage width of turn-on voltage shift in transfer curve, among the evaluated controlled devices, as shown in Fig. 5(c). When the V_G sweep range was varied from ±10 to ±20 V, the MW for the MTFT using 83/17 mol% ZTO channel annealed at 400 °C increased from 2.4 to 5.9 V. On the contrary, for the MTFT using 50/50 mol% ZTO channel annealed at 500 °C, much larger value of MW was obtained to be in the range from 5.6 to 10.6 V. Because the E_c was estimated to be approximately 690 kV/cm at the applied voltage of ±20 V (dotted line in Fig. 3(a)), the MW was expected to be more than 25 V. However, this estimation cannot be generally applicable in the real

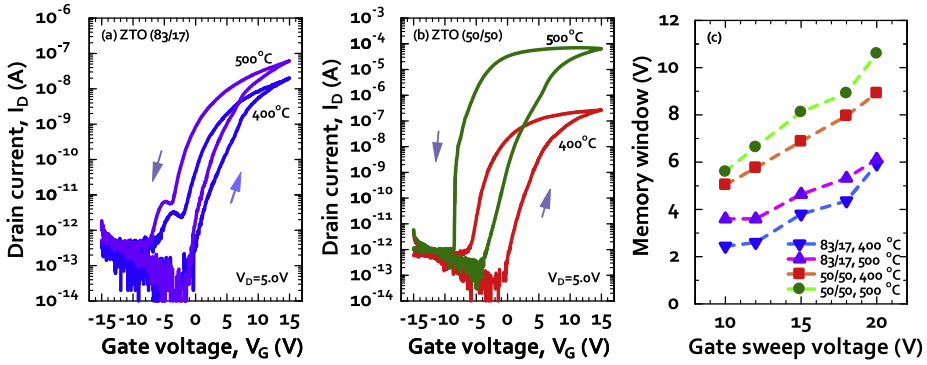

Fig. 5. I_D–V_G characteristics of the fabricated MTFT using the (a) 83/17 mol% and (b) 50/50 mol% ZTO channels. The annealing temperature for the ZTO channels were varied to 400 and 500 °C. All measurements were performed in a double sweep mode of V_G in the range of ±15 V at the V_D of 5.0 V. Arrows indicated in the plots represent the direction of hysteresis in I_D. (c) Variation of memory window for each MTFT when the sweep range of V_G was varied from ±10 to ±20 V.

Table 1
Summary of main process parameters and device characteristics of the fabricated MTFTs using the solution-processed ferroelectric P(VDF-TrFE) gate insulator and ZTO active channel.

Composition (Zn/Sn, mol%)	Annealing temp. (°C)	Threshold voltage (V)	Field-effect mobility (cm^2/V s)	S-Swing (V/dec)	Memory window (15 V) (V)	On/off ratio
83/17	400	4.7	0.007	2.85	3.8	4.3×10^4
	500	4.0	0.02	1.81	4.6	1.4×10^5
50/50	400	3.9	0.07	1.46	6.9	3.8×10^5
	500	4.0	15.8	1.07	8.1	6.4×10^7

situation. We have to remind couple of important issues for the device operation of the proposed ferroelectric-driven MTFTs. The first investigation is related to the fact that the oxide channel layer is fully or partially depleted at the negative V_G region (at *off* operation). Once the depletion layer is formed within in the channel, it remains an insulating layer at the *off* state, because the inversion carriers cannot be formed easily for the oxide semiconductor such as ZTO unlike the case of Si. Therefore, the voltage applied to the gate stack is distributed with the capacitance coupling. This feature of oxide semiconductor channel results in the second consideration. Considering that this MTFT operates in accumulation/depletion mode, it would be very difficult to establish the condition to fully compensate for the ferroelectric polarization charge at the ferroelectric/semiconductor interface. Moreover, because the film thickness of channel layer for this application is generally in the range of several nano-meters, only a small charge density is induced at the surface of semiconducting channel even for the accumulation state. Assuming that the carrier concentration (N_D) of the 40-nm thick ZTO film is $10^{18}/cm^2$, the induced semiconductor charge (qN_Dd, where d is semiconductor channel thickness) is roughly estimated to be approximately 0.6 μC/cm^2, which is much smaller than the ferroelectric P_r. Therefore, the channel thickness [5] and initial carrier concentration of the oxide channel layer have an important effect on the memory margin, which is expressed as the MW and memory *on*/*off* ratio. Actually, the variations in MW obtained for each device were observed to be sensitively affected by the differences of the ZTO channel conductance (Fig. 5(c)). Eventually, it was found that the solution-processed 83/17 mol% ZTO channels were not so suitable for a memory device as well as for a conventional TFT because of their too low carrier concentration and field-effect mobility.

In order to examine the differences in channel conductance and conduction mechanism of solution-processed ZTO channels with different film compositions, the variation in electrical conductivity (σ_c) was measured at the forward and reverse sweeps in temperature, as shown in Fig. 6. The ramping rate was set to be 5 °C/min. The σ_c typically increased and decreased with the increase and decrease of temperature, respectively, in the range from 250 to 400 °C. This reveals that the semiconducting behaviors of the prepared ZTO films appeared in this temperature range. However, obvious differences were observed with the changes in film composition, such as the activation energies of *in-situ* σ_c during the ramp-up ($E_{a,up}$) and ramp-down ($E_{a,down}$) periods, the value of σ_c at 400 °C, and the final σ_c after the ramp-down process. When the temperature approached to 400 °C, the σ_c's of 83/17 and 50/50 mol% ZTO films were approximately 1.4×10^{-5} and 7.3×10^{-5} S/cm, respectively. Although we could not increase the temperature up to 500 °C owing to the temperature limit of the measurement system, the σ_c difference between the films was expected to be much larger at 500 °C. It is also noticeable for the 50/50 mol% ZTO film that there was a significant variation between the $E_{a,up}$ and $E_{a,down}$ of *in-situ* σ_c, and that two distinct temperature region representing different values of $E_{a,up}$ ($E_{a,up1}$ and $E_{a,up2}$) were observed at

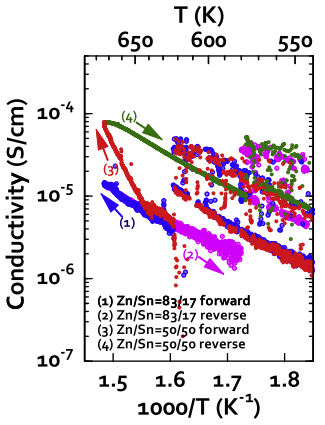

Fig. 6. Variation of electrical conductivity for the ZTO film with 83/17 and 50/50 mol% in terms of Arrhenius plot, which was *in-situ* measured for the forward and reverse directions in temperature from RT to 400 °C. The ramping rate was 5 °C/min. The data points of (1) in blue, (2) in pink, (3) in red, and (4) in green correspond to the forward and reverse sweeps for the 83/17 mol% and those for the 50/50 mol% ZTO film, respectively. (For interpretation of the references to color in this figure legend, the reader is referred to the web version of this article.)

the vicinity of 370 °C. The values of $E_{a,up}$ and $E_{a,down}$ for each film were summarized in Table 2. For the case of 83/17 mol% ZTO film, the $E_{a,up}$ and $E_{a,down}$ were calculated to be similar values of 0.87 and 0.82 eV, respectively. While the $E_{a,up1}$ and $E_{a,down}$ for the 50/50 mol% ZTO film was also in the range from 0.80 to 0.77 eV, the $E_{a,up2}$ abruptly increased to 2.23 eV above the temperature of 370 °C. These results suggest some important insights related to the effect of annealing temperature and corresponding electrical behaviors of ZTO channel layers. The observed activation energies of lower than 1 eV can be mainly explained by the simple thermal excitation of the electrons in the semiconducting films [36], in which the conduction mechanism activated below the given critical temperature range was not so varied with the Zn/Sn compositions. On the contrary, the larger $E_{a,up2}$ values observed at higher temperature region for the 50/50 mol% ZTO film may result from the additionally generated free electrons. Consequently, the σ_c could be modulated by controlling the annealing temperature and film composition. The electronic configuration and effective density of states, which are intrinsically varied with the Zn/Sn molar ratio, have a critical impact on the semiconducting behaviors of the solution-processed ZTO films. Once free carriers are activated by the appropriate thermal treatment, they work even when the temperature was reversed to RT. The $E_{a,down}$ observed for the 50/50 mol% ZTO film well reflects this investigation. The second scenario is closely related to the fact that the H_2 and/or H_2O-based species incorporated in the ZTO films diffused out at high temperature. This process generates ionized oxygen vacancies and free electrons doped into the film [36]. These phenomena can be accelerated by the increase in Sn composition within the ZTO film.

Table 2
Summary of activation energies of *in-situ* electrical conductivity with the forward ($E_{a,up}$) and reverse ($E_{a,down}$) sweeps in temperature, which were calculated by Arrhenius plots for the solution-processed ZTO films with different compositions of 83/17 and 50/50 mol%.

	Zn/Sn (83/17)	Zn/Sn (50/50)
$E_{a,up1}$ (eV)	0.87	0.80
$E_{a,up2}$ (eV)	–	2.23
$E_{a,down}$ (eV)	0.82	0.77

As results, we can conclude that the most desirable behaviors for the proposed MTFT could be obtained when the ZTO channel composition was controlled to be 50/50 mol% and the annealing process was performed at 500 °C. In most previous literatures, the conventional oxide TFTs using the solution-processed ZTO channel were fabricated with the bottom gate structure, in which the μ_{FE} was reported to be in the range from 0.7 to 14 $cm^2\ V^{-1}\ s^{-1}$ at the annealing temperature of 500 °C [27–29]. The TFT *on/off* ratios of those devices were approximately from 10^7 to 10^8. Although a larger μ_{FE} of 16 $cm^2\ V^{-1}\ s^{-1}$ was obtained for the ZTO channel annealed at 600 °C, the *on/off* ratio was degraded to 10^5 owing to the marked increase of *off* current level (10^{-8}) [26]. Besides, the process temperatures of higher than 500 °C cannot be conventionally applicable for the large-area electronics employing low-cost glass substrates. From these investigations, we can say that the TFT performances obtained in this work were sufficiently good compared with those for the previously reported devices using the solution process for the ZTO channel layer.

4. Conclusions

The nonvolatile memory TFT using a solution-processed ZTO channel and a ferroelectric P(VDF-TrFE) gate insulator was fabricated for the first time. The spin-coated ZTO films were essentially amorphous phase and their surfaces were very smooth. The electrical natures of the ZTO films were found to be sensitively affected by the film composition and/or annealing temperature. Although all MTFTs exhibited ferroelectric field-effect-driven memory window in their I_D–V_G characteristics, there were marked variations in device performances. While the film composition of Zn-rich phase and the annealing temperature of lower than 500 °C were not so desirable in realizing the proposed MTFT with good performances, the excellent device characteristics of the MTFT were successfully confirmed when the 50/50 mol% ZTO channel was treated at 500 °C. The memory window at V_G sweep of ±15 V, μ_{FE}, SS, and *on/off* ratio were approximately 8.1 V, 15.8 $cm^2\ V^{-1}\ s^{-1}$, 1.1 V/dec, and 6.4×10^7, respectively. It is also inspiring that the *off* current could be suppressed as low as 10^{-12} A. A relatively high thermal budget is one of the issues to be considered as future works. We conclude that the electrical properties of the ZTO film could be improved by controlling the process conditions, and that the solution-processed amorphous ZTO film is very promising as a semiconducting channel for our proposed memory device using organic ferroelectric GI. These embeddable memory transistors fabricated via simple solution process could enhance the functionality of next-generation large-electronic devices and systems.

Acknowledgement

This work was supported by the Industrial Strategic Technology Development program [Project No. 10035225, Development of Core Technology for High Performance AMOLED on Plastic] funded by MKE/KEIT.

References

[1] T. Osada, K. Akimoto, T. Sato, M. Ikeda, M. Tsubuku, J. Sakata, J. Koyama, T. Serikawa, S. Yamazaki, Jpn. J. Appl. Phys. 49 (2010) 03CC02.
[2] J.S. Park, T.W. Kim, D. Stryakhilev, J.S. Lee, S.G. An, Y.S. Pyo, D.B. Lee, Y.G. Mo, D.U. Jin, H.K. Chung, Appl. Phys. Lett. 95 (2007) 013503.
[3] S.H. Noh, W. Choi, M.S. Oh, D.K. Hwang, K. Lee, S. Im, S. Jang, E. Kim, Appl. Phys. Lett. 90 (2007) 253504.
[4] K.H. Lee, G. Lee, K. Lee, M.S. Oh, S. Im, S.M. Yoon, Adv. Mater. 21 (2009) 4287.
[5] S.M. Yoon, S. Yang, S.H. Ko Park, S.W. Jung, C.W. Byun, D.H. Cho, S.Y. Kang, C.S. Hwang, B.G. Yu, J. Phys. D 42 (2009) 245101.
[6] N. Ueda, Y. Ogawa, K. Tanaka, K. Yamamoto, Y. Yamauchi, Dig. Tech. Papers SID 2010, p. 615.
[7] T. Sekitani, T. Yukota, U. Zschieschang, H. Klauk, S. Bauer, K. Takeuchi, M. Takamiya, T. Sakurai, T. Someya, Science 326 (2009) 1516.
[8] S.M. Yoon, S. Yang, C. Byun, S.H. Ko Park, D.H. Cho, S.W. Jung, O.S. Kwon, C.S. Hwang, Adv. Funct. Mater. 20 (2010) 921.
[9] S.M. Yoon, C.W. Byun, S. Yang, S.H. Ko Park, D.H. Cho, S.W. Jung, S.Y. Kang, C.S. Hwang, IEEE Electron Device Lett. 31 (2010) 138.
[10] T. Sekitani, K. Zaitsu, Y. Noguchi, K. Ishibe, M. Takamiya, T. Sakurai, T. Someya, IEEE Trans. Electron Device 56 (2009) 1027.
[11] R.C.G. Naber, C. Tanase, P.W.M. Blom, G.H. Gelinck, A.W. Marsman, F.J. Touwslager, S. Setayesh, D.M. de Leeuw, Nat. Mater. 4 (2005) 243.
[12] S.J. Kang, I. Bae, Y.J. Park, T.H. Park, J. Sung, S.C. Yoon, K.H. Kim, D.H. Choi, C. Park, Adv. Funct. Mater. 19 (2009) 1609.
[13] C.S. Li, Y.N. Li, Y.L. Wu, B.S. Ong, R.O. Loutfy, J. Phys. D: Appl. Phys. 41 (2008) 125102.
[14] C. Yang, K. Hong, J. Jang, D.S. Chung, T.K. An, W.S. Choi, C.E. Park, Nanotechnology 20 (2009) 465201.
[15] G.H. Kim, H.S. Shin, B.D. Ahn, K.H. Kim, W.J. Park, H.J. Kim, J. Electrochem. Soc. 156 (2009) H7.
[16] J.H. Lim, J.H. Shim, J.H. Choi, J. Joo, K. Park, H. Jeon, M.R. Moon, D. Jung, H. Kim, H.J. Lee, Appl. Phys. Lett. 95 (2009) 012108.
[17] D.H. Lee, Y.J. Chang, G.S. Herman, C.H. Chang, Adv. Mater. 19 (2007) 843.
[18] C.G. Choi, S.J. Seo, B.S. Bae, Electrochem. Solid State Lett. 11 (2008) H7.
[19] Y.H. Hwang, J.H. Jeon, S.J. Seo, B.S. Bae, Electrochem. Solid State Lett. 12 (2009) H336.
[20] S.M. Yoon, S.H. Yang, S.W. Jung, C.W. Byun, S.H. Ko Park, C.S. Hwang, H. Ishiwara, Electrochem. Solid State Lett. 13 (2010) H141.
[21] H.Q. Chiang, J.F. Wager, R.L. Hoffman, J. Jeong, D.A. Keszler, Appl. Phys. Lett. 86 (2005) 013503.
[22] W.B. Jackson, R.L. Hoffman, G.S. Herman, Appl. Phys. Lett. 87 (2005) 193503.
[23] R.L. Hoffman, Solid State Electrochem. 86 (2005) 013503.
[24] P. Görrn, M. Sander, J. Meyer, M. Kröger, E. Becker, H.H. Johannes, W. Kowalsky, T. Riedl, Adv. Mater. 18 (2007) 738.
[25] P. Görrn, P. Hölzer, T. Riedl, W. Kowalsky, J. Wang, T. Weimann, P. Hinze, S. Kipp, Appl. Phys. Lett. 90 (2007) 063502.
[26] Y.J. Chang, D.H. Lee, G.S. Herman, C.H. Chang, Electrochem. Solid State Lett. 10 (2007) H135.
[27] S.K. Park, Y.H. Kim, H.S. Kim, J.I. Han, Electrochem. Solid State Lett. 12 (2009) H256.
[28] S.J. Seo, C.G. Choi, Y.H. Hwang, B.S. Bae, J. Phys. D 42 (2009) 035106.
[29] Y. Jeong, K. Song, D. Kim, C.Y. Koo, J. Moon, J. Electrochem. Soc. 156 (2009) H808.
[30] T. Nakajima, R. Abe, Y. Takahashi, T. Furukawa, Jpn. J. Appl. Phys. 44 (2005) L1385.
[31] R. Gysel, I. Stolichnov, A.K. Tagantsev, N. Setter, P. Mokry, J. Appl. Phys. 103 (2008) 084120.
[32] T. Furukawa, T. Nakajima, Y. Takahashi, IEEE Trans. Dielectr. Electr. Insulat. 13 (2006) 1120.
[33] T. Furukawa, S. Kanai, A. Okada, Y. Takahashi, R. Yamamoto, J. Appl. Phys. 105 (2009) 061636.
[34] R.V. Gaynutdinov, O.A. Lysova, S.G. Yudin, A.L. Tolstikhina, A.L. Kholkin, V.M. Fridkin, S. Ducharme, Appl. Phys. Lett. 95 (2009) 023303.
[35] S.M. Yoon, S.H. Yang, C.W. Byun, S.H. Ko Park, S.W. Jung, D.H. Cho, S.Y. Kang, C.S. Hwang, H. Ishiwara, Jpn. J. Appl. Phys. 49 (2005) 04DJ06.
[36] K. Nomura, T. Kamiya, H. Ohta, M. Hirano, H. Hosono, Appl. Phys. Lett. 93 (2008) 192107.

Organic Electronics 11 (2010) 1753–1758

Contents lists available at ScienceDirect

Organic Electronics

journal homepage: www.elsevier.com/locate/orgel

Mobility with negative coefficient in Poole–Frenkel field dependence in conjugated polymers: Role of injected hot electrons

Awnish Kumar Tripathi [a,c], Ashish [c], Y.N. Mohapatra [a,b,c,*]

[a] Department of Physics, Indian Institute of Technology Kanpur, Kanpur 208 016, India
[b] Materials Science Programme, Indian Institute of Technology Kanpur, Kanpur 208 016, India
[c] Samtel Center for Display Technologies, Indian Institute of Technology Kanpur, Kanpur 208 016, India

ARTICLE INFO

Article history:
Received 21 April 2010
Received in revised form 17 June 2010
Accepted 23 July 2010
Available online 4 August 2010

Keywords:
Conjugated polymers
Polymer light emitting diodes
Electroluminescence transient
Charge carrier mobility
Density of states

ABSTRACT

In this work we study the electric field dependence of mobility extracted from Electroluminescence Transient (ELT) measurements in both single carrier and double carrier Polymer Light emitting Diode (PLED) configurations by varying the cathode. We have chosen two different families of conjugated light emitting polymers (structurally different hole transporting materials). The Poole–Frenkel (P–F) plot of mobility μ as a function electric field F ($\log \mu \propto \sqrt{F}$) shows negative slope ($\beta < 0$) in the case of double carrier injection, while positive slope is observed as expected in the case of dominantly single carrier injection. The mobility values and their corresponding field dependent parameters for both the carriers are derived. It is shown that electrons injected to higher lying transport states can have high mobilities behaving as hot electrons. We propose a phenomenological model based on alignment of Gaussian local density of states (DOS) to explain the occurrence of reduction of mobility with increasing electric field for electrons, which do not fully relax into equilibrium distribution within the DOS in the timescales of transit time.

© 2010 Elsevier B.V. All rights reserved.

1. Introduction

Since the discovery of electroluminescence (EL) in conjugated polymers, both the science and technology of conjugate polymer based electronics have progressed unabated for the last two decades [1,2]. Their potential applicability in flat panel and flexible displays, lighting and thin film transistors motivate much of the current research. In these electronic systems, most of the opto-electronic processes and properties have been described using the framework of Gaussian density of states (DOS). The Bässler's Gaussian disorder model consisting of energetic and positional disorder have been successful in the interpretation and understanding of charge carrier transport in thin films of conjugated polymers, and specifically the temperature and electric field dependence of carrier mobility [3,4]. Carrier mobility, being one of the most significant parameters from both understanding and application points of view, has been studied by many methods. Often however, the results from different methods are not consistent and get mired in interpretative difficulties. In contrast to steady state methods involving J–V characteristics of specially designed samples [5], the most reliable methods of determination of mobility involve transient experiments such as Time-of-Flight (TOF) technique [6], transient current method [7], Charge Extraction by Linearly Increasing Voltage (CELIV) [8], and Electroluminescence Transient (ELT) [9]. The mobility in these cases is deduced from the transit time (t_{tr}) or delay time (t_d) for charge carrier in organic layer as

$$\mu = \eta \frac{d^2}{t \times V} \tag{1}$$

where t is the transit time or delay time observed, d is layer thickness of sandwiched device and V is the voltage drop

* Corresponding author. Address: Department of Physics, Materials Science Programme, Indian Institute of Technology Kanpur, Kanpur 208 016, India. Tel.: +91 512 2597033, 2597538; fax: +91 512 2590914.
E-mail address: ynm@iitk.ac.in (Y.N. Mohapatra).

1566-1199/$ - see front matter © 2010 Elsevier B.V. All rights reserved.
doi:10.1016/j.orgel.2010.07.019

across it. Here η is a correction factor for different situations, for example, in case of TOF and ELT, the value of η is unity while for current transient $\eta = 0.786$.

The carrier mobility has been observed to increase with increasing electric field following Poole–Frenkel (P–F) model [5,10,11]. However, decrease in mobility with increasing electric field has also been observed for a variety of conjugated polymers [12,13], molecularly doped polymers [14,15], regioregular poly (alkylthiophenes) [8,16] polymer blends [17] etc., with Al or Au as cathode (except the case in Ref. [15] where Ca cathode was used). This phenomena has been sought to be understood using a variety of ideas such as Peled's empirical approach [14], Hirao's emphasis on correct determination of transit time free from field assisted diffusion [18], use of CELIV method [8,16], Marcus models in inverted regime [19], and Bässler's positional disorder formalism [19,20]. Among these, Bässler's positional disorder correction and their variants have been invoked most often to explain the occurrence of negative P–F coefficient in field dependence [21].

In this paper, we specifically focus on the occurrence of decrease in mobility with increasing electric field contrary to standard expectations. A coherent understanding of such observations is yet to emerge. Within the Gaussian disorder model, or their more refined correlated disorder versions, it is now widely recognized that diagonal disorder gives rise to P–F type electric field dependence of mobility (i.e. $\mu \propto \exp(\beta\sqrt{F})$), while a strong off-diagonal disorder yields a mobility that may decrease with electric field. However, there have been reports of observation of negative P–F coefficient in field dependence where nature of the disorder cannot be invoked as being responsible. We show that for two well characterized conjugate polymer systems the P–F coefficient (β) can be either positive or negative depending on different choice of cathodes even for the same material. This allows us to understand the dependence of mobility on the energy states to which the carriers are injected and the relaxation of carriers within the DOS. A phenomenological model is proposed to account for such observations which are both insightful and significant for applications.

2. Experimental

We have chosen two different families of conjugated polymers viz. *poly [2-methoxy-5-(2-ethylhexyloxy)-1,4-phenylenevinylene]* (MEH-PPV) and *Arylenevinylene-co-pyrrolenevinylene* with *octyloxy* side-chain (C8-AVPV) [22] in single layer LED configuration (Fig. 1(a) and (b)). All the devices were fabricated in controlled laboratory conditions to avoid as much as possible extrinsic effects on material's electronic property. Commercial ITO coated glass substrates were used to realize transparent anode. The patterned and RCA cleaned ITO substrates were subjected to 15 min ozone treatment followed by spin-coating of a thin layer of polyethylene dioxythiophene/polystyrenesulfonate (PEDOT:PSS) and dried at 120 °C for 1 h under 10^{-7} mbar vacuum. The PEDOT:PSS layer serves as conducting planar layer to avoid high electric field associated with roughness of the ITO substrates. The solution of MEH-PPV (commercial source, Sigma Aldrich) was prepared with concentration of 6 mg/cc in chloroform: toluene (50:50) mixture, which was optimized from the point of view of device fabrication in our laboratory [23,24]. C8-AVPV polymer solution is prepared in chlorobenzene with a concentration of 10 mg/cc. Active layers are spin-coated and dried under 10^{-7} mbar vacuum at 120 °C for 1 h. The thickness (~1000 Å) of the active layer was kept the same in all the devices. For single carrier and double carrier situations, we have used Al and Ca metals, respectively. A thick Al layer was deposited to cap the Ca layer in polymer/Ca devices. All the cathodes were deposited through shadow mask without breaking the vacuum to avoid any contamination at the active layer–cathode interface.

We have used ELT technique to monitor the electric field dependent transport parameters. The method is essentially based on monitoring time lag in EL on the application of a rectangular voltage pulse. Fig 1(c) and (d) show the schematics of the experimental setup and typical transients obtained in response to square voltage pulse, respectively. The carriers injected from the respective electrodes have to drift towards the other electrode, and give rise to exciton formation on meeting the opposite carriers. For a single layer of PLED, the fastest carrier controls the observed delay in luminescence in response to a rising edge of the voltage pulse, and the time delay (t_d) is given by

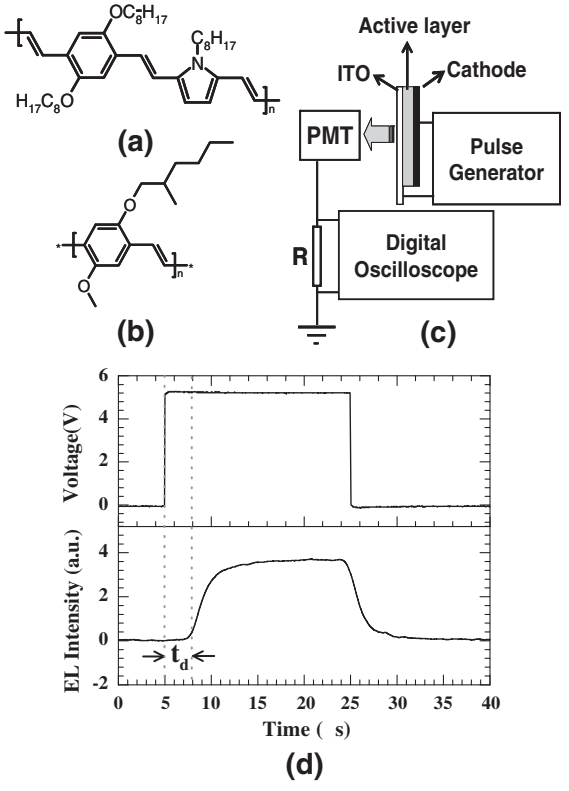

Fig. 1. (a) and (b) shows chemical structure of active material C8-AVPV and MEH-PPV, respectively. (c) Schematic diagram of experimental setup for measuring Electroluminescence Transient (ELT) for PLED device, and (d) typical ELT curve depicting the method of determining time delay (t_d).

$$t_d = \frac{d^2}{\mu_{eff} \times (V - V_{BI})} \quad (2)$$

where $\mu_{eff} = \mu_e + \mu_h$ is the effective mobility, V_{BI} is the built-in voltage and $(V - V_{BI})$ the corrected potential drop across the device.

The finished device was mounted on a home made copper sample mounting stage inside a vacuum chamber having an optical window. A 50 Hz HP 81101A pulse generator, with rise time 10 ns, was used to apply rectangular voltage pulses of different magnitude and pulse width across the devices. The pulse repetition rate was fixed 1 kHz to ensure no interference between the subsequent pulses and their corresponding ELT responses. A photomultiplier tube (S100 response) with time resolution < 1 ns was mounted near the optical window facing the emitting area of the device to detect the EL intensity. The PMT was connected to a 500 MHz digital oscilloscope (model HP 54615B) to record the time dependent EL signals. The RC time constant of the setup, including the PLED devices, was ensured to be smaller than the time scales of the transients.

3. Results and discussion

The effective mobility (μ_{eff}) as a function of electric field (F) was derived using Eq. (2) for two different materials viz. MEH-PPV and C8-AVPV. For each case, the electron injection into the single layer PLED was controlled by varying cathode material, aluminum (Al) to hinder electron injection and calcium (Ca) to provide copious electrons. The schematic band diagrams of the two types of devices are shown in the Fig. 2(a) and (b). The mobilities derived from time delay in each case are plotted as a function of $\sqrt{F}$, where F is the electric field taking into account correction for built-in voltage in Fig. 2(c). There are several important features in this plot as listed below:

- For both the materials, when Al is used as a cathode we obtain traditional P–F type behavior, in which $\mu_{eff} \propto e^{\beta\sqrt{F}}$, where β is positive, i.e. mobilities increase exponentially with increase in F as expected.
- For both the materials, when Ca is used as a cathode, the μ_{eff} decreases with β being negative in contrast to the Al case.
- The absolute values of μ_{eff} for Ca-cathode case is more than Al-cathode by an order of magnitude for lower electric fields, attaining similar values towards higher electric field.

In a typical determination of mobility using ELT, one assumes that the mobility of one of the charge carriers is higher by at least an order of magnitude than the other, and hence the measured mobility is that of the faster carrier. However, if they are comparable one would measure an effective mobility ($\mu_{eff} = \mu_e + \mu_h$). In this work, both the materials chosen are otherwise well characterized as hole transport materials. There is little doubt in ascertaining that for the case of Al-cathode, the transit time is dominated by the mobility of the holes. As expected we obtain

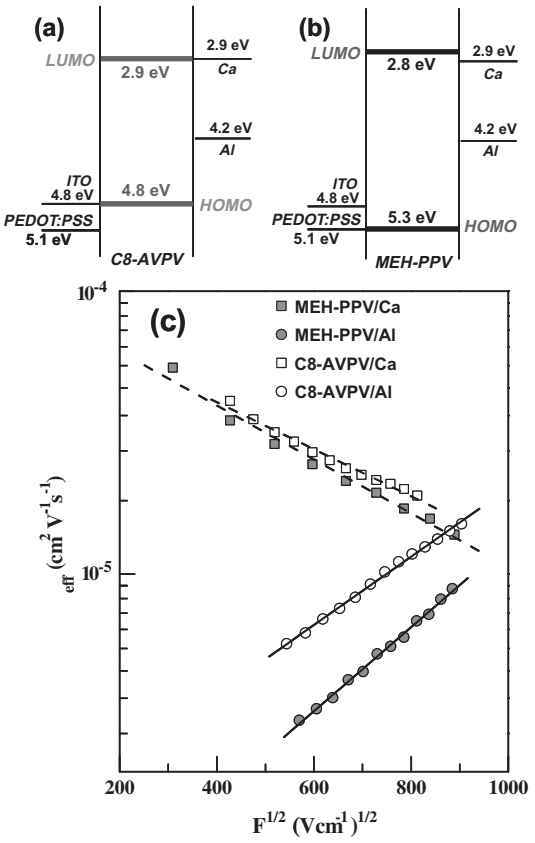

Fig. 2. The Schematic band diagram of PLED structures studied, (a) C8-AVPV/Ca, and (b) MEH-PPV/Ca. Note the energy barrier for electron injection is negligible for Ca in both polymeric systems. (c) Poole–Frenkel plots for charge carrier mobility in MEH-PPV/Ca (grey filled square), MEH-PPV/Al (grey filled circle), C8-AVPV/Ca (white filled square), and C8-AVPV/Al (white filled circle) device structures.

field activated dependence for hole mobility $\mu_h \propto e^{\beta_h\sqrt{F}}$. However, in both the cases when cathode is Ca, the field dependence is reversed. Ca being the low work-function cathode can inject electrons copiously without a barrier as shown in Fig. 2(a) and (b). Hence the measured mobility must be μ_{eff} due to both electrons and holes. In that case, the electron mobility must be unusually large and have negative field dependence. The values of $\mu_{0,eff}$, $\mu_{0,h}$, and $\mu_{0,e}$ along with their corresponding β_{eff}, β_h, and β_e can be determined using μ_h values obtained for the case of Al cathode [25]. The results so obtained are summarized in Table 1. Note that the P–F coefficients for Ca-cathode case (i.e. β_{eff} and β_e) are negative. The $\mu_{0,h}$ and β_h values for MEH-PPV agree well with the published literature. The reported hole mobility parameters ($\mu_{0,h}$) are 1.0×10^{-7} cm^2 V^{-1} s^{-1}–5.7×10^{-7} cm^2 V^{-1} s^{-1} [26–30]. There are only two reported measurements for electron mobility (μ_e) in MEH-PPV, in specially made electron-only structures using steady state J–V characteristics [5,30]. The values ($\mu_{0,e} \sim 1.0 \times 10^{-8}$ cm^2 V^{-1} s^{-1}–2.0×10^{-7} cm^2 V^{-1} s^{-1} and $\beta_e \sim 8.0 \times 10^{-3}$ cm$^{1/2}$ V$^{-1/2}$) are much lower than those obtained here. The fact that electrons can become the dominant carriers in single layer PLED of

Table 1
Transport parameters extracted from P–F mobility plot for both the polymers.

Material/cathode	$\mu_{0,eff}$ ($cm^2\ V^{-1}\ s^{-1}$)	$\mu_{0,h}$ ($cm^2\ V^{-1}\ s^{-1}$)	μ_{0e} ($cm^2\ V^{-1}\ s^{-1}$)	β_{eff} $(cm\ V^{-1})^{1/2}$	β_h $(cm\ V^{-1})^{1/2}$	β_e $(cm\ V^{-1})^{1/2}$
MEH-PPV/Ca	9.48×10^{-5}	–	1.19×10^{-4}	-2.19×10^{-3}	–	-2.84×10^{-3}
C8-AVPV/Ca	8.71×10^{-4}	–	1.83×10^{-4}	-1.91×10^{-3}	–	-3.72×10^{-3}
MEH-PPV/Al	4.20×10^{-7}	4.20×10^{-7}	–	3.42×10^{-3}	3.42×10^{-3}	–
C8-AVPV/Al	1.25×10^{-6}	1.25×10^{-6}	–	2.78×10^{-3}	2.78×10^{-3}	–

MEH-PPV with Ca as the cathode has been noted earlier [31,32]. In Fig. 2, we also note that the μ_{eff} data has an upward curvature and is within a factor of two of the μ_h at higher electric fields. This clearly indicates that the μ_{eff} has an increasingly large contribution from holes at higher field thus tending to flatten the overall field dependence. This can be used to refine the fitting obtained though its effect in the values is small.

Our observations clearly indicate that electrons are involved and are responsible for the unusual behavior. Since the Ca work-function is much lower compared to that of Al, it is reasonable to assume that electrons being injected into the material occupy directly the transport states, and would need to relax within a Gaussian DOS to equilibrate. However, if this process of equilibration is slow, the injected electrons can be considered as hot and hence transport of such charge carriers within the transport states would be different. For equilibrium carriers, we observe P–F type activated transport due to existence of mobility-gap like barrier between localized states and transport states as is well known from Bässler formalism. This would be true for holes in both the polymer cases. This would also hold for electron mobility measurements reported in the literature using steady state techniques such as J–V characteristics in electron only devices and impedance analysis. The hot electron behavior can be observed only in transient experiments using sufficiently low work-function cathodes.

Further, we propose a phenomenological model to account for negative coefficient of field dependence for hot electrons through a series of schematics as shown in Fig 3. The injected electrons into the layers immediately in contact with the cathode have to tunnel into the transport states of the local DOS (shown as Gaussians) of the subsequent layer. However, because of the electric field the two Gaussian DOS would be misaligned in energy reducing the number of transport states accessible for transport in the subsequent layers. This misalignment increases further at higher electric field reducing probability of tunneling into the subsequent layers and hence the mobility of the hot electrons. However in case of Al, the concentration of electrons are low and are primarily injected into the localized/trap states and hence do not result in hot electrons. This is a scenario which provides a compelling rationale for observation of reduced mobility with increasing electric field. By changing the cathode only, we do not expect to alter the nature or degree of positional (i.e. off-diagonal) disorder, which are generally invoked to explain the negative coefficient of P–F field dependence in presence of dopants or other similar situations. However it is possible that at the microscopic level the hot electrons may be more sensitive to off-diagonal disorder—an effect that must be explicitly simulated to justify. In other words, our results indicate that in the case of Al-cathode, electrons are injected to localized states and hence are already equilibrated within the DOS with extremely low electron mobility. Effectively only holes move to recombine with electrons very near to the Al-cathode. The injected holes relax much faster within the DOS to obey the usual field dependence as predicted by Gaussian disorder model.

The above account that transport of electrons would involve simultaneously two processes – movement across the transport states towards the anode, and relaxation within the DOS towards the minimum of transport states and to localized states lying lower in energy. During the drift, the competition between the two processes would determine an effective mobility and hence a single value of mobility would loose its well-defined meaning. We believe that this is indeed the case for electrons in these materials. It is worth reemphasizing that this can only be observed in transient experiments with thin films as is typically used in OLED applications and any steady state experiment would completely miss this possible time dependent contribution to drift phenomena. Our results also indicate that the time-scale of relaxation of electrons is slower than that of the holes, and are longer than the transit time in our experiments which is in order of microseconds. This would need further empirical test. The mechanism of relaxation for holes and electrons seem to be very different probably owing to the nature and occupancy of localized/trap levels. It is plausible that electron trapping states get occupied very quickly and have low emission rates thus effectively getting eliminated as a source of equilibration in the timescales of the experiment.

In order to further test the idea that energetics and DOS play a crucial role in determining the behavior of injected electrons, we use a blend system in which C8-AVPV is blended with high gap non-luminescent PVK material as the active layer. The blend with PVK is uniformly miscible across the range. Ca as a cathode would not be able to inject electrons into LUMO bands of PVK. The mixtures of the two polymers only ensure that the local DOS corresponding to C8-AVPV gets decreased as compared to the pure C8-AVPV case. The comparison of results of pure C8-AVPV with blend of 60% PVK and 40% C8-AVPV is shown in Fig. 4. The negative field dependence occurs in both the devices except that the absolute value of mobility for corresponding electric field is decreased due to reduction in C8-AVPV local DOS, responsible for hot electron transport. This reinforced the idea that the occurrence of negative coefficient in P–F dependence of mobility using low work-function cathode is a robust phenomena and its origin can be traced to transport of hot electrons.

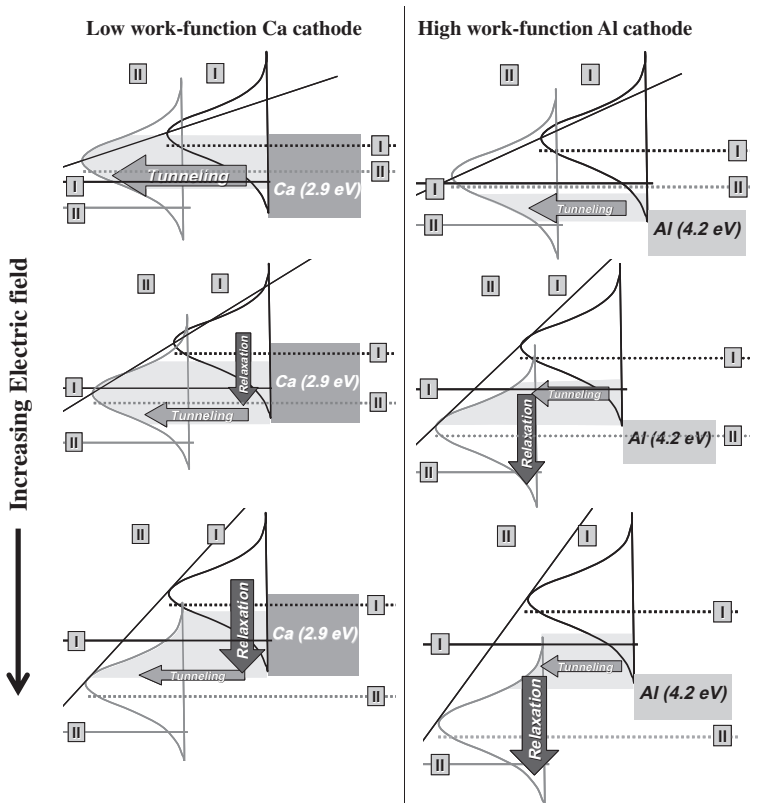

Fig. 3. Schematics (not to scale) depicting the transport mechanism for polymer/Ca (left column) and polymer/Al (right column) configuration. The dotted line represents lower edge of transport states and solid line represents upper edge of localized/trap states. Here shaded area shows overlapping of energy states between populated interfacial DOS and empty states in the localized DOS of next layer. The first interfacial and second next DOS are denoted as *I* and *II*, respectively. At low electric field (small band bending), for polymer/Ca, matching of Ca Fermi level with LUMO of polymer, favors electron population in transport states of interfacial DOS and subsequent tunneling to transport states of the next layer DOS. While due to limited injection efficiency and nature of band bending in case of Al, only localized trap states are filled first with very small tunneling probability to transport and trap levels of next DOS (first row). At moderate electric field (steeper band bending) (second row), for polymer/Ca, the probability of tunneling is slowly diminished. At higher electric field (steepest band bending) (third row), for polymer/Ca, the charge carriers' relaxation dominates over tunneling to next DOS, while in the case of Al the probability of tunneling from localized/trap states increase, i.e. trapping precedes tunneling to transport states of the next layer.

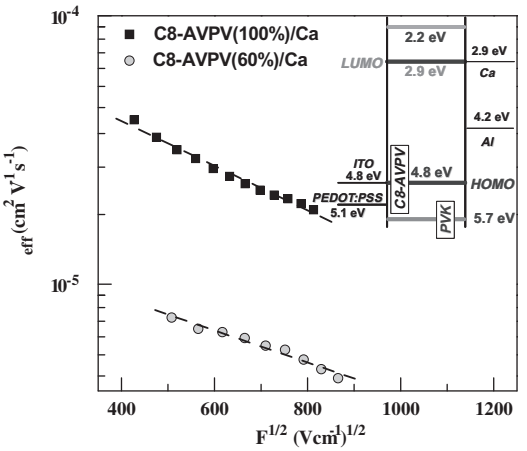

Fig. 4. log μ vs. $\sqrt{F}$ plot for blend of 60% (C8-AVPV: PVK) with Ca cathode (grey filled square). The 100% case is pure C8-AVPV (black filled square) showing the difference observed in magnitude for both the cases. Inset of the plot shows band diagram of the blended device.

4. Conclusions

In summary, we have demonstrated that the effective mobility and its field dependence measured in electroluminescence transient experiment can be strongly dependent on the nature of cathode used. The parameters describing field dependence for both carriers have been derived, and shown to have negative coefficient for electrons injected from Ca cathode. In this case carriers are injected into higher energies of transport states, and do not relax to equilibrium soon enough, the mobility of electrons can be significantly higher than the hole mobility even in traditional hole transporting layers. This is invoked to explain the occurrence of negative coefficient of field dependence for two different material systems (MEH-PPV and C8-AVPV) having Ca as the low work-function cathode. The proposed phenomenological model of field dependence is based on the idea that injected hot electrons are unable to find accessible transport states due to increasing misalignment of local DOS of subsequent layers with increasing electric field.

Acknowledgements

We are thankful to Dr. Anand K. Biswas for help in material preparation and device standardization. We are also thankful to Department of Science and Technology, New Delhi and Samtel Group of Industries, New Delhi for financial support.

References

[1] J.H. Burroughes, D.D.C. Bradley, A.R. Brown, R.N. Marks, K. Macky, R.H. Friend, P.L. Burn, A.B. Holmes, Nature 347 (1990) 539.
[2] D. Braun, A.J. Heeger, Appl. Phys. Lett. 58 (1991) 1982.
[3] H. Bässler, Phys. Status Solidi B 175 (1993) 15.
[4] I.I. Fishchuk, A.K. Kadashchuk, J. Genoe, Mujeeb Ullah, H. Sitter, Th.B. Singh, N.S. Sariciftci, H. Bässler, Phys. Rev. B 81 (2010) 045202.
[5] L. Bozano, S.A. Carter, J.C. Scott, G.G. Malliaras, P.J. Brock, Appl. Phys. Lett. 74 (1999) 1132.
[6] E. Lebedev, Th. Dittrich, V. Petrova-Koch, S. Karg, W. Brütting, Appl. Phys. Lett. 71 (1997) 2686.
[7] D. Poplavskyy, W. Su, F. So, J. Appl. Phys. 98 (2005) 014501.
[8] G. Juška, K. Genevičius, K. Arlauskas, R. Österbacka, H. Stubb, Phys. Rev. B 65 (2002) 233208.
[9] D.J. Pinner, R.H. Friend, N. Tessler, J. Appl. Phys. 97 (2004) 014504.
[10] H.H. Poole, Philos. Mag. 32 (1916) 112.
[11] J. Frenkel, Phys. Rev. 54 (1938) 647.
[12] M. Gailberger, H. Bässler, Phys. Rev. B 44 (1991) 8643.
[13] M. Redecker, D.D.C. Bradley, M. Inbasekaran, E.P. Woo, Appl. Phys. Lett. 74 (1999) 1400.
[14] A. Peled, L.B. Schein, Chem. Phys. Lett. 153 (1988) 422.
[15] Z. Chen, D. Ma, J. Appl. Phys. 102 (2007) 024510.
[16] A.J. Mozer, N.S. Sariciftci, Chem. Phys. Lett. 389 (2004) 438.
[17] J. Huang, G. Li, Y. Yang, Appl. Phys. Lett. 87 (2005) 112105.
[18] A. Hirao, H. Nishizawa, M. Sugiuchi, Phys. Rev. Lett. 75 (1995) 1787.
[19] R.H. Young, N.G. Rule, Phys. Rev. Lett. 72 (1994) 388.
[20] L. Pautmeier, R. Richert, H. Bässler, Synth. Met. 37 (1990) 271.
[21] Gaussian disorder model predicts the temperature and field dependent mobility as $\mu_{GDM} = \mu_\infty \exp\left[-\left(\frac{2\sigma}{3k_BT}\right)^2 + C\left(\left(\frac{\sigma}{k_BT}\right)^2 - \Sigma^2\right)\sqrt{F}\right]$ in Ref. [3] above.
[22] A.K. Biswas, Ashish, A.K. Tripathi, Y.N. Mohapatra, A. Ajayaghosh, Macromolecules 40 (2007) 2657.
[23] A.K. Biswas, A.K. Tripathi, S. Singh, Y.N. Mohapatra, Synth. Met. 155 (2005) 340.
[24] G.S. Samal, A.K. Tripathi, A.K. Biswas, S. Singh, Y.N. Mohapatra, Synth. Met. 155 (2005) 344.
[25] The values of mobility are interpolated for any electric field for which data points are not available while carrying out the separation of μ_e and μ_h from measured value of μ_{eff}.
[26] G.G. Malliaras, J.R. Salem, P.J. Brock, C. Scott, Phys. Rev. B 58 (1998) R 13411.
[27] P.W.M. Blom, M.J.M. de Jong, M.G. van Munster, Phys. Rev. B 55 (1998) R 656.
[28] I.H. Campbell, P.S. Davids, D.L. Smith, N.N. Barashkov, J.P. Ferraris, App. Phys. Lett. 72 (1998) 1863.
[29] I.H. Campbell, D.L. Smith, C.J. Neef, J.P. Ferraris, App. Phys. Lett. 74 (1999) 2809.
[30] H.C.F. Martens, J.N. Huiberts, P.W.M. Blom, App. Phys. Lett. 77 (2000) 1852.
[31] J.C. Scott, G.G. Malliaras, W.D. Chen, J.C. Breach, J.R. Salem, P.J. Brock, S.B. Sachs, C.E.D. Chidsey, Appl. Phys. Lett. 74 (1999) 1510.
[32] G.G. Malliaras, J.C. Scott, J. Appl. Phys. 85 (1999) 7426.

Organic Electronics 11 (2010) 1759–1766

Contents lists available at ScienceDirect

Organic Electronics

journal homepage: www.elsevier.com/locate/orgel

White organic light-emitting diodes showing nearly 100% internal quantum efficiency

Ji Hoon Seo [a], Seok Jae Lee [a], Bo Min Seo [a], Se Jin Moon [a], Kum Hee Lee [b], Jung Keun Park [b], Seung Soo Yoon [b,*], Young Kwan Kim [a,**]

[a] Department of Information Display, Hongik University, Seoul 121-791, South Korea
[b] Department of Chemistry, Sungkyunkwan University, Suwon, Kyeonggi-do 440-746, South Korea

ARTICLE INFO

Article history:
Received 2 February 2010
Received in revised form 13 July 2010
Accepted 18 July 2010
Available online 7 August 2010

Keywords:
White organic light-emitting diodes
Various electron-transporting materials
Various 100% internal quantum efficiency

ABSTRACT

The authors have demonstrated white organic light-emitting diodes (WOLED) using all phosphorescent emitters for blue, green, and red, such as FCNIrpic, $Ir(ppy)_3$ and $Ir(pq)_2$(acac). Various electron-transporting materials such as $Bebq_2$, BPhen, TAZ, BAlq, and TPBI were also investigated for improving quantum efficiency of phosphorescence of WOLED by fabricating and characterizing white devices using these materials as an electron-transporting layer (ETL). It was found that WOLED with an ETL of TPBI exhibits a peak external quantum efficiency (EQE) of 19.5% and a peak power efficiency of 39.2 lm/W at very low light intensity. The optimized device also shows an EQE of 16.4% at 1000 cd/m^2. It was also found that the optimized white device with TPBI shows minimal change with Δ Commission Internationale de l'Eclairage coordinates of ±(0.02, 0.00) from 100 to 10,000 cd/m^2. In order to understand the mechanism for achieving nearly 100% IQE with this device structure, various analyses were also executed, such as UV/visible absorbance measurements of FCNIrpic and photoluminance (PL) measurements of mCP, fabrications of hole- and electron-only devices, UV/visible absorbance measurements of $Ir(ppy)_3$ and $Ir(pq)_2$(acac) and PL of FCNIrpic, and surface roughness measurements of various ETL films.

© 2010 Elsevier B.V. All rights reserved.

1. Introduction

White organic light-emitting diodes (WOLEDs) have drawn increasing attention as a solid-state light (SSL) source and backlights in liquid crystal displays and full-color OLEDs due to their light weight, low operating voltage, thinness, diffusiveness, and harmlessness for the restriction of certain hazardous substances directive/waste electrical and electronic equipment [1–6]. There are two ways of realizing WOLEDs as SSL in the aspects of materials used. One is phosphorescent WOLEDs (PHWOLEDs), which use all phosphorescent emitters, and the other is hybrid WOLEDs (HWOLEDs), which use fluorescent blue and phosphorescent red–green emitters. Sun et al. have demonstrated highly efficient HWOLEDs using fluorescent blue and phosphorescent red–green emitters, where a spacer of 4,4′-*N*,*N*′-dicarbazole-biphenyl was used in order to prevent singlet energy transfer from fluorescent blue emitter to phosphorescent red–green emitters; the exchange energy losses were minimized to increase the efficiency and lifetime [7]. Nevertheless, they showed low external quantum efficiency (EQE) and power efficiency (PE) to be about 10% and 14 lm/W at 500 cd/m^2, respectively [8]. PHWOLEDs have also been investigated intensively because we can harvest both singlet and triplet excitons with PHWOLEDs [9–11]. Unfortunately, PHWOLEDs, despite the possibility of achieving 100% internal quantum efficiency (IQE), do not yet have a proper phosphorescent blue emitter with high-energy gap, long life, or host materials for this emitter.

* Corresponding author. Tel.: +82 31 290 7071; fax: +82 31 290 7075.
** Corresponding author. Tel.: +82 2 320 1646; fax: +82 2 3141 8928.
E-mail addresses: ssyoon@skku.edu (S.S. Yoon), kimyk@hongik.ac.kr (Y.K. Kim).

1566-1199/$ - see front matter © 2010 Elsevier B.V. All rights reserved.
doi:10.1016/j.orgel.2010.07.015

Nevertheless, lately, a few researchers have reported highly efficient phosphorescent deep-blue OLEDs and have also investigated the synthesis of novel blue Ir and Pt complexes [12,13].

White light emission can be obtained from monomeric or polymeric emitters [14,15], depending on molecular length, from all phosphorescent, fluorescent or hybrid phosphorescent–fluorescent materials [16–18], depending on the emission mechanism, and from single-emitting layer (EML) or multi-EML [19,20], excimer or exciplex [21,22], microcavity, down conversion, *p–i–n*, and tandem junction [23–26], depending on device structures. Among these options, we have investigated multi-EML junctions using all phosphorescent emitters in this paper.

Materials for hole-transporting layers (HTL) have been investigated widely in various aspects such as hole mobility, band gap, triplet exciton energy, and glass transition temperature. As a results, *N*′-bis-(1-naphyl)-*N*,*N*′-diphenyl-1,1′-biphenyl-4,4′-diamine (NPB) is now used as a common HTL material because it shows the most outstanding characteristics such as thermal stability, high hole mobility, and appropriate band gap. Even though there are many kinds of electron-transporting layers (ETL), such as bis(10-hydroxybenzo[h]quinolinato)beryllium complex ($Bebq_2$), 4,7-diphenyl-1,10-phenanthroline (BPhen), 3-(4-biphenylyl)-4-phenyl-5-tert-butylphenyl-1,2,4-triazole (TAZ), bis-(2-methyl-8-quinolinolate)-4-(phenylphenolato)aluminum (BAlq), and 2,2′,2″-(1,3,5-benzinetriyl)-tris(1-phenyl-1-H-benzimidazole) (TPBI), there were no systematic investigations to improve the efficiency of WOLEDs having multi-EML junctions using all phosphorescent emitters in the aspects of various physical properties. In this paper, we investigated the effects of photophysical analysis for host-dopant trade-off of 1,3-bis(9-carbazolyl)benzene (mCP) and iridium(III) bis[(5-cyano-4-fluorophenyl)pyridinato-N,C2′]picolinate (FCNIrpic) and various ETL materials on the efficiency of these WOLEDs by analyzing hole block ability, lowest unoccupied molecular orbital (LUMO) level, electron mobility, triplet energy level, and surface morphology of various ETL materials. Hence, 100% IQE and 19.5% EQE were achieved by using the optimized WOLEDs with TPBI as an ETL material.

The structure of all devices and energy level diagrams of WOLEDs fabricated in this study are shown in Fig. 1(a) and b), respectively, where the device structure was indium-tin oxide (ITO) (150 nm)/NPB (50 nm)/mCP (10 nm)/FCNIrpic:mCP (7 nm)/*fac*-tris(2-phenylpyridine)iridium ($Ir(ppy)_3$):iridium(III) bis(2-phenylquinoline) acetylacetonate($Ir(pq)_2(acac)$):TPBI (3 nm)/various ETLs (30 nm)/lithium quinolate (Liq) (2 nm)/Al (100 nm), respectively. $Bebq_2$, BPhen, TAZ, BAlq, and TPBI were used as ETL material in devices A, B, C, D, and E, respectively. The doping concentrations of FCNIrpic in mCP, $Ir(ppy)_3$, and $Ir(pq)_2(acac)$ in TPBI were optimized to 8%, 8%, and 3%, respectively. The thickness of EML was optimized to 10 nm since this thickness has many advantages such as low operating voltage, higher efficiency, and lower color shift [9]. NPB as an HTL, mCP as an exciton-blocking layer (XBL) and a phosphorescent blue host, FCNIrpic, as a phosphorescent blue emitter, TPBI as a phosphorescent red host and an ETL, $Ir(ppy)_3$, as a phosphorescent green emitter, $Ir(pq)_2(acac)$ as a phosphorescent red emitter, and Liq as an electron injection layer were also used in these device structures. In device E, TPBI was used as a red host and ETL simultaneously, for this set-up makes the fabrication process simple.

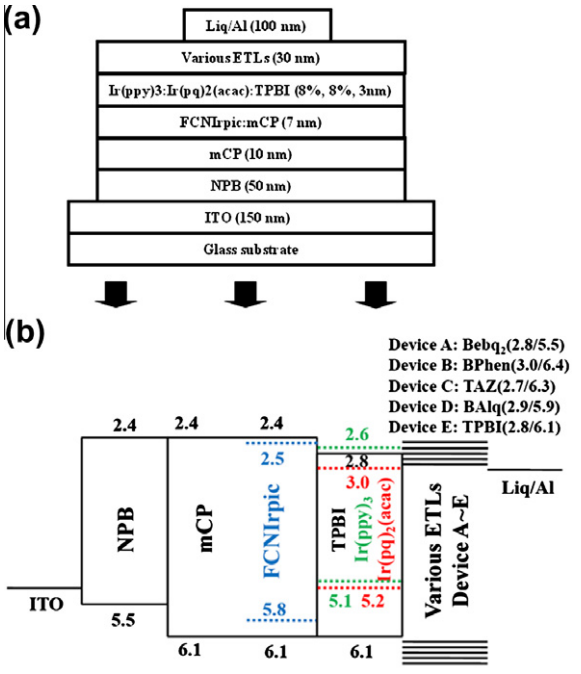

Fig. 1. (a) The structures of all devices fabricated in this study. (b) Energy level diagrams for all white devices. Numbers denote the energy level for the HOMO and LUMO of various materials used in this study, where the HOMO and LUMO of FCNIrpic, $Ir(ppy)_3$, and $Ir(pq)_2(acac)$ are presented by blue, green, and red dotted line, respectively. (For interpretation of the references to colour in this figure legend, the reader is referred to the web version of this article.)

The highest occupied molecular orbital (HOMO), LUMO, electron mobility, and triplet emission energy for various ETLs are listed in Table 1 [27–33]. It is clear in Table 1 that $Bebq_2$ and BPhen have a considerably higher electron mobility of 10^{-4} cm^2/V s compared to TAZ, BAlq, and TPBI, which has an electron mobility of 10^{-5} cm^2/V s. TAZ and TPBI have higher triplet emission energies than FCNIrpic (2.65 eV).

2. Experimental

An indium-tin oxide (ITO)-coated glass substrate was cleaned in an ultrasonic bath using the following sequence of solvents: acetone, methanol, distilled water, and isopropyl alcohol. Thereafter, a precleaned ITO layer was treated with O_2 plasma under the following conditions: 2×10^{-2} Torr and 125 W for 2 min. HWOLEDs were fabricated by the high-vacuum (5×10^{-7} Torr) thermal evaporation of organic materials onto the surface of the ITO-coated glass substrate (10 Ω/sq, emitting area was 3×3 mm^2). The deposition rates were 0.1 nm/s for all organic materials and 0.01 nm/s for Liq.

Without breaking the vacuum, after the deposition of the organic layers, the Al cathode was deposited at a rate of 1 nm/s. The ultraviolet (UV)/visible absorption and PL

Table 1
HOMO, LUMO, electron mobility, and triplet energy level of various electron transporting layers.

ETL	HOMO (eV)	LUMO (eV)	Electron mobility (cm^2/V s)	Triplet energy (eV)
$Bebq_2$	5.5	2.8	$\sim10^{-4}$ [27]	2.5 [28]
BPhen	6.4	3.0	$\sim10^{-4}$ [29]	2.5 [30]
TAZ	6.3	2.7	$\sim10^{-5}$ [31]	3.3 [28]
BAlq	5.9	2.9	$\sim10^{-5}$ [32]	2.6 [33]
TPBI	6.1	2.8	$\sim10^{-5}$ [31]	2.8 [27]

spectra were measured with HP-8453 (Hewlett Packard) and LS-55 (Perkin Elmer). In a presence of a DC voltage bias, the optical and electrical properties of WOLEDs such as the current density, luminance, PE, EQE, Commission Internationale de l'Eclairage ($CIE_{x,y}$) coordinates, and EL spectra of the emission characteristics were measured with Keithley 2400 (Keithley) and Chroma meter CS-1000A (Konica Minolta) instruments simultaneously. The films of various ETLs on silicon wafer substrates were used for atomic force microscopy (AFM) imaging. The various ETLs were deposited at a thickness of 20 nm at a rate of 0.1 nm/s. The AFM images were obtained with an XE-150 (Park Systems) instrument. The film conditions for the AFM measurements were kept the same as for OLEDs. All measurements were carried out under ambient conditions at room temperature.

3. Results and discussion

3.1. Photophysical analysis for host-dopant trade-off

Fig. 2 shows the UV/visible absorption spectrum of FCNIrpic and PL spectra of FCNIrpic, and of mCP in chlorobenzene, respectively. It was found in Fig. 2 that FCNIrpic shows the maximum UV/visible absorption peak at 250 nm with a sub-peak at 293 nm and peaks also at 375 and 413 nm, which are due to spin-allowed ^{1}metal–ligand charge transfer band (MLCT) and spin-forbidden ^{3}MLCT, respectively. It was also found in Fig. 2 that the PL emission peaks of FCNIrpic and mCP were located at 465.5 nm, with vibrational peaks at 492 nm and at 361.5 nm, respectively.

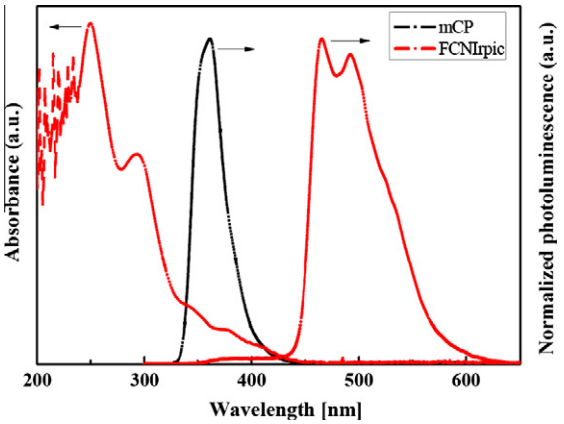

Fig. 2. UV/visible absorption spectrum of FCNIrpic and normalized PL spectra of mCP and FCNIrpic.

Since FCNIrpic is an iridium derivative having a strong electron-withdrawing substituent of CN at the position of fluorine in iridium(III) bis(4,6-(difluorophenyl)pyridinato-*N*,$C^{2'}$)picolinate (FIrpic), FCNIrpic has a wider bandgap (2.5/5.8 eV) than that of FIrpic (2.5/5.7 eV). It can be expected that the efficient Förster energy transfer would be possible from mCP to FCNIrpic since ^{1}MLCT and ^{3}MLCT absorption spectra of FCNIrpic has broader spectral overlap with fluorescence spectra of mCP from 330 to 450 nm. Efficient Dexter energy transfer is also possible from phosphorescence of mCP (430 nm) to ^{3}MLCT absorption of FCNIrpic (413 nm) [34]. Therefore, both Förster and Dexter energy transfers occur through the paths as follows; singlet excited state (S_1) of mCP → S_1 of FCNIrpic → intersystem crossing → triplet exited state (T_1) of FCNIrpic and T_1 of mCP → T_1 of FCNIrpic, respectively [19].

3.2. Mechanism analysis for achieving nearly 100% IQE of WOLEDs

Fig. 3(a) and (b) show EQE and PE-luminance characteristics of all devices, respectively. It was found in Fig. 3(a) and (b) that devices A, B, C, D, and E have peak EQEs of 8.9%, 11.8%, 12.0%, 15.1%, and 19.3% and peak PEs of 19.5, 28.9, 26.2, 33.5, and 39.2 lm/W at very low light intensities, respectively. The EQE of 19.3% and the PE 39.2 lm/W at very low light intensity are equivalent to nearly 100% IQE [35,13]. All devices also show EQEs of 7.2%, 9.1%, 9.1%, 12.0%, and 16.4% at 1000 cd/m^2. Device E, having TBPI as an ETL which is one of the highest values for the previously reported WOLEDs to the best of our knowledge. These excellent experimental results seem to be due to the following reasons: (1) blue device (10.70%) using FCNIrpic had an efficiency 1.5 times that of the control blue device (7.43%) using FIrpic [36] (see Ref. [36]); (2) TPBI as an ETL has an ideal hole-blocking property (see Section 3.2.2); (3) all the electrons injected into the EML pass without electron leakage since the same material was used as the red host and ETL (see Section 3.2.2); (4) since TPBI (2.8 eV) has a higher triplet energy than FCNIrpic (2.65 eV), device E, having TPBI as an ETL, can confine triplet energy of FCNIrpic to EML effectively (see Section 3.2.4); (5) TPBI film exhibits a very smooth surface with $\sigma \sim 0.14$ nm, which is the lowest value among those of $Bebq_2$, BPhen, TAZ, BAlq, and TPBI film (see Section 3.2.5). Thus, these five factors may contribute partially to the achievement of excellent efficiency in WOLEDs shown in this study. We will discuss some experimental results obtained by various analyses in detail in order to explain excellent efficiency in the next chapter.

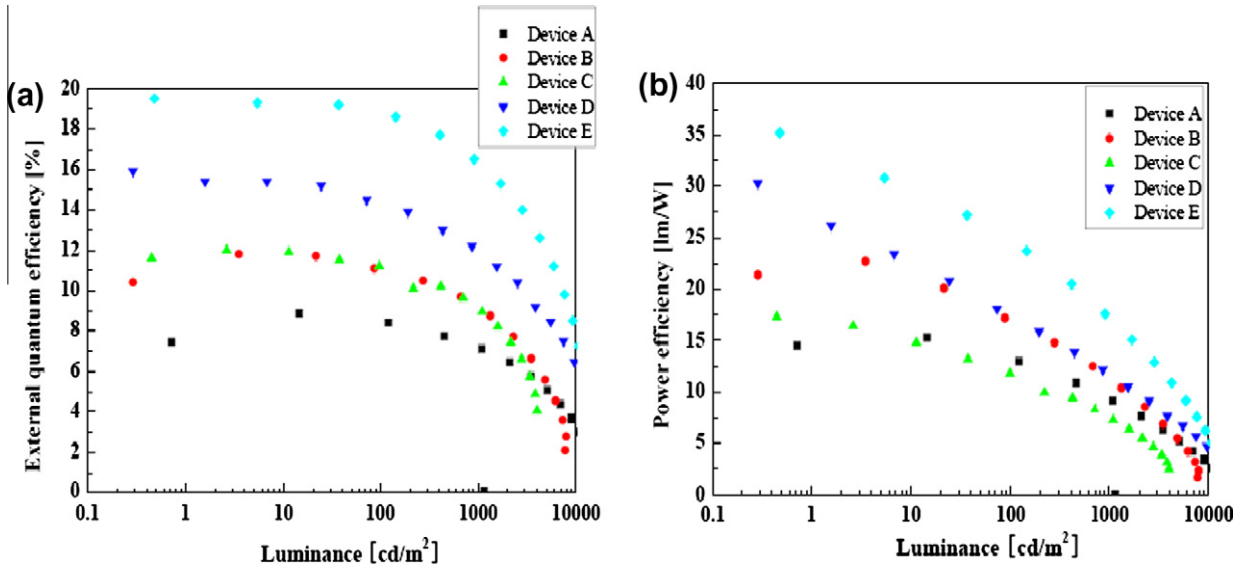

Fig. 3. (a) EQE versus luminance characteristics of all devices with various ETLs. (b) PE versus luminance characteristics of all devices with various ETLs.

3.2.1. Electrical and optical characteristics of WOLEDs using various ETLs

Fig. 4 and the inset in Fig. 4 show current density–voltage and luminance–voltage characteristics of all five devices, respectively. It was found in Fig. 4 that they have maximum current densities of 600, 143, 19, 64, and 113 mA/cm^2 at 10 V and luminances of 13,200, 7910, 2780, 9620, and 11,500 cd/m^2 at 10 V, respectively.

Device A shows the highest current density at operating voltages, which seems to be due to the inadequate role of $Bebq_2$ having the low HOMO (5.5 eV) as a hole-blocking layer. On the other hand, device C shows the lowest current density among other devices, which also seems to be due to the largest electron injection barrier between the Liq-Al and LUMO of TAZ and its lower electron mobility of 10^{-5} cm^2/V s compared to $Bebq_2$ and BPhen as shown in Table 1. It was also found that although BAlq in device D and TPBI in device E have the same electron mobility as shown in Table 1, device D shows lower current density than device E.

This can be explained as follows: device E did not have an electron injection barrier between the red EML and ETL because the same material, TPBI, was used for both the EML and ETL in device E. It is shown in the inset of Fig. 4 that devices A and B have similar saturation characteristics at driving voltages higher than 9.5 V, which seems to be due to the inadequate hole-blocking ability of $Bebq_2$ in device A and also bad surface morphology of the Bphen layer in device B (see Sections 3.2.2 and 3.2.5).

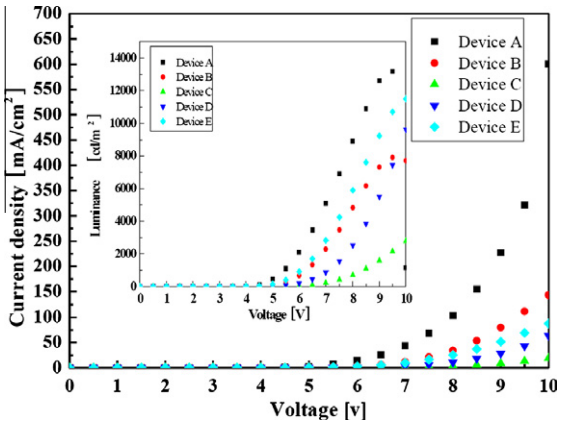

Fig. 4. Current density versus voltage characteristics of all devices. Inset: luminance versus voltage characteristics of all devices.

3.2.2. Fabrication and characterization of unipolar devices

Hole-only devices (HODs) and electron-only devices (EODs) were fabricated to prove the previous assumption. Fig. 5 and the inset of Fig. 5 show current density–voltage

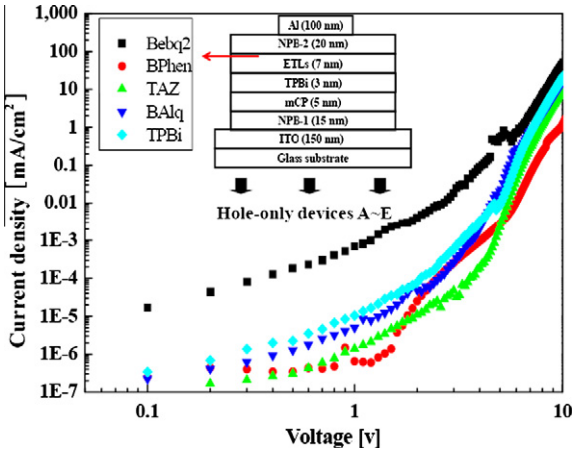

Fig. 5. Current density versus voltage characteristics of HODs. Inset: HODs structure which have five structures of ITO (150 nm)/NPB-1 (15 nm)/mCP (5 nm)/TPBI (3 nm)/various ETLs (7 nm)/NPB-2 (20 nm)/Al (100 nm).

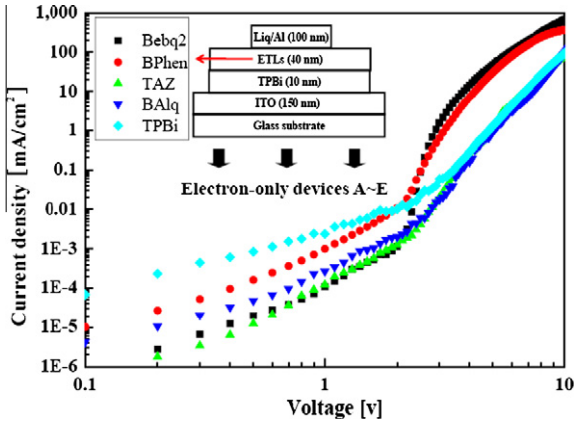

Fig. 6. Current density versus voltage characteristics of EODs. Inset: EODs structure which have five structures of ITO (150 nm)/TPBI (10 nm)/ETLs (40 nm)/Liq-Al (100 nm).

characteristics of HODs, and the device structure for five HODs is as follows: ITO (150 nm)/NPB-1 (15 nm)/mCP (5 nm)/TPBI (3 nm)/various ETLs (HOD-1–5) (7 nm)/NPB-2 (20 nm)/Al (100 nm), where various ETLs are $Bebq_2$ (HOD-1), BPhen (HOD-2), TAZ (HOD-3), BAlq (HOD-4), and TPBI (HOD-5). To maintain the same HOMO value in HODs as that of white devices, NPB-1, mCP, and TPBI were used as the HTL and NPB-2 was used as the electron-blocking layer. It was found in Fig. 5 that the HODs show current densities of 7.0×10^{-4}, 6.5×10^{-7}, 1.4×10^{-6}, 5.0×10^{-6}, and 9.0×10^{-6} mA/cm^2 at 1 V and also 0.538, 0.003, 0.002, 0.020, and 0.009 mA/cm^2 at 5 V. HOD-1 shows the highest current density at the whole voltage, and this trend becomes more conspicuous at a lower voltage. Therefore, this indicates that $Bebq_2$ could not play an adequate role of hole-blocking in device A. The lower the HOMO level of ETLs, the more holes that pass through toward the cathode; all ETLs except $Bebq_2$ can effectively prevent a hole from passing through an EML and, therefore, confine hole carriers within the EML.

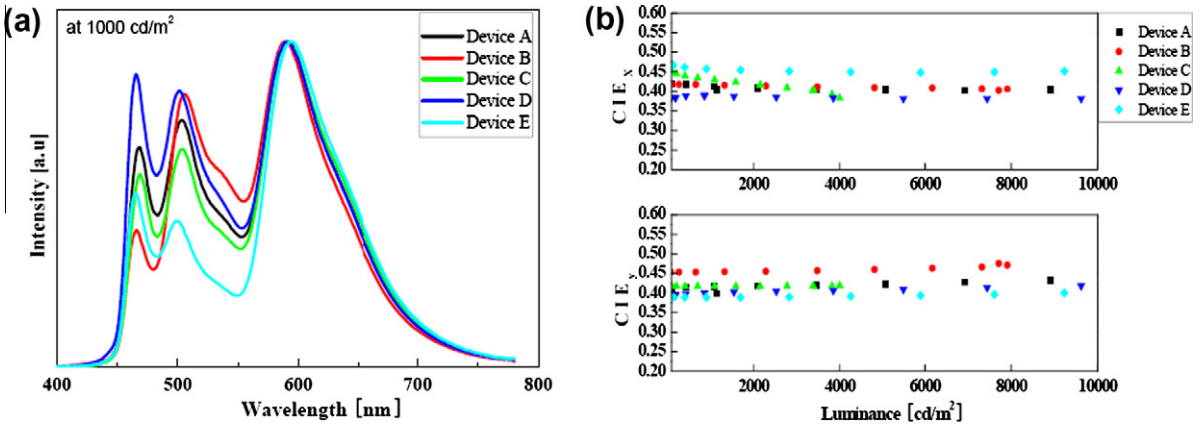

Fig. 7. (a) EL spectra of all white devices at 1000 cd/m^2. (b) CIE$_{x,y}$ coordinates versus luminance characteristics from 100 to 10,000 cd/m^2 of all white devices.

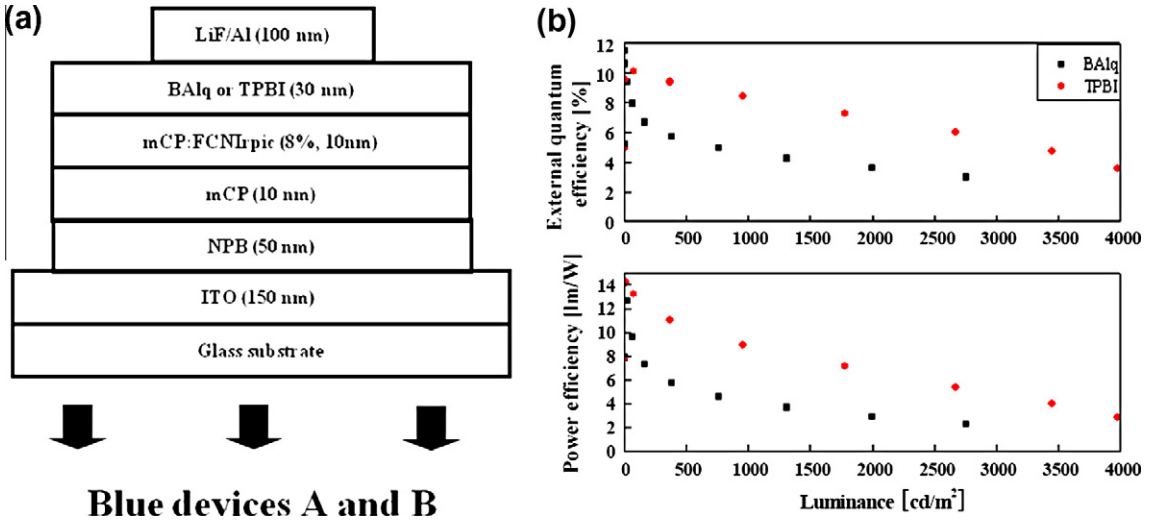

Fig. 8. (a) Blue device A and B where the device structures were ITO (150 nm)/NPB (50 nm)/mCP (10 nm)/FCNIrpic:mCP (8%, 10 nm)/BAlq (blue device A) or TPBI (blue device B) (30 nm)/LiF (2 nm)/Al (100 nm), respectively. (b) EQE and PE versus luminance characteristics of blue device A and B.

Fig. 6 and the inset of Fig. 6 show current density–voltage characteristics of EODs, and the device structure for five EODs is as follows: ITO (150 nm)/TPBI (10 nm)/various ETLs (40 nm)/Liq (2 nm)/Al (100 nm), where various ETLs are $Bebq_2$ (EOD-1), BPhen (EOD-2), TAZ (EOD-3), BAlq (EOD-4), and TPBI (EOD-5). To maintain the same LUMO value in EODs as that of white devices, TPBI was used as an HTL. It was found in Fig. 6 that the EODs show current densities of 1.54, 0.66, 0.02, 0.02, and 0.06 mA/cm^2 at 3 V and 47.8, 30.9, 1.2, 0.9, and 1.3 mA/cm^2 at 5 V, where the current densities of EODs having $Bebq_2$ and BPhen were much higher than those of other devices. This indicates that the electron mobility of ETLs plays a more important role in the current density of EODs than the LUMO value of ETLs.

3.2.3. EL characteristics of WOLEDs using various ETLs

Fig. 7(a) shows the EL spectra of five white OLEDs at 1000 cd/m^2. It was found in Fig. 7(a) that all devices have blue peaks at 465–469 nm, green peaks at 501–503 nm, and red peaks at 592–594 nm. Fig. 7(b) also shows $CIE_{x,y}$ coordinates-luminance characteristics from 100 to 10,000 cd/m^2 for all devices, where they have an emission of $CIE_{x,y}$ coordinates from (0.42, 0.41), (0.42, 0.45), (0.45, 0.42), (0.38, 0.40), and (0.47, 0.40) at 100 cd/m^2 to (0.40, 0.42), (0.41, 0.46), (0.38, 0.42), (0.38, 0.41), and (0.45, 0.40) at 5000 cd/m^2. It was found in Fig. 7(b) that device E has minimal change with $\Delta CIE_{x,y}$ of ±(0.02, 0.00) from 100 to 10,000 cd/m^2. It was also found in Fig. 7(a) that red peak intensity in devices C and E is enhanced compared to that in other devices, which means that devices C and E have more warmish white-emission characteristics rather than coldish white-emission characteristics compared to other devices.

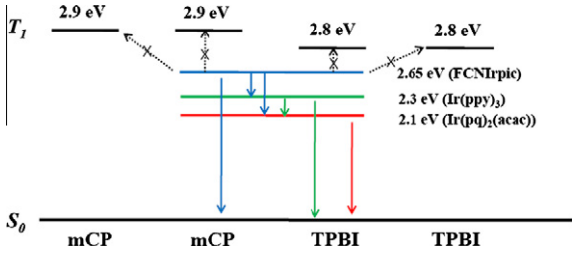

Fig. 9. Possible triplet energy transfer paths for all emitters in the two hosts and ETLs.

3.2.4. Efficiency comparison of white devices with BAlq and TPBI having different triplet energy

Device E with an ETL of TPBI showed higher efficiency than device D with an ETL of BAlq because TPBI (2.8 eV) has higher triplet energy than FCNIrpic (2.65 eV). On the other hand, BAlq (2.6 eV) has lower triplet energy than FCNIrpic as shown in Table 1. Therefore, device E could confine triplet energy in EML well. To confirm this result, as shown in Fig. 8(a), we fabricated blue devices A and B that had the following structure: ITO (150 nm)/NPB (50 nm)/mCP (10 nm)/FCNIrpic:mCP (8%, 10 nm)/BAlq (blue device A) or TPBI (blue device B) (30 nm)/LiF (2 nm)/Al (100 nm), where the doping concentrations of FCNIrpic in mCP were the same as those used for white devices. Fig. 8(b) also showed EQE and PE-luminance charac-

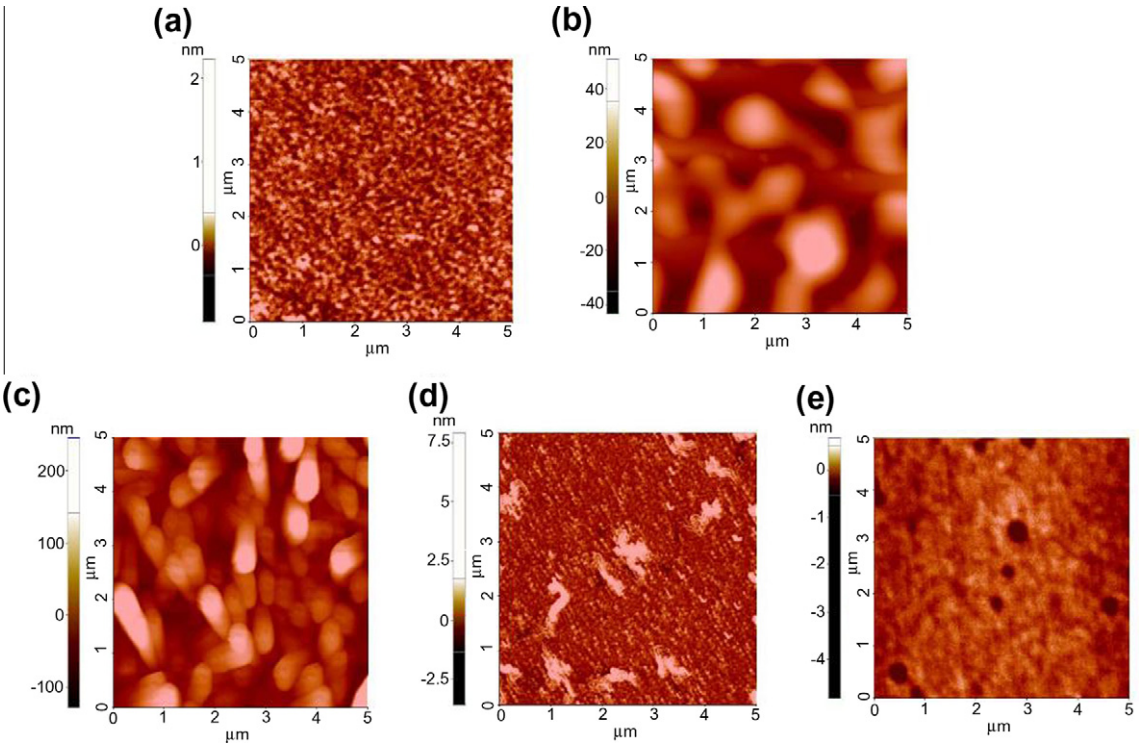

Fig. 10. AFM images of various ETLs. AFM images of various ETLs showing a 5 × 5 μm surface area: (a) $Bebq_2$, (b) BPhen, (c) TAZ, (d) BAlq, and (e)TPBI.

teristics of blue devices A and B, where an EQE of blue devices A and B was 7.55% and 10.01% at 100 cd/m^2 and 4.62% and 8.42% at 1000 cd/m^2, respectively. It was also found in Fig. 8(b) that a PE of blue devices A and B was 8.63 and 13.18 lm/W at 100 cd/m^2 and 4.16 and 8.94 lm/W at 1000 cd/m^2, respectively. Blue device B with an ETL of TPBI showed higher efficiency by a factor of 1.3 and two at 100 and 1000 cd/m^2 than blue device A with an ETL of BAlq, respectively. The efficiency difference between blue devices A and B explains the reason why device E has higher efficiency than device D. In other words, the ETL of TPBI, which has a higher triplet energy level than that of FCNIrpic, could confine triplet energy in EML well. Fig. 9 shows possible triplet energy transfer paths for all emitters in the two hosts and ETLs, where mCP used as a host for FCNIrpic and XBL, and TPBI, used as a host for Ir(ppy)$_3$ and Ir(pq)$_2$(acac), had higher triplet energy leading to effective confinement of triplet excitons in EML.

3.2.5. Surface morphology of various ETLs

Fig. 10 shows the AFM images of Bebq$_2$, BPhen, TAZ, BAlq, and TPBI films. It was found in Fig. 10 that for the films of BPhen and TAZ, the surfaces were very rough with r.m.s. roughness values (σ) of 14.75 and 54.60 nm, respectively. On the other hand, TPBI film showed the smoothest σ, at 0.14 nm, among them. Bebq$_2$ and BAlq films also showed σ of 0.15 and 0.56 nm, respectively. We can expect that the smooth surface of the film may be one of the important factors for achieving high efficiency in OLEDs due to less defective sites at the smooth interface of films. Therefore, the highest efficiency of device E with TPBI as the ETL may be partially due to the good film-forming property of TPBI.

4. Conclusions

WOLEDs were fabricated using blue, green, and red phosphorescent emitters such as FCNIrpic, Ir(ppy)$_3$, and Ir(pq)$_2$(acac) and various ETLs such as Bebq$_2$, BPhen, TAZ, BAlq, and TPBI. White devices with an ETL of TPBI exhibited nearly IQE of 100% and PE of 39.2 lm/W, which had a doubly higher efficiency than the control white device. Remarkably, it also showed high EQE of 16.4% at 1000 cd/m^2. In order to understand the reason why white devices with an ETL of TPBI exhibit nearly 100% IQE, many devices with various structures were fabricated and characterized in this study. In summary, the reasons for nearly 100% IQE are as follows: (1) high-efficiency phosphorescent blue emitter of FCNIrpic: the efficiency of phosphorescent blue emitters is generally lower than that of phosphorescent green and red emitters. But, the blue device with FCNIrpic in this study was found to have 1.5 times higher efficiency than the blue device with FIrpic; (2) good hole-blocking ability: TPBI has a deep HOMO value of 6.2 eV, which is similar to BPhen (6.4 eV) and TAZ (6.3 eV); (3) no electron leakage: no electron leakage can occur at the interface of red EML and ETL since the optimized white device E used TPBI as a host for the red emitter and also as ETL material; (4) higher triplet energy than blue emitter: TPBI can play the role of hole- and exciton-blocking layer simultaneously. Therefore, white devices with TPBI showed good confinement of triplet excitons within the EML; (5) a very smooth surface: TPBI has the smoothest morphology of $\sigma \sim 0.14$ nm among other ETLs. Thus, white devices with TPBI do not seem to show a saturated luminance–voltage curve at high voltage. We have exhibited high-efficiency PHWOLEDs along with a suggestion for the mechanism for achieving nearly 100% IQE. PHWOLEDs fabricated using device structures and materials described here may be expected to be applicable for SSL.

Table 2
Various characteristics of all devices, including, external quantum efficiency, current efficiency, power efficiency, and Commission Internationale de L'Eclairage (CIE$_{x,y}$) coordinates at 500 cd/m^2.

Device	External quantum efficiency (%)	Current efficiency (cd/A)	Power efficiency (lm/W)	CIE$_{x,y}$
A	7.70	17.14	10.87	0.42, 0.41
B	9.93	22.15	13.20	0.42, 0.45
C	10.04	24.46	9.07	0.44, 0.42
D	12.92	28.51	13.54	0.39, 0.40
E	17.47	35.74	19.85	0.46, 0.39

Various characteristics of all devices are summarized in Table 2, such as EQE, current efficiency, PE, and CIE$_{x,y}$ coordinates at 500 cd/m^2.

Acknowledgements

This work was supported by the ERC program of the Korea Science and Engineering Foundation (KOSEF) grant funded by the Korea Ministry of Education, Science and Technology (MEST) (No. R11-2007-045-03001-0).

References

[1] B.W. D'Andrade, S.R. Forrest, Adv. Mater. 16 (2006) 1585.
[2] J.H. Seo, J.H. Park, Y.K. Kim, J.H. Kim, G.W. Hyung, K.H. Lee, S.S. Yoon, Appl. Phys. Lett. 90 (2007) 203507.
[3] K.S. Yook, J.Y. Lee, Appl. Phys. Lett. 92 (2008) 193308.
[4] Q.X. Tong, S.L. Lai, M.Y. Chan, J.X. Tang, H.L. Kwong, C.S. Lee, S.Y. Lee, Appl. Phys. Lett. 91 (2007) 023503.
[5] M.H. Ho, S.F. Hsu, J.W. Ma, S.W. Hwang, P.C. Yeh, C.H. Chen, Appl. Phys. Lett. 91 (2007) 113518.
[6] Y. Sun, S.R. Forrest, Appl. Phys. Lett. 91 (2007) 263503.
[7] Y. Sun, N.C. Giebink, H. Kanno, B. Ma, M.E. Thompson, S.R. Forrest, Nature 440 (2006) 908.
[8] G. Schwartz, S. Reineke, T.C. Rosenow, K. Walzer, K. Leo, Adv. Funct. Mater. 19 (2009) 1319.
[9] S.J. Su, E. Gonmori, H. Sasabe, J. Kido, Adv. Mater. 20 (2008) 4189.
[10] S. Reineke, F. Lindner, G. Schwartz, N. Seidler, K. Wazer, B. Küssem, K. Leo, Nature 459 (2009) 234.
[11] Q. Wang, J. Ding, D. Ma, Y. Cheng, L. Wang, X. Jing, F. Wang, Adv. Funct. Mater. 19 (2008) 84.
[12] Y. Zheng, S.H. Eom, N. Chopra, J.W. Lee, F. So, J. Xue, Appl. Phys. Lett. 92 (2008) 223301.
[13] E.L. Williams, K. Haavisto, J. Li, G.E. Jabbour, Adv. Mater. 19 (2007) 197.
[14] H.I. Baek, C.H. Lee, J. Appl. Phys. 108 (2008) 124504.
[15] F. Hide, P. Kozodoy, S.P. DenBaars, A.J. Heeger, Appl. Phys. Lett. 70 (1997) 2664.
[16] S. Tokito, T. Lijima, T. Tsuzuki, F. Sato, Appl. Phys. Lett. 83 (2003) 2459.

[17] Y.S. Wu, S.W. Hwang, H.H. Chen, M.T. Lee, W.J. Shen, C.H. Chen, Thin Solid Films 486 (2005) 265.
[18] J.H. Seo, I.H. Park, G.Y. Kim, K.H. Lee, M.K. Kim, S.S. Yoon, Y.K. Kim, Appl. Phys. Lett. 92 (2008) 183303.
[19] B.W. D'Andrade, R.J. Holmes, S.R. Forrest, Adv. Mater. 16 (2004) 624.
[20] D. Qin, Y. Tao, Appl. Phys. Lett. 86 (2007) 113507.
[21] J.Y. Li, D. Liu, C. Ma, O. Lengyel, C.S. Lee, C.H. Tung, S. Lee, Adv. Mater. 16 (2004) 1538.
[22] S.P. Singh, Y.N. Mohapatra, M. Qureshi, S.S. Manoharan, Appl. Phys. Lett. 86 (2005) 113505.
[23] M. Kashiwabara, K. Hanawa, R. Asaki, I. Kobori, R. Matsuura, Society of Information Display '04 Digest (2004) 1017.
[24] M. Mazzeo, D. Pisignano, L. Favaretto, G. Sotgiu, G. Barbarella, R. Cingolani, G. Gigli, Synth. Met. 139 (2003) 675.
[25] M.H. Ho, T.M. Chan, P.C. Yeh, S.W. Hwang, C.H. Chen, Appl. Phys. Lett. 91 (2007) 233507.
[26] C.C. Chang, J.F. Chen, S.W. Hwang, C.H. Chen, Appl. Phys. Lett. 87 (2005) 253501.
[27] Y. Liu, J. Guo, J. Feng, H. Zhang, Y. Li, Y. Wang, Appl. Phys. Lett. 78 (2001) 2300.
[28] T.J. Park, W.S. Jeon, J.J. Park, S.Y. Kim, Y.K. Lee, J. Jang, J.H. Kwon, R. Pode, Appl. Phys. Lett. 92 (2008) 113308.
[29] S. Naka, H. Okada, H. Onnagawa, T. Tsutsui, Appl. Phys. Lett. 76 (2000) 197.
[30] J.W. Lee, N. Chopra, S.H. Eom, Y. Zheng, J. Xue, F. So, J. Shi, Appl. Phys. Lett. 93 (2008) 123306.
[31] D. Gebeyehu, K. Walzer, G. He, M. Pfeiffer, K. Leo, J. Brandt, A. Gerhard, P. Stößel, H. Vestweber, Synth. Met. 148 (2005) 205.
[32] G. Schwartz, Doctor Rerum Naturalium, "Novel Concepts for High-Efficiency White Organic Light-Emitting Diodes" (2007) 75.
[33] T.Y. Chu, Y.S. Wu, J.F. Chen, C.H. Chen, Chem. Phys. Lett. 404 (2005) 121.
[34] M.-F. Wu, S.-J. Yeh, C.-T. Chen, H. Murayama, T. Tsuboi, W.-S. Li, I. Chao, S.-W. Liu, J.-K. Wang, Adv. Funct. Mater. 17 (2007) 1887.
[35] C. Adachi, M.A. Baldo, M.E. Thompson, S.R. Forrest, Appl. Phys. Lett. 90 (2001) 5048.
[36] J.H. Seo, G.Y. Kim, J.H. Kim, J.S. Park, K.H. Lee, S.S. Yoon, Y.K. Kim, Jpn. J. Appl. Phys. 48 (2009) 082103.

Organic Electronics 11 (2010) 1767–1771

Contents lists available at ScienceDirect

Organic Electronics

journal homepage: www.elsevier.com/locate/orgel

Plasma-polymerized multistacked bipolar gate dielectric for organic thin-film transistors

Woo-Jun Yoon [a,1,3], Dhiman Bhattacharyya [b,2,3], Richard B. Timmons [b], Paul R. Berger [a,c,*]

[a] Department of Electrical and Computer Engineering, The Ohio State University, Columbus, OH 43210, USA
[b] Department of Chemistry and Biochemistry, University of Texas at Arlington, Arlington, TX 76019, USA
[c] Department of Physics, The Ohio State University, Columbus, OH 43210, USA

ARTICLE INFO

Article history:
Received 27 April 2010
Received in revised form 17 July 2010
Accepted 24 July 2010
Available online 6 August 2010

Keywords:
Plasma polymerization
Polymer gate dielectrics
Organic thin-film transistor

ABSTRACT

A 10-layer stack of bipolar gate dielectric was formed by sequential layer-by-layer deposition using pulsed radio frequency (RF) plasma polymerization of allylamine and vinyl acetic acid monomers. Due to polar groups localized at the interfaces between each consecutive layer by alternating amine (–NH_2) and carboxylic acid (–COOH) functional groups, a 60 nm thick multilayer structure demonstrated relatively high dielectric constant of 4.4 with extremely smooth and crack/pin-hole free surfaces. Without any post-deposition thermal annealing, a 10-layer stack of bipolar dielectric layers shows a low leakage current density ($\sim 1 \times 10^{-6}$ A/cm^2 at 2 MV/cm) with high breakdown fields (>4 MV/cm). With a 10-layer stack of bipolar gate dielectrics, low supply voltage regioregular poly-(3-hexythiophene) (P3HT) organic thin-film transistors (OTFT) were tested. P3HT OTFTs demonstrated low-voltage operation and moderate field-effect mobility up to $\sim 3.4 \times 10^{-3}$ cm^2/V s in the saturation region with the drain voltage a −12 V. The threshold voltage in the saturation region and on–off current ratio were measured to be +1.4 V and $\sim 1.2 \times 10^2$, respectively.

© 2010 Elsevier B.V. All rights reserved.

1. Introduction

Organic-based gate dielectrics with high dielectric constant (k) have made remarkable progress toward high performance and low-voltage operation organic thin-film transistors (OTFT) in the last two decades [1–8]. Among various gate dielectric deposition methods, plasma polymerization has gained increasing interest for its ability to develop new thin gate dielectrics toward electronic application due to simple processing, wide selection of monomers, and low deposition temperature [9,10]. For example, both high- and low-k dielectric have been successfully plasma-polymerized using different monomers [11–15]. More recently, high-k gate dielectrics deposited under plasma polymerization have been implemented in OTFTs, greatly reducing OTFT's operating voltages while exhibiting good device performances [11,12].

Pulsed RF plasma polymerization can be employed to alter systematically the density of the monomer functional groups through controlled variation of the plasma on/off duty cycle. As a result, functional groups present in the monomer can be retained significantly in the polymerized films [13,14]. Under pulsed plasma polymerization conditions, the k values of deposited films can be tailored by employing different polarizability of monomer functional groups. Recently, a 50 nm thick multilayer structure demonstrated relatively high dielectric constant of ~6 without employing any post-deposition thermal annealing, which was attributed to the presence of polar groups, specifically ammonium ($-NH_3^+$) and carboxylate ($-COO^-$) localized at the interfaces between each consecutive plasma deposited

* Corresponding author at: Department of Electrical and Computer Engineering, The Ohio State University, Columbus, OH 43210, USA. Tel.: +1 614 247 6235; fax: +1 614 292 7596.
E-mail address: pberger@ieee.org (P.R. Berger).
[1] Present address: Air Force Institute of Technology, Wright-Patterson AFB, OH 45433, USA.
[2] Present address: Department of Chemical Engineering, Massachusetts Institute of Technology, Cambridge, MA 02139, USA.
[3] Contributed equally to this work.

1566-1199/$ - see front matter © 2010 Elsevier B.V. All rights reserved.
doi:10.1016/j.orgel.2010.07.022

layer [14]. It should be noted that carbon-based materials, like polyimides, generally exhibit a dielectric constant of only 2.0–2.5.

The significant advantage of multistacked bipolar films is that the leakage current can be effectively suppressed, while the film can be synthesized thin, typically less than 50 nm [14]. In our previous study, we found the leakage current is decreased two orders of magnitude even though the total thickness of film is decreased while increasing the number of multilayers in the stack, indicating the number of interfaces within each deposited film is an important factor to control the leakage current in multilayer stacked bipolar polymer films [14].

In this article, we report low-voltage operation regioregular poly-(3-hexylthiophene) (P3HT) OTFTs with pulsed RF plasma-polymerized multistacked bipolar gate dielectric.

2. Experimental

A carboxylic acid (–COOH) containing monomer, vinyl acetic acid (VAA), and an amine ($-NH_2$) containing monomer, allylamine (AA), were polymerized under pulsed RF plasma operational conditions. The monomers were used as-received without further purification. A polymeric thin film of AA was first deposited by pulsed RF plasma polymerization on the substrate which was then followed by the deposition of a thin film of VAA. The sequential layer-by-layer deposition of these films was performed to obtain a total 10-layer stacked structure of pulsed RF plasma-polymerized AA (PP-AA) and VAA (PP-VAA), containing polar groups localized at the interfaces between each consecutive layer. For pulsed plasma deposition of VAA, a plasma duty cycle of 2/30 (plasma on-time, ms/plasma off-time, ms) was used at a monomer pressure 160 mTorr and 150 W power input. Allylamine was plasma polymerized at a duty cycle of 10/30, monomer pressure 70 mTorr and 100 W power input. Substrate temperature was nominally held at room temperature. Further details of condition for pulsed RF plasma polymerization of VAA and AA can be found elsewhere [14]. The nominal total thicknesses and the refractive index of the deposited films were estimated to be ~60 nm, corresponding to individual layers of ~6 nm, and 1.61, respectively, as measured by single wavelength ellipsometry. The surface morphologies of a 10-layer stack of polymeric films were studied using a Dimension 3100 atomic force microscopy (AFM) (Veeco Instruments) in tapping mode.

For capacitance–voltage (C–V) characterization with an LCR meter (Agilent 4284A), the polymer films were deposited on p-type silicon wafers with a resistivity of 4.4 Ω cm for metal–insulator–semiconductor (MIS) capacitors. After deposition of 10-layer stack of PP-AA and PP-VAA, the MIS capacitors were completed by shadowmask electron beam evaporation (~10^{-7} Torr) of a 100 nm thick Au gate metal, directly onto the multilayer stack surface. The final MIS structure fabricated was a p-Si/10-layer stack of PP-AA and PP-VAA/Au. The active area of each MIS capacitor studied was 0.283 mm^2. Leakage current density versus electric field characteristics ($J_{Leakage}$–E) of MIS capacitors were measured with a semiconductor parameter analyzer (Agilent 4156) at room temperature under darkness. All MIS capacitors fabricated were tested without any post-deposition annealing.

A 10-layer stack of film as the gate dielectric was used for a bottom contact OTFTs. The Si substrates were processed using standard silicon degreasing and RCA cleaning procedures prior to plasma polymerization. A heavily doped n-type silicon substrate with a resistivity of 0.003 Ω cm was used as the gate. After deposition of multilayer stacks of thin films, the Au source and drain contacts are formed by standard photolithography and lift-off, defining a channel length of 7 μm and width of 135 μm. It was shown that the plasma-polymerized multistacked gate dielectrics are resistant to immersion in typical chemical solvents for standard photolithography and lift-off. They are robust enough to withstand conventional photolithographic processing with no observable film shrinkage, warping or peeling.

Thin films of the P3HT were then deposited by spin coating from a concentration of 8 mg/ml in chloroform in an inert glove box environment with ⩽1 ppm level of oxygen and moisture. The regioregular P3HT (Merck Chemicals Ltd.) with 94.5% regioregularity was used without further purification. The P3HT used here has a weight-average molecular weight (M_w) of 26,200 g/mol, corresponding to a number-average molecular weight (M_n) of 13,000 g/mol, and with a polydispersity (M_w/M_n) of ~2. The P3HT OTFTs were kept in a vacuum at pressures below 10^{-6} Torr for 10 h to remove any unintended doping. Prior to the measurement, the completed P3HT OTFTs were briefly annealed at 110 °C for 10 min in N_2 atmosphere. Electrical characterizations of the P3HT OTFTs were performed with a semiconductor parameter analyzer (Agilent 4156) at room temperature under darkness in ambient air.

3. Results and discussion

The chemical structures of monomers used for plasma polymerization are shown in Fig. 1. Each AA and VAA monomer has the requisite monomer functionalities, $-NH_2$ and –COOH groups, respectively. Under pulsed plasma operational conditions, these functional groups in the monomer structure are retained significantly in the films. Explicit evidence for the presence of the $-COO^-$ and $-NH_3^+$ polar entities in the interface of the multilayer structure was provided using X-ray photoelectron spectroscopy and attenuated total reflectance Fourier transform-IR spectroscopy, described in detail elsewhere [14].

Fig. 2 shows the AFM tapping mode height images (1 μm × 1 μm) for a 10-layer stack of PP-AA and PP-VAA films deposited on a silicon substrate by pulsed RF plasma polymerization. The root-mean-square (RMS) roughness of the deposited film is ~0.129 nm in the image Z range of 1.703 nm, demonstrating pulsed RF plasma polymerization could be very effective for producing extremely smooth surfaces. In addition, no crack/pin-holes were observed over different positions on the surface scanned by AFM.

Fig. 3a shows a typical C–V response of an MIS capacitor (p-Si/10-layer stack of alternating AA and VAA/Au) at

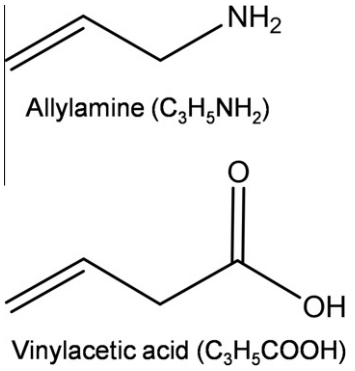

Fig. 1. Chemical structure of monomers used for polymerization under pulsed RF plasma condition: an amine ($-NH_2$) containing monomer, allylamine ($C_3H_5NH_3$), and a carboxylic acid (–COOH) containing monomer, vinyl acetic acid (CH_3COOH).

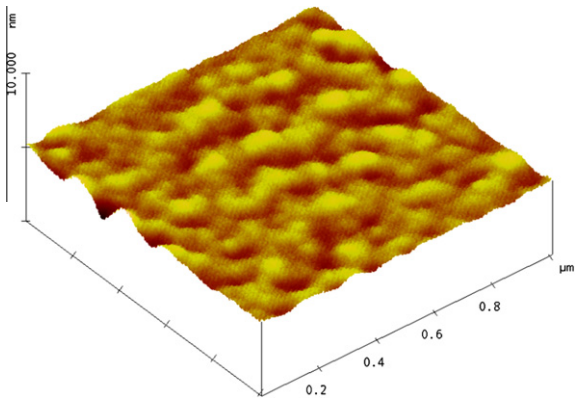

Fig. 2. AFM images (1 μm × 1 μm) for a 10-layer stack of gate dielectric layers deposited by pulsed RF plasma polymerization. The RMS roughness of the gate dielectric layers was 0.129 nm with the image Z range of 1.703 nm.

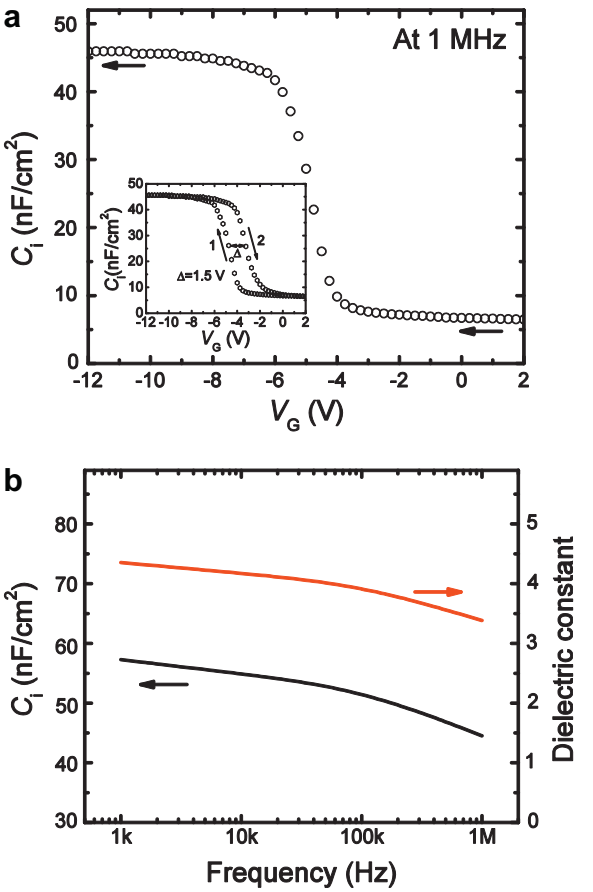

Fig. 3. (a) *C–V* characteristics of MIS capacitors at 1 MHz for a pulsed RF plasma-polymerized gate dielectric (~60 nm). The inset shows the hysteresis behavior of the MIS capacitor. (b) Frequency dependency of the gate capacitance per area (C_i) in accumulation and the dielectric constant. The dielectric constant extracted at 1 kHz is ~4.4.

1 MHz frequency clearly showing depletion at positive gate voltage (V_G) and accumulation at negative V_G when the V_G was swept from $+V_G$ to $-V_G$. It shows the shift to more negative values of V_G along the voltage axis of a *C–V* curves with respect to the ideal *C–V* curve due to uniformly distributed trapped charges during plasma polymerization process across the polymerized films thickness [15]. The inset of Fig. 3a shows the hysteresis behavior of the capacitor for a sweep of $+V_G$ to $-V_G$ and a return sweep $-V_G$ to $+V_G$, which exhibits a ~1.5 V voltage shift at 1 MHz. The voltage shift of the *C–V* curves could be attributed to positive mobile charges associated with the multilayered bipolar gate dielectric. For positive V_G, positive mobile ions drift to the insulator–semiconductor interface, giving a negative voltage shift. For large negative V_G, the positive mobile charges are attracted to the gate-insulator interface where it exhibits less influence upon the measured *C–V* curves. The total voltage shift, ΔV (V) is given as $\Delta V = -Q/C_i$ where Q is the effective net charge per unit area (cm^{-2}), and C_i is the measured gate capacitance per unit area (F/cm^2). The effective net charge density in the gate dielectric layer is estimated to be $\sim 4.4 \times 10^{12}\ cm^{-2}$. The C_i tends to shift to slightly higher values when decreasing the frequency for all capacitors, as shown in Fig. 3b. An observed frequency dependent dispersion in the accumulation region can be attributed to the slow polarization of the gate dielectric at higher frequencies and this polarization can lead to an increase in the induced charge at lower frequencies [16]. The k values of the multilayer gate dielectric were calculated at four different frequencies using $k = C_i \cdot t/\varepsilon_0$, where ε_0 is the permittivity in vacuum, and t is the thickness. The calculated dielectric constant was 4.4 at 1 kHz (Fig. 3b). For the extraction of field-effect mobility values of P3HT OTFTs in the saturation region, the C_i equal to 57.3 nF/cm^2 at 1 kHz was considered.

Fig. 4 illustrates the leakage current density versus electric field, $J_{Leakage}$–E, for the 10-layer stack of gate dielectric. The leakage current density was $7.34 \times 10^{-6}\ A/cm^2$ at 2 MV/cm. The breakdown field was estimated to be larger than 4 MV/cm. The inset of Fig. 4 is the leakage current density versus the voltage ($J_{Leakage}$–V) characteristics for the MIS capacitors. It should be noted that all the multilayer gate dielectrics in this study were measured without any post-deposition annealing.

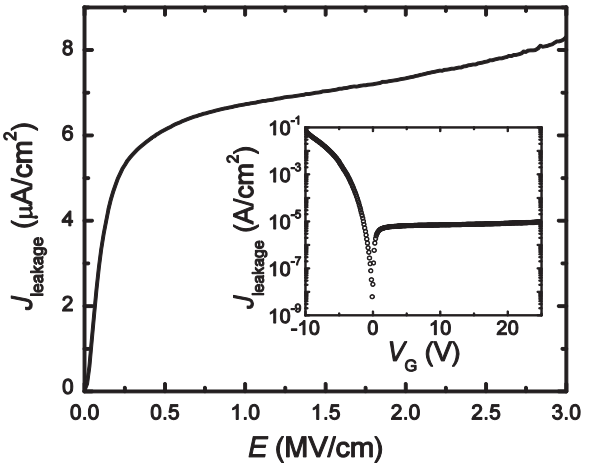

Fig. 4. $J_{Leakage}$–E characteristics of MIS capacitors. The breakdown field is estimated >4 MV/cm. The inset shows $J_{Leakage}$–V characteristics of the capacitors.

Fig. 5a shows the output characteristics for P3HT OTFTs with applied drain voltage (V_D) ranging from 0 to −15 V with V_G varying from 4 to −6 V. The devices operate at relatively low supply voltages. However, a large off-state I_D at the level of $\sim 1 \times 10^{-9}$ A at $V_G = 0$ was observed using fresh devices tested in air without any encapsulation immediately after completion of the fabrication process. Although a non-zero I_D could be reduced by applying a positive V_G, the I_D at $V_G = 4$ V was only one order of magnitude lower than that at $V_G = 0$ V. It has been known that an off-state I_D could increase over the extended exposure in ambient air due to the high bulk conductivity of P3HT attributed from unreduced P3HT and oxygen doping [17,18]. However, considering that the fresh devices were tested immediately after completion of fabrication, a high off-state I_D at a positive V_G could be due to doping to P3HT by oxygen from the surfaces of plasma-polymerized films since plasma-polymerized films have a strong affinity for oxygen and moisture [19]. For the transfer characteristic in the saturation region at $V_D = -10$ V and $V_D = -12$ V, the plot of $I_D^{1/2} - V_G$ is shown in Fig. 5b. The mobility in the saturation region (μ_{sat}), and the threshold voltage (V_T) are calculated from

$$I_D = \frac{W}{2L} C_{total} \mu (V_G - V_T)^2 \quad (1)$$

At $V_D = -12$ V, the μ_{sat} and V_T are estimated to be 3.4×10^{-3} cm^2/V s and +1.4 V, respectively, while $V_D = -10$ V, the μ_{sat} and V_T are 2.9×10^{-3} cm^2/V s and +1.5 V, respectively. The devices showed a dependence of μ_{sat} on V_G (not shown here). Due to a large off-state I_D, an on–off current ratio ($I_{on/off}$) of only $\sim 1.2 \times 10^2$ was measured. No significant variation of estimated μ_{sat}, V_T, and $I_{on/off}$ was recorded over more than 5 devices.

4. Conclusions

In conclusion, pulsed RF plasma polymerization could be very effective for producing extremely smooth and crack/pin-hole free gate dielectrics. It was shown that the plasma-polymerized multistacked gate dielectrics are robust enough to withstand conventional photolithographic processing with no observable film shrinkage, warping or peeling. Finally it was demonstrated that the P3HT OTFTs operate at low supply voltages due to high-k values of pulsed RF plasma-polymerized multistacked gate dielectrics, achieved without post-production annealing. Further work is required to reduce possible oxygen doping to P3HT from the surface of plasma-polymerized gate dielectrics through surface passivation.

Acknowledgement

This work was supported by the Center for Photovoltaics Innovation and Commercialization (PVIC) and the Institute for Materials Research (IMR).

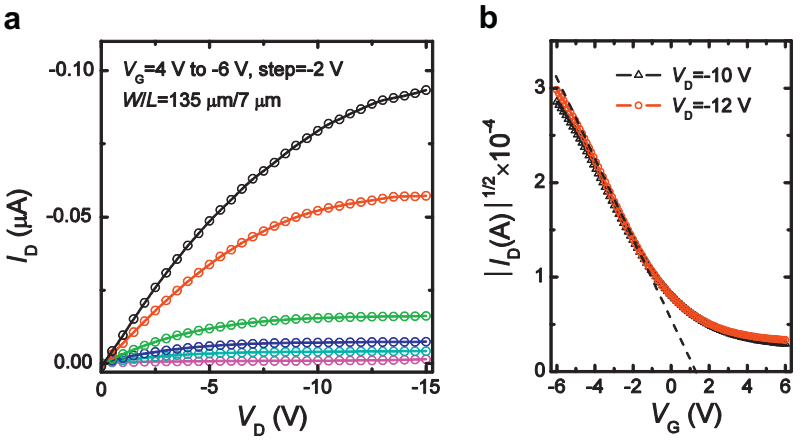

Fig. 5. (a) V_D–I_D characteristics of the P3HT OTFT with the applied V_D ranging from 0 to −15 V with V_G varying from 4 to −6 V in steps of −2 V. (b) $I_D^{1/2} - V_G$ characteristics of the P3HT OTFT with the V_G ranging from 6 to −6 V with V_D of −10 and −12 V.

References

[1] L.-L. Chua, P.K.H. Ho, H. Sirringhaus, R.H. Friend, Appl. Phys. Lett. 84 (2004) 3400.
[2] X. Peng, G. Horowitz, D. Fichou, F. Garnier, Appl. Phys. Lett. 57 (1990) 2013.
[3] Z. Bao, V. Kuck, J.A. Rogers, M.A. Paczkowski, Adv. Funct. Mater. 12 (2002) 526.
[4] Z. Bao, Y. Feng, A. Dodabalapur, V.R. Raju, A.J. Lovinger, Chem. Mater. 9 (1997) 1299.
[5] R. Parashkov, E. Becker, G. Ginev, T. Riedl, H.H. Johannes, W. Kowalsky, J. Appl. Phys. 95 (2004) 1594.
[6] I.M. Rutenberg, O.A. Scherman, R.H. Grubbs, W. Jiang, E. Garfunkel, Z. Bao, J. Am. Chem. Soc. 126 (2004) 4062.
[7] F.-C. Chen, C.-W. Chu, J. He, Y. Yang, J.-L. Lin, Appl. Phys. Lett. 85 (2004) 3295.
[8] Y.-Y. Noh, H. Sirringhaus, Org. Electron. 10 (2009) 174.
[9] H. Biederman (Ed.), Plasma Polymer Films, Imperial College Press, London, 2004.
[10] H. Biederman, Y. Osada, Plasma Polymerization Processes, Elsevier Science, 1992.
[11] Y. Xu, P.R. Berger, J. Cho, R.B. Timmons, J. Appl. Phys. 99 (2006) 014104.
[12] J.-S. Lim, P.-K. Shin, B.-J. Lee, S. Lee, Org. Electron. 11 (2010) 951.
[13] Y. Xu, P. Berger, J. Cho, R. Timmons, J. Electron. Mater. 33 (2004) 1240.
[14] D. Bhattacharyya, W.-J. Yoon, P.R. Berger, R.B. Timmons, Adv. Mater. 20 (2008) 2383.
[15] J.E. Klemberg-Sapieha, S. Sapieha, M.R. Wertheimer, A. Yelon, Appl. Phys. Lett. 37 (1980) 104.
[16] P.J. Brown, H. Sirringhus, M. Harrison, M. Shkunov, R.H. Friend, Phys. Rev. B 63 (2001) 1252041.
[17] M.S.A. Abdou, F.P. Orfino, Y. Son, S. Holdcroft, J. Am. Chem. Soc. 119 (1997) 4518.
[18] D.B.A. Rep, A.F. Morpurgo, T.M. Klapwijk, Org. Electron. 4 (2003) 201.
[19] H. Jiang, J.T. Grant, J. Enlow, W. Su, T.J. Bunning, J. Mater. Chem. 19 (2009) 2234.

Organic Electronics 11 (2010) 1772–1778

Contents lists available at ScienceDirect

Organic Electronics

journal homepage: www.elsevier.com/locate/orgel

Synthesis of an alternating thienylenevinylene–benzothiadiazole copolymer with high hole mobility for use in organic solar cells

Bogyu Lim [1], Jang Jo [1], Dongyoon Khim, Hyung-Gu Jeong, Byung-Kwan Yu, Juhwan Kim, Dong-Yu Kim *

Heeger Center for Advanced Materials (HCAM), Department of Materials Science and Engineering, Gwangju Institute of Science and Technology, 1 Oryong-Dong, Buk-Gu, Gwangju 500-712, Republic of Korea

ARTICLE INFO

Article history:
Received 27 June 2010
Received in revised form 30 July 2010
Accepted 8 August 2010
Available online 18 August 2010

Keywords:
Bulk-heterojunction solar cell
Low band-gap polymer
Poly(thienylenevinylene)

ABSTRACT

A new thienylenevinylene–benzothiadiazole copolymer, poly{1,2-(*E*)-bis[2-(5-bromo-3-dodecyl-2-thienyl)-5-thienyl]ethene-2,1,3-benzothiadiazole} (**PETVTBT**), was synthesized and characterized for potential use in solar cells. The polymer had broad absorption over the entire visible region and a low band gap of 1.57 eV. In addition, the polymer had a relatively low HOMO level of about 5.1 eV. Although **PETVTBT** was a donor–acceptor-type copolymer, the hole mobility reached 0.025 $cm^2/V\,s$ using field-effect transistors. Bulk-heterojunction solar cells that used a **PETVTBT**:$PC_{[71]}BM$ blend as the active layer showed a power conversion efficiency of 1.0% under a simulated AM 1.5 G solar irradiation at 100 mW/cm^2.

© 2010 Elsevier B.V. All rights reserved.

1. Introduction

Polymer solar cells (PSC) have attracted considerable attention recently because of their low manufacturing costs, solution processing and use in flexible devices [1]. Recently, the power conversion efficiencies (PCE) of bulk-heterojunction (BHJ) solar cells that are based on poly (3-hexylthiophene):[6,6]-phenyl-C61-butyric acid methyl ester (P3HT:$PC_{[61]}BM$) were reported to be approximately 5% [2]. Although P3HT is one of the most promising materials ever tested for use in polymer solar cells, P3HT absorbs only within the visible region of the solar spectrum, which limits device performance. To better match the solar spectrum, development of new low band-gap (LBG) polymers is critically important. The most successful approach to designing LBG-conjugated polymers is alternation of conjugated electron-rich and conjugated electron-deficient units within the polymer chain. These polymers have been termed donor (D)–acceptor (A) semiconducting polymers [3]. The D–A semiconducting polymers reduce the optical band-gap via intramolecular charge transfer (ICT) [4].

A large number of D–A-type LBG polymers have been reported by many research groups [5,6]. Among the various acceptor units, 2,1,3-benzothiadiazole and 4,7-di-2-thienyl-2,1,3-benzothiadiazole are most frequently used as acceptor molecules in the D–A-type LBG polymers [7]. For example, the silole-containing thiophene-2,1,3-benzothiadiazole copolymer PSBTBT has a high power conversion efficiency of 5.1% and a relatively high hole mobility of 3×10^{-3} $cm^2/V\,s$ [8]. Recently, Bazan and co-workers reported that modification of the alkyl side-chain of this polymer resulted in a very high efficiency of 5.9% when it was blended in a BHJ composite with $PC_{[71]}BM$ [9].

On the other hand, charge carrier mobility is also a very attractive feature that is critically important for high-performance solar cells [10]. The low hole mobility of the donor polymer is one of the limiting factors to achieve high efficient BHJ solar cells due to the efficient charge collection to each electrodes [11]. Therefore, high-mobility

* Corresponding author. Tel.: +82 62 715 2319; fax: +82 62 715 2304.
E-mail address: kimdy@gist.ac.kr (D.-Y. Kim).
[1] Present address: Center for Polymers and Organic Solids, University of California Santa Barbara, Santa Barbara, CA 93106, USA.

1566-1199/$ - see front matter © 2010 Elsevier B.V. All rights reserved.
doi:10.1016/j.orgel.2010.08.004

LBG-conjugated polymers with broad absorption spectra are very attractive for PSC applications.

Recently, we reported a strong interchain interaction polymer in the solid state, poly(1,2-(*E*)-bis[2-(5-bromo-3-dodecyl-2-thienyl)-5-thienyl]ethene) (PETV12T) [12], which also had a high charge carrier mobility of 0.15 cm^2/V s. However, PETV12T has a relatively large band gap (~1.85 eV), which prevents its application as an absorber in a BHJ solar cell. To further enhance the absorption of sunlight, the band gap must be reduced.

The present study describes the synthesis of an alternating copolymer comprised of electron-rich 1,2-(*E*)-bis[2-(5-bromo-3-dodecyl-2-thienyl)-5-thienyl]ethene and electron-deficient 2,1,3-benzothiadiazole units, which was abbreviated as **PETVTBT**. This D–A copolymer had broad absorption over the entire visible region and a low band gap of 1.57 eV. In addition, this LBG polymer had a high hole mobility of 0.025 cm^2/V s. The BHJ solar cells that used a **PETVTBT**:$PC_{[71]}BM$ blend as the active layer showed a power conversion efficiency of 1.0% under simulated AM 1.5 G solar irradiation at 100 mW/cm^2. The relatively low power conversion efficiency, despite a low band gap and a high mobility, was due to a change in the electronic properties of **PETVTBT** that resulted from blending the polymer with the acceptor $PC_{[71]}BM$.

2. Experimental section

2.1. Materials

All starting materials were purchased from Aldrich Chemical Co., and were used without further purification. THF and diethyl ether were dried over calcium hydride. 1,2-(*E*)-bis[2-(5-bromo-3-dodecyl-2-thienyl)-5-thienyl]ethene and 4,7-dibromo-2,1,3-benzothiadiazole were prepared as previously described [12,13].

2.2. Synthesis

2.2.1. 4,7-Bis(4,4,5,5-tetramethyl-1,3,2-dioxaborolan-2-yl)-2,1,3-benzothiadiazole (**2**)

A solution of 4,7-dibromo-2,1,3-benzothiadiazole (1.5 g, 5.1 mmol), bis(pinacolato)diboron (3 g, 11.81 mmol), PdCl2 (dppf)-MC complex (0.75 g, 0.92 mmol), and potassium acetate (3 g, 30.57 mmol) in degassed 1,4-dioxane (20 ml) was stirred at 80 °C overnight. The reaction was quenched by addition of water, and the resulting mixture was washed with diethyl ether, dried over $MgSO_4$, and concentrated *in vacuo* to yield a dark red solid. The solid was purified by silica gel chromatography using 3% ethyl acetate in hexane to give the desired compound as a pink solid. Yield: 21%. ^1H NMR ($CDCl_3$, 400 MHz, [ppm]): δ 8.12 (s, 2H), 1.43 (s, 24H). GCMS (EI): *m/z* 388, calcd 388.10.

2.2.2. Poly{1,2-(E)-bis[2-(5-bromo-3-dodecyl-2-thienyl)-5-thienyl]ethene-2,1,3-benzothiadiazole} (**PETVTBT**)

2 (0.31 g, 0.8 mmol) and 1,2-(*E*)-bis[2-(5-bromo-3-dodecyl-2-thienyl)-5-thienyl]ethane (0.68 g, 0.8 mmol), degassed K_2CO_3 (8 ml, 2 M) and 1 drop of Aliquat 336 (2 mol%) were dissolved in 10 ml of toluene in a 100-ml flask. The solution was purged with nitrogen for 30 m, and then tetrakis(triphenylphosphine)palladium (92 mg, 0.08 mmol) was added. The reaction was stirred at 100 °C for 48 h. After completion of the reaction, bromobenzene (0.1 equiv) was added to the reaction mixture, followed by stirring for 2 h. The resulting mixture was poured into a mixture of methanol and concentrated hydrochloric acid (2:1) and stirred overnight. The precipitated dark black solid was redissolved in THF and added dropwise to methanol (200 ml). The resulting solid was removed by filtration and then was subjected to Soxhlet extraction with methanol, acetone, and hexane to remove the low-molecular-weight fraction. The residue was extracted with chlorobenzene to give a dark black solid. Yield: 0.272 g (41%). ^1H NMR ($CDCl_3$, 400 MHz, [ppm]): δ 7.51 (s, 2H), 7.04–6.99 (br, 8H), 2.85 (br, 4H), 1.75 (br, 4H), 1.25 (br, 36H), 0.87 (br, 6H).

2.2.3. Characterization and measurements

Materials were characterized by ^1H NMR spectroscopy (JEOL JNM-LA300WB 400 MHz). Thermo-gravimetric analysis (TGA) was performed using a TA Instrument 2050 series. Differential scanning calorimetry (DSC) was performed using a TA Instrument 2010 series at a heating rate of 10 °C/min under a nitrogen atmosphere. Absorption spectra were measured using a UV–vis spectrophotometer (Lambda 750, Perkin–Elmer). Mass spectra were obtained by gas chromatography mass spectrometry (GCMS, Shimadzu GCMS-QP2010). The molecular weight of the polymer was confirmed by gel-permeation chromatography (GPC, Futecs, NS2001). Cyclic voltammetry (CV) was conducted using an Autolab, PGSTAT 30 Potentiostat/Galvanostat in an acetonitrile solution with 0.1 M tetrabutylammonium perchlorate (Bu_4NClO_4) as the supporting electrolyte, indium tin oxide (ITO) as the working electrode, a Pt wire as the counter electrode, and a Ag wire as the reference electrode at a scan rate of 50 mV/s. Atomic force microscopy (AFM) measurements were performed using an Autoprobe CP, PSI.

2.2.4. OTFT fabrication and characterization

The glass substrate was cleaned in an ultrasonic bath with DI water and acetone, followed by 2-propanol, and was then stored in a vacuum oven prior to electrode deposition. The source and drain electrodes were deposited on the cleaned glass substrates by thermal evaporation (Ni/Au = 5/30 nm). The channel length was 50 μm and the width was 1.0 mm. After deposition of the source and drain electrodes, the patterned surface was treated with 1H,1H,2H,2H-perfluorodecanethiol (PFDT) vapor to produce hydrophobic surfaces on the bottom-contact Au electrodes. **PETVTBT** films with a thickness of 80 nm were spin-coated from a 10 mg/ml solution in chlorobenzene and annealed at 130 °C for 10 min in a glove box. After annealing, 500-nm thick PMMA films, which served as gate dielectric layers, were spin-coated from an 80 mg/ml solution in *n*-butylacetate and baked at 80 °C for 2 h in a glove box. Subsequently, aluminium electrodes were deposited at a thickness of 30 nm by thermal evaporation. OTFT devices were characterized using a Keithley 4200-SCS characterization system under ambient conditions.

2.2.5. BHJ solar cell fabrication and characterization

The patterned indium tin oxide (ITO)-coated glass substrates were cleaned according to a conventional method. After cleaning the substrate, UV-O_3 treatment was carried out for 30 min prior to deposition of PEDOT:PSS (Baytron P VP AI4083). The PEDOT:PSS was spin-coated (5000 rpm, 1 min) onto the ITO-coated glass, which was then baked at 140 °C for 10 min in air before being transferred to an N_2-filled glove box for additional processing. The thickness, as measured with a surface profiler (Kosaka ET-3000i), was almost 25 nm. Films of **PETVTBT** blended with $PC_{[71]}BM$ (Nano-C) were used for the active layers of the solar cells. The weight ratios of **PETVTBT** to $PC_{[71]}BM$ in the blended solutions were 1:1, 1:2, 1:3, and 1:4. **PETVTBT** and $PC_{[71]}BM$ (total 25 mg) were dissolved in 500 μl of 1,2-dichlorobenzene and stirred at 60 °C overnight in an N_2-filled glove box. The active layers of each device were formed by spin coating, with the blended solutions passing through a 0.2-μm PTFE filter prior to deposition on the PEDOT:PSS layer. After spin coating, solvent annealing was performed at room temperature for 2 h in a jar. The Ca (25 nm)/Al (100 nm) top electrodes were deposited on the active layers by thermal evaporation under a high vacuum ($<3 \times 10^{-6}$ torr) with a shadow mask, and the area (4.66 mm^2) was defined as the photoactive area of the corresponding devices. *J–V* curves were measured with a Keithley 4200 source measurement unit. The solar cell devices were illuminated at an intensity of 100 mW/cm^2 using a 1-kW Oriel solar simulator with an AM 1.5 G filter in an N_2-filled glove box. For accurate measurements, the light intensity was calibrated using a radiant power meter and two reference silicon solar cells certified by the NREL.

3. Results and discussion

3.1. Synthesis and characterization

Scheme 1 shows the synthesis of **PETVTBT**. The monomer **1** was synthesized according to an established method [13]. The bromination of 2,1,3-benzothiadiazole with bromine to form **1** was performed at room temperature. The diboronic esters **2** were synthesized by the $PdCl_2$ (dppf)-catalyzed reaction of the corresponding dibromo starting material **1**, bis(pinacolato)diboron, and KOAc in degassed 1,4-dioxane [14]. The pure product **2** was isolated by chromatography on silica gel using a mixture of ethyl acetate and hexane as the eluent. After chromatography, **2** was recrystallized from dichloromethane/ethanol to afford the product as a pale pink solid. The D–A **PETVTBT** polymer was synthesized from a combination of diborolane 2 with a dibromooligothiophene 1,2-(*E*)-bis[2-(5-bromo-3-dodecyl-2-thienyl)-5-thienyl]ethane by Suzuki coupling in the presence of 10 mol% of $Pd(pph_3)_4$ as a catalyst, K_2CO_3 as a base, and 1 drop of Aliquat 336 as a phase-transfer catalyst. After polymerization, soxhlet extraction was performed using methanol, acetone, hexane and chlorobenzene in sequence. The **PETVTBT** in the chlorobenzene fraction gave a dark black solid in 41% yield. The molecular weight of the **PETVTBT** was estimated by gel-permeation chromatography (GPC) analysis in a THF solution relative to polystyrene standards. The number-average molecular weight (M_n) was 8000 with a polydispersity index (M_w/M_n) of 1.4.

TGA and DSC were used to investigate the thermal properties of the polymers. **PETVTBT** exhibited very good thermal stability, losing less than 5% of its weight on heating to 390 °C, as determined by thermo-gravimetric analysis (TGA) (Fig. 1a). The differential scanning calorimetry (DSC) thermogram for the polymer was determined to have a glass transition temperature of 149 °C (Fig. 1b).

3.2. Optical and electrochemical properties

The normalized UV–vis absorption spectra of a solution of **PETVTBT** in chlorobenzene, and films spin-coated from chlorobenzene onto a glass substrate are shown in Fig. 2. The dilute chlorobenzene solution of **PETVTBT** showed a broad absorption band, ranging from 350 to 700 nm. The absorption maximum (λ_{max}) located at 563 nm was due to the ICT transition [15]. The absorption maximum was accompanied by a strong absorption band at a shorter

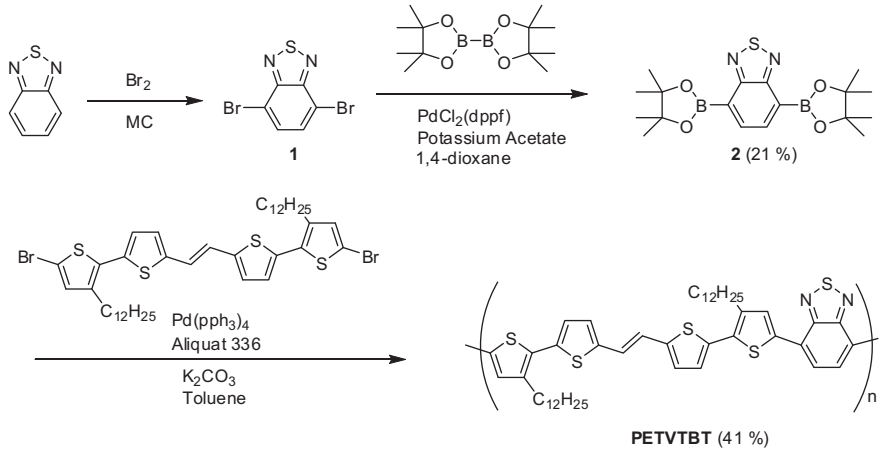

Scheme 1. Synthetic scheme for **PETVTBT**.

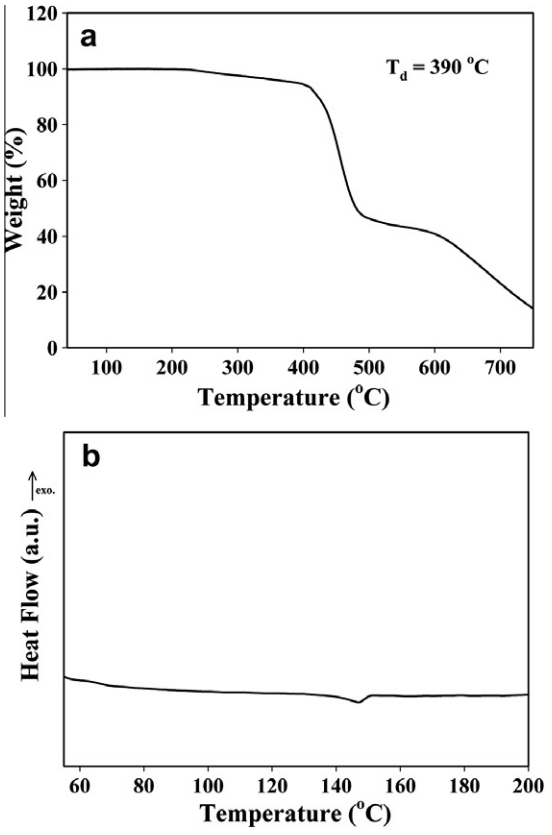

Fig. 1. TGA curve (a) and DSC thermogram (b) of **PETVTBT**.

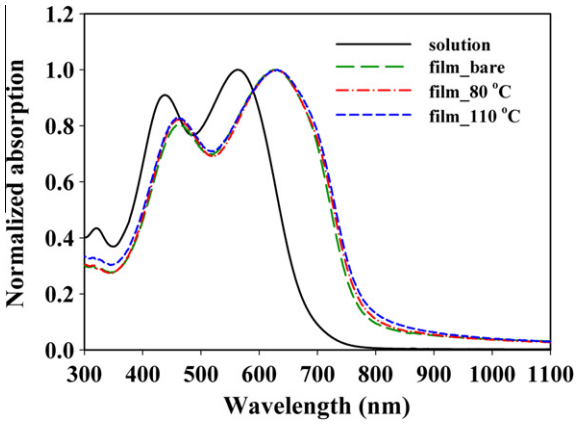

Fig. 2. UV–vis spectra of **PETVTBT** in chlorobenzene solution, unannealed thin film, and annealed film.

wavelength of 438 nm, which corresponded to the π–π^* transition of the quarterthiophene-vinylene units [16].

The normalized UV–vis absorption spectra of the **PETVTBT** films are also depicted in Fig. 2. Compared with the UV–vis absorption spectrum of the solution, the spectra of the polymer films showed pronounced peak broadening and a very large red-shift. When the thin film was annealed at 80 °C or 110 °C, the absorption maximum underwent an additional red-shift from 625 to 632 nm. This result implies that the polymer chains formed a more planar geometry with strong interchain interactions in the solid state

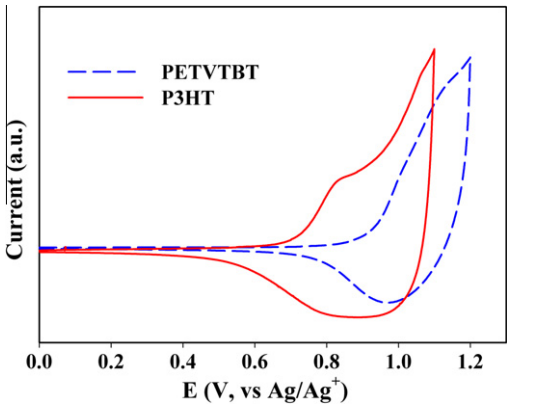

Fig. 3. Cyclic voltammogram of **PETVTBT** and P3HT.

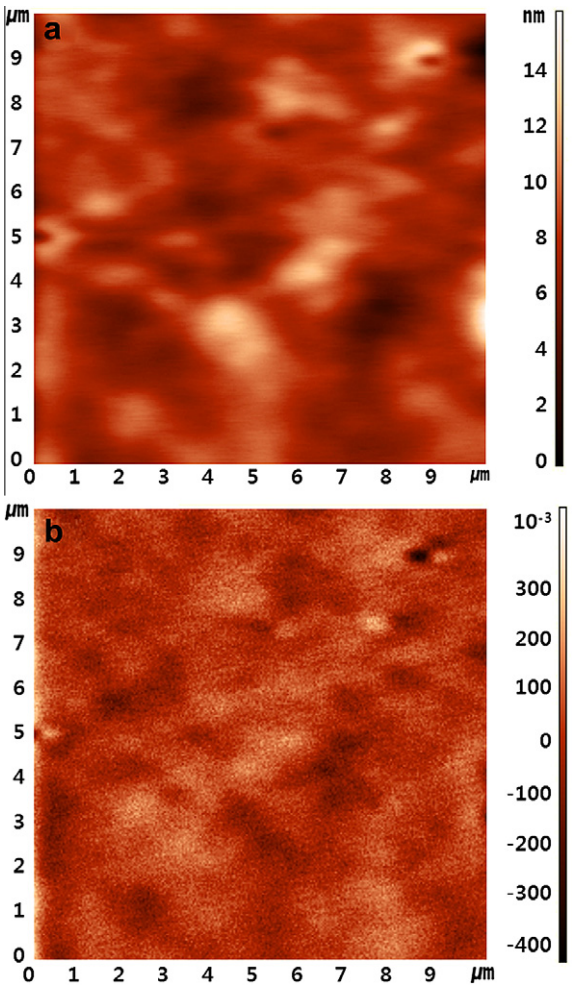

Fig. 4. AFM images of spin-coated **PETVTBT**:$PC_{[71]}BM$ (1:2, w/w ratio) films on silicon wafer; (a) topographic and (b) phase images.

[17]. More importantly, the UV–vis absorption spectrum of **PETVTBT** covered the entire visible region, which was indicative of a black polymer. This property is very attractive for fabrication of high-performance polymer solar cells due to the improved light harvesting. The optical band gap of the polymer was determined from the onset of UV–vis absorption in the solid state. The optical band gap of **PETVTBT** was 1.57 eV, which is very close to the ideal band gap for a polymer solar cell [18].

To investigate the electrochemical characteristics of **PETVTBT** and to estimate the highest occupied molecular orbital (HOMO) and lowest unoccupied molecular orbital (LUMO) levels of the polymers, cyclic voltammetry (CV) measurements were performed with 0.1 M tetrabutylammonium perchlorate ($Bu_4NC\,lO_4$) as the supporting electrolyte at a scan rate of 50 mV/s. To estimate the energy levels of the polymer from the vacuum energy level, we used the ferrocene/ferrocenium (Fc/Fc^+) redox couple as a calibration reference. The half-wave potential ($E_{1/2}$) for oxidation of the Fc/Fc^+ redox couple is 4.8 eV, below the vacuum level [19]. The HOMO level of **PETVTBT** was 5.1 eV (Fig. 3), which was 0.2 eV less than that of rr-P3HT (4.9 eV) when measured under the same conditions. The HOMO energy level of **PETVTBT** was lower than that of rr-P3HT, which is important for achieving large open-circuit voltage (V_{oc}) and high air stability.

3.3. Surface morphology of *PETVTBT*:$PC_{[71]}BM$ blend film

The roughness and surface morphology of the **PETVTBT**:$PC_{[71]}BM$ blend film were observed using atomic force microscopy (AFM). The blend film was prepared by spin coating from a 1:2 weight ratio of **PETVTBT**:$PC_{[71]}BM$ in 1,2-dichlorobenzene, and solvent annealing was performed at room temperature for 2 h in a jar. Fig. 4 shows the topographic and phase images of the blend film. The blend film was very smooth, and the root-mean-squared (RMS) surface roughness of the blend film was 1.58 nm, as shown in the topographic image.

3.4. Hole mobility

High hole mobility in the donor polymer is critically important for effective BHJ solar cells [20]. To characterize hole mobility, a **PETVTBT**-based organic thin-film transistor (OTFT) with a bottom-contact/top-gate (BC/TG) configuration was fabricated on a glass substrate. Before deposition of the active layer, the patterned substrate was treated with PFDT. The PFDT treatments reduced the contact resistance between the Au electrodes and the polymer active layer by increasing the Au electrode work function [21]. Fig. 5 shows transfer and output curves typical of a device with **PETVTBT** as the active layer. The hole

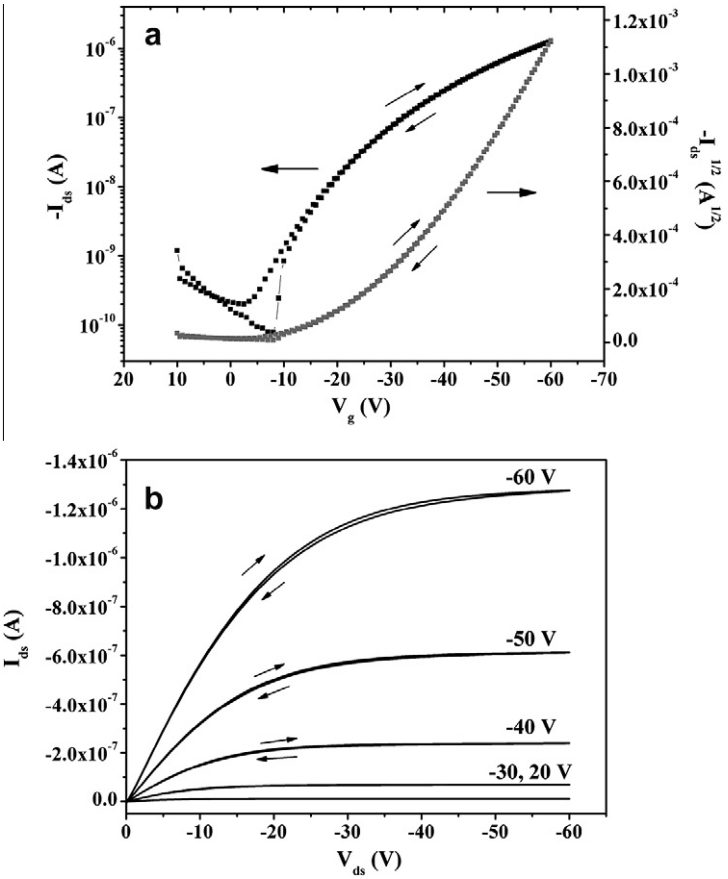

Fig. 5. *I–V* characteristics of a bottom-contact/top-gate (BC/TG) OTFT device of **PETVTBT** as semiconductor: (a) transfer curve at $V_d = -60$ V; (b) output curves at different gate voltages ($L = 50$ μm, $W = 1.0$ mm).

mobility was calculated from the slope of the linear fit of the transfer curve using the saturation regime. The hole mobility was 0.025 $cm^2/V\,s$, which was relatively high value than that of other D–A-type LBG polymers [22]. In addition, forward and reverse scans of the transfer curves showed that this polymer has very low hysteresis.

3.5. Photovoltaic performance

Bulk-heterojunction polymer solar cells were fabricated using **PETVTBT** as the donor, $PC_{[71]}BM$ as the acceptor, and Ca/Al as the negative electrode. The device structure was ITO/PEDOT:PSS/photoactive layer/Ca/Al. The active layer was spin-coated from a 1,2-dichlorobenzene solution, followed by solvent-assisted annealing at room temperature for 2 h in a jar [23]. The thicknesses of the thin film of the photoactive **PETVTBT**:$PC_{[71]}BM$ layer ranged from 60 to 100 nm. Although **PETVTBT** has a low solubility in 1,2-dichlorobenzene at low temperatures, the film morphology that formed upon heating a solution of **PETVTBT**:$PC_{[71]}BM$ was very smooth, as shown in the AFM images. Fig. 6 shows the current density–voltage characteristics of the photovoltaic cells fabricated using **PETVTBT**:$PC_{[71]}BM$ weight ratios of 1:1, 1:2, 1:3, and 1:4 under 1 sun AM 1.5 G of simulated irradiation at 100 mW/cm^2. Table 1 summarizes the photovoltaic characteristics as a function of $PC_{[71]}BM$ weight ratios. Maximal values of J_{sc}, and PCE were observed for the photovoltaic device with a 1:2 ratio of **PETVTBT**:$PC_{[71]}BM$. Both J_{sc} and PCE decreased at $PC_{[71]}BM$ weight ratios greater than 1:2. This result was attributed to increased aggregation of the $PC_{[71]}BM$, which would influence the separation of charges. Furthermore, an unbalanced charge transport was established due to the large fullerene ratio. Hence, both J_{sc}, and PCE decreased at higher fullerene weight ratios because of the two reasons described above. In addition, the values for V_{oc} decreased monotonically when the $PC_{[71]}BM$ content of the blend films was increased. A similar drop in the V_{oc} of MDMO-PPV/PCBM devices has been observed [24]. The decrease in V_{oc} could be explained by the formation of a charge-transfer complex (CTC) in a polymer/PCBM film, which reduces the effective LUMO level of PCBM [25]. Therefore,

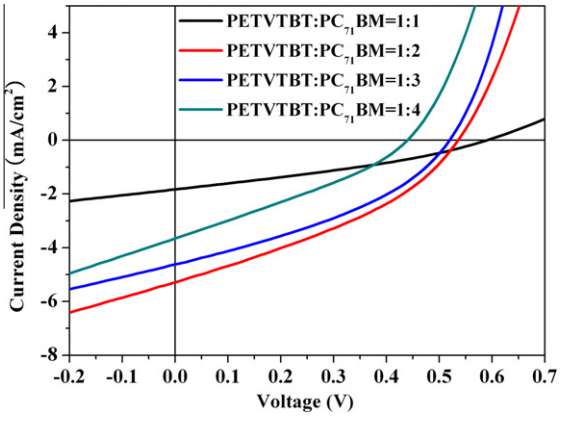

Fig. 6. The *J–V* curves of the **PETVTBT**:$PC_{[71]}BM$ based BHJ solar cell under 1 sun illumination. Device configuration – glass/ITO/PEDOT:PSS (25 nm)/**PETVTBT**:$PC_{[71]}BM$/Ca (25 nm)/Al (100 nm).

Table 1
A summary of the cell performance of parameters, indicating J_{sc}, V_{oc}, *FF* and PCE as functions of $PC_{[71]}BM$ concentration.

Device	Thickness (nm)	*FF* (%)	J_{sc} (mA/cm^2)	V_{oc} (V)	PCE (%)
1:1	100	32	1.83	0.59	0.35
1:2	80	35	5.29	0.54	1.00
1:3	60	37	4.62	0.52	0.88
1:4	80	30	3.66	0.44	0.49

the decrease in V_{oc} was proportional to the increase in the $PC_{[71]}BM$ concentration. The best performance was obtained with an active layer thickness of approximately 80 nm and a **PETVTBT**:$PC_{[71]}BM$ weight ratio of 1:2, which resulted in a J_{sc} of 5.29 mA/cm^2, a V_{oc} of 0.54 V, a *FF* of 0.35, and a PCE of 1.00%. These relatively lower efficiencies could be mainly attributed to the poor absorption and dissociation of low energy region excitons after blended with PCBM. Fig. 7 shows an incident photon-to-current conversion efficiency (IPCE) spectrum and UV–vis absorption spectrum of the 1:2 ratio of **PETVTBT**:$PC_{[71]}BM$ film. In contrast with the UV–vis absorption spectrum of the neat polymer, the IPCE spectrum of the **PETVTBT**:$PC_{[71]}BM$ blend film was decreased at longer wavelengths (~600–800 nm), and the absorption spectrum of the blend film was also diminished in the long-wavelength region unlike other high-performance polymers (Supplementary information, Fig. S1). These phenomena were also observed in

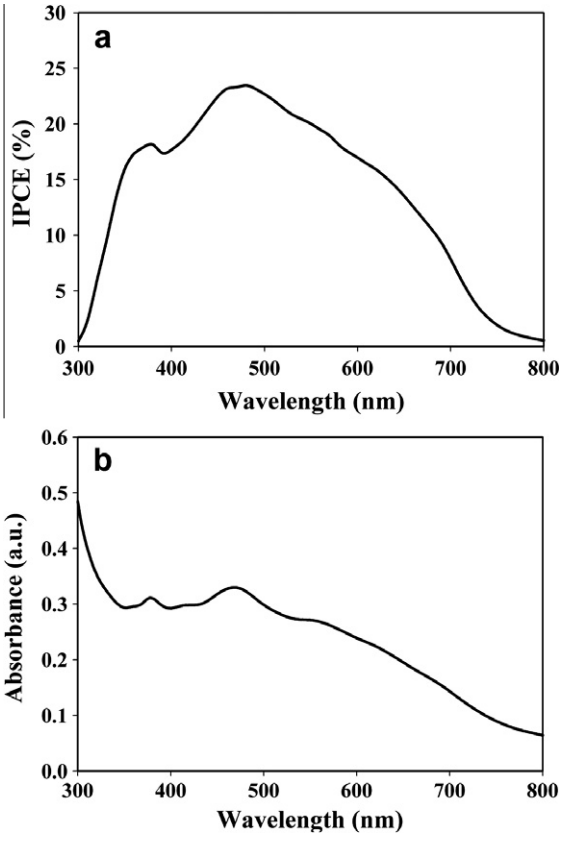

Fig. 7. The IPCE spectrum (a) and UV–vis absorption spectrum (b) of 1:2 ratio of **PETVTBT**:$PC_{[71]}BM$ film.

the UV–vis absorption spectrum of the **PETVTBT**:$PC_{[71]}BM$ solution (Supplementary information, Fig. S2). This result indicates that the electronic properties of **PETVTBT** were altered by blending with $PC_{[71]}BM$. Additional studies aimed at explaining this phenomenon are currently under way.

4. Conclusions

An alternating copolymer comprised of electron-rich thienylenevinylene and electron-deficient benzothiadiazole, **PETVTBT**, was synthesized. The thermal, optical, electrochemical, and photovoltaic properties of the copolymer were investigated in detail. The polymer was thermally stable with a decomposition temperature of 390 °C. The UV–vis absorption spectrum of **PETVTBT** covered the entire visible region, and the optical band gap of **PETVTBT** was 1.57 eV, which is very close to the ideal band gap for a polymer solar cell. In addition, the polymer had a low HOMO level of about 5.1 eV. Furthermore, the polymer had relatively high hole mobility of 0.025 cm^2/V s. These properties indicate that the polymer has potential for use in polymer solar cell applications. The photovoltaic properties of **PETVTBT** were investigated in a bulk-heterojunction solar cell that used $PC_{[71]}BM$ as the electron acceptor. A power conversion efficiency of 1.00% was achieved. In spite of the low band-gap, low HOMO energy level, and high hole mobility of the **PETVTBT**, the photovoltaic efficiency was relatively low, because the electronic properties of **PETVTBT** were changed after blending with $PC_{[71]}BM$.

Acknowledgment

This work was financially supported by the Ministry of Education, Science and Technology (MEST) of Korea through the Brain Korea 21 (BK21) program, a National Research Foundation of Korea Grant funded by the Korean Government (MEST) (NRF-2009-C1AAA001-2009-0092950), NCRC grant (No.R15-2008-006-02001-0), the New and Renewable Energy R&D program (2008-N-PV08-P-01) under the Korea Ministry of Knowledge Economy (MKE), the World Class University (WCU) program at GIST through a grant provided by the MEST (Project No. R31-20008-000-10026-0), the BioImaging Research Center at GIST, and the Heeger Center for Advanced Materials (HCAM).

Appendix A. Supplementary data

Supplementary data associated with this article can be found, in the online version, at doi:10.1016/j.orgel.2010.08.004.

References

[1] (a) G. Yu, J. Gao, J.C. Hummelen, F. Wudl, A.J. Heeger, Science 270 (1995) 1789;
(b) F.C. Krebs, S.A. Gevorgyan, Jan Alstrup, J. Mater. Chem. 19 (2009) 5442;
(c) S.H. Eom, S. Senthilarasu, P. Uthirakumar, S.C. Yoon, J. Lim, C. Lee, H.S. Lim, J. Lee, S.-H. Lee, Org. Electron. 10 (2009) 536.
[2] W. Ma, C. Yang, X. Gong, K. Lee, A.J. Heeger, Adv. Funct. Mater. 15 (2005) 1617.
[3] Y.P. Zou, D. Gendron, R. Badrou-Aich, A. Najari, Y. Tao, M. Leclerc, Macromolecules 42 (2009) 2891.
[4] G. Brocks, A. Tol, J. Phys. Chem. 100 (1996) 1838.
[5] (a) E. Zhou, S. Yamakawa, K. Tajima, C. Yang, K. Hashimoto, Chem. Mater. 21 (2009) 4055;
(b) J.-Y. Lee, W.-S. Shin, J.-R. Haw, D.-K. Moon, J. Mater. Chem. 19 (2009) 4938;
(c) H.A. Becerril, N. Miyaki, M.L. Tang, R. Mondal, Y.-S. Sun, A.C. Mayer, J.E. Parmer, M.D. McGehee, Z. Bao, J. Mater. Chem. 19 (2009) 591;
(d) I.H. Jung, H. Kim, M.-J. Park, B. Kim, J. -H. Park, E. Jeong, H.Y. Woo, S. Yoo, H.-K. Shim, J. Polym. Sci. Part A: Polym. Chem. 48 (2010) 1423.
[6] (a) M. Helgesen, S.A. Gevorgyan, F.C. Krebs, R.A.J. Janssen, Chem. Mater. 21 (2009) 4669;
(b) L. Biniek, C.L. Chochos, N. Leclerc, G. Hadziioannou, J.K. Kallitsis, R. Bechara, P. Lévêque, T. Heiser, J. Mater. Chem. 19 (2009) 4946;
(c) X. Chen, G.L. Schulz, X. Han, Z. Zhou, S. Holdcroft, J. Phys. Chem. C 113 (2009) 8505.
[7] (a) E. Bundgaard, S.E. Shaheen, F.C. Krebs, D.S. Ginley, Sol. Energy Mater. Sol. Cells 91 (2007) 1631;
(b) W. Yue, Y. Zhao, S. Shao, H. Tian, Z. Xie, Y. Geng, F. Wang, J. Mater. Chem. 19 (2009) 2199;
(c) L. Huo, H.-Y. Chen, J. Hou, T.L. Chen, Y. Yang, Chem. Commun. (2009) 5570;
(d) N. Blouin, A. Michaud, M. Leclerc, Adv. Mater. 19 (2007) 2295;
(e) S.H. Park, A. Roy, S. Beaupré, S. Cho, N. Coates, J.S. Moon, D. Moses, M. Leclerc, K. Lee, A.J. Heeger, Nat. Photon. 3 (2009) 297.
[8] J. Hou, H.-Y. Chen, S. Zhang, G. Li, Y. Yang, J. Am. Chem. Soc. 130 (2008) 16144.
[9] R.C. Coffin, J. Peet, J. Rogers, G.C. Bazan, Nat. Chem. 1 (2009) 657.
[10] D. Muhlbacher, M. Scharber, M. Morana, Z.G. Zhu, D. Waller, R. Gaudiana, C. Brabec, Adv. Mater. 18 (2006) 2884.
[11] K.M. Coakley, M.D. McGehee, Chem. Mater. 16 (2004) 4533.
[12] B. Lim, K.-J. Baeg, H.-G. Jeong, J. Jo, H. Kim, J.-W. Park, Y.-Y. Noh, D. Vak, J.-H. Park, J.-W. Park, D.-Y. Kim, Adv. Mater. 21 (2009) 2808.
[13] R. Yang, R. Tian, J. Yan, Y. Zhang, J. Yang, Q. Hou, W. Yang, C. Zhang, Y. Cao, Macromolecules 38 (2005) 244.
[14] M. Zhang, H.N. Tsao, W. Pisula, C. Yang, A.K. Mishra, K. Müllen, J. Am. Chem. Soc. 129 (2007) 3472.
[15] P. Sonar, S.P. Singh, S. Sudhakar, A. Dodalapur, A. Sellinger, Chem. Mater. 20 (2008) 3184.
[16] J.M. Tour, R. Wu, Macromolecules 25 (1992) 1901.
[17] T.-A. Chen, X.M. Wu, R.D. Rieke, J. Am. Chem. Soc. 117 (1995) 233.
[18] M.C. Scharber, D. Mühlbacher, M. Koppe, P. Denk, C. Waldauf, A.J. Heeger, Christoph J. Brabec, Adv. Mater. 18 (2006) 789.
[19] (a) E. Beltrán, J.L. Serrano, T. Sierra, R. Giménez, Org. Lett. 12 (2010) 1404;
(b) J.H. Kim, H. Lee, Synth. Met. 139 (2003) 471.
[20] J. Chen, Y. Cao, Acc. Chem. Res. 42 (2009) 1709.
[21] J.-F. Chang, H. Sirringhaus, Adv. Mater. 21 (2009) 2530.
[22] (a) J. Kim, S.H. Kim, I.H. Jung, E. Jeong, Y. Xia, S. Cho, I.-W. Hwang, K. Lee, H. Suh, H.-K. Shim, H.Y. Woo, J. Mater. Chem. 20 (2010) 1577;
(b) H.A. Becerril, N. Miyaki, M.L. Tang, R. Mondal, Y.-S. Sun, A.C. Mayer, J.E. Parmer, M.D. McGehee, Z. Bao, J. Mater. Chem. 5 (2009) 591;
(c) L. Bürgi, M. Turbiez, R. Pfeiffer, F. Bienewald, H.-Jörg Kirner, C. Winnewisser, Adv. Mater. 20 (2008) 2217.
[23] J. Jo, S.-I. Na, S.-S. Kim, T.-W. Lee, Y. Chung, S.-J. Kang, D. Vak, D.-Y. Kim, Adv. Funct. Mater. 19 (2009) 2398.
[24] J.K.J. van Duren, X. Yang, J. Loos, C.W.T. Bulle-Lieuwma, A.B. Sieval, J.C. Hummelen, R.A.J. Janssen, Adv. Funct. Mater. 14 (2004) 425.
[25] (a) J.J. Benson-Smith, L. Goris, K. Vandewal, K. Haenen, J.V. Manca, D. Vanderzande, D.D.C. Bradley, J. Nelson, Adv. Funct. Mater. 17 (2007) 451;
(b) M.A. Loi, S. Toffanin, M. Muccini, M. Forster, U. Scherf, M. Scharber, Adv. Funct. Mater. 17 (2007) 2111;
(c) K. Vandewal, A. Gadisa, W.D. Oosterbaan, S. Bertho, F. Banishoeib, I.V. Severen, L. Lutsen, T.J. Cleij, D. Vanderzande, J.V. Manca, Adv. Funct. Mater. 18 (2008) 2064.

Organic Electronics 11 (2010) 1779–1785

Contents lists available at ScienceDirect

Organic Electronics

journal homepage: www.elsevier.com/locate/orgel

Direct determination of the electronic structure of the poly(3-hexylthiophene):phenyl-[6,6]-C61 butyric acid methyl ester blend

Ze-Lei Guan [a,*], Jong Bok Kim [b], He Wang [a,b], Cherno Jaye [c], Daniel A. Fischer [c], Yueh-Lin Loo [b], Antoine Kahn [a]

[a] Department of Electrical Engineering, Princeton University, Princeton, NJ 08544, USA
[b] Department of Chemical Engineering, Princeton University, Princeton, NJ 08544, USA
[c] Materials Science and Engineering Laboratory, National Institute of Standards and Technology, Gaithersburg, MD 20899, USA

ARTICLE INFO

Article history:
Received 9 March 2010
Received in revised form 17 June 2010
Accepted 24 July 2010
Available online 10 August 2010

Keywords:
Electronic structure
Bulk heterojunction
Blend
P3HT
PCBM
Interface dipole

ABSTRACT

This article focuses on the electronic structure of the poly(3-hexylthiophene):phenyl-[6,6]-C61 butyric acid methyl ester (P3HT:PCBM) blend, widely used in bulk heterojunction (BHJ) solar cells. Given the fact that the surface of the blend film is a nearly pure P3HT wetting layer, we use a lift-off method to access the originally buried surface, which is rich in both P3HT and PCBM and thus representative of the BHJ. The combination of direct and inverse photoemission spectroscopy on this surface leads to a determination of the energy gap between the lowest unoccupied molecular orbital (LUMO) of the acceptor and the highest occupied molecular orbital (HOMO) of the donor. The gap is ~1.4 eV, which implies a 0.5–0.6 eV interface dipole barrier between the two materials. The energy gap is found to be stable versus *in situ* annealing up to 100 °C.

© 2010 Elsevier B.V. All rights reserved.

1. Introduction

The ubiquity and fundamental role of organic–organic heterojunctions (OOH) in most organic-based devices have led to in-depth investigations of their molecular and electronic structures [1–4]. In organic photovoltaic (OPV) cells in particular, OOH molecular level offsets dominate exciton dissociation and charge transfer, and define open-circuit voltage and other characteristics of the device [5–7]. A detailed understanding of OOH electronic structure is therefore of general interest and is directly relevant to the control and optimization of these organic-based devices. A number of planar OOHs have been experimentally and theoretically investigated [7,8], and models have been proposed to provide a first-order evaluation of their electronic structure. Both experimental measurements and theoretical computations point out that vacuum level alignment generally does not describe OOHs adequately, and that interface dipoles should be taken into consideration for a proper description of their electronic structure [7–9]. Yet, in spite of their increasing popularity in high efficiency OPV devices, bulk heterojunctions (BHJ) have not received the same degree of scrutiny. The problem is both experimental and theoretical, given the difficulty in identifying molecular features of the various constituents and the complexity and lack of specific information on the molecular structure of the various phases of the film.

The present study focuses on the electronic structure of a BHJ system composed of a poly(3-hexylthiophene) (P3HT):phenyl-[6,6]-C61 butyric acid methyl ester (PCBM) blend. The P3HT:PCBM blend is widely used in BHJ solar cells, resulting in open-circuit voltages (V_{oc}) of the order of 0.6 V and power conversion efficiencies in the range of

* Corresponding author.
E-mail address: zeleig@princeton.edu (Z.-L. Guan).

1566-1199/$ - see front matter © 2010 Elsevier B.V. All rights reserved.
doi:10.1016/j.orgel.2010.07.023

4–6% [10–12]. The study combines structural and composition determination of the film via near edge X-ray absorption fine structure (NEXAFS) and X-ray photoemission spectroscopy (XPS), and electronic structure determination of filled and empty states via ultraviolet and inverse photoemission spectroscopy (UPS, IPES). The key result is the experimental determination of the fundamental gap between the lowest unoccupied molecular orbital (LUMO) and highest occupied molecular orbital (HOMO) of the blend. Comparison with the gap expected from the difference between the ionization energy (IE) and electron affinity (EA) of separated P3HT and PCBM, respectively, indicates a significant departure from vacuum level alignment at that interface, with formation of a 0.5–0.6 eV interface dipole barrier.

2. Experimental

In the course of this investigation, we measured (i) the main energy levels, i.e. HOMO and LUMO, of the separate constituents P3HT and PCBM, (ii) the electronic structure of the P3HT/C_{60} interface, and (iii) the electronic structure of the P3HT/PCBM blend. The organic films were formed on two different types of surfaces: silicon (Si) with a native oxide; and gold (Au, 30 nm) on Ti (2 nm)/Si. The Si substrates were cleaned by sonication in acetone and isopropyl alcohol, followed by a rinse of a few seconds in de-ionized water and a 10 min ultraviolet/ozone treatment to remove organic contaminants. The Au films were evaporated on Ti/Si shortly before use, without further treatment. The P3HT films prepared for spectroscopy were spin-coated from a 1 wt% P3HT chlorobenzene solution at 1000 rpm for 60 s. PCBM and 1:1 P3HT:PCBM blend films were prepared under similar conditions. C_{60} films were evaporated in a chamber connected to the photoemission analysis chamber.

All the films and heterojunctions were investigated with UPS and IPES to determine the vacuum level, the HOMO and LUMO positions, and the IE and EA. The resolution of the UPS measurements, using a He discharge lamp (HeI, 21.22 eV and HeII, 40.84 eV) and a double-pass cylinder mirror analyzer, was 0.15 eV, and the resolution of the IPES measurements was 0.45 eV [13]. *In situ* annealing of the blend films up to 100 °C was done to simulate post-fabrication processing of BHJ solar cells.

Samples prepared for NEXAFS analysis were spin-coated on glass substrates from a 24 mg/ml, 1:0.8 P3HT:PCBM solution, at 500 rpm for 2 min, yielding 150 nm thick films. NEXAFS experiments were carried out at the NIST/Dow soft X-ray materials characterization facility located at beamline U7A at the National Synchrotron Light Source at Brookhaven National Laboratories. Partial electron yield (PEY) NEXAFS spectra were acquired at the carbon K-edge per previously published procedures [14,15]. Step scans of 2 eV were used to acquire data between 250 and 270 eV; 0.5 eV increments between 270 and 280 eV; 0.1 eV increments between 280 and 300 eV; 0.5 eV increments between 300 and 330 eV; and 2 eV increments between 330 and 350 eV. The spectra were collected in vacuum (1×10^{-8} Torr) at ambient temperature. Raw PEY NEXAFS spectra were normalized by the corresponding incident beam intensity, I_0, obtained concomitantly from the photon yield of a freshly coated gold grid that is located upstream from the sample chamber. This normalization accounts for any incident beam intensity fluctuations and monochromator absorption features.

3. Results and discussion

The combined UPS and IPES spectra of separate films of pure P3HT and PCBM are shown in Fig. 1a. The vacuum level is used as energy reference, thus the IE and EA of the two materials (Fig. 1b and Table 1) can be directly obtained from the positions of the onsets of filled and empty states, respectively. The P3HT IE of 4.65 eV is consistent with data obtained by other groups [6,16,17], and the 2.5 eV transport gap is in good agreement with the UPS/IPES result by Deibel et al. [17]. Note that the assumption of vacuum

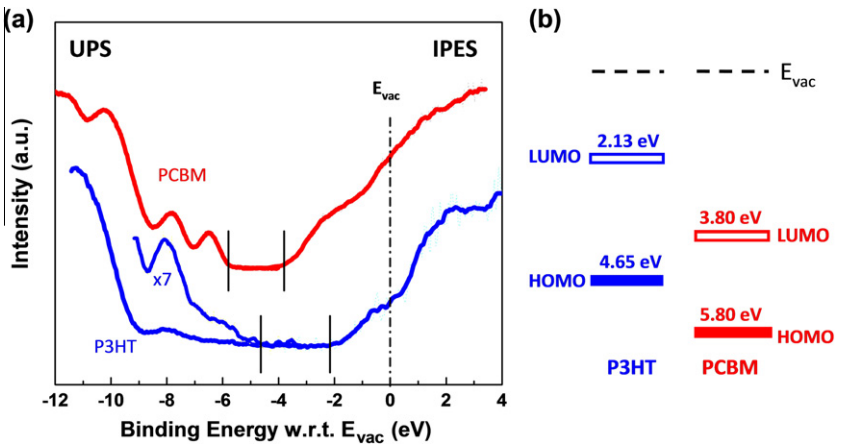

Fig. 1. The left panel shows the combined UPS and IPES spectra of pure P3HT (blue curves) and pure PCBM (red curves) with the energy position referenced to the vacuum level (E_{vac}, dash dotted line). HOMO and LUMO edges are shown in solid lines. The right panel presents the corresponding electronic structure with positions of molecular levels. (For interpretation of the references to colour in this figure legend, the reader is referred to the web version of this article.)

Table 1
Measured ionization energy (IE), electron affinity (EA) and transport gap for all materials used in this work, as determined by UPS and IPES.

Materials	IE (eV)	EA (eV)	Gap (eV)
P3HT	4.65	2.13	2.52
PCBM	5.80	3.80	2.00
C_{60}	6.35	3.98	2.37
P3HT:PCBM top surface	4.69	2.14	2.55
P3HT:PCBM once-buried surface, on Si	5.22	3.76	1.46
P3HT:PCBM once-buried surface, on Au	4.63	3.29	1.34

level alignment between P3HT and PCBM would place the PCBM LUMO at 0.85 eV above the P3HT HOMO (Fig. 1b). OOHs with similarly small predicted LUMO (organic 2)–HOMO (organic 1) gap have been experimentally shown to display an interface dipole that increases this gap by several hundreds of millivolts [3,9]. No specific calculations have been done on these materials. However, electronic structure computations of OOHs comprising constituents with widely different EAs and IEs, based on the model of alignment of charge neutrality levels [9,18], have also predicted significant interface dipoles [3,9].

A first-cut approach to the actual electronic structure of the P3HT:PCBM blend is obtained by looking at the single heterojunction formed by vacuum deposition of C_{60} on a P3HT film (prepared *ex situ* by spin-coating). Obvious similarities between C_{60} and PCBM molecules in terms of molecular size and large IE and EA (Table 1) make C_{60} a good candidate for a first electronic structure evaluation. C_{60} films have been extensively investigated in the past via UPS and IPES [6,19,20], and electronic parameters like IE and EA are well established. Vacuum level alignment at the P3HT/C_{60} interface would place the fullerene LUMO only 0.65 eV above the polymer HOMO. In the present experiment, C_{60} is incrementally deposited on P3HT, and valence states and onset of photoemission are measured at each step. The spectra of the P3HT film, bare and covered with 80 Å C_{60}, are shown in Fig. 2a. The shift of the photoemission onset indicates a 0.5 eV dipole at the P3HT/C_{60} interface, which moves the C_{60} molecular levels upwards, toward lower binding energy with respect to those of P3HT (care was taken to ensure that P3HT molecular levels were not shifting during C_{60} deposition). This is in good agreement with results previously reported by Osikowica et al. [16]. The energy difference between the P3HT and C_{60} HOMO edges is 1.30 eV, and the energy difference between the LUMO edges is deduced from this value, using

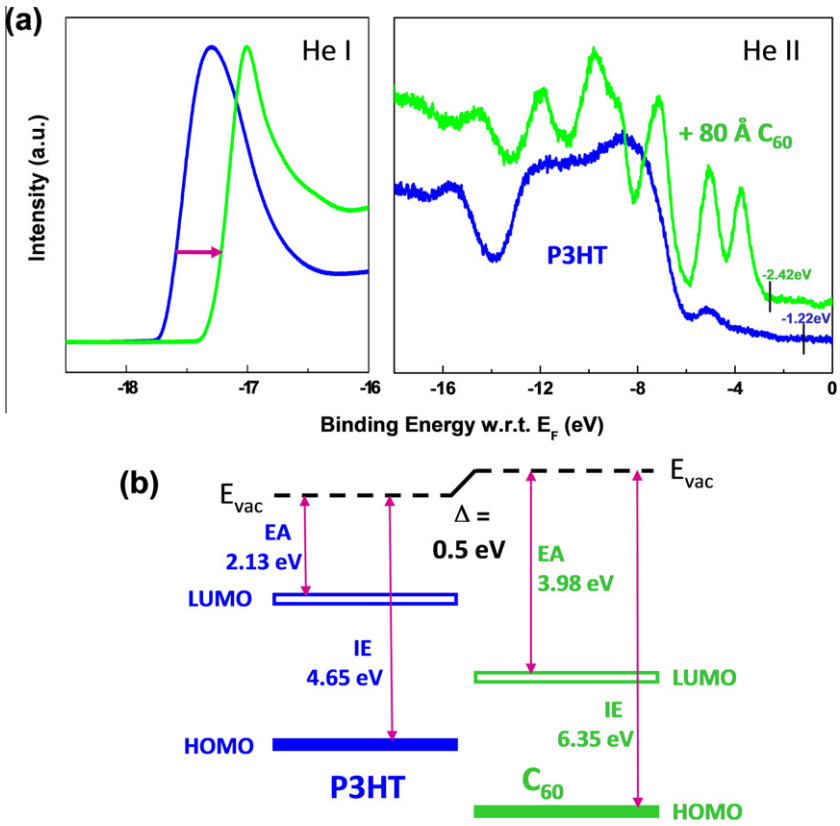

Fig. 2. (a) Valence UPS spectra of pure P3HT (blue curves) and 80 Å P3HT/C_{60} heterojunction (green curves). The right panel shows the different features of P3HT and P3HT/C_{60}, while the left panel shows the shift of the photoemission onset, indicating the presence of an interface dipole. All energies are taken Fermi level (E_F) as reference. (b) Corresponding schematic heterojunction energy diagram. The interface dipole is about 0.5 eV. (For interpretation of the references to colour in this figure legend, the reader is referred to the web version of this article.)

the transport gap of the two materials (Table 1). The energy diagram of the heterojunction is displayed in Fig. 2b.

The UPS and IPES spectra of the surface of a ~400 Å P3HT:PCBM blend film prepared on Si as described above are shown in Fig. 3a. Both spectra look remarkably similar to those of pure P3HT (Fig. 1), and the measurements of LUMO and HOMO positions yield IE, EA and energy gap identical to those of the pure polymer (Fig. 3b). In particular, the 2.55 eV gap is considerably larger than that anticipated between the PCBM LUMO and P3HT HOMO (Fig. 1b). This surprising result is explained by subsequent investigations of the vertical composition of the blend film by NEXAFS and XPS.

The pre- and post-edge normalized NEXAFS PEY spectra acquired at the carbon edge of thin films of PCBM, P3HT, as well as those of a film comprising P3HT:PCBM blended at 1:0.8 mass ratio are shown in Fig. 4. The spectra is magnified in the C1s – to – π^* transition region to facilitate discussion. The results of a full NEXAFS analysis of these films will be presented elsewhere [21]. Comparison of the NEXAFS spectra of PCBM and P3HT reveals C1s – to – π^* transitions occurring at different energies; these are highlighted in Fig. 4 for comparison. PCBM exhibits C1s – to – π^* transitions at 284.5 eV and 285.8 eV whereas the C1s – to – π^* transition of P3HT occurs at 285.13 eV [22]. Carefully monitoring the NEXAFS spectra in this region thus provides a unique fingerprint for the species in question. The NEXAFS spectrum acquired on the surface of the P3HT:PCBM film (labeled "Top", in Fig. 4) largely resembles that of neat P3HT. This observation is consistent with the presence of a thin P3HT wetting layer at the film surface [23,24] and explains why only the energy levels associated with P3HT are accessed when UPS and IPES measurements are conducted on the film surface (Fig. 3). The thickness of the P3HT wetting layer, estimated by NEXAFS, is around 5 nm [21].

Access to the blend, or mixed part of the film, was obtained in the following way. For UPS/IPES and XPS experiments, the P3HT:PCBM blend film was lifted off the substrate by soaking in water for a few seconds. The film was then picked up from the top with a second Si substrate and flipped over to expose the previously buried, PCBM-rich, surface of the film, referred to as "once-buried surface". The films for NEXAFS studies were delaminated using polydimethylsiloxane (PDMS) stamps. Note that the quality and composition of these films should not depend on the delamination method. The NEXAFS spectrum acquired on the once-buried surface of the P3HT:PCBM film (labeled "Bottom", in Fig. 4) reveals signatures of both P3HT and PCBM. In fact, quantitative analysis of the NEXAFS spectrum [21] indicates that this once-buried interface comprises 65 wt% P3HT and 35 wt% PCBM. It is thus the

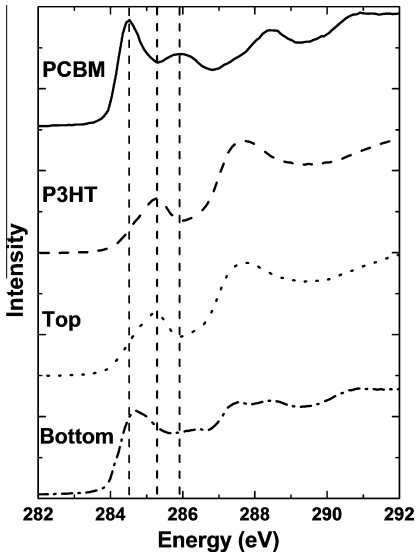

Fig. 4. Carbon-edge pre- and post-edge normalized NEXAFS PEY spectra of PCBM (solid), P3HT (dash), as well as those of a P3HT:PCBM blend taken at the original surface (dot) and the once-buried surface (dash dot) at 55°, the magic angle. The traces have been displaced along the *y*-axis for clarity.

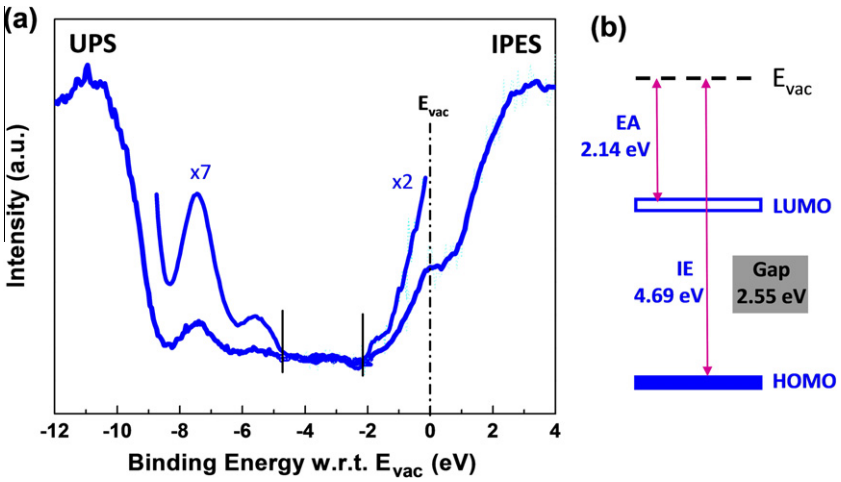

Fig. 3. (a) Combined UPS and IPES spectra of the blend original surface. All energies are taken E_{vac} as reference. (b) The schematic electronic structure deduced from UPS and IPES.

characterization performed on this once-buried interface that provides a more realistic picture of the electronic structure of the polymer blend.

The chemical composition of the film was further analyzed via XPS on pure PCBM as well as on the original and once-buried surfaces of a 1:1 blend film formed on Si. The analysis of the O1s, C1s and S2p core levels measured from the blend film (Fig. 5) shows that the once-buried surface is richer in O than the top surface (Table 2), consistent with a larger concentration of PCBM. The O1s – to – C1s ratio is 1/20 for the once-buried blend surface, versus 1/15 for the pure PCBM film, as expected from the presence of the P3HT carbon in the blend. Furthermore, the original top surface yields no O signal, consistent with the fact that it contains very little PCBM, and in spite of the fact that the surface was exposed to air and water. An analysis of the line-shape of the oxygen core level on the PCBM and once-buried blend surface reveals the presence of two components, O=C–O (533.9 eV) and O–C=O (532.4 eV), corresponding to the two non-equivalent O species of the PCBM molecule [25]. Finally, the S2p – to – C1s ratio is at least in qualitative agreement with the compositions of the original and once-buried surfaces, when the enhancement in carbon content corresponding to PCBM is taken into consideration. All the XPS data confirm that the once-buried surface contains a mixture of the two molecules, although the precise ratio is difficult to establish with precision.

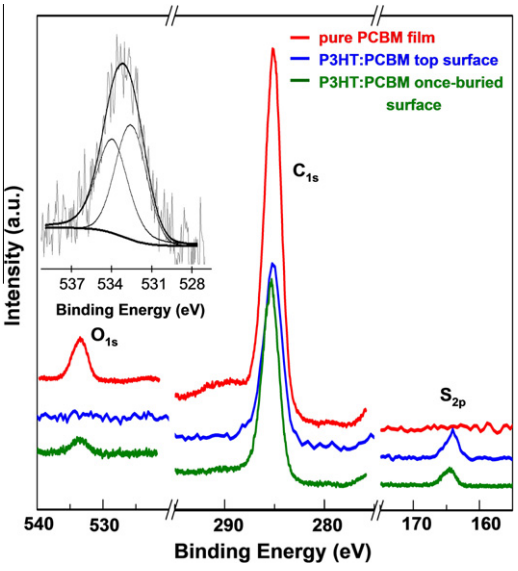

Fig. 5. XPS data of O1s, C1s and S2p core levels. The inset shows the detailed analysis of the O1s peak of the once-buried surface of the blend film. The two components correspond to the two different oxygen species of PCBM, indicating that there is no impact from H_2O on the increased O-signal.

Table 2
Normalized intensity of the O1s, C1s and S2p core levels measured from PCBM and the original and once-buried surfaces of the 1:1 blend P3HT:PCBM film.

Film	O1s	C1s	S2p
PCBM	1	15	0
P3HT:PCBM top surface	0	14	1
P3HT:PCBM once-buried surface, on Si	1	20	0.9

The UPS and IPES spectra of the once-buried surface of the blend film on Si are shown in Fig. 6a. This surface yields a significantly smaller transport gap (Fig. 6b) than the exposed surface (Fig. 3), i.e. 1.46 eV versus 2.55 eV, and an IE of 5.22 eV and an EA of 3.76 eV. Given that this part of the film is a true mixture of the two elements of the blend, and considering the electronic structure of the separate constituents (Fig. 1b and Table 1), we attribute the top of the filled states to the HOMO edge of the donor P3HT, and the bottom of the empty states to the LUMO edge of the acceptor PCBM. The energy gap is larger than would be expected from a simple vacuum level alignment between the donor and the acceptor phases in the blend (0.85 eV, Table 1), and fairly close to the LUMO(C_{60})–HOMO(P3HT) described above. This implies that a displacement of the PCBM molecular levels upwards with respect to those of P3HT has taken place. Such a displacement, which corresponds to the formation of a dipole at the interface between P3HT and PCBM, was expected from considerations of alignment of charge neutrality levels given above, and from the preliminary experiment with P3HT/C_{60}. The magnitude of the dipole is ~0.5–0.6 eV, and the electronic structure of the D/A interface in the blend is given in Fig. 6b. Note that the dipole value is in good agreement with the 0.4 eV value reported by Xu et al., who used a different experimental approach [24].

In the experiment described above, the Fermi level of the blend film (dashed vertical line in Fig. 6a) picked-up on the Si substrate is relatively high in the LUMO(PCBM)–HOMO(P3HT) gap. To verify that the substrate Fermi level did not have a significant impact on the molecular level alignment in the blend, and thus on the critical LUMO(PCBM)–HOMO(P3HT) gap, all experiments described above were repeated on Au (Au/Ti/Si) substrates. The energy levels of the separate constituents, i.e. P3HT and PCBM, and the electronic structure of the P3HT/C_{60} interface were re-measured on Au substrates (not shown here), and found in very good agreement with those obtained on Si. Measurements on the exposed surface of the blend film showed identical IE, EA and energy gap to those of pure P3HT, indicating here again the presence of a thin P3HT wetting layer at the film surface.

The UPS and IPES spectra of the once-buried surface of the blend film were also measured on a film picked-up on an Au sample following lift-off in water. As can be seen in Fig. 7a, the Fermi level is significantly lower in the LUMO(PCBM)–HOMO(P3HT) gap than in the Si substrate case. The IE and EA measured at this surface are different from those measured in the Si substrate case, indicating a different position of the overall vacuum level of the blend (issues related to the precise nature of the vacuum level at the surface of such a blend are complex, and beyond the scope of this work). Yet, the surface yields a 1.34 eV transport gap, nearly identical to that obtained on Si, implying

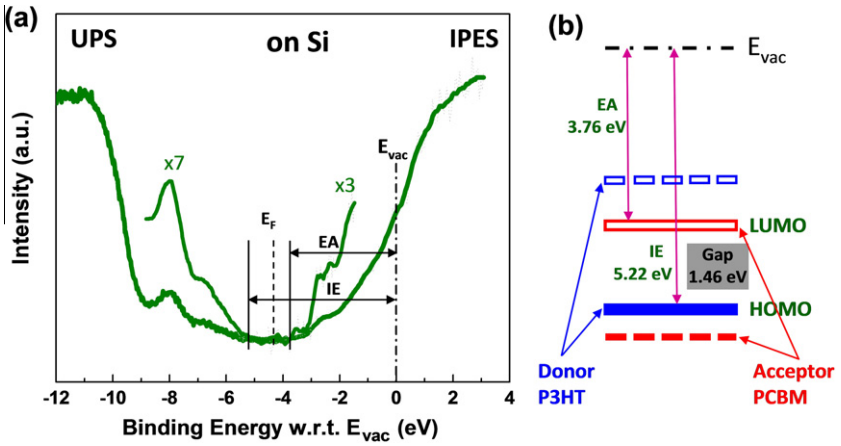

Fig. 6. (a) Combined UPS and IPES spectra of once-buried surface of the blend film on a Si substrate. The reference (0 eV) energy is the vacuum level E_{vac}. The position of the Fermi level E_F is indicated. (b) Corresponding energy diagram outlining, in particular, the relative positions of the donor (P3HT) HOMO and acceptor (PCBM) LUMO. The energy gap of the real blend film is 1.46 eV.

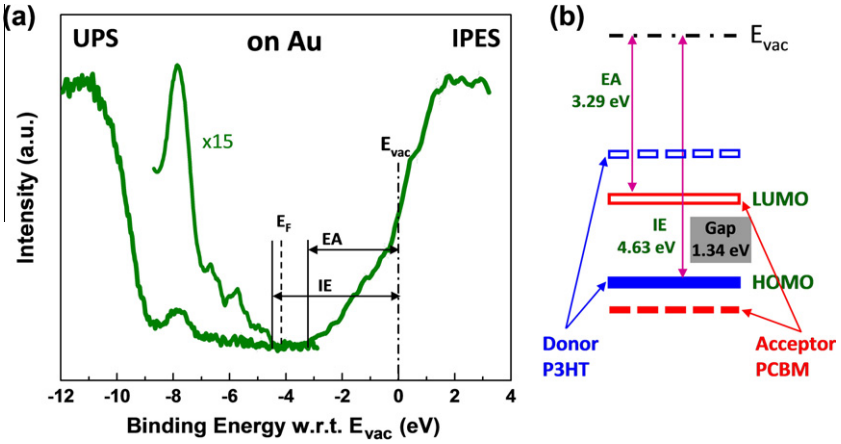

Fig. 7. (a) Combined UPS and IPES spectra of the once-buried surface of the blend film on an Au substrate. The reference (0 eV) energy is the vacuum level E_{vac}. The position of the Fermi level E_F is indicated. (b) Corresponding energy diagram outlining, in particular, the relative positions of the donor (P3HT) HOMO and acceptor (PCBM) LUMO. The energy gap is 1.34 eV.

the existence of a similar dipole at the donor/acceptor interface. The electronic structure of the blend is given in Fig. 7b.

Annealing is known to improve the performance of P3HT:PCBM solar cells [26,27]. A series of *in situ* annealing steps at temperatures up to 100 °C for 10 min each were therefore performed to detect eventual changes in the electronic structure of the blend film on Si. Interestingly, the UPS and IPES spectra (not shown here) demonstrated that the position of the LUMO and HOMO edges with respect to the Fermi level, as well as the gap of the blend, remain the same as for the non-annealed film, which places origin of the improvement on something else than the donor/acceptor LUMO–HOMO gap. On the other hand, the work function of the blend film was reduced by 0.30 eV by annealing, possibly due to a change in film morphology, to an evolution of the phase separation between P3HT and PCBM [26,27], or simply to desorption of some contaminants from the surface.

Finally, the measurements presented here show that the donor/acceptor LUMO–HOMO gap is significantly larger than the best open-circuit voltage (V_{oc}) developed by a P3HT:PCBM cell: ~1.4 eV versus ~0.6–0.65 eV. Recent investigations of excitonic molecular and polymer cells have clearly established correlations between increase or decrease in the gap and in V_{oc} [28–32]. These correlations were coupled with models based on equivalent circuits of the cells, which include leakage and resistance paths for the photo-generated current, to explain the difference between the electronic structure of the donor/acceptor heterojunction and the cell performance. It is clear that further development of such models will be possible only if at least one of the most important parameters of the junction, i.e. the molecular level alignment at the OOH, is independently determined.

4. Summary

Measurements presented here have lead to the first direct determination of the donor/acceptor LUMO/HOMO energy gap in the widely used P3HT:PCBM bulk heterojunction. Using a lift-off technique to expose the once-buried surface of the thin blend film, and analysis with direct and inverse photoemission spectroscopy complemented by NEXAFS, we showed that this surface is rich in both donor (P3HT) and acceptor (PCBM) components, and thus representative of the blend. The LUMO/HOMO gap of the blend is found to be $\sim$1.4 eV, from which we infer a 0.5–0.6 eV interface dipole barrier between the donor and acceptor phases. This dipole widens the gap of the blend. The dipole and LUMO/HOMO gap are stable in a series of *in situ* annealing steps up to 100 °C.

Acknowledgments

Support of this work by the Department of Energy (DE-FG02-04ER46165), the Office of Science DOE Energy Frontier Research Center for Interface Science: Solar Electric Materials (DE-S0001084), the Princeton MRSEC (DMR-0819860) and the Organic Photovoltaic Program at ONR (N000140811175) is gratefully acknowledged.

References

[1] P. Peumans, A. Yakimov, S.R. Forrest, J. Appl. Phys. 93 (2003) 7.
[2] D.M. Guldi, C. Luo, M. Prato, A. Troisi, F. Zerbetto, M. Scheloske, E. Dietel, W. Bauer, A. Hirsch, J. Am. Chem. Soc. 123 (2001) 9166.
[3] W. Zhao, E. Salomon, Q. Zhang, S. Barlow, S.R. Marder, A. Kahn, Phys. Rev. B 77 (2008) 165336.
[4] W. Chen, D.C. Qi, Y.L. Huang, H. Huang, Y.Z. Wang, S. Chen, X.Y. Gao, A.T.S. Wee, J. Phys. Chem. C 113 (2009) 12832.
[5] C.J. Brabec, N.S. Sariciftci, J.C. Hummelen, Adv. Funct. Mater. 11 (2001) 15.
[6] F.J. Zhang, A. Aollmer, J. Zhang, Z. Xu, J.P. Rabe, N. Koch, Org. Electron. 8 (2007) 606.
[7] A. Kahn, N. Koch, W.Y. Gao, J. Polym. Sci. B 41 (2003) 2529.
[8] A. Kahn, W. Zhao, W. Gao, H. Vázquez, F. Flores, Chem. Phys. 325 (2006) 129.
[9] H. Vázquez, W. Gao, F. Flores, A. Kahn, Phys. Rev. B 71 (2005) 041306(R).
[10] W. Ma, C. Yang, X. Gong, K. Lee, A.J. Heeger, Adv. Funct. Mater. 15 (2005) 1617.
[11] G. Li, V. Shrotriya, J. Huang, Y. Yao, T. Moriarty, K. Emery, Y. Yang, Nat. Mater. 4 (2005) 864.
[12] K. Kim, J. Liu, M.A.G. Namboothiry, D.L. Carroll, Appl. Phys. Lett. 90 (2007) 163511.
[13] C.I. Wu, Y. Hirose, H. Sirringhaus, A. Kahn, Chem. Phys. Lett. 272 (1997) 3.
[14] D.A. Krapchetov, H. Ma, A.K.Y. Jen, D.A. Fischer, Y.-L. Loo, Langmuir 21 (2005) 5887.
[15] D.A. Krapchetov, H. Ma, A.K.Y. Jen, D.A. Fischer, Y.-L. Loo, Langmuir 22 (2006) 9491.
[16] W. Osikowica, M.P. de Jong, W.R. Salaneck, Adv. Mater. 19 (2007) 4213.
[17] C. Deibel, D. Mack, J. Gorenflot, A. Schöll, S. Krause, F. Reinert, D. Rauh, V. Dyakonov, Phys. Rev. B 81 (2010) 085202.
[18] H. Vázquez, F. Flores, R. Oszwaldowski, J. Ortega, R. Pérez, A. Kahn, Appl. Surf. Sci. 234 (2004) 107.
[19] W. Zhao, A. Kahn, J. Appl. Phys. 105 (2009) 123711.
[20] Y. Ge, J.E. Whitten, Chem. Phys. Lett. 448 (2007) 65.
[21] H. Wang, E.D. Gomez, Z.L. Guan, C. Jaye, A. Kahn, D.A. Fischer, J. Schwartz, Y.-L. Loo, in press.
[22] D.S. Germack, C.K. Chan, B.H. Hamadani, L.J. Richter, D.A. Fischer, D.J. Gundlach, D.M. DeLongchamp, Appl. Phys. Lett. 94 (2009) 233303.
[23] Z. Xu, L.-M. Chen, G. Yang, C.-H. Huang, J. Hou, Y. Wu, G. Li, C.-S. Hsu, Y. Yang, Adv. Funct. Mater. 19 (2009) 1227.
[24] Z. Xu, L.-M. Chen, M.-H. Chen, G. Li, Y. Yang, Appl. Phys. Lett. 95 (2009) 013301.
[25] G.P. López, D.G. Castner, B.D. Ratner, Surf. Interface Anal. 17 (1991) 267.
[26] M. Al-Ibrahim, O. Ambacher, S. Sensfuss, G. Gobsch, Appl. Phys. Lett. 86 (2005) 201120.
[27] G. Li, V. Shrotriya, Y. Yao, Y. Yang, J. Appl. Phys. 98 (2005) 043704.
[28] B.P. Rand, D.P. Burk, S.R. Forrest, Phys. Rev. B 75 (2007) 115327.
[29] M. Brumbach, D. Placencia, N.R. Armstrong, J. Phys. Chem. 112 (2008) 3142.
[30] C.J. Brabec, A. Cravino, D. Meissner, N.S. Sariciftci, T. Fromherz, M.T. Rispens, L. Sanchez, J.C. Hummelen, Adv. Funct. Mater. 11 (2001) 374.
[31] A. Gadisa, M. Svensson, M.R. Andersson, O. Inganas, Appl. Phys. Lett. 84 (2004) 1609.
[32] M.C. Scharber, D. Muhlbacher, M. Koppe, P. Denk, C. Waldauf, A.J. Heeger, C.J. Brabec, Adv. Mater. 18 (2006) 789.

Organic Electronics 11 (2010) 1786–1791

Contents lists available at ScienceDirect

Organic Electronics

journal homepage: www.elsevier.com/locate/orgel

Letter

Evolution of the electronic structure of alkali metal-doped copper-phthalocyanine (CuPc) on different metal substrates

Huanjun Ding *, Yongli Gao

Department of Physics and Astronomy, University of Rochester, Rochester, NY 14627, United States

ARTICLE INFO

Article history:
Received 7 August 2009
Received in revised form 28 May 2010
Accepted 24 July 2010
Available online 20 August 2010

Keywords:
Photoemission spectroscopy
Alkali metal doping
Organic semiconductors

ABSTRACT

The evolutions of the electronic structure in Cs-doped copper-phthalocyanine (CuPc) on different metal substrates have been investigated with photoemission spectroscopy. As the Cs doping ratio increases, the Fermi level of the system starts to shift towards the lowest unoccupied molecular orbital (LUMO) of CuPc, and then becomes saturated, as it aligns with the LUMO. The shift of all the energy levels has a linear dependence on the logarithm of the Cs doping ratio, with a slope of about 0.13 eV. By comparing the results of the samples deposited on different metal substrates, we found out that this slope indicates the broadening of the LUMO induced by alkali metal doping and is independent of the work-function of the metal substrate.

© 2010 Elsevier B.V. All rights reserved.

In the past few decades, there has been extensive interest in the development of semiconductor electronic devices based on organic molecules and polymers [1–3]. Organic semiconductors posses many potential advantages over their inorganic counterparts, which make them particularly attractive for large-area and low-cost applications [4]. In the development of organic electronics, many well-established techniques developed for inorganic semiconductors have been successfully adopted, such as doping. As for the inorganic semiconductors, doping has proven to be one of the most efficient techniques to adjust the electronic properties of the organic semiconductors [1,5,6]. However, due to the distinctive nature of the organic molecules, the understanding of the interactions between the organic host and the dopant is still quite limited, and the conventional doping theories based on the band structure in crystalline inorganic semiconductors are usually assumed without careful verification for the case of organic system. It is thus important to investigate the doping-induced evolution of the electronic structures of the organic molecules, in order to understand the fundamental mechanism of the interactions in the guest–host system. Such studies have been carried out by many groups for different kinds of dopants, such as oxygen [7], organic molecules [8], and alkali metals [9,10]. Among them, alkali metals, which donate their single outmost s-electrons, are usually considered as good candidates for prototypical studies, due to their simple electronic structures comparing to other possible dopants [11–14]. Generally, doping of the alkali metal atoms results in the energy level shift in the organic semiconductors [13,14]. Our previous studies suggest that such shift cannot be explained by the equations derived for crystalline inorganic semiconductors [15,16]. However, there is also doubt if the energy level shift is simply from the change of the substrate work-function by the alkali metals diffusing through the organic film. Therefore, it is interesting to investigate doping-induced electronic structure modification of organic thin films prepared on different metal substrates.

In this paper, we report our photoemission investigations on the evolution of the electronic structure for Cs-doped copper-phthalocyanine (CuPc) prepared on different metal substrate, such as Ag and Al. With ultraviolet and X-ray photoemission spectroscopy (UPS and XPS), we find out that, before saturation, the CuPc energy levels shift linearly as a function of the logarithm of the Cs doping ratio, with a slope of about 0.13 eV which is independent of the

* Corresponding author.
E-mail address: hjding@pas.rochester.edu (H. Ding).

1566-1199/$ - see front matter © 2010 Elsevier B.V. All rights reserved.
doi:10.1016/j.orgel.2010.07.027

substrate workfunction. The slope is much larger than k_BT as predicted by theory for inorganic semiconductors, and it can be understood as the broadening of the lowest unoccupied molecular orbital (LUMO) induced by metal–organic interaction.

The UPS and XPS studies were performed using a VG ESCA Lab system equipped with a He I (21.2 eV) gas discharge lamp and an Mg Kα X-ray source (1253.6 eV). The ultrahigh vacuum (UHV) system consists of a spectrometer chamber and an evaporation chamber, in which samples could be prepared in UHV and transferred directly into the spectrometer chamber. The base pressure of the spectrometer chamber is typically 8×10^{-11} torr. A fresh metal substrate (Ag or Al) was prepared inside the spectrometer chamber by thermal evaporation onto a Au-coated Si wafer cleaned with Ar^+ sputtering. The workfunction and the surface cleanness of the metal substrates were checked by UPS and XPS before the deposition of a 200 Å CuPc film. Cs was evaporated at 5.5 Amps from a SEAS getter source in the spectrometer chamber. The Cs doping ratio (R_{Cs}), calibrated as the number of Cs atoms per CuPc molecule, is derived from the XPS core level intensities with careful calibration of the atomic sensitive factor. The evolution of the doping ratio as a function of evaporation time (not shown) turns out to be very reliable for each experiment. The UPS spectra were recorded with the samples biased at −5.0 V to observe the low-energy secondary cutoff. The typical instrumental resolution for UPS measurements ranges from ∼0.03 to 0.2 eV with photon energy dispersion of less than 20 meV. The XPS resolution is ∼1.4 eV. All measurements were done at room temperature.

Fig. 1 shows the evolution of the UPS spectra of the highest occupied molecular orbital (HOMO) region of Cs-doped CuPc prepared on clean Ag (a) and Al (b) substrates as a function of R_{Cs}, the number ratio between the Cs atoms and the CuPc molecules. The workfunction of the metal substrate is measured with UPS (not shown), and is determined to be 4.32 eV and 4.09 eV for Ag and Al, respectively, which are consistent with the handbook values [17]. The spectra of the pristine CuPc films on both metal substrates agree very well with our previous observations [18] and those published in literature [13,14,19]. For the films prepared on Ag and Al substrates, the HOMO onset, which is usually determined by the linear extrapolation of the leading edge of the HOMO peak, is located about 1.2 eV and 1.4 eV below the Fermi level, respectively. The difference in the HOMO position at those two interfaces can be attributed mostly to the metal workfunction, which determines charge transfer at the interface and the formation of interface dipole. Other factors, such as push-back effect and screening, may also contribute in this case, as discussed in the review of metal organic interface [20]. Upon Cs doping, energy levels of the CuPc films prepared on both Ag and Al substrates start to shift towards higher binding energy, in other words, the Fermi levels of the two samples shift upwards inside the energy gap of the CuPc. This is in good agreement with our earlier studies of Cs-doped CuPc film prepared on Au substrate [15,21]. As the Cs doping ratio increases, the valence features of the CuPc molecules are well preserved, indicating that there is no destructive chemical interaction between the organic molecules and the doped alkali metal atoms. The full width at half maximum (FWHM) of HOMO in pristine CuPc film is estimated to be about 0.47 eV and 0.49 eV for films prepared on Ag and Al, respectively. Doping of Cs leads to a slight broadening of the HOMO peak. At higher doping ratios, the FWHM of the HOMO increases to about 0.50 eV for both samples. However, the shape of the HOMO peak remains symmetric and the simultaneous shift can also be noticed at the onset position. These observations rule out the presence of coexisting phases with different Cs stoichiometry. For both samples, the shift of the energy levels becomes saturated at higher doping ratios. However, the saturation occurs at different doping levels for the two

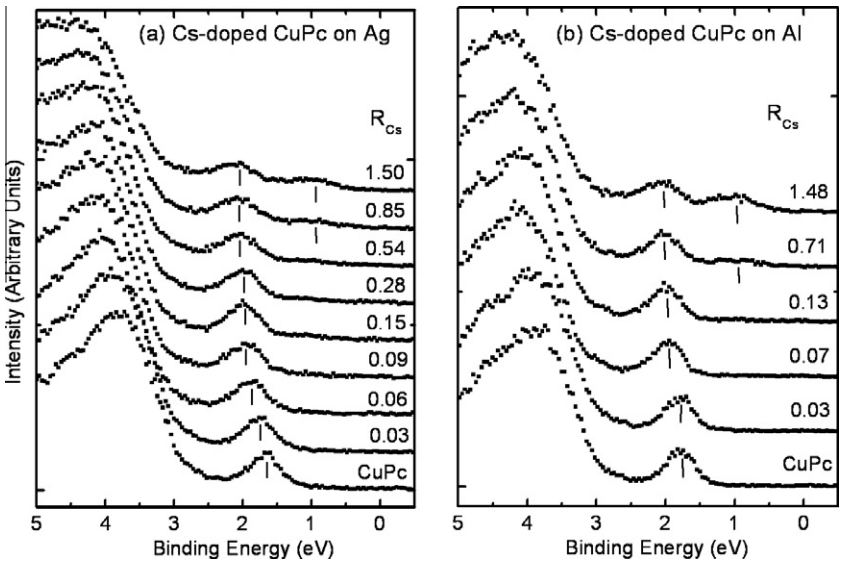

Fig. 1. UPS spectra of the HOMO region of Cs-doped CuPc film prepared on (a) Ag and (b) Al substrates as a function of Cs doping ratio R_{Cs}, derived from XPS core level intensities. The spectra are plotted in binding energy relative to the Fermi level.

samples prepared on different metal substrates. For the sample prepared on Ag, the shift of the HOMO peak becomes saturated after R_{Cs} reaches 0.25, when the total shift of the HOMO is about 0.4 eV. On the other hand, the saturation of the energy level shift happens much sooner when Al is used as the substrate. The HOMO shifts for a total of 0.2 eV and then becomes saturated at R_{Cs} equals 0.13. Those values are significantly different from our previous doping experiment on clean Au substrate, where the saturation occurs at R_{Cs} equals 0.4, and a much larger shift (0.8 eV) is observed before the saturation [15]. Another issue one should note here is that, at high Cs doping ratios, a new state emerges from the former energy gap in the UPS spectra, and its intensity increases monotonically as R_{Cs} increases. Similar to our earlier observation for samples prepared on Au substrate, the gap state lies about 1.1 eV above the HOMO peak. It is believed to be originated from the filling of the former LUMO in the CuPc molecules due to charge transfer [15]. For samples prepared on both metal substrates, the gap state can only be clearly identified after the saturation of the energy level shift and when the Cs doping ratio is large enough (0.54 for Ag and 0.71 for Al). Before that the features are too weak to be seen.

The evolution of the C 1s, N1s and Cu $2p_{3/2}$ core levels of Cs-doped CuPc prepared on Ag substrate are shown in Fig. 2. The C 1s core level spectrum of pristine CuPc (see bottom spectrum in Fig. 2(a)) consists of two main components: the leading peak C 1s(A), which can be easily associated with the aromatic carbon of the benzene rings, and the second peak C 1s(B) at 1.4 eV higher binding energy, which is due to the pyrrole carbon in contact with N [13]. A satellite of C 1s(A) overlaps with C 1s(B), whose contribution must be accounted for to get the proper intensity ratio of these two peaks. Both components shift simultaneously towards higher binding energy for about 0.4 eV at initial doping ratios, which is quite consistent with what has been observed for the valence features. After that, they merge into one broad and asymmetry peak, as a result of the slightly reverse shift of C 1s(B) towards lower binding energy. Both N 1s and Cu $2p_{3/2}$ core levels appear to have a single component in the XPS spectra. They shift towards higher binding energy for similar amount as that of C 1s core level for the initial doping ratios. A reverse shift can be identified for these two elements as the doping ratio is beyond 0.85, which coincides with the appearance of the gap state in the UPS spectra. This may be attributed to the correlation effect induced by the doped electrons, when they fill in the unoccupied sates of CuPc and become more localized at one molecular site. We have not observed any new components in the core level spectra, which further corroborate the absence of any strong chemical interactions, except for a doping-induced broadening. Finally, it has been reported that alkali metals readily diffuse into CuPc. For example, the Li diffusion length in CuPc has been measured to be 700 Å [22]. We therefore expect the distribution of Cs atoms inside CuPc reasonably uniform within the probing depth of photoemission (~15 Å for UPS and ~50 Å for XPS) [13,15].

The energy level shifts in Cs-doped CuPc film prepared on Ag and Al substrates are summarized in Fig. 3 (a) and (b), respectively. The vacuum level cutoff was obtained at the maximum of the differential curve of the UPS spectra. The core level shifts were deduced by fitting the spectra with Gaussian curves for C 1s, N 1s, and Cu $2p_{3/2}$ after careful deduction of the background. Note that R_{Cs} is in logarithmic scale to emphasize the initial shift. It has been reported that complete ionization of the doped Cs atoms can be easily achieved even at high doping ratios [15]. One can thus safely treat R_{Cs} simply as the electron doping density, as each Cs atom donates single electron to the organic molecules. The overall evolution of the electronic structure turns out to be similar to the case of the Cs-doped CuPc samples on Au substrate [23]. The energy level shift induced by Cs doping can be seen in two stages. At the first stage where the Cs doping ratio is low, all energy levels shift simultaneously and linearly towards higher binding

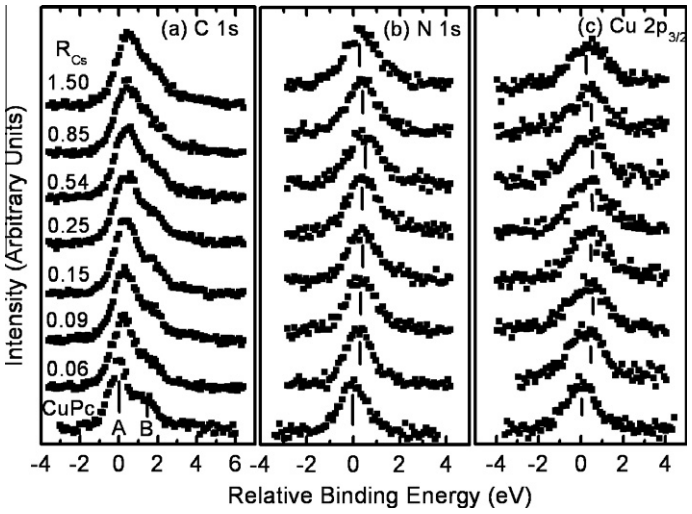

Fig. 2. XPS spectra of C 1s, N 1s and Cu $2p_{3/2}$ core levels as a function of the Cs doping ratio (R_{Cs}) for CuPc thin film prepared on clean Ag substrate. The peak positions are noted by short bars.

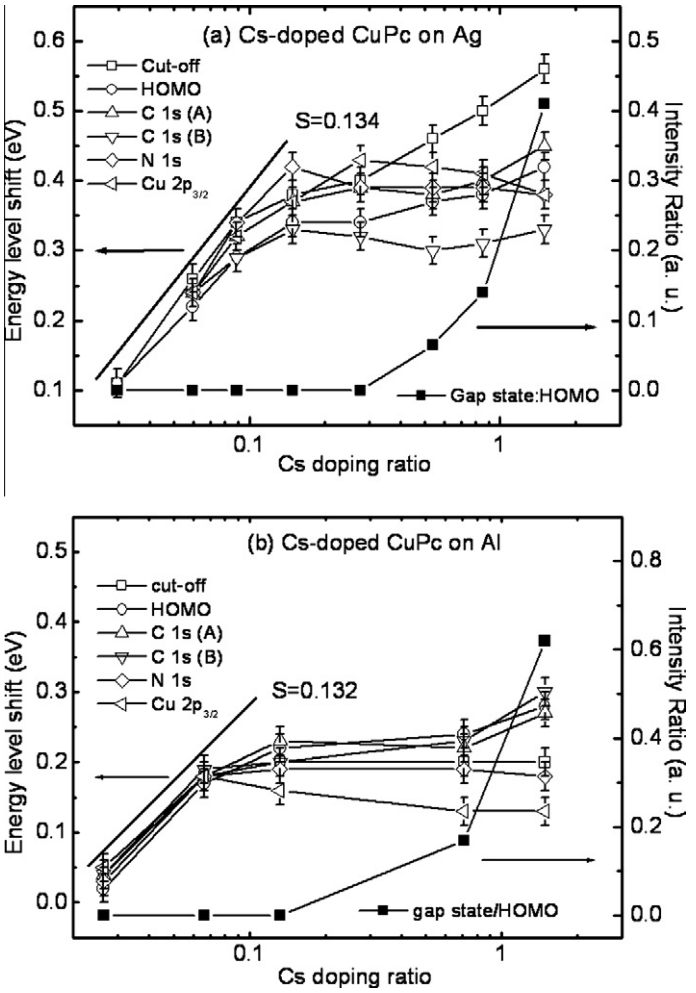

Fig. 3. The summary of the doping-induced energy level shift for CuPc samples prepared on (a) Ag and (b) Al substrates. Note that R_{Cs} is in logarithmic scale to emphasize the initial shift. For both samples, the doping-induced energy level shift can be seen in two stages, and the slopes of the initial stage are almost identical.

energy in the semi-log plot. As the doping density increases, the shift of the energy levels becomes diverse. For CuPc film prepared on Ag, the workfunction shift continuously, reaching 3.34 eV at $R_{Cs} = 1.50$, whereas the workfunction of the sample on the Al substrate becomes saturated quickly, leading to a final value of 3.28 eV. One should also note that both values are much larger than the workfunction of metallic Cs (2.14 eV), indicating strong intermixing at the sample surface, as suggested in our previous studies of intensive doping of CuPc with Na [18]. On the other hand, the shift of HOMO becomes saturated and a reverse shift can be observed for some core levels, such as N 1s and Cu $2p_{3/2,}$ for both samples. Such saturation and reversion have also been reported in our previous studies [14,15,24]. However, the saturation turns out to be substrate-dependent, as it occurs at different doping levels with different amount of shift for samples prepared on Ag, Al and Au substrates. To understand the discrepancy here, one needs to first learn about the energy level alignment at the interfaces between the pristine CuPc film and the metal substrates with different workfunctions. The location of the Fermi level inside the band gap of CuPc can be estimated by the HOMO energy shown in Fig. 1 and the gap energy of the pristine CuPc molecules, which is about 1.6 eV [25]. Thus, the energy separation between the Fermi level and the LUMO is derived to be 0.4, 0.2 and 0.8 eV for Ag, Al and Au substrates, respectively, which agrees very well with the total energy shift before saturation for doped-samples prepared on each of the three substrates. In fact, our previous inverse photoemission (IPES) studies also provide direct evidence that the doping-induced energy level shift becomes saturated as the Fermi level is aligned with the onset of the LUMO of the organic molecules [15]. We can then conclude that the amount of doping-induced energy level shift depends on the position of the Fermi level inside the energy gap of organic semiconductors. More importantly, despite of the workfunction difference of the metal substrates, the slopes derived from the linear shift region in the semi-log plot are in perfect agreement, being about 0.13 eV [15]. On one hand, this is

a clear indication that alkali metal doping-induced energy level shift is determined primarily by metal–organic interaction, which is independent from the choice of the metal substrates. On the other hand, it also suggests the failure of the predictions of the classical doping theories developed for inorganic semiconductors, as a slope of k_BT (0.026 eV) would be expected. The much larger slope in the case of Cs-doped CuPc should be attributed to the absence of the band structure in the amorphous organic thin films. However, if we first assume an infinitely sharp distribution of the molecular orbital, which can be simulated by a δ-function, the energy level shift will still be determined by the Fermi distribution, which again leads to a small slope of k_BT [23]. In order to have a large slope, as being observed in this experiment, a broadening of the LUMO has to be introduced, as one would actually expect when organic molecules are doped with impurities. In this context, the slope of 0.13 eV for Cs-doped CuPc may be used as an estimation of the broadening of the LUMO due to the presence of the excess electrons from alkali metals or other impurities. At a low doping ratio, the electronic structure of organic molecule remains almost intact, except for the rigid shift of all the energy levels. The absence of a discernable gap state suggests that the interactions between the dopants and the organic molecules are weak. Instead of the formation of a new state, the charge transfer at this stage is characterized by the partial occupation of the broadened exponential tail of the LUMO. It should be noted here that all energy levels shift simultaneously in the doping experiment at low doping ratios. No phase separation can be observed in the CuPc film, for the investigated doping ratios, which is much less than 1 at this stage. This suggests that the electronic structures of all CuPc molecules within the probing depth have been modified, and the doped electrons are shared by several surrounding molecules. The alkali metals are fully ionized even for moderately heavy doping ration ~1, another evidence that these dopants are not aggregated among themselves nor phase separated [15].

The independence of the slope of the energy level shift in the semi-log plot on the substrate workfunction indicates that the shift is the result of dopant-organic interaction instead of the substrate workfunction change induced by the alkali metal. Further assessment of the statement can be obtained from the Debye length considerations. As a measure of the screening of an electric field by a semiconductor, the intrinsic Debye length is inversely proportional to the doping density [26]. The Debye length for 1% doping, assuming 100% ionization, is about 7 Å in the organics, supporting the notion that the substrate contribution to the measured energy level shift is insignificant given the probing depth (~20 Å) and the film thickness (200 Å).

As doping density increases, the energy level shift saturates because of the pinning of the Fermi level at the LUMO [25]. Further doping leads to the second stage of charge transfer, when the doped electron concentrates at the center of CuPc and a strong correlation of the electronic states takes place [13,14,18,27]. This leads to the reversed shift of core levels of atoms at the center, including those of Cu and N, as well as the growth of the gap state. When low workfunction metal is used as the substrate, the energy level shift becomes saturated at much smaller doping ratio, comparing to the case of Au. In the UPS measurements, the gap state may not be clearly identified at this time, due to the weak signal intensity. However, as the LUMO now is aligned with the Fermi level, the doped electrons can easily fill in the unoccupied sates in organic molecules and stay localized at a single molecular site, leading to a strong correlation that can effectively modify the electronic structure of the doped molecule. The charge transfer at the second stage is therefore characterized by the formation of gap and strong correlation of the organic energy levels.

In conclusion, the evolution of the electronic structure of Cs-doped CuPc prepared on different metal substrates has been investigated with UPS and XPS. We found out that the shift of the energy levels depend on the energy level alignment at the interface between the pristine CuPc film and the metal substrate. However, the slope of the shift in the semi-log plot is independent of the substrate metal workfunction, being about 0.13 eV, which is much larger than the prediction by inorganic semiconductor theory. This is attributed to the doping-induced broadening of the CuPc LUMO.

Acknowledgments

This work is supported in part by in part by NSF DMR-0602870.

References

[1] L.S. Hung, C.H. Chen, Materials Science and Engineering R-Reports 39 (2002) 143.
[2] C.R. Newman, C.D. Frisbie, D.A. da Silva, J.L. Bredas, P.C. Ewbank, K.R. Mann, Chemistry of Materials 16 (2004) 4436.
[3] H. Hoppe, N.S. Sariciftci, Journal of Materials Research 19 (2004) 1924.
[4] S.R. Forrest, Nature 428 (2004) 911.
[5] A.B. Kaiser, Reports on Progress in Physics 64 (2001) 1.
[6] A. Pron, P. Rannou, Progress in Polymer Science 27 (2002) 135.
[7] A. Vollmer, O.D. Jurchescu, I. Arfaoui, I. Salzmann, T.T.M. Palstra, P. Rudolf, J. Niemax, J. Pflaum, J.P. Rabe, N. Koch, European Physical Journal E 17 (2005) 339.
[8] W.Y. Gao, A. Kahn, Applied Physics Letters 79 (2001) 4040.
[9] N. Koch, G. Leising, L.M. Yu, A. Rajagopal, J.J. Pireaux, R.L. Johnson, Journal of Vacuum Science and Technology A: Vacuum Surfaces and Films 18 (2000) 295.
[10] J. Wusten, S. Berger, K. Heimer, S. Lach, C. Ziegler, Journal of Applied Physics 98 (2005) 10.
[11] M.F. Craciun, S. Rogge, M.J.L. den Boer, S. Margadonna, K. Prassides, Y. Iwasa, A.F. Morpurgo, Advanced Materials 18 (2006) 320.
[12] M.G. Betti, F. Crispoldi, A. Ruocco, C. Mariani, Physical Review B 76 (2007).
[13] T. Schwieger, H. Peisert, M.S. Golden, M. Knupfer, J. Fink, Physical Review B 66 (2002) 155207.
[14] O.V. Molodtsova, V.M. Zhilin, D.V. Vyalikh, V.Y. Aristov, M. Knupfer, Journal of Applied Physics 98 (2005) 093702.
[15] H.J. Ding, Y.L. Gao, Applied Physics Letters 92 (2008) 053309.
[16] H.J. Ding, Y.L. Gao, Applied Physics Letters 86 (2005) 213508.
[17] CRC Handbook on Chemistry and Physics, The Chemical Rubber Co., Cleveland, OH, 2008.
[18] H.J. Ding, K.W. Park, K. Green, Y.L. Gao, Chemical Physics Letters 454 (2008) 229.
[19] I.G. Hill, A. Kahn, Z.G. Soos, R.A. Pascal, Chemical Physics Letters 327 (2000) 181.
[20] H. Ishii, K. Seki, IEEE Transactions on Electron Devices 44 (1997) 1295.
[21] H.J. Ding, Y.L. Gao, Applied Surface Science 252 (2006) 3943.

[22] G. Parthasarathy, C. Shen, A. Kahn, S.R. Forrest, Journal of Applied Physics 89 (2001) 4986.
[23] Y.L. Gao, L. Yan, Chemical Physics Letters 380 (2003) 451.
[24] L. Giovanelli, P. Vilmercati, C. Castellarin-Cudia, J.M. Themlin, L. Porte, A. Goldoni, Journal of Chemical Physics 126 (2007) 044709.
[25] L. Yan, N.J. Watkins, S. Zorba, Y.L. Gao, C.W. Tang, Applied Physics Letters 79 (2001) 4148.
[26] S.M. Sze, Physics of Semiconductor Devices, John Wiley, New York, 1981.
[27] H.J. Ding, Y.L. Gao, Journal of Applied Physics 102 (2007) 043703.

Organic Electronics 11 (2010) 1792–1795

Contents lists available at ScienceDirect

Organic Electronics

journal homepage: www.elsevier.com/locate/orgel

Enhanced sensitivity of an organic field-effect transistor pH sensor using a fatty acid Langmuir–Blodgett film

Supachai Ritjareonwattu, Youngjun Yun, Christopher Pearson, Michael C. Petty *

School of Engineering and Computing Sciences and Centre of Molecular and Nanoscale Electronics, Durham University, Durham DH1 3LE, United Kingdom

ARTICLE INFO

Article history:
Received 25 May 2010
Accepted 26 July 2010
Available online 6 August 2010

Keywords:
Organic thin film transistor
pH sensor
Langmuir–Blodgett film

ABSTRACT

An ion-sensitive organic field-effect transistor (ISOFET) has been fabricated by using poly(3-hexylthiophene) as the semiconductor and polymethylmethacrylate as the gate insulator. With the gate metallization replaced by an Ag/AgCl reference electrode, and following suitable encapsulation, the ISOFETs exhibit transistor behavior in an aqueous environment. Moreover, the devices are shown to respond to changes in pH of the solution. A significant increase in the sensitivity of the ISOFET to H^+ ions was found by depositing a Langmuir–Blodgett film of arachidic acid on top of the gate insulator.

© 2010 Elsevier B.V. All rights reserved.

1. Introduction

The development of effective devices for the identification and quantification of chemical and biochemical substances for process control and environmental monitoring is a growing need. Many sensors do not conform to existing or forthcoming legislation; some systems are too bulky or expensive for use in the field. The ion-sensitive field-effect transistor (ISFET) has been developed since the 1970s [1,2]. In essence, the ISFET is a metal-oxide field-effect transistor (MOSFET) in which the gate connection is separated from the silicon substrate in the form of a reference electrode.

The field of organic electronics is concerned with replacing the 'traditional' inorganic materials used in electronic devices (e.g. Si, SiO_2) with their organic counterparts. This technology should allow for the fabrication of organic ISFETs (ISOFETs) which are cheap, relatively easily to fabricate and offer additional advantages such as mechanical flexibility [3,4]. To date, most work in this area has been reported for devices in which an organic semiconductor has been combined with an inorganic gate dielectric, e.g. Si_3N_4 or Ta_2O_5, to provide hydrogen ion selectivity [5,6]. Here, we fabricate ISOFET structures in which both the semiconducting layer and the gate insulator are organic materials, and show that their pH sensitivity can be enhanced by coating the gate insulator with a few layers of a fatty acid Langmuir–Blodgett (LB) film.

2. Experiment

The devices use poly(3-hexylthiophene) (P3HT) as the semiconductor and polymethylmethacrylate (PMMA) as the gate insulator. We have previously described the incorporation of PMMA into organic FETs and inverter structures [7,8]. This particular insulator exhibits low leakage currents and can be used to produce devices with high carrier mobility and minimal hysteresis.

PMMA (molecular weight 93,000) and P3HT were purchased from Sigma–Aldrich. The PMMA was dissolved in anisole (methoxybenzene) to a concentration of 42 mg ml^{-1}, while the P3HT was dissolved in chloroform to a concentration of 10 mg ml^{-1}. A standard silver/silver chloride (Ag/AgCl) reference electrode was used as the gate electrode to provide a stable electrical contact in the solution. The pH of the solution in contact with the ISOFET surface was changed by adding quantities of acetic acid (buffers containing Cl^- ions were avoided); the pH was

* Corresponding author. Tel.: +44 (0) 191 334 2419; fax: +44 (0) 191 334 2407.
E-mail address: m.c.petty@durham.ac.uk (M.C. Petty).

1566-1199/$ - see front matter © 2010 Elsevier B.V. All rights reserved.
doi:10.1016/j.orgel.2010.07.025

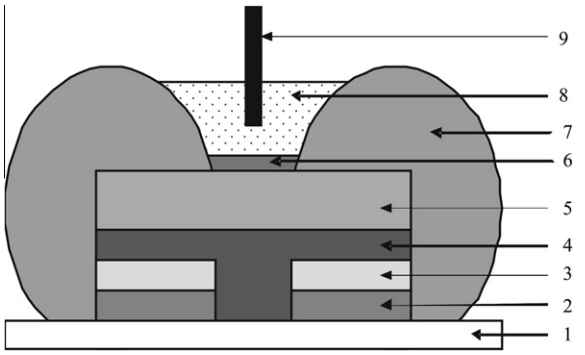

Fig. 1. A typical structure for ISOFET; 1 – glass substrate, 2 – chromium, 3 – gold, 4 – P3HT, 5 – PMMA, 6 – LB film, 7 – epoxy resin, 8 – electrolyte solution, 9 – reference (gate) electrode.

monitored using a Philips PW9420 pH meter. The electrical characteristics of the ISOFET were recorded using an HP 4140B picoammeter/voltage source. All the measurements were undertaken at room temperature and with the devices in the dark.

Fig. 1 shows a schematic diagram of the top-gate ISOFET structure. After cleaning in an ultrasonic bath, the glass substrate was rendered hydrophobic by immersion in dimethyldichlorosilane solution. An interdigitated pattern of source and drain electrodes, formed using conventional photolithographic methods, was used; the channel width, W, and length, L, were 22,000 μm and 25 μm, respectively. The electrode materials were deposited by the thermal evaporation of Cr (20 nm) followed by Au (20 nm). The P3HT (thickness about 55 nm) was deposited using spin-coating at a spin speed of 5000 rpm for 45 s. This was followed by spin-coating the PMMA (thickness approximately 130 nm) using a two-step process: spinning at 500 rpm for 10 s followed by 3000 rpm for 50 s. The resulting device structure was baked in a vacuum oven at 135 °C for 120 min. For some devices, 10 LB layers of arachidic acid were deposited on top of the PMMA (Y-type deposition, with the first layer transferred on the initial downward traversal of the substrate through the air/water interface). An epoxy resin was used to encapsulate the final device by hand. This allowed the electrolyte solution to come into direct contact with only the gate insulator.

3. Results and discussion

The electrical measurements were first undertaken with the device in deionized water (pH 5.5) and at source-to-drain voltages, V_d, and gate-to-source voltages, V_g, below 1 V to prevent the occurrence of unwanted electrolytic processes, which led to device instability. The device was normally left in solution for about 2 h before the measurements were started. If the ISOFET bias conditions were changed (V_g and/or V_d), relatively long current transients generally resulted. For example, Fig. 2 shows the effect of changing the value of V_g. During this measurement, V_d was scanned over the range 0 V → −1 V → 0 V in 50 mV steps, while the source-to-drain current, I_d, was monitored. Fig. 2 reveals that, following a decrease in the

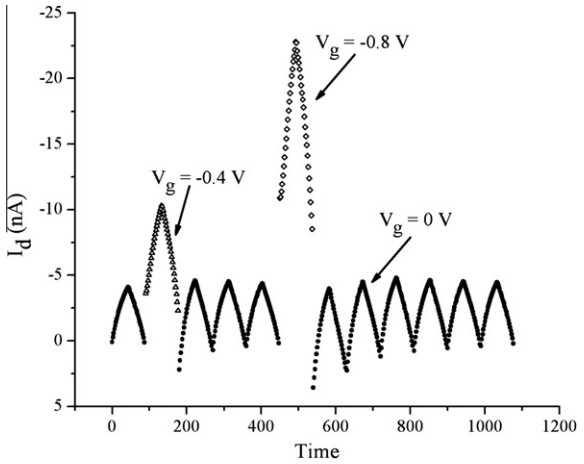

Fig. 2. Effect of changing the gate bias V_g on the drain current I_d of the ISOFET (without LB layer). The increase and decrease of I_d correspond to a scan in V_d over the range 0 V → −1 V → 0 V. Measurements in the dark at room temperature.

magnitude of the gate voltage (e.g. −0.8 V → 0 V), the drain current initially changed polarity and took several cycles (each cycle of V_d lasted approximately 90 s) to stabilize at its new value. This recovery time increased with increasing magnitude of the change in V_g. These effects were attributed to the charging and discharging of the surface of the PMMA resulting from changes in the gate voltage (applied via the reference electrode). Consequently, a systematic method of recording the electrical characteristics of the ISOFET was devised to avoid ambiguous results.

Fig. 3 shows the output currents of the P3HT/PMMA ISOFET (the basic structure without the LB layer). Each I_d versus V_d curve was recorded following the stabilization of I_d using the procedure discussed above. Results for both increasing and decreasing V_d (at a constant value of V_g) are included in Fig. 3. The data reveal that the ISOFET is work-

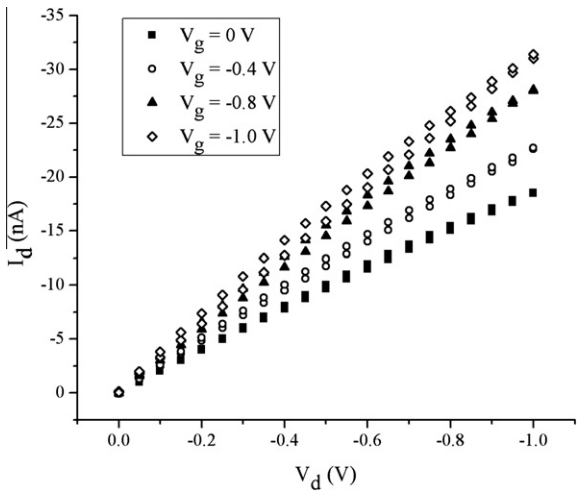

Fig. 3. Output characteristics of ISOFET (without LB layer). Voltage scans are shown for both increasing and decreasing V_d. Measurements in the dark at room temperature.

ing as a transistor in the linear regime, with very little hysteresis evident on reversing the drain voltage scan [9].

To investigate the pH response of our ISOFETs, acetic acid was added to samples of deionized water; the solutions were stirred and left overnight to provide a series of test solutions at different pHs. The ISOFET was placed initially in deionized water for 2 h, removed and immersed in the highest pH test solution. The drain voltage was then scanned over the range 0 V → −0.2 V → 0 V, with V_g = 0 V in 20 mV steps until the I_d values were stable; this process generally took 5 min. The gate voltage was then changed to V_g = −0.2 V and the drain voltage scanned between 0 V and −0.20 V until I_d was again stable. The ISOFET was removed from the solution, placed in a different pH test solution and the measurement procedure repeated. Results for V_g = −0.2 V and V_d = −0.2 V are summarized in Fig. 4a; the error bars reflect the average of 5 measurements at each pH value. The magnitude of the drain current clearly decreases with increasing acidity of the solution. This is similar to the pH effects reported other ion-sensitive transistors based on P3HT [4].

The pH response of the ISOFET with the LB film deposited on the gate insulator, Fig. 4b, shows a similar trend to

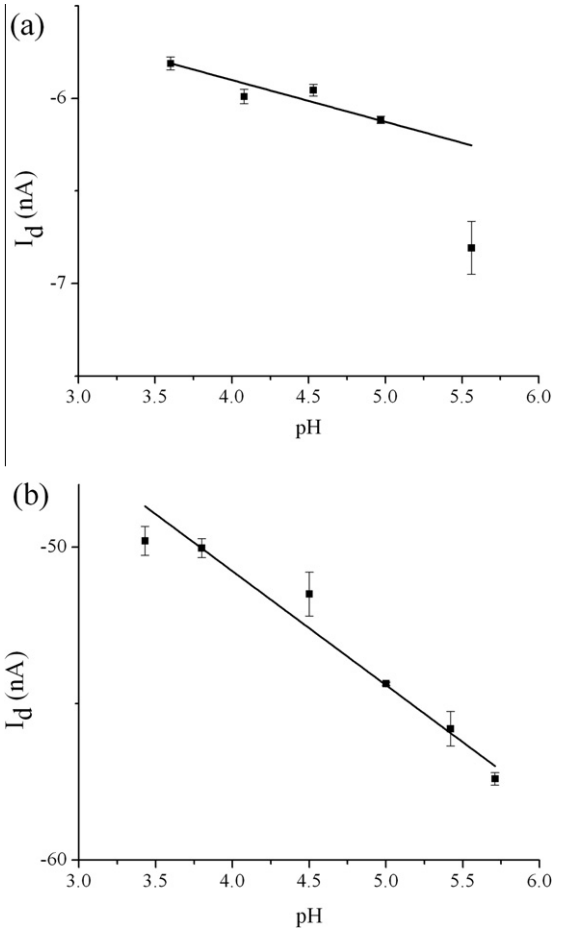

Fig. 4. (a) pH response of the ISOFET without the LB layer (V_g = −0.2 V, V_d = −0.2 V). (b) pH response of the ISOFET with the LB layer (V_g = −0.2 V, V_d = −0.2 V).

that of the uncoated device. However, the drain currents are significantly larger and the hydrogen-ion sensitivity (slope of the graph) has increased by about an order of magnitude. Osa has reported a similar result by depositing LB layers onto both Si_3N_4 and parylene gate ISFETs [10].

In the linear regime, the dependence of the FET drain current I_d on the drain to source voltage V_d is given by [9]

$$I_d = \frac{\mu C_i W V_d}{L}\left[(V_g - V_t) - \frac{V_d}{2}\right] \quad (1)$$

where V_t is the threshold voltage of the transistor. In the case of the ISFET, the introduction of new interfaces between the solution and the gate insulator leads to the modification of Eq. (1) [9]. If the gate insulator is assumed to be ideal (i.e. no charge can cross it and it is thicker than the electron tunneling distance) and that the interface between the solution and the gate insulator can be considered to be non-polarized (i.e. ions can permeate reversibly into and out of the insulator) the relevant equation is

$$I_d = \frac{\mu C_i W V_d}{L}\left[(V_g - V_t^*) - \frac{V_d}{2} \pm \frac{RT}{z^i F}\ln a^i - E_{ref}\right] \quad (2)$$

where V_t^* is the modified threshold voltage for the ISFET, a^i is the activity of the ion in solution, z^i is the number of charges per ion, E_{ref} is the reference electrode potential, T is the temperature, R is the gas constant and F is Faraday's constant. The effect of the ion concentration on the drain current is provided through the term containing the activity in Eq. (2).

Based on the site-binding model [5,11], the charges at the surface of the insulating layer are affected directly by the H^+ concentration in solution; this in turn changes the drain current of the ISOFET. An increase in the pH (i.e. to a more basic solution) will decrease the positive charge density, leading to an increase in the density of holes in the accumulation layer of the P3HT. As a consequence, the magnitude of the drain current increases, as observed in Fig. 4a and b. The opposite effect occurs when the solution is made more acidic. The change in the drain current with pH for our P3HT/PMMA ISOFET is approximately 0.5 nA per pH unit. This is significantly smaller than the variation of 30–40 μA/pH reported for Si/Si_3N_4 ISFETs [12], and also much less than figures reported for devices based on $P3HT/Ta_2O_5$ (0.3 μA/pH) [6] and those based on $P3HT/Si_3N_4$ (25 nA/pH) [5]. The low sensitivity is directly related to the small transconductance, $\left(\frac{\partial I_d}{\partial V_g}\right)_{V_d=\text{constant}}$, of the organic-based ISOFET and to the low affinity of the ester groups in the PMMA to hydrogen ions.

By coating 10 LB layers on the PMMA layer of the ISOFET, the change in the drain current with pH is approximately 3.5 nA per pH unit, an increase of almost an order of magnitude. We suggest that the enhanced drain current and increased pH response of the LB film-coated ISOSFET both arise from the presence of the carboxylic acid head groups in the LB film. These will become ionized on the surface of the aqueous subphase during monolayer formation and will subsequently be incorporated into the ISOFET structure [13]. The increased negative charge increases the conductivity of the channel, thereby increasing I_d. A variation in

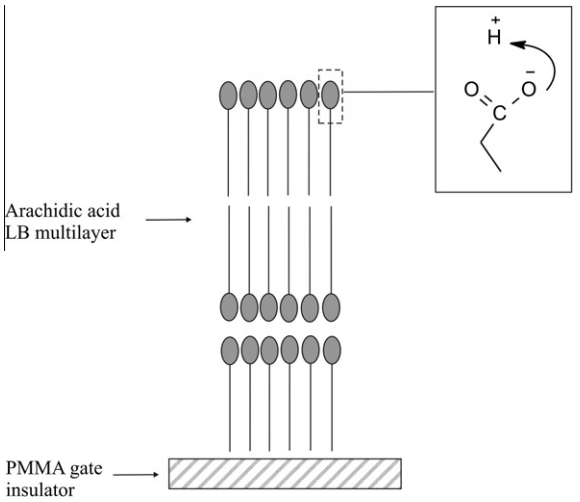

Fig. 5. Schematic diagram showing ionization of carboxylic acid head-group in outer layer of LB multilayer.

the solution pH subsequently changes the degree of ionization of the carboxylic acid head groups, as depicted in Fig. 5 (although the alkyl chain will be outermost for the LB film in air, it is likely that the top monolayer is removed following immersion of the LB film-coated ISOFET in the test solution). These groups more readily dissociate (lower pK_a) in the solution than the ester groups in the PMMA.

The sensitivity of the LB film-modified ISOFET is also less than that of its inorganic counterpart. However, it is anticipated that higher values can be obtained using an improved device design (e.g. larger W/L ratios, thinner gate dielectrics). The organic device offers significant advantages in terms of mechanical flexibility, cost and potential biocompatibility. Moreover, the LB layer, to some extent emulates a biological membrane. It should therefore be possible to incorporate additional components in the fatty acid matrix (e.g. ionophores) to sensitize the ISOFET to other species.

4. Conclusions

An organic field-effect transistor, fabricated by using P3HT as the semiconductive layer and PMMA as the gate insulator, has been shown to operate in an aqueous environment, with the metallic gate electrode replaced by an Ag/AgCl reference electrode. The resulting device exhibits a small sensitivity to hydrogen ions and indicates that such transistor structures might form the basis of organic-based chemical sensors. Furthermore, results with Langmuir–Blodgett film-coated devices suggest a strategy to make the ISOFET more sensitive and more selective to the target ions in a solution.

Acknowledgement

S.R. would like to thank the Royal Thai Government for the provision of a studentship.

References

[1] P. Bergveld, Sens. Actuat. B 88 (2003) 1.
[2] J. Janata, Electroanalysis 16 (2004) 1831.
[3] J.T. Mabeck, G.G. Malliaras, Anal. Bioanal. Chem. 384 (2006) 343.
[4] C. Bartic, G. Borhs, Anal. Bioanal. Chem. 384 (2006) 354.
[5] C. Bartic, B. Palan, A. Campitelli, G. Borghs, Sens. Actuat. B 83 (2002) 115.
[6] C. Bartic, A. Campitelli, S. Borghs, Appl. Phys. Lett. 82 (2003) 475.
[7] Y. Yun, C. Pearson, M.C. Petty, J. Appl. Phys. 105 (2009) 034508.
[8] Y. Yun, C. Pearson, M.C. Petty, IET Circ. Dev. Syst. 3 (2009) 182.
[9] J. Janata, R.J. Huber, in: H. Freiser (Ed.), Ion-Selective Electrodes in Analytical Chemistry, vol. 2, Plenum Press, 1980.
[10] T. Osa, Appl. Biochem. Biotechnol. 41 (1993) 35.
[11] D.E. Yates, S. Levine, T.W. Healy, J. Chem. Soc. Faraday I 70 (1974) 1807.
[12] S.D. Moss, J.B. Smith, P.A. Comte, C.C. Johnson, in: P. Cheung, D.G. Fleming, W.H. Ko, M.R. Neuman (Eds.), Theory, Design, and Biomedical Applications of Solid State Chemical Sensors, CRC Press, Cleveland, OH, 1978.
[13] E. Pezron, P.M. Claesson, J.M. Berg, D. Vollhardt, J. Colloid Interf. Sci. 138 (1990) 245–254.

Organic Electronics 11 (2010) 1796–1801

Contents lists available at ScienceDirect

Organic Electronics

journal homepage: www.elsevier.com/locate/orgel

A conductor/insulator/semiconductor polymer solar cell by an ultra-thin polymer insulator

Hsing-Wang Tsai [a], Zingway Pei [b,*], Ting-Hsiang Huang [b], Pei-Wen Li [a], Yi-Jen Chan [c]

[a] Department of Electrical Engineering, National Central University, Chungli 32001, Taiwan, ROC
[b] Graduate Institute of Optoelectronic Engineering, Department of Electrical Engineering, National Chung Hsing University, Taichung 40227, Taiwan, ROC
[c] Electronics and Optoelectronics Research Laboratories (EOL), Industrial Technology Research Institute (ITRI), Hsinchu 31040, Taiwan, ROC

ARTICLE INFO

Article history:
Received 13 June 2010
Received in revised form 29 July 2010
Accepted 8 August 2010
Available online 18 August 2010

Keywords:
Anode structure
Insulator
Lifetime
Polymer solar cell

ABSTRACT

In the letter, a conductor/insulator/semiconductor (CIS) polymer solar cell was demonstrated with higher performance and stability than standard polymer solar cell. The random copolymer, poly(styrene-co-methyl-methacrylate) (PS-r-PMMA), was used as the insulator. By control the annealing temperature, a 2 nm-thick insulator could provide dark current suppress function and ensure carrier tunneling simultaneously. The efficiency of the CIS solar cell was improved from 2.09 to 2.37%, around 11% improvement. Meanwhile, the half-efficiency lifetime increase from 58 to 97 h by the applying of PS-r-PMMA protection layer.

© 2010 Elsevier B.V. All rights reserved.

1. Introduction

The solar cell based on polymer material is an attractive technology for developing low cost and large area renewable energy because of its solution process and simple cell structure [1–3]. The structure of the polymer solar cell consists of a polymer photoactive layer placed between anode and cathode electrodes [4]. The photoactive layer for the most efficient polymer solar cell is based on a bulk hetero-junction (BHJ) structure [5,6]. The BHJ intermixes the polymer donor and acceptor materials to form a percolated conducting network. The excitations generate by photon absorption in photoactive material and separate at BHJ interfaces into holes and electrons, transporting through the percolation-conducting path toward the anode and cathode [7]. The generally used polymer donor and acceptor is poly-3-hexthiophene (P3HT) and [6,6]-phenyl-C61 butyric acid methyl ester (PCBM) [8,9]. A conducting polymer, poly(3,4-ethylenedioxythiophene)/poly(styrenesulfonate), abbreviated as PEDOT:PSS is generally inserted between the anode electrode and the active layer as a buffer layer to improve device performance, increasing and modifying the work function and surface morphology of the indium-tin oxide (ITO) anode [10]. The interface between ITO/PEDOT:PSS and BHJ is not stable because the moisture and oxygen in PEDOT:PSS oxidizes the photoactive polymer [11,12], forming poor contact that reduces the fill factor (*FF*) and opens the circuit voltage (V_{oc}) after high temperature annealing or storage in air for a period of time [13].

This work places an ultra-thin polymer insulator between PEDOT:PSS and the photoactive layer to make a conductor/insulator/semiconductor (CIS) solar cell. The polymer insulator may improve the interface, blocking the dark current that improves the V_{oc} and *FF*. This research uses the poly(styrene-co-methyl-methacrylate) (PS-r-PMMA) for this concept. The PS-r-PMMA is a copolymer randomly combines polystyrene (PS) and poly methyl methacrylate (PMMA) in which some PS-r-PMMA contains the hydroxyl group (OH–) after copolymer formation. The

* Corresponding author. Present address: Department of Electrical Engineering, National Chung Hsing University, 250, Kuo Kuang Rd., Taichung 40227, Taiwan, ROC. Tel.: +886 4 22851549x801; fax: +886 4 22851410.
E-mail address: zingway@dragon.nchu.edu.tw (Z. Pei).

1566-1199/$ - see front matter © 2010 Elsevier B.V. All rights reserved.
doi:10.1016/j.orgel.2010.08.006

hydrophobic surface of the PS-r-PMMA may cause better surface morphology and better P3HT/PCBM phase separation in the active layer to form an efficient percolation-conducting path. Research on the organic thin film transistor has demonstrated that the PS-r-PMMA attaches on the hydroxyl surface forming a very thin polymer layer in amorphous form by a condensation process. An adequate solvent removes the excess un-attached PS-r-PMMA material. The amounts of attached PS-r-PMMA vary with thermal annealing time and temperature, controlling the thickness of the PS-r-PMMA film on silicon oxide from 2 to 6 nm [14]. A thin enough PS-r-PMMA ensures photocurrent tunneling, as in the inorganic metal–insulator–semiconductor solar cell, and serves as a protection layer for the photoactive layer. This layer could suppress oxygen and moisture penetration from PEDOT:PSS into the photoactive layer.

2. Experimental

Fig. 1(a) shows the device structure of the conduction/insulator/organic semiconductor (CIS) solar cell. A pre-patterned ITO glass was cleaned by acetone, DI water, and isopropanol sequentially, for 10 min. After cleaning, the ITO surface was treated by UV-ozone for 30 min. The conducting layer, PEDOT:PSS was spin coated on the ITO substrate and thermally dried at 140 °C for 10 min. The thickness of the dried PEDOT:PSS layer was about 40–50 nm. The polymer insulator, PS-r-PMMA was applied on the PEDOT:PSS. Fig. 1(a) depicts the chemical structure of PS-r-PMMA. To prepare the PS-r-PMMA solution, the PS-r-PMMA random copolymer (Aldrich, M_w = 1000.000–150.000) was dissolved in toluene in a concentration of 10 mg/ml and stirred overnight. Fig. 1(b) shows the formation procedure of ultra-thin PS-r-PMMA film. The PS-r-PMMA solution was first spin coated on the PEDOT:PSS layer at 500 rpm for 60 s. Three temperatures, 140, 180, and 220 °C were used to anneal PS-r-PMMA film for 2 h. After annealing, the samples were rinsed in toluene for 10 s. Since the toluene removes the un-attached PS-r-PMMA polymer to form a flat film, the thickness of the remained PS-r-PMMA film was approximately 2, 3, and 6 nm for the 140, 180, and 220 °C annealed sample. The thickness of the PS-r-PMMA layers was determined by measuring the thickness of PS-r-PMMA on the silicon oxide with the same processes by an ellipsometer with calibrated parameters [15]. The photoactive layer was a mixed solution of P3HT and PCBM organic semiconductors. The P3HT and PCBM were dissolved in 1,2-dichlorobenzene (DCB) separately in a concentration of 16 mg/ml. The photoactive layer solution was achieved

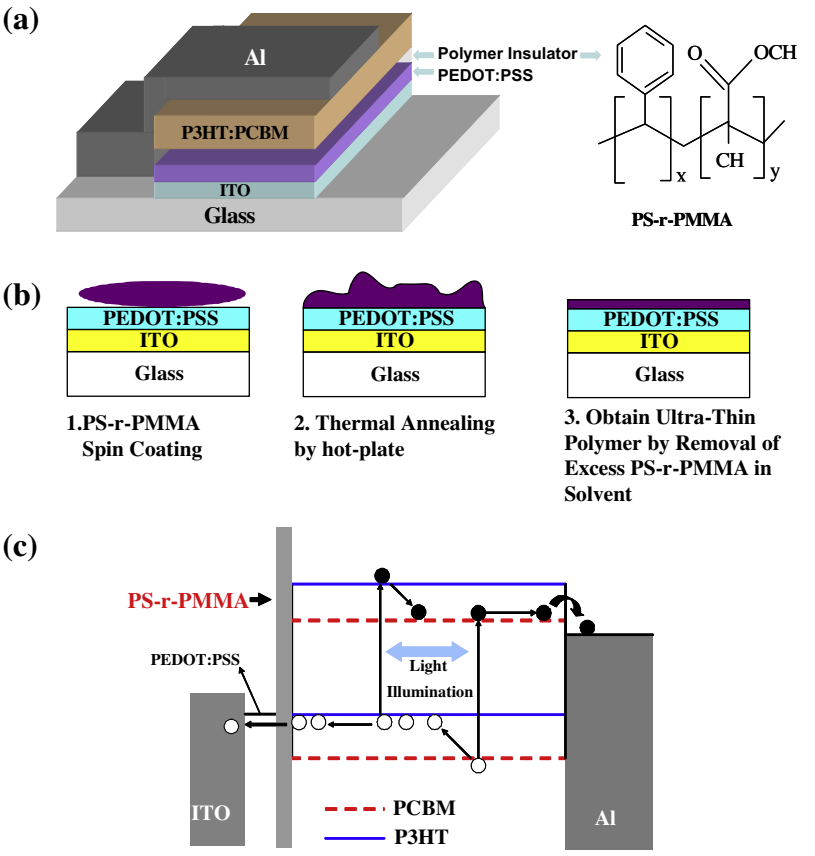

Fig. 1. (a) The schematic diagram of CIS solar cell with ultra-thin PS-r-PMMA random copolymer as insulator. The chemical structure and processing for PS-r-PMMA layer is also shown. (b) The coating process for ultra-thin PS-r-PMMA. After rinsed in toluene, a smooth and ultra-thin PS-r-PMMA was obtained. (C) The band alignment of CIS polymer solar cell.

by mixing P3HT and PCBM solution in a 1:1 ratio. The active layer was spin coated on the PS-r-PMMA layer at 500 rpm for 60 s and naturally dried in a glove box. Finally, a 100 nm thick Al layer was deposited on the photoactive layer as the cathode electrode and annealed at 110 °C for 10 min in a N_2 filled glove box. The active area for all devices was 4 mm^2. The photovoltaic effect was performed by a (Peccell-PEC-L11) solar simulator under AM1.5G illumination (100 mW/cm^2), calibrated by a reference silicon solar cell. The atomic force microscopy (AFM) images were obtained using a PicoPlusII scanning probe microscope. All device characterizations were performed under an ambient condition.

3. Results and discussion

Fig. 1(c) sketches the band alignment of the CIS cell and an ultra-thin PS-r-PMMA layer between PEODT:PSS and the photoactive layer. Inserting a thick layer of PS-r-PMMA might blocks the hole transport, reducing the dark saturation current since PS-r-PMMA is an insulator. However, if the thickness of PS-r-PMMA is thin enough, the holes can transport through it with less reduction. After light illumination, the photo-generated holes could tunnel through the ultra-thin insulator to the anode to achieve high photocurrent [16]. To find the appropriate thickness of PS-r-PMMA, the dark current for polymer solar cells with several PS-r-PMMA thickness was shown in Fig. 2(a). The reverse saturation leakage current for 2 nm thick PS-r-PMMA in CIS solar cell is slightly less than standard solar cell. The reduction of dark leakage saturation current is not clear. This reverse saturation leakage current decreases obviously for the CIS solar cell with 3 and 6 nm thick PS-r-PMMA layer. This implies the thickness of PS-r-PMMA less than 2 nm might be suitable for carrier transport with less blocking effect. However, for PS-r-PMMA graft to the hydroxyl group (OH–) of the underlying OH– surface, the temperature equal or higher than 140 °C is required [14]. Further decrease the thickness less than 2 nm is hardly to obtain and control. Compare the dark current at the forward bias, the current for the CIS solar cell with 2 nm thick PS-r-PMMA is also slightly less than standard cell. However, for CIS solar cell with 3 and 6 nm thick PS-r-PMMA, the forward current is strongly blocked which would not have acceptable photovoltaic performance. Fig. 2(b) shows the photovoltaic effect of the four polymer solar cell conditions. The standard cell denotes the polymer solar cell without the PS-r-PMMA protection layer. The J_{sc}, V_{oc} and fill factor (*FF*) for the standard cell is 8.90 mA/cm^2, 0.48 V and 0.49, respectively, leading to a 2.09% power conversion efficiency (PCE). With 2 nm thickness of the PS-r-PMMA insulator layer, the J_{sc}, V_{oc}, and *FF* of a polymer solar cell increase to 9.11 mA/cm^2, 0.52 V and 0.50, leading to a 2.37% PCE, around 11.26% enhancement, compared to a standard cell. The Fig. 2 inset shows the J_{sc} and V_{oc} for several CIS and standard cells. In general, CIS cells exhibit higher J_{sc} and V_{oc} than standard cells. Inserting an ultra-thin layer of PS-r-PMMA, slightly decreases the leakage current and enhances photocurrent leading to an slightly increase of V_{oc} by the following equation:

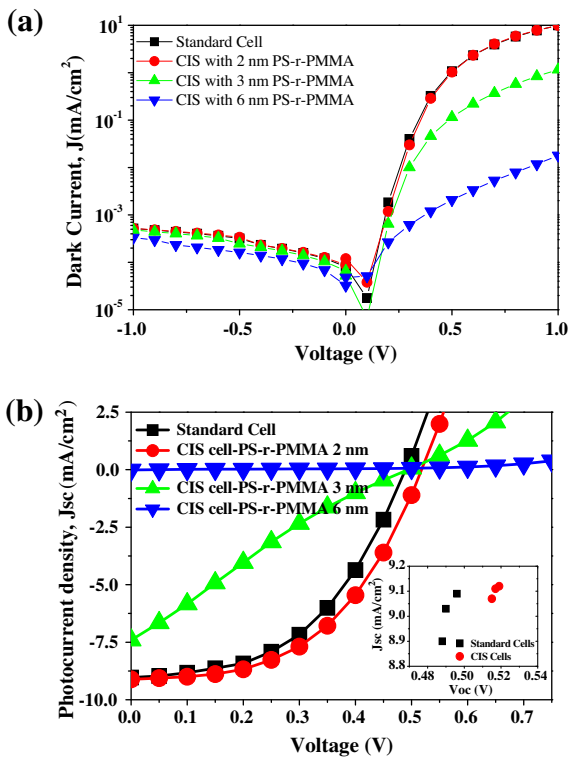

Fig. 2. (a) The dark saturation leakage current density–voltage characteristic for standard solar cell and CIS solar cells with 2, 3, and 6 nm thick PS-r-PMMA insertion layer. (b) The photo-current density–voltage characteristics for the polymer solar cell with standard and CIS structure under AM1.5 illumination. Inset shows the J_{sc} and V_{oc} of several standard and CIS polymer solar cells.

$$V_{oc} = \frac{nKT}{q} \ln\left(\frac{J_{sc}}{J_0} + 1\right)$$

in which n is the ideal factor, K is the Boltzman constant, T is the absolute temperature, J_{sc} is the photocurrent, and J_0 is the dark current [17]. The V_{oc}, J_{sc}, *FF*, PCE, series resistance and shunt resistance for standard solar cell, and CIS solar cells with 2, 3, and 6 nm thick PS-r-PMMA were listed in Table 1. From the table, the insertion of 2 nm thick PS-r-PMMA will not increase the series resistance extensively. This agrees well with the similar current density–voltage (*J–V*) characteristics of standard and CIS (2 nm) solar cell. However, increase the thickness of PS-r-PMMA to 3 nm, the series resistance increase dramatically from 11.89 to 93.6 Ω cm^2. Further increase the thickness of PS-r-PMMA to 6 nm, no photovoltaic effect was observed. We could still try to extract the series resistance. It increases to 468 Ω cm^2, which is around 42 times higher than CIS solar cell with 2 nm thick PS-r-PMMA. With insertion a layer of PS-r-PMMA with thickness higher than 3 nm, the carriers will be blocked cause high series resistance and poor photovoltaic performance. By the mechanism for CIS solar cell described above, the J_{sc} should decrease instead of increase, compared to a standard cell. This could be explained by the surface of the photoactive layer deposition. Inserting an ultra-thin layer of PS-r-PMMA

Table 1
Photovoltaic performance parameters for standard and CIS polymer solar cells with 2, 3, and 6 nm thick PS-r-PMMA.

	J_{sc} (mA/cm^2)	V_{oc} (V)	Fill factor (%)	Efficiency (%)	Series resistance (Ω cm^2)	Shunt resistance (Ω cm^2)
Standard cell	8.90	0.48	49	2.09	11.63	862
PS-r-PMMA (2 nm)	9.11	0.52	50	2.37	11.82	917
PS-r-PMMA (3 nm)	7.52	0.47	25	0.88	93.6	63.6
PS-r-PMMA (6 nm)	–	–	–	0	468	20,846

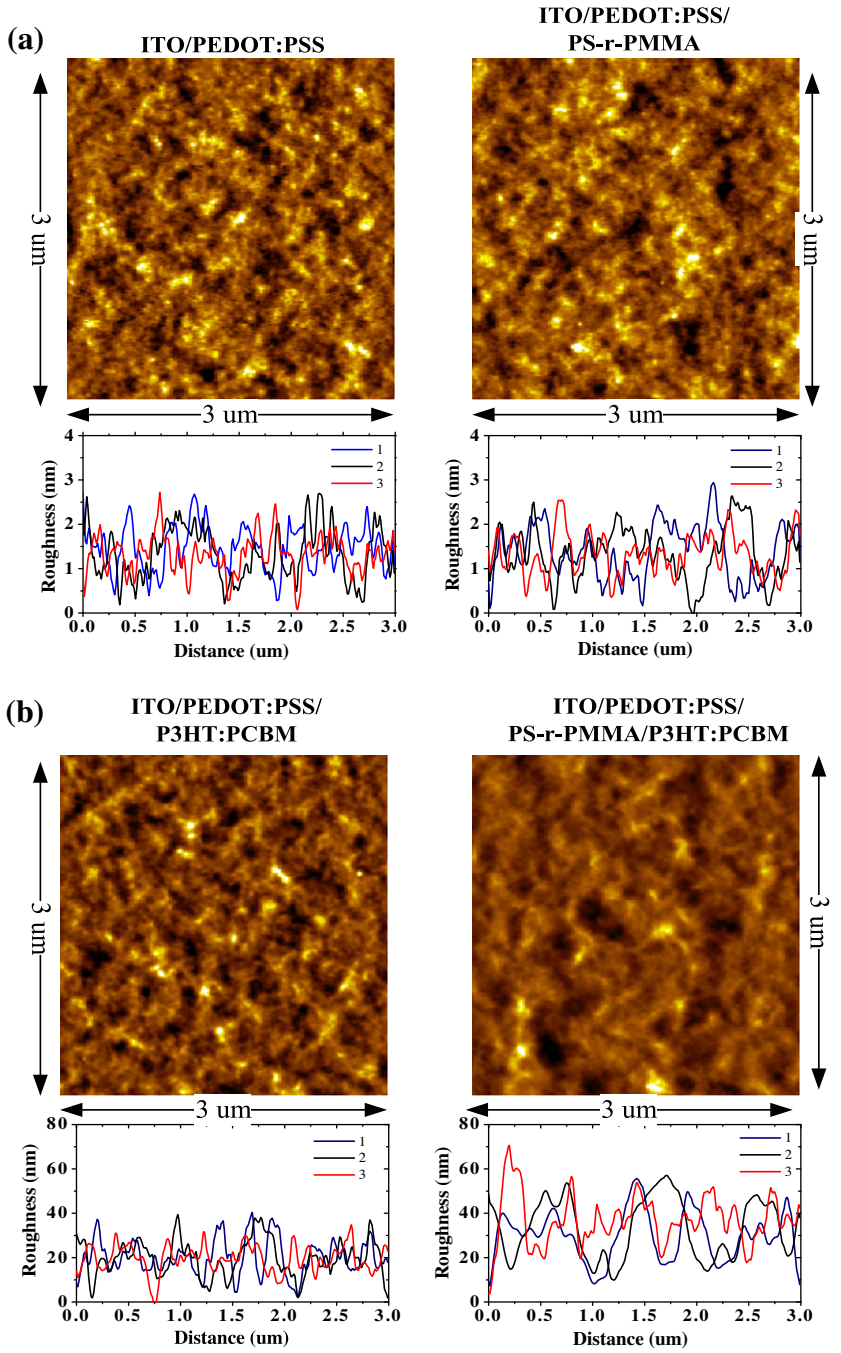

Fig. 3. The atomic force microscope (AFM) surface morphology on (a) PEDOT:PSS and PS-r-PMMA surface. The scales are 3 μm × 3 μm. The roughness is similar for both surface, (b) on P3HT/PCBM with PEDOT:PSS and PS-r-PMMA underlying layer. The roughness of the P3HT:PCBM layer on the PEDOT:PSS layer exhibits rms around 18.7–19.5 nm with small P3HT and PCBM domains. In comparison, the roughness of the P3HT:PCBM film on the PS-r-PMMA surface exhibits rms around 23.75–32.5 nm with a large P3HT and PCBM domain.

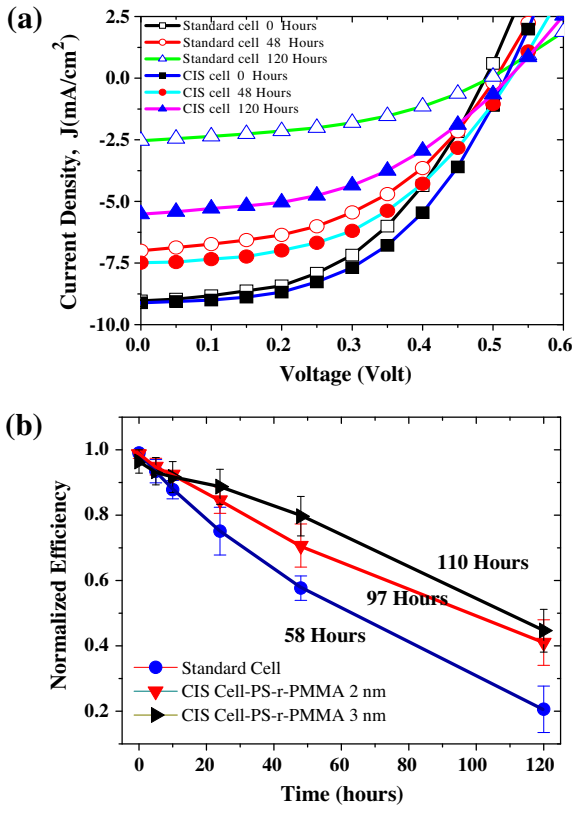

Fig. 4. (a) The photo-current density–voltage characteristic for standard and CIS (2 nm PS-r-PMMA layer) solar cells after storage in ambient for 0 (pristine), 48, and 120 h. (b) The normalized efficiency respect to the storage time for standard and CIS solar cells. The half-efficient for standard, CIS (2 nm) and CIS (3 nm) polymer solar cell are 58, 97, and 110 h, respectively.

modifies the surface from hydrophilic to hydrophobic. The hydrophobic surface is favorable for better P3HT/PCBM growth and phase separation [18]. The increase in the photocurrent due to better morphology of the active layer compensates for photocurrent reduction by the ultra-thin insulator, resulting in obtaining a similar J_{sc} in CIS and the standard cell. Further increases in the thickness of PS-r-PMMA causes a current density leakage far below the photocurrent of the polymer solar cell. Carrier blocking makes the J_{sc} of the polymer solar cell too small to have good photovoltaic performance. Fig. 3(b) shows a totally blocked photocurrent by a 6 nm thick PS-r-PMMA film.

To verify modification in the P3HT/PCBM active layer on different underlying layers, the surface morphology was measured by AFM on the area of $3 \times 3\ \mu m^2$. Fig. 3(a) shows the surface for PEDOT:PSS film and PS-r-PMMA covered PEDOT:PSS film. The roughness of the PEDOT:PSS/ITO surface is flat with a root-mean-square (rms) approximately 1.1–1.3 nm. Covering with PS-r-PMMA does not alter uniformity of the rms at approximately 1.1–1.5 nm. This indicates the uniform coverage of the PEDOT:PSS surface by PS-r-PMMA. The PS-r-PMMA layer also modifies the surface energy. The contact angle measurements determine the surface energy of a material surface [19]. The aqueous contact angle increases from 25° of PEDOT:PSS to around 62°, meaning that the hydrophilic surface modifies to slightly hydrophobic. Fig. 3(b) shows the AFM surface morphology for the P3HT:PCBM layer on PEDOT:PSS and on PS-r-PMMA. The roughness of the P3HT:PCBM layer on the PEDOT:PSS layer exhibits rms around 18.7–19.5 nm with small P3HT and PCBM domains. In comparison, the roughness of the P3HT:PCBM film on the PS-r-PMMA surface exhibits rms around 23.75–32.5 nm with a large P3HT and PCBM domain. This indicates that the P3HT and PCBM on PS-r-PMMA separate well into a better percolation path for electron and hole-conduction by a self-organization process. The rough surface also enhances internal light scattering and light absorption, leading to higher J_{sc}, resulting in the J_{sc} for the CIS cell not less than the standard cell [20].

For the lifetime measurement, this research encapsulated the polymer solar cell at the cathode side by covering it with a glass sheet and sealing with epoxy. Fig. 4(a) shows the photo-current density–voltage (J–V) characteristic of standard and CIS cells. The measurement time is 0 (pristine), 48, and 120 h after cell fabrication. The J_{sc} of the standard cell decreased from 8.90 to 7.00 mA/cm^2, for the first 48 h, and decreased rapidly from 7.00 to 2.53 mA/cm^2 from 48 to 120 h. Within 120 h, the J_{sc} decreased around 72%. In comparison, the J_{sc} in the CIS cell with 2 nm PS-r-PMMA protection layer reduced from 9.11 to 7.48 mA/cm^2 in 48 h, and further decreased to 5.51 mA/cm^2 after 120 h. Within 120 h, the J_{sc} decreased only 39.5%. Table 2 lists the details. Fig. 4(b) shows the efficiency trend to a prolonged time. Efficiency for the standard and CIS cells decreases along the store time. The half-efficiency lifetime for the standard cell is around 58 h and around 97 h for the CIS cell. The lifetime for the CIS cell exceeds the standard cell by 40 h, around 67% enhanced. The half-efficiency lifetime further increases to 110 h when using the 3 nm thick PS-r-PMMA layer. Although J_{sc} and efficiency for both

Table 2
Photovoltaic performance parameters for standard and CIS polymer solar cells with 2 nm thick PS-r-PMMA after 0 (pristine), 48, and 120 h.

	Time (h)	J_{sc} (mA/cm^2)	V_{oc} (V)	Fill factor (%)	Efficiency (%)	Series resistance (Ω cm^2)	Shunt resistance (Ω cm^2)
Standard	Pristine	8.90	0.48	49	2.09	11.63	862
	48	7.00	0.50	35	1.23	18.48	422
	120	2.53	0.50	33	0.42	56.30	564
PS-r-PMMA (2 nm)	Pristine	9.11	0.52	50	2.37	11.82	917
	48	7.48	0.52	43	1.67	18.30	701
	120	5.51	0.52	34	0.97	32.94	386

the standard and CIS cell decrease with time, the trend is different. The efficiency decreases faster than the short circuit current, explained by the series resistance (R_s). Table 1 shows that the R_s for the pristine standard cell is 11.63 and 11.82 $\Omega\,cm^2$ for the CIS cell. After 120 h, the R_s for the standard cell increases to 56.30 $\Omega\,cm^2$. The R_s for the CIS cell only increases to 32.94 $\Omega\,cm^2$, far smaller than the standard cell. The increase in R_s causes the decrease of the *FF*, with efficiency decreasing faster than J_{sc}. This is because the moisture and oxygen in the PEDOT:PSS film that oxidizes the photoactive polymers decreases conductivity to enhance the R_s device. Inserting a layer of PS-r-PMMA may help block the oxygen and moisture penetration. Only 2 nm thick PS-r-PMMA has significant effect in oxygen and moisture blocking. To explain this effect, this study measured the water vapor transmission rate (WVTR) of PS-r-PMMA. The WVTR is around 0.9676 (gm/m^2 day) at 22 h in the H_2O 90 RH% environment [21]. In polymer materials, insulator materials are more stable than conductive materials in an atmosphere environment. PS-r-PMMA as an insulator material is rather stable in an oxygen and moisture environment. In the AFM measurement, the P3HT and PCBM form a better percolation loop on the PS-r-PMMA surface to resist oxidation longer to preserve the conduction path, which is indicated by R_s measurement as in the table.

4. Conclusion

This study demonstrates a conductor/insulator/organic semiconductor solar cell by covering PEDOT:PSS with an ultra-thin polymer, PS-r-PMMA. The 2 nm thick PS-r-PMMA improves the *FF* and V_{oc} leading to improving efficiency from 2.13 to 2.37%, around 11% enhancement. This research extends the lifetime of the polymer solar cell from 58 to 97 h. This technique provides higher performance and longer lifetime for the polymer solar cell, compatible to the roll-to-roll large area printing process on a plastic substrate.

Acknowledgement

This work is supported by Electronic and Optoelectronic Research Laboratories, Industrial Technology Research Institute (EOL/ITRI) and National Science Council of Taiwan by Grant NSC 99-ET-E-005-001-ET.

References

[1] F.C. Krebs, H. Spanggard, T. Kjær, M. Biancardo, J. Alstrup, Mater. Sci. Eng., B 138 (2007) 106.
[2] F.C. Krebs, M. Jørgensen, K. Norrman, O. Hagemann, J. Alstrup, T.D. Nielsen, J. Fyenbo, K. Larsen, J. Kristensen, Sol. Energy Mater. Sol. Cells 93 (2009) 422.
[3] R. Tipnis, J. Bernkopf, S. Jia, J. Krieg, S. Lia, M. Storch, D. Laird, Sol. Energy Mater. Sol. Cells 93 (2009) 442.
[4] C.W. Tang, Appl. Phys. Lett. 48 (1986) 183.
[5] N.S. Sariciftic, L. Smilowitz, A.J. Heeger, F. Wudl, Science 258 (1992) 1474.
[6] N.S. Sariciftic, D. Braun, C. Zhang, V.I. Srdanov, A.J. Heeger, G. Stuchy, F. Wudl, Appl. Phys. Lett. 62 (1993) 585.
[7] G. Yu, J. Gao, J.C. Hummelen, F. Wudl, A.J. Heeger, Science 270 (1995) 1789.
[8] X. Wang, D. Zhang, K. Braun, H.J. Egelhaaf, C.J. Brabec, A.J. Meixner, Adv. Funct. Mater. 20 (2010) 492.
[9] M. Koppe, H.J. Egelhaaf, C. Dennler, M.C. Scharber, C.J. Brabec, P. Schilinsky, C.N. Hoth, Adv. Funct. Mater. 20 (2010) 338.
[10] T.M. Brown, J.S. Kim, R.H. Friend, F. Cacialli, R. Daik, W.J. Feast, Appl. Phys. Lett. 75 (1999) 1679.
[11] P. de Jong, L.J. van Ijzendoom, M.J.A. de Voigt, Appl. Phys. Lett. 77 (2000) 2255.
[12] T.P. Nguyena, S.A. de Vos, Appl. Surf. Sci. 221 (2004) 330.
[13] M. Jorgensen, K. Norrman, F.C. Krebs, Sol. Energy Mater. Sol. Cells 92 (2008) 686.
[14] P. Mansky, Y. Liu, E. Huang, T.P. Russell, C. Hawker, Science 275 (1997) 1458.
[15] T.H. Huang, H.C. Huang, Z. Pei, Org. Electron. 11 (2010) 618.
[16] W.A. Nevin, G.A. Chamberlain, IEEE Trans. Electron Devices 40 (1993) 75.
[17] N. Li, B.E. Lassiter, R.R. Lunt, G. Wei, S.R. Forrest, Appl. Phys. Lett. 94 (2009) 023307.
[18] J.S. Kim, J.H. Park, J.H. Lee, J. Jo, D.Y. Kim, K. Cho, Appl. Phys. Lett. 91 (2007) 112111.
[19] H.H. Liao, L.M. Chen, Z. Xu, G. Li, Y. Yang, Appl. Phys. Lett. 92 (2008) 173303.
[20] G. Li, V. Shrotriya, J.S. Huang, Y. Yao, Moriarty, K. Emery, Y. Yang, Nat. Mater. 4 (2005) 864.
[21] J.A. Hauch, P. Schilinsky, S.A. Choulis, S. Rajoelson, C.J. Brabec, Appl. Phys. Lett. 93 (2008) 103306.

Organic Electronics 11 (2010) 1802–1808

Contents lists available at ScienceDirect

Organic Electronics

journal homepage: www.elsevier.com/locate/orgel

Novel self-directed dual surface metallisation via UV-curing technique for flexible polymeric capacitors

Jijeesh R. Nair [a], Vijaykumar S. Ijeri [a,*], C. Gerbaldi [b,**], S. Bodoardo [a], R. Bongiovanni [a], N. Penazzi [a]

[a] Department of Materials Science and Chemical Engineering, Politecnico di Torino, C.so Duca degli Abruzzi 24, 10129 Turin, Italy
[b] IIT@POLITO Center for Space Human Robotics, IIT-Italian Institute of Technology, Corso Trento 21, 10129 Turin, Italy

ARTICLE INFO

Article history:
Received 4 May 2010
Received in revised form 2 August 2010
Accepted 7 August 2010
Available online 18 August 2010

Keywords:
Ag nanoparticle
Methacrylate
Polypyrrole
UV-curing
Polymeric capacitor

ABSTRACT

Polymer composites with metal nanoparticles have attracted considerable attention over the past years due to numerous solid state potential applications in organic electronics and microelectronic devices. Here we report the first example of a novel, rapid and convenient self-directed dual surface nano-silvering of a polymer film by a simple single-stage process of free-radical photopolymerisation (UV-curing). The major component of the composite is bisphenol A ethoxylate dimethacrylate (BEMA) which can be photopolymerised by a photo-reactive initiator (Darocur 1173) under UV light. Under the same conditions of UV irradiation, silver nitrate decomposes and the silver ion is deposited as metal while the pyrrole is oxidised to polypyrrole. It is demonstrated that this versatile method can open up promising prospective in obtaining innovative composite polymeric capacitors for highly flexible and/or non-planar electronics application. The obtained films are characterised by Scanning Electron Microscopy (SEM) and electrical measurements.

© 2010 Elsevier B.V. All rights reserved.

1. Introduction

The rapid development of portable electronic devices has increased the demand for compact, lightweight, high capacity electronics [1–3]. Capacitors are important elements in electrical circuits. In this context, polymer networks offer the obvious advantages of being light in weight, flexible, elastic, and less fragile with respect to other inorganic supports such as glasses, ceramics, or native metals. Silver has been a material of great interest as it has the highest electrical and thermal conductivity among the metals. Metal–polymer and ceramic–polymer composites are being studied as embedded capacitors in organic substrates [4–7]. In particular, polymer composites with silver nanoparticles are receiving considerable attention due to numerous solid state potential applications in many fields, e.g. organic electronics, catalysts, plasmonics, coatings, antimicrobials, etc., [8–14]. Very often the polymeric capacitors are prepared by multi-step methods like spin or spray coating, layer by layer deposition or Langmuir–Blodgett techniques followed by vapour deposition of a metal for conducting contacts [15–18].

Free-radical photopolymerisation (UV-curing) is a well established polymerisation technique which takes place at room temperature under UV light. Upon irradiation, a liquid poly-functional monomer containing a proper photo-initiator forms a solid highly cross-linked film. A typical formulation may consist of more than one monomer and oligomer, but is usually solvent free. The irradiation time ranges from few seconds to few minutes and light is the only energy source for building up the polymeric thermo-set matrix. Therefore, the process is well known for being fast and environmentally friendly, as the energy consumption is low and there is no emission of

* Corresponding author. Tel.: +39 011 654 4641; fax: +39 011 564 4699.
** Corresponding author. Tel.: +39 011 090 3402; fax: +39 011 090 3401.
E-mail addresses: vijayijeri@gmail.com (V.S. Ijeri), claudio.gerbaldi@polito.it, claudio.gerbaldi@iit.it (C. Gerbaldi).

1566-1199/$ - see front matter © 2010 Elsevier B.V. All rights reserved.
doi:10.1016/j.orgel.2010.08.003

volatile organic compounds [19]. For these reasons the UV-curing is a consolidated technique for the production of coatings and inks; it is widely applied in the field of photolithography for the production of electronic and optical devices and is gaining interest in other areas, such as biomedical applications. We have previously demonstrated the use of this versatile technique to prepare in a single-step plasticized polymer electrolyte membranes for Li-based batteries application [20–22].

There is abundant literature on one side metalised polymeric films for various applications [23–27]. Southward and Stoakely [23] have reviewed the single-stage thermal curing of selected Ag^+ containing poly(amic acids) leading to cyclo-imidization of the polyimide precursor with concomitant Ag^+ reduction and surface aggregation of the metal, yielding a reflective and/or conductive silver surface. They have also highlighted the disadvantages of multi-stage processes like chemical vapour deposition, sputtering, electroless plating, etc. which often result in poor adhesion at polymer–metal interface. Photo-induced (mainly UV) polymerisation has been used to obtain silver nanoparticles in different polymer composite matrices like trisacrylates [8], acrylamide cryogels [28] and also polypyrrole [29,30]. However, all these methods involved time-consuming multiple steps in preparation.

Recently we had reported a simple single-step UV-curing method to obtain conducting polymer surfaces with silver nanoparticles [31]. Here we report the first example of dual surface nano-silvering of a polymer film by a simple single-stage process of UV-curing. The term "single-stage" refers to a procedure in which the metallised film is directly developed from a single homogeneous solution that contains both the metal precursor and the desired reactive precursors of the final polymeric network. That is, the sample is obtained in a single-stage and no subsequent distinct metallisation stage is involved, as is the usual route to prepare metallised films/coatings [23]. To the best of our knowledge, such an approach to dual surface metallisation has not been reported so far. This kind of polymeric film metalised on both sides is conceived to be, in principle, a capacitor.

2. Experimental section

2.1. Materials

The reactive formulation for the preparation of the dual-surface conducting polymer composite membranes was based on bisphenol A ethoxylate (15 EO/phenol) dimethacrylate (BEMA), a methacrylic-based di-functional oligomer having an average molecular weight of 1700, obtained from Aldrich. The free radical photo-initiator was 2-hydroxy-2-methyl-1-phenyl-1-propanone (Darocur 1173/D1173) provided by Ciba Specialty Chemicals. Silver nitrate ($AgNO_3$, 99.5%), methanol (CH_3OH, 99.8%) and pyrrole (C_4H_5N, $\geqslant$98%) were obtained from Aldrich and used as such.

2.2. Procedure

$AgNO_3$ (1.27 g) was dissolved in 5.00 g of 50% (v/v) $CH_3OH + H_2O$ mixture. This methanol + distilled water mixture enabled the dissolution of silver nitrate and pyrrole and homogenized the mixture with BEMA and the photo-initiator. To this solution, 7.43 g of BEMA, 1.00 g of pyrrole and 0.30 g of initiator were added subsequently and mixed thoroughly. This gives a molar ratio of 2:1 for pyrrole to silver nitrate, and ensures complete reduction of Ag^+ to its metallic form [31]. The mixture was then poured into Petri dishes and then exposed to UV irradiation for 3 min on each side (sample A) and for 3 min on only one side (sample B). The photochemical curing was performed by using a medium vapour pressure Hg UV lamp (Helios Italquartz, Italy), with a radiation intensity on the surface of the sample of 28 ± 2 mW cm^{-2}. For this process, the samples were held under a pure N_2 atmosphere in small sealed boxes equipped with a quartz window. These conditions assure maximum curing (disappearance of the band attributable to the double bonds of the methacrylate groups at 1630 cm^{-1}, checked by real time FT-IR spectroscopy) [20]. Free composite polymer films were then easily detached from the dishes.

In the absence of UV light (i.e., under ambient laboratory conditions), the reaction between silver nitrate and

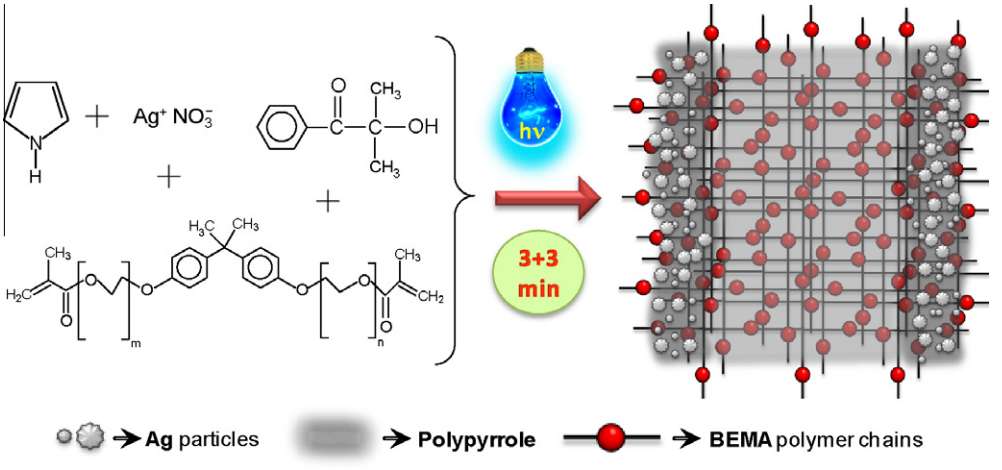

Scheme 1. Schematic illustration of the single-stage UV-curing process to self-directed dual surface polymer metallisation.

pyrrole is very slow, and the black colour of polypyrrole formation starts to be visible after about an hour. Also, there is no film formation as BEMA does not polymerise in absence of UV.

Experiments were repeated at least three times and were found to be reproducible.

2.3. Instrumental techniques and characterisation

Morphological characterisation of the films was performed employing a FEI Quanta Inspect 200 LV Scanning Electron Microscope (max magnification of 1.5×10^5). Scanning Electron Micrographs were obtained using a microscope operated at an accelerating voltage of 15.00 kV, both as secondary and backscattered electron images. The samples for the cross-sectional Scanning Electron Microscopy (SEM) images were prepared by fracturing the given film in liquid nitrogen in order to avoid any change in the morphology.

The surface resistances of the films were calculated from the current–voltage (I–V) curves recorded at ambient temperature over the voltage range of ±1.0 V by a CHI 760 D Electrochemical Workstation, with constant pressure spring loaded gold-plated pin probes (spring force 1.26 N,

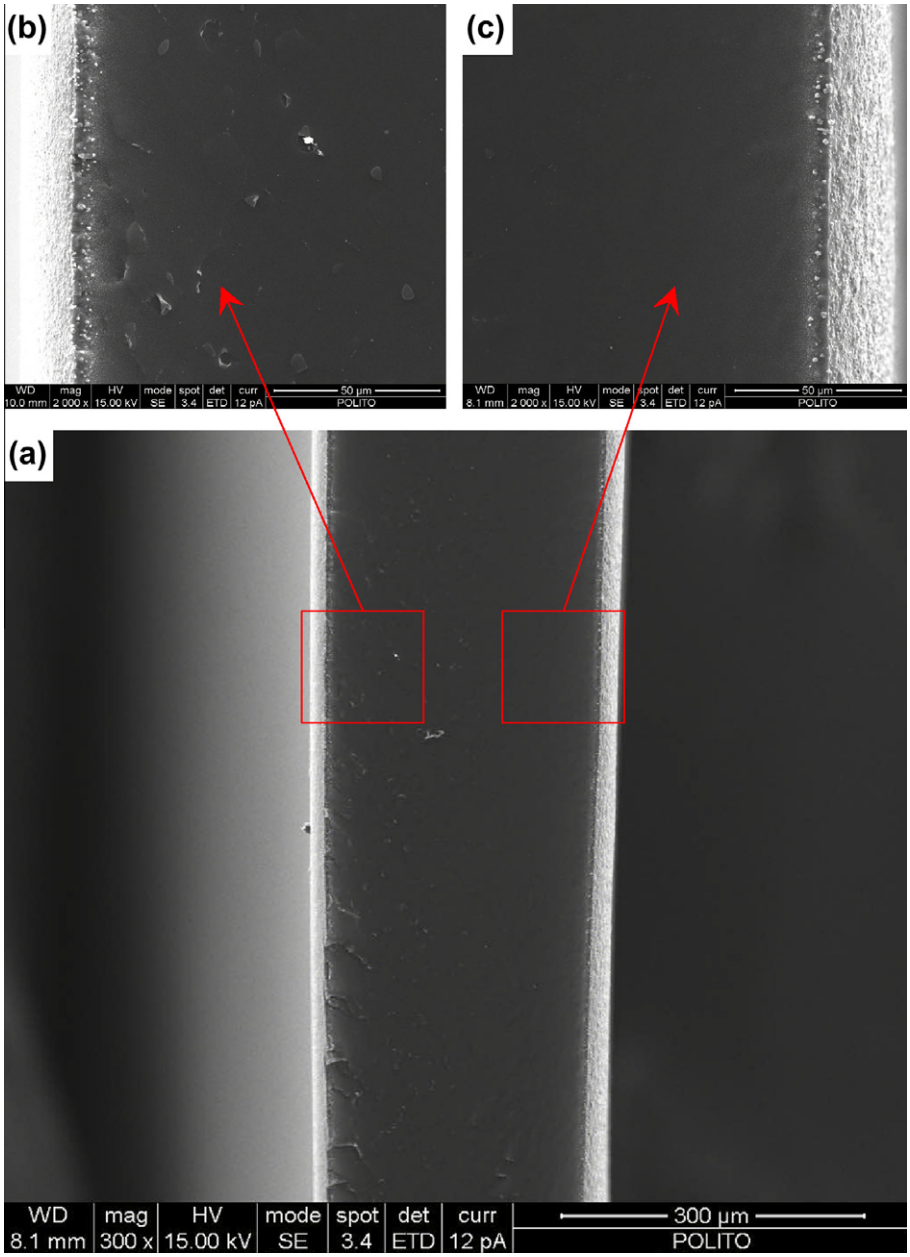

Fig. 1. SEM micrographs of sample A (UV exposed on both sides) at different magnifications: (a) cross-sectional image, (b) cross-section left edge (upper side, exposed first) and (c) right edge (lower side).

contact resistance 50 mΩ, P25-0822 Flat Head, Harwin). There was a fixed distance of 1.0 cm between the probes, and measurements were made at five different points on the surface of the films.

The same CHI 760 D Electrochemical workstation was used to obtain the capacitance versus voltage plot. Two-electrodes Teflon-made Swagelok test cells were assembled by sandwiching discs of 0.785 cm^2 of the given film (sample A: average thickness ≅ 500 μm, average weight ≅ 50 mg) between two stainless-steel 316 (SS-316) cylindrical blocking electrodes (1.0 cm in diameter and resistance of less than 1 Ω).

3. Results and discussion

The major component of the composite is bisphenol A ethoxylate dimethacrylate (BEMA) which can be photopolymerised by a photo-reactive initiator under UV light. The complete process involves multiple reactions, simultaneously. A schematic representation is shown in Scheme 1. On irradiation with UV, the initiator generates radicals by intramolecular scission. Then, the monomer BEMA undergoes free radical polymerisation, the details of which have been already discussed [20]. Under the same conditions of UV irradiation, silver ion is reduced to metallic form while the pyrrole is oxidized to polypyrrole. All these reactions occur within few minutes. This process gave methacrylate films with one side conducting surface of 7–10 μm composed mostly of silver nanoparticles and polypyrrole. Interestingly, when the sample is turned over to expose the other surface to UV light we get a polymer film with both sides silvered to more or less the same extent. It is this interesting and intriguing phenomenon that forms the core of this communication.

Two kinds of samples have been prepared, namely sample A (UV irradiated on both sides) and sample B (irradiated only on the top surface). The obtained samples were then characterised by Scanning Electron Microscopy (SEM) and electrical measurements.

Fig. 1 shows the cross-sectional SEM micrographs of the film that was exposed on both sides (sample A). It is clearly evident that the silvered layer is present on both sides, extending to about 8 ± 2 μm into the interior. In Fig. 2, the SEM micrographs are reported of the cross-section of sample B (UV exposed only on top side). Clearly it is seen that only the top surface is silvered, even when checked in backscattered mode. Correspondingly, the electrical measurements show low resistances on both surfaces for the sample exposed to UV light on both sides; whereas the sample exposed on only one side demonstrated a high resistance on the unexposed surface, as shown in Table 1.

Table 1
Average surface resistance values.

Sample	Resistance [Ω]	
	Upper surface[a]	Lower surface[a]
A	256 ± 8	201 ± 9
B	326 ± 15	>620 K

[a] Values obtained as an average from *I–V* curves recorded at five different point on the surface of the samples. One example is reported in Fig. 3.

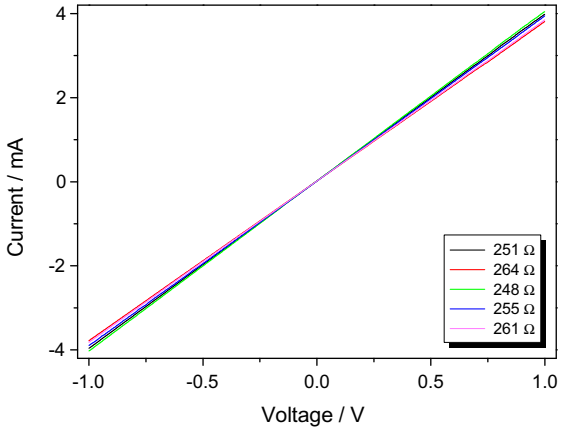

Fig. 3. Current–voltage (*I–V*) plots at five different locations on the upper surface (exposed first) of sample A.

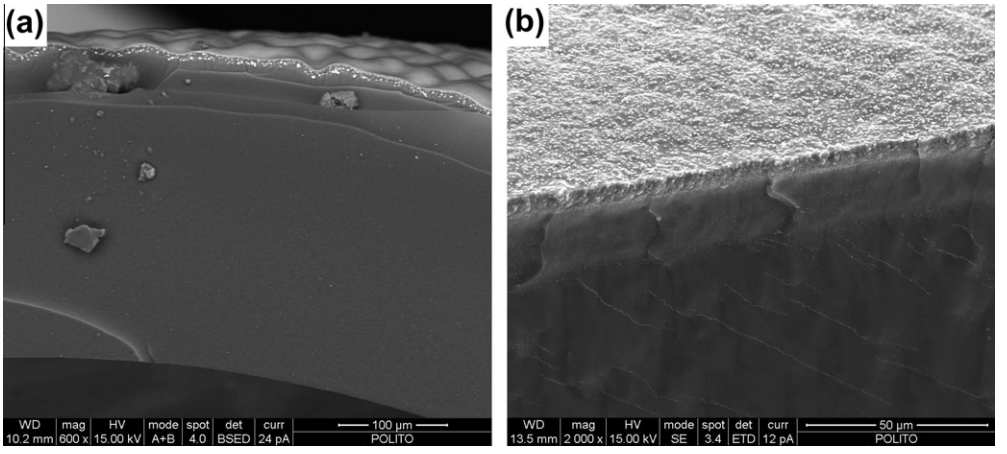

Fig. 2. SEM micrographs of sample B (UV exposed only on the top side) at different magnifications: (a) backscattered electron mode and (b) secondary electron mode.

The surface resistances of the films were calculated from the current–voltage (I–V) curves recorded at ambient temperature over the voltage range of ±1.0 V, with constant pressure spring loaded gold-plated pin probes. There was a fixed distance of 1.0 cm between the probes, and measurements were made at five different points on the surface of the films. An example of the results obtained for sample A is shown in Fig. 3. As the five curves are nearly

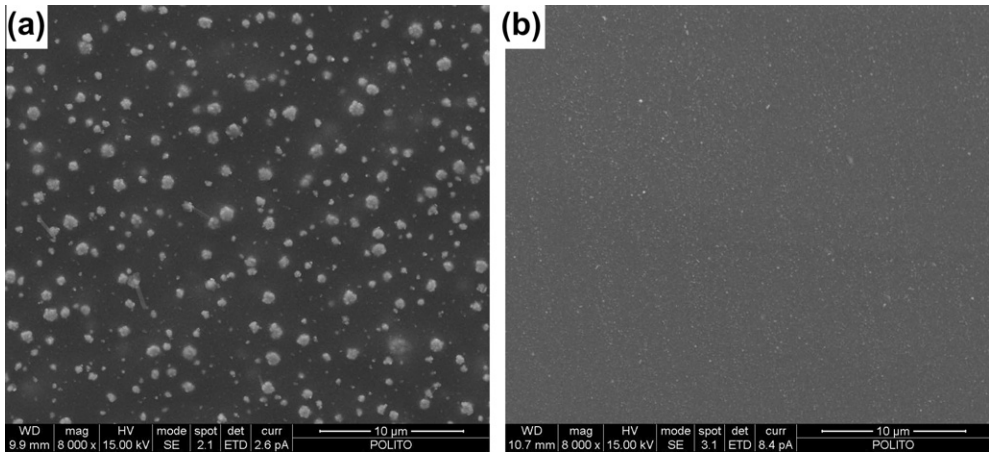

Fig. 4. SEM micrographs of film B: (a) topography of the exposed surface and (b) topography of the unexposed surface.

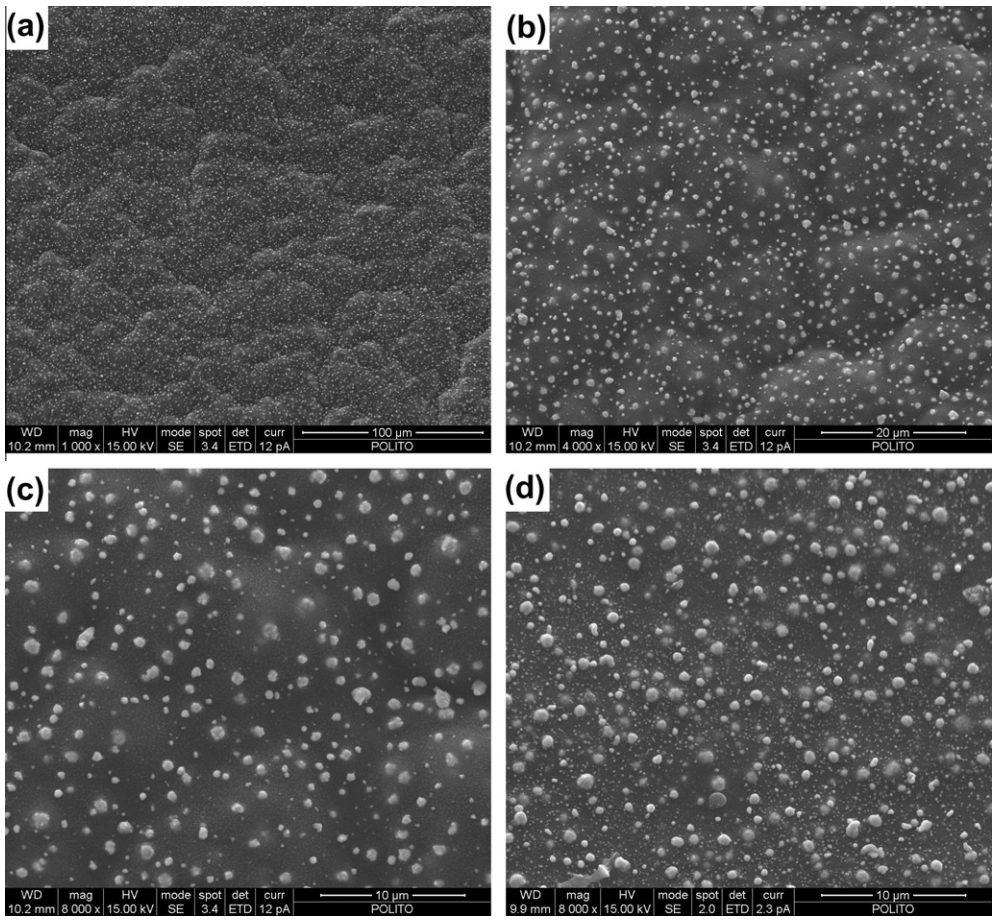

Fig. 5. SEM micrographs of sample A: (a, b, c) top surface (exposed first) at different magnifications and (d) lower surface (exposed next). Ag nanoparticles embedded in polypyrrole are clearly visible on both surfaces.

overlapping, it indicates highly homogenous conductivity all over the surface of the film.

We found a large variance associated with the resistance values measured on the unexposed side which is indicative of several non-homogeneities on the surface. This is somewhat expected due to some random reduction of silver ions with large areas of non-conducting material. The same is confirmed from Fig. 4, which illustrates the comparison between the SEM micrographs of the exposed (Fig. 4a) and unexposed (Fig. 4b) surfaces of sample B. In fact, the exposed side shows homogenous distribution of Ag nanoparticles, whereas no such particles can be seen on the unexposed surface.

On the contrary, in the case of sample A there is formation of well-distributed Ag nanoparticles on both the surfaces (see Fig. 5). Moreover, at low magnifications, the characteristic wrinkles of polypyrrole are clearly visible with Ag nanoparticles studded more or less uniformly, as shown in (Fig. 5a and b) [32]. The silver particles on the surface have an average size of 150 nm, while the agglomerates were of the order of 700 nm. Uniformity in high conductivity is maintained all over the surface by the conducting polymer polypyrrole studded with the Ag nanoparticles.

The formation of silvered layers on both surfaces indicates that there is migration of silver ions and pyrrole towards both surfaces under UV irradiation. From complexation studies and the "hard and soft acid–base" (HSAB) concept [33], it is known that transition metal ions (viz. silver) being a soft acid would form stronger complex with nitrogen-containing pyrrole than the polyether oxygen of BEMA, and hence both silver and pyrrole migrate together to the surfaces. The causes for such migration are not clear yet. We hypothesize that since the photo-initiated reaction of BEMA [20] is much faster than the redox reactions of pyrrole and Ag^+, the formation of cross linked BEMA polymer pushes out the Ag^+ and pyrrole contained in aqueous domains.

Southward and Stoakley reported the observation of such migration in thermally cured polyimides, and it seems there is still no explanation as to why and how it

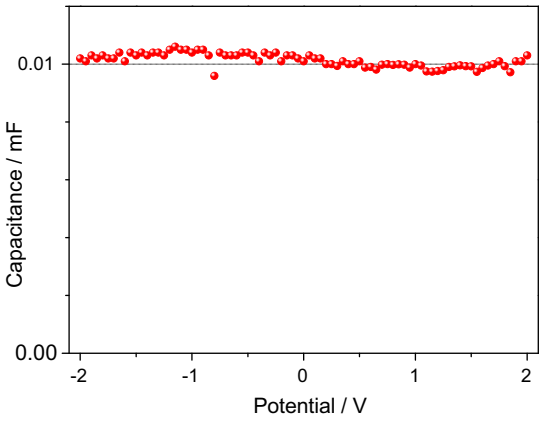

Fig. 7. Capacitance versus voltage plot of sample A at a frequency of 100 Hz.

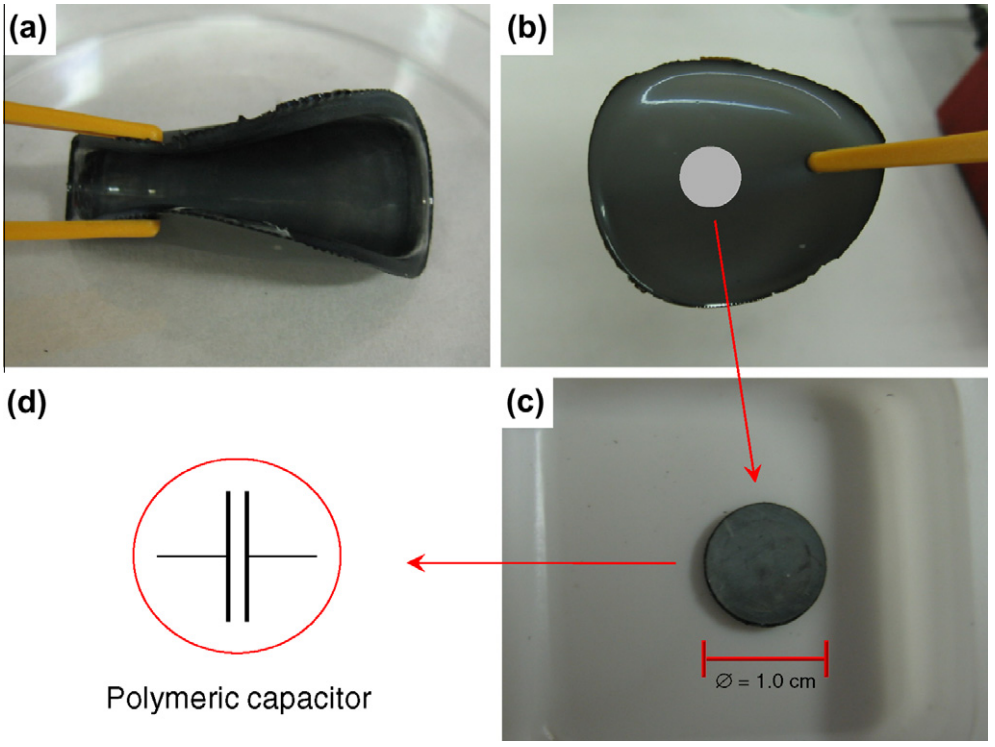

Fig. 6. (a) Illustration of the flexibility of the polymer composite (highly suitable for flexible and/or non-planar electronics application); (b, c, d) a disc of 1.0 cm in diameter is cut out to be used as a capacitor (results obtained are shown in Fig. 7).

happens [23]. However, they discussed about migration of silver towards only one surface. Probably, we are the first to observe this intriguing migration towards both the surfaces of the composite polymer films and we are now trying to ascertain its exact mechanism and causes by changing various preparation conditions and compositions of the materials. Nevertheless, the formation of two conducting layers on either sides of an insulating polymer in a single-step opens up possibilities of rapid production of highly flexible polymeric capacitors, which until now are made by time-consuming multiple steps procedures. In this respect, Fig. 6 shows the bendability of the film. Circular discs of 1.0 cm in diameter were cut out from the master film, as shown in the figure, and tested for capacitive properties. Fig. 7 shows the capacitance versus potential curve for sample A at a frequency of 100 Hz. A two-electrode Teflon-made Swagelok test cell was used for this experiment, which was assembled by sandwiching a 0.785 cm^2 disc of the given film between two SS-316 cylindrical blocking electrodes. The capacitance behaviour over the voltage range of ±2.0 V is similar to the curve reported by Liu et al. for their polymer capacitor made by multi-step inkjet printing [18]; however, the capacitance value obtained for our sample is rather high (about 0.01 mF) compared to what is reported in the reference above. We suspect this could be because of the presence of a very small amount of Ag nanoparticles and/or conducting polymer trapped in the bulk of the insulating (BEMA) polymer matrix, which act as multiple nano-capacitors thus leading to a huge increase in the overall capacitance value. Work is in progress to get a deeper insight into this aspect.

4. Conclusions

In summary, we have successfully introduced a novel but simple and efficient method that allows excellent dual surface metallisation of a methacrylic-based polymer network, in a single-stage. The whole process is remarkably convenient, with short reaction time, ‘‘environmentally friendly”, and no need for any complex equipment or manipulation. For certain applications, such an approach can increase the production efficiency when compared to traditional multistage techniques. We believe that exploiting the potential and versatility of UV-curing technique can open up promising perspectives in obtaining innovative polymeric capacitors with high flexibility, which is well suited for flexible and/or non-planar electronics application. In this respect, further work and optimization is currently directed towards a better understanding of the silver migration phenomenon and extending the method to other metals and polymer matrices.

Acknowledgements

The authors would like to thank Mr. Mauro Raimondo, Department of Materials Science and Chemical Engineering – Politecnico di Torino for the SEM analysis of the samples. Dr. V.S. Ijeri would like to thank Italian Regione Piemonte Council for the research grant.

References

[1] B. Park, K.-J. Im, K. Cho, S. Kim, Org. Electron. 9 (2008) 878.
[2] D. Mao, M.A. Quevedo-Lopez, H. Stiegler, B.E. Gnade, H.N. Alshareef, Org. Electron. 11 (2010) 925.
[3] F. Maddalena, M. Spijkman, J.J. Brondijk, P. Fonteijn, F. Brouwer, J.C. Hummelen, D.M. de Leeuw, P.W.M. Blom, B. de Boer, Org. Electron. 9 (2008) 839.
[4] L. Qi, B.I. Lee, S. Chen, W.D. Samuels, G.J. Exarhos, Adv. Mater. 17 (2005) 1777.
[5] Z.M. Dang, Y.H. Lin, C.W. Nan, Adv. Mater. 15 (2003) 1625.
[6] M. Kakimoto, A. Takahashi, T. Tsurumi, J. Hao, L. Li, R. Kikuchi, T. Miwa, T. Oono, S. Yamada, Mater. Sci. Eng. B 132 (2006) 74.
[7] H.R. Kricheldorf, A. Stricker, Macromol. Chem. Phys. 200 (1999) 1726.
[8] C. Damm, H. Münstedt, Surf. Coat. Technol. 202 (2008) 5122.
[9] F.W. Campbell, R.G. Compton, Anal. Bioanal. Chem. 396 (2010) 241.
[10] T. Pradeep Anshup, Thin Solid Films 517 (2009) 6441.
[11] D. Basak, S. Karan, B. Mallik, Solid State Commun. 141 (2007) 483.
[12] S. Li, S. Gong, Adv. Funct. Mater. 19 (2009) 2601.
[13] Y. Shen, Y. Lin, C.W. Nan, Adv. Funct. Mater. 17 (2007) 2405.
[14] J. Puiso, I. Prosvcevas, A. Guobiene, S. Tamulevicius, Mater. Sci. Eng. B 149 (2008) 230.
[15] J. Matsui, Y. Sato, T. Miyashita, Colloid. Surf. A: Physicochem. Eng. Aspects 313–314 (2008) 452.
[16] N. Venkat, T.D. Dang, Z. Bai, V.K. McNier, J.N. DeCerbo, B.H. Tsao, J.T. Stricker, Mater. Sci. Eng. B, in press, doi:10.1016/j.mseb.2009.12.038.
[17] S. Muruganand, S.K. Narayandass, D. Mangalaraj, T.M. Vijayan, Polym. Int. 50 (2001) 1089.
[18] Y. Liu, T. Cui, K. Varahramyan, Solid State Electron. 47 (2003) 1543.
[19] J.P. Fouassier, J.F. Rabek, Radiation Curing in Polymer Science and Technology, vol. I–IV, Elsevier, London, 1993.
[20] J.R. Nair, C. Gerbaldi, G. Meligrana, R. Bongiovanni, S. Bodoardo, N. Penazzi, P. Reale, V. Gentili, J. Power Sources 178 (2008) 751.
[21] J.R. Nair, C. Gerbaldi, A. Chiappone, E. Zeno, R. Bongiovanni, S. Bodoardo, N. Penazzi, Electrochem. Commun. 11 (2009) 1796.
[22] C. Gerbaldi, J.R. Nair, Shahzada Ahmad, G. Meligrana, R. Bongiovanni, S. Bodoardo, N. Penazzi, J. Power Sources 195 (2010) 1706.
[23] R.E. Southward, D.M. Stoakley, Prog. Org. Coat. 41 (2001) 99.
[24] J. Puiso, I. Prosycevas, A. Guobiene, S. Tamulevicius, Mater. Sci. Eng. B 149 (2008) 230.
[25] C. Girotto, B.P. Rand, S. Steudel, J. Genoe, P. Heremans, Org. Electron. 10 (2009) 735.
[26] S.M. Lee, B.S. Lee, T.G. Byun, K.C. Song, Colloid. Surf. A: Physicochem. Eng. Aspects 355 (2010) 167.
[27] W.J. Yoon, K.Y. Jung, J. Liu, T. Duraisamy, R. Revur, F.L. Teixeira, S. Sengupta, P.R. Berger, Sol. Energy Mater. Sol. Cells 94 (2010) 128.
[28] P. Petrov, E. Petrova, C.B. Tsvetanov, Polymer 50 (2009) 1118.
[29] X. Yang, Y. Lu, Mater. Lett. 59 (2005) 2484.
[30] C. Zhao, Q. Zhao, Q. Zhao, J. Qiu, C. Zhub, S. Guo, J. Photochem. Photobiol. A: Chem. 187 (2007) 146.
[31] V.S. Ijeri, J.R. Nair, C. Gerbaldi, R.S. Gonnelli, S. Bodoardo, R.M. Bongiovanni, Soft Matter, in press, doi:10.1039/C0SM00530D.
[32] J.S. Shapiro, W.T. Smith, Polymer 38 (1997) 5505.
[33] V.S. Ijeri, A.K. Srivastava, J. Chem. Eng. Data 47 (2002) 346.

Organic Electronics 11 (2010) 1809–1814

Contents lists available at ScienceDirect

Organic Electronics

journal homepage: www.elsevier.com/locate/orgel

Letter

Hysteresis-type current–voltage characteristics in Au/eumelanin/ITO/glass structure: Towards melanin based memory devices

Marianna Ambrico [a,*], Antonio Cardone [b], Teresa Ligonzo [c], Vincenzo Augelli [c], Paolo Francesco Ambrico [a], Stefania Cicco [b], Gianluca M. Farinola [d], Michele Filannino [c], Giuseppe Perna [e], Vito Capozzi [e]

[a] Institute for Inorganic Methodologies and Plasmas (IMIP), CNR UOS Bari, Via Orabona 4, 70126 Bari, Italy
[b] CNR-ICCOM-UOS di Bari, Via Orabona 4, 70126 Bari, Italy
[c] Dipartimento Interateneo di Fisica, Università degli Studi di Bari, Via Amendola 172, 70126 Bari, Italy
[d] Dipartimento di Chimica, via Orabona 4, 70126 Bari, Italy
[e] Department of Biomedical Sciences, University of Foggia, Viale L. Pinto, 1, 71100 Foggia, Italy

ARTICLE INFO

Article history:
Received 6 April 2010
Received in revised form 30 July 2010
Accepted 1 August 2010
Available online 14 August 2010

Keywords:
Eumelanin layer
Hysteresis effect
Memory device

ABSTRACT

Hysteresis behaviour of the current–voltage characteristics collected on spin coated synthetic eumelanin layer embedded in the Au/eumelanin/ITO/glass structure is shown. The effect has been observed under dark both in air and vacuum environment and its magnitude has been found related to the eumelanin hydration state. Moreover, in vacuum and under white light illumination, enhancement of the hysteresis loop area respect to those collected under dark has been observed. Space charge storage and charge trapping/detrapping as possible mechanisms responsible of the observed current–voltage behaviour are discussed. Preliminary experimental results have evidenced the possible integration of eumelanin layers in electro-optical charge storage based memory devices.

© 2010 Elsevier B.V. All rights reserved.

1. Introduction

Eumelanins are ubiquitous pigments present throughout nature responsible for the color of hair, skin and eyes ranging from red, yellow, brown to black. It is ascertained worldwide that eumelanins exert several functions such as photoprotection, photosensitization, antibiotic activity and thermal regulation. A pioneering work by Mc Ginnes et al. disclosed that eumelanin electrical properties are similar to those of amorphous semiconductors and envisaged its possible implementation as active material in switching devices [1]. Following this original hint, a great deal of work is currently in progress in order to investigate the various optoelectronic properties and possible technological applications of eumelanins. Most research efforts mainly concerned the investigation on synthetic eumelanin powders or pellets: absorption coefficient, dark electrical conductivity, photoconductivity and ac response were explored [2–9] but all of them under the picture of eumelanin as an amorphous semiconductor. However, its broadband absorption that does not strictly follow a Tauc law [5,6,10] pointed out also that the picture of eumelanin as an amorphous structure has to be taken with care [11–13] and the chemical disorder model has been invoked to explain the α vs λ behaviour [3]. The eumelanin conductivity is furthermore strongly related to the hydration state and external environment and can lowers several order of magnitude when water is desorbed [8,9]. The dependence of conductivity on the humidity degree stems in the presence of two forms of water bonded to the macromolecules: one adsorbed on the surface and easily removable under vacuum or by drying, and the other incorporated in the inner polymer

* Corresponding author.
E-mail address: marianna.ambrico@ba.imip.cnr.it (M. Ambrico).

1566-1199/$ - see front matter © 2010 Elsevier B.V. All rights reserved.
doi:10.1016/j.orgel.2010.08.001

structure. In the last case the removal can require thermal treatments. The presence of these two kind of water bonding has been assessed by several studies and mainly on pellets [[8,9] and Ref. therein]. Specifically, in air water bridges and/or hydrogen bonds between individual molecules and carboxy, hydroxyl and amino groups are present but, during dynamic vacuum treatment, weakening or partial breaking of hydrogen bonds between planar layer occurs influencing (i.e. lowering) then the conductivity. The residual conductivity is then due to the remaining strong bonded water. Eumelanin is nowadays recognized as primarily formed by various combinations, still unknown at this stage, of 5,6-dihydroxyindole (DHI or HQ) and 5,6-dihydroxyindole-carboxylic acid (DHICA) and their corresponding redox forms.

One of major drawbacks in the application of melanin as active material in electronic devices is represented by its scarce solubility in common solvents, preventing easy deposition of homogeneous layers. As a consequence, in recent years, the focus is on eumelanin layer deposition on various substrates in order to better study electrical properties aiming to foresee a possible integration of this intriguing material in hybrid optoelectronic devices [2,14]. To date, eumelanin layer has been electrochemically deposited on gold, or spin coated and/or spray coated on quartz substrates [2,14,15].

To the best of our knowledge, no paper has been published so far concerning the study of the electrical properties of eumelanin layers on ITO/glass substrates. While, in our opinion this approach is a priority in the view of technological applications. It is well known, in fact, that ITO/glass is a widely used conductive support for organic semiconductors, and the feasibility of building up such a eumelanin/ITO junction, opens the possibility to witness the intriguing electrical properties of eumelanin and to compare its behaviour with that of the widely studied layer of organic molecular or polymeric semiconductors.

Up to now the electrical characterization of eumelanin layers have been interpreted under the picture of melanin as an amorphous semiconductor [14]. However, it was stated that in order to perform conductivity measurements on melanin under stationary conditions, the current should be collected after a certain time interval thus evidencing the presence of transient phenomena which cannot be overcome in any way [14]. However, such effects can be useful to shed light on the nature of a carrier (electron or hole) dominating the transport which is still an open issue. As a matter of fact, current relaxation phenomena have been well known and studied in several organic Au/polymers/ITO/glass interfaces and ascribed to space charge storage or to trapping/detrapping mechanisms under voltage application. Based on these phenomena, a possible integration of these materials in memory devices has been foreseen [16–18]. The experimental evidence of space charge storage or charge trapping effect is the hysteresis-type behaviour of current–voltage (I vs V) characteristics [16,17]. This communication shows for the first time similar hysteresis behaviour in I vs V characteristics observed in Au/eumelanin/ITO/glass interfaces and a first insight on the mechanisms responsible of this behaviour will be discussed.

2. Materials and methods

Eumelanin layers have been spin coated on ITO/glass substrates starting from synthetic melanin powder (140 mg, Sigma–Aldrich) dissolved in water (1 mL) and 28% aq. ammonia solution (2 mL). The solution was stirred and sonicated for 1 h, and subsequently centrifuged at 3500 rpm for 15 min. Before layer deposition, ITO/glass substrates were submitted to an oxygen plasma treatment (30 min, room temperature), in order to improve the adhesion of organic layers onto ITO/glass substrates [19].

AFM measurements were performed in air, in the weak repulsive regime of contact mode. Gold coated Si_3N_4 cantilevers with a force constant of 0.05 N/m and a statistical apical radius of 5–20 nm were used. Constant force images were acquired with a scan rate of 3.0–4.0 s/row.

The optical absorption spectrum has been calculated following the Ritter–Weiser expression on reflectance (R) and transmittance spectra (T) collected in air in the wavelength range $\lambda = 400$–800 nm by using a Perkin–Elmer Lambda 9 spectrophotometer [20]. The chosen wavelength range was dictated by the glass absorption at $\lambda < 330$ nm and high ITO reflectance at $\lambda = 800$ nm. Moreover, T and R spectra were collected from both the film and substrate side to estimate the film roughness and scattering effects on the absorption [21]. The film thickness was estimated from reflectance interference fringes.

Current–voltage (I vs V) characteristics have been performed on Au/eumelanin/ITO/glass structure at room temperature by using an electrometer and a power supply. For these measurements an Au slab ($0.25 * 0.25$ cm^2) has been gently placed on top of the melanin layer in order to avoid possible macromolecule modification induced by metal evaporation contacting procedure. The I vs V loops have been collected in air and in vacuum ($p = 10^{-5}$ mbar), and waiting several minutes between consecutive sweeps, under dark and white light irradiation at different voltage sweep speed starting from zero bias to a maximum positive value $+V_L$, and then alternating back and forth between $+V_L$ and $-V_L$. A halogen lamp simulating the solar spectrum at a power of AM 1.5 (100 mW/cm^2) was used for white light irradiation.

3. Results and discussion

The optical absorption spectra (Fig. 1(a)) display the characteristic broadband absorption observed in spin coated 400 nm thick eumelanin layer on quartz [2,3,7]. The α values have been found varying between 5×10^5 m^{-1} and 3×10^6 m^{-1} in the wavelength range $\lambda = 400$–800 nm, thus confirming the good film density. Also the calculated surface roughness (10 nm) agrees with values observed by AFM measurements. The estimate of the scattering coefficient was around 2–3% in the range 400–700 nm, i.e. <6% in the overall λ range, so that scattering has practically no influence in determining the layer broadband absorption [22]. AFM acquisitions (see Fig. 1(b and c) and inset herein) show that the surface of eumelanin layer is homogeneous, with a RMS roughness [23] of about 7 nm estimated over the entire area imaged in

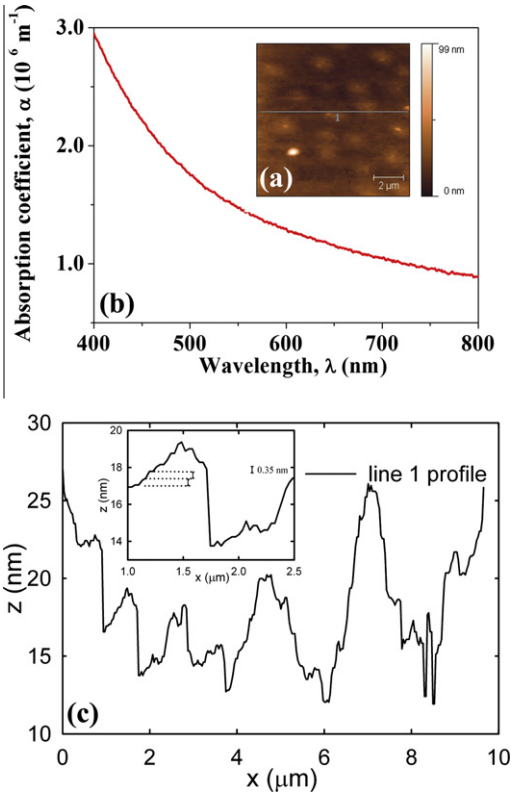

Fig. 1. (a) AFM height image acquisition and (b) broadband optical absorption spectra of a 400 nm thick eumelanin layer deposited by spin coating on ITO/glass substrate and corresponding (c) typical cross-section of the film height profile as derived from AFM height image acquisition. The profile refers to scan along the line 1 corresponding to the same region indicated in the AFM image (see inset).

Fig. 1(c) and a stacked structure about 0.35 nm apart, as illustrated in the inset. This supports the expected structural organization of eumelanin, consisting of stacked layers of several DHI- and DHICA-based monomers self assembled forming the so called eumelanin 'protomolecule' [24]. A strong anisotropy in the conduction has been also found thus validating the model that the melanin structure can be considered similar to that of graphite-like materials [25]. In fact, the in plane layer dark conductivity at room temperature was of 10^{-7} $(\Omega\,\mathrm{cm})^{-1}$ in air and of 10^{-12} $(\Omega\,\mathrm{cm})^{-1}$ in vacuum respectively, while the transverse conductivity was found 10^{-15} $(\Omega\,\mathrm{cm})^{-1}$ in air and 10^{-19} $(\Omega\,\mathrm{cm})^{-1}$ in vacuum, respectively. It can be noted that the transverse conductivity has been found around height order of magnitude lower than the planar conductivity both in air and in vacuum. While both the in plane and transverse conductivity decrease of around four order of magnitude under vacuum.

Fig. 2(a.1) and (b.1) shows the hysteresis loop of the current–voltage (I vs V) characteristics on Au/eumelanin/ITO/glass structure in the voltage range (−1 V, 1 V) in air under dark only and at different voltage sweep speed (Fig. 2(a.1)) and the hysteresis behaviour which occurs in vacuum, under dark and white light illumination at a sweep rate of 9 mV/s (Fig. 2(b.1)). This because in air, no relevant modification on the hysteresis curves has been evidenced under white light irradiation. Similar hysteresis behaviour has been observed on several conjugated polymers [16–18].

The origin of the hysteresis loop lies in the presence of a displacement current I_d adding to the conductive part I_r and shifting upwards or downwards the I vs V characteristics. The $I_d = d(CV)/dt$ is due to both voltage variation ($C dV/dt$) and capacitance variation $V(dC/dt)$. The first contribution is typically due to voltage sweep speed (dV/dt)

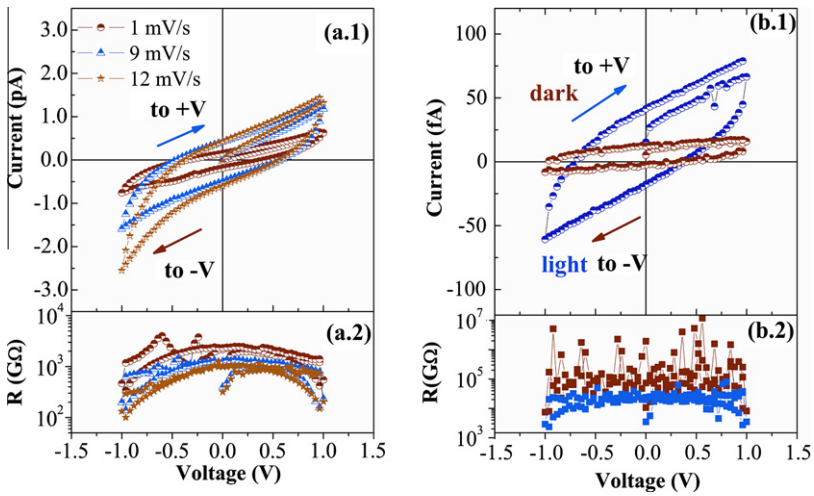

Fig. 2. (a.1) Hysteresis-type current–voltage (I vs V) characteristics collected in air of Au/eumelanin/ITO/glass structure at different voltage speed rate for 1 V loop amplitude at a voltage speed rate of 1 mV/s, 9 mV/s and 12 mV/s. (a.2) Corresponding semilog plot of $(dI/dV)^{-1} = R$ vs V. (b.1) Hysteresis-type current–voltage (I vs V) characteristics of Au/eumelanin/ITO/glass structure collected in vacuum under dark (red circles) and white light exposure ($P = 100$ mW/cm^2) (blue circles) at a voltage speed rate of 9 mV/s. The I vs V characteristics collected in vacuum have been magnified by a factor of 50 for sake of clarity. (b.2) Corresponding semilog plot of $(dI/dV)^{-1} = R$ vs V. The red and blue arrows show the reverse (towards negative voltages) and forward (towards positive voltages) voltage sweep direction. (For interpretation of color in this figure readers are referred to web version of this article.)

whereas the second one $V(dC/dt)$, is more or less enhanced by the hysteresis loop amplitude (i.e. voltage interval). The magnitude of these contributions determines the total value of the detected current.

In Fig. 2(a.1) the hysteresis curves in air show asymmetry and higher current values in the negative voltage bias region while in vacuum are rather symmetric, but with different V_{oc} values in the two voltage branches and I_{sc} values lower than in air. As for other metal/polymer interfaces the mechanisms generating the hysteresis behaviour in present case could be ascribed to the space charges accumulation at metal/polymer interface, screening the applied electric field and limiting further carrier injection in the eumelanin layer [16,24]. As a matter of fact the asymmetry observed in Fig. 2(a.1) indicates that the space charge accumulates mainly near one of the electrodes (Au or ITO) depending on carrier signs (electron or holes) which at this stage is still unknown. Also, one cannot exclude the presence of layer defect sites producing trapping centres, so that, the hysteresis behaviour could be due to trapping (i.e. charge reduction) or detrapping (charge release) mechanisms as well [18]. The amount of space charges or effectiveness of a trapping mechanism can both have a fundamental role in determining the hysteresis behaviour and conversely affect the possible device operation.

Under the hypothesis of stored charges, carriers injection occurs when increasing the applied voltage from 0 V to $+V_L$ and space charges accumulate at one of the eumelanin/electrode (Au or ITO) and then spatially distributed in the structure [16]. By reversing the voltage sweep (from positive voltage to 0 V) the device retains its charges with no further carriers injection due to screening effect, so that, the device current decreases. During the reverse sweep and at a certain value of the applied voltage (called open circuit voltage $V_{oc}(+)$) a balance establishes between the external and the electric field due to space charge and a zero current is detected. At zero voltage a non zero current is observed (short circuit current $I_{sc}(-)$) representing the flowing back of the stored charges through the external circuit. In a similar way, charge storage occurs when the voltage is swept from 0 V to negative voltage and in the subsequent forward sweep direction (i.e from negative to 0 V) an open circuit voltage ($V_{oc}(-)$) and short circuit current ($I_{sc}(+)$) are again observed. The magnitude of I_{sc} and V_{oc} in both sweep directions depends on the amount of stored charges at electrode/polymer interface and may differ in the two hysteresis branches due to the different electrodes (Au and ITO) work functions [16].

Hysteresis curves can be also the effect of carrier trapping/detrapping mechanisms within the organic layer [17,18]. A hint of the presence of such a mechanism is the dependence of the hysteresis curve from the voltage sweep speed [17]. But, mostly to discriminate between the prevalence of this mechanism or space charge accumulation, an useful method is the analysis of the oscillation in the resistance vs voltage $R(V)$ characteristics (where $R = (dI/dV)^{-1}$) [18]. These oscillations have been observed on several materials, from layered to structure embedding nanoclusters and have been ascribed to discrete (single electron for example) carrier transport or trapping and emission of carriers [25,26].

The hysteresis loop parameters (i.e. $V_{oc}(+)$, $V_{oc}(-)$, $I_{sc}(+)$, $I_{sc}(-)$, loop area A_L) extracted from in air *I vs V* of Fig. 2(a.1) have been summarized in Table 1. Also the parameters observed by performing the *I* vs *V* in air at the same sweep speed (9 mV/s) and for different V_L values (*I vs V* loops not shown) have been reported. Moreover, the V_{oc} values have been found in the range of those observed on other conjugated polymers [16,18]. Respect to what has been assumed and observed elsewhere, the loop area shrinks at low speed rate evidencing that the current component depending on voltage sweep speed also contributes to the displacement current [17,19]. However, loop parameters values are only slightly dependent on the sweep rate and, apart $I_{sc}(-)$, they saturate when increasing the voltage sweep speed. Conversely, when maintaining the same voltage sweep speed (9 mV/s) a general linear increase of all loop parameters has been observed for increasing values of V_L.

The loop parameters extracted from the dark *I vs V* collected under vacuum ($p = 1 \times 10^{-5}$ mbar, see Table 1) shows values of V_{oc} higher than those collected under light exposure. Interestingly, *I vs V* collected under white light illumination proves a detectable increase of the loop area (about four times of those collected under dark), together with higher values of the I_{sc} in both voltage sweep direction and lower values of the V_{oc}. The large enlargement of the hysteresis curve areas indicates the presence of a displacement current adding to that measured under dark together with a DC photocurrent effect producing the rotation of the hysteresis axis. This conversely explains also the observed V_{oc} values lower than those seen under dark.

Table 1
Open circuit voltage (V_{oc}), short circuit current (I_{sc}), and loop area (A_L) values extracted from the hysteresis loops collected: (a) in air, at different voltage sweep speeds and 1 V loop amplitude; (b) in air, at a voltage sweep speed of 9 mV/s and different loop amplitudes; (c) in vacuum under dark and white light irradiation at a voltage sweep speed of 9 mV/s and 1 V loop amplitude.

Voltage sweep speed (mV/s)	Measurements conditions	$V_{oc}(+)$ (V)	$V_{oc}(-)$ (V)	$I_{sc}(+)$ (pA)	$I_{sc}(-)$ (pA)	A_L (10^{-12} a.u.)
1	Air/dark	0.41	−0.35	0.15	−0.19	0.88
9	Air/dark	0.56	−0.46	0.42	−0.49	2.16
12	Air/dark	0.55	−0.39	0.40	−0.61	2.43
Voltage loop amplitude V_L						
(−1 V, 1 V)	Air/dark	0.56	−0.46	0.42	−0.49	2.16
(−2 V, 2 V)	Air/dark	1.00	−0.92	1.27	−1.02	15.0
(−3 V, 3 V)	Air/dark	1.47	−1.50	3.83	−1.27	50.7
(−1 V, 1 V)	Vacuum/dark	0.44	−0.98	1.2×10^{-2}	-2.3×10^{-3}	3.8×10^{-2}
(−1 V, 1 V)	Vacuum/light	0.36	−0.78	1.8×10^{-2}	-4.2×10^{-2}	1.5×10^{-1}

As stated above two principal mechanisms can be responsible for hysteresis behaviour: space charge storage and/or trapping/detrapping mechanisms at organic layer defect sites that can be discriminate by the presence/absence of conductivity oscillation when representing the $R = (dI/dV)^{-1}$. The $R(V)$ characteristics shown in Fig. 2(a.2) and (b.2) clearly indicate that under dark carrier flow due to trapped/detrapped charges at layer defect sites is detectable in vacuum while in air space charges are mostly stored at the Au/ or ITO/eumelanin interface, although with a different density. In air, this has been furthermore observed also when changing the voltage sweep speed. In vacuum and under white light exposure, although a certain amount of detrapped charges can be also released, the large enhancement of the loop area (about a factor of four) and absence of (or not detectable) trapping/detrapping mechanisms (see Fig. 2(b.2)) indicates that space charge storage is still the predominant mechanism. In order to explain the predominant space charge effect in air and discrete charge trapping/detrapping mechanisms in vacuum we refer to the dependence of melanin transport properties on hydration states. As state before, the water weakly bonded to carboxy, hydroxyl and amino groups can be responsible of a continuous distribution of trap across the layer and promote the charge injection from the contact inside the melanin layer. In vacuum, these traps are removed and only a discrete trap distribution is expected so that trapping/detrapping mechanisms are present explaining the conductivity oscillation behaviour.

Eumelanin memory capabilities have been verified by preliminary tests. Fig. 3(a) shows that a writing stage occurs at a voltage of −3.7 V and −2.8 V in air and vacuum respectively; however, no erasing voltage has been till now clearly identified. The current on/off ratio has been found of around 100 in both cases and consistent with similar ones observed in other organic polymers [27]. The charge storage effect under white light has been evidenced by the reduction of the photocurrent collected under consecutive light pulse switches (Fig. 3(c)). This because during the first light pulse the photo-generated space charges are stored in the eumelanin layer; during the second light pulse the space charges oppose to the further photo-carrier injection resulting in a decrease of the detected photocurrent.

In conclusion, this work represents a first experimental insight into the electrical transport in Au/eumelanin/ITO/glass structure. The good optical quality and staking of eumelanin layers have been evidenced by optical absorption spectra and AFM characterization. The hysteresis loops when performing I vs V measurements suggest that space charges are retained in the layer and the charge storage is the predominant mechanism in air and in vacuum also under white light irradiation whereas trapping/detrapping generates the loop in vacuum. More experiments are in progress aiming to better clarify first the nature of the majority carriers (holes or electrons) and the characteristics of memory effect under voltage or light pulses and possible erasing procedure. At this stage, the

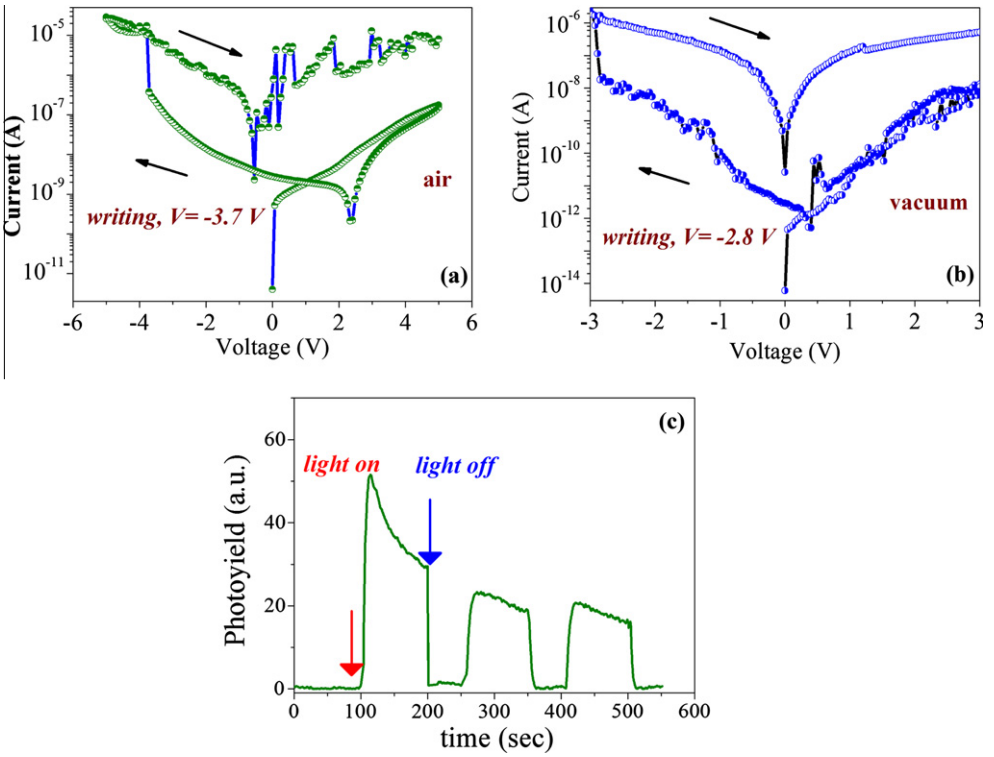

Fig. 3. (a) I vs V characteristics collected in air on Au/eumelanin/ITO/glass structure showing a writing state at −3.7 V. (b) I vs V characteristics collected in vacuum on Au/eumelanin/ITO/glass structure showing a writing state at −2.8 V. The arrows indicate the voltage sweep direction. (c) Transient photoresponse (Y vs t) determined under consecutive white light pulse switches. The light pulses duration and delay between consecutive light switching was of 60 s.

above results aim to foresee a possible of integration of eumelanin layer in voltage or light sensitive memory devices in a fashion similar to conjugated polymer or molecular materials layers.

Acknowledgements

This work was financially supported by Ministero dell'Istruzione, dell'Università e della Ricerca (MIUR), "Progetto PRIN 2007 PBWN44" and by Università degli Studi di Bari.

References

[1] J. Mc Ginnes, P. Corry, P. Proctor, Science 183 (1974) 853.
[2] J.P. Pothma, J. deBoor, U. Divakar, P.E. Schwenn, P. Meredith, Adv. Mat. 20 (2008) 3539.
[3] P. Meredith, B.J. Powell, J. Riesz, S.P. Nighswander-Rempel, M.P. Pederson, E.V. Moore, Soft Matt. 2 (2006) 37.
[4] M.A. Rosei, L. Mosca, F. Galluzzi, Synth. Met. 76 (1996) 331.
[5] J.E. de Albuquerque, C. Giacomantonio, A.G. White, P. Meredith, Appl. Phys. Lett. 87 (2005) 0161920.
[6] V.P. Grishchuk, S.A. Davidenko, I.D. Zholner, A.B. Verbitsckii, M.V. Kurik, Y.P. Piryatinskii, Techn. Phys. Lett. 28 (2002) 896.
[7] T. Ligonzo, M. Ambrico, V. Augelli, G. Perna, L. Schiavulli, M.A. Tamma, P.F. Biagi, A. Minafra, V. Capozzi, J. Non-Cryst. Solids (2009), doi:10.1016/j.noncrystol.2009.05.014.
[8] M. Jatstrzebska, A. Kocot, L. Tajber, J. Photochem. Photobiol. B, Biology 66 (2002) 201.
[9] M. Jatstrzebska, A. Kocot, J.K. Vij, J. Zalewska-Rejdak, T. Witecki, J. Mol. Struct. 606 (2002) 205.
[10] P.R. Crippa, V. Cristofoletti, N. Romeo, Biochim. Biophys. Acta 538 (1978) 164.
[11] K.B. Stark, J.M. Gallas, G.W. Zajac, M. Eisner, J.T. Golab, J. Phys. Chem. B 107 (2003) 3061.
[12] K.B. Stark, J.M. Gallas, G.W. Zajac, M. Eisner, J.T. Golab, J. Phys. Chem. B 107 (2003) 11558.
[13] K.B. Stark, J.M. Gallas, G.W. Zajac, J.T. Golab, S. Gidanian, T. McIntire, P.J. Farmer, J. Phys. Chem. B 109 (2005) 1970.
[14] M. Abbas, F. D'Amico, L. Morresi, R. Gunnella, N. Pinto, M. Ficcadenti, R. Natali, M. Cuccioloni, M. Angeletti, Eur. Phys. J. E 28 (2009) 285–291.
[15] P. Diaz, Y. Gimeno, P. Carro, S. Gonzales, P.L. Schilardi, G. Benitez, R.C. Salvarezza, A.H. Creus, Langmuir 21 (2008) 5924.
[16] H.S. Majumdar, A. Bandyopadhyay, A. Bolognesi, A.J. Pal, J. Appl. Phys. 91 (2002) 2433.
[17] W. Brutting, H. Riel, T. Beierlein, W. Reiss, J. Appl. Phys. 89 (2001) 1704.
[18] Y.-J. Lin, J. Appl. Phys. 103 (2008) 063702.
[19] Z. Zhong, S. Yin, C. Liu, Y. Zhong, W. Zhang, D. Shi, C. Wang, Appl. Surf. Sci. 207 (2003) 183.
[20] D. Ritter, K. Weiser, Opt. Comm. 57 (1986) 336.
[21] A. Fejfar, A. Poruba, M. Vanecek, J. Kocka, J. Non-Cryst. Sol. 198 (1996) 304.
[22] J. Riesz, J. Gilmore, P. Meredith, J. Biophys. 90 (2006) 1.
[23] The root mean square roughness R_{rms} is a measure of the root mean square value of the height distribution, according to $R_{rms} = \sqrt{\sum_{i=1}^{N} \frac{(z_i - z_m)^2}{(N-1)}}$ where N is the total number of data points, z_i is the height of the ith point and z_m is the mean height.
[24] J. Cheng, S.C. Moss, M. Eisner, Pigm. Cell. Res. 7 (1994) 263–273.
[25] M.Y. Seyidov et al., Solid State Sci. 10 (2008) 1666.
[26] A.I. Yakimov, V.A. Markov, A.V. Dvurechenskii, O.P. Pchelyakov, J. Phys.: Condens. Matter 6 (1994) 2573–2582.
[27] L. Li, Q.D. Ling, S.L. Lim, Y.P. Tan, C. Zhu, D.S.H. Chan, E.T. Kang, K.G. Neoh, Org. Electron. 8 (2007) 401.

Organic Electronics 11 (2010) 1815–1820

Contents lists available at ScienceDirect

Organic Electronics

journal homepage: www.elsevier.com/locate/orgel

Complementary organic thin film transistor circuits fabricated directly on silicone substrates

Ingrid M. Graz *, Stéphanie P. Lacour

Nanoscience Centre, University of Cambridge, 11 JJ Thomson Avenue, Cambridge CB3 0FF, United Kingdom

ARTICLE INFO

Article history:
Received 30 June 2010
Received in revised form 6 August 2010
Accepted 7 August 2010
Available online 19 August 2010

Keywords:
Organic electronics
Elastomeric substrates
Thin-films
Low temperature process

ABSTRACT

The present work demonstrates organic circuits on a new class of substrate, silicone elastomers. The fabrication method relies on dry, additive processes performed at ultra-low substrate temperature (<100 °C). P-type pentacene and n-type C_{60} organic thin-film transistors (TFTs) in a bottom gate, top contact architecture are prepared directly on polydimethylsiloxane (PDMS) membranes without any surface pre-treatment. Simple logic elements including complementary inverters and ambipolar transistors patterned on PDMS perform similarly to their counterparts fabricated on substrates thousands times stiffer. The processing options and mechanical compliance of the elastomeric substrate combined with organic device materials open new opportunities for compliant, lightweight, low-power and large area thin-film circuitry.

© 2010 Elsevier B.V. All rights reserved.

1. Introduction

Organic materials have been successfully employed for CMOS-circuitry [1]. Their applications stand in circuits of low complexity such as RF ID tags [2] or in active matrices for displays [3] and electronic skins [4]. Complementary organic electronics have been reported on silicon, polyimide or polyethylene naphtalate (PEN) substrates [5,6]. Non-volatile memories and non-volatile memory transistors for flexible sensor arrays have recently been demonstrated by Sekitani [7,8].

To date, polydimethylsiloxane (PDMS) elastomers are mainly used in microfabricated devices for microfluidics, sensors, MEMS and biomedical applications [9–13]. Their implementation as substrates for microelectronics is a recent evolution. When integrated circuits, first manufactured on and cut into small silicon [14] or plastic [15] platforms, are transferred onto an elastomeric wiring board, the electronic circuit becomes mechanically compliant and even stretchable. The results provide unique electronic systems, which can integrate clothes [16], conform spherical surfaces [14] and more recently organs [17]. Several strategies for elastic interconnects have been developed and patterned directly onto the elastomeric substrates [14,18–21]. We now propose to also fabricate the electronic circuits directly onto PDMS employing organic small molecules semiconductors. The device process flow is straightforward [22] and compatible with organic thin-film electronics manufacturing.

2. Experimental

PDMS substrates of 1 mm thickness are prepared by casting polydimethylsiloxane (PDMS, Sylgard 184, Dow Corning) in a 10:1 mixing ratio into Petri dishes and curing at 65 °C for 24 h. Alternatively 1 mm thick PDMS membranes (Speciality Manufacturing Inc., MI, USA) are leached for 48 h in isopropanol alcohol followed by blow-drying with nitrogen. A bilayer of 5 nm/50 nm thick Chromium/Gold films is thermally evaporated (rate ~0.1 Å/s) to form the transistor bottom gate electrode. The gate dielectric is formed by vapour deposition of 600 nm thick poly-para-xylylene (Parylene C) film with a capacitance of 4.6 μF/cm^2 using a Labcoater 2010 (Speciality Coating Systems, UK). Organic semiconductor films of 50 nm

* Corresponding author. Tel.: +44 1223 760303; fax: +44 1223 760309.
E-mail address: img21@cam.ac.uk (I.M. Graz).

1566-1199/$ - see front matter © 2010 Elsevier B.V. All rights reserved.
doi:10.1016/j.orgel.2010.08.008

pentacene (Sigma Aldrich, 98% purity) (p-type) and C_{60} (MER Corp., 99% purity) (n-type) respectively are evaporated with a rate of $r = 0.4$ Å/s, followed by 30 nm of gold to form the source and drain electrodes for the top contacts. Pentacene and C_{60} TFTs have identical channels with $W/L = 3000\ \mu m/200\ \mu m = 15$. Complementary organic inverters are further prepared by patterning adjacent p-type and n-type transistor channels. Fig. 1a presents 18 complementary inverters on a transparent 1 mm thick PDMS substrate. Each pair of TFTs shares a common 1 mm gate electrode. The n-type and p-type devices are clearly distinguished from their resulting multilayer colour (Fig. 1b). Fig. 1c shows the schematic view of the inverter. For ambipolar TFTs, the semiconductor layer is formed by evaporating a 50 nm thick pentacene film on a 50 nm thick C_{60} film (C_{60}/pentacene device) or vice versa (pentacene/C_{60} device). Channel dimensions for ambipolar TFTs are $W/L = 3000\ \mu m/150\ \mu m = 20$. Electrodes and the semiconductor layer are patterned through stainless steel shadow masks; the gate dielectric deposited through a PDMS shadow mask. The devices are not annealed.

AFM micrographs of the topography of the thin films on PDMS are obtained using a Pico Plus AFM system (Molecular Imaging) and an NSC36noAl cantilever (MikroMasch) with a 1.75 N/m force constant.

TFTs and inverter circuits are characterised in a nitrogen environment using an HP4155 semiconductor parameter analyser.

3. Results and discussion

Fig. 2 summarizes the electrical response of n-type, p-type TFTs and complementary inverters on PDMS. The transfer and I(V) characteristics of a p-channel pentacene TFT on PDMS are shown in Fig. 2a and b. The TFT channel is 3000 μm wide and 200 μm long ($W/L = 15$). The off state current is below 5 nA and the on/off ratio is 10^4 for $V_{GS} \cdot \varepsilon \cdot [-60\ V;\ 10\ V]$. Low leakage gate current is maintained during linear and saturation TFT operation with $I_{GS} < 1$ nA. The threshold voltage is −4 V, and carrier mobility in the saturation regime is 0.16 cm^2/V s. Symmetric results are obtained for the n-type C_{60} TFT on PDMS (Fig. 2c and d) with equal channel dimensions ($W/L = 15$). Saturation electron mobility and threshold voltage are measured to be 0.16 cm^2/V.s and 12 V, respectively. On current at $V_{DS} = 60$ V is 10 μA. Both n-type and p-type TFTs show negligible hysteresis suggesting good gate stability.

C_{60} and pentacene TFTs are then integrated into complementary inverters (Fig. 1). Fig. 2e shows the transfer curves of an inverter with equally sized n- and p-type channels ($W/L = 3000\ \mu m/200\ \mu m$) and for supply voltages V_{DD} of 40, 50 and 60 V. The gate is common to both transistors and is the circuit input node V_{in}. The circuit exhibits sharp switching at nearly $V_{DD}/2$. In the off state ($V_{in} = 0$ V), V_{out} matches V_{DD}. Voltage gains as high as 21 are recorded from the inverter. This confirms that both transistors have matching performance (Fig. 2f).

Small tensile flexion (bending radius of 6.5 cm) is then applied to the inverters on PDMS. The circuits remain functional inverters after one bending cycle but their performance degrades quickly with further bending. This is expected because the TFT stack is sitting on top of the PDMS membrane without any encapsulation, i.e. away from the mechanical neutral plane, where the tensile strain is about one percent [23].

Ambipolar transistors and inverters based on heterojunctions of pentacene/C_{60} or C_{60}/pentacene semiconductor films are prepared as an alternative to complementary TFT inverters. Fig. 3a and d show the transfer characteristics for transistors with pentacene/C_{60} or C_{60}/pentacene semiconductor channels for V_{DS} at 10 V and 60 V. Their channel is 3000 μm wide and 150 μm long ($W/L = 20$). Both devices exhibit a typical ambipolar response with V-shaped transfer curves. On currents for both device configurations are in the micro ampere range, and gate leakage currents are below 10 nA. In the electron accumulation mode, the pentacene/C_{60} device has a threshold voltage $V_{Th,n}$ of 40 V and yields a saturation electron mobility of 0.12 cm^2/V.s, close to that of the C_{60} TFT (Fig. 2c). In the hole accumulation mode, the device's threshold voltage $V_{Th,p}$ is −30 V and the corresponding hole mobility is low, 3×10^{-2} cm^2/V.s. The C_{60}/pentacene transistor presents poorer performance with electron mobility of 0.02 cm^2/V s and $V_{Th,n} = 12$ V, and hole mobility of $\sim 6.5 \times 10^{-3}$ cm^2/V s and $V_{Th,p} = -40$ V.

The obtained mobilities for either of our ambipolar device configurations are higher than those reported for similar devices fabricated on Si/SiO_2 or Mylar substrates

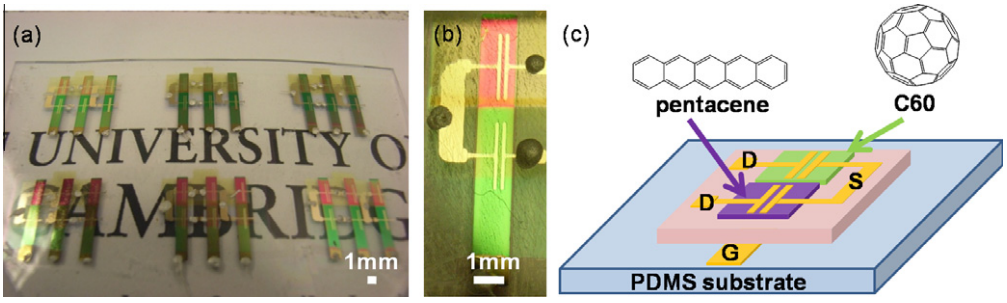

Fig. 1. (a) Photograph of an array of complementary organic inverters on 1 mm thick transparent PDMS. (b) Photograph of a complementary organic inverter prepared on PDMS. The n-type C_{60} transistor is the top (pink) device; the p-type pentacene transistor is the bottom (green) device. (c) Schematic view of the complementary inverter stack directly prepared on PDMS. (For interpretation of the references to colour in this figure legend, the reader is referred to the web version of this article.)

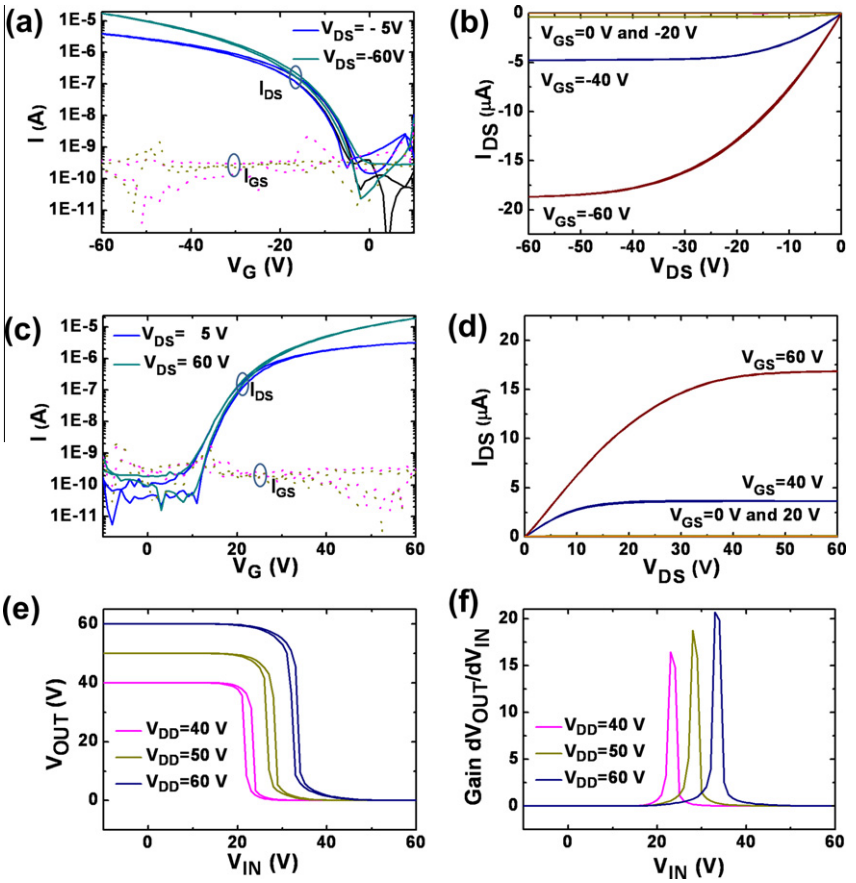

Fig. 2. (a) Transfer curves of a pentacene TFT on PDMS. V_{DS} is −5 V and −60 V. (b) $I(V)$ curves of the same device. The gate voltage decreases from 0 V to −60 V in −20 V steps. (c) Transfer and (d) output curves for a C_{60} TFT on PDMS with similar but opposite V_{DS} and V_{GS}. (e) Transfer characteristics of a pentacene and C_{60} complementary inverter for V_{DD} = 40, 50, 60 V and (f) corresponding inverter gain.

[24,25]. Clearly, the semiconductor stack construction, C_{60} on pentacene or vice versa, affects the resulting carrier mobilities and overall device performance. Several studies have reported on the electronic structures on the pentacene/C_{60} interfaces [26,27]. In particular, Kang et al. have measured the HOMO and LUMO offsets at the pentacene/C_{60} interface as a function of the stack preparation (pentacene on C_{60} versus C_{60} on pentacene) and showed the offsets are minimal when C_{60} is deposited on pentacene films [27]. This may therefore result in better carrier injection in the pentacene/C_{60} device and higher mobilities than in the pentacene/C_{60} device. Further investigation of the electronic properties of the pentacene/fullerene interfaces grown on parylene on PDMS will help analysing the electrical performance of the devices.

Complementary inverters are prepared using two identical ambipolar transistors where the common gate is the input voltage. Channels' geometry is $W/L = 20$. Typical transfer curves of pentacene/C_{60} or C_{60}/pentacene ambipolar inverters are shown Fig. 3b, c, e and f. The pentacene/C_{60} device performs well. In the first quadrant, a voltage gain of up to 20 is measured for V_{DD} = 60 V. Negligible hysteresis is observed. In the third quadrant, the hysteresis is more pronounced and probably indicates charge trapping at the parylene/pentacene interface. Nevertheless, the ambipolar inverter has a gain of 20 for $V_{DD} = -60$ V. The C_{60}/pentacene ambipolar inverter also presents reliable switching in the first and third quadrants. High inverter gains are measured (gain ~25 for $V_D = 60$ V). However the threshold voltages in both quadrants are low, much lower than half of V_{DD}, possibly due to the poor and unbalanced hole and electronic mobilities. In both ambipolar inverter configurations, low V_{out} never reaches 0 V when V_{in} is high. This is explained by the fact that the individual ambipolar devices never fully turn off (as shown Fig. 3a and d).

The morphology of each layer of the devices' stack was analysed using scanning electron (SEM) and atomic force microscopies (AFM). Fig. 4a shows an SEM image of the gold gate electrode on PDMS. The film has a complex topography where gold ligaments are separated by short, micro-scale cracks [28]. A 9 μm × 9μm scan is recorded on each layer of the TFT stack. Representative AFM micrographs are presented in Fig. 4b. Overall the topography of the thin films deposited on PDMS is complex and rough. The as-prepared PDMS surface is smooth with an RMS roughness of 5 nm (Fig. 4b-i).

After deposition of the gate electrode (Fig. 4b-ii), the RMS roughness increases to 16 nm as a result of the built-in micro-crack network in the gold film on PDMS

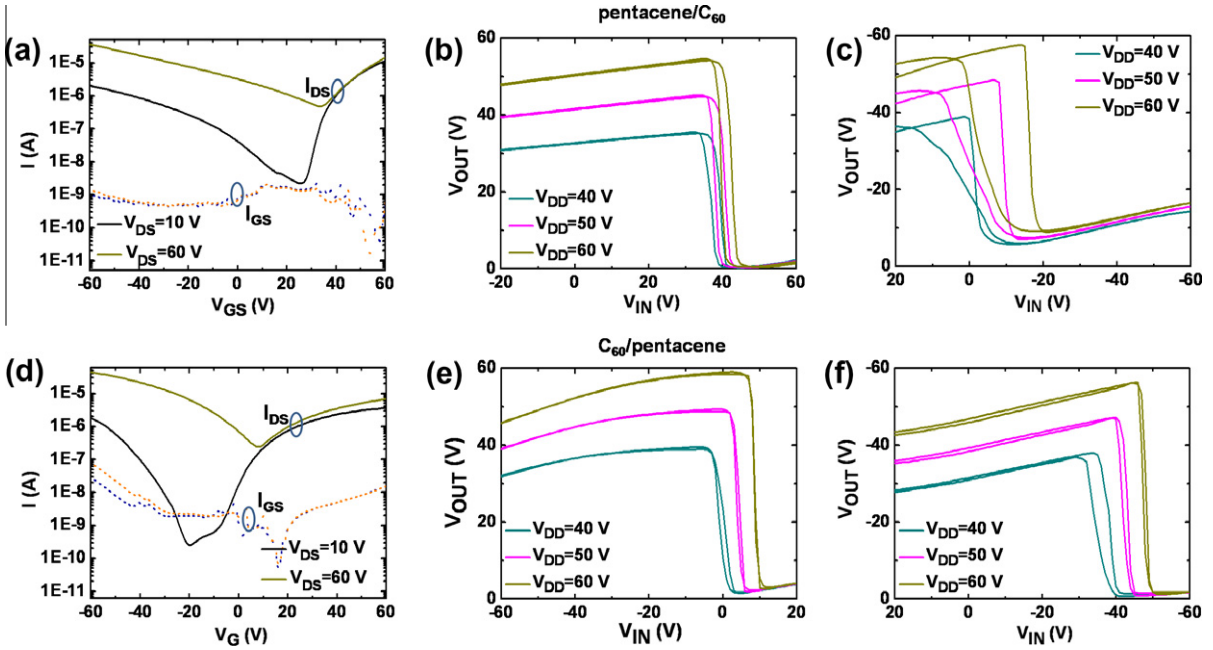

Fig. 3. (a) Transfer characteristics of an ambipolar pentacene/C_{60} TFT on PDMS; V_{DS} is 10 V and 60 V. (b) First and (c) third quadrants $I(V)$ curves of a pentacene/C_{60} inverter on PDMS; V. (d) Transfer characteristics of the ambipolar C_{60}/pentacene TFT; V_{DS} is −10 V and −60 V. (e) First and (f) third quadrants I(V) curves of a C_{60}/pentacene inverter on PDMS. V_{DD} is 40 V, 50 V and 60 V for all transfer characteristics.

(Fig. 4a). AFM micrographs (Fig. 4b-iii) and (Fig. 4b-iv) show that the parylene film grows differently on the bare PDMS substrate than on the gate gold electrode. On PDMS, the parylene forms a smooth coating with an RMS roughness of 12 nm and features or grains of 100 nm diameter and 5 nm height. On the microstructured gold film, the parylene appears very rough with a resulting RMS roughness of 16.2 nm and raised features as tall as 100 nm are observed. Metallic surfaces, including gold, inhibit parylene deposition [29,30]. Vaeth et al. reports that the resulting polymer film grows into large and sparse grains rather than small and uniformly distributed grains, thereby leading to films with high roughness [30]. Parylene growth inhibition combined with the initially micro-cracked gold film on PDMS lead to a gate dielectric surface with a chaotic and rugged topography showing features of 0.5–1 μm width and 20–100 nm height. The roughness of the parylene film is therefore significantly higher than that of typical polymer dielectrics with RMS roughness between 0.2 nm and 2 nm [31]. As a result, the parylene's morphology sets that of the subsequently deposited films of pentacene (Fig. 4b-v) and C_{60} (Fig. 4b-vi). For pentacene, grains with 100–300 nm diameter superimposed onto a complex wavy topography are observed (Fig. 4b-v); the RMS roughness is 16.7 nm. For the C_{60} devices, no grain is clearly visible (Fig. 4b-vi) and the film RMS roughness is 17 nm. Finally, the source/drain metal film conforms the semiconductor surface (RMS roughness = 18.9 nm, AFM micrograph not shown).

The channel surface of the ambipolar devices is shown Fig. 4b-vii and Fig. 4b-viii. Grains of 100–300 nm in diameter are observed in the C_{60} films grown on pentacene. Pentacene films grown on C_{60} exhibit significantly smaller grains with 50–100 nm in diameter. Surface RMS roughness is about 17 nm for both stacks of organic semiconductors. Further investigation on the structural and electrical properties of the semiconductor bi-layers is now required to explain the different electrical performance of the pentacene-on-C_{60} and C_{60}-on-pentacene devices.

4. Conclusion

In summary, we have demonstrated that complementary organic field-effect transistor circuits can be manufactured on ultra-compliant silicone substrate. Their process flow is straightforward and does not require extensive substrate or dielectric surface treatment or annealing to obtain devices with carrier nobilities in the 0.2 $cm^2/V\,s$ range. Only modest bending can be sustained by the devices on PDMS but various strategies including placing the device stack in the neutral plane of the structure or onto rigid platforms embedded in the silicone matrix, can be readily implemented to add flexibility and even stretchability to the organic CMOS-like circuits on PDMS.

The ability of depositing and patterning active device materials directly onto silicone elastomers is a promising and exciting opportunity for the fabrication of truly integrated circuits on elastomers. Our results clearly show that organic circuitry on elastomer is feasible and competitive with organic electronics on plastic. Thin-film circuitry on elastomer promises diverse and multiple applications in the fields of microfluidics, active matrices for sensory platforms and large-area electronics. With optimised mechanical design, TFT circuits on PDMS will become flexible and even fully elastic.

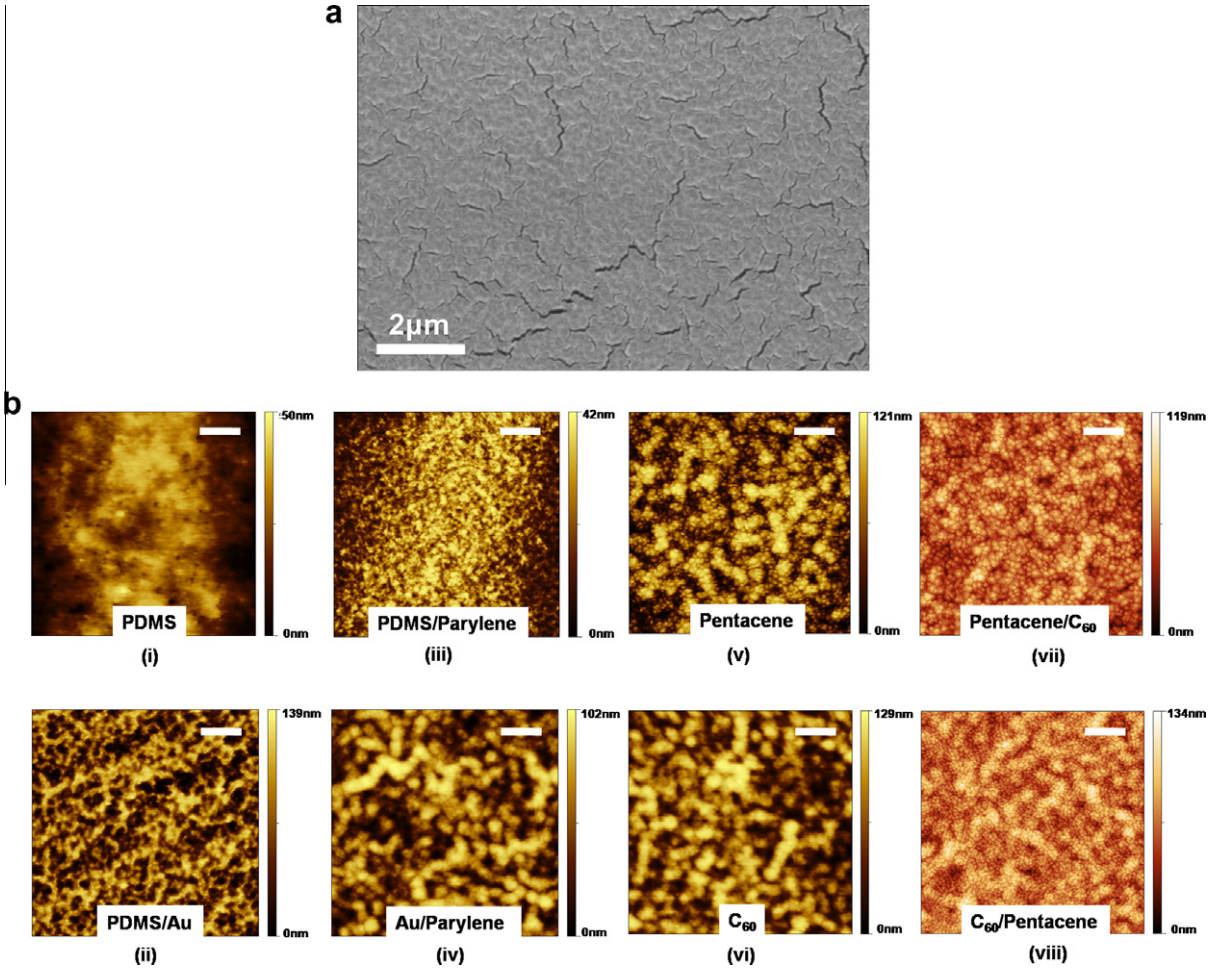

Fig. 4. (a) Scanning Electron Microscope (SEM) image of 50 nm thick gold electrode on PDMS. The built-in micro-cracks are typically 0.5–2 μm long and randomly distributed. (b) Atomic Force Microscopy (AFM) images of (i) the PDMS substrate (1 mm), (ii) the gold gate electrode (50 nm), (iii) the parylene C film (600 nm) on plain PDMS, (iv) the parylene C dielectric layer (600 nm) on the gold gate electrode, (v) the pentacene film (50 nm) on parylene C, (vi) the C_{60} film (50 nm) on parylene C, (vii) the C_{60} film (50 nm) on the pentacene channel and (viii) the pentacene film (50 nm) on the C_{60} channel. Scale bar for *x* and *y* direction is 2 μm, scale bars for *z* direction are in nanometer.

Acknowledgements

This research is supported by the Royal Society and by the collaboration on Nanotechnology between the University of Cambridge and Nokia. We would like to thank Prof. H. Sirringhaus for providing access to the electrical characterisation glovebox, Dr. M. Caironi for fruitful discussions, Prof. Mark Welland, Dr. Christoph Meier and Alex Buell for their help with the atomic force microscopy.

References

[1] H. Klauk, U. Zschieschang, J. Pflaum, M. Halik, Nature 445 (2007) 745–748.
[2] S. Steudel, K. Myny, V. Arkhipov, C. Deibel, S. De Vusser, J. Genoe, P. Heremans, Nat. Mater. 4 (2005) 597–600.
[3] G.H. Gelinck, H.E.A. Huitema, E. van Veenendaal, E. Cantatore, L. Schrijnemakers, J.B.P.H. van der Putten, T.C.T. Geuns, M. Beenhakkers, J.B. Giesbers, B.-H. Huisman, E.J. Meijer, E.M. Benito, F.J. Touwslager, A.W. Marsman, B.J.E. van Rens, D.M. de Leeuw, Nat. Mater. 3 (2004) 106–110.
[4] T. Sekitani, Y. Noguchi, U. Zschieschang, H. Klauk, T. Someya, PNAS 105 (2008) 4976–4980.
[5] C.J. Drury, C.M.J. Mutsaers, C.M. Hart, M. Matters, D.M. De Leeuw, Appl. Phys. Lett. 73 (1998) 108–110.
[6] H. Klauk, M. Halik, U. Zschieschang, F. Eder, G. Schmid, C. Dehm, Appl. Phys. Lett. 82 (2003) 4175–4177.
[7] T. Sekitani, K. Zaitsu, Y. Noguchi, K. Ishibe, M. Takamiya, T. Sakurai, T. Someya, IEEE Trans. Electron. Dev. 56 (5) (2009) 1027–1035.
[8] T. Sekitani, T. Yokota, U. Zschieschang, H. Klauk, S. Bauer, K. Takeuchi, M. Takamiya, T. Sakurai, T. Someya, Science 326 (2009) (1516) 1519.
[9] J.T. Mabeck, J.A. DeFranco, D.A. Bernards, G.G. Malliaras, S. Hocde, C.J. Chase, Appl. Phys. Lett. 87 (2005) 013503.
[10] J.C. McDonald, G.M. Whitesides, Acc. Chem. Res. 35 (2002) 491–499.
[11] C. Liu, Adv. Mater. 19 (2007) 3783–3790.
[12] D.P.J. Cotton, I.M. Graz, S.P. Lacour, Proceedings of the Eurosensors XXIII Conference, Proc. Chem. 1 (2009) 152–155.
[13] Z. Yu, O. Graudejus, C. Tsay, S.P. Lacour, S. Wagner, B. Morrison, J. Neurotrauma 26 (2009) 1–11.
[14] H.C. Ko, M.P. Stoykovich, J. Song, V. Malyarchuk, W.M. Choi, C.-J. Yu, J.B. Geddes III., J. Xiao, S. Wang, Y. Huang, J.A. Rogers, Nature 454 (2008) 748–753.
[15] T. Someya, Y. Kato, T. Sekitani, S. Iba, Y. Noguchi, Y. Murase, H. Kawaguchi, T. Sakurai, PNAS 102 (2005) 12321–12325.
[16] T. Löher, R. Vieroth, M. Seckel, A. Ostmann, H. Reichl, in: 9th IEEE Workshop of Japan on VLSI Packaging, IEEE, pp. 9–12.

[17] J. Viventi, D.-H. Kim, J.D. Moss, Y.-S. Kim, J.A. Blanco, N. Annetta, A. Hicks, J. Xiao, Y. Huang, D.J. Callans, J.A. Rogers, B. Litt, Science Translational Medicine 2 (2010) 4ra22.
[18] S.P. Lacour, J.E. Jones, S. Wagner, T. Li, Z. Suo, Proc. IEEE 93 (2005) 1459–1467.
[19] D.S. Gray, J. Tien, C.S. Chen, Adv. Mater. 16 (2004) 393–397.
[20] D. Brosteaux, F. Axisa, M. Gonzalez, J. Vanfleteren, IEEE Electron. Dev. Lett. 28 (2007) 552–554.
[21] T. Sekitani, H. Nakajima, H. Maeda, T. Fukushima, T. Aida, K. Hata, T. Someya, Nat. Mater. 8 (2009) 494–499.
[22] I. Graz, S.P. Lacour, Appl. Phys. Lett. 95 (2009) 243305.
[23] S. Wagner, H. Gleskova, I.-C. Cheng, H. Sturm, Z. Suo, Mechanics of TFT technology on flexible substrates, in: G.P. Crawford (Ed.), Flexible Flat Panel Displays, Chichester, Wiley, 2005, pp. 263–283 (Chapter 14).
[24] E. Kuwahara, H. Kusai, T. Nagano, T. Takayanagi, Y. Kubozono, Chem. Phys. Lett. 413 (2005) 379–383.
[25] P. Cossedu, A. Bonfiglio, I. Salzmann, J.P. Rabe, N. Koch, Org. Electron. 9 (2008) 191–197.
[26] I. Salzmann, S. Duhm, R. Opitz, R.L. Johnson, J.P. Rabe, N. Koch, J. Appl. Phys. 104 (2008) 114518.
[27] S.J. Kang, Y. Yi, C.Y. Kim, S.W. Cho, M. Noh, K. Jeong, C.N. Whang, Synth. Met. 156 (2006) 32–37.
[28] S.P. Lacour, D. Chan, S. Wagner, T. Li, Z. Suo, Appl. Phys. Lett. 88 (2006) 204101–204103.
[29] K.M. Vaeth, R.J. Jackman, A.J. Black, G.M. Whitesides, K.F. Jensen, Langmuir 16 (2000) 8495–8500.
[30] K.M. Vaeth, K.F. Jensen, Chem. Mater. 12 (2000) 1305–1313.
[31] C. Kim, A. Facchetti, T.J. Marks, Adv. Mater. 19 (2007) 2561–2566.

Organic Electronics 11 (2010) 1821–1827

Contents lists available at ScienceDirect

Organic Electronics

journal homepage: www.elsevier.com/locate/orgel

Enhanced efficiency in double junction polymer:fullerene solar cells

D.J.D. Moet [a,*], P. de Bruyn [a,b], J.D. Kotlarski [a], P.W.M. Blom [a,c]

[a] Zernike Institute for Advanced Materials, University of Groningen, Nijenborgh 4, 9747 AG Groningen, The Netherlands
[b] Dutch Polymer Institute, P.O. Box 902, 5600 AX Eindhoven, The Netherlands
[c] Holst Centre, High Tech Campus 31, 5605 KN Eindhoven, The Netherlands

ARTICLE INFO

Article history:
Received 5 July 2010
Received in revised form 23 July 2010
Accepted 12 August 2010
Available online 27 August 2010

Keywords:
Polymer
Solar cells
Tandem
PF10TBT
Optoelectronic modeling

ABSTRACT

Polymer solar cells based on the polyfluorene copolymer poly[9,9-didecanefluorene-alt-(bis-thienylene) benzothiadiazole] (PF10TBT) and the fullerene derivative [6,6]-phenyl C_{61}-butyric acid methyl ester (PCBM) exhibit a power conversion efficiency of 4%. However, the optimum thickness of the photoactive layer is only 80 nm, such that these solar cells absorb only half of the photons available in their absorption bandwidth. Thicker cells are subject to electronic losses due to space charge effects and recombination. We demonstrate both from simulations and experiments that the optical and electronic losses can be decoupled in a double junction solar cell. For the PF10TBT:PCBM blend, the integration of two thin cells in a double junction device leads to an enhancement of the measured power conversion efficiency with 13% up to a value of 4.5%.

© 2010 Elsevier B.V. All rights reserved.

1. Introduction

The active layer of the most efficient polymer solar cells to date consists of a bulk heterojunction (BHJ) of a conjugated polymer with the buckminster fullerene derivative [6,6]-phenyl C_{61}-butyric acid methyl ester (PCBM). Such a bulk heterojunction is characterized by nanoscale intermixing of the electron donor and acceptor materials in order to maximize their cross-sectional area [1]. Compared to inorganic solar cells, thin film polymer devices produce high photovoltages. However, the power conversion efficiency is limited by a relatively low photocurrent as a result of a higher bandgap and narrower absorption bandwidth. Efforts to increase the efficiency are therefore primarily focused on the harvesting of more photons.

The most direct way to increase absorption is increasing the thickness of the photoactive layer. However, in many polymer:fullerene systems the combined effects of charge carrier recombination and the formation of space charge reduce the fill factor and consequently the overall device efficiency of thick cells [2]. In a BHJ solar cell the reflective back electrode introduces optical interference effects inside the photoactive layer between incoming and reflected light [3]. Therefore, it has been suggested that the photocurrent can be increased by introducing an optical spacer that enhances light absorption in thin polymer solar cells by redistributing the optical electric field [4,5]. However, the spacer effect is only beneficial if the BHJ film thickness does not coincide with a local maximum of optical power dissipation [6].

Alternatively, the optical properties of the photoactive materials can be tuned. Promising results have been reported for solar cells in which narrow bandgap polymers were introduced in order to absorb low-energy photons [7–9]. The electron-accepting material can be modified as well: substitution of PCBM with its more strongly absorbing C_{70}-analogue generally results in a larger contribution to the photocurrent [10]. A further improvement of the spectral coverage of the solar irradiance spectrum can be realized by incorporation of multiple heterojunctions with complementary absorption spectra in a tandem solar cell [11–13].

In this paper we present an alternative approach to improve the performance of thin film polymer photovoltaics. As a model system we use polymer solar cells based on the

* Corresponding author.
E-mail address: d.j.d.moet@rug.nl (D.J.D. Moet).

1566-1199/$ - see front matter © 2010 Elsevier B.V. All rights reserved.
doi:10.1016/j.orgel.2010.08.010

polyfluorene copolymer poly[9,9-didecanefluorene-alt-(bis-thienylene) benzothiadiazole] (PF10TBT) and PCBM with a power conversion efficiency of 4%. An efficiency increase of 13% is realized by combining two optimized PF10TBT:PCBM solar cells in one double junction device, without any change to the constituents of the photoactive layer. The approach concurrently utilizes the enhanced absorption of thick films and the superior electronic performance of thin films.

2. Experimental

2.1. Device fabrication

ITO patterned glass substrates were thoroughly cleaned with soap water, acetone, propanol and a UV ozone treatment before application of a layer of PEDOT:PSS (Clevios VP AI4083 SG, H.C. Starck). PF10TBT (TNO, M_w = 1.9 $\times$ 10^5 g/mol, PDI = 3.5) and PCBM (Solenne) were used as received. Photoactive layers were spin coated under ambient conditions from hot (90 °C) chlorobenzene solutions of PF10TBT:PCBM in a 1:4 weight ratio and capped with a 1 nm LiF/100 nm Al cathode. For the middle electrode of double junction devices, ZnO nanoparticles with a diameter of 5–10 nm were synthesized in methanol via hydrolysis and condensation of zinc acetate dihydrate by KOH, as described elsewhere [14,15]. After centrifugation, the ZnO gels were dispersed in acetone [16], followed by sonication and filtration. The acidity of PEDOT:PSS (Clevios PH500, H.C. Starck) was tuned by addition of a 1:8 dilution of 2-dimethylaminoethanol in water [17]. Nafion perfluorinated resin solution (5 wt% in a mixture of lower aliphatic alcohols and water, Aldrich) was diluted 1:20 with ethanol before spin coating at high rpm on top of pH-modified PEDOT:PSS layers in a nitrogen-flushed compartment under ambient atmosphere.

2.2. Characterization

Current–voltage characteristics were recorded with a Keithley 2400 SourceMeter. The results of Fig. 1 were recorded under illumination from a Steuernagel SolarConstant 1200, producing white light with an intensity of 1.3 kW/m^2. The light intensity was determined by (a) comparison of the measured J_{sc} with the expected short-circuit current density as calculated from the convolution of the spectral responsivity curve with the AM1.5 global reference spectrum, taking into account the linear dependence of J_{sc} on light intensity and (b) the deviation of the setpoint of a multicrystalline silicon reference cell from the value determined using accurate mismatch correction [18]. The same lamp was used for the measurements of Fig. 6, using spectral mismatch correction (M = 1.40) and a GG385 filter, resulting in a light intensity equivalent to 0.9 sun. Contributions to the photocurrent from regions outside the anode/cathode overlap area were eliminated using illumination masks with slightly smaller apertures. Incident photon to current conversion efficiency (IPCE) spectra were measured from 400 to 1100 nm using a custom-built setup comprising a 50 W quartz tungsten halogen lamp, 28 narrow band-pass interference filters, a transimpedance amplifier and a lock-in amplifier. The spectral response was measured relative to that of a calibrated monocrystal-

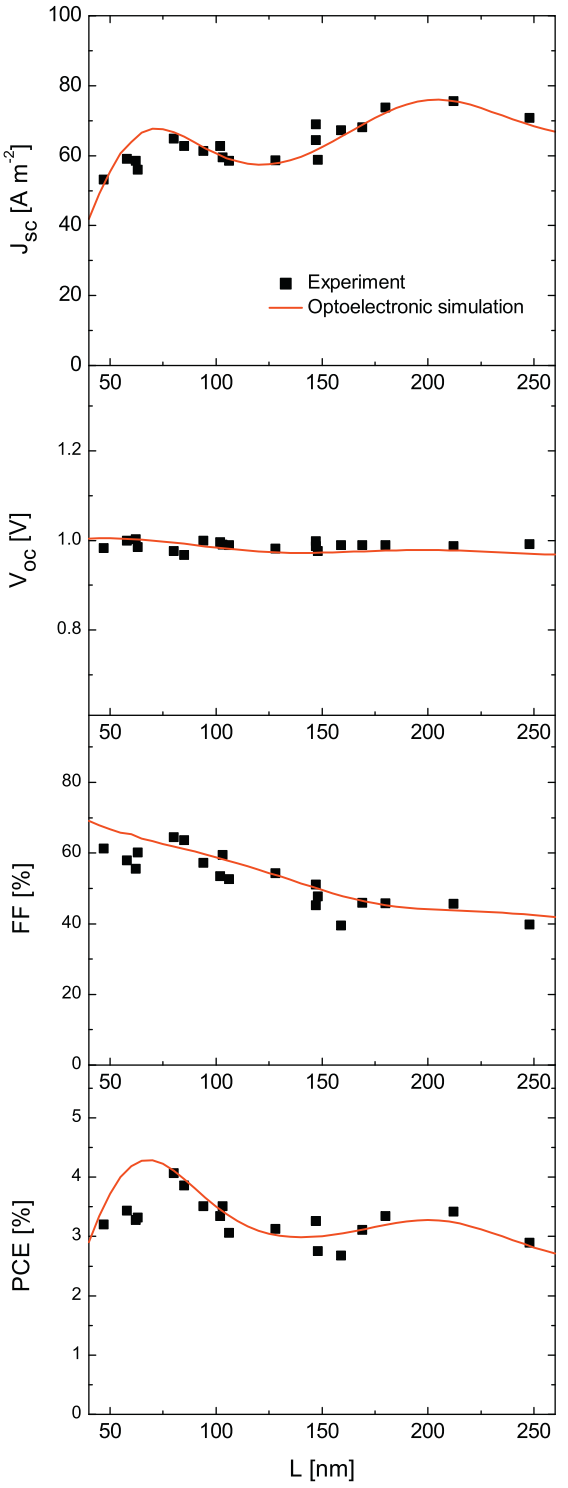

Fig. 1. Squares: experimental photovoltaic data of PF10TBT:PCBM solar cells with varying active layer thickness. The lines denote the result of the combined optoelectronic simulation.

line silicon photodiode (Newport 818-SL). Layer thickness measurements were done with a Veeco Dektak 6 M or 150 profilometer. Optical absorbance was measured with a Perkin–Elmer Lambda 900 spectrophotometer.

3. Results and discussion

3.1. Single junction solar cells

The efficiency of PF10TBT:PCBM solar cells is known to increase with the molecular weight of the polymer. This is caused by a reduced recombination rate of bound electron–hole pairs at high molecular weights, which leads to more efficient generation of free charges [19]. Therefore, the solar cells studied here are based on bulk heterojunctions of PCBM and high molecular weight PF10TBT. The donor/acceptor weight ratio was fixed to the optimum of 1:4 and all devices were processed from hot chlorobenzene solutions.

The variation of the short-circuit current density J_{sc}, open-circuit voltage V_{oc}, fill factor FF and power conversion efficiency PCE with photoactive layer thickness L is displayed in Fig. 1. Each data point (squares) represents the average of three or more current density–voltage (J–V) measurements. The values of J_{sc} and PCE were corrected for spectral mismatch of the lamp with the solar spectrum (see Section 2.2). Noticeable is the oscillatory behavior of J_{sc}, characterized by maxima at L = 80 nm and L = 210 nm. Thicker cells clearly absorb more light as J_{sc} is highest for L > 150 nm. However, since the open-circuit voltage is virtually independent of layer thickness and the fill factor strongly decreases with increasing L, the overall experimental PCE reaches its highest value of 4.0% already at L = 80 nm.

Next, we use combined optoelectronic modeling to gain insight in the major limitations of PF10TBT:PCBM solar cells of varying thickness. In order to describe the experimental results, we use an optical model based on the transfer matrix formalism in combination with a numerical electronic device model [20].

3.1.1. Optical simulations

Most conjugated polymers exhibit strong absorption with a high peak absorption coefficient [21]. As a result, layers as thin as several hundreds of nanometers can effectively absorb most solar photons with energy higher than the bandgap of the polymer. Since the wavelength of the incoming light is of a similar length scale and the back electrode in polymer solar cells is usually highly reflective, optical interference effects have to be taken into account in the description of the photocurrent of such devices [3].

As input for the optical model, the index of refraction n, extinction coefficient k and thickness of each layer in the device architecture are used. The optical constants were determined previously using variable-angle spectroscopic ellipsometry [19]. The light intensity $I(\lambda,x)$ is calculated for each wavelength and position inside the entire layer stack, taking into account the optical properties of each layer as well as the interference of light that is incident on the device (AM1.5G, 1000 W/m^2) with light that is reflected by the back electrode. The exciton generation rate at each position in the polymer:fullerene layer is given by the convolution of the local spectral photon flux and the absorption spectrum of the active layer [20]. In the calculation the relevant wavelength range is discretized at exponentially equidistant values λ_i and the integral is consequently replaced by a summation:

$$G(x) = \sum_i \frac{4\pi k(\lambda_i)}{hc} I(\lambda_i, x)\Delta\lambda_i \quad (1)$$

where $G(x)$ is the exciton generation rate at position x, h is Planck's constant, c is the speed of light and $I(\lambda_i,x)$ is the light intensity at wavelength λ_i and position x. The exciton generation profiles $G(x)$ are used below as an input for the electronic device model. A final integration of $G(x)$ over the position in the device gives the total generation rate G_{tot} of excitons inside the photoactive layer.

By definition, the amount of absorbed photons is equal to the amount of photogenerated excitons G_{tot}. For the AM1.5G reference spectrum, the number of *incident* photons with wavelengths within the effective absorption bandwidth of PF10TBT:PCBM layers, i.e., 300 < λ < 650 nm, is $N_{ph} = 1.05 \times 10^{21}$ m^{-2} s^{-1}. A measure of the absorption efficiency is now given by the ratio of G_{tot} to N_{ph}, which is plotted versus layer thickness in Fig. 2 (solid line). At L = 80 nm, which is the point of the first maximum of the experimental J_{sc}, only 48% of the available photons are absorbed. Poor light absorption thus strongly limits the current these thin PF10TBT:PCBM solar cells can produce. As expected, this conclusion is not altered by the introduction of an optical spacer in the form of a thin ZnO layer between the active layer and the cathode, since the incoupling of light is already optimal, giving a local maximum of the dissipated optical power at L = 80 nm. At the other local maximum of the experimental short-circuit current density, L = 210 nm, two-thirds of the available photons are absorbed. This shows that the available light can be used more efficiently in order to increase cell performance, without reducing the bandgap of the polymer.

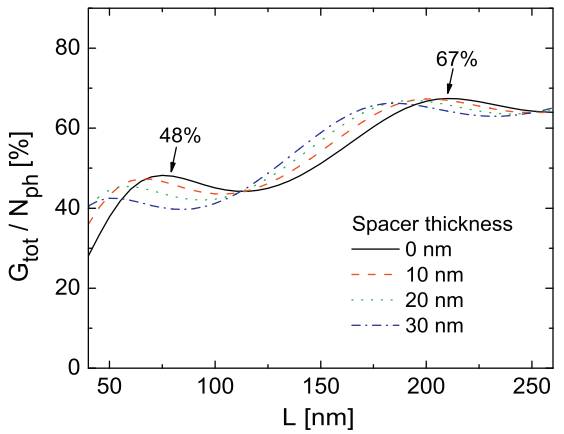

Fig. 2. Ratio of photogenerated excitons G_{tot} to the amount of photons N_{ph} with wavelength between 300 and 650 nm as a function of layer thickness. The lines denote different optical spacer thicknesses as indicated in the legend.

3.1.2. Electronic simulations

In polymer:fullerene solar cells, photogeneration of excitons is followed by diffusion of the excitons towards a donor–acceptor interface, charge transfer at the interface, dissociation of the resulting bound electron–hole (e–h) pair and charge carrier transport to and extraction at separate electrodes. Each of these processes generally introduces electrical losses that reduce the amount of extracted charges. The cumulative effect of these losses at short-circuit conditions is represented in the internal quantum efficiency, defined as the number of electrons in an external circuit per absorbed photon, or IQE = J_{sc}/qG_{tot}, where q is the elementary charge. The IQE can thus directly be determined from the measured J_{sc} (Fig. 1) and calculated G_{tot} (Fig. 2). In Fig. 3, the resulting IQE is plotted versus photoactive layer thickness. Approximately 80% of the absorbed photons contribute to the photocurrent in thin cells. For thicker layers this fraction decreases monotonically to around 70%, which is in good agreement with previously reported results [22].

Next, the current–voltage characteristics are simulated for each L in the range of experimental layer thicknesses. Here we use our numerical device model that includes drift and diffusion of charge carriers, a temperature- and field-dependent generation rate of free carriers, bimolecular recombination and the effect of space charge on the electric field in the device [23]. Ultrafast electron transfer from the photoexcited polymer to PCBM is assumed to occur with unity quantum yield, i.e., each exciton generates a bound e–h pair at an interface of donor and acceptor molecules. The dissociation rate of bound pairs into free carriers is described by Onsager–Braun theory [24,25], using an initial e–h separation distance a with a Gaussian distribution in energy and a bound pair decay rate k_f to parameterize the dependence of the dissociation probability P on electric field and temperature. Recombination of free carriers is assumed to be of the Langevin type, with a recombination constant dominated by the slowest carrier [26], and results in a bound pair that can either dissociate again or decay to the ground state. Other relevant parameters are the electron and hole mobilities μ_e and μ_h, the spatially averaged relative dielectric constant ε_r and the effective energy gap E_{gap} between the highest occupied molecular orbital (HOMO) energy of the donor and the lowest unoccupied molecular orbital (LUMO) energy of the acceptor.

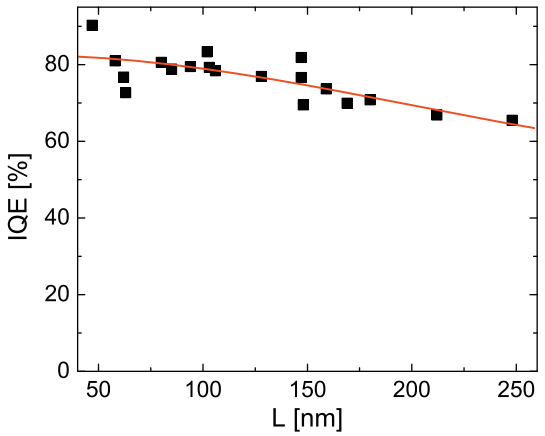

Fig. 3. The internal quantum efficiency IQE = J_{sc}/qG_{tot} versus photoactive layer thickness. The line serves as a guide to the eye.

The exciton generation profiles obtained by optical modeling are used as an input for the electronic model. The values that were used for the parameters in the electronic model are in excellent agreement with those previously derived for high molecular weight PF10TBT:PCBM cells [19] and are summarized in Table 1. In Fig. 1, the results of the optoelectronic simulations are depicted by the solid lines. Clearly, the oscillations of the short-circuit current density and power conversion efficiency with thickness are reproduced, as well as the strongly decreasing fill factor. The simulations indicate an optimal thickness of around 70 nm, which is close to the experimental value of 80 nm. The ratio of the amount of excitons that are lost due to quenching at the electrodes to the total amount of photogenerated excitons is large in very thin cells. As this quenching effect is not incorporated in the model, the calculations slightly overestimate the fill factor and short-circuit current in thin cells and, consequently, the predicted value of the maximum PCE of 4.3% is somewhat higher than the optimal experimental value.

Based on the optical simulations of Section 3.1.1, a relative increase of 40% in J_{sc} would be expected for a 210 nm thick cell compared to the 80 nm thick device. As can be seen in Fig. 1, enhanced absorption in thicker cells does indeed enable the extraction of a higher current. However, limited by the combined effects of space charge and recombination, the short-circuit current at L = 210 nm is only 16% higher than that at L = 80 nm. The same limitation causes the fill factor to drop considerably, resulting in a reduction of the PCE to 3.2%.

This clearly demonstrates that the increased absorption in thick cells is opposed by less favorable electronic properties. As a result the processing window for optimized solar cells is limited to thin layers. In the following section, the interlocking of optics and electronics is reduced by using double junction solar cells consisting of two optimized thin layer devices.

3.2. Double junction solar cells

Multijunction solar cells are generally used to compensate for the relatively narrow absorption bandwidth of conjugated polymers. By inclusion of a second bulk heterojunction with a lower optical bandgap, photon harvesting

Table 1
Overview of the model parameters used in the simulations.

Parameter	Symbol	Value
Bandgap	E_{gap}	1.37 eV
Electron mobility	μ_e	1×10^{-7} m^2 V^{-1} s^{-1}
Hole mobility	μ_h	6×10^{-9} m^2 V^{-1} s^{-1}
Effective density of states	N_c	2.5×10^{25} m^{-3}
Relative dielectric constant	ε_r	3.6
Initial e–h pair distance	a	2.2 nm
e–h Pair decay rate	k_f	5×10^5 s^{-1}

can be extended from the visible towards the near infrared. However, as discussed above, thin solar cells based on high bandgap materials fail to absorb a lot of photons with sufficient energy. In this section we therefore choose to investigate the possibility to enhance absorption of these high energy photons.

The photovoltaic properties of a multijunction solar cell depend on the method of interconnection of the subcells. A polymer tandem cell containing two subcells in a parallel configuration is feasible and is generally capable of producing higher currents [27]. However, charges need to be extracted at the middle electrode, which should consequently be based on materials with high sheet conductivity, such as metals. So far this has been incompatible with processing from solution. A much more practical approach is the series-connected multijunction, in which an increase in the amount of absorbed photons is utilized to deliver a higher photovoltage rather than a high current. As conduction now mainly occurs perpendicular to the interface, less conductive materials such as conjugated polymers and metal oxides are suitable candidates for the interlayer as well.

Here, we employ a previously reported device architecture in which the two subcells are connected in series by a composite middle electrode of ZnO nanoparticles and pH-modified PEDOT:PSS [16]. For practical reasons, the thicknesses of these layers are fixed to 20 and 30 nm, respectively.

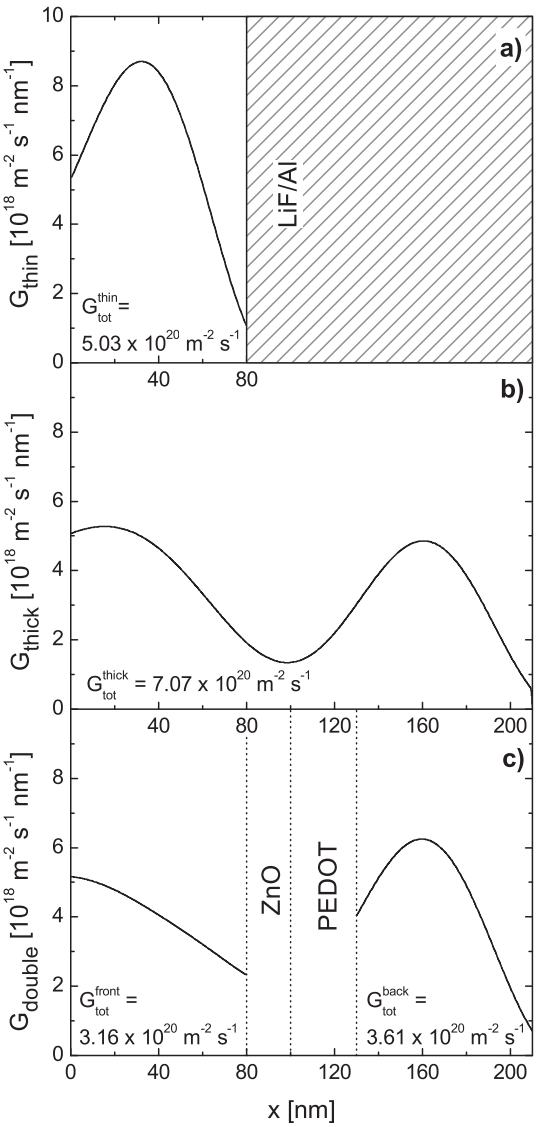

Fig. 4. Calculated exciton generation rate profiles plotted versus the position x in (a) a thin, (b) a thick and (c) a double junction solar cell. The total (integrated) exciton generation rate G_{tot} for each profile is indicated in the relevant figure panel.

3.2.1. Simulations

As a reference, we first take a step back to examine the exciton generation profiles of a thin and a thick device, as shown in Fig. 4a and b. Again we consider the layer thicknesses at the maxima of the experimental J_{sc} and PCE, i.e., L = 80 nm and L = 210 nm. Position x = 0 corresponds to the interface of PEDOT:PSS with the photoactive layer and the cathode is located at $x = L$. The light can thus be considered incident from the left side of the figure. As expected, both profiles show excellent incoupling of the incident light. Furthermore, as discussed above, the ratio of the total exciton generation rates amounts to $G_{tot}^{thick}/G_{tot}^{thin} = 1.40$, which means that the thick cell absorbs 40% more photons than the thin one.

In Fig. 4c, the exciton generation profiles inside the two subcells of a double junction device are plotted. As a one-to-one extension of the optimized single layer cell, the tandem device is chosen to incorporate two thin PF10TBT:PCBM cells of 80 nm thickness. These are separated by a ZnO cathode (20 nm) for the front cell and PEDOT:PSS anode (30 nm) for the back cell, which results in a

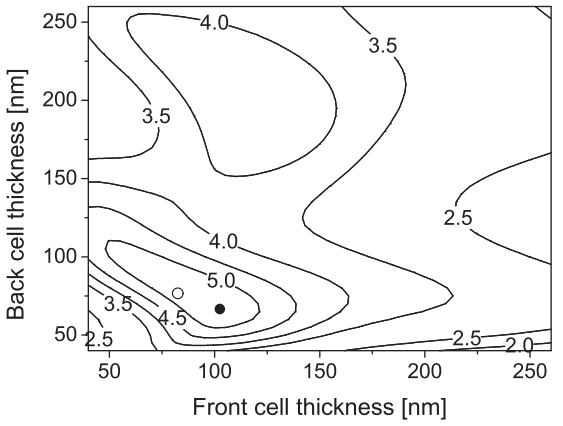

Fig. 5. Layer thickness dependence of the efficiency of a double junction device (labels) as predicted by combined optoelectronic simulations. For each combination of layer thicknesses, the exciton generation profiles inside the subcells were calculated and used as an input for our numerical device model. The J–V curves of tandem cells were constructed from the subcell characteristics [28]. The symbols indicate the optimal combination of subcell thicknesses (filled circle) and the case of two 80 nm thick subcells (open circle).

total device thickness of 210 nm. It can be seen that the shape of the generation profile in the back cell is similar to the one of the single thin layer because it is closest to the reflective cathode. As expected the magnitude of $G(x)$ in the back cell is lower than in the single layer thin cell due to optical interference effects and absorption in the front cell. However, *in total* the double junction absorbs more photons, in fact nearly as much (96%) as the 210 nm thick single layer device. In contrast, a single layer of 160 nm thickness absorbs only 81% of G_{tot}^{thick}. In other words, the double junction device absorbs more photons per nanometer of photoactive material than thick single layer cells due to the presence of the transparent middle electrode.

In order to predict the photovoltaic properties of the double junction device, we consider the general properties of a series-connected tandem cell. First, since each subcell is as thick as the thin single layer device and based on the same donor–acceptor system, it is reasoned that they will exhibit a similar IQE, FF and V_{oc}. Similarly, this also means that the FF of the double junction device will be the same as the FF of the subcells whereas its V_{oc} will be twice as large. Of the two subcells in the particular device considered in Fig. 4c, the front cell produces the least amount of excitons ($G_{tot}^{front} < G_{tot}^{back}$). As the IQE is invariant, this subcell will be current-limiting under short-circuit conditions and thus determine J_{sc} of the double junction device. Then, the ratio of the short-circuit current densities of the double junction cell and the thin, optimized single layer cell is close to $G_{tot}^{front}/G_{tot}^{thin} = 0.63$. It is thus predicted that a stack of two thin cells produces a J_{sc} that amounts to ca. 63% of the value for the single layer device. Combined with a doubled V_{oc} and an unchanged FF, an ideal double junction device is expected to have a 26% higher efficiency than the optimized single layer device.

The efficiency increase that is obtained with the use of a double junction structure can be enlarged slightly when the layer thicknesses of the subcells are chosen such that light absorption is more balanced. As indicated in Fig. 5, combined optoelectronic simulations of double junction devices predict that the highest performance would be expected for a device with a front cell thickness of 100 nm and a back cell thickness of 70 nm. However, since a more straightforward double junction device with two 80 nm thick subcells should perform much better than a single junction cell as well, we will employ this structure in the experimental section below.

3.2.2. Comparison with experiment

To determine the advantageous effect of a double junction structure on the performance of a real device, a slight modification to the anode of the back cell was necessary. The work function of pH-modified PEDOT:PSS is lower than that of unmodified PEDOT:PSS, which would result in a reduction of the open-circuit voltage of the back cell. To prevent this, an ultrathin layer of a perfluorinated ionomer was spin coated on the middle electrode [17]. Since the perfluorinated ionomer layer is presumably only a few monolayers thick, it is not expected to affect the optical properties of the layer stack. Fig. 6 shows the measured and simulated J–V curves of single and double junction cells with active layers of 80 nm thickness. At a light intensity of 0.9 sun, the experimental double junction device delivers a J_{sc} of 34.9 A/m^2 compared to 56.0 A/m^2 for the 80 nm thick single layer cell. The J_{sc} ratio thus amounts to 62%, which is in excellent agreement with the calculated value of 63%. At 1.92 V the V_{oc} of the double junction cell is very close to but slightly lower than the sum of the subcell voltages (1.94 V). Unfortunately, the fill factor shows a small drop as well, from 66% to 61%, which is most probably caused by an additional series resistance due to the thin insulating layer between the back photoactive layer and its anode. Nevertheless, the power conversion efficiency increases with 13% from 4.0% for the optimized single layer device to 4.5% for the double junction device. The decoupling of optical and electronic limitations thus clearly enables an enhancement of the photovoltaic performance. The working principle is therefore generic to all polymer:fullerene systems that show optimum performance at small layer thicknesses.

4. Conclusions

The photovoltaic properties of PF10TBT:PCBM solar cells are described with combined optoelectronic modeling to identify the processes that limit the power conversion

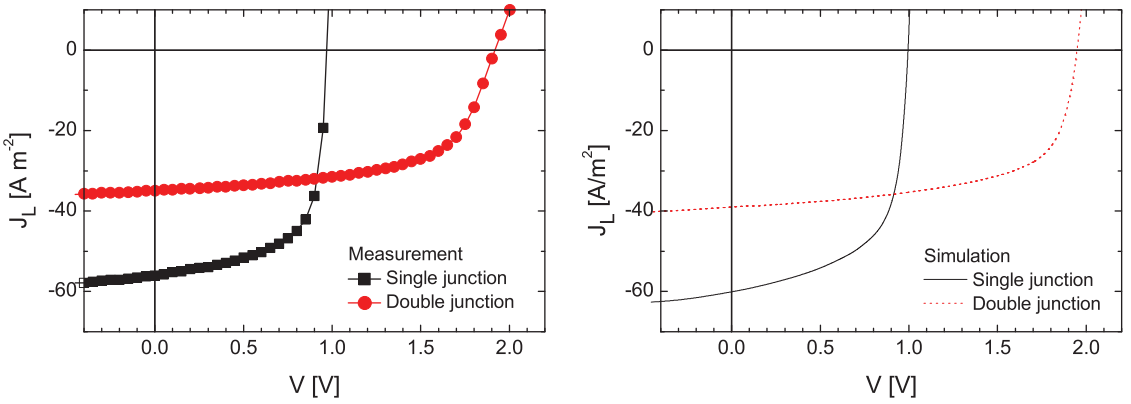

Fig. 6. Experimental (left) and calculated (right) current density versus voltage curves of a single and a double junction cell at a light intensity of 0.9 sun. The (sub)cells are all 80 nm thick.

efficiency. It is shown that 4%-efficient solar cells with an optimized layer thickness of 80 nm absorb only 48% of the photons that are available within the absorption bandwidth. Optical modeling reveals that this figure can be increased to 67% if the PF10TBT:PCBM layer is made 210 nm thick. However, a concurrent decrease in fill factor limits the efficiency of thick cells to 3.2%. It is shown that a double junction solar cell consisting of two optimized PF10TBT:PCBM layers absorbs photons more efficiently than thick single layer cells, as its structure disentangles the optical and electronic limitations. Simultaneously, the subcells have the high internal quantum efficiency and fill factor associated with thin cells. Overall, the power conversion efficiency is improved from 4.0% for an optimized single layer cell to 4.5% for the double junction device.

Acknowledgements

The authors thank J. Sweelssen and M.M. Koetse for the supply of PF10TBT and J. Harkema and F. van der Horst for technical assistance. This work was funded by Senter Novem via the EOS Long Term program ZOMER (EOS LT 03026) and partly supported by the Dutch Polymer Institute (DPI), Project DPI No. 660.

References

[1] G. Yu, J. Gao, J.C. Hummelen, F. Wudl, A.J. Heeger, Science 270 (1995) 1789.
[2] M. Lenes, L.J.A. Koster, V.D. Mihailetchi, P.W.M. Blom, Appl. Phys. Lett. 88 (2006) 243502.
[3] L.A.A. Pettersson, L.S. Roman, O. Inganäs, J. Appl. Phys. 86 (1999) 487.
[4] J.Y. Kim, S.H. Kim, H. Lee, K. Lee, W. Ma, X. Gong, A.J. Heeger, Adv. Mater. 18 (2006) 572.
[5] J. Gilot, I. Barbu, M.M. Wienk, R.A.J. Janssen, Appl. Phys. Lett. 91 (2007) 113520.
[6] B.V. Andersson, D.M. Huang, A.J. Moulé, O. Inganäs, Appl. Phys. Lett. 94 (2009) 043302.
[7] J. Peet, J.Y. Kim, N.E. Coates, W.L. Ma, D. Moses, A.J. Heeger, G.C. Bazan, Nat. Mater. 6 (2007) 497.
[8] M.M. Wienk, M. Turbiez, J. Gilot, R.A.J. Janssen, Adv. Mater. 20 (2008) 2556.
[9] R. Kroon, M. Lenes, J.C. Hummelen, P.W.M. Blom, B. de Boer, Polym. Rev. 48 (2008) 531.
[10] M.M. Wienk, J.M. Kroon, W.J.H. Verhees, J. Knol, J.C. Hummelen, P.A. van Hal, R.A.J. Janssen, Angew. Chem. Int. Ed. 42 (2003) 3371.
[11] A. Hadipour, B. de Boer, P.W.M. Blom, Adv. Funct. Mater. 18 (2008) 169.
[12] J. Gilot, M.M. Wienk, R.A.J. Janssen, Adv. Mater. 22 (2010) E67.
[13] J.Y. Kim, K. Lee, N.E. Coates, D. Moses, T. Nguyen, M. Dante, A.J. Heeger, Science 317 (2007) 222.
[14] C. Pacholski, A. Kornowski, H. Weller, Angew. Chem. Int. Ed. 41 (2002) 1188.
[15] W.J.E. Beek, M.M. Wienk, M. Kemerink, X. Yang, R.A.J. Janssen, J. Phys. Chem. B 109 (2005) 9505.
[16] J. Gilot, M.M. Wienk, R.A.J. Janssen, Appl. Phys. Lett. 90 (2007) 143512.
[17] D.J.D. Moet, P. de Bruyn, P.W.M. Blom, Appl. Phys. Lett. 96 (2010) 153504.
[18] J.M. Kroon, M.M. Wienk, W.J.H. Verhees, J.C. Hummelen, Thin Solid Films 403–404 (2002) 223.
[19] D.J.D. Moet, M. Lenes, J.D. Kotlarski, S.C. Veenstra, J. Sweelssen, M.M. Koetse, B. de Boer, P.W.M. Blom, Org. Electron. 10 (2009) 1275.
[20] J.D. Kotlarski, P.W.M. Blom, L.J.A. Koster, M. Lenes, L.H. Slooff, J. Appl. Phys. 103 (2008) 084502.
[21] K.M. Coakley, M.D. McGehee, Chem. Mater. 16 (2004) 4533.
[22] L.H. Slooff, S.C. Veenstra, J.M. Kroon, D.J.D. Moet, J. Sweelssen, M.M. Koetse, Appl. Phys. Lett. 90 (2007) 143506.
[23] L.J.A. Koster, E.C.P. Smits, V.D. Mihailetchi, P.W.M. Blom, Phys. Rev. B 72 (2005) 085205.
[24] C.L. Braun, J. Chem. Phys. 80 (1984) 4157.
[25] V.D. Mihailetchi, L.J.A. Koster, J.C. Hummelen, P.W.M. Blom, Phys. Rev. Lett. 93 (2004) 216601.
[26] L.J.A. Koster, V.D. Mihailetchi, P.W.M. Blom, Appl. Phys. Lett. 88 (2006) 052104.
[27] A. Hadipour, B. de Boer, P.W.M. Blom, J. Appl. Phys. 102 (2007) 074506.
[28] A. Hadipour, B. de Boer, P.W.M. Blom, Org. Electron. 9 (2008) 617.

Organic Electronics 11 (2010) 1828–1834

Contents lists available at ScienceDirect

Organic Electronics

journal homepage: www.elsevier.com/locate/orgel

Sol–gel processed CuO_x thin film as an anode interlayer for inverted polymer solar cells

Ming-Yi Lin [a], Chun-Yu Lee [a], Shu-Chia Shiu [a], Ing-Jye Wang [a], Jen-Yu Sun [a], Wen-Hau Wu [a], Yu-Hong Lin [a], Jing-Shun Huang [a], Ching-Fuh Lin [a,b,*]

[a] Graduate Institute of Photonics and Optoelectronics, National Taiwan University, No. 1, Sec. 4, Roosevelt Road, Taipei 10617, Taiwan, ROC
[b] Graduate Institute of Electronics and Engineering, National Taiwan University, No. 1, Sec. 4, Roosevelt Road, Taipei 10617, Taiwan, ROC

ARTICLE INFO

Article history:
Received 26 January 2010
Received in revised form 7 August 2010
Accepted 11 August 2010
Available online 24 August 2010

Keywords:
Polymer solar cells
CuO_x
Cu_2O
Sol–gel

ABSTRACT

We have used sol–gel derived copper oxide (CuO_x) thin film as an interlayer at the organic/metal interface to improve the performance of the inverted P3HT:$PC_{61}BM$ solar cells. The resulting interlayer can form an ohmic contact between the P3HT:$PC_{61}BM$ and electrode. Due to the formation of the ohmic contact, the series resistance of device has been decreased from 2.77 to 1.29 (Ω/cm^2). Simultaneously, the CuO_x interlayer can redistribute the light intensity to enhance light absorption and thereby increases the current density form 11.0 to 11.9 (mA/cm^2). Thus, the power conversion efficiency (PCE) is improved from 3.11% to 4.02%.

© 2010 Elsevier B.V. All rights reserved.

1. Introduction

Polymer solar cells (PSCs) have great potential for renewable energy due to their low cost, mass production and low temperature fabrication. Recently, the conventional bulk-heterojunction solar cells, which consist of donor and acceptor blend inserted between a high work function transparent semiconducting oxide anode and a low-work-function metal cathode with PCE of 7.73%, have been reported [1]. However, the conventional structures of PSCs have the drawback of fast degradation partly due to the poly(3,4-ethylenedioxythiophene):poly(styrenesulfonate) (PEDOT:PSS) and the low-work-function metal cathode. The PEDOT:PSS layer will etch the ITO and cause interface instability due to its acidic nature. The low-work-function metals are easily oxidized, increasing the series resistance (R_s) at the metal/organic layer interface. Hence, the inverted structures are used to overcome the above deficiencies. They reverse the nature of charge collection and replace both the PEDOT:PSS and the electrode. This significantly improves the life time of the solar cells [2,3].

Generally, the metal electrodes used in most studies are Ag or Au for effective hole collection [4,5]. However, the work function of Au will decrease in the air due to the contamination by carbon and oxide [6]. This will lead to the degradation in the device's performance. Nevertheless, in the case of the Ag electrode, the oxidization of Ag will increase its work function from 4.3 to 5.0 eV [2,7], which will benefit the hole transportation from P3HT to Ag and improve the device's performance. Thus, in this study, we choose Ag metal as the anode electrode.

In order to further increase the efficiency of the inverted structure device, the oxide interlayer, such as P–NiO [8], V_2O_5 [9], WO_3 [10], Cs_2CO_3 [11], ZnO [12], and MoO_3 [13] have been applied to the organic solar cell as a blocking layer. They are mostly deposited by using vacuum evaporation. Nevertheless, the process of vacuum evaporation is expensive. Consequently, low-cost solution process becomes the strategic principle for the preparation of metal oxide interlayer on polymer solar cell.

* Corresponding author at: Graduate Institute of Photonics and Optoelectronics, National Taiwan University, No. 1, Sec. 4, Roosevelt Road, Taipei 10617, Taiwan, ROC. Tel.: +886 2 33663540; fax: +886 2 23642603.
E-mail address: cflin@cc.ee.ntu.edu.tw (C.-F. Lin).

1566-1199/$ - see front matter © 2010 Elsevier B.V. All rights reserved.
doi:10.1016/j.orgel.2010.08.009

Using solution-processed metal oxide as an anode interlayer is challenging because of the hydrophobicity of the polymer active layer [2]. Therefore, the selection of solvent for sol–gel is an important issue. 2-methoxyethanol (2MOE) is usually used as the solvent in sol–gel methods [14]. However, to be compatible with the polymer active layer, we use isopropanol (IPA) instead of 2MOE as the solvent. In addition to the solvent selection, the metal selection is also critical. We found that the copper oxide is a good choice for the metal oxide layer. The highest occupied molecular orbital (HOMO) energy of P3HT is located at 5.2 eV [15]. The work function of copper oxide is about 5.3 eV [16,17] which is close to HOMO of P3HT. This leads to the better hole transportation at the organic/inorganic interface. Therefore, copper oxide complexes have great potential to function as hole transportation layer. Here, we have fabricated CuO_x interlayer on P3HT:$PC_{61}BM$ blend by using low-cost sol–gel process in inverted structure device.

The CuO_x film which mainly consists of Cu_2O can form an ohmic contact between P3HT:$PC_{61}BM$ blend and metal because the Cu_2O can modulate the barrier height of schottky contact and form an ohmic contact at P3HT:$PC_{61}BM$ blend/metal interface. With the CuO_x interlayer, the device increases the shunt resistance (R_{sh}) from 412.42 to 1030.71 (Ω/cm^2) and decreases the R_s from 2.77 to 1.29 (Ω/cm^2). In addition, the photocurrent density (J_{sc}) also enhances from 11.0 to 11.9 (mA/cm^2). Thus, the FF (fill factor) of our device is dramatically improved from 53.4% to 63.7% while the efficiency of device increases from 3.11% to 4.02%.

2. Experimental details

The inset of Fig. 1 is the structure of the inverted polymer solar cell with CuO_x. The devices were fabricated on cleaned ITO-coated glass substrates (~7 Ω/sq.). The ZnO seed layer (50 nm) was spin-coated from a 0.5-mol solution of zinc acetate in 2MOE. Then, a blend of P3HT:$PC_{61}BM$ (1:1 by weight) was prepared on the ZnO seed layer by spin-coating a 1.5-wt.% dichlorobenzene solution. After spinning the active layer, the CuO_x layer was spin-coated from a 0.25-mol solution of copper (II) acetate monohydrate in IPA mixed with monoethanolamine and deionized water. For comparison, another sample without the CuO_x layer was also prepared. Finally, silver film (~250 nm) was deposited on top of the blend under high vacuum ($\sim 3 \times 10^{-6}$ torr). The electrical measurements were carried out with the devices under air atmosphere at room temperature. Fig. 1 is the current density–voltage (J–V) curve of the devices illuminated at 100 mW/cm^2 from a 150 W Oriel solar simulator using an air mass 1.5 global (AM 1.5G) filter. The R_s and R_{sh} of the devices are obtained from the J–V curve. The R_s and the R_{sh} are calculated by the $(slope)^{-1}$ of curve at $V = 1$ and $V = 0$, respectively. The reflectance spectrum of the devices with the CuO_x layer was obtained by using a Perkin–Elmer Lambda 35 UV–vis spectrophotometer with an integrating sphere. To investigate the sol–gel derived thin film, the scanning electron microscopy (SEM) and Fourier Transform Infrared Spectroscopy (FTIR) were used for identifying the thickness and structure.

3. Results and discussion

To characterize the contact behavior between the CuO_x and electrode, we measure the surface J–V characteristic of metal/P3HT:$PC_{61}M$ [18], as shown in Fig. 2(a). The inset of Fig. 2(a) shows the device structure for surface J–V curve measurement. It can be seen that the schottky barrier formed between P3HT:$PC_{61}BM$ and aluminum (black line). The schottky contact may lead to the decrease in V_{oc} (open-circuit voltage) of the device [19]. However, the sample with CuO_x shows good ohmic contact at the interface (red line). The CuO_x can be applied to modulate schottky barrier as the oxide of Cu_2O in CuO_x is very easily reduced and a copper rich phase will form near the Cu_2O/metal interface [20]. These decrease barrier height and result in an ohmic contact between P3HT:$PC_{61}BM$ and aluminum.

On the other hand, ohmic contact has also established at the interface between the P3HT:$PC_{61}BM$ and silver

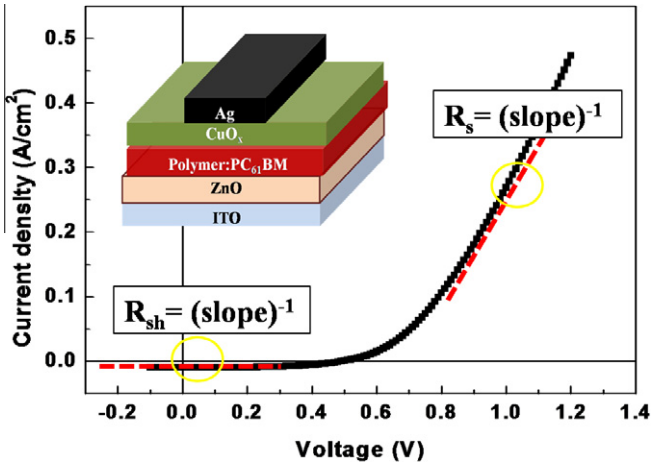

Fig. 1. Device structure and the J–V curve of the device illuminated at 100 mW/cm^2 from a 150 W Oriel solar simulator using an air mass 1.5 global (AM 1.5G) filter.

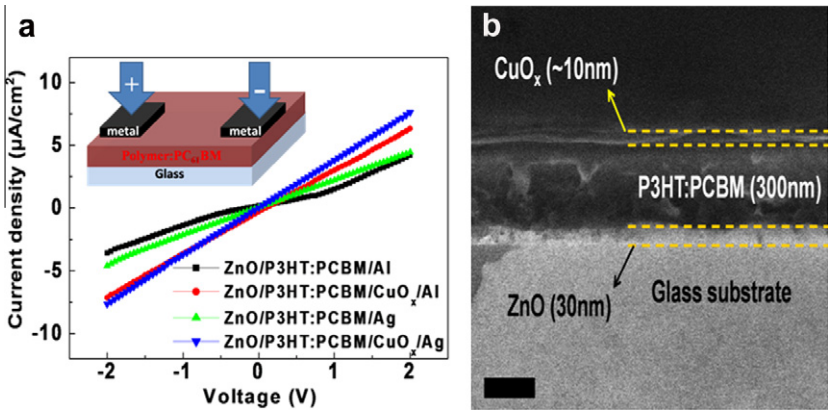

Fig. 2. (a) The structure diagram for surface *J–V* measurement and the surface *J–V* curve of the contact between P3HT:$PC_{61}BM$ and electrode with and without the CuO_x interlayer. (b) SEM cross-sectional image of Si/ZnO/P3HT:$PC_{61}BM$/ CuO_x, scale bar: 200 nm.

electrode (green line). In this case, the slope for CuO_x/Ag contact at the interface is 77% higher than that on P3HT:$PC_{61}BM$ /Ag contact (blue line). It reveals that the devices with CuO_x interlayer have low-resistance ohmic contact to the Ag electrode, which makes the R_s decrease.

The R_s in the solar cell is attributed to the conductivity of each layer and the contact resistance between them. The materials with high charge carrier mobility and ohmic contact at the interfaces are required to obtain high J_{sc} values [19]. Although the ohmic contact has formed at active layer/Ag interface, by introducing the CuO_x interlayer, the R_s and R_{sh} can still be dramatically improved due to the low-resistance ohmic contact. This will lead to the increase in the J_{sc} and the FF. However, since the ohmic contact has formed, there will be no V_{bi} at the interface. As a result, the contributions to the performance of devices by the CuO_x are mainly on FF, J_{sc} and efficiency [21]. In addition, by introducing the CuO_x, the Fermi levels of electrodes are close to the HOMO of donor and LUMO of acceptor due to the energy level alignment between CuO_x interlayer and the Ag anode, which can slightly increase the V_{oc}.

Fig. 2(b) shows the SEM cross-sectional image of the Si/ZnO/P3HT:$PC_{61}BM$/CuO_x. The thicknesses of ZnO film and active layer are about 30–50 and 300 nm, respectively. The sol–gel derived CuO_x thin film (10 nm) can cover the active layer well, preventing the organic layer from oxygen and moisture which can lead to the degradation of active layer.

To further clarify whether the CuO_x protect the polymer blend underneath against moisture and oxygen, we investigate the FTIR spectrum of the polymer thin films with and without CuO_x prepared and placed in the air for 9 days as shown in Fig. 3(a) and (b). In the Fig. 3(a), it is observed that the C=O peak at 1740 cm^{-1} [22,23] of the sample with oxide layer appears clearly after 3 days and then becomes stable, revealing that the CuO_x can prevent the polymer

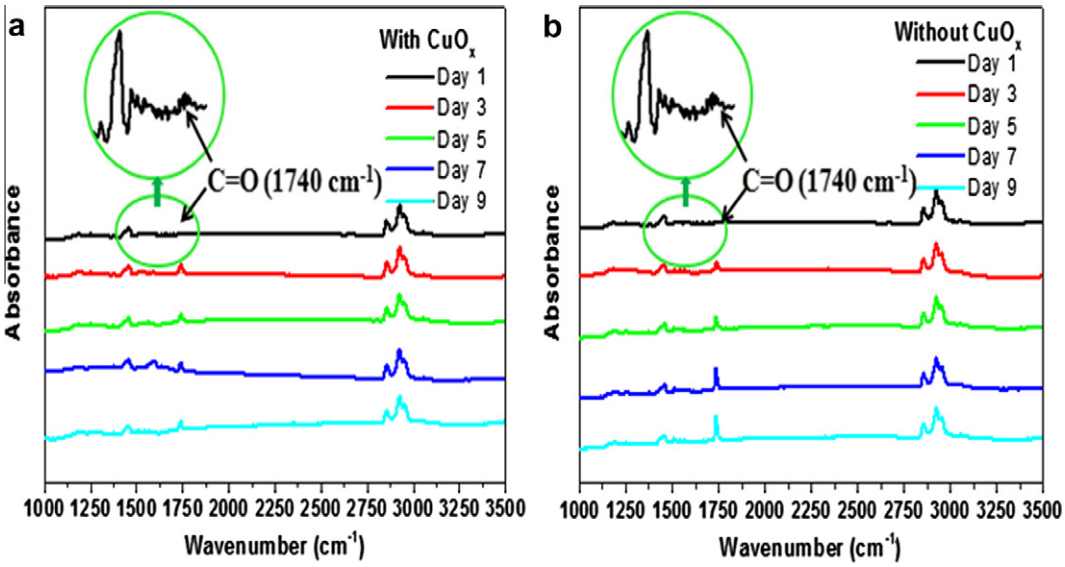

Fig. 3. (a) The FTIR spectrum of the polymer thin film with CuO_x in the air for 9 days. (b) The FTIR spectrum of the polymer thin film without CuO_x in the air for 9 days.

layer from oxygen. In the Fig. 3(b), the peak at 1740 cm^{-1} of the sample without oxide layer gradually enhances as the time increases, revealing that the thin film is continually oxidized. It implies that the CuO_x can prevent the photoactive from oxygen.

Irradiation of inverted polymer solar cells at ambient air leads to the formation of oxidation products attributed to P3HT and to $PC_{61}BM$. The variation of the peak at 1740 cm^{-1} can be observed in the FTIR spectrum. As a result, we need to further identify the peak derived from P3HT or $PC_{61}BM$. The C=O peak observed at 1740 cm^{-1} in IR spectrum can be assigned to be carbonyl part of $PC_{61}BM$ [23]. The carbonyl group of $PC_{61}BM$ has been found to be sensitive to local environments [23]. Therefore, it implies that oxidation products in this study may be attributed to $PC_{61}BM$.

In order to observe the variation of $PC_{61}BM$ in ambient environment, we performed atomic force microscopy (AFM) examinations of the surface morphology of the $PC_{61}BM$ thin film which was only spin-coated from a 20 mg mL^{-1} solution of $PC_{61}BM$ in dichlorobenzene. Moreover, we measured the FTIR spectra to identify whether or not $PC_{61}BM$ is oxidized in the air. The course of photo- and thermo-oxidation was followed by FTIR spectra monitoring the increase of carbonyl absorption at 1740 cm^{-1}, caused by oxidation products [24]. Fig. 4 is the AFM and FTIR spectra of the $PC_{61}BM$ thin film observed with aging. The AFM images show root-mean-square (rms) roughness values of 1.05 nm at day 1, 2.35 nm at day 3, 3.51 nm at day 5, 6.89 nm at day 7 and 7.32 nm at day 9. The surface roughness of $PC_{61}BM$ thin film increases from day 1 to day 9, revealing $PC_{61}BM$ may be deteriorated with aging. Furthermore, the peak at 1740 cm^{-1} also becomes stronger from day 1 to day 9, representing that oxidation products in devices should be attributed to $PC_{61}BM$.

Fig. 5 is the device performance of unencapsulated inverted PSCs with and without the CuO_x interlayer over 1000 h in air. The device without CuO_x reaches a maximum PCE of ~3.1% and then reduces to ~1.5% after 1000 h, a ~51% degradation. In contrast, the PCE of the device with the CuO_x interlayer reaches a maximum of ~4.0% and then declines to ~3.5% after 1000 h, only 13% degradation. The improved stability is mainly attributed to the CuO_x

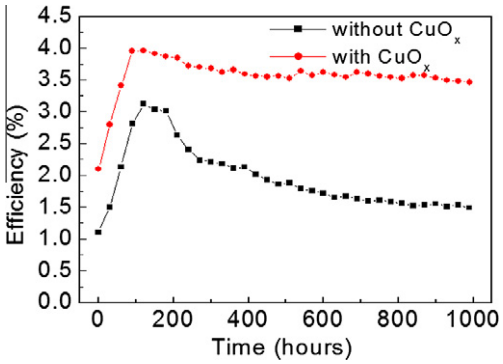

Fig. 5. The device performance of unencapsulated inverted polymer solar cells with and without the CuO_x interlayer over 1000 h in air.

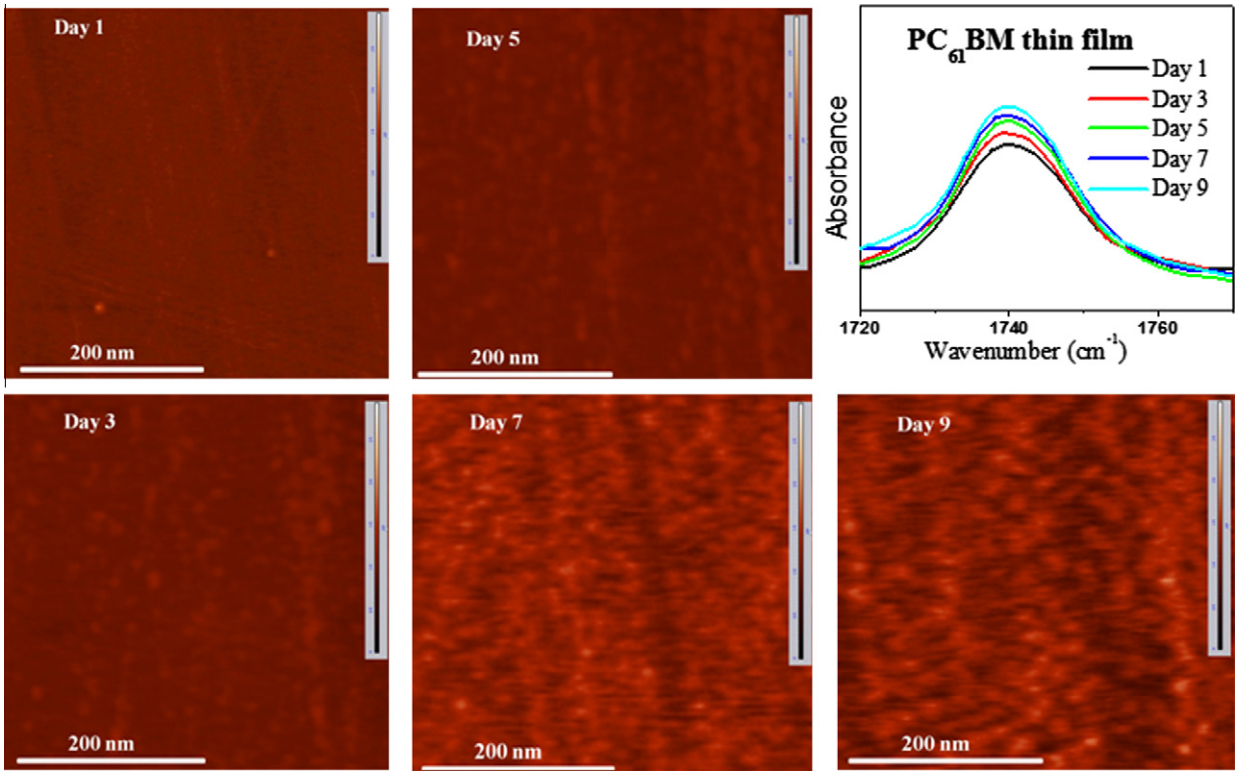

Fig. 4. The AFM and FTIR spectra of the $PC_{61}BM$ thin film observed with aging.

interlayer. Furthermore, in both devices, the maximum performance is only obtained by 100 h of storage in air after device preparation. This phenomenon has also been observed in previous report [25]. In this study, it is found that the oxidization of the photoactive layer may result in the variation in morphology of photoactive layer with aging, which may lead to the improvement in efficiency.

In order to identify the thin film composition, we further compare the FTIR spectrum with and without CuO_x, as shown in Fig. 6(a). The CuO_x film consists of Cu_2O (630, 606 and 588 cm^{-1}) [26,27], Cu_2S (617 cm^{-1}) [28] and CuO_2 (646 cm^{-1}) [29]. The CuO_x may react with S atom of the P3HT at the interface, resulting in the peak at 617 cm^{-1} [28]. The weak signal at 646 and 617 cm^{-1} indicate that the CuO_2 and Cu_2S contained in the CuO_x thin film are both rare.

To further clarify the containment of CuO_2 and Cu_2O in the CuO_x thin film, we simulated the spectra by the Gauss function with 588, 630 and 646 cm^{-1} peak, as shown in Fig. 6(b). By calculating the area under the individual peak, we can roughly estimate the containment of variety structures [30]. Here, the containment of CuO_2 in CuO_x is about 1%, which is much smaller than the Cu_2O.

To realize the role of the CuO_x interlayer, we measured the reflectance spectrum of the devices with and without the CuO_x interlayer. Perkin–Elmer Lambda 35 with an integrating sphere was used to measure the reflectance of devices. Since the two devices are identical except the addition of the interlayer, we can compare the reflectance yield information on the additional absorption. Fig. 7(a) is the absorption spectra through the equation: $A = 1 - R - T$. The CuO_x interlayer enhances the absorption of the devices at 400–600 nm and only slightly increases the absorption above 600 nm. The increased photogeneration of charge carriers are resulted from the spatial redistribution of the light intensity. To further identify the function of CuO_x, the additional absorption, $\Delta\alpha(\lambda)$, as a result of spatial redistribution of light intensity by the CuO_x interlayer is estimated by [9,15].

$$\Delta\alpha(\lambda) \cong (-1/2d)\ln(I'_{out}(\lambda)/I_{out}(\lambda)) \quad (1)$$

where $I'_{out}(\lambda)$ is the reflection from a device with the CuO_x interlayer, $I_{out}(\lambda)$ is the reflection from a device without the CuO_x interlayer, and d is the thickness of the photoactive layer (d is ~300 nm in both). Fig. 7(b) is the change in the absorption spectrum $\Delta\alpha(\lambda)$ resulting from the Eq. (1). The result shows a clear increase in absorption over the spectral region. Furthermore, this spectrum reveals four peaks at 450, 512, 556, and 602 nm, respectively. It implies that the contribution of the CuO_x interlayer in photocurrent is

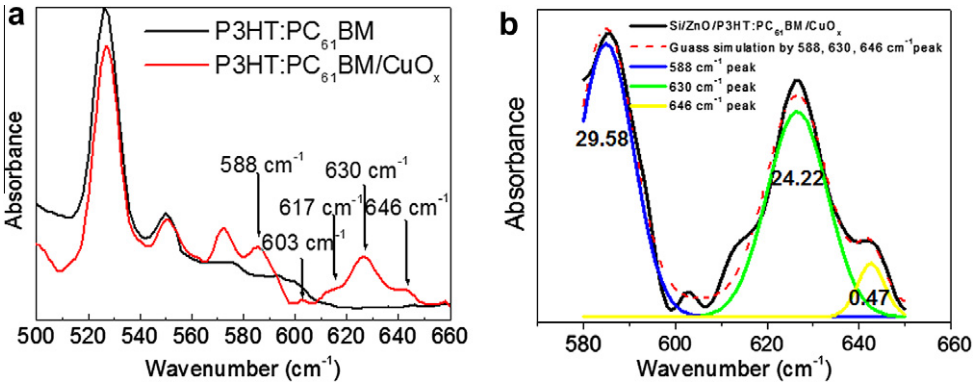

Fig. 6. (a) The FTIR spectrum of the polymer thin film with and without CuO_x. (b) The FTIR spectra of the CuO_x thin film and the spectra simulated by variety peaks.

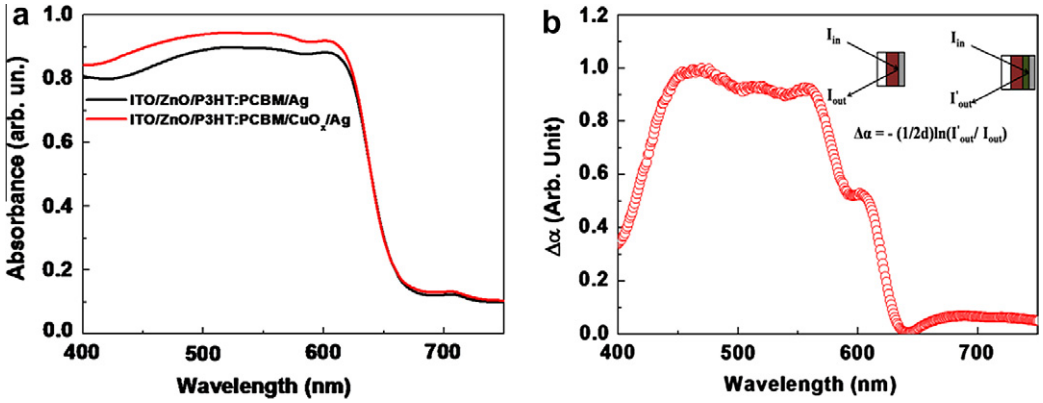

Fig. 7. (a) The absorbance spectrum of active layer with and without CuO_x thin film. (b) The change in the absorption spectrum $\Delta\alpha(\lambda)$ resulting from the Eq. (1).

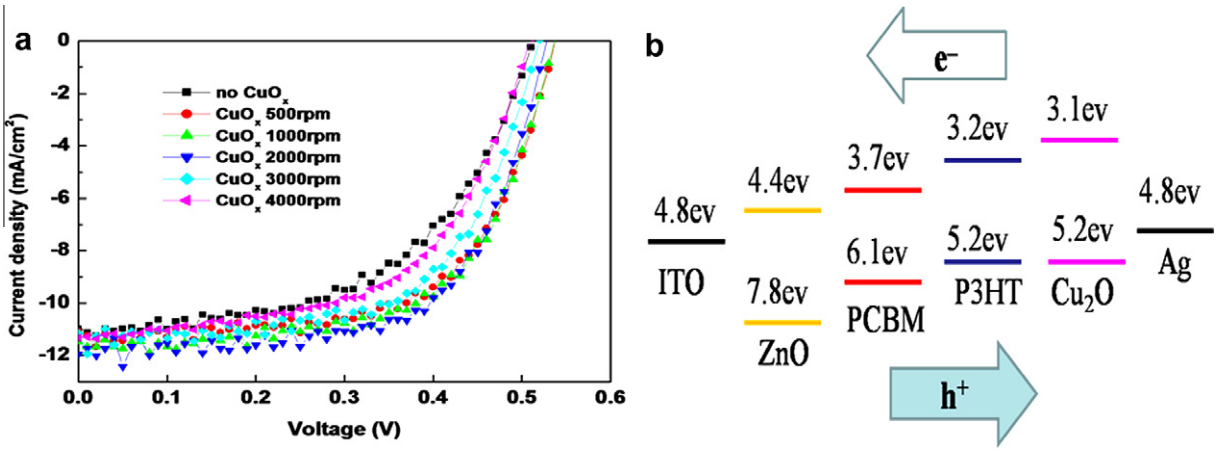

Fig. 8. (a) The *J–V* curve of the photovoltaic devices with different spin rates of the oxide layer under 100 mW/cm^2 AM 1.5G irradiation. (b) Energy band diagram for the photovoltaic cells in this study. The HOMO and LUMO energies of used materials are referred to the Ref. [15].

Table 1
The device performance of inverted P3HT:$PC_{61}BM$ bulk-heterojunction solar cells.

Device	V_{oc} (V)	J_{sc} (mA/cm^2)	FF (%)	PCE (%)	R_s (Ω/cm^2)	R_{sh} (Ω/cm^2)
No CuO_x	0.53	11.0	53.4	3.11	2.77	412.42
CuO_x 500 rpm	0.54	11.1	63.5	3.81	1.88	446.42
CuO_x 1000 rpm	0.53	11.6	64.2	3.93	1.73	473.91
CuO_x 2000 rpm	0.53	11.9	63.7	4.02	1.29	1030.71
CuO_x 3000 rpm	0.53	11.5	59.5	3.63	1.46	431.32
CuO_x 4000 rpm	0.53	11.3	54.3	3.25	2.12	382.48

mainly at these peaks which are vibronic features from the P3HT molecules [31,32].

Fig. 8(b) shows energy band diagram for the photovoltaic cells in this study. The conduction band and the valence band of Cu_2O are located at near 3.1 and 5.2 eV, respectively [33,34]. The HOMO of P3HT is 5.2 eV [35], which is similar to the valence band energy of Cu_2O. Thus, the interface between the P3HT:$PC_{61}BM$ blend and CuO_x can easily form an ohmic contact. To optimize the device efficiency, we controlled the thickness of the oxide by varying spin rate from 500 to 4000 rpm. The oxide film with lower spin rate has the higher thickness. Fig. 8(a) is the *J–V* curve of the photovoltaic devices with different spin rates of the oxide layer under 100 mW/cm^2 AM 1.5G irradiation. The higher thickness of CuO_x does not only contribute to the R_s of the device but lead to a lower photocurrent. In contrast, the thinner CuO_x film has higher photocurrent and lower R_s. These results are similar to the previous reports [13,36].

Table 1 illustrates the efficiency of unencapsulated inverted P3HT:$PC_{61}BM$ bulk-heterojunction solar cells using CuO_x film as an interlayer with different spin rates. The efficiency initially increases as the spin rate increases from 500 to 2000 rpm. Nevertheless, the efficiency starts to decline at 3000 rpm. When the spin rate of the CuO_x film is 2000 rpm, the devices exhibit a PCE of 4.02% with J_{sc} of 11.90 mA/cm^2 and V_{oc} of 0.53 V. The R_s and the R_{sh} are also improved. As the spin rate reaches over 2000 rpm, the high spin rate could result in the broken CuO_x film that leads to a lower PCE.

Furthermore, the devices with CuO_x all have higher FF value than the device without CuO_x. Except for the better ohmic contact formation at the interface, the other reason for these is because the states of Cu_2O at the top of valence band are derived from fully occupied Cu 3d states and are more mobile when converted into holes [35], which makes it a great hole transportation layer.

4. Conclusions

In conclusion, we have fabricated the CuO_x film well on P3HT:PC61BM blend of inverted structure by all solution process. The CuO_x has similar valence band energy with the HOMO of P3HT and serves as an interlayer which modulates the ohmic contact at the organic/metal interface. This leads to the better transportation that causes the improvement in FF, R_{sh} and R_s of the device. Hence, the PCE is improved from 3.11% to 4.02%. Moreover, the CuO_x layer can redistribute the light intensity to enhance the light absorption and increase current density. Furthermore, the CuO_x interlayer can prevent the organic layer from oxygen and moisture, which can cause the degradation of active layer.

Acknowledgement

This project was supported by the National Science Council, Taiwan, Republic of China. The NSC numbers are: NSC96-2221-E-002-277-MY3, NSC98-2218-E-002-002, NSC97-2221-E-002-039-MY3, and NSC98-3114-E-002-001.

References

[1] H.Y. Chen, J. Hou, S. Zhang, Y. Liang, G. Yang, Y. Yang, L. Yu, Y. Wu, G. Li, Polymer solar cells with enhanced open-circuit voltage and efficiency, Nat. Photonics 3 (2009) 649.

[2] L.M. Chen, Z. Hong, G. Li, Y. Yang, Recent progress in polymer solar cells: manipulation of polymer:fullerene morphology and the formation of efficient inverted polymer solar cells, Adv. Mater. 21 (2009) 1434.

[3] C.Y. Chou, J.S. Huang, C.H. Wu, C.Y. Lee, C.F. Lin, Lengthening the polymer solidification time to improve the performance of polymer/ZnO nanorod hybrid solar cells, Sol. Energy Mater. Sol. Cells 93 (2009) 1608.

[4] C. Waldauf, M. Morana, P. Denk, P. Schilinsky, K. Coakley, S.A. Choulis, C.J. Brabec, Highly efficient inverted organic photovoltaics using solution based titanium oxide as electron selective contact, Appl. Phys. Lett. 89 (2006) 233517.

[5] C. Tao, S. Ruan, G. Xie, X. Kong, L. Shen, F. Meng, C. Liu, X. Zhang, W. Dong, W. Chen, Role of tungsten oxide in inverted polymer solar cells Role of tungsten oxide in inverted polymer solar cells, Appl. Phys. Lett. 94 (2009) 043311.

[6] A. Wan, J. Hwang, F. Amy, A. Kahn, Impact of electrode contamination on the a-NPD/Au hole injection barrier, Org. Electron. 6 (2005) 47.

[7] M.S. White, D.C. Olson, S.E. Shaheen, N. Kopidakis, D.S. Ginley, Inverted bulk-heterojunction organic photovoltaic device using a solution-derived ZnO underlayer, Appl. Phys. Lett. 89 (2006) 143517.

[8] M.D. Irwin, D.B. Buchholz, A.W. Hains, R.P.H. Chang, T.J. Marks, P-type semiconducting nickel oxide as an efficiency-enhancing anode interfacial layer in polymer bulk-heterojunction solar cells, Proc. Natl Acad. Sci. USA 105 (2008) 2783.

[9] J.S. Huang, C.Y. Chou, M.Y. Liu, K.H. Tsai, W.H. Lin, C.F. Lin, Solution-processed vanadium oxide as an anode interlayer for inverted polymer solar cells hybridized with ZnO nanorods, Org. Electron. 10 (2009) 1060.

[10] S. Han, W.S. Shin, M. Seo, D. Gupta, S.J. Moon, S. Yoo, Improving performance of organic solar cells using amorphous tungsten oxides as an interfacial buffer layer on transparent anodes, Org. Electron. 10 (2009) 791.

[11] H.H. Liao, L.M. Chen, Z. Xu, G. Li, Y. Yang, Highly efficient inverted polymer solar cell by low temperature annealing of Cs_2CO_3 interlayer, Appl. Phys. Lett. 92 (2008) 173303.

[12] N. Sekine, C.H. Chou, W.L. Kwan, Y. Yang, ZnO nano-ridge structure and its application in inverted polymer solar cell, Org. Electron. 10 (2009) 1473.

[13] A.K.K. Kyaw, X.W. Sun, C.Y. Jiang, G.Q. Lo, D.W. Zhao, D.L. Kwong, An inverted organic solar cell employing a sol–gel derived ZnO electron selective layer and thermal evaporated MoO_3 hole selective layer, Appl. Phys. Lett. 93 (2008) 221107.

[14] M. Kakihana, Invited. Review, Invited review "sol–gel" preparation of high temperature superconducting oxides, J. Sol–Gel Sci. Technol. 6 (1996) 7.

[15] J.Y. Kim, S.H. Kim, H.H. Lee, K. Lee, W. Ma, X. Gong, A.J. Heeger, New architecture for high-efficiency polymer photovoltaic cells using solution-based titanium oxide as an optical spacer, Adv. Mater. 18 (2006) 572.

[16] H.H. Lin, C.Y. Wang, H.C. Shih, J.M. Chen, C.T. Hsieh, Characterizing well-ordered CuO nanofibrils synthesized through gas–solid reactions, J. Appl. Phys. 95 (2004) 5889.

[17] Y. Liu, L. Liao, J. Li, C. Pan, From copper nanocrystalline to CuO nanoneedle array: synthesis, growth mechanism, and properties, J. Phys. Chem. C 111 (2007) 5050.

[18] C.Y. Lee, J.Y. Wang, Y. Chou, M.Y. Liu, W.F. Su, Y.F. Chen, C.F. Lin, Enhanced ultraviolet electroluminescence from ZnO nanowires in TiO_2/ZnO coaxial nanowires/pol (3,4-ethylenedioxythiophene)-poly(styrenesulfonate) heterojunction, J. Appl. Phys. 107 (2010) 034310.

[19] H.L. Yip, S.K. Hau, N.S. Baek, H. Ma, A.K.Y. Jen, Polymer solar cells that use self-assembled-monolayer-modified ZnO/metals as cathodes, Adv. Mater. 20 (2008) 2376.

[20] P.E. de Jongh, D. Vanmaekelbergh, J.J. Kelly, Photoelectrochemistry of electrodeposited Cu_2O, J. Electrochem. Soc. 147 (2000) 486.

[21] V.D. Mihailetchi, P.W.M. Blom, J.C. Hummelen, M.T. Rispens, Cathode dependence of the open-circuit voltage of polymer:fullerene bulk heterojunction solar cell, J. Appl. Phys. 94 (2003) 6849.

[22] A.M. Shanmugharaj, S. Sabharwal, A.B. Majali, V.K. Tikku, A.K. Bhowmick, Surface characterization of electron beam modified dual phase filler by ESCA, FT-IR and surface energy, J. Mater. Sci. 37 (2002) 2781.

[23] L.W. Barbour, M. Hegadorn, J.B. Asbury, Watching electrons move in real time: ultrafast infrared spectroscopy of a polymer blend photovoltaic material, J. Am. Chem. Soc. 129 (2007) 15884.

[24] B. Pawelke, Cs. KoÂsa, S.Ï. Chmela, W.D. Habicher, New stabilisers for polymers on the basis of isophorone diisocyanate, Polym. Degrad. Stab. 68 (2000) 127.

[25] K.H. Tsai, J.S. Huang, M.Y. Liu, C.H. Chao, C.Y. Lee, S.C. Hung, C.F. Lin, High efficiency flexible polymer solar cells based on PET substrates with a nonannealing active layer, J. Electrochem. Soc. 156 (2009) B1188.

[26] A. Jagminas, J. Kuzmarskyte, G. Niaura, Electrochemical formation and characterization of copper oxygenous compounds in alumina template from ethanolamine solutions, Appl. Surf. Sci. 201 (2002) 129.

[27] Y.C. Zhang, J.Y. Tang, G.L. Wang, M. Zhang, X.Y. Hu, Facile synthesis of submicron Cu_2O and CuO crystallites from a solid metallorganic molecular precursor, J. Cryst. Growth 294 (2006) 278.

[28] A. Lachkar, A. Selmani, E. Sacher, M. Leclerc, R. Mokhliss, Metallization of polythiophenes I. Interaction of vapor-deposited Cu, Ag and Au with poly (3-hexylthiophene) (P3HT), Synth. Met. 66 (1994) 209.

[29] C.A. Melendres, G.A. Bowmaker, J.M. Leger, B. Beden, In-situ synchrotron far infrared spectroscopy of surface films on a copper electrode in aqueous solutions, J. Electroanal. Chem. 449 (1998) 215.

[30] C.J. Burke, G. Sanyal, M.W. Bruner, J.A. Ryan, R.L. LaFemina, H.L. Robbins, A.S. Zeft, C.R. Middaugh, M.G. Cordingley, Structural implications of spectroscopic characterization of a putative zinc finger peptide from HIV-1 integrase, J. Biol. Chem. 267 (1992) 9639.

[31] R. Radbeh, E. Parbaile, J. Boucle, C.D. Bin, A. Moliton, V. Coudert, F. Rossignol, B. Ratier, Nanoscale control of the network morphology of high efficiency polymer fullerene solar cells by the use of high material concentration in the liquid phase, Nanotechnology 21 (2010) 035201.

[32] A. Zen, M. Saphiannikova, D. Neher, J. Grenzer, S. Grigorian, U. Pietsch, U. Asawapirom, S. Janietz, U. Scherf, I. Lieberwirth, G. Wegner, Effect of molecular weight on the structure and crystallinity of poly(3-hexylthiophene), Macromolecules 39 (2006) 2162.

[33] L.H. Tjeng, M.B.J. Meinders, J. van Elp, J. Ghijsen, G.A. Sawatzky, Electronic structure of Ag_2O, Phys. Rev. B: Condens. Matter Mater. Phys. 41 (1990) 3190.

[34] S.S. Jeong, A. Mittiga, E. Salza, A. Masci, S. Passerini, Electrodeposited ZnO/Cu_2O heterojunction solar cells, Electrochim. Acta 53 (2008) 2226.

[35] M. Nolan, S.D. Elliott, The p-type conduction mechanism in Cu_2O: a first principles study, Phys. Chem. Chem. Phys. 8 (2006) 5350.

[36] V. Shrotriya, G. Li, Y. Yao, C.W. Chu, Y. Yang, Transition metal oxides as the buffer layer for polymer photovoltaic cells, Appl. Phys. Lett. 88 (2006) 073508.

Organic Electronics 11 (2010) 1835–1843

Contents lists available at ScienceDirect

Organic Electronics

journal homepage: www.elsevier.com/locate/orgel

Role of structural disorder in charge transport properties of cobalt phthalocyanine thin films grown by molecular-beam epitaxy

Ajay Singh [a,*], Soumen Samanta [a], Arvind Kumar [a], A.K. Debnath [a], D.K. Aswal [a], S.K. Gupta [a], J.V. Yakhmi [a], Y. Hayakawa [b], S.K. Deshpande [c]

[a] Technical Physics Division, Bhabha Atomic Research Center, Mumbai 400 085, India
[b] Research Institute of Electronics, 3-5-1 Johoku, Naka-Ku, Hamamatsu 432-8011, Japan
[c] University Grant Commission, Department of Atomic Energy (UGC-DAE) Consortium for Scientific Research, Mumbai 400 085, India

ARTICLE INFO

Article history:
Received 24 February 2010
Received in revised form 20 August 2010
Accepted 23 August 2010
Available online 17 September 2010

Keywords:
Cobalt phthalocyanine
Space-charge-limited conduction
Disordered films

ABSTRACT

The charge transport properties of 100 nm thick cobalt phthalocyanine (CoPc) films grown on single crystal Al_2O_3 (0 0 0 1 oriented) and quartz substrates using molecular-beam epitaxy, have been investigated as a function of applied bias (±50 V) and temperature (300–75 K). Films grown on Al_2O_3 are highly ordered and exhibited non-hysteretic current–voltage (*J–V*) characteristics. The *J–V* characteristics in this case are well described by space-charge-limited conduction (SCLC) mechanism. On the other hand, films grown on quartz substrates are highly disordered and exhibited hysteretic *J–V* characteristics. Analyses of complex hysteretic *J–V*'s in disordered films indicated a transition from trap-controlled SCLC mechanism to Poole–Frankel emission with lowering temperature. Various parameters, such as, hole density, trap concentration and space charge limited motilities have been estimated. X-ray photoelectron spectroscopy data show that charge trapping centers in the films grown on quartz substrates are created by chemisorbed oxygen.

© 2010 Elsevier B.V. All rights reserved.

1. Introduction

Molecular organic semiconductors (OSC) are promising materials for future low cost and large area electronics. Among various OSCs, metal phthalocyanines (MPcs) due to high mobility, high thermal and chemical stability and ease of preparation make them suitable for a wide range of applications, such as, dyes, light emitting diodes, solar cells, field effect transistors, gas sensors, field emission applications etc. [1–4]. However, in order to estimate a full potential of these materials, a better understanding of charge transport mechanisms in thin films forms is needed. The charge transport in OSC's is either electrode-limited (due to a mismatch of energy levels between the electrode work function and the corresponding transport levels of the OSC) or bulk-limited. If an ohmic contact is established between OSC and electrode material, then the current is dominated by bulk transport. Efficient charge transport in a film requires that charges move from molecule to molecule and do not trap or scatter. Therefore, charge carrier mobility is influenced by several factors, including molecular packing or crystallinity, disorders, temperature, electric field and charge-carrier density. In literature, several experimental studies have been reported on the understanding of the impact of these parameters on charge transport in OSCs. Unfortunately, such studies are made on films having different OSC materials (e.g., phthalocyanines, pentacene etc.), which were grown on substrates of different materials as well as crystallinity under varying experimental conditions [5]. Several interesting findings have been reported. These include: (i) an enhancement of mobility by nearly six orders in magnitude in pentacene thin films by controlling the substrate temperature, nature of substrate and films thickness [6]; (ii) a

* Corresponding author. Tel.: +91 22 25586822; fax: +91 22 25505296.
E-mail address: asb_barc@yahoo.com (A. Singh).

1566-1199/$ - see front matter © 2010 Elsevier B.V. All rights reserved.
doi:10.1016/j.orgel.2010.08.014

systematic decrease of mobility with increasing background pressure/deposition rates ratio in copper phthalocyanine thin films, which has been attributed to an increase in trap concentrations [7]; (iii) presence of hysteretic current–voltage (J–V) characteristics along with a negative differential resistance (NDR) in copper phthalocyanine thin films, which depend on the deposition parameters etc. [8]. Such a high sensitivity of transport properties essentially depends on the disorders created in the films due to deposition conditions and/or the substrates employed [9–12]. Generalization of disorder induced charge transport in OSC films by comparing data of different groups can be tricky as films of different OSCs are prepared on different substrate materials with varying deposition conditions. Therefore, in order gain an insight into the role of disorders in the charge transport of OSC films, it is essential to delineate the origins of disorders created in the films due to substrates and processing conditions. This demands that films of a particular OSC are grown on different substrates under identical conditions and their charge transport studies are investigated.

In this work, we present results of a detailed investigation carried out on the role of substrate-induced disorders in charge transport properties of cobalt phthalocyanine (CoPc) films. For this purpose, 100 nm CoPc films were deposited under identical conditions on amorphous quartz and crystalline (0 0 0 1 oriented) Al_2O_3 (sapphire) substrates using molecular-beam epitaxy. We demonstrate that films grown on quartz substrates exhibit the J–V characteristics with a pronounced hysteresis, whereas those grown on Al_2O_3 substrates exhibit J–V without any hysteresis. The hysteresis in films grown on quartz substrates is attributed to the deep traps created by chemisorbed oxygen.

2. Experimental

CoPc films (thickness ~100 nm) were deposited on quartz and (0 0 0 1 oriented) Al_2O_3 substrates using molecular-beam epitaxy, MBE, (RIBER system, model EVA 32) under identical conditions. The details of the deposition process are described in our earlier paper [13]. Briefly, cleaned quartz and sapphire substrates were introduced in the introduction chamber of the system and heated at 300 °C under 10^{-8} torr vacuum for removal of moisture and impurities present at the surfaces. The substrates were then transferred in situ to the deposition chamber and CoPc films were deposited using an effusion cell loaded with pure α-CoPc powder (Aldrich make, which was purified by thermal gradient sublimation technique as described in the literature [14]). Prior to the film deposition, the loaded material was heated at 300 °C for 2 days to remove the moisture. All the films were grown at a substrate temperature of 200 °C using a deposition rate of 2 Å/s under a base vacuum of better than 10^{-8} torr. The X-ray photoelectron spectroscopy (XPS) of the deposited films was carried out in situ using MgK_α (1253.6 eV) source and a MAC-2 electron analyzer. The binding energy scale was calibrated to Au $4f_{7/2}$ line at 83.95 eV. The C 1s peak from the adventitious carbon-based contaminant, with the binding energy of 285 eV, was used as the reference for calibration of the charging effect. The structure of the grown films was determined by grazing incidence X-ray diffraction (GIXRD) using CuK_α radiation (Seifert-XRD 3003TT) in out-of-the-plane geometry with an incidence angle of 0.1°. The surface morphology of the films was studied by scanning electron microscopy, SEM, (Tescan make VEGA MV2300T/40 system).

The charge transport measurements were carried out using in-plane electrode geometry. For this purpose, two planar gold electrodes of length 3 mm, width 2 mm separated by 12 μm were thermally deposited onto films using a metal mask and silver wires were attached to the gold pads with silver paint. We may like to add that we have varied the width of gold electrode from 1 to 5 mm, and no significant effect of width on the J was observed. The in-plane geometry has following distinct advantages over out-of-plane geometry (i.e., electrodes are made across the film thickness). (i) In the out-of-plane geometry, metal ions can get incorporated in the films, which can act as the charge trapping centers and hence can create hysteresis in the J–V characteristics [15]. This can make it difficult to differentiate intrinsic origin of hysteresis. This problem will not arise in the in-plane geometry, as the electrodes are far apart (12 μm). (ii) Larger electrode spacing also indicates that the contribution of contact resistance is very small as compared to the film resistance. The J–V measurements were carried out using Keithley 6487 picoammeter/voltage source and computer based data acquisition system. The measurements at low temperatures (20–300 K) were carried out using a closed cycle cryostat. All measurements were carried out in dark to avoid the problem of photoconductivity. In order to rule out the effect of film inhomogeneities, J–V measurements were carried out using at least three pairs of electrodes deposited on a film at different locations.

3. Results

The morphology and GIXRD spectra of the 100 nm CoPc films grown under identical conditions on Al_2O_3 and quartz substrates are shown in Fig. 1. The morphology of films grown on Al_2O_3 substrates has a very dense structure, whereas for quartz substrates the film morphology is granular with a rough surface. For films grown on Al_2O_3 substrates, the presence of GIXRD peaks at $2\theta = 6.94°$, 15.56° and 22.23° indicate that the film is polycrystalline. The least-square fitting of the XRD pattern indicated the monoclinic unit cell structure with lattice parameters $a = 2.58(8)$ nm, $b = 3.75(3)$ nm and $c = 2.40(8)$ nm, $\beta = 90.2°$, which is in agreement with the reported values [16,17]. On the other hand, for quartz substrate presence of only one peak at $2\theta = 6.94°$ (i.e., (2 0 0) orientation) with very low intensity, along with granular morphology, indicates weak crystallization of the film. This difference in CoPc film morphology and structure on two different substrates is attributed to the interaction between the CoPc molecules and the surface of the substrates. On Al_2O_3 substrates, due to strong reactivity of Al-terminated surface, the CoPc molecules initially stack with face-on configura-

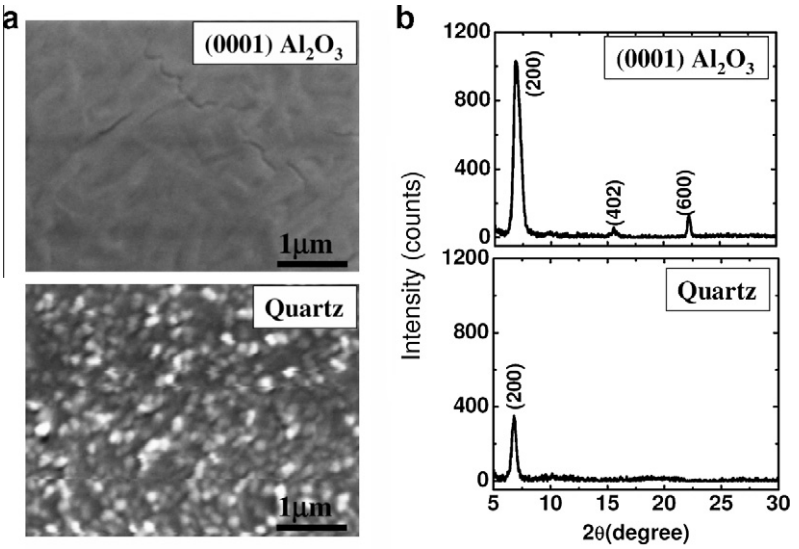

Fig. 1. GIXRD patterns (a) and scanning electron micrographs (b) for the films grown on (0001) Al_2O_3 and quartz substrates.

tion [18,19]. However, as the thickness increases the substrate-molecule interaction weakens, which allows other planes to grow and, in turn, a polycrystalline film is grown. On the other hand, due to inert nature of quartz substrates, the CoPc molecules stack randomly on the substrate resulting in a more disordered state.

The in situ XPS data of CoPc films grown on both substrates indicated absence of oxygen and presence of cobalt in Co^{2+} state. However, exposing films to ambient conditions for 24 h showed a marked difference in the XPS spectra, as shown in Fig. 2. For CoPc films grown on Al_2O_3, O-1s spectrum exhibited single peak at 531 eV (corresponding to physisorbed oxygen) [20]. This indicates that films on Al_2O_3 substrates are not reactive with atmospheric oxygen, which is attributed to a dense packing of the molecules. On the other hand, CoPc films on quartz substrates are found to be reactive with atmospheric oxygen. This is evident from the O-1s spectrum, which has two distinct components at binding energies of 531 and 535 eV, corresponding

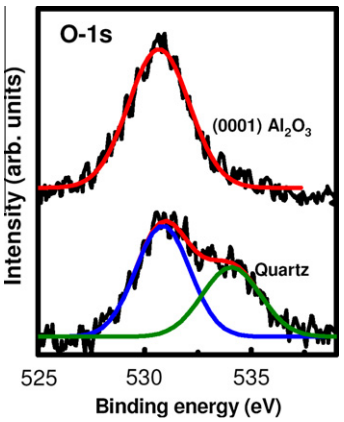

Fig. 2. O-1s XPS spectra recorded for the films grown on Al_2O_3 and quartz substrates.

to physisorbed and chemisorbed oxygen, respectively [21]. The XPS data, therefore, indicates that the charge transport properties of the CoPc films grown on Al_2O_3 and quartz substrates are likely to be very different, which is in agreement with transport properties discussed in the following.

The *J–V* characteristics recorded for films grown on Al_2O_3 and quartz substrates in the bias range of ±50 V are shown in Fig. 3a and b, respectively. The striking difference between the two films is that while for films on Al_2O_3 substrates the *J–V* characteristics are non-hysteretic and highly reproducible with repeated bias scans; for films on quartz substrates a hysteresis in *J–V* characteristics is observed it increases with number of scans. However, hysteresis becomes highly reproducible after 12th scan. Before making further analysis, we would like to mention that space-charge-limited conduction (SCLC) is a commonly reported charge transport mechanism in the OSC films. In the case of ohmic interface between the metallic electrodes and organic films, if the density of injected carriers is lower than the thermally generated carriers in the films (as occurs at low bias) one expects an ohmic (linear *J–V*) behavior. The *J* in this case is given by [22]:

$$J = n_0 e \mu V / d \tag{1}$$

where J is the current density, n_0 is the concentration of thermally generated holes, e is the electronic charge, μ is the hole mobility and V is the applied bias and d is the electrode separation. At sufficiently high bias, concentration of injected carriers exceeds the thermally generated carrier density and SCLC mechanism becomes dominant. In the presence of shallow traps, the SCLC is described by [22]:

$$J = \frac{9\varepsilon_0 \varepsilon_r \theta \mu V^2}{8d^3} \tag{2}$$

where ϵ_0 is the permittivity of free space, and ϵ_r is the static dielectric constant of the film and θ is the ratio of free to total (trapped and free) charge-carrier density.

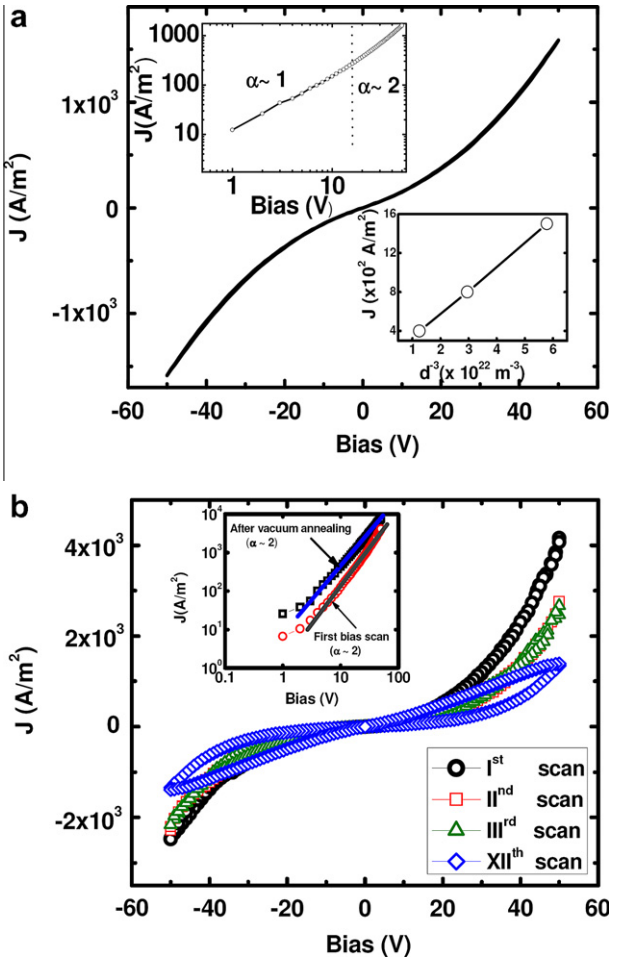

Fig. 3. Room temperature J–V characteristics recorded for the films grown on (a) Al_2O_3 and (b) quartz substrates (for repeated bias scans). Inset of Fig. 3(b) shows the J–V plots for the first bias scan and for the vacuum annealed films on Quartz substrate.

A large amount of structural disorder in films can result in high concentration of trapping centers. Often, the disorder does not have a uniquely defined environment and results in a broad smearing of the trap level distribution. In many cases an exponential distribution of trap levels with a maximum at valence band edge has been reported. In such a case, the J–V characteristics are described by [22]:

$$J = e\mu N_V \left(\frac{\varepsilon_0 \varepsilon_r}{eP_0 kT_t}\right)^l \frac{V^{l+1}}{d^{2l+1}} \tag{3}$$

Where N_V is the effective density of states in the valence band, P_0 is the trap density per unit energy at valence band edge, $l = T_t/T$, where T is the measurement temperature and T_t is the temperature characterizing the trap distribution. Current–voltage characteristics with exponent $(l+1) > 2$ suggest SCLC mechanism in the presence of exponentially distributed traps. We may add that SCLC (Eqs. (2) and (3)) assumes field independent mobility. In case of field dependent mobility, the expressions for J–V characteristics will be modified [23]. In case of exponential distribution of traps, total trap density is given by:

$$N_t = P_0 kT_t \tag{4}$$

In the light of above discussion, we make interpretation of the data presented in Fig. 3 and will first analyze data on sapphire. It is known that the energy barrier at Au/CoPc interface is very small (0.2 eV), which indicates an ohmic contact between Au and CoPc film [24]. For films on Al_2O_3 substrates, a log–log plot of data, as shown in inset of Fig. 3a, indicates a power law behavior of J–V characteristics, i.e., J–V^α, with a crossover in exponent (α) from 1 to 2 at a bias of ~20 V. This indicates that charge transport is ohmic in the bias range 0–20 V, and at higher bias the transport mechanism changes to shallow trap mediated SCLC [22] as described by Eq. (2). In case of SCLC mechanism with shallow traps, linear dependence of J on d^{-3} has been predicted. Therefore, we had made measurements on a single film with different spacing between electrodes (d = 12, 15 and 20 μm) and the results shown in the lower inset of Fig. 3a confirm the validity of SCLC mechanism. Using slope of J–V^2 plots and assuming literature value of $\varepsilon_0\varepsilon_r$ (2.43×10^{-11} F/m), value of mobility (μ) was determined (using Eq. (2)) to be 9.8×10^{-5} m^2/Vs [22]. Using this value of μ, we find (using Eq. (1)) the thermally generated hole concentration (n_0) of 9.6×10^{18} m^{-3} (at 300 K). Here, we have assumed $\theta = 1$ (as justified later, by

very low trap density found for sapphire substrate). Values of different parameters calculated above are given in Table 1.

We can estimate the injected carrier concentration n_{inj} as well as show field independent mobility (assumed in above analysis on sapphire substrate) using the approach of Wu et al. [25]. Under SCLC conditions, Eq. (1) with carrier density n_{inj} may be written as:

$$J = n_{inj}(x)e\mu E(x) \tag{5}$$

Electric field $E(x)$ is related to injected carrier density by:

$$\frac{\varepsilon}{e}\frac{dE(x)}{dx} = n_{inj}(x) \tag{6}$$

We define a function $g = g(E)$ satisfying $\mu(E)E = dg(E)/dE$ with $g(0) = 0$. For an ohmic contact at $x = 0$ and $E = 0$ (at $x = 0$) we obtain:

$$\frac{J}{\varepsilon}x = g(E) \text{ or } E = g^{-1}\left(\frac{J}{\varepsilon}x\right) \tag{7}$$

Where g^{-1} is the inverse function of g. We define another function $F = F(y)$ such that $dF/dy = g^{-1}(y)$ and integration of Eq. (7) with respect to x from $x = 0$ (injecting electrode) to $x = d$ (collecting electrode) gives:

$$\frac{VJ}{\varepsilon} = \left[F\left(\frac{dJ}{\varepsilon}\right) - F(0)\right] \tag{8}$$

Taking derivative of Eq. (8) with respect to J, we get:

$$G\left(\frac{V}{d} + \frac{J}{d}\frac{dV}{dJ}\right) = \frac{dJ}{\varepsilon} \tag{9}$$

Using Eq. (9) and experimental J–V characteristics, one can calculate the g as a function of E. For a fixed value of J, we can also find (from Eq. (7)) the $g(E)$ for different x. By comparing these two data set for $g(E)$, we can find out E as a function of x. The $n_{inj}(x)$ can be calculated using Eq. (6). Mobility (μ) as function of E can be determined using:

$$\mu = \frac{1}{E}\frac{dg(E)}{dE} \tag{10}$$

It can be seen from the Fig. 4, the mobility is field independent and very closely matches with earlier derived SCLC mobility assuming θ as 1. The field independent mobility confirms application of SCLC model to data on sapphire. Further, as required for SCLC mechanism, injected carrier density (at bias of 50 V) shown in the inset of Fig. 4a is significantly larger than thermally generated carrier density (Table 1).

In order to estimate the concentration of shallow traps, we have measured J–V characteristics for films on sapphire substrates at lower temperatures and results for temperatures in 300–75 K range are shown in Fig. 5a. It is seen that the J–V characteristics are non-hysteretic even at low temperatures though the value of J decreases significantly. In Fig. 5b, we plot the data's of Fig. 5a in log–log scale. It is seen that J–V characteristics at different temperatures converge to $V_c = 460$ V, indicating that the current is temperature independent (for $V = V_c$) and the activation energy is zero. The voltage V_c is related to trap density N_t by equation: $V_c = qN_t d^2/2\varepsilon_0\varepsilon_r$ [26]. Using this equation, we obtain $N_t = 9.8 \times 10^{20}/m^3$. The trap characteristic temperature T_t can be determined using exponent of J–V characteristics ($\alpha = l + 1$) determined at different temperatures from data of Fig. 5b. A plot of α versus $1/T$ is shown in the inset of Fig. 5a. Using $\alpha = l + 1 = T_t/T + 1$, the slope of the curve gives the value of T_t (~236 K). Using the values of N_t and T_t, we determine the value of P_0 using Eq. (4) as 1.9×10^{22} eV^{-1} m^{-3}. A transition from trap free SCLC regime at room temperature to exponentially distributed trap-controlled SCLC at low temperature can occur due to free carrier density at room temperature being higher than the trapped

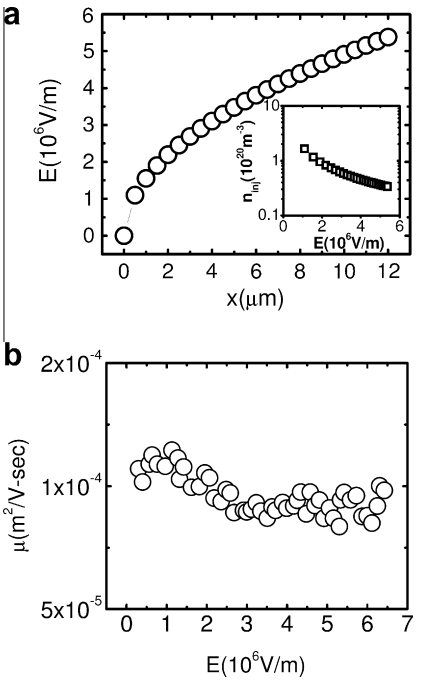

Fig. 4. (a) Spatial distribution of the electric field E at bias voltage of 50 V, inset shows the injected hole concentration n_{inj} (at bias of 50 V) as a function of field and (b) Field dependence of mobility for the films on Al_2O_3 substrates.

Table 1
Values of hole concentration (n_0), trap characteristics temperature (T_t), trap concentration per unit energy at valence band edge (P_0) and Mobility (μ), determined using J–V characteristics for CoPc films grown on (0001) Al_2O_3 and quartz substrates.

Films	n_0 (m^{-3})	T_t (K)	N_t (m^{-3})	P_0 (eV^{-1} m^{-3})	μ (m^2/Vs)
Quartz					
Increasing bias (12th scan)	2.5×10^{18}	600	4.5×10^{23}	8.7×10^{24}	
1st scan	4.5×10^{18}				1.2×10^{-4}
Vac. Ann.	5.5×10^{18}				1.9×10^{-4}
Al_2O_3 (0001)	9.6×10^{18}	236	9.8×10^{20}	1.9×10^{22}	9.8×10^{-5}

carrier density. However, as the temperature is reduced the free carrier density is reduced and the trapped carrier density increases, resulting in exponentially distributed trap-controlled SCLC characteristics.

The value of Fermi energy E_F (at room temperature) may be determined [using $n_0 = N_v \exp[-(E_v - E_F)/kT]$ from free carrier density (n_0) and literature value of effective density of states in valence band $N_V = 10^{27}\ m^{-3}$ to be 0.46 eV above valence band edge [22]. Schematic of trap distribution and band diagram is shown in Fig. 6. It is seen that the traps are on the average at $E_t \sim 0.1$ eV from E_v. Density of trapped carriers (n_{t0}) can be estimated from $n_{t0} = N_t \cdot \exp\{(E_t - E_F)/kT\}$ to be $\sim 5.5 \times 10^{14}/m^3$. A very small concentration of trapped carriers compared to n_0 justifies use of $\theta = 1$ in our analysis earlier.

Now we analyze room temperature data of J–V characteristics measured on quartz substrate [as shown in Fig. 3b]. As seen from Fig. 3b, the current reduces as J–V characteristics are scanned repeatedly. The hysteresis in characteristics is negligible for 1st scan, increases on further scans and characteristics stabilize after about 12 scans. In each scan, the current during increasing voltage is smaller than that during decreasing voltage. The results indicate that trap states are created (on application of voltage) as the J–Vs are measured resulting in reduced current

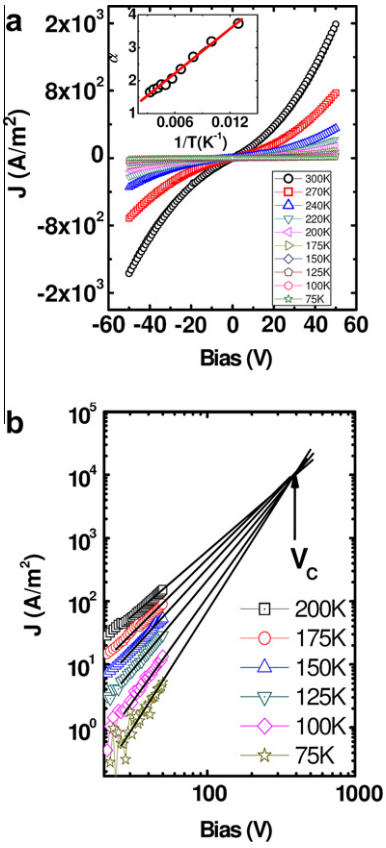

Fig. 5. (a) Temperature dependence of J–V characteristics for films on Al_2O_3 substrate. Inset shows the temperature dependence of exponent (α, J–V^{α}) (b) Power law fit of data of Fig. 5(a). The fits meet at cross over voltage $V_c = 460$ V.

after each scan. Similar bias dependent generation of charge traps has been reported in the other organic semiconductors, such as, pentacene single crystals, polyfluorene etc. [27–29]. Fig. 7a shows the stability of the room temperature J–V characteristics obtained after 12th scan. Higher current during reducing voltage (12th scan) is attributed to filling of deep trap states during increasing current part of scan. This is also indicated by V^2 dependence of current on voltage during reducing voltage scan in Fig. 7b, as the deep traps are filled and shallow trap characteristics (of Eq. (2)) are realized. To confirm that the traps are created by adsorbed oxygen, film was vacuum annealed and characteristics were measured in vacuum. The results are shown in the inset of Fig. 3b. It is found that the current density is higher than in 1st scan in air, due to annealing of trap states on removal of oxygen (removal of oxygen was independently confirmed by XPS, data not shown here).

Now we analyze the J–V characteristics of 1st scan and vacuum annealed sample. We note that the current density at each voltage is quite large (similar to that on sapphire) and V^2 dependence of current indicates SCLC mechanism with shallow traps (shown in the inset of Fig. 3b). This is also indicated by absence of hysteresis that arises on filling of deep traps. Analysis of linear and SCLC characteristics (assuming $\theta = 1$) using Eqs. (1) and (2) yield mobility and free carrier density as given in Table 1. The trap distribution during 12th scans can be estimated using the increasing part of J–V characteristics shown in Fig. 7b. We find that in the bias range >25 V, exponent $\alpha = l + 1 = 3$. This implies that the value of trap characteristic temperature T_t (defined as: $l = T_t/T$) is 600 K. The value of the trap density per unit energy range at valence band edge (P_0), estimated (using Eq. (3)) from slope of J–V plot and literature value of $N_V = 10^{27}\ m^{-3}$ [22], is $8.7 \times 10^{24}\ eV^{-1}\ m^{-3}$. We have used mobility value as determined from characteristics of 1st scan. The mobility for 12th scan may not be calculated as there could be large number of trapped carriers and value of θ is not known. Value of $\theta\mu$ may however be calculated using slope J–V^2 part of the characteristics and Eq. (2). This is found to be nearly five times lower at $2.5 \times 10^{-5}\ m^2/V\text{-}s$ and is minimum value of mobility assuming limiting value of $\theta = 1$. Using this value of mobility, estimated trap density is $2.6 \times 10^{25}\ eV^{-1}\ m^{-3}$, i.e., a factor of nearly 3 higher compared to that given earlier and this is maximum possible error in calculation of trap density. Total concentration of traps (N_t) given in Table 1, has been calculated from the value of P_0 and T_t using Eq. (4) [22]. Thermally generated hole concentration (n_0) for increasing current (of 12th scan) has been estimated from ratio of conductivity of 1st and 12th scan and the hole concentration of 1st scan. Values of parameters T_t, N_t and P_0, as given in Table 1, are within the range of reported values for various metal phathalocyanines [22]. A significantly smaller value of n_0 for 12th scan (compared to first scan) indicates large number of trapped carriers in this case.

As seen by data of Fig. 7c, the hysteresis in J–V characteristics is a function of maximum bias applied. This is understandable as with the increasing applied bias more and more traps gets filled, which results in increase in the hysteresis. As seen earlier, application of bias also re-

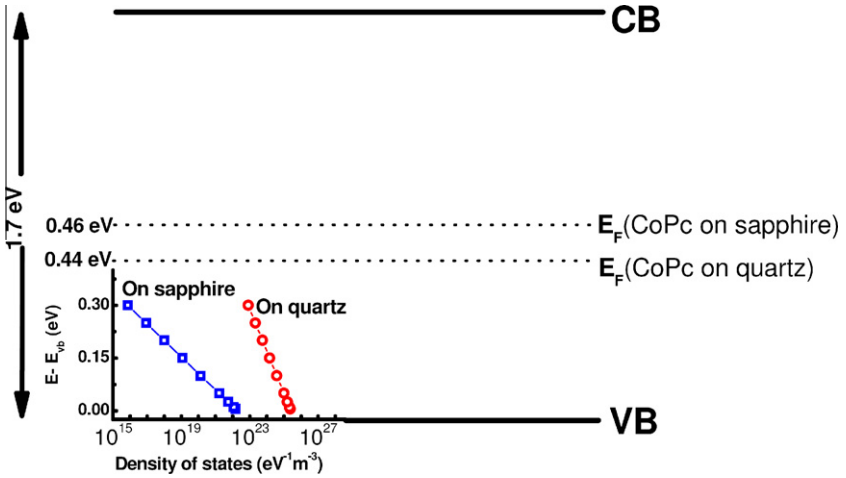

Fig. 6. Fermi energy levels (E_F) position is shown with respect to the conduction band and valence band for films grown on sapphire and quartz. In the left side show the plot of density of traps states as a function of energy.

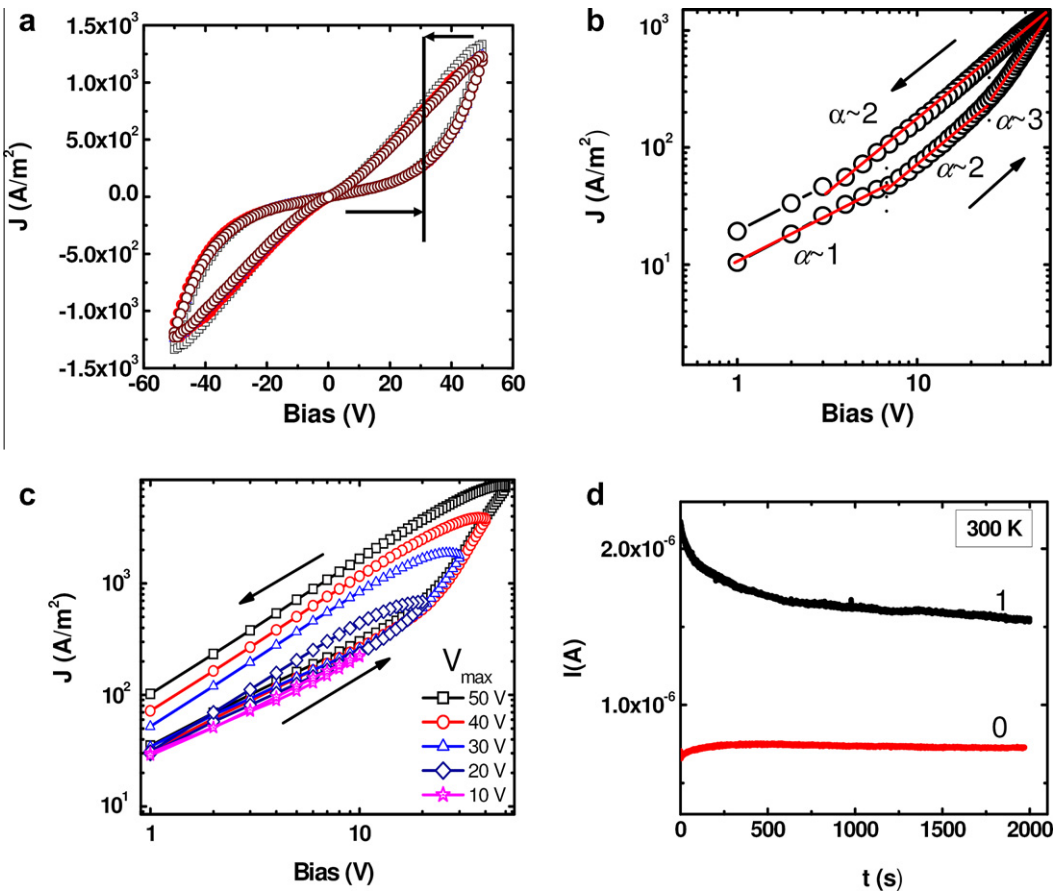

Fig. 7. (a) Stable *J–V* data (obtained after12th bias scan) for CoPc films on quartz substrates; (b) log *J* – log *V* data (at 300 K) plot for data of Fig. 7(a); (c) *J–V* characteristics for different voltage sweep range (as indicated in the figure). (d) High (i.e. denoted by 1) and low conducting state (i.e. denoted by 0) of the CoPc films on quartz substrate. 1 state is obtained by application of + 50 volts for 100 s. and read at + 30 volt, 0 state is obtained by application of 0 volts and read at + 30 volt. The arrow marked in Fig 7(a) shows the bias sequence applied to obtain 1 and 0 states.

sults in creation of traps and some increase in hysteresis on increasing bias could be due to such additional traps. Stability of two high and low conduction states was studied by measurement of time dependence of current at 30 V by ramping bias from 50 to 30 V and 0 to 30 V and the results are shown in Fig. 7d. We may like to add

that hysteresis with current ratio of 10^9 has been reported in the organic semiconductors based devices. In most of these devices the metal nano-particles have been embedded in organic/polymer matrix to achieve the bistability [30]. Hysteresis in the present case is intrinsic to the films and arises due to oxygen induced deep traps in the films on quartz.

For films grown on quartz substrates, as shown in Fig. 8a, the hysteresis decreases systematically with lowering temperature, and eventually vanishes at 220 K. Moreover, below 150 K, films do not transport any current. As shown in the inset of Fig. 8a, the value of α decreases with lowering temperature and becomes <2 for temperatures below 230 K. This implies in the temperature range 230 – 150 K, the SCLC transport mechanism is not valid. This is because due to disorder present in the films, at low temperatures there is strong charge localization, density of free carriers is very small and conduction occurs by hopping of trapped charges.

The charge transport mechanisms in temperature range 230–150 K were analyzed using Poole-Frankel (PF) and Schottky-emission (SC) models. The PF effect essentially is a field-assisted lowering of the coulomb potential barrier of the trap levels, which is given by the expression: $\Delta\phi = \beta_{PF}V^{1/2}/d^{1/2}$ where $\beta_{PF} = (e^3/\pi\varepsilon_0\varepsilon_r)^{1/2}$ is the PF field lowering coefficient. The J–V characteristics in this case are described by [22]:

$$J = J_0 \exp(-\frac{\beta_{PF}V^{1/2}}{kTd^{1/2}}) \tag{11}$$

The electrode-limited analogue of PF effect is Schottky effect [22]. In this case due to field-assisted lowering of a potential barrier at the injection electrode J–V characteristics are given by:

$$J = AT^2 \exp(-\frac{\phi_0}{kT}) \exp(\frac{\beta_s V^{1/2}}{kTd^{1/2}}) \tag{12}$$

Where A is Richardson constant $A = \frac{4\pi mk^2e}{h^3}$ $\mathrm{Am^{-2}K^{-2}}$, m and e are the mass and charge of the charge carries, h is the Planck constant, φ_0 is the Schottky barrier height at injecting electrode interface, k is boltzmann constant and, β_S is the Schottky field lowering coefficient. In principle the Schottky and PF effects can be distinguished by the measured value of field lowering coefficient, which is twice as high in the PF case as in Schottky case.

$$2\beta_S = \beta_{PF} = (\frac{e^3}{\pi\varepsilon_0\varepsilon_r})^{1/2} \tag{13}$$

For phthalocyanines, the theoretically determined values for PF and Schottky field lowering coefficients are $\beta_{PF} \sim 4 \times 10^{-5}\ \mathrm{eVm^{1/2}\,V^{-1/2}}$ and $\beta_S \sim 2 \times 10^{-5}\ \mathrm{eVm^{1/2}\,V^{-1/2}}$ [22].

Linear dependence of $\ln J$ on $V^{1/2}$ for $T < 220$ K, as shown in Fig. 8b, indicates agreement with PF or SC model. Average value of β determined from slopes of characteristics at different temperatures was found to be $\sim 3.5 \times 10^{-5}\ \mathrm{eVm^{1/2}\,V^{-1/2}}$. Value of β was also calculated from the slope of $\ln J$ versus $1/T$ (measured at 50 V) characteristics shown in inset of Fig. 8b to be $4.7 \times 10^{-5}\ \mathrm{eVm^{1/2}\,V^{-1/2}}$. These values of β indicate PF mechanism of charge transport. We may note that contact dominated SC mechanism, if present, should be more dominant for films on sapphire substrates due to higher current density (at low temperatures). The absence of SC transport in sapphire supports absence of SC and presence of PF mechanism for quartz substrate.

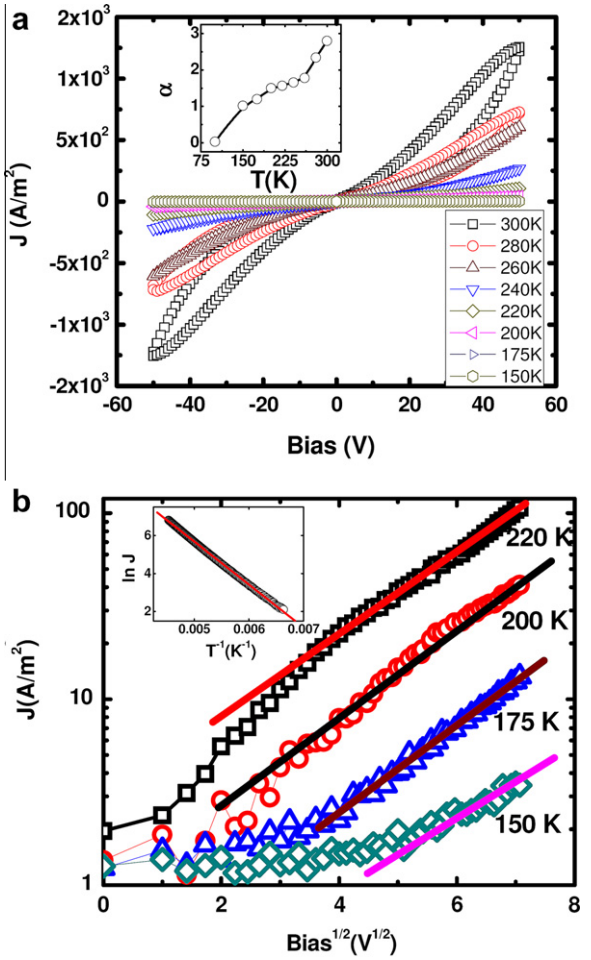

Fig. 8. (a) Temperature dependence of J–V characteristics for the films grown on quartz substrate. Inset shows the temperature dependence of voltage exponent α. (b) $\ln J$ vs $V^{1/2}$ plots at different temperatures. Inset shows the $\ln J$ versus $1/T$ plot obtained at bias of 50 V.

4. Conclusions

By carrying out the temperature dependent J–V measurements of 100 nm thick CoPc films grown under identical conditions on single crystal Al_2O_3 and quartz substrates – we have demonstrated that charge transport is strongly governed by the structural disorders present in the films. The films grown on Al_2O_3 are polycrystalline and have densely packed molecules, which exhibit non-hysteretic J–V characteristics. On the other hand, films grown on quartz substrates are more disordered and exhibit hysteretic J–V characteristics. This difference in charge transport is attributed to the chemisorbed oxygen present in the films grown on quartz substrates owing to the disordered nature. The chemisorbed oxygen acts as charge traps. For films grown

on Al_2O_3, the *J–V* characteristics are well described by SCLC mechanism in the temperature range of 300–75 K. However, for the films grown on quartz substrates, a change in charge transport mechanism from SCLC to PF with lowering temperature has been observed.

Acknowledgements

This work is supported by "DAE-SRC Outstanding Research Investigator Award" (2008/21/05-BRNS) and "Prospective Research Funds" (2008/38/02-BRNS) granted to D.K.A.

References

[1] C.W. Tang, S.A. Van Slyke, Appl. Phys. Lett. 51 (1987) 913;
J.H. Burroughs, D.D.C. Bradley, A.R. Brown, R.N. Marks, K. Mackay, R.H. Friend, P.L. Bums, A.B. Holmes, Nature (London) 347 (1990) 539.
[2] F. Garnier, R. Hajlaoui, A. Yassar, P. Srivastava, Science 265 (1994) 1684.
[3] N.S. Sariciftci, L. Smilowitz, A.J. Heeger, F. Wudl, Science 258 (1992) 1474.
[4] L. Ma, J. Liu, S. Pyo, Y. Yang, Appl. Phys. Lett. 80 (2002) 362;
J.C. Scott, Science 304 (2004) 62.
[5] V. Coropceanu, J. Cornil, D.A. da Silva Filho, Y. Olivier, R. Silbey, J.-L. Brédas, Chem. Rev. 107 (2007) 92.
[6] C.D. Dimitrakpoulous, D.J. Mascaro, IBM J. Res. Dev. 45 (2001) 11.
[7] R.D. Gould, J. Phys. D. Appl. Phys. 9 (1986) 1785.
[8] J. Lin, D. Ma, Org. Electron. 10 (2009) 275.
[9] G. Horowitz, Adv. Mater. 10 (1998) 365.
[10] Z. Hu, B. Li, A. Zhao, J. Yang, J.G. Hou, J. Phys. Chem. C 112 (2008) 13650.
[11] L. Chen, Z. Hu, A. Zhao, B. Wang, Y. Luo, J. Yang, J.G. Hou, Phys. Rev. Lett. 99 (2007) 146803.
[12] J. Zhang, H. Wang, X. Yan, J. Wang, J. Shi, D. Yan, Adv. Mater. 17 (2005) 1191.
[13] A.K. Debnath, S. Samanta, A. Singh, D.K. Aswal, S.K. Gupta, J.V. Yakhmi, S.K. Deshpande, A.K. Poswal, C. Suergers, Physica E 41 (2008) 154.
[14] S.R. Forrest, Chem. Rev. 97 (1997) 1793.
[15] D. Tondelier, K. Lmimouni, D. Vuillaume, Appl. Phys. Lett. 85 (2004) 5763.
[16] S.I. Shihub, R.D. Gould, Phys. Stat. Sol. (a) 139 (1993) 129.
[17] F.F. Gracia, A.S. Sanchez, J.L.S. Sanchez, Mater. Charact. 58 (2007) 829.
[18] P.J. Eng, T.P. Trainor, G.E. Brown Jr., G.A. Waychunas, M. Newville, S.R. Sutton, M.L. Rivers, Science 288 (2000) 1029.
[19] S.A. Chambers, T. Droubey, D.R. Jennison, T.R. Mattsson, Science 297 (2002) 827.
[20] J.F. Moulder, W.F. Stickle, P.E. Sobol, K.D. Bombson, Handbook of X-ray Photoelectron Spectroscopy, Physical Electronics Inc., Minnesota, 1995.
[21] T. Kawabe, K. Tabata, E. Suzuki, Y. Yamaguchi, Y. Nagasawa, J. Phys. Chem. B 105 (2001) 4239.
[22] R.D. Gould, Coordin. Chem. Rev. 156 (1996) 237.
[23] P.W.M. Blom, M.J.M. de Jong, M.G. van Munster, Phys. Rev. B 55 (1997) R656.
[24] A.K. Mahapatro, S. Ghosh, Appl. Phys. Lett. 80 (2002) 4840.
[25] Y.Z. Wu, C.R. Chang, D.J. Zhang, Appl. Phys. Lett. 95 (2009) 033508.
[26] M.A. Rafiq, Y. Tsuchiya, H. Mizuta, S. Oda, S. Uno, Z.A. Durrani, W.I. Mine, Appl. Phys. Lett. 87 (2005) 182101.
[27] D.V. Lang, X. Chi, T. Siegrist, A.M. Sergent, A.P. Ramirez, Phys. Rev. Lett. 93 (2004) 076601.
[28] M. Arif, M. Yun, S. Gangopadhyay, K. Ghosh, L. Fadiga, F. Galbrecht, U. Scherf, S. Guha, Phys. Rev. B 75 (2007) 195202.
[29] A. Benor, D. Knipp, J. Northrup, A.R. Volkel, R.A. Street, J. Non-Crystal. Solids 354 (2008) 2875.
[30] J. Ouyang, C.-W. Chu, C.R. Szmanda, L. Ma, Y. Yang, Nat. Mater. 2 (2004) 918.

Organic Electronics 11 (2010) 1844–1852

Contents lists available at ScienceDirect

Organic Electronics

journal homepage: www.elsevier.com/locate/orgel

Deep-blue OLEDs using novel efficient spiro-type dopant materials

Young-Min Jeon [a], Jun-Yeop Lee [b], Joon-Woo Kim [c], Chil-Won Lee [c], Myoung-Seon Gong [d,*]

[a] Department of Chemistry, Dankook University, Chungnam 330-714, Republic of Korea
[b] Department of Polymer Engineering, Dankook University, Yongin, Kyung-gi 448-701, Republic of Korea
[c] OLED Team, Daejoo Electronic Materials, Siheung, Kyung-gi 429-848, Republic of Korea
[d] Department of Nanobiomedical Science and WCU Research Center of Nanobiomedical Science, Dankook University, Cheonan, Chungnam 330-714, Republic of Korea

ARTICLE INFO

Article history:
Received 31 March 2010
Received in revised form 16 May 2010
Accepted 6 August 2010
Available online 19 August 2010

Keywords:
Deep blue
Spiro[fluorene-benzofluorene]
Dopant
Color purity
OLED
Host

ABSTRACT

The deep blue fluorescent spiro-type dopant materials *N,N,N′,N′*-tetraphenylspiro[fluorene-7,9′-benzofluorene] (**SFBF**)-5,9-diamine (BD-6DPA), *N,N′*-di-(2-naphthyl)-*N,N′*-diphenyl-**SFBF**-5,9-diamine (BD-6NPA), *N,N′*-diphenyl-*N,N′*-di-*m*-tolyl-**SFBF**-5,9-diamine (BD-6MDPA) and *N,N′*-diphenyl-*N,N′*-bis(4-(trimethylsilyl)phenyl)-**SFBF**-5,9-diamine (BD-6TMSA) were designed and successfully prepared by amination reactions. The EL characteristics of MADN as the blue host material doped with the above blue dopant materials were evaluated. The electroluminescence spectra of ITO/*N,N′-diphenyl-N,N′*-bis-[4-(phenyl-*m*-tolyl-amino)-phenyl]-biphenyl-4,4′-diamine (DNTPD/*N,N′*-di(1-naphthyl)-*N,N′*-diphenylbenzidine (NPB)/2-methyl-9,10-di(2-naphthyl)anthracene (MADN):BD-6MDPA/tris(8-hydroxyquinoline)aluminum (Alq_3)/LiF/Al devices show a narrow emission band with a full width at half maximum of 48 nm and a $\lambda_{max}(\varepsilon)$ = 463 nm. The device obtained from MADN doped with BD-6MDPA showed a good color purity (0.135, 0.156), high luminance efficiency (9.11 cd/A at 6.5 V) and high external quantum efficiency (8.16%).

© 2010 Elsevier B.V. All rights reserved.

1. Introduction

Organic light emitting diodes (OLEDs) have attracted considerable attention due to their many advantages for commercial applications, such as their high brightness, low power consumption, capability of emitting a wide range of colors, and applications in full color organic displays [1]. For full color displays, three primary colors (red, green, blue) are necessary. Many new materials with red, green, and blue emitting colors have been developed to meet these requirements [2]. Developing blue light emitters is essential for the development of full color displays. In spite of the considerable advances that have been made in the field of OLEDs, it is difficult to find appropriate blue emitting materials because of their low solution and low solid-state photoluminescence (PL) quantum yields [3]. OLED devices have a short lifetime because of the deterioration of the luminescent layers. Their lifetimes can be lengthened by the introduction of thermally stable substituents on the host and dopant materials [4]. Generally, host and supporting layer materials having a high glass transition temperature are needed to obtain a long lifetime. Especially, the lifetime of the luminescent layers is closely related to the specific host material in use [5].

The color purity of a blue light emitter is determined by the dopant, and is improved by shifting the emission region to a shorter wavelength. The maximum emission range of some commercial dopant materials are close to the blue sky region (450–470 nm), but wavelengths lower than 450 nm are also considered to have reasonable color purity [6,7]. In addition, many problems still remain to be solved regarding durability over time due to long-term usage, and deterioration caused by oxygen and moisture in air. In addition, many other problems remain related to the need for good color purity of blue luminescence in applications such as full color displays [8].

* Corresponding author. Tel./fax: +82 41 5501476.
E-mail address: msgong@dankook.ac.kr (M.-S. Gong).

1566-1199/$ - see front matter © 2010 Elsevier B.V. All rights reserved.
doi:10.1016/j.orgel.2010.08.007

On the other hand, spiro compounds with specific steric configurations has been attracting attention as an organic functional material because of the specific physical properties of the material, such as high glass transition temperature, which makes them a very promising approach for optoelectric materials [9]. Much of the recent research into blue light-emitting materials has centered on spiro-based derivatives because of their high solution and solid-state photoluminescence quantum yields [10]. Representative organic spiro materials as blue light-emitting materials include spiro-oligophenyl [11], spirofluorenes (**SFs**) with asymmetric substitution [12],spiro-substituted **SF** [13], **SF**-linked phenylanthracene [14] and anthracene [15], heteroatom-substituted spiro compounds [16], pyrene-substituted **SFs** [17] and difluorene-indenofluorene compounds [18]. Many studies have dealt with the spiro[fluorene-7,9′-benzofluorene] (**SFBF**) as organic electroluminescent host materials. The performance of OLEDs (the color purity and luminescence efficiency) based on **SFBF** was determined by the position of substitution and aryl moieties with a variety of conjugation chain length [19].

In this study, we report the synthesis of a series of new deep-blue emitting dopant materials, *N,N,N′,N′*-tetraphenyl-**SFBF**-5,9-diamine(BD-6DPA), *N,N′*-di-(2-naphthyl)-*N,N′*-diphenyl-**SFBF**-5,9-diamine (BD-6NPA), *N,N′*-diphenyl- *N,N′*-di-*m*-tolyl-**SFBF**-5,9-diamine (BD-6MDPA) and *N,N′*-diphenyl-*N,N′*-bis(4-(trimethylsilyl)phenyl)-**SFBF**-5,9-diamine (BD-6TMSA) by amination reactions of both 5- and 9-positions on the **SFBF**. Multilayered OLEDs were fabricated by using these deep-blue materials as the emitting layer and the dopant for MADN. A high quantum efficiency of 8.16% with CIE coordinates of (0.135, 0/156) was achieved, and this is one of the best efficiency value of deep blue fluorescence OLEDs ever reported in the literature.

2. Experimental

2.1. Materials and measurements

Tetrakis(triphenylphosphine)palladium(0) and bromine (Aldrich Chem. Co.) were used without further purification. Diphenyl-[4-(2-[1,1;4,1]terphenyl-4-yl-vinyl)-phenyl]-amine (BD-1) and 2-methyl-9,10-di(2-naphthyl)anthracene (MADN) were prepared using a method reported elsewhere [22]. Tetrahydrofuran and toluene were distilled over sodium and calcium hydride. Diphenylamine, *N*-phenyl-2-naphthylamine and 3-methyldiphenylamine (Aldrich Chem. Co.) were used as received. *N*-phenyl-4-(trimethylsilyl)aniline was prepared by the literature method previously reported [23]. Tri-*t*-butylphosphine, potassium *t*-butoxide (Aldrich Chem. Co.), palladium(II) acetate (TCI Co.) were used as received for amination. 5-Bromo-**SFBF** and 5,9-bromo-**SFBF** [19] were prepared as previously reported.

The FT-IR spectra were obtained using a Biorad Excaliber FTS-3000MX spectrophotometer, and the ^{1}H NMR and ^{13}C NMR spectra were recorded on a Bruker Avance 500 (500 MHz for ^{1}H and 125 MHz for ^{13}C) spectrometer. The photoluminescence (PL) spectra were recorded on a fluorescence spectrophotometer (Jasco FP-6500) and the UV–vis spectra were obtained using a UV–vis spectrophotometer (Shimadzu, UV-1601PC). Elemental analyses were performed using a CE Instrument (EA1110), and the differential scanning calorimetry (DSC) measurements were performed using a Mettler DSC 822^{e} under nitrogen at a heating rate of 10 °C/min. The low and high resolution mass spectra were recorded using a mass spectrometer (JEOL, JMS-AX505WA) in FAB mode. The energy levels were measured using a low energy photoelectron spectrometer (Riken-Keiki AC-2). The current–voltage characteristics of the encapsulated devices were measured using a Keithley 2400 source measurement unit and CS 1000 spectroradiometer.

2.2. General procedure for the coupling reaction

The 5,9-dibromo-**SFBF** (**1**) (5 g, 9.53 mmol), diarylamine derivative (24.79 mmol) and palladium acetate (0.150 g, 0.67 mmol) were dissolved in anhydrous toluene under nitrogen atmosphere. To the reaction mixture was added a solution of tri-*t*-butylphosphine (1 M, 0.42 g, 1.91 mmol) and potassium *t*-butoxide (4.28 g, 38.15 mmol) dropwise slowly. The reaction mixture was stirred for 12 h at 100 °C. The mixture was diluted with dichloromethane and washed with distilled water (150 mL) three times. The organic layer was dried over anhydrous $MgSO_4$ and evaporated in vacuo to give the crude product, which was purified by column chromatography by *n*-hexane. The final product was obtained, a yellow-green powder.

N,N,N′,N′-Tetraphenyl-**SFBF**-5,9-diamine (BD-6DPA). Yield 65%. Mp 270 °C. ^{1}H NMR (500 MHz, $CDCl_3$) δ 8.77–8.76 (d, J = 8.47 Hz, 1H, Ar-CH– naphthalene), 8.23–8.22 (d, J = 8.54 Hz, 1H, Ar-CH–naphthalene), 8.02–8.00 (d, J = 8.37 Hz, 1H, Ar-CH–benzene), 7.69–7.67 (d, J = 7.61 Hz, 2H, Ar-CH–fluorene), 7.61–7.59 (t, J = 8.15 Hz, 1H, Ar-CH–naphthalene), 7.39–7.38 (t, J = 8.00 Hz, 1H, Ar-CH–naphthalene), 7.28–7.26 (t, J = 7.05 Hz, 2H, Ar-CH–fluorene), 7.12–7.10(s, 2H, Ar-CH–benzene), 7.12–7.10 (t, 4H, Ar-CH–benzene), 7.10–7.08 (d, 2H, Ar-CH–fluorene), 6.96–6.94(t, 4H, Ar-CH–benzene), 6.90–6.89(t, 4H, Ar-CH–benzene), 6.89–6.87 (d, 1H, Ar-CH–naphthalene), 6.82–6.81 (d, 4H, Ar-CH–benzene), 6.71–6.69 (d, 1H, Ar-CH–benzene), 6.56–6.56 (d, 1H, Ar-CH–benzene). ^{13}C NMR ($CDCl_3$) δ 151.6, 148.0, 147.9, 147.8, 147.5, 146.8, 142.7, 142.1, 137.1, 135.4, 131.9, 130.8, 129.2, 127.9, 127.8, 127.0, 126.1, 125.7, 124.4, 124.1, 123.9, 123.5, 123.4, 122.9, 121.5, 121.4, 120.3. 119.5, 77.4, 77.2, 76.9, 66.4 ppm.

*N,N′-D*i-(2-naphthyl)-N,N′-diphenyl-**SFBF**-5,9-diamine (BD-6NPA). Yield 62%. Mp 295 °C. ^{1}H NMR (500 MHz, CDCl3) δ 8.80–8.78 (d, J = 8.50 Hz, 1H, Ar-CH- naphthalene), 8.26–8.24 (d, J = 8.54 Hz, 1H, Ar-CH–naphthalene), 8.06–8.05 (d, J = 8.39 Hz, 1H, Ar-CH–benzene), 7.69–7.68 (d, J = 7.62 Hz, 1H, Ar-CH–naphthalene), 7.65–7.63 (d, 2H, Ar-CH–fluorene), 7.65–7.63 (d, 2H, Ar-CH–naphthalene), 7.60–7.57 (t, 1H, Ar-CH–naphthalene), 7.51–7.50 (d, 1H, Ar-CH–naphthalene), 7.43–7.42 (d, 1H, Ar-CH–naphthalene), 7.40–7.38 (d, 2H, Ar-CH–naphthalene), 7.28–7.27 (t, 2H, Ar-CH–fluorene), 7.26–7.24 (t, 2H,

Ar-CH–naphthalene), 7.24–7.21 (d, 2H, Ar-CH–naphthalene), 7.18–7.16 (d, 2H, Ar-CH–naphthalene), 7.16–7.14 (d, 2H, Ar-CH–naphthalene), 7.12–7.10(s, 2H, Ar-CH–benzene), 7.10–7.08(d, 2H, Ar-CH–benzene), 7.08–7.06(d, 1H, Ar-CH–benzene), 7.06–7.04(d, 2H, Ar-CH–benzene), 6.99–6.97 (d, 2H, Ar-CH–fluorene), 6.96–6.94(d, 1H, Ar-CH–benzene), 6.92–6.91(d, 2H, Ar-CH–benzene), 6.90–6.88(d, 1H, Ar-CH–benzene), 6.89–6.87 (d, 1H, Ar-CH–naphthalene), 6.85–6.83(s, 1H, Ar-CH–benzene), 6.73–6.71 (s, 1H, Ar-CH–benzene), 6.63–6.62 (d, 1H, Ar-CH–benzene). ^{13}C NMR ($CDCl_3$) δ 151.7, 148.0, 147.9, 147.7, 147.5, 146.7, 145.7, 145.1, 142.7, 142.1, 137.2, 135.5, 134.4, 131.8, 130.8, 130.1, 129.5, 129.3, 129.1, 128.8, 128.7, 127.9, 127.8, 127.6, 127.1, 127.0, 126.9, 126.3, 126.2, 125.7, 124.6, 124.5, 124.2, 124.1, 124.0, 123.8, 123.5, 123.3, 122.6, 121.8, 121.6, 120.4, 120.0, 119.4, 117.2, 77.4, 77.2, 76.9, 66.4.

N,N′-Diphenyl-*N,N′*-di-*m*-tolyl-**SFBF**-5,9-diamine (BD-6MDPA). Yield 64%. Mp 248 °C. ^{1}H NMR (500 MHz, CDCl3) δ 8.77–8.75 (d, *J* = 8.47 Hz, 1H, Ar-CH–naphthalene), 8.22–8.20 (d, *J* = 8.53 Hz, 1H, Ar-CH–naphthalene), 8.02–8.01 (d, *J* = 8.45 Hz, 1H, Ar-CH–benzene), 7.69–7.67 (d, *J* = 7.60 Hz, 2H, Ar-CH–fluorene), 7.60–7.59 (t, *J* = 8.00 Hz, 1H, Ar-CH–naphthalene), 7.39–7.38 (t, *J* = 7.57 Hz, 1H, Ar-CH–naphthalene), 7.28–7.27 (t, *J* = 7.90 Hz, 2H, Ar-CH–fluorene), 7.12–7.10(s, 2H, Ar-CH–benzene), 7.12–7.10(t, 4H, Ar-CH–benzene), 7.10–7.08 (d, 2H, Ar-CH–fluorene), 7.04–7.02 (d, 2H, Ar-CH–benzene), 6.96–6.94(d, 1H, Ar-CH–benzene), 6.90–6.89(t, 4H, Ar-CH–benzene), 6.89–6.87 (d, 2H, Ar-CH–naphthalene), 6.80–6.78 (d, 2H, Ar-CH–benzene), 6.74–6.72 (d, 2H, Ar-CH–benzene), 6.71–6.68 (d, 2H, Ar-CH–benzene), 6.62–6.60 (d, *J* = 7.92 Hz, 1H, Ar-CH–benzene), 6.57–6.57 (s, 1H, Ar-CH–benzene), 2.08–2.09 (s, 6H, Ar-CH_3). ^{13}C NMR ($CDCl_3$) δ 151.5, 148.1, 147.9, 147.8, 147.5, 147.4, 146.8, 142.7, 142.1, 139.0, 138.8, 136.9, 135.4, 131.9, 130.8, 129.2, 129.0, 128.8, 127.9, 127.8, 126.9, 126.1, 125.7, 124.5, 124.4, 124.1, 123.8, 123.6, 123.3, 123.0, 122.5, 122.1, 121.4, 121.3, 121.1, 120.4, 119.2, 118.6, 77.4, 77.2, 76.9, 66.4, 21.5, 21.4.

N,N′-Diphenyl-*N,N′*-bis(4-(trimethylsilyl)phenyl)-**SFBF**-5,9-diamine (BD-6TMSA). Yield 60%. Mp 256 °C. ^{1}H NMR (500 MHz, $CDCl_3$) δ 8.78–8.76 (d, *J* = 8.50 Hz, 1H, Ar-CH–naphthalene), 8.24–8.23 (d, *J* = 8.53 Hz, 1H, Ar-CH–naphthalene), 8.02–8.00 (d, *J* = 8.42 Hz, 1H, Ar-CH–benzene), 7.69–7.67 (d, *J* = 7.60 Hz, 2H, Ar-CH–fluorene), 7.61–7.59 (t, *J* = 7.38 Hz, 1H, Ar-CH–naphthalene), 7.39–7.38 (t, *J* = 7.70 Hz, 1H, Ar-CH–naphthalene), 7.28–7.27 (t, 2H, Ar-CH–fluorene), 7.24–7.22(d, 2H, Ar-CH–benzene), 7.12–7.10(s, 2H, Ar-CH–benzene), 7.12–7.10(t, 4H, Ar-CH–benzene), 7.10–7.08 (d, 2H, Ar-CH–fluorene), 6.96–6.94(d, 2H, Ar-CH–benzene), 6.90–6.89(d, 2H, Ar-CH–benzene), 6.89–6.87 (d, 1H, Ar-CH–naphthalene), 6.82–6.81 (d, 4H, Ar-CH–benzene), 6.71–6.69 (s, 1H, Ar-CH–benzene), 6.567–6.56 (s, 1H, Ar-CH–benzene), 0.21–0.20 (s, 9H Ar-Si–$(CH_3)_3$), 0.16–0.15 (s, 9H Ar-Si–$(CH_3)_3$). ^{13}C NMR ($CDCl_3$) δ 151.7, 148.5, 148.1, 148.0, 147.8, 147.6, 147.3, 146.6, 142.4, 142.1, 137.3, 135.6, 134.3, 134.2, 133.7, 132.0, 131.8, 130.8, 129.2, 129.1, 127.9, 127.8, 127.0, 126.2, 125.7, 124.4, 124.3, 123.9, 123.8, 123.4, 123.1, 122.7, 121.9, 121.4, 120.3, 120.0, 119.9, 77.4, 77.2, 76.9, 66.4.

2.3. OLED fabrication

A basic device configuration of indium tin oxide(ITO, 150 nm)/*N,N′*-diphenyl-*N,N′*-bis-[4-(phenyl-*m*-tolyl-amino)-phenyl]-biphenyl-4,4′-diamine (DNTPD, 60 nm)/*N,N′*-di(1-naphthyl)-*N,N′*-diphenylbenzidine (α-NPB, 30 nm)/2-methyl-9,10-di(2-naphthyl) anthracene (MADN): dopant (30 nm, x%)/tris(8-hydroxyquinoline)aluminum (Alq_3, 20 nm)/LiF (1 nm)/Al (200 nm) was used for device fabrication. All organic materials except for dopants were deposited at a deposition rate of 1 Å/s. The doping concentration of the dopant materials was varied at 3, 5 and 7%. The devices were encapsulated with a glass lid and a CaO getter after cathode deposition. Current density–voltage-luminance and electroluminescence characteristics of the blue fluorescent OLEDs were measured with a Keithley 2400 source measurement unit and CS 1000 spectroradiometer. Lifetime measurement of the blue OLEDs was carried out at a luminance of 5000 cdm^{-2} at constant current mode.

3. Results and discussion

3.1. Synthesis and characterization

The key intermediate in this synthesis is the introduction of diarylamine substituents into the 5- and 9-position of the **SFBF** by amination reactions, to tune the electro-optical properties of the deep-blue emitting dopant materials. 5,9-Dibromo- **SFBF** (**1**) was prepared by selective bromination of **SFBF** via 5-bromo-**SFBF** using carbon tetrachloride and chloroform solvent as shown in Scheme 1. The dopant materials *N,N,N′,N′*-tetraphenyl-**SFBF**-5,9-diamine (BD-6DPA), *N,N′*-di-(2-naphthyl)-*N,N′*-diphenyl-**SFBF**-5,9-diamine (BD-6NPA), *N,N′*-diphenyl-*N,N′*-dim-tolyl-**SFBF**-5,9-diamine (BD-6MDPA) and *N,N′*-diphenyl-*N,N′*-bis(4-(trimethylsilyl)phenyl)-**SFBF**-5,9-diamine (BD-6TMSA) were prepared by amination reactions of compounds **1** with diphenylamine, *N*-phenyl-2-naphthylamine, 3-methyldiphenylamine and *N*-phenyl-4-(trimethylsilyl)aniline in the presence of a palladium catalyst. The synthetic routes to the four dopant materials are described in Scheme 1. The chemical structures and compositions of the resulting precursor and spiro-compounds were characterized by ^{1}H NMR, ^{13}C NMR, FT-IR and GC–MS.

3.2. Optical properties and energy levels

Table 1 shows the UV–vis absorption and photoluminescence (PL) spectra data of the dopant materials, respectively. The solution absorption maxima of BD-6DPA, BD-6NPA, BD-6MDPA and BD-6TMSA showed at 407, 411, 408 and 407 nm, respectively, whereas the BD-6 series showed at 416, 421, 416 and 413 nm in film. The emission maximum of BD-6DPA, BD-6NPA, BD-6MDPA and BD-6TMSA were located at 478, 464, 468 and 459 nm in solution, respectively, whereas the BD-6 series showed an absorption maximum at 484, 491, 487 and 484 nm in film. The introduction of a diphenylamine group to both the 5- and 9-positions in **SFBF** caused a significant red-shift in

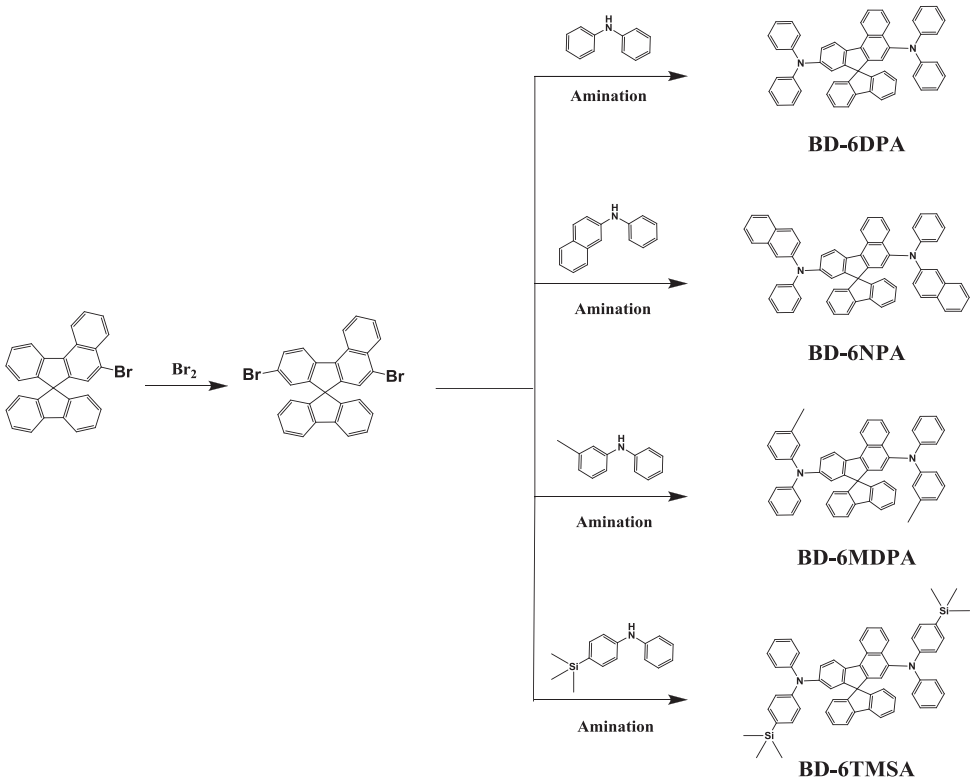

Scheme 1. Synthetic scheme and chemical structure of dopant materials.

Table 1
UV absorption, PL, energy levels and thermal properties of four dopant materials.

Properties	Abs (nm)		PL (nm)		Energy level (eV)		Thermal properties (°C)			Φ_f[a]
Sample	Solution	Film	Solution	Film	HOMO	LUMO	T_g	T_m	T_d	
BD-6DPA	407	416	478	484	5.48	2.77	120	270	429	0.747
BD-6NPA	411	421	464	491	5.44	2.77	154	295	477	0.656
BD-6MDPA	408	416	468	487	5.42	2.70	130	248	436	0.736
BD-6TMSA	407	413	459	484	5.45	2.70	144	256	437	0.672

[a] Fluorescence quantum efficiency, relative to 9,10-diphenylanthracene in cyclohexane (Φ_f = 0.90).

the PL spectrum of BD-6DPA to 478 nm as a result of increased electron donation. The solution fluorescence quantum efficiency (Φ_f) of dopant materials are 0.65 and 0.75, which were determined relative to 9,10-diphenylanthracene in cyclohexane (Φ_f = 0.90). The relatively higher fluorescence quantum efficiency values of BD-6DPA and BD-6MDPA compared to those of BD-6NPA and BD-6TMSA is due to the introduction of the phenyl and tolyl group, which maintains the intermolecular interaction between the emitting materials. A molecular simulation of DPA, NPA, MDPA and TMSA was carried out to understand the physical properties of DPA, NPA, MDPA and TMSA at the molecular level. Density functional theory (DFT) calculations have also been performed to characterize the three-dimensional geometries and the frontier molecular orbital energy levels of DPA, NPA, MDPA and TMSA at the B3LYP/6-31G* level [20] by using the Gaussian 03 program. The optimized structures and the HOMO/LUMO orbitals for DPA, NPA, MDPA and TMS are shown in Fig. 2. Energy gaps for DPA, NPA, MDPA and TMSA were calculated as 3.31 eV, 3.25 eV, 3.31 eV, and 3.30 eV, which corresponded to the absorption wavelengths of 416, 421, 416, and 413 nm, respectively. The calculated geometries of DPA, NPA, MDPA and TMSA in Fig. 1 show that the fluorene and benzofluorene are significantly twisted against each other because of the spiro center, resulting in a non-coplanar structure in each molecule. These geometrical characteristics can effectively prevent intermolecular interactions between π-systems and, thus, suppress molecular recrystallization, which improves the morphological stability of these molecules. Calculated highest occupied molecular orbital (HOMO) and lowest unoccupied molecular orbital (LUMO) density maps of DPA, NPA, MDPA and TMSA are also included in Fig. 1. The electron densities of the HOMOs and

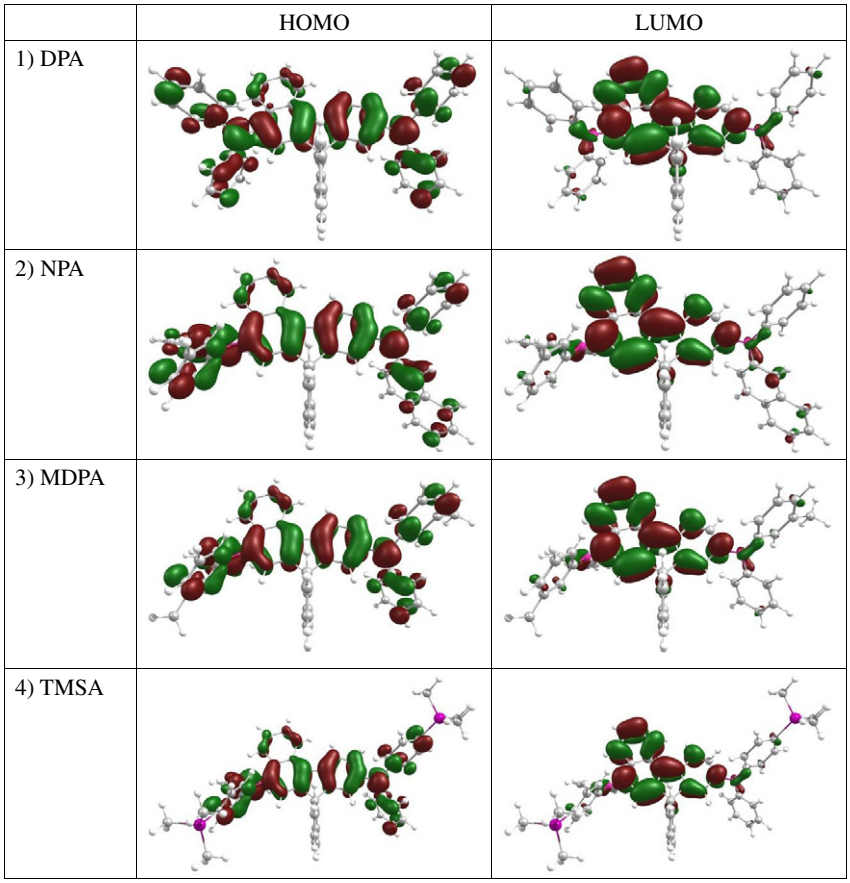

Fig. 1. Molecular simulation results of (a) DPA, (b) NPA, (c) MDPA, and (d) TMSA , showing the HOMO and LUMO orbital distribution (calculated at the DFT/B3LYP/6-31G* for optimization and Time Dependent DFT (TDDFT) using Gaussian 03).

LUMOs are mostly localized on the benzofluorene unit, implying that the absorption and emission processes can only be attributed to the π–π^* transition centered at the benzofluorene unit. As a result, the molecular orbital analysis clearly indicates that the substituents in fluorene unit do not influence the blue emission at all.

3.3. Thermal properties

The thermal properties of the resulting deep-blue emitting materials were characterized with DSC and TGA in a nitrogen atmosphere. The onset decomposition temperatures were 429, 477, 436 and 437 °C for BD-6DPA, BD-6NPA, BD-6MDPA and BD-6TMSA, respectively. Table 1 summarizes the DSC and TGA data for four dopant materials. The purified samples of BD-6DPA, BD-6NPA, BD-6MDPA and BD-6TMSA showed a melting point (T_m) of 270, 295, 248 and 256 °C, respectively. On the second heating, no melting points were observed, even though it was given enough time to cool in air. Once it becomes an amorphous solid, it does not revert to the crystalline state at all. After the sample had cooled to room temperature, a second DSC scan performed at 10 °C/min revealed a high glass transition temperature (T_g) between 120 and 154 °C because of their rigid spiro-type backbone. As a result, the amorphous glassy state of the transparent film of the four dopant materials was a good candidate as an EL material. This suggests that thermal stability was improved significantly by the introduction of various diarylamine groups.

3.4. EL properties

In order to find an optimized dopant concentration, EL spectra were gathered of MADN doped by BD-6 series dopants with different weight concentrations. The emission band increases with the increase of dopant concentration from 3 to 7% by weight. However, it is noted that CIE color coordinates of blue emission did not deviate from deep blue when the doping concentration of BD-6MDPA dopant increases from 5 to 7%. The CIE coordinates of the four devices made of MADN: 7%, 5%, 3%, 0% BD-6MDPA were (0.135, 0.153), (0. 135, 0.156), (0.138, 0.144) and (0.154, 0.164), respectively. It was found that sufficiently deep-blue emission was obtained in the sample with 5% concentration of BD-6MDPA with the CIE coordinates (0.135, 0.156).

OLEDs were fabricated by thermal evaporation onto a cleaned glass substrate precoated with transparent and conductive indium tin oxide (ITO). All the organic layers were grown by thermal evaporation at a deposition rate

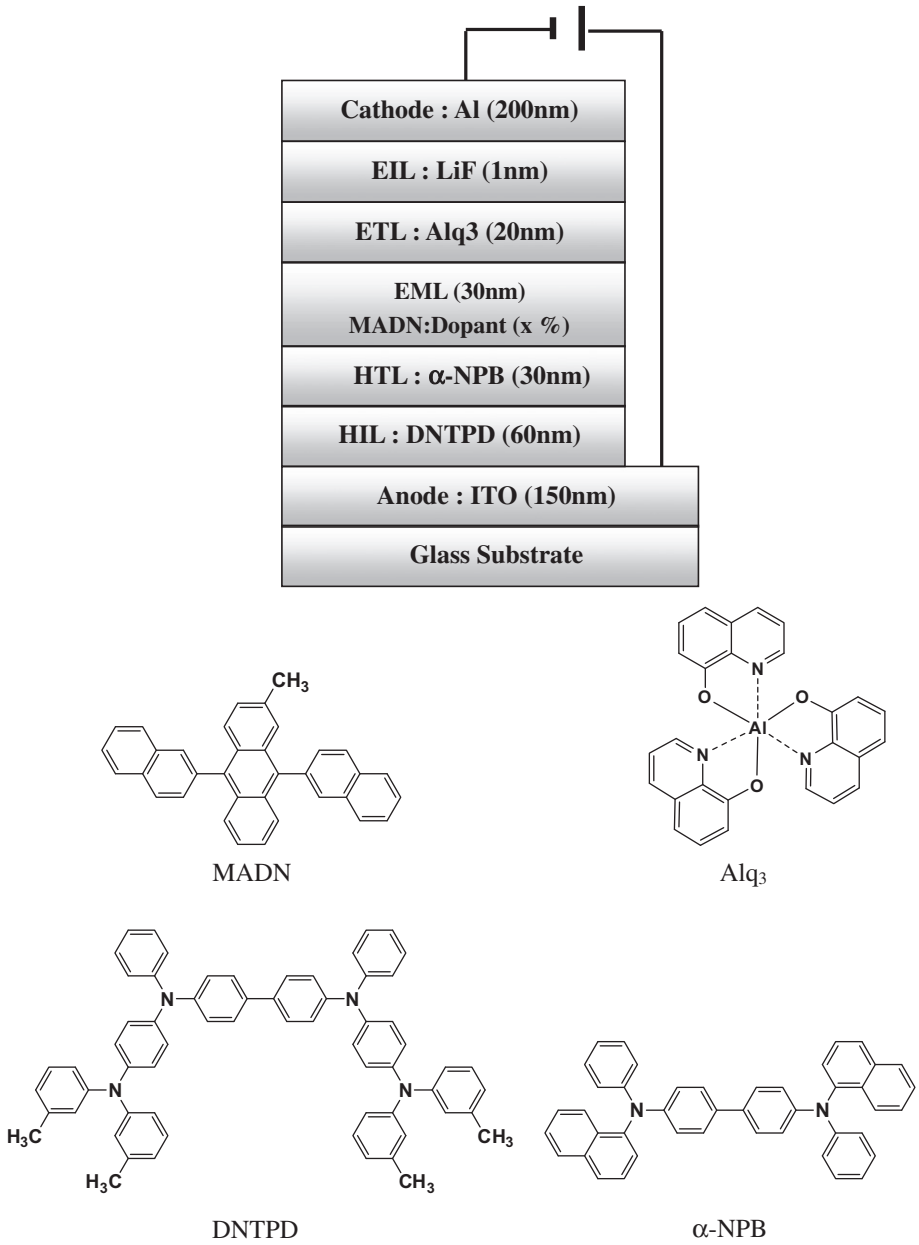

Fig. 2. The device configuration and the chemical structure of the materials used in the devices.

of 1 Å/s. The EL properties of the BD-6DPA, BD-6NPA, BD-6MDPA and BD-6TMSA dopant materials were examined by fabricating multilayer devices with the following configuration: glass ITO anode/HIL/HTL/EML/ETL/EIL/Al cathode. DNTPD was used as the HIL, α-NPB as the HTL, MADN:5% dopant as the EML and Alq3 as the ETL; a 10 Å LiF layer was used as the EIL, as shown in Fig. 2.

Fig. 3 shows the normalized EL spectra of a device composed of MADN doped with BD-6DPA, BD-6NPA, BD-6MDPA and BD-6TMSA at 7 V. All the devices showed intense blue emission in the EL spectra at 465, 463, 462 and 462, respectively. The maximum wavelength of the EL spectra varied significantly according to the dopant material. Based on the EL spectrum, the CIE coordinates of the emitting layer MADN doped with 5% BD-6DPA, BD-6NPA, BD-6MDPA and BD-6TMSA were measured to be (0.135, 0.175), (0.134, 0.168), (0.135, 0.156) and (0.135, 0.151), respectively.

3.5. OLED device properties

Figs. 4 and 5 shows the luminance–voltage and current density–voltage characteristics of the OLEDs with MADN:5% dopant as the EML. The threshold voltage for

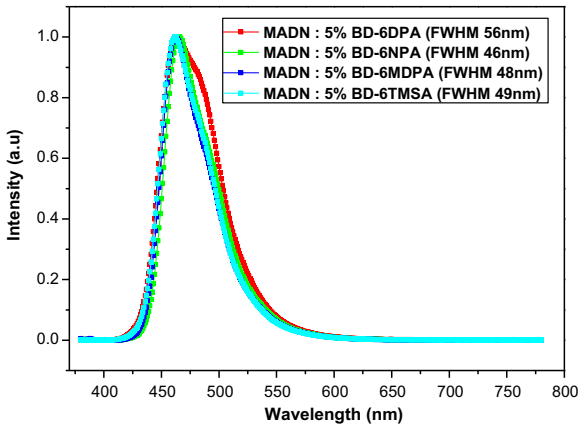

Fig. 3. EL spectra of the devices obtained from MADN host doped with various dopant materials.

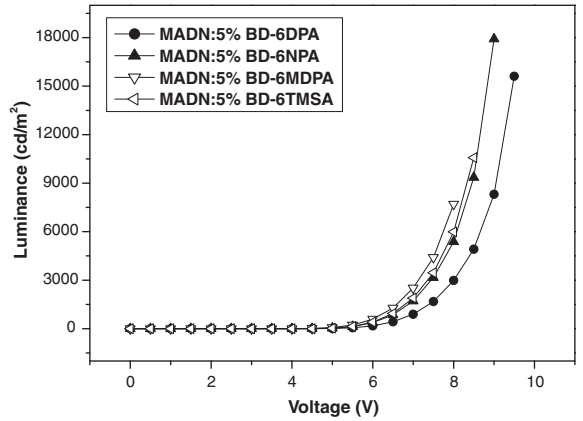

Fig. 4. Luminance–voltage characteristics of the device using MADN:5% dopant.

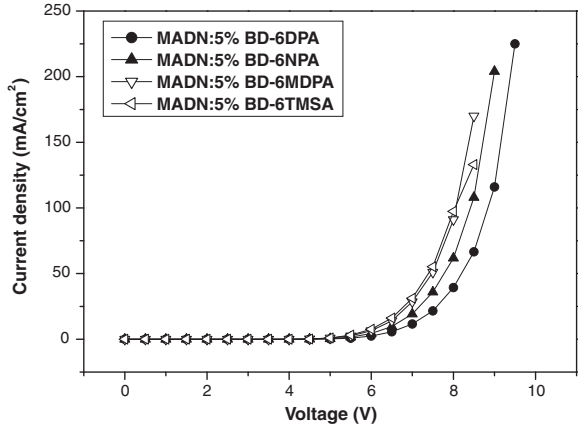

Fig. 5. Current density–voltage characteristics of the device using MADN:5% dopant.

luminescence was about 4.5 V in all the devices. In the case of the device using MADN doped with 5% BD-6MDPA, the maximum brightness of 7699 cdm^{-2} occurs at approximately 8.0 V. Table 2 summarizes the device characteristics at 7 V.

The luminance efficiency of the devices made using MADN:5% dopant were more than 4–6 times higher those of the device without the dopant. This suggests that the dopant is significantly effective in enhancing the EL properties of the spiro-type emitting layer.

The maximum power efficiency of the device obtained from MADN doped with 5% BD-6MDPA was 6.13 l mW^{-1}, which is five times that of the device without the dopant (1.28 l mW^{-1}). The device shows the maximum EQE of 7.95% and the efficiency increased rapidly to a maximum of approximately 8.84 cd A^{-1} at a low current density of 28.50 mA cm^{-2} at 7 V. The holes injected from α-NPB as HTL is transferred to the blue lighting layer and can be trapped to dopant sites. HOMO values of four dopant materials decreased in the order of BD-6DPA (5.48) > BD-6TMSA (5.45) > BD-6NPA (5.44) > BD-6MDPA (5.42). In the case of BD-6DPA having a little difference between the HOMO values of dopant and host materials, the holes from NPB were transferred to ETL as well as EML to causing the loss of holes. However the BD-6MDPA have the large capacity to catch the holes strongly, they minimized the loss of holes to result in the good electroluminescent efficiency. Thus the HOMO level of BD-6MDPA is suitable for holes trapping and the hole transporting properties of the dopant and MADN host is appropriate for balancing holes and electrons in the emitting layer. There was a large difference in EL efficiency between BD-6DPA and BD-6MDPA, even though both materials have almost same PL efficiencies and spectra.

Fig. 6 shows the dependence of luminescence efficiency on the current density of four devices. It can be seen that MADN doped with 5% BD-6NPA shows high efficiency and a small decrease of efficiency as the current density increased from 0 to 175 mA cm^{-2}, *i.e.*, a weak-current-induced fluorescent quenching. It reached a current efficiency of 8.56 cd A^{-1}. This suggests that an exciton is formed and light is emitted at specific thresholds. It should be noted that the efficiencies of these devices remained stable when the current density was increased to 175 mA cm^{-2}. The PL spectrum of MADN overlaps with a major portion of the absorption spectrum of BD-6MDPA. This indicates that BD-6MDPA can effectively accept energy from the host through Förster energy transfer or function as a direct recombination center due to the higher HOMO levels [21]. By using BD-6TMSA as the fluorescent dopant, the PE was successfully enhanced to 5.12 l mW^{-1}, which is four times higher than that of the undoped device. The EQE of OLEDs using BD-6TMSA as the fluorescent dopant with a doping concentration of 5 wt.% was 7.43% with CIE coordinates of (0.135, 0.151).

The device with MADN:5% BD-6-MDPA as EML shows the maximum EQE 8.16% at a current density of 14.0 mA cm^{-2} (6.5 V, 1275 cd m^{-2}) with an luminance efficiency of 9.11 cd A^{-1}, power efficiency of l mW^{-1} and the CIE coordinates of (0.135, 0.157). To our knowledge, this is one of the highest EQE in deep-blue OLEDs. Combined

Table 2
EL properties of the devices obtained from MADN host and four dopant materials.

Devices		MADN			
Properties		BD-6DPA	BD-6NPA	BD-6MDPA	BD-6TMSA
EL at 7 V	λ_{max} (nm)	463	465	462	462
	FWHM (nm)	56	46	48	39
	mA cm^{-2}	11.6	30.3	28.5	31.2
	cd A^{-1}[a]	7.69	8.40	8.84	8.02
	cd A^{-1}[b]	7.79 (7.5 V)	8.56 (6.5 V)	9.11 (6.5 V)	8.11 (6.5 V)
	l mW^{-1}[a]	3.82	4.17	4.39	3.98
	l mW^{-1}[b]	4.43 (5.5 V)	4.61 (6 V)	6.13 (4.5 V)	5.12 (5 V)
	cd m^{-2}	892.6	2544	2520	2503
	CIE-*x*	0.135	0.134	0.135	0.135
	CIE-*y*	0.175	0.168	0.156	0.151
	EQE[a] (%)	6.44	7.2	7.95	7.40
	EQE[b] (%)	6.54 (7.5 V)	7.32 (6.5 V)	8.16 (6.5 V)	7.45 (6.5 V)

[a] Values at 7 V.
[b] Values at a peak.

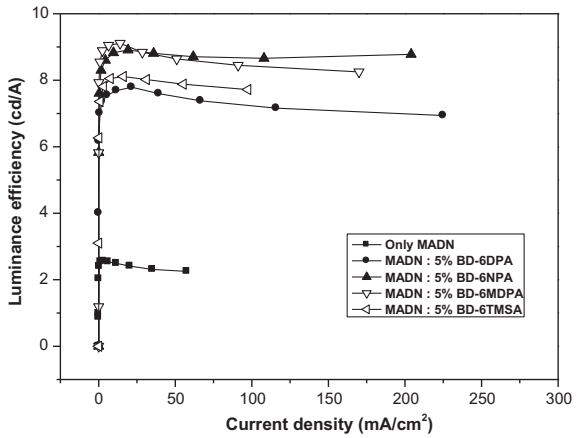

Fig. 6. Efficiency-current density characteristics of the device using MADN:5% dopant.

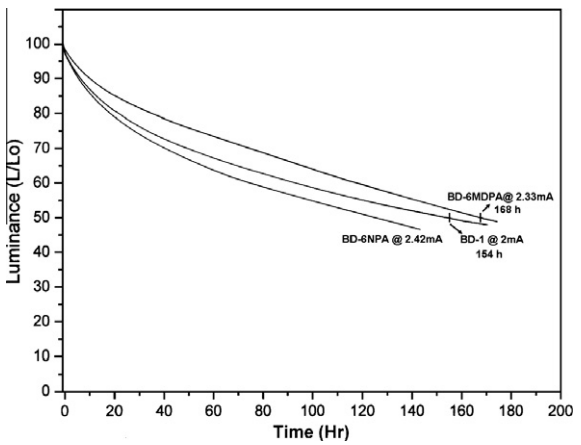

Fig. 7. Lifetime of MADN:5% dopant devices under initial luminance of 5000 cd/m^2 at a constant current.

good efficiency and color purity enables the dopant materials to be a good candidate as a deep-blue emitter for OLEDs.

Among synthesized compounds, the lifetime of BD-6MDPA, which showed the best EL efficiency in this series, was measured as the operational lifetime ($t_{1/2}$) of the blue devices under initial luminance of 5000 cd/m^2 at a constant current. Its lifetime (168 h@2.33 mA) was more than that of MADN:5% BD-1 (154 h@2 mA) as shown in Fig. 7.

4. Conclusion

A series of new deep-blue light emitting spiro-type dopant materials (BD-6DPA, BD-6NPA, BD-6MDPA and BD-6TMSA) were successfully prepared by amination reactions of 5,9-dibromo-**SFBF** with various diarylamines. When the device configuration of ITO/DNTPD/NPB/MADN:dopant/Alq_3/LiF/Al was constructed, the EL emissions of the devices (doped with 5% BD-6MDPA) are observed at 463 nm. In optimized structures, the device obtained using MADN:5% BD-6MDPA had greatest resulted in high performance OLEDs with a high external quantum efficiency of 8.16% and deep-blue emission, having CIE coordinates (0.135, 0/156). According to these characteristics, these deep-blue emitting materials have sufficient potential for display applications.

Acknowledgement

This research was supported by WCU (World Class University) program through the National Research Foundation of Korea funded by the Ministry of Education, Science and Technology (R31-10069).

References

[1] C.W. Tang, S.A. VanSlyke, Appl. Phys. Lett. 51 (1987) 913–915;
L.S. Hung, C.H. Chen, Mater. Sci. Eng. 39 (2002) 143;
U. Mitschke, P. Bäuerle, J. Mater. Chem. 10 (2000) 1471;
Y. Shirota, J. Mater. Chem. 10 (2000) 1.
[2] C.H. Chen, C.W. Tang, J. Shi, K.P. Klubek, Thin Solid Films 363 (2000) 327;
P. Wang, Z. Hong, Z. Xie, S. Tong, O. Wong, C.S. Lee, N. Wong, L. Hung, S. Lee, Chem. Commun. 14 (2003) 1664;
G. Cheng, Y.F. Zhang, Y. Zhao, S.Y. Liu, S. Tang, Y.G. Ma, Appl. Phys. Lett. 87 (2005) 151905;
W.J. Shen, R. Dodda, C.C. Wu, F. Wu, T.H. Liu, C.H. Chen, C.F. Shu, Chem. Mater. 16 (2004) 930;

S. Tao, Z. Hong, Z. Peng, W. Ju, X. Zhang, P. Wang, S. Wu, S. Lee, Chem. Phys. Lett. 397 (2004) 1;
H.T. Shih, C.H. Lin, H.H. Shin, C.H. Cheng, Adv. Mater. 14 (2002) 1409;
K. Danel, T.H. Huang, J.T. Lin, Y.T. Tao, C.H. Chuen, Chem. Mater. 14 (2002) 3860;
Y.H. Kim, H.C. Jeong, S.H. Kim, K. Yang, S.K. Kwon, Adv. Funct. Mater. 15 (2005) 1799;
C. Huang, C.G. Zhen, S.P. Su, K.P. Loh, Z.K. Chen, Org. Lett. 7 (2005) 391.

[3] Y. Xiong, W. Xu, C. Li, B. Liang, L. Zhao, J. Peng, Y. Cao, J. Wang, Org. Electron. 9 (2008) 533.

[4] A. Kadashchuk, A. Vakhnin, Yu. Skryshevski, V.I. Arkhipov, E.V. Emelianova, H. Bässler, Chem. Phys. 291 (2003) 243.

[5] S. Tokito, H. Tanaka, K. Noda, A. Okada, Y. Taga, Appl. Phys. Lett. 70 (1997) 1929.

[6] M.T. Lee, H.H. Chen, C.H. Tsai, C.H. Liao, C.H. Chen, Appl. Phys. Lett. 85 (2004) 3301.

[7] Q. Pei, Y. Yang, J. Am. Chem. Soc. 118 (1996) 7416;
Y. Ohmori, M. Uchida, K. Muro, K. Yoshino, Jpn. J. Appl. Phys. 30 (1991) L1941.

[8] S.M. Kelly, Flat Panel Displays: Advanced Organic Materials, Royal Society of Chemistry, Cambridge, UK, 2000.

[9] P.I.S. Tobat, S. Till, S. Achim, F.L. Thomas, S. Josef, Chem. Rev. 107 (2007) 1011;
H. Xiao, H. Shen, Y. Lin, J. Su, Dyes Pigm. 73 (2007) 224;
J. Pei, J. Ni, X.H. Zhou, X.Y. Cao, Y.H. Lai, J. Org. Chem. 67 (2002) 4924;
J.H. Fournier, T. Maris, J.D. Wuest, J. Org. Chem. 69 (2004) 1762;
H. Lee, J. Oh, H.Y. Chu, J.I. Lee, S.H. Kim, Y.S. Yang, G.H. Kim, L.-M. Do, T. Zyung, J. Lee, Y. Park, Tetrahedron 59 (2003) 2773.

[10] C.T. Chen, C.H. Chien, J. Am. Chem. Soc. 128 (2006) 10992;
K.T. Wang, C.L. Wang, Org. Lett. 3 (2001) 2285.

[11] F. Milota, C. Warmuth, A. Tortschanoff, J. Sperling, T. Fuhrmann, J. Salbeck, H.F. Kauffmann, Synth. Met. 121 (2001) 1497.

[12] V. Prelog, D. Bedekovic, Helv. Chim. Acta 62 (1979) 2285;
N. Harada, H. Ono, T. Nishiwaki, H. Uda, Chem. Commun. 24 (1991) 1753;
V. Alcazar, F. Diederich, Angew. Chem. 104 (1992) 1503;
T. Spehr, A. Siebert, T. Fuhrmann-Lieker, S. Salbeck, T. Rabe, T. Riedl, H.H. Johannes, W. Kowalsky, J. Wang, T. Weimann, P. Hinze, Appl. Phys. Lett. 87 (2005) 161103.

[13] K.T. Wong, Y.L. Liao, Y.T. Lin, H.C. Su, C.C. Wu, Org. Lett. 7 (2005) 5131.

[14] D. Gebeyehu, K. Walzer, G. He, M. Pfeiffer, K. Leo, J. Brandt, A. Gerhard, P. Stoessel, H. Vestweber, Synth. Met. 148 (2005) 205.

[15] Y.H. Kim, D.C. Shin, S.H. Kim, C.H. Ko, H.S. Yu, Y.S. Chae, S.K. Kwon, Adv. Mater. 13 (2001) 1690.

[16] R. Pudzich, J. Salbeck, Synth. Met. 138 (2003) 21.

[17] S. Tao, Z. Peng, X. Zhang, P. Wang, C.S. Lee, S.T. Lee, Adv. Funct. Mater. 15 (2005) 1716–1721.

[18] D. Horhant, J.J. Liang, M. Virboul, C. Poriel, G. Alcaraz, J. Rault-Berthelot, Org. Lett. 8 (2006) 257.

[19] S.O. Jeon, Y.M. Jeon, J.W. Kim, C.W. Lee, M.S. Gong, Org. Electron. 9 (2008) 522;
S.O. Jeon, Y.M. Jeon, J.W. Kim, C.W. Lee, M.S. Gong, Synth. Met. 159 (2009) 1147;
S. Hamai, F. Hirayama, J. Phys. Chem. 87 (1983) 83;
K.S. Kim, H.S. Lee, Y.M. Jeon, J.W. Kim, C.W. Lee, M.S. Gong, Dyes Pigm. 81 (2009) 174;
Y.M. Jeon, J.W. Kim, C.W. Lee, M.S. Gong, Dyes Pigm. 83 (2009) 66;
S.O. Jeon, Y.M. Jeon, J.W. Kim, C.W. Lee, M.S. Gong, Synth. Met. 159 (2009) 1147;
K.S. Kim, Y.M. Jeon, H.S. Lee, J.W. Kim, C.W. Lee, M.S. Gong, Synth. Met. 158 (2008) 870;
K.S. Kim, Y.M. Jeon, J.W. Kim, C.W. Lee, M.S. Gong, Org. Electron. 9 (2008) 797;
J.H. Kim, Y.M. Jeon, J.G. Jang, S. Ryu, H.J. Chang, C.W. Lee, J.W. Kim, M.S. Gong, Bull. Korean Chem. Soc. 30 (2009) 647;
S.O. Jeon, H.S. Lee, Y.M. Jeon, J.W. Kim, C.W. Lee, M.S. Gong, Bull. Korean Chem. Soc. 30 (2009) 863.

[20] M.J. Frisch et al., GAUSSIAN 03, Revision B.05, Gaussian, Inc., Pittsburgh, PA, 2003.

[21] S.J. Lee, J.S. Park, K.J. Yoon, Y.I. Kim, S.H. Jin, S.K. Kang, Y.S. Gal, S.W. Kang, J.Y. Lee, J.W. Kim, S.H. Lee, H.D. Park, J.J. Kim, Adv. Funct. Mater. 18 (2008) 3922.

[22] M.T. Lee, C.H. Liao, C.H. Tsai, C.H. Chen, Adv. Mater. 17 (2005) 2493.

[23] W. Norbert, A. Mitzel, S.H. Klaus, Chem. Ber. 127 (1994) 841.

Organic Electronics 11 (2010) 1853–1857

Contents lists available at ScienceDirect

Organic Electronics

journal homepage: www.elsevier.com/locate/orgel

Letter

Unoccupied states in copper phthalocyanine/fullerene blended films determined by inverse photoemission spectroscopy

Kouki Akaike [a,*], Andreas Opitz [b], Julia Wagner [b], Wolfgang Brütting [b], Kaname Kanai [c], Yukio Ouchi [a], Kazuhiko Seki [a]

[a] Department of Chemistry, Graduate School of Science, Nagoya University, Furo-cho, Chikusa-ku, Nagoya 464-8602, Japan
[b] Institute of Physics, University of Augsburg, 86135 Augsburg, Germany
[c] Department of Physics, Faculty of Science and Technology, Tokyo University of Science, Yamazaki 2641, Noda 278-8510, Japan

ARTICLE INFO

Article history:
Received 8 May 2010
Received in revised form 3 July 2010
Accepted 18 August 2010
Available online 22 September 2010

Keywords:
Donor/acceptor blend
Unoccupied states
Inverse photoemission spectroscopy
Electronic structure
Organic photovoltaics

ABSTRACT

Blends of copper phthalocyanine (CuPc) and fullerene (C_{60}) have successfully been used for organic field-effect transistors and photovoltaic cells. In this work we investigate the unoccupied states of CuPc/C_{60} blends by inverse photoemission spectroscopy. The energies of the lowest unoccupied molecular orbitals of CuPc and C_{60} vary linearly with the mixing ratio, which is consistent with the energy shifts of the vacuum level, the highest occupied molecular orbitals and core levels. The observed results can be interpreted as unchanged electron affinities of CuPc and C_{60} in the blended films due to nano-phase separation.

© 2010 Elsevier B.V. All rights reserved.

1. Introduction

Donor/acceptor (DA) blends have been used for improving the performance of various organic electronic devices so far. For example, DA blended films were introduced in organic photovoltaics (OPVs) as an active layer. Using blends the power conversion efficiency of small molecule-based OPVs has been improved significantly [1–4]. The success in employing DA blends for OPVs is due to an increase in the magnitude of the DA interface and improved efficiency of exciton dissociation, which consequently enhances the photocurrent. DA blended films have also been used in organic field-effect transistors (OFETs) leading to ambipolar character, where balanced mobility can be adjusted by the mixing ratio of the DA blend [5].

For understanding and describing the performance of these devices, knowledge on the electronic structure of the DA blend is important. Previously, Opitz et al. investigated the occupied states of CuPc/C_{60} blends with ultraviolet photoelectron spectroscopy (UPS) and X-ray photoelectron spectroscopy (XPS) [6]. It was found that the vacuum level, the highest occupied molecular orbitals (HOMOs) and core levels vary linearly with C_{60} concentration. Recently, the investigation of the electronic structure in occupied states has also been extended to P3HT/PCBM blended films for bulk heterojunction OPVs by Xu et al. [7]. However, the unoccupied states in DA blends have been elusive. So far, the energies of the lowest unoccupied molecular orbitals (LUMOs) in the blended films have only been estimated using the band gaps of neat films of donor and acceptor, which assume that the energy shift of the LUMO is the same as that of the HOMO. However, recently, it was found that the change in the polarization energy leads to the opposite shift of the LUMOs and HOMOs at the planar C_{60}/CuPc interface [8]. These results suggest that the constant band gap is not always a valid assumption at

* Corresponding author. Present address: Graduate School of Natural Science and Technology, Okayama University, Tsushima-naka 3-1-1, Okayama 700-8530, Japan. Tel.: +81 86 251 7797; fax: +81 86 251 7903.
E-mail address: akaike-k@cc.okayama-u.ac.jp (K. Akaike).

1566-1199/$ - see front matter © 2010 Elsevier B.V. All rights reserved.
doi:10.1016/j.orgel.2010.08.011

an interface, and that the direct measurements of the energies of the LUMOs for donor and acceptor are important to understand the dominant factor which determines the electronic structure.

In this letter, we have investigated the LUMO energies in CuPc/C_{60} blends with various mixing ratios by inverse photoemission spectroscopy (IPES), which can detect the energies of unoccupied states, directly [9]. We found that the LUMOs of CuPc and C_{60} vary linearly with increasing C_{60} concentration. This trend is consistent with the results on the vacuum level, the HOMOs and the core levels. The observed results indicate that electron affinities of CuPc and C_{60} are the same in the blend as in the neat film, which can be attributed to phase separation between CuPc and C_{60} in the blend, as observed by atomic force microscopy and X-ray scattering.

2. Experimental

As substrates we used clean polycrystalline Au films prepared by thermal evaporation on naturally oxidized Si (100) substrate in ultra-high vacuum (base pressure $< 1 \times 10^{-7}$ Pa). The CuPc/C_{60} mixed films were fabricated in situ on the Au substrate by co-evaporation using two glass cells with different evaporation rates to achieve the required mixing ratio. The thickness of the blended films was monitored by a quartz microbalance and adjusted to be 10 nm. IPES measurements were performed in situ in the isochromat mode using a home-made apparatus [10]. The band-pass type detector for photons with an energy of $h\nu = 9.3$ eV consists of a channeltron coated with KCl and is placed behind a SrF_2 window. A low energy electron gun was used to produce a mono-energetic electron beam. The substrate temperature during sample preparation and measurement was kept at room temperature. The morphology of blended films were also analyzed by atomic force microscope (AFM, Seiko Instrument: SPA300) in non-contact mode under ambient atmosphere.

3. Results and discussion

Fig. 1 shows the IPES spectra of the CuPc/C_{60} blend films as a function of C_{60} concentration. The abscissa is energy measured from the Fermi level (E_F) of clean Au substrates. Peaks marked with horizontal lines or solid filling are assigned to unoccupied states of CuPc and C_{60}, respectively. The composition of the blended films were determined by fitting each spectra with Voigt functions using the spectral shapes of neat CuPc and C_{60} films. Here, Gaussian width was set to be 0.75 eV including the total energy resolution of IPES measurements at room temperature. Lorentzian widths were properly taken to fit each peak. The spectra of the neat films (0% and 100% C_{60}) are in good agreement with the reported results [11–14]. The spectra of the mixed films in Fig. 1 can be described by a superposition of the spectra for neat CuPc and C_{60} films with proper energy shifts. No additional features are required in the fitting procedure, which indicates that there is no strong interaction between CuPc and C_{60}. From Fig. 1, it was found that

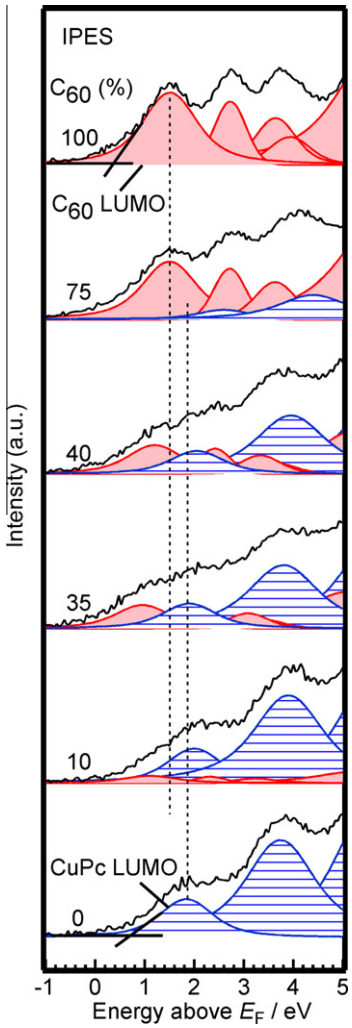

Fig. 1. The IPES spectra of blended films are shown as a function of C_{60} concentration. Peaks marked with striped lines or solid filling are assigned to unoccupied states of CuPc and C_{60}, respectively. Dashed lines are visual aids for recognizing the energy shifts of the LUMOs. The onsets of the LUMO peaks were determined from the cross-point as indicated by solid lines in neat CuPc and C_{60} films (0% and 100% C_{60}).

the LUMO peaks of CuPc and C_{60} move away from E_F with increasing C_{60} concentration.

The energy shifts of the LUMOs are consistent with those of the vacuum level and the HOMOs. Fig. 2 shows the concentration dependence of the observed energies for vacuum level (triangles in Fig. 2(a)), HOMO (squares in Fig. 2(a)) and LUMO (Fig. 2(b)). The upper and lower axes are CuPc and C_{60} concentrations, respectively. The energies of the HOMOs and LUMOs were deduced from the peak onsets. The data of vacuum level and the HOMOs were taken from the UPS spectra that the Augsburg group reported in Ref. [6]. Considering mixed films, the LUMOs of CuPc and C_{60} shift upward by 0.7 and 0.5 eV, respectively, with increasing C_{60} concentration, which is close to the shift of the vacuum level and the HOMOs.

Important to mention are the differences of the two analyses. Whereas the study presented here was carried

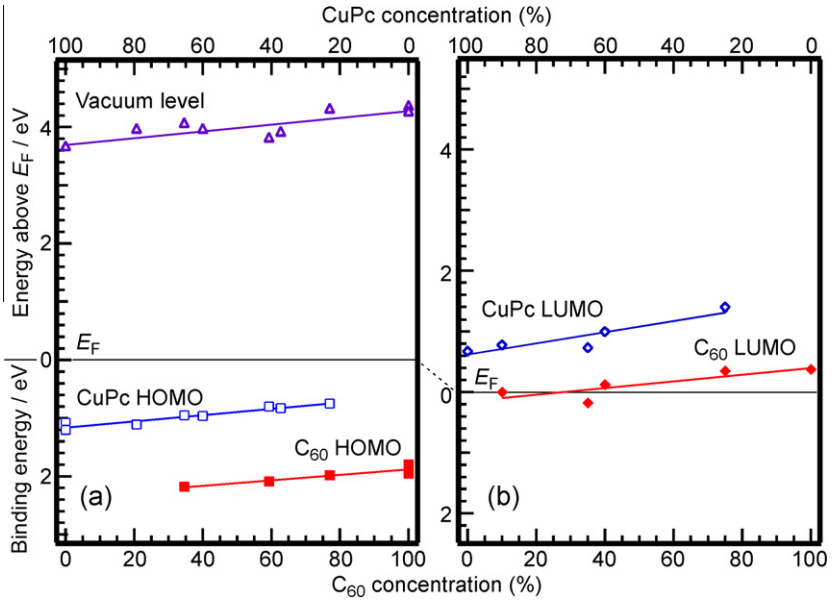

Fig. 2. Dependence of vacuum level and the HOMO (a) and LUMO (b) energies of CuPc and C_{60} on different mixing ratio. The data of vacuum level and HOMOs are deduced from the UPS spectra reported in [6]. Error bars in the LUMO data of CuPc in (b) are derived from an uncertainty of spectral fitting. The lines are linear fits of the corresponding energy levels. The data in (a) and (b) are collected on thin films prepared on contaminated and clean Au substrates, respectively. For a clearance of the difference in work function, *y*-axis in (b) is shifted by 0.35 eV.

out on a clean gold surface (Fig. 2(b)) the substrate of the previous study was contaminated with hydrocarbons (Fig. 2(a) and [6]). After deposition of CuPc and C_{60} on contaminated-Au substrate, the vacuum levels of CuPc and C_{60} films are found at 3.8 and 4.3 eV from E_F, respectively [6]. On the other hand, the vacuum levels of CuPc and C_{60} films prepared on clean Au surfaces are located at 4.21 and 4.63 eV, respectively [15]. Thus a difference in the Fermi levels should be taken into account for the analysis of the energy values of the materials. Assuming a difference of 0.35 eV in the vacuum levels for the semiconducting films, the HOMO–LUMO gap determined from the onset of the peaks is 2.2 eV for CuPc and 2.6 eV for C_{60}, respectively. These values are in between the energy gap derived from peak maxima and onsets which were reported in the literature [11–14]. The differences to the values in the literature are based on the experimental broadening of the peak width which is not accounted here and which is in the range of 0.3–0.4 eV in total for both experiments, UPS and IPES.

Even though different substrates were used for UPS and IPES measurements, similar energy shifts were observed in the vacuum level, HOMO and LUMO. Thus, the difference in substrate work functions can be neglected to discuss nature of electronic properties in the blended films. The similar shift of all levels indicates that the ionization energies and electron affinities of CuPc and C_{60} are constant even in their blended film. The observed constant ionization energies and electron affinities as well as the common vacuum level can be related to nano-phase separation in the mixed film (see below) [16].

In Fig. 3, AFM images of the mixed films with C_{60} concentration of 10%, 35% and 75% are shown. The maximum height increases with increasing C_{60} concentration, which can be attributed to higher roughness of C_{60} films than CuPc films [13]. We also notice that the maximum height exceeds the nominal thickness of the mixed films (10 nm), which also reflects the growth of C_{60} grains. These results can be related to phase separation between CuPc and C_{60} in the blend. Actually, X-ray diffraction (XRD) measurements of a CuPc/C_{60} blend with mixing ratio of 1:1 show the formation of the α-phase of CuPc and the *fcc*-phase of C_{60} even in the blended film [13]. The results of the XRD study indicate that both CuPc and C_{60} crystallites formed in blends are similar to neat films, and that phase separation occurs between the two materials. This can explain the fact that the ionization energies and electron affinities of CuPc and C_{60} in the mixture are similar to those of neat films in the whole range of concentration (Fig. 2). Nevertheless, phase separation occurs only on a length scale of about 10 nm which allows for the preservation of a common vacuum level [6,16–17].

The behavior of the energy levels in planar and bulk heterojunction solar cells is reported in the literature [18] for layers grown on the device relevant electrode PEDOT:PSS. It was found that the energy gap between the HOMO of CuPc and the LUMO of C_{60} is comparable for blended films and planar heterojunctions in contrast to our previous expectation [6]. This is because the HOMO of CuPc stays constant and the LUMO of C_{60} is also expected to be located at the same energy in the planar heterojunction and blended films [18]. As for CuPc, the hole polaron level of CuPc is pinned to the Fermi level of the electrode material [19] which prevents changes by the variation of the blend ratio. One can therefore expect that the open circuit voltage in planar heterojunction, whose value

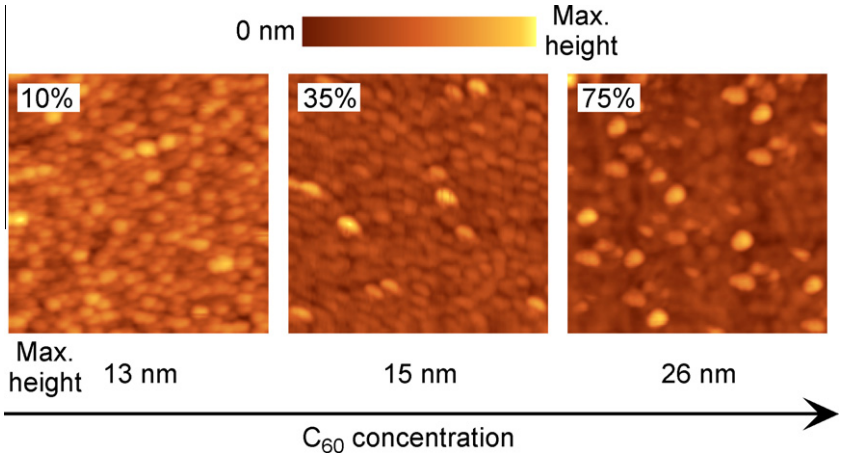

Fig. 3. AFM images for CuPc/C_{60} blends with C_{60} concentration of 10%, 35% and 75%. The maximum heights of each film were deduced from the lowest and highest values in each image. The image size is 1 μm^2.

can be related to the energy gap between the HOMO of the donor and LUMO of the acceptor [20], will be similar to that in blended films. However, this expectation contradicts with the fact that the open circuit voltage in blended films is by 0.2 V smaller than that in planar heterojunction [16–17]. The reduced open circuit voltage in bulk heterojunction solar cells in comparison to planar heterojunction cells are reported to be explained with additional recombination losses [21] or insufficient energy level alignment at contacts [22].

It is also noted that in the case of CuPc/Au interface the Fermi level seems to be near mid-gap of CuPc (Fig. 2(a)), similar to various phthalocyanines/Au substrate interfaces [23], when the work function difference in Au substrates between UPS and IPES studies is considered. However, the pinning of the energy levels is not expected at the present CuPc/Au interface, since Kelvin probe study indicated that the interfacial dipole induced by the push-back effect lowers the energy levels of CuPc on Au substrate and no band bending was observed up to CuPc thickness of 20 nm [24]. On the other hand, for C_{60} films, the energy level pinning occurs at 10–50 nm thickness on Au substrate [25]. This can be attributed to the pinning of the LUMO edge of C_{60} to the Fermi level of Au substrate [26]. Actually, the LUMO edge of C_{60} at C_{60} concentration = 100% is very close to the Fermi level of Au substrate as shown in Fig. 2(b). With increasing C_{60} concentration in CuPc/C_{60} blended films, the energy level alignment gradually changes between CuPc/Au and C_{60}/Au systems.

4. Conclusion

We performed the first investigations on the LUMO energies of CuPc and C_{60} in blends of both materials using inverse photoemission spectroscopy. It was found that the LUMOs of CuPc and C_{60} shift away from E_F by 0.7 and 0.5 eV, respectively, which is similar to the energy shifts of the vacuum level and the HOMO peaks. The coincidence of the energy shifts for the LUMOs with the vacuum level indicates that the electron affinities of CuPc and C_{60} are unchanged in blended films as compared to the neat materials. This can be attributed to nano-phase separation between CuPc and C_{60}, which is indicated by AFM measurements of the blended films. The present results provide information on unoccupied states in DA blends, which will be beneficial for understanding the energetics in DA solar cells.

Acknowledgements

This work was supported by the Grant-in-Aid for Scientific Research (Grant No. 19105005) and Global COE program on Molecular Functions at Nagoya University from the Ministry of Education, Culture, Sports, Science and Technology of Japan (MEXT) and Special Coordination Funds for Promoting Sciences and Technology of MEXT. K.A. thanks Global COE program at Nagoya University for Independent Research Expenses. The Augsburg group acknowledges financial support by the Deutsche Forschungsgemeinschaft (DFG) within priority program 1355 ('Elementary processes of organic photovoltaics'). W.B. thanks the Japan Society for the Promotion of Science (JSPS) for providing a fellowship for research in Japan.

Reference

[1] M. Hiramoto, H. Fujiwara, M. Yokoyama, Appl. Phys. Lett. 58 (1991) 1062.
[2] J. Rostalski, D. Meissner, Sol. Energy Mater. Sol. C 61 (2000) 87.
[3] P. Peumans, A. Yakimov, S.R. Forrest, J. Appl. Phys. 93 (2003) 3693.
[4] B.P. Rand, J. Genoe, P. Heremans, J. Poortmans, Prog. Photovolt: Res. Appl. 15 (2007) 659.
[5] A. Opitz, M. Bronner, W. Brütting, J. Appl. Phys. 101 (2007) 063709.
[6] A. Opitz, M. Bronner, W. Brütting, M. Himmerlich, J.A. Schaefer, S. Krischok, Appl. Phys. Lett. 90 (2007) 212112.
[7] Z. Xu, L.M. Chen, M.H. Chen, G. Li, Y. Yang, Appl. Phys. Lett. 95 (2009) 013301.
[8] K. Akaike, K. Kanai, Y. Ouchi, K. Seki, Adv. Funct. Mater. 20 (2010) 715.
[9] K. Kanai, K. Akaike, K. Koyasu, K. Sakai, T. Nishi, Y. Kamizuru, T. Nishi, Y. Ouchi, K. Seki, Appl. Phys. A 95 (2009) 309.
[10] T. Nishi, T. Iwahashi, H. Yamane, Y. Ouchi, K. Kanai, K. Seki, Chem. Phys. Lett. 455 (2008) 213.
[11] K. Akaike, K. Kaname, H. Yoshida, J. Tsutsumi, T. Nishi, N. Sato, Y. Ouchi, K. Seki, J. Appl. Phys. 104 (2008) 023710.

[12] R.W. Lof, M.A. Veenendaal, B. Koopmans, H.T. Jonkman, G.A. Sawatzky, Phys. Rev. Lett. 68 (1992) 3924.
[13] I.G. Hill, A. Kahn, Z.G. Soos, R.A. Pascal Jr., Chem. Phys. Lett. 327 (2000) 181.
[14] S. Krause, M.B. Casu, A. Schöll, E. Umbach, New J. Phys. 10 (2008) 085001.
[15] O.V. Molodtsova, M. Knupfer, J. Appl. Phys. 99 (2006) 053704.
[16] A. Opitz, J. Wagner, W. Brütting, A. Hinderhofer, F. Schreiber, Phys. Status Solidi A 206 (2009) 2683.
[17] A. Opitz, J. Wagner, W. Brütting, I. Salzmann, N. Koch, J. Manara, J. Pflaum, A. Hinderhofer, F. Schreiber, IEEE J. Sel. Top. Quantum Electron, in press.
[18] A. Wilke, T. Mizokuro, R.-P. Blum, J.P. Rabe, N. Koch, IEEE J. Spec. Top. Quantum Electron, in press.
[19] H. Peisert, A. Petr, L. Dunsch, T. Chassé, M. Knupfer, Chem. Phys. Chem. 8 (2007) 386.
[20] B.P. Rand, D.P. Burk, S.R. Forrest, Phys. Rev. B 75 (2007) 115327.
[21] T. Kirchartz, B.E. Pieters, K. Taretto, U. Rau, Phys. Rev. B 80 (2009) 035334.
[22] C. Uhrich, D. Wynands, S. Olthof, M.K. Riede, K. Leo, S. Sonntag, B. Maennig, M. Pfeiffer, J. Appl. Phys. 104 (2008) 043107.
[23] H. Peisert, M. Knupfer, J. Fink, Appl. Phys. Lett. 81 (2002) 2400.
[24] Y. Tanaka, K. Kanai, Y. Ouchi, K. Seki, Org. Electron. 10 (2009) 990.
[25] N. Hayashi, H. Ishii, Y. Ouchi, K. Seki, J. Appl. Phys. 92 (2002) 3784.
[26] T.R. Ohno, Y. Chen, S.E. Harvey, G.H. Kroll, J.H. Weaver, R.E. Haufler, R.E. Smalley, Phys. Rev. B 44 (1991) 13747.

Organic Electronics 11 (2010) 1858–1863

Contents lists available at ScienceDirect

Organic Electronics

journal homepage: www.elsevier.com/locate/orgel

Simple write-once-read-many-times memory device based on a carbon sphere-poly(vinylphenol) composite

Messai A. Mamo [a,b], Wagner S. Machado [c], Willem A.L. van Otterlo [b], Neil J. Coville [a,b], Ivo A. Hümmelgen [c,*]

[a] DST/NRF Centre of Excellence in Strong Materials, University of the Witwatersrand, PO Wits, 2050, Johannesburg, South Africa
[b] Molecular Sciences Institute, School of Chemistry, University of the Witwatersrand, PO Wits, 2050, Johannesburg, South Africa
[c] Departamento de Física, Universidade Federal do Paraná, Caixa Postal 19044, 81531-990 Curitiba, Brazil

ARTICLE INFO

Article history:
Received 25 June 2010
Received in revised form 14 August 2010
Accepted 23 August 2010

Keywords:
Organic memories
Carbon spheres
WORM memory

ABSTRACT

We report on the electrical properties of a thin film of carbon spheres and cross-linked poly(4-vinylphenol) composites, sandwiched between an Al bottom contact and a Au or Al top contact. These simple sandwich structure memory devices show write-once-read-many-times (WORM) characteristics with an ON/OFF current ratio of 10^8 at 1 V bias when Au is used as top contact and the write operation corresponding to an OFF/ON transition can be made at low voltages, of *ca.* 2 V.

© 2010 Elsevier B.V. All rights reserved.

1. Introduction

There is an always increasing need to enhance data processing and data storage in our society, which imposes higher demands for memory devices. In some electronic devices used for this purpose the information is written or erased by changing the conductivity through an external input. This input changes the device conductivity in order to achieve a stable state different from the initial one, characterizing bistability. This bistability allows the introduction of binary information that can then be read by measuring the current that flows through the device submitted to a known voltage [1].

In the last years several attempts have been made to substitute inorganic semiconductors and related processes by simpler processes and device architectures using organic semiconductors [2–19], motivated by the perception that existing technologies are inadequate in one or more memory operating parameters [20]. Additionally, there is a need for memories whose production processes are compatible with generally adopted procedures in organic device based circuits, in order to allow simple incorporation of memories in organic electronics.

In this letter we report on the electrical non-volatile memory properties of a thin film of carbon spheres (CSs) and cross-linked poly(4-vinyl phenol) (CPVP) composites, sandwiched between an Al bottom contact and a Au or Al top contact layer. These simple memory devices show write-once-read-many-times (WORM) characteristics, *i.e.*, if the device is turned from the OFF to ON-state, the change is irreversible.

Despite the fact that there are several groups working on CS synthesis, characterization and applications [21], the use of CSs in electronic devices has been under reported.

2. Experimental

All chemicals, except the carbon spheres, were obtained from Sigma–Aldrich and used without further purification. Carbon spheres (see Fig. 1) were synthesized by passing a continuous flow of acetylene gas (100 mL/min) for

* Corresponding author. Tel./fax: +55 41 3361 3645.
E-mail address: iah@fisica.ufpr.br (I.A. Hümmelgen).

1566-1199/$ - see front matter © 2010 Elsevier B.V. All rights reserved.
doi:10.1016/j.orgel.2010.08.013

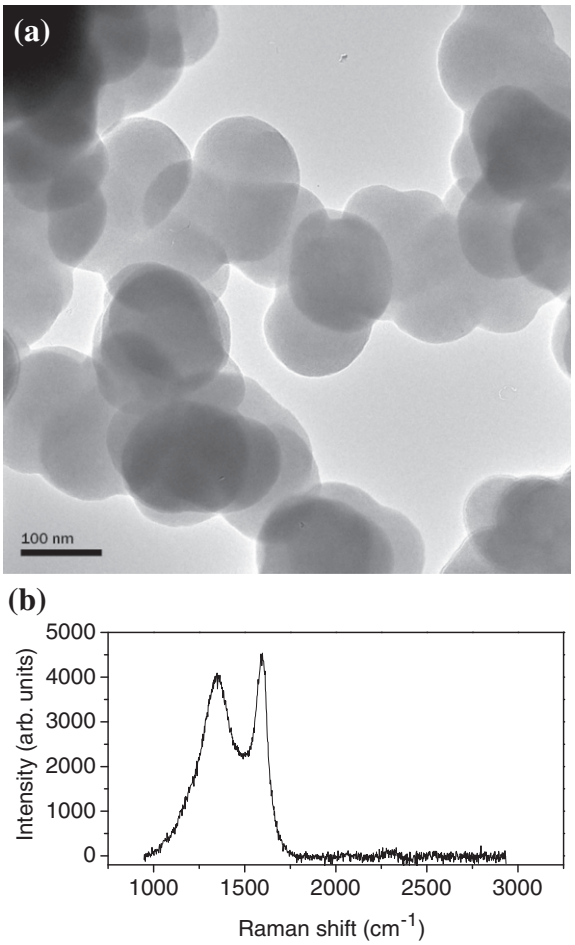

Fig. 1. (a) Transmission electron micrograph and; (b) Raman spectrum of the carbon spheres.

10 min at 900 °C under an argon atmosphere (100 mL/min) through a quartz tube placed vertically in a furnace. The acetylene and the argon gases were allowed to flow from top to bottom through the quartz tube and the carbon material collected in a 500 mL round bottom flask. This synthesis is based on a process reported by Jin et al. [22].

The carbon spheres thus synthesized were characterized by transmission electron microscopy (TEM) using a FEI Tecnai G2 Spirit electron microscope at 120 kV. Raman spectroscopy (J-Y T64000) was used to measure the intensity of the D and G bands of the CSs.

The memory device was prepared by the simple construction of ~450 nm (composite A) and ~300 nm (composite B) thick CPVP-CS composite film sandwiched between a 100 nm thick Al bottom electrode and a 100 nm thick, either Au or Al, top electrode (Al/CPVP-CS/Au or Al), as schematically represented in Fig. 2. The device active area, corresponding to the overlap of the top and bottom electrode, was 4 mm^2. The thickness of the PVP film was estimated by the capacitance measurements of the CPVP film, assuming a relative dielectric constant equal to 3.5 [23].

For the fabrication of the devices, poly(4-vinylphenol) (PVP) and methylated poly(melamine-*co*-formaldehyde) (PMF) as a cross-linker, were dissolved in propylene glycol monomethyl ether acetate, at concentrations equal to 11% and 4%, respectively (sample A), and 7% and 2.5%, respectively (sample B). The concentration was varied in order to vary the viscosity of the solution to obtain spin-coated films with different thickness, while maintaining the same PVP/PMF w/w ratio. CSs were then added to these two solutions (A and B), to prepare devices with four different ratios of CS to host polymer matrix, specifically [CS]/[PVP + PMF] w/w concentrations of 5%, 10%, 15% and 20%), as summarized in Table 1.

The composite mixtures were sonicated for *ca* 3 h at room temperature and 100 μL of suspension, in each case, were then spin-coated onto an Al electrode at 2000 rpm.

Table 1
PVP and PMF concentrations used for the preparation of solutions before CS addition; and the relative CS to PVP + PMF concentration in the solutions after CS addition. This is also the concentration in the prepared films.

Sample	Solution		Film
	PVP concentr. (w/w%)	PMF concentr. (w/w%)	[CS]/[PVP + PMF] (w/w%)
A-00	11.0	4.0	0
A-05	11.0	4.0	5
A-10	11.0	4.0	10
A-15	11.0	4.0	15
A-20	11.0	4.0	20
B-00	7.0	2.5	0
B-05	7.0	2.5	5
B-10	7.0	2.5	10
B-15	7.0	2.5	15
B-20	7.0	2.5	20

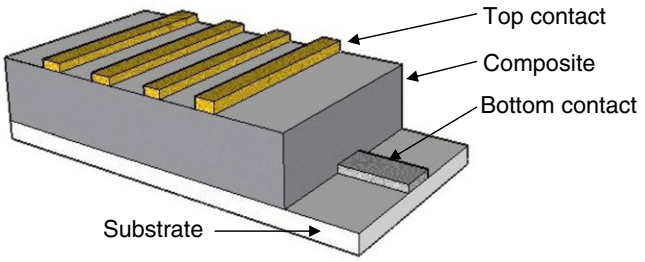

Fig. 2. Schematic representation of the memory device structure.

The devices were then annealed in air at 200 °C for an hour in order to cross-link the polymer [24–26]. Then, either Au or Al metal was thermally evaporated onto the composite surface at 10^{-6} Torr base pressure using a shadow mask for device patterning. The devices, 8 for each concentration, were characterized using a programmable Keithley 2602. The OFF–ON transition time was determined measuring the voltage drop in a 10 Ω resistor in series with a 81101A Agilent pulse generator (50 MHz) and the memory device. The voltage drop in the resistor was measured with a DSO 6104A Agilent 4-channel oscilloscope (1 GHz).

3. Results and discussion

Fig. 1a shows the transmission electron microscope (TEM) image of the CSs. The synthesized carbon spheres were obtained in good yield (about 250 mg) and size distributions (diameter: 124 ± 13 nm). The Raman spectrum of the CSs (Fig. 1b) shows two bands at 1356 cm^{-1} (D band) and at 1595 cm^{-1} (G band), indicating that the synthesized material is graphitic in nature. The good yield and the simple production procedure constitute an advantage in using this material, when compared to more expensive carbon materials such as carbon nanotubes and fullerenes, which have been also demonstrated to be suitable for memory devices [9],[27]. As a consequence, the CS-CPVP composite, constitutes a very cheap material option as active layer in memory devices.

Current–voltage (I–V) measurements were carried out to investigate the electrical properties of the devices. The I–V characteristics of devices made from composites A and B are qualitatively similar, both displaying distinctly bistable electrical conductivity states. Starting with a low-conductivity (OFF) state in the devices containing composite A and B (Fig. 3a–b, and Fig. 4a–b, respectively) the current increases gradually with an the increase in applied negative voltage (bottom Al electrode negatively biased). The current density, J, remains in the low 10^{-9}–10^{-7} A cm^{-2} range, corresponding to sweep 1 (up to −2 V in Fig. 3a-b), until the threshold voltage of about −4 V is reached. At the threshold voltage, J increases suddenly from 10^{-4}–10^{-1} A cm^{-2} (sweep 2), indicating a device transition from the low-conductivity OFF-state to the high conductivity ON-state. A similar OFF–ON transition occurs if a threshold voltage is achieved at positive applied voltage (not shown here).

However, there is a quantitative difference between devices shown in Figs. 3 and 4. In the case of Fig. 4, the ob-

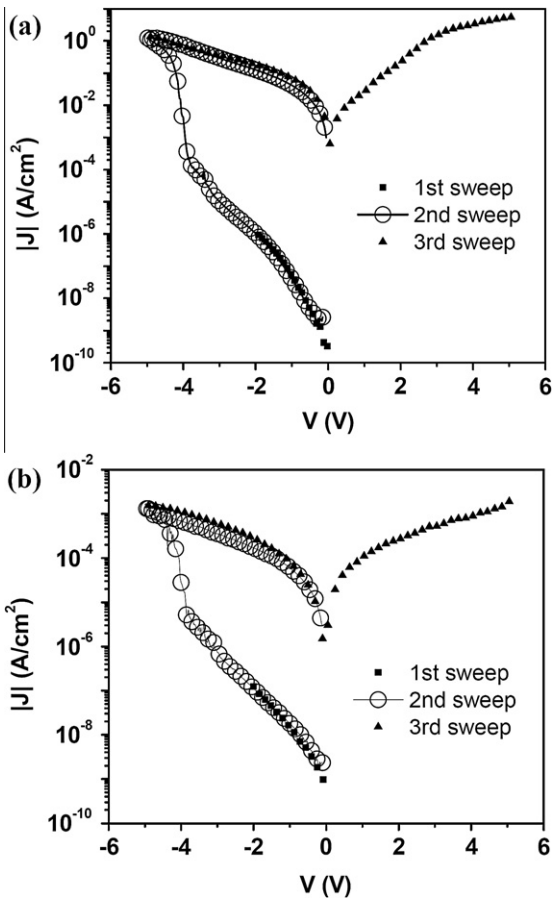

Fig. 3. $J(V)$ characteristic of the: (a) Al/CPVP-CS(A-10)/Au device; (b) Al/CPVP-CS(A-10)/Al devices.

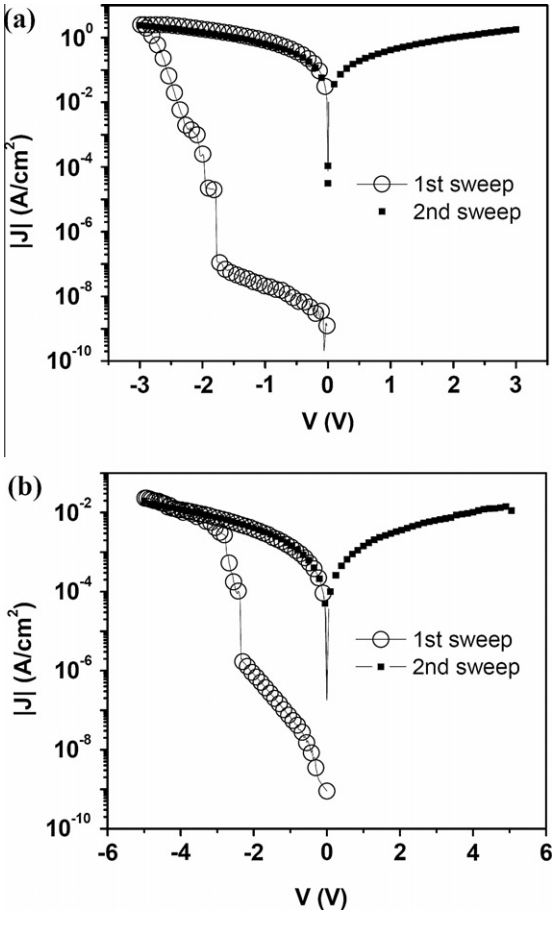

Fig. 4. $J(V)$ characteristic of the: (a) Al/CPVP-CS(B-15)/Au; (b) Al/CPVP-CS(B-15)/Al.

served threshold voltages are around −1.8 and −2.3 V for the Au and Al electrodes, respectively, values that are much lower than the ∼−4 V value obtained for devices like that of Fig. 3. This presumably relates to the different thickness of the two composites.

For the composites used in the samples, whose data are presented in Figs. 3 and 4, the device readily transformed from a low-conductivity state (OFF-state) to a high conductivity state (ON-state). The ON/OFF current ratio at $V = -1$ V is of the order of $\sim 10^6$ and $\sim 10^4$ for the Au and Al electrodes (Fig. 3a–b), respectively for composite A −10; and $\sim 10^8$ and $\sim 10^4$ for Au and Al electrode, respectively, for composite B-15 (Fig. 4a–b).

For comparative purposes, devices having a structure of Al/CPVP/Au or Al were also fabricated. The *J–V* characteristics of the devices are shown in Fig. 5. The Al/CPVP/Au or Al devices show low-conductivity, corresponding to an OFF-state, in the full voltage range used for CS-CPVP composite devices. This implies that the memory effect is due to the presence of carbon spheres in the polymer composites.

When Au was used as top metal electrode, the device performed better than when Al metal was used, showing a higher ON/OFF current ratio. Moreover, according to our results, even using a relatively thin film in a simple device architecture, permits control of the threshold voltage and the ON/OFF current, through top electrode material choice and thickness of the composite film. In the case of composite B-10, these values were measured to be *ca.* −2 V and $\sim 10^8$, respectively. This constitutes a very simple strategy for adjustment of the device characteristics, representing a big advantage when a production process is considered. Furthermore, this threshold voltage is low and the ON/OFF ratio high enough to allow compatibility with most conventional electronics and available circuitry, without further need of sophisticated improvements.

The relative concentration of CSs in the composites used in our devices influence the electrical characteristics trends, as shown in Fig. 6a and b. When the CS relative concentration increases (15% CS and 20% CS) there is an increase in the OFF current density while the ON current density is lowered when low CS concentration (5% CS) is used. As a consequence, the highest ON/OFF current density ratio is always observed in samples with a 10% CS concentration (A-10 and B-10, in Table 1). The variation of the threshold voltages with CS concentration is small, of the order of 0.5 V, which is similar to the maximum dispersion of values observed in a set of 8 different devices prepared at the same CS concentration.

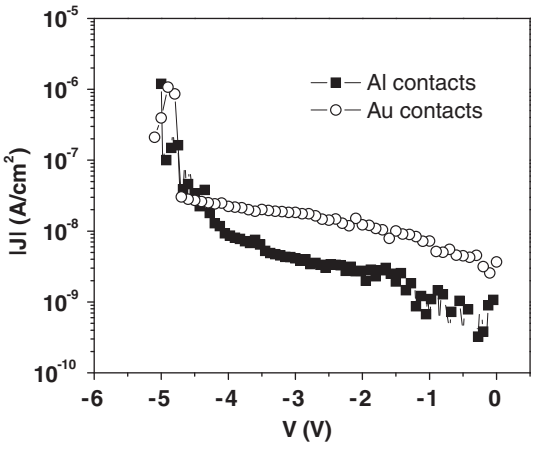

Fig. 5. *J*(*V*) characteristic of the Al/CPVP/Au and Al/CPVP/Al device.

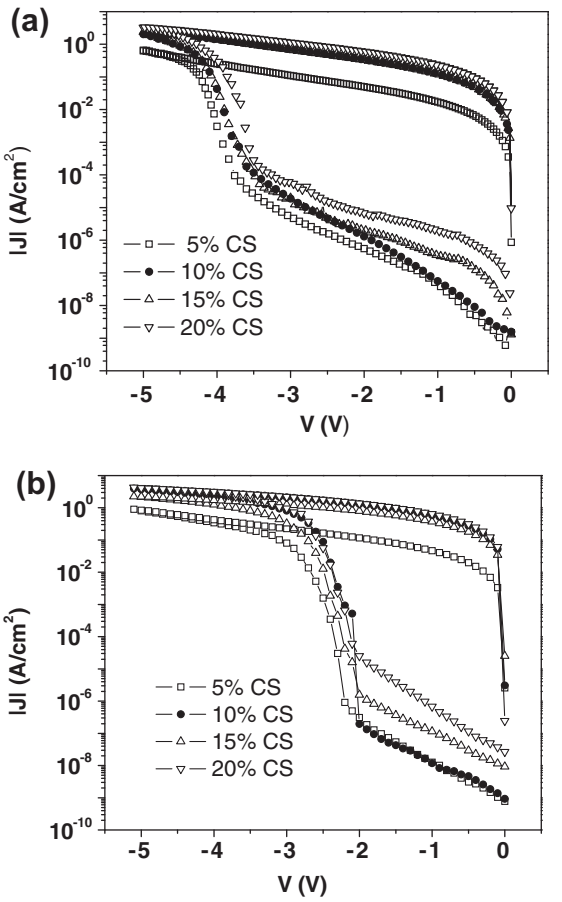

Fig. 6. *J*(*V*) characteristic of Al/CPVP-CS/Au devices prepared with (a) composites A and; (b) with composites B, for different relative CS concentrations.

This electrical transition voltage threshold from the OFF-state to the ON-state, considering the absolute values, serves as the lowest limit of the voltage applied during the "write" operation for the memory device. In contrast, the "read" operations have to be performed in the range below the threshold voltage, where the two states are clearly separated. The "0" and "1" can be encoded from the low-conductivity state and high conductivity state, respectively, allowing application of Boolean algebra.

The most interesting feature of these memory device is that it remains in the ON-state even after turning off the power and in the subsequent voltage scans. Thus the devices exhibit write-once-read-many-times (WORM) memory behavior. The current and WORM memory effect of these memory devices are largely dependent on the type of metal electrode used, as also observed by other authors [28,29]. Moreover, the devices exhibit stability in the OFF-state as well as in the ON-state during the subsequent for-

ward and reverse voltage scans. The stability of the devices is demonstrated in Fig. 7. In Fig. 7(a) the device current density is presented as a function of time for a device which was biased at the READ voltage (−1 V), before and after the application of the WRITE voltage (two pulses). It can be seen that the current density value is stable. In Fig. 7(b) and (c) we present the current obtained from devices that were periodically submitted to the READ voltage for 24 h (see inset for pulse characteristics and measurement moment). The higher current density corresponds to the current during the READ condition (−1 V), whereas the bottom curve corresponds to the current of the device at rest (0 V) for devices in both states: a device in the OFF-state (Fig. 7(b)) and a device in the ON-state (Fig. 7(c)). The ON-state device current density during the READ operation decays by ~50%, following a simple exponential decay with time constant of 7 h. The variation of the *J(V)* characteristics of the device with temperature (between 20 and 70 °C) is not significant for its use as memory, as illustrated in Fig. 8. The most important finding is that the threshold voltage is only slightly displaced and the ON/OFF current ratio remains almost the same.

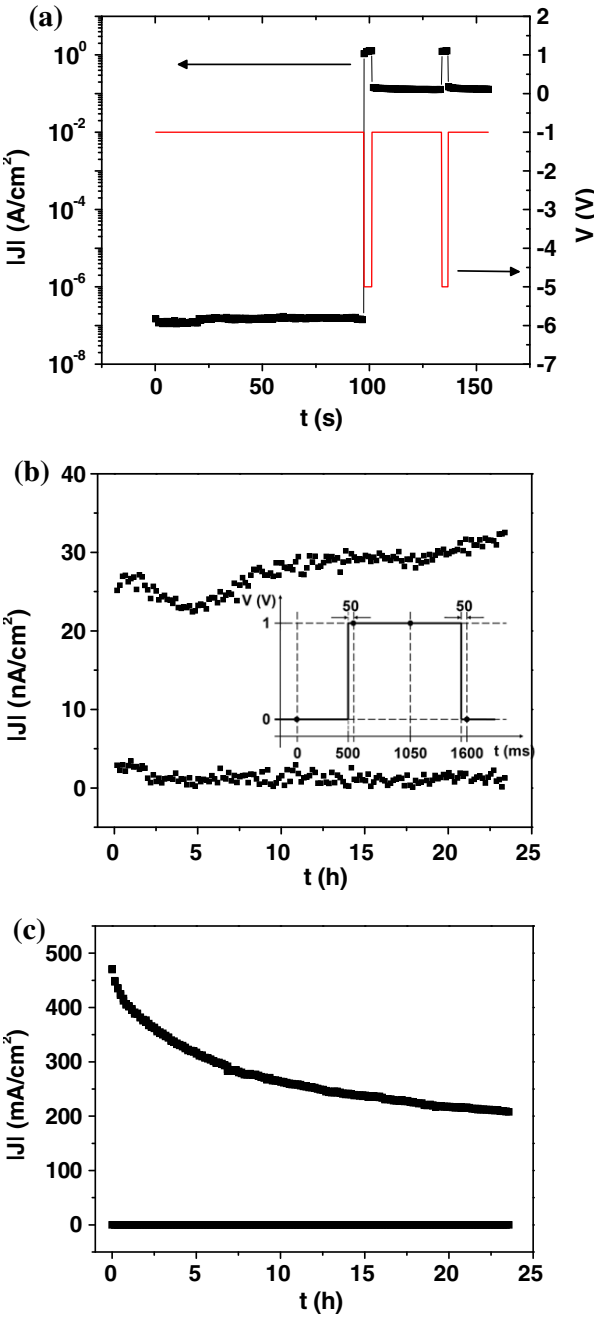

Fig. 7. (a) *J*(*t*) behavior of a Al/CPVP-CS(A-05)/Au device at READ voltage (−1 V) in the OFF-state (up to ~100 s), during and after a WRITE pulse (−5 V) and the subsequent ON current at READ voltage. (b) Long term measurement applying a pulse every 10 min for a Al/CPVP-CS(B-10)/Au device in the OFF-state [inset: pulse form indicating the time for the four measurements made during every pulse, as full circles]. (c) Same as in (b), after application of the WRITE pulse, *i.e.*, ON-state.

The slight threshold displacement that occurs with an increase in the relative CS to CPVP composite concentration in the composite and with temperature, as well as the strong threshold voltage displacement with device thickness, suggests that the OFF–ON transition is controlled by the thickness of the composite film. This threshold then occurs at a critical electrical field strength. However, since the relationship between these two quantities is not a simple proportionality, this subject must be investigated in more details. This observation is under investigation and will be reported in due course.

The formation of percolation paths throughout the CSs inside the CPVP insulator layer is easier when the relative amount of CSs is equal to or larger than 10% (Fig. 6). Percolation paths may be formed through the displacement of the CSs at the high fields achieved in the device, which are larger than 10^6 V/m. The irreversible character of the OFF–ON transition suggests again that the new CS positions are stabilized after high current passage, which also leads to higher local temperatures facilitating molecular conformation modification. Even at the high ON-state current, fusion of CSs occurs, leading to the formation of permanent conducting filaments [19]. In the case of the formation of a filamentary current, high temperatures are easily achieved since the current density is then locally

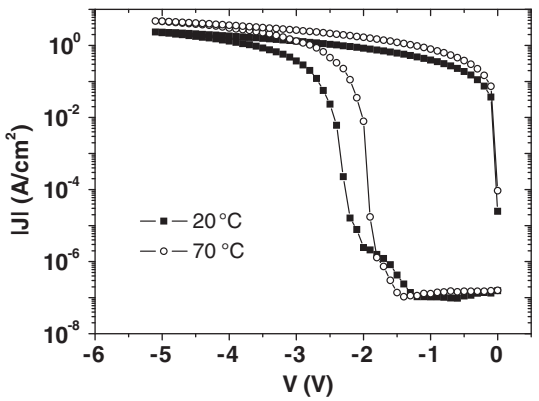

Fig. 8. *J*(*V*) characteristics of two Al/CPVP-CS/Au devices of the same sample prepared with composite B-10, measured at different temperatures.

much higher than the value calculated for the average device current density considering the superposition of top and down electrodes. And it is important to remember that even this value is very high for organic devices, in some cases achieving more than 1 A/cm^2, which corresponds to more than 2 W/cm^2 in the ON-state.

The reproducibility of the results is very good, since from 64 prepared devices all demonstrated the OFF–ON transition, except three devices that presented short-circuit between the electrodes.

We measured the transition time from the OFF to the ON-state during the WRITE operation. In all measurements made using 10 devices prepared with composites B-05, B-10, B-15, B-20 and A-10 the current stabilizes at the ON value in less than 2 μs.

Simple memory elements have been developed for organic electronics, such as conducting polymer strips that make a conducting bridge between metal electrodes. When a current above a certain threshold passes through this bridge, the Joule heat degrades the polymeric material producing at least a partial interruption of the bridge, and in this way the current state is modified [30]. Compared to such devices, our memory elements have the advantage offered by the vertical architecture, which allows smaller device size and consequently a higher integration level.

In summary, we have demonstrated WORM memory devices made using a thin film of a composite of carbon spheres and cross-linked poly(vinylphenol) sandwiched between two metallic electrodes, which show OFF/ON transitions at low voltages and show ON/OFF current ratios $\sim 10^8$.

Acknowledgements

The authors would like to thank CNPq and Renami (Brazil) and DST/NRF (South Africa) for research grants. MAM gratefully acknowledges funding from Pró-África-CNPq for financial travel support.

References

[1] Q.D. Ling, D.J. Liaw, C.X. Zhu, D.S.H. Chan, E.T. Kang, K.G. Neoh, Prog. Polym. Sci. 33 (2008) 917.
[2] D. Ma, M. Aguiar, J.A. Freire, I.A. Hümmelgen, Adv. Mater. 12 (2000) 1063.
[3] L.P. Ma, J. Liu, Y. Yang, Appl. Phys. Lett. 80 (2002) 2997.
[4] R.M.Q. Mello, E.C. Azevedo, A. Meneguzzi, M. Aguiar, A. Ackcelrud, I.A. Hümmelgen, Macromol. Mater. Eng. 287 (2002) 466.
[5] S. Möller, C. Perlov, W. Jackson, C. Taussig, S.R. Forrest, Nature 426 (2003) 166.
[6] A. Bandyopadhyay, A.J. Pal, J. Phys. Chem. B 107 (2003) 2531.
[7] L.D. Bozano, B.W. Kean, V.R. Deline, J.R. Salem, J.C. Scott, Appl. Phys. Lett. 84 (2004) 607.
[8] J. Chen, D. Ma, Appl. Phys. Lett. 87 (2005) 023505.
[9] S. Paul, A. Kanwal, M. Chowalla, Nanotechnology 17 (2006) 145.
[10] B. Mukherjee, A.J. Pal, Chem. Mater. 19 (2007) 1382.
[11] S. Sahu, A.J. Pal, Org. Electron. 9 (2008) 873.
[12] B.C. Das, A.J. Pal, Philos. Trans. R. Soc. A 367 (2009) 4181.
[13] D. Tsoukalas, Philos. Trans. R. Soc. A 367 (2009) 4169.
[14] D. Fazzi, C. Castiglioni, F. Negri, Phys. Chem. Chem. Phys. 12 (2010) 1600.
[15] T.Y. Chang, Y.W. Cheng, P.T. Lee, Appl. Phys. Lett. 96 (2010) 043309.
[16] H. Houili, E. Tutiš, R. Izquierdo, Org. Electron. 11 (2010) 514.
[17] Y. Yang, J. Ouyang, L. Ma, R.J. Tseng, C.W. Chu, Adv. Funct. Mater. 16 (2006) 1001.
[18] J.C. Scott, L.D. Bozano, Adv. Mater. 19 (2007) 1452.
[19] D. Prime, S. Paul, Philos. Trans. R. Soc A 367 (2009) 4141.
[20] L.D. Bozano, B.W. Kean, M. Beinhoff, K.R. Carter, P.M. Rice, J.C. Scott, Adv. Funct. Mater. 15 (2005) 1933.
[21] Y. Li, J. Chen, Q. Xu, L. He, Z. Chen, J. Phys. Chem. C 113 (2009) 10085 (references therein).
[22] Y.Z. Jin, C. Gao, W.H. Hsu, Y. Zhu, A. Huczko, M. Bystrzejewski, M. Roe, C.Y. Lee, S. Acquah, H. Kroto, D.R.M. Walton, Carbon 43 (2005) 1944.
[23] F.C. Chen, C.W. Chu, J. He, Y. Yang, J.L. Lin, Appl. Phys. Lett. 85 (2004) 3295.
[24] T.F. Guo, Z.J. Tsai, S.Y. Chen, T.C. Wen, C.T. Chung, J. Appl. Phys. 101 (2007) 124505.
[25] J. Zhou, F. Zhang, L. Lan, S. Wen, J. Peng, Appl. Phys. Lett. 91 (2007) 253507.
[26] K. Sethuraman, S. Ochiai, K. Kojima, T. Mizutani, Appl. Phys. Lett. 92 (2008) 183302.
[27] C.E. Cava, R. Possagno, M.C. Schnitzler, P.C. Roman, M.M. Oliveira, C.M. Lepienski, A.J.G. Zarbin, L.S. Roman, Chem. Phys. Lett. 444 (2007) 307.
[28] J. Oyang, Y. Yang, Appl. Phys. Lett. 96 (2010) 063506.
[29] H. Ha, O. Kim, IEEE Electron Device Lett. 31 (2010) 368.
[30] D.M. de Leeuw, C.M. Hart, G.H. Gelinck, Patent WO 01/73845 A1.

Organic Electronics 11 (2010) 1864–1869

Contents lists available at ScienceDirect

Organic Electronics

journal homepage: www.elsevier.com/locate/orgel

Efficient bulk-heterojunction photovoltaic cells with transparent multi-layer graphene electrodes

Minhyeok Choe [a,1], Byoung Hoon Lee [a,1], Gunho Jo [a], June Park [c], Woojin Park [a], Sangchul Lee [b], Woong-Ki Hong [a,2], Maeng-Je Seong [c], Yung Ho Kahng [a], Kwanghee Lee [a,b,*], Takhee Lee [a,b,**]

[a] Department of Materials Science and Engineering, Gwangju Institute of Science and Technology, Gwangju 500-712, Republic of Korea
[b] Department of Nanobio Materials and Electronics, Gwangju Institute of Science and Technology, Gwangju 500-712, Republic of Korea
[c] Department of Physics, Chung-Ang University, Seoul 156-756, Republic of Korea

ARTICLE INFO

Article history:
Received 9 August 2010
Received in revised form 29 August 2010
Accepted 30 August 2010
Available online 9 September 2010

Keywords:
Graphene
Photovoltaics
Transparent electrode
TiOX
Chemical vapor deposition

ABSTRACT

We present the results of applying multi-layer graphene (MLG) films as transparent conductive electrodes in organic photovoltaic devices (OPVs). The MLG films synthesized at different growth temperatures by chemical vapor deposition were applied to OPVs. The performance of OPVs with 1000 °C-grown MLG films was found to be the best with a power conversion efficiency (PCE) of ~1.3%. The PCE was further enhanced when a hole-blocking TiO_X layer was inserted in the device structure, resulting in a PCE of ~2.6% which is a significantly higher efficiency compared to other previously reported graphene-adopted photovoltaic cells. Our demonstration of the PCE-increase in the graphene-electrode OPVs may foster the application of the fast-progressing graphene technology toward more practical OPV technology.

© 2010 Elsevier B.V. All rights reserved.

1. Introduction

Graphene, a two-dimensional sheet of covalently bonded carbon atoms, has been attracting great attention in the field of optoelectronics of organic and inorganic materials. This is because of its outstanding electronic, optical, and mechanical properties, such as quantum electronic transport properties, transparency, mechanical and chemical stability, stretchability, and flexibility [1–6]. Currently, graphene films that can be deposited on arbitrary substrates are prepared by various techniques, including mechanical exfoliation of graphite crystals, reduction of graphene oxide films, and growth by chemical vapor deposition (CVD) [6–11]. In this study, we used the CVD method for graphene production. This method offers several advantages, including the capability to grow large and continuous uniform films with low sheet resistances, transferability to arbitrary substrates, and controllability of the synthesized film properties. It has been reported that the graphene films produced by CVD typically have sheet resistances of 300–1000 Ω/□ and mobilities of 300–4000 $cm^2/V\,s$ [4,8,9].

In this work, our focus is on the application of graphene films as the electrodes in organic photovoltaic cells. In the optoelectronics, the need for a noble material to replace indium tin oxide (ITO) that can be produced cheaply while providing high transparency and conductivity has emerged [12,13]. Graphene films potentially fulfill all of these required properties and are therefore currently being vigorously researched [4,5,10,11,14–23]. Wang et al. [11] first reported the application of graphene films in dye-sensitized photovoltaic cells and obtained a power conversion efficiency (PCE) of 0.26%. A number of reports followed.

* Corresponding author at: Department of Materials Science and Engineering, Gwangju Institute of Science and Technology, Gwangju 500-712, Republic of Korea. Tel.: +82 62 715 2325; fax: +82 62 715 2304.
** Corresponding author at: Department of Materials Science and Engineering, Gwangju Institute of Science and Technology, Gwangju 500-712, Republic of Korea. Tel.: +82 62 715 2313; fax: +82 62 715 2304.
E-mail addresses: klee@gist.ac.kr (K. Lee), tlee@gist.ac.kr (T. Lee).
[1] These authors contributed equally to this work.
[2] Present address: Nanoscience Centre, University of Cambridge, Cambridge CB3 0FF, UK.

1566-1199/$ - see front matter © 2010 Elsevier B.V. All rights reserved.
doi:10.1016/j.orgel.2010.08.018

Tung et al. [5] reported organic bulk-heterojunction (BHJ) photovoltaic cells with modified graphene films composited with carbon nanotubes and demonstrated a 0.85% PCE. More recently, Wang et al. [14] used functionalized graphene films in organic BHJ photovoltaic cells and reported an improved PCE of 1.71%. Overall, BHJ photovoltaic cells with graphene electrodes have exhibited PCEs below 2% to date [5,11,14–17]. These PCEs are only proof-of-concept and are far below the best performance obtained from organic solar cells made with ITO electrodes. Values of 6.1% [24], with a BHJ structure, and 6.5% [25], with a tandem cells structure, have both been reported by the research group of Heeger and Lee, one of co-authors of this paper. Recently, a PCE of 6.7% has been reported from an organic BHJ structure with low bandgap polymers having an enhanced open-circuit voltage [26,27]. On the contrary, the poor performance of photovoltaic cells incorporating graphene electrodes is apparently due to the poor quality of graphene films: high sheet resistances and interfacing problems with the active layers.

In this paper, we report an application of CVD-synthesized multi-layer graphene (MLG) films incorporated as transparent and conductive electrodes of organic BHJ photovoltaic cells (OPVs). Particularly, the growth temperature of the graphene films was studied as a control paramter on the PCE of the graphene-OPVs. Overall, the MLG films showed good performance as electrodes for OPVs, and among tested graphene-OPVs the1000 °C-grown MLG films were found to yield the best PCE. Furthermore, when a thin sol–gel processed titanium sub-oxide (TiO_X) layer was inserted in the cell, the PCE was further increased to ~2.60%. Our results show the control of the graphene film quality and the cell structure optimization with a TiO_X layer can increase the performance of OPVs beyond the proof-of-concept level.

2. Experimental

The device structure of a photovoltaic cell with graphene as a transparent and conducting electrode is shown in Fig. 1(a). To synthesize graphene films, 300 nm thick Ni-deposited substrates were placed into the CVD chamber and heated to 800, 900, or 1000 °C under the flow of a 4% H_2 in Ar gas mixture. Then, a graphene film was grown by adding CH_4 gas to the flow. After growth, the substrate was rapidly cooled to room temperature (>200 °C/min initially and slower later) to suppress excessive precipitation of carbon atoms. Finally, the graphene film was released from the Ni substrate by etching Ni in an aqueous solution of iron chloride ($FeCl_3$) [4]. The CVD-synthesized MLG film was transferred onto a glass substrate to form the anode for OPV. Before a poly(3,4-ethylenedioxythiophene) poly(styrenesulfonate) (PEDOT:PSS) layer was spin coated on top of the graphene film, the graphene film was undergone an ozone treatment to produce the hydrophilic surface, which was a necessary step to increase the coating efficiency of PEDOT:PSS on graphene. Next, the photoactive BHJ composite of poly(3-hexylthiophene) (P3HT) and [6,6]-phenyl-C61 butyric acid methyl ester (PCBM) was spin coated on top of the PEDOT:PSS layer. Then, a TiO_X film was spin coated for some devices. Finally, aluminum was thermally evaporated to form the cathode. A cross-sectional high-resolution transmission electron microscopy (HRTEM) image of a prepared photovoltaic cell (Fig. 1(b)) clearly shows that the individual layers were nicely formed with distinctive interfaces; the TiO_X film and MLG film are shown in the upper and lower inset of Fig. 1(b), respectively.

3. Results and discussion

3.1. Characteristics of multi-layer graphene films

Before applying the MLG films in photovoltaic cells, we investigated the properties of these films using various techniques. To determine the morphological features and thicknesses of the MLG films, we used an atomic force microscope (AFM) to image a transferred MLG film on a 300-nm-thick SiO_2 layer on a Si substrate, as shown in Fig 2(a). The thinnest part measured on our graphene film is 1.13 nm, as shown in the cross-sectional profile in Fig. 2(b). This thickness corresponds to the thickness of a monolayer; due to the chemical contrast between graphene and substrate, the monolayer thickness has been measured as ~1 nm by AFM [7,9,28–30]. Fig. 2(c) shows the TEM images for a graphene film. Our graphene films consisted of mono to multi-layer regions and contained rippled regions, as marked by a square in the lower image. By counting the number and the distance of the bright and dark stripes in the rippled region, the number of

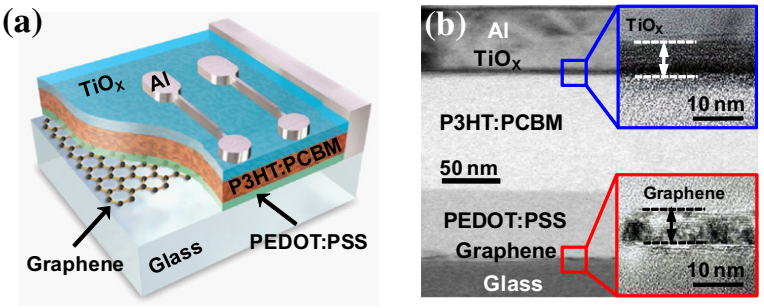

Fig. 1. (a) Schematic diagram of the photovoltaic device structure with MLG electrodes and a hole-blocking TiO_X layer. (b) TEM cross-sectional image of a photovoltaic device. The insets show HRTEM images near the TiO_X layer (top) and near the MLG films (bottom).

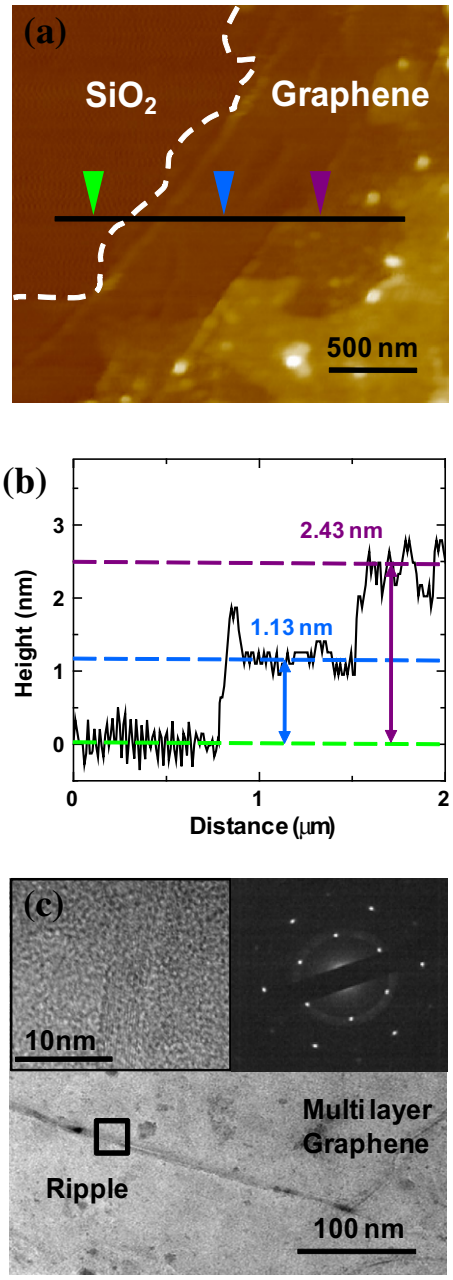

Fig. 2. (a) AFM image of a MLG film showing the edge of the MLG layers (dashed) on a SiO_2 substrate. (b) Topographic height profiles across the solid line indicated in (a). (c) TEM image of a region of MLG. The insets show an HRTEM image of the rippled region (top left) and an electron diffraction pattern (top right) of MLG.

graphene layers (~15) and the interlayer distance (3.5 ± 0.1 Å) were obtained; the results were found consistent with values reported previously [9,31]. The electron diffraction (ED) pattern (upper right inset, Fig. 2(c)) taken on a monolayer region shows a hexagonal spot pattern, confirming the threefold symmetry of the arrangement of carbon atoms in the graphene film.

Raman spectroscopy using the 514 nm line of an Ar+ laser was used to analyze the properties of MLG films grown at three different temperatures (Fig. 3). Raman spectroscopy is a non-destructive analysis tool which provides high-throughput and unambiguous identification of the properties of graphene films with three most intense peaks: D peak at ~1350 cm^{-1}, G peak at ~1580 cm^{-1}, and 2D peak at ~2700 cm^{-1} [32–34]. Our CVD-grown graphene films typically showed multi-layer-type Raman features (i.e., G-peak intensity > 2D-peak intensity) and small D peaks that were related to defects on MLG. The integrated intensity ratios of the observed Raman peaks are shown in Fig. 3(b) and (c). The ratios of the G-peak intensity to the 2D-peak intensity (I_G/I_{2D}) shown in Fig 3(b) indicate that the average thickness of the graphene film increased as the growth temperature increased since the higher ratio corresponds to the thicker graphene film. The ratios of the D-peak intensity to the G-peak intensity (I_D/I_G) shown in Fig. 3(c) correspond with the average density of defects [33–35], and these ratios indicate that the defect density decreased as the growth temperature increased. From the comparison of Raman peak ratios, we conclude that the growth temperature significantly affects the properties of the graphene in terms of the film thickness and defect density.

Furthermore, the film property that is directly relevant to the performance of the organic photovoltaics was investigated: the optical transmittances and the sheet resistances of the MLG films synthesized at three different growth temperatures. Results are summarized in Fig. 4. Fig. 4(a) shows the representative transmittances of MLG films prepared at different growth temperatures and the inset shows the transmittance of 90.7 ± 1.5, 88.8 ± 2.2, and 86.9 ± 1.2% at 515 nm wavelength according to the growth temperatures of 800, 900, and 1000 °C, respectively. The plot of mobility versus resistance, shown in Fig. 4(b), was obtained by taking the statistical means and standard deviations of 8–10 synthesized-MLG films at each growth temperature. As expected from Raman analysis, higher temperature grown thicker MLG films yielded less transparency and lower sheet resistance. Specifically, MLG films prepared at growth temperatures of 800, 900, and 1000 °C showed the sheet resistances of 1730 ± 600, 990 ± 400, and 610 ± 140 Ω/□, and the mobility of 660 ± 270, 1030 ± 440, and 1180 ± 260 $cm^2/V\,s$ respectively. Furthermore, we measured the work function of the MLG films by using a Kelvin probe measurement system. As shown in Fig. S2(b) in Supplementary material, the work function of the graphene films was 4.45 ± 0.04 eV and did not change significantly with the growth temperature change.

3.2. Performance of the organic photovoltaic cells with graphene electrode

Fig. 5(a) shows the representative current density–voltage (*J–V*) data of the fabricated OPVs without TiO_X layers under AM 1.5 G irradiation by a solar simulator with an irradiation intensity of 100 mW/cm^2. The three different MLG films prepared at different growth temperatures (800, 900, and 1000 °C) were used to compare the performance as electrodes in OPVs. The best performance was achieved from the devices using MLG films that were

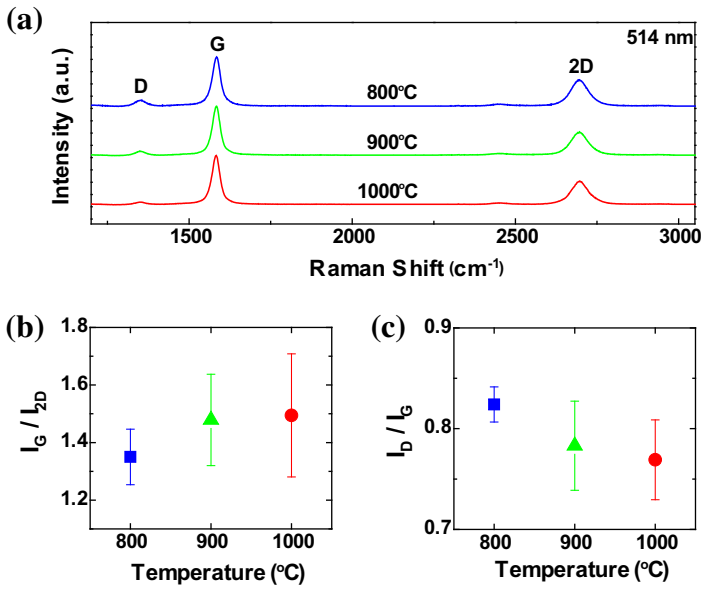

Fig. 3. (a) Raman spectra of MLG films synthesized at different growth temperatures (800, 900, and 1000 °C). (b) Integrated intensity ratios of G peak and 2D peak (I_G/I_{2D}), and (c) of D peak and G peak (I_D/I_G) as a function of growth temperature. These integrated intensity peaks are from the Raman spectra of graphene films.

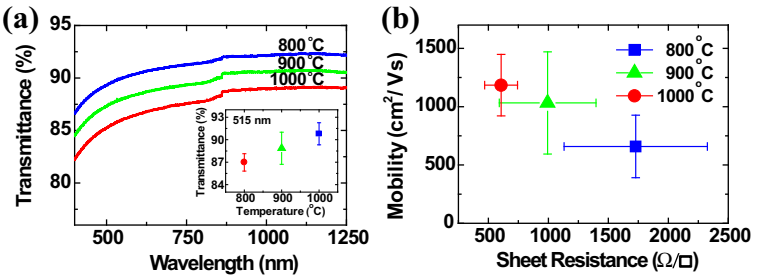

Fig. 4. (a) Transmission spectra of MLG films. The inset shows the transmittance of 90.7 ± 1.5, 88.8 ± 2.2, and 86.9 ± 1.2% at 515 nm wavelength, 800, 900, and 1000 °C, respectively. (b) Mobility versus sheet resistance of MLG films prepared at different growth temperatures (800, 900, and 1000 °C).

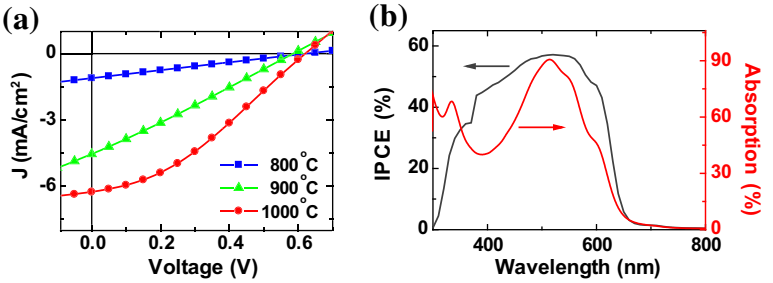

Fig. 5. (a) J-V curves of photovoltaic cells with MLG films grown at different growth temperatures under AM 1.5 G irradiation conditions. (b) Incident photon-to-current efficiency (IPCE) and absorption spectra of a photovoltaic device fabricated with a 1000 °C-grown MLG film.

prepared at 1000 °C. Specifically, for the case of the 1000 °C-graphene OPV, the representative parameters obtained were short-circuit current density (J_{SC}) of 6.25 mA/cm^2, open-circuit voltage (V_{OC}) of 0.62 V, and fill factor (FF) of 0.35. These values yielded PCE = $J_{SC}V_{OC}$FF/P_{inc} (here P_{inc} is the intensity of incident light) of 1.34%. The parameters for the devices with graphene films prepared at 800 and 900 °C are summarized in Table 1. Fig. 5(b) compares

Table 1
Summary of the performance parameters of graphene-electrode organic photovoltaic devices fabricated with graphene films that were synthesized at different growth temperatures (800, 900, and 1000 °C) and ITO-electrode devices. Short-circuit current density (J_{SC}), open-circuit voltage (V_{OC}), fill factor (FF), and power conversion efficiency (PCE) are listed. The improvement of the performance parameters by the insertion of the TiO_X layer as a hole-blocking layer (HBL) was compared in all the device types.

Temp. (°C)	HBL	V_{OC} (V)	J_{SC} (mA/cm^2)	FF	PCE (%)
800	–	0.62	1.11	0.25	0.17
800	TiO_x	0.59	6.45	0.32	1.22
900	–	0.59	4.54	0.26	0.70
900	TiO_x	0.62	7.57	0.46	2.13
1000	–	0.62	6.25	0.35	1.34
1000	TiO_x	0.60	9.03	0.48	2.60
ITO	–	0.63	7.50	0.50	2.34
ITO	TiO_x	0.63	9.02	0.67	3.80

the incident photon-to-current collection efficiency (IPCE) spectrum and absorption spectrum of a device fabricated using MLG films prepared at 1000 °C. The graphene-electrode photovoltaic cell without a TiO_X layer showed the typical spectral response of P3HT:PCBM composites with a maximum IPCE of approximately 57% at 515 nm.

The performance of the graphene photovoltaic devices was further enhanced when a TiO_X film was added between the aluminum cathode and the photo-active layer. Fig. 6(a) compares the *J–V* curves of the photovoltaic devices with 1000 °C-grown MLG electrodes and with ITO electrodes with and without the TiO_X layer. The performance parameters obtained from the MLG-electrode devices with the TiO_X layer shown in this figure are J_{SC} of 9.03 mA/cm^2, V_{OC} of 0.60 V, and FF, which was dramatically increased, of 0.48. The corresponding PCE was significantly increased to 2.60%. Such performance enhancement by adding a TiO_X film was also observed in photovoltaic cells with ITO electrodes. The representative parameters obtained for the case of the ITO-electrode devices with the TiO_X layer were J_{SC} of 9.02 mA/cm^2, V_{OC} of 0.63 V, and FF of 0.67, and the PCE was determined as 3.80%. The enhancement of PCE for our graphene-electrode and ITO-electrode photovoltaic devices by inserting a TiO_X layer can be explained by the role of the TiO_X layer that creates a higher density of photo-generated charge carriers as an optical spacer [36,37] and facilitates better transport of charge carriers to each electrode as a hole-blocking layer [24,25,38,39], thereby increasing J_{SC}. Recently, Roy et al. [37] have compared the calculated and the experimentally measured total absorption spectra of photovoltaic devices with and without the TiO_X layer and confirmed the effect of the TiO_X layer as an optical spacer. Also, Cho et al. [38] have demonstrated the hole-blocking property of TiO_X using multilayer bipolar field-effect transistors (FETs). In their device, the TiO_X layer was inserted to separate the n-channel material and the p-channel material. Because the TiO_X layer retained the injected holes within the p-channel material and transferred the injected electrons into the n-channel material, their device successfully showed the *J–V* characteristics. As a result, the PCE of our photovoltaic devices with TiO_X was improved by the effects of the TiO_X layer both as an optical spacer and as a hole-blocking layer. Moreover, the TiO_X layer reduced the contact resistance between the aluminum cathode and the P3HT:PCBM photo-active layer, consequently increasing the FF in the device. Fig. 6(b) presents detailed statistical data for PCE values that were statistically determined from all the measured graphene-electrode devices in comparison with the ITO-electrode devices, with and without the TiO_X layers. Each statistical value in Fig. 6(b) was extracted from all the measured devices shown in the Supplementary material (Fig. S1). For devices without the TiO_X layer, the PCEs (the mean and standard deviation) of the photovoltaic devices were determined as 0.19 ± 0.08, 0.56 ± 0.10, and 1.38 ± 0.35% with the graphene-electrodes grown at 800, 900, and 1000 °C, respectively, in comparison to 1.20 ± 0.27, 1.79 ± 0.31, and 2.58 ± 0.45% for the devices with TiO_X layer and the graphene-electrodes grown at 800, 900, and 1000 °C, respectively. Also, we found that the PCE of the ITO-electrode photovoltaic devices without TiO_X was 2.53 ± 0.42% compared to 3.74 ± 0.31% of those with TiO_X. It can be noticed that the PCEs for ITO-electrode devices were higher than those for graphene-electrode devices, partly due to higher conductivity of ITO film than that of graphene films. Furthermore, the best PCE observed was 3.63% from a 1000 °C-grown graphene-electrode device with the TiO_X layer. However, this value was outside of the one sigma criterion, i.e., the 3.63% value was beyond

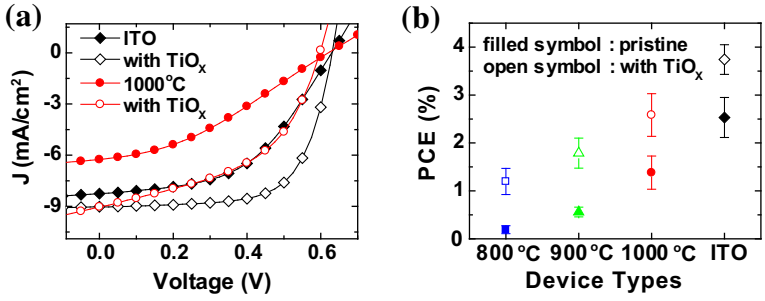

Fig. 6. (a) *J–V* curves of photovoltaic devices with 1000 °C-grown MLG electrodes (circles) and with ITO electrodes (diamonds). The curves without the TiO_X layer (filled symbols) are compared to the ones with the TiO_X layer (open symbols). (b) The PCEs for graphene-electrode photovoltaic devices in comparison with those for the ITO-electrode photovoltaic devices with the TiO_X layers and without the TiO_X layers (pristine). This statistical means and standard deviations were extracted from Supplementary material. The types of the devices are indicated on the *x*-axis (800, 900, and 1000 °C: graphene-electrode devices, ITO: ITO-electrode devices).

one $\sigma = 0.45\%$ (standard deviation) from the mean of $m = 2.58\%$. The performance parameters for all types of photovoltaic devices measured in this study are summarized in Table 1. Although our results indicate that the efficiency of OPVs can be significantly enhanced by graphene film quality control and by inserting a TiO_X layer, there are rooms for improvements to compete with the efficiency of ITO-electrode OPVs. With more research to further enhance the graphene film quality and to further optimize the device structure, graphene films may soon be widely used as an alternative material to ITO films in organic photovoltaics.

4. Conclusions

In summary, we reported the application of MLG films grown by chemical vapor deposition to organic photovoltaic cells. The effect of graphene synthesis temperature on the performance as anode in OPVs was studied. The 1000 °C-grown MLG films, that possessed sheet resistances of ~606 Ω/□ at transmittances of ~87%, showed the best performance as electrodes in OPVs. Furthermore, a cell structure optimization with an inserted TiO_X layer enhanced the observed power conversion efficiency up to $2.58 \pm 0.45\%$. Our demonstration of efficiency improvements in graphene-adopted photovoltaic cells may foster the application of fast-progressing graphene technology into the practical realm of organic photovoltaic cells.

Acknowledgements

This work was supported by the National Research Laboratory Program, the National Core Research Center grant, the World Class University program, and the National Research Foundation of Korea (Grant No. 20090093869) from the Korean Ministry of Education, Science and Technology, and the Program for Integrated Molecular System at GIST. The authors thank Yun Chang Park at the National Nanofab Center for his comments and assistance in analyzing and obtaining the TEM images.

Appendix A. Supplementary material

Supplementary data associated with this article can be found, in the online version, at doi:10.1016/j.orgel.2010.08.018.

References

[1] K.S. Novoselov, A.K. Geim, S.V. Morozov, D. Jiang, M.I. Katsnelson, I.V. Grigorieva, S.V. Dubonos, A.A. Firsov, Nature 438 (2005) 197.
[2] X. Du, I. Skachko, A. Barker, E.Y. Andrei, Nat. Nanotechnol. 3 (2008) 491.
[3] D.V. Kosynkin, A.L. Higginbotham, A. Sinitskii, J.R. Lomeda, A. Dimiev, B.K. Price, J.M. Tour, Nature 458 (2009) 872.
[4] K.S. Kim, Y. Zhao, H. Jang, S.Y. Lee, J.M. Kim, K.S. Kim, J.-H. Ahn, P. Kim, J.-Y. Choi, B.H. Hong, Nature 457 (2009) 706.
[5] V.C. Tung, L.-M. Chen, M.J. Allen, J.K. Wassei, K. Nelson, R.B. Kaner, Y. Yang, Nano Lett. 9 (2009) 1949.
[6] H.A. Becerril, J. Mao, Z. Liu, R.M. Stoltenberg, Z. Bao, Y. Chen, ACS Nano. 2 (2008) 463.
[7] K.S. Novoselov, A.K. Geim, S.V. Morozov, D. Jiang, Y. Zhang, S.V. Dubonos, I.V. Grigorieva, A.A. Firsov, Science 306 (2004) 666.
[8] X. Li, W. Cai, J. An, S. Kim, J. Nah, D. Yang, R. Piner, A. Velamakanni, I. Jung, E. Tutuc, S.K. Banerjee, L. Colombo, R.S. Ruoff, Science 324 (2009) 1312.
[9] A. Reina, X. Jia, J. Ho, D. Nezich, H. Son, V. Bulovic, M.S. Dresselhaus, J. Kong, Nano Lett. 9 (2009) 30.
[10] G. Jo, M. Choe, C.-Y. Cho, J.H. Kim, W. Park, S. Lee, W.-K. Hong, T.-W. Kim, S.-J. Park, B.H. Hong, Y.H. Kahng, T. Lee, Nanotechnology 21 (2010) 175201.
[11] X. Wang, L. Zhi, K. Mullen, Nano Lett. 8 (2008) 323.
[12] S.K. Hau, H.-L. Yip, J. Zou, A.K.Y. Jen, Org. Electron. 10 (2009) 1401.
[13] R.C. Tenent, T.M. Barnes, J.D. Bergeson, A.J. Ferguson, B. To, L.M. Gedvilas, M.J. Heben, J.L. Blackburn, Adv. Mater. 21 (2009) 3210.
[14] Y. Wang, X. Chen, Y. Zhong, F. Zhu, K.P. Loh, Appl. Phys. Lett. 95 (2009) 063302.
[15] G. Eda, Y.-Y. Lin, S. Miller, C.-W. Chen, W.-F. Su, M. Chhowalla, Appl. Phys. Lett. 92 (2008) 233305.
[16] J. Wu, H.A. Becerril, Z. Bao, Z. Liu, Y. Chen, P. Peumans, Appl. Phys. Lett. 92 (2008) 263302.
[17] X. Wang, L. Zhi, N. Tsao, Z. Tomovi, J. Li, K. Mullen, Angew. Chem. Int. Ed. 47 (2008) 2990.
[18] J. Wu, M. Agrawal, H.A. Becerril, Z. Bao, Z. Liu, Y. Chen, P. Peumans, ACS Nano. 4 (2010) 43.
[19] Z. Yin, S. Wu, X. Zhou, X. Huang, Q. Zhang, F. Boey, H. Zhang, Small 6 (2010) 307.
[20] P. Blake, P.D. Brimicombe, R.R. Nair, T.J. Booth, D. Jiang, F. Schedin, L.A. Ponomarenko, S.V. Morozov, H.F. Gleeson, E.W. Hill, A.K. Geim, K.S. Novoselov, Nano Lett. 8 (2008) 1704.
[21] N. Yang, J. Zhai, D. Wang, Y. Chen, L. Jiang, ACS Nano. 4 (2010) 887.
[22] S. Sun, L. Gao, Y. Liu, Appl. Phys. Lett. 96 (2010) 083113.
[23] S. Bae, H. Kim, Y. Lee, X. Xu, J.-S. Park, Y. Zheng, J. Balakrishnan, T. Lei, H.R. Kim, Y.I. Song, Y.-J. Kim, K.S. Kim, B. Özyilmaz, J.-H. Ahn, B.H. Hong, S. Iijima, Nat. Nanotechnol. 5 (2010) 574.
[24] S.H. Park, A. Roy, S. Beaupre, S. Cho, N. Coates, J.S. Moon, D. Moses, M. Leclerc, K. Lee, A.J. Heeger, Nat. Photonics 3 (2009) 297.
[25] J.Y. Kim, K. Lee, N.E. Coates, D. Moses, T.-Q. Nguyen, M. Dante, A.J. Heeger, Science 317 (2007) 222.
[26] J. Hou, H.-Y. Chen, S. Zhang, R.I. Chen, Y. Yang, Y. Wu, G. Li, J. Am. Chem. Soc. 131 (2009) 15586.
[27] H.-Y. Chen, J. Hou, S. Zhang, Y. Liang, G. Yang, Y. Yang, L. Yu, Y. Wu, G. Li, Nat. Photonics 3 (2009) 649.
[28] C. Gomez-Navarro, R.T. Weitz, A.M. Bittner, M. Scolari, A. Mews, M. Burghard, K. Kern, Nano Lett. 7 (2007) 3499.
[29] S. Gilje, S. Han, M. Wang, K.L. Wang, R.B. Kaner, Nano Lett. 7 (2007) 3394.
[30] M.J. Allen, V.C. Tung, L. Gomez, Z. Xu, L.-M. Chen, K.S. Nelson, C. Zhou, R.B. Kaner, Y. Yang, Adv. Mater. 21 (2009) 2098.
[31] X. Wang, H. You, F. Liu, M. Li, L. Wan, S. Li, Q. Li, Y. Xu, R. Tian, Z. Yu, D. Xiang, J. Cheng, Chem. Vap. Dep. 15 (2009) 53.
[32] Y.y. Wang, Z.h. Ni, T. Yu, Z.X. Shen, H.m. Wang, Y.h. Wu, W. Chen, A.T.S. Wee, J. Phys. Chem. C 112 (2008) 10637.
[33] A.C. Ferrari, Solid State Commun. 143 (2007) 47.
[34] L.G. Cancado, K. Takai, T. Enoki, M. Endo, Y.A. Kim, H. Mizusaki, A. Jorio, L.N. Coelho, R. Magalhaes-Paniago, M.A. Pimenta, Appl. Phys. Lett. 88 (2006) 163106.
[35] M.J. Matthews, M.A. Pimenta, G. Dresselhaus, M.S. Dresselhaus, M. Endo, Phys. Rev. B 59 (1999) R6585.
[36] J.Y. Kim, S.H. Kim, H.-H. Lee, K. Lee, W. Ma, X. Gong, A.J. Heeger, Adv. Mater. 18 (2006) 572.
[37] A. Roy, S.H. Park, S. Cowan, M.H. Tong, S. Cho, K. Lee, A.J. Heeger, Appl. Phys. Lett. 95 (2009) 013302.
[38] S. Cho, J. Yuen, J.Y. Kim, K. Lee, A.J. Heeger, S. Lee, Appl. Phys. Lett. 92 (2008) 063505.
[39] S. Cho, J.H. Seo, K. Lee, A.J. Heeger, Adv. Funct. Mater. 19 (2009) 1459.

of the adjacent layers when the environmental temperature changes [5]. External stress comes from the application of an external bending moment [6]. For example, when the FOLED device is bent, strain is introduced in the thin-films and stress is generated. Stress can make each film to crack or buckle when the deformation exceeds what it can bear. In a conventional multilayer OLED device structure, the indium-tin-oxide (ITO) is the most vulnerable film with the Young's Modulus of 120 GPa and yield stress of 1.2 GPa. Mechanical studies of ITO under external stress have been widely conducted [7]. Stretching-type stress can cause ITO to crack and increase its sheet resistance [8]. However, compression-type stress could promote buckling at first, and eventually crack or delaminate when the stored energy exceeds what the film can bear. When the ITO/plastic composite film is bent, the ITO film can suffer from either compressive or tensile stress, and this depends on the way it is bent.

Comparing these two types of strain conditions, people have found the increase in sheet resistance behaves asymmetrically. This might arise from the residual stress of the ITO/plastic composite, which is usually compressive in terms of the ITO layer [9] or the different course for the cracking or buckling to the electrical resistance. Thus the two different types of stress may also change the electroluminescence (EL) of OLED device differently. Apart from these stress effects, creep [10] (which is more likely to happen to the metal thin-film and plastic substrate) and film delamination [11] are two other key factors which affect soft multilayer thin-film structures.

2. Experimental

The ITO/polyethylene terephthalate (PET) composite substrate used in this study was purchased from Sigma–Aldrich, with the ITO thickness to be 100 nm and sheet resistance to be 60 Ω/□. The substrate was then cleaned with acetone and isopropanol in the ultrasonic bath for 7 min each, and exposed in the UV–Ozone Oven for another 7 min.

The component layers of the OLED device with the structure aluminum (100 nm)/lithium fluoride (0.8 nm)/tris–(8-hydroxyquinoline) aluminum (Alq_3) (40 nm)/*N*,*N*′-bis(naphthalen-1-yl)–*N*,*N*′-bis(phenyl)benzidine (NPB) (50 nm)/ITO (100 nm)/PET (0.127 mm) were deposited by evaporation under vacuum (2×10^{-7} mbar) using the Kurt J. Lesker small molecule deposition system. The FOLED device was mounted on the sample holder and the brightness was measured by the Konica-Minolta LS-110 Luminance meter as shown in Fig. 1a. The holder enables the device to be bent about one axis with three different conditions: R_1 = position A, R_2 = position B, and R_3 = position C in both concave and convex directions. Furthermore, the device pattern (as shown in Fig. 2) was designed in order that during the bending tests, the active area (5 mm × 10 mm) was located around the furthest point of the curve from the electrical contact caused by bending, i.e., the axis referred to above was parallel to the short side and the area between the electrical contacts and the active area was relatively flat.

In order that uninterrupted optical access can be made in the "bent" positions, a 2-point bending method was used. However, this method has the disadvantage of having to define the radius of curvature at the device position (R_c). Two methods were applied to estimate R_c for bending

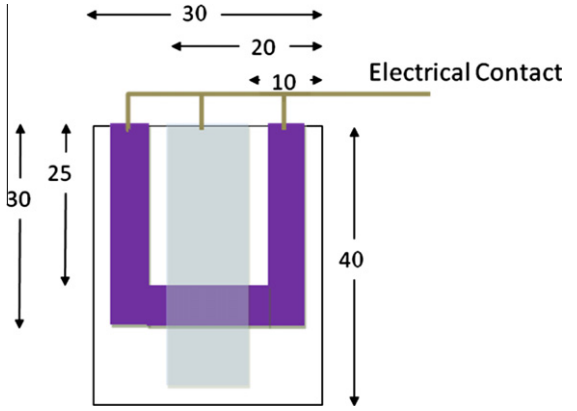

Fig. 2. The FOLED device plan. The darker area is the ITO layer. The lighter oblong shape covered on it is the aluminum layer. The dimensions are in unit of mm. The OLED is thermal evaporated everywhere on the 40 mm × 30 mm PET substrate and between these two electrodes. The OLED active area is 10 mm × 5 mm.

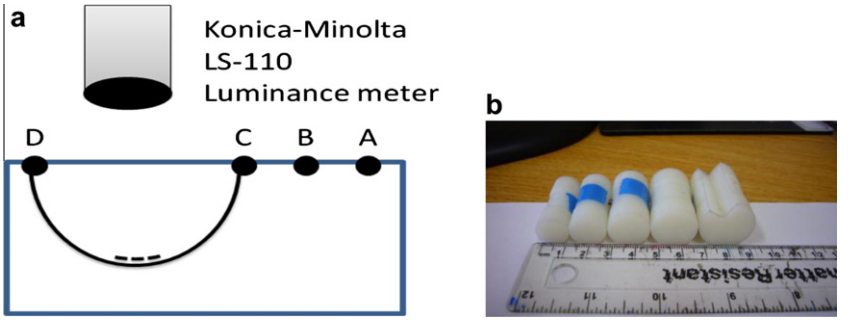

Fig. 1. The FOLED device was mounted and bent on the sample holder to be measured by the Konica-Minolta LS-110 Luminance meter fixed above the sample holder as shown in (a). The curved line is the FOLED device. It is fixed at the left end of the long side (position D). The dash line is the active OLED area which emits light. The right end is to be fixed at the positions A, B, and C for different radius of curvature. $\overline{DC}$ = 25 mm, $\overline{DB}$ = 35 mm, $\overline{DA}$ = 45 mm. (b) The cylindrical rods used to estimate the bending radius of curvature of the device.

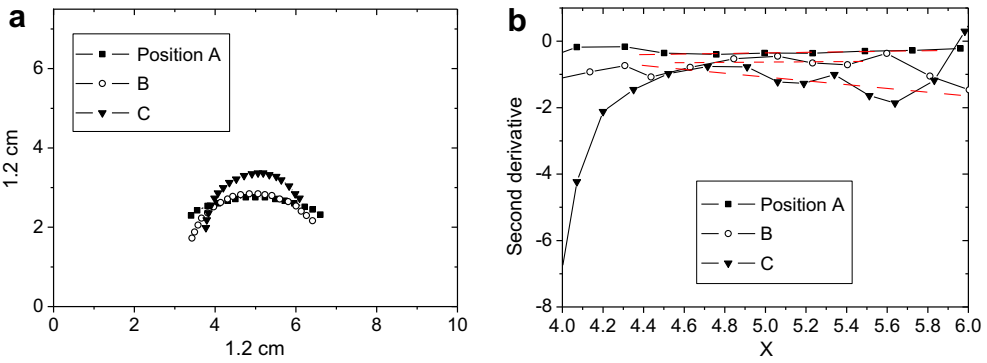

Fig. 3. Traced curves (a) from the 2.5× images of the FOLED device bent with positions A, B, and C. (b) Their second derivative around the active OLED area ($x = 5$).

Table 1
The radius of curvature (R_c) of the devices investigated in each of the test runs.

Test run	1	2	3	4	5	6	7	8	9	10	11	12	13	14	15
R_c of FOLED in Expt. 1	N/A	R_1	R_2	R_3	R_2	R_1	N/A	R_1	R_2	R_3	R_2	R_1	N/A	R_3	N/A
R_c of FOLED in Expt. 2	N/A	R_1	R_2	R_3	N/A	R_3	N/A								
R_c of FOLED in Expt. 3	N/A	R_3	N/A	R_3	N/A										
R_c of FOLED in Expt. 4	N/A	R_3	N/A	R_3	N/A										

R_1 = position A, R_2 = position B, and R_3 = position C.

positions A, B, and C. First, five cylindrical rods were fabricated with radius 7 mm, 8 mm, 9 mm, 10 mm, and 12 mm as shown in Fig. 1b, and used to compare with the curvature at the three positions. As a result, R_c for positions A, B, and C are approximately 12 mm, 10 mm, and 8 mm. For confirmation, the second method was also applied in each case, but is more complicated. Images of the FOLED devices bent at the three positions were taken separately and input to the software Origin 7.0 with a magnification of 2.5. Three curves were then traced and centered on $x = 5$ as shown in Fig. 3a, and the second derivative was calculated and plotted in Fig. 3b. The semi-circle as a function of x centered on (x_0, y_0) is:

$$y(x) = y_0 + \sqrt{R_c^2 - (x - x_0)^2} \quad (1)$$

and the second derivative of (1) when $x = x_0$ is:

$$y''(x_0) = \frac{-1}{R_c} \quad (2)$$

From Fig. 3b, the average of the second derivative of bending positions A, B, and C between $x = 4.4$ and 5.6 are about −0.37, −0.68, and −0.8. Therefore, the R_c of Fig. 3a are 3.2 cm, 1.9 cm, and 1.5 cm. But because the curves were traced from a 2.5× image, so the real R_c of the FOLED device of bending positions A, B, and C are 12.8 mm, 7.6 mm, and 6 mm.

Finally, when the device was bent, the focus of Konica-Minolta LS-110 Luminance meter was adjusted in order to focus on the active area and make the accurate measurement of the device brightness.

3. Results and discussion

The experiments included several runs with different R_c and bending stress type as listed in Table 1. It is to be noticed that the device in Expt. 1, 2, 3, and 4 are not the same device in order to control the defect type caused by each direction of stress. Second, the device was not encapsulated, which means the EL efficiency would decay with time under normal operation in the air, even without bending. Consequently, the EL lifetime experiment was first conducted at a current density of 9.4 mA/cm^2 (about 4.6 V and 100 cd/m^2) as shown in Fig. 4. It showed that after about 10 min, the device was relatively stable at least for the next 50 min. Therefore, the bending experiments were only conducted after the fresh devices were operated

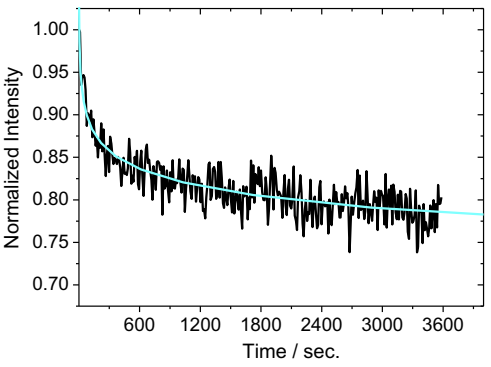

Fig. 4. The lifetime measurement of the non-encapsulated FOLED device under constant current supply at 9.4 mA/cm^2.

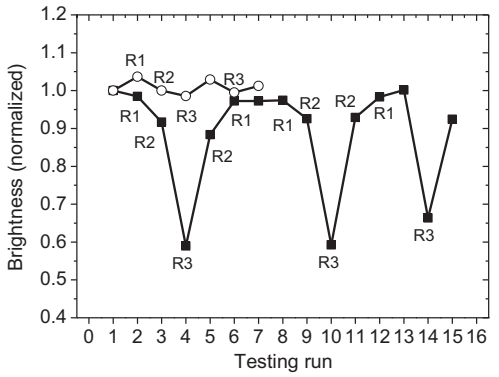

Fig. 5. The brightness of the FOLED device against the testing runs. In the Expt. 1 (filled square), the OLED device was given a stretched stress while in the Expt. 2 (open circle), a compressive stress. R_x denotes the radius of curvature: R_1 = position A, R_2 = position B, and R_3 = position C.

at 9.4 mA/cm^2 after 10 min and did not extend beyond 1 h in duration. This ensured that the EL performance change in the experiment was mainly caused by the mechanical bending process.

Fig. 5 shows how the brightness (normalized) of the OLED device changed with the different bending conditions. The OLED was stretched in Expt. 1 (filled square), and compressed in Expt. 2 (open circle). With the constant current supply at 9.4 mA/cm^2, the brightness of the device in Expt. 1 reduced slightly first when being stretched with R_c = position A, and lowered to 90% with R_c = position B. When it was bent more tightly with R_c = position C, the brightness drops dramatically to under 60%. It seemed that the device was sustainable under the strain up to a critical point: in this case R_c between positions B and C. The strain of the thin-film caused by bending can be calculated by Eq. (3) if the bending is homogeneous and R_c is known.

$$\varepsilon = \frac{y}{R_c} \tag{3}$$

ε is the strain, and y is the distance between the layer and the neutral axis (the layer-element within the complete stack that is neither stretched nor compressed in the bending). With the condition of the described 2-point bending method, it is assume that over the small area of the device, the strain produced is homogeneous. It is also assumed that the position of the neutral axis was at the midpoint of the substrate (as the substrate is much thicker than the coated films) → y = 0.0635 mm. Therefore, for the case of R_c = 10 mm and 6 mm for bending positions B and C, the strain of the OLED layers ~0.65–1%, respectively. After this point, one or more layers appear to crack. Candidate layers could be the ITO anode, as it is the most brittle material of the device, or the ductile aluminum cathode layer as the yield stress decreases dramatically when being as thin as 100 nm [12], or even the organic layers, of which the Young's modulus is between 60 and 120 GPa when being coated on a harder substrate such as the silicon waver [13]. Surprisingly, this damage was reversible as shown in the testing runs 5–7 where the device was relieved gradually until completely flattened. The cycle was then repeated one more time. The brightness again was decreased to lower than 60% after the critical bending point and recovered to almost 100% in run 13 when the bending was relieved again. In the third cycle, the device was bent with R_c = position C directly and relieved again in the next run. It shows that although the brightness did not drop as much as the previous two cycles, the recovery was nevertheless not complete. The damage caused by sudden hard bending seems to be more pronounced. On the other hand, when comparing run 2 and run 8 (with R_c = position A in both runs), although the run 8 was after a likely severe damage to the device that had been caused in run 4, the brightness of each run was not too different. This may be due to the fact that when the device was operated, the higher temperature allowed the layers to creep when the strain was less severe. When the OLED was compressed as in Expt. 2, the brightness was almost unchanged even when R_c = position C.

In order to confirm this result, two more devices were tested and measured by the integrated sphere (Labsphere LMS-100), which had been calibrated according to the FOLED sample holder, as Expt. 3 and Expt. 4 in Table 1. The integrating sphere is a hollow spherical chamber with

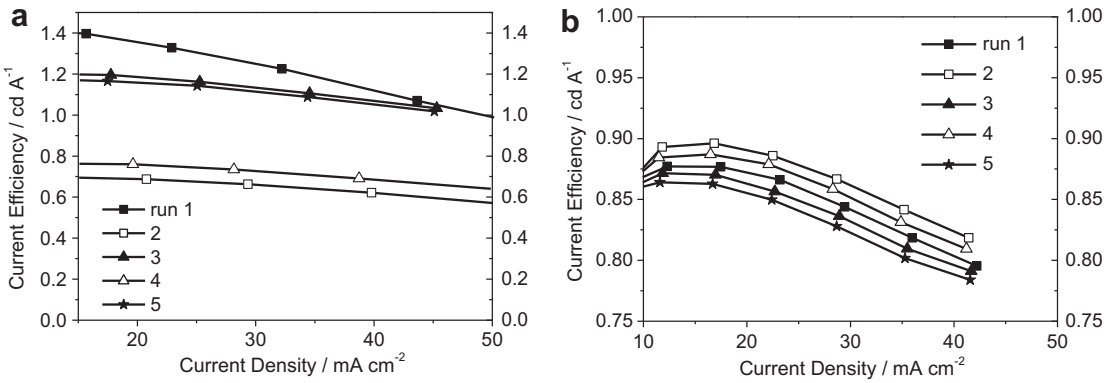

Fig. 6. The current efficiency of the FOLED device against the current density. In the Expt. 3 (a), the OLED device was given a tensile stress while in the Expt. 4 (b), a compressive stress. The filled symbols plots the runs when the device was unbent, while the open symbols plots the runs when the device was bent such that R_c = position C.

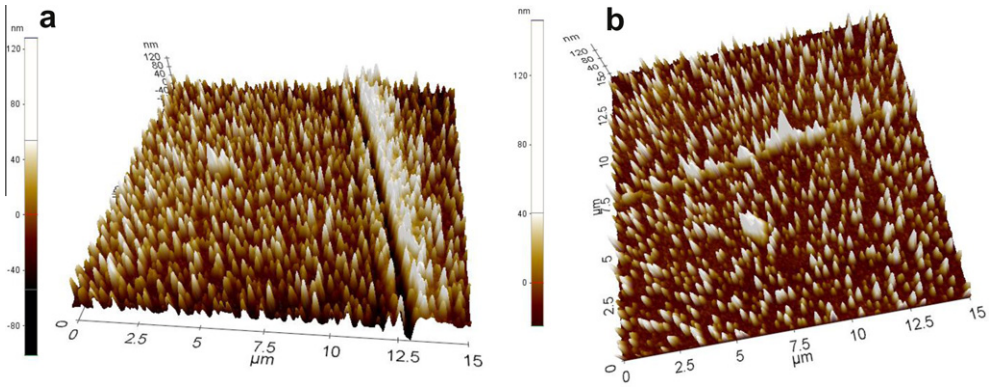

Fig. 7. The AFM images of the aluminum surface of the Expt. 1 (a) and Expt. 2 (b) FOLED device after the bending tests.

a highly reflective material coated on the inner surface and a small photodiode. The sample to be measured is mounted in the middle of the chamber so that ideally all the out-coupled light can be collected by the photodiode. In Fig. 6a (Expt. 3), the device was bent in a concave manner to produce a tensile stress with R_c = position C in the runs 2 and 4, and relieved in the runs 1, 3, and 5. In Fig. 6b (Expt. 4), on the other hand, the device was bent in a convex manner to produce a compressive stress with R_c = position C in the runs 2 and 4, and relieved in the runs 1, 3, and 5. Both experiments repeated the two important results observed by the luminance meter in Fig. 5: the recovery of EL when tensile stress was removed and the different response of the device EL to the opposite direction of the stress.

To understand more about these observations, the devices were examined by atomic force microscopy (AFM) immediately after the bending experiments, and the images are shown in Fig. 7a (Expt. 1) and 7b (Exp. 2). The rough surfaces in the images were the typical thermal evaporated aluminum layer surface as it was the outmost layer of the device. Although it was reported that for a free-standing or polymer-supported aluminum thin-film, the rupture strain is normally between 1% and 2% [14], which is about the maximum strain caused by bending position C in Expt. 1 (~1%). Therefore, the deep and clear cracks were observed in Fig. 7a. On the other hand, in the Fig. 7b only some buckle-like lines were observed, and these lines were merely rougher surfaces with taller spikes, and this may explain why the EL brightness of the Expt. 2 and Expt. 4 remained relatively unchanged as shown in Figs. 5 and 6b. Although the AFM images could only reveal the surface of the aluminum layer as it was the outermost layer, the other layers of the OLED, notably the ITO layer, might have the same types of defects, cracks or buckling, as the aluminum layer. One thing to be noticed here is that these AFM measurements were not conducted during the bending experiments but 1–2 h after, therefore, some cracks or buckles might recover already thus were not observable, but they still provide some information about how these two kinds of stress damaged the devices differently. It is also worth mentioning here that although the compressive strain looks harmless to the FOLED device, it did, however, cause the outermost aluminum layer to detach initially. It means the device completely failed when being bent tighter than some critical radius. This is a known issue for multilayer thin-films when adherence of the layers is poor. But as long as the whole active area did not completely delaminate, and it was still adherent in the flat regions either side of it, i.e., it was still held in place, the layers would come back into contact when the bending moment was removed. Nevertheless, creep, which accelerates as the temperature rises as a result of the resistive heating while the device is operated, would improve the adherence. This process only takes 10s of seconds. For example, the Expt. 2 device would completely fail initially when under a compressive strain with R_c = position C. On removing the bending moment, the device would come back to work with the original EL efficiency. By operating the device for 10–20 s further at the current density of 9.4 mA/cm^2 (about 4.6 V), and then bending the device with R_c = position C again, the device would then not fail but would perform as well as before the bending, as shown in curve Expt. 2 of Fig. 5.

4. Conclusion

It has been shown here that the conventional bottom emitting FOLED device can work with at least 90% of the original efficiency when the OLED layers were subjected to bending in a cylindrical sense about one axis and given a tensile stress with R_c = position B, and almost 100% of the original efficiency when given a compressive stress with R_c = position C. The damage caused by the bending is reversible. For the case of tensile stress (stretching), the device recovered better when bending was applied slowly and step by step from R_c = positions A–C. When it was bent with R_c = position C directly, the device only recovered to 95% after the bending was removed. For the case of compression, one possibility may be that the aluminum cathode detaches initially when being bent with R_c = position C. But after the bending is relieved and the device operated for another 20 s at the current density of 9.4 mA/cm^2 (about 4.6 V), thus giving the aluminum layer enough time to creep, the device could function while being bent with

R_c = position C, and with the same efficiency as before the bending. In both situations, the results give reason to be optimistic about FOLEDs, provided the bending radius of curvature does not fall below 10 mm. To reduce the critical bending radius of curvature further would require a modified substrate architecture. In addition, to avoid delamination when a compressive stress is applied, the adhesion of the OLED layers needs to be improved.

Acknowledgments

C.-J.C. gratefully acknowledges the support of a Ph.D. studentship from Kodak European Research, and Dr. Zhi-Yong Zhou of Electronic Engineering Department, Newcastle University, UK for doing AFM measurement, and Dr. Ben P. Lyon of Department of Physics, Durham University, UK for science consultancy.

References

[1] C.W. Tang, S.A. Vanslyke, Organic electroluminescence diodes, Appl. Phys. Lett. 51 (1987) 913–915.
[2] Y.C. Yang, D.K. Yang, Wider viewing angle in in-plane switching mode liquid crystal displays by self-compensated phase retardation films, in: J. Morreale (Ed.), SID International Symposium Digest of Technical Papers, vol. XI, Books I–Iii, Society Information Display, Campbell, 2009, pp. 1563–1566.
[3] Y.C. Lu, C.S. Cheng, C.J. Hu, C.M. Chang, F.Y. Gan, SID, New multi-domain vertical alignment LCD with high contrast ratio, in: SID International Symposium, Digest of Technical Papers, vol. Xxxviii, Books I and Ii, vol. 38, Society Information Display, Playa Del Rey, 2007, pp. 725–727.
[4] F.M. Dheurle, J.M.E. Harper, Note on the origin of intrinsic stresses in films deposited via evaporation and sputtering, Thin Solid Films 171 (1989) 81–92.
[5] C.H. Hsueh, Thermal stresses in elastic multilayer systems, Thin Solid Films 418 (2002) 182–188.
[6] C.J. Chiang, C. Winscom, S. Bull, A. Monkman, Mechanical modeling of flexible OLED devices, Org. Electron. 10 (2009) 1268–1274.
[7] G.P. Crawford, Flexible flat panel displays, in: A.C. Lowe (Ed.), Wiley-SID Series in Display Technology, Brown University, USA, John Wiley & Sons Ltd., 2005, pp. 99–120.
[8] Y. Leterrier, L. Medico, F. Demarco, J.A.E. Manson, U. Betz, M.F. Escola, M.K. Olsson, F. Atamny, Mechanical integrity of transparent conductive oxide films for flexible polymer-based displays, Thin Solid Films 460 (2004) 156–166.
[9] C.F.Y. Leterrier, L. Médico, F. Demarco, J.-A.E. Månson, P. Bouten, J. DeGoede, J.A. Nairn and Nairn, Mechanical properties of transparent functional thin films for flexible displays, in: 46th Annual Technical Conference Proceedings, Society of Vacuum Coaters, 2003, 505/856-7188.
[10] J.S.L. William, N. Findley, Kasif Onaran, Creep and Relaxation of Nonlinear Viscoelastic Materials with an Introduction to Linear Viscoelasticity vol. 18, North-Holland Publishing Company, Amsterdam, New York, Oxford, 1976. p. 191.
[11] S. Li, J. Wang, M.D. Thouless, The effects of shear on delamination in layered materials, J. Mech. Phys. Solids 52 (2004) 193–214.
[12] G.T. Mearini, R.W. Hoffman, Tensile properties of aluminium alumina multilayered thin-films, J. Electron. Mater. 22 (1993) 623–629.
[13] C.J. Chiang, S. Bull, C. Winscom, A. Monkman, A nano-indentation study of the reduced elastic modulus of Alq(3) and NPB thin-film used in OLED devices, Org. Electron. 11 (2010) 450–455.
[14] T. Li, Z.Y. Huang, Z. Suo, S.P. Lacour, S. Wagner, Stretchability of thin metal films on elastomer substrates, Appl. Phys. Lett. 85 (2004) 3435–3437.

Organic Electronics 11 (2010) 1877–1885

Contents lists available at ScienceDirect

Organic Electronics

journal homepage: www.elsevier.com/locate/orgel

Combination of donor characters in a donor–acceptor–donor (DAD) type polymer containing benzothiadiazole as the acceptor unit

Merve Sendur [a], Abidin Balan [a], Derya Baran [a], Baris Karabay [a], Levent Toppare [a,b,c,*]

[a] Middle East Technical University, Department of Chemistry, 06531 Ankara, Turkey
[b] Department of Biotechnology, Middle East Technical University, 06531 Ankara, Turkey
[c] Department of Polymer Science and Technology, Middle East Technical University, 06531 Ankara, Turkey

ARTICLE INFO

Article history:
Received 3 August 2010
Received in revised form 2 September 2010
Accepted 2 September 2010
Available online 16 September 2010

Keywords:
Conjugated polymers
Electrochromism
Donor–acceptor theory
Copolymers
p- and n-doping

ABSTRACT

A benzothiadiazole bearing donor–acceptor–donor (D–A–D) type monomer (M_3) was synthesized using the combination of 3, 4-ethylenedioxythiophene (EDOT) and thiophene donor units to understand the effect of donor strength on the optoelectronic and electrochemical properties. The resulting monomer was polymerized electrochemically (P_3) and compared with its symmetrical thiophene (P_1) and EDOT (P_2) bearing homologues whether there exists a combination of the electrochemical and optical characteristics. Also, copolymer studies were performed with symmetrical thiophene (M_1) and EDOT (M_2) containing monomers in order to compare the results with P_3. Cyclic voltammetry (CV) and spectroelectrochemistry results revealed that P_3 is a low band gap polymer (1.18 eV) having both p-and n-type property which is superior to the copolymers synthesized using M_1 and M_2.
© 2010 Elsevier B.V. All rights reserved.

1. Introduction

Due to their favorable electronic, optical and mechanical properties conductive polymers (CPs) are used in a wide range of applications such as photovoltaics [1], light-emitting diodes [2], field-effect transistors [3], sensors [4], and electrochromic devices [5]. CPs as a class of electrochromic materials have attracted great interest due to several superior properties over their inorganic counterparts such as coloration efficiency [6], fast switching ability [7], multiple colors with the same material [8], and fine-tuning of the band gap with small structural modifications [5b,6–9]. Due to the fact that electrochromic and non emissive applications of CPs provide stimuli effect (viewing angle, light intensity or sunlight exposure) free, light-weight and flexible displays, their development is considered to be important for future display technologies [10].

In order to use CPs in electrochromic devices, there are two issues to be resolved; to have a low band gap to maximize the conductivity of the polymers and satisfy three additive colors in the neutral state to obtain full color space [11]. Approaches to achieve RGB (red, green, blue) colors with CPs have become the subject of many studies; however, only handful of them revealed true red [12], blue [13] or green [14] neutral state polymers. Up to date, donor–acceptor–donor (DAD) route has been considered as the most effective way to obtain low band gap polymers with desired neutral state colors. DA structured monomers are usually obtained with electropolymerizable heterocycles as the end group in order to achieve the necessary polymers electrochemically [15].

Electrochemical copolymerization is also a facile method to obtain desired neutral state colors for these types of materials. In copolymerization, electroactive monomers are polymerized from a bulk containing the co-monomers. Resulting polymer generally shows unique optical and electronic properties with enhanced mechanical and kinetic properties compared to those of the homo-polymers [16]. Fine tuning in the band gap and neutral state color

* Corresponding author at: Middle East Technical University, Department of Chemistry, 06531 Ankara, Turkey. Tel.: +90 3122103251; fax: +90 3122103200.
E-mail address: toppare@metu.edu.tr (L. Toppare).

1566-1199/$ - see front matter © 2010 Elsevier B.V. All rights reserved.
doi:10.1016/j.orgel.2010.09.001

can be achieved by tailoring the co-monomer feed ratio as well as the working potential of copolymerization [17]. However, exact structures of electrochemical copolymers are hard to determine due to the insolubility of the deposited films which hinders the solution characterizations.

Recently, poly(4,7-di(2,3-dihydro-thieno[3,4-b][1,4]dioxin-5-yl)benzo[1,2,5] thiadiazole) [14d] (P_2) was characterized in terms of its electrochromic properties in our group. It was shown to be the first green to transmissive electrochromic material with two simultaneous maximum absorptions placed at around 400 and 750 nm. Its homologue with lower electron density, poly(4,7-dithien-2-yl-2,1,3-benzothiadiazole) [18] (P_1) has an absorption maximum at around 560 nm where its second transition is in UV region. At the first glance, it seems that a copolymer obtained from these two monomers should have an absorption covering the entire visible region, but the copolymers reported in this manuscript revealed neutral state colors in between the two, since absorption maximum of the copolymer usually lies between the two homo-polymers.

Herein, we report our approach to explain the effect of different donor groups on the electronic and optical properties of DAD type polymers. An asymmetric monomer having both 3,4-ethylenedioxytiophene and thiophene as the donor groups was synthesized and electrochemically polymerized. Since the monomer contains two different donor units, we anticipated that its polymer may behave as a copolymer of the symmetric monomer having the same donor groups. Hence, the properties of copolymers achieved with the co-monomers having either thiophene or 3,4-ethylenedioxythiophene as the donor group were also reported.

2. Results and discussion

2.1. Synthesis

Donor–acceptor–donor type materials 4,7-di(thiophen-2-yl)benzo[c][1,2,5]thiadiazole (M_1) [18,19], 4,7-di(2,3-dihydro-thieno[3,4-b][1,4]dioxin-5-yl)benzo[1,2,5]thiadiazole (M_2) [14d,20] and 4-(2,3-di hydrothieno[3,4-b][1,4]dioxin-5-yl)-7-(thiophen-2-yl)benzo[c][1,2,5]thiadiazole (M_3) were synthesized as shown in Scheme 1 according to previously reported methods. In order to synthesize the asymmetric monomer (M_3) 4,7 dibromobenzothiadiazole was first coupled with tributyl(2,3-dihydrothieno[3,4-b][1,4]dioxin-5-yl)stannane and then the isolated compound was coupled with tributyl(thiophen-2-yl) stannane.

2.2. Cyclic voltammetry

M_3 was polymerized potentiodynamically between −0.3 V and 1.5 V vs. Ag wire pseudo reference electrode (0.3 V vs. Fc/Fc^+) in a 0.1 M dichloromethane (DCM)/acetonitrile (AN) (5:95, v:v) / tetrabutylammonium hexafluorophosphate ($TBAPF_6$) solution onto ITO-coated glass slides in order to observe the polymer characteristics. During polymerization, a characteristic oxidation peak of monomer was observed at 1.2 V accompanied by a reversible redox couple of the polymer. In Fig. 1, the increase in current density with the number of scans clearly shows the deposition of an electroactive film of P_3 on ITO. The resultant polymer revealed reversible p-type doping properties where the p doping/de-doping was indicated by the peaks at 1.06 V and 0.85 V, respectively. The P_3 film is blue in its neutral state and reveals light blue color when oxidized.

Generally, EDOT bearing DAD type molecules have lower monomer oxidation potentials than thiophene bearing ones under identical experimental conditions owing to the electron rich ethylenedioxythiophene group. As reported M_1, revealed a monomer oxidation at 0.85 V in 0.1 M DCM/AN (5:95, v:v)/$TBAClO_4$ vs. the Ag/Ag^+ reference electrode and its EDOT bearing homologue M_2 has a monomer oxidation at 0.95 V in DCM/$TBAPF_6$. In order to have a reliable comparison with M_3, we performed all experiments in DCM/AN/$TBAPF_6$ system vs. Ag wire pseudo reference electrode. As a result, M_3 revealed a monomer oxidation at 1.2 V vs. Ag wire pseudo reference electrode which was lying between the two others. Since M_3

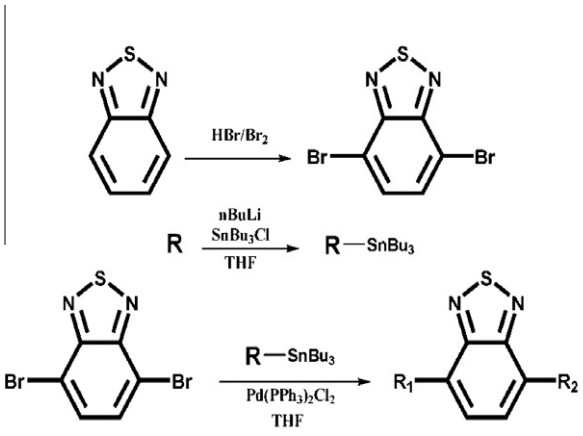

Monomer	R_1	R_2
M_3	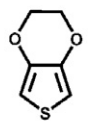	
M_2	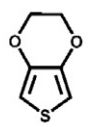	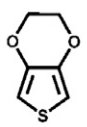
M_1		

Scheme 1. Synthesis scheme of the monomers; M_1, M_2 and M_3.

contains both ethylenedioxythiophene and thiophene groups, its oxidation potential value is between the values of the monomers containing only EDOT or thiophene as shown in Fig. 2.

Since the polymer structure consists of electron withdrawing benzothiadiazole units, a rare property; n-type doping was observed for P_3 with reversible peaks at −1.6 V and −0.9 V vs. the same reference electrode (Fig. 3). Oxidation and reduction onset values were used to determine the band gap energies for P_1, P_2 and P_3 since all the polymers are both p- and n-type dopable. HOMO and LUMO energies were calculated as −5.75 and −4.65 eV, respectively for P_3 (the value of NHE was used as −4.75 eV throughout this study) [1j]. As seen from Table 1, the LUMO levels of three polymers are same since benzothiadiazole was used as the acceptor unit. However, as the donor strength increases the HOMO energy levels decrease due to the electron rich EDOT units incorporated into the polymer structure. Calculated optical and electrochemical band gap values for P_1 (1.65 eV), P_2 (1.1 eV) and

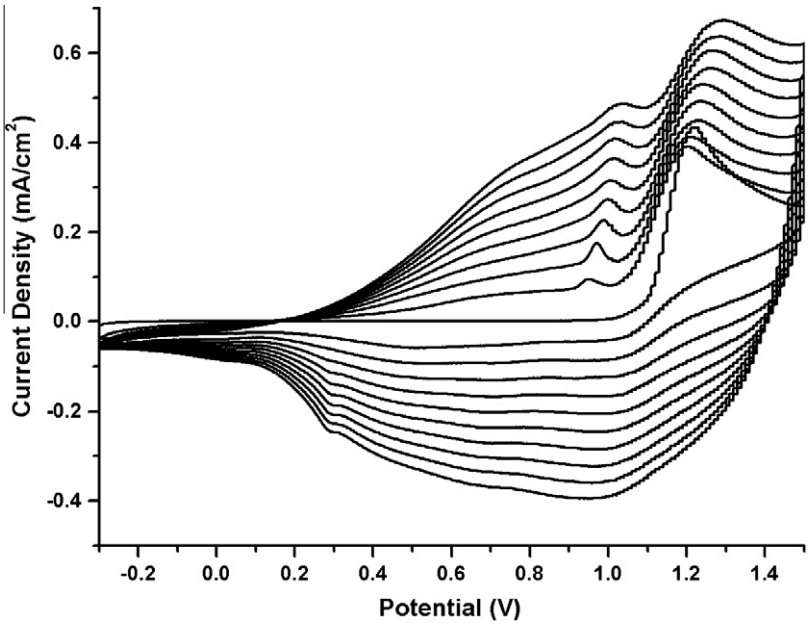

Fig. 1. Electrochemical deposition of P3 on ITO-coated glass slide in a 0.1 M DCM/AN/$TBAPF_6$ solvent-electrolyte couple.

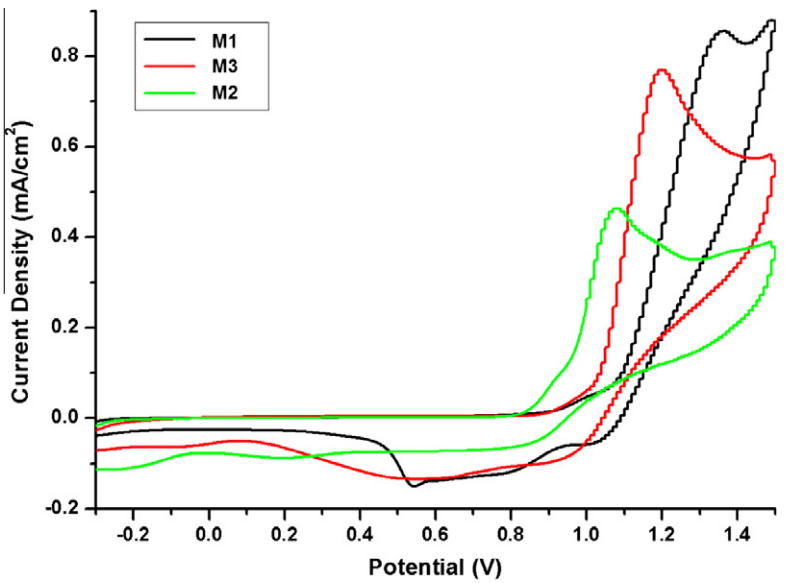

Fig. 2. First cycles of M_1, M_2 and M_3 in 0.1 M DCM/AN/$TBAPF_6$ solvent-electrolyte couple during electrochemical polymerization.

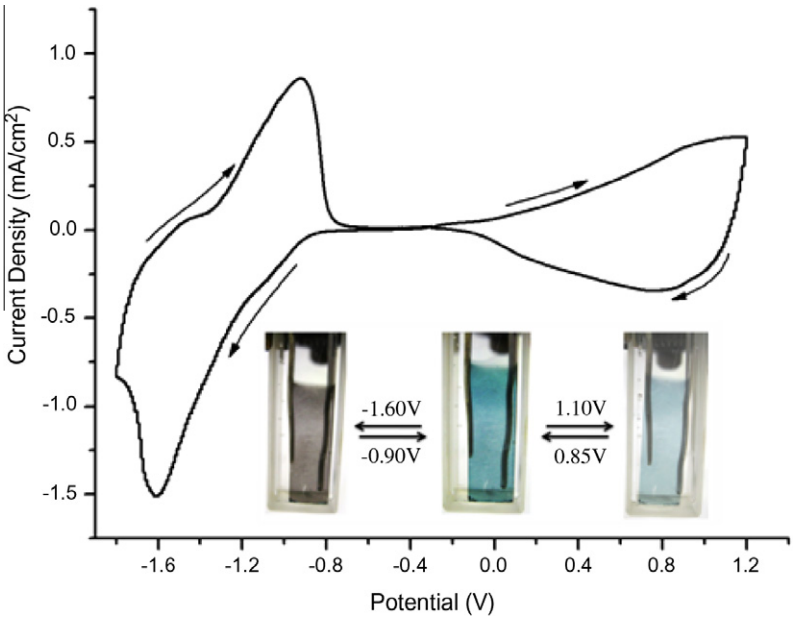

Fig. 3. p- and n-type doping of P_3 in 0.1 M AN/$TBAPF_6$.

Table 1
Monomer oxidation, corresponding polymer redox potentials, band energies (HOMO/LUMO values), optical and electronic band gap values of P_1, P_2 and P_3.

Polymer	E_m^{ox} (V)	E_p^{ox} (V)	E_p^{red} (V)	HOMO/LUMO energies (eV)	Optical band gap (eV)	Electrochemical band gap (eV)
P_1	1.36	1.09	0.61	−4.85/−3.75	1.50	1.65
P_2	1.07	0.90	0.70	−5.40/−3.75	1.20	1.10
P_3	1.20	1.06	0.85	−5.00/−3.75	1.18	1.20

P_3 (1.2 eV) are in good agreement confirming the identical electrochemical processes for both methods (CV and spectroelectrochemistry).

The scan rate dependence of the P_3 film was investigated using CV. A direct proportionality between the scan rate and the current intensity indicates a well adhered electroactive film on ITO and a non-diffusion controlled electrochemical process. The linear relationship can be seen even at very low and high scan rates which demonstrates that the number of electrons in the diffusion layer is always constant during the scans but increases as the scan rate increases [21] (Fig. 4).

Copolymer studies were performed with M_1 and M_2 in order to observe whether the resulting copolymer will have the same properties with P_3. Since M_3 has both thiophene and EDOT units on its polymer backbone, its polymer P_3 may reveal the similar electrochemical and optical characteristics with the copolymer (M_1 and M_2 as the co-monomers). A three-electrode cell with ITO working electrode was used to deposit polymers potentiodynamically. Oxidative polymerizations were achieved by repeated cycling between −0.3 V and +1.5 V with different feed ratios. For 1:1 (M_1:M_2) ratio 10^{-6} moles of each co-monomers were used and the other ratios were determined according to the mole ratios. DCM/AN (5:95 v: v)/ $TBAPF_6$ solvent-electrolyte system was used for polymerization at a scan rate of 100 mV s^{-1} for 1:1, 1:2, 1:4, 1:10 and 2:1 (M_1:M_2) ratios. Table 2 summarizes the monomer and polymer redox potentials for electrochemically prepared copolymers. During potentiodynamic scans, two monomer oxidations were observed for M_1 and M_2 distinctively and reversible redox peaks were determined for the copolymers. As the amount of M_1 was increased in the feed, the polymer redox peaks were slightly shifted to higher potentials due to the increased amount of thiophene units on the polymer backbone. Likewise, P_3 showed similar electrochemical properties with those of the copolymers prepared from different feed ratios.

2.3. Optical studies

In its neutral state, P_3 showed maximum absorption at 408 nm and 642 nm in the visible region which resulted in a greenish-blue color. Likewise P_2 also has two absorption maxima due to π–π^* transition at around 428 nm and 755 nm corresponding to green color in its neutral state. In order to have a green color, there should be two transitions at around 400 nm and 700 nm in the visible region. P_1 has only one transition at 560 nm whereas its second transition is not in the visible region. As we incorporated EDOT moieties into the P_3 polymer structure the absorption in the UV region shifts to 408 nm which is

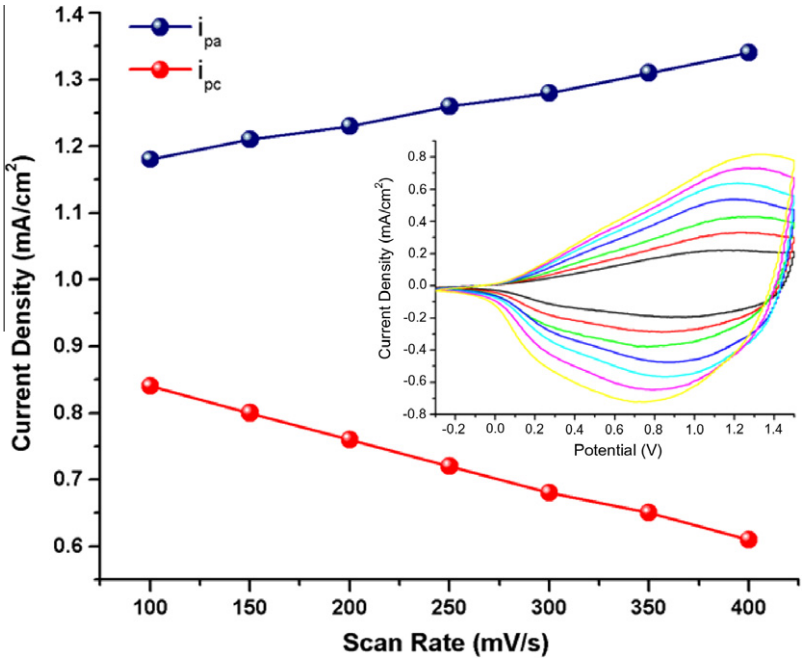

Fig. 4. Scan rate dependence of P_3 film for p-doping in 0.1 M AN/$TBAPF_6$ solvent-electrolyte couple at 100, 150, 200, 250, 300, 350 and 400 mV s−1.

Table 2
Monomer oxidation and accompanied polymer redox potentials of copolymers prepared from co-monomers M_1 and M_2.

Co-monomer composition	$2M_1$:$1M_2$	$1M_1$:$1M_2$	$1M_1$:$2M_2$	$1M_1$:$4M_2$	$1M_1$:$10M_2$
E^{ox}_{poly} (V)	1.34	1.30	1.28	1.28	1.26
E^{red}_{poly} (V)	0.94	0.91	0.85	0.75	0.58

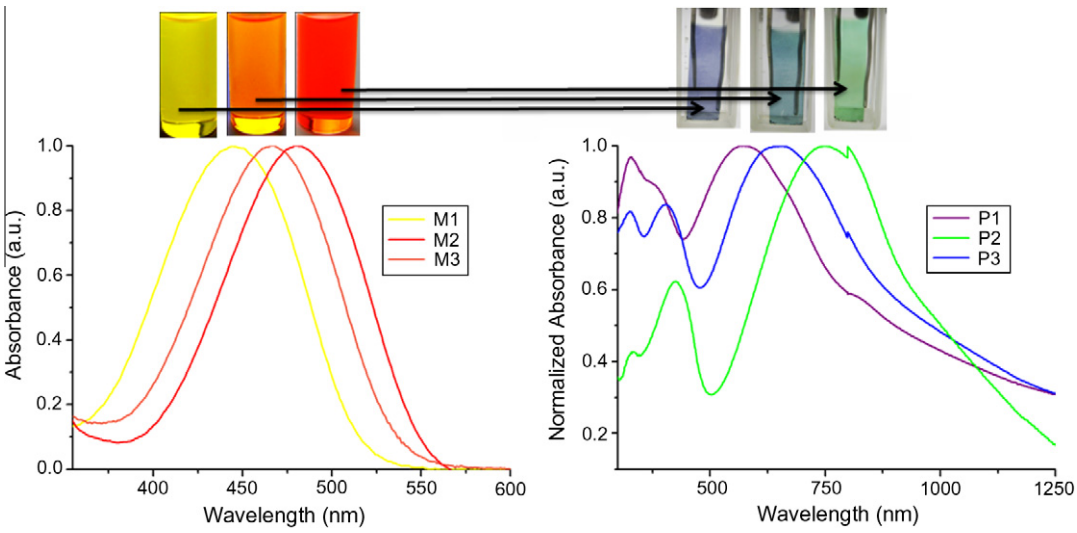

Fig. 5. Electronic absorption spectra of monomers M_1, M_2 and M_3 (left) in $CHCl_3$ and polymers P_1, P_2 and P_3 in thin film form (right).

in the visible region but still does not correspond to green color since the second π–π^* transition is not at around 700 nm. The normalized monomer and resulting polymer film absorptions of P_1, P_2 and P_3 are shown in Fig. 5. It can be seen that when thiophene units were replaced by EDOT units, monomer absorbance values were shifted to lower energies. This trend was also observed in the absorbance values of polymer films. Also, since the conjugation

length was increased, all dominant wavelengths were shifted to right for polymers P_1, P_2 and P_3 compare to the ones for their monomers.

Fig. 6 displays the normalized absorbance of each copolymer film in neutral state prepared from different compositions. P_1, P_2 and P_3 demonstrate a clear shift in the dominant wavelength as the co-monomer composition is varied from pure P_1 to pure P_2. As the concentration of M_2 is increased in the copolymer chain, the π–π^* absorptions of the copolymers were shifted to lower energies from 391 nm to 422 nm and 596 nm to724 nm. The observed red shift indicated a "tunable" electrochromic material can be synthesized by varying the amount of any monomer in the copolymer backbone. Here, it is noteworthy to emphasize that P_3 showed the electrochemical and optical properties of the copolymer (1:4, M_1:M_2 ratio) hence P_3 can be used like a copolymer. Most of the copolymer studies in the literature state that the copolymerization of two co-monomers often results in a random copolymer. However, we achieved a controlled polymerization with similar properties to that of copolymers using M_1 and M_2 as the co-monomers. Table 3 summarizes λ_{max} values and band gap energies for P_1, P_2, P_3 and the copolymers obtained from M_1 and M_2. The band gap of P_3 was calculated as 1.18 eV from the lowest π–π^* transition which is very similar to the one reported for the copolymer obtained using 1:4 M_1:M_2 ratio.

In order to probe the spectral response of P_3 upon applied potential spectroelectrochemical studies were performed in 0.1 M AN/$TBAPF_6$ solvent-electrolyte couple. During stepwise oxidation, the potential was gradually increased from −0.3 V to 1.2 V and the absorbance changes were observed for P_3. In its neutral form P_3 revealed only two transitions with no absorbance in NIR region. Upon p-type doping, as the peaks at 408 nm and 642 nm were decreased new bands in near-IR region intensified due to the charge carrier formation such as polarons and bipolarons (Fig. 7). Since P_3 still absorbs after 600 nm in its doped

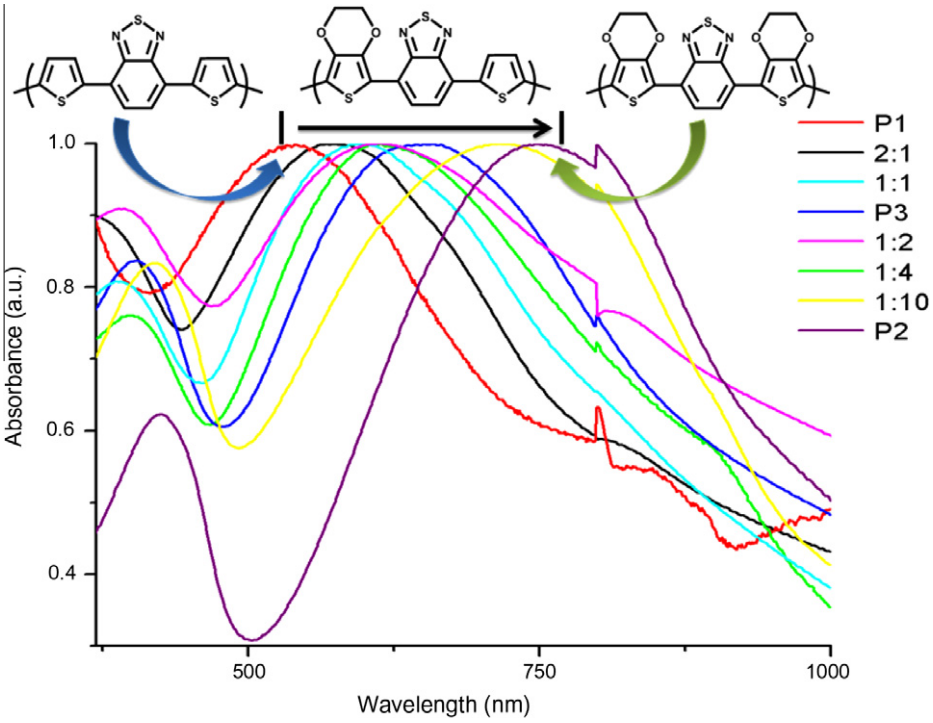

Fig. 6. Normalized absorbance spectra of P_1, P_2, P_3 and the copolymer films prepared from different compositions (all in neutral state).

Table 3
Maximum wavelength values and band gap energies of P_1, P_2, P_3 and resulting copolymers.

Polymer	P1	2:1 (M_1:M_2)	1:1 (M_1:M_2)	1:2 (M_1:M_2)	1:4 (M_1:M_2)	P3	1:10 (M_1:M_2)	P2
Neutral state colors								
λ_{max} (nm)	–	384	391	395	404	408	422	428
	560	574	596	613	619	642	724	755
Optical band gap (eV)	1.5	1.41	1.36	1.06	1.18	1.18	1.2	1.2

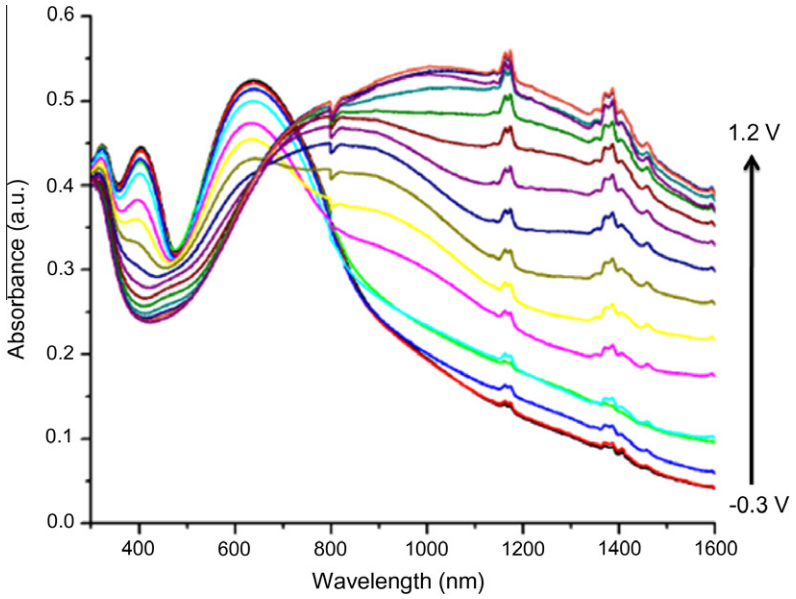

Fig. 7. Electronic absorption spectra of P_3 in 0.1 M AN/$TBAPF_6$ system upon p-type oxidation.

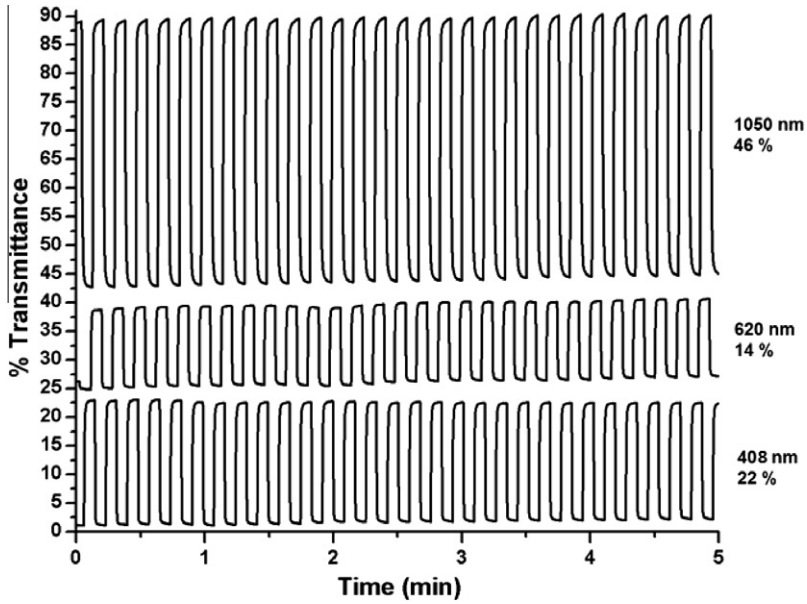

Fig. 8. Optical transmittance changes of P_3 at 408 nm, 620 nm and 1050 nm in 0.1 M AN/$TBAPF_6$ system while switching the potentials between its neutral and oxidized states.

state, the polymer was light blue. To have a transmissive state in the doped form the bands in the visible region should have depleted completely [13b].

Transmittance changes and switching abilities of P_3 were determined while sweeping the potentials between its fully oxidized and reduced states within 5 s time intervals. The studies were performed in a monomer free 0.1 M AN/$TBAPF_6$ solvent-electrolyte system. P_3 revealed 22% transmittance change upon doping/de-doping process at 408 nm, 14% at 620 nm and 46% at 1050 nm (Fig. 8). Switching time is the duration for the polymer to switch between the two extreme states and it was calculated as 0.6 s, 0.75 s and 0.8 s at corresponding wavelengths.

3. Conclusion

An EDOT, thiophene and benzothiadiazole bearing donor–acceptor type monomer was synthesized and

polymerized electrochemically as an alternative to copolymer studies. The polymer was characterized by electrochemically and optically. The resulting polymer is both p- and n-type dopable and showed the characteristics of a copolymer where two monomers are required. The results revealed that P_3 can be synthesized and its polymerization can be controlled to avoid the formation of a random copolymer.

4. Experimental

4.1. General

All chemicals were purchased from Aldrich except THF (tetrahydrofuran) which was purchased from Acros. Tributyl(thiophene-2-yl)stannane [22] and tributyl(2,3-dihydrothieno[3,4-b][1,4]dioxin-5-yl)stannane [23] were synthesized according to a previously described method. All reactions were carried out under argon atmosphere unless otherwise mentioned. All electrochemical studies were performed under ambient conditions using a Voltalab 50 potentiostat. Electropolymerizations were performed in a three-electrode cell consisting of an indium tin oxide doped glass slide (ITO) as the working electrode, platinum wire as the counter electrode, and a silver wire pseudo reference electrode. After each measurement the reference electrode was calibrated with ferrocene. The potential of quasi reference electrode was determined as 50 mV vs. the normal hydrogen electrode (NHE).

^{1}H and ^{13}C NMR spectra were recorded in $CDCl_3$ on a Bruker Spectrospin Avance DPX-400 Spectrometer. Chemical shifts are given in ppm downfield from tetramethylsilane. A Varian Cary 5000 UV–Vis spectrophotometer was used to perform the spectroelectrochemical studies of the polymer at a scan rate of 2000 nm/min. Column chromatography of all products was performed using Merck Silica Gel 60 (particle size: 0.040–0.063 mm, 230–400 mesh ASTM). Reactions were monitored by thin layer chromatography using silica gel coated aluminum sheets. Solvents used for spectroscopy experiments were spectrophotometric grade.

4.2. Synthesis of 4,7-dibromobenzo[c] [1,2,5] thiadiazole

A mixture of hydrobromic acid (16 ml) and bromine (2 ml) was added slowly to a mixture containing hydrobromic acid (36 ml) and benzothiadiazole (2.0 g, 0.015 mol) via continuous stirring at 150 °C. The reaction was left for overnight reflux. Then, the mixture was kept in ice bath; orange crystals were produced in 3–4 h. The crystals were filtered, and dissolved in dichloromethane. The organic phase was extracted by two portions of sodium bisulfide solution, and then with saturated sodium chloride solution. After the washing process, mixture was dried over $MgSO_4$ and the solvent DCM was evaporated by rotary evaporator. The yellowish solid was collected after drying in oven for overnight. ^{1}H NMR (400 MHz, $CDCl_3$): δ(ppm) 7.65 (s, 2H). ^{13}C NMR (100 MHz, $CDCl_3$): δ(ppm) 152.75, 132.13, 113.70.

4.3. Synthesis of 4-bromo-7-(2,3-dihydrothieno[3,4-b][1,4]dioxin-5-yl)benzo[c][1,2,5]thiadiazole

4,7-Dibromobenzo[c] [1,2,5] thiadiazole (1.5 g, 5.1 mmol) and tributyl(2,3-dihydrothieno[3,4-b][1,4]dioxin-5-yl)stannane (3.3 g, 7.7 mmol) were dissolved in dry tetrahydrofuran (THF) (60 ml) and set for refluxing under argon atmosphere. The catalyst, dichlorobis(triphenylphosphine)-palladium(II) (60 mg, 0.085×10^{-3} mmol) was added and the mixture was stirred at 100 °C under argon atmosphere for 16 h while monitoring the reaction with TLC. At the end of 16 h, the mixture was cooled and THF was removed from the mixture by rotary evaporator. Then the residue was subjected to column chromatography (Chloroform: Hexane, 3:1) to afford a purple solid, 4-bromo-7-(2,3-dihydrothieno[3,4-b][1,4]dioxin-5-yl)benzo[c][1,2,5]thiadiazole. ^{1}H NMR (400 MHz, $CDCl_3$): δ(ppm) 7.77 (d, 1H), 8.16 (d, 1H), 6.54 (s, 1H), 4.24 (m, 2H), 4.34 (m, 2H). ^{13}C NMR (100 MHz, $CDCl_3$): δ(ppm) 61.95, 62.73, 100.63, 105.36, 115.65, 123.47, 124.02, 127.67, 127.84, 130.21, 139.34, 151.15.

4.4. Synthesis of 4-(2,3-dihydrothieno[3,4-b][1,4]dioxin-5-yl)-7-(thiophen-2-yl)benzo[c][1,2,5]thiadiazole (M_3)

4-Bromo-7-(2,3-dihydrothieno[3,4-b][1,4]dioxin-5-yl) benzo[c][1,2,5]thiadiazole (1 g, 2.8 mmol), and tributyl(thiophen-2-yl)stannane (2.1 g, 5.6 mmol) were dissolved in THF (60 ml) and dichlorobis(triphenylphosphine)-palladium(II) (50 mg, 0.071×10^{-3} mmol) was added at room temperature. The mixture was refluxed for 12 h under argon atmosphere. Solvent was evaporated under vacuum and the crude product was purified by column chromatography (Cholorform: Hexane, 3:1) to obtain a dark red solid, 4-(2,3-dihydrothieno[3,4-b][1,4]dioxin-5-yl)-7-(thiophen-2-yl)benzo[c][1,2,5]thiadiazole (M_3) . ^{1}H NMR (400 MHz, $CDCl_3$): δ(ppm) 6.5 (s, 1H), 7.8 (d, 1H), 6.9 (s, 2H), 8.3 (d, 1H), 8.0 (m, 1H), 7.1 (m, 1H), 7.4 (m, 1H), 4.3 (m, 2H), 4.2 (m, 2H); ^{13}C NMR (100 MHz, $CDCl_3$): δ(ppm) 151.56, 151.38, 140.70, 140.66, 140.37, 139.21, 138.32, 126.64, 125.90, 125.11, 124.92, 124.85, 123.51, 101.13, 63.75, 63.04.

4.5. Electrochemical polymerization of M_3

For electrochemical polymerization, anodic electrodeposition of the polymer was performed from a dichloromethane (DCM) and acetonitrile (AN) mixture (5/95, v/v) with 0.1 M $TBAPF_6$ (tetrabutylammonium hexafluorophosphate) solvent-electrolyte couple at a scan rate of 100 mV s^{-1}. ITO-coated glass slides, Pt wire and Ag wire were used as working, counter and pseudo reference electrodes, respectively. The potentiodynamic scans were carried out between −0.3 and 1.5 V. After polymerization, the film was washed with ACN to remove the unreacted monomers and the supporting electrolyte.

4.6. Synthesis of copolymers

A three-electrode cell containing ITO-coated glass slide as the working electrode was used to deposite copolymer films potentiodynamically. 4,7-Di(thiophen-2-yl)benzo[c]-

[1,2,5]thiadiazole (M_1) and 4,7-bis(2,3-dihydrothieno[3,4-b][1,4]dioxin-5-yl)benzo[c][1,2,5]thiadiazole (M_2) were synthesized according to the previously reported method [14d,18,20b]. The oxidative electrochemical copolymerizations were achieved by repeated potential cycling in different solutions. M_1 and M_2 were used as the co-monomers in 0.1 M tetrabutylammonium hexafluorophosphate ($TBAPF_6$)/acetonitrile (AN)/dichloromethane (DCM) (95:5, v: v) solvent-electrolyte couple at a scan rate of 100 mV s^{-1}. All polymerizations were done under the same conditions for comparison purposes. For 1:1 (M_1:M_2) ratio 10^{-6} moles of each co-monomer were used and the other ratios; 1:2, 2:1, 1:4 and 1:10 (M_1:M_2) were determined accordingly to mimic M_3. Potentiodynamic runs were between −0.3 and 1.5 V for all copolymer depositions with a scan rate of 100 mV s^{-1}. After electrolysis, the films were washed with ACN to remove the supporting electrolyte and the unreacted monomers.

Acknowledgement

The authors thank TUBA for financial support.

References

[1] (a) F. Huang, K.S. Chen, H.L. Yip, S.K. Hau, O. Acton, Y. Zhang, J. Luo, A.K.Y. Jen, J. Am. Chem. Soc. 131 (2009) 13886;
(b) J.C. Bijleveld, A.P. Zoombelt, S.G.J. Mathijssen, M.M. Wienk, M. Turbiez, D.M. de Leeuw, R.A.J. Janssen, J. Am. Chem. Soc. 131 (2009) 16616;
(c) K.M. Coakley, M.D. McGehee, Chem. Mater. 16 (2004) 4533;
(d) H. Hoppe, N.S. Sariciftci, J. Mater. Res. 19 (2004) 1924;
(e) C.J. Brabec, N.S. Sariciftci, J.C. Hummelen, Adv. Funct. Mater. 11 (2001) 15;
(f) S. Gunes, D. Baran, G. Gunbas, F. Ozyurt, A. Fuchsbauer, N.S. Sariciftci, L. Toppare, Sol. Energy Mater. Sol. Cells. 92 (2008) 1162;
(g) A.P. Zoombelt, M. Fonrodona, M.M. Wienk, A.B. Sieval, J.C. Hummelen, R.A.J. Janssen, Org. Lett. 11 (2009) 903;
(h) K. Colladet, S. Fourier, T.J. Cleij, L. Lutsen, J. Gelan, D. Vanderzande, L.H. Nguyen, H. Neugebauer, S. Sariciftci, A. Aguirre, G. Janssen, E. Goovaerts, Macromology 40 (2007) 65;
(i) G. Dennler, N.S. Sariciftci, Proc. IEEE 93 (2005) 1429;
(j) D. Baran, A. Balan, S. Celebi, B.M. Esteban, H. Neugebauer, N.S. Sariciftci, L. Toppare, Chem. Mater. 22 (2010) 2978.
[2] (a) A. Kraft, A.C. Grimsdale, A.B. Holmes, Angew. Chem. Intl. Ed. 37 (1998) 402;
(b) N.R. Evans, L.S. Devi, C.S.K. Mak, S.E. Watkins, S.I. Pascu, A. Kohler, R.H. Friend, C.K. Williams, A.B. Holmes, J. Am. Chem Soc. 128 (2006) 6647;
(c) Q. Huang, G.A. Evmenenko, P. Dutta, P. Lee, N.R. Armstrong, T.J. Marks, J. Am. Chem. Soc. 127 (2005) 10227.
[3] (a) H.H. Fong, V.A. Pozdin, A. Amassian, G.G. Malliaras, D.M. Smilgies, M. He, S. Gasper, F. Zhang, M. Sorensen, J. Am. Chem. Soc. 130 (2008) 13202;
(b) M.H. Hoang, M.J. Cho, D.C. Kim, K.H. Kim, J.W. Shin, M.Y. Cho, J. Joo, D.H. Choi, Org. Elec. 10 (2009) 607;
(c) P.M. Beaujuge, W. Pisula, H.N. Tsao, S. Ellinger, K. Mullen, J.R. Reynolds, J. Am. Chem. Soc. 131 (2009) 7514;
(d) S. Pang, H.N. Tsao, X. Feng, K. Mullen, Adv. Mater. 21 (2009) 3488;
(e) S. Cho, K. Lee, A.J. Heeger, Adv. Mater. 21 (2009) 1941;
(f) N. Marjanović, T.B. Singh, G. Dennler, S. Günes, H. Neugebauer, N.S. Sariciftci, R. Schwödiauer, S. Bauer, Org. Elec. 7 (2006) 188;
(g) I. McCulloch, M. Heeney, C. Bailey, K. Genevicius, I. MacDonald, M. Shkunov, D. Sparrowe, S. Tierney, R. Wagner, W. Zhang, M.L. Chabinyc, R.J. Kline, M.D. McGehee, M.F. Toney, Nat. Mater. 5 (2006) 328.
[4] D.T. McQuade, A.E. Pullen, T.M. Swager, Chem. Rev. 100 (2000) 2537.
[5] (a) A. Argun, A. Cirpan, J.R. Reynolds, Adv. Mater. 15 (2003) 1338;
(b) P.M. Beaujuge, J.R. Reynolds, Chem. Rev. 110 (2010) 268.
[6] G. Sonmez, H. Meng, F. Wudl, Chem. Mater. 16 (2004) 574.
[7] (a) S.A. Sapp, G.A. Sotzing, J.R. Reynolds, Chem. Mater. 10 (1998) 2101;
(b) A. Kumar, D.M. Welsh, M.C. Morvant, F. Piroux, K.A. Abboud, J.R. Reynolds, Chem. Mater. 10 (1998) 896;
(c) Y. Coskun, A. Cirpan, L. Toppare, J. Mater. Sci. 42 (2007) 368;
(d) L. Groenendaal, G. Zotti, P.H. Aubert, S.M. Waybright, J.R. Reynolds, Adv. Mater. 15 (2003) 855;
(e) J.M. Nadeau, T.M. Swager, Tetrahedron 60 (2004) 7141;
(f) P. Schottland, K. Zong, C.L. Gaupp, B.C. Thompson, C.A. Thomas, I. Giurgiu, R. Hickman, K.A. Abboud, J.R. Reynolds, Macromology 33 (2000) 7051;
(g) C.L. Gaupp, K. Zong, P. Schottland, B.C. Thompson, C.A. Thomas, J.R. Reynolds, Macromology 33 (2000) 1132.
[8] (a) A. Balan, D. Baran, G. Gunbas, A. Durmus, F. Ozyurt, L. Toppare, Chem. Commun. 44 (2009) 6768;
(b) F. Ozyurt, E.G. Gunbas, A. Durmus, L. Toppare, Org. Elec. 9 (2008) 296.
[9] E. Kose Unver, S. Tarkuc, Y. Arslan Udum, C. Tanyeli, L. Toppare, J. Polym. Sci. Polym. Chem. 48 (2010) 1714.
[10] F.C. Krebs, Nature Mater. 7 (2008) 766.
[11] G. Sonmez, H.B. Sonmez, C.K.F. Shen, F. Wudl, Adv. Mater. 16 (2004) 1905.
[12] R.M. Walczak, J.R. Reynolds, Adv. Mater. 18 (2006) 1121.
[13] (a) M. Amb, P.M. Beaujuge, J.R. Reynolds, Adv. Mater. 22 (2010) 724;
(b) A. Balan, G. Gunbas, A. Durmus, L. Toppare, Chem. Mater. 20 (2008) 7510.
[14] (a) A. Durmus, G.E. Gunbas, P. Camurlu, L. Toppare, Chem. Commun. 31 (2007) 3246;
(b) A. Durmus, G.E. Gunbas, L. Toppare, Chem. Mater. 19 (2007) 6247;
(c) G.E. Gunbas, A. Durmus, L. Toppare, Adv. Mater. 20 (2008) 691;
(d) G.E. Gunbas, A. Durmus, L. Toppare, Adv. Funct. Mater. 18 (2008) 2026;
(e) P.M. Beaujuge, S. Ellinger, J.R. Reynolds, Adv. Mater. 20 (2008) 2772.
[15] C.A. Thomas, K. Zong, K.A. Abboud, P.J. Steel, J.R. Reynolds, J. Am. Chem. Soc. 126 (2004) 16440.
[16] (a) S. Celebi, D. Baran, A. Balan, L. Toppare, Electrochimi. Acta 55 (2010) 2373;
A.T. Taskin, A. Balan, Y. Arslan Udum, L. Toppare, Smart Mater. Struct. 19 (2010) 065005;
(c) G.A. Cetin, A. Balan, A. Durmus, G. Gunbas, L. Toppare, Org. Elec. 10 (2009) 34.
[17] (a) C.L. Gaupp, J.R. Reynolds, Macromology 36 (2003) 6305;
(b) E. Yildiz, P. Camurlu, C. Tanyeli, I. Akhmedov, L. Toppare, J. Electroanal. Chem. 612 (2008) 247.
[18] O. Atwani, C. Baristiran, A. Erden, G. Sonmez, Synth. Met. 158 (2008) 83.
[19] C. Kitamura, S. Tanaka, Y. Yamashita, Chem. Mater. 8 (1996) 570.
[20] (a) D. Aldakov, M.A. Palacios, P.Jr. Anzenbacher, Chem. Mater. 17 (2005) 5238;
(b) P. Blanchard, J.M. Raimundo, J. Roncali, Synth. Met. 119 (2001) 527.
[21] G. Sonmez, I. Schwendeman, P. Schottland, K. Zong, J.R. Reynolds, Macromology 36 (2003) 639.
[22] S.S. Zhu, T.M. Swager, J. Am. Chem. Soc. 119 (1997) 12568.
[23] J.T. Pinhey, E.G. Roche, J. Chem. Soc. Perkin Trans. 1 (1988) 2415.

Organic Electronics 11 (2010) 1886–1890

Contents lists available at ScienceDirect

Organic Electronics

journal homepage: www.elsevier.com/locate/orgel

N-channel organic field-effect transistors containing carbonyl-bridged bithiazole derivative fabricated using polyfluorene derivatives as solution-processed buffer layers

Hirotake Kajii [a,*], Yutaka Ie [b], Masashi Nitani [b], Youhei Hirose [a], Yoshio Aso [b], Yutaka Ohmori [a]

[a] Center for Advanced Science and Innovation, Osaka University, 2-1 Yamada-oka, Suita, Osaka 565-0871, Japan
[b] The Institute of Scientific and Industrial Research, Osaka University, 8-1 Mihogaoka, Ibaraki, Osaka 567-0047, Japan

ARTICLE INFO

Article history:
Received 24 March 2010
Received in revised form 17 August 2010
Accepted 30 August 2010
Available online 9 September 2010

Keywords:
N-channel organic field-effect transistor
Polyfluorene
Buffer layer
Surface free energy
Carbonyl-bridged bithiazole

ABSTRACT

The effects of adding solution-processed polyfluorene derivatives as buffer layers between the polymer insulator and active layer of n-channel organic field-effect transistors (OFETs) containing a carbonyl-bridged bithiazole derivative were investigated. The surface free energy was modified by the polyfluorene derivatives. A poly(9,9-dioctylfluorene) (F8) buffer layer, which has a hydrophobic nature, a low surface free energy, and consists almost entirely of a dispersion component, improved the growth morphology of the OFET active layer. An OFET with an F8 buffer layer exhibited n-channel characteristics, and an electron field-effect mobility of 0.025 $cm^2 V^{-1} s^{-1}$.

© 2010 Elsevier B.V. All rights reserved.

1. Introduction

Organic semiconductors have attracted considerable attention due to their simple, low-cost processing and potential electronic and optoelectronic applications. They have potential application as electronic and optoelectronic devices, especially when fabricated by solution processing for large-area, flexible devices. Recently, organic field-effect transistors (OFETs) have been extensively studied for their potential application in low-cost, large-area, flexible electronics [1–9]. However, most of the high field-effect-mobility OFETs have been based on p-channel materials. Although n-channel semiconductor materials are important in the manufacture of ambipolar transistors and complementary circuits, they are relatively rare compared to p-channel materials. N-channel OFETs containing carbonyl-bridged bithiazole derivatives have been reported to have a relatively high electron field-effect mobility [10]. These n-channel OFETs, fabricated on organic self-assembled monolayer (SAM)-treated SiO_2, had an electron mobility on the order of 10^{-2} $cm^2 V^{-1} s^{-1}$.

Recently, polymer gate insulators have attracted attention due to their novel properties, such as solution-processed fabrication, smooth surface, optical transparency, and thermal stability. The electrical characteristics of OFETs depend on the interface state between the organic active layer and the gate insulator, so the choice of gate insulator is important. Chua et al. demonstrated that hydroxyl bonds at the interface between SiO_2 and the organic active layer interfered with n-type carrier transport [8]. On the other hand, Nakayama et al. also demonstrated that insertion of an electronically active interfacial layer of an organic semiconductor is more effective in eliminating electron traps at the insulator surface [11]. Therefore, surface treatment could be an effective means of improving the performance of OFETs. In general, the application of an organic SAM, such as octadecyltrichlorosilane ($C_{18}H_{37}SiCl_3$, OTS) or hexamethyldisilazane ($(CH_3)_3$-Si-NH-Si-$(CH_3)_3$, HMDS), forms an effective channel coating

* Corresponding author. Tel./fax: +81 6 6879 4213.
E-mail address: kajii@casi.osaka-u.ac.jp (H. Kajii).

1566-1199/$ - see front matter © 2010 Elsevier B.V. All rights reserved.
doi:10.1016/j.orgel.2010.08.016

[8,12,13]. However, because the SAM is only a monolayer, it is difficult to quantify its formation, and the surface treatment time required to form the SAM is relatively long.

Fluorene-type polymers have emerged as an important class of conducting polymers, due to their efficient emission, high stability, and relatively high mobility [8,14,15]. Various characteristics, such as electrical and optical properties, of polymers can be modified by copolymerization with fluorene units and various functional groups.

In this study, we anticipated that a fluorene-type polymer could be utilized as a hydroxyl-bond-free solution-processable buffer layer, instead of a SAM. We investigated the interface effect of adding polyfluorene derivatives as solution-processable buffer layers between the polymer insulator and the active layer in n-channel OFETs containing a carbonyl-bridged bithiazole derivative.

2. Experimental procedure

Fig. 1 shows the device structure, with a polyfluorene derivative buffer layer, and the molecular structure of the active layer used in this study. Poly(9,9-dioctylfluorene) (F8), which has a fluorene backbone and alkyl side-chains, and fluorene copolymers of poly[(9,9-dioctylfluorenyl-2,7-diyl)-co-bithiophene] (F8T2) and poly[(9,9-dioctylfluorenyl-2,7-diyl)-co-(1,4-benzo-{2,1′,3}-thiadiazole)] (F8BT) were used as buffer layers. Polished indium tin oxide (ITO), commercially pre-coated on a glass substrate, was used as the gate electrode. The surface morphology was observed by atomic force microscopy (AFM; JEOL JSPM-5200), from which the average surface roughness of the ITO was estimated to be about 0.5 nm. The polyvinylphenol (PVP) and poly(methyl methacrylate) (PMMA) used to make the insulator were spun onto a patterned ITO-coated glass substrate, and then baked above 150 °C in air. To form the buffer layer, polyfluorene derivatives with a 15 nm thickness were spun onto PVP and baked at 70 °C. The typical thickness of the gate insulator was about 400 nm.

It is well-known that the electrical properties of OFETs are strongly affected by the surface roughness of the gate insulator. The average surface roughness of gate insulators

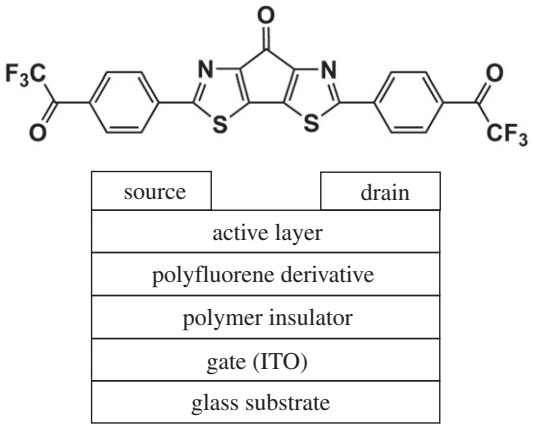

Fig. 1. The device configuration and the molecular structure of the active layer used in this study.

and buffer layers was estimated to be less than 0.3 nm from AFM images. The gate leakage of the PVP was on the order of 10 nA/cm^2 at a gate bias of 50 V. An electric permittivity of 5.3 for the PVP insulator was calculated from capacitance measurements. Material containing trifluoroacetyl groups at the terminal positions of a π-conjugated oligomer was observed to lower the lowest unoccupied molecular orbital energy level and invoke strong intermolecular interactions [16,17]. The material shown in Fig. 1 was synthesized using a previously published procedure [10], and used as the organic active layer in an OFET. An organic active layer 15 nm thick was deposited by organic molecular beam deposition, without substrate annealing, at a background pressure of about 10^{-5} Pa. The growth rate was monitored using a quartz crystal oscillator, and was on the order of 1 Å/min. 30-nm-thick source and drain Au electrodes were evaporated at a background pressure of about 10^{-4} Pa. The channel length and width were 0.1 and 2 mm, respectively. All measurements of electrical characteristics of the OFETs were performed at room temperature in a vacuum chamber at a background pressure of about 10^{-4} Pa. The current–voltage characteristics were obtained using 2400 and 6517A source meters (Keithley). To analyze the surface state of the buffer layers, the surfaces were characterized by measuring the contact angles with distilled water, ethylene glycol, and diiodomethane [18,19].

3. Results and discussion

PVP, which has a relatively high electric permittivity, is a candidate polymer insulator for p-channel OFETs [20]. In OFETs, it is well-known that the charge carriers run a few nm around the insulator/semiconductor interface, and OH groups at the interface between the polymer gate insulator and the organic active layer interfere with n-type carrier transport [8]. Therefore, OFETs with unmodified PVP gate insulators cannot exhibit good electron transport, because the hydroxyl groups trap electrons. PMMA, which contains no electron trapping groups, has also been used as a gate insulator for n-channel OFETs [9,15].

Carrier mobility depends on the microstructure and morphology of the organic layer. Moreover, the surface morphology of the first few layers, where charge transport occurs, can strongly influence the mobility. Fig. 2a–c show phase images of organic layers on PVP, PMMA, and PVP/F8, respectively, with deposited organic active layers approximately 1 nm thick. As shown in Fig. 2, AFM images demonstrated that larger monolayer grains grew on the F8 buffer layer, compared to PVP and PMMA. That is, the molecular ordering in the initial layer was better on the F8 buffer layer.

It is widely known that the growth of organic thin films is highly sensitive to the surface free energy of the substrate. Thus, the optimization of surface free energy by SAMs influences the two-dimensional growth of the organic layers. In the initial stage of vacuum deposition of the semiconductor, crystal growth is affected by the surface free energy of the insulator or buffer layer. We investigated the surface free energy to determine why polymer insula-

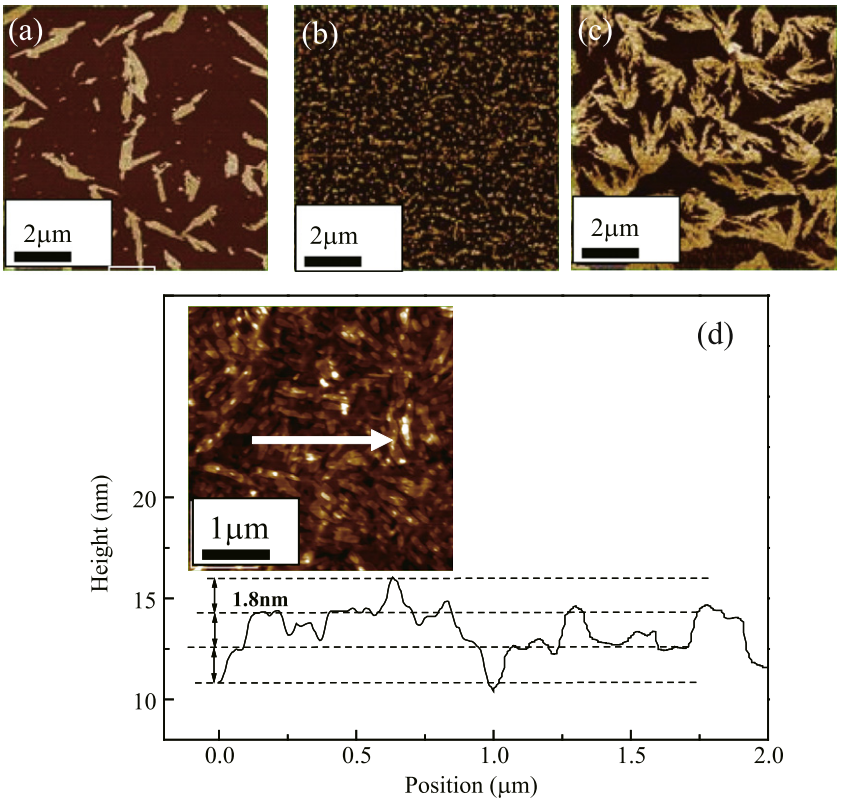

Fig. 2. Phase images of 1-nm-thick active layers on (a) PVP, (b) PMMA, and (c) PVP/F8, and (d) cross-sectional profile along the arrow shown in the inset. The inset shows a topographic image of a 15-nm-thick active layer on PVP/F8.

tor and polyfluorene derivatives yielded different morphologies. The surface free energy was estimated from contact angle measurements using distilled water, ethylene glycol ($C_2H_6O_2$), and diiodomethane (CH_2I_2). To calculate the surface free energy, we employed a solid–liquid adhesion (W) equation based on Owen's theory [18] as follows,

$$W = \gamma_{LV}(1+\cos\theta) = 2(\gamma_s^d\gamma_{LV}^d)^{1/2} + 2(\gamma_s^p\gamma_{LV}^p)^{1/2}, \quad (1)$$

where the superscript d refers to the dispersion (non-polar) component, and p refers to the polar (non-dispersion) component including all interactions established between the solid and liquid, such as dipole–dipole, dipole-induced dipole, and hydrogen bonding. γ_s and γ_{LV} refer to the solid and liquid surface free energies, respectively.

Since it contains OH groups, PVP is hydrophilic. The static contact angles of polyfluorene derivatives were larger than those of polymer insulators. Unsaturated hydrocarbons tend to exhibit $\gamma_s^p = 0$ [18]. PVP and PMMA have both dispersion and polar components, as shown in Table 1. The surfaces of polyfluorene derivatives are believed to be hydrophobic because of their alkyl side-chains, which have $\gamma_s^p = 0$. Their surfaces consist almost entirely of a dispersion (non-polar) component, as shown in Table 1. The characteristics of surfaces consisting almost entirely of a dispersion component are the same as those of OTS [12]. The F8 buffer layer had a lower surface free energy than the polymer insulators, and its surface free energy was lower than that of HMDS (~40 mJ/m^2) and close to that of OTS (~30 mJ/m^2) [12,13]. Therefore, fluorene-type polymers without OH could be applied to the buffer layer to modify the surface free energy at the interface between the insulator and the active layer, as an alternative to an SAM.

The low surface free energy and predominant dispersion component of F8 resulted in improved molecular ordering in the initial layer. The differences in the phase images were consistent with the differences in surface states of the insulators and F8. In a 15-nm-thick film on F8, crystal growth was governed by a layer-by-layer mechanism, as shown in Fig. 2d. The step size of a grain was estimated to be approximately 1.8 nm, and the molecules were oriented parallel to each other, with their long axis tilted away from normal to the substrate plane [10]. The grain structure of the active layer favored current flow, with a nearly upright orientation of molecules on the substrate, when the maximum change transport was realized in the direction perpendicular to the plane of the bithiazoles. Therefore, n-channel OFETs with an organic layer on the polyfluorene buffer layer should be expected to have a high mobility.

The output characteristics, at various gate voltages, of OFETs containing different polyfluorene derivatives as buffer layers are shown in Fig. 3. For all devices, the saturation characteristics were typical of an n-channel OFET function-

Table 1
Contact-angle measurements and the corresponding surface free energy of polymer insulators and fluorene derivatives, and the mobilities, threshold voltages, and current on/off ratios of OFETs with polyfluorene-derivative buffer layers.

Surface	Contact angle (°)			γ_s^d (mJ/m^2)	γ_s^p (mJ/m^2)	γ_s (mJ/m^2)	Mobility (cm^2 V^{-1} s^{-1})	Threshold voltage (V)	On/off ratio
	H_2O	$C_2H_6O_2$	CH_2I_2						
PVP	37.9	19.8	19.7	35.7	25.7	61.4	–	–	–
PMMA	64.1	49.2	37.6	33.4	12	45.4	–	–	–
F8BT	96.7	63.6	27.1	46.5	0.2	46.7	0.001	23	10^3
F8T2	83.8	53.2	37.4	41.6	0.9	42.5	0.007	17	10^3
F8	92.5	73.9	53.3	30.8	1.6	32.4	0.025	23	10^3

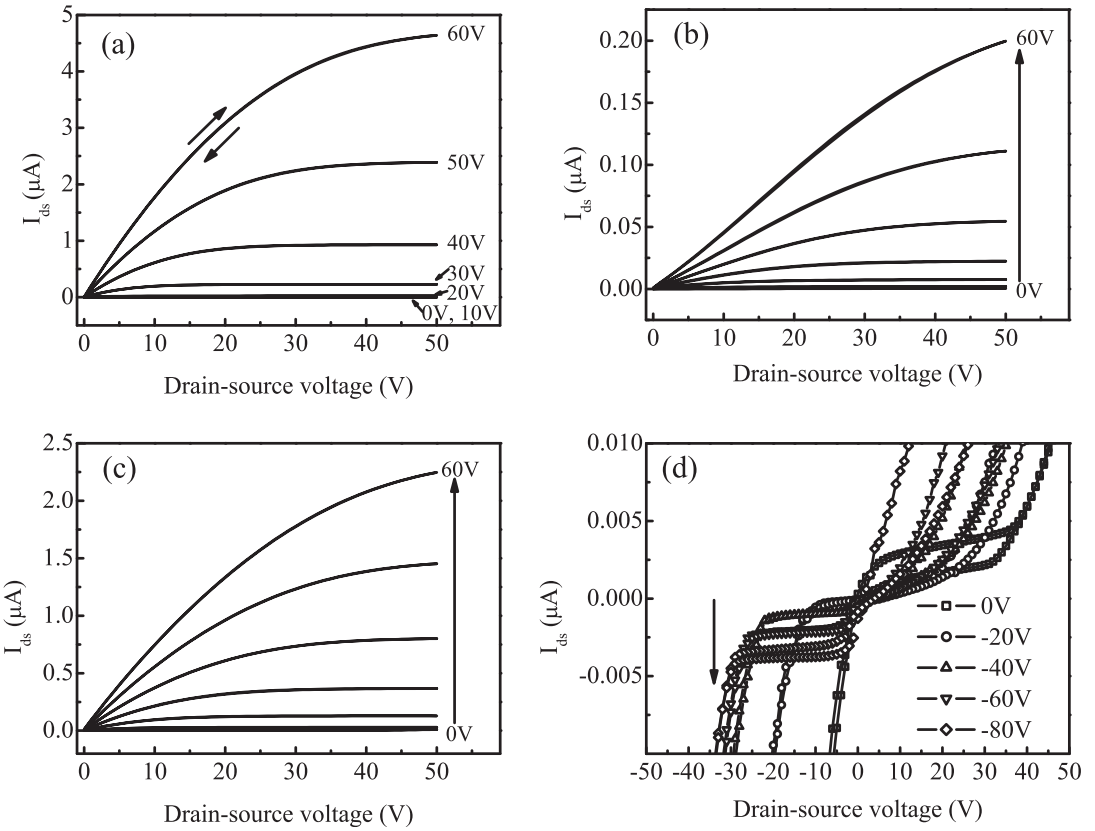

Fig. 3. Output characteristics of OFETs with F8 (a), F8BT (b), and F8T2 (c), (d) buffer layers at different gate voltages.

ing in electron enhancement mode. However, for a device with F8T2, the saturation characteristics of a p-channel OFET functioning in hole enhancement mode were also observed. Therefore, the F8T2 layer functioned as a p-channel active layer.

Fig. 4 shows transfer characteristics of OFETs with F8, F8T2, and F8BT buffer layers at a drain voltage of 50 V. The field-effect mobility and threshold voltage were estimated from the square root of the drain current versus gate voltage, by plotting the saturated drain current at a drain voltage of 50 V. The field-effect mobilities, threshold voltages, and current on/off ratios of various OFETs are summarized in Table 1. The OFET with an F8 buffer layer had a field-effect electron mobility of 0.025 cm^2 V^{-1} s^{-1}, and a threshold voltage of 23 V. The current on/off ratios of OFETs with F8, F8T2, and F8BT buffer layers at a drain voltage of 50 V were about 10^4, 10^3, and 10^3, respectively, as shown in Fig. 4 when the gate voltage was scanned from 0 to 100 V. The carrier mobility and current on/off ratio of an OFET with an F8 buffer layer, which had the lowest surface free energy, were higher than those of OFETs with F8T2 and F8BT layers. One possible explanation for this is that the effect of grain boundaries was dominant in determining the electron mobility in OFETs, since the hydrophobic surface of the F8 improved the molecular ordering in the initial layer. It is also possible that the mobility of an OFET with an F8T2 buffer layer decreased because the F8T2 also functioned as the active layer. The interface between the insulator and organic layer encountered problems, not only with the growth morphology of the

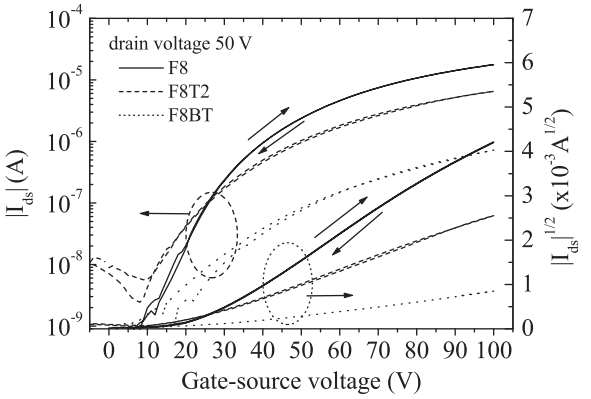

Fig. 4. Transfer characteristics of OFETs with F8, F8T2, and F8BT buffer layers at a drain voltage of 50 V.

overlaying films, but also with carrier traps. Since PVP insulator with OH groups has a hydrophilic nature, the OFETs had hysteresis characteristics related to carrier traps at the interface [21]. For an F8 device, no significant hysteresis was observed in the output or transfer characteristics. This suggests that the carrier traps decreased due to the hydrophobic surface of the F8. Due to the presence of alkyl groups on the F8 surface, instead of an SAM, devices with an F8 buffer layer would have performed comparably to those fabricated on SAM-treated surfaces [10].

4. Conclusions

We investigated the effect of inserting solution-processable polyfluorene derivatives as buffer layers between the insulator and the active layer in n-channel OFETs containing a carbonyl-bridged bithiazole derivative. The surface free energy was modified by the polyfluorene derivatives. An F8 buffer layer with a hydrophobic nature, low surface free energy, and consisting almost entirely of a dispersion component improved the growth morphology of the active layer. An OFET with an F8 buffer layer exhibited n-channel characteristics, with an electron field-effect mobility on the order of 10^{-2} cm^2 V^{-1} s^{-1}. The combination of a polymer insulator and F8 exhibited the same order of n-type performance as a conventional SiO_2-SAM system, demonstrating that our findings may help enable an all-OFET device. Polyfluorene derivatives, the characteristics of which can be modified by copolymerization of fluorene units with various functional groups, can be applied as a solution-processable buffer layer to modify the surface free energy at the insulator to active layer interface.

Acknowledgements

This research was partially supported by Industrial Technology Research Grant Program in 2000 from New Energy and Industrial Technology Development Organization (NEDO) of Japan, and by the Ministry of Education, Culture, Sports, Science and Technology in Japan (MEXT) under a grant for the Osaka University Global COE Program, "Center for Electronic Devices Innovation". The authors thank Sumitomo Chemical Co., Ltd. for providing fluorene derivatives.

References

[1] K. Kudo, D.X. Wang, M. Iizuka, S. Kuniyoshi, K. Tanaka, Synth. Met. 111–112 (2000) 11.
[2] H. Sirringhaus, T. Kawase, R.H. Friend, T. Shimoda, M. Inbasekaran, W. Wu, E.P. Woo, Science 290 (2000) 2123.
[3] K. Kaneto, W.Y. Lim, W. Takashima, T. Endo, M. Rikukawa, Jpn. J. Appl. Phys. 39 (2000) L872.
[4] M. Ando, M. Kawasaki, S. Imazeki, H. Sasaki, T. Kamata, Appl. Phys. Lett. 85 (2004) 1849.
[5] H. Kawaguchi, T. Someya, T. Sekitani, T. Sakurai, IEEE J. Solid-State Circuits 40 (2005) 177.
[6] T. Someya, Y. Kato, S. Iba, H. Kawaguchi, T. Sakurai, IEEE Trans. Electron Devices 52 (2005) 2502.
[7] K. Nakayama, S. Fujimoto, M. Yokoyama, Appl. Phys. Lett. 88 (2006) 153512.
[8] L.L. Chua, J. Zaumseil, J.F. Chang, E.C.-W. Ou, P.K.-H. Ho, H. Sirringhaus, R.H. Friend, Nature 434 (2005) 194.
[9] T. Takenobu, S.Z. Bisri, T. Takahashi, M. Yahiro, C. Adachi, Y. Iwasa, Phys. Rev. Lett. 100 (2008) 066601.
[10] Y. Ie, M. Nitani, M. Karakawa, H. Tada, Y. Aso, Adv. Funct. Mater. 20 (2010) 907.
[11] K. Nakayama, M. Ishikawa, M. Yokoyama, Appl. Phys. Express 2 (2009) 021501.
[12] T. Kobayashi, H. Uda, T. Nagase, M. Watanabe, K. Matsukawa, H. Naito, Thin Solid Films 517 (2008) 1340.
[13] S.C. Lim, S.H. Kim, J.H. Lee, M.K. Kim, D.J. Kim, T. Zyung, Synth. Met. 148 (2005) 75.
[14] Y. Ohmori, M. Uchida, K. Muro, K. Yoshino, Jpn. J. Appl. Phys. 30 (1991) L1941.
[15] H. Kajii, K. Koiwai, Y. Hirose, Y. Ohmori, Org. Electron. 11 (2010) 509.
[16] Y. Ie, M. Nitani, Y. Aso, Chem. Lett. 36 (2007) 1326.
[17] Y. Ie, M. Nitani, T. Uemura, Y. Tominari, J. Takeya, Y. Honsho, A. Saeki, S. Seki, Y. Aso, J. Phys. Chem. C 113 (2009) 17189.
[18] D.K. Owens, R.C. Wendt, J. Appl. Pol. Sci. 13 (1969) 1741.
[19] D.Y. Kwok, A.W. Neumann, Adv. Colloid. Interface Sci. 81 (1999) 167.
[20] U. Zschieschang, H. Klauk, M. Halik, G. Schmid, C. Dehm, Adv. Mater. 15 (2003) 1147.
[21] S.H. Kim, H. Yang, S.Y. Yang, K. Hong, D. Choi, C. Yang, D.S. Chung, C.E. Park, Org. Electron. 9 (2008) 673.

Organic Electronics 11 (2010) 1891–1895

Contents lists available at ScienceDirect

Organic Electronics

journal homepage: www.elsevier.com/locate/orgel

Efficient top-emitting organic light-emitting devices using Fe_3O_4 modified Ag anode

Dan-Dan Zhang [a], Jing Feng [a,*], Yu-Qing Zhong [a], Yue-Feng Liu [a], Hai Wang [a,b], Yu Jin [a], Yu Bai [a], Qi-Dai Chen [a], Hong-Bo Sun [a,b,**]

[a] State Key Laboratory on Integrated Optoelectronics, College of Electronic Science and Engineering, Jilin University, 2699 Qianjin Street, Changchun 130012, People's Republic of China
[b] College of Physics, Jilin University, 119 Jiefang Road, Changchun 130023, People's Republic of China

ARTICLE INFO

Article history:
Received 24 March 2010
Received in revised form 26 June 2010
Accepted 28 August 2010
Available online 8 September 2010

Keywords:
Top-emitting organic light-emitting devices
Fe_3O_4
Anodic buffer

ABSTRACT

Highly efficient top-emitting organic light-emitting devices (TOLEDs) using a Fe_3O_4 modified Ag anode have been demonstrated. The tris-(8-hydroxyquinoline) aluminum-based TOLEDs exhibit a very low turn-on voltage of 2.5 V and a high current efficiency of 8.1 cd/A. The improved properties for the TOLEDs is mainly due to the enhanced hole injection by introducing the anodic buffer. The mechanism of this enhanced hole injection is studied by the X-ray and ultra-violet photoemission spectroscopy, which demonstrated that the dipole layer is formed at the anode/organic interface and the hole-injection barrier is therefore reduced after introducing the thin Fe_3O_4 film between the Ag anode and the hole-transport layer.

© 2010 Elsevier B.V. All rights reserved.

1. Introduction

Top-emitting organic light-emitting devices (TOLEDs) are of considerable interest for their application in high resolution active matrix display because they provide better image quality, higher aperture ratio and allows fabrication on an opaque substrate, such as Si wafers [1]. The bottom anode with both high reflectivity and high work function are essential for achieving efficient TOLEDs. Ag is an excellent candidate due to its highest reflectivity in visible light range among various metals. However, its work function (4.3 eV) [2] is not sufficient high for efficient hole injection. Serious efforts, therefore, have been devoted to overcome the problem. For example, MoO_x [3], Ag_2O [4], V_2O_5 [5], CFx [6], etc. have been reported to modify the Ag anode and improve the hole injection from the Ag anode. A self-assembled monolayer appears to be another way of tuning the work function of the Ag anode [7]. Therefore, using an anodic buffer in the TOLEDs is effective in realizing its high performance, and more works are needed to explore other materials as the anodic buffer to further improve the performance of the TOLEDs.

In previous work [8,9], we have reported that Fe_3O_4 is not only an effective buffer on the ITO anode but also an effective p-dopant in hole-transport layer in bottom emitting OLEDs. In this work, the application of the Fe_3O_4 was further explored into the TOLEDs and much improved performance due to the anodic modification of the Fe_3O_4 on the Ag anode was observed. Systematic investigation on the role of Fe_3O_4 as the buffer in the TOLEDs was performed by *in situ* ultra-violet photoemission spectroscopy (UPS) and X-ray photoemission spectroscopy (XPS) measurements, as well as the characteristics of the hole-only devices. These studies reveal that the hole-injection efficiency is enhanced due to the reduction of the injection barrier after introducing the ultra thin film of Fe_3O_4 at the Ag anode and the hole-transport layer interface. As a

* Corresponding author.
** Corresponding author at: State Key Laboratory on Integrated Optoelectronics, College of Electronic Science and Engineering, Jilin University, 2699 Qianjin Street, Changchun 130012, People's Republic of China. Tel./fax: +86 431 85168281.
E-mail addresses: jingfeng@jlu.edu.cn (J. Feng), hbsun@jlu.edu.cn (H.-B. Sun).

1566-1199/$ - see front matter © 2010 Elsevier B.V. All rights reserved.
doi:10.1016/j.orgel.2010.08.017

result, the brightness, the current density and the efficiency of the TOLEDs are highly improved.

2. Experimental details

The TOLEDs were fabricated by depositing 80 nm thick Ag as the reflective anode onto 1600 nm thick SiO_2-covered Si substrate. An ultra thin film of Fe_3O_4 as the anode buffer with the different thickness changing from 1 nm to 4 nm was then deposited, followed by deposition of 50 nm thick hole-transporting layer of *N*,*N*′-diphenyl-*N*,*N*′-bis(1,1′-biphenyl)-4,4′-diamine(NPB), 50 nm thick emitting layer of tris-(8-hydroxyquinoline) aluminum (Alq_3), and semi-transparent cathode of LiF (1 nm)/Al (1 nm)/Ag (20 nm). Here, all layers were prepared by thermal evaporation in a high vacuum system with the pressure of less than 5×10^{-4} Pa. The active area of the devices was 2×2 mm^2. Their current density–luminance–voltage (*J*–*L*–*V*) characteristics were measured by Keithley 2400 programmable voltage–current source and Photo Research PR-655 spectrophotometer. The UPS data were measured with a Thermo ESCALAB 250, and the samples were biased at −4.0 V to observe the low energy secondary cutoff during the measurement. The XPS measurements were performed with Mg Kα X-ray source (1253.6 eV) (Specs XR50).

3. Results and discussion

3.1. Effects of Fe_3O_4 modified Ag anode on electroluminescence performance of TOLEDs

The *J*–*L*–*V* characteristics of the TOLEDs with the various thickness of Fe_3O_4 as the anodic buffer are shown in Fig. 1. The inset of Fig. 1a shows the electroluminescence (EL) spectra of the TOLEDs at viewing angle of 0°, 20°, and 40° off the surface normal. The EL spectra of the TOLEDs with the various Fe_3O_4 thickness are similar, and the TOLEDs show narrowed and angular shift of the peak wavelength and intensity of the EL spectra due to the existence of microcavity effects. Both the current density and the luminance in the normal direction are strongly dependent on the presence and the thickness of the Fe_3O_4 buffer layer. They markedly increase when increasing the Fe_3O_4 thickness, and reach the maximum at 3 nm. With further increment of the Fe_3O_4 layer thickness, the current density and the luminance are decreased. The devices without the buffer layer shows much lower EL properties compared to the Fe_3O_4 buffered devices. The turn-on voltage of 2.5 V to obtained the luminance of 1 cd/m^2 and the maximum luminance of 108,297 cd/m^2 at 14 V have been observed from the TOLEDs with an optimum Fe_3O_4 thickness of 3 nm, while it is 5.0 V and 13,680 cd/m^2 at 13 V for the TOLEDs without the anodic buffer. The current efficiency versus voltage in the normal direction of these TOLEDs shows a similar behavior to that of *J*–*L*–*V* performance (Fig. 2b), and also exhibits an optimum thickness of 3 nm. The maximum current efficiency is around 8.1 cd/A for the Fe_3O_4 buffered TOLEDs, while it is only around 4.0 cd/A for the devices without the anodic buffer. These results indicate

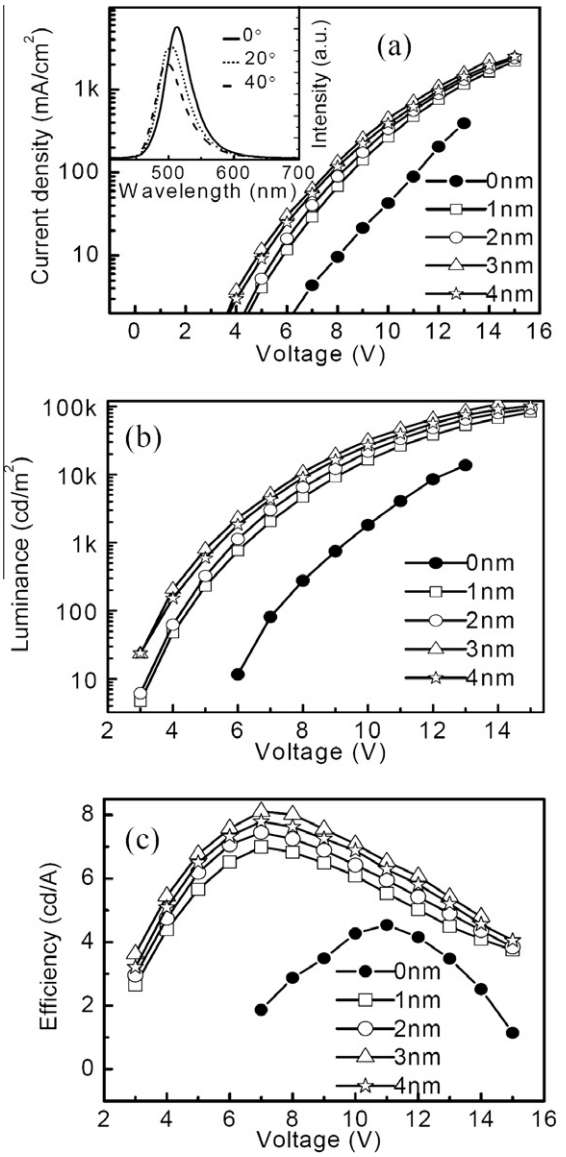

Fig. 1. EL performance of the Fe_3O_4 buffered OLEDs. (a) Current density–voltage, (b) luminance–voltage, and (c) current efficiency–voltage characteristics of the devices with various thickness of Fe_3O_4 film as the buffer layer. Inset in (a) shows the EL spectrum of the Fe_3O_4 buffered device at different observation angle.

that high EL performance of the TOLEDs is obtained by employing the Fe_3O_4 modified Ag anode.

Various metal oxides have been demonstrated as effective anodic buffer in the TOLEDs [3–5]. In order to study the relative effectiveness of the anodic modification of the Fe_3O_4, we have fabricated the devices with MoO_3 as the buffer layer for comparison, which is one of the most effective anodic buffer for the Ag anode [3,10]. The *J*–*L*–*V* characteristics of both Fe_3O_4 and MoO_3 buffered TOLEDs with the same device structure and optimized thickness of the buffer layer are compared in Fig. 2a. The optimized thickness is 3 nm and 4 nm for the buffer of Fe_3O_4 and MoO_3, respectively. The operating voltage at the current

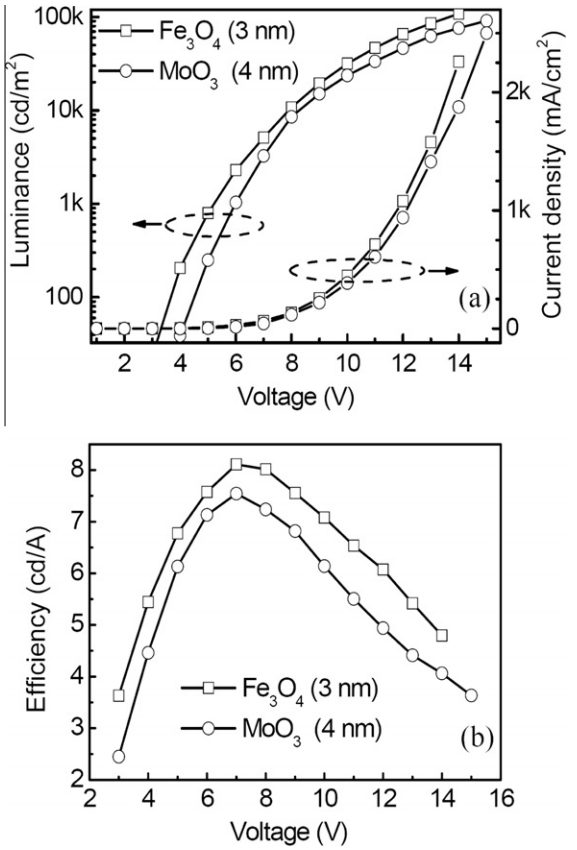

Fig. 2. (a) Current density–luminance–voltage and (b) current efficiency–voltage characteristics of the Fe_3O_4 and MoO_3 buffered devices.

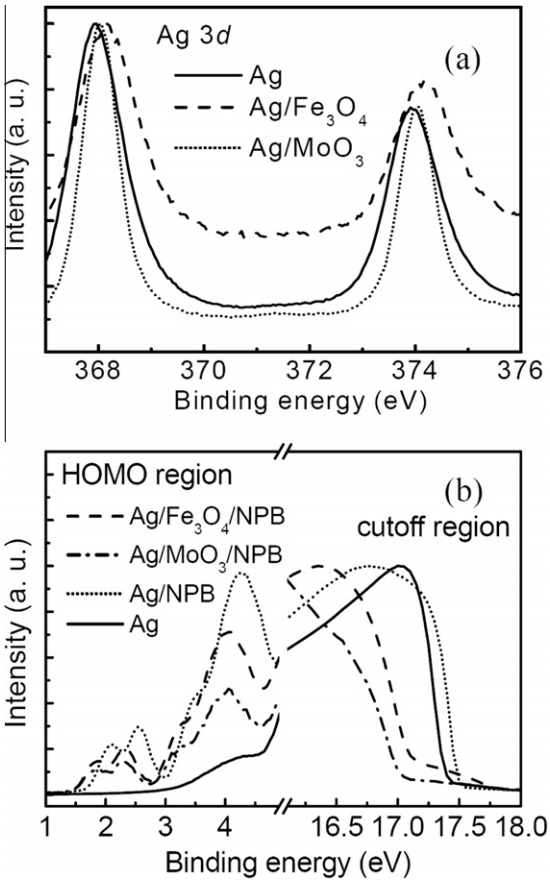

Fig. 3. (a) XPS spectra of Ag (80 nm) and Ag (80 nm)/Fe_3O_4 (3 nm). (b) UPS spectra of Ag (80 nm), Ag (80 nm)/NPB (15 nm) and Ag (80 nm)/Fe_3O_4 (3 nm)/NPB (15 nm).

density of 100 mA/cm^2 is 9.1 V and 9.3 V, and the operating voltage for obtaining a luminance of 300 cd/m^2 is 4.3 V and 5.1 V for the Fe_3O_4 and MoO_3 buffered devices, respectively. The turn-on voltage of the Fe_3O_4 buffered devices (2.5 V) is 0.2 V lower than that of the MoO_3 buffered devices (2.7 V), and its current efficiency is also higher than that of the MoO_3-based device as shown in Fig. 2b. These results indicate that Fe_3O_4 has comparable and even appreciably superior effect in modifying the Ag anode and improving the properties of the TOLEDs to the MoO_3.

3.2. Effects of Fe_3O_4 as anodic buffer on hole injection of TOLEDs

Generally, the reduced operating voltage and enhanced EL performance in OLEDs with the insertion of the anodic buffer are attributed to the reduced hole-injection barrier and therefore enhanced hole-injection efficiency. We have carried out the XPS measurements to analyze the interface between the anode and the hole-transport layer. The XPS spectra of the Ag 3*d* peaks are measured from the bare Ag (80 nm), Ag (80 nm)/Fe_3O_4 (3 nm) and Ag (80 nm)/MoO_3 (2 nm) as shown in Fig. 3a. It can be seen that the Ag 3*d* peaks shift towards higher binding energy by approximately 0.25 eV after depositing the ultra thin Fe_3O_4 layer on the Ag film, while it is ~0.15 eV in case of MoO_3 buffered Ag film. The peak shift indicates an electron transfer from Ag to Fe_3O_4 at the interface [10], which would result in a formation of a dipole layer at the interface and leading to an abrupt shift of the potential across the dipole layer [11,12]. Therefore, the hole-injection barrier is reduced as a result of the potential shift.

To further clarify the effects of the Fe_3O_4 on the hole injection, UPS spectra are investigated to evaluate the reduction of the hole-injection barrier. Fig. 3b shows the UPS spectra of the Ag (80 nm), Ag (80 nm)/Fe_3O_4 (3 nm)/NPB (15 nm), Ag (80 nm)/MoO_3 (4 nm)/NPB (15 nm) and Ag (80 nm)/NPB (15 nm). There are clear spectra changes after the insertion of the ultra thin film of Fe_3O_4 or MoO_3 between Ag and NPB compared to that of Ag/NPB sample. Both the highest occupied molecular orbital (HOMO) onset position and the cut off position shift towards the lower binding energy. The shift of the HOMO onset position indicates that the HOMO level of NPB is reduced after introducing the Fe_3O_4 or MoO_3 buffer layer, which will result in the reduction of the hole-injection barrier [12]. Moreover, it is noticeable that the shift of the secondary electron cutoff position indicates the formation of the interface dipoles at the Ag/NPB interface, which is coincident with the XPS results. The energy diagrams of the Ag/NPB, Ag/Fe_3O_4/

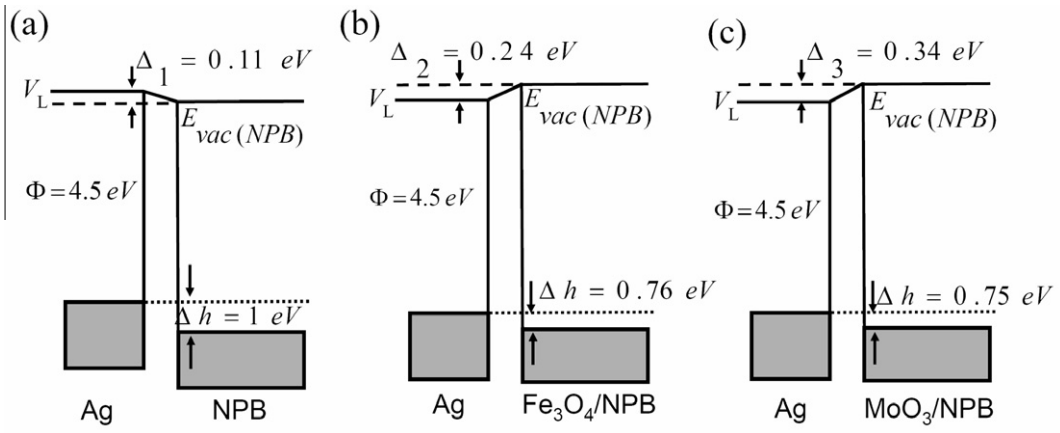

Fig. 4. Schematic energy diagram of Ag/NPB (a), Ag/Fe_3O_4/NPB (b), and Ag/MoO_3/NPB (c).

NPB, Ag/MoO_3/NPB extracted from the UPS spectra [13–15] are shown in Fig. 4. The work function of Ag is calculated to be 4.5 eV from the UPS spectra. The hole-injection barrier from Ag to NPB is reduced by 0.24 eV after inserting the Fe_3O_4 buffer. While in case of the MoO_3, the injection barrier is reduced by 0.25 eV. Both the XPS and UPS results demonstrate that the Fe_3O_4 as the anodic buffer has similar effect to MoO_3 in lowering the energy barrier of the hole injection at the interface, which should contribute to the reduction of the operating voltage and the improvement of the EL efficiency.

The efficient hole injection of the Fe_3O_4 modified devices are further confirmed by the *J–V* characteristics of the hole-only devices [16,17]. The hole-only devices with and without the anodic buffer were fabricated to demonstrate the role of the anodic buffer in the hole-injection ability of the TOLEDs. Fig. 5 shows the current density versus voltage characteristics of the hole-only devices with the structures of Ag (80 nm)/Fe_3O_4 (3 nm)/NPB (80 nm)/Ag (20 nm), Ag (80 nm)/MoO_3 (4 nm)/NPB (80 nm)/Ag (20 nm) and Ag (80 nm)/NPB (80 nm)/Ag (20 nm). The electron injection from the Ag cathode to the NPB is prohibited, because the work function of Ag is around 4.5 eV while the lowest occupied molecular orbital level of the NPB is around 2.4 eV, and there exists very large injection barrier. It can be seen that the current density of the hole-only devices with the anodic buffer is obviously higher than that of the device without the buffer, and the Fe_3O_4 buffered devices shows even higher current density than that of the MoO_3 buffered devices. It further confirms that Fe_3O_4 is an efficient anodic buffer in enhancing the hole injection of the TOLEDs.

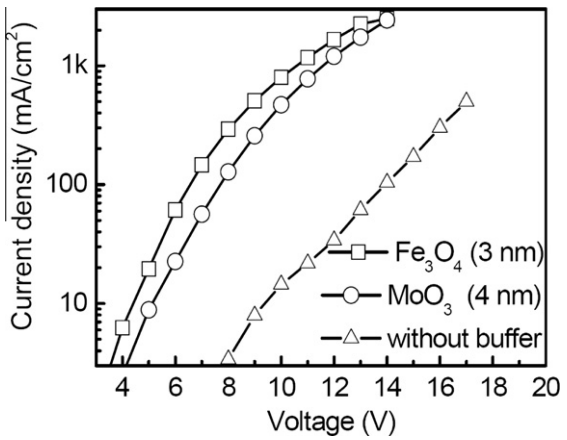

Fig. 5. The current density–voltage characteristics of the hole-only devices with and without the anodic buffer.

4. Conclusions

In summary, we report the thin film of Fe_3O_4 as the Ag anodic buffer for efficient TOLEDs. The Fe_3O_4 exhibits its effect in lowering the driving voltage and improving the brightness and current efficiency of the TOLEDs. The XPS and UPS measurements indicate that the introduction of the thin film Fe_3O_4 can greatly reduce the hole-injection barrier, and the enhancement of the hole injection has been further confirmed by the investigation of *J–V* characteristics of the hole-only devices. Our results reveal that Fe_3O_4 is a prospective material in modifying the Ag anode and realizing the high performance of the TOLEDs.

Acknowledgements

This research was supported by NSFC (Grant Nos. 60677016, 60977025 and 60877019), NECT (Grant No. 070354) and Jilin Provincial Science and Technology Foundation (Grant No. 20070109).

References

[1] C.W. Chu, C.W. Chen, S.H. Li, E.H. Wu, Y. Yang, Appl. Phys. Lett. 86 (2005) 253503.
[2] H.B. Michaelson, IBM J. Res. Dev. 22 (1978) 72.
[3] J. Cao, X.Y. Jiang, Z.L. Zhang, Appl. Phys. Lett. 89 (2006) 252108.
[4] C.W. Chen, P.Y. Hsieh, H.H. Chiang, C.L. Lin, H.M. Wu, C.C. Wu, Appl. Phys. Lett. 83 (2003) 5127.
[5] J. Wu, J.H. Hou, Y.X. Cheng, Z.Y. Xie, L.X. Wang, Semicond. Sci. Technol. 22 (2007) 824.
[6] Y.Q. Li, J.X. Tang, Z.Y. Xie, L.S. Hung, S.S. Lau, Chem. Phys. Lett. 386 (2004) 128.

[7] M.C. Hung, K.Y. Wu, Y.T. Tao, H.W. Huang, Appl. Phys. Lett. 89 (2006) 203106.
[8] D.D. Zhang, J. Feng, Y.F. Liu, Y.Q. Zhong, Y. Bai, Y. Jin, G.H. Xie, Q. Xue, Y. Zhao, S.Y. Liu, H.B. Sun, Appl. Phys. Lett. 94 (2009) 223306.
[9] D.D. Zhang, J. Feng, H. Wang, Y. Bai, Q.D. Chen, S.Y. Liu, H.B. Sun, Appl. Phys. Lett. 95 (2009) 263303.
[10] F. Wang, X. Qiao, T. Xiong, D. Ma, Organ. Elect. 9 (2008) 985.
[11] T. Matsushima, Y. Kinoshima, H. Murata, Appl. Phys. Lett. 91 (2007) 253504.
[12] H. Ishii, K. Sugiyama, E. Ito, K. Seki, Adv. Mater. 11 (1999) 605.
[13] H. Yanagi, M. Kikuchi, K.B. Kim, H. Hiramatsu, T. Kamiya, M. Hirano, H. Hosono, Org. Electron. 9 (2008) 890.
[14] Y. Lee, J. Kim, S. Kwon, C.K. Min, Y. Yi, J.W. Kim, B. Koo, M. Hong, Org. Electron. 9 (2008) 407.
[15] J.G. Xue, S.R. Forrest, Phys. Rev. B 69 (2004) 245322.
[16] T. Matsushima, Y. Kinoshita, H. Murata, Appl. Phys. Lett. 91 (2007) 253504.
[17] J.H. Lee, Dong S. Leem, H.J. Kim, J.J. Kim, Appl. Phys. Lett. 94 (2009) 123306.

Organic Electronics 11 (2010) 1896–1900

Contents lists available at ScienceDirect

Organic Electronics

journal homepage: www.elsevier.com/locate/orgel

Letter

Encapsulation of organic solar cells with ultrathin barrier layers deposited by ozone-based atomic layer deposition

Smita Sarkar, Jason H. Culp, Jon T. Whyland, Margret Garvan, Veena Misra *

Department of Electrical and Computer Engineering, North Carolina State University, Raleigh, NC 27695-7911, USA

ARTICLE INFO

Article history:
Received 18 June 2010
Received in revised form 23 August 2010
Accepted 28 August 2010
Available online 9 September 2010

Keywords:
Organic solar cell
Encapsulation
Atomic layer deposition
Ozone

ABSTRACT

Ultrathin Al_2O_3 layers, deposited using atomic layer deposition (ALD), have been utilized as the primary barrier layers for encapsulation of organic solar cells. This work shows that the encapsulation characteristics of a barrier layer can be accentuated by replacing H_2O with O_3 as the ALD oxidant. The Al_2O_3 layers deposited using O_3 offered superior device encapsulation compared to the films deposited using H_2O. The organic solar cell efficiency has also been studied as a function of Al_2O_3 thickness and effective encapsulation has been monitored for two different ALD temperatures.

© 2010 Elsevier B.V. All rights reserved.

1. Introduction

Organic solar cells comprising conjugated polymer–fullerene bulk heterojunctions (BHJs) have the potential of becoming ubiquitous sources of renewable energy owing to their cost-effectiveness and ease of fabrication on lightweight, flexible substrates [1–4]. However, these cells have primarily been tested in controlled laboratory environment as they undergo rapid degradation upon exposure to oxygen and water [5,6]. Therefore, adequate encapsulation from ambient oxygen and water is an essential requirement for the commercial viability of organic photovoltaic (OPV) cells. The encapsulating layer in turn should be thin, defect-free, light weight, and offer ease of processing. Amongst various methods reported in literature, the ultrathin barrier layers grown by atomic layer deposition (ALD) have emerged as promising candidates for device encapsulation [7,8]. ALD is particularly suitable for organic and flexible electronics as passivation layers with excellent film conformity can be grown at low temperatures. In this regard, the encapsulation of OPVs by ALD has been reported using Al_2O_3 [7] and Al_2O_3/HfO_2 nanolaminates [8]. However, both approaches use H_2O as the oxidant along with trimethylaluminum (TMA) as the precursor for Al_2O_3 or tetrakis(dimethylamido) for growing HfO_2 layers. It is well known that films deposited by ALD using H_2O as oxidant have high impurity content, especially hydrogen [9]. Also, it takes longer time to purge out water molecules from the surface as water has a high surface affinity owing to its large dipole moment [9,10]. This reduces throughput of the process especially when lower temperatures are used for deposition and high aspect ratio structures are in consideration [10]. In the current semiconductor technology, O_3 is the preferred oxidant for growing dielectric layers by ALD [9–11]. The MIS (Metal–Insulator–Semiconductor) capacitors with Al_2O_3 films grown using O_3 (O_3–Al_2O_3) show a smaller hysteresis, lower leakage current density, and higher breakdown field strength compared to the Al_2O_3 films grown using H_2O (H_2O–Al_2O_3) at the same growth temperature [9,11]. O_3-based ALD offer higher throughput as the time required for surface reactions and purging out of the unreacted surface adsorbed species is much shorter than H_2O-based processes. This is because

* Corresponding author. Address: Department of Electrical and Computer Engineering, 2410 Campus Shore Drive, North Carolina State University, Raleigh, NC 27695-7911, USA. Tel.: +1 919 515 7356; fax: +1 877 570 5514.
E-mail address: vmisra@ncsu.edu (V. Misra).

1566-1199/$ - see front matter © 2010 Elsevier B.V. All rights reserved.
doi:10.1016/j.orgel.2010.08.020

of the high chemical reactivity between TMA and O_3 and that O_3 can be purged out more efficiently than H_2O [9–11]. O_3–Al_2O_3 film also shows a smaller residual hydrogen concentration as compared to H_2O–Al_2O_3 film [9]. This work describes how encapsulation of OPVs with ultrathin Al_2O_3 layers is significantly improved by replacing water with ozone as the oxidant in ALD. Unlike previous reports, this work utilizes only Al_2O_3 as the primary barrier layer and does not require a UV-curable epoxy resin film as an additional sealant for protecting OPVs from ambient moisture or oxygen. The OPV efficiency has been studied as a function of Al_2O_3 thickness and effective encapsulation has been monitored for two different ALD temperatures – 140 °C and 150 °C.

2. Experimental

Fig. 1a shows schematics of the encapsulated OPV structure discussed in this work. The pre-patterned indium tin oxide (ITO) coated glass substrates [12] were cleaned by ultrasonic treatment in acetone and isopropyl alcohol followed by a UV–ozone treatment. These substrates were then spun coated with poly-3,4-ethylenedioxythiophene–poly-styrenesulphonate (PEDOT:PSS, Aldrich) at 4000 rpm for 40 s and annealed at 120 °C for 1 h. For the active layer, 1 wt% of poly-3-hexylthiophene-2,5-diyl (P3HT, Rieke Metals) was blended with 0.8 wt% of 6,6-phenyl-C61-butyric acid methyl ester (PCBM, Nano-C) in 1,2-dichlorobenzene for 12 h inside a N_2-filled glovebox. The PEDOT-coated ITO substrates were transferred into the glovebox and spun coated with the P3HT/PCBM blend at 600 rpm for 60 s [13]. Immediately after spin casting, these films were dried in a covered Petri dish for 20 min to yield 100 nm of the active layer. The samples were then briefly exposed to ambient air while being transferred into the thermal evaporator. Al was deposited through a shadow mask to define an active device area of 10 mm^2. An unencapsulated OPV (control sample) underwent post metal anneal for 20 min at 150 °C in order to increase the device efficiency [14]. Thermal annealing induces aggregation of the P3HT and PCBM domains, which facilitates transport of charge carriers through these domains and increases the device efficiency [14]. No post metal anneal was done for the samples that were encapsulated using ALD as the ALD process also served as the annealing step. For ALD encapsulation, the devices were again briefly exposed to the ambient conditions while being transferred into the ALD chamber (Savannah100, Cambridge Nanotech, Inc.). A typical ALD cycle comprised an initial pulse of TMA for 0.015 s followed by a 5 s purge with N_2 and a subsequent pulse of O_3/H_2O for 0.015 s followed by a 5 s purge with N_2. The growth rates for Al_2O_3 using O_3 and H_2O at 140 °C are 0.85 Å and 1.05 Å per cycle, respectively. The encapsulated devices were stored outside the glovebox under ambient conditions. The current density–voltage (J–V) characteristics were measured with a Keithley 2400 source meter under simulated AM1.5G illumination (100 mW/cm^2) using Oriel solar simulator. All electrical measurements were done in ambient conditions and averaged over six devices patterned on a single substrate.

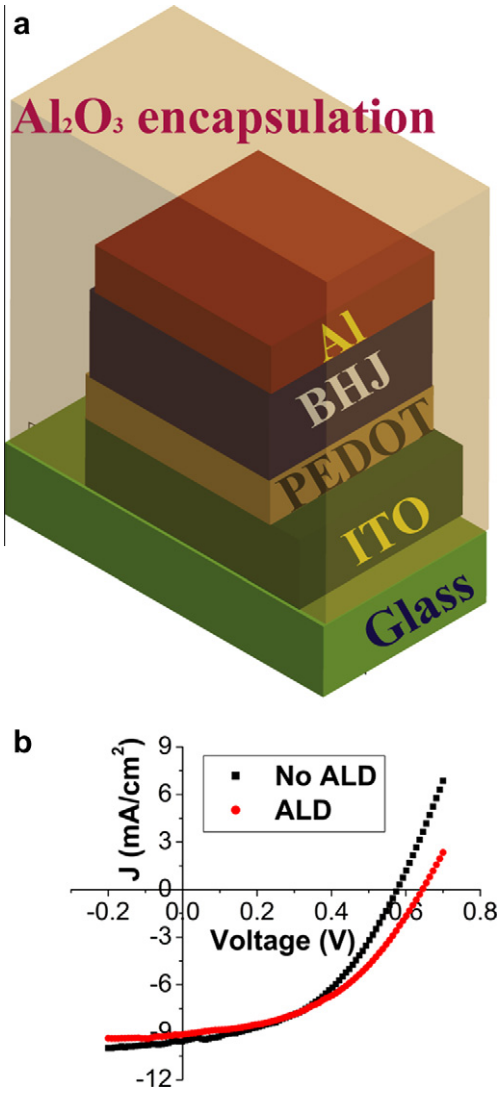

Fig. 1. (a) Schematics of the device structure encapsulated with Al_2O_3. BHJ signifies the P3HT–PCBM bulk heterojunction layer. (b) J–V characteristics of the control device (black squares) and an OPV encapsulated with 210 cycles of Al_2O_3 deposited at 140 °C (red circles) under illumination. (For interpretation of the references to color in this figure legend, the reader is referred to the web version of this article.)

3. Results and discussion

Fig. 1b shows the J–V characteristics under illumination for a control device (black squares) and an OPV encapsulated with O_3–Al_2O_3 (red circles). The open circuit voltage (V_{OC}), short circuit current (J_{SC}), efficiency (η), and fill factor (FF) for both the devices are listed in Table 1. The FF and η

Table 1
The performance characteristics of OPVs with and without Al_2O_3 encapsulation based on J–V characteristics in Fig. 1b.

	J_{SC} (mA/cm^2)	V_{OC} (V)	FF (%)	η (%)
Control device	9.58	0.574	46	2.54
Encapsulated device	9.15	0.646	45	2.7

for the control device is lower than that is typically reported [7,8,13,14] because of the following reasons (i) these devices were exposed to ambient conditions while being transferred into thermal evaporator and (ii) electrical measurements were done outside the glovebox. After ALD encapsulation, the V_{OC} increased from 0.57 V to 0.64 V and η increased from 2.54% to 2.7% as seen in Table 1. Additionally, there was a minimal change in the FF and J_{SC} for the encapsulated device as compared to the control sample. This indicates that ALD precursors, especially O_3 that is known to be highly reactive, did not cause any damage to the organic layer. This is primarily because the organic layer is initially exposed to O_3 for a short period of 0.015 s per cycle however, as Al_2O_3 continues to grow on top of the organic layer, the effect of this exposure gets severely attenuated with each ALD cycle. When stored outside the glovebox, the control sample underwent severe degradation and the device efficiency reduced by more than 80% in less than 24 h. This further highlights the importance of OPV encapsulation.

The efficiency for two sets of encapsulated OPVs were tested over time, where one set was encapsulated with O_3–Al_2O_3 and the other with H_2O–Al_2O_3 as shown in Fig. 2a and b. Four different thicknesses of Al_2O_3, i.e., 90, 120, 150, and 210 cycles of ALD were deposited for each set at 140 °C. The encapsulating ability of Al_2O_3 in both sets increased with increase in ALD thickness, which is expected (Fig. 2a and b). The most effective encapsulation was offered by 210 cycles of O_3–Al_2O_3 (210-O_3–Al_2O_3) as the efficiency for that device reduced by just 20% over a period of 500 h (Fig. 2c). In contrast, efficiency for OPV encapsulated with 210-H_2O–Al_2O_3 decreased by 67% within 350 h (Table 2). The efficacy of O_3-based ALD for device encapsulation is further highlighted by the fact that even 10.2 nm of O_3–Al_2O_3 (120 cycles) offers better encapsulation than 20 nm of H_2O–Al_2O_3 (210 cycles). Hence, this work shows that O_3–Al_2O_3 offers excellent device encapsulation for a much lower effective oxide thickness when compared with the H_2O–Al_2O_3 layer. This is further substantiated when the blocking characteristics observed in the present work is compared with that reported in literature. Potscavage et al. [7] required a thick film of 200 nm for an effective protection of OPV from ambient conditions and they deposited Al_2O_3 layer using H_2O at a growth rate of 10 nm/h. In another work, Chang et al. [8] did employ a thinner capping layer (26 nm of Al_2O_3) for OPV encapsulation. However, they reported a 60% degradation in device efficiency within 100 h, indicating extremely poor encapsulation by the Al_2O_3 layer grown using H_2O. In comparison, a device capped with 18 nm of O_3–Al_2O_3, in the present work, showed 80% retention of the initial efficiency in over 500 h. Hence, an ultrathin barrier layer of 18 nm offers excellent blocking for OPVs from ambient conditions. As the market for organic solar cells is growing, the importance of having a more effective encapsulation with a thinner capping layer can be readily realized. This would bring down the fabrication time and manufacturing cost, thereby making organic solar cells commercially more viable. The more effective blocking behavior offered by O_3–Al_2O_3 layer is attributed to higher density, lesser defects, lower leakage current and higher breakdown field as compared to the H_2O–Al_2O_3 layer [9,11].

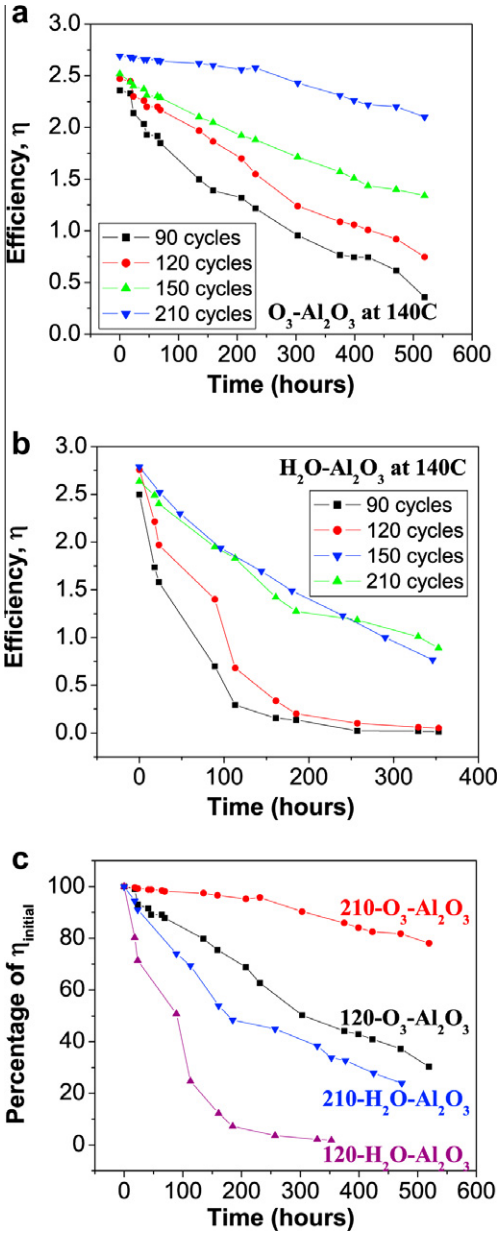

Fig. 2. (a) A time dependent study of efficiency for OPVs encapsulated with four different thicknesses of Al_2O_3 deposited using O_3 at 140 °C. (b) The degradation profile of device efficiency over time for OPVs capped with four different thicknesses of H_2O–Al_2O_3 deposited at 140 °C. (c) A comparison of the percentages of initial efficiencies studied over time for four different organic solar cells encapsulated with 120 cycles of O_3–Al_2O_3 (black squares), 210 cycles of O_3–Al_2O_3 (red circles), 120 cycles of H_2O–Al_2O_3 (purple triangles), and 210 cycles of H_2O–Al_2O_3 (blue inverted triangles). (For interpretation of the references to color in this figure legend, the reader is referred to the web version of this article.)

In literature, the efficiency of a polymer solar cell is typically enhanced by doing a post metal deposition anneal at either 140 °C or 150 °C [8,13,14]. Since the anneal

Table 2
The initial efficiency ($\eta_{initial}$), efficiency after 350 h ($\eta_{350\ h}$) and percentage of initial efficiency retained after 350 h (% $\eta_{retention}$) for OPVs encapsulated with 90, 120, 150, and 210 cycles of Al_2O_3 deposited at 140 °C.

ALD cycles	O_3–Al_2O_3			H_2O–Al_2O_3		
	$\eta_{initial}$	$\eta_{350\ h}$	% $\eta_{retention}$	$\eta_{initial}$	$\eta_{350\ h}$	% $\eta_{retention}$
90	2.36	0.82	35	2.50	0.01	0.4
120	2.47	1.13	46	2.76	0.05	2
150	2.52	1.61	64	2.64	0.74	28
210	2.69	2.35	87	2.78	0.91	33

temperature is key in determining the BHJ morphology and device efficiency, ALD encapsulation of OPVs was also studied at 150 °C. This is particularly because the process of ALD also serves as a thermal anneal step. Four different OPVs were encapsulated with 90, 120, 150, and 210 ALD cycles of O_3–Al_2O_3. Chang et al. [8] reported that device efficiency increases with increase in anneal time, typically peaking at 30 min for 150 °C but the trend reverses after reaching the maximum value. A similar trend was also observed here as the thermal budget was increased by 10 °C. The η at 150 °C peaked at 120 cycles with a marginal change at 150 cycles but decreased for the device encapsulated with 210 cycles. The peak value of η obtained at 150 °C is about 20% lower than that obtained at 140 °C. The effectiveness of encapsulation by O_3–Al_2O_3 increased with increase in number of ALD cycles with the exception of 210-O_3–Al_2O_3 (Fig. 3a). The deterioration of device characteristics for the OPV capped with 210-O_3–Al_2O_3 is attributed to prolonged heating of the solar cell at 150 °C. Prolonged heating causes over aggregation of the P3HT and PCBM domains, reducing the effective BHJ area that is critically required for charge generation [8]. Amongst the different Al_2O_3 thicknesses deposited at 150 °C, 150-O_3–Al_2O_3 offered the most effective encapsulation and the device retained 60% of the initial efficiency after 500 h. As a comparison, three other OPVs were also encapsulated with 90, 120, and 150 cycles of H_2O–Al_2O_3 at 150 °C and their efficiencies were monitored over time. As seen in Fig. 3b, devices capped with H_2O–Al_2O_3 showed rapid degradation in efficiencies as compared to devices capped with O_3–Al_2O_3. Hence, independent of anneal temperature, Al_2O_3 films deposited using O_3 offer superior encapsulation characteristics as compared to the films deposited using H_2O.

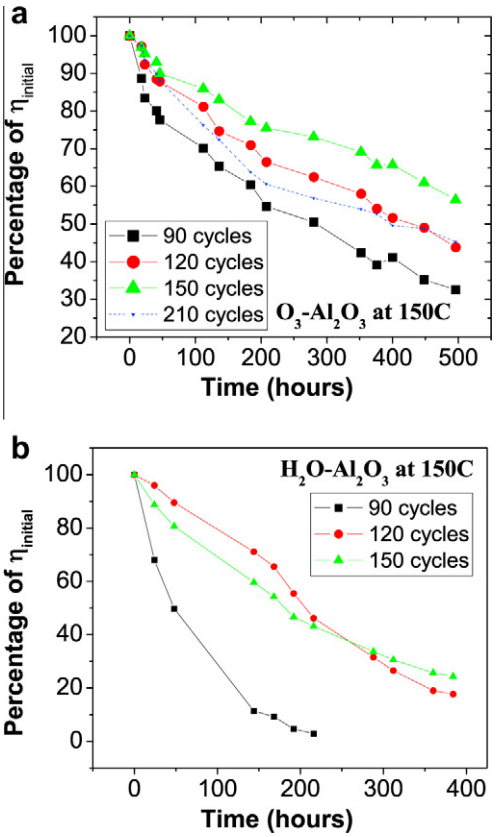

Fig. 3. (a) Percentages of initial efficiencies monitored over time for four OPVs capped with four different thicknesses of Al_2O_3 deposited using O_3 at 150 °C. (b) A time dependent study of the percentage of initial efficiencies for OPVs encapsulated with three different Al_2O_3 layers deposited using H_2O at 150 °C.

4. Conclusions

This work shows that encapsulation behavior of ultrathin Al_2O_3 films is significantly enhanced by replacing H_2O with O_3 as the ALD oxidant. This work utilizes Al_2O_3 grown using O_3 as the primary barrier layer without the requirement of any additional UV-curable epoxy resin film as a sealant for protecting OPVs from ambient moisture or oxygen. Amongst the various Al_2O_3 thicknesses monitored, 210 cycles of O_3–Al_2O_3 offered the best device encapsulation and the OPV retained 80% of its initial efficiency over a period of 500 h. The barrier layer thickness of 18 nm, utilized in the present work, provides excellent protection from ambient water and oxygen. Since ALD also serves as the annealing step, the effective encapsulation was studied for two different ALD temperatures. Irrespective of the anneal temperature, the O_3–Al_2O_3 layers showed superior encapsulation as compared to the H_2O–Al_2O_3 film. The device efficiency was studied as a function of Al_2O_3 thickness. The O_3–Al_2O_3 films demonstrated excellent encapsulation characteristics for a much lower effective oxide thickness compared to the H_2O–Al_2O_3 films.

Acknowledgments

The authors would like to acknowledge DOE # 08NT0001925 for supporting this project.

References

[1] H. Hoppe, N.S. Sariciftci, J. Mater. Res. 19 (2004) 1924.
[2] S. Günes, H. Neugebauer, N.S. Sariciftci, Chem. Rev. 107 (2007) 1324.
[3] G. Dennler, M.C. Scharber, C.J. Brabec, Adv. Mater. 21 (2009) 1323.
[4] B.C. Thompson, J.M.J. Fréchet, Angew. Chem. Int. Ed. 47 (2008) 58.
[5] K. Kawano, R. Pacios, D. Poplavskyy, J. Nelson, D.D.C. Bradley, J.R. Durrant, Sol. Energy Mater. Sol. Cells 90 (2006) 3520.
[6] M. Jorgensen, K. Norrman, F.C. Krebs, Sol. Energy Mater. Sol. Cells 92 (2008) 686.

[7] W.J. Potscavage, S. Yoo, B. Domercq, B. Kippelen, Appl. Phys. Lett. 90 (2007) 253511.
[8] C. Chang, C. Chou, Y. Lee, M. Chen, F. Tsai, Org. Electron. 10 (2009) 1300.
[9] S.K. Kim, S.W. Lee, C.S. Hwang, Y. Min, J.Y. Won, J. Jeong, J. Electrochem. Soc. 153 (2006) F69.
[10] M. Rose, J. Niinsito, I. Endler, J.W. Bartha, P. Kucher, M. Ritala, ACS Appl. Mater. Interfaces 2 (2010) 347.
[11] J.B. Kim, D.R. Kwon, K. Chakrabarti, C. Lee, K.Y. Oh, J.H. Lee, J. Appl. Phys. 92 (2002) 6739.
[12] Patterned ITO substrates were procured from Thin Film Devices, Inc. (thickness, resistivity and transmission of ITO are 280 nm, 8–10 ohms/sq and $\geqslant$85%, respectively).
[13] G. Li, V. Shrotriya, J. Huang, Y. Yao, T. Moriarty, K. Emery, Y. Yang, Nat. Mater. 4 (2005) 864.
[14] W. Ma, C. Yang, X. Gong, K. Lee, A.J. Heeger, Adv. Funct. Mater. 15 (2005) 1617.

Organic Electronics 11 (2010) 1901–1908

Contents lists available at ScienceDirect

Organic Electronics

journal homepage: www.elsevier.com/locate/orgel

Impedance spectroscopy and equivalent circuits of conductively doped organic hole-transport materials

Chung-Chia Chen, Bo-Chao Huang, Ming-Shiang Lin, Yin-Jui Lu, Ting-Yi Cho, Chih-Hao Chang, Kun-Cheng Tien, Su-Hao Liu, Tung-Hui Ke, Chung-Chih Wu *

Department of Electrical Engineering, Graduate Institute of Photonics and Optoelectronics and Graduate Institute of Electronics Engineering, National Taiwan University, Taipei 10617, Taiwan, ROC

ARTICLE INFO

Article history:
Received 4 July 2010
Received in revised form 15 August 2010
Accepted 4 September 2010
Available online 18 September 2010

Keywords:
OLEDs
Conductive doping
Impedance spectroscopy
Equivalent circuit

ABSTRACT

In this work, the impedance spectroscopy was adopted to characterize conductively doped organic hole-transport layers. We performed comparative studies of the impedance spectroscopy of undoped and doped hole-transport materials, by both experiment and simulation approaches. The impedance spectroscopy of the non-doped hole-transport material can be well understood by simply adopting the conventional RC equivalent circuits and considering the dielectric response frequency-independent. For the conductively doped organic hole-transport materials, however, successful modeling of the impedance spectroscopy results need to take into account the more complicated situations: including the difference between the bulk region and the depletion region near the electrode, and dispersion (i.e. frequency dependence) in the dielectric response of the conductively doped transport layer. As such, it is found necessary to include the complex dielectric response and the non-conventional complex impedance element in the equivalent circuit to achieve tight matching of simulated results with experiment results over wide bias and frequency ranges.

© 2010 Elsevier B.V. All rights reserved.

1. Introduction

Since first reports of efficient organic light-emitting diodes (OLEDs) in 1980s [1], OLEDs have attracted substantial research efforts and have now become one of the most promising technologies for displays and solid-state lighting [2–5]. To further enhance OLED performances, conductive doping of carrier-transport materials in OLEDs has been adopted and is becoming an important technology due to their various merits [6–12]. Conductive doping of carrier-transport materials in OLEDs could largely facilitate carrier injection and increase the conductivity of organic semiconductors, both capable of reducing operation voltages and increasing efficiencies of OLEDs. Thus, more detailed understanding of the operation mechanisms and electrical properties of conductively doped organic carrier-transport materials could be of use to applications and advancement of such technologies.

Impedance spectroscopy has been a useful tool for probing the electrical/dielectric properties and operation mechanisms of organic and inorganic semiconductors/devices [13–16]. With the aid of impedance spectroscopy, one in principle can construct the equivalent circuits of the devices and thereby obtain more insights about the operation of the materials and devices [17–19]. In this work, we adopted the impedance spectroscopy to characterize conductively doped organic hole-transport layers for OLEDs. We performed comparative studies of the impedance spectroscopy of undoped and doped hole-transport materials, by both experiment and simulation approaches. The impedance spectroscopy of the non-doped hole-transport material can be well understood by simply

* Corresponding author. Tel.: +886 2 3366 3636; fax: +886 2 3366 9404.
E-mail address: chungwu@cc.ee.ntu.edu.tw (C.-C. Wu).

1566-1199/$ - see front matter © 2010 Elsevier B.V. All rights reserved.
doi:10.1016/j.orgel.2010.09.005

adopting the conventional RC equivalent circuits and considering the dielectric response frequency-independent [18]. For the conductively doped organic hole-transport materials, however, successful modeling of the impedance spectroscopy results need to take into account the more complicated situations: including the difference between the bulk region and the depletion region near the electrode, and dispersion (i.e. frequency dependence) in the dielectric response of the conductively doped transport layer. As such, it is found necessary to include the non-conventional complex impedance element in the equivalent circuit to achieve tight matching of simulated results with experiment results over wide bias and frequency ranges.

2. Experimental: sample preparation and characterization

The organic carrier-transport material studied in this work is the widely used hole-transport/hole-injection material 4,4′,4″-tris(3-methylphenylphenylamino)triphenylamine (*m*-MTDATA) [20]. For comparative studies, *m*-MTDATA was vacuum-deposited as an intrinsic non-doped layer or with 2 wt.% p-type conductive dopants 2,3,5,6-tetrafluoro-7,7,8,8-tetracyanoquinodimethane (F_4-TCNQ) [21]. F_4-TCNQ is a very strong electron acceptor that can act as effective p-type dopant materials. The undoped device structure for impedance spectroscopy was ITO/*m*-MTDATA (100 nm)/Ag (100 nm), while the doped device structure was ITO/*m*-MTDATA: F_4-TCNQ (2 wt.%, 100 nm)/Ag (100 nm). The LUMO level of *m*-MTDATA is 1.9 eV [20] while the work function of silver is around 4.28 eV. Such a difference in energy levels results in a large barrier for electron injection. Together with the much better hole-transport capability vs. electron-transport capability in *m*-MTDATA, both undoped and doped *m*-MTDATA devices were mainly single-carrier (hole-only) devices.

The devices were fabricated on the ITO (indium tin oxide)-coated glass substrates with organic layers sandwiched between the bottom anode and the top metal cathode. ITO was cleaned and UV–ozone-treated before use. All the organic and metal layers were deposited by thermal evaporation in a vacuum chamber with a base pressure of $<10^{-6}$ torr. The F_4-TCNQ-doped *m*-MTDATA layer was deposited by co-evaporation. The deposition rate of organic layers was kept at ~0.2 nm/s. The deposition system permitted the fabrication of the complete device structure in a single pump-down without breaking vacuum. The active area of the device was 1×1 mm^2, as defined by the shadow mask for cathode deposition. The impedance spectroscopy was measured by an impedance analyzer (Wayne Kerr 6440B) together with a dc power supply used to provide the dc bias voltage. For all measurements, the amplitude of ac signals was kept at 0.1 V. The frequency range of the generated impedance data was from 20 to 3×10^6 Hz.

3. Results and discussions

The *I*–*V* curves of the undoped and the doped devices are shown in Fig. 1. With the conductive doping, the current is increased by orders of magnitude (vs. the undoped device) and the current rises sharply with the bias.

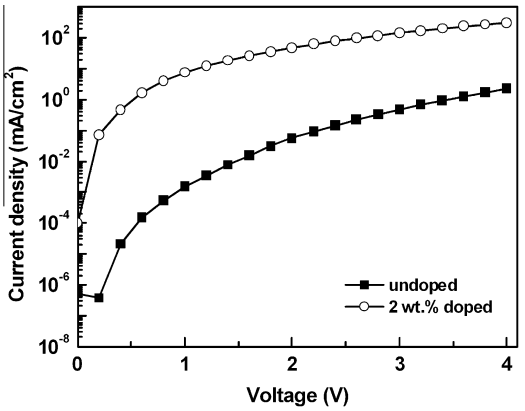

Fig. 1. *I*–*V* characteristics of ITO/*m*-MTDATA: F_4-TCNQ (0 wt.%, 2 wt.%, 100 nm)/Ag (100 nm).

Fig. 2 shows the measured Cole–Cole plots of the undoped *m*-MTDATA device under different dc bias voltages. The Cole–Cole plot depicts the imaginary part of the impedance (i.e. Im(*Z*)) versus the real part of the impedance (i.e. Re(*Z*)) when continuously sweeping the small-signal frequency (under a particular dc bias) [17]. Under each dc bias, the Cole–Cole plot of the undoped device resembles a single-semicircle in continuously sweeping the frequency, which is typical for a single-layer single-carrier device [18]. Such single-semicircle impedance characteristics in the Cole–Cole plot can usually be reproduced with an equivalent circuit as shown in Fig. 3. In Fig. 3, the series resistance R_s is associated with the contribution from the electrode. The parallel resistance R_p in the parallel RC network is associated with the layer resistance (i.e. *m*-MTDATA), while C_p is associated with the geometric capacitance of the *m*-MTDATA layer. As also shown in Fig. 2, by carefully adjusting the parameters (R_s, R_p, C_p), each curve in the Cole–Cole plot (each associated with a particular bias voltage) can be well reproduced using the equivalent circuit of Fig. 3. The parameters (R_s, R_p, C_p) used

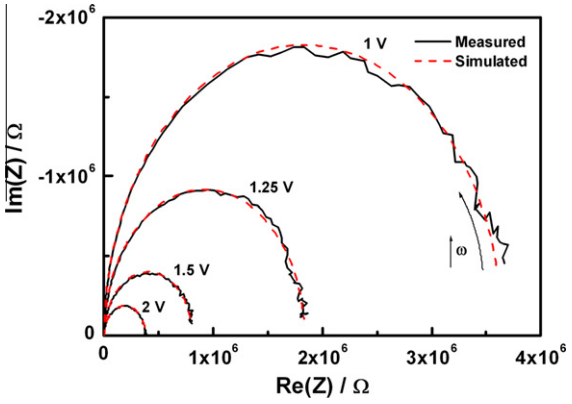

Fig. 2. Measured and simulated Cole–Cole plots of the undoped *m*-MTDATA device, ITO/*m*-MTDATA (100 nm)/Ag (100 nm), under different dc bias voltages. The simulated curves are generated using the equivalent circuit shown in Fig. 3 and parameters listed in Table 1.

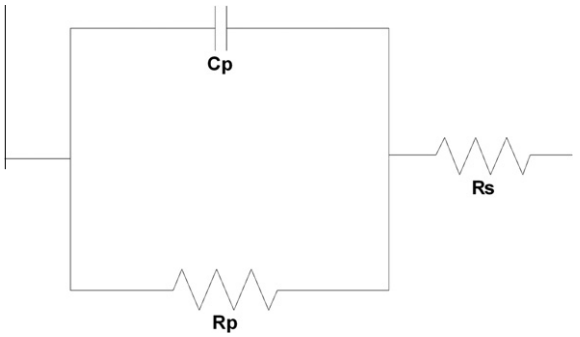

Fig. 3. The equivalent circuit used to simulate impedance characteristics shown in Fig. 2 for the undoped *m*-MTDATA device.

to fit the curves under different bias voltages are shown in Table 1. In Table 1, one sees that C_p remains rather constant versus bias voltage for the frequency range measured (as the geometric capacitance is supposed to be) and R_p drops significantly as the bias voltage increases. It makes sense since more carrier are injected into the device (leading to higher carrier concentrations) and thus the layer resistance drops when the dc bias voltage is raised. By assuming a nominal dielectric constant of ~3 typical for organic layers, the thickness of the *m*-MTDATA film is estimated to be 107 nm from the C_p value, which is consistent with the deposited m-MTDATA thickness verified by ellipsometry.

Fig. 4 shows the measured Cole–Cole plots of the F_4-TCNQ-doped (2 wt.%) *m*-MTDATA device under different dc bias voltages. In contrast to the undoped device, the doped device exhibits two semicircle-like features, particularly at lower dc bias conditions. When the dc bias increases, one feature shrinks quickly and the two semicircles appear to merge together. The difference in impedance spectroscopy for undoped and doped devices can be further manifested by comparing Re(Z) and Im(Z) of both devices as a function frequency. Fig. 5a and b shows Re(Z) versus frequency under different bias voltages for undoped and doped devices, respectively. Fig. 6a and b shows $-$Im(Z) versus frequency under different bias voltages for undoped and doped devices, respectively. From results of Figs. 4–6, one sees that under a similar dc bias, in general the doped device exhibits a much smaller (absolute) magnitude of the impedance (much smaller semicircles in the Cole–Cole plots, much smaller Re(Z) and Im(Z) at lower frequencies). It manifests that with the conductive doping, the carrier conduction in the carrier-transport layer is largely enhanced.

For Cole–Cole plots containing two semicircles, an equivalent circuit consisting of series connection of two parallel RC circuits, like that shown in Fig. 7, is often effective. A series connection of two parallel RC circuits is usually associated with a device containing two layers or two regions of different electrical characteristics. For the present case, although the organic layer was deposited as a single doped layer, yet Riess et al. [13] previously reported that in the conductively doped organic carrier-transport layer, a depletion region could occur near the electrode with larger energy level mismatch. Thus, for the present F_4-TCNQ-doped (2 wt.%) *m*-MTDATA device,

Table 1
Device parameters used to simulate the measured Cole–Cole plots of Fig. 2 (for the non-doped device) using the equivalent circuit of Fig. 3.

	R_s (Ω)	C_p (F)	R_p (Ω)
1 V	175.4	2.48E−10	3.65E6
1.25 V	175.3	2.47E−10	1.83E6
1.5 V	175.9	2.47E−10	8.03E5
2 V	177.2	2.46E−10	3.78E5

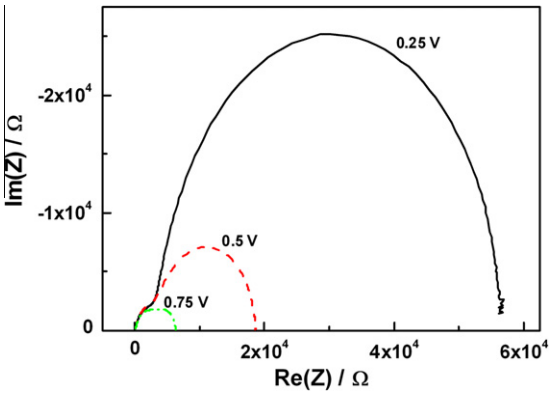

Fig. 4. Measured Cole–Cole plots of the F_4-TCNQ-doped *m*-MTDATA device, ITO/*m*-MTDATA: F_4-TCNQ (2 wt.%, 100 nm)/Ag (100 nm), under different dc bias voltages.

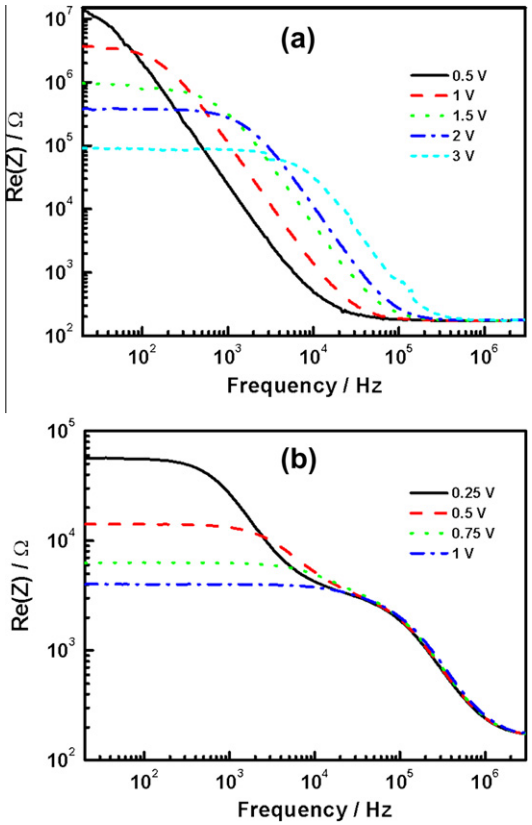

Fig. 5. Re(Z) versus frequency under different bias voltages for (a) the undoped and (b) the 2 wt.% doped devices.

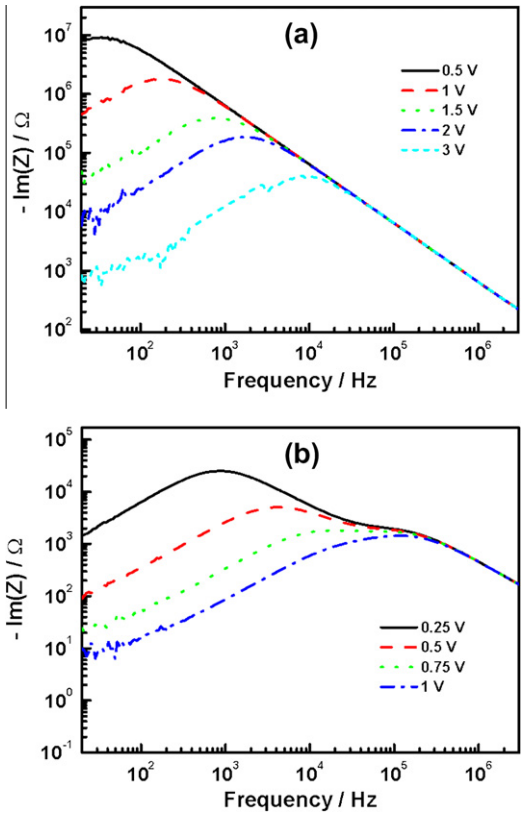

Fig. 6. −Im(*Z*) versus frequency under different bias voltages for (a) the undoped and (b) the 2 wt.% doped devices.

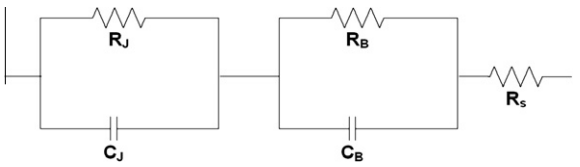

Fig. 7. An equivalent circuit consisting of a series connection of two parallel RC circuits.

two regions of different electrical characteristics, a depletion region near the Ag electrode and a more conducting bulk region near the ITO electrode, might occur and the equivalent circuit in Fig. 7 might be appropriate. In such a case, in Fig. 7, R_B and C_B represent the resistance and capacitance of the conducting bulk region, while R_J and C_J represent the resistance and capacitance of the depletion region. The optimized fittings to the measured Cole–Cole plots (under different dc biases) using such an equivalent circuit and the parameters listed in Table 2 are shown in Fig. 8. In assigning fitting values of equivalent circuit elements to the bulk or the junction under different biases (throughout this whole work), particular attention was paid to the consistency of the characteristic frequency ranges and their transitions vs. biases with the frequency responses of corresponding circuit elements. From Fig. 8, one sees that even in the optimized case, it is difficult to

Table 2
Device parameters used to simulate the measured Cole–Cole plots of Fig. 4 (for the 2 wt.% doped device) using the equivalent circuit of Fig. 7.

	R_s (Ω)	C_B (F)	R_B (Ω)	C_J (F)	R_J (Ω)
0.25 V	181.3	4.04E−10	3154	3.44E−9	5.2E4
0.5 V	178.2	4.27E−10	2906	3.22E−9	1.1E4
0.75 V	175.6	3.91E−10	2595	3.22E−9	3479

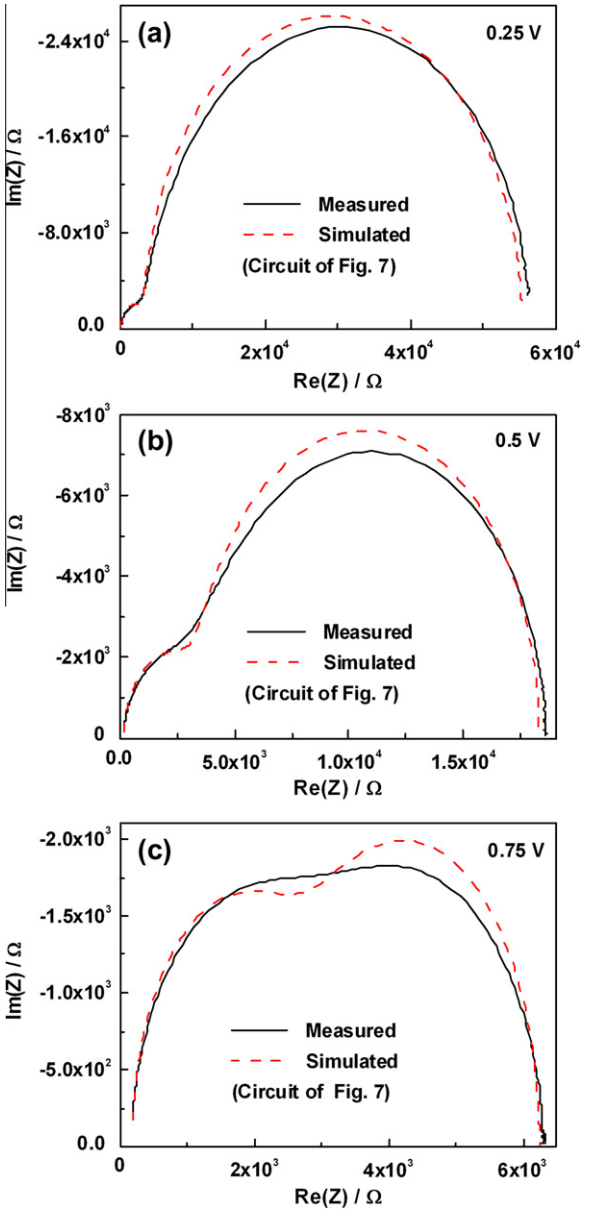

Fig. 8. The optimized fitting to the measured Cole–Cole plots of the 2 wt.% doped device in Fig. 4 using the equivalent circuit in Fig. 7 and parameters listed in Table 2 (for different bias voltages): (a) 0.25 V, (b) 0.5 V, and (c) 0.75 V.

obtain satisfactory fittings for a wide range of dc biases and frequencies. The simulated curves have the difficulty to truthfully follow the shapes/forms of the measured

curves, indicating the equivalent circuit in Fig. 7 is not good/complete enough. Also, with the circuit model of Fig. 7, one would expect a dependence of C_J on the bias [13]. Yet from the fitting values shown in Table 2, one notices that the junction capacitance C_J does not show a strong dependence on biases. This is partially due to the limited bias range shown (more significant increase of C_J can be seen at higher forward biases). On the other hand, with doubts on the accuracy and completeness of the simple RC model, one suspects how much the extracted C_J values reflect the real situations.

Riess et al. [13] also similarly observed significant deviations in fittings of impedance spectroscopy results of the conductively doped carrier-transport layer using the equivalent circuit of Fig. 7. Riess el al. [13] mentioned that the imperfect fittings might result from the frequency (ω) dependence of the conductivity $\sigma(\omega)$ and dielectric constant $\varepsilon(\omega)$ and spatial inhomogeneities in the thickness and dopant concentration etc., whose effects are not included in the simple equivalent circuit of Fig. 7. Thus, a more accurate and physically meaningful equivalent circuit/model is needed to reproduce impedance characteristics of the conductively doped organic transport layer. Later, Leo et al. [22] suggested the adoption of a distributed circuit element called constant phase element (CPE) [17,23,24] to replace the regular capacitance, for taking into account the dispersive properties (e.g. frequency dependence of the dielectric properties) and for better modeling impedance characteristics of conductively doped organic carrier-transport films. The impedance of a CPE has the general form of $Z(\omega) = Q(j\omega)^{-\alpha}$, where Q is a constant parameter and the parameter α can assume values between 0 and 1. The parameter α describes the degree of the capacitive character; when $\alpha = 1$, the CPE is like a regular capacitance. The introduction of this CPE distributed element may include effects of the distribution of energy states and/or spatially distributed conductivity etc. By replacing the regular capacitances in Fig. 7 with the corresponding CPE elements, the modified equivalent circuit is shown in Fig. 9. The optimized fittings to the measured Cole–Cole plots (under different dc biases) of the F_4-TCNQ-doped *m*-MTDATA device using such an equivalent circuit and the parameters listed in Table 3 are shown in Fig. 10. Compared to results of Fig. 8 using the equivalent circuit of Fig. 7, the fittings are improved, but still deviations from measured curves are apparently visible and there is room for further improvement of the model/equivalent circuit.

Results of Fig. 10 based on the equivalent circuit of Fig. 9 indicate that simply replacing regular capacitances

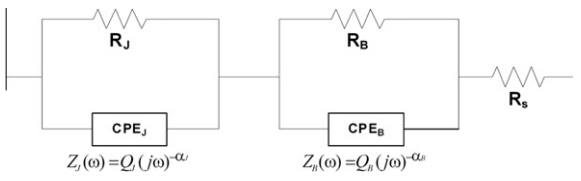

Fig. 9. An equivalent circuit consisting of a series connection of two parallel *R*/CPE circuits, (which is modified from Fig. 7 by replacing regular capacitances with constant phase elements).

Table 3
Device parameters used to simulate the measured Cole–Cole plots of Fig. 4 (for the 2 wt.% doped device) using the equivalent circuit of Fig. 9.

	R_S (Ω)	CPE_B (Q_B/α_B)	R_B (Ω)	CPE_J (Q_J/α_J)	R_J (Ω)
0.25 V	181.3	7.42E8/ 0.9201	3092	1.78E8/ 0.9413	5.40E4
0.5 V	178.2	7.83E8/ 0.9259	3099	1.81E8/ 0.9306	1.54E4
0.75 V	175.6	1.05E9/ 0.9437	2664	9.31E7/ 0.8997	3517

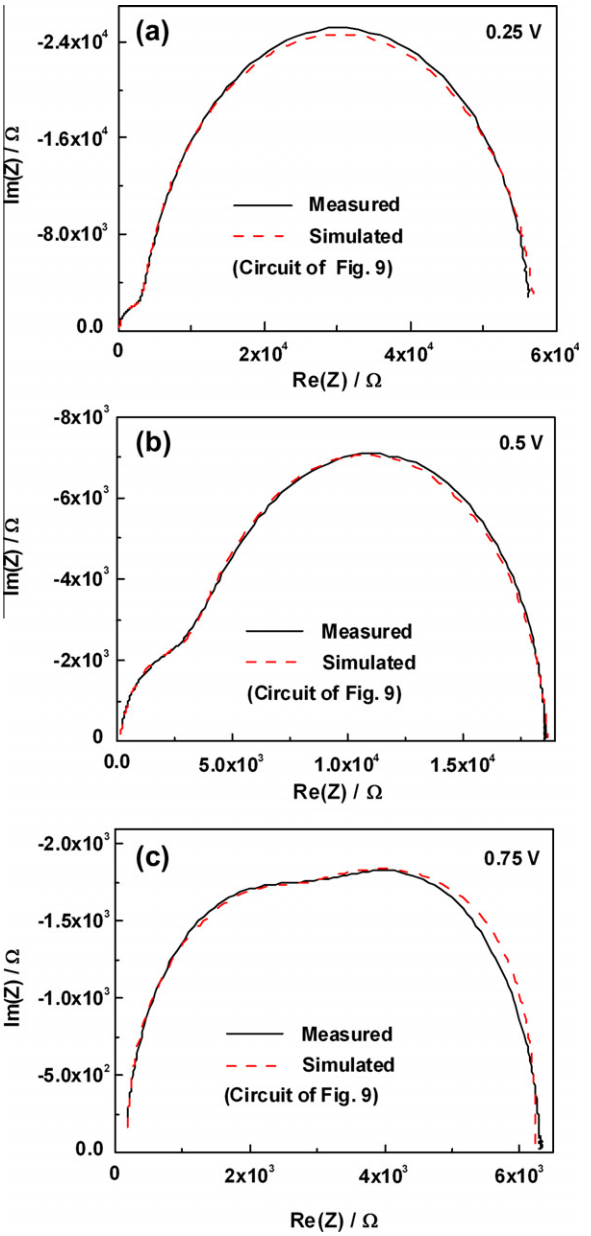

Fig. 10. The optimized fitting to the measured Cole–Cole plots of the 2 wt.% doped device in Fig. 4 using the equivalent circuit in Fig. 9 and parameters listed in Table 3 (for different bias voltages): (a) 0.25 V, (b) 0.5 V, and (c) 0.75 V.

with the CPE elements is not sufficient (or accurate enough) to model dispersive characteristics of the conductively doped organic carrier-transport layers. A more complete/accurate model is needed. A more general formula for including the dispersion in the dielectric constants, that was first reported by Cole and Cole [25] and is found to well represent dielectric properties of many inorganic and organic electrochemical systems, has the complex form of:

$$\varepsilon - \varepsilon_\infty = \frac{(\varepsilon_s - \varepsilon_\infty)}{[1 + (j\omega\tau_0)^{1-\alpha}]} \quad (1)$$

In this formula, ε is the dielectric constant at a angular frequency ω, ε_∞ is the high-frequency dielectric constant, ε_s is the static (low-frequency) dielectric constant, and τ_0 is the average relaxation time. The parameter α can assume values between 0 and 1. ε_∞ represents the non-dispersive component of ε, which remains from low-frequencies to high frequencies. Meanwhile, $(\varepsilon_s - \varepsilon_\infty)/[1 + (j\omega\tau_0)^{1-\alpha}]$ represents the dispersive part of ε, the transition of ε from the static dielectric constant ε_s to the high-frequency dielectric constant ε_∞.

When an electric field is applied to an electrochemical system, an almost instant polarization due to the displacement of electrons with the respect to the (molecular) nuclei, which corresponds to the high-frequency dielectric constant ε_∞. If there is reorientation of electric dipole moments associated with the applied electric field (often associated with complexes, defect electronic species, ionic interstitials etc.), a time-dependent polarization (at the time-scale of interest) and dispersion in dielectric responses, however, could occur. In such a case, the static dielectric constant ε_s is associated with the total polarization if the electric field remains in place for long enough time. As for the detailed dispersion characteristics, it depends on the detailed relaxation processes. For instance, if the polarization process can be described by a single relaxation time, a Debye dispersive relation is usually derived [17,25]. On the other hand, when there is a distribution in the relaxation times, the dispersion behaviors in the dielectric response are most widely described by Eq. (1), in which τ_0 represents the average of the relaxation times, not the single relaxation time. For the present F_4-TCNQ-doped *m*-MTDATA, the p-type conductive doping (increase of hole carriers) is based on the ground-state electron transfer between host and dopant molecules. If for some of the molecules the electron transfer is not complete (due to energetic and spatial distributions associated with the amorphous/disordered morphology), then charge-transfer complexes (between donor host *m*-MTDATA and acceptor dopant F_4-TCNQ) with electric dipole moments could form. F_4-TCNQ dopant molecules are surrounded by much more *m*-MTDATA host molecules and thus reorientation of electric dipole moments of the complexes could very possibly occur when an ac field is applied. Since the present F_4-TCNQ-doped *m*-MTDATA is an amorphous system, the corresponding polarization relaxation could also very possibly exhibit a distribution in the relaxation times, showing a dielectric dispersion like Eq. (1).

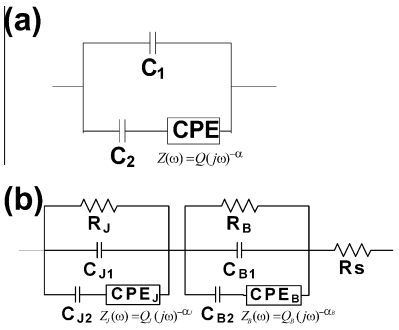

Fig. 11. (a) The equivalent circuit for a material layer having a dispersive dielectric response like Eq. (1). (b) The equivalent circuit modified from Fig. 7 by replacing regular capacitances with the equivalent circuit of Fig. 11a.

For a material layer having a dispersive dielectric response as described by Eq. (1), in impedance spectroscopy, such a dispersive dielectric response represents a more complicated equivalent circuit as shown in Fig. 11a [17,25]. The equivalent circuit in Fig. 11a can be understood by considering a general capacitance that is equal to the complex dielectric constant multiplied by the area *A* and divided by the layer thickness *d*. As such, the effects of dielectric response function of Eq. (1) can naturally be decomposed into an equivalent circuit like Fig. 11a. $C_1 = A\varepsilon_\infty/d$ represents the geometric layer capacitance associated with the non-dispersive component of ε in Eq. (1) (i.e. ε_∞, which remains same from low-frequencies to high frequencies) [17]. Meanwhile, $C_2[=A(\varepsilon_s - \varepsilon_\infty)/d]$ in series with the constant phase element [CPE, $Z = Q \times (j\omega)^{-\alpha}$, $Q = (\tau_0^{1-\alpha} \times d)/(\varepsilon_s - \varepsilon_\infty)/A]$ represents the contributions from the dispersive part of ε in Eq. (1), i.e. $(\varepsilon_s - \varepsilon_\infty)/[1 + (j\omega\tau_0)^{1-\alpha}]$.

By replacing the regular capacitances in Fig. 7 with the circuit of Fig. 11a that now gives more general/complete description of dispersive characteristics, the equivalent circuit for the conductively doped carrier-transport-layer device is modified as Fig. 11b. The optimized fittings to the measured Cole–Cole plots (under different dc biases) using such an equivalent circuit and parameters listed in Table 4 are shown in Fig. 12. As shown in Fig. 12, nearly perfect matching between the measured and simulated results is

Table 4
Device parameters used to simulate the measured Cole–Cole plots of Fig. 4 (for the 2 wt.% doped device) using the equivalent circuit of Fig. 11b.

	R_S (Ω)	R_S (Ω)	C_{B1} (F)	C_{B2} (F)	CPE_B (Q_B/α_B)	R_J (Ω)	C_{J1} (F)	C_{J2} (F)	CPE_J (Q_J/α_J)
0.25 V	152.2	1781	9.55E−11	5.97E−10	7.55E4/0.9966	5.44e4	5.34E−10	2.85E−9	9.63E4/0.3081
0.5 V	154.7	1502	7.73E−10	7.73E−10	7.43e4/0.8919	1.69E4	4.75E−10	2.05E−9	8.68E4/0.2711
0.75 V	158.8	1196	1.07E−10	9.43E−10	7.39E4/0.8674	5265	4.21E−10	1.52E−9	8.36E4/0.2312

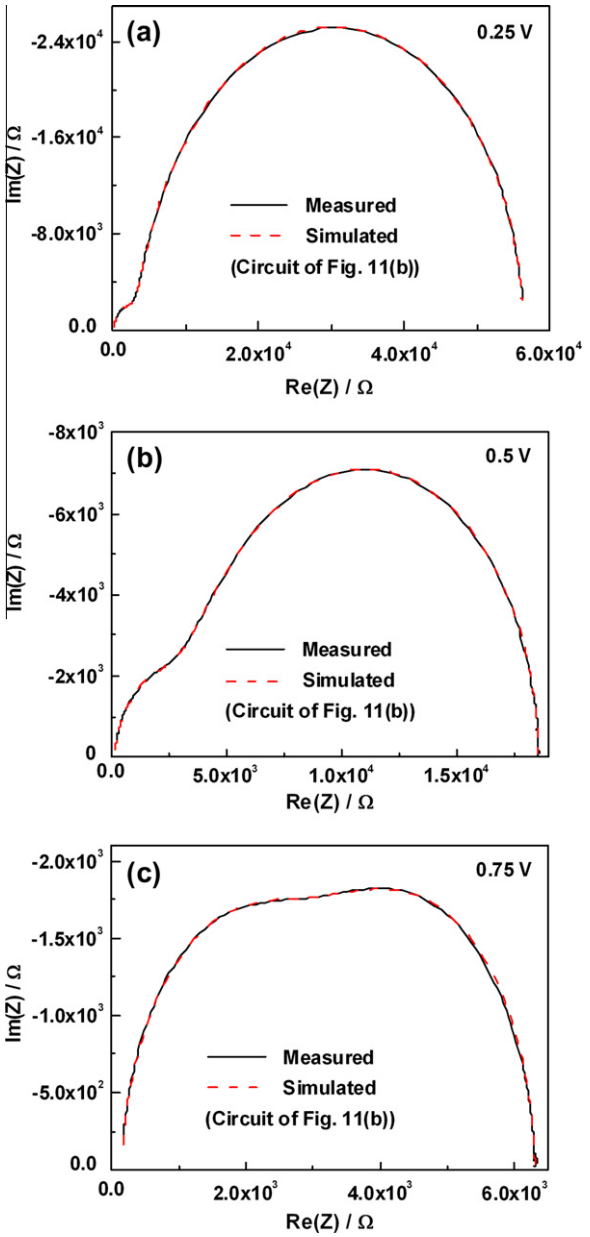

Fig. 12. The optimized fitting to the measured Cole–Cole plots of the 2 wt.% doped device in Fig. 4 using the equivalent circuit in Fig. 11b and parameters listed in Table 4 (for different bias voltages): (a) 0.25 V, (b) 0.5 V, and (c) 0.75 V.

obtained over a wide bias and frequency range by using the equivalent circuit of Fig. 11b. These results indicate the effectiveness of the equivalent circuits of Fig. 11a and b for the conductively doped organic carrier-transport layer. In Table 4, one notices that the CPE for the depletion region (CPE_J) has the α value significantly lower than 1, suggesting of more dispersive character. One also notices that the layer resistances of doped devices are much smaller than R_P in the non-doped device. With increasing bias, the resistance of the depletion region (R_J) decreases significantly. From the extracted values of equivalent circuit elements (e.g. comparing C_J and C_B) in Table 4, one can estimate the thicknesses of the bulk region and the junction region to be 70–90 nm and 10–30 nm, respectively, for the bias range shown. From the Q and capacitance values, one can also estimate the average relaxation time τ_0 to be on the order of 10^{-5} s, which is within the frequency range studied here and thus has noticeable influences on impedance spectroscopy.

The impedance spectroscopy of conductively doped hole-transport layers in this work indicates that a higher-impedance depletion region would occur when the energy level of the conductively doped hole-transport layer does not well match that of the adjacent layer in the OLED device (e.g. undoped hole-transport layer, emitting layer, electrode etc.). If occurring, that might degrade benefits provided by the conductively doped hole-transport layer (improved injection and conductivity, lowered operation voltage etc.). Thus to optimize OLED performances, even with adoption of conductively doped carrier-transport layers in devices, it is still worthy of carefully considering matching of energy levels of relevant materials layers to avoid/minimize such depletion phenomena. Furthermore, the dispersive dielectric responses induced by the conductively doping (and corresponding polarization relaxation) could have impacts on high-frequency operation (e.g. >10 kHz) of organic devices, in addition to regular RC effects.

4. Conclusions

In summary, the impedance spectroscopy was adopted to characterize conductively doped organic hole-transport layers for OLEDs. We performed comparative studies of the impedance spectroscopy of undoped and doped hole-transport materials, by both experiment and simulation approaches. The impedance spectroscopy of the non-doped hole-transport material can be well understood by simply adopting the conventional RC equivalent circuits and considering the dielectric response frequency-independent. For the conductively doped organic hole-transport materials, however, successful modeling of the impedance spectroscopy results need to take into account the more complicated situations: including the difference between the bulk region and the depletion region near the electrode, and dispersion (i.e. frequency dependence) in the dielectric response of the conductively doped transport layer. As such, it is found necessary to include the complex dielectric response and non-conventional complex impedance element in the equivalent circuit to achieve tight matching of simulated results with experiment results over wide bias and frequency ranges.

Acknowledgements

The authors gratefully acknowledge the financial support from National Science Council and Ministry of Economic Affairs of Taiwan.

References

[1] C.W. Tang, S.A. VanSlyke, Appl. Phys. Lett. 51 (1987) 913.

[2] J.R. Sheats, H. Antoniadis, M. Hueschen, W. Leonard, J. Miller, R. Moon, D. Roitman, A. Stocking, Science 273 (1996) 884.
[3] M.A. Baldo, D.F. O'Brien, Y. You, A. Shoustikov, S. Sibley, M.E. Thompson, S.R. Forrest, Nature 395 (1998) 151.
[4] Y. Sun, N.C. Giebink, H. Kanno, B. Ma, M.E. Thompson, S.R. Forrest, Nature 440 (2006) 908.
[5] S. Reineke, F. Lindner, G. Schwartz, N. Seidler, K. Walzer, B. Lüssem, K. Leo, Nature 459 (2009) 234.
[6] J. Huang, M. Pfeiffer, A. Werner, J. Blochwitz, S. Liu, K. Leo, Appl. Phys. Lett. 80 (2002) 139.
[7] C.L. Lin, T.Y. Cho, C.H. Chang, C.C. Wu, Appl. Phys. Lett. 88 (2006) 081114.
[8] T.Y. Cho, C.L. Lin, C.C. Wu, Appl. Phys. Lett. 88 (2006) 111106.
[9] C.I. Wu, C.T. Lin, Y.H. Chen, M.H. Chen, Y.J. Lu, C.C. Wu, Appl. Phys. Lett. 88 (2006) 152104.
[10] T. Matsushima, C. Adachi, Appl. Phys. Lett. 89 (2006) 253506.
[11] M.H. Ho, S.F. Hsu, J.W. Ma, S.W. Hwang, P.C. Yeh, C.H. Chen, Appl. Phys. Lett. 91 (2007) 113518.
[12] K. Walzer, B. Maennig, M. Pfeiffer, K. Leo, Chem. Rev. 107 (2007) 1233.
[13] M. Meier, S. Karg, W. Riess, J. Appl. Phys. 82 (1997) 1961.
[14] S. Berleb, W. Brütting, Phys. Rev. Lett. 89 (2002) 286601.
[15] J. Bisquert, G. Garcia-Belmonte, A. Pitarch, H.J. Bolink, Chem. Phys. Lett. 422 (2006) 184.
[16] N.D. Nguyen, M. Schmeits, H.P. Loebl, Phys. Rev. B 75 (2007) 075307.
[17] J.R. MacDonald, Impedance Spectroscopy – Emphasizing Solid Materials and Systems, Wiley, New York, 1987.
[18] C. Jonda, A.B.R. Mayer, Chem. Mater. 11 (1999) 2429.
[19] L.S.C. Pingree, B.J. Scott, M.T. Russell, T.J. Marks, M.C. Hersam, Appl. Phys. Lett. 86 (2005) 073509.
[20] Y. Shirota, Y. Kuwabara, H. Inada, T. Wakimoto, H. Nakada, Y. Yonemoto, S. Kawami, K. Imai, Appl. Phys. Lett. 65 (1994) 807.
[21] J. Blochwitz, M. Pfeiffer, T. Fritz, K. Leo, Appl. Phys. Lett. 73 (1998) 729.
[22] J. Drechsel, M. Pfeiffer, X. Zhou, A. Nollau, K. Leo, Synth. Met. 127 (2002) 201.
[23] H. Göhr, J. Schaller, C.-A. Schiller, Electrochim. Acta 38 (1993) 1961.
[24] A.K. Jonscher, Phys. Status Solidi A 32 (1975) 664.
[25] K.S. Cole, R.H. Cole, J. Chem. Phys. 9 (1941) 341.

Organic Electronics 11 (2010) 1909–1915

Contents lists available at ScienceDirect

Organic Electronics

journal homepage: www.elsevier.com/locate/orgel

Heterojunction organic solar cells based on donor-π-acceptor small molecule layers with controlled interface morphology

Shanshan Wang, Zuqiang Bian *, Xinyuan Xia, Chunhui Huang

Beijing National Laboratory for Molecular Sciences (BNLMS), State Key Laboratory of Rare Earth Materials Chemistry and Applications, Peking University, Beijing 100871, PR China

ARTICLE INFO

Article history:
Received 6 July 2010
Received in revised form 24 August 2010
Accepted 4 September 2010
Available online 17 September 2010

Keywords:
Organic solar cells
Morphology
Interface
Heterojunction
Aromatic amines
DCM

ABSTRACT

Small molecules have a great potential in developing organic solar cells owing to their well-controlled structure and tunable electronic properties by functionalization. Here, we use a classical fluorescent dye with a D-π-A structure, 4-(dicyanomethylene)-2-methyl-6-(4-dimethyl-aminostyryl)-4H-pyran (DCM), as an efficient light absorption layer with sensitivity at wavelengths of 400–600 nm where the aromatic amine/C_{60} cells have low absorbance. Combined with a p-type transporting layer of selected aromatic amines, the much improved layer and interface morphology yield solar cell power conversion efficiency up to 1.68% under AM 1.5 and 100 mW cm^{-2} illumination. The morphology of active organic layers, their interface, and the influence on the cell performance have been systematically studied.

© 2010 Elsevier B.V. All rights reserved.

1. Introduction

Organic solar cells (OSCs) have the potential to offer device flexibility and inexpensive power generation [1–4]. Developing materials with useful physical properties and exploring novel device architecture have been a general strategy in improving the power conversion efficiency of OSCs [5–7]. Small molecules with π-conjugated donor–acceptor (D-π-A) structure constitute an important group of material that possess many distinct advantages in the design and fabrication of OSCs [8,9]. The intramolecular charge transfer between π-conjugated electron donating and accepting units results in reduced optical band gap and enhanced light absorption in solar spectrum. Small molecules offer great flexibility in modifying the molecular structures and tailoring the electronic properties, and can be processed (e.g. by vacuum evaporation) into high-purity thin films consisting of mono-dispersed molecules. Recently, there has been increasing interest in studying new D-π-A type materials and their potential application in making bulk-heterojunction OSCs. Current results show that slight modification of the molecular structure by reducing the linker length could lead to nearly 2-fold increase of cell efficiency [10,11]. Despite these progresses, it remains a great challenge in developing D-π-A molecules with appropriate structures and optimizing device configuration for substantial improvement of OSC performance.

Here, we show that a commercially available dye, 4-(dicyanomethylene)-2-methyl-6-(4-dimethyl-aminostyryl)-4H-pyran (DCM), which has a simple D-π-A structure with an electron-rich dimethylamino group linked to two electron-withdrawing cyano groups, can be used as photoactive materials in OSCs. One of the advantages is that DCM has high absorption coefficient to visible light (42,000 M^{-1} cm^{-1} at 468 nm) [12], thus DCM layers can be made into very small thickness (less than 10 nm) for exciton transport but still have strong light absorption. Previous study on laboratory-synthesized materials consisting of triphenylamine and DCM moieties has shown promising results including high open-circuit voltages

* Corresponding author.
E-mail address: bianzq@pku.edu.cn (Z. Bian).

1566-1199/$ - see front matter © 2010 Elsevier B.V. All rights reserved.
doi:10.1016/j.orgel.2010.09.006

(>0.9 V) and efficiencies in the range of 0.79–1.5% [10,11], however, OSCs directly using DCM have not been reported. Our devices were made by stacking electron accepting (C_{60}), photoactive (DCM), and selected p-type transporting layers into a heterojunction structure. Systematic study reveals that the DCM layer morphology, thickness, and interface with underlying layers are critical factors that dominate the cell performance. A combination of 10 nm thick DCM with 4,4′-bis[*N*-(1-naphthyl)-*N*-phenyl-amino]biphenyl (NPB) yields uniform layers with smooth interface, and cell efficiencies up to 1.68%.

2. Experimental

All materials were purchased from Sigma–Aldrich. Except for C_{60} (99%), they were purified by thermal gradient sublimation before deposition.

All devices were fabricated on indium tin oxide (ITO) coated glass substrates with an ITO thickness of 600 Å. The substrates were routinely pre-cleaned using isopropanol, ethanol and de-ionized water. PEDOT:PSS was spun onto the ITO anode at 4500 rpm for 60 s and then it was annealed at 120 °C for 15 min under atmosphere to form a 600 Å thick film. Organic layers were deposited at a 0.2 Å s^{-1} rate by thermal evaporation under high vacuum (7×10^{-7} Torr). Organic layers were annealed at 140–160 °C before Al electrodes were evaporated on their surfaces, followed the work of Osasa et al. [13]. Then the Al cathode was thermally evaporated on the top through a shadow mask giving an active device area of 5 mm^2. The film thicknesses were monitored by a quartz-crystal microbalance. The *J*–*V* characteristics were recorded using a Keithley 4200 Semiconductor Characterization System under ambient conditions. An Oriel 300W solar simulator (Thermo Oriel 91160-1000) with AM 1.5 G filter provides 100 mW cm^{-2} illumination, determined using a standard silicon solar cell.

Except where noted, all samples were prepared identically to the cells and all measurements were performed under ambient conditions. AFM images were obtained in the taping model using an SPA400 SPM (Seiko Instrument Inc.). The cross-section images of samples were observed using SEM (SIRION, FEI, USA). PL and polarized PL spectra were obtained using a Spectrometer FLS920 equipped with excitation and emission polarizers. The absorption spectra were recorded on a UV-3100 spectrophotometer (Shimadzu, Japan).

3. Results and discussion

A typical cell structure (from bottom to top, shown in Fig. 1a) is described as ITO/PEDOT:PSS (60 nm)/NPB (or TPD) (10 nm)/DCM (10 nm)/C_{60} (50 nm)/BCP (10 nm)/Al (80 nm) (here ITO, PEDOT:PSS, BCP and TPD denote indium tin oxide, poly(3,4-ethylenedioxythiophene):poly(styrenesulfonate), bathocuproine and *N*,*N*′-diphenyl-*N*,*N*′-di(m-tdyl)benzidine, respectively. BCP serves as an exciton-blocking layer [5]). A proposed energy level scheme is shown in Fig. 1b, where the highest occupied molecular orbital levels are measured by cyclic voltammetry. The band gap energies are estimated from optical absorption edge of each material (Table S1). Here, the energy levels of the materials measured under the same condition are not absolute values but on trend in the energy diagram.

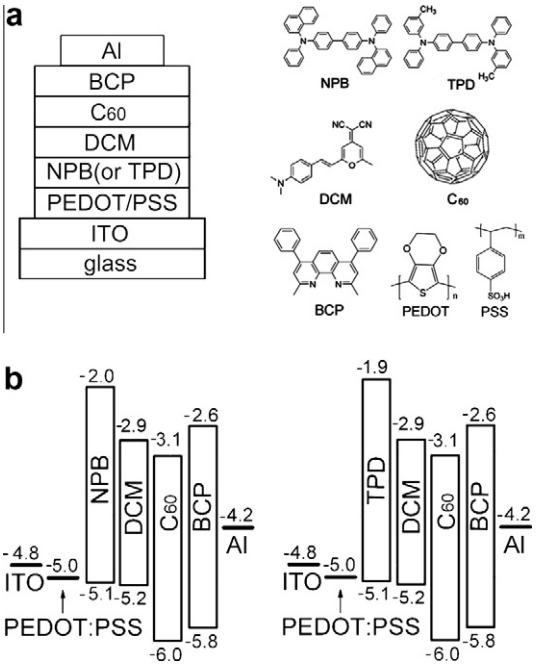

Fig. 1. Illustration of solar cell structure and energy level. (a) (Left) Illustration of a heterojunction cell with ITO/PEDOT:PSS/NPB (or TPD)/DCM/C_{60}/BCP/Al structure. (Right) The chemical structure of materials used in this work. (b) Energy level diagram for NPB (or TPD)/DCM/C_{60} cells assembly as determined by cyclic voltammetry.

Fig. 2a and b show the *J*–*V* characteristics of the NPB/DCM/C_{60} and TPD/DCM/C_{60} cell, respectively. The NPB/DCM/C_{60} cell (DCM thickness = 10 nm) annealing at 160 °C shows an open-circuit voltage (V_{oc}) of 0.75 V, a short-circuit current density (J_{sc}) of 4.62 mA cm^{-2}, a fill factor (*FF*) of 48.4%, and a power conversion efficiency (η) of 1.68% under AM 1.5, 100 mW cm^{-2} simulated solar light (Fig. 2a). The cell efficiency is higher or comparable to OSCs based on the similar materials TPA–DCM–TPA or DADP reported by other groups (0.79% and 1.5%, respectively) [10,11]. At the same condition, control sample of NPB/C_{60} (without DCM layer) shows slightly higher V_{oc} (0.86 V) but much decreased J_{sc} (2.47 mA cm^{-2}) and efficiency (0.81%). It was reported that OSCs made of α-NPD (NPB) or TPD layers in combination with C_{60} showed a large open-circuit voltage (>0.8 V) and maximum cell efficiency of about 1% [3,13]. This indicates that the incorporation of DCM is essential for improving the cell efficiency from 0.81% to 1.68%. In our cells, *J*–*V* curves from a comparative study demonstrate that annealing process has a favorable effect on the V_{oc} and fill factor (Fig. S1). The enhanced cell performance is most likely attributed to the improvement of carrier mobility in the organic layers [14,15].

Compared with the NPB/DCM/C_{60} structure, the TPD/DCM/C_{60} cell (DCM thickness = 10 nm) annealing at 140 °C shows significantly reduced V_{oc} (0.25 V) and

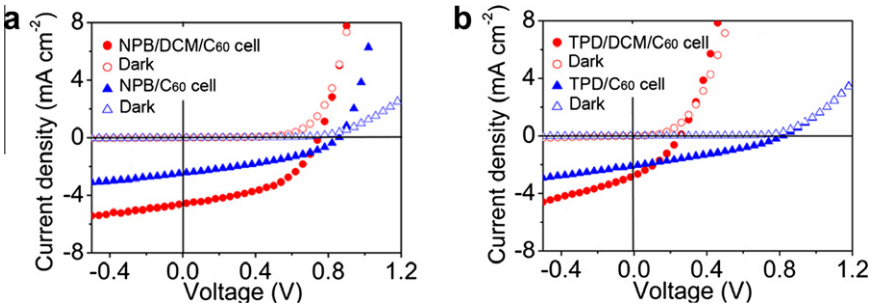

Fig. 2. *J–V* characteristics of solar cells. Dark (open) and photo (solid) current density–voltage characteristics of (a) the NPB/C_{60} cell (up triangle) and NPB/DCM (10 nm)/C_{60} cell (circle), and (b) TPD/C_{60} cell (up triangle) and TPD/DCM/C_{60} cell (circle).

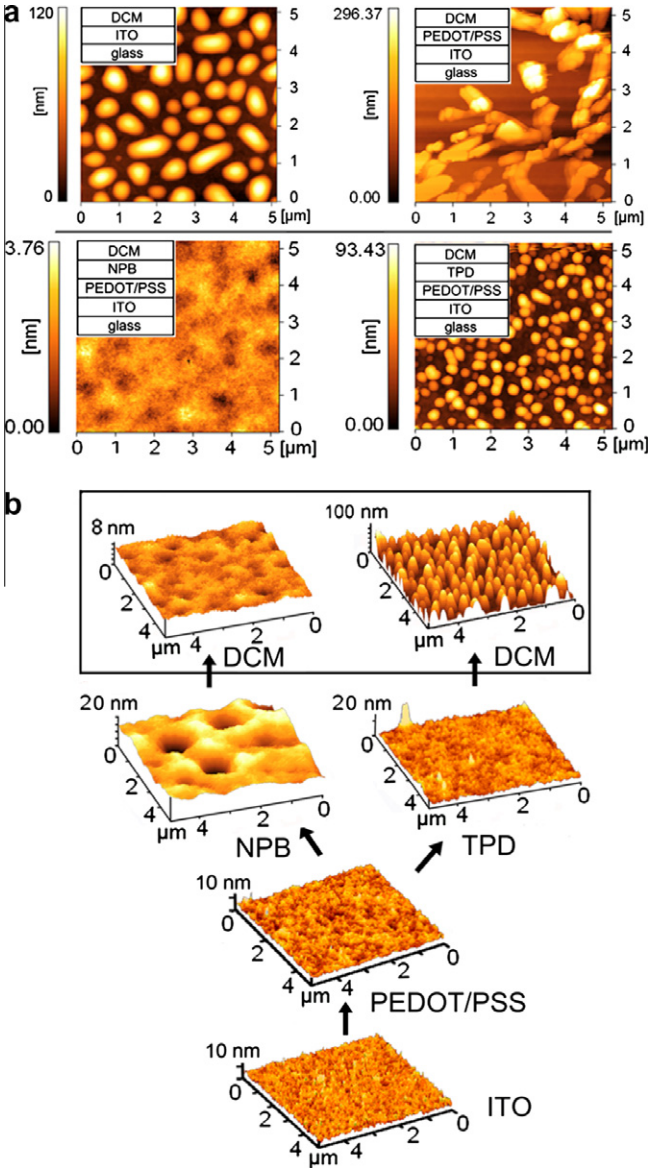

Fig. 3. Characterization of DCM film morphology. (a) Illustration of multi-layer film deposition where DCM was vacuum evaporated onto ITO/glass substrates with various pre-deposited organic layers, including bare ITO and PEDOT:PSS (top panel), NPB and TPD (bottom panel), and AFM images of the corresponding DCM film morphology. (b) AFM characterization and film roughness of each layer from the ITO to the DCM layer: ITO (roughness ~8.0 nm rms), PEDOT/PSS (roughness ~6.9 nm rms), NPB (roughness ~15.0 nm rms), TPD (roughness ~11.2 nm rms), DCM (on NPB layer, roughness ~10.1 nm rms), DCM (on TPD layer, roughness ~93.4 nm rms). AFM image scans are 5 × 5 μm.

efficiency (0.24%) (Fig. 2b and Table S2). It is known that V_{oc} strongly depends on HOMO–LUMO offset between donor and acceptor materials [16]. Since NPB and TPD only has slight difference in their energy levels, the energy band diagrams (Fig. 1b) of NPB/DCM/C_{60} and TPD/DCM/C_{60} heterojunctions indicate that both configurations are favorable for exciton dissociation and transport to outer electrodes in theory. In other words, there is no significantly different between TPD/DCM/C_{60} and NPB/DCM/C_{60} heterojunctions in their energy levels, which means there are other reasons leading to the different results. In practice the morphology of active layers and their interface are important factors because processes such as exciton transport and dissociation occur at these sites in a heterojunction cell structure [14].

We characterized the morphology of DCM deposited on substrates with different pre-deposited layers. Atomic force microscopy (AFM) images show that the layer and interface morphology of DCM is strongly influenced by the underlying substrate, and can be tuned from separated small islands to a uniform thin film by introducing an NPB layer. DCM molecules directly deposited on ITO or PEDOT:PSS substrates aggregate into microscale islands with irregular shapes, which is undesirable for subsequent device fabrication (Fig. 3a, top panel). A DCM layer deposited on TPD pre-deposited on PEDOT:PSS/ITO still shows island-like morphology, with considerable surface roughness of 100 nm. In contrast, deposition of DCM on NPB pre-deposited on PEDOT:PSS/ITO resulted in a smooth layer with a surface roughness of <10 nm (Fig. 3a, bottom panel and Fig. 3b). The surface morphology of DCM films largely depends on the wettability of the underlying layer to DCM molecules. These wetting process are determined by many factors related to the hydrophilic–hydrophobic property of materials (Table S3) at the macroscale (larger than 1 μm) and the long range force (e.g. van der Waals force) at the microscopic level (from 3 nm to 1 μm) [17].

We also characterized the interface morphology between active layers by means of scanning electron microscopy (SEM) and atomic force microscopy (AFM). The cross-section of the NPB/DCM/C_{60} cell shows a compact structure that is efficient for carrier transport and collection

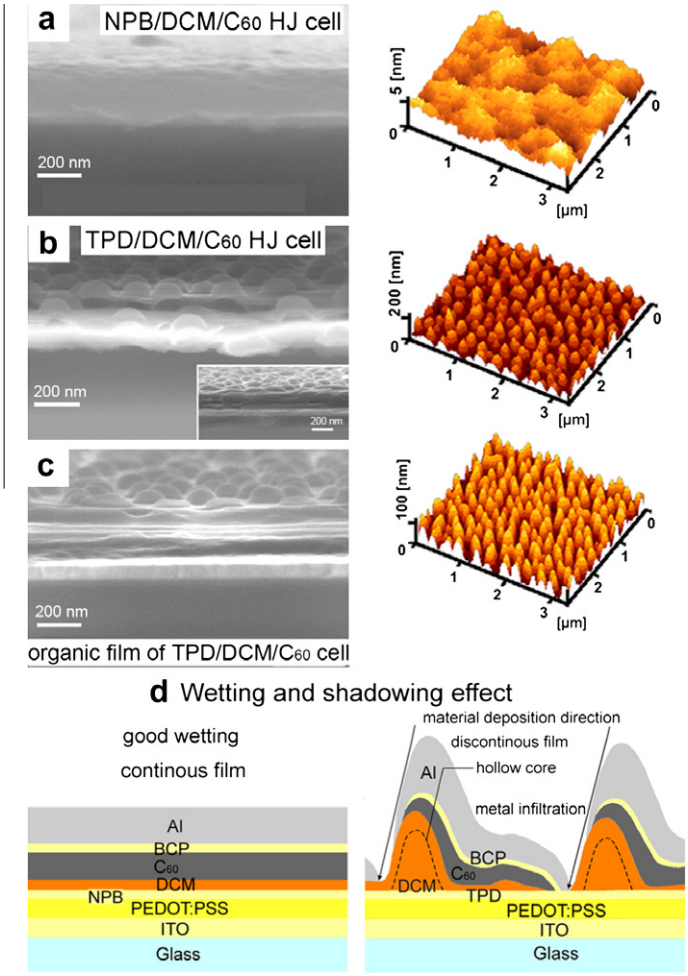

Fig. 4. Interface morphology of solar cells. Cross-sectional SEM and the film surface AFM images of (a) the ITO/PEDOT:PSS/NPB/DCM/C_{60}/BCP/Al cell, (b) the TPD/DCM (10 nm)/C_{60} cell after and (c) before Al electrode deposition. (d) Illustrations of the interface structure of the NPB/DCM/C_{60} cell with continuous and uniform layers (left), and the TPD/DCM/C_{60} cell with discontinuous layers and penetration of Al electrode due to shadowing effect (right).

(Fig. 4a). In contrast, the TPD/DCM/C_{60} cell shows an uneven layer interface with many structural defects like encapsulated hollow spheres. The formation of these defects can have significant influence on cell performance. First, the shadowing effect [18] can give a reasonable explanation for the lower V_{oc} of the TPD/DCM/C_{60} cells. The DCM film deposited on the TPD substrate shows an "island-like" morphology with a roughness of about 100 nm. After deposition of a 50 nm thick C_{60} layer and 10 nm thick BCP layer, the surface roughness is still about 100 nm (Fig. 4c). The DCM islands were too high to be completely covered by the subsequent organic layers, therefore cannot form a continuous layer to prevent penetration of Al electrode into the bottom organic layers. Fig. 4b shows that the surface roughness increased to 200 nm after depositing 80 nm Al as the top electrode. The shadowing of the high DCM islands could cause nonuniform organic layer deposition, and in some areas (e.g. around the islands) the organic layer might be very thin. In this case Al electrode could easily penetrate into deeper layers (even contact ITO/PEDOT:PSS anode), as illustrated in Fig. 4d, thus promote charge recombination in the organic layers and result in shortage of current and decrease of V_{oc}.

Although the TPD/DCM/C_{60} cell has a relatively large interface area similar to the bulk-heterojunction solar cells [6] the presence of structural defects is detrimental for exciton dissociation. In comparison, the results show that a smooth, continuous DCM film deposited on NPB is important for high performance of the heterojunction cells.

In addition to the layer morphology, the thickness of DCM film also determines the cell performance. Systematic study on the NPB/DCM/C_{60} cell with a DCM thickness in the range of 0–20 nm shows that the cell efficiency reaches maximum value (1.68%) at a DCM thickness of 10 nm (Fig. 5a). The increase of efficiency is accompanied by simultaneous increase of J_{sc} and *FF* due to improved light absorption and more exciton generation. The hole mobility of DCM derivatives is around 10^{-6}–10^{-5} $cm^2\,V^{-1}\,s^{-1}$ [10,11]. The highest *FF* is achieved through control of DCM layer thickness so that the low hole mobility does not significantly impact the cell performance. However, the cell efficiency drops monotonically from 1.68% down to <0.7% with increasing film thickness from 10 to 20 nm, indicating that the DCM thickness is limited to 10 nm therefore a film thicker than that is not favorable for good charge transport. At the same time, V_{oc} shows little change with DCM thickness in the range of 5–15 nm, since the HOMO–LUMO offset of DCM/C_{60} is similar to that of NPB/C_{60} heterojunction.

For the TPD/DCM/C_{60} cell in which the active layers formed islands during deposition, the efficiency–thickness relationship is very different compared with the NPB/DCM/C_{60} cell with smooth layers. There is no optimized layer thickness for maximum cell efficiency as V_{oc} drops significantly from 0.8 V to below 0.4 V when the thickness of DCM increases to >5 nm, and the cell efficiency drops to only 0.24% at a DCM thickness of 10 nm (Fig. 5b). In comparison, a uniform 10 nm DCM layer in the NPB/DCM/C_{60} cell has improved the efficiency by 2-fold (Fig. 5a).

The optimized DCM layer morphology and thickness (10 nm) suggests that incorporating DCM with appropriate structure is helpful for achieving maximum efficiencies in energy conversion processes such as photon absorption, exciton diffusion, and carrier collection. Such processes in both NPB/DCM/C_{60} and TPD/DCM/C_{60} cells have also been studied by the absorption and photoluminescence spectrum.

First, we show that the combination of a DCM and NPB (or TPD) layer has extended the photo absorption to UV and visible region (Fig. 6a). Without DCM, NPB or TPD

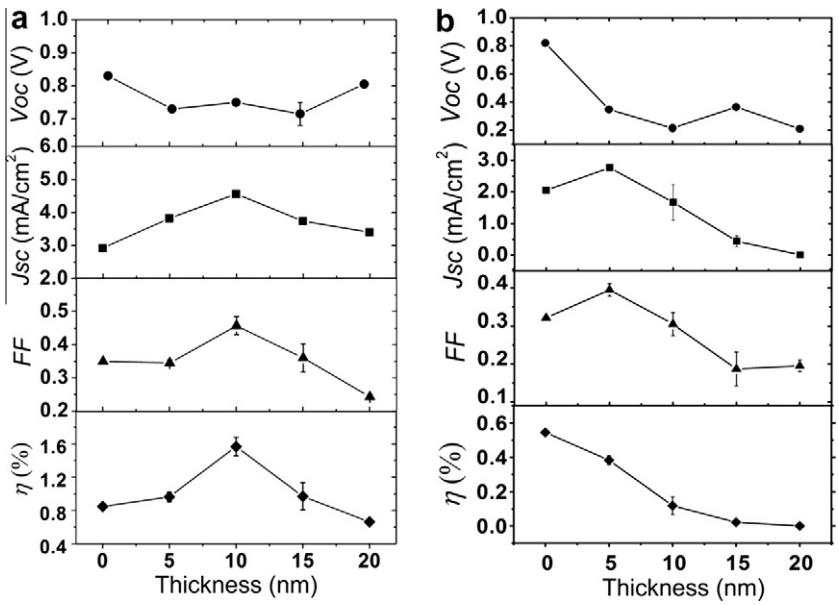

Fig. 5. Effect of DCM thickness on PV performance. (a) Photovoltaic response (e.g. V_{oc}, I_{sc}, *FF* and η, respectively) of the NPB/DCM/C_{60} cell with varying DCM thickness from 0 to 20 nm. (d) Photovoltaic response of the TPD/DCM/C_{60} cell with varying DCM thickness.

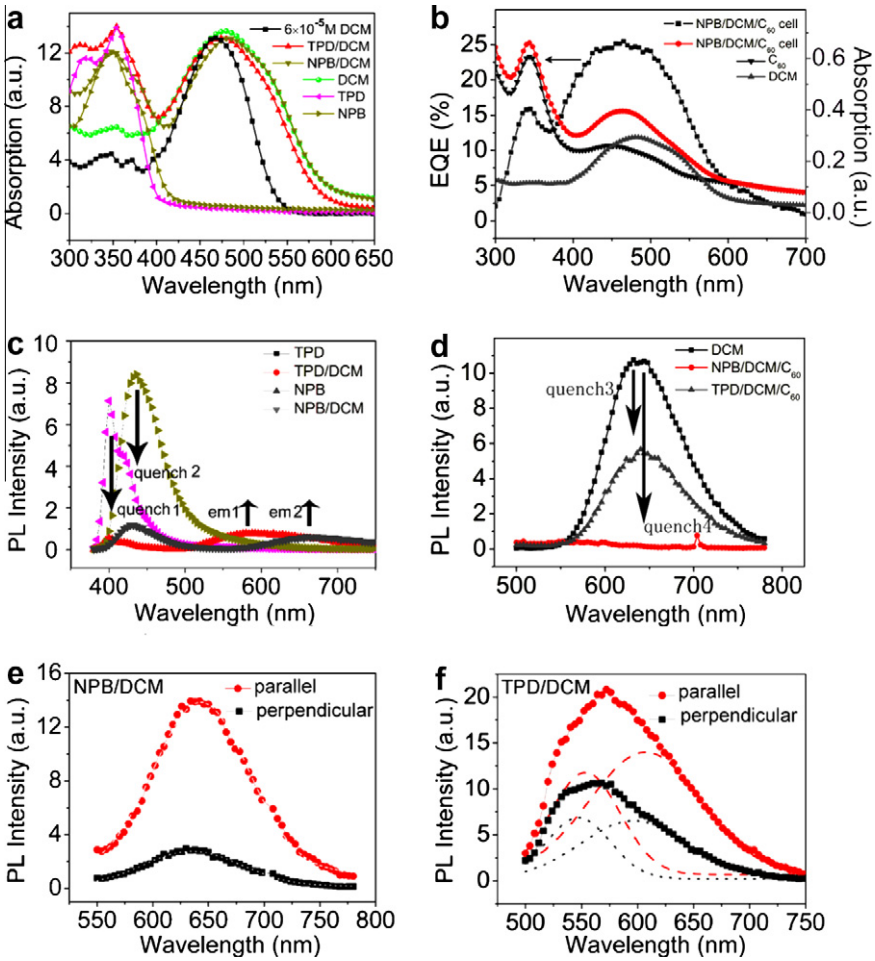

Fig. 6. Absorption and photoluminescence characterization. (a) UV absorption spectra of DCM, TPD, NPB, TPD/DCM and NPB/DCM films on ITO and 6×10^{-5} M DCM solution in CH_2Cl_2. (b) External quantum efficiency (EQE) spectrum and absorption spectra of NPB/DCM/C_{60} cell, C_{60} and DCM films. (c) PL spectra of NPB, TPD, NPB/DCM and TPD/DCM films on the ITO/PEDOT:PSS substrates (λ_{ex} = 352 nm). (d) PL spectra of DCM, NPB/DCM/C_{60} and TPD/DCM/C_{60} films (λ_{ex} = 467 nm). Polarized PL spectra for DCM deposited on (e) NPB, (f) TPD films, respectively, in parallel and perpendicular to the substrate under 352 nm polarized excitation, in which the parallel (dash lines) and perpendicular (dot lines) emissions were both fit with Gaussian. (The thicknesses of NPB, TPD, DCM and C_{60} are 10, 10, 10 and 50 nm, respectively.)

layers show little absorption in the range of 400–600 nm. Second, the order and interaction of DCM molecules in the film could be inferred from the absorption peak positions. In a diluted CH_2Cl_2 solution (6×10^{-5} M), DCM monomers show a relatively narrow absorption peak centered at λ_{max} = 468 nm (Fig. 6a). For DCM (islands) deposited on ITO substrate by vacuum evaporation, the absorption spectrum was broadened and red-shifted about 10 nm, indicating the formation of *J* aggregates [19]. Since the absorption band of TPD/DCM is slightly broadened on the blue-side compared with the NPB/DCM film, the DCM intermolecular interactions in these two films could be different, which is also verified by the PL spectra. The external quantum efficiency (EQE) of the NPB/DCM/C_{60} cell is shown in Fig. 6b followed absorptions of the cell and constituent photoactive materials with the photocurrent contribution from C_{60} generated between $320 < \lambda < 550$ nm, while DCM layer contributes from $400 < \lambda < 600$ nm.

Fig. 6c shows the emission spectra of the TPD and NPB films with maxima at λ_{max} = 400 nm and λ_{max} = 436 nm, respectively, under excitation at 352 nm. After depositing 10 nm DCM, the emission maxima of the TPD/DCM and NPB/DCM layer were mostly quenched. Since there is an overlap between the emission band of TPD (or NPB) and the absorption band of DCM, the energy transfer occurred from TPD (or NPB) to DCM via the Förster mechanism is responsible for the quenching of emission [20]. At the same time, new emissions originating from the DCM layer with maximum at λ_{max} = 586 nm (for TPD/DCM) and λ_{max} = 671 nm (for NPB/DCM) were observed. The emission maximum of the NPB/DCM film at λ_{max} = 671 nm was close to that of DCM crystal at λ_{max} = 693 nm [19] and red-shifted by ca. 100 nm compared with that of DCM in CH_2Cl_2 solution (λ_{max} = 582 nm). It is suggested that the intermolecular force of DCM in NPB/DCM films is high, close to the force in the crystal of DCM. On the other hand, the

emission band of the TPD/DCM film is very broad, overlapping both the band of DCM in CH_2Cl_2 solution and that of the NPB/DCM film, which means that the DCM molecules existed in the form of both monomers and aggregates after deposition on TPD. The emission from excited DCM layers was thoroughly quenched by the C_{60} layer in the NPB/DCM/C_{60} cell indicating an electron donating and accepting process occurred across their interface (Fig. 6d). While the emission of DCM was only half quenched in the TPD/DCM/C_{60} cell, since DCM layer is too rough (roughness around 100 nm) to be completely covered by C_{60} in the TPD/DCM/C_{60} cell (Figs. 3a and 6d).

Fig. 6e and f show polarized PL spectra for NPB/DCM and TPD/DCM films, respectively, excited at 352 nm. For the NPB/DCM film, both emission peaks in parallel and perpendicular polarization could be fitted with one Gaussian peak (around 634 nm) (Fig. 6e). The polarization ratio (parallel to perpendicular) was estimated to be 5.0, and the molecular order degree (R) was estimated to be 0.57 (see Table S4). These values suggest that most DCM molecules deposited on the NPB surface packed in an order form. However, the polarized emission peaks from TPD/DCM film are broad and can be fitted with two Gaussians centered at 553 and 607 nm, respectively, with smaller polarization ratios (1.7 and 2.1) and molecular order degrees (0.19 and 0.27). This result indicates a disorder form of DCM molecules on the TPD surface without obvious polarization. It can be seen that increasing order (alignment) of DCM molecules would cause their PL emission more red-shifted. The alignment of DCM molecules allows fast exciton diffusion to the interface through the ordered pathway, and also can significantly influence the optical and electrical properties of the devices [21].

4. Conclusions

To summarize, we demonstrated the application of a classical small molecule D-π-A material, DCM, in making heterojunction OSCs. Combined with appropriate underlying p-type layers, the cell efficiencies reach 1.68% due to extended solar spectrum coverage and improved exciton dissociation and transport path. We show that in the design and fabrication of OSCs, a smooth morphology of active layers and their interface is important for preventing device short-circuiting and achieving higher efficiencies. Simple small molecules such as DCM therefore are promising materials to make inexpensive OSCs.

Acknowledgements

This work was supported by The National Basic Research Program (2006CB601103) and NNSFC (50772003, 90922004, and 20821091). The authors wish to express their sincerely thanks to Prof. Anyuan Cao (Department of Advanced Materials and Nanotechnology, College of Engineering, Peking University) for helpful discussions and suggestions.

Appendix A. Supplementary data

Supplementary data associated with this article can be found, in the online version, at doi:10.1016/j.orgel.2010.09.006.

References

[1] C.W. Tang, Appl. Phys. Lett. 48 (1986) 183.
[2] F. Yang, S.R. Forrest, ACS Nano 2 (2008) 1022.
[3] G.P. Kushto, W.H. Kim, Z.H. Kafafi, Appl. Phys. Lett. 86 (2005) 093502.
[4] Q.L. Song, M.L. Wang, E.G. Obbard, X.Y. Sun, X.M. Ding, X.Y. Hou, C.M. Li, Appl. Phys. Lett. 89 (2006) 251118.
[5] P. Peumans, V. Bulovic, S.R. Forrest, Appl. Phys. Lett. 76 (2000) 2650.
[6] F. Yang, M. Shtein, S.R. Forrest, Nat. Mater. 4 (2005) 37.
[7] J.Y. Lee, S.T. Connor, Y. Cui, P. Peumans, Nano Lett. 10 (2010) 1276.
[8] P.F. Xia, X.J. Feng, J.P. Lu, S.W. Tsang, R. Movileanu, Y. Tao, M.S. Wong, Adv. Mater. 20 (2008) 4810.
[9] K. Schulze, C. Uhrich, R. Schuppel, K. Leo, M. Pfeiffer, E. Brier, E. Reinold, P. Bauerle, Adv. Mater. 18 (2006) 2872.
[10] C. He, Q.G. He, X.D. Yang, G.L. Wu, C.H. Yang, F.L. Bai, Z.G. Shuai, L.X. Wang, Y.F. Li, J. Phys. Chem. C 111 (2007) 8661.
[11] L.L. Xue, J.T. He, X. Gu, Z.F. Yang, B. Xu, W.J. Tian, J. Phys. Chem. C 113 (2009) 12911.
[12] M. Meyer, J.C. Mialocq, B. Perly, J. Phys. Chem. 94 (1990) 98.
[13] T. Osasa, S. Yamamoto, M. Matsumura, Adv. Funct. Mater. 17 (2007) 2937.
[14] P. Peumans, S. Uchida, S.R. Forrest, Nature 425 (2003) 158.
[15] Y. Shao, S. Sista, C.W. Chu, D. Sievers, Y. Yang, Appl. Phys. Lett. 90 (2007) 103501.
[16] B.A. Gregg, MRS Bull. 30 (2005) 20.
[17] P.G. Degennes, Rev. Mod. Phys. 57 (1985) 827.
[18] F. Yang, M. Shtein, S.R. Forrest, J. Appl. Phys. 98 (2005) 014906.
[19] H. Tong, Y. Dong, M. Haussler, Y. Hong, J.W.Y. Lam, H.H.Y. Sung, I.D. Williams, H.S. Kwok, B.Z. Tang, Chem. Phys. Lett. 428 (2006) 326.
[20] A.D. Peng, D.B. Xiao, Y. Ma, W.S. Yang, J.N. Yao, Adv. Mater. 17 (2005) 2070.
[21] M. Misaki, Y. Ueda, S. Nagamatsu, M. Chikamatsu, Y. Yoshida, N. Tanigaki, K. Yase, Appl. Phys. Lett. 87 (2005) 243503.

Organic Electronics 11 (2010) 1916–1919

Contents lists available at ScienceDirect

Organic Electronics

journal homepage: www.elsevier.com/locate/orgel

Letter

Quantifying angular color stability of organic light-emitting diodes

Alexander Isphording *, Manfred Pralle

Philips Technologie GmbH, Business Center OLED Lighting, Philipsstr. 8, 52068 Aachen, Germany

ARTICLE INFO

Article history:
Received 14 June 2010
Received in revised form 30 August 2010
Accepted 30 August 2010
Available online 15 September 2010

Keywords:
OLED
Chromaticity
Angle
Color stability

ABSTRACT

We show the need for a quantity that describes the angular dependence of the chromaticity emitted from organic light-emitting diodes (OLEDs), present different quantities that may be suitable for describing this color stability and compare these quantities to ratings obtained from a perception test to determine which quantity correlates most strongly with the observer ratings.

© 2010 Elsevier B.V. All rights reserved.

1. Introduction

In the past years, organic light-emitting diodes have undergone significant development towards becoming a new generation of light source for general illumination. Not only are monochromatic OLEDs available, white OLEDs are also starting to enter the markets [1]. Due to the completely novel nature of these two-dimensional light sources, some challenges that are not present in previous luminaires must still be overcome. One such challenge is the angular dependence of the chromaticity. This angular dependence is especially prevalent in microcavity OLEDs [2], but also significantly distracting in white non-microcavity OLEDs.

Before attempting to reduce the angular color dependence, a quantity is required that successfully describes how strong the angular dependence is. While quantities like a shift in the peak wavelength [2,3] can be used for monochromatic OLEDs, this does not work well for white non-microcavity OLEDs where multiple emission-peaks are present that change their relative intensity but whose peak wavelengths do not shift significantly.

Because humans will ultimately decide whether the color shift is acceptable for use as a luminaire, the figure of merit against which color dependence must be judged should always be the color stability as perceived by a human observer. For this reason we have focused our research on finding a quantity that will successfully predict, from the measurement results, how a human observer judges the color stability with viewing angle of an OLED.

Several quantities that might describe the angular color stability well were identified. These quantities were calculated for a range of different color gradients (Fig. 1) and compared to observer ratings to determine which, if any, showed the best correlation.

2. Color difference

As stated above, the figure of merit must be the perceived color stability for a human observer. This means that color must be described in a suitable color space. David MacAdam showed that the CIE 1931 *xy* color space is not suited for comparing color differences [4] and it has been an ongoing effort to find a uniform color space that is perfectly equidistant with respect to perceived color difference. Albeit far from perfect, one such color space is the CIE (comission international de l'eclairage) 1976 $u'v'$ color space [5].

While still not perfectly uniform, it seems nonetheless justified to use the $u'v'$ color space because the OLEDs to be studied only exhibit a relatively small variation in color and OLEDs that are compared to each other will have a similar chromaticity (in the direction of the surface nor-

* Corresponding author.
E-mail address: alexander.isphording@rwth-aachen.de (A. Isphording).

1566-1199/$ - see front matter © 2010 Elsevier B.V. All rights reserved.
doi:10.1016/j.orgel.2010.08.022

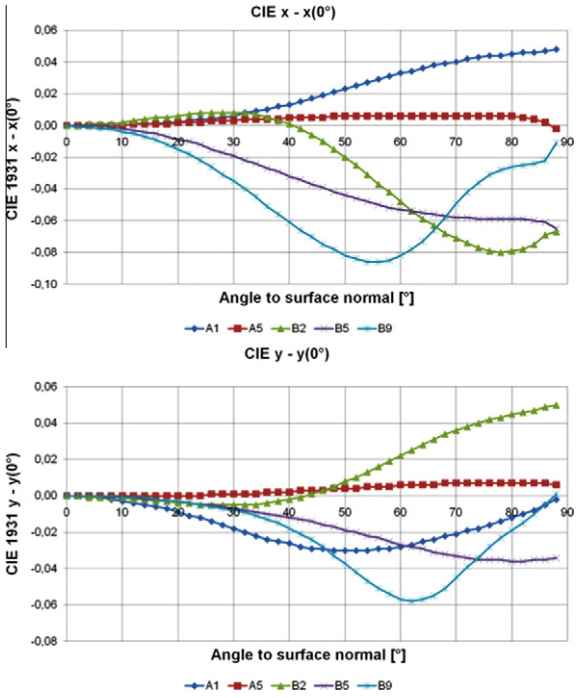

Fig. 1. Relative change of CIE x and y coordinates for selected samples. All samples had a chromaticity near color point A (≈ 0.44/0.40).

mal). Comparisons between OLEDs with similar color are, therefore, feasible with a color difference based on the CIE 1976 $u'v'$ color space.

Luminance changes with viewing angle are not taken into account in order to focus solely on the color. As OLEDs are (almost) Lambertian emitters, the luminance does not vary significantly with viewing angle, which allows for this simplification.

Color differences in a uniform color space, which the CIE $u'v'$ color space is assumed to be for our purposes, can simply be calculated as the Euclidean distance between two color points. This distance is calculated as

$$\Delta E_{i,j} = \sqrt{(\Delta u')^2 + (\Delta v')^2} \tag{1}$$

$$= \sqrt{\left(u'(\vartheta_i) - u'(\vartheta_j)\right)^2 + \left(v'(\vartheta_i) - v'(\vartheta_j)\right)^2} \tag{2}$$

where ϑ_i, ϑ_j denote the angles under which the chromaticity is measured with $i,j = 1,2,\ldots n$ and $0^\circ \leqslant \vartheta_i \leqslant 90^\circ$.

The color difference Eq. (2) can be used to describe the difference between two colors, for example an OLED under different viewing angles. It is not yet, however, suitable for judging the continuously changing color of an OLED viewed under varying angles. The color difference is, therefore, not the final solution for determining the color stability. Instead, it forms the basis for the following formulae that take into account the gradual change with viewing angle.

2.1. Maximum color difference

The maximum color difference is the largest value of ΔE that occurs between any two angles ϑ_i, ϑ_j and can be expressed as

$$CD_{max} = max(\Delta E_{i,j}). \tag{3}$$

2.2. Maximum color difference to vertical

Similarly, the maximum color difference to the color emitted in the direction of the surface normal can be calculated as

$$CD_{vert} = max(\Delta E_{1\,j}) \tag{4}$$

where $\vartheta_1 = 0^\circ$.

2.3. Average color difference to vertical

Rather than determining the maximum value of the color difference between the vertical direction and any angle, as calculated in Eq. (4), one can also calculate the average color difference to the vertically emitted color:

$$CD_{avg,vert} = \frac{1}{n-1}\sum_{j=2}^{n} \Delta E_{1,j}. \tag{5}$$

2.4. Average color difference between all angles

Similar to the average color difference to the vertical, an average color difference between all viewing angles ϑ_i, ϑ_j, $i \neq j$ can be calculated as

$$CD_{avg} = \sum_{1 \leqslant i \leqslant n} \sum_{i < j \leqslant n} \frac{\Delta E_{i,j}}{\frac{n(n+1)}{2} - n}. \tag{6}$$

2.5. Maximum rate of change

The previous concepts have focused on the absolute values of color difference only. An aspect that can also influence perceived color stability is the rate at which a color changes. The rate of color change might, therefore, also give an indication of the perceived color stability. The maximum rate of change is defined as

$$ROC_{max} = max\left(\frac{\Delta E_{i-1,i}}{\vartheta_i - \vartheta_{i-1}}\right). \tag{7}$$

2.6. Average rate of change

As the maximum rate of change might be high, even if only a small but very rapid color change is present, a more relevant quantity could be the average rate of change

$$ROC_{avg} = \frac{1}{n-1}\sum_{i=2}^{n} \frac{\Delta E_{i-1,i}}{\vartheta_i - \vartheta_{i-1}}. \tag{8}$$

2.7. Average rate of change between angles with maximum color difference

As a last quantity that might describe the perceived color stability well, we have identified the average rate of change between the angles with maximum color difference. The angles with maximum color difference are the angles ϑ_i, ϑ_j for which Eq. (3) yields the maximum. The average rate of change between these angles is

$$ROC = \frac{\Delta E_{ij}}{|\vartheta_i - \vartheta_j|}. \quad (9)$$

To determine which of these formulae is best suited for describing the perceived color stability, a perception test was carried out.

3. Perception test

A number of participants were shown different OLEDs with different color gradients (Fig. 1) at a luminance of 1000 cd/m^2. These OLEDs were attached to a goniometer and could be viewed under angles between 0° and 90°. Participants were free to adjust the angle as they desired. The participants were first shown the worst (i.e. with the largest angular color dependence) sample that would be used during the test. They were then asked to judge the following samples on a scale from 1 (good, no visible color change) to 6 (bad). They were only told to pay attention to the color change, but were otherwise not pointed to any details (i.e. rate of change, range of colors etc.). The group of participants consisted of men and women and people with and without experience in judging colors and working with OLEDs. The test was later repeated with a different set of OLEDs with different (more noticeable) color gradients and a different group of participants.

A repeatability and reproducibility study was carried out to judge how suitable this test is. The difference between a first and second rating of an OLED by the same observer was, on average, lower than 0.5, which is acceptable for such a visual perception test. As for the reproducibility, a difference was observed between different observers, as also expressed by the standard deviation on the average ratings. However, most participants put the OLEDs in the same order and only the absolute values of the ratings differed. This error is minimized by averaging over a large number of observer ratings.

4. Results

The participant ratings and calculated results are given in Tables 1 and 2. A scatter plot of CD_{avg} versus participant rating is shown in Fig. 2. A linear fit is applied to the data and the coefficient of determination, R^2, is used to judge how well the formula compares to the observer ratings. The results for all formulae are summarized in Table 3. The threshold for R^2, above which the correlation is statistically significant, is 0.36 for eight samples and a significance level of 95%.

From these results it is clear that ROC_{max} shows no or very little correlation with the perceived color stability. This is to be expected, because a very small color change that happens rapidly will significantly affect this quantity but will be hardly noticed by a human observer. ROC and ROC_{avg} must also be eliminated as quantities to describe the color instability of an OLED because the correlation with the ratings was weak on at least one test. CD_{vert} and CD_{avg}, on the other hand, are more promising quantities and CD_{max} and $CD_{avg,vert}$ can also not be ignored completely. From these findings it is suggested that CD_{avg} is used as a measure for OLED color instability. This quantity can be

Table 1
Calculated color instabilities and ratings for the different samples of test A.

	A1	A2	A3	A4	A5	A6	A7	A8
Rating	4.37	2.84	2.76	4.71	1.59	3.87	1.52	2.05
σ	0.67	0.84	1.08	0.91	0.62	0.92	0.60	0.70
$CD_{max} \cdot 10^2$	3.20	1.02	1.03	2.72	0.57	1.87	0.63	0.85
$CD_{vert} \cdot 10^2$	3.20	1.02	0.76	2.72	0.39	1.26	0.42	0.72
$CD_{avg,vert} \cdot 10^2$	1.89	0.60	0.30	1.66	0.23	0.55	0.28	0.46
$CD_{avg} \cdot 10^2$	1.53	0.52	0.37	1.24	0.20	0.72	0.25	0.41
$ROC_{max} \cdot 10^3$	1.00	0.48	1.13	0.92	1.11	1.70	1.11	0.81
$ROC_{avg} \cdot 10^3$	0.52	0.27	0.32	0.43	0.12	0.57	0.16	0.22
$ROC \cdot 10^3$	0.43	0.21	0.57	0.40	0.12	0.67	0.14	0.18

Table 2
Calculated color instabilities and ratings for the different samples of test B.

	B1	B2	B3	B4	B5	B6	B7	B8	B9
Rating	4.40	4.82	2.25	4.32	2.94	4.03	2.47	1.85	4.16
σ	1.04	0.92	1.03	1.10	0.71	1.29	0.76	0.91	1.12
$CD_{max} \cdot 10^2$	3.77	7.50	2.75	6.47	3.80	4.21	3.27	2.52	5.05
$CD_{vert} \cdot 10^2$	3.77	6.72	2.75	6.47	3.80	4.21	3.27	2.52	5.05
$CD_{avg,vert} \cdot 10^2$	2.23	2.58	1.34	2.99	1.99	2.56	1.77	1.14	2.43
$CD_{avg} \cdot 10^2$	1.73	3.23	1.03	2.86	1.56	1.86	1.36	0.88	2.20
$ROC_{max} \cdot 10^3$	1.30	2.55	1.35	1.79	1.52	1.36	2.29	1.35	3.06
$ROC_{avg} \cdot 10^3$	0.58	1.02	0.37	0.86	0.49	0.69	0.79	0.33	1.30
$ROC \cdot 10^3$	0.51	1.34	0.31	0.81	0.43	0.68	0.54	0.29	0.90

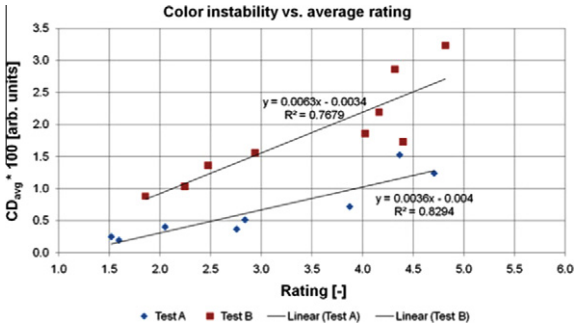

Fig. 2. Scatter plot of observer ratings versus CD_{avg}.

Table 3
Coefficients of determination R^2 for both tests.

	Test A	Test B
CD_{max}	0.88	0.69
CD_{vert}	0.81	0.71
$CD_{avg,vert}$	0.72	0.83
CD_{avg}	0.83	0.77
ROC_{max}	0.02	0.14
ROC_{avg}	0.83	0.47
ROC	0.47	0.65

used to compare different OLEDs to each other, characterize, for example, outcoupling structures, or serve as an optimization target for computer simulations.

It is also interesting to note that the quantities that performed worst were the ones that incorporated the rate of change in some way, indicating that the absolute color difference is more distracting to the human observer than the rate at which this change occurs.

To summarize these conclusions, the procedure for calculating the angular color stability of an OLED can be broken down into the following steps:

1. Measure the angle-dependent chromaticity of an OLED using a goniophotometer.
2. Ensure that color points are expressed in CIE 1976 $u'v'$ color space; convert measurement results if necessary. The $u'v'$ color space must be used as it is more equidistant with respect to perceived color difference than the widely used CIE 1931 xy color space.
3. Calculate color difference Eq. (2) for every pair of color points (with $i \neq j$) once.
4. Average over these color differences. This average value quantifies the angular color instability.

Steps three and four correspond to Eq. (6).

The following should be observed when using this procedure to rate OLEDs:

- Angular color instabilities of different OLEDs *should not* be compared if different measurement resolutions are used (e.g. color points measured every 2° or 5°). Higher resolutions yield more accurate results.
- Color instability *cannot* be compared for different angular ranges (e.g. measurements from 0° to 70° or 0° to 90°). Ideally, measurements should be conducted from 0° to 90° to cover all directions of emission.

5. Outlook

In the future, further perception tests must be performed before a definitive quantity for OLED color stability can be agreed upon. Once these tests have been carried out, it might also be worthwhile to look at combinations of the above formulae, like, for example, the product of the maximum color difference and a rate of change. The quantity that turns out to have the highest correlation with observer ratings should then be normalized to a range that is easier to handle and understand for people unfamiliar with the involved procedures.

6. Summary

In summary, we have explained why a quantity describing angular color stability of an OLED is required. We have compared several potentially suitable quantities to observer ratings of the color stability. From these results, the average color difference between all angles was determined to show the best agreement with the perceived color stability as rated by observers. Some other quantities may also be able to describe the color stability well although they performed slightly worse, while others can be eliminated completely.

Acknowledgement

The work leading to these results has received funding from the European Community's Seventh Framework Programme under grant agreement No. FP7-224122 (OLED100.eu).

References

[1] <http://www.lumiblade.com>.
[2] N. Tessler, S. Burns, H. Becker, R.H. Friend, Suppressed angular color dispersion in planar microcavities, Appl. Phys. Lett. 70 (1997) 556.
[3] W.C.H. Choy, C.Y. Ho, Improving the viewing angle properties of microcavity OLEDs by using dispersive gratings, Opt. Express 15 (2007) 13288.
[4] D.L. MacAdam, Visual sensitivities to color differences in daylight, J. Opt. Soc. Am. 32 (1942) 247.
[5] Y. Ohno, CIE Fundamentals for color measurements, in: IS&T NIP16 Conference, Vancouver, Canada, October 16–20, 2000.

Organic Electronics 11 (2010) 1920–1927

Contents lists available at ScienceDirect

Organic Electronics

journal homepage: www.elsevier.com/locate/orgel

Review

Effect of active layer thickness on the electrical characteristics of polymer thin film transistors

L. Reséndiz [a,*], M. Estrada [b], A. Cerdeira [b], B. Iñiguez [c], M.J. Deen [d]

[a] Sección de Estudios de Posgrado e Investigación, UPIITA – IPN, Av. IPN No. 2580, 07340, D.F., Mexico
[b] Sección de Electrónica del Estado Sólido, Departamento de Ingeniería Eléctrica, CINVESTAV, Av. IPN No. 2508, 07360, D.F., Mexico
[c] Departament dÉnginyeria Electronica Electrica i Automatica, Universitat Rovira i Virgili, Avda. Paisos Catalans 26, 43007 Tarragona, Spain
[d] Electrical and Computer Engineering Department (CRL 226) McMaster University, 1280 Main Street West, Hamilton, ON, Canada L8S 4K1

ARTICLE INFO

Article history:
Received 17 May 2010
Received in revised form 30 August 2010
Accepted 1 September 2010
Available online 16 September 2010

Keywords:
PTFT
P3HT
Thickness

ABSTRACT

In this paper, we analyze the variation of the threshold voltage V_T and carrier mobility μ_{fet} with the active layer thickness of polymer thin film transistors (PTFTs). The value of V_T was observed to become more negative as the active layer thickness decrease, while mobility slightly increased. Simulations obtained for different active layer thickness were first validated with experimental data from measured devices with known active layer thickness. Then using the calibrated simulator, it was found that as the semiconductor thickness decreased, the charge per square units in the active layer changes, establishing the cause of both of these behaviors.

© 2010 Elsevier B.V. All rights reserved.

1. Introduction

During the past decade, organic and polymeric materials have received increased attention from the research and industrial communities, particularly for application as electronic devices for low-cost, flexible, large-area displays. Among these devices, small molecules organic thin film transistors (OTFTs) already reached performance similar to amorphous silicon TFTs, especially OTFTs based on pentacene [1]. Polymeric TFTs (PTFTs) are also been intensively studied, with poly (3-hexyl-thiophene) (P3HT). P3HT has attracted considerable interest because it can be solution-processed and has been reported to show the highest reported field effect mobility, up to 0.1 $cm^2/V\,s$ [2–7].

It has been observed that the structure and ordering of the organic active layer has a great impact on the value of the mobility [3,6,8], which is related to the charge carrier transport mechanism. The increase in mobility with charge carrier concentration is described in many publications, for example in [9–11].

Another factor that may affect mobility is the interface between the dielectric and the semiconductor polymer, which is much related to the threshold voltage, V_T, as well as to its stability [12,13]. For the above reasons, the device current voltage characteristics and mobility are related to many factors, which include the characteristics of the active layer material, its interface with the dielectric, as well as details of the fabrication process [14] and the device structure [6–8].

Less attention, however, has been dedicated to the optimization of device geometry for a more efficient device operation, where the thickness of the active layer has been reported to affect in different ways device characteristics. In [15] the effect of the active layer thickness on-current–voltage characteristics for pentacene bottom gate and top drain and source contacts devices was studied. It was reported that drain current and mobility (determined from the square root of drain current vs. gate voltage curve) increased as active layer thickness t_S is reduced down to 16 nm. However, it was observed that the on/off-current ratio reduced with t_S, which they associated with an off-state leakage that was not clearly understood. On the other hand, the authors in [16] observed that the

* Corresponding author. Tel.: +52 55 572960000
E-mail address: lresendiz@ipn.mx (L. Reséndiz).

1566-1199/$ - see front matter © 2010 Elsevier B.V. All rights reserved.
doi:10.1016/j.orgel.2010.09.002

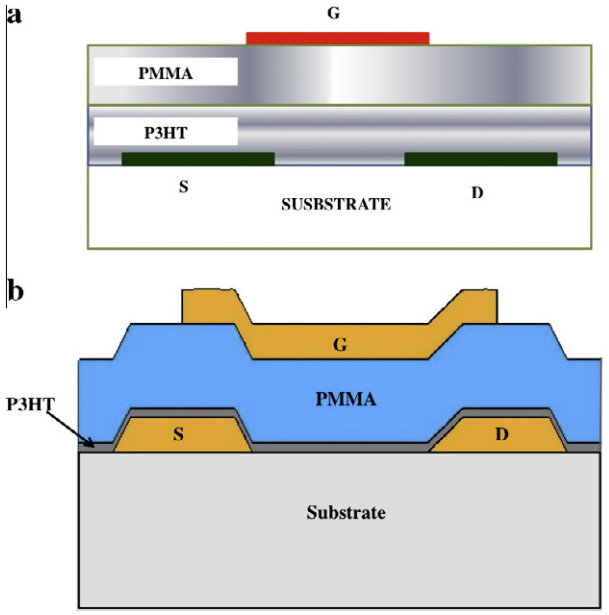

Fig. 1. Device structure of the P3HT-based PTFTs used in simulations. (a) Planar structure in ATLAS and (b) real structure in ATHENAS.

gate current decreased as pentacene thickness was reduced from 80 to 10 nm, which they found related to the presence of series resistance. Also, the thickness of the pentacene layer has been observed to affect device stability [17,18].

For polymer active layers, variation of drain current and mobility with active layer thickness was observed as early as 1988 [19], when quality of the P3HT and optimization of the fabrication processes were still in their infancy. Since then, much work has been done regarding PTFTs with different structures and materials. The effect of ambient conditions on the stability of PTFTs has been investigated [13,18]. More recently the dependence of organic thin film transistor characteristics with pentacene thickness was analyzed [20], they observed that the drain current increases at any drain voltage until a pentacene thickness of 35 nm, and then the current decreases; they show that in all the devices with varying pentacene thickness, most of the current flows through a very thin region, approximately 5 nm, near the dielectric surface.

In this work, we report and analyze the effect of the active layer thickness on the current voltage characteristics of top gate P3HT-based PTFTs. First, we validate results from a two-dimensional simulation in ATLAS [21] with measured characteristics of PTFTs fabricated with PMMA on P3HT, as reported in [4,5]. This was done to confirm the simulation, with the structure and input parameters to represent correctly the behavior of measured devices. With this calibration completed, simulation to study the effect of t_S on threshold voltage and mobility can be performed. The structure and geometrical input parameters were taken from measurements on fabricated devices. Other parameters were extracted using the procedure described in [22]. Since, as indicated above, the PTFT electrical characteristics depend on many technological parameters and conditions, and then using simulation allows for the separation of the effect of layer thickness from the effect of other factors (source/drain contact resistances, surface roughness, etc.) that may arise from processing conditions during the fabrication process, either intentionally or non-intentionally. Simulation also allows for fixing with precision the desired device dimensions. At the same time, simulation provides the means to determine charge carrier distribution, electric fields and other physical parameters for a given operating condition of the device, thus making it is possible to better understand the observed electrical behavior.

2. Experimental part

A schematic cross section of the TFTs under study is depicted in Fig. 1. Upper gate polymer TFTs were fabricated with a PMMA layer on top of a P3HT layer, both deposited by spin coating. Transistors with the following dimensions were fabricated, channel width W of 210, 150 and 110 mm and channel length L = 50 mm, L = 30 mm, L = 20 mm and 10 mm. The PTFTs with expected thickness of the P3HT layer of 80, 30 and 16 nm and the above dimensions, were fabricated. Details on their fabrication can be found in [4,5].

3. Simulation

For simulation, we have used the commercial device simulator ATLAS. The band gap for P3HT was taken as 1.8 eV as provided by supplier Sigma Aldrich. The dielectric constant of P3HT and PMMA was taken as 6.5 and 2.6, respectively, as obtained in [4]. The density of states *gdo* and the characteristic temperature T_o were extracted from

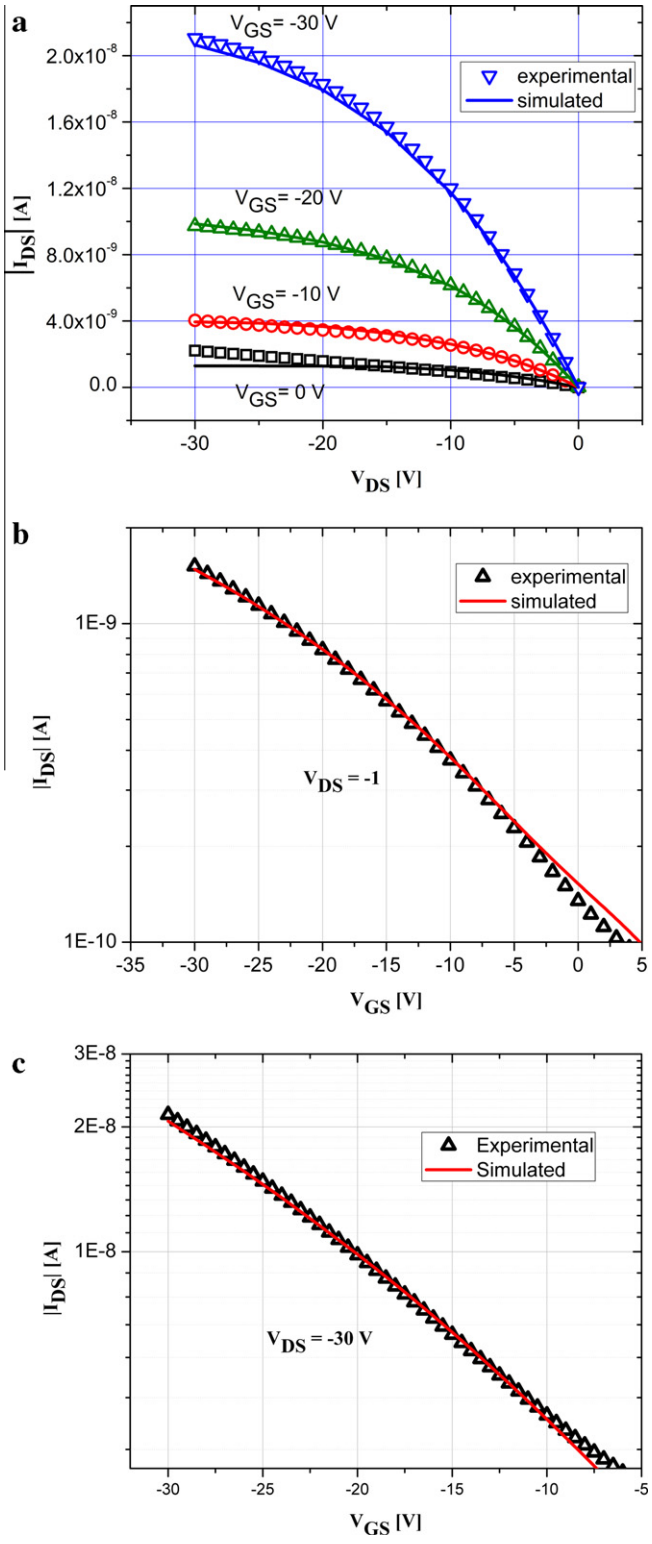

Fig. 2. (a) Output, (b) linear transfer and (c) saturation transfer characteristics for top gate PMMA on P3HT transistor, measured and simulated.

measurements following the procedure described in [22]. The P3HT film was considered non-intentionally doped *p*-type, with a concentration in the range of 5×10^{16} to 1×10^{17} cm^{-3}, as was determined in [22]. The effective density of states in the conduction band N_C and valence band N_V were both assumed to be 1×10^{21} cm^{-3}, which

is a typical value considered for organic materials. Simulations were done using a planar structure in ATLAS, where drain and source were located at the bottom and the gate on top, and also using the more real representation done in ATHENAS, as indicated in Fig. 1(a) and (b), respectively.

4. Results and discussion

Fig. 2 shows the good agreement obtained between simulated and measured characteristics, indicating that simulations, with the extracted parameters, can be used to study the effect of active layer thickness on the device parameters. It is worth to remark, that for this device, with active layer thickness of 80 nm, the I_{DS}–V_{DS} curve for V_{GS} = 0 V is the same as reported in [4], a drain current is present due to the conductivity of the P3HT layer between drain and source, which depends on the non-intentional doping of the P3HT layer.

The output characteristics of the TFTs with a P3HT active layer of 20, 30, 40, 80, 120 and 160 nm, simulated with the extracted parameters indicated above are shown in Fig. 3 for two gate voltages. In Fig. 3(a) can be observed that the drain current increases with the P3HT thickness, the same behavior was observed in [23,24], for P3HT film thickness below 200 nm.

Reducing the P3HT layers thickness can eliminate the drain current related to the conductivity of the unintentionally doped P3HT, Fig. 3(a). For 20 nm thickness there is no effect, while for 160 nm thickness, the effect is much more pronounced than the observed for 80 nm, this was also obtained experimentally in [23].

The transfer characteristics of the TFTs with a P3HT layer for the same thicknesses above were simulated with V_{DS} = −1 V and −30 V, Fig. 4. An important effect observed, that is also related with the unintentional doping of the P3HT layer, is that decreasing the active layer thickness, t_S, leads to a lower off-current.

The on/off ratio was calculated from the highest on-current and the lowest off-current from the transfer curve of the P3HT PTFTs (V_{GS} = + 7 to −30 V at V_{DS} = −30 V), Fig. 5.

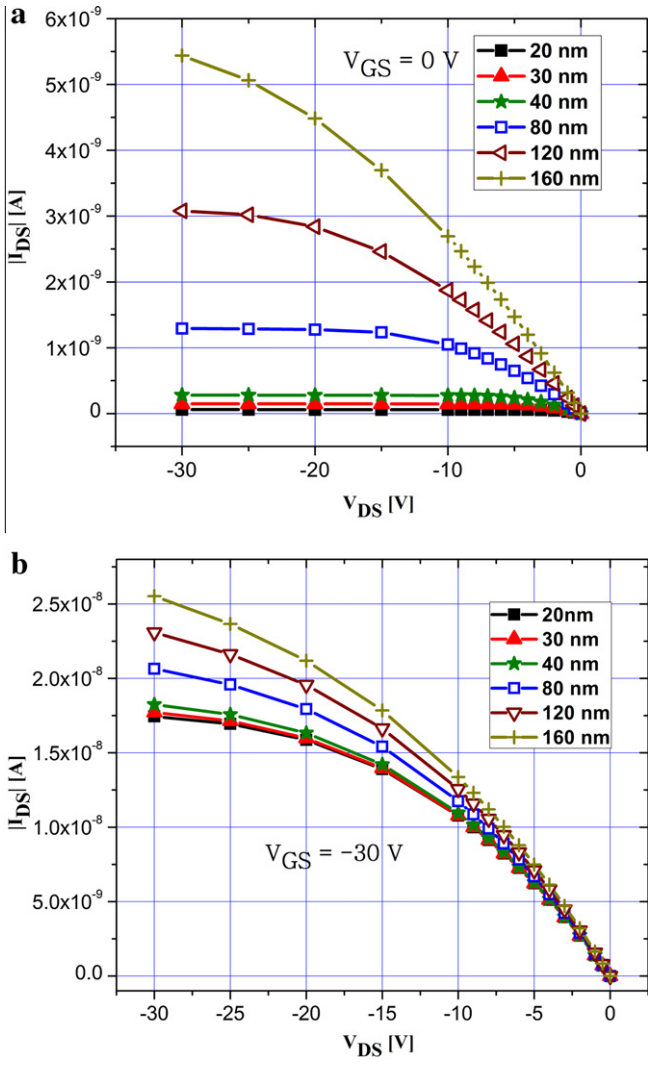

Fig. 3. Simulated output characteristic for the PTFT transistor (a) *VGS* = 0 V and (b) V_{GS} = −30 V.

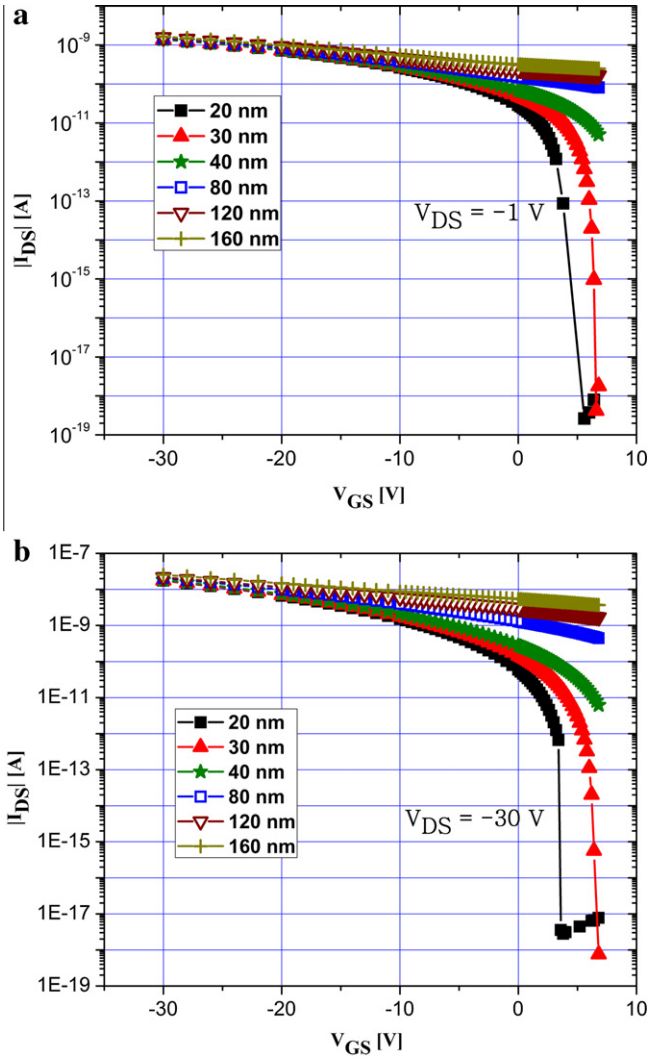

Fig. 4. Simulated transfer characteristics for PTFTs with various active layers thickness, (a) $V_{DS} = -1$ V and (b) $V_{DS} = -30$ V.

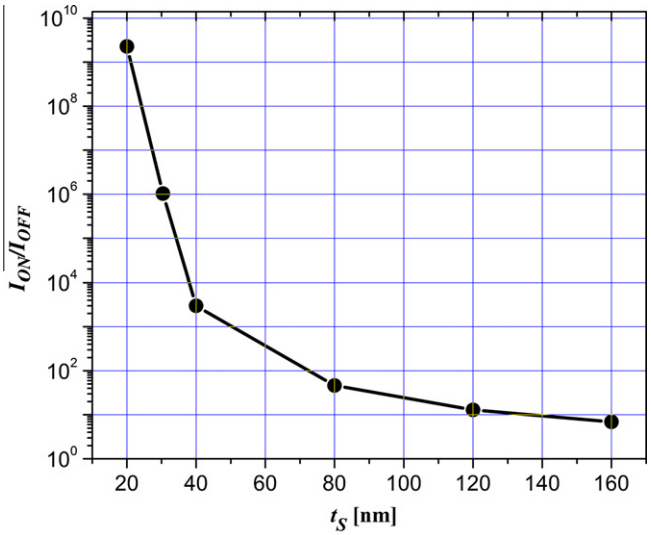

Fig. 5. P3HT film thickness dependence of on/off ratio in P3HT devices.

The devices with thicker films have lower on/off ratios. Since the on-current slightly increases, the reason for low on/off ratios is the faster increase of the off-current.

For the same operating conditions used to simulate the transfer and output characteristics, the charge per unit area in the active layer was analyzed, and the results are shown in Fig. 6. It was observed that for V_{GS} below V_T, active layers with thickness smaller than 40 nm are fully depleted, and for this reason, the off-current is low. For active layers with thickness greater than or equal to 80 nm, at some depth, the charge per unit area is high enough to provide current path between drain and source even for V_{GS} below V_T. As the active layer thickness increases, the part of the layer where current can flow increases, and so the off-current also increases.

In Fig. 4(a) and (b), it is seen that the on-current also increases as the thickness of the active layer increases, for same reason described above. At high values of V_{GS}, the active layer surface will be accumulated. The charge per unit area in the active layer in a plane near the drain, for $V_{GS} = -30$ V is shown in Fig. 7 as function of film depth.

For further analysis, we calculated the V_T for each active layer thickness using the procedure described in [22] and the simulated current–voltage curves. It can see in Fig. 8, there is a variation in the curvature of the $I_{DSsat}^{1/1+\gamma}$–V_{GS} profiles in the low V_{GS} region, suggesting that the deviation of the drain current from the potential law of V_{GS} has influence on the determination of the V_T values, and has been ascribed to a decrease in the field effect mobility at low V_{GS} values [25].

The variation of V_T with t_S is shown in Fig. 9, where V_T becomes more positive as t_S increases. As the semiconductor layer becomes thinner, the charge per square units decreases, so there is less charge to compensate, Fig. 6 [6].

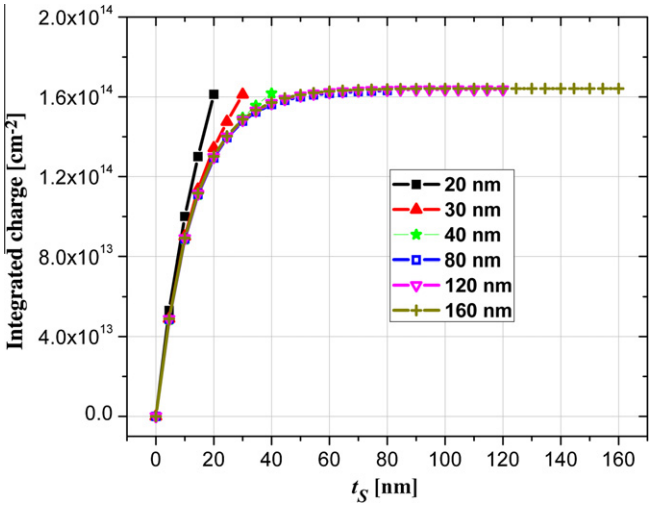

Fig. 6. Charge per square unit in the active layer in a plane located near the drain, obtained from simulation for $V_{DS} = -1$ V and $V_{GS} = 0$ V.

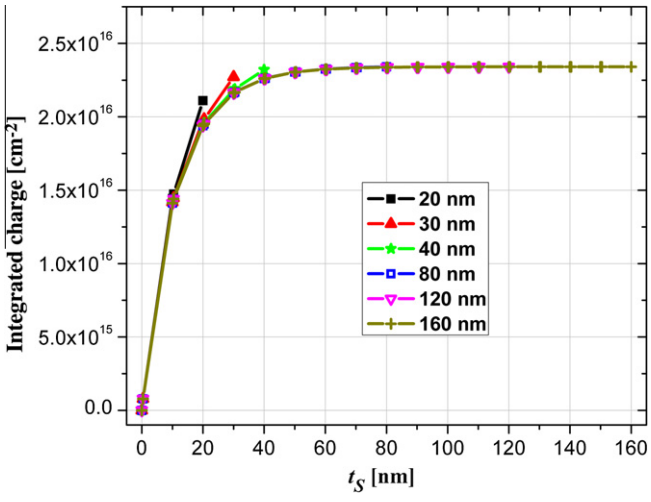

Fig. 7. Charge per square unit in the active layer in a plane located near the drain, obtained from simulation for $V_{DS} = -1$ V and $V_{GS} = -30$ V.

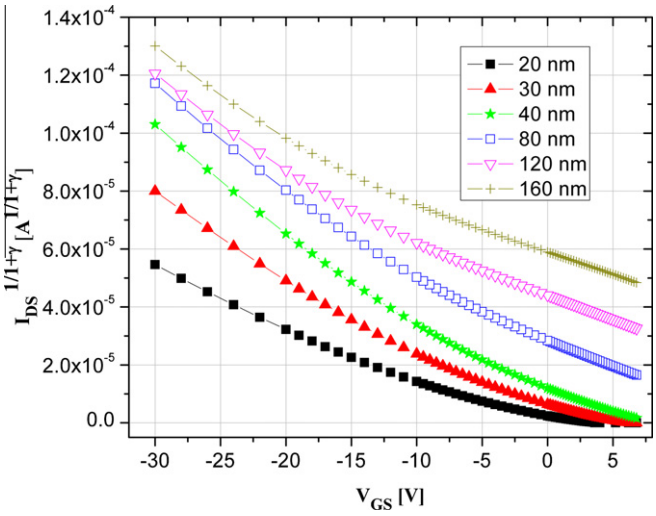

Fig. 8. $I_{DSsat}1/1+^{\gamma}$–V_{GS} curves (V_{DS} = −30 V) of PTFTs with various P3HT thicknesses.

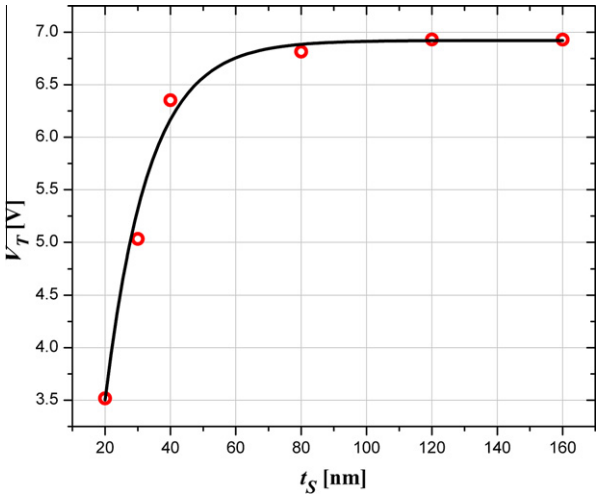

Fig. 9. Variation of threshold voltage [22] with the active layer thickness.

Table 1
Mobility values for different active layer thickness.

t_s (nm)	m_{fet}
160	1.762e−3
120	1.764e−3
80	1.770e−3
40	1.788e−3
30	1.835e−3
20	1.919e−3

This however cannot explain the behavior of I_{DS}, if the drain current increase is solely because of the bulk conductance increase, the output characteristic would not saturate, so other factors must be present.

Finally, the field-effect mobilities (μ_{fet}), according to the method described in [22] were extracted, the behavior of mobility with active layer thickness is shown in Fig. 10 and Table 1, where it is observed, as the active layer

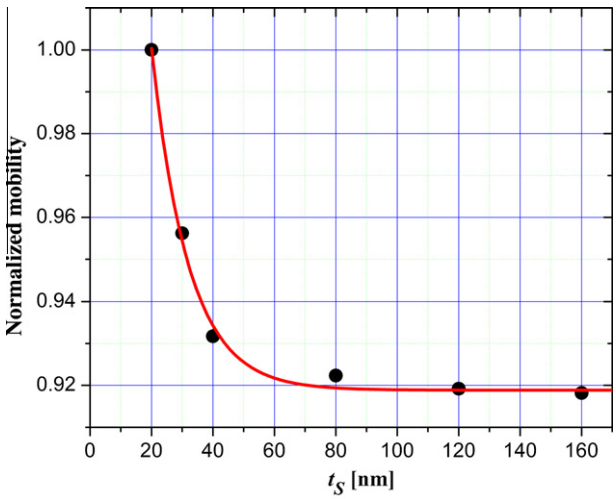

Fig. 10. Variation of normalized field effect mobility (calculated as in [22]) with the active layer thickness.

thickness decreases, the mobility slightly increases. The degeneration of mobility seems to be dependent on thickness, as seen in Fig. 8, this behavior can be caused by the increase of the average value of the charge, as the thickness of the active layer decreases, which is confirmed by simulation.

5. Conclusions

In this paper, we studied the dependence on thickness of V_T and mobility in PMMA on P3HT PTFTs. The value of V_T was observed to become more positive as the active layer thickness is increased, while mobility slightly decreased. Using simulation we confirmed that, as the semiconductor layer becomes thinner, the charge per square units decreases, which can explain the observed shift of V_T. The increase in mobility can be explained by the increase of the average value of the charge as the thickness of the active layer decreases, which was confirmed from simulations.

Acknowledgements

This work was supported by SIP-IPN Project 20101653 and CONACYT Projects 82783, 45689 and 56461 in Mexico, PCI2005-A7-0492, CSD2007-00007 (“HOPE”) from the Spanish Government, and the ICREA Academic Award”.

References

[1] H. Klauk, M. Halik, U. Zschieschang, G. Schmid, W. Radlik, High mobility polymer gate dielectric pentacene thin film transistors, J. Appl. Phys. 92 (2002) 5259–5263.
[2] Z. Bao, A. Dodabalapur, A. Lovinger, Soluble and processable regioregular poly(3-hexylthiophene) for thin-film field-effect transistor application with high mobility, Appl. Phys. Lett. 69 (1996) 4108–4110.
[3] H. Sirrnghaus, N. Tessler, R.H. Friend, Integrated, high-mobility polymer field-effect transistors driving polymer light-emitting diodes, Synth. Met. 102 (1999) 857–860.
[4] M. Estrada, I. Mejia, A. Cerdeira, B. Iñiguez, MIS polymeric structures and OTFTs using PMMA on P3HT layers, Solid-State Electron. 52 (2008) 53–59.
[5] I. Mejia, M. Estrada, M. Avila, Improved upper contacts PMMA on P3HT PTFTS using photolithographic processes, Microelectron. Reliab. 48 (2008) 1795–1799.
[6] M.J. Deen, M.H. Kazemeini, Y.M. Haddara, J. Yu, G. Vamvounis, S. Holdcroft, W. Woods, Electrical Characterization of Polymer-Based Field-Effect Transistors Fabricated by Spin-Coating Poly(3-alkylthiophene)s, IEEE Trans. Electron. Dev. 50 (2004) 1892–1901.
[7] M. Xu, M. Nakamura, K. Kudo, Thickness dependence of mobility of pentacene planar bottom-contact organic thin-film transistors, Thin Solid Films 516 (2008) 2776–2778.
[8] O. Marinov, M.J. Deen, B. Iñiguez, Charge transport in organic and polymer thin-film transistors: recent issues, IEE Proc. Circ. Dev. Syst. 152 (2005) 189–209.
[9] L. Li, G. Meller, H. Kosina, Carrier concentration dependence of the mobility in organic semiconductors, Synth. Met. 157 (2007) 243–246.
[10] G. Paasch, T. Lindner, S. Scheinert, Variable range hopping as possible origin of a universal relation between conductivity and mobility in disordered organic semiconductors, Synth. Met. 132 (2002) 97–104.
[11] M.J. Deen, M.H. Kazemeini, S. Holdcroft, Contact effects and extraction of intrinsic parameters in Poly(3-alkylthiophene) thin-film field-effect transistors, J. Appl. Phys. 103 (2008) 124509.
[12] H.L. Gomes, P. Stallinga, F. Dinelli, M. Murgia, F. Biscarini, D.M. de Leeuw, T. Muck, J. Geurts, L.W. Molenkamp, V. Wagner, Bias-induced thershold voltages shifts in thin-film organic transistors, Appl. Phys. Lett. 84 (2004) 3184–3186.
[13] O. Marinov, M.J. Deen, J. Yu, G. Vamvounis, S. Holdcroft, W Woods, Variable current transport in polymer thin film transistors, J. Vac. Sci. Technol., A 22 (2008) 755–759.
[14] N. Zhao, O. Marinov, G.A. Botton, M.J. Deen, B.S. Ong, Y. Wu, P. Liu, Characterization of MOS structures based on poly(3,3‴-dialkyl-quaterthiophene), IEEE Trans. Electron. Dev. 52 (2005) 2150–2156.
[15] J. Lee, K. Kim, S. Im, Optimum channel thickness in pentacene-based thin-film transistors, Appl. Phys. Lett. 82 (2003) 4169–4171.
[16] L. Mariucci, D. Simeone, S. Cipolloni, L. Maiolo, A. Pecora, G. Fortunato, S. Brotherton, Effect of active layer thickness on electrical characteristics of pentacene TFTs with PMMA buffer layer, Solid-State Electron. 52 (2008) 412–416.
[17] J.B. Chang, V. Subramanian, Effect of active layer thickness on bias stress effect in pentacene thin-film transistors, Appl. Phys. Lett. 88 (2006) 233513.
[18] M.H. Choi, S.H. Han, S.H. Lee, D.J. Choo, J. Jang, S.K. Kwon, Effect of active layer thickness on environmental stability of printed thin-film transistor, Org. Electron. 10 (2009) 421–425.
[19] A. Assadi, C. Svensson, M. Willander, O. Inganas, Field-effect mobility of poly(3-hexylthiophene), Appl. Phys. Lett. 53 (1988) 195–197.
[20] D. Gupta, D.Y. Hong, Undestanding the effect of semiconductor thickness on device characteristics in organic thin film transistors by two dimensional simulation, Org Electron. doi:10.1016/j.orgel.2009.10.009.
[21] Silvaco_Inc., ATLAS Usefs Manual, vol. 1, Santa Clara, CA, 2000.
[22] M. Estrada, I. Mejia, A. Cerdeira, L.F. Marsal, B. Iñiguez, Mobility model for compact device modeling of OTFTs made with different materials, Solid-State Electron. 52 (2008) 787–794.
[23] H. Jia, S. Gowrisanker, G.K. Pant, R.M. Wallace, B.E. Gnade, Effect of poly (3-hexylthiophene) film thickness on organic thin film transistor properties, J. Vac. Sci. Technol., A 24 (2006) 1228–1232.
[24] X.J. Zhou, K.E. Mutkins, D. Elkington, K. Sirois, W. Belcher, P.C. Dastoor, Effects of device architecture on the performance of organic thin film transistors, Mater. Res. Soc. Sym. Proc. 1138 (2009) 27–32.
[25] Z. Bao, A.J. Lovinger, A. Dodabalapur, Organic field-effect with high mobility based on copper phthalocyanine, Appl. Phys. Lett. 69 (1996) 3066–3068.

Organic Electronics 11 (2010) 1928–1934

Contents lists available at ScienceDirect

Organic Electronics

journal homepage: www.elsevier.com/locate/orgel

Control of charge mobility in single-crystal rubrene through surface chemistry

Keke K. Zhang [a], Kejie Tan [a], Changji Zou [a], Magnus Wikberg [b], Laurie E. McNeil [c], Subodh G. Mhaisalkar [a], C. Kloc [a,*]

[a] School of Materials Science and Engineering, Nanyang Technological University, 50 Nanyang Avenue, 639798, Singapore
[b] Uppsala University, The Ångström Laboratory, Department of Engineering Science, Division of Solid State Physics, SE-751 21 Uppsala, Sweden
[c] Department of Physics and Astronomy, The University of North Carolina at Chapel Hill, Chapel Hill, NC 27599-3255, USA

ARTICLE INFO

Article history:
Received 11 July 2010
Accepted 30 August 2010
Available online 9 September 2010

Keywords:
Rubrene
Single crystal
Oxidation
Reduction
Mobility

ABSTRACT

The mobility of rubrene single-crystal field-effect transistors has been measured in the presence of hydrogen and oxygen gas. The mobility of as-grown crystals is ~10 cm^2/V s but falls to 0.01 cm^2/V s during reduction in a hydrogen environment, and returns to nearly its original value in oxygen. Several cycles of surface reduction and oxidation have been done, which indicates that the surface reactions are reversible and the mobility can be changed to any value between that of the oxidized surface (10 cm^2/V s) and that of the reduced surface (0.01 cm^2/V s). Fourier-transform infrared (FTIR) spectroscopy and photoluminescence (PL) spectroscopy have been applied to examine the oxidized and reduced surface of the rubrene single crystal. FTIR, Raman and PL spectroscopies reveal differences between the rubrene surface and bulk depending on the state of surface oxidation. We conclude that high field-effect mobility in rubrene crystals is a result of surface doping by an oxidized layer on the crystal surface and not due to the intrinsic molecular and crystal structure of rubrene.

© 2010 Elsevier B.V. All rights reserved.

1. Introduction

Fundamental studies over the past 50 years [1–3] of carrier transport properties in organic semiconductors have led to applications in low cost, flexible organic electronics such as foldable displays, organic solar cells and printed microelectronic circuits. In particular, the increase in electron and hole mobilities from the range of 10^{-5} to above 10 cm^2/V s achieved as a result of the exploration of new and higher-quality crystalline materials promises numerous new applications, especially in high-frequency electronics.

Single crystals provide a good platform for studying the fundamental physics of the charge transport mechanism and to evaluate its limits in organic semiconductors. Numerous studies have been done on single crystals of polycyclic aromatic hydrocarbons such as tetracene [4,5], pentacene [6], anthracene [7] and similar compounds [8,9]. However, the transport mechanism is still controversial and the limit of the charge-carrier mobility, a parameter critical for device applications, is not yet known due to the presence of impurities and other defects at far higher levels than in typical inorganic semiconductors. Despite dramatic improvements in the mobility measured in field-effect transistors made from organic semiconductors from initial levels in the 10^{-5} cm^2/V s range, during the last few years improvements in the mobility have stagnated in both thin films and single crystals at values of order 10 cm^2/V s.

Rubrene (5,6,11,12-tetraphenylnaphthacene) appears to be an exceptional material in this regard, as very high values for its mobility have been consistently reported [10–12]. However, the composition and the molecular and crystalline structure of rubrene are in no way excep-

* Corresponding author. Tel.: +65 6790 4716; fax: +65 67909081.
E-mail address: ckloc@ntu.edu.sg (C. Kloc).

1566-1199/$ - see front matter © 2010 Elsevier B.V. All rights reserved.
doi:10.1016/j.orgel.2010.08.019

tional compared with other organic semiconductors, although the intermolecular coupling is known to be extremely low, and so the origin of this high mobility remains a subject of controversy.

Conduction in FET devices takes place in a shallow surface channel, which in rubrene is subject to oxidation under ambient conditions. Photo-oxidation of rubrene in solution has been reported since the compound was first synthesized [13], and a red toluene solution of rubrene fully bleaches in the presence of air and light, forming an endoperoxide of rubrene that is not very stable. The dry endoperoxide loses oxygen during heating and decomposes back to rubrene. However, bulk rubrene single crystals appear not to bleach, presumably due to steric obstacles in the crystalline lattice because the formation of the endoperoxide requires bending of the tetracene backbone of the molecule. Materials with large surface area such as commercial powders have been shown to contain endoperoxide, and the oxide has also been detected on the surface of single crystals [14]. To date a connection between the transport properties and the oxidation state of the rubrene surface has not been directly established.

In the present paper, we report the growth of rubrene single crystals from the gas phase and measurements of conductivity, field-effect mobility, infrared transmission and reflection, and photoluminescence on the crystals during oxidation in an oxygen atmosphere and reduction in hydrogen atmosphere. We observed significant changes in the transport parameters due to oxidation and reduction of the rubrene single-crystal surface. The field-effect mobility of a rubrene single-crystal transistor decreased by at least three orders of magnitude, from 10 to 10^{-2} cm^2/V s, during reduction of the rubrene surface. Upon re-oxidation the mobility returned to close to the original value of 10 cm^2/V s. We have shown that the process is repeatable and reproducible. Our measurements of IR transmission and reflection, photoluminescence, Raman scattering and chemical purity all indicate that surface oxidation and reduction change the doping of the active layer in a rubrene field-effect transistor. We explore here whether surface doping is the primary parameter producing the high mobility of organic semiconductors, with the structure–property relations being a secondary factor in the search for high-performance organic semiconductors.

2. Experimental

Rubrene single crystals were grown by the physical vapor transport (PVT) technique [15,16], using hydrogen, forming gas (4% H_2 and 96% N_2) or argon (Ar) for transport of the rubrene molecules in the gas phase. The rubrene source powder (purchased from Sigma–Aldrich) was purified by sublimation before crystal growth. The temperature of two-zone furnance was set to 300 and 260 °C, respectively. The carrier gas hydrogen was produced by a hydrogen generator via electrolysis of water. Before using it, water was eliminated by passing it through a dry column. After growth, the furnace was cooled to room temperature without any additional temperature control, keeping the carrier gas flowing throughout the cooling process. We collected the crystals from the furnace in laboratory atmosphere and evaluated their quality under a polarized microscope, selecting some for further measurements.

Two-terminal devices were fabricated with contacts made with Ag paint. A Keithley 6517 electrometer was used to make two-point current vs. voltage measurements. The sample was kept in oxygen or hydrogen atmosphere at 100 °C overnight before the room-temperature conductivity measurements were made.

Rubrene air-gap field-effect transistors (FET) were fabricated by gently pressing the smooth surface of the rubrene crystal onto a pre-fabricated polydimethylsiloxane (PDMS) stamp [17]. The air gap was 4.2 μm thick. We deposited a 20-nm layer of Au on the PDMS stamps at rate of 0.2 Å/s by an electron beam evaporator, forming the source, drain and gate electrodes and allowing us to achieve adhesion of the rubrene crystals to the source and drain electrodes. A schematic of a transistor is shown in the insert of Fig. 1. After the transistors were fabricated we placed them inside a quartz tube of a transparent tube furnace where the temperature, pressure and gas atmosphere could all be controlled. Electrical wires attached to transistor led to the measurement instrument outside the furnace, allowing us to make transport measurements while using oxygen and hydrogen gas in the oxidation and reduction process. To study the reproducibility of the oxidation/reduction process, we cycled the gas flow between oxygen and hydrogen repeatedly, measuring the output and transfer characteristics of the transistors continuously during processing, using a Keithley 4200-Semiconductor Characterization System.

Perkin–Elmer FTIR spectrum GX was used to perform FTIR measurement on rubrene crystals in both transmission and attenuated total reflection (ATR) modes. We selected thin flexible rubrene single crystals (approximately 20 μm thick) for the ATR-FTIR measurement, as the

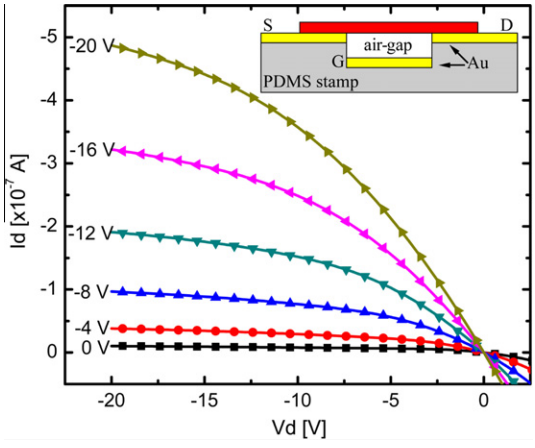

Fig. 1. Output characteristics of an air-gap rubrene single-crystal FET used in this study. The numbers at the end of curves indicate the corresponding gate voltage (V_g). The inset is a schematic of the air-gap rubrene single-crystal FET. The red part represents the rubrene single crystal. The yellow part represents the 20 nm gold film. The grey part represents the polydimethylsiloxane (PDMS) stamp.

measurement required good adhesion between a quartz window and the rubrene single-crystal surface. For transmission-mode measurements we used crystals a few hundred micrometers in thickness. The crystals used in infrared experiments were grown in Ar and stored in dry air for several days. Photoluminescence spectrum were collected using a confocal photoluminescence spectroscope, the Witec α-300. Excitation was provided by the 488-nm wavelength of an Ar+ laser focused through a 100× objective (N.A. 0.95) onto the rubrene single-crystal surface. Laser power is of approximately 15 μW/cm^2 to avoid damaging the sample.

3. Results and discussion

Charge-carrier transport in an FET takes place in the near-surface region, therefore any modification of the chemical or physical properties of this region in an organic semiconductor affects the transport properties of the device [18,19]. In order to demonstrate that the oxidation state of the semiconductor surface controls the mobility of a rubrene FET, we have conducted two types of transport experiments in which the crystal is cycled between the oxidized and reduced state while the surface conductivity or the charge-carrier mobility is measured.

Our first measurements were of conductivity, using samples prepared with two electrodes painted on the surface of the as-grown crystals. We observed a significantly larger current in the oxidized samples than in the reduced. The largest currents were observed in the as-grown samples, which we assume were already oxidized from extended contact with air. The change in the conductivity upon oxidation or reduction is shown in Fig. 2. Since silver (Ag) was used as a contact material, there were concerns that changes affecting only the contacts might have occurred, especially since contacts always play a large role in charge injection and thus in conductivity measurements of organic semiconductors. We therefore produced additional samples with silver paste, evaporated Ag, copper (Cu) and aluminum (Al) as contacts. We observed changes in the conductivity of the same order of magnitude for oxidation and reduction in all of the crystals regardless of the type of contacts. While highly suggestive, these experiments did not allow us to distinguish between changes in the charge injection and changes in the doping of the conduction channel as potential causes of the dramatic change in conductivity observed upon oxidation and reduction. We therefore performed FET measurements to resolve this ambiguity.

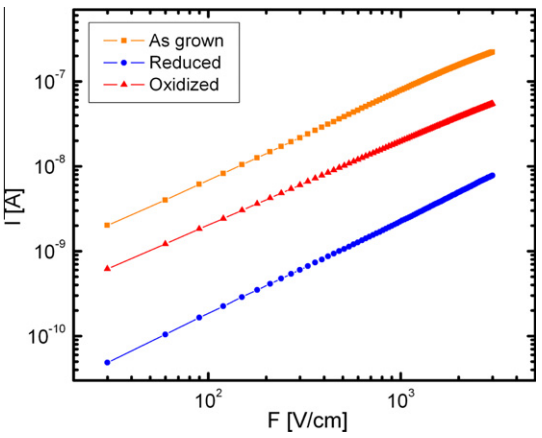

Fig. 2. Change of rubrene single-crystal surface conductivity under different conditions. The oxidation and reduction were done in O_2 and H_2 environment at 100 °C, respectively. The measurements were done at room temperature.

To measure the charge-carrier mobility we fabricated rubrene FETs with air-gap dielectric where the conduction channel is accessible to flowing oxygen or hydrogen gas, as shown in the insert of Fig. 1. At the start of the experiment in our FET measurements of transistors made on as-grown crystals, we observed a typical output characteristic as shown in Fig. 1. In the low source-drain voltage (V_d) range (−1 to 1 V), the source-drain current (I_d) shown a symmetric and linear curve crossing the origin, which indicates good contact between the Au electrode and the rubrene crystal with low contact resistance. In the higher V_d region the current saturated.

We placed the device in a quartz tube with pure oxygen or pure hydrogen gas flowing at room temperature and connected the source, drain and gate terminals to the measurement apparatus. We observed significant changes in the FET characteristic curves with time during hydrogen or oxygen treatment, as shown in Fig. 3. During the reduction process the source-drain current I_d decreased by almost three orders of magnitude within 1 h. When the

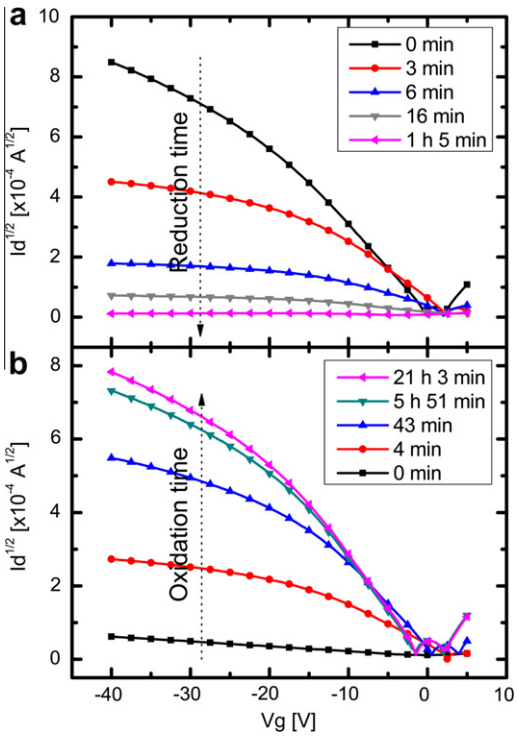

Fig. 3. Transfer characteristic with $V_d = -8$ V, V_g swept from 5 to −40 V. (a) Shows the reduction process. (b) Shows the oxidation process. The measurements are done at 1 atm, 25 °C.

same device was subsequently put through the oxidation process under flowing oxygen gas in the quartz tube, I_d returned to almost its original magnitude over a period of about 20 h.

The mobility of a typical rubrene FET measured in air before oxidation or reduction treatment did not depend on the carrier gas used in crystal growth. Because the FET was fabricated in air, we assume that the surface of the rubrene FET channel area was always oxidized in the initial measurement. The devices always shown relatively high initial mobility in the range of >1 cm^2/V s, and in some samples above 10 cm^2/V s, before the reduction/oxidation cycle was begun.

The field-effect mobility was extracted from the transfer characteristic using the equation

$$\mu = \frac{L}{CWV_d} \cdot \frac{dI_d}{dV_g}.$$

Fig. 4 shows the mobility change with time in three reduction/oxidation cycles. In the presence of hydrogen the mobility drops steeply from its initial value of ~10 to ~0.01 cm^2/V s in less than 1 h. When the flowing gas is switched to oxygen, the mobility increases rapidly in the first few minutes, followed by slow saturation in the next 20 h. The mobility never fully recovered to its original value in this time period, rather the saturation value decreased a little in each cycle. In a chemical reaction resulting from the oxygen or hydrogen treatment, water molecules would be formed. Therefore we suspect that build-up of defects may occur after repeated cycling and may interfere with the charge flowing in the channel area.

The three-order-of-magnitude change in the hole mobility observed in this experiment between the reduced and the oxidized state is surprising, since conventional wisdom from studies of transport properties of inorganic semiconductors suggests that in order to observe the intrinsic (or at least as high as possible) mobilities of charge carriers it is necessary to remove defects and dopants. Our previous work [15] shows that multiple sublimations of rubrene may remove solvent molecules or other molecules used for synthesis, but the dominant contaminants, which are oxidized forms of rubrene, need to be removed from the growth environment to avoid oxidization of the purified materials during the crystal growth process. The recent literature on rubrene transport properties indicates that the room-temperature mobility of rubrene may be as high as 20 cm^2/V s [9], or perhaps even higher [12]. All of those reports claim very high quality and purity of rubrene single crystals used in the measurement, but our analysis of the details given in those reports does not allow us to exclude the possibility of surface oxidation of the crystals during handling or contact preparation. It is not clear if the oxide is fully removed when the surface of the device is exposed to vacuum at room temperature, but it appears that the mobility changes slowly, if at all [10].

In order to examine that surface more closely, and to distinguish its state from that of the bulk crystal, we conducted two types of optical measurements: Fourier-transform infrared (FTIR) and photoluminescence (PL). We performed transmission FTIR measurements to examine the bonds in bulk rubrene (~300 μm in thickness), and attenuated total reflection (ATR) FTIR measurements to analyze the surface region (to a depth of ~700 nm). The results are shown in Fig. 5, in which selected peaks are magnified for clarity. We observed new peaks at the rubrene surface, and those are indicated by black arrows in the figure. The changes we have observed in the oxidized rubrene surface indicate the formation of oxidized species such as rubrene endoperoxide, rather than just intercalation of O_2 into the rubrene crystal. This conclusion is consistent with our previous observation of the endoperoxide in our chemical analysis of rubrene crystals [15].

To explore the effect of oxidation on the electronic states of rubrene, we performed photoluminescence measurements. Immediately after the crystal growth, the

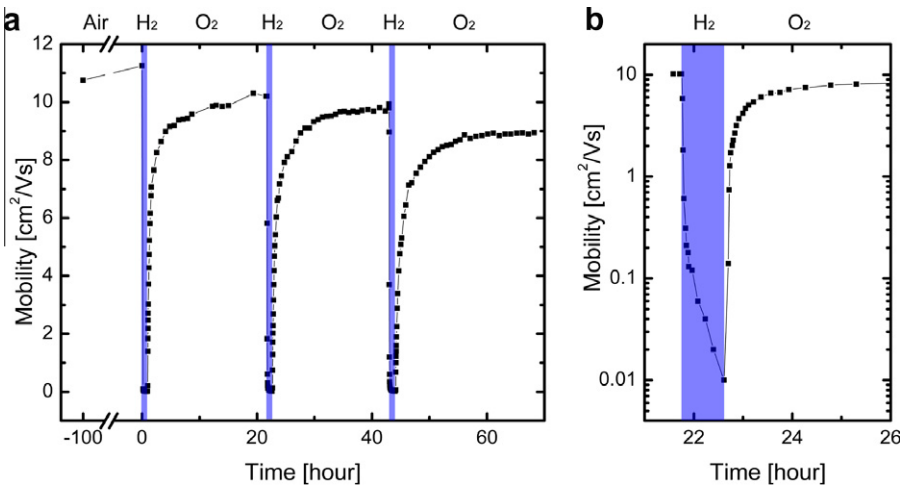

Fig. 4. (a) Effective mobility change in reductive gas H_2 and oxidative gas O_2 in three cycles. Reversible change in the mobility is observed. Before time 0, the device is stored in a dry box under laboratory atmosphere. Beginning at time 0 the device is purged under pure H_2 gas, followed by purging with O_2 gas. (b) Is the effective mobility from the second cycle on a log scale.

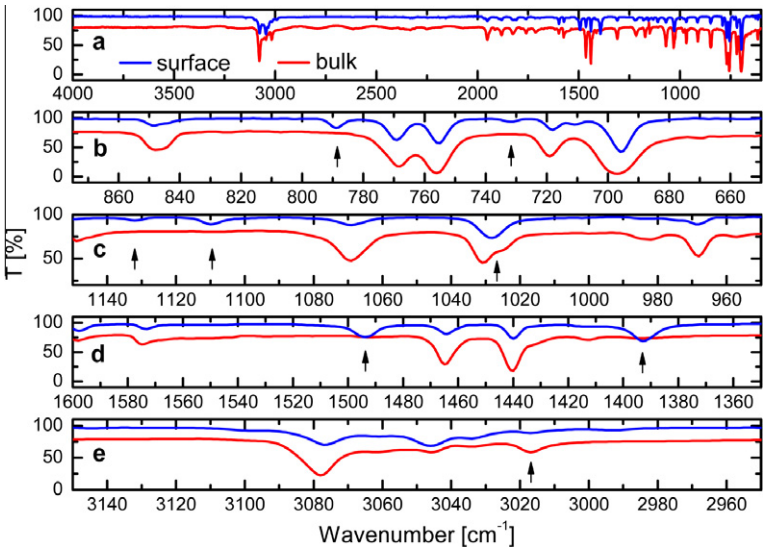

Fig. 5. Fourier-transform infrared spectroscopy (FTIR), (a) complete spectra, (b)–(e) magnification of selected areas. Arrows are to guide the eye. The blue line is the spectrum from the rubrene surface, collected by attenuated total reflection (ATR) FTIR. The red line is the bulk spectrum, collected by transmission FTIR.

room-temperature PL spectrum (measured in laboratory air) of rubrene crystals grown in a hydrogen atmosphere shows two peaks, one at near 570 nm (2.18 eV) and the other near 600 nm (2.06 eV) [20]. These emissions, which are intrinsic to rubrene, most likely result from molecular (Frenkel) excitons [21]. For the rubrene crystals grown in air or oxidized in air at a temperature of approximately 100 °C, the intrinsic rubrene peaks at 570 nm are reduced in intensity in comparison with the peaks at 650 nm (1.91 eV) and 700 nm (1.77 eV). Fig. 6 shows the PL spectrum observed during a dynamic process of oxidation of an ultra thin (<100 nm) rubrene single crystal on a SiO_2 substrate. It illustrates the change of intensity of the aforementioned three peaks during oxidation at 100 °C. However it is worth noting that the intensities of these peaks do not change significantly after growth of rubrene single crystals and storage for several weeks in a laboratory-air atmosphere, suggesting that the oxidation is confined to the surface at room temperature. However, the excitation wavelength for the PL measurement was 488 nm and the optical absorption coefficient for rubrene at this wavelength means that the incident beam intensity will decay to half its initial value by a depth of approximately 1.1 μm [22]. The PL measurement will therefore not be sensitive to a few layers (<10 nm) of oxidation product which may be formed at room temperature over a period of a few weeks. However at elevated temperature and over a longer time the oxidation may proceed deeper into the crystals (for example along dislocations or other structural defects) and therefore be detected by PL measurements. Similarly, Raman measurements performed with long-wavelength excitation that penetrates deeply into the crystal [21] do not display vibrational modes attributable to oxide molecules. However, those measurements were likewise performed on rubrene crystals stored in laboratory air, not those oxidized at higher temperatures in pure oxygen. It is likely that Raman measurements made with short wavelength on crystals oxidized at high temperature would display such modes, as do the ATR infrared measurements shown in Fig. 5.

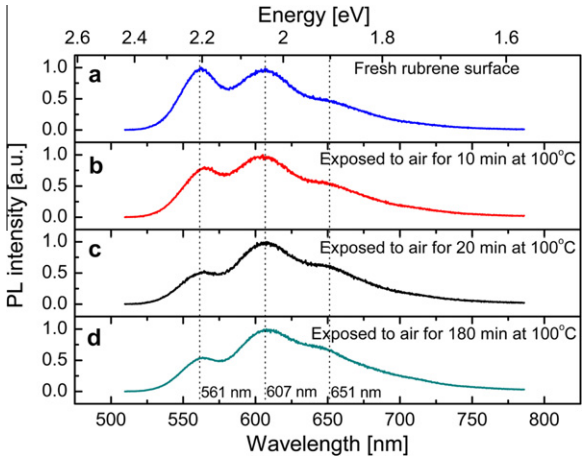

Fig. 6. Photoluminescence spectrum of rubrene showing change with time. (a) Pristine rubrene at room temperature, (b) pristine rubrene heated in air at 100 °C for 10 min, (c) for 20 min, (d) for 180 min. The thickness of the rubrene crystal is less than 100 nm, cleaved on a clean SiO_2 substrate.

Because the mobility measurement in an FET is determined by only the conditions in the near-surface region, it is not necessary for the entire crystal to be oxidized in order to observe the dramatic effect shown in Fig. 4. To examine the fraction of the material that is oxidized, we performed X-ray powder diffraction measurements on our oxidized and reduced crystals. The diffraction patterns of both oxidized and reduced rubrene were identical to

that of the published structure [23]. Assuming that impurities need to constitute approximately 1% of the volume of the substance to be detected in our routine X-ray powder diffraction measurements, this suggests that only the thin surface layer may be oxidized and the bulk of the crystal was composed of pristine rubrene.

Our results, in which we achieve the highest mobility in oxidized samples, may appear to be in contradiction with a long series of reports by the group of Prof. N. Karl of the University of Stuttgart [24]. The group measured carrier transport in very-thoroughly-purified single crystals of organic semiconductors (though not in rubrene) by time-of-flight methods and shown that the lifetime of the charge carriers increases significantly if impurities are removed from the crystal. We believe that this observation is general for all organic semiconductors. However, field-effect measurements of mobility probe only the very shallow channel on the surface of the semiconductor and therefore do not measure bulk mobility. This can be seen by the different mobilities recorded for FETs made from rubrene but with different dielectric layers [25,26]. However, our mobility values measured in rubrene crystals reduced in a hydrogen environment, as well as the value reported by Iwasa and co-workers [27] for ambipolar transport measured in vacuum and the value measured by Podzorov et al. [28] under vacuum in the presence of a hot-cathode vacuum gauge are likely to be closer to the intrinsic value than are the maximum values measured on samples in which significant surface oxide is present. It appears that the high value of the mobility measured in FET structures results from the presence of the oxidized layer at the surface, perhaps through radical cation hole carriers doping generated by oxygen assisted electron transfer mechanism [29] at the interface with the pristine rubrene.

4. Conclusion

We have grown rubrene single crystals in flowing hydrogen, argon or air. The mobility measured in FET structures made from as-grown crystals was more than 10 $cm^2/V\,s$ at room temperature. When the FET was treated with flowing hydrogen gas the mobility decreased by more than three orders of magnitude as a result of reduction of the rubrene surface. The mobility increased back to nearly its original value when the crystal was subsequently oxidized, a cycle that could be repeated multiple times. Fourier-transform infrared spectroscopy confirmed that oxidation appears only at the surface, and changes in the photoluminescence spectrum resulting from oxidation or reduction were also observed. We conclude that the high value of the mobility reported for rubrene is not an intrinsic property of the bulk crystal but is determined by the oxidation state of the rubrene surface. Therefore we believe that the current effort to tailor the molecular structure of organic semiconductors to achieve high-mobility charge-carrier transport should be complemented by efforts to control the state of the surface of organic semiconductors by defect control, and doping by electron transfer through interfaces or in binary organic compounds.

Acknowledgements

We thank Prof. Rogers for providing the PDMS mould. We acknowledge the support of Nanyang Technological University.

References

[1] M. Pope, C.E. Swenberg, Electronic Processes in Organic Crystals and Polymers, second ed., Oxford University Press, New York, 1999.
[2] F. Garnier, G. Horowitz, X.H. Peng, D. Fichou, An all-organic soft thin-film transistor with very high carrier mobility, Advanced Materials 2 (1990) 592–594.
[3] C.D. Dimitrakopoulos, S. Purushothaman, J. Kymissis, A. Callegari, J.M. Shaw, Low-voltage organic transistors on plastic comprising high-dielectric constant gate insulators, Science 283 (1999) 822–824.
[4] R.W.I. de Boer, T.M. Klapwijk, A.F. Morpurgo, Field-effect transistors on tetracene single crystals, Applied Physics Letters 83 (2003) 4345–4347.
[5] T. Takahashi, T. Takenobu, J. Takeya, Y. Iwasa, Ambipolar light-emitting transistors of a tetracene single crystal, Advanced Functional Materials 17 (2007) 1623–1628.
[6] J. Takeya, C. Goldmann, S. Haas, K.P. Pernstich, B. Ketterer, B. Batlogg, Field-induced charge transport at the surface of pentacene single crystals: a method to study charge dynamics of two-dimensional electron systems in organic crystals, Journal of Applied Physics 94 (2003) 5800–5804.
[7] N. Karl, J. Marktanner, Electron and hole mobilities in high purity anthracene single crystals, Molecular Crystals and Liquid Crystals 355 (2001) 149–173.
[8] T. Hasegawa, J. Takeya, Organic field-effect transistors using single crystals, Science and Technology of Advanced Materials 10 (2009) 024314.
[9] M.E. Gershenson, V. Podzorov, A.F. Morpurgo, Colloquium: electronic transport in single-crystal organic transistors, Reviews of Modern Physics 78 (2006) 973–989.
[10] R.W.I. de Boer, M.E. Gershenson, A.F. Morpurgo, V. Podzorov, Organic single-crystal field-effect transistors, Physica Status Solidi a-Applied Research 201 (2004) 1302–1331.
[11] E. Menard, V. Podzorov, S.H. Hur, A. Gaur, M.E. Gershenson, J.A. Rogers, High-performance n- and p-type single-crystal organic transistors with free-space gate dielectrics, Advanced Materials 16 (2004) 2097–2101.
[12] J. Takeya, M. Yamagishi, Y. Tominari, R. Hirahara, Y. Nakazawa, T. Nishikawa, T. Kawase, T. Shimoda, S. Ogawa, Very high-mobility organic single-crystal transistors with in-crystal conduction channels, Applied Physics Letters 90 (2007) 102120.
[13] M. Yamada, I. Ikemoto, H. Kuroda, Photooxidation of the evaporated-films of polycyclic aromatic-hydrocarbons studied by X-ray photoelectron-spectroscopy, Bulletin of the Chemical Society of Japan 61 (1988) 1057–1062.
[14] D. Kafer, G. Witte, Growth of crystalline rubrene films with enhanced stability, Physical Chemistry Chemical Physics 7 (2005) 2850–2853.
[15] C. Kloc, K.J. Tan, M.L. Toh, K.K. Zhang, Y.P. Xu, Purity of rubrene single crystals, Applied Physics a-Materials Science and Processing 95 (2009) 219–224.
[16] C. Kloc, P.G. Simpkins, T. Siegrist, R.A. Laudise, Physical vapor growth of centimeter-sized crystals of alpha-hexathiophene, Journal of Crystal Growth 182 (1997) 416–427.
[17] V.C. Sundar, J. Zaumseil, V. Podzorov, E. Menard, R.L. Willett, T. Someya, M.E. Gershenson, J.A. Rogers, Elastomeric transistor stamps: reversible probing of charge transport in organic crystals, Science 303 (2004) 1644–1646.
[18] K.P. Pernstich, S. Haas, D. Oberhoff, C. Goldmann, D.J. Gundlach, B. Batlogg, A.N. Rashid, G. Schitter, Threshold voltage shift in organic field effect transistors by dipole monolayers on the gate insulator, Journal of Applied Physics 96 (2004) 6431–6438.
[19] A. Vollmer, O.D. Jurchescu, I. Arfaoui, I. Salzmann, T.T.M. Palstra, P. Rudolf, J. Niemax, J. Pflaum, J.P. Rabe, N. Koch, The effect of oxygen exposure on pentacene electronic structure, European Physical Journal E 17 (2005) 339–343.
[20] O. Mitrofanov, D.V. Lang, C. Kloc, J.M. Wikberg, T. Siegrist, W.Y. So, M.A. Sergent, A.P. Ramirez, Oxygen-related band gap state in single crystal rubrene, Physical Review Letters 97 (2006) 166601.

[21] J.R. Weinberg-Wolf, L.E. McNeil, S. Liu, C. Kloc, Evidence of low intermolecular coupling in rubrene single crystals by Raman scattering, Journal of Physics-Condensed Matter 19 (2007) 276204.
[22] H. Najafov, I. Biaggio, V. Podzorov, M.F. Calhoun, M.E. Gershenson, Primary photoexcitations and the origin of the photocurrent in rubrene single crystals, Physical Review Letters 96 (2006) 056604.
[23] O.D. Jurchescu, A. Meetsma, T.T.M. Palstra, Low-temperature structure of rubrene single crystals grown by vapor transport, Acta Crystallographica Section B-Structural Science 62 (2006) 330–334.
[24] N. Karl, Charge carrier transport in organic semiconductors, Synthetic Metals 133 (2003) 649–657.
[25] A.F. Stassen, R.W.I. de Boer, N.N. Iosad, A.F. Morpurgo, Influence of the gate dielectric on the mobility of rubrene single-crystal field-effect transistors, Applied Physics Letters 85 (2004) 3899–3901.
[26] I.N. Hulea, S. Fratini, H. Xie, C.L. Mulder, N.N. Iossad, G. Rastelli, S. Ciuchi, A.F. Morpurgo, Tunable Frohlich polarons in organic single-crystal transistors, Nature Materials 5 (2006) 982–986.
[27] T. Takahashi, T. Takenobu, J. Takeya, Y. Iwasa, Ambipolar organic field-effect transistors based on rubrene single crystals, Applied Physics Letters 88 (2006) 033505.
[28] V. Podzorov, E. Menard, S. Pereversev, B. Yakshinsky, T. Madey, J.A. Rogers, M.E. Gershenson, Interaction of organic surfaces with active species in the high-vacuum environment, Applied Physics Letters 87 (2005) 093505.
[29] A.J. Maliakal, J.Y.C. Chen, W.Y. So, S. Jockusch, B. Kim, M.F. Ottaviani, A. Modelli, N.J. Turro, C. Nuckolls, A.P. Ramirez, Mechanism for oxygen-enhanced photoconductivity in rubrene: electron transfer doping, Chemistry of Materials 21 (2009) 5519–5526.

Organic Electronics 11 (2010) 1942–1946

Contents lists available at ScienceDirect

Organic Electronics

journal homepage: www.elsevier.com/locate/orgel

Towards high efficiency solution processable inverted bulk heterojunction polymer solar cells using modified indium tin oxide cathode

Xiaohong Chen [a,b], Jiaxiang Yang [a], Lim Yi Xuan Candy Haley [a], Jiong Lu [a], Furong Zhu [c], Kian Ping Loh [a,*]

[a] Department of Chemistry, National University of Singapore, 3 Science Drive, Singapore 117543, Singapore
[b] Engineering Research Center for Nanophotonics and Advanced Instrument and Department of Physics, East China Normal University, Shanghai 200062, China
[c] Department of Physics and Centre for Advanced Luminescence Materials, Hong Kong Baptist University, 224 Waterloo Road, Kowloon Tong, Hong Kong

ARTICLE INFO

Article history:
Received 21 June 2010
Received in revised form 8 September 2010
Accepted 8 September 2010
Available online 23 September 2010

Keywords:
Inverted bulk heterojunction polymer solar cells
ITO cathode
Carbon nanoparticles

ABSTRACT

High efficiency inverted regioregular poly(3-hexylthiophene) (P3HT) and [6,6]-phenyl C_{61}-butyric acid methyl ester (PCBM)-based polymer solar cells (PSCs) using an indium tin oxide (ITO) cathode, modified with a solution-processed ionic liquid-functionalized carbon nanoparticles (ILCNs) layer, was demonstrated. ILCNs-modified ITO cathode has a very good thermal stability and a superior surface electronic property suited for application in polymer solar cells. A power conversion efficiency (PCE) of 3.2% was obtained for inverted PSCs measured under AM1.5G illumination of 100 mW/cm^2, which is comparable to PCE of a reference P3HT:PCBM-based solar cell having a conventional structure. There was almost no deterioration in the performance of inverted PSCs that were aged over a post-annealing temperature range from 100 to 200 °C. The work function of ILCNs-modified ITO cathode annealed at different temperatures was also measured using ultraviolet photoelectron spectroscopy. It was found that the work function of 4.4 eV, measured for a bare ITO electrode, decreased to 3.8 eV when it was modified with ILCNs, and was not dependent on the post-annealing temperature.

© 2010 Elsevier B.V. All rights reserved.

1. Introduction

The development of the emerging polymer solar cell technology has attracted a lot of interests due to its great potential of low-cost non-vacuum process photovoltaic technology. Polymer solar cells (PSCs) can be flexible, large-area and prepared using solution processable technologies. PSCs have enjoyed significantly development in the past decades. The power conversion efficiency (PCE) of 4–5% for bulk heterojunction (BHJ) PSCs using regioregular poly(3-hexylthiophene) (P3HT) and [6,6]-phenyl C_{61}-butyric acid methyl ester (PCBM) blend system has been achieved. A PCE of 6.0% was reported for BHJ polymer solar cells using low-bandgap alternating co-polymers of poly (2,7-carbazole) derivatives with deeper highest occupied molecular orbital (HOMO) energy and [6,6]-phenyl C_{70}-butyric acid methyl ester [1]. PCE of 6.77% was reported recently for heterojunction PSCs [2]. New device processes based on the control of film morphology, optimization of the active layer thickness [3], modification of electrode using surface plasmonic effect to boost the light absorption [4,5], and use of p- and n-types metal oxides [6–11] to improve the charge collection efficiency were demonstrated.

In a conventional P3HT:PCBM-based polymer solar cell, the hole-transporting layer, poly(3,4-ethylenedioxythiophene):poly(styrenesulfonate) (PEDOT:PSS) is spin-coated on top of indium tin oxide (ITO) surface to prevent electron leakage and to aid in hole extraction. The active layer of P3HT:PCBM is sandwiched between an ITO/PEDOT:PSS anode and a low work function metal cathode. However,

* Corresponding author.
E-mail address: chmlohkp@nus.edu.sg (K.P. Loh).

1566-1199/$ - see front matter © 2010 Elsevier B.V. All rights reserved.
doi:10.1016/j.orgel.2010.09.011

PEDOT:PSS layer is detrimental to ITO anode and the active polymer layer due to its acidic nature. In conventional PSCs, the top cathode, often made with a low work function metal cathode, such as calcium or barium cathode, is easily oxidized even with a delicate encapsulation, leading to reduced device lifetime [12]. The p- and n-types transparent metal oxides have been recently introduced as anode and cathode contacts in PSCs, providing greater process freedom for new device structures including inverted PSCs [6–8,10,11]. The use of transparent metal oxides can also offer a better choice to fabricate inverted PSCs. More importantly, the inverted PSCs can overcome some disadvantages of the regular PSCs with PEDOT:PSS anode contact layer. Therefore, several inverted polymer solar cell structures have been developed. For example, p-type metal oxide, such as vanadium oxide (V_2O_5) [11,13] and molybdenum trioxide (MoO_3) [10] were deposited on top of the active layer as a hole selective layer before a less air-sensitive and high work function metal was deposited as a back hole collecting electrode [8,10]. Solution-processed ZnO [7] and TiO_x [6] when applied as electron selective layer have been reported to achieve 2.58% and 3% PCE, respectively. However the high temperature annealing needed to improve the film properties of these metal oxides is not compatible with the active polymer layer.

Liao et al. [14] demonstrated that work function of ITO electrode was decreased from 4.5 to 3.06 eV by spin-coating an ultrathin cesium carbonate (Cs_2CO_3) onto ITO surface. The Cs_2CO_3 layer can be decomposed into low work function cesium oxide by annealing under 150 °C, which is consistent with the fabrication procedures of the active polymer layer. The PCE of inverted PSCs with Cs_2CO_3-modified ITO cathode reaches 4.2% after annealing, which is comparable to the regular structure device on the same system. However, Cs_2CO_3 is very sensitive to moisture and the property of Cs_2CO_3-modified ITO cathode can be easily degraded due to air-leakage through the edges of the encapsulation. Solution-processed V_2O_5 as an anode interlayer without annealing have been reported, the PCE of devices made with V_2O_5 modified ITO anode was shown to increase from 2.5% to 3.56% compared to PSCs without the V_2O_5 interlayer [11]. This solution-processed V_2O_5 is relatively insensitive to moisture and oxygen and its advantage of non-annealing treatment, as compared to a post-annealing treatment required for solution-processed TiO_x [6] and ZnO [7], offers a simple and effective approach for fabrication of low-cost and large-area PSCs.

In this work, a thermally stable, transparent cathode of ionic liquid-functionalized carbon nanoparticles (ILCNs)-modified ITO was developed. A layer of ILCNs was solution-processed and its low annealing temperature offers additional advantage for fabrication of PSCs. The ILCNs was used to modify ITO electrode; the work function of the modified ITO electrode decreased from 4.5 to 3.8 eV after spin-casting a ~1–3 nm thick ILCNs film on top of the ITO electrode. The PCEs of inverted PSCs made with modified ITO cathode increased to 3.2%, after post-annealing at a temperature of 120 °C, which is comparable to that of a reference PSC using the same system [15,16].

2. Experimental

The ILCNs was synthesized by the electrochemical exfoliation of graphite electrode in 1-butyl-3-methylimidazolium tetrafluoroborate ($[C4mim]^+[BF4]^-$) and water mixture [17]. The ILCNs consists of ionic liquid molecules and graphite-like carbon nanoparticles held together by hydrogen bonding, van der Waals forces, $\pi-\pi$ stacking interactions or/and covalent interactions in a gel-like matrix. The transmission electron microscopy image shows that the average size of ILCNs is below 4 nm [15]. The details of ILCNs synthesis and its properties have been reported [15,17]. In this work, the ILCNs layer was spin-coated on the surface of ITO-coated glass substrates (15 Ω/sq), pretreated with UV-ozone, and followed by annealing with different temperature in the glove box with an O_2 level and a H_2O level <2 ppm. P3HT (Sigma–Aldrich) and PCBM (American Dye Source) were dissolved in 1,2-dichlorobenzene with 1:0.8 wt. ratio. ILCNs were dissolved in ethanol. P3HT:PCBM film was spin-coated on top of the ILCNs-modified ITO in the glove box. The P3HT:PCBM film was spin-coated at 800 rpm for 60 s, and then kept in a petri dish for slow growth. After 12 h, P3HT:PCBM films were annealed at 120 °C for 10 min. The 5 nm thickness MoO_3 and 100 nm Al metallic layers were thermally deposited with a background pressure of 5×10^{-7} Torr. The active area of PSCs is 3.0 mm × 3.0 mm. Current density–voltage (J–V) characteristics of PSCs were measured in nitrogen under AM1.5G illumination of 100 mW/cm^2 (SAN-EI Electric Xe-Lamp controller). The surface work function of bare ITO and ILCNs-modified ITO cathode was examined using ultraviolet photoelectron spectroscopy with Helium line (21.2 eV).

3. Results and discussion

The atomic force microscopy (AFM) image measured for ILCNs layer on ITO surface is shown in Fig. 1(a). The ILCNs film was spin-coated at the speed of 1500 rpm for 60 s. The average thickness of the ILCNs layer was estimated to be 2.8 nm with corresponding rms roughness of ~0.85 nm, as shown in Fig. 1(b). The optical transmission spectra of ILCNs films spin-coated at 1500 and 2500 rpm, respectively onto ITO/glass substrates are shown in Fig. 1(c). The transmission spectra measured for ILCNs-modified ITO glass substrate show a slight decrease in the light wavelength range from 350 to 450 nm, as the thickness of ILCNs over layer increases. The overall transparency of the ILCNs-modified ITO glass substrates is almost identical to that of the bare ITO glass over the light wavelength from 450 to 800 nm. This reveals clearly that modification of the ILCNs layer on ITO electrode does not affect its transparency. This is in agreement with the results showing that absorption in PSCs made with ILCNs-modified ITO glass is almost the same as PSCs with bare ITO glass.

In order to carry out a systematic study of the effect of the ILCNs-modified ITO cathode on the performance of inverted P3HT:PCBM-based PSCs, a set of structurally identical polymer solar cells made with ITO cathode modified differently by ILCNs was fabricated. To get optimal

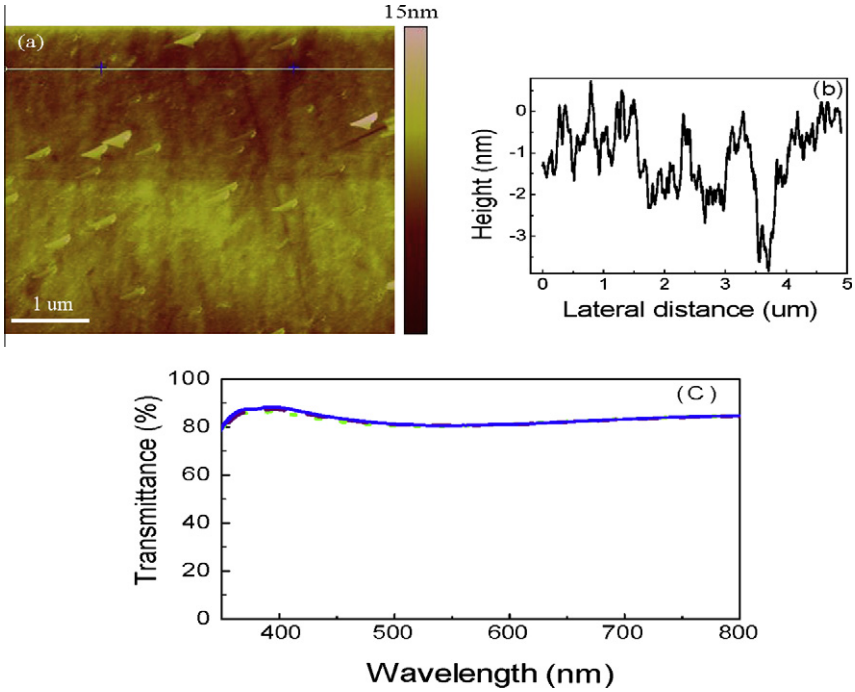

Fig. 1. (a) AFM images measured for ILCNs-modified ITO surface. (b) Topographical height of ILCNs layer on ITO. (c) Optical transmission spectra measured for ITO surface modified with ILCN layers prepared at different spin-coating speeds of 1500 rpm (dot), 2500 rpm (dash) and pure ITO (solid).

thickness of ILCNs layer, the ILCN films were spin-coated at 1500, 2000 and 2500 rpm for 60 s, respectively, followed by annealing at 120 °C for 10 min. The layer thickness of ILCNs prepared at different spin-casting speeds was estimated to be 1–3 nm using AFM. However, the PCE of devices within these spin-coating speed range is close and the optimal device of PCE is 3.20% at the spin-coating speed of 2000 rpm. The results reveal that the PCE of devices is insensitive to thickness of ILCNs layer. This is probably attributed to the sp^2-bonded aromatic structure of carbon nanoparticles and the formation of the electric double layers between ITO and the active layer. The sp^2-bonded aromatic structure of carbon nanoparticles can transport electrons and decrease tunneling barrier height at the interfacial contacts [18]. The ions of ILCNs are expected to form electric double layers with large polarization fields at the interface between the active layer and ILCN, as well as between ILCN and ITO cathode [19]. The presence of electric double layers and carbon nanoparticles helps to reduce the electron injection/extraction barrier and, unlike the tunnel theory [20], is not significantly sensitive to barrier height and tunnel thickness.

The schematic energy diagram of an inverted PSC is shown in the inset of Fig. 2a. The thickness of P3HT:PCBM blend layer and MoO_3 is 200 and 5 nm, respectively. Fig. 2a shows *J–V* characteristics corresponding to PSCs prepared with ILCNs-ITO cathode that was pre-annealed at different temperatures. The ILCNs films were annealed at 120 °C (device A), 160 °C (device B) and 200 °C (device C) for 10 min after spin-casting ILCNs solution at 2000 rpm for 60 s. As-prepared ILCN-ITO cathode, which was done at room temperature (RT) without the post-annealing treatment, was also used for the control PSC (device D) for comparison study. The PCE of PSCs with ITO-only cathode is far lower than that of PSCs with ILCNs-ITO cathode, which is attributed to the higher interface barrier and the elevated reverse saturation current, as shown in Fig. 2(b). Fig. 3 presents the statistical graph of PCE of PSCs made with ILCNs-modified cathode that was annealed at different temperature. The PCE of inverted PSCs made with ILCNs-modified ITO under optimum annealing temperature of 120 °C can reach up to 3.2% and the highest efficiency of 3.37% was obtained for PSCs made with ITO-cathode pre-annealed at 160 °C. The PCE of PSCs made with ILCNs-modified ITO cathode that was annealed over the temperature from 120 and 160 °C is slightly higher than efficiency of PSCs made with the cathode that was at 200 °C (device C). It is noted that PCE of device C is comparable to the efficiency of devices A, B and D, suggesting that ILCNs-modified cathode has a very good thermal stability suitable for application in inverted PSCs. In addition to its thermal stability, the nature of the solution processability also makes ILCNs practically more attractive over the materials commonly used for electrode modification, such as TiO_x, ZnO and Cs_2CO_3. This is because the performance of inverted PSCs made with ITO, modified with these materials, is very sensitive to the annealing temperature. The solution-processed ILCNs-modified ITO can be also easily integrated with the fabrication of PSCs using solution processable materials.

In order to understand the changes in the surface properties of ILCNs-modified ITO cathode, the surface hydrophobic property of ILCNs-modified ITO was measured using contact angle measurement, and the ILCNs-modified

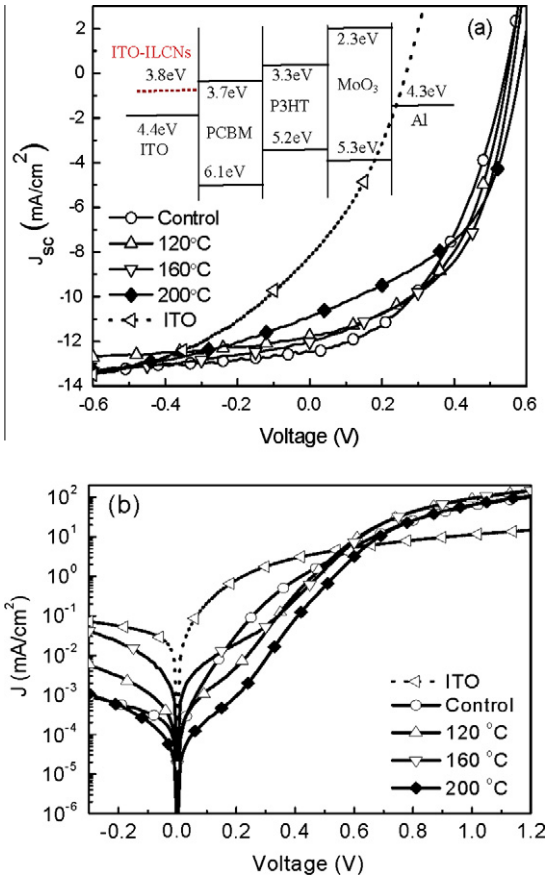

Fig. 2. (a) The *J–V* characteristics of PSCs made with ITO-only cathode (◁), ILCNs-modified ITO cathodes prepared at different pre-annealing temperature, for example, the as-prepared ILCNs layer at room temperature (Control ○), annealed at temperatures of 120 °C (△), 160 °C (▽) and 200 °C (♦). The inset illustrates the schematic energy diagram of an inverted PSC studied in this work. (b) The *J–V* characteristics measured for the PSCs in the dark condition.

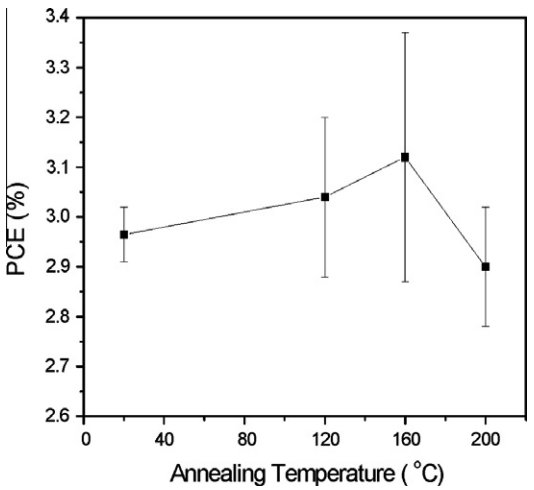

Fig. 3. PCE of devices made with ILCNs-modified ITO cathode as a function of pre-annealing temperature.

ITO cathode was studied using UPS measurements to determine the electronic structures on both bare ITO and ILCNs-modified ITO surfaces. Fig. 4(a) shows the secondary electron edge in UPS spectra measured for ILCNs-modified ITO surface, which can provide information of the work function of ILCNs-modified ITO surface. The work function of modified ITO cathode as a function of ILCNs annealing temperature is further presented in Fig. 4(b). As shown in Fig. 4(b), the surface hydrophobic property of ILCN films gradually increased with the post-annealing temperature. The increase in the contact angle seen in ILCNs surface is ascribed to the ionic liquid deficiency in ILCNs, due to the increase in the annealing temperature. The work function of UV-ozone treated ITO surface was 4.4 eV. The work function of the bare ITO decreased to about 3.8 eV when its surface was modified with a thin layer of ILCNs. The 0.6 eV decrease in work function of ILCNs-modified ITO electrode suggests that ILCNs-modified ITO can be an effective cathode for application in inverted PSCs. It was found that the work function of ILCNs-modified ITO further decreased to 3.7 eV after annealing at 200 °C for 10 min. However, the PCE of device C annealed at 200 °C was a little lower, which means that other possible factors such as hydrophobic property may affect the morphology of the

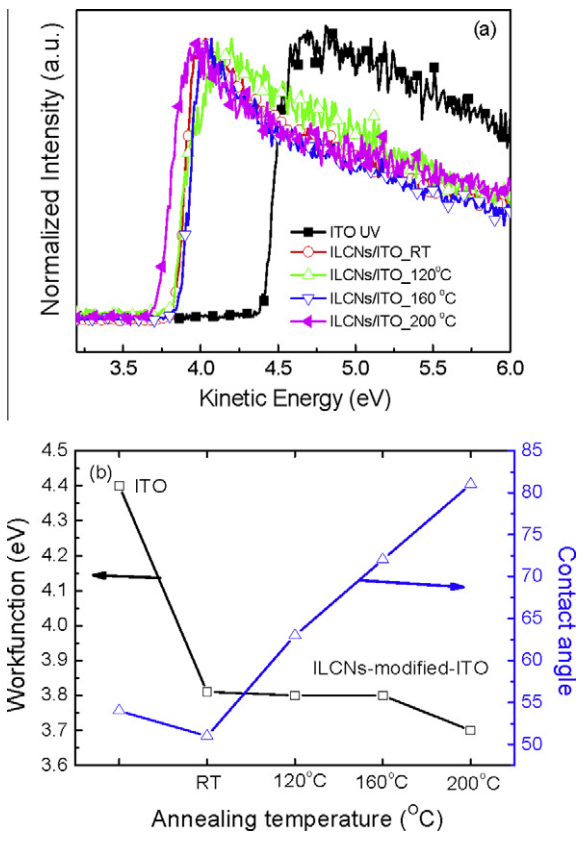

Fig. 4. (a) Evolution of secondary electron edge in UPS spectra measured for ILCNs layer modified ITO annealed at different temperatures; (b) Work function (□) and the contact angle (△) of modified-ITO cathode as a function of ILCNs annealing temperature, the values of work function and the contract angle obtained for a bare ITO are also plotted for comparison.

active polymer layer and the interface barrier between cathode electrode and P3HT:PCBM blend layer [14].

4. Conclusion

In summary, a high performance solution processable ILCNs-modified ITO cathode was developed. ILCNs-modified ITO cathode has very good thermal stability and a surface work function of 3.8 eV. Transparent ILCNs-modified ITO cathode was used for P3HT:PCBM-based inverted polymer solar cells, resulting in a PCE of 3.2% measured under AM1.5G illumination of 100 mW/cm^2. The device performance of the inverted PSCs is comparable to that of a reference PSC having the same material system and device structure [15,16]. The ILCNs-modified ITO cathode developed here has the advantages of solution processability, thermal stability and the desired electronic properties, and is superior to the cathode contacts that are modified using traditional materials such as TiO_x, ZnO and Cs_2CO_3, for application in inverted polymer solar cells.

Acknowledgement

The authors acknowledge financial support from the NRF-CRP grant "Graphene and Related Materials and Devices R-143-000-360-281".

References

[1] S.H. Park, A. Roy, S. Beaupr, S. Cho, N. Coates, J.S. Moon, D. Moses, M. Leclerc, K. Lee, A.J. Heeger, Bulk heterojunction solar cells with internal quantum efficiency approaching 100 percent, Nature Photonics 3 (2009) 297–302.
[2] H.Y. Chen, J. Hou, S. Zhang, Y. Liang, G. Yang, Y. Yang, L. Yu, Y. Wu, G. Li, Polymer solar cells with enhanced open-circuit voltage and efficiency, Nature Photonics 3 (2009) 649–653.
[3] G. Li, V. Shrotriya, J. Huang, Y. Yao, T. Moriarty, K. Emery, Y. Yang, High-efficiency solution processable polymer photovoltaic cells by self-organization of polymer blends, Nature Materials 4 (2005) 864–868.
[4] G.M. Ng, E.L. Kietzke, T. Kietzke, L.W. Tan, P.K. Liew, F. Zhu, Optical enhancement in semitransparent polymer photovoltaic cells, Applied Physics Letters 90 (2007) 103505.
[5] X. Chen, C. Zhao, L. Rothberg, M.K. Ng, Plasmon enhancement of bulk heterojunction organic photovoltaic devices by electrode modification, Applied Physics Letters 93 (2008) 123302.
[6] C. Waldauf, M. Morana, P. Denk, P. Schilinsky, K. Coakley, S.A. Choulis, C.J. Brabec, Highly efficient inverted organic photovoltaics using solution based titanium oxide as electron selective contact, Applied Physics Letters 89 (2006) 233517.
[7] M.S. White, D.C. Olson, S.E. Shaheen, N. Kopidakis, D.S. Ginley, Inverted bulk-heterojunction organic photovoltaic device using a solution-derived ZnO underlayer, Applied Physics Letters 89 (2006) 143517.
[8] L.M. Chen, Z. Hong, G. Li, Y. Yang, Recent progress in polymer solar cells: manipulation of polymer: fullerene morphology and the formation of efficient inverted polymer solar cells, Advanced Materials 21 (2009) 1434–1449.
[9] J.Y. Kim, K. Lee, N.E. Coates, D. Moses, T.Q. Nguyen, M. Dante, A.J. Heeger, Efficient tandem polymer solar cells fabricated by all-solution processing, Science 317 (2007) 222.
[10] C. Tao, S. Ruan, X. Zhang, G. Xie, L. Shen, X. Kong, W. Dong, C. Liu, W. Chen, Performance improvement of inverted polymer solar cells with different top electrodes by introducing a MoO buffer layer, Applied Physics Letters 93 (2008) 193307.
[11] J.S. Huang, C.Y. Chou, M.Y. Liu, K.H. Tsai, W.H. Lin, C.F. Lin, Solution-processed vanadium oxide as an anode interlayer for inverted polymer solar cells hybridized with ZnO nanorods, Organic Electronics 10 (2009) 1060–1065.
[12] M. Jorgensen, K. Norrman, F.C. Krebs, Stability/degradation of polymer solar cells, Solar Energy Materials and Solar Cells 92 (2008) 686–714.
[13] V. Shrotriya, G. Li, Y. Yao, C.W. Chu, Y. Yang, Transition metal oxides as the buffer layer for polymer photovoltaic cells, Applied Physics Letters 88 (2006) 073508.
[14] H.H. Liao, L.M. Chen, Z. Xu, G. Li, Y. Yang, Highly efficient inverted polymer solar cell by low temperature annealing of Cs_2CO_3 interlayer, Applied Physics Letters 92 (2008) 173303.
[15] X. Chen, J. Yang, J. Lu, K.K. Manga, K.P. Loh, F. Zhu, Ionic liquid-functionalized carbon nanoparticles-modified cathode for efficiency enhancement in polymer solar cells, Applied Physics Letters 95 (2009) 3305.
[16] Y. Wang, X. Chen, Y. Zhong, F. Zhu, K.P. Loh, Large area, continuous, few-layered graphene as anodes in organic photovoltaic devices, Applied Physics Letters 95 (2009) 063302.
[17] J. Lu, J. Yang, J. Wang, A. Lim, S. Wang, K.P. Loh, One-pot synthesis of fluorescent carbon nanoribbons, nanoparticles, and graphene by the exfoliation of graphite in ionic liquids, ACS Nano 3 (2009) 2367–2375.
[18] C. Ganzorig, K.J. Kwak, K. Yagi, M. Fujihira, Fine tuning work function of indium tin oxide by surface molecular design: enhanced hole injection in organic electroluminescent devices, Applied Physics Letters 79 (2001) 272.
[19] C.V. Hoven, J. Peet, A. Mikhailovsky, T.Q. Nguyen, Direct measurement of electric field screening in light emitting diodes with conjugated polyelectrolyte electron injecting/transport layers, Applied Physics Letters 94 (2009) 033301.
[20] R.G. Forbes, Simple good approximations for the special elliptic functions in standard Fowler–Nordheim tunneling theory for a Schottky–Nordheim barrier, Applied Physics Letters 89 (2006) 113122.

Organic Electronics 11 (2010) 1947–1953

Contents lists available at ScienceDirect

Organic Electronics

journal homepage: www.elsevier.com/locate/orgel

Origin of high field-effect mobility in solvent–vapor annealed anthradithiophene derivative

Chia-Hsin Wang [a], Yung-Chiuan Cheng [b], Jing-Wen Su [b], Liang-Jen Fan [a], Peng-Yi Huang [c], Ming-Chou Chen [c], Yaw-Wen Yang [a,b,*]

[a] National Synchrotron Radiation Research Center, Hsinchu 30076, Taiwan
[b] Department of Chemistry, National Tsing-Hua University, Hsinchu 30013, Taiwan
[c] Department of Chemistry, National Central University, Jhongli 32001, Taiwan

ARTICLE INFO

Article history:
Received 25 April 2010
Received in revised form 7 September 2010
Accepted 8 September 2010
Available online 23 September 2010

Keywords:
Functionalized anthradithiophene
Solvent–vapor annealing
Organic field effect transistor

ABSTRACT

Solvent–vapor annealing was used to increase the field-effect mobility of soluble triethylsilylethynyl anthradithiophene spin-coated on organosilane-terminated silicon dioxide, yielding a high value of 1.2 $cm^2 V^{-1} s^{-1}$. The cause of improvement was investigated by atomic force microscopy, X-ray diffraction, and near-edge X-ray absorption fine structure spectroscopy. Vapor annealing exerts little effect on the molecular tilt and the crystallinity normal to the surface, but improves the film morphology significantly, yielding larger grains with perhaps better in-plane crystallinity.

© 2010 Elsevier B.V. All rights reserved.

1. Introduction

Solution-processable organic semiconducting materials have gained tremendous popularity in recent years due to the anticipated low-cost and flexible engineering approaches to electronic device fabrication [1–4]. Organic field effect transistors (OFETs) have been envisaged to have active applications in the fields of radio-frequency identification tags [5], active matrices displays [6], and smart cards. For practical usage, OFET should have mobility comparable to that of amorphous silicon, i.e., 1 $cm^2 V^{-1} s^{-1}$, an on/off ratio larger than 10^6, and an operational stability in ambient [1,7,8]. Solvent–vapor annealing has been demonstrated to improve the electrical performance of organic electronics materials via the recrystallization induced by solvent vapor [9–11]. However, the effect of the vapor annealing on the molecular orientation and the crystalline state remains to be elucidated.

Due to a favorable two-dimensional π-stacking, solution-processable triethylsilylethynyl-anthradithiophene (TESADT) was demonstrated to yield a hole mobility of 1 $cm^2 V^{-1} s^{-1}$, based on a bottom contact OFET with TESADT spread across the device surface [12]. However, the typical processing techniques like spin-coating only produce OFET of low mobility, which can be remedied by vapor annealing. Improved mobility values of 0.11 and 0.43 $cm^2 V^{-1} s^{-1}$ have been reported [13,14]. The modification of SiO_2 dielectric surface with self-assembled monolayers (SAM) of organosilanes has established itself as an effective means of improving the field-effect mobility of OFET via improved thin film quality and better interfacial property [15]. Along the line, a phenyl-terminated SAM of phenethlytrichlorosilane grown on SiO_2 was reported to increase the mobility and also improve the air-stability of pentacene OFET [16].

In this report, we used a phenyl-SAM-modified SiO_2 as the substrate for growing TESADT and the as-grown films were further subject to the solvent–vapor annealing to accelerate the grain growth, thereby achieving an OFET saturation mobility higher than what have been reported so far. By combining several structural characterization

* Corresponding author at: National Synchrotron Radiation Research Center, Hsinchu 30076, Taiwan. Tel.: +886 3 578 0281x7314; fax: +886 3 578 3813.
E-mail address: yang@nsrrc.org.tw (Y.-W. Yang).

1566-1199/$ - see front matter © 2010 Elsevier B.V. All rights reserved.
doi:10.1016/j.orgel.2010.09.010

techniques, we offer a plausible explanation for the mobility enhancement.

2. Experimental

The *n*-type heavily-doped silicon wafer capped with 300 nm thick thermally-grown SiO_2 served as a gate dielectric. The wafer was cleaned by hot Piranha solution, an acid mixture of H_2SO_4 and H_2O_2 at a volume ratio of 7:3, heated through water bath for 3–5 h to remove the organic contaminants, and then thoroughly rinsed with deionized water and dried with nitrogen gas before use. TESADT films were grown on two types of substrates: SiO_2 and SiO_2 terminated with 4-phenylbutyltrichlorosilane (4-PBTS) SAM. As-produced samples were labeled as **I** and **II**, respectively. For growing SAM, the SiO_2 was placed in a 1 wt.% solution of 4-PBTS in toluene for 1 h. TESADT was spin-coated using a 20 μl of 1 wt.% solution of TESADT in toluene at two speeds, 1000 rpm for 2 s and then 1500 rpm for 28 s. The thickness of as-produced films was estimated as 30 nm by Atomic Force Microscopy (AFM). Afterward, vapor-annealing was performed by separately placing samples **I** and **II** faceup near the bottom of a 100 ml PFA bottle filled with 50 μl dichloromethane solvent with its vapor agitated by a Teflon bar spinning at 120 rpm for 15 min. These samples were labeled as **III**, and **IV**. The fabrication of top-contact, bottom gate OFETs was complete by forming Au electrodes on top of TESADT films via vacuum-depositing gold through a shadow mask patterned with a fixed channel length of 80 μm, but variable channel widths of 400, 800, and 1600 μm, respectively.

The morphology of the organic films was characterized by AFM operated in contact mode (Digital instruments, NanoScope E). X-ray diffraction (XRD) study was carried out using MAC MXP-18 and BRUKER AXS D8 ADVANCE diffractometer with Cu K_α radiation. The Near-Edge X-ray Absorption Fine Structure (NEXAFS) spectroscopy were performed in Wide-Range beamline (BL24A) of NSRRC based on Auger-electron yield (AEY) detection mode with an electron energy analyzer (SPECS PHOBOIS 150). The output characteristics of the OFETs were measured in ambient condition using a Keithley 2636A dual-channel source-meter instrument.

3. Results and discussion

Fig. 1 shows a set of AFM images for samples **I**–**IV**. The SiO_2 surface in sample **I** is covered by small TESADT grains uniformly, producing a film with an rms roughness of 1.0 nm (Fig. 1a). In comparison, a growth of larger grains up to several hundred nm is noted in sample **II**, yielding a roughness of 1.8 nm (Fig. 1b). As a reference, the typical roughness values for the SiO_2 after Piranha cleaning and after 4-PBTS modification are 0.9 and 0.6 nm, respectively. After the vapor annealing, a dramatic change of surface morphology is observed. For sample **III** (Fig. 1c), mound-like structures with sizable voids in-between are formed, resulting in a larger roughness of 2.4 nm. Meanwhile, for sample **IV** (Fig. 1d), continuous, platelet-shaped structures are produced with a reduced roughness of 1.0 nm.

Fig. 2 shows the θ–2θ XRD patterns obtained for samples **I**–**IV**. The diffraction patterns consist of (0 0 *l*) reflections only as the 2θ angle is varied between 3° and 18°. A (0 0 1) reflection at $2\theta = 5.34°$ corresponds to an interlayer spacing of 16.54 Å, given the X-ray wavelength of 1.5406 Å. The numerical closeness between the interlayer spacing and the *c* axis value [17] together with the observation of (0 0 *l*) reflections only strongly indicate that TESADT crystallites are oriented with silyl group in close proximity to the surface and *a*, *b* crystallographic axes are parallel to

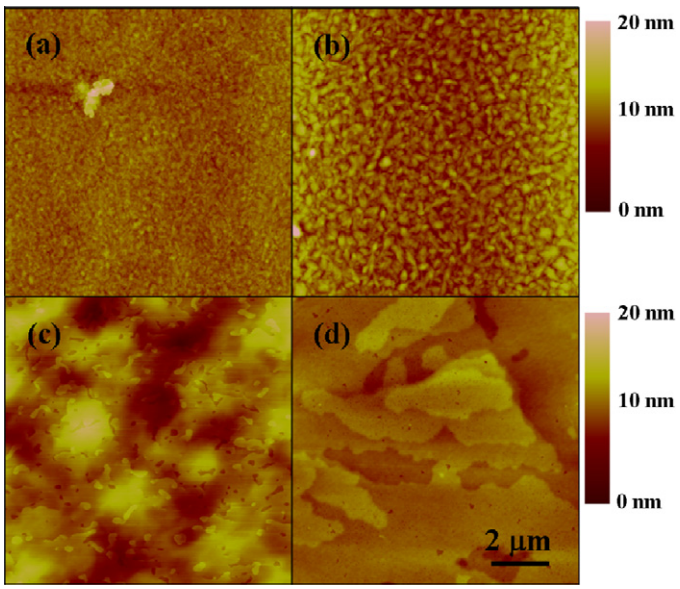

Fig. 1. AFM images for samples **I–IV**. (a) sample **I**, TESADT on SiO_2 surface; (b) sample **II**, TESADT on the SiO_2 modified with 4-PBTS; (c) sample **III**, vapor-annealed sample **I**, and (d) sample **IV**, vapor-annealed sample **II**.

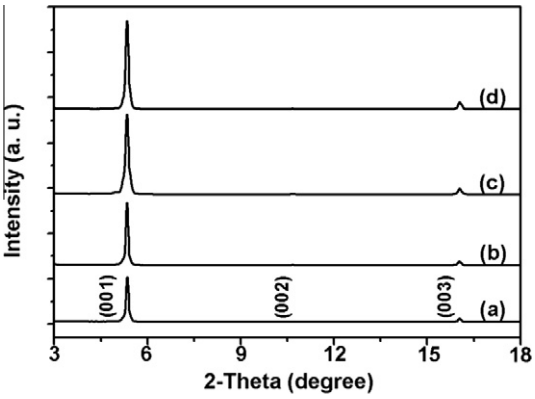

Fig. 2. XRD patterns for (a) sample **I**; (b) sample **II**; (c) sample **III**, and (d) sample **IV**.

the substrate surface within a few degrees. This finding corroborates with the results deduced from NEXAFS data (*vide infra*). Sample **IV** has the strongest (0 0 1) reflection as compared with the weakest reflection for sample **I**, yielding a 2:1 intensity ratio but similar peak width. Sample **IV** is deemed to possess the best out-of-plane crystallinity, but perhaps not by much. Moreover, the distribution of sub-grain tilt is assessed by measuring the ω-scan rocking curve of (0 0 1) peak and two types of slightly misoriented crystallites are identified (data not shown).

The intermolecular carrier transport crucially depends on the molecular orientation ordering, a physical parameter amenable to the NEXAFS techniques. Briefly speaking, the carbon *K*-edge NEXAFS spectroscopy measures the transition probabilities of an electron from the C1s core level into its various unoccupied molecular orbitals with the transitional intensity (I) dependent on the X-ray incidence angle (θ), and the orientation of transitional dipole

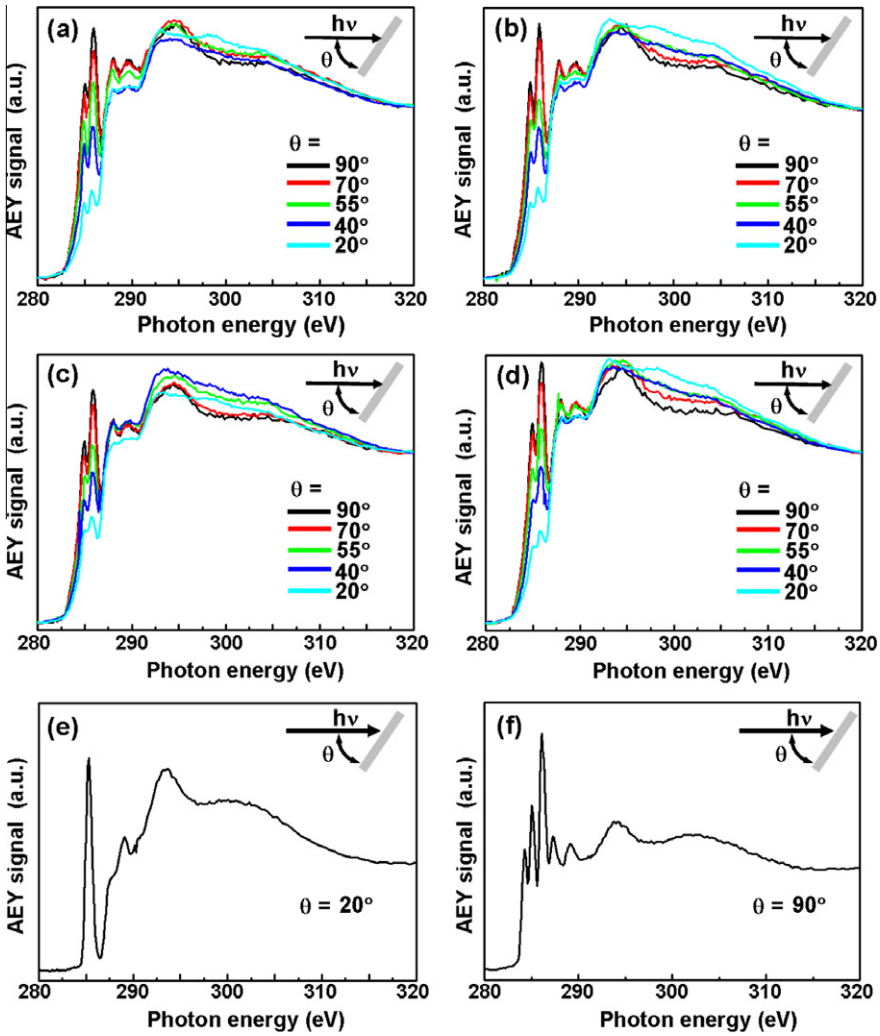

Fig. 3. (a–d) Polarization dependent, edge-jump normalized carbon *K*-edge NEXAFS spectra for (a) sample **I**; (b) sample **II**; (c) sample **III**, and (d) sample **IV**; (e) NEXAFS spectrum for 4-PBTS on SiO_2; (f) NEXAFS spectrum of ADT multilayer on SiO_2. All the spectra were acquired using Auger electron detection (AEY) method with the electron energy window set at 260 eV.

moment investigated. For the molecules adsorbed on a surface, the dependence on the azimuthal angle often vanishes due to the crystallographic symmetry exhibited by the surface atomic plane and the tilt angle of the dipole moment (α) becomes the remaining angle dependent term. The angular dependence is expressed in the following equation:[18]

$$I(\theta,\alpha) \propto P\cos^2\theta\left(1-\frac{3}{2}\sin^2\alpha\right)+\frac{1}{2}\sin^2\alpha, \quad (1)$$

where P is the polarization factor and determined to be 0.85 for carbon K-edge energy at a bending beamline of NSRRC, and θ and α are measured from the surface plane and surface normal, respectively. For the π-conjugated molecule investigated here, the lower-energy X-ray absorption peaks are due to the transitions from C1s to π* orbitals with the transition dipole moment vectors perpendicular to the aromatic-ring plane of the molecule. Therefore, by analyzing how the intensity of X-ray transition depends on the X-ray incidence angle, the molecular tilt angle can be inferred.

Fig. 3a–d show four sets of polarization-dependent carbon NEXAFS spectra for samples **I–IV**. The major spectral features and their angular dependence are all similar despite the different surface treatment. Also shown for comparison are the spectra of 4-PBTS (Fig. 3e) and multilayered anthradithiophene (ADT), a five-member-ring constituent of TESADT, grown on SiO_2 (Fig. 3f). The contribution of 4-PBTS SAM to the total signal is found to be negligible owing to its attenuation by the TESADT overlayer. The spectroscopic assignment of the salient features of TESADT spectra is relatively straightforward.[18] The first region from 284 to 287 eV containing several sharp absorption peaks is assigned to the transitions from C1s core level to the lower unoccupied orbitals of π character; the second region from 287 to 290 eV is assigned to the transitions form C1s to mostly π* states but perhaps mixed with some σ^*_{C-H} and σ^*_{C-S} characters [19]; the broad absorption features from 290 to 320 eV are due to the transitions from C1s to various σ^* states.

For the determination of inclination angle of the ring plane of TESADT, the total intensity of sharp1s to π* transitions located in the spectral region from 284 to 287 eV is included in the analysis. These peaks bear strong resemblance with those of ADT and the anthracene [20] and can be regarded as originated from ADT in spite of slightly larger transitional energy for TESADT. Note that the dependence of NEXAFS signal on the X-ray incidence angle for an amorphous sample like SiO_2 used here is the same as that for a substrate possessing 3-fold symmetry like fcc(1 1 1) [21]. A fitting of the intensity of the X-ray transition to the theoretical curves described by Eq. (1) is presented in Fig. 4a in which an inclined angle of 72° is concluded. The ADT rings of samples **I–IV** are found to be inclined from the surface plane by 70°, 71°, 68°, and 72°, respectively. The derived inclination angles agree closely with the 71° tilt of the ADT ring from the surface to the *a*, *b* plane of the crystallographic unit cell [12], as presented in Fig. 4b. The close similarity among these tilt angles suggests that *a*, *b* plane of the TESADT crystallites aligns

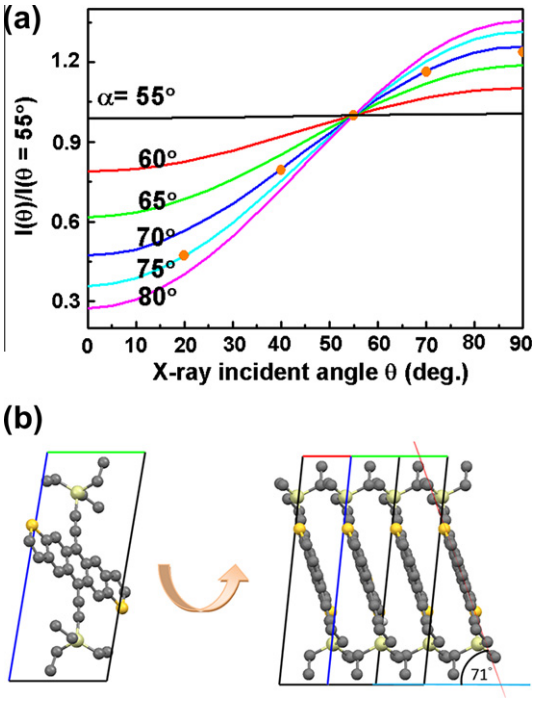

Fig. 4. (a) Angle-dependent intensity of 1s to π* transition for the sample **IV** (solid dots) plotted against the theoretical curves generated from Eq. (1). The intensity of each curve, corresponding to a given inclination angle of aromatic ring made with the surface, is normalized to its intensity at the so-called magic angle of $\theta = 54.7°$. (b) (Left) view of TESADT unit cell along the *a*-axis with crystallographic data taken from Ref. [12]. (Right) The 71° inclination angle of ADT ring made with the *a*, *b* plane is revealed by rotating the unit cell in the *a*, *b* plane.

closely with the substrate surface. It is worth noting that the NEXAFS and XRD data corroborate with each other despite their different structure sensitivity. Whereas XRD is sensitive to long-range structural ordering, NEXAFS technique has no direct bearing on the structural ordering other than yielding an averaged molecular tilt from the surface normal because the azimuthal dependence is often averaged out.

The electrical properties of the samples were assessed by measuring their OFETs characteristics. The field-effect mobility (μ) is extracted from the saturation regime using the relationship:

$$I_{DS} = \frac{W}{2L}\left[C_i\mu(V_{GS}-V_T)^2)\right] \quad (2)$$

where I_{DS} is the source-drain saturation current, W and L are channel width and length, respectively, C_i is the capacitance per unit area of the gate dielectric (= 10.8 nF/cm^2) [14], V_{GS} is the gate voltage relative to source electrode, and V_T is the threshold voltage. The latter can be estimated as the x intercept of the linear section of the plot of $(I_{DS})^{1/2}$ vs. V_{GS}. Fig. 5 shows the typical output characteristics (left) of the OFETs fabricated from samples **I–IV** and the corresponding transfer characteristics evaluated at V_{GS} of −50 V are shown in the right. The distribution of the

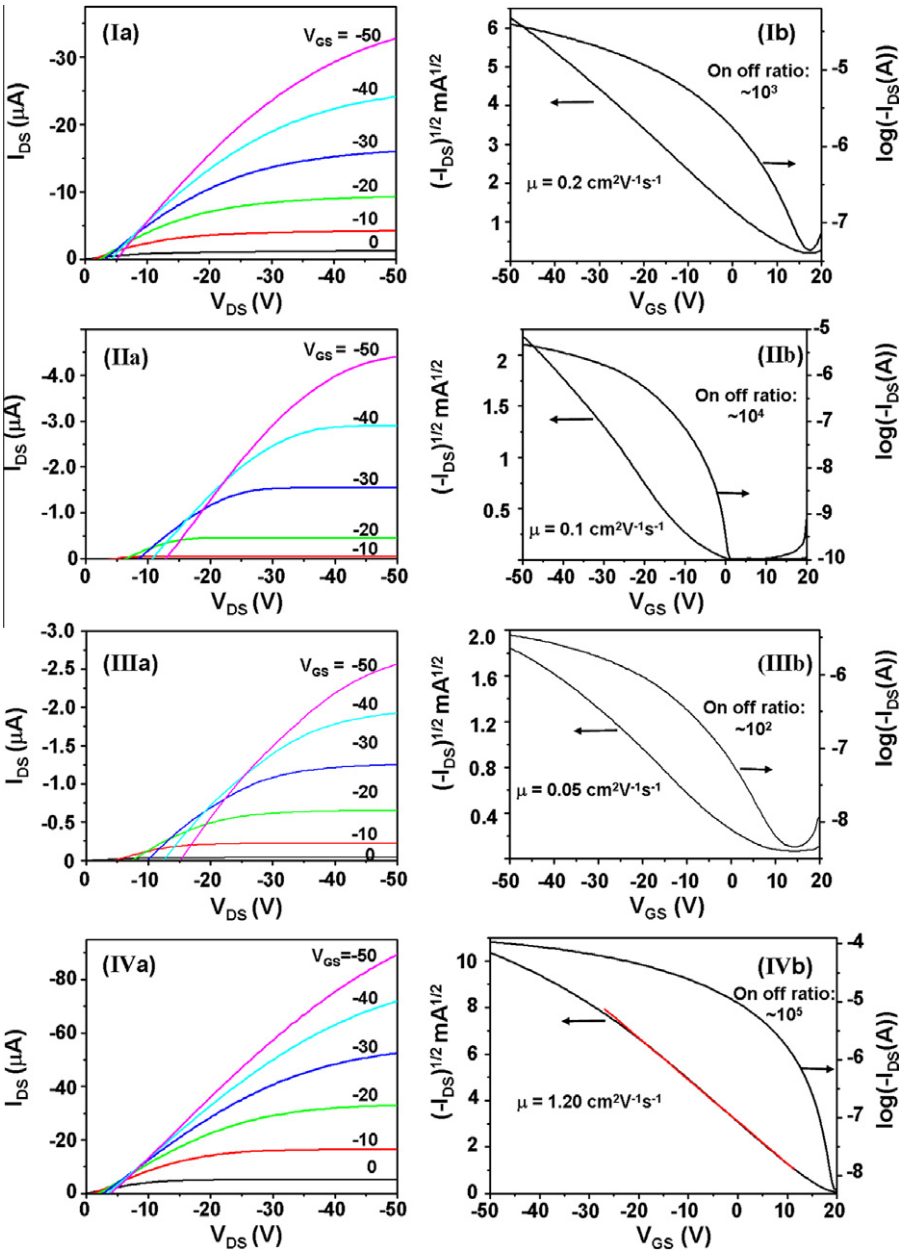

Fig. 5. (Left) output characteristics of the OFETs fabricated from samples **I–IV**; (right) saturated transfer characteristics ($I_{DS}^{1/2}$ vs. V_{GS}) of the corresponding OFETs. *W/L* for samples **II–IV** OFETs is 400 μm/80 μm, whereas *W/L* for sample **I** OFET is 800 μm/80 μm. For each device, the output curves were first acquired by having V_{GS} varied by a 10 V step between 0 and −50 V, and for each V_{GS}, the V_{DS} was swept from 0 to −50 V and back to 0 V. The transfer curves were next obtained by keeping V_{DS} at −50 V with V_{GS} swept from 20 to −50 V (off-to-on).

mobility values determined for all devices is presented in a linear scatter plot shown in Fig. 6. Note that the mobility for samples **I–III** OFETs ranges from several hundredths to several tenths of a $cm^2\,V^{-1}\,s^{-1}$; and a number of data points clustered around $\mu = 0$ are omitted for clarity in Fig. 6. In stark contrast, the sample **IV** OFET yields a consistently larger mobility, though of a broader spread, and averages 0.46 $cm^2\,V^{-1}\,s^{-1}$ over ten devices. The highest mobility obtained is 1.2 $cm^2\,V^{-1}\,s^{-1}$ and the on/off ratio is 10^5. The output and transfer characteristics of this device are shown in Fig. 5-IVa and 5-IVb. We note that our value tops the mobility list of TESADT OFETs reported so far [12–14]. The performance of OFETs fabricated with samples **I–IV** is compiled in Table 1. The gate induced leakage current, or drain current offset, signaled by non-zero drain current at zero V_{DS} in the output characteristics curve [22], is sometimes found in devices such as those shown in Fig. 5-IIa and 5-IIIa. This undesirable feature can be greatly reduced by spatially confining the semiconducting materials in the intended channel region.

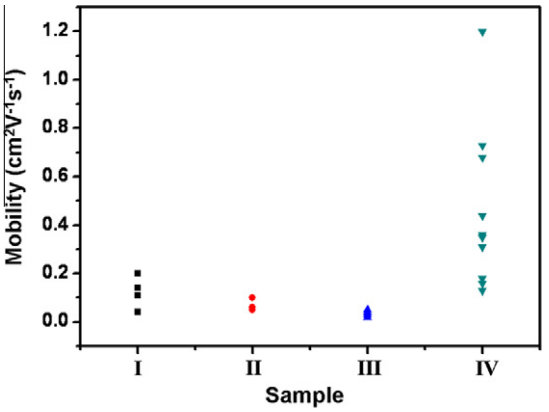

Fig. 6. Distribution of OFET mobility determined from the devices fabricated with samples **I–IV**.

Table 1
Performances summary of the OFETs fabricated from samples **I–IV**.

Sample	Sample condition	μ ($cm^2\ V^{-1}\ s^{-1}$)		Avg. on/off ratio
		Avg.	Max.	
I	TESADT/SiO_2	0.11	0.20	4.84×10^2
II	TESADT/4-PBTS/SiO_2	0.08	0.10	5.94×10^4
III	TESADT/SiO_2 (p.a.s.v.)	0.03	0.05	4.18×10^4
IV	TESADT/4-PBTS/SiO_2 (p.a.s.v.)	0.46	1.20	1.17×10^5

p.a.s.v., Post-annealed with solvent vapor.

Here we digress to examine the hysteresis in current–voltage characteristics in the devices. For example, in the sample **IV** OFET, the last measurement in the output-curve scan ($V_{GS} = V_{DS} = -50$ V) gives an I_{DS} of 89 μA, but in the subsequent transfer-curve scan with the transistor changing from the off-to on-mode (V_{GS} swept from 20 to −50 V while V_{DS} fixed at −50 V), the corresponding I_{DS} increases to 107 μA. The increase of I_{DS} for the off-to-on sweep in the transfer characteristics has been reported for the pentacene OFET, with the hysteresis accounted for by the formation of long-lifetime traps at pentacene–dielectric interface [23,24]. Since the present study is focused on the investigation of origin of high mobility in solvent-annealed TESADT films, the hysteresis is not pursued further. How the saturation mobility, determined by the rate of change of $(I_{DS})^{1/2}$ with the V_{GS}, is affected by the hysteresis must await further studies. However, it is interesting to note that for the typical pentacene OFET with hysteresis, as reported in the Fig. 1 of Ref. [23], the saturation mobility determined from the off-to-on scan is estimated to be lower by ~10% than that from an on-to-off scan, despite a higher I_{DS} produced from the off-to-on scan. Linear mobility determined from the on-to-off scan also increases by ~25%, counter to the effect of decreasing I_{DS}.

We now return to the discussion of origin of mobility enhancement. Samples **I–IV** are all crystalline, and even more interesting is that sample **I** possesses crystallinity and thus fares better than the amorphous samples reported earlier [13]. The similar tilt angle between samples I–IV and TESADT single crystal, inferred from NEXAFS data, suggests that all four samples have adopted a favorable cofacial π–π stacking characteristic of a single crystal. As a result, the intermolecular transfer integral that is crucial in charge transport should be similar if the molecular spacing in all four samples is close [25]. Moreover, considering that samples **I–IV** are all crystalline and terminated with TESADT of the same orientation, there is no a prior reason not to expect the formation of similar metal–semiconductor interface that gives rise to equivalent charge injection as Au is deposited on TESADT. The presence of 4-PBTS creates a permanent interface dipole that changes the surface potential and shifts the threshold voltage of OFET but not the carrier mobility [26].

Because the charge injection and the transfer integral for samples **I–IV** are argued to be similar in quantity, the size of crystallite distribution should be scrutinized next because the carrier transport critically depends on the carrier scattering at the grain boundary. It has been well established that a smaller crystal grain decreases the carrier transport efficiency [25]. AFM image of sample **III** is typified by an increasing number of disconnected, mound-like features after annealing; therefore, a mobility increase is not to be expected. In stark contrast, sample **IV** forms smooth, continuous, platelet-like structures after annealing, thereby leading to a tenfold increase in mobility.

Why is there such a difference in the regrowth initiated by solvent vapor? An effective vapor annealing depends complicatedly on many parameters including solubility, solvent vapor pressure, spreading of solution on surface, interfacial free energy, recrystallization rate, to name a few. We speculate that different interfacial interaction between TESADT and the substrate might be responsible for the morphology difference that in turn affects the mobility. TESADT interacts with 4-PBTS more strongly than with SiO_2 due to the phenyl termination in the former. As a result, more two-dimensional-like growth of TESADT on 4-PBTS is favored due to the stronger interfacial interaction. In comparison, three-dimensional mound-like formation is found for TESADT on SiO_2.

In conclusion, we have used a phenyl-terminated SAM on SiO_2 to enable a larger grain growth of TESADT. Dichloromethane-vapor annealing promotes the formation of better-connected, platelet-shaped crystallites, thereby increasing the saturation OFET mobility to 1.2 $cm^2\ V^{-1}\ s^{-1}$. The formation of TESADT crystallites on SiO_2 is noted in the present study, which paves the way for growing larger crystallites during vapor annealing. Vapor annealing neither changes the molecular orientation nor improves the out-of-plane crystallinity markedly, but significantly improves the morphology and yields larger grains with perhaps better in-plane crystallinity.

Acknowledgements

The authors wish to thank Ching-Shun Ku for the help and useful discussion in XRD measurements. YWY acknowledges the financial support from NSRRC and National Science Council of ROC (Grant No. NSC 96-2113-M-213-008-MY3).

References

[1] C.D. Dimitrakopoulos, P.R.L. Malenfant, Adv. Mater. 14 (2002) 99.
[2] J.E. Anthony, Chem. Rev. 106 (2006) 5028.
[3] D.J. Gundlach, J.E. Royer, S.K. Park, S. Subramanian, O.D. Jurchescu, B.H. Hamadani, A.J. Moad, R.J. Kline, L.C. Teague, O. Kirillov, C.A. Richter, J.G. Kushmerick, L.J. Richter, S.R. Parkin, T.N. Jackson, J.E. Anthony, Nat. Mater. 7 (2008) 216.
[4] H. Sirringhaus, Adv. Mater. 17 (2005) 2411.
[5] P.F. Baude, D.A. Ender, M.A. Haase, T.W. Kelley, D.V. Muyres, S.D. Theiss, Appl. Phys. Lett. 82 (2003) 3964.
[6] Y.H. Kim, S.K. Park, D.G. Moon, W.K. Kim, J.I. Han, Jpn. J. Appl. Phys. 43 (2004) 3605.
[7] M.L. Tang, A.D. Reichardt, T. Siegrist, S.C.B. Mannsfeld, Z. Bao, Chem. Mater. 20 (2008) 4669.
[8] D. Braga, G. Horowitz, Adv. Mater. 21 (2009) 1.
[9] A. Babel, J.D. Wind, S.A. Jenekhe, Adv. Funct. Mater. 14 (2004) 891.
[10] J. Liu, Y. Shi, L. Ma, Y. Yang, J. Appl. Phys. 88 (2000) 605.
[11] Y. Zhao, Z.Y. Xie, Y. Qu, Y.H. Geng, L.X. Wang, Appl. Phys. Lett. 90 (2007) 3.
[12] M.M. Payne, S.R. Parkin, J.E. Anthony, C.-C. Kuo, T.N. Jackson, J. Am. Chem. Soc. 127 (2005) 4986.
[13] K.C. Dickey, J.E. Anthony, Y.-L. Loo, Adv. Mater. 18 (2006) 1721.
[14] W.H. Lee, D.H. Kim, J.H. Cho, Y. Jang, J.A. Lim, D. Kwak, K. Cho, Appl. Phys. Lett. 91 (2007) 092105.
[15] S. Kobayashi, T. Nishikawa, T. Takenobu, S. Mori, T. Shimoda, T. Mitani, H. Shimotani, N. Yoshimoto, S. Ogawa, Y. Iwasa, Nat. Mater. 3 (2004) 317.
[16] D. Kumaki, M. Yahiro, Y. Inoue, S. Tokito, Appl. Phys. Lett. 90 (2007) 133511.
[17] The triclinic structure of TESADT contains the following unit cell parameters: a = 6.73 Å, b = 7.25 Å, c = 16.70 Å, α = 98.14°, β = 94.53°, and γ = 103.9°, from Ref. [12].
[18] J. Stöhr, NEXAFS Spectroscopy, Springer-Verlag, Berlin, 1992.
[19] P. Väterlein, M. Schmelzer, J. Taborski, T. Krause, F. Viczian, M. Bäßler, R. Fink, E. Umbach, W. Wurth, Surf. Sci. 452 (2000) 20.
[20] P. Yannoulis, K.H. Frank, E.E. Koch, Surf. Sci. 241 (1991) 325.
[21] W.-S. Hu, S.-Z. Weng, Y.-T. Tao, H.-J. Liu, H.-Y. Lee, L.-J. Fan, Y.-W. Yang, Langmuir 23 (2007) 12901.
[22] H.P. Jia, G.K. Pant, E.K. Gross, R.M. Wallace, B.E. Gnade, Org. Electron. 7 (2006) 16.
[23] G. Gu, M.G. Kane, J.E. Doty, A.H. Firester, Appl. Phys. Lett. 87 (2005) 243512.
[24] C. Ucurum, H. Goebel, F.A. Yildirim, W. Bauhofer, W. Krautschneider, J. Appl. Phys. 104 (2008) 084501.
[25] V. Coropceanu, J. Cornil, D.A. da Silva, Y. Olivier, R. Silbey, J.L. Bredas, Chem. Rev. 107 (2007) 926.
[26] K.P. Pernstich, S. Haas, D. Oberhoff, C. Goldmann, D.J. Gundlach, B. Batlogg, A.N. Rashid, G. Schitter, J. Appl. Phys. 96 (2004) 6431.

Organic Electronics 11 (2010) 1954–1959

Contents lists available at ScienceDirect

Organic Electronics

journal homepage: www.elsevier.com/locate/orgel

Novel cyclometalated platinum (II) complex containing alkyl-trifluorene picolinic acid as emitter for single-layer white PLEDs

Yafei Wang [a], Yu Liu [a], Xiaoshuang Li [a], Hongrui Qi [a], Meixiang Zhu [a], Lei Wang [a], Gangtie Lei [a], Qiliang Wei [a], Weiguo Zhu [a,*], Junbiao Peng [b], Yong Cao [b,*]

[a] College of Chemistry, Key Lab of Environment-Friendly Chemistry and Application of the Ministry of Education, Xiangtan University, Xiangtan 411105, China
[b] Institute of Polymer Optoelectronic Material and Devices, South China University of Technology, Guangzhou 510640, China

ARTICLE INFO

Article history:
Received 4 June 2010
Received in revised form 12 September 2010
Accepted 14 September 2010
Available online 25 September 2010

Keywords:
Electrophosphorescence
Platinum (II) complex
White polymer light-emitting devices
Excimers
Synthesis

ABSTRACT

To explore the influence of molecular structure on formation excimers and obtain high-efficiency white polymer light-emitting devices, two novel blue-emitting cyclometalated platinum (II) complexes of (dfppy)Pt(Tfl-pic) and (C_{16}dfppy)Pt(Tfl-pic) have been successfully synthesized and characterized, where dfppy is 2-(2,4-difluoro-phenyl)pyridine, C_{16}dfppy is 5-hexdecanyl-2-(2,4-difluorophenyl)pyridine and Tfl-pic is alkyltrifluorene-containing picolinic acid derivative. Compare to (dfppy)Pt(pic), both of platinum (II) complexes exhibited high thermal stability, good solubility and excellent photoluminescent quantum efficiency (about 94% ± 10%) at room temperature. Deep blue emission at about 418 nm in dilute dichloromethane (10^{-5} M) and red-shifted emission at about 619 nm in the neat film were observed under opto-excitation. Pure white light with a CIE coordinates (0.33, 0.33) at 10 V was obtained in the (dfppy)Pt(Tfl-pic)-doped devices and a red emission was obtained in the (C_{16}dfppy)Pt(Tfl-pic)-doped devices with the same device configuration using a blend of polyvinylcarbazole and 2-(4-biphenyl)-5-(4-*tert*-butylphenyl)-1,3,4-oxadiazole as a host matrix, respectively.

© 2010 Elsevier B.V. All rights reserved.

1. Introduction

Recently, white organic light-emitting devices (WOLEDs) have attracted much increasing interest because of their potential applications in full color displays, back lighting of flat-panel displays and solid-state lighting [1–16]. An ideal white emission is generally composed of three primary colors (blue, green and red) and covers the whole visible range from 400 to 700 nm. So far, most of the reported white-emitting devices were multilayer configuration fabricated by consecutive evaporations or co-evaporation of different emission compounds [6–8]. However, this class of multilayer devices requires complicated processes, high cost and high turn-on voltage. Compared to the multilayer devices, the single-layer devices fabricated by a blend of different emitters with three primary colors have a more cost-effective. Nevertheless, this class of single-layer devices could have poor stability and can hardly get pure white emission due to phase separation and undesired Förest energy transfer from the high-energy emitter to the low-energy one. In order to obtain high-efficiency single-layer WOLEDs, an effective method, in which planar blue-emitting platinum (II) complexes were used as emitter, has been developed in these years. The white emission results from a blend of itself blue short-wavelength emission and excimer's long-wavelength emission in these devices [3,17,18]. For example, Forrest et al. made a WOLED using a bidentate platinum (II) complex (FPt) doped into 1,3-bis(N-carbazolyl)-benzene (mCP) with a power efficiency of 8.1 lm W^{-1} [17]. Jabbour et al. used the same FPt complex as dopant to fabricate similar WOLEDs using a 2,6-bis

* Corresponding authors. Tel.: +86 731 58298280; fax: +86 731 58292251 (W. Zhu).
E-mail addresses: zhuwg18@126.com (W. Zhu), poycao@scut.edu.cn (Y. Cao).

1566-1199/$ - see front matter © 2010 Elsevier B.V. All rights reserved.
doi:10.1016/j.orgel.2010.09.012

(N-carbazolyl)pyridine (26mCPy) as a host with external quantum efficiency (*EQE*) of 15.9% and a power efficiency of 12.6 lm W^{-1} [18]. However, to our best knowledge, the reports on the platinum (II) complex-doped white polymer light-emitting devices (WPLEDs) are very rare [19–21].

With this mind, to study the influence of cyclometalated platinum (II) complexes on formation excimers in polymer host and obtain high-efficiency WPLEDs, we designed and synthesized a new ancillary ligand of the oligomer-fluorene-based picolinic acid derivative (Tfl-picH) and its heteroleptic platinum (II) complexes of (dfppy)Pt(Tfl-pic) and (C_{16}dfppy)Pt(Tfl-pic), where dfppy is 2-(2,4-difluorophenyl)pyridine and C_{16}dfppy is 5-hexadecanyl-2-(2,4-difluorophenyl)pyridine. The synthetic route of two platinum (II) complexes is shown in Scheme 1. As oligomer-fluorene possesses a rigid π-π aryl system and good solubility [22], it is expected to facilitate its square-planar platinum (II) complexes to form excimers in high concentration, even in thin films [23–25]. As expected, intense excimers's emissions were observed for these two platinum (II) complexes in their neat films under photo-excitation and in their-doped PLEDs under electronic-excitation. Significant influence of cyclometalated ligand on the excimer emission of its platinum (II) complexes was presented. Employing (dfppy)Pt(Tfl-pic) as guest, a blend of polyvinylcarbazole (PVK) and 2-(4-biphenyl)-5-(4-*tert*-butylphenyl) -1,3,4-oxadiazole (PBD) as a host matrix, the simple single-layer PLEDs exhibited pure white emission with the CIE coordinates (0.33, 0.33) at 10 V. In contrast, the (C_{16}dfppy)Pt(Tfl-pic)-doped PLED with the same device configuration displayed only red emission with the CIE coordinate around (0.40, 0.41).

2. Results and discussion

2.1. Synthesis

The trialkyl-fluorene-based picolinic acid (Tfl-picH) was prepared with a moderate yield based on the procedures [26]. The platinum (II) complexes of (dfppy)Pt(Tfl-pic) and (C_{16}dfppy)Pt(Tfl-pic) were synthesized by two-step procedures with a chloride-bridged process of K_2PtCl_4 with cyclometalated ligand and a chloride cleavage of the resulting chloro-bridged dimmers with the ancillary ligand of Tfl-picH in a moderate condition based on the literatures [27,28].

As this trifluoene-based ancillary ligand has a steric block and the platinum atom has a planar structure with a bigger atom radius, it was more difficult to gain (dfppy)-Pt(Tfl-pic) and (C_{16}dfppy)Pt(Tfl-pic) than (dfppy)Pt(pic). Both of platinum (II) complexes have been confirmed with ^{1}H NMR and elemental analysis.

2.2. Optical analysis

Fig. 1 shows the UV–vis absorption spectra of platinum (II) complexes in dilute dichloromethane (DCM, 10^{-5} M) at room temperature and their UV absorption data are summarized in Table 1. As shown in Fig. 1, a moderate high-energy UV absorption band at 267 nm and much intense low-energy absorption bands at about 354 nm were observed for each of two alkyltrifluorene-based platinum (II) complexes. The influence of alkyltrifluorene-based picolinic acid on UV–vis absorption property of its platinum (II) complex is similar to that of its iridium (III) complex reported in our previous work [26]. Compared to UV–vis spectrum of (dfppy)Pt(pic), the high-lying absorption band is assigned to the intraligand-based π–π* transitions, and the low-lying absorption band is attributed to the mixed single and triplet metal-to-ligand charge transfer transitions (MLCT) for these alkyltrifluorene-based platinum (II) complexes [29]. Furthermore, the low-energy absorption of both alkyltrifluorene-based platinum (II) complexes are more intense than that of (dfppy)Pt(pic). This means that incorporating alkyl-trifluorene group into the common ancillary ligand of picolinic acid is available for enhancing UV absorption of its platinum (II) complexes and enlarges spectral overlap between UV absorption of platinum (II) complexes and PL of PVK employed as host matrix in the latter devices.

The photoluminescence (PL) spectra of these three platinum (II) complexes are shown in Fig. 2 and their emission data are summarized in Table 1. Nearly identical PL profiles containing an emission peaks at 396 nm with a shoulder at 418 nm are exhibited for these two alkyltrifluorene-based platinum (II) complexes (dfppy)Pt(Tfl-pic) and (C_{16}dfppy)-Pt(Tfl-pic) in dilute DCM (10^{-5} M). Compared to PL spectrum of (dfppy)Pt(pic) in dilute DCM (10^{-5} M), these two deep blue emission peaks are attributed to the emission

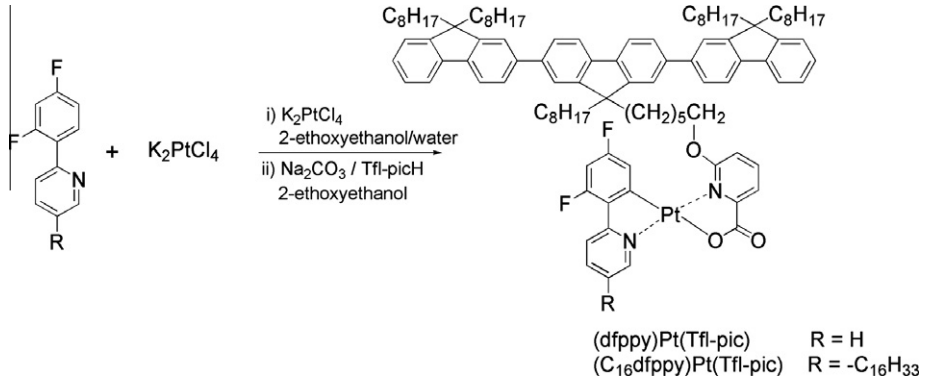

Scheme 1. Synthesis route of (dfppy)Pt(Tfl-pic) and (C_{16}dfppy)Pt(Tfl-pic).

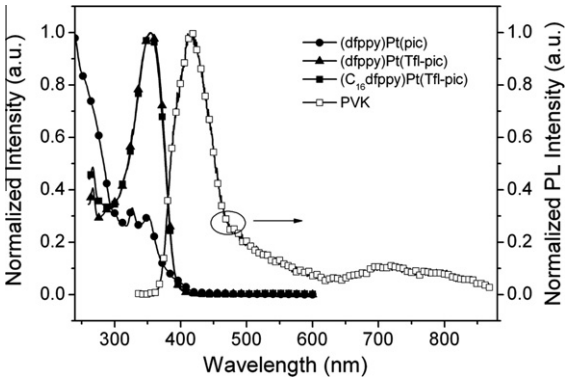

Fig. 1. Normalized UV–vis absorption spectra of (dfppy)Pt(pic), (dfppy)Pt(Tfl-pic) and (C_{16}dfppy)Pt(Tfl-pic) in dilute DCM (10^{-5} M) and PL spectrum of PVK film at room temperature.

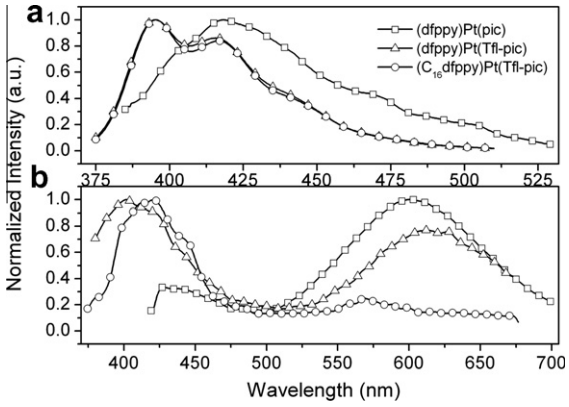

Fig. 2. Normalized PL spectra of (dfppy)Pt(pic), (dfppy)Pt(Tfl-pic) and (C_{16}dfppy)Pt(Tfl-pic) in dilute DCM (10^{-5} M) (a), and their neat films at room temperature(b).

of platinum (II) complexes. However, these two trifluorene-based platinum (II) complexes exhibited higher photoluminescent quantum yield (Φ_f) than (dfppy)Pt(pic) in degassed DCM at room temperature. The Φ_f was determined to be 0.94 for (dfppy)Pt(Tfl-pic), 0.81 for (C_{16}dfppy)Pt(Tfl-pic) and 0.58 for (dfppy)Pt(pic) by using 9,10-diphenylanthrancene as the standard (Φ_f = 0.9) [30]. Therefore, an introduction of alkyl-trifluorene group into the ancillary ligand of picolinic acid did improve the PL quantum efficiency of its platinum (II) complexes obviously.

In contrary, the PL spectra of (dfppy)Pt(Tfl-pic) and (C_{16}dfppy)Pt(Tfl-pic) in their neat films exhibit two emission peaks, respectively. The high-energy emission peak locates at 402 nm for (dfppy)Pt(Tfl-pic) and 421 nm for (C_{16}dfppy)Pt(Tfl-pic) while the low-energy emission peak locates at 619 nm for the former and 569 nm for the latter. They are different from the PL spectrum of (dfppy)Pt(pic) in the neat film which exhibit only an emission peak at 601 nm. As we know, platinum (II) complexes have a planar molecular configuration and have a potential to form excimers and give the excimers emission in their neat film [31]. Compared to (dfppy)Pt(Tfl-pic), (C_{16}dfppy)Pt(Tfl-pic) with a substituted alkyl chain in 2,4-difluorophenylpyridine presented obviously weak emission in long-wavelength area. The weak low-energy emission for (C_{16}dfppy)Pt(Tfl-pic) may be relative to the excimer emission quenching resulting from facile aggregation by the flexibility of long alkyl chain in 2,4-difluorophenylpyridine core.

2.3. Thermal property

The thermal stability of platinum (II) complexes was evaluated by thermogravimetric analysis (TGA) under N_2 stream with a scanning rate of 20 °C/min and their TGA curves are shown in Figure S1. The decomposition temperature (T_d) values are 292 °C for (dfppy)Pt(Tfl-pic), 295 °C for (C_{16}dfppy)Pt(Tfl-pic) and 294 °C for (dfppy)Pt(pic), which correspond to a 5% weight loss. This result suggests incorporating a trifluorene group into picolinic acid has a minor effect on thermal stability of its platinum (II) complexes.

2.4. Electrochemical property

The electrochemical behavior of these cyclometalated platinum (II) complexes was studied by cyclic voltammetry using ferrocene as the internal standard and their data are listed in Table 1. Irreversible oxidation peaks were found from each compound. On the basis of these onset oxidation potentials (E^{ox}) and formula $E_{HOMO} = E^{ox} + 4.34$ eV, the highest occupied molecular orbital energy levels (E_{HOMO}) of (dfppy)Pt(Tfl-pic) and (C_{16}dfppy)Pt(Tfl-pic) were calculated as −6.28 and −5.94 eV, respectively. The lowest unoccupied molecular orbital energy levels (E_{LUMO}) of (dfppy)Pt(Tfl-pic) and (C_{16}dfppy)Pt(Tfl-pic) were −2.23 and −2.0 eV based on the equation $E_{LUMO} = E_{HOMO} + E_g$, respectively, in which energy band gap (E_g) was estimated from the UV–vis absorption threshold[32]. Compared to (dfppy)Pt(pic) complex, (dfppy)Pt(Tfl-pic) present an increased energy gap due to introduction of trialkylfluorene group into picolinic acid. Moreover, an additional introduction of alkyl to the cyclometalated ligand further results in energy gap decrease of (C_{16}dfppy)Pt(Tfl-pic).

Table 1
Optophysical, electrochemistry and thermal stability data of (dfppy)Pt(pic), (dfppy)Pt(Tfl-pic) and (C_{16}dfppy)Pt(Tfl-pic).

Compounds	UV–vis (nm)	Emission[a](nm)	Emission[b](nm)	Φ_{em}	HOMO (eV)	LUMO(eV)	E_g (eV)
(dfppy)Pt(pic)	264, 325, 350, 404	418	601	0.58	−6.63	−3.46	3.17
(dfppy)Pt(Tfl-pic)	354, 266, 404	396, 418	402, 616	0.94	−6.28	−2.23	4.05
(C_{16}dfppy)Pt(Tfl-pic)	354, 266, 404	396, 418	421, 569	0.81	−5.94	−2.0	3.94

[a] measured in DCM at room temperature.
[b] measured in the neat film at room temperature.

2.5. Electroluminescent property

To investigate electroluminescence (EL) properties of these platinum (II) complexes, the single-layer devices were fabricated with a structure of ITO/PEDOT : PSS (50 nm)/dopant + PVK–PBD (45 nm)/Ba (4 nm)/Al (150 nm), in which ITO is used as the anode, PEDOT:PSS is used as a hole-injection layer and Ba/Al is employed as a cathode. The emitting layer is consist of the dopant of platinum (II) complexes and host matrix of PVK-PBD blend, in which doping weight concentration of (dfppy)Pt(Tfl-pic) and (C_{16}dfppy)Pt(Tfl-pic) is 10 wt.%, respectively, PBD weight ratio is 30% in the PVK–PBD blend.

The EL spectra of the (dfppy)Pt(Tfl-pic) and (C_{16}dfppy)Pt(Tfl-pic)-doped PVK–PBD devices at different applied voltage are shown in Fig. 3. EL spectrum of the (dfppy)Pt(Tfl-pic)-doped device covers whole visible range from 400 to 700 nm (Fig. 3a). Two emission peaks at about 590 nm and 418 nm are observed. Compared to PL spectrum of the (dfppy)Pt(Tfl-pic)-based neat film, the high-energy emission is attributed to itself blue emission and the low-energy emission is assigned to its excimer's emission. With increasing applied voltage, the low-energy emission intensity become stronger and the high-energy emission intensity turn weaker. Their CIE 1931 chromaticity diagram is shown in Figure S2. While the driving voltage increases from 7 V to 13 V, CIE coordinates of the (dfppy)Pt(Tfl-pic)-doped device vary from (0.27, 0.22) to (0.39, 0.41), which locates in white area. At 10 V, this (dfppy)Pt(Tfl-pic)-doped device displayed bright white light with a CIE coordinate of (0.33, 0.33). The luminance was 650 cd m^{-2} and current efficiency 0.40 cd A^{-1} were obtained in this situation. As far as we know, this is the purest white emission ever reported for platinum (II) complex-doped single-layer PLEDs. However, (C_{16}dfppy)Pt(Tfl-pic)-doped device only presented red emission at the different applied voltages in the same device configuration (Fig. 3b). The CIE coordinates of the (C_{16}dfppy)Pt(Tfl-pic)-doped device have a minor change around (0.40, 0.41) with increased bias from 7 V to 13 V. This implies that a hexadecyl group attached into 5-position of 2-(2,4-difluorophenyl)pyridine plays an positive role in facilitating the excimer's formation for its trialkylfluorene-based platinum (II) complexes under electric-excition. In order to explain why the trifluorene-based platinum (II) complexes-doped PLEDs exhibit different EL spectra, we measured the surface morphologies of (dfppy)Pt(Tfl-pic) and (C_{16}dfppy)Pt(Tfl-pic) in PVK–PBD film by atomic force microscopy (AFM) as shown in Fig. 4, respectively. The (dfppy)Pt(Tfl-pic)-doped film displayed a significantly decreased roughness with R_a = 1.79 nm (a) while the (C_{16}dfppy)Pt(Tfl-pic)-doped film exhibited a roughness with R_a = 46.0 nm (b). It indicates that (dfppy)Pt(Tfl-pic) has a better dispersibility than (C_{16}dfppy)Pt(Tfl-pic). It may be attributed to that the hook junction effect of this flexible hexadecyl chain can make easily the (C_{16}dfppy)Pt(Tfl-pic) molecules aggregation in the host matrix.

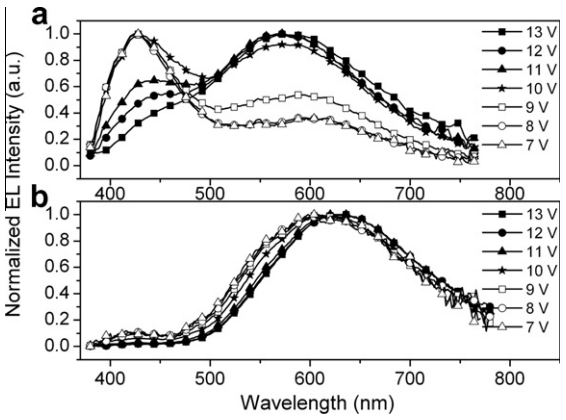

Fig. 3. (a) EL spectra of the (dfppy)Pt(Tfl-pic)-doped PVK–PBD device at 10% dopant concentration under different applied voltages; (b) EL spectra of the (C_{16}dfppy)Pt(Tfl-pic)-doped PVK–PBD device at 10% dopant concentration under different applied voltages.

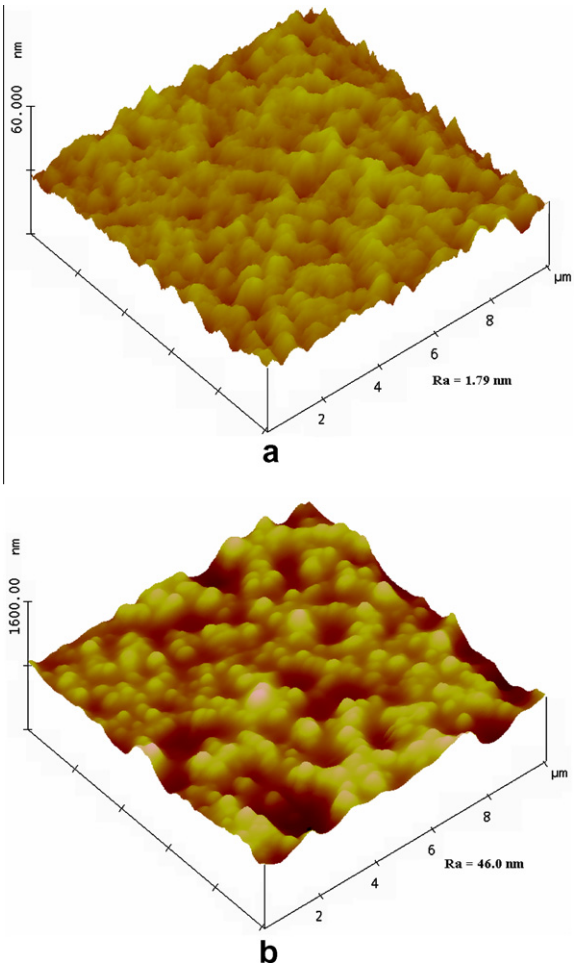

Fig. 4. Atomic force microscope images for: (a) the (dfppy)Pt(Tfl-pic)-doped PVK–PBD film; (b) the (C_{16}dfppy)Pt(Tfl-pic)-doped PVK–PBD film. The film thickness was about 80 nm.

3. Conclusion

In summary, two alkyl trifluorene-based cyclometalated platinum (II) complexes were obtained. The alkyl-

trifluorene group in ancillary ligand and hexadecyl chain in cyclometalated ligand present significantly influence on optophysical and EL properties of its cyclometalated platinum (II) complexes. The device using (dfppy)Pt(Tfl-pic) as dopant presented a white emission with CIE coordinate of (0.33, 0.33) at 10 V, but the other device using (C_{16}dfppy)Pt(Tfl-pic) as dopant displayed a red emission with the same single layer device configuration. This work provide an improved approach to control formation excimers of platinum (II) complex by tuning molecular structure with alkyl-trifluorene group in ancillary ligand and long alkyl chain in cyclometalated ligand. The pure white PLEDs can be obtained using this kind of platinum (II) complex as dopant.

4. Experimental

All solvents were carefully dried and distilled prior to use. Commercially available reagents were used without further purification unless otherwise stated. Tfl-picH was prepared according to the reported process [26]. All reactions were performed under nitrogen atmosphere and were monitored by thin-layer chromatography (TLC). Flash column chromatography and preparative TLC were carried out using silica gel from Merck (200–300 mesh). All ^{1}H NMR spectra were acquired at a Bruker Dex-400NMR instrument using $CDCl_3$ as a solvent. Elemental analysis was performed on a Harrios elemental analysis instrument. The UV absorption and photoluminescence spectra were measured with a Varian Cray50 and Perkin-Elmer LS50B Luminescence Spectrometer, respectively. EL spectra were recorded with an Insta-Spec IV CCD system (Oriel). Luminance was measured with a Si photodiode and calibrated by using a PR-705 spectrascan spectrophotometer (Photo Research).

4.1. Synthesis of (dfppy)Pt(Tfl-pic)

To a mixture of K_2PtCl_4 (0.3 g, 0.84 mmol) and water (5 mL) was added 2,4-difluoropyphenylpyridine (0.4 g, 2.1 mmol) and 2-ethoxyethanol (15 mL). The mixture was stirred vigorously under inert gas atmosphere for 20 h. After cooled, the colored precipitate was filtered off, washed with water and hexane, respectively. A red solid of dimmer of $[(dfppy)PtCl]_2$ was obtained (0.42 g, 78.0%). Then a mixture of the dimmer (0.2 g, 0.24 mmol), compound Tfl-picH (0.75 g, 0.60 mmol) and sodium carbonate (90 mg, 0.85 mmol) in 2-ethoxyethanol (15 mL) at about 80–90°Cwas stirred vigorously under inert gas atmosphere for 24 h. After cooling to room temperature, the mixture was extracted with DCM and the resulting organic layer was dried over anhydrous magnesium sulfate and distilled to gain black fused liquid. This crude product was purified by a dry flash silica gel column using DCM as eluent to gain the goal product (0.28 g, 53.0%) as a brown red solid. ^{1}H NMR ($CDCl_3$, 400 MHz), δ (ppm): 9.19–9.20 (1H, d, J = 5.2), 7.82–7.64 (16H, m), 7.37–7.33 (9H, m), 7.12–7.10 (1H, t), 6.90–6.85 (1H, t), 6.47–6.42 (1H, t), 4.10–4.06 (2H, t), 2.07–2.03 (12H, m), 1.26–1.01 (56H, m), 0.81–0.71 (27H, m). Anal. Calcd for $C_{102}H_{126}F_2N_2O_3Pt$: C 73.75, H 7.65, N 1.69. Found: C 73.48, H 7.60, N 1.73%.

4.2. Synthesis of (C_{16}dfppy)Pt(Tfl-pic)

It was prepared according to the synthetic procedure of (dfppy)Pt(Tfl-pic). A brown red solid was obtained with a yield of 36.0%.δ (ppm): 9.98 (1H, s), 7.82–7.63 (16H, m), 7.38–7.32 (9H, m), 6.89–6.85 (1H, t), 6.45–6.40 (1H, t), 4.09–4.04 (2H, t), 2.64–2.62 (2H, t), 2.08–2.03 (12H, m), 1.25–1.07 (84H, m), 0.81–0.78 (30H, m). Anal. Calcd for $C_{118}H_{158}F_2N_2O_3Pt$: C 75.16, H 8.45, N 1.49. Found: C 75.08, H 8.53, N 1.55%.

Acknowledgements

Financial support from The National Natural Science Foundation of China (20772101 and 20872124), The Science Foundation of Hunan Province (2009FJ2002 and 2007FJ3017) and The Postgraduate Science Foundation for Innovation in Hunan Province (S2008 yjscx09).

Appendix A. Supplementary data

Supplementary data associated with this article can be found, in the online version, at doi:10.1016/j.orgel.2010.09.012.

References

[1] Z.J. Zhao, B. Xu, Z.F. Yang, H.Y. Wang, X.M. Wang, P. Lu, W.J. Tian, J. Phys. Chem. C 112 (2008) 8511.
[2] K.T. Kamtekar, A.P. Monkman, M.R. Bryce, Adv. Mater. 22 (2010) 572.
[3] Y. Liu, M. Nishiura, Y. Wang, Z.M. Hou, J. Am. Chem. Soc. 128 (2006) 5592.
[4] Z.J. Zhao, Y.X. Zhao, P. Lu, W.J. Tian, J. Phys. Chem. C 111 (2007) 6883.
[5] M. Mazzeo, V. Vitale, F. DellaSala, M. Anni, G. Barbarella, L. Favaretto, G. Sotgiu, R. Cingolani, G. Gigli, Adv. Mater. 17 (2005) 34.
[6] (a) Y. Hamada, T. Sano, H. Fujii, Y. Nishio, H. Takahashi, K. Shibata, Jpn. J. Appl. Phys. (1996) L1339;
(b) B.W. D'Andrade, S.R. Forrest, Adv. Mater. 16 (2004) 1585;
(c) R. Duggal, J.J. Shiang, C.M. Heller, D.F. Foust, Appl. Phys. Lett. 80 (2002) 470;
(d) K.L. Paik, N.S. Baek, H.K. Kim, J.H. Lee, Y. Lee, Macromolecules 35 (2002) 6782.
[7] J. Kido, M. Kimura, K. Nagai, Science 267 (1995) 1332.
[8] R.S. Deshpande, V. Bulovic, S.R. Forrest, Appl. Phys. Lett. 75 (1999) 888.
[9] M. Strukelj, R.H. Jordan, A. Dodabalapur, J. Am. Chem. Soc. 118 (1996) 1213.
[10] B.W. D'Andrade, M.E. Thompson, S.R. Forrest, Adv. Mater. 14 (2002) 147.
[11] J. Kido, H. Shionoya, K. Nagai, Appl. Phys. Lett. 67 (1995) 2281.
[12] A. Dodabalapur, L.H. Rothberg, T.M. Miller, Appl. Phys. Lett. 65 (1994) 2308.
[13] J. Thompson, R.I.R. Blyth, M. Mazzeo, M. Anni, G. Gigli, R. Cingolani, Appl. Phys. Lett. 79 (2001) 560.
[14] S. Tasch, E.J.W. List, O. Ekstrom, W. Graupner, G. Leising, P. Schlichting, U. Rohr, Y. Geerts, U. Scherf, K. Mullen, Appl. Phys. Lett. 71 (1997) 2883.
[15] Z. Deng, S.T. Lee, D.P. Webb, Y.C. Chan, W.A. Gambling, Synth. Met. 107 (1999) 107.
[16] R.G. Kepler, P.M. Beeson, S.J. Jacobs, R.A. Anderson, M.B. Sinclair, V.S. Valencia, P.A. Cahill, Appl. Phys. Lett. 66 (1995) 3618.
[17] B.W. D'Andrade, J. Brooks, V. Adamovich, M.E. Thompson, S.R. Forrest, Adv. Mater. 14 (2002) 1032.
[18] E.L. Williams, K. Haavisto, J. Li, G.E. Jabbour, Adv. Mater. 19 (2007) 197.
[19] S.U. Pandya, K.C. Moss, M.R. Bryce, A.S. Batsanov, M.A. Fox, V. Jankus, H.A.A. Attar, A.P. Monkman, Eur. J. Inorg. Chem. 2010 (1963).
[20] X.H. Yang, Z.X. Wang, S. Madakuni, J. Li, G.E. Jabbour, App. Phys. Lett. 93 (2008) 193305.
[21] J. Kalinowski, M. Cocchi, D. Virgili, V. Fattori, J.A.G. Williams, Adv. Mater. 19 (2007) 4000.

[22] K.T. Wong, Y.Y. Chien, R.T. Chen, C.F. Wang, Y.T. Lin, H.H. Chiang, P.Y. Hsieh, C.C. Wu, C.H. Chou, Y.O. Su, G.H. Lee, S.M. Peng, J. Am. Chem. Soc. 124 (2002) 11576.
[23] S.W. Lai, M.C.W. Chan, K.K. Cheung, C.M. Che, Inorg. Chem. 38 (1999) 4262.
[24] S.W. Lai, M.C.W. Chan, T.C. Cheung, S.M. Peng, C.M. Che, Inorg. Chem. 38 (1999) 4046.
[25] P.I. Kvam, M.V. Puzyk, K.P. Balashev, J. Songstad, Acta Chem. Scand. 49 (1995) 335.
[26] Y.F. Wang, H. Tang, Y. Liu, C.X. Jiang, Z.Y. Hu, M.X. Zhu, L. Wang, W.G. Zhu, Y. Cao, Tetrahedron 66 (2010) 1483.
[27] S. Lamansky, P. Djurovich, D. Murphy, F. Abdel-Razzaq, H.E. Lee, C. Adachi, P.E. Burrows, S.R. Forrest, M.E. Thompson, J. Am. Chem. Soc. 123 (2001) 4304.
[28] X. Chen, J.L. Liao, Y. Liang, M.O. Ahmed, H.E. Tseng, S.A. Chen, J. Am. Chem. Soc. 125 (2003) 636.
[29] F. Lafolet, S. Welter, Z. Popović, L. De Cola, J. Mater. Chem. 15 (2005) 2820.
[30] Q. Peng, J. Xu, M.J. Li, W.X. Zheng, Macromolecules 42 (2009) 5478.
[31] V.N. Kozhevnikov, B. Donnio, D.W. Bruce, Angew. Chem., Int. Ed. 47 (2008) 6286.
[32] Z.J. Si, J. Li, B. Li, Z.R. Hong, S.Y. Liu, W.L. Li, J. Phys. Chem. C 112 (2008) 3920.

Organic Electronics 11 (2010) 1960–1965

Contents lists available at ScienceDirect

Organic Electronics

journal homepage: www.elsevier.com/locate/orgel

Fabrication of organic thin-film transistors by spray-deposition for low-cost, large-area electronics

Natalia A. Azarova [a], Jack W. Owen [a], Claire A. McLellan [a], Marsha A. Grimminger [b], Eric K. Chapman [a], John E. Anthony [b], Oana D. Jurchescu [a,*]

[a] Department of Physics, Wake Forest University, Winston-Salem, NC, USA
[b] Department of Chemistry, University of Kentucky, Lexington, KY, USA

ARTICLE INFO

Article history:
Received 27 July 2010
Received in revised form 3 September 2010
Accepted 4 September 2010
Available online 26 September 2010

Keywords:
Organic thin-film transistors
Organic semiconductors
High-mobility
Solution processing
Spray-coating

ABSTRACT

We report on high performance organic thin-film transistors fabricated by spray-deposition, an innovative coating technique for organic electronic devices. This method is simple and inexpensive, compatible with room-temperature processing and easily scalable from laboratory-based devices to large-area electronics. Our spray-deposited 2,8-difluoro-5,11-bis (triethylsilylethynyl) anthradithiophene transistors show very good homogeneity, with mobilities of 0.2 cm^2/V s, and on/off ratios of 10^7. This performance is comparable to that of our best spin-coated devices fabricated on the same substrate type, while offering additional advantages such as using 20 times less organic semiconductor and facilitating fast coating of large-areas.

© 2010 Elsevier B.V. All rights reserved.

1. Introduction

The scope of applications emerging from large-area electronics has broaden considerably with the latest successes demonstrated in the field of organic electronics [1–4]. Organic devices offer an attractive balance between cost and performance, complemented by versatility and functionality accomplished by means of molecular engineering. The applications envisioned for organic semiconductors have expanded beyond conventional silicon, and include flexible displays, chemical and biological sensors, wearable electronics, medical applications, etc. The fabrication methods presently employed in research labs, such as spin-coating or drop-casting, offer advantages of low cost and allow demonstration of very good device performance [5–7]. Nevertheless, they are not compatible with large-areas, and thus present limited usability. New methods have emerged to design alternative processing routes that can meet the manufacturing requirements for large-area electronics, and at the same time maintain the cost-efficiency. Several techniques such as inkjet printing [8], screen printing [9], or doctor blading [10] have endeavored to deliver fast deposition over large-areas. In the frame of these efforts, spray-coating captures increasing attention, with both organic semiconductors [11–17] and contact materials [18,19] spray-deposition being demonstrated. However, while an intense effort is involved in developing spray-deposition technologies for manufacturing organic photovoltaics (OPVs) and organic light emitting diodes (OLEDs) [11–15], to the best of our knowledge, with the exception of a few reports [16,17], little attention is given to designing and developing methods that match organic thin-film transistors (OTFTs) materials and device structures.

In this article we report on high performance OTFTs fabricated by spray-deposition of organic semiconductor layer and demonstrate the viability of this approach by comparing the performance of spray-deposited devices with that of the spun-coated devices. While previous reports presented a detailed study of the spray-deposition of polymer semiconductors [16,17], here we demonstrate for the

* Corresponding author. Tel.: +1 3367584407; fax: +1 3367586142.
E-mail address: jurcheod@wfu.edu (O.D. Jurchescu).

1566-1199/$ - see front matter © 2010 Elsevier B.V. All rights reserved.
doi:10.1016/j.orgel.2010.09.008

first time spray-deposited small molecule OTFTs. In spite of the impressive electronic properties measured in single crystals of materials from this class [20–22], their use in combination with cost-effective fabrication techniques was inhibited by their poor solubility. Recently, various molecular design approaches have succeeded in increasing solubility, allowing for demonstration of solution deposited OTFTs [5,6,23]. In this study we use 2,8-difluoro-5,11-bis (triethylsilylethynyl) anthradithiophene (diF-TES ADT) [5](chemical formula shown in the inset of Fig. 1) and demonstrate that spray-coating is a processing technique suitable for fast large-area coating, while maintaining device performance of small molecules organic TFTs. DiF-TES ADT has received much attention lately given the high performance it demonstrated in thin films [6] and single crystals devices [24], as well as the interesting film forming properties which allow low-cost, room-temperature patterning approaches [25]. Charge mobilities as high as 6 cm^2/V s have been demonstrated in field-effect transistors of vapor grown single crystal diF-TES ADT, together with large current on/off ratios ($I_{on}/I_{off} = 10^8$), small subthreshold slopes (S = 1 V/dec) and negligible hysteresis in the current–voltage characteristics [24]. In solution deposited devices, mobilities of 1.5 cm^2/V s have been reported in films drop-casted from a chlorobenzene solution [5], 0.2 cm^2/V s in diF-TES ADT TFTs, when the organic material was spun-casted from a chlorobenzene solution on pentafluorobenzenethiol (PFBT) treated contacts, and 0.4 cm^2/V s for PFBT treated contacts and hexamethyldisilazane (HMDS) modified gate dielectric [26]. Our spray-deposited diF-TES ADT TFTs exhibit performance comparable with spun-deposited devices on the same substrate (mobilities as high as $\mu = 0.2$ cm^2/V s, and $I_{on}/I_{off} = 10^7$ for PFBT treated contacts), while offering the advantage of being faster and less complex to manufacture on any size device structure, and utilizing 20 times smaller the amount of organic semiconductor.

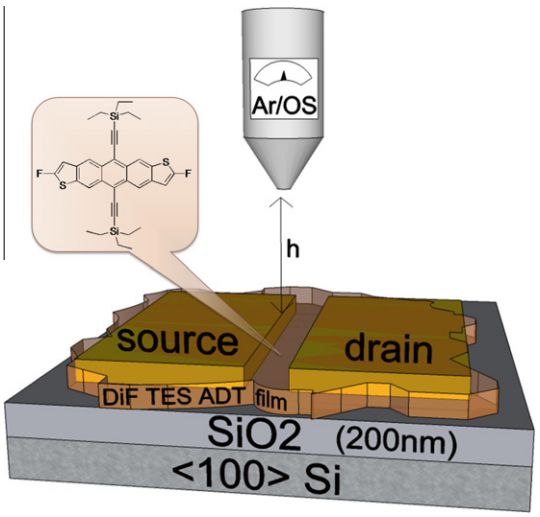

Fig. 1. Schematic drawing of the spray-deposition system. Organic semiconductor solution (OS) was sprayed under argon directly onto the device structure. h is the distance between the sample and airbrush. Field-effect transistor device structure is also shown, as well as the chemical formula of the organic semiconductor used in this study.

2. Experimental

A schematic of our spray-deposition system is presented in Fig. 1. We have used an Iwata Kustom TH K9200 airbrush with a nozzle diameter of 0.50 mm and pressurized argon as the carrier gas (5N purity). The organic semiconductor solution in chlorobenzene was aerosolized under high pressure argon, and the droplets were collected on the device structure, positioned at distance h below the airbrush. The concentration of the organic solution was carefully controlled, and systematically modified to improve transistor performance. The spray process was performed in ambient conditions, under the hood. Argon pressure, as well as the aforementioned distance h, were accurately adjusted, as they are critical parameters that dictate thin-film quality and, consequently, device performance, as we will demonstrate later. The airbrush was set in a fixed position, aiming perpendicular towards the sample. The sample and the airbrush were held steady during the spraying process, and the deposition time was monitored. Typical spraying times were in the order of 20–30 s (continuous spraying).

We have fabricated bottom-contact TFTs (see cross-section of the device structure in Fig. 1) by spraying the organic semiconductor solution over the 1.2 cm × 1.2 cm substrate containing 63 pre-fabricated device structures. We used a heavily doped Silicon wafer as the substrate and gate electrode with a 200 nm thermally grown SiO_2 layer that served as the gate oxide. The source and drain Ti/Au contacts (5 nm Ti/45 nm Au) were deposited by e-beam evaporation. Discrete devices had well defined geometries by using photolithography and lift-off, with channel lengths L between 5 and 100 μm and channel widths W between 200 and 1000 μm. Prior to spray-deposition of the organic semiconductor, the substrates were cleaned by soaking in hot acetone, isopropyl alcohol, followed by UV ozone cleaning and DI water rinse. The contacts were chemically treated by immersing the substrates for 30 min in a $5 \cdot 10^{-2}$ mol/L PFBT solution in ethanol. The fabrication parameters have been optimized by performing systematic tests and correlating processing parameters with resulting device performance. We have investigated the electrical properties of our transistors in ambient air and at room temperature, using a commercially available probe station, and an Agilent 4155C Semiconductor Parameter Analyzer. A minimum number of 50 devices were fabricated and characterized for each set of parameters that were investigated in this study. Optimum spraying parameters were found to be: argon pressure 5 psi, spray distance 13 cm, solution concentration $c = 0.1$ wt% (1.1 mg/mL), and spray time 30 s. In parallel with spray-deposited devices, spin-coated TFTs were also fabricated for comparison studies. These devices were fabricated in air, on the same substrate type (held at room temperature), from a solution in room-temperature chlorobenzene. No subsequent thermal treatment was applied to the spray or spin-coated samples.

3. Results and discussion

Fig. 2 shows the current–voltage characteristics of a device having channel length $L = 20$ μm, and channel width $W = 200$ μm. It can be observed from these graphs that the drain current I_D increases with increased negative gate–source voltage V_{GS}, typical for a hole-transporting organic layer. In the upper panel of Fig. 2 we plot the $\log(I_D)$ vs. V_{GS} (right axis) and $\sqrt{I_D}$ vs. V_{GS} (left axis) graphs in the saturation regime (drain–source voltage $V_{DS} = -40$ V).

The mobility for this device was calculated to be $\mu = 0.2$ cm^2/V s by using the following expression:

$$I_D = \frac{W}{L}\frac{C_i}{2}\mu(V_{GS} - V_T)^2 \quad (1)$$

where V_T is the threshold voltage, C_i is the gate oxide capacitance per unit area ($C_i = 1.7 \times 10^{-4}$ F/m^2), and W and L are the channel width and length, respectively. We have estimated the threshold voltage $V_T = 4.4$ V by extrapolating the linear fit of $\sqrt{I_D}$ vs. V_{GS} plot to $I_D = 0$ A (intercept with V_{GS} axis). The current on/off ratio for this device was $I_{on}/I_{off} = 10^7$. The evolution of the drain current (I_D) with the drain voltage (V_{DS}) is presented in the lower panel of Fig. 2 for different gate voltages (V_{GS}). The gate voltage was varied in 10 V steps from 0 to −40 V. A strong field-effect modulation of the channel conductance can be observed in this plot, with a linear variation of I_D with V_{DS} at small voltages and reaching saturation regime at high voltages. The performance of this OTFT is clearly altered by contact effects. This observation is supported by the current compression in the linear regime [27,28]. We have previously demonstrated using scanning Kelvin probe microscopy (SKPM) that such a current compression in the linear regime is accompanied by a several volts potential drop at the electrode/organic semiconductor interface [29]. Therefore, only a small fraction of the applied voltage is gradually dropped across the organic semiconductor itself, indicating that the electrical performance of the devices is contact-limited. The potential profile gives valuable insight into device operation, and we believe higher mobilities can be achieved in air-brushed diF-TES ADT TFTs, by improving device contacts.

The promise for low-cost electronics converges expectations of cost efficiency in processing, as well as materials used in devices. Spray-deposition is more efficient than spin-coating, where most solution is wasted during spinning. With spray-coating, the waste is highly minimized and most of the starting material is efficiently used to fabricate the active film. To increase the material usage efficiency even further, we have investigated the effect of the concentration of the organic solution used for spraying, with the goal of determining the minimum amount of material required to fabricate high-mobility devices. Fig. 3 presents the effect of the concentration of the solution on the properties of the devices, for diF–TES ADT TFTs fabricated from a chlorobenzene solution, under constant flow rate, 5 psi argon carrier gas pressure, spray time 30 s, and spraying distance of 13 cm. The plot in the lower panel of this figure suggests the presence of three distinct

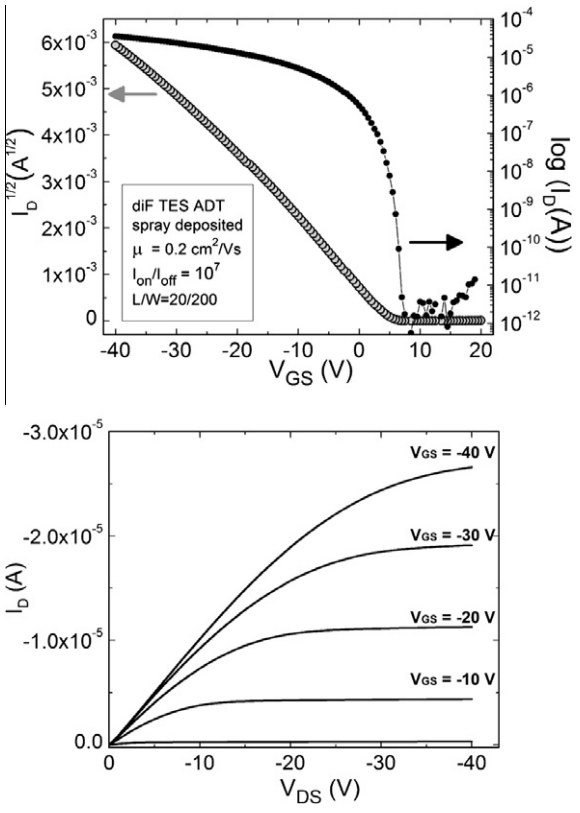

Fig. 2. Electrical characteristics of a spray-deposited diF-TES ADT TFT. Upper graph: current–voltage characteristics ($\log(I_D)$ vs. V_{GS}) in the saturation regime, at $V_{DS} = -40$ V. Left axis: $\sqrt{I_D}$ vs. V_{GS} plot used to calculate the mobility. Lower graph: Source–drain (I_D) current vs. drain voltage (V_{DS}) measured at different gate voltages (V_{GS}). The dimensions of channel length (L) and channel width (W) are indicated.

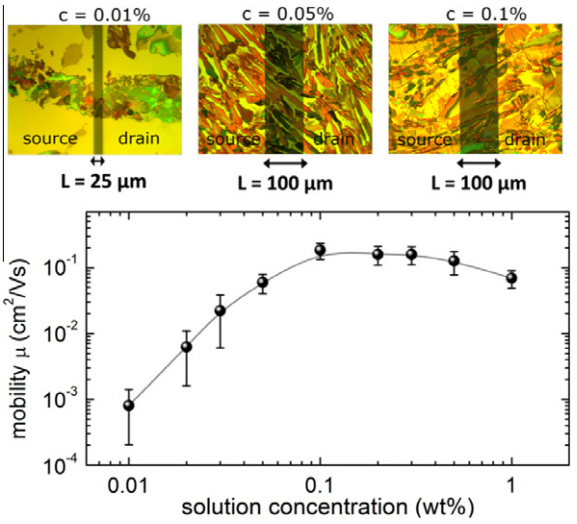

Fig. 3. Upper panel: Optical micrographs of the spray-deposited thin-film transistors, showing the difference in coverage for three different concentrations. The concentration of the organic semiconductor solution used for fabrication is indicated above each photo. Lower panel: Variation of mobility with the concentration of the solution.

regimes: mobility increases with concentration (regime I), it reaches the highest value for $c = 0.1$ wt% (1.1 mg/mL – regime II), and it decreases slightly after that (regime III). We believe the improved mobility as a function of concentration for the first segment of this graph is a result of better coverage achieved at higher concentrations. Our observations are supported by the optical micrographs presented in the upper panel of Fig. 3. At $c = 0.01$ wt% (0.11 mg/mL) the coverage is very poor, consistent with the low average mobility of 8×10^{-4} cm^2/V s. As the concentration increases, the coverage gradually improves and consequently the mobility increases, reaching the value of 0.06 ± 0.02 cm^2/V s for $c = 0.05$ wt% (0.55 mg/mL), and 0.18 ± 0.05 cm^2/V s at $c = 0.1$ wt%. With further increase in concentration, for $c > 0.1$ wt%, a small decrease in mobility is observed (regime III). This behavior may stem from anisotropy in mobility [30,31], a non-uniform vertical structural profile in the film structure or/and the presence of the structural phase transition around room-temperature, which was found in diF–TES ADT, and which leads to the existence of two polymorphs with different inter-layer spacings and distinct electrical properties [32].

Fig. 4 reveals the channel length dependence of the mobilities measured in the saturation regime for spray- (black circles) and spin-coated (red squares) films of diF-TES ADT from chlorobenzene, on PFBT treated contacts, for comparison. Here we focus on the values of mobilities in the saturation regime, to minimize contact effects. For each of the two techniques, the fabrication process has been extensively optimized, and the conditions that promoted the best performance are presented. We recall the parameters for the spray-deposited films, which include $c = 0.1$ wt%, argon pressure 5 psi, spray distance 13 cm, spray time 30 s. For the spun-coated devices, a concentration of $c = 2$ wt%, and spinning speed of 1000 rpm were used. Devices fabricated on the same substrate presented very little spread in performance for a given channel length, and devices fabricated on different days, following the same conditions, demonstrated good reproducibility. The mobilities at small channel lengths are similar for spray- and spin-deposited devices. Nevertheless, the newly introduced spray-deposition uses 20 times diluted solution, thus a considerably smaller quantity of organic semiconductor material to achieve the same performance, allowing impressive cost reduction for organic devices fabricated by spray-coating. While this achievement is itself remarkable, it presents additional advantages over spin-coating, such as offering the opportunity of being used in fast large-area coating. Another notable aspect is that the entire fabrication process takes place in air, at room temperature, with no high-temperature steps involved. The modest thermal budget required by our method opens new routes towards fabrication of large-area, light-weight, low-cost flexible electronics on plastic substrates. Both device types exhibit increased mobility with decreasing channel length. This behavior seems to contradict our earlier statement of contact-limited devices, which would lead to lower mobility for short channel length due to the fact that contact resistance effects are more severe here [27]. However, it was previously demonstrated that with diF-TES ADT devices, microstructure effects play an important role in the device operation [25,26]. Organic thin-film microstructure and contact effects are competing effects in this case. For short channel devices, only a small number of grains/grain-boundaries are necessary to bridge the channel, but barriers at the organic/electrode interfaces dominate the charge transport. For long channel length devices, film microstructure governs the electrical properties, in agreement with Ref. [29]. It is clear from this behavior of mobility with channel length that both contacts and microstructure act simultaneously, and the interplay between the two effects is complex. A detailed model of the effect of microstructure and contact effects is currently under development. A closer look over Fig. 4a reveals a very distinct behavior for the two types of devices. For spray-coated films the mobility changes from $\mu = 0.18$ (± 0.05) cm^2/V s at $L = 5$ μm to $\mu = 0.05$ (± 0.01) cm^2/V s at $L = 100$ μm. On the contrary, for spun films, the mobility starts from roughly the same value, $\mu = 0.16$ (± 0.03) cm^2/V s at $L = 5$ μm, but decreases more abruptly, to $\mu = 0.001$ ($\pm 4.02 \times 10^{-4}$) cm^2/V s at $L = 100$ μm. Optical microscopy performed on films consisting of 100 μm

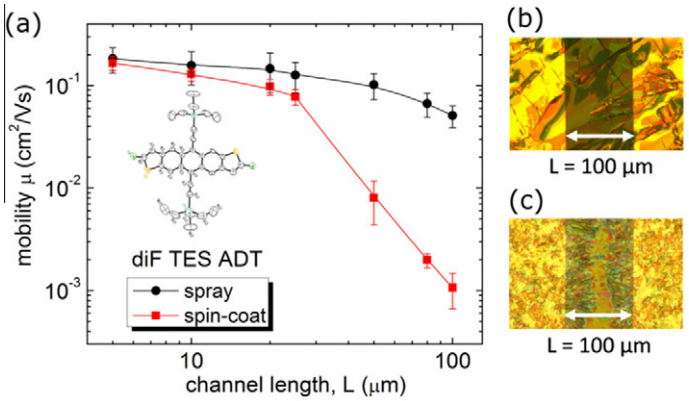

Fig. 4. (a) Saturation mobility μ vs. channel length L for diF-TES ADT TFTs fabricated by spray-deposition (black circles) and spin-coating (red squares). Optical micrograph of a spray-deposited device (b) and spin-coated device (c) with channel length L = 100 μm. (For interpretation of references to colors in this figure legend, the reader is referred to see the web version of this article.)

channel length TFTs of diF-TES ADT deposited by spray- and spin-deposition, respectively, on PFBT treated Au contacts (Fig. 4b and c) shows very different structural features characteristic for the two types of fabrication approaches, and elucidate the origin of the differences measured in electrical properties. In the spray-deposited devices, the mobility varies monotonically with L, pointing to an uniform film structure in the transistor channel [33,34]. This behavior is consistent with the optical micrograph in Fig. 4b, which shows that both the channel and contacts are covered with a nominally continuous, uniform film consisting of large plate-like crystals. The large crystalline grain size obtained in spray-deposited films is controlled by the fabrication conditions such as gas pressure, solvent boiling point, solution flow, surface tension, and more importantly, the distance h between the spray nozzle and the substrate [17]. For short distances the solution is easily blown away by the incoming flow. On the contrary, for large h distances, the solvent present in small aerosolized droplets, with large solution-air surface contact area, will evaporate before the solution reaches the substrate. For intermediate distances, which we have determined to be $h = 13$ cm for our system, the droplets will reach the substrate, coalesce there, and the organic semiconductor film will grow from the nucleation sites that form here. For the spin-coated devices, the film formation is very different. Here, the solvent evaporates almost instantaneously. This effect, together with the interactions present at the surface of the chemically treated contacts, leads to formation of a very distinct film microstructure. As a result of this microstructure, the mobility vs. channel length graph shown in Fig. 4 kinks at $L = 25$ μm. This behavior is in good agreement with our earlier reports on diF-TES ADT thin-film devices fabricated on PFBT treated contacts, and is a result of a transition between two distinct channel microstructures [26]. Following PFBT treatment, spin-coated devices consist of unique structural features, with plate-like crystals covering the contact area and extending into the channel, and small grains in the middle of the channel. We have demonstrated that these contact-nucleated features form a highly ordered film, consisting of co-facially packed molecules, with the long axis of the ADT core forming the π stacking along the charge transport path and, consequently, exhibiting high mobility. In TFTs with sufficiently short channels, the contact-nucleated features bridge the source and drain contacts and a high mobility is observed. At long channel lengths the mobility dramatically decreases as a result of the formation of a poorly ordered film within the channel consisting of mixed molecular orientations and promoting low mobility regions [25]. Fig. 4c shows the unique film microstructure at large channel lengths, consisting of the two different film types and provides an explanation for this peculiar behavior.

4. Conclusions

In summary, we have fabricated high performance organic thin-film transistors by using spray-deposition. We have shown that the electrical performance of our devices is strongly dependent on solution concentration, with the best TFTs exhibiting mobilities of $\mu = 0.2$ cm^2/V s, and current on/off ratios of 10^7. Our results demonstrate the viability of spray-deposition, a low-cost, high-throughput method that provides a robust route to fabricating reliable organic TFTs, with remarkable properties, and open new routes to low-cost fabrication of organic electronic devices.

Acknowledgements

We acknowledge C. Chan, B. Conrad and D. Gundlach from the National Institute of Standards and Technology for supplying the pre-fabricated substrates, and C. Day (Chemistry Department, Wake Forest University) for valuable discussions. NAA and JWO have contributed equally to the work.

References

[1] E.C.P. Smits, S.G.J. Mathijssen, P.A. van Hal, S. Setayesh, T.C.T. Geuns, K.A.H.A. Mutsaers, E. Cantatore, H.J. Wondergem, O. Werzer, R. Resel, M. Kemerink, S. Kirchmeyer, A.M. Muzafarov, S.A. Ponomarenko, B. de Boer, P.W.M. Blom, D.M. de Leeuw, Bottom-up organic integrated circuits, Nature 455 (2008) 956–959.
[2] T. Sekitani, H. Nakajima, H. Maeda, T. Fukushima, T. Aida, K. Hata, T. Someya, Stretchable active-matrix organic light-emitting diode display using printable elastic conductors, Nat. Mater. 8 (2009) 494–499.
[3] A.S. Molinari, H. Alves, Z. Chen, A. Facchetti, Alberto F. Morpurgo, High electron mobility in vacuum and ambient for PDIF-CN2 single-crystal transistors, J. Am. Chem. Soc. 131 (7) (2009) 2462–2463.
[4] J. Ho Cho, J. Lee, Y. Xia, B. Kim, Y. He, M.J. Renn, T.P. Lodge, C.D. Frisbie, Printable ion-gel gate dielectrics for low-voltage polymer thin-film transistors on plastic, Nat. Mater. 7 (2008) 900–906.
[5] S. Subramanian, S.K. Park, S.R. Parkin, V. Podzorov, T.N. Jackson, J.E. Anthony, Chromophore fluorination enhances crystallization and stability of soluble anthradithiophene semiconductors, J. Am. Chem. Soc. 130 (2008) 2706–2707.
[6] S.K. Park, D.A. Mourey, S. Subramanian, J.E. Anthony, T.N. Jackson, High-mobility spin-cast organic thin film transistors, Appl. Phys. Lett. 93 (2008) 043301.
[7] T. Uemura, Y. Hirose, M. Uno, K. Takimiya, J. Takeya, Very high mobility in solution-processed organic thin-film transistors of highly ordered [1]benzothieno[3,2-b]benzothiophene derivatives, Appl.Phys. Express 2 (2009) 111501.
[8] Tsuyoshi Sekitani, Yoshiaki Noguchi, Ute Zschieschang, Hagen Klauk, Takao Someya, Organic transistors manufactured using inkjet technology with subfemtoliter accuracy, Proc. Nat. Acad. Sci. 105 (2009) 4976–4980.
[9] S.E. Shaheen, R. Radspinner, N. Peyghambarian, G.E. Jabbour, Fabrication of bulk heterojunction plastic solar cells by screen printing, Appl. Phys. Lett. 79 (2001) 2996–2998.
[10] F. Padinger, C.J. Brabec, T. Fromherz, J.C. Hummelen, N.S. Sariciftci, Fabrication of large area photovoltaic devices containing various blends of polymer and fullerene derivatives by using the doctor blade technique, Opto-Electron. Rev. 8 (2000) 280–283.
[11] S.F. Tedde, J. Kern, T. Sterzl, J. Frst, P. Lugli, O. Hayden, Fully spray coated organic photodiodes, Nano Lett. 9 (2009) 980–983.
[12] C.N. Hoth, R. Steim, P. Schilinsky, S.A. Choulis, S.F. Tedde, O. Hayden, C.J. Brabec, Topographical and morphological aspects of spray coated organic photovoltaics, Org. Electron. 10 (2009) 587–593.
[13] R. Green, A. Morfa, A.J. Ferguson, N. Kopidakis, G. Rumbles, S.E. Shaheen, Performance of bulk heterojunction photovoltaic devices prepared by airbrush spray deposition, Appl. Phys. Lett. 92 (2008) 033301.
[14] T. Ishikawa, M. Nakamura, K. Fujita, T. Tsutsui, Preparation of organic bulk heterojunction photovoltaic cells by evaporative spray deposition from ultradilute solution, Appl. Phys. Lett. 84 (2004) 2424–2426.
[15] D.J. Vak, S.S. Kim, J. Jo, S.H. Oh, S.I. Na, J.W. Kim, D.Y. Kim, Fabrication of organic bulk heterojunction solar cells by a spray deposition

method for low-cost power generation, Appl. Phys. Lett. 91 (2007) 081102.
[16] C.K. Chan, L.J. Richter, B. Dinardo, C. Jaye, B.R. Conrad, H.W. Ro, D.S. Germack, D.A. Fischer, D.M. DeLongchamp, D.J. Gundlach, High performance airbrushed organic thin film transistors, Appl. Phys. Lett. 96 (2010) 133304.
[17] A. Abdellah, B. Fabel, P. Lugli, G. Scarpa, Spray deposition of organic semiconducting thin-films: Towards the fabrication of arbitrary shaped organic electronic devices, Org. Electron. 11 (2010) 0311038.
[18] Y.-F. Lim, S. Lee, D.J. Herman, M.T. Lloyd, J.E. Anthony, G.G. Malliaras, Spray-deposited poly(3,4-ethylenedioxythiophene):poly(styrenesulfonate) top electrode for organic solar cells, Appl. Phys. Lett. 93 (2008) 193301.
[19] C. Girotto, B.P. Rand, S. Steudel, J. Genoe, P. Heremans, Nanoparticle-based, spray-coated silver top contacts for efficient polymer solar cells, Org. Electron. 10 (2009) 735–740.
[20] E. Menard, V. Podzorov, S.-H. Hur, A. Gaur, M.E. Gershenson, J.A. Rogers, High-performance n- and p-type single-crystal organic transistors with free-space gate dielectrics, Adv. Mater. 16 (2004) 2097–2101.
[21] A.L. Briseno, S.C.B. Mannsfeld, M.M. Ling, S. Liu, R.J. Tseng, C. Reese, M.E. Roberts, Y. Yang, F. Wudl, Z. Bao, Patterning organic single-crystal transistor arrays, Nature 444 (2006) 913–917.
[22] O.D. Jurchescu, M. Popinciuc, B.J. van Wees, T.T.M. Palstra, Interface-controlled, high-mobility organic transistors, Adv. Mater. 19 (2007) 688–692.
[23] S.K. Park, T.N. Jackson, J.E. Anthony, D.A. Mourey, High mobility solution processed 6,13-bis(triisopropyl-silylethynyl) pentacene organic thin film transistors, Appl. Phys. Lett. 91 (2007) 063514.
[24] O.D. Jurchescu, S. Subramanian, R.J. Kline, J. E Anthony, T.N. Jackson, D.J. Gundlach, Organic single-crystal field-effect transistors of a soluble anthradithiophene, Chem. Mater. 20 (2008) 6733–6737.
[25] D.J. Gundlach, J.E. Royer, S.K. Park, S. Subramanian, O.D. Jurchescu, B.H. Hamadani, A.J. Moad, R.J. Kline, L.C. Teague, O. Kirillov, C.A. Richter, J.G. Kushmerick, L.J. Richter, S.R. Parkin, T.N. Jackson, J.E. Anthony, Contact-induced crystallinity for high-performance soluble acene-based transistors and circuits, Nat. Mater. 7 (2008) 216–221.
[26] O.D. Jurchescu, B.H. Hamadani, H.D. Xiong, S.K. Park, S. Subramanian, N.M. Zimmerman, J.E. Anthony, T.N. Jackson, D.J. Gundlach, Correlation between microstructure, electronic properties and flicker noise in organic thin film transistors, Appl. Phys. Lett. 92 (2008) 132103.
[27] D.J. Gundlach, L. Zhou, J.A. Nichols, T.N. Jackson, P.V. Necliudov, M.S. Shur, An experimental study of contact effects in organic thin film transistors, J. Appl. Phys. 100 (2006) 024509.
[28] C. Reese, Z. Bao, Detailed characterization of contact resistance, gate-bias-dependent field-effect mobility, and short-channel effects with microscale elastomeric single-crystal field-effect transistors, Adv. Funct. Mater. 19 (2009) 763–771.
[29] L.C. Teague, B.H. Hamadani, O.D. Jurchescu, S. Subramanian, J.E. Anthony, T.N. Jackson, D.J. Gundlach, J.G. Kushmerick, Surface potential imaging of solution processable acene-based thin film transistors, Adv. Mater. 20 (2008) 4513–4516.
[30] O. Ostroverkhova, D.G. Cooke, F.A. Hegmann, R.R. Tykwinski, S.R. Parkin, J.E. Anthony, Anisotropy of transient photoconductivity in functionalized pentacene single crystals, Appl. Phys. Lett. 89 (2006) 192113.
[31] C.W. Sele, B.K.C. Kjellander, B. Niesen, M.J. Thornton, J.B.P.H. van der Putten, K. Myny, H.J. Wondergem, A. Moser, R. Resel, A.J.J.M. van Breemen, N. van Aerle, P. Heremans, J.E. Anthony, G.H. Gelinck, Controlled deposition of highly ordered soluble acene thin films: effect of morphology and crystal orientation on transistor performance, Adv. Mater. 21 (2009) 4926–4931.
[32] O.D. Jurchescu, D.A. Mourey, S. Subramanian, S.R. Parkin, B.M. Vogel, J.E. Anthony, T.N. Jackson, D.J. Gundlach, Effects of polymorphism on charge transport in organic semiconductors, Phys. Rev. B 80 (2009) 085201.
[33] L.H. Jimison, M.F. Toney, I. McCulloch, M. Heeney, A. Salleo, Charge-transport anisotropy due to grain boundaries in directionally crystallized thin films of regioregular poly(3-hexylthiophene), Adv. Mater. 21 (2009) 1568–1572.
[34] S.S. Lee, C.S. Kim, E.D. Gomez, B. Purushothaman, M.F. Toney, C. Wang, A. Hexemer, J.E. Anthony, Y.-L. Loo, Controlling nucleation and crystallization in solution-processed organic semiconductors for thin-film transistors, Adv. Mater. 21 (2009) 3605–3609.

Organic Electronics 11 (2010) 1966–1973

Contents lists available at ScienceDirect

Organic Electronics

journal homepage: www.elsevier.com/locate/orgel

Bi- or ter-pyridine tris-substituted benzenes as electron-transporting materials for organic light-emitting devices

Musubu Ichikawa [a,b,*], Kenta Wakabayashi [a], Shuichi Hayashi [c], Norimasa Yokoyama [c], Toshiki Koyama [a], Yoshio Taniguchi [d]

[a] Functional Polymer Science Course, Faculty of Textile Science and Technology, Shinshu University, 3-15-1 Tokita, Ueda City, Nagano 386-8567, Japan
[b] Presto, Japan Science and Technology Agency (JST), 4-8-1 Honcho, Kawaguchi, Saitama 332-0012, Japan
[c] Hodogaya Chemical Co. Ltd., 45 Miyukigaoka, Tsukuba, Ibaraki 305-0841, Japan
[d] Faculty of Textile Science and Technology, Shinshu University, 3-15-1 Tokita, Ueda, Nagano 386-8567, Japan

ARTICLE INFO

Article history:
Received 7 June 2010
Received in revised form 30 August 2010
Accepted 4 September 2010
Available online 28 September 2010

Keywords:
Electron transporting
Hole blocking
OLED
Phosphorescent device
Mobility
Bipyridine

ABSTRACT

We demonstrated that 1,3,5-tris([2′,2″]bipyridin-6′-yl)benzene (BpyB) and 1,3,5-tris([2′,2″,6″,2‴]terpyridin-6'-yl)benzene (TpyB) are good electron-transport (ET) layer materials for organic light-emitting devices (OLEDs). The new materials exhibit high electron mobilities of around 10^{-4} cm^2 V^{-1} s^{-1}, and OLEDs comprising the materials operate at lower voltage than the OLEDs with tris(8-hydroxyquinolinato) aluminum (Alq) as an ET material. The new materials are also useful for phosphorescent OLEDs in blue-, green-, and red-light-emitting devices, where they function as both electron-transporting and hole-blocking materials. Phosphorescent OLEDs with the new materials operate at lower voltage (while maintaining comparable external quantum efficiencies of electroluminescence) than does the corresponding reference device with bathocuproine/Alq as electron-transporting and hole-blocking layers.

© 2010 Elsevier B.V. All rights reserved.

1. Introduction

Organic light-emitting devices (OLEDs) are of interest for potential application in various fields such as flat televisions, mobile displays, lights, and optical communication light sources. OLEDs generally comprise functionally divided organic multilayers – for example, hole-transporting (HT), emissive, and electron-transporting (ET) layers [1,2]. In the last decade, many kinds of amorphous molecular semiconductor materials [3,4], HT materials [5–12], and ET materials [13–23], have been proposed. Among these, HT molecular semiconducting materials have become practical due to their high charge-carrier mobility and excellent operational durability, but few reports exist to date on ET organic semiconducting amorphous materials that perform well in terms of high-speed transport of electrons, easy injection of electrons from the cathode, and good operational durability [16]. Tris (8-hydroxyquinolinato) aluminum(III) (Alq) was used in the first bright OLED reported by Tang and VanSlyke in 1987 [1]; it is still conventionally used as an ET material, despite its slow electron mobility [24], because of its relatively good operational durability. However, as a reflection of the imbalanced performance between ET and HT materials, electron-feeding from the cathode into an emissive layer controls device characteristics. As a result, the development of efficient ET organic amorphous semiconducting materials remains an important challenge.

* Corresponding author at: Functional Polymer Science Course, Faculty of Textile Science and Technology, Shinshu University, 3-15-1 Tokita, Ueda, Nagano 386-8567, Japan. Tel.: +81 268 21 5498; fax: +81 268 21 5413.
E-mail address: musubu@shinshu-u.ac.jp (M. Ichikawa).

1566-1199/$ - see front matter © 2010 Elsevier B.V. All rights reserved.
doi:10.1016/j.orgel.2010.09.004

ET materials with high electron mobilities provide some advantages, including lower operating voltage and lower power consumption. Moreover, if ET materials have wide band gaps – that is, deep highest occupied molecular orbitals (HOMOs) – they can also work as hole-blocking (HB) materials. Hole-blocking is desirable because complete confinement of holes in emissive layers by the HB layer raises the quantum efficiency (QE) of electroluminescence (EL). Furthermore, when considering phosphorescent OLEDs (PHOLEDs) that can theoretically provide the 100% internal electron–photon conversion efficiency theoretically [25], a complete confinement for triplet exciton energies of phosphorescent light-emitters also becomes important to attain extremely high QE.

We have frequently reported on ET materials with high electron mobilities based on one molecular design concept: hybridizing bipyridine with common ET units such as oxadiazole or triazole [26–28]. Can we now make good ET materials based on bipyridine only? Bathophenanthroline, a common good ET material, is similar in structure to bipyridine. Kido et al. recently reported that tris-pyridine-substituted triphenylbenzenes exhibit very good electron-transport properties, with electron mobilities as high as 7.9×10^{-3} cm^2 V^{-1} s^{-1} [29]. As a result, we can assume that the tris-bipyridine-substituted benzene (BpyB) and tris-terpyridine-substituted benzene (TpyB) examined in this study will be good ET-layer materials for OLEDs. As described herein, OLEDs with these new materials clearly operate at lower voltage than do OLEDs with Alq, a conventional ET material. The new materials are also useful for phosphorescent OLEDs, where they work not only as ET but also as HB materials.

2. Experimental

2.1. Materials

Fig. 1 shows chemical structures of the newly developed materials BpyB and TpyB, synthesized from bipyridine or terpyridine bromides with tris(pinacolboryl) benzene by Suzuki–Miyaura coupling reaction. BpyB and TpyB were purified, before evaluation and measurements, by temperature-gradient sublimation in a flow stream of pure Ar gas. Other OLED materials were obtained from industrial companies as sublimation grades and used without further purification.

2.2. Synthesis

2.2.1. 6-Bromo[2,2′]bipyridine (Br-Bpy)

Br-Bpy was synthesized from 2,6-dibromopyridine (11.8 g, 52.8 mmol) and 2-pyridyl zinc bromide (55.0 mmol) that was contained in 110 ml of its tetrahydrofuran (THF) solution (0.5 M) using 50 ml of THF as additional solvent and tetrakis(triphenylphosphine)Pd(0) (1.7 g, 2.5 mmol) as catalyst. With the reaction solution kept below 10 °C with an ice bath, the 2-pyridyl zinc bromide solution was added dropwise. The ice bath was removed and the solution was stirred continuously for 48 h. Then, 10 wt.% ethylenediamine-*N*,*N*,*N*′,*N*′-tetraacetic acid, disodium salt (EDTA 2Na) aqueous solution (500 ml) was added in small steps. Chloroform extraction and distillation of the solvent gave a crude brown powder. Purification by silica gel chromatography with a toluene/ethyl acetate mixture as eluent yielded Br-Bpy as white powder (7.0 g; 54% yield). δ_H (600 MHz, $CDCl_3$): 8.67 (d, 1H, J 4.8 Hz), 8.41 (d, 1H, J 7.8 Hz), 8.38 (d, 1H, J 8.4), 7.82 (dd, 1H, J 8.7 Hz), 7.67 (dd, 1H, J 7.8 Hz), 7.49 (d, 1H, J 7.2 Hz), 7.32 (dd, 1H, J 6.3 Hz).

2.2.2. 6-Bromo[2,2′,6′,2″]terpyridine (Br-Tpy)

Br-Tpy was synthesized from 6,6′-dibromo[2,2']bipyridine (10.0 g, 31.4 mmol) essentially as described for Br-Bpy to yield a white powder (5.2 g; 52.4% yield). δ_H (600 MHz, $CDCl_3$): 8.70 (d, 1H, J 4.8 Hz), 8.58 (d, 1H, J 6.6 Hz), 8.57 (d, 1H, J 9.0 Hz), 8.46 (m, 2H), 7.95 (dd, 1H, J 7.8 Hz), 7.85 (dd, 1H, J 6.0 Hz, J 7.8 Hz), 7.70 (dd, 1H, J 8.1 Hz), 7.50 (d, 1H, J 7.2 Hz) 7.34 (m, 1H).

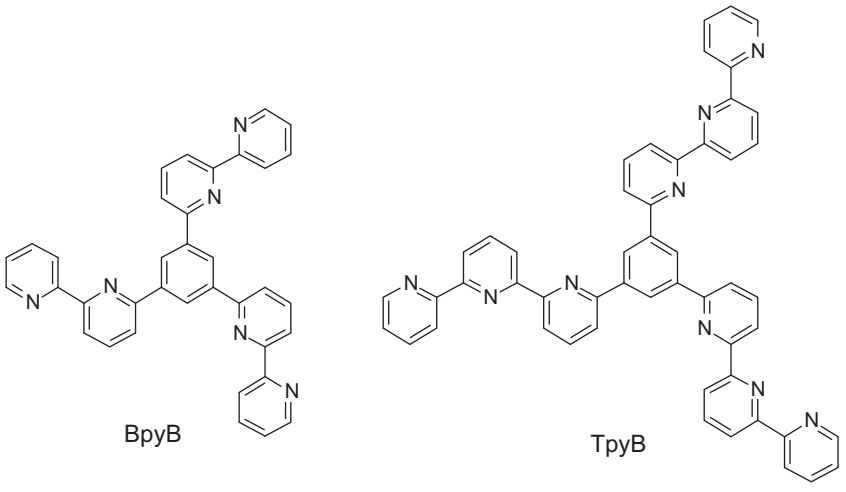

Fig. 1. Chemical structures of BpyB and TpyB.

2.2.3. 1,3,5-Tris(pinacorato boryl)benzene ((PinB)$_3$B)

(PinB)$_3$B was synthesized by Suzuki–Miyaura coupling reaction using 1,3,5-tribromobenzene (8.6 g, 27.3 mmol), bis(pinacorato)diboron (25.0 g, 98.4 mmol), potassium acetate (24.1 g, 245.7 mmol), and [1,1′-bis(diphenylphosphino)ferrocene] dichloropalladium(II) as catalyst in dimethyl sulfoxide. The reaction mixture was refluxed for 21 h, and then cooled to room temperature. Pure water (1000 ml) was added and the mixture was stirred for 30 min and filtered to remove precipitates. Addition of methanol gave a crude white crystalline powder, which was dissolved in ethyl acetate, filtered to remove the catalyst, and distilled to yield pure (PinB)$_3$B (7.1 g; 57% yield). δ_H (600 MHz, $CDCl_3$): 8.37 (s, 3H), 1.33 (s, 36H).

2.2.4. 1,3,5-Tris([2′,2″]bipyridin-6′-yl)benzene (BpyB)

BpyB was synthesized from (PinB)$_3$B (2.5 g, 5.5 mmol) and Br-Bpy (3.8 g, 15.0 mmol) by Suzuki–Miyaura coupling reaction using 1 M K_2CO_3 aqueous solution (32.4 ml, 32.4 mmol) as base, tetrakis(trisphenylphosphine)palladium(0) (0.32 g, 0.28 mmol) as catalyst, and 135 ml of a 4/1 ethanol/toluene mixture as solvent. The reaction mixture was refluxed with stirring for 33 h, and then cooled to room temperature. Pure water (500 ml) was added and the mixture was stirred for 30 min. Extraction by chloroform, drying with $MgSO_4$, filtration to remove precipitates, and distillation to remove the chloroform gave a crude brown powder. Purification by silica gel column chromatography with a 1/3 chloroform/hexane mixture as eluent yielded BpyB as a white crystalline powder (1.1 g; 41% yield). δ_H (600 MHz, $CDCl_3$): 9.01(s, 3H), 8.76 (d, 3H, J 7.2 Hz), 8.74 (d, 3H, J 4.8 Hz), 8.47 (d, 3H, J 7.2 Hz), 8.01 (dd, 3H, J 8.7 Hz), 7.98 (d, 3H, J 7.8 Hz), 7.88 (dd, 3H, J 7.8 Hz), 7.36 (dd, 3H, J 6.3 Hz). δ_C (150 MHz, $CDCl_3$): 156.43, 156.31, 155.90, 149.14, 140.43, 137.82, 136.82, 126.25, 123.78, 121.37, 120.65, 119.65.

2.2.5. 1,3,5-Tris([2′,2″,6″,2‴]terpyridin-6′-yl)benzene (TpyB)

TpyB was synthesized by Suzuki–Miyaura coupling reaction using (PinB)$_3$B (2.4 g, 5.26 mmol) and Br-Tpy (5.0 g, 16.0 mmol) essentially as described for BpyB using 1 M K_2CO_3 aqueous solution (32.3 g, 32.4 mmol), tetrakis(trisphenylphosphine)palladium(0) (0.32 g, 0.28 mmol), and 150 ml of a 4/1 ethanol/toluene mixture. The reaction mixture was refluxed for 3 h, cooled, and then filtered. Recrystallization from *o*-dichlorobenzene solution yielded TpyB as a white powder (2.7 g; 67% yield). δ_H (600 MHz, $CDCl_3$): 9.06 (s, 3H), 8.81 (d, 3H, J 7.8 Hz), 8.73(d, 3H, J 3 Hz), 8.68 (d, 3H, J 8.4 Hz), 8.67 (d, 3H, 7.8 Hz), 8.50 (d, 3H, J 8.4 Hz), 8.03 (m, 9H), 7.89 (dd, 3H, J 7.8 Hz), 7.35 (d, 3H, J 7.8 Hz). δ_C (150 MHz, $CDCl_3$): 156.21, 155.85, 155.54, 155.30, 149.15, 140.28, 137.77, 136.87, 130.51, 127.70, 126.17, 123.75, 121.26, 121.21, 121.05, 120.60, 119.69.

2.3. Device fabrication and measurements

All OLEDs were fabricated on 150-nm-thick layers of indium-tin oxide (ITO) that were commercially precoated onto glass substrates with a sheet resistance of 14 Ω/sq. The solvent-cleaned ITO surface was treated with O_2 plasma for 5 min and then the substrate was immediately loaded into a high-vacuum chamber (base pressure below $\sim 6 \times 10^{-4}$ Pa) where organic layers, 0.5-nm-thick LiF, and 200-nm-thick aluminum cathode layers were deposited by thermal evaporation. Deposition rates were 0.6 Å/s for organic materials, 0.1 Å/s for LiF, and 6 Å/s for Al. The current density-applied voltage–luminance (*J–V–L*) characteristics of the OLEDs were measured with a commercial OLED-characteristics measurement system (Precise Gauge EL1003) and a source meter (Keithley 2400). Electroluminescence (EL) spectra were recorded simultaneously with the EL1003 during *J–V–L* measurements.

^{1}H- and ^{13}C NMR spectra were recorded on an FT–NMR spectrometer (JEOL JNM-ECA600). Thermal analyses were performed on a differential scanning calorimeter (Seiko Instruments DSC-6200) at a heating rate of 10 °C/min under N_2 gas. Ultraviolet (UV) and visible absorption spectra were recorded with a spectrophotometer (Shimadzu UV-3150); photoluminescence (fluorescence and phosphorescence) spectra were recorded with a spectrofluorometer (Horiba FluoroMax4P). HOMO energy was determined with a photoelectron emission yield spectrometer (Riken Keiki AC-3), and the HOMO energy was defined as being equal to the ionization potential measured by photoelectron emission spectroscopy. Optical band gaps were determined by the spectral onset of each UV–visible absorption spectrum; the lowest unoccupied molecular orbital (LUMO) energy was then estimated to be the difference between the HOMO energy and the optical bandgap. Spectroscopic measurements were conducted with thin films prepared by thermal evaporation on quartz substrates.

Electron mobility was measured by conventional time-of-flight (TOF) techniques. The excitation light was a 500-ps-duration optical pulse from an N_2 gas laser (λ = 337 nm, Usho Optical Systems KEN-150). Test samples were prepared by thermal evaporation in vacuum and encapsulated with fresh desiccant under a highly inert atmosphere of N_2 at the dew point of almost −60 °C and O_2 concentration of <10 ppm. A 100-nm-thick fullerene C_{60} layer was used as a charge-generation layer for optical excitation [27].

Computational chemistry was conducted with commercial software (Wavefunction Spartan 06W) on a personal computer with a dual-core processer. Density function theory (DFT) was used to determine conformations, with a B3LYP hybrid functional and a 6-311G* basis set for determining optimized geometries and estimating activation energies for conformation change. During the estimation of activation energies, we constrained the dihedral angle that was responsible for the conformation change and conducted each geometry optimization with the dihedral constraint at several angles.

3. Results and discussion

3.1. Thermal and electronic properties

Fig. 2 shows differential scanning calorimetry (DSC) curves for BpyB and TpyB. During the first heating procedure, endothermic peaks due to melting are observed for

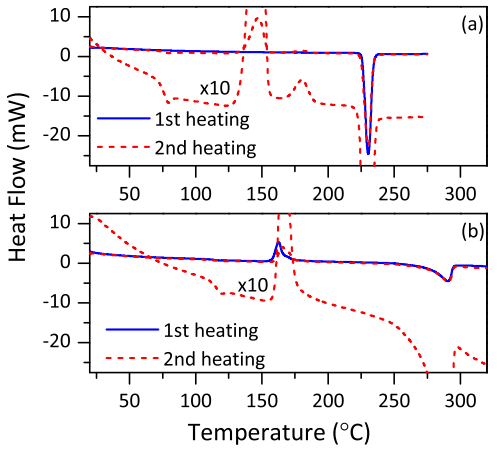

Fig. 2. DSC curves of BpyB and TpyB during first and second heating procedures.

the two powders at 240 °C and 305 °C, respectively. For BpyB, during the second heating procedure, a baseline shift due to glass transition and an exothermic peak at 146 °C due to recrystallization are observed; the glass transition temperature T_g is 75 °C. For TpyB, during the second heating procedure, the same transitions occur: recrystallization at 166 °C and T_g at 110 °C. These results confirm that both powders can form stable glassy thin films by vacuum evaporation. T_g is higher for TpyB (110 °C) than for NPB (94 °C), a practical HT material (Fig. 5).

Fig. 3a shows the optimized geometry for BpyB, obtained by means of computational chemistry. The geometry shows C3 symmetry and resembles a three-blade propeller. The dihedral angle between the center phenyl ring and the adjacent pyridine ring is 23° because of steric hindrance between the two hydrogen atoms at the ortho position of each ring. In contrast, the pyridine units are coplanar. These angles are reasonable from the viewpoint of general chemistry. Fig. 3b shows a bipyridyl wing of BpyB rotated 180° around the single bond that connects the bipyridine unit with the center phenyl ring, significantly changing the molecular geometry. Note that the energy of this rotated geometry is the third lowest and the energy difference ΔE between the two conformers is estimated to be only 1.77 kJ mol^{-1}. Such rotation is known to occur easily in the case of conformation with a single bond that links two aromatic rings. Fig. 3c shows the energy profile for dihedral rotation. Through computational chemistry, we estimate the activation energy to be 15.5 kJ mol^{-1}, only ~6 times larger than the thermal energy at room temperature (2.48 kJ mol^{-1}). This result indicates that conformation change between the two conformers occurs frequently, and a population of the higher energy conformer must be defined by the Boltzmann distribution with the energy difference ΔE. The exact population must depend on the energy distributions of all the

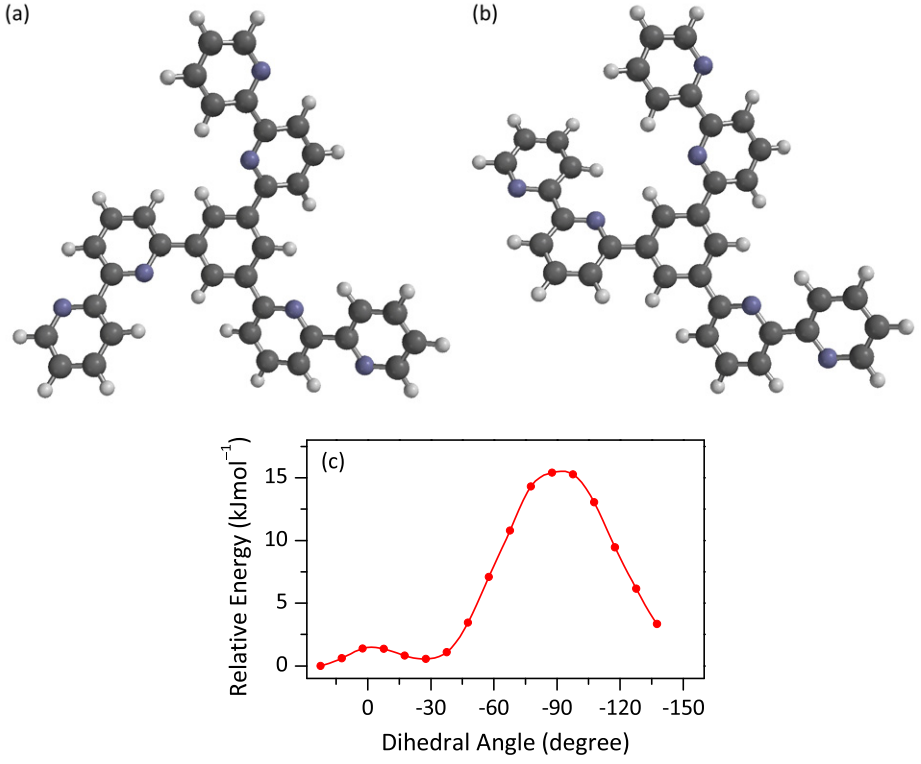

Fig. 3. (a) and (b) Lowest-energy and third-lowest-energy computational optimized geometries, respectively, of BpyB. (c) Energy profile of the conformation change between these two geometries. Another local minimum exists at a dihedral angle of 30°. The structure of the second-lowest-energy geometry is close to that of (a).

conformers of BpyB, but this small ΔE suggests that a large number of BpyB molecules exist as conformers other than the lowest energy one, and thus thin films of BpyB are composed of several conformers. We believe that this is one reason why BpyB displays an amorphous nature [27].

Fig. 4a shows UV–visible absorption and fluorescence spectra of neat thin films of each material. The absorption maxima are at 274 nm for BpyB and 293 nm for TpyB, and both materials emit bright UV fluorescence. Optical interference by the sample thin film causes broad absorption around 500–600 nm. The band gaps (E_g = 3.60 eV) for both BpyB and TpyB from the absorption spectra are clearly wide.

Fig. 4b shows phosphorescent spectra of dilute 2-methyltetrahydrofuran (meTHF) solutions of BpyB and TpyB at liquid-nitrogen temperature (77 K). We determined the triplet bandgap energy E_g^T from an apparent peak at the shortest wavelength, indicated by an arrow in the figure; for BpyB, $E_g^T = 2.77$ eV and for TpyB, $E_g^T = 2.79$ eV. For BpyB, the LUMO level (2.85 eV) in neat solid is low enough to easily accept electrons from a cathode metal. For TpyB, the LUMO level is deeper (3.00 eV) due to three additional pyridine units, implying easier injections of electrons from a cathode metal. In addition, for both materials, the HOMO levels (6.45 eV for BpyB and 6.60 eV for TpyB) are sufficiently deep to suppress hole leakages from the emissive layer, and hole confinement in the emissive layer leads to high QE of EL. As a result, BpyB and TpyB can be used as efficient ET and HB materials. The thermal and electronic properties of BpyB and TpyB are summarized in Table 1.

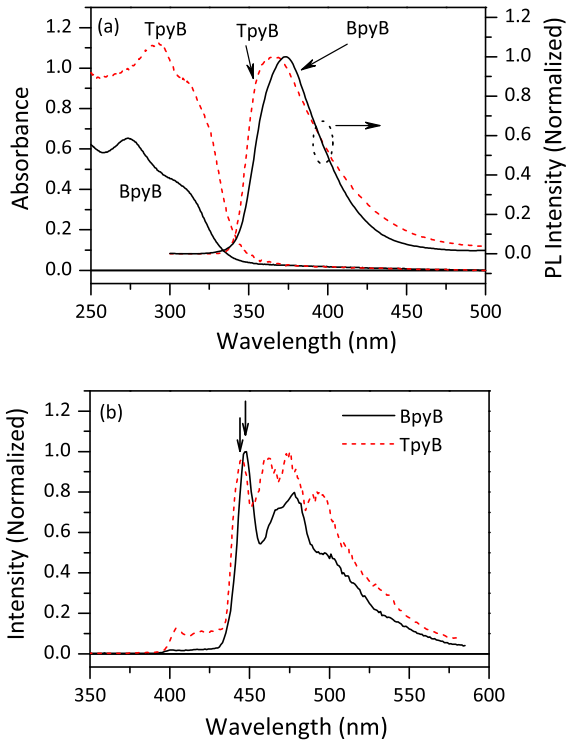

Fig. 4. (a) UV and visible absorption spectra (left axis) and PL spectra (right axis) of thin films of BpyB (thickness 77 nm) and TpyB (thickness 88 nm). (b) Phosphorescence spectra of meTHF solutions of the materials at liquid-nitrogen temperature (77 K). Weak bands around 400–425 nm are assigned to phosphorescence from the stabilizer contained in meTHF, 3,5-di-*tert*-butyl-4-hydroxytoluene (BHT).

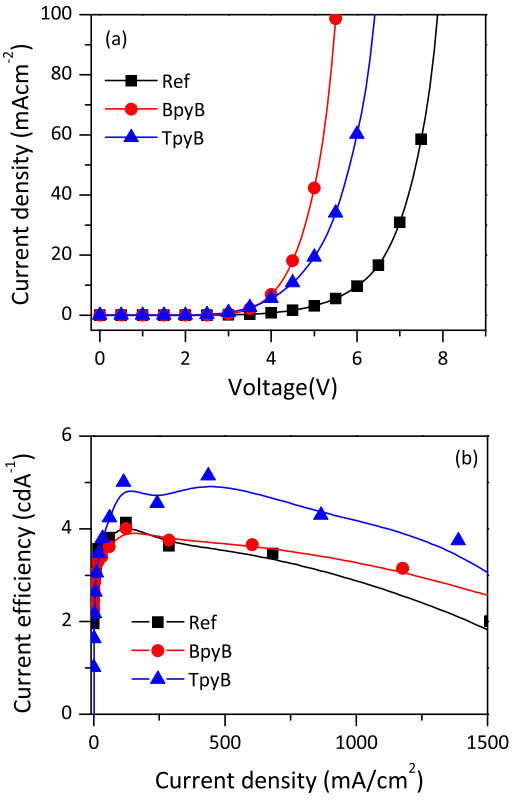

Fig. 5. *J–V–L* characteristics of OLEDs with BpyB or TpyB as electron-transporting materials and of a reference OLED with Alq: (a) Current density as a function of voltage (*J–V*); (b) Luminous current efficiency as a function of current density (*L–J*).

Table 1
Thermal and electronic properties of BpyB and TpyB.

	I_p (eV)	E_a (eV)	E_g (eV)	E_g^T (eV)	T_m (°C)	T_g (°C)
BpyB	6.45	2.85	3.60	2.77	240	75
TpyB	6.60	3.00	3.60	2.79	305	110

3.2. OLED properties

Fig. 5 shows the current density–applied voltage (*J–V*) characteristics of OLEDs with BpyB or TpyB as an ET material as well as of a reference device without the new materials. Fig. 6 shows the structure of the associated OLED and the various chemicals used in it. OLEDs with the new materials perform better (operate at lower voltage) than a reference OLED with Alq. Therefore, we conclude that we can make a good ET material with bipyridine and/or terpyridine only. The BpyB device shows almost the same luminous efficiency (4.0 cdA^{-1}) as does the reference device with Alq. The TpyB device shows even higher luminous efficiency (5.0 cdA^{-1}), probably due to the deeper HOMO

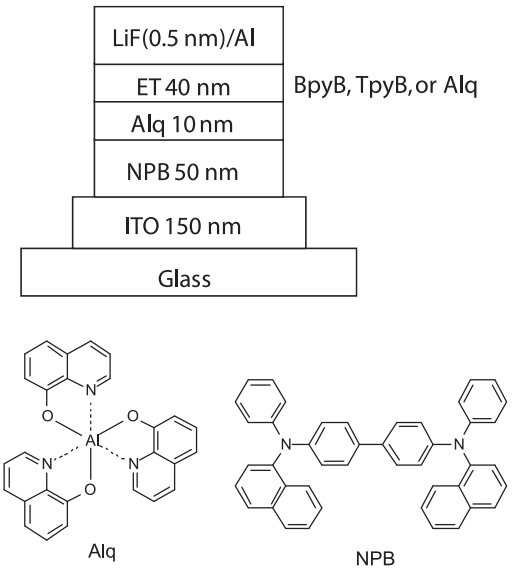

Fig. 6. OLED device: (top) device structure; (bottom) chemical structures of two of the materials used in the device.

of TpyB, which is effective for preventing hole leakages from the emissive layer. As noted earlier, hole-blocking is important for attaining high QE of EL. While we observed no increase in efficiency for BpyB, the lower operation voltage of the device with BpyB implies high electron mobility of BpyB, and the high mobility might move the electron–hole recombination zone for the NPB/Alq interface. The move of the recombination zone is probably a reason no increase of the QE because a very recent report indicated that an interaction between NPB and Alq apparently reduces the luminescence efficiency of Alq [30]. We believe that BpyB should also have HB properties because of its sufficiently deep HOMO.

Because BpyB and TpyB perform well not only as ET materials but also as HB materials, we investigated their use as double-function ET/HB materials. Recent highly efficient phosphorescent OLEDs have both an HB layer and an ET layer. In particular, an HB layer is important for obtaining high QE because hole leakage seriously reduces efficiency. Moreover, it is more important to consider triplet energy dissipation from the emissive layer to the hole-blocking layer for attaining high QE. At present, only a few materials are used as HB materials for phosphorescent OLEDs, including bathocuproine (BCP) and bis (2-methyl-8-quinolinolato) (*p*-phenylphenolato) aluminum (BAlq).

Fig. 7 shows the *J*–*V* characteristics of phosphorescent OLEDs with BpyB or TpyB as a double-function ET/HB material as well as of a reference OLED. Fig. 8 shows the structure of the associated phosphorescent OLED and the various chemicals used in it. Phosphorescent OLEDs with both new materials perform better (operate at much lower voltage) than a conventional double-layer reference OLED comprising BCP and Alq layers [31]. Since devices with both new materials show high external QE (almost 10%), BpyB and TpyB are both useful as double-function ET/HB materials for phosphorescent OLEDs. As shown in Table 1, the E_g^T for each new material is so large that no triplet en-

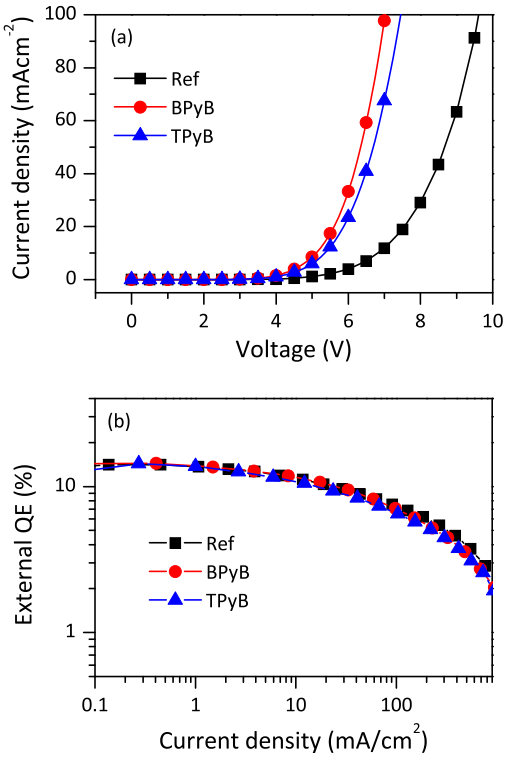

Fig. 7. *J*–*V*–*L* performance characteristics of phosphorescent OLEDs with BpyB or TpyB as dual-function hole-blocking and electron-transporting materials and of a reference OLED with the conventional structure: (a) current density as a function of voltage (*J*–*V*); (b) external quantum efficiency (QE) as a function of current density.

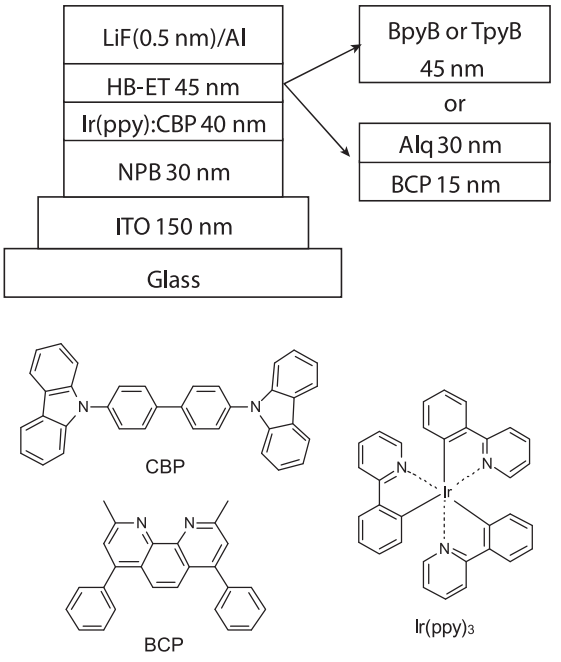

Fig. 8. Phosphorescent OLED device: (top) device structure; (bottom) chemical structures of three of the materials used in the device.

ergy leakage from the Ir-complex phosphorescent light emitter occurs.

The new materials appear to be effective even for blue-light-emitting Ir complex because the E_g^Ts of the materials are sufficiently large enough to prevent leakages of the triplet energy in blue-lights-emitting Ir complexes such as Ir(III) bis(2-(4,6-difluorophenyl)pyridinato-N,C^2)picolinate (FIrpic) of which E_g^T is 2.62 eV [32]. This is clearly evident from Fig. 9, which shows the *J*–*V*-external QE characteristics of blue- and red-light-emitting PHOLEDs with the corresponding dopants (Ir(III) bis(2-(4,6-difluorophenyl)pyridinato-N,C^2)picolinate (FIrpic) for blue and Ir(III) bis(2-(2′-benzothienyl)pyridinato-N,$C^{3'}$)acetylacetonate (BtpIracac) for red. Note that we fabricated those devices based on the same structure shown in Fig. 8 except for the dopants. Fig. 9 clearly shows that using the new materials reduce operation voltages in both colors. In addition, as one can see from Fig. 9, the devices comprising the new materials in both luminescent colors showed comparable external QEs to the corresponding reference devices with BCP and Alq. However, a slight but obvious difference in the QEs between the BpyB and TpyB devices could be observed in the blue devices. Because both E_g^Ts are almost the same, the difference probably results from a change of the recombination zone due to higher electron mobility of BpyB – the triplet energies of FIrpic and also maybe CBP possibly leak to NPB. The lower operation voltages and the comparable external QEs indicate that both BpyB and TpyB are also useful for phosphorescent OLEDs in both colors. Further optimization of device structures, including changes of host and other materials, should lead to higher external QEs at low operating voltage.

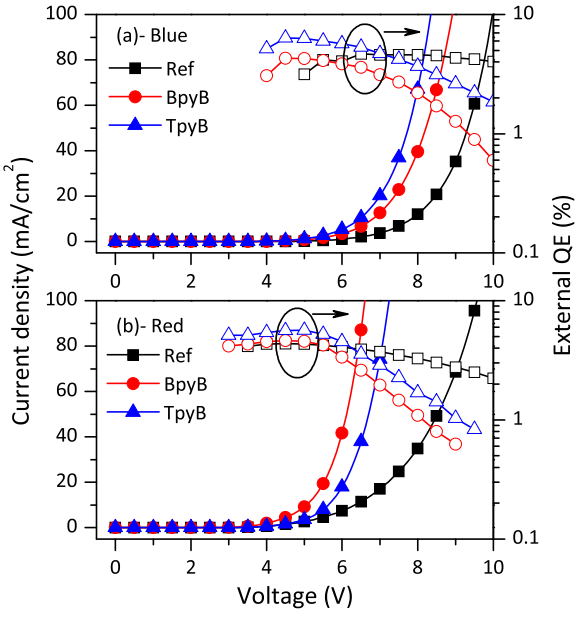

Fig. 9. *J*–*V*-external QE characteristics of phosphorescent OLEDs with BpyB or TpyB as dual-function hole-blocking and electron-transporting materials and of a reference OLED with the conventional structure: (a) blue-light-emitting phosphorescent OLED with FIrpic as the dopant; (b) red-light-emitting phosphorescent OLED with BtpIracac as the dopant. Device structures are the same as shown in Fig. 8 except for the dopants.

3.3. Electron mobility

Finally, we would like to briefly discuss electron mobility in the new materials. Fig. 10 shows the transient electron photocurrent waveform with double logarithmic scale, obtained by TOF measurement, for the BpyB film. Although each photocurrent waveform was not clear non-dispersive, we could clearly see that the transits of photogenerated charge carriers – electrons in this case become faster with increasing applied voltages because the photocurrents decayed faster with the increasing. In accordance with the conventional method to determine a transit time (t_T) for dispersive transportations, we drew the two auxiliary straight lines as shown in the figure and determined the t_T at the crossing point of the auxiliary lines. Note that the two slopes of the two auxiliary lines for each photocurrent are almost the same as each other, and this also endorses that the observed photocurrents are due to drift motions in the film. If we take electron mobility μ to be.

$$\mu = Dd/(t_T V) \tag{1}$$

where D is the distance between the two electrodes (4.0 μm), d is the thickness of the prepared BpyB layer (3.9 μm), and V is the applied voltage, we can determine, for example, that $\mu = 2.6 \times 10^{-4}$ cm^2 V^{-1} s^{-1} at the electric field $E = V/D = 1.13 \times 10^6$ V cm^{-1}. This mobility is two orders of magnitude higher than that for Alq (1.3×10^{-6} cm^2 V^{-1} s^{-1}) at approximately the same electric field [33]. This high mobility probably accounts for the better *J*–*V* curve for the OLED with BpyB than for the OLED with the corresponding reference.Fig. 11 shows electron mobility as a function of the square root of the applied electric field for several materials, including BpyB and TpyB. Both BpyB and TpyB show mobility that is at least an order of magnitude higher than that of Alq. This high mobility is comparable to that of a representative ET material with high electron mobility: a silole derivative, 2,5-bis(6′-(2′,2″-bipyridine))-1,1-dimethyl-3,4-diphenylsilole (PyPySiPyPy) [33,34]. The

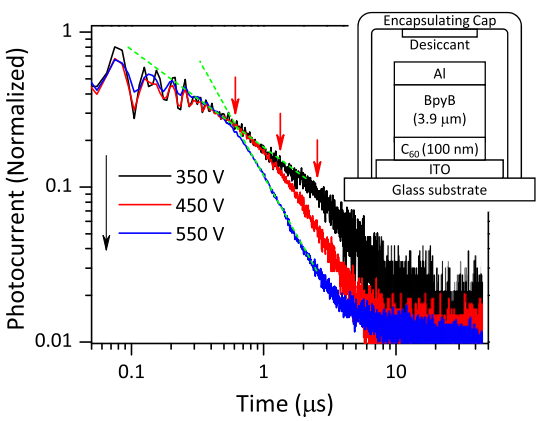

Fig. 10. Electron transient photocurrent for time-of-flight measurements of BpyB at applied voltages, to the Al cathode, of 350, 450, and 550 V. The dashed lines in green are for guides to determine the transit time of the photocurrent at 550 V and the three short red arrows represent each transit time. The inset shows the structure of the OLED device used.

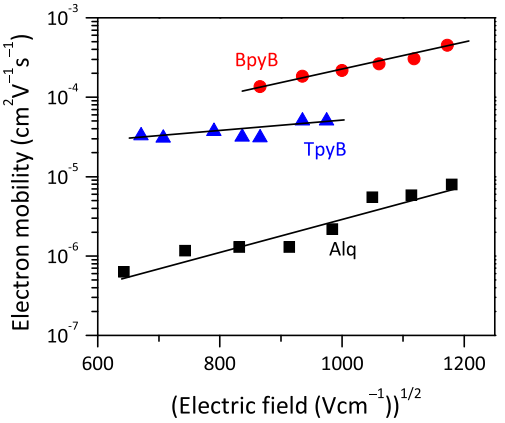

Fig. 11. Electron mobility as a function of electric field for BpyB, TpyB, and Alq. Data for Alq are from Murata (refer text).

mobility was relatively high but lower than that (1.0×10^{-3} cm^2 V^{-1} s^{-1} at 6.4×10^5 V cm^{-1}) of tris-pyridyl substituted 1,3,5-triphenylbenzene (TmPyPB) reported by Kido et al. [29] of which structure was similar to BpyB, and we are unsure about the reasons for the difference at present. In addition, mobility is lower for TpyB than for BpyB. Although we are also not sure at present about the reason, the lower mobility reflects the higher operating voltages for TpyB devices than for BpyB devices, as shown in all of the figures showing *J–V* characteristics.

4. Conclusion

We demonstrated that tris-bipyridine-substituted benzene (BpyB) and tris-terpyridine-substituted benzene (TpyB) are good ET-layer materials for OLEDs. Electron mobilities for these new materials ($\sim 10^{-4}$ cm^2/Vs) are much higher than that for Alq and almost the same as that for conventional high-mobility ET materials such as bathophenanthroline and silole derivatives. OLEDs with these new materials operate at lower voltages than does an OLED with Alq as an ET material. The new materials are also useful for phosphorescent OLEDs in blue-, green-, and red-light-emitting devices, where they work as both electron-transporting and hole-blocking materials. Phosphorescent OLEDs with the new materials operate at lower voltage (while maintaining comparable external quantum efficiencies) than do the corresponding reference devices with BCP/Alq as electron-transporting and hole-blocking layers.

Acknowledgements

We thank Dr. Y. Nakajima of Riken Keiki for measuring the ionization potential of compounds with their photoelectron yield spectroscopic equipment (Riken Keiki AC-3). This work was supported by Regional Innovation Cluster Program of Nagano, granted by the Ministry of Education, Culture, Sports, Science, and Technology, Japan. This article is dedicated to the first principal of the Faculty of Textile Science and Technology, Shinshu University, Chotaro Harizuka, on the occasion of the 100th anniversary of the faculty.

References

[1] C.W. Tang, S.A. VanSlyke, Appl. Phys. Lett. 51 (1987) 913.
[2] C. Adachi, T. Tsutsui, S. Saito, Appl. Phys. Lett. 57 (1990) 531.
[3] Y. Shirota, J. Mater. Chem. 10 (2000) 1.
[4] U. Mitschke, P. Baeuerle, J. Mater. Chem. 10 (2000) 1471.
[5] S.A. VanSlyke, C.H. Chen, C.W. Tang, Appl. Phys. Lett. 69 (1996) 2160.
[6] M. Thelakkat, H.-W. Schmidt, Adv. Mater. 10 (1998) 219.
[7] K. Katsuma, Y. Shirota, Adv. Mater. 10 (1998) 223.
[8] H. Tanaka, S. Tokito, Y. Taga, A. Okada, Chem. Commun. (1996) 2175.
[9] M. Ichikawa, K. Hibino, N. Yokoyama, T. Miki, T. Koyama, Y. Taniguchi, Synth. Met. 156 (2006) 1383.
[10] Y.-L. Liao, W.-Y. Hung, T.-H. Hou, C.-Y. Lin, K.-T. Wong, Chem. Mater. 19 (2007) 6350.
[11] C.-Y. Lin, Y.-M. Chen, H.-F. Chen, F.-C. Fang, Y.-C. Lin, W.-Y. Hung, K.-T. Wong, R.C. Kwong, S.C. Xia, Org. Electron. 10 (2009) 181.
[12] Z. Jiang, Z. Liu, C. Yang, C. Zhong, J. Qin, G. Yu, Y. Liu, Adv. Funct. Mater. 19 (2009) 3987.
[13] C. Adachi, T. Tsutsui, S. Saito, Appl. Phys. Lett. 55 (1989) 1489.
[14] Y. Hamada, C. Adachi, T. Tsutsui, S. Saito, Jpn. J. Appl. Phys. 31 (1992) 1812.
[15] K. Tamao, M. Uchida, T. Izumizawa, K. Furukawa, S. Yamaguchi, J. Am. Chem. Soc. 118 (1996) 11974.
[16] M. Uchida, T. Izumizawa, T. Nakano, S. Yamaguchi, K. Tamao, K. Furukawa, Chem. Mater. 13 (2001) 2680.
[17] J. Bettenhausen, P. Strohriegl, Adv. Mater. 8 (1996) 507.
[18] S.B. Heidenhain, Y. Sakamoto, T. Suzuki, A. Miura, H. Fujikawa, T. Mor, S. Tokito, Y. Taga, J. Am. Chem. Soc. 122 (2000) 10240.
[19] G. Hughes, M.R. Bryce, J. Mater. Chem. 15 (2005) 94.
[20] Y.J. Pu, M. Yoshizaki, T. Akiniwa, K.i. Nakayama, J. Kido, Org. Electron. 10 (2009) 877.
[21] H. Sasabe, E. Gonmori, T. Chiba, Y.-J. Li, D. Tanaka, S.J. Su, T. Takeda, Y.J. Pu, K.i. Nakayama, J. Kido, Chem. Mater. 20 (2008) 5951.
[22] H. Tsuji, K. Sato, Y. Sato, E. Nakamura, J. Mater. Chem. 19 (2009) 3364.
[23] L. Na, W. Pengfei, L. Shiu-Lun, L. Weimin, L. Chun-Sing, L. Shuit-Tong, L. Zengtao, Adv. Mater. 22 (2010) 527.
[24] R.G. Kepler, P.M. Beeson, S.J. Jacobs, R.A. Anderson, M.B. Sinclair, V.S. Valencia, P.A. Cahill, Appl. Phys. Lett. 66 (1995) 3618.
[25] M.A. Baldo, D.F. O'Brien, Y. You, A. Shoustikov, S. Sibley, M.E. Thompson, S.R. Forrest, Nature 395 (1998) 151.
[26] M. Ichikawa, T. Kawaguchi, K. Kobayashi, T. Miki, K. Furukawa, T. Koyama, Y. Taniguchi, J. Mater. Chem. 16 (2006) 221.
[27] M. Ichikawa, N. Hiramatsu, N. Yokoyama, T. Miki, S. Narita, T. Koyama, Y. Taniguchi, Phys. Status Solidi (RRL) 1 (2007) R37.
[28] M. Ichikawa, S. Fujimoto, Y. Miyazawa, T. Koyama, N. Yokoyama, T. Miki, Y. Taniguchi, Org. Electron. 9 (2008) 77.
[29] S.-J. Su, T. Chiba, T. Takeda, J. Kido, Adv. Mater. 20 (2008) 2125.
[30] N. Matsumoto, C. Adachi, J. Phys. Chem. C 114 (2010) 4652.
[31] M.A. Baldo, S. Lamansky, P.E. Burrows, M.E. Thompson, S.R. Forrest, Appl. Phys. Lett. 75 (1999) 4.
[32] Y. Han et al., J. Phys. D: Appl. Phys. 40 (2007) 1363.
[33] H. Murata, G.G. Malliaras, M. Uchida, Y. Shen, Z.H. Kafafi, Chem. Phys. Lett. 339 (2001) 161.
[34] S. Tabatake, S. Naka, H. Okada, H. Onnagawa, M. Uchida, T. Nakano, K. Furukawa, Jpn. J. Appl. Phys. 41 (2002) 6582.

Organic Electronics 11 (2010) 1974–1990

Contents lists available at ScienceDirect

Organic Electronics

journal homepage: www.elsevier.com/locate/orgel

Environmentally sustainable organic field effect transistors

Mihai Irimia-Vladu [a,f,*], Pavel A. Troshin [b], Melanie Reisinger [a], Guenther Schwabegger [c], Mujeeb Ullah [c], Reinhard Schwoediauer [a], Alexander Mumyatov [b], Marius Bodea [d], Jeffrey W. Fergus [e], Vladimir F. Razumov [b], Helmut Sitter [c], Siegfried Bauer [a], Niyazi Serdar Sariciftci [f]

[a] Department of Soft Matter Physics, Johannes Kepler University, A-4040 Linz, Austria
[b] Institute of Problems of Chemical Physics of Russian Academy of Sciences, Semenov Prospect 1, 142432, Chernogolovka, Moscow Region, Russia
[c] Institute of Semiconductor and Solid State Physics, Johannes Kepler University, A-4040 Linz, Austria
[d] Institute of Applied Physics, Johannes Kepler University, A-4040 Linz, Austria
[e] Materials Research and Education Center, Auburn University, Auburn, AL 36849, USA
[f] Linz Institute for Organic Solar Cells (LIOS), Physical Chemistry, Johannes Kepler University, A-4040 Linz, Austria

ARTICLE INFO

Article history:
Received 16 July 2010
Received in revised form 3 September 2010
Accepted 4 September 2010
Available online 26 September 2010

Keywords:
Environmentally sustainable electronics
Organic field effect transistors
Natural materials
Biodegradable electronics
Biocompatible electronics
Edible electronics

ABSTRACT

Environmentally sustainable systems for the design, production, and handling of electronic devices should be developed to solve the dramatic increase in electronic waste. Sustainability in plastic electronics may be the production of electronic devices from natural materials, or materials found in common commodity products accepted by society. Thereby biodegradable, biocompatible, bioresorbable, or even metabolizable electronics may become reality. Transistors with an operational voltage as low as 6 V, a source drain current of up to 0.5 μA and an on–off ratio up to four orders of magnitude, with saturated field effect mobilities in the range of 1.5×10^{-4} to 2×10^{-2} cm^2/V s, have been fabricated with such materials. Our work comprises steps towards environmentally safe devices in low-cost, large volume, disposable or throwaway electronic applications, such as in food packaging, plastic bags, and disposable dishware. In addition, there is significant potential to use such electronic items in biomedical implants. As such, organic materials offer a unique opportunity to guide electronics industry towards an environmentally safe direction.

© 2010 Elsevier B.V. All rights reserved.

1. Introduction

Two major concerns in the world nowadays are plastic consumption and waste. Due to the economic growth and the increased demand in developing countries, plastics consumption is projected to increase by a factor of two to three during the current decade [1]. A consequence of this incessant demand of plastics in the world is the accumulation of non-biodegradable solid waste and plastic litter with negative effects on our environment. As an example, the amount of municipal solid waste per person per year averages ~440 kg/yr for China, ~550 kg/yr for the European Union and ~790 kg/yr for the United States, with roughly half of the waste being electronic products and plastics [1,2]. Taking into account the expected increase of plastic electronics in low-cost, large volume, disposable or throwaway applications, plastic waste problems may become even more dramatic. More effort will be necessary in order to minimize the negative impact of the increasing production, consumption and disposal of both polymer materials and electronic circuits [3].

There have been so far several initial reports addressing the use of biodegradable substrates in organic electronics, such as poly (L-lactide-co-glycolide) [4], paper [5–9],

* Corresponding author at: Department of Soft Matter Physics and Linz Institute for Organic Sollar Cells, Johannes Kepler University, Altenberger Strasse Nr. 69, 4040 Linz, Austria. Tel.: +43 732 2468 9293; fax: +43 732 2468 9273.
E-mail address: Mihai.Irimia-Vladu@jku.at (M. Irimia-Vladu).

1566-1199/$ - see front matter © 2010 Elsevier B.V. All rights reserved.
doi:10.1016/j.orgel.2010.09.007

leather [10] or even silk [11,12]. Here we present an initial study of using natural, nature-inspired and common commodity materials which are widely accepted by society for sustainable electronics. The rationale for choosing materials from sugar family, small molecular nucleobases, beta-carotene, indigo, food colors (indanthrenes) and cosmetic colors (perylene diimide) on substrates such as glucose, hard gelatine and biodegradable polymers is to show how large the materials base may become for organic electronics, when low cost and sustainability is a concern. We limit our work to the electrical characterization of these materials and to the demonstration of field-effect transistors, a first step towards building more complex electronic integrated circuits. We consider unusual substrates, such as Ecoflex, hard gelatine capsules and caramelized glucose, to enhance the substrate materials base for organic electronics. High-performance, biocompatible and biodegradable organic field-effect transistors operating at low voltages are demonstrated by the evaporation of ultrathin layers of natural nucleobase dielectrics (adenine and guanine) on inorganic oxide dielectrics, a viable alternative to the passivation of such oxide dielectrics with self-assembled monolayers [13,14]. Semiconductors chosen include natural compounds like beta-carotene and indigo, as well as perylene diimide (a lipstick colorant), indanthrene yellow G and indanthrene brilliant orange RF, colorants used for example in textile and food industry. Having identified natural and nature-inspired p- and n-type semiconductors, opens ways to fabricate integrated circuits, based on inverters, ring oscillators, logical elements, etc. We hope that this initial study initiates an intense search for new materials and material combinations to finally end up with sustainable plastic electronic products.

2. Experimental

2.1. Preparation and/or purification of materials

Dielectric and semiconductor compounds employed (adenine, guanine, cytosine, thymine, caffeine, indigo, indanthrene yellow G) were purchased from Sigma–Aldrich and additionally purified by two vacuum sublimation cycles performed in a closed quartz tube. Indanthrene brilliant orange RF was purchased from Shanghai Jucheng Chemical Co., and purified by three vacuum sublimation cycles; its chemical composition was proven by mass spectrometry. Poly (vinyl alcohol) (Mowiol®40-88, electronic grade) was purchased from Kuraray Specialities Europe GmbH and used as received. D-(+)-glucose, lactose, and beta-carotene were purchased from Sigma–Aldrich and used without further purification. Ecoflex foil was purchased from BASF and hard gelatine capsules from a local pharmacy in Linz, Austria.

2.1.1. Perylene diimide: synthesis and analysis

Perylene diimide (EH-PDI) was synthesized as shown in Scheme 1. Perylene-3,4,9,10-tetracarboxylic acid dianhydride (5 g, 12.8 mmol) was mixed with 60 ml of freshly distilled quinoline, 15 g (116 mmol) of 2-ethylhexylamine and ca. 100 mg of $Zn(OAc)_2 \cdot H_2O$.

The obtained mixture was heated at reflux for 2 h, cooled down to room temperature and poured into 600 ml of 10% aqueous hydrochloric acid. The precipitate formed was removed by filtration, extracted with methanol and dried in air. The resulting crude sample of perylene diimide was purified by column chromatography. Elution with a CH_2Cl_2–methanol mixture (95.5:0.5 v/v) produced a pure compound EH-PDI. The final purification was performed by sublimation at 450–500 °C under a reduced pressure of $\sim 10^{-2}$ mbar. The yield of EH-PDI was in the range of 45–55%.

The NMR and FTIR spectra are summarized below:

^{1}H NMR (400 MHz, $CDCl_3$,) δ = 8.83 (d, 4H, *H*-Ar), 8.75 (d, 4H, *H*-Ar), 4.31 (m, 4H, NCH_2), 2.14 (m, 2H, C*H*), 1.58 (m, 8H, CH_2), 1.50 (m, 8H, CH_2), 1.13 (t, 6H, CH_3), 1.06 (t, 6H, CH_3), ppm. Chemical analysis: $C_{40}H_{42}N_2O_4$.

Calculated: C, 78.15; H, 6.89; N, 4.56. Found: C, 77.95; H, 6.97; N, 4.61.

IR spectrum (KBr pellet): ν = 745, 809, 1178, 1247, 1308, 1346, 1380, 1403, 1441, 1577, 1594, 1615, 1650, 1695, 2859, 2873, 2930, 2958 cm^{-1}.

2.2. Device fabrication

2.2.1. Glucose/caffeine-beta-carotene OFET on glass

Precursor solution of D-(+)-glucose (0.9 g/ml) and caffeine (0.02 g/ml) was prepared in deionized water (~18 MΩ cm). The mixture was stirred for 60 min at 60 °C. Beta-carotene solutions (10 mg/ml in chloroform) were prepared under inert atmosphere in a glove bow. Thin films of glucose containing also caffeine were spun at 2000 rpm on top of a 100 nm thick patterned aluminium gate on a 1.5 × 1.5 cm glass substrate. The spun samples were dried overnight in a vacuum oven at 55 °C. Beta-carotene thin film was spin coated at 2000 rpm for 60 s under inert atmosphere. A 100 nm thick gold layer was evaporated through a shadow mask to pattern the top source and drain electrodes. The channel dimensions (length and width) was L = 100 μm, and W = 1 mm. The measured capacitance per unit area (by impedance spectroscopy) of a 3.1 μm thick dielectric film of glucose with caffeine was C_{0d} = 1.9 nF/cm^2. The measured unit capacitance of a 2.6 μm thick film cast from glucose solution (0.9 g/ml in deionized water, with no caffeine addition) was 2.15 nF/cm^2.

2.2.2. PVA/Indigo OFET on glass

Precursor solution of PVA (0.08 g/ml) was prepared in deionized water (~18 MΩ cm) and the mixture was stirred for 24 h at 90 °C. Thin films of PVA were spun at 2000 rpm on top of a 100 nm thick patterned aluminium gate on a 1.5 × 1.5 cm glass substrate. 100 nm thick indigo layer was vacuum processed in an Edwards evaporator. A 100 nm thick aluminium layer was evaporated through a shadow mask to pattern the top source and drain electrodes. The evaporation rate of indigo was 0.1 nm/s. The channel dimensions (length and width) was L = 100 μm, and W = 1 mm. The measured capacitance per unit area (by impedance spectroscopy) of a 2 μm thick dielectric film of PVA was C_{0d} = 3.1 nF/cm^2.

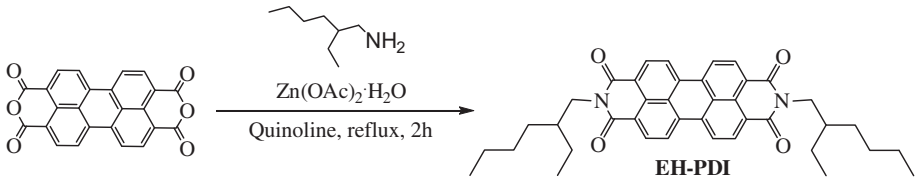

Scheme 1. Fabrication route of the perylene diimide semiconductor.

2.2.3. Glucose/C_{60} and lactose/C_{60} OFET on glass

Precursor solutions of D-(+)-glucose (0.9 g/ml in deionized water) and lactose (0.3 g/ml in DMSO) were spun at 2000 rpm on top of a 100 nm thick patterned aluminium gate electrodes on 1.5 × 1.5 cm glass substrates. Thick film of fullerene (100 nm), C_{60}, was evaporated in an Edwards vacuum evaporator. Thick aluminium (100 nm) was evaporated through a shadow mask to pattern the top source and drain electrodes. The evaporation rate of fullerene was 0.1 nm/s. The channel dimensions (length and width) was L = 100 μm, and W = 1 mm. The measured capacitances per unit area (by impedance spectroscopy) for a 2.6 μm thick dielectric film of glucose, C_{0d}, was 2.15 nF/cm^2 and for a 0.85 μm thick dielectric film of lactose was 6.8 nF/cm^2.

2.2.4. Guanine–C_{60} OFET on glass

A 1 mm wide-100 nm thick aluminium was evaporated onto 1.5 × 1.5 cm^2 glass slides to pattern the gate electrode. Thick guanine (425 nm) and C_{60} (100 nm) formed the organic dielectric and semiconductor layers, respectively, whereas 100 nm aluminium was used to pattern the source and drain electrodes. The evaporation rates of guanine and fullerene were 0.75 nm/s and 0.1 nm/s, respectively. The channel dimensions for the source and drain electrodes were: L = 100 μm and W = 1 mm. The measured unit capacitance of the dielectric was C_{0d} = 9.25 nF/cm^2.

2.2.5. Cytosine–C_{60} OFET on glass

A 1 mm wide-100 nm thick aluminium was evaporated onto 1.5 × 1.5 cm^2 glass slides to pattern the gate electrode. Thick cytosine (300 nm) and C_{60} (100 nm) were vacuum deposited to form the organic dielectric and semiconductor layers, respectively, whereas 100 nm aluminium was used to pattern the source and drain electrodes. The evaporation rates of cytosine and fullerene were 2 nm/s and 0.1 nm/s, respectively. The channel dimensions for the source and drain electrodes were: L = 100 μm and W = 1 mm. The measured unit capacitance of the dielectric was C_{0d} = 13.8 nF/cm^2.

2.2.6. Aluminium oxide–adenine–C_{60}/pentacene OFET on glass

A 1 mm wide-100 nm thick aluminium gate was evaporated onto 1.5 × 1.5 cm^2 glass slides and subsequently anodized by immersing in citric acid solution and passing a step voltage (up to a maximum of 40 V) at a constant current of 0.06 mA. Adenine (i.e., 10 nm thick for the sample with C_{60} and 150 nm thick for sample with pentacene) was vacuum deposited on top of AlOx to form the combined inorganic–organic dielectric. A 100 nm thick C_{60} and 100 nm pentacene, respectively, formed the organic semiconductors for the n- and p-type of OFETs. A 100 nm thick aluminium formed the source and drain electrodes for the sample with fullerene semiconductor; a 100 nm thick gold formed the source and drain electrodes for the sample with pentacene semiconductor. The evaporation rate of adenine was 3 nm/s, whereas pentacene and C_{60} and were evaporated at 0.1 nm/s, respectively. The channel dimensions for the source and drain electrodes were: L = 100 μm and W = 1 mm. The measured unit capacitances of the dielectrics were C_{0d} = 99 nF/cm^2 for the dielectric built for the n-type sample, and 19.55 for the dielectric of the p-type OFET.

2.2.7. Aluminium oxide–thymine–C_{60} OFET on glass

A 1 mm wide-100 nm thick aluminium gate was evaporated onto 1.5 × 1.5 cm^2 glass slides and subsequently anodized using the same method as described above. Thymine (i.e., 75 nm thick) was vacuum deposited on top of AlOx to form the combined inorganic–organic dielectric. A 100 nm thick C_{60} formed the organic semiconductor. A 100 nm thick aluminium formed the source and drain electrodes. The evaporation rate of thymine and C_{60} was 0.1 nm/s. The channel dimensions for the source and drain electrodes were: L = 100 μm and W = 1 mm. The measured unit capacitances of the combined dielectric was C_{0d} = 23.6 nF/cm^2.

2.2.8. Aluminium oxide–guanine/adenine–indanthrene yellow G OFET on glass

A 1 mm wide-100 nm thick aluminium gate was evaporated onto 1.5 × 1.5 cm^2 glass slides and subsequently anodized by immersing in citric acid solution and passing a step voltage (up to a maximum of 40 V) at a constant current of 0.06 mA. A transmission electron microscopy (TEM) picture of a cross-section of the anodized electrode revealed a thickness of ~55 nm of aluminium oxide. Two alternating layers of guanine and adenine (i.e., 2.5 nm thick guanine and 15 nm thick adenine) were vacuum deposited on top of AlOx to form the combined inorganic–organic dielectric. A 100 nm thick indanthrene yellow G and 100 nm aluminium formed the semiconductor and source/drain electrodes, respectively. The evaporation rates of adenine, guanine and indanthrene yellow G were 3 nm/s, 0.75 nm/s and 0.1 nm/s, respectively. The channel dimensions for the source and drain electrodes were: L = 100 μm and W = 1 mm. The measured unit capacitance of the dielectric was C_{0d} = 81.6 nF/cm^2.

2.2.9. Aluminium oxide–adenine/guanine–perylene diimide OFET on glass

A 1 mm wide-100 nm thick aluminium gate was evaporated onto 1.5 × 1.5 cm^2 glass slides and subsequently anodized by immersing in citric acid solution and passing

a step voltage (up to a maximum of 40 V) at a constant current of 0.06 mA. Two alternating layers of guanine and adenine (i.e., 2.5 nm thick guanine and 15 nm thick adenine) were vacuum deposited on top of aluminium oxide to form the combo inorganic–organic dielectric. A 100 nm thick perylene diimide and 100 nm aluminium patterned the semiconductor and source and drain electrodes, respectively. The evaporation rates of adenine, guanine and perylene diimide were 3 nm/s, 0.75 nm/s and 0.1 nm/s, respectively. The source and drain electrodes had the channel dimensions: $L = 100$ μm, $W = 1$ mm. The measured capacitance per unit area of the combined dielectric was $C_{0d} = 81.6$ nF/cm^2. The measured capacitance per unit area of the plain AlOx was 140 nF/cm^2.

2.2.10. Aluminium oxide–adenine/guanine–indanthrene brilliant orange RF OFET on glass

A 1 mm wide-100 nm thick aluminium gate was evaporated onto 1.5×1.5 cm^2 glass slides and subsequently anodized by immersing in citric acid solution, using the method described. Two alternating layers of guanine and adenine (i.e., 2.5 nm thick guanine and 15 nm thick adenine) were vacuum deposited; followed by 100 nm thick indanthrene brilliant orange RS and 100 nm gold source and drain electrodes. The source and drain electrodes had the channel dimensions: $L = 35$ μm, $W = 7$ mm. Gold, rather than aluminium, was used for contacting the n-type semiconductor. Adenine was evaporated at a rate of 3 nm/s, guanine at 0.75 nm/s and indanthrene brilliant orange RF at a rate of 0.1 nm/s. The measured capacitance per unit area of the dielectric was $C_{0d} = 81.6$ nF/cm^2.

2.2.11. Adenine–perylene diimide OFET on Ecoflex

Aurin (0.1 g/ml in pure ethyl alcohol) was spun at 2000 rpm for 60 s onto 1.5×1.5 cm^2 Ecoflex foils to act as a smoothening layer. A 1 mm wide-100 nm thick aluminium gate was evaporated through a shadow mask; A 1.1 μm thick adenine and 100 nm thick perylene diimide were evaporated in an Edwards high vacuum evaporation system at a pressure of 10^{-6} torr to pattern the gate dielectric and semiconductor, respectively. A 100 nm thick aluminium layer formed the top drain and source electrodes. The evaporation rate was 3 nm/s for adenine, and 0.1 nm/s for perylene diimide. The channel dimensions were $L = 100$ μm, $W = 1$ mm. The measured capacitance per unit area of the dielectric was $C_{0d} = 3.1$ nF/cm^2.

2.2.12. Adenine/guanine–indanthrene yellow G OFET on caramelized glucose

As received powder of D-(+)-glucose was melted on top of a hot plate at ~225–250 °C and droplets were deposited with a glass rod on aluminium foil wrapped around 1.5×1.5 cm glass slides. Wrapping aluminium around the glass slides was necessary to prevent the solidified glucose from cracking during cooling to room temperature. A thin layer of rosolic acid (50 nm) was vacuum evaporated to serve a double role: (1) to act as a smoothening layer and (2) to prevent the caramelized glucose substrate to swollen during the gold gate electrode patterning. A 100 nm thick-1 mm wide gold gate electrode was evaporated in a metal evaporator. The gate dielectric was formed by four alternating layers of guanine and adenine (75 nm thick each of the first three layers of guanine and adenine, and 400 nm thick adenine-the fourth layer), and 100 nm indanthrene yellow G was used as organic semiconductor. Adenine was evaporated at a rate of 3 nm/s, whereas guanine and indanthrene yellow G at a rate of 0.1 nm/s. A 100 nm thick layer of gold patterned the source and drain electrodes. The channel dimensions were: $L = 100$ μm and $W = 1$ mm. The measured unit capacitance of the combined dielectric was $C_{0d} = 5.6$ nF/cm^2.

2.2.13. Adenine/guanine–perylene diimide OFET on hard gelatine capsules

Hard gelatine capsules were cut open and stuck with the aid of a double-side scotch tape on 1.5×1.5 cm^2 glass substrates in order to force the gelatine substrate remain in a flat-open position. Rosolic acid (0.1 g/ml in pure ethylalcohol) was spun at 2000 rpm for 60 s on top of capsule substrates to act as a smoothening layer. A 1 mm wide-100 nm thick gold gate was evaporated through a shadow mask followed by four alternating layers of guanine and adenine (75 nm thick the first and the third layer of guanine, 100 nm and 500 nm thick the second and fourth layer of adenine) to form the gate electrode and gate dielectric, respectively. A 100 nm thick perylene diimide was evaporated to pattern the semiconductor layer and a 100 nm thick gold source and drain electrodes were subsequently evaporated. The evaporation rate was 1 nm/s for guanine, 3 nm/s for adenine, and 0.1 nm/s for perylene diimide. The source and drain electrodes had the channel dimensions: $L = 100$ μm, $W = 1$ mm. The measured capacitance per unit area of the dielectric was $C_{0d} = 5.1$ nF/cm^2.

2.3. Device characterization

Steady state current–voltage measurements were performed with an Agilent E5273A instrument. Both transfer and output characteristics were measured at a sweep rate of 66 mV s^{-1}, with 1 s for each of the hold, delay and step delay times, respectively.

Dielectric characterization of the gate dielectrics was performed with metal–insulator–metal capacitors using a Novocontrol Alpha Analyzer. X-ray diffraction was performed using a Bruker AXS X-ray Diffractometer (Cu Kα) X-ray Diffractometer. AFM investigation was performed using a Digital Instruments Dimension 3100 microscope working in tapping mode.

3. Results and discussion

3.1. Field effect transistors

Field effect transistors rely on an electric field (supplied by the gate voltage, V_{gs}, applied between the grounded source and the gate) to control the conductivity of a channel at the interface between the semiconductor and the insulator, and hence the current between source and drain contacts I_{ds}. A measure of the quality of the dielectric is given by the leakage current from the gate to the source contacts through the insulator layer, I_{gs}. Field effect

transistor preparation requires substrates, smoothing layers when the substrate is rough, metal electrodes, gate dielectrics and organic semiconductors. Fig. 1 illustrates such a transistor with all the components employed in this work presented in the schematic form. In the following, we start discussing first substrates, then gate dielectrics and

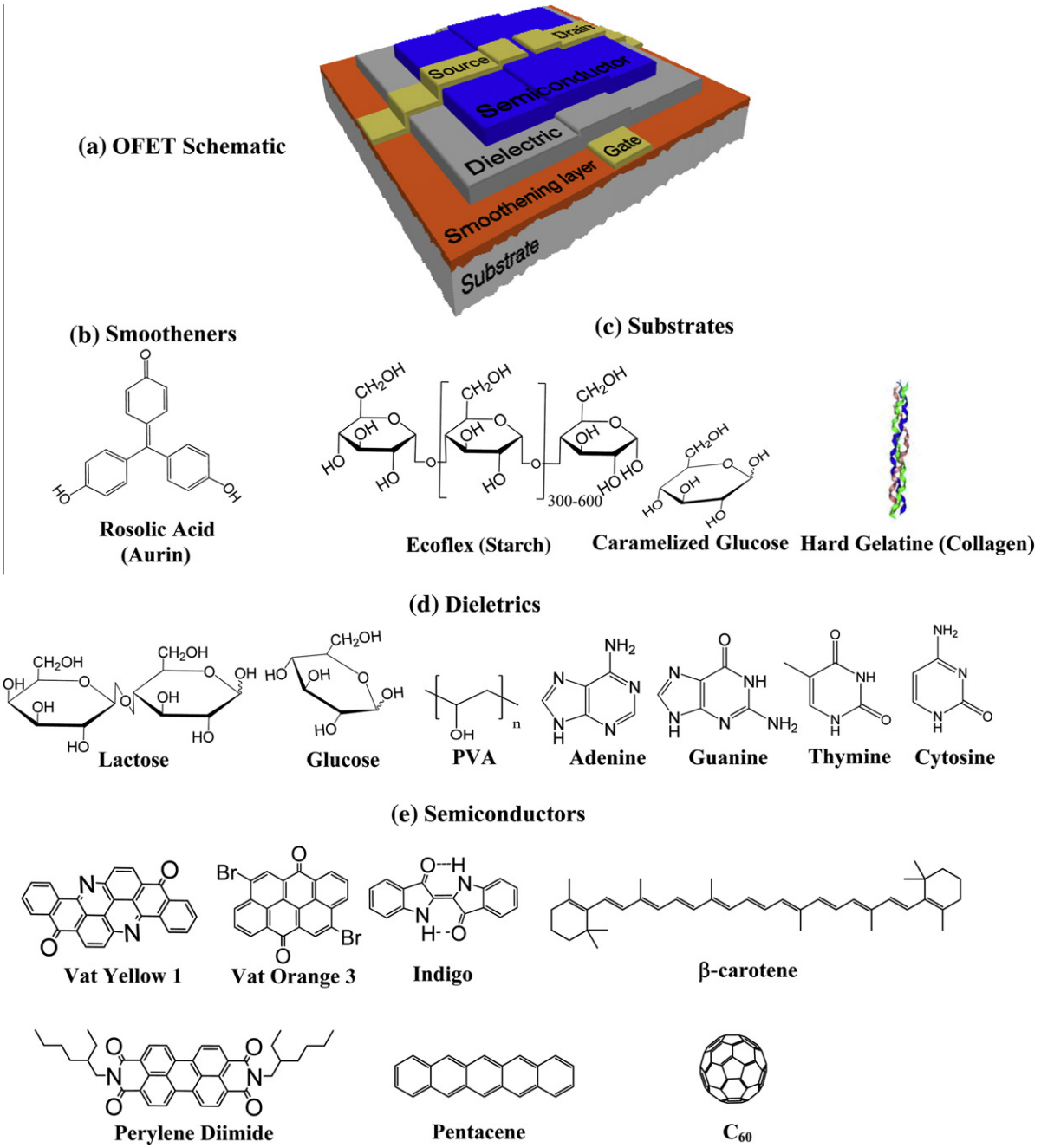

Fig. 1. Natural materials or materials inspired by nature used for fabrication of environmentally sustainable organic field effect transistors. (a) Schematic of bottom-gate, top-contact OFET employed in this work; (b) schematic of rosolic acid (aurin), used here as smoothener; (c) substrates investigated: Ecoflex produced from potato and corn starch, hard gelatine capsule originating from collagen and caramelized glucose; (d) natural dielectrics materials in the nucleobase and sugar families: adenine, guanine, cytosine, thymine glucose and lactose; (e) semiconductor materials: β-carotene and indigo are natural p- and n-type organic semiconductors; indanthrene yellow G and indanthrene brilliant orange RF are semiconductors derived from natural anthraquinone and perylene diimide, a cosmetic color. Glass, aluminium oxide, poly(vinyl alcohol), C_{60} and pentacene are examples of workhorse substrate, dielectric and semiconductor materials widely employed in the field, used here for comparison. Transistors and integrated circuits produced from natural or nature inspired materials may ultimately provide the basis for "sustainable green electronics".

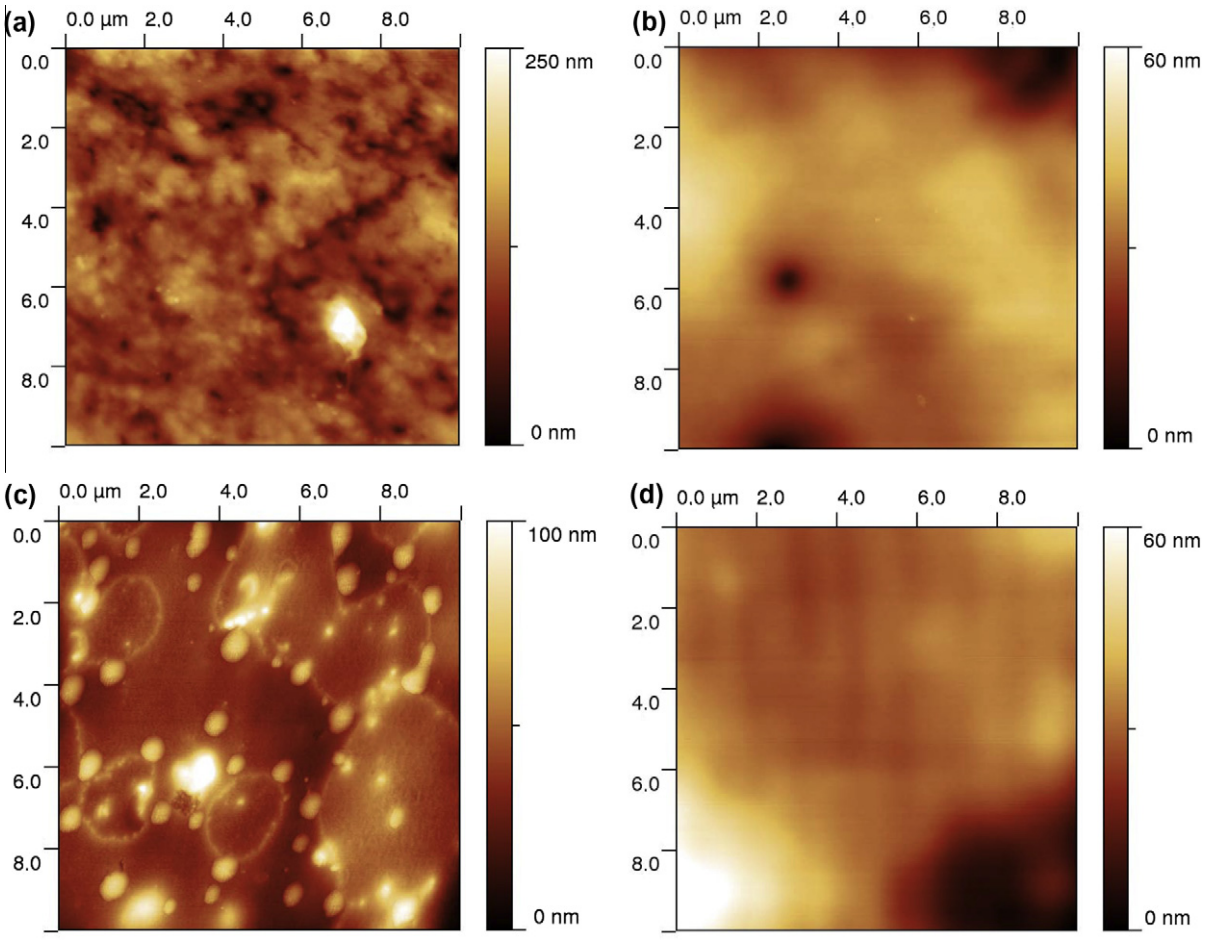

Fig. 2. AFM pictograms of (a) plain Ecoflex foil (rms ~70 nm); (b) aurin-coated Ecoflex foil (rms ~8 nm); (c) plain hard gelatine capsule (rms ~30 nm); (d) aurin-coated hard gelatine capsule (rms ~9 nm).

organic semiconductors, together with examples of field-effect transistors built on either glass or biodegradable/biocompatible substrates.

3.1.1. Substrates for sustainable electronics

Fabric, hot-pressed cotton-fiber paper, leather and silk have been recently reported as examples of biodegradable and biocompatible-sustainable substrates for organic field effect transistors [4,5,10,11]. Other examples of such substrates are presented here; they include hard gelatine, commercially available biodegradable polymers and even caramelized sugar for edible devices.

Hard gelatine capsule is a fully biocompatible and biodegradable substrate employed extensively in the pharmaceutical field for oral drug delivery. Gelatine capsules are made from pork skin and bones and may contain small additions of plasticizers (e.g., glycerin and sorbitol), preservatives, colors, flavors (e.g., ethylvanilin and essential oil), sugars, etc. Their widespread availability, the ease of production in various forms and the complete biodegradability make gelatine capsules an interesting substrate for electronics. Such electronics may even be ingested in the body in biomedical applications. Ecoflex is a commercially available (BASF) biodegradable polymer based on potato starch, corn and polylactic acid. Ecoflex degrades in compost in 6 months without leaving any residue [15]. Since the use of such polymers for various low-end, biodegradable applications will most likely increase, it is interesting to explore them also as a substrate for organic electronics. Caramelized glucose is employed as another example of substrates for the preparation of OFETs; it allows for the

Table 1
Dielectric performance of investigated materials.

Material	Dielectric constant (at 1 kHz)	Breakdown field (MV/cm)	Loss tangent (at 100 mHz)
Dielectrics			
Adenine	~3.85	~1.5	$\sim 4 \times 10^{-3}$
Cytosine	~4.65	~3.4	$\sim 5 \times 10^{-3}$
Guanine	~4.35	~3.5	$\sim 7 \times 10^{-3}$
Thymine	~2.4	~0.9	$\sim 1 \times 10^{-2}$
Glucose	~6.35	~1.5	$\sim 5 \times 10^{-2}$
Lactose	~6.55	~4.5	$\sim 2 \times 10^{-2}$
Caffeine	~4.1	~2	$\sim 9 \times 10^{-2}$
PVA	~6.1	~2	$\sim 4 \times 10^{-2}$
AlOx	~9	~3.5	$\sim 4 \times 10^{-3}$

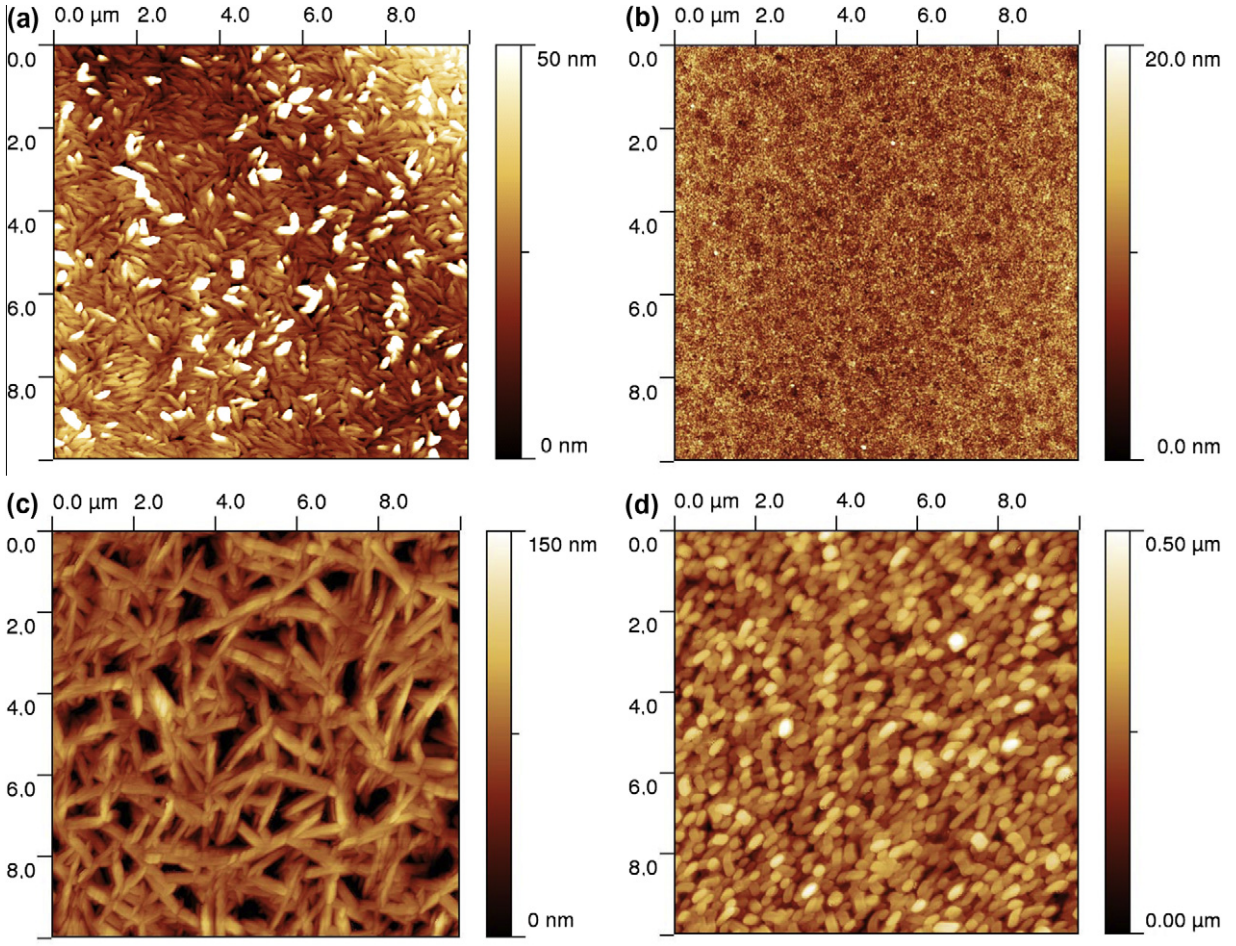

Fig. 3. AFM of nucleobase thin films on aluminium covered glass a) 1000 nm adenine (rms ~14.5); (b) 425 nm guanine (rms ~3); (c) 350 nm cytosine (rms ~24); (d) 450 nm thymine (rms ~65).

fabrication of bio-metabolizable (edible) electronics. All substrates mentioned here have large surface roughnesses, with root-mean-square (rms) values between 30 nm and 80 nm, necessitating the addition of a smoothing layer in order to decrease their roughness to values that allow fabrication of electronic components on such materials.

3.1.2. Smoothening layer

Initial work on paper substrates employed a smoothening layer formed by a thin spin-coated polymer film (polydimethylsiloxane, PDMS) to reduce the inherent roughness of the substrate [5,10]. While being biocompatible and solution processible, the polymer film required thermal cross-linking to render the structure amenable for the patterning of electrodes and further device preparation. Aurin (rosolic acid), a compound with a simple synthetic chemistry (i.e., produced by the reaction of phenol with oxalic acid in concentrated sulfuric acid bath) and which occurs also naturally (being extracted from the rhizomes of a free growing plant (*Plantago asiatica* L.)) [16,17] is used here as a smoothing layer. In traditional Chinese medicine, *Plantago asiatica* L. is known for its medicinal properties, used as anti-inflammatory, antiseptic, diuretic, expectorant, etc. [18]. In the medical and pharmacological fields, aurin is currently explored as heme-oxygenase activity regulator in aortic endothelial cells or as a generator of androgen receptors in binding assays that mimic the functions of natural hormones [17,19]. Being a naturally occurring compound with a simple chemistry and easy biodegradability, aurin represents an interesting candidate for the smoothening layer of various rough substrates. Fig. 2a and c shows the surface roughness of Ecoflex and gelatine capsules, with rms roughness values of ~70 nm and ~30 nm, respectively. As presented in Fig. 2b and d, the substrate roughness, rms, is reduced to 8 nm for Ecoflex and 9 nm for hard gelatine after spin-coating aurin, solution processed in ethyl-alcohol.

3.1.3. Natural dielectrics for sustainable organic field effect transistors

Nature provides an overwhelming number of materials that are degradable, so looking for natural dielectrics appears to be a promising route for sustainability in organic electronics. We first describe dielectrics from the sugar family, followed by dielectrics from the nucleobase family, both groups comprising naturally occurring-biodegradable

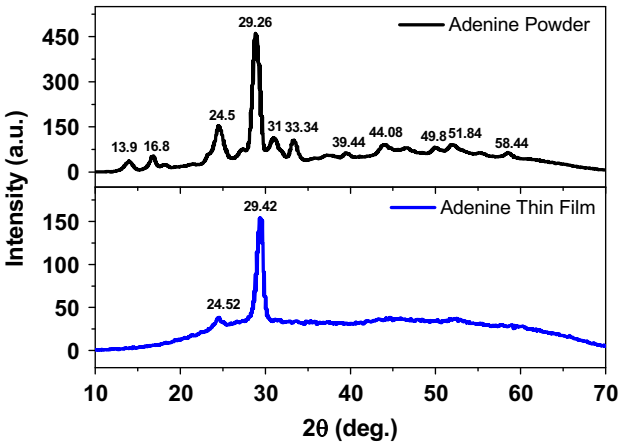

Fig. 4. X-ray diffraction profiles of precursor adenine (a) and evaporated adenine (b); the corresponding crystallographic planes are conforming to the pattern in a standard card.

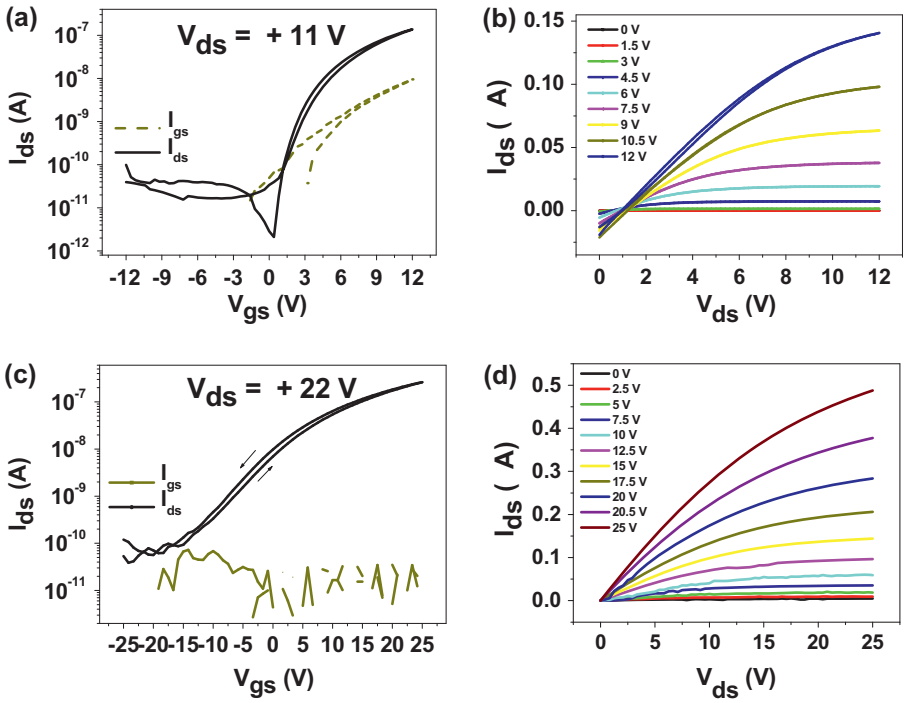

Fig. 5. Transfer and output characteristics of OFETs with (a and b) solution processed lactose gate and C_{60} semiconductor channel; capacitance per unit area, C_{0d} = 6.8 nF/cm^2, field-effect mobility μ = 0.055 cm^2/V s, subthreshold swing S = 2 V/dec and normalized subthreshold swing S_n = 13.6 V nF/cm^2 dec; (c and d) solution processed glucose gate and C_{60} channel. Capacitance: C_{0d} = 2.15 nF/cm^2, field-effect mobility μ = 0.085 cm^2/V s, subthreshold swing S = 6.2 V/dec and normalized subthreshold swing S_n = 13.3 V nF/cm^2 dec.

compounds with a long history in chemistry or biochemistry.

3.1.3.1. Dielectrics from the sugar family (lactose, glucose). Glucose and lactose are two of many other simple small molecules in the sugar family. They are industrially produced on a very large scale, are non-toxic and have excellent film forming properties, when solution processed from water and/or DMSO. The measured dielectric properties of films of glucose and lactose (dielectric constant, breakdown field and loss tangent) are displayed in Table 1. AFM graphs of the spin-cast films are essentially featureless and display a root-mean-square (rms) roughness in the range of 0.5–1 nm. In addition to their excellent film

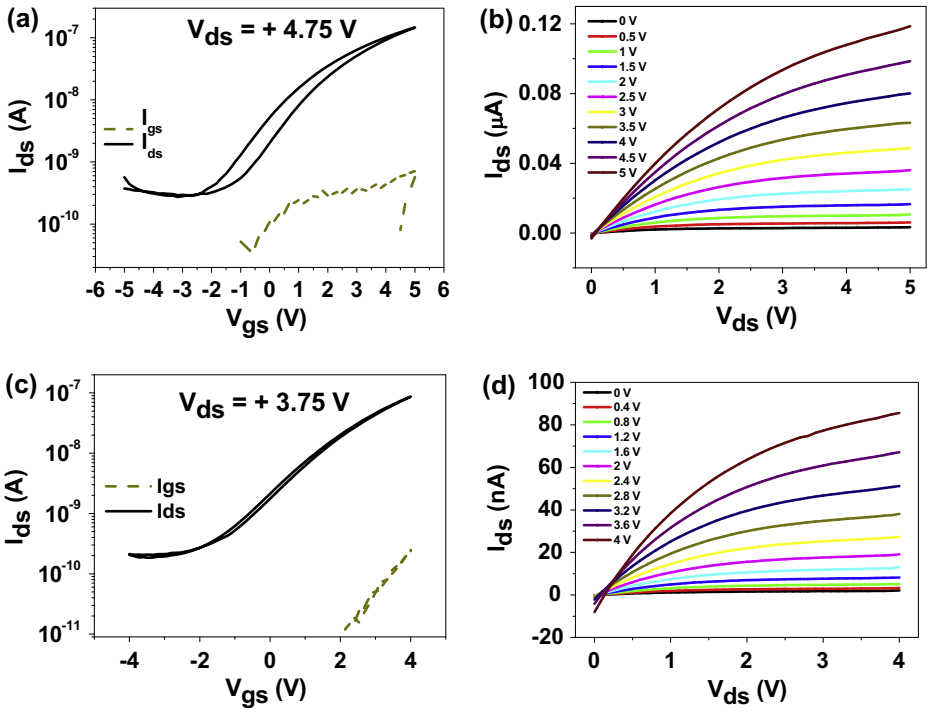

Fig. 6. Transfer and output characteristics of OFETs with (a and b) Guanine gate and C_{60} channel. Capacitance per area, C_{0d} = 9.25 nF/cm^2, field effect mobility μ = 0.12 cm^2/V s, subthreshold swing S = 1.4 V/dec and normalized subthreshold swing S_n = 12.9 V nF/cm^2 dec; (c and d) cytosine gate and C_{60} channel. Capacitance per area, C_{0d} = 13.8 nF/cm^2, field effect mobility μ = 0.09 cm^2/V s, subthreshold swing S = 1.2 V/dec and normalized subthreshold swing S_n = 16.6 V nF/cm^2 dec.

forming properties, the two small molecules are good insulators as shown by the low dielectric losses measured over a wide frequency range (10 kHz to 10 mHz). In addition, glucose and lactose have relatively high breakdown voltages of ~1.5 MV/cm and ~4.5 MV/cm, respectively.

3.1.3.2. Dielectrics from the nucleobase family (adenine, guanine, cytosine and thymine). DNA, recently considered for photonics as well as other electronic applications [20,21], has been employed also as gate dielectric in organic field effect transistors [22–24]. The main drawback of the use of DNA as an organic dielectric is the occurrence of hysteresis in the transfer characteristics of organic field effect transistors [22–24], probably caused by the presence of mobile ionic impurities in the natural DNA dielectric. However, DNA is composed of alternating sequences of four nucleobases (adenine, guanine, cytosine and thymine). Being small molecules, nucleobases are amenable for scrupulous purification and can be vacuum processed in thin films of thicknesses scaled down to 2.5 nm, as it will be shown in this work. Their natural abundance, low cost and low toxicity make these materials interesting candidates for organic electronics. Guanine and adenine, for example, occur naturally in many biological systems. Guanine can be extracted from bat droppings, as well as fish skin and scales [25]. Currently, the cosmetic industry relies on small additions of guanine into shampoo, facial creams and nail enamels to render them an iridescent bluish-white tint. Adenine is also a natural product, freely produced in most of the fruits, whole grains, raw honey and propolis, etc.

The dielectric properties of thin evaporated films of adenine, guanine, cytosine and thymine presented in Table 1 show low losses and featureless dielectric functions over a wide frequency window, ranging from 10 kHz to 10 mHz. The breakdown voltage of the four investigated nucleobases ranges from 0.9 MV/cm to 3.5 MV/cm, which makes these materials suitable for use as gate dielectric in field effect transistors.

AFM surface investigations of thin films of adenine, guanine, cytosine and thymine are presented in Fig. 3a–d. Vacuum processed nucleobase thin films show a tendency for crystallization, with increasing surface roughness starting from guanine (rms ~3 nm) to adenine (rms ~14.5 nm), cytosine (rms ~24 nm) and thymine (rms ~65 nm). The investigation of the fifth nucleobase, uracil, proved difficult because of its extreme tendency for crystallization. With this respect, thin films of uracil displayed pin-holes, whereas thicker films had a roughness with root-mean-square values greater than 100 nm.

An example of the X-ray diffraction investigation for adenine in the forms of precursor powder and 1 μm thick evaporated film on aluminium coated glass slide is presented in Fig. 4. The crystallographic planes are conforming to the pattern available in the standard card (JSPDS no. 24-1654) of the instrument. As shown in Fig. 4, adenine thin films display crystallinity and preferred orientation compared to precursor powder, as it is suggested by strong

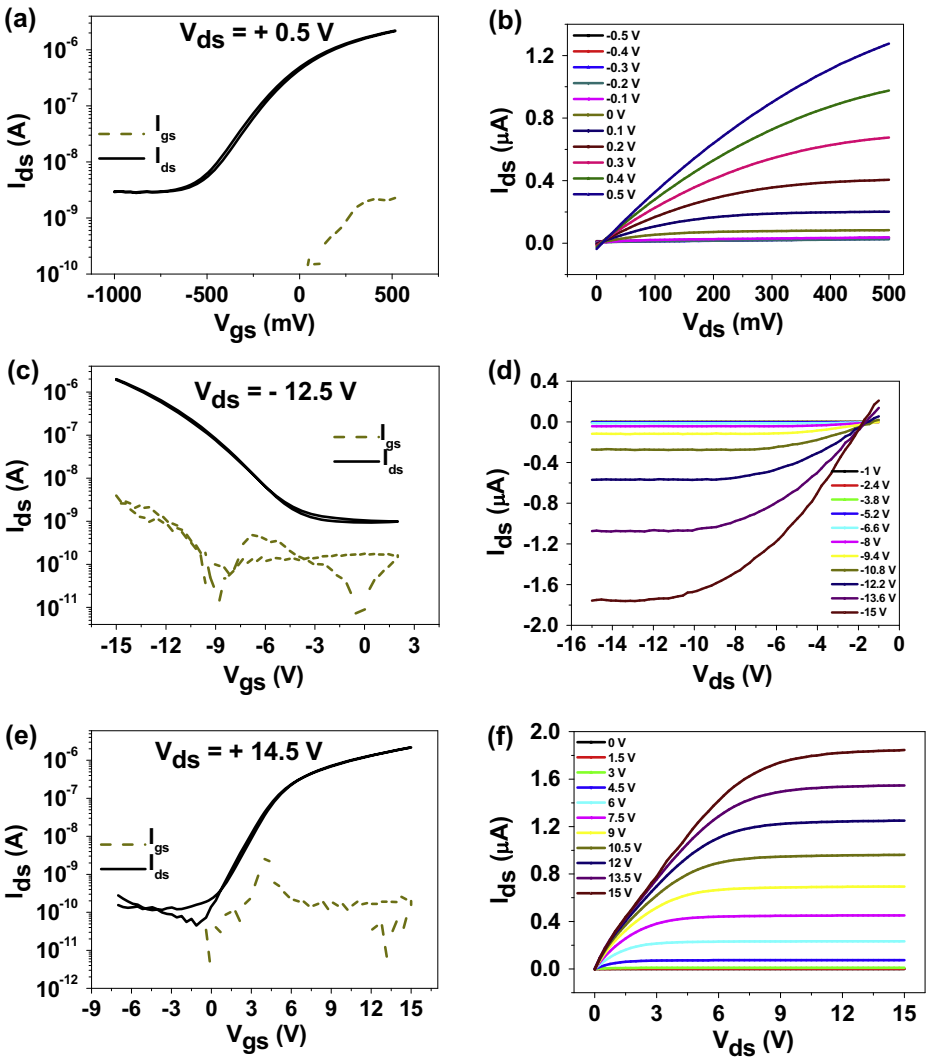

Fig. 7. Transfer and output characteristics of OFETs with (a and b) an AlOx–adenine gate and hot-wall epitaxial deposited C_{60} channel. Capacitance per area, C_{0d} = 99 nF/cm^2, field effect mobility μ = 5.5 cm^2/V s, subthreshold swing S = 0.25 V/dec and normalized subthreshold swing S_n = 24.7 V nF/cm^2 dec; (c and d) AlOx–adenine gate and pentacene channel. Capacitance per area, C_{0d} = 19.6 nF/cm^2, field effect mobility μ = 0.35 cm^2/V s, subthreshold swing S = 2.5 V/dec and normalized subthreshold swing S_n = 49 V nF/cm^2 dec; (e and f) AlOx–thymine gate and C_{60} channel. Capacitance per area, C_{0d} = 23.6 nF/cm^2, field effect mobility μ = 0.5 cm^2/V s, subthreshold swing S = 2 V/dec and normalized subthreshold swing S_n = 47.2 V nF/cm^2 dec.

domination of the peak centered at $2\theta = 29.42°$. Nevertheless, more work is required to understand the mechanisms of film growth in nucleobase materials.

3.1.3.3. Natural dielectrics-based OFETs. Organic field effect transistors with solution processed thin film gate dielectrics of glucose (in deionized water) and lactose (in DMSO) and vacuum processed fullerene, C_{60}, as semiconductor are presented in Fig. 5a–d. The transfer and output characteristics display a minimal hysteresis, which being counterclockwise can be attributed to the finite presence of mobile ionic impurities in the two dielectric films [26,27]. The field effect mobility of the organic semiconductor, C_{60}, deposited on lactose and glucose dielectrics was in the range of 5.5×10^{-2} to 8.5×10^{-2} cm^2/V s, and the capacitances per area of the two dielectrics employed were 6.8 nF/cm^2 for lactose and 2.15 nF/cm^2 for glucose dielectric. The method used to calculate the field effect mobility was reported in Ref. [28]. The measured subthreshold swing values of the fullerene were 2 V/dec for the OFET with a lactose dielectric and 6.2 V/dec for the glucose dielectric device. As described in the review article (Ref. [28]), the normalized subthreshold swing (the product of the dielectric capacitance per area and the subthreshold swing) is a more useful metric of comparison of semiconductor films deposited on different dielectrics or on dielectrics of various thicknesses. The values of the normalized subthreshold swing (S_n) for fullerene grown on lactose and glucose dielectrics are 13.6 V nF/cm^2 dec and 13.3 V nF/cm^2 dec, respectively. The saturated electron mobility of C_{60} deposited on solution processed small molecules in the sugar family is somewhat lower compared to

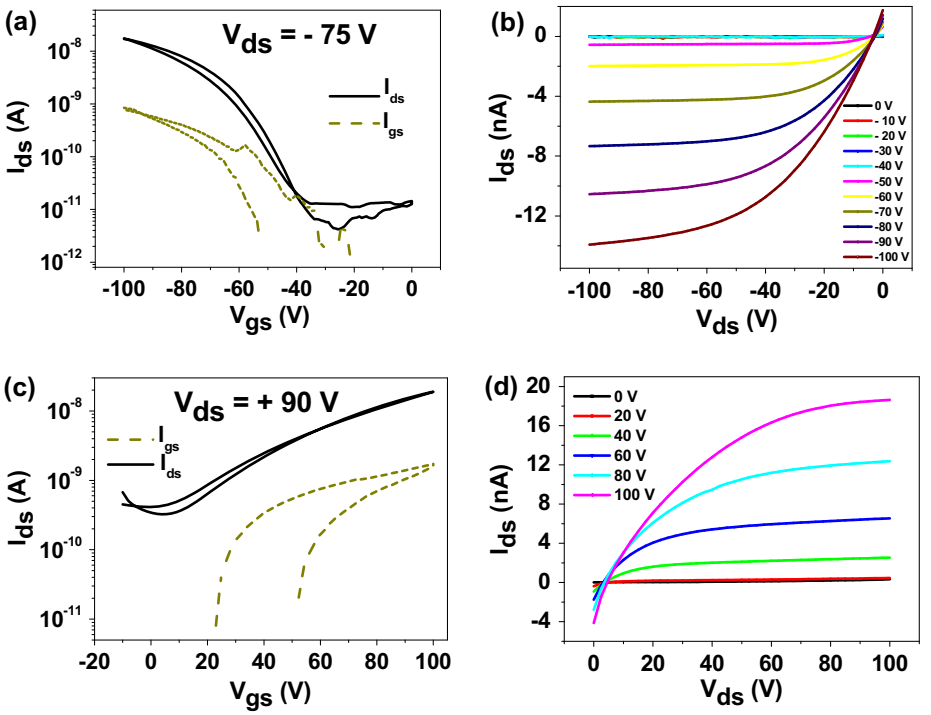

Fig. 8. (a and b) Transfer and output characteristics of organic field effect transistors with glucose and caffeine gate and solution processed beta-carotene (from chloroform) channel. Capacitance per unit area, C_{0d} = 1.9 nF/cm^2, field effect mobility $\mu = 4 \times 10^{-4}$ cm^2/V s, subthreshold swing S = 11 V/dec and normalized subthreshold swing S_n = 21 V nF/cm^2 dec; (c and d) transfer and output characteristics of organic field effect transistors with poly(vinyl alcohol) (PVA) gate and vacuum processed indigo organic semiconductor channel. Capacitance per unit area C_{0d} = 3.1 nF/cm^2, field effect mobility $\mu = 1.5 \times 10^{-4}$ cm^2/V s, subthreshold swing S = 34 V/dec and normalized subthreshold swing S_n = 105.4 V nF/cm^2 dec.

values reported elsewhere for fullerene semiconductors [29,30]. This lower electron mobility may be explained by the finite presence of moisture in the two dielectric films.

Vacuum processed organic dielectrics on the other hand allow fabrication of OFETs operating at low voltages [31,32]. Organic field effect transistors with vacuum processed guanine and cytosine gate and C_{60} channel are displayed in Fig. 6a–d, for transistors operating at voltages as low as 4–5 V. The measured saturated field effect mobility of C_{60} vacuum processed on cytosine and guanine dielectrics was 0.09 cm^2/V s and 0.12 cm^2/V s, respectively; the dielectric capacitance per area was 9.25 nF/cm^2 for guanine and 13.8 nF/cm^2 for cytosine. The measured subthreshold swing and normalized subthreshold swing values for the structure built on guanine were S = 1.4 V/dec and S_n = 12.9 V nF/cm^2 dec, respectively; the respective values for the fullerene film grown on cytosine were 1.2 V/dec and 16.6 V nF/cm^2 dec.

Higher operating currents as well as higher saturated field effect mobilities are possible when organic and inorganic dielectrics (i.e., anodized aluminium) are combined in hybrid structures [33]. Transistors with such hybrid gate structures are shown in Fig. 7a–f where thin layers of adenine (a–d) and thymine (e and f) were evaporated on aluminium oxide electrochemically grown in citric acid to produce high performance gate dielectrics. The calculated field effect mobility of transistors with hot-wall epitaxially deposited C_{60} and the hybrid gate (capacitance per area, C_{0d} = 99 nF/cm^2) listed in Fig. 7a and b was 5.5 cm^2/V s, with a calculated subthreshold swing of 0.25 V/dec and a normalized subthreshold swing of 24.7 V nF/cm^2 dec. The operating voltage of the respective device was as low as 500 mV. It is important to note that all the vacuum processed nucleobase dielectrics are also amenable to work in combination with p-type semiconductors (e.g., pentacene); an example of such an OFET is shown in Fig. 7c and d. In the latter case, 150 nm adenine was vacuum processed on 55 nm aluminium oxide (AlOx with a capacitance per unit area, C_{0d} = 140 nF/cm^2). The field effect mobility in the saturation regime of pentacene was 0.35 cm^2/V s, subthreshold swing S = 2.5 V/dec and normalized subthreshold swing S_n = 49 V nF/cm^2 dec, for a capacitance per unit area of the combined dielectric C_{0d} = 19.6 nF/cm^2. Despite its relatively low dielectric constant (i.e., 2.4 as shown in Table 1) and its high tendency of crystallization that renders films of high roughness (Fig. 3d), thymine passivates aluminium oxide very well. In the transistor shown in Fig. 7e and f, a 75 nm thick thymine film was vacuum processed on top of anodized aluminium, and vacuum processed C_{60} was used for the organic semiconductor. The respective OFET was hysteresis free in both transfer and output characteristics, while displaying a C_{60} mobility of 0.5 cm^2/V s, a subthreshold swing of 2 V/dec and a normalized subthreshold swing of 47.2 V nF/cm^2 dec, for a capacitance per unit area of

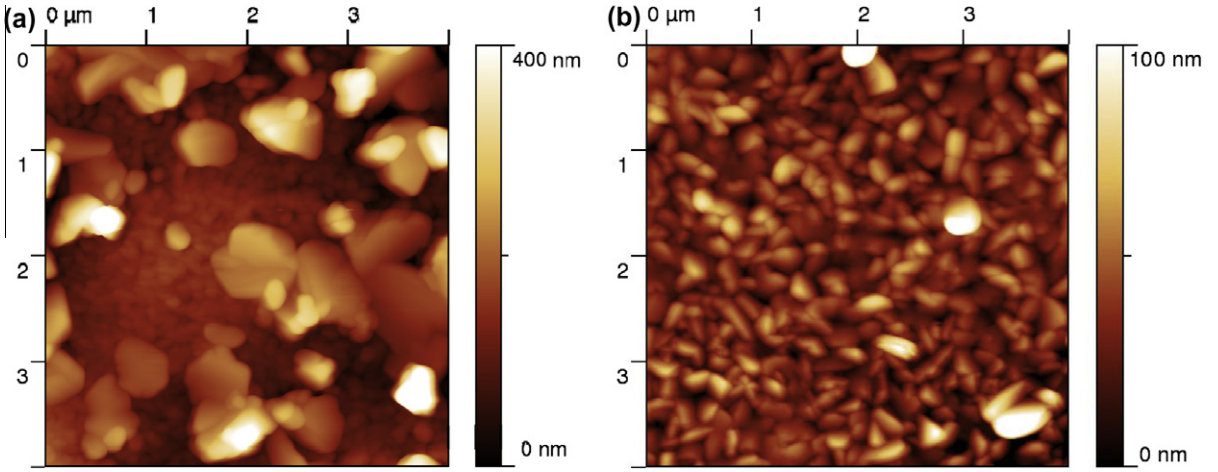

Fig. 9. AFM of natural semiconductor thin films (a) solution processed beta-carotene in chloroform on glucose + caffeine dielectric. Average roughness, rms = ~19 nm, measured in the shallow region of small grains; (b) vacuum processed indigo on poly(vinyl alcohol) dielectric. Average roughness, rms = ~17 nm. Measurements were recorded in the channel of OFETs devices displayed in Fig. 8.

23.6 nF/cm^2 of the hybrid gate dielectric. Surprisingly, the extreme roughness of vacuum processed small molecule dielectrics described here (adenine, cytosine and thymine), as well as in our previous work (melamine), Ref. [32]), was not a deterrent in generating hysteresis-free devices. The only exception was guanine. Interestingly, guanine formed smoother films when compared with adenine, cytosine, thymine or even melamine. We presume that the intimate binding that occurs at the interface between the dielectric and the semiconductor layers generates the occurrence of hysteris-free behavior in various OFETs. Further investigations at the molecular level are required to elucidate the mechanism of hysteresis formation in transistors with vacuum processed small molecules dielectrics and semiconductors of high purity.

3.1.4. Semiconductors for sustainable electronics

Encouraged by the performance of our transistors based on vacuum processible sustainable dielectrics and traditional workhorse semiconductors we went on identifying organic semiconductors, which may be viewed sustainable. A short, and by no means comprehensive list of such semiconductors, includes natural (indigo, beta-carotene), nature-inspired (anthraquinone vat dyes), and common commodity materials (perylene diimide). All these semiconductors have in common large scale production, ease of synthesis and low price, coupled with low toxicity, biodegradability and wide social acceptance [34].

3.1.4.1. Natural semiconductors for organic field effect transistors. Beta-carotene is a material with an old history. It was first reported by the German chemist Hernan Wachenroder, who in 1831 extracted red crystals from carrot roots, that he ultimately called "carotene" [35]. Until now, applications of beta-carotene and related products have been limited to the medical/biomedical field, as anti-aging and heart-disease prevention drug [36]. However, the optical, non-linear optical, fluorescence and even semiconducting properties of beta-carotene have been recently investigated by various groups [37–41].

Indigo is a naturally occurring compound, which has historically been extracted from plants in the *Indigofera* genus. Nowadays the synthetic production of indigo (initiated by Adolf Baeyer in 1882) has made possible high scale production of blue cotton yarn cloths with the main application of the compound remaining in the blue jeans industry [42]. Although the electronic and energetic levels of indigo were recently investigated, no report of using indigo as organic semiconductor in field effect devices appeared so far [43,44].

Organic field effect transistors with solution processed p-type beta-carotene and vacuum processed n-type indigo as organic semiconductors are presented in Fig. 8a–d. The organic dielectrics are glucose with small additions of caffeine in a and b and poly(vinyl alcohol) in c and d. The AFM investigations of the two dielectrics (glucose + caffeine and PVA) revealed featureless surfaces with rms ~1.5 nm and ~1 nm, respectively. The calculated field effect mobilities of the two natural semiconductors were 4×10^{-4} cm^2/V s for beta-carotene and 1.5×10^{-4} cm^2/V s for indigo for capacitances per area C_{0d} = 1.9 nF/cm^2 for glucose and caffeine dielectric and C_{0d} = 3.1 nF/cm^2 for PVA dielectric. The calculated subthreshold swing and normalized subthreshold swing values of the two natural semiconductors were 11 V/dec and 21 V nF/cm^2 dec for beta-carotene; 34 V/dec and 105.4 V nF/cm^2 dec for indigo, respectively. Higher performance may be achieved by optimizing transistor design and fabrication, corroborated with scrupulous purification of the chemicals.

AFM measurements of beta-carotene and indigo, performed in the channel of the measured devices shown in Fig. 8, are depicted in Fig. 9. The top surface of beta-carotene revealed small grains with a diameter in the range of 60–150 nm and an average size of 105 nm. However, in all the locations investigated (like for example the region shown in Fig. 9a), large grains were also visible, with diameters scaling up to 900 nm. The average roughness, rms, of

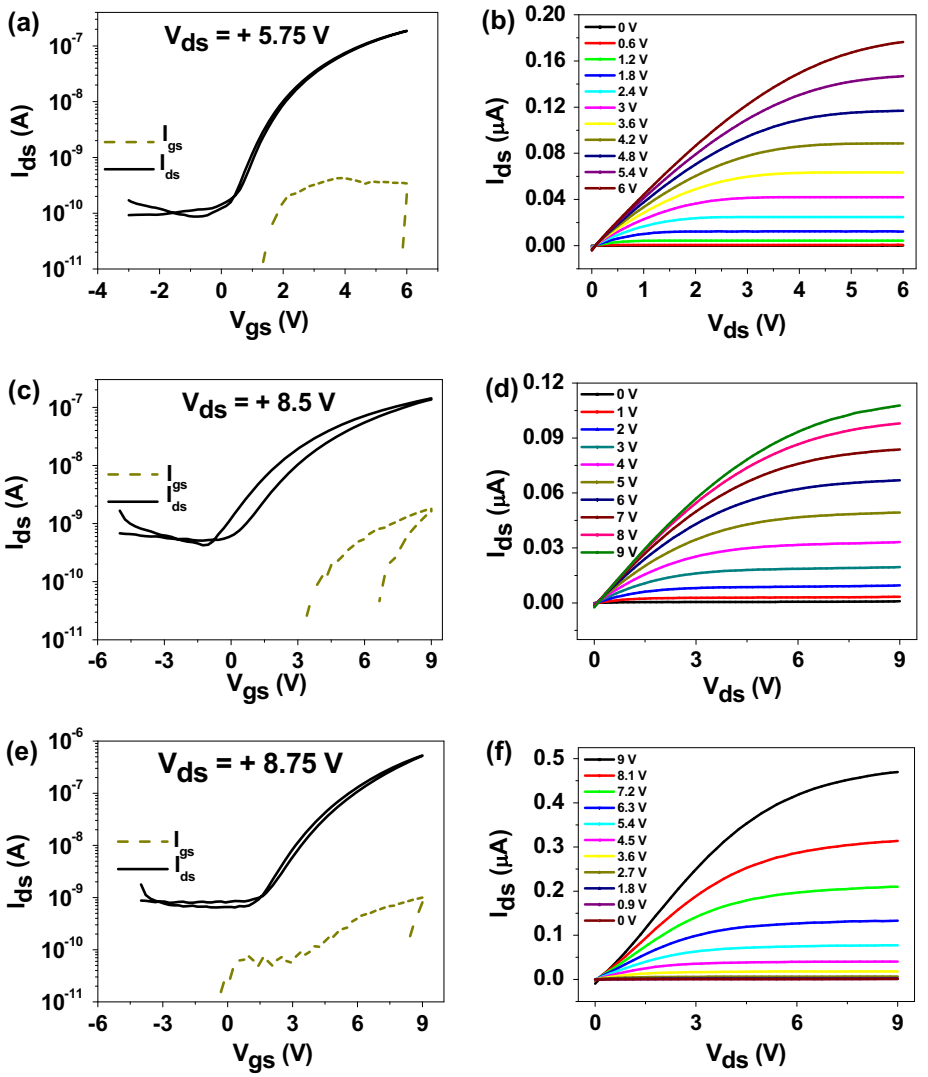

Fig. 10. (a and b) Transfer and output characteristics of organic field effect transistors with AlOx–guanine–adenine gate and perylene diimide channel. Capacitance per unit area C_{0d} = 81.6 nF/cm^2, field effect mobility μ = 0.016 cm^2/V s, subthreshold swing S = 1.5 V/dec and normalized subthreshold swing S_n = 122.4 V nF/cm^2 dec; (c and d) OFET with AlOx–guanine–adenine gate dielectric and indanthrene yellow G channel. Capacitance per unit area C_{0d} = 81.6 nF/cm^2, field effect mobility μ = 0.01 cm^2/V s, subthreshold swing S = 2.4 V/dec and normalized subthreshold swing S_n = 196 V nF/cm^2 dec; (e and f) OFET with AlOx–guanine–adenine gate and indanthrene brilliant orange RF channel. Capacitance per unit area C_{0d} = 81.6 nF/cm^2, field effect mobility $\mu = 1.9 \times 10^{-3}$ cm^2/V s, subthreshold swing S = 1.9 V/dec and normalized subthreshold swing S_n = 155 V nF/cm^2 dec.

beta-carotene measured in the shallow regions of small grains was ~19 nm. Indigo on the other hand displayed a more uniform surface in terms of grain size and distribution. Most of the indigo grains were elongated in shape and had a diameter in the range of 150–550 nm, with an average of 250 nm.

3.1.4.2. Nature-inspired semiconductors for organic field effect transistors. Indanthrene yellow G and indanthrene brilliant orange RF (derivatives of natural occurring anthraquinone-a well known laxative drug [45]) are both used widely in textile industry as vat dyes for fabrics coloring as well as in electronics industry as color filter in image forming applications [46,47]. However, their low toxicity [48], biodegradability [49,50] and ability to metabolize [51] has led to these compounds being proposed for coloring sausage skin in food industry [52,53].

Although having a synthetic route that can be distantly considered as starting from natural naphthalene, perylene diimide is not a truly nature-inspired compound [54]. Nevertheless, we want to list it here as environmentally sustainable material. The chemical inertness of perylene diimides is a prerequisite for their very low acute toxicity that opens up numerous applications in cosmetic industry as red pigments for hair colorants, nail enamels and lipsticks. Nowadays many perylene dyes are produced on an industrial scale and commercially available under trade names such as Red Dye 190 or Lumogen®F [55]. Perylene

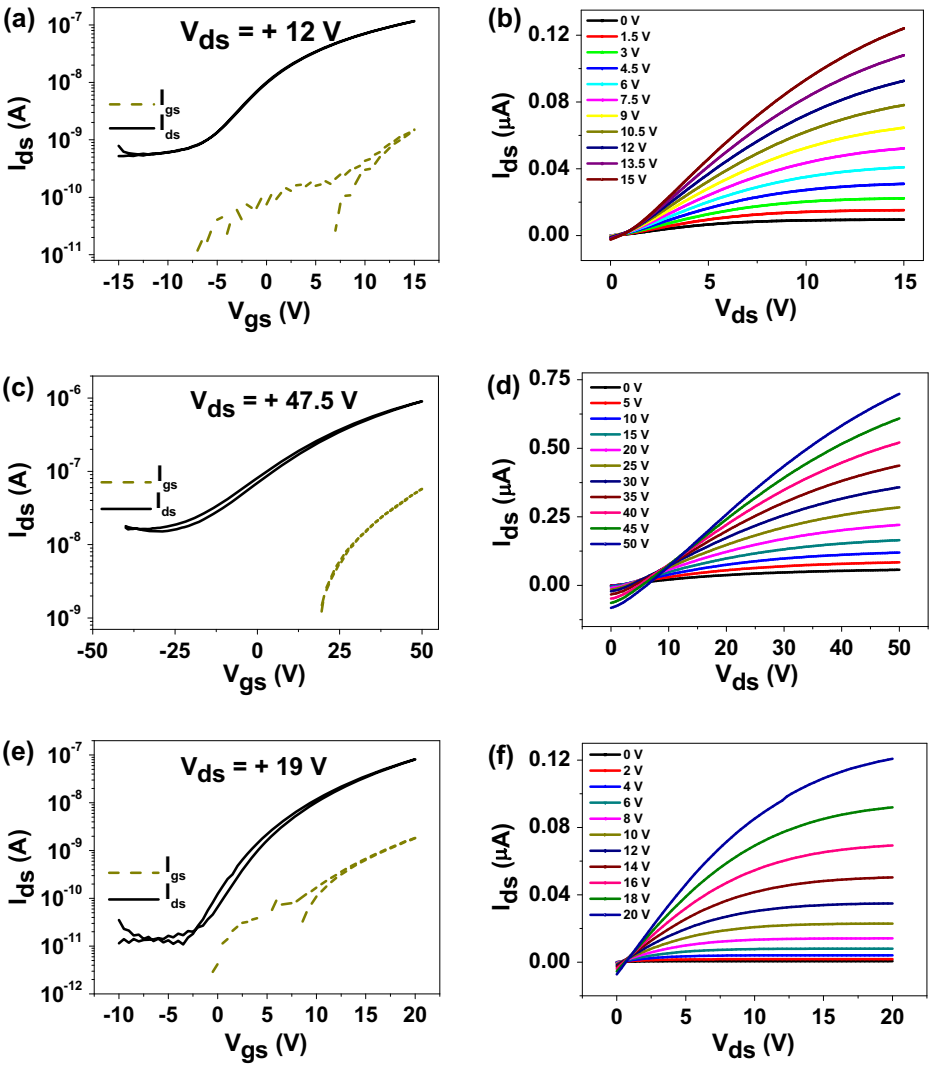

Fig. 11. (a and b) Transfer and output characteristics of an OFET on a biodegradable Ecoflex substrate; the roughness of the Ecoflex foil is reduced with a smoothing layer of aurin. Adenine forms the dielectric and perylene diimide is the semiconductor; C_{0d} = 3.1 nF/cm^2, μ = 0.01 cm^2/V s, S = 3.6 V/dec and S_n = 11.1 V nF/cm^2 dec; (c and d) Transfer and output characteristics of biocompatible and biodegradable OFETs on caramelized glucose substrates; guanine and adenine form the gate dielectric and indanthrene yellow G is the organic semiconductor. C_{0d} = 5.6 nF/cm^2, $\mu = 8 \times 10^{-3}$ cm^2/V s; (e and f) Transfer and output characteristics of an edible OFET on a hard gelatine capsule substrate; adenine and guanine form the gate dielectric and perylene diimide is the organic semiconductor; C_{0d} = 5.1 nF/cm^2, μ = 0.02 cm^2/V s, S = 3.1 V/dec and S_n = 15.8 V nF/cm^2 dec. Electrodes are aluminium (a and b) and gold (c and f).

diimides are also known as good n-type organic semiconductors widely used in organic solar cells [56].

3.1.4.3. OFETs with sustainable semiconductors on glass substrates. After having shown a large number of potential low cost organic semiconductors, we now proceed by presenting field effect transistors of these materials on glass substrates. Fig. 10a–f display transistors formed with indanthrene yellow G and indanthrene brilliant orange RF, as well as perylene diimide. Thin layers of these organic semiconductors have been evaporated on hybrid inorganic–organic gate dielectrics (55 nm aluminium oxide and thin alternating layers of guanine (2.5 nm) and adenine (15 nm), with a total capacitance per area of 81.6 nF/cm^2. The reason for using different organic dielectric layers was the intention to produce dense and pinhole free layers at lower thickness than using one organic dielectric layer alone. The saturated field effect mobilities of perylene diimide and indanthrene yellow G were ~0.015 cm^2/V s, indanthrene brilliant orange RF had a mobility of $\sim 2 \times 10^{-3}$ cm^2/V s. The mobilities of these materials of low cost and large scale availability are on par with mobilities reported recently for synthetic poly(p-phenylene vinylene) or for ambipolar polyselenophene organic semiconductors [57,58]. The calculated subthreshold swing values for the investigated nature-inspired semiconductors fell in a close range: 1.5 V/dec for perylene diimide, 2.4 V/dec for indanthrene yellow G and 1.9 V/dec for indanthrene brilliant orange RF. The OFET devices in Fig. 10 have been fabricated using identical

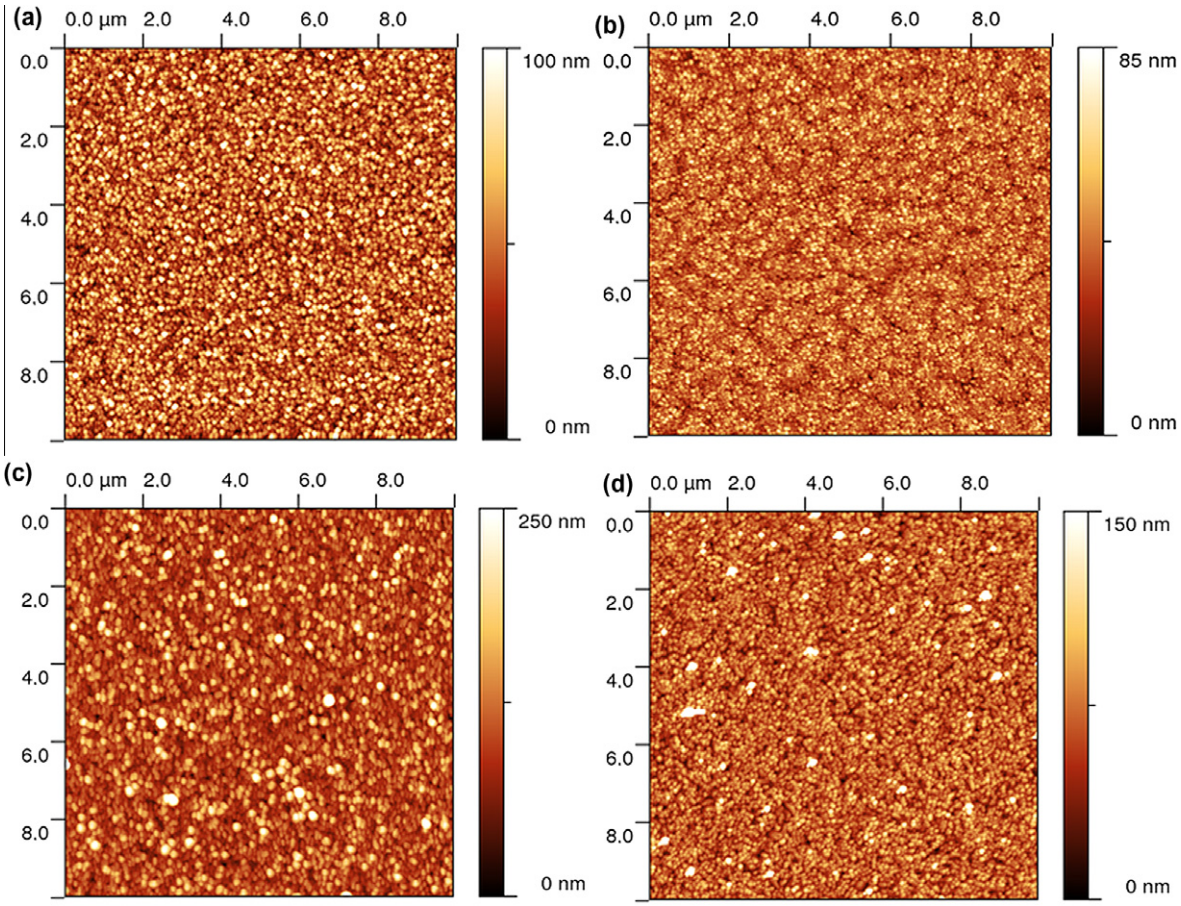

Fig. 12. AFM of various nature-inspired semiconductors employed in this work. Measurements were performed in the channel of the OFET devices shown here; (a) perylene diimide displayed in Fig. 10a and b; average surface roughness, rms ~17.5 nm (b) indanthrene yellow G displayed in Fig. 10c and d; average surface roughness, rms ~10.5 nm; (c) indanthrene brilliant orange RF displayed in Fig. 10e and f; average surface roughness, rms ~34 nm; (d) indanthrene yellow G displayed in Fig. 11c and d; average surface roughness, rms ~22 nm.

dielectric material (a hybrid inorganic–organic layer, having a capacitance per area $C_{0d} = 81.6$ nF/cm^2). The much lower values of the subthreshold swing recorded for the nature-inspired semiconductors displayed in Fig. 10, compared to the respective values of the natural semiconductors (beta-carotene and indigo) shown in Fig. 8, are not a surprise, since the subthreshold swing is highly dependent on both the semiconductor mobility and the dielectric capacitance per unit area [28]. It also shows the need for more detailed investigations on naturally occurring organic semiconductors.

3.1.4.4. OFETs with sustainable semiconductors on biodegradable and biocompatible substrates. Having been able to demonstrate transistors with sustainable gate dielectrics and semiconductors, we have tried to fabricate such devices also on natural caramelized glucose, biodegradable Ecoflex and biocompatible hard gelatine capsule substrates. OFET transfer and output characteristics for such devices are presented in Fig. 11a–f where small molecule-vacuum processed nucleobases (adenine in Fig. 11a and b or alternating layers of adenine and guanine in Fig. 11c–f) have been used for gate dielectrics; perylene diimide and indanthrene yellow G have been used for organic semiconductors. The on–off ratio of transistors fabricated with these sustainable materials ranged from 10^2 to 10^5, whereas the mobility of organic semiconductor was 8×10^{-3} for indanthrene yellow G and $\sim 1 \times 10^{-2}$ to 2×10^{-2} cm^2/V s for perylene diimide. The calculated subthreshold swing values of the perylene diimide semiconductor employed in Fig. 11a, b e, and f were 3.6 V/dec and 3.1 V/dec, respectively; the normalized subthreshold swing values were 11.1 V nF/cm^2 and 15.8 V nF/cm^2. The recorded values of normalized subthreshold swing show a good correlation of its dependence on mobility and dielectric capacitance (i.e., 3.1 nF/cm^2 for adenine dielectric in Fig. 11a and b and 5.1 nF/cm^2 for guanine and adenine in Fig. 11e and f).

AFM investigations of the nature-inspired semiconductors employed here (perylene diimide, indanthrene yellow G and indanthrene brilliant orange RF), performed in the channel of the measured devices presented in Figs. 10a–f and 11c and d are displayed in Fig. 12. The grain size of uniformly distributed perylene diimide (Fig. 12a) is in the range of 80–160 nm, with an average size of 125 nm. Indanthrene yellow G and indanthrene brilliant orange

RF form also grains with a uniform distribution (Figs. 12b and c, respectively). The indanthrene yellow G grain size spans the range from 60 nm to 130 nm, with an average size of 90 nm, whereas the indanthrene brilliant orange RF grains are somewhat larger, ranging from 100 nm to 300 nm, with an average grain size of 200 nm. Fig. 12d) shows the surface of indanthrene yellow G deposited on alternating layers of guanine and adenine on caramelized glucose substrate, the OFET device displayed in Fig. 11c and d). The surface of the latter material shows a uniform grain distribution, with grain diameters from 70 nm to 190 nm, and an average grain size of 125 nm.

It is interesting to observe that the grain sizes of the two semiconductor materials displaying on par mobilities in Fig. 10 (perylene diimide and indanthrene yellow G) were also comparable, whereas materials that rendered films of larger grain sizes (indanthrene brilliant orange RF, beta-carotene and indigo) recorded significantly lower mobilities. Moreover the subthreshold swing of various OFET devices was in the same range for devices showing similar semiconductor mobilities and having dielectrics of comparable capacitances per unit area.

4. Conclusions

In this work, we have initiated a search on low cost materials that may find applications in sustainable biodegradable and biocompatible organic field effect transistors. We have shown that different gate dielectrics from sugars and nucleobases can be used in field effect transistors based on workhorse p and n-type organic semiconductors such as C_{60} and pentacene. Large volume prepared dyes used in textiles, cosmetics or food industry have shown surprisingly large mobilities in field effect devices on glass and biodegradable/biocompatible substrates. Transistors on degradable substrates, such as Ecoflex, gelatine and caramelized sugars, could be operated with voltages around 15–20 V and source drain currents of 0.15 μA. We hope to have initiated with this work an intense search for new materials for organic electronics, to make the vision of sustainability in plastics electronics coming closer to reality.

Acknowledgements

The work was financially funded by the Austrian Science Foundation "FWF" within the National Research Network NFN on Organic Devices (P20772-N20, S09712-N08, S09706-N08 and S9711-N08) as well as by the Russian Foundation for Basic Research (grant 10-03-00443), by the Russian Ministry for Science and Education (contract 02.740.11.0749) and by the Russian President Foundation (grant MK-4305.2009.3). We thank Philipp Stadler, Michael Ramsay, Roland Resel and Christian Teichert for valuable discussions and suggestions.

References

[1] E. Rudnik, Compostable Polymer Materials, first ed., Elsevier, Amsterdam, 2008.
[2] R.J. Slack, J.R. Gronow, N. Voulvoulis, Hazardous components of household waste, Crit. Rev. Environ. Sci. Technol. 34 (2004) 419–445.
[3] (a) C.J. Bettinger, Z. Bao, Biomaterials-based organic electronic devices, Polym. Int. 59 (2010) 563–567;
(b) M. Irimia-Vladu, P.A. Troshin, M. Reisinger, L. Shmygleva, Y. Kanbur, G. Schwabegger, M. Bodea, R. Schwödiauer, A. Mumyatov, J. W. Fergus, V. F. Razumov, H. Sitter, N. S. Sariciftci, S. Bauer, Biocompatible and biodegradable materials for organic field effect transistors, Adv. Funct. Mater. in press, doi:10.1002/adfm.2010.01.031.
[4] C.J. Bettinger, Z. Bao, Organic thin-film transistors fabricated on resorbable biomaterial substrates, Adv. Mater. 22 (2010) 651–655.
[5] F. Eder, H. Klauk, M. Halik, U. Zschieschang, G. Schmid, C. Dehm, Organic electronics on paper, Appl. Phys. Lett. 84 (14) (2004) 2673–2675.
[6] B. Lamprecht, R. Thünauer, M. Osterman, G. Jakopic, G. Leising, Organic photodiodes on newspaper, Phys. Status Solidi (a) 202 (5) (2009) R50–R52.
[7] A.C. Siegel, S.T. Phillips, M.D. Dickey, N. Lu, Z. Suo, G.M. Whitesides, Foldable printed circuit boards on paper substrates, Adv. Funct. Mater. 20 (2010) 28–35.
[8] A.C. Siegel, S.T. Phillips, B.J. Wiley, G.M. Whitesides, Thin, lightweight, foldable thermochromic display on paper, Lab Chip 9 (2009) 2775–2781.
[9] R. Martins, P. Barquinha, L. Pereira, N. Correira, G. Goncalves, I. Fereira, E. Fortunato, Selective floating gate non-volatile paper memory transistor, Phys. Status Solidi RRL 9 (2009) 308–310.
[10] D.-H. Kim, Y.-S. Kim, J. Wu, Z. Liu, J. Song, H.-S. Kim, Y.Y. Huang, K.-C. Hwang, J.A. Rogers, Ultrathin silicon circuits with strain-isolation layers and mesh layouts for high-performance electronics on fabric, vinyl, leather, and paper, Adv. Mater. 21 (2009) 3703–3707.
[11] D.-H. Kim, Y.-S. Kim, J. Amsden, B. Panilaitis, D.L. Kaplan, F.G. Omenetto, M.R. Zakin, J.A. Rogers, Silicon electronics on silk as a path to bioresorbable, implantable devices, Appl. Phys. Lett. 95 (2009) 133701.
[12] D.-H. Kim, J. Viventi, J.J. Amsden, J. Xiao, L. Vigeland, Y.-S. Kim, J.A. Blanco, B. Panialitis, E.S. Frechette, D. Contreras, D.L. Kaplan, F.G. Omenetto, Y. Huang, K.-C. Hwang, M.R. Zakin, B. Litt, J.A. Rogers, Dissolvable films of silk fibroin for ultrathin conformal bio-integrated electronics, Nat. Mater. 9 (2010) 511–517.
[13] L. Miozzo, A. Yassar, G. Horrowitz, Surface engineering for high performance organic electronic devices: the chemical approach, J. Mater. Chem. 20 (2010) 2513–2538.
[14] T. Sekitani, T. Yokota, U. Zschieschang, H. Klauk, S. Bauer, K. Takeuchi, M. Takamiya, T. Sakurai, T. Someya, Organic nonvolatile memory transistors for flexible sensor arrays, Science 326 (5959) (2009) 1516–1519.
[15] Information about Ecoflex® is provided on the BASF internet page <http://www2.basf.us/businesses/plasticportal/ksc_ecoflex_biodegradable_plastic_literature.htm>.
[16] E. Fischer, O. Fischer, Ueber das Aurin (On Aurin), Ber. Deut. Chem. Ges. 11 (1878) 473–474.
[17] R. Foresti, M. Hoque, D. Monti, C.J. Green, R. Motterlini, Differential activation of heme oxygenase-1 by chalcones and rosolic acid in endothelial cells, J. Pharmacol. Exp. Therap. 312 (2005) 686–693.
[18] H.C. Yeung, Handbook of Chinese Herbs and Formulas, first ed., Institute of Chinese Medicine, Los Angeles, 1985.
[19] H. Fang, W. Tong, W.S. Branham, C.L. Moland, S.L. Dial, H. Hong, Q. Xie, R. Perkins, W. Owens, D.M. Sheehan, Study of 202 natural, synthetic, and environmental chemicals for binding to the androgen receptor, Chem. Res. Toxicol. 16 (2003) 338–1358.
[20] A.J. Steckl, DNA-A new material for photonics?, Nat Phot. 1 (2007) 3–5.
[21] Y.-W. Kwon, C. H Lee, D.-H. Choi, J.-I. Jin, Materials science of DNA, J. Mater. Chem. 19 (2009) 1353–1380.
[22] P. Stadler, K. Oppelt, B. Singh, J. Grote, R. Schwödiauer, S. Bauer, H. Piglmayer-Brezina, D. Bäuerle, N.S. Sariciftci, Organic field-effect transistors and memory elements using deoxyribonucleic acid (DNA) gate dielectric, Org. Electr. 8 (2007) 648–654.
[23] C. Yumusak, Th.B. Singh, N.S. Sariciftci, J.C. Grote, Bio-organic field effect transistors based on crosslinked deoxyribonucleic acid (DNA) gate dielectric, Appl. Phys. Lett. 95 (2009) 263304.
[24] Y.S. Kim, K.W. Jung, U.R. Lee, K.H. Kim, M.H. Hoang, J.I. Jin, D.H. Choi, High-mobility bio-organic field effect transistors with photoreactive DNAs as gate insulators, Appl. Phys. Lett. 96 (2010) 103307.
[25] D.M. Cohen, S.P. Atsaides, Additions to a revision of Argentine fishes, Fishery Bull. U.S. Dept. Int. 68 (1970) 13–36.
[26] J. Lancaster, D.M. Taylor, P. Sayers, H.L. Gomes, Voltage- and light-induced hysteresis effects at the high-k dielectric-poly(3-hexylthiophene) interface, Appl. Phys. Lett. 90 (2007) 103513.
[27] M. Egginger, M. Irimia-Vladu, R. Schwödiauer, A. Tanda, I. Frischauf, S. Bauer, N.S. Sariciftci, Mobile ionic impurities in poly(vinyl alcohol) gate dielectric. Possible source of the hysteresis in organic field effect transistors, Adv. Mater. 20 (2008) 1018.

[28] C.R. Newman, C. Daniel Frisbie, D.A. da Silva Filho, J.-L. Bredas, P.C. Ewbank, K.R. Mann, Introduction to organic thin film transistors and design of n-channel organic semiconductors, Chem. Mater. 16 (2004) 4436–4451.
[29] S. Kobayashi, T. Takenobu, S. Mori, A. Fujiwara, Y. Iwasa, Fabrication and characterization of C60 thin film transistors with high field-effect mobility, Appl. Phys. Lett. 82 (25) (2003) 4581–4583.
[30] Th.B. Singh, N. Marjanovic, G.J. Matt, S. Gunes, N.S. Sariciftci, A. Montaigne Ramil, A. Andreev, H. Sitter, R. Schwoediauer, S. Bauer, High-mobility n-channel organic field-effect transistors based on epitaxially grown C60 films, Org. Electron. 6 (2005) 105–110.
[31] M. Irimia-Vladu, N. Marjanovic, A. Vlad, A Montaigne Ramil, G. Hernandez-Sosa, R. Schwödiauer, S. Bauer, N.S. Sariciftci, Vacuum processed polyaniline-C60 organic field effect transistors, Adv. Mater. 20 (20) (2008) 3887–3892.
[32] M. Irimia-Vladu, N. Marjanovic, M. Bodea, G. Hernandez-Sosa, A. Montaigne Ramil, R. Schwödiauer, S. Bauer, N.S. Sariciftci, F. Nüesch, Small-molecule vacuum processed melamine-C60, organic field-effect transistors, Org. Electron. 10 (2009) 408–415.
[33] L.A. Majewski, M. Grell, S.D. Ogier, J. Veres, A novel gate insulator for flexible electronics, Org. Electron. 4 (2003) 27–32.
[34] The biodegradability of perylene diimide remains however questionable. Nevertheless, the low toxicity of the material made possible its large scale applicability in cosmetic industry as a lip stick and nail polish chromophore.
[35] H. Wachenroder, Concerning the oil extracted from carrot roots, carotene, carotene sugars and components of carrot juice, Geiger's Mag. Pharm. 33 (1831) 144–172.
[36] J.A. Olson, N. Krinsky, Introduction: the colourful, fascinating world of carotenoids: important physiologic modulators, FASEB J. 9 (1995) 1547–1550.
[37] S.M. Bachilo, T. Gillbro, Beta-carotene S1 fluorescence, Proc. SPIE 2370 (1995) 719–723.
[38] M. Fujiwara, Large third-order optical nonlinearity realized in symmetric nonpolar carotenoids, Phys. Rev. B 78 (2008) 161101.
[39] T.N. Misra, B. Rosenberg, R. Switzer, Effect of adsorption of gases on the semiconductive properties of all-trans beta-carotene, J. Chem. Phys. 48 (1968) 2096–2102.
[40] E. Ehrenfreund, T.W. Hagler, D. Moses, F. Wudl, A.J. Heeger, Gap states of iodine-doped β-carotene, Synth. Met. 49 (1-3) (1992) 77–82.
[41] R.R. Burch, Y.H. Dong, C. Fincher, M. Goldfinger, P.E. Rouviere, Electrical properties of polyunsaturated natural products: field effect mobility of carotenoid polyenes, Synth. Met. 146 (2004) 43–46.
[42] A. Baeyer, V. Drewsen, Darstellung von Indigblau aus Orthonitrobenzaldehyd. (Description of indigo blue from orthonitro bennzaldehyde), Ber. Deut. Chem. Ges. 15 (1882) 2856–2864.
[43] M. Klwessinger, The origin of color of indigo dyes, Dyes Pigm. 3 (1982) 235–241.
[44] V.T. Ngan, G. Gopakumar, T.T. Hue, M.T. Nguyen, The triplet state of indigo: electronic structure calculations, Chem. Phys. Lett. 449 (2007) 11–17.
[45] Natural Anthraquinone Drugs International Journal of Experimental and Clinical Pharmacology, 20(Suppl. 1) (1980).
[46] M. Fukaya, Method of making photosensors, United States Patent No. 4746535, 1988.
[47] S. Nakamura, I. Shimamura, Color image forming process, United States Patent No. 4242441, 1980.
[48] Substance Profile for the Challenge Benzo[h]benz[5,6]acridino[2,1,9,8-klmna]acridine-8,16-dione (Pigment Yellow 24). Chemical Abstracts Service Registry Number 475-71-8, Environment Canada, March 2009.
[49] J. Liu, H. Luo, Degradation of anthraquinone dyes by ozone, Trans. Nonferrous Met. Soc. China 17 (2007) 880–886.
[50] S. Sirianuntapiboon, K. Chairattanawan, S. Jungphungsukpanich, Some properties of a sequencing batch reactor system for removal of vat dyes, Bioresour. Technol. 97 (2006) 1243–1252.
[51] R. Olaganathan, J. Patterson, Decolorization of anthraquinone vat blue 4 by the free cells of an autochthonous bacterium, Bacillus subtilis, Water Sci. Technol. 16 (12) (2009) 3225–3232.
[52] D. Wearing, Method of producing colored structures, United States Patent No. 3293340, 1966.
[53] K. D. Blumenberg, W. Neuschulz, Method for producing transparent, colored cellulose sleeves, United States Patent No. 6797015, 2004.
[54] R. Scholl, C. Seer, R. Weitzenbock, Perylen, ein hoch kondensierter aromatischer Kohlenwasserstoff $C_{20}H_{12}$ (perylene, a high aromatic hydrocarbon), Ber. Deut. Chem. Ges. 43 (1910) 2202–2209.
[55] M. Medelnick, E. Pfrommer, T. Clemens, P. Erk, A. Bohm, S. Kielhorn-Bayer, H. Witteler, W. M. Dausch, H. Westenfelder, T. Wunsch, K. Mathauer, T. Habeck, T. Ikeda, H. Ichihara, Use of finely divided dye-containing polymers PD as color-imparting constituent in cosmetic compositions, United States Patent No. 6541032, 2003.
[56] L.A. Schmidt-Mende, A. Fechtenkoetter, K. Muellen, E. Moons, R.H. Friend, J.D. MacKenzie, Self-organized discotic liquid crystals for high-efficiency organic photovoltaics, Science 293 (2001) 1119–1122.
[57] A.J.J.M. van Breemen, P.T. Herwig, C.H.T. Chlon, J. Sweelssen, H.F.M. Schoo, E.M. Benito, D.M. de Leeuw, C. Tanase, J. Wildeman, P.W.M. Blom, High-performance solution-processable poly(p-phenylene vinylene)s for air-stable organic field-effect transistors, Adv. Funct. Mater. 15 (5) (2005) 872–876.
[58] Z. Chen, H. Lemke, S. Albert-Seifried, M. Caironi, M.M. Nielsen, M. Heeney, W. Zhang, I. Mc. Culloch, H. Sirringhaus, High mobility ambipolar charge transport in polyselenophene conjugated polymers, Adv. Mater. 22 (21) (2010) 2371–2375.

Organic Electronics 11 (2010) 1991–1998

Contents lists available at ScienceDirect

Organic Electronics

journal homepage: www.elsevier.com/locate/orgel

Band alignment engineering in organized rrP3HT/C_{60} bulk heterojunction

Arnaud Maillard *, Alain Rochefort

Département de génie physique et Regroupement québécois sur les matériaux de pointe (RQMP), École Polytechnique de Montréal, C.P. 6079, succ. Centre-Ville, Montréal, Qué., Canada H3C 3A7

ARTICLE INFO

Article history:
Received 7 August 2010
Received in revised form 15 September 2010
Accepted 20 September 2010
Available online 30 September 2010

Keywords:
Organic solar cell
Bulk heterojunction
Organic semiconductor
Polythiophene
Fullerene
Density functional theory

ABSTRACT

The influence of structural ordering in a blend of rrP3HT polymer and C_{60} molecules has been investigated with first principles DFT calculations. An increasing packing density of rrP3HT chains and C_{60} component favors an increasing open-circuit voltage (V_{oc}), leaving the absorption properties of rrP3HT nearly intact. In contrast, an increasing size of π-crystal domains of rrP3HT within the blend tends to strongly enhance the magnitude of π-electron delocalization, leading to a decrease of both the rrP3HT band gap and V_{oc}.

© 2010 Elsevier B.V. All rights reserved.

1. Introduction

The development of clean, renewable and sustainable energy sources considers multiple technologies, including photovoltaic cells, with the aim of replacing more traditional energy sources. A large-scale implantation of photovoltaic cells that would sustain the actual energetic demand is strongly hindered by their manufacturing cost [1]. The use of organic semiconductors to manufacture photovoltaic devices with large-scale and low-cost printing techniques associated with the facility to process polymer could overcome the cost limitation of traditional inorganic photovoltaic cells [2–5]. However, the power conversion efficiency of organic photovoltaic cells has to reach a minimal 10% target in order for such devices to be economically competitive [6,7]. State-of-the-art organic photovoltaic cells, presently achieving power conversion efficiencies up to 7.9% [8,9], rely on a bulk heterojunction (BHJ) made of π-conjugated polymer acting as electron donor and fullerene derivative acting as electron acceptor [10–12]. Therefore, before attaining the 10% target with high-efficiency BHJ organic photovoltaic cells, more experimental and theoretical efforts are needed to provide a comprehensive representation of the electronic properties of the blend at the donor–acceptor interface.

The present work is a theoretical investigation of the electronic properties of an important BHJ model system in which we focus on the influence of structural order at the donor–acceptor interface. In the investigated BHJ models, regioregular head-to-tail poly(3-hexylthiophene-2,5-diyl) (rrP3HT) polymer is used as electron donor and buckminsterfullerene (C_{60}) molecule as electron acceptor. The photophysical interest for such rrP3HT/C_{60} blend is mainly motivated by an ultrafast electron transfer that occurs between the conjugated polymer and the C_{60} moiety [2,13,14]. Due to its significant solubility [15], [6,6]-phenyl-C_{61}-butyric acid methyl ester (PCBM) molecule is more often used in high-efficiency organic photovoltaic cells [4]. Nevertheless, one may assume that the physical characteristics of a BHJ containing C_{60} are similar to one with PCBM because the side chain attached to C_{60} in PCBM does not actively participate in the electron transfer process, and

* Corresponding author.
E-mail addresses: arnaud.maillard@polymtl.ca (A. Maillard), alain.rochefort@polymtl.ca (A. Rochefort).

1566-1199/$ - see front matter © 2010 Elsevier B.V. All rights reserved.
doi:10.1016/j.orgel.2010.09.013

hence does not modify the electronic properties of frontier orbitals. Experimentally, an improved solubility translates into a better film morphology which in turn leads to an improved efficiency of the photovoltaic cell [14]. However, an appropriate use of recent fabrication techniques can improve the morphology of BHJ made of C_{60} without requiring the use of PCBM [16]. Finally, considering the high electron mobility of C_{60} networks ($\sim 1\ cm^2/Vs$) [17] over PCBM networks ($\sim 10^{-3}\ cm^2/Vs$) [18], BHJs based on C_{60} would lead to organic photovoltaic cells with higher efficiency.

Concerning the rrP3HT polymer, it is composed of a rigid π-conjugated backbone combined with alkyl side chains providing the required solubility to polythiophene for the processing steps used to build the devices [19]. A high degree of regioregularity in the polymer favors the self-assembly of the rrP3HT chains into microcrystalline domains through a π-stacking of the polythiophene backbones [20,21]. This self-assembly leads to an highly anisotropic mobility for the two-dimensional charge transport observed in high-performance organic field-effect transistors. The charge carrier mobility reaches $0.1\ cm^2/Vs$ for transport in the plane containing the π-conjugated backbone and π-stacked directions, while a mobility more than a 100 times smaller is observed for transport in the plane containing the π-conjugated backbone and alkyl side chains directions [22,23]. The influence of ordering on the photophysical properties of P3HT have been extensively studied at both theoretical [24] and experimental [25] level. The existence of structural ordering in rrP3HT solution is usually associated to the formation of H-aggregate nanostructures that lead to the emergence of new absorption bands that are significantly redshifted with respect to the main absorption peak observed in diluted and disordered solution [25]. From these observations, we may then anticipate that well-ordered rrP3HT polymer have a higher band dispersion and a smaller optical band gap than the disordered phase.

In this paper, we first briefly describe the computational details considered in the study of organic BHJ. These BHJs were constructed by varying the domain size of the rrP3HT π-crystal region in the rrP3HT/C_{60} blend. Then, we discuss the geometry optimization of the BHJs, analyze their electronic properties and compare the results with the electronic properties previously obtained for pure rrP3HT π-crystals [26]. Finally, we examine the influence of interface between domains of rrP3HT and C_{60} on the electronic properties of the BHJs.

2. Computational details

We have performed first principles density functional theory (DFT) computations with the SIESTA software package [27] to determine the structural and electronic properties of different rrP3HT/C_{60} blends. The DFT calculations were mostly performed within the local density approximation (LDA), which still remain an adequate approach to determine accurate equilibrium distances in periodic π-stacked systems even though it does not formally consider dispersion interactions [26,28]. In fact, computations performed on graphite involving π—π interactions show a small underestimation of the interlayer separation with LDA compared to a large overestimation with the generalized gradient approximation (GGA) [29]. Our interpretation based on the comparison of relative energies and electronic properties of different BHJs drastically reduces the importance of artifacts related to well-known shortcomings of LDA, such as the underestimation of the band gap, on the general conclusions of this work. Nevertheless, we also tested the approach of Dion [30,31] (vdW-DF) to evaluate the magnitude of van der Waals interactions for the rrP3HT/C_{60} blend.

All computations were performed using periodic boundary conditions in conjunction with norm-conserving Troullier–Martins pseudopotentials and double-ζ polarized linear combination of numerical atomic orbitals basis sets. The pseudopotentials generated with the ATOM software [27] for the different atomic species reproduce the all-electron eigenvalues and excitation energies of multiple atomic configurations within a 1 mRy error. The geometry of the BHJs studied were optimized using the DFT-LDA calculated forces and stresses within a quasi-Newton method updating the Hessian matrix with a Broyden–Fletcher–Goldfarb–Shanno (BFGS) procedure. The geometry optimizations were stopped when the maximum force in the unit cell was less than 7.5 meV/Å (20 meV/Å for the largest systems) and the total energy variation between two iterations was less than 0.5 meV.

3. Results and discussion

3.1. Structural properties of well-organized blend

In experimental rrP3HT/C_{60} BHJ, suitable electronic coupling exists between C_{60} and rrP3HT frontier states to establish charge transfer across the interface. Considering that the rrP3HT crystal frontier states are centered on the π-conjugated backbones while the alkyl side chains states are further away from the Fermi level, we built the BHJ by placing C_{60} between rrP3HT backbones in the π-stacked direction in order to promote electronic donor–acceptor coupling. As shown in Fig. 1, the BHJ unit cell used to model an amorphous disordered blend is composed by one C_{60} and one rrP3HT chain containing four hexylthiophene monomers. We define the three orthogonal vectors **a**, **b** and **c** lying, respectively, in the alkyl side chains, the π-stacked and the π-conjugated backbone directions. The unit cell vectors **a** and **c** are fixed at the optimized values for a pure rrP3HT π-crystal [26], that are $|\mathbf{a}| = 15.82$ Å and $|\mathbf{c}| = 15.66$ Å. The dimension of $|\mathbf{b}|$, as well as the orientation and relative position of the C_{60} along the rrP3HT chain were fully optimized. In order to appropriately describe the C_{60}—rrP3HT interface, the geometry optimization was performed for the four different configurations illustrated in Fig. 1 as a function of the distance d ($d = |\mathbf{b}|/2$) separating the rrP3HT chain from the center of the C_{60} molecule. Configuration I, the most stable configuration found at DFT-LDA level, gives a cohesive energy ($E_{rrP3HT} + E_{C_{60}} - E_{BHJ}$) of 1.87 eV. This value compares well to the cohesive energy 1.55–1.99 eV reported for solid C_{60}

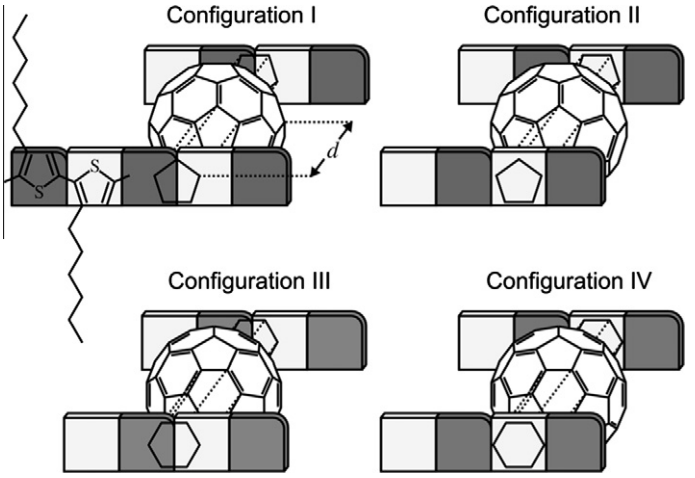

Fig. 1. Representation of the four rrP3HT/C_{60} BHJ configurations studied.

Table 1
Equilibrium distances and relative stabilities of optimized BHJ configurations with LDA and vdW-DF.

	LDA		vdW-DF	
	d (Å)	ΔE (meV)	d (Å)	ΔE (meV)
Conf. I	6.35	0	6.68	0
Conf. II	6.43	4	6.71	−109
Conf. III	6.35	24	6.56	57
Conf. IV	6.47	75	6.63	−12

[32], but is significantly lower than the cohesive energy of 3.50 eV previously calculated for bulk rrP3HT with a DFT-LDA approach [26]. This result indicates that the formation of ordered rrP3HT/C_{60} BHJ is favorable even though the interactions between component are relatively weak.

As reported in Table 1, the energy differences (ΔE) between the four configurations considered with LDA and vdw-DF are within nearly 100 meV, indicating that C_{60} is almost free to rotate and to move along the rrP3HT chain in the backbone direction. The LDA method seems to favor configurations for which a pentagon of C_{60} is facing the rrP3HT chain, while the vdw-DF method favors configurations where C_{60} is simply aligned with an hexylthiophene ring. The energy difference between configurations where pentagon or hexagon of C_{60} is facing the hexylthiophene chain is similar to the calculated value obtained by Kanai and Grossman with a similar DFT-LDA approach [33].

The equilibrium distances given in Table 1 also differ for both computational approximations, the vdw-DF giving larger separation between rrP3HT chain and C_{60} than LDA. The periodicity of the BHJ crystal given by the value of 2d varies from 12.70 to 13.42 Å for both LDA and vdW-DF, which is shorter than the summation of individual bulk distances for C_{60} (10.02 Å) [34] and P3HT (3.42–3.60 Å) [26,35–38]. This result is fully consistent with a previous work on rrP3HT/C_{60} system [33]. As mentioned above, these dimensions are coherent with rather weak interactions between the rrP3HT and C_{60} in the BHJ crystal. In addition, considering the very good agreement between LDA and experimental values we previously obtained for the equilibrium distance between rrP3HT chains in a rrP3HT crystal [26], and including the fact that this not well tested vdw-DF approach tends to overestimate equilibrium distances [30,31], we believe that LDA results remain the most reliable.[1] Therefore, configuration I, the LDA most stable configuration, will be used in further calculations.

It is well accepted experimentally that annealing of a rrP3HT/C_{60} blend leads to the crystallization of domains made of pure polymeric or molecular phase [39–42]. Even with this partial phase segregation, the overall physical and electrical characteristics of the blend are usually enhanced with respect to mixed and disordered phase by allowing higher charge carrier mobilities [43–45]. Those variations should also be somehow related to the quality of the interface between C_{60} and rrP3HT domains. Hence, from the most stable configuration I at LDA level, we have studied the influence of the domain size of the π-crystal, or in other words the size of H-aggregates of rrP3HT, by introducing C_{60} within the rrP3HT crystal network. This would contribute to describe the variation of C_{60}—rrP3HT interface properties when the blend becomes gradually well-organized with a demixing of the two components. The different BHJ unit cells studied, illustrated in Fig. 2, are composed of 1, 2, 3 or 4 chains of rrP3HT in the π-stacked direction where each chain is made of four hexylthiophene monomers in the conjugated backbone direction. The distance between the center of C_{60} and the nearest rrP3HT chain is set at 6.35 Å with the shortest distance between the hydrogens of the alkyl side chains and the C_{60} carbons at approximatively 2 Å, as in configuration I. Furthermore,

[1] We have also compared LDA and PBE-vdW energies with the help of NwChem software on finite models of configuration I–IV where P3HT oligomers where considered instead of a periodic polymer. For these test cases, we found similar ordering in stability between LDA and PBE-vdW approaches, but where, as expected, the stability is increasing with consideration of dispersion corrections.

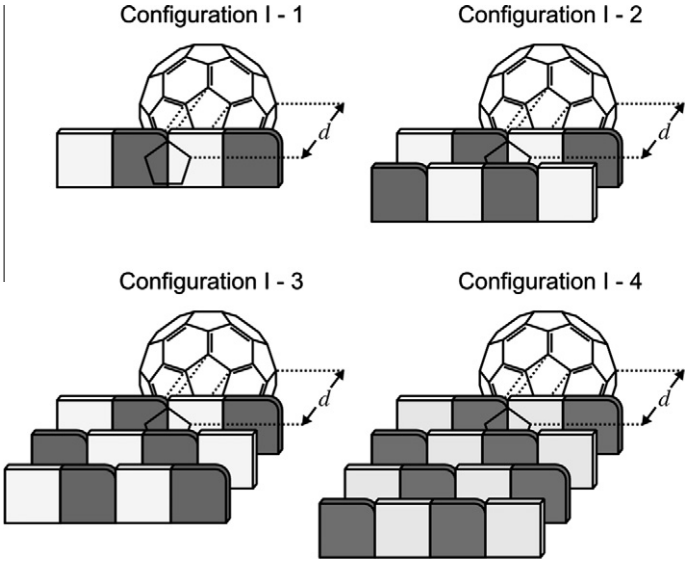

Fig. 2. Illustration of configuration I-*X* where *X* indicates the number of rrP3HT chains per unit cell considered in the π-crystal domain.

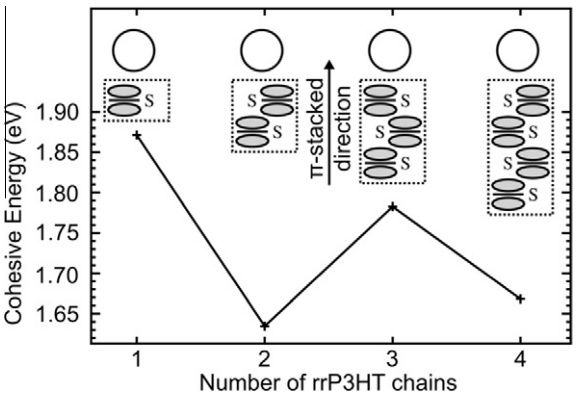

Fig. 3. Cohesive energy of the BHJ as a function of number of rrP3HT chains between C_{60} in the π-stacked direction. A representation of the HOMO wavefunction is illustrated above the curve.

the distance between rrP3HT chains in the π-stacked direction is fixed at 3.42 Å as in the periodic rrP3HT π-crystal [26].[2]

After full relaxation of the atomic coordinates inside the fixed unit cell, the cohesive energy of the BHJ is evaluated as a function of number of the rrP3HT chains in the unit cell. The variation of cohesive energy reported in Fig. 3 clearly shows an oscillation between 1.63 and 1.87 eV, with values greater for odd numbers of rrP3HT chains than for even numbers. This stability oscillation is related to boundary conditions in the π-stacked direction where an odd number of rrP3HT chains allow the formation of symmetric delocalized wavefunctions through the thiophene units (A, ABA, ABABA,...) that stabilize the system. This contrast with an even number of stacked chains (AB, ABAB,...) that does not allow the formation of symmetric delocalized wavefunctions which leads to a less stable system.

3.2. Electronic properties of nanostructured blend

In this section, we first present the electronic structure properties of a BHJ in configuration I with a rrP3HT/C_{60} ratio of 1 (see configuration I-1, Fig. 2). Such rrP3HT/C_{60} mixture can be compared to a disordered blend in which there is no H-aggregates or domains of rrP3HT nanocrystallite. The band structure of this BHJ is displayed in Fig. 4a for the π-stacked direction from Γ to $X = (0, \pi/\mathbf{b}, 0)$ and for the π-conjugated backbone direction from Γ to $X' = (0, 0, \pi/\mathbf{c})$. As illustrated by the three shaded areas in Fig. 4a, the presence of C_{60} in the polymer has few impacts on the band structure of rrP3HT in the π-stacked direction. C_{60} mainly introduces three nearly degenerate states in the rrP3HT band gap defined by the position of the highest occupied molecular orbital (HOMO) and the lowest unoccupied molecular orbital (LUMO). These three empty states are originating from the threefold degenerate t_{1u} state of isolated C_{60}, and are weakly dispersed in both $X\Gamma$ and $\Gamma X'$ directions of the blend. Those results suggest that C_{60} interacts weakly with rrP3HT and other C_{60} molecules forming the crystal blend. As revealed by the wavefunctions in Fig. 4b, the C_{60} acceptor states remain strongly localized in the blend and no overlap between rrP3HT and C_{60} states can be clearly identified.

Similarly, as observed for an isolated rrP3HT chain, the dispersion of both HOMO and LUMO bands of rrP3HT in

[2] In a previous DFT study, the rrP3HT crystal configuration was determined the most stable configuration among multiple probable configurations. We consider this configuration to be highly probable since it allows an uniform distribution of the alkyl side chains in a structure similar to a polyethylene crystal ($|\mathbf{a}| = 7.46$ Å and $|\mathbf{b}| = 4.98$ Å [46]) with comparable lattice parameters ($|\mathbf{a}| = 6.83$ Å and $|\mathbf{b}| = 5.72$ Å). Furthermore, we view this configuration as truly representative of real rrP3HT crystal samples considering the very good agreement between calculated and experimental results [37,47–49].

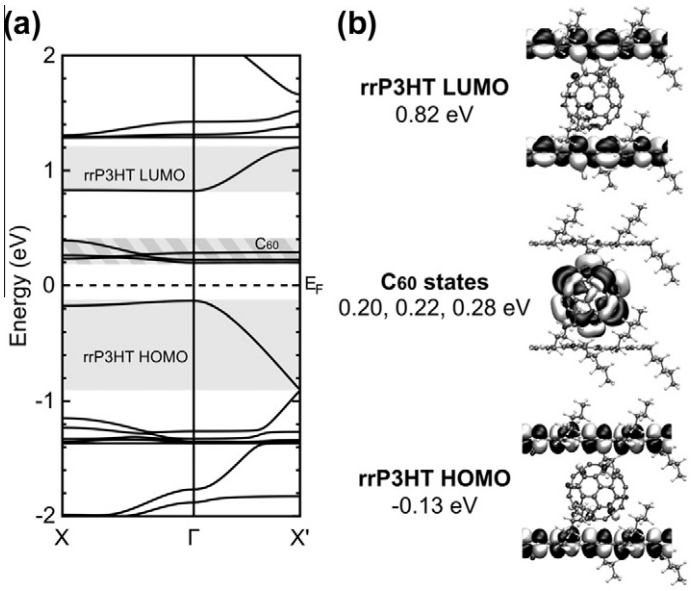

Fig. 4. (a) Band structure of BHJ in configuration I. (b) Wavefunction contours of frontier orbitals in a configuration I BHJ with the energy levels taken at Γ point.

the π-stacked direction ($X\Gamma$) is nearly zero while it is significantly larger in the π-conjugated backbone direction ($\Gamma X'$) [26]. The calculated HOMO–LUMO gap at Γ-point for rrP3HT (0.97 eV) is substantially lower than the experimental band gap ($\sim$ 1.9 eV), as generally observed with an DFT-LDA approach. A similar trend is observed for C_{60} where the calculated HOMO–LUMO gap (1.60 eV) is lower than the experimental value (2.6 eV) [50]. Although band gaps are usually underestimated with DFT-LDA, the relative alignment of HOMO–LUMO bands between rrP3HT and C_{60} are more appropriately described. For example, the calculated energy shift between LUMOs of rrP3HT and C_{60} is 0.62 eV as compared to 0.50 eV observed experimentally [51,52]. A similar trend is observed between HOMO's where the calculated value (1.13 eV) is in good agreement with experimental value (1.00 eV) [51,52]. Hence, the relative variation of electronic properties observed in this study and their impact on our general conclusions should not be affected by the absolute band gap values.

The two diagrams in Fig. 5 show the position of HOMO and LUMO of rrP3HT along with the three C_{60} energy levels in different BHJ systems. The position of HOMO and LUMO taken at Γ are clearly identified by a thick line located at, respectively, the top of the valence band and the bottom of the conduction band. The dispersion of these bands is represented by the shaded area. The influence of the distance d separating the nearest rrP3HT chain from the C_{60} on the electronic properties of the BHJ is presented in Fig. 5a. The effect of the domain size of rrP3HT crystal on the position of frontier orbital is reported in Fig. 5b.

The most noticeable impact of modulating the unit cell dimension in the π-stacked direction (see Fig. 5a), or in other words in varying the rrP3HT/C_{60} packing density, is to modify the position of energy levels. A decrease in d causes a simultaneous displacement of HOMO and LUMO levels of rrP3HT toward higher binding energy (BE) by approximately the same amount, while the splitting between the three C_{60} states increases with their shift toward lower BE. These energy shifts are consistent with the trend and magnitude of the total induced dipole moment variation observed at a pentacene–fullerene heterojunction upon reduction of the intermolecular distance [53]. The direct consequences of these shifts are (1) a decrease of $\Delta\epsilon_{LUMO}$ for the blend when d decreases, i.e. a decrease in the energy offset between LUMOs of the donor (rrP3HT) and the acceptor (C_{60}) and (2) an increase in energy separation between $HOMO^{rrP3HT}$ and empty states of C_{60} ($LUMO^{C60}$) with a decreasing d. Finally, energy shifts observed for HOMO and LUMO of rrP3HT with a variation of d leave the band gap of rrP3HT nearly constant.

The band gap of rrP3HT and the $HOMO^{rrP3HT}$—$LUMO^{C60}$ separation have their own importance in the photovoltaic process : the rrP3HT band gap is an approximation of the optical gap for the photon absorption by the donor component in the BHJ; and the $HOMO^{rrP3HT}$—$LUMO^{C60}$ separation is proportional to the maximum theoretical open-circuit voltage (V_{oc}) of the organic photovoltaic cell [54]. To maximize the efficiency of the device, the optical gap has to be minimized to allow the harvesting of a broader range of the solar spectrum while V_{oc}, which limits the efficiency of state-of-art bulk heterojunction organic photovoltaic cells, has to be maximized. Although a concurrent optimization of both parameters remains a difficult task, it is facilitated by employing a bulk heterojunction to decouple the optical band gap from V_{oc} [55]. For example, new acceptor materials are being developed to raise their LUMO level in order to optimize simultaneously both parameters [56].

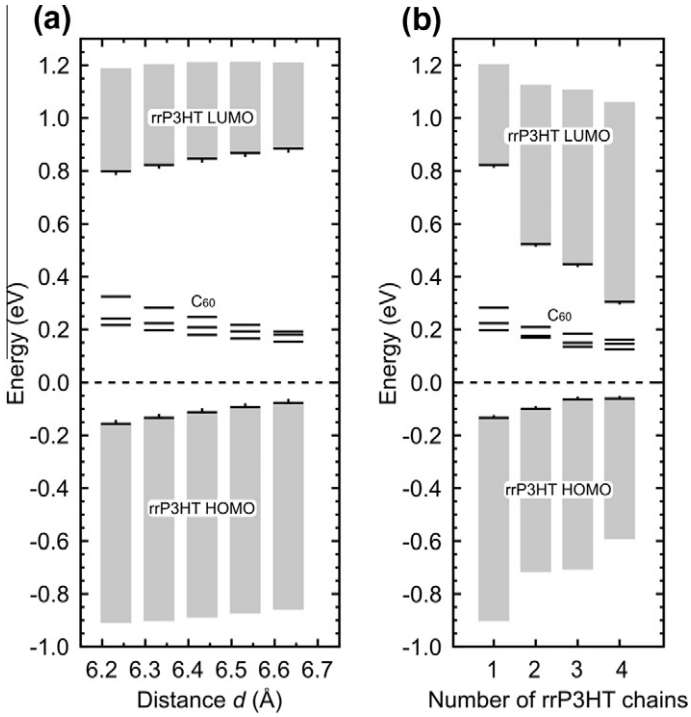

Fig. 5. Diagrams of the rrP3HT HOMO and LUMO and of the three C_{60} energy levels taken at Γ for a BHJ in configuration I as a function of (a) the distance d and (b) the number of rrP3HT chains in the crystal domain.

From Fig. 5a, artificially increasing the pressure on the unit cell in the π-stacked direction to reduce the dimension d would not modulate the optical gap and therefore it cannot rectify the mismatch between the solar spectrum and the rrP3HT absorption spectrum [57]. Nonetheless, a reduction of the interface distance d would still noticeably increase the efficiency of the organic photovoltaic cell through an increase of V_{oc} since the efficiency is more sensitive to a variation of V_{oc} than to a variation of the donor band gap [54].

The influence of rrP3HT crystal domain size as shown in Fig. 2 on the electronic properties of the BHJ is reported in Fig. 5b. The bottom of the LUMO band of rrP3HT is displaced toward higher BE by approximately 0.54 eV when the number of rrP3HT chains goes from 1 to 4, which also results in a major increase of its bandwidth and a large decrease of the rrP3HT band gap. The trend observed for the rrP3HT band gap with respect to the number of chains in the polymer π-stack will converge rapidly to the band gap value of the rrP3HT crystal. Considering π-stacked molecular systems, the band gap usually converges within 10 stacked molecules [58,59]. The calculated decrease of rrP3HT band gap (~ 0.6 eV) upon the formation of a π-crystal domain is consistent with the significant redshift observed experimentally (~ 0.5 eV) with the presence of H-aggregation [25]. Since we have considered periodic rrP3HT into the π-conjugated backbone direction which also contributes to maximize the π—π interactions between chains, the agreement with experimental results obtained on H-aggregates in solution is quite satisfying. Furthermore, the lowering of the rrP3HT LUMO band pushes the three C_{60} states toward higher BE which, combined with the shift of the top HOMO band toward lower BE, closes the $HOMO^{rrP3HT}$—$LUMO^{C60}$ separation. In contrast to the influence of d, an increasing size of rrP3HT crystal domains induces a significant decrease of rrP3HT band gap, and would also significantly decrease the value of V_{oc}. The variation of the rrP3HT band gap and $HOMO^{rrP3HT}$—$LUMO^{C60}$ separation have the same trend which suggests that the optical gap and V_{oc} cannot be optimized simultaneously. These theoretical results clearly reproduce and explain the V_{oc} decrease and the increase of spectral overlap with solar emission observed upon the formation of rrP3HT crystallite following the annealing of the BHJ [12,60].

It is also possible to notice in Fig. 5b an increase of the $LUMO^{rrP3HT}$ bandwidth with increasing rrP3HT crystal domain size, while an overall decrease of the $HOMO^{rrP3HT}$ bandwidth is observed simultaneously. Increasing the rrP3HT crystal domain size increases the number of $HOMO^{rrP3HT}$ like and $LUMO^{rrP3HT}$ like states between nearly fixed C_{60} states. Furthermore, due to the respective symmetry of the $HOMO^{rrP3HT}$ and $LUMO^{rrP3HT}$, the former is not allowed to cross the lower lying C_{60} states which forces a reduction of the $HOMO^{rrP3HT}$ bandwidth, while the latter is allowed to cross the higher lying C_{60} states which helps to increase the $LUMO^{rrP3HT}$ bandwidth.

4. Conclusions

We have investigated the structural and electronic properties of bulk heterojunctions formed by the inclusion of C_{60} in a rrP3HT π-crystal network. Among the different rrP3HT/C_{60} configurations considered, we found a cohesive

energy of around 1.9 eV per unit cell which is not significantly influenced by the relative position and orientation of the C_{60} molecule along the polymer chain. An increase in the size of crystal domain of rrP3HT induces the appearance of π-electron delocalization in both π-stacked and conjugated backbone directions. We have theoretically altered the levels alignment through a modulation of the interface distance between the nearest rrP3HT chain and the C_{60} molecule, and we corroborated the strong influence of the number of rrP3HT chains in the crystal domain mixed with C_{60} on the rrP3HT band gap and V_{oc}. These results suggest a potential optimization of photovoltaic devices through the use of an engineered mixture of C_{60} and nanostructured rrP3HT crystal domains.

Further calculations involving the presence of excited states (excitons) within the BHJ system are necessary to support this ground state band alignment, and to understand the influence of structural organization on the photophysical properties of excitons in such bulk heterojunction.

Acknowledgments

This work was supported by the Natural Sciences and Engineering Research Council of Canada (NSERC). Computational resources were provided by the Réseau québécois de calcul de haute performance (RQCHP) and Compute Canada. Arnaud Maillard is grateful to the Fonds Québécois de la Recherche sur la Nature et les Technologies (FQRNT) and to the NSERC for financial support.

References

[1] R. Kannan, K.C. Leong, R. Osman, H.K. Ho, Life cycle energy, emissions and cost inventory of power generation technologies in Singapore, Renewable Sustainable Energy Rev. 11 (2007) 702–715.
[2] N.S. Sariciftci, L. Smilowitz, A.J. Heeger, F. Wudl, Photoinduced electron transfer from a conducting polymer to buckminsterfullerene, Science 258 (1992) 1474–1476.
[3] C.J. Brabec, Organic photovoltaics: technology and market, Sol. Energy Mater. Sol. Cells 83 (2004) 273–292.
[4] A.C. Mayer, S.R. Scully, B.E. Hardin, M.W. Rowell, M.D. McGehee, Polymer-based solar cells, Mater. Today 10 (2007) 28–33.
[5] N.S. Sariciftci, Plastic photovoltaic devices, Mater. Today 7 (2004) 36–40.
[6] N.S. Lewis, Toward cost-effective solar energy use, Science 315 (2007) 798–801.
[7] H. Larsen, L. Sønderberg Petersen, RisøEnergy Report 5, 2006.
[8] Solarmer Energy Inc., Press Release, December 2, 2009.
[9] M.A. Green, K. Emery, Y. Hishikawa, W. Warta, Solar cell efficiency tables (version 35), Prog. Photovoltaics Res. Appl. 18 (2010) 144–150.
[10] J.K. Lee, W.L. Ma, C.J. Brabec, J. Yuen, J.S. Moon, J.Y. Kim, K. Lee, G.C. Bazan, A.J. Heeger, Processing additives for improved efficiency from bulk heterojunction solar cells, J. Am. Chem. Soc. 130 (2008) 3619–3623.
[11] J. Peet, J.Y. Kim, N.E. Coates, W.L. Ma, D. Moses, A.J. Heeger, G.C. Bazan, Efficiency enhancement in low-bandgap polymer solar cells by processing with alkane dithiols, Nat. Mater. 6 (2007) 497–500.
[12] G. Dennler, M.C. Scharber, C.J. Brabec, Polymer–fullerene bulk-heterojunction solar cells, Adv. Mater. 21 (2009) 1323–1338.
[13] S. Morita, A.A. Zakhidov, K. Yoshino, Doping effect of buckminsterfullerene in conducting polymer: change of absorption spectrum and quenching of luminescence, Solid State Commun. 82 (1992) 249–252.
[14] C.J. Brabec, N.S. Sariciftci, J.C. Hummelen, Plastic solar cells, Adv. Funct. Mater. 11 (2001) 15–26.
[15] G. Yu, J. Gao, J.C. Hummelen, F. Wudl, A.J. Heeger, Polymer photovoltaic cells: enhanced efficiencies via a network of internal donor–acceptor heterojunctions, Science 270 (1995) 1789–1791.
[16] J.K. Lee, Y.-M. Wang, S. Cho, F. Wudl, A.J. Heeger, New approach for forming bulk-heterojunction solar cells comprising a π-conjugated polymer and C60, Org. Electron. 10 (2009) 1223–1227.
[17] K. Itaka, M. Yamashiro, J. Yamaguchi, M. Haemori, S. Yaginuma, Y. Matsumoto, M. Kondo, H. Koinuma, High-mobility C60 field-effect transistors fabricated on molecular-wetting controlled substrates, Adv. Mater. 18 (2006) 1713–1716.
[18] C. Waldauf, P. Schilinsky, M. Perisutti, J. Hauch, C.J. Brabec, Solution-processed organic n-type thin-film transistors, Adv. Mater. 15 (2003) 2084–2088.
[19] R.L. Elsenbaumer, K.Y. Jen, R. Oboodi, Processible and environmentally stable conducting polymers, Synth. Met. 15 (1986) 169–174.
[20] T.J. Prosa, M.J. Winokur, J. Moulton, P. Smith, A.J. Heeger, X-ray structural studies of poly(3-alkylthiophenes): an example of an inverse comb, Macromolecules 25 (1992) 4364–4372.
[21] S.V. Meille, V. Romita, T. Caronna, A.J. Lovinger, M. Catellani, L. Belobrzeckaja, Influence of molecular weight and regioregularity on the polymorphic behavior of poly(3-decylthiophenes), Macromolecules 30 (1997) 7898–7905.
[22] H. Sirringhaus, P.J. Brown, R.H. Friend, M.M. Nielsen, K. Bechgaard, B.M.W. Langeveld-Voss, A.J.H. Spiering, R.A.J. Janssen, E.W. Meijer, P. Herwig, D.M. de Leeuw, Two-dimensional charge transport in self-organized, high-mobility conjugated polymers, Nature 401 (1999) 685–688.
[23] Y. Kim, S. Cook, S.M. Tuladhar, S.A. Choulis, J. Nelson, J.R. Durrant, D.D.C. Bradley, M. Giles, I. McCulloch, C.-S. Ha, M. Ree, A strong regioregularity effect in self-organizing conjugated polymer films and high-efficiency polythiophene:fullerene solar cells, Nat. Mater. 5 (2006) 197–203.
[24] F.C. Spano, J. Clark, C. Silva, R.H. Friend, Determining exciton coherence from the photoluminescence spectral line shape in poly(3-hexylthiophene) thin films, J. Chem. Phys. 130 (2009) 074904.
[25] J. Clark, C. Silva, R. Friend, F. Spano, Role of intermolecular coupling in the photophysics of disordered organic semiconductors: aggregate emission in regioregular polythiophene, Phys. Rev. Lett. 98 (2007) 1–4.
[26] A. Maillard, A. Rochefort, Structural and electronic properties of poly(3-hexylthiophene)-stacked crystals, Phys. Rev. B: Condens. Matter Mater. Phys. 79 (2009) 115207.
[27] J.M. Soler, E. Artacho, J. Gale, A. García, J. Junquera, P. Ordejón, D. Sánchez-Portal, The SIESTA method for ab initio order-N materials simulation, J. Phys.: Condens. Matter 14 (2002) 2745–2779.
[28] A. Rochefort, J.D. Wuest, Interaction of substituted aromatic compounds with graphene, Langmuir 25 (2009) 210–215.
[29] M. Hasegawa, K. Nishidate, Semiempirical approach to the energetics of interlayer binding in graphite, Phys. Rev. B: Condens. Matter Mater. Phys. 70 (2004) 205431.
[30] M. Dion, H. Rydberg, E. Schröder, D. Langreth, B. Lundqvist, van der Waals density functional for general geometries, Phys. Rev. Lett. 92 (2004) 246401.
[31] G. Román-Pérez, J.M. Soler, Efficient implementation of a van der Waals density functional: application to double-wall carbon nanotubes, Phys. Rev. Lett. 103 (2009) 096102.
[32] F. Bo, Relationship between the structure of C60 and its lubricity: a review, Lubr. Sci. 9 (1997) 181–193.
[33] Y. Kanai, J.C. Grossman, Insights on interfacial charge transfer across P3HT/fullerene photovoltaic heterojunction from ab initio calculations, Nano Lett. 7 (2007) 1967–1972.
[34] P.W. Stephens, L. Mihaly, P.L. Lee, R.L. Whetten, S.-M. Huang, R. Kaner, F. Deiderich, K. Holczer, Structure of single-phase superconducting K3C60, Nature 351 (1991) 632–634.
[35] L. Scifo, M. Dubois, M.E.L. Brun, P. Rannou, S. Latil, A. Rubio, B. Grévin, Probing the electronic properties of self-organized poly(3-dodecylthiophene) monolayers by two-dimensional scanning tunneling spectroscopy imaging at the single chain scale, Nano Lett. 6 (2006) 1711–1718.
[36] B. Grévin, P. Rannou, R. Payerne, A. Pron, J.-P. Travers, Scanning tunneling microscopy investigations of self-organized poly(3-hexylthiophene) two-dimensional polycrystals, Adv. Mater. 15 (2003) 881–884.
[37] M. Brinkmann, P. Rannou, Effect of molecular weight on the structure and morphology of oriented thin films of regioregular poly(3-hexylthiophene) grown by directional epitaxial solidification, Adv. Funct. Mater. 17 (2007) 101–108.
[38] M. Brinkmann, P. Rannou, Molecular weight dependence of chain packing and semicrystalline structure in oriented films of regioregular poly(3-hexylthiophene) revealed by high-resolution transmission electron microscopy, Macromolecules 42 (2009) 1125–1130.

[39] A.C. Mayer, M.F. Toney, S.R. Scully, J. Rivnay, C.J. Brabec, M. Scharber, M. Koppe, M. Heeney, I. McCulloch, M.D. McGehee, Bimolecular crystals of fullerenes in conjugated polymers and the implications of molecular mixing for solar cells, Adv. Funct. Mater. 19 (2009) 1173–1179.
[40] J. Zhao, A. Swinnen, G. Van Assche, J. Manca, D. Vanderzande, B. Van Mele, Phase diagram of P3HT/PCBM blends and its implication for the stability of morphology, J. Phys. Chem. B 113 (2009) 1587–1591.
[41] W.D. Oosterbaan, V. Vrindts, S. Berson, S. Guillerez, O. Douhéret, B. Ruttens, J. D'Haen, P. Adriaensens, J. Manca, L. Lutsen, D. Vanderzande, Efficient formation, isolation and characterization of poly(3-alkylthiophene) nanofibres: probing order as a function of side-chain length, J. Mater. Chem. 19 (2009) 5424.
[42] S. van Bavel, E. Sourty, G. de With, S. Veenstra, J. Loos, Three-dimensional nanoscale organization of polymer solar cells, J. Mater. Chem. 19 (2009) 5388.
[43] R.J. Kline, M.D. McGehee, E.N. Kadnikova, J. Liu, J.M.J. Fréchet, M.F. Toney, Dependence of regioregular poly(3-hexylthiophene) film morphology and field-effect mobility on molecular weight, Macromolecules 38 (2005) 3312–3319.
[44] X. Yang, J. Loos, S.C. Veenstra, W.J.H. Verhees, M.M. Wienk, J.M. Kroon, M.A.J. Michels, R.A.J. Janssen, Nanoscale morphology of high-performance polymer solar cells, Nano Lett. 5 (2005) 579–583.
[45] R.J. Kline, M.D. McGehee, Morphology and charge transport in conjugated polymers, J. Macromol. Sci. Part C: Polym. Rev. 46 (2006) 27–45.
[46] K. Tashiro, I. Tanaka, T. Oohara, N. Niimura, Extraction of hydrogen-atom positions in polyethylene crystal lattice from wide-angle neutron diffraction data collected by a two-dimensional imaging plate system: comparison with the X-ray and electron diffraction results, Macromolecules 37 (2004) 4109–4117.
[47] K. Tashiro, M. Kobayashi, T. Kawai, K. Yoshino, Crystal structural change in poly(3-alkyl thiophene)s induced by iodine doping as studied by an organized combination of X-ray diffraction, infrared/Raman spectroscopy and computer simulation techniques, Polymer 38 (1997) 2867–2879.
[48] T.J. Prosa, M.J. Winokur, R.D. McCullough, Evidence of a novel side chain structure in regioregular poly(3-alkylthiophenes), Macromolecules 29 (1996) 3654–3656.
[49] N. Kayunkid, S. Uttiya, M. Brinkmann, Structural model of regioregular poly(3-hexylthiophene) obtained by electron diffraction analysis, Macromolecules 43 (2010) 4961–4967.
[50] X.-B. Wang, C.-F. Ding, L.-S. Wang, High resolution photoelectron spectroscopy of C60, J. Chem. Phys. 110 (1999) 8217–8220.
[51] B.C. Thompson, J.M.J. Fréchet, Polymer–fullerene composite solar cells, Angew. Chem. Int. Ed. 47 (2008) 58–77.
[52] K.L. Mutolo, E.I. Mayo, B.P. Rand, S.R. Forrest, M.E. Thompson, Enhanced open-circuit voltage in subphthalocyanine/C60 organic photovoltaic cells, J. Am. Chem. Soc. 128 (2006) 8108–8109.
[53] M. Linares, D. Beljonne, J. Cornil, K. Lancaster, J.-L. Brédas, S. Verlaak, A. Mityashin, P. Heremans, A. Fuchs, C. Lennartz, J. Idé, R. Méreau, P. Aurel, L. Ducasse, F. Castet, On the interface dipole at the pentacene–fullerene heterojunction: a theoretical study, J. Phys. Chem. C 114 (2010) 3215–3224.
[54] M. Scharber, D. Mühlbacher, M. Koppe, P. Denk, C. Waldauf, A.J. Heeger, C.J. Brabec, Design rules for donors in bulk-heterojunction solar cells towards 10% energy-conversion efficiency, Adv. Mater. 18 (2006) 789–794.
[55] A. Moliton, Optoelectronics of Molecules and Polymers, Springer, New York, 2006.
[56] F.B. Kooistra, J. Knol, F. Kastenberg, L.M. Popescu, W.J.H. Verhees, J.M. Kroon, J.C. Hummelen, Increasing the open circuit voltage of bulk-heterojunction solar cells by raising the LUMO level of the acceptor, Org. Lett. 9 (2007) 551–554.
[57] K.M. Coakley, M.D. McGehee, Conjugated polymer photovoltaic cells, Chem. Mater. 16 (2004) 4533–4542.
[58] A. Rochefort, P. Boyer, Tailoring electronic and charge transport properties of molecular pi-stacked heterojunctions, Appl. Phys. Lett. 89 (2006) 092115.
[59] A. Rochefort, P. Boyer, B. Nacer, Resonant tunneling transport in highly organized oligoacene assemblies, Org. Electron. 8 (2007) 1–7.
[60] V.D. Mihailetchi, H. Xie, B. de Boer, L.J.A. Koster, P.W.M. Blom, Charge transport and photocurrent generation in poly(3-hexyl-thiophene): methanofullerene bulk-heterojunction solar cells, Adv. Funct. Mater. 16 (2006) 699–708.

Organic Electronics 11 (2010) 1999–2011

Contents lists available at ScienceDirect

Organic Electronics

journal homepage: www.elsevier.com/locate/orgel

Impact of energy alignment and morphology on the efficiency in inorganic–organic hybrid solar cells

M. Gruber [a,b,*], B.A. Stickler [a,b], G. Trimmel [b], F. Schürrer [a], K. Zojer [a,**]

[a] Institute of Theoretical and Computational Physics, Graz University of Technology, Petersgasse 16, 8010 Graz, Austria
[b] Institute for Chemistry and Technology of Materials and Christian Doppler Laboratory for Nanocomposite Solar Cells, Graz University of Technology, Stremayrgasse 9, 8010 Graz, Austria

ARTICLE INFO

Article history:
Received 14 July 2010
Received in revised form 12 August 2010
Accepted 23 August 2010
Available online 25 September 2010

Keywords:
Hybrid inorganic–organic solar cells
Drift diffusion
Two-dimensional model

ABSTRACT

Carrier transport in hybrid inorganic–organic solar cells has been studied by means of a two-dimensional drift-diffusion-based model including the generation and motion of excitons. The devices consist of a polymer serving as donor material and a semiconducting small-band gap inorganic component as acceptor material. For the first time it is taken into account that, in strong contrast to purely organic or inorganic cells, charge carriers can be generated at the heterojunction (due to dissociation of the donor excitons) *and* in the bulk of the acceptor material (due to band to band generation in the inorganic material). The efficiencies of devices were investigated dependent on (i) the donor–acceptor interface geometry, (ii) the transport level offsets at the heterojunction, and (iii) the energy barriers formed at the contacts. For each case, a detailed analysis of the behavior is given. We demonstrate that, depending on the particular scenario, each of these three factors can be responsible for profoundly reduced efficiencies and pronounced s-shaped sections in the *I–V* curves. Moreover, we show that each of the investigated factors may give rise to equally serious efficiency losses. However, it is not possible to identify a dominant effect. Depending on the particular combination, the efficiency can vary by two orders of magnitudes. In order to avoid such losses, our theoretical assessment reveals that suitable material combinations are required to form (i) ohmic contacts, (ii) preclude formation of isolated islands or nanoparticles during growth, and (iii) possess a hole-blocking offset in the transport levels at the heterojunction.

© 2010 Elsevier B.V. All rights reserved.

1. Introduction

Inorganic–organic hybrid solar cells (hsc) represent one of the currently persued routes to produce low-cost solar cells. The introduction of an inorganic component rather than an organic material promises a good control over the morphology to arrive at an interdigited heterointerface, e.g., by incorporating nanowires of ZnO or TiO_2 [1,2] as acceptor materials. To combine these advantages with the desire to efficiently harvest sun light, the absorption spectra of the organic and inorganic phase are required to cover the solar spectrum in a preferably complementary fashion. One promising route to achieve this is to employ an organic material that covers the high-irradiance portion of the solar spectrum, i.e., visible light between 1.7 and 3.0 eV, and an inorganic component that absorbs in the long-wavelength tail well below 1.7 eV. Suitable inorganic semiconductors are, e.g., CdSe , CdTe, and $CuInS_2$ [3,4]. In hsc containing these materials, the organic and inorganic phase contribute differently to charge carrier generation. Upon light absorption, excitons are formed in the organic phase and need to diffuse to the heterojunction interface within their lifetime in order to dissociate into free

* Corresponding author.
** Principal Corresponding author.
E-mail addresses: gruberm@sbox.tugraz.at (M. Gruber), karin.schmidt@tugraz.at (K. Zojer).

1566-1199/$ - see front matter © 2010 Elsevier B.V. All rights reserved.
doi:10.1016/j.orgel.2010.08.015

charges. In the inorganic semiconductor, carriers are generated directly via band-to-band absorption throughout the bulk. Therefore, the question arises to which extent these two strongly differing generation mechanisms influence the efficiency of such cells. In particular, the impact on efficiency-related factors such as morphology, contact materials, and transport level alignment requires detailed investigation.

Hybrid inorganic–organic heterojunctions can be prepared in several distinct types of morphologies: Besides bilayer structures, (i) nanoporous inorganic templates infiltrated with polymers and (ii) blends of organic polymers co-deposited with inorganic (isotropic) nanoparticles or nanorods have been prepared. A comprehensive overview can be found, e.g., in Refs. [1b,2a]. Morphologies in which the photoactive materials are segregated perpendicular to the electrodes are particularly sought after, since this vertical alignment reduces shortenings and recombination [1e,2a]; such structures were achieved by co-deposition [4(b–f)] or a template approach [1a,4(g,h)]. Compared to hybrid bilayer structures, blend devices usually exhibit relatively low open-circuit voltages and fill factors, cf., e.g., Ref. [1a]. Devices made of blends containing nanorods of high aspect ratios systematically outperform nanoparticle blends in terms of short circuit currents, open circuit voltages, and higher efficiencies [1a,4(e,f)]. The performance of excitonic solar cells consisting either of hybrid blends/template structures containing wide bandgap inorganic semiconductors such as ZnO or TiO_2 [1a] or pure organic blends (containing C_{60}-derivatives or small molecules) [4j] is strongly dependent on the morphology. Previous studies related this effect to (i) an effective generation efficiency [5–7], (ii) the apparent length of the interface available for exciton cleavage [1a,8–13], (iii) the connectivity of transport paths [15], and (iv) a change in the effective mobility [16]. Moreover, the occurrence of an s-shaped *I–V* curve [1(a,b),9,14,17–19] has been linked to the selectivity of the contact materials [9,18], and the alignment of transport levels [19].

The optimization of the morphologies in purely excitonic solar cell targets structure sizes being comparable to typical exciton diffusion lengths of ca. 15 nm [1b]. The use of low-band gap inorganic materials can presumably obliterate the need for such small inorganic domain sizes, since generation due exciton migration is replaced by carrier generation in the bulk. Then, large inorganic domains offer the advantages of (i) providing efficient carrier generation due to bulk generation, (ii) a more efficient carrier abstraction at the contacts and, thus, less efficient recombination due to higher intrinsic mobilities, (iii) ensuring a better connectivity [4a], and, (iv) presumably leading to a higher average carrier mobility due to a significantly reduced number of interparticle hops [4a].

The main aim of this work is to theoretically investigate the impact of (i) cell morphology, (ii) transport level alignment, and (iii) choice of contacts on the carrier transport and, consequently, the efficiency of such hybrid inorganic–organic solar cells. Under consideration of the two charge generation mechanisms, the abovementioned effects were cast into a two-dimensional drift-diffusion model for both charge carrier and exciton transport. Based on this model, current–density voltage (*I–V*) curves of the entire device were simulated. The devices studied below consist of $CuInS_2$ as prototypical acceptor and P3EBT (poly[3-(ethyl-4-butanoate)thiophene-2,5-diyl]) as donor material (Fig. 1(d)). From a theoretical point of view, the combination of P3EBT with $CuInS_2$ is particularly intriguing due to a vanishing offset between the hole transport levels. Such a level alignment cannot be encountered in hsc based on wide-band gap semiconductors, such as ZnO and TiO_2. P3EBT can be of potential practical relevance due to an improved processability in comparison to the archetypical P3HT (poly(3-hexylthiophene)).

After introducing the details of the model, we will investigate the impact of the interface morphology on the carrier transport for selected heterojunction geometries. In a next step, the degeneracy in the hole transport levels is lifted to point out the impact of transport level alignment. In a last series of simulations, the dependence of the *I–V* curves and the power conversion efficiency on the nature of the imposed contacts is studied for the chosen representative morphologies. Based on these simulations we will derive criteria for material properties according to which major efficiency losses can be avoided.

2. The model

To get a deeper understanding of the device behavior due to variations (i) of the transport level offsets between the donor and acceptor material and (ii) their interface morphology, as well as the role of bulk vs. interface carrier generation, a two-dimensional drift-diffusion model for the device simulation is proposed. Such a two-dimensional model offers the possibility to regard actual morphologies such as isolated particles or ideal, i.e., interdigitated structures. Note that the feature size of the assumed interface geometries must be sufficiently large (ca. 15–20 nm) in order to define valid material parameters for the photoactive components as model input. Typical structure sizes in nanocomposite hybrid inorganic–organic solar cells are 5–20 nm for particle diameters, domain sizes, and nanorod diameters; nanorods of high aspect ratio are ca. 50–100 nm long [1b,2a]. Thus, it is possible to construct artifical interface geometries that represent limiting cases of real morphologies and feature structure sizes known from actual heterojunctions.

In contrast to drift-diffusion models, microscopic simulations are able to safely tackle morphologies with typical length scales below 15 nm. However, due to the extensive computational costs, most of the publications focus on interface generation and recombination processes [5,6,20,21]. Apart from the pioneering works of Marsh et al. [5] and Meng et al. [21a], subsequent carrier transport is not evaluated at the same level of complexity. Rather, it is either described by means of equivalent circuit models [21b] or by one-dimensional drift-diffusion models [16]. The former is not able to reflect a departure of the *I–V* curve from the ideal diode characteristic and the latter cannot take into account the actual morphology. Given that the hybrid inorganic–organic systems exhibit generation not only at the interface but also throughout the bulk,

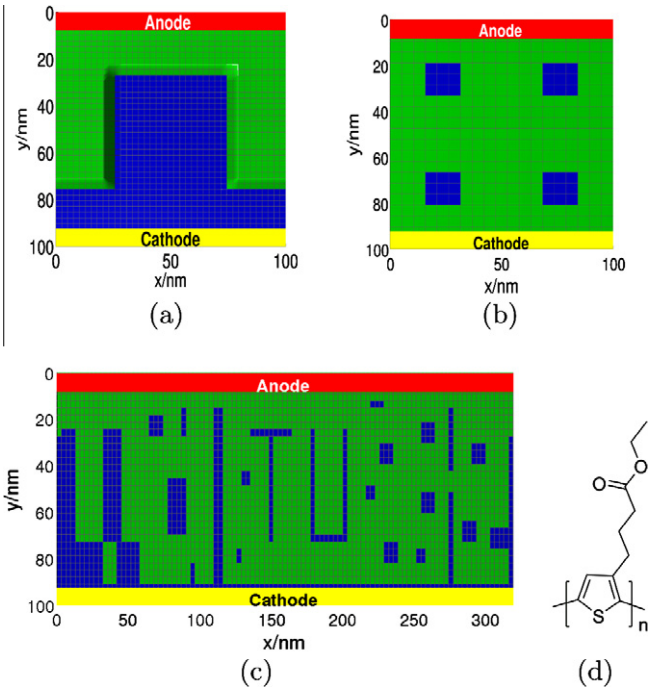

Fig. 1. Interface morphologies: (a) comblike structure, (b) single nanoparticle structure, and (c) a superposition of (a) and (b). The area corresponding to the donor (P3EBT) is indicated in green (/light gray), the one of the acceptor ($CuInS_2$) in blue (/dark gray). (d) Schematic structure of P3EBT. (For interpretation of references to color in this figure legend, the reader is referred to see the web version of this article.)

models as proposed in Refs. [5,21a] are neither computationally feasible nor are they suited to immediately interpret the results in terms of relevant macroscopic transport parameters.

Charge transport equations: In a drift-diffusion model, the motion of the charge carriers is caused by the electric field and carrier density gradients. The resulting current density is carried by electrons and holes in their respective transport levels. According to [22], the current density reads

$$\mathbf{J}(x,y) = \mathbf{J}_p(x,y) + \mathbf{J}_n(x,y) \tag{1}$$

with

$$\mathbf{J}_{n(p)}(x,y) = qn[/p](x,y)\mu_{n(p)}(x,y)\mathbf{E}_{n(p)}(x,y) \pm D_{n(p)}(x,y)q\nabla n[/p](x,y). \tag{2}$$

Here, $\mu_{n(p)}(x,y)$ denotes the electron (hole) mobility; k_B, the Boltzmann constant; T, the temperature; and q, the elementary charge ($q > 0$). Moreover, $n(x,y)$ and $p(x,y)$ are the density distributions and $\mathbf{E}_{n(p)}(x,y)$ the generalized electric fields (for definition see below) for electrons and holes, respectively. The electron (hole) diffusion constant is defined by the Einstein relation:

$$D_{n(p)} = \mu_{n(p)}(x,y)k_BT/q. \tag{3}$$

The current densities are coupled with the continuity equation for electrons and holes

$$\frac{\partial n[/p](x,y)}{\partial t} \mp \frac{1}{q}\nabla \mathbf{J}_{n(p)}(x,y) = G(x,y) - R(x,y) \tag{4}$$

where $G(x,y)$ and $R(x,y)$ are the charge carrier generation and recombination terms.

Generalized potentials: By defining a generalized potential $\widehat{\Psi}_{n(p)}$, the actual electrostatic potential Ψ and the "driving forces" excerted on the carrier at the heterojunction can be cast into one quantity [23,24]:

$$\widehat{\Psi}_{n(p)}(x,y) = \Psi(x,y) - \Theta_{n(p)}(x,y)/q. \tag{5}$$

Herein, the potential $\Psi(x,y)$, resulting from the Poisson equation

$$\nabla[\epsilon_0\epsilon_r(x,y)\nabla\Psi(x,y)] = q[n(x,y) - p(x,y)], \tag{6}$$

is caused by the charges in the active layer and the effective applied voltage V at the electrodes; ϵ_0 is the dielectric constant of vacuum and $\epsilon_r(x,y)$ the relative dielectric constant. V is the difference of the external applied voltage and the built-in voltage. At the non-conducting surfaces periodic boundary conditions were imposed. The additional terms $\Theta_{n(p)}(x,y)$ in Eq. (5) are the band parameters that are associated to the spatial energetic alignment of the transport levels [23,24]. In disordered materials, $\Theta_{n(p)}(x,y)$ is directly given by the relative spatial alignment of the transport levels [23]. For convinience, we set the band parameters to zero in the organic donor ($\Theta_{n(p)} = 0$) and to the transport level offsets in the inorganic acceptor ($\Theta_n = E_C - \text{LUMO}$; $\Theta_p = E_V - \text{HOMO}$). Thus, the generalized potential multiplied by the charge of the carrier yields the actual potential energy landscape in which the carrier traverses the device. Carrying out the spatial derivative of the generalized potential yields a generalized electric field that was formally introduced in Eq. (2):

$$\mathbf{E}_{n(p)}(x,y) = -\nabla \widehat{\Psi}_{n(p)}(x,y). \quad (7)$$

It consists of the true electric field across the device superimposed with an additional term occurring solely at the interface. For abrupt heterojunctions, this generalized electric field has no physical meaning due to the singularity at the interface. However, once cast in the final form, the transport equations (2) and (4) contain the generalized potential rather than its spatial derivative [24]. The associated terms account for the "driving force" acting on the carrier at the interface [23]; they penalize uphill and encourage downhill motion by means of an exponential factor containing the potential difference.

Recombination rates: The recombination term in Eq. (4) is assumed to be of Langevin type which reads

$$R(x,y) = \gamma n(x,y)p(x,y) \quad (8)$$

with $\gamma = q\mu/\epsilon_0\epsilon_r$ and $\mu = min[\mu_p, \mu_n]$ [25,26]. Note that this rate expression does not allow to explicitely discriminate between geminate pair and nongeminate pair recombination.

Generation rates and exciton motion: Assuming a Lambert–Beer type absorption profile across the device, an absorption rate $A(x,y)$ accounting for the number of photons absorbed per second and volume can be introduced as

$$A(x,y) = \int_0^{\frac{hc}{E_{gap}}} \Phi_0(\lambda)\frac{\lambda\alpha(\lambda)}{hc}e^{-\alpha(\lambda)x}d\lambda. \quad (9)$$

where $\alpha(\lambda)$ denotes the absorption coefficient related to the organic and inorganic species; c, the speed of light; h, the Planck constant; E_{gap}, the optical bandgap; and $\Phi_0(\lambda)$, the solar spectrum used (AM 1.5 with 1000 Wm^{-2}). In this formulation, Eq. (9) yields the photon number as a function of the material-dependent absorption and, in reasonable first approximation, the morphology of the device. As we intend to focus on investigating the role of the morphology for *carrier transport*, we will exclude additional morphology-related effects that may originate from strongly spatially varying absorption profiles [27] by introducing the following simplifications: (i) α enters Eq. (9) as a wavelength- and material-independent parameter and (ii) the optical band gap E_{gap} is treated as material-independent. This means that both materials are considered to be capable of absorbing the same number of photons per volume and time. Then, the actual number of photons absorbed anywhere in the device is only determined by Lambert–Beer's law, i.e., is solely dependent on the position of the considered volume element with respect to the transparent electrode. The coefficient α is set to the representative value of 2×10^7 m^{-1}. With the help of the simplifications made above, we are able to compare also materials whose optical absorption is not known quantitatively.

In the inorganic phase, light absorption leads directly to free charges. The generation rate $G(x,y)$ associated to this process is, thus, directly given by $G(x,y) = A(x,y)$ [28]. Within the organic phase, the absorbed photons give rise to an exciton density distribution $ex(x,y)$. Since excitons have no charge, exciton migration, described by a flux density $\Phi_{ex}(x,y)$, is determined only by diffusion:

$$\Phi_{ex}(x,y) = -k_B T \mu_{ex} \nabla ex(x,y) \quad (10)$$

with μ_{ex} being the exciton mobility. The continuity equation contains an exciton generation rate $G_{ex}(x,y) = A(x,y)$ and has the form [29]

$$\frac{\partial ex(x,y)}{\partial t} + \frac{1}{q}\nabla(\Phi_{ex}(x,y)) = G_{ex}(x,y) + \frac{1}{4}R(x,y) - R_{ex}(x,y) - G(x,y). \quad (11)$$

Herein, an exciton recombination rate R_{ex} is defined as

$$R_{ex}(x,y) = \frac{ex(x,y)}{\tau_{ex}} \quad (12)$$

where τ_{ex} is the exciton lifetime. Carrier recombination $R(x,y)$ (cf. Eq. (4)) can give rise to the formation of singlet excitons and, thus, increases the exciton density. Thus, the fraction of $R(x,y)$ yielding singlet states needs to be considered in Eq. (11) and is taken here as 1/4. Excitons dissociate into free charge carriers if they reach the organic–inorganic interface within their lifetime, i.e., the charge carrier generation rate $G(x,y)$ reads

$$G(x,y) = \begin{cases} 0, & x,y \text{ within organic material} \\ \frac{1}{\tau_{diss}} ex(x,y), & x,y \text{ at organic—inorganic interface.} \end{cases} \quad (13)$$

As a further simplification of Eqs. (10) and (12), the parameters μ_{ex} and τ_{ex} are set to fixed values. We chose the values to 3.86×10^{-6} m^2 V^{-1} s^{-1} and 1 ns [30], respectively, to arrive at a mean exciton diffusion length of 15 nm. The values of all constants used in our simulations to describe exciton formation and migration are summarized in Table 1.

The resulting coupled system of equations (Eqs. (2), (4)–(6), (10) and (11)) is solved self-consistently on a two-dimensional mesh with variable grid spacing by using the discretization of the current density equations according to Scharfetter and Gummel [31].

Important device parameters of solar cells are the fill factor (FF) and the power conversion efficiency (PCE) which are related to the open circuit voltage V_{oc}, the short circuit current density j_{sc}, the voltage V_{mpp}, and the current density j_{mpp} at the maximum power point by

$$FF = \frac{V_{mpp}j_{mpp}}{V_{oc}j_{sc}}$$

and

Table 1
Material parameters used in the device simulations

Donor: P3EBT HOMO/LUMO	−5.6 eV/−3.7 eV
Acceptor: $CuInS_2$ E_C/E_V	−5.6 eV/ −4.1 eV [32]
Relative dielectric constant: ϵ_r	3.0
Electron and hole mobility: $\mu_n = \mu_p$	10^{-8} $m^2/(V\,s)$
Exciton lifetime: τ_{ex}	1 nm [30]
Exciton mobility: μ_{ex}	3.86×10^{-6} $m^2/(V\,s)$
Absorption coefficient: α	2×10^7 m^{-1}
Optical bandgap: E_{gap}	1.5 eV
Hole concentration at the anode	10^{22} m^{-3}
Electron concentration at the cathode	10^{22} m^{-3}

$$PCE = \frac{V_{mpp} j_{mpp}}{P_{in}}$$

with P_{in} being the incident light power ($1000\,W/m^2$). All simulations were carried out for room temperature.

3. Results and discussion

At first, we define a model system that allows us to discriminate between the effects arising from (i) the cell morphology, (ii) the choice of contacts, and (iii) the transport level alignment. To prevent such effects to be obscured by a possible dependence on additional material parameters, we will use identical parameter values for the donor and acceptor phase whenever possible (see below).

In order to implement representative model morphologies, one needs to bear in mind that the shape of the interface between the organic donor and the inorganic acceptor material in nanocomposite solar cells depends strongly on the actual fabrication procedure, cf., e.g., [4(a–d)]. Such procedures aiming at obtaining a continuous phase of the acceptor material [1b,4(a–d)]. However, there are often acceptor nanoparticles that are fully surrounded by the organic material [4(a–d)]. Varying the processing conditions may give rise to many different degrees of conglomeration [4a,4b,4c,4d]. To capture the influence of such different interface morphologies, the following interface geometries were assumed in the simulation.

As a first limiting case, an interdigitated array of donor and acceptor, a "comb-like" structure, was considered (cf. Fig. 1(a)). Such a geometry ensures (i) continuous pathways for the charge carriers to travel from the interface to the contacts and (ii) promises the highest sensitivity of the short circuit current with respect to a varying digit width [33]. Nanoparticles entirely embedded into the donor polymer matrix are investigated as second limiting case (cf. Fig. 1(b)). Provided that the mobility of the phases can be assumed to be independent of the morphology, all other interface geometries can be considered as superpositions of interdigited phases and nanoparticles. A morphology as depicted in Fig. 1(c) is a mixture of a comblike and a single nanoparticle structure and may serve as a more realistic description of the donor–acceptor interface.

The material parameters assumed in the simulation are listed in Table 1. The position of the transport levels, i.e., the HOMO/LUMO levels of P3EBT, as determined from cyclovoltammetry, and E_C/E_V of $CuInS_2$ [32] are depicted in Fig. 2(a). The remaining transport-related parameters, the carrier mobilities and the dielectric constants, are not varied throughout the simulations. The impact of these quantities and variations thereof are beyond the scope of this paper. The mobility is set to be the same for electrons and holes and independent of the donor and acceptor. Eventhough the mobilities of the materials most likely differ from each other and change when tuning the interface structure in an actual device, our choice has, nevertheless, two advantages for the theoretical assessment: (i) We can independently study effects arising from the interface morphology and effects related to different mobilities in the donor and acceptor phase. Moreover, it guarantees that all considered morphologies are studied using the same set of mobility values. (ii) As will be shown in detail elsewhere [34], the ratio between the mobilities of the two materials has, as can be expected, a significant impact on the I–V characteristic. In the hybrid solar cells considered here, however, mobility effects can be shown to (i) occur largely independent from morphology-related effects and (ii) be less pronounced than the latter [34]. Also the dielectric constant is assumed to be identical in both materials. This simple choice constitutes a valid starting point for our investigations, since, as shown in detail elsewhere [34], the effect of differing dielectric constants on the I–V curve is independent of and less marked than the three factors studied below.

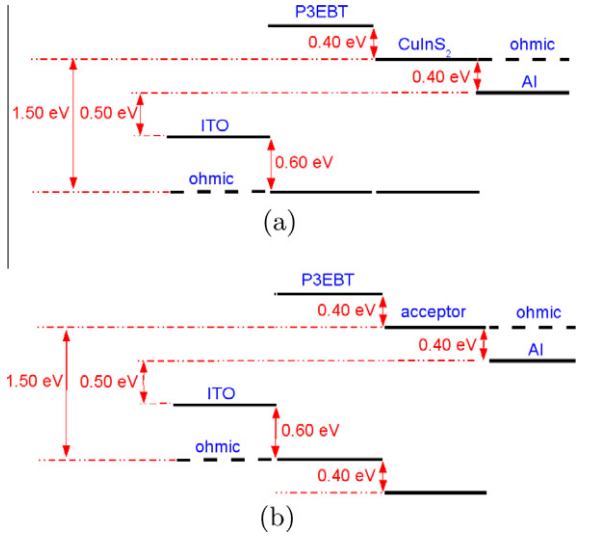

Fig. 2. Position of HOMO and LUMO levels in P3EBT and E_C, E_V for (a) $CuInS_2$ or (b) an idealized acceptor with equivalent transport level offsets with respect to P3EBT. Further shown is the alignment of the contact workfunctions corresponding to ohmic (dashed lines) contacts for holes towards P3EBT and for electrons towards the acceptor, or to an ITO anode and Al cathode (solid lines).

Two types of contacts were investigated. In a first case, ohmic contacts for holes towards P3EBT and electrons towards $CuInS_2$, respectively, were chosen (Fig. 2a). [35] In a second scenario, ITO as cathode and Al as anode were chosen as actual contacts. These contact materials give rise to substantial barriers for electrons and holes towards the contacts, cf. Fig. 2(a), i.e., form non-ohmic contacts. Throughout this work, we define the built-in voltage $V_{built\text{-}in}$ as the difference between the work functions of the contacts, i.e., the bias necessary to compensate the potential difference across the device imposed by the contacts [38]. In case of ohmic contacts, we obtain a built-in voltage of $V_{built\text{-}in} = 1.5$ V for the interdigitated structure (cf. Fig. 2(a)). For the nanoparticle structure, however, $V_{built\text{-}in}$ assumes the value of 1.9 V, since the cathode workfunction is aligned with the P3EBT donor LUMO level to ensure an ohmic contact. In case of the "real" structure, $V_{built\text{-}in} = 1.5$ V coincides with the value of the interdigitated structure.

Impact of interface geometry: In the following, we will turn our attention to the relationship between the three

aforementioned heterojunction morphologies and transport studied for a P3EBT/$CuInS_2$ device with ohmic contacts.

Interdigitated structures whose combwidth d is varied while keeping the area of the acceptor phase constant, give rise to I–V curves shown in Fig. 3(a). Table 2 lists the corresponding open circuit voltages V_{oc}, short circuit currents j_{sc}, fill factors (FF), and power conversion efficiencies (PCE). As can be seen from Fig. 3(a), the open circuit voltage V_{oc} remains constant at a value of 1.5 V independent of the combwidth d. This value coincides $V_{built\text{-}in} = 1.5$ V of this system, as expected for ohmic contacts [36]. The short circuit current density j_{sc} increases with reducing the finger width d, since an increased number of donor excitons are able to reach the interface. This behavior has already been observed experimentally when changing (i) the combwidth of nanoimprinted organic solar cells [13] and (ii) the surface roughness of the donor–acceptor interface in a layered solar cell [12,17]. Interestingly, as can be seen in Fig. 3(b), there is a pronounced dependence of j_{sc} on d. In the limit of small d, the d-dependent contribution to j_{sc} becomes nearly as large as the constant current contribution stemming from the acceptor phase due to bulk generation. A closer inspection of the evolution of $j_{sc}(d)$ reveals two distinct regimes: (i) As long as the width exceeds ca. 100 nm, essentially those excitons migrating perpendicular to the contacts (y-direction in Fig. 1(a)) reach the interface and contribute to the current. As a consequence, only small changes in $j_{sc}(d)$ are observed. (ii) However, once the structure size drops below 100 nm, $j_{sc}(d)$ is quickly rising with decreasing d. For such d, there is a non-neglible fraction of excitons migrating parallel to the contacts (x-direction in Fig. 1(a)) that is able to reach heterojunction facets that are oriented perpendicular to the contacts. This result is in full agreement with previous theoretical studies on excitonic solar cells [9,14,29]. When further decreasing d, $j_{sc}(d)$ begins to saturate as soon as d reaches the mean exciton diffusion length of 15 nm, as seen also in [9]. However, the maximum value of $j_{sc}(d)$ is reached at d considerably smaller than 15 nm. Then, however, the actual values j_{sc} have to be considered with care, as a macroscopic description is not necessarily valid at such small structure sizes.

To gain insight into the role of the two different carrier generation mechanisms for the formation of I–V curves, we consult a representative spatial distribution of electron and hole concentration within the power quadrant. The steady state quantities associated to the maximum power point are illustrated in Fig. 4; the generalized potential for electrons (upper potential) and holes (lower potential), and charge carrier distributions of the interdigited structure are shown in the left column. Note here that the generalized potential incorporates the electrostatic potential superimposed with the transport level offsets. At V_{mpp}, the potential across the interdigitated device (Fig. 4(a)) drops approximately linearly from the anode to the

Table 2
Open circuit voltage, short circuit current density, fill factor, and power conversion efficiency for devices varying in interface geometry, and contact type.

Assumed morphology	V_{oc}(V)	j_{sc} (A m^{-2})	FF (%)	PCE (%)
P3EBT/CuInS$_2$; ohmic				
Comblike (combwidth 50 nm)	1.48	38.3	61.3	3.25
Nanoparticle structure	1.57	10.2	44.0	0.69
"Real" structure	1.48	28.5	50.8	2.21
P3EBT/CuInS$_2$; Al/ITO				
Comblike (combwidth 50 nm)	0.77	34.9	23.2	0.75
Nanoparticle structure	0.48	1.8	10.0	0.01
"Real" structure	0.77	18.4	36.6	0.59
P3EBT/acceptor; ohmic				
Comblike (combwidth 50 nm)	1.88	39.1	58.6	4.31
Nanoparticle structure	1.80	30.8	35.7	1.98
"Real" structure	1.86	37.9	43.2	3.42
P3EBT/acceptor; Al/ITO				
Comblike (combwidth 50 nm)	1.01	37.0	39.5	1.46
Nanoparticle structure	0.49	12.7	47.2	0.30
"Real" structure	0.99	25.4	38.8	0.97

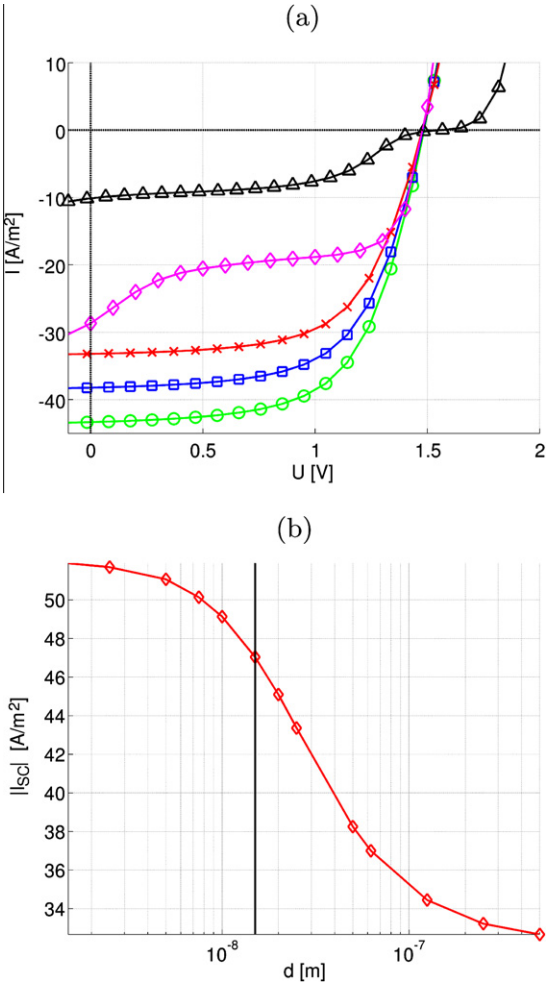

Fig. 3. (a) I–V curves for the P3EBT/$CuInS_2$ interdigitated interface with finger width $d = 250$ nm (crosses, ×), 50 nm (squares, □), and 25 nm (circles, ○), nanoparticles (triangles, △), and real structure (diamonds, ◇) in a device with ohmic contacts. (b) Dependence of the short circuit current density j_{sc} on finger width d for the interdigitated device with ohmic contacts. The exciton mean free path length of 15 nm is indicated by a vertical line.

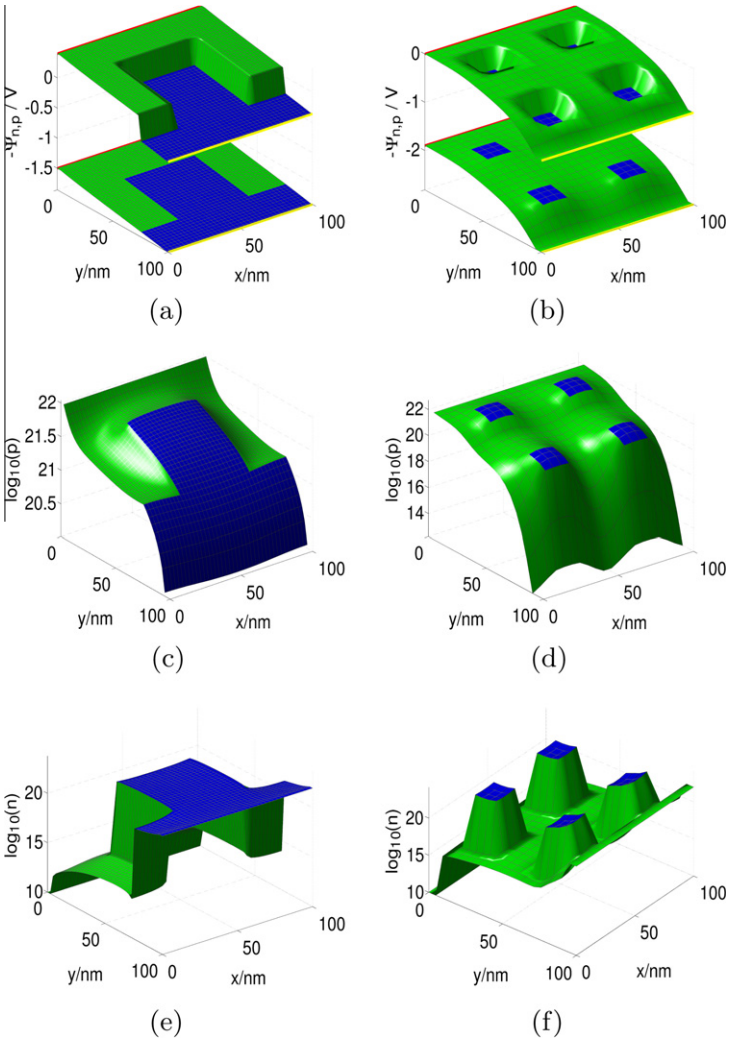

Fig. 4. Steady state distribution of the potential (a,b), hole (c,d), and electron concentration (e,f) related to the comblike structure (left column) and isolated nanoparticle structure (right column). The area corresponding to the donor (P3EBT) is indicated in green (/light gray), the one of the acceptor ($CuInS_2$) in blue (/dark gray). (For interpretation of references to color in this figure legend, the reader is referred to see the web version of this article.)

cathode. It resembles, as usually anticipated for this type of cells, the potential evolution predicted by the MIM model [37]. The resulting electric field, that is uniform in strength and position, ensures that electrons and holes being generated across the acceptor region can be spatially separated prior direct recombination. Driven by the field, the carriers accumulate at the contacts, i.e., the hole [electron] concentration (Fig. 4(c,e)) is highest at the anode [cathode].

However, a closer inspection of the two carrier distributions shown in Figs. 4(c,e) reveals profound differences: (i) The hole concentration drops continuously from anode to cathode, while there is a pronounced step in the electron distribution and (ii) the carrier concentrations at the heterojunction interface are enhanced with respect to the surrounding bulk. The first observation is a direct consequence of the level arrangement of the particular donor and acceptor materials investigated here. As a result of the vanishing barrier between donor and acceptor hole transport levels, holes lack a driving force enabling them to leave the acceptor region. Without being able to escape the acceptor, the holes are subject to significant recombination, since also electrons are confined to the acceptor region due to the barrier formed by the LUMO offset. The local enhancement of the carrier density at the interfaces is due to the *donor* excitons (formed throughout the organic bulk) that dissociate at the heterojunction. As we assume bulk carrier generation throughout the inorganic acceptor rather than exciton transport with subsequent interface cleavage, the local gradient in hole concentration is much more pronounced in the donor phase (Fig. 4(c)). Moreover, the effect is less pronounced among the electrons (Fig. 4(e)).

When turning to isolated nanoparticles, a profoundly different *I–V* characteristic is observed (cf. Fig. 3(a)). To provide a quantitative comparison to the interdigited case, the interface length of the nanoparticles is chosen to coincide with the corresponding length of 50 nm wide fingers. I.e., in both cases the same area for exciton dissociation

(i.e., interface carrier generation) is available. While V_{oc} is approximately the same, j_{sc} is reduced by a factor of almost four. Moreover, a pronounced plateau appears in the power quadrant that gives rise to an s-shaped curve. As a result of this shape, the fill factor of the cell is reduced (cf. Table 2). In combination with the low j_{sc}, PCE is reduced by a factor of five with respect to the cell with comb-like interface. The strong reduction of the photocurrent compared to the comb geometry results from the combination of two factors: (i) As the LUMO level is lower in the acceptor than in the P3EBT donor, electrons are accumulated in the, at least in part, inorganic nanoparticles (cf. Fig. 4(b,f)). Thus, the number of carriers reaching the cathode is reduced. (ii) In addition to a lacking support for hole migration into the donor (cf. HOMO and E_V level in Fig. 2(a)), generated holes prefer to stay close to the acceptor due to the space charge caused by the high electron density in the acceptor material, as can be seen well when comparing the carrier distributions in Fig. 4(d,f). As a result, recombination processes are strongly reducing the hole concentration within the inorganic phase. Thus, the reduction in PCE is to a large extent, as will be shown below, a consequence of the particular combination of semiconductors considered here.

The *I–V* curve which corresponds to an "actual" structure (Fig. 3(a)) is located between the characteristics of the single nanoparticle structure and the comblike structures, but exhibits the same V_{oc}. It possesses a pronounced plateau the onset of which is located at voltages lower than in the nanoparticle curve. In Fig. 5, the generalized potential and the current density distribution in *y*-direction corresponding to the maximum power point, i.e., an external voltage of 1.3 V, are depicted. The distribution of potential and carrier concentrations are reminiscent to those seen in the individual cases. Since the net dark current is zero at this bias, the current close to cathode is a pure electron photocurrent and at the anode a pure hole photocurrent. The pronounced negative maxima in the current density shown in Fig. 5(b) indicate that the main part of the electron current to the cathode is transported in the

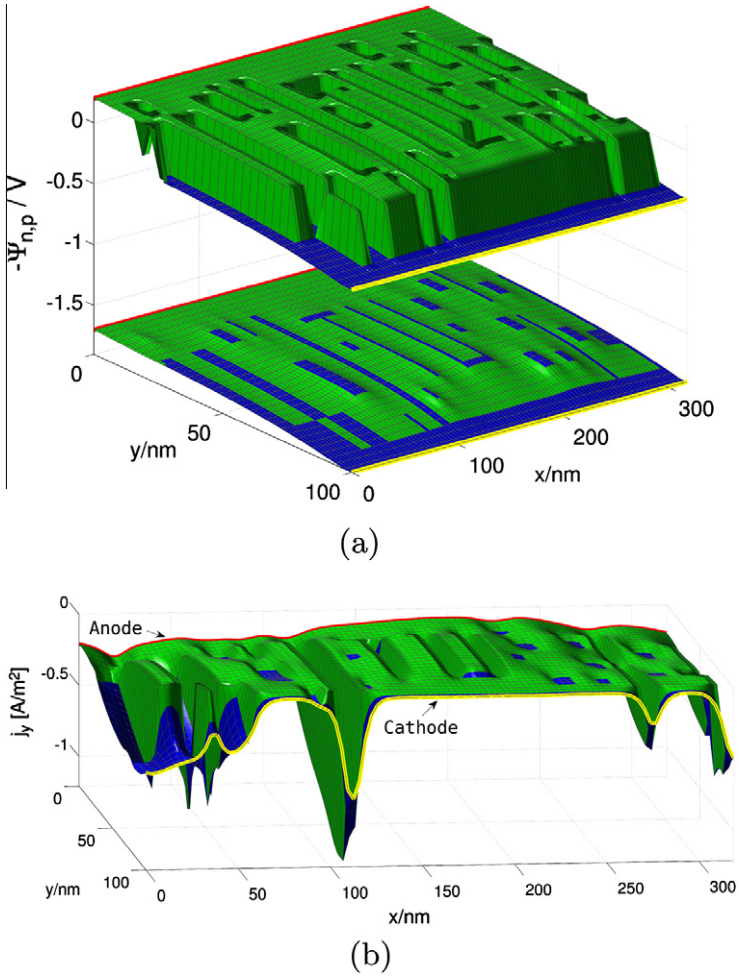

Fig. 5. Generalized potential $\tilde{\Psi}_{n(p)}$ for electrons (holes) (a) and current density distribution in *y*-direction (b) of the intermediate structure at the maximum power point ($V_{mpp} = 1.3$ V) of an illuminated cell. The area corresponding to the donor (P3EBT) is indicated in green (/light gray), the one of the acceptor ($CuInS_2$) in blue (/dark gray). The vertical position of the yellow line in the lower panel indicates the electron current density at the cathode and the vertical position of the the red line the hole current density at the anode. (For interpretation of references to color in this figure legend, the reader is referred to see the web version of this article.)

through-going acceptor paths. This adduces further evidence that comblike structures lead to best efficiencies. Moreover, it can be seen in regions close to the contacts depicted in Fig. 5(b) that the current is confined to the acceptor region, while the hole current appears to be spatially more uniform in the vicinity of the anode. This lack of confinement is related to the vanishing offset in the hole transport levels in donor and acceptor (Fig. 5(a)).

Impact of the level offset: To discriminate between the effect of morphology and the disadvantageous lack of an HOMO level offset, we replace $CuInS_2$ by a fictitious acceptor material whose HOMO and LUMO are equidistantly set off by 0.4 eV with respect to the P3EBT levels (Fig. 2(b)). All other parameters including $V_{\text{built-in}}$ were kept the same. The corresponding *I–V* characteristics for the three model geometries assuming ohmic contacts are shown in Fig. 6(b,filled symbols). Compared to the curves obtained in the original P3EBT/$CuInS_2$ device Fig. 6(a), the following differences arise: Independent from the interface structure, j_{sc}, V_{oc}, and PCE are increased (cf. also Table 2) for the idealized acceptor. However, the shape and, thus, FF are less ideal. While, e.g., the comb-like structure gives rise to an FF of 61.3% in P3EBT/$CuInS_2$, FF drops to 58.6% when changing the acceptor. At the same time, the enhanced values of j_{sc} and V_{oc} compensate for the loss in FF and effectively increase PCE from 3.25% to 4.31%.

The origin of the decrease in FF and increase in V_{oc} is presumably discussed best for the case of the interdigitated interface. The apparent departure of the *I–V* curve from an ideal diode-like shape (Fig. 6(b)) turns out to be related to the bias-dependence of hole transport. Fig. 6(c) schematically depicts the general transport scenario valid for biases within the power quadrant. As discussed already in Fig. 4(a,e), the contribution from electrons to the overall current is not affected by the actual bias. For voltages not exceeding V_{oc}, the corresponding electric field is not able to lift the electrons across the barrier at the interface. Therefore, all generated electrons diffuse towards the cathode (Fig. 6(c)). Holes that are generated throughout the acceptor and via exciton dissociation at the interface, give rise to a gradient in the concentration p that induces a desired diffusion current through the donor towards the cathode (cf. Fig. 6(c)). However, due to the external bias there is a non-vanishing electric field that drives holes, in particular those generated close to the anode, towards the wrong contact. The higher *V*, the higher the loss in hole current due to such drift currents. With the introduction of an offset between the hole transport levels, holes regard the transfer from the interface into the donor region as energetically favorable (cf. Fig. 6(c)). I.e., there is an effective diffusion process that (i) diminishes p within the acceptor and, thus, (ii) counteracts the disadvantegeous drift current. As a result, the photocurrent "decays" slowlier with *V* than in a device without level offset. Thus, V_{oc} is increased beyond $V_{\text{built-in}}$ and FF is reduced. Note that this effect is significantly less pronounced in purely exciton-based solar cells, since the predominant amount of holes contributing to the detrimental drift current, i.e., those generated in bulk, does not exist.

The most profound dependence of j on the type of acceptor is observed for the nanoparticle geometry. Aided

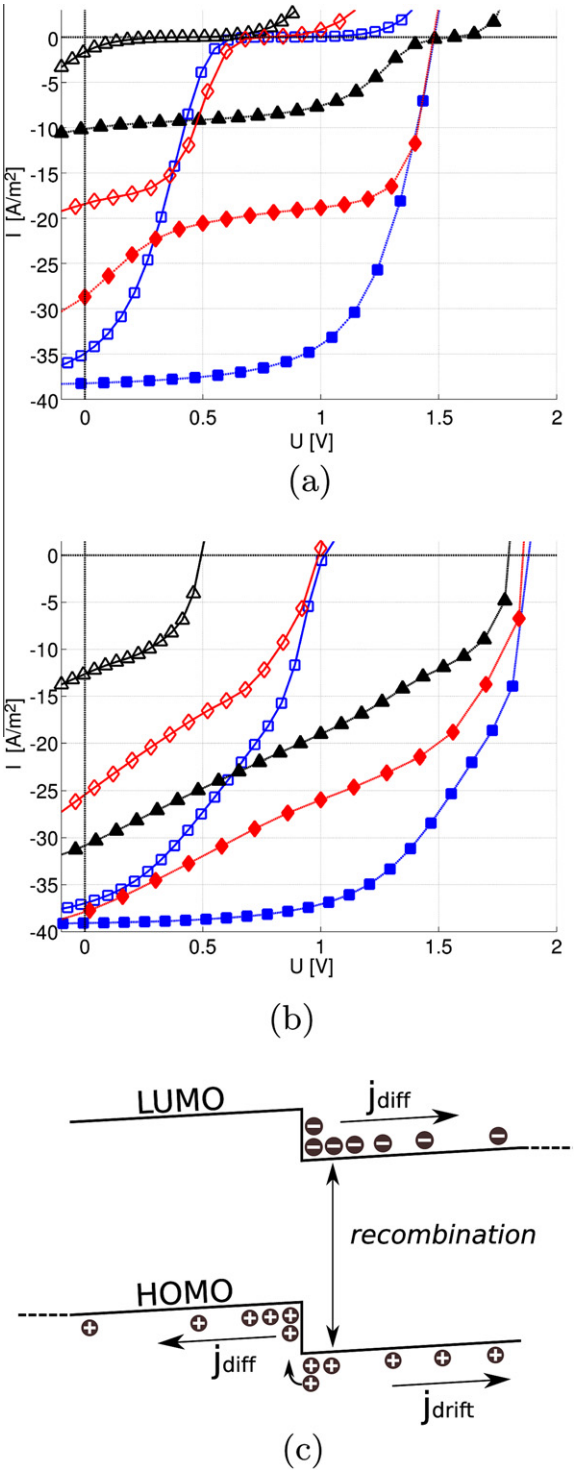

Fig. 6. *I–V* curves for the interfaces of (a) P3EBT/$CuInS_2$ and (b) P3EBT/idealized acceptor in a device with Al and ITO contacts (open symbols) and ohmic contacts (filled symbols). Shown are the curves for the interdigitated interface (squares) with a finger width $d = 50$ nm, nanoparticles (triangles), and real structure (diamonds). (c) Sketch of the current contributions for a P3EBT/idealized acceptor device operating in the power quadrant.

by a non-vanishing hole level offset, holes generated in the acceptor better escape into the donor and, thus, from the region of trapped electrons. Thus, recombination losses are strongly reduced.

Impact of contacts: To study the impact of actual contacts, aluminum with a workfunction of $\theta = -4.50$ eV (intrinsic electron concentration of 10^{29} m^{-3}) for the cathode and indium tin oxide (ITO) with a workfunction of $\theta = -5.0$ eV (intrinsic hole concentration of 10^{27} m^{-3}) have been considered. The position of the contact workfunctions with respect to the transport levels of P3EBT and $CuInS_2$ is depicted in Fig. 2(a). As the difference in the contact workfunctions is exclusively dictating the built-in voltage, we arrive at $V_{\text{built-in}} = 0.5$ V. The *I–V* curves considering Al/ITO contacts and interface geometries as introduced above are shown in Fig. 6(a) for P3EBT/$CuInS_2$ and in Fig. 6(b) for a P3EBT/idealized acceptor combination. In Table 2 the corresponding figures of merit can be compared between devices with ohmic and real contacts.

In comparison to the curves representing the ohmic case (indicated by closed symbols in Fig. 6), the *I–V* curves possess a lower V_{oc} (cf. also Table 2). This can be seen best for devices containing an idealized acceptor and through-going paths (Fig. 6(b), squares and diamonds): Actual contacts (open symbols) appear to shift the curves obtained for ohmic contacts (closed symbols) towards lower voltages by an amount of ca. 0.9 V. This value corresponds to $V_{\text{built-in}}^{ohmic} - V_{\text{built-in}}^{non-ohmic} = 1.0$ V corrected by small differences in diffusion contributions. As a result, PCE is reduced by at least a factor of 3, e.g., from 4.3 to 1.5 for the interdigitated interface. Note, that V_{oc} exceeds $V_{\text{built-in}}$ by ca. 0.4 V due to the aforementioned effective diffusion induced by

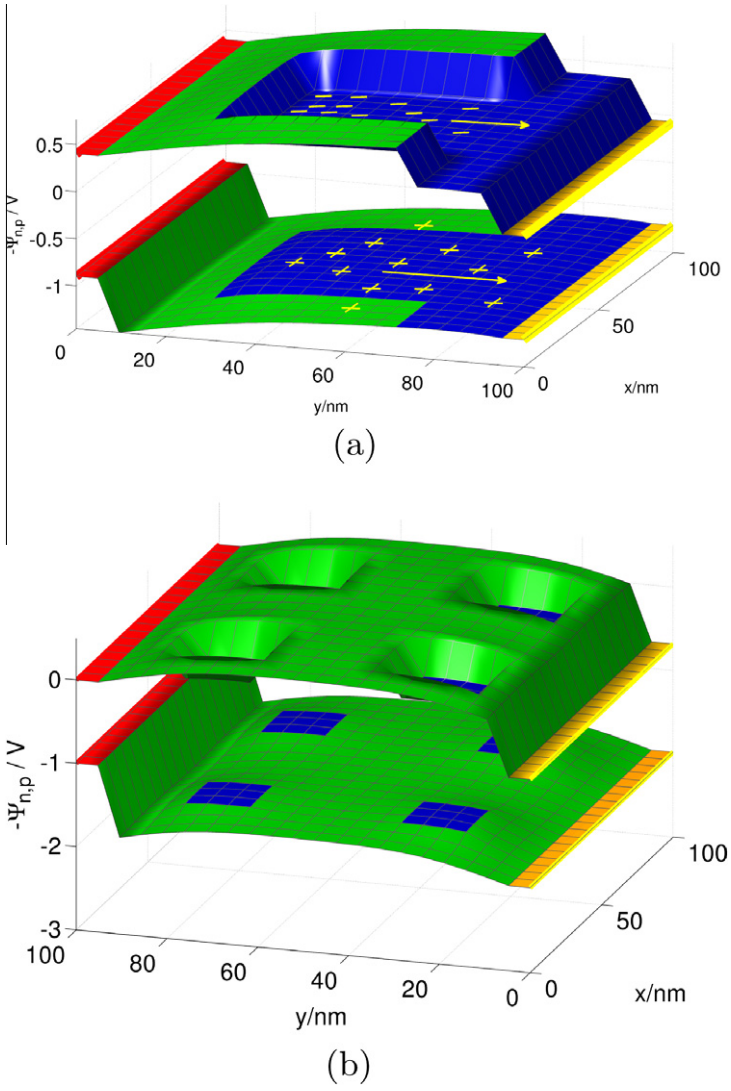

Fig. 7. Generalized potential $\widehat{\Psi}_{n(p)}$ for electrons (holes) of a device with (a) a comb-like interface at $V_{\text{ext}} = 0.83$ V bias and (b) a nanoparticle interface and Al/ITO contacts at $V_{\text{ext}} = 0.32$ V bias. The area corresponding to the donor (P3EBT) is indicated in green (/light gray), the one of the acceptor ($CuInS_2$) in blue (/dark gray). Electrons [/holes] in the E_C [/E_V] level are schematically indicated by "−" [/"+"]. (For interpretation of references to color in this figure legend, the reader is referred to see the web version of this article.)

the hole transport level offset. When turning to P3EBT/$CuInS_2$ devices, however, real contacts additionally induce strong changes in the shape with respect to their ohmic counterparts, as can be deduced from Fig. 6(a) and the FF values in Table 2. Correspondingly, both j_{sc} and PCE values are affected. Even for the most ideal heterojunction geometry, PCE drops by more than a factor of 4 from 3.25 to 0.75. For devices with through-going paths (Fig. 6(a), squares and diamonds), this change in shape is due to a photocurrent that (i) drops more rapidly with increasing V and (ii) collapses into a pronounced plateau that is approximately centered at V_{oc}. Already at biases beyond 0.6 V, the net *photocurrent* vanishes. Electron and hole photo currents *cancel* each other exactly. This can be readily understood from the corresponding generalized potential distribution, shown for a representative external bias $V_{ext} = 0.83$ V near V_{oc} in Fig. 7(a): The electron current is essentially caused by diffusion, as discussed previously (cf. Fig. 6(c)). All holes are driven by the drift force towards the cathode as their motion is not hampered by a band offset, and are, thus, moving into the same direction as the electrons (Fig. 7(a)). This condition, of course, promotes a further reduction of the carrier concentrations due to efficient recombination. A similar mechanism was revealed by Uhrich et al. [19] when changing the level offset between hole transporting moities in a layered organic solar cell. In the vicinity of V_{oc}, the I–V curves are already dominated by the dark characteristic. The onset of the dark electron current eventually occurs at a voltage of about 0.9 V, i.e., an appreciable amount of electrons can cross the non-illuminated device at biases exceeding the sum of $V_{built\text{-}in} = 0.5$ V and the barrier posed by the LUMO/LUMO band offset of 0.4 V. Note that the corresponding hole dark current is very small, since (i) the hole concentration at the ITO contact is small and (ii) a large injection barrier from ITO into P3EBT is present. The degree to which the s-shape evolves can be further influenced by the height of the injection barrier present at the contacts. For a given built-in voltage, an increase of the injection barrier height associated to thermoionic injection was shown to induce a sigmoidal shape in the I–V curve while not affecting V_{oc} [9].

The most significant influence of the contacts is seen for the nanoparticle devices (Fig. 6, upper triangles). The open circuit voltage is with $V_{oc} \approx V_{built\text{-}in} = 0.5$ V independent from the acceptor material. A vanishing photocurrent at voltages beyond $V_{built\text{-}in}$ is an indication for a loss in selectivity of the contacts. Indeed, when inspecting the generalized potential at a bias of 0.32 V near $V_{built\text{-}in}$ shown in Fig. 7(b), we recognize a strong deviation from a linear voltage drop from anode to cathode. Rather, the potential is almost flat and bends slightly downward from the device's center towards the contacts due to electron accumulation in the nanoparticle regions and close to the cathode. Therefore, electrons and holes experience an average similar driving forces towards each of the contacts; the *net* photo current vanishes.

For the P3EBT/$CuInS_2$ device, i.e., in the device lacking a hole transport level offset, j_{sc} vanishes almost to zero. Here, acceptor-generated holes do not leave the nanoparticles sufficiently fast and, thus, are subject to efficient recombination with electrons trapped in the acceptor. As a result, its I–V curve is characterized by a very small j_{sc} value of 2 A m^{-2}, and a broad plateau centered around V_{oc}, i.e., the fill factor is lowered from 0.23 to 0.10 (cf. Table 2). In comparison to the device with ideal contacts, the resulting PCE drops by an order of magnitude from 0.69 to 0.01.

4. Conclusion

The carrier transport in hybrid cells has been studied in the light of interplay between (i) energy barriers formed at the contacts, (ii) barriers at the donor–acceptor interface, and (iii) representative shapes of the heterojunction. Particular attention has been paid to the fact that carrier generation can occur at the heterojunction (due to dissociation of the donor excitons) *and* in the bulk of the acceptor material (due to band to band generation in the inorganic material).

Each of the three factors consitutes a major loss factor that profoundly determines the power conversion efficiency of hybrid organic–inorganic solar cells. As expected, the choice of the interface geometry has a crucial influence on the device efficiency even if perfect contacts are considered. In accord with previous investigations [5,33,42], interdigitated structures are found to yield the highest efficiencies. In such highly ordered systems, j_{sc} is limited by the digit width and, thus, by the exciton diffusion length [8,10]. This is true independent from the nature of the contacts.

The presence of isolated islands in the device, be them formed by the donor and/or acceptor material, reduces the overall efficiency. The extent of this reduction strongly depends on the actual ratio between through-going pathways and isolated particles. The location of the maximum power point is determined by an interplay of two essential effects: The more through-going paths exist, (i) the more short circuit current can be obtained and (ii) the larger the area at which advantageous contact barriers can be offered, i.e., the more the plateau (s-shape) formation in the I–V curve can be suppressed.

As a second factor, it turns out that a vanishingly small or a negative hole transport level offset leads to an accumulation of holes in the nominally electron transporting acceptor zone. The resulting reduction of the photocurrent due to (i) direct hole and electron photocurrent compensation and (ii) recombination represents a major contribution to the overall efficiency loss. A straightforward way to avoid losses due to non-ideally shaped I–V curves is, therefore, to select the semiconducting materials so that the hole transport level offset at the heterojunction promotes hole diffusion into the donor. Note, that this criteria for chosing transport levels has to be distinguished from other, already well employed rules: As a first requirement it is commonly accepted that a significant offset in the LUMO levels ensures efficient exciton dissociation [36]. Secondly, it is advantageous to block the charge carriers prior entering the opposing contact (see, e.g., in [41]); however, there are no restrictions in which part of the solar cell this blocking needs to occur.

Despite the determining influence of the level offsets, the efficiency of the device is strongly influenced by the choice of contacts. As soon as non-ohmic contacts to the

semiconductors are formed, the open circuit voltage is dictated by the contact workfunctions; V_{oc} differs from $V_{built\text{-}in}$ only by a small possible amount corresponding to the smallest transport level offset arising from diffusion. For our choice of materials, V_{oc} is halved when introducing Al/ITO contacts. Moreover and less expectedly, barriers at the semiconductor metal interfaces give rise to a substantial deviation from the ideal diode-shaped *I–V* curve and, thus, reduce the fill factor. As shown by Yip et al. [40] for ZnO-based bilayer hybrid solar cells, the systematic tuning of just the cathode workfunction via SAMs revealed fill factors varying by a factor of two.

From the considerations above it is possible to conclude that the three investigated factors give rise to equally serious efficiency losses. As each of these factors directly relates to the properties and processing of the chosen materials, we can derive the following guidelines to select suitable material combinations: (i) The formation of ohmic contacts ensures contact-independent open circuit voltages *and* high fill factors. (ii) A successful suppression of the formation of donor or acceptor islands is boosting the FF. And, (iii), holes need to be driven from the acceptor into the donor at the heterojunction by means of an effective diffusion induced by a transport level offset.

Acknowledgments

This work has been supported by the Austrian Federal Ministry of Economy, Family, and Youth (bmwfj), ISOVOLTAIC GmbH, and the Austrian Nanoinitiative (FFG) through the NILsimtos project as part of the NILaustria cluster.

References

[1] (a) P. Ravirajan, A.M. Peiro, M.K. Nazeeruddin, M. Graetzel, D.D.C. Bradley, J.R. Durrant, J. Nelson, J. Phys. Chem. B 110 (2006) 7635;
(b) J. Boucle, P. Ravirajan, J. Nelson, J. Mater. Chem. 17 (2007) 3141;
(c) J. Boucle, S. Chyla, M.S.P. Shaffer, J.R. Durrant, D.D.C. Bradley, J. Nelson, Adv. Funct. Mater. 18 (2008) 622–633;
(d) S. Tepavcevic, S.B. Darling, N.M. Dimitrijevic, T. Rajh, S.J. Sibener, Small 5 (2009) 1776–1783;
(e) K. Shankar, G.K. Mor, H.E. Prakasam, O.K. Varghese, C.A. Grimes, Langmuir 23 (2007) 12445–12449.

[2] (a) B.R. Saunders, M.L. Turner, Adv. Coll. Interf. Sci. 138 (2008) 1–23;
(b) Y.-Y. Lin, T.H. Chu, S.S. Li, C.H. Chuang, C.H. Chang, W.F. Su, C.P. Chang, M.W. Chu, C.-W. Chen, J. Am. Chem. Soc. 131 (2009) 3644–3649;
(c) W.J.E. Beek, M.M. Wienk, R.A.J. Janssen, J. Mater. Chem. 15 (2005) 2985–2988.

[3] B.G. Streetman, S. Banerjee, Solid State Electronic Devices, 5th ed., Prentice Hall, New Jersey, 2000.

[4] (a) I. Gur, N.A. Fromer, C.P. Chen, A.G. Kanaras, A.P. Alivisantos, Nano Lett. 7 (2007) 409–414;
(b) S. Gupta, Q. Zhang, T. Emrick, T.-P. Russell, Nano Lett. 6 (2006) 2066–2069;
(c) K.M. Ryan, A. Mastroianni, K.A. Stancil, H. Liu, A.-P. Alivisatos, Nano Lett. (2006) 6 1479–1482;
(d) Z. Hu, M.D. Fischbein, C. Querner, M. Drndic, Nano Lett. 6 (2006) 2585;
(e) B. Sun, H.J. Snaith, A.S. Dhoot, S. Westerhoff, N.C. Greenham, J. Appl. Phys. 97 (2005) 014914;
(f) W.U. Huynh, J.J. Dittmer, A.P. Alivisatos, Science 295 (2002) 2425–2427;
(g) H.J. Snaith, G.L. Whiting, B. Sun, N.C. Greenham, W.T.S. Huck, R.H. Friend, Nano Lett. 5 (2005) 1653–1657;
(h) Y. Kang, N.G. Park, D. Kim, Appl. Phys. Lett. 86 (2005) 113101;
(i) E. Arici, H. Hoppe, F. Schäffler, D. Meissner, M.A. Malik, N.S. Sariciftci, Appl. Phys. A 79 (2004) 59;
(j) G. Dennler, M.C. Scharber, C.J. Brabec, Adv. Mater. 21 (2009) 1323–1338.

[5] R.A. Marsh, C. Groves, N.C. Greenham, J. Appl. Phys. 101 (2007) 083509.

[6] C. Groves, R.A. Marsh, N.C. Greenham, J. Chem. Phys. 129 (2008) 114903.

[7] P.K. Watkins, A.B. Walker, G.L.B. Verschoor, Nano Lett. 5 (2005) 1814.

[8] C.M. Martin, V.M. Burlakov, H.E. Assender, Sol. Ener. Mater. Sol. Cells 90 (2006) 900–915.

[9] C.M. Martin, V.M. Burlakov, H.E. Assender, D.A.R. Barkhouse, J. Appl. Phys. 102 (2007) 104506.

[10] G.A. Buxton, N. Clarke, Mod. Sim. Mat. Sci. Eng. 15 (2007) 13.

[11] H. Al-Dmour, D.M. Taylor, J.A. Cambridge, J. Appl. Phys. D 40 (2007) 5034.

[12] A. Keawprajak, P. Piyakulawat, C. Saekung, U. Asawapirom, J. Micr. Soc. Thailand 23 (2009) 134.

[13] M.S. Kim, J.S. Kim, J.C. Cho, M. Shtein, L.J. Guo, J. Kim, Appl. Phys. Lett. 90 (2007) 123113.

[14] K. Maturova, S.S. van Bavel, M.M. Wienk, R.A.J. Janssen, M. Kemerik, Nano Lett. 9 (2009) 3032.

[15] H. Hoppe, N.S. Sariciftci, J. Mater. Chem. 16 (2006) 45.

[16] C. Groves, L.J.A. Koster, N.C. Greenham, J. Appl. Phys. 105 (2009) 094510.

[17] A. Kumar, G. Li, Z. Hong, Y. Yang, Nanotechnology 20 (2009) 165202.

[18] (a) M. Glatthaar, M. Riede, N. Keegan, K. Sylvester-Hvid, B. Zimmermann, M. Niggemann, A. Hinsch, A. Gombert, Sol. Ener. Mater. Sol. Cells 91 (2007) 390;
(b) K. Schulze, M. Riede, E. Brier, E. Reinold, P. Bäuerle, K. Leo, J. Appl. Phys. 104 (2008) 074511;
(c) J. Nelson, J. Kirkpatrick, P. Ravirajan, Phys. Rev. B 69 (2004) 035337.

[19] C. Uhrich, D. Wynands, S. Olthof, M. Kiede, K. Leo, S. Sonntag, B. Maennig, M. Pfeiffer, J. Appl. Phys. 104 (2008) 043107.

[20] C. Groves, N.C. Greenham, Phys. Rev. B 78 (2008) 155205.

[21] (a) L. Meng, Y. Shang, Q. Li, Y. Li, X. Zhan, Z. Shuai, R.G.E. Kimber, A.B. Walker, J. Phys. Chem. B 114 (2010) 36–41;
(b) J. Williams, A.B. Walker, Nanotechnology 19 (2008) 424011.

[22] E.A. Schiff, J. Non-Cryst. Sol. 190 (1995) 1.

[23] J.E. Sutherland, J.R. Hauser, IEEE Trans. Electron Dev. 24 (1977) 363.

[24] C.M. Snowden, Introduction to Semiconductor Device Modeling, World Scientific, 1986.

[25] L.J.A. Koster, V.D. Mihailetchi, P.W.M. Blom, Appl. Phys. Lett. 88 (2006) 052104.

[26] *We use this convenient rate expression also for the pristine inorganic bulk. For the particular mobilities that will be used below (cf. Table 1), this expression is applicable and differs by the smallest possible factor of two [6] from the standard Langevin expression [39]. The actual recombination rate in bulk heterojunction cannot be expressed in a simple form using the mobilities [6]; for the ratio of mobilities employed in our work, however, the actual rate is limited from below by rate expression according to Koster et al. [25] and from above by the Langevin rate [6]. Careful testing revealed that the type of recombination rate had no detectable impact on the I–V curves. This result is supported by Maturova et al. [14], who showed that the standard Langevin rate and a Koster-type rate equivalently describe the bimolecular recombination in two-dimensional simulation.*

[27] *The consideration of the actual distribution of the electromagnatic field is beyond the scope of this paper.*

[28] *To be consistent with the numerical treatment of exciton dissociation, our implementation mimicks the direct charge generation by assuming that an incoming photon generates an exciton first which dissociates immediately into free charges. This somewhat underestimates the number of carriers generated in the inorganic phase; the corresponding relative error in $\Delta G/G$ does not exceed* 10^{-3}.

[29] G.A. Buxton, N. Clarke, Phys. Rev. B 74 (2006) 085207.

[30] E.J.W. List, C.-H. Kim, A.K. Naik, U. Scherf, G. Leising, W. Graupner, J. Shinar, Phys. Rev. B 64 (2001) 155204.

[31] D.L. Scharfetter, H.K. Gummel, IEEE Trans. Electron Dev. 16 (1969) 64.

[32] E. Arici, N.S. Sariciftci, D. Meissner, Adv. Funct. Mater. 13 (2003) 165.

[33] K.O. Sylvester-Hvid, S. Rettrup, M.A. Ratner, J. Phys. Chem. B 108 (2004) 4296.

[34] B.A. Stickler, Master Thesis, University of Technology, Graz, 2009.; B.A. Stickler, M. Gruber, G. Trimmel, F. Schürrer, K. Zojer, in preparation.

[35] *That implies that (i) no injection barrier is present and that (ii) the intrinsic charge carrier concentration in the contacts is sufficiently small (cf. values in Table 1). The latter property avoids a strong 'band bending', i.e., significant correction of the transport level energies due to the*

potential of accumulated charges. A carrier concentration of 10^{22} m^{-3} *in the contact was found not to influence the potential close to the contacts.*
[36] P.W. Blom, V.D. Mihailetchi, L.J.A. Koster, D.E. Markov, Adv. Mater. 19 (2007) 1551–1566.
[37] H. Hoppe, N.S. Sariciftci, J. Mater. Res. 19 (2004) 1924.
[38] *This definition adheres to the MIM model for organic solar cells [37] and, thus, differs from the standard definition related to semiconductor p–n homojunctions [39].*
[39] S.M. Sze, Physics of Semiconductors, Wiley, New York, 1981.
[40] H. Yip, S.K. Hau, N.S. Baek, H.M. Ma, A.K. Jen, Adv. Mater. 20 (2008) 2376–2382.
[41] A.W. Hains, J. Liu, A.B.F. Martinson, M.D. Irwin, T.J. Marks, Adv. Funct. Mater. 20 (2010) 595–606.
[42] P. Peumans, S. Uchida, S.R. Forrest, Nature 425 (2003) 158.

Organic Electronics 11 (2010) 2012–2018

Contents lists available at ScienceDirect

Organic Electronics

journal homepage: www.elsevier.com/locate/orgel

Core-type polyfluorene-based copolymers for low-cost light-emitting technologies

Umberto Giovanella [a,*], Paolo Betti [a], Alberto Bolognesi [a], Silvia Destri [a], Manuela Melucci [b,c], Mariacecilia Pasini [a], William Porzio [a], Chiara Botta [a]

[a] Istituto per lo Studio delle Macromolecole, CNR, Via Bassini 15, 20133 Milano, Italy
[b] Istituto per la Sintesi Organica e la Fotoreattività, CNR, via Gobetti 101, 40129 Bologna, Italy
[c] Istituto di Chimica dei Composti Organometallici, CNR, via Madonna del Piano 10, 50019 Sesto F.no (Fi), Italy

ARTICLE INFO

Article history:
Received 18 May 2010
Received in revised form 6 September 2010
Accepted 7 September 2010
Available online 23 September 2010

Keywords:
Polyfluorene
WOLED
Energy transfer
Benzothiadiazole
Suzuki coupling
Electroluminescence

ABSTRACT

Single layer white organic light emitting diodes (WOLED) are obtained with a polymeric blend, whose constituents are three polyfluorene (PF) based materials emitting in the three fundamental colours thanks to the insertion of a single monomeric unit with different chemical nature at the core of the PF chain. The peculiar choice of three fully compatible polymers allows us to obtain stable and homogeneous active layers for highly performing WOLEDs. The high quality white electroluminescence with chromaticity coordinates (0.32; 0.33), correlated colour temperature of 5893 K and colour rendering index of 90, makes these compounds good candidates for low-cost solid-state lighting technologies.

© 2010 Elsevier B.V. All rights reserved.

1. Introduction

White organic light emitting diodes (WOLEDs) have gained increasing interest both in the scientific and in the industrial communities thanks to their great potential in lighting applications and as back-lights in liquid-crystal displays [1]. Lighting uses a significant part of the world energy resources, now partially wasted by inefficient incandescent lamps. In the future WOLEDs can represent a valuable alternative to incandescent lamps thanks to both their higher efficiencies and their unique properties such as large-area emission and processability in transparent and flexible devices. White-light emission can be obtained either by mixing the three fundamental colours or with two complementary colours and devices have been reported with multiple and single layer architectures [2,3]. Among many different approaches, devices based on soluble and processable polymeric materials are of particular interest since they provide a simple technology which allows for low-cost large area and flexible devices. The drawbacks of these materials are the poorer device performances when compared to devices fabricated with small molecules by using vacuum-deposition technologies, the incompatibility among different chemical components of the blends (with unwanted time-evolution of phase separation) and the voltage dependence of the emitted colour caused by the different nature of the emitting states.

An alternative approach is the use of blends of macromolecules with the same chemical nature, able to combine the colours to obtain white light [4]. Even though the efficiency of devices fabricated with only fluorescent materials is lower with respect to those employing phosphorescent ones, the advantages in terms of device stability, robustness, white light quality and ease of fabrication make them of great interest in indoor lighting applications. Most of the polymeric materials used in WOLEDs contain polyfluorene (PF) based polymers as blue emitting material, combined with lower energy gap materials to which only

* Corresponding author. Tel.: +39 02 23699733.
E-mail address: u.giovanella@ismac.cnr.it (U. Giovanella).

1566-1199/$ - see front matter © 2010 Elsevier B.V. All rights reserved.
doi:10.1016/j.orgel.2010.09.009

a limited amount of energy is transferred through a controlled resonant energy transfer (RET) mechanism [5] by a proper supramolecular structure of the materials [6].

In this work, we report on the fabrication and characterization of a single layer WOLED obtained with a polymeric blend whose constituents are three PF based polymers emitting in the three fundamental colours. The different emission colours of two of the three polymers, i.e. green and red, are achieved by an unprecedented core-type design approach which reduces the chemical effort in the synthesis and improve the reproducibility of the material composition with respect to random synthesized copolymer. Here, a molecular dye of different structure and emission colour, is inserted as bridging core between two identical polymeric arms. The polymeric arms, as well as the pure blue-emitting compound, consist of a fluorene-based alternating copolymer (hereafter **1**) made by a triphenylamine (TPA) substituted fluorene unit alternated with an alkyl substituted fluorene one. Worthy to mention, we have already shown that the insertion of TPA moiety resulted in reduced interchain interactions, an enhanced hole injection, and increased morphological stability with respect to conventional PFs [7]. Central yellow–green and red emitting molecules based on benzothiadiazole moiety are used as molecular dye core.

We demonstrate that the peculiar choice of such core-type polymers emitters, possessing the same chemical nature and therefore fully compatible, allows us to obtain stable and homogeneous active layers (AL) for high quality WOLEDs.

2. Materials and methods

2.1. Synthesis and characterization of core-type copolymers

Polymer **1-borolane** was synthesized by reacting 9,9-dioctylfluorene-2,7-diboronic acid bis(1,3-propanediol) ester (356 mg 0.62 mmol) with 9,9-bis(4-diphenylaminophenyl)-2,7-dibromofluorene (500 mg 0.62 mmol) for 10 h at 90 °C before adding the capper phenylboronic acid pinacol ester (3:1 M ratio) and stirring for further 15 h at 90 °C. The solution diluted with 10 ml of toluene was filtered through Celite, concentrated and **1-borolane** was recovered by precipitation in methanol. After extraction with acetone using a Soxhlet apparatus and drying 190 mg (42% yield) was obtained. 75 mg of **1-borolane** was dissolved in toluene and (0.32 mg, 0.27 μmol) of $Pd(Ph_3P)_4$ from a previously prepared toluene solution together with 7.5 ml of [2 M] K_2CO_3 aqueous solution and a droop of Aliquat were added. A toluene solution of 4,7-dibromo-benzothiadiazole (2.8 mg, 6.8 μmol in 4.0 ml) or 4,7-bis(5-bromothiophen-2-yl)benzothiadiazole (3.1 mg, 6.8 μmol in 4 ml) to get **2** and **3** core-type polymers respectively was slowly dropped in 8 h maintaining the reaction at 90 °C under stirring. The mixture was further stirred for 15 h, then phenylbromide (373 mg, 2.38 mmol) was added as a quencher of unreacted **1-borolane** and the stirring and heating were prolonged during 24 h. The solution was filtered through a Celite column and the polymer was precipitated in methanol. Extraction with acetone was used to remove any residue of dyes obtaining 50 mg of **2** and 62 mg of **3**, respectively.

^{1}H NMR of **2** (toluene-d_6, 298 K) δ (ppm): 8.11 (s, fluorenyl), 7.8–7.6 (m, fluorenyl + BT), 7.42 (m, fluorenyl), 7.2–6.8 (m, N-Ph), 2.07 (br, αCH_2 alkyl chain), 1.05 (br, CH_2), 0.81 (m, CH_3).

^{1}H NMR of **3** (toluene –d_6, 298 K) δ (ppm): 8.11 (m, fluorenyl + Th), 7.8–7.6 (m, fluorenyl + BT), 7.42 (m, fluorenyl), 7.25–6.8 (m, N-Ph + Th), 1.99 (br, αCH_2 alkyl chain), 1.05 (br, CH_2), 0.81 (m, CH_3).

A GPC determination of the molecular weight (Mn) of compounds **1**, **2** and **3** and **1-borolane** gave 10075 (Mw/Mn 1.95), 6887 (2.00), 8574 (2.29) and 6016 (1.92), respectively. The Mn values were referred to standard of polystyrene.

2.2. Measurements

^{1}H spectra were recorded with a Bruker ARX400 MHz spectrometer.

Gel permeation chromatography (GPC) measurements were carried out on Waters SEC system consisting of a pump, a 410 differential refractometer, and a 490 UV spectrophotometer as detectors. The column was a Ultrastyragel Waters; THF as solvent and polystyrene as standard were used.

Electrochemical experiments were performed at room temperature under nitrogen in three electrode cells. The counter electrode was platinum; reference electrode was a silver/0.1 M silver perchlorate in acetonitrile (0.34 V vs SCE). The core-polymers were generally investigated in millimolar concentration in acetonitrile + 0.1 M Bu_4NClO_4. The voltammetric apparatus (AMEL, Italy) included a 551 potentiostat modulated by a 568 programmable function generator and coupled to a 731 digital integrator. The working electrode for cyclic voltammetry was a platinum minidisc electrode (0.003 cm^2).

Photoluminescence (PL) and electroluminescence (EL) were obtained with monochromator equipped with a CCD detector, by exciting with a monochromated Xenon lamp, or by applying a constant bias, respectively. Solid-state PL quantum yields (PL-QY) were obtained by using a home-made integrating sphere [8]. Device optimization and characterization were performed following the methods reported elsewhere [9,10]. PL and EL microscopy images were obtained using a Nikon Eclipse TE2000-U inverted confocal microscope.

2.3. Film and OLED fabrication

Macromolecules were dissolved in toluene 15 mg/ml. Indium tin oxide (ITO; 15 Ω per square) substrates were cleaned by sonication in distilled water, acetone, and isopropyl alcohol. After treatment with nitrogen plasma, a 50 nm thick film of poly-(3,4-ethylenedioxythiophene)-poly(styrenesulfonic acid) (PEDOT:PSS) (Clevios P VP AI 4083, H.C. Starck) used as a hole-injection layer at the anode interface was spin-coated onto the ITO substrate, and then dried under nitrogen atmosphere at 100 °C for 15 min. Poly(vinylcarbazole) (PVK; Aldrich, MW 10^6 Da) from chlorobenzene solution was subsequently deposited

on top of the dried PEDOT:PSS layer and treated at 150 °C for 30 min. A thin film of copolymers or blends were then spin-coated inside a nitrogen-filled drybox. The active layer thickness was around 80–100 nm. A thin layer of Calcium (30 nm) or Barium (5 nm) and subsequently 100 nm layers of Aluminium were deposited on the top by vacuum (10^{-7} mbar) thermoevaporation. All device preparation steps and performance measurements were performed inside a MBraun drybox system.

3. Results and discussion

The chemical structure of the materials utilized in the paper is reported in Fig. 1. In a previous work [11] we reported the preparation of polymer **1** functionalized with a borolane group (**1-borolane**). The newly synthesized core-type copolymers **2** and **3** were prepared by reacting via a Suzuki coupling a large excess of **1-borolane** with 4,7-dibromo-benzothiadiazole (Aldrich) as the green core dye and 4,7-bis(5-bromothiophen-2-yl)benzothiadiazole as the red emitter [12].

UV–visible absorption spectra are dominated by fluorene backbone 388 nm band and absorption of core dyes is visible as weak shoulder at 450 nm and weak broad band at 520 nm for **2** and **3**, respectively (Fig. 2a). PL emission spectra of **1**, **2**, **3**, **blend1** (**3**:**2**:**1**) (1.5:1.75:96.75) and **blend2** (**3**:**2**:**1**) (0.3:0.45:99,25) films are reported in Fig. 2b and the corresponding PL-QY are summarized in Table 1.

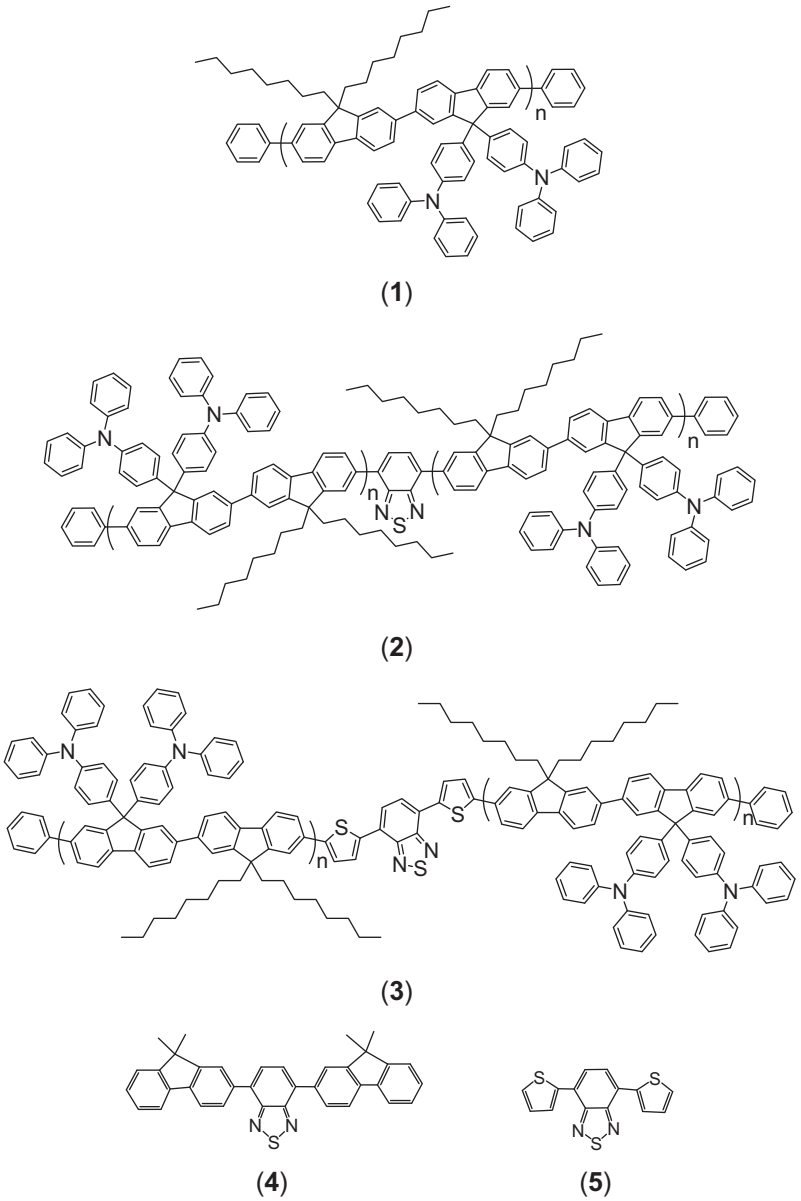

Fig. 1. Chemical structure of homopolymer (**1**) and core-type copolymers (**2**–**3**) and model compounds, oligomers (**4**–**5**).

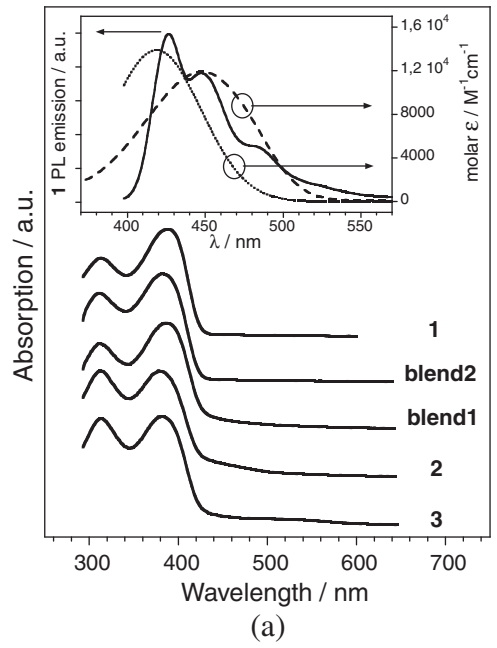

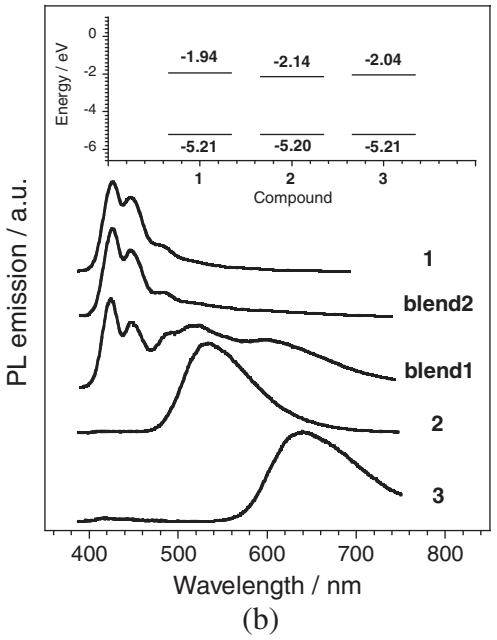

Fig. 2. (a) Normalized absorption spectra of **1**, **2**, **3**, **blend1** and **blend2** films. Spectra are vertically shifted for clarity. Inset: overlap between solid-state PL emission of **1** (solid line) and **4** (dotted line), **5** absorption in solution (dashed line); (b) PL spectra of **1**, **2**, **3**, **blend1** and **blend2** films. Spectra are vertically shifted for clarity. Inset: energy levels of the compounds.

The oligomers **4** 4,7-bis(9,9-dimethyl-9H-fluoren-2-yl)benzothiadiazole [13] and **5** 4,7-di(thiophen-2-yl) benzothiadiazole [14] are used as model compounds to theoretically investigate RET from the PF backbone towards the core dyes. Almost complete spectral overlap between the absorption of both the **4** and **5** dyes and the emission of **1** is obtained (see inset of Fig. 2a). This condition satisfies the request for an efficient RET from **1**, the excitation donor, to the core dyes, which behave as the acceptors.

The values of critical radius R_0, defined as the average distance between donor and acceptor when the RET rate is equal to the sum of all other relaxation rates of the donor are 3.1 and 3.2 nm for **2** and **3**, respectively.

The energy levels of the highest occupied molecular orbital (HOMO) and lowest unoccupied molecular orbital (LUMO) have been derived from cyclovoltammetric measurements [15] for **1**, **2**, **3** compounds and are reported in the inset of Fig. 2b. For PVK we measured only the oxidation potential, derived the HOMO, while the LUMO value is obtained by using the optical energy gap of the polymer.

The effect of the substitution at the C9 position of fluorene moiety of functional groups for linear alkyl chains on supramolecular structure and optical properties of PF copolymers has been already reported [16]. The insertion of TPA groups increases stability with respect to radical oxidation, suppressing low-energy emission band related to keto-defect formation and leading to a stable blue emission. Moreover, as we have shown in our previous work, through hindering fluorene backbone aggregation, TPA contributes to tune RET process towards the acceptor [17], otherwise too efficient to observe the contemporary emission of all the chromophores.

To obtain white emission with high quality and efficiency, a series of devices with various compounds ratios were fabricated and evaluated. Devices were prepared with the standard architecture ITO/PEDOT:PSS/AL/Ca/Al for all compounds and blends, and the multilayer ITO/PEDOT:PSS/PVK/AL/Ba/Al ones for **1**, **blend1** and **blend2** only. By using a thin conductive polymeric interlayer between PEDOT:PSS and the emitting layer, the efficiency and lifetime can be improved [18]. In fact, PEDOT:PSS acidic nature may contribute to the active polymer degradation [19] and its poor electron blocking capability does not favour a good charge balancing [20]. After annealing treatment, the low solubility of the high molecular weight PVK interlayer allows to fabricate multilayer architecture by successive solution deposition. We think that a PVK interlayer, thanks to its HOMO and LUMO energy levels position, i.e. −5.44 and −1.84 eV, respectively, is able to block the radiative excitons from direct quenching by PEDOT:PSS and thus remove a nonradiative decay channel introduced by PEDOT:PSS itself. Moreover, due to both the electrons confinement into the emissive layer (produced by the energy barrier between PVK and active layer LUMO levels), and the rising of the energy barrier at the anode that could compensate the high hole mobility of the active layer based on **1**, **2**, **3** polymers, a better charge balance is feasible. Further investigations are in progress. [21] EL spectra (Fig. 3) were measured together with their current density–luminance–voltage (*J*–*L*–*V*) curves (see Fig. 4). All devices performances are summarized in Table 1.

Electro-optical characterization of **1** showed stable EL spectrum after several operating hours, under ambient conditions differently from the easily oxidable PF-based devices. Thus Polymer **1** provides a stable blue emitter and energy donor for both **2** and **3** copolymers. In **2** and **3** EL spectra, emission of the core dyes dominates, with peaks at 538 and 625 nm, respectively.

Table 1
PL-QY, devices performances (EQE, LE, L_{MAX}), CIE of **1**, **2**, **3** compounds, **blend1** and **blend2**.

Copolymer	PL-QY [%]	EQE [%]	LE [cd/A] (Bias [V])	L_{MAX} [cd/m^2]	CIE (1931)	
					PL	EL
1	52	0.5[a]	0.11 /(6.6)	411[a]	(0.16; 0.08)	(0.18; 0.11)
		1.5[b]	0.35 (12)	295[b]		
2	91	0.7[a]	2.75 (6.6)	20200[a]	(0.36; 0.58)	(0.37; 0.58)
3	76	0.6[a]	0.96 (5)	5900[a]	(0.63; 0.33)	(0.62; 0.37)
Blend1	47	0.2[b]	0.90 (6)	8300[b]	(0.31; 0.32)	(0.30; 0.42)
Blend2	40	1.3[b]	5.80 (6.4)	21250[b]	(0.19; 0.13)	(0.32; 0.33)

[a] ITO/PEDOT:PSS/AL/Ca/Al.
[b] ITO/PEDOT:PSS/PVK/AL/Ba/Al.

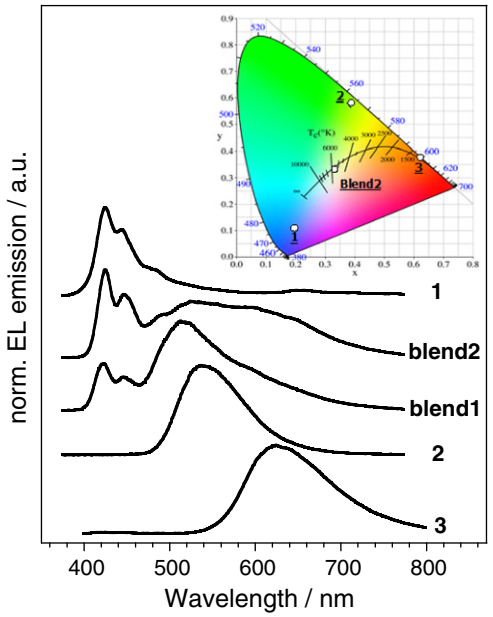

Fig. 3. EL spectra of ITO/PEDOT:PSS/AL/Ca/Al. Spectra are vertically shifted for clarity. Inset: CIE 1931 chromaticity space, also showing Planckian locus.

The high quality WOLED, with CIE (1931) chromaticity coordinates [22] (0.32; 0.33) at 7 V, a correlated colour temperature [23] of 5893 K (inset of Fig. 3) and an excellent colour rendering index [24] as high as 90, is obtained by blending **3**, **2** and **1** in the weight ratio (0.3:0.45:99.25) (**blend2**). The CIE coordinates remain in the region of white, with a slight shift to (0.34; 0.35) when the voltage is lowered to 6 V. The colour shift upon variation of the applied voltage is common in single emissive layer WOLEDs based on polymers or polymer–dye mixtures. It is usually attributed to the fact that the concentrations of acceptor chromophores (i.e. core molecular dyes with a lower energy gap with respect to the main polymer) are usually very low thus the possibility of charge trapping (see later) on such sites will decrease by increasing voltage as the low energy excited states are saturated [25]. Alternatively, the change in the emission spectra could be explained by a shift or broadening of the emission zone or a competition between electron trapping on low energy gap emitting sites and unperturbated charge transport through the organic layer [26]. By a proper balancing of relative concentration of **1**, **2** and **3** in a blend, EL spectra can be addressed in terms of the colour of the emission. Moreover, the same chemical nature, and therefore full compatibility of the components leads to a homogeneous and amorphous film with suppressed demixing tendency

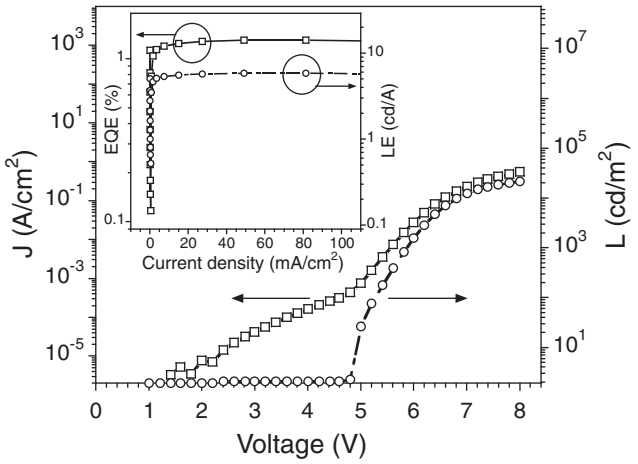

Fig. 4. *J–L–V* curves for ITO/PEDOT:PSS/PVK/**blend2**/Ba/Al device; Inset, EQE-J and LE-J curves.

as confirmed by AFM technique investigation of PFTPA-based film [11] and by PL spectra (see Fig. 5) of **blend2**, upon thermal treatment up to 150 °C for 1 h in room atmosphere. According to literature data [27], performances are further improved by optimizing device's architecture, reaching maximum EQE of 1.3% and luminance (L) of about 21250 cd/m^2 at 7 V. The corresponding maximum luminous efficiency (LE) of 5.8 cd/A (inset of Fig. 4) and power efficiency of 2.8 lm/W are remarkable for this type of blend [28]. In fact, the upper limit for device's EQE [29] based on **blend2** is expected to be around 5%. Further optimization steps are possible to reach this theoretical upper limit: we have observed on PFTPA-based polymers that, due to their amorphous character, the thermal treatments can be used to improve the efficiency of devices through the improvement of the cathode/polymer interfacial adhesion [27].

The coincidence of the current and light onsets [30] (4.8 V, Fig. 4) implies holes–electron balancing into the active layer. The observed pronounced difference in blend EL spectra as compared with corresponding PL, i.e. white PL emission from **blend1** but white EL from **blend2**, is due to a trapping of injected charge carriers on **2** and **3** compounds beside the RET mechanism discussed above. In fact, as could be deduced from energy band diagram of the compounds, the holes, once injected, can move freely in the whole bulk without energy barriers (same ionization potential for **1**, **2** and **3**) while electron would be trapped by **2** and **3** due to the lower electron affinity. Electron–hole pairs are then formed and its recombination mainly occurs on the core molecular dye. The similar energy transfer efficiency from the blue emitting polymer to the green and the red emitting copolymers, and the comparable electron-trapping aptness of the two low energy gap materials, makes the EL quite stable upon voltage variations.

Typical PL and EL micrographs of ITO/PEDOT:PSS/PVK/**blend2**/Ba/Al device are reported in Fig. 6. EL images are obtained in high luminance regime by applying a constant bias (15 V). Random areas with weaker emission are noticeable, corresponding to brighter spots in the PL micrograph. This difference in light intensity is related to preexisting defects associated with the device fabrication and not evidence of EL diode degradation. The typical dark spots previously observed in organic LEDs [31], i.e. none-missive areas due to degradation, are not visible here even after 2 h of operation in aerobic exposure.

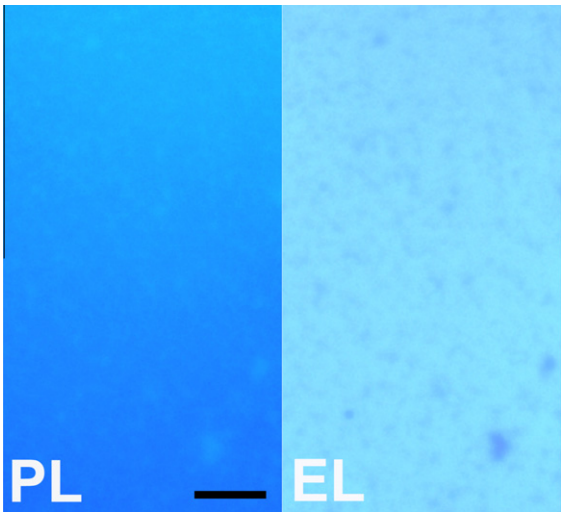

Fig. 6. PL and EL micrographs of ITO/PEDOT:PSS/PVK/**blend2**/Ba/Al device. Colours of micrographs doesn't match with real colours. The bar corresponds to 10 μm.

To support the fundamental antioxidant role of TPA groups, the comparison between PL spectra of **blend1** and **blend2** as fresh film and after 18 months aging in room atmosphere is shown in the inset of Fig. 5. Only a very weak low-energy emission band, commonly related to fluorenone formation, that usually heavily affects fluorene-based compounds emission, is observed for **blend2**, while **blend1** spectrum remains unchanged.

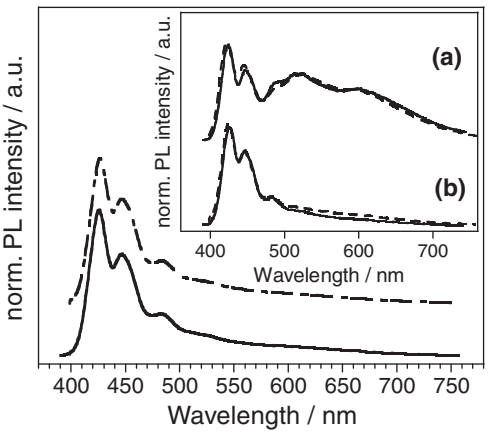

Fig. 5. Normalized PL spectra of pristine (solid line) and annealed **blend2** film (dashed line). Spectra are vertically shifted for clarity. In the inset, normalized PL spectra of fresh (solid line) and 18 months aged (dashed line) **blend1** (a) and **blend2** film (b).

4. Conclusions

In conclusion, high quality white emitting OLED in terms of CIE coordinates, EQE, CRI and stability is obtained from an all polymeric and solution processable single layer device. The excellent performance of the polymeric blend relies on both the high stability and the fully compatibility of the blue emitting PF copolymer and two green and red emitting PF based copolymers. The latter are obtained by an unprecedented core-type design approach which reduces the chemical effort in the synthesis and improve the reproducibility of the material composition with respect to random synthesized copolymers. The polymeric arms, as well as the pure blue-emitting compound, consist of an almost unoxidable fluorene-based alternating copolymer made by a triphenylamine substituted fluorene unit alternated with an alkyl substituted fluorene one. Well balanced energy transfer and electron trapping mechanisms control the colour emission in the highly homogeneous active layer blend.

Acknowledgements

This work was partially supported by Italian project MIUR-PRIN 2007PBWN44, FIRB RBIP0642YL LUCI, FIRB-RBIP06JWBH NODIS, and Fondazione Cariplo project DANAE and WOLED. The authors wish to thank to Dr. Gianni Zotti and Dr. Barbara Vercelli for cyclovoltammetric measurements. Thanks to Dr. Wojciech Mróz and to Dr. Andrea Arcari for the development of colour calculator and electrical measurements software, respectively.

References

[1] Y. Sun, N.C. Giebink, H. Kanno, B. Ma, M.E. Thompson, S.R. Forrest, Nature 440 (2006) 908–912.
[2] J.-H. Jou, M.-H. Wu, S.-M. Shen, H.-C. Wang, S.-Z. Chen, S.-H. Chen, C.-R. Lin, Y.-L. Hsieh, Appl. Phys. Lett. 95 (2009) 13307.
[3] P.-I. Shih, Y.-H. Tseng, F. -Iy Wu, A.K. Dixit, C.-F. Shu, Adv. Funct. Mater. 16 (2006) 1582–1589.
[4] X. Guo, C. Qin, Y. Cheng, Z. Xie, Y. Geng, X. Jing, F. Wang, L. Wang, Adv. Mater. 21 (2009) 3682.
[5] J.R. Lakowicz, Principles of Fluorescence Spectroscopy, second ed., Kluwer Academic Plenum Publishers, New York, 1999.
[6] S. Brovelli, F. Meinardi, G. Winroth, O. Fenwick, G. Sforazzini, M.J. Frampton, L. Zalewski, J.A. Lewitt, F. Marinello, P. Schiavuta, K. Suhling, H.L. Anderson, F. Cacialli, Adv. Funct. Mat. 20 (2010) 272–280.
[7] U. Giovanella, M. Pasini, S. Destri, W. Porzio, C. Botta, Synth. Met. 158 (2008) 113–119.
[8] J. Moreau, U. Giovanella, J-P. Bombenger, W. Porzio, V. Vohra, L. Spadacini, G. Di Silvestro, L. Barba, G. Arrighetti, S. Destri, M. Pasini, M. Saba, F. Quochi, A. Mura, G. Bongiovanni, M. Fiorini, M. Uslenghi, C. Botta, Chem. Phys. Chem. 10 (2009) 647–653;
(a) L.-O. Pålsson, A.P. Monkman, Adv. Mat. 14 (2002) 757.
[9] U. Giovanella, M. Pasini, C. Freund, C. Botta, W. Porzio, S. Destri, J. Phys. Chem. C 113 (2009) 2290–2295.
[10] X. Gong, M.R. Robinson, J.C. Ostrowski, D. Moses, G.C. Bazan, A.J. Heeger, Adv. Mater. 14 (2002) 581–585;
(a) Z.-Q. Chen, F. Ding, Z.-Q. Bian, C.-H. Huang, Org. El. 11 (2010) 369–376.
[11] A. Bolognesi, P. Betti, C. Botta, S. Destri, U. Giovanella, J. Moreau, M. Pasini, W. Porzio, Macromolecules 42 (2009) 1107.
[12] F. Huang, L. Hou, H. Shen, J. Jiang, F. Wang, H. Zhen, Y. Cao, J. Mater. Chem. 15 (2005) 2499–2507.
[13] X. Liu, R. Zhu, Y. Zhang, B. Liu, S. Ramakrishna, Chem. Commun. (2008) 3789–3791.
[14] H.A.M. van Mullekom, J.A.J.M. Vekemans, E.W. Meijer, Chem. Eur. J. 4 (1998) 1235–1243.
[15] S. Janietz, D.D.C. Bradley, M. Grell, M. Giebeler, M. Inbasekaran, E.P. Woo, Appl. Phys. Lett. 73 (1998) 2453.
[16] S.-F. Lim, R.H. Friend, I.D. Rees, J. Li, Y. Ma, K. Robinson, A.B. Holmes, E. Hennebicq, D. Beljonne, F. Cacialli, Adv. Funct. Mater. 15 (2005) 981–988.
[17] M. Pasini, U. Giovanella, P. Betti, A. Bolognesi, C. Botta, S. Destri, W. Porzio, B. Vercelli, G. Zotti, Chem. Phys. Chem. 10 (2009) 2143–2149. 12.
[18] M. Shakutsui, H. Matsuura, K. Fujita, Org. Electron. 10 (2009) 834–842;
(a) N.C. Yang, M.C. Suh, Curr. Appl. Phys. 9 (2009) 505–509;
(b) L. Duan, B.D. Chin, N.C. Yang, M.-H. Kim, H.D. Kim, S.T. Lee, H.K. Chung, Synth. Met. 157 (2007) 343–346.
[19] K.W. Wong, H.L. Yip, Y. Luo, K.Y. Wong, W.M. Lau, K.H. Low, H.F. Chow, Z.Q. Gao, W.L. Yeung, C.C. Chang, Appl. Phys. Lett. 80 (2002) 2788.
[20] H. Yan, B.J. Scott, Q. Huang, T.J. Marks, Adv. Mater. 16 (2004) 1948.
[21] U. Giovanella, P. Betti, C. Botta, S. Destri, J. Moreau, M. Pasini, W. Porzio, B. Vercelli, A. Bolognesi, Chem. Mater. (2010). doi:cm-2010-02154q.
[22] The colour space created by the International Commission on Illumination (CIE) in 1931.
[23] J. Schanda, Colorimetry: Understanding the CIE System, Wiley, 2007;
(a) N. Ohta, A.R. Robertson, Colorimetry: Fundamentals and Applications, Wiley, 2005.
[24] Colour rendering index (CRI) is a numerical measurement of how "true" colour looks when viewed with the lighting source. CRI values range from 0 to 100 with 100 represents true colour reproduction;
(a) J. Liu, L. Chen, S. Shao, Z. Xie, Y. Cheng, Y. Geng, L. Wang, X. Jing, F. Wang, Adv. Mater. 19 (2007) 4224–4228.
[25] T.-H. Kim, H.K. Lee, O.O. Park, B.D. Chin, S. Lee, J.K. Kim, Adv. Funct. Mater. 16 (2006) 611.
[26] M.C. Gather, R. Alle, H. Becker, K. Meerholz, Adv. Mater. 19 (2007) 4460–4465.
[27] J. Luo, X. Li, Q. Hou, J. Peng, W. Yang, Y. Cao, Adv. Mater. 19 (2007) 1113–1117.
[28] J.H. Kim, P. Herguth, M.-S. Kang, A.K.-Y. Jen, Y.-H. Tseng, C.-F. Shu, Appl. Phys. Lett. 85 (2004) 1116.
[29] D.Y. Kondakov, T.D. Pawlik, T.K. Hatwar, J.P. Spindler, J. Appl. Phys. 106 (2009) 124510.
[30] Current density (J) onset is defined as the bias at which current behaviour switch from ohmic to exponential one; ligh onset is defined as the bias at which $1cd/m^2$ is measured.
[31] J. McElvain, H. Antoniadis, M.R. Hueschen, J.N. Miller, D.M. Roitman, J.R. Sheats, J. Appl. Phys. 80 (1996) 6002–6007.

Organic Electronics 11 (2010) 2019–2025

Contents lists available at ScienceDirect

Organic Electronics

journal homepage: www.elsevier.com/locate/orgel

The effect of a MoO_x hole-extracting layer on the performance of organic photovoltaic cells based on small molecule planar heterojunctions

I. Hancox, P. Sullivan, K.V. Chauhan, N. Beaumont, L.A. Rochford, R.A. Hatton, T.S. Jones *

Department of Chemistry, University of Warwick, Coventry CV4 7AL, UK

ARTICLE INFO

Article history:
Received 18 June 2010
Received in revised form 4 August 2010
Accepted 21 September 2010
Available online 26 October 2010

Keywords:
Organic photovoltaics
Molecular heterojunctions
Metal oxides
Phthalocyanines
Work function
Electronic structure

ABSTRACT

We report a significant increase in the open circuit voltage (V_{oc}) and power conversion efficiency in both chloroaluminium phthalocyanine (ClAlPc)/fullerene (C_{60}) and boron subphthalocyanine chloride (SubPc)/C_{60} organic photovoltaic (OPV) cells with the insertion of a thin molybdenum oxide (MoO_x) hole-extracting layer. This improvement was not seen with copper phthalocyanine (CuPc)/C_{60}, and the addition of the MoO_x layer leads to reduced device performance for pentacene/C_{60} cells. Cells containing the MoO_x layer demonstrated significantly improved stability compared to the cells deposited on bare indium-tin oxide (ITO). External quantum efficiency (EQE) measurements taken before and after constant AM1.5G illumination for 60 min showed reduced current losses for all cells containing the MoO_x layer, especially in spectral regions where the donor layer contributes. We attribute this improvement to the increased stability at the MoO_x/donor interface.

© 2010 Elsevier B.V. All rights reserved.

1. Introduction

Organic photovoltaic (OPV) cells show great potential to be a low cost source of renewable energy. Interest in the field has grown substantially since Tang's initial discovery of the donor–acceptor small molecule planar heterojunction [1], with improvements in cell performance brought about by the use of new materials, the insertion of exciton blocking layers, and the nanostructuring of the interfaces [2,3]. Cells are now approaching the efficiencies and lifetimes required for niche commercial market applications [4], however it is widely accepted that significant further improvements in performance are still needed for commercialisation with higher power conversion efficiencies (η_p) requiring increases in open circuit voltage (V_{oc}), short circuit current density (J_{sc}) and fill factor (*FF*).

By utilising donor layers with different properties, the performance of small molecule OPV cells is constantly being improved. Wide band gap materials have enabled larger V_{oc} values, materials with high absorption coefficients give improved J_{sc}, and those with a large exciton diffusion length allow more efficient charge separation and photocurrent generation [5]. The non-planar molecule, chloroaluminium phthalocyanine (ClAlPc), has shown particular promise for small molecule OPVs due to its absorbance in the near infra-red [6], allowing greater coverage of the solar spectrum than the more commonly used planar copper phthalocyanine (CuPc) molecule [7]. Boron subphthalocyanine chloride (SubPc) has also shown recent promise as a donor material, as it produces a larger V_{oc} value due to a favourable energy level offset with the commonly employed C_{60} acceptor [8]. Heterojunctions based on oligoacenes, in particular pentacene, have also being extensively studied and benefit from the relatively long exciton diffusion length of >50 nm, allowing comparatively thicker layers to be used to increase light absorption [5,9].

Indium-tin oxide (ITO) is the most commonly used hole-extracting electrode for OPVs due to its good transparency and conductivity [10,11]. However, ITO has several disadvantages for use in organic electronics, in particular inhomogeneous electrical characteristics across

* Corresponding author. Tel.: +44 (0)24 7652 8265; fax: +44 (0)24 7652 4112.
E-mail address: t.s.jones@warwick.ac.uk (T.S. Jones).

1566-1199/$ - see front matter © 2010 Elsevier B.V. All rights reserved.
doi:10.1016/j.orgel.2010.09.014

its surface, the diffusion of indium into organic layers, poor energy level alignment with many organic materials, and variation in its properties due to processing conditions [11]. Layers of poly(ethyleneoxythiophene):poly(styrenesulfonate) (PEDOT:PSS) have been spin-coated directly on top of ITO to provide better energy level alignment with the donor material due to the higher work function of PEDOT:PSS compared to bare ITO [12]. PEDOT:PSS has been shown to give significantly improved cell performance compared to ITO for both polymer and some small molecular based OPV systems [13]. However PEDOT:PSS still retains many undesirable characteristics, in particular significant device degradation and electrical inhomogenity [14]. Additionally the acidity of the PEDOT:PSS layer can lead to damage of the underlying ITO electrode, making the material unsuitable for future commercialisation [15,16].

The recognised problems with ITO and PEDOT:PSS has resulted in considerable recent research into the development of alternative hole-extracting materials for OPV cells, in particular metal oxides. Notably, Irwin et al. incorporated a 10 nm nickel oxide (NiO) film between ITO and a poly(3-hexylthiophene) (P3HT)/[6,6]-phenyl-C_{61} butyric acid methyl ester (PCBM) blend, improving the overall cell efficiency as well as providing increased device stability [14]. Tungsten oxide (WO_3) and vanadium oxide (V_2O_5) have also been used by several groups to improve the performance of polymer-based bulk heterojunction OPV cells [17,18]. Molybdenum oxide (MoO_x) has also been investigated as a potential hole-extracting layer for both polymer and small molecule based OPV cells [17,19,20]. It has the advantage of easily controlled deposition by thermal evaporation, with little variation in properties unless deposited at extremely fast rates [21]. However different groups have reported vastly different values of the optimal MoO_x layer thickness for OPV cells, varying between 3.5 and 50 nm, with the most commonly reported value being 5 nm [17,22]. The impact the MoO_x layer has on cell performance also varies widely in the literature. For example, Shrotriya et al. state that with a 5 nm layer of MoO_x, a P3HT/PCBM bulk heterojunction demonstrates a significantly improved V_{oc}, J_{sc} and *FF* when compared with the same cells fabricated on bare ITO [17]. By contrast, Kinoshita et al. showed that the V_{oc} of a tetraphenylporphyine/C_{60} cell increased greatly with an optimal MoO_x layer thickness of 50 nm, but J_{sc} remained comparable to the same cells fabricated on bare ITO [19]. Kim et al. found the insertion of MoO_x gave a significant increase in the *FF* in both a CuPc/C_{60} and a ClAlPc/C_{60} bulk heterojunction, due to a decrease in series resistance, R_s. They also reported an increased *FF* for a P3HT/PCBM bulk heterojunction compared to deposition on PEDOT:PSS/ITO [23].

Initial studies of thermally evaporated MoO_x layers indicated that the valence band and conduction band are at 5.3 and 2.3 eV, respectively [17,24,25]. More recently reported results show that these values are far greater, ranging between 9.37–9.70 eV and 6.18–6.70 eV, respectively [25–27]. The same reports suggest that MoO_x is a strongly *n*-type material, with the work function only 0.16–0.60 eV below the LUMO, and that there is a large positive vacuum level (V_l) shift for the MoO_x compared to that of the ITO substrate [25–27]. A negative V_l shift occurs from the MoO_x to the V_l of the organic material, due to formation of an interface dipole as a result of charge transfer. However, this still leads to a substantial barrier to hole-extraction through the MoO_x valence band for OPV devices. Kanai et al. reported evidence from ultra-violet photoemission spectroscopy (UPS) measurements of gap states within the MoO_x layer due to oxygen deficiencies, that facilitate hole-extraction from the organic layer [26]. Kröger et al. did not directly observe the gap states [25]. In the same study, WO_x was found to have a conduction band of 6.27 eV, a work function of 6.47 eV and a valence band of 9.66 eV, which are 0.53, 0.39 and 0.02 eV smaller than the corresponding MoO_x values.

In this paper we compare the performance of four different donor/C_{60} small molecule OPV cells using pentacene, CuPc, ClAlPc and SubPc, showing the different effects of inserting an optimised MoO_x interlayer on planar heterojunctions possessing different electronic energy levels (Fig. 1). Significant improvements in performance are seen for ClAlPc and SubPc, but not with CuPc or pentacene, the latter having a poorer performance after inclusion of the MoO_x layer. In all four systems the incorporation of MoO_x results in significantly improved cell stability. The changes in cell performance are attributed to the different electronic structure at the MoO_x/donor interface, whilst the improved overall stability is rationalised by the thin oxide layer providing a more stable electrode/donor interface.

2. Experimental methods

Devices were fabricated on commercially available ITO-coated glass substrates (Psiotec, 100 nm ITO thickness) after initial solvent cleaning. The ITO was then treated in ultraviolet/ozone to remove carbon residues. Organic layers were grown by vacuum deposition in a Kurt J. Lesker Spectros system with a base pressure of about 5×10^{-8} mbar. The organic materials used: pentacene (Aldrich – 99.9%), CuPc (Aldrich – 97%), ClAlPc (Acros Organics – 98%), SubPc (Aldrich – 85%), C_{60} (MER Corp – 99.5%) and bathocuproine (BCP, Aldrich), were all purified by thermal gradient sublimation before deposition. MoO_x and WO_x (Aldrich – 99.99%) were used as received. A deposition rate of 0.10 nm s^{-1} was used for pentacene, CuPc, ClAlPc, SubPc and BCP, with C_{60} grown at 0.05 nm s^{-1}. The aluminium cathodes were deposited *in situ* by evaporation through a shadow mask, to a thickness of 100 nm, to give an active

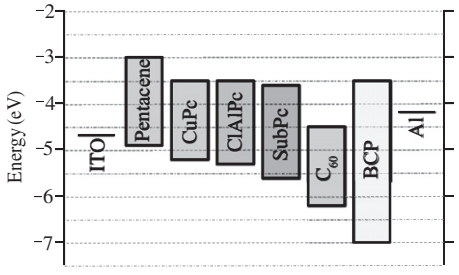

Fig. 1. Summary of the electronic energy levels for each material used in the OPV devices.

area of 0.16 cm^2. Data for direct comparison was obtained by simultaneous deposition of the same cells on both bare ITO and ITO/MoO_x.

Current–voltage (*J–V*) curves were measured using a Keithley 2400 sourcemeter under AM1.5G solar illumination at 100 mW cm^{-2} (1 sun) from a Newport Oriel solar simulator. External quantum efficiency (EQE) measurements were also carried out using this source, calibrated to a photodiode and signal measured using a Stanford research SR 830 lock-in amplifier. Atomic force microscopy (AFM) images were obtained using an Asylum Research MFP-3D (Santa Barbara, USA) in AC mode. A PANalytical X'Pert PRO diffractometer with Cu Kα radiation was used for X-ray diffraction (XRD). UV/vis absorption spectra were obtained using a Perkin-Elmer Lambda 25 spectrometer.

3. Results and discussion

Throughout this work the basic planar heterojunction cell architecture grown was ITO/*d* nm MoO_x/donor material/40 nm C_{60}/8 nm BCP/Al, with each donor layer thickness stated where appropriate. The optimum MoO_x layer thickness (*d*) was found to be 5 nm for cells fabricated with an optimised 20 nm ClAlPc donor layer. Deposition of $d < 5$ nm resulted in incomplete coverage of the ITO surface, with the donor layer in contact with both the ITO and MoO_x, and a range of V_{oc} values obtained in between that of the bare ITO cells and the optimised MoO_x/ITO system. Increasing *d* beyond 5 nm results in a reduction in both J_{sc} and *FF;* there is no additional gain in V_{oc} and so η_p decreases from 2.6% when $d = 5$ nm to 1.8% with $d = 50$ nm. The *J–V* curves shown in Fig. 2 show a clear increase in series resistance, R_s, with increased *d.* This detrimental increase in R_s is caused by the increased MoO_x layer thickness weakening the built-in electric field of the cells. Table 1 provides a summary of the data obtained for optimisation of *d* in the ClAlPc system.

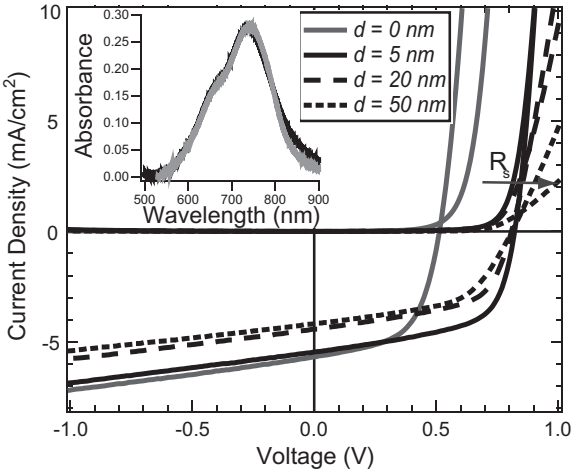

Fig. 2. *J–V* curves obtained under AM1.5G illumination for OPV devices with structures ITO/*d* nm MoO_x/20 nm ClAlPc/40 nm C_{60}/8 nm BCP/Al. The inset shows the corresponding UV–vis data for the ClAlPc/C_{60} heterojunction on bare ITO (grey line) and ITO/5 nm MoO_x (black line).

Table 1
Summary of cell performance parameters obtained from OPV cells grown on ITO/MoO_x, with the thickness (*d*) of the MoO_x layer varying between $d = 0$ and 50 nm, for the cell architecture ITO/*d* nm MoO_x/20 nm ClAlPc/40 nm C_{60}/8 nm BCP/Al.

d (nm)	V_{oc} (V)	J_{sc} (mA cm^{-2})	*FF*	η_p (%)
0	0.51 ± 0.03	5.68 ± 0.20	0.57 ± 0.01	1.6
2.5	0.78 ± 0.03	5.28 ± 0.40	0.50 ± 0.09	2.0
5	0.82 ± 0.01	5.46 ± 0.10	0.58 ± 0.01	2.6
10	0.81 ± 0.01	4.68 ± 0.10	0.58 ± 0.03	2.2
20	0.81 ± 0.01	4.43 ± 0.05	0.56 ± 0.01	2.0
50	0.81 ± 0.01	4.02 ± 0.05	0.55 ± 0.03	1.8

Table 2
Summary of cell performance parameters obtained from OPV planar heterojunction cells grown on bare ITO ($d = 0$ nm) and MoO_x ($d = 5$ nm) and WO_x ($d = 5$ nm) using four different donor materials.

Donor material; *d* (nm)	V_{oc} (V)	J_{sc} (mA cm^{-2})	*FF*	η_p (%)
ClAlPc; 0	0.51 ± 0.03	5.68 ± 0.20	0.57 ± 0.01	1.6
ClAlPc; 5	0.82 ± 0.01	5.46 ± 0.10	0.58 ± 0.01	2.6
ClAlPc; 5 (WO_x)	0.77 ± 0.01	5.47 ± 0.18	0.56 ± 0.01	2.3
SubPc; 0	0.82 ± 0.03	5.22 ± 0.23	0.47 ± 0.01	2.0
SubPc; 5	1.05 ± 0.05	5.49 ± 0.10	0.51 ± 0.01	3.0
CuPc; 0	0.47 ± 0.02	4.47 ± 0.40	0.53 ± 0.02	1.1
CuPc; 5	0.46 ± 0.01	4.37 ± 0.26	0.51 ± 0.05	1.0
Pentacene; 0	0.42 ± 0.02	6.43 ± 0.66	0.51 ± 0.02	1.4
Pentacene; 5	0.43 ± 0.03	6.06 ± 0.60	0.48 ± 0.03	1.2

For both the 20 nm ClAlPc and 14 nm SubPc cells, a large increase in V_{oc} and η_p is seen with the insertion of $d = 5$ nm MoO_x compared to bare ITO. In the ClAlPc cell, V_{oc} increases from 0.51 V (ITO) to 0.82 V (ITO/5 nm MoO_x), resulting in a substantial increase in η_p from 1.6% to 2.6%. Insertion of the MoO_x layer gives a similar *FF* but marginally lower J_{sc} when compared to the same cell fabricated on bare ITO. It is worth noting that the work function of the ITO substrates were measured by Kelvin probe to be 4.7 eV, leading to a relatively low V_{oc} for the ClAlPc cells fabricated on bare ITO. As a comparison, ITO/5 nm WO_x/20 nm ClAlPc/40 nm C_{60}/8 nm BCP/Al cells were also fabricated generating the device results shown in Table 2. The WO_x cells produce V_{oc} and η_p values in between those of the same cells grown on bare ITO and on MoO_x, with 0.77 V and 2.3%, respectively. For the SubPc system there is a similar improvement in η_p, from 2.0% to 3.0% for ITO and ITO/5 nm MoO_x respectively, mainly due to the increase in V_{oc} from 0.82 to 1.05 V (Fig. 3). The use of MoO_x also leads to a slight improvement in J_{sc} and *FF*, and the cell data is summarised in Table 2.

For the 30 nm CuPc cell the introduction of the MoO_x layer causes a small drop in η_p from 1.1% for bare ITO to 1.0% with ITO/5 nm MoO_x, as shown in Fig. 4. The V_{oc} values are similar in both cases, but the *FF* and J_{sc} both decrease slightly with the introduction of the MoO_x layer. The performance of the 43 nm pentacene cell decreases significantly with the insertion of the MoO_x, with η_p reduced from 1.4% to 1.2% for $d = 5$ nm. This reduction in performance is mainly due to the lower values obtained for J_{sc} and *FF* for the cells fabricated with MoO_x. Fig. 5 shows that the insertion of a 5 nm MoO_x layer leads to increased R_s and a less ideal shunt resistance, R_{sh}.

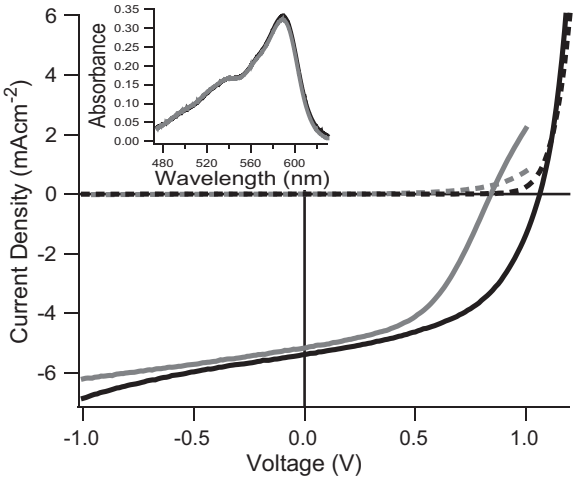

Fig. 3. *J–V* curves obtained under AM1.5G illumination for OPV devices with structures ITO/*d* nm MoO_x/14 nm SubPc/40 nm C_{60}/8 nm BCP/Al, for *d* = 0 nm (grey line) and *d* = 5 nm (black line). The inset shows the corresponding UV–vis data for the SubPc/C_{60} heterojunction on bare ITO (grey line) and ITO/5 nm MoO_x (black line).

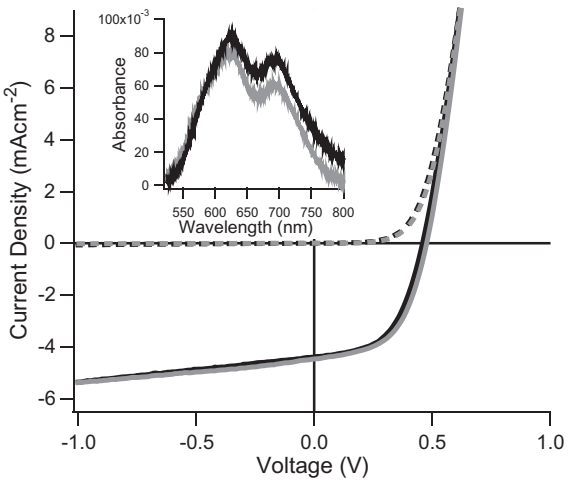

Fig. 4. *J–V* curves obtained under AM1.5G illumination for devices with structures ITO/*d* nm MoO_x/30 nm CuPc/40 nm C_{60}/8 nm BCP/Al, for *d* = 0 nm (grey line) and *d* = 5 nm (black line). The inset shows the corresponding UV–vis data for the CuPc/C_{60} heterojunction on bare ITO (grey line) and ITO/5 nm MoO_x (black line).

The factors influencing the changes in cell performance were explored for each of the four OPV heterojunction systems. To establish whether the changes in cell performance can be attributed to any modification of the structure and morphology of the donor layers as a consequence of deposition on the MoO_x layer, AFM, UV/vis absorption and XRD measurements were performed on each of the four donor layer films. The root mean square roughness (R_q) of the surfaces of bare ITO and ITO/5 nm MoO_x were extracted from topographic AFM images and are very similar, with R_q = 4.2 and 4.0 nm respectively. Similar topological features were seen in both cases, suggesting that a homogenous coverage of the ITO surface by a thin 5 nm MoO_x

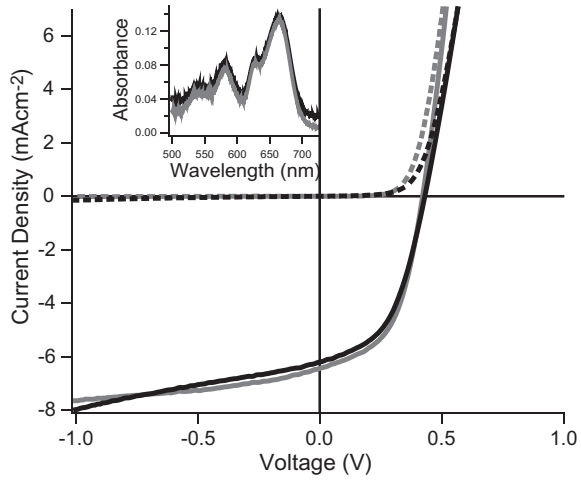

Fig. 5. *J–V* curves obtained under AM1.5G illumination for devices with structures ITO/*d* nm MoO_x/43 nm pentacene/40 nm C_{60}/8 nm BCP/Al, for *d* = 0 nm (grey line) and *d* = 5 nm (black line). The inset shows the corresponding UV–vis data for the pentacene/C_{60} heterojunction on bare ITO (grey line) and ITO/5 nm MoO_x (black line).

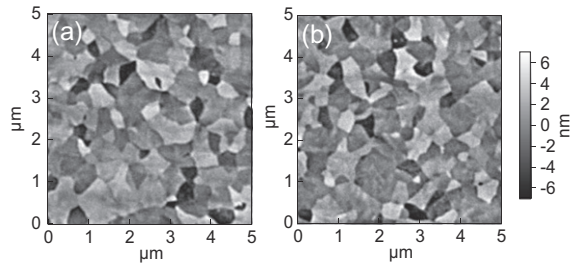

Fig. 6. AFM topography images of (a) ITO/14 nm SubPc and (b) ITO/5 nm MoO_x/14 nm SubPc.

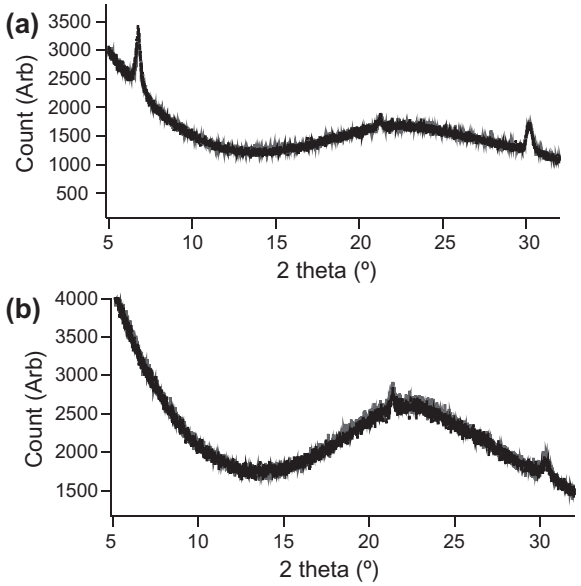

Fig. 7. Thin film XRD scans for (a) ITO/80 nm CuPc (grey line) and ITO/5 nm MoO_x/80 nm CuPc (black line), and (b) ITO/80 nm ClAlPc (grey line) and ITO/5 nm MoO_x/80 nm ClAlPc (black line).

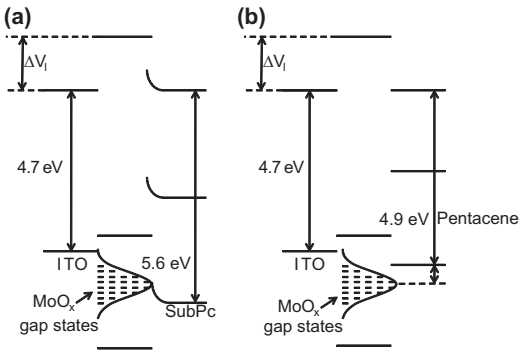

Fig. 8. Schematic of the effect of the MoO_x layer to device performance in (a) SubPc/C_{60} and (b) pentacene/C_{60} OPV cells.

layer does not lead to an electrode surface with its own distinct morphology. Each donor layer also gave a negligible change in R_q when deposited on 5 nm MoO_x. As an example, the AFM images in Fig. 6 compare the morphology of a thin SubPc layer grown on ITO and ITO/MoO_x. The similar R_q values of 2.3 and 2.4 nm suggest that surface morphology does not cause any significant changes in device behaviour when incorporating the MoO_x layer. The UV/vis absorption spectra of each donor material also showed negligible difference for thin films deposited on bare ITO and ITO/MoO_x; the main absorption peaks are shown in the insets of Figs. 2–5 for ClAlPc, SubPc, CuPc and pentacene, respectively. Fig. 7 shows XRD data obtained for 80 nm thick layers of CuPc (Fig. 7a) and ClAlPc (Fig. 7b) on both bare ITO and MoO_x. The XRD shows no shift in the main CuPc peak at $2\theta = 6.8^\circ$ after growth on MoO_x, indicating very little change in molecular stacking. Similarly, for ClAlPc layers the XRD results show the material to be essentially amorphous on both bare ITO and MoO_x (Fig. 7b). This rules out any effects such as templating, that have been recently demonstrated when using thin organic interlayers such as 3,4,9,10-perylenetetracarboxylic dianhydride (PTCDA) [28,29]. These results demonstrate clearly that the MoO_x layer has very little influence on the molecular stacking within the donor layer and the resulting thin film structure, morphology and absorption properties [17,19,20,23].

We propose that a possible reason for the increase in V_{oc} with the insertion of the thin MoO_x layer for the SubPc and ClAlPc cells is the difference in the electronic properties at the MoO_x/donor interface. These donor materials have

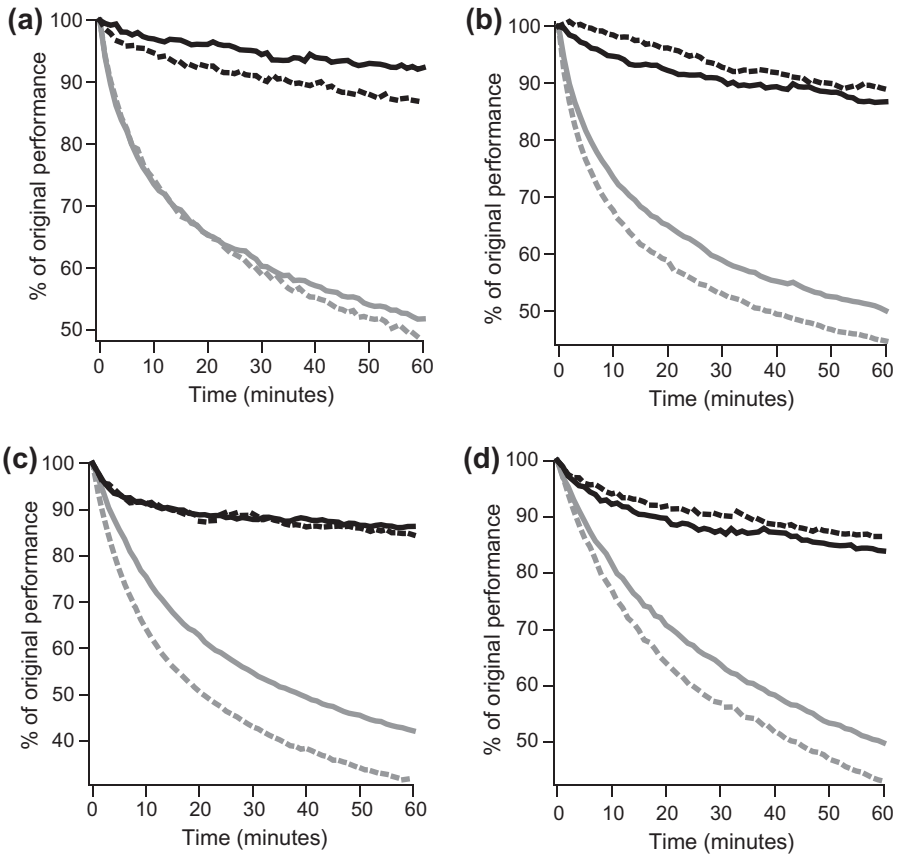

Fig. 9. Device degradation data for percentage decrease of η_p under constant illumination at 1 sun for 60 min for (a) ITO/d nm MoO_x/20 nm ClAlPc/40 nm C_{60}/8 nm BCP/Al, (b) ITO/d nm MoO_x/14 nm SubPc/40 nm C_{60}/8 nm BCP/Al, (c) ITO/d nm MoO_x/30 nm CuPc/40 nm C_{60}/8 nm BCP/Al, (d) ITO/d nm MoO_x/43 nm pentacene/40 nm C_{60}/8 nm BCP/Al. For each grey and black lines are for $d = 0$ and 5 nm, respectively, with solid lines and dashed lines representing N_2 and air atmospheres respectively.

relatively high ionisation potentials and are therefore likely to exhibit significant band bending towards the gap states in the MoO_x layer, due to interface dipole effects from charge transfer [23,27], thus allowing more efficient hole-extraction from the more favourable electronic energy level alignment at the hole-extracting electrode. A very recent study by Kanai et al. on α-NPD/MoO_x/Au interfaces suggested that defects in the MoO_x layer allow charge collection from gap states [26]. We speculate that a similar favourable energy level alignment exists for the ClAlPc and SubPc OPV cells grown on MoO_x, as shown schematically in Fig. 8a. This alignment leads to a reduced loss in the built-in field of the cells and facilitates an increase in V_{oc}, as seen in the data in Table 2. The gap states within WO_x interlayers are likely to be positioned between the work function of bare ITO and the position of the gap states of MoO_x [25]. For ClAlPc and SubPc, the ability of the WO_x layers to extract holes efficiently should be better than bare ITO but not as favourable as MoO_x. This is shown in the resulting cell performance, with the V_{oc} values obtained being higher than for bare ITO, but not as large as the values obtained for the same cells fabricated on MoO_x.

For the CuPc OPV cell, the J_{sc} and *FF* are marginally decreased with the insertion of MoO_x, and for the pentacene cells, insertion of the MoO_x layer has a significant detrimental impact on cell performance. The smaller ionisation potential of these donor materials leads to a less favourable alignment with the MoO_x gap states and there is no benefit from any band bending effects, leading to less efficient hole-extraction compared to bare ITO (Fig. 8b). In this case there is an approximately 6% decrease in charge collection and a concomitant reduction in *FF*.

Although insertion of the MoO_x layer did not result in improved cell efficiencies for all of the four planar heterojunction systems studied, the overall stability of the cells was significantly improved in every case. Device variation for all cells grown on MoO_x was less (Table 2), the MoO_x layer providing an electrode surface with a more homogeneous work function and eliminating the 'hot' and 'dead' spots commonly present on bare ITO.

Each cell was tested under 60 min of continuous illumination at 100 mW cm^{-2} AM1.5G for both d = 0 and 5 nm of MoO_x. These measurements were performed under both N_2 and air atmospheres in order to test the degradation characteristics of each cell. Fig. 9 shows the change in η_p for each system, in terms of a percentage of the original performance of the cell. For ClAlPc on bare ITO, η_p dropped by 51% and 46% in air and N_2, respectively. This significant reduction in performance is due to the large decrease in V_{oc} and J_{sc}, which also produces a loss in *FF*. However, with the insertion of 5 nm MoO_x, η_p is reduced by only 13% and 8% under air and N_2 respectively. In this case there is little change in V_{oc} and *FF*, and a smaller loss in J_{sc} compared to the cell fabricated on bare ITO.

Fig. 9 shows comparable degradation performances for cells fabricated with the different donor layers. With d = 0 nm in an air atmosphere, η_p drops by 55%, 69% and 57% for SubPc, CuPc and pentacene cells, respectively. The degradation is only marginally less in an N_2 atmosphere. Inserting the 5 nm MoO_x layer greatly improves the stability of each cell with similar performances in both air and N_2 for each system. Of particular note is the stability of V_{oc} for the cells fabricated using the MoO_x interlayer, in addition to less degradation in J_{sc} and *FF*. Due to the severity of the degradation for the pentacene and CuPc cells on bare ITO, and the relative stability of the same cells after inserting MoO_x, it appears that it is still advantageous to fabricate these cells on the oxide interlayer for improved stability, despite the lower initial performance with these particular donor materials.

EQE measurements were performed before and after cell degradation under constant illumination and are shown in Fig. 10 for the SubPc system on both bare ITO and ITO/MoO_x. On MoO_x the overall degradation is less across the whole spectrum when compared to bare ITO, but the least degradation is between 550 and 650 nm, which is the region corresponding to the SubPc contribution. This indicates increased stability for the MoO_x/SubPc interface compared to ITO/SubPc. The large degradation for the bare ITO cells is likely to be due to diffusion of oxygen from the ITO into the active layer, a process that has been well documented in the literature [30–32]. Illumination is also known to accelerate the oxidation of the donor

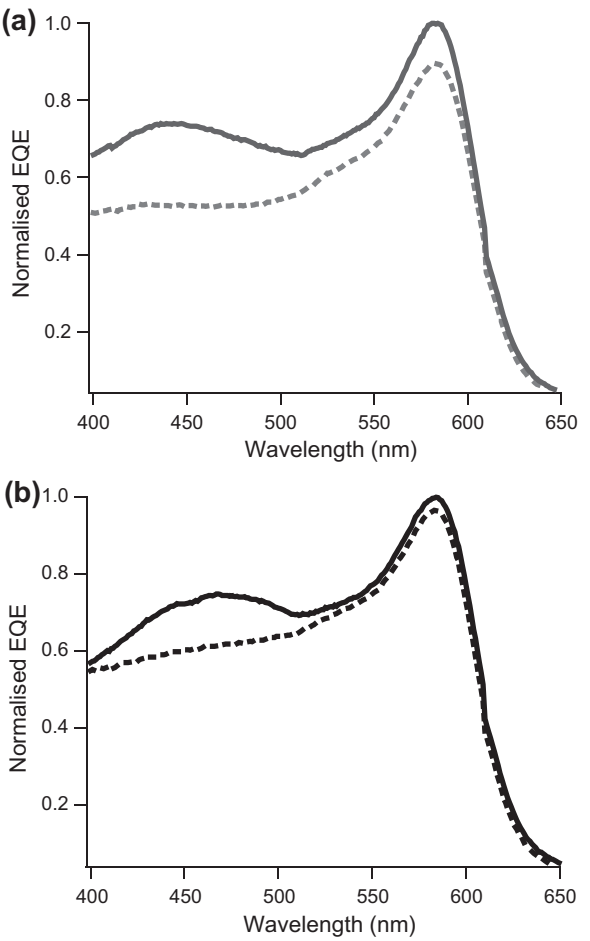

Fig. 10. EQE data taken before (solid lines) and after (dashed lines) degradation for 1 h under constant illumination for (a) ITO/14 nm SubPc/40 nm C_{60}/8 nm BCP/Al and (b) ITO/5 nm MoO_x/14 nm SubPc/40 nm C_{60}/8 nm BCP/Al.

layers [32]. These undesirable reactions cause disruption to the charge transport paths and morphology, reducing J_{sc}, and leading to charge build up. This charge build up opposes the built-in electric field of the cell and hence lowers the resulting V_{oc} for the ITO cells. However the MoO_x layer is able to act as a barrier and also has the advantage of being oxygen deficient and so is an ideal layer to minimise the chance of oxidation reactions being able to occur. Therefore the cells containing the MoO_x layer show increased stability, due to the interface between MoO_x and the donor materials.

4. Conclusions

We have demonstrated how the performance of OPV cells fabricated using planar molecular heterojunctions is influenced by the insertion of a 5 nm thin film of MoO_x for four different donor materials. Using ClAlPc and SubPc donor layers the η_p of the cells increases by ~60% and 50% respectively, predominantly due to increases in V_{oc} in both cases. The inclusion of MoO_x produces a marginally lower performance for CuPc based cells, and hinders the performance of cells with pentacene as a donor layer. We propose that the increase in V_{oc} for the ClAlPc and SubPc systems with the insertion of the MoO_x layer is likely to be due to band bending of the donor layers towards the more favourable energy alignment with the MoO_x gap states in comparison to the bare ITO, allowing more efficient extraction of holes at the interface. The performance decreases in the CuPc and pentacene systems are possibly due to detrimental energy alignment and band bending to the MoO_x layer for hole-extraction, leading to reduced hole-extraction efficiency.

Insertion of the MoO_x hole-extracting layer reduces the variability of the cells in each heterojunction system, a consequence of the more homogeneous work function across the surface. With cell degradation often overlooked in small molecule OPVs, degradation studies were carried out for each system on both bare ITO and MoO_x, in air and N_2 atmospheres. Incorporating MoO_x improves significantly improves the characteristics of the cells compared to bare ITO. Higher relative cell performance was obtained for all systems with the MoO_x layer inserted after 60 min of constant illumination at 1 sun, regardless of whether initial performance was preferable on bare ITO.

Acknowledgements

This work was supported through the Energy Programme of the Research Councils UK as well as the Advantage West Midlands Science City Materials Initiative (Project 2). R.A.H. is supported by a Royal Academy of Engineering/EPRSC Research Fellowship and I.H. is supported by Asylum Research UK.

References

[1] C.W. Tang, Appl. Phys. Lett. 48 (1986) 183–185.
[2] S. Schumann, S.A.F. Bon, R.A. Hatton, T.S. Jones, Chem. Commun. 42 (2009) 6478–6480.
[3] P. Sullivan, S. Heutz, S.M. Schultes, T.S. Jones, Appl. Phys. Lett. 84 (2004) 1210.
[4] M. Reide, T. Mueller, W. Tress, R. Schueppel, K. Leo, Nanotechnology 19 (2008) 424001.
[5] P. Peumans, A. Yakimov, S.R. Forrest, J. Appl. Phys. 93 (2003) 3693.
[6] R.F. Salzman, B.P. Rand, S.R. Forrest, Appl. Phys. Lett. 91 (2007) 013508.
[7] J. Xue, S. Uchida, B.P. Rand, S.R. Forrest, Appl. Phys. Lett. 84 (2004) 3013.
[8] K.L. Mutolo, E.I. Mayo, B.P. Rand, S.R. Forrest, M.E. Thompson, J. Am. Chem. Soc. 128 (2006) 8108.
[9] P. Sullivan, T.S. Jones, Org. Electron. 9 (2008) 656.
[10] J. Cui, A. Wang, N.L. Edleman, J. Ni, P. Lee, N.R. Armstrong, T.J. Marks, Adv. Mater. 13 (2001) 1476.
[11] N.R. Armstrong, P.A. Veneman, E.L. Ratcliff, D. Placencia, M. Brumbach, Acc. Chem. Res. 42 (2009) 1748.
[12] M. Granstrom, A.C. Arias, A. Lux, M.R. Andersson, R.H. Friend, Nature 395 (1998) 257.
[13] Y. Kim, A.M. Ballantyne, J. Nelson, D.D.C. Bradley, Org. Electron. 10 (2009) 205.
[14] M.D. Irwin, A.W. Hains, R.P.H. Chang, T.J. Marks, Proc. Natl. Acad. Sci. USA 105 (2008) 2783.
[15] E.L. Ratcliff, P.A. Lee, N.R. Armstrong, J. Mater. Chem. 20 (2010) 2672.
[16] M. Girtan, M. Rusu, Sol. Energy Mater. Sol. Cells 94 (2010) 446.
[17] V. Shrotriya, G. Li, Y. Yao, C.W. Chu, Y. Yang, Appl. Phys. Lett. 88 (2006) 073508.
[18] C. Tao, S. Ruan, G. Xie, X. Kong, L. Shen, F. Meng, C. Liu, X. Zhang, W. Dong, W. Cheng, Appl. Phys. Lett. 94 (2009) 043311.
[19] Y. Kinoshita, R. Takenaka, H. Murata, Appl. Phys. Lett. 92 (2008) 243309.
[20] L. Cattin, F. Dahou, Y. Lare, M. Morsli, R. Tricot, S. Houari, A. Mokrani, K. Jondo, A. Khelil, K. Napo, J.C. Bernede, J. Appl. Phys. 105 (2009) 034507.
[21] C.T. Lin, M.H. Chen, S.H. Hsu, C.I. Wu, T.W. Pi, J. Appl. Phys. 107 (2010) 053703.
[22] I. Hancox, K.V. Chauhan, P. Sullivan, R.A. Hatton, A. Moshar, C.P.A. Mulcahy, T.S. Jones, Energy Environ. Sci. 3 (2010) 107.
[23] D.Y. Kim, J. Subbiah, G. Sarasqueta, F. So, H. Ding, Irfan, Y. Gao, Appl. Phys. Lett. 95 (2009) 093304.
[24] C. Tao, S. Ruan, X. Zhang, G. Xie, L. Shen, X. Kong, W. Dong, C. Liu, W. Chen, Appl. Phys. Lett. 93 (2008) 193307.
[25] M. Kroeger, S. Hamwi, J. Meyer, T. Riedl, W. Kowalsky, A. Kahn, Appl. Phys. Lett. 95 (2009) 123301.
[26] K. Kanai, K. Koizumi, S. Ouchi, Y. Tsukamoto, K. Sakanoue, Y. Ouchi, K. Seki, Org. Electron. 11 (2010) 188.
[27] Irfan, H. Ding, Y. Gao, D.Y. Kim, J. Subbiah, F. So, Appl. Phys. Lett. 96 (2010) 073304.
[28] P. Sullivan, T.S. Jones, A.J. Ferguson, S. Heutz, Appl. Phys. Lett. 91 (2007) 233114.
[29] K.V. Chauhan, P. Sullivan, J.L. Yang, T.S. Jones, J. Phys. Chem. C 114 (2010) 3304.
[30] J.C. Scott, J.H. Kaufman, P.J. Brock, R. DiPietro, J. Salem, J.A. Goitia, J. Appl. Phys. 79 (1996) 2745–2751.
[31] F.C. Krebs, K. Norrman, Prog. Photovolt. Res. Appl. 15 (2007) 697–712.
[32] M. Jorgensen, K. Norrman, F.C. Krebs, Sol. Energy Mater. Sol. Cells 92 (2008) 686–714.

Organic Electronics 11 (2010) 2026–2031

Contents lists available at ScienceDirect

Organic Electronics

journal homepage: www.elsevier.com/locate/orgel

Letter

Complementary transfer-assisted patterning of high-resolution heterogeneous elements on plastic substrates for flexible electronics

Wonsuk Choi, Min-Hoi Kim, Yu-Jin Na, Sin-Doo Lee *

School of Electrical Engineering and Computer Science, #32, Seoul National University, Kwanak, P.O. Box 34, Seoul 151-600, Republic of Korea

ARTICLE INFO

Article history:
Received 6 July 2010
Received in revised form 12 August 2010
Accepted 28 September 2010
Available online 26 October 2010

Keywords:
Complementary transfer-assisted patterning
OTFT
Short-channel
High-resolution patterning

ABSTRACT

We developed a versatile platform to construct heterogeneous organic and metallic elements with micrometer features on a plastic substrate in a complementary transfer-assisted patterning (CTAP) scheme. The underlying concept relies on a high-resolution transfer-printing process of a sacrificial layer, producing complementary patterns of the elements, in combination with a lift-off technique for removing the sacrificial layer to leave only active patterns on a variety of substrates. No detrimental errors in sequentially defining patterns of both an organic material and a metal are involved during lifting-off the sacrificial layers in multilayer architecture. We demonstrated the generic principle of the CTAP in the fabrication of short-channel organic thin film transistors on glass substrates and organic inverters on plastic substrates for flexible electronics.

© 2010 Elsevier B.V. All rights reserved.

Recently, organic electronic materials have been attracted for the fabrication of a new class of electronic components needed for low-cost and flexible applications ranging from smart cards [1–3] and e-papers [4,5] to flexible information displays [6–9]. For such applications, the construction of basic components such as organic thin-film-transistors (OTFTs) and inverters satisfying proper levels of the driving current, the current on–off ratio, and the operational speed requires a simple and reliable patterning scheme of precisely defining active channels of an organic semiconductor and gate/source/drain electrodes in multilayered structures on a variety of substrates. In heterogeneous organic multilayers that necessarily form interfaces at a semiconductor–insulator, a semiconductor–electrode, and an insulator–electrode, it is critical to pattern each functional layer without causing the degradation of the material characteristics in the subsequent layer formation. Among the recently developed patterning techniques, an advanced photolithographic method, based on the use of an orthogonal solvent dissolving a new type of a photoresist [10,11], is promising for fabricating organic electronic devices. However, this photolithography still involves the patterning complexity and may experience the deterioration of underlying organic layers in multilayer architecture by the exposure of strong ultraviolet (UV) light. An interesting variant approach is based on the use of a screen-printed photoresist layer as a shadow mask [12], which is rather simple but limits feature resolutions. As another type, a dry-lift off method using metal patterns to peel-off residual layers of active organic materials has been demonstrated in organic patterns down to 4 μm [13] but it inevitably requires high pressure and temperature during patterning the metals.

In this work, we developed a complementary transfer-assisted patterning (CTAP) approach as a simple and generic platform to pattern heterogeneous organic/metal elements in high-resolution. The basic principle is the generation of high-resolution patterns of a sacrificial layer by transfer printing, complementary to active element patterns, and the lift-off of the sacrificial layer using a chemically inert solvent to leave only active patterns on a substrate. The unit process of the CTAP technique is described as follows: (i) high-resolution patterns of a sacrificial layer of a fluorous-polymer prepared on an elastomeric

* Corresponding author. Tel.: +82 2 880 1823; fax: +82 2 874 9769.
E-mail address: sidlee@plaza.snu.ac.kr (S.-D. Lee).

1566-1199/$ - see front matter © 2010 Elsevier B.V. All rights reserved.
doi:10.1016/j.orgel.2010.09.017

stamp are directly transfer-printed onto a substrate, (ii) an organic or a metallic layer is blanket-deposited over the entire surface of the substrate having transfer-printed patterns of the sacrificial layer, and (iii) the sacrificial layer is subsequently removed using an inert fluorous-solvent to leave only active regions that are complementary to the transfer-printed patterns of the sacrificial layer on the substrate. Fabrication of organic thin film transistors (OTFTs) using sequential CTAP processes of an organic semiconductor and metals is illustrated in Fig. 1. For preparing a sacrificial layer, a fluorous-polymer (Novec™ EGC-1700, 3M) dissolved in a fluorous-solvent (Novec™ HFE-7100, 3M) was first coated on the surface of an elastomeric stamp with predefined patterns. The fluorous-solvent is known to be chemically compatible to most of organic materials, and thus it involves essentially no disruption of heterogeneous multilayers during repetitive CTAP processes. Polydimethylsiloxane (PDMS) was chosen for fabricating a stamp to ensure low adhesion at the interface between the stamp and the fluorous-polymer layer because of a low surface energy. Note that, in contrast to a metal-based dry lift-off method [12] requiring high pressure or heat, intimate contact between the sacrificial layer and the substrate is spontaneously produced when the stamp is placed on the substrate. Thus any mechanical and/or physical damage on the underlying layer will be avoided during the transfer-printing. The formation of an organic semiconductor (OS) layer on a gate insulator (I) was shown in Fig. 1(a). In our study, poly(vinyl cinnamate) (PVCi) dissolved in cyclopentanone in 10 wt.% was spin coated at the rate of 3000 rpm for 30 s for a gate insulator [14]. Patterns of the sacrificial layer (SL) of about 600 nm thick, prepared on stamp 1 from a fluorous-polymer solution of 4% in concentration, were transfer-printed on the top of the PVCi film. The pentacene film for the OS layer was then blanket-deposited at the rate of 0.5 Å s^{-1} to be the thickness of 50 nm over the whole area. For lifting-off the OS on the SL to leave only active regions, the substrate was immersed in the fluorous-solvent for a few seconds. The complementary patterns, i.e., the regions covered with the sacrificial layer were then removed and only the active OS patterns were left on the substrate. We now describe a

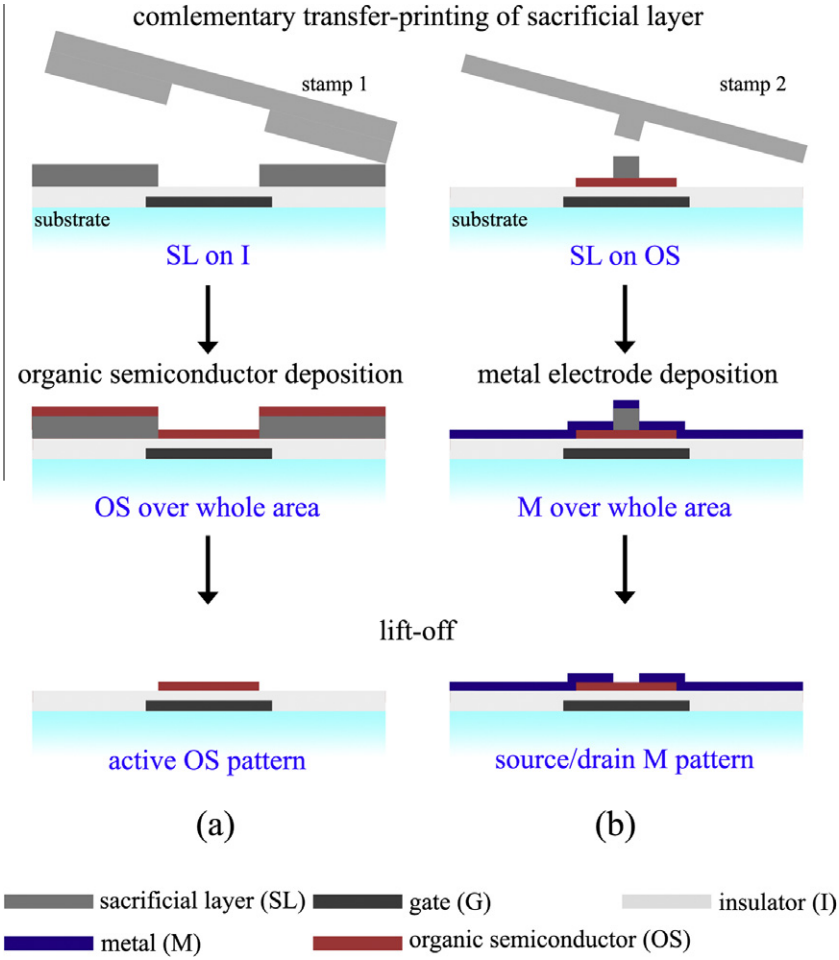

Fig. 1. Schematic illustration of each step of the CTAP for fabricating a top-contact OTFT with a short channel. Two serial processes of the CTAP are depicted for (a) active patterns of an organic semiconductor and (b) electrode patterns of a metal, respectively. Two elastomeric stamps of the PDMS, stamp 1 and stamp 2, are used for the two processes where different feature sizes may be adopted.

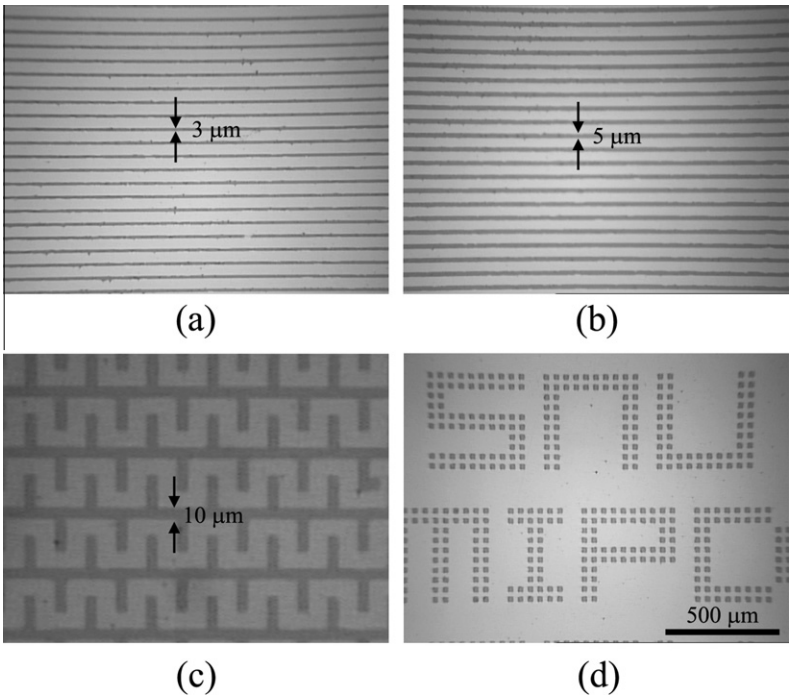

Fig. 2. Optical microscopic images of pentacene patterns showing (a) lines of 3 μm, (b) lines of 5 μm, (c) lines with branched segments (10 μm in resolution), and (d) different characters composed of squares of 25 μm in each side.

subsequent CTAP process of fabricating metal patterns on the OS layer to provide the source and drain electrodes. As shown in Fig. 1(b), the patterns of the sacrificial layer, complementary to the electrode patterns, were transfer-printed using stamp 2. A gold film of 80 nm thick was first deposited onto the entire substrate at the rate of 1 Å s^{-1}. The sacrificial layer was then lifted-off to leave only the electrode patterns on the top of the OS, yielding an OTFT in a top-contact configuration. Note that our CTAP is a powerful method of directly forming a very short channel length (down to a few micrometers) over the OS layer. A shadow mask, providing an easy and direct method, gives typically about 30 μm in resolution.

We first describe the pattern fidelity and the pattern resolution achieved in our CTAP approach. Basically, the feature resolutions of the heterogeneous patterns are governed by the complementary patterns of the sacrificial layer that were transfer-printed using a stamp. Three different types of patterns (lines, lines with branched segments, characters composed of isolated squares) with different resolutions ranging from 3 to 25 μm were shown in Fig. 2. As shown in Fig. 2(a) and (b), the resolution of 3 and 5 μm can be easily achieved and down to submicrometers depending on the pattern resolution of the stamp. A variety of patterns like lines with branched segments (10 μm in resolution) in Fig. 2(c) and different characters (25 μm in resolution) with high fidelity as shown in Fig. 2(d) were produced over the area of a few square centimeters using the CTAP technique.

Let us now examine both the morphology of the pentacene film on the PVCi gate insulator and the resultant

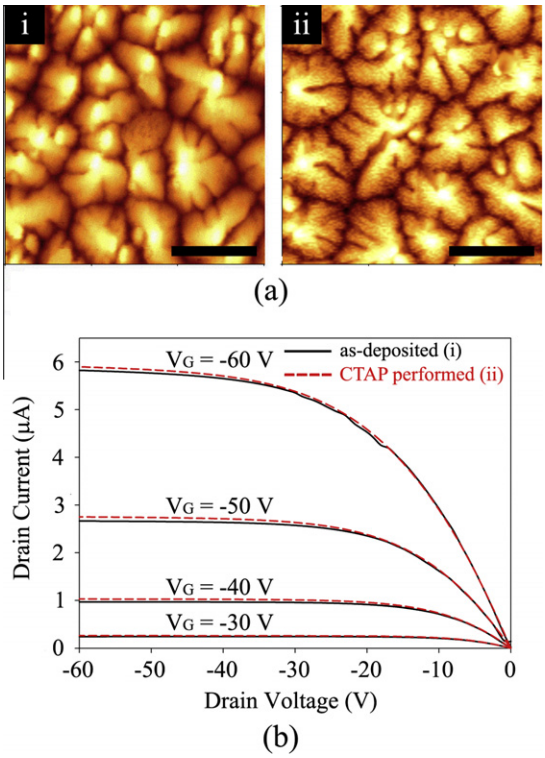

Fig. 3. (a) The AFM images of (i) an as-deposited pentacene layer and (ii) a pentacene layer experienced the transfer-printing and lifting-off processes of the sacrificial layer. The scale bar represents 1 μm. (b) The output characteristics of two OTFTs, one of which was fabricated using a shadow mask and the other using the CTAP.

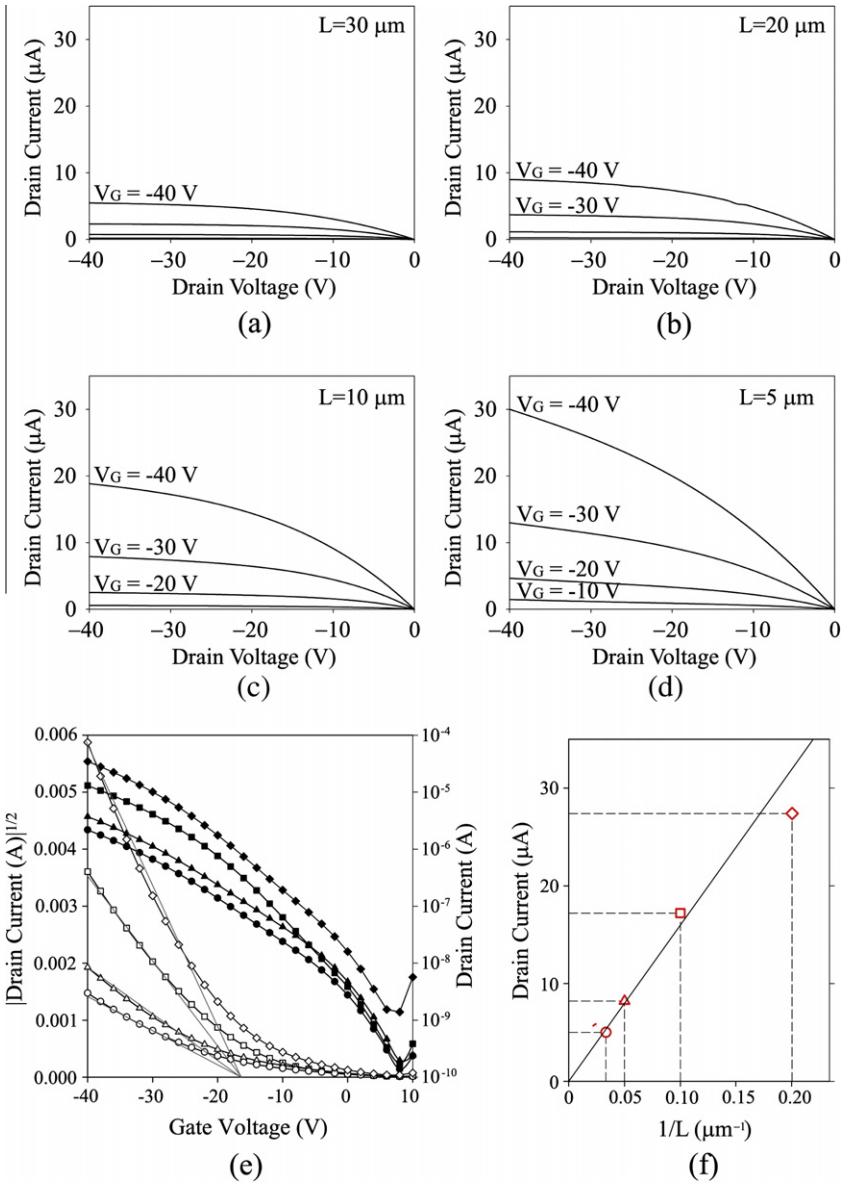

Fig. 4. The output characteristics of four OTFTs with different channel lengths of (a) 30 μm, (b) 20 μm, (c) 10 μm, and (d) 5 μm. (e) The transfer curves of the OTFTs with different channel lengths in linear and semi-logarithmic plots. (f) The drain current in the saturation regime as a function of $1/L$ at the gate voltage of −40 V. The solid line represents a linear fit. The circle, triangle, square, and diamond symbols represent the characteristics of the OTFTs with the channel of 30, 20, 10, and 5 μm, respectively.

electrical properties of the top-contact OTFT fabricated using the CTAP. In Fig. 3(a), the atomic force microscopic image (the surface morphologies) of an as-deposited pentacene film and that of a pentacene film experienced the transfer-printing and lift-off processes of the sacrificial layer were shown in (i) and (ii), respectively. Clearly, no considerable difference in the surface morphology was observed. Fig. 3(b) shows the output characteristic curves of two top-contact OTFTs made with the two types of the pentacene films described above. The drain current was measured as a function of the drain voltage for several different values of the gate voltage ranging from −30 to −60 V. It should be noted that the electrical properties of the two OTFTs are nearly identical. This indicates that the lift-off process in the CTAP approach essentially does not alter the morphological and electrical properties of the pentacene film.

More specifically, in pentacene-based OTFTs with different channel lengths (L) of 5, 10, 20, and 30 μm, we demonstrate the high-resolution patterning capability and the performance reliability of the CTAP approach. The channel width (W) was fixed as 1 mm. Fig. 4(a–d) shows the output curves of the four OTFTs whose channel length varies from 30 to 5 μm. Clearly, the saturation behavior of the drain current always appears irrespective of L. The transfer characteristic curves of the four OTFTs with different channel

lengths in linear and semi-logarithmic plots are shown in Fig. 4(e). From Fig. 4(e), it was found that the carrier mobility was about 0.10 $cm^2/V\,s$ and the current on–off ratio was on the order of 10^5 irrespective of the channel length. A slight off-current was observed only for the short channel case of $L = 5$ μm in Fig. 4(e). The turn-on voltage was estimated to be about 8 V. For fixed gate voltage ranging from −10 to −40 V, the drain current increases monotonically with decreasing L at a given drain voltage. For example, in the saturation regime, the drain current increases from 5.47 to 30.00 μA with decreasing L from 30 to 5 μm at the gate voltage of −40 V. Fig. 4(f) shows the drain current in the saturation regime at the gate voltage of −40 V as a function of $1/L$. As shown in Fig. 4(f), except for a very short channel case, a linear relationship between the drain current in the saturation regime and $1/L$ as expected from the following equation:

$$I_D = \frac{W}{2L} C_i \mu_{sat} (V_G - V_T)^2 \quad (1)$$

where I_D is the drain current, C_i is the capacitance per unit area of an insulator, μ_{sat} is the carrier mobility, and V_G and V_T are the gate voltage and the threshold voltage, respectively. A deviation from the linear relationship in the short channel case ($L = 5$ μm) may be attributed to the contact resistance which is believed to be critical in short channel devices [15]. Such contact resistance is one of the important issues to be explored from the device physics viewpoint which is beyond the scope of our work.

We now describe the applicability of the CTAP technique for the fabrication of flexible electronic devices on plastic substrates such as polyethersulphone (PES). An organic inverter, two OTFTs in series, was fabricated on the PES substrate by simultaneously forming all the source and drain electrodes on the OS patterns produced through the CTAP. The two OTFTs have the same dimensions of the channel length (10 μm) and the channel width (1 mm). A solvent dropping method was used for forming via holes required for the interconnection between two transistors. Fig. 5(a) shows a microscopic image of a single organic inverter with $L = 10$ μm together with a photographic image of inverter arrays fabricated on the PES substrate (3 cm × 4 cm in size) in bent environment. Neither delamination of organic and/or metal layers nor deterioration of the electric characteristics of the inverter was observed under a bent state with the curvature radius of a few centimeters. The voltage transfer characteristics (VTCs) of the organic inverter scanned for the input voltage from 0 to −60 V at $V_{DD} = -60$ V are shown in Fig. 5(b). The operation scheme of the organic inverter was depicted in the logic diagram of Fig. 5(b). In our inverter, the inversion voltage in the VTCs at $V_{DD} = -60$ V was found to be around −7 V at which the maximum gain of 9.5 was obtained. Note that our OTFT can be used as a load transistor in a zero drive load logic [16], requiring a turn-on state of the OTFT at the gate voltage of 0 V, since our OTFT has a positive turn-on voltage (8 V). The high and low states of the output voltage were well distinguished in the input voltage swing from 0 to −60 V. As shown in Fig. 5(b), the hysteresis measured during increasing and decreasing the input voltage between −60 and 0 V was negligibly small (<0.8 V).

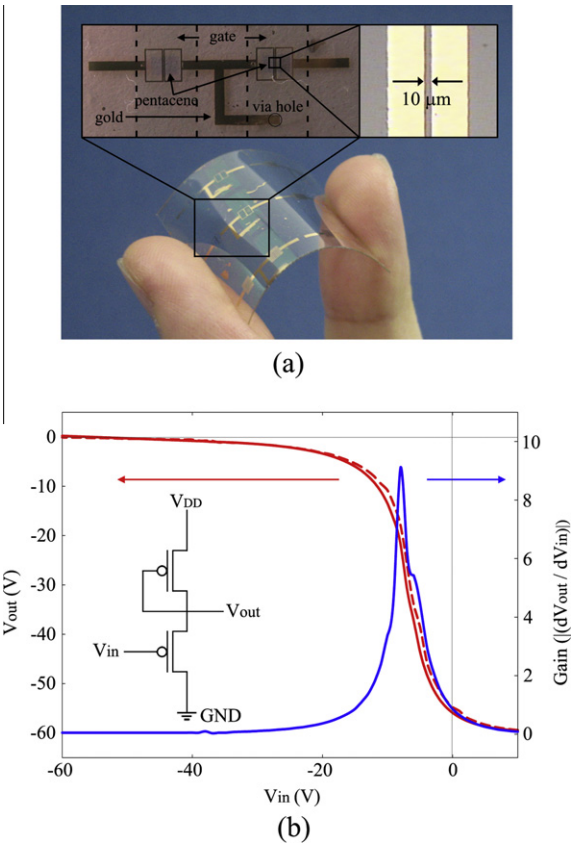

Fig. 5. (a) A microscopic image of a single organic inverter and a photographic image of inverter arrays (in the left inset) fabricated on a PES substrate. The channel of 10 μm in resolution was shown in the right inset. (b) The VTCs of an organic inverter as function of the input voltage. The red solid and dashed lines represent the VTC curves for the input voltage on increasing from −60 to 0 V and decreasing from 0 to −60 V, respectively. The blue line shows the gain of the organic inverter. The logic diagram represents the organic inverter in a zero drive load logic. (For interpretation of the references to colour in this figure legend, the reader is referred to the web version of this article.)

The optimization of the VTCs can be achieved through the variations of the channel length and width of an individual OTFT on the basis of the driving capability of each transistor (load or drive transistor) for specific applications. Moreover, it should be emphasized that on simply repeating the CTAP process, a variety of short channel inverters and circuits can be easily fabricated on a single plastic substrate and their electrical performances are well preserved under mechanically deformed environment such as in a bent state.

In summary, we developed a viable tool of patterning heterogeneous functional elements of organic and metallic materials in high resolution multilayer architecture for flexible electronics. The underlying mechanism comes from the lift-off of the sacrificial patterns complementary to active patterns on a variety of the substrates including a plastic film. We demonstrated that the simple repetition of the CTAP on successive layers in series enables to fabricate short channel OTFTs and organic inverters with high pattern fidelity and reliability. In principle, no detrimental

error was involved in defining high-resolution patterns down to submicrometers on the basis of the CTAP depending on the stamp resolution. The CTAP approach presented here is expected to be applicable for advanced flexible electronic systems including high-resolution organic light-emitting displays and highly integrated organic electronic circuits.

Acknowledgement

This work was supported in part by Korea Ministry of Knowledge Economy through the 21st Century Frontier Research and Development Program.

References

[1] D. Dimitrakopoulos, P.R.L. Malenfant, Adv. Mater. 14 (2002) 99.
[2] S.R. Forrest, Nature 428 (2004) 911.
[3] B. Crone, A. Dodabalapur, Y.Y. Lin, R.W. Filas, Z. Bao, A. LaDuca, R. Sarpeshkar, H.E. Katz, W. Li, Nature 403 (2000) 521.
[4] H.E. Edzer, A. Huitema, G.H. Gellink, J. Bas, P.H. van der Putten, K.E. Kuijk, K.M. Hart, E. Cantatore, D.M. de Leeuw, Adv. Mater. 14 (2002) 1201.
[5] J.A. Rogers, Z. Bao, K. Baldwin, A. Dodabalapur, B. Crone, V.R. Raju, V. Kuck, H. Katz, K. Amundson, J. Ewing, P. Drzaic, Proc. Natl. Acad. Sci. USA 98 (2001) 4835.
[6] H. Sirringhaus, N. Tessler, R.H. Friend, Science 280 (1998) 1741.
[7] M. Mizukami, N. Hirohata, T. Iseki, K. Ohtawara, T. Tada, S. Yagyu, T. Abe, T. Suzuki, Y. Fujisaki, Y. Inoue, S. Tokito, T. Kurita, IEEE Electron Device Lett. 27 (2006) 249.
[8] C.D. Sheraw, L. Zhou, J.R. Huang, D.J. Gundlach, T.N. Jackson, Appl. Phys. Lett. 80 (2002) 1088.
[9] P. Mach, S.J. Rodriguez, R. Nortrup, P. Wiltzius, J.A. Rogers, Appl. Phys. Lett. 78 (2001) 3592.
[10] A.A. Zakhidov, J.-K. Lee, H.H. Fong, J.A. DeFranco, M. Chatzichristidi, P.G. Taylor, C.K. Ober, G.G. Malliaras, Adv. Mater. 20 (2008) 3481.
[11] H.S. Hwang, A.A. Zakhidov, J.-K. Lee, X. Andre, J.A. DeFranco, H.H. Fong, A.B. Holmes, G.G. Malliaras, C.K. Ober, J. Mater. Chem. 18 (2008) 3087.
[12] Y. Noguchi, T. Sekitani, T. Someya, Appl. Phys. Lett. 91 (2007) 133502.
[13] K.-H. Kim, K.-W. Bong, H.H. Lee, Appl. Phys. Lett. 90 (2007) 093505.
[14] J.-H. Bae, W.-H. Kim, H. Kim, C. Lee, S.-D. Lee, J. Appl. Phys. 102 (2007) 063508.
[15] M.J. Panzer, C.D. Frisbie, Contact effect in organic field-effect transistors, in: Z. Bao, J. Locklin (Eds.), Organic Field Effect Transistors, CRC press, Boca Raton, FL, 2007, pp. 139–157.
[16] E. Cantatore, D.J. Meijer, in: Proceeding of the 29th European Solid-State Circuits Conference, Estoril, Portugal, 16–18 September, 2003, p. 29.

Organic Electronics 11 (2010) 2032–2036

Contents lists available at ScienceDirect

Organic Electronics

journal homepage: www.elsevier.com/locate/orgel

Short-circuit current density and spectral response modelling of bulk-heterojunction solar cells

Suman Banerjee [a,b,*], S. Sundar Kumar Iyer [b,c]

[a] Department of Physics, Indian Institute of Technology Kanpur, Kanpur 208 016, Uttar Pradesh, India
[b] Samtel Centre for Display Technologies, Indian Institute of Technology Kanpur, Kanpur 208 016, Uttar Pradesh, India
[c] Department of Electrical Engineering, Indian Institute of Technology Kanpur, Kanpur 208 016, Uttar Pradesh, India

ARTICLE INFO

Article history:
Received 15 July 2010
Received in revised form 7 September 2010
Accepted 25 September 2010
Available online 26 October 2010

Keywords:
Spectral response
Bulk-heterojunction solar cell
Optical modelling

ABSTRACT

A general model to calculate short circuit current and spectral response of the bulk-heterojunction solar cell is discussed here. In order to get the short circuit current density at each wavelength the generation rate of electron and holes are calculated by the optical modelling based on transfer matrix approach. The drift–diffusion equation is then solved to get the current density at each wavelength using the calculated generation rate. Spectral response is found to be very similar to the experimental data of (3-hexylthiophene) (P3HT): [6,6]-phenyl C61-butyric acid methylester (PCBM) based bulk-heterojunction solar cell. The variation of short circuit current as a function of active layer thickness has been calculated using the model which matches with the experimental observations taken from literature. The sub-linear dependence of short circuit current on incident light intensity has also been explained by the model.

© 2010 Elsevier B.V. All rights reserved.

1. Introduction

Organic solar cells (OSC) have been gaining much attention recently because of its low cost and large area application [1]. Among various types of OSC, the bulk-heterojunction (BHJ) solar cells are becoming important as after absorbing light, photo-generated excitons break down to electron and holes directly due to the presence of the interpenetrating donor and acceptor material, thus the choice of the active layer thickness is not restricted by the small exciton diffusion length [2] typically of the order of 10 nm [3]. The ease of fabrication of BHJ solar cells by wet processing is also an important factor for its popularity as it makes the solar cell low cost. High efficiency 7.4% has recently [4] been reported for these devices. One of the typical shortcomings of BHJ devices is low spectral absorption range which can be observed from spectral response measurement. Recently it has been shown that inclusion of other material into the P3HT: PCBM active layer can enhance the spectral response range and hence the efficiency of the solar cells [5]. But a significant special overlap of different materials can make the charge collection and hence the BHJ solar cells inefficient. So to design efficient devices it is necessary to understand spectral response of such solar cells. Spectral responses of single layer organic devices [6] and bilayer organic solar cells [3] have been modelled recently. Elaborate device modelling for bulk-heterojunction solar cells of Koster et al. [7] and Lacic and Inganäs [8] discuss about the current voltage characteristics, charge generation inside the device etc. Dependence of the short circuit current on blend layer thickness has been discussed by Monestier et al. [9]. In this paper we shall discuss about the dependence of the short circuit current on the wavelength of incident light or spectral response of the bulk-heterojunction solar cells. We shall also show the effect of various loss mechanisms on short circuit current density (J_{sc}) of blend solar cells.

* Corresponding author. Tel.: +91 512 259 6070; fax: +91 512 259 6620.
E-mail address: sumanb@iitk.ac.in (S. Banerjee).

1566-1199/$ - see front matter © 2010 Elsevier B.V. All rights reserved.
doi:10.1016/j.orgel.2010.09.016

2. Theory

In this section we shall discuss about the mechanism and model of the external quantum efficiency (η_{EQE}) in the BHJ solar cells. After absorption of light excitons are generated in the active layer of the solar cells. Because of the presence of interpenetrating donor and acceptor layers in the blend, excitons dissociate efficiently at the donor–acceptor (D–A) interface and generates electron and holes. Then the electrons and holes diffuse through the active layer by the help of built-in potential present in the device and collected at the respective electrodes. The η_{EQE} of the BHJ solar cells can be described in terms of the product of several other efficiencies [2]:

$$\eta_{EQE} = \eta_A \times \eta_{ED} \times \eta_{CT} \times \eta_{CC} \tag{1}$$

where η_A, η_{ED}, η_{CT} and η_{CC} are the absorption efficiency of the active material, exciton diffusion efficiency (efficiency of excitons to reach the D–A interface), charge transfer efficiency of the D–A interface leading to holes in the donor and electron in the acceptor material and charge collection efficiency respectively. The generation of exciton (η_A) can be accurately modelled using optical modelling by the transfer matrix approach [3]. The presence of D–A interfaces makes both η_{ED} and η_{CT} very efficient [10,11], so we assumed η_{ED} and η_{CT} equal to one. But as a significant special overlap exists between the electron and holes in the active layer, trap generated and bimolecular recombination [2,9] become a dominant factor making η_{CC} less than one. To model the η_{CC} accurately the calculated generation rate is included in the drift–diffusion equation for electron and holes. The basic set of equations for the bulk-heterojunction solar cells are given below:

$$\frac{1}{e}\frac{dJ_n}{dx} = R - G \tag{2}$$

$$\frac{1}{e}\frac{dJ_p}{dx} = -(R - G) \tag{3}$$

where J_n and J_p are electron and hole current density, respectively and given by:

$$J_n = \mu_n eEn + \mu_n k_B T\frac{dn}{dx} \tag{4}$$

$$J_p = \mu_p eEp - \mu_p k_B T\frac{dp}{dx} \tag{5}$$

Here R and G are the recombination and generation rate of the electron and holes, n and p are the density of electron and holes inside the device, e is the electron charge, μ_n and μ_p are the electron and hole mobility of the active material, E is the electric field inside the device, k_B is the Boltzman constant and T is the temperature of the system taken in the absolute scale. The first and second part of the Eqs. (4) and (5) are the drift and diffusion part of the electron and hole current respectively. Both trap generated and bimolecular recombination are taken into consideration in the model. Generation rate of electron and holes are calculated using the optical modelling where optical constants and thicknesses of all the layers are taken into account. Current densities are calculated by solving the Eqs. (2)–(5) described above. The external quantum efficiency of the full device is then calculated by normalising the current by the incident photon flux using Eq. (6) below.

$$\eta_{EQE} = \frac{j/q}{\frac{1}{2}\varepsilon_0 c|\bar{E}_0|^2/(hc/\lambda)} \tag{6}$$

Short circuit current density of the solar cell has been calculated by integrating η_{EQE} with the solar spectrum using Eq. (7) below.

$$J_{sc} = q\int_{SolarSpectrum} S(\lambda)\eta_{EQE}(\lambda)d\lambda \tag{7}$$

where $S(\lambda)$ is the spectral shape of the solar spectrum. Trap generated recombination of electron and holes in the presence of impurities and inhomogeneity in D–A mixture can be described by $R_n \approx \frac{n}{\tau_n}$, $R_p \approx \frac{p}{\tau_p}$ for electrons and holes, respectively, where τ_n and τ_p are the electron and hole lifetime. Bimolecular recombination rate depends on both the electron and hole density and can be modelled as $R \approx rnp$, where r is the recombination rate constant. The boundary conditions are $n = 0$ and $J_n = 0$ at the ITO:PEDOT junction and $p = 0$ and $J_p = 0$ at the Ca:Al junction. As PEDOT and Ca:Al make ohmic contact with P3HT and PCBM, respectively, the electron and hole density at anode and cathode is assumed to be $n(\text{anode}) \approx N_c \exp\left(-\frac{E_{barrier}}{\kappa T/q}\right)$ and $p(\text{cathode}) \approx N_c \exp\left(-\frac{E_{barrier}}{\kappa T/q}\right)$, where N_c is the effective density of states typically $10^{26}/m^3$ for these materials and $E_{barrier}$ is the gap between HOMO of P3HT and the LUMO of PCBM. So the presence of electron and holes in the anode and cathode respectively would be extremely small. In the presence of large built-in electric field it is energetically favourable for the electrons and holes to go to cathode and anode, respectively which justifies the boundary conditions on current densities. Parameters like τ_n, τ_p and r are taken as free parameters to fit the model to the experimental data of the spectral response. Electric field inside the device is taken to be constant [9,12] and equal to V_{bi}/d where V_{bi} is the built in potential present in the device which is equal to 1.3 V [13]. Here the cathode work function becomes pinned close to the LUMO level of PCBM. The value of μ_n and μ_p are taken from the literature for similar condition (3-hexylthiophene) (P3HT): [6,6]-phenyl C61-butyric acid methylester (PCBM) system where $\mu_n = 3 \times 10^{-7}$ m^2 V^{-1} S^{-1} and $\mu_p = 2 \times 10^{-8}$ m^2 V^{-1} S^{-1} [14]. Similar values of mobility has been reported and used in literature [8,9,15]. Optical constants of the material used here are also taken from the literature [9,16–18].

3. Experimental details

We fitted our model on the spectral response of P3HT:PCBM based solar cells. In order to make the devices PEDOT:PSS is spin coated on cleaned and patterned indium tin oxide (ITO) substrates. After that 1:1 weight ratio P3HT:PCBM solution is spin coated on it and dried at 120 °C before depositing Ca:Al or cathode layer by shadow mask. Devices are exposed as less as possible in atmosphere before encapsulating it in glove box. So the final structure

of the solar cells becomes 140 nm indium tin oxide (ITO)/ 50 nm PEDOT:PSS/70 nm P3HT:PCBM/5 nm Ca/100 nm Al. These samples were then annealed in 110 °C for 1 h. Spectral responses of these solar cells are carefully measured in the system described elsewhere [6].

4. Results and discussion

Fig. 1(a) and (b) shows the simulated optical field distribution and the generation profile of excitons inside the device. The current density distribution inside the device at an electric field 3×10^5 V/m is shown in Fig. 2. In such built-in electric field both the drift and diffusion current has a considerable contribution in the total current. Our simulation result shows that at high field (5×10^6 V/m) diffusion current becomes around 3% of the total current. This satisfies the assumption of Ray et al. [19] of neglecting the diffusion current in the single layer TPD devices where the photogeneration was caused by the bulk generation of carriers. The comparison between experimentally achieved spectral response data and the fitted models is shown in Fig. 3. r, τ_n and τ_p are used as free parameter in this fitting. The model fits the experimental data quite well with the best fitted parameter $\tau_p = 0.2$ μs. At very low intensity of incident light used in SR measurement r does not play a critical role. Although this model fits the experimental data very well the slight discrepancy between the model and experimental data especially in the lower wavelength range can be attributed to the possibilities of inaccuracies in optical constant taken from literature for our devices. The effect of thickness on J_{sc} is also calculated by the process described above. Recently Monestier et al. [9] and Li et al. [20] have studied the effect of thickness on J_{sc}. Both the experimental data can be well described by our model as seen in Fig. 4. The thickness dependent J_{sc} data of Li et al. can be best described by $r = 1 \times 10^{-15}$ m^3/s and $\tau_p = 0.8$ μs where as the data of Monestier et al. can be described by $r = 1 \times 10^{-18}$ m^3/s and neglecting trap generated recombination. The experimental data in this case were found shifted by a constant amount from the modelled data. Here we have taken η_{ED} and η_{CT} is 100%, but for practical devices because of these efficiencies can be slightly lower than one depending upon the morphology.

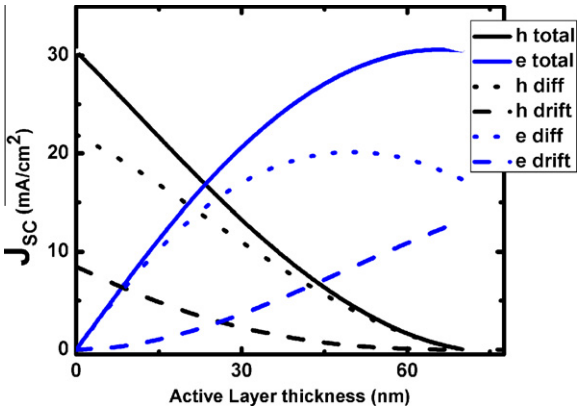

Fig. 2. Simulated current density distribution inside the device calculated using the model. The parameters used in the calculation are $E = 3 \times 10^5$ V/m, $\tau_p = 7$ μs and $r = 1 \times 10^{-16}$ m^3/s. The hole current is higher and the electron current is negligibly small at the anode. The electron current is higher and hole current is almost zero at the cathode.

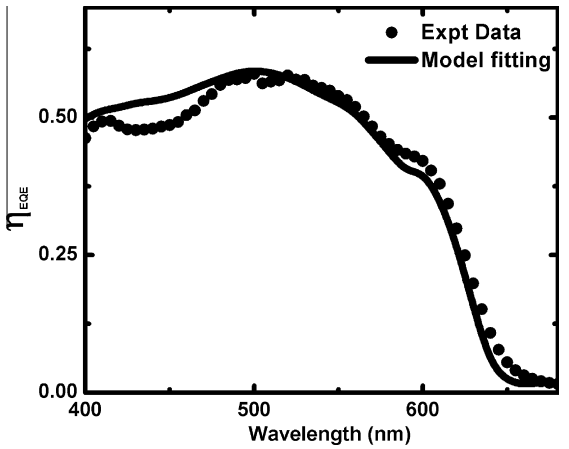

Fig. 3. Comparison between experimental data and fitted model is shown in the figure. The model fits the experimental data very well, but slight discrepancy is observed for lower wavelengths. The best fitted parameters are $\tau_n = 1$ μs, $\tau_p = 0.2$ μs.

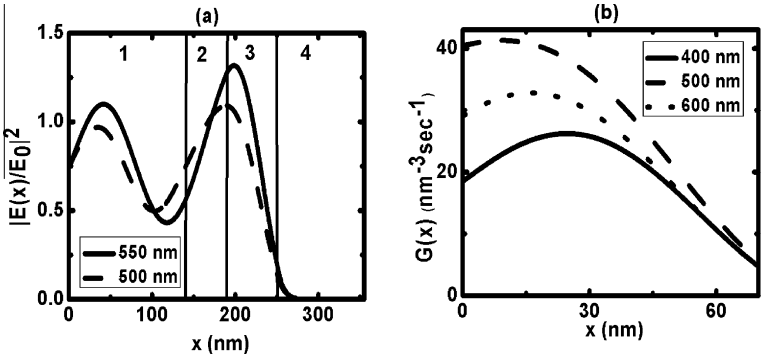

Fig. 1. The simulated electric field distribution inside the device is shown here. Layers 1–4 denoted in the (a) are 140 nm ITO, 50 nm PEDOT, 70 nm P3HT:PCBM and 105 nm Ca:Al, respectively and (b) is the generation profile of excitons inside the P3HT:PCBM layer. The generation rate is used in the drift–diffusion equation.

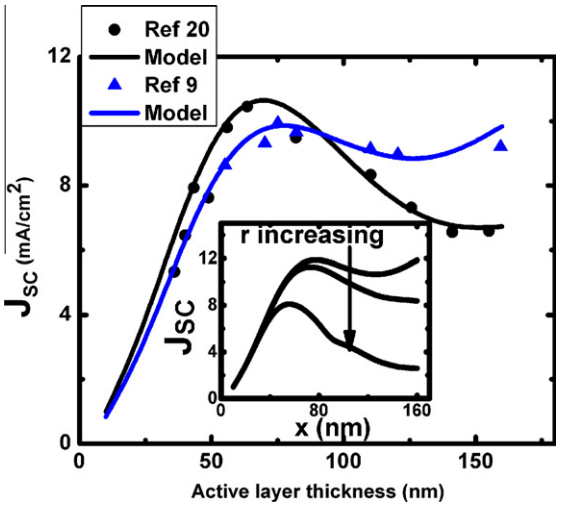

Fig. 4. Comparison between experimental data taken from the literature and fitted model is shown in the figure. The model fits the experimental data very well. The best fitted parameters are $\tau_p = 0.8\ \mu s$ and $r = 1\times 10^{-15}\ m^3/s$ for the data of Li et al. (Ref. [20]). The data of Monestier et al. (Ref. [9]) can be best fitted by $r = 1 \times 10^{-18}\ m^3/s$ and neglecting the trap generated recombination. Effect of bimolecular recombination coefficient on J_{sc} is shown in the inset. It can be seen as recombination increases J_{sc} decreases.

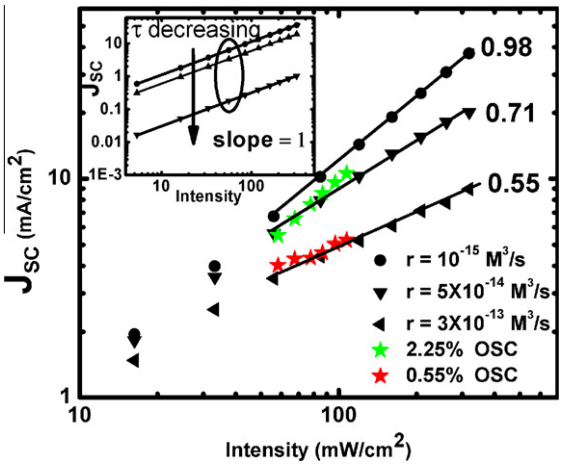

Fig. 5. Effect of intensity on J_{sc} is shown in the figure. At very low recombination J_{sc} follows linear behaviour with incident light intensities. For high recombination devices sub-linear dependence of J_{sc} on I_{LIGHT} is found. Experimental data of our low and high efficiency devices are also shown in the figure. In the inset the effect of I_{LIGHT} on J_{sc} in the case of trap generated recombination is shown. The power exponent in this case is found to be equal to one.

So J_{sc} can be lower than the calculated model. Finally we have calculated the effect of the incident light intensity on J_{sc}. We have found that for the devices with very low bimolecular recombination, J_{sc} increases with the incident light intensity I_{LIGHT} and follows a linear relation with I_{LIGHT} i.e. $J_{sc} \propto I_{LIGHT}^{1.0}$. But for the devices with high bimolecular recombination J_{sc} follows a sub-linear relation with I_{LIGHT} i.e. the power exponent is less than one. We have also seen in our low efficiency (0.55%) devices J_{sc} follows the sub-linear behaviour with the power exponent equal to 0.55 and from our modelling and calculation we can clearly see that the bimolecular recombination is limiting our device efficiency. But for our high efficiency (2.25%) devices we found fully linear behaviour due to almost no bimolecular recombination. We can compare this r to the Langevin bimolecular recombination coefficient $r_{LANGEVIN}$ where $r_{LANGEVIN} = \frac{q}{\varepsilon_r \varepsilon_0}(\mu_n + \mu_p)$.

We can assume $r = \xi \times r_{LANGEVIN}$ for our devices where ξ is the Langevin recombination prefactor. The prefactor value ξ varies order of magnitude starting from 10^{-4} to 1 [8,21] for various blend solar cells. The small value of ξ indicates the presence of extremely low bimolecular recombination. For P3HT: PCBM solar cells this low value of ξ can be attributed to extremely good morphology [8] of the blend and formation of fibrils in nanoscale and lamella-like chain packing [21]. In the intensity vs. J_{sc} curve we did not see any notable difference in α in the region $\xi \leqslant 1$. For instance the intensity vs. J_{sc} data of the 2.25% OSC can be fitted with $\xi \approx 1$ whereas the data of 0.55% solar cell can be fitted with $\xi = 148$. This high bimolecular recombination may cause due to the experimental condition. We think more controlled atmosphere experiment will lead to less recombination and small ξ value in the devices. For the case of monomolecular recombination, J_{sc} decreases as recombination increases but J_{sc} follows a linear behaviour with I_{LIGHT}. The effect of light intensity on J_{sc} is shown in Fig. 5. In the inset of Fig. 5 the effect of I_{LIGHT} on J_{sc} is shown for the case of trap generated recombination. In literature various authors [22,23] found the sub-linear relation of J_{sc} with incident light intensity, which they concluded is a signature of bimolecular recombination, also validates our model.

5. Conclusions

A general method to calculate the spectral response of a bulk-heterojunction solar cell has been described here. The generation rate of exciton and electron hole is calculated using optical interference method based on transfer matrix approach. First order and bimolecular recombination are taken into consideration in the model. Spectral response of the bulk-heterojunction solar cell has been found by solving the drift–diffusion equation. The simulated result matches with the spectral response of 1:1 P3HT:PCBM based bulk-heterojunction solar cell. We have also described the effect of thickness on short circuit current which matches with the experimental observations. We found that the best short circuit current density can be achieved from the devices of 60–75 nm. We have also described the effect of incident light intensity on short circuit current density which also matches with the experimental observations.

Acknowledgements

We are thankful to Mr. Anirban Bagui and Mr. Arun Tej Mallajosyula for the sample preparation. Financial supports of the Department of Science and Technology (DST)

of the Government of India in various projects at SCDT is deeply acknowledged.

References

[1] M.D. McGehee, M.A. Topinka, Nat. Mater. 5 (2006) 675.
[2] J. Xue, B.P. Rand, S. Uchida, S.R. Forrest, J. Appl. Phys. 98 (2005) 124903.
[3] P. Peumans, A. Yakimov, S.R. Forrest, J. Appl. Phys. 93 (2003) 3693.
[4] Y. Liang, Z. Xu, J. Xia, S.-T. Tsai, Y. Wu, G. Li, C. Ray, L. Yu, Adv. Mater. 22 (2010) 1.
[5] W.J. Belcher, K.I. Wagner, P.C. Dastoor, Sol. Energy Mater. Sol. Cells 91 (2007) 447.
[6] S. Banerjee, A.P. Parhi, S.S.K. Iyer, S. Kumar, Appl. Phys. Lett. 94 (2009) 223303.
[7] L.J.A. Koster, E.C.P. Smits, V.D. Mihailetchi, P.W.M. Bolm, Phys. Rev. B 72 (2005) 085205.
[8] S. Lacic, O. Inganäs, J. Appl. Phys. 97 (2005) 124901.
[9] F. Monestier, J.-J. Simon, P. Torchio, L. Escoubas, F. Flory, S. Bailly, R. de Bettignies, S. Guillerez, C. Defranoux, Sol. Energy Mater. Sol. Cells 91 (2007) 405.
[10] G. Yu, J. Gao, J. Hummelen, F. Wudl, A.J. Heeger, Science 270 (1995) 1789.
[11] P.A. van Hal, R.A.J. Janssen, G. Lanzani, G. Cerullo, M. Zavelani-Rossi, S.D. Silvestri, Chem. Phys. Lett. 345 (2001) 33.
[12] P. Schilinsky, C. Waldauf, J. Appl. Phys. 95 (2004) 2816.
[13] V.D. Mihailetchi, P.W. Bolm, J.C. Hummelen, M.T. Rispens, J. Appl. Phys. 94 (2003) 6849.
[14] V.D. Mihailetchi, H. Xie, B. de Boer, L. Jan, A. Koster, P.W.M. Blom, Adv. Mater. 16 (2006) 699.
[15] T.A. Skotheim, J.R. Reynolds, Conjugated Polymer Processing and Applications, third ed., CRC Press.
[16] R.A. Synowicki, Thin Solid Films 313 (1998) 394.
[17] C.M. Ramsdale, N.C. Greenham, J. Phys. D: Appl. Phys. 36 (2003) L29.
[18] S. Liu, W. Xie, Jpn. J. Appl. Phys. 42 (2003) 2545.
[19] D. Ray, M.P. Patankar, G.H. Döhler, K.L. Narasimhan, J. Appl. Phys. 100 (2006) 113727.
[20] G. Li, V. Shrotriya, Y. Yao, Y. Yang, J. Appl. Phys. 98 (2005) 043704.
[21] A. Pivrikas, N.S. Sariciftci, G. Juška, R. Österbacka, Prog. Photovolt: Res. Appl. 15 (2007) 677.
[22] V. Dyakonov, Appl. Phys. A 79 (2004) 21.
[23] Y. Kim, S.A. Choulis, J. Nelson, D.D.C. Bradley, S. Cook, J.R. Durrant, J. Mater. Sci. 40 (2005) 1371.

Organic Electronics 11 (2010) 2037–2044

Contents lists available at ScienceDirect

Organic Electronics

journal homepage: www.elsevier.com/locate/orgel

Fully gravure and ink-jet printed high speed pBTTT organic thin film transistors

Alejandro de la Fuente Vornbrock *, Donovan Sung, Hongki Kang, Rungrot Kitsomboonloha, Vivek Subramanian

Department of Electrical Engineering and Computer Sciences, University of California, Berkeley, CA 94720, USA

ARTICLE INFO

Article history:
Received 30 April 2010
Received in revised form 31 August 2010
Accepted 1 September 2010
Available online 28 September 2010

Keywords:
Gravure
Thin film transistors
pBTTT
Ink-jet
Switching speed
Printed electronics

ABSTRACT

Organic thin film transistors with channel lengths below 20 μm have been fabricated on plastic substrates using a combination of rotogravure and ink-jet printing exclusively. Gravure is utilized to deposit thin, smooth, and narrow metal lines ideal for gate electrodes; a poly(4-vinylphenol) dielectric; and a poly(2,5-bis(3-tetradecylthiophene-2-yl)thieno[3,2-b]thiophene) (pBTTT) semiconductor using a heated roll. A novel fluid guiding technique is used to maintain closely spaced ink-jet printed source and drain (S/D) contacts. Together these printing processes yield aggressively scaled yet easily manufacturable TFTs with operating frequencies of 18 kHz.

© 2010 Elsevier B.V. All rights reserved.

1. Introduction

Printed electronics has received attention as a technology for the realization of low-cost circuits such as flexible displays, RFID tags, and sensors. While substantial work towards these goals has been performed using lithography and ink-jet printing, relatively little progress has been made in transferring these advances to higher speed processes such as gravure printing, flexography, etc. A few early demonstrations of OTFTs as well as simple circuits have been made [1–4] proving the feasibility of using rotogravure in combination with other printing techniques such as flexo and inkjet. However these devices suffered from large feature sizes, hampering their usability in any realistic applications.

We have developed a custom high-resolution rotogravure printer suitable for the development of printed electronics processes on a laboratory scale. Using this machine, an organometallic silver precursor ink and planarized polyethylene napthalate (PEN) films, we have previously demonstrated printed lines with feature sizes as small as 17.5 μm and a line edge roughness of <2 μm [5]. Scaling transistors with printed contacts, particularly gates, has been challenging to date because the processes used have provided relatively thick and rough films causing early breakdown and decreased yield [6]. In this work, by exploiting the small, well-controlled volume of our gravure wells and the use of an organometallic precursor ink, we demonstrate patterns of sufficient quality for use in fully-integrated devices with films as thin as 100 nm, allowing for the realization of high-performance, well-scaled devices.

In this paper we fabricate thin film transistors using these features, thus realizing the smallest rotogravure printed devices to date. In particular, we introduce a hybrid process using gravure for patterning high-resolution lines, thin dielectrics, and pBTTT semiconductor which until now, has been difficult to print; and using inkjet with a novel fluid guiding technique for precisely aligned upper electrodes to achieve an overall optimized process flow for

* Corresponding author. Present address: Hewlett Packard Laboratories, Long Down Avenue, Stoke Gifford, Bristol, BS34 8QZ, United Kingdom. Tel.: +44 07788 852 123.
E-mail address: delafuentea@gmail.com (A. de la Fuente Vornbrock).

1566-1199/$ - see front matter © 2010 Elsevier B.V. All rights reserved.
doi:10.1016/j.orgel.2010.09.003

highly scaled printed devices offering high performance in a scalable, manufacturing-friendly process.

2. Experiment

Both a top gate and bottom gate transistor process was developed to explore the possibility of using gravure as a printing technique for TFTs. In the bottom gate process (Fig. 1 (left)), the gate and dielectric were printed using gravure followed by ink-jet printed source and drain contacts and gravure printed semiconductor. In the top gate process (Fig. 1 (right)) gravure was used to print the source and drain contacts, followed by the semiconductor and dielectric, and finally the gate was printed using ink-jet. A direct comparison of representative devices can be made in Figs. 5 and 6.

Details of the process to print and scale the feature sizes of the first gravure printed metal layer and dielectric are described elsewhere [5]. In brief, the metal lines were gravure printed using Inktec PR-010 silver precursor ink on planarized Q65FA PEN substrates by DuPont Teijin, which had been cleaned using an N_2 gun, and treated with UV ozone for 5 min. The line patterns where composed of 30 μm wide gravure cells with ~32 μm spacing such that the wells almost touched. For all gravure steps reported here prints were made at a speed of 1 m/s, which despite being slow compared with the speed used in the graphic arts (>10 m/s), is suitable for electronics. A doctor blade pressure of 12 PSI per inch, and a 3 mm nip contact where used. After printing, the lines were annealed in an oven at 150 °C for 15 min. Line widths were 20–21 μm with a thickness of 70 nm and a dome shaped profile giving a low roughness of 5.8 nm RMS and 20 nm peak to peak. Poly(4-vinylphenol) with 20% poly(melamine co-formaldehyde)methylated cross-linker was used as a dielectric by dissolving 1 g of the dielectric and cross-linker into 15 mL of propylene glycol monomethyl ether acetate and printing with electromechanically engraved gravure wells on a 40 l/cm pitch yielding an areal volume of 6.6 mL/m^2. After printing, the dielectric was cross-linked at 220 °C for 5 min.

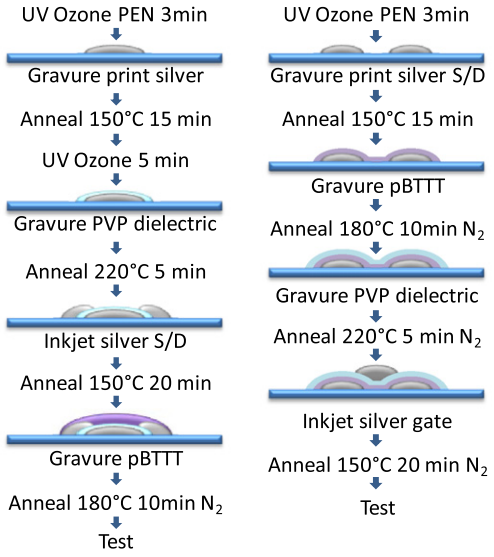

Fig. 1. Hybrid gravure/ink-jet process flow for bottom gate transistors (left) and top gate transistors (right).

2.1. Ink-jet printed contacts

A unique printing process was developed to allow the source and drain contact lines to be ink-jet printed close enough to each other to ensure overlap with the gate (<20 μm line spacing), yet avoid shorting the source and drain due to bulging, which is a common problem found when ink-jet printing two straight rows of drops (Cabot CCI-300 nanoparticle silver ink) in close proximity as seen in Fig. 2.

The growth mechanism for the bulges seen on the left side of the micrograph is also presented in Fig. 2. Drops merging at the beginning of an ink-jet printed line will try to adopt the least energetic shape possible: a larger, circular drop. As the line begins to get drawn out, ink deposited at the end of the line will flow towards the initial drop due to a pressure differential between the small deposited drop, the line, and the larger drop or bulge that was initially formed and is now growing. Eventually the pressure between the bulge and the line is equilibrated in part due to the increased size of the bulge, and in part due to the flow resistance of the long line, and the bulge ceases to grow [7,8].

The bulge is thus a natural result of steady state line formation that could be minimized using a few approaches including the use of larger drop spacing at the beginning of a line and higher print speeds [8]. Such a strategy is

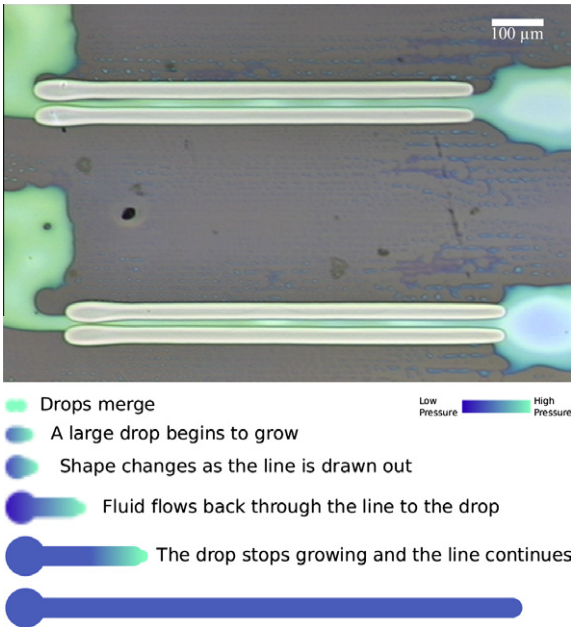

Fig. 2. Two printed thin film transistors (top) with channel lengths ~15 μm showing the risk of a source/drain short failure due to the bulge on the left side of the ink-jet printed lines. The bulge in these lines is due to the nature of line formation, as shown in the diagram (bottom).

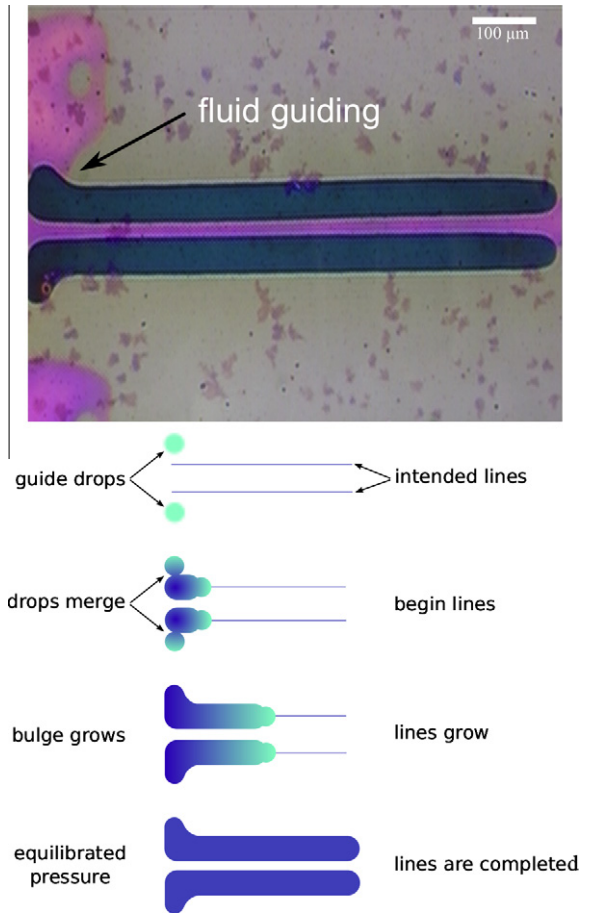

Fig. 3. Optical micrograph of a pBTTT TFT with ink-jet printed contacts employing fluid guiding to allow for a 15 μm channel length (top). Diagram of the fluid guiding process flow (bottom). Guide drops printed above and below contact lines, direct fluid flow away from the channel during the initial process of line formation.

not attractive for high-speed manufacturing, since rasterized constant-space printing is much more attractive from a throughput perspective. Instead, a novel fluid guiding approach was implemented where guiding drops are placed at the beginning of the source and drain lines, off-axis and away from the channel, such that the bulge that forms early in the print process contacts the guiding drops and is guided away from the channel (Fig. 3). Lines printed in this manner have a much reduced line edge waviness in the channel region allowing for much better control of the channel length and overlap to the gate, these features are now limited by the deposition accuracy of the drop which is ±5 μm. Transistor structures with channel lengths as small as 15 μm and leakage below 10^{-6} A/cm^2 at 1 MV/cm fields as tested before semiconductor deposition can be reliably made. These S/D contacts compare favorably with gravure printed ones where channel lengths below 20 μm are currently difficult to achieve.

2.2. Gravure printed semiconductor

pBTTT has been demonstrated to provide some of the highest field effect mobility and ambient stability obtained from a polymeric semiconductor [9]. However the polymer is difficult to dissolve into a solution and requires the use of hot solvents, which make it difficult to print this material with techniques such as ink-jet (due to the rapid evaporation of the heated solvents, causing clogging) or flexography (due to the swelling effects organic aromatic solvents can have on polymer masters). Gravure rolls and doctor blades are metallic and thus impervious to organic solvents regardless of their temperatures. Further they can be heated [10] to maintain pBTTT solubility and also to maintain consistent ink viscosity, thus making gravure a good candidate for depositing this material.

To test the thickness and uniformity of pBTTT films formed with gravure, an electromechanically engraved roll with eight different engravings as detailed in Table 1 was used. The gravure roll was heated prior to printing in an oven. Because of its high thermal mass, the roll could easily maintain its temperature through the print process which lasted approximately 5 min. Ink was delivered to the roll via a heated syringe just before the print. Substrates were treated with UV ozone for 4 min prior to printing to improve wetting of the pBTTT ink. After printing, the substrates were dried in an oven at 100 °C.

The optimal film thickness for pBTTT is known to be between 30 and 60 nm to provide high-quality film formation while minimization bulk leakage effects. Typical ink transfer volumes were found to be approximately half the cell volume; therefore, optimal ink dilutions could be estimated and inks with five different concentrations were prepared. Table 1 provides the expected film thicknesses printed from these solutions.

The prints were visually inspected to determine which patterns produced the most uniform films, and which concentration provided the most adequate thickness. Direct measurements of the film thickness where difficult to obtain because the flexibility of the PEN substrate prevents

Table 1
Gravure cell parameters–cell depth and areal volume for wells electromechanically engraved on a 40 l/cm pitch- and estimated film thicknesses provided from solutions of pBTTT as shown.

pBTTT concentration		% Vol.	Cell depth (μm)	45	50	55	60	65	70	75	80
(mg/mL)	(mg/mg)		Area volume (mL/m^2)	6.1	8	10	13.1	15.6	19.3	20.7	23.3
5	3.85	0.5	Thickness (nm):	30.5	40	50	65.5	78	96.5	103.5	116.5
2	2.31	0.3		18.3	24	30	39.3	46.8	57.9	62.1	69.9
3	1.54	0.2		12.2	16	20	26.2	31.2	38.6	41.4	46.6
1	0.77	0.1		6.1	8	10	13.1	15.6	19.3	20.7	23.3

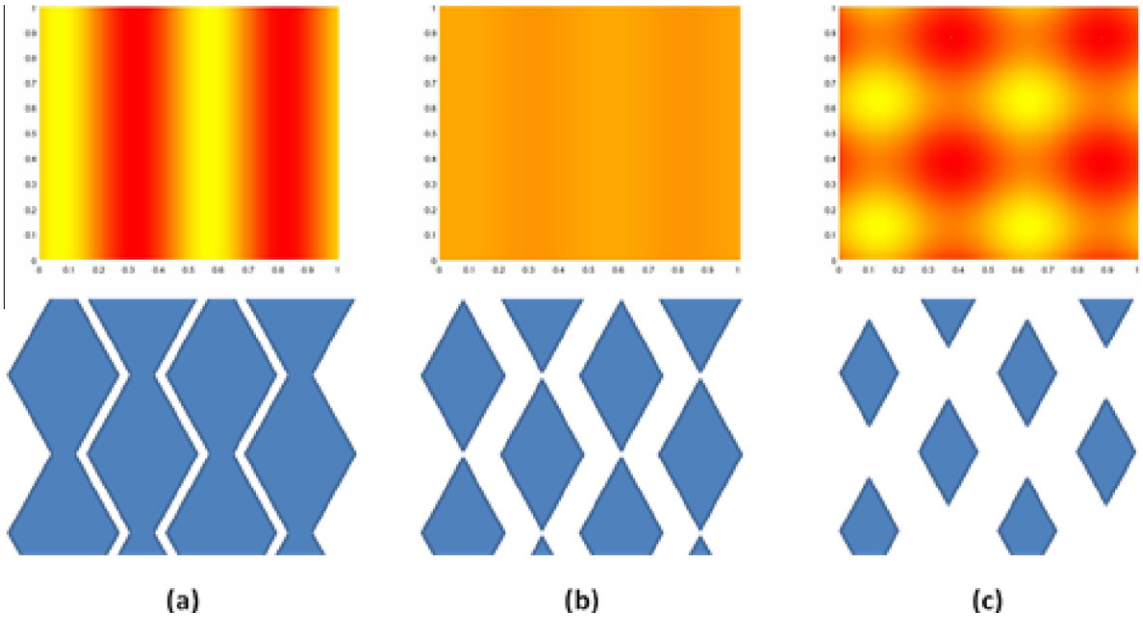

Fig. 4. Schematic of film thickness variation (top) and equivalent gravure cell volume (bottom) for gravure printed pBTTT films. Cells are spaced by 250 μm on the gravure. Large cells (a) merge in the vertical print direction causing band-like thickness variation. Small cells (c) are too far apart to allow ink to uniformly spread. An ideal cell spacing (b) allows for fluid flow to form uniform films.

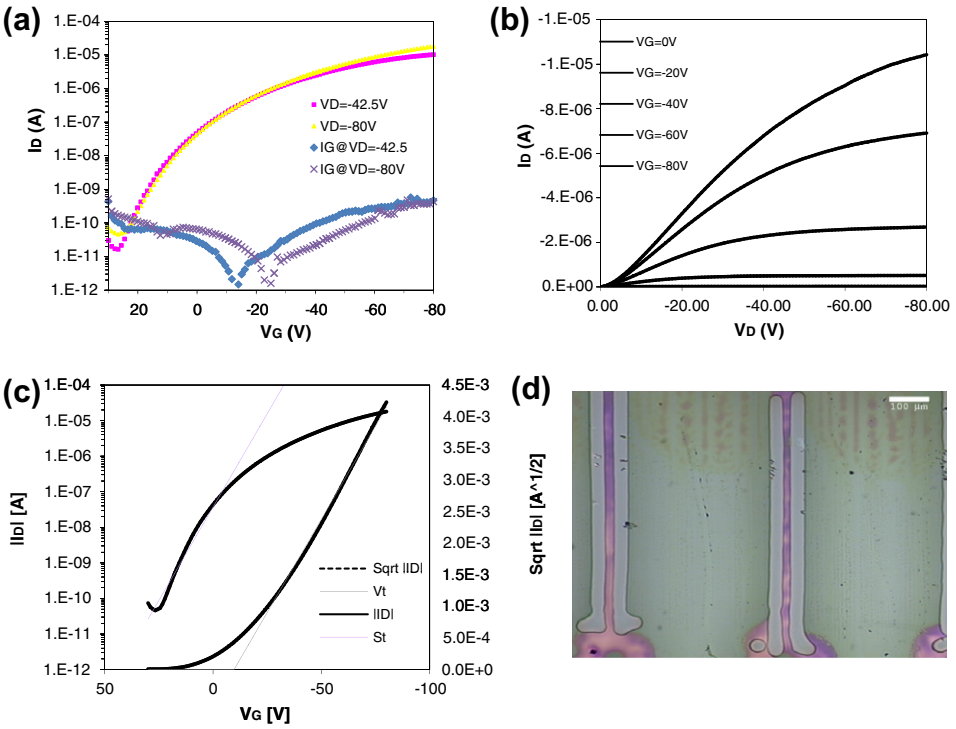

Fig. 5. (a) Transfer characteristics, (b) output characteristics, (c) transfer characteristic and $\sqrt{I_D}$ showing square law behavior with a −4 V V_T, and subthreshold slope of 9.5 V/dec. The transfer characteristic shows a low gate current throughout the operation range, and provides a μ_{SAT} = 1.5e−2 cm^2/Vs, on/off of 3.7e−5, μ_{LIN} = 2.6e−2 cm^2/Vs. d) Shows an optical micrograph of the device (center), W = 754 μm and L = 18 μm.

a flat reference to be obtained for step-height measurements and is too wavy for optical methods such as ellipsometry. The optimal pattern/concentration was thus determined by looking for the best uniformity and comparing the color of the printed film to a test sample which was spin coated with a 50 nm thick pBTTT film.

Variation of film thickness was observable when viewing the substrate at an oblique angle despite appearing uniform when viewed head on. The variation was too faint to be captured by camera or microscope. Instead, a schematic of these results is shown in Fig. 4. Patterns printed with a high print volume (21 or 23 mL/m^2) presented an oscillatory thickness perpendicular to the print direction but good uniformity in the print direction (Fig. 4(a)). Patterns printed with a low print volume (6 and 8 mL/m^2) had an incomplete film as wells were spaced too far apart for the deposited ink to spread and merge. Patterns with a slightly higher print volume (10 mL/m^2) were continuous films, but exhibited a similar color oscillation as for the dithered patterns (Fig. 4(c)), while a few print volumes (13 and 15.6 mL/m^2) yielded optically uniform films (Fig. 4(b)). Best results were found using a concentration of 3 mg/mL of pBTTT in dichlorobenzene and a 13.1 mL/m^2 pattern.

3. Results and discussion

3.1. DC results

DC characteristics where obtained in air using an Agilent 4156C semiconductor parameter analyzer. Mobilities where extracted using the square-law equations for linear and saturation mobility as appropriate and the peak transconductance extracted from the first derivative of the transfer characteristics in order to avoid including errors in extracting the threshold voltage.

As printed, the bottom gate devices exhibited reasonable saturation mobilities of 0.06 cm^2/Vs and a modest on/off ratio of 10^3. It was determined that the poor on/off ratios were due to leakage through the gate to the probe tip during testing, as the semiconductor had not been patterned over the gate contact. After eliminating the semiconductor around the gate contact, the off current decreased dramatically yielding devices with on/off ratios of 10^6. pBTTT is quite air-stable, and mobility stabilized at 0.01–0.02 cm^2/Vs after storing in air for 3 weeks. Transfer and output characteristics for a prototypical device are presented in Fig. 5. The onset voltage and threshold voltage for these devices have had a positive shift from their initial state, which could be an indication of the incorporation of moisture into the film [9]. These are among the highest performing gravure printed organic TFTs to date.

A top gate device structure was also investigated. In the process flow for this device, shown on the right of Fig. 1, gravure is utilized to define the source and drain. These contacts are printed first, using PR-010 and are printed in the same manner as the gate contacts for bottom gate devices. A key advantage to printing S/D contacts with gravure is that the spacing between the lines is determined on the roll, and can be accurately controlled during the print process because of the contact nature of the print technique. However a key disadvantage is that the non-image areas of a gravure roll remain coated with residual ink as ink removal by the doctor blade is never perfect [5]. This residual ink can cause chemical contamination of the semiconductor, and increase the roughness of the surface onto which the semiconductor is to be deposited decreasing its crystallinity and performance [11,12].

The electrical characteristics of these devices, shown in Fig. 6, exhibit very high off currents. The off-state leakage was determined not to be caused by gate leakage, but by S/D leakage. This could be caused by a poor semiconductor limited by the roughness of the surface onto which it was deposited, or by chemical doping and contamination from the residual ink in the channel. Further, test devices fabricated on silicon samples rule out that the performance of the material was compromised by subsequent processing of the dielectric and gate. Considering that the channel for these devices is formed on the top surface of the semiconductor which because of its roughness should cause increased carrier scattering, the saturation mobility, 0.015 cm^2/Vs, is comparable to that observed on bottom gate devices.

Removal of the scum deposited during gravure printing of the contacts is thus imperative to improving the performance of these devices, and will be necessary to realize top-gated devices by gravure printing.

3.2. AC performance

The DC characterization of printed pBTTT TFTs is essential to understanding the materials properties and electronic behavior of the devices. Performance parameters extracted from DC characterization are used to model how

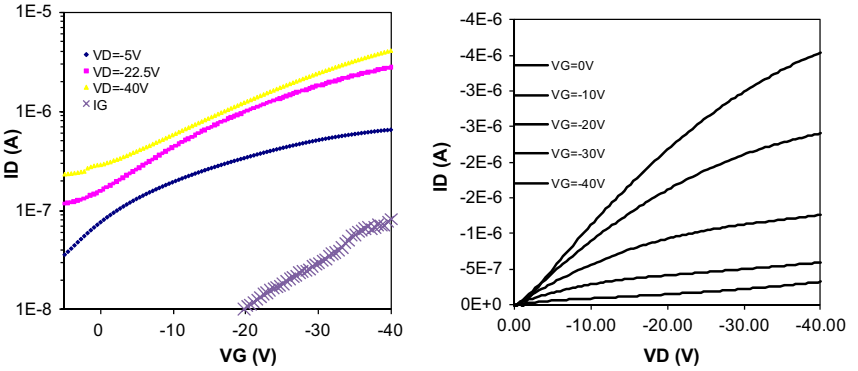

Fig. 6. Transfer and output characteristics for top gate, gravure printed TFTs. W = 854 μm, L = 21 μm, μ_{FE} = 6.8e−3, on/off = 17.5.

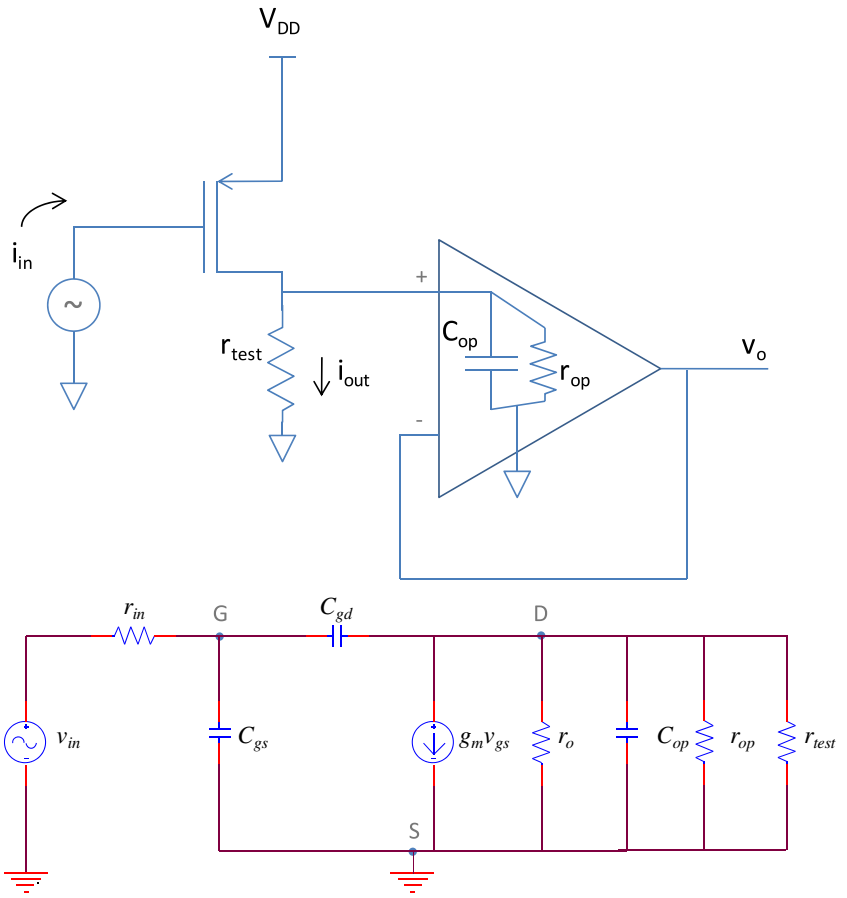

Fig. 7. Schematic of experimental setup (top) for f_T extraction and equivalent small signal circuit (bottom).

a device will operate in a real circuit. However, for actual applications, AC analysis and characterization is crucial, since DC characterization alone does not provide sufficient information about how a transistor will operate under these conditions. At high frequencies, capacitances dominate a transistors performance, shorting the signal from the gate to channel due to overlap capacitance, decreasing the gain of a transistor in an analog circuit; and ever increasing the drive current required to charge capacitive loads, limiting the rise and fall times of digital signals.

For organic thin film transistors, the operating speed of the device can also be limited by charge injection from the source/drain contacts into the channel [13–15]. In this case injection is limited by trapping and de-trapping rates at the metal/semiconductor interface, which can be difficult to measure directly.

A direct form of assessing the AC performance of a transistor is through the measurement of its *transition frequency*, f_T. The transition frequency is defined as the frequency at which an unloaded transistor exhibits unity current gain. This measurement is particularly useful for analog circuitry where f_T gives a clear bound on the maximum frequency an analog circuit can be expected to provide amplification. The relation of f_T to device parameters and its importance in understanding the scalability of such devices has been recently reviewed in this journal by Hoppe and coworkers [16].

In high performance transistors, the transition frequency is measured using high frequency test structures with load matched transmission lines connecting the contacts of the device and measurement results are fitted to a small signal model to obtain f_T [17,18]. For OTFTs, operating frequencies are much lower and microwave techniques can be avoided. Instead, a direct measurement of f_T can be made by the circuit in Fig. 7. The transistor is operated at its standard DC bias point (saturation), a small signal current is applied to the gate, and the corresponding output current is measured at the drain of the device.

In an ideal case, the ammeter at the drain behaves as a short in small signal and thus the output resistance of the transistor and any output capacitance are shorted. Ignoring r_{in}, which should be negligible for a good voltage source, $v_{in} = v_{gs}$ and the input current can then be expressed as

$$i_{in} = j\omega(C_{gs} + C_{gd})v_{gs} \tag{1}$$

the output current is

$$i_o = g_m v_{gs} \tag{2}$$

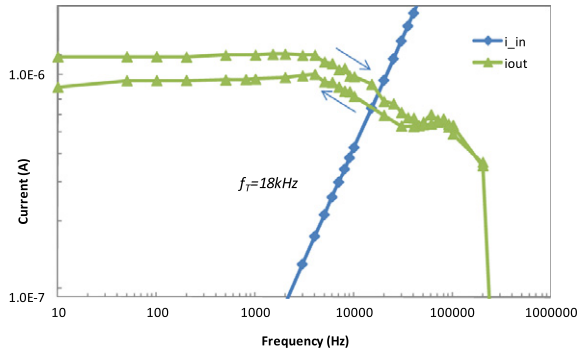

Fig. 8. Input and ouput current vs. frequency for an all printed pBTTT transistor. f_T is measured at the intersection of the two curves, indicating unity current gain. Data is for transistor presented in Fig. 5.

by substituting v_{gs} from Eq. (1), the current gain is given as

$$\frac{i_o}{i_{in}} = \frac{gm}{j\omega(C_{gs}+C_{gd})} \tag{3}$$

Which, when $\frac{i_o}{i_{in}} = 1$ gives f_T

$$f_T = \frac{g_m}{2\pi(C_{gs}+C_{gd})} \tag{4}$$

A low current small load ammeter was emulated by placing a test resistor in series with the drain such that $r_{test} << r_o$ and connecting a high impedance probe to accurately measure a voltage drop across the load such that the output current could be measured

$$i_o = \frac{v_o}{r_{test}}. \tag{5}$$

To further improve measurement accuracy, the impedance of the high impedance probe was taken into account and the circuit model in Fig. 7 was used to accurately extract i_o.

The input capacitance of the transistor was determined by using the measured dielectric capacitance per unit area, the size of the transistor, and the overlap area of the source and drain contacts (determined using optical microscopy) such that

$$C_{gs}+C_{gd} = C_{ins}W\left(\frac{2}{3}L + L_{S_{OL}}\right) + C_{ins}WL_{D_{OL}} \tag{6}$$

where C_{ins} is the dielectric capacitance per unit area in F/cm^2 W and L are the transistor width and length, respectively, and L_{SOL} and L_{DOL} are the overlap lengths for the source and drain contacts. The channel capacitance was assumed to be 2/3 of the channel length in saturation as is common practice. Assuming that the overlap lengths are the same for both source and drain, and expressing these lengths as a percentage ϕ of the channel length, the input capacitance can be written as

$$C_{gs}+C_{gd} = C_{ins}W\left(\frac{2}{3}L + 2\phi L\right) \tag{7}$$

With these equations and the measured output voltage, the small signal output current (i_{out}) and the input current (i_{in}) can be plotted to determine the f_T of the device. Biasing an all printed pBTTT TFT with V_{DS} = −60 V and V_{GS} = −56 V, and applying a 2 V peak-to-peak sinusoidal signal to the gate while sweeping its frequency measurements of i_{in} and i_o where made. The data in Fig. 8 show a transition frequency of 18 kHz which is an excellent result that compares quite favorably to other gravure printed transistors [1,2].

To better understand the source of this performance, Eq. (4) can be expanded to reflect the influence of device parameters by substituting $g_m = \mu C_{ins}\frac{W}{L}(V_{GS}-V_T)$ and Eq. (7) to yield

$$f_T = \frac{\mu(V_{GS}-V_T)}{2\pi\left(\frac{2}{3}L^2 + 2\phi L^2\right)} \tag{8}$$

which is similar to Eq. (11) from [16], where the contact resistance term has been ignored.

For the device presented here, a transition frequency of 27 kHz was calculated with Eq. (8), which is in good agreement with the measured value.

4. Conclusion and outlook

In this work, we have presented highly scaled gravure printed organic transistors offering excellent performance, including some of the highest switching speeds reported to date for fully-printed transistors. It is evident that though clear improvements to f_T can be obtained through improvements in field effect mobility, the operation of the device is extremely sensitive to its channel length, and substantial improvement can be achieving through proper device scaling. Herein lays the success of the presented devices where gravure printed features were scaled down to 20 μm providing devices with channel lengths of 18 μm. By comparison, the work from Huebler [1] and Jung [2], where channel lengths of 100 and 200 μm were printed, respectively, yielded devices with operation frequencies well below 1 kHz. With a 10× improvement in mobility that can be expected from the pBTTT semiconductor devices operating near 200 kHz could be fabricated using this process. Further, if the channel length can be reduced to 10 μm, a transition frequency of 900 kHz would be expected making these printed devices suitable for standards compliant RFID and high-resolution displays.

References

[1] A.C. Huebler, F. Doetz, H. Kempa, H.E. Katz, M. Bartzsch, N. Brandt, I. Hennig, U. Fuegmann, S. Vaidyanathan, J. Granstrom, et al., Ring oscillator fabricated completely by means of mass-printing technologies, Organic Electronics 8 (2007) 480–486.
[2] M. Jung, J. Kim, J. Noh, N. Lim, C. Lim, G. Lee, J. Kim, H. Kang, K. Jung, A.D. Leonard, J.M. Tour, G. Cho, All-printed and roll-to-roll-printable 13.56-MHz-operated 1-bit RF tag on plastic foils, IEEE Transactions on Electron Devices 57 (2010) 571–580.
[3] G. Cho, R2R Printed TFTs and RFID Tags: Demonstration of All Printed 13.56 MHz Operated 1 Bit RFID Tags, Hsinchu, Taiwan: ISFED, 2008.
[4] J. Jo, J. Yu, T. Lee, D. Kim, Fabrication of printed organic thin-film transistors using roll printing, Japanese Journal of Applied Physics 48 (2009) 04C181.
[5] A. de la Fuente Vornbrock, J.M. Ding, D. Sung, Huai-Yuan Tseng, V. Subramanian, Printing and Scaling of Metallic Traces and Capacitors Using a Laboratory-Scale Rotogravure Press, 2009 Flexible Electronics and Displays Conference and Exhibition, Phoenix, AZ, USA, 2009, pp. 1–7.
[6] D. Sung, A. de la Fuente Vornbrock, V. Subramanian, Scaling and optimization of gravure-printed silver nanoparticle lines for printed

electronics, IEEE Transactions on Components and Packaging Technologies 33 (2010) 105–114.
[7] P.C. Duineveld, The stability of ink-jet printed lines of liquid with zero receding contact angle on a homogeneous substrate, Journal of Fluid Mechanics 477 (2003).
[8] D. Soltman, V. Subramanian, Inkjet-printed line morphologies and temperature control of the coffee ring effect, Langmuir 24 (2008) 2224–2231.
[9] I. McCulloch, M. Heeney, C. Bailey, K. Genevicius, I. MacDonald, M. Shkunov, D. Sparrowe, S. Tierney, R. Wagner, W. Zhang, M.L. Chabinyc, R.J. Kline, M.D. McGehee, M.F. Toney, Liquid-crystalline semiconducting polymers with high charge-carrier mobility, Nature Materials 5 (2006) 328–333.
[10] H. Kipphan et al., Handbook of Print Media, Springer, Heidelberg, 2001.
[11] M.L. Chabinyc, R. Lujan, F. Endicott, M.F. Toney, I. McCulloch, M. Heeney, Effects of the surface roughness of plastic-compatible inorganic dielectrics on polymeric thin film transistors, Applied Physics Letters 90 (2007) 233508.
[12] Y. Jung, R.J. Kline, D.A. Fischer, E.K. Lin, M. Heeney, I. McCulloch, D.M. DeLongchamp, The effect of interfacial roughness on the thin film morphology and charge transport of high-performance polythiophenes, Advanced Functional Materials 18 (2008) 742–750.
[13] Y. Majima, D. Kawakami, S. Suzuki, Y. Yasutake, Simultaneous measurements of drain-to-source current and carrier injection properties of top-contact pentacene thin-film transistors, Japanese Journal of Applied Physics Part 1 Regular Papers Short Notes and Review Papers 46 (2007) 390.
[14] T. Miyadera, T. Minari, K. Tsukagoshi, H. Ito, Y. Aoyagi, Frequency response analysis of pentacene thin-film transistors with low impedance contact by interface molecular doping, Applied Physics Letters 91 (2007) 013512.
[15] K. Seshadri, C.D. Frisbie, Potentiometry of an operating organic semiconductor field-effect transistor, Applied Physics Letters 78 (2001) 993.
[16] A. Hoppe, D. Knipp, B. Gburek, A. Benor, M. Marinkovic, V. Wagner, Scaling limits of organic thin film transistors, Organic Electronics, 2010.
[17] S. Lee, Direct extraction technique for a small-signal MOSFET equivalent circuit with substrate parameters, Microwave and Optical Technology Letters 39 (2003) 344–347.
[18] J. Raskin, R. Gilon, G. Dambrine, J. Chen, D. Vanhoenacker, J. Colinge, Accurate characterization of silicon-on-insulator mosfets for the design of low-voltage, Low-Power RF Integrated Circuits, Analog Integrated Circuits and Signal Processing 25 (2000) 133–155.

Organic Electronics 11 (2010) 2045–2054

Contents lists available at ScienceDirect

Organic Electronics

journal homepage: www.elsevier.com/locate/orgel

Conjugated small molecules with broad absorption containing pyridine and pyran units: Synthesis and application for bulk heterojunction solar cells

J.A. Mikroyannidis [a,*], D.V. Tsagkournos [a], S.S. Sharma [d], Y.K. Vijay [e], G.D. Sharma [b,c,*]

[a] Chemical Technology Laboratory, Department of Chemistry, University of Patras, GR-26500 Patras, Greece
[b] Physics Department, Molecular Electronic and Optoelectronic Device Laboratory JNV University, Jodhpur, Rajasthan 342005, India
[c] R&D Center for Engineering and Science, Jaipur Engineering College, Kukas, Jaipur, Rajasthan, India
[d] Department of Physics, Government Engineering College for Women, Ajmer, Rajasthan, India
[e] Thin Film and Membrane Science Laboratory, University of Rajasthan, Jaipur, Rajasthan, India

ARTICLE INFO

Article history:
Received 20 August 2010
Received in revised form 29 September 2010
Accepted 3 October 2010
Available online 14 October 2010

Keywords:
Conjugated small molecules
Photovoltaic
Bulk heterojunction solar cells
Low band gap
Pyridine
Pyran

ABSTRACT

Two new conjugated small molecules (SMs), **M1** and **M2**, of low band gap with pyridine and pyran units, respectively, were synthesized by a convenient two-step reaction. They were soluble in common organic solvents and showed broad absorption ranging from 300 to 750 nm. Their long-wavelength absorption maximum was at 601–640 nm and the optical band gap was 1.60–1.67 eV. These SMs and [6,6]-phenyl-C61-butyric acid methyl ester (PCBM) were used as donor and acceptor respectively to fabricate bulk heterojunction organic photovoltaic (OPV) devices through solution processing. The power conversion efficiencies (PCEs) for the OPV devices based on the as cast **M1**:PCBM and **M2**:PCBM are 1.42% and 1.80%, respectively. The higher PCE for the **M2**:PCBM based devices is attributed to the higher hole mobility, broader absorption spectra and lower band gap of **M2** as compared to **M1**. The PCEs have been improved up to 1.75% and 2.18% for the solvent treated **M1**:PCBM and **M2**:PCBM blends, respectively. Finally, they have been further enhanced to 2.03% and 2.77% for the thermally annealed solvent treated **M1**:PCBM and **M2**:PCBM blends, respectively. This improvement has been attributed to the increase in the crystallinity of the blend and balance charge transport of the devices based on the solvent treated and thermally annealed solvent treated blends.

© 2010 Elsevier B.V. All rights reserved.

1. Introduction

Intense research in the field of organic photovoltaics (OPVs) has led to a significant increase in their power conversion efficiencies (PCEs) over the past decade [1]. One of the most important advances in OPVs has been the introduction of the bulk heterojunction (BHJ) architecture [2], in which the photoactive thin film consists of an interpenetrating blend of electron donor and electron acceptor components. Extensive research efforts have focused on improving the polymeric electron donor component of the BHJ while retaining fullerene derivatives as the electron acceptor [3]. In BHJ devices using 6,6-phenyl-C61-butyric acid methyl ester (PC61BM) as the acceptor, a desirable processable polymer donor should exhibit not only a band gap between 1.2 and 1.9 eV with broad absorption to maximize sunlight absorption but also a highest occupied molecular orbital (HOMO) energy level between −5.2 and −5.8 eV and a lowest unoccupied molecular orbital (LUMO) energy level between −3.7 and −4.0 eV to ensure efficient charge separation while maximizing the

* Corresponding authors at: Chemical Technology Laboratory, Department of Chemistry, University of Patras, GR-26500 Patras, Greece. Tel.: +30 2610 997115; fax: +30 2610 997118 (J.A. Mikroyannidis), tel.: +91 0291 2720857; fax: +91 0291 2720856 (G.D. Sharma).
E-mail addresses: mikroyan@chemistry.upatras.gr (J.A. Mikroyannidis), sharmagd_in@yahoo.com (G.D. Sharma).

1566-1199/$ - see front matter © 2010 Elsevier B.V. All rights reserved.
doi:10.1016/j.orgel.2010.10.002

open-circuit voltage (V_{oc}). In addition, good hole mobility is needed to allow adequate charge transport [1c]. On the other hand, the use of donor–acceptor structures has become an efficient strategy for obtaining low-band-gap polymers and modulating their electronic properties [4]. Recent developments concerning processes for the production of flexible large area polymer and generally organic solar cells have been reported [5].

Small-molecule (SM) donor materials can also form useable BHJ solar cells by solution processing, although it is more challenging to obtain high-quality films. The highest reported efficiencies for such devices have remained low relative to solution processed solar cells using polymeric donor materials. SM materials, however, offer advantages over polymeric materials in terms of ease of synthesis and purification, which greatly improve fabrication reproducibility, as well as possessing a greater tendency to self assemble into ordered domains, which leads to high charge carrier mobilities [6,7]. SMs do not suffer from batch to batch variations, broad molecular-weight distributions, end-group contamination, or difficult purification methods, which can be significant problems for polymeric materials. These considerations make SMs a promising class of donor material for BHJ solar cell applications [8]. PCE up to 2.3% and 3.0% have been reported [9] using an oligothiophene with dialkylated diketopyrrolopyrrole chromophere as donor and soluble fullerenes PCBM or [6,6]-phenyl C71 butyric acid methyl ester as an acceptor, respectively. The best performance of solution processed SM solar cells with a PCE of 4.4% has been reported by Nguyen et al. [9a]. Theoretical and experimental advances in OSCs have demonstrated that the donor–acceptor (D–A) type SMs have great potential as one class of promising materials in solution processed OPVs [10]. These encouraging results stimulate scientists to develop and investigate more solution processable organic donors for high performance OPVs.

Pyridine has been inserted into a bithiophene template to create a donor monomer. This monomer has been copolymerized with 2,1,3-benzothiadiazole and with thiophene and the resulting copolymers have been used for BHJ solar cells [11]. On the other hand, various polymers and SMs containing (4*H*-pyran-4-ylidine)propanedinitrile have been widely used for fabrication of BHJ solar cells [12–16].

Recently, we have synthesized a series of SMs of low band gap containing cyanovinylene 4-nitrophenyl segments which have been used as donors with PCBM as acceptor for BHJ solar cells [17–21]. In continuation of this research line, in the present article we report the synthesis, characterization and the BHJ solar cells performance of two new conjugated SMs, **M1** and **M2**, which contain pyridine and substituted-pyran as central unit, respectively. Besides, they contained terminal cyanovinylene 4-nitrophenyl units, which broadened and red-shifted their absorption spectrum, as well as a phenylenevinylene spacer. Pyridine is an electron-donating segment, while (4*H*-pyran-4-ylidine) propanedinitrile is a coplanar electron-withdrawing segment with high oxidative stability. These SMs were successfully synthesized by a two-step reaction sequence from inexpensive and widely used starting materials. The SMs, were used as electron donor materials along with PCBM as electron acceptor, to fabricate BHJ organic photovoltaic devices through solution processing. The PCEs for the OPV devices based on the as cast **M1**:PCBM and **M2**:PCBM are 1.42% and 1.80%, respectively. The higher PCE for the **M2**:PCBM based devices is attributed to the lower optical (1.60 vs. 1.67 eV) and electrochemical (1.70 vs. 1.75 eV) band gap, the higher hole mobility (7.8×10^{-6} vs. 4.5×10^{-6} cm^2/Vs) and broader absorption spectrum of **M2** as compared to **M1**. Since these SMs are differentiated only by their central unit, (4*H*-pyran-4-ylidine) propanedinitrile seems to be superior to pyridine from the viewpoint of PV performance. Moreover, the effect of solvent vapour treatment of blends and thermal annealing on the photovoltaic (PV) performance of the devices has been investigated. PCEs of 2.03% and 2.77% were achieved for OPVs based on thermally annealed solvent treated **M1**:PCBM and **M2**:PCBM blends, respectively.

2. Experimental

2.1. Reagents and solvents

(2,6-Dimethyl-4*H*-pyran-4-ylidine)propanedinitrile (**1b**) was synthesized from the condensation of 2,6-dimethyl-4-pyrone with malononitrile in acetic anhydride [22]. 4-Nitrobenzylcyanide was synthesized from the nitration of benzyl cyanide with concentrated nitric and sulfuric acid [23]. It was recrystallized from ethanol. Terephthaldehyde was recrystallized from water. *N*,*N*-dimethylformamide (DMF) and tetrahydrofuran (THF) were dried by distillation over CaH_2. All other reagents and solvents were commercially purchased and were used as supplied.

2.2. Preparation of compounds

2.2.1. 2,6-di(E)-4-formylstyrylpyridine (*2a*)

A flask was charged with a mixture of 2,6-dimethylpyridine (**1a**) (0.75 g, 6.99 mmol), terephthaldehyde (1.88 g, 13.98 mmol) and acetic anhydride (25 mL). It was stirred and refluxed for 12 h under N_2. The reaction product precipitated upon cooling at room temperature. It was filtered off, washed thoroughly four times with hot water and dried to afford **2a** (2.06 g, 87%).

FT-IR (KBr, cm^{-1}): 1696 (carbonyl); 3032, 1598, 1448 (aromatic).

^{1}H NMR ($CDCl_3$) ppm: 9.95 (s, 2H, formyl); 7.76 (m, 4H, phenylene ortho to formyl); 7.42 (m, 1H, pyridine H4); 7.32 (m, 4H, phenylene meta to formyl); 7.21 (m, 4H, vinylene); 6.93 (m, 2H, pyridine H3, H5).

Anal. Calcd. for $C_{23}H_{17}NO_2$: C, 81.40; H, 5.05; N, 4.13. Found: C, 80.63; H, 5.38; N, 4.52.

2.2.2. 2-(2,6-bis((E)-4-formylstyryl)-4H-pyran-4-ylidene)-malononitrile (*2b*)

Compound **2b** was prepared in 82% yield from the reaction of (2,6-dimethyl-4*H*-pyran-4-ylidine)propanedinitrile (**1b**) with terephthaldehyde in a mol ratio 1:2 in acetic anhydride according to the procedure described for **2a**.

FT-IR (KBr, cm^{-1}): 1700 (carbonyl); 2208 (cyano); 3056, 1578, 1508, 1430 (aromatic).

^1H NMR ($CDCl_3$) ppm: 9.98 (s, 2H formyl); 7.76 (m, 4H, phenylene ortho to formyl); 7.32 (m, 4H, phenylene meta to formyl); 7.21 (m, 4H, vinylene); 6.60 (s, 2H, pyran).

Anal. Calcd. for $C_{26}H_{16}N_2O_3$: C, 77.22; H, 3.99; N, 6.93. Found: C, 76.62; H, 3.68; N, 6.42.

2.2.3. 2-(2,6-bis((1Z,1E)-4-((Z)-2-cyano-2-(4-nitrophenyl)-vinyl)styryl)pyridine (*M1*)

A flask was charged with a solution of **2a** (0.2315 g, 0.682 mmol) and 4-nitrobenzylcyanide (0.2212 g, 1.364 mmol) in DMF (15 mL). Sodium hydroxide (0.20 g, 5.00 mmol) dissolved in ethanol (8 mL) as added to this solution. The reaction mixture was stirred for 1 h at room temperature under N_2 and then was concentrated under reduced pressure. Water was added to the concentrate and **M1** precipitated as a dark green solid. It was recrystallized from DMF/water (0.2967 g, 69%).

FT-IR (KBr, cm^{-1}): 2156 (cyano); 1524, 1346 (nitro); 3028, 1584, 1504, 1446 (aromatic).

^1H NMR ($CDCl_3$) ppm: 8.19 (m, 4H, phenylene ortho to nitro); 7.83 (s, 2H, cyanovinylene); 7.52–7.30 (m, 4H, phenylene meta to nitro; 1H, pyridine H4; 8H, other phenylene); 7.21 (m, 4H, vinylene); 6.93 (m, 2H, pyridine H3, H5).

Anal. Calcd. for $C_{39}H_{25}N_5O_4$: C, 74.63; H, 4.01; N, 11.16. Found: C, 74.15; H, 4.28; N, 11.51.

2.2.4. 2-(2,6-bis((1Z,1E)-4-((Z)-2-cyano-2-(4-nitrophenyl)-vinyl)styryl)-4H-pyran-4-ylidene)malononitrile (*M2*)

Compound **M2** was prepared as a dark green solid in 75% yield from the reaction of **2b** with 4-nitrobenzylcyanide in DMF in the presence of sodium hydroxide.

FT-IR (KBr, cm^{-1}): 2193, 2170 (cyano); 1520, 1346 (nitro); 3032, 1590, 1508, 1458 (aromatic).

^1H NMR ($CDCl_3$) ppm: 8.19 (m, 4H, phenylene ortho to nitro); 7.83 (s, 2H, cyanovinylene); 7.52 (m, 4H, phenylene meta to nitro); 7.48–7.30 (m, 8H, other phenylene); 7.21 (m, 4H, vinylene); 6.60 (s, 2H, pyran).

Anal. Calcd. for $C_{42}H_{24}N_6O_5$: C, 72.83; H, 3.49; N, 12.13. Found: C, 72.35; H, 3.68; N, 11.75.

3. Characterization methods

IR spectra were recorded on a Perkin–Elmer 16PC FT-IR spectrometer with KBr pellets. ^1H NMR (400 MHz) spectra were obtained using a Brucker spectrometer. Chemical shifts (δ values) are given in parts per million with tetramethylsilane as an internal standard. UV–vis spectra were recorded on a Beckman DU-640 spectrometer with spectrograde THF. Elemental analyses were carried out with a Carlo Erba model EA1108 analyzer.

The electrochemical properties of **M1** and **M2** were studied by cyclic voltammetry (CV) (CH Instruments). A glassy carbon coated with **M1** or **M2**, a Pt plate and an Ag/Ag^+ electrode were used as the working-, counter- and reference-electrode, respectively. The electrolyte solution was 0.1 M tetrabutylammonium hexafluorophosphate (Bu_4NPF_6) in anhydrous accetonitrile. The potential scan rate was 100 mV s^{-1}. The films for the electrochemical measurements were coated from their THF solutions.

The crystallinity of the films was studied using the X-ray diffraction (XRD) technique (panalytical make USA) having CuKα, as radiation source of wavelength λ = 1.5405 A° with the films coated on the quartz substrates.

3.1. Device fabrication and characterization

The BHJ devices were fabricated by the following ways. The indium doped tin oxide (ITO) coated glass serving as transparent anode was cleaned with detergent, acetone and isopropyl alcohol in an ultrasonic bath and then dried in oven. A 60 nm poly-[ethylenedioxy-thiophene]:(poly-(styrene sulphonic acid) (PEDOT:PSS) (BARTRON AG) as modified layer was then spin coated onto the pre-cleaned ITO glass substrate and dried at 80 °C for 15 min in vacuum oven. After cooling the substrate to room temperature, a solution of **M1** or **M2** (5 mg/mL) and PCBM (5 mg/mL) in THF was spin coated onto the top of PEDOT:PSS layer. For the solvent vapour treatment, the spin coated blend film was transferred into a jar filled with THF and remained there for 20 min. The thermal annealing of solvent vapour treated film was carried out at 100 °C for 2 min on the hot plate. Finally, an aluminum (Al), electrode (60 nm) was deposited on the top of the active BHJ layer through the thermal evaporation method. We have also fabricated the devices based on pure **M1** and **M2** having configuration ITO/PEDOT:PSS/**M1** or **M2**/Al to get information for the electrical and PV properties of these materials.

Current–voltage (*J–V*) characteristics of the PV devices were measured using a computer controlled Keithley 238 source meter in dark as well as under illumination intensity of 100 mW/cm^2. A xenon light source was used to give a simulated irradiance of 100 mW/cm^2 (equivalent to AM1.5 irradiation) at the surface of the device. The hole only and electron only devices having ITO/PEDOT:PSS/**M1** or **M2**: PCBM/Au and Al/**M1** or **M2**:PCBM/Al structures, respectively, were fabricated and *J–V* characteristics in dark at room temperature were recorded to estimate the hole and electron mobilities in the BHJ active layers.

4. Results and discussion

4.1. Synthesis and characterization

In this work we attempted to synthesize broadly absorbing SMs which are candidates for BHJ solar cells. Scheme 1 outlines the two-step reaction sequence of the target SMs. In particular, 2,6-dimethylpyridine (**1a**) and 2,6-dimethyl-4*H*-pyran-4-ylidine)propanedinitrile (**1b**) reacted with double molar amount of terephthaldehyde in acetic anhydride to afford dialdehydes **2a** and **2b**, respectively. In this reaction, the ratio of the reactants is crucial to limit the formation of poly(styrylpyridine). Moreover, the reaction product was thoroughly washed with hot water to dissolve possible unreactive terephthaldehyde. Dialdehydes **2a** and **2b** were condensed with 4-nitrobenzylcyanide in DMF in the presence of sodium hydroxide

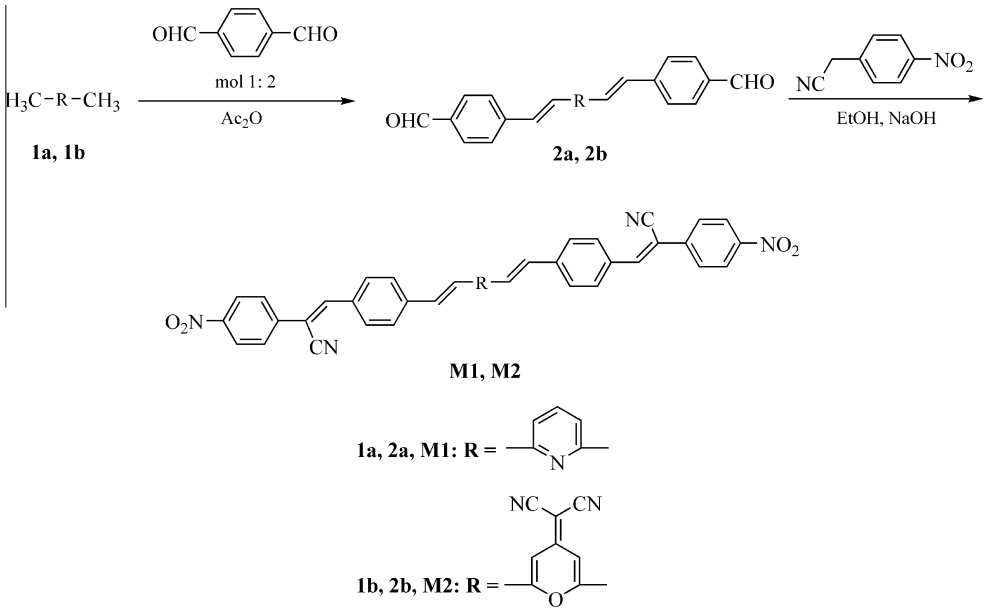

Scheme 1. Synthesis of SMs **M1** and **M2**.

to give **M1** and **M2**, respectively as dark green solids in 69–75% yield. Even though these SMs lacked solubilising aliphatic chains, they were soluble in common organic solvents such as chloroform, dichloromethane and THF. Thin films of SMs could be obtained from their solutions by spin-casting.

The SMs were characterized by FT-IR and ^{1}H NMR spectroscopy. The IR spectra showed characteristic absorption bands around 2160 (cyano); 1520, 1346 (nitro) and 3030, 1590, 1500, 1450 cm^{-1} (aromatic). The ^{1}H NMR spectra displayed common signals at 8.19 (phenylene ortho to nitro); 7.83 (cyanovinylene) and 7.52 ppm (phenylene meta to nitro). It is worth mentioning that the unsubstituted vinylene protons resonated at lower shift (7.21 ppm) than the cyanovinylene protons (7.83 ppm) due to the electron-withdrawing cyano substituents of the latter.

4.2. Photophysical properties

The photophysical properties of SMs were investigated by UV–vis absorption spectroscopy in dilute (10^{-5} M) THF solution as well as in thin film (Fig. 1). All photophysical and electrochemical characteristics of SMs are summarized in Table 1. The absorption spectra were broad and extended from 300 nm up to approximately 750 nm which is a desirable feature for PV applications. The long-wavelength absorption maximum ($\lambda_{a,max}$) was at 601–640 nm which for **M1** could be attributed to an intramolecular charge transfer (ICT) between the electron-donating central pyridine and the electron-withdrawing terminal cyanovinylene 4-nitrophenyl. Upon going from solution to thin film, the $\lambda_{a,max}$ was red-shifted by ~35 nm owing to intermolecular interactions in solid state. The thin film absorption onset for **M1** and **M2** was located at 744 and

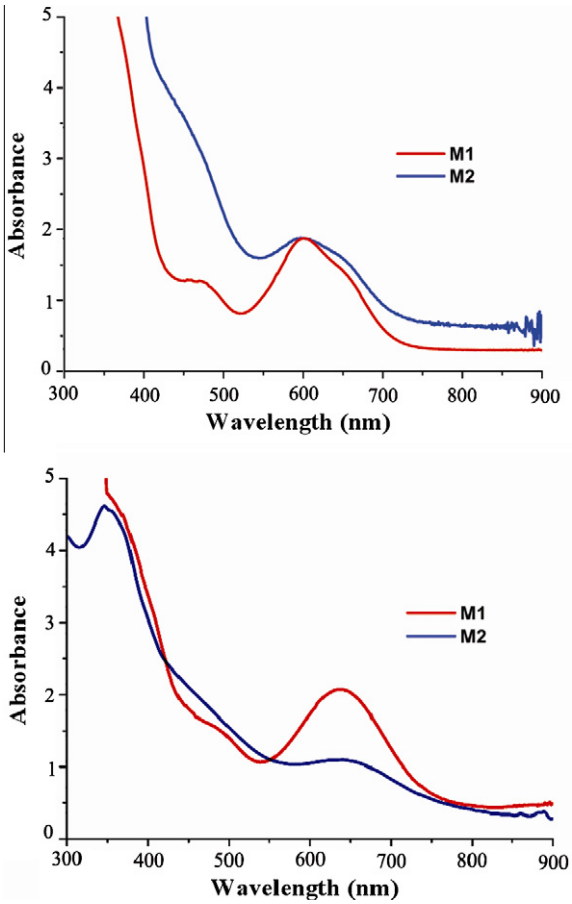

Fig. 1. UV–vis absorption spectra of SMs in THF solution (top) and thin film (bottom).

Table 1
Optical and electrochemical properties of SMs.

Molecule	M1	M2
$\lambda_{a,max}$[a] in solution (nm)	601	604
$\lambda_{a,max}$[a] in thin film (nm)	636	640
Thin film absorption onset (nm)	744	777
E_g^{opt} (eV)[b]	1.67	1.60
E_{onset}^{ox} (V)	0.65	0.45
E_{onset}^{red} (V)	−1.10	−1.25
HOMO (eV)	−5.35	−5.15
LUMO (eV)	−3.60	−3.45
E_g^{el} (eV)[c]	1.75	1.70

[a] $\lambda_{a,max}$: The absorption maxima from the UV–vis spectra in THF solution or in thin film.
[b] E_g^{opt}: optical band gap determined from the absorption onset in thin film.
[c] E_g^{el}: electrochemical band gap determined from cyclic voltammetry.

777 nm which corresponds to an optical band gap (E_g^{opt}) of 1.67 and 1.60 eV respectively. These values of E_g^{opt} are in line with those of other related SMs which have been synthesized in our laboratory [17–21]. Since both SMs showed comparable photophysical characteristics, the different chemical structure of the central unit did not influence considerably their photophysical properties.

4.3. Electrochemical properties

The electrochemical properties of **M1** and **M2** were studied by CV measurements as shown in Fig. 2. The onset reduction potential and oxidation potential have been measured with respect to a Ag/Ag^+ electrode. The values of the highest occupied molecular orbital (HOMO) and lowest unoccupied molecular orbital (LUMO) energy levels were estimated from the following equations [24].

$$E_{HOMO}(eV) = -q(E_{onset}^{ox} + 4.7)$$
$$E_{LUMO}(eV) = -q(E_{onset}^{red} + 4.7)$$

where the unit of the potential is V vs. Ag/Ag+. The onset oxidation potential (E_{onset}^{ox}), onset reduction potential (E_{onset}^{red}), positions of HOMO and LUMO levels and electrochemical band gap of SMs are summarized in Table 1.

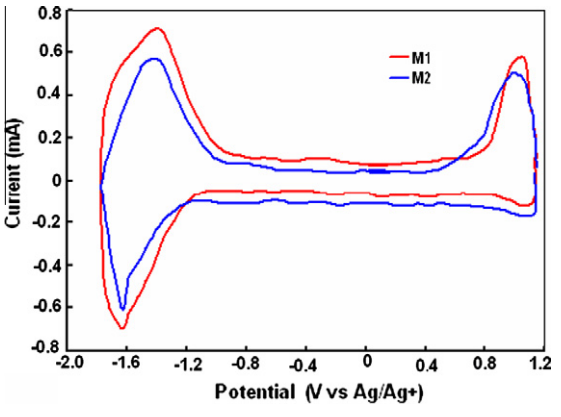

Fig. 2. Cyclic voltammogram of SMs **M1** and **M2** at scan rate of 50 mV/s.

The LUMO level of both M1 (−3.60 eV) and M2 (−3.45 eV) is higher than that of PCBM (−4.0 eV). The electrochemical band gap (E_g^{el}) of these materials is slightly higher than the corresponding E_g^{opt}, which is a common feature of most of the organic semiconductors due to the exciton binding energy [25]. It has been generally accepted that an energy difference of 0.35 eV between the LUMO levels of acceptor and donor materials (i.e. LUMO–LUMO offset) used in BHJ layer is necessary for efficient photoinduced electron transfer between donor to acceptor [26]. As it can be seen from Table 1, the difference between the LUMO levels of M1 or M2 and PCBM is greater than the binding energy of the excitons. Therefore, it is expected that excitons can be easily dissociated at the interface between M1 or M2 and PCBM in the organic solar cells based on blends with M1 or M2 as electron donor and PCBM as electron acceptor. Furthermore, the HOMO energy levels of M1 (−5.35 eV) and M2 (−5.15 eV) are well aligned with the HOMO level of PEDOT:PSS (−5.2 eV), indicating that holes can be easily transported from the HOMO level of M1 or M2 to PEDOT:PSS hole transport layer.

4.4. Electrical and photovoltaic properties of M1 and M2

We have measured the *J–V* characteristics of the devices based on pure SM sandwiched between the PEDOT:PSS and Al electrodes, in dark as well as under illumination and are shown in Fig. 3. The *J–V* characteristics (Fig. 3a) of both devices show a rectification effect, when positive potential is applied to PEDOT:PSS/ITO electrode with respect to the Al electrode. The HOMO level of the PEDOT:PSS (−5.2 eV) is very close to the HOMO level of **M1** (−5.35 eV) or **M2** (−5.15 eV) and forms a nearly Ohmic contact for hole injection from PEDOT:PSS into the HOMO of **M1** or **M2** in the respective devices. However, the LUMO level of both **M1** (−3.60 eV) or **M2** (−3.45 eV) is very far from the work function of Al (4.2 eV) and forms the Schottky barrier for the electron injection from the Al into the LUMO level of **M1** or **M2**. Therefore, the rectification effect observed in these devices is due to the formation of Schottky barrier at the Al-**M1** or Al-**M2** interfaces in the respective devices. From the *J–V* characteristics of the devices in dark, we concluded that both **M1** and **M2** behave as *p* type organic semiconductors.

The charge carrier mobilities of the organic materials used as photoactive layer is an important factor, which influences the PV performance of the organic solar cells. We have measured the hole mobilities of these molecules, using the *J–V* characteristics of the devices in dark with configuration ITO/PEDOT:PSS/**M1** or **M2**/Au, using the space charge limited current model [27]. The *J–V* characteristics of the devices, in dark at room temperature were plotted as $\ln [Jd^3/V_{app}–V_{bi})]$ vs. $[(V_{app}–V_{bi})/d]^{0.5}$, where V_{bi} is the built-in potential, and the hole mobilities of **M1** and **M2** estimated from the intercept on current axis of corresponding lines. The estimated values of hole mobility for **M1** and **M2** are 4.5×10^{-6} and 7.8×10^{-6} cm^2/Vs, respectively.

The PV parameters i.e. short circuit current (J_{sc}), open-circuit voltage (V_{oc}) and fill factor (FF) and power conversion efficiency (PCE) were extracted from the *J–V*

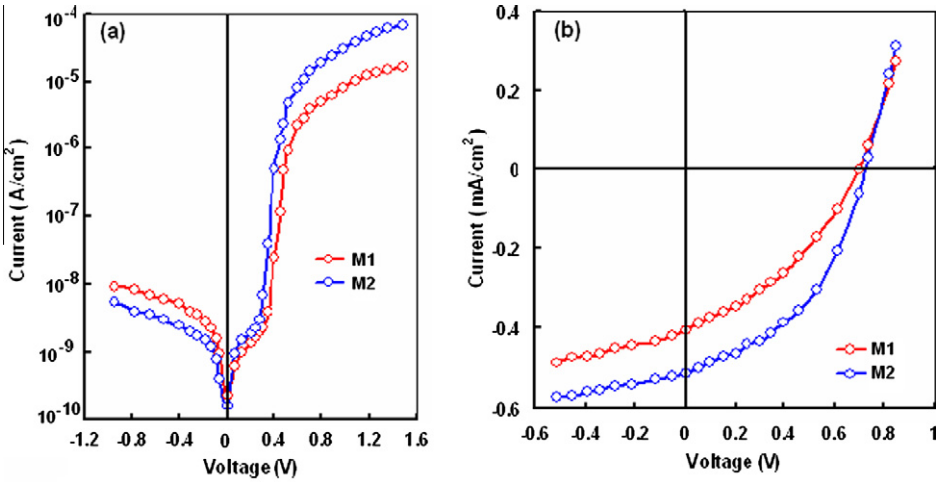

Fig. 3. Current–voltage characteristics of ITO/PEDOT:PSS/**M1** or **M2**/Al devices in (a) dark and (b) under illumination.

Table 2
Photovoltaic parameters of the ITO/PEDOT:PSS/**M1**or **M2**/Al devices.

Material	J_{sc} (mA/cm^2)	V_{oc} (V)	FF	PCE (%)
M1	0.40	0.70	0.32	0.09
M2	0.52	0.72	0.36	0.13

characteristics under illumination intensity of 100 mW/cm^2 (Fig. 3b) and are summarized in Table 2. It can be seen from this table that the values of J_{sc} and PCE are higher for the device based on **M2** in comparison to the device based on **M1** under the same experimental conditions. This can be attributed to the higher hole mobility of **M2** as compared to **M1**. The broader absorption band and lower E_g^{opt} of **M2** as compared to **M1** may contribute to the higher PCE of the device based on **M2** because more excitons are generated in this device. Moreover, the HOMO level of **M2** is very close to the HOMO level of PEDOT:PSS indicating better hole collection in the device of **M2**, which may also be a reason for higher PCE in this device. However, in the case of the device of **M1**, the holes may be trapped in the interface between **M1** and PEDOT:PSS, due to the difference between the HOMO levels of **M1** and PEDOT:PSS, which causes a slight band bending at the interface. The lower band gap, the higher hole mobility and the broader absorption band of **M2** as compared to **M1**, as well as the matching of the HOMO level of **M2** to the HOMO level of PEDOT:PSS are responsible for the higher photovoltaic effect of the **M2** device.

4.5. Electrical and photoelectrical properties of BHJ devices

The BHJ organic solar cells were fabricated with a structure of ITO/PEDOT:PSS/**M1** or **M2**:PCBM (1:1 w/w):Al, with **M1** and **M2** as electron donors and PCBM as electron acceptor. Fig. 4 shows the *J–V* characteristics of these devices in dark. It can be seen from this figure that the *J–V* characteristics in dark, clearly show a rectifying behaviour and exhibit three regions:

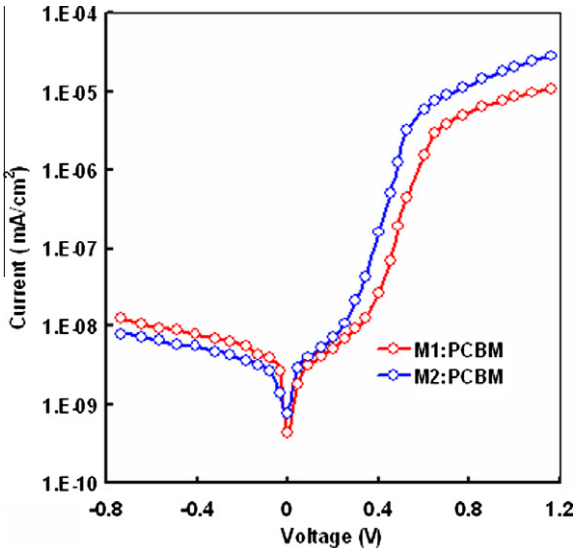

Fig. 4. Current–voltage (*J–V*) characteristics of ITO/PEDOT:PSS/**M1**or **M2**:PCBM/Al devices, using as cast blend, in dark.

(i) A linear region at reverse bias voltages and low forward bias voltages, where the current is controlled by the shunt resistance (R_s)
(ii) An exponential behaviour at intermediate forward bias voltages, where the current is controlled by diode, and
(iii) A second linear region at high forward bias voltages, where the current is controlled by the series resistance (R_{sh}).

Even though the physical and electrical properties of the organic semiconductors may be different, the principal loss mechanisms in the device are the same and consequently the *J–V* characteristics of the organic solar cells can be modelled using the one diode model [28]. The exponential region in the forward *J–V* characteristics is

attributed to the donor-acceptor (*D–A*) interface existing in the device. In the case of the device based on BHJ active layer, a well defined *D–A* interface is not formed as for the p–n junction and schottky barrier devices. In this case, the *D–A* interfaces are spread throughout the bulk of the active layer sandwiched between the two electrodes. The two materials used in the active layer, are arranged like the *D–A* interface, connect the electrode as pure phase or one material is completely enclosed by the other. The exponential behaviour of *J–V* characteristics depends on the properties of the two materials involved in the active layer. The slope of the *J–V* characteristics in exponential region depends upon the two parameters, i.e. ideality factor and reverse saturation current. The ideality factor gives an idea about the recombination process in the device, whereas the saturation current gives an idea about the number of charge carriers which are able to overcome the energetic barrier in the reverse bias. From the slope of *J–V* characteristics in exponential region, we have estimated the ideality factor of the devices, which is 1.50 and 1.23 for the devices based on **M1**:PCBM and **M2**:PCBM, indicating that the recombination of charge carriers is lower for the device fabricated from **M2**:PCBM as compared to the **M1**:PCBM, which may also be a reason for the higher photovoltaic response for the device based on **M2**:PCBM.

Photoluminescence (PL) measurements were performed to get information weather the photoinduced charge transfer or energy transfer is taking place in the blend after the absorption of light. Fig. 5 compares the PL spectra of **M1**, **M1**:PCBM and **M2**:PCBM in solid state. Both **M1** and **M2** show similar PL spectra with maximum emission at 820 nm. The intensity of both **M1**:PCBM and **M2**:PCBM is quenched by addition of PCBM, indicating that photoinduced charge transfer takes place effectively from SM to PCBM. The PL quenching in **M2**:PCBM is relatively higher than that for **M1**:PCBM, which supports the assumption that a more efficient charge transfer occurs in the former.

Fig. 6 shows the *J–V* characteristics of the devices based on the as cast, solvent vapour treated and thermally annealed solvent vapour treated blend under illumination intensity of 100 mW/cm^2 and the corresponding PV parameters are summarized in Table 3. It can seen from this Table that the J_{sc} (3.6 mA/cm^2) and PCE (1.42%) for the device based on the as cast **M2**:PCBM blend is higher than that for device based on the as cast **M1**:PCBM(J_{sc} = 4.57 mA/cm^2 and PCE = 1.81%) blend. The J_{sc} is directly related to the product of absorbed photons and external quantum efficiency (EQE). Since the absorption band of **M2**:PCBM blend is broader than that of **M1**:PCBM, more photons are absorbed by the former blend. Thus more excitons are generated in the **M2**:PCBM blend as compared to **M1**:PCBM due to the absorption of light. The EQE is determined by three processes: (i) migration/diffusion of photogenerated excitons towards the D/A interfaces, (ii) exciton dissociation into free charge carriers at the D/A interfaces, and (iii) collection of charge carriers by the electrodes i.e. holes by PEDOT:PSS/ITO and electrons by Al electrode. The process (i) depends on the nanoscale phase separation between the donor and acceptor materials used in the BHJ active layer. We have observed almost the same surface roughness for both **M1**:PCBM and **M2**:PCBM through the atomic force microscopic images, which indicates that the phase separation in both blends is almost the same. Therefore, we assume that the contribution in EQE or J_{sc} from the process (i) is the same. The process (ii) is related with difference between the LUMO energy levels of donor and acceptor, which is required for ultra fast photoinduced charge transfer in the device. This difference in **M2**:PCBM (0.55 eV) is higher that that in **M1**:PCBM (0.40 eV). This indicates that the exciton dissociation into free carriers and photoinduced charge transfer in the device of **M2**:PCBM blend is faster than that in the device of **M1**:PCBM blend. Process (iii) depends on the percolated path for electrons and holes in the photoactive layer, mobility of holes and also on the HOMO and LUMO energy level of the donor and acceptor materials, relative to the work function of anode and cathode. The HOMO level of **M2** (−5.15 eV) is closer to the HOMO level of PEDOT:PSS (−5.2 eV) and the mobility of holes in **M2**, results in more efficient hole collection. Therefore, we concluded that the higher PCE is due to the higher photocurrent generated in the device of **M2**:PCBM. This has been attributed to the broader absorption band, lower band gap and higher mobility of **M2**. Moreover, the PL quenching in the **M2**:PCBM blend is higher than that in **M1**:PCBM blend indicating faster photoinduced charge transfer in the device of **M2**:PCBM, which affords higher photocurrent in this device.

The V_{oc} (0.96 V) for the device of **M1**:PCBM blend is higher than that (0.88 V) for the device of **M2**:PCBM blend. Mixing of acceptor material with donor material completely modifies the nature of the photoactive layer. In the case of Ohmic contact, the work function of cathode (Al) and the HOMO level of anode (PEDOT:PSS) match the LUMO level of acceptor and HOMO level of donor, respectively. The maximum voltage in this case will be $(V_{oc})_{max} = E_{LUMO}$ (A)$-E_{HOMO}$ (D). The observed value of V_{oc} in the present devices is lower than that for the theoretical value. The HOMO level of **M1** (−5.35 eV) and **M2** (−5.15 eV) does not closely match the HOMO level of PEDOT:PSS (−5.2 eV), resulting in a nearly Ohmic contact for holes with some band bending. Moreover, the LUMO level of PCBM also does not closely match the work function of

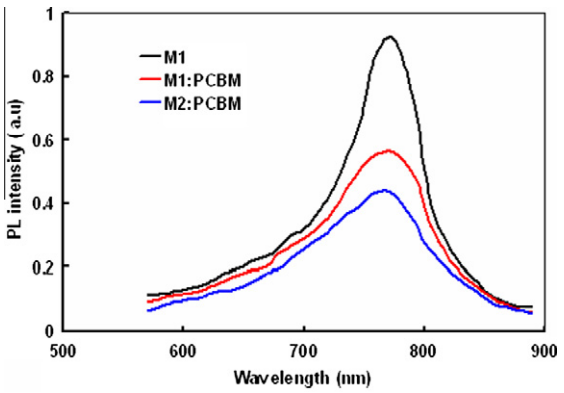

Fig. 5. Photoluminescence (PL) spectra of **M1**, **M1**:PCBM and **M2**:PCBM.

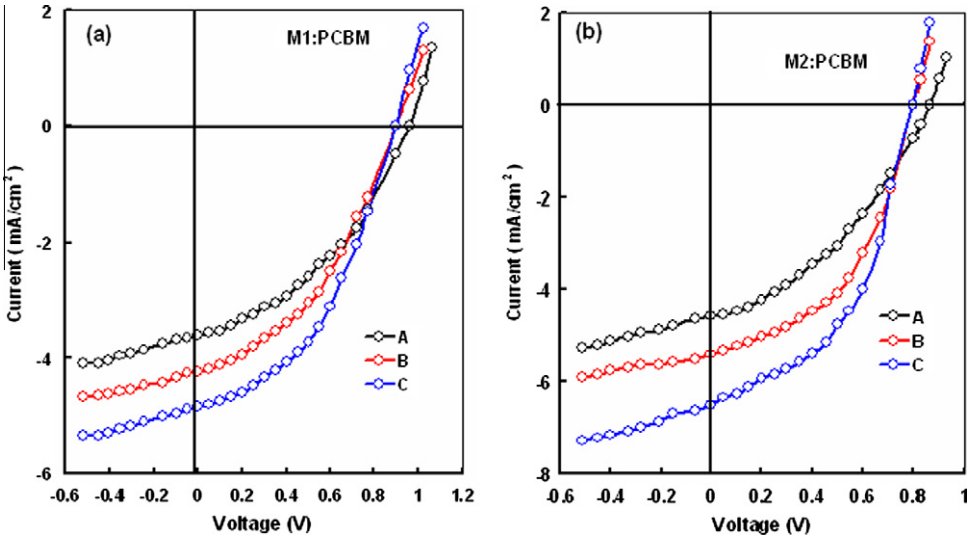

Fig. 6. Current–voltage (J–V) characteristics of ITO/PEDOT:PSS/**M1**or **M2**:PCBM/Al devices using (A) as cast, (B) solvent vapour treatment and (C) thermally annealed solvent vapour treated under illumination.

Table 3
Photovoltaic parameters of the ITO/PEDOT: PSS/**M1** or **M2**:PCBM/Al devices.

Material	J_{sc} (mA/cm^2)	V_{oc} (V)	FF	PCE (%)
M1:PCBM[a]	3.60	0.96	0.41	1.42
M2:PCBM[a]	4.57	0.88	0.45	1.80
M1:PCBM[b]	4.22	0.92	0.45	1.75
M2:PCBM[b]	5.40	0.84	0.48	2.18
M1:PCBM[c]	4.85	0.88	0.47	2.05
M2:PCBM[c]	6.50	0.82	0.52	2.77

[a] As cast film.
[b] Solvent vapour treated film.
[c] Thermally annealed solvent treated film.

the Al electrode and a small band bending also occurs at the Al-PCBM interface. The V_{oc} can be expresses as $V_{oc} = [E_{LUMO}(D) - E_{HOMO}(A)] - \Delta V_b$, where ΔV_b is the voltage losses due to the band bending at the interfaces [29]. Therefore, the experimentally observed V_{oc} is smaller than the theoretical value. The difference between the LUMO–HOMO energy levels for **M1**:PCBM (1.35 eV) is higher than that for **M2**:PCBM (1.15 eV), which is attributed to the lower value of V_{oc} for the device of **M2**:PCBM as compared to that of **M1**:PCBM.

We have observed that the solvent and thermal annealing of blend film changes the thin film absorption spectra significantly. The absorption peak corresponding to the donor (**M1** or **M2**) is shifted after solvent and thermal annealing and in addition their intensities are higher than that in the as cast film. These absorption changes indicate increased crystallinity in both solvent and thermal annealed films.

Thin film XRD was used to determine the differences between the crystallinity of the as cast and annealed films. Fig. 7 gives the diffraction patterns of the as cast and annealed **M2** films. It can be seen that the pure **M2** films exhibit a peak around $2\theta = 7.5°$ corresponding to an interplanar distance of 13.2 A°. The annealing leads to higher peak intensity, indicating a higher degree of the crystallinity. Similar XRD patterns were also observed with **M1** films. When **M1** or **M2** blended with PCBM, this diffraction peak is not observed, suggesting the effectiveness of the PCBM acceptor in interfering the **M1** or **M2** molecular packing. However, when the blends are solvent and thermaly annealed, the diffraction peaks reappear. The diffraction peak for **M1**:PCBM and **M2**:PCBM is broad and centered at $2\theta = 8.4°$ and $2\theta = 7.64°$, respectively. The increase in the peak intensity in the XRD pattern after annealing leads to an increase in the crystallinity of the blend. These changes in film crystallinity after thermal annealing agree with the changes observed in the absorption data. A high degree of **M1** or **M2** crystallinity was also indicated by a red shift in the absorption band, clear vibronic shoulders appearance at long wavelengths owing to the enhanced interchain π–π^* stacking, and increased absorption intensity. The improved crystallinity in the annealed blend, facilitated through self organized chain stacking, can enhance not only the hole transport but also the light harvesting capabilities, improving the device photocurrent [27a].

The J–V characteristics of the devices based on the solvent treated and thermally annealed solvent treated blends are shown in Fig. 6 and the PV parameters are summarized in Table 3. It can be seen from Fig. 6 and Table 3, the device performance changes significantly after annealing (solvent vapour as well as thermal). These changes correlate well with the significant changes in the morphologies of the blended films. The devices fabricated with solvent vapour treated **M1**:PCBM and **M2**:PCBM showed PCE about 1.73% and 2.17%, respectively, which has been further enhanced up to 2.03% and 2.77% for the thermally annealed solvent treated **M1**:PCBM and **M2**:PCBM blends. The improvement of the PCE has been attributed mainly to the increase in the J_{sc} and FF. As we have discussed earlier, the absorption band is red shift

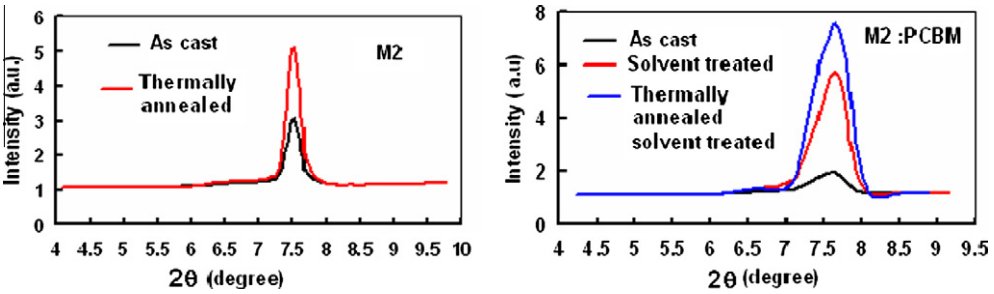

Fig. 7. XRD patterns of pure as cast and thermally annealed **M2**, and as cast, solvent vapour treated and thermally annealed solvent vapour treated **M2**:PCBM blends.

Table 4
Electron and hole mobilities of **M1**:PCBM and **M2**:PCBM blends with different conditions.

Blend	Electron mobility (μ_e) (cm^2/Vs)	Hole mobility (μ_h) (cm^2/Vs)	μ_e/μ_h
M1:PCBM[a]	4.5×10^{-5}	1.8×10^{-6}	25
M1:PCBM[b]	5.5×10^{-5}	3.5×10^{-6}	15.70
M1:PCBM[c]	6.2×10^{-5}	$8. \times 10^{-6}$	6.9
M2:PCBM[a]	5.2×10^{-5}	6.7×10^{-6}	7.76
M2:PCBM[b]	5.8×10^{-5}	1.3×10^{-5}	4.46
M2:PCBM[c]	6.1×10^{-5}	5.6×10^{-5}	1.08

[a] As cast film.
[b] Solvent vapour treated film.
[c] Thermally annealed solvent treated film.

upon the solvent treatment and thermal annealing, which was interpreted as arising from the **M1** or **M2** crystallinity and the resulting hole mobility, which will be discussed later.

It can be seen from Table 3, a drop in V_{oc} occurred for all devices based on solvent treated and thermally annealed blend. It is widely accepted that the V_{oc} for the BHJ PV devices is determined by the energy difference between the HOMO level of donor and LUMO level of acceptor used in the BHJ active layer. The crystallization **of M1** or **M2** in the solvent treatment and subsequent thermal annealing reduced their optical band gaps, assuming that the HOMO level of **M1** or **M2** shifted upward due to the extension of the conjugation length as a result of interchain overlap, as we have observed in the absorption spectra of **M1** and **M2** films [30]. Therefore, the devices containing **M1** or **M2**:PCBM films with higher crystallinity resulting from solvent vapour treatment and thermal annealing, showed lower V_{oc} than the devices with films which have lower crystallinity.

To obtain efficient charge transport of the carriers, it is necessary to enhance the hole and electron mobilities to achieve a balanced mobility ratio [27a,31]. The SCLC method was employed to evaluate the hole and electron mobilities of devices prepared with the various thin active layers. SCLC *J–V* characteristics were obtained in dark from the hole only devices (ITO/PEDOT:PSS/**M1**or **M2**:PCBM/Au) and electron only devices (Al/M1 or M2:PCBM/Al) as a function of the applied bias voltage, which was corrected with the built in potential: $V = V_{appl} - V_{bi}$. The hole and electron mobilities were estimated by the dark *J–V* curves at low voltages, where the current is described by the Mott–Gurney square law i.e. $J = (9/8)\,\varepsilon\,\mu\,(V^2/L^3)$ [32], where the ε is the permittivity of the blend, μ is the charge carrier mobility, and L is the film thickness of the active layer. The values of the hole and electron mobilities are listed in Table 4. It can be seen from this table, that both electron and hole mobilities increase after solvent vapour treatment and thermal treatment. The increase in the hole mobility is higher than the electron mobility. The ratio between the electron and hole mobilities has been reduced for devices based on solvent vapour treated blend and thermally annealed blends, resulting in more balanced carrier transport. The well controlled morphology of the blend, obtained from the solvent vapour treatment and thermal annealing increased the carrier mobilities, particularly the hole mobility through the increase in the crystallinity of **M1** or **M2**, leading to balanced charge transport in the active layer and enhancement of the photocurrent.

5. Conclusions

Two new conjugated SMs, **M1** and **M2**, were successfully synthesized. They were soluble in common organic solvents, showed long-wavelength absorption maximum at 601–640 nm and optical band gap 1.60–1.67 eV. The band gap of these SMs is smaller than that of P3HT. The HOMO and LUMO levels estimated from cyclic voltammetry suggest that **M1** and **M2** can be used as electron donor materials and PCBM as electron acceptor for BHJ organic PV devices. The PCE of the devices based on **M1**:PCBM and **M2**:PCBM is 1.42% and 1.80%, respectively, which is attributed to the higher hole mobility, improved PL quenching and broader absorption spectra for **M2**:PCBM

blend. Moreover, the ratio of electron and hole motilities is lower for the **M2** device relative to **M1** thus supporting the higher value of PCE for the **M2**:PCBM based device. Solution processed organic PV devices with **M1** or **M2** and PCBM were fabricated with as cast, solvent vapour treated and thermally annealed solvent vapour treated blends. The PCEs for the devices fabricated with thermally annealed solvent vapour treated **M1**:PCBM and **M2**:PCBM blends were 2.05% and 2.77%, respectively, which are higher than those for the as cast blends. This improvement in the PCE has been attributed to the increase in crystallinity of the blend, induced by the thermal annealing and solvent vapour treatment and balanced charge transport in the device.

References

[1] (a) B.C. Thompson, J.M.J. Fréchet, Angew. Chem. Int. Ed. 47 (2008) 58;
(b) B. Kippelen, J.-L. Brédas, Energy Environ. Sci. 2 (2009) 251;
(c) G. Dennler, M.C. Scharber, C.J. Brabec, Adv. Mater. 21 (2009) 1323;
(d) M. Helgesen, R. Søndergaard, F.C. Krebs, J. Mater. Chem. 20 (2010) 36;
(e) S.H. Park, A. Roy, S. Beaupré, S. Cho, N. Coates, J.S. Moon, D. Moses, M. Leclerc, K. Lee, A.J. Heeger, Nat. Photonics 3 (2009) 297;
(f) Y. Liang, Z. Xu, J. Xia, S.–T. Tsai, Y. Wu, G. Li, C. Ray, L. Yu, Adv. Mater. 3 (2010) 297, doi:10.1002/adma.200903528.

[2] (a) G. Yu, A.J. Heeger, J. Appl. Phys. 78 (1995) 4510;
(b) G. Yu, J. Gao, J.C. Hummelen, F. Wudl, A.J. Heeger, Science 270 (1995) 1789.

[3] (a) N. Blouin, A. Michaud, M. Leclerc, Adv. Mater. 19 (2007) 2295;
(b) J. Hou, H.–Y. Chen, S. Zhang, Y. Yang, J. Am. Chem. Soc. 130 (2008) 16144;
(c) L. Huo, J. Hou, S. Zhang, H. -Y. Chen, Y. Yang, Angew. Chem. Int. Ed. 49 (2010) 1500.

[4] Y. Li, Y. Zou, Adv. Mater. 20 (2008) 2952.

[5] (a) F.C. Krebs, T. Tromholt, M. Jorgensen, Nanoscale 2 (2010) 873;
(b) F.C. Krebs, T.D. Nielsen, J. Fyenbo, M. Wadstrom, M.S. Pedersen, Energy Environ. Sci. 3 (2010) 512;
(c) F.C. Krebs, M. Jorgensen, K. Norrman, O. Hagemann, J. Alstrup, T.D. Nielsen, J. Fyenbo, K. Larsen, J. Kristensen, Sol. Energy Mater. Sol. Cells 93 (2009) 422.

[6] M.T. Lloyd, J.E. Anthony, G.G. Malliaras, Mater. Today 11 (2007) 34.

[7] B.P. Rand, J. Genoe, P. Heremans, J. Poortmans, Prog. Photovoltaics: Res. Appl. 15 (2007) 659.

[8] J. Roncali, P. Frere, P. Blanchard, R. de Bettignies, M. Turbiez, S. Roquet, P. Leriche, Y. Nicolas, Thin Solid Films 567 (2006) 511.

[9] (a) B. Walker, A.B. Tamayo, X.D. Dang, P. Zalar, J.H. Seo, A. Garcia, M. Tantiwiwat, T.Q. Nguyen, Adv. Funct. Mater. 19 (2009) 3063;
(b) T. Rousseau, A. Cravino, T. Bura, G. Ulrich, R. Ziessel, J. Roncali, Chem. Commun. (2009) 1673;
(c) A.B. Tamayo, B. Walker, T.Q. Nguyen, J. Phys. Chem. C 112 (2008) 11545;
(d) A.B. Tamayo, X.D. Dang, B. Walker, J. Seo, T. Kent, T.Q. Nguyen, Appl. Phys. Lett. 94 (2009) 103301.

[10] (a) N. Mataga, H. Chosrowjan, S. Taniguchi, J. Photochem. Photobiol. 6 (2005) 37;
(b) J. Hou, M. Park, S. Zhang, Y. Yao, L. Chen, J. Li, Y. Yang, Macromolecules 41 (2008) 6012.

[11] S.C. Price, A.C. Stuart, W. You, Macromolecules 43 (2010) 797.

[12] L. Xue, J. He, X. Gu, Z. Yang, B. Xu, W. Tian, J. Phys. Chem. C 113 (2009) 12911.

[13] Y. Li, Z. Li, C. Wang, H. Li, H. Lu, B. Xu, W. Tian, J. Polym. Sci. Part A: Polym. Chem. 48 (2010) 2765.

[14] Y. Li, H. Li, B. Xu, Z. Li, F. Chen, D. Feng, J. Zhang, W. Tian, Polymer 51 (2010) 1786.

[15] Y. Li, L. Xue, H. Li, Z. Li, B. Xu, S. Wen, W. Tian, Macromolecules 42 (2009) 4491.

[16] Q. Peng, K. Park, T. Lin, M. Durstock, L. Dai, J. Phys. Chem. B 112 (2008) 2801.

[17] J.A. Mikroyannidis, S.S. Sharma, Y.K. Vijay, G.D. Sharma, ACS Appl. Mater. Interfaces 2 (2010) 270.

[18] J.A. Mikroyannidis, M.M. Stylianakis, P. Balraju, P. Suresh, G.D. Sharma, ACS Appl. Mater. Interfaces 1 (2009) 1711.

[19] J.A. Mikroyannidis, M.M. Stylianakis, P. Suresh, P. Balraju, G.D. Sharma, Org. Electron. 10 (2009) 1320.

[20] J.A. Mikroyannidis, A.N. Kabanakis, A. Kumar, S.S. Sharma, Y.K. Vijay, G.D. Sharma, Langmuir 26 (2010) 12909.

[21] J.A. Mikroyannidis, P. Suresh, G.D. Sharma, Org. Electron. 11 (2010) 311.

[22] B.-Y. Hsieh, Y. Chen, Macromolecules 40 (2007) 8913.

[23] (a) G.R. Robertson, Org. Synth. Coll. 1 (1941) 396;
(b) G.R. Robertson, Org. Synth. Coll. 2 (1922) 57.

[24] (a) Y. Li, Y. Cao, J. Gao, D. Wang, G. Yu, A.J. Heeger, Synth. Met. 99 (1999) 243;
(b) Q.J. Sun, H.Q. Wang, C.H. Yang, Y.F. Li, J. Mater. Chem. 13 (2003) 800.

[25] (a) Y. Zhu, R.D. Chempion, S.A. Jeneke, Macromolecules 39 (2006) 8712;
(b) T. Johansson, W. Mammo, M. Svensson, M.R. Andersson, O. Inganas, J. Mater. Chem. 13 (2003) 1316;
(c) H. Shang, H. Fan, Q. Shi, S. Li, Y. Li, X. Zhan, Sol. Energy Mater. Sol. Cells 94 (2010) 457.

[26] (a) G. Li, V. Shrotriya, J. Huang, Y. Yao, T. Moriarity, K. Emery, Y. Yang, Nat. Mater. 4 (2005) 864;
(b) A.P. Zoombelt, M. Fonrodona, M.G.R. Turbiez, M.M. Wienk, R.A.J. Janssen, J. Mater. Chem. 19 (2009) 5336;
(c) R. Po, M. Maggni, N. Camaioni, J. Phys. Chem. C 114 (2010) 695.

[27] (a) V.D. Mihailetchi, H.X. Xie, B. de Boer, L.J.A. Koster, P.W.M. Blom, Adv. Funct. Mater. 16 (2006) 699;
(b) Y.Y. Liang, D.Q. Feng, Y. Wu, S.T. Tsai, G. Li, C. Ray, L.P. Yu, J. Am. Chem. Soc. 131 (2009) 7792.

[28] (a) C. Waldauf, M.C. Scharber, P. Schilinsky, J.A. Hauch, C.J. Brabec, J. Appl. Phys. 99 (2006) 104503;
(b) C.J. Brabec, A. Cravino, G. Zerza, N.S. Sariciftci, R. Kiebooms, D. Vanderzande, J. Phys. Chem. B 105 (2001) 1528.

[29] M.S. Roy, P. Balraju, Y.S. Deol, S.K. Sharma, G.D. Sharma, J. Mater. Sci. 43 (2008) 5551.

[30] (a) C. Muller, T.A.M. Ferenczi, M. Campoy-Quiles, J.M. Frost, D.D.C. Bradley, P. Smith, N. Stingelin-Stutzmann, J. Nelson, Adv. Mater. 20 (2008) 3510;
(b) J. Cornil, D. Beljonne, J.P. Calbert, J.L. Bredas, Adv. Mater. 13 (2001) 1053.

[31] V.D. Mihailetchi, J. Wildeman, P.W.M. Blom, Phys. Rev. Lett. 94 (2005) 126602.

[32] M.A. Lampert, P. Mark, Current Injection in Solids, Academic Press, New York, USA, 1970.

Organic Electronics 11 (2010) 2055–2059

Contents lists available at ScienceDirect

Organic Electronics

journal homepage: www.elsevier.com/locate/orgel

Highly efficient top-emitting white organic light-emitting diodes with improved contrast and reduced angular dependence for active matrix displays

Guohua Xie, Zhensong Zhang, Qin Xue, Shiming Zhang, Li Zhao, Yang Luo, Ping Chen, Baofu Quan, Yi Zhao *, Shiyong Liu *

State Key Laboratory on Integrated Optoelectronics, College of Electronic Science and Engineering, Jilin University, 2699 Qianjin Street, Changchun 130012, PR China

ARTICLE INFO

Article history:
Received 6 July 2010
Received in revised form 30 September 2010
Accepted 2 October 2010
Available online 14 October 2010

Keywords:
Top-emitting
White light
Cu
Capping layer

ABSTRACT

Highly efficient top-emitting white organic light-emitting diodes (TEWOLEDs) on silicon substrates based on complementary blue and yellow phosphors are demonstrated. The bottom copper anode with medium reflectance, which is compatible with standard complementary metal oxide semiconductor (CMOS) technology, and the semitransparent cathode with a top capping layer, are introduced to facilitate white light emission with improved contrast and reduced angular dependence. Both TEWOLEDs, with and without the capping layers, exhibit nearly lambertian-type emission. The spectrum of TEWOLED with a capping layer is similar to that of the bottom-emitting counterpart. Our TEWOLED reaches high efficiencies of 27.7 cd/A and 17.6 lm/W at a current density of 10 mA/cm^2, and low voltage of 4.4 V at 1000 cd/m^2.

© 2010 Elsevier B.V. All rights reserved.

1. Introduction

Organic light-emitting diodes (OLEDs) are considered as one of the most powerful candidates for the next generation mainstream flat panel displays and solid-state lighting sources [1–5]. In active matrix displays, top-emitting architectures are preferable due to their intrinsic large aperture ratio and the less risk of cross-talk in high resolution and large area displays. For full color and high resolution displays, white light combined with color filters is one of the best schemes for low-cost mass production due to the avoidance of precise and time-consuming shadow mask process for red-green-blue (RGB) pixilation [6,7]. It's pointed out that the technique which is capable of directly patterning the pixels in small dimensions (~10 μm pitch for RGB pixels) is not available so far [8]. Note that the pixel pitch of OLED microdisplays now is reduced to several micrometers to achieve high resolution. However, it's a great challenge to achieve uniform and angular independent white light emission in the top-emitting architectures due to intrinsic strong microcavity effects. Basically, a low reflective bottom anode and a highly transparent top cathode stack are beneficial for white light extraction from top-emitting architectures avoiding constructive interference inside the devices [3,9–17]. In order to achieve high resolution and high information-content Si-based microdisplays, which have vast potential application in military and consumer electronics market, TEWOLED is one of the prerequisites as well as CMOS process selection. As mentioned above, no technique is competent enough to directly pattern the full color OLED pixels in microdisplays. The solution now is based on white light and RGB color filters. For low cost mass production, a suitable active matrix driving circuit scheme introducing the standard CMOS metal interconnection (Al or Cu) is crucial, as it has to meet the requirement of fabricating OLEDs directly on the top metal layer of the chips. In addition, TEWOLEDs based on Cu foil with high flexibility are very promising for flexible full color active matrix displays.

* Corresponding authors. Tel.: +86 431 85168242-8301.
E-mail addresses: zhao_yi@jlu.edu.cn (Y. Zhao), syliu@jlu.edu.cn (S. Liu).

1566-1199/$ - see front matter © 2010 Elsevier B.V. All rights reserved.
doi:10.1016/j.orgel.2010.10.001

In this letter, we demonstrate highly efficient TEWOLEDs based on Cu bottom anode, which is compatible with the standard foundry CMOS technology (for deep submicron and below), paving the way for integrating organic optoelectronic devices directly with the readily available Si wafer. It's reported that the production cost comes from the interconnect metallization process in integrated circuits is over 50% of the total budget [18]. A new choice of metal process, which is not compatible with the standard foundry technology, will cost even much more. Undoubtedly, this is a great obstacle for mass production. In previous reported TEWOLEDs, Ag [11,16], Ag/ITO [14], Al [17], Al/Ag [17], Al/Au [13], Al/ITO [19], Al/Ni [10], and Mo [15] are selected as anodes, respectively. However, only limited candidates are competent for commercialization. Here, a Cu anode is adopted for TEWOLED to meet the requirement of integrating OLEDs with foundry CMOS circuitry. Cu can then be used as contact material and as via connection in the CMOS process [18,20]. In contrast, an Al interconnect requires a W plug for via and subsequently creates an additional interface of Al and W. No such interface is existing between the via and interconnect for Cu as via and anode material for OLEDs. This does significantly simplify the fabricating process for OLED microdisplays aiming for low cost and small size with augmented reality that requires high resolution [4]. In addition, due to the excellent thermal conductivity, Cu-based devices usually exhibit superior heat dissipation [21], thus the issue of thermal management in highly dense integrated devices tends to be less severe. In order to further reduce the OLED microcavity effect, an additional capping layer, 4,4′,4″-tris(N-3-methylphenyl-N-phenyl-amino)triphenylamine (m-MTDATA), is deposited directly over the semitransparent cathode. It's proved here that the manipulation of white light emission profiles towards angular independence and broad spectral coverage is much easier in Cu-based TEWOLEDs than those based on highly reflective electrodes, such as Ag and Al.

2. Experimental

The white OLED is based on the blue emitter iridium(III) bis[(4,6-difluorophenyl)-pyridinato-N,$C^{2'}$] (FIrpic) and the yellow emitter bis(2-(2-fluorphenyl)-1,3-benzothiozolato-N,$C^{2'}$) ((F-BT)$_2$Ir(acac)) doped into a common host, N, N′-dicarbazolyl-3,5-benzene (mCP), respectively. Pristine m-MTDATA, N,N′-bis(naphthalene-1-yl)-N, N′-bis(phenyl)-benzidine (NPB), and 7-diphenyl-1,10-phenanthroline (BPhen) serve as hole injecting layer, hole transporting layer, and hole blocking/electron transporting layer, respectively. The Cu anode is thermally deposited onto Si substrate covered with insulating SiO_2, following with m-MTDATA:MoO_x p-doping layer to reduce the ohmic loss. The structures are listed below, Si/SiO_2/Cu (60 nm)/m-MTDATA:MoO_x (15wt.%, 10 nm)/m-MTDATA (18 nm)/NPB (5 nm)/mCP (15 nm)/mCP:FIrpic (10wt.%, 5 nm)/BPhen (2 nm)/mCP:(F-BT)$_2$Ir(acac) (4wt.%, 5 nm)/BPhen (40 nm)/LiF (1 nm)/Al (2 nm)/Ag (18 nm)/m-MTDATA (0 and 50 nm). For comparison, ITO/m-MTDATA:MoO_x(15wt.%, 10 nm)/m-MTDATA (18 nm)/NPB (5 nm)/mCP (15 nm)/mCP:FIrpic (10wt.%, 5 nm)/BPhen (2 nm)/mCP:(F-BT)$_2$Ir(acac) (4 wt.%, 5 nm)/BPhen (40 nm)/LiF (1 nm)/Al (100 nm), a bottom-emitting white OLED (BEWOLED) is also fabricated. In order to achieve high efficiency, the pristine 15 nm mCP is introduced to prevent the high energy triplet exciton of blue emitter from diffusing into the NPB layer, and 2 nm BPhen spacer is inserted between the blue and yellow emitters to balance white emission. The current–voltage–luminance characteristics were measured with a PR650 spectrascan spectrometer and a Keithley 2400 programmable voltage–current source. All the devices without encapsulation were measured in ambient atmosphere at room temperature.

It's reported that the out-coupling characteristics are significantly dependent on the interference effects in the cavity [22,23]. As depicted, the top light out-coupling stack design strongly influences the emission profiles [9–11,13–17,19,23,24]. In order to reveal the effects, we investigate the influences of the capping layer on the reflectance, transmittance and absorbance of the stack of BPhen/LiF/Al/Ag/m-MTDATA (x nm) with software SETFOS [25].

3. Results and discussion

For monochromatic emission, the out-coupling efficiency is not simply dependent on the transparency of the top electrode [23]. It's even more complicated in TEWOLEDs, because of the complex interplay of wide-angle and multiple-beam interference effects. As indicated in Fig. 1a and b, the stack with 50 nm capping layer exhibits a low reflectance and high transmittance in the blue region, but medium values in the yellow region. Additionally, the stack with above 50 nm capping layer has low absorbance over the visible region (Fig. 1c). However, the devices with a capping layer above 50 nm do not exhibit improved luminance (not shown here).

As shown in Fig. 2, TEWOLED with (Device A) and without (Device B) 50 nm capping layer exhibit similar luminance–voltage characteristics, while Device A has superior luminance due to the improved light out-coupling efficiency. In contrast, the luminance of BEWOLED (Device C) tends to grow more slowly as the voltage increased. One of the reasons may be attributed to the different series resistance of the electrodes. And also, the lower thermal conductivity of the ITO/glass substrate than that of Cu/SiO_2/Si substrate may play a role, as great joule heat generated on the poor thermal conductive substrate may accelerate the degradation at high luminance level. In view of practical use, the capping layer is not only beneficial for the improvement of luminance of TEWOLED, but also for the achievement of high contrast active matrix displays. Device A with the capping layer reaches a contrast ratio of 199, while that of Device B is only 66, under an ambient illumination of 140 lx [26,27]. A high contrast ratio is necessary to achieve high gray scale and reduce eyestrain in near-eye microdisplays with relative low perceptible luminance level. As for head-mount displays, the ambient illumination could be much lower. Taking 10 lx for example, the contrast ratio of Device A is up to 351 when the on-state brightness is set to 200 cd/m^2.

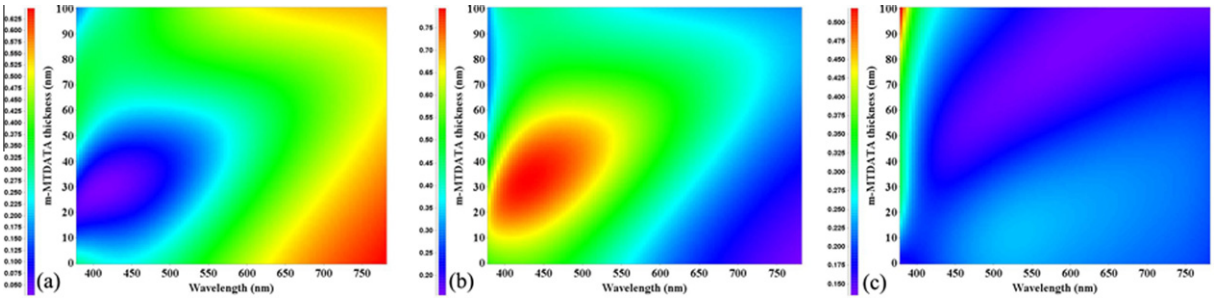

Fig. 1. (a–c) Calculated reflectance, transmittance and absorbance of the stack BPhen (40 nm)/LiF (1 nm)/Al (2 nm)/Ag (18 nm)/m-MTDATA (*x* nm) as a function of m-MTDATA capping layer thickness and the wavelength, respectively. The optical constants used in the calculation are obtained by variable-angle spectroscopic ellipsometry measurements. The dispersion of the complex refractive indices is also taken into account, as the emission profiles are dependent on the dispersion.

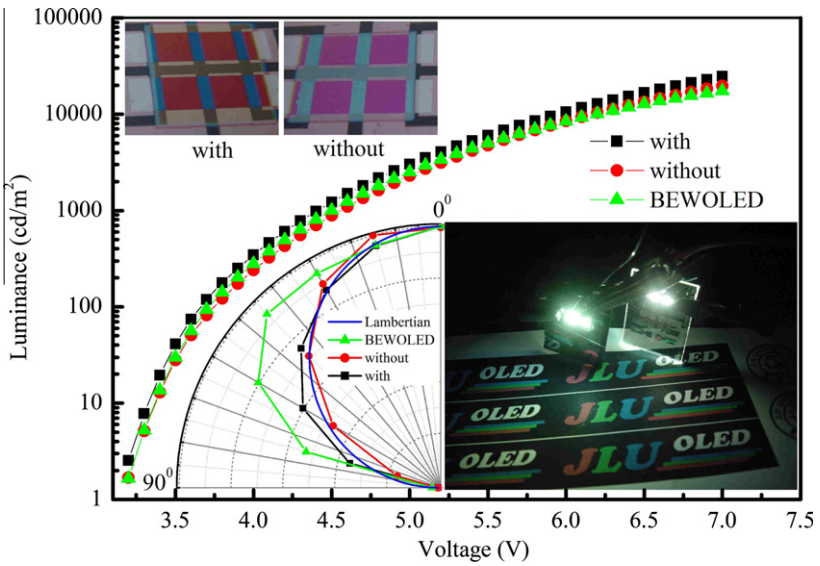

Fig. 2. Luminance–voltage characteristics of Device A, B and C, respectively. The lower left-hand inset indicates the measured angular distribution of the devices and the bluish solid line represents a Lambertian-type distribution. The upper left-hand inset shows the photos of TEWOLEDs with and without the capping layer, respectively. TEWOLED with the capping layer and BEWOLED radiate at a high brightness level are also presented in the lower right-hand inset.

The current efficiency–current density–power efficiency characteristics of the three devices are compared in Fig. 3. Apparently, TEWOLEDs exhibit lower efficiency at low luminance, while peak efficiency at low luminance is observed in BEWOLED, and subsequently the efficiency gradually decreases due to triplet–triplet annihilation as the current density increases [23]. At the current density of 10 mA/cm^2, the efficiencies are 27.7 cd/A (17.6 lm/W), 24.8 cd/A (15.4 lm/W) and 26.8 cd/A (16.5 lm/W) for Device A, B and C, respectively. As shown in the inset of Fig. 3, the spectra of TEWOLEDs are narrower in the red region due to interference effects and the poor transmittance of the cathode stack at long wavelengths, which have been indicated in Fig. 1. According to our calculation, the BEWOLED is not optimized with the structure used here. The optimized current efficiency is expected to be improved by 40%, simply adjusting the thicknesses of m-MTDATA:MoO_x and m-MTDATA layer to improve light out-coupling in BEWOLED. Hence the optimized BEWOLED would still have slightly superior efficiencies. A thick p-doping layer with negligible voltage drop is also expected to improve the yield of both TEWOLEDs and BEWOLEDs in mass production.

With the capping layer, the angular dependence of the spectrum in TEWOLED is reduced, while the spectrum of TEWOLED without the capping layer changes dramatically as the viewing angle changes, shown in Fig. 4a and b. BEWOLED exhibits almost no angular dependence of the spectrum (Fig. 4c). The Commission Internationale de L'Eclairage (CIE) coordinates measured in forward direction of Device A only change from (0.306, 0.430) to (0.330, 0.445) over the luminance range of 100–4000 cd/m^2, and the variation is only (±0.003, ±0.001) over 4000–20000 cd/m^2. Due to the dominant yellow emission as a result of constructive interference in Device B, the CIE coordinates are quite stable over 100–20000 cd/m^2, with negligible variation of (±0.009, ±0.004). Device C (BEWOLED) has a convoluted shape of the CIE coordinates over

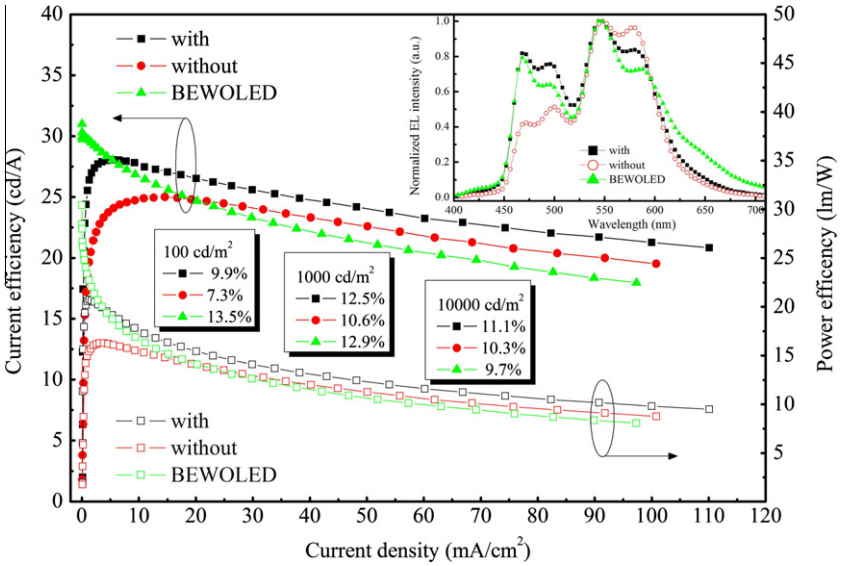

Fig. 3. Current efficiency–current density–power efficiency characteristics of Device A, B and C, respectively. The external quantum efficiencies at a luminance of 100, 1000, 10000 cd/m^2 are also shown in the boxes. Inset: the electroluminescent (EL) spectra of the devices at a current density of 40 mA/cm^2.

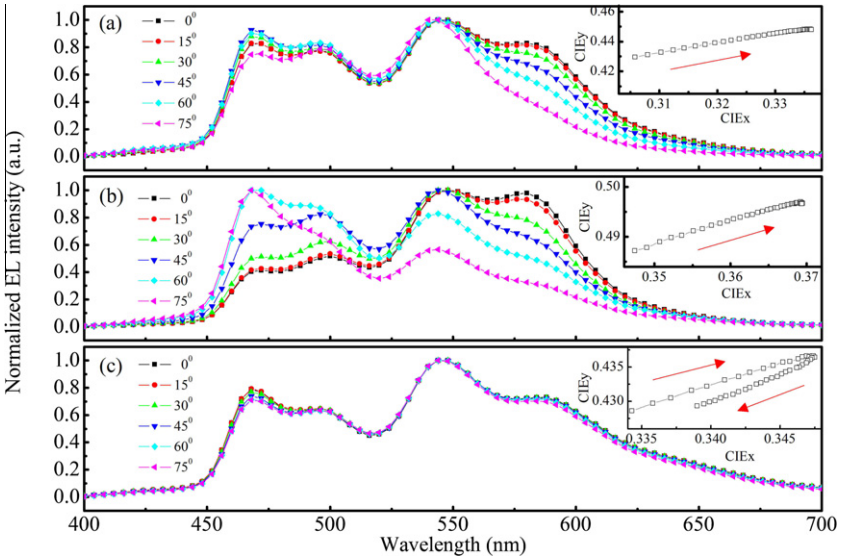

Fig. 4. Spectra of Device A, B and C at a current density of 40 mA/cm^2, respectively. CIE 1931 color coordinates measured in forward direction over a luminance range of 100–20,000 cd/m^2 are also plotted in the insets, respectively.

the luminance range, corresponding to a variation of (±0.006, ±0.004). The blue-shift of the color in Device C may be caused by the slightly increased residual NPB emission under high driving voltage. However, this emission is suppressed in TEWOLEDs with an optical cavity length of ~100 nm as the low light out-coupling efficiency in the deep-blue region, which is also indicated by the whole device simulation with software SETFOS. That's why the variation of the CIE coordinates with luminance of TEWOLEDs is different to that of BEWOLED.

4. Conclusions

In summary, we have demonstrated efficient TEWOLED based on Cu anode for potentially full color small and large area active matrix displays, or flexible OLED displays. In this embodiment, we have deliberately considered the technologic compatibility of integrating OLEDs with CMOS circuitry, aiming for commercially low-cost OLED microdisplays. In order to improve the contrast ratio (typical for microdisplays), and reduce the angular dependence

(typical for flexible displays), a low absorption loss capping layer is used to balance the degree of constructive and destructive interference for white light extraction.

Acknowledgements

We wish to acknowledge funding for this research from the National Key Basic Research and Development Program of China under grant No. 2010CB327701, and the National Natural Science Foundation of China (grant Nos. 60977024 and 60907013). The authors gratefully acknowledge Dr. Liying Zhang and Dr. Bin Li for providing $(F\text{-}BT)_2Ir(acac)$.

References

[1] O. Prache, Displays 22 (2001) 49.
[2] J.Y. Lee, J.H. Kwon, H.K. Chung, Org. Electron. 4 (2003) 143.
[3] S. Kim, S. Lee, M. Kim, J. Song, E. Hwang, S. Tamura, S. Kang, H. Kim, C. Kim, J. Lee, J. Kim, S. Cho, J. Cho, M.C. Suh, H. Kim, J. Soc. Inf. Disp. 17 (2009) 145.
[4] A.P. Ghosh, T.A. Ali, I. Khayrullin, F. Vazan, O.F. Prache, I. Wacyk, Proc. SPIE 7415 (2009) 74150Q.
[5] S. Reineke, F. Lindner, G. Schwartz, N. Seidler, K. Walzer, B. Lüssem, K. Leo, Nature 459 (2009) 234.
[6] K. Mameno, R. Nishikawa, K. Suzuki, S. Matsumoto, T. Yamaguchi, K. Yoneka, Y. Hamada, H. Kanno, Y. Nishio, H. Matsuoka, Y. Saito, S. Oima, N. Mori, G. Rajeswaran, S. Mizukoshi, T.K. Hatwar, Proc. IDW'02, The Ninth International Display Workshop, Hiroshima, Japan (2002) 235.
[7] W. den Boer, Active Matrix Liquid Crystal Displays: Fundamentals and Applications, Elsevier, Amsterdam, 2005.
[8] D. Armitage, I. Underwood, S.-T. Wu, Introduction to Microdisplays, Wiley, New York, 2006. pp. 269.
[9] T. Feng, T.A. Ali, E.S. Ramakrishnan, R. Campos, W.E. Howard, Proc. SPIE 4105 (2001) 30.
[10] H. Kanno, Y. Sun, S.R. Forrest, Appl. Phys. Lett. 86 (2005) 263502.
[11] S.-F. Hsu, C.-C. Lee, S.-W. Hwang, C.H. Chen, Appl. Phys. Lett. 86 (2005) 253508.
[12] J.P. Spindler, T.K. Hatwar, S.A. Van Slyke, SID IDRC (2006) 51.
[13] X. Zhu, J. Sun, X. Yu, M. Wong, H.-S. Kwok, Jpn. J. Appl. Phys. 46 (2007) 4054.
[14] M.S. Kim, C.H. Jeong, J.T. Lim, G.Y. Yeom, Thin Solid Films 516 (2008) 3590.
[15] M.-T. Lee, M.-R. Tseng, Curr. Appl. Phys. 8 (2008) 616.
[16] M. Thomschke, R. Nitsche, M. Furno, K. Leo, Appl. Phys. Lett. 94 (2009) 083303.
[17] P. Freitag, S. Reineke, M. Furno, B. Lüssem, K. Leo, Proc. SPIE 7722 (2010) 77221D.
[18] K.N. Tu, J. Appl. Phys. 94 (2003) 5451.
[19] R.S. Cok, J.D. Shore, J. Soc. Inf. Disp. 17 (2009) 617.
[20] R. Doering, Y. Nishi, Handbook of Semiconductor Manufacturing Technology, 2nd ed., Taylor & Francis, CRC, London, 2007.
[21] Y.-S. Tsai, S.-H. Wang, C.-H. Chen, C.-L. Cheng, T.-C. Liao, Appl. Phys. Lett. 95 (2009) 233306.
[22] H. Riel, S. Karg, T. Beierlein, B. Ruhstaller, W. Rieß, Appl. Phys. Lett. 82 (2003) 466.
[23] Q. Huang, K. Walzer, M. Pfeiffer, V. Lyssenko, G. He, K. Leo, Appl. Phys. Lett. 88 (2006) 113515.
[24] Q. Wang, Z. Deng, J. Chen, D. Ma, Opt. Lett. 35 (2010) 462.
[25] www.fluxim.com
[26] J.A. Dobrowolski, B.T. Sullivan, R.C. Bajcar, Appl. Opt. 31 (1992) 5988.
[27] In the calculation, the brightness of the devices at off-and on-state is set to be 0 and 1000 cd/m^2. The standard illuminating source D65 is referenced as the spectral power distribution of the light source to determine the luminous reflectance taking into account the response of human eyes.

ORGANIC ELECTRONICS
materials • physics • chemistry • applications

Editors:

Prof. Chihaya Adachi — Center for Future Chemistry, Kyushu University, 744 Motooka, Nishi, Fukuoka 819-0395, Japan. Fax: +81-92-802-3294, e-mail: adachi@cstf.kyushu-u.ac.jp

Prof. Stephen R. Forrest — EECS, MS&E, and Physics, University of Michigan, 4080 Fleming Building, 503 Thompson Street, Ann Arbor, MI 48109-1340, USA. Fax: +1-734-763-0085, e-mail: stevefor@umich.edu

Prof. Paul Heremans — Imec, Kapeldreef 75, B-3001 Leuven, Belgium. Tel: +32 16 281521, e-mail: heremans@imec.be

Prof. René Janssen — Molecular Materials and Nanosystems, Eindhoven University of Technology, P.O. Box 513, 5600 MB Eindhoven, The Netherlands. Fax: +31 40 2451036, e-mail: r.a.j.janssen@tue.nl

Prof. Antoine Kahn — Electrical Engineering Department, Princeton University, Engineering Quadrangle, Princeton, NJ 08544, USA

Associate Editorial Board:

V.M. AGRANOVICH (Moscow)
Y. CAO (Guangzhou)
A. DODABALAPUR (Austin)
M. FUJIHIRA (Yokohama)
N. PEYGHAMBARIAN (Tucson)
Z. POPOVIC (Mississauga)
W. RIESS (Rüschlikon)
Y. SHIROTA (Osaka)
C. TALIANI (Bologna)
T. TSUTSUI (Fukuoka)
E. UMBACH (Würzburg)

Founding Editors:

Prof. Donal Bradley, Prof. Stephen Forrest, Prof. Norbert Karl and Prof. Kazuhiko Seki

Aims and scope

Organic Electronics is a primary journal whose interdisciplinary focus is organic materials, devices and phenomena, with application to devices such as organic light emitting diodes, thin film transistors, photovoltaic cells, etc.

Papers suitable for publication in this journal cover such topics as photoconductive and electronic properties of organic materials, thin film growth and characterization, charge and exciton transport, organic electronic and optoelectronic devices, etc.

Organic Electronics provides the only forum for both applied and fundamental contributions spanning the many different disciplines addressing the wide range of electronic properties and applications of organic materials. A Letters section is included for rapid publication of short articles announcing significant and highly original results.

Advertising information

If you are interested in advertising or other commercial opportunities please e-mail Commercialsales@elsevier.com and your enquiry will be passed to the correct person who will respond to you within 48 hours.

Abstracted/indexed in:

Current Contents: Engineering, Technology and Applied Sciences; El Compendex Plus; Engineering Index; INSPEC; Physics Briefs; Science Citation Index, expanded; Chemistry Citation Index; Current Contents: Physics, Chemistry and Engineering Science. Also covered in the abstract and citation database SCOPUS®. Full text available on ScienceDirect®.

Publication information: *Organic Electronics* (ISSN 1566-1199). For 2010, Volume 11 (12 issues) is scheduled for publication. Subscription prices are available upon request from the Publisher or from the Elsevier Customer Service Department nearest you or from this journal's website (http://www.elsevier.com/locate/orgel). Further information is available on this journal and other Elsevier products through Elsevier's website (http://www.elsevier.com). Subscriptions are accepted on a prepaid basis only and are entered on a calendar year basis. Issues are sent by standard mail (surface within Europe, air delivery outside Europe). Priority rates are available upon request. Claims for missing issues should be made within six months of the date of dispatch.

Orders, claims, and journal enquiries: please contact the Elsevier Customer Service Department nearest you:

St. Louis: Elsevier Customer Service Department, 3251 Riverport Lane, Maryland Heights, MO 63043, USA; phone: (877) 8397126 [toll free within the USA]; (+1) (314) 4478878 [outside the USA]; fax: (+1) (314) 4478077; e-mail: JournalCustomerService-usa@elsevier.com

Oxford: Elsevier Customer Service Department, The Boulevard, Langford Lane, Kidlington, Oxford OX5 1GB, UK; phone: (+44) (1865) 843434; fax: (+44) (1865) 843970; e-mail: JournalsCustomerService-EMEA@elsevier.com

Tokyo: Elsevier Customer Service Department, 4F Higashi-Azabu, 1-Chome Bldg, 1-9-15 Higashi-Azabu, Minato-ku, Tokyo 106-0044, Japan; phone: (+81) (3) 5561 5037; fax: (+81) (3) 5561 5047; e-mail: JournalsCustomerServiceJapan@elsevier.com

Singapore: Elsevier Customer Service Department, 3 Killiney Road, #08-01 Winsland House I, Singapore 239519; phone: (+65) 63490222; fax: (+65) 67331510; e-mail: JournalsCustomerService-APAC@elsevier.com

USA mailing notice: *Organic Electronics* (ISSN 1566-1199) is published monthly by Elsevier B.V., Radarweg 29, 1043 NX Amsterdam, the Netherlands. Periodical postage paid at Rahway NJ and additional mailing offices.

USA POSTMASTER: Send change of address to *Organic Electronics*, Elsevier Customer Service Department, 3251 Riverport Lane, Maryland Heights, MO 63043, USA.

AIRFREIGHT AND MAILING in USA by Mercury International Limited, 365 Blair Road, Avenel, NJ 07001.

Printed in the Netherlands

For a full and complete Guide for Authors, please go to: http://www.elsevier.com/locate/orgel

Contents lists available at ScienceDirect

Organic Electronics

journal homepage: www.elsevier.com/locate/orgel

Publisher's Note

As of June 1st, after a decade as Editor of Organic Electronics, Stephen Forrest, one of the Founding Editors will retire from his role. In this time, the journal has grown from 4 issues per year to 12 issues and has a major influence in the community. I would like to thank Steve very much for his expertise and dedication in making this journal a success.

Although I am very sorry to see Steve go, I am delighted that Paul Heremans will join the board of Editors as of May 1st. Paul is currently a fellow of IMEC, a world-leading independent research centre in nanoelectronics and nanotechnology, and Professor at the Katholieke Universiteit Leuven, Belgium. Please join me in welcoming Paul to the journal!

Karien van Wetering
Publisher

doi:10.1016/S1566-1199(10)00158-8